Global COE Program

International Urban Earthquake Engineering Center
for Mitigating Seismic Mega Risk

JOINT CONFERENCE PROCEEDINGS

7th International Conference on Urban Earthquake Engineering (7CUEE)

5th International Conference on Earthquake Engineering (5ICEE)

Center for Urban Earthquake Engineering
Tokyo Institute of Technology

Tokyo Tech
CUEE

Global COE Program

International Urban Earthquake Engineering Center

for Mitigating Seismic Mega Risk

JOINT CONFERENCE PROCEEDINGS

7th International Conference on Urban Earthquake Engineering (7CUEE)

5th International Conference on Earthquake Engineering (5ICEE)

Center for Urban Earthquake Engineering

Tokyo Institute of Technology

Tokyo Tech

CUEE

Executive and Editorial Committee
Kazuhiko Kasai (Chair)
Hiroyasu Sakata
Akihiro Takahashi
Kohji Tokimatsu
Satoshi Yamada
Troy Morgan

Global COE program entitled **"International Urban Earthquake Engineering Center for Mitigating Seismic Mega Risk"**

Center for Urban Earthquake Engineering (CUEE), Tokyo Institute of Technology
CUEE O-okayama Office TEL/FAX: +81-(0) 3-5734-3200
CUEE Suzukakedai Office TEL/FAX: +81-(0) 45-924-5576/5199
URL: http://www.cuee.titech.ac.jp

PREFACE

Jointly on behalf of both Organizers, it is a great pleasure to welcome you to this specially coordinated event (March 3–5, 2010) combining two of the major recurring events in international earthquake-engineering studies:

7TH CUEE (SEVENTH INTERNATIONAL CONFERENCE ON URBAN EARTHQUAKE ENGINEERING)

5TH ICEE (FIFTH INTERNATIONAL CONFERENCE ON EARTHQUAKE ENGINEERING).

Our 7th CUEE is an integral component of the research activities of the Center for Urban Earthquake Engineering (CUEE), Tokyo Institute of Technology, Japan, where it is supported by the Ministry of Education, Culture, Sport, Science and Technology (MEXT), as part of the mission of our university's Global Center of Excellence (COE) in the field of earthquake engineering. The conference has been held annually since 2003 under two consecutive COE programs (FY 2003-2007 and FY 2008-2012). The current program aims not only to promote research to mitigate the seismic "mega" risk confronting vast modern cities in earthquake regions throughout the world, but also to produce next-generation researchers and other professionals who will develop new strategies and practices for seismic risk reduction. As always it is hoped to stimulate intensive information dissemination and technology transfer, as well as promote and sustain an international network directed toward nurturing young researchers through an international collaborative effort.

The 5th ICEE is a core activity of the Asian-Pacific Network of Centers for Earthquake Engineering Research (ANCER). The ICEE was conceived in 2000 on the occasion of the China-US Millennium Symposium on Earthquake Engineering held at Beijing. The China-US Millennium Symposium had the clear aim of creating a detailed research plan for US-China cooperative research in the field of earthquake engineering and hazard mitigation. In 2001, based on the mandated resolutions of the China-US Symposium, ANCER was established by seven national earthquake engineering research centers: the Korean Earthquake Engineering Research Center (ROK), Institute of Engineering Mechanics of China Seismological Bureau (PRC), Multidisciplinary Center for Earthquake Engineering Research (USA), Mid-America Earthquake Center (USA), Pacific Earthquake Engineering Research Center (USA), Disaster Prevention Research Institute of Kyoto University (Japan), and the National Center for Research on Earthquake Engineering (ROC). The aim of ANCER is to create a significant impact on current seismic hazard mitigation practice by way of cooperative research activities best advanced through center-to-center collaboration focused on areas of common interest.

We the organizers of both the 7th CUEE and 5th ICEE are excited by the opportunity to merge the two meetings. In this joint conference, a broad range of research topics are showcased in order to set a new multilateral research platform disseminating state-of-the-art information, illustrating new and emerging mitigation technologies, and promoting new education initiatives. The conference will also reaffirm the commitment of CUEE and ANCER to international collaboration and open exchange of state-of-practice research findings in the aim of improving pre-earthquake preparedness, emergency response, and post-earthquake recovery as well as reinforcing a strong international network for the next generation. We are thus committed to four major investigative themes: 1) Vulnerability of megacities to seismic hazard; 2) Multi-hazard mitigation solutions; 3) Adoption of sensor, actuation, and control technologies within the context of future mitigation strategies; 4) Educational initiatives aimed at cultivating interdisciplinary and cross-cultural earthquake engineering curricula.

This Joint Conference comprises seven state-of-the-art Keynote Talks as well as over 300 additional oral presentations (inclusive of some 70 presentations by young researchers and graduate students during the midday Inter-COE Special Sessions). An exceptional session is also planned on the "12th January 2010 Haiti Earthquake" that has resulted in catastrophic damage with an estimated death toll above 200,000. We wish to express sincere sympathy to those who experienced this tragedy and vow to work toward the future mitigation of such occurrences and resultant loss of life.

A beneficent reduction in the potential huge damage and loss occasioned by a catastrophic earthquake cannot however be attained by merely strengthening single buildings and/or infrastructures, nor by the short-term efforts of a small number of people. An integrated and collaborative effort is decisively called for, through which various professions and technologies in divers disciplines must join together worldwide. To this end, we greatly appreciate your participation, contributions, and discussion during the present Joint Conference and further solicit your continued advice, guidance, and collaboration, towards achieving this profound mutual objective that is our overarching mission. Our hope is that the Joint Conference will prove a stimulating opportunity for all dedicated, as each of us is, to Urban Earthquake Engineering.

Kohji Tokimatsu
Global COE Program Leader and
Director of CUEE at Tokyo Tech

Table of contents

Keynote Lectures

00-211 Engineering Seismology: Directions in Probabilistic Seismic Hazard Analysis 1
John G. Anderson

00-284 Full-Scale Shake Table Tests of 5-Story Steel Building with Various Dampers 11
Kazuhiko Kasai, Hiroshi Ito, Yoji Ooki, Tsuyoshi Hikino, Koichi Kajiwara, Shojiro Motoyui, Hitoshi Ozaki, and Masato Ishii

00-452 Demand Spectra and SFSI for the Performance Based Design 23
Kyriazis Pitilakis, Dimitris Pitilakis, and Anna Karatzetzou

00-450 Self-Centering Damage-Free Seismic-Resistant Steel Frame Systems 39
Richard Sause, James M. Ricles, Ying-Cheng Lin, Choung-Yeol Seo, David Roke, and Brent Chancellor

00-657 Seismic Design for Resilient Society 49
Akira Wada

00-241 Seismic Performance of Concentrically Braced Steel Frames: Past and Future 57
Stephen Mahin, Jiun Wei Lai, Chiu Hsin Chen, and Yuli Huang

Special Lecture

00-478 Preliminary Reconnaissance Report - 12 January 2010 Haiti Earthquake..... 63
Eduardo A. Fierro and Cynthia L. Perry

Engineering Seismology

01-461 Site Specific Ground Motion Estimations for the Vulnerability Assessment of Historic Buildings in Istanbul 75
Atilla Ansal, Dina D'Ayala, Aslı Kurtuluş, and Gökçe Tönük

01-267 Site Response at Mexico City. Progress Made and Pending Issues 81
Francisco J. Chavez-Garcia

01-195 Microzonation and site Effect Studies in Istanbul 89
O. Ozel, N. Ozel, and M. Erdik

01-060 Site Characteristics of Strong-Motion Earthquake Stations in Metropolitan Izmir, Aegean Region of Turkey 97
Elcin Gok, Orhan Polat, Doguser Yilmaz, Ulubey Ceken, Mehmet Kuruoglu, Ahmet Turan Arslan, Bekir Tuzel, and Zafer Akcig

01-204 Attenuation Characteristics of Peak Ground Motions during the M8.0 Wenchuan Earthquake, China 103
Hongjun Si, Ken X. Hao, Yang Xu, Shigeki Senna, Hiroyuki Fujiwara, Hiroyuki Yamada, Hideaki Tsutsumi, Changjiang Wu, Saburoh Midorikawa, and Kojiro Irikura

01-606 An Empirical Arias Intensity Relationship for Rock Sites in Stable Continental Regions 109
Jongwon Lee and Russell A. Green

01-192 Site Effect Study in Taiwan Area From Dense Microtremor Survey..... 111
Kuo-Liang Wen and Jyun-Yan Huang

01-197 Analysis of Love-Wave Components in Microtremors 115
Taku Tada, Ikuo Cho, and Yuzo Shinozaki

01-158 A Study on Array Microtremors Survey with Motions Generated by 3D Finite Element Models with Irregular Bedrock..... 125
Huei-Tsyr Chen, Jun-An Wei, and Hitoshi Morikawa

01-292 Evaluation of Site Effects in the Onikobe Basin in Miyagi Prefecture, from Ground Motion Data from Aftershocks of the Iwate-Miyagi Nairiku Earthquake in 2008 and Microtremor Measurements 131
Kentaro Motoki, Hiroaki Yamanaka, Kazuoh Seo, and Haruhiko Suzuki

01-390 Estimation of Ground Structure around Damaged Area by 2008 Iwate-Miyagi Nairiku Earthquake..... 137
Hitoshi Morikawa, Masachika Tanigawa, Taiyo Kobayashi, and Hiroko Matsuo

01-205 A Detailed Receiver Function Study of the Southern Dead Sea Transform (SDST) 141
Ayman Mohsen, Rainer Kind, Guenter Asch, Michael Weber, Rami Hofstetter, and Khalil Abu-Ayyash

01-099 Extracting the Multiscale Coherence of Strong Ground Motions Using Wavelet Analysis . 147
Michalis F. Vassiliou and Nicos Makris

01-194 Long-Period Ground Motion Simulation of Osaka Sedimentary Basin for a Hypothetical Nankai Subduction Earthquake 157
Tomotaka Iwata, and Asako Iwaki

01-012 Effects of Shallow Soil Layers on Propagation of Long-Period Ground Motion in Large Basin in 3D Numerical Simulation 163
Hiroaki Yamanaka and Sho Akeda

01-335 Broadband Strong-Motion Evaluation by a Hybrid Method for The Miyagi-Oki Earthquakes, Japan 169
Susumu Ohno

01-023 3D Subsurface Structural Model for Strong Motion Simulation around Lake Biwa Using Earthquake Ground Motion Records..... 175
Haruhiko Suzuki and Hiroaki Yamanaka

01-170 An Evaluation of Long-Period Earthquake Motion for the Purpose of Structural Design ... 181
Izuru Okawa, Toshimi Satoh, Toshiaki Sato, Takao Nishikawa, and Matsutaro Seki

01-187 Shaking Table Test for Indoor Human Response and Evacuation Limit 187
Toru Takahashi, Toshiko Suzuki, Taiki Saito, Tatsuya Azuhata, and Koichi Morita

01-191 Disaster Mitigation Activities of a High-Rise Building in the Shinjuku Station Area by Collaborating with Local Government and Communities 195
Yoshiaki Hisada, Masahiro Murakami, and Tomohiro Kubo

01-319 Seismic Hazards of Gyeongju Historic Areas 199
Heon Joon Park, Derk Moon Kim, Hyung Choon Park, and Dong Soo Kim

01-271 Signal Processing and Probabilistic Seismic Hazard Analysis Tools for Characterizing the Impact of Near-Fault Directivity 207
Shrey K. Shahi and Jack W. Baker

01-239 The Gutenberg-Richter b-Value of The Korean Peninsula for a Seismic Hazard Analysis . 213
Jeong-Moon Seo, Hyun-Me Rhee, and In-Kil Choi

01-280 Upthrow of Objects during Recent Earthquakes in Japan 217
Saburoh Midorikawa and Hiroyuki Miura

01-276 Survey of Seismic Demands on California High Speed Rail 223
Tat S. Fu and J. P. Bardet

01-148 Distribution of Building Damage Areas Detected from Satellite Optical Images of the 2006 Central Java, Indonesia, Earthquake 229
Hiroyuki Miura and Saburoh Midorikawa

01-321 Building Damage Estimation Using Seismic Intensity and Satellite L-band SAR Imagery 235
Masashi Matsuoka and Nobuoto Nojima

01-303 Detailed Mapping of Engineering Geomorphologic Classification Using High Resolution Satellite Image and Digital Elevation Model for Seismic 243
Kazunori Ishii, Saburoh Midorikawa, and Hiroyuki Miura

01-030 Analysis of the Bicep Borehole Array 251
Liam Wotherspoon and Rolando Orense

01-341 Three-Dimensional Site Response at KiK-net Downhole Arrays 259
Eric M Thompson, Yasuo Tanaka, Laurie G Baise, and Robert E Kayen

01-482 Ground Motion Selection and Scaling for Site Response Analysis 269
Gokce Tonuk and Atilla Ansal

01-015 Imaging Sedimentary Layers of Metro Manila, Philippines from the Joint Inversion of Receiver Function and Surface-Wave Phase Velocity 277
Rhommel Grutas and Hiroaki Yamanaka

01-083 Site Characterization Using Spatial Autocorrelation Method in Linear and Triangular Arrays by Means of Ambient Vibration Measurements 285
Fabio M. Upegui-Botero, Carlos I. Huerta-Lopez, Jorge A. Caro-Corts, and Jose A. Martinez-Cruzado

01-423 Time-frequency Energy Distribution of Wenchuan Earthquake Motions Based on Matching Pursuit Decomposition..... 291
Dongwang Tao and Hui Li

01-025 A Quantitative Approach to Estimate Coseismic Displacements in the Near-Field from Strong-Motion Accelerographs: Example of the 2007 Niigata-Ken Chuetsu-Oki Earthquake, Japan. 299
Emmanuel H. Javelaud, Tatsuo Ohmachi, Yoichiro Murakami, and Shusaku Inoue

01-129 Development of a Forward-Inversion Crust Modeling Scheme for Accurate Strong-Ground Motion Prediction 305
Pher Errol B. Quinay, Tsuyoshi Ichimura, and Muneo Hori

01-010 Effects of Water Depth Variation on Seismogram Synthesis in Oceanic Structures Based on a Hybrid Boundary Element Method..... 309
Zheng-Hua Qian, Hiroaki Yamanaka, and Sohichi Hirose

01-176 Development of Earthquake Experience System Using Ground Motion Simulator "JISHIN the VUTON" 317
Sou Adachi, Masayuki Matsudaira, Yoshiharu Hirayama, Minoru Yoshida, Saburoh Midorikawa, and Shigeo Hirose

01-279 Ground-motion Selection for PEER Transportation Research Program 321
Nirmal Jayaram and Jack W. Baker

Geotechnical Engineering

02-312 Seismic Earth Pressure Acting on Cantilevered Retaining Walls..... 331
Akihiro Takahashi, Hideki Sugita, and Shunsuke Tanimoto

02-306 Investigation on the Seismic Performance of Under Ground Efficient Tie-rod System, a New Existing Quay Reinforcement Method, by the Centrifuge Experiment..... 335
Shunichi Higuchi, Kenichi Miki, Takashi Matsuda, and Masami Hoshino

02-286 Evaluation of Damage in Geogrid Reinforced Soil Walls Based on Wall Displacement 343
Jun Izawa and Jiro Kuwano

02-240 The Study of Relationship between Landslide Geometry and Run-out Distance of Landslide Mass 347
Muneyoshi Numada and Kazuo Konagai

02-308 Mechanism and Sliding Distance of Earthquake-Induced Amayachi Landslide Estimated by Modified Newmark Method 353
Atsuo Onoue and Junichi Onda

02-376 Centrifuge Model Tests and Deformation Analyses on Seismic Behaviors of Embankments in Mountainous Areas 357
Susumu Nakajima, Tadao Enomoto, and Tetsuya Sasaki

02-305 Difference between Viscous Damping and Hysteresis Damping in Earthquake Response Analysis of Ground 367
Nozomu Yoshida

02-289 Seismic Damages of Mountain Tunnels in Japan and Case Studies 375
Kazuhide Yashiro, Jun Saito, Tomomi Iura, and Jiro Takemura

02-186 Isolation Method for Existing Cut and Cover Tunnel Using Polymer Material 381
Satoshi Kiryu, Yoshitaka Murono, and Hitoshi Morikawa

02-021 Initial Shear Modulus of Auckland Residual Soil from Field and Laboratory Tests 391
Norazzlina M.Sa'don, Anas Ibrahim, Rolando Orense, Michael Pender, and Naotaka Kikkawa

02-232 Liquefaction Potential at Padang City : Comparison of Predicted and Observed Soil Liquefaction during the Padang Earthquake 401
Adrin Tohari and Eko Soebowo

02-460 Performance-based Earthquake Evaluation of a Single Column Bridge System 407
Jinchi Lu, Kevin Mackie, and Ahmed Elgamal

02-307 Effects of Roughness of Shallow Foundations Surface on Superstructure Response during a Strong Earthquake 413
Shuji Tamura, Keisuke Adachi, and Kohji Tokimatsu

02-291 Centrifugal Modeling of Road Embankments Engulfed by Tsunami for its Damage Prediction 419
Akihiko Hirooka, Kousuke Tanaka, Hiroshi Fujii, and Hideo Nagase

02-358 Boundary Effects of Laminar Container in Centrifuge Shaking Table Test 425
Chung-Jung Lee, Yu-Chieh Kuo, and Yu-Chen Wei

02-380 Distinct Element Analysis on Uplift Resistance of Belled Pile and Multi-belled Piles 433
Tsuyoshi Honda, and Yoshio Hirai

02-481 Site Amplification Formula from Bedrock to Surface using Average Vs in Equivalent Surface Layer based on Vertical Array Records 441
Takaji Kokusho

02-466 Where Topographic Effects Responsible for Building Collapses in the 2001 Southern Peru Earthquake? 447
Joseph Wartman and Nicholas E. Malasavage

02-026 H/V Method Used to Qualify the Modification of Dynamic Soil Characteristics Due to Ground Improvement Work by Means of Heavy Compaction Process. A Case Study: the Former Givors's Glass Factory Area 451
Stephane Brule, Emmanuel H. Javelaud, Tastsuo Ohmachi, Yutaka Nakamura, and Shusaku Inoue

02-322 Simulation of Strong Ground Motions at K-NET Kashiwazaki during the 2007 Niigata-ken Chuetsu-oki Earthquake 457
Kohji Tokimatsu, Kota Katsumata, and Hiroshi Arai

02-350 Non-linear Dynamic Modeling of Bridge Embankments Underlain by Liquefied Soil..... 463
Armstrong, R. J., Boulanger, R. W., and Beaty, M. H.

02-290 Seismic Stability of Gravity Type Quay Wall on Desaturated Loose Sand..... 467
Jiro Takemura, Komatsumoto Naomi, Seki Sakae, and Jun Izawa

02-310 Centrifuge Model Tests on Effect of Deep Mixing Wall Spacing on Liquefaction Mitigation..... 473
Masaki Kitazume and Hidenori Takahashi

02-309 In-situ Air Injection as Liquefaction Countermeasure and its Evaluation by Multiphase Flow Simulation..... 479
Mitsu Okamura and Kazuyuki Hayashi

02-353 Effects of Calcite Precipitation on Liquefaction Resistance of Sand..... 485
Kazuyuki Hayashi, Hideaki Yasuhara, and Mitsu Okamura

02-462 A 3D Soil-Structure Interaction Computational Framework 493
Ahmed Elgamal, Jinchi Lu, Zhaohui Yang, and Thomas Shantz

02-130 Response Characteristics and Failure Mechanisms of Pile Foundations in Liquefiable Soil 499
Sumanta Haldar and G.L. Sivakumar Babu

02-260 Effects of Spatial Variation of Laterally Spreading Ground on Stress Distributions within Pile Groups..... 507
Hiroko Suzuki, Kohji Tokimatsu, Masayoshi Sato, and Tabata Kentaro

02-056 Kinematic Bending Moments of Piles in Layered Soils: An Experimental Study 513
S.Bhattacharya, L.Dihoru, C.A.Taylor, G.Mylonakis, F.Moccia, and A.L.Simonelli

02-281 Simulation of Soil-pile-structure Interaction through Multi-dimensional Shaking Table Tests Using E-Defense Facility 519
Hiroyuki Yoshida, Youhao Zhou, Hiroko Suzuki, Yasushi Nukui, and Kohji Tokimatsu

02-230 Simulation Analyses of Shaking Table Test on Soil-pile-structure Model with Semi-rigid Pile Head Connections 525
Sadayuki Ishizaki, Masato Majima, and Toshiaki Nagao

02-076 Characterization of ERT as A New Non-invasive Monitoring Method of Liquefaction Process 531
Suresh R Dash, Anthony Blakeborough, and Subhamoy Bhattacharya

02-449 Large Deformation Analysis of Dynamic Behavior of Embankment on Liquefiable Sand Deposit Using a Strain Space Multiple Mechanism Model 537
Kyohei Ueda, Susumu Iai, and Tetsuo Tobita

02-137 Additional Anchor Influence on Dynamic Behavior of Anchored Retaining Wall..... 547
Ali Derakhshani , Mohammad Sajjad Fayyazi, and Khosrow Bargi

02-287 Effect of Stress State around Tunnel on Pseudo-static Response of Urban Mountain Tunnel in Sand 553
Shuhei Shibayama, Jun Izawa, Akihiro Takahashi, Jiro Takemura, and Osamu Kusakabe

02-063 Dynamic Field Testing of Shallow Foundations Subjected to Rocking 561
Thomas B Algie, Rolando P Orense, and Michael J Pender

02-288 Mechanical Behavior of Piled Raft Foundation in Sand Subjected to Static Horizontal Load 571
Kohei Sawasa, Jiro Takemura, Jun Izawa, and Sakae Seki

02-115 Simplified Dynamic Analysis of Pile Supported Structures in Liquefiable Soils 579
Domenico Lombardi, Suresh R. Dash, and Subhamoy Bhattacharya

02-135 Evaluation of Pile Diameter Effect on p-y Method Precision, in Seismic Analysis of Pile Supported Wharves 589
Mohammad Sajjad Fayyazi, Ali Derakhshani, and Khosrow Bargi

02-387 Lateral Resistance Reduction for Static Analysis of Lateral Spreading 593
Christopher R McGann, Pedro Arduino, and Peter Mackenzie-Helnwein

02-426 Vertical Loads Effect on Lateral Pile Group Response on the Basis of Soil-pile-cap Interactions 601
Mahmoud N. Hussien, Tetsuo Tobita, Susumu Iai, and Kyle M. Rollins

Lifeline Systems and Multihazards

03-352 Earthquake Damage Assessment of Multiple Lifelines for System Interaction Analysis 609
Nobuoto Nojima

03-351 Earthquake Disaster Evaluation and Restoration Support Technologies for Electric Power Distribution Equipment 617
Yoshiharu Shumuta and Shingo Sunagawa

03-360 Modeling of Restoration Process associated with Critical Infrastructures and the Interdependencies due to a Seismic Disaster 623
Gaku Shoji and Ayumi Toyota

03-270 Multi-Hazard Resilient Bridges: Facts and Challenges 633
George C. Lee, and Zach Liang

03-275 Application of Disaster Chain Principle in the Earthquake Disaster Mitigation 639
Yu Shizhou, Zhao Zhendong, and Li Tianqi

03-346 Seismic Performance and Communication Failure of Cell Phone Towers in Iran's Seismic Zones, Case Study: Developing Structural and Communicational Fragility Curves for 24M Monopole Tower 643
Mehdi Sadeghi, Farzad Mohajeri, and Erfan Khalaghi

03-378 Bayesian Network for Infrastructure Seismic Risk Assessment: Challenges and Opportunities 649
Michelle T. Bensi, Armen Der Kiureghian, and Daniel Straub

Concrete Building

04-159 An Overlooked Failure Mechanism of Reinforced Concrete Beam-Column Joints - An Experimental Verification - 659
Hitoshi Shiohara and Fumio Kusuhara

04-147 Study on Compressive Strength of R/C Columns by Using the Upper Bound Theorem 667
Koshiro Nishimura, Hisato Hotta, and Katsuki Takiguchi

04-006 Large-Scale Testing of High Performance Fiber Reinforced Concrete Coupled Walls 671
Remy D. Lequesne, James K.Wight, and Gustavo J. Parra-Montesionos

04-424 Analytical Study of Shear Stud Behavior in High Strength Concrete 681
Haibei Xiong, Wei Zhang, Xilin Lu, and Xiaone Wei

04-162 Strengthening of Masonry Infill Panels with GRP Fabric for Out-of-plane Seismic Loads 685
Luiza Dihoru, Adam Crewe, Olafur Oddbjornsson, and Colin Taylor

04-122 Verification of Pushover Analysis with Chi-Chi Earthquake Damage Database of School Buildings 695
Fu-Pei Hsiao，Yeong-Kae Yeh, Lap-Loi Chung, and Shyh-Jiann Hwang

04-034 Seismic Performance Evaluation of Industrial Building Structures in Turkey using Capacity Spectrum Method 701
Baki Ozturk and Melih Sadak

04-008 System Identification and Damage Detection of Degrading Hysteresis of Reinforced Concrete Frames 707
Chin-Hsiung Loh, Chien-Hong Mao, and Jhih-Ren Huang

04-210 Earthquake Response Evaluation Using Equivalent SDOF System for Single-Story Asymmetric Buildings 715
Hiroshi Kumamoto

04-105 Seismic Performance of RC Building by Cyclic Pushover Analysis 723
Phaiboon Panyakapo

04-136 Effects of Aspect Ratios on Seismic Behaviour of Concrete-filled Rectangular Steel Tubular Columns under Low Cycle Reversed Loading 729
Wang Lai, Li Wensheng, and Liu Ming

04-188 Seismic Retrofit of RC or SRC Buildings with Prestressed Braces 735
Susumu Kono, Takeshi Katayama, and Fumio Watanabe

04-018 Seismic Evaluation and Retrofit of RC Buildings by Using Structural Walls 745
Chao-Lin Huang, Yeou-Fong Li, and Chih-Tsung Lin

04-175 Structural Retrofit for Depth Reduced Beams in Mid-rise Existing Reinforced Concrete Boxed Wall-buildings 751
Yo Hibino, Hiroki Tauchi, Masaomi Teshigawara, Hiroshi Fukuyama, and Yoshio Inoue

04-128 A Brief Introduction to the New Standard for Seismic Appraisal of Existing Buildings in China 761
Cheng Shaoge, Shi Tiehua, and Bai Xueshuang
04-044 Seismic Evaluation of Existing Facilities of Primary and Secondary Schools in Shanghai, China 767
Haibei Xiong, Wei Zhang, Xilin Lu, and Xiaone Wei
04-005 Structural Retrofit of the Taipei Camphor Factory 773
Chao-Hsun Huang, Sheng-Feng Zeng, and Cheng-Guan Lin
04-372 Modeling of Diagonally Reinforced Concrete Coupling Beams 779
David Naish, John Wallace, J. Andrew Fry, and Ron Klemencic
04-237 The Effect of Angle's Crack on The Debonding of The Reinforced Beams by Polymer's Fiber of The FRP (Experimental and Modeling) 785
Zaniar Saimi and Hassan Afshin
04-328 Effect on the Nonlinear Performance of Tall Buildings under the Earthquake due to the Simplification to Structural Systems for the Earthquake Risk Analysis 791
Du Wenxue and Zhang Ligxin
04-363 An Evaluation of Vibration Comport on Reaction Mass Foundation with Shake Table System 797
DaJung Jung, JungWoo Kim, HyoungSuk Choi, and JinHwan Cheung
04-212 Analytical and Experimental Study on RC Exterior Beam-Column Joints without Transverse Reinforcement 803
Sangjoon Park and Khald M. Mosalam
04-302 Damage Distribution of Buildings in Istanbul During the 1894 Marmara Sea, Turkey, Earthquake..... 813
Masashi Morita and Saburoh Midorikawa
04-381 The Analysis of Non-linear Seismic Response between A Collapsed and A Serious Damage Infilled Frame Structure in Yingxiu Town - The Heavy Disaster Areas of Wenchuan 8.0 Earthquake 821
Yan Peilei, Sun Baitao, and Chen Hongfu
04-397 Hysteresis Model of Square Reinforced Concrete Columns with Non-seismic Detailing ... 827
Wilson Y.M. Chung, Eddie S.S. Lam, Bo Wu, and Ivy F.Y. Ho
04-405 Seismic Analysis of RC Frame Structure with Passive Energy Dissipation Devices Using Modal Pushover Analysis..... 835
Gao Ma, Hui Li and Jinping ou
04-373 Experimental Study of Unreinforced Masonry Pier Sub-Structures 841
Charlotte Knox, Alistair Russell, and Jason Ingham
04-455 Strength Deterioration Model Based on Effective Hysteretic Energy Dissipation for RC Members under Cyclic Loading 851
Zhe Qu and Leping Ye

04-042 Simulation-Based Fragility Relationships for Unreinforced Masonry Buildings 857
Thomas M. Frankie and Amr S. Elnashai

Steel Structures (Building)

05-142 Full Scale Shaking Table Collapse Experiment on 4-Story Steel Moment Frame: Part 1 Outline of the Experiment 867
Satoshi Yamada, Keiichro Suita, Yuichi Matsuoka, Yuko Shimada, Motohide Tada, and Kazuhiko Kasai

05-369 Full Scale Shaking Table Collapse Experiment on 4-Story Steel Moment Frame: Part 2 Detail of Collapse Behavior 873
Keiichiro Suita, Satoshi Yamada, Yuichi Matsuoka, and Yuko Shimada

05-145 Numerical Simulation of Collapse using Collaborative Structural Analysis System 879
Motohide Tada, Akinobu Horimoto, Atsushi Mitani, Seiji Mukaide, Kazuhiko Kasai, Keiichiro Suita, and Satoshi Yamada

05-163 Parallel FE-Analysis for Collapse Simulation of 4-Story Steel Building Frame 887
Tomoshi Miyamura, Makoto Ohsaki, Masayoshi Kohiyama, Kunizo Onda, Daigoro Isobe, Hiroshi Akiba, Muneo Hori, Koichi Kajiwara, and Tatsuhiko Ine

05-193 A Steel Database for Component Deterioration of Tubular Hollow Square Steel Columns under Varying Axial Load for Collapse Assessment of Steel Structures under Earthquakes 893
Dimitrios G. Lignos and Helmut Krawinkler

05-118 Collapse Mechanism for Steel Moment Resisting Frames with Different Column Bases ... 899
Katsunori Kaneda, Yoshihiro Kimura, Shinichi Hamasaki, and Akira Wada

05-050 Performance of Steel Frame Structures with Controlled Buckling Mechanism in the Knee Braces 905
H. L. Hsu and C. H. Peng

05-082 Shake Table Study of Dynamic Friction between Steel and Mortar for Seismic Applications in Structures 909
Jason McCormick, Masahiro Ikenaga, Takuya Nagae, and Masayoshi Nakashima

05-138 Effect of Vertical Non-Uniform Ground Motion on Seismic Response of Large Span Structures 917
Feng Liu and Xilin Lu

05-336 Cyclic Behavior and Collapse Mode of High Strength Steel H-Section Beams 925
Kikuo Ikarashi, Ryota Suekuni, and Tao Wang

05-112 Plastic Deformation Capacity and Post Buckling Behavior of H-Shaped Beam with Large Depth-Thickness Ratio under Cyclic Loading 931
Tao Wang and Kikuo Ikarashi

05-043 Crack Fracture of H-Section Cantilever Beam under Strong Cyclic Load 937
Katsuhiko Goto and Motoo Saisho

05-096 Assessment of the Seismic Performance of a Suspended Zipper Frame with Hybrid Testing 943
Andreas Stavridis and Benson P. Shing

05-231 Effects of Reinforcements on Shear Resistance Capacity of Anchor Bolt with Deep Embedment Located Close to Free Edges 953
Hayato Asada, Shoichi Kishiki, and Satoshi Yamada

05-301 Seismic Performance Evaluation of the Steel Intermediate Moment Frame Systems with RBS with Bolted Web 959
Seong-Hoon Hwang, Sang Whan Han, Ki-Byung Kang, and Ki-Hoon Moon

05-265 Evaluation of Plastic Energy Dissipation Capacity of Steel Beams under Various Loading Histories 963
Yu Jiao, Satoshi Yamada, Shioichi Kishiki, and Yuko Shimada

05-327 The Influence of the Lateral Load Pattern on the Minimum Column-to-Beam Moment Strength 973
Se Woon Choi, Sung Woo Park, Bub Ryur Kim, and Hyo Seon Park

05-294 Seismic Behavior of a New Steel Beam-column Connection using Steel Fiber Reinforced Cementitious Composite (SFRCC) 977
Yao Cui, Toru Tai, Shuhai Song, Toko Hitaka, and Masayoshi Nakashima

05-272 System-level Seismic Evaluation of Partial-strength Semi-rigid Steel Frames using Hybrid Simulation 983
Hussam Mahmoud, Amr Elnashai, Billie Spencer, and David Bennier

05-297 Numerical Simulation of Large Scale Seismic Frame Structures 989
Yi-Jer Yu and Keh-Chyuan Tsai

05-296 Test on Retrofit Effects of Steel Beam-to-Column Connections with RC Floor Slabs..... 997
Yulin Chung, Tomohiro Matsumiya, Takuya Nagae, Kunio Fukuyama, Toko Hitaka, and Masayoshi Nakashima

05-300 Evaluation of Rotation Capacity for Reduced Beam Section with Bolted web 1003
Ki-Hoon Moon, Sang Whan Han, Seong-Hoon Hwang, and Sang-Jae Lee

05-317 Applicability of Simulated Ground Motions in Design of Tall Buildings in California 1007
Pierson Jones and Farzin Zareian

Timber Structures

07-084 Testing of a Full-Scale Apartment Building at E-Defense: Design and Performance 1017
John van de Lindt, Shiling Pei, Steven E. Pryor, Hidemaru Shimizu, Kazuki Tachibana, Hiroshi Isoda, and Izumi Nakamura

07-104 Seismic Assessment for Restoration of Prambanan World Heritage Temples Damaged by the Central Java Earthquake of 2006, Indonesia 1025
Toshikazu Hanazato, Satoshi Yamato, Yasufumi Uekita, Chikahiro Minowa, Suprapt Siswosukarto, Subagyo Pramumijyo, Kunihiko Ono, Noriko Koresawa, and Mai Taneichi

07-146 Experimental Study on Shear Behavior of Thick Structural Plywood Sheet Floor Framing with Opening 1033
Hiroyasu Sakata, Shota Nakano, Hiromichi Ito, Azuma Fujishiro, and Hitoshi Ooguchi

07-180 Recent Large-scale Wood Construction in Japan - Development and Consideration of Mid-rise Timber Based Structure - 1041
Hiroshi Isoda, Naohito Kawai, and Mikio Koshikara

07-314 Instrumental Earthquake Intensities vs. Ductility Demand: Correlation Study Using Data from Europe & The Middle East 1047
J.Enrique Martinez-Rueda and Tilemachos Vlachos

07-177 Indian Bamboo as An Alternate to Timber : A Critical Evaluation from Strength of Material Perspective 1053
Parthasarathi Mukhopadhyay and Sekhar Dutta

07-223 Analytical Study on Seismic Response Controlled Effect of Wooden Houses Using Frame Model 1063
Kazuhiro Matsuda, Kazuhiko Kasai, and Hiroyasu Sakata

Advanced Technologies

08-244 Seismic Resilience of Self-Centering Steel Braced Frames with Replaceable Energy-Dissipating Fuses ; Part 1: Large-Scale Cyclic Testing 1071
Jerome F. Hajjar, Matthew Eatherton, Xiang Ma, Gregory G. Deierlein, Helmut Krawinkler, and Sarah Billington

08-243 Seismic Resilience of Self-Centering Steel Braced Frames with Replaceable Energy-Dissipating Fuses ; Part 2: E-Defense Shake Table Test 1079
Gregory G. Deierlein, Xiang Ma, Jerome F. Hajjar, Matthew Eatherton, Helmut Krawinkler, Toru Takeuchi, Mitsumasa Midorikawa, Tsuyoshi Hikino, and Kazuhiro Kasai

08-167 Seismic Behavior of Steel Rocking Frames by Three-dimensional Shaking Table Tests 1085
Mitsumasa Midorikawa, Tadashi Ishihara, Tatsuya Azuhata, Tetsuhiro Asari, Hirotake Hori, and Takayoshi Kusakari

08-106 Shaking Table Tests on Controlled Rocking Frame of Wooden Structures 1091
Shoichi Kishiki and Akira Wada

08-174 Three-dimensional Analysis for Square Seismic Isolation Bearings under Large Shear Deformation and High Axial Loads 1097
Masaru Kikuchi, Ken Ishii, Takahito Nakamura, and Ian D. Aiken

08-062 Structural Response Control by Controllable Dampers setting at Inter-Story of Buildings . 1105
Hideto Kanno, Tetsuya Nishida, Jun Kobayashi, and Norio Inoue

08-103 Experimental Validation Of Market-Based Control Using Wireless Sensor And Actuator Networks 1111
R. Andrew Swartz, Yang Wang, Jerome P. Lynch, Kincho H. Law, and Chin-Hsiung Loh

08-182 Performance-Based Seismic Design Of Building Systems With Dampers: Experimental Validation Using Real-Time Hybrid Simulation 1119
James M. Ricles, Richard Sause, Theodore L. Karavasilis, and Cheng Chen

08-121 Experimental Seismic Response of a Full-Scale Seven-Story Mixed-Use Steel/Wood Apartment Building 1125
Steven E. Pryor, John W. van de Lindt, and Shiling Pei

08-032 Cyclic Loading Tests on Buckling-restrained Braces Using Round Steel Bar Cores and Double Steel Tubes 1133
Shunji Fujii and Hiroshi Tagawa

08-415 Parametric Studies of Particle Dampers under Multi-Axis Excitations 1137
Xilin Lu, Zheng Lu, and Sami F. Masri

08-246 A Tracking System to Maximize the Efficiency of TMD 1143
Ali Bozer and Gulay Altay

08-097 Practical Nonlinear Response Analysis Method of Viscoelastic Damper considering Temperature, Frequency, and Stain Dependencies 1151
Naohiro Nakamura, Takuya Suzuki, Kazuhiko kasai, and Yoji Ooki

08-164 Seismic Risk Evaluation of School Gymnasia based on Dynamic Nonlinear Response Analysis 1161
Shoji Nakazawa and Shiro Kato

08-144 Response Control of Lattice Dome Roofs using Seismic Isolation 1167
Toru Takeuchi, Kengo Takamatsu, Tomohiko Kumagai, and Toshiyuki Ogawa

08-233 Shaking Table Tests of Cylindrical Lattice Shell Roofs Supported by Substructure with Viscous Damper Subjected to Horizontal Earthquake Motions 1173
Tomohiko Kumagai, Toru Takeuchi, Fumi Ushiwata, and Toshiyuki Ogawa

08-266 Structural Design and Research of A Large-span Single-layer Ellipsoid Latticed Shell with Complex Boundary 1181
Zhang Hui, Yang Lianping, Li Yaming, Zhang Lianglan, and Zhou Deyuan

08-161 Implementation of Bio-informatics on Structural Health Monitoring 1189
Tzu-Kang Lin, Chang-Hung Ku, Li-Chen Yu, Chih-Shiuan Lin, and Kuo-Chun Chang

08-139 Structural Control Using Global Vibration Sensing and Model Updating Based on Local Infrared Imaging 1195
Chun-Hung Lin, Nebojsa Sebastijanovic, Henry T.Y. Yang, and Xiaoyan Han

08-149 Statistical-based Structural Damage Detection Using Strain Power Mode Shape 1203
Eun Hyung Cho, and Jae Kwan Kim

08-190 A High Resolution Distributed Moisture Sensing System to Quantify Earthquake Induced Void Redistribution 1211
Jonathon Fagert, Bin Zhang, and Xiong (Bill) Yu
08-446 Application of Different Continuous Wavelet Functions on Cylindrical Guided Wave Signals for Underground Pipe Inspection 1217
Rais Ahmad, and Tribikram Kundu
08-340 Experimental and Theoretical Study on Self-centering Isolators Made of Shape Memory Alloy Metallic Rubber 1225
Suchao Li, Chenxi Mao, Hui Li, Yagebai Zhao, and Wentao Wang
08-019 Passive Energy Dissipation Device Using U-shaped Steel Dampers Based on Quasi-Linear Motion Mechanism 1231
Jinhe Gao and Hiroshi Tagawa
08-113 Adaptive Noise Variance Identification for Fusion of Acceleration and Displacement 1237
Zhen Li and Chih-Chen Chang
08-263 Effective Buckling Length for Buckling Restrained Braces Considering Rotational Stiffness at Restrainer Ends..... 1245
Ryota Matsui, Toru Takeuchi, Kohji Nishimoto, Satoshi Takahashi, and Tatsuya Ohyama
08-132 An Experimental Study on ASNLSE Method for Health Monitoring of Base-Isolated Structures 1255
Qiang Yin, Li Zhou, and Jann N. Yang
08-451 A Study on the Stability of Step-over Isolated Structure..... 1261
Yosuke Yamamoto, Toru Takeuchi, Yasuhiro Nakata, and Eiichirou Saeki
08-416 Optimum Design of Particle Dampers under Random Excitation 1269
Zheng Lu, Xilin Lu, and Sami F. Masri
08-379 Measurement of Performance and Estimation of Scalability for Enhanced IES with High Performance Computing Techniques 1275
Gholamreza Sobhaninejad, Muneo Hori, Ichimura Tsuyoshi, and Maddegedara L.L.Wijerathne
08-035 A New Model Parameter Identification Technique for Magnetorheological Dampers..... 1283
Aditya Venkatesan
08-282 Torsional Seismic Response Reduction by Passive Control Devise for Conventional Post-and-beam One-story Wooden House with Stiffness Eccentricity 1289
Yoshihiro Yamazaki, Kazuhiko Kasai, and Hiroyasu Sakata

Non-Structural Components and Contents

09-066 Analysis and Experimental Approaches on Seismic Performance of Architectural Curtain Walls..... 1299
Wensheng Lu, Baofeng Huang, and Shiming Chen
09-392 Dynamic Characteristics of Japanese Style of Ceiling 1307
Shojiro Motoyui, Yasuaki Satoh, and Takuto Kawanishi

09-093 Estimation of Floor Acceleration Design Spectra 1313
Hossein Akhlaghi, and Abdolreza S. Moghadam

New Design Criteria and Methods

10-016 The Development and Use of the Continuous Column Concept 1319
Gregory MacRae
10-156 A Novel Approach to Performance-based Seismic Design of Bridge Using Fuzzy Genetic Optimization 1327
Yu-Chi Sung, Chin-Kuo Su, and Dyi-Wei Chang
10-131 Study on Seismic Retrofitting Using Rocking Walls and Steel Dampers 1335
Hiroshi Ito, Yuta Uchiyama, Hiroyasu Sakata, Shojiro Motoyui, and Akira Wada
10-081 A Study on Earthquake Response Analyses of Buildings Using Energy Transmitting Boundary in the Time Domain 1341
Naohiro Nakamura
10-442 Performance Based Seismic Design for the Shanghai Tower 1349
Jiemin Ding, Xin Zhao, and Si Chao
10-268 Prescriptive Seismic Codes: Societal Inconveniences 1355
F. Casciati, A. Narcellini, A. Tento, and D. Gerosa
10-299 A Methodology for the Seismic Design of Tall Buildings Incorporating Base Isolation Devices 1361
Troy A. Morgan and Kazuhiko Kasai
10-053 Scaling the Ground Motion Records in Order to Estimate the Probabilistic Seismic Demand Using Bayesian Statistics 1369
Mehdi Banazadeh and Mehdi Mahdavi Adeli
10-467 Evaluation of the Dynamic Pressure Envelopes in Embedded Storage Tanks under Near Field Earthquakes 1379
Fayaz R. Rofooei, Nader K. A. Attari, and Navid K. A. Attari
10-453 A New Design Idea for Mitigating Seismic Damage of Frame Columns by Using SMA Related Device 1387
Yun Chen and Xilin Lu
10-318 Fiber Reinforced Polymer (FRP) Strengthening of Unreinforced Masonry Bearing Wall Buildings - A New Approach 1393
Geoff Sharp, Bill Tremayne, Paul Littler, Meng, and Zander Sivyer
10-166 A Design Approach Using Viscous-type Damper to Control Seismic Vibration of Slip-hysteretic Structure 1401
Wuchuan Pu and Kazuhiko Kasai
10-476 Structural Damage Assessment Based on 3D Nonlinear Dynamic Response and Its Seismic Design 1407
Yongle Zhang, Jianqun Jiang, and Jiajin Liu

10-472 Seismic Response of Rocking Bridges Self-Centering Due to Gravity 1415
Mostafa Masoudi

Earthquake Engineering Practice

11-382 Analysis of Earthquake Damage for Various Types of Buildings Structures in Wenchuan Earthquake 1423
Sun Bai-tao and Zhang Gui-xin

11-114 Bi-spectra for Two-way Asymmetric-plan Structures under Bi-directional Ground Excitations 1427
Jui-Liang Lin, Wen-Chia Yang, and Keh-Chyuan Tsai

11-401 Selection of Earthquake Records for Time-history Analysis of Structures 1435
Abbas Moustafa, Izuru Takewaki, and Anil Wijeyewickrema

11-456 An Evaluation of Cost Effectiveness of New Technology for Seismic Mitigation in Gansu during Wenchuan Earthquake 1445
Yohgfeng Du and Hui Li

11-326 Approximate Incremental Dynamic Analysis Using Modal Pushover 1449
SW Han and TS Lee

11-028 Analysis and Comparison of An Innovative Partial Isolation Method and Traditional Isolation Method for A Shaking Table Laboratory 1453
Yifei Ma, Xilin Lu, Yonghui Ruan, and Xueping Li

11-024 Static-Dynamic Analysis Method for Energy-Dissipated Design of Frame-Shear-Wall Structures with Dampers 1461
Gengwen Zhao, Aiqun Li, and Ruixin Huang

11-377 Response of RC Buildings under Multiple Earthquakes 1466
Adel E. Abdelnabi and Amr S. Elnashai

11-264 Experimental Study on In-plane and Out-of-plane Behavior of PP-Band Retrofitted Masonry Wallette Made of Shapeless Stones 1473
Kotaro Sakurai, Navaratnarajah Sathiparan, and Kimiro Meguro

Earthquake Loss Estimation

12-430 Rapid Visual Seismic Vulnerability Assessment Tool and its Application in Disaster Risk Mitigation in Urban Areas 1479
Youb Raj Paudyal, Ryuichi Yatabe, Netra Prakash Bhandary, Jishnu Subedi, and Rekha Shrestha

12-171 Damage Estimation of Water Distribution Pipes following Recent Earthquakes in Japan 1487
Yoshihisa Maruyama and Fumio Yamazaki

12-181 Post Quake Microzoning Study on Pisco and Tambo de Mora due to August 15th 2007 Pisco Quake 1493
Carlos Zavala, Zenon Aguilar, and Miguel Estrada

12-196 Enhancement of Earthquake and Tsunami Disaster Mitigation Technology In Peru: A SATREPS Project 1501
Fumio Yamazaki, Carlos Zavala, Shoichi Nakai, Shunichi Koshimura, Taiki Saito, and Saburoh Midorikawa
12-480 Seismic Loss Estimation for Three Major Cities in Bangladesh 1507
Pennung Warnitchai, Matrin Suthasit, Chaiyapat Suesutajit, and Kawin Worakanchana

Information and Computing Technology
14-359 Urban Structural Damage Characterization Using Optical Imagery 1517
Tara C. Hutchinson and ZhiQiang Chen
14-206 Prediction and Utilization of Spatial Geotechnical Information for Administrative Decision Support on Earthquake Disaster in Urban Area..... 1523
Chang-Guk Sun
14-342 A New Disaster Management Manual for Disaster Reduction..... 1531
Shinya Kondo and Kimiro Meguro
14-331 Parallelized Fast Multiple BEM for Seismic Analysis in Time-Domain..... 1537
Sohichi Hirose and Takahiro Saitoh
14-386 Analytical Evaluation for Local Buckling Behavior of Steel Framed Structures..... 1543
Takahiro Ohtsuka and Shojiro Motoyui

Socio-Economic Issues
16-338 Development of Integrated Disaster Information System and Information Management.... 1549
Kimiro Meguro and Shinya Kondo
16-184 The Meanings of the Approval System for Business Continuity Ability of Construction Companies..... 1557
Hiroaki Maruya
16-073 Mining Critical Infrastructure Interdependency Relationships to Mitigate Disasters Using GSP..... 1563
Ssu-Min Tseng, Te-Che Chen, and Chien-Cheng Chou
16-357 Estimation of Interregional Commodity Flows under Utility and Transportation Infrastructure Damages..... 1567
Yoshio Kajitani
16-157 Relative Analysis between a Community Disaster Recovery Potential and Social Capital . 1577
Emi Ishibashi, Eiichi Itoigawa, Michitaka Umemoto, and Yoshio Kumagai
16-119 Effectiveness of a Sports Festival Style of Disaster Drill by Picked Community Groups in Their Capacity Building for Responding to Earthquake Disasters 1587
Masaki Fujioka, Hideki Kaji, Jun Mihira, and Yoshinari Takanashi
16-209 Globalization and Localization of Disaster Impacts: Examination for Global Propagation . 1591
Yasuhide Okuyama

Human Behavior

17-511 Emergency and Transitional Shelter Post Earthquake: The Role of Social Capital in Javanese Community 1599
Ika Putra

17-454 Housing Reconstruction and Community 1609
Yoshimitsu Shiozaki

17-293 Human Behavior in Preparation for Earthquake Damage Mitigation 1613
Haruyuki Fujii

17-277 Spatiotemporal Distribution of Railroad Users Facing Difficulty in Returning Home After A Devastating Earthquake 1617
Toshihiro Osaragi and Ikuko Otani

17-311 A Human Behavior Model in Replacement of Wooden Housing for Earthquake Damage Mitigation 1623
Yusuke Meshitsuka

17-402 Educational Activities To Promote Earthquake Preparedness Using A Portable Virtual Reality System 1627
Shinsuke Tsubota and Ryuzo Ohno

17-361 Residents' Evaluation in Java 2006 Earthquake Post Disaster Settlement - Case Study of New Ngelepen, Sleman, Yogyakarta- 1631
Syam Rachma Marcillia

17-120 Survey on Causes of Fatalities in Recent Japanese Earthquakes 1639
Masahiro Yoshimura and Saburoh Midorikawa

17-334 Workshop for Disaster Imagination Improvement of Nursery School Leaders 1645
Mariko Abe, Kimiro Meguro, and Mari Yokoya

Tsunami

18-383 Introduction of Japanese Coastal Wave Monitoring Network 1649
Toshihiko Nagai

18-417 Field Survey of the 2009 Samoa Earthquake Tsunami 1655
Shunichi Koshimura, Yuichi Nishimura, Yugo Nakamura and Yuichi Namegaya, Gerard Flyer, Akapo Akapo, Don Vargo, and Laura Kong

18-396 Differences of Tsunami Waves induced by Earthquakes, Submarine Landslides and Sea Floor Collapse 1659
K.T. Chau

18-283 Verification of a Dynamic Tsunami Simulation Technique Based on Observation Records in Near-field 1665
Shusaku Inoue and Tatsuo Ohmachi

18-375 Recent Progress on Offshore Tsunami Observation 1671
Hiroyuki Matsumoto, and Yoshiyuki Kaneda

18-477 Tsunami Loading-From Experiments to Field Load Test 1677
Panitan Lukkunaprasit, Nuttawut Thanasisathit, and Anat Ruangrassamee
18-362 Numerical Simulation of Tsunami Generation 1681
Taro Kakinuma
18-413 Numerical Simulation of Hydroacoustic Effects in Tsunami Source 1687
Sergey Kolesov, Anna Bolshakova, Shusaku Inoue, Hiroyuki Matsumoto, Mikhail Nosov, and Tatsuo Ohmachi .....
18-395 Hydrodynamics of Boulder Transport on a Shore Platform on Phi Phi Island during the 2004 Tsunami 1693
K.T. Chau and Bao J.Q.
18-431 Real-Time Tsunami Simulation accelerated by GPU 1701
Marlon Arce Acuna and Takayuki Aoki

Structures Miscellaneous Issues

19-425 Bamboo As A Green Building Material 1709
Shyam K Paudel
19-470 Fire Resistant Testing and Analysis of Light-gauge Steel Earthquake Disaster Relief Shelters 1715
Q. Zhou, Y. Xiao, and L.Y. She
19-295 Sustainable Rural House Design in Post-quake Reconstruction 1719
Hu Rongrong, Liu Jiaping, Cheng Hui, and Zhou Wei
19-471 Glubam Buildings for Earthquake Relief in Sichuan 1725
B. Shan, Y. Xiao, L. Y. She, Q. Zhou, G. Chen, and R. Z. Yang
19-479 Behavior of Concrete Horizontal-hole Hollow Block Masonry 1729
Wu Fangbo, Chen Wei, Huang Hilin, and Zhou Xuhong
19-469 Design and Construction of Lightweight Glubam Frame Residential Houses 1733
G. Chen, Y. Xiao, B. Shan, R. Z. Yang, and L. Y. She
19-274 Educational Programs at the PEER Center That Encourage Multidisciplinary Understanding 1737
Heidi Faison and Stephen Mahin
19-189 Improving Seismic Performance of Brick Masonry Junctions 1745
Sekhar Chandra Dutta, Parthasarathi Mukhopadhyay, and Kundan Goswami
19-208 Earthquake Resistance Analysis on A Double Circuit Intermediate Tower Consisted of Steel Tubes and Angel Steels 1753
Wang Lai, Liu Ming, and Yang Ning
19-229 Protection of Mediterranean Historical Structures against Earthquakes Using Fragility Curves 1761
Syrmakezis A. Costas, and Kosta T. Margarita

19-348 Towards Earthquake Safer Non-engineering Houses by Technological and Social Approaches 1769
Kimiro Meguro
19-152 The Investigation and Analysis of Structure Earthquake Damage in Dujiangyan 1775
Zhong Jiangrong, and Lin Junqi
19-079 Retrofit of Historical Structures against Earthquakes: A Case Study on Minarets 1781
Ahmet Murat Turk

Structural Engineering (Civil)

20-475 Damage Analysis of High Arch Dam including Contraction Joint and Cracking Nonlinearity 1789
Xiaowen Yao, Jianqun Jiang, and Yikang Xu
20-330 Nonlinear Behavior of Reinforced Concrete Columns Impacted by Tsunami Water-borne Shipping Containers 1795
Kavinda M. Madurapperuma, and Anil C. Wijeyewickrema
20-285 Comparison of Seismic Response in Skewed Bridges to Near Vs. Far Field Motions 1805
Peyman Kaviani, Farzin Zareian, and Majid Sarraf
20-324 Effect of Fiber Reinforced Cement Composites on the Seismic Performance of Bridge Columns 1811
Richelle Zafra, Tomohiro Sasaki, Kazuhiko Kawashima, Koichi Kajiwara, and Manabu Nakayama
20-320 Effect of Finger Expansion Joints on Seismic Response of Bridges 1819
Guilian Quan and Kazuhiko Kawashima
20-332 Nonlinear Finite Element Analysis of Seismic Pounding between Adjacent Multi-Story Reinforced Concrete Buildings 1829
Deepak Raj Pant, Anil C. Wijeyewickrema, and Tastsuo Ohmachi
20-234 Experimental Testing of Innovative Confinement Techniques for Seismic Retrofitting of RC Bridge Columns 1841
Moochul Shin and Bassem Andrawes
20-333 Experimental Study on Static and Dynamic Behavior of PP-band Mesh Retrofitted Adobe Masonry Structures 1845
Navaratnarajah Sathiparan, Paola Mayroca, and Kimiro Meguro
20-037 Effect of Rubber Bearing's Modeling on Seismic Response of Base Isolated Highway Bridge 1855
M. K. Razzaq, A. R. Bhuiyan, Y. Okui, H. Mitamura, and T. Imai
20-116 Mitigation of Residual Deformations of Rc Bridge Piers Using Steel Fiber Composite Bars as Longitudinal Reinforcement 1863
Mohamed F.M. Fahmy, Zhishen Wu, and Gang Wu

Seismic Diagnosis and Strengthening

22-444 Seismic Retrofitting of RC Columns by CF Rope and its Computational Model 1873
Takumi Shimomura

22-440 Train Running Safety during Seismicity on Railway Viaduct Group and its Improvement 1879
Mamichi Sogabe, Kouji Matsuhashi, Keiichi Goto, Yukihiro Tanimura, and Kiyoshi Asanuma

22-077 Shear Retrofitting Method for RC Beams Using UFC Panels 1887
Koji Matsumoto, Kou Shibata, and Junichiro Niwa

22-048 A Comparative Experimental Study on Alternative Strengthening Methods for Historical Masonry Walls 1899
Necdet Torunbalci and Fatih Sutcu

22-169 Seismic Resistance of Beam-Column Joints in Scaled Framed Bridges 1907
Kabir Shakya, Ken Watanabe, and Junichiro Niwa

22-155 Rocking Behavior of Bridge Piers with Spread Footing under Cyclic Loadings and Earthquake Excitations 1913
H. H. Hung, K C. Chang, and K. Y. Liu

Isolation, Seismic Response Control System and Seismic Response

23-036 Experimental Study of Rate-Dependent Mechanical Behavior of Laminated Rubber Bearings 1923
T. Imai, A.r. Bhuiyan, M.k. Razzaq, Y. Okui, and H. Mitamura

23-269 Viscous Fluid Devices for an Italian Viaduct..... 1929
Lucia Faravelli, Sara Casciati, and Agostino Marioni

23-020 Nonlinear Modeling and Seismic Performance of a Multi-Span Simply Supported Viaduct..... 1935
Sourabh Agrawal and Ashok K. Jain

23-433 Shake Table Test and Non-Linear Dynamic Analysis for a Bridge Model Using Rigid-Plastic Dampers..... 1941
Takao Okada, Shigeki Unjoh, and Jun-Ichi Hoshikuma

23-100 "Complete Similarities" in the Response of Seismic Isolated Structures 1947
Nicos Makris and Michalis F. Vassiliou

Dynamic Analysis and Failure

24-447 Shake-Table Tests and Numerical Study of the Seismic Performance of Non-Ductile RC Frames with Masonry Infill Walls 1957
P. Benson Shing, Andreas Stavridis, and Ioannis Koutromanos

24-414 Damping Characteristics of a Cable-stayed Bridge based on Strong Motion Records 1967
Kazuhiko Kawashima, Hidenori Ogimoto, Gakuho Watanabe, and Hiroshi Nishi

24-022 Seismic Progressive Collapse of Reinforced Concrete Frames and Bridges 1975
David T. Lau, and Hartanto Wibowo
24-298 Predicting In-Cabinet Response Spectrum by Using Impact Hammer Tests 1985
Jintao Cui, Sung Gook Cho, Dookie Kim, and Do-Gyeum Kim
24-441 Cracking Behavior of Reinforced Concrete Beams Repaired with Strain Hardening Cement-based Composites 1989
Yuichi Uchida, Seungchan Lim, and Mamoru Moriyama

Steel Structures and Cable-stayed Bridges

25-434 Fatigue Behavior of Load-Carrying Cruciform Joints with Weld Defect under Cyclic Plastic Strain 1997
Takeshi Hanji, Saiprasertkit Kawin, and Chitoshi Miki
25-435 Effect of Plate Thickness on Low Cycle Fatigue Strength of Cruciform Welded Joints 2005
Koji Kinoshita and Kiyohiro Ueda
25-436 Residual Strength of Damaged Steel Bridge Pier with Circular Cross Section and its Repair Method 2011
Moriaki Suzuki, Yoshiyuki Shimaguchi, and Tetsuhiko Aoki
25-437 Elasto-Plastic Behavior of Spiral Steel Pipes under Cyclic Loading 2017
Kiyoshi Ono, Mitsuyoshi Akiyama, and Hideki Naito
25-439 The Application to the Viaduct of the Energy Dissipation Connectors of Girders in Consideration of Axial and Transverse Directions 2023
Kentaro Tanaka, Masahide Matsumura, Takeshi Kitahara, Hiroshi Zui, and Toshiyuki Kitada
25-014 Seismic Fragility Analysis of Long-span Cable-stayed Bridges 2027
Jiao Chi-yu, Li Jian-Zhong, and Long Pei-Heng
25-033 Identifying Cable Tension Loss and Deck Damage in a Cable-Stayed Bridge Using a Moving Vehicle 2035
Shih-Hsun Yin and Chung-Yu Tang

Structural Concrete

26-443 Piezoresistive Cement-Based Sensors For Real-time Structural Health Monitoring During Earthquakes 2045
N. Banthia, F. Azhari, and B. Raheja
26-273 A Precast Concrete Bent System for Bridges in Seismic Regions 2053
Eberhard, M. O., Stanton, J.F., Pang, J.P.K., and Haraldsson, O.
26-438 Experimental Study on Shear Failure Mechanism of Circular Reinforced Concrete Beams 2061
Ken Watanabe, Syunya Oishi, Moe Yonehana, and Junichiro Niwa

26-168 Experimental Study for Shear Carrying Capacity of Segmental Concrete Beams with External Tendons and Dry Joint 2067
Dinh Hung Nguyen, Ken Watanabe, Junichiro Niwa, and Tsuyoshi Hasegawa

26-261 Seismic Response of R/C Structures Subjected to Simulated Ground Motions Compatible with Design Spectrum 2073
Dae-Han Jun

General and Miscellaneous Issues

27-038 Testing of an Earthquake-Damaged Unreinforced Masonry Building..... 2081
Dmytro Dizhur, Ronald Lumantarna, Hossein Derakhshan, and Jason Ingham

27-127 Comparison Shaking Table Test Study on Seismic Strengthening of Single Story Masonry School Building 2093
Shi Tiehua and Cheng Shaoge

27-448 Life-Cycle Cost Estimation of Open-Type Wharf Based on Seismic Damage Risk 2101
Hirohi Yokota, Hiroshi Yamauchi, Ema Kato, and Mitsuyasu Iwanami

27-445 Shear Carrying Capacity of RC Beams Having Partially Corroded Longitudinal Reinforcement 2109
Tomohiro Miki and Yasuhito Takeuchi

27-398 Strengthening Reinforced Concrete Columns by High Performance Ferrocement 2115
Ivy F.Y. Ho and Eddie S.S. Lam

27-329 Diagnosis, Analysis and Retrofitting of an Old Masonry Building in Algeria 2125
Nadir Boumechra, Fabio Casciati, and Karim Hamdaoui

E-Defense Blind Analysis Contest

30-463 3-D Blind Analyses of Full-Scale 5-Story Building with Steel Dampers..... 2133
Naohiro Nakamura, Takuya Suzuki, Soshi Nakamura, Masashi Yamamoto, Takayuki Sone, and Harumi Yoneda

30-464 2-D Blind Analyses of Full-Scale 5-Story Building with Steel Dampers..... 2139
Harumi Yoneda, Masashi Yamamoto, Takayuki Sone, Naohiro Nakamura, Takuya Suzuki, and Soshi Nakamura

30-465 2- and 3-D Blind Analyses of Full-Scale 5-Story Building with Viscous Dampers..... 2145
Tadamichi Yamashita, Jun Kawabata, Masayuki Ninomiya, Norikazu Sakaba, and Yukimori Yanagawa

30-468 Overview of 2009 E-Defense Blind Analysis Contest Results 2153
Tsuyoshi Hikino, Makoto Ohsaki, Kazuhiko Kasai, and Masayoshi Nakashima

03-140 Numerical Simulation of Underground Pipeline under Lateral Non-uniform Earthquake Wave Excitation and Comparison with Shaking Table Tests 2159
Xiaoyu Qi and Jun Chen

27-242 Consideration on Process of Seismic Retrofit using Environmentally Friendly Materials in Existing Bridge 2165
Jang, Won-Rak, Jeon, Gyoo-Shick, Kim, Eun-Kyum, and Park, Chul-Sung

JOINT CONFERENCE PROCEEDINGS
7th International Conference on Urban Earthquake Engineering (7CUEE) &
5th International Conference on Earthquake Engineering (5ICEE)
March 3-5, 2010, Tokyo Institute of Technology, Tokyo, Japan

ENGINEERING SEISMOLOGY: DIRECTIONS IN PROBABILISTIC SEISMIC HAZARD ANALYSIS

John G. Anderson
Nevada Seismological Laboratory and Department of Geological Sciences and Engineering, University of Nevada, Reno, Nevada
Earthquake Research Institute, The University of Tokyo, Japan.

Abstract

The goal of probabilistic seismic hazard analysis (PSHA) is to estimate the answer to a question that is conceptually simple: how often do different levels of ground motion occur at the site. Obviously, since engineering interest is in the answer to this question at occurrence rates of 10^{-3} per year or lower, the experiment is impossible to perform. However, based on geological observations, comparison with the largest observed ground motions, and/or comparisons of different regions, the estimates of some specific PSHA studies are very surprising, particularly at small exceedance rates. High standard deviations in ground motion prediction equations are a leading candidate to explain the surprising hazard predictions. The high standard deviation is caused by the use of an ergodic assumption in development of the ground motion prediction equations. Especially thanks to the development of relatively dense strong motion networks in Taiwan and Japan, it is now possible to partially remove the ergodic assumption, and recent studies indicate that the result is a significant reduction of the standard deviation. The median reduction of the standard deviation from five studies is applied to simplified PSHA models for Yucca Mountain, Nevada, and for the central United States. Estimated ground motions at annual occurrence rates below 10^{-3} per year are significantly reduced in both cases.

INTRODUCTION

Probabilistic seismic hazard analysis (PSHA) has become a widely used procedure. Over the past decade the number of articles addressing issues in PSHA has exploded. Consequently, any brief paper on the topic of "current directions" cannot possibly cover the full scope of important directions in the field.

PSHA is valuable because it estimates the answer to an important question: how often does ground motion from earthquakes at a site exceed an amplitude of interest? Since the answer is relevant to seismic resistant construction and societal risks, it is critical that PSHA be tested as rigorously as possible. PSHA methodology is a sound, straightforward application of probability theory, but the results of are subject to input model parameters. These parameter issues may be local issues such as the activity rate of particular faults or seismic zones, but some are more general. The treatment of the uncertainty parameters in the ground motion prediction equations is probably the most important of the general issues. This paper briefly reviews PSHA methodology and how the analysis can be tested. It identifies two surprising PSHA results and shows how the results might be less surprising if more information is available to reduce the aleatory uncertainty.

PSHA METHODOLOGY

A calculated *exceedance rate curve*, $\lambda_C(Y)$, estimates the number of times per year that an earthquake motion will exceed the amplitude Y. If the Poisson model holds, the probability of exceeding Y in a time interval of duration T is:

$$P(Y,T) = 1 - \exp(-\lambda_C(Y)T) \quad (1)$$

The curve $P(Y,T)$ is the *hazard curve.* For $\lambda_C(Y)T<<1$, $P(Y,T) \approx \lambda_C(Y)T$. Hazard maps (e.g. Frankel et al, 2000, 2002; Stirling et al, 2002; Marin et al, 2004; Fujiwara et al, 2006; Pace et al, 2006; Petersen and others, 2008; Kalkan et al, 2009) select an annual probability and contour the values of Y obtained from hazard curves calculated on a grid of points.

Methods to estimate hazard curves and deaggregations are described by, e.g. Cornell (1968), McGuire (1995), SSHAC (1997), and Bazzurro and Cornell (1999). Recent articles dealing with implementation issues include Scherbaum et al (2004a,b, 2005, 2006, 2009), Albarello et al (2005), and Bommer et al (2005).

A general integral to calculate $\lambda_C(Y)$ is:

$$\lambda_C(Y) = \iint n(M,R(\mathbf{x}))\Phi(y \geq Y \mid \hat{Y}(M,R(\mathbf{x})),\sigma_T)dMd\mathbf{x} \quad (2)$$

The term $\Phi(y \geq Y \mid \hat{Y}(M,R(\mathbf{x})),\sigma_T)$ is developed from a ground motion prediction equation (GMPE), and gives the probability that an earthquake with magnitude M at location $\mathbf{x}$ will cause a ground motion that equals or exceeds Y, where $\hat{Y}(M,R(\mathbf{x}))$ is the median value of Y from the GMPE and σ_T is the standard deviation. The seismicity model $n(M,\mathbf{x})dMd\mathbf{x}$ gives the number of earthquakes per year in a magnitude range of width dM and an area (or volume) of size $d\mathbf{x}$. $R(\mathbf{x})$ is the distance from the earthquake at location $\mathbf{x}$ to the site of interest.

The integrals in Equation 2 are over relevant magnitudes and the relevant volume of the Earth. Equation 2 is a standard equation, from probability theory, to estimate the mean of a multi-dimensional probability distribution.

There are some typical ways to quantify *n(M,x)*. The first is as "area sources", for which an earthquake within the zone has either a uniform probability of occurring anyplace or obeys a smoothed spatial dependence (e.g. Lapajne et al, 2003). The second is as "line sources" that represent faults. The development of seismicity models consistent with the geology, geodesy and historical seismicity is difficult, even in the best-studied regions such as California (e.g. Working Group on California Earthquake Predictability, 1996; Field et al, 1999; Petersen et al 2000; Page and Carlson, 2006; Plesch et al, 2007; Field et al, 2009). Where detailed study of all the faults in a complex network is impractical, the development of models consistent with geology, seismicity, and geodesy still needs more research, and the development of *n(M,x)* requires making practical decisions on how to best represent the available data (e.g. Frankel et al, 2002; Pancha et al, 2007; Pace et al, 2007; Marzocci, 2007; Peruzza, 2007).

TWO SURPRISING PSHA RESULTS

Cases where PSHA has generated surprising results are valuable opportunities to explore the input parameters. Locations of two such places in the United States are shown on the seismicity map in Figure 1.

Yucca Mountain

Figure 2 shows an approximation to the median hazard curve for peak acceleration generated by for a hypothetic hard rock site at Yucca Mountain, Nevada (Stepp et al., 2001; Stepp and Wong, 2003). At rates of 10^{-6}, 10^{-7}, and 10^{-8} per year, the Yucca Mountain study computed mean peak accelerations of 2.9 g, 5.8 g, and 11 g, and peak velocities (not shown) of 3.0 m/s, 6.5 m/s, and 14 m/s (Stepp, 2001; Hanks et al, 2005, 2006; Wong et al, 2006). These values are much above the median in Figure 2, are mostly greater than the highest recorded ground motions (e.g. Anderson, 2010), and have been labeled "extreme" by Hanks et al (2005, 2006). Brune and Anderson (2003) suggest that these extreme values are suspect due to an overestimate of σ_T due to the ergodic assumption (discussed below).

New Madrid

Figure 3 compares hazard curves, from the 2007 USGS National Seismic Hazard Map, for San Francisco, California, and Paducah, Kentucky. From Figure 1, the seismicity is clearly much higher near San Francisco, which is on the boundary between the Pacific and North American plates, than near Paducah, which is in the geologically stable continental interior, but near the presumed fault responsible for a major earthquake sequence in 1811-1812. Hazard curves in the 1997 and 2002 hazard maps were similar (USGS web pages). At high annual probabilities, the hazard in San Francisco is greater, as expected from the seismicity. However, the slope of the hazard curve for Paducah is smaller, and crosses the curve for San Francisco at about $\lambda_C = 5 \times 10^{-4}$ per year. The question of whether this is reasonable has tended to focus on the seismicity model (e.g. Stein et al, 2003). However, as will be shown, the hazard curve for Paducah would fall off faster if σ_T were decreased.

TESTING EXCEEDANCE RATE CURVES

It is important to recognize that $\lambda_C(Y)$ can be measured, at least conceptually. If an accelerograph has operated for *N* years, the number of records that exceed *Y*, divided by *N*, gives an estimate of one point on the hazard curve. Such tests, and especially proxies that bound the hazard curve at low probabilities, can occasionally be found. Abrahamson and Hanks (2008) refer to data of this nature in general as "points in hazard space". If these proxies are inconsistent with the corresponding curve, then at least some part of the input for that curve is not correct. These inconsistencies may point to important global problems.

Instrumental observations are available to test the high-exceedance rate range. Milne and Davenport (1969), Anderson et al. (1988), and Ward (1995) synthesized hazard curves based on the earthquake catalog and a ground motion prediction equation. Anderson and Brune (1999a) emphasized the connection of the hazard curve and historical ground motion observations at a site, and Anderson et al (1988) used accelerographic data as a check on a hazard curve but did not show the results in a figure. Ordaz and Reyes (1999) and Beauval et al (2008) have published hazard curves based entirely on accelerographic data. Beauval et al. (2008) also analyzed the potential resolution of this approach. For $\lambda_C(Y) > \sim 0.1$ per year, one could now generate large suites of empirical hazard curves, using data from strong motion networks such as KiK-net or K-NET, to evaluate whether the variability of the observed hazard curves follow the statistics predicted by Beauval et al (2008).

Records of seismic intensity in historical earthquakes may date back to over 1000 years in some regions. Thus by use of an empirical conversion from intensity to ground motion, intensity data may be compared with hazard curves. Stirling and Petersen (2006) used this approach with data from the United States and New Zealand. They find general agreement, and attribute disagreements to seismicity models, site conditions, and uncertainty in correlating intensity to peak acceleration. Mucciarelli et al (2008) compared the historical seismic intensity in Italy with a 50 year mean repeat time to a hazard map predicting PGA with a probability of 10% in 50 year. Miyazawa and Mori (2009) compared maximum observed seismic intensity in Japan over the past 500 years with the corresponding probabilistic seismic hazard. For subduction zone earthquakes, Miyazawa and Mori (2009) found satisfactory agreement. For crustal earthquakes, both Mucciarelli et al (2008) and Miyazawa

and Mori (2009) found similar patterns of hazard on the maps and attributed disagreement to the seismicity model. In summary these studies have all suggested that the PSHA results are reasonable to first order, but may have some biases that depend on regional factors associated with the inputs *n(M,x)* and/or uncertainties associated with the comparison methods and data.

In contrast to the above, at rates under 10^{-3} per year many of the points in hazard space are inconsistent with corresponding hazard curves. Brune (1996) suggested that precariously balanced rocks can be used as low-resolution seismoscopes that are important points in hazard space. The overturning of unstable features is a highly nonlinear process, studied by Shi et al (1996) and Anooshehpoor et al (1999, 2004) to test this idea. Brune (1999) suggested that the ages and fragilities of numerous precarious rock observations in southern California are inconsistent with some recent PSHA maps, and Anderson and Brune (1999a) suggested that a leading candidate for the inconsistency is the uncertainty, σ_T, in the GMPE. Anderson and Brune (1999b) used estimated ages of rocks, estimated peak accelerations to topple the rocks, and a simplified assumption about the hazard curves to estimate the probability that several rocks in Nevada were consistent with the hazard curve. They concluded that there was a high probability that many of the rocks were too fragile to be consistent with the hazard curves, and primarily focused on the GMPEs as the cause of the discrepancies. Similarly, Stirling and Anooshehpoor (2006) found some precarious rocks in New Zealand that appear to be inconsistent with the national hazard map. Because the toppling of rocks depends strongly on the low frequency content of an accelerogram in addition to the peak acceleration (e.g. Anooshehpoor et al, 2004), Purvance et al (2008) improved on the technique by integrating over the joint distribution of PGA and PGV. Purvance et al (2008) suggested that discrepancies between precarious rocks and the 2002 national seismic hazard maps in southern California are largely eliminated by use of newer GMPEs which reduce the median ground motions in large earthquakes compared to GMPE's used for the 2002 maps.

At even smaller probabilities, perhaps the only way to test PSHA is to resort resort to fundamental physics. Andrews et al (2007) take that approach to address the problem for Yucca Mountain. In their 2D simulation of a "worst case" earthquake for the underground repository site, they find peak horizontal and vertical velocity to be bounded by 3.6 m/s and 5.7 m/s, respectively. These points in hazard space are smaller than those on the mean hazard curve for Yucca Mountain.

Considering the nature of $\lambda_C(Y)$, inconsistency with a point in hazard space indicates that the input needs to be modified. Furthermore, considering Equation 2, changes to the input will generally affect all probabilities, not only low probabilities. In this way, demonstrating that $\lambda_C(Y)$ is consistent with constraints at small exceedance rates will improve confidence in $\lambda_C(Y)$ at all exceedance rates. For this reason, study of points in hazard space at the very low rates, testable only by geological features like precarious rocks or fundamental physical considerations, are perhaps the most important tests that can be applied.

COMMENTS ON σ_T

The tests of PSHA at small exceedance rates have pointed to GMPEs as a possible global cause of discrepancies. These discrepancies can come in two forms: the median ground motion may not be estimated correctly, or the uncertainty may be incorrect. However, especially at low exceedance rates, the value of σ_T and the shape of the tail of the probability distribution is more important (e.g. Bommer and Abrahamson, 2006).

Douglas (2003) and Strasser et al (2009) have shown that σ_T estimates have not changed much over the past 40 years. Anderson and Brune (1999a) suggested that σ_T is artificially inflated through making an ergodic assumption, which is that σ_T measured via the spatial variability of ground motion in a single event is appropriate to use for the variability of motion at a single site in a PSHA. They envision a thought experiment in which a single characteristic ground motion earthquake occurs repeatedly on a single fault. In this case the ground motions at every site would repeat identically in multiple realizations of the earthquake. For this "characteristic ground motion earthquake", the procedure of estimating σ_T from the spatial variability of ground motion is clearly wrong. Several recent studies (Atkinson, 2006; Morikawa et al, 2008; Lin et al., 2010; Anderson and Uchiyama, 2010) have attempted to partially overcome this ergodic assumption, taking advantage of the large numbers of accelerograms that are available from individual sites. The data, available thanks to the expansion of high quality digital networks in the 1990's, can be used to determine site and path contributions to σ_T. Strasser et al (2009) suggest that this is the most promising approach to reducing σ_T below the range of historical regressions.

REDUCING SIGMA

Anderson and Uchiyama (2010) suggest the following procedure for reducing the impact of the ergodic assumption.

I. Find a basic GMPE to model the records.

II and III. Find station corrections and source terms as random effects and determine the variance reduction.

IV. Find path terms that will be unique to each station. Contour the average spatial distribution of the path terms, and use the contoured value to determine the resulting variance reduction.

Stages I, II, and III.

It is important to start with the best possible regional model, since otherwise stages II, III, and IV will first attempt to compensate for weaknesses in the basic GMPE, and the full benefits of the method will not be realized.

Let Y_{ij} represent one observation of an amplitude of ground motion, observed at a station at location $\mathbf{x}_j$ from an earthquake at location $\mathbf{x}_i$. One can write:

$$\ln Y_{ij} = f\left(\mathbf{Z}_{ij},\theta\right) + \varepsilon_{ij}^{I} \quad (3)$$

where Z_{ij} is a vector of parameters characterizing the earthquake and the station (e.g. magnitude, distance, Vs30…), and θ is a vector of parameters determined by regression. The GMPE is $\ln\hat{Y}_{ij}^{I} = f\left(\mathbf{Z}_{ij},\theta\right)$, and the residual, ε_{ij}^{I}, is assumed to be normally distributed with zero mean and standard deviation σ^{I}. The superscript indicates stage I of the procedure. The effects of Stages II, III, and IV are, respectively to represent Y_{ij} as:

$$\ln Y_{ij} = f(\cdot) + S_j + \varepsilon_{ij}^{II} \quad (4)$$

$$\ln Y_{ij} = f(\cdot) + S_j + E_i + \varepsilon_{ij}^{III} \quad (5)$$

$$\ln Y_{ij} = f(\cdot) + S_j + E_i + P_j(\mathbf{x}) + \varepsilon_{ij}^{IV} \quad (6)$$

where S_j is the mean station term, E_i is the mean event term, and $P_j(\mathbf{x})$ is the mean path term. Standard deviations of ε_{ij}^{II}, ε_{ij}^{III}, ε_{ij}^{IV} are σ^{II}, σ^{III}, and σ^{IV}, respectively. An estimate of the uncertainty in predicting the ground motion at the individual station is:

$$\sigma_j^{IV} = \sqrt{\frac{1}{I_j}\sum_{i=1}^{I_j}\left(\varepsilon_{ij}^{IV}\right)^2} \quad (7)$$

where I_j is the number of observations at the ith station.

E_i is a random effect (e.g. Abrahamson and Youngs, 1992; Abrahamson and Silva, 2008) with standard deviation σ_{events}. Although related to measurable physical properties at the site, Joyner and Boore (1993) recognized that with enough data, S_j can also be treated as a random effect with standard deviation $\sigma_{station}$, and more recently this has become possible (e.g. Atkinson, 2006). The order of Stages II and III is arbitrary, and the terms are best estimated using a method that finds optimized values (e.g. Joyner and Boore, 1993).

Stage IV

The motivation for Stage IV is observations such as those shown in Figure 4, showing clear asymmetry in the distribution of ground motion. The cause of this asummetry was modeled by Furumura and Kennett (2005). The Stage III residuals, ε_{ij}^{III}, will not correct for the types of spatial anomalies seen in Figure 4. Spatial patters in ε_{ij}^{III} for station j can be visualized by plotting each residual on a map (or more generally in a volume) at the hypocenter of earthquake i, with different symbols to represent different values.

To use the path residuals in a predictive sense, one needs a value for every location on the map or in the volume, and not just for points where a prior earthquake has occurred. Anderson and Uchiyama (2010) define $P_j(\mathbf{x})$ as the path term for the jth station. It is reasonable to assume that the similarity of paths from nearby earthquakes will cause $P_j(\mathbf{x})$ to be a relatively smooth function of the general location $\mathbf{x}$. A spatial average of the residuals ε_{ij}^{III} is the best way to estimate $P_j(\mathbf{x})$. There is not a unique way to smooth the residuals ε_{ij}^{III}, but a general approach is to determined $P_j(\mathbf{x})$ from a weighted average of the observed residuals:

$$P_j(\mathbf{x}) = \frac{\sum_i w_i \varepsilon_{ij}^{III}}{\sum_i w_i} \quad (8)$$

Since each value of ε_{ij}^{III} is associated with the earthquake location ($\mathbf{x}_i$), the weight w_i must be a function of $\mathbf{x}$ and $\mathbf{x}_i$.

Anderson and Uchiyama (2010) determined $P_j(\mathbf{x})$ as a weighted average of two sets of information. The observed residuals, ε_{ij}^{III} were supplemented with a second sparse set of uniformly spaced points, at which zero residuals are artificially introduced for "regularization". The relative weight assigned to a residual at location $\mathbf{x}_i$, both observed and introduced for regularization, is:

$$w_i = \exp\left[-\left(\frac{\left|\mathbf{x}_j - \mathbf{x}_i\right|}{r_S}\right)^2\right] \quad (9)$$

where $\left|\mathbf{x}_j - \mathbf{x}_i\right|$ is the distance from the datum to the point $\mathbf{x}$ and r_S is a smoothing parameter. The regularization is necessary so that the source-station correction goes to zero at locations far from any of the available earthquakes. These artificial data tend to bias the estimates of average residuals towards zero everyplace. Where earthquakes are sparse, that is appropriate, considering that in the limit where there are no historical earthquakes, the best estimate of the correction is zero.

Anderson and Uchiyama (2010) point out that $P_j(\mathbf{x})$ is expected to be a smooth function of space, and suggest that for a station location between existing stations, it may be reasonable to consider an appropriate average of the observed path corrections to the existing stations.

Additional Comments

Anderson and Uchiyama (2010) and Lin et al (2010) point out that event correction terms (Equation 5) may have some spatial correlation. For instance, there might be regions with systematically high or low stress drop. Thus, the procedure for finding $P_j(\mathbf{x})$ could also be used to develop a contour of mean event terms, $E(\mathbf{x})$. Unlike the path terms, the same function $E(\mathbf{x})$ would be used for all stations. This would allow the source terms in the total uncertainty to be divided into two independent components, the local mean value, and the residuals relative to that local mean. Only the residuals would need to be counted as part of σ_T in Eqn. 2.

Station terms S_j (Equation 4) could also be contoured. However for most frequencies of interest for strong motion prediction and most strong-motion networks, the near-surface geology that controls the station correction varies rapidly compared to the station spacing, so the observed station terms provide only a highly aliased

sample of the true spatial variability and contouring is not justified. On the other hand, it is possible to measure station response directly by simply operating a seismic station at critical sites to monitor frequent weak events.

RESULTS

Pilot Application In Japan

Anderson and Uchiyama (2010) show results for two pilot studies. The first examined the variability of peak ground acceleration (PGA) and peak ground velocity (PGV) in Japan. Their Stage I model is the ground motion prediction equation by Si and Midorikawa (1999). This relationship is used in the National Seismic Hazard Map Project in Japan [National Research Institute for Earth Science and Disaster Prevention, 2005]. Table 1 and Figures 5-7 show their results. Figure 5 shows the earthquakes ($M \geq 5.5$)used by Anderson and Uchiyama (2010). Table 1 gives the value of σ^I for all earthquakes with $R \leq 200$ km.

Anderson and Uchiyama (2010) estimated σ^{II} from subsets of 73 stations in the Kanto-Niigata region (Figure 5b) and 35 stations in the Tohoku region (Figure 5c). Each station in the Kanto-Niigata region has more than 12 records, and each station in the Tohoku region has at least 10 records. The station corrections for individual stations in the Kanto-Niigata region due to the regional earthquake sources and estimates of σ_j^{II} at each station are shown in Figure 6. The average of the station standard deviations for the 73 stations ($\overline{\sigma}_j^{II} \approx \sigma^{II}$) is about 24% smaller than σ^I for peak acceleration, and 28% smaller for peak velocity. Results for the Tohoku region (Figure 7) show similar reduction.

Anderson and Uchiyama (2010) assume E_i=0 for all events and apply a scaled-down version of Stage IV by determining point estimates of $P_j(\mathbf{x}_C)$ for only the location $\mathbf{x}_C$ of clusters of earthquakes. In the Kanto-Niigata region, $\mathbf{x}_C$ is the location of the 2004 Niigata-Chuetsu earthquake (M_W6.6) and its aftershocks. In the Tohoku region the small volume encloses the 2003 northern Miyagi earthquake and its foreshock and aftershocks. Figures 6 and 7 show the mean station residuals and standard deviations (σ_j^{IV}, Equation 10) for the two regions on the same plots as the regional values. The average standard deviation ($\overline{\sigma}_j^{IV} \approx \sigma^{IV}$) in both regions (Table 1) is less than half of σ^I for both PGA and PGV. As in Morikawa et al (2006, 2008), they propose that the similarity in the propagation path from the small source regions allow the small standard deviation.

Application In Guerrero, Mexico

Anderson and Uchiyama (2010) also tested this procedure using data recorded in Mexico, above the Guerrero subduction zone. They used 351 records from 32 events recorded at ten or more stations of the Guerrero accelerograph network (Anderson et al, 1994).

The initial GMPE is given by Anderson and Uchiyama (2010). Residuals for Stages I, II, and III are given in Table 2. The Stage II station residuals for PGA are shown on Figure 8. The uncertainties in these residuals are large compared to the mean value. This is perhaps why Anderson and Lee (1994), using less data, failed to recognize the site term. The net effect of these residuals (Table 2) is to reduce the standard deviations by 16% for PGA and by 12% for PGV. The net effect of adjusting the GMPE in Stage III is to reduce the overall uncertainty in the ground motion prediction equations by an additional 13% for PGA and 14% for PGV.

Figure 9 maps the Stage III residuals for station ATYC. The contours (Equation 8) are based on smoothed residuals on a grid with spacing of 0.1 degrees in latitude and longitude. The regularization data are on grid points with a spacing of 0.5 degrees, and r_S=0.5 degrees. After finding $P_j(\mathbf{x})$ in this way for all stations, Anderson and Uchiyama (2010) find that the mean misfit was reduced by an additional 19% for both PGA and PGV (Table 2).

Figure 8 compares the residuals after Stage IV on a station-by-station basis with the residuals determined in Stage II. As with the pilot application in Japan, the standard deviation is significantly reduced at every station by using the path corrections. Anderson and Uchiyama (2010) demonstrated that some adjacent stations show similar patterns of path corrections.

Summary of Variance Reduction

Table 3 summarizes three studies (Morikawa et al, 2008; Lin et al, 2010; Anderson and Uchiyama, 2010) that have developed path terms for PGA in five regions. The median reduction in sigma is to 46% of the original.

Figures 2 and 3 suggest the effects that reducing sigma to 46% of the values used in the original study might have on the PSHA results in Yucca Mountain and New Madrid. These curves, developed for simplified inputs that approximately replicate the original curves, show the advantages that gathering information to reduce the aleatory standard deviation might provide, and also that an overestimate of sigma might contribute to the surprising results shown in both places.

DISCUSSION AND CONCLUSIONS

The results summarized here describe a process that has the potential to improve the results of PSHA studies in the future. Motivated by observations that some PSHA studies appear to give surprising results by testing them against a few points in hazard space, and recognizing that making the ergodic assumption is a probable cause of this overestimate, current research is focusing on finding ways to shift uncertainty in GMPEs from the aleatory to the epistemic category. The initial results summarized here suggest that reducing the impact of the ergodic assumption by including the path terms has the potential to achieve this goal in particular in two cases where

supplementary data can reduce the epistemic uncertainty. The first is for regions instrumented with networks of digital instruments that record moderate as well as strong earthquakes with a good signal-to-noise ratio. The second is for locations that receive special studies, such as a critical structure that is under consideration. For special studies, a strong motion and broad band seismic station could be installed at the site as soon as it is selected, and the weak motion records from relatively abundant small earthquakes used to calibrate the site. Care needs to be taken to adjust for the changing frequency content of small and large earthquakes.

Figures 7 and 8 suggest that some stations have smaller standard deviations than others. The differences might be caused by more complicated subsurface geology. This suggests the possibility that site-specific aleatory uncertainties could further refine probabilistic seismic hazard analyses that utilize site-specific recordings.

FUTURE DIRECTIONS

Perhaps the greatest hope, in the long run, for further reduction of sigma is through replacing GMPEs with models that use the representation theorem to simulate the entire physical process, including regional source, path, and site contributions, in either the time or frequency domain (e.g. see review by Anderson, 2007). Widely used waveform simulation methods including stochastic source and path contributions are now available (e.g. Boore, 1983; Anderson and Yu, 1996; Miyake et al, 2003), and these simulations have been used as guidance for development of GMPEs (e.g. Atkinson and Boore, 2006). Models for essential components of these simulations have been developed (e.g. Anderson, 2007; Assimaki et al., 2008; Nakamura, 2009). In one study that brings the components together, Kawase (2006, 2008) reports excellent standard deviations (comparable to σ^{III}) for a model of the Fourier spectrum including source, attenuation, and site amplification in the range from 0.53 to 0.64, depending on frequency, for a frequency-domain model. Wave-form simulations are also proven effective in modeling ground motions at low frequencies (e.g. Graves, 2008, Olsen et al, 2009) and in understanding some features of higher frequencies (e.g. Furumura and Kennett, 2005). The limits to sigma reduction via these approaches have not yet been estimated.

ACKNOWLEDGEMENTS

I thank Norm Abrahamson for providing a draft of the Lin et al manuscript describing their important results in reducing sigma through path effects in Taiwan, UNR for granting a sabbatical leave, and ERI at the Univ of Tokyo for inviting me to spend my sabbatical leave in Japan.

REFERENCES

Abrahamson, N. A. and T. C. Hanks (2008). Points in hazard space: a new view of PSHA (abstract), Seismol. Res. Lett. 79, 285.

Abrahamson, N. A. and W. Silva (2008). Summary of the Abrahamson & Silva NGA ground-motion relations, Earthquake Spectra 24, 67-97.

Abrahamson, N. A. and R. R. Youngs (1992). A stable algorithm for regression analyses using the random effects model, Bull. Seism. Soc. Am. 82, 505-510.

Albarello, D. and V. D'Amico (2005). *Short Notes* Validation of intensity attenuation relationships, Bull. Seism. Soc. Am., Vol. 95, No. 2, pp. 719–724, April 2005, doi: 10.1785/0120040062.

Anderson, J. G. (2007). Physical Processes That Control Strong Ground Motion. In Hiroo Kanamori, Volume Editor; Gerald Schubert, Editor in Chief (Ed.), Treatise on Geophysics, Volume 4, Earthquake Seismology (vol. 4, pp. 513-565). Amsterdam: Elsevier.

Anderson, J. G., T. K. Rockwell and D. C. Agnew (1988). Past and possible future earthquakes of significance to the San Diego region, Earthquake Spectra 299-335.

Anderson, J. G. and J. N. Brune (1999a). Probabilistic seismic hazard analysis without the ergodic assumption, Seismol. Res. Lett. 70, 19-28.

Anderson, J. G. and J. N. Brune (1999b). Methodology for using precarious rocks in Nevada to test seismic hazard models, Bull. Seism. Soc. Am., 89, 456-467.

Anderson, J. G. and Y. Uchiyama (2010). A methodology to improve ground motion prediction equations by including source-to-site corrections (submitted for publication).

Anderson J.G. and Yu G (1996) Predictability of strong motions from the Northridge, California, earthquake. Bull. Seism. Soc. Am. 86: S100–S114.

Andrews, D. J., T. C. Hanks, and J. W. Whitney (2007). Physical limits on ground motion at Yucca Mountain, Bull. Seism. Soc. Am. 97, 1771–1792, doi: 10.1785/0120070014.

Anooshehpoor, A., T. H. Heaton, B. Shi, and J. N. Brune (1999). Estimates of the ground acceleration at Point Reyes Station during the 1906 San Francisco earthquake, Bull. Seismol. Soc. Am. 89, 845–853.

Anooshehpoor, A., T. H. Heaton, B. Shi, and J. N. Brune (2000). Reply to "Comment by J. Zhang and N. Makris on 'Estimates of the ground accelerations at Point Reyes Station during the 1906 San Francisco earthquake'", Bull. Seismol. Soc. Am. 90, 1349–1351.

Anooshehpoor, A., J. N. Brune, and Y. Zeng (2004). Methodology for obtaining constraints on ground motion from precariously balanced rocks, Bull. Seism. Soc. Am. 94, 285–303.

Assimaki, D., W. Li, J. H. Steidl and K. Tsuda (2008). Site amplification and attenuation via downhole array seismogram inversion: a comparative study of the 2003 Miyagi-Oki aftershock sequence, Bull. Seism. Soc. Am 98, 301-330.

Atkinson, G. M. (2006). Single-station sigma, Bull. Seism. Soc. Am. 96, 446–455, doi: 10.1785/0120050137.

Atkinson, G. M. and D. M. Boore (2006). Earthquake ground-motion prediction equations for eastern North America, Bull. Seism. Soc. Am. 96, 2181-2205.

Bazzurro, P. and C. A. Cornell (1999). Disaggregation of seismic hazard, Bull. Seism. Soc. Am. 89, 501-520.

Beauval, C. and O. Scotti (2004). Quantifying sensitivities of PSHA for France to earthquake catalog uncertainties, truncation of ground-motion variability, and magnitude limits, Bull. Seism. Soc. Am. 94, 1579–1594.

Beauval, C., P.-Y. Bard, S. Hainzl, and P. Guéguen (2008). Can strong-motion observations be used to constrain probabilistic seismic-hazard estimates? Bull. Seism. Soc. Am. 98, 509–520, doi: 10.1785/0120070006.

Bommer, J. J., and N. A. Abrahamson (2006). Why do modern probabilistic seismic-hazard analyses often lead to increased hazard estimates?, Bull. Seismol. Soc. Am. 96, 1967–1977.

Bommer, J. J., F. Scherbaum, H. Bungum, F. Cotton, F. Sabetta, and N. A. Abrahamson (2005). On the use of logic trees for ground-motion prediction equations in seismic-hazard analysis, Bull. Seism. Soc. Am. 95, 377–389, doi: 10.1785/0120040073.

Boore, D. M. (1983) Stochastic simulation of high-frequency ground motions based on seismological models of the radiated spectra. Bulletin of the Seismological Society of America 73(6): Part A, 1865–1894 (Dec 1983).

Bragato, P. L., G. Laurenzano, and C. Barnaba (2007). Automatic zonation of urban areas based on the similarity of H/V spectral ratios, Bull. Seismol. Soc. Am. 97, 1404–1412.

Bragato, P. L. (2008). Limits for the improvement of ground-motion relations in Europe and the Middle East by accounting for site effects, Bull. Seism. Soc. Am., 98, 2061–2065, doi: 10.1785/0120070249.

Brune, J.N. (1996). Precariously balanced rocks and ground-motion maps for southern California: Bull. Seism. Soc. Am. 86, 43-54.

Brune, J. N. (1999). Precarious rocks along the Mojave section of the San Andreas fault, California: constraints on ground motion from great earthquakes, Seism. Res. Lett. 70, no. 1, 29–33.

Brune, J. N. and J. G. Anderson (2003). Precarious rocks, shattered rock, and seismic hazard at low probabilities for Yucca Mountain, Presentation to the US Nuclear Waste Technical Review Board, Panel on the Repository / Panel on Site Characterization, Las Vegas, Feb. 24, 2003. (http://www.nwtrb.gov/meetings/2003/feb/03feb24.html)

Cornell, C. A. (1968). Engineering seismic risk analysis, Bull. Seism. Soc. Am. 58, no. 5, 1583–1606.

CRWMS M&O [Civilian Radioactive Waste Management System Management and Operating Coordinator] (1998). Probabilistic seismic hazard analysis for fault displacement and vibratory ground motion, Ivan G. Wong and J. Carl Stepp, report coordinators, U.S. Department of Energy DE-AC04-94AL85000, Prepared for the U.S. Geological Survey, February 23, 3 vols., MOL. 1998 1207.0393, 3 vols.

Douglas, J. (2003). Earthquake ground motion estimation using strong-motion records: a review of equations for the estimation of peak ground acceleration and response spectral ordinates, Earth-Science Reviews 61 (2003) 43–104.

Field, E. H., David D. Jackson, and James F. Dolan (1999). A mutually consistent seismic-hazard source model for southern California, Bull. Seism. Soc. Am., 89, pp. 559-578.

Field, E. H., T. E. Dawson, K. R. Felzer, A. D. Frankel, V. Gupta, T. H. Jordan, T. Parsons, M. D. Petersen, R. S. Stein, R. J. Weldon II, and C. J. Wills (2009). Uniform California earthquake rupture forecast, version 2 (UCERF 2), Bull. Seism. Soc. Am. 99, 2053–2107, doi: 10.1785/0120080049.

Frankel, A. (1995). Mapping seismic hazard in the central and eastern United States, *Seism. Res. Lett.* **66,** 8–21.

Frankel, A., C. Mueller, T. Barnhard, E. Leyendecker, R. Wesson, S. Harmsen, F. Klein, D. Perkins, N. Dickamn, S. Hanson, and M. Hopper (2000). USGS national seismic hazard maps, *Earthquake Spectra* **16,** 1–20.

Frankel, A.D., Petersen, M.D., Mueller, C.S., Haller, K.M., Wheeler, R.L., Leyendecker, E.V., Wesson, R.L., Harmsen, S.C., Cramer, C.H., Perkins, D.M., Rukstales, K.S.,(2002). Documentation for the 2002 update of the National Seismic Hazard Maps: U.S. Geological Survey Open-File Report 2002–420, 39 p.

Fujiwara, H., S. Kawai, S. Aoi, N. Morikawa, S. Senna, K. Kobayashi, T. Ishii, T. Okumura and Y. Hayakawa (2006). National seismic hazard maps of Japan, Bull. Earthquake Res. Inst, Univ. Tokyo, 81, 221-232.

Furumura, T. and B. L. N. Kennett (2005). Subduction zone guided waves and the heterogeneity structure of the subducted plate: intensity anomalies in northern Japan, J. Geophys. Res. 110, B10302, doi: 10.1029/2004JB003486.

Goda, K. and G. M. Atkinson (2009). Probabilistic characterization of spatially correlated response spectra for earthquakes in Japan, Bull. Seism. Soc. Am. 99, 3003–3020, doi: 10.1785/0120090007.

Graves, R. W. (2008). The seismic response of the San Bernardino basin region during the 2001 Big Bear Lake earthquake, Bull. Seism. Soc. Am. 98, 241-252.

Hanks, T. C., N. A. Abrahamson, M. Board, D. M. Boore, J. N. Brune and C. A. Cornell (2005). Observed ground motions, extreme ground motions, and physical limits to ground motions, in P. Gulkan and J. G. Anderson (eds.), Directions in Strong Motion Instrumentation, NATO Science Series IV. Earth and Environmental Sciences Vol. 58, Springer, Dordrecht, The Netherlands, 55-59.

Hanks, T. C., N. Abrahamson, M. Board, D. Boore, J. Brune, and A. Cornell (2006).Workshop on extreme ground motion at Yucca Mountain, U.S. Geol. Surv. Open-File Rept. OF2006-1277.

Jayaram, N and J. W. Baker (2008). Statistical tests of the joint distribution of spectral acceleration values, Bull. Seism. Soc. Am. 98, pp. 2231–2243, doi: 10.1785/0120070208.

Joyner, W. B. and D. M. Boore (1993). Methods for regression analysis of strong-motion data, Bull. Seism. Soc. Am. 83, 469-487.

Kalkan, E, P. Gülkan, N. Yilmaz, and M. Çelebi (2009). Reassessment of probabilistic seismic hazard in the Marmara region, Bull. Seism. Soc. Am. 99, 2127–2146, doi: 10.1785/0120080285.

Kawase, H. (2008). Site amplification characteristics and their variations derived from K-NET, KiK-Net, and JMA strong motion records in Japan, Eos Trans. AGU, 89(53), Fall Meet. Suppl., Abstract 51C-1173.

Kreemer, C., Blewitt, G., and Hammond, W.C., 2009, Geodetic constraints on contemporary deformation in the northern Walker Lane: 2. Velocity and strain rate tensor analysis, in Oldow, J.S., and Cashman, P.H., eds., Late Cenozoic Structure and Evolution of the Great Basin–Sierra Nevada Transition: Geological Society of America Special Paper 447, p. 17–31, doi: 10.1130/2009.2447(02).

Lapajne, J., B. Sˇ. Motnikar, and P. Zupancˇic (2003). Probabilistic seismic hazard assessment methodology for distributed seismicity, Bull. Seism. Soc. Am. 93, 2502–2515.

Lin, P., N.Abrahamson, M. Walling, C.-T. Lee, B. Chiou and C. Cheng (2010). Repeatable path effects on the standard deviation for empirical ground motion models, submitted for publication.

Marin, S., J.-P. Avouac, M. Nicolas, and A. Schlupp (2004). A probabilistic approach to seismic hazard in metropolitan France, Bull. Seism. Soc. Am. 94, 2137–2163.

Marzocchi, W (2007). Comment on "Layered seismogenic source model and probabilistic seismic-hazard analyses in central Italy" by Bruno Pace, Laura Peruzza, Giusy Lavecchia, and Paolo Boncio, Bull. Seism. Soc. Am., 97, 1763–1765, doi: 10.1785/0120060192.

McGuire, R. K. (1995). Probabilistic seismic hazard analysis and design earthquakes: closing the loop, Bull. Seism. Soc. Am. 85, 1275-1284.

Milne, W. G. and A. G. Davenport (1969). Distribution of earthquake risk in Canada, Bull. Seism. Soc. Am. 59, 729-754.

Miyake, H., T. Iwata and K. Irikura (2003). Source

characterization for broadband ground-motion simulation: kinematic heterogeneous source model and strong motion generating area, Bull. Seism. Soc. Am. 93, 2531-2545.

Miyazawa, M. and J. Mori (2009). Test of seismic hazard map from 500 years of recorded intensity data in Japan, Bull. Seism. Soc. Am. 99, 3140–3149, doi: 10.1785/0120080262.

Morikawa, N., T. Kanno, A. Narita, H. Fujiwara, T. Okumura, Y. Fukushima and A. Guerpinar (2008). Strong motion uncertainty determined from observed records by dense network in Japan, J. Seismol 12, 529-546, DOI 10.1007/s10950-008-9106-2.

Mucciarelli, M., D. Albarello, and V. D'Amico (2008). Comparison of probabilistic seismic hazard estimates in Italy, Bull. Seism. Soc. Am. 98, pp. 2652–2664, December 2008, doi: 10.1785/0120080077.

Nakamura, R. (2009). 3-D attenuation structure beneath the Japanese islands, source parameters and site amplification by simultaneous inversion using short period strong motion records and predicting strong ground motion, Univ. of Tokyo, Ph. D thesis, 205 pp. (in Japanese).

Olsen, K. B., S.M. Day, L.A. Dalguer, J. Mayhew, Y. Cui, J. Zhu, V.M. Cruz-Atienza, D. Roten, P. Maechling, T.H. Jordan, D. Okaya & A. Chourasia, ShakeOut-D: Ground motion estimates using an ensemble of large earthquakes on the southern San Andreas fault with spontaneous rupture propagation, Geophys. Res. Lett., 36, L04303, doi:10.1029/2008GL036832, 2009.

Ordaz, M., and C. Reyes (1999). Earthquake hazard in Mexico City: observations versus computations, Bull. Seismol. Soc. Am. 89, 1379–1383.

Pace, B., L. Peruzza, G. Lavecchia, and P. Boncio (2006). Page, M. T. and J. M. Carlson (2006). Methodologies for earthquake hazard assessment: model uncertainty and the WGCEP-2002 Forecast, Bull. Seism. Soc. Am. 96, 1624–1633, doi: 10.1785/0120050195

Layered seismogenic source model and probabilistic seismic-hazard analyses in central Italy, Bull. Seism. Soc. Am. 96, 107–132, doi: 10.1785/0120040231.

Pancha, A., J. G. Anderson, and C. Kreemer (2006). Comparison of seismic and geodetic scalar moment rates across the Basin and Range province, Bull. Seism. Soc. Am. 96, 11-32.

Peruzza, L., B. Pace, G. Lavecchia, and P. Boncio (2007). Reply to "Comment on 'Layered seismogenic source model and probabilistic seismic-hazard analyses in central Italy' by B. Pace, L. Peruzza, G. Lavecchia, and P. Boncio" by W. Marzocchi, Bull. Seism. Soc. Am. 97, 1766–1768, doi: 10.1785/0120070043.

Petersen, M. D. and others (2008). Unites States National Seismic Hazard Maps: U. S. Geological Survey Fact Sheet 2008-3017, 4 p.

Petersen, M. D., C. H. Cramer, M. S. Reichle, A. D. Frankel, and T. C. Hanks (2000). Discrepancy between earthquake rates implied by historic earthquakes and a consensus geologic source model for California, Bull. Seism. Soc. Am., 90, 1117–1132.

Plesch, A., J. H. Shaw, C. Benson, W. A. Bryant, S. Carena, M. Cooke, J. Dolan, G. Fuis, E. Gath, L. Grant, E. Hauksson, T. Jordan, M. Kamerling, M. Legg, S. Lindvall, H. Magistrale, C. Nicholson, N. Niemi, M. Oskin, S. Perry, G. Planansky, T. Rockwell, P. Shearer, C. Sorlien, M. P. Süss, J. Suppe, J. Treiman, and R. Yeats (2007). Community fault model (CFM) for southern California, Bull. Seism. Soc. Am. 97, 1793–1802, doi: 10.1785/0120050211.

Rhoades, D. A., J. X. Zhao, and G. H. McVerry (2008). A simple test for inhibition of very strong shaking in ground-motion models, Bull. Seism. Soc. Am., Vol. 98, 448–453, doi: 10.1785/0120070133.

Purvance, M. D., J. N. Brune, N. A. Abrahamson, and J. G. Anderson (2008). Consistency of precariously balanced rocks with probabilistic seismic hazard estimates in southern California, Bull. Seism. Soc. Am. 98 2629–2640, doi: 10.1785/0120080169.

Scherbaum, F., J. Schmedes, and F. Cotton (2004a). On the conversion of source-to-site distance measures for extended earthquake source models, *Bull. Seism. Soc. Am.* **94,** 1053–1069.

Scherbaum, F., F. Cotton, and P. Smit (2004b). On the use of response spectral reference data for the selection and ranking of ground motion models for seismic hazard analysis in regions of low to moderate seismicity, *Bull. Seism. Soc. Am.* **94,** 2164–2185.

Scherbaum, F., J. J. Bommer, H. Bungum, F. Cotton, and N. A. Abrahamson (2005). Composite ground-motion models and logic trees: methodology, sensitivities, and uncertainties, Bull. Seism. Soc. Am. 95 1575–1593, doi: 10.1785/0120040229

Scherbaum, F., F. Cotton, and H. Staedtke (2006). The estimation of stochastic host region models for host-to-target-region conversions, *Bull. Seism. Soc. Am.* (in press).

Scherbaum, F., E. Delavaud, and C. Riggelsen (2009). Model selection in seismic hazard analysis: an information-theoretic perspective, Bull. Seism. Soc. Am. 99, 3234–3247, doi: 10.1785/0120080347.

Shi, B., A. Anooshehpoor, Y. Zeng, and J. Brune (1996). Rocking and overturning of precariously balanced rocks by earthquakes, Bull. Seismol. Soc. Am. 85, 1364–1371.

Stein, S., J. Tomatello and A Newman (2003). Should Memphis build for California's earthquakes, Eos, Transactions of the American Geophysical Union, 84, pages 177, 184-185.

Stepp, J.C., I. Wong, J. Whitney, R. Quittmeyer, N. Abrahamson, G. Toro, R. Youngs, K. Coppersmith, J. Savy, and T. Sullivan (2001). Probabilistic seismic hazard analyses for ground motions and fault displacement at Yucca Mountain, Nevada, Earthquake Spectra, 17, 113-151.

Stepp, J.C. and I. Wong (2003). Probabilistic seismic hazard analysis for Yucca Mountain, Presentation to the US Nuclear Waste Technical Review Board, Panel on the Repository / Panel on Site Characterization, Las Vegas, Feb. 24, 2003. (http://www.nwtrb.gov/meetings/2003/feb/03feb24.html)

Stirling, M. W., G. H. McVerry, and K. R. Berryman (2002). A new seismic hazard model for New Zealand, Bull. Seism. Soc. Am. 92, 1878–1903.

Stirling, M. and M. Petersen (2006). Comparison of the historical record of earthquake hazard with seismic-hazard models for New Zealand and the continental United States, Bull. Seism. Soc. Am., Vol. 96, 1978–1994, doi: 10.1785/0120050176.

Strasser, F. O., J. J. Bommer and N. A. Abrahamson (2008). Truncation of the distribution of ground-motion residuals, J Seismol 12:79-105, DOI 10.1007/s10950-007-9073-z.

Strasser, F. O., N. A. Abrahamson, and J. J. Bommer (2009). Sigma: issues, insights, and challenges, 40 Seismological Research Letters 80, 40-56.

Ward, S. (1995). A multidisciplinary approach to seismic hazard in southern California, Bull. Seism. Soc. Am. 84, 1293–1309.

Wong, I., W. Silva, P. Thomas, R. Quittmeyer, M. Dober, C. Law Pattanapong, R. Lee, G. Toro, K. Stokoe, and J. C. Stepp (2006). Development of earthquake ground motions for Yucca Mountain, paper number 1420, Proceedings of the 8th U.S. National Conference on Earthquake Engineering, April 18–22, 2006, San Francisco, California.

Working Group on California Earthquake Probabilities (1996). Seismic hazards in southern California: Probable earthquakes 1994-2024, Bull. Seism. Soc. Am. 86, 379-439.

Yamada, M., A. H. Olsen, and T. H. Heaton (2009). Statistical features of short-period and long-period near-source ground motions, Bull. Seism. Soc. Am., Vol. 99, 3264–3274, doi: 10.1785/0120090067.

Table 1. Standard deviation of the Si and Midorikawa (1999) model for the expanded data, Stage II results after applying station corrections and narrowing the included earthquakes to regional subsets, and Stage IV after selecting localized source zones.

	All R<200	Kanto&Niigata		Tohoku	
	σ^I	σ^{II}	σ^{IV}	σ^{II}	σ^{IV}
PGA	0.85	0.64	0.25	0.53	0.30
PGV	0.76	0.55	0.28	0.51	0.35

Table 2. Aleatory uncertainty in Guerrero, Mexico, after each stage of the procedure.

Stage	PGA	PGV
σ^I	.90	.87
σ^{II}	.76	.77
σ^{III}	.65	.66
σ^{IV}	.53	.53
$\sigma_{station}$	.48	.42
σ_{events}	.38	.39
σ_{path}	.39	.39

Table 3. Summary of studies on the reduction in sigma for PGA by including path effects.

Study	σ^I	σ^{IV}/σ^I
Morikawa et al (2008)	.78	.46
Lin et al (2010)	.68	.54
Mexico	.90	.59
Kanto & Niigata	.85	.28
Tohoku	.85	.35

FIGURES

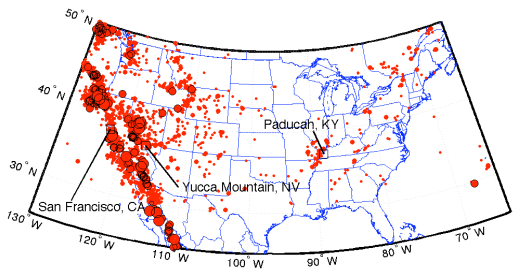

Figure 1. Seismicity of the United States from the: ANSS catalog (Nov, 2009) north of 31N, M>=4, and the Engdahl Centenniel Catalog south of 31N.

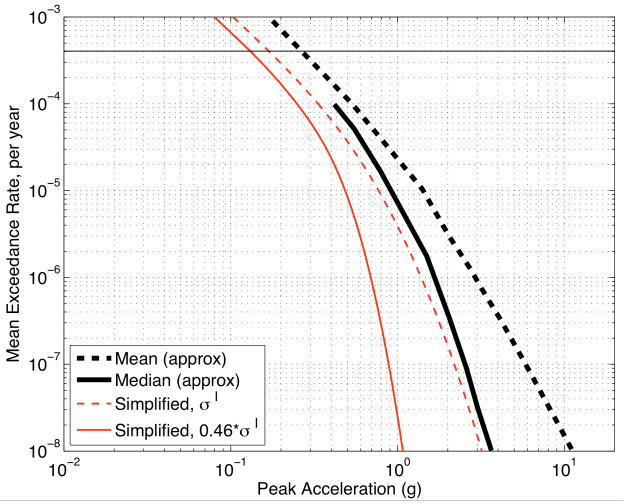

Figure 2. Black lines approximate mean and median of the hazard curve (CRWMS M&O,1998; Stepp et al., 2001) for a point on Yucca Mountain (116.4622° W, 36.8444° N). Solid red shows an alternative unqualified hazard curves using the Anderson GMPE (CRWMS M&O, 1998) and a simplified seismicity model that, with this GMPE, approximately replicates the median curve. The dashed line uses $\sigma_T = \sigma^I$ of the Anderson GMPE, while the solid line uses $\sigma_T = 0.46\sigma^I$.

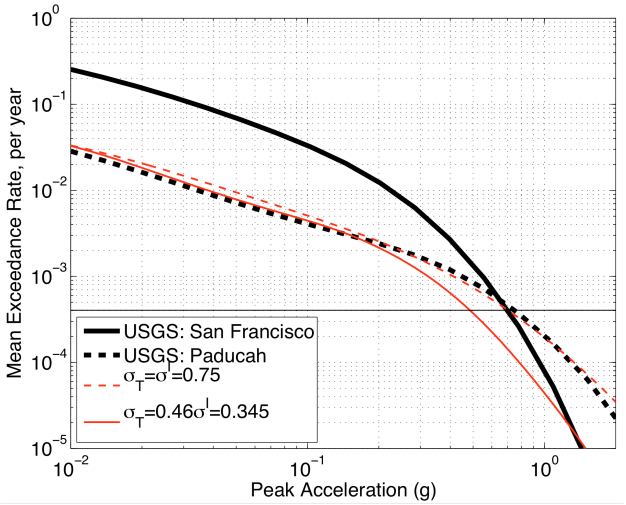

Figure 3. Black lines show 2008 USGS exceedance rate curves for San Francisco, CA, and Paducah, KY. Locations are shown on Figure 1. Red dashed line shows a hazard curve using a similar seismicity model and one of the GMPEs as used by USGS. Red solid line shows effect of using $\sigma_T = 0.46\sigma^I$ in the simplified model.

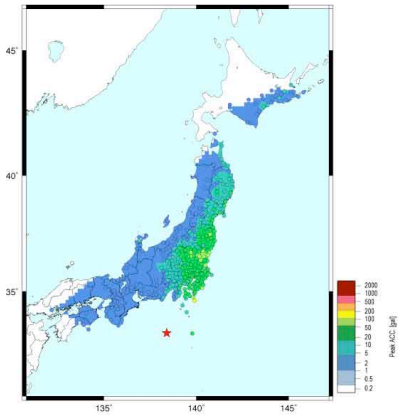

Figure 4. Contours of peak acceleration in the deep Aug. 9, 2009 (M_W=7.1, HRV) Izu Islands, Japan earthquake (from K-NET web site, www.-knet.bosai.go.jp). Red star is at the epicenter. Note the asymmetry of intensity distribution.

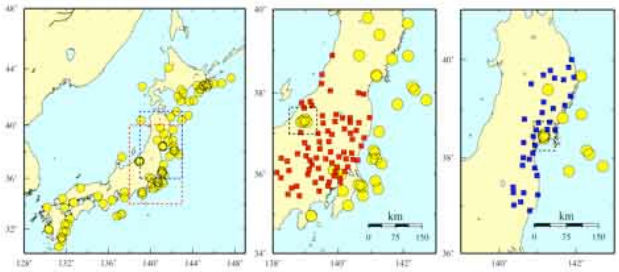

Figure 5. (**a**) All epicenters (yellow) used in the pilot application to Japanese data. (**b**) Red squares show strong motion stations for the subset of data from the Kanto-Niigata region (red outline on **a**). The black rectangle shows the area of 2004 Niigata-Chuetsu earthquake and its aftershocks. (**c**) Blue rectangles represent strong motion stations for the subset of data from the Tohoku region (blue outline on **a**). The black rectangle shows the area of 2003 Northern Miyagi earthquake, and its foreshock and aftershocks. (From Anderson and Uchiyama, 2010)

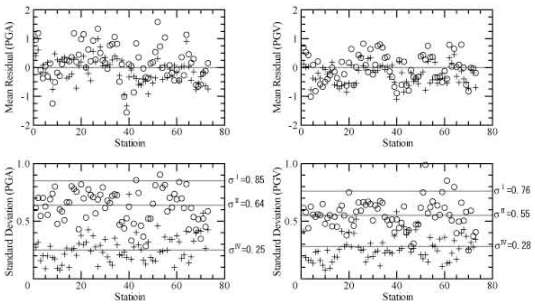

Figure 6. Mean residuals and standard deviation for individual stations in the Kanto-Niigata region for PGA (left) and PGV (right). Circles indicate the mean residual and the standard deviation for the earthquakes throughout the region. Plus symbols indicate the mean residual and the standard deviation for the earthquakes in the compact single source volume. All quantities are given in natural log units. (From Anderson and Uchiyama, 2010)

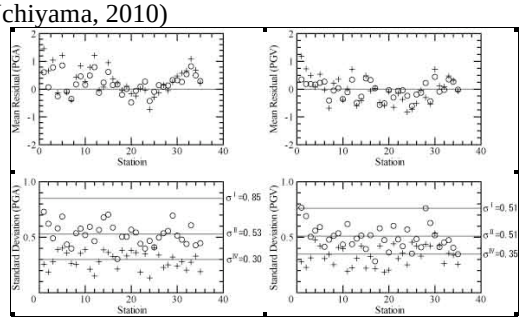

Figure 7. Equivalent of Figure 6 for the Tohoku region. (From Anderson and Uchiyama, 2010)

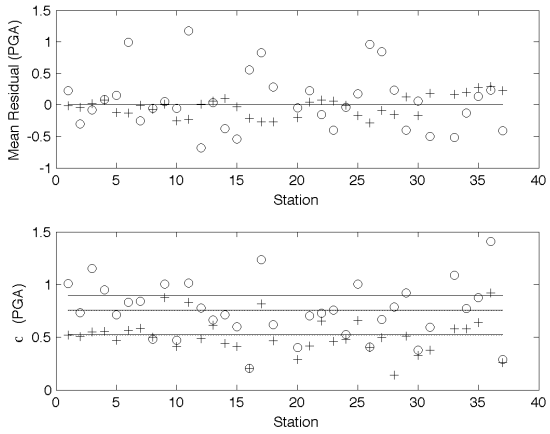

Figure 8. Equivalent of Figure 6 for PGA in the Guerrero region. (From Anderson and Uchiyama, 2010)

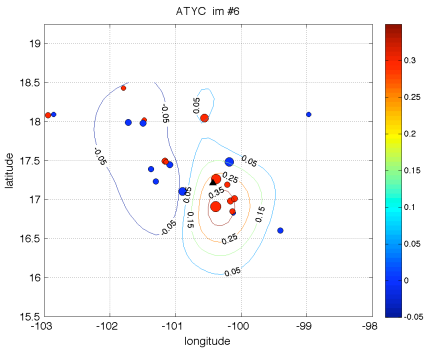

Figure 9. Path residuals for the station ATYC, and contours determined in Stage IV. (From Anderson and Uchiyama, 2010)

JOINT CONFERENCE PROCEEDINGS
7th International Conference on Urban Earthquake Engineering (7CUEE) &
5th International Conference on Earthquake Engineering (5ICEE)
March 3-5, 2010, Tokyo Institute of Technology, Tokyo, Japan

FULL-SCALE SHAKE TABLE TESTS OF 5-STORY STEEL BUILDING WITH VARIOUS DAMPERS

Kazuhiko Kasai [1], Hiroshi Ito[2], Yoji Ooki[3], Tsuyoshi Hikino[4], Koichi Kajiwara[4], Shojiro Motoyui[5], Hitoshi Ozaki[6], and Masato Ishii[6]

1) Professor, Structural Engineering Research Center, Tokyo Institute of Technology, Japan
2) Researcher, Structural Engineering Research Center, Tokyo Institute of Technology
3) Assistant Professor, Center on Urban Earthquake Engineering, Tokyo Institute of Technology
4) Researcher, National Research Institute for Earth Science and Disaster Prevention
5) Associate Professor, Interdisciplinary Graduate School of Science and Engineering, Tokyo Institute of Technology
6) Nikken Sekkei Ltd.
kasai@serc.titech.ac.jp, ito.h.ac@m.titech.ac.jp, ooki@serc.titech.ac.jp, hikino@bosai.go.jp, kaji@bosai.go.jp, motoyui.s.aa@m.titech.ac.jp, ozaki@nikken.co.jp, ishiim@nikken.co.jp

Abstract: Realistic simulations of earthquake responses were conducted in March 2009 for the full-scale 5-story building specimens with dampers using the E-Defense, the world's largest three-dimensional shake table. The building was tested repeatedly, inserting and replacing each of 4 damper types, i.e., steel damper, oil damper, viscous damper, and viscoelastic damper. This paper discusses test concept, method and test results as well as details of the 5-story building specimen. Performance improvement by the dampers will be addressed for moderately tall buildings that constitute a major portion of the building stock.

1. INTRODUCTION

The E-Defense shaking table facility, whose construction was completed in early 2005, is the largest earthquake simulator capable of subjecting full-scale structures to the strongest earthquakes recorded in the world.

Using the facility, three major research projects were completed on geostructures, wooden buildings, and reinforced concrete buildings, respectively. Currently, projects on steel buildings and bridges are being pursued. Figure 1 shows overall organizations for the steel building project that focuses on moment-resisting frames, innovative methods for new or existing buildings, nonstructural elements, and protective systems. It is pursued by four working groups (WG's) shown in Figure 1.

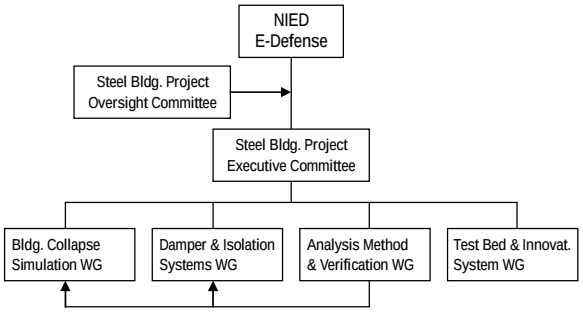

Figure 1. Organization of E-Defense Steel Project

This paper addresses the work of Damper and Isolation Systems WG. This paper discusses test concept, method and test results, as well as details of the 5-story building. The building was tested repeatedly, inserting and re-placing each of 4 damper types, i.e., steel damper, oil damper, viscous damper, and viscoelastic damper. Moderately tall buildings that constitute a major portion of the building stock will be considered.

2. TEST CONCEPT AND METHOD

2.1 Validation of Passive Control Technology

Japan has constructed the largest number of passively-controlled buildings, and is believed to have conducted the most extensive research to realize various control schemes. A variety of dampers are being produced by more than twenty manufacturers and more than ten general construction companies in Japan. Numerous technical papers on the schemes are also published.

Most major Japanese buildings designed and constructed after the 1995 Kobe earthquake are either base-isolated or passively-controlled in order to better protect the building and its contents. However, because of their short histories, the schemes have never been attested under the major and catastrophic quakes, while they are increasingly used in Japan. Thus, it is extremely important to validate these advanced schemes by realistic experiments, before occurrence of such earthquakes.

The full-scale shake table test made possible by the E-Defense would be the best option for such validation.

2.2 Moderately Tall Steel Buildings

A 5-story steel building is considered as the specimen, since it represents many office buildings seen in Japan; it is about the tallest of the majority of steel building stock, and; it tends to deform, if not damped, much more than taller steel buildings under the major quake. The last point is discussed below:

Figure 2 shows spectral displacement S_d vs. acceleration S_a for the design basis earthquake (DBE) and maximum considered earthquake (MCE). The spectra for the ground motion recorded at JR Takatori Station during the 1995 Kobe Earthquake are also shown. Damping ratio 5% is considered. The plots are for elastic responses, but they will be used here as crude estimates for inelastic responses.

It is customary in Japan to estimate the building vibration period T by the building height H. Possible range of T for a building with H=16m, similar to the specimen height (Sec. 3) is shown in Figure 2. Story drift angle averaged over the building height θ_{avg} is also shown, by approximating it as $S_d/(2H/3)$. The $2H/3$ is the effective height, corresponding to a case of straight mode shape.

It was statistically found that the Japanese code formula T=0.03H is reasonably accurate for taller Japanese MRFs. In contrast, for moderately tall MRFs considered here, the range of T=0.05H to even 0.07H is found to be more appropriate. From Figure 2, this would lead to θ_{avg}=0.017 to 0.027 under the DBE, suggesting significant structural and no-structural damage, as vibration period is longer.

Such an MRF would be vulnerable against stronger quakes such as the Takatori motion whose spectra are much larger (Fig. 2). Moreover, consequently large ductility demand will produce θ_{avg} larger than estimated by this elastic approach. Further, inelastic drift may be highly non-uniform and concentrate in a particular story, largely exceeding θ_{avg}. These were demonstrated by the Building Collapse Simulation WG (Fig. 1), testing a full-scale 4-story steel building (H=14.4m) with T=0.063H (Suita 2009, Yamada 2009). The building collapsed under the Takatori ground motion, due to the large drift and non-ductile column behavior at the 1st story.

Accordingly, moderately tall steel MRF tends to be vulnerable due to its larger deformation caused by the relatively long vibration period. The Japanese code limits the story drift angle to 1/200 under the static force estimated from the acceleration spectrum similar to that of DBE (Fig. 2). However, since acceleration is constant and thus limited in the shorter period range (Fig. 2), the drift limit is easily satisfied by the short and moderately tall buildings. This results in larger flexibility and thus longer vibration of such buildings.

Based on these, and since simply increasing the MRF member sizes to control drift would be very uneconomical, the use of dampers is believed to be an alternative and attractive option. In spite, passive control is hardly utilized for short and moderately tall buildings in Japan, since the code does not yet adequately address such applications. Moderately tall building, therefore, was selected as the specimen, because of its significant potential to impact the above circumstances.

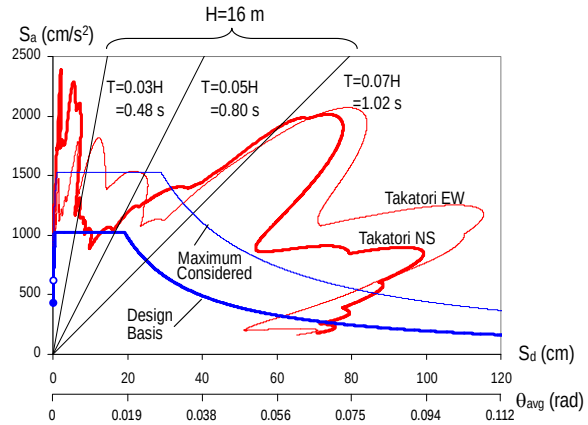

Figure 2. Displacement vs. Acceleration Spectra (Design Basis Earthquake, Maximum Considered Earthquake, and JR Takatori Ground Motions, 5% Damping Ratio)

2.3 Test Method

The objective of the present test is to validate reliability of the passive control technology by conducting realistic experiments. Four major types of dampers are selected, and for the economical reason the building will be tested repeatedly, inserting and replacing each of the damper types. In this regard, the frame members must be kept almost elastic without much residual deformation. Such requirement is considered to be important for design of actual damped building, thus, a practical beam column connection detail to enhance the elastic limit of the frame is developed and used for the specimen.

The aforementioned JR Takatori ground motion that caused collapse of the 4-story specimen is used in order to demonstrate contrasting performance and appeal to the community for promoting safer seismic environments. In this regard, the building without dampers will be tested at the end of the test series, which is expected to demonstrate that even the MRF with improved design will suffer significant deformation and damage in contrast to the damped case. The JR Takatori motion will be scaled 0.05, 0.1, 0.2, 0.4, and 1.0 times, in order to compare the performance among the four damped frames as well as un-damped frame at various seismic levels. White noise excitation as well as free vibration test will be pursued. Ambient vibration frequencies and modes are also constantly monitored after erection of steel skelton, until end of the tests. Dynamic properties at moderate shaking will be also measured by operating two vibrating machines set on the building roof, during the break between the shake table tests.

The number of data channels will be about 1,350 which is the largest among all the tests performed previously at E-Defense. The quantities to be measured are as follows:

(1) Strains: columns strains, beam strains, damper

strains, anchor bolt strains, slab reinforcement strains, slab surface strains, panel zone strains, and cladding support member strains, etc.

(2) Deformations and Displacements: story drift and twisting deformation, damper deformation, foundation rocking, column rotation, beam rotation, ceiling displacement, stairway displacement, exterior panel in- and out-of-plane displacement, partition in-plane displacement, door shear deformation, and ceiling edge and partition relative displacement, etc.

(3) 3D-Accelerations: shake table accelerations, each floor accelerations, story drift support accelerations, ceiling accelerations, and cladding accelerations, etc.

(4) Others: pressure between ceiling edge and partitions, ceiling hanger reaction force, motion records outside and inside the building (including axial and transverse damper deformation) etc.

3. BUILDING FRAMES WITH DAMPERS

Japanese dampers can be categorized into five major types shown in Figure 3, and four types such as shown in Figure 4 are considered: they are steel, oil, viscous, and viscoelastic dampers. The building will have 12 dampers of the same type with three to four different sizes. For each type, full-scale dampers of three different sizes were dynamically tested at Tokyo Institute of Technology (Kasai et al. 2008). Detailed descriptions for the test results and analytical models are described elsewhere (Ooki et al. 2009).

As shown in Fig. 5, the building is 5-story with two bays in each direction. Due to the reduction in budget, the building is made smaller than originally planned and described elsewhere (Kasai et al. 2007, 2008). The plan dimension is 10m × 12m, and total height from the upper surface of a stiff foundation beam is 15.8 m (Fig. 5). Seismically active weight of the superstructure is 4,730 kN, including all structural/non-structural components and a portion of live load (Table 1).

The frame members of the superstructure consist of either rolled or built-up wide-flange beam sections of 400 mm deep (Table 2), and cold-formed square box column sections of 350 mm × 350 mm (Table 3). Note that each

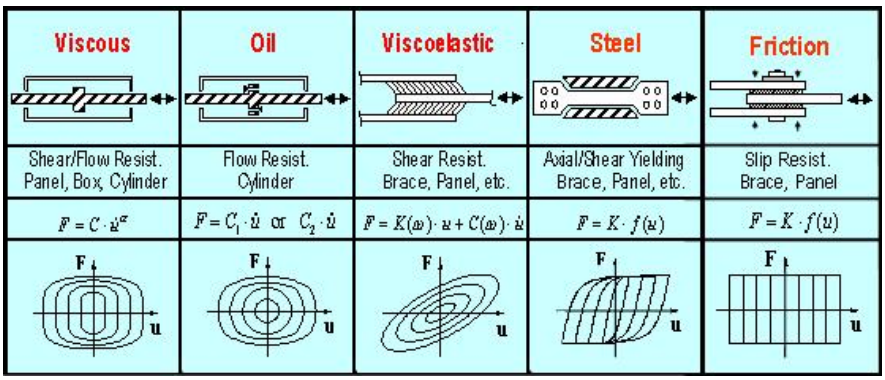

Figure 3. Five major types of dampers used in Japan.

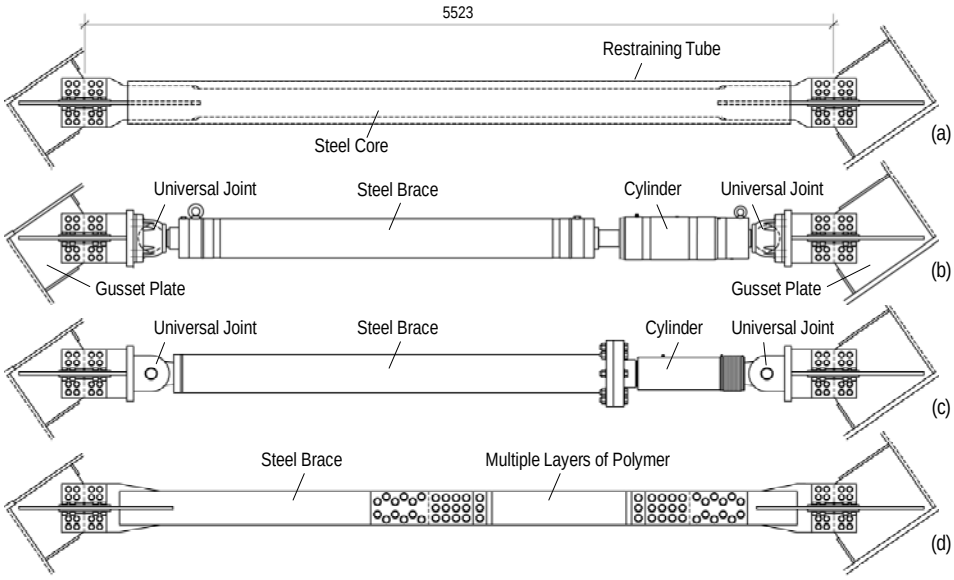

Figure 4. Sizes and configurations of 4 types of dampers to be used (between 2nd and 3rd floors) : (a) steel, (b) oil, (c) viscous, and (d) viscoelastic dampers

span consists of three beam portions, a center beam portion and two end beam portions that are bolt-connected through the splice plates on flanges and webs. For the beams of MRF bays (G2, G3, G12, and G13 in Fig. 5), the the center portion uses smaller cross section, as indicated by Table 2. And for the beams of damper bays (G1 and G11), the same sections are used for all the three portions in order to resist large axial forces transmitted from the damper. The coupon tests for all members indicate actual yield stresses of the columns and beams were in average about 1.2 times the nominal values (Table 4).

All the beam and column connections will be a fully-restrained type. For the beams of MRF bays, the flange is haunched to increase yield rotation and to delay onset of yielding. And for the beams of damper bays, haunch was considered unnecessary due to large sections created by the gusset plate (Kasai et al. 2009).

Figure 6 shows exterior views of the building. The precast light-weight curtain walls and glass curtain walls are provided to the 1st and 2nd story levels only. The walls are not attached to the damper bays for ease of dismantling/mantling the dampers. Figure 7 shows four types of damper inserted in the building specimen.

The steel deck with normal concrete on top will be considered and fully composite beams will be created (Fig. 8). The concrete thickness is 80 mm above the corrugated metal deck of 75 mm high. The stairway (Fig. 5) is detailed to slide during shaking, thus, it does not produce significant twisting against building. At every story level above the 1st, partitions with doors are constructed. Two types of ceilings with sprinkler systems, as well as mechanical equipment are placed at some story levels.

Figure 9 shows measurement system of damper stroke and displacement of damper brace.

Table 1. Breakdown of seismically active weight for the full-scale 5-story building specimen (Unit: kN)

Floor	Floor	Steel frame	Exterior wall	Interior wall	Live load	Others	Total weight
RF	963.4	111.6	127.8	20.3	81.7	150.0	1454.8
5F	436.2	99.5	100.3	26.5	98.8	37.5	798.8
4F	436.2	117.4	100.3	26.5	98.8	37.5	816.7
3F	436.2	122.7	100.3	26.5	98.8	37.5	822.0
2F	436.2	131.3	108.8	28.7	98.8	37.5	841.3
Total	2708.2	582.5	537.5	128.5	476.9	300.0	4733.6

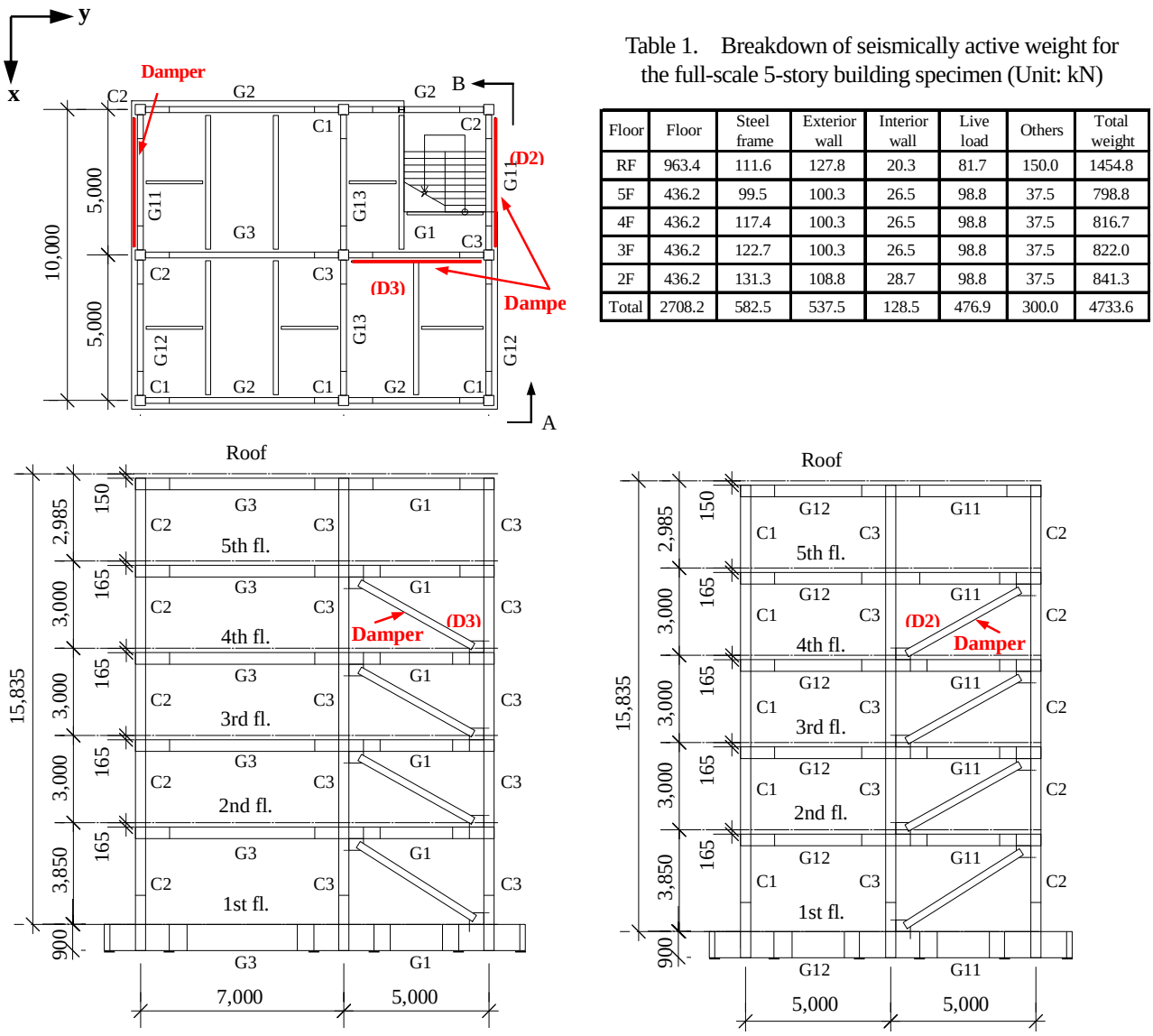

Figure 5. Plan and elevations for full-scale 5-story building specimen

Table 2. List of cross section sizes for all girders

Floor	G1(Full portion)	G2(End portion)	G2(Center portion)	G3(End portion)	G3(Center portion)
RF	H-400x200x9x12	BH-400x200x9x12	H-400x200x9x12	BH-400x200x12x16	H-400x200x9x12
5F	BH-400x200x12x16	BH-400x200x12x16	H-400x200x9x12	BH-400x200x12x16	H-400x200x9x12
4F	BH-400x200x12x19	BH-400x200x12x19	H-400x200x9x16	BH-400x200x12x19	H-400x200x9x16
4F	H-400x200x12x22	BH-400x200x12x19	H-400x200x9x16	BH-400x200x12x19	H-400x200x9x16
2F	H-400x200x12x22	BH-400x200x12x19	H-400x200x9x16	BH-400x200x12x19	H-400x200x9x16
1F	BH-900x500x16x28	BH-900x500x16x28		BH-900x500x16x28	

Floor	G11(Full portion)	G12(End portion)	G12(Center portion)	G13(End portion)	G13(Center portion)
RF	H-400x200x9x12	BH-400x200x9x12	H-400x200x9x12	BH-400x200x9x12	H-400x200x9x12
5F	BH-400x200x12x16	BH-400x200x12x16	H-400x200x9x12	BH-400x200x12x16	H-400x200x9x12
4F	BH-400x200x12x16	BH-400x200x12x19	H-400x200x9x16	BH-400x200x12x19	H-400x200x9x16
4F	BH-400x200x12x19	BH-400x200x12x19	H-400x200x9x16	BH-400x200x12x19	H-400x200x9x16
2F	H-400x200x12x22	BH-400x200x12x19	H-400x200x9x16	BH-400x200x12x19	H-400x200x9x16
1F	BH-900x500x16x28	BH-900x500x16x28		BH-900x500x16x28	

Table 3. List of cross section sizes for all columns

Story	C1	C2	C3
5	□-350x350x12x12	□-350x350x12x12	□-350x350x12x12
4	□-350x350x12x12	□-350x350x12x12	□-350x350x12x12
3	□-350x350x16x16	□-350x350x16x16	□-350x350x19x19
2	□-350x350x16x16	□-350x350x19x19	□-350x350x19x19
1	□-350x350x19x19	□-350x350x22x22	□-350x350x22x22

Table 4. Yield and ultimate strengths of steel used (actual vs. nominal values)

	σ_y(N/mm^2)	σ_u(N/mm^2)
Column	346-398	430-470
(BCR295)	295	400
Beam	331-422	510-557
(SN490B)	325	490
Gusset plate	342-365	510-520
(SN490B)	325	490



Figure 6. Exterior views of the building specimen under construction (Dec. 2008 and Jan. 2009)



Figure 7. Four types of damper inserted in the building specimen (Feb. and Mar. 2009)



Figure 8. Interior views of the building specimen under construction (Dec. 2008 and Jan. 2009)



Figure 9. Measurement system of damper stroke and displacement of whole damper brace (Feb. and Mar. 2009)

4. OBSERVED RESPONSES

Measured responses of main structural components such as dampers, frame and system during the shake table test are as follows.

Figure 10 shows comparison between the story shear based on inertia forces and the story shear based on member forces at 1st, 3rd, and 5th story in x-direction for the building with steel dampers under the 100% Takatori motion. As Figure 10 shows, both story shear based on inertia forces and story shear based on member forces match well. In addition, the former is about 10% larger than the latter probably because of the contribution from non-structural components.

Figure 11 shows relationship between damper forces and damper stroke of each of the four types of dampers at 1st story under the 15%, 50% and, 100% Takatori motions. As shown in Figure 11(a), steel dampers behave elastically under 15% Takatori motion, and elasto-plastically under 50% and 100% Takatori motions. As Figure 11(c) shows, oil dampers behave linearly under 15% and 50% Takatori motions, and non-linearly under 100% Takatori motion due to working of relief valve. As shown in Figure 11(d), viscoelastic dampers behave linearly regardless of shaking intensity.

Figure 12 shows relationship between story shear based on inertia force and story drift for the building with steel dampers. As Figure 12 shows, hysteresis curves at 1st and 3rd stories with dampers indicate significant energy dissipation by the steel damper. On the other hand, hysteresis curve at 5th story without damper indicates elastic behavior.

Figure 13 shows peak responses such as story shear, story drift angle and floor acceleration of building specimen with four types of dampers under 50% and 100% Takatori motion. In addition, peak responses of building specimen without damper are shown in Figure 13 for comparison. Note that, for the 100% Takatori motion, they are extrapolated as 2 times those for 50% Takatori, because shaking was limited up to the level of 70% Takatori motion for the safety reason. As shown in Fig. 13, story drift angle under 100% Takatori motion for the building with each type of damper is less than the design target value of 1% radian. As a whole, peak responses of the building having dampers are considerably less than those without dampers.

The recorded damper deformation is used as input for analytical prediction of damper force, and thus-obtained damper force appears to match well with that recorded during the test. Figure 14 shows comparison of these two damper forces for each damper type. Analysis gives good estimation for viscous, oil, and viscoelastic dampers except for the steel damper, that is not very accurately predicted by using the bilinear model. Analysis model including Bauschinger effect, strain hardening and dependency for velocity and frequency has been developed for improved accuracy.

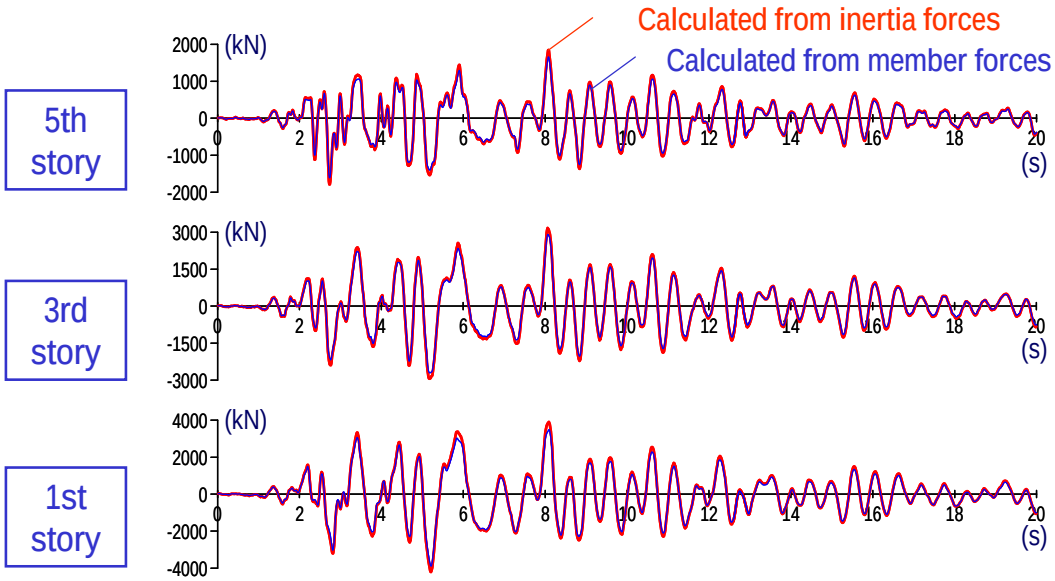

Figure 10. Comparison between story shear based on inertia forces and story shear member forces (with Steel dampers, Takatori 100%, X-Dir.)

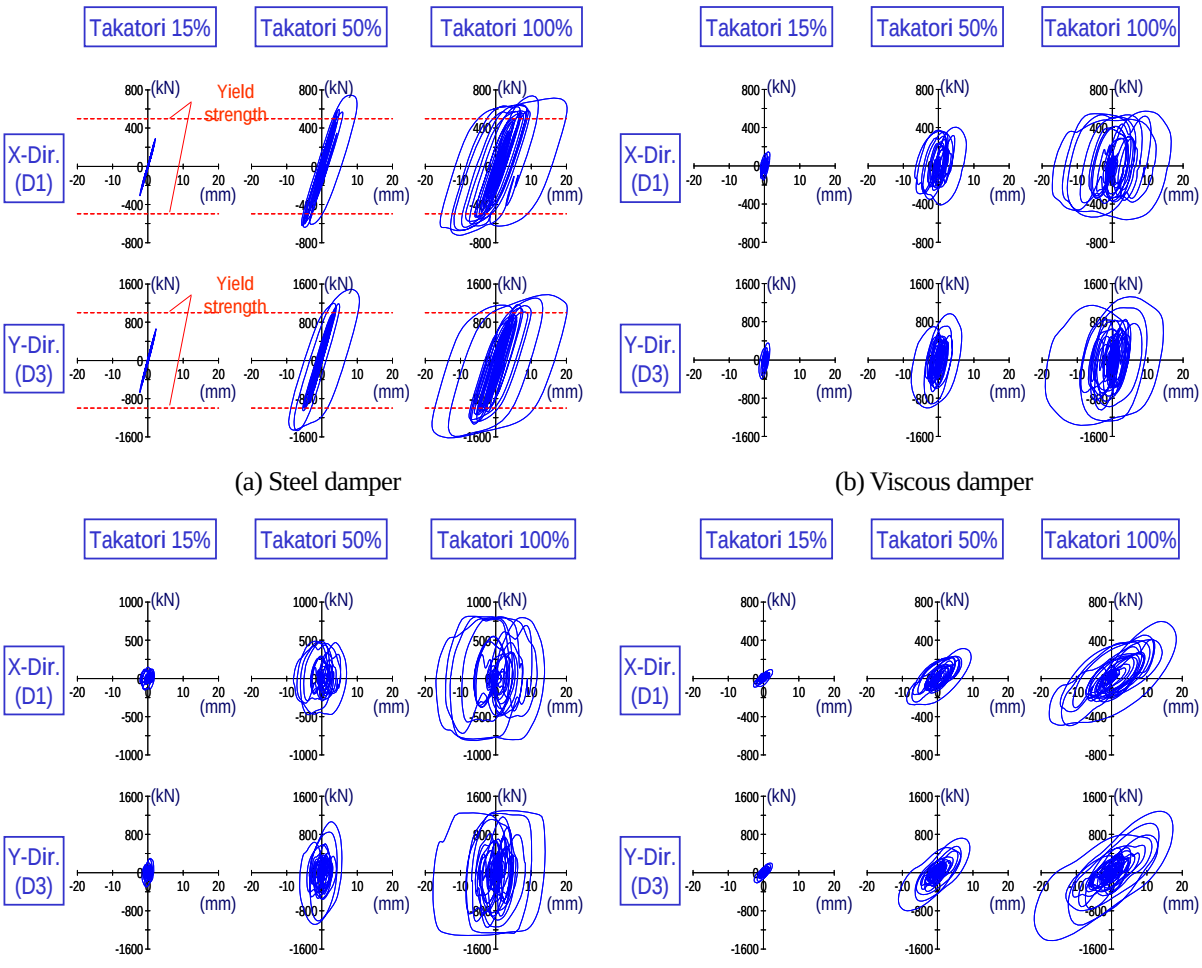

(a) Steel damper

(b) Viscous damper

(c) Oil damper

(d) Viscoelastic damper

Figure 11. Relationship between axial damper forces and damper stroke of four types of dampers (1st story)

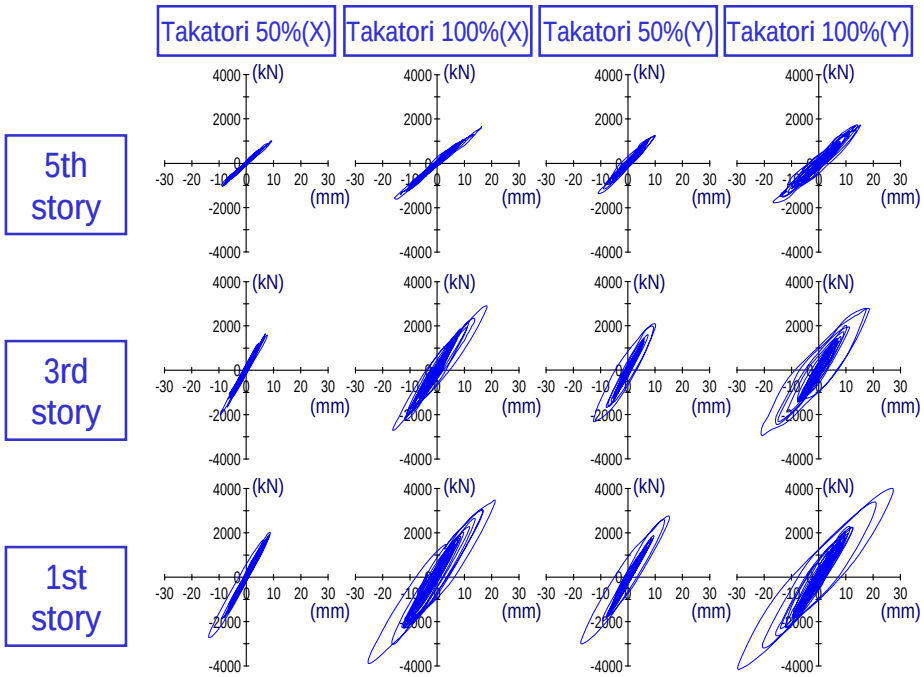

Figure 12. Relationship between story shear based on inertia force and story drift (with steel dampers)

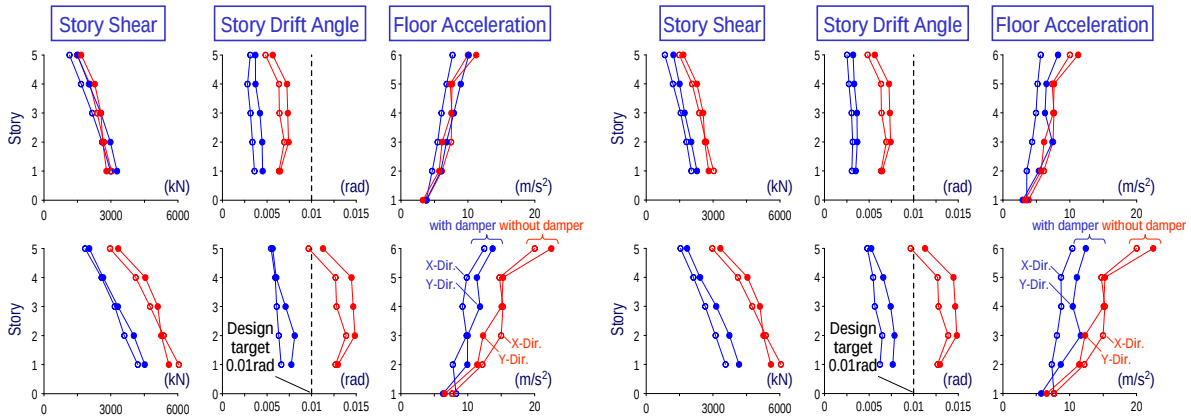

(a) Steel damper

(b) Viscous damper

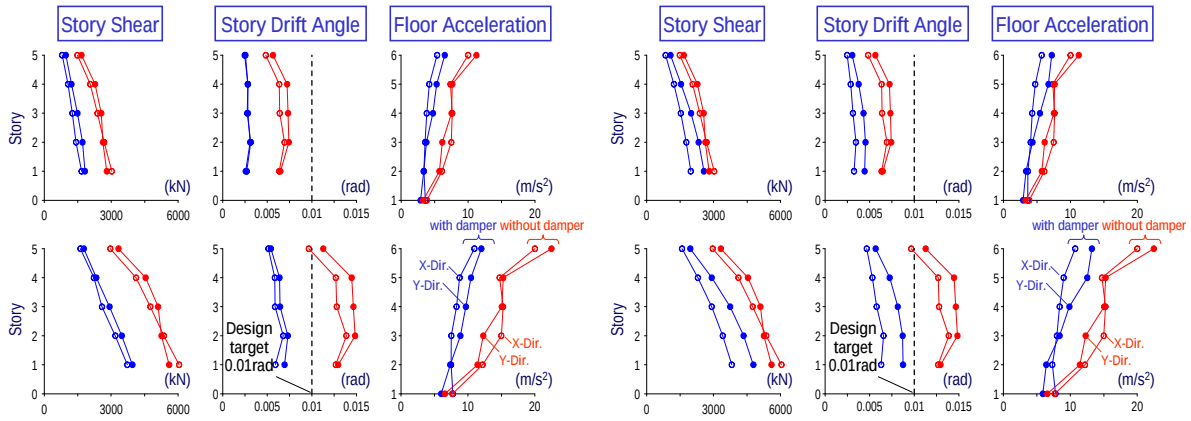

(c) Oil damper

(d) Viscoelastic damper

Figure 13. Peak responses of building specimen with four types of dampers

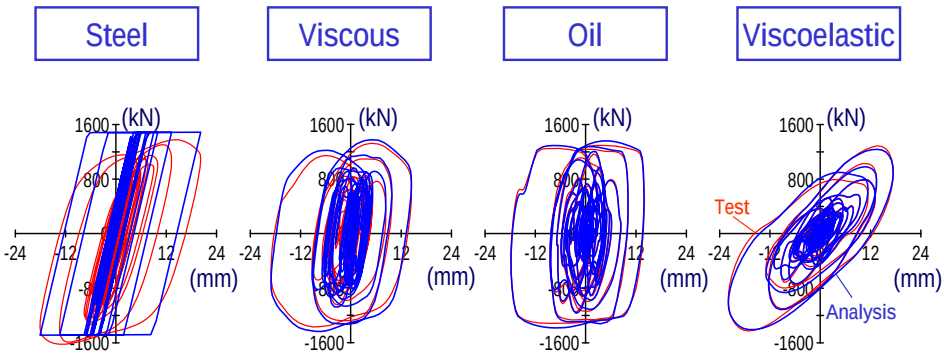

Figure 14. Validation study for analysis model of four types of dampers (Takatori 100%)

5. DYNAMIC PROPERTIES

As described above, the building was subjected many table motions, and changes in dynamic properties of the building were successfully monitored through the extensive measurement explained earlier.

Figure. 15 shows the cracks observed from the second floor concrete slab, prior to the tests, after the tests with steel dampers, viscous dampers, oil dampers, and viscoelastic dampers, and the tests without dampers, respectively. Cracks formed when the story drift reached approximately 0.5% rad. and significant increase in cracks was observed after the test with steel damper using 100% Takatori motion, as well as the test without dampers using 70% Takatori motion.

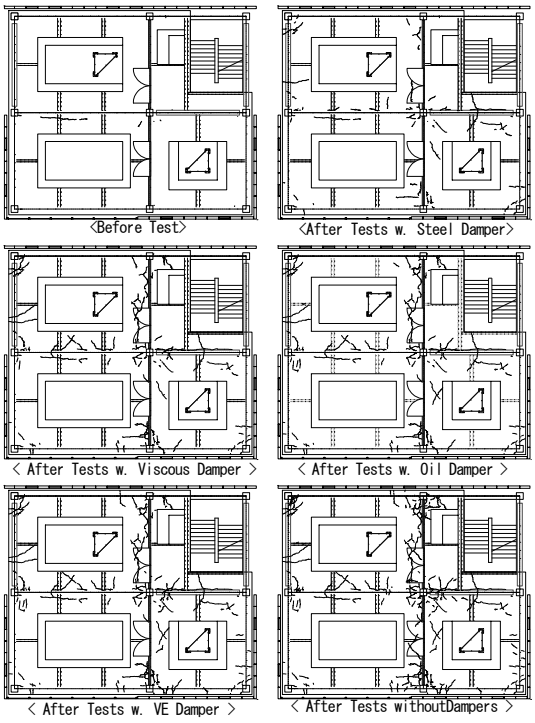

Figure 15 Cracks on second floor concrete slab

At each story level, story shear force is obtained from member forces (Fig. 10) excluding those of dampers, and it is compared with the story drift to obtain the story stiffness. Figure 16 shows change of thus-estimated story stiffness at each story level. The frame had the largest stiffness before the test, and about 10 to 15% loss in stiffness occurred at the end of all the tests. The cracks in the floor slabs noted above could be major source of such change.

Non-structural components are partially attached to the building. As Figures 6 to 8 show, curtain walls and ALC (autoclaved light-weight concrete) panels are attached to the exterior surface of the buildings at the 1st and 2nd story level except where the dampers are installed. The interior partitions with doors (e.g., Fig. 8) are also provided except for the 1st story level. The stiffness contribution of these non-structural components were estimated by using the difference between the story shear forces obtained from inertia force and those from member forces (Fig. 10).

Figure 17 shows change of thus-estimated stiffness of the non-structural components at each story level. The peak average story drift, the value obtained by averaging the drifts of all stories is also shown for every test conducted (Fig. 17 above), in order to indicate intensity of shaking.

It should be noted that the stiffness of nonstructural components is as much as 0.3 times that of the steel frame, at earlier tests. Thereafter, the former deteriorates much more rapidly than the latter, and as much as 70% loss of the non-structural component is observed from Figure 17. The loss is significant when large shaking took place.

Although not shown, energy dissipated by the non-structural components are also estimated. As the smallest energy contribution, it was only 0.1 times the overall energy dissipation for the building with oil dampers that showed about 20% damping ratio. However, the contribution increases for the building that indicated smaller damping ratio, using different dampers. As the largest energy contribution, it was as much as 0.3 times the overall energy dissipation for the building without dampers.

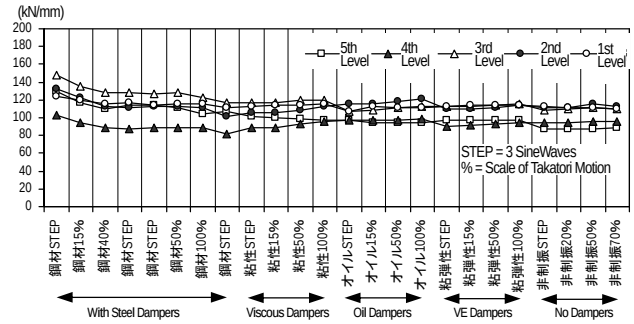

Figure 16 Change in steel frame lateral stiffness (x-direction)

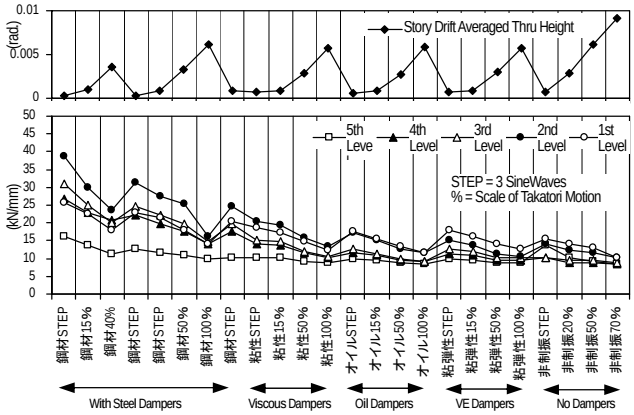

Figure 17 Change in non-structural components' lateral stiffness (x-direction)

Vibration periods and damping ratios are also estimated from the responses recorded. Several different tests and/or evaluation methods were employed. In this paper, only the shake table tests will be referred to, and a basic system identification technique using real modes is used. The control of the shake table considers interaction between the specimen and table, and it is used to calibrate shaking of the subsequent test. The target translational acceleration histories along x-, y-, and z-axes are given, and target rotational acceleration with respect to the three axes are set zero. However, due the shake table occasionally rocks with respect to the x- and y-axes (Fig. 18), especially at the earlier shaking where little calibration is done.

Significant error will develop when one considers the transfer function between only the shake table horizontal acceleration and building response acceleration. It is necessary to decompose the response acceleration into the acceleration due to rigid-body rotation caused by table rocking and acceleration relative to the shake table surface. A technique to consider this was developed by the writers. It will be explained elsewhere and only the results will be shown in this paper.

Figure 19 shows the recorded roof displacement of the building with or without dampers. Prediction using the writers' system identification technique is also shown. Remarkable correration is obtained between the prediction and test result. In spite of different nonlinear behavior of

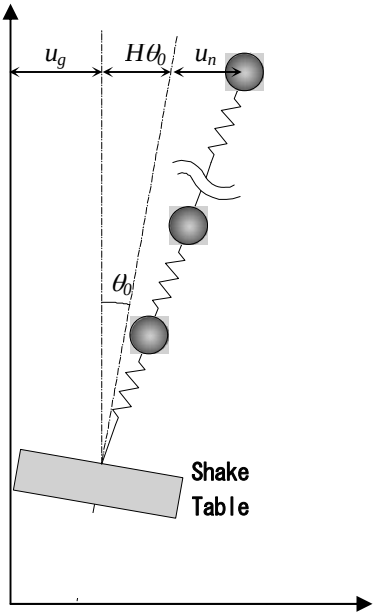

Figure 18 Rocking of E-Defense shake table

the damper and the building, the linear identification method assuming real vibration mode still produces excellent results. Note however that the method showed less accuracy for the frame without dampers at the 70% Takatori motion, probably due to yielding of the members and connections of the building.

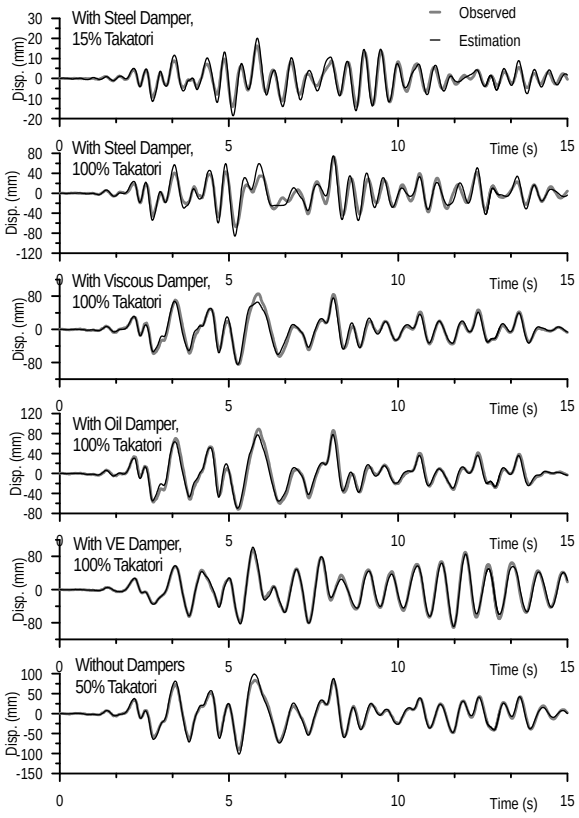

Figure 19 Roof displacements: test vs. prediction using system ID and modal superposition

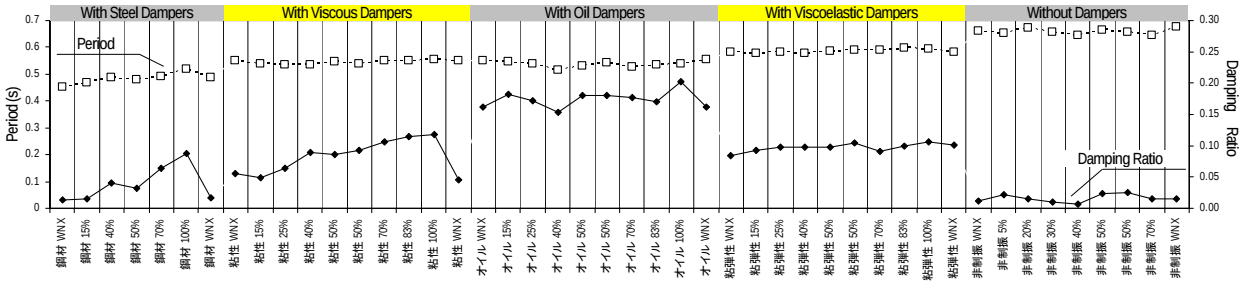

Figure 20 Vibration periods and damping ratios in x-direction

Figure 20 shows the vibration periods and damping ratios obtained for all the tests, using the above-mentioned technique. The building with steel dampers shows shortest period and smallest damping ratio among those with dampers, and they become longer and larger, respectively, at larger shaking. The building with oil dampers shows the largest damping ratio of about 17%, and the smallest responses (Fig. 13). Note that the oil dampers were somewhat over-sized compared with other types dampers, which is one of the reasons for the above trend. The building with either viscous dampers or viscoelastic dampers shows damping ratios of about 10%, and performed well.

6. SUMMARIES AND CONCLUSIONS

Realistic three-dimensional shaking table tests were conducted for full-scale 5-story building specimens with (March 2009) or without (April 2009) dampers. This paper has described the test concept, method and test results, as well as details of the 5-story building specimen.

Acknowledgements:

This study is a part of "NEES/E-Defense collaborative research program on steel structures," and was pursued by the Damper and Isolation WG. The Japan team leader for the overall program and the leader for the WG is Kazuhiko Kasai, Tokyo Institute of Technology. The WG members not listed as the authors also contributed to the present effort, and their contributions are greatly appreciated. The authors also acknowledge the financial support provided by the National Research Institute for Earth Science and Disaster Prevention (NIED).

References:

Kasai, K., Motoyui, S., Ozaki, H., Ishii, M., Ito, H., Kajiwara, K., and Hikino, T. (2009). Full-Scale Tests of Passively-Controlled 5-Story Steel Building Using E-Defense Shake Table, Part 1: Test concept, method, and building specimen, STESSA 2009, Philadelphia.

Kasai, K., Ooki, Y., Ito, H., and Motoyui, S., Hikino, T. and Sato, E. (2009). Full-Scale Tests of Passively-Controlled 5-Story Steel Building Using E-Defense Shake Table, Part 2: Preliminary Analysis Results, STESSA 2009, Philadelphia.

Ooki, Y., Kasai, K., Motoyui, S., Kaneko, K., Kajiwara, K., and Hikino, T. (2009) Full-Scale Tests of Passively-Controlled 5-Story Steel Building Using E-Defense Shake Table, Part 3: Full-Scale Tests for Dampers and Beam-Column Subassemblies, STESSA 2009, Philadelphia.

Kasai, K., Ooki, Y., Motoyui S., Takeuchi T., and Sato, E. (2007). "E-Defense Tests on Full-Scale Steel Buildings: Part 1 – Experiments Using Dampers and Isolators", ASCE Str. Congress, Long Beach, CA, May 16-19

Yamada, S., Suita, K., Tada, M., Kasai, K., Matsuoka, Y., and Shimada, Y. (2009). Full Scale Shaking Table Collapse Ex-periment on 4-Story Steel Moment Frame: Part 1 Outline of the Experiment, STESSA 2009, Philadelphia, USA.

Suita, K., Yamada, S., Kasai, K., Shimada Y., Tada, M., and Matsuoka, Y. (2009). Full Scale Shaking Table Collapse Experiment on 4-Story Steel Moment Frame: Part 2 Detail of Collapse Behavior, STESSA 2009, Philadelphia, USA.

Kasai, K., Ooki, Y., Motoyui S., Takeuchi T., Kajiwara, K., and Sato, E. (2008). "Results of Recent E-Defense Tests on Full-Scale Steel Buildings: Part 3 – Experiments on Dampers and Frame Subassemblies", ASCE Structures Congress, Vancouver, B.C., April 24-26.

Ohsaki M., Kasai, K., Hikino, T., and Matsuoka, Y. (2008a). "Overview of 2007 E-Defense Blind Analysis Contest Re-sults", 14WCEE , Beijing, Oct. 12-17

Ohsaki M., Kasai, K., Yamamoto, M., Kiriyama, S. (2008b). "2-D Analysis Methods for 2007 Blind Analysis Contest", 14WCEE , Beijing, Oct. 12-17

Ohsaki M., Kasai, K., Thiagarajan, G., Yang, Y., and Komiya, Y. (2008c). "3-D Analysis Methods for 2007 Blind Analysis Contest", 14WCEE , Beijing, Oct. 12-17

JOINT CONFERENCE PROCEEDINGS
7th International Conference on Urban Earthquake Engineering (7CUEE) &
5th International Conference on Earthquake Engineering (5ICEE)
March 3-5, 2010, Tokyo Institute of Technology, Tokyo, Japan

DEMAND SPECTRA AND SFSI FOR THE PERFORMANCE BASED DESIGN

Kyriazis Pitilakis[1)], Dimitris Pitilakis[2)], Anna Karatzetzou[3)]

1) Professor, Aristotle University of Thessaloniki, Greece
2) Lecturer, Aristotle University of Thessaloniki, Greece
3)MSc, PhD student, Aristotle University of Thessaloniki, Greece
pitilakis@civil.auth.gr , dpitlak@civil.auth.gr , akaratze@civil.auth.gr

Abstract: Performance based design is traditionally performed assuming a fixed-base model. The free-field soil response is evaluated and simply applied at the base of the structure in order to calculate the demand spectrum and thus the dynamic response of superstructure. In this study the soil – structure - interaction (SFSI) is taken into account in the estimation of the demand spectrum at the foundation level. The dynamic response of the foundation – structure system is known to depend on the foundation input motion, which in turn depends on the interaction of the superstructure with the underlying soil, when subjected to strong ground motion. Consequently, the dynamic response of a compliant foundation differs from the free field soil ground motion and therefore the demand spectrum for the structure will be affected. In case the superstructure has inelastic behavior, a pushover analysis is needed in order to estimate the capacity of the structure. It will be also affected by the soil compliance in case of strong seismic excitations. The paper presents and discusses several issues related to the above problems. Moreover we present results proving that the EC8 demand spectra for certain soil categories need further improvement and calibration.

1. INTRODUCTION

Performance-based seismic design requires the estimation and selection of elastic acceleration and displacement spectra for different damping ratios in a wide range of periods. Traditionally the selected design elastic demand spectra are the free field demand spectra proposed in seismic codes, based on the available soil and site classification. However the real demand spectra for every structure are affected by the soil-foundation-structure interaction, the effective soil compliance under strong seismic excitations and the potential ground improvement. The aim of the present study is to highlight and discuss the potential differences of the traditional approach in case we are considering the soil-foundation-structure interaction, as well as the potential soil improvement. Moreover, at least in Europe, there is a warm discussion on the accuracy of the EC8 response spectra.

The aim of this study is to validate the reliability of traditionally proposed demand spectra with a large sample of high quality worldwide records, and to highlight some important aspects of the selection of the design elastic demand spectra in view of the performance based design. Real structures on good or poor soil conditions are rarely subjected to the elastic demand spectra proposed by seismic codes, which correspond to an ideal free-field ground motion. SFSI, soil non-linearity and soil improvement may modify considerably the design elastic demand spectra.

In the first part of this study, demand spectra from a well constraint database of strong ground motion records from Japan (Kik-net), Greece and United States, (COSMOS and NSMPD), in well defined soil conditions from the surface to the bedrock basement, are computed. The results are presented for different soil categories, and for two different seismic excitation levels, as it is suggested in Eurocode (EC8). The discussion is focused on the differences between the design demand spectra of EC8 and the computed demand spectra from a large worldwide data set of real records. The aim of this research is to compare actual recordings for different soil conditions with demand spectra proposed in EC8 and in Pitilakis et al (2004).

The second part of the paper is devoted on the effect of soil – foundation – structure interaction (SFSI) on the demand spectra, as it is known to affect significantly the dynamic structural response (D.Pitilakis, 2009). This approach is traditionally considered to be beneficial for the structure, but the 1985 Mexico City and many recent earthquakes have

proved that this is a simplifying and, sometimes, a misleading generalization. The soil – foundation – structure system is more flexible than the traditionally assumed fixed base model (Avilés. and Pérez-Rocha, 2003, 2004, Aviles and Suarez, 2001).

For this reason, the SFSS has a longer natural period and a higher damping ratio than the fixed base structure. Since 1970's many researchers tried to estimate the elastic response of structures (Chopra. and Gutierrez, 1974, Veletsos, 1997) taking into account the SFSI effects. On the other hand, the inelastic response did not receive considerable attention.

Since 1990s, a new approach based on the performance based design is proposed, which is tackling some of the problems of the traditional approach (Mirada and Bertero, 1994, Miranda, 2001, Lin and Miranda, 2007, Priestley et al., 2007). However the demand spectra under free-field soil conditions remain at the basis of this improved approach. The aim of this study is exactly to investigate, always in the framework of the performance based design, the actual response of the structure, taking into consideration SFSI effects.

Finally in the third part of the paper we shortly investigate the effects of ground improvement on the demand spectra. In many real cases where important structures are founded on soft soils of low strength, it is necessary to improve soil conditions applying different techniques. Among the most popular is the use of stone columns to strengthen the foundation soft-loose soil and to increase its permeability. .A recently developed alternative technique replace at a given depth the initial soil with a compacted mixture of rubber and sand material (RSM)(Anastasiadis et al., 2009)

The elastic demand spectra under these conditions may differ considerably from the demand spectra of the initial soil, as adopted in the codes. The behavior of a simple soil – foundation – structure system (SFSS) founded on a soft cohesive soil that corresponds to soil category C according to EC 8, replaced with rubber-sand compacted layer is examined in the present paper. Three RSM materials having 0%, 5% and 25% rubber by mixture weight ratio are used in this study. The overall depth of the replacement columns is 20m, and the ratio of face replacement is on the order of 10%. The effect of the soft soil RSM reinforcement on the demand spectra of a single degree of freedom (SDOF) structure is depicted for the seismic input of the Athens, Greece 1999 earthquake. Similar analysis where performed for the traditional stone column improvement.

2. REAL GROUND MOTIONS AND DESIGN DEMAND SPECTRA

Ground motion selection

A large number (~1000) of well-documented strong ground motion recordings with different PGA values, Mw magnitudes and epicenter distances, were selected for the soil classes propose in EC8 and studied in this paper (Figure 1). The selection is based on the very good knowledge of dynamic soil properties (mainly Vs values), and the knowledge of the depth of the bedrock basement. In this paper we present a selected sample of about 300 records. They were provided from Japan (164 KiK-Net records), Greece, (58 records) and from USA- California (86 strong ground records from the COSMOS Virtual Data Center and the National Strong Motion Project Datasets) (Figure 2a). The seismic records are classified in two main categories depending on the level of seismic intensity, Mw>5.5 (or approximately PGA>0.2g) and Mw<5.5 (or approximately PGA<0.2g). Actually this is not always true, as in some cases even for low seismicity regions it is possible to have higher acceleration.

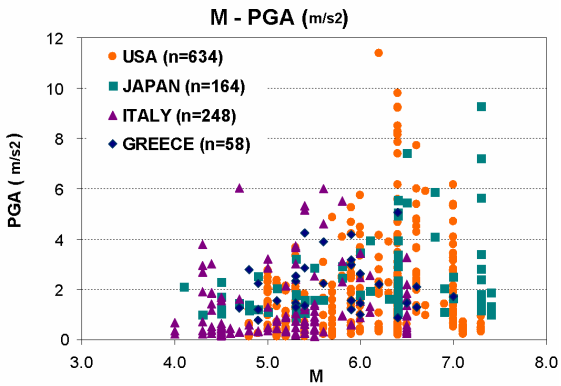

Figure 1 Mw – PGA pairs for the selected strong motion records

In Figure 2b the total number of the seismic records used for each soil class B, C and E according to EC8 are presented, classified in two main categories depending on the level of seismicity. In total, 138 records were selected for soil class B, 122 for soil class C and 48 for soil class E. We present herein only the results for stiff soils B (360m/s<$V_{s,30}$<800m/s) and soft soils C (180m/s<$V_{s,30}$<360m/s, 15<N_{spt}<50) according to EC8.

Soil class B

Based on the available detailed geotechnical soil profiles 138 records are classified in the soil class B. 92 records are classified in the high seismicity (M>5.5) and 46 in the low seismicity range. Among the 92 records there are 56 records from (Japan), 18 from the Greece and 18 from California, USA. The PGA values vary between 0.63m/s^2 and 9.24m/s^2, a range that includes certain very strong earthquake recordings.

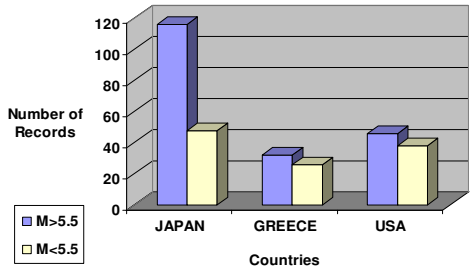

a)

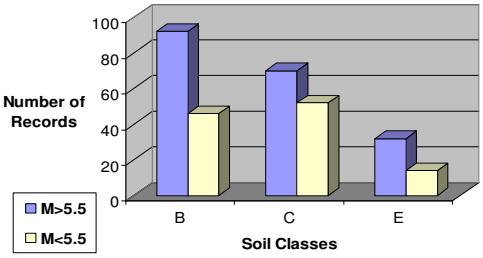

b)

Figure 2 (a) Geographical distribution of records used and (b), number of records used for each soil class B, C and E according to EC8 classification, for different seismic magnitudes Mw.

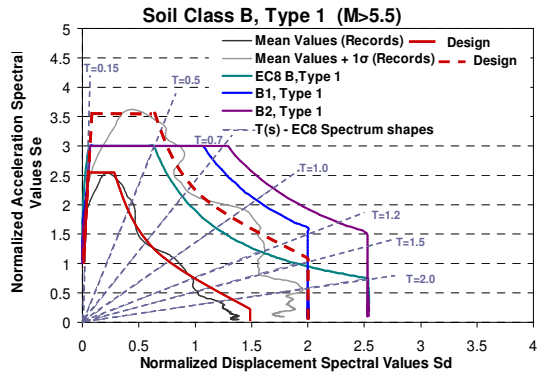

a)

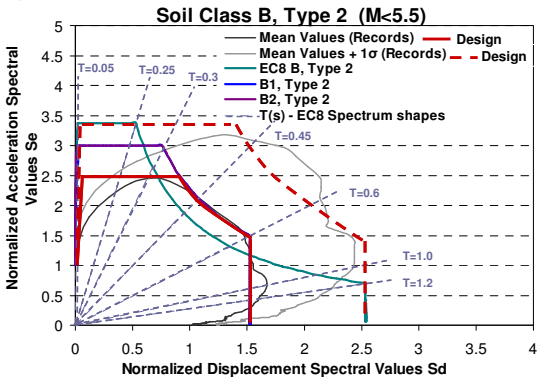

b)

Figure 3 Soil class B: Mean values (+1SD) of the normalized demand spectra (a) for M>5.5, n=92 records and (b) for M<5.5, compared with the design demand spectra of EC8 and Pitilakis et al., (2004).

The absolute Sd values vary from 0.01m to 0.2m, while absolute peak PSA values vary from 2m/s2 to 32m/s2. Figure 3 presents the mean and mean+1SD demand spectra (smoothing lines as well) for the two intensity levels, along with the corresponding demand spectra according to EC8 and Pitilakis et al (2004).

Given the scatter of the values, it is observed that at the set of the strong earthquakes (M>5.5), the design demand spectra of EC8 and the proposed demand spectra by Pitilakis et al. (2004) are better correlated with the mean values +1SD (Figure 3a). For earthquakes with M<5.5 the mean values of the recorded demand spectra are in good agreement with both design curves (Figure 3b), while the mean+1SD curve gives much higher values.

Soil class C

The total number of records in soil class C is 122. For M>5.5 there are 70 records; 28 records from Japan, 14 from the Greece and 28 from California. The range of PGA values varies between 0.59m/s^2 and 7.41m/s^2. For M<5.5 there are 22 records from Japan, 12 from Greece and 12 from USA; 52 records in total. The PGA values range between 0.10m/s^2 and 3.20m/s^2, meaning that this sample includes both weak and strong recordings mainly due to variable near field conditions.

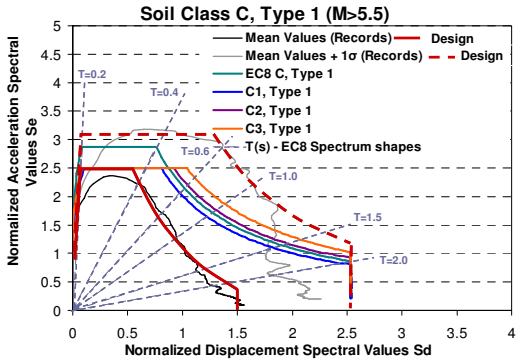

a)

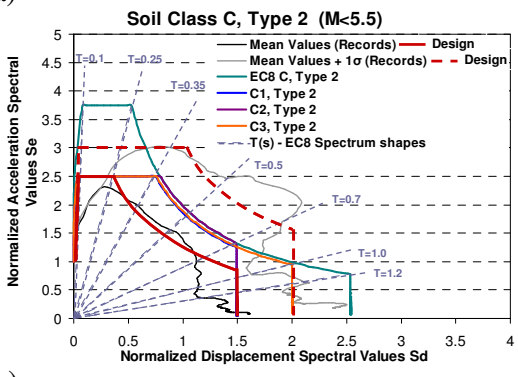

b)

Figure 4 Soil class B: Mean values (+1SD) of the normalized demand spectra (a) for M>5.5, n=92 records and (b) for M<5.5, compared with the design demand spectra of EC8 and Pitilakis et al., (2004).

From Figure 4a it is observed that the mean values of the computed demand spectra for M>5.5 are well compared with the corresponding design demand spectra of EC8 and the proposed demand spectra by Pitilakis et al. (2004), especially for the spectral values which correspond to the constant plateau. For small earthquakes with M<5.5, (Figure 4b), the mean values of the computed demand spectra appear significantly lower, compared to the design demand spectral values, while mean+1SD values are practically identical with the corresponding design demand spectra of EC8.

3. EFFECT OF SFSI AND NONLINEAR SOIL BEHAVIOR ON THE DEMAND SPECTRA AND THE PERFORMANCE BASED DESIGN

The Capacity Spectrum Method (Fajfar, 2000, Freeman, 1998) compares the capacity of the structure (inelastic analysis → capacity curve), with the demand of earthquake ground motion to be applied on the structure (e.g. equivalent linear analysis → demand spectrum). In order to compare the two curves efficiently, concerning the pushover curve, the base shear forces and the roof displacements are converted to equivalent spectral acceleration and spectral displacements. The intersection of the two curves produces the performance of the specific structure to the specific earthquake. The SFSI may be introduced in the capacity curve through the soil-foundation compliance but not in the demand spectra. However the demand spectra are seriously affected as well.

In the following we first examine the effect of several parameters, affecting the SFSI phenomenon, Such parameters are the soil – to – structure stiffness ratio index, the slenderness of the structure, the structural mass and the strong ground motion dynamic characteristics. At this step, the structure is considered to have elastic response and thus the structural response is the intersection of the modified, due to SFSI effects, demand curve, with the radial line which corresponds to the structural effective period.

At the second part, we examine the inelastic behavior of the superstructure, and thus the real structural response is the intersection of demand curve with the actual capacity curve. In both curves, SFSI phenomena are taken into consideration.

3.1 Effect of SFSI and soil non-linear behavior on the demand spectra

3.1.1 Description of the problem

A simple soil-foundation-structure model (Figure 5) is used to elucidate the effects of the nonlinear soil behaviour and the soil-foundation-structure interaction on the system response. The combined effect of the two abovementioned phenomena on the system response is investigated in the context of demand spectra. The aim is to investigate the effects of SFSI and soil non-linearity in the computed elastic demand spectra at the foundation and to compare them with the free field demand spectra. In this part the effect of SFSI on the demand spectra, will be investigated in case the structure behaves elastically.

The simplified structural characteristics vary, with a lumped mass at the top of the SDOF system of 22.5t, 45t and 180t, height over a rigid surface of 5m, 10m and 15m, square foundation of dimensions 10m x 10m, fixed base natural frequency of the linear structure at 2Hz and 4Hz and damping at 5% for the first mode of the system (according to Rayleigh). The soil profile consists of clay. The soil beneath the structure is considered as a homogeneous equivalent linear elastic half space and is modeled using quadrilateral shaped elements. The system is then subjected to five different input ground motions to the level of rock.

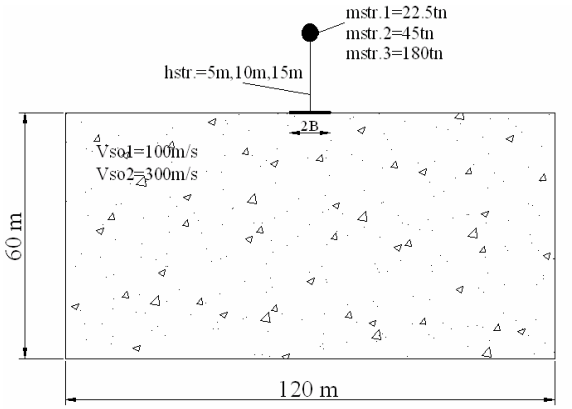

Figure 5 Soil – Foundation – Structure model

Firstly, a series of 1D seismic ground response analyses carried out in order to estimate the reduced shear modulus because of the inelastic response of soil. Required inputs for this kind of analyses include stiffness and material damping information for soil. G – γ – d curve was chosen according to Zhang (2005). Small – strain shear wave velocity is directly related to small – strain shear modulus G_{max} by:

$$G_{max} = \rho \cdot V_{So}^{2} \qquad (1)$$

where: ρ = 1800 kg/m^3 (mass density of soil), V_{So} is selected equal to 100m/s and 300m/s corresponding to very soft and medium stiffness clays. Secondly, a series of 2D time – history seismic soil – foundation – structure response analyses were carried out in order to estimate the response in the centre of the foundation and thus to compute the respective demand spectra curves.

Finally, a series of harmonic analyses took place in order to estimate the structural effective period (T_{SSI}).

3.1.2. Traditional evaluation of demand spectra versus present approach.

Traditional approach

A demand spectrum is traditionally a plot of the peak acceleration (y axis) and displacement (x axis) response of a series of oscillators of varying natural frequency, that are forced into the same input motion. The structure is assumed fixed on its base and the foundation input motion (F.I.M.) is the response at the top of a linear elastic soil (free field conditions). The well known procedure is as following (Figure 6).

Step 1: Perform 1D seismic ground elastic response analysis to obtain the foundation input motion (F.I.M).

Step 2: Apply the input motion from the previous step to a series of single degree of freedom systems of varying natural frequency.

Step 3: Plot the maximum response (acceleration – displacement) at the top of all the oscillators on the same graph in order to calculate the demand curve. Each point of the curve refers to the response of a structure with specific geometrical and dynamic characteristics (Figure 6). The critical point here is that the demand curve is the same for all structures, because the F.I.M. is the same irrespective of structural materials, sections and dynamic proprieties. Shortly, no S.F.S.I. effects are taken into consideration.

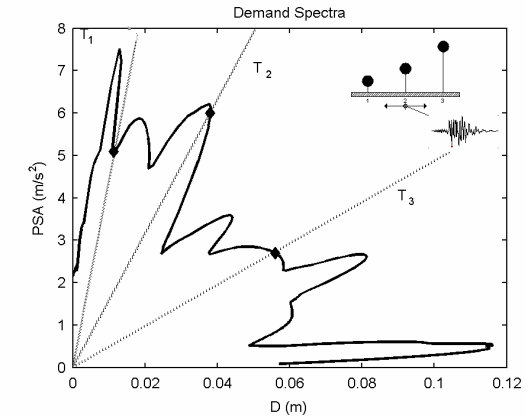

Figure 6 Conventional evaluation of Demand Spectra

The actual problem

When the S.F.S.I effects are taken into account, the procedure of calculating the demand curve is different from that represented above. Each parametric analysis includes not only the soil, but also the foundation and the structure. Using the direct method for analyzing the SFSI phenomenon, the ground motion (acceleration time history) at the center of the foundation differs from that assuming free field conditions, and therefore the demand spectrum for the structure will be affected. The difference between the two curves depends on the severity of soil – structure – interaction. The procedure is then the following (Figure 7):

Step 1: Calculate the ground motion in the middle of foundation through a step by step time history analysis for the whole SFSS.

Step 2: The demand spectrum curve that results from the response of the previous step concerns only the specific structural dynamic characteristics, and thus only one point of this curve is 'correct', and that is the point which corresponds to the structural effective period. Another structure with different characteristic will have a different demand spectra curve. Assuming elastic response of the structure, the intersection point of the two curves (demand and T_{SSI}) is the response for each specific structure.

Step 3: To estimate the final demand spectrum, a series of analyses is needed, with different structural characteristics each time.

It is of great importance to note here that the main difference with the traditional approach is the different input motion.

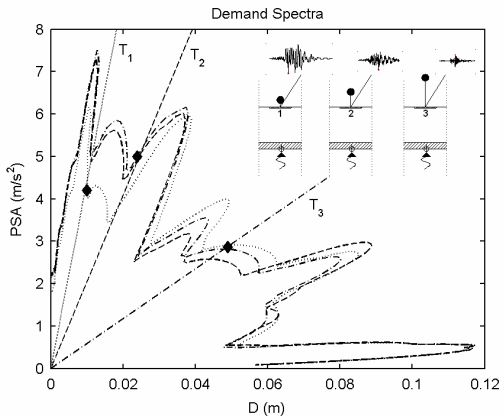

Figure 7 Evaluation of demand spectra in this study.

3.1.3 Input motions

Five acceleration time – histories are used as input motion.. Three of these motions were recorded during the Kozani- Greece 1995 Mw6.4 earthquake, the Aegion-Greece 1995 Mw6.5 earthquake and the 1976 Friuli earthquake. The other two motions are Ricker wavelets with different fundamental periods. All input motions were scaled to peak ground acceleration of 0.16g and 0.36g.

The earthquake input motions in terms of acceleration – time and the demand spectra curves are shown in Figure 8 and Figure 9. The predominant period of the input motions are: Ricker 1: T_p=0.25 s, Ricker 2: T_p=0.50 s, Aegion 1995: T_p: 0.425 s, Friuli 1976: T_p: 0.25 s and Kozani 1995: T_p: 0.20 s.

3.1.4 Effective period of structures

The effective structural period including interaction, is calculated theoretically and numerically. The theoretical calculation is made using the eequation proposed by Veletsos and Meek (1974) (Equation 2):

$$T_{SSI} = T\sqrt{1+\bar{k}/K_y\left(1+\bar{k}\cdot\bar{h}^2/K_r\right)} \qquad (2)$$

where T is the fixed base period, Ky and Kr the spring stiffness values to lateral and rocking motions calculated, $\bar{k}$ and $\bar{h}$ the stiffness and effective height of the fixed base structure. Concerning the numerical calculation, the results of harmonic analyses are employed. The response period of the structure in each soil – structure combination is identified, using the Fourier transform of the corresponding response time – histories at free field conditions and at the top of the structure. Indeed the top-to-free field ratio of the response histories depicted in the frequency domain (transfer function), can be utilized for the determination of the resonance period at the point of maximum motion amplification.

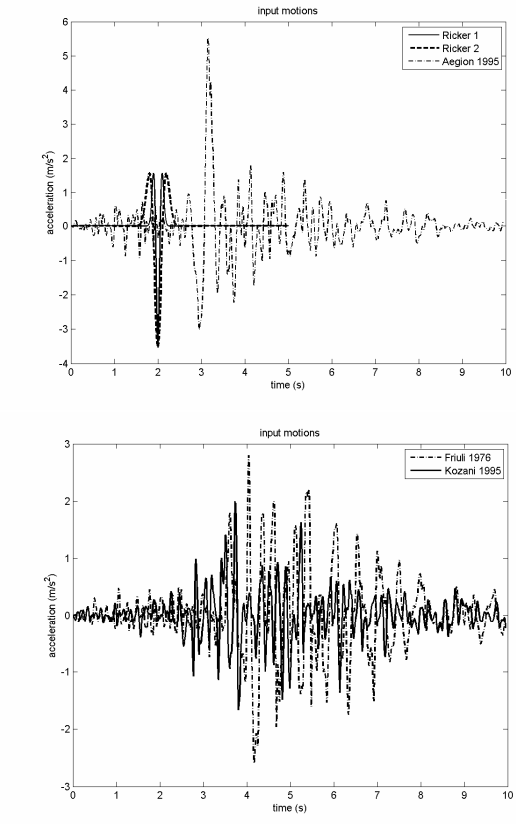

Figure 8 Earthquake input motions

The T_{SSI} values in the following paragraphs result from the numerical analyses. Numerical and analytical values of T_{SSI} are quite close (Figure 10 and Figure 11). Numerical analyses give in general slightly greater values. The differences are greater in case of strong earthquake input motions, very soft soil profiles and more flexible structures (Figure 11).

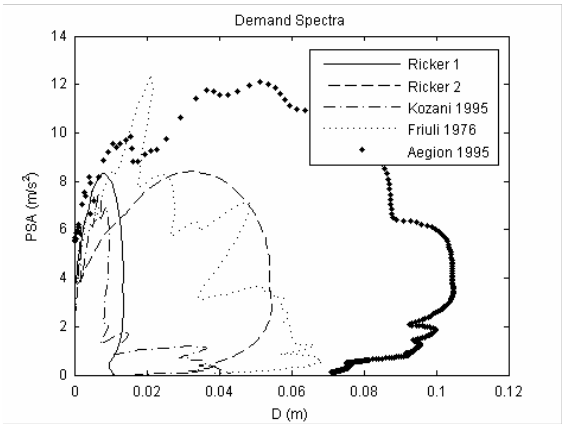

Figure 9 Demand Spectra (free field conditions) of the five selected earthquake input motions spectra curves

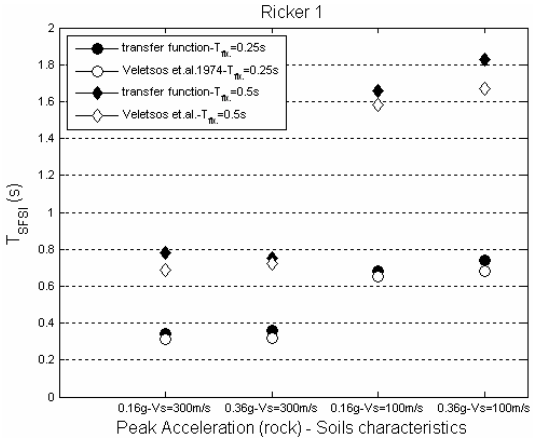

Figure 10 Comparison of structural effective period between theoretical and numerical calculation for Ricker 1 wavelet and for two structures with different dynamic characteristics $T_{fix.1}$=0.25s & $T_{fix.2}$=0.5s

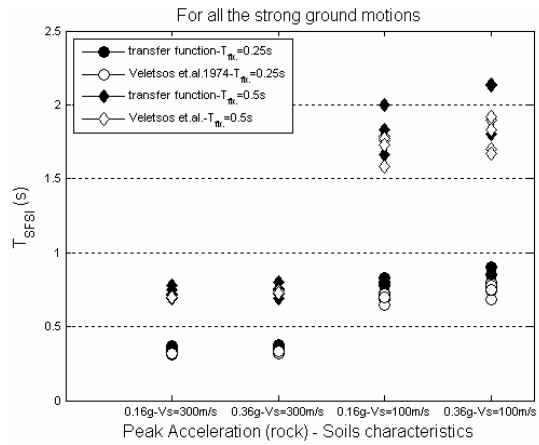

Figure 11 Comparison of structural effective period between theoretical and numerical calculation for all five input motions and for two structures with different dynamic characteristics $T_{fix.1}$=0.25s & $T_{fix.2}$=0.5s

It's worthy to note here that Figures 10 and 11 concern structures with a lumped mass of 180t. This

great lumped mass justifies the high values of effective structural period (up to 2.15s for strong input motion and very soft soil profiles figure 11). Taking for example a structure of 5m height, a lumped mass of 180t and period in fixed base conditions of 0.25s laying on a very soft soil profile (Vs=75m/s), the values for T_{SSI} are $0.68s<T_{SSI}<0.83s$ according to harmonic analyses, compared to $0.65s<T_{SSI}<0.73s$ according to equation 2, and $T_{SSI}\approx0.83s$ according to Wolf (1985). Kirtas et al. (2007), for a structure of $T_{fix.}= 0.2s$ laying on a very soft soil profile with a lumped mass of $\bar{m}=2$ ($\bar{m}=m_{str}/\rho B^3=2m_{pl.str}/\rho B^2$), gives $0.488s<T_{SSI}<0.622s$. Its worthy to note here that $m_{str.}=180t$ corresponds to $\bar{m}=8$.

3.1.5 Effect of V_s on seismic Demand

The sensitivity of structural response is investigated through a detailed parametric analysis. The first parameter under investigation is the soil's shear wave velocity.

Firstly, the soil is subjected to the Friuli 1976, earthquake record with 0.16g maximum acceleration on rock. The small – strain shear wave velocity of soil is $V_{So}=100m/sec$, but because the soil behaves in the inelastic range, the actual value is decrease to 75m/sec for the first 30m and 71m/sec for the next 30m of the soil profile. These two values resulted from a 1D seismic ground response analysis. From the ground accelerogram of the time history analysis results the demand spectrum of Figure 12. The peaks of the graph (points 1-6) correspond with the periods of soil. The maximum values of the graph in terms of accelerations and displacements relate to the frequency domain of the input motion.

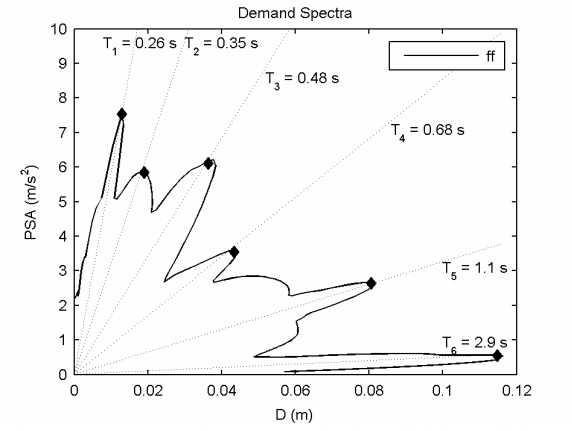

Figure 12 Demand spectrum for free field conditions for Friuli 1976, earthquake input motion, Vs=75m/sec and lines radiating from the origin and represent soils response periods

Vs= 100m/s

Secondly, the full soil – foundation – structure system is subjected to the same ground motion. The dynamic soil characteristics remain the same. The structure is 5m high and its period for fixed base conditions is $T_{fix.}=0.25s$. The superstructure mass is 180t. The SFSI effects are controlled through the soil – to - structure stiffness ratio index $\sigma=V_{So}T_{fix.}/h_{str.}$. In Figure 13, points 1 and 2 refer to the elastic structural response according to the traditional and the actual approach, respectively. Due to SFS interaction, the structural effective period increases by 220%, the spectral response values reduce by 64% in terms of accelerations and increase by 72% in terms of displacements.

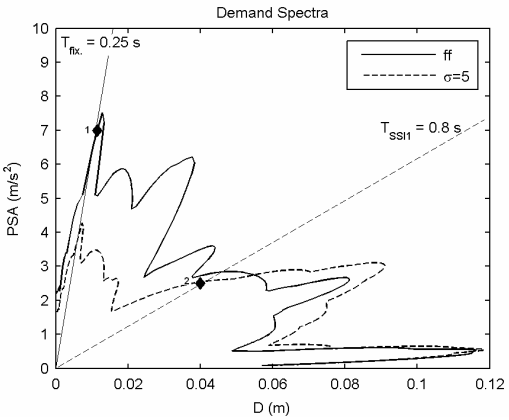

Figure 13 Demand Spectra for Friuli 1976, Italy earthquake as input motion, shear wave velocity of Vs=75m/sec, for a 5m high structure and structural mass of 180t, structural period in fixed - base conditions of $T_{fix.}=0.25s$ ff: free field conditions $\sigma=5$: soil – structure – interaction system

V_{So}=300m/s

All the input data remain the same. That is Friuli 1979 earthquake, $h_{str.}=5m$, $T_{fix.}=0.25s$. The only parameter that changes is the soil shear wave velocity which is estimated equal to 250m/sec for the first 30m of the soils profile and 223m/sec for the next 30m. Not only the shape, but the spectral values change also substantially (Figure 14 against Figure 13). The role of site effects emerges to be significant to the structural response. The spectral acceleration's reduction is 7% in comparison with free field - fixed base conditions.

The comparison between Figure 13 and Figure 14 leads to the conclusion that for soft soils (Figure 13) the SFSI phenomena are much more severe, as it was expected.

3.1.6 Effect of m_{str} on seismic Demand

0.16g peak acceleration on rock

The soil – foundation – structure system is then subjected to the Ricker 1 wavelet with 0.16g maximum acceleration. The small – strain shear wave velocity of soil is 100m/sec, but because of the inelastic behavior of soil the values are now become 86m/sec for the first

30m and 83m/sec for the next 30m of the soil profile. Figure 15 concerns the above-mentioned soil and strong motion's characteristics and three different structures. The first one is assumed to de fixed on its base and the response of the structure is described by point 1. The second one, with a lumped structural mass of 22.5t, has $T_{fix.}$=0.25s but because of the SFSI effects the normal period of structure increases to 0.35s. The third structure has a lumped structural mass of 180t. The reduction of the spectral accelerations in comparison with the response that results assuming the traditional approach is 40% for the small structural mass (point 1 against point 2) and 85% for greater one (point 1 against point 3). The effect of structural mass on seismic structural response seems to be important.

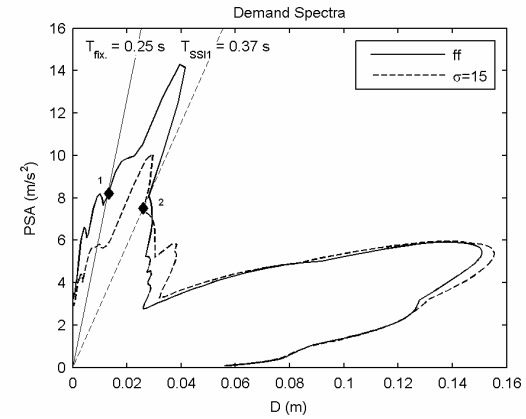

Figure 14 Demand Spectra for Friuli 1976, input motion, Vs=250m/sec, H= 5m and structural mass of 180t, Structural period in fixed - base conditions of $T_{fix.}$=0.25s.ff: free field conditions. σ=15: soil – structure – interaction system

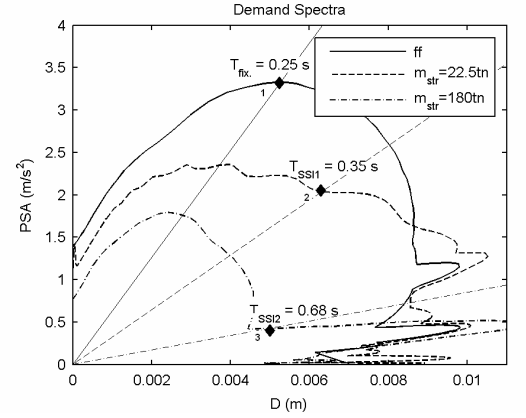

Figure 15 Demand Spectra for Ricker 1_PGA=0.16g as input motion, Vs=83m/sec, H= 5m , structural period in fixed - base conditions of $T_{fix.}$=0.25s and a structural lumped mass of 22.5t and 180t.

0.36g peak acceleration on rock

Keeping all the above parameters the same and changing the intensity of the input motion and the corresponding shear wave velocity, due to the greater inelastic soils behavior, Figure 16 presents the results of the analysis. The small – strain shear velocity of soil is now 81m/sec for the first 30m and 74m/sec for the next 30m of the soil profile As it can be seen the reduction in terms of spectral accelerations - displacements is almost the same with that results from Figure 15. However, the spectral values are greater, something that is expected due to the intensity of the input motion.

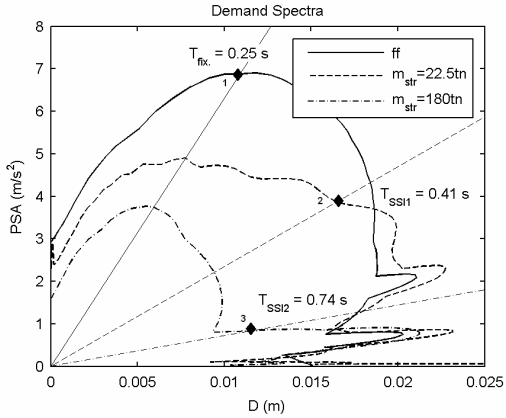

Figure 16 Demand Spectra for Ricker 1_PGA= 0.36g wavelet , Vs=81m/sec, H=,5m, structural period in fixed base conditions of $T_{fix.}$=0.25s and structural mass of 22.5tn and 180t.

3.1.7 Effect of k_{str} on seismic Demand

The soil – foundation – structure system is subjected to the Ricker 2_0.16g pulse. The soil has now an equivalent shear wave velocity of 76m/s for the first 30m and 72m/sec for the next 30m of the investigated soil profile. The two examined structures have in case of fixed base conditions $T_{fix.1}$=0.25s and $T_{fix.2}$=0.5s, respectively (Figure 17).

The performance points are points 1 and 2 for the stiff and flexible structure respectively. Taking into account the SFSI effects the performance points are 1' and 2'. T_{SSI} is the same for the two structures. The structure of fixed base period equal to 0.25s approaches an effective SSI period value of 0.8s, whereas the structure with fixed base period equal to 0.5s approaches the effective period value of 0.8s also. Natural period modification due to soil structure interaction is more pronounced in the case of the stiffer structure (220%), while on the other hand, maximum effective period alteration is reduced for the more flexible structure (60%). At first sight, the interaction effects seem to be more significant for the rigid structure. However, as far as the impact of interaction on structural response for the specific input motion is concerned, the spectral reduction of the acceleration values comparing with the traditional approach is more significant for the more flexible structure (70%_point 2

against point 2'). This can be explained through the frequency domain of input motion (T_p=0.5s).

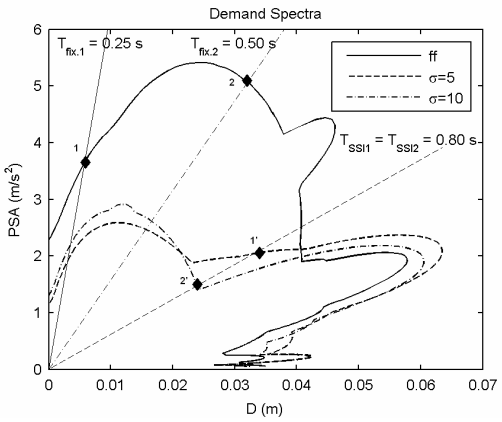

Figure 17 Demand Spectra for Ricker 2_0.16g wavelet as input motion, Vs=76m/sec, H=5m , structural periods in fixed base conditions of Tfix.1=0.25s and Tfix.2=0.5s, and structural mass of 180t.

3.1.8 Effect of h_{str} on seismic Demand

In order to examine the effect of structural height on seismic demand, Friuli_0.16g, Italy earthquake is used as input motion to a soil profile with V_{So}=100m/s. The analyses that were carried out are the following:

1. Analysis for the soil profile only. For two structures of $T_{fix.1}$= $T_{fix.2}$ =0.50s, the performance points and thus the response of the structures (traditionally) concerns point 1=2 (PSA=6m/s^2, D=0.038m).

2. Analysis for the whole system (including structure), where $h_{str.}$=5m, T_{SSI1}=0.54s (Figure 18). In this case the performance point is point 1'(PSA=3m/s^2, D=0.023m). This means that interaction leads to a decrease on response 50% and 40% in terms of accelerations and displacements respectively. It is worthy to note here that traditionally it is believed that the structural accelerations, and thus the forces that the system is subjected, decrease due to the interaction. On the other hand, the structural displacements increase. This is opposed to the abovementioned conclusion.

3. Analysis for the whole system like analysis 2, but now the structural height is $h_{str.}$=10m, and T_{SSI2}=0.79s. In this case the performance point is point 2' (PSA=2.8m/s^2, D=0.043m). This means that interaction leads to a decrease on response (comparing to analysis 1) of 53% in terms of accelerations and increase of 13% in terms of displacements.

To sum up, two structures with variable height but with the same stiffness (different section), traditionally are designed for the same loads. From the above analysis the conclusion is that this is not accurate, because interaction may reduce and sometimes increase the design loads. For the specific case examined herein the structural normal period increases 8% and 37% for the short and high structure, respectively. This means that interaction affects mainly the higher structure. However, because of the demand spectrum shape, which depends on the frequency content of the input motion and the dynamic soil characteristics, it seems that the interaction is in favor of the small structure, decreasing not only the accelerations but the displacements as well. On the contrary, the high structure will have larger displacement of that expected from the traditional approach (point 1-2).

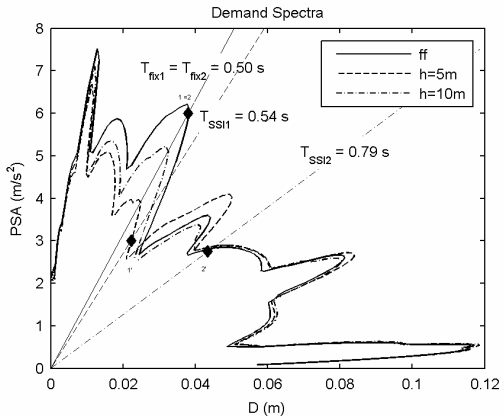

Figure 18 Demand Spectra for Friuli_0.16g, Italy earthquake as input motion, V_{So}=100m/sec, H=5m and 10m high, structural period in fixed conditions of $T_{fix.1}$=0.5s and structural mass of 180t.

3.1.9 Effect of input motion intensity

In case of free field conditions, for a very soft soil (Vs=76m/s for the top 30m and Vs=70m/s for the next 30m), the demand spectra that result when triggering the system with the Aegion 1995_0.16g and _0.36g earthquake are illustrated in Figure 19. It's worthy to notice that the shape of the demand spectrum remains unchanged while the spectral values, are actually much greater. As the soil responses further into the inelastic range for the 0.36g (peak acceleration on the rock) , the peak values are displaced at higher periods.

On the soil profile that has been described above, lays now a structure with $T_{fix.}$ =0.25s (Figure 20). This system is triggered with the Aegion_0.16g 1995 earthquake and afterwards with Aegion_0.36g 1995 earthquake. The modification for the normal period is greater for the stronger ground motion. (T_{SFSI}=0.85s). The reduction (spectral accelerations) compared with the traditional approach is 17.8% (from point 1 to 1') for the earthquake with peak acceleration 0.16g and 30% (from point 2 to 2') for the stronger earthquake input motion.

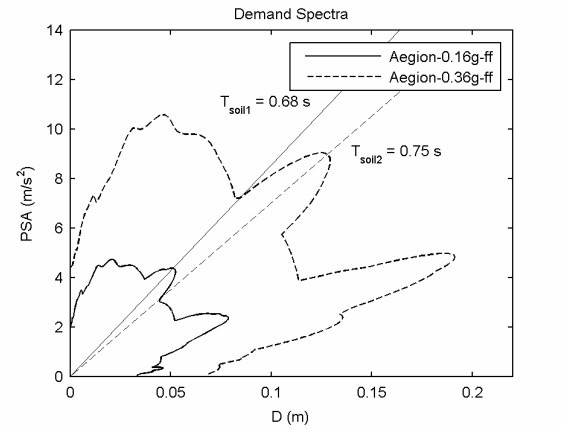

Figure 19 Demand Spectra for ff conditions for Aegion 1995_0.16g and Aegion 1995_0.36g, Greece earthquake, and equivalent VSo=76m/sec

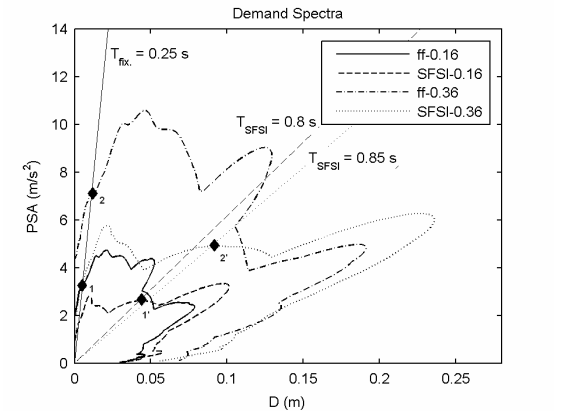

Figure 20 Demand Spectra for Aegion_0.16g and Aegion 0.36g, input motions, Vs=76m/sec, H=5m , structural period in fixed conditions of $T_{fix.}$=0.25s and a structural lumped mass of 180t.

3.2. Seismic capacity

Until now all conclusions concern the elastic response of structures. Although elastic analysis is a useful tool for estimating the dynamic structural response, it can not evaluate the structural behavior in the inelastic range and the identification of the locations of structural weaknesses. Over the last decades (Fajfar and Krawinkler, 1997), it has been recognized that damage control must become a more explicit design consideration. The way this aim can be achieved is by introducing some kind of non linear analysis into the seismic design methodology.

3.2.1 Pushover analysis – Input data

In pushover analysis the response of the structure is controlled by its fundamental mode. When the structure is fixed on its base this is accurate, because the examined structure is an SDOF system. On the other hand, when the whole system is examined, the fundamental mode concerns the first mode of the whole system, which is no longer a single degree of freedom system. For this reason pushover analysis for the whole system (soil-foundation-superstructure). is controlled by a horizontal load at the top of the structure, which scales up until the collapse of the structure. To perform the non linear analysis the constitutive law was determined according to FEMA 356 (Figure 21).

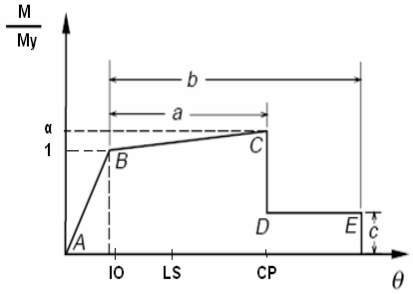

Figure 21 Constitutive law (FEMA 356)

For the inelastic pushover analyses the data of the soil profiles and the structures, remain the same with the time history analyses. Each structure was designed according to the Greek Seismic Code (E.A.K.2000) for Seismic Zones II (PGA=0.16g) & III (PGA=0.36g), using the design Spectrum. The force reduction factor corresponding to the assessed ductility capacity of the structural system and material is assumed 1 (q=1). For each structure two analyses are carried out. One for the fixed - base model and one for the whole soil – structure – interaction system.

It's worthy to note here that the structures are designed for q=1. This means that they are expected to behave elastically during the design earthquake. The earthquakes that trigger the model have maximum acceleration of 0.16g and 0.36g on the rock.

Figure 22 depicts the PGA for the five examined input motions that result from the 1D analyses The peak ground acceleration at stiffer soil profiles, (V_{So}=300m/s), is expected greater than peak acceleration on rock (Figure 22). On the other hand, at very soft soil profiles, because soil responds into the inelastic range, it is expected a decrease in PGA in comparison with the maximum acceleration on the rock (Figure 22). Consequently, the inelastic response of structures is pronounced in cases of high ground amplification.

3.2.2. Capacity curves

We assume the case of a soil profile of V_{So}=300m/s with a Vs value appropriately adjusted to consider the non-linear soil behavior, and a structure H= 5m high, with a fixed base period T= 0.25s and 180t structural mass. The system is triggered by Friuli 1976,

earthquake with 0.36g peak acceleration on the rock.. After the pushover analysis the base shear forces and the roof displacements are converted to equivalent spectral accelerations and spectral displacements, respectively. These spectral values define the capacity spectrum. For the above mentioned characteristics, the capacity curves when taking into account the interaction (SFSI) or not (fixed –base), are depicted in Figure 23. The whole system becomes more flexible because of the interaction and the soil compliance.

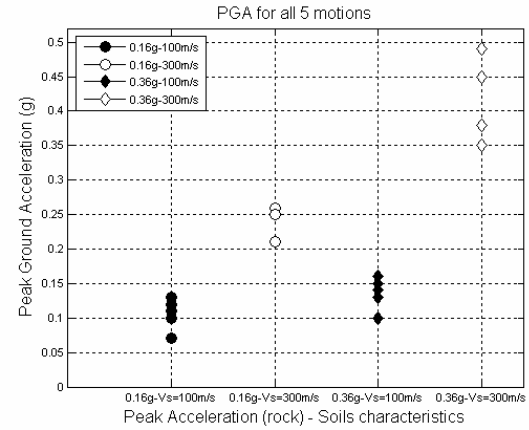

Figure 22 Free field PGA values for all five input motions from the 1D equivalent linear response analyses

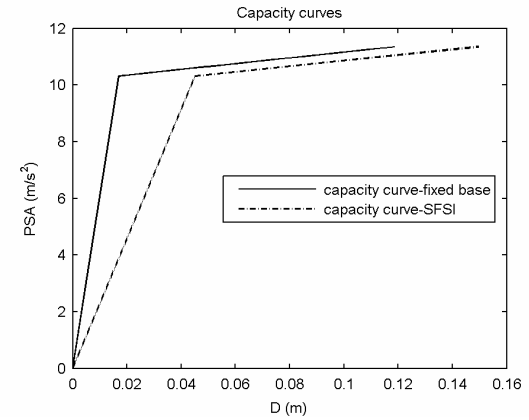

Figure 23 Capacity curves with and without SFS interaction. V_{So}=300m/s, $h_{str.}$=5m, $m_{str.}$=180t, $T_{fix.}$=0.25s, Friuli 1976_0.36g

3.2.3. Modified demand spectrum

The modified demand spectrum due to the SFSI effects is defined with the following steps:

1. The structural normal period is $T_{fix.}$=0.25s, for fixed base conditions. The effective period is expected to be between 0.25s and 0.8s.For this reason a series of 10 analyses take place with a variety of structural periods ($T_{fix.1}$=0.1s, $T_{fix.2}$=0.15s,…,$T_{fix.10}$=0.7s).

2. Evaluate T_{SSI} values (T_{SSI1}=0.27s, T_{SSI2}=0.28s,.., T_{SSI10}=0.75s).

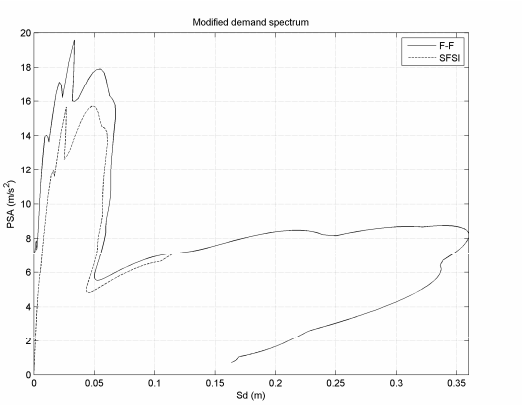

Figure 24 Demand curves with and without interaction for a soil profile of V_{So}=300m/s, $h_{str.}$=5m, $m_{str.}$=180t, Friuli 1976_0.36g, Italy Earthquake.

3. Estimate the average modified demand spectra curve for every T_{SSI}

Figure 24 depicts the modified demand spectra curve compared with the initial one under free-field conditions.

3.2.4. Equivalent viscous damping

When a structure responds inelastically for a given earthquake excitation, there is a need to estimate the level of equivalent viscous damping. The demand curve does not concern the elastic damping ratio anymore ($\xi_{el.}$=5%).

The relationships between hysteric damping and ductility, were obtained by Dwairi (2004), are shown in Figure 25 and given by Equation 3 for Takeda's hysteretic model.

$$\xi_{eq} = \xi_{el} + \frac{50}{\pi} \cdot \left(\frac{\mu - 1}{\mu}\right)\% \qquad (3)$$

where μ is the displacement ductility ($\mu = D_{max}/D_y$) and $\frac{50}{\pi} \cdot \left(\frac{\mu - 1}{\mu}\right)\%$ is the hysteric damping depends on the hysteresis rule appropriate for the structure being designed. D_{max} is the maximum inelastic displacement of the structure and D_y is the yield structural displacement (the values are taken from the pushover curve). Once ξ_{eq} is calculated then the new demand curve is calculated for this damping ratio.

3.2.5. Structural response according to performance based design.

V_{So}=300m/s

Considering all the above, Figures 26 and 27 illustrate the differences of the two approaches in the case of the example used in this paper. Figure 26 concerns the traditional design approach and Figure 27 when SFSI effects are taken into consideration.

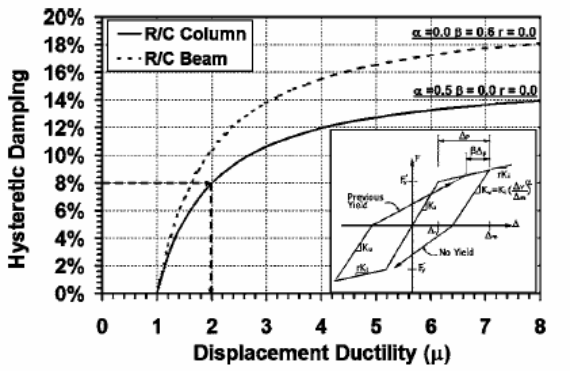

Figure 25 Hysteretic damping relationship for Takeda's hysteretic model (Dwairi et. al., 2006)

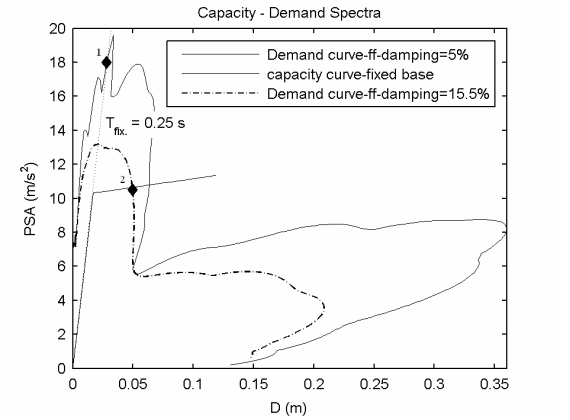

Figure 26 Capacity Spectrum method for free field – fixed base conditions. Soils characteristics: V_{So}=300m/s. Structural characteristics: h=5m, $T_{fix.}$=0.25s, $m_{str.}$=180t. Friuli 1976_0.36g, Italy Earthquake

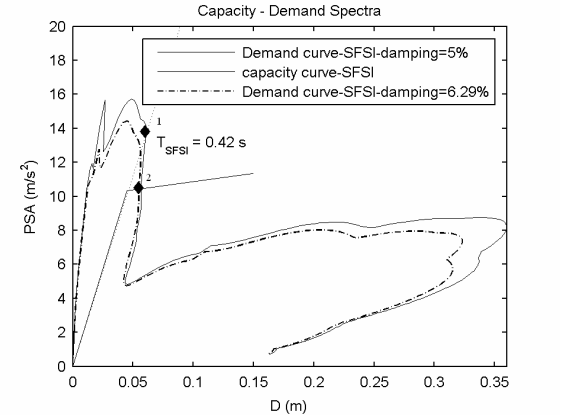

Figure 27 Capacity Spectrum method taking into account SFS interaction effects. Soils characteristics: V_{So}=300m/s. Structural characteristics: h=5m, $T_{fix.}$=0.25s, $m_{str.}$=180t. Friuli 1976_0.36g, Italy Earthquake

In Figure 26 the demand spectra curves are computed for 5% and 15.5% damping ratio, (free field conditions), and the capacity curve is estimated for a structure fixed on its base. In Figure 27 both demand (5% and 6.29%) and capacity curves, concern the whole soil – structure – interaction system. In both figures, point 1 concerns elastic structural response, while point 2 a structure that behaves in the inelastic range.

When taking into account the inelastic structural behavior the spectral acceleration values decrease by 42% (traditional approach) and 25% (SFSI model). In terms of displacements we observe a 50% increase and 4% decrease, for the traditional approach and the whole SFSI system, respectively.

The final response (point 2) for the two approaches has a slight change, in this case. The differences may be more important depending on the parameters of the examined model.

V_{So}=100m/s

Changing now the soils properties and keeping all the other parameters the same, the results are depicted in Figures 28, 29 and 30. It is obvious that the interaction affect more (comparing with the stiffer soil), not only the capacity but the demand curve also.

The final response when taking into account the structural inelastic behavior, is PSA=9m/s^2 D= 0.015m (point 2_Figure 29) for the traditional approach, while the real response (with SFSI effects) is PSA=3.2m/s^2 and D=0.1m. The acceleration is in this case decreased by 64% while the displacements are increased by 57%.

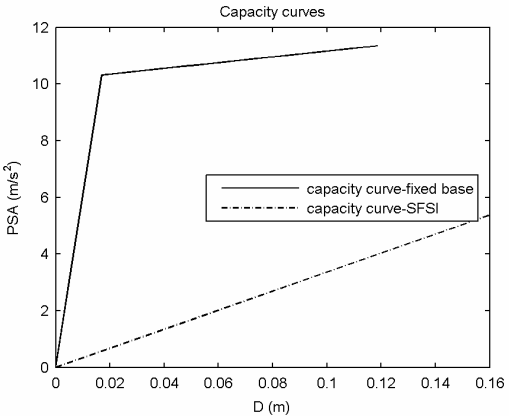

Figure 28 Capacity curves with and without interaction for a soil profile of V_{So}=100m/s, $h_{str.}$=5m, $m_{str.}$=180t, $T_{fix.}$=0.25s, Friuli 1976_0.36g

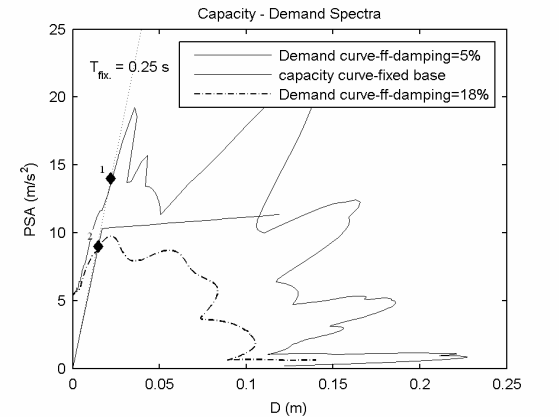

Figure 29 Capacity Spectrum method for free field – fixed base conditions. Soils characteristics: V_{So}=100m/s. Structural characteristics: h=5m, $T_{fix.}$=0.25s, $m_{str.}$=180t. Friuli 1976_0.36g, Italy Earthquake

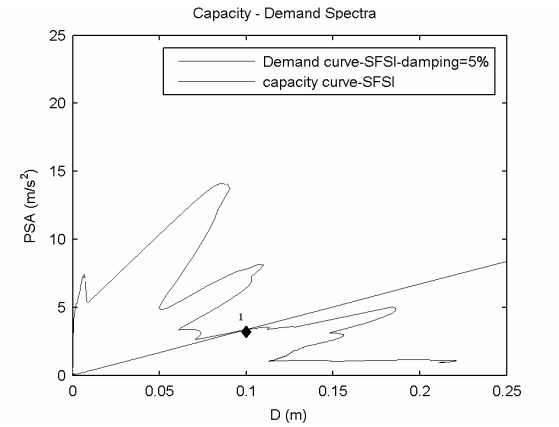

Figure 30 Capacity Spectrum method taking into account interaction effects. Soils characteristics: V_{So}=100m/s. Structural characteristics: h=5m, $T_{fix.}$=0.25s, $m_{str.}$=180t. Friuli 1976_0.36g, Italy Earthquake

4. DEMAND SPECTRA IN CASE OF SOIL IMPROVEMENT

The demand spectra and the behavior of a simple SFS system founded on a soft cohesive soil (soil C according to EC8) are examined next, in case of foundation soil improvement.

Figure 31 shows the effect of soil replacement with Rubber - Soil Mixtures (RSM) for the seismic input of the Athens, Greece 1999 earthquake. They were computed using a coupled soil-structure FEM model under plane strain conditions, in the frequency domain. The shear modulus of the soil layers were reduced from their initial values according the last iteration of equivalent of linear 1D analysis. The damping ratio was set up accordingly for each layer. The dynamic soil properties of the RMS mixtures were deduced from specific resonant column tests (Anastasiadis, 2009, Senetakis et al., 2009).

Four characteristic dynamic analyses are considered: two with the initial or replaced soil without the SDOF structure, and two with the structure. In particular: (i) the computed initial free-field demand spectra, (ii) the same soil replaced in a depth of 5m and 15m by RSM (noted as "5% and "15% RSM" according to the weight ratio of the mixture), (iii) the SDOF on the original soil ("SDOF initial") and (iv) the SDOF on the replaced soil ("SDOF, RSM"). It is observed that in the case of s soft soil profile (type C), the appropriate use of a well-selected RSM replacement, (RSM5 instead of RSM15), may produce significant beneficial effects in the coupled system seismic demand, in almost all frequencies of interest. Similar analysis performed for a stiff soil B, (which is not presented here), proved that the RSM replacement leads to a considerable increase of the seismic demand especially in high frequencies. The softer the replacement material (RSM15) the greater the seismic demand. However the increase was lower when SFSI effects are considered compared to the initial soil.

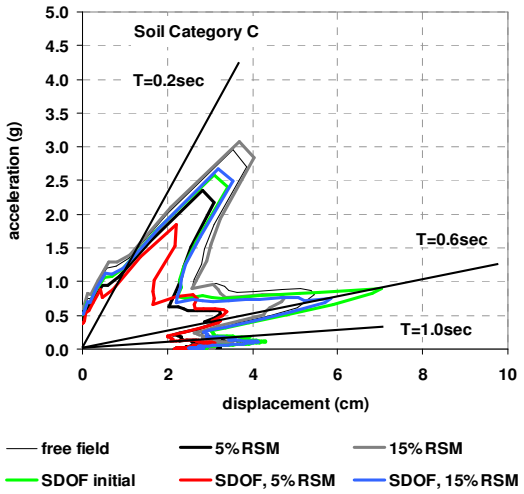

Figure 31 Effect of foundation soil replacement with RSM on the demand spectra calculated at the foundation level of a SDOF system (Senetakis et al., 2009)

5. CONCLUSIONS

A comparison is presented between recorded demand spectra for different seismic intensities and soil-site conditions, and design spectra proposed in codes. Moreover the effects of SFSI on the earthquake response of structures in the framework of the performance based design are investigated. A short discussion is also made for the potential difference that we may have in the demand spectra in the case of soil

improvement. From trends of results of the present study following conclusions may be drawn.

1. Further research is required in order to enrich the available data with digital recordings from well-documented sites, focusing in the contribution of near field conditions, as well as source and path effects, to the design displacement and the respective demand spectra.
2. The effect of the soil improvement on the demand spectra is also demonstrated for the case of the ground replacement with compacted rubber and sand mixtures. The elastic demand spectra under these conditions may differ considerably from the demand spectra of the initial soil. It is shown that the appropriate use of a well selected RSM replacement may result into significant beneficial effects in the coupled system seismic demand in almost all frequencies of interest.
3. The shape of demand spectra and thus the structural response depends on the local geology at the examined site and the frequency domain of earthquake input motion. Generally, the design response spectra, such as those in building codes are smooth in shape. However response that results from actual earthquake input motions are irregular and have spikes at the predominant soils periods. For this reason, it is only a generalization the assumption that SFSI effects are in favor of the structure, reducing accelerations and thus the seismic loads that structures should resist during an earthquake. Taking for example a structure with a lumped mass of 45t, a height of 5m and fundamental period, in fixed – base conditions, of 0.25s, laying on a soil profile with small - strain shear velocity (Vs=100m/s), the modified demand spectra are shown in Figure 32. For the specific structure without interaction the response point is described by point 1, while when taking into account interaction effects the structural response point is point 2. This means that the specific structure, laying on the specific soil profile will receive during the specific earthquake 162% higher forces than the forces that were used during the design of the structure.
4. The effects of the SFSI in the framework of performance based design are severe for (a) stiff structures laying on soft soil profiles, (b) structures with .large lumped mass, 9c) intense earthquake input motions and 9d) for high structures, and thus structures with great slenderness.

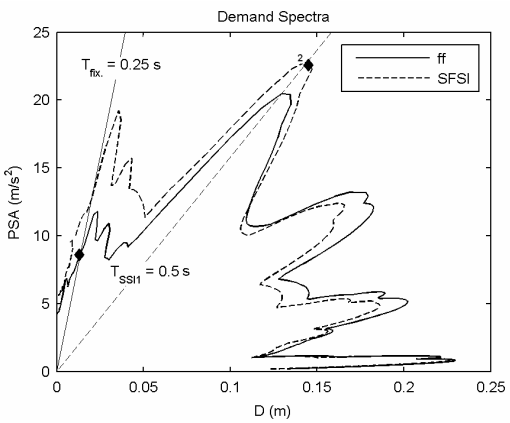

Figure 32 Demand spectra for Friuli 1976_0.36g Vs=100m/sec, for a structure of 5m high, structural period in fixed base conditions of $T_{fix.}$=0.25s, and structural mass of 45t.

5. Intense earthquake input motions, cause modification of soils proprieties during shaking. Thereby, the more intense the input motion is, the higher the soils response periods are. This happens because for strong input motions soil behaves further in the inelastic range.
6. The final decision in what cases the soil – foundation – structure interaction effects should be taken into account during the seismic design of structure depends on the structural – soil – earthquake characteristics.
7. When it is assumed during the analysis that the structure will respond in the inelastic range, the differences from the traditionally use approach may be even more pronounced.. In this case the design values in terms of accelerations are usually lower than the assuming values for elastic structural response, (not always), but it is of great importance to have ensured, that the system has the essential available ductility at the critical locations of potential plastic hinging in order to avoid the total collapse of structure.

5. REFERENCES

Anastasiadis, A., Pitilakis, K. and Senetakis, K. (2009), "Dynamic shear modulus and damping ratio curves of sand/rubber mixtures," *Proceedings of the XVII ICSMGE Satellite Conference on Earthquake Geotechnical Engineering. Alexandria, Egypt.*

Aviles, J., Pérez-Rocha Luis, E., (2003), "Soil–structure interaction in yielding systems", *Earthquake Engineering and Structural Dynamics 2003*;32:1749–71

Avilés, J., Pérez-Rocha Luis, E., (2004), "Design concepts for yielding structures on flexible foundation", *Engineering Structures 2005*, 27: 443–454.

Aviles J., Suarez, M., (2001), "Effective periods and

dampings of building-foundation systems including seismic wave effects'', *Engineering Structures 2002;*24:553–62.

Chopra, AK. and Gutierrez, JA. (1974) ''Earthquake response analysis of multistory building including foundation interaction,'' *Earthquake Engineering and Structural Dynamics*; 3:65–77.

Dwairi, H., (2004), ''Equivalent Damping in Support of Direct Displacement Based Design with applications to Multi – Spam Bridges'', *P.H.D. dissertation, North Carolina, State University,* Raleigh, NC.

Dwairi, H. and Kowalsky, M., (2006), ''Implementation of inelastic displacement patterns in Direct Displacement-Based Design of continuous bridge structures'', *Earthquake Engineering Research Institute*, *Earthquake Spectra 2006*, Volume 22, No. 3, pages 631–662

Fajfar P., (2000), ''A nonlinear analysis method for performance based seismic design'', *Earthquake Spectra 2006*, Volume 22, No. 3, pages 631–662

Fajfar, P. and Krawinkler, H., (1997), ''Seismic Design Methodologies for the next Generation of Codes'', *Balkema, Rotterdam.*

Freeman, Sigmund, A., (1998), ''The Capacity Spectrum Method as a tool for seismic design'', *Proceedings of the Eleventh European Conference on Earthquake Engineering*, Paris, France

Kirtas, E., Trevlopoulos, K. , Rovithis, E., Pitilakis, K. (2007) "Fundamental Period of SDOF systems Including Soil-Structure Interaction and Soil Improvement", *Proceedings of the 2nd Japan – Greece Workshop on Seismic Design, Observation and Retrofit of Foundations,* Athens, Greece.

Lin, Y. and Miranda, E., ''Kinematic soil-structure interaction effects on maximum inelastic displacement demands of SDOF systems'', (2007), *Bulletin of Earthquake Engineering, Earth and Environmental Science*, p: 241-259.

Miranda, E, Bertero, V., (1994), ''Evaluation of strength reduction factors for earthquake resistant design. Earthquake'', *Spectra 1994*, 10(2):357–379.

Miranda, E., (2001), "Estimation of inelastic deformation demands of SDOF systems", *Journal of Structural. Engineering,* 127(9), 1005–1012.

Pitilakis, D, (2009), ''Nonlinear soil–foundation–structure interaction aiming in performance based design''. *Proceedings of the International Conference on Performance-Based Design in Earthquake Geotechnical Engineering*, Tokyo, Japan, pp.635-642

Pitilakis, K., Gazepis, C. and Anastasiadis, A., (2004), ''Design response spectra and soil classification for seismic code provisions'', *13th World Conference on Earthquake Engineering, Proc., Vancouver, 1-6 August 2004. Paper No. 2904.*

Priestley, M.J.N., Calvi, G.M., Kowalsky, M.J., (2007), ''Displacement – Based seismic design of structures''

Senetakis, K., Anastasiadis, A., Trevlopoulos, K., Pitilakis, K., (2009), ''Dynamic Response Of SDOF Systems On Soil Replaced With Sand/Rubber Mixture". *COMPDYN 2009 ECC0MAS Thematic Conference on Computational Methods in Structural Dynamics and Earthquake Engineering*, Papadrakakis M, Lagaros N D, Fragiadakis M (eds.), June 22-24, Rhodes, Greece.

Wolf, J. P., (1985)., ''Dynamic soil – structure interaction'', Prentice Hall, Englewood Cliffs, NJ.

Veletsos, A. S. and Meek, J. W., (1974), ''Dynamic Behaviour of Building-Foundation System'', *Earthquake Engineering and Structural Dynamics,* Vol. 3, No. 2, pp. 121-138.

Veletsos, AS., (1997), ''Dynamic of structure-foundation systems'', In: Hal WJ, *editor. Structural and Geotechnical Mechanics,* Englewood Cliffs (NJ): Prentice-Hall; p. 333–61. A Volume Honoring N.M. Newmark.

Zhang, J., Andrus, R. D. and Juang, C., Hsein, (2005), ''Normalized shear modulus and material damping ratio relationships'', *Journal of Geotechnical and Geoenvironmental Engineering*, ASCE, p:453-464.

JOINT CONFERENCE PROCEEDINGS
7th International Conference on Urban Earthquake Engineering (7CUEE) &
5th International Conference on Earthquake Engineering (5ICEE)
March 3-5, 2010, Tokyo Institute of Technology, Tokyo, Japan

SELF-CENTERING DAMAGE-FREE SEISMIC-RESISTANT STEEL FRAME SYSTEMS

Richard Sause[1], James M. Ricles[2], Ying-Cheng Lin[3], Choung-Yeol Seo[4], David Roke[3], and Brent Chancellor[3]

1) Joseph T. Stuart Professor of Structural Engineering, ATLSS Center, Dept. of Civil and Env. Engineering, Lehigh University, USA
2) Bruce G. Johnston Professor of Structural Engineering, ATLSS Center, Dept. of Civil and Env. Engineering, Lehigh University, USA
3) Graduate Research Assistant, ATLSS Center, Dept. of Civil and Env. Engineering, Lehigh University, USA
4) Post-Doctoral Research Associate, ATLSS Center, Lehigh University, USA
rsause@lehigh.edu, jricles@lehigh.edu, ycl206@lehigh.edu, cys4@lehigh.edu, dar305@lehigh.edu, nbc208@lehigh.edu

Abstract: Innovative self-centering (SC) moment resisting frames (SC-MRFs) and concentrically-braced frames (SC-CBFs) are being developed. In the SC-MRF, the beams are post-tensioned to the columns using high strength post-tensioning (PT) strands. A beam web friction device (WFD) is included in each beam-column connection to dissipate energy under seismic loading. The connection behavior is characterized by gap opening and closing at the beam-column interface. In the SC-CBF, the columns at the base are designed to decompress and uplift at a selected level of lateral loading, initiating a rigid-body rotation (rocking) of the frame. Vertically-aligned post-tensioning (PT) bars resist this uplift and provides a restoring force to return the SC-CBF to its support (to re-center the system). The SC-MRFs and SC-CBFs in this study are designed to meet two primary seismic performance objectives, namely, (1) no damage or residual drift under the Design Basis Earthquake (DBE), leading to immediate occupancy performance after the DBE, and (2) collapse prevention performance under the Maximum Considered Earthquake. A 4-story SC-MRF prototype building and a 4-story SC-CBF prototype building were designed for a stiff soil site in the Los Angeles area using performance-based design procedures with the above performance objectives. A 0.6-scale model of the SC-MRF and a 0.6-scale model of the SC-CBF were developed and tested at Lehigh University using the hybrid simulation method. Experimental results from these earthquake simulations are used to assess the design procedures.

1. INTRODUCTION

Conventional moment resisting frames (MRFs) soften and dissipate energy under the design basis earthquake by developing yielding and associated damage in critical regions of the main structural members. This damage can result in significant damage and residual drift after the earthquake. To avoid this damage and residual drift, post-tensioned (PT) beam-column connections for the self-centering moment-resisting frame (SC-MRF) system were developed by Ricles et al. (2001, 2002) and others. The behavior of these connections is characterized by gap opening and closing at the beam-column interface. Energy dissipation occurs in special devices designed for the beam-column connection regions. Together, the PT strands and the energy dissipation devices provide the flexural resistance of the connections.

Conventional steel concentrically-braced frame (CBF) systems are stiff and economical earthquake-resistant steel frame systems, which often exhibit limited system ductility capacity. The ductility capacity can be increased using buckling-restrained braces (e.g., Fahnestock et al. 2003); however, the buckling-restrained braced frame (BRBF) system sometimes exhibits significant residual drift after an earthquake. To increase the ductility and reduce the residual drift of CBFs, the self-centering concentrically-braced frame (SC-CBF) system is being developed.

This paper presents experimental studies of an SC-MRF system and an SC-CBF system. Using performance based design (PBD) procedures both the SC-MRF and the SC-CBF are designed to remain damage-free under the Design Basis Earthquake (DBE) to enable immediate occupancy, while also achieving the collapse prevention performance level under the Maximum Considered Earthquake (MCE). The paper summarizes design concepts and criteria for SC-MRF and SC-CBF systems. Experimental results from earthquake simulations are used to assess the PBD procedures.

2. SC-MRF SYSTEM

2.1 System Overview

Figure 1(a) shows an SC-MRF with PT strands and web friction devices (WFDs). The PT strands run across multiple bays. The WFD, shown in Figure 1(b), includes two friction channels welded to the column flange. Brass plates are sandwiched between the friction channels and beam to provide reliable friction conditions. Normal force on the friction surface between the channels and beam is provided by friction bolts shown in Figure 1(b). The friction channels are welded to the column flange after the friction bolts are tightened. The friction channel shape was selected to reduce the effect of weld shrinkage on the friction surface normal

force. Slotted holes are used in the beam web to accommodate the travel of the friction bolts during the gap opening and closing of the connection (discussed later). The shim plates shown in Figure 1(a) are welded to the column flange to provide good contact surfaces for the beam flanges. Reinforcing plates are welded on the outside faces of the beam flanges to avoid excessive yielding in the beam flanges.

The conceptual moment-relative rotation ($M\text{-}\theta_r$) behavior of the connection shown in Figure 1(b) is shown in Figure 1(c). From event 0 to 2, the connection has stiffness similar to that of a conventional welded moment connection. After the connection moment M reaches the imminent gap opening moment at event 2 (M_{IGO}), the beam tension flange loses contact with the shim plate at the column face and gap opening occurs. M_{IGO} is the sum of the decompression moment M_d due to the initial PT force (event 1) and the moment M_{Ff} due to friction in the WFD. After M_{IGO} is exceeded, M increases with increases in the PT strand force due to gap opening (event 2 to 3). Excessive gap opening will eventually yield the PT strands at event 4. During unloading between events 3 and 5, θ_r remains constant but M decreases by $2M_{Ff}$ due to the reversal in direction of the WFD friction force. Continued unloading between events 5 and 6 reduces θ_r to zero as the beam tension flange comes in contact with the shim plate at the column face. Further unloading (between events 6 and 7) decreases M to zero as the beam tension flange fully compresses against the shim plate. Similar behavior occurs under load reversal.

After M_{IGO}, M is controlled by the axial force in the beam, P and the WFD friction force resultant, F_f, as follows:

$$M = Pd_2 + F_f r \quad (1)$$

where d_2 is the distance from the beam cross section centroid to the center of rotation (COR) of the connection, and r is the distance from F_f to the COR. The COR is at the point of contact of the beam compression flange with the column. P includes the PT force, T, and the effects of interaction between the SC-MRF and floor system (e.g., floor diaphragm forces), F_{fd}, as follows (Garlock et al. 2005):

$$P = F_{fd} + T \quad (2)$$

T depends on the initial PT force, T_o, and the strand elongation due to θ_r.

2.2 Performance-Based Design

The performance-based design (PBD) procedure proposed for SC-MRFs (Garlock et al. 2005) considers two seismic hazard (ground motion intensity) levels, as defined by FEMA 450 (FEMA 2003): (1) a Design-Basis Earthquake (DBE) and (2) a Maximum Considered Earthquake (MCE). The DBE has two-thirds the intensity of the MCE (FEMA 2000) and an approximate 10% probability of being exceeded in 50 years. The MCE has a 2% probability of being exceeded in 50 years. Under the DBE, an SC-MRF is designed to achieve immediate occupancy (IO) performance (FEMA 2003), with limited structural and nonstructural damage. Under the MCE, an SC-MRF is designed to achieve collapse prevention (CP) performance (FEMA 2003).

The design objectives and the limit states of an SC-MRF with WFDs are shown in a conceptual base shear-roof drift ($V\text{-}\theta_{roof}$) response in Figure 2. Before the IO performance limit, connection decompression and yielding at the column bases of the SC-MRF are permitted to occur. Panel zone yielding, beam web yielding, and a beam flange strain greater than twice the yield strain (i.e., $2\varepsilon_y$) are permitted to occur between the IO and CP performance limits. Before the CP limit, PT strand yielding, beam web buckling, and excessive story drift are not permitted.

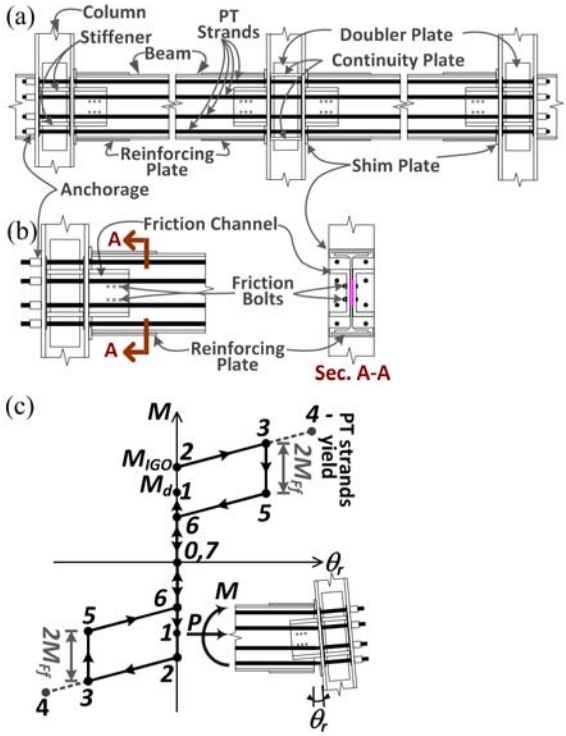

Figure 1 (a) 2-Bay SC-MRF with PT Strands and WFDs, (b) Connection Details, and (c) Conceptual $M\text{-}\theta_r$ Behavior of Connection.

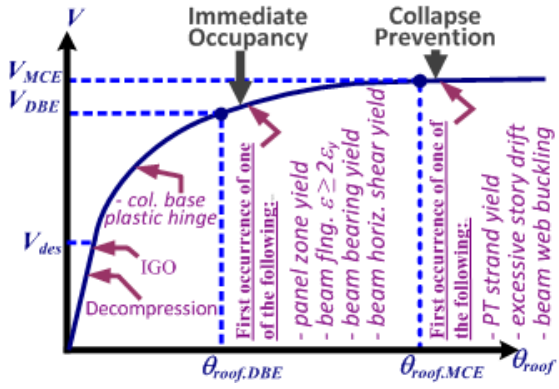

Figure 2 SC-MRF Performance-Based Design

The PBD procedure permits the use of an equivalent lateral force analysis of the SC-MRF, using an analysis model with rigid beam-column connections that is subjected to the design forces defined in ASCE 7-05 (2005) with a

response modification factor R equal to 8. The design moment M_{des} from this analysis is used to establish an initial value of M_{IGO} approximately equal to $0.95M_{des}$. The effective energy dissipation ratio of the SC-MRF connections, $\beta_E = M_{Ff} / M_{IGO}$, is used to establish the proportion of M_{IGO} provided by M_{Ff}. To provide the SC-MRF with sufficient energy dissipation to achieve a satisfactory seismic response, Seo and Sause (2005) recommend that $\beta_E \geq 0.25$, however to enable connection re-centering, $\beta_E \leq 0.40$. The PBD procedure includes numerous steps to control the limit states shown in Figure 2. In this procedure, estimates of the θ_r demand under the DBE and MCE are critical for determining whether these limit states are reached. The details of the PBD procedure are given in Garlock et al. (2005).

2.3 Experimental Program

The PBD procedure described above was used to design SC-MRFs for the 7x7-bay 4-story prototype building shown in plan in Figure 3(a). The building is located on a stiff soil site in the Los Angeles area. The perimeter frames include SC-MRFs. Each perimeter frame has two 2-bay SC-MRFs with WFDs. Figure 3(a) shows the floor diaphragm is attached to one bay of each SC-MRF in each perimeter frame to avoid restraining gap opening of the SC-MRF connections.

The test structure is a 0.6-scale model of one SC-MRF from the prototype building, as shown in Figure 3(b). The test frame has A992 steel members which were scaled down from the prototype SC-MRF. Table 1 gives the design demands for roof drift (θ_{roof}), story drift (θ_s), and connection relative rotation (θ_r) at the DBE and MCE levels. The initial PT forces T_o, shown in Figure 3(b), are less than 45% of strand ultimate strength (T_u). Design values of β_E are shown in Figure 3(b). During the experiments, lateral force is applied at each floor level by hydraulic actuators through a simulated floor diaphragm attached near the middle of the North-bay beam shown in Figure 3(b).

The hybrid simulation method was used for earthquake simulations. In these simulations, the test structure was the experimental substructure, while the gravity load bearing system, gravity loads, and the seismic mass tributary to the test structure were included in the analytical substructure. The hybrid simulation used 2% damping in the 1st mode and 5% damping in the 3rd mode. The explicit unconditionally stable CR integration algorithm by Chen and Ricles (2008) was used to solve the equations of motion. Table 2 shows the test matrix of hybrid simulations. Ground motions at the frequently occurring earthquake (FOE), DBE, and MCE level were used. Three different DBE level ground motion records were used and are denoted DBE-1, DBE-2 and DBE-3. Each of these records was one of a pair of recorded orthogonal components of horizontal ground acceleration. To develop a set of DBE-level ground motions, fifteen such pairs were selected from earthquake ground motion data bases, and scaled so that the geometric mean of the spectral accelerations S_a of the record pair was equal to the S_a value at a period of 1.5 seconds for the uniform hazard spectrum (UHS) for the site of the prototype building in the Los Angeles area. To use these records for the hybrid simulations, the time step for the records were scaled by $(0.6)^{1/2}$ (=0.77), where 0.6 is the scale factor of the test frame.

The selected records, DBE-1, DBE-2 and DBE-3, cause a maximum story drift that is approximately one-standard deviation lower than, similar to, and one-standard deviation higher than, respectively, the mean maximum story drift from nonlinear dynamic analyses of the test frame for the set of DBE-level ground motion records. Figure 4 compares the design (DBE) spectrum based on ASCE7-05 (2005), the uniform hazard spectrum, UHS, which has a 10% probability of exceedance in 50 years at the prototype building site, and the individual response spectra for the DBE-1, DBE-2 and DBE-3 records. In this figure, all periods are scaled by the time scale factor of $(0.6)^{1/2}$ (=0.77). It should be noted that S_a for the DBE design spectrum at the period of 1.16 sec (which is approximately the fundamental period of the test structure with the associated seismic mass) is slightly higher than the corresponding S_a of the UHS (i.e., 0.4g vs. 0.35g), because the DBE design spectrum is defined to have two-thirds the intensity of the MCE design spectrum (FEMA 2000), and is not directly equal to the UHS which has 10% probability of exceedance in 50 years. The S_a of the individual response spectra for DBE-1, DBE-2, and DBE-3 at 1.16 sec. vary from 0.32g to 0.4g because each record was not scaled individually to the target S_a value, rather, each record pair was scaled by a single scale factor so that the geometric mean of S_a for the record pair equaled the target S_a value.

Table 1 Design Demands (Radians)

$\theta_{roof,DBE}$	$\theta_{s,DBE}$	$\theta_{r,DBE}$	$\theta_{roof,MCE}$	$\theta_{s,MCE}$	$\theta_{r,MCE}$
0.026	0.039	0.031	0.039	0.059	0.047

Table 2 Test Matrix of Hybrid Simulations

Tests	Description	Record	Scale Factor
FOE-1	1979 Imperial Valley	H-CXO225	-0.70
FOE-2			-1.41
DBE-1	1979 Imperial Valley	H-ECC002	0.94
DBE-2	1989 Loma Prieta	SJTE315	-2.23
DBE-3	1994 Northridge	LOS000	1.18
MCEs	1994 Northridge	Varied w/ tests	
Aftershock	1989 Loma Prieta	SJTE315	-2.23

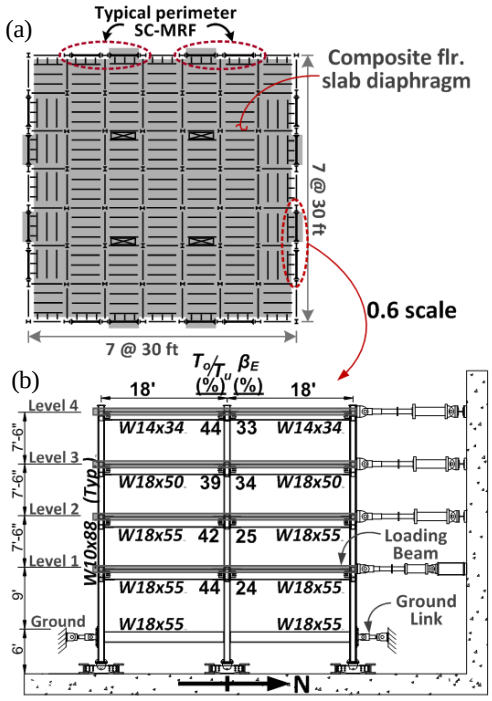

Figure 3 Schematic of (a) Plan of Prototype Building, and (b) Elevation of 0.6-Scale 4-Story 2-Bay SC-MRF Test Structure (1′ = 1ft = 305mm, 1″= 1in = 25.4mm)

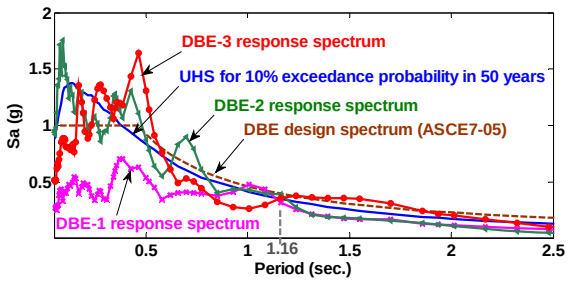

Figure 4 Pseudo-Acceleration Response Spectra

2.4 Experimental Results

Floor displacement time histories from the DBE-2 hybrid simulation are shown in Figure 5(a). The residual story drifts of the test frame are given in Table 3 and were obtained by dividing the difference in residual displacements of adjacent floors by the story height. Table 3 shows the maximum residual story drift after DBE-2 is 0.00061 radians, which demonstrates the self-centering capability of the SC-MRF. Table 4 shows results from the DBE-2 simulation, and includes the maximum story drift $\theta_{s\ max}$, maximum relative rotation $\theta_{r\ max}$, maximum PT force T_{max} and loss of PT force during the simulated earthquake, ΔT, normalized by the strand tensile strength T_u. The maximum $\theta_{s\ max}$ is 2.9% radians, which is less than the expected design demand of 3.9% radians (Table 1) for the DBE. The maximum $\theta_{r\ max}$ is 2.7% radians, which is less than the expected design demand of 3.1% radians for the DBE. The maximum PT force in the DBE-2 simulation was $0.6T_u$. No yielding occurred in the PT strands. The PT force decreased slightly due to seating of the PT strand anchorage, and ΔT is less than 1% of T_u.

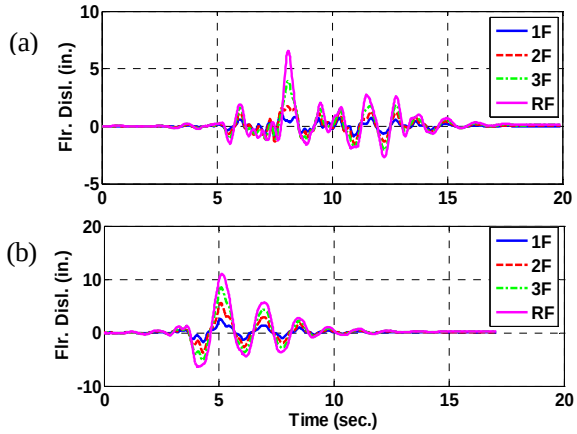

Figure 5 Floor Displacements Time Histories from (a) DBE-2, and (b) DBE-3.

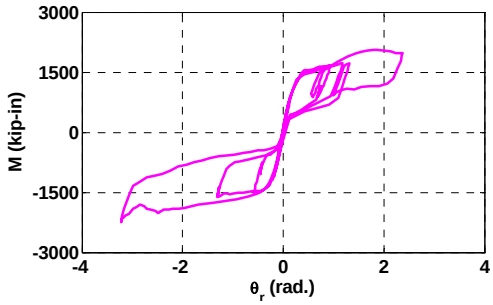

Figure 6 Moment vs. θ_r of 3FSN Connection from DBE-3

Figure 5(b) shows floor displacement time histories from DBE-3. The maximum residual story drift after DBE-3 is 0.00074 radians, which further demonstrates the self-centering capability of the SC-MRF. The 1st story residual drift from the DBE-3 simulation is larger than that from the DBE-2 simulation due to yielding in the columns at the ground level. Table 4 shows the maximum $\theta_{s\ max}$ is 3.9% radians, which equals the design demand for the DBE (Table 1). The maximum $\theta_{r\ max}$ is 3.8% radians, which is slightly larger than the design demand of 3.1% radians for the DBE. The maximum PT force in the DBE-3 simulation was $0.65T_u$. No yielding occurred in the PT strands. ΔT is less than 1.5% of T_u. The self-centering behavior of the SC-MRF beam-column connections is illustrated by the typical M-θ_r response from the DBE-3 simulation for the North-end connection of the 3rd floor South-bay beam (denoted 3FSN), shown in Figure 6. After gap opening, the stiffness differs in the positive and negative moment directions due to the floor diaphragm forces (i.e., the lateral force from the actuators) acting on the North-bay beam. When the test frame is loaded in the North direction by the floor diaphragm, a tension axial force is imposed on the South-bay beam. When test frame is loaded to the South, a compression axial force is imposed on

the South-bay beam. Therefore, the axial force P in the South bay is different for the North and South loading directions. β_E estimated from the DBE-3 simulation results is around 30%. Overall, the SC-MRF achieved the DBE performance objectives.

Table 3 Residual Story Drift (Radians)

Test	Story			
	1st	2nd	3rd	4th
DBE-2	0.00014	0.00035	0.00061	0.00045
DBE-3	0.00074	0.00063	0.00023	0.00008

Table 4 Test Results from DBE-2 and DBE-3

	Level	$\theta_{s\,max}$ (rad.)	$\theta_{r\,max}$ (rad.)	T_{max}/T_u (%)	$\Delta T_i/T_u$ (%)
DBE-2	RF	0.029	0.027	60	-0.5
	3F	0.025	0.024	54	-0.4
	2F	0.014	0.014	51	-0.0
	1F	0.008	0.005	46	-0.0
DBE-3	RF	0.039	0.038	65	-0.7
	3F	0.035	0.034	60	-0.7
	2F	0.035	0.031	61	-1.3
	1F	0.021	0.025	59	-1.0

3. SC-CBF SYSTEM

3.1 System Overview

The SC-CBF system and its idealized behavior are shown schematically in Figure 7. The system consists of beams, columns, and braces in a conventional arrangement (Figure 7(a)), with column base details that permit the columns to uplift at the foundation (Figure 7(c)). Gravity loads and post-tensioning (PT) forces (from PT bars arranged along the column lines in the system shown in Figure 7(a)) resist column uplift and provide a restoring force after uplift. The beams, columns, and braces are intended to remain essentially elastic under the design earthquake, and the column uplift provides a mechanism for controlling the force levels that develop in the frame under earthquake loading.

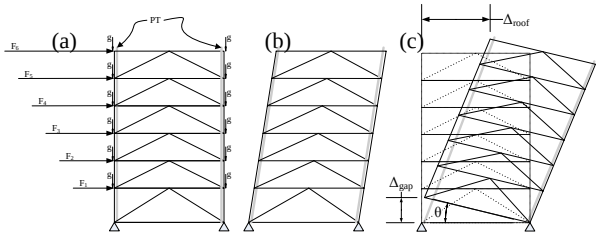

Figure 1 SC-CBF System: (a) Schematic of Members and Loads; (b) Elastic Response Prior to Column Uplift; (c) Rigid-Body Rotation after Column Uplift.

Figure 7(a) shows loads used in a lateral force seismic analysis of an SC-CBF. Gravity loads (g) are applied at the columns at each floor level. The lateral load profile (F_i) is similar to that used in an equivalent lateral force procedure (ASCE 7-05 2005). Under low levels of lateral force, the structure deforms elastically as shown schematically in Figure 7(b). This deformation is similar to that of a conventional CBF. Under higher levels of lateral force, the overturning moment at the base of the frame becomes large enough for the "tension" column to decompress, and uplift of the column occurs, as shown in Figure 7(c). After column decompression and uplift, the lateral displacement of the frame is dominated by rigid body rotation of the SC-CBF about the base of the "compression" column (i.e., frame rocking), although some additional forces and deformations develop in the beams, columns, and braces of the frame. The PT bars elongate from the uplift of the frame, leading to an increase in PT force, which provides a positive stiffness to the lateral force-lateral drift behavior after column decompression and uplift.

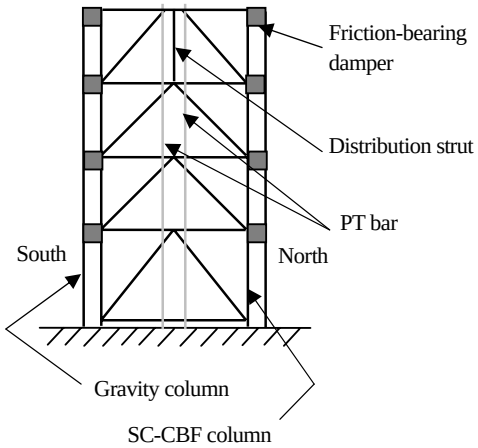

Figure 8 Frame Configuration D_{DIST}

Several SC-CBF configurations have been studied (Roke et al. 2006, 2009). From these configurations, Frame D_{DIST}, was selected for detailed study. Frame D_{DIST}, shown in Figure 8, consists of an SC-CBF placed between two additional columns that are attached to the gravity load system of the building. These two "gravity columns," which do not uplift, separate the gravity load carrying function from the rocking of the SC-CBF. "Friction-bearing" dampers are located so that slip can occur due to the relative vertical displacement between the gravity columns and the SC-CBF columns. Each friction-bearing damper has a small initial gap between the gravity column and SC-CBF column, which is closed by the transfer of floor diaphragm inertial forces in bearing between the gravity column and the SC-CBF column. A brass shim is located at the friction surface of the friction bearing dampers. The normal force on the friction surface equals the floor diaphragm inertial force transferred to the SC-CBF at a floor level. The steel-on-brass friction surface has a friction coefficient of approximately

0.5. To reduce the elongation demand on the PT steel, the PT steel is located at midbay of the SC-CBF. As the tension column uplifts and a gap opens at the column base, the elongation demand of the PT steel is half of the gap-opening displacement of the uplifting column, Δ_{gap} (Figure 7(c)). A vertical "distribution" strut is located in the upper story. This strut distributes the force of the midbay PT steel to the braces over multiple stories, thereby reducing the concentration of force in the braces in the upper story.

3.2 Performance-Based Design

The primary limit states considered in the performance-based seismic design (PBD) of an SC-CBF are: (1) decompression and uplift of the "tension" column at the base of the SC-CBF; (2) yielding of the PT steel; (3) significant yielding of the beams, columns, or braces of the SC-CBF; and (4) failure of the beams, columns, or braces. Again, two seismic hazard (ground motion intensity) levels are considered: (1) a Design-Basis Earthquake (DBE) and (2) a Maximum Considered Earthquake (MCE). The performance objectives are immediate occupancy (IO) performance under the DBE and collapse prevention (CP) performance under the MCE. To reach these objectives, the four primary limit states are considered as follows (Figure 9).

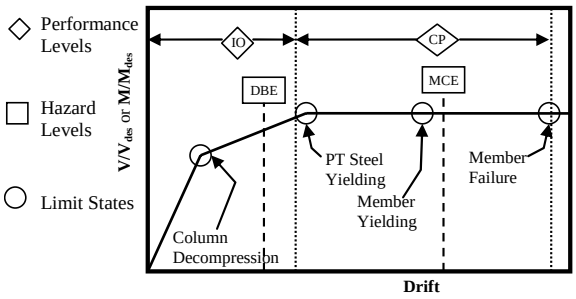

Figure 9 SC-CBF Performance-Based Design

Decompression and uplift of the SC-CBF columns will not produce structural damage if the column bases and the attachment of the SC-CBF to the floor system are properly detailed, so this limit state conforms to the IO performance level. The prestress force in the PT steel is important to the self-centering behavior of SC-CBFs. Therefore, significant yielding of the PT steel, which produces a subsequent loss in prestress force (or fails the PT steel) could have serious consequences. Some types of PT steel and associated anchorage systems, for example, certain high strength PT bar systems, can yield and provide ductile behavior without immediate failure (Perez et al. 2003). However, other types of PT steel and associated anchorage systems, for example, certain high strength PT strand systems, may fail at the anchorages shortly after yielding (Garlock et al. 2005). The SC-CBF system studied here employs high strength PT bars, and, therefore, the primary consequence of PT bar yielding is the subsequent loss of prestress force under cyclic loading. This loss of prestress is a form of structural damage that does not compromise the safety of the SC-CBF system, however, it must be repaired after an earthquake (by re-stressing or replacing the PT bars). Therefore, yielding of the PT bars is a limit state that conforms to the CP performance level, but not to the IO performance level (Figure 9).

Significant yielding of the beams, columns, or braces of the SC-CBF is the initiation of significant structural damage to the SC-CBF system. To control the amount of damage that must be repaired after ground motions at an intensity level between the DBE and MCE levels, this limit state should be reached only after yielding of the PT bars (Figure 9). Yielding of the PT bars provides a mechanism to control force levels in the SC-CBF, making it possible to control significant yielding of the other structural members. The PBD approach uses a capacity design method for the beams, columns, and braces of the SC-CBF to keep these members essentially elastic at seismic input levels that cause PT bars to yield. Failure (buckling or fracture) of the beams, columns, or braces of the SC-CBF is a limit state that may not conform to the CP performance level (Figure 9). The force level control provided by yielding of the PT bars as well as the inherent ductility of these steel members are used to control this limit state.

3.3 Experimental Program

A prototype structure was designed using the SC-CBF system. The prototype structure is a four-story office building designed for a stiff soil site in Van Nuys, California. A 0.6-scale model of the prototype structure is shown schematically in Figure 10, where SC-CBFs are shown located symmetrically throughout the plan. The test structure represents one SC-CBF with the adjacent gravity columns. Estimated gravity loads and seismic masses were determined using the following assumptions. The dead load includes the concrete floor slab, steel floor deck, mechanical equipment, floor and ceiling finishes, cladding weight, and an estimated weight per square foot of structural steel. The seismic mass of each floor is determined from the dead load plus the weight of interior partitions. The tributary seismic masses for the test structure, from the first floor to the roof, are: 135900 kg, 134800 kg, 134800 kg, and 142200 kg. The gravity loads carried by the associated 1/4th of the gravity load bearing system of the building, from the first floor to the roof, are: 1495 kN, 1484 kN, 1484 kN, and 1556 kN.

The design of the SC-CBF system is based upon an equivalent lateral force (ELF) procedure (ASCE 7-05 2005) modified to meet the performance-based design objectives described above. An initial value for the response modification factor, R, of 8 is used. R is modified during the design process. The value of R is controlled by the design objective of avoiding PT bar yielding under the DBE. The drift capacity at PT bar yielding is determined from the rigid-body rotation of the SC-CBF (after column decompression) and the elastic deformation of the SC-CBF at PT bar yield. The rigid-body rotation elongates the PT bars, while the elastic deformation does not. The DBE drift demand equals the drift at decompression amplified by μ, which is calculated from μ-R relationships developed for self-centering systems (Seo 2005). As R decreases μ decreases, and therefore, R is decreased in the design process

until a sufficient margin of safety between the DBE drift demand and the drift demand at PT bar yielding is provided.

The SC-CBF beams, columns, and braces (members) are designed according to the PBD criteria discussed earlier. The member force demands were determined using a response spectrum procedure modified to meet the performance-based design objectives described above, as discussed by Roke et al. (2009). The first mode demand is controlled by the overturning moment at the PT yield limit state. The higher mode demands are determined from a linear response spectrum analysis of the SC-CBF. The first mode and higher mode demands are then combined using the complete quadratic combination rule (Roke et al. 2009). The PT bars selected for the test structure are six 1 in (25.4 mm) nominal diameter PT bars, for a total PT bar area of 5.1 in^2 (3290 mm^2). The A992 steel sections selected for the test structure are W8x67 gravity columns; W10x112 frame columns; W12x50 beams; W8x48 first, second, and third story braces and distribution strut; and W8x58 fourth story braces.

To provide context for the SC-CBF test structure design, it was compared to the design of a special CBF (SCBF) and a BRBF. Table 5 summarizes R values for the SC-CBF test structure, the SCBF, and the BRBF. Other design quantities, such as the design base shear and design brace forces, are also compared. The design base shear, V_{bdes}, varies inversely with R. For the SCBF and the BRBF, the design brace force in each story (F_{b1des} through F_{b4des}) is estimated by assuming each brace in a story resists half of the story shear corresponding to the design lateral forces. The design brace forces are much higher for the SC-CBF system because the braces are specifically designed to account for higher mode response as described earlier. In addition, the design brace forces for the 3rd and 4th stories of the SC-CBF include the effects of the force in the midbay PT bars.

Table 5 Summary of Design Values (1k = 4.448kN)

System	R	V_{bdes} (k)	F_{b1des} (k)	F_{b2des} (k)	F_{b3des} (k)	F_{b4des} (k)	θ_r (%)
SC-CBF	7.8	155.7	384.9	231.7	376.0	479.1	1.1
SCBF	6	201.6	157.5	126.5	98.0	54.5	--
BRBF	8	151.2	118.1	94.9	73.5	40.8	--

The seismic response of the SC-CBF test structure was characterized initially using nonlinear time history analyses performed using OpenSEES (Mazzoni 2006). A suite of 30 scaled DBE-level recorded ground motions and a suite of 30 scaled MCE-level recorded ground motions were used. The beams, columns, and braces of the SC-CBF were modeled as linear elastic so the member force demands required to keep the members linear elastic could be determined. The PT steel was modeled using nonlinear beam-column elements. The gap opening behavior and friction behavior at the column bases and at the friction-bearing dampers were modeled using contact friction elements. Rayleigh damping was used with 2% and 5% damping in the 1st and 3rd modes, respectively.

The analytical response to the DBE and MCE records is summarized in Table 6. From the 30 DBE records and 30 MCE records, the ground motion records shown in Table 6 were chosen to represent the mean, the mean-minus-one-standard-deviation, as well as the mean-plus-one-standard-deviation responses for each hazard level. Mean values for the DBE and MCE are also presented in the table. The tabulated values are SF, the scale factor applied to each ground motion; V_b/V_{bdes}, the maximum base shear demand normalized by the design base shear; θ_r, the maximum roof drift; and θ_s, the maximum story drift from any story.

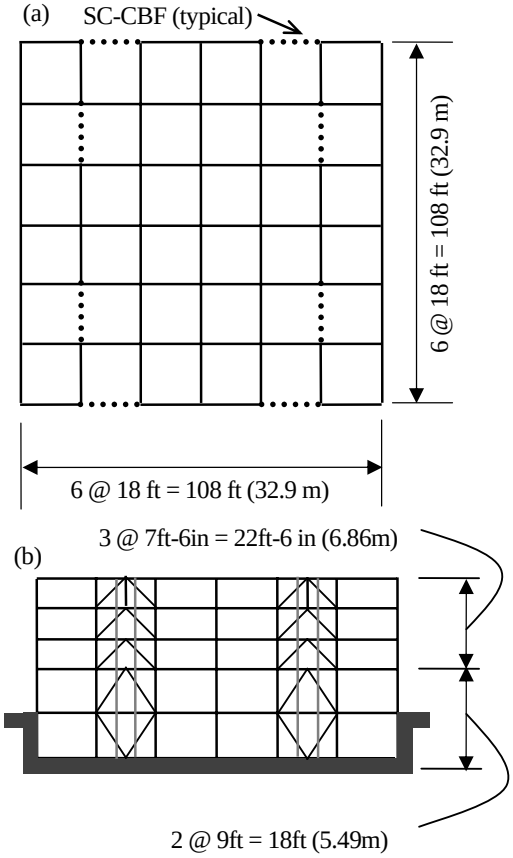

Figure 10 Prototype Structure at 0.6 Scale: (a) Plan; (b) Elevation of Column Line with SC-CBFs

3.4 Experimental Results

The test structure was subjected to numerous simulated earthquakes using the hybrid simulation method. During these laboratory simulations, a lateral force at each level was applied by hydraulic actuators through a floor diaphragm model consisting of a loading beam system attached to both the north and south gravity columns shown in Figure 8. This load was then transferred to the SC-CBF columns through the friction-bearing dampers described earlier. In the hybrid simulations, the test structure (SC-CBF and 2 adjacent gravity columns) was the experimental substructure, while the remaining gravity load bearing system, gravity loads, and seismic mass tributary to the test structure were included in the analytical substructure. The hybrid simulations used Rayleigh damping with 2% and 5% damping in the 1st and 3rd modes, respectively. Table 7 summarizes the experimental response of the test structure.

Each response quantity is well-predicted by the analytical model. Examples of the experimental response from the laboratory simulations are given in Figures 11 through 15.

Table 6 Summary of analytical response

Identifier	Input Level	SF	V_b/V_{bdes}	θ_r (%)	θ_s (%)
Mean	DBE	--	2.62	0.880	0.981
Mean	MCE	--	3.18	1.467	1.582
cls000	DBE	0.73	1.79	0.641	0.720
5108-090	DBE	2.49	2.85	0.827	0.909
h-shp270	DBE	1.75	3.01	0.912	1.023
arl090	DBE	1.40	2.92	1.389	1.521
stn110	MCE	1.98	2.91	1.622	1.747
a-tmz270	MCE	2.55	3.48	1.120	1.246
lp-hda255	MCE	2.24	3.38	1.477	1.588
nr-pel360	DBE	1.55	3.38	0.952	1.156
cap000	MCE	1.45	3.31	2.068	2.221
h-cpe237	MCE	3.85	3.70	1.741	1.831

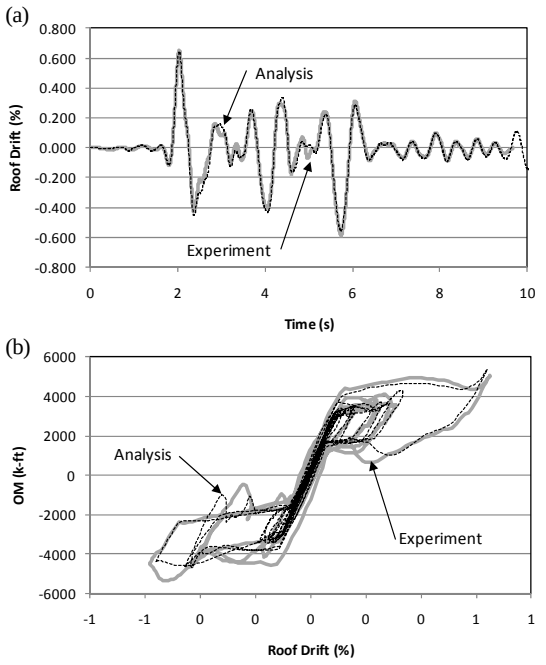

Figure 11 Response to DBE cls000: (a) Roof Drift Time History; (b) Overturning Moment versus Roof Drift Hysteresis Loops (1 k-ft = 1.356 kN-m)

Figures 11 and 12 show the response to the low-level DBE Corralitos ground motion (cls000) from the 1989 Loma Prieta earthquake. The response shown in Figure 11(a) is the lateral roof drift time history. The roof drift is determined from the roof displacement measured at the centerline of the north gravity column. The peak drift, 0.650% in the positive direction, occurs early in the response. Figure 11(b) shows the base overturning moment-roof drift hysteresis response. The flag-shaped loops are typical of self-centering systems. Note that the SC-CBF fully re-centers at the conclusion of the earthquake response. No structural damage was observed. Figure 12 shows brace force time histories. The first story brace forces (Figure 12(a)) reflect the base shear response. The fourth story brace forces (Figure 12(b)) reflect both the roof-level inertial force and the PT force responses. Overall, the analytical predictions agree with the experimental responses.

Table 7 Summary of experimental response

Identifier	Input Level	SF	V_b/V_{bdes}	θ_r (%)	θ_s (%)
cls000	DBE	0.73	1.92	0.650	0.760
5108-090	DBE	2.49	3.01	0.781	0.910
h-shp270	DBE	1.75	3.12	0.916	1.035
arl090	DBE	1.40	3.00	1.342	1.443
stn110	MCE	1.98	2.88	1.553	1.718
a-tmz270	MCE	2.55	2.93	1.120	1.234
lp-hda255	MCE	2.24	3.54	1.412	1.549
nr-pel360	DBE	1.55	3.35	0.982	1.134
cap000	MCE	1.45	3.43	1.872	1.964
h-cpe237	MCE	3.85	3.22	1.637	1.706

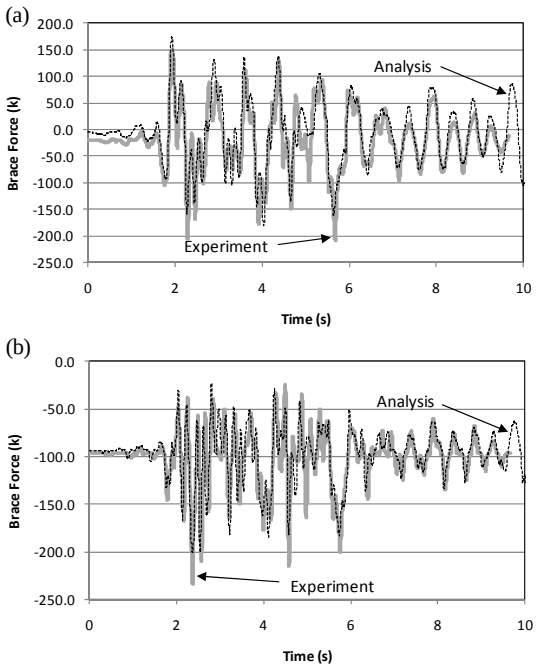

Figure 12 Response to DBE cls000: (a) 1st Story South Brace Force Time History; (b) 4th Story South Brace Force Time History (1 k = 4.448 kN)

Figures 13, 14, and 15 show the response to the mean-plus-one-standard-deviation MCE Capitola ground motion (cap000) from the 1989 Loma Prieta earthquake. The lateral roof drift, as measured at the north gravity column, is shown in Figure 13(a). The experimental peak response, the negative peak occurring at about 8 seconds of

response, is 1.9%. The corresponding analytical peak response is 2.1%. These values are about twice the design roof drift of 1.1% (Table 5). Figure 13(b) shows the base overturning moment-roof drift hysteresis response. As in Figure 11(b), the hysteresis loops are flag-shaped. Due to the larger roof drift response under this record, the PT bars yielded slightly during the response. The plastic elongation of the PT bars reduced the prestress in the PT bars by 7%, which did not significantly affect the performance of the system. Figure 13(a) shows that SC-CBF fully re-centers at the conclusion of the earthquake response. Figure 14 shows the brace force response. Figure 15 shows the uplift displacement at the base of the SC-CBF columns. The peak values of column uplift are about 3 in (76mm). Overall, the analytical predictions agree with the experimental responses.

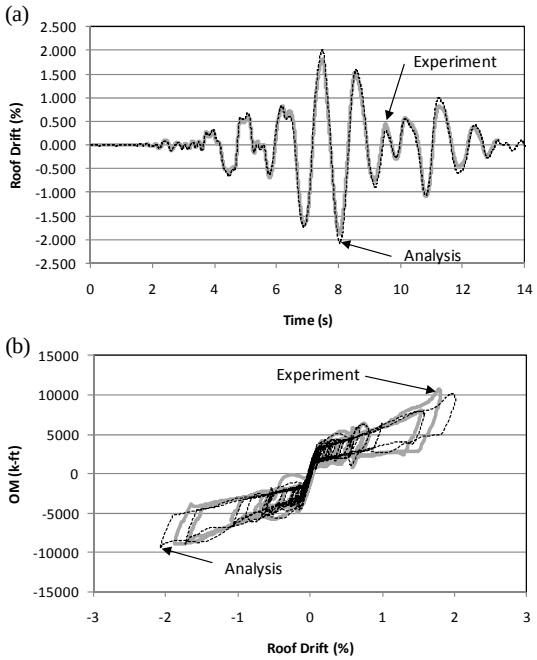

Figure 13 Response to MCE cap000: (a) Roof Drift Time History; (b) Overturning Moment versus Roof Drift Hysteresis Loops (1 k-ft = 1.356 kN-m)

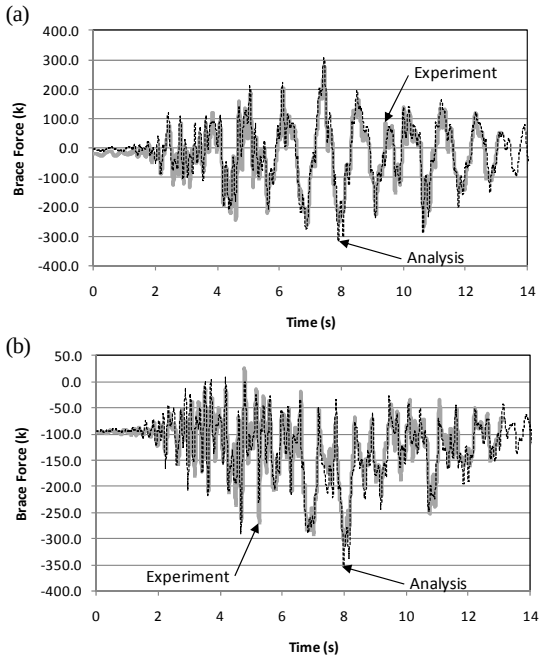

Figure 14 Response to MCE cap000: (a) 1st Story South Brace Force Time History; (b) 4th Story South Brace Force Time History (1 k = 4.448 kN)

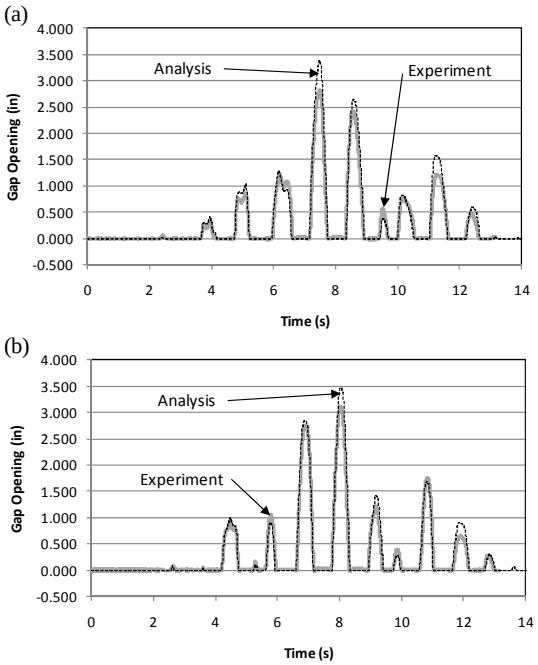

Figure 15 Response to MCE cap000: (a) South Column Uplift; (b) North Column Uplift (1 in = 25.4 mm)

4. SUMMARY AND CONCLUSIONS

This paper presents experimental studies of a self-centering (SC) moment resisting frame (SC-MRF) system and a self-centering (SC) concentrically-braced frame (SC-CBF) system. These self-centering systems are motivated by the goal of minimizing structural damage under seismic loading and are intended to provide significant non-linear drift capacity while limiting damage and residual drift. Using a performance based design (PBD) approach both the SC-MRF and the SC-CBF are designed to remain damage-free under the Design Basis Earthquake (DBE) to enable immediate occupancy, while also achieving the collapse prevention performance level under the Maximum Considered Earthquake (MCE). The paper summarizes design concepts and criteria for SC-MRF and SC-CBF systems.

The SC-MRF had post-tensioning (PT) strands which clamped the beams to the columns to provide self-centering, and beam web friction devices (WFDs) at the beam-column connections to provide energy dissipation. Experimental results from hybrid earthquake simulations on a large-scale test structure demonstrated the self-centering behavior of the SC-MRF with WFDs under the DBE. The SC-MRF performed well and satisfied the objectives of the PBD procedure. No significant damage occurred during the DBE-level tests. The beam-column connection M-θ_r behavior was as intended, and the WFDs provided reasonable levels of energy dissipation. Overall, the SC-MRF achieved the IO performance level under the DBE. The results of the MCE simulations are not shown in the paper due to space limitations, however the SC-MRF sustained modest damage during the MCE simulations and achieved at least the CP performance level.

Experimental results from several hybrid simulations on a large-scale test structure demonstrated the self-centering behavior of the SC-CBF under the DBE and MCE. The SC-CBF exceeded the objectives of the PBD procedure. Related analytical predictions were quite close to the experimental results, demonstrating the accuracy of the analytical model. Under DBE-level ground motions, no significant structural damage occurred, and under MCE-level ground motions only a small loss of prestress occurred. In all cases the SC-CBF re-centered after the seismic response.

Acknowledgements:

This research was conducted at the NEES Real-Time Multi-Directional (RTMD) Earthquake Simulation Facility in the ATLSS Center at Lehigh University. This paper is based upon work supported by the National Science Foundation under Award No. CMS-0420974, within the George E. Brown, Jr. Network for Earthquake Engineering Simulation Research (NEESR) program and Award No. CMS-0402490 NEES Consortium Operation. Any opinions, findings, and conclusions or recommendations expressed in this material are those of the authors and do not necessarily reflect the views of the National Science Foundation.

References:

ASCE 7-05 (2005), Minimum design loads for buildings and other structures, American Society of Civil Engineers, Reston, VA.

Chen, C, and Ricles, J.M. (2008). Development of direct integration algorithms for structural dynamics using discrete control theory. Journal of Engineering Mechanics, 134(8), pp. 676-683.

Fahnestock, L.A., Sause, R., Ricles, J.M., and Lu, L.-W. (2003), Ductility demands on buckling restrained braced frames under earthquake loading, Journal of Earthquake Engineering and Engineering Vibration, 2(2), 255-268.

FEMA. (2003), NEHRP Recommended Provisions for Seismic Regulations for New Buildings and Other Structures. Part 1 – Provisions and Part 2 – Commentary, FEMA 450, Federal Emergency Management Agency, Washington, D.C.

Garlock, M.M., Ricles, J.M., and Sause, R. (2005), Experimental studies on full-scale post-tensioned steel connections, Journal of Structural Engineering, ASCE, 131(3), 438-448.

Mazzoni, S., McKenna, F., Scott, M.H., Fenves, G.L., et al. (2006), Open System for Earthquake Engineering Simulation User Command-Language Manual, Pacific Earthquake Engineering Research Center, University of California, Berkeley.

Perez, F.J., Pessiki, S., Sause, R., and Lu, L.-W. (2003), Lateral load tests of unbounded post-tensioned precast concrete walls, Large-Scale Structural Testing, ACI SP-211, 161-182.

Ricles J.M., Sause, R., Garlock, M., and Zhao, C. (2001), Post-tensioned seismic-resistant connections for steel frames, Journal of Structural Engineering, 127(2), 113-121.

Ricles, J.M., Sause, R., Peng, S.W., and Lu, L.-W. (2002), Experimental evaluation of earthquake resistant post-tensioned steel connections, Journal of Structural Engineering, 128(7), 850-859.

Roke, D., Sause, R., Ricles, J.M., Seo, C.-Y., and Lee, K.S. (2006), Self-centering seismic-resistant steel concentrically-braced frames. Proceedings, Eighth U.S. National Conference on Earthquake Engineering, San Francisco, April, EERI.

Roke, D., Sause, R., Ricles, J.M., and Gonner, N. (2009), Damage-free seismic-resistant self-centering steel concentrically-braced frames, STESSA 2009, Proceedings of the 6th International Conference on Behavior of Steel Structures in Seismic Areas, Philadelphia, August.

Seo, C-Y, and Sause, R. (2005), Ductility demands on self-centering systems under earthquake loading, ACI Structural Journal, 102(2), pp. 275-285.

Seo, C.-Y. (2005), Influence of ground motion characteristics and structural parameters on seismic responses of SDOF systems, Ph.D. Dissertation, Civil and Environmental Engineering Dept., Lehigh University, Bethlehem, PA.

JOINT CONFERENCE PROCEEDINGS
7th International Conference on Urban Earthquake Engineering (7CUEE) &
5th International Conference on Earthquake Engineering (5ICEE)
March 3-5, 2010, Tokyo Institute of Technology, Tokyo, Japan

SEISMIC DESIGN FOR RESILIENT SOCIETY

Akira Wada

Professor, Structural Engineering Research Center, Tokyo Institute of Technology, Japan
wadai@serc.titech.ac.jp

Abstract: Advances in seismic design technology today enable structural engineers to design buildings with a variety of seismic safety levels corresponding to different demands of the society. However, target of design is basically limited to secure life safety level within relatively short time span, i.e., serviceable life of each building. Aspects of constructing sustainable and resilient cities, which consists of buildings with long life, are not taken into account in general.
Strong earthquakes occur at intervals that are longer than life of individual building or people. On the other hand, as life of cities is obviously much longer, the corresponding seismic action is stronger than the design action and may cause serious damage in buildings designed for their life only. Taking these into account, we have to design each building for earthquakes considering the life of cities in order to secure continuity of urban activities over disastrous earthquakes.
However, there are problems to be solved in order to implement such seismic design. In this paper, factors in seismic engineering that hinder to realize long life city are identified and discussions on future steps of structural engineers to contribute in constructing sustainable and resilient society are indicated.

DEVELOPMENT OF SEISMIC DESIGN METHOD

Starting with a simple seismic resistant design where strength of building structures only is the bases for seismic performances, new technologies and design methods to provide various levels of seismic safety in buildings have been studied and developed. They are grouped into:

Seismic isolation where seismic energy input to building is remarkably reduced;

Passive control system where energy absorption devices of various types are installed;

Orthodox strength dependent system where seismic safety is mainly provided by the strength of structures; and

Ductility dependent system where seismic safety is mainly provided by ductility of structures.

Making use of these design methods, buildings of various types and structural characteristics are being built. The difference in design method usually produces difference in seismic performances. Among the listed design methods, seismic isolation can realize the highest seismic performance of buildings and, generally speaking, the order of the above list indicates decreasing performances.

Although we should not be too haughty of our present technology nor forget that there are certain limits of scope of application in each design method, it is possible to state that the structural engineers today can provide appropriate design solutions to demands for any level of seismic performances in buildings with a variety of height if only characteristics and intensities of design input earthquake ground motions are defined. *Fig. 1* on the next page shows which design method can realize what level of seismic performance in buildings corresponding to their heights. In *Fig. 1*, seismic performance is classified into four (4) levels. The seismic performances here mean those of buildings as a whole and not limited to structural issues. The "minimum" level corresponds to the level of performance which can be obtained by satisfying requirements of the Building Standard Law and Enforcement Order only and design target for this level is to ensure life safety under very rare (expectation for approx. 500 years) seismic action.

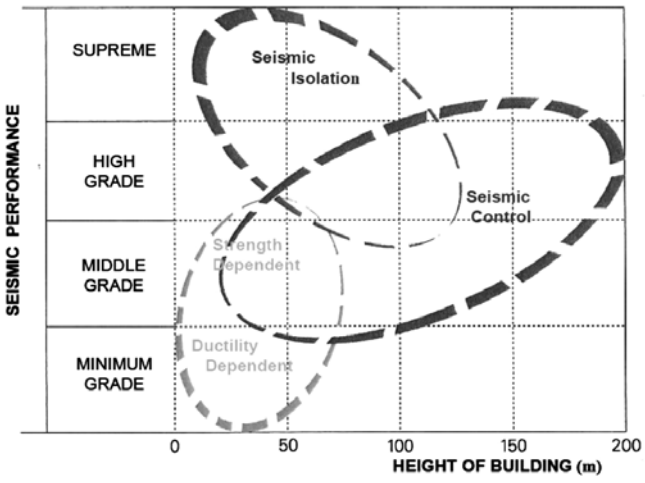

Figuer 1 Design Method and Seismic Performance

SEISMIC ISOLATED BUILDINGS

We have more than 5,000 seismic isolated small houses and more than 1500 seismic isolated buildings such as big apartment, computer centre, hospital, school and government in Japan. In our campus, 20 story steel building was constructed on the seismic isolation devices 4 years ago.

PASSIVE CONTROLLED STRUCTURES

After Kobe earthquake in 1995, more than 80% of new constructions of tall buildings are designed using passive control system. We have many kinds of supplemental damping devices such as Buckling Restrained Braces, Viscous Damping Walls and Oil Dampers. We designed three passive controlled steel tall buildings in down town Tokyo about 10 years ago. Many buckling restrained braces were installed to the 40 story steel structure as shown in the photographs.



Figuer 2 Seismic Isolated Steel Tall Building in Tokyo Institute of Technology



Figuer 3 Three Steel Tall Buildings Installed Buckling Restrained Braces

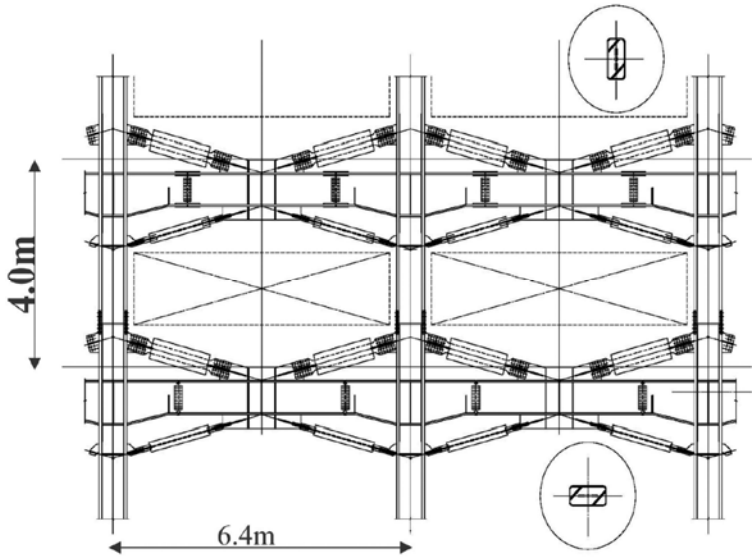

Figuer 4 Steel Columns, Steel Beams and Buckling Restrained Braces



Figuer 5 Construction of Frames and Installing Buckling Restrained Braces

COST INCREASE FOR PERFORMANCE ENHANCEMENT

As prescribed, the development in structural design methods makes it possible to realize remarkably high seismic performances. Consequently, targets of seismic design today are of great variety including life safety, functionality after seismic action, damage mitigation, etc. In addition, objects of design are not limited to structures but include all elements consisting buildings. However, there are still bottlenecks in popularizing such high performances in the society. It is the problem of the construction cost increase.

The enhancement of seismic performances is not

achieved without increase in their construction cost. As the seismic performance is not limited to structural safety, cost increase is inevitable not only in structure but also in cladding, finishes, and MEP system.

An example of calculation of increase in cost associated with enhancement of seismic performance of a model building designed with strength dependent system is shown in *Fig. 6*. Here, minimum grade, middle grade and high grade corresponds performance of life safety, limited function secured and main function secured respectively after very rare earthquakes. Design seismic strength of a middle grade and high grade building is 125% and 150% respectively of that of minimum grade building. It should be noted that increase in total construction cost is influenced by types of the buildings and cost allocations for various works. *Fig. 6* shows results of a case study on just an example model building which is based on relatively old data and a fairly conservative estimation taking into account possible increase in non-structural elements and MEP system.

Fig. 7 shows results of another example calculation. Nine (9) model buildings with various numbers of stories are designed to have seismic performances of minimum grade, middle grade and high grade with base isolation and their construction costs are compared. Although there is relatively high fluctuation, several to 30 percent cost increase is necessary to achieve high seismic grade by introducing seismic isolation system compared with buildings with minimum seismic performances.

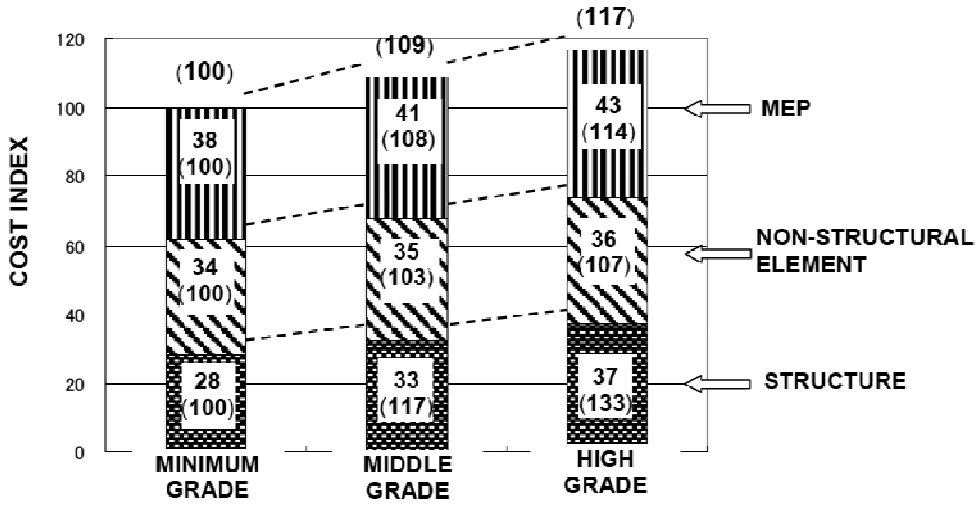

Figuer 6 Seismic Performance Upgrading and Cost Increase

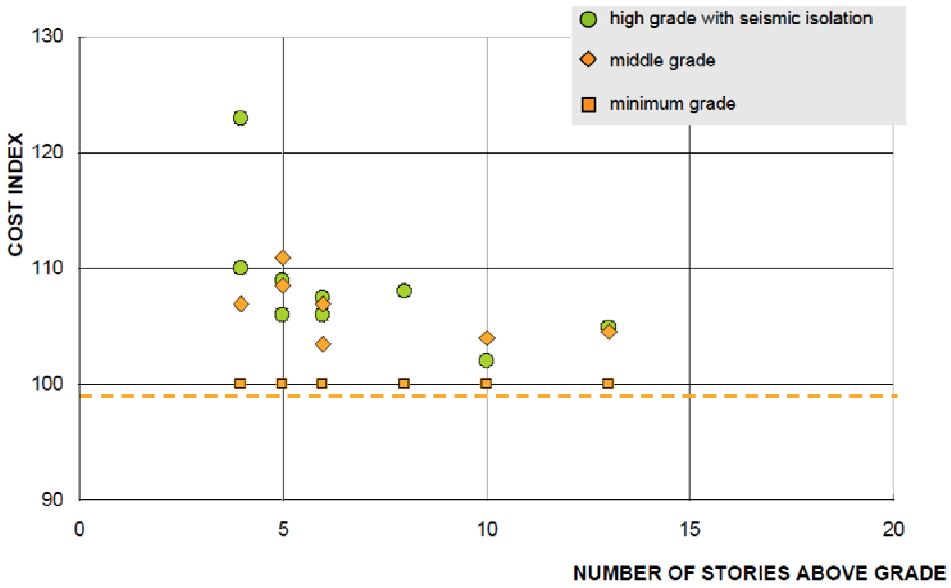

Figuer 7 Construction Cost Index (Minimum Grade = 100)

WIDESPREAD MOMENT-RESISTING FRAME STRUCTURE

The spread of performance based seismic design philosophy has positively affected in improving seismic performances of buildings. However, due to lack of sufficient understanding of damage levels in buildings caused by strong earthquakes, the developments in seismic design technology sometimes resulted in increase of rather vulnerable buildings of which the structural design is too much focused on satisfying the minimum requirements of codes and standards.

Diversification in seismic design method does not necessarily result in reduction of potential earthquake damage in buildings. The most representative example is the excessive reliance on structural ductility. It is possible to evaluate ductility of structures more precisely today and obviously the result of the evaluation in moment resisting frames is more reliable than that in frames with shear walls. This fact tends to increase risk of misunderstandings that the most popular and simple moment-resisting frame system without shear walls or vertical braces is the best type of structures as their characteristics and seismic performance can readily be calculated. The structures which can be easily analyzed and designed are not necessarily those with preferable performances. These are the most rational structures in a sense but they are the ductility dependent structures. Their seismic performances are provided mainly by capability of structure to support vertical loads in large deformation ranges where there is high potential that finishing, claddings, MEP systems, etc. are seriously damaged. In fact, their coefficient of structural characteristics, ***Ds***, which is equivalent to inverse of ***R***-factor, is from 0.25 to 0.30. On the other hand, ***Ds*** in the buildings with strength dependent earthquake resistant system are from 0.45 to 0.55. It is obvious that ultimate lateral shears in the ductility dependent buildings are less and damage in the buildings will be serious once they are hit by strong earthquakes even if the life safety requirements are satisfied.

The revised Building Standard Law (BSL) went into effect in this June and stipulations in the revised law and relevant regulations require more precise evaluation and calculation with high accountability on the characteristics of earthquake resisting elements, especially those of shear walls. These requirements are intended to and perhaps efficient to prevent falsifications in structural calculation but contain high risk of a side effect to facilitate design of ductility dependent buildings with high potential of seismic damage.

In the current seismic design regulation in Japan, intensity of very rare seismic action expressed in terms of standard shear coefficient, ***Co*** = 1.0 is 5 times that of rare earthquakes for which ***Co*** = 0.2. Although there is a certain possibility that ground motions due to strong earthquakes may partly exceed this design condition, most buildings in urban areas will be hit by the ground motion within this bound. As the result, buildings with strength dependent resisting system suffer serious damage only in limited zones where quite intense ground motions occur but those with simple moment-resisting frames suffer the same level of damage in wider areas. It is understood that design targets in current BSL are to maintain functionality for rare earthquakes and life safety for very rare earthquakes. The people seems to understand that all buildings are designed to possess the same level of performances as a minimum standard stipulated by BSL and no explicit difference exists excluding special cases. However, the actual damage in buildings will be not same as considered.

Today, damage control issues are often highlighted and PML has become an important factor to evaluate seismic performance. In addition, business continuity issues after earthquakes in various types of facilities are frequently discussed. On the other hand, however, it is a quite unfavourable trend from the viewpoint of design for durable, sustainable and resilient buildings that the simple moment-resisting frame structures, in which large plastic deformations under intense seismic motions is predicted, are becoming widespread.

DESIGN SEISMIC ACTION FOR BUILDING AND CITY

The prescribed two problems, namely, cost increase necessary to enhance performance and widespread of ductility depending structures are the factors which may hinder the effort to mitigate earthquake damage in buildings. These problems are even more serious when we consider issue of how to keep functionality of urban activity over disastrous earthquakes and to realize sustainable and resilient cities.

Earthquakes are natural phenomena and the most fundamental problem in seismic design of buildings is that we cannot predict precisely what the intensity of the critical earthquake is and when it occurs. In this context, it is perhaps a rational engineering judgment considering impacts on construction cost, not to take into account explicitly the maximum possible earthquake that is with very low probability of occurrence in designing individual building. As such earthquakes will occur only quite rarely, this is an appropriate approach from probabilistic viewpoint and works well to ensure a certain level of seismic safety of each individual building against design seismic actions established based on the life of the building. However, this design philosophy concerning seismic action will be a risky choice from the viewpoint of creating sustainable and resilient cities due to the synergy effect of two factors, namely: expected life of cities is much longer than that of buildings; and buildings should be treated as being not replaceable but component parts of cities when seismic actions are concerned.

Although the serviceable life of each building is 60 years or less in general, the life of a city is much longer and ranging from several hundreds to over a thousand years. The risk of strong earthquakes in the life of a city is much higher than that of each building. In other words, the critical earthquakes to be considered in discussing the continuous functionality of cities throughout their expected life should be much stronger

than that to be considered in securing safety of each building only. Under ordinary situation, each building is deemed to be a replaceable part of a city. Buildings can be replaced one by one as the end of the life comes and sustainability of the city will be secured even if design life of each individual building is shorter than that of the city. However, the same principle cannot be applied in case of very rare earthquakes. If a very rare and strong earthquake hit a city, most of the buildings there will suffer serious damages and the function of the city will be lost for a considerably long period.

There may be argument that importance factor can provide some solutions to the problem. Concepts of importance factor are not stipulated in BSL but increase of required ultimate lateral shear for important governmental facilities and buildings accommodating hazardous materials are stipulated in "General Seismic Design Standard for Governmental Building with Commentary". Such increase is efficient in mitigating probable damages of important facilities and in improving social preparedness for emergency operation immediately after earthquakes. However, the improvements are limited to performance of so classified important facilities. All remaining buildings are out of scope of application. When discussing sustainable and resilient cities, seismic performance of not only facilities for emergency operation but also ordinary buildings for maintaining urban functionality is the key issue.

LIMIT OF LEGAL CONTROL

Despite all of the prescribed arguments, it is not easy to design individual buildings to be free from any damage for the maximum possible seismic action which we cannot predict when to occur only because they are basic components of a city. If the buildings are not subjected to strong ground motion for several decades until end of their life, we can't help being blamed that we have forced our clients to make useless additional investment. In Japan, it is a common understanding that the average life of ordinary buildings is 40 years or less. Provided that these buildings are designed to withstand strong ground motions that occur once in 400 years, as they are demolished and rebuilt 10 times in the 400 years and it means that only one out of the 10 is hit by the design earthquake and demonstrate the fruit of seismic design. The rest 9 buildings end their life without experiencing design seismic action and it will be judged that they are over-designed for seismic safety.

Under this situation, it seems that the restriction or control by laws or codes will be most effective to construct sustainable and resilient cities through enhancing required minimum seismic performance level of buildings. However, there are limits also in laws and codes and it is difficult to regulate obligations of owners or private companies to make their buildings having higher level of seismic performance beyond the target of life safety within their expected life because such regulation involves extra financial loads on the owners and/or private companies as explained before. If the government put such requirements, it may be deemed an infringement of the people's right to control their own property, which is protected by the Constitution of Japan. Consequently, not the preservation of functionality nor property but life safety level by preventing failure or collapse only is required for very rare intense earthquakes in BSL.

NEEDS FOR SUPREME SEISMIC PERFORMANCE WITHOUT COST INCREASE

Recently, concepts of performance based design are often discussed and issues such as PML and BCP are becoming more popular in structural engineering. Other methods to evaluate seismic performances are being studied and developed from various aspects. At the same time, we need to have practical methods to respond various requests for enhancement of seismic performance.

The prescribed arguments call for the development of structural systems which realize supreme seismic performance without or with very slight increase of cost compared with those required in ordinary buildings. If substantial increase in cost is not required, then, it is rational to design buildings which suffer substantially no damage from very rare earthquakes and such design will be accepted by the society. As the results of enhancement of seismic performance of individual building in a city, the performance of the city itself will be improved remarkably. Development of such structural system will make it reasonable to design buildings for the seismic action based on the return period corresponding to the life of a city, say 1000 to 2000 years. Of course we should be aware of the fact that our knowledge is still limited and further researches and studies are necessary to identify the seismic actions corresponding to such long return periods.

Today, studies of seismic engineering in the countries or areas where risk of destructive earthquakes is high should be focused on developing the technology to realize supreme seismic performance. Since the methods of reinforced concrete and steel structures were introduced to Japan in approximately 100 years ago, lots of buildings had been designed and constructed based on the methods. They have suffered from various earthquakes and it seams that the limit of seismic performances obtained based on such orthodox technology is becoming evident today. We are at the time to make effort to enhance seismic performance of cities by enhancing those of individual buildings. What we are requested today is to seek not for cost reduction keeping same performance level but for higher performance level without cost increase and to promote building structures with higher seismic performance which contribute to develop a long lasting therefore sustainable and resilient society.

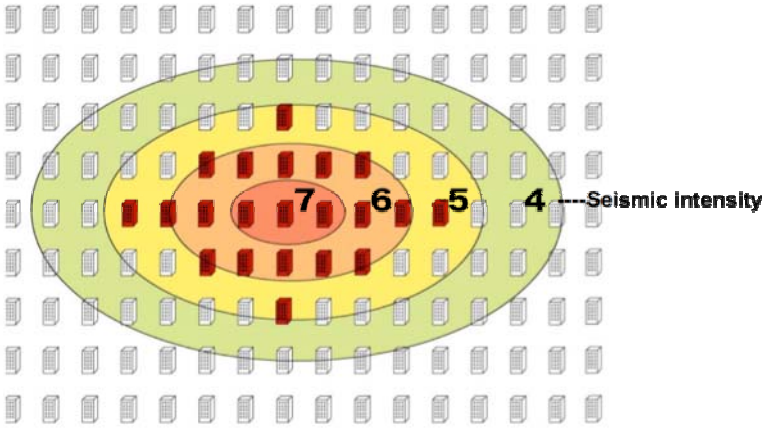

Figuer 8　Damages of buildings in the city after big earthquake, in the case that all buildings were designed as ductile frame structure.

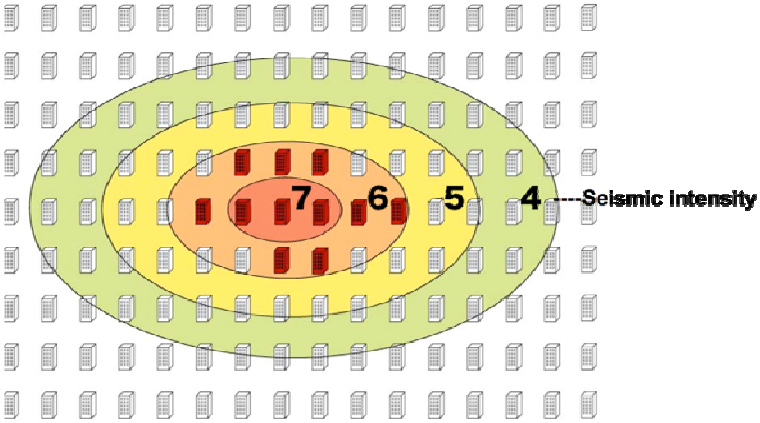

Figuer 9　Damages of buildings in the city after big earthquake, in the case that all buildings were designed as strength oriented structure.

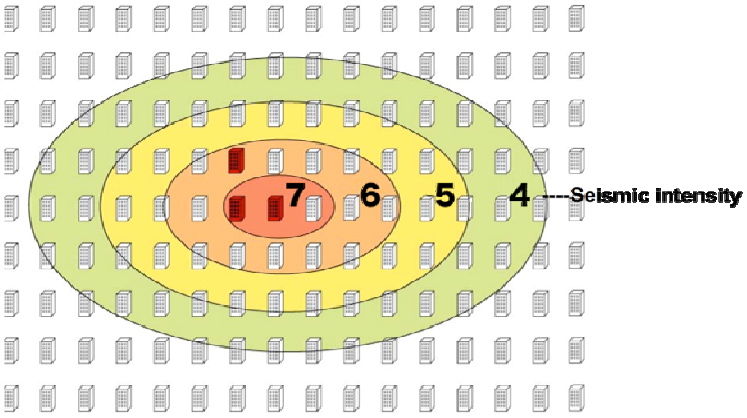

Figuer 10　Damages of buildings in the city after big earthquake, in the case that all buildings were designed as passive controlled structures.

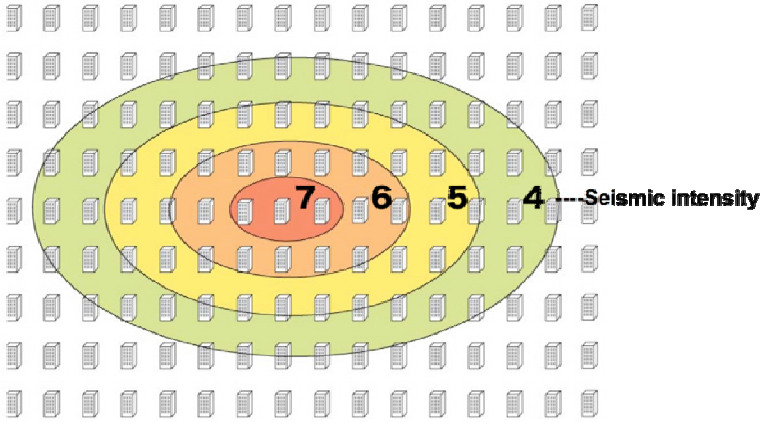

Figuer 11 All buildings were designed as seismic isolated structures.

CONCLUDING REMARK

Sustainability and resilience are obviously two of the most important and common key-words all over the world today. The most important role of structural engineers in this relation is perhaps to contribute by providing long-lasting buildings. Especially in areas where risk of destructive earthquake is high, the key issue is to secure functionality of cities over earthquakes of the intensity corresponding to their life but there are obstructions for the implementation. The most serious obstruction is the increase in cost required for this purpose. Therefore, we should changeover the direction of technology development from "cost reduction keeping same performance level" to "higher performance level without cost increase". In addition, we should note that it is one of the important duties of structural engineers to explain the true merits for clients and all stakeholders of enhancing the seismic performances of buildings.

Finally, one other important issue should be pointed out. It is the increasing risk brought about by the advance in civilization. Torahiko Terada, a famous scientist and essayist once stated that the more the civilizations advance, the more the disasters evolve. One of depopulated areas in Japan, Noto Peninsula district was hit by an earthquake in March 2007. One month was necessary to provide the temporary houses for the refugees. It is predicted that 10 years will be necessary for the same purpose in case a strong earthquake hit Tokyo even if there are sufficient spaces for temporary houses. The structural engineers, based on the knowledge in physics, mathematics, structural dynamics, etc, and complying with the laws, have been striving effort to complete many project for satisfaction of request from society. Transportation system such as railways and roads, life lines including water, gas and electricity supply and lots of buildings have been constructed. The large cities so constructed are highly efficient and active in normal situation. They have provided bases for activating economy and spaces for people to enjoy modern civilization. As the result, excessive concentration of population as well as social function to main cities has been brought about. The excessive concentration is most remarkable in Japan. Among the total population of 80 million in Germany, only 3.4 million (4%) is living in the largest city, Berlin and there are many other active cities all over the country. In US, 8.2 million among the total population of 290 million is in New York and there are also many large cities. On the other hand, approximately 25% of total population of Japan is living in Tokyo and the surroundings. Once Tokyo is damaged by destructive earthquakes, the whole country may be put into functional disorder for a long period. It is obvious that the social system of Japan is quite vulnerable strong earthquakes.

The pursuits of excessive concentration to mega cities inspired by people's demand and facilitated by activation of economy, high efficiency obtained by the concentration, highly controlled traffic network and pleasant social life supported by mass use of energy, all these will produce contrary effects to weaken the resistance against natural disasters.

Perhaps most of the citizens including engineers are honest in their activities. However, we shall perceive and alarm today that civilization resulted from integration of individual honest activity creates a high risk society and start actions in our discipline to mitigate such risk.

JOINT CONFERENCE PROCEEDINGS
7th International Conference on Urban Earthquake Engineering (7CUEE) &
5th International Conference on Earthquake Engineering (5ICEE)
March 3-5, 2010, Tokyo Institute of Technology, Tokyo, Japan

SEISMIC PERFORMANCE OF CONCENTRICALLY BRACED STEEL FRAMES: PAST AND FUTURE

Stephen Mahin[1)], Jiun-Wie Lai[2)], Chui-Hsin Chen[2)] and Yuli Huang[3)]

1) Byron and Elvira Nishkian Professor, Dept of Civil and Environmental Engineering;
Director, Pacific Earthquake Engineering Research Center, Univ. of California, Berkeley USA
2) Graduate Student, Dept. of Civil and Environmental Engineering, Univ. of California, Berkeley USA
3) Structural Engineer, ARUP Engineers, San Francisco, California, USA
mahin@berkeley.edu, adrian.jwlai@gmail.com, chchen@berkeley.edu, yuli.huang@arup.com

Abstract: This paper briefly summarizes on going experimental and computational studies on steel concentrically braced frames. Experimental results are presented herein for a NEES small group project entitled "International Hybrid Simulation of Tomorrow's Braced Frames". Results for two large-scale two-story braced frames with different bracing member cross-sections are presented from the first part of this test series. Test results are primarily used to refine the analytical models, confirm the current design practice and also validate the seismic performance of steel concentrically braced frames. Test validated numerical models are then used to simulate the performance of concentrically braced frames for ground motions representing the full hazard level. Various types of analytical models are discussed and results compared. Preliminary observations and future research directions are discussed.

1. INTRODUCTION

The steel braced frame is thought by many to be one of the most efficient and economical seismic load resisting systems to control the deformation of structures. Several severe earthquakes around the world have exposed some anticipated and unanticipated damages (AIJ, 1995; Bonneville and Bartoletti, 1996; Kelly et al., 2000). Several approaches have been proposed to enhance braced frame system behavior by making changes at the component level by using innovative devices, such as buckling restrained braces (Watanabe et al., 1988) and self-centering braces (Christopoulos et al., 2008). Some other research focuses on reducing concentration of drifts in a few stories by better distributing inelastic demand along the full height of the structure (Khatib et al., 1988; Tremblay and Merzouq, 2004). Although many experimental studies of the conventional buckling brace components and some braced frame specimens have performed in the past three decades (Black et al., 1980; Ballio and Perotti, 1987; Lee and Goel, 1987; Bertero et al., 1989; Tremblay, 2002; Yang and Mahin, 2005; Uriz and Mahin, 2008; Lehman and Roeder, 2008), the number of tests of large-scale concentric braced frame specimens is still limited. Seismic design requires that the strength and deformation capacities of a structure be sufficiently large compared to the demands. As such, test validated analytical line and finite element models are sued and compared to help assess the performance of concentrically braced frames. This paper highlights the findings of a set of experimental and numerical simulations of steel concentric braced frame building systems.

2. EXPERIMENTAL PROGRAM AT UC BERKELEY

2.1 TEST SETUP

The experiments are conducted in the NEES facility at UC Berkeley. The test setup is shown in Fig. 1. Thirty reconfigurable reaction blocks are post-tensioned vertically and horizontally to create an integrated reaction wall. The maximum base shear capacity of the test setup is 4000 kN under the loading configuration illustrated in Fig. 1. Large actuators with ±30 cm stoke are attached to each floor, which can impose around 5% story drift.

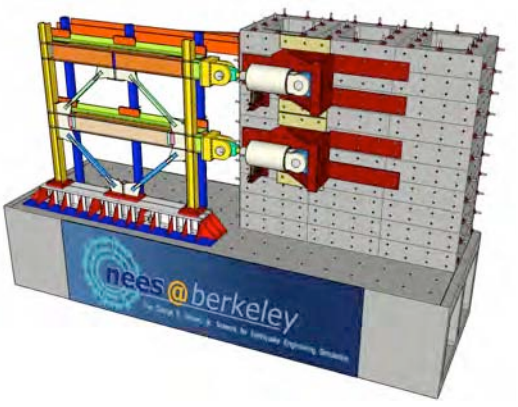

Fig 1. Overview of Test Setup

2.2 Description of Test Specimens

Four braced frame specimens are included in the special concentric braced frame test program. Each test specimen consists of a two-story, single bay concentric braced frame that is designed and detailed in compliance with the AISC Seismic Provisions for Structural Steel Buildings (AISC, 2005). The story height is 2.74 m, measured from beam centerline-to-centerline distance, and the bay width is 6.1 m, measured from column centerline-to-centerline. The name, member size, material type and test method of each specimen are shown in Table 1. Figure 2 shows the overview of specimen TCBF-B-2 before testing. The roof beam, two columns and base plates are re-used after the testing of TCBF-B-1 specimen.

Table 1 Member Specifications

Name	Column & Beam	Brace	
TCBF-B-1	W12 x 96 (Column) (ASTM A992) W24 x 117 (Roof Beam) W24 x 68 (Lower Beam) (ASTM A992)	HSS 5 x 5 x 5/16 HSS 6 x 6 x 3/8	ASTM A500B
TCBF-B-2		HSS 5 x 1/2 HSS 6 x 1/2	ASTM A500B
TCBF-B-3		W 8 x 21 W 8 x 28	ASTM A992
TCBF-B-4		HSS 5 x 5 x 5/16 HSS 6 x 6 x 3/8	ASTM A500B



Fig. 2 Specimen TCBF-B-2

The tapered gusset plates that connect braces from both stories in each specimen are 3/4" thick, and constructed as a single piece. Two fingerplates are welded on them to mimic the situation if the beam flanges continued to the column face. The fingerplates are CJP spliced to the W24 x 68 lower beam. The end of the brace was separated from the beam or column by twice the thickness of the gusset plate as recommended by AISC (2005) for out-of-plane buckling of the braces. Reinforcing plates at the net section of the braces are provided to prevent premature failure of bracing components (Fig. 6). More detail descriptions of test specimens are presented by Lai (2009).



Fig. 3 Typical Net Reduced Section Reinforcement

2.3 Loading Sequence and Instrumentation

For the first three SCBF specimens, the displacement of the roof beam is monitored and displacement controlled during the entire test process. The lower level actuator is force controlled to have one-half of the force developed in the upper level actuator. This makes the lateral force pattern an inverted triangular distribution. The test protocol is modified from the Appendix T of AISC Seismic Provisions (AISC, 2005) in order to compare with the results of future BRBF tests. Fig. 4 shows the cyclic loading protocol.

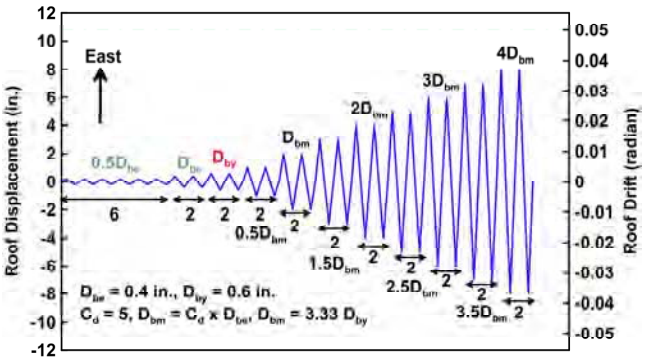

Fig. 4 Top Beam Displacement History

Each specimen is instrumented with displacement transducers to measure the story drifts, relative displacements and local deformation of members or connections. Linear type strain gages and rosettes are also used to measure the internal strain distributions during the tests. The specimens are whitewashed to facilitate observation of local yield patterns.

2.4 Specimen TCBF-B-1 (Square HSS Braces)

The story shear vs. story drift is shown in Fig. 5. This shows that while both stories yield for low-level cycles, more drift is concentrated in the lower level during the later cycles. In the first cycles to D_{by}, all four braces exhibit small out-of-plane buckling. Local buckling begins at the mid-length of the braces as well as at the ends of the lower level beam at the face of the gusset plates during the first cycle to D_{bm}. Cracks in the local buckles in both braces on the lower level began in the first half cycle at $1.5D_{bm}$. The

cracks in both lower level braces fractured across the entire section during the remaining cycles at $1.5D_{bm}$. AISC (2005) requires BRBF systems to be able to develop $2D_{bm}$. The flanges in the lower level beam fractured at cycles at $2D_{bm}$ and $2.5D_{bm}$. This failure of beams or columns adjacent to gusset plates was noted previously by Uriz and Mahin (2005) at drifts in excess of about 2%. One of the upper level braces almost completely fractured in the $2.5D_{bm}$ cycles.

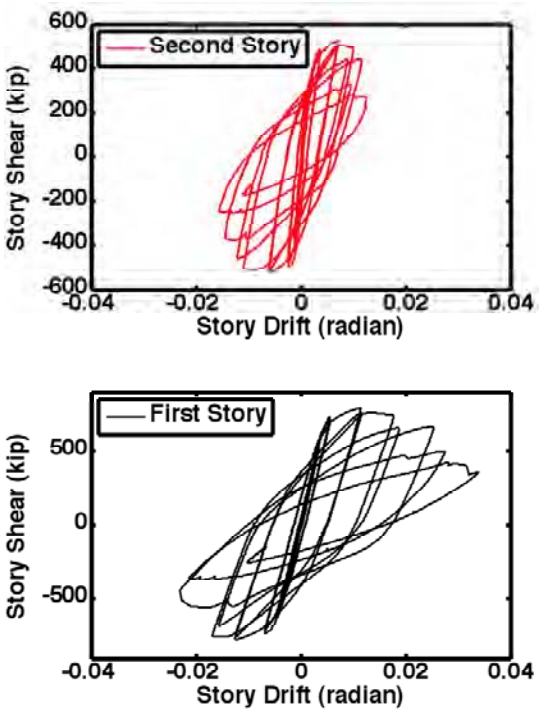

Fig. 5 Story Shear-Story Drift Relations for Specimen with Square HSS Braces

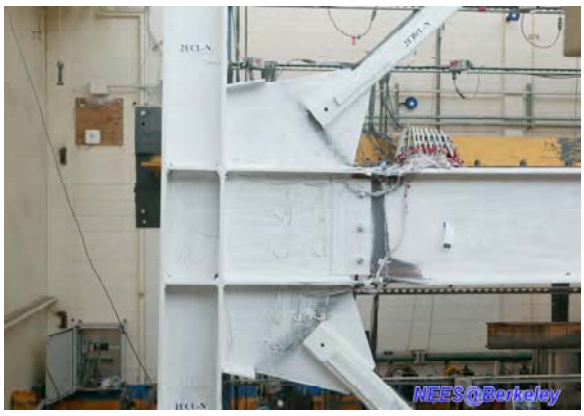

Fig. 6 Local Bucking and Fracture of Beam Flanges

2.5 Specimen TCBF-B-2 (Round HSS Braces)

The second specimen was build by repairing the TCBF-B-1. The roof beam, columns and base plates were reused, and the lower beam and all of the gussets and braces were replaced. Some weld repairs were made at the column bases due to small fractures detected there in the CJP welds. During the second cycle at 1.5 D_{bm}, one column base fractured (Fig. 8), and ribs were added to reinforce both column bases before continuing with the test.



Fig. 7 Complete Fracture of Lower Level Square HSS Brace



Fig. 8 Fracture of Weld to Base Plate in TCBF-B-2

The relationships between story shear and story drift for specimen TCBF-B-2 is shown in Fig. 9. This specimen exhibited a more even distribution of story drifts.

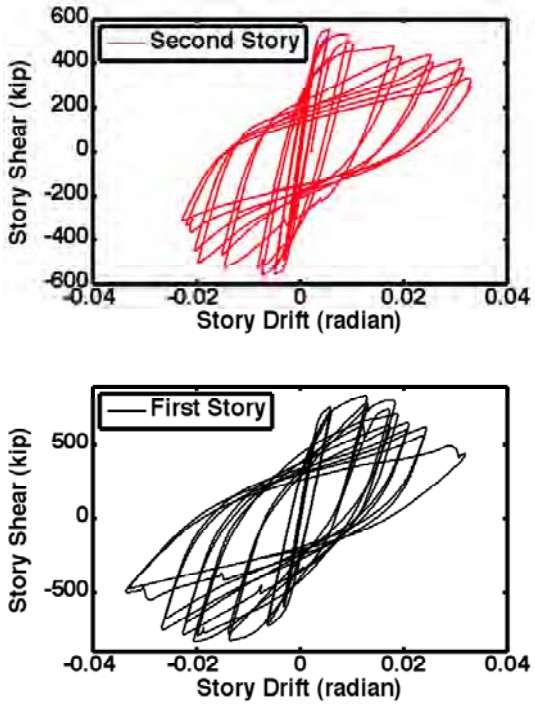

Fig. 9 Story Shear - Story Drift 3relations for Specimen with Round HSS Braces

Because the round HSS sections selected were more resistant to local buckling than the square ones used for TCBF-B-1, local buckling was delayed until the first half cycle at $2.5D_{bm}$ compared to $1.0D_{bm}$ for TCBF-B-1. One lower level brace buckled out-of-plane during the first 0.5 D_{bm} cycle, and the remainder buckled at both levels during the $1.0D_{bm}$ cycles. Substantial out-of-plane brace displacements were observed during the test (Fig. 10).



Fig. 10 Lateral Buckling of Braces During Test



Fig. 11 Local Buckle and Fracture of Beam at Gusset

As noted, one of the column to base plate connections fractured during the second 1.5 D_{bm} cycle (Fig. 8). After this was repaired and testing continued, the flanges at both ends of the beam where they connected to the gusset plates (and webs) locally buckled and fractured during the 2.0 D_{bm} cycles (Fig. 11). Cracks did not appear in one of the round HSS braces at the bottom story until the last cycle at $2.5D_{bm}$, and this brace fractured during the first cycle at 3.0 D_{bm}. The remaining brace at the lower level did not fracture until the first cycle to 3.5 D_{bm}. Considerable damage was observed at the column bases.



Fig. 12 Fracture of Round HSS Brace

2.6 Observations from Tests

From the results shown above, we can see that for designs having similar configuration and base shear capacity, the specimen with round HSS braces exhibits better ductility capacity than the one with square HSS braces, and that the envelop of base shear degrades more slowly. This is attributed to the superior local buckling characteristics of the braces selected. In addition, the story drift at each story of TCBF-B-2 specimen tends to be more uniform than TCBF-B-1 specimen.

The brace and gusset plate configuration of both specimens tends to amplify the rotation demand at both ends of lower beam-to-gusset splices. Once a plastic hinges forms at either end of the lower beam, local buckling and flange fracture rapidly ensue. The frame specimen with these fractured flanges is able to redistribute the internal forces needed for frame stability and the frame is able to withstand even larger roof lateral displacements. Thus, it may be reasonable to use pinned beam-to-gusset details to help avoid local damage at this region. In specimen TCBF-B-2, a net reduced section failure mode happened in the fingerplate of one-piece-gusset, which indicates a modified fingerplate to gusset plate details should be used.

Yield patterns on the column flanges also indicate that significant torsion and biaxial bending occurred in the columns under large deformation. This is associated with the large out of plane displacement of the braces. Once a brace fractures, the story hysteretic loops for the structure are not symmetric. Frame action not typically considered in the design of concentric braced frames played an important role in the overall behavior prior to and subsequent to the brace fractures, and further research is needed on this topic.

2.7 Future Tests

Two additional SCBF specimens are planned. One will involve wide flange bracing, and the other will be a repeat of TCBF-B-1, but with hybrid testing to better assess the likely

seismic response of conventional concentric braced frames. Following these tests, several tests of frames incorporating buckling resistant braces are planned.

3. NUMERICAL SIMULATION

Numerical simulations are essential to understand the behavior of concentrically braced frames, and to develop reliable methods for designing them to withstand the effects of earthquakes. Because of the highly complex behavior of braces, and the unintended important role of frame action, modeling of braced frames is quite complex. Three approaches have been undertaken in the past. One of these represents the braces as simple pin ended truss elements that have rule-based hysteresis characteristics that mimic the behavior of actual braces. Increasingly fiber models are being used whereby a brace is able to withstand both axial load and bidirectional bending. A brace member is divided in to a series of line elements, each of which model a number of sections along their length. By representing the section by a series of uniaxial fibers the cross section of the member can be geometrically modeled, and realistic uniaxial properties can be accounted for in the model, including the effects of low cycle fatigue and rupture. By using large displacement geometric effects when formulating and computing the mechanical characteristics of the member, yielding and lateral buckling can be modeled. A summary of such approaches has been described by Uriz and Mahin (2008). These fiber models can give good indications of response, but do not account for the effects of local buckling. As such, these models must be calibrated against tests of similar members. Moreover, line models are often unable to realistically represent the behavior of beam-column-gusset plate regions.

As a result, increasing attention is being placed on finite element models based on shell and solid elements. While many studies have been done in the past, only recently have investigators focused on models that predict the deterioration and rupture of materials (Kavinde and Deierlein, 2004), especially during the analysis so that the redistribution of loads and deformations due to member failure can be simulated (Huang and Mahin, 2009). Such modeling approaches are time consuming, but they can provide information not obtainable by other numerical means, and execution speeds are becoming reasonable for many problems of interest due to increasing computer capabilities.

4. STRUCTURAL PERFORMANCE ASSESSMENT

The availability of advanced numerical models makes it possible to investigate the performance of buildings having different heights, configurations, member types, design criteria, and details considering many ground motions selected to represent the full range of seismic hazard appropriate for the building site and design criteria. Such studies have been undertaken by Uriz and Mahin (2008), Chen, Lai and Mahin (2008), Chen, Huang and Mahin (2009) an others.

Such studies tend to show that concentrically braced frames tend to concentrate damage in one of a few stories, but that this tendency is slightly less for BRBFs. The studies also show that inelastic deformation demands can be quite large in comparison with brace capacities, especially for short period structures incorporating conventional braces that buckle. For taller structures, weak story responses can occur, especially where the demand to capacity ratio for the structure is not uniform over height. P-Δ effects can be important for taller buildings where damage concentrates in one or a few stories. By designing a structure to be stronger, providing more uniform demand/capacity characteristics over the height of a structure, or by providing a strong continuous spine or mast vertically throughout the building height, the adverse effects of these damage concentrations can be mitigated.

3. CONCLUSIONS

Concentrically braced frames are widely used around the world. In spite of this, and their often inadequate performance in past earthquakes, considerable research remains to be done to develop reliable design procedures capable of achieving specified performance. However, results indicate various problems with braced frames, but also suggest solutions.

Acknowledgements:
This paper is based upon research work which is part of research project entitled "International Hybrid Simulation of Tomorrow's Concentrically Braced Frames" funded by the National Science Foundation through the research program of the George E. Brown Jr. Network for Earthquake Engineering Simulation (Grant No. CMMI-0619161) and "Robust Performance-based Design of Concentrically Braced Steel Frame Buildings" (Grant No. CMS-0600625). Financial and in-kind support from NSF, the Herrick Corporation and the Nishkian Chair in Structural Engineering is greatly appreciated. Any opinions, findings and conclusions in this paper are those of the authors and do not necessary reflect the views of the sponsors.

References

AIJ (1995), *Reconnaissance report on damage to steel building structures observed from the1995 Hyogoken-Nanbu (Hanshin/Awaji) earthquake*, Steel Committee of Kinki Branch, Architectural Institute of Japan, Tokyo, Japan.

AISC, 2005. *Seismic Provisions for Structural Steel Buildings*, American Institute of Steel Construction, Chicago, Illinois 60601.

Ballio, G. and Perotti, F., (1987), "Cyclic Behavior of Axially Loaded Members: Numerical Simulation and Experimental Verification," *Journal of Constructional Steel Research*, 7, 3–41.

Bertero, V. V., Uang, C.-M., Llopiz, C. and Igarashi, K. (1989). "Earthquake Simulator Testing of Concentric Braced Dual System," *ASCE Journal of Structural Engineering*, 115(8), 1877–1894.

Black, G. R., Wenger, B. A. and Popov, E. P. (1980). Inelastic Buckling of Steel Struts Under Cyclic Load Reversals, UCB/EERC-80/40, Earthquake Engineering Research Center, University of California, Berkeley, CA.

Bonneville, D. and Bartoletti, S. (1996), "Case Study 2.3: Concentric Braced Frame, Lankershim Boulevard, North Hollywood," *1994 Northridge Earthquake; Building Case Studies Project; Proposition 122: Product 3.2*, SSC 94–06, Seismic Safety Commission State of California, 305–324.

Chen, C.-H., Lai, J.-W. and Mahin, S. (2008). "Seismic Performance Assessment of Concentrically Braced Steel Frame Buildings," *Proceedings*, 14th World Conference on Earthquake Engineering, Beijing, China, Oct. 12-17, 2008.

Chen, C-H, Huang, Y. and Mahin, S. (2009), "Comparison of Seismic Demands for a Three-Story SCBF System Considering Fiber and Finite Element Models," *Proceedings*, Annual Convention of the Structural Engineers Association of California, San Diego, CA.

Chen, C-H, AND Mahin, S. (2010), "Example Collapse Performance Evaluation of Steel Concentrically Braced Systems," *Proceedings*, US National Conference on Earthquake Engineerng, Toronto, Canada (in press).

Christopoulos, C., Tremblay, R., Kim, H. J. and Lacerte M. (2008), "Self-Centering Energy Dissipative Bracing System for the Seismic Resistance of Structures: Development and Validation," *ASCE Journal of Structural Engineering*, 134(1), 96–107.

Huang, Y. and Mahin, S. (2008), "Evaluation of Steel Structure Deterioration with Cyclic Damaged Plasticity," *Proceedings*, 14WCEE, Beijing, China.

Kanvinde, A., and Deierlein, G. G. (2004). "Micromechanical Simulation of Earthquake Induced Fractures in Steel Structures." *Blume Center Report TR145*, Stanford University, Stanford, CA.

Kelly, D. J., Bonneville, D. and Bartoletti, S., 2000. "1994 Northridge earthquake: damage to a four-story steel braced frame building and its subsequent upgrade," *Proceedings*, 12th World Conference on Earthquake Engineering, New Zealand Society for Earthquake Engineering, Upper Hutt, New Zealand.

Khatib, I.F., Mahin, S.A. and Pister, K.S. (1988), "Seismic Behavior of Concentrically Braced Steel Frames," *UCB/EERC-88/01*, Earthquake Eng. Research Center, University of California, Berkeley, CA.

Lehman**,** D. and Roeder, C. (2008), "Improved Seismic Design of Concentrically Braced Frames and Gusset Plate Connections**,"** *Proceedings*, 2008 Structures Congress: Crossing Borders; Vancouver, BC; Canada; 24-26 Apr. 2008.

Lai, J.W. (2009), Test Results of Two Special Concentric Braced Frame Specimens," *CE299 Report*, University of California, Berkeley, CA. (in press)

Lee, S. and Goel, S. C. (1987). "Seismic Behaviour of Hollow and Concrete Filled Square Tubular Bracing Members," *UMCE87-11*, University of Michigan, Ann Arbor, MI.

Tremblay, R. (2002), "Inelastic seismic response of steel bracing members," *Journal of Constructional Steel Research*, 58, 665–701.

Tremblay, R. and Merzouq, S. (2004), "Dual Buckling Restrained Braced Steel Frames for Enhanced Seismic Response," *Proceedings*, Passive Control Symposium 2004, November 15-16, Yokohama, Japan.

Uriz, P. and Mahin, S. A. (2008), "Toward Earthquake-Resistant Design of Concentrically Braced Steel-Frame Structures," *PEER 2008/08*, Pacific Earthquake Engineering Research Center, University of California, Berkeley, CA.

Watanabe, A., Hitomi, Y., Saeki, E., Wada, A., and Fujimoto, M. (1988). "Properties of Brace Encased in Buckling-Restraining Concrete and Steel Tube," *Proceedings*, Ninth World Conference on Earthquake Engineering, Japan, Paper No. 6-7-4, 719–724.

Yang, F. and Mahin, S. A. (2005), "Limiting Net Section Failure in Slotted HSS Braces," Structural Steel Education Council, Moraga, CA.

JOINT CONFERENCE PROCEEDINGS
7th International Conference on Urban Earthquake Engineering (7CUEE) &
5th International Conference on Earthquake Engineering (5ICEE)
March 3-5, 2010, Tokyo Institute of Technology, Tokyo, Japan

PRELIMINARY RECONNAISSANCE REPORT - 12 JANUARY 2010 HAITI EARTHQUAKE

Eduardo A. Fierro[1)] and Cynthia L. Perry[2)]

1) President, BFP Engineers, Inc., Berkeley, California USA
2) Vice President, CFO, BFP Engineers, Inc., Berkeley, California USA
efa@bfpeq.com, clp@bfpeq.com

Abstract: After 240 years, the Enriquillo Plantain Garden Fault ruptured on 12 January 2010 at 4:53PM, resulting in a 7.0 Magnitude (USGS) earthquake in the vicinity of Port-au-Prince, Haiti. The epicenter was located at 18.457°N and 72.533°W and 25 km (15 miles) WSW of Port-au-Prince. The earthquake has been a disaster for Haiti; at the time of this writing there are 212,000 confirmed deaths. The National Palace, Palace of Justice, National Assembly, Supreme Court, Prison Civile de Port-au-Prince, and buildings housing the ministries of finance, education, public works, communication and culture have all been damaged. Power, water, and communications have been disrupted. This report is based on field reconnaissance by Eduardo Fierro. Mr. Fierro was on the ground in Port-au-Prince on Thursday January 14. His photos and observations were made from January 14 to 20, 2010. The primary objective of this initial trip was to observe the performance of building structures, industrial facilities, and infrastructure from a structural engineering perspective. This report documents places and structures that Mr. Fierro personally observed during his initial visit including Port-au-Prince, Cite Soleil, Petion Ville, Carrefour and other towns en route to Leogane.

1. INTRODUCTION

After 240 years of inactivity, the Enriquillo Plantain Garden Fault ruptured on 12 January 2010 at 4:53PM local time, resulting in a 7.0 Magnitude (USGS) earthquake in the vicinity of Port-au-Prince, Haiti. The epicenter was located at 18.457°N and 72.533°W and 25 km WSW of Port-au-Prince. The rupture occurred at a shallow depth of 13km.

The earthquake has been an unmitigated disaster for Haiti; as of February 5th the Haitian government stated there were 212,000 deaths, but the actual number of deaths may never be known. Thousands more are injured, thousands are homeless, and thousands have already fled Port-au-Prince. The Haitian government is in shambles; the National Palace, Palace of Justice, National Assembly, Supreme Court, Prison Civile de Port-au-Prince, and buildings housing the ministries of finance, education, public works, communication and culture have all been damaged. Municipal government buildings in Port-au-Prince suffered similar damage. Power, water, and communications have been disrupted. In spite of international efforts, there are desperate shortages of water, food, and medical care. The Minister of Education stated that the education system in Haiti had "totally collapsed;" half the nation's schools and the three main universities suffered severe damage. (Wikipedia)

As the poorest nation in the western hemisphere, Haiti has been struggling to pull its people out of poverty. It is perhaps not surprising that few Haitians appeared to have an awareness that they were living in an active seismic zone; 240 years is a long time to nurture a memory of earthquakes when hunger and hurricanes are more immediately pressing concerns. Nevertheless, the consequences of building without seismic detailing have been staggering.

This preliminary report is based on field reconnaissance by Eduardo Fierro. Mr. Fierro has performed reconnaissance after many previous earthquakes and has established relations with the seismic engineering community in the Dominican Republic (DR) where he and Prof. Vitelmo Bertero have been lecturing on seismic design since 2003. A center promoting protection against natural disasters was founded in Santiago, DR in 2008 bearing the name of Prof. Bertero (Instituto Dominicano de Ingenieria Superior y Desastres Naturales "Vitelmo Bertero" Inc. (IDISDEN)).

Mr. Fierro left Berkeley on January 12, traveled to Santiago, DR, and along with several Dominican engineers from IDISDEN, was on the ground in Port-au-Prince, Haiti on Thursday January 14; his photos and observations were made between January 14th and 20th. The primary objective of this initial trip was to observe the performance of building structures, industrial facilities, and infrastructure from a structural engineering perspective. Extensive information about this earthquake and its effects is available on the internet and from various media sources. This report documents places and structures that Mr. Fierro personally observed during his initial visit including Port-au-Prince, Cite Soleil, Petion Ville, Carrefour and other towns en route to Leogane.

2. SEISMIC SETTING

Haiti shares the island of Hispaniola with the Dominican Republic; Haiti occupies roughly the western third of the island. The northern shore of Hispaniola lies near the boundary separating the Caribbean plate and the North America plate. This plate boundary is dominated by left-lateral strike slip motion and compression, and accommodates about 20 mm/y slip, with the Caribbean plate moving eastward with respect to the North America plate. The island is crossed by several strike-slip faults including those which make up the Enriquillo Plantain Garden Fault Zone on the south. This fault zone starts offshore to the west of Haiti, bisects the Haitian peninsula, and then extends eastward towards Santo Domingo, DR (see Figure 1).

Although there have been no recent significant earthquakes in Haiti, several earthquakes were recorded by French historian Moreau de Saint-Méry (1750–1819) during the French colonial period. He wrote that in Port-au-Prince, "only one masonry building had not collapsed" in the earthquake of 1751 and that the "whole city collapsed" in the earthquake of 1770 (Wikipedia). At the 18th Caribbean Geological Conference in 2008, Paul Mann et al stated that the fault had been locked for many years and the period of inactivity was likely at an end (Mann, 2008).

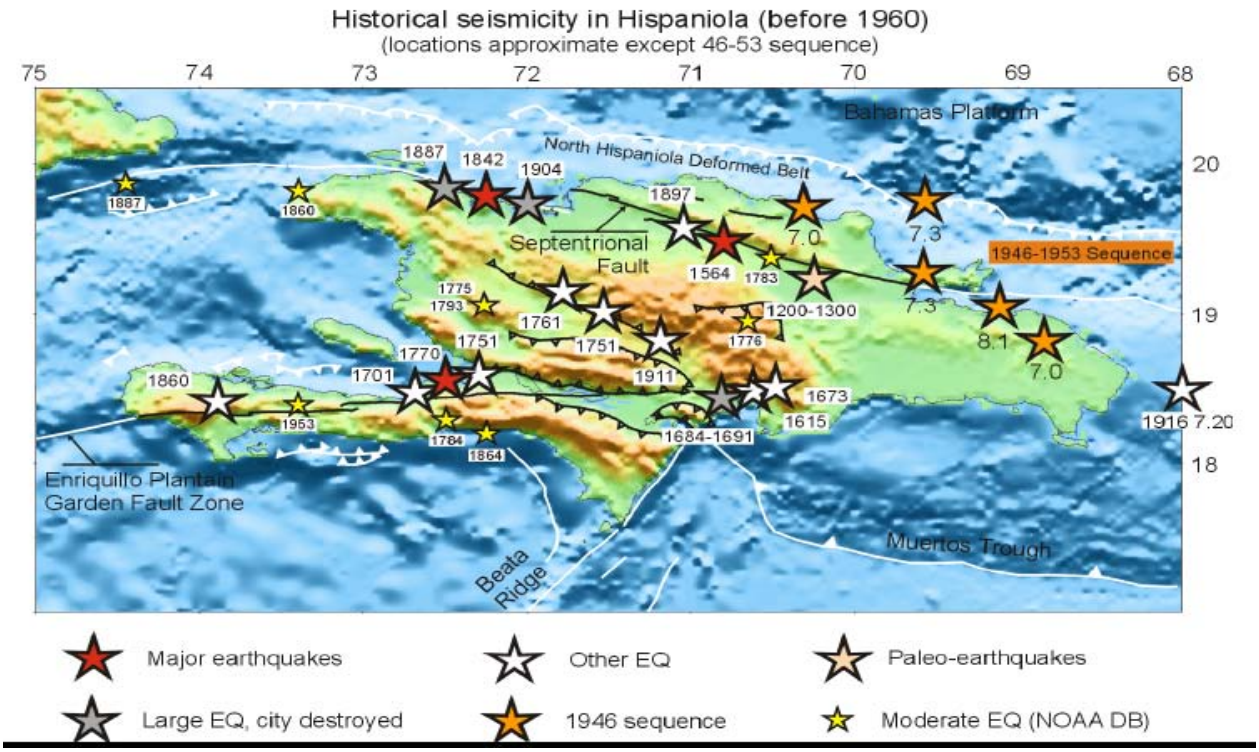

Figure 1 Historical Seismicity in Hispaniola prior to 1960. Last major earthquake near Port-au-Prince was in 1770.

3. GROUND MOTION ESTIMATES

The USGS has published Shakemap instrumental intensity estimates (Figure 2) and estimated peak ground accelerations (PGA) (Figure 3). Note that the blue dots in Figure 3 indicate instrument locations; the one instrument located in Haiti is along the north coast, far from the epicenter. Figure 3 shows a maximum PGA of 0.30g. Based on the observed damage, Mr. Fierro estimates the PGA was more likely 0.45g in Port-au-Prince and possibly higher west of the epicenter. Structures in Leogane and other communities to the west suffered a higher level of damage than similar construction in Port-au-Prince.

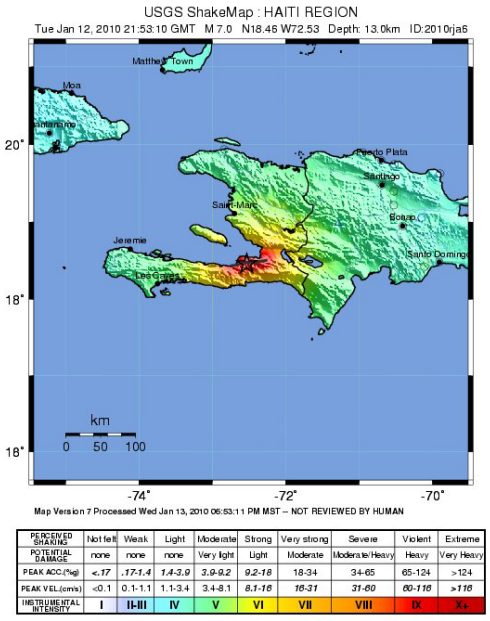

Figure 2 Instrumental Intensity (USGS Shakemap)

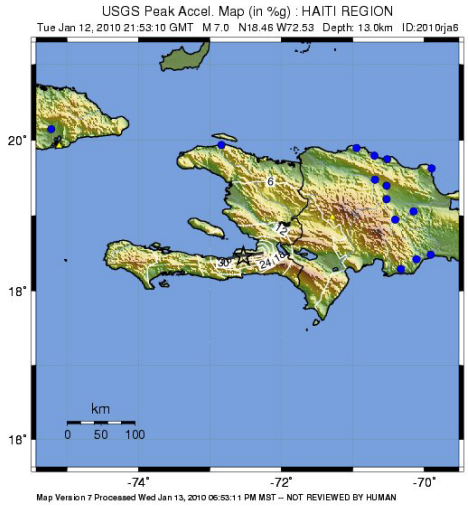

Figure 3 Peak ground acceleration (USGS)

4. GEOTECHNICAL OBSERVATIONS

The epicentral region includes low lying coastal areas as well as coastal mountains with elevations in the range of 500-2000 meters. Landslides were a common sight on hillsides surrounding Port-au-Prince. Landslides and rock falls blocked roads, brought down utility poles, and resulted in damage or collapse of many hillside structures. Maps of damaged areas in Port-au-Prince show pockets with relatively more or less damage than the surrounding areas; indicating that local soil conditions may have contributed to the variation in damage. Dramatic evidence of liquefaction and lateral spreading was evident at the port where several docks and port structures were damaged or disappeared completely into the harbor.



Figure 4 Landslide caused collapse of utility pole.



Figure 5 Failure of rubble and unreinforced masonry retaining walls.



Figure 6 Landslides contributed to damage of shanties on hillside near Petion Ville



Figure 7 Landslide west of Port-au-Prince

5. CONSTRUCTION STANDARDS FOR BUILDINGS IN HAITI

The most striking aspect of the Haitian earthquake is the complete absence of seismic detailing in Haitian construction, from informal housing to recent multistory buildings in downtown Port-au-Prince, only a handful appeared to have been built with any awareness of the most basic principles of seismic design and construction. It appears there is no building code in Haiti and there are no licensing requirements for architects, engineers, or contractors. Seismic design is not included in the engineering curriculum in Haiti. Engineers who use any type of code have apparently used the French code (Beton Arme aux Etats Limites (BAEL)) which does not include any provisions for seismic design, or they have used the gravity load provisions from the American Concrete Institute code (ACI-318). While there are some laws on the books requiring building permits and inspections, it appears these are neither followed nor enforced. (Fouche, 2010)

The predominant style of construction is what is known in some parts of the developing world as confined masonry; relatively small reinforced concrete frames with unreinforced concrete masonry unit (CMU) infill. In this style of construction, the concrete members are cast after the masonry walls are in place. Tragically, the Haitian version has the outward appearance of confined masonry but had been built without the requisite seismic detailing to provide the confinement, resulting in thousands of catastrophic failures. Thus, this unconfined masonry construction had been used on multistory buildings up to 5-6 stories but performed no better than unreinforced masonry construction.

Nonductile concrete, unreinforced masonry, and unconfined masonry are all structural systems with little lateral capacity and known to perform poorly in earthquakes. Irregular configurations with soft, weak stories or captive columns are also known to perform poorly. Poor quality materials, poor workmanship, poor maintenance, and use of corrosive materials such as beach sands in the concrete result in structures that perform poorly. Construction without any engineering design or oversight, without any standards, much less seismic standards, and without any type of inspection cannot be expected to fare well during a major earthquake.

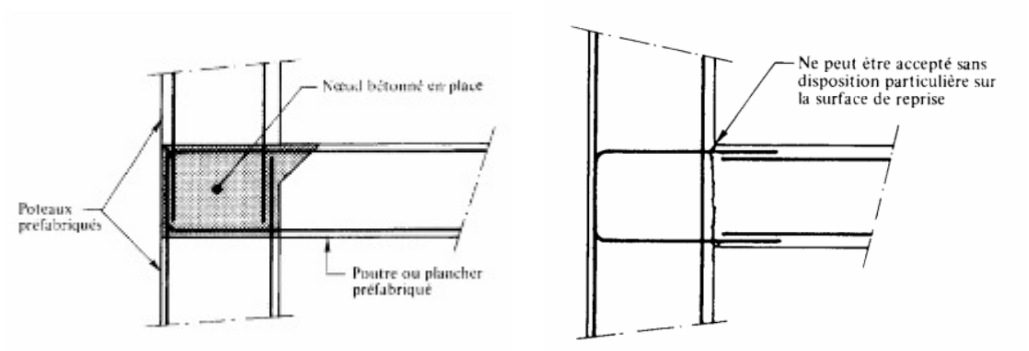

Figure 8: Beam-column joint details A & B from Regles BAEL 91 (Beton Arme aux Etats Limites), 2006. Details show column bars spliced in the beam-column joint and beam bars spliced at the face of the joint





Figures 9, 10, 11 (clockwise): Typical concrete details with undersized members, mixed use of smooth and deformed rebar, undersized rebar, small open hoops, no hoops in joint. Columns often sized to match width of 0.15m or 0.20m CMU block. Poor quality concrete, lack of consolidation, and corrosion of bars also seen widely. The combination of heavy construction and lack of ductility resulted in thousands of collapsed structures and many thousands of fatalities.

6. RESPONSE OF BUILDING STRUCTURES

As noted above, the building stock in Haiti is largely brittle and weak and was not designed to resist earthquakes. The difference between those that collapsed and those still standing may be a very small margin of reserve strength since virtually none of these structures were designed for seismic forces. Although there are many buildings still standing, buildings of all sizes, materials, and vintages did poorly. A small sample of these is shown below:



Figure 12: Presidential Palace. E-shaped plan; completed 1920; partial collapse. Many 1st story windows unbroken but most of the structure above 1st story collapsed.



Figure 13: Port-au-Prince Cathedral. Built 1884-1914; collapse of roof and upper walls. Archaic reinforcing dangling from above; light steel roof framing in debris.



Figure 14: Modern 4-story colonial-style building (est. 5 yrs old), partial collapse of bottom 2 floors.



Figure 15: 5-story building; bottom two stories collapsed. Close-up of 1st-2nd story joints in Fig. 11.



Figure 16: 3-story structure; never completed; collapsed at 1st floor and leaning on adjacent structure. Few transverse walls, heavy slabs, undersized and weak columns, and complete lack of ductile detailing all contributed to collapse.



Figure 17: Close-up from 3-story collapse at left. Column dimensions 0.15m x 0.30m. Note column bars spliced inside the beam-column joint.



Figure 18: 2-story school in Leogane; complete collapse with many fatalities.



Figure 19: 3-story university building in Leogane, still under construction with weak columns and little or no masonry infill. Complete collapse.

7. RESPONSE OF INFRASTRUCTURE

The infrastructure of Haiti will take many years to recover from this devastating earthquake. The main port in Port-au-Prince had two primary docks; one of these collapsed completely and the other suffered a partial collapse (see

Figures 20-23). The adjacent fuel port lost the seaward end of the dock and the piles supporting the remaining section were all misaligned (Figures 24-27). The glazing all fell from the control tower at the international airport and masonry infill walls in the terminal were cracked, closing the airport temporarily. The team visited two electric power plants; neither one was in operation. The first was out primarily due to failures in the distribution system outside the plant; the second was down due to the failure of a fire water tank. The tank farm adjacent to the fuel port suffered extensive damage. Roads and bridges throughout the area suffered damage.

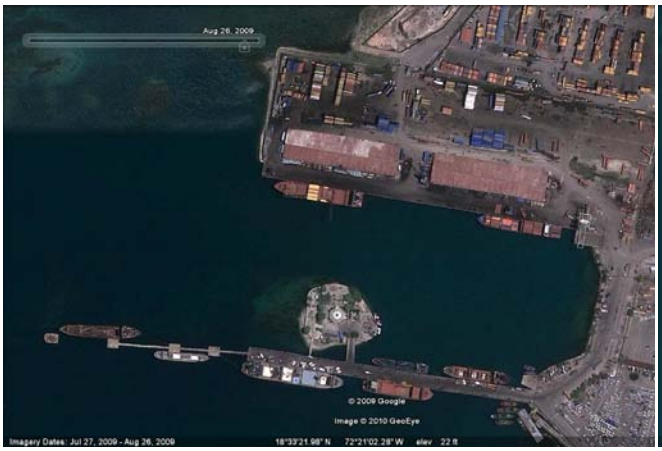

Figure 20: Port-au-Prince main commercial port prior to earthquake. (Google Earth images used for Figures 20, 21, 24, and 25).

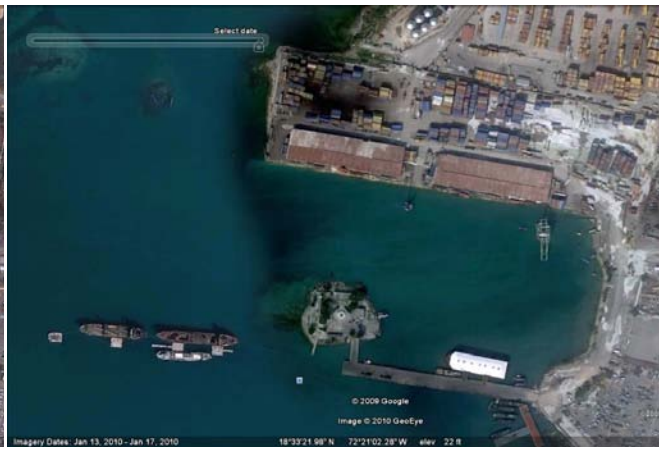

Figure 21: Note traveling crane at top of photo now immersed in water; no sign of dock. Half of dock at bottom of photo also gone. Note white patches onshore indicating residue from sand boils.



Figure 22: Commercial port; dock collapsed and crane immersed underwater. Signs of liquefaction, sand boils, and lateral spreading were seen throughout port area.

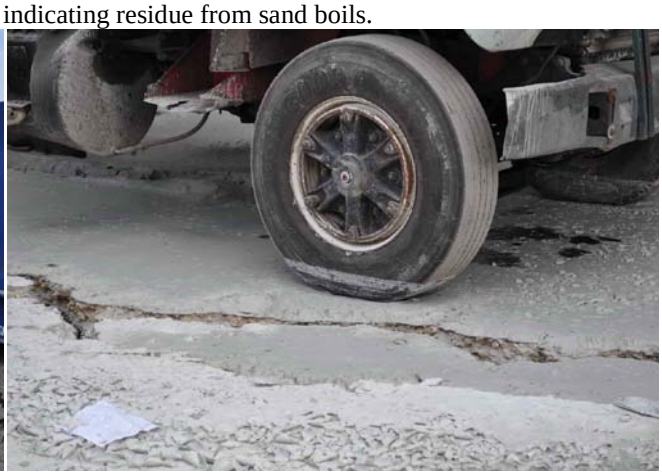

Figure 23: Mark on tire indicates height of sand flow at commercial port.



Figure 24: Fuel port prior to earthquake.

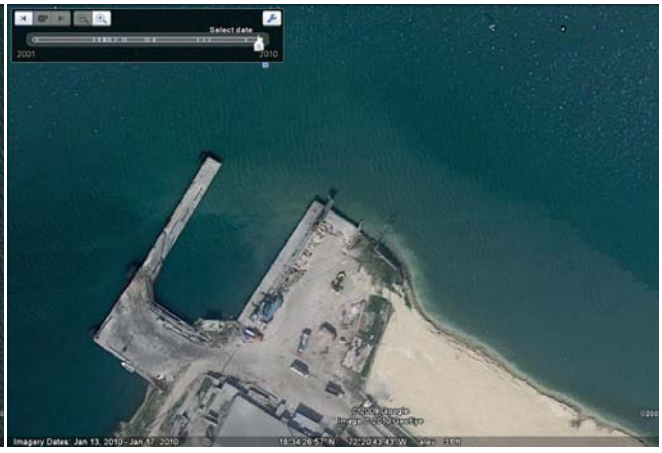

Figure 25: Fuel port; dock collapsed (note green truck visible hanging off end of remaining section).



Figure 26: Fuel port, end of remaining section of dock.



Figure 27: Precarious support for remaining section of dock at fuel port; all piles misaligned.



Figure 28: All glazing fell from control tower; Port-au-Prince International Airport. Infill walls in terminal cracked; mostly nonstructural damage.



Figure 29: Bridge along main road into Port-au-Prince from the east. Damage at girder seats; all locations.



Figure 30: Electric power plant; one of six unanchored transformers jumped the rails. No damage to ceramic components.



Figure 31: Tank farm at fuel port. Widespread tank damage; tank shown had “elephant foot” and “elephant knee.”

8. RESPONSE OF INDUSTRIAL FACILITIES

Mr. Fierro visited a steel factory in Port-au-Prince and a cement plant located near Aubry to the north of Port-au-Prince. The cement plant was still operating the day of the visit. This plant had a dedicated pier, many conveyors, silos,

tanks, etc. While the team observed damage to many structures at the plant, the plant manager indicated that most of the observed damage affected structures or equipment that was not actively in use. The steel plant imports large rolls of Dominican steel wire and cuts and straightens the bars for sale as deformed #3 bars, deformed #4 bars, and smooth ¼" diameter bar used for transverse ties. The roof of the steel plant collapsed the facility was not in operation.

9. EMERGENCY RESPONSE

One of the most tragic aspects of this earthquake was the complete absence of emergency responders in the initial hours and days following the earthquake. Haitian government officials were overwhelmed by family tragedies of their own; government ministries were in ruins; and communications were severed. On January 14, Mr. Fierro did not see any search and rescue teams, any police presence, any caution tape, any clean-up crews, any heavy equipment, any food or aid stations, any assistance of any kind. While this situation changed in the following days, as international aid poured in, the lack of immediate assistance may have cost many their lives.

10. CONCLUSIONS AND RECOMMENDATIONS

It would be easy for those in the developed world to look at this tragedy and think that this cannot happen here. Unfortunately for all of us, there are many locations in the world that build today without appropriate seismic detailing; there are many vintage structures throughout both the developed and developing world without appropriate seismic detailing; there are many locations where the current generation has no memory of seismic activity and earthquake preparedness is not on the list of priorities. As the world population grows and urban areas become more densely populated, the worldwide earthquake hazard is increasing rather than decreasing.

Nevertheless, successful seismic resistant schools, hospitals, commercial structures and residences can be built utilizing the same concrete, steel, and concrete block used in Haiti. Other countries such as Peru and Turkey share many of the problems seen in Haiti and use confined masonry for the majority of their building structures. Since 1999, schools in Peru have been built following a standard design that has been shown to resist ground motion on the order of 0.50g without any damage. The government of Peru also sponsored the production and dissemination of a handbook for property owners and laborers showing cartoon-style how to build a confined masonry home, including step by step instructions for digging footings, mixing concrete, arranging the bars, etc. (Blondet). Several pages from the Spanish language version of this booklet are shown in Figure 34.

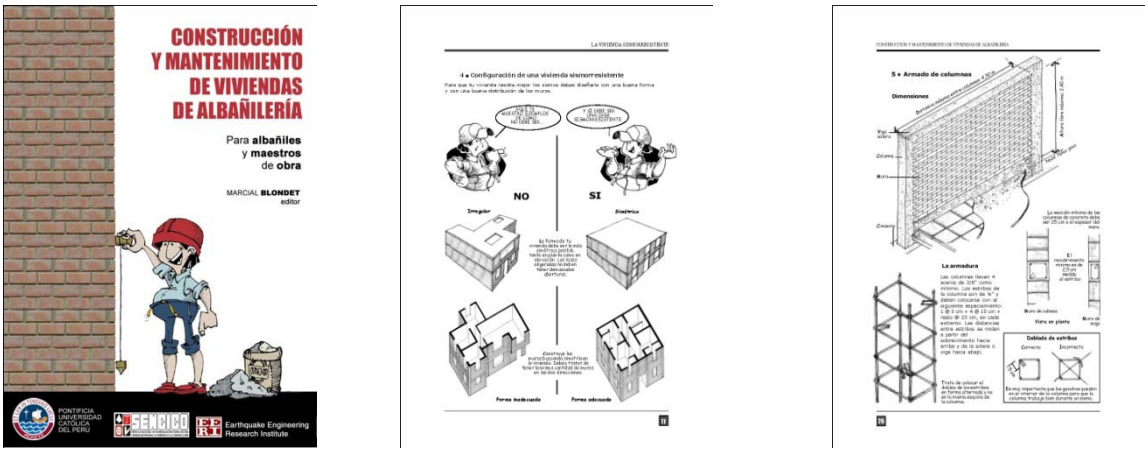

Figure 32: Peruvian booklet on confined masonry construction; sample pages from Spanish edition. (Blondet)

The people of Haiti need to rebuild quickly; on January 19th Mr. Fierro saw masons reconstructing collapsed walls using the exact technology that caused them to fall. The international aid and engineering communities need to help educate Haitians regarding the earthquake hazards and provide basic, easy to understand guidance on how to rebuild their society in a more earthquake resilient fashion. This should not involve reinventing the wheel; most of Haiti's construction problems have previously been addressed elsewhere. Some ideas might include:

1. Provide immediate assistance to the government of Haiti to develop and adopt a provisional building code that includes seismic provisions. Countries such as the Dominican Republic or Peru have codes that might be readily adapted for Haiti. The Association of Caribbean States has been working on model codes; ACI also has a document which might be adapted for Haiti (*ACI IPS-1, Essential Requirements for Reinforced Concrete Buildings*).
2. Translate the Peruvian booklet on confined masonry construction into Creole and French and make it available for free; provide training and demonstrations in public parks, schools, or locations that sell building supplies to show proper construction techniques. In addition, a simpler 2-4 page pamphlet or series of posters directed at homeowner's may also be needed. This effort is currently underway using volunteer translators.
3. Provide immediate assistance to existing Haitian architecture, engineering and construction professionals to educate them on the principles of seismic design and construction; such educational seminars should be organized as soon as possible since reconstruction is already underway.
4. Use international aid money to sponsor the construction of one seismically resistance school in each affected town following the plans developed in Peru; these plans are readily available and show a proven technology that utilizes reinforced concrete and masonry infill, the materials currently in use in Haiti.
5. Devise a mechanism to tie aid money for reconstruction to the use of seismic detailing and seismic resistant construction.
6. Create an avenue for engineers and inspectors from developed countries to help with design, plan review, and construction inspection during the initial reconstruction period. We have received a number of requests from international professionals asking how they can volunteer.
7. Provide scholarships to existing Haitian students studying architecture and engineering to go abroad to finish their studies since many Haitian universities are not currently able to function and do not have the appropriate curriculum in seismic design. This could involve both short and long term scholarship arrangements.

In closing, here are photos of school construction in Peru (Figures 33-34). The school shown in Figure 33 and the school in the background in Figure 34 both experienced ground motion of 0.5g during the 2007 Pisco, Peru Earthquake. This was a magnitude 7.9 event; 80,000 structures collapsed in Pisco, but these schools were undamaged. The wing in the foreground (Figure 34) was under construction during July 2008. At that time, we met a woman who identified herself as the Engineer of Record and had designed the school; she was in the field personally tying all the bars for the column cages because she said no one else could be trusted with such an important task. While this may not be practical in Tokyo or San Francisco, it is critical that architects, engineers and contractors throughout the world assume a sense of personal responsibility for the lives of those who occupy the buildings that we design and build.



Figure 33: School in Pisco, Peru survived 7.9M 2007 Pisco earthquake without damage (PGA 0.5g). Peruvian government developed standard plans for school construction in 1999.



Figure 34: School under construction, Pisco, Peru July 2008. Building has 1m T-shaped longitudinal wall at location of each transverse wall; rest of transverse wall is solid unreinforced concrete block masonry infill.

Acknowledgements:

We would like to acknowledge the invaluable assistance of Ing. Victor Suarez of IDISDEN in Santiago DR for making all of the arrangements for travel, lodging, meals, Creole translation, and security for the trip into Haiti. In addition to Ing. Suarez, several other Dominican engineers accompanied Mr. Fierro including Ing. Luis Peña, Ing. Hector O'Reilly, and Ing.Felipe Roman. Thanks also to Estrella Ingenieria including Ing. Alejandro Adames, Ing. Álvarez, and; to Palito for security; to drivers Daniel and Ronald; and to Cecelia the cook. The reconnaissance was supported jointly by BFP Engineers, Inc., IDISDEN, and the Pacific Earthquake Engineering Research Center at the University of California, Berkeley (PEER). Unless otherwise indicated, all photos were taken by Eduardo Fierro.

References

USGS, Haiti earthquake statistics and maps. http://earthquake.usgs.gov/earthquakes/eqinthenews/2010/us2010rja6/

Fouche, Pierre. Phd student at SUNY Buffalo. Personal communication 23 January 2010.

Regles BAEL 91 (Beton Arme aux Etats Limites), 2006 edition. Paris, France.

Wikipedia article on 2010 Haiti Earthquake as of Jan. 28, 2010. http://en.wikipedia.org/wiki/2010_Haiti_earthquake

Blondet, Marcial, editor. Construcción y Mantenimiento de Viviendas de Albañilería, Second edition 2005. Lima, Peru.

Mann, Paul et al, "Enriquello-Plantain Garden strike-slip fault zone: A major seismic hazard affecting Dominican Republic, Haiti, and Jamaica," 18th Caribbean Geological Conference, Santo Domingo, Dominican Republic, 2008.

JOINT CONFERENCE PROCEEDINGS
7th International Conference on Urban Earthquake Engineering (7CUEE) &
5th International Conference on Earthquake Engineering (5ICEE)
March 3-5, 2010, Tokyo Institute of Technology, Tokyo, Japan

SITE SPECIFIC GROUND MOTION ESTIMATIONS FOR THE VULNERABILITY ASSESSMENT OF HISTORIC BUILDINGS IN ISTANBUL

Atilla Ansal[1], Dina D'Ayala[2], Aslı Kurtuluş[3] and Gökçe Tönük[3]

1) Professor, Bogaziçi University, Kandilli Observatory and Earthquake Research Institute, Istanbul, Turkey
2) Professor, Department of Architecture and Civil Engineering, University of Bath, Bath, United Kingdom
3) Dr. Bogaziçi University, Kandilli Observatory and Earthquake Research Institute, Istanbul, Turkey
ansal@boun.edu.tr, absdfda@bath.ac.uk, asli.kurtulus@boun.edu.tr, gokce.tonuk@boun.edu.tr

Abstract: The objectives of the Istanbul Seismic Risk Mitigation and Emergency Preparedness Project are to improve Istanbul's preparedness for a potential earthquake. Within this framework "Risk Assessment of Cultural Heritage Buildings" was designed to address the vulnerability of cultural assets, specifically buildings with global cultural heritage value. One of the components of the project was vulnerability and risk assessment of 170 historical buildings. The choice of the appropriate earthquake scenario and the methodology used for assessing the effects of local site conditions in earthquake performance of selected cultural heritage buildings is presented. The purpose is to estimate the earthquake characteristics on the ground surface based on the earthquake characteristics on the engineering bedrock outcrop obtained from the probabilistic and deterministic hazard studies conducted by Erdik et al. (2007). The site specific elastic design spectra for each site are determined to further obtain site specific non linear displacement spectra. As a case studies, the results of site specific evaluations are presented for two historical heritage building sites (Kariye Museum and Ragıp Pasha Library) to demonstrate the applicability of the proposed approach.

1. INTRODUCTION

The locations of the most of the cultural heritage building are shown in Figure 1 (D'Ayala and Ansal, 2009). Local site conditions were evaluated using available reports on geotechnical and geophysical investigations conducted in the near vicinity of the sites. Most of the information came from previously conducted geotechnical investigations and geotechnical projects on the study area. Consequently, it should be noted that the results obtained include some uncertainties concerning the compiled geotechnical data. Using all the relevant information, representative soil profiles with shear wave velocity profiles extending down to the engineering bedrock with estimated shear wave velocity of 750m/s are determined for all building sites. Each soil profile contains information on soil stratification, depth of bedrock, ground water table, and shear wave velocity with depth.

1D site response analyses were carried out at each building site using representative soil profiles and regional seismic hazard parameters. Regional seismic hazard was evaluated using deterministic as well as probabilistic time dependent Poisson model by Erdik et al. (2007). Seismic hazard parameters in terms of PGA and spectral accelerations at periods T=0.2s and T=1s on the engineering bedrock outcrop were assigned at each site (Ansal et al, 2007b).

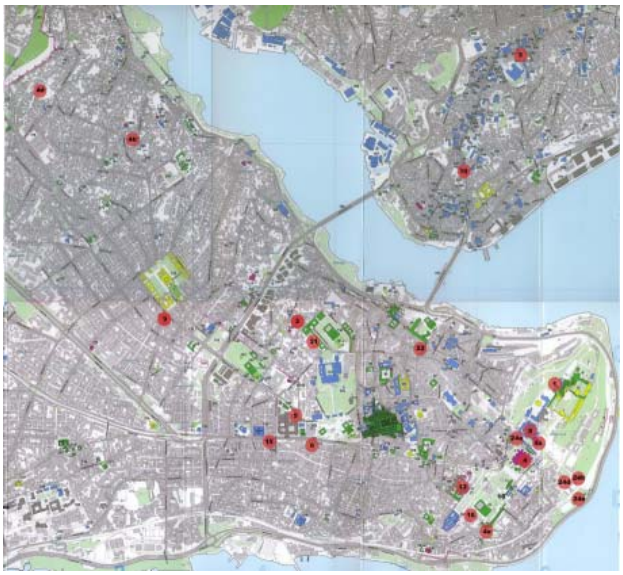

Figure 1 Locations of the most of the historical buildings evaluated in this study

2. SITE CHARACTERIZATION

Based on previous investigations and evaluation of the findings of borings carried out in the area, the local geological sequence and soil profiles were established.

These studies indicate that Neocene deposits outcrop in the regions which comprise a sequence of stratus overlying the Lower Carboniferous greywacke layers (Trakya Formation). The Neocene sequence, deposition of which started in Late Oligocene, is composed of from bottom to top, basal gravel and conglomerate, interbedded overconsolidated clay and sand. In the upper zone, due to a lacustrine environment getting shallower at the end of the Miocene, sand, organic clay, marl and fossiliferous limestone interbedded with clay (Bakırköy formation) are located as an uninterrupted sequence. The site has outcrops of limestone/marl interbedded with limey clay, belonging to the Bakırköy formation. The lithologies forming the Bakırköy formation are not only marls and low-strength limestone, but also may be composed of sequence of interbedded sand, clay, marl and limestone. The underlying Gürpınar formation is composed of fissured, overconsolidated clays occasionally interbedded with sand layers.

2.1 Geotechnical Site Conditions

Local geological and geotechnical site conditions were evaluated using all the available and relevant information and representative soil profiles with shear wave velocity profiles extending down to the engineering bedrock with estimated shear wave velocity of 750m/s are determined for all building sites. Each soil profile contains information on soil stratification, soil classification for each layer, layer thickness, depth of bedrock, ground water table elevation, and shear wave velocity with depth.

The variation of shear wave velocity with depth was determined from SPT-N blow counts using an empirical relationship proposed by Iyisan (1996) as well as based in-hole and surface shear wave velocity measurements conducted in the vicinity of the borings. The shear wave velocity profiles determined from SPT values were compared with measured or calculated shear wave velocity data reported in available geophysical reports and modifications were made if necessary.

The site classification at each site was determined according to both Turkish Earthquake Code TEC (2007) and National Earthquake Hazards Reduction Program NEHRP (2001). Soil stratification, soil types and related index laboratory test results, SPT blow counts, and shear wave velocities were used to establish site classifications. The equivalent (average) shear wave velocities for the top most 30m were used to determine site classifications according to NEHRP (2001).

2.2 Dynamic Soil Properties

Soil profiles at each site included information about soil stratification, thickness, soil type, shear wave velocity for each soil layer. Empirical relationships available in the literature for different soil types were used to define variations of G/G_{max} and damping ratio with strain. The G/G_{max} and damping ratio relationships that were used in this study are listed in Table 1 and the variation of modulus ratio and damping are illustrated in Figure 2.

Table 1 G/G_{max} and damping ratio - shear strain relationships used in site response analysis

Material No	Soil Type	Reference
1	Clay (CH) PI=60%	Vucetic & Dobry (1991)
2	Clay (CL) PI=45%	Vucetic & Dobry (1991)
3	Clay (CH) PI=30%	Vucetic & Dobry (1991)
4	Clay (CL) PI=15%	Vucetic & Dobry (1991)
5	Silt	Darendeli (2001)
6	Sand (SC-SM)	Darendeli (2001)
7	Sand	Seed et al.(1986)
8	Gravel	Seed et al.(1986)
9	Gravel	Menq et al.(2003)
10	Rock 0-6 m	EPRI (1993)
11	Rock 6-16 m	EPRI (1993)
12	Rock 16-37 m	EPRI (1993)
13	Rock 37-76 m	EPRI (1993)

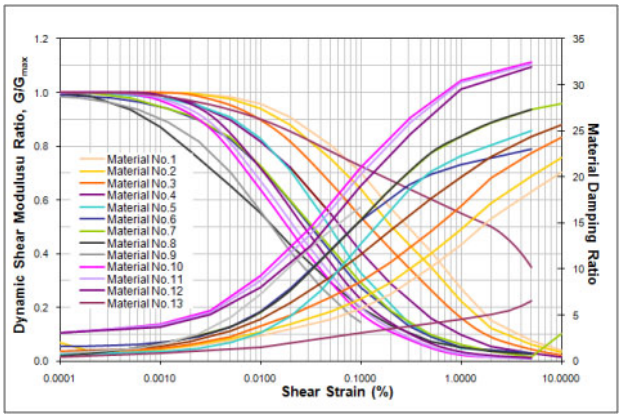

Figure 2 Empirical shear modulus reduction and damping ratio relationships used for site response

3 SITE RESPONSE ANALYSES FOR GROUND SHAKING INTENSITY

Site specific response analysis was carried out at each building site using representative soil profiles and regional seismic hazard parameters. Regional seismic hazard was evaluated using deterministic as well as probabilistic time dependent Poisson model for the return period of 475 years that corresponds approximately to 10% probability of exceedance in 50 years by Erdik et al. (2007). Seismic hazard parameters in terms of PGA and spectral accelerations at periods T=0.2s and T=1s on the engineering bedrock outcrop were assigned at each site. 1D equivalent-linear model site response code Shake91 (Idriss and Sun, 1991) was used to conduct site response analyses.

3.1 Earthquake Input

24 acceleration time histories compatible with the earthquake hazard in terms of probable magnitude, distance and fault mechanism were selected as the input rock outcrop motion (Ansal and Tönük, 2007). The main purpose was to account for the variability arising from the differences observed in the real acceleration time histories (Table 2).

Table 2 Acceleration time histories that were used for site response analysis (from PEER)

Earthquake	Station	Magnitude	Component	PGA (g)
Duzce 11/12/99	375 Lamont	7.1	375E	0.514
Duzce 11/12/99	375 Lamont	7.1	375N	0.970
Duzce 11/12/99	531 Lamont	7.1	531E	0.118
Duzce 11/12/99	531 Lamont	7.1	531N	0.159
Duzce 11/12/99	1059 Lamont	7.1	1059E	0.133
Duzce 11/12/99	1059 Lamont	7.1	1059N	0.147
Duzce 11/12/99	1061 Lamont	7.1	1061E	0.134
Duzce 11/12/99	1061 Lamont	7.1	1061N	0.107
Duzce 11/12/99	1062 Lamont	7.1	1062E	0.254
Duzce 11/12/99	1062 Lamont	7.1	1062N	0.114
Duzce 11/12/99	Bolu	7.1	BOL000	0.728
Duzce 11/12/99	Bolu	7.1	BOL090	0.822
Kocaeli 08/17/99	Arçelik	7.4	ARC000	0.219
Kocaeli 08/17/99	Arçelik	7.4	ARC090	0.150
Kocaeli 08/17/99	Gebze	7.4	GBZ000	0.244
Kocaeli 08/17/99	Gebze	7.4	GBZ270	0.137
Kocaeli 08/17/99	Duzce	7.4	DZC180	0.312
Kocaeli 08/17/99	Duzce	7.4	DZC270	0.358
Imperial Valley 5/19/40	El Centro Array #9,	7.0	I-ELC180	0.313
Imperial Valley 5/19/40	El Centro Array #9,	7.0	I-ELC180	0.215
Landers 6/28/92	Morango Valley	7.3	MVH090	0.182
Landers 6/28/92	Morango Valley	7.3	MVH000	0.138
Landers 6/28/92	Joshua Tree	7.3	JOS000	0.274
Landers 6/28/92	Joshua Tree	7.3	JOS090	0.284

The selected input acceleration time histories were then scaled with respect to the peak ground horizontal accelerations obtained from earthquake hazard study at each site and were used as outcrop input motions for site response analyses (Ansal et al., 2006, Durukal et al., 2005).

3.2 Evaluation of Ground Shaking Parameters

Two approaches were adopted to evaluate site-specific free field earthquake characteristics on the ground surface. In the first approach 1D site response analysis using Shake91 (Idriss and Sun, 1992) was conducted and average from all 24 analyses at each site was computed to determine average peak ground acceleration (PGA), average peak ground velocity (PGV) and average elastic acceleration response spectrum on the ground surface at each site (Ansal et al., 2007a). In the second approach empirical relationship proposed by Borcherdt (1994) was employed to determine peak spectral accelerations corresponding to 0.2s and 1s using equivalent (average) shear wave velocities at each site. PGA, PGV, and SA for T=0.2s and 1s values evaluated for each site are determined both for deterministic and probabilistic analyses.

In order to be used for seismic vulnerability assessments of buildings two more parameters; site-specific short period (corresponding to 0.2s) and long period (corresponding to 1s) spectral acceleration values were evaluated. The average acceleration response spectrum obtained for each cell from site response analyses were used to determine spectral accelerations for the short period (Ss) and for the long period (S1). An approach was adopted to determine the best fit envelope to the calculated average acceleration response spectra (Ansal et al. 2006). All the requirements of the NEHRP design spectra were applied in obtaining the short (Ss) and long (S1) period spectral ordinates. The two independent variables in the developed optimization algorithm were (Ss) and (S1). The best fit NEHRP envelope obtained by this approach with respect to average elastic acceleration response spectra. The NEHRP design spectrum is preferred because of its flexibility in defining short period spectral accelerations and for vulnerability assessment of the building stock (Erdik and Fahjan 2005).

4 KARIYE MUSEUM

One of the historical heritage buildings investigated was the Kariye Museum located on the north part of the Istanbul historical peninsula very near to the outer city walls of that period. The Kariye Museum was constructed as a church during sixth century (Figure 3).



Figure 3 East facade of the Kariye Museum (ISMEP, 2007)

The main building is dated to 11th century. Second church, inner and outer narthexes, parecclesion and northern annex are dated 14th century. To structurally strengthen the bema section an abutment was placed on 14th century. The church was converted into a mosque on 15th century and the minaret was added (Figure 4 and Figure 5).



Figure 4 The Kariye Museum (ISMEP, 2007)

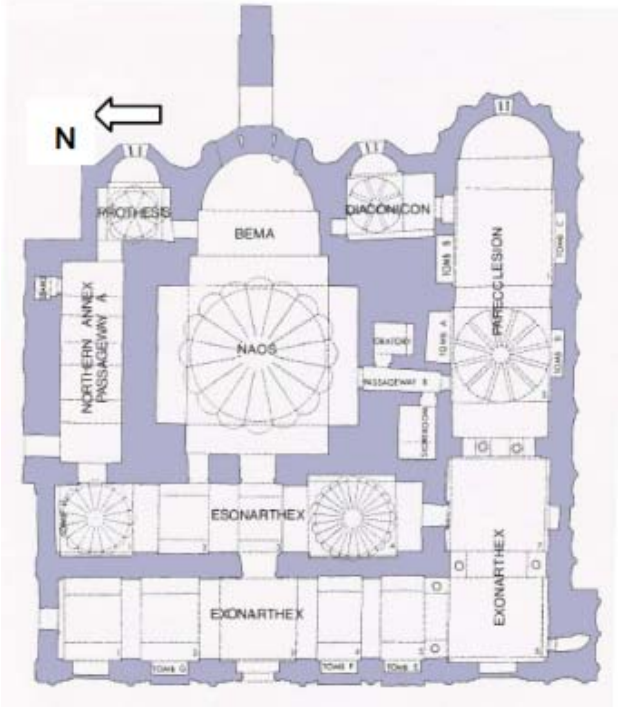

Figure 5 Schematic ground floor plan (ISMEP, 2007)

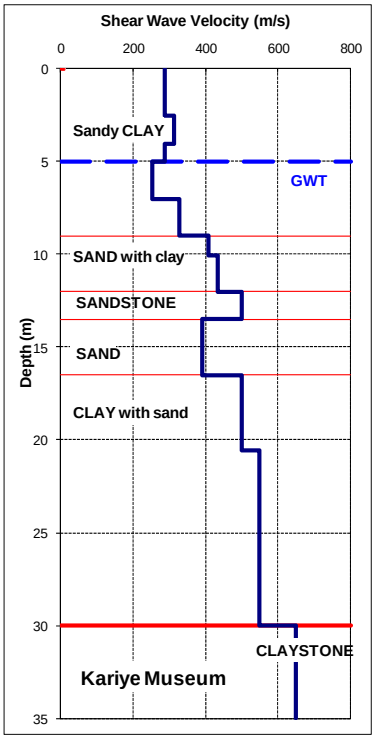

Figure 6 Soil profile for Kariye Museum

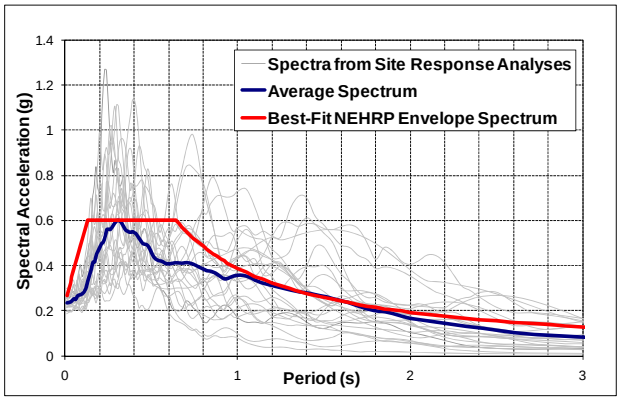

Figure 7 Best envelop NEHRP spectrum fitted to average acceleration response spectrum calculated from site response analyses the soil profile for the Kariye Museum

After 1766 earthquake extensive repairs have been undertaken, including the replacement of the brick dome of naos with a timber dome. According Oztin (1994) the minaret of the museum partially collapsed and some cracking was observed in different parts of the museum during the 1894 earthquake.

Based on the available borings in the vicinity of the investigation area (app. 150m), the representative soil profile consists of approximately 9m of sandy clay overlying 7.5m of sandy layers, upper 3m of which is sand with clay, underlain by 1.5m of sandstone and the lower 3m is with sand (Figure 6). The profile enters a layer of clay with sand starting from 16.5m and continues until 30m depth. Beneath clay layer claystone is encountered that was assumed as the engineering bedrock. Ground water table is at 5m below the ground surface. The site is located on the Güngören Formation (Ansal et al, 2007).

Shear wave velocities in the transitional clayey and sandy soil layers over claystone vary between 254-550m/s. Equivalent shear wave velocity (weighted average for the uppermost 30m from the ground) was estimated as 405m/s. The NEHRP site classification is class C, described as stiff soils. According to Turkish Earthquake Code, the site can be classified as Z3 (partly Group C soils; stiff clay or medium sand and gravel; with 15m<h≤50 m, partly Group D soils; soft clay or loose sand; with h≤10m).

The average PGA on the ground surface was calculated as 0.30g for the probabilistic and 0.23g for the deterministic earthquake scenarios. The acceleration response spectra obtained on the ground surface from site response analysis for all of the input motions, the average of these spectra and the best fit envelope NEHRP spectrum on the average are shown in Figure 7 for the deterministic scenario.

5 RAGIP PASHA LIBRARY

One of the other historical heritage buildings investigated was the Ragıp Pasha Library located somewhat in the central part of the Istanbul historic peninsula. The library was established by Ragıp Pasha in 1762, the building has a unique architectural design in the Baroque style and possesses typical details of the period, such as the European tiles adorning the inner walls The walls of the reading hall are decorated with exquisite ceramic tiles (Figure 8).



Figure 8 Entrance of the Ragıp Pasha Library (ISMEP,2007)

Based on the available borings in the vicinity of the investigation area (app. 100m), the representative soil profile consists of 4.5m of artificial fill overlying almost 30m thick clay and sand layers in transition, upper 1.5m of which is clay with sand continued by 15m thick clayey sand layer and the lower 14m is clay with sand. Greywacke layers are encountered starting from 30m depth. Beneath the weathered portion, the greywacke layers were assumed as the engineering bedrock located at 48m depth. Ground water table is at 3m below the ground surface. The surface clay layers are of Güngören Formation where greywacke layers encountered deeper belong to Trakya Formation (Figure 9).

Shear wave velocities in the artificial fill and clay layer vary between 193-485m/s. Equivalent shear wave velocity (weighted average for the uppermost 30m from the ground) was estimated as 301m/s. The NEHRP site classification is class D, described as stiff soils. According to Turkish Earthquake Code, the site can be classified as Z3 (partly Group C soils; stiff clay; with 15m<h≤50 m, and mostly Group D soils; soft clay; with h≤10m).

The average PGA on the ground surface was calculated as 0.60g for the probabilistic and 0.47g for the deterministic earthquake scenarios. The acceleration response spectra obtained on the ground surface from site response analysis for all of the input motions, the average of these spectra and the best fit envelope NEHRP spectrum on the average are shown in Figure 10 for the deterministic scenario. All the related spectral acceleration amplitudes for the probabilistic and the deterministic earthquake scenarios are calculated.

The site (clayey sand layers between 6m and 21m depths) has high liquefaction susceptibility, with liquefaction potential index PL=16 for the deterministic scenario.

The library has experienced some minor damages during the 1999 Kocaeli earthquake. As can be observed in comparison between Figure 10 and Figure 7, the maximum spectral calculated for the Ragıp Pasha Library site was around 2.5 times higher than the Kariye Museum site.

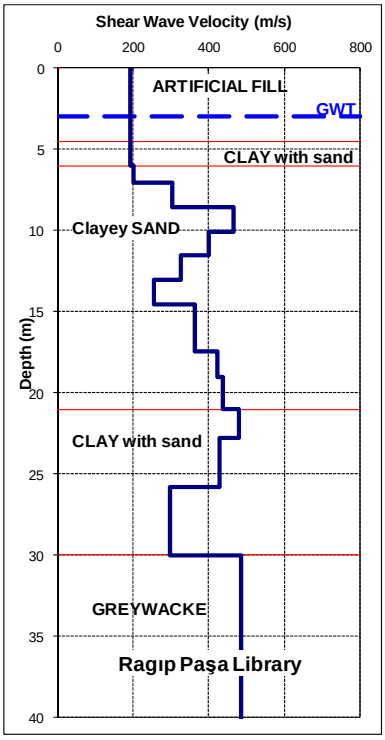

Figure 9 Soil profile for Ragıp Pasha Library

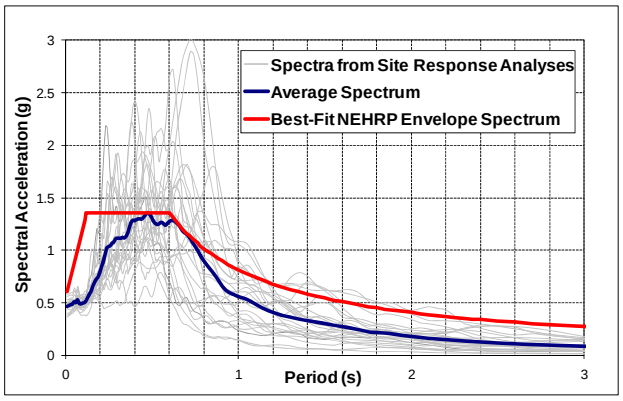

Figure 10 Best envelop NEHRP spectrum fitted to average acceleration response spectrum calculated from site response analyses the soil profile for the Ragıp Pasha Library

6 CONCLUSIONS

A detailed study was conducted to evaluate site-specific ground shaking parameters at the cultural heritage building sites based on available geotechnical and geophysical data. The results obtained from the probabilistic earthquake hazard study for a Poisson model with a return period of 475 years that corresponds to 10% probability of exceedance in 50 were used to define the earthquake hazard at NEHRP (2001) B/C boundary site conditions. 24 real earthquake records that are compatible with the earthquake hazard in terms of probable magnitude, distance and fault mechanism were selected and scaled with respect to the PGA values

from hazard studies and were used as outcrop input motions for site response analyses.

Site response analyses based on 1D equivalent-linear model was used to predict free-field earthquake shaking parameters on the ground surface. The ground motion parameters that were computed using results of site response analyses included average values of PGA, PGV and elastic response spectrum on the ground surface and spectral acceleration values corresponding to short (0.2s) and long (1s) periods.

References:

A.Ansal, G.Tönük (2007) "Source And Site Effects For Microzonation", *Earthquake Geotechnical Engineering, 4th International Conference on Earthquake Geotechnical Engineering-Invited Lectures*, Springer Editor.: K.Pitilakis, Chapter 4, pp.73-92

Ansal, A., Kurtuluş, A., & Tönük, G. (2007a) Earthquake Damage Scenario Software for Urban Areas. Keynote Lecture, Computational Methods in Structural Dynamics and Earthquake Engineering, M. Papadrakakis, D.C.

Ansal, A., Kurtuluş, A., Tönük, G. (2007b) "Evaluation Of Site-Specific Earthquake Characteristics On The Ground Surface", *Istanbul Seismic Risk Mitigation and Emergency Preparedness Project (ISMEP) on Inventorization and Multi-Hazard and Earthquake Performance Evaluation of the Cultural Heritage Buildings in Istanbul*, the Ministry of Culture and Tourism

Ansal, A., Durukal, E., Tönük, G. (2006) "Selection and Scaling of Real Acceleration Time Histories for Site Response Analyses", *Proc. of ETC12 Workshop*, Athens, Greece.

Ansal, A., Tönük, G., Demircioglu, M., Bayraklı,Y., Sesetyan,K., Erdik,M (2006) "Ground Motion Parameters for Vulnerability Assessment", *Proceedings of the First European Conference on Earthquake Engineering and Seismology*, Geneva, Paper Number: 1790

Borcherdt, R.D. (1994) "Estimates of Site Dependent Response Spectra For Design (Methodology And Justification)" *Earthquake Spectra*, 10(4), 617-654

BSSC-Building Seismic Safety Council (2001) NEHRP (National Earthquake Hazards Reduction Program) Recommended Provisions for Seismic Regulations for new buildings and other structures, 2000 Edition, Part 1: Provisions (FEMA 368), Ch. 4, Washington, D.C.

Darendeli, M. B. (2001) A New Family of Normalized Modulus Reduction and Material Damping Curves, PhD Dissertation, University of Texas at Austin, 362 p.

D'Ayala,D. and Ansal,A. "Non linear push over assessment of historic buildings in Istanbul to define vulnerability functions" *Proceedings of the Conference on Earthquakes and Tsunamis - Civil Engineering Disaster Mitigation Activities - Implementing Millennium Development Goals*., Paper No.128

Durukal, E., Ansal, A., and Tönük, G. (2005) "Effect of Ground Motion Scaling in Site Response Analyses", *Proceedings of the Earthquake Geotechnical Engineering Satellite Conference*, 16th ICSMGE, Osaka, Japan

Erdik,M., E.Durukal, K.Şeşetyan, M.B.Demircioğlu (2007) "Assessment Of Site-Specific Earthquake Hazard At Reference Ground Conditions", *Istanbul Seismic Risk Mitigation and Emergency Preparedness Project (ISMEP) on Inventorization and Multi-Hazard and Earthquake Performance Evaluation of the Cultural Heritage Buildings in Istanbul*, the Ministry of Culture and Tourism

Erdik M, Fahjan Y (2006) Damage Scenarios and Damage Evaluation, *Assessing and Managing Earthquake Risk Geo-scientific and Engineering Knowledge for Earthquake Risk Mitigation: developments, tools, techniques*, Ch.10, Book Series: Geotechnical, Geological, and Earthquake Engineering, Eds: Oliveira CS, Roca A, Goula X (Eds.)

EPRI (1993) "Guidelines for Determining Design Basis Ground Motions", Electric Power Research Institute, Palo Alto, CA, Vol1, EPRI TR-102293.

Idriss, I. M. and Sun J. I. (1992) "Shake91, A Computer Program for Conducting Equivalent Linear Seismic Response Analysis of Horizontally Layered Soil Deposits Modified based on the original SHAKE program Published in December 1972 by Schnabel, Lysmer and Seed"

ISMEP(2007) Inventorization and Multi-Hazard and Earthquake Performance Evaluation of the Cultural Heritage Buildings in Istanbul, Istanbul Seismic Risk Mitigation And Emergency Preparedness Project Reports, Republic of Turkey, Ministry of Culture and Tourism, Istanbul Directorate of Surveying and Monuments

Iyisan, R. (1996) "Correlations between Shear Wave Velocity and In-situ Penetration Test Results", *Technical Journal of Turkish Chamber of Civil Engineers*, 7(2),1187-1199 (in Turkish)

Iwasaki, T., Tokida, K., Tatsuoka, F., Watanabe, S., Yasuda, S., & Sato, H. (1982) "Microzonation of Soil Liquefaction Potential Using Simplified Methods", *Proc. 3rd Int. Conf. On Microzonation*, Seattle, 3:1319-1330

Oztin,F (1994) 10 July 1894 Istanbul Earthquake Report, Ministry of Construction and Settlement, General Directorate of Disaster Affairs, Earthquake Research Division.

PEER Strong Motion Data Bank, http:// peer.berkeley.edu

Turkish Earthquake Code (2007) "Specification for Structures to be Built in Earthquake Areas", Ministry of Public Works and Settlement, Government of Republic Turkey/

Seed, H.B., Wong, R.T., Idriss, I.M. and Tokimatsu, K. (1986). "Moduli and Damping Factors for Dynamic Analyses of Cohesionless Soils", Univ. of California, Berkeley, Earthquake Engineering Research Center, Report No. UCB/EERC-84/14, 37 p.

Menq, F. Y., K. H. Stokoe, E. Kavazanjian (2003) "Linear dynamic properties of sandy and gravelly soils from largescale resonant tests," *International Symposium IS Lyon 03, Deformation Characteristics of Geomaterials*, (Lyon, France)

Vucetic, M and R. Dobry (1991). "Effect of soil plasticity on cyclic response", *Journal of Geotechnical Engineering*, American Society of Civil Engineers, 117(1), 89-107

JOINT CONFERENCE PROCEEDINGS
7th International Conference on Urban Earthquake Engineering (7CUEE) &
5th International Conference on Earthquake Engineering (5ICEE)
March 3-5, 2010, Tokyo Institute of Technology, Tokyo, Japan

SITE RESPONSE AT MEXICO CITY. PROGRESS MADE AND PENDING ISSUES

Francisco J. Chávez-García[1)]

1) Professor, Instituto de Ingeniería, Universidad Nacional Autónoma de México, Mexico
paco@pumas.iingen.unam.mx

Abstract: The case of site effects in Mexico City is paradigmatical in Earthquake Engineering. The city was severely affected during the great 1985, Michoacan, earthquake. The aftermath of this event left hundreds of buildings destroyed or damaged beyond repair (including well designed structures) and thousands of casualties. Economic losses exceeded 4 billion dollars. Seismic intensities at Mexico City surpassed by far provisions in the building code in force at the time. It was immediately recognized that site effects were a major factor in the consequences of what was a large earthquake but with an epicenter that was farther than 350 km from Mexico City. Moreover, the damage toll was smaller at many other places, even closer to the source. During the last 24 years, many efforts have been made to prevent the disaster from repeating. This paper reviews the efforts made to understand site effects at Mexico City. The questions that have been solved regarding the prediction of local amplification are discussed and the modifications included in the current version of the building code at this city are presented. The issues that remain unsolved regarding the prediction of site response at this large city are also discussed.

1. INTRODUCTION

Site effects in Mexico are paradigmatical. The very soft soil layers that cover the lake-bed zone amplify ground motion by factors up to 40 relative to firm ground sites nearby. This was the main factor behind the large effects of the great 1985 Michoacan earthquake (Ms 8.1). The consequences of this event, with an epicenter farther than 350 km from Mexico City, were hundreds of buildings destroyed or damaged beyond repair (including well designed structures) and thousands of casualties. Since that earthquake, many efforts have been made to understand the seismic response of Mexico's basin (Figure 1) to prevent the disaster from repeating, especially having in mind that the segment of the subduction zone at the origin of the Michoacan earthquake was not the one expected to rupture. The section to the south of Acapulco is considered a more mature gap expected to generate an earthquake at least as large as that of 1985 at a closer distance to the city.

This paper presents a brief review of the progress made since 1985. The questions that have been solved regarding local amplification are discussed and the modifications included in the current version of the building code at this city are presented. The issues that remain unsolved are also discussed. Foremost among them is an accepted model of ground motion. In addition, firm soil ground motion at Mexico City is already amplified relative to sites with different paths between the subduction zone and central Mexico. The relation between this "regional amplification" and crustal structure is poorly understood. Finally, some comments are offered regarding current work to predict ground motion at Mexico City for future earthquakes.

2. OBSERVED LOCAL EFFECTS

Site effects are known to be an important factor in Mexico's basin at least since 1957, when intensities were estimated for the July 28 event and the amplification on soft soils estimated at three MMI units (Duke and Leeds, 1959). In 1962, the analysis of the first accelerograms recorded in Mexico City for two large events (magnitude 7), 260 km away from Mexico City, showed amplifications factors in undamped reponse spectra between a site at the basement of a building and a free field site up to 5 at the dominant period (Zeevaert, 1964). Thus, the large amplifications observed in spectral ratios computed using the records of the great 1985 event and its aftershock (Singh et al., 1988) came as no surprise. More surprising was the almost linear behavior of the clay layer demonstrated by the similar amplification between the main shock and its aftershock and the very long duration of strong ground motion. Figure 2 shows the horizontal strong motion records obtained at two stations in Mexico City: TACY on firm soil and SCT on the lake-bed zone. The explanation of the differences between these two records, separated less than 10 km, both recording the same earthquake more than 350 km away, has challenged the ingenuity of many researchers during these 24 years.

3. 1D MODELS

It was quickly recognized that the impedance contrast at

the base of the very soft clay layer that characterizes the lake-bed zone was the major factor explaining the large amplification observed. 1D models are the first and most logical to use in Mexico City. Both the horizontal extent of that clay layer as compared to its thickness (40 to 60 m) and the large impedance contrast at the base of this layer (shear wave velocity is about 80 m/s in the clay and more than 600 m/s in its substratum) argue in favor of simple, vertical S-wave propagation models. Seed et al. (1988) made the most comprehensive 1D analysis. They used linear equivalent models. The 1D profile at each site was obtained from borehole measurements, adjusted to improve the fit between observed and computed response spectra. Seed et al. (1988) claimed a "fair to very good match" between observed and computed response spectra (Figure 3). However, when the same geotechnical model was used to compare frequency domain transfer functions with spectral ratios relative to a firm soil site, the discrepancy between model and observations was very large (Kawase and Aki, 1989), as shown in Figure 4. In a similar way, if the geotechnical model was adjusted to get a good fit between observed and computed transfer functions, then comparison of the synthetics with the observed traces showed a very poor agreement: duration was too short and amplitudes were too large (Chávez-García and Bard, 1994). 1D models then, can explain part of the observations but not all of them together. Thus, although site response should be 1D, it is not. This contradiction spurred many hypotheses, some of them quite wild, to explain site response. Given that the level of amplification could be easily explained in terms of impedance contrast, research concentrated on the very large duration of strong ground motion.

4. LINEAR OR NON-LINEAR BEHAVIOR

The intensity of ground motion imposed the possibility that non-linear behavior of the soft soil layers could have had a large impact. However, this possibility was quickly discarded as a major factor throughout the valley. Romo et al. (1988) showed that samples of the clay layer had a very large range of linear behavior, which was related to the large plasticity index of the clay. In addition, the large duration of ground motion had been observed as early as 1964 for a small earthquake (Rosenblueth, 1966). The very large duration was also observed for small, more recent earthquakes, well documented by the accelerograph array put in place in the city after the 1985 event. There is consensus that there may be some small non-linear effects but that the long duration of ground motion is independent from them. Non-linear effects are expected (and were indeed seen to occur) in localized points (e.g., small volumes of clay under the foundations of buildings, where the stresses generated by the building were already large and only a small increment was required to tilt its behavior into the non-linear domain) but it is clearly irrelevant to understand the seismic response of the basin.

In spite of the previous arguments, a peculiar explanation of ground motion based on the non-linearity of the clay layer was proposed in a series of papers by Lomnitz (e.g., 1990). This author claimed that non-linear effects could bring about a phase transition where Rayleigh waves in the soil would be transformed into gravity waves, akin to those in fluids. This speculation was not supported on observations other than the presumed prograde elliptical particle motion of the largest amplitudes in the SCT record (Figure 2) nor on any modeling whatsoever. Moreover, the statement that surface waves in the SCT record show prograde particle motion record requires two prior conditions that are impossible to meet: confidence in the direction of propagation and confidence in the polarity of the recorded signals, besides ignorance of the possibility that the fundamental mode of Rayleigh waves shows prograde particle motion in some cases (see e.g., Mooney and Bolt, 1966). The difficulty to show the opposite (i.e., that non-linear phase transitions did not occur in Mexico City clay), however, imposed waiting 8 years until that speculation was shown to be unfounded (Chávez-García and Bard, 1993a, 1993b, 1995), and the flow of papers with gravity waves from Lomnitz was put out.

5. 2D AND 3D MODELS

Simple 1D models proved inadequate to explain observed ground motion, especially its long duration. For this reason, attention turned to 2D models. Two possibilities were proposed: 2D horizontal wave resonance and surface waves generated by the lateral heterogeneities in the basin.

Long, sustained ground motion strongly suggests some resonance phenomenon. Given that 1D resonance was inadequate to explain the observations, a 2D resonant model was proposed in a series of papers (e.g., Flores et al., 1987; Seligman et al., 1989; Mateos et al., 1993). In this model, two dimensions were considered in the horizontal plane and the vertical direction was neglected. Those authors proposed that 2D resonance aroused from the horizontal propagation of P waves generated by S to P conversion in the clay layer-substratum interface. Those horizontally propagating P waves would be completely trapped within a horizontally closed basin. This model was tested in Chávez-García and Bard (1994) in great detail. It was observed that there exists indeed a 2D resonance for the homogeneous valley proposed in the papers by Flores and colleagues. However, this 2D resonance occurs at an extremely low frequency (0.06 Hz) and for a very unrealistic velocity distribution (the model requires a constant S-wave velocity of 400 m/s from the surface down to 2500 m depth). A more realistic velocity model for the sediments indicates that laterally propagating waves are the governing phenomenon for their model of Mexico basin. Lateral propagation of surface waves appears for frequencies as low as 0.2 Hz. Chávez-García and Bard (1994) give additional arguments that allowed us to discard completely this possibility to explain ground motion duration in Mexico City.

A closed basin generates locally diffracted surface

waves that can increase significantly observed amplification and duration of strong ground motion (Bard and Bouchon, 1980a, 1980b). Lateral irregularities are then a natural factor to investigate. The computation of the effects on ground motion of lateral heterogeneity in Mexico's basin faces two large challenges. The first is the need to include in the models an irregular soft layer, thin and with extremely low shear-wave velocities, essential to understand observed ground motion. This layer imposes a very small spatial sampling rate on any numerical modeling scheme, which, at the same time, must discretize a basin tens of km wide. The second is that we do not have the data that is needed to constrain the structure and properties of the large portion of the crust that should be included in that model. The first limitation curbed early results. The second checks today's efforts concerning the modeling of the seismic response of Mexico's basin.

2D models of the large scale Mexico's basin were presented in several papers. Two representative studies are those of Kawase and Aki (1989), see Figure 5 and 6, and Fäh et al. (1994). The restrictions discussed above limited the usefulness of the results, as the influence of the clay layer or anelastic attenuation was not included. Chávez-García and Bard (1994) discussed those models and showed that the effect of the clay layer would not only be to increase ground motion amplitude, as speculated in papers that did not include it (see Figure 7 and 8). The very large contrast at its base as well as the low velocity of its Q value (Chávez-García et al., 1995; Ramos-Martínez et al., 1997) makes it impossible for locally generated surface to propagate far within the basin. The surface waves generated at the basin's edge are obliterated very rapidly because of dispersion and anelastic attenuation. Chávez-García and Bard (1994) considered in addition small-scale models of lateral irregularities of the thin clay layer, either in its thickness or its velocity structure (See Figure 9, 10, and 11). They concluded that lateral heterogeneities allow understanding the large differences in ground motion between neighboring stations. However, they do not explain the arrival of the late, energetic phases observed in the lake-bed zone.

The lack of data to construct a 2D model of Mexico's basin is exacerbated when 3D modeling is attempted. In spite of this, several 3D models have been explored to understand ground motion in this valley. The best results so far are those of Furumura and Kennett (1998), who also include an interesting parametric analysis of 2D, large scale, simulations. The results presented in this paper were limited to low frequencies (3 sec period). They showed that the complex 3D structure of the crust between the subduction zone and central Mexico has a large impact on ground motion from subduction earthquakes. They concluded that Sn and Lg phases were guided efficiently by the subducted plate and their amplitude and duration enhanced by scattering and P wave conversions along the path. Furumura and Kennett (1998) concluded that, in the case of Mexico City, simultaneous consideration of source, path, and site effects was required to understand ground motion.

A general observation regarding many of the models advanced to explain ground motion in Mexico City is that the soft clay layer at the surface is not included in the model, as mentioned above. However, the idea that its effect could be neglected because the amplification it brings about would cancel out with its associated attenuation has been shown to be incorrect. Different results point in the same direction: the necessity of considering simultaneously source, path, and site effects, to understand ground motion in this basin. It seems clear that we should dedicate a lot more effort to the determination of the geometry and mechanical properties of the subsoil structure at many different scales.

6. THE CONTRIBUTION OF THE BUILDINGS

When we study site effects in a sedimentary basin, we usually assume that the free surface is flat and empty. The existence of buildings at the surface in a city is usually neglected in seismological models, even if they are the prime motivation to understand ground motion at that site in the first place. It has been suggested (P.-Y. Bard, pers. comm.) that the presence of buildings could contribute to the long duration of earthquake motion by storing kinematic energy absorbed from the ground and liberating it slowly afterwards. A first exploration of this idea was presented in Chávez-García and Bard (1994), where an irregular, rigid, surface layer was proposed to model the presence of foundations on top of the clay layer. A more refined model was presented in Guéguen et al. (2002). In this paper, oscillators were modeled at the surface mimicking the real building distribution of "colonia Roma" (Figure 12), a heavily touched neighborhood in 1985. The results were evaluated in terms of comparisons between the ground motion modeled on the empty free-surface and that including the buildings. It was shown that the influence of the buildings on the free-surface ground motion cannot be neglected (Figure 13). Surface motion is effectively modified by the presence of the structures. However, in terms of significant increase in the duration of strong ground motion, the results were not relevant. These conclusions were complemented by additional studies involving not only analytical models of soil-structure interaction but incorporating analyses of simultaneous measurements of ambient vibration in the free-field and in buildings in Mexico City (Cárdenas et al., 1998, 2000; Chávez-García and Cárdenas, 2002). Nearby structures may affect significantly our estimates of ground motion amplification (effectively blurring the limits between hazard and vulnerability). However, they do not explain the long duration of strong ground motion observed.

7. DISCUSSION AND PERSPECTIVES

A paradox regarding site effects in Mexico City is that although 1D models were shown to be useless to understand ground motion, the observed amplification due to the thin,

very soft clay layer at the surface can be usefully modeled using such models. This was recognized early because of the large importance that dominant frequency has in this basin (e.g., Lermo and Chávez-García, 1994). Dominant frequency is due only to the clay layer and varies between 1 and more than 4 sec. It can be easily measured and conditions the frequencies for which amplification is observed at each site. For these reasons, current design provisions in Mexico City are based on this quantity. Ground motion in the firm zone is specified with a single design spectrum. In contrast, in the lake-bed zone, it is made to depend on the value of the dominant period at each site. That dominant period is specified in the code through a program that gives the dominant frequency value once a location is specified within the city. Once the dominant frequency is known, the code specifies rules to build the design spectrum using five parameters based on the dominant frequency. In this way, Mexico City boasts a "nanozonation map" (Figure 14), where the building code provides rules to compute a design spectrum that varies continuously throughout the city. This solution agrees with the fact that dominant frequency shows continuous variation through the lake-bed zone and avoids the problem of defining boundaries between zones of constant design spectra. The same map of dominant period is being used to estimate roughly peak motion parameters using a record of ground motion obtained on firm ground. Those estimates of peak motion may be used as a preliminary estimate of ground motion in the city using only one record, a sort of computed "shake-map". It is interesting that a model that is clearly wrong is so useful.

Observed ground motion in Mexico City has been studied very much during the past 24 years. Different hypotheses were advanced, often based on speculation. A lot of effort was necessary to discard those that were unfounded. It has been shown that local conditions cannot explain site effects in Mexico. Because of this, attention has turned to more regional effects. Soon after 1985, Singh et al. (1988) already pointed out that firm soil sites at Mexico City were amplified relative to similar site conditions at the same distance but at sites located parallel to the coast. This observation was confirmed by Ordaz and Singh (1992). Firm soil sites along paths perpendicular to the coast showed amplification by factors as large as 10 in a frequency band from 0.3 to 1 Hz. This "regional amplification", however, was unexplained by those authors, except for a speculation on impossibly large alluvial valleys. More complete studies of this regional amplification were presented in Cárdenas et al. (1997) and Cárdenas and Chávez-García (2003) where it was related to the crustal structure. In Mexico, the volcanic belt related to the subduction zone along the Pacific coast runs obliquely to the coast. This peculiar geometry has been related to differences of the subduction angle, steep to the north and shallower to the shouth. It has been suggested (Chávez-Garcia et al., 1995; Chávez-García and Salazar, 2002) that site effects in Mexico City cannot be considered separated from the crustal structure. The heterogeneity due to the volcanic belt conditions incident wavefield in Mexico's basin. Long duration of ground motion would result from the interaction of different surface wave modes, generated in the irregular crustal structure, with the very local soil conditions in Mexico City. This is the most promising idea to date and is supported by the modeling results of Furumura and Kennett (1998) and by other, more recent, results by Cruz-Jiménez et al. (2009). The constraints for a crustal model of central Mexico, however, are painfully few. We still have much progress to do to construct a model of this structure.

8. CONCLUSIONS

This paper has reviewed the efforts made to understand site effects at Mexico City. The questions that have been solved regarding the prediction of local amplification were discussed. Many hypotheses had been published, claiming to explain observed ground motion, often based on simple speculation. Much effort was necessary to show some of them to be unfounded. Space limitations forced this review to be schematic and only the main ideas were outlined. This paper should be considered more an invitation to interested readers to approach the abundant literature published on this subject, than a complete presentation in itself. The references cited in this paper are the more important, in the opinion of the author. However, the papers cited in each one of the articles listed below are often worth reading.

There are several points that have been demonstrated without doubt since the 1985 Michoacan earthquake. Ground motion is mostly linear in Mexico City, in spite of the very large amplitudes observed for that event. Although the very soft clay layer is fundamental to understand that amplitude, 1D site effects are only part of explanation of ground motion. The large duration of strong ground motion, which greatly contributed to the observed damage, cannot be explained using 1D models. It is also clear that locally generated surface waves cannot be a major factor in the seismic response of this basin. The very large dispersion due to the huge impedance contrast at the base of the clay layer, together with anelastic attenuation, inhibits their propagation over significant distances. Lateral heterogeneity at many different scales, including the presence of the buildings at the surface, must contribute to ground motion and to its variation throughout the valley. However, those irregularities cannot explain observed ground motion.

The seismic response of Mexico City seems to be as contradictory as its inhabitants. A model that is patently wrong is useful and is at the base of the building code currently in force. In addition, it seems that site effects cannot be considered separated from source and path, even for earthquakes hundreds of km away. Current work is directed to the understanding of the interaction between the crustal structure and the very local soft soils in the lake bed-zone. Their dominant frequencies are surprisingly close (thick layers with high S-wave velocities have similar dominant frequencies as very thin layers with exceptionally small S-wave velocities). The development of a model for the region and its use to predict ground motion for the

expected future large earthquakes in this region is one of the major goals of current research.

Acknowledgements:

The author would like to thank the organizers of the meeting for their kind invitation to prepare and present this paper.

References:

Bard, P.-Y. and Bouchon, M. (1980a), "The seismic response of sediment-filled valleys. Part 1. The case of incident SH waves", *Bulletin of the Seismological Society of America*, **70**, 1263-1286.

Bard, P.-Y. and Bouchon, M. (1980b), "The seismic response of sediment-filled valleys. Part 2. The case of incident P and SV waves", *Bulletin of the Seismological Society of America*, **70**, 1921-1941.

Bard, P.-Y. and Chávez-García, F.J. (1993), "On the decoupling of surficial sediments from surrounding geology at Mexico City", *Bulletin of the Seismological Society of America*, **83**, 1979-1991.

Cárdenas, M. and Chávez-García, F.J. (2003), "Regional path effects on seismic motion in central Mexico", *Bulletin of the Seismological Society of America*, **93**, 973-985.

Cárdenas, M. and Chávez-García, F.J. (2007), "Earthquake ground motion in Mexico City. An analysis of data recorded at Roma array", *Soil Dynamics and Earthquake Engineering*, **27**, 475-486.

Cárdenas, M., Chávez-García, F.J., and Gusev, A. (1997), "Regional amplification of ground motion in central Mexico. Results from coda magnitude data and preliminary modeling", *Journal of Seismology*, **1**, 341–355.

Cárdenas, M., Bermúdez, M.L., and Chávez-García, F.J. (1998), "Ground motion in Mexico City: contributions of building stock", in K. Irikura, K. Kudo, H. Okada y T. Sasatani (eds.) *The effects of surface geology on seismic motion. Recent progress and New horizons on ESG study, Proc. of the 2nd. Int. Symp. on the Effects of Surface Geology on Seismic Motion*, diciembre 1-3, Yokohama, A.A. Balkema, **2**, 421-426.

Cárdenas, M., Bard, P.-Y., Guéguen, P., and Chávez-García, F.J. (2000), "Soil- structure interaction in Mexico City. Wave field radiated away from Jalapa building: data and modeling", *Proc. of the 12th World Conference on Earthquake Engineering*, Auckland, New Zeland, 30 enero-4 febrero, paper 0385.

Chávez-García, F.J. and Bard, P.-Y. (1993a), "Gravity waves in Mexico City? I. Gravity perturbed waves in an elastic solid", *Bulletin of the Seismological Society of America*, **83**, 1637–1655.

Chávez-García, F.J. and Bard, P.-Y. (1993b), "Gravity waves in Mexico City? II. Coupling between an elastic solid and a fluid layer", *Bulletin of the Seismological Society of America*, **83**, 1656–1675.

Chávez-García, F.J. and Bard, P.-Y. (1994), "Site effects in Mexico City eight years after the September 1985 Michoacan earthquakes", *Soil Dynamics and Earthquake Engineering*, **13**, 229–247.

Chávez-García, F.J. (1995), "Dispersión de ondas superficiales en el Valle de México y su influencia en la respuesta sísmica de la zona de lago en septiembre de 1985", in *La Sismología en México: 10 años después del temblor de Michoacán del 19 de septiembre de 1985*, F. Medina-Martínez, L.A. Delgado-Argote, and G. Suárez-Reynoso (eds.), Monografía No. 2, Unión Geofísica Mexicana, 143-156.

Chávez-García, F.J. and Bard, P.-Y. (1995), "Reply to comment on 'Comment on two articles on gravity waves by Chávez-García and Bard (1993a, b)' by C. Lomnitz", *Bulletin of the Seismological Society of America*, **85**, 1272-1274.

Chávez-García, F.J. and Cárdenas, M. (2002), "The contribution of the built environment to the 'free-field' ground motion", *Soil Dynamics and Earthquake Engineering*, **22**, 773-780.

Chávez-García, F.J. and Salazar, L. (2002), "Strong motion in central Mexico: a model based on data analysis and simple modeling", *Bulletin of the Seismological Society of America*, **92**, 3087–3101.

Chávez-García, F.J., Ramos Martínez, J., and Romero-Jiménez, E. (1995), "Surface wave dispersion analysis in Mexico City", *Bulletin of the Seismological Society of America*, **85**, 1116–1126.

Cruz-Jiménez, H., Chávez-García, F.J., and Furumura, T. (2009), "Differences in attenuation of ground motion perpendicular to the Mexican subduction zone between Colima and Guerrero: an explanation based on numerical modeling", *Bulletin of the Seismological Society of America*, **99**, 400-406.

Duke, M. and Leeds, D.J. (1959), "Soil conditions and damage in the Mexico earthquake of July 28, 1957", *Bulletin of the Seismological Society of America*, **49**, 179-191.

Fäh, D., Suhadolc, P., Mueller, St., and Panza, G.F. (1994), "A hybrid method for the estimation of ground motion in sedimentary basins: quantitative modeling for Mexico City", *Bulletin of the Seismological Society of America*, **84**, 383-399.

Flores, J., Novaro, O., and Seligman, T. (1987), "Possible resonance effect in the distribution of earthquake damage in Mexico City", *Nature*, **326**, 783-785.

Furumura, T. and Kennett, B.L.N. (1998). "On the nature of regional seismic phases III. The influence of crustal heterogeneity on the wavefield for subduction earthquakes: the 1985 Michoacan and 1995 Copala, Guerrero, Mexico earthquakes", *Geophysical Journal International*, **135**, 1060–1084.

Guéguen, P., Bard, P.-Y., and Chávez-García, F.J. (2002), "Site-city seismic interaction in Mexico City-like environments: an analytic study", *Bulletin of the Seismological Society of America*, **92**, 794-811.

Kawase, H. and Aki, K. (1989), "A study on the response of a soft soil basin for incident S, P, and Rayleigh waves with special reference to the long duration observed in Mexico City", *Bulletin of the Seismological Society of America*, **79**, 1361–1382.

Lermo, J. and Chávez-García, F.J. (1994), "Site effect evaluation at Mexico City: dominant period and relative amplification from strong motion and microtremor records", *Soil Dynamics and Earthquake Engineering*, **13**, 413–423.

Lomnitz, C. (1990), "Mexico 1985: the case for gravity waves", *Geophysical Journal International*, **102**, 569-572.

Mateos, J.L., Flores, J., Novaro, O., Seligman, T.H., and Alvarez-Tostado, J.M. (1993), "Resonant response models for the Valley of Mexico–II. The trapping of horizontal P waves", *Geophysical Journal International*, **113**, 449-462.

Mooney, H.M. and Bolt, B.A. (1966), "Dispersive characteristics of the first three Rayleigh modes for a single surface layer", *Bulletin of the Seismological Society of America*, **56**, 43–67.

Ordaz, M. and Singh, S.K. (1992), "Source spectra and spectral attenuation of seismic waves from Mexico earthquakes, and evidence of amplification in the hill zone of Mexico City", *Bulletin of the Seismological Society of America*, **82**, 24–43.

Ramos-Martínez, J., Chávez-García, F.J., Romero-Jiménez, E., Rodríguez-Zúñiga, J.L., and Gómez-González, J.M. (1997), "Site effects in Mexico City: constraints from surface wave inversion of shallow refraction data", *Journal of Applied Geophysics*, **36**, 157-165.

Romo, M.P., Jaime, A., and Reséndiz, D. (1988), "General soil conditions and clay properties in the Valley of Mexico", *Earthquake Spectra*, **4**, 731-752.

Rosenbuelth, E. (1966), "Consideraciones sobre diseño sísmico", *Ingeniería Civil*, 132, 6-25.

Seed, H.B., Romo, M.P., Sun, J.I., Jaime, A., and Lysmer, J. (1988), "Relationships between soil conditions and earthquake ground motions", *Earthquake Spectra*, **4**, 687–729.

Seligman, T.H., Alvarez-Tostado, J.M., Mateos, J.L. Flores J., and Novaro, O. (1989), "Resonant response models for the Valley of Mexico–I. The elastic inclusion approach", *Geophysical Journal International*, **99**, 789-799.

Singh, S.K., Mena, E., and Castro, R. (1988), "Some aspects of source characteristics of the 19 September 1985 Michoacan earthquake and ground motion amplification in and near Mexico City from strong motion data", *Bulletin of the Seismological Society of America*, **78**, 451–477.

Zeevaert, L. (1964), "Strong ground motions recorded during the earthquakes of May the 11th and 19th, 1962 in Mexico City", *Bulletin of the Seismological Society of America*, **54**, 209-231.

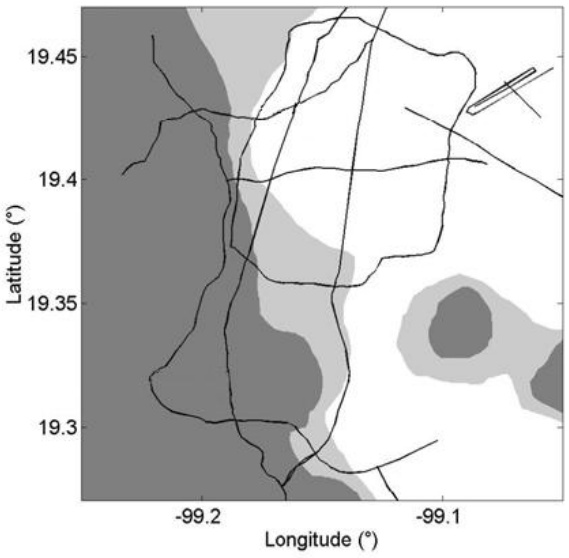

Figure 1 Map of Mexico City showing the three geotechnical zones. Dark grey: hill zone (firm soil). Light grey: transition zone. White: lake-bed zone, with the infamous thin layer of very soft clay. Lines indicate main streets and the airport (at the top, right hand corner).

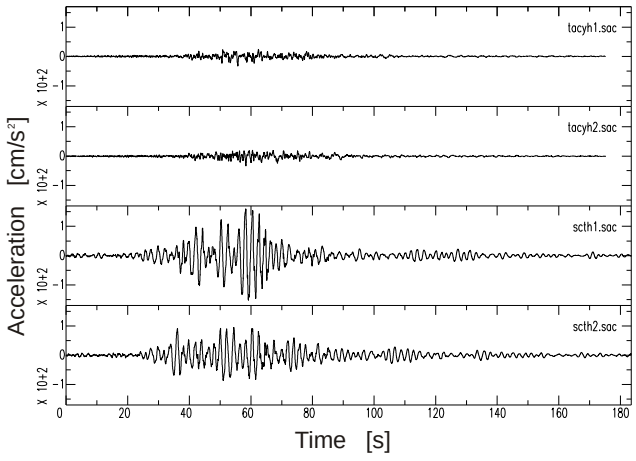

Figure 2 Horizontal accelerograms recorded at two sites in Mexico City during the great Michoacan earthquake of September 19, 1985. The two top traces correspond to a hill zone site. The two lower traces were recorded at SCT site in the lake-bed zone.

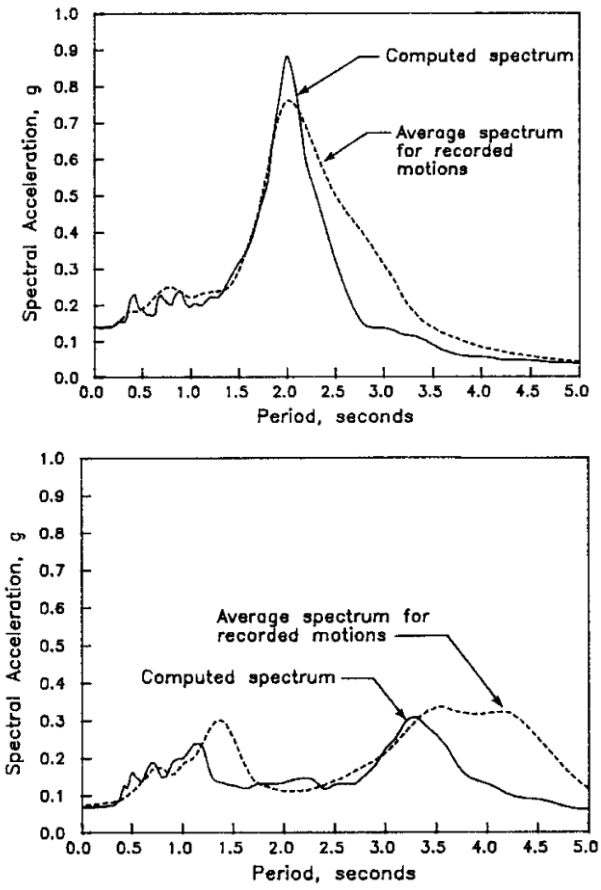

Figure 3 Comparison between observed and computed response spectra at two soft soil sites in Mexico City for the records of the main shock of the Michoacan earthquake. Computations were made using a linear equivalent 1D model for sites SCT (upper diagram) and CDA) (lower diagram). [After Seed et al., 1988.]

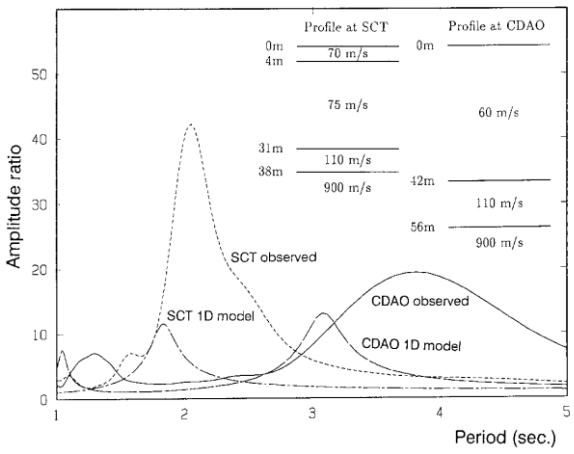

Figure 4 Comparison between observed and computed transfer functions. Computed amplification corresponds to a 1D model using the stratigraphy proposed by Seed et al. (1988) for each site. Observed amplification is the average of spectral ratios relative to TACY, a firm soil site in Mexico City. [After Kawase and Aki, 1989.]

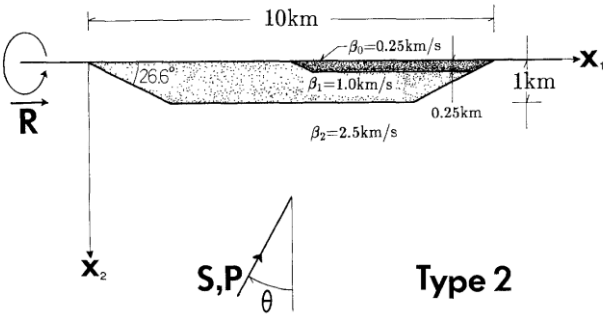

Figure 5 Deep basin structure with a soft surface layer proposed in Kawase and Aki (1989) to investigate seismic response of Mexico's basin. The soft clay layer was not included in the model, and it was argued that the amplification it would generate would cancel out its attenuation. [After Kawase and Aki, 1989.]

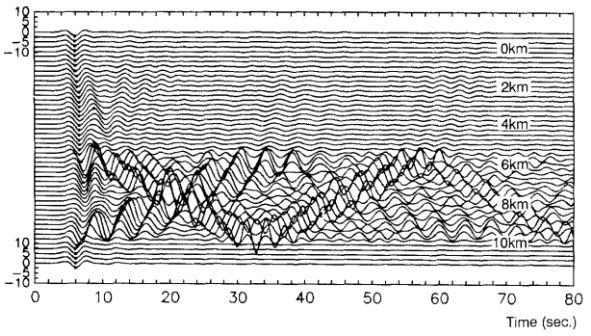

Figure 6 Response of the model shown in the previous figure to vertically incident SH waves. The input signal is a Ricker wavelet with 0.25 Hz dominant frequency. A very long duration of ground motion due to locally generated Love waves is observed. [After Kawase and Aki, 1989.]

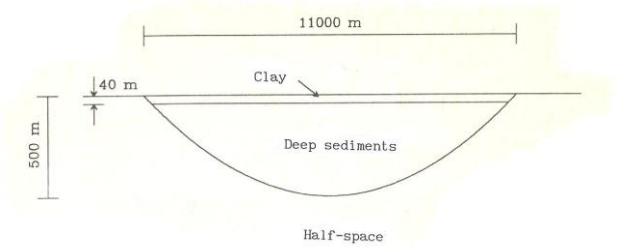

Figure 7 2D model of the large structure of Mexico City. S-wave velocity of the clay layer was fixed at 80 m/s. Different models were considered for the velocity of the deep sediments [after Chávez-García and Bard, 1994].

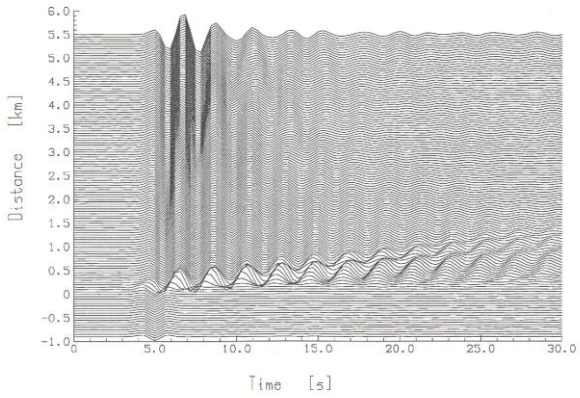

Figure 8 Synthetic seismograms computed for the model shown in the preceding figure for vertical incidence of SH waves. Only half of the valley is shown due to the symmetry of the problem. The velocity of the deep sediments was considered constant at 1000 m/s. Group velocity of the Love wave generated at the edge is 18 m/s. [After Chávez-García and Bard, 1994.]

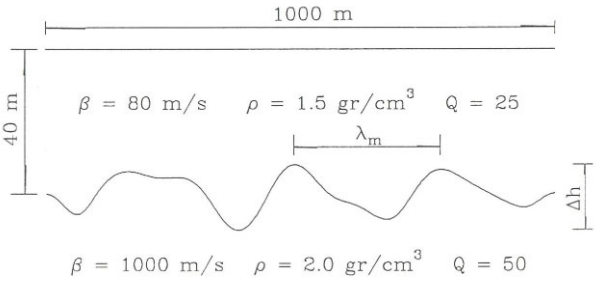

Figure 9 Example of a model of irregular thickness of a homogeneous clay layer. The irregularity of the layer is stochastic, with a fixed mean wavelength (λ_m) of the variations of 132 m and a maximum amplitude of $\Delta H = 20$ m. [After Chávez-García and Bard, 1994.]

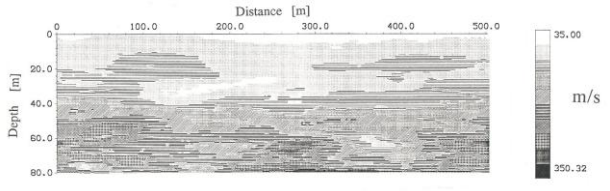

Figure 10 Example of a model with continuous variation of S-wave velocity within the clay layer. Heterogeneities are correlated through von Karman's function of zero order with a correlation distance of 2 m in the vertical direction and 20 m in the horizontal direction. [After Chávez-García and Bard, 1994.]

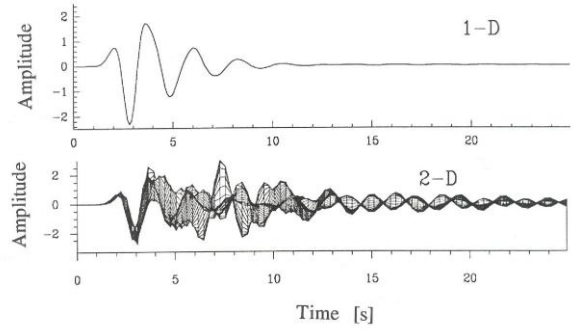

Figure 11 Synthetic seismograms computed for vertical incidence of SH waves in the model shown in the preceding figure. The input signal is a Ricker wavelet of 0.5 Hz dominant frequency. The upper trace shows the result for the average 1D model. The lower traces are the superposition of the 251 sythetic seismograms computed at the surface of the 2D model. [After Chávez-García and Bard, 1994.]



Figure 12 Building distribution in "colonia Roma" in Mexico City. Solid squares show buildings taller than six stories. Open squares show instrumented buildings. [After Guéguen et al., 2002.]

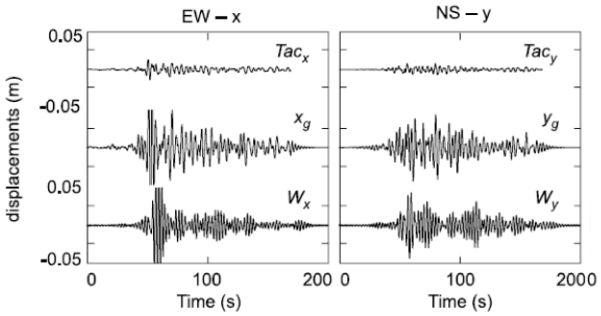

Figure 13 Example of the results obtained from the analytical procedure to estimate the importance of the contamination of seismic ground motion due to the vibration of the buildings shown in the preceding figure. Each diagram corresponds to a horizontal direction. The upper trace shows the records obtained at TACY, on firm ground, station during the Michoacan, 1985, earthquake. Middle traces: simulation of ground motion at the location of "colonia Roma" without including the buildings. Lower traces: ground motion computed at an observation point (Co56 in Figure 12) due to the radiation of the buildings excited by the incident field. The lower traces do not include the free-field ground motion (middle traces). Note that the amplitude of the ground motion radiated by the buildings has an amplitude equivalent to the free-field ground motion (without the buildings) indicating the large importance of the energy radiated by the vibrating buildings. [After Guéguen et al., 2002.]

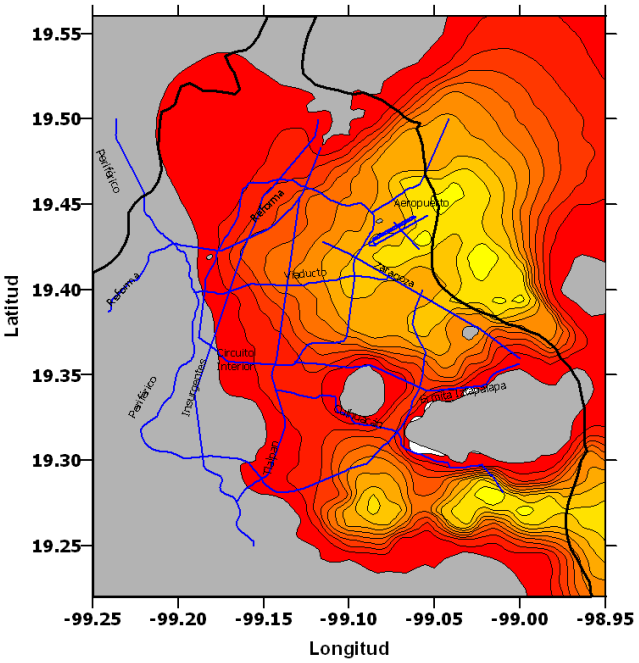

Figure 14 Dominant period map for Mexico City. Red is 1 sec and yellow is 4.5 sec. This map is, effectively, a "nanozonation" map of the city. A design spectrum is constructed at each point based on dominant period only.

JOINT CONFERENCE PROCEEDINGS
7th International Conference on Urban Earthquake Engineering (7CUEE) &
5th International Conference on Earthquake Engineering (5ICEE)
March 3-5, 2010, Tokyo Institute of Technology, Tokyo, Japan

Microzonation and site effect studies in Istanbul

O. Ozel[1], N. Ozel[2] and M. Erdik[2]

[1] Istanbul University, Engineering Faculty, Geophysical Engineering Department
[2] Bogazici University, Kandilli Observatory and Earthquake Research Institute
oguzozel@istanbul.edu.tr, ozeln@boun.edu.tr, erdik@boun.edu.tr

Abstract

On August 17, 1999, a devastating earthquake with a moment magnitude of Mw=7.4 struck the Kocaeli and Sakarya (Adapazari) provinces, and part of suburbs of Istanbul in the northwestern of Turkey, a very densely populated region in the industrial heartland of Turkey. This earthquake caused about 30.000 losses of life and collapsed thousands of buildings. Thus, total loss figure amounted to about US$ 16 Billion. Following the losses during this large earthquake, there has been a broad recognition among Turkey governmental, non-governmental and academic organizations of the need for extensive response planning based on detailed risk analysis of likely seismic hazard, microzonation studies and ground-motion researches in Turkey, in general and, Istanbul particular. In this frame, the metropolitan municipality of Istanbul (IMM), in cooperation with Japan International Cooperation Agency (JICA), implemented a project on disaster prevention/mitigation basic plan in Istanbul. The main objective of this project is to develop seismic microzonation maps which will serve as the basis for disaster prevention and mitigation plan for Istanbul city. On the other hand, as part of the preparations for the future earthquake in Istanbul, Kandilli Observatory and Earthquake Research Institute of Bogazici University (KOERI) in cooperation with other agencies have installed a Rapid Response and Early Warning system (IERREWS) in the metropolitan area. In addition to ground motion research, the data from this dense urban network is used to provide rapid post-earthquake loss information. Besides, KOERI, in co-operation with German GeoForshungs Zentrum (GFZ) scientists has implemented another multi-disciplinary project in Istanbul. One of the aims of the project is to improve the knowledge about the influence of local geology in the city on the expected earthquake ground motion. For this purpose, both single station measurements and array measurements of microtremors were conducted at each IERRS site (hundred sites). In addition to these projects, a complimentary project funded by Bogazici University was implemented at the IERRS sites to study the distribution of the fundamental frequencies beneath these stations using microtremors and small magnitude events' recordings. In the frame of a currently proposed project to Istanbul University, all the results from both single station and array microtremor measurement have been compiled, and additional array measurements where are needed have being performed to determine bedrock depth distribution beneath the European side of Istanbul. According to preliminary results, bedrock (Vs > 1500 m/s) dips from north-northeast towards south-southeast. Based on these results, site effects will be evaluated.

1. INTRODUCTION

Istanbul is a megacity of 12 million inhabitants, who are exposed to a significant earthquake hazard. Moreover, the considerable rate of urbanization combined with uncontrolled land use makes such hazard even higher (Erdik et al., 2003).

During the Izmit and Duzce 1999 earthquakes, this scenario was worsened by the recognition of site amplifications that were observed to locally modify the ground motion inside the metropolitan area. In particular, as shown by several studies (e.g., Ansal et al.,2004; Ozel et al., 2004), the Avcilar district in the western part of Istanbul suffered significant damage, largely due to the

amplification of the earthquake ground motion (Figure 1). In fact, for this area, an intensity of VII (MSK) was assigned, while in the other districts of the metropolitan area an intensity of VI (MSK) was generally observed. The anomalous amplification of the ground motion observed in the western part of the city is considered to be mainly related to the presence of soft sediments overlaying a competent seismic bedrock. In fact, the thickness and the velocity of the sedimentary layers, as well the impedance contrast between the sediments and the underlying bedrock, are the main parameters affecting the frequency band of the seismic motion that may be strongly amplified by the local conditions. Therefore, recent studies (Ergin et al., 2004; Sorenson et al., 2004; Kudo et al., 2002) have focused on estimating possible site effects in the metropolitan area of Istanbul, and in particular in its western part.

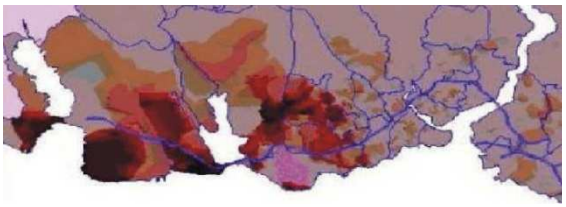

Figure 1. Distribution of damage in Istanbul 17August 1999 Kocaeli Earthquake (after Istanbul Governorate Disaster Management Center)

A suitable characterization of local site effects can be performed by estimating local S-wave velocity profiles, or by determining the resonance frequency of the soft soil layers. Often, information is obtained through invasive techniques, such as drilling, down/cross-hole measurements, etc. However, due to their expensive nature, the widespread application of such techniques is only able to be performed after coming to a compromise with respect to cost, resulting in a limited exploration depth. In fact, microzonation works are frequently based on the use of the average shear-wave velocity in the uppermost 30m (Vs30), which is adopted by the National Earthquake Hazard Reduction Program (NEHRP) classification in the USA.

This paper is the compilation of the related parts of the project report of "Disaster Mitigation Basic Plan in Istanbul", implemented in cooperation of IMM and JICA, and of the report of "Istanbul Megacity Project" by IMM, KOERI and GFZ. Moreover, the results of some other studies (e.g. Erdik et al. 2003; Birgoren et al., 2009; Picozzi et al. 2009) are also included to this paper. The purpose of this compilation is to give information about what have been performed for disaster mitigation and microzonation after Izmit (17th August, 1999) and Duzce (12th November, 1999) earthquakes in Istanbul.

2. MICROZONATION AND SITE EFFECT STUDIES IN ISTANBUL

2.1. Disaster mitigation basic plan in Istanbul

In response to a request from the Government of the Republic of Turkey, the Government of Japan decided to conduct "The Study on A Disaster Prevention / Mitigation Basic Plan in Istanbul including Seismic Microzonation in the Republic of Turkey" and entrusted the Study to the Japan International Cooperation Agency (JICA). The objectives of the Study are to compile the seismic microzonation maps which can serve as the basis of seismic disaster prevention/mitigation plan for Istanbul city and prefecture, to make recommendations for construction of earthquake resistant urbanization and to conduct effective technical transfer on relevant planning technique.
Specifically, the study intends to:
1) Integrate and develop seismic microzonation studies being carried out in Istanbul as scientific and technical basis for disaster prevention/mitigation planning;
2) Recommend a citywide prevention/mitigation program against damage of buildings and infrastructures based on the detailed seismic microzonation study and buildingThe Study on a Disaster Prevention/Mitigation Basic Plan in Istanbul including Seismic Microzonation in the Republic of Turkey vulnerability evaluation of areas;
3) Recommend disaster prevention considerations to be incorporated in urban planning of Istanbul City including land use plan and earthquake-resistant design regulation, etc; and
4) Pursue technology transfer of planning techniques to Turkish counterpart personnel in the course of the study.

2.2. Scenario Earthquakes

From the beginning of the study, many extensive discussions have occurred with elevant institutes/researchers in order to determine the scenario earthquakes. Based on these discussions and the recent amount of research work on the North Anatolian Fault (NAF), the scenario earthquakes were identified so that the appropriate damage estimation is taken into consideration in disaster prevention planning. The location of the NAF, in the Marmara Sea, was determined based on the most recent study result by Le Pichon et al. (2001).

The following the four scenario earthquake models were determined as show in Figure 2.
Model A: This section is about 120 km long from west of 1999 Izmit earthquake fault to Silivli. This model is the most probable model of these four scenario earthquakes because the seismic activity is progressing to the west. The moment magnitude (Mw) is assumed to be 7.5.
Model B: This section is about 110 km long from the eastern end of 1912 Murefte-Sarkoy earthquake fault to Bakılkoy. The moment magnitude is assumed to be 7.4.
Model C: This model supposes a simultaneous break of the entire 170 km section of the NAF in the Marmara Sea. The moment magnitude is assumed to be 7.7. This is the largest magnitude that this area has ever experienced, as the maximum magnitude of historical earthquakes in the Marmara Sea area is 7.6.

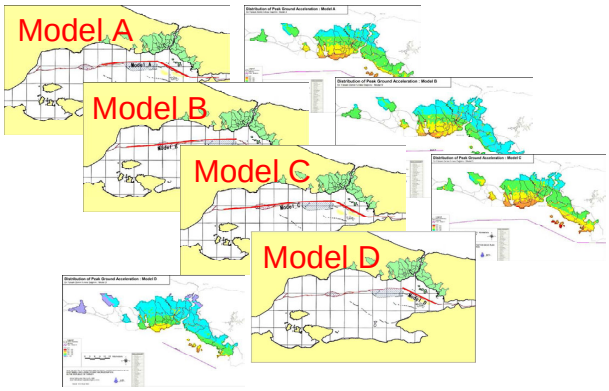

Figure 2. Scenario earthquakes based on four models (after "Disaster Mitigation Basic Plan" report). Also shown are the PGA distributions based on these scenario earthquakes (Project report by JICA and IMM).

There is no evidence of a simultaneous break of the entire section in the past, though the eastern one-third did rupture on May 1766 and the rest on August 1766. If a rupture of the maximum length of the faults is assumed, this is the worst case within reason.
Model D: The continuous fault that was found in the north of the Marmara Sea follows the base of the northern steep slope of the Cinarcık Basin. A normal fault model was developed, which follows the northern slope of the Cinarcık Basin with reference to many recent researched works. The moment magnitude (Mw) was assumed to be 6.9 with the empirical formula for a normal fault.

2.3. Building damages

Based on scenario earthquakes Model A and Model C, every type of building included in the building census for the year 2000 is included. Buildings are calculated as "heavily," moderately," or "partly" damaged (Figure 4). "Heavily" damaged buildings are buildings that are severely damaged or have collapsed, and these buildings are unfit to occupy until they are repaired or rebuilt. "Moderately" damaged buildings are buildings that are able to used for evacuation purposes just after the hazard, but they need to be repaired before occupied permanently.

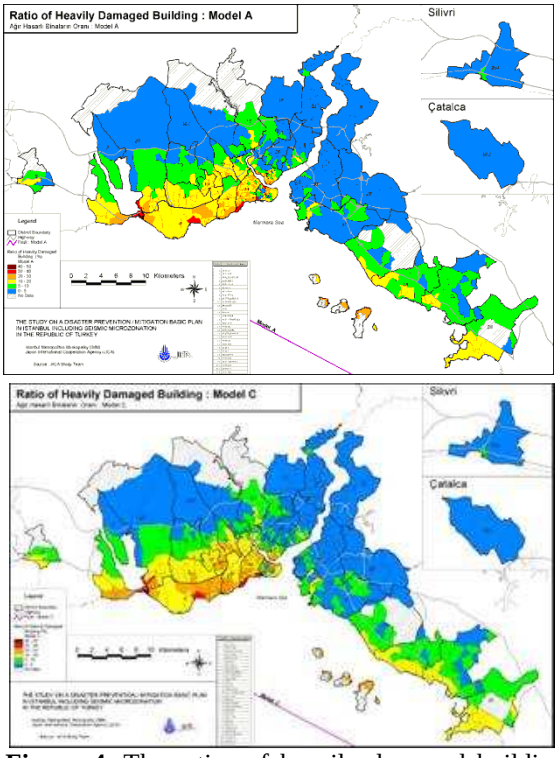

Figure 4. The ratios of heavily damaged buildins based on the scenario models of A and C (Project report by JICA and IMM).

"Partly" damaged buildings can be used for living, but it is desirable they be repaired because the structure is partly damaged and its earthquake-resistance has been compromised. The cause of damage is limited to the seismic vibration itself. Damage due to other causes such as liquefaction, landslide, and fire is not included. This assumption will not affect the results because these phenomena are not main causes of earthquake disasters in Istanbul.

2.4. Ground Classification

Shear wave velocities were measured comprehensively by suspension PS logging in every 500 m-grid. Ground shear- wave velocities for very 1 m-pitch of the boreholes were directly correlated to the most of the geological units in the Study Area. Average shear wave velocities of the upper 30 m of every 500 m grid model are calculated. Ground classification of each grid model was

determined according to NEHRP. The compiled ground classification map is shown in Figure 5.

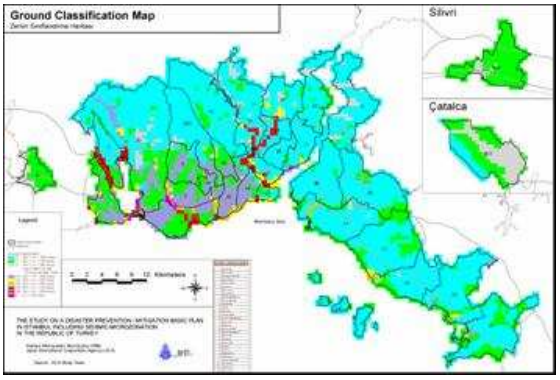

Figure 5. Ground classification map (Project report by JICA and IMM).

3. ISTANBUL MEGACITY PROJECT

This project is implemented by the co-operation of Istanbul Metropolitan Municipaility (IMM), Kandilli Observatory and Earthquake Research Institute (KOERI) and Geoforshung Zentrum (GFZ). The purpose of the project is;

-Detailed Probabilistic Seismic Hazard Assessment for the Area of Istanbul

- Numerical Stress Field Modelling of the Istanbul Region
- Modelling the Crustal Deformation and Stress at the North Anatolian Fault Zone – a Contribution to the Time-Dependent Seismic Hazard Analysis for the Region of İstanbul
- Microzonation and Modelling - Site Effects in İstanbul
- Vulnerability and Risk
- Vulnerability Study of Istanbul Metropolitan Area with Respect to an Earthquake Event Estimated by Means of Remote Sensing and GIS
- Flooding due to Alibeykoy Dam Failure
- Indirect Economic Losses

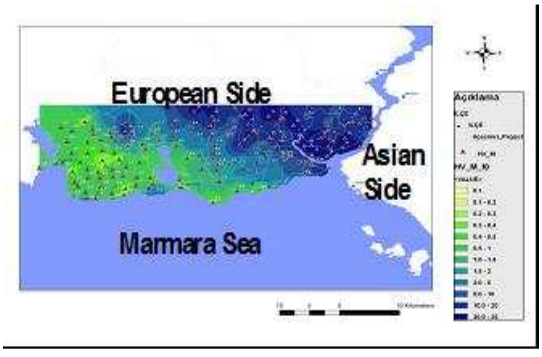

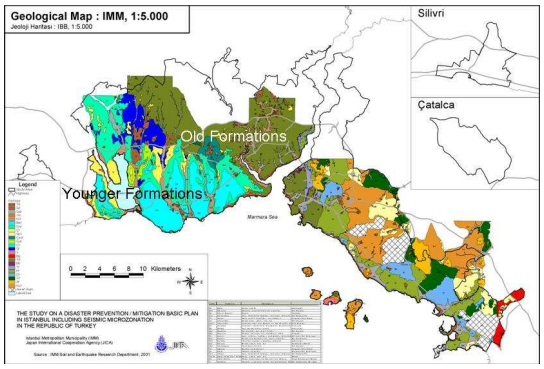

Figure 6. The combined fundamental frequency distribution map for the European side of Istanbul (modified from Picozzi et al. 2009; above). Blue scaled colors show higher frequncies. The map at the bottom show geology of Istanbul (Report by JICA-IMM, 2002).

Because of the large scope of this project, we mention only the microzonation and site effects part. In this part, as a preliminary activity for the microzonation characterization of Istanbul, 192 single station measurements for the estimation of the H/V curves were carried out in the western part of the metropolitan area, in order to estimate the fundamental frequencies of the sedimentary cover. In particular, 42 of these noise measurements were performed at sites where accelerometers belonging to the permanent and temporary networks operated by KOERI are located. Thus, for 29 sites of the considered accelerometric stations, the H/V curves from noise recording were compared with those calculated using weak motion recordings. This comparison of the results provided by the different methods was in fact directed towards performing a calibration of the passive seismic techniques in the area investigated, allowing a preliminary validation for the reconstructed sediment–bedrock interface geometry and the site effects estimates. Furthermore, single station microtremor measurements in the frame the other projects implemented by KOERI (Ozel et al., 2005) and Istanbul University (Ozel et al., 2009) were also performed in the European side of Istanbul. The combined fundamental frequency distribution map is given in Figure 6(upper). The fundamental frequency map is in remarkable agreement with the geological map (Figure 6, bottom), both in identifying the boundaries of the Paleozoic bedrock outcrops in the northern and eastern parts of the investigated area (characterized by H/V curves without amplification or fundamental resonance frequencies over 10 Hz), and the identification of areas with soft sedimentary covers in the southwestern part.

In addition, in order to provide additional useful information for site effects and microzonation studies, a series of eight 2D micro-array measurements utilizing short-period sensors and

high dynamic digitizers were carried out in selected sites of the study area (Picozzi et al. 2009). The extended spatial autocorrelation technique (ESAC; Okada, 2003), and frequency–wavenumber analysis (maximum likelihood method; Capon, 1969) were used for the estimation of the Rayleigh wave dispersion curves and wavefield analysis. For the first time, the resulting dispersion curves were used together with the H/V curve in a joint inversion scheme for the estimation of the S-wave velocity profiles in a megacity. Figure 7 shows the single-station and array mictrotremor measurements' locations.

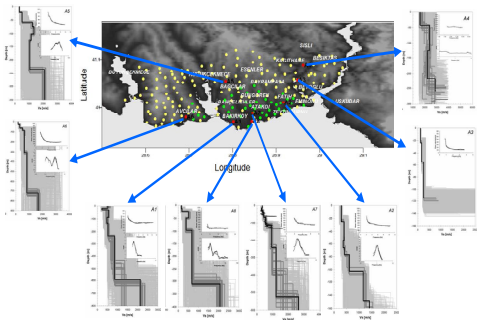

Figure 7. Locations of single stations (yellow dots, from Picozzi et al. 2009; and green dots, from Ozel et al. 2005) and array microtremor measurements (red dots).

4. ISTANBUL EARTHQUAKE RAPID RESPONSE AND EARLY WARNING (IERREEW) PROJECT

To assist in the reduction of losses in a disastrous earthquake in Istanbul a dense strong motion network is established. One hundred (100) of the strong motion recorders are stationed in dense settlements in the Metropolitan area of Istanbul in dial-up mode for Rapid Response information generation (Figure 8).

The Rapid Response part of the IERREWS has the objective of providing:

• Reliable information for accurate, effective characterization of the shaking and damage by other rapid post-earthquake maps (Shake, Damage and Casualty maps) for rapid response;

• Recorded motion for post-earthquake performance analysis of structures;

• Empirical basis for long-term improvements in seismic microzonation, seismic provisions of building codes and construction guidelines; and

• Seismological data to improve the understanding of earthquake generation at the source and seismic wave propagation.

The Early Warning part of the IERREWS ten strong motion stations were located as close as possible to the Great Marmara Fault in 'on-line' mode.(Figure 8). Considering the complexity of fault rupture and the short fault distances involved, a simple and robust EarlyWarning algorithm, based on the exceedance of specified threshold time domain amplitude levels is implemented. The early warning information (consisting three alarm levels) will be communicated to the appropriate servo shut-down systems of the recipient facilities, which will automatically decide proper action based on the alarm level. Depending on the location of the earthquake (initiation of fault rupture) and the recipient facility the alarm time can be as high as about 8s.

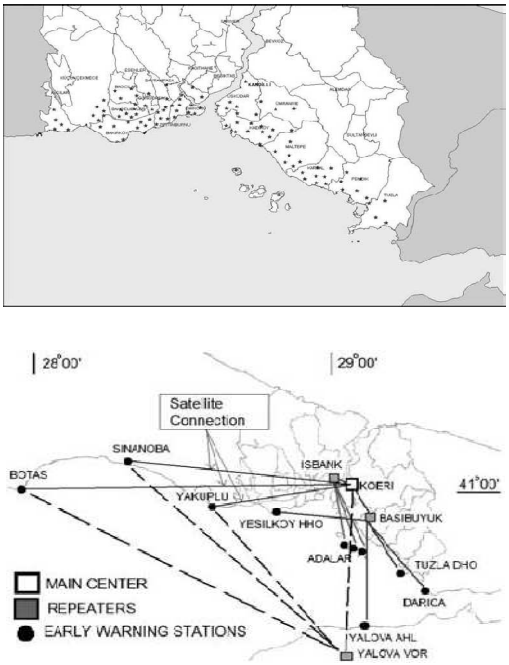

Figure 8. Istanbul Earthquake Rapid Response stations (top) and Early Warning stations (botom).

5. BEDROCK MAPPING PROJECT AND RESONANCE FREQUENCY DISTRIBUTION FOR THE EUROPEAN SIDE OF ISTANBUL

Several earthquake scenerio studies on earthquake risk mitigation have been performed in Istanbul where is threated by a large earthquake in near future. In these studies, efforts are given to estimation of building damage and loss of life by producing synthetic waveforms for such an damaging earthquake in close distances to Istanbul. The S-wave velocity structure and the distribution of bedrock depth are the key parameters for evaluating the effects of a large earthquake, such as ground motion simulations (e.g. Sorensen et al., 2007; Pulido et al., 2004).

The purpose of this project is to determine the 3-dimensional bedrock depth distribution underlying the Oligocene and Miocene formations beneath the European side of Istanbul. To determine the bedrock distribution or in other words the total thickness of the sedimentary layers, an empirical relationship between thickness and dominant

frequency has been derived by using single-station microtremor measurements (Birgoren and Ozel, 2009). Figure 9 shows the derived relationship between resonance frequency and cover thickness above bedrock.

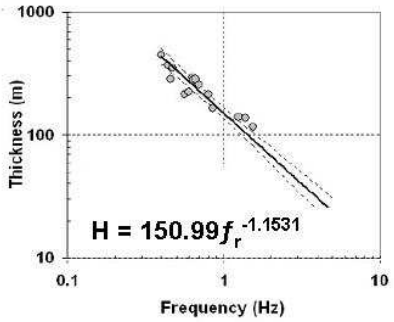

Figure 9. The relationship between cover thickness and resonance frequency for the European side of Istanbul. The confidence limits of 95% are also shown by dashed lines (Birgoren and Ozel, 2009).

On the other hand, array microtremor measurements have been performed (still an ongoing project) by 2-4 km spacing in the European side of Istanbul to estimate the S-wave velocity structure above the bedrock. Figure 10 shows the locations of the array microtremor measurements (Intermediate project report, Ozel et al., 2009). These locations are chosen on the profiles crossing the area of interest from north to south and from east to west (Figure 10). Spatial Auto-Correlation (SPAC) method have been applied to the acquired data (Okada, 2003).

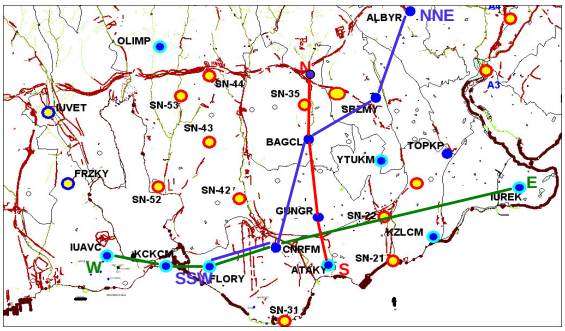

Figure 10. The locations of the array microtremor measurements. Blue dots show already performed locations and yellow dots show those which will be performed in this year. Also shown by straith lines are the profiles along which the cross-sections are taken (Intermediate project report, Ozel et al., 2009).

The results from array microtremor measurements are given in Figure 11. According to the preliminary results, the depths to the bedrock (>1500 m/s) beneath the locations in the north and the northeast are quite shallow while deeper beneath those in the south and southwest, suggesting that the bedrock dips towards south-southwest (Figure 12). This is also evident from the geological information and the distribution of fundamental frequency (Figure 6).

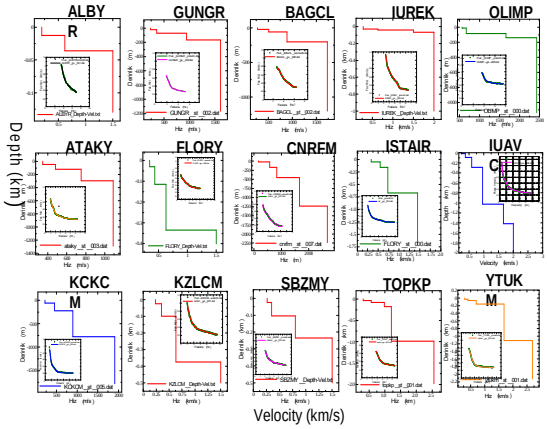

Figure 11. The S-wave velocity-Depth profiles obtained from the array microtremor measuremnts. Inlets show the Rayliegh wave dispersion curves (Ozel et al., 2009).

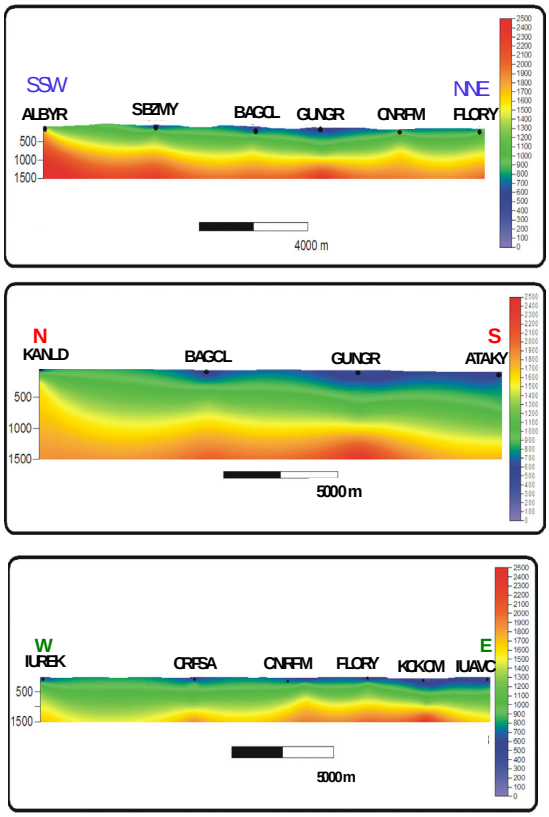

Figure 12. Cross sections along the profiles; NNE-SSW oriented (top), N-S oriented (middle) and E-W oriented (bottom).

6. CONCLUSION

The outputs of these studies will be the basic input for the researchers who have been modeling the strong-ground motion instead of using rough velocity models and sediment thicknesses. At the same time, the distribution of the fundamental

frequencies will help the completeness of the microzonation studies in Istanbul.

ACKNOWLEDGEMENTS

The authors thank to the IMM and to the authors of the studies included in this paper, as well, for their permissions to use their results. We also thanks to the reviewers for their contributions. This work was partially funded by İstanbul University Research Fund under Project Number UDP-3564.

REFERENCES

Ansal A, Laue J, Buchheister J, Erdik M, Springman SM, Studer J, Koksal D. (2004). Site characterization and site amplification for a seismic microzonation study in Turkey. In: Proceedings of the 11th international conference on soil dynamics and earthquake engineering (11th ICSDEE) and the 3rd international conference on earthquake geotechnical engineering (3rd ICEGE), Berkeley, CA, 7–9 January, p. 53–60.

Birgoren G, Ozel O. (2006) Determination of site effects and ground motion lengthening in Istanbul area derived from small earthquake recordings. In: Proceedings of the 8th US national conference on earthquake engineering, San Francisco, CA, USA, 18–22 April, paper no. 1908.

Birgoren, G. Siyahi, B. and Ozel O. (2009). Bedrock Depth Mapping of the Coast South of İstanbul: Comparison of Analytical and Experimental Analysesö Turkish Journal of Earth Sciences (Turkish J. Earth Sci.), Vol. 18.

Capon J. (1969). High-resolution frequency–wavenumber spectrum analysis. Proc. IEEE 1969;57(8):1408–18.

Erdik M, Aydinoglu N, Fahjan Y, Sesetyan K, Demircioglu M, Siyahi B. (2003) . Earthquake risk assessment for Istanbul metropolitan area. Earthquake Eng Eng Vib.;2:1.

Ergin M, Ozalaybey S, Aktar M, Yalcin MN. (2004) Site amplification at Avcilar, Istanbul. Tectonophysics; 391 :335–46.

Istanbul Governorate Disaster Management Center (1999) Damage Distribution Map.

JICA & IMM (Japan International Cooperation Agency & İstanbul Metropolitan Municipality) (2002). The Study on a Disaster Prevention/Mitigation Basic Plan in İstanbul Including Seismic Microzonation. Field Report (2) Appendix1.

Kudo K, Kanno T, Okada H, Ozel O, Erdik M, Sasatani T. (2002) . Site-specific issues for strong ground motions during the Kocaeli, Turkey, earthquake of 17 August 1999, as inferred from array observations of microtremors and aftershocks. Bull Seism Soc Am., 92(1):448–65.

Le Pichon, X., Şengör, A.M.C. Demirbağ, E., Rangin, C., İmren, C. Armijo, R., Görür, N., Çağatay, N., Mercier de Lepinay, B., Meyer, B., Saatçiler, R., Tok, B., (2001), The active Main Marmara Fault. Earth Planet. Sc. Lett., 192, 595-616.

Okada H. (2003). The Microtremor Survey Method (Geophysical Monograph Series 12). Washington: American Geophysical Union; 2003.

Ozel O, Sasatani T, Kudo K, Okada H, Kanno T, Tsuno S, et al. (2004) Estimation of S-wave velocity structures in Avcilar–Istanbul from array microtremor measurements. Geophysics, 12:2.

Ozel, O., Bırgoren, G. Fahjan, Y., Alcık, H. & Erdık, M. (2006). İstanbul Deprem Acil Mudahale ve Erken Uyarı Sisteminin Kalibrasyonu ve İstasyon Yerlerinin Depreme Karşı Yerel Tepkilerinin Belirlenmesi [Determination of Site Response and Calibration of İstanbul Early Warning and Rapid Response Stations]. BU-SRP Project no. 05T102 (in Turkish).

Ozel O., Ozel N., Pinar A., Karabulut S., Fırat B.,Tanırcan G., Yılmazer M. (2009). Istanbulda Avrupa Yakası altında Anakaya derinlik dagılımını ve S-dalga hız yapısını belirleyerek deprem yer tepkisini incelemek. Istanbul Universitesi BAP Projesi, Ara Raporu (in Turkish).

Picozzi, M., Strollo, A., Parolai, S., Durukal, E., Ozel, O., Karabulut, S., Zschau, J., Erdik, M. (2008). Site characterization by seismic noise in Istanbul, Turkey. Soil Dyn Earthquake Eng, doi:10.1016/j.soildyn.2008.05.007

Pulido N.,, Ojeda A., Atakan K.,, Kubo T., (2004). Strong ground motion estimation in the Sea of Marmara region (Turkey) based on a scenario earthquake, Tectonophysics 391, 357–374.

Sørensen M, Oprsal I, Bonnefoy-Claudet S, Atakan K, Martin Mai P. (2006). Local site effects in Atakoy, Istanbul, Turkey, due to a future large earthquake in the Marmara Sea. Geophys J Int., 167:1413–24.

JOINT CONFERENCE PROCEEDINGS
7th International Conference on Urban Earthquake Engineering (7CUEE) &
5th International Conference on Earthquake Engineering (5ICEE)
March 3-5, 2010, Tokyo Institute of Technology, Tokyo, Japan

SITE CHARACTERISTICS OF STRONG-MOTION EARTHQUAKE STATIONS IN METROPOLITAN IZMIR, AEGEAN REGION OF TURKEY

Elcin Gok[1)], Orhan Polat[2)], Doguser Yilmaz[2)], Ulubey Ceken[3)], Mehmet Kuruoglu[4)], Ahmet Turan Arslan[1)], Bekir Tuzel[3)], and Zafer Akcig[1)]

1) Earthquake Research and Implementation Center of Dokuz Eylul University, Izmir, Turkey
2) Seismology Division of the Department of Geophysics, Engineering Faculty of Dokuz Eylul University, Izmir, Turkey
3) Earthquake Research Directorate, General Directorate of Disaster Affairs, Ankara, Turkey
4) Geotechnical Division of the Civil Engineering Department, Engineering Faculty of Dokuz Eylul University, Izmir, Turkey
elcin.gok@deu.edu.tr, orhan.polat@deu.edu.tr, doguser.yilmaz@ogr.deu.edu.tr, ceken@deprem.gov.tr, mehmet.kuruoglu@deu.edu.tr, tuzel@deprem.gov.tr, zafer.akcig@deu.edu.tr

Abstract: This article is mainly concerned with analyzing the accelerometric data that has been recorded by the local strong-motion IzmirNET array (Polat et. al. 2009), located in Western Anatolia, Turkey. The main conceptual aims of this new network are: 1) adequate coverage of the various sedimentary environments in Izmir and surroundings, 2) installing the stations settlement area which is close to potential fault planes, 3) free-field establishments wherever logistically possible, 4) remote accessibility to the data, and 5) continuous recording (as opposed to triggered recording). More than 80 good quality triaxial acceleration time histories have been recorded Most of the events are moderate-size records. Commonly-used ground motion estimation equations for shallow crustal earthquakes were poorly estimated yet from the available data due to the smaller earthquakes for greater distances, regional dependence of ground motions, differing tectonics or crustal structures in the study area. The site response in the city was initially evaluated by using horizontal-to-vertical spectral ratio (HVSR) technique from the strong motion recordings.

1. INTRODUCTION

The study area is located in the central Aegean Region-*AR* of Turkey including North Anatolian Fault Zone-*NAFZ* and East Anatolian Fault Zone-*EAFZ* (Figure 1 inset). The AR is commonly considered as under N-S extension in response to westward motion of Anatolian Plate which is in collision with Arabian and African plates (Jackson and McKenzie 1984).

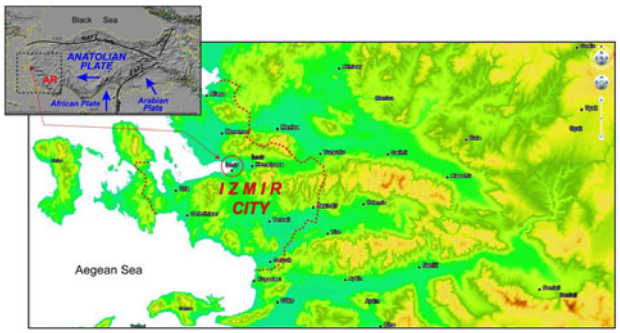

Figure 1 Topography map of Izmir and its vicinity. Political boundary was indicated in red-colored dashed line. Inset shows regional tectonic features and relative motion of the plates. Image was prepared by using SRTM 90m topographic data in Google Earth.

Izmir city, 3rd biggest city of Turkey following Istanbul and capital Ankara, is located very close to the active faults (i.e; Izmir Fault-IF, Orhanli-Tuzla Fault-OTF), and is sited on thick Quaternary sediments (Figure 2).

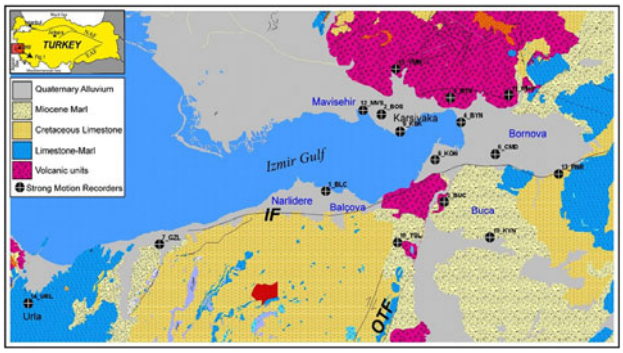

Figure 2 Main geologic and tectonic features of Izmir.

A small-aperture local accelerometric array, IzmirNET, has been installed in 2008 in the frame of a national cooperation between Dokuz Eylul University-DEU and Earthquake Research Department-ERD (Polat et al. 2009).

The accelerometers were mainly installed on the sediments. Basin-type structures are in Bornova, Karsiyaka, Mavisehir area, and Narlidere-Urla seashore of the Gulf of

Izmir. Since unconsolidated deposits in Izmir basin may significantly change the propagation of ground motions to the surface, the assessment of seismic hazard for the city is an important issue (Pamukcu and Yurdakul 2008, Polat et al. 2008). Considering these necessities in engineering seismology and earthquake engineering, we completed installation of IzmirNET in August 2008. This will be a complementary and on-going effort of TURDEP project for the Izmir area (Inan et al. 2007). We acquired, processed and interpreted the data as a preliminary analysis for the following questions:

- Present seismicity, seismotectonic and stress regime
- Amplification and spectral ratio changes
- Distribution of Peak Ground Amplification (PGA)
- Attenuation relationships
- Source parameters

2. ANALYSIS OF STRONG-MOTION DATA

2.1 Seismicity, seismotectonic, and stress regime

In this work, we analyzed the earthquakes ($2.1 \leq M \leq 3.5$) that occurred between 2008 and 2009 August. These events are recorded by the IzmirNET seismic network. The dataset consists of 76 events recorded by at least eight stations, on average, resulting in a total of about 1.800 P-wave, and 1.300 S-wave arrival time picks. The location of the earthquakes reveals a swarm at the NW of Narlidere. Whether some locations exhibit 30km depth, most of the events concentrate in the upper part of the earth crust for about 20 km. Other seismic activity can be observed in the south of Guzelbahce, and NW of the study area (26.8^{o}E-38.5^{o}N). But location quality is poor due to the weak station coverage over there (Figure 3).

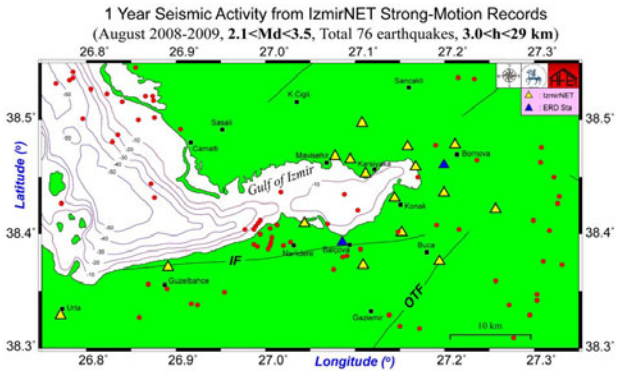

Figure 3 Distribution of main settlements and one year seismic activity around Metropolitan city of Izmir. Bathymetry was taken from Duman et al. (2004).

We estimated the focal mechanisms for the events from the P-wave first-motion polarities using the FocMec algorithm (Snoke 2003). The dataset consists of 9 earthquakes recorded by 15 stations, resulting in a total of about 135 P-wave polarity recordings. To compute the high-quality focal mechanisms for the selected dataset of the Izmir earthquakes, we decided to reject the events with an RMS larger than 0.3 s, and with azimuthal gaps larger than 180◦. Whether computed focal mechanisms are discrepant, most of them belong to normal component faulting (pure normal or dominant normal with a minor strike-slip component). In Figure 4, examples of the fault plane solutions are shown. Only some solutions show strike-slip or reverse faulting.

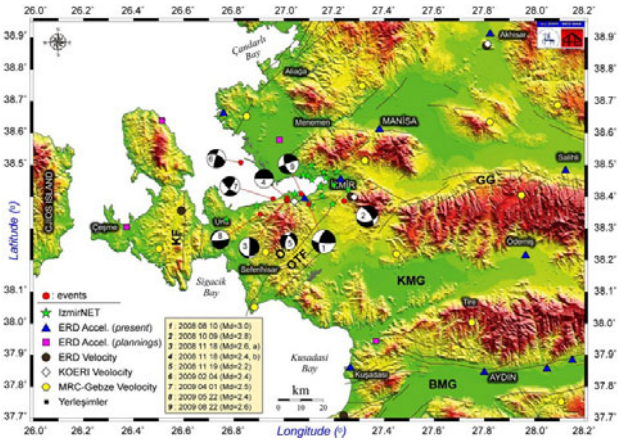

Figure 4 Focal mechanism solutions from IzmirNET (August 2008 - 2009, number of investigated earthquake is 9, $2.2 \leq Md \leq 3.0$). KF: Karaburun Fault, KMG, BMG, GG: Kucuk, Buyuk Menderes, Gediz graben systems.

In the present study, we used the method developed by Michael (1987) to determine the stress tensor from the 9 focal mechanisms. Applying the Michael's technique, we obtain the best stress tensor that fits the data and is represented by the orientation of the three principal stress axes (σ_1, σ_2 σ_3) , and the shape factor (R) expressed as $R = (\sigma_2 - \sigma_1)/(\sigma_3 - \sigma_1)$ where σ_1, σ_2, and σ_3 are the maximum, intermediate, and the minimum compressive principal stress axis, respectively. Generally the *P*- and *T*-axis of a single fault plane solution coincide with the maximum and minimum stress orientations acting in the area (Jackson and McKenzie 1984). Small pre-existing faults in the shallow crust may be conducive to slip when only a small component of shear stress is resolved along the fault surface. In accordance with the prevailing N–S extensive stress regime, the exact method of stress inversion indicates that the maximum principal stress axis (σ_1) is oriented N310°E with a dip (δ=50°). The shape factor, R, is 0.6. The pattern of stresses proves that the extensive stress regime is dominant in Izmir area (because σ_1 is closer to vertical, σ_2 and σ_3 are almost horizontal (Figure 5). This result is in good agreement with the available seismological, geophysical and geological information of the area (Uzel and Sozbilir 2008). This indicates that the stress field in Izmir and surrounding area are relatively uniform. The minimum principal stress axis (σ_3), with the orientation about NNE–SSW, might be predictive on the basis of current plate motion from the directions of the P-axes.

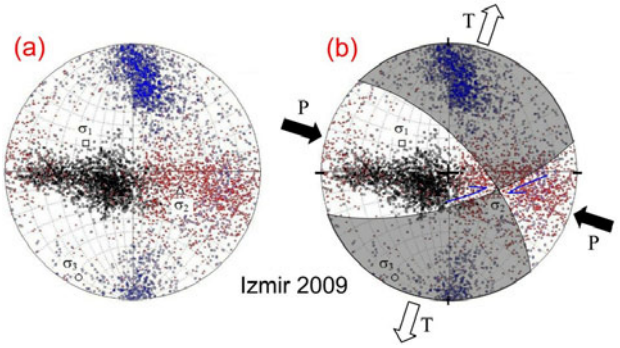

Figure 5 Stress tensor analysis from IzmirNET; (a) Raw data obtained from focal mechanisms of 9 events, (b) Preliminary interpreted results for Izmir area according to Michael (1987). The σ_1, σ_2, and σ_3 show principal stress axes (maximum, intermediate, minimum; respectively).

2.2 Amplifications and Spectral Ratio Changes

The site response and amplifications at 15 stations (except GZL in the SW) in the Izmir is calculating simultaneously for the recorded events. An example of the earthquake that occurred on August 22, 2009 (Mw=3.5), was shown in Figure 6 by using the Horizontal-to-Vertical Spectral Ratio (HVSR) method.

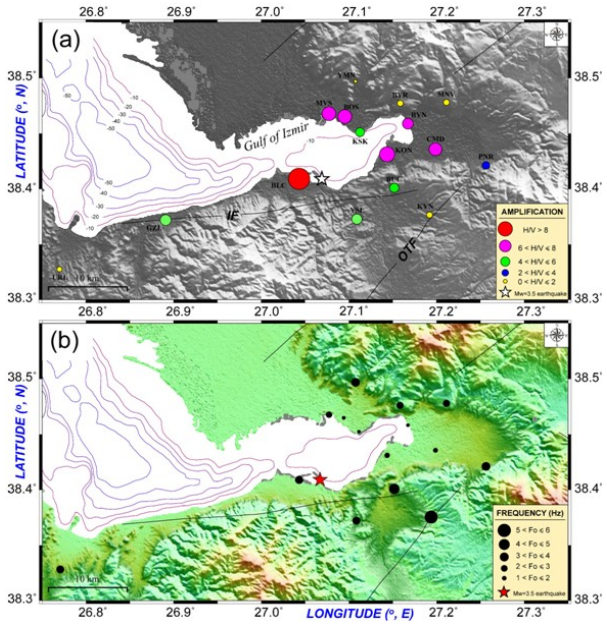

Figure 6 Analysis of strong-motion data for a local event (Mw=3.5) which is occurred on August 22, 2009 (19h21 GMT) near Balcova-Izmir (27.069°E - 38.409°N); Distribution of; (a) Horizontal-to-Vertical Spectra Ratio (HVSR), and (b) Fundamental frequencies (Fo, Hz)

Results are in good harmony at many stations in determining the site spectral ratio (Figure 6a). Higher amplification was observed in BLC station near Narlidere-Balcova area. Other serious ratios were detected at the eastern and northern part of the city where they are usually higher than 6. Distribution of the fundamental frequencies (Fo) has been shown in Figure 6b. The soil frequency characterizes the damage properties for the buildings and structures. Amplifications and frequencies are in good agreement generally. Most of the stations reveal similar results by using HVSR method. But at URL station, resonance frequency and amplification are not consistent. Low amplification was estimated for the lower frequencies at about 2 Hz. This may indicate that the source effect and azimuthal directivity could play an important role in the estimations.

The YMN is a typical rock station and convenient for the usage of Reference Site Method (RSM). In near future, amplification level and spectral ratios will be investigated together by using different methods such as RSM and HVSR.

2.3 Distribution of Peak Ground Amplification (PGA)

An earthquake with a magnitude of Mw=4.9 detected by IzmirNET has been shown in Figure 7a. The IzmirNET is free-field and equipped with three-component CMG-5TD accelerographs (Guralp Systems, Reading-UK) with CMG-5T force balance accelerometer and built-in 24-bit AD converter for data acquisition. A three component accelerogram is also given in Figure 7b for the YMN station.

The PGA mapping for the event that occurred at the northern half of the Gulf of Izmir in January 19, 2009 (19h17), indicates that the Narlidere-Balcova area at the south and Mavisehir-Bostanli area at the North reveal peak acceleration distribution (Figure 8). Thus, it is reasonable to assume that a potential seismic hazard during future earthquakes is crucial over these areas and potential damage for the lifeline systems (gas, water, electricity, sewage, etc) of the city.

2.4 Attenuation relationships

There are many attenuation relationships available for the prediction of ground motions as a function of distance and earthquake magnitude. For a study area, the rates of attenuation could be different from expected relationships due to the scarcity of strong-motion data. In the present study, we used the models developed by Boore et al. (1997), Kalkan and Gulkan (2004), Sadigh et al. (1997) and, Ulusay et al. (2004) to compare recorded peak values.

The attenuation equations are plotted in Figure 9 to show its overall compatibility on different sites (site class A, B, C, D according to the TDY2007 and Eurocode8) for an earthquake Mw=4.9 that occured nearly 90 km far from the IzmirNET array. It is apparent that the relationship by Sadigh et al. (1997) agrees reasonably well with observed PGA's.

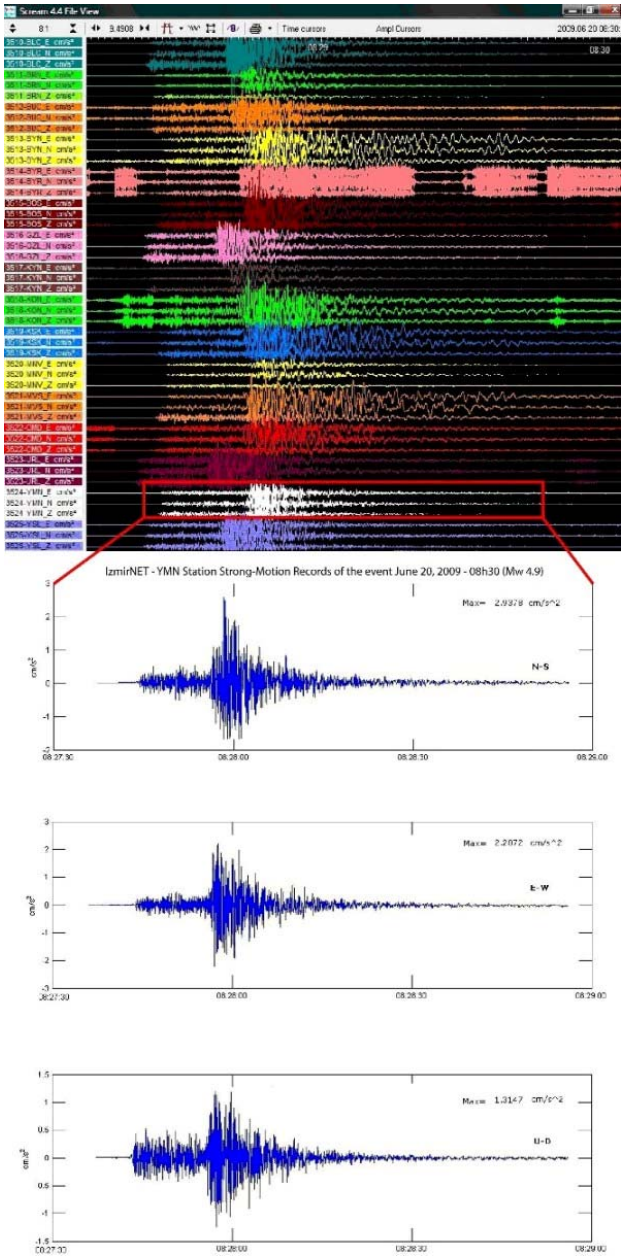

Figure 7 Acceleration records of the event 20.06.2009 (Mw 4.9) detected by the IzmirNET. (a) Triggered seismograms on Scream! software, (b) 3-component recordings of the event at the YMN station (a rock site) in the northern part of the Gulf of Izmir

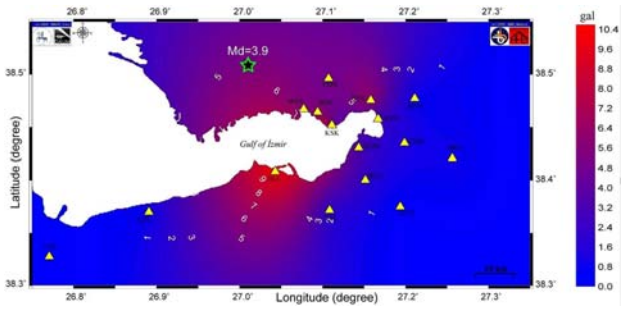

Figure 8 PGA mapping for a local event where occurred in the North of the Izmir Gulf in January 19, 2009 (19h17) with a magnitude of Mw=3.9.

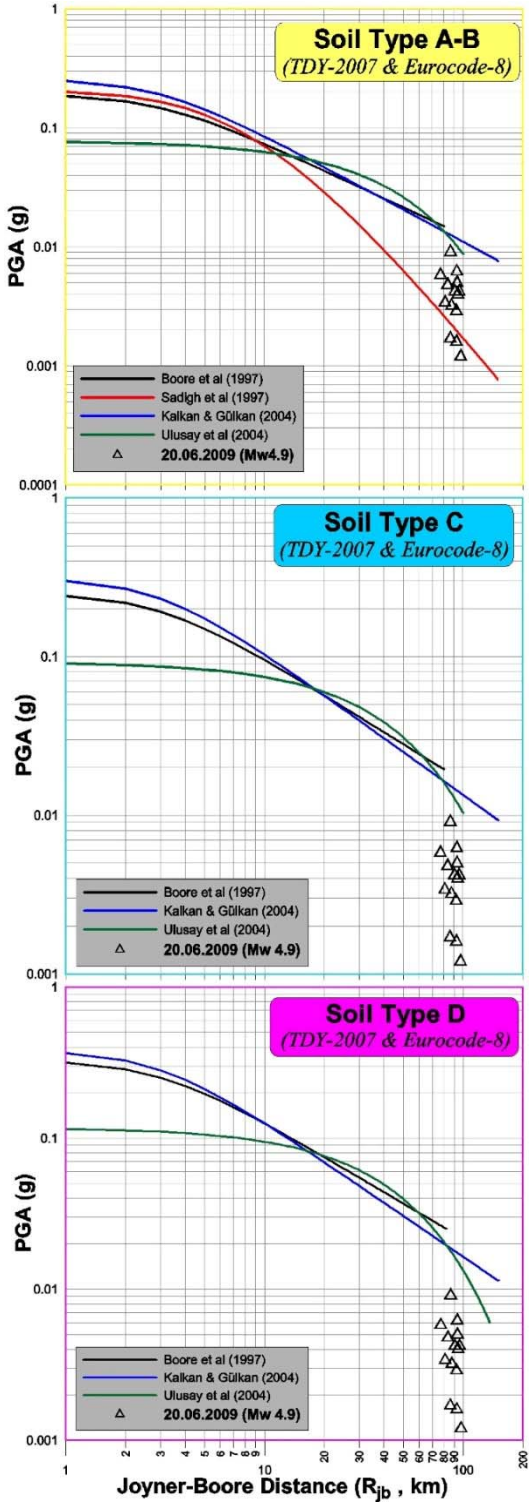

Figure 9 Comparison of an observed (Kusadasi-Sisam Island) earthquake which is occurred on June 20, 2009 (Mw=4.9) along Turkish-Greek border, with some attenuation curves.

2.5 Source parameters

Source parameter study is still an ongoing investigation in the frame of this project. Seismic moment (Mo), source radius (r), stress drop ($\Delta\sigma$), and seismic energy (Es) will be

computed by using Brune (1970)'s circular source model starting from corner frequency (f_c) and stress drop (Ω_0) on acceleration and displacement spectra. The Mo will be calculated from the equation as defined by Keilis-Borok (1960):

$$M_o(S) = \frac{\Omega_o(S) \cdot 4\pi \cdot \rho \cdot R \cdot \beta^3}{k_s \cdot R_\beta(\theta,\phi)} \qquad (1)$$

where Mo is seismic moment (dyne.cm) obtained from SH-wave spectrum, $\Omega_o(S)$ is spectral level (cm.sn), ρ denotes density (gr/cm^3), R indicates hypocentral distance (km), β is S-wave velocity (km/sn), k_s means free surface correction for S-wave, and ve $R_\beta(\theta,\phi)$ is coefficient of radiation pattern. In the present study, we accepted ρ as 2.7 gr/cm^3, β=3.3 km/sn, k_s=2 and $R_\beta(\theta,\phi)$= 0.6.

Calculation of source radius will ve performed by using the equation of Brune (1970):

$$r(S) = \frac{2.34 \cdot \beta}{2\pi \cdot f_o(S)} \qquad (2)$$

Here; r(S) denotes circular source radius (km), $f_c(S)$ is corner frequency of SH-wave spectra as observed from acceleration or displacement spectra (Figure 10).

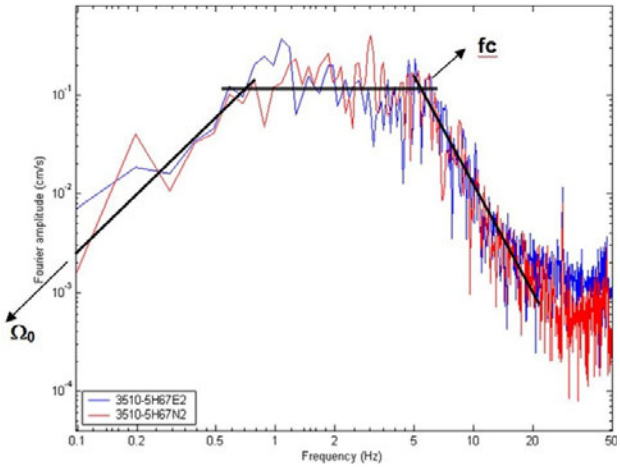

Figure 10 Acceleration spectrum for the Kusadasi-Sisam Island occurred (20.06.2009, Mw=4.9). Readings of the corner frequency (Fo), spectral level (Ω_0) and Fmax (from Displ. Spectra) will be used to calculate source parameters according to the Brune's (1970) circular source model.

Stress drop (Δσ, bar) could be defined as a function of Mo and r. Relationship among them could be written as:

$$\Delta\sigma = \frac{7}{16} \cdot \frac{M_o}{r^3} \qquad (3)$$

defined by Brune (1970). Computations of Mo and r were given in the equations (1) and (2).

Unlike stress drop, the S-wave seismic energy (Es) is a parameter which is a independent of any model. Hanks and Wyss (1972) expressed Es (dyne.cm) by the relation:

$$E_s = \frac{0.454 \cdot (\Delta\sigma)^2 \cdot r^3}{\mu} \qquad (4)$$

where μ is rigidity coefficient (dyne.cm^2).

All computations will be performed following the procedures defined in Sellami et al. (1997) for the Bursa city, Marmara region of Turkey. Site effect of frequency dependent attenuation wil be removed by using the equation of Archuleta et al. (1982):

$$Q_s(R, f) = e^{-\frac{\pi \cdot f \cdot R}{Q \cdot \beta}} \qquad (5)$$

Here; $Q_s(R,f)$ is source- and path-dependent attenuation spectrum for SH-wave, f denotes frequency (Hz), and Q means quality factor (1/km).

A parameter, called later as F_{max} by Hanks (1982), has been revealed during the investigations on source spectrum. Its origin is still ongoing debate whether source or site. In the frame of the cooperative project between DEU and ERD, we will also examined the origin of the second spectral decay (after Fc) in strong-motion spectra after removing attenuation effect as defined in equation (5). Dynamic range and response spectra of the instruments installed in IzmirNET permit us very well to perform this study (Figure 11).

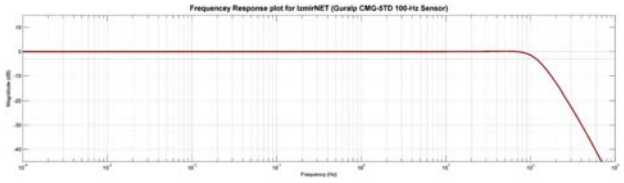

Figure 11 Response spectra of the Guralp 100Hz CMG-5TD recorder which is being used in IzmirNET accelerometric array. Spectral values are flat from DC up to 80 Hz, approximately.

3. CONCLUSIONS

Our preliminary results should be only used for the hazard analysis study in Izmir if the underlying assumptions and input parameters are in agreement with more accurate and reliable local accelerometric data. It should be pointed out that the values shown in the present study, are the function of several variables such as recurrence, attenuation, magnitude, distance, and source area parameters. Thus, the obtained results should be thought (whether they are not hard evidences) are suitable for preliminary planning and further study for the design of some facilities and plannings. Seismic hazard determinations by using PGA distributions and attenuation curves, are strongly influenced by the location of source zones and used PGA equations. Hence, we believe that alternative and different relationships, included NGA (Next Generation Attenuation) models, will lead to evaluate of the seismic hazard for Izmir area for the following two years.

The IzmirNET will describe the parameters of site characteristic and seismic hazard. These parameters include seismicity and seismotectonics, stress tensor, amplification, PGA, attenuation relationship, amplitude, fundamental frequency, dominant period and source parameters. First results reveal potential hazard near Barlidere-Balcova at the South, and Mavisehir-Bostanli area at the North of the Gulf of Izmir. According to the seismic activity and PGA distribution, taller buildings could be a subject to more damage on unconsolidated sediments, observed widely over there. Sediment type contributes largely to the extent of damage to buildings and lifeline systems that result from shaking. Shaking is amplified greatly on unconsolidated surficial deposits or non engineered fillings, especially in Narlidere, Balcova and Mavisehir areas. An example of this determination had been already seen in M=7.4 August 1999 Izmit-Kocaeli (Polat et al. 2002a, b), and Mw=5.9 October 2005 Sigacik Bay-Izmir (Aktar et al. 2007, Benetatos et al. 2006) which is 80 km far from the city center (refer Figure 4 for the location of Sigacik Bay), earthquakes.

Acknowledgements:

The present study was supported by TUBITAK-KAMAG (106G159) with a grant of 2 billion USD in 2008 (for three years). This support makes possible to install the first local accelerometric network in Metropolitan Izmir in a cooperation between Ministry of Public Works & Settlement, and Metropolitan Municipality of Izmir. Preliminary results of this collaborative effort have been first presented during this conference (5thICEE) in Tokyo-Japan. This is a contribution of Seismology Work Group (Deliverable 5.1.1 of Work Package-1). We thank to the staff of all officers, geophysicists, geologists, civil engineers of Dokuz Eylul University-Izmir, Earthquake Research Department-Ankara. Special thank to Dr. Murat Nurlu for his efforts during the realizing this project, and to Dr. Senol Ozyalin in preparing of Figure 2. We are also greateful to the Governorship of Izmir and Mayors of Metropolitan Izmir for their helps during the installation of IzmirNET strong-motion stations.

References:

Archuleta, R.J., Cranswick, E., Mueller, C., and Spudich, P. (1982), "Source parameters of the 1980 Mammoth Lakes, California-Earthquake Sequence", *Journal of Geophysical Research*, **87**, 4595-4607.

Aktar, M., Karabulut, H., Ozalaybey, S., and Childs, D. (2007), "A conjugate strike-slip fault system within the extensional tectonics of Western Turkey", *Geophysical Journal International*, doi: 10.1111/j.1365-246X.2007.03598.x, 1-13.

Benetatos, C., Kiratzi, A., Ganas, A., Ziazia, M., Plessa, A.. and Drakatos, G. (2006), "Strike-slip motions in the Gulf of Sigacik (Western Turkey): Properties of the 17 October 2005 earthquake seismic sequence", *Tectonophysics*, **426**, 263-279.

Boore, D.M., Joyner, W.B., and Fumal, T.E. (1997), "Equations for Estimating Horizontal Response Spectra and Peak Acceleration from Western North American Earethquakes: A Summary of recent Work", *Seismological Research Letters*, **(68)**1, 128-153.

Brune, J.N. (1970), "Tectonic stress and the spectra of seismic shear waves from earthquakes", *Journal of Geophysical Research*, **75**(4), 4997-5009.

Duman, M., Avci, M., Duman, S., Demirkurt, E., Duzbastilar, and M.K. (2004), "Surficial sediment distribution and net sediment transport pattern in Izmir Bay, Western Turkey", *Continental Shelf Research*, **24**, 965-981.

Eurocode-8 (2004), "Design of structures for earthquake resistance Part 1: general rules, seismic actions and rules for buildings", European Norm. European Committee for Standardisation, European Committee for Standardisation Central Secretariat, Brussels-Belgium.

Hanks, T., and Wyss, M., (1972), "The use of body waves spectra in the determination of seismic source parameters", *Bulletin of the Seismological Society of America*, **62**, 561-589.

Hanks, T., (1982), "Fmax", *Bulletin of the Seismological Society of America*, **71**(6), 1867-1879.

Inan, S., Ergintav, S., Saatcilar, R., Tuzel, B., and Iravul, Y. (2007). "Turkey makes major investment in earthquake research", *EOS Transactions*, American Geophysical Union, **88**(34), 333–334.

Jackson, J. A., and McKenzie, D.P. (1984), "Active tectonics of Alpine–Himalayan belt between western Turkey and Pakistan", *Geophysical Journal of the Royal Astronomical Society*, **77**, 185–265.

Kalkan, E., and Gulkan, P. (2004), "Site-Dependent Spectra Derived from Ground Motion Records in Turkey", *Earthquake Spectra*, **20**(4), 1111–1138.

Keilis-Borok, V.I. (1960), "Investigation of the mechanism of earthquakes", *Sov. Res. Geophys.*, 4-Am. Geophys. Union Consultants Bureau, NY, 201 p.

Michael, A.J. (1987), "Use of focal mechanisms to determine stress: a control study", *Journal Geophysical Research*, **92**, 357-368.

Pamukcu, O., and Yurdakul, A. (2008), "Isostatic compensation in western Anatolia with estimate of the effective elastic thickness", *Turkish Journal of Earth Sciences*, **17**, 545–557.

Polat, O., Ceken, U., Uran, T., Gok, E., Yilmaz, N., Beyhan, M., Koc, N., Arslan, B., Yilmaz, D., and Utku, M. (2009), "IzmirNet: A Strong-Motion Network in Metropolitan Izmir, Western Anatolia, Turkey", *Seismological Research Letters*, **80**(5), 831-838.

Polat, O., Gok, E., and Yilmaz, D. (2008), "Earthquake hazard of the Aegean extension region (West Turkey)", *Turkish Journal of Earth Sciences*, **17**, 593–614.

Polat O., Haessler, H., Cisternas, A., Philip, H., Eyidoğan, H., Aktar, M., Frogneux, M., Comte, D., and Gürbüz, C. (2002a), The Izmit (Kocaeli) Turkish earthquake of August 17, 1999: Previous seismicity, aftershocks and seismotectonics", *Bulletin of the Seismological Society of America*, **92**(1), 361-375.

Polat O., Haessler, H., Cisternas, A., Philip, H., and Eyidoğan, H. (2002b), "Analysis and interpretation of the aftershock sequence of the August 17, 1999, Izmit (Turkey) earthquake", *Journal of Seismology*, **6**, 287-306.

Sadigh, K., Chang, C.Y., Egan, J.A., Makdisi, F., and Youngs, R.R., (1997), "Attenuation relationships for shallow crustal earthquakes based on California strong motion data", *Seismological Research Letters*, **68**, 180-189.

Sellami, S., Pavoni, N., Mayer-Rosa, D., Mueller, S., Eyidogan, H., Aktar, M., Gurbuz, C., Baris, S., Polat, O. and Yalcin, N. (1997), "Seismicity and Seismotectonics of the Bursa Region", (Editors: Schindler, C. and Pfister, M., Active Tectonics of Northwestern Anatolia : The Marmara Poly Project, 570 p.), vdf Publications Zurich-Swiss, ISBN No: 3-7281-2425-5, 449-486.

Snoke, J.A. (2003), "FocMec: Focal Mechanism Determinations", Local Report of Virginia Tech, Blacksburg, VA-USA, 21 pp.

TDY (1997), "Specification for Structures to be Built in Disaster Areas", Ministry of Public Works and Settlement Government of Republic of Turkey, http://www.deprem.gov.tr

Ulusay, R., Tuncay, E., Sonmez, H. and Gokceoglu, C. (2004), "An attenuation relationship based on Turkish strong motion data and isoacceleration map of Turkey", *Engineering Geology*, **74**, 265-291.

Uzel, B., and Sozbilir, H. (2008), "A First record of strike-slip basin in Western Anatolia and its tectonic implication: The Cumaovasi basin as an example", *Turkish Journal of Earth Sciences* **17**, 559-591.

JOINT CONFERENCE PROCEEDINGS
7th International Conference on Urban Earthquake Engineering (7CUEE) &
5th International Conference on Earthquake Engineering (5ICEE)
March 3-5, 2010, Tokyo Institute of Technology, Tokyo, Japan

ATTENUATION CHARACTERISTICS OF PEAK GROUND MOTIONS DURING THE M_W7.9 WENCHUAN EARTHQUAKE, CHINA

Hongjun Si[1], Ken X. Hao[2], Yang Xu[3], Shigeki Senna[2], Hiroyuki Fujiwara[4], Hiroyuki Yamada[5], Hideaki Tsutsumi[6], Changjiang Wu[7], Saburoh Midorikawa[8], and Kojiro Irikura[9]

1) Senior Research Engineer, Kozo Keikaku Engineering Inc., Japan
2) Researcher, National Research Institute for Earth Science and Disaster Prevention, Japan
3) Researcher, Earthquake Administration of Shanxi Province, China
4) Senior Researcher, National Research Institute for Earth Science and Disaster Prevention, Japan
5) Senior Researcher, Japan Nuclear Energy Safety Organization, Japan
6) Director, Japan Nuclear Energy Safety Organization, Japan
7) Senior Researcher, Japan Nuclear Energy Safety Organization, Japan
8) Professor, Tokyo Institute of Technology, Japan
9) Visiting Professor, Aichi Institute of Technology, Japan
shj@kke.co.jp, hao@bosai.go.jp, senna@bosai.go.jp, fujiwara@bosai.go.jp, smidorik@enveng.titech.ac.jp, irikura@geor.or.jp

Abstract: In this study, we analyzed the peak horizontal motion recorded during the M_w7.9 Wenchuan earthquake, which occurred on 2008 May 12, Sichuan, China. The results show that, (1) the observed data are generally consistent with the predictions by Si and Midorikawa (1999, 2000) both for PGA on soil and PGV on stiff ground within 200 km, but larger than the attenuation curves for PGA on stiff ground and less than that for PGV on soil sites. This implies that the observation of the peak motion may show an average strength for a crustal earthquake with an Mw of 7.9. However, supposedly most of the observation stations are located on soft soil sites, the strong motion from the Wenchuan earthquake may be weaker than the average; (2) Forward directivity effects may have occurred; (3) the basin effects amplified PGV or longer period components, but the mountain makes motion weaker; (4) in the far field area the strong motion may become relatively larger.

1. INTRODUCTION

The M_w7.9 Wenchuan earthquake, which occurred on 2008 May 12, caused over 87,000 people to be killed or missing, and more than 370,000 injured. According to the results of co-seismic surface rupture investigation (e.g., Xu et al. 2008, Hao et al. 2009) and the results of rupture process inversion (Ji and Hayes 2008, Koketsu et al. 2008), the rupture length of the earthquake was about 300 km, and the moment magnitude was 7.9. A fault with a fault length of 300 km is one of the largest crustal earthquakes in the world. Since the Chinese government has established a national strong motion observation network in China, including the source area, the strong motions are well recorded during the earthquake. This made it possible to understand the characteristics of the strong motion from an M8 class crustal earthquake. Before this earthquake, the strong motion generated from M8 class earthquakes is not well understood since there are not enough recordings. There are some recordings from the 2002 M_w7.9 Denali earthquake, but in the near source area there are only 4 stations.

In this study, we analyze the attenuation characteristics of peak ground motion recorded during the earthquake and compared them with the attenuation models proposed in the previous studies. The residuals between the observations and prediction are also discussed. From this analysis, it can be known whether the strong motions from this earthquake are stronger or weaker than the average ones predicted by an attenuation model. This may be helpful to understand the cause of the severe damages.

2. DATA

2.1 Strong Motion Data and Processing Method

During the 2008 Wenchuan earthquake, the strong motion records including near-source records ones were obtained by the National Strong Motion Observation Network System (NSMONS) of China, which was formally operated from March 2008, just two months before the occurrence of the earthquake. During the earthquake, over 400 records are obtained nationwide. Among them more than 200 records are obtained at stations in Sichuan, Shaanxi and Gansu province, including about 20 records in the near source area, with source distances less than 50 km. In this study, the strong motion records derived in Sichuan, Gansu and Shaanxi province are used. The distribution of the

observation stations is shown in Fig.1. The peak ground acceleration (PGA) is derived after filtering the seismic waves and the peak velocity (PGV) is derived by integrating the filtered acceleration waveform to velocity waveform. The larger value of two horizontal components is used in the analysis. The rupture distance was calculated based on the source model proposed by Ji and Hayes. (2008).

2.2 Geological setting

In Figure 1, we can see that most of the stations are located in the mountainous area, and some of them are located in the Sichuan basin and the Weihe basin. In the information companying the dataset provided by the CSMNC, only stations located on bedrock can be identified. No information of soil profile, such as AVS30, is available at present. As a reference, here, we employ an estimation system for AVS30 provided by USGS (Allen and Wald, 2007, http://earthquake.usgs.gov/hazards/apps/vs30/, last accessed on 16/01/2010) to evaluate the AVS30s in the area. Figure 2 shows the distribution of estimated AVS30 and the NEHRP site classification in the area. From the figure, it can be predicted that most of the stations located in the mountain area are NEHRP B or C, and also stations in the basin areas are NEHRP D. The results are generally consistent with the geological condition. Since most of the stations seem to be located on stiff ground, the discussions made hereafter are based on the original values of PGA and PGV.

3. RESULTS

3.1 Attenuation Characteristics of the Wenchuan Earthquake

Fig. 3 shows distance dependency of the observations of peak acceleration and velocity. In the figure, since the detailed soil profiles for the observation stations are not yet available at present, the site condition is simply classified into two categories according to the information provided by the CSMNC database: soil or unknown, and bedrock. Note here that it is possible that a station located on stiff ground may be classified into a soil site. From the figure, the following observations can be made: (1) the peak motions decay with distance. (2) Generally, amplitude at bed rock sites is weaker than those at soil sites. (3) In the near source sites, peak motions are ranged from 600 cm/s^2 - 1000 cm/s^2 for PGA, and 50 cm/s – 110 cm/s for PGV. (4) The high PGA and PGV area corresponding to the severely damaged area.

In the figure, the predictions calculated by the attenuation model proposed by Si and Midorikawa (1999, 2000), both on soil and stiff ground for PGA and PGV are plotted. The attenuation model for crustal earthquake is shown in Eq.(1) and Eq.(2).

$$\log PGA = 0.50M_w + 0.0043D + d - \log(X + 0.0055 \cdot 10^{0.5Mw}) - 0.003X + 0.61 \quad (1)$$

$$\log PGV = 0.58M_w + 0.0038D + d - \log(X + 0.0028 \cdot 10^{0.5Mw}) - 0.002X - 1.29 \quad (2)$$

where X, M_w show closest distance to the rupture fault and moment magnitude, respectively. D is the depth to center of a fault plane. d shows the coefficient for earthquake types: PGA: 0.0 for crustal, 0.02 and 0.22 for inter- and intra-plate events; PGV: 0.0 for crustal, -0.02 and 0.12 for inter- and intra-plate events, respectively.

The results show that the observation data are generally consistent with the predicted ones by Si and Midorikawa (1999, 2000) both for PGA on soil ground and PGV on stiff ground with distances less than 200 km, but larger than the attenuation curves for PGA on stiff ground and less than PGV on soil sites. These results imply that, the PGA, PGV observed during the earthquake may show an average strength for a crustal earthquake with an M_w of 7.9. However, supposedly most of the observation stations are located on soft soil sites, the strong motion from the Wenchuan earthquake may be weaker than the average strength predicted by Si and Midorikawa (1999, 2000).

On the other hand, for the stations located far from the rupture faults, especially in Weihe basin area, the number of observations larger than the predicted ones increases, especially for PGV. This result implies that the amplification factor in the basin area, the forward directivity, and the attenuation characteristics of surface waves may caused the difference.

3.2 Spatial distribution of strong motion

Figure 4 shows the distribution of the residual between the observations and predictions by Si and Midorikawa (1999). The residual is defined in Eq.(3).

$$\text{Residual} = \log_{10} Observed/Predicted \quad (3)$$

In the figure, a circle, indicating positive value, shows the observation at a station is larger than the prediction, and a triangle shows the reverse. The size of the circles and the triangles shows the value of the residual at the station. The area is divided into four areas based on two criterions. The first two areas are derived by solid lines, i.e., A: rupture forward area, B: rupture backward area. The second two areas are derived by broken lines, i.e., H: Hanging wall area, F: Foot wall area. From the figures, the following observations can be made: (1) the data at stations located in area A are generally larger; in Weihe basin area, the differences rise to over 10 times greater than the predictions; (2) in the area B, generally the strong motions are smaller; but become larger in the far field; (3) the area H and F are most complicated. In the hanging wall area, since it is also a mountain area, the amplitudes are not significantly larger than the predictions, while in the foot wall area, since it is also a basin area, the residual is not so much weaker. For PGV the data all in the foot wall even larger than the predictions. This result implies that the longer period component may be dominant in the basin area.

From the discussions above, the following observations

can be made: (1) Forward directivity effects may have occurred; (2) the basin effects amplified PGV or longer period components, but the mountain makes motion weaker; (3) in the far field areas the strong motion may become relatively larger.

3.3 Comparison with the 2002 Denali earthquake

In Fig. 5, we compared the PGA and PGV derived from the Wenchuan earthquake and a recent M_w7.9 earthquake, the 2002 Delali earthquake, Alaska, the USA. The fault lengths of the two earthquakes are almost the same too. The peak ground motions for the Denali earthquake are collected from the database of the NGA project. In the figure, the stations for the Denali earthquake are classified into 3 categories based the NEHRP classification criterion. From the figures, we found that, in general, the PGV from the two earthquakes is almost the same, but the PGA from Denali earthquake seems weaker in the near field. Note that the strong motion data from Denali earthquake are not enough for a definitive comparison.

4. CONCLUSIONS

From the discussion above, the following conclusion can be made. (1) the observed data are generally consistent with the predictions by Si and Midorikawa (1999, 2000) both for PGA on soil and PGV on stiff ground within 200 km, but larger than the attenuation curves for PGA on stiff ground and less than that for PGV on soil sites. This implies that the observation of the peak motion may show an average strength for a crustal earthquake with an Mw of 7.9. However, supposedly most of the observation stations are located on soft soil sites, the strong motion from the Wenchuan earthquake may be weaker than the average; (2) Forward directivity effects may have occurred; (2) Forward directivity effects may have occurred; (3) the basin effects amplified PGV or longer period components, but the mountain makes motion weaker; (4) in the far field area the strong motion may become relatively larger.

Acknowledgements:

The authors thank CSMNC and PEER, NGA project to provide us strong motion data derived during the 2008 Wenchuan earthquake and the 2002 Denali earthquake. Dr. Akemi Noda draws part of the figures in this article. Figures are drawn using GMT and Plots. This study is partially supported by the Japan Nuclear Energy Safety Organization (JNES).

References:

Allen, T.I., and Wald, D.J. (2007), "Topographic slope as a proxy for global seismic site conditions (VS30) and amplification around the globe," U.S. Geological Survey Open-File Report 2007-1357, 69 p.

Chiou, B., Darragh, R., Gregor, N., and Silva, W. (2008), "NGA project strong-motion database", Earthquake Spectra, 24, 23–44.

Hao, K. X., H. Si, H. Fujiwara, and T. Ozawa (2009), "Coseismic surface-ruptures and crustal deformations of the 2008 Wenchuan earthquake M_w7.9", China, Geophys. Res. Lett., 36, L11303, doi:10.1029/2009GL037971.

Ji, C. and Hayes G. (2008), "Preliminary result of the May 12, 2008Mw 7.9 eastern Sichuan, China earthquake," (http://earthquake.usgs.gov/eqcenter/eqinthenews/2008/us2008ryan/finite_fault.php).

Koketsu, K., K. Hikima, H. Miyake, T. Maruyama, Z. Wang (2008), "Source process and ground motions of the 2008 Wenchuan, China, earthquake", Eos Trans. AGU, Vol. 89, No. 53, Fall Meet. Suppl., Abstract S31B-1914

Si and Midorikawa (2000), "Attenuation Relationships of Peak Ground Acceleration and Velocity Considering Effects of Fault Type and Site Condition", *Proceedings of the 12th World Conference on Earthquake Engineering*, Paper No. 532.

Wessel, P. and Smith, W. H. F. (1998), "New improved version of generic mapping tolls released", EOS Trans. AGU, 79-47, 579.

Xu, X., et al. (2008), "The Ms8.0 wenchuan earthquake surface ruptures and its seismogenic structure" (in Chinese), Seismol. Geol., 30, 597– 629.

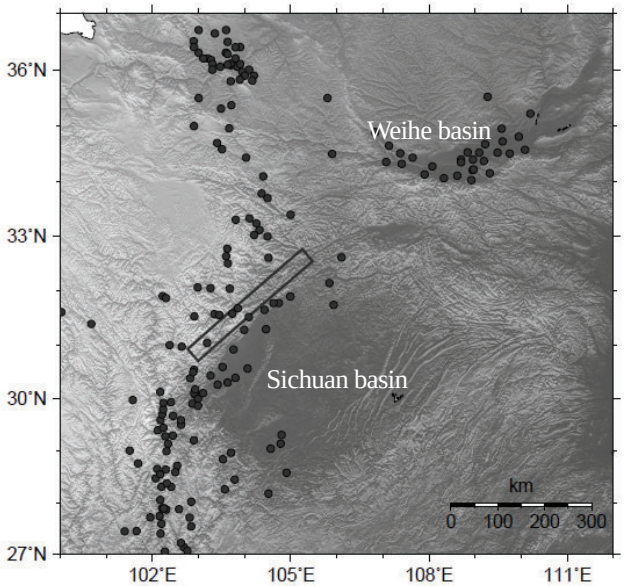

Figure 1 The distribution of observation stations used in this study and the fault model proposed by Ji and Hayes (2008)

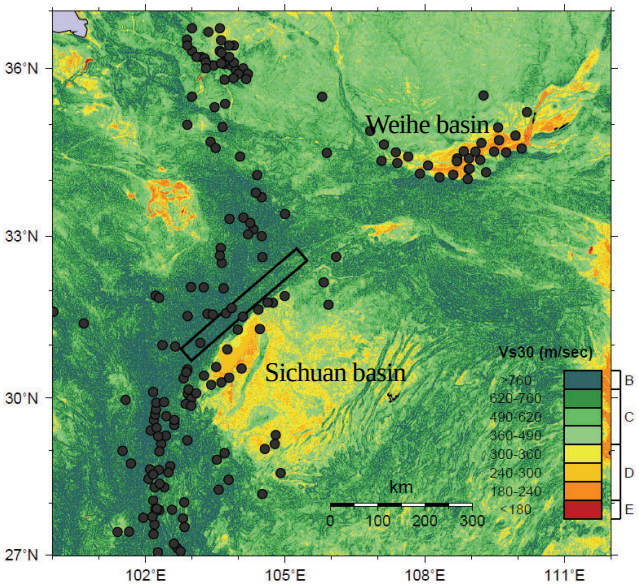

Figure 2 The distribution of observation stations and the estimated AVS30 used in this study. Alphabets show the classification of soil condition defined by NEHRP.

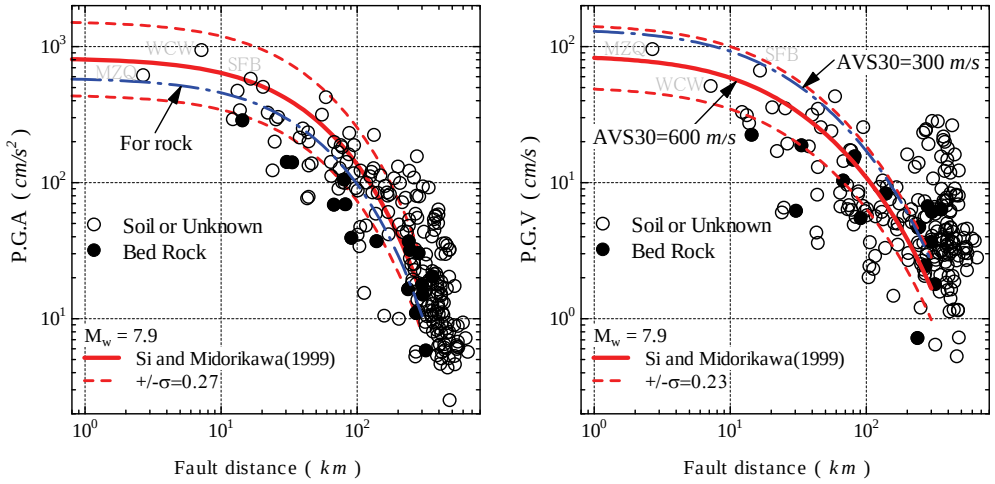

Figure 3 Distance dependency for peak ground motion recorded during the wenchuan earthquake. (Left panel: for PGA; right panel: for PGV; Blue lines are calculated by Si and Midorikawa 1999 on ground with different soil condition labeled in the figure; site names in 3 gray alphabets show the near source stations)

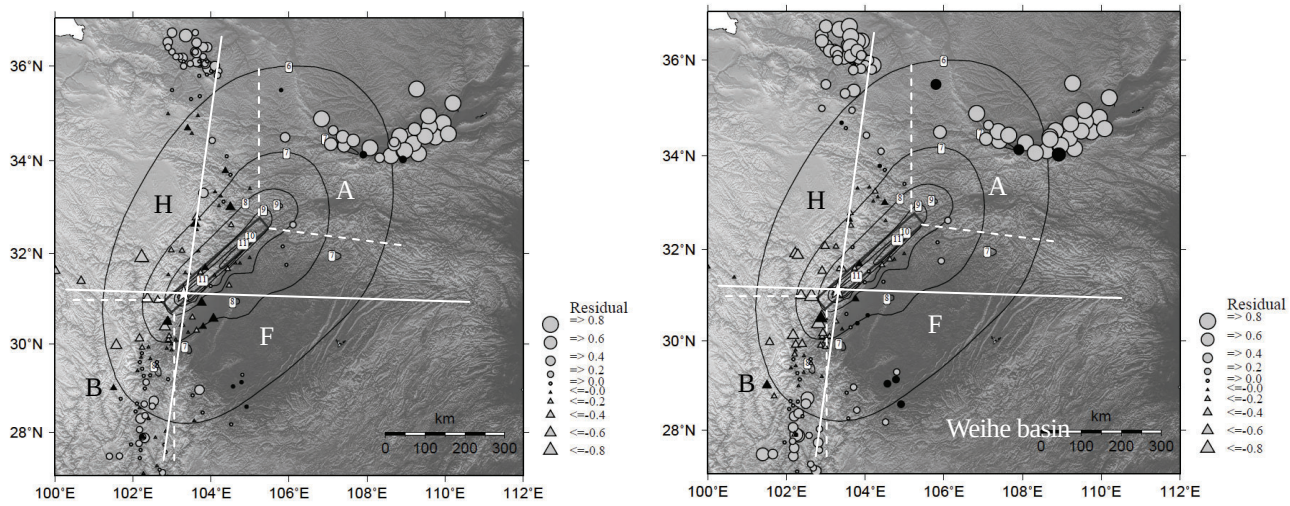

Figure 4 Distribution of residuals for PGA and PGV between the observations and the predictions by Si and Midorikawa (1999, 2000) (Left panel: for PGA, right panel: for PGV. Circle: positive residual; Triangle: negative residual. Open circles and triangles: soil or unknown sites; Solid circles and triangles: bed rock. A, B: the areas divided by the solid lines; H, F: the areas divided by the broken lines)

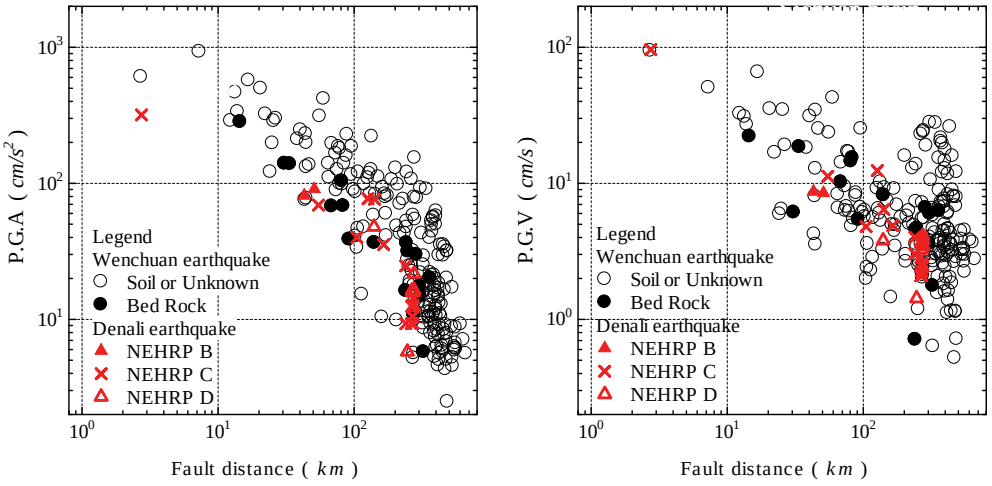

Figure 5 Comparison of the PGA and PGV from the 2002 Denali earthquake (red symbols) and the 2008 Wenchuan earthquake (black symbols) (Left panel: for PGA, right panel: for PGV)

JOINT CONFERENCE PROCEEDINGS
7th International Conference on Urban Earthquake Engineering (7CUEE) &
5th International Conference on Earthquake Engineering (5ICEE)
March 3-5, 2010, Tokyo Institute of Technology, Tokyo, Japan

AN EMPIRICAL ARIAS INTENSITY RELATIONSHIP FOR ROCK SITES IN STABLE CONTINENTAL REGIONS

Jongwon Lee[1] and Russell A. Green[2]

1) Postdoctoral Research Fellow, Charles E. Via, Jr. Dept. of Civil and Environmental Engineering, Virginia Tech, Blacksburg, VA, USA
2) Associate Professor, Charles E. Via, Jr. Dept. of Civil and Environmental Engineering, Virginia Tech, Blacksburg, VA, USA
jongwonl@vt.edu, rugreen@vt.edu

Abstract: Presented herein is an empirical predictive relationship correlating Arias intensity to earthquake magnitude and site-to-source distance for rock sites in stable continental regions. The correlation was developed from data derived from 302 representative horizontal rock motions for stable continental regions, consisting of 22 recorded motions and 280 scaled motions. The non-linear mixed-effects regression technique was used to fit a predictive model to the Arias intensity data. Similar to the trend observed from active shallow crustal region motions, Arias intensity predicted for stable continental region motions decreases with increasing site-to-source distance, but increases with increasing earthquake magnitude. In comparing the Arias intensities in the two tectonic regions (i.e., active shallow crustal versus stable continental regions), it is shown that Arias intensity of stable continental earthquake motions is systematically greater than that of active shallow crustal earthquake motions.

1. INTRODUCTION

The objective of the study presented herein is to develop an Arias intensity predictive relationship for stable continental regions (e.g., central/eastern North America: CENA). Specifically, the relationship is for horizontal motions at rock sites and relates Arias intensity to earthquake magnitude and site-to-source distance.

Earthquake motions are a complex combination of various wave types, having a range of amplitudes and frequencies. As a result, the development of engineering indices for quantifying the potential destructiveness of earthquake motions to the built environment is an ongoing endeavor. In this vein, Arias (1970) proposed an index that has become to be known as "Arias intensity," which is a function of the amplitude, frequency content, and duration of ground shaking. Several studies have shown that Arias intensity correlates well to observed earthquake damage to building and geotechnical structures (e.g., Cabanas et al. 1997; Harp and Wilson 1995; Kayen and Mitchell 1997).

Arias intensity "… is the sum of the energy absorbed by a population of simple oscillators evenly spaced in frequency" (Kayen and Mitchell 1997). For a single component of motion (e.g., x-direction), Arias intensity is computed as:

$$I_{xx} = \frac{\pi}{2g}\int_0^{t_d} a_x^2(t)\,dt \qquad (1)$$

where: g is the coefficient of acceleration due to gravity; t_d is total duration of earthquake shaking; and $a_x(t)$ is the acceleration time history in the x-direction. Accordingly, I_{xx} will have units of velocity. Because ground motion amplitude, frequency content, and duration all influence the damage potential of the motions, as well as influence Arias intensity per Eq. (1), Arias intensity is seemingly a reliable index to use in the seismic design.

An empirical Arias intensity relationship for rock sites in stable continental regions is developed herein. Also, this relationship is compared with a similarly developed relationship for rock sites in active shallow crustal regions (e.g., western North America: WNA). This latter relationship was proposed by Lee and Green (2008), and allows for consistent comparisons to be made for the two regions. Although there are existing relationships for Arias intensity for WNA, the authors felt that in order to avoid issues related to differences in the intensity due to disparities in database size, analysis techniques, etc., consistently developed relationships for the two regions were needed to make valid comparisons.

Regarding the organization of this paper, first the strong ground motion database used in this study is described. Then, basic concepts of the NLME regression method are reviewed, and the proposed functional form of the predictive model is introduced. Next, the results of the regression analyses and a comparison of Arias intensity predicted for stable continental and active shallow crustal rock motions are presented. Finally, it is noted that the acronyms "CENA" and "WNA" in this paper are used to refer to "stable continental" and "active shallow crustal"

regions, respectively, not just to the central/eastern NA and western NA.

2. STRONG GROUND MOTION DATABASE

In total, 302 representative horizontal earthquake motions at rock sites for CENA were used to develop the empirical Arias intensity relationship in this study. These rock motions for CENA were taken from a ground motion dataset assembled by McGuire et al. (2001). Primarily, this dataset was intended to provide a library of strong ground motion time histories suitable for engineering analyses. Because there are few recorded strong ground motions in stable continental regimes, only 22 of the motions in the dataset are recorded motions, with the remaining 280 motions being "scaled" WNA motions. McGuire et al. (2001) scaled the motions using response spectral transfer functions generated from the single-corner point source model (e.g., Boore 1983; McGuire et al. 2001; Silva and Lee 1987). The transfer functions account for the differences in seismic source, wave propagation path properties, and site effects between the WNA and CENA regions. The moment magnitudes of these motions range from 4.5 to 7.6, and the site-to-source distances range from 0.1 km to 199.1 km; the site-to-source distance is defined as the closest distance to the fault rupture plane. The recorded motions include motions from the 1988 Saguenay (M 5.9 main shock and M4.5 aftershock) and the 1985 Nahanni (M 6.8) earthquakes. Figure 1 shows the magnitude and site-to-source distance distribution of these CENA rock motion data.

The ground motions were classified as either "rock" or "soil" based on the site conditions at the respective seismograph stations. The site classification scheme used by McGuire et al. (2001) is based on the third letter of the Geomatrix 3-letter site classification system shown in Table 1. Site categories A and B were considered to represent rock sites, and site categories C and D were considered to represent soil sites.

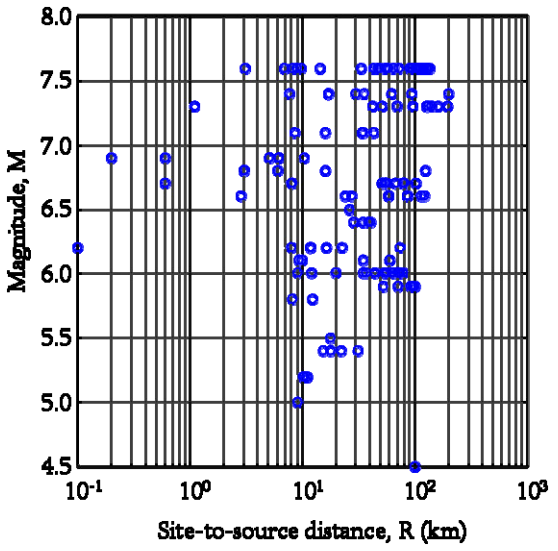

Figure 1 Earthquake magnitude and site-to-source distance distributions

Table 1. Third letter: Geotechnical subsurface characteristics of Geomatrix 3-letter site classification.

Third letter	Site description	Comments
A	Rock	Instrument on rock (V_S > 600 m/s) or < 5 m of soil over rock.
B	Shallow (stiff) soil	Instrument on/in soil profile up to 20 m thick overlying rock.
C	Deep narrow soil	Instrument on/in soil profile at least 20 m thick overlying rock, in a narrow canyon or valley no more than several km wide.
D	Deep broad soil	Instrument on/in soil profile at least 20 m thick overlying rock, in a broad valley.
E	Soft deep soil	Instrument on/in deep soil profile with average V_S < 150 m/s.

3. REGRESSION ANALYSIS

3.1 Non-linear Mixed-effects Regression

The non-linear mixed-effects (NLME) regression technique was used to develop the empirical relationships in this study. NLME modeling is a maximum likelihood method based on normal (Gaussian) distribution and is primarily used for analyzing grouped data (i.e., datasets comprised of subsets). The NLME regression method allows regression models to account for both random-effects that vary from subset to subset and fixed-effects that do not. In this study, a subset consists of motions recorded during a given earthquake event. In comparison to applying a fixed-effects regression technique (e.g., the least squares method) to the entire dataset, a mixed-effects regression method allows both inter- and intra-earthquake uncertainty to be quantified. The inter-earthquake error is designated by η_i where the subscript, i represents the ith earthquake (i.e., group) and has mean of zero and variance of τ^2. The intra-earthquake error is designated by ε_{ij} where the subscript, ij indicates the jth record of the ith earthquake and has a mean of zero and variance of σ^2. The standard deviation of the total error can be determined by the following equation:

$$\sigma_{total} = \sqrt{\tau^2 + \sigma^2} \qquad (2)$$

where, σ_{total} is the standard deviation of total error.

In more traditional regression techniques (e.g., least squares method), the entire dataset is regressed in a single analysis. However, because the dataset is comprised of motions from different earthquakes, with the number of recordings from each earthquake varying, the resulting regression is inherently unduly influenced by the earthquake having the largest number of motions. On the

contrary, the NLME regression method produces unbiased fittings for each subset having different numbers of ground motion recordings. This is important because of the number of motions from each earthquake can vary significantly. The statistical analysis program R (version 2.5.0) was used to perform the NLME regression analyses (e.g., Lee, 2009).

3.2 Regression Model and Result

The predictive relationship developed herein is for the average Arias intensity, I_a, of the two horizontal components motions recorded at a given seismograph station (i.e., $I_a = (I_{xx} + I_{yy})/2$), where I_{xx} and I_{yy} are Arias intensities in the x- and y-directions, respectively. The distribution of the computed I_a values was observed to be log-normally distributed. Therefore, the regression analyses were performed on $\ln(I_a)$.

The functional form of the predictive relationship used in this study was a variant of that proposed by Travasarou et al. (2003). Their model was based on Brune's point source model (Brune 1970; 1971) for the smoothed Fourier amplitude spectrum of ground motions. Using Parseval's theorem, the definition of Arias intensity (i.e., Eq. (1)) was rewritten by substituting the integral of the squared acceleration in Eq. (1) with the integral of the squared Brune's point source model (i.e., the square of Fourier amplitude spectrum). Then, the regression model was built based on observing the magnitude and site-to-source distance dependencies of Arias intensity from trend plots.

Assuming a log-normal distribution of the data, the proposed functional form of the predictive relationship is:

$$\ln I_a = C_1 + C_2(M-6) + C_3(M-6)^2 + C_4 \ln(M/6) + C_5 \ln\left(\sqrt{R^2+h^2}\right) \quad (3)$$

where: I_a is the average Arias intensity of two horizontal components (m/sec), C_1 through C_5 and h are regression coefficients, M is the moment magnitude, and R is the closest distance to the fault rupture plane (km). The term $(M-6)^2$ was added to the Travasarou et al. (2003) model, which considerably lowered the total standard deviation of the regression results for CENA.

The results from the NLME regression analyses using the model given by Eq. (3) are shown in Table 2. For a comparison of magnitudes of the standard deviations for CENA and WNA (Lee and Green 2008), the regression results for WNA are also shown in Table 2. It is noted that the coefficient C_3 for WNA is zero. This is because the term $C_3(M-6)^2$ was actually removed from the model for the regression analyses for WNA because it reduced the total standard deviation. However, for consistency in form, $C_3 = 0$ for the proposed predictive relationship for WNA. Comparing the standard deviations for CENA and WNA, they have a similar level of uncertainty.

The medians of the average Arias intensities predicted for CENA rock motions using Eq. (3), in conjunction with the coefficients listed in Table 2, are shown in Figure 2. As may be observed from this figure, the Arias intensity decreases with increasing site-to-source distance but increases with increasing earthquake magnitude. The comparisons of CENA and WNA for rock sites are also shown in Figure 2. As may be observed from this figure, CENA motions have larger intensities than those for WNA. Particularly, CENA motions for large magnitude earthquakes (i.e., M7.5) are estimated to have significantly greater intensities than WNA motions by factors of 3 to 8 at distances of 0.1 km to 200 km, respectively.

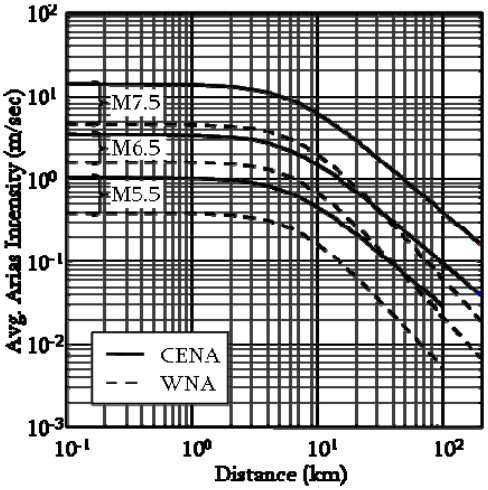

Figure 2 Comparison of CENA and WNA for rock sites

Table 2 Regression coefficients and standard deviations of inter-earthquake, intra- earthquake, and total errors.

CENA								
C_1	C_2	C_3	C_4	C_5	h	τ_{ln}	σ_{ln}	$\sigma_{ln\,total}$
3.2	-107.6	7.9	651.1	-1.28	6.06	0.67	0.89	1.11
WNA[*]								
C_1	C_2	C_3	C_4	C_5	h	τ_{ln}	σ_{ln}	$\sigma_{ln\,total}$
3.0	-1.1	0	15.1	-1.65	7.24	0.68	0.84	1.08

[*]From Lee and Green (2008)

4. CONCLUSIONS

An empirical predictive relationship for Arias intensity for horizontal ground motions at rock sites in stable continental regions has been developed in this study. This relationship shows that the, Arias intensity for CENA decreases with increasing site-to-source distance and increases with increasing earthquake magnitude. In comparing Arias intensities for CENA and WNA motions, CENA motions are predicted to have consistently larger intensities than WNA motions.

Acknowledgements:
This material is based upon work supported in part by the National Science Foundation under Grant No. CMMI 0644580.

This support is gratefully acknowledged. However, any opinions, findings, and conclusions or recommendations expressed in this material are those of the authors and do not necessarily reflect the views of the National Science Foundation.

References:

Arias, A. (1970). "A measure of earthquake intensity." Seismic Design for Nuclear Power Plants, R. J. Hansen, ed., The MIT press, Cambridge, MA, 438-483.

Boore, D. M. (1983). "Stochastic simulation of high-frequency ground motions based on seismological models of the radiated spectra." *Bulletin of the Seismological Society of America*, **73**(6A), 1865-1894.

Brune, J. N. (1970). "Tectonic stress and spectra of seismic shear waves from earthquakes." *Journal of Geophysical Research*, **75**(26), 611-614.

Brune, J. N. (1971). "Correction." *Journal of Geophysical Research*, **76**(20), 1441-1450.

Cabanas, L., Benito, B., and Herraiz, M. (1997). "An approach to the measurement of the potential structural damage of earthquake ground motions." *Earthquake Engineering & Structural Dynamics*, 26, 79-92.

Harp, E. L., and Wilson, R. C. (1995). "Shaking intensity thresholds for rock falls and slides: Evidence from 1987 Whittier Narrows and Superstition Hills earthquake strong-motion records." *Bulletin of the Seismological Society of America*, 85, 1739-1757.

Kayen, R. E., and Mitchell, J. K. (1997). "Assessment of liquefaction potential during earthquakes by Arias intensity." *Journal of Geotechnical and Geoenvironmental Engineering*, **123**(12), 1162-1174.

Lee, J. (2009). "Engineering Characterization of Earthquake Ground Motions." Ph.D. dissertation, Department of Civil and Environmental Engineering, University of Michigan, Ann Arbor, MI, 246pp.

Lee, J., and Green, R. A. (2008). "An empirical earthquake Arias intensity relationships for the western US." *International Workshop on Signal Processing and its Applications*, March 18-20, Sharjah, UAE.

McGuire, R. K., Silva, W. J., and Costantino, C. J. (2001). "Technical basis for revision of regulatory guidance on design ground motions: Hazard-and risk-consistent ground motion spectra guidelines.", US Nuclear Regulatory Commission, Washington, DC.

Program-R. (version 2.5.0). "A language and environment for statistical computing and graphics: http://www.r-project.org."

Silva, W. J., and Lee, K. (1987). "WES RASCAL Code for Synthesizing Earthquake Ground Motions: State-of-the-art for assessing earthquake hazards in the United States." *Report 24*, US Army Engineering Waterways Experiment Station Vicksburg, MS.

Travasarou, T., Bray, J. D., and Abrahamson, N. A. (2003). "Empirical attenuation relationship for Arias intensity." *Earthquake Engineering & Structural Dynamics*, **32**(7), 1133-1155.

JOINT CONFERENCE PROCEEDINGS
7th International Conference on Urban Earthquake Engineering (7CUEE) &
5th International Conference on Earthquake Engineering (5ICEE)
March 3-5, 2010, Tokyo Institute of Technology, Tokyo, Japan

SITE EFFECT STUDY IN TAIWAN AREA FROM DENSE MICROTREMOR SURVEY

Kuo-Liang Wen[1, 2] and Jyun-Yan Huang[3]

1) Professor, Institute of Geophysics, National Central University, Taiwan
2) Division head, National Center for Research on Earthquake Engineering, Taiwan
3) PHD student, Institute of Geophysics, National Central University, Taiwan
wenkl@earth.ncu.edu.tw, 986402005@cc.ncu.edu.tw

Abstract: The site effects of Taiwan region were analyzed from dense microtremor survey, including 3917 survey points in this study. The interval of each point was two to three kilometers in most of the region, and it is five hundred meters to one kilometer far in the city. Data processing is from H/V spectral ratio method, which could analysis site responds of the station without reference rock site. After data processing, the dominant frequency was analyzed in every single station, and displayed with contours. It represented the information of deposit thickness and S-wave velocity of the main alluvium layer, and the P-S logging results can be compared. The amplification factors at different frequencies can be shown, it reflects the site response at that frequency. Finally, all the results are combined with the GIS system, and hope these results can be used in many purposes like earthquake engineering, disaster prevention, seismological study, and land use planning.

1. INTRODUCTION

Taiwan is located on the seismic zone of rounding Pacific Ocean area. There are lots of earthquakes occurred every years, so we need to consider about earthquake ground motion. The inference of the earthquake ground motion can divided into source, path, and site effects. Moreover, the site effect usually plays the most important rule in earthquake disaster, so many people using reference site spectral ratio method to study the site effect (Borcherdt, 1970; Chávez-Gracía *et al.*, 1990; Field *et al.*, 1992). After calculating the spectral ratio, site amplification factor will be identifiable.

But it's hard to find the reference rock site after all. Nakamura (1989) investigated that the site amplification factor can be identified from microtremor which been recorded by a single station, the method is so-called H/V spectral ratio method. This method improves the site effect researches very much. Economize on its cost, time and manpower, the greatest advantage is no need to wait earthquake occurred. So the site characteristics of Taiwan region were analyzed by dense microtremor survey in this study.

2. MEASUREMENTS AND DATA PROCESSING

2.1 Microtremor Measurements

The microtremor survey had been constructed during 2001 to 2006, including 3917 survey points spread in plain, basin, and hill region of Taiwan (Figure 1). Each point measured microtremor for 18 minutes, and the sampling rate is 200 points per second. Three-component acceleration and velocity had been recorded. The position of each point was carefully selected to avoid artificial noise. The seismometer we used is made from Tokyo Sokushin, including the recorder SAMTAC-801B with 24 bits resolutions and the sensor VSE-311C with the frequency response from 0.07 to 100 Hz.

2.2 H/V Ratios analysis

After the data been recorded in every survey points, they were cut into many time windows of 40.96 seconds long. The windows with notable noise were eliminated. Three-component spectra of these windows were calculated with Fast Fourier Transform (FFT). Following H/V spectral ratio method's step, the horizontal spectra were composed by NS and EW component, and divided by vertical spectra to get H/V ratios for each window. After all, the mean H/V spectral ratio was calculated for all windows, and plotted with plus and minus one standard deviation (Figure 2). The H/V ratios for all survey points were used to find out the variation of site characteristics in the studying region.

H/V spectral ratio can show the site characteristics. The

dominant frequency of each station was marked and the contours for Taiwan region can be plotted (Figure 3). The dominant frequency reflects the main site characteristic of underground structures at the survey points.

In order to verify the dominant frequency, the shear-wave velocity data from borehole measurements were used. Based on the 1D resonant relationship:

$$F = V_s/4h \qquad (1)$$

where F is resonant frequency in *Hz*, V_s is shear-wave velocity in *m/s*, and *h* is thickness of the deposit in *m*. Figure 4(a) shows the shear-wave velocity measured from borehole survey near the strong motion station ILA033. And the H/V spectral ratio from nearest microtremor station was also plotted in Figure 4(b).

The site amplification factors of different frequency bands were plotted in Figure 5. The contour for each frequency band could provide the reference for land used planning and engineering consideration for seismic safety.

3. RESULTS AND CONCLUSIONS

The dominant frequency distribution seems can be related to geological or topography distribution. Around 1.2 *Hz* or less appeared located at basin and plain regions, and 3 to 4 *Hz* at hill zone (Figure 3). This results can roughly reflected the deposit thickness at the position of survey points. The dominant frequency distribution and other contours in this study were constructed on GIS (Geographic Information System). So the figure could zoom in to consider the local variations and characteristics, such as Figure 6 (b) which shows the local site conditions in Taipei basin. The dominant frequency in the Taipei basin is mostly ranging from 1 to 2 *Hz*, reveals soft alluvium deposit of the surface layer.

Except Taipei basin, the other regions in Taiwan also appeared different frequency characteristics. The regions which's dominant frequency occurred below 1.2 Hz are Yilan plain, Chianan plain, and Kaohsiung region. Taoyuan, Hsinchu , Miaoli, and Taidong area are shown in 2 to 5 *Hz*. And the highest dominant frequency which is above 6 *Hz* appeared at Taichung region (Figure 3).

Figure 4 shows the comparison between shear-wave velocity from borehole measurements near the strong motion station and the H/V spectral ratio of the nearest microtremor station. A clear velocity contrast appeared at about 28 meters depth, the mean shear-wave velocity of this layer is 245.83 *m/s*. Calculated the 1D resonant frequency by equation (1) is 2.27 *Hz*, and the dominant frequency from nearest microtremor station is 2.19 Hz. It shows that the dominant frequency of microtremor can reflect the resonant frequency of the surface main layer very well. Because the borehole measurements are expensive and need lots of time, the microtremor survey can be a useful tool for estimating the dominant frequency of the soil layer.

The distribution of H/V ratios on different frequency bands (Figure 5) can be a good reference for engineering application. Generally, the characteristic frequency of a twenty floors building is about 0.5 Hz, and site selection should avoid the high amplification regions in that frequency. So, Figure 5 can be used for land-used planning.

Wang *et al.* (2004) used seismic reflection survey to determine the bottom of Sungshan layer in Taipei basin. The isobath of Sungshan layer was shown in Figure 6(a). This isobath compared very well with the microtremor dominant frequency (Figure 6(b)). So, microtremor H/V spectral ratio can roughly determine the thickness of the soil layer if the velocity structure was known.

Acknowledgements:

The borehole data used in this study was based on the Geologic Surveyed Database of CWB Strong Motion Stations, which provided by National Center for Research on Earthquake Engineering, Taiwan and Central Weather Bureau. This study was supported by National Science Council under the grant no. NSC96-2119-M-008-007 and NSC97-2116-M-008-005.

References:

Borcherdt, R. D. (1970), "Effects of local geology on ground motion near San Francisco Bay," *Bull. Seism. Soc. Am.*, **60**, 29-61.

Chávez-Gracía F. J., G. Pedotti, D. Hatzfeld, and P.-Y. Bard (1990), "An experimental study of site effects near Thessaloniki (Northern Greece)," *Bull. Seism. Soc. Am.*, **86**, 646-654.

Field, E. H., K. H. Jacob, and S. E. Hough (1992), "Earthquake site response estimation : a weak-motion case study," *Bull. Seism. Soc.Am.*, **82**, 2283-2306.

Nakamura, Y. (1989), "A method for dynamic characteristics estimation of subsurface using microtremor on the ground surface," *QR of RTRI*, **30**(1), 25-33.

Wang, C. Y., Y. H. Lee, M. L. Ger, and Y. L. Chen (2004), "Investigating subsurface structures and P- and S-wave velocities in the Taipei basin," *Terr. Atm. Oce. Sci.*, **15**(4), 609-627.

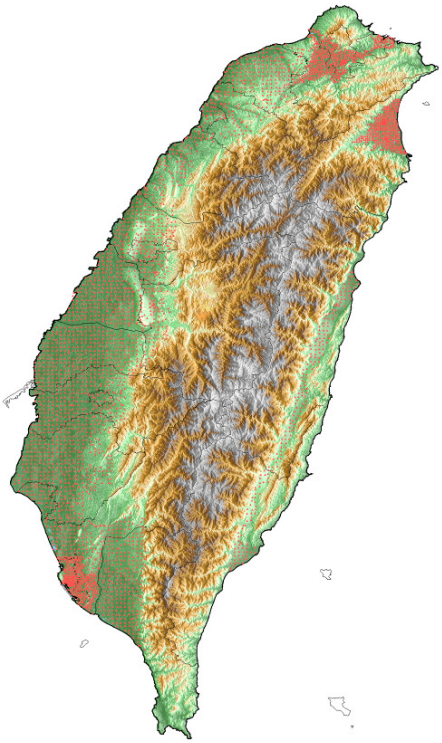

Figure 1　Location of the dense microtremor survey points (red dots) in Taiwan region, station interval is 500 meters to 3 kilometer far.

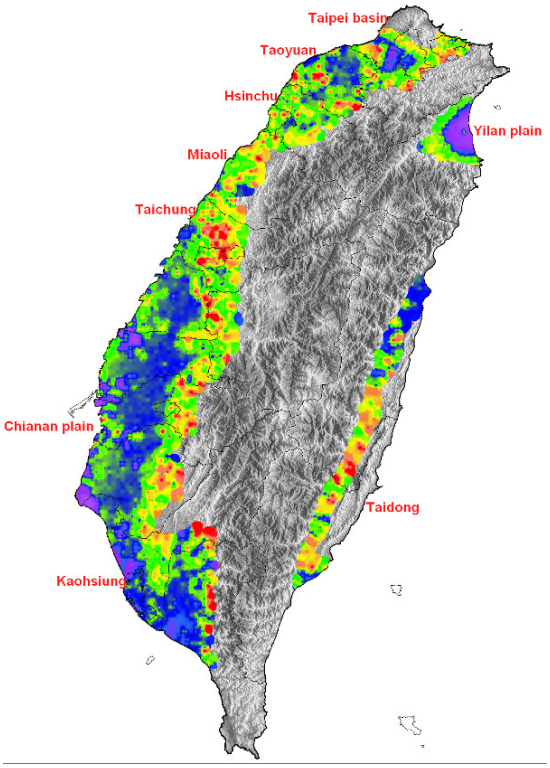

Figure 3　Contour of dominant frequency distribution in the Taiwan region. Color bar shows different frequency values, monochromatic background shows the topography.

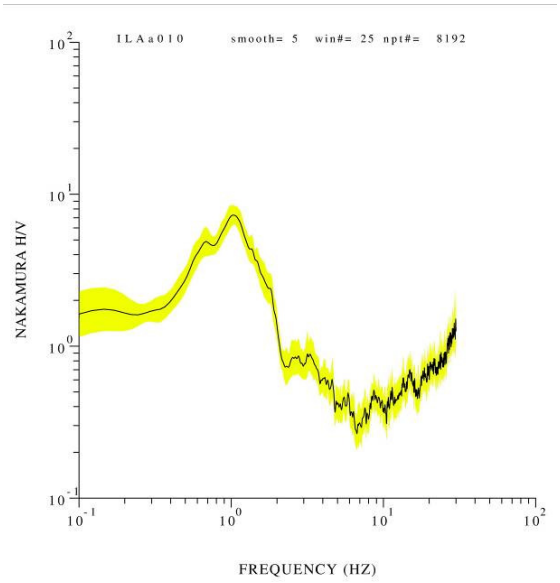

Figure 2　Example of the H/V spectral ratio, which shows the results of station ILAa010. Yellow region shows the one standard deviation area.

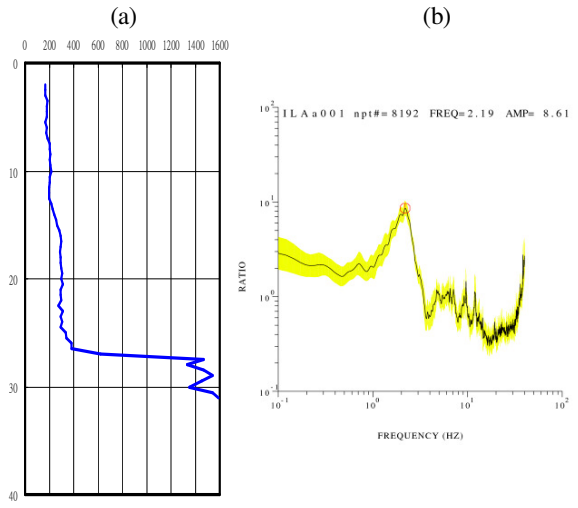

Figure 4　(a) Shear-wave velocity at station ILA033, horizontal axis is velocity (unit in *m/s*) and vertical axis shows depth from ground surface (unit in *m*). (b) Microtremor H/V spectral ratio of station ILAa001 which is near the station ILA033, the red circle shows the dominant frequency.

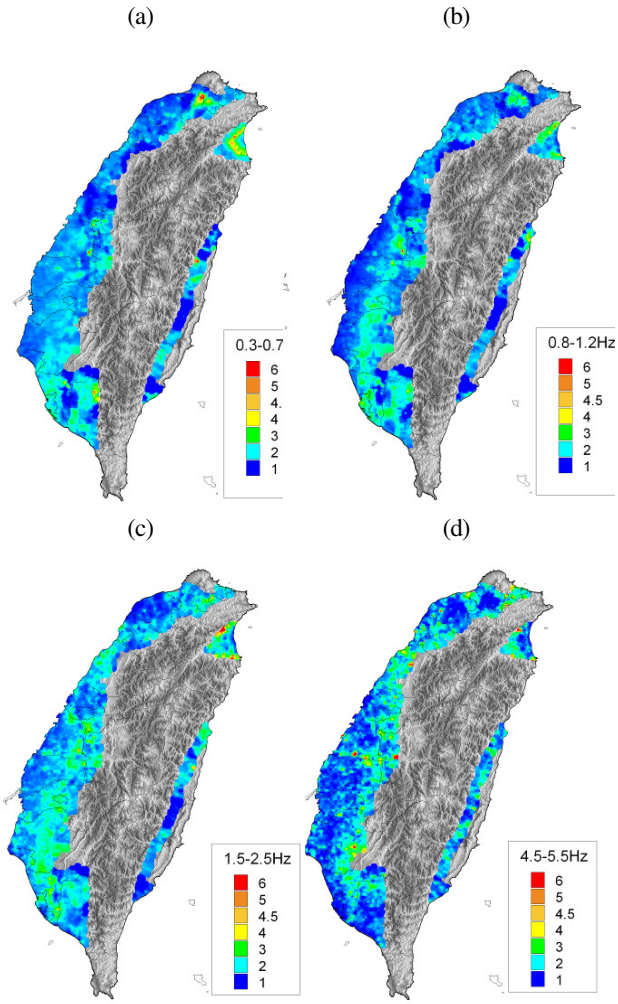

Figure 5 (a) Contour of the H/V ratios at 0.3-0.7 *Hz*. (b) Contour of H/V ratios at 0.8-1.2 *Hz*. (c) Contour of H/V ratios at 1.5-2.5 *Hz*. (d) Contour of H/V ratios at 4.5-5.5 *Hz*.

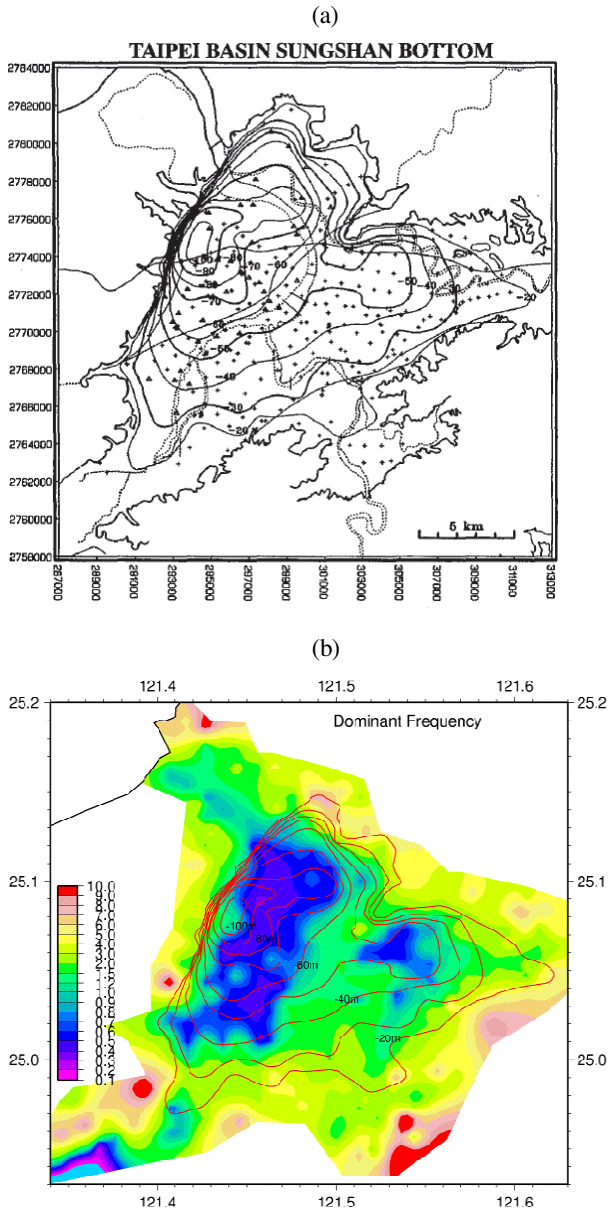

Figure 6 (a) Isobath of Sungshan layer bottom in the Taipei basin (Wang *et al.*, 2004). (b) Comparison of the dominant frequency distribution with Isobath of Sungshan layer's bottom.

JOINT CONFERENCE PROCEEDINGS
7th International Conference on Urban Earthquake Engineering (7CUEE) &
5th International Conference on Earthquake Engineering (5ICEE)
March 3-5, 2010, Tokyo Institute of Technology, Tokyo, Japan

ANALYSIS OF LOVE-WAVE COMPONENTS IN MICROTREMORS

Taku Tada[1)], Ikuo Cho[2)], and Yuzo Shinozaki[3)]

1) Technical Staff Member, Geological Survey of Japan, National Institute of Advanced Industrial Science and Technology (AIST), Japan
2) Research Scientist, Geological Survey of Japan, National Institute of Advanced Industrial Science and Technology (AIST), Japan
3) Professor, Department of Architecture, Faculty of Engineering, Tokyo University of Science, Japan
kogutek@ni.aist.go.jp, ikuo-chou@aist.go.jp, sinozaki@rs.kagu.tus.ac.jp

Abstract: We present new and simple formulas, obtained by expanding the SPAC method, that allow one to infer (1) Love-wave phase velocities and (2) Rayleigh-to-Love power partition ratios using records of microtremors around a circle and at its center. Love-wave velocities can be inferred by simple inversion of an observational equation that involves Bessel functions. Two-component horizontal-motion records are the only input required. Rayleigh-to-Love power partition ratios can be inferred by simple forward algebra. Vertical- and radial-component horizontal-motion records around a circle, plus three-component records at its center, suffice for this purpose. We have released BIDO, a package of free software, that automatically implements the SPAC method plus a broad variety of circular-array microtremor techniques that we have so far developed on its basis. Application of the BIDO software to field data from two sites in Japan indicates preponderance of Love-wave components over Rayleigh-wave components in horizontal-motion microtremors, although further investigations are necessary before any conclusion can be drawn with certainty.

1. INTRODUCTION

The spatial autocorrelation (SPAC) method is a popular technique of microtremor (ambient noise) exploration that employs circular arrays (Aki 1957, Okada 2006, Cho et al. 2008). It is most typically used to infer phase velocities of Rayleigh waves (c^R) using vertical-motion records of microtremors (e.g. Ekström et al. 2009, Picozzi et al. 2009, Prieto et al. 2009, Stephenson et al. 2009; see references in Cho et al. 2008 and Tada et al. 2009 for more).

A derivative form of the technique, known as the three-component SPAC method because it relies on the use of three-component microtremor records, provides the possibility to simultaneously infer (i) c^R, (ii) phase velocities of Love waves (c^L), and (iii) ratios of power partition between Rayleigh waves and Love waves (Okada and Matsushima 1989, Ferrazzini et al. 1991, Endrun et al. 2010). Availability of information related to Love-wave properties, such as (ii) c^L and the (iii) power partition ratios, should provide better constraint on subsurface soil structures than when (i) c^R alone is available. In the three-component SPAC method, however, a nonlinear set of simultaneous equations has to be solved for the three unknown parameters, so that the solution process can be fairly complicated.

By expanding the SPAC method, we have recently developed novel formulas that allow one to infer c^L independently by simple inversion of an observational equation, and also to infer Rayleigh-to-Love power partition ratios independently by simple forward algebra, with no need to solve simultaneous equations (Tada et al. 2009). Just like in the case of the SPAC method, records of microtremors around a circle and at its center are all that is required of the input. Two-component horizontal-motion records suffice for the estimation of c^L, whereas vertical- and one-component horizontal-motion records around the circle, plus three-component records at its center, suffice for the estimation of the power partition ratios. Our new methods therefore substantially facilitate the evaluation of Love-wave properties using circular microtremor arrays.

This article reviews the flow of algorithm in our new techniques, and presents examples of field data analysis results, with relative emphasis on the Rayleigh-to-Love power partition ratios.

2. METHOD DESCRIPTIONS

2.1 Method for Estimating Love-Wave Velocities (the SPAC+L Method)

Let $R(t, r, \theta)$ and $T(t, r, \theta)$ be the radial and tangential components, respectively, of the horizontal-motion seismogram of microtremors at radius r and azimuth θ as seen from the array center. The sign of $R(t, r, \theta)$ is taken to be positive in the centrifugal direction, whereas $T(t, r, \theta)$ is taken to be positive in the counterclockwise direction.

We define $R_1(t, r)$ as a weighted average of $R(t, r, \theta)$ over the azimuth θ:

$$R_1(t,r) = \int_{-\pi}^{\pi} R(t,r,\theta)\exp(-i\theta)d\theta\,. \qquad (1)$$

In the special case of $r = 0$, Eq. (1) reduces to

$$R_1(t,0) = \pi[R(t,0,0) - iT(t,0,0)] \quad (2)$$

(Tada et al. 2009, eq. 8). We also define $T_0(t, r)$ as a non-weighted azimuthal average of $T(t, r, \theta)$:

$$T_0(t,r) = \int_{-\pi}^{\pi} T(t,r,\theta)d\theta . \quad (3)$$

Our formula for evaluating Love-wave phase velocities $c^L(\omega)$, which vary with frequency ω, is

$$\frac{G_{R1T0}(r,r;\omega)}{G_{R1T0}(0,r;\omega)} = J_0(r\omega/c^L(\omega)) + J_2(r\omega/c^L(\omega)), \quad (4)$$

where $G_{R1T0}(r, r; \omega)$ is the cross-spectral density between $R_1(t, r)$ and $T_0(t, r)$; $G_{R1T0}(0, r; \omega)$ is the cross-spectral density between $R_1(t, 0)$ and $T_0(t, r)$; and $J_m(\cdot)$ denotes the mth-order Bessel function of the first kind. Eq. (4) holds true under the assumption that the field of Love waves is dominated by a single mode (most typically the fundamental mode, but not necessarily). The c^L evaluation method, based on the use of Eq. (4), was named by Tada et al. (2009) the "SPAC+L method," where the plus sign refers to the one that appears on the right-hand side of Eq. (4) and the letter L is short for Love waves.

Once the cross-spectral densities $G_{R1T0}(r, r; \omega)$ and $G_{R1T0}(0, r; \omega)$ are calculated using field measurement records, it is quite straightforward to infer $c^L(\omega)$ by simple inversion of Eq. (4). The only input required is the two-component horizontal-motion records around a circle of radius r and at its center.

2.2 Method for Estimating the Power Share of Rayleigh Waves

Let $Z(t, r, \theta)$ be the vertical-motion seismogram of microtremors at radius r and azimuth θ, and let us define $Z_1(t, r)$ as a weighted average of $Z(t, r, \theta)$ over the azimuth θ:

$$Z_1(t,r) = \int_{-\pi}^{\pi} Z(t,r,\theta)\exp(-i\theta)d\theta . \quad (5)$$

We also define $R_0(t, r)$ as a non-weighted azimuthal average of $R(t, r, \theta)$:

$$R_0(t,r) = \int_{-\pi}^{\pi} R(t,r,\theta)d\theta . \quad (6)$$

Our formula for evaluating the share of Rayleigh waves in the total power of horizontal motion, which we denote by $\gamma^R(\omega)$, is

$$\gamma^R(\omega) = \frac{G_{Z0Z0}(0,0;\omega)\,G_{R0R0}(r,r;\omega)}{4G_{Z1Z1}(r,r;\omega)\,G_{R1R1}(0,0;\omega)} \quad (7)$$

(Tada et al., 2009, appendix C), where $G_{Z1Z1}(r, r; \omega)$ is the power-spectral density of $Z_1(t, r)$; $G_{R0R0}(r, r; \omega)$ is the power-spectral density of $R_0(t, r)$; $G_{R1R1}(0, 0; \omega)$ is the power-spectral density of $R_1(t, 0)$ (Eq. 2), which equals the sum of the power-spectral densities of the two horizontal components at the array center; and $G_{Z0Z0}(0, 0; \omega)$ is the power-spectral density of vertical motion at the center. Eq. (7) holds true under the assumption that (i) the field of microtremors is composed of Rayleigh and Love waves alone, and that (ii) the field of Rayleigh waves is dominated by a single mode (most typically the fundamental mode, but not necessarily). There is no theoretical requisite regarding the mode composition of Love waves. Because of assumption (i), the share of Love waves in the total power of horizontal motion is $1 - \gamma^R(\omega)$.

Once the four power-spectral densities appearing in Eq. (7) are calculated using field records, $\gamma^R(\omega)$ can be inferred by means of simple forward algebra. The only input required is the Z- and R-component records around a circle of radius r, plus three-component records at its center.

2.3 The BIDO Software Package

Our above-described new techniques of Love-wave properties analysis, namely the SPAC+L method (Eq. 4) and the γ^R estimation method (Eq. 7), are both part of the software package BIDO, which we are offering free on the user's demand (visit our BIDO Web site: http://staff.aist.go.jp/ikuo-chou/bidodl_en.html). BIDO, which we named after the Japanese word *bidō* for microtremors, is a bundle of analysis codes that implement the SPAC method plus a number of kindred techniques which we have developed by expanding it. When fed with appropriately formatted input seismograms, BIDO produces, in both numerical and graphical output, estimates of quantities including:

(i) Rayleigh-wave phase velocities (c^R) [SPAC method (Aki 1957); CCA method (Cho et al. 2006a); noise-compensated CCA, H0, H1, and V methods (Tada et al. 2007); SPAC+R, SPAC-R, and CCA-R methods (Tada et al. 2009, appendix B)],

(ii) Love-wave phase velocities (c^L) [SPAC+L, SPAC-L and CCA-L methods (Tada et al. 2009)],

(iii) Share of Rayleigh waves in the total power of horizontal motion (γ^R) (Tada et al. 2009, appendix C),

(iv) Horizontal-to-vertical amplitude ratios (ellipticities) of Rayleigh waves (Cho et al. 2006b, appendix E),

(v) Horizontal-to-vertical spectral ratios (HVSRs) of total motion, and

(vi) Noise-to-signal (NS) power ratios in vertical motion (Cho et al. 2006a).

When the input data lack records at the array center, the output lacks (iii) γ^R and (vi) NS ratios. When the input is composed of vertical-motion records alone, the output lacks (ii) c^L, (iii) γ^R, (iv) ellipticities, and (v) HVSRs. When, on the contrary, the input is composed of horizontal-motion records alone, the output lacks (iii) γ^R, (iv) ellipticities, (v) HVSRs, and (vi) NS ratios.

2.4 Error Factors

There are at least three categories of factors which can introduce errors into the estimates of c^L and γ^R that are derived by way of Eqs (4) and (7) using field records.

One is called directional aliasing. The time series $R_1(t, r)$, $R_0(t, r)$, $T_0(t, r)$, and $Z_1(t, r)$, or weighted and non-weighted azimuthal averages of seismograms around a circle, have to be inferred, in practice, by summing up seismograms at a finite number of stations. This introduces errors in the estimates of the spectral densities appearing in Eqs (4) and (7), because information on the directional characteristics of microtremors slips away partially. The effects of directional aliasing grow larger with increasing frequency (e.g. Cho et al. 2006b, Okada 2006, Tada et al. 2007, Cho et al. 2008).

Another factor is the presence of multiple modes in surface waves (Rayleigh and Love waves). Eq. (4) relies on the assumption that all Love waves are made up of a single mode, whereas Eq. (7) presupposes that all Rayleigh waves consist of a single mode. When these assumptions fail, so does the accuracy of the c^L and γ^R estimates. Like directional aliasing, the effects of multiple modes tend to grow larger in higher frequency ranges.

The third factor, the presence of incoherent noise, affects Eq. (7) but not Eq. (4). This is because the power-spectral densities, appearing in Eq. (7), get inflated by amounts that depend on the power of noise, whereas the cross-spectral densities, appearing in Eq. (4), are not affected (Cho et al. 2006b).

Quantitative evaluation of these error factors is beyond the scope of the present study. For the convenience of future investigations, however, we present relevant mathematical formulas in the Appendix (Sections A.1-A.5).

A fourth category of error factors, or stochastic uncertainties due to the finite length of available data, were theorized and quantitatively evaluated by ourselves with reference to the H0, H1, and CCA methods (Tada et al. 2007) and the SPAC method (Cho et al. 2008). Theorization of stochastic uncertainties in Eqs (4) and (7), however, remains yet to be done (see Section A.6 in the Appendix).

3. FIELD IMPLEMENTATION

3.1 Input Data and Analysis Output

We applied the BIDO software package to real microtremor data from the field with a view to evaluating the relative content of Rayleigh and Love waves in them. The input data are the same as those described in the work of Tada et al. (2009): six data sets from two measurement sites, one lying in a quiet residential area in the northern suburbs of Tokyo (KSKB: Kasukabe), and the other close to a street of heavy traffic near central Tokyo (KIBA: Kiba Park). At each site, circular arrays of six seismic sensors, with five of them distributed evenly around a circle and the sixth at its center, were deployed successively at three different array radii of r = 3, 12, and 36 m. The data sampling rate was 100 Hz and the duration was 30 min in all measurement sessions.

Figures 1 and 2 show, in the left columns, the share of Rayleigh waves in the total power of horizontal motion (γ^R) evaluated with Eq. (7), and in the right columns, the phase velocities of Love waves (c^L) inferred with the SPAC+L method (Eq. 4). The bold curves in the γ^R plots and the plus signs in the c^L plots indicate averages of estimates obtained from different portions of the data. Standard deviations are indicated by pairs of thin curves in the γ^R plots and by vertical error bars in the c^L plots. In both categories of plots, the horizontal axis denotes the frequency. Incidentally, estimates of γ^R based on Eq. (7) may exceed unity, although the true values of γ^R should lie between 0 and 1.

3.2 Estimates of Love-Wave Velocities

In the c^L plots (right columns of Figures 1 and 2), the bold and smooth curves, sloping left up, indicate phase velocities of fundamental-mode Love waves that were calculated theoretically from subsurface soil structure models (see Tada et al. 2009 for details). The gray shades highlight frequency intervals where agreement between the theoretical and inferred c^L is relatively good. These shades were drawn by visual inspection, and their locations are not necessarily based on objective criteria.

The pairs of thin and smooth curves, sloping right up, correspond to wavelengths (λ^L) of twice and ten times the array radius r, respectively. The area bordered on both sides by a pair of these curves ($2r < \lambda^L < 10r$) gives a rule-of-thumb measure of the interval in which one can most typically expect to obtain relatively accurate estimates of c^L, even though there are obvious exceptions (e.g. KSKB, r = 36 m; KIBA, r = 12 m).

3.3 Estimates of the Power Share of Rayleigh Waves

We have highlighted the frequency intervals of good agreement between the theoretical and inferred c^L not only in the c^L plots but also in the plots of γ^R (left columns of Figures 1 and 2). We focus our attention on the estimates of γ^R in those highlighted intervals, although we still need theoretical and empirical evidences to find out the frequency ranges in which the γ^R estimates are the most reliable.

In the cases of (i) KSKB, r = 12 m, (ii) KSKB, r = 36 m, and (iii) KIBA, r = 36 m, the γ^R estimates, derived from Eq. (7), take values of around 0.2 everywhere in the highlighted frequency ranges. This implies that about 80% of all power of horizontal-motion microtremors is made of Love-wave components, in contrast to only about 20% for the Rayleigh-wave components.

In the other cases, namely (iv) KSKB, r = 3 m, (v) KIBA, r = 3 m, and (vi) KIBA, r = 12 m, the γ^R estimates vary significantly within the highlighted frequency intervals. In these cases, the highlighted intervals lie at higher frequencies than in cases (i)-(iii), and therefore are expected to be more susceptible to potential effects of directional aliasing and of multiple modes (Section 2.4). The reliability of the γ^R estimates in cases (iv)-(vi) should therefore be taken with more caution.

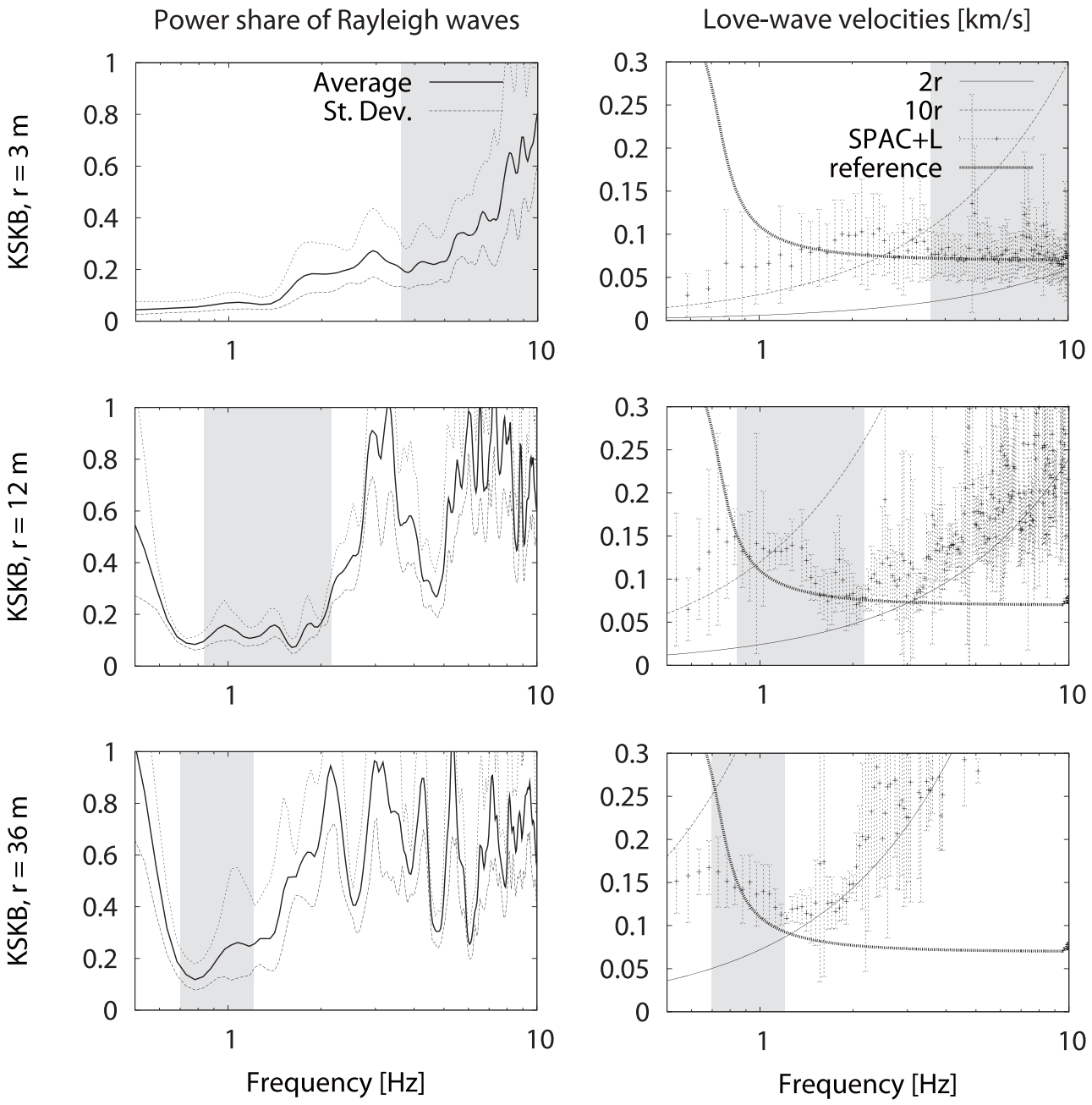

Figure 1 (Left) Share of Rayleigh waves in the total power of horizontal-motion microtremors (γ^R) at KSKB, evaluated using Eq. (7). The bold curves denote averages of estimates obtained from different portions of the data, whereas standard deviations are indicated by pairs of thin curves. The horizontal axis denotes the frequency.

From top to bottom, the plots show estimates using six-sensor, circular seismic arrays of radii r = 3, 12, and 36 m, respectively.

(Right) Phase velocities of Love waves (c^L) at KSKB, inferred with the SPAC+L method (Eq. 4). The plus signs denote averages of estimates obtained from different portions of the data, whereas standard deviations are indicated by vertical error bars. The horizontal axis denotes the frequency. The bold and smooth curves, sloping left up, indicate phase velocities of fundamental-mode Love waves that were derived theoretically from a subsurface soil structure model (Tada et al. 2009). The pairs of thin and smooth curves, sloping right up, correspond to wavelengths of twice and ten times the array radius r, respectively.

The shades highlight frequency intervals where agreement between the theoretical and inferred Love-wave phase velocities is relatively good.

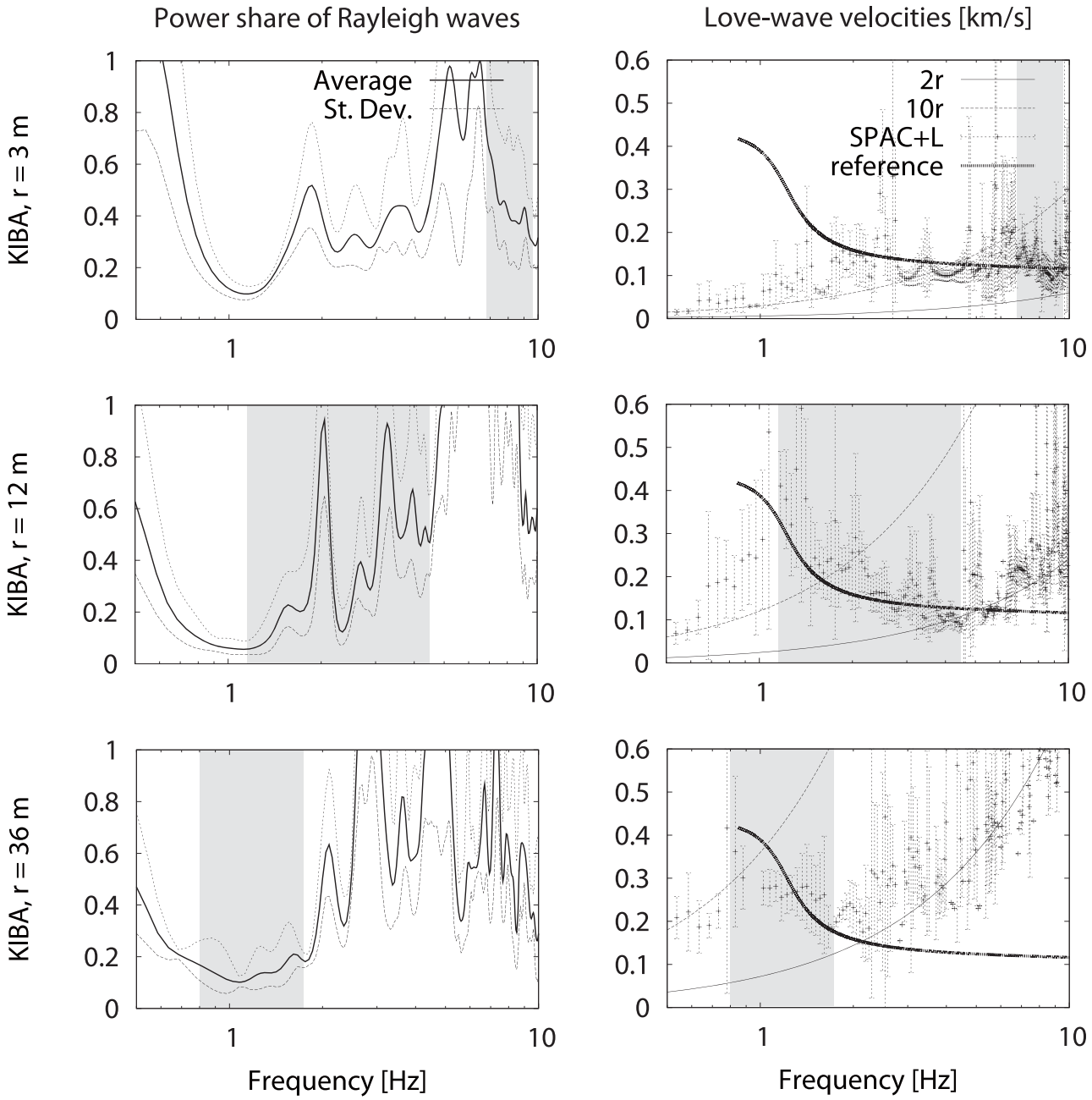

Figure 2 (Left) Share of Rayleigh waves in the total power of horizontal-motion microtremors (γ^R) at KIBA, evaluated using Eq. (7). (Right) Phase velocities of Love waves (c^L) at KIBA, inferred with the SPAC+L method (Eq. 4). From top to bottom, the plots show estimates using six-sensor, circular seismic arrays of radii r = 3, 12, and 36 m, respectively.

See caption to Figure 1 for the meaning of the curves, symbols and shades. The theoretical c^L dispersion curves (the bold and smooth curves that slope left up in the right column panels) are due to Tada et al. (2009).

A closer look reveals that γ^R estimates in the highlighted frequency bands stay around 0.2 everywhere if we limit our attention on low frequency ranges of less than 2 Hz (cases (i)-(iii) and part of case (vi)).

Previous studies that used the three-component SPAC method (Section 1) to evaluate γ^R in microtremors argued that the power of Rayleigh waves accounted for about half (Métaxian et al. 1997, Saccorotti et al. 2003) or less than half (Matsushima and Okada 1990, Arai and Tokimatsu 1998, Chouet et al. 1998, Yamamoto 2000, Köhler et al. 2007) of the total power of horizontal motion. Endrun et al. (2010) found γ^R to be variable, but consistently found it to be either at about half or below half. The results of our present study, implying the preponderance of Love waves, largely agree with the arguments of those earlier investigations.

4. CONCLUSION

We have applied new techniques of circular-array microtremor analysis to field data from two sites in the Tokyo conurbation. The results implied preponderance of Love waves over Rayleigh-wave components in horizontal-motion microtremors, at least in relatively low frequency ranges of less than 2 Hz. This finding is largely consistent with the arguments made by earlier studies, although further investigations are necessary before any conclusion can be drawn with certainty.

Ratios of power partition between Rayleigh and Love waves play an important part, e.g., in methods to interpret subsurface soil structures using horizontal-to-vertical spectral ratios (HVSRs) of microtremors. In practice, however, power partition ratio values have often been prescribed *a priori* (e.g. Arai and Tokimatsu 2004). Accumulation of reliable estimates for the power partition ratios should therefore be useful for enhancing the precision and utility of the microtremor HVSR exploration methods.

Acknowledgements:

The present work was partially supported by Grants-in-Aid for Scientific Research of the Japan Society for the Promotion of Science (JSPS) and of the Japanese Ministry of Education, Culture, Sports, Science, and Technology (MEXT).

References:

Aki, K. (1957), "Space and Time Spectra of Stationary Stochastic Waves, with Special Reference to Microtremors," *Bulletin of the Earthquake Research Institute, University of Tokyo*, **35**(3), 415-457.

Arai, H. and Tokimatsu, K. (1998), "Evaluation of Local Site Effects Based on Microtremor H/V Spectra," in *The Effects of Surface Geology on Seismic Motion*, Irikura, K., Kudo, K., Okada, H., and Sasatani, T. (editors), Balkema, Rotterdam, **2**, 673-680.

Arai, H. and Tokimatsu, K. (2004), "*S*-Wave Velocity Profiling by Inversion of Microtremor H/V Spectrum," *Bulletin of the Seismological Society of America*, **94**(1), 53-63.

Cho, I., Tada, T., and Shinozaki, Y. (2006a), "Centerless Circular Array Method: Inferring Phase Velocities of Rayleigh Waves in Broad Wavelength Ranges Using Microtremor Records," *Journal of Geophysical Research*, American Geophysical Union, **111**, B09315, doi:10.1029/2005JB004235.

Cho, I., Tada, T., and Shinozaki, Y. (2006b), "A Generic Formulation for Microtremor Exploration Methods Using Three-Component Records from a Circular Array," *Geophysical Journal International*, **165**(1), 236-258.

Cho, I., Tada, T., and Shinozaki, Y. (2008), "Assessing the Applicability of the Spatial Autocorrelation Method: A Theoretical Approach," *Journal of Geophysical Research*, American Geophysical Union, **113**, B06307, doi:10.1029/2007JB005245.

Chouet, B., De Luca, G., Milana, G., Dawson, P., Martini, M., and Scarpa, R. (1998), "Shallow Velocity Structure of Stromboli Volcano, Italy, Derived from Small-Aperture Array Measurements of Strombolian Tremor," *Bulletin of the Seismological Society of America*, **88**(3), 653-666.

Ekström, G., Abers, G. A., and Webb, S. C. (2009), "Determination of Surface-Wave Phase Velocities across USArray from Noise and Aki's Spectral Formulation," *Geophysical Research Letters*, American Geophysical Union, **36**, L18301, doi:10.1029/2009GL039131.

Endrun, B., Ohrnberger, M., and Savvaidis, A. (2010), "On the Repeatability and Consistency of Three-Component Ambient Vibration Array Measurements," *Bulletin of Earthquake Engineering*, in press, doi:10.1007/s10518-009-9159-9.

Ferrazzini, V., Aki, K., and Chouet, B. (1991), "Characteristics of Seismic Waves Composing Hawaiian Volcanic Tremor and Gas-Piston Events Observed by a Near-Source Array," *Journal of Geophysical Research*, American Geophysical Union, **96**(B4), 6199-6209.

Köhler, A., Ohrnberger, M., Scherbaum, F., Wathelet, M., and Cornou, C. (2007), "Assessing the Reliability of the Modified Three-Component Spatial Autocorrelation Technique," *Geophysical Journal International*, **168**(2), 779-796.

Matsushima, T. and Okada, H. (1990), "An Exploration Method Using Microtremors (2)—An Experiment to Identify Love Waves in Long-Period Microtremors" (in Japanese with English abstract), *Proceedings of the 82nd SEGJ Conference*, Society of Exploration Geophysicists of Japan, 5-8.

Métaxian, J.-P., Lesage, P., and Dorel, J. (1997), "Permanent Tremor of Masaya Volcano, Nicaragua: Wave Field Analysis and Source Location," *Journal of Geophysical Research*, American Geophysical Union, **102**(B10), 22,529-22,545.

Okada, H. (2006), "Theory of Efficient Array Observations of Microtremors with Special Reference to the SPAC Method," *Exploration Geophysics*, Australian Society of Exploration Geophysicists, **37**(1); *Butsuri-Tansa*, Society of Exploration Geophysicists of Japan, **59**(1); *Mulli-Tamsa*, Korean Society of Exploration Geophysicists, **9**(1), 73-85.

Okada, H. and Matsushima, T. (1989), "An Exploration Method Using Microtremors (1)—A Theory to Identify Love Waves in Microtremors" (in Japanese with English abstract), *Proceedings of the 81st SEGJ Conference*, Society of Exploration Geophysicists of Japan, 15-18.

Picozzi, M., Strollo, A., Parolai, S., Durukal, E., Özel, O., Karabulut, S., Zschau, J., and Erdik, M. (2009), "Site Characterization by Seismic Noise in Istanbul, Turkey," *Soil Dynamics and Earthquake Engineering*, **29**(3), 469-482.

Prieto, G. A., Lawrence, J. F., and Beroza, G. C. (2009), "Anelastic Earth Structure from the Coherency of the Ambient Seismic Field," *Journal of Geophysical Research*, American Geophysical Union, **114**, B07303, doi:10.1029/2008JB006067.

Saccorotti, G., Chouet, B., and Dawson, P. (2003), "Shallow-Velocity Models at the Kilauea Volcano, Hawaii, Determined from Array Analyses of Tremor Wavefields," *Geophysical Journal International*, **152**(3), 633-648.

Stephenson, W. J., Hartzell, S., Frankel, A. D., Asten, M., Carver, D. L., and Kim, W. Y. (2009), "Site Characterization for Urban Seismic Hazards in Lower Manhattan, New York City, from Microtremor Array Analysis," *Geophysical Research Letters*, American Geophysical Union, **36**, L03301,

doi:10.1029/2008GL036444.
Tada, T., Cho, I., and Shinozaki, Y. (2007), "Beyond the SPAC Method: Exploiting the Wealth of Circular-Array Methods for Microtremor Exploration," *Bulletin of the Seismological Society of America*, **97**(6), 2080-2095.
Tada, T., Cho, I., and Shinozaki, Y. (2009), "New Circular-Array Microtremor Techniques to Infer Love-Wave Phase Velocities," *Bulletin of the Seismological Society of America*, **99**(5), 2912-2926.
Yamamoto, H. (2000), "An Experiment for Estimating Phase Velocities of Love Waves from Three-Component Microtremor Array Observations" (in Japanese with English abstract), *Butsuri-Tansa*, Society of Exploration Geophysicists of Japan, **53**(2), 153-166.

APPENDIX. EFFECTS OF DIRECTIONAL ALIASING, MULTIPLE MODES OF SURFACE WAVES, AND INCOHERENT NOISE

In this appendix we present mathematical formulas that describe the effects of the three error factors mentioned in Section 2.4—directional aliasing, multiple modes of surface waves, and incoherent noise—on the estimates of the quantities given by Eqs (4) and (7). Numerical evaluation of these error factors, however, is beyond the scope of the present paper and we leave that for future investigations.

A.1 Basic Formula of Directional Aliasing

Let us denote, by the letter X, either one of the three letters R, T, and Z, which stand for the radial-, transverse-, and vertical-component seismograms of microtremors, respectively. Let us also denote, by

$$X_m(t,r) = \int_{-\pi}^{\pi} X(t,r,\theta)\exp(-im\theta)d\theta\,, \qquad \text{(A.1)}$$

the mth-order coefficient in the Fourier series expansion of $X(t, r, \theta)$ with respect to the azimuth θ. Under the assumption that (i) a finite number of N seismic sensors are distributed evenly around a circle of radius r, with one of them lying in the direction of zero azimuth, the estimate for $X_m(t, r)$, obtained by taking a weighted sum of seismograms at the N stations, is related to the true values of $X_m(t, r)$ by

$$\hat{X}_m(t,r) = \sum_{j=-\infty}^{\infty} X_{m+jN}(t,r) \qquad \text{(A.2)}$$

(e.g. Cho et al. 2006b).

There is no directional aliasing when $r = 0$.

A.2 Notation for the Modes of Surface Waves

We use the letter q to denote the qth mode of surface waves (Rayleigh or Love waves), and N^R and N^L to denote the total number of modes for the Rayleigh and Love waves, respectively.

A.3 Cross- and Power-Spectral Densities of Incoherent Noise

Let $G_{XmYn}(r_1, r_2; \omega)$ denote the cross-spectral density between two time series $X_m(t, r_1)$ and $Y_n(t, r_2)$. When the latter two represent Fourier coefficients of an identical order ($m = n$) for an identical component ($X = Y$) of seismograms around an identical circle ($r_1 = r_2 = r$), $G_{XmYn}(r_1, r_2; \omega) = G_{XmXm}(r, r; \omega)$ represents the power-spectral density of the time series $X_m(t, r)$.

Suppose that (ii) seismograms include noise that is uncorrelated with the microtremor signals (i.e. propagating Rayleigh- and Love-wave components). In this case, the estimate (which we indicate by a superscript hat) of the cross- or power-spectral density $G_{XmYn}(r_1, r_2; \omega)$, obtained using the noise-inclusive seismograms, equals the sum of a spectral density estimate relevant to the signals (which we indicate by a superscript s) and a spectral density estimate relevant to the noise (which we denote by a superscript n):

$$\hat{G}_{XmYn}(r_1,r_2;\omega) = \hat{G}^{s}_{XmYn}(r_1,r_2;\omega) + \hat{G}^{n}_{XmYn}(r_1,r_2;\omega)\,. \qquad \text{(A.3)}$$

The signal term includes the effects of both directional aliasing and multiple modes.

If (iii) the noise is incoherent (uncorrelated) from one sensor to another, the noise term in Eq. (A.3) is non-zero when and only when the two radii, r_1 and r_2, coincide.

If (iv) the noise is incoherent from one component to another in the records of an identical sensor, the noise term in Eq. (A.3) is non-zero when and only when the combination of the two component indicators, (X, Y), is either (Z, Z), (R, R), (T, T), (R, T), or (T, R). The noise term does not necessarily vanish for (R, T) and (T, R), because both the R and T records contain contributions from the east-west and north-south component seismograms.

Let us further assume that (v) the noise has identical intensities for all sensors, that (vi) the noise has identical intensities for the two components of horizontal motion at an identical station, and that (i) N seismic stations are distributed at equal distances around a circle of radius r. Cho et al. (2006b) demonstrated that, for $r \neq 0$,

$$\hat{G}^{n}_{ZmZn}(r,r;\omega) = 4\pi^2\delta_{mn} f_Z(\omega)/N \qquad \text{(A.4)}$$

$$\hat{G}^{n}_{RmRn}(r,r;\omega) = \hat{G}^{n}_{TmTn}(r,r;\omega) = 2\pi^2\delta_{mn} f_H(\omega)/N \qquad \text{(A.5)}$$

$$\hat{G}^{n}_{RmTn}(r,r;\omega) = \hat{G}^{n}_{TmRn}(r,r;\omega) = 0\,, \qquad \text{(A.6)}$$

where δ_{mn} denotes the Kronecker delta, $f_Z(\omega)$ is the power of noise in vertical motion, and $f_H(\omega)$ is the total power of noise in the two components of horizontal motion. The power of noise in either the east-west or the north-south component is given by (1/2) $f_H(\omega)$. Eqs (A.4)-(A.6) indicate that the noise term in Eq. (A.3) is non-zero when and only when the two component indicators, X and Y, are identical (the combinations (R, T) and (T, R) are no longer included), and the two order numbers, m and n, are also identical.

For the case of $r_1 = r_2 = 0$, Cho et al. (2006b)

demonstrated that

$$\hat{G}^{n}_{Z0Z0}(0,0;\omega) = 4\pi^2 f_Z(\omega) \tag{A.7}$$

$$\hat{G}^{n}_{R1R1}(0,0;\omega) = \hat{G}^{n}_{T1T1}(0,0;\omega) = \pi^2 f_H(\omega) \tag{A.8}$$

$$\hat{G}^{n}_{R1T1}(0,0;\omega) = -i\pi^2 f_H(\omega)\,. \tag{A.9}$$

A.4 SPAC+L Method

Let us denote, by $\rho_{\mathrm{SPAC+L}}$, the spectral ratio that appears on the left-hand side of Eq. (4):

$$\rho_{\mathrm{SPAC+L}} = \frac{G_{R1T0}(r,r;\omega)}{G_{R1T0}(0,r;\omega)}\,. \tag{A.10}$$

Both the denominator, $G_{R1T0}(0, r; \omega)$, and the numerator, $G_{R1T0}(r, r; \omega)$, are free from the effects of incoherent noise under the assumptions described in Section A.3:

$$\hat{G}^{n}_{R1T0}(0,r;\omega) = \hat{G}^{n}_{R1T0}(r,r;\omega) = 0\,. \tag{A.11}$$

The denominator is the cross-spectral density (which we denote CSD in equations that follow) between the estimates of $R_1(t, 0)$ and $T_0(t, r)$. Its estimate, to be obtained by records of N sensors around the circle, is

$$\begin{aligned}
\hat{G}_{R1T0}(0,r;\omega) &= \hat{G}^{s}_{R1T0}(0,r;\omega) = \mathrm{CSD}[\hat{R}_1(t,0), \hat{T}_0(t,r)] \\
&= \mathrm{CSD}\left[R_1(t,0), \sum_{j=-\infty}^{\infty} T_{jN}(t,r) \right] \\
&= \sum_{j=-\infty}^{\infty} \mathrm{CSD}[R_1(t,0), T_{jN}(t,r)] \\
&= \sum_{j=-\infty}^{\infty} G_{R1T(jN)}(0,r;\omega)\,.
\end{aligned} \tag{A.12}$$

All terms other than $j = 0$ represent the effects of directional aliasing.

A general mathematical expression for $G_{RmTn}(r_1, r_2; \omega)$, in the presence of multiple modes of surface waves, is given in the work of Tada et al. (2009, eq. 18). Substituting that expression into Eq. (A.12), one obtains

$$\begin{aligned}
\hat{G}_{R1T0}(0,r;\omega) = -\pi^2 \sum_{j=-\infty}^{\infty} &\exp(ijN\pi/2) \\
\times \Bigg[\sum_{q=1}^{N^R} &(J_{jN-1} + J_{jN+1})(rk_q^R(\omega))\, f^R_{q/-jN+1}(\omega) \\
+ \sum_{q=1}^{N^L} &(J_{jN-1} - J_{jN+1})(rk_q^L(\omega))\, f^L_{q/-jN+1}(\omega) \Bigg].
\end{aligned} \tag{A.13}$$

In Eq. (A.13), $k_q^R(\omega) = \omega/c_q^R(\omega)$ represents the wavenumber of the qth-mode Rayleigh waves, whereas $f_{q/m}^R(\omega)$ denotes the mth-order component in the Fourier series expansion of the intensity-versus-arrival-azimuth profile of the qth-mode Rayleigh waves in horizontal motion—the component that undulates sinusoidally over m cycles during one rotation. The symbols $k_q^L(\omega)$ and $f_{q/m}^L(\omega)$ denote the Love-wave counterparts of $k_q^R(\omega)$ and $f_{q/m}^R(\omega)$.

For the sake of simplicity, we introduce two additional assumptions here: (vii) $N \geq 3$, and (viii) $f_{q/m}^R(\omega) = f_{q/m}^L(\omega) = 0$ for all $m \geq 2$ and $m \leq -2$. The latter assumption means that the intensity-versus-arrival-azimuth profile of the surface waves is made up only of a homogeneous (or isotropic) component ($m = 0$) plus dipolar components ($m = \pm 1$). These assumptions eliminate all terms with $j \neq 0$ in Eq. (A.13):

$$\hat{G}_{R1T0}(0,r;\omega) = 2\pi^2 \sum_{q=1}^{N^L} f^L_{q/1}(\omega)\, J_1(rk_q^L(\omega))\,. \tag{A.14}$$

Likewise, the estimate for the numerator is

$$\begin{aligned}
\hat{G}_{R1T0}(r,r;\omega) &= \hat{G}^{s}_{R1T0}(r,r;\omega) = \mathrm{CSD}[\hat{R}_1(t,r), \hat{T}_0(t,r)] \\
&= \mathrm{CSD}\left[\sum_{j=-\infty}^{\infty} R_{1+jN}(t,r), \sum_{l=-\infty}^{\infty} T_{lN}(t,r) \right] \\
&= \sum_{j,l=-\infty}^{\infty} \mathrm{CSD}[R_{1+jN}(t,r), T_{lN}(t,r)] \\
&= \sum_{j,l=-\infty}^{\infty} G_{R(1+jN)T(lN)}(r,r;\omega)\,.
\end{aligned} \tag{A.15}$$

All terms other than $j = l = 0$ represent the effects of directional aliasing. Substituting eq. (18) of Tada et al. (2009) into Eq. (A.15), one obtains

$$\begin{aligned}
\hat{G}_{R1T0}(r,r;\omega) = -\pi^2 \sum_{j,l=-\infty}^{\infty} &\exp\left[i(l-j)N\pi/2\right] \\
\times \Bigg[\sum_{q=1}^{N^R} &(J_{jN} - J_{jN+2})(rk_q^R(\omega)) \\
&\times (J_{lN-1} + J_{lN+1})(rk_q^R(\omega))\, f^R_{q/(j-l)N+1}(\omega) \\
+ \sum_{q=1}^{N^L} &(J_{jN} + J_{jN+2})(rk_q^L(\omega)) \\
&\times (J_{lN-1} - J_{lN+1})(rk_q^L(\omega))\, f^L_{q/(j-l)N+1}(\omega) \Bigg].
\end{aligned} \tag{A.16}$$

Assumptions (vii) and (viii) eliminate all terms other than $j = l$ in Eq. (A.16):

$$\hat{G}_{R1T0}(r,r;\omega) = -\pi^2 \sum_{q=1}^{N^R} f_{q/1}^R(\omega) \sum_{j=-\infty}^{\infty} (J_{jN} - J_{jN+2})(rk_q^R(\omega)) \times (J_{jN-1} + J_{jN+1})(rk_q^R(\omega)) - \pi^2 \sum_{q=1}^{N^L} f_{q/1}^L(\omega) \sum_{j=-\infty}^{\infty} (J_{jN} + J_{jN+2})(rk_q^L(\omega)) \times (J_{jN-1} - J_{jN+1})(rk_q^L(\omega)). \quad \text{(A.17)}$$

Finally, the estimate for the spectral ratio $\rho_{\mathrm{SPAC+L}}$, to be obtained by using the cross-spectral density estimates (A.14) and (A.17) in Eq. (A.10), is given by

$$\hat{\rho}_{\mathrm{SPAC+L}} = \frac{\hat{G}_{R1T0}(r,r;\omega)}{\hat{G}_{R1T0}(0,r;\omega)} = -\left[\sum_{q=1}^{N^R} f_{q/1}^R(\omega) \sum_{j=-\infty}^{\infty} (J_{jN} - J_{jN+2})(rk_q^R(\omega)) \times (J_{jN-1} + J_{jN+1})(rk_q^R(\omega)) + \sum_{q=1}^{N^L} f_{q/1}^L(\omega) \sum_{j=-\infty}^{\infty} (J_{jN} + J_{jN+2})(rk_q^L(\omega)) \times (J_{jN-1} - J_{jN+1})(rk_q^L(\omega)) \right] \Bigg/ \left[2\sum_{q=1}^{N^L} f_{q/1}^L(\omega) J_1(rk_q^L(\omega)) \right]. \quad \text{(A.18)}$$

In Eq. (A.18), all terms other than $j = 0$, involving Bessel functions of the third or higher orders (recall our assumption (vii) that $N \geq 3$), represent the effects of directional aliasing. Summations over q represent the effects of multiple modes. Both effects remain insignificant in low frequency ranges ($rk^R(\omega) = r\omega/c^R(\omega)$ and $rk^L(\omega) = r\omega/c^L(\omega)$ tend to zero when $\omega \to 0$). The point where they cease to be negligible defines the upper limit on the valid frequency range of the SPAC+L method.

To the extent that our assumptions stated in Section A.3 are valid, the effects of incoherent noise do not enter Eq. (A.18). It therefore remains beyond one's power, as long as one relies on the theoretical framework presented here, to evaluate how noise affects or limits the validity of the SPAC+L method.

A.5 Power Partition Ratio Estimation Method

The four power-spectral densities, which enter Eq. (7), are all subject to the effects of incoherent noise, and their magnitudes are given by Eqs (A.4), (A.5), (A.7), and (A.8). Let us introduce new symbols, $\varepsilon_Z(\omega)$ and $\varepsilon_H(\omega)$, for the noise-to-signal (NS) power ratios of the vertical and horizontal motions, respectively:

$$\varepsilon_Z(\omega) = \frac{f_Z(\omega)}{\sum_{q=1}^{N^R} |h_q(\omega)|^2 \; f_{q/0}^R(\omega)} \quad \text{(A.19)}$$

$$\varepsilon_H(\omega) = \frac{f_H(\omega)}{\sum_{q=1}^{N^R} f_{q/0}^R(\omega) + \sum_{q=1}^{N^L} f_{q/0}^L(\omega)}. \quad \text{(A.20)}$$

In Eqs (A.19)-(A.20), the quantities ${f_{q/0}}^R(\omega)$ and ${f_{q/0}}^L(\omega)$ correspond to the horizontal-motion intensity, in the most usual definition of the word, of the qth mode of Rayleigh and Love waves, respectively, whereas $|h_q(\omega)|$ denotes the vertical-to-horizontal amplitude ratio of the qth-mode Rayleigh waves. Using these symbols, the noise terms (see Eq. A.3) in the power-spectral density estimates may be rewritten as

$$\hat{G}_{Z0Z0}^n(0,0;\omega) = 4\pi^2 \varepsilon_Z(\omega) \sum_{q=1}^{N^R} |h_q(\omega)|^2 \; f_{q/0}^R(\omega) \quad \text{(A.21)}$$

$$\hat{G}_{Z1Z1}^n(r,r;\omega) = 4\pi^2 \frac{\varepsilon_Z(\omega)}{N} \sum_{q=1}^{N^R} |h_q(\omega)|^2 \; f_{q/0}^R(\omega) \quad \text{(A.22)}$$

$$\hat{G}_{R1R1}^n(0,0;\omega) = \pi^2 \varepsilon_H(\omega) \left[\sum_{q=1}^{N^R} f_{q/0}^R(\omega) + \sum_{q=1}^{N^L} f_{q/0}^L(\omega) \right] \quad \text{(A.23)}$$

$$\hat{G}_{R0R0}^n(r,r;\omega) = 2\pi^2 \frac{\varepsilon_H(\omega)}{N} \left[\sum_{q=1}^{N^R} f_{q/0}^R(\omega) + \sum_{q=1}^{N^L} f_{q/0}^L(\omega) \right]. \quad \text{(A.24)}$$

In the meantime, general mathematical expressions for $G_{ZmZn}(r_1, r_2; \omega)$ and $G_{RmRn}(r_1, r_2; \omega)$, in the presence of multiple modes, are presented in the works of Cho et al. (2006b, eqs 58-59) and Tada et al. (2009, eqs A7-A8). Using those formulas, and applying assumptions (vii) and (viii) that were described in Section A.4, we obtain the following expressions for the signal terms (see Eq. A.3) in the power-spectral density estimates:

$$\hat{G}_{Z0Z0}^s(0,0;\omega) = G_{Z0Z0}(0,0;\omega) = 4\pi^2 \sum_{q=1}^{N^R} |h_q(\omega)|^2 \; f_{q/0}^R(\omega) \quad \text{(A.25)}$$

$$\hat{G}_{Z1Z1}^s(r,r;\omega) = \sum_{j,l=-\infty}^{\infty} G_{Z(1+jN)Z(1+lN)}(r,r;\omega) = 4\pi^2 \sum_{q=1}^{N^R} |h_q(\omega)|^2 \; f_{q/0}^R(\omega) \sum_{j=-\infty}^{\infty} J_{jN+1}^2(rk_q^R(\omega)) \quad \text{(A.26)}$$

$$\hat{G}_{R1R1}^s(0,0;\omega) = G_{R1R1}(0,0;\omega) = \pi^2 \left[\sum_{q=1}^{N^R} f_{q/0}^R(\omega) + \sum_{q=1}^{N^L} f_{q/0}^L(\omega) \right] \quad \text{(A.27)}$$

$$\hat{G}^{s}_{R0R0}(r,r;\omega) = \sum_{j,l=-\infty}^{\infty} G_{R(jN)R(lN)}(r,r;\omega)$$
$$= \pi^2 \sum_{q=1}^{N^R} f^R_{q/0}(\omega) \sum_{j=-\infty}^{\infty} (J_{jN-1} - J_{jN+1})^2 (rk^R_q(\omega))$$
$$+ \pi^2 \sum_{q=1}^{N^L} f^L_{q/0}(\omega) \sum_{j=-\infty}^{\infty} (J_{jN-1} + J_{jN+1})^2 (rk^L_q(\omega)). \quad \text{(A.28)}$$

Directional aliasing terms ($j \neq 0$) appear in the estimates of $G_{Z1Z1}(r, r; \omega)$ and $G_{R0R0}(r, r; \omega)$, which use records around the circle (Eqs A.26 and A.28), but do not do so in the estimates of $G_{Z0Z0}(0, 0; \omega)$ and $G_{R1R1}(0, 0; \omega)$, which use records at the center alone (Eqs A.25 and A.27).

Adding up the signal terms and noise terms, we get

$$\hat{G}_{Z0Z0}(0,0;\omega) = \hat{G}^{s}_{Z0Z0}(0,0;\omega) + \hat{G}^{n}_{Z0Z0}(0,0;\omega)$$
$$= 4\pi^2 (1+\varepsilon_Z(\omega)) \sum_{q=1}^{N^R} |h_q(\omega)|^2 \; f^R_{q/0}(\omega) \quad \text{(A.29)}$$

$$\hat{G}_{Z1Z1}(r,r;\omega) = \hat{G}^{s}_{Z1Z1}(r,r;\omega) + \hat{G}^{n}_{Z1Z1}(r,r;\omega)$$
$$= 4\pi^2 \sum_{q=1}^{N^R} |h_q(\omega)|^2 \; f^R_{q/0}(\omega) \left[\sum_{j=-\infty}^{\infty} J^2_{jN+1}(rk^R_q(\omega)) + \frac{\varepsilon_Z(\omega)}{N} \right] \quad \text{(A.30)}$$

$$\hat{G}_{R1R1}(0,0;\omega) = \hat{G}^{s}_{R1R1}(0,0;\omega) + \hat{G}^{n}_{R1R1}(0,0;\omega)$$
$$= \pi^2 (1+\varepsilon_H(\omega)) \left[\sum_{q=1}^{N^R} f^R_{q/0}(\omega) + \sum_{q=1}^{N^L} f^L_{q/0}(\omega) \right] \quad \text{(A.31)}$$

$$\hat{G}_{R0R0}(r,r;\omega) = \hat{G}^{s}_{R0R0}(r,r;\omega) + \hat{G}^{n}_{R0R0}(r,r;\omega)$$
$$= \pi^2 \sum_{q=1}^{N^R} f^R_{q/0}(\omega) \left[\sum_{j=-\infty}^{\infty} (J_{jN-1} - J_{jN+1})^2 (rk^R_q(\omega)) + \frac{2\varepsilon_H(\omega)}{N} \right]$$
$$+ \pi^2 \sum_{q=1}^{N^L} f^L_{q/0}(\omega) \left[\sum_{j=-\infty}^{\infty} (J_{jN-1} + J_{jN+1})^2 (rk^L_q(\omega)) + \frac{2\varepsilon_H(\omega)}{N} \right]. \quad \text{(A.32)}$$

Finally, the estimate for the power share of Rayleigh waves, $\gamma^R(\omega)$, to be obtained by using the power-spectral density estimates (A.29)-(A.32) in Eq. (A.7), is given by

$$\hat{\gamma}^R(\omega) = \frac{\hat{G}_{Z0Z0}(0,0;\omega)\,\hat{G}_{R0R0}(r,r;\omega)}{4\hat{G}_{Z1Z1}(r,r;\omega)\,\hat{G}_{R1R1}(0,0;\omega)}$$
$$= \frac{1+\varepsilon_Z(\omega)}{1+\varepsilon_H(\omega)}$$
$$\times \left[\frac{\sum_{q=1}^{N^R} f^R_{q/0}(\omega) \sum_{j=-\infty}^{\infty} (J_{jN-1} - J_{jN+1})^2 (rk^R_q(\omega))}{4\left(\sum_{q=1}^{N^R} f^R_{q/0}(\omega) + \sum_{q=1}^{N^L} f^L_{q/0}(\omega) \right)} + \frac{\varepsilon_H(\omega)}{2N} \right]$$
$$+ \frac{\sum_{q=1}^{N^L} f^L_{q/0}(\omega) \sum_{j=-\infty}^{\infty} (J_{jN-1} + J_{jN+1})^2 (rk^L_q(\omega))}{4\left(\sum_{q=1}^{N^R} f^R_{q/0}(\omega) + \sum_{q=1}^{N^L} f^L_{q/0}(\omega) \right)} + \frac{\varepsilon_H(\omega)}{2N} \Bigg]$$
$$\Bigg/ \left[\frac{\sum_{q=1}^{N^R} |h_q(\omega)|^2 \; f^R_{q/0}(\omega) \sum_{j=-\infty}^{\infty} J^2_{jN+1}(rk^R_q(\omega))}{\sum_{q=1}^{N^R} |h_q(\omega)|^2 \; f^R_{q/0}(\omega)} + \frac{\varepsilon_Z(\omega)}{N} \right]. \quad \text{(A.33)}$$

In Eq. (A.33), all terms other than $j = 0$, involving Bessel functions of the second or higher orders, represent the effects of directional aliasing. Summations over q represent the effects of multiple modes. The effects of incoherent noise enters Eq. (A.33) by way of the NS ratios, $\varepsilon_Z(\omega)$ and $\varepsilon_H(\omega)$.

The effects of directional aliasing and multiple modes remain insignificant in low frequency ranges, and the point where they cease to be negligible defines the upper bound on the valid frequency range of the γ^R estimation method.

The effects of incoherent noise, on the contrary, are the most significant in low frequency ranges. The point where $J_1(rk^R(\omega))$ of the fundamental-mode Rayleigh waves becomes so small that $\varepsilon_Z(\omega)/N$ and $\varepsilon_H(\omega)/N$ are no longer negligible in comparison to $J_1^2(rk^R(\omega))$ defines the lower bound on the valid frequency range of the γ^R estimation method. Using the asymptotic expression for the Bessel function $J_1(\cdot)$ near a zero argument, this lower bound may be redefined as the frequency ω that satisfies

$$\frac{(rk^R(\omega))^2}{4} \approx \max\left(\frac{\varepsilon_Z(\omega)}{N}, \frac{\varepsilon_H(\omega)}{N} \right). \quad \text{(A.34)}$$

A.6 Stochastic Uncertainties

The quantities given by Eqs (4) and (7) should be subject to a fourth category of error factors, namely stochastic uncertainties arising from the finite length of available data (Section 2.4).

Tada et al. (2007) presented theoretical expressions for the magnitude of stochastic uncertainties with respect to a number of spectral ratios used in circular-array microtremor techniques. Their theoretical framework, however, works only for ratios of two power-spectral densities. Using a different approach, Cho et al. (2008) derived a mathematical expression for the magnitude of stochastic uncertainties accompanying the SPAC coefficient, a quantity playing a central role in the SPAC method. The SPAC coefficient has the form of a cross-spectral density divided by a power-spectral density.

Theorization remains yet to be done, however, for a ratio of two cross-spectral ratios, like Eq. (4), and for a ratio involving four power-spectral ratios, like Eq. (7).

JOINT CONFERENCE PROCEEDINGS
7th International Conference on Urban Earthquake Engineering (7CUEE) &
5th International Conference on Earthquake Engineering (5ICEE)
March 3-5, 2010, Tokyo Institute of Technology, Tokyo, Japan

A STUDY ON ARRAY MICROTREMORS SURVEY WITH MOTIONS GENERATED BY 3D FINITE ELEMENT MODELS WITH IRREGULAR BEDROCK

Huei-Tsyr Chen[1], Jun-An Wei[2], and Hitoshi Morikawa[3]

1) Professor, Department of Civil Engineering, National Central University, Taiwan
2) Graduate Student, Department of Civil Engineering, National Central University, Taiwan
3) Associate Professor, Department of Built Environment, Tokyo Institute of Technology, Japan
chenht@cc.ncu.edu.tw, Morika@enveng.titech.ac.jp

Abstract: When AMS is adopted to characterize the shear wave velocity profile of a site, a theoretical dispersion curve of 1D soil stratum is used; however, in reality, the ground structure of a target site may not be so. In this study, a three-dimensional finite element method is employed to simulate the microtremors of a soil stratum underlain by irregular (protruding) bedrock to investigate the validity of applying 1D theoretical dispersion curve to determining the soil profile of an irregular soil stratum. From the study it is found that if the area of an array is smaller than that of protruding rock and the soil boring data is obtained just outside of the protruding rock, use of 1D theoretical dispersion curve model as a basis for inversion will lead to a soil profile which is very different from the real one. The differences in surface ground motions between the real and the inversed soil stratum with Ricker wavelet as input motion may result from the configuration of the bedrock and the differences in the number of soil layers and shear wave velocity profile. Thus, to characterize the soil profile more accurately, two or more geophysical means should be adopted.

1. INTRODUCTION

It has been well known through theoretical analyses and field observations that not only the near-surface soil deposits but also the configurations of deep underground bedrock structures affect the surface ground motions during the earthquakes. Thus, it becomes a common consensus that to realistically estimate the effects of strong earthquakes, the three-dimensional underground structure of a target site should be identified as accurately as possible. The gravity anomaly is frequently adopted to identify the configuration of deep underground structure (Morikawa et al. 2007) which is then followed by the characterizing the shear wave velocity profile of the near surface soil deposit using geophysical approaches (Goto et al. 2005, Morikawa et al. 2008).

Many geophysical means have been developed to determine the shear wave velocity profile such as soil boring, PS well logging, seismic refraction method, seismic reflection method, microtremor measurement, etc. Each method has its own merits and disadvantages. Among them, microtremor measurement has been frequently employed nowadays due to easy operation, low cost and friendly to environment. When microtremor measurement is adopted to characterize the shear wave velocity profile of a soil stratum, it is arranged in a predefined array, called Array Microtremor Survey (AMS). It uses the fact that the microtremors which are feeble ground motions due to man-made activities and natural phenomena and consists of mainly surface wave which is dispersive. The dispersion curve of Rayleigh wave extracted from the AMS will be established using either F-K spectrum method (Capon 1969) or spatial auto-correlation method (SPAC) (Aki 1957). This observed dispersion curve is then used as the basis for comparing with the inversed result which uses the theoretical dispersion curve for 1D soil stratum (Haskell 1953). There are abundant of papers and reports on the use of AMS to characterize of shear wave velocity profile of soil and for more information on AMS readers may refer to a series paper by Tokimatsu et al. [1991,1992a, 1992b] where the name of Rayleigh wave method is used.

For the inversion process to determine the shear wave velocity profile a theoretical formulation based on 1D soil stratum is used; however, in reality, the ground structure of a target site may not be so. In this study, a three-dimensional finite element method is employed to simulate the microtremors of a soil stratum underlain by irregular (protruding) bedrock. These results are then used to generate dispersion curve by using spatial auto-correlation method. Finally through forward inversion process, the validity of applying 1D theoretical dispersion curve to determining the soil profile of an irregular soil stratum is investigated.

2. METHOD OF ANALYSIS

2.1 Generation of Surface Ground Motion

Despite that there may be scattering soil boring data, the subsurface conditions of a large area are in general unknown and it would be very difficult to use the data of AMS recorded in the field to achieve the goal of this paper. A heuristic thinking may be to adopt a numerical approach to generate the surface ground motions which are then used as the measured microtremors for generating the dispersion curve. The advantage for this approach is that the soil profile generating the surface ground motions is exactly known which can then be used as the benchmark for verifying the soil profile determined through the inversion process.

As a result, in this study we adopted a linearly elastic three-dimensional finite element method to generate the surface ground motions at nodes which are arranged in the form of double concentric equilateral triangles. Within a specified region on the surface, a concentrated load of unity was applied at a node which was determined by using the random number generator to simulate the randomly applied load. The surface ground motions at these nodes were taken as microtremors and the vertical components of these motions were then used for establishing the dispersion curve.

2.2 Spatial Auto-Correlation Method

In this study the dispersion curve was obtained by using the spatial auto-correlation method developed by Aki [Aki 1957]. From the derivation, it can be seen that the array is arranged in circular shape; however, in application an equilateral triangle is frequently adopted. For N stations $S_i(r,\theta_i)$ (i=1,2,…,N) on the periphery and the station at the center O(0,0), a relation shown in Eq. 1 can be obtained.

$$\overline{\rho(r,\omega)} = \frac{1}{N}\sum_{i=1}^{N}\rho_{OS_i}(r,\omega_0) = J_0\left(\frac{\omega r}{C(\omega)}\right) \quad (1)$$

where $\overline{\rho}$ is the average of auto-correlation coefficients over the azimuth angles, $C(\omega)$ is the phase velocity at frequency ω, J_0 is the zero-order Bessel function of first kind and ρ is defined as

$$\rho(r,\omega) = \frac{\phi(r,\omega)}{\phi(0,\omega)} \quad (2)$$

and

$$\phi(r,\omega) = \frac{1}{T}\int_0^T v_O(t)v_{S_i}(t)dt \quad (3)$$

where $\varphi(r,\omega)$ is the auto-correlation equation between the stations on the periphery and center and V_{si} and V_o are the measured microtremors at station i on the periphery and the center, respectively. With the above equations the phase velocity associated with each frequency can then be calculated and plotted in the form of dispersion curve.

2.3 Summary of Procedures

The processes adopted in this study are summarized as follows.

1. Pair two stations where the angle between the stations is 60 or 120 degrees and the distance between the stations is the same. The set of such pairs is called a "sub-array", which includes three different directions at least and each pair has the same distance.
2. Calculate the spatial auto-correlation (SPAC) coefficients for each pair of stations.
3. Average the SPAC coefficients obtained from all directions for each sub-array.
4. Estimate the phase velocities from the SPAC coefficients for each sub-array using grid search technique.
5. Select the good portions of phase velocities obtained from each sub-array and merge them into one dispersion curve.
6. Conduct forward inversion analysis to obtain the shear wave velocity profile.

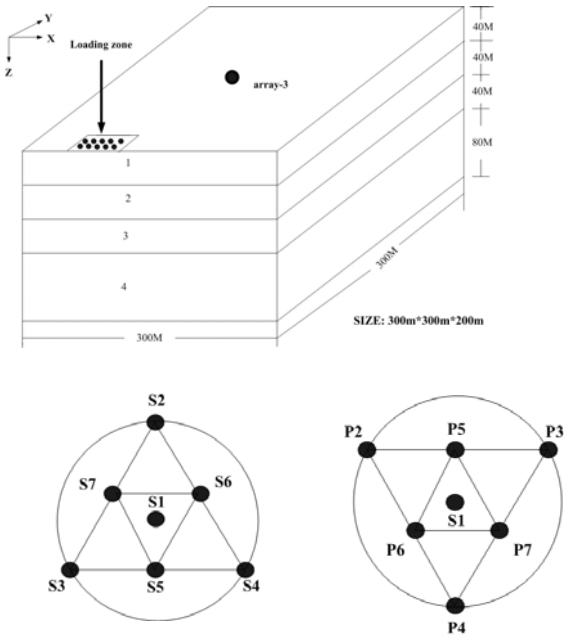

Figure 1 Finite element model and array arrangement

3. RESULTS AND DISCUSSIONS

3.1 Model Description

Shown in Figure 1 is the three-dimensional finite element model adopted in this study. It is a 4-layer soil stratum underlain by rigid rock and along the four lateral sides the viscous boundaries are assigned. The size of the model is 300m x 300m x 100m and that of an element is 10m x 10m x10m which is based on our computational capability. The properties of this 4-layer soil stratum are shown in Table 1. For the case of irregular bedrock, a protruding rock was set at the center of the model. Three cases were considered: 200m x 200m x 30m, 100m x 100m x 30m and 60m x 60m x 30m. That is, only the area was changed while the height was not varied. Shown in Figure 2 is the cross-sectional view of the model 60m x 60m x 30m cut from the center of the model.

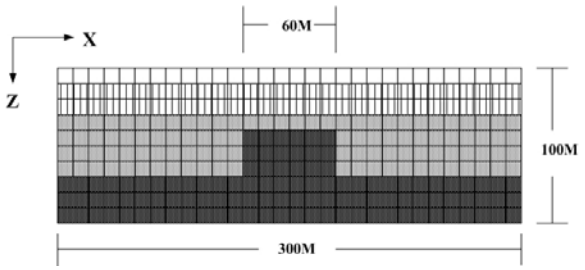

Figure 2 Side view of 4-layer model with protruding bedrock at the center of model

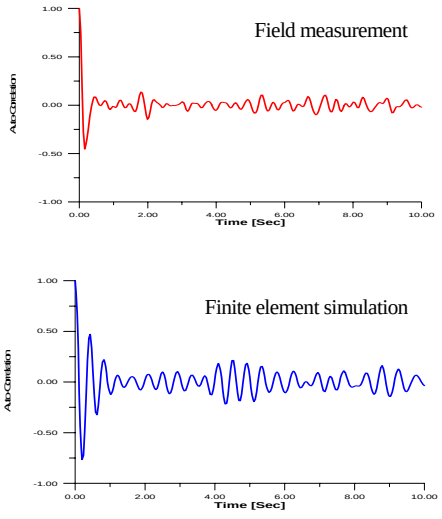

Figure 3 Auto-correlation for field motion and motion of finite element simulation

The dot on the surface of the model shown in Figure 1 is the site where microtremor measurement was made. The configuration of the array arrangement is also shown in the figure which is concentric double equilateral triangles with both triangles lying on the periphery of an outer circle and an inner circle. In this study, we adopted two arrangements: one has the outer diameter of 80m and inner diameter of 40m with station prefix s, denoted as M-array, and the other has the outer diameter of 70m and inner diameter of 30m with station prefix p, denoted as S-array. Figure 1 also shows these two arrangements. In our pilot analysis, it showed that good results can be obtained if the distance between the center of each array and the loading zone is more than 100m and thus, for both arrays, we took the distance as 140m.

Near the edge of the model a loading zone of 20 nodes was specified so that a concentrated load of unity can be applied at the nodes within it; the random application of the load at a node is determined by random number technique. The load was applied at 0.01-second interval for a period of 25 seconds. Figure 3 compares auto-correlation functions of the motion measured in the field and that of numerical simulation and the trend is very similar.

Table 1 Soil properties of original model

Layer	V_p (m/sec)	V_s (m/sec)	ρ (t/m^3)	Thickness (m)
1	937	450	1.8	10
2	1145	550	1.9	20
3	1353	650	1.95	40
4	2498	1200	2.0	30

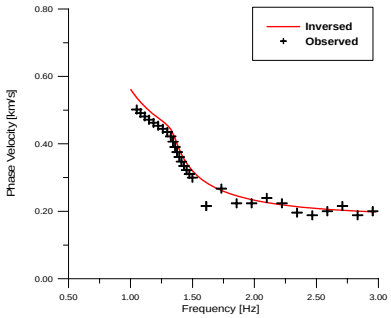

Figure 4 Dispersion curves of observed motions and inversion for regular soil stratum

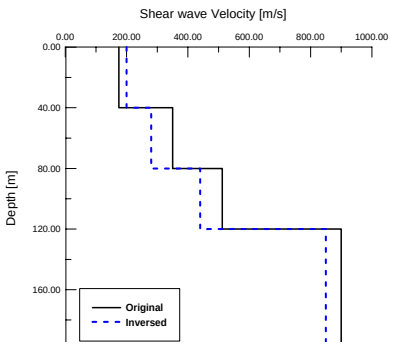

Figure 5 Original and Inversed soil profile for regular soil stratum

3.2 Verification of the Present Approach

In checking the validity of present approach, a case with flat bedrock was adopted. The dispersion curves from the simulated motions and that from forward inversion are shown in Figure 4 and Figure 5 shows the original and the inversed soil shear velocity profiles. Good agreement can be observed. Thus, it indicates the validity of applying AMS to determining the shear wave velocity profile of a horizontally layered soil stratum and that of present approach.

3.3 Discussions

As mentioned previously, in the study of soil stratum with protruding bedrock, three cases were considered. The soil properties described in Table 1 was treated as the soil boring data of the borehole which is just outside of the protruding bedrock. In this table and the tables to be appeared in the following discussions, V_p denotes the compressive velocity, V_s shear wave velocity, ρ the mass density of soil. The set of properties given in Table 1was used as the data of initial trial for the forward inversion analysis. In each figure of dispersion curve, there are four curves. The curve labeled as "observed" is obtained from the simulated microtremors. The curve labeled as "inversion" is obtained from forward inversion analysis, permitting to change the number of soil layers, layer thickness and shear velocity of each layer. The curve labeled as "borehole 1" is the theoretical dispersion curve computed using the soil properties described in Table 1 and that labeled as "borehole 2" is the dispersion curve where the forward inversion is performed by changing the shear velocity of each layer while keeping soil mass density, number of soil layers and layer thickness constant. It should be pointed out that the inversed soil profile is underlain by flat bedrock.

Figure 6 shows the dispersion curves for the case 200m x 200m x 30m and Tables 1, 2 and 3 are the soil properties from borehole data, "borehole 2" and "inversion", respectively. The shape of dispersion curves for "borehole 1" and "borehole 2" are very different from that of "observed". The inversed soil profile, although its dispersion curve can give good agreement with that of "observed", the soil profile is completely different from the original one. Similar trend can also be seen for the case 100m x 100m x 30m. Shown in Figure 7 are the dispersion curves for the case 60m x 60m x 30m and Tables 1, 4 and 5 are the soil properties from borehole data, "borehole 2" and "inversion", respectively. In this case the areas of M-array and S-array are larger than that of protruding rock. The shape of dispersion curve for "borehole 1" is nearly parallel to that of "observed" with not much difference. The dispersion curve of "Borehole 2" coincides with that of "inversion", indicating that only adjustment in the shear velocity is needed for this case. From the above discussions, it can be seen that if the area of an array is smaller than that of protruding rock and the soil boring data is obtained just outside of the protruding rock, use of 1D theoretical dispersion curve model as a basis for inversion will lead to a soil profile which is very different from the real one.

To further investigate the differences in the ground motions between the real and the inversed soil stratum, a Ricker wavelet was applied at the bottom of the finite element model for all three directions simultaneously. Figure 8 presents the acceleration response spectrum in the y direction at station S1 which is the center of the array. The inversed soil stratum has larger response for period less than period of 0.5 seconds and smaller response between the period of 0.5 seconds and 1.5 seconds, as compared with the original soil stratum. Such differences may result from the configuration of the bedrock and the differences in the number of soil layers and shear wave velocity profile.

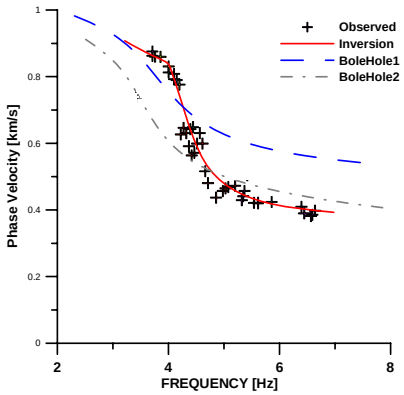

Figure 6 Dispersion curves obtained from different inversion processes for case 200m x 200m x 30m

Table 2 Soil properties of inversed model ("Bohole2") for case200m x 200m x30m

Layer	V_p (m/sec)	V_s (m/sec)	ρ (t/m^3)	Thickness (m)
1	625	300	1.8	10
2	937	450	1.9	20
3	1249	600	1.95	40
4	2498	1200	2.0	30

Table 3 Soil properties of inversed model ("Inversion") for case 200m x 200m x30m

Layer	V_p (m/sec)	V_s (m/sec)	ρ (t/m^3)	Thickness (m)
1	833	450	1.8	40
2	2498	550	2.0	60

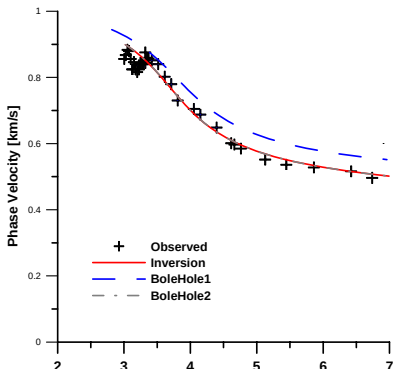

Figure 7 Dispersion curves obtained from different inversion processes for case 60m x 60m x 30m

Table 4 Soil properties of inversed model ("Bohole2") for case 60m x 60m x30m

Layer	V_p (m/sec)	V_s (m/sec)	ρ (t/m^3)	Thickness (m)
1	625	300	1.8	10
2	937	450	1.9	20
3	1249	600	1.95	40
4	2498	1200	2.0	30

Table 5 Soil properties of inversed model ("Inversion") for case 60m x 60m x30m

Layer	V_p (m/sec)	V_s (m/sec)	ρ (t/m^3)	Thickness (m)
1	833	400	1.8	10
2	1041	500	1.9	20
3	1312	630	1.95	40
4	2498	1200	2.0	30

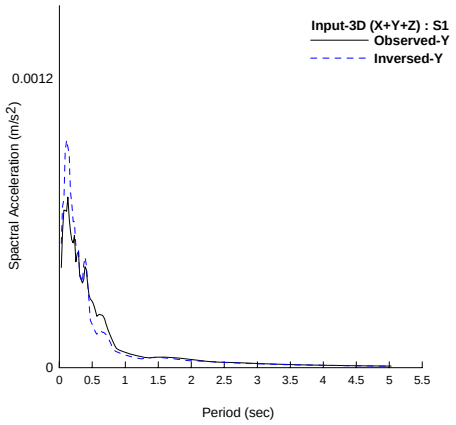

Figure 8 Acceleration response spectrum for station S1 for original and inversed models

4. CONCLUSIONS

When AMS is adopted to characterize the shear wave velocity profile of a site, the inversion process uses a theoretical dispersion curve of 1D soil stratum; however, in reality, the ground structure of a target site may not be so. In this study, a three-dimensional finite element method is employed to simulate the microtremors of a soil stratum underlain by irregular (protruding) bedrock to investigate the validity of applying 1D theoretical dispersion curve to determining the soil profile of an irregular soil stratum. From the study it is found that if the area of an array is smaller than that of protruding rock and the soil boring data is obtained just outside of the protruding rock, use of 1D theoretical dispersion curve model as a basis for inversion will lead to a soil profile which is very different from the real one. The differences in surface ground motions between the real and the inversed soil stratum with Ricker wavelet as input motion may result from the configuration of the bedrock and the differences in the number of soil layers and shear wave velocity profile. Thus, to characterize the soil profile more accurately, two or more geophysical means should be adopted.

References:

Aki, K. (1957), "Space and Time Spectra of Stationary Stochastic Waves with Special Reference to Microtremors," Bulletin of Earthquake Research Institute, Tokyo University, 35, 415-456.

Capon, J. (1969), "High-Resolution Frequency-Wavenumber Spectrum Analysis," Proc. IEEE, 57(8), 1408-1418.

Goto, H., Sawada, S., Morikawa, H., Kiku, H. and Ozalaybey S. (2005), "Modeling of 3D Subsurface and Numerical Simulation of Strong Ground Motion in Adapazari Basin During the 1999 Kocaeli Earthquake, Turkey," Bulletin of the Seismological Society of America, 95(6), 2197-2215.

Haskell, N.A. (1953), "The Dispersion of Surface Waves on Multilayered Media," Bulletin of the Seismological Society of America, 41(1), 17-34.

Morikawa, H., Komazawa, M., Chen, H.T., Shosaka, T. and Takahashi, C. (2007) "A Model of Bedrock Structure for HsinChu Basin, Taiwan Using Gravity Survey," Proceedings of 4th International Conference on Urban Earthquake Engineering, Tokyo, March 5-6, 227-230.

Morikawa, H., Chen, H.T., Takahashi, C., Kawatsure, H. and Komazawa, M. (2008), "Detailed Study on Ground Structure around Hsinchu City, Taiwan using Gravity and Microtremors," Proceedings of 5th International Conference on Urban Earthquake Engineering, Tokyo, March 4-5, 89-94.

Tokimatsu, K., Kuwayama, S., Tamura, S. and Miyadera, Y. (1991), "V_s Determination from Steady State Rayleigh Wave Method," Soils and Foundations, 31(2), 153-163.

Tokimatsu, K., Tamura S. and Kojima, H. (1992a), "Effects of Multiple Modes on Rayleigh Wave Dispersion Characteristics," Journal of Geotechnical Engineering, ASCE, 118(10), 1529-1543.

Tokimatsu, K., Shinzawa K. and Kuwayama, S. (1992b), "Use of Short Period Microtremors for V_s Profiling," Journal of Geotechnical Engineering, ASCE, 118(10), 1544-1558.

EVALUATION OF SITE EFFECTS IN THE ONIKOBE BASIN IN MIYAGI PREFECTURE, FROM GROUND MOTION DATA FROM AFTERSHOCKS OF THE IWATE-MIYAGI NAIRIKU EARTHQUAKE IN 2008 AND MICROTREMOR MEASUREMENTS

Kentaro Motoki[1)], Hiroaki Yamanaka[2)], Kazuoh Seo[3)] and Haruhiko Suzuki[4)]

1) Assistant Professor, Dept. of Built Environment, Tokyo Institute of Technology, Japan
2) Associate Professor, Dept. of Environmental Science and Technology, Tokyo Institute of Technology, Japan
3) Professor, Dept. of Built Environment, Tokyo Institute of Technology, Japan
4) Tokyo Technical Center, Oyo Corporation, Japan
kmoto@enveng.titech.ac.jp, yamanaka@depe.titech.ac.jp, seo@enveng.titech.ac.jp, suzuki-haruhiko@oyonet.oyo,co.jp

Abstract: A disastrous earthquake with Mjma of 7.2, Iwate-Miyagi Nairiku earthquake, Japan, occurred in 2008. Noticeable earthquake motion records at the 2 sites where are not 10 km far from each other were observed in the Onikobe area, Miyagi prefecture. Long period ground motions predominated at the one site, and the PGV at this site is 3 times more than the other one. We conducted aftershock observation and microtremor measurements in Onikobe to understand how the earthquake motions were amplified from the view point of the effects of surface geology for the Onikobe area. The aftershock motions were observed significantly high amplitude in Onikobe basin. The spectral ratios against the record at the rock site show that the predominant periods are around 3 seconds. This predominant period can be confirmed in the H/V spectral ratio of the microtremors. But the predominant period cannot be explained with the S-wave velocity profile estimated with microtremor array exploration. Addition to it, the amplification factor evaluated with observed motions is much higher than calculated transfer function by 1-D S wave analysis. It can be interpreted that the site amplification is affected not only by the 1-D structure, but also by the effects of the irregular structure.

1. INTRODUCTION

The Iwate-Miyagi Nairiku earthquake in 2008 with an Mj of 7.2 is an inland earthquake took place by an active fault. The damage during this earthquake is mostly damage by land failures (Fire and Disaster Management Agency, 2009). The damage of houses by earthquake motions is not so much for an Mj of 7.2. Very high amplitude acceleration was recorded about 4 times of gravity acceleration in vertical component near the source region (Aoi et. al., 2008). Addition to it, noticeable earthquake records at the 2 sites where are not 10 km far from each other were observed in the Onikobe area, Miyagi prefecture. Long period ground motions predominated at the one site, and the PGV at this site is 3 times more than the other one. The velocity amplitude in Onikobe area is higher than those near the source region including a 4G record.

We conducted aftershock observation and microtremor measurements in Onikobe to understand how the earthquake motions were amplified from the view point of the effects of surface geology for the Onikobe area.

2. CHARACTERISTICS of EARTHQUAKE MOTIONS around the PREDOMINANT PERIOD

The station of K-NET at Onikobe MYG005 has successfu-lly observed high amplitude earthquake motions for several times. Figure 1 shows velocity waveforms and pseudo velocity response spectra with 5 % damping listed in TABLE 1. The EQ6 is the Iwate-Miyagi Nairiku Earthquake. These waveforms are normalized with maximum amplitude. The later phases are remarkable in each earthquake and rather long period motions are dominant for long duration in each earthquake. The predominant periods of these earthquake can be seen at 3 seconds from response spectra. The response value around 3 seconds during the 2008 Iwate-Miyagi Nairiku Earthquake are prominent and the highest at Onikobe comparing with all records.

Next, the characteristics of earthquake motions were examined in terms of epicentral azimuth using aftershocks of the 2008 Iwate-Miyagi Nairiku Earthquake. Figure 2 shows the variance of predominant periods with epicentral azimuth. The azimuth indicates the clockwise angle from the north in degree. The predominant period are derived from horizontal spectral ratio at MYG005 against

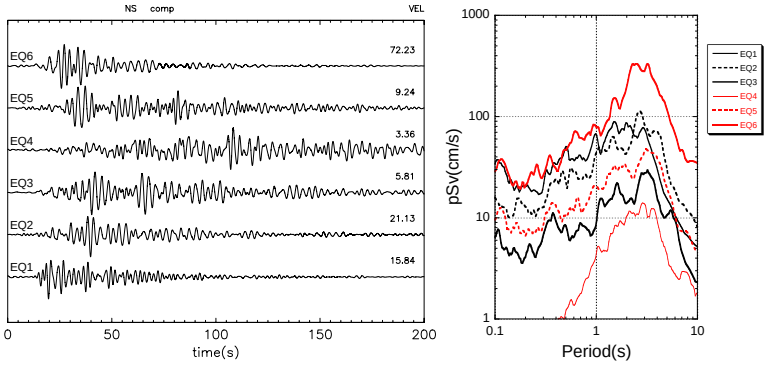

Figure 1 Velocity waveforms (left) and pseodo velocity response spectra (right), which recorded at MYG005 during past earthquakes

Table 1 List of the earthquakes used in Fig.1

	Date	D(km)	M
EQ1	1996/8/11	7	5.9
EQ2	2003/5/26	71	7
EQ3	2003/7/26	12	6.2
EQ4	2003/9/26	45	8
EQ5	2005/8/16	42	7.2
EQ6	2008/6/14	8	7.2

MYGH02, where is rock site. The predominant period is related to an arrival direction of seismic waves. The similar examination were conducted for magnitudes and depths of an earthquake, and the predominant periods have little correlation to them. The phenomena of variable predominant period depending on epicentral azimuths imply that the shape of the subsuface structure of the basin makes a difference in predominant period and it appears as the consequence of the 3 dimensional effect of the basin.

3. AFTERSHOCK OBSERVATION and MICROTREMOR MEASUREMENTS

The observation of ground motion during aftershocks was conducted in the Onikobe basin. The locations of the temporary stations in the aftershock observation are shown in Figure 3. The equipment was arranged to fill between MYG005 (K-NET site) and MYGH02 (KiK-net site) with from 03 to 07 stations. The stations of 03, 04, 05 and MYG005 are located on the Onikobe basin and the stations of 06 and 07 correspond to near the edge of this basin. Only 08 station was installed on the other area where 25 percents of tomb stones, which is the highest ratio around the Onikobe area, were overturned. Onikobe basin forms a caldera around Mt. Araodake and Araogawa river flows there. The caldera is covered with Quaternary soils over Tertiary rock that exists outside of the Onikobe and Mt. Araodake3). At each station, an accelerometer and a 24 bit-digital recorder were installed on the surface. Ground motions were recorded continuously from 18th, June to 5th, July and sampled with 100Hz. The ground motions during the aftershocks were picked up based on earthquake information provided by Hi-net and magnitudes of the earthquakes used in this study are larger than 2.8, because earthquake motions were buried under microtremors during smaller events. The data set of 18 earthquakes is used and the epicenters of these earthquakes are shown in right figure of Figure 3.

The Microtremors were recorded at MYG005 continuously while other mobile measurements and for 5 minutes at other stations. The instruments were used a same type of the accelerometer for aftershock observation as mentioned above. The purpose of microtremor measurements is to understand the spatial distribution of the effects of surface geology of Onikobe basin. The measurement points are set to cover all Onikobe basin and the distances from adjacent points are around 1 km as shown in Figure 4 with crosses.

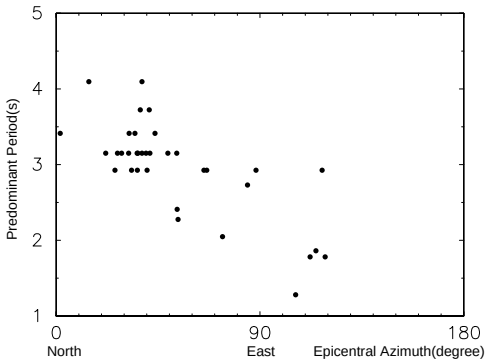

Figure 2 Variation of predominant periods relative to epicentral azimuth

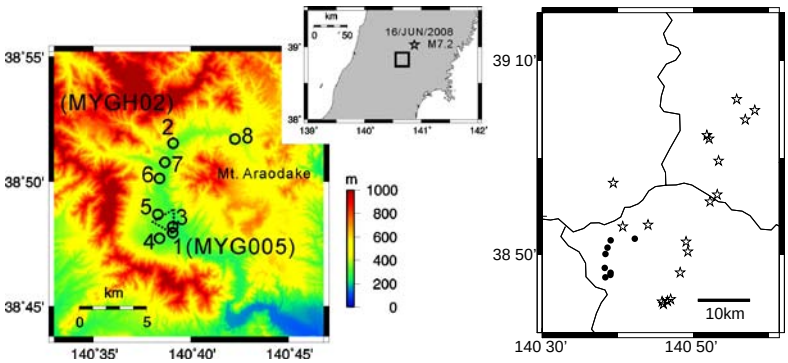

Figure 3 Station map for the aftershock observation (left), and the distribution of the epicenter of the aftershock used in this study (right)

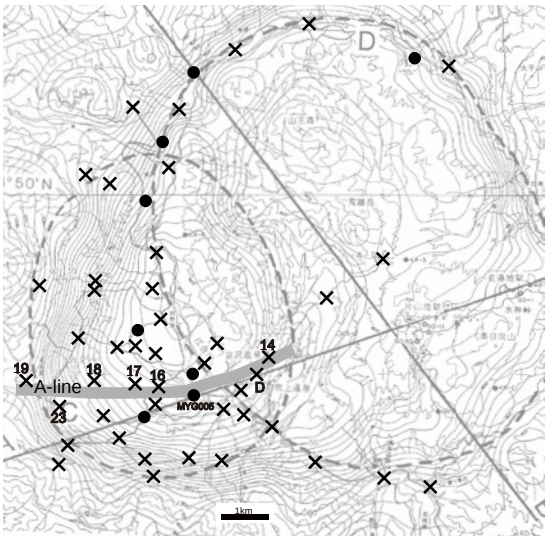

Figure 4 Distribution map of microtremor measurements points and Bourguer anomaly evaluated by Komasama and Murata(1988)

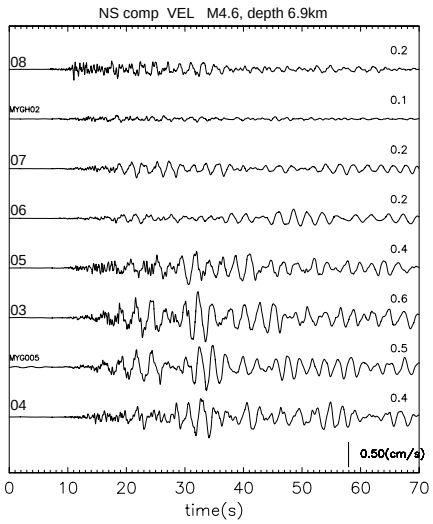

Figure 5 Velocity waveforms of an Mj of 4.6

4. CHARACTERISTICS of AFTERSHOCK MOTIONS

Velocity waveforms recorded for one of the events with an Mj of 4.6 are displayed in Figure 5. These are integrated from the original accelerations and filtered with a highpass filter having a cut-off frequency of 0.1 Hz. It can be seen that the later phase at on the Onikobe basin is amplified comparing with the earthquake motion at MYGH02, 06 and 07. The amplitudes on the Onikobe basin are much higher than those of others. The amplitude at MYGH02 is the lowest of all stations and same for the other earthquakes. In this study, MYGH02 is regarded as a reference point to estimate the effects of surface geology. The differences of seismic intensity in JMA scale from MYGH02 are calculated as shown in Figure 6(a). The seismic intensity was a maximum at 08 and the differences are between 0.6 and 0.8 on the Onikobe basin. The ratio of the peak ground velocity (PGV) is also displayed in Figure 6 (b). The ratio of non-filtered PGV at 08 is the highest similar to seismic intensity and that at other stations is low. The ratio of PGV filtered in a frequency range from 0.1 to 1.0 Hz is larger on the Onikobe basin than that at other stations. The difference of seismic intensity shows a distribution that has a characteristic of both of non-filtered PGV and filtered PGV and seismic intensity is partically affected by a high frequency motions. The geometrical averages of the ratio of the Fourier Spectra of the horizontal component (H/H ratio hereafter) against records at MYGH02 are shown in Figure 7. The Fourier spectra were calculated with the data for about 40 seconds from S-wave arrivals. The H/H ratio has similar feature having peaks in a period range from 2 to 3 seconds. However, the amplitude of the ratio on the Onikobe basin is higher than those of other sites. The variance in the peak periods from each other is the smaller than that in the amplitude of the ratio. High frequency component is dominant at 08 and it can be inferred that it is the cause of the local effect.

The comparison of the observed H/H ratio to

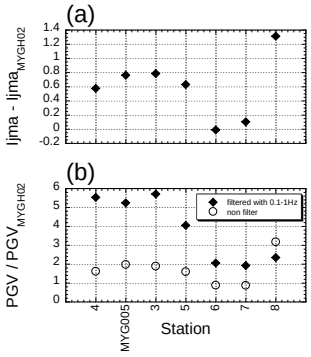

Figure 6 Distribution of (a) difference of seismic intensity and (b) ratio of PGV

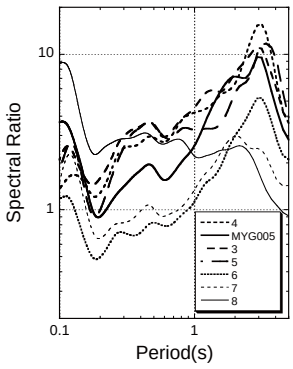

Figure 7 H/H spectral ratio against records of MYGH02

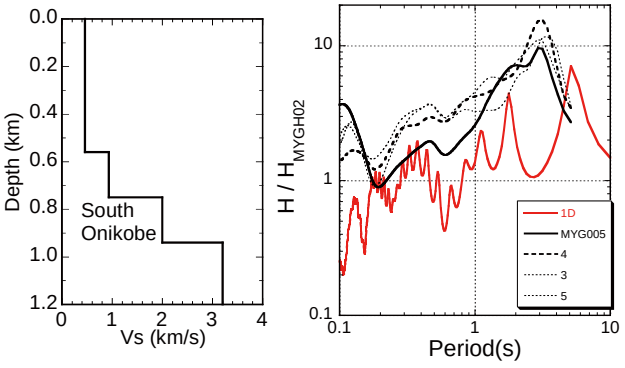

Figure 8 Subsurface structure model evaluated by Yamanaka et. al. (2008) (left), and the comparison of amplification factor betwee evaluated from aftershock motions and 1-D analysis (right)

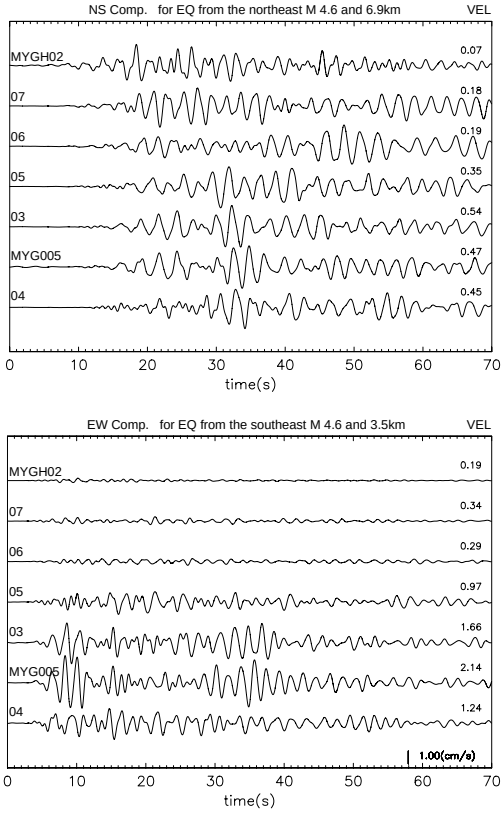

Figure 9 Velocity waveforms of earthquakes from the northeast direction (upper) and the southeast direction (lower)

theoretical amplification estimated with the subsurface structure model evaluated by Yamanaka et. al. (2008) is shown in Figure 8. For the MYGH02, S wave profile provided by KiK-net is used for this calculation. The microtremor array site is around the center of the Onikobe basin near the MYG005, 03, 04 and 05 stations. The amplification by the 1-D analysis is smaller and the 1st predominant period is longer than that evaluated from the aftershock records. It can be considered that the predominant period is shortened because surrounding hard rock restricts the motions of the Onikobe basin. And the seismic waves are trapped in the Onikobe basin by surrounding hard rock. Therefore the Onikobe basin was more amplified than due to the 1-D structure.

In the former section, it mentioned that a predominant period during earthquake depends on an epicentral azimuth. The feature of wavefield influenced by an epicentral azimuth is shown, noticing the difference in later phase in this section. Figure 9 shows waveforms during earthquakes of which epicenters are located to the northeast and the southeast direction from the Onikobe. Significant later phases can be seen in both earthquakes. However, despite the southeast earthquake is nearer than another, it takes more time to arrive these later phases from the first S-wave arrivals. This feature can be seen in other earthquakes, and suggest that the arrival direction of seismic waves relates to how to amplify earthquake motions. Figure 10 shows the result of the Sembrance

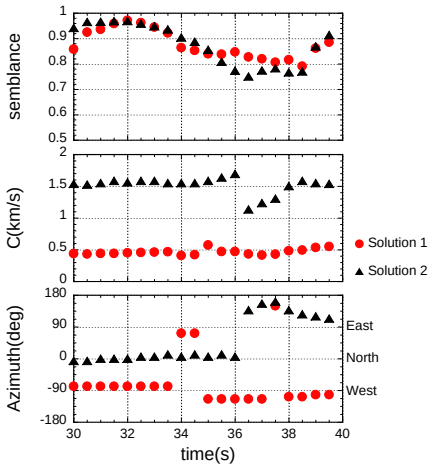

Figure 10 Result of Sembrance analysis for the earthquake from the northeast direction shown in Fig. 9

analysis for the later phase part of the earthquake from the northeast direction shown in the upper figure in Fig. 9. 2 solutions are calculated and the Sembrance values are high from 30.5 to 33.5 seconds in both solutions. The differences of these is arrival azimuth and phase velocity. The phase velocity of solution 2 is consistent with the that evaluated by Yamanaka et. al. (2008). In the case of solution2, the later phase is composed of the surface waves. In each solution, the noticing later phase propagates from the differenct direction from the epicenteral azimuth. In the excitation at the basin edge or the propagating in the basin, the propagating path is bent. For the southeast earthquake, the Sembrance analysis was performed similarly. But a reasonable result could not be derived, because it takes more time to arrive the later phase and it can be considered that the complicated wavefield at this time makes this analysis difficult.

5. CHARACTERISTICS of MICROTREMORS

Records without any disturbances were divided into segments with duration of 40.96 seconds for the calculation of spectra. First, we used an FFT to obtain spectra and smoothed them with a logarithmic window.

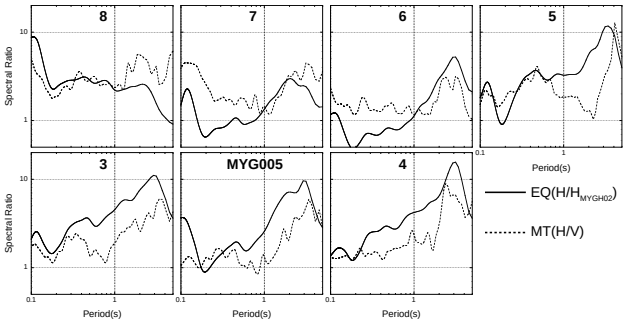

Figure 11 Comparison of spectral ratio between H/H ratio of aftershock and H/V ratio of microtremors

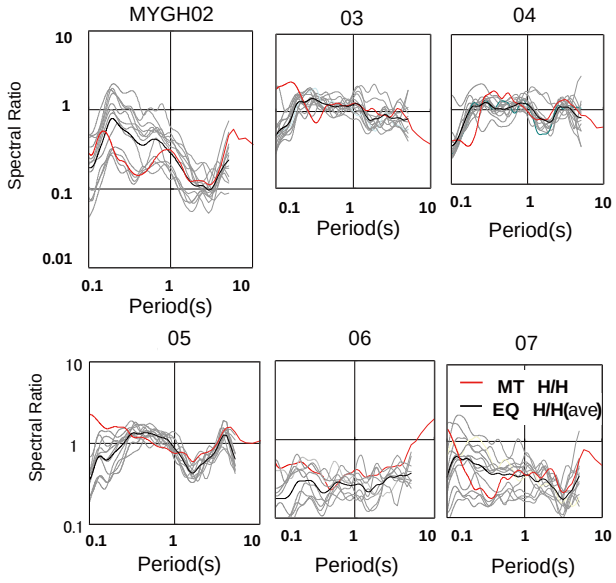

Figure 12 Consistency in H/H ratio of aftershock motions and microtremors

Next, we calculated ensemble averages of the spectra of more than 3 segments. The comparison between the H/H ratio of the aftershock records and the horizontal to vertical amplitude ratio (H/V ratio hereafter) of the microtremors is shown in Figure 11. In some of stations, we can find the difference in the peak period in Figure 11, but the peak period of the H/V ratio correspond to those of the H/H ratio around 3 seconds by and large.

Figure 12 shows how the H/H ratio of the microtremors fits that of the aftershock motions. In this figure, MYG005 is set as the reference because the amplitude of microtremors is extremely low on the rock site as MYGH02. Both of the data of the reference and mobile stations are used for recording at same time. The shapes of the H/H ratio of microtremors are similar to those of aftershock motions, especially in a period range longer than 1 second. In comparison between microtremors and aftershock motions, the H/H ratio

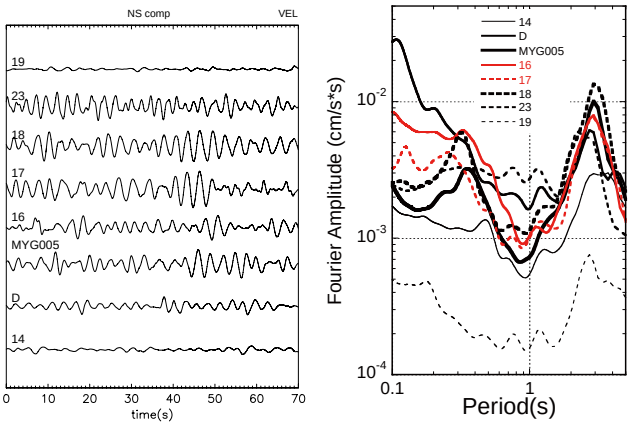

Figure 13 Velocity waveforms of microtremors (left) and Fourier Spectra (right) along A-line in Fig. 4

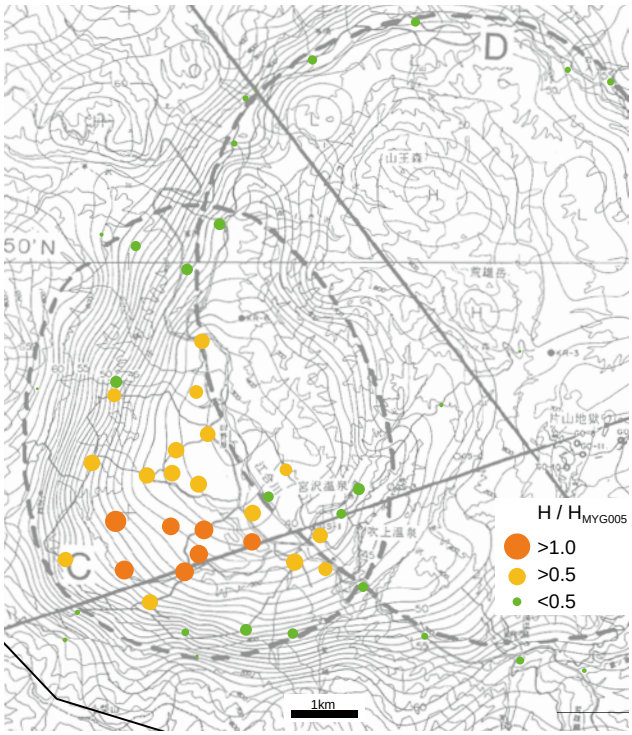

Figure 14 Distribution map of H/H ratio of microtremors in a period range from 2 to 4 seconds

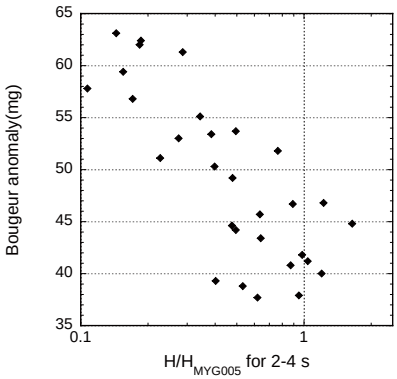

Figure 15 Comparison of H/H ratio to Bouguer anomary

has higher consistency than the H/V ratio. It can be said that the microtremors in horizontal component are able to substitute of the earthquake motions around the predominant period of 3 seconds in the Onikobe basin. The waveforms and the spectra of microtremors measured at stations along A line shown Figure 4 are displayed in Figure 13. The variation of the predominant period is not recognized in this measurement at even the station near the edge of the Onikobe basin, but the amplitudes are changed. This phenomenon is not appeared only in the A-line, but also for all on the Onikobe basin. It can be considered that it is caused by the proportion of the subsurface structure of the Onikobe basin that the width is narrow for the depth of about 1km. Addition to it, this shape of the Onikobe basin might influence to what the predominant periods are getting shorter than those estimated by 1-D structure.

Figure 14 shows the distribution of the average of the ratio in a period range from 2 to 4 second. The ratio is getting higher around the east of MYG005, and Figure 15 shows the relation between Bouguer anomaly and the H/H ratio. Although the correlation can be seen in Figure 14 and this distribution mostly corresponds to that of Bouguer anomaly, the locations of the extreme values are different from each other. Gravity anomaly is more strongly affected by the rock of the outside than the amplitude of microtremors that are sensitive to subsurface structure, because the variation of S wave velocity from surface to the bedrock is much higher than that of density.

6. CONCLUSIONS

We performed aftershock observation and microtremor measurements to understand the characteristics of the earthquake motions during the Iwate-Miyagi Nairiku earthquake in 2008. The predominant periods are around 3 seconds all over the Onikobe basin from both of earthquake motions and microtremors. The predominant periods and the amplification factors can not be estimated only by 1-D structure of subsurface geology. It can be considered that the amplification is strongly affected by the irregular subsurface structures. As future works, we will demonstrate the features revealed in this study using a numerical earthquake simulation.

Acknowledgements:

We thank those who allowed us to install the instruments during the observations of ground motions during aftershocks. The strong motion data, velocity profiles, event information and sea wave height userd in this study are provided by the K-NET, KiK-net and Hi-net of the National Research Institute of Earth Science and Disaster Prevention and by the NOWPHAS of the Port and Airport Research Institute. This study was supported by Global COE Program titled International Urban Earthquake Engineering Center for Mitigating Seismic Mega Risk from the Ministry of Education, Culture, Sports, Science, and Technology.

References:

Aoi,Shin, et.al., characteristics of extreme ground acceleration during the 2008 Iwate-Miyagi Nairiku Earthquake, Programme and abstracts of the 7th General Assembly of Asian Seismological Commision and The 2008 Fall meeting of Seismological Society of Japan, 6, 2008

Fire and Disaster Management Agency, 2009. The 78th Report of the 2008 Iwate-Miyagi Nairiku Earthquake, http://www.fdma.go.jp/data/010906061520038874.pdf (in Japanese)

Geological Survey of Japan, Geological map Onikobe S=1:75000, 1958

Komasawa, and Yasuaki Murata, The gravimetric analysis of the Kurikoma geothermal areas, Northeast Japan, Reports, Geological Survey of Japan, No. 268, 285-313, 1988

Yamanaka, Hiroaki, et.al., Observation of Ground motion of Aftershocks of the 2008 Iwate-Miyagi Nairiku Earthquake and Microtremors in the Onikobe Area, Programme and abstracts of the 7th General Assembly of Asian Seismological Commision and The 2008 Fall meeting of Seismological Society of Japan, 30, 2008

JOINT CONFERENCE PROCEEDINGS
7th International Conference on Urban Earthquake Engineering (7CUEE) &
5th International Conference on Earthquake Engineering (5ICEE)
March 3-5, 2010, Tokyo Institute of Technology, Tokyo, Japan

PRELIMINARY ANALYSIS FOR GROUND STRUCTURE AROUND DAMAGED AREA BY 2008 IWATE-MIYAGI NAIRIKU EARTHQUAKE

Hitoshi. Morikawa[1)], **Masachika Tanigawa**[2)], **Taiyo Kobayashi**[3)], **and Hiroko Matsuo**[4)]

1) Associate Professor, Department of Built Environment, Tokyo Institute of Technology, Japan
2) Under Graduate Student, Department of Civil Engneering, Tokyo Institute of Technology, Japan
3) Engineer, Goverment of Kanagawa Prefecture, Japan
4) Graduate Student, Department of Civil Engneering, Tokyo Institute of Technology, Japan
morika@enveng.titech.ac.jp

Abstract: To obtain a detailed model of the three-dimensional ground structure, the microtoremor and gravity surveys were carried out around Kurikoma area, Japan, where is the source reagion of 2008 Iwate-Miyagi nairiku earthquake and is located about 90 km north of Sendai. Using the microtremor data, velocity structures of shallow sediments are estimated and the results at some of the sites are reported preliminarily. We could not find the detailed velocity structure to bedrock, because small arrays for the microtremor observation were applied. However, significant structures are observed for shallow velocity structure at some sites. Furthermore, gravity data provided Bouguer anomaly, which is one of gravity anomalies, around the target area. From the Bouguer anomaly, area with low anomaly is found around the south-eastern area of the fault plane.

1. INTRODUCTION

2008 Iwate-Miyagi nairiku earthquake of M7.2 has occurred on June 14. The source area was Kurikoma area where is located about 90 km north of Sendai, Japan. After the earthquake, we found distinctive behaviors of gravestone around some specific area close to the source region.

For example, some gravestones fell similarly at Hozo-ji (HZOJ in the map of Figure 1). The photograph after the earthquake is shown as Figure 2. This type of uniform behavior of gravestones is found rarely. On the other hand, we could find the different type of behaviour of gravestones at Kongo-ji (KNGJ): that is, many of gravestones turned similarly but very few gravestones were fallen. Altough the distance between HOZJ and KNGJ is not so far, only 4.7 km, and the distance to the fault plane from these two sites are not so different, the behaviors of gravestones were definitely different.

Many reasons why this kind of differences are occurred can be considered: source effects, path effects, and local site effects, and so on. Thus, we would like to focus the site effect to konw the behaviour of gravestone at HZOJ and KNGJ. For this purpose, some microtremor and gravity surveys are carried out around the Kurikoma area.

2. OBSERVATIONS AND RESULTS OF MICROTREMOR ARRAY OBSERVATIONS

To determine the velocity structure, we carried out array observations of microseisms at HOZJ and KNGJ as shown in Figure 1, during August, 2008. For this observation, we used moving-coil-type velocity sensors, whose

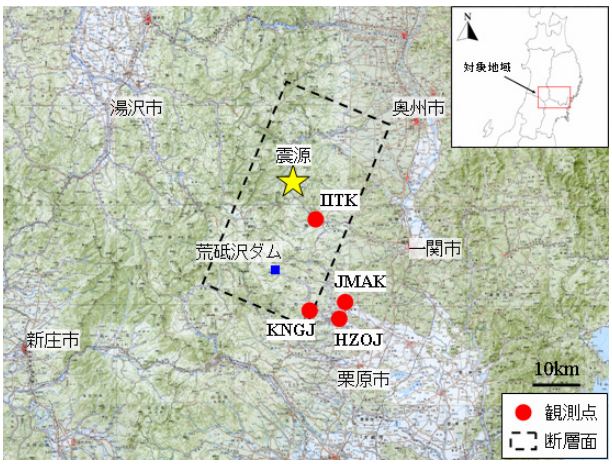

Figure 1 Map of the target area. The square with dashed line shows the fault plane and HOZJ and KNGJ are observation sites of microtremor array. JMAK is the location of the observation site of strong motion by Japan Meteorological Agency.



Figure 2 Fallen gravestones at Hozo-ji (HZOJ) after 2008 Iwate-Miyagi nairiku earthquake.

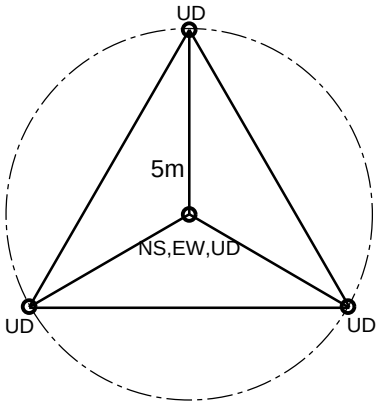

Figure 3 Array collocation for observations. Three components are set at center and vertical component at the vertexes of the array.

natural period is 2 seconds, and digital recorder with 24-bit resolution $\Delta\Sigma$-type A/D converter, which includes an analog gained filter and GPS clock system. The time is synchronized by the GPS clock and data is recorded by sampling rate 800 Hz after passing the low pass filter with cut off frequency of 10 Hz.

Before the observations, a step response of the pendulum is recored to perform the correction of instrumental characteristics during the process of analysis. Duration of the observation is 30 minutes at each site. Radii of the arrays are 5 m with 4 stations as shown in Figure 3.

For the analysis, the spatial auto-correlation (SPAC) method (Matsushima and Okada, 1990) is applied and phase velocities are estimated. Figure 4 shows the results.

Furthermore, we calculate the spectral ratio of horizontal and vertical components (hereafter, H/V), which includes NS/UD and EW/UD, where NS, EW, UD stand for the north-to-south, east-to-west, and vertical components, respectively. H/Vs at HZOJ and KNGJ are shown in Figure 5. The peak period of H/V is not clear at HZOJ, but they can be found in the very high frequency range around 10 Hz. This means that these peaks reflect the very shallow structures at the sites.

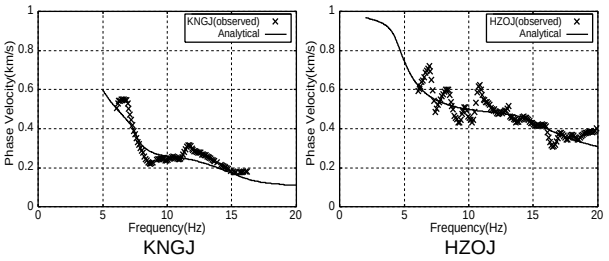

Figure 4 Estimated phase velocities at KNGJ and HZOJ. The solid lines show the analytical dispersion curves of the fundamental mode of Rayleigh wave obtained from the estimated velocity structures at the sites.

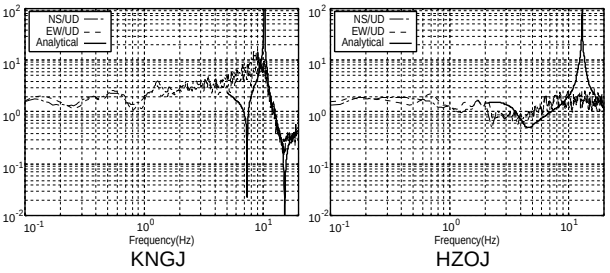

Figure 5 H/V obtained from observed data at KNGJ and HZOJ. The solid lines show the analytical ellipticity of the fundamental mode of Rayleigh wave obtained from the estimated velocity structures at the sites.

3. OBSERVATIONS AND RESULTS OF GRAVITY SURVEY

To obtain the three-dimensional ground structure around Kurikoma area accurately, we carried out the measurements of gravity at the area: 38°47'N – 38°54'N × 140°50'E – 141°03'E: that is, 15km NS × 19km EW. The observation area is shown in Figure 6. In this figure, the background (grayish colored) map is the topography.

Firstly, we set a reference site with absolute gravity value in Tsukidate area through the comparison between our reference site and the official gravity base site. Then, using the reference site, we carried out the relative observations of gravity and the absolute values of the gravity were determined at each site. The data at 146 sites were obtained during 15th to 26th December, 2009. The location of the observation sites are shown as small open circles in Figure 6.

For the observation, we used a G-type gravimeter by La-Coste & Romberg (S/N G911). To determine the position of the observation site accurately, the differential survey using the GPS (Global Positioning System) is performed. As a result, errors of the horizontal and vertical position are less than 1m. The observation system is shown in Figure 7.

We analyze our own data at 146 sites with the existent gravity data (Geological Survey of Japan, 2004), which were obtained in the area. After some data correction such as corrections for height of the instrument, tide, drift, terrain, free-air, and Bouguer correction, the Bouguer anomaly can be obtained. For the Bouguer cor-

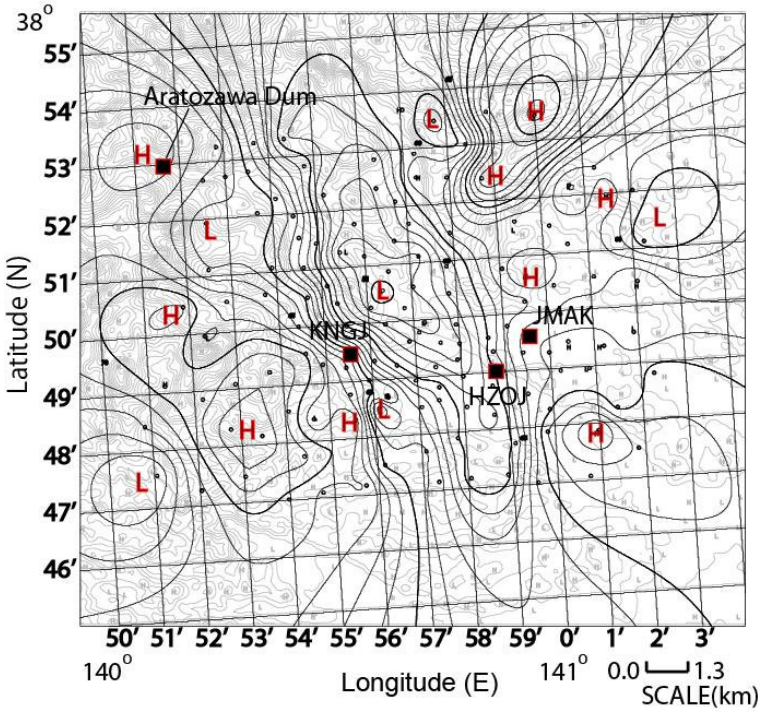

Figure 6 Obtained Bouguer anomaly map around HZOJ. The assumed density is set at 2.4 [t/m^3] and the interval of the contour lines are 1 [mGal]. Small open circles denote observation sites of gravity. Bouguer anomaly is positive in the area. Background (grayish colored) map is topography. The interval of the contour lines is 20 m for the topography.



Figure 7 Observation system for the gravity. GPS receiver and its antenna on the tripod, and LaCoste & Romberg Gravimeter (Type G) below them.

rection, we have to give a value of assumed density ρ. For this purpose, some methods are proposed such as the G-H relation method (Komazawa, 1998), and a method to check the correlation between the Bouguer anomaly map and topography. We apply the latter technique and determine temporarily ρ as 2.4 t/m^3, which corresponds to the density of baserock. The obtained Bouguer anomaly map is shown in Figure 6. The value of anomaly is positive in this area.

4. DISCUSSION

To estimate the velocity structure, we search an appropriate structure to satisfy the observed phase velocity and H/V using a heuistic approach based on forward calculations. For this calculations, we assume that the microtremors propagate through the horizontal and parallell layered medium and that they consist of the waves with fundamental mode of Rayleigh wave.

As a result, the layers with some different shear wave velocities (hereafter, V_S) are determined for very shallow structure. Roughly speaking, the values of V_S can be divided into three categories: that is, about 250 m/s for soft soil such as alluvium, 500 to 750 m/s for hard soil such as diluvium, and 1000 m/s for soft rock. The profiles of the velocity structures are shown in Table 1 and Figure 8. The dispersion curves and ellipticities obtained analytically can be found as solid lines in Figures 4 and 5.

Although it is difficult to know the depth to bedrock (for example, $V_S = 3.0$ [km/s]) using small arrays, we can recognize the difference of the shallow structure between HZOJ and KNGJ. There is no layer of soft soil at KNGJ, thus, the large contrast of acoustic impedance is located at the boundary between soft soil and soft rock: namely, about 200m depth. On the other hand, there is no soft soil at HZOJ and the contrast of the velocity can be found at the boundary between very soft soil and hard soil, that is, only 2m depth.

The difference of the velocity structure at KNGJ and HZOJ may cause the difference of the responses of the gravestone. However, the predominant frequency of the gravestone can be estimated about 1.0 Hz using an empirical equation (Kaneko and Hayashi, 2000). This suggests that the cotribution of the shallow structure is not so large for the response of the gravestone. Thus, we may need to consider the deep structure using the gravity survey.

From the gravity survey, a low gravity anomaly is observed around northern area of KNGJ and HZOJ. These two sites are located on the slope of the Bouguer anomaly: especially, KNGJ is located on the very steep slope.

This suggests that the basement is very deep in this area. However, the depth to the bedrock estimated by the microtremors is not so deep at site CR. This may be caused by the very low density structure around site CR. In the present time, it is difficult to explain this inconsistency between density and velocity structure.

Table 1 The estimated structures at HZOJ and KNGJ

Layer No.	V_P [km/s]	V_S [km/s]	Density [g/m^3]	Thickness [km]
HZOJ				
1	1.000	0.130	1.000	0.002
2	1.600	0.520	1.970	0.033
3	1.800	0.750	2.000	0.033
4	2.100	1.100	2.600	∞
KNGJ				
1	0.700	0.103	1.000	0.003
2	1.000	0.270	1.500	0.016
3	1.600	1.000	2.000	∞

* V_P and V_S stands for P- and S-wave velocitis, respectively.

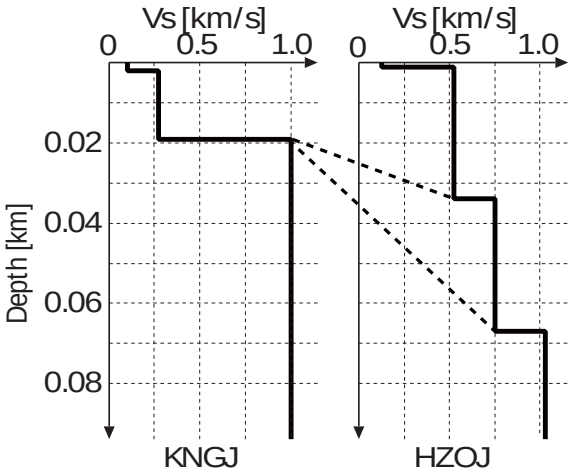

Figure 8 Estimated velocity structures at HZOJ and KNGJ. The dashed lines show the corresponding layers.

5. CONCLUSIONS

We have carried out the observations of microtremor array and gravity around Kurikoma area, Japan. Using microtremor data, we estimated the phase velocities and velocity structures at the sites using the spatial autocorrelation method and a heuistic approach based on forward calculations. Furthermore, the Bouguer anomaly is obtained from gravity data. The results from this research are listed as follows:

- The shallow velocity structure is significantly different between two sites closely located. However, the contribution of the shallow structure may be not so large for the seismic response of gravestone.
- In the sediment, 3 or 4 layers are determined: 250 m/s for soft soil, 750 m/s for hard soil, and 1.1 km/s for soft rock.
- The low Bouguer anomaly is observed around the south-eastern area of the fault plane of 2008 Iwate-Miyagi nairiku earthquake.
- To determine the gravity basement accurately, we need more information about the velocity structure to bedrock. For this, we may consider microtremor observations with large scale array.

References:

Geological Survey of Japan (2004), *Gravity CD-ROM of Japan Ver. 2*, Geological Survey of Japan, AIST.

Kaneko, M. and Hayashi, Y. (2000), "Proposal of a Curve to Describe Overturning Ratios of Rigid Bodies," *Journal of Structural and Construction Engineering*, (536), Architectural Institute of Japan, 55–62.

Komazawa, M. (1998), "Gravity Survey," *Handbook of Exploration Geophysics*, Vol. 4, Society of Exploration Geophysicists of Japan, 431–471.

Matsushima, T. and Okada, H. (1990), "Determination of Deep Geological Structures under Urban Areas using Long-Period Microtremors," *Butsuri-Tansa*, **43**, 21–33.

JOINT CONFERENCE PROCEEDINGS
7th International Conference on Urban Earthquake Engineering (7CUEE) &
5th International Conference on Earthquake Engineering (5ICEE)
March 3-5, 2010, Tokyo Institute of Technology, Tokyo, Japan

A Detailed Receiver Function Study of the Southern Dead Sea Transform (SDST)

Ayman Mohsen1,2), Rainer Kind 1,3), Guenter Asch 1,3), Michael Weber 1,4), Rami Hofstetter 5), and Khali Abu-Ayyash 6)

1) Dr., Geophysical Deep Sounding, Deutsches GeoForschungsZentrum (GFZ), Potsdam, Germany
2) Al-Najah National University, Nablus, Palestine
3) Professor, Dept. of Seismology, Freie Universität, Berlin, Germany
4) Professor, Universität Potsdam, Potsdam, Germany
5) Dr., Geophysical Institute of Isreal, Israel
6) Dr., Natural Resources Authority, Amman, Jordan

ayman@gfz-potsdam.de, kind@gfz-potsdam.de, asch@gfz-potsdam.de, mhw@gfz-potsdam.de, rami@seis.mni.gov.il, rayd@nets.com.jo

Abstract: We report on a receiver function study of the crust within DESERT and DESIRE, two multi-national geophysical projects, across the southern Dead Sea Transform (DST) in Araba Fault (AF) and the Dead Sea Basin (DSB), respectively. The depth of the Moho increases smoothly from about 30 to 34-38 km towards the east across the SDST. These Moho depth estimates from receiver function analysis are consistent with results from steep and wide-angle controlled-source techniques. Steep-angle reflections and receiver functions reveal an additional discontinuity in the lower crust, but only east of the DST in Araba Fault.

1. INTRODUCTION

The Dead Sea Transform (DST) has accommodated left-lateral transform motion of 105 km between the African and Arabian plates since early Miocene (?20 My), creating during this process also the prime example of a pull-apart basin, the Dead Sea Basin (DSB). The DST strikes in a north-northeast direction and extends over some 1000 km from the active spreading centre of the Red Sea, along the Wadi Araba, Dead Sea , Jordan Valley, Lake Tiberias and central Lebanon to the continental collision zone in the Taurus-Zagros mountain belt (Quennell 1958, Garfunkel 1981, El-Isa 1990) (Figure 1). DESERT and DESIRE, two multi-national geophysical projects, have imaged the crustal structure across the southern DST in Araba Fault (AF) and the DSB, respectively.

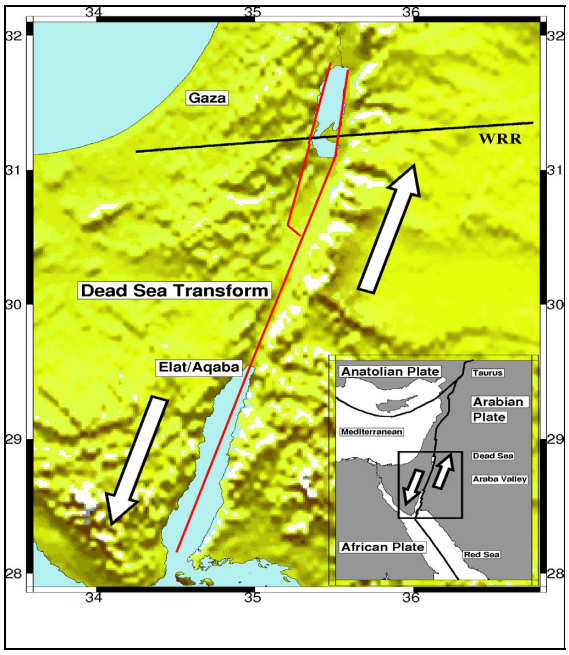

Figure 1 Tectonic map of the Dead Sea Transform area. WRR is the Wide-angle Reflection-Refraction profile across the Dead Sea Basin.

2. RECEIVER FUNCTION TECHNIQUE

We applied the receiver function technique to determine the thickness of the crust, and the average crustal Vp/Vs ratio. The background of the receiver function technique has been reported in a number of papers (e.g. Vinnik 1977, Owens et al. 2000). A very valuable feature of the receiver function technique is the use of crustal multiples for determination of accurate crustal thickness and average Vp/Vs ratios (Zhu & Kanamori 2000). The usual processing is: rotation of the three components Z-N-E into the local ray coordinate system P-SV-SH (Kind et al. 1995), deconvolution of the SV component by the P component, distance move-out correction for the direct conversions at a standard slowness of 6.4 s per degree and summation (Yuan et al. 1997).

3. DATA

We dug holes at each site of a seismic station with a depth of at least one meter, with a cemented base-plate to achieve good ground coupling and reduce meteorological noise. All stations were equipped with 50 W solar panels, 100 Ah batteries, and GPS, to guarantee synchronized continuous recording over the whole duration of the experiment. DESERT and DESIRE, two multi-national geophysical projects, have imaged the crustal structure across the southern DST in Araba Fault (AF) and the DSB, respectively. They include a number of controlled and natural source seismic experiments. Within DESERT, a temporary seismic network (Figure 2) was operated on both sides of the DST between April 2000 and June 2001. Within DESIRE the DSB, the largest basin along the DST. A temporary seismic network of 30 broadband and 45 short-period seismic stations has been set up on both sides of the DSB (Figure 3). During one and a half year of successful operation (October 2006-April 2008), data were continuously recorded in the field at 100 Hz and 200 Hz sample frequency for the broadband and short-period seismic stations, respectively. The raw data were converted to miniseed format and archived as full seed volume in the GEOFON data center of the GFZ.

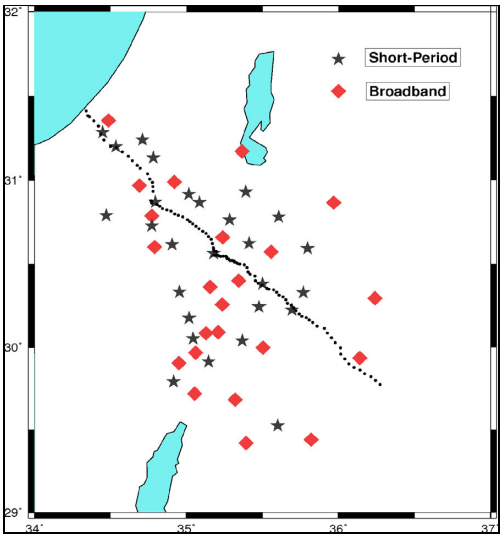

Figure 2 Location map of seismic stations in the region of the Dead Sea Transform in Araba Fault. The dotted line shows the steep-and wide-angle control source profiles.

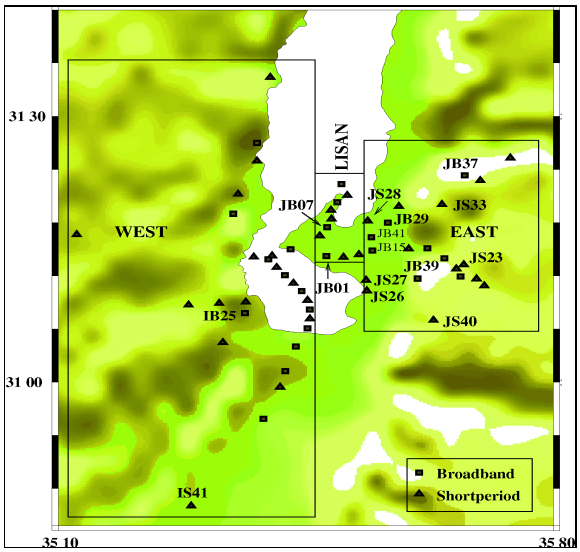

Figure 3 Location map of seismic stations in the region of the Dead Sea Basin. Stations are grouped in three regions: EAST, LISAN and WEST.

4. RECEIVER FUNCTION RESULTS

Within DESERT, the Moho depth increases smoothly from about 30 to 34-38 km towards the east across the DST, with significant north-south variations east of the DST (Figure 4). These Moho depth estimates from receiver functions are consistent with results from steep and wide angle controlled source techniques. Steep angle reflections and receiver functions reveal an additional discontinuity in the lower crust, however only east of the DST (Mohsen et al. 2005) (Figure 5). This leads to the conclusion that the internal crustal structure east and west of the DST is different.

Within DESIRE the DSB, the largest basin along the DST. Unusual negative phases at about 1s delay time have been observed at several stations in the Dead Sea region on the top of the assumed salt diapir. First preliminary receiver function analysis reveals a crustal thickness of about 30-35 km in the investigated area and possibly low-velocity layer beneath the Moho. It also shows a basin which is possibly filled with salt about 10 km thick beneath the Lisan peninsula (Dead Sea).

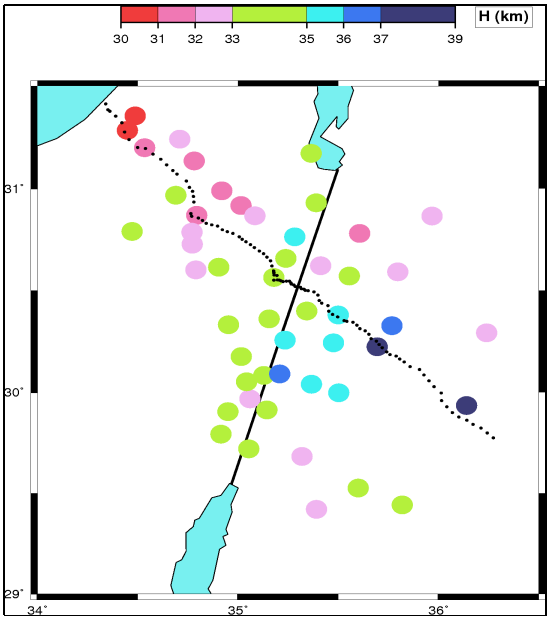

Figure 4 Map of Moho depth values obtained by the application of Zhu and Kanamori.

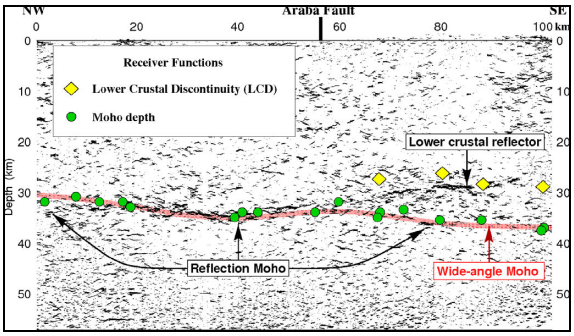

Figure 5 Comparison of depth determinations of the Moho and Lower Crustal Discontinuity by steep-and wide-angle controlled-source techniques and the receiver functions. The error in the Moho depth determined with receiver functions is estimated at less than 3 km at most stations.

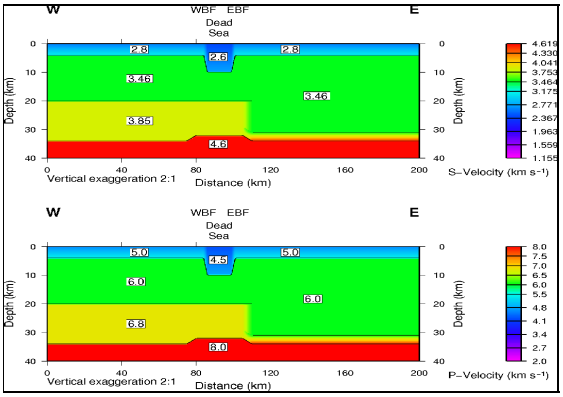

Figure 6 Two dimensional P and S wave velocity models.

5. CONCLUSIONS

Different seismic techniques have been applied to study the crustal structure across the DST in Araba Fault and the Dead Sea Basin. These are steep-and-wide-angle controlled-source techniques along a linear profiles perpendicular to the DST and the natural source-receiver function technique . The resulting Moho depth profiles agree very well in all techniques. The Moho depths smoothly increase across the DST along the linear profiles, without any indication of a sudden difference. However, an additional discontinuity in the lower crust was identified only to the east of the DST in Araba Fault in the receiver function and steep-angle data. This indicates that the internal crustal structure is different to the east and west of the DST in Araba Falut.. In order to examine the effects of the DSB, 2-D waveform modelling along a profile perpendicular to the trend of the DSB. The model which through visual inspection seems to fit the data best (Figure 6) comprises a basin 15-20 km wide and about 10 km deep, a high velocity lower crustal layer beneath and west of the basin and a 2 km shallower Moho beneath the DSB.

Acknowledgments:

The DESERT & DESIRE projects were funded by the Deutsche ForschungsGemeinschaft. Al-Najah National University in Nablus, Palestine, the Natural Resources Authority of Jordan and the National Ministry of Infrastructure of Israel are thanked for support. The instruments were provided by the Geophysical Instrument Pool of the Deutsches GeoForschungsZentrum Potsdam (GFZ). The first author (Ayman Mohsen) is deeply acknowledges the support from the organizers.

References:

Quennell, A. M. (1958), "The structural and geomorphic evolution of the Dead Sea Rift," The geological society of London CXIV: 1-24, London.

Garfunkel, Z. (1981), "Internal structure of the Dead Sea Leaky Transform (rift) in relation to plate Kinematrics." In R. Freund and Z. Garfunkel (Edits.). The Dead Sea rift, *Tectonophysics*, **80**, 81-108.

El-Isa, Z. H. (1990), "Lithospheric structure of the Jordan Dead Sea Transform from earthquake data," *Tectonophysics*, **180**, 29-36

Vinnik, L.P. (1977), Detection of waves converted from P to SV in the mantle, *Phys. Earth planet., Int*., **15**, 39-45.

Owens, T.J., Nyblade, A.A., Gurrola, H. & Langston, C.A. (2000), "Mantle transition zone structure beneath Tanzania, East Africa," *Geophys. Res. Lett*., **27**, 827-830.

Zhu, H. & Kanamori, H. (2000), "Moho depth variation in southern California from teleseismic receiver functions," *J. geophys. Res*., **105**, 2969-2980.

Kind, R., Kosarev, G.L. & Petersen, N.V. (1995), "Receiver functions at the stations of the German Regional Seismic Network (GRSN)," *Geophys. J. Int*., **121**, 191-202.

Yuan, X., Ni, J., Kind, R., Mechie, J. & Sandvol, E. (1997), "Lithospheric and upper mantle structure of southern Tibet from a seismological passive source experiment," *J. geophys. Res.*, **102**, 27491-27500.

Mohsen, A., Hofstetter, R., Bock, G., Kind, R., Weber, M., Wylegalla, K., Rümpker, G. & DESERT Group 2005, A receiver function study across the Dead Sea Transform," *Geophys. J. Int*., **160**, 948-960.

JOINT CONFERENCE PROCEEDINGS
7th International Conference on Urban Earthquake Engineering (7CUEE) &
5th International Conference on Earthquake Engineering (5ICEE)
March 3-5, 2010, Tokyo Institute of Technology, Tokyo, Japan

EXTRACTING THE MULTISCALE COHERENCE OF STRONG GROUND MOTIONS USING WAVELET ANALYSIS

Michalis F. Vassiliou[1] and Nicos Makris[2]

1) PhD Graduate Student, Dept. of Civil Engineering, University of Patras, Greece, GR 26500
2)Professor, Dept. of Civil Engineering, University of Patras, Greece, GR 26500
mfvassiliou@gmail.com, nmakris@upatras.gr

Abstract: This paper is motivated from the need to extract the characteristic time scales and length scales of strong ground motions with a mathematically formal and easily reproducible procedure. The investigation uses wavelet analysis to identify and approximate energetic acceleration pulses (not velocity pulses) together with their associated frequency and amplitude. The processing of acceleration records with wavelet analysis is capable to extract acceleration pulses which are not detected visually in the acceleration records; yet, they become coherent and distinguishable in the velocity records. The capability of several popular symmetric and antisymmetric wavelets to locally match the energetic acceleration pulse is examined; and it is concluded that the exercise to identify the best matching wavelet shall incorporate, in addition to the standard translation and dilation-contraction of the wavelet transform, a phase modulation together with a manipulation of the oscillatory character (addition of cycles) of the wavelet. This need leads to the extension of the wavelet transform to a more general wavelet transform during which the mother wavelet is subjected to the four abovementioned modulations.

1. INTRODUCTION

During the last three decades an ever increasing database of recorded ground motions has shown that the kinematic characteristics of the ground motion near the fault of major earthquakes contain distinguishable velocity and displacement pulses (Somerville and Graves 1993, Abrahamson and Somerville 1996, Papageorgiou 1998, Somerville 1998 among others). In some events the pulse is also distinguishable in the acceleration history and in this case the ground motions are particularly destructive to most civil structures. In other cases acceleration records contain high frequency spikes and resemble random motions; however, their velocity and displacement histories uncover a coherent long-duration pulse that results from the nonzero mean of the acceleration fluctuations. These motions have a much smaller destructive potential to most civil structures (Ts < 4s) even when they produce ground displacements as large as 3m. A comprehensive comparison between the destructive potential of these two classes of near–source ground motions has been presented by Makris and Black (2004c). The area under the acceleration pulse was coined by Bertero the ‘‘incremental’’ ground velocity in an effort to distinguish between the net increment of the ground velocity along a monotonic segment of its time history and the peak ground velocity that might be the result of a succession of high-frequency one-sided acceleration spikes. As an example, Fig. 1 (left) shows the fault parallel components of the acceleration, velocity, and displacement histories of the June 18, 1992 Landers, California earthquake (Mw=7.2) recorded at the Lucerne Valley station. The coherent 8.3s long pulse, responsible for a 1.8 m forward displacement, can also be distinguished in the velocity history; whereas, the acceleration history is crowded with high-frequency spikes without exhibiting any distinguishable acceleration pulse. The acceleration pulse associated with the 8.3s velocity pulse has so feeble inertia effects that is immaterial to most engineering structures.

Fig. 1 (right) shows the acceleration, velocity and displacement time histories recorded during the March 13, 1992 Erzinkan, Turkey earthquake with Mw = 6.7. What distinguishes this record is that the velocity pulse is a result of a distinguishable acceleration pulse–not the sum of many acceleration spikes with nonzero mean as is the case in the Lucerne Valley record, shown in Fig. 1 (left). This paper focuses on matching and extracting coherent acceleration pulses (not velocity pulses) of strong ground motions.

Given that the maximum inelastic displacement of structures scales with (the period of the predominant acceleration pulse) the need for a mathematically formal, objective and easily reproducible procedure to extract pulse periods and pulse amplitudes from near source ground motions becomes apparent. This need is the main motivation for this work.

While the aforementioned studies focused on the

mathematical representation of distinguishable acceleration and velocity pulses, the first systematic study for quantitatively identifying coherent velocity pulses in near-fault ground motions has been presented by Baker (2007). Baker's work uses wavelet analysis to extract automatically the largest velocity pulse (not acceleration pulse) in a given earthquake record; therefore, it offers some characteristic time and length scales of the ground motion.

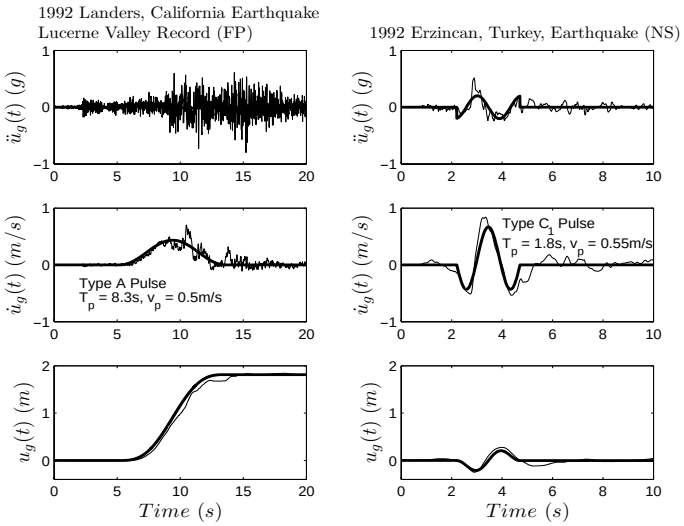

Fig. 1.Left: Fault-parallel component of the acceleration, velocity and displacement time histories recorded at Lucerne Valley during the June 18, 1992, Landers, California earthquake. Heavy line is a one-sine (Type A) acceleration pulse. Right: North-South component of the acceleration, velocity and displacement histories recorded during the 1992 Erzinkan, Turkey earthquake. Heavy line is a Type-C_1 pulse (Makris and Chang 2000 and Table 1 of this paper).

This article essentially builds upon the work of Baker (2007), Mavroeidis and Papageorgiou (2003), Gabor (1946) and Makris and Black (2004c) in an effort to extract in a mathematically rigorous way the most representative time scales and length scales in earthquake acceleration records. In this work we first examine with continuous wavelet transform 183 acceleration records using five (5) elementary mother wavelets and we conclude that not only the period (dilation-contraction of the wavelet) but also the phase and number of cycles (oscillatory character) need to be manipulated in order to achieve the best local matching of the prevailing acceleration pulse. Accordingly the acceleration records of strong ground motions are represented mathematically by the Gabor (1946) wavelet (or its variation proposed by Mavroeidis and Papageorgiou (2003)) and the concept of wavelet transform is extended so that the mother wavelet is not only translated and dilated but also subjected to an appropriate phase shift and enhanced with additional cycles.

2. WAVELET AN ALYSIS

Over the last two decades, wavelet transform analysis has emerged as a unique new time-frequency decomposition tool for signal processing and data analysis. Wavelets are simple wavelike functions localized on the time axis. Examples of wavelets can be found in Table 1.

In order for a wavelike function to be classified as a wavelet, the wavelike function must have: (a) finite energy

$$E = \int_{-\infty}^{\infty} \left|\psi(t)\right|^2 dt < \infty \qquad (1)$$

and (b) a zero mean. In this work we are merely interested to achieve the best local matching of any acceleration record with a wavelet that will offer the best estimates of the period (T_p = time scale) and amplitude (a_p, since $a_p T_p^2$= length scale) of the prevailing energetic pulse. Accordingly, we perform a series of inner products (convolutions) of the ground acceleration signal, $\ddot{u}_g(t)$, with the wavelet by manipulating the wavelet through a process of translation (i.e. movement along the time axis) and a process of dilation-contraction (i.e. spreading out or squeezing of the wavelet)

$$C(s,\xi) = w(s)\int_{-\infty}^{\infty} \ddot{u}_g(t)\,\psi\left(\frac{t-\xi}{s}\right)dt \qquad (2)$$

The values of s = S and ξ = Ξ for which the coefficient, $C(s,\xi)=C(S,\Xi)$ becomes maximum offer the scale and location of the wavelet $w(s)\psi\left(\frac{t-\xi}{s}\right)$ that locally matches best the acceleration record, $\ddot{u}_g(t)$. Equation (2) is the definition of the wavelet transform. The quantity $w(s)$ outside the integral in Equation (2) is a weighting function. Typically $w(s)$ is set equal to $1/\sqrt{s}$ in order to ensure that all wavelets $\psi_{s,\xi}(t) = w(s)\psi\left(\frac{t-\xi}{s}\right)$ at every scale s have the same energy.

The same energy requirement among all the daughter wavelets $\psi_{s,\xi}(t)$ is the default setting in the MATLAB wavelet toolbox (2007) and what has been used by Baker (2007); however, the same energy requirement is, by all means, not a restriction.

A weighting function $w(s) = 1/s^1 = 1/s$ suppresses the large scale wavelets; therefore it accentuates the presence of shorter period pulses; whereas a weighting function, $w(s) = 1/s^0 = 1$ accentuates the presence of longer period pulses. For instance, in order to capture the long velocity pulse of the Lucerne Valley record shown in Fig. 1, the weighting

function needs to promote the long periods. Therefore a weighting function $w(s) = 1/s^0 = 1$ had to be used to capture the 8.3s long velocity pulse of the Lucern Valley record.

3. SELECTION OF THE BEST MATCHING WAVELET

Fig. 1 shows that a Type-A cycloidal pulse (one sine acceleration pulse) was selected to approximate the impulsive character of the 1992 Lucerne Valley record; whereas a Type – C_1 (one cycle displacement pulse) was selected to approximate the 1992 Erzikan record . The question that arises is which wavelet matches better the majority of records so that it can be used with confidence to extract invariably the pulse period and pulse amplitude of any pulse-like acceleration record. This paper examines the performance of the five wavelets listed in Table 1. Note that the mathematical expressions appearing in Table 1 are for the mother wavelets (scale $s=1$) and this is why the symbol of frequency, f, does not appear in the expressions. Each of these wavelets was used to match to the extend possible the 183 records listed in (Vassiliou and Makris 2009).

As an example, the top five graphs of Fig. 2 show the performance of each of the five candidate wavelets listed in Table 1 when matching the El Centro Array #5 record from the 1979 Imperial valley Earthquake. The measure used to evaluate the capability of a wavelet to locally match the predominant acceleration pulse (matching index) is the inner product of the extracted mathematical pulse, $\lambda(S,\Xi)\psi_{S,\Xi}(t)$, with the acceleration record, normalized with the energy of the record. $\lambda(S,\Xi)$ is defined in (Vassiliou and Makris 2009)

$$e = \frac{\int_{-\infty}^{\infty} \ddot{u}_g(t) \cdot \lambda(S,\Xi)\psi_{S,\Xi}(t)\,dt}{\int_{-\infty}^{\infty} \left(\ddot{u}_g(t)\right)^2 dt} \qquad (3)$$

The scores of the five wavelets appearing in Table 1 during the contest of best matching all 183 acceleration records are obtained as follows. When matching each record, the wavelet with the highest matching index, e, takes 4 points, the second best takes 3 points, the third takes 2 points, the one before last takes one point and the last one takes zero points. Fig. 3 (top) portraits the scores of all five (5) wavelets in the form of an histogram. Clearly there is no clear winner since the outcome of the contest depends on the set of ground motions which includes probably more records with antisymmetric coherent pulses than symmetric pulses. The above exercise indicates that in order to satisfy the request of matching satisfactorily the majority of records with a single mother wavelet; this wavelet should allow for a manipulation of its phase and number of cycles.

Table 1. Elementary symmetric and antisymmetric wavelets used in this study.

Name	Equation	Graph	Energy
One-cosine (Type B Cyclodial)	$\cos(2\pi t), \quad 0 \le t \le 1$	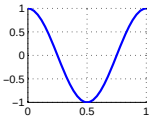	$1/2$
Symmetric Ricker (2nd Derivative of Gaussian, Mexican Hat)	$\left(1-t^2\right)e^{-\frac{t^2}{2}}$	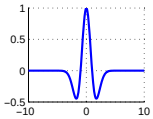	$\frac{3}{4}\sqrt{\pi}$
Antisymmetric Ricker (3rd Derivative of Gaussian)	$te^{-\frac{t^2}{2}}\left(t^2-3\right)$	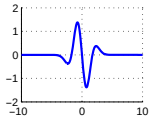	3.323
Type C1 Cyclodial	$\cos(2\pi t + 0.0697\pi), \quad 0 \le t \le 1.4303$	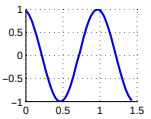	0.681
Type C2 Cyclodial	$\cos(2\pi t + 0.0410\pi), \quad 0 \le t \le 2.459$	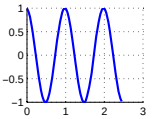	1.209

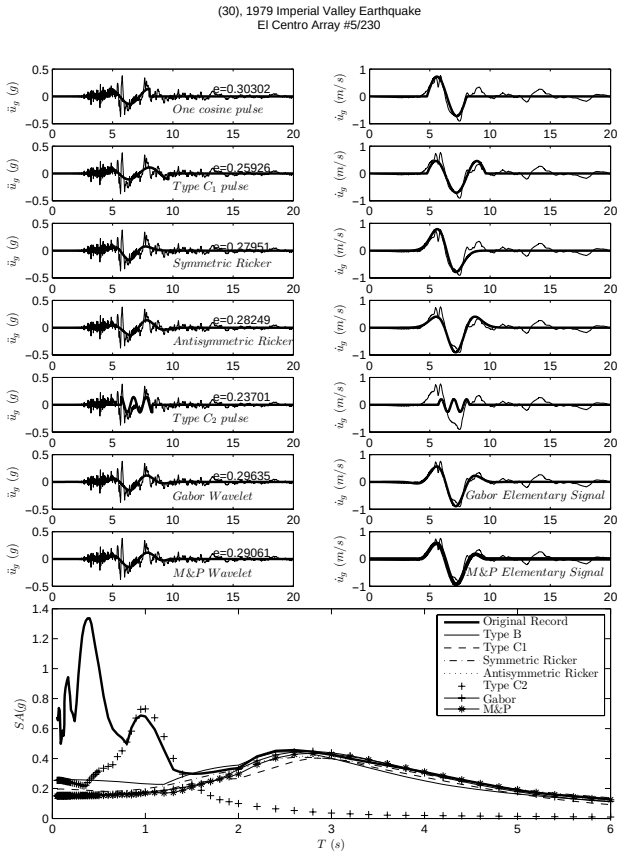

Fig. 2. *Matching of the acceleration record with various elementary wavelets (left) and the resulting velocity signals (right). In the wavelet transform, all daughter wavelets have same energy. Bottom: Comparison of the elastic acceleration response spectra with 5% viscous damping.*

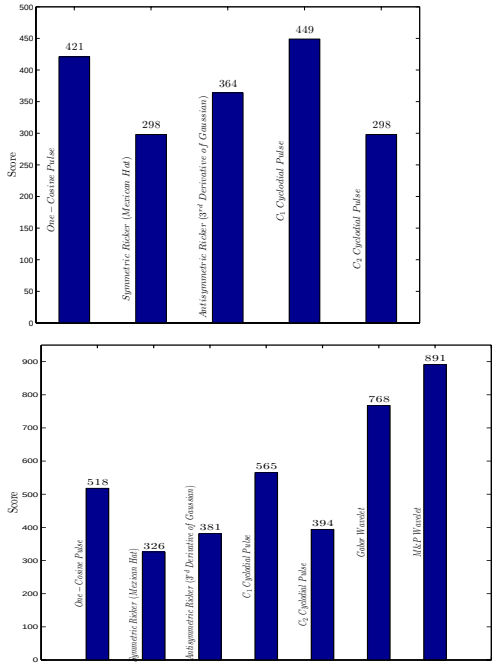

Fig. 3 *Scores of the five wavelets listed in Table 1 from the contest of best matching the 183 records (Top) Scores of all seven (7) wavelets of interest. The M&P wavelet ranks first ahead of the Gabor wavelet, while the other five wavelets listed in Table 1 which do not allow for phase modulation and manipulation of their oscillatory character are falling far behind.*

4. EXTENSION OF THE WAVELET TRANSFORM BY ALSO MODULATING THE PHASE AND THE OSCILLATORY CHARACTER OF THE ELEMENTARY SIGNAL

In the classical wavelet transform defined with equation (2) the mother wavelet is only subjected to a translation together with a dilation-contraction, $\psi\left(\frac{t-\xi}{s}\right)$. The dilation contraction is controlled with the scale parameter *s*; while, the movement of the wavelet along the time axis is controlled with the translation time, ξ. For instance, any daughter wavelet of the symmetric Ricker mother wavelet appearing in Table 1 assumes the form

$$\psi\left(\frac{t-\xi}{s}\right)=\left[1-\left(\frac{t-\xi}{s}\right)^2\right]e^{-\frac{1}{2}\left(\frac{t-\xi}{s}\right)^2} . \qquad (4)$$

The need to include four parameters in a mathematical expression of a simple wavelike function that is a good candidate to express the coherent component of a recorded ground motion has been presented and addressed by Mavroeidis and Papageorgiou (2003). They suggested that a sound analytical model for pulse like records should include four parameters–that is the pulse duration (or period), the pulse amplitude, the number of cycles and the phase of the pulse. They identified as the most appropriate analytical expression the Gabor (1946) "elementary signal" which they slightly modified to facilitate derivations of closed-form expressions of the spectral characteristics of the signal and response spectra.

One of the earliest and most seminal publications in time frequency analysis has been presented by Gabor (1946).

$$g(t)=e^{-\left(\frac{2\pi f_p}{\gamma}\right)^2 t^2}\cos\left[2\pi f_p t+\varphi\right] \qquad (5)$$

which is merely the product of a harmonic oscillation with a Gaussian envelop. In equation (5), f_p is the frequency of the harmonic oscillation, φ is the phase angle and γ is a parameter that controls the oscillatory character of the signal. The Gabor wavelike signal given by equation (5) does not have a zero mean; therefore, it cannot be a wavelet within the context of the wavelet transform.

Nevertheless, the derivative of the Gabor (1946) elementary signal,

$$\frac{dg(t)}{dt}=-\frac{2\pi f_p}{\gamma^2}e^{-\left(\frac{2\pi f_p}{\gamma}\right)^2 t^2}\left(\gamma^2\sin\left(2\pi f_p t+\varphi\right)+4\pi f_p t\cos\left(2\pi f_p t+\varphi\right)\right) \qquad (6)$$

is by construction a zero-mean signal and is defined in this paper as the Gabor wavelet. According to the notation used in this paper for the wavelet functions the frequency, f_p, in equation (6) is replaced with the inverse of the scale parameter, *1/s*; while ξ denotes the translation time. Accordingly the Gabor wavelet is expressed as

$$\psi\left(\frac{t-\xi}{s},\gamma,\varphi\right)==-\frac{2\pi}{\gamma^2}\frac{1}{s}e^{-\left(\frac{2\pi}{\gamma}\right)^2\left(\frac{t-\xi}{s}\right)^2}\cdot \cdot\left(\gamma^2\sin\left(2\pi\left(\frac{t-\xi}{s}\right)+\varphi\right)+4\pi\left(\frac{t-\xi}{s}\right)\cos\left(2\pi\left(\frac{t-\xi}{s}\right)+\varphi\right)\right) \quad (7)$$

In the expression for the Gabor wavelet given by equation (7), the dilation-contraction is controlled with the parameter *s* while the movement of the wavelet along the time axis is controlled with translation parameter ξ, the same way as is done in the Ricker wavelet given by equation (4). The novel attraction in the Gabor wavelet given by equation (7) is that in addition to the dilation-contraction and translation $\left(\frac{t-\xi}{s}\right)$, the wavelet can be further manipulated by modulating the phase, φ, and the parameter γ, which controls the oscillatory character (number of half cycles). We can now define the four parameter wavelet transform as

$$C\left(s,\xi,\gamma,\varphi\right)=w\left(s,\gamma,\varphi\right)\int_{-\infty}^{\infty}\ddot{u}_g\left(t\right)\psi\left(\frac{t-\xi}{s},\gamma,\varphi\right)dt \quad (8)$$

The inner product given by equation (8) is performed repeatedly by scanning not only all times, ξ, and scales, *s*, but also by scanning various phases φ={0, π/4, π/2, 3π/4} and various values of the oscillatory nature of the signal γ={1.0, 1.5, 2.0, 2.5, 3.0}. When needed more values of φ and γ may be scanned. The quantity *w(s,γ,φ)* outside the integral is a weighting function which is adjusted according to the application. Vassiliou and Makris (2009) have demonstrated that the weighting function determines whether a long or a short duration pulse will be extracted.

The values of *s=S, ξ=Ξ, γ=Γ, φ=Φ* for which the coefficient *C(s,ξ,γ,φ)=C(S,Ξ,Γ,Φ)* becomes maximum offer the scale, location, phase and number of half cycles of the wavelet $\psi\left(\frac{t-\xi}{s},\gamma,\varphi\right)$ that locally matches best the acceleration record, $\ddot{u}_g\left(t\right)$. Fig. 4 plots the magnitude of the extended wavelet transform, *C(s,ξ,γ,φ)*, of the El Centro Array #5 acceleration record for various scales as a function of time and four different values of the phase φ={0, π/4, π/2, 3π/4} when γ=3. The maximum value of the wavelet transform *C(s,ξ,γ,φ)* is located at $s=T_p$=3.8s and φ=3π/4..

Fig. 2 (sixth plot from the top) plots the shape of the

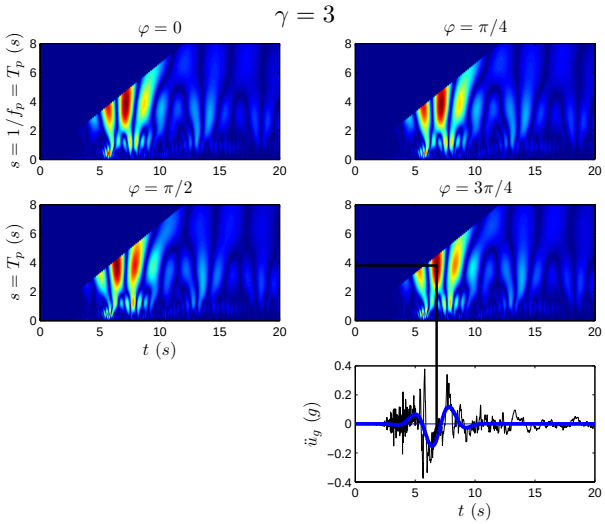

Fig. 4. *Scalograms of the extended wavelet transform defined by equation (26) exercised on the El Centro Array #5 acceleration record from the 1979 Imperial Valley earthquake with the Gabor wavelet (γ = 3). The maximum value of the wavelet transform is located at s = T_p= 3.8s, γ = 3 and φ=3π/4.*

Gabor wavelet $\lambda\left(S,\Xi,\Gamma,\Phi\right)\cdot w\left(S,\Gamma,\Phi\right)\cdot\psi\left(\frac{t-\Xi}{S},\Gamma,\Phi\right)$ where the values (S,Ξ,Γ and Φ) are those that maximize the extended wavelet transform given in (8) in which $\ddot{u}_g\left(t\right)$ is the El Centro Array #5 acceleration record from the 1979 Imperial Valley earthquake.

The elementary signal proposed by Mavroeidis and Papageorgiou (2003) to approximate velocity pulses is a slight modification of the Gabor signal given by equation (5) where the Gaussian envelope has been replaced by an elevated cosine function.

$$v\left(t\right)=\frac{1}{2}\left(1+\cos\left(\frac{2\pi f_p}{\gamma}t\right)\right)\cos\left(2\pi f_p t+\varphi\right) \quad (9)$$

Clearly the wavelike signal given by equation (9) does not always have a zero mean; therefore it cannot be a wavelet within the context of wavelet transform. Nevertheless, the time derivative of the elementary velocity signal given by equation (10)

$$\frac{dv\left(t\right)}{dt}=\frac{\pi f_p}{\gamma}\left(\begin{array}{l}\sin\left(\frac{2\pi f_p}{\gamma}t\right)\cos\left(2\pi f_p t+\varphi\right)+\\ +\gamma\sin\left(2\pi f_p t+\varphi\right)\left(1+\cos\left(\frac{2\pi f_p}{\gamma}t\right)\right)\end{array}\right) \quad (10)$$

is by construction a zero-mean signal and is defined in this

paper as the Mavroeidis and Papageorgiou (M&P) wavelet. After replacing the oscillatory frequency, fp, with the inverse of the scale parameter the M&P wavelet is defined as

$$\psi\left(\frac{t-\xi}{s},\gamma,\varphi\right)=\left(\begin{array}{l}\sin\left(\frac{2\pi}{s\gamma}(t-\xi)\right)\cos\left(\frac{2\pi}{s}(t-\xi)+\varphi\right)+\\ \gamma\sin\left(\frac{2\pi}{s}(t-\xi)+\varphi\right)\end{array}\right)\left(1+\cos\left(\frac{2\pi}{\gamma s}(t-\xi)\right)\right) \quad (11)$$

Clearly, when selecting the appropriate weighting function w(s,γ,φ) the wavelet transform on the acceleration records proposed in this paper leads to the velocity pulses presented by Mavroeidis and Papageorgiou (2003) and Baker (2007); yet, most importantly the coherence of the ground motion extracted with this work is directly related to the inertia effects on structures given that it originates from the acceleration records.

The last time history plot on the left of Fig. 2 plots with a heavy line the shape of the M&P wavelet where the values of s=S, ξ=Ξ, γ=Γ and φ=Φ are those that maximize the extended wavelet transform given by equation (8) in which

$\ddot{u}_g(t)$ is respectively the 1979 El Centro, Array #5.

The parameters (T_p=period=s=scale, γ=oscillatory character and φ=phase) of the Gabor and M&P wavelets that maximize the outcome of the extended wavelet transform given by equation (8) for three well known records are offered in Table 2. The extended version of Table 2 for 183 strong motions is presented in (Vassiliou and Makris 2009).

In order to address the question, which wavelet matches better the majority of records, the scores of the seven (7) wavelets under examination (5 wavelets appearing in Table 1 plus the Gabor and M&P wavelets defined by equations (7) and (11) are obtained following the protocol defined in constructing Fig. 3. When matching each record, the wavelet with the highest matching index, e, takes 6 points the second best takes 5 points, all the way to the last matching index which takes zero points.

5. TIME SCALES AND LENGTH SCALES OF STRONG GROUND MOTIONS

The parameters of the M&P wavelets that maximize the extended wavelet transform of the strong ground motions listed in Table 3 are extracted by setting the weighting function $w(s,\gamma,\varphi)$ in equation (8) such that all daughter wavelets have (a) the same area, (b) the same energy and (c) the same amplitude. The parameters of the M&P wavelets when $w(s,\gamma,\varphi)$ is chosen so that all the daughter wavelets have the same energy are listed in Table 2.

In several occasions, even the same energy requirement on the wavelet transform results in energetic acceleration pulses which do not correspond to the long velocity pulses derived visually. For instance Fig. 5 shows the performance of each of the seven wavelets examined in this paper when matching the Parachute Test Site–225 record from the 1981 Westmorland Earthquake. With the same energy requirement, the first two wavelets capture a long duration pulse which becomes apparent in the velocity time histories shown in the right of Fig. 5. On the other hand, the same energy requirement on the next five wavelets (from the symmetric Ricker to the M&P wavelet) extracts a higher frequency pulse–not the longer period pulse that dominates the velocity record. Note that the higher score goes to the M&P Wavelet, e=0.1687. The acceleration spectra of a linear single degree of freedom structure shown at the bottom of Fig. 5 indicates that the shorter period acceleration pulse

Table 2. Parameters of the Gabor and M&P wavelets that maximize the Extended Wavelet Transform given by equation (8). (same energy scaling function is used)

			Gabor (1946)				M&P (2003)			
	Event	Station	a_p (g)	T_p (s)	γ	φ (rad)	a_p (g)	T_p (s)	γ	φ (rad)
1	Parkfield	CO2/065	0.47	0.7	3	1.57	0.41	0.6	3	1.57
2	San Fernando	Pacoima Dam 164	0.42	1.5	3	0.79	0.59	0.5	3	0.79
3		Pacoima Dam 254	0.69	0.6	3	2.36	0.61	0.5	3	2.36

Table 3. Strong ground motion records and the parameters of the Mavroeidis & Papageorgiou (M&P) wavelets for different weighting functions.

	Same Area							Same Energy							Same amplitude						
	a_p (g)	A (m/s)	T_p (s)	γ	φ (rad)	Sa(g) T=0.5s	Sa(g) T=2.5s	a_p (g)	A (m/s)	T_p (s)	γ	φ (rad)	Sa(g) T=0.5s	Sa(g) T=2.5s	a_p (g)	A (m/s)	T_p (s)	γ	φ (rad)	Sa(g) T=0.5s	Sa(g) T=2.5s
1	0.50	0.55	0.70	1	1.57	1.45	**0.04**	0.41	0.38	0.60	3	1.57	**2.19**	0.03	0.35	0.40	0.70	3	0	1.37	0.03
2	0.73	0.26	0.20	1	0	0.21	0.01	0.59	0.42	0.45	3	0.79	**2.17**	0.02	0.30	0.68	1.35	3	0	0.38	**0.19**
3	0.69	0.37	0.30	1	0	0.46	0.02	0.61	0.48	0.50	3	2.36	**2.96**	**0.03**	0.58	0.48	0.50	3	0	2.90	0.03

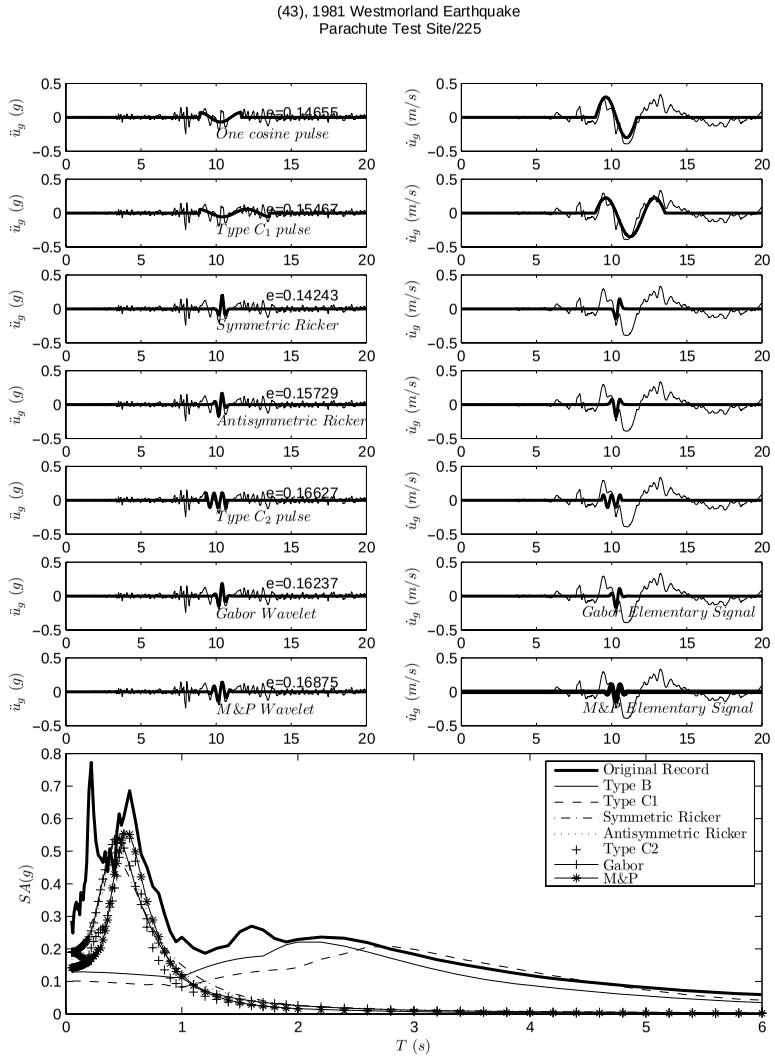

Fig. 12. *Matching of the acceleration record with various wavelets (left) and the resulting velocity signals (right). In the wavelet transform all daughter wavelets have same energy. Bottom: Comparison of the elastic acceleration response spectra with 5% viscous damping.*

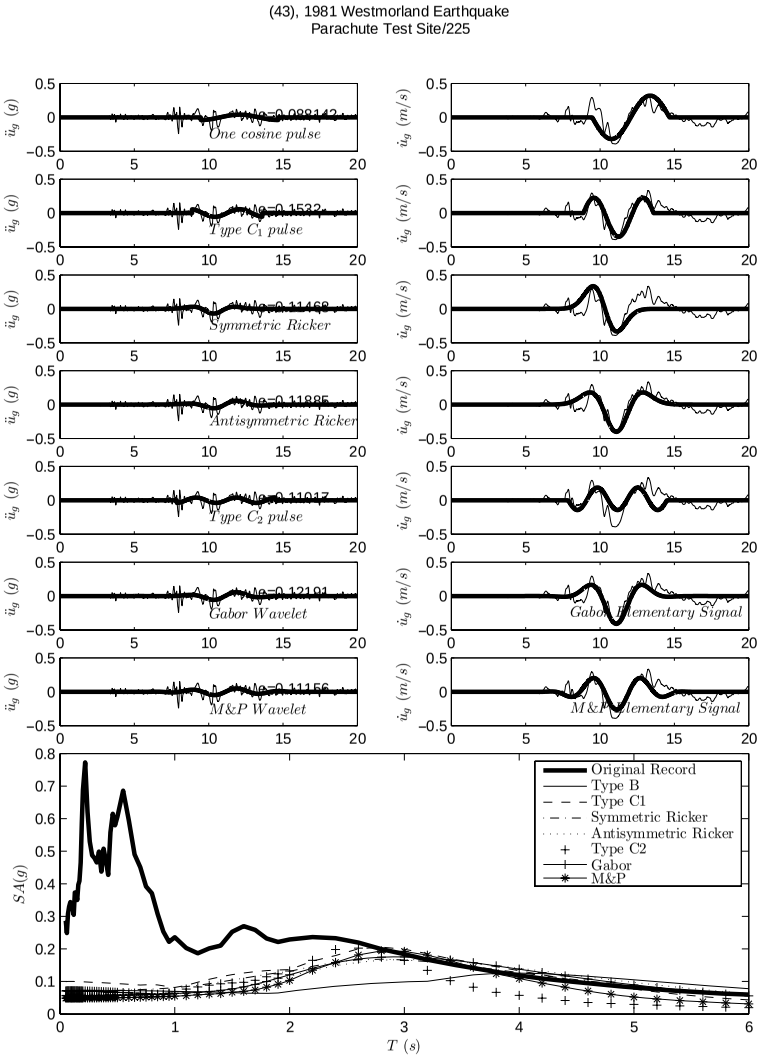

Fig. 13. *Matching of the acceleration record with various wavelets (left) and the resulting velocity signals (right). In the wavelet transform all daughter wavelets have same amplitude. Bottom: Comparison of the elastic acceleration response spectra with 5% viscous damping.*

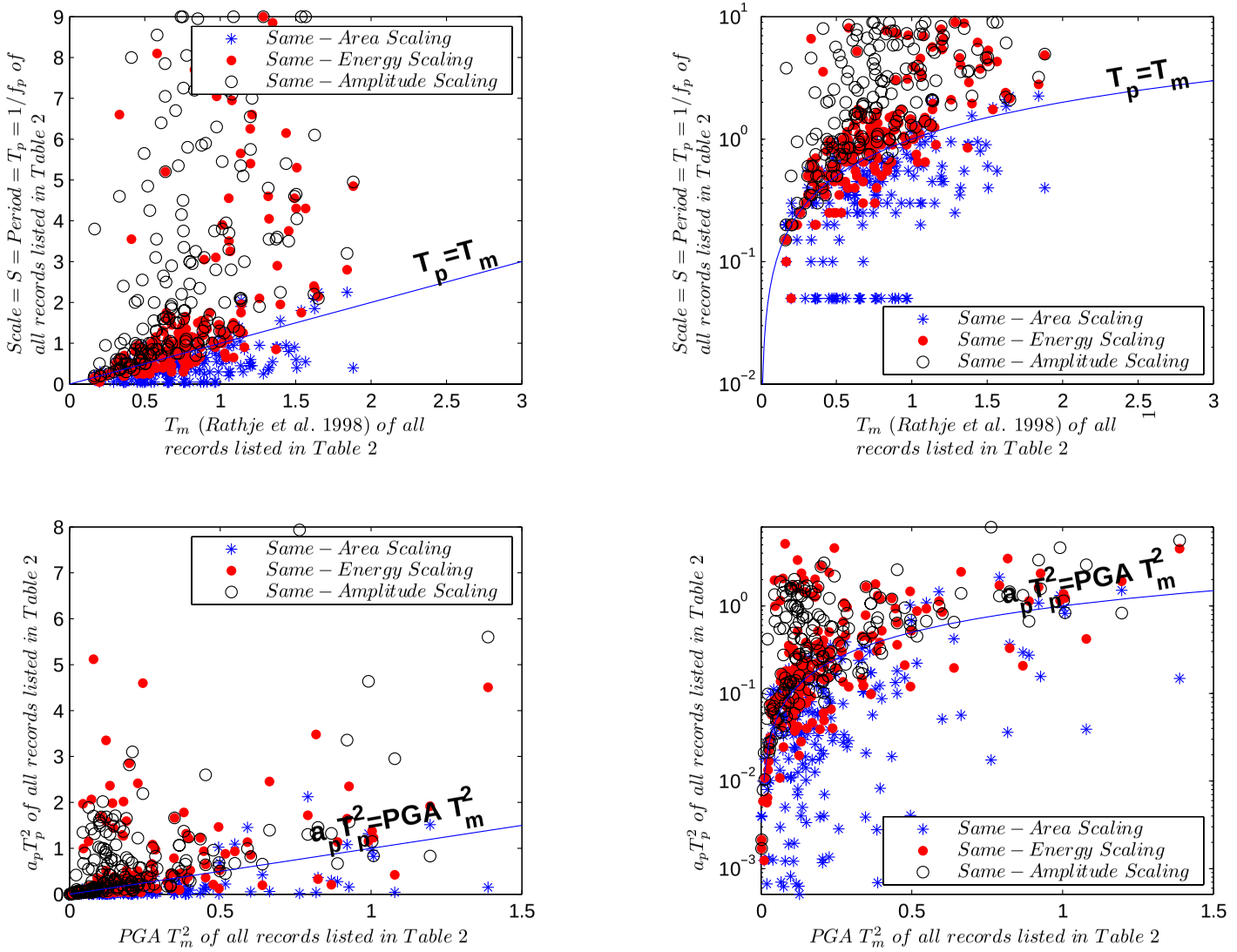

Fig. 13. Top: Comparison of the length scale T_p=S as a result from the extended wavelet transform of the records when convolved with the M&P wavelets, together with the period T_m (Rathje et al., 1998). Bottom: Comparison of the corresponding energetic length scales, $a_p T_p^2$, resulted from the M&P wavelets together with the length scale $L_e = PGA \cdot T_m^2$.

(T_p=0.6s) extracted with the last five wavelets (from symmetric Ricker to the M&P wavelet) is most relevant to structures with a fundamental period = 0.6s (3-6 story buildings); while the longer period acceleration pulse extracted with the first two wavelets (one cosine and Type C_1 pulses) is most relevant to the structures with fundamental period above 3s (e.g. seismic isolated structures and longer period bridges). In order for the last five wavelets (from the symmetric Ricker to the M&P wavelet) to capture the longer acceleration pulse that dominates the velocity signal, the same energy requirements needs to be replaced by the same amplitude requirement (a weighting function that suppresses less the longer scales) as shown in Fig. 6.

In conclusion, in any given record different pulses may be extracted with each weighting function, *w(s)*. For instance, the parameters of the pulses that result to the maximum pseudoacceleration of two elastic SDOF oscillators with natural periods T_0=0.5s and T_0=2.5s are marked with bold face in Table 3.

In calculating the maximum pseudoacceleration response, the closed form expressions offered in the paper by Mavroeidis et al. (2004) are used. Similarly, using the charts of Fig. 6 of Mavroeidis et al. (2004) one can determine which pulse is the most destructive to a given inelastic SDOF. The parameter *A* which controls the amplitude of the velocity pulse appearing in the closed form expression of Mavreoeidis and Papageorgiou (2003) is also offered in Table 3.

The challenge to extract a representative time scale of an earthquake is not new. About a decade ago Rathje et al. (1998) examined three popular frequency content parameters and concluded that the mean period ,

$$T_m = \frac{\sum_j C_j^2 \frac{1}{f_j}}{\sum_j C_j^2} \quad \text{for } 0.25\text{Hz} \le \text{fj} \le 20\text{Hz}, \qquad (12)$$

appears to be the best simplified time–scale characterization parameter. In equation (12) C_j = Fourier amplitudes of the entire acceleration record, and f_j = Discrete Fourier Transform Frequencies between 0.25Hz and 20Hz. Fig. 7 plots along the horizontal axis the computed mean period, T_m, of the earthquake records listed in Table 3, and in the vertical axis the corresponding periods of the records extracted with the M&P wavelets when the weighting function in the extended wavelet transform enforces that all daughter wavelets have (a) the same area, (b) the same energy and (c) the same amplitude. Fig. 7 indicates that when the same-area scaling is selected (stars) in the extended wavelet transform (suppression of the long-periods) the extracted pulses are mostly short period with pulse periods below the values of T_m as expressed by equation (12). When the same energy scaling is selected (dark circles), the extracted pulses have pulse periods close to the values of T_m up to approximately values of T_p=1s and beyond this value the pulses extracted with the wavelet transform have pulse periods much larger than T_m. Finally when the same amplitude scaling is selected (empty circles) in the extended wavelet transform (accentuation of large periods) the extracted pulses have consistently period larger than those predicted by T_m. As a conclusion, for structures which have natural period below 1s the time-scale of the acceleration record offered by Tm as given by equation (12) is dependable and can be used with confidence. This good agreement explains the good correlation of the results reported in the dimensional analysis study reported by Dimitrakopoulos et al. (2009) and Karavassilis et al. (2009).

6. CONCLUSIONS

In this paper we develop and validate a mathematically formal procedure to extract the characteristic time scales and length scales of strong ground motions. The procedure uses wavelet analysis to identify and approximate energetic acceleration pulses (not velocity pulses). The study shows that the weighting function in the definition of the wavelet transform has a dominant role in extracting a specific pulse. For instance longer pulses which are often detected visually in the velocity records (and have attracted the attention of Mavroeidis and Papageorgiou (2003) and Baker (2007) among others) can be systematically captured with the wavelet transform of the acceleration records by implementing a less suppressive weighting function.

The capability of several popular symmetric and antisymmetric wavelets to locally match the energetic acceleration pulse is examined; and it is concluded that the exercise to identify the best matching wavelet shall incorporate, in addition to the standard translation and dilation–contraction of the traditional wavelet transform, a phase modulation together with a manipulation of the oscillatory character (addition of cycles) of the wavelet. This need leads to the extension of the wavelet transform to a more general wavelet transform during which the mother wavelet is subjected to the four abovementioned functions.

The paper examines the performance of two similar elementary signals–the seminal elementary signal proposed by Gabor (1946) and its variation proposed by Mavroeidis and Papageorgiou (2003) which in addition to a period (scale) parameter and an amplitude parameter, include a phase parameter, φ, and an oscillatory character parameter γ. The time derivatives of these abovementioned elementary signals satisfy the conditions for a wavelike function to be a wavelet and are defined as the Gabor and the Mavroeidis and Papageorgiou (M&P) wavelets.

The paper examines the capability of the Gabor anf M&P wavelets to locally match the energetic acceleration pulse of 183 strong ground motions and it shows that the performance of the proposed extended wavelet transform which convolves the acceleration record with the abovementioned four-parameter wavelets outshines the performance of the traditional wavelet transform which convolves the acceleration record with any two–parameter wavelet.

Finally the paper compares the resulted time scales of the 183 records examined with the mean period that has been proposed by Rathje et al. (1998) as a dependable time–scale characterization parameter of an acceleration record. When the same-area scaling is selected (stars) in the extended wavelet transform (suppression of the long-periods) the extracted pulses are mostly short period with pulse periods below the values of T_m as expressed by equation (12). When the same energy scaling is selected (dark circles), the extracted pulses have pulse periods close to the values of Tm up to approximately values of T_p=1s and beyond this value the pulses extracted with the wavelet transform have pulse periods much larger than T_m. Finally when the same amplitude scaling is selected (empty circles) in the extended wavelet transform (accentuation of large periods) the extracted pulses have consistently period larger than those predicted by T_m. As a conclusion, for structures which have natural period below 1s the time-scale of the acceleration record offered by T_m as given by equation (12) is dependable and can be used with confidence.

Acknowledgements:

Partial financial support for this study has been provided to the first author by the Alexander S. Onassis Public Benefit Foundation.

References:

Abrahamson NA and Somerville P(1996). Effects of the hanging wall and foot wall on ground motions recorded during the Northridge earthquake, Bull. Seism. Soc. Am. 86, S93–S99.

Baker WJ, (2007) Quantitative classification of near fault ground motions using wavelet analysis, Bull. Seism. Soc. Am., 97, 1486-1501

Dimitrakopoulos E., A. J. Kappos and N. Makris (2009). Dimensional analysis of yielding and pounding structures for records without distinct pulses, Soil Dynamics and Earthquake Engineering 29, 1170-1180

Gabor, D (1946). Theory of communication. I. The analysis of information, IEEE 93, 429–441.

Karavasilis T.L., N. Makris, N. Bazeos, and D.E. Beskos (2009). Dimensional response analysis of multi-storey regular steel MRF subjected to pulse-like earthquake ground motions" J. Struct. Eng. (ASCE) (under review)

Makris, N., and S. Chang. (2000). Effect of viscous, viscoplastic and friction damping on the response of seismic isolated structures. Earthquake Eng. Struct. Dyn., 29, 85–107.

Makris N, and Black C (2004c). Evaluation of peak ground velocity as a ''good'' intensity measure for near-source ground motions, J. Eng. Mech., ASCE 130, 1032-1044

MATLAB. High-performance Language Software for Technical Computation. The MathWorks, Inc.: Natick, MA, 2002

Mavroeidis GP, Papageorgiou AS (2003) A mathematical representation of near-fault ground motions, Bull. Seism. Soc. Am., 93, 1099-1131

Mavroeidis GP, G. Dong, AS. Papageorgiou Near-fault ground motions, and the response of elastic and inelastic single-degree-of-freedom (SDOF) systems. Earthquake Engineering and Structural Dynamics 2004; 33, 1023–1049.

Papageorgiou AS (1998). The character of near-source ground motions and related seismic design issues, in Proc. of the Structural Engineers World Congress, San Francisco, California, 18–23 July 1998.

Rathje, E. M., N. A. Abrahamson, J. D. Bray, (1998) Simplified Frequency Content Estimates of Earthquake Ground Motions, J. Geotech. and Geoenvir. Engrg. 124, 150-159

Ricker N (1944). Wavelet functions and their polynomials, Geophysics 9, 314–323.

Somerville P and Graves R (1993). Conditions that give rise to unusually large long period ground motions, Struct. Design Tall Buildings 2, 211–232.

Somerville P (1998). Development of an improved representation of near-fault ground motions, SMIP98-CDMG, Oakland, California, 1–20.

Vassiliou MF, Makris N (2009) Estimating Time Scales and Length Scales in Earthquake Acceleration Records, Bull. Seism. Soc. Am. (Submitted)Newmark, N.M. and Rosenblueth, E. (1971), "Fundamentals of Earthquake Engineering," Prentice-Hall Inc.

Trifunac, M.D. and Brady, A.G. (1975), "A Study on Duration of Strong Earthquake Ground Motion," *Bulletin of the Seismological Society of America*, **65**(3), 581-626.

JOINT CONFERENCE PROCEEDINGS
7th International Conference on Urban Earthquake Engineering (7CUEE) &
5th International Conference on Earthquake Engineering (5ICEE)
March 3-5, 2010, Tokyo Institute of Technology, Tokyo, Japan

LONG-PERIOD GROUND MOTION SIMULATION OF OSAKA SEDIMENTARY BASIN FOR A HYPOTHETICAL NANKAI SUBDUCTION EARTHQUAKE

Tomotaka Iwata[1] and Asako Iwaki[2]

1) Professor, Disaster Prevention Research Institute, Kyoto University, Japan
2) Graduate Student, Disaster Prevention Research Institute, Kyoto University, Japan
iwata@egmdpri01.dpri.kyoto-u.ac.jp, iwaki@egmdpri01.dpri.kyoto-u.ac.jp

Abstract: Long-period ground motion simulations for the hypothetical Nankai subduction earthquake are studied. We confirmed the Osaka basin and crustal velocity structure model that covers the source area of the Nankai earthquake and the Osaka basin by modeling of long-period ground motion of the largest aftershock of the 2004 off Kii peninsula earthquake. The simulated ground motions by our velocity model reproduce the observed ground motions well. Then we simulate long-period ground motions for the hypothetical Nankai earthquake using that velocity model and discuss the ground motion characteristics in the Osaka sedimentary basin.

1. INTRODUCTION

Ground motion simulations and predictions based on the source model and the underground velocity structure model are quite important for understanding of the strong ground motion characteristics and related earthquake disaster. Since the 1994 Northridge, USA, and the 1995 Kobe, Japan, earthquakes occurred, strong motion simulations using the heterogeneous source and realistic three-dimensional underground velocity structure models have become successful and quite popular in the research field of applied seismology and earthquake engineering.

In Japan, Kinki area has higher seismic hazard potentials, especially in the Osaka sedimentary basin that has a large population. The Headquarters for earthquake research promotion, the Ministry of Education, Culture, Sports, Science, and Technology (MEXT), Japan, reported that occurrence potentials of the next M8-class Nankai and Tonankai earthquakes are high: about 60 to 70 percent within the next 30 years starting from the 2009 (Headquarters for Earthquake Research Promotion 2009). We have already experienced long-period ground motions from the M8-class events rocked facilities on basin or sedimentary sites located at 200-300 km away from the source region, e.g. well known damages in Mexico-city during the 1985 Michoacan earthquake, and in the Tomakomai, Hokkaido, Japan, during the 2003 Tokachi-Oki earthquake. In case of Tomakomai, the long-period ground motions, generated from the source and then amplified and elongated in the Yufutsu basin, damaged the fuel tanks (Koketsu *et al.*, 2005).

The Osaka sedimentary basin is located approximately 250 km away from the source regions of the hypothetical Tonankai and Nankai earthquakes. It is expected that modern mega-cities consisting of a large number of skyscrapers and fuel storage tanks of Osaka and Kobe, located in that basin, will surely be shaken by disastrous long-period ground motions. Therefore, reliable strong motion predictions at those sites are required for reducing earthquake disaster by long-period ground motions.

The velocity structure models for long-period ground motion simulation are already constructed by several organizations and research groups. In this study, first, we demonstrate the applicability of one of the velocity structure models for the strong motion evaluations through simulations of the ground motions observed by the dense strong motion observation network in Kinki area. Next, we simulate long-period ground motions for a hypothetical Nankai earthquake and discuss the ground motion characteristics of the Osaka sedimentary basin.

2. OSAKA SEDIMENTARY BASIN AND CRUSTAL VELOCITY STRUCTURE

In this study, we refer an Osaka basin and crustal velocity structure model given by Iwata et al. (2008). The Osaka sedimentary basin is filled with the late Cenozoic sediments (Ikebe et al. 1970) and surrounded by the Rokko Mountains (northwest), Hokusetsu Mountains (northeast), Ikoma Mountains (east), Izumi Mountains (south), and Awaji Island (west). It has a nearly ellipsoid shape with a length of 60 km in the NE-SW direction and a width of 40 km in the NW-SE direction. The central part of the basin is covered by the Alluvium that is 15–35 m thick. Below the Alluvium, there lie the sedimentary layer mainly composed of the Osaka group that contains marine clay layer in the upper part. The bedrock chiefly consists of granite rocks.

Geophysical investigation of the underground velocity structure by exploration surveys started as early as 1960 in

Osaka area (Kagawa *et al.* 2004a), which enabled several groups of researchers to construct basin structure models. Kagawa *et al.* (1993) incorporated the bedrock depth information obtained from refraction surveys, reflection surveys, gravity anomaly surveys, microtremor array measurements, down-hole logging, etc., and interpolated them using a two-dimensional third-order B-spline function (*e.g.* Koketsu and Higashi 1992) to model the bedrock geometry. They divided the sedimentary layer into three layers according to seismic wave velocities and densities estimated from the results of the reflection surveys and microtremor array measurements. As the spline model, composed only of a set of spline coefficients, can be easily modified by adding new control points, they have been continuously adopting new exploration information to improve their basin velocity structure model (Miyakoshi *et al.* 1997, 1999; Kagawa *et al.* 1998, 2004a). Iwata *et al.* (2008) introduced the improved basin structure model that includes new additional bedrock depth control points from exploration survey information, such as gravity anomaly data and microtremor survey results, in areas where those data were coarse in Kagawa *et al.* (2004).

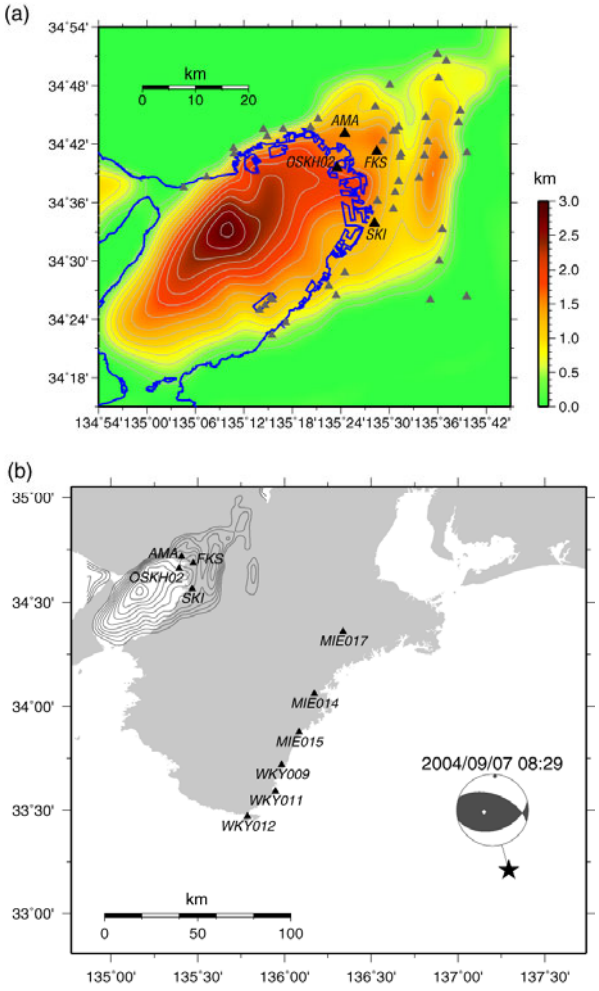

Figure 1 (a) Map of strong motion observation stations used in this study. Color and contour lines indicate the bedrock distribution of the Osaka basin model by Iwata et al. (2008). (b) Model area of for the ground motion simulation. The epicenter determined by JMA and mechanism by F-net, NIED, are shown. The triangles denote the observation stations.

The crustal velocity model by Iwata et al. (2008) covers the crust from the seismic bedrock and Moho discontinuity as well as the subducting Philippine-Sea plates. It was constructed by compiling great amount of data available such as OBS (Ocean Bottom Seismometer) velocity models, deep seismic profiles, receiver function inversion results, and 1D velocity models used for routine-work hypocenter determinations. They modeled the crustal velocity model as the stack of uniform velocity layers, same as the basin. The geometry of the interface depth of each layer is also represented using a two-dimensional third-order B-spline function.

3. VELOCITY STRUCTURE MODEL VALIDATION BY LONG-PERIOD GROUND MOTION SIMULATION

To validate the basin and crustal velocity structure model, we conduct a long-period ground motion simulation for the observed records during the largest aftershock 2004/09/07 08:29JST, M_{JMA}6.5) of the 2004 off the Kii peninsula earthquake (2004/09/05 23:57JST, M_{JMA}7.4). The reason we try to analyze the largest aftershock records is that the source time functions of the mainshock and the foreshock are complex (*e.g.* Yamada and Iwata 2005) and that of the largest aftershock is relatively simple.

We use the strong motion records of this event provided by the Committee of Earthquake Observation and Research in the Kansai Area (CEORKA; Kagawa *et al.* 2004b), K-NET (Kinoshita 1998) and KiK-net (Aoi *et al.* 2001) maintained by the National Research Institute for Earth

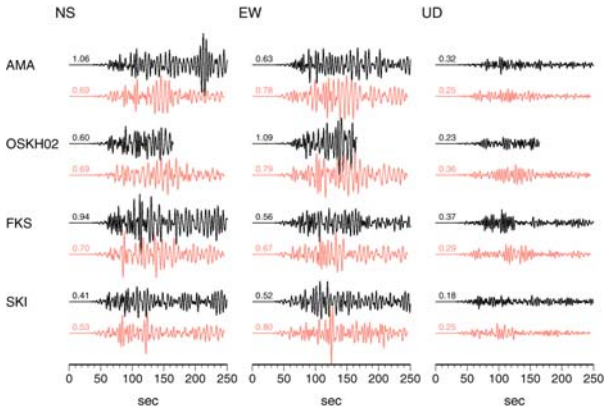

Figure 2 Comparison of the observed (black trace) and synthetic (red trace) velocity waveforms at stations inside the Osaka basin. The waveforms are band-pass filtered at 3 – 10 sec.

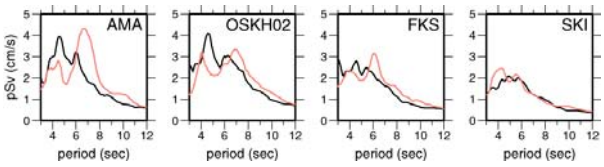

Figure 3 Comparison of the observed (black trace) and synthetic (red trace) pseudo velocity response spectra with 5% damping factor.

Science and Disaster Prevention (NIED), the seismic intensity observation network of Japan Meteorological Agency (JMA), and the strong motion network project of 10 electric power companies (Denkyo-net). In addition to the seismograms listed above that had been open to researchers, we have also collected the seismograms of two organizations: the Osaka City Waterworks Bureau (OCWB) and Kansai International Airport Co., Ltd (KIAC). In total, we use data from as many as 54 strong motion stations in and around the Osaka basin shown in Figure 1(a). The computation of seismic wave propagation is performed by a fourth-order 3D finite-difference method (FDM) using staggered grids with non-uniform spacing (Pitarka 1999). The model area size of the computation is 280 km (EW) × 250 km (NS) × 70 km (depth). The basin model is included in the northwest corner of the model with a volume of 105 km (EW) × 93 km (NS) × 3 km (depth). The model area is illustrated in Figure 1(b).

The source is modeled as a double couple point source, using the epicenter determined by JMA and the source mechanism by F-net of NIED. The source time function is represented by a bell-shaped function $f(t) = [1 - \cos(2\pi t/T_d)]/T_d$ with a duration time T_d. The source duration T_d as well as the source depth is estimated so as to fit the waveforms observed at K-NET stations outside of the Osaka basin in Kii peninsula. The source duration and source depth are estimated to be 4.5 s and 11 km, respectively.

We then simulate long-period ground motions and validate the basin model by comparing the observed and the synthetic waveforms in terms of velocity waveforms and pseudo-velocity response spectra (pSv). Figure 2 shows examples of the observed and synthetic velocity waveforms. AMA, OSKH02, FKS, and SKI are the stations in the central bay area where the bedrock depth is represented as 1.4 – 1.7 km in the model (see Figure 1(a)). In Figure 3, we show 5% pseudo-velocity response spectra of horizontal component. Not only waveforms but also peak periods and levels of ground motions in pSv are well reproduced. Iwaki and Iwata (2010) pointed out the simulations fairly well reproduced the observations except those at some stations at North-Eastern area of Osaka basin.

4. SIMULATION OF LONG-PERIOD GROUND MOTIONS FOR THE HYPOTHETICAL NANKAI EARTHQUAKE

Based on the simulation results discussed in the previous section, the Osaka basin and crust velocity structure model by Iwata *et al.* (2008) could be used as a reference velocity model for long-period ground motion simulations. We would like to conduct the prediction of the ground motion during a hypothetical Nankai earthquake. We use the hypothetical Nankai earthquake source model proposed by Sekiguchi *et al.* (2008), Their source model is based on the characterized source model (Irikura and Miyake 2001) by Central Disaster Management Council of Japan (2003) that consists of five asperities and a background area. They applied multi-scale heterogeneity to the slip and rupture velocity distributions so as to be fit for more realistic simulation in a broadband frequency range. Each of the six areas slips according to a slip velocity time function by Nakamura and Miyatake (2002) with different maximum slip and duration time.

The simulation is carried out by the 3D FDM (Pitarka 1999) at the periods 3s and longer. The size of the velocity structure model is 400 km (EW) × 344 km (NS) × 70 km (depth) that includes the entire source model and the Osaka basin area (Figure 4).

The source model by Sekiguchi et al. (2008) is composed of subfaults distributed every 1.5 km over the

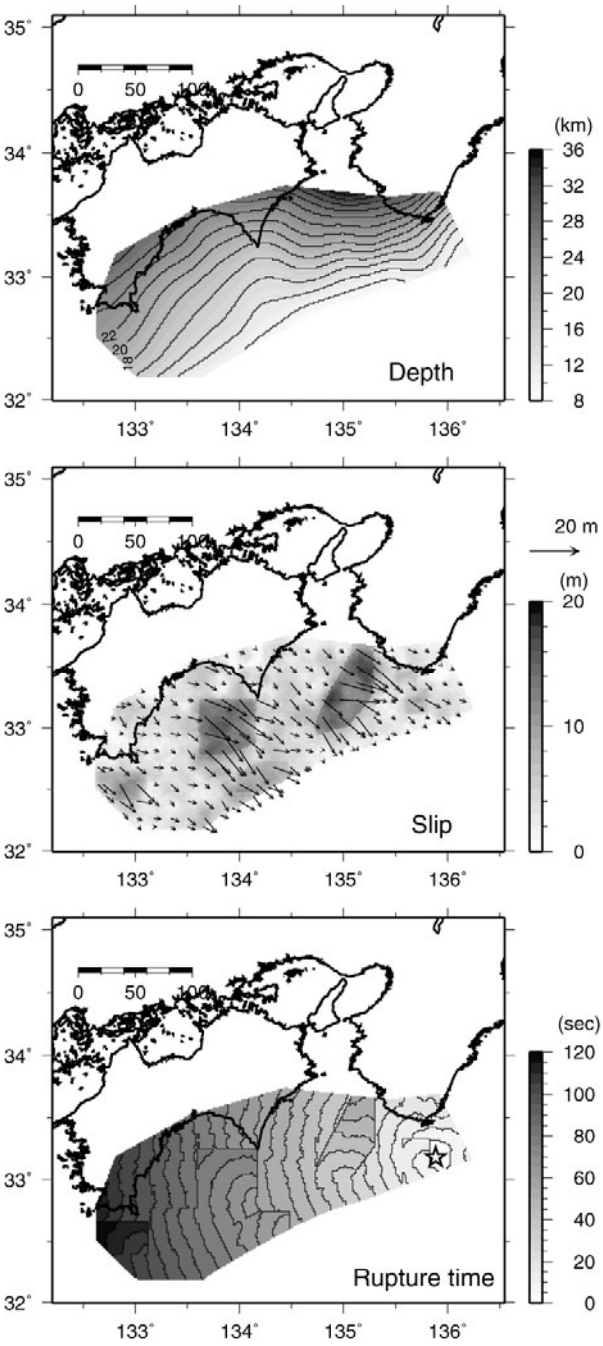

Figure 4 Source depth distribution (top), slip distribution and direction (middle), and rupture time distribution (bottom) of the hypothetical Nankai earthquake source model used in this study.

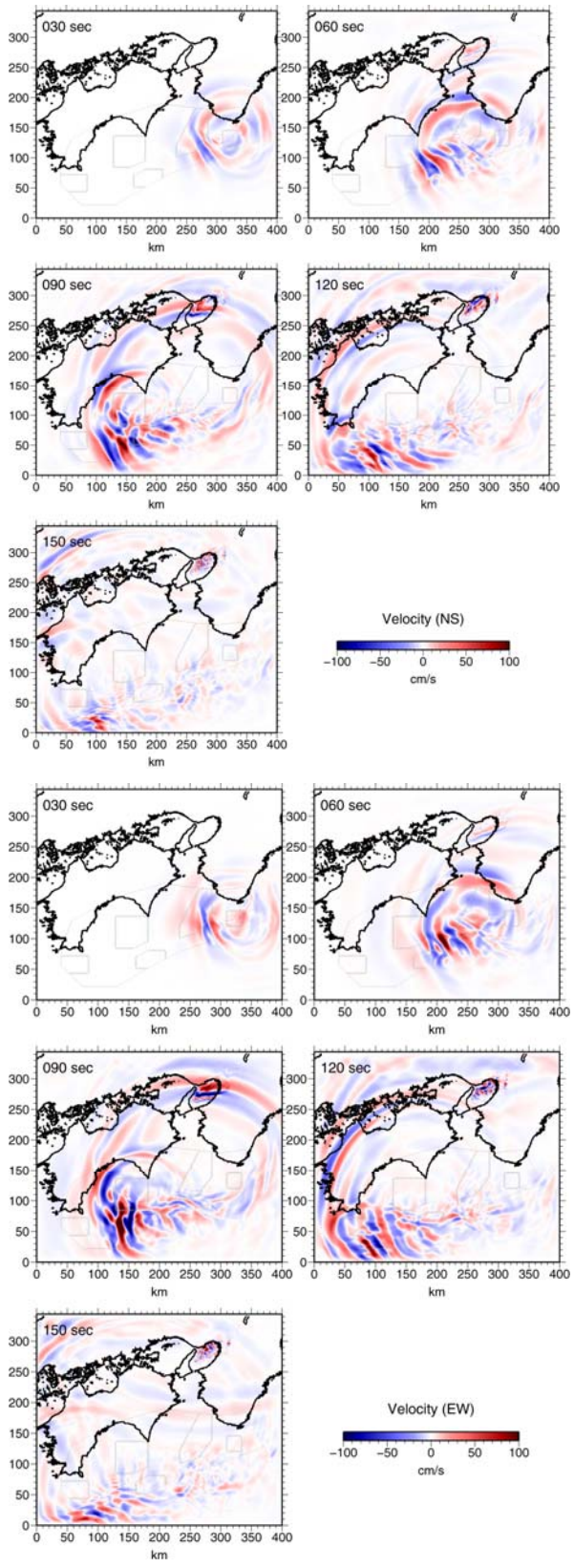

Figure 5 Snapshots of the ground velocity for NS (top) and EW(bottom) components at 30 to 150 seconds after the rupture starting time.

source area. We changed the depth of each subfault so that they are pasted on the upper surface of the Philippine Sea Plate of our crustal model. Consequently, our subfault depths

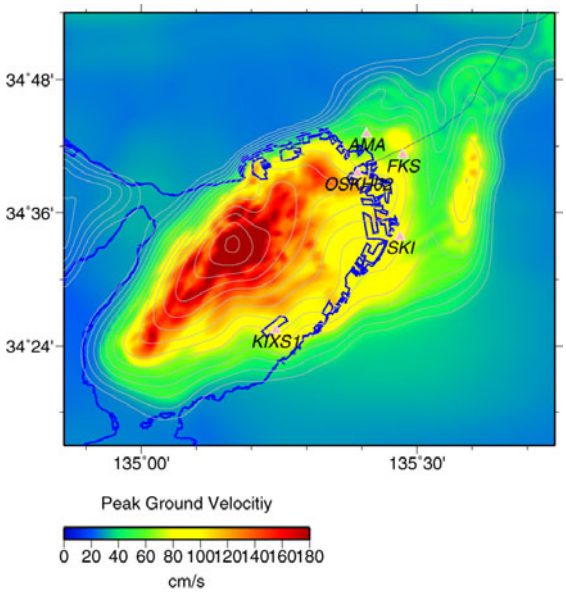

Figure 6 Distribution of the simulated maximum horizontal ground velocity in the Osaka basin.

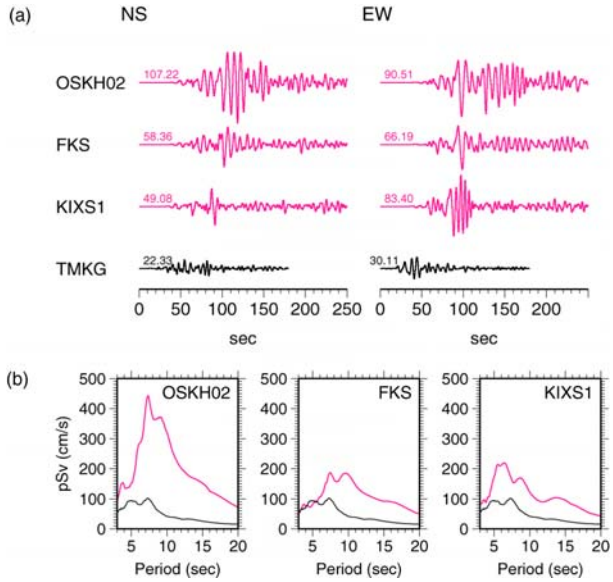

Figure 7 The simulated (a) velocity waveforms and (b) pSv for the hypothetical Nankai earthquake at stations in the Osaka basin (pink traces) compared with the observed pSv during the 2003 Tokachi-oki earthquake at Tomakomaoi port (black traces).

are systematically shallower than those of Sekiguchi *et al.* (2008) because the plate depth of our velocity model is shallower than theirs. The depth, slip, and rupture time distribution of the source model used in this study are shown in Figure 4.

Figure 5 shows the snapshots of the horizontal components of the velocity wavefield (bandpass filtered at 3–20 s). As the rupture starts at off Shionomisaki (southern promontory of Kii peninsula) area and propagates westward, large ground motions can be clearly observed on the west side of the rupture front at 60, 90, and 120 sec after the

rupture starting time. On the other hand, the Osaka basin experiences remarkable amplification of the long-period ground motions at approximately 60 sec, which still continues at 150 sec after the rupture starting time. In the Osaka basin area, at 60 second and 90 second, that is approximately the *S* -wave arrival time, the ground motions in the east-west component seems to be larger than that in the north-south component, which would be caused by the slip direction of the source. Figure 6 shows the distribution of peak horizontal ground velocity (PGV), i.e. the vector sum of the two horizontal components, in the Osaka basin area. The PGV value reaches 80 – 100 cm/s in the central area and the eastern area of the basin. In Figure 7, we compare the simulated ground motions and pSv (horizontal component) at OSKH02, FKS and KIXS1 (Kansai air-port island) with the observed ones during the 2003 Tokachi-oki earthquake at Tomakomai port. The maximum velocities at these Osaka coastal are higher than approximately 80 cm/s. The pSv value at period 6 s is approximately 480 cm/s at OSKH02 and higher than 200 cm/s at FKS and KIXS1, They are twice to five times as large as the pSv value observed at Tomakomai port.

4. CONCLUSIONS

We conducted a long-period ground motion simulation during a hypothetical Nankai earthquake using the validated Osaka basin and crustal velocity structure model. The simulated peak ground velocity reached 80 - 100 cm/s at the center and east part of Osaka. The pSv at period 6 s was as high as 480 cm/s at the bay area, which is nearly five times as large as the pSv observed at Tomakomai port during the 2003 Tokachi-oki earthquake. Discussion on plausible source scenarios of the hypothetical earthquake is needed in the future study.

Acknowledgements:

Strong motion data provided by the Committee of Earthquake Observation and Research in the Kansai Area, K-NET and KiK-net of the National Research Institute for Earth Science and Disaster Prevention (NIED), Japan Meteorological Agency (JMA), the strong motion network project of 10 electric power companies, the Osaka City Waterworks Bureau, Kansai International Airport Co., Ltd., Disaster Prevention Research Institute of Kyoto University, and the Port and Airport Research Institute were used in this study. The moment tensor solution by the F-net of NIED and the hypocenter information by JMA are also acknowledged. The figures in this thesis were drawn with the Generic Mapping Tools (Wessel and Smith, 1998).

References:

Aoi, S., Obara, K., Hori, S., Kasahara, K., and Okada, Y. (2001), "New Japanese uphole/downhole strong-motion observation network: KiK-net," *Seismological Research Letters*,**72**, 239.

Central Disaster Management Council of Japan (2003), Conference document, 16th conference of the Special Board of Inquiry on Tonankai and Nankai earthquake, http://www.bousai.go.jp/jishin/chubou/nankai/16/ (in Japanese).

The Headquarters for Earthquake Research Promotion (2009), Abstract of long term evaluation of subduction earthquakes, http://www.jishin.go.jp/main/choukihyoka/kaikou.htm (in Japanese).

Ikebe, N., Iwatsu, J. and Takenaka, J. (1970), "Quaternary geology of Osaka with special reference to land subsidence," *Journal of Geosciences. Osaka City University*, **13**, 39-98.

Irikura, K. and H. Miyake (2001), "Prediction of strong ground motions for scenario earthquakes," *Journal of Geography*, **110**, 849-875 (in Japanese with English abstract)

Iwaki, A. and T. Iwata (2010), "Simulation of long-period ground motion in the Osaka sedimentary basin: performance estimation and thte basin structure effects," submitted to *Geophysical Journal International*.

Iwata, T., Kagawa, T., Petukhin, A. and Onishi, Y. (2008), "Basin and crustal velocity structure models for the simulation of strong ground motions in the Kinki area, Japan," *Journal of Seismology*, **12**, 223-234.

Kagawa, T., Sawada, S., Iwasaki, Y., and Nanjo, J. (1993), "Modeling the deep sedimentary structure in the Osaka basin," *Proceedings of the 22nd JSCE Earthquake Engineering Symposium*, pp.199–202 (in Japanese).

Kagawa, T., Sawada, S., Iawasaki, Y., and Nanjo, J. (1998), "*S* -wave velocity structure model of the Osaka sedimentary basin derived from microtremor array observations," *Zisin 2* (*Journal of the Seismolgical Society of Japan.*), **51**, 31–40 (in Japanese with English abstract).

Kagawa, T., Zhao, B., Miyakoshi, K., and Irikura, K. (2004a), "Modeling of 3D basin structures for seismic wave simulations based on available information on the target area: case study of the Osaka basin," *Bulletin of the Seismological Society of America*, **94**, 1353–1368.

Kagawa, T., Iemura, H., Irikura, K., and Toki, K. (2004b), "Strong ground motion observation by the Committee of Earthquake Observation and Research in the Kansai area (CEORKA)," *Journal of Japan Association for Earthquake Engineering*, **4**(3), 128–133.

Kinoshita, S. (1998), "Kyoshin Net (K-NET)," *Seismological Research Letters*, **69**, 309–332.

Koketsu, K., Hatayama, K., Furumura, T., Ikegami, Y., and Akiyama, S. (2005), "Damaging long-period ground motions from the 2003 *MW*8.3 Tokachi-oki, Japan, earthquake," *Seismological Research Letters*, **76**, 67–73.

Koketsu, K. and Higashi, S. (1992), "Three-dimensional topography of the sediment/basement interface in the Tokyo metropolitan area, central Japan," *Bulletin of the Seismological Society of America*, **82**, 2328–2349.

Miyakoshi, K., Kagawa, T., Sawada, S., Echigo, T. and Horie, Y. (1997), "Modeling the deep sedimentary structure in the Osaka basin (2)," *Proceedings of the 24th JSCE Earthquake Engineering Symposium*, 33–36 (in Japanese).

Miyakoshi, K., Kagawa, T., Zhao, B., Tokubayashi, M., and Sawada, S. (1999), "Modeling the deep sedimentary structure in the Osaka basin (3)," *Proceedings of the 25th JSCE Earthquqke Engineering Symposium*, 185–188 (in Japanese).

Nakamura, H. and Miyatake, T. (2000), "An approximate expression of slip velocity time function for simulation of near-field strong ground motion," *Zisin 2 (Journal of the Seismological Society of Japan)*, **53**, 1-9.

Pitarka, A. (1999), "3D elastic finite-difference modeling of seismic motion using staggered grids with nonuniform spacing," *Bulletin of the Seismological Society of America*, **89**, 54–68.

Sekiguchi, H., Yoshimi, M., Horikawa, H., Yoshida, K., Kunimatsu, S., and Satake, K. (2008), "Prediction of ground motion in the Osaka sedimentary basin associated with the hypothetical Nankai earthquake," *Journal of Seismology*, **12**, 185-195.

Wessel, P. and Smith, W. H. F. (1998), "New, improved version of the Generic Mapping Tools released," *EOS Transactions, American Geophysical Union*, **79**, 579.

Yamada, N. and Iwata, T. (2005), "Long-period ground motion simulation in the Kinki area during the *MJ*7.1 foreshock of the 2004 off the Kii peninsula earthquakes," *Earth Planets Space*, **57**, 197-202.

JOINT CONFERENCE PROCEEDINGS
7th International Conference on Urban Earthquake Engineering (7CUEE) &
5th International Conference on Earthquake Engineering (5ICEE)
March 3-5, 2010, Tokyo Institute of Technology, Tokyo, Japan

EFFECTS OF SHALLOW SOIL LAYERS ON PROPAGATION OF LONG-PERIOD GROUND MOTION IN LARGE BASIN IN 3D NUMERICAL SIMULATION

Hiroaki Yamanaka[1], and Shou Akeda[2]

1) Associate Professor, Dept. of Environmental Science and Technology, Tokyo Institute of Technology, Japan
2) Graduate Student, Dept. of Environmental Science and Technology, Tokyo Institute of Technology, Japan
yamanaka@depe.titech.ac.jp

Abstract: Shallow surface layers with S-wave velocities less than 0.4 km/s over the engineering bedrock are usually excluded in a model used in 3D numerical simulations of long-period earthquake ground motion in a large basin, because of limitations of computational resources. Therefore, the effects of the shallow soil layers are estimated by multiplying the 1D amplification factors of the shallow soils to the synthetic motion on the surface of the 3D basin model having no shallow soils with an assumption of the vertical propagation of S-waves in hybrid approaches. The appropriateness of the procedure is not examined because of the above-mentioned difficulties in numerical computations. In this study we investigated the effects of the shallow soils over the engineering bedrock by comparing synthetic motions calculated for 3D basin models with and without the shallow soils layers. In order to calculate high frequency synthetic motion in the basin models having the surface layers with very low S-wave velocities, the large parallel computer, TSUBAME, in Tokyo Institute of Technology is used with 900 CPUs and total core memories of 1.6TB. We calculate the synthetic motions for the basins from finite-difference simulations by Yamada and Yamanaka (2003). The shallow soils with an S-wave velocity of 0.2km/s and a thickness of 100 meters affect the ground motion so much at periods less than 2 seconds at irregular parts of the shallow basin, because of generation of surface waves. The effects can not be sufficiently estimated by the above 1D amplification of the shallow soils.

1. INTRODUCTION

Numerical simulations of seismic wave propagation in 3D basin models have been often used in estimation of long-period earthquake ground motion due to a large earthquake for providing fundamental materials in seismic design of high rise buildings, base-isolation buildings and so on (AIJ, 2009). In particular, the simulation based on finite difference approximation of the equation of motion in elastic Earth's model is very popular in strong motion seismology (e.g., Frankel and Vidale, 1992). The recent increase of computer performance and accumulation of data in subsurface structure also allow us to use the 3D simulation in practical estimation of strong motion at a site during a future large event. However, the period range in the 3D simulations is usually limited in long-period motion, such as at periods more than 1 second. The estimation of ground motion at periods less than 1 second is still a tough computational task. Therefore, a subsurface structural model is digitized with the spatial interval that is as large as possible in the upper limit of the allowable range. Shallow near-surface soils are also neglected in models used in the 3D simulations. The high frequency ground motion is estimated in a hybrid approach that is a combination of 3D simulation in the long-period range and 1D simulation in the short-period range (AIJ, 2009). Shallow soils are included into the subsurface structural model that is used in the 1D simulation of the hybrid approaches. However, only vertically propagating S-waves are included in the estimation of the high frequency motion in the hybrid approaches, and the effects of laterally propagating waves are neglected. The appropriateness of the treatments of the shallow soils in the hybrid approaches is not sufficiently examined. In particular, the accuracy of estimated ground motion is not clearly known at around the connecting period of the 3D and 1D simulations in the hybrid methods. The connecting period is usually set at 1 to 2 seconds in many of the hybrid simulations (e.g., AIJ, 2009). This period range is of important in earthquake engineering, because earthquake damage of wooden houses are mainly controlled by ground motion in this period ranges (Sakai, 2001).

In this study, we discussed effects of modeling shallow near-surface soils in 3D numerical simulation by computing ground motion using a massive parallel computer. The appropriateness of treatment of the shallow soils in the hybrid approaches are also discussed in this paper.

2. METHOD AND SIMULATION MODEL

2.1 Basin and Source Models

The subsurface structural model used in this study is

shown in Figure 1. The physical parameters for the layers of the model are also tabulated in Table 1. The model has a shallow low-velocity layer (layer 1 in Figure 1) with an S-wave velocity of 200m/s at the top of the shallow basin part of the model. The second layer corresponds to the engineering bedrock having an S-wave velocity of 500m/s. The depth to the second layer is 60meters or 100meters in the main part of the shallow basin part. It is noted that the thickness of the shallow soil in this model is similar to the actual depth of the Holocene layers in the downtown area of the Tokyo bay (Endo et al., 1884). The deep sedimentary basin consists of 3 layers having S-wave velocities of 0.5, 1.0, 1.5km/s as similar to those in Kanto basin (Yamanaka and Yamada, 2006). The S-wave velocity of the seismic bedrock is 3km/s. The layers beneath the seismic bedrock correspond to the Crustal and Mantle. These layers are modeled as a flat layered model as can be seen in Figure 1. We call this model as Model 1. The cross section of the model is also displayed in Figure 1.

The second model (Model 2) without any shallow layers is also examined for the comparison with Model 1. This model has the same layers with the same geometry as those of Model 1 except for the top shallow layer with the low velocity. The physical parameters of the top low velocity layer in Model 1 are replaced with those of the second layer in Model 2.

The computational area is 50×50km in the horizontal direction and 45km in vertical direction. A double couple point source is applied to the models. The point source is located at a depth of 20 km shown by a star in Figure 1. The double couple source is characterized with a strike, dip and rake of 190, 45, 60 degrees, and the seismic moment is 1.26 $\times 10^{18}$ Nm. The source time function used is the smoothed ramp function with a rise time of 1 second.

Table 1. Physical parameters

Layer	Vp(km/s)	Vs(km/s)	ρ(g/cm^3)
1	1.6	0.2	1.8
2	1.8	0.5	1.9
3	2.4	1.0	2.1
4	3.2	1.5	2.3
5	5.5	3.0	2.5
6	6.7	3.8	2.9
7	8.0	4.2	3.3

2.2 Finite Difference Computation

A finite difference approximation of the equation of motion in elastic media was used in the 3D simulation of wave propagation. We followed the finite difference algorithm by Yamada and Yamanaka (2003) in this study. The algorithm is based on the staggered grid approximation of the equation expressed with stress and velocity with a fourth-order and second order accuracy in space and time, respectively. The subsurface structural models were discretized with rectangular grid cells. The horizontal grid spacing is 25 meters, while the grid spacing in the vertical direction is 25 meters down to 0.5km from the surface, 100 meters down to 3km and 300 meters to the bottom of the model. The total number of the grid cells is 2000×2000×180. The minimum S-wave velocity of the model and minimum grid spacing allows us to estimate ground motion at periods longer than 0.6 second in the following simulations.

We used a massive parallel computer 'TSUBAME' at the computer center of Tokyo Institute of Technology. The parallel computer consists of 10612 CPUs (Mainly Opteron Dual Core 2.4GHz) with 85 Tflops/s Linpack performances at the peak. We could use 900 CPUs of the computer in this study. The total core memory used is approximately 3.6TB. The original FD code by Yamada and Yamanaka, 2003) was parallelized using the Message Passing Interface (MPI) for the use of the parallel computer. In the programming we used the same approach by Kasamatsu and Yamanaka (2006). The computational area of the subsurface structural model was divided into 5×5×36 sub-spaces in horizontal and vertical directions. The calculation of velocity and stress in each subspace was conducted with each CPU, and those at the interface between the subspaces are exchanged at each time step using the MPI.

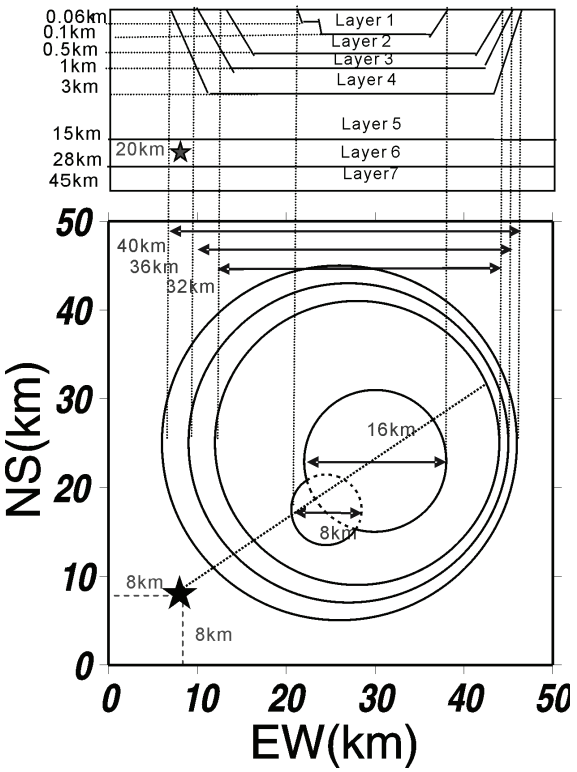

Figure 1. Subsurface structural model used in 3D simulation. The double couple point source by a star is used. The synthetic motions in Figure 2 were computed at the surface along a dotted line.

3. RESULTS OF 3D COMPUTATIONS

Figure 2 shows the three components of the ground velocity computed at the surface of the Model 1 and 2 at the sites along the dotted line in Figure 1 with an interval of 1.8km. It is noted that the calculated motions were filtered using a bandpass filter at periods from 0.6 to 10 seconds in the following. The ground motions for the two models with and without the low velocity model near the surface are not so significantly different in the area outside of the shallow basin (distance less than 16.2kmin the figure). However, the ground motions in the shallow basin differ from each other. The ground motions for Model 1 are larger and more complex than those for Model 2, because of the amplification of S-waves and generation of surface waves in the low velocity layer. The differences between Model 1 and 2 are significant in the horizontal motions in a comparison with the vertical one, although the surface wave generation can be identified in the vertical component similar to the horizontal one.

Figure 3 shows the distributions of the peak values of ground velocities in the east-west direction on the surface of Model 1 and Model 2. The peak values are large near the marginal parts of the shallow basin in Model 1. The spatial variations of the peak velocity in Model2 are more moderate than that of Model 1. The ground velocities at site A, B, and C in Figure 3 are displayed in Figure 4. The ground motions at the same locations for the Model 2 are also shown in the figure by solid lines. The ground motions for Model 1 and 2 are almost the same up to 10 second after the initial P-wave arrival. The slight differences of the wave forms are caused by the arrival time differences due to the existence of the low velocity layer in Model 1. The motions after the S-wave arrivals are significantly different from each other. In particular the later phase at 34 seconds at site A exhibits large amplitude at a period of about 1 second. Similar later phases can be also seen in the synthetics at sites B and C with different arrival times. It is therefore suggested that the large later arrivals in the synthetics for Model 1 show very a low propagation velocity, indicating major contributions of the surface wave. The snap shots of the ground velocity on the surface for Model 1 are displayed in Figure 5. The spatial variations of the amplitudes are large as can be seen in the figures. We can easily understand that the later arriving phases with large amplitudes have a propagation apparent velocity of about 300 m/s. This velocity is similar to group velocity of Love waves for the 1D model in the shallow basin. Figure 6 shows the theoretical group velocities for fundamental modes of Love and Rayleigh waves in the 1D models without the shallow soils (Model2) and with shallow soils having thicknesses of 60 and 100meters (Model 1).

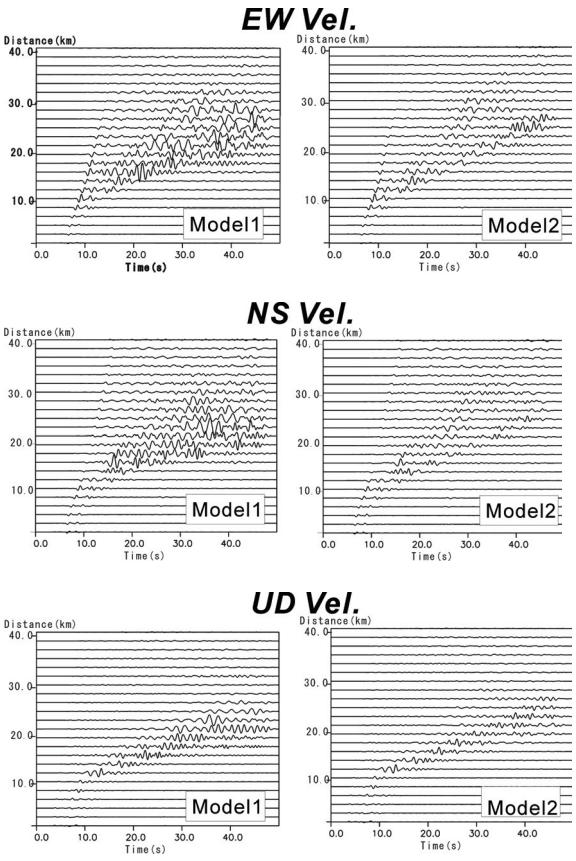

Figure 2 Ground velocities in east-west (top), north-south (middle) and vertical (bottom) components for Model 1 (left) and 2 (right).

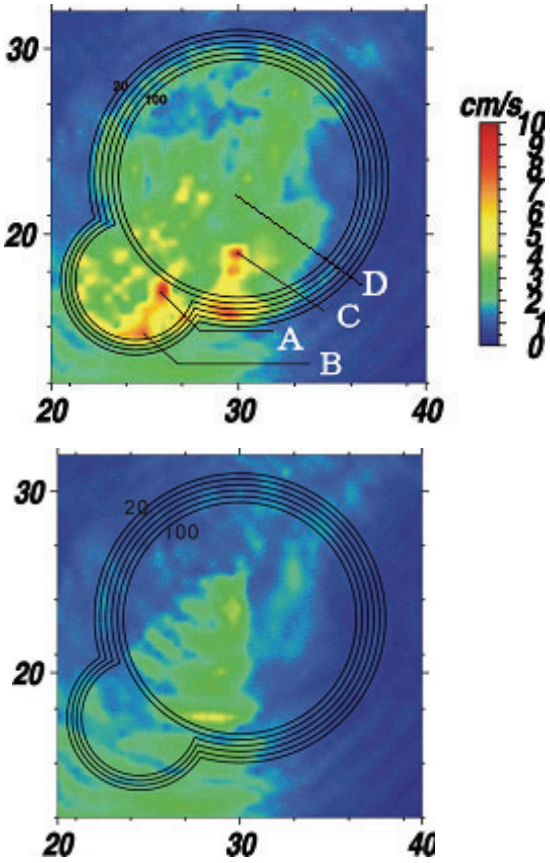

Figure 3 Distribution of peak ground velocity in east-west direction at the surface for Model l (top) amd 2 (bottm)

These features of the synthetic motions indicate that the later phases are generated at the edge of the shallow basin, and propagate as Love wave in the shallow basin.

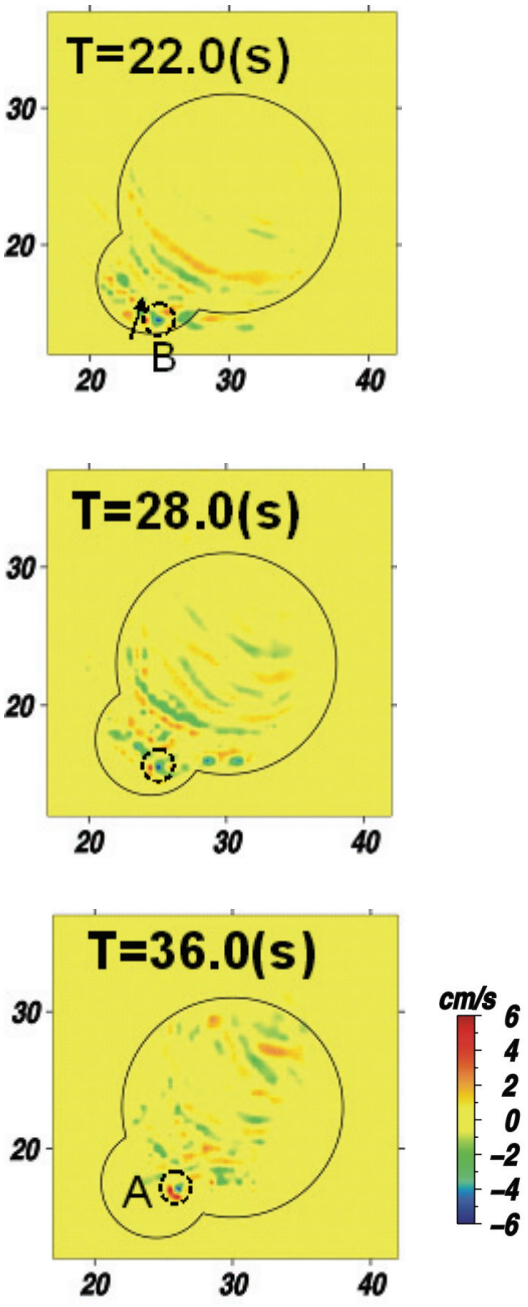

Figure 5 Snap shots of east-west oriented ground velocities at times of 22, 28, 36 seconds for Model 1.

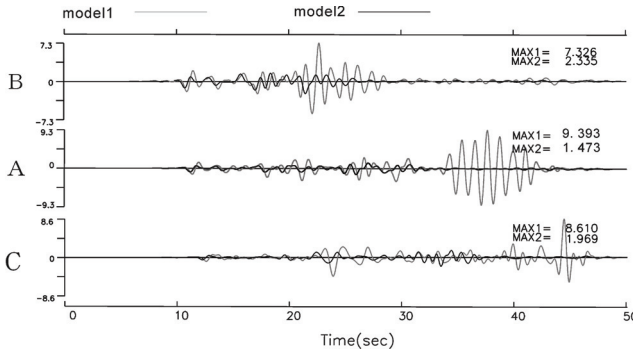

Figure 4 Comparison between synthetic ground velocities at site A, B, and C for Model 1 (dotted lines) and 2 (solid lines). All the traces are filtered at periods from 0.6 to 10 sec.

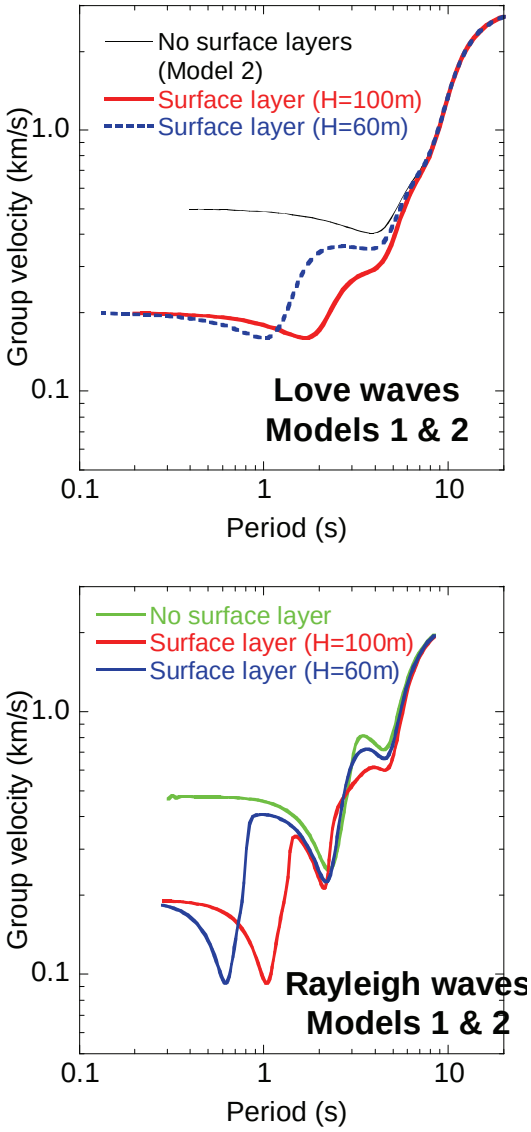

Figure 6 Group velocities for Love (Top) and Rayleigh (bottom) waves for Model 1 with shallow soils having thicknessed of 60 and 100 meters and Model2.

4. COMPARISON WITH 1D AMPLIFICATION

We compared spectral characteristics of the synthetic motions for Model 1 and 2. Figure 7 shows the Fourier spectra of the synthetic velocities at sites of A, B, C and D (see Figure 4 for their locations). The spectral shapes for the ground motions in Model 1 and 2 are similar at periods more than 2 or 3 seconds, indicating the appropriateness of neglecting the effects of the shallow layer over the engineering bedrock in long-period ground motion estimation. We also compared the spectra for Model 1 with spectra calculated from the hybrid approach. The 1D amplification factors for the shallow soil with an S-wave velocity of 200m/s in Model 1 are shown in Figure 8. The amplification factor for sites A and B has a dominant peak at a period of 1 second, while that for sites C and D is characterized by peak at 2 seconds. These amplification factors are multiplied with the spectra on the engineering bedrock of Model 2 in Figure 8 as similar to the hybrid approach. These amplified spectra are shown by broken lines in Figure 7. The amplified spectra at the sites of B and D are almost the same in a wide period range. However, the spectra for Model 1 at A and C are not well reconstructed with the hybrid approach. In particular, the dominant peak at site A can not be estimated by the broken line. This peak is attributed by the generation of the surface waves in the shallow basin, which is not included in the 1D amplifications in the hybrid approach. Similar differences of the ground motions for Model 1 and 2 can be identified in the vertical component as in Figure 9. Since surface waves are dominant at periods of 1 to 2 seconds in the horizontal components as explained above, Rayleigh wave contributes so much to the peak motion in the vertical component.

The appearance of short-period surface wave at periods of about 1 second is sometimes indicated from analysis of later phases in observed strong ground motions (e.g., Phillips et al., 1993). Furthermore, it is also pointed out that surface

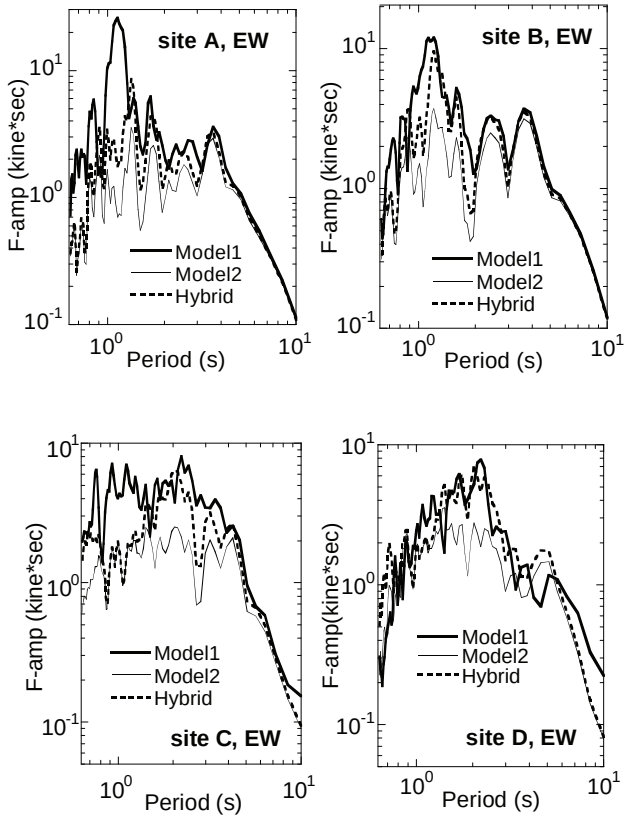

Figure 7 Comparison of spectra for Model 1 (solid line) and 2 (thin line).The spectra estimated with hybrid approach is also shown by broken line.

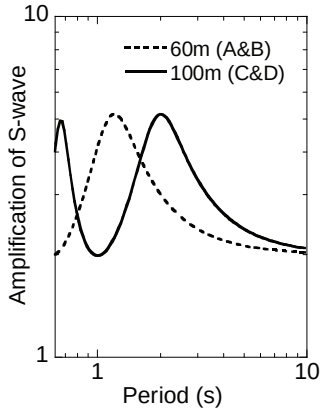

Figure 8 Amplification factors for shallow layer with an S-wave velocity of 200m/s.

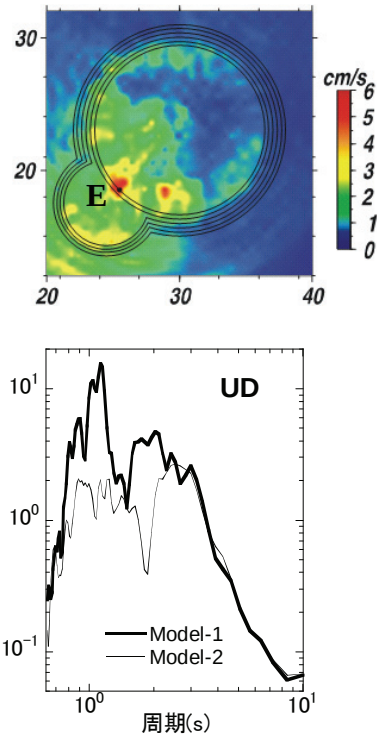

Figure 9 Comparison of spectra of vertical motions for Model 1 (solid line) and 2 (thin line) at point E in the top figure.

wave contributions are larger than that of S-waves in 1-second ground motions observed in the downtown of Tokyo where deep Quaternary layers exist (Iida et al., 2005). These observational results are in agreement with what we concluded from the simulations.

5. CONCLUSIONS

The effects of shallow low velocity layers over the engineering bedrock having an S-wave velocity of about 500m/s were investigated using 3D simulation of wave propagation. The shallow soils that are usually neglected in 3D simulations can generate short-period surface waves at periods of about 1 to 2 seconds at a site with thick Quaternary layers, such as downtown part of Tokyo area. This kind of short-period surface waves can not be estimated with 1D amplification of S-waves in the shallow soils. Therefore, the hybrid approach for broad band ground motion simulation underestimates ground motion at site with thick Quaternary layers. These effects must be included appropriately in strong ground motion estimation in a basin using 2D/3D simulation.

Acknowledgements:

The authors acknowledge financial support from the Japan Ministry of Education, Culture, Sport, Science, and Technology (MEXT).

References:

Endo K., T. Takano, and K. Sekimoto (1984), "Soft soils in Kanto plain," *The Earth Monthly*, 6-11, 672-676 (in Japanese).

Frankel, A, and J. Vidale (1992), "A three-dimensional simulation of seismic waves in the Santa Clara Valley, California, from a Loma Prieta aftershock," *Bull. Seism. Soc. Am.*, 82, 2045 – 2074, 1992.

Iida, M., H. Yamanaka, and N. Yamada (2005), "Wave field estimation by borehole recordings in the reclaimed zone of Tokyo Bay," *Bull. Seism. Soc. Am*., 95, 1101-1119, 2005.

Kasamatsu, K., and H. Yamanaka (2006), "Estimation of a 3D basin model around the fault area of the 2004 Mid Niigata prefecture earthquake using simulation of earthquake ground from small events,", *Geophysical Exploration*, 59, 475-484, (in Japanese).

AIJ (Architectural Institute of Japan) (2008), "Generation guide for seismic input motions based on the recent advancement of ground motion studies, 72-74 (in Japanese).

Phillips, W.S., S. Kinoshita, and H. Fujiwara (1993), "Basin-induced Love waves observed using the strong-moiton array at Fuchu, Japan," *Bull. Seism. Soc. Am.*, 83, 64-84.

Sakai, Y., Y. Tsuno, K. Koketsu, T. Kanno (2001), "Destructive power of design ground motion in the revised enforcement order of the building standard law," Proc. 29th symposium of earthquake ground motion, 111-122, (in Japanese).

Yamada, N., and H. Yamanaka (2003), "Ground motion simulations of moderate earthquakes for comparison of performance of 3D subsurface structural models in Kanto plain for strong motion prediction," *J. Seism. Soc. Japan*, 56, 111-123 (in Japanese).

Yamanaka, H., and N. Yamada (2006), "Modeling 3D S-wave velocity structure of Kanto basin for estimation of earthquake ground motion," *Geophysical Exploration*, 59, 549-560 (in Japanese).

JOINT CONFERENCE PROCEEDINGS
7th International Conference on Urban Earthquake Engineering (7CUEE) &
5th International Conference on Earthquake Engineering (5ICEE)
March 3-5, 2010, Tokyo Institute of Technology, Tokyo, Japan

BROADBAND STRONG-MOTION EVALUATION BY A HYBRID METHOD FOR THE MIYAGI-OKI EARTHQUAKES, JAPAN

Susumu Ohno[1)]

1) Associate Professor, Disaster Control Research Center, Tohoku University, Japan
ohnos@archi.tohoku.ac.jp

Abstract: For the forthcoming Miyagi-oki earthquakes, Japan, a subsurface structure model in the Miyagi-oki area is developed based on strong motion simulation. A characterized asperity model for the 1978 Miyagi-oki earthquake is proposed and it is found that the asperity is concentrated in small areas compared with average subduction-zone earthquakes in Japan. It is also found that strong motions from the far-offshore fault could dominate at long periods in Sendai.

1. INTRODUCTION

In and around the Miyagi-oki area, northeastern part of Japan, damage causative earthquakes of magnitude about 7.5 to 8 have occurred repeatedly about 40-year period. It is very important to make reliable source models for the past Miyagi-oki earthquakes and a subsurface structure model to estimate ground motions for the forthcoming earthquakes in this area.

In this paper, the following investigations are conducted: 1) a subsurface structure model for the Miyagi-oki area is constructed and its validity is checked by strong motion simulation, 2) a characterized asperity model of the 1978 Miyagi-oki earthquake is proposed, 3) contribution from far-offshore area for the forthcoming earthquake is estimated.

2. STRONG-MOTION SIMULATION USING 3-D SUBSURFACE STRUCTURE MODEL FOR MIDDLE EARTHQUAKES

2.1 Long-period Simulation

Fig.1 shows the area of strong motion simulation. Rectangles are fault models of the expected Miyagi-oki earthquakes proposed by the Headquarters for Earthquake Research Promotion (2005). Filled triangles are strong-motion stations of NIED and JMA.

A 3-D subsurface structure model is constructed by the following procedure. For the part shallower than seismic basement (S-wave velocity of 3.0km/s), a 3-D model is constructed based on the report by the Central Disaster Prevention Council (2004). Basement depth of the model is shown in Fig. 1. For the part deeper than the seismic basement, the 1-D model of Niimi (2009), which is based on travel-time simulation, is adopted. A layer of oceanic crust is also included as shown in the E-W section in Fig. 1. Table 1 is the velocity model of the subsurface structure.

To check the validity of the model, long-period ground motion simulations for two middle (M6.0) earthquakes are conducted. One is the 12/17/2005 earthquake, occurred at a relatively deep position (depth of 40km) near A1- fault and the 1978 Miyagi-oki faulting area. The other is the 08/31/2005 earthquake, occurred at a shallow position (depth of 13km) of far offshore area. CMT solutions of these earthquakes are plotted at their epicenters in Fig. 1.

Figure 2 shows the observed and simulated velocity traces. Simulation is conducted by 3D-FDM using GMS (Aoi and Fujiwara, 1999), with a point source of smoothed ramp function. See the caption of Fig.2 for the other parameters. Q-values are determined as Table 1 to simulate amplitudes of later phases in Fig. 2.

For both of the deep and shallow earthquakes, amplitudes and durations of the simulated waves generally agree with the observed waves, both in S-wave and later arrivals.

2.2 Short-period and Hybrid Simulation

For the above two M6.0 earthquakes, short-period strong motion simulations are conducted using the stochastic simulation method by Boore (1983) with SH-wave amplification due to surface soil. $Q(f) = 100f$, f is frequency, is used as Q-value of the propagation path based on the spectral inversion results by Ohno (2008).

As the velocity models shallower than the engineering bedrock (S-wave velocity of 0.7km/s), PS-profiles are used for the NIED stations, while velocity models in the report of Miyagi Prefecture (2004) are used for the other stations.

Using results of the long-period 3D-FDM simulations

and the short-period stochastic simulations, broadband waveforms are evaluated by the hybrid procedure of Irikura and Kamae (1999). The connecting period is 1s for the 12/17/2005 earthquake and 0.5s for the 08/31/2005 earthquake.

Figure 3 shows pseudo velocity response spectra (5% damping) of the observed records and the hybrid simulation waveforms. For both of the deep and shallow earthquakes, spectra of the simulated waves agree well with those of the observed waves, except that the simulations overestimate at period shorter than 0.2s for the 08/31/2005 earthquake. This is probably due to difference in fmax or Q of the propagation path, and further investigation is needed.

3. STRONG-MOTION SIMULATION FOR THE 1978 MIYAGI-OKI EARTHQUAKE

3.1 Long-period Simulations

The last disastrous earthquake in the Miyagi-oki area was the 06/12/1978 (M7.4) earthquake. Recently, several researchers investigated variable-slip and characterized asperity models for this earthquake (e.g., Wu et al., 2008; Kamae et al., 2002; Nozu, 2008). Kato et al. (2005) estimated a variable-slip model by waveform inversion of strong motion records. Okutsu et al. (2008) found that simulation results by Kato's model underestimate amplitude in Sendai, the largest city in the Tohoku region. They adjusted Kato's model to explain the long-period amplitude of observed records at SU2B in central Sendai, based on DWM simulation using 1-D subsurface structure model.

Fig. 4(a) shows a map of the fault model by Kato et al. (2005) with stations where strong-motions were recorded during the 1978 earthquake. Fig. 4(b) is slip-velocity time functions of the adjusted variable slip model (case number cs22) by Okutsu et al. (2008).

Based on the cs22 model, the slip-velocity functions are characterized as shown in Fig. 4(c). Table 2 shows summary of parameters of the asperity model. In this model, the asperity/total area ratio (6%) is clearly smaller than those of usual subduction earthquakes (20%) in Japan (Murotani et al., 2008). This tendency agrees with the result from the spectral inversion analysis that the high-frequency radiation strength of the Miyagi-oki earthquakes is larger than those of the earthquakes in the other Tohoku regions (Ohno, 2008).

Table 2 Parameters of the characterized asperity model for the 1978 earthquake

	Total	Asperity	Background	Asp./Total
Seismic Moment (N•m)	3.5E+20	1.0E+20	2.5E+20	29%
Area (km^2)	3200	192	3008	6%
slip (m)	1.9	8.8	1.4	-
rake (deg.)	-	45	90	-

For the cs22 and the characterized asperity models in Figs. 4(b) (c), long-period ground motions are simulated by 3D-FDM using the subsurface structure model constructed in chapter 2.1. Figure 5 shows the observed and simulated velocity waveforms. It is confirmed that both models reproduce the large pulses, commonly observed at all records, while overestimation at TRMD may need further investigation.

3.2 Short-period and Hybrid Simulation

Short-period ground motions for the 1978 earthquake are simulated by a stochastic green's function method. An element wave from each subfault is calculated by the Boore's method as chapter 2.2. The method of Dan and Sato (1999) is used for synthesis over the fault plane. Broadband waveforms are evaluated by the hybrid technique as chapter 2.2, with the connecting period of 1s.

Figure 6 shows pseudo velocity response spectra (5% damping) of the observed records and the hybrid simulations. The spectra of the simulated waves generally agree with those of the observed waves, while the simulation at SU2B significantly underestimate at periods of 0.5-1s. The reason of this gap is not clear at this stage, but a concept of superasperity could be one reason, as indicated by Matsushima and Kawase (2006).

4. LONG-PERIOD STRONG-MOTION EVALUATION FOR THE HYPOTHETIC MIYAGI-OKI EARTHQUAKES INCLUDING FAR-OFFSHORE FAULT

The Headquarters for Earthquake Research Promotion (2005) estimate that the fault at far-offshore area (fault B in Fig. 1) could rupture jointly with the faults at near-onshore area (faults A1 and A2).

To investigate contribution of the fault at far offshore area, long-period ground motions are estimated by 3D-FDM. Characterized source models proposed by Dan et al. (2005) are used. Figure 7 shows the evaluation results at SU2B, central Sendai, and it is found that the contribution from far-offshore area could be dominant at periods longer than 5s.

5. CONCLUSIONS

For the forthcoming Miyagi-oki earthquakes, Japan, a subsurface structure model in the Miyagi-oki area is developed based on strong motion simulation. A characterized asperity model for the 1978 Miyagi-oki earthquake is proposed and it is found that the asperity is concentrated in small areas compared with average subduction-zone earthquakes in Japan. It is also found that contribution from the far-offshore fault could dominate at long periods in Sendai.

Acknowledgements:

Strong motion records from National Research Institute for Earth Science and Disaster Prevention (NIED), Port and Airport Research Institute (PARI), and Japan Meteorological Agency (JMA) are used. GMS of Aoi and Fujiwara (1999) is used for 3D-FDM. The author thanks Mr. Cao Miao at Tohoku University for his help to make the subsurface structure model.

References:

Aoi, S. and Fujiwara, H. (1999). "3-D finite difference method using discontinuous grids," *Bulletin of the Seismological Society of America*, **89**, 918-930.

Boore, D. M (1983) "Stochastic simulation of high-frequency ground motions based on seismological models of the radiated spectra, " *Bulletin of the Seismological Society of America*, **73**, 1865-1894

Central Disaster Prevention Council (2004) http://www.bousai.go.jp/jishin/nihonkaikou/3/index.html

Dan, K. and Sato, T. (1999) "A Semi-empirical Method for Simulating Strong Ground Motions Based on Variable-Slip Rupture Models for Large Earthquakes," *Bulletin of the Seismological Society of America*, **89**(1), 36-53.

Dan, K., Hata, N., Muto, T., Miyakoshi, J., and Kanda J. (2005) "Probabilistic Design Earthquake Ground Motion Considering Scenario Earthquakes, Part 3: Faulting Scenario of the Plate-Boundary Earthquakes Off Miyagi Prefecture and Strong Ground Simulation, " *Summaries of Technical Papers of Annual Meeting, Architectural Institute of Japan*, B-1, 97-98.

Irikura, K. and Kamae, K. (1999) "Strong Ground Motions during the 1948 Fukui Earthquake. Estimation of Broad-band Ground Motion Using a Hybrid Simulation Technique," *Journal of the Seismological Society of Japan. Second Series*, **52**, 129-150

Kamae, K., kawabe, H., and Irikura, K. (2002) "Source model for the 1978 Miyagi-Oki earthquake (M7.4) in Japan," *Abstracts the Seismological Society of japan, 2007, Fall Meeting*, A24.

Matsushima, S., and Kawase, H. (2006) "Source model of a subduction zone earthquake with super-asperity," *Chikyu Monthly*, **55**, 98-102.

Miyagi Prefecture (2004) The 3rd Miyagi-prefecture Earthquake Damage Estimation Report, http://www.pref.miyagi.jp/kikitaisaku/jishin_chishiki/3higaishin/index.htm

Murotani, S., Miyake, H., and Koketsu, K. (2008) "Scaling of characterized slip models for plate-boundary earthquakes," *Earth Planets Space*, **60**, 987–991.

Niimi, M. (2009) Study on 3-D subsurface structure and long-period ground motion in Sendai City, *Master Thesis of Tohoku University*.

Nozu, A. (2008) "Site Amplification Factor at Kaihoku Bridge and Asperity size of the 1978 Miyagi-oki earthquake," *Proc. of the 6th Annual Meeting of Japan Association for Earthquake Engineering*, 266-267.

Okutsu, T., Motosaka, M., Yamamoto, Y., and Ohno, S. (2008) "Wide band wave form simulation of the 1978 Miyagiken-Oki earthquake in Sendai City, " *Tohoku Journal of Natural Disaster Science*, **44**, 57-62.

Ohno, S. (2008) "Development Of A Statistical Strong-Motion Evaluation Method Considering Regional Variation Of Source And Path Effects In The Tohoku Region, Japan," *14th World Conf. Earthq. Eng.*, 02-0072.

The Headquarters for Earthquake Research Promotion (2005) http://www.jishin.go.jp/main/kyoshindo/05dec_miyagi/index.htm

Wu, C., K. Koketsu and H. Miyake (2008) "Source processes of the 1978 and 2005 Miyagi-oki, Japan, earthquakes: Repeated rupture of asperities over successive large earthquakes," *J. Geophys. Res.*, **113**, B08316.

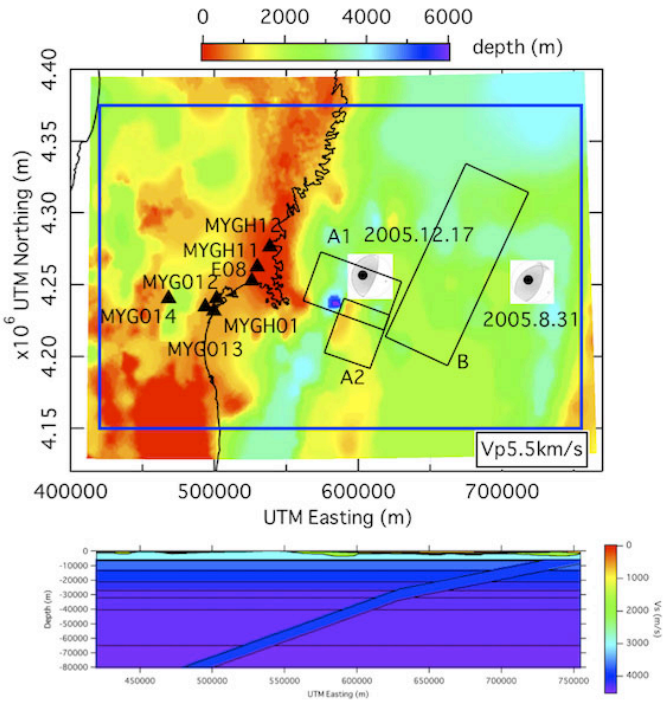

Table 1 Subsurface Velocity Structure Model

No	Vp (m/s)	Vs (m/s)	density (kg/m^3)	Q_0* (1Hz)	Depth(m)
1	2100	700	2000	500	
2	2100	700	2000	500	
3	2500	1000	2150	500	
4	3300	1400	2300	500	variable
5	4000	1800	2400	850	
6	4800	2400	2500	850	
7	5500	3000	2600	850	
8	5820	3500	2640	850	6500
9	6090	3660	2650	900	13000
10	6560	3950	2700	1250	21000
11	6940	4180	2750	1750	27000
12	7750	4350	2900	1750	32000
13	7780	4360	3100	2000	40000
14	7850	4400	3150	2500	65000
15	7920	4450	3200	2500	90000
16	8000	4500	3300	2500	12000
17	8100	4540	3350	2500	-
18	6800	3930	3000	2000	(oceanic crust)

$Q(f) = Q_0 f$, f: frequency (Hz)

Figure 1 Map of Fault Models, CMT Solutions of Middle Earthquakes, and Strong-motion Observation Stations. Basement Depth and E-W Section of the Subsurface Model are also shown.

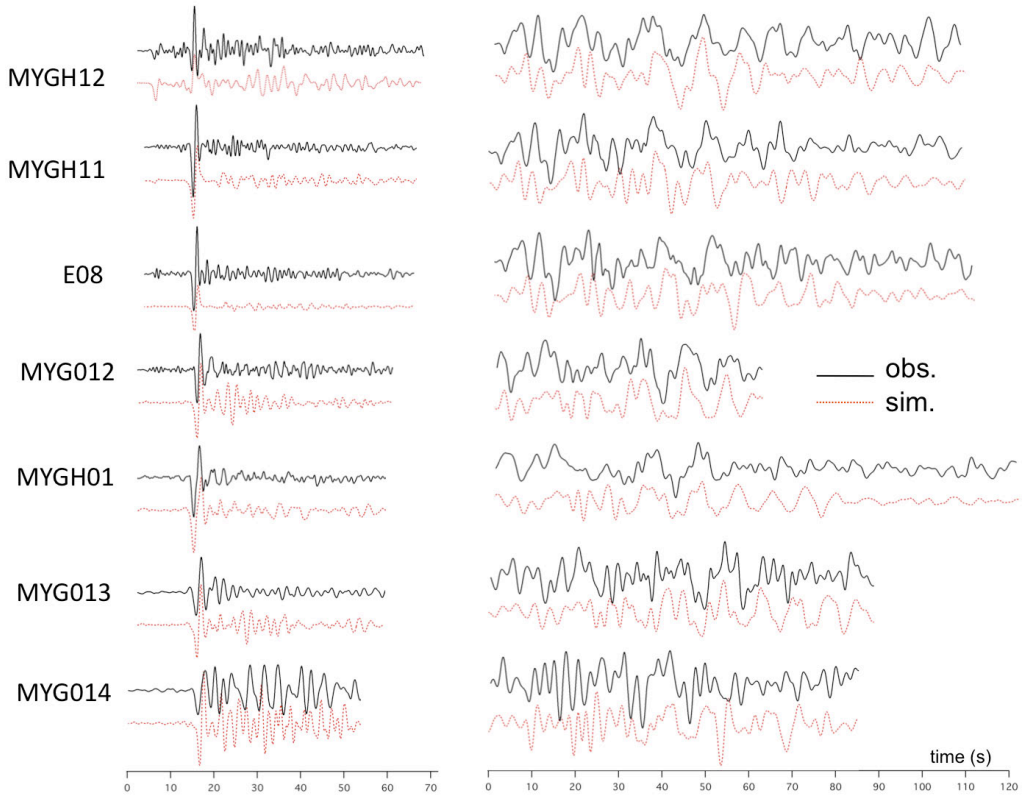

(a) 2005.12.17 NS (0-1Hz) (b) 2005.8.31 EW (0-0.5Hz)

Figure 2 Velocity Waveforms of Observation and 3D-FDM Simulation
(a) 12/17/2005 EQ. M6.0, F-net CMT Solution, Centroid Depth 40km, Width of Source Time Function 2.5s.
(b) 08/31/2005 EQ. M6.0, Global CMT Solution, Centroid Depth 13km, Width of Source Time Function 3.5s.
(Vertical axis is normalized by each record.)

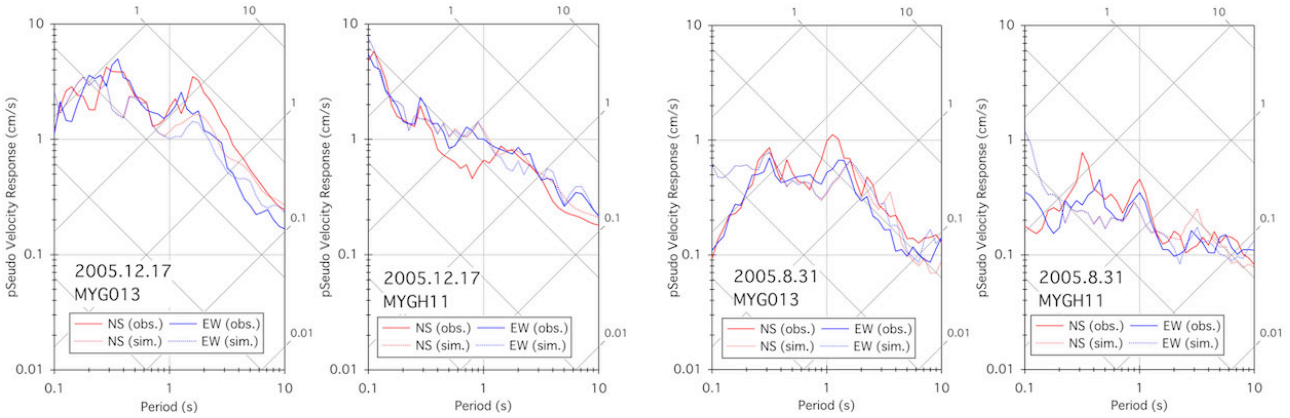

(a) 2005.12.17 (b) 2005.8.31

Figure 3 Response Spectra of Observation Records and Hybrid Simulation Results (fmax=10Hz, Radiation pattern coefficient Rθϕ = 0.63)

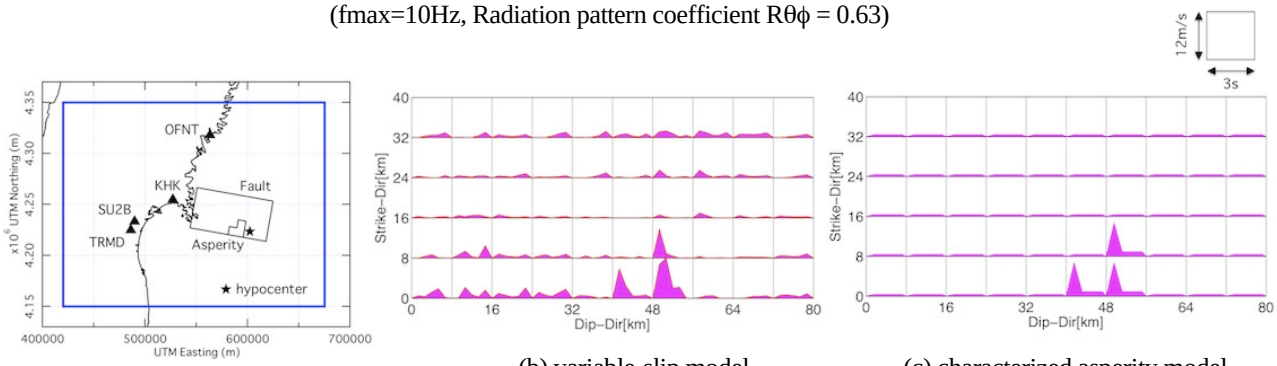

(a) map of fault and station (b) variable-slip model (cs22 by Okutsu et al., 2008) (c) characterized asperity model

Figure 4 Fault Model of the 1978 Miyagi-oki earthquake

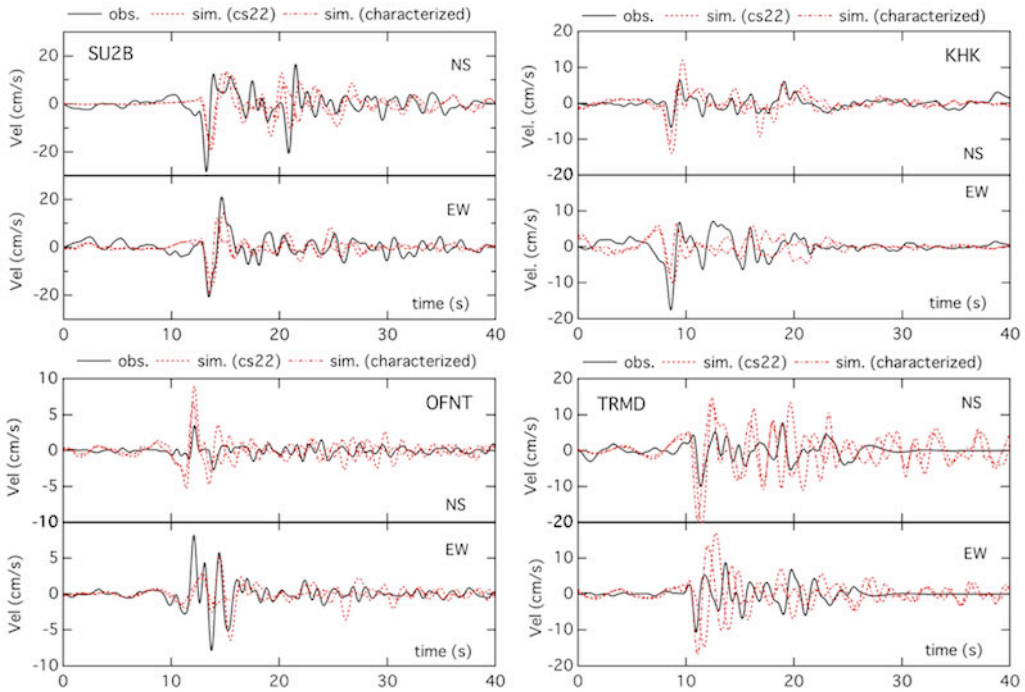

Figure 5 Velocity Waveforms of Observation and FDM Simulation using Variable Slip Model (cs22) and Characterized Asperity Model. Band-Pass Filter of 0.1-1Hz is applied for SU2B and KHK, 0.2-1Hz is applied for OFNT and TRMD.

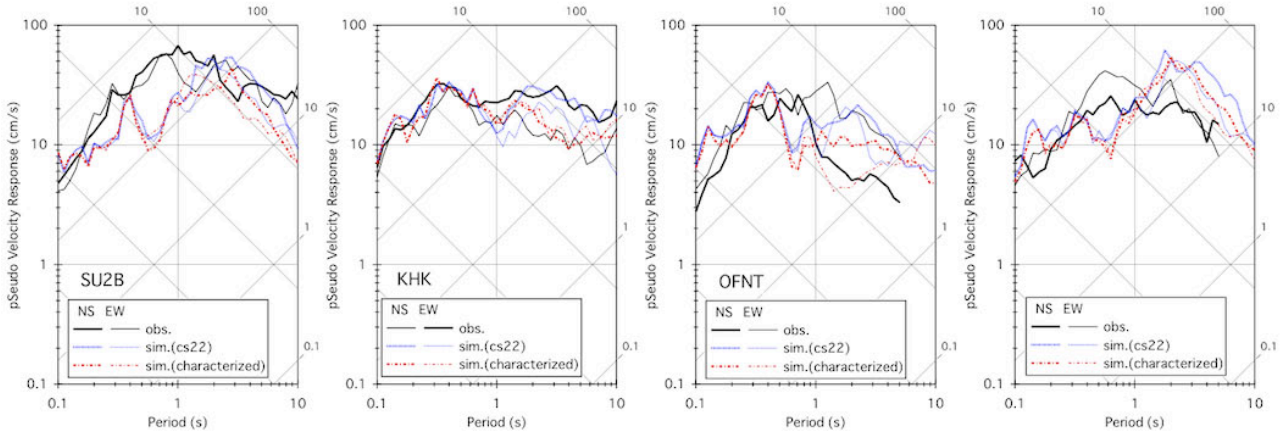

Figure 6 Response Spectra of Observation Records and Hybrid Simulation using Variable Slip Model (cs22) and Characterized Asperity Model.

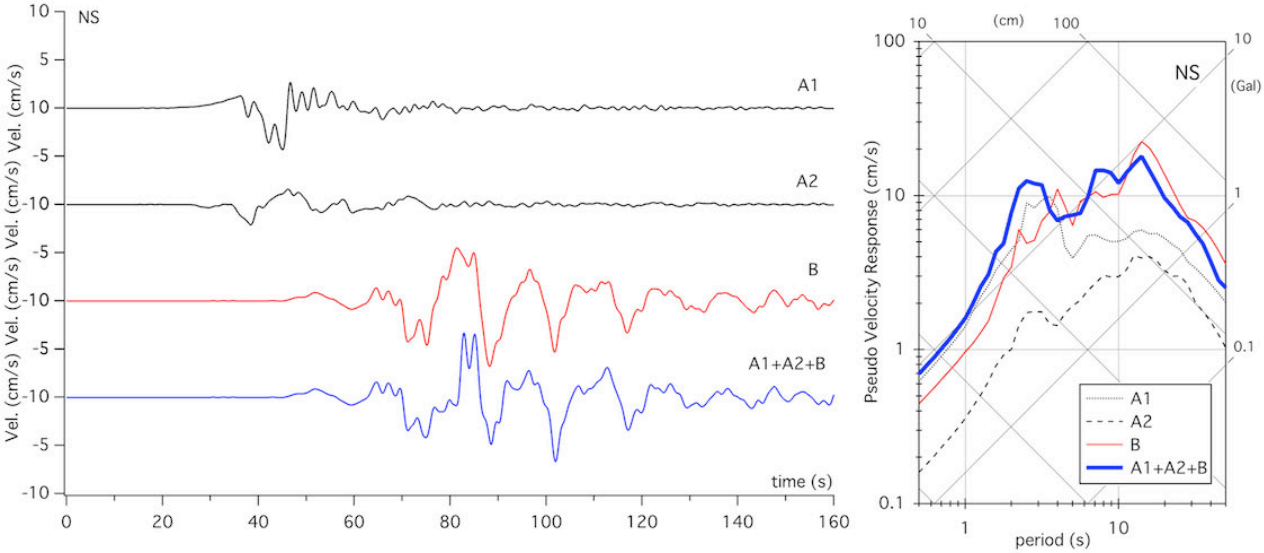

Figure 7 Long-period Ground Motion Evaluation for A1, A2, and B Faults of the Forthcoming Miyagi-oki earthquakes. See Fig.1 for the Fault Geometries.

JOINT CONFERENCE PROCEEDINGS
7th International Conference on Urban Earthquake Engineering (7CUEE) &
5th International Conference on Earthquake Engineering (5ICEE)
March 3-5, 2010, Tokyo Institute of Technology, Tokyo, Japan

3D SUBSURFACE STRUCTURAL MODEL FOR STRONG MOTION SIMULATION AROUND LAKE BIWA USING EARTHQUAKE GROUND MOTION RECORDS

Haruhiko Suzuki[1)] and Hiroaki Yamanaka[2)]

1) OYO Corp., Japan
2) Associate Professor, Department of Environmental Science and Technology, Tokyo Institute of Technology, Japan
suzuki-haruhiko@oyonet.oyo.co.jp, yamanaka@depe.titech.ac.jp

Abstract: We construct the 3D subsurface structural model using the data of geophysical and geological surveys in and around Lake Biwa. And we have modified the model using the S-wave parts of earthquake records, H/V spectral ratio of S-coda and phase velocity of microtremor. In the waveform inversion of S-wave, we assume a simple source time function and plane wave incident to a layered model from the basement. And In the waveform inversion of H/V spectral ratio, we use only the period of H/V spectral ratio because the amplitude of H/V spectral ratio are influenced by S/N ratio in long period range and the amplitude ratio between Rayleigh and Love wave amplitude in the surface wave. A genetic algorithm is used in the inversion to find an optimal model that has the minimum misfit between observed and synthetic data. Using three 3D subsurface structural models, we simulate ground motions for moderate earthquake. The first model is the model using only boring and reflection survey data; the second one is the model by adjusting the peak period of theoretical H/V spectral ratio to observed one; the last one is the model by joint inversion of S-wave, H/V spectra and phase velocity of microtremor. As the results, simulated waveforms of ground velocity by using joint inversion model agree with observed ones better. It is possible to construct 3D subsurface structural model which is applicable to strong motion simulation by using earthquake ground motion records, even though there are few data of geophysical surveys.

1. INTRODUCTION

We proposed joint inversion method to avoid trade-off problems between shear wave velocity and thickness in S-wave form inversion (Suzuki and Yamanaka, 2009). We try to apply this method to the subsurface model around Lake Biwa. Suzuki et al. (2005) constructed 3D subsurface structural model by the geological and H/V spectral data of earthquakes. This studies purpose is confirming applicability of joint inversion method.

2. GEOLOGICAL AND GEOPHYSICAL DATA AROUND LAKE BIWA

The geology around Lake Biwa is composed by Tanba group and Ryoke metamorphic rocks, Ryoke granite, Koto Rhyolites(Cretaceous~Paleogene), First Setouchi supergroup (Miocene), Kobiwako group(Pliocene~Pleistocene), Biwako Formation (Pleistocene), Terrace deposits and Alluvium (Figure1).

Location of deep boreholes in and around Lake Biwa is displayed in Figure1. Solid circles indicate the deep borehole reached basement rocks. Numbers in the parenthesis indicate depth of basement rocks in meter. Gray lines, Solid triangles and solid stars indicate the location of reflection surveys, microtremor array surveys and K-net observation point, respectively.

3. 3D SUBSURFACE STRUCTURAL MODEL

3.1 Initial Model

Initial model is made by the borehole, reflection and refraction data. 3D model there is a few geological data is constructed using gravity data. The component ratio of sediment is decided by the Karasuma borehole(in Lake Biwa). P-wave velocity of Biwako Formation is 1.6km/s. Kobiwako group is divided by two layers (1.8km/s and 2.0km/s). The depths of top of the layers of initial model are displayed in Figre2. Physical parameter decided from PS logging results. Physical parameter indicates in Table1.

3.2 Model Modification using H/V spectra (HV model)

Initial model is modified based on comparison observed and synthetic H/V spectral ratio at K-net observation points. The earthquakes Mj more than 5.0 and focal depth less than 50km are used. Spectra of Radial and UD components are calculated by the waveform 20sec after S-wave. The data length is 163s. Comparison between observed H/V spectral ratio for earthquakes and synthetic ellipticity of Rayleigh wave is displayed in Figure3. The component ratios of sediment and basement rocks are fixed as initial model. 3D model is same in Lake Biwa. Figure4

indicate the contour maps of the top of layers modified by H/V spectra. Figure4b indicates the difference between initial and HV model.

3.3 Joint Inversion of S-wave, H/V spectra and phase velocity (JI model)

HV model is modified by the joint inversion wave forms of S-wave part, peak periods of H/V spectra of earthquake and phase velocity of microtremors at SIG002, SIG003, SIG005, SIG006, SIG007 and SIG010. At SIG005, we used the waveform of S-wave, H/V spectra and phase velocity of microtremors (Miyakoshi et al., 1998). At other site, we used the waveform of S-wave and H/V spectra.

The bandpass data from 1~6.7sec are used in the wave form inversion of S-wave. In the inversion process, S-wave velocity is fixed 0.4, 0.6, 1.8, 2.2, 3.1km/s. And the component ratio of basement rocks is fixed as initial model.

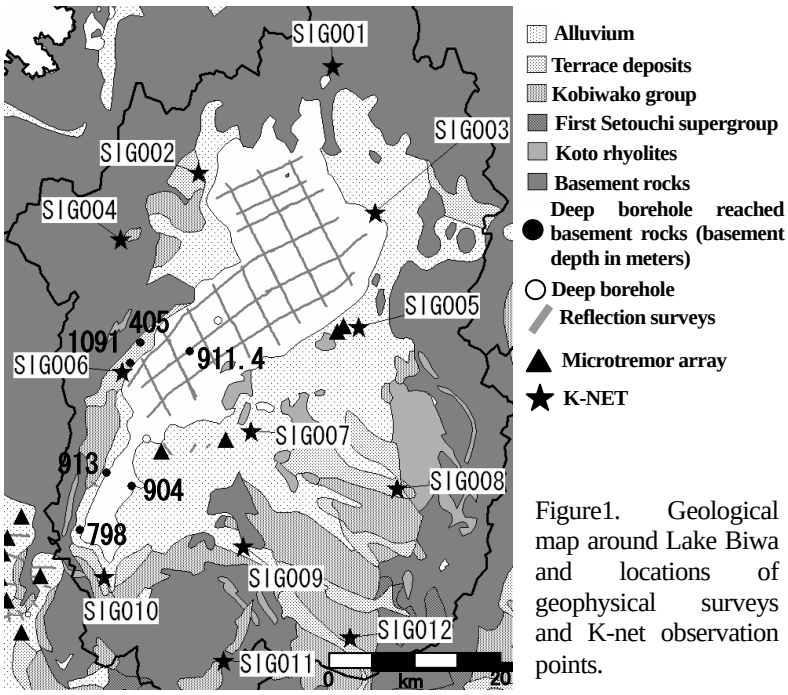

Figure1. Geological map around Lake Biwa and locations of geophysical surveys and K-net observation points.

We defined the misfit between observed and synthetic data of S-wave as Eq. (1).

$$E_{SH} = \left(1/N^{SH}\right)\sum_{t=t_2}^{t_3}\left[\left(S^o(t) - S^c(t)\right)/A^o\right]^2 \quad (1)$$

Here, S^o, A^o, S^c and N^{SH} are observed velocity wave, observed maximum amplitude, synthetic SH wave, and number of S-wave data, respectively. We calculate velocity wave form at surface using Haskell method (Haskell, 1960). *t2* and *t3* indicate the end time of first S-wave and the end time of analysis, respectively. *t3* is decided 5sec after S-wave first break.

We defined the misfit between observed and synthetic peak period of H/V spectra as Eq. (2).

$$E_{HV} = \left[\left(T^o - T^c\right)/T^o\right]^2 \quad (2)$$

Here, T^o and T^c are observed and synthetic peak period of of H/V spectra, respectively. From fundamental to 4th mode of Rayleigh wave is considered.

We defined the misfit between observed and synthetic phase velocity of Rayleigh wave as Eq. (3).

$$E_{PV} = \left(1/N^{PV}\right)\sum_{j=1}^{N^{PV}}\left[\left(C^o(f_j) - C^c(f_j)\right)/C^o(f_j)\right]^2 \quad (3)$$

Here, C^o, C^c and N^{PV} are observed and synthetic phase velocity of Rayleigh wave and number of phase velocity data, respectively.

We defined the misfit between observed and synthetic data as Eq. (4) in the joint inversion process.

$$E = p_{SH}E_{SH} + p_{HV}E_{HV} + p_{PV}E_{PV} \quad (4)$$

Here, p_{SH}, p_{HV} and p_{PV} are ratio of each misfit defined as Eq (5).

$$p_{SH} + p_{HV} + p_{PV} = 1 \quad (5)$$

For example, p_{SH} and p_{SH} are 0.5 the case of joint inversion of S-wave and H/V spectra. p_{SH}, p_{HV} and p_{PV} are 0.33 the case of all data used. Minimization of E is performed by genetic algorithm (GA; Yamanaka and Ishida, 1996) .

The inversion results are displayed in Figure 5. The S-wave velocity structures displayed in Figure 5-1. The results of S-wave form inversion displayed in Figure 5-2. The results of inversion of H/V spectra and phase velocity displayed in Figure 5-3. The basement and top of Vs0.6km/s layer presumed shallower than that of HV model at SIG002. The basement depth didn't change and top of Vs0.6km/s layer presumed about 60m shallower than that of initial model at SIG005. The top of Vs0.6km/s layer presumed

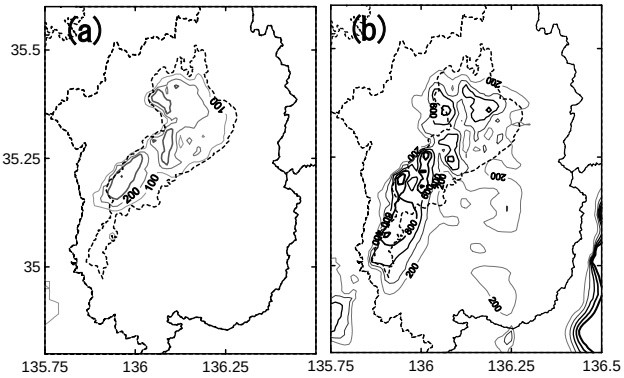

Figure 2 Contour maps showing the depths of top of the layers of initial model.
(a)Vs0.43km/s contour interval:100m
(b)Vs1.8km/s contour interval:200m

about 120m shallower than that of HV model at SIG006. The basement (Vs 1.8 km/s) depth is displayed in Figure6a. Figure6b indicates the difference between SH and HV model. Around site SIG002, SIG003 and SIG006 the basement depth estimated shallower, around site SIG007 deeper than HV model.

4. EXAMINATION OF THE VALIDITY OF 3D STRUCTURAL MODEL BY THE EARTHQUAKE GROUND MOTION SIMULATION

We examined the validity of the 3D structural model by calculating of moderate earthquake occurred on 22/04/1998. We calculated mid western GIF pref. Focal mechanism is displayed in Table2. The crust and upper mantle structure by Zhao et al. (1994) is used. Q-value of sedimentary layer is 110; from basement to 5km depth is 200; from 5km depth to Conrad discontinuity is 300; deeper than Conrad discontinuity is 500. We simulate long-period ground motions using a 3D FD simulation with variable grids. The minimum and maximum grid spacing is 150m and 600m, respectively.

The comparisons between the observed and synthetic ground velocities are displayed in Figure 7. These traces are bandpass-filtered in the period range from 2.5 to 10s. Though synthetic wave of NS component is underestimating for each model's results, EW and UD component are showing good agreement for the JI model results at SIG002 and SIG005. At SIG005, because the initial model is almost same the HV model, the synthetic wave calculated by both model is almost similar. Because the thickness of 1st and 2nd layer is thicker than that of the HV model, the maximum amplitude of synthetic wave is lager than that of the HV model. At SIG010, because the basement depth of JI model is shallower, the duration of the synthetic wave form is shorter than that of initial model.

5. CONCLUSIONS

The 3D subsurface structural model is constructed using the data of geophysical and geological surveys in and around Lake Biwa. And we have modified the model using the S-wave parts of earthquake records, H/V spectral ratio of S-coda and phase velocity of

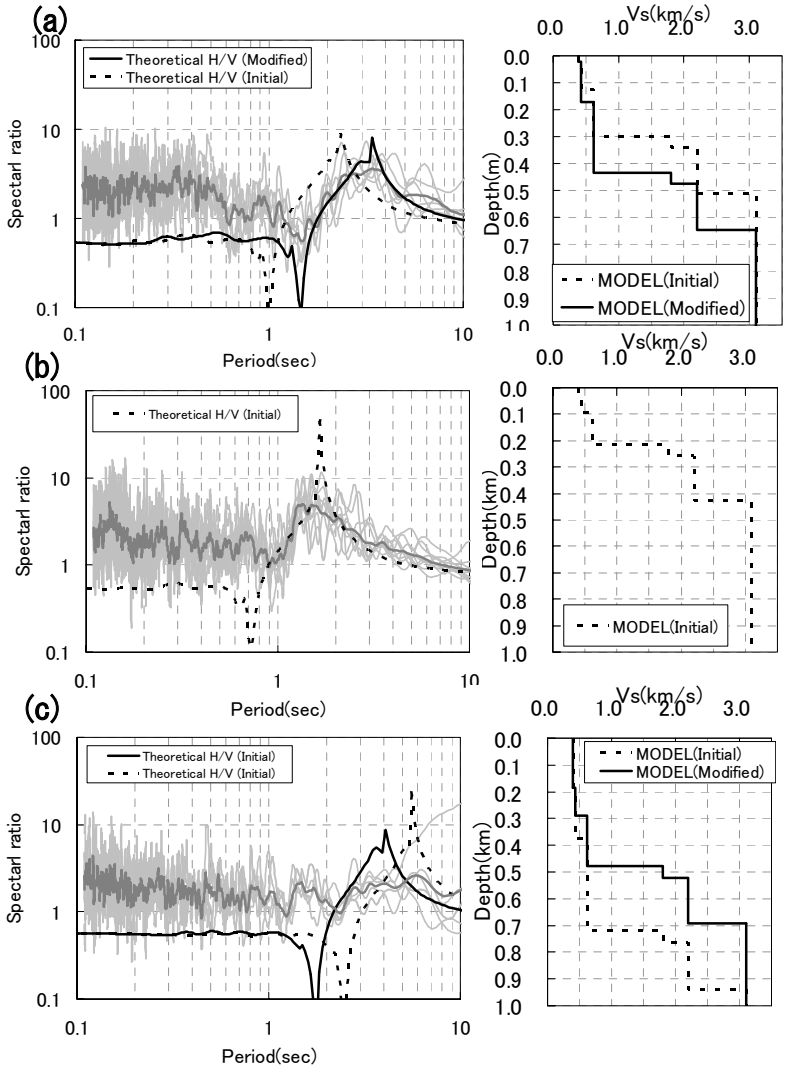

Figure 3 Comparison between H/V spectral ratio and synthetic ellipticity of Rayleigh wave (a) SIG002 (b) SIG005 (c) SIG006.
(left) Gray thin lines, gray thick lines, black dotted lines and black thick lines indicate observed H/V spectra, ensemble average of observed H/V spectra, synthetic ellipticity for initial model and synthetic ellipticity, respectively for HV model. (right) The 1-D velocity structure of initial model (dotted lines) and HV model (thick lines).

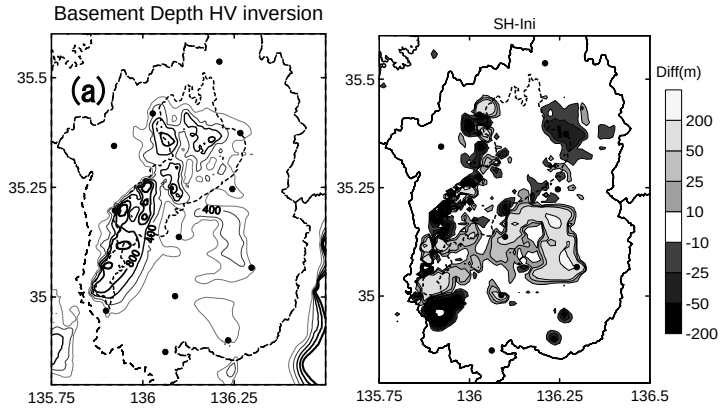

Figure4 (a) Contour maps showing the depths of top of the Vs1.8km/s layers of HV model. Contour interval 200m (b) The difference between initial and HV model.

microtremor. Then effectiveness of joint inversion is confirmed by the earthquake ground motion simulation. So It is possible to construct 3D subsurface structural model which is applicable to strong motion simulation by using earthquake ground motion records, even though there are few data of geophysical surveys.

Acknowledgements:

Main part of this study was conducted during one (H.S.) of the authors' stay at Tokyo Institute of Technology as a graduate student.

The authors acknowledge support from the Japan Ministry of Education, Culture, Sport, Science, and Technology (MEXT).

References:

Haskell, N. A. (1960), Crustal reflection of plane SH waves, J. Geophys. Res., 65, 4147-4150.

Miyakoshi, K., T. Kagawa, M. Tsurugi, T. Akazawa, B. Zhao, T. Noguchi, K. Fukumoto, T. Fujiwara (1998), Estimation of underground structures in Hikone city by seismic-array observations of microtremors (in Japanese) , Proceedings of the 99th SEGJ conference ,164-167.

Suzuki, H., M. Morino, K. Iwamoto, L. Ying, H. Fujiwara and Y. Hayakawa(2005), 3D subsurface structural model for strong motion simulation around Lake Biwa, southwest Japan (in Japanese with English abstract), Zisin, 58, 91-106.

Suzuki, H. and H. Yamanaka (2009), Joint Inversion of S-wave, receiver function and phase velocity of Rayleigh wave to S-wave profile of deep sedimentary layers, Sixth International Conf. Earthq. Eng., 149-153.

Yamanaka, H and H. Ishida (1996): Application of genetic inversion to inversion of surface wave dispersion, Bull. Seism. Soc. Am., 86, 436-444.

Table1 Physical parameters of initial model

No.	Geology	Vs(km/s)	Vp(km/s)	ρ (g/cm^3)
1	Biwako F.	0.39	1.6	1.8
2	Kobiwako G.	0.43	1.8	2.0
3		0.62	2.0	2.0
4	Basement Rocks	1.8	3.8	2.4
5		2.2	4.4	2.5
6		3.1	5.2	2.6

Table2 Focal mechanism of the earthquake used for the 3D FD simulation

Origine Time	1998/4/22 20:32
Depth(km)	5.0
Mj	5.4
Strike	163
Dip	29
Rake	53
Moment(Nm)	6.74E+16
Rise time(s)	0.6

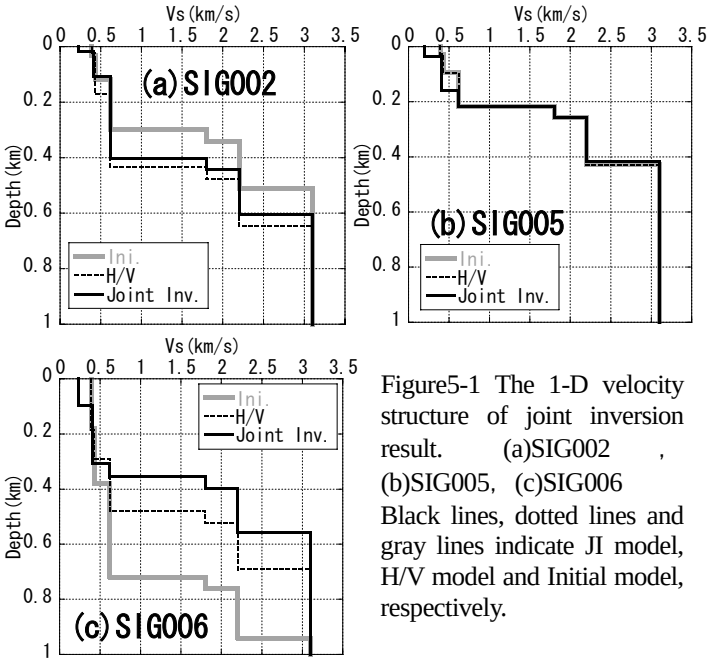

Figure5-1 The 1-D velocity structure of joint inversion result. (a)SIG002 , (b)SIG005, (c)SIG006 Black lines, dotted lines and gray lines indicate JI model, H/V model and Initial model, respectively.

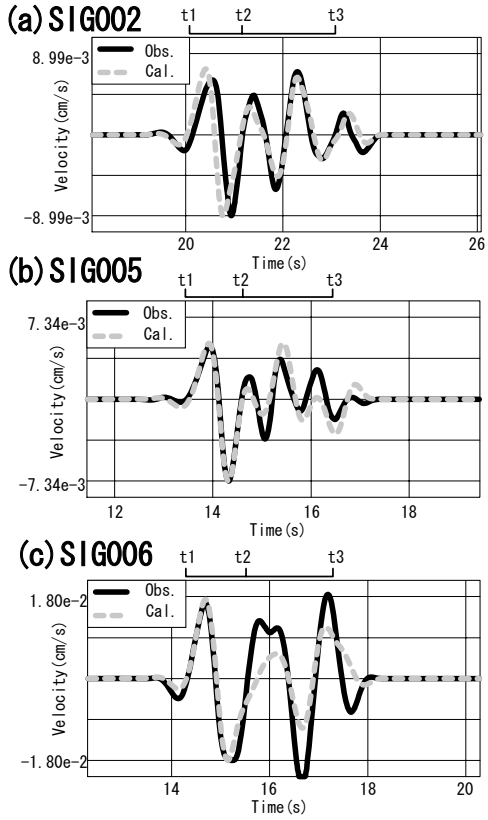

Figure 5-2 Joint inversion results. (a)SIG002 , (b)SIG005, (c)SIG006 Thick lines and gray dotted lines indicate observed velocity wave forms and synthetic SH wave forms, respectively.

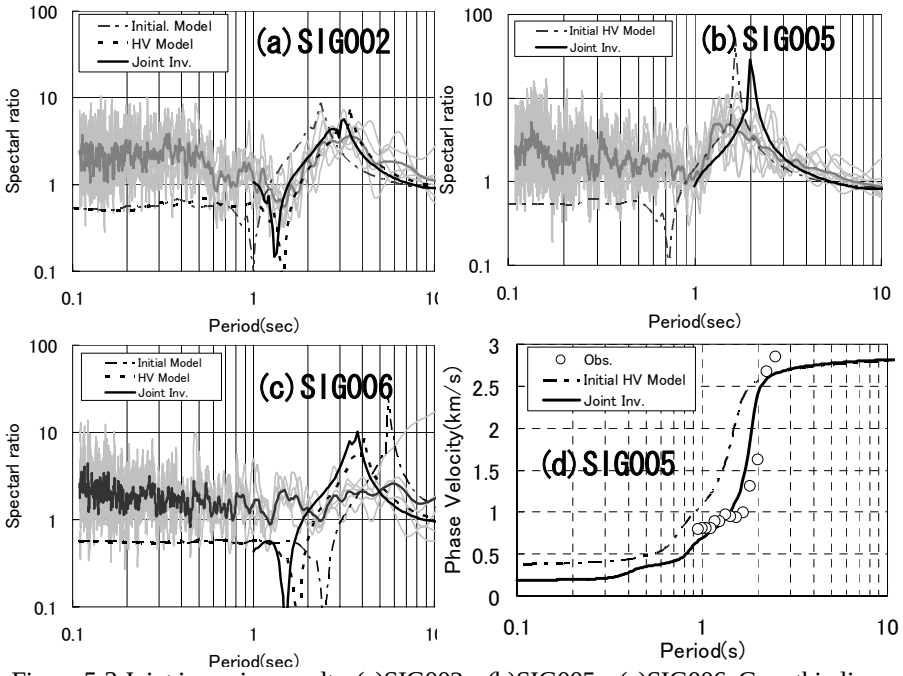

Figure 5-3 Joint inversion results. (a)SIG002, (b)SIG005, (c)SIG006. Gray thin lines, gray thick lines, black dashed lines, black dotted lines and black thick lines indicate observed H/V spectra, ensemble average of observed H/V spectra, synthetic ellipticity for initial model, synthetic ellipticity for HV model and synthetic ellipticity for JI model, respectively. (d) Comparison between observed phase velocity and synthetic phase velocity of Rayleigh wave at SIG005. Open circle, dashed line and solid line indicate observed phase velocity, synthetic phase velocity for initial model and for JI model, respectively.

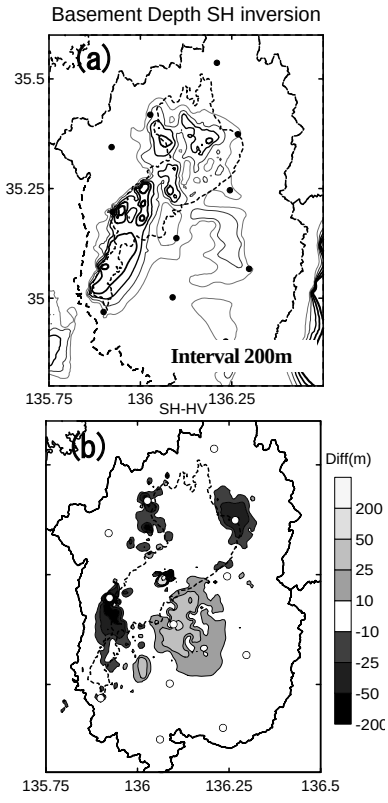

Figure 6 (a) Contour maps showing the depths of top of the Vs1.8km/s layers of SH model. (b) The difference between HV and SH model.

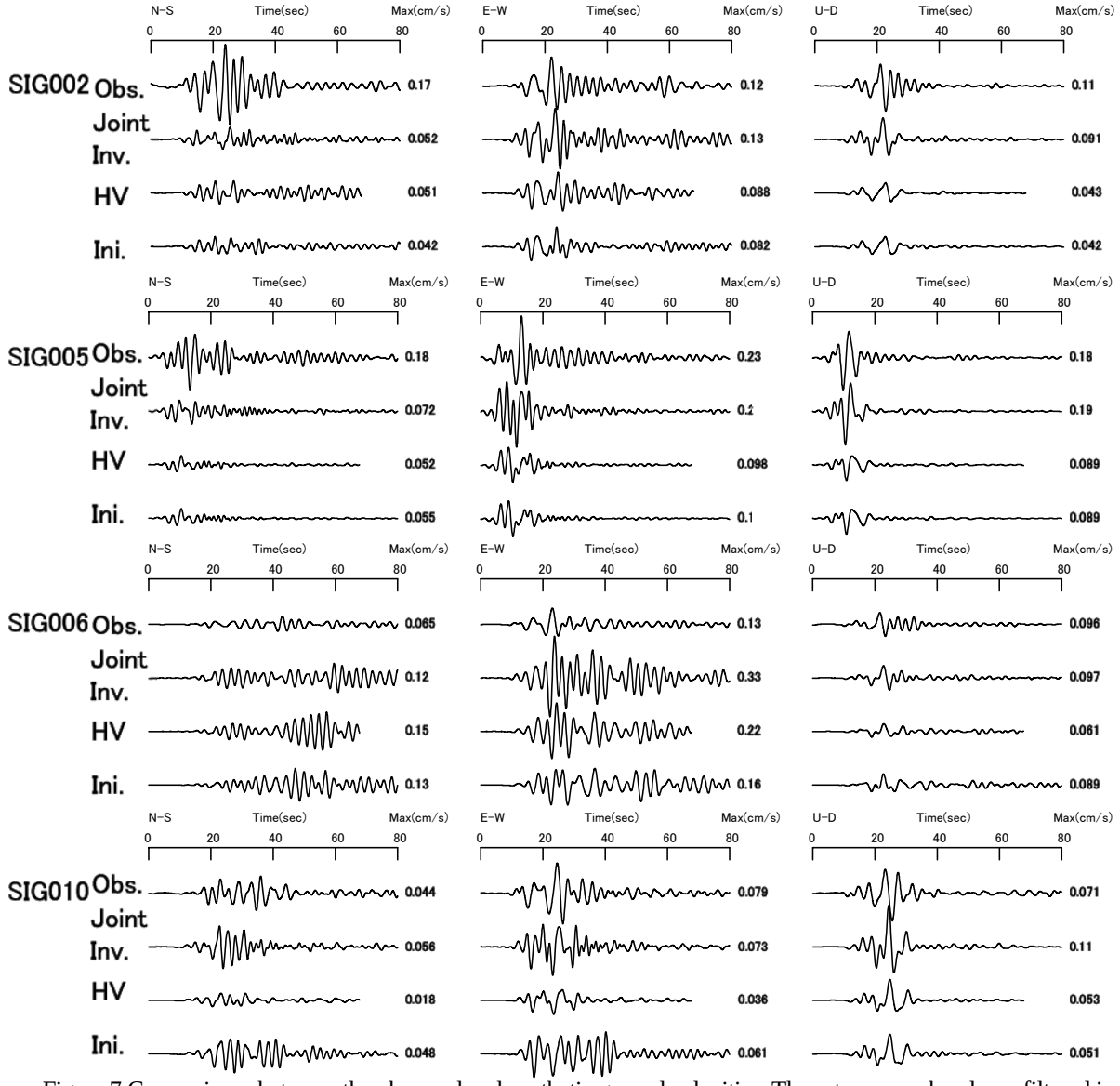

Figure 7 Comparisons between the observed and synthetic ground velocities. These traces are bandpass-filtered in the period range from 2.5 to 10s. Top rows indicate observed ground velocities. Second rows indicate synthetic ground velocities for SH model. Third rows indicate synthetic ground velocities for HV model. Forth rows synthetic ground velocities for initial model. Attached number to each trace indicates the maximum velocity in cm/s.

JOINT CONFERENCE PROCEEDINGS
7th International Conference on Urban Earthquake Engineering (7CUEE) &
5th International Conference on Earthquake Engineering (5ICEE)
March 3-5, 2010, Tokyo Institute of Technology, Tokyo, Japan

AN EVALUATION OF LONG-PERIOD EARTHQUAKE MOTION FOR THE PURPOSE OF STRUCTURAL DESIGN

Izuru Okawa[1], Toshimi Satoh[2], Toshiaki Sato[3], Takao Nishikawa[4] and Matsutaro Seki[5]

1) Senior Research Fellow, Structural Engineering Department, Building Research Institute of Japan, Tsukuba, Japan
2) Principal Researcher, Ohsaki Research Institute, Tokyo, Japan
3) General Manager, Center for Atomic Energy Eng., Institute of Technology, Shimizu Corp., Tokyo, Japan
4) Professor Emeritus, Tokyo Metropolitan Univ., Tokyo, Japan
5) Senior Technical Adviser, the Japan Building Disaster Prevention Association, Tokyo, Japan
okawa@kenken.go.jp, toshimi.satoh@shimz.co.jp, toshiaki.sato@shimz.co.jp,
tanishi@river.dti.ne.jp, seki@kenchiku-bosai.or.jp

Abstract: The large earthquakes are supposed to occur on subduction zones around Japan in near future. Therefore, we have serious concerns on structural damage due to the long-period ground motions generated by those earthquakes.
We have made a method to evaluate the ground motion in longer period range both in spectral and time-history formats, and have applied it to develop method to construct design long-period ground motion.
This technique is expected to show the average characteristics and over-all features of the recorded long-period ground motions. This newly developed method will be applied to construct the design long-period ground motions for high-rise buildings and base-isolated buildings with concurrently performed earthquake response analysis results using the generated waves as input motions.

1. INTRODUCTION

The long-period ground motions were known as part of the earthquake motions excited with events of large magnitude and relatively long distance. After the 2003 Tokachi-oki, Hokkaido, earthquake that caused fire-damage to large oil tanks, its influence on structures with longer natural period has become a matter of concern to earthquake engineers. Although we have no experience of structural damage due to the long-period motions except for the fire-damage, recently we have had some damage to non-structural elements and equipments of buildings such as the elevators with excess deformation of high-rise buildings during the subsequent inland earthquakes such as 2007 Niigata-ken Chuetsu-oki earthquake.
In Japan, the construction of high-rise buildings was started in the late 60's. Since then, large subduction zone earthquake that may possibly excite long-period motion have not occurred to date yet.
By the way, in the Japanese Building Standard Law, the high-rise buildings taller than 60 meters shall confirm the structural earthquake safety through the response history analysis using the input motion considering the regional earthquake activity and the geological conditions under the construction site.
Seeing the ground motion records with long duration during the afore-mentioned 2003 Hokkaido earthquake, we have recognized the design input motions adopted at present do not reflect the reality, we need to re-evaluate the actual property patterns of long–period ground motions with newly collected data.

2. Status Quo, Design Motions for Buildings in Japan

In Japan, the construction of high-rise buildings over 60 meters (hereafter, referred to as HR building) started in late 60's. The recorded motions available to design were not enough in number and quality. Therefore, a magnified motions recorded in Japanese large cities were used as well as the well-known records El Centro NS component for 1940 Imperial Valley Eq. or Taft EW component for 1952 Kern County Eq. records that were already in use. The maximum amplitude levels used for magnification were 200-300 cm/s^2 for elastic design, and 300-500cm/s^2 for elastic-plastic design. Afterwards, the scaling with maximum velocity amplitude level was replaced as appropriate for relatively longer-period dominant ground motions. The scaling with max velocity amplitude with 25cm/s for damage-protection design and 50cm/s for collapse-protection was established in mid 80's. (BCJ, 1986)

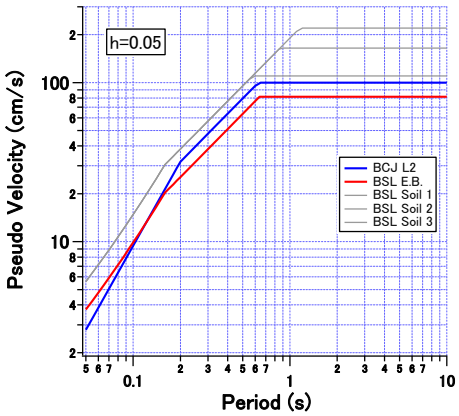

Figure 1 BCJ (L2) wave

The scaling scheme is still maintained for parts of the design motions. In mid-90's, a project left a fruit that proposes a design motions for HR buildings. The project was conducted as a cooperated research work between the Building Center (BCJ) of Japan and the Building Research Institute (BRI) of Japan.

At the same time, the design motion was defined at the outcropped hard soil surface, that was referred 'Engineering Bedrock'. This motion is named BCJ-wave. The pseudo velocity response spectrum is shown in Fig.1. (BRI&BCJ, 1992)

The Building Standard Law was revised in 2000, consequently, the design spectrum for response history analysis was added as one of notifications. The spectrum was corresponding to the conventional design seismic force and was lower than the previously shown BCJ-spectrum as shown in Fig.1. In Fig.2, an example of notification waveform is shown. The notification also requests site-specific motions referred to as 'site-wave' considering the earthquake environment of the site such as influence of an active fault, etc. In 2003, the Hokkaido earthquake occurred and gave impact on the significance on the long-period wave and made it informed that the duration time of the recorded long-period motion is much larger than as assumed at present. The problems are as follows;

(1) The design motion has been changing. The one used for older buildings is not for newer buildings. This is caused mainly gradual application of acquired knowledge but inevitable.
(2) The site-wave should be evaluated using site dependent conditions such as location of earthquake sources and the influence of deep ground structure.
(3) The long-duration time is important.
(4) The structural response recording in buildings is as important as ground motion for structural design purposes.
(5) Average characteristics of long period motions need to be made clear in terms of eq. sources, regions, etc.
(6) Urgent need exists on the evaluation of ground motions with large earthquakes expected to occur in near future.
(7) A technical guideline is necessary for judging the plausibility of evaluated motions

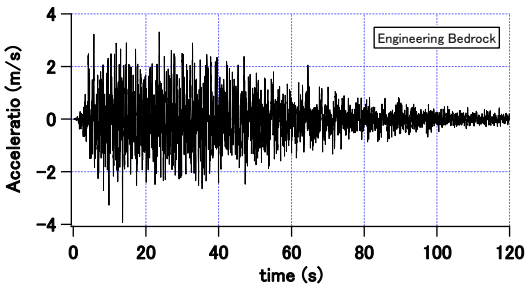

Figure 2 BSL Notification wave

3. Status Quo, Long-Period Ground Motions in Japan

Recently, the Architectural Institute of Japan (AIJ), and the Japan Society for Civil Engineers (JSCE) have cooperatively evaluated the ground motions due to the hypothetical, Tokai, Nankai, Tonankai, and Kanto earthquakes.

According to their reports, the important points for evaluating the long-period motions at the construction site are, (1) the source size, the distribution of asperities, and the rupture velocity. (2)The attenuation property of motion due to distance between hypocenter and the construction site, (3) the deep geological structure beneath the wide area around the construction site.

The other activities for the purpose include,

(1) A new correction coefficient using new zoning scheme for evaluation of the long-period motion was proposed and enforced for the oil storage tanks. (Zama, 2006)

(2) The Cabinet Office made and published the nationwide map for the natural period of ground using underground structural data, and the H/V spectrum with recorded earthquake motions. (CAO, 2008)

(3) AIJ working group made a strong motion simulation with the 3D FEM model including Kanto, Nobi, and Osaka plains for Tokai-Tonankai earthquake made comparisons of motions between different rupture patterns. (AIJ, 2007)

(4) The Headquarters for Earthquake Research Promotion is now conducting the research on the nationwide deep underground structure and also publishing the long-period motion map, a trial version, for the major three hypothetical subduction zone earthquakes, i.e., the Miyagiken-oki, the Tokai, and the Tonankai earthquakes, in September, 2009.

(5) Others

Other active organizations on these topics include, the Committee of Earthquake Observation and Research in the Kansai Area (CEORKA), for Kansai region (Hayashi, 2006), and the Research Council on the Design Earthquake Ground Motion in Aichi Prefecture. (Sato, 2006) Kataoka (2008) proposed an attenuation formula for estimating long-period ground motion using the nationwide recorded data.

4. Evaluation of Long-period Ground Motion with Subduction-Zone Mega-Earthquake Based on the Empirical Method

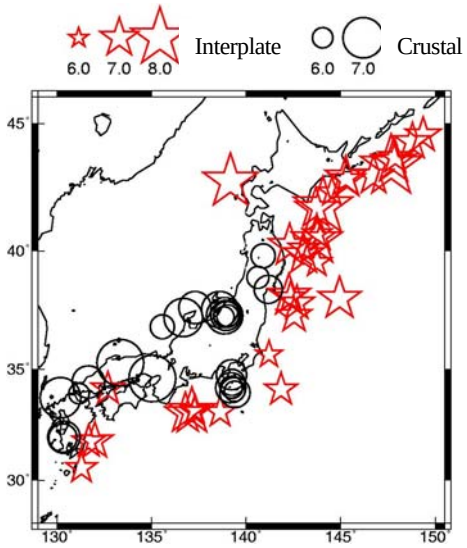

Figure 3 Earthquake Epicenters Used

The research on the evaluation of long-period motions are widely conducted using theoretical method such as the 3D-FDM. On the other hand, the researches on the empirical evaluation of the long-period motions are very few. Kataoka (2008) showed the attenuation formula. However, the research targeted on the time history generation was almost none.

Considering the usefulness of the formula and the data accumulation in future, the empirical method will become much more useful in engineering sense. In addition, the evaluated motion with empirical method will be useful enough to judge the plausibility of the theoretical method.

Here, we used nationwide many ground motion records to make an empirical model to predict the ground motion for 0.1 to 10 second period broadband. Furthermore, based on this formula, we investigated the method to construct the long-period ground motion time histories for hypothetical earthquakes. (Satoh, 2010)

4.1 Attenuation Formula for Acc. Response Spectra with 5% damping in Longer Period

(1) Dataset used in the study;

The data used here are from JMA87, K-NET, and KiK-net. The selecting criteria of records are,

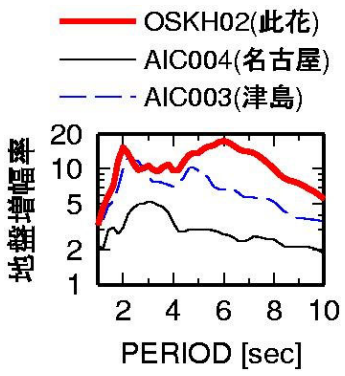

Figure 4 Site Amplification Factors

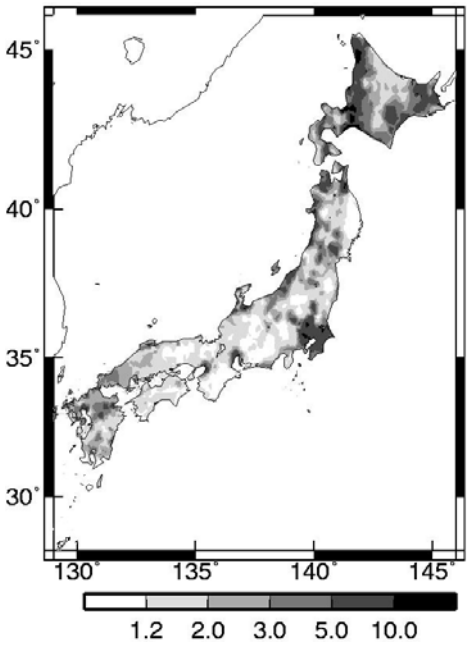

Figure 5 Nationwide Map for Site Amplifications for Period T=5 second

1) Subduction Type :Mj≧6.5 for hypothetical distance≦400km
2) Crustal Type: Mj≧6.0 for hypothetical distance≦350km
3) Hypocenter depth≦60km

The location of earthquake sources and their magnitudes are shown in Fig.3. It is seen that the subduction type earthquakes are mainly on the Pacific Ocean side.

In the least square analysis, the 5% damping acc. Response spectra are related with the moment magnitude and the shortest distance from recording station to the assumed source area of each recorded event, i.e.,

$$\log_{10} S_a(T) = a(T)M_w + b(T)R - \log_{10}(R^{p(T)} + d(T)10^{0.5M_w}) + c(T) + c_j(T) \quad (1)$$

Where, M_w: moment magnitude and R:the shortest distance from the recording site to the source area, and the a(T), b(T), d(T), p(T), c(T), cj(T) are coefficients to be determined with the Least Square Method. The c(T) is assumed to be the site amplification factor for KiK-net FKSH19 station which is regarded as station on the seismic bedrock and cj(T) is a site amplification factor for the j-th recoding station.

The least square analysis was conducted separately for subduction and crustal earthquake type datasets. However, the final cj(T) was taken as a weighted average of cj(T) coefficients for both cases with data number taken as weight. Therefore, the cj(T) is treated as identical for subduction and crustal earthquakes.

Figure 4 shows the site amplification factors for three sites, OSKH02, AIC003, and AIC004. It is seen that the site amplification factor that shows the amplification from seismic bedrock to surface becomes nearly 20 at around 6

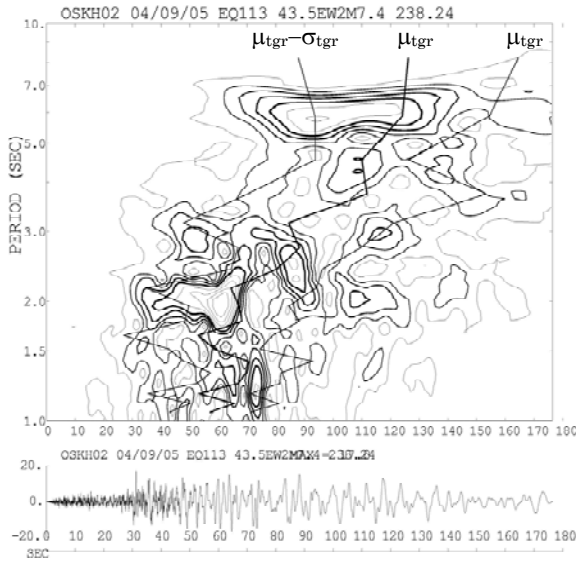

Figure 6 Non-stationary Spectrum for Recorded Motion at OSKH02 During 2004 Off- Kii Peninsula Earthquake

second for OSKH02 site, located at the coast of the Osaka Bay. The sites AIC003 and AIC004 are both in the Aichi prefecture, but it is seen that the site amplification factors are different within the Nobi plain. In addition, the site amplification map for whole Japan area is shown in Fig.5. It is seen that the factor takes large value for area such as Kanto, Osaka, Nobi, Niigata, Sakata, Ishikari-Yufutsu, and Tokachi plains that holds thick overlying soft soil medium.

4.2 Empirical Formula for Frequency-dependent Average and Variance of Narrow-band Group Delay Time

The average value μ_{tgr} of the group delay time corresponds to the gravity center of arriving time of wave group in a narrowband. The standard deviation σ_{tgr} of the group delay time corresponds to the scatter of the arriving time that is the duration time of the wave group in the narrowband. (Izumi et.al., 1983)

Since the group delay time is the first derivative of the Fourier phase spectra, once the initial phase angle is fixed, the other phase angles are recursively calculated assuming a normal distribution with the average and standard deviation values within the narrowband. The method holds an advantage to realize the spectral non-stationarity of the wave seemingly caused by the dispersion of surface waves. The average values are corrected so that the rupture initiation time should be zero. The Fig.6 shows the non-stationary spectrum and the average group delay time μ_{tgr} and its standard deviation σ_{tgr} using the recorded motion at site OSKH02 (Konohana) during the 2004 Off Kii-peninsula earthquake. Since both of the average group delay time μ_{tgr}, and the standard deviation σ_{tgr} of group delay time can be represented as sum of the source property, path effect and the site property, both μ_{tgr} and σ_{tgr}^2 can be eventually related in the following relationship.

$$Y(f) = A(f)M_0^{1/3} + B(f)X + C_j(f) \qquad (2)$$

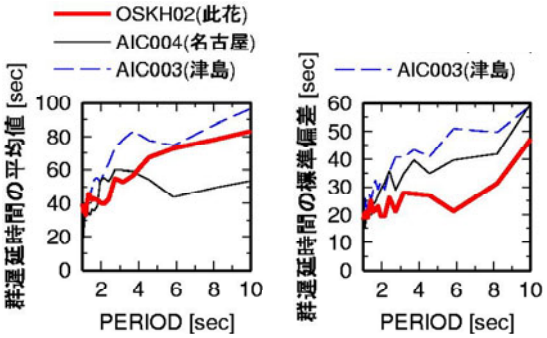

Figure 7 Site Coefficient for Inter-plate Earthquakes

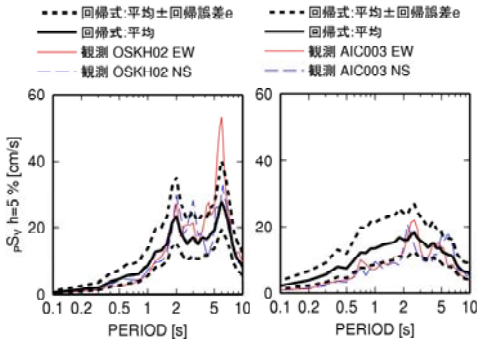

Figure 8 Comparison of Recorded and Simulated Motion with Pseudo Velocity Spectra for OSKH02 and AIC003

Where, Y(f) are either μ_{tgr} or σ_{tgr}^2, M_0 is seismic moment in dyne-cm, X is the hypocentral distance, i.e., the distance between the rupture initiation point and the recording site. F is frequency. A(f), B(f) and Cj(f) are determined by the least square analysis. The seismic moment M_0 has a well-known relationship with M_w.

$$\log M_0 = 1.5M_w + 16.1 \qquad (3)$$

The site coefficient for μ_{tgr} and σ_{tgr}^2 with horizontal component for OSKH02, AIC003, AIC004 sites are shown in Fig.7 It is seen from the figure, for longer period both site coefficients become larger.

4.3 Generation of Waves with Empirical Formula

For generation of the time history, the Fourier phase angles are firstly determined using the regression formula with μ_{tgr} and σ_{tgr} and giving initial phase angles and random numbers with normal distribution of μ_{tgr} and σ_{tgr}. Then, the 5% damping acc. response spectrum are determined with the attenuation formula. The Fourier amplitudes will be corrected so that the generated wave holds the acc. Response spectrum by correcting the Fourier amplitudes cyclically. (Ohsaki, 1994)

At first, the method was testified by simulating the recorded motions during the 2004 Off-Kii-Peninsula earthquake (Mw=7.4). Figure.8 shows the comparison of response spectra between recorded and generated waves for 2004 earthquake. Figure 9 also shows comparison of waveforms for the OSKH02 site. The duration times of generated velocity waveforms are, much less for OSKH02 and

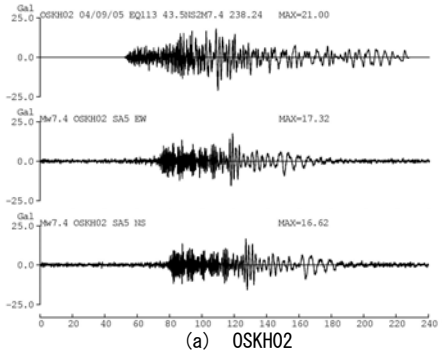

Figure 9 Comparison of Waveforms between Recorded and Simulated Motions for OSKH02

AIC004 than the recorded, and much larger for AIC003, when the average values with the group delay time standard deviation is used. These comparison shows the method can reproduce the recorded motion when a regression error is taken into account.

Subsequently, we generated the waves for Nankai (Mw=8.5) earthquake with site OSKH02, and for Tokai-Tonankai (Mw=8.3) earthquake with sites AIC003 and AIC004 sites. The macroscopic fault plain modeled as a rectangle for Nankai earthquake (Tsurugi, et. al., 2005) and the rupture initiation points and the location of the predicting site are indicated in Fig.10(a). In Fig. 10(b), the rectangular fault plain model for Tokai-Tonankai earthquake based on Sato, et. al. (2006) etc. are shown. When the multiple plain fault model is assumed, each generated wave from single component fault model will be added considering rupture time differences to get the final total waveform.

The pseudo response spectra for the Nankai earthquake using the method was shown in Fig.11, and compared with the preceding simulations by Kamae (2006), Tsurugi (2005) and Sekiguchi (2006). Kamae's result includes components longer than 2.5 second. Other simulations include short period components. The generated velocity waveforms are also shown in Fig.12.

In addition, the pseudo velocity response spectra for AIC003 and AIC004 were compared in Fig.13 with the simulated wave for NST site, located at downtown Nagoya, that was estimated with so-called hybrid procedure. It is seen that the spectral levels at longer period for AIC004 and NST are comparable. In Fig.14, the predicted waveforms for both

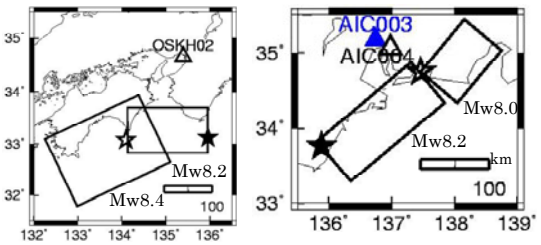

(a) Nankai Eq. (b) Tonankai-Tokai Eq.

Figure 10 Earthquake Source Models

★ First rupture, ☆ Second rupture

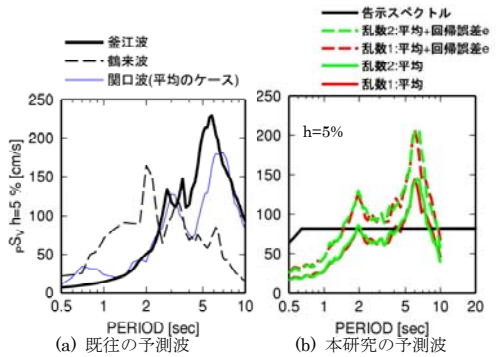

(a) 既往の予測波 (b) 本研究の予測波

Figure 11 Comparison of pSv with other research(left) and this work(right)

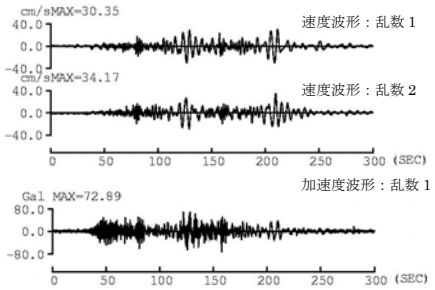

Figure 12 Velocity and Acceleration waveforms of OSKH02 for Nankai earthquake

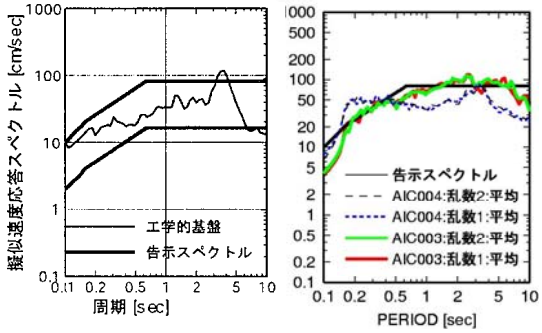

Figure 13 Comparison of pSv's for Tokai-Tonankai Earthquake between Previous Study(left) and This Study(right) at Downtown Nagoya

sites are also compared in Fig.14. The maximum velocity amplitudes and the effective duration times for both waves are almost equivalent.

5. CONCLUSIONS

In this paper, a method was proposed that will produce a broadband long-period (0.1-10sec.) earthquake motion waveforms using parameters, such as, the seismic moment, the macroscopic fault plain model, rupture initiation position, time difference among ruptures for multiple events.

It was suggested that the empirical formula for long-period

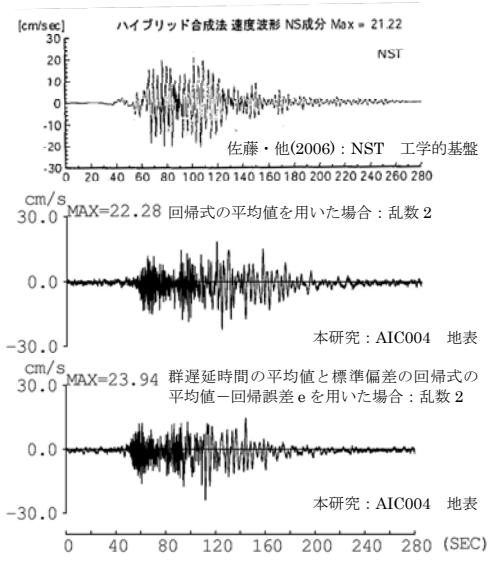

Figure 14 Comparison of Waveforms between Previous Study(upper) and This Study(middle and bottom) for Tokai-Tonankai at Downtown Nagoya

earthquake motions even in spectral property was very few. However, the method presented here will be useful for generating earthquake time history.

The simulated waves using the proposed method was in general comparable to the results in the preceding research results, except for that the number of the long-period earthquake records are in general very small and the situation makes the statistical study using those data unreliable and also that there are some cases in which the duration time of the records are not enough.

In view of that these research results will be applied to the very limited field, seismic design of buildings, it is necessary to make studies in parallel on the earthquake responses of the HR buildings and/or the base-isolated buildings to these simulated motions and their uncertainties.

Acknowledgements:

The authors express their sincere thanks to the members of the Committee on the Study of the Long-Period Earthquake Motions established in the Japan Building Disaster Prevention Association for their relevant ideas and suggestions. The financial support of the Japan Ministry of Land, Infrastructure, Transport and Tourism is also acknowledged.

References:

The Building Center of Japan (1986), Building Letter 1986.6, BCJ

BRI and BCJ (1992), "Technical Guideline for Making Design Earthquake Motions," BC J

Zama, S. (2006), "Revision of Design Spectra for Liquid Sloshing of Oil Storage Tank," The *12th Japan Symposium on Earthquake Engineering, No. 0164*, pp. 1550-1553

Central Disaster Management Council, CAO (2008), Published Committee material, Committee for Technical Investigation on Tonankai-Nankai earthquake.

AIJ (2007), "Structural Response and Performance for Long Period Seismic Ground Motions," AIJ.

AIJ (2009), Proceedings of the Workshop on the countermeasures against long-period earthquake motions

Hayashi, Y. (2006), "On the activity of the working group for structural response evaluation of long-period buildings in and around Osaka Plain for Tonankai-Nankai earthquake', CEORKA

Sato, T., et. al. (2006), "Strong Motion Prediction for Hypothetical Tokai Earthquake by the Research Council on Design Input Motions in Aichi Prefecture," Proceedings of the Symposium on the Prediction of the Broadband Strong Motions (2), JSCE and AIJ.

Kataoka, S.(2008), "Attenuation Relationship and Amplification Map for Ground Motion in Rather-Long Period Range", Journal of the Japan Society for Civil Engineers

Satoh, T. et.al. (2010), "Prediction of Waveforms of Long-Period Ground Motions for Hypothetical Earthquakes Using Empirical Regression Relations of Response Spectra and Phase Spectra," Transactions of AIJ (to be published)

Izumi, M., et.al., (1983), "A Fundamental Study on Extraction of Phase-Information in Earthquake Motions, Transactions of AIJ

Ohsaki, Y., (1994), "Introduction to Spectral Analysis of Earthquake Motions", Kajima Publishing Co. Ltd.

Tsurugi, M., et.al., (2005), "A Strong Motion Prediction in Osaka Area for Tonankai-Nankai earthquake", Proceedings of the Symposium on the Prediction of the Broadband Strong Motions, JSCE and AIJ.

Sekiguchi, H., et.al., (2006), "A Multi-Scale Inhomogeneous Model for the Prediction of Broadband Seismic Wave due to Mega-Interplate Earthquake and Its Application to Nankai Earthquake", Proceedings of the Symposium on the Prediction of the Broadband Strong Motions (2), JSCE and AIJ.

Kamae, K., et.al. (2006), "Strong Motion Prediction in Kinki Region for Nankai Earthquake," Proceedings of the 34th Symposium on Ground Vibration," AIJ

JOINT CONFERENCE PROCEEDINGS
7th International Conference on Urban Earthquake Engineering (7CUEE) &
5th International Conference on Earthquake Engineering (5ICEE)
March 3-5, 2010, Tokyo Institute of Technology, Tokyo, Japan

SHAKING TABLE TEST FOR INDOOR HUMAN RESPONSE AND EVACUATION LIMIT

Toru Takahashi[1], Toshiko Suzuki[2], Taiki, Saito[3], Tatsuya Azuhata[4], and Koichi Morita[3]

1) Professor, Department of Architecture, Chiba University, Japan
2) Nakata Katsuo Laboratory, Tokyo, Japan
3) Building Research Institute, Japan
4) National Institute for Land and Infrastructure Management, Japan
takahashi.toru@faculty.chiba-u.jp, danjiro@msn.com, tsaito@kenken.go.jp, azuhata-t92ta@nilim.go.jp, morita@kenken.go.jp

Abstract: Shaking table tests were performed to clarify the performance limit of human actions in the room under strong motions. These tests were performed in 2000, 2002, 2005 to 2009 using shaking tables of Building Research Institute (2000, 2005 to 2009) and Fujita Corporation. Especially, in 2006 to 2009 the BRI long range shaking table was used for the test. The input motions were sine waves and totally 352 patterns of actions were tested for 15 to 30 subjects in the experiment. The authors asked each subject for his/her feeling at the test for each input. The subjects' feelings of difficulty for actions, anxiousness for shaking, and action impossibility for real earthquakes were considered. As a result, performance limit curves for strong motions were proposed.

1. INTRODUCTION

Structural performance has been usually represented with structural capacity against earthquakes. The capacity has been mainly explained with strength and/or deformation capacity of structural resistance against earthquakes. The authors have paid attention with indoor human response and evacuation action in the strong ground motion (Takahashi 2003, 2004, 2006, 2007). The evacuation action does not mean refuge from the building, but means hiding under the table or turning off the kitchen stove, for example. The reason why the authors pay attention with the evacuation action was that the safety of human inside the buildings was more important than the safety of the buildings itself. The concept might lead us to the situation that the structural performance could represent with the ease of evacuation action.

Although Shibata and Nagai (1990) studied the human error of operators for the safety of facilities, Noguchi (1994) studied on habitability to the motion in floating ocean structures, Tsukagoshi et al. (1997, 1999) studied the relation between strong motion and perspiration, Shindo and Goto (2002) studied human visual perception, there have been no studies for evacuation action in strong motion except of the authors' work (2003, 2004, 2006, 2007). In these days, scientists have paid attention with long period ground motion because of the effect for tall buildings. Therefore, the authors performed shaking table test using BRI long range shaking table in 2006 to 2009. The authors asked each subject to explain his/her feeling after each input. The performance of each subject was recorded by motion capture system and analyzed as three-dimensional motion. Their feelings of difficulty for actions, anxiousness for shaking, and impossibility of actions in future earthquakes by questionnaire survey were considered in the analysis.

2. SHAKING TABLE TEST

The shaking table tests were performed in 2000, 2002, 2005 to 2009. Except of 2002, shaking table in the Building Research Institute was used. In 2002, shaking table at Fujita Corporation was used because its stroke was longer than that of BRI, but it was clarified that further long stroke shaking would be necessary. Therefore, the authors developed wire-driven long stroke shaking table as shown in Figure 1. This table is driven by wire connected with dynamic actuator and its displacement is increased by 6 sets of tackles and 13 times of actuator's deformation, theoretically.

2.1 Outline of the test

Shaking table tests in 2000 were performed from September 25 to 29 at Building Research Institute, Tsukuba, Japan. Three subjects on one day and totally 15 subjects joined the tests. Four subjects were female. Input motions were sine waves. The combinations were chosen based on floor response of various buildings in the strong ground motions. Tests in 2002 were performed on August 26, 29, September 11, 19 and 20, at Technology Center, Fujita Corporation, Atsugi, Japan. Total number of subjects were 15. Three subjects were female. Tests in 2005 were performed on August 22 to

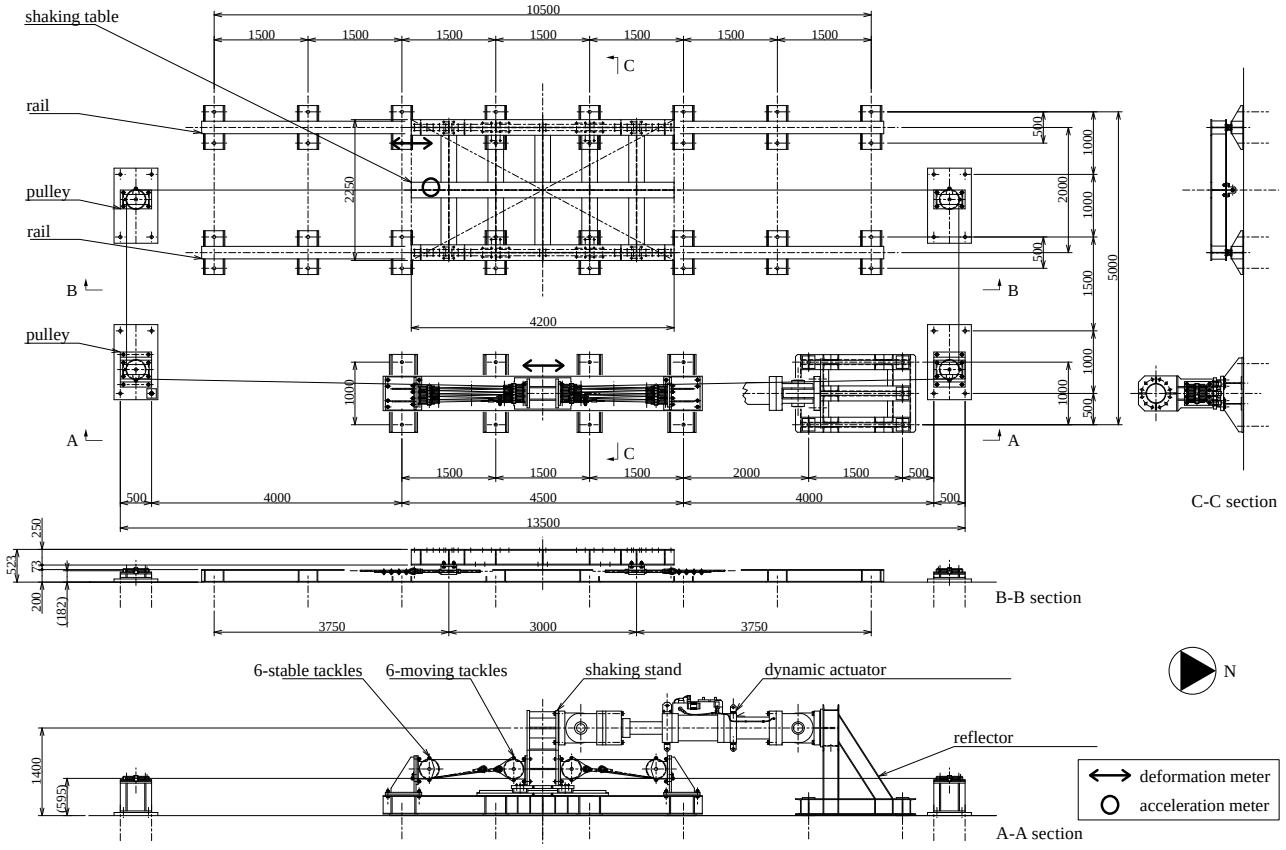

Figure 1. BRI Long-stroke shaking table.

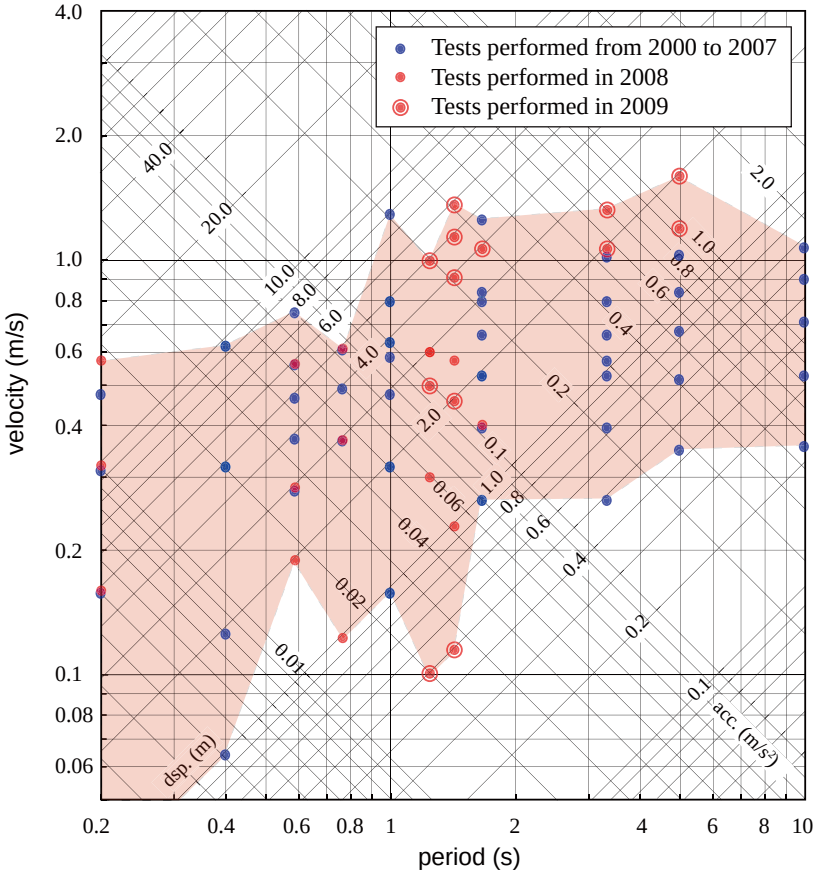

Figure 2. Chart of input motions.

26 at BRI. Total number of subjects were 14. Two subjects were female. Tests in 2006 were performed on May 13, 27, 28, June 3, 11, 16 at BRI. Total number of subjects were 21. Seven subjects were female. Test in 2007 was performed on Feburuary 27 at BRI. Total number of subjects were 4. Two subjects were female. Test in 2008 was performed from August 4 to 9 at BRI. Total number of subjects were 18. 7 subjects were female. Test in 2009 was performed from January 5 to 8 at BRI. Total number of subjects were 19. 8 subjects were female. Combinations of input sine waves are shown in Figure 2. Totally 106 subjects (33 of them were female) joined in the test.

Each subject wore protectors for head, elbows and knees. Then they put markers for motion capture system on head, chest, belly, elbows, knees and toes. One scene of the shaking table test in 2007 is shown in Photo 1. The authors tested two kinds of evacuation actions, i.e., standing up and walking. In the test of walking, metronome (114/min.) was used for reference of action. The authors tested two directions for

input, i.e., back and forth, and right and left motions. Therefore, totally 352 patterns of actions were tested. The authors asked subjects to answer the questionnaire shown in Table 1 after each input motion.

Table 1. Questionnaire list (standing up test).

A. How did you feel about difficulty in action?
0. No difficulty for standing up.
1. There was slight difficulty but I could.
2. There was difficulty but I could.
3. There was difficulty for standing up.
4. I could not stand up.
B. How did you feel in the test?
0. There was no anxiety.
1. I felt anxiety a little.
2. I felt anxiety.
3. I felt rather strong anxiety.
4. I felt anxiety very much.
C. What do you think that it is the real earthquake?
0. I can action.
1. I am not sure whether I can or not.
2. I do not think I can action.

2.2 Analysis method

Results of the questionnaire survey were used in this paper. The influence of habituation against the input motion was varidated by random order of input and masked the same level of input motion. Figure 3 shows the result of varidation test for habituation. The bable chart shows almost the same level were answered for different order of input motion. Therefore, the influence of habituation may be neglected.

Results of questionnaires were plotted on the vertical axis of the graph with input velociity as the abscissa axis. The authors fitted the distributions with Weibull distribution function. The formula is explained as follows:

$$F(x) = 1 - \exp\left[-\left(\frac{x-\gamma}{\eta}\right)^{m}\right] \quad (1)$$

Where, m is a shape parameter, η is a scale parameter, and γ is a position parameter. The authors set the minimum and maximum value of the result of questionnaire as the range of the function. Therefore, the value of γ is assumed to 0. The authors calculated the value of the parameters m and η using moment method.

3. TEST RESULTS

3.1 Result of questionnaires

Example results of questionnaires are shown in Figures 4 and 5. The figure of 5.0 Hz shows that in high frequency motion, they felt more anxiousness than low frequency motion, in the same velocity. Each index seems approximately in proportion to velocity, therefore, the authors performed linear regression analysis on these graphs and got performance limit curves as shown in Figure 4 and Figure 5. In Figure 4, there seems small gap in the line of level 1 (slight difficulty). The authors got the same results in 2005 and 2007 using different equipment with different subjects. Therefore, some human origin characteristics lie around the period (0.6 s to 1.0 s). Except of this, the performance curves for action difficulty seems proportional to velocity in the range of 0.2 s to 3.3 s. For more long range, it seems



Photo 1. One scene of right and left shaking test on the long-stroke shaking table at BRI.

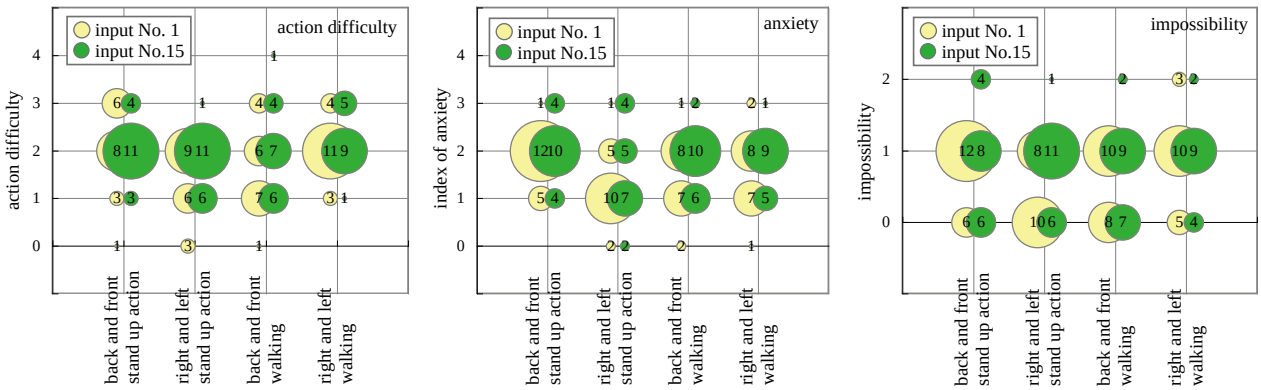

Figure 3. Varidation test for habituation.

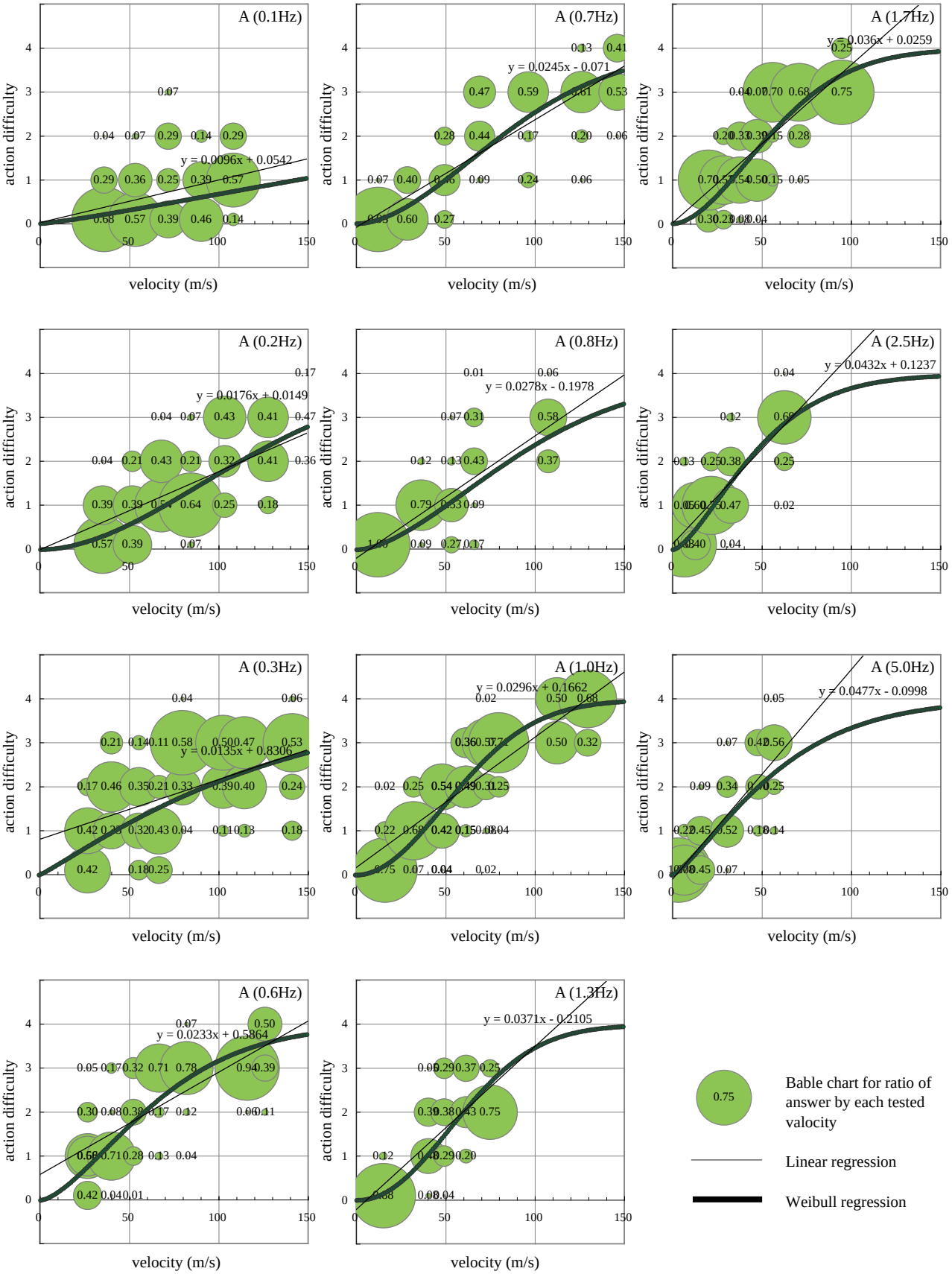

Figure 4. Test results of questionaire for action difficulty.

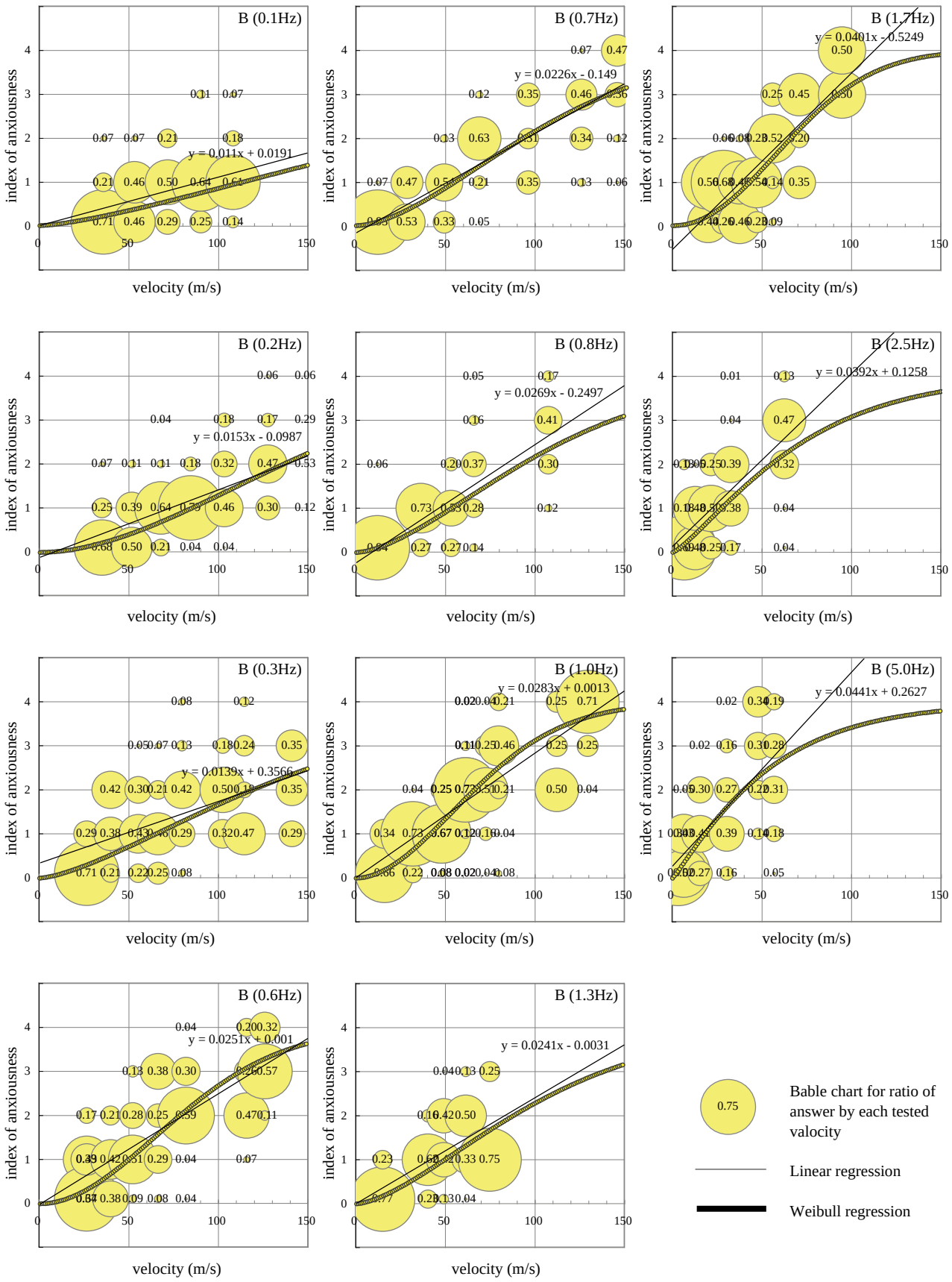

Figure 5. Test results of questionaire for anxiety.

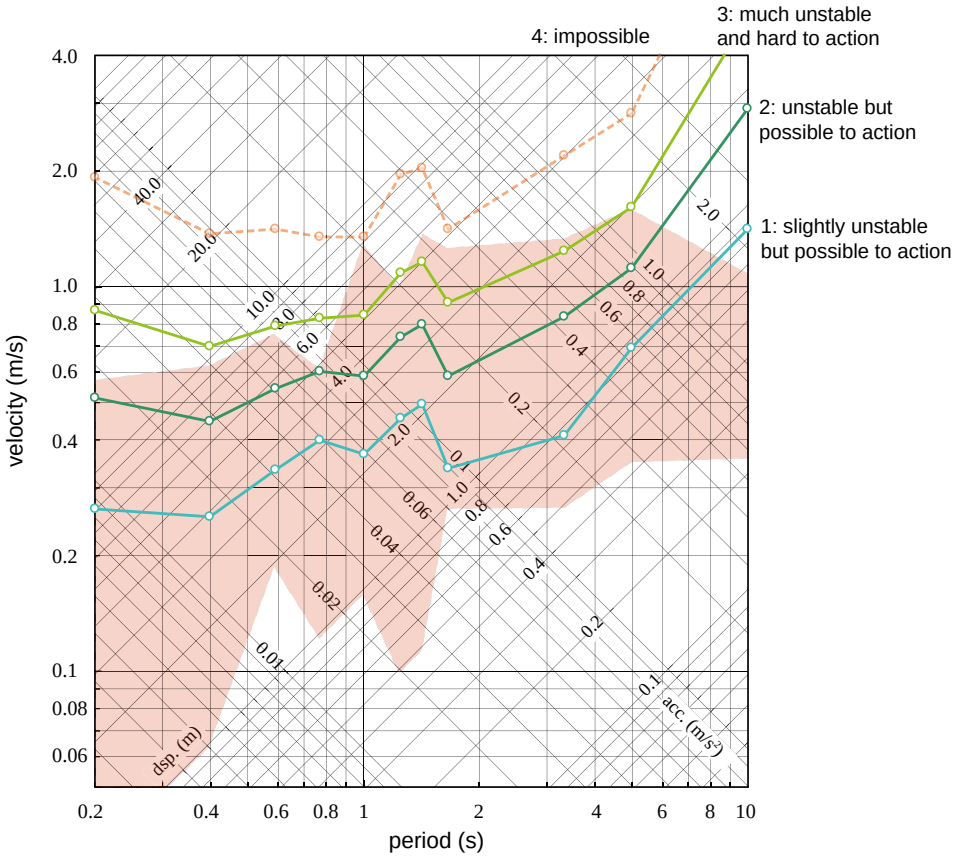

(A) Action difficulty

Figure 6. Human performance limit curves for action difficulty (average).

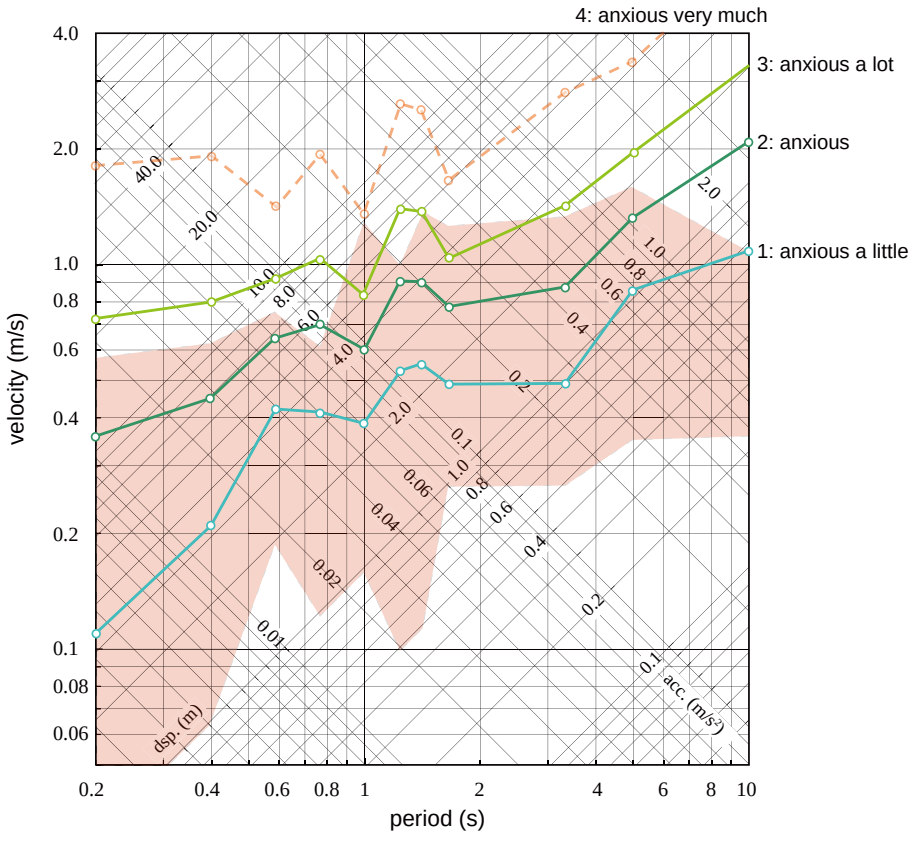

(B) Anxiety

Figure 7. Human performance limit curves for anxiety (average).

proportional to acceleration. When comparing Figure 4 with Figure 5, the most different point is the sensitivity of anxiety in high frequency, as mentioned above. However, no clear proportion with velocity nor acceleration is seen in anxiety, except of level 1 for 0.6 s to 3.3 s.

4. CONCLUSIONS

Shaking table tests were performed for the sake of making new criterion for structural performance. It could be said that high frequency floor response causes strong anxiety for indoor people. Low frequency floor response cause stagger for indoor people proportional with velocity in the range of 1.0 s to 3.3 s. For longer period than 3.3 s, it seems proportional with acceleration. After the analysis with motion capture system, the authors got unsteadiness indices and one of them (index using the record of 1.6 s) has very strong correlation with action difficulty.

Acknowledgements:

This study was partially supported by the Grant in Aid for Scientific Research, JSPS, No.17360264 (Delegate: Shunsuke Otani, former Professor, Chiba University.) The authors very appreciate it. The basic patent on the BRI long stroke shaking table is held by Chikahiro Minowa (Japanese Patent No.2003-130755) The device was assembled by Tomoe Giken Co.,Ltd.

References:

Kotake J. and Tsukagoshi I. (1999), Damping Ratio of Structures To Physiological Responses : Part 2 On the perspiration of palms due to exposure to vibration in sitting and standing postures, *Journal of Structural and Construction Engineering. Transactions of AIJ*, No.515 53-57.

Noguchi K. (1994), Experimental Study on Difficulties in Walking of Usual Motion Condition, Study on acceptable motion of floating ocean structures for human activities Part 1. *Journal of Architecture, Planning and Environmental Engineering*, AIJ, No.456, 273-282.

Saito T., Takahashi T., Azuhata T., Noguchi K. and Minowa C. (2006), Development of BRI Large Stroke Shaking Table for Simulating Earthquake Response of Long Period Buildings, *Proc. of 12JEES*, Paper No.0343

Shibata H., Nagai A. (1990), On Human Effect in Design Process to Seismic Failure of Industrial Facilities, *Seisan Kenkyu* Vol.42, No.3, 161-164.

Shindo S. and Goto T. (2002), Effects of Long Period Torsional Motion on Human Visual Perception, *Journal of Architecture, Planning and Environmental Engineering, Transactions of AIJ*, No.553 23-28

Takahashi T., Azuhata T., Saito T., Ohtomo K. (2003), Structural performance considering human response limit during strong earthquake, *Proceedings of JCOSSAR2003*, JSME, Vol.5 825-828.

Takahashi T., Saito T., Azuhata T., Ohtomo K. (2004), Shaking table test on Indoor Human Response and Evacuation Action Limit in Strong Ground Motion, *Proc. of 13WCEE*, Paper No.1320.

Takahashi T., Mazaki A., Saito T., Azuhata T. and Noguchi K. (2006), Shaking Table Test on Indoor Human Performance Limit in Strong Motion, *Proc. of 12JEES*, Paper No.0322.

Toru Takahashi, Masaharu Sadahiro, Toshiko Suzuki, Taiki Saito, Tatsuya Azuhata, Kazuya Noguchi, and Chikahiro Minowa (2007), Shaking Table Test on Indoor Human Performance Limit in Strong Motion for High-Rise Buildings, *Proceedings of 8th Pacific Conference on Earthquake Engineering*, 5-7 December 2007, Paper No.131, Singapore.

Tsukagoshi I., Kotake J. and Umemura T. (1997), Damping of Structure and Physiological Response, *Journal of Structural and Construction engineering. Transactions of AIJ*, No.497 39-46.

JOINT CONFERENCE PROCEEDINGS
7th International Conference on Urban Earthquake Engineering (7CUEE) &
5th International Conference on Earthquake Engineering (5ICEE)
March 3-5, 2010, Tokyo Institute of Technology, Tokyo, Japan

DISASTER MITIGATION ACTIVITIES OF A HIGH-RISE BUILDING IN THE SHINJUKU STATION AREA BY COLLABORATING WITH LOCAL GOVERNMENT AND COMMUNITIES

Yoshiaki Hisada[1)], Masahiro Murakami[2)], and Tomohiro Kubo[3)]

1) Professor, Dept. of Architecture, Kogakuin University, Japan
2) Associate Professor, Dept. of Architecture, Kogakuin University, Japan
3) Research Associate, Dept. of Architecture, Kogakuin University, Japan

Abstract: We introduce various earthquake disaster mitigation activities of a 28-strories building (the Shinjuku campus of Kogakuin University) in the Shinjuku Station area, by collaborating with local governments, residents, and companies. The activities are combination of researches, educations and drills, including simulations of building response, estimation of the damage, developing RSMS (Real-time Strong Motion Monitoring System), and EEWS (Earthquake Early Warning System), organizing community committees, holding seminars/symposium, and carrying out earthquake/emergency drills.

1. INTRODUCTION

The probabilities of large earthquakes in the Tokyo metropolitan area are very high, approximately 70% and 86, in the next 30 years for an M7 near earthquake and the Tokai Earthquake, respectively, according to the Headquarters for Earthquake Research Promotion. Thus, high-rise buildings may suffer severe damage because of not only for near source strong ground motions from a M7 earthquake, but also the long-period ground motions from a M8 subduction earthquake. In order to mitigate those anticipated damage, we have been conducting various activities by collaborating with Kogakuin University (Picture 1), the local government, residents, and companies in the Shinjuku Station area. The area is one of the largest places for business, amusement and entertainments in Japan: numbers of business institutions and daytime population are about 20,000 and 710,000, respectively. To cope with anticipated earthquake damage in the area, the Earthquake Disaster Mitigation Committee of the Shinjuku Station Area was organized in 2007, which includes Kogakuin University, the local government (Shinjuku Ward), Japan Red-Cross, local companies and shopping district promotion associations, hospitals and so on. Our activities includes numerical simulations of strong ground motions and building response, shake-table tests of a office room, estimations of damage, preparation of emergency response teams, carrying out of earthquake drills, and holding seminars/symposium.

2. Disaster Mitigation Activities of the Shinjuku Campus of Kogakuin University

2.1 Simulations of Strong Ground Motions and High-Rise Building Response

Figures 1 and 2 show the locations of the hypothesis M7 earthquake in the Tokyo metropolitan area, and the M8 Tokai-Tonankai combined earthquake, respectively. Figure 3 shows the simulated strong ground motions at Kogakuin University using the hybrid method, which is the combination of the wavenumber integration method (Hisada, 1995) and FEM (Yoshimura et al., 2008) for long-periods, and the empirical Green's function methods for short periods. The acceleration waves of the M7 earthquake are large in amplitudes, but short in duration, whereas those for the M8 earthquake are moderate in amplitudes, but very long in duration.

The Shinjuku Campus of Kogakuin University is a 28-story building of approximately 143 meters high with a primary natural period of 3 seconds (see Picture 1). Figure 4 shows a 3D moment frame model of the building, and Figure 5 shows the building response of the top floor. The maximum acceleration for the M7 earthquake is nearly 1 g, and the maximum displacement is about 0.7 m. On the other hand, the duration is extremely long and the maximum amplitude is close to 1 m for the M8 quake because of the long-period ground motion. We also conducted shake table experiments by collaborating

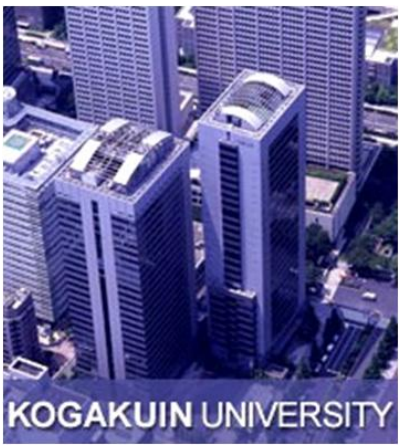

Picture 1 The Shinjuku Campus of Kogakuin University

with BRI (Building Research Institute) and NHK (Japan Broadcasting Corporation), and demonstrated that an office room suffer severe damage due to the strong shaking of the JMA intensity 7 at the top floor. Those results are useful for the local people to visually understand the necessity of the disaster mitigation activities.

2.2 RSMS (Real-time Strong Motion Monitoring System), and EEWS (Earthquake Early Warning System)

At the Shinjuku campus buildings, RSMS (Real-time Strong Motion Monitoring System), and EEWS (Earthquake Early Warning System) have been working since 2007 (e.g., Kubo et al., 2008). Figure 6 shows an example of the RSMS, which shows animations of the building vibration and the information of the building safety using the JMA intensities and the story drift angles. If a building is actually deformed substantially, the system provides information the security control center (located at the B1 floor) to quickly understand the building situation and deliver announcements.

On the other hand, EEWS (Earthquake Early Warning System) of the Kogakuin University provides the information not only of the arrival time and the estimated JMA intensities, but also those of long-period strong ground motions (Kubo et al., 2008). Figure 7 shows the example of the Ibaraki Offshore Earthquake of May 8, 2008. The blue, red, and green circles indicate the estimated wave front of the P, S and surface waves, respectively. Using this information, the system controls the elevator operations, and provides informative messages to the security control center. These systems allow the members of the center to make prompt announcements when disaster strikes.

2.3 Emergency Response Team and Earthquake Drill

In order to carry out prompt emergency response after an large-scale earthquake, Kogakuin University organized a task-force team under the board of directors in 2007. It also organized the disaster management headquarter including the university president and the chief director, and emergency response teams including faculties/students at all the floors. The task-force have carried out simulation exercises and made the disaster prevention maps of the campus by checking the locations of emergency items and hazardous objects/places.

Since 2007, we have been carrying out earthquake drills in the campus under realistic earthquake damage situations, which includes smoke, injured people, and panels showing various earthquake damage, such as fire breaking, falling objects, and trapped people. Pictures 2 to 10 show the 2008 drill. When the drill started, an EEWS announcement was derived from the security control center, and people carried out quick safety activities from falling objects (Picture 2). Then, the emergency response teams at the all floors stared various activities, such as fire extinction activities for fire panels (Picture 3), and first-aid activities for injured students (Picture 4). When a serious situation occurred, the head of the teams called the security center using the emergency phone (Pictures 5 and 6). On the other hand, the disaster management headquarter assembled spontaneously at the second floor, and started to obtain the information of the serious damage and injured people using various communication tools such as IP phones and portable wireless devices (Picture 7). After those emergency activities, all the students/faculty members at upper floors evacuated to the assigned lower floors to check the safety of the people (Pictures 7 and 8). In addition, the member excised various drills including fire extinctions and first aids (Picture 10), and then held a meeting to improve the activities.

3. Community Disaster Management Activities of the Shinjuku Station Area

Kogakuin University and the Earthquake Disaster Mitigation Committee of Shinjuku Station Area have been conducting various community activities since 2007, making disaster prevention maps, holdings workshops, seminars, and symposiums, and conducting earthquake drills. The Shinjuku campus is expected to be the local management headquarter of the Westside of the Shinjuku station, and provide student/faculty as volunteers. Pictures 11 to 13 show the 2008 earthquake drill. The management headquarter, which consisted of the university faculties and office workers of the local companies, summarized and shared the information of local damage, injured people, hospital, public transportations, and so force (Picture 11). All the data were shared on the Web GIS system (Picture 12). In addition, student volunteers helped vulnerable people and provided the information to the local people (Picture 13).

4. CONCLUSIONS

We introduced various community activities of Kogakuin University in the Shinjuku station area, which is one of the busiest places in Japan; the activities are combination of researches, educations and drills. Although those activities just started by trial and error, we believe that those are useful and applicable to other mega-cities.

Acknowledgements:

The authors acknowledge support from the Research Center for Urban Disaster Mitigation of Kogakuin University, and a research fund of Ministry of Land, Infrastructure, Transport and Tourism (MLIT), and education programs of the Japan Ministry of Education, Culture, Sport, Science, and Technology (MEXT). Early warning system and data are provided by National Research Institute of Earth Science and Disaster Prevention (NIED).

References:

Hisada, Y. (1995), An Efficient Method for Computing Green's Functions for a Layered Half-Space with Sources and Receivers at Close Depths (Part 2) (Graphic Only), Bulletin of the Seismological Society of America, Vol.85, No.4, pp. 1080-1093.

Kubo, T., Y. Hisada, S. Horiuchi and S. Yamamoto (2008), "Application of Earthquake Early Warning System and Real-time Strong-motion Monitoring System to Earthquake Disaster Mitigation of a High-Rise Building in Tokyo, Japan", Proc. 14th World Conf. Earthq. Engng., CD-ROM.

Yoshimura, C. Y. Yamamoto1 and Y. Hisada (2008), "Long-Period Ground Motion Simulation of 2004 off the KII Peninsula Earthquakes and Prediction of Future M8 Class Earthquakes along Nankai Trough Subduction Zone, South of Japan Island", Proc. 14th World Conf. Earthq. Engng., CD-ROM.

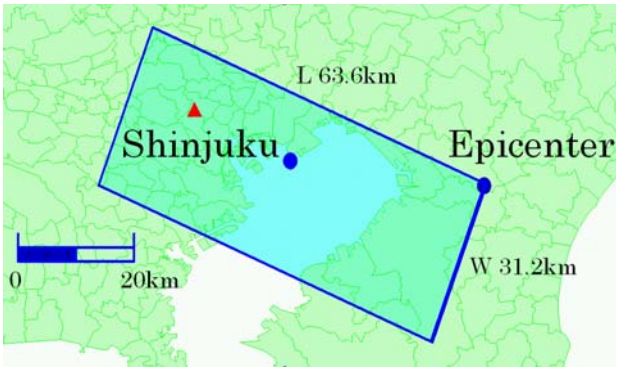

Figure 1 The hypothesis M7 earthquake in the Tokyo metropolitan area, and the Shinjuku area

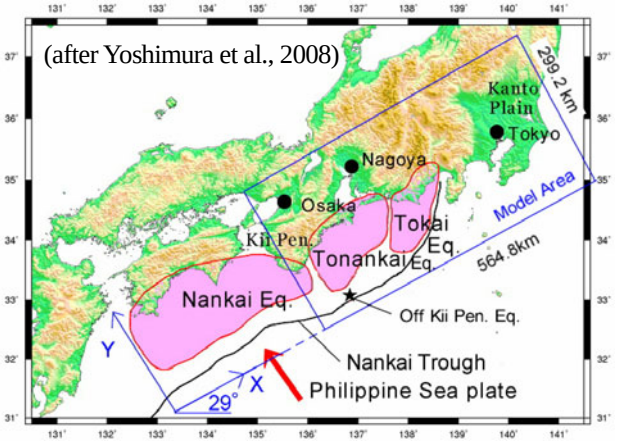

Figure 2 The M8 Tokai and Tonankai earthquakes

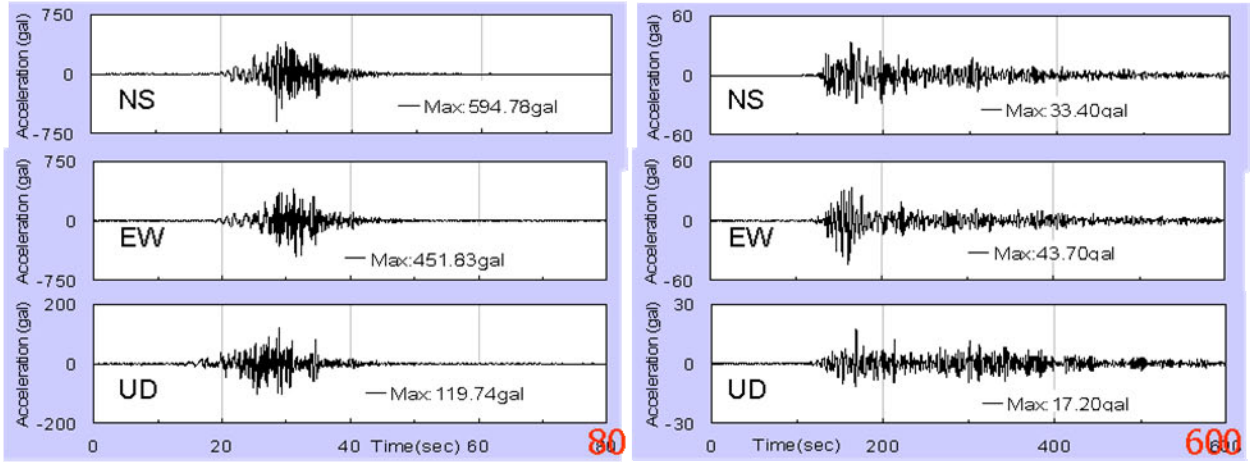

Figure 3 The simulated ground motion at Shinjuku for the M7 earthquake (left) and the M8 earthquake (right)

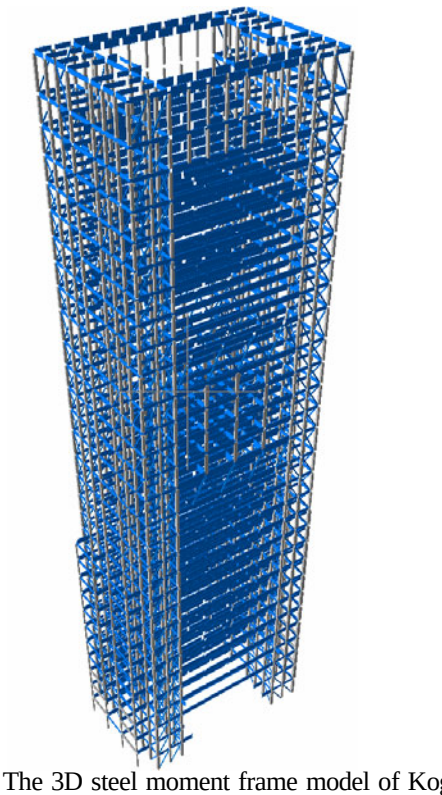

Figure 4 The 3D steel moment frame model of Kogakuin University for building response simulations

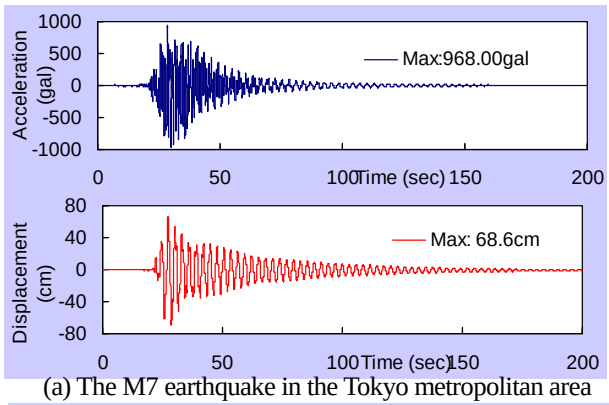

(a) The M7 earthquake in the Tokyo metropolitan area

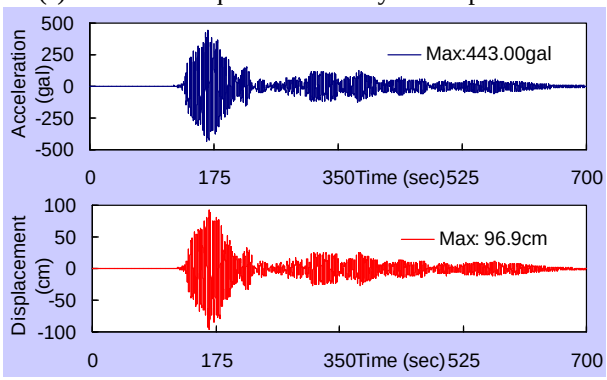

(b) The M8 Tokai and Tonankai combined earthquake

Figure 5 Simulated response of the Kogakuin University

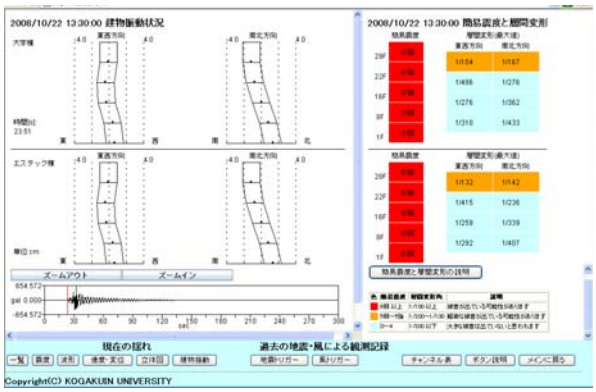

Figure 6 The Web page system of RSMS (Real-time Strong Motion Monitoring Systems) of Kogakuin University

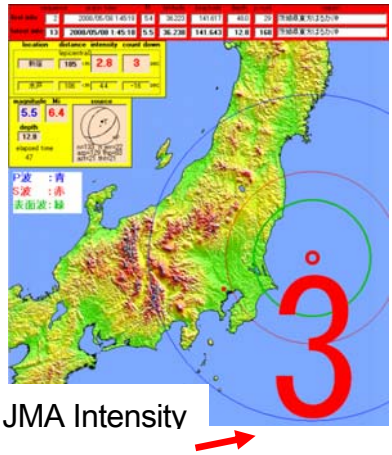

Provide by NIED

Figure 7 EEWS (Earthquake Early Warning System)



Picture 2 Safety drill using EEWS



Picture 3 Fire Extinguishing drill (NHK news)



Picture 4 First aid drill



Picture 5 Emergency Communication



Picture 6 Emergency Control Center



Picture 7 Disaster Headquarter drill



Picture 8 Evacuation drill (NHK news)



Picture 9 Safety check drill



Picture 10 Emergency relief drill



Picture 11 Headquarter of Westside area



Picture 12 Web GIS for sharing information



Picture 13 Providing Information

JOINT CONFERENCE PROCEEDINGS
7th International Conference on Urban Earthquake Engineering (7CUEE) &
5th International Conference on Earthquake Engineering (5ICEE)
March 3-5, 2010, Tokyo Institute of Technology, Tokyo, Japan

SEISMIC HAZARDS OF GYEONGJU HISTORIC AREAS

Heon Joon Park[1], Derk Moon Kim[2], Hyung Choon Park[3] and Dong Soo Kim[4]

1) Doctoral Student, Department of Civil and Environmental Engineering, KAIST, Korea
2) Research Division of Architectural Heritage, National Research Institute of Cultural Heritage, Korea
3) Professor, Department of Civil and Environmental Engineering, Chungnam National University, Korea
4) Professor, Department of Civil and Environmental Engineering, KAIST, Korea
heonjoon@kaist.ac.kr, kimdmn@nricp.go.kr, civilman@cnu.ac.kr, dskim@kaist.ac.kr

Abstract: The evaluation of seismic hazards was conducted for the cultural heritage sites in Gyeongju, the capital of ancient Silla Kingdom. The Gyeongju Historic Areas, which are one of the UNESCO World Heritage sites, contain remarkable sites of Korean Buddhist art in the form of pagodas, fortresses, bridges, and the remains of temples and palaces. Site characterization through field seismic tests and site-specific ground response analysis were performed on thirty historical sites. The peak ground accelerations were between 0.144g and 0.269g when there was a collapse level I earthquake and between 0.205g and 0.379g when there was a special collapse level earthquake, respectively. Gyeongju has the potential for site amplification. The fundamental site periods were distributed in the range from 0.04 to 0.45 seconds. Seismic hazards distribution mapping based on the geotechnical information system made a reliable estimation of the spatial geotechnical data for the Gyeongju areas. The seismic ground response analysis for each cultural heritage site and the seismic zonation for Gyeongju Historic Areas present a methodology on proper disaster mitigation of cultural heritage and historic sites.

1. INTRODUCTION

The earthquake's motion on the earth surface, which has caused seismic hazard such as casualties and property damage, is the result of seismic wave propagation from the epicenter. It is also seriously affected by the local ground condition as a delivery media. In other words, the seismic intensity is shown to be different according to the characteristics of the local ground, even if it is the same distance from the epicenter when the earthquake occurs.

The local site conditions have a profound influence upon the characteristics of earthquake ground motion and the corresponding response spectra. Site conditions give an impact on the amplification of ground motions together with the dominant site period range in the response spectra, because earthquake motions at the bedrock can be drastically modified in frequency and amplitude during the propagation of seismic waves through the soil strata.

As one of the most important aspects in geotechnical earthquake engineering practice involves evaluation of the effects of local soil conditions on surface ground motion (Kim et al. 2002, Sun et al. 2005, and Fujiwara et al. 2006), the sensitivity analysis for the spatial earthquake-induced motions based on the site characterization, as well as the studies on the geotechnical information system based on geographic information system (GIS), were the focus of this study.

The earthquake ground motions in the seismic design guide of Korea were determined based on the relations between the ground motions and earthquake intensities in the historical earthquake events. Most of the historical earthquake events were experienced at the ground surface of the soil sites and the effects of site amplification were included in the earthquake intensities. The evaluation of site amplification considering local site effects is essential, because it can estimate the rock outcropping motion based on historical earthquake intensities as well as it can identify the potential consequences of an earthquake (Kim et al. 2002).

In this study, the effects of the local site condition for the cultural heritages were evaluated in the Gyeongju area. Gyeongju, the capital of the ancient Silla Kingdom, is the one of the most glorious historic cities in Korea. The Gyeongju Historic Areas, a UNESCO World Heritage site, contain remarkable sites of Korean Buddhist art in the form of pagodas, fortresses, bridges, and the remains of temples and palaces. The Gyeongju area also has frequent historical records of seismic damages and is located in a relatively higher earthquake prone region due to the Yangsan fault line.

In-situ test sites around these cultural heritage sites were selected and site characterization was performed at each site. The ground response analysis was conducted through the pre-existing data for the site investigation and in-situ test results. Based on these studies, GIS based seismic microzonation for the geotechnical information systems was constructed.

Table 1 Cultural Heritage Sites for Field Test in Gyeongju

Cultural Heritage Sites					Classification in Korea	Historical Earthquake Records
UNESCO World Heritage Sites	Seokguram Grotto • Bulguksa Temple (Registered in Dec. 1995)		2-1	Dabotap pagoda of Bulguksa Temple	National Treasures No. 20	
			2-2	Three storied stone pagoda at Bulguksa Temple	National Treasures No. 21	O
			2-3	Yeonhwagyo and Chilbogyo bridges of Bulguksa Temple	National Treasures No. 22	
			2-4	Cheongungyo and Baegungyo bridges of Bulguksa Temple	National Treasures No. 23	
			2-5	Sarira pagoda of Bulguksa Temple	Treasures No. 61	
	Gyeongju Historic Areas (Registered in Dec. 2000)	The Mount Namsan Belt	3-1	Najeong well in Gyeongju	Historic Sites No. 245	
			3-2	Standing stone buddhist triad in Bae-dong	Treasures No. 63	
			3-3	Poseokjeong pavilion site	Historic Sites No. 1	
			7-4	Seochulji lake	Historic Sites No. 138	
			7-3	Three storied stone pagoda in Namsan-ri	Treasures No. 124	
		The Wolseong Belt	1-1	Cheomseongdae observatory	National Treasures No. 31	
			4-1	Gyerim forest in Gyeongju	Historic Sites No. 19	
			4-2	Wolseong fortress	Historic Sites No. 16	
			4-3	Imhaejeon hall site	Historic Sites No. 18	
		The Tumuli Park Belt	5-1	Royal tomb of King Michu of Silla	Historic Sites No. 175	
			5-2	Jaemaejeong well	Historic Sites No. 246	
		The Hwangnyongsa Belt	6-1	Hwangnyongsa Temple site	Historic Sites No. 6	O
			6-2	Stone pagoda of Bunhwangsa Temple	National Treasures No. 30	
		The Fortress Belt	6-4	Myeonghwalsanseong fortress	Historic Sites No. 47	
Tentative World Heritage Sites	Yangdong Village (Registered in Jan. 2002)		8-0	Yangdong village of Wolseong	Important Folklore Materials No.189	
			8-1	Gwangajeong	Treasures No. 442	
			8-2	Hyangdan	Treasures No. 412	
Cultural Heritage Sites with Earthquake Records			7-1	Mangdeoksa Temple site	Historic Sites No. 7	O
			7-2	Flagpole support of in Mangdeoksa Temple site	Treasures No. 69	
Other National Architectural Treasure Sites			9-1	Monument of King Taejongmuyeol of Silla Period	National Treasures No. 25	
			4-4	Three storied stone pagoda of Goseonsa Temple site, Gyeongju National Museum	National Treasures No. 38	
			6-3	Three storied stone pagoda in Guhwang-dong	National Treasures No. 37	
			10-1	Five storied stone pagoda in Nawon-ri, Wolseong	National Treasures No. 39	
			11-1	Thirteen storied stone pagoda of Jeonghyesa Temple site	National Treasures No. 40	
			12-1	Three storied stone pagoda of Gameunsa Temple site	National Treasures No. 112	

2. SELECTION OF IN-SITU TEST SITES AROUND GYEONJU HISTORIC AREAS

In order to evaluate the seismic hazards for the Gyeongju Historic Areas, a zone of 10km by 10km area, which includes the historic area and current downtown area, was selected. The various pre-existing site investigation results in this zone were used (Kim et al. 2002, Sun et al. 2005, NRICH 2009). The sixty site characterization data, such as boring, standard penetration test, seismic tests, and laboratory tests were collected for this study.

Among the many cultural heritages in Gyeongju city, UNESCO World Heritage sites, cultural heritage sites with earthquake records and other national architectural treasure sites were selected for the site investigation and for site-specific ground response analysis. The UNESCO World Heritage sites selected for this study include for 'Seokguram grotto • Bulguksa temple' and 'Gyeongju Historic Areas', as well as the tentative world heritage sites for 'Yangdong village' in Gyeongju city. The cultural heritage sites that have historical earthquake records include the 'three storied stone pagoda at Bulguksa temple,' 'Hwangnyongsa temple site,' and 'Mangdeoksa temple site'.

The mountain and rock outcrop have relatively lower possibilities of local site amplification and seismic hazards. Therefore, cultural properties in the mountain area were excluded from this study. Thirty cultural heritage sites in Gyeongju were selected for the in-situ test, as shown in Table 1.

3. SITE CHARACTERIZATION USING FIELD TEST

The best way for determining the design ground motion is the site-specific ground response analysis through an in-situ site investigation of the subsurface ground. When the soil profile and material property are obtained, the reliable ground response analysis results, such as peak ground acceleration, response spectrum, or site period can be evaluated.

The maximum shear modulus below the elastic threshold strain, which is a fundamental stiffness in design ground motion, is usually inferred from the shear wave velocity obtained by seismic wave propagation tests (Kim et al. 2009).

The Harmonic Wavelet Analysis of Wave (HWAW) test, a kind of seismic test, was mostly performed around the thirty cultural heritage sites in order to measure the shear wave velocity profile of the site. In the 'Cheomseongdae

observatory', the boring and downhole tests were executed to check the reliability of HWAW method.

The HWAW test is a non-intrusive test that use surface waves. The HWAW method is based on the harmonic wavelet transform that can evaluate dispersive phases and group velocities of surface waves. The HWAW method mainly uses the signal portion of the maximum local signal to noise ratio in order to evaluate the phase velocity and it can minimize the effects of noise (Park and Kim 2001). For the site characterization, the HWAW method generally uses short receiver spacing setup. In the short receiver spacing setup (Fig. 1), the source-receiver spacing (D) is 6~12 m and the receiver spacing (R) is 1~3 m.

In the HWAW method, the single array inversion process can be possible without increasing the calculation time and any complexity because the HWAW method uses just one test setup in the field. Because the HWAW method uses a short receiver spacing setup, it can minimize the possibility of error due to lateral non-homogeneity and can determine a detailed local soil profile (Park and Kim 2001).

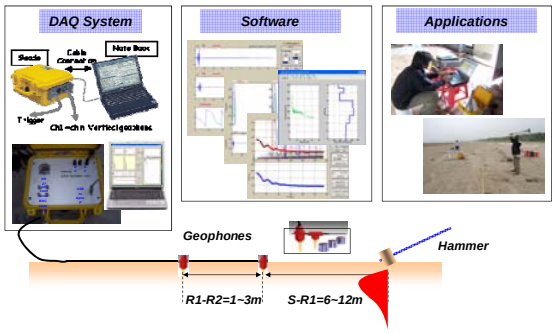

Figure 1 The HWAW Method for Site Characterization

4. GROUND RESPONSE ANALYSIS

4.1 Design Rock Outcrop Motion

One of the most important problems in geotechnical earthquake engineering is the evaluation of the ground response. Ground response analyses are used to predict ground surface motions during earthquake. The effects of the local site can play an important role in ground response analysis (Kramer, 1996). Therefore, the development of site-specific design ground motion is required prior to determining the earthquake-induced forces.

The earthquake resistant design guide for the cultural heritage sites was not yet proposed in the Korean seismic design guide. Considering the importance of a ripple effect on the collapse of the architectural heritage sites, the design rock outcropping accelerations were considered for special seismic category and/or category I structures in this study. The design rock outcropping accelerations at Gyeongju were 0.20g at the special collapse level for earthquakes (2400 year return period) and 0.14g at collapse level I for earthquakes (1000 year return period) based on the Korean seismic hazard map.

4.2 Input Ground Motions and Soil Properties

Since ground motion is significantly affected by the local site conditions, the composition of the entire soil strata that were determined by individual boring and seismic investigations were separately utilized in the analyses. Input soil properties, such as shear wave velocity profile, mass density, and modulus reduction and damping curves were determined for each layer while the bedrock properties of higher than 760m/s of shear wave velocity were determined from seismic tests.

One artificial synthetic earthquake, three strong motion recordings and one weak motion recording were used as input ground motions. The input rock outcropping accelerations were modified to the levels of collapse level earthquakes. Among the input motions, three strong motion recordings include El Centro, Hachinohe, and Ofunato earthquake motions, which were recorded in strong seismic regions, because of the lack of strong motion records of earthquakes in Korea. To reflect the characteristics of regional seismicity, an earthquake acceleration waveform recorded in Gyeongju was also applied to the estimation of site-specific response.

4.3 One-dimensional Ground Response Analysis

Site response analyses of Gyeongju were performed by using a one-dimensional equivalent linear scheme of a SHAKE program (Schnabel et al. 1972). The equivalent linear analysis provides relatively reliable results when the strain level caused by an earthquake is lower than one percent, which is a typical range in at moderate seismic zone such as in Gyeongju (Kim et al. 2002).

Figure 2 shows the summary of heritage information, field test results and site-specific ground response analysis results for the Cheomseongdae Observatory site. Cheomseongdae, the astronomical observatory, was estimated to have been built in the period of Queen Seondeok (A.D. 632~647) in the Silla Era. It is highly valued as the oldest astronomical observatory in Asia.

According to the results from the boring test, deep alluvial soil layers that consisted of gravel with sand were found at the subsurface of Cheomseongdae. The bedrock was composed of granite soft rock and 17.7 meters deep. The representative shear wave velocity, the mean value of downhole and HWAW test results, was used for the site response analysis of the Cheomseongdae ground.

In the case of Cheomseongdae, the peak ground accelerations were 0.370g at the special collapse level earthquake and 0.259g at collapse level I earthquake. Depending on the local site conditions, a maximum of 1.85 times site amplification is expected and the deep alluvial layers, which are common in Gyeongju area, show high potential for amplification. The site periods of the Cheomseongdae ground are 0.21~0.23 seconds.

The cultural heritage information and site-specific analysis results were summarized at thirty heritage sites by using the same way like Figure 2.

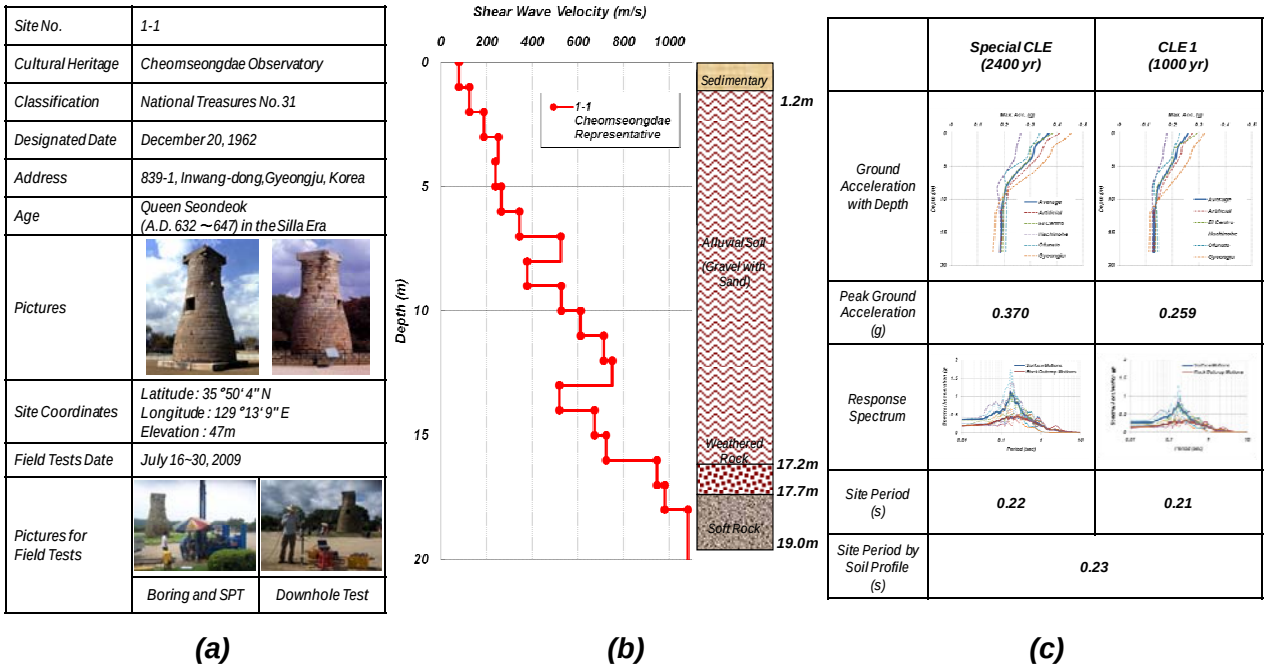

Figure 2 The Cultural Heritage Information and Site-specific Analysis Results: (a) Cultural Heritage Information and Pictures; (b) Field Test Results; (c) Ground Response Analysis Results

4.4 Two-dimensional Dynamic Response Analysis

One dimensional ground response analysis is useful for level or gently sloping sites. For many other problems, however, the assumptions of one-dimensional wave propagation are not acceptable. Irregular surface topography requires two-dimensional analysis.

The Bulguksa temple area is in the irregular surface topography of Toham Mountain. The necessity of two-dimensional analysis, therefore, as well as one-dimensional free surface motion analysis exists in this study. A two-dimensional dynamic response analysis for the Bulguksa temple area was conducted by using FLAC2D (Itasca 1996). Figure 3 shows a mesh for the two-dimensional ground response analysis of the Bulguksa temple site.

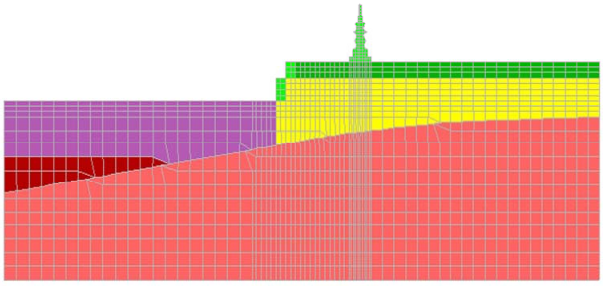

Figure 3 The Construction of Two-dimensional Mesh for the Ground Response Analysis of Three Storied Stone Pagoda at Bulguksa Temple.

Figure 4 shows the result of site response analysis that used one-dimensional and two-dimensional analysis for three storied stone pagoda ground at Bulguksa Temple. The peak ground accelerations of surface through FLAC analysis were 0.329g at special collapse level and 0.244g at collapse level I earthquake. These results were thirteen percent higher for one-dimensional analysis at the special collapse level and were the similar value as the collapse level I.

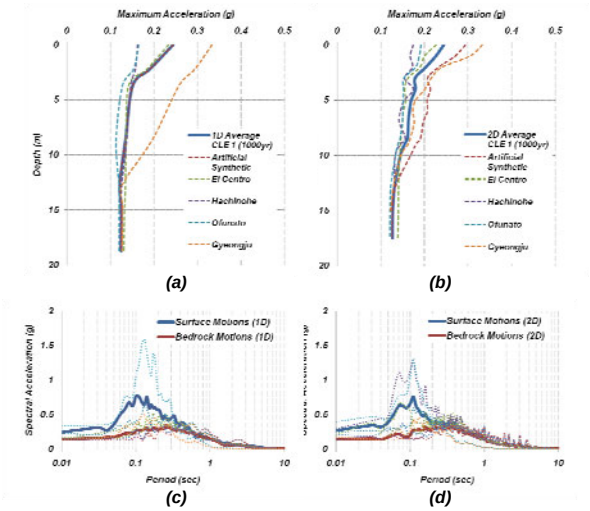

Figure 4 The Ground Response Analysis Results for Three Storied Stone Pagoda at Bulguksa Temple: (a) The Ground Accelerations with Depth for One-dimensional Analysis; (b) The Ground Accelerations with Depth for Two-dimensional Analysis; (c) Response Spectrum for SHAKE Analysis; (d) Response Spectrum for Two-dimensional Analysis

Table 2 The Results of Ground Response Analysis for Cultural Heritage Sites

Site No.	Cultural Heritage Sites	Latitude (°N)	Longitude (°E)	Elevation (m)	Bedrock Depth (m)	Average Peak Ground Acceleration (g)		Site Period (Sec)		
						Special CLE (2400yr)	CLE 1 (1000yr)	Special CLE (2400yr)	CLE 1 (1000yr)	by Soil Profile
2-1	Dabotap pagoda of Bulguksa Temple	35°47'24"	129°19'57"	249	12.7	0.291	0.244	0.15	0.14	0.15
2-2	Three storied stone pagoda at Bulguksa Temple	35°47'24"	129°19'56"	249	12.7	1D: 0.291 2D: 0.329	1D: 0.244 2D: 0.244	0.15	0.14	0.15
2-3	Yeonhwagyo and Chilbogyo bridges of Bulguksa Temple	35°47'23"	129°19'56"	243	13.5	0.267	0.187	0.26	0.23	0.18
2-4	Cheongungyo and Baegungyo bridges of Bulguksa Temple	35°47'23"	129°19'57"	243	13.5	0.267	0.187	0.26	0.23	0.18
2-5	Sarira pagoda of Bulguksa Temple	35°47'26"	129°19'55"	251	20.0	0.298	0.211	0.27	0.24	0.20
3-1	Najeong well in Gyeongju	35°48'55"	129°12'46"	56	26.0	0.255	0.200	0.35	0.32	0.29
3-2	Standing stone buddhist triad in Bae-dong	35°48'5"	129°12'40"	74	14.0	0.260	0.184	0.12	0.13	0.14
3-3	Poseokjeong pavilion site	35°48'25"	129°12'46"	53	14.0	0.298	0.200	0.14	0.13	0.14
7-4	Seochulji lake	35°47'45"	129°14'32"	95	31.0	0.274	0.205	0.31	0.28	0.31
7-3	Three storied stone pagoda in Namsan-ri	35°47'35"	129°14'40"	75	32.0	0.359	0.269	0.44	0.39	0.42
1-1	Cheomseongdae observatory	35°50'4"	129°13'9"	47	17.7	0.370	0.259	0.22	0.21	0.23
4-1	Gyerim forest in Gyeongju	35°49'56"	129°13'7"	45	14.0	0.298	0.205	0.14	0.13	0.15
4-2	Wolseong fortress	35°49'59"	129°13'28"	60	14.0	0.315	0.253	0.30	0.27	0.22
4-3	Imhaejeon hall site	35°50'3"	129°13'36"	56	18.0	0.379	0.261	0.18	0.17	0.20
5-1	Royal tomb of King Michu of Silla	35°50'18"	129°12'39"	41	22.0	0.366	0.264	0.21	0.19	0.22
5-2	Jaemaejeong well	35°49'43"	129°12'47"	37	22.0	0.337	0.235	0.17	0.16	0.21
6-1	Hwangnyongsa Temple site	35°50'11"	129°14'2"	57	26.0	0.263	0.189	0.20	0.19	0.22
6-2	Stone pagoda of Bunhwangsa Temple	35°50'27"	129°14'2"	60	18.0	0.258	0.177	0.16	0.15	0.17
6-4	Myeonghwalsanseong fortress	35°30'37"	129°15'44"	92	16.0	0.274	0.198	0.38	0.34	0.26
8-0	Yangdong village of Wolseong	36°0'1"	129°15'15"	17	29.2	0.293	0.235	0.45	0.40	0.42
8-1	Gwangajeong	35°59'59"	129°15'7"	28	1.8	0.205	0.144	0.04	0.04	0.04
8-2	Hyangdan	36°0'0"	129°15'10"	28	3.0	0.208	0.145	0.05	0.05	0.05
7-1	Mangdeoksa Temple site	35°48'59"	129°14'37"	49	30.0	0.331	0.249	0.32	0.30	0.35
7-2	Flagpole support of in Mangdeoksa Temple site	35°48'57"	129°14'40"	48	30.0	0.330	0.254	0.44	0.39	0.41
9-1	Monument of King Taejongmuyeol of Silla Period	35°49'30"	129°11'11"	49	31.2	0.270	0.196	0.34	0.31	0.32
4-4	Three storied stone pagoda of Goseonsa Temple site, Gyeongju National Museum	35°49'46"	129°13'46"	56	32.0	0.323	0.235	0.27	0.25	0.29
6-3	Three storied stone pagoda in Guhwang-dong	35°49'54"	129°14'33"	71	10.0	0.266	0.193	0.13	0.12	0.11
10-1	Five storied stone pagoda in Nawon-ri, Wolseong	35°53'36"	129°12'45"	47	3.1	0.250	0.173	0.04	0.04	0.06
11-1	Thirteen storied stone pagoda of Jeonghyesa Temple site	36°1'7"	129°9'27"	96	11.8	0.287	0.195	0.11	0.10	0.12
12-1	Three storied stone pagoda of Gameunsa Temple site	35°44'52"	129°28'41"	19	24.8	0.275	0.215	0.39	0.34	0.30

The peak ground accelerations, site periods, and site information were determined at thirty heritage sites, and are tabulated in Table 2.

Considering the maximum site amplification factor between rock outcrop motion and free surface motion for the thirty cultural heritage sites, the 'three storied stone pagoda in Namsan-ri', the 'Cheomseongdae observatory' and the 'flagpole support of in Mangdeoksa temple site' were expected to have more than one-point-five times site amplification. On the contrary, 'Gwangajeong' and 'Hyangdan' in Yangdong village, the 'five storied stone pagoda in Nawon-ri, Wolseong', the 'standing stone buddhist triad in Bae-dong', and the 'Stone pagoda of Bunhwangsa temple' had relatively low potentials for site amplification.

The cultural heritage information and site-specific ground response analysis results considering local site effect at thirty heritage sites were compiled and summarized as shown in Table 2. The evaluation of site amplification can estimate the rock outcropping motion based on historical earthquake intensities as well as it can identify the potential of an earthquake. Based on this study, the re-evaluation of historical earthquake records is possible. And it can be evaluated whether that the architectural heritages are consistent with the site period or not through the structural analysis.

5. GIS BASED SEISMIC MICROZONATION

The seismic geotechnical information determined by site-specific ground response analysis were interpreted using GIS tool. In order to analyze the seismic sensitivity in geotechnical earthquake engineering, the spatial data were collected for assessing synthetically the earthquake hazard in Gyengju Historic Areas.

Seismic microzonation, which is a city scale hazards distribution mapping based on the geotechnical information system, made a reliable estimation of spatial geotechnical data for the Gyeongju Historic Areas. This system incorporates a geostatistical kriging interpolation technique, which can be adopted for reliable prediction of geotechnical data values. Kriging is considered to be the best linear unbiased estimate and optimal interpolation method for geological and geotechnical predictions in space, because it is a linear combination of weighted sample values that have

minimum variance (Oliver and Webster 1990).

A study area of interest for the GIS based seismic microzonation is Gyeongju city, which is centered around 10km by 10km. The sixty pre-existing site investigation data and 21 in-situ test data are collected from the microzonation area. The geotechnical information component contains computation modules on depth to bedrock, site period, peak ground acceleration and amplification factors.

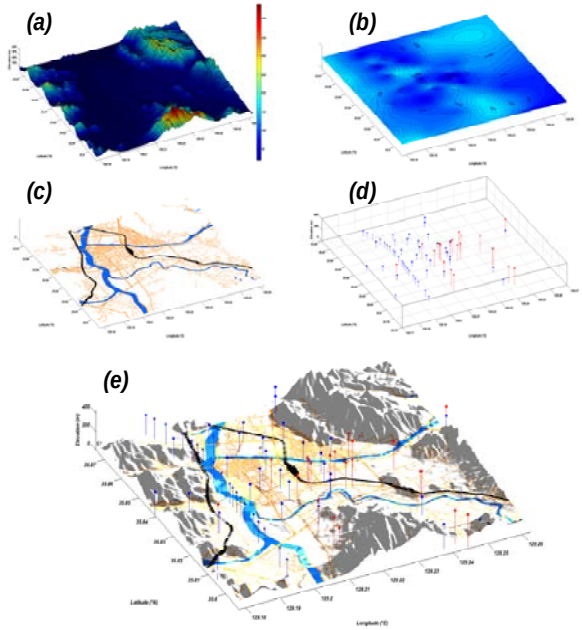

Figure 5 The Procedure of Seismic microzonation: (a) Three-dimensional digital elevation map by the Triangulated Irregular Network; (b) Kriging Interpolation with Depth; (c) Standard Geographical Information Map; (d) Coordinate System; (e) Combination of Digital Maps

A two-dimensional numerical topographical map, three-dimensional digital elevation map, and standard geographical information map were used to construct the geotechnical information system. Figure 5 shows the system construction procedure.

Each geotechnical information system is shown in Figure 6. The bedrock depth, site period, and site amplification factor information systems are interrelated and can be considered as reasonable results. The area of 'Cheomseongdae observatory' and 'Imhaejeon hall site', the plain area from 'Mangdeoksa temple site', and the 'three storied stone pagoda in Namsan-ri' have relatively high potentials for amplification.

The construction of the GIS based seismic microzonation system can be used as a method for seismic disaster mitigation of cultural heritage and historic sites. This system can involve very important information on the overall countermeasures against earthquake disasters and the seismic hazards of historic areas, such as Gyeongju

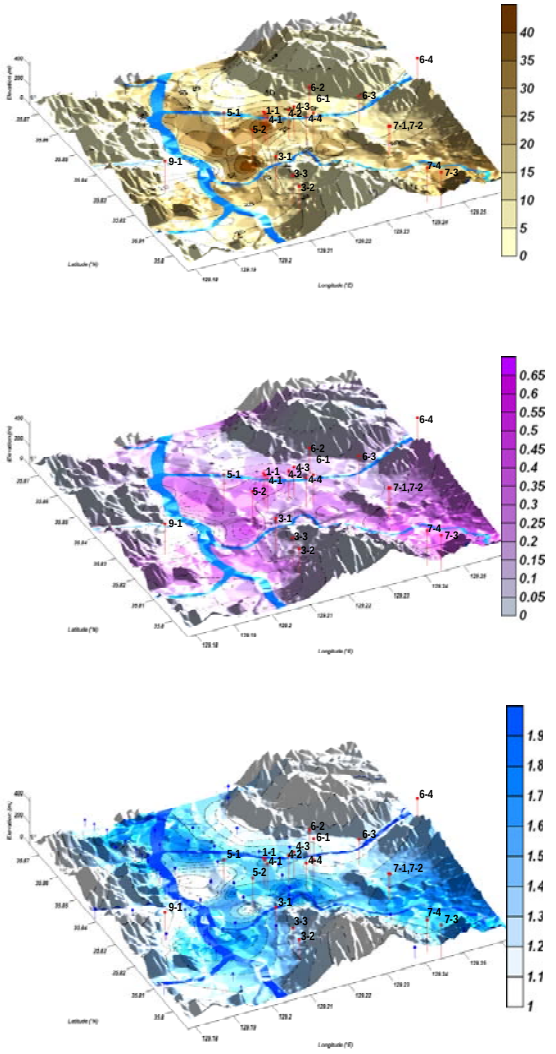

Figure 6 GIS based Geotechnical Information System; The Bedrock Depth, Site Period, and Site Amplification Factor

6. CONCLUSION

Gyeongju is the one of the most glorious historic cities in Korea, and is even considered a huge historic site with a lot of cultural heritage for nearly a thousand years. In this study, the local site effect during an earthquake on Gyeongju, which has frequent historical earthquake damage records, was evaluated.

The necessity of estimating the seismic hazard of the historic area was recognized. In-situ test sites around the cultural heritage sites were selected. Field tests and ground response analysis were conducted after pre-existing data of site investigation were analyzed. Based on these results, GIS based seismic microzonation and constructions of geotechnical information systems have been proposed.

Acknowledgements:

The authors acknowledge support from the National Research Institute of Cultural Heritage, Cultural Heritage Administration of Korea for "Research and Development of the Technology for Conservation and Restoration".

References:

Fujiwara, H., Kawai, S., Aoi, S. Ishii, T., Okumura, T., Hayakawa, Y., Morikawa, N., Senna, S., Kobayashi, K. and Hao, K.X.S. (2006), "Japan seismic hazard information station, J-SHIS," *Proceedings of 4th International Conference on Earthquake Engineering*, Oct. 12-14, Taipei, Taiwan, CD-ROM, Paper No. 274.

Itasca Consulting Group, I. (1996), "FLAC: Fast Langrangian Analysis of Continua"

Kim, D.S., Chung, C.K., Sun, C.G. and Bang, E.S. (2002), "Site assessment and evaluation of spatial earthquake ground motion of Kyeongju," *Soil Dynamics and Earthquake Engineering*, **22**(5), 371-387.

Kim, D.S., Park, H.J., Kim, J.T., Kim, N.R. and Bang, E.S. (2009), "Evaluation of spatial variations in soil stiffness using stress wave propagations," *Proceedings of International Conference on Performance-Based Design in Earthquake Geotechnical Engineering (IS-Tokyo2009)*, June 15-18, Tsukuba, Japan

Kramer, S.L. (1996), "Geotechnical earthquake engineering," Prentice Hall.

National Research Institute of Cultural Heritage (2009), "Study on the Evaluation Method for Flood and Seismic Risks of Architectural Heritage," Research Report in Korean

Oliver, M.A. and Webster, R. (1990), "Kriging: a method of interpolation for geographical information systems," *International Journal of Geographical Information Systems*, **4**(3), 313-332.

Park, H.C. and Kim, D.S. (2001), "Evaluation of the dispersive phase and group velocities using harmonic wavelet transform," *NDT&E International*, **34**(7), 457-467.

Schnabel, P.B., Lysmer, J. and Seed, H.B. (1972), "SHAKE: a computer program for earthquake response analysis of horizontally layered sites," Report EERC 72-12, Earthquake Engineering Research Center, University of California, Berkeley.

Sun, C.G., Kim, D.S. and Chung, C.K. (2005), "Geologic site conditions and site coefficients for estimating earthquake ground motions in the inland areas of Korea," *Engineering Geology*, **81**(4), 446-469.

JOINT CONFERENCE PROCEEDINGS
7th International Conference on Urban Earthquake Engineering (7CUEE) &
5th International Conference on Earthquake Engineering (5ICEE)
March 3-5, 2010, Tokyo Institute of Technology, Tokyo, Japan

SIGNAL PROCESSING AND PROBABILISTIC SEISMIC HAZARD ANALYSIS TOOLS FOR CHARACTERIZING THE IMPACT OF NEAR-FAULT DIRECTIVITY

Shrey K. Shahi [1] and Jack W. Baker[2]

1) Graduate Research Assistant; Dept. of Civil & Environmental Engineering; Stanford University, Stanford, CA 94305
2) Assistant Professor; Dept. of Civil & Environmental Engineering; 473 Via Ortega; Stanford University, Stanford, CA 94305
shrey@stanford.edu, bakerjw@stanford.edu

Abstract: Near-fault ground motions containing strong velocity pulses are of interest to engineers designing systems close to active faults. These ground motions, which are here referred to as 'pulse-like ground motions,' have been identified as imposing extreme demands on structures, but methods of accounting for their effects in design are still relatively ad hoc. This paper reviews a recently proposed quantitative ground motion classification system that is being utilized to identify these ground motions, study their unique effects on structures, and account for their occurrence in probabilistic seismic hazard analysis. Example results are shown to illustrate the classification scheme, how it can be used to develop statistical models that predict the occurrence and severity of this effect in future ground motions, and what impact these models have on probabilistic seismic hazard analysis calculations.

1. INTRODUCTION

Pulse-like near-fault ground motions resulting from directivity effects are a special class of ground motions that are particularly challenging to characterize for seismic performance assessment. These motions contain a 'pulse' in the velocity time history of the motion, typically in the direction perpendicular to the fault rupture, and generally occur at locations near the fault where the earthquake rupture has propagated towards the site. It has been observed that these motions have, on average, larger elastic spectral acceleration values at moderate to long periods. Additionally, these motions tend to cause severe response of nonlinear multi-degree-of-freedom structures to an extent not entirely accounted for by measuring the intensity of the ground motion using spectral acceleration at the elastic first-mode period of a structure. Despite our growing understanding of these ground motions, many questions remain when trying to incorporate these effects into design codes. How can one distinguish between 'pulse-like' and ordinary ground motions, other than through a visual identification that relies on user judgment? How should directivity effects be accounted for when determining the target ground motion intensity level used for design? If one is performing dynamic analysis of the structure, what fraction of input ground motions should have directivity pulses, given that not all near-fault ground motions contain pulses? Should the ground motions be input in a 'worse case' fault-normal/fault-parallel orientation, or is some other orientation more appropriate?

Forward directivity results when the fault rupture propagates towards the site at a velocity nearly equal to the propagation velocity of the shear waves and the direction of fault slip is aligned with the site. This causes the wave front to arrive as a single large pulse. Forward directivity effects in the near-fault region can cause large-amplitude pulses that occur early in the velocity time history. A more detailed description of this phenomenon is given by, e.g., Somerville et al. (1997). For both strike-slip and dip-slip faults, forward directivity typically occurs in approximately the fault normal direction, although this is not always the case. Another near-fault effect, fling step, is mentioned for completeness but not considered here. This permanent displacement of the ground resulting from fault rupture can be important for structures such as lifelines crossing a fault, but is less important for general structural design than the effects of directivity.

This paper summarizes recent work in ground motion processing and seismic hazard analysis that facilitates the incorporation of directivity effects into the widely used probabilistic seismic hazard analysis (PSHA) procedure. This work is then used to perform an example PSHA for a near-fault site with and without accounting for directivity effects, to examine the impact of directivity. The results are used to illustrate how the above questions can be answered in a systematic manner, and to speculate as to how near-fault factors might be incorporated into building codes in a more systematic manner. These results are also compared to previous results using the widely used model of Somerville et al. (1997), and the distinctions and advantages of the

approach used here are described.

2. WAVELET-BASED GROUND MOTION ANALYSIS AND PULSE EXTRACTION

Directivity pulses are known to occur in near-fault ground motions, but the presence and severity varies due to variations in source properties and source-to-site geometry (which affects the constructive interference of seismic waves as they propagate towards the site of interest). For this reason, it is not always clear whether a particular near-fault ground motion contains a velocity pulse; see Figure 1 for example ground motions having velocity pulses of varying severity.

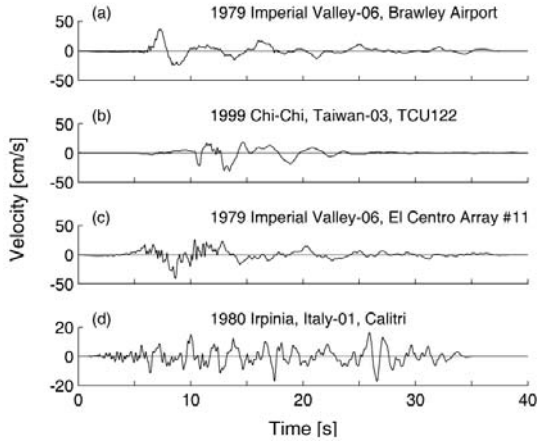

Figure 1. Example fault-normal near-fault ground motions (from Baker 2007).

Several researchers have developed detailed analytical models describing the shapes of velocity pulses resulting from directivity (Fu and Menun 2004; Makris and Black 2004; Mavroeidis and Apostolos S. Papageorgiou 2003; Rodríguez-Marek and Bray 2004). These models are useful when specifying dynamic loading for parametric studies of structural response to velocity pulses. A critical component of these models is the period, or frequency, of the velocity pulse. This pulse period has been seen to be correlated with the magnitude of the causative earthquake (Bommer et al. 2001; Mavroeidis and Apostolos S. Papageorgiou 2002; Somerville 2003). None of these models, however, is able to determine whether an arbitrary ground motion contains a pulse; they are only used to characterize pulses that have previously been identified by user judgment.

To empirically determine the probability of observing a directivity pulse under a given set of conditions, it is necessary to classify an existing library of near-fault ground motions according to whether or not they contain a pulse. Typically, users classify records manually using their best visual judgment, but this results in classifications that vary from author to author (Fu and Menun 2004; Mavroeidis and Apostolos S. Papageorgiou 2003; Somerville 2003; Akkar et al. 2005; Cox and Ashford 2002). Relying on user judgement is also time consuming when processing large ground motion libraries. For a quantitative classification procedure to be effective, several criteria are important. First, the procedure should be able to distinguish between pulse-like and ordinary ground motions. Additionally, the classification procedure should require minimal intervention or judgment from the analyst and should produce a reproducible result so that classifications of a given ground motion are consistent from analyst to analyst. A computationally inexpensive procedure is also preferable, because thousands of recorded ground motions will need to be processed. The authors have recently developed a classification concept that uses wavelet-based signal processing to identify and extract the largest velocity pulse from a ground motion (Baker 2007). If the extracted pulse is 'large' relative to the remaining features in the ground motion, the ground motion is classified as pulse-like. Quantitative descriptions of pulse amplitude are produced using the proposed technique, so there is a precise definition of a 'large pulse.' The period of the detected velocity pulse, a needed parameter for the proposed assessment approach, is also easily determined. The algorithm requires only a few seconds to analyze and classify a given ground motion.

The proposed classification technique utilizes wavelet analysis, as illustrated schematically in Figure 2. Similar to a Fourier Transform, which decomposes a signal into a set of sine and cosine waves, the wavelet transform decomposes the signal into a series of "wavelets." In Fourier analysis, the sine and cosine waves serve as basis functions; each wave is very precise in terms of the frequency it represents, but not at all precise in the time range it represents (because it is infinite in length). In contrast, a wavelet basis function is somewhat precise in both the time and frequency range it represents. This time localization is particularly advantageous when studying short-duration phenomena such as directivity pulses. As seen in Figure 2, a single wavelet can substantially represent the strongest velocity pulse present in the example ground motion. This efficient representation of short-duration pulses makes the wavelet transform an ideal mathematical tool for identifying and analyzing the presence of strong velocity pulses.

Figure 3 illustrates further how the wavelet decomposition of a signal can be used to detect velocity pulses. The first panel of this figure illustrates the original ground motion velocity time history, along with the wavelet having the largest amplitude (which again identifies the strong velocity pulse). The second panel shows the identified velocity pulse, which consists of the largest wavelet, plus several additional wavelets having the same frequency and located adjacent in time to the original wavelet. The third panel shows the residual ground motion, obtained by subtracting the pulse from the original ground motion. This decomposition can be performed for any ground motion, as some wavelet is always the largest. So, in order to classify a ground motion as pulse-like, the residual ground motion is compared to the original ground motion to see if the intesity of the motion has decreased significantly

(in terms of its energy and peak ground velocity). Baker (2007) provides a quantitative measure of this comparison that can be used toclassify any ground motion.

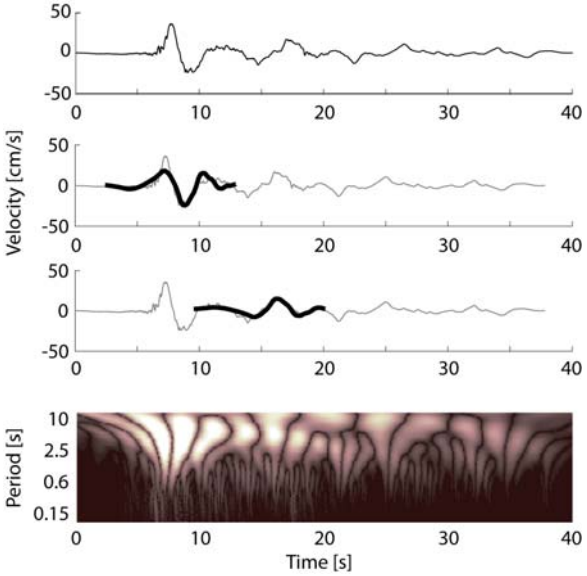

Figure 2. Example results for the wavelet decomposition of a velocity time history. The top panel shows the original time history. The second panel shows the largest single wavelet coefficient that appears in the ground motion (which typically matches the large velocity pulse in the ground motion, if one is present). The third panel shows the largest remaining wavelet coefficient if the first coefficient is removed from the time history. The final panel shoss the continuous wavelet transform coefficients for all periods and locations in the time history(light shading indicates a large absolute value of the coefficient with the specified period and location in time).

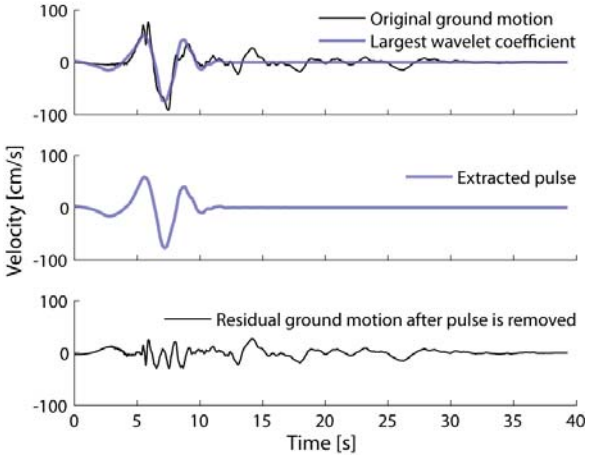

Figure 3. Illustration of the proposed decomposition procedure used to extract the pulse portion of a ground motion. (from Baker 2008).

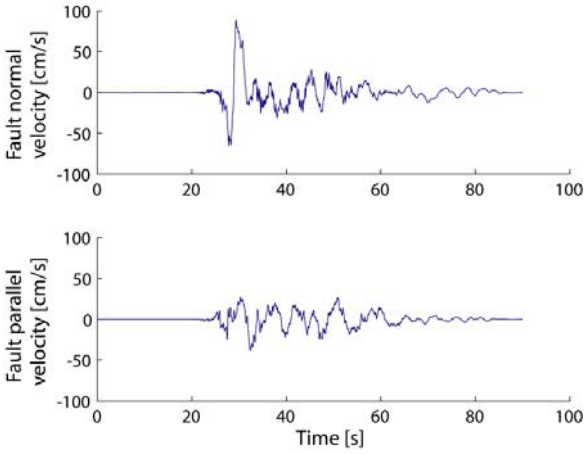

(a)

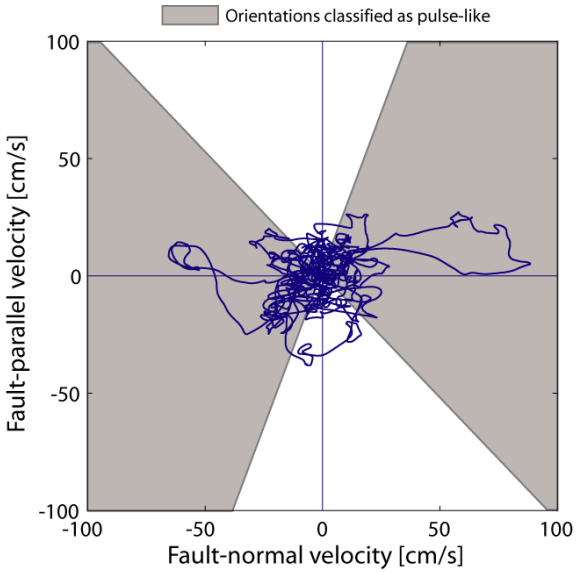

(b)

Figure 4. Velocity time history of the Chi-Chi, Taiwan, Tsaotun (TCU075) ground motion. (a) Fault normal and fault parallel velocity time histories. (b) Fault normal versus fault parallel velocity, with shaded regions denoting orientations classified as pulse-like using the proposed procedure (adapted from Baker 2007).

The classification procedure that has been described thus far is applicable to individual components of a ground motion. But the procedure can be applied to multi-component ground motions that have been rotated to arbitrary orientations, to see the range of orientations over which a strong pulse is present. Figure 4a shows the fault normal and fault parallel components of an example ground motion, illustrating a strong pulse in the fault normal direction but not in the fault parallel direction (as theory would suggest should be the case). The ground motions velocity profile is plotted in two dimensions in Figure 4b, showing the large velocity pulse orientied largely in the fault normal direction. But by rotating the ground motion to other orientations, we can repeatedly re-classify it, and identify

the range of orientations over which the pulse is strong. This range of orientations is denoted by the shading in Figure 4b. Ongoing research by the authors suggests that velocity pulses are often very clear over a wide range of orientations, and that the strongest orientation is not always fault normal. This emperical finding is justified theoretically by noting that "fault normal" is somewhat of an abstraction for non-planar ruptures, and by noting that variability in the rupture and wave-propagation path may disrupt primary orientations of directivity effects.

3. Seismic hazard analysis

Basic calculations have been performed to evaluate the effects of directivity on seismic hazard analysis (Abrahamson 2000). This work has utilized the simple response spectrum modification of Somerville et al. (1997) discussed in the previous section. Abrahamson (Abrahamson 2000) found that, as expected, directivity effects increased the ground motion intensity associated with a given return period at sites located near active faults. But because only a simple spectrum modification was used, this approach provides no information regarding the period of the pulses responsible for the increased ground motion intensity. As seen in the previous section, this pulse period is important when estimating structural response and thus it is important to consider when selecting ground motions for use in dynamic structural analysis. Tothong et al. (2007) have recently proposed a new framework for seismic hazard analysis that can include pulse periods explicitly, and has thus been modified and calibrated for implementation as part of this work.

Once the pulse-like ground motions have been identified, their effects can be incorporated into probabilistic seismic hazard analysis. The technique adopted by the authors is adapted from that proposed by Tothong et al. (2007). Some highlights are provided here. For reference, let us first consider the standard Probabilistic Seismic Hazard Analysis calculations (for more details see, e.g., Kramer 1996; McGuire 2004). Without loss of generality, we can consider the case with one seismic source as follows

$$\nu_{S_a}(x) = \nu_{eq} \iint_{m,r} P(Sa > x \mid m,r)\, f(m,r)\, dm\, dr \qquad (1)$$

where $\nu_{S_a}(x)$ is the annual rate of spectral acceleration at a given period (*Sa*) exceeding *x*, ν_{eq} is the annual rate of earthquakes on the source, $P(Sa > x \mid m,r)$ is the probability that spectral acceleration at the given period exceeds *x* given an earthquake with magnitude *m* and distance *r* (as characterized by standard ground motion prediction models), and $f(m,r)$ is the joint probability density function of *m* and *r*. The integration over *m* and *r* is an application of the total probability theorem.

To consider near-fault directivity, equation (1) is modified as follows

$$\nu_{S_a}(x) = \nu_{eq} \iiint_{m,r,z} P^*(Sa > x \mid m,r,z)\, f(m,r,z)\, dm\, dr\, dz \qquad (2)$$

where *z* is a new parameter or vector of parameters describing source-to-site geometry properties that predict occurrence of near-fault velocity pulses, $P^*(Sa > x \mid m,r,z)$ is an updated ground motion prediction model that accounts for possible directivity pulses as a function of *z*, and $f(m,r,z)$ is the joint probability density function for *m*, *r* and *z*. Implementation of this model requires the updated prediction model $P^*(Sa > x \mid m,r,z)$, and the identification and characterization of the parameter(s), *z*, that are effective in predicting occurrence of velocity pulses.

The updated prediction model can be constructed from a variety of existing models along with modification functions, so that the considerable body of knowledge that was used to create an existing ground motion model can be retained. The updated model can be formulated using the Total Probability Theorem as follows:

$$\begin{aligned} P^*(Sa > x \mid m,r,z) = {} & P(Pulse \mid z) P_{Pulse}(Sa > x \mid m,r,z) \\ & + \left(1 - P(Pulse \mid z)\right) P(Sa > x \mid m,r) \end{aligned} \qquad (3)$$

where $P(Pulse \mid z)$ predicts the probability of observing a pulse-like ground motion, given a source-to-site geometry parameterization defined by *z* (e.g., Iervolino and Cornell 2008). $P_{Pulse}(Sa > x \mid m,r,z)$ is a ground motion prediction for pulse-like ground motions, which here is assumed to consist of a standard ground motion prediction model plus a "pulse amplification function" that increases predicted ground motions to account for the effect of the velocity pulse; this function assumes occurrence of a pulse (as this occurrence is accounted for by the $P(Pulse \mid z)$ term), and amplifies spectral amplitudes in some range around the pulse period (e.g., Baker 2008; Shahi and Baker 2010). This requires a predictive model for pulse periods, which is available from several sources (Baker 2007; Bray and Rodríguez-Marek 2004; Mavroeidis et al. 2004; Somerville 2003). The new predictive models have been termed "narrow-band" in that they are dependent upon the period of the pulse rather than amplifying all periods due to pulse effects (Somerville 2003).

Non-pulse-like ground motions are accounted for in the second term of the summation of equation (3). Currently, the $P(Sa > x \mid m,r)$ predictions for non-pulse-like ground motoins are assumed to be reasonably predicted by standard ground motoin prediction models, but ongoing work is investigating whether that prediction might be overly conservative, as standard ground motion prediction models are calibrated using both pulse-like and non-pulse-like ground motions, while this model should represent only non-pulse-like motions (which presumably have lower intensities).

While further mathematical details of the calibration

and combination of these models is omitted here for brevity, they are available from other sources (Shahi and Baker 2010; Tothong et al. 2007). Another portion of the mathematical details of this calculation whose details are omitted is the deaggregation of input parameters, conditional upon exceeding a given spectral acceleration intensity. Deaggregation on magnitude, distance and ε can be performed as with standard PSHA, but now it is also possible to deaggregate on directivity parameters. Conditional upon exceedance of a spectral acceleration threshold, it is possible to compute the associated probability of observing a velocity pulse and the distribution of pulse periods.

4. Example analysis

Using the framework and predictive models cited in the previous section, an example analysis can be performed to highlight the impact of considering near-fault directivity. The geometry of the example site considered is illustrated in Figure 5, and is further quantified by the following parameters. The single fault in the region has a truncated Gutenberg-Richter distribution of earthquake magnitudes (with a minimum magnitude of five and maximum magnitude of seven). The Gutenburg-Richter "b-value" is 0.9. The site being considered is located 6.7 km from the fault and has an average shear-wave velocity over the top 30 meters (V_{s30}) of 250 m/s. These choices were made to approximately represent conditions of the Imperial Valley Fault in Southern California, and the El Centro Array #4 station that experienced a strong velocity pulse in the 1979 Imperial Valley earthquake.

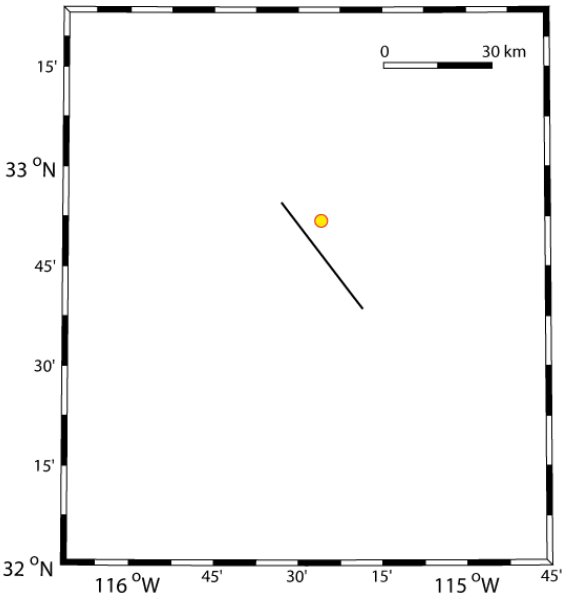

Figure 5. Map of fault and site geometry the example analysis.

Using this information PSHA was performed using three techniques, and 2% in 50 years uniform hazard spectra (UHS) for the site are shown in Figure 6. The analysis was first performed using the standard PSHA equation of equation (1). The second analysis was performed using the proposed PSHA equation given in equation (2). For reference, the PSHA approach proposed by Abrahamson (2000), using the ground motion prediction model adjustment by Somerville et al. (1997), is also shown in the figure. While the Somerville prediction model always gives directivity amplifications that increase monotonically with period, the proposed technique has amplifications with period that depend upon the earthquake magnitudes most likely to cause strong ground shaking at the site. In this case, the uniform hazard spectrum is dominated by earthquakes with magnitudes close to seven, causing the amplification model to amplify periods near two seconds by the greatest amount. In this analysis, the proposed PSHA approach causes spectral values at two seconds to be amplified by 13% relative to the corresponding UHS value obtained without explicit directivity considerations. It should be noted that these exact numerical values are still tentative. Further refinement of the amplification model, and a more comprehensive study of PSHA analysis, are expected to lead to more precise and more general results of this type in the near future.

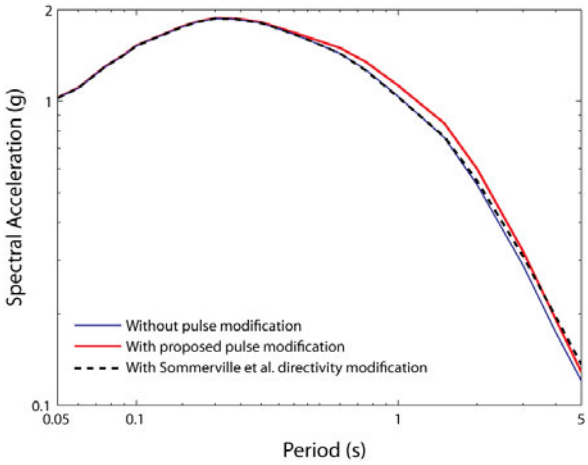

Figure 6. Uniform hazard spectra with 2% probability of exceedance in 50 years, obtained for the example site using three Probabilistic Seismic Hazard Analysis techniques.

5. CONCLUSIONS

This paper has highlighted some recent progress in ground motion pulse classification, seismic hazard analysis, and ground motion intensity predictions that facilitate a new quantitative approach for assessing the potential effects of these ground motions. Bringing these tools together will help engineers and seismologists more fundamentally understand the effect of this phenomenon, and will give stakeholders greater confidence that projects are being

designed using rational tools to account for all effects of ground shaking. A more quantitative representation of pulses, pulse occurrence, and their effect on structural response will also be useful to seismologists working on simulation of synthetic ground motion time histories. These new models will provide target results and a better understanding of important ground motion properties for seismologists to use in validation of their simulations.

Some major features of the proposed signal processing and hazard analysis approach have been presented here. It is hoped that this brief overview will present some important characteristics of the technique, and point interested readers towards other references providing more mathematical details (Baker 2007; Shahi and Baker 2010; Tothong et al. 2007).

The effort described here will result not only in new models to address the impacts of near-fault velocity pulses, but also in a variety of software tools and data sets to support extension and application of this work by other researchers and practitioners. Relevant signal processing software and example analysis results are currently available at *http://stanford.edu/~bakerjw/pulse-classification.html*. These offerings will continue to be updated and expanded as refined analysis models are developed.

Acknowledgements:

This material is based upon work supported by the Pacific Earthquake Engineering Research (PEER) Center and also by the National Science Foundation under NSF grant number CMMI 0726684. This support is gratefully appreciated. Any opinions, findings and conclusions or recommendations expressed in this material are those of the authors and do not necessarily reflect the views of the National Science Foundation (NSF).

References:

Abrahamson, N. A. (2000). "Effects of rupture directivity on probabilistic seismic hazard analysis." *Sixth International Conference on Seismic Zonation*, Earthquake Engineering Research Inst., Oakland, California.

Akkar, S., Yazgan, U., and Gulkan, P. (2005). "Drift Estimates in Frame Buildings Subjected to Near-Fault Ground Motions." *Journal of Structural Engineering*, 131(7), 1014-1024.

Baker, J. W. (2007). "Quantitative Classification of Near-Fault Ground Motions Using Wavelet Analysis." *Bulletin of the Seismological Society of America*, 97(5), 1486-1501.

Baker, J. W. (2008). "Identification of near-fault velocity pulses and prediction of resulting response spectra." *Geotechnical Earthquake Engineering and Soil Dynamics IV*, Sacramento, California, 10.

Bommer, J., Georgallides, G., and Tromans, I. J. (2001). "Is there a near-field for small-to-moderate magnitude earthquakes?." *Journal of Earthquake Engineering*, 5(3), 395-423.

Bray, J. D., and Rodríguez-Marek, A. (2004). "Characterization of forward-directivity ground motions in the near-fault region." *Soil Dynamics and Earthquake Engineering*, 24(11), 815-828.

Cox, K. E., and Ashford, S. A. (2002). *Characterization of large velocity pulses for laboratory testing*. Pacific Earthquake Engineering Research Center, University of California at Berkeley, Berkeley, California, 60.

Fu, Q., and Menun, C. (2004). "Seismic-environment-based simulation of near-fault ground motions." *Proceedings, 13th World Conference on Earthquake Engineering*, Vancouver, Canada, 15.

Iervolino, I., and Cornell, C. A. (2008). "Probability of occurence of velocity pulses in near-source ground motions." *Bulletin of the Seismological Society of America*, 98(5), 2262-2277.

Kramer, S. L. (1996). *Geotechnical earthquake engineering*. Prentice Hall, Upper Saddle River, N.J.

Makris, N., and Black, C. J. (2004). "Dimensional Analysis of Bilinear Oscillators under Pulse-Type Excitations." *Journal of Engineering Mechanics*, 130(9), 1019-1031.

Mavroeidis, G. P., Dong, G., and Papageorgiou, A. S. (2004). "Near-Fault Ground Motions, and the Response of Elastic and Inelastic Single-Degree-of-Freedom (SDOF) Systems." *Earthquake Engineering & Structural Dynamics*, 33(9), 1023-1049.

Mavroeidis, G. P., and Papageorgiou, A. S. (2002). "Near-source strong ground motion: characterizations and design issues." *7th U.S. National Conference on Earthquake Engineering*, Earthquake Engineering Research Institute, Boston, MA, 1 CD-ROM.

Mavroeidis, G. P., and Papageorgiou, A. S. (2003). "A Mathematical Representation of Near-Fault Ground Motions." *Bulletin of the Seismological Society of America*, 93(3), 1099-1131.

McGuire, R. K. (2004). *Seismic Hazard and Risk Analysis*. Earthquake Engineering Research Institute, Berkeley.

Rodríguez-Marek, A., and Bray, J. D. (2004). "Site Effects for Near-Fault Forward-Directivity Motions." *8th National Conference on Earthquake Engineering*, San Francisco, CA, 10.

Shahi, S., and Baker, J. W. (2010). "A comprehensive model to include the effects of near-fault ground motions in Probabilistic Seismic Hazard Analysis." *Bulletin of the Seismological Society of America*, (in preparation).

Somerville, P. G. (2003). "Magnitude scaling of the near fault rupture directivity pulse." *Physics of the earth and planetary interiors*, 137(1), 12.

Somerville, P. G., Smith, N. F., Graves, R. W., and Abrahamson, N. A. (1997). "Modification of Empirical Strong Ground Motion Attenuation Relations to Include the Amplitude and Duration Effects of Rupture Directivity." *Seismological Research Letters*, 68(1), 199-222.

Tothong, P., Cornell, C. A., and Baker, J. W. (2007). "Explicit-Directivity-Pulse Inclusion in Probabilistic Seismic Hazard Analysis." *Earthquake Spectra*, 23(4), 867-891.

JOINT CONFERENCE PROCEEDINGS
7th International Conference on Urban Earthquake Engineering (7CUEE) &
5th International Conference on Earthquake Engineering (5ICEE)
March 3-5, 2010, Tokyo Institute of Technology, Tokyo, Japan

THE GUTENBERG-RICHTER B-VALUE OF THE KOREAN PENINSULA FOR A SEISMIC HAZARD ANALYSIS

Jeong-Moon Seo[1)], Hyun-Me Rhee[2)], and In-Kil Choi[3)]

1) Manager, Nuclear Safety Research, Korea Atomic Energy Research Ins., Korea
2) Post Master, Nuclear Safety Research, Korea Atomic Energy Research Ins., Korea
3) Manager,, Nuclear Safety Research, Korea Atomic Energy Research Ins., Korea
jmseo@kaeri.re.kr, rhhm@kaeri.re.kr, cik@kaeri.re.kr

Abstract: The Gutenberg-Richter b-value of the Korean Peninsula was estimated by an expert panel by assigning weighting factors on study results currently available and combining other seismological information. The b-values have been suggested by many researchers based on historical and (or) instrumental earthquake data. The panel's assessment yielded that the Gutenberg-Richter b-value was rather constant over the whole Korean Peninsula with an average value of 0.96, independent of the seismic zone. A case study was performed for the Shinuljin Nuclear Units 1&2 site to investigate the effects on the seismic hazard. A significant reduction in the mean hazard level was identified when the revised b-value was used. Use of the constant b-value of 0.95 is recommended for all seismic source zones for engineering purposes.

1. INTRODUCTION

It was identified from an analysis of input parameters used for PSHAs (Probabilstic Seismic Hazard Analysis) for nuclear plants that the uncertainty of the Gutenberg-Richter parameter was larger than that of attenuation relations (Seo et al., 2009a). This could be a result of Korean PSHA practice combined with the uncertainty of the Gutenberg-Richter parameter. During PSHAs, only area sources were considered, and seismicity parameters such as the a-value, b-value, maximum magnitude, and depth of hypocenter were defined for each source zone. The a- and b-values provided by experts showed wide variations among seismic source zones, and these values were generally low compared with those of other stable continents. Most of the experts assigned high weights to the historical earthquake data in the estimation of seismicity parameters. This is probably due to low seismicity characteristics and insufficient instrumental earthquake data.

The consensus of opinion on the b-value for the PSHA in Korea was reached in the seismological society through a workshop held in May 2009. Topics specific to Korea were presented and discussed by experts during the workshop. A panel was organized, and a questionnaire was prepared after the workshop. This paper summarized the results of the questionnaire replied to by panel members and a case study obtained by applying the revised b-value to a PSHA for a nuclear power plant site. Finally, a constant b-value was recommended for a PSHA in Korea, which is characterized by a low seismicity.

2. b-VALUE OF THE KOREAN PENINSULA

2.1 Seismicity Characteristics and Previous Studies

The Korean Pennsula belongs to a stable continental region and is characterized by a low seismicity. Based on the instrumental earthquake data obtained after the late 1970s, the average annual earthquake activity rates are estimated to be nine for M>3, one for M>4, and 0.2 for M>5 (Seo et al. 2009b). No earthquake larger than M 6 was recorded in the 20th century. Figure 1 shows the epicenters of earthquakes that occurred from 1978 to 2008 (KMA 2009).

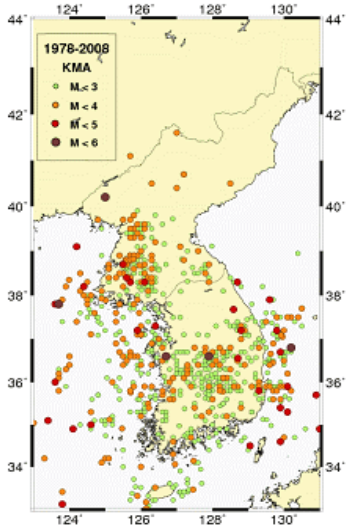

Figure 1. Epicenters of Earthquakes which occurred from 1978 to 2008 (KMA 2009)

Table 1. Comparison of a- and b-values for the Korean Peninsula (Seo et al. 2009b)

Researcher	a-value	b-value	Catalog and data period considered
Lee and Jung (1980)	-	0.8	Instrumental earthquake catalog (1926-1943)
Noh et al. (2000)	5.66	1.11	Instrumental earthquake catalog (1978-2000)
Kyung et al. (2009)	4.45-4.27	0.76-0.78	Instrumental earthquake catalog (1978-2007)
Yun (2009)	-	0.99-1.04	Instrumental earthquake catalog (1905-2008)
Lee et al. (1999)	-	0.98 0.89-0.92	Instrumental earthquake catalog (1905-1989, raw data) Instrumental and historical earthquake catalogs, complete data
Lee and Yang (2006)	6.09	0.71	Historical earthquake catalog (2-1904)
Seo et al. (2010b)	5.32	0.95	Historical earthquake catalog (2-1904)

The historical earthquake catalog lists damage records from 2 A.D. to 1904. The maximum magnitude estimated is about M 6.5 and the number of inland events with M>5.5 is less than ten (Seo et al. 2010b). The epicenters of the historical events are generally recognized to be similar to those of the instrumental earthquakes. However, a revision is required due to large uncertainty.

Many researchers have studied the Gutenberg-Richter parameter of the Korean Peninsula, as shown in Table 1 (Seo et al. 2009b). The results of Table 1 were obtained from instrumental and historical earthquake catalogs. It is noted that the b-values are quite different among researchers. The ranges of the b-value of instrumental and historical earthquakes are 0.76-1.11 and 0.71-0.95, respectively. The results of Kyung et al. (2009) and of Lee and Yang (2006) are quite low compared with others. The study of Lee et al. (1999) showed that, when the incompleteness of the historical earthquake data was considered, the b-value notably varied depending on a data period. However, the b-value based on revised historical data showed little deviation among the data period for a certain magnitude level (Seo et al. 2010b). The diversity of the b-value is primarily caused by the incompleteness of the earthquake catalog (especially the historical earthquake catalog) and the modeling method in getting the parameter value (linear regression or maximum likelihood).

2.2 Current Study Through an Expert Panel

The expert panel consisted of nine seismologists (four professors, four researchers, and one engineer) who have much experience in PSHAs. KAERI (Korea Atomic Energy Research Inst.) organized a workshop on "Improvement of the Reliability of PSHA in Korea" in May 2009, and topics such as tectonic structure, a logic tree, an analysis of the incompleteness of the historical earthquake catalog, the Gutenberg-Richter parameter in the regions of low-to-intermediate seismicity, and attenuation formula were presented and discussed. After the workshop, a questionnaire prepared by some panel members was distributed to the panel.

The questionnaire related with the Gutenberg-Richter b-value was as follows:

1) Is it necessary and important to consider the incompleteness of the earthquake catalog?

2) Assign weighting factors to the b-values of Table 1 and other study results if necessary.

3) Is the difference in b-values among seismic source zones in the Korean Peninsula small or large?

4) If the b-value is excessively small or large, is it necessary to set lower and upper bounds?

5) If it is necessary to set a threshold level on the b-value, provide the lower and upper bound value (or values) with weighting factors.

The results of the panel assessment, item-by-item, were as follows: 1) All panel members agreed on the importance of the incompleteness analysis. 2) Table 2 shows the

Table 2. Assessment result of Expert Panels for Confidence in b-Values (Seo et al. 2010a)

Researcher	b-value	Weight (%)	Remarks
Lee and Yang	0.71	5.8	weighted average b-value =0.96
Lee and Jung	0.80	7.4	
Noh et al.	1.11	23.0	
Lee et al.	0.90	16.3	
Yun	1.10	20.8	
Seo et al.	0.84	19.2	
China	1.01	5.2	
Kyung et al.	0.77	2.2	

summary of the panel's assessment of the b-value. A weighted mean b-value of 0.96 was obtained. The portions of contribution of the instrumental and historical earthquakes were about 50% and 25%, respectively. 3) Most of the panel members except for three had the same opinion that the difference in b-values among seismic source zones is small. 4) Most of the panel members except for two agreed on setting the bounds in the b-value. 5) The weighted mean b-value of the upper and lower bounds were 1.06 and 0.74, respectively.

Summing up the results of the panel assessment, it can be concluded that the application of the constant b-value to all source zones is acceptable for engineering purposes in Korea. A mean b-value of 0.96 was estimated by the panel, and this was similar to those of stable continental regions.

3. COMPARISON OF SEISMIC HAZARD-CASE STUDY

3.1 Input Data

The Shinuljin Nuclear Units 1&2 site was selected for a case study, and a PSHA was performed. Four expert teams provided input data for the seismic source parameters, and two independent experts gave attenuation formulas for the PSHA. A sensitivity analysis was performed for the same site regarding the range of each seismicity parameter used for the PSHA (Seo et al. 2009a).

Figure 2 shows an example of the seismic source map and the b-value of each source zone provided by an expert team. Also shown in this figure is the υ (M>5.0), the annual occurrence rate of earthquakes greater than M>5.0, which was obtained from the a-value provided by an expert.

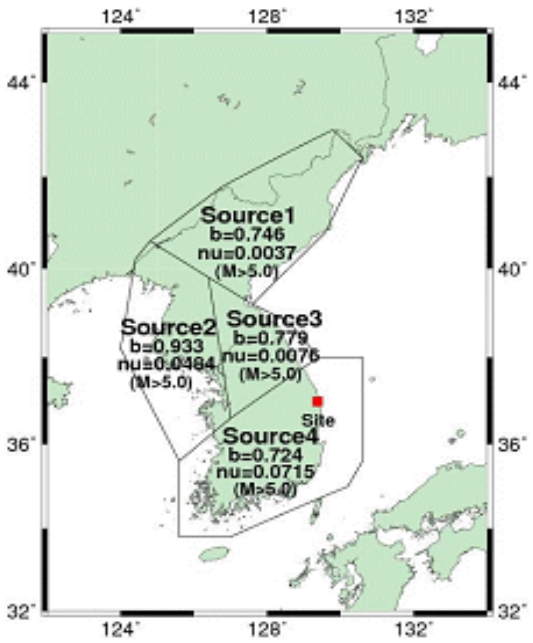

Figure 2. Example of a Seismic Source for the Shinuljin 1&2 Site

Seismic hazards for two cases were considered in this study: case 1 for the original b-value used during the PSHA and case 2 for the b-value obtained from this study. The b-value of case 1 ranged from 0.43 to 0.99, depending on the seismic source. Other input parameter values used for the sensitivity analysis of the study site (Seo et al. 2009a) were equally applied to both cases, viz. the maximum and minimum magnitudes of M 6.7 and M 5.0, respectively, were used in the case study. The depth of 10 km hypocenter was applied. The a-value of the seismic source used for both cases varied from 4.32 to 6.25. This is equivalent to υ (M>5.0)=0.037-0.0869. Eight attenuation equations and their weights of the original PSHA were equally considered in this study.

3.2 Seismic Hazard

Figure 3 shows the seismic hazard curves (median, mean, 15th and 85th percentile curve) of the study site for each case. Seismic hazards for certain acceleration levels are summarized in Table 3. As expected, the uncertainty of the seismic hazard and the mean hazard level decreased in case 2 which used a rather large b-value. At the design level of 0.2g for nuclear power plant in Korea, the mean hazard level of case 2 (2.51E-5) decreased by approximately 80% (or 0.7 order) when compared to case 1 (1.37E-4). The uncertainty width of case 1 at 0.2g for 15th-85th percentile curves was 2.76E-5~2.19E-4, and it gradually increased with an increasing acceleration level. In case 2, the uncertainty width at the same acceleration level was 5.83E-6~3.12E-5, which showed a similar trend as case 1.

Table 3. Comparison of Seismic Hazards for the Shinuljin Units 1&2 Site (Seo et al. 2010a)

Ground acceleration level	Seismic Hazards (1/year)			
	case 1		case 2	
	median	average	median	average
0.1 g	3.132E-4	5.615E-4	1.197E-4	1.113E-4
0.2 g	5.652E-5	1.367E-4	2.808E-5	2.507E-5
0.5 g	4.329E-6	1.268E-5	2.439E-6	2.108E-6
1.0 g	4.060E-7	1.190E-6	2.199E-7	1.883E-7

3. CONCLUSIONS

The Gutenberg-Richter b-value of the Korean Peninsula was assessed for engineering purposes by an expert panel that consisted of seismologists. The panel's assessment yielded that the Gutenberg-Richter b-value was rather constant over the whole Korean Peninsula with an average value of 0.96, independent of a seismic zone. A case study was performed for the Shinuljin Nuclear Units 1&2 site to

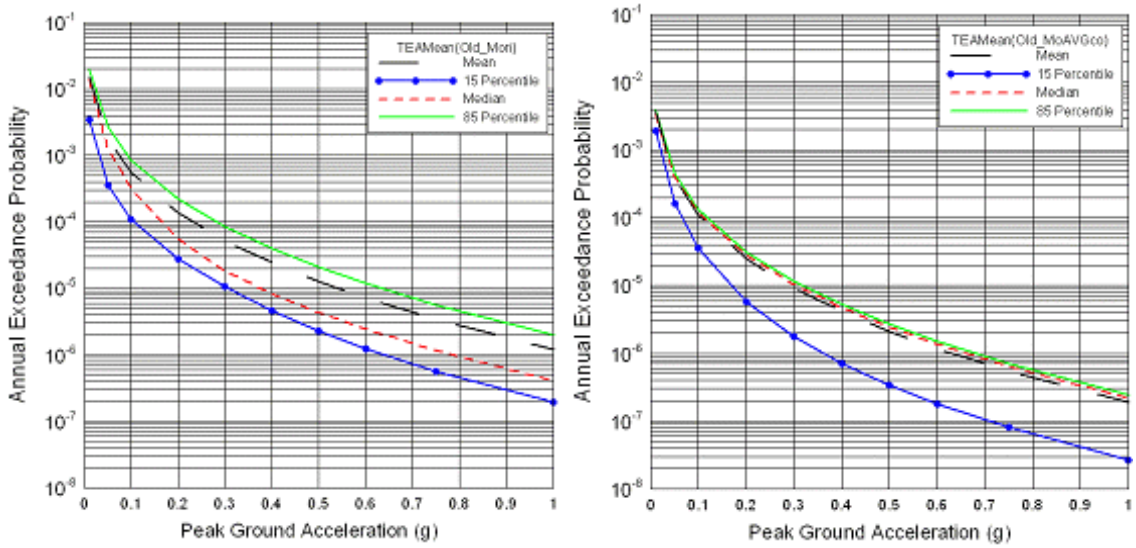

Figure 3. Comparison of Seismic Hazard for the Shinuljin Units 1&2 site: case1 (left) for original seismic source and original b-value, and case 2 (right) for original seismic source and revised average b-value of 0.96 (Seo et al. 2010a).

investigate effects on seismic hazards. The mean hazard level at the design level of 0.2g was reduced by about 80% (or 0.7 order), and the uncertainty width decreased a little for the case when the b-value of this study was used.

The b-value of this study is one of many possible cases, and the result of the case study is an example showing the reduction of a seismic hazard. The result of this study can be considered in a logic tree, or the b-value of 0.95 may be used for engineering purposes in PSHAs in the future.

Acknowledgements:

The authors acknowledge the support from the Korea Meteorological Administration Research and Development Program under Grant CATER 2009-5208.

References:

Choi, I.K., Nakajima Masato, Choun, Y.S., and Ohtori Yasuki (2009),"Development of the Site Specific Uniform Hazard Spectra for Korean Nuclear Power Plant Sites," *Nuclear Engineering and Design.*

Korea Meteorological Administration (2009), http//:www.kma.go.kr/ (in Korean)

Kyung, J.B. et al. (2009), "Seismic Activity of Korea since 1978," *Proc. of Earthquake Engineering Society of Korea Conference* (in Korean)

Lee, J.R. et al. (1999), Improvement of Uncertainty in Probabilistic Seismic Hazard Analysis, Korea Electric Power Research Institute (in Korean).

Lee, K. and Jung, H. O. (1980),"A study of instrumental earthquake data of Korea", *J. Geol. Soc. Korea*, 16(1), 32-45.

Lee, K. and Yang, W.-S. (2006), "Historical Seismicity of Korea," Bulletin of Seismological Society of America, Vol. 96, No. 3, pp. 846-855.

Noh, M.H., Lee, S.K., and Choi, K.R. (2000),"Minimum Magnitude of Earthquake Catalog of Korea Meteorological Agency for the Estimation of Seismicity Parameters," *J. of Korean Geophy. Soc., 3(4), 261-268.*

Seo, J.M., Rhee, H.M., Choi, I.K., and Yoo, H.J. (2009a),"A Study on the Sensitivity of the Gutenberg-Richter Parameter Value on the Seismic Hazard in Korea," *Proc. of Earthquake Engineering Society of Korea Conference* (in Korean).

Seo, J.M., Noh, M., Chang, C.J., and Yun, K.H. (2009b),"Status of the PSHA in Korea for Nuclear Power Plant Sites," *Nuclear Engineering and Design, 41(10).*

Seo, J.M., Rhee, H.M., Choi, I.K. (2010a),"A Study on the Best Estimate of Seismicity Parameter b-value and Its Application for the Seismic Hazard Analysis of the Korean Peninsula," *J. of Earthquake Engineering Society of Korea* (in Korean)(accepted for publication in Feb. 2010).

Seo, J.M., Choi, I.K., and Rhee, H.M. (2010b),"A Study on the Historical Earthquake Catalog and Gutenberg-Richter Parameter Values of the Korean Peninsula," *Nuclear Engineering and Technology* (accepted for publication in 2010).

Yun, K.H. (2009)," Method and Example for Completeness Analysis of Historical Earthquakes," *Workshop on Probabilistic Seismic Hazard Analysis, Daejeon* (in Korean).

JOINT CONFERENCE PROCEEDINGS
7th International Conference on Urban Earthquake Engineering (7CUEE) &
5th International Conference on Earthquake Engineering (5ICEE)
March 3-5, 2010, Tokyo Institute of Technology, Tokyo, Japan

UPTHROW OF OBJECTS DURING RECENT EARTHQUAKES IN JAPAN

Saburoh Midorikawa[1] and Hiroyuki Miura[2]

1) Professor, Department of Built Environment, Tokyo Institute of Technology, Japan
2) Assistant Professor, Department of Built Environment, Tokyo Institute of Technology, Japan
smidorik@enveng.titech.ac.jp, hmiura@enveng.titech.ac.jp

Abstract: In order to deepen understanding of near-field earthquake motion, case histories of upthrow of objects during recent Japanese earthquakes including the 1995 Kobe earthquake are compiled and examined. In most cases, the upthrows were observed in the area of the JMA intensity 6 upper or more. The displacements of upthrown objects are 0.7 to 1.5 m and 0.3 to 1 m at the JMA intensities 7 and 6 upper, respectively. This suggests that the displacement of 1m or more indicates the ground shaking of the intensity 7 which corresponds to the ground motion with the peak ground velocity larger than 1 m/s.

1. INTRODUCTION

In seismic design of critical structures located in the proximity of an active fault, near-field ground motion from the fault should be considered as the input seismic motion. To discuss the intensity of near-field ground motion, observed strong-motion records with large amplitudes have been compiled (Strasser and Bommer 2009, Anderson 2009). The number of the records, however, is limited, and factors for the large-amplitude records have not been fully understood.

To supplement the near-field records, Ohmachi and Midorikawa (1992) analyzed the upthrow of boulders during the 1984 Western Nagano earthquake to estimate the intensity of near-field ground motion. They concluded that the required intensity to produce the upthrow is as large as 1.5 g in peak ground acceleration and 150 cm/s in peak ground velocity.

Considering the importance of observation of upthrow as an indicator of strong shaking, Midorikawa (1994) compiled the case histories of upthrow of objects observed during earthquakes occurred in 1891 to 1992. In recent Japanese earthquakes including the 1995 Kobe earthquake, many upthrown objects have been also observed. This paper describes observations of upthrow of objects during Japanese earthquakes occurred in 1995 to 2008.

2. CASE HISTORIES OF UPTHROW OF OBJECTS

2.1 The 1995 Kobe Earthquake (Mw6.9)

The 1995 Kobe earthquake produced very strong ground shaking. As shown in Fig. 1, the intensity 7 which is the highest degree in the J.M.A. scale was observed, and high peak ground velocities over 100 cm/s were observed in the area of the intensity 7. Along the earthquake fault, many boulders were displaced by upthrow as shown in Fig. 2 (Umeda 1998). The observed displacements, however, are rather small such as 54 or 75 cm at Nashimoto, the Awaji island.

At Ichinomiya town, the Awaji island, a bell house was displaced by jumping (Ohmachi et al. 1997). As schematically shown in Fig. 3, a traditional bell house at a temple consists of wooden columns and beams, a tiled roof, shoe-stones and a bronze bell hanging under its ceiling. The observed displacement of the bell house is 75 cm to the south-southeast which corresponds to the fault-normal direction (See Photo 1 and Fig. 4).

At Tsuchi town, Higashinada ward in Kobe city, displacement of a wooden house by two jumps was observed (Tohiguchi 1995). By the first jump, the house was displaced 75 cm to the west-northwest, and 42 cm to the west-southwest by the second jump. Evidence of jumping was also observed at some other houses in the disastrous area (Tohiguchi 1995).

Among the reports on upthrown objects, many of them are on cars in Kobe. The careful observations at fire and police stations are reported by Midorikawa (1996). Figure 5 shows the displacements of fire trucks at Ohgi fire station in Kobe. Two trucks were displaced about 1.5 m sideways to the north. At Hyogo fire station, a small fire truck was displaced about 3 m fore without leaving visible skid marks on the floor (See Photo 2).

At Suma fire station, a fire truck was jumping and moved more than 1 m aft. A fire man standing on the step of the car was thrown to ground. At Fukiai fire station, two fire trucks moved about 1 m aft. At the vicinities of Suma and Fukiai stations, the strong motion records with the peak horizontal velocity of about 150 and 120 cm/s were observed, respectively.

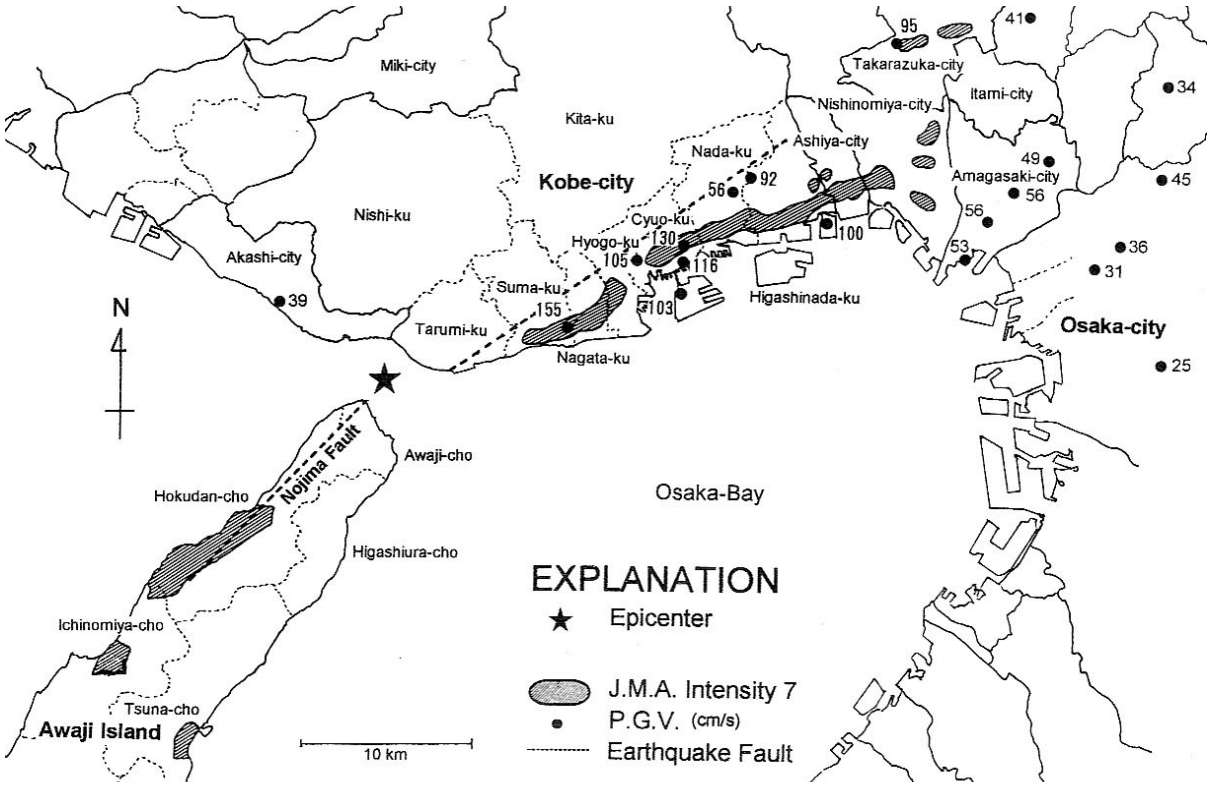

Figure 1. Map of Affected Area by the 1995 Kobe Earthquake with Observed Peak Ground Velocities and Earthquake Fault

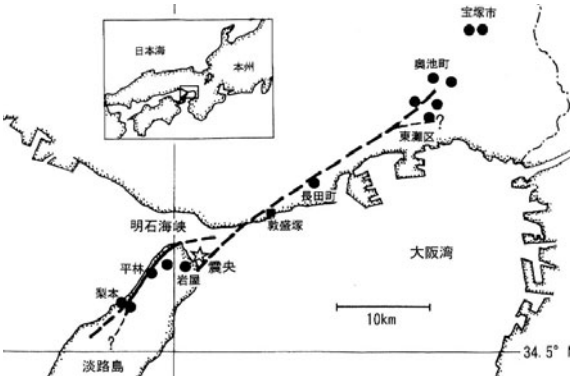

Figure 2. Location of Sites where Upthrow of Boulders was observed (Umeda 1998)



Photo 1. Upthrown Bell House at Ichinomiya

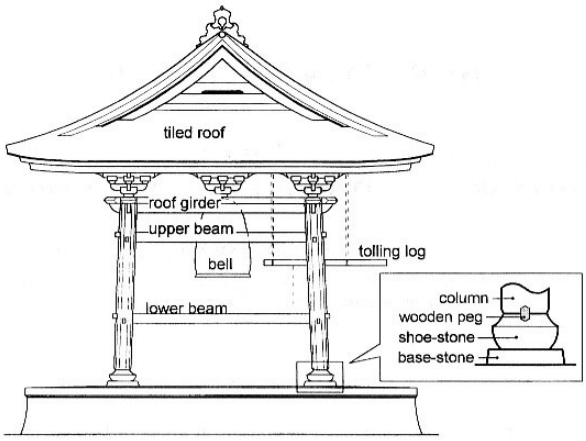

Figure 3. Schematic Explanation of Bell House

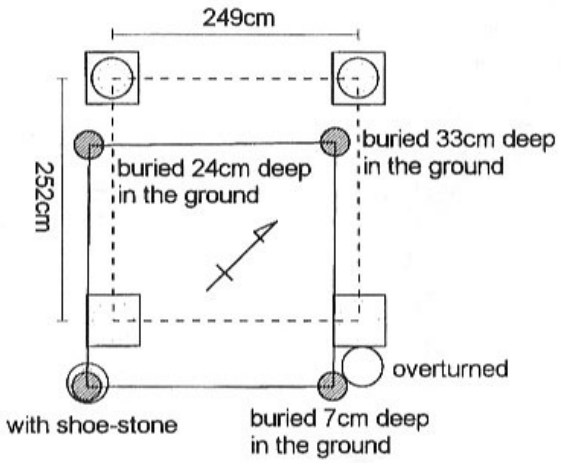

Figure 4. Displacement of Bell House at Ichinomiya

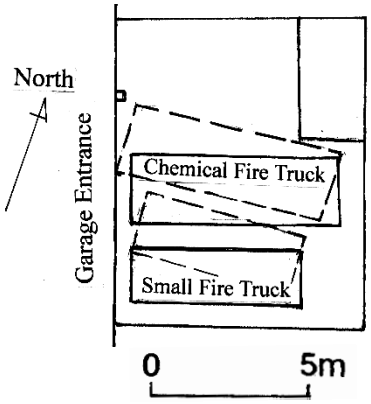

Figure 5. Displacement of Fire Trucks at Ohgi Fire Station



Photo 2. Displaced Fire Truck at Hyogo Fire Station

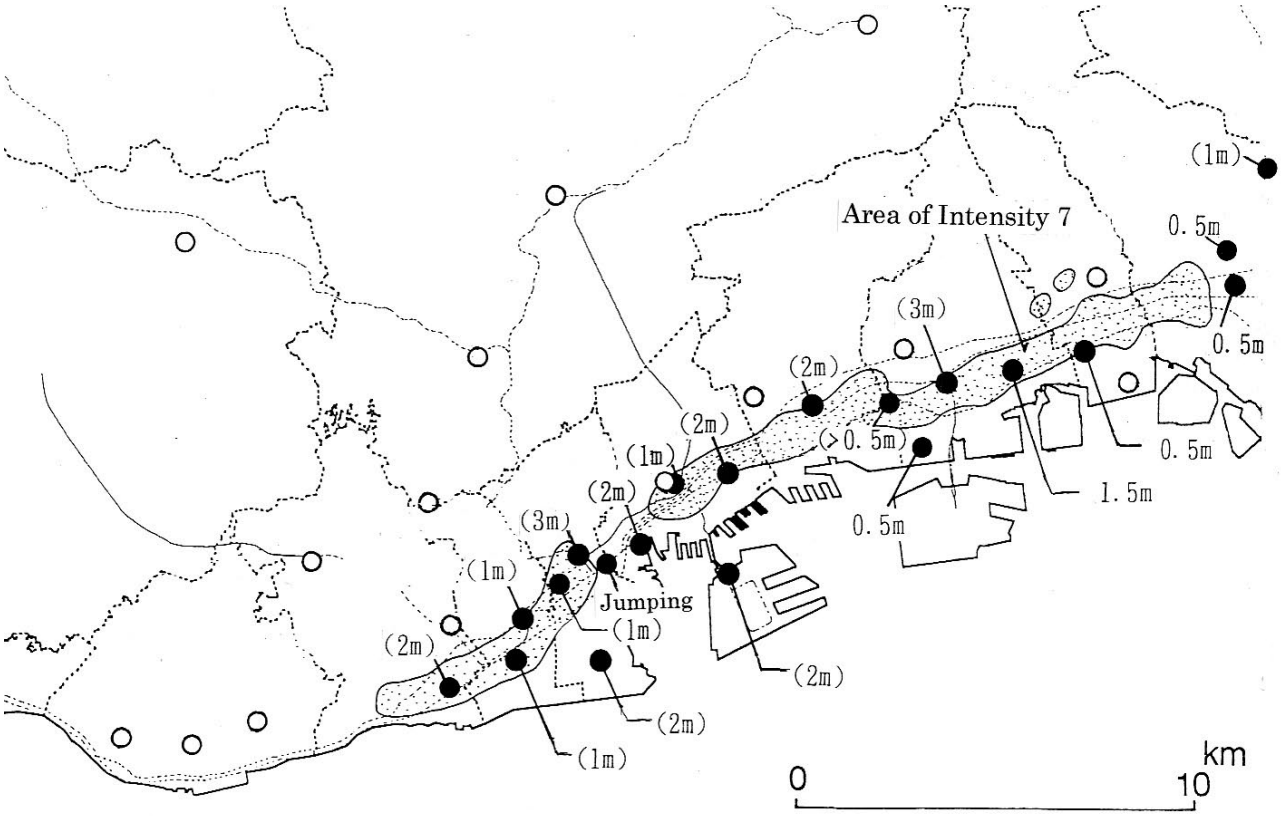

Figure 6. Distribution of Displacements of Trucks or Cars. Numbers with and without Parentheses are Fore-Aft and Sideways Displacements, respectively.

Figure 6 shows the distribution of the displacements of fire trucks or cars. The numbers with and without parentheses are the fore-aft and sideways displacements, respectively. The open circle indicates the station where no displacement is reported. Many of the displacements are observed in the area of the intensity 7. The maximum displacements are about 3 m fore and aft and 1.5 m sideways, respectively. It should be noted that there are some observations that large fore-aft displacements were produced by several jumps, not by a single jump. In many cases, the directions are north or south which corresponds to the fault normal direction.



Photo 3. Upthrown Boulders at Shindoshima (Arakawa and Watanabe 2005)

2.2 The 2004 Niigata-ken-chuetsu Earthquake (Mw6.6)

In the area of the seismic intensity 7, large boulders are displaced with the maximum displacement of about 1m to the north-northwest at Shindojima district of Horinouchi town as shown in Photo 3 (Arakawa and Watanabe 2005, Kataoka et al. 2006) and a small car was displaced about 1 m fore at Kawaguchi town (Midorikawa et al. 2004).

In the area of the seismic intensity 6 upper, a temple house was displaced about 20 cm at Ojiya city (Kazaoka 2005) and a shrine house was displaced about 50 cm at Oh-imokawa district of Hirokami village (Arakawa and Watanabe 2005). It should be noted that Chinese radishes were thrown out from the soil by strong shaking at Shindojima as shown in Photo 4 (Arakawa and Watanabe 2005). The distribution of the observed displacements with observed seismic intensities is summarized in Fig. 7.

2.3 The 2007 Noto-hanto-oki Earthquake (Mw6.7)

At the central part of Monzen town where the instrumental seismic intensity 6.4 was observed, a temple gate was displaced several tens cm to the southeast. At Doge and Kuroshima districts of Monzen town located a few km west of the central part, bell houses are displaced about 60 cm to the south. At Kuroshima district, a shrine gate was also displaced about 60 cm to the northwest (Photo 5). At Kaiso and Tsurugiji districts, bell houses were displaced about 30 cm and 20 cm, respectively (Midorikawa and Miura 2007, Kamata 2007).

At Anamizu town where the instrumental seismic intensity 6.3 was observed, a bell house was displaced by two jumps. The first and second jumps produced displacements of about 30 cm and 25 cm to the east-northeast and northeast, respectively, as shown in Photo 6 (Midorikawa and Miura, 2007). The distribution of the observed displacements with observed seismic intensities is summarized in Fig. 8.

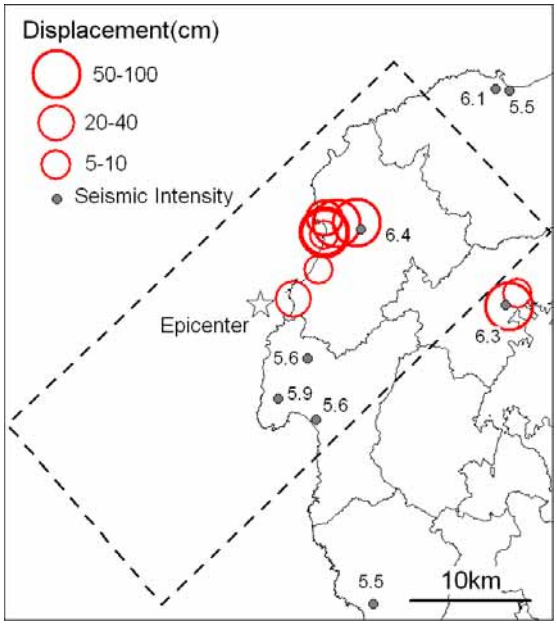

Figure 8. Displacements in the Noto-hanto-oki Earthq.



Photo 4. Chinese Radishes Thrown out by Strong Shaking (Arakawa and Watanabe 2005)

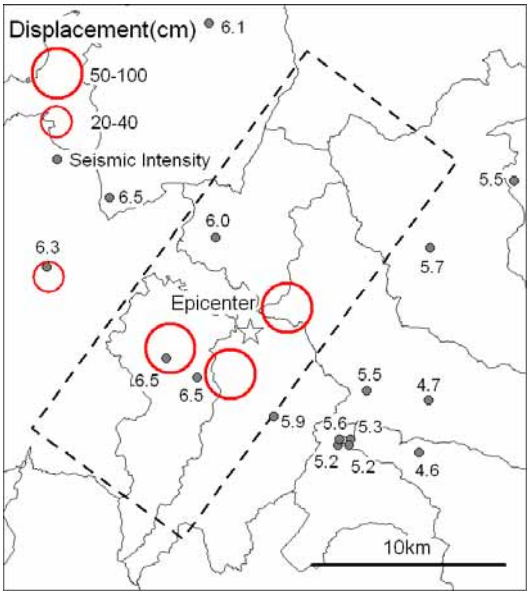

Figure 7. Displacements in the Niigata-ken-chuetsu Earthq.



Photo 5. Upthrown Shrine Gate at Kuroshima



Photo 6. Evidence of Two Jumps of Bell House at Anamizu

2.4 The 2007 Niigata-ken-chuetsu-oki Earthquake(M_w6.6)

At Kashiwazaki city where the instrumental seismic intensity 6.3 was observed, a bell house was displaced about 60 cm to the east-southeast. Fire trucks at the Kashiwazaki fire station were moved with the maximum displacement of 2 m fore and aft and about 1 m sideways (Tokyo Fire Department 2007). Many of them were displaced to the south.

At Nagasaki district of Kashiwazaki city located several km northeast of the central part, a shrine gate was displaced about 40 cm to the southeast as shown in Photo 7. At Takiya and Terao districts of Kariwa village, temple gates were displaced 20 to 30 cm (Midorikawa and Miura 2007)

At Nishiyama town of Kashiwazaki city where the instrumental seismic intensity 6.2 was observed, a shrine gate was displaceed about 70 cm (Fujimoto and Kasukawa 2007). The distribution of the observed displacements with observed seismic intensities is summarized in Fig. 9.

2.5 The Other Earthquakes

In the 2000 Tottori-ken-seibu earthquake (Mw6.6), a temple house was displaced 15 cm to the north-northeast at Hayata district, Saihaku town (Fukuzawa et al. 2000). In the 2003 Northern Miyagi earthquake (Mw6.1), a stone monument was displaced about 50 cm at Naruse town (Motosaka and Ohno 2004). A boulder was displaced about 15 cm at Yamoto town (Motosaka and Ohno 2004). The estimated seismic intensities at these places were 6 upper. In the 2008 Iwate-Miyagi-Nairiku earthquake (Mw6.9), a shed was displaced about 20 cm by jumping at Matsurube where the peak horizontal and vertical accelerations of 1 g and 4 g were observed respectively (Kimura 2008).

3. DISPLACEMENT OF UPTROWN OBJECTS AND GROUND MOTION INTENSITY

Owing to recent advancement of strong motion instrumentation in Japan such as the K-Net. KiK-net, and JMA network, many strong ground motion data are available in recent earthquakes. This enables reliable estimation of the seismic intensities at the sites where upthrow of objects were observed. Figure 10 shows the relation between the displacement of the upthrown object and the estimated JMA seismic intensity. In this figure, the data on the fore-aft displacement of a car are not plotted because the displacement might be caused by several jumps as mentioned earlier.

As there are very few case histories of the upthrow at the intensity 6 lower, the upthrow of objects would be an evidence of ground shaking of the intensity 6 upper or greater. The displacements are 0.7 to 1.5 m and 0.3 to 1 m at the JMA intensities 7 and 6 upper, respectively. This may suggest that the displacement of 1m or more indicates the ground shaking of the intensity 7.

If an object is emitted with the initial velocity of 5 m/s and the angle of 60 degrees to the air, it is displaced about 1



Photo 7. Upthrown Shrine Gate at Nagasaki

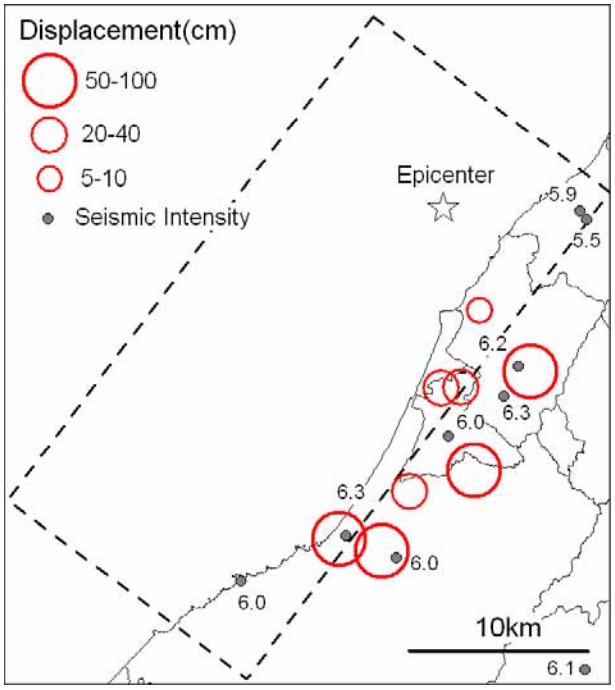

Figure 9. Displacements in the Niigata-ken-chuetsu-oki Earthq.

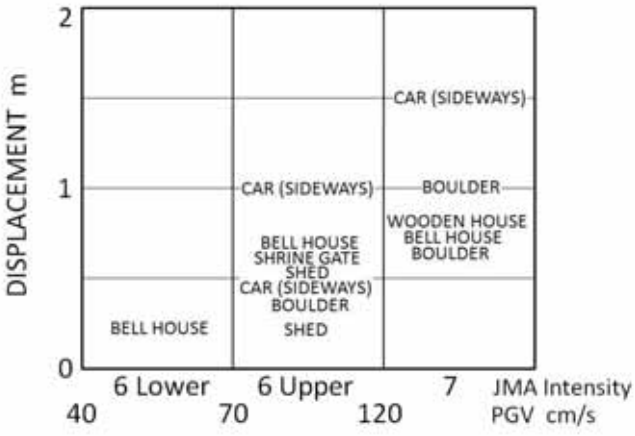

Figure 10. Relation of Displacement of Objects with Ground Motion Intensity

m. The initial velocity of the object corresponds to the velocity response of the soil-object interaction system (Ohmachi and Midorikawa 1992). If the amplification of the interaction system is assumed to be three to five, the ground motion with the peak ground velocity of 1 or 1.5 m/s could produce the displacement of 1 m. This rough estimate is consistent with the obsevations shown in Fig. 10 because the ground motion of the intensity 7 roughly corresponds to the peak ground velocity of 120 cm/s or more (Fujimoto and Midorikawa 2005).

4. CONCLUSIONS

In order to deepen understanding of near-field earthquake motion, upthrow of objects observed during large earthquakes could be used as the supplementary data of near-field strong motion records. For this purpose, case histories of upthrow of objects during recent Japanese earthquakes including the 1995 Kobe earthquake are compiled and examined. In most cases, the upthrows were observed in the area of the JMA intensity 6 upper or more. The displacements of upthrown objects are 0.7 to 1.5 m and 0.3 to 1 m at the JMA intensities 7 and 6 upper, respectively. This suggests that the displacement of 1 m or more indicates the ground shaking of the intensity 7 which corresponds to the ground motion with the peak ground velocity larger than 1 m/s.

Acknowledgements:

This study was partially supported by the 21st Century COE Program "Evolution of Urban Earthquake Engineering" and the Global COE Program "International Urban Earthquake Engineering Center for Mitigating Seismic Mega Risk" supported by Ministry of Education, Culture, Sports, Science and Technology (MEXT), Japan.

References:

Anderson, J.G. (2009), "Source and Site Characteristics of Earthquakes that have caused Exceptional Ground Accelerations and Velocities," *Bulletin of the Seismological Society of America* (in Press).

Arakawa, K. and Watanabe, T. (2005), "Damage in Uonuma city," *The Mid Niigata Prefecture Earthquake in 2004 – Relation of earthquake damage with geomorphic and geologic setting* -, The Association for the Geological Collaboration in Japan, 78-82.

Fujimoto, K. and Kasukawa, M. (2007), "Damage Survey of Cultural Assets in Kashiwazaki City during the 2007 Niigata-ken-chuetsu-oki Earthquake," http://www.cis.ac.jp/~kfujimoto/, Chiba Science University (in Japanese).

Fujimoto, K. and Midorikawa, S. (2005), "Empirical Methods for Estimating J.M.A. Instrumental Seismic Intensity from Ground Motion Parameters Using Strong Motion Records during Recent Major Earthquakes," *Journal of Social Safety Science*, **7**, 241-246 (in Japanese with English abstract).

Fukuzawa, E., Arita, T., Maruta, M., Iwata, T. Hatamoto, H., and Hokan, H. (2000), "Damage of Building Structures," *Report on the 2000 Tottori-ken-seibu Earthquake*, Kajima Corporation, 3.1-3.77 (in Japanese).

Kamata, M. (2007), Personal communication.

Kataoka, S., Matsumoto, T., Nagaya, K., and Kusakabe, T. (2006), "Earthquake and Ground Motion," *Report on Damage to Infrastructures by the 2004 Mid Niigata Prefecture Earthquake*, Public Works Research Institute, 1.1-1.8 (in Japanese).

Kazaoka, O. (2006), "Strong Motion Distribution," *The Niigata-ken-chuetsu Earthquake*, Niigata Nippo Enterprise, 34-42 (in Japanese).

Kimura, T. (2008), "Strong Motion Observation, the 2008 Iwate-Miyagi-Nairiku Earthquake," http://taro.eri.u-tokyo.ac.jp/saigai/iwate/kansoku.html, Earthquake Research Institute, University of Tokyo (in Japanese).

Midorikawa, S. (1994), "Case Histories of Upthrow of Objects during Earthquakes," Journal of the Seismological Society of Japan, **47**, 333-340 (in Japanese with English abstract).

Midorikawa, S. (1996), "Jumping of Cars due to Strong Ground Shaking of the Kobe Earthquake," *Jishin Journal*, **22**, 38-43 (in Japanese).

Midorikawa, s. and Miura, H. (2007), "Displaced Objects during the 2007 Noto-hanto-oki and Niigata-ken-chuetsu-oki earthquakes," *Proceedings of the 5th Annual Meeting of Japan Association for Earthquake Engineering*, 460-461 (in Japanese).

Midorikawa, S., Miura, H. and Akiba S. (2004), " Strong Ground Motions during the 2004 Niigata-ken-chuetsu Earthquake," *Research Reports on Earthquake Engineering*, **92**, 1-10 (in Japanese).

Motosaka, M. and Ohno, S. (2004), "Survey of Tomb Stones and Other Rigid Bodies," *Report on the Damage Investigation of the May 26, 2003 off Miyagi Prefecture Earthquake and the July 26, 2003 Northern Miyagi Prefecture Earthquake*, Architectural Institute of Japan, 171-177.

Ohmachi, T. and Midorikawa, S. (1992), "Ground-motion Intensity Inferred from Upthrow of Boulders during the 1984 Western Nagano Prefecture, Japan, Earthquake," *Bulletin of the Seismological Society of America*, **82**, 44-60.

Ohmachi, T., Midorikawa, S. and Honda, M. (1997), "Jumping of Bell Houses Caused by Near-Field Ground Motion. Case Histories and Shaking Table Experiment," *Earthquake Engineering and Structural Dynamics*, **26**, 657-665.

Strasser, F.O. and Bommer, J.J. (2009), "Large-amplitude Ground-motion Recordings and Their Interpretations," *Soil Dynamics and Earthquake Engineering*, **29**, 1305-1329.

Tohiguchi, M. (1995), "Damage of Wooden Houses and Problem on Upgrading of Their Seismic Performance," *Chikyu Monthly Extra Edition*, **13**, 207-218 (in Japanese).

Tokyo Fire Department (2007), "Damage at Kashiwazaki Fire Station," *Report on the damage investigation of the 2007 Niigata-ken-chuetsu-oki Earthquake*, 32-44 (in Japanese).

Umeda, Y. (1998), "Upthrown Objects," *Report on the Hanshin-Awaji Earthquake Disaster, General Issues Volume 2*, Maruzen Co. Ltd., 302-306 (in Japanese).

JOINT CONFERENCE PROCEEDINGS
7th International Conference on Urban Earthquake Engineering (7CUEE) &
5th International Conference on Earthquake Engineering (5ICEE)
March 3-5, 2010, Tokyo Institute of Technology, Tokyo, Japan

SEISMIC DEMANDS ON CALIFORNIA HIGH SPEED RAIL

Tat S. Fu[1)], and Jean-Pierre Bardet[2)]

1) Postdoctoral Researcher, Sonny Astani Department of Civil and Environmental Engineering, University of Southern California, USA
2) Professor and Chair, Sonny Astani Department of Civil and Environmental Engineering, University of Southern California, USA
tsf@usc.edu, bardet@usc.edu

Abstract: In 2008, California voters approved Proposition 1A to build a high speed rail stretching over 800 miles from San Diego to San Francisco. The high speed rail (HSR), which is still under consideration, will have to be designed to meet the demands of earthquakes in California. This paper surveys these technical considerations including fault crossing and spatial variation of spectral acceleration along the HSR alignment.

1. INTRODUCTION

In 2008, California voters approved Proposition 1A which released 9.95 billion US dollar worth of bonds to build a high speed rail (HSR) stretching over 800 miles from San Diego to San Francisco. In 2009, the US Congress passed the Reinvestment and Recovery Act that allocates $8 billion US dollars for rail projects with priority in HSR. In 2010, California will be awarded $2.25 billion federal funding in HSR (Simon, 2010). The increased interests from the federal and state levels help speed up the construction of California HSR (CHSR), which is under preliminary planning and consideration.

There are technological considerations to design and build HSR in California. Since there is no existing HSR in America, appropriate design specifications, safety, and operation requirements have to be invented to suit California needs, an earthquake prone region. This paper surveys the existing literature on seismic design of HSR and the seismic demands on the CHSR by examining the proposed alignment along different seismic regions in California.

2. HIGH SPEED RAIL

High speed rail (HSR) is commonly defined as passenger rail exceeding 200km/h. The first HSR is Japan's Shinkansen that opened in 1964. Since then, there have been steady increases in the number of HSR in European countries (France, Germany, Spain, *etc.*) and other Asian countries (China, South Korea, Taiwan, *etc.*).

There is a wealth of technical papers and reports on HSR. However, the literature on seismic issues of HSR is noticeably less in comparison. Figure 1 compares the number of keyword search results from well-known data bases (listed in Figure 1) for technical papers on HSR. Although the literature on seismic designs in HSR has been increasing over the years, they are a small fraction compared to the overall literature on HSR.

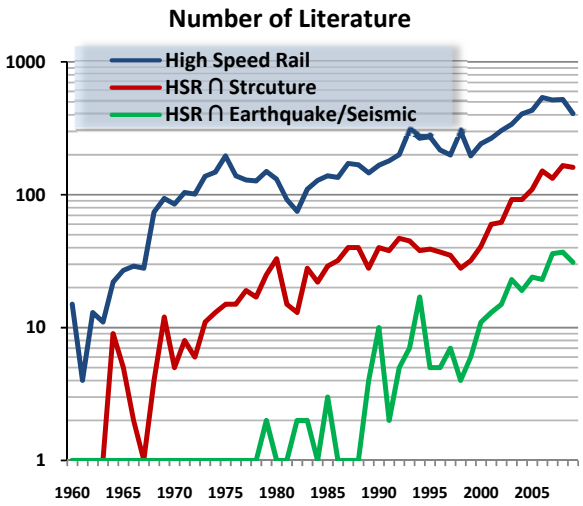

Keyword Searches: Web of Science, Engineering Village, ASCE Research Library, Proquest/CSA, Transportation Research Information Services (from TRB), and Select Science Direct Databases

Figure 1: Literature on high speed rail

There are two leading agencies in railway technologies and practices: the International Union of Railways (UIC: Union Internationale des Chemins de fer) and the Railway Technical Research Institute (RTRI) of Japan. UIC has 199 members including railway authorities from various countries. One of its most important publications is the UIC leaflets that aim to "standardization and improvement of location and operating conditions of railways with a view to international traffic" (ETF, 2010). UIC leaflets are vital in ensuring compatibility among railways from various countries such as between France and Germany.

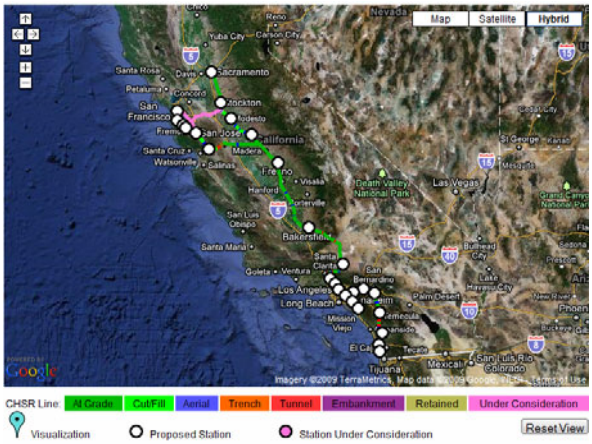

Figure 2: California HSR alignments (California HSR Authority, 2010)

RTRI conducts research for Japan's railways. Since Japan is an earthquake prone region, similar to California. RTRI publishes many technical reports on seismic issues on railways and HSR. RTRI's researchers study ground motion on railway vehicles (Kawanishi *et al.*, 2009), structural damages due to seismicity (Tadokoro *et al.*, 2008; Toyooka *et al.*, 2005), structural design for seismic forces (Sawada and Nishimura, 1999; Takase *et al.*, 1999), running safety (Miyamoto and Ishida, 2008), and many other topics related to HSR and/or earthquakes. Both UIC and RTRI are great information resources for designing HSR in California.

3. CALIFORNIA HIGH SPEED RAIL

3.1 Proposed Alignment

The proposed CHSR is 856 mile long with the main 502 mile segment (San Francisco-to-Irvine) connecting San Francisco and Los Angeles. It will take an estimate of 2 hours and 38 minutes to travel from San Francisco to Los Angeles (432 miles trip) with about half the cost of airfares (California HSR Authority, 2009). The CHSR also connects San Diego to Los Angeles and Sacramento to Fresno. The segment connecting Sacramento and the Bay Area is still under consideration.

Figure 2 illustrates the proposed CHSR alignment on Google Map. This interactive map is available online (Figure 2) and provides details such as rail types and stations. The information from this map was used to tally the lengths of each rail/structure types (shown in Table 1) and to assess the seismic demands of the HSR throughout California.

3.2 California Faults

In California, there are many seismic faults that can cause earthquakes. Both San Francisco and Los Angeles — the two biggest cities in California — are located seismic active areas. The CHSR passes through many faults in its 856 miles of railways. Using fault data from the U.S. Geological Survey, or USGS, (2009) and the proposed alignment shown in Figure 2, Figure 3 superimposes California faults on the CHSR alignment.

These faults are classified by age of their last known movement:

- Historic (most recent, less than 150 years),
- Holocene to Latest Pleistocene (younger than 15,000 years),
- Late Quaternary (younger than 130,000 years),
- Mid to Late Quaternary (younger than 750,000 years), and
- Quaternary (younger than 1,600,000 years).

Figure 3 clearly shows the interactions between the CHSR alignment and the faults. In Northern California, the San Francisco/San Jose segments of the CHSR are especially subjected to seismic demands; while the Los An-



Figure 3: California faults and HSR alignments (USGS, 2009)

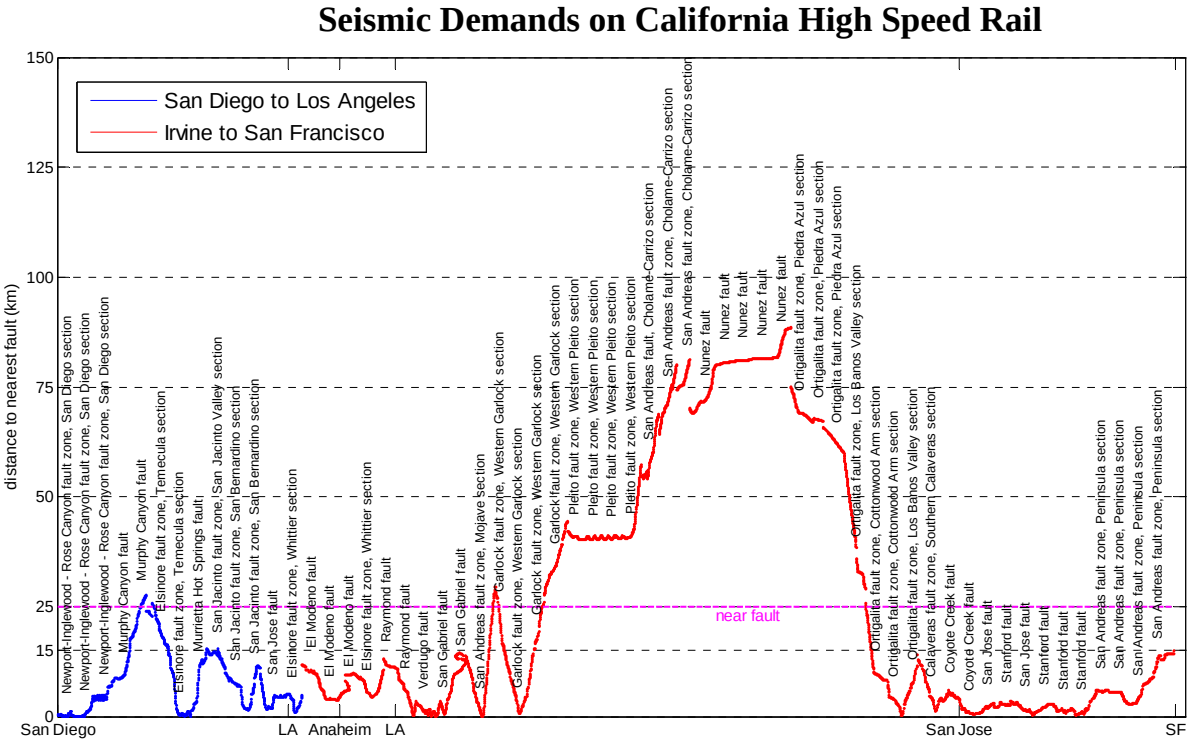

Figure 4: Distance between HSR and faults (LA: Los Angeles; SF: San Francisco)

geles and San Diego segments of Southern California are earthquake prone.

Readers should note that not all faults should be treated equally in terms of seismogenicity. Larger faults can cause larger ruptures and larger earthquakes. Several faults can also rupture together to generate multi-fault earthquakes. Faults with more ancient "last known movements" can be viewed as inactive or overdue.

4. SEISMIC DEMAND

4.1 HSR Alignment and Earthquake Faults

The proposed CHSR passes through many regions with seismic faults that are potential sources of earthquakes (Figure 3). The seismic demand of the CHSR is related to the likelihoods of seismic events and distances from these faults. Figure 4 shows the distances between the CHSR and its nearest faults along its alignment. The closest faults, for some of the segments, are also named in the figure. The segment under consideration (Sacramento-to- Bay Area) is not shown in Figure 4 because it is still under consideration. The Sacramento-to-Fresno segment is also not presented because of the scarcity of faults in these areas.

The central California (near Fresno) is relatively fault-free. In both northern and southern California, almost all of the CHSR is in the near-fault regions (less than 25 km). In fact, most of the alignment is less than 15 km from the nearest faults. Figure 4 illustrates the distances from the nearest faults; it, however, disregards information on the fault sizes and slip rates and the likelihoods of seismic events by these faults.

4.2 Fault Crossing

Also shown in Figure 4, there are many segments of the CHSR that intersect the faults. These are referred as fault crossing. Since ground surfaces can deform permanently and substantially over short distances during a seismic event, fault crossing can be very disruptive for long structures such as railways and pipelines. Figure 5 illustrates the disruptive nature of fault crossing on railways occurred at Taiwan during the Chichi Earthquake in 1999.

Fault crossing still poses challenges to design appropriately for the large localized displacements that structures have to endure. Pipelines had been constructed to allow large displacements with movable tracks attached to foundations (Newman and Hall, 1975). However, such design may not be completely feasible for HSR. The authors believe that an effective post-disasters recovery strategy is



Figure 5: Railway failure at fault crossing

key to CHSR design for fault crossing.

Table 1 lists the number of fault crossings categorized by rail segments. There are possible 33 fault crossings in the proposed CHSR alignment. At the present design stage, aerial and at-grade segments of the CHSR, which collectively account 65% of the 1379.7 km of alignment, have most of the crossings. Interestingly, the CSHR segment (Sacramento to Bay Area) under consideration accounts for 36.4% (22/33) of the fault crossings when it accounts only 12.2% in railway length.

Table 1: Fault crossing in HSR alignments

Rail Type	Length (km)	Length (miles)	Fault Crossing
Aerial	201.7	125.2	7
At Grade	703.7	437	9
Cut & Fill	195.9	121.6	2
Embankment	2.1	1.3	0
Retaining Wall	28.8	17.9	0
Trench	11.6	7.2	1
Tunnel	67.6	42	2
Under Consideration	168.3	104.5	12
total	1379.7	856.8	33

4.3 Response Spectra

Besides fault crossing, another source of seismic demands is ground acceleration, which can be estimated using acceleration response spectra. A response spectrum represents the maximum responses of an elastic system of variable periods subjected to a particular seismic input. It is typically used for seismic designs and evaluations. Recently, California Department of Transportation (Caltrans), in collaboration with the Pacific Earthquake Engineering Research (PEER) Center, developed an online tool to compute probabilistic acceleration response spectra for any location in California (Caltrans, 2009). The probabilistic method

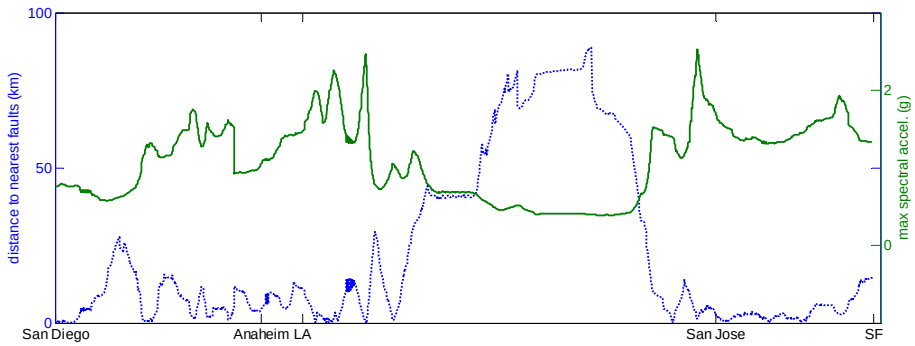

Figure 7: Spectral accelerations compared to distances to the nearest faults

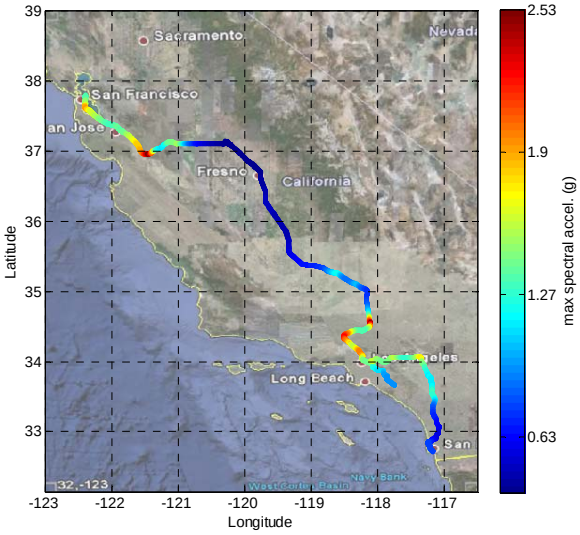

Figure 6: Spectral accelerations along CHSR

of this tool is used to estimate spectral acceleration values (for peak ground acceleration and periods of 0.2, 0.3 and 1 second) with a probability of exceedence 5% in 50 years. The source data of spectral accelerations are obtained from USGS based on a 0.05 degree grid in both longitude and latitude (USGS, 2008). The maximum spectral accelerations along the CHSR alignments are presented in Figure 6. In Figure 7, the maximum spectral accelerations are plotted with distances to the nearest faults. Clearly, spectral accelerations decrease with the distance to faults.

5. CONCLUSIONS

The proposed California high-speed rail (CHSR) will have to be designed to meet earthquakes. This paper surveys the seismic demands on the CHSR. Most of the demands concentrate on the northern and southern regions of California, where there are many seismic faults in both San Francisco and Los Angeles areas — the two biggest cities in California.

The locations with highest seismic demands coincide with the shortest distances to faults for the entire CHSR alignment. Moreover, the authors identified 33 possible fault crossings with the CHSR. Finally, spectral accelerations are calculated along the CHSR alignment. This study is only a preliminary estimate of seismic demands. Additional in-depth analyses are warranted to determine more accurately actual seismic demands at particular locations along the alignment.

Acknowledgements:

The authors acknowledge the financial support from the

Pacific Earthquake Engineering Research (PEER) Center. They also thank John Chirco (Parsons-Brinckerhoff), Bruce Hilton (Kleinfelder) and Vince Jacob (SC Solutions) for valuable discussion. Any opinions, findings, and conclusion or recommendations expressed herein are those of the authors and do not necessarily reflect the views of PEER.

References:

California High-Speed Rail Authority (2010), "High-Speed Rail on Google Map," <http://www.cahighspeedrail.ca.gov/google-map/>.

Caltran (2009), "Caltran ARS Online," <http://dap3.dot.ca.gov/shake stable/technical.php>.

ETF – Railway Technical Publications (2010), "UIC Code: Catalogue of UIC Leaflets," *Railway Technical Publications.*

Kawanishi, T., Murono Y., Miyamoto, and T., Sogabe, M. (2009), "Influence of Seismic Motion with Ground Irregularity on Railway Vehicles," *Quarterly Report of Railway Technical Research Institute*, **50**(2): 89-94.

Miyamoto, T. and Ishida, H. (2008), "Numerical Analysis on the Running Safety of an Improved Bogie during Seismic Vibration," *Quarterly Report of Railway Technical Research Institute*, **49**(3): 173-177.

Newmark, N. M., and Hall, W. J. (1975), "Pipeline design to resist large fault displacement," *U.S. National Conference on Earthquake Engineering Proceedings*, University of Michigan, Ann Arbor, 416-425.

Sawada, R. and Nishimura, A. (1999), "Design Method of Structure Considering Liquefaction and Subsequent Lateral Flow,",*Quarterly Report of Railway Technical Research Institute*, **40**(3): 146-151.

Simon, R. (2010), "California to get $2.25 billion in high-speed rail funding," Los Angeles Times, Jan 28, 2010, <http://www. latimes.com/news/nation-and-world/la-na-high-speed-rail28-2010 jan28,0,2948055.story>.

Tadokoro, T., Tanimura., Y., and Murono, Y. (2008), "Evaluation Method of Limit State of Collapse for Viaduct Columns to Repetitive Seismicit," *Quarterly Report of Railway Technical Research Institute*, **49**(4): 215-221.

Takase, N., Ikegame, M., Tanamura, S., Nishimura, A., and Kondou, M. (1999), "Seismic Design of Pile Foundation," *Quarterly Report of Railway Technical Research Institute*, **40**(3): 152-157.

Toyooka, A., Ikeda, M., Yanagawa, H., Kataoka, H., Iemura, H., and Murata, K. (2005) "Effects of Track Structure on Seismic Behavior of Isolation System Bridges," *Quarterly Report of Railway Technical Research Institute*, **46**(4): 238-243.

U.S. Geological Survey (2009), "Quaternary Faults in Google Earth," <http://earthquake.usgs.gov/hazards/qfaults/google.php>.

U.S. Geological Survey (2008), "Spectral Accelerations Points," <http://earthquake.usgs.gov/research/hazmaps/products_data/2008/data/>.

U.S. Congress (2009), "The American *Recovery* and *Reinvestment Act* of 2009," *Public Law*, 111-5.

JOINT CONFERENCE PROCEEDINGS
7th International Conference on Urban Earthquake Engineering (7CUEE) &
5th International Conference on Earthquake Engineering (5ICEE)
March 3-5, 2010, Tokyo Institute of Technology, Tokyo, Japan

DISTRIBUTION OF BUILDING DAMAGE AREAS DETECTED FROM SATELLITE OPTICAL IMAGES OF THE 2006 CENTRAL JAVA, INDONESIA, EARTHQUAKE

Hiroyuki Miura[1] and Saburoh Midorikawa[2]

1) Assistant Professor, Department of Built Environment, Tokyo Institute of Technology, Japan
2) Professor, Department of Built Environment, Tokyo Institute of Technology, Japan
hmiura@enveng.titech.ac.jp, smidorik@enveng.titech.ac.jp

Abstract: In order for rapid identification of building damage areas in a large earthquake, a semi-automated damage detection method is applied to satellite optical images observed before and after the 2006 Central Java, Indonesia earthquake (Mw6.3). The satellite FORMOSAT images whose spatial resolution is 2 m are used. In the damage detection, the difference of digital numbers between pre- and post-event images is mainly used. The distribution of the building damage detected by the proposed method is compared to the village-level damage statistical data. The result shows that the distribution of the detected pixels approximately corresponds to the severely damaged areas while the damage in the densely vegetated areas is not well detected because the buildings are obscured by vegetation.

1. INTRODUCTION

In order for emergency response and early recovery assessment after a large-scale disaster, it is important to evaluate distribution of the building damage as soon as possible. Remote sensing technology would be useful to identify building damage areas. The Central Java, Indonesia, earthquake (M_W6.3) on May 27, 2006 caused severe building damage in and around Yogyakarta city. About 5,800 people were killed and 38,000 people were injured due to the earthquake. About 130,000 houses were completely collapsed, and 450,000 houses were damaged (USGS 2006).

Damage distribution maps were estimated using high-resolution satellite images such as QuickBird observed after the earthquake (e.g., UNOSAT 2006 and RESPOND 2006). According to the accuracy assessment of the maps (Kerle 2009), the building damage was accurately detected when the damage is severe and extensive. In the area where buildings are obscured by vegetation, clouds and cloud shadow, however, the damage could not be accurately detected. The maps were delineated by visual detection of the satellite images. The visual detection, however, requires a great demand for time and labor. Automated or semi-automated damage detection technique is necessary to quickly identify damaged areas for more rapid post-earthquake assessment.

Authors has examined a semi-automated damage detection method using pre- and post-event satellite optical images (Miura and Midorikawa 2008). The applicability, however, has not been fully discussed. In this study, the building damage detection method is applied to satellite optical images observed before and after the 2006 Central Java earthquake, and the validity of the method is discussed by comparing to damage distribution by village-level damage statistical data.

2. CHARACTERISTICS OF SATELLITE IMAGES

2.1 Pre- and Post-event FORMOSAT Images

Images of the satellite FORMOSAT launched by Taiwan in May 2004 are used in this study. The satellite provides a panchromatic (black/white) image whose spatial resolution is 2 m and a multi-spectral (color) image whose resolution is 8 m. The multi-spectral image consists of four bands (Band1: Blue, Band2: Green, Band3: Red, and Band4: Near infrared). The off-nadir view angle of the satellite is usually constant, while the view angles of other high-resolution commercial satellites such as QuickBird and IKONOS are often changed from observation to observation in order to capture a target area in a short time interval. The constant view angle would make it easier to precisely overlay a pair of images acquired in different date. Besides, the image width of FORMOSAT is about 25 km, while the width of the other high-resolution satellite images is only 10-15 km. These are advantages of FORMOSAT images in widely detecting changes between before and after the earthquake.

Figure 1 shows the map of the epicentral area of the

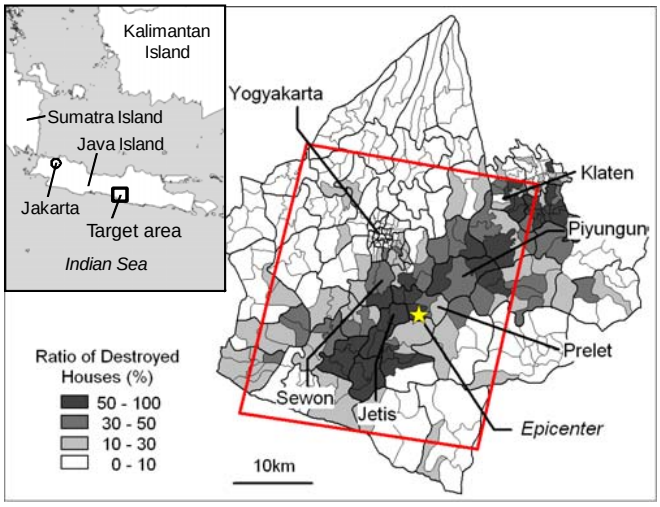

Figure 1 Coverage of FORMOSAT Image and Damage Distribution of the 2006 Central Java Earthquake

2006 Central Java earthquake with the damage distribution compiled by the local governments (International Federation of Red Cross 2006). Solid square indicates the coverage of the FORMOSAT images used in this study. Figures 2 show the pre- and post-event images. The images cover the epicentral area of 40 km x 35 km for NS and EW direction.

To detect the building damage, color images pan-sharpened from panchromatic and multi-spectral images would be appropriate for pre- and post-event images. Panchromatic image, however, is used as a pre-event image because the coverage of the pre-event multi-spectral image covers only the northern part of the target area. As a post-event image, not only panchromatic image but also pan-sharpened image are used. The spatial resolution of the images is 2 m. The characteristics of the images such as the observation dates, the satellite angles and the sun angles are shown in Table 1. The pre-event image was observed nine days before the earthquake and the post-event image was acquired fifteen days after the earthquake. The time interval of the images is about one month.

2.2 Spectral and Spatial Characteristics of Damaged Area

The close-ups of severely damaged area in the pre- and post-event panchromatic images are shown in Figs. 3(a) and (b). The cross-sections of digital numbers (DN) along the dotted line in the images are illustrated in Fig. 3(e). Black and red lines indicate the digital numbers of pre- and post-event images, respectively. As indicated by arrow in Fig. 3(e), the digital numbers in the damaged area after the earthquake is higher than those before the earthquake.

In the severely damaged area, numbers of wall bricks and debris of buildings are exposed on the ground surface due to the collapse of buildings. According to the observed spectral reflectance of typical building materials (Miura *et al.* 2007), the spectral reflectance of wall brick is higher than those of roof tile and asphalt. The difference of the digital numbers between the images would be caused by the

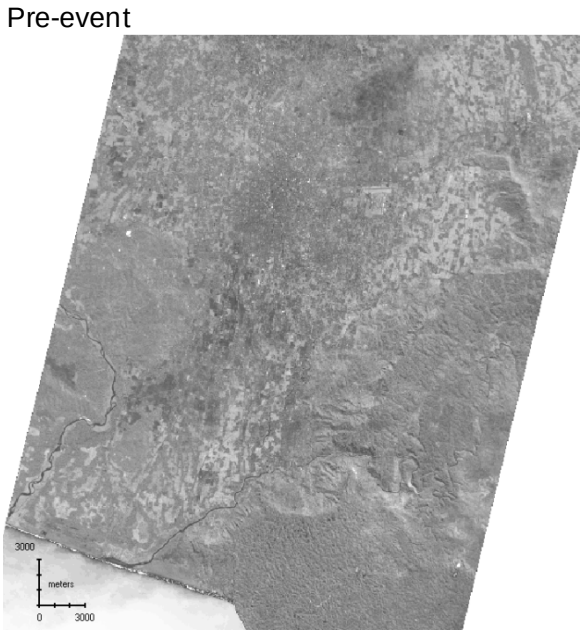

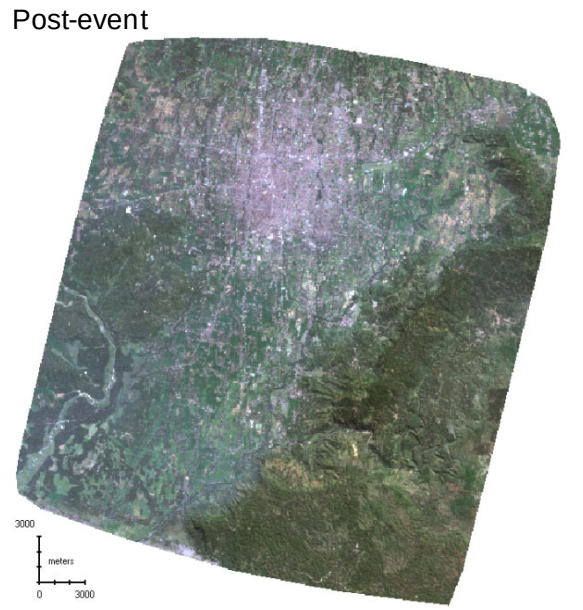

Figures 2 Pre- and Post-event FORMOSAT Images

Table 1 Characteristics of FORMOSAT Images

Event	Date	Time	Satellite		Sun		Spatial Resolution (m)
			Azimuth (deg.)	Elevation (deg.)	Azimuth (deg.)	Elevation (deg.)	
Before	May 18, 2006	AM 09:09	N103.2E	28.8	N52.3E	44.9	2.0
After	Jun 11, 2006	AM 09:09	N102.8E	28.5	N48.7E	42.2	2.0

difference of spectral reflectance of building materials. This suggests a possibility to identify damaged areas from the difference of the digital numbers between the images.

In order to detect only the change of the buildings, non built-up areas should be eliminated. Figures 3(a) and (b) also cover vegetated areas and bare ground areas. NDVI (normalized difference vegetation index) would be appropriate to extract vegetated areas. NDVI is calculated from the digital numbers of near infrared band an red band

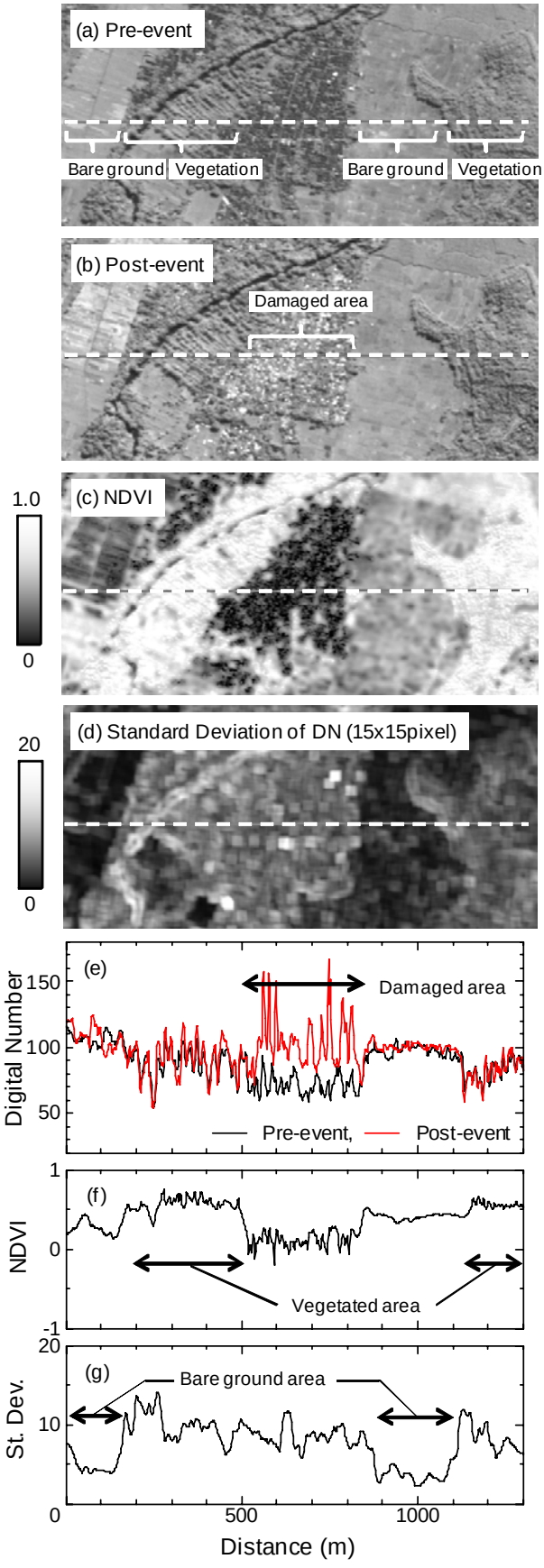

Figures 3 Close-up of damaged area in (a) Pre-event Image, (b) Post-event Image, (c) NDVI Image, (d) Standard Deviation of DN, and Cross-sections of (e) Digital Number, (f) NDVI, (g) Standard Deviation of DN

using pan-sharpened image. Higher NDVI indicates a higher density of green leaves in the image. In this study, the post-event pan-sharpened image is used to calculate NDVI in each pixel. The distribution of NDVI and the cross-section of NDVI is shown in Figs. 3(c) and (f), respectively. As indicated by arrow, NDVI in the vegetated areas is higher than that in other areas.

As shown in Figs. 3 (a) and (b), the digital numbers in bare ground areas seem to be uniformly distributed. This suggests that texture index would be useful to extract the bare ground areas. Standard deviation (SD) of digital numbers calculated in windowed area that is one of the texture index is used in this study. The distribution of SD of the digital numbers for 15 x 15 pixel windowed area using pre-event image and its cross-section are shown in Fig. 3(d) and (g), respectively. As indicated by arrows, SD in the bare ground areas is lower than the other areas.

3. Distribution of Building Damage Areas

3.1 Detection of Building Damage Areas

Flowchart of proposed damage detection method is shown in Fig. 4. Firstly, the post-event image is geometrically corrected to superpose the pre-event image. The pixels of the image are classified into three categories; vegetated area, bare ground area, and built-up area. The vegetated areas such as paddy fields, grasses and forests are extracted using NDVI calculated from the post-event image. In this study, the pixels whose NDVI is higher than 0.4 are classified into vegetated area.

Bare ground areas are extracted using SD of digital numbers computed for 15 x 15 pixel windowed area. The threshold value to distinguish bare ground area from built-up area is determined by comparing the distribution of bare ground areas with that of the SD. The pixels whose SD are lower than 6.0 in the pre-event image are classified into bare ground areas. The other pixels are classified into built-up areas.

The difference of the digital numbers between the pre- and post-event images is computed for the pixels classified as built-up areas. The threshold value to distinguish damaged area from undamaged area is determined from the distribution of the difference of digital numbers between obviously damaged areas and undamaged areas. In this study, the pixels whose difference of digital numbers is higher than 20 are extracted as damaged areas.

Figures 5(a) and (b) show the close-up of the pre- and post-event image in a built-up area. The pixels whose brightness is higher after the earthquake represent severely damaged buildings, indicating that most of the buildings are severely damaged in this area. Figure 5(c) shows the result of the damage detection. Red pixels indicate the pixels detected by the proposed method. The comparison of the figures shows that the severely damaged buildings are well detected because most of the buildings are classified into damage.

The damage detection is applied to whole area of the

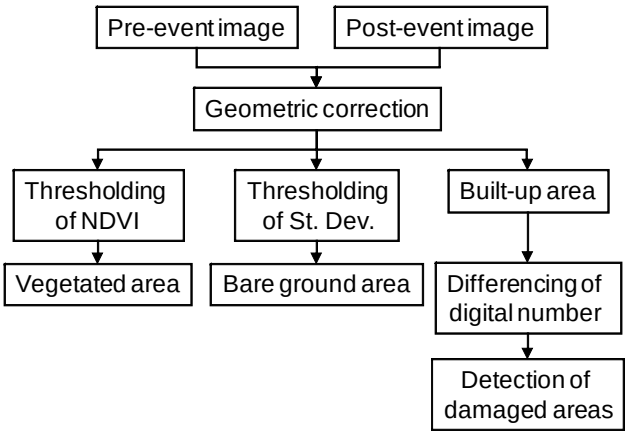

Figure 4 Flowchart for Detection of Building Damage Areas

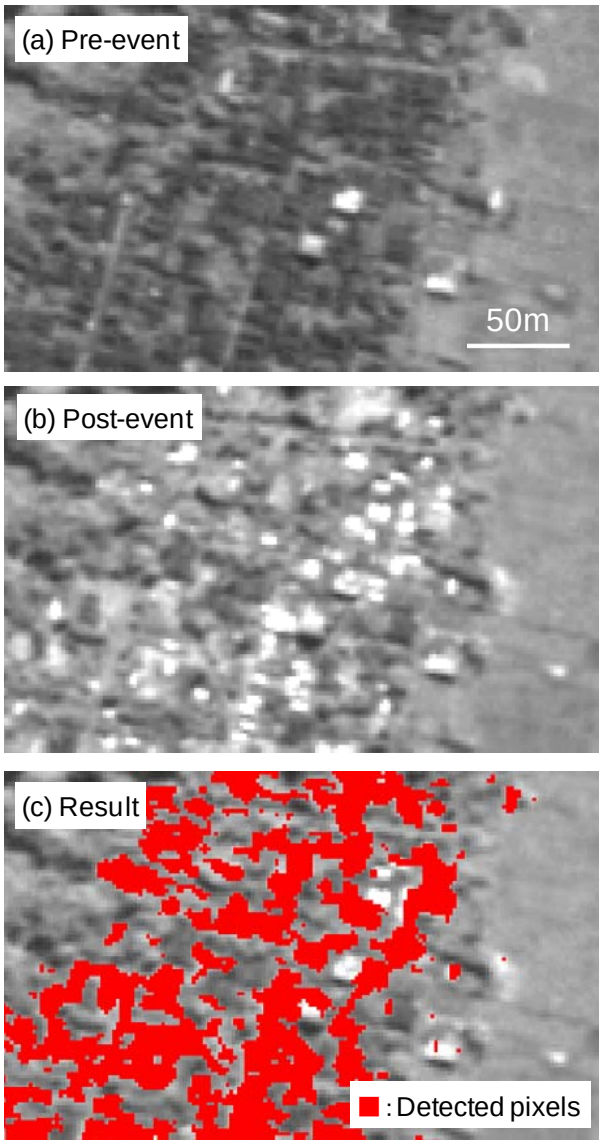

Figures 5 Result of Damage Detection, (a) Pre-event Image, (b) Post-event Image, (c) Detected Pixels

image. Since the method is a pixel-based analysis of the 2m-resolution images, it is difficult to identify the detected pixels in a small scale map. In this study, the detected pixels are evaluated by 200 m mesh system. The mesh size is determined to cover several tens of buildings with a mesh. The number of the detected pixels divided by total number of pixels in a 200 m mesh is defined as ratio of detected pixels. Figure 6 shows the distribution of the ratio of the detected pixels on the pre-event image. The meshes whose ratio of the detected pixels is higher than 10 % are distributed in the central (Pleret, Jetis and Sewon), southern (Imogiri and Pundong) and northeastern (Piyungan and Klaten) part of the area.

3.2 Evaluation of Damage Distribution

The village-level statistical data of building damage compiled by the regional officials of Yogyakarta and Central Java is used to compare to the detected damage distribution. The statistical data includes total population, number of households, and number of damaged houses in each village (International Federation of Red Cross 2006). The damage is classified into three categories; destroyed, heavy damage, and slight damage. The damage ratio is calculated from the number of destroyed houses divided by the number of households for each village.

Figure 7 shows the distribution of the damage ratios. The severely damaged villages whose damage ratio is higher than 70% are distributed in the central (Pleret and Jetis), southern (Imogiri and Pundong), and northeastern (Piyungan and Klaten) part of the area. The comparison of the distribution between the damage detection (Fig. 6) and the damage ratios (Fig. 7) shows that the meshes whose ratio of the detected pixels is higher than 10 % are distributed in the villages whose damage ratio is higher than 70% such as Pleret, Jetis, Imogiri, Piyungan and Klaten. This indicates that the severely damaged areas are well detected by the proposed method.

The number of the detected pixels in the southern part of the area such as Pundong is relatively small although the severely damaged villages whose damage ratio is higher than 70 % is widely distributed. Figures 8 show the results of the damage detection in the built-up area (Figs. 8(a-1) and (a-2)) and the vegetated rural area (Figs. 8(b-1) and (b-2)). Although the damage ratios in both villages are higher than 70%, the number of the detected pixels in the vegetated area is smaller than that in the built-up area. As shown in Fig. 8(b-1), some buildings seem to be obscured by trees of the vegetation. As described in Kerle (2009), it is difficult to identify the damage of buildings obscured by vegetation using satellite images. The vegetated rural areas are widely distributed in the southern part of the target area. The obscuration of buildings by vegetation might be one of the reasons for underestimation of the damage in the southern area.

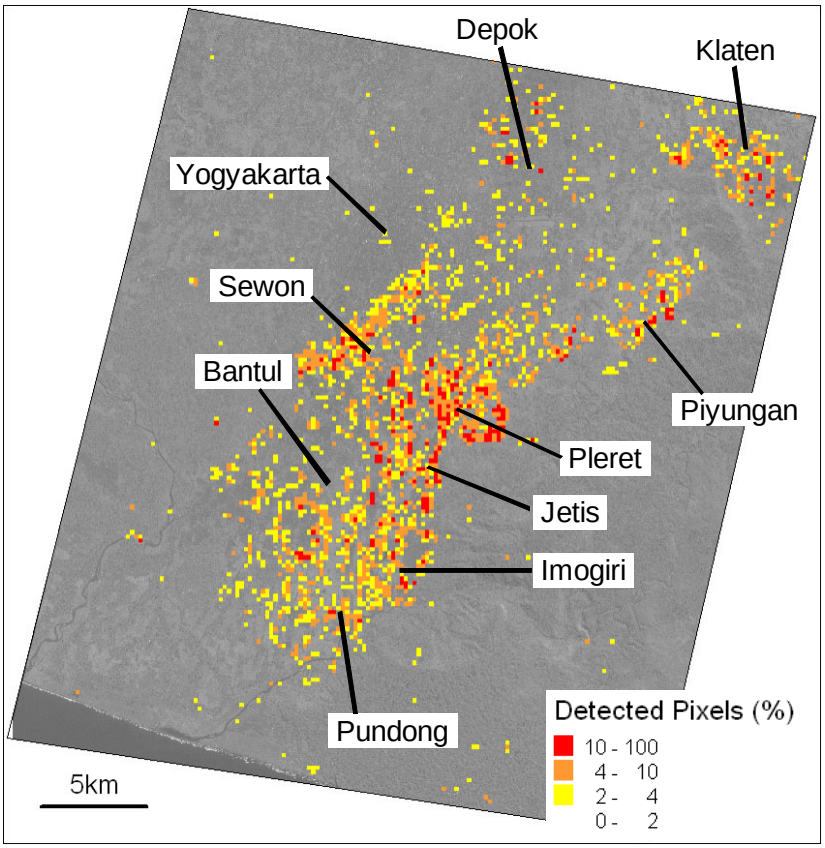

Figure 6 Distribution of Building Damage Detected from Satellite Images

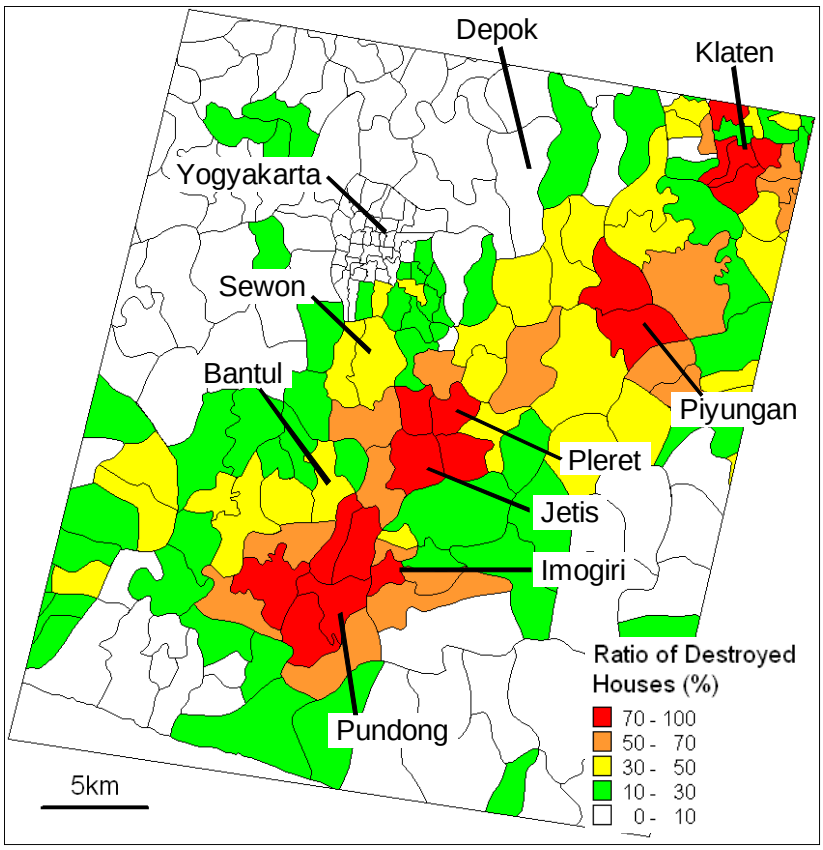

Figure 7 Distribution of Damage Ratios by Village-level Damage Statistical Data

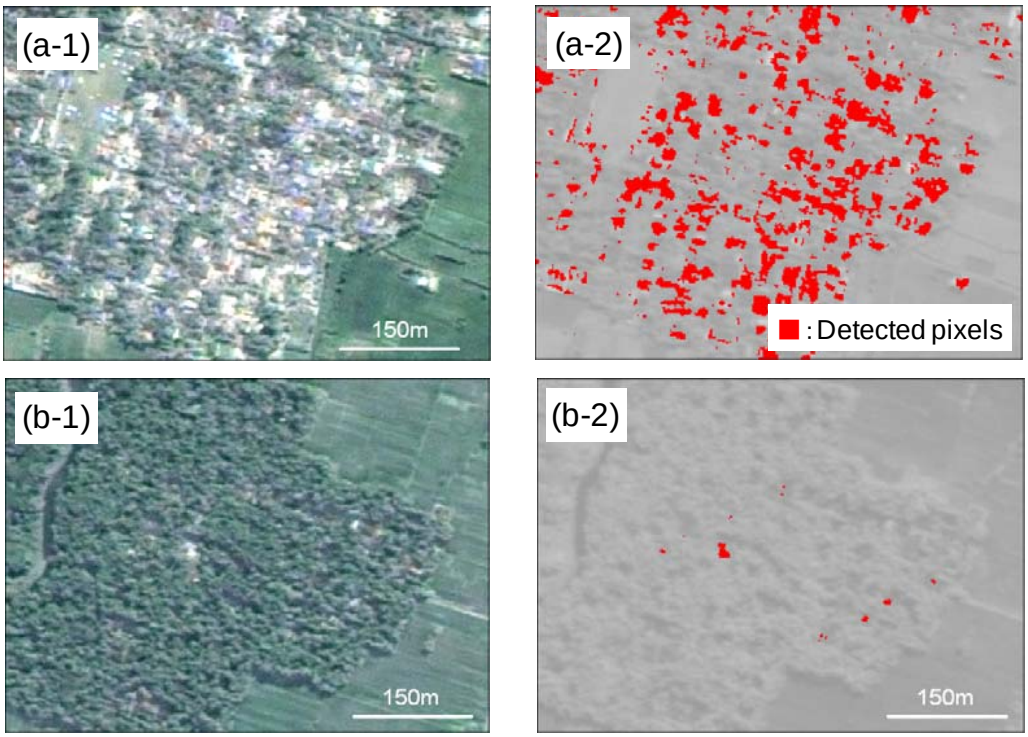

Figures 8 Post-event Image and Detected Pixels
in (a) Built-up Area and (b) Vegetated Rural Area

4. CONCLUSIONS

A semi-automated damage detection technique is applied to the satellite optical images observed before and after the 2006 Central Java, Indonesia, earthquake. Using NDVI and standard deviation of the digital numbers, the pixels of the image are classified into three categories; vegetated area, bare ground area and built-up area. The damaged areas are detected from the difference of the digitalnumbers in the built-up areas between the pre- and post-event images. The distribution of the pixels detected by the proposed method is compared to the damage distribution by the village-level damage statistical data. The result shows that the distribution of the detected pixels approximately corresponds to the severely damaged areas while it is difficult to detect the building damage in densely vegetated areas.

Acknowledgements:

This study is supported by the Global COE Program "International Urban Earthquake Engineering Center for Mitigating Seismic Mega Risk" sponsored by Ministry of Education, Culture, Sports, Science and Technology (MEXT), Japan.

References:

International Federation of Red Cross (IFRC) (2006), "Damage, Distribution and Preliminary Needs Assessment", http://www.reliefweb.int/library/documents/2006/IFRC/ifrc-idn-20jun.xls.

Kerle, N. (2009), "Satellite-based Damage Mapping Following the 2006 Indonesia Earthquake –How Accurate Was It ?-", *International Journal of Applied Earth Observation and Geoinformation* (submitted).

Miura, H., Yamazaki, F. and Matsuoka, M. (2007), "Identification of Damaged Areas due to the 2006 Central Java, Indonesia Earthquake Using Satellite Optical Images", *Proceedings of Urban Remote Sensing Joint Event*, Paper No.DIS4.

Miura, H. and Midorikawa, S. (2008), "Detection of Building Damage Areas due to the 2006 Central Java, Indonesia, Earthquake Using High-resolution Satellite Images", *Proceedings of 14th World Conference on Earthquake Engineering*, Paper ID 07-0010.

RESPOND (2006), "Damage Assessment of the Earthquake on May 27", http://respond-int.org/respondlive/index.html.

UNOSAT (2006), "Preliminary Damage Assessment: Java Earthquake", http://unosat.web.cern.ch/unosat/asp/.

USGS (2006), "Magnitude 6.3 – Java Indonesia", http://earthquake.usgs.gov/earthquakes/eqinthenews/2006/usneb6/#summary.

JOINT CONFERENCE PROCEEDINGS
7th International Conference on Urban Earthquake Engineering (7CUEE) &
5th International Conference on Earthquake Engineering (5ICEE)
March 3-5, 2010, Tokyo Institute of Technology, Tokyo, Japan

BUILDING DAMAGE ESTIMATION USING SEISMIC INTENSITY AND SATELLITE L-BAND SAR IMAGERY

Masashi Matsuoka[1] and Nobuoto Nojima[2]

1) Senior Research Scientist, Information Technology Research Institute, AIST, Japan
2) Professor, Dept. of Civil Engineering, Faculty of Engineering, Gifu University, Japan
m.matsuoka@aist.go.jp, nojima@gifu-u.ac.jp

Abstract: For quick and stable estimation of damaged buildings due to earthquakes all over the world using PALSAR (Phased Array type L-band Synthetic Aperture Radar) loaded on the ALOS satellite, a model using combined usage of satellite SAR imagery and seismic intensity is proposed. In order to expand the existing C-band SAR based damage estimation model into L-band SAR, this paper rebuilds a likelihood function for severe damage ratio on the basis of dataset from JERS-1/SAR (L-band SAR) images observed the 1995 Kobe earthquake and its detailed ground truth data. The model which integrates the fragility functions of building damage in terms of seismic intensity and proposed likelihood function is then applied to PALSAR images taken over the areas affected by the 2007 Pisco, Peru earthquake. The accuracy of the proposed damage estimation model is examined by comparing the results of the analyses with field investigations and/or interpretation of high-resolution satellite images.

1. INTRODUCTION

Remote monitoring from space of natural disasters worldwide, such as earthquakes, tsunamis, and floods, is becoming more familiar in recent years, with a launch of a system (International Charter Space and Major Disaster) which allows observation of disaster-stricken regions immediately after a natural disaster using earth observation satellites around the year 2000, and access to high-resolution satellite images with a ground resolution of under 1m for commercial use at about the same time. Broadly speaking, two types of sensors are used in satellite remote sensing of Earth; optical sensors which observe reflective and radiometric characteristics in the visible light, near and mid-infrared, and thermal infrared regions, and radar sensors which use microwaves with wavelengths between several centimeters to several tens of centimeters. Each type of sensor has advantages using which various types of natural disasters are studied. High-resolution optical sensor images can be used to assess damage at building level (Yamazaki et al. 2005, Gusella et al. 2005) or to evaluate damage to ground, such as landslides, in regions where field investigation may be difficult (Miura and Midorikawa 2007), making them a promising observation method in terms of use in emergency responses following disasters. However, this method also has a disadvantage in that incidence of cloud cover or cloud shadows in the target area would prevent damage assessment. On the other hand, radar sensors are capable of observing the ground irrespective of weather conditions or the time of day and are therefore more reliable, and have been gaining prominence as a means of grasping the overall picture of damages. In particular, crustal deformation monitoring technology (Massonnet et al. 1993) based on interferometric processing of synthetic aperture radar (SAR) phase information has been undergoing refinement through numerous case examples (e.g. Hao et al. 2009), and is now reaching a level where it can be utilized at a practical level.

For effective disaster response and reconstruction efforts, it is crucial to be informed of direct damages to social infrastructure such as buildings and their spatial distribution. Against such a background, comparative studies of backscattering intensity information or phase information of SAR images with building damage have been actively performed (Matsuoka and Yamazaki 2001, Yonezawa and Takeuchi 2001, Ito and Hosokawa 2002) using dataset from the 1995 Kobe earthquake. Integration with seismic intensity information has also been attempted (Hosokawa et al. 2008). Then, Matsuoka and Yamazaki (2004) proposed a linear discriminant score that uses as variables the correlation coefficient and difference in backscattering coefficient before and after the earthquake as an indicator which correlates strongly with areas of building damage, using ERS-1/SAR images from the European Space Agency which observed the area hit by the Kobe earthquake before and after the event. Furthermore, in order to evaluate the building damage ratio from SAR images, and to allow integrated analysis with other types of information such as seismic intensity information, Nojima et al. (2006) derived a regression discriminant function that relates to the building

damage ratio from the difference and correlation coefficient, and created a model for quantitatively estimating the severe building damage ratio from a modeled likelihood function based on the regression discriminant function. The versatility of this model has been qualitatively demonstrated, as it is not very susceptible to the effects of satellite observation conditions and regional characteristics because it uses intensity information in the form of backscattering coefficient in order to extract areas of damage (Matsuoka and Yamazaki 2002a). However, Nojima et al.'s estimation model is based on C-band (wavelength of about 5.7cm) ERS-1/SAR images, which means that it cannot strictly be applied to L-band (wavelength of about 23cm) JERS-1/SAR and ALOS/PALSAR images owned by Japan. This is because at different wavelengths, there are variations in backscatter characteristics of target objects resulting from their permeability, permittivity and surface roughness.

The aim of this paper is to follow the procedure used by Nojima et al. in order to create an estimation model for the severe building damage ratio that can be applied to PALSAR images from ALOS which has been conducting several observations of earthquake damage since the launch of the satellite in January 2006. In this paper, we will determine a modeled likelihood function for the severe building damage ratio from JER-1/SAR images of the 1995 Kobe earthquake, and will demonstrate that the building damage distribution can be accurately estimated through integration with fragility functions for building damage in terms of seismic intensity. Furthermore, the created model will be applied to PALSAR images from ALOS which observed the areas of the 2007 Peru earthquake, and assessed through comparisons with field investigations.

2. LIKELIHOOD FUNCTION FROM JERS-1/SAR

2.1 SAR Images and Ground Truth Data

The JERS-1 satellite launched by Japan in 1992 was operational until 1998, and made observations of the region affected by the 1995 Kobe earthquake. This satellite was boarded with an optical sensor (OPS) and a radar sensor (SAR). SAR images for before and after the earthquake (before: May 17, 1994; after: May 4, 1995) are shown in Fig. 1(a) and Fig. 1(b). Fig. 1(c) shows the data for building damage (Building Research Institute 1996) by the Building Research Institute, used as the ground truth data. Areas where the severe damage ratio was more than 30% are colored black. There are significant linear noise patterns on the image, due to the fact that SAR sensors at the time had a relatively low signal-to-noise ratio. Although the effects of noise in the subsequent analysis is unavoidable, we have decided to use this dataset because no other earthquake that has been observed by L-band SAR has such an availability of data for building damage which is sufficiently detailed for statistical analyses. As a matter of note, the post-quake image was taken approximately 4 months after the earthquake, which means that it is probable that some of the buildings which were damaged by the quake had been either partly or fully demolished or dismantled; however, this image was chosen so as to allow a comparison with an ERS/SAR image which was taken in the same period. The size of 1 pixel in the SAR image is about 30m.

2.2 Derivation of Regression Discriminant Function and Likelihood Function

Following Nojima et al., (2006) the regression

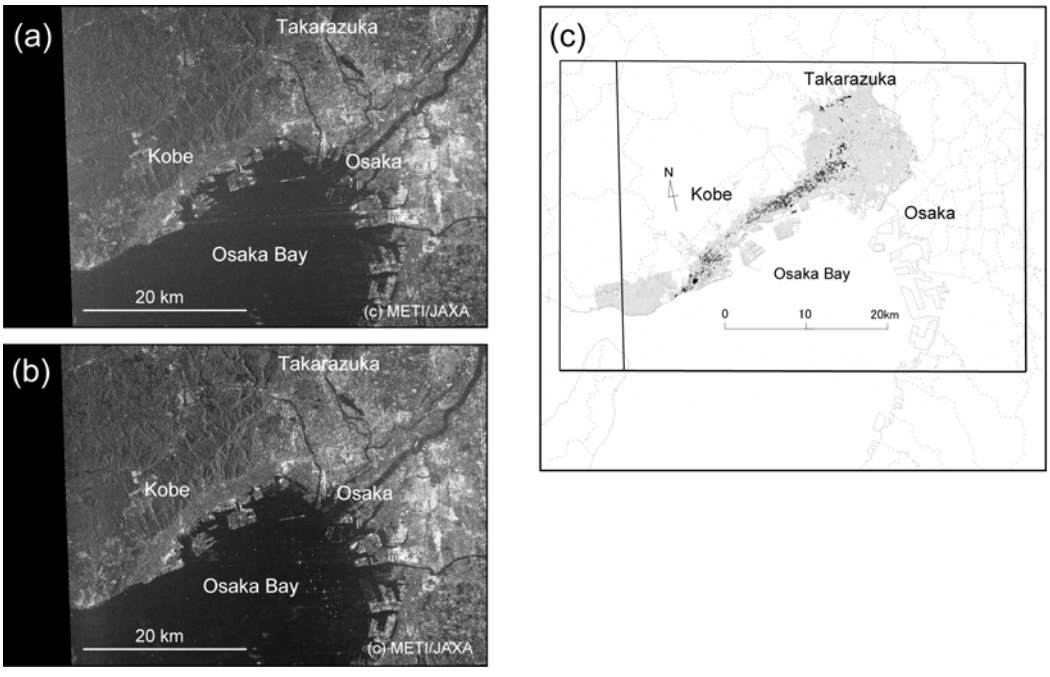

Figure 1 JERS-1/SAR image before and after the 1995 Kobe earthquake and target area of analysis. (a) Image taken May 17, 1994. (b) Image taken May 4, 1995. (c) With building damage data (black areas indicate severe damage ratio of over 30%).

discriminant function for building damage is calculated from two characteristic values, the correlation coefficient and the difference in backscattering coefficient of pre-event and post-event SAR images. First, following accurate positioning of the two SAR images, a speckle noise filter with a 21×21 pixel window (Lee 1980) is applied to each image. The difference value is calculated by subtracting the average value of the backscattering coefficient within a 13×13 pixel window of the pre-event image from the post-event image, and the correlation coefficient is also calculated from the same 13×13 pixel window (Matsuoka and Yamazaki 2002b).

$$d = 10 \cdot \log_{10} \bar{I}a_i - 10 \cdot \log_{10} \bar{I}b_i \quad (1)$$

$$r = \frac{N\sum_{i=1}^{N} Ia_i Ib_i - \sum_{i=1}^{N} Ia_i \sum_{i=1}^{N} Ib_i}{\sqrt{\left(N\sum_{i=1}^{N} Ia_i^2 - \left(\sum_{i=1}^{N} Ia_i\right)^2\right) \cdot \left(N\sum_{i=1}^{N} Ib_i^2 - \left(\sum_{i=1}^{N} Ib_i\right)^2\right)}} \quad (2)$$

Here, d represents the difference in backscattering coefficient [dB], r represents the correlation coefficient, and N represents the number of pixels within the target window. N is 169 because a 13×13 pixel window is used. Ia_i, Ib_i represent the i-th pixel values of the post-event and pre-event images respectively, and $\bar{I}a_i$, $\bar{I}b_i$ are the average values of 13×13 pixels surrounding the i-th pixel.

Then, the images are overlapped with the data for building damage, and 2,000 pixels are randomly extracted from areas corresponding to each of the seven damage severity rankings as shown on Table 1 (total of 14,000 pixels) to create a training sample. Fig. 2 shows a scatter diagram of d and r for each damage severity ranking. In areas with more severe damage, the difference in backscattering coefficient tends to have a larger absolute value in the negative, and the correlation coefficient tends to be smaller. This is because when microwaves hit undamaged pre-event buildings, multiple reflections between the ground and the building (cardinal effect) result in a large backscatter returning to the satellite; whereas in destroyed buildings and empty plots, microwaves scatter in various directions, reducing the amount which returns to the satellite, resulting in a negative difference. Additionally, damage to buildings cause the regularity of spatial distribution of backscattering coefficient to decrease in comparison to before the earthquake, resulting in a decrease in correlation coefficient.

The result of applying regression discriminant function (Okuno et al. 1981), a method of multiple-group discrimination, using d and r of the seven damage severity rankings, for a quantitative evaluation of the severe damage ratio, is shown in equation 3.

$$z_{Rj} = -1.277\, d - 2.729\, r \quad (3)$$

Here, Z_R represents the discriminant score derived from JER-1/SAR. Fig. 3 shows the distribution of Z_{Rj} determined from pre-and post-event JERS-1/SAR images. Z_{Rj} is fairly large in an area extending north-east direction from Nagata Ward, Kobe. It should be noted that the target

Table 1 Range of severe damage ratios and mean values for each damage severity ranking

Damage Ranking	Severe Damage Rate D (%)	Med-value (%)
C1	$D = 0$	0.0
C2	$0.0 \leqq D < 6.25$	3.13
C3	$6.25 \leqq D < 12.5$	9.38
C4	$12.5 \leqq D < 25$	18.75
C5	$25 \leqq D < 50$	37.5
C6	$50 \leqq D < 100$	75.0
C7	$D = 100$	100.0

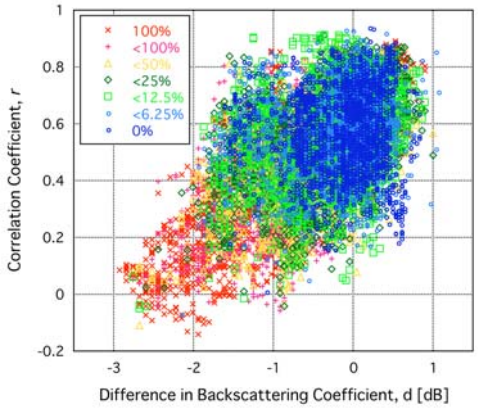

Figure 2 Scatter diagram of difference in backscattering coefficients and correlation coefficients for each damage severity ranking

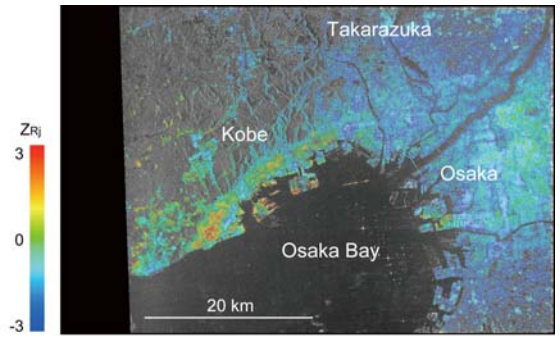

Figure 3 Distribution of discriminant score Z_{Rj} obtained from JERS-1/SAR

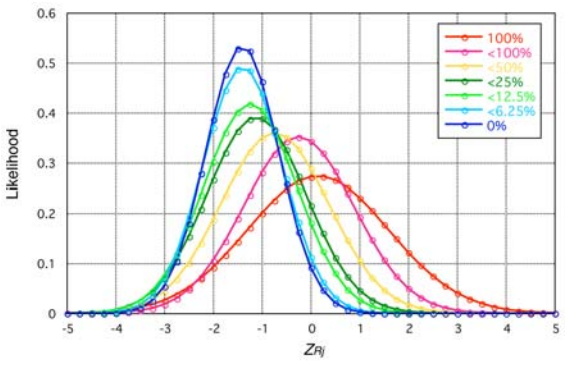

Figure 4 Normal distribution model of discriminant score Z_{Rj} frequency distribution

area is restricted to urban areas where the cardinal effect can be expected; therefore, areas whose pre-event backscattering coefficient is small (under -7dB) are masked.

Next, the likelihood function for estimating the severe damage ratio from the discriminant score Z_{Rj} is created. Fig.4 shows the frequency distribution of Z_{Rj} for 2,000 pixels for each damage severity ranking, modelled using normal distribution. Table 2 shows the average values and standard deviations of Z_{Rj} for each damage severity ranking. The discriminant score Z_{Rj} is larger with higher damage severity ranking. However, similar to the case of ERS-1/SAR, the distribution curves cross for some damage severity rankings in regions with small discriminant scores; therefore, there is a limit to the abilities of the discriminant

Table 2 Average values and standard deviations of likelihood function of SAR intensity image information

Damage Ranking	Average value of Z_{Rj}	Standard Deviation
C1	-1.399	0.747
C2	-1.390	0.809
C3	-1.233	0.955
C4	-1.110	1.018
C5	-0.733	1.107
C6	-0.241	1.134
C7	0.151	1.457

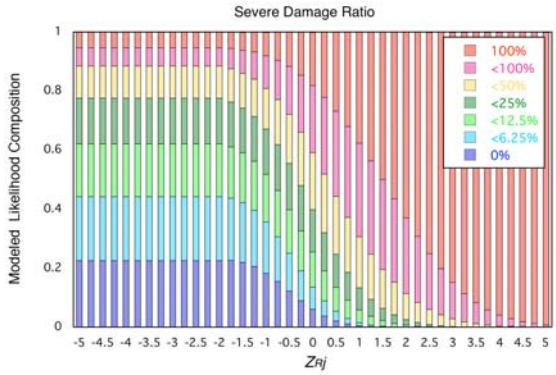

Figure 5 Modeled likelihood functions by discriminant score Z_{Rj}

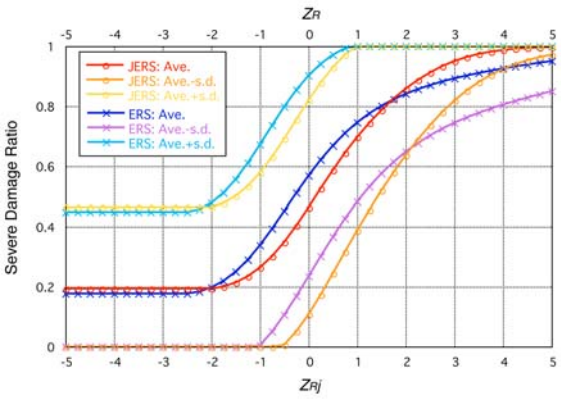

Figure 6 Relationship between the discriminant scores Z_{Rj} (JERS) and Z_{rj}(ERS), and severe damage ratio (average values and standard deviations)

analysis in areas with a low damage severity ranking. Fig. 5 shows modeled likelihood functions. For the region where Z_{Rj} is under -2.0, a constant value obtained by extrapolating the value at Z_{Rj} = -2.0 is used in order to avoid a reversal of sequence of the severe damage ratio caused by the distribution curves crossing. The average values and standard deviations of the estimated severe damage ratio against the discriminant score Z_{Rj} can be obtained from the central values of the damage severity rankings in Table 1, Table 2, and the distribution shown in Fig. 5. Fig. 6 shows the curves for the average values and the average values ± standard deviation of the severe damage ratio estimated from Z_{Rj}. This curve is equivalent to the fragility function for damage without seismic intensity information, and the severe damage ratio increases with increasing Z_{Rj}.

3. DAMAGE RATIO ESTIMATION BY INTEGRATION WITH SEISMIC INTENSITY INFORMATION

3.1 Integration of SAR Images and Seismic Intensity Information

Fig. 7(a) shows the average values and standard deviations of the severe damage ratio for seven discriminant scores Z_{Rj} when data from SAR images only are used. When $Z_{Rj} < -2.0$, the distributions overlap as shown on Fig. 4 and Fig. 5, and contain an amount of information which is only marginally more in comparison to complete non-information (average severe damage ratio of 34.8% and standard deviation of 35.8% at an equal probability of 1/7 for each damage severity ranking). Therefore, seismic intensity information is used as supplementary information for a highly accurate estimation which includes regions of low severe damage ratio. Already, the fragility function for damage in terms of seismic intensity information has been created (Nojima et al. 2006), and Fig. 7(b) shows the average values and standard deviations of the severe damage ratio at seven degrees of seismic intensities, when only the seismic intensity information is used. Next, Fig. 8(a) and Fig. 8(b) respectively show the average values and the standard deviations of the severe damage ratio after integration and probability updates for all 49 possible combinations of the two. An example of integration in the Kobe earthquake is shown in the next section.

3.2 Estimation of the severe damage ratio in the Kobe earthquake

The seismic intensity information is estimated by multiplying the seismic intensity on stiff soil layer with the amplification factor of the subsurface layer. A model by Wald (1996) was used for the locations of the fault lines, and the attenuation relationship of maximum velocity by Si and Midorikawa (2000) (crustal earthquake, using shortest distance to fault plane) were used for the seismic intensity on stiff soil layer. For the amplification distribution of the surface layer, the average S-wave velocity for the ground was calculated from the 250m grid-version (Matsuoka et al.

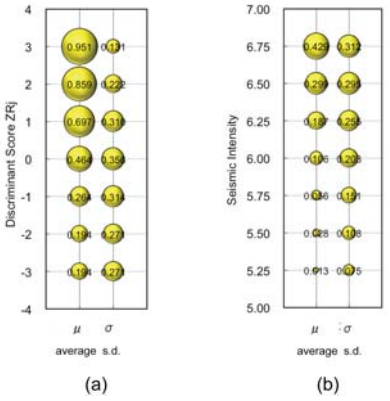

Figure 7 Average values and standard deviations of estimated severe damage ratios when estimated from one source of information only. (a) SAR information. (b) Seismic intensity information

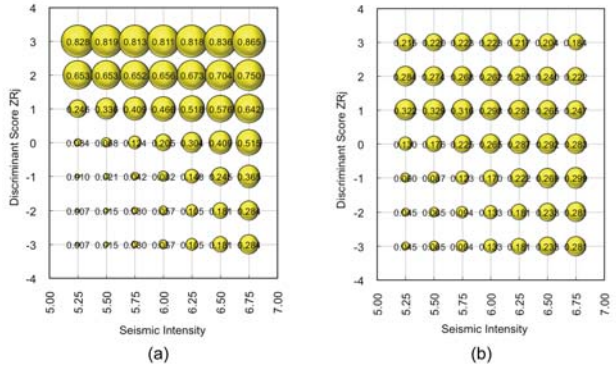

Figure 8 Estimated severe damage ratio from integration of SAR information and seismic intensity information. (a) Average values. (b) Standard deviations

2006, Wakamatsu and Matsuoka 2006) of the Japan Engineering Geomorphologic Classification Map (Wakamatsu et al. 2005) and the amplification was estimated using a formula (Fujimoto and Midorikawa 2006). The values for peak ground velocities (PGV) at the surface thus obtained were converted to instrumental seismic intensity using the relationship by Fujimoto and Midorikawa (Fujimoto and Midorikawa 2005).

Seismic intensity distribution and the severe damage ratio (average values) distribution estimated from the fragility function for damage, overlaid onto a shaded relief map, is shown in Fig. 9. It can be seen that seismic intensity tends to be larger on lower ground. Additionally, we can estimate, purely from the seismic intensity information, that the severe damage ratio is likely to be large in the coastal regions of Kobe. However, because this is based on a simple method which does not account for factors such as the direction of fault rupture, the estimated seismic intensities are lower than the actual intensities in the area around Takarazuka where the effect of such factors was significant.

Fig. 10 shows the estimated severe damage ratio (average values) obtained through an integration of discriminant scores Z_{Rj} of the SAR images (Fig. 3) and seismic information (Fig. 9). Compared to the severe damage ratio estimation using seismic intensity information only, the contrast between severely damaged areas and lightly damaged areas is more pronounced, and a distribution which resembles the so-called "earthquake damage belt" from Kobe to Nishinomiya (black areas in Fig. 1(c)) is obtained. As for Takarazuka whose seismic intensity has been underestimated, the severe damage ratio estimated by the integration is also underestimated due to small discriminant score Z_{Rj} from the SAR data (see Fig. 3). The requirement for more accurate seismic intensity estimation, and the capacity of JERS-1/SAR images, are issues which need to be examined in detail in the future.

4. APPLICATION TO ALOS/PALSAR IMAGES OF THE 2007 PERU EARTHQUAKE

The severe building damage ratio estimation model for L-band SAR image proposed above is applied to ALOS/PALSAR images for the 2007 Peru earthquake, and the accuracy of the model is examined through comparisons between the results of integration with seismic intensity information with the actual damage situation. For the seismic

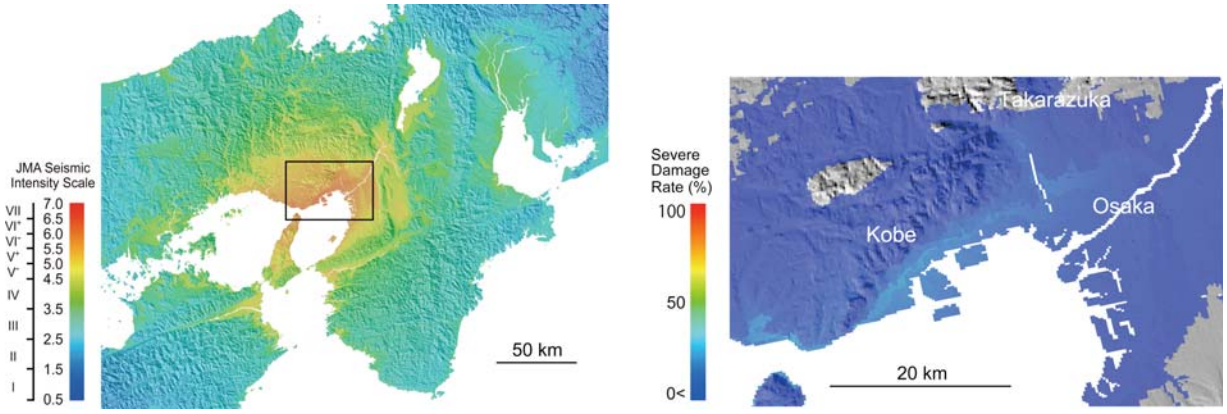

Figure 9 Distribution of estimated seismic intensities (left) and distribution of estimated severe damage ratios from seismic intensity information (average values) (right) for the Kobe earthquake

intensity information, we used the grid data for PGV from ShakeMap (USGS 2009a, Wald et al. 2006) and PAGER (USGS 2009b) which are published by the US Geological Survey (USGS) immediately after the events, and obtained the instrumental seismic intensities from the PGV using a formula (Fujimoto and Midorikawa 2005). Additionally, in order to take into consideration the seismic resistance of buildings in this country, we amended the fragility function for damage (added the 30% standard deviation on top of the average values for the severe damage ratio) so that it more or less corresponds with previous fragility functions for damage (Coburn and Spence 2002, O'Rourke et al. 2000).

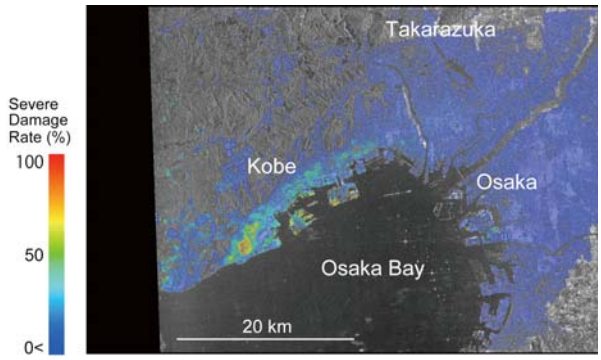

Figure 10 Distribution of estimated severe damage ratios (average values), estimated from an integrated processing of the discriminant score Z_{Rj} of the JERS-1/SAR image and seismic intensity information

The Peru Earthquake, which measured (Mw) 8.0 and occurred 40 km north-west of the city of Chincha on August 15, 2007, caused serious damage in the city of Pisco and surrounding areas, with more than 500 dead or missing and more than 35,000 buildings completely destroyed. The coastal area affected by the quake was observed by ALOS/PALSAR in high-resolution mode about two weeks after the event. Pre- and post-event images are shown in Figs. 11(a) and (b) (pre-event: July 12, 2007; post-event: August 27, 2007). The ground resolution is approximately 10m. The PGV distribution from the USGS is shown

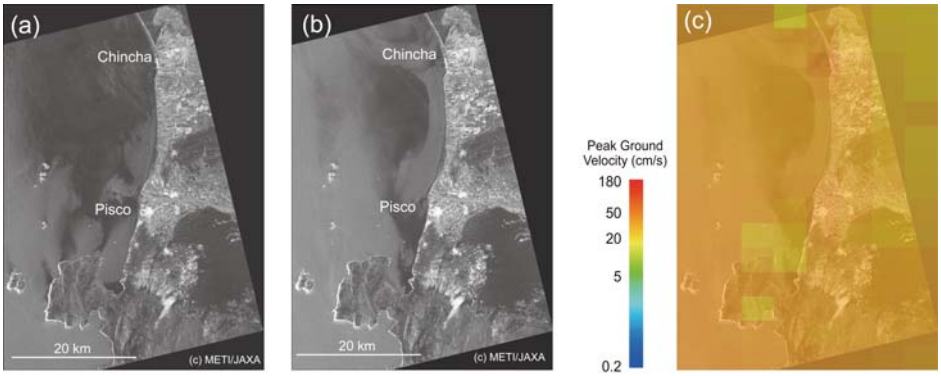

Figure 11 ALOS/PALSAR image before and after the 2007 Peru earthquake, and strong motion distribution
(a) Image taken July 12, 2007. (b) Image taken August 27, 2007. (c) PGV estimated by USGS

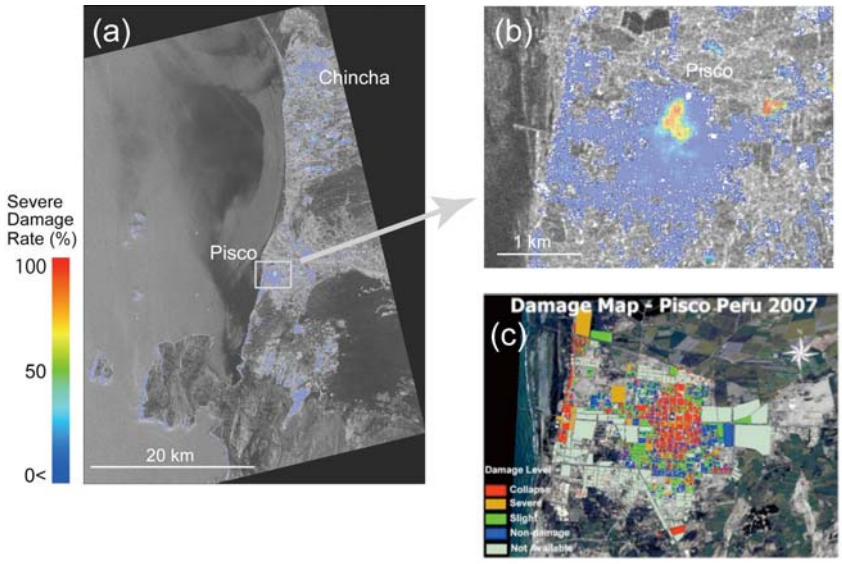

Figure 12 Distribution of severe damage ratios (average values) estimated from an integration of PALSAR images and seismic intensity information, and comparison with damage study data. (a) All areas of image. (b) Close up of Pisco area. (c) Building study data in Pisco (red = destroyed, orange = severe damage, green=slight damage, blue = no damage, brown=out of survey)

superimposed on the PALSAR image in Fig. 11(c). A discriminant score Z_{Rj} is obtained from the PALSAR image and PGVs are converted to instrumental seismic intensities; the two results are integrated using the modeled likelihood function and the fragility function for damage to arrive at estimations of the severe damage ratio, the results of which are shown on Fig. 12(a). Fig. 12(b) shows a close-up of the Pisco area. Because built-up areas are the target, areas with backscattering coefficient of under -5dB are hidden. When compared to the distribution of building damage in Pisco (Estrada 2008) according to the results of ground investigation after the earthquake shown on Fig. 12(c), there is good agreement between areas in the city center with a high concentration of destroyed or severely damaged buildings and areas with high severe damage ratio estimated from the PALSAR image. It must be noted that damage in the western coastal area of Pisco have not been detected using the PALSAR image. It is possible that the extent of damage are localized and over a small area, thereby rendering the change too small to be adequately detected from the image with a ground resolution of 10m.

5. CONCLUSIONS

We proposed a modeled likelihood function for severe building damage ratio from discriminant scores obtained via regression discriminant analysis, using the difference values and correlation coefficients from pre-event and post-event JERS-1/SAR images of the areas affected by the 1995 Kobe earthquake, as well as damage severity rankings obtained from building damage data of the quake, as explaining variables. We demonstrated that the severe building damage ratio distribution can be estimated from SAR images through integration with the fragility function for damage in terms of seismic intensity of this earthquake. Furthermore, we applied the proposed model to ALOS/PALSAR images of the 2007 Peru earthquake, and examined the accuracy of the proposed model through comparisons with local field investigations.

In terms of application of the model for early-stage estimations following earthquakes abroad, a realistic option would be to use a seismic intensity estimation system that is in global use. Although ShakeMap has been used in this instance, the estimation should ideally be updated when detailed seismic intensity distribution information through strong motion observations and high-precision simulations become available. For estimations of building damage, the function for the Kobe earthquake was used; however, it is preferable that a fragility function for damage that is appropriate for the situation of the relevant country (Jaiswal and Wald 2008) be used in order to further increase the accuracy of damage estimation. This is an issue to be addressed in the future.

Acknowledgements:

The PALSAR data is the property of METI and JAXA, and is provided by ERSDAC. We received a grant, for part of the research, from the "Development of real-time tsunami damage detection technology for expeditious disaster response of Japan and ASEAN countries (Project ID: 08E52010a) ", a NEDO Industrial Technology Research Grant Program. We would like to express our gratitude.

References:

Building Research Institute (1996), *Final Damage Report of the 1995 Hyogo-ken Nanbu Earthquake (with CD-ROM)*, 303p. (in Japanese).

Coburn, A., Spence, R. (2002), *Earthquake Protection -Chapter 9 Earthquake Risk Modeling-* , John Wiley & Sons, 436p.

Estrada, M. (2008), "Damage Study of the Pisco, Peru Earthquake using GIS and Satellite Images," *International Workshop for Safer Housing*, Building Research Institute.

Fujimoto, K., Midorikawa, S. (2005), "Empirical Method for Estimating J.M.A. Instrumental Seismic Intensity from Ground Motion Parameters Using Strong Motion Records during Recent Major Earthquakes," *Journal of Institute of Social Safety Science*, No.7, pp.214-246 (in Japanese with English abstract).

Fujimoto, K., Midorikawa, S. (2006), "Relationship between Average Shear-Wave Velocity and Site Amplification Inferred from Strong Motion Records at Nearby Station Pairs," *Journal of Japan Society for Earthquake Engineering*, Vol.6, No.1, pp.11-22 (in Japanese with English abstract).

International Charter Space and Major Disaster, http://www.disasterscharter.org, as of June 2009.

Gusella, L., Adams, B. J., Bitelli, G., Huyck, C. K., Mognola A. (2005), "Object-Oriented Image Understanding and Post-Earthquake Damage Assessment for the 2003 Bam, Iran, Earthquake," *Earthquake Spectra*, Vol.21, No.S1, pp.S225-S238.

Hao, K. X., Si, H., Fujiwara, H., Ozawa, T. (2009), "Coseismic Surface-Ruptures and Crustal Deformations of the 2008 Wenchuan Earthquake Mw7.9, China," *Geophysical Research Letters*, Vol.36, L11303, 5p.

Hosokawa, M., Jeong, B., Takizawa, O., Matsuoka, M. (2008), "Disaster Risk Evaluation and Damage Detection Using Remote Sensing Data for Global Rescue Operations," *Proc. 21st International Society for Photogrammetry and Remote Sensing (ISPRS) Congress 2008*, Vol.XXXVII, B8, VIII, pp.183-186.

Ito, Y., Hosokawa, M. (2002), "An Estimation Model of Damage Degree Using Interferometric SAR Data," *Journal of Institute of Electrical Engineers of Japan*, Vol.122-C, No.4, pp.617-623 (in Japanese with English abstract).

Jaiswal, K., Wald, D. J. (2008), "Creating a Global Building Inventory for Earthquake Loss Assessment and Risk Management," *Open-file Report 2008-1160*, US Geological Survey, 103p.

Lee, J. S. (1980), "Digital Image Enhancement and Noise Filtering by Use of Local Statistics," *IEEE Trans. Pattern Analysis and Machine Intelligence*, Photographic Surveying and Remote Sensing, Vol.2, No.2, pp.165-168.

Massonnet, D., Rossi, M., Carmona, C., Adragna, F., Peltzer, G., Fiegl, K., Rabaute, T. (1993), "The displacement Field of the Landers Earthquake Mapped by Radar Interferometry," *Nature*, Vol.364, pp.138-142.

Matsuoka, M., Yamazaki, F. (2001), "Characteristics of Satellite SAR Intensity Images in Building Damage Areas due to the 1995 Hyogo-ken Nanbu Earthquake," *Journal of Struct. Constr. Engng*, Architectural Institute of Japan, No.546, pp.55-61 (in Japanese with English abstract).

Matsuoka, M., Yamazaki, F. (2002a), "Detection of Building Damage Areas due to Earthquakes Using Satellite SAR Intensity Images," *Journal of Struct. Constr. Engng*, Architectural Institute of Japan, No.551, pp.53-60 (in Japanese with English abstract).

Matsuoka, M., Yamazaki, F. (2002b), "Effect on Speckle Noise for Detection of Building Damage Area Using SAR Intensity Images," *Journal of the Japan Society of Photogrammetry and*

Remote Sensing, Vol.41, No.5, pp.4-14 (in Japanese with English abstract).
Matsuoka, M. Yamazaki, F. (2004), "Use of Satellite SAR Intensity Imagery for Detecting Building Areas Damaged due to Earthquakes," *Earthquake Spectra*, Vol.20, No.3, pp.975-994.
Matsuoka, M., Wakamatsu, K., Fujimoto, K, Midorikawa, S. (2006), "Average Shear-wave Velocity Mapping Using Japan Engineering Geomorphologic Classification Map," *Journal of Structural Engineering and Earthquake Engineering*, Japan Society of Civil Engineers, Vol.23, No.1, pp.57s-68s.
Miura, H., Midorikawa, S. (2007), "Detection of Slope Failure Areas due to the 2004 Niigata-ken Chuetsu Earthquake Using High-Resolution Satellite Images and Digital Elevation Model," *Journal of Japan Association of Earthquake Engineering*, Vol.7, No.5, pp.1-14 (in Japanese with English abstract).
Nojima, N., Matsuoka, M., Sugito, M., Ezaki, K. (2006), "Quantitative Estimation of Building Damage based on Data Integration of Seismic Intensities and Satellite SAR Imagery," *Journal of Structural Mechanics and Earthquake Engineering*, Japan Society of Civil Engineers, Vol.62, No.4, pp.808-821 (in Japanese with English abstract).
Okuno, T., Kume, H., Haga, T., Yoshizawa, T. (1981), *[Revised] Multivariate Statistical Methods*, Union of Japanese Scientists and Engineers, pp.259-321 (in Japanese).
O'Rourke, T. D., Sang-Soo, J., Eguchi, R. T., Huyck, C. K. (2000), "Advanced GIS for Loss Estimation and Rapid Post-Earthquake Assessment of Building Damage," *Research Progress and Accomplishment*, Multidisciplinary Center for Earthquake Engineering Research, pp.157-164.
Si, H, Midorikawa, S. (2000), "New Attenuation Relations for Peak Ground Acceleration and Velocity Considering Effects of Fault Type and Site Condition," *Proc. 12th World Conference on Earthquake Engineering*, CD-ROM, ID532.
US Geological Survey, *ShakeMap*, http://earthquake.usgs.gov/eqcenter/shakemap/, as of June 2009.
US Geological Survey, *PAGER: Prompt Assessment of Global Earthquakes for Response*, http://earthquake.usgs.gov/eqcenter/pager/, as of June 2009.
US Geological Survey, *ShakeMap* us2007gbcv, http://earthquake.usgs.gov/eqcenter/shakemap/global/shake/2007gbcv/, as of June 2009.
Wald, D.J. (1996), "Slip History of the 1995 Kobe, Japan, Earthquake Determined from Strong Motion, Teleseismic and Geodetic Data," *Journal of Physical Earth*, Vol.44, pp.489-503.
Wald, D. J., Worden, B. C., Quitoriano, V., Pankow, K. L. (2006), *ShakeMap Manual: Technical Manual, User's Guide, and Software Guide Ver. 1.0*, Techniques and Methods 12-A1, US Geological Survey, 156p.
Wakamatsu, K., Kubo, S., Matsuoka, M., Hasegawa, K., Sugiura, M., (2005), *Japan Engineering Geomorphologic Classification Map*, University of Tokyo Press (in Japanese with English abstract, GIS data in CD-ROM),112p.
Wakamatsu, K., Matsuoka, M. (2006), "Development of the 7.5-Arc-Second Engineering Geomorphologic Classification Database and its Application to Seismic Microzoning," *Bulletin of Earthquake Research Institute*, The University of Tokyo, Vol.81, pp.317-324.
Yamazaki, F., Yano, Y., Matsuoka, M. (2005), "Visual Damage Interpretation of Buildings in Bam City Using QuickBird Images Following the 2003 Bam, Iran, Earthquake," *Earthquake Spectra*, Vol.21, No.S1, pp.S329-S336.
Yonezawa, C., Takeuchi, S. (2001), "Decorrelation of SAR Data by Urban Damages Caused by the 1995 Hyogoken-Nanbu Earthquake," *International Journal of Remote Sensing*, Vol.22, No.8, pp.1585-1600.

JOINT CONFERENCE PROCEEDINGS
7th International Conference on Urban Earthquake Engineering (7CUEE) &
5th International Conference on Earthquake Engineering (5ICEE)
March 3-5, 2010, Tokyo Institute of Technology, Tokyo, Japan

DETAILED MAPPING OF GEOMORPHOLOGIC CLASSIFICATION USING HIGH RESOLUTION SATELLITE IMAGE AND DIGITAL ELEVATION MODEL FOR SEISMIC HAZARD ASSESSMENT

Kazunori Ishii[1], Saburoh Midorikawa[2], and Hiroyuki Miura[3]

1) Doctoral Student, Dept. of Build Environment, Tokyo Institute of Technology, Japan
2) Professor, Dept. of Build Environment, Tokyo Institute of Technology, Japan
3) Assistant Professor, Dept. of Build Environment, Tokyo Institute of Technology, Japan
kazishii@enveng.titech.ac.jp, smidorik@enveng.titech.ac.jp, hmiura@enveng.titech.ac.jp

Abstract: For detailed seismic hazard assessment, 50m-mesh engineering geomorphologic classification map is estimated using the existing 250m-mesh map, high-resolution satellite image (QuickBird) and digital elevation model (DEM) in the southern part of the Kanto area, Japan. The spatial resolution of the satellite image and DEM are 0.7m and 1m, respectively. The spatial spectral characteristic of the image computed by two-dimensional fast Fourier transformation is used for the detailed mapping in the lowland. Based on the characteristic of the image and the DEM for each geomorphologic unit, the rules for the detailed mapping are constructed. The result of the detailed mapping shows that the estimated the mesh map almost agrees with the manually classified map.

1. INTRODUCTION

In order to obtain a ground shake map due to a scenario earthquake, the distribution of site amplification factors is indispensable. The geomorphologic classification map whose mesh size is 1km has been used to compute the distribution of site amplification factors for the national seismic hazard map for Japan. The Central Disaster Prevention Council of Japan is encouraging detailed ground shake mapping with mesh size of 50m as an incentive to citizens' disaster mitigation actions such as seismic retrofit of their own houses.

The detailed mapping requires a high-resolution digital map of soil information such as geomorphologic classification. It is, however, a time and labor consuming task to create such a digital map from the existing analog maps. Authors have examined a semi-automated detailed mapping of 50m-mesh geomorphologic classification using the exiting 250m-mesh map, digital elevation model (DEM) and satellite image (Ishii *et al.* 2007 and 2009). The detailed mapping means to increase the resolution of the existing map by estimating the smoother boundary of the geomorphology as shown Fig.1.

In the previous study(Ishii *et al.* 2009), not only the topographical characteristics in DEM but also the spatial spectral characteristics of high-resolution satellite images evaluated by two-dimensional Fourier transformation were used for detailed mapping in the lowland. In the previous study, almost the detailed mapping for lowland area was mainly discussed. However, in order for detailed mapping with wider area, the characteristic of the geomorphology that were not examined in the previous study should be discussed.

In this study, the relationship of the characteristics between the geomorphologies such as mountain, hill, and alluvial fan area are examined. Based on the characteristics, a classification rules for semi-automated detailed mapping is proposed and applied to the data with wide area.

2. TARGET AREA AND DATA USED

The target area of this study is the southern part of Kanto, Japan. The target area is extending about 50km in NS direction by about 40km in EW direction. The area covers the major cities such as Yokohama and Kawasaki.

The 250m-mesh geomorphologic classification in Japan was constructed by Wakamatsu and Matsuoka (2009).

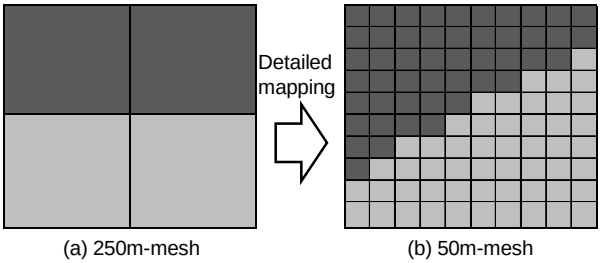

Figure 1 Schematic Diagram of Detailed Mapping

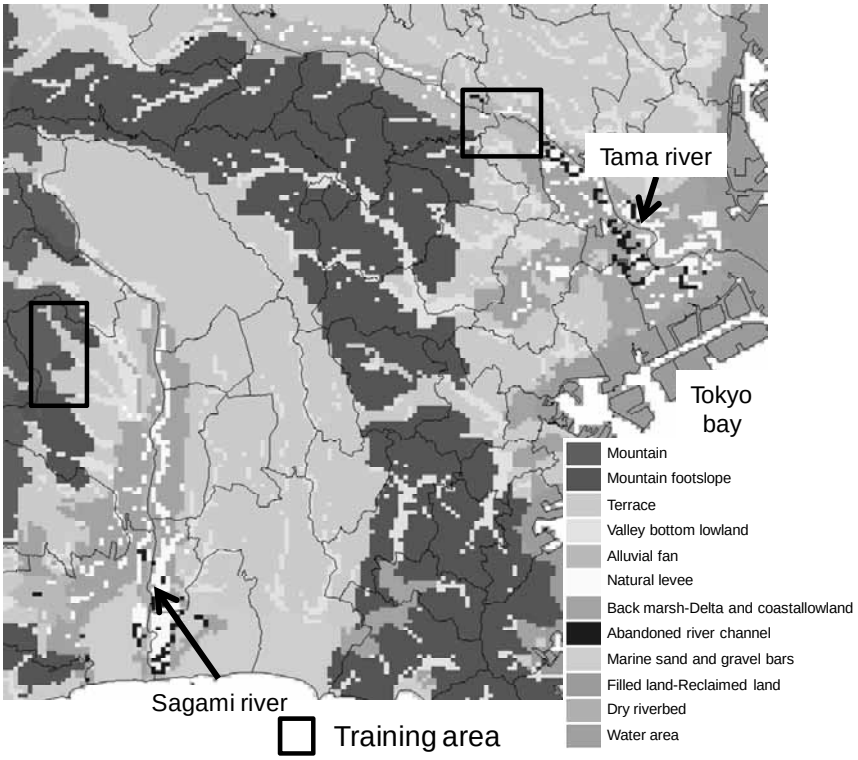

(a) 250m-Mesh Geomorphologic Classification Map

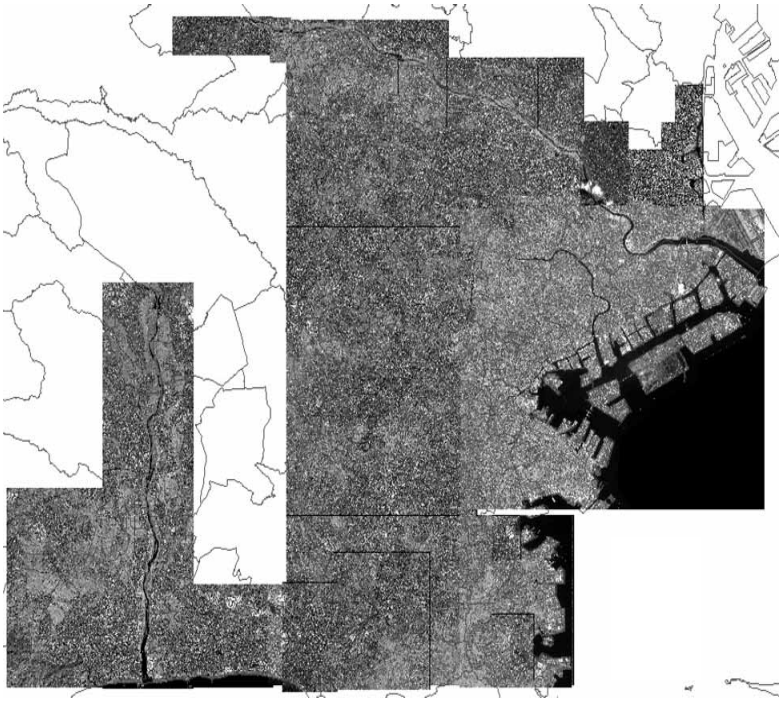

(b) Satellite QuickBird Image

Figures 2 (a) 250m-Mesh Geomorphologic Classification Map, (b) Satellite QuickBird Image

In the map, 24 geomorphologic units such as the mountain, hill, filled land and lowland are included. Figure 2(a) shows the exiting 250m-mesh geomorphologic classification map in the target area. In the area, various geomorphologic units are distributed such as the mountain, the hill, the lowland and the filled land.

Figure 2(b) shows the satellite QuickBird image of the study area. These images were observed in 2002 to 2008.

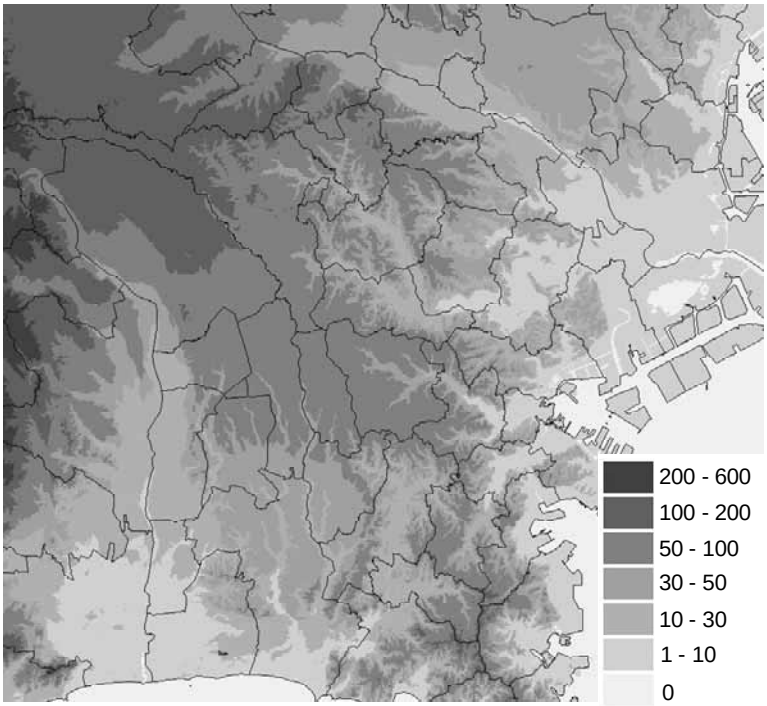

(c) DEM

Figures 2 (c) DEM (Continued)

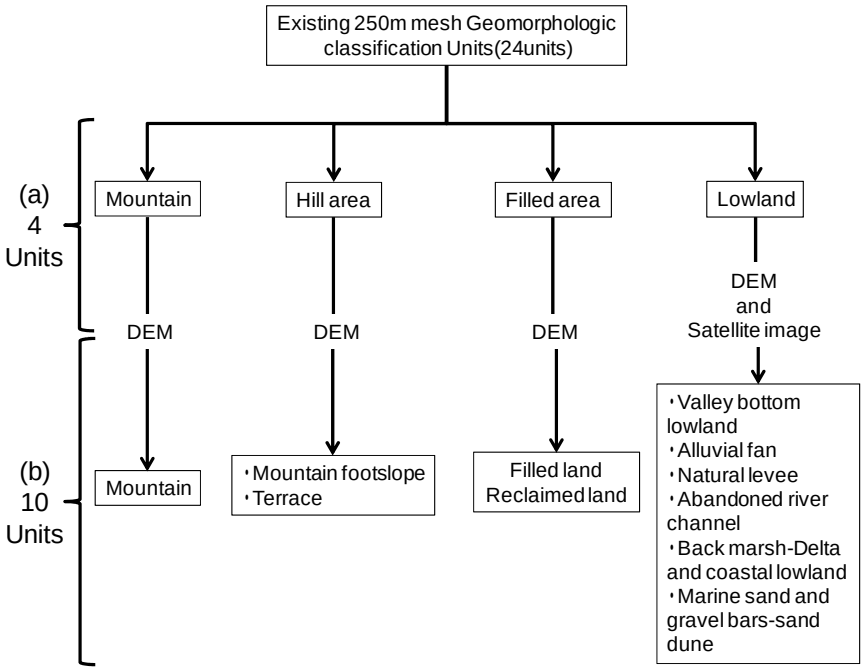

Figure 3 Flow of Detailed Mapping

The spatial resolution of the images is 0.7m. The image consists of 4 bands. Bands 1, 2 and 3 indicate blue, green and red bands, respectively. The band 4 indicates near infrared band. To evaluate vegetation activity in a pixel, NDVI (Normalized difference of vegetation index) is computed.

Figure 2(c) shows the distribution of elevation with the resolution of 50m. Slope, relief and difference of elevation between 250m-mesh and 50m-mesh (difference of elevation) are computed to evaluate the topographical characteristics. In the lowland area, it is difficult to evaluate topographic characteristics by the 50m-mesh DEM. High-resolution DEM with the resolution of 1m is also used.

3. CHARACTERISTICS OF DEM AND SATELLITE IMAGES

In the existing mesh map, 24 geomorphology units are included. It is, however, difficult to classify all the units by semi-automated classification. Figure 3 shows the flowchart of the proposed detailed mapping. To simplify the classification rules, all the units are broadly classified into four major geomorphologies; mountain area, hill area, filled area and lowland area. By considering ground shaking characteristics estimated from the geomorphologies, the geomorphologies are simply classified into 10 units as shown in Fig. 3.

Firstly, the characteristics of the DEM and the satellite images are examined in training areas where the characteristics between the geomorphologies were not examined in the previous study. Solid squares indicate the training areas in this study, including the boundaries between (A) mountain and hill, (B) alluvial fan and the other lowlands.

Figures 4(a) and (b) show the comparison of the exiting 250m-mesh map and manually classified 50m-mesh map in the boundary of mountain and hill. Figures 5 show the histograms of the elevation and the relief between the

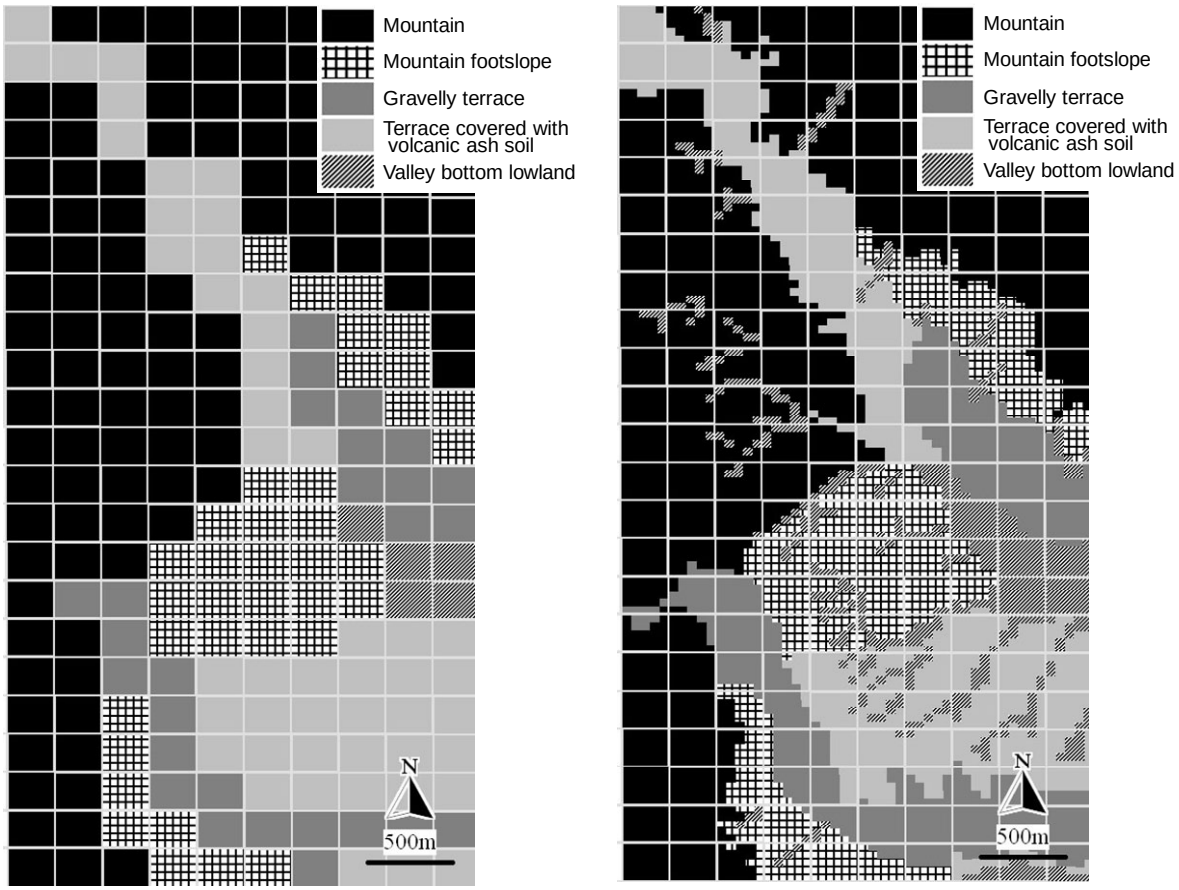

(a) 250m-Mesh Map (b) Manually Classified 50m-Mesh Map

Figures 4 Geomorphologic Classification Maps in Mountain and Hill Area

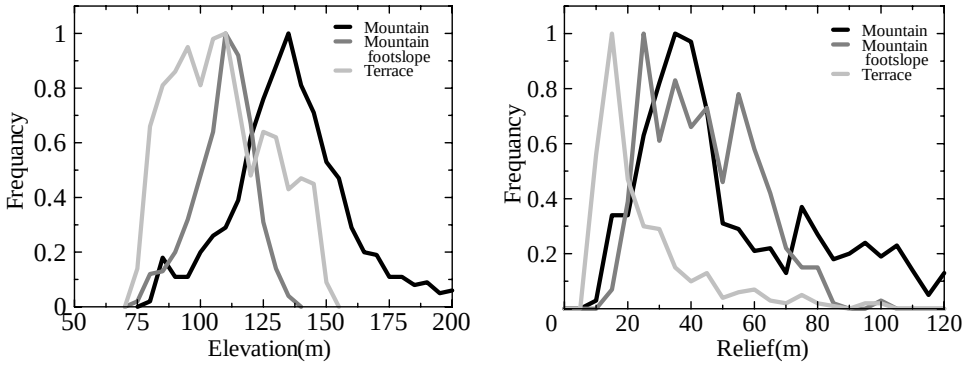

Figures 5 Histogram of Elevation and Relief

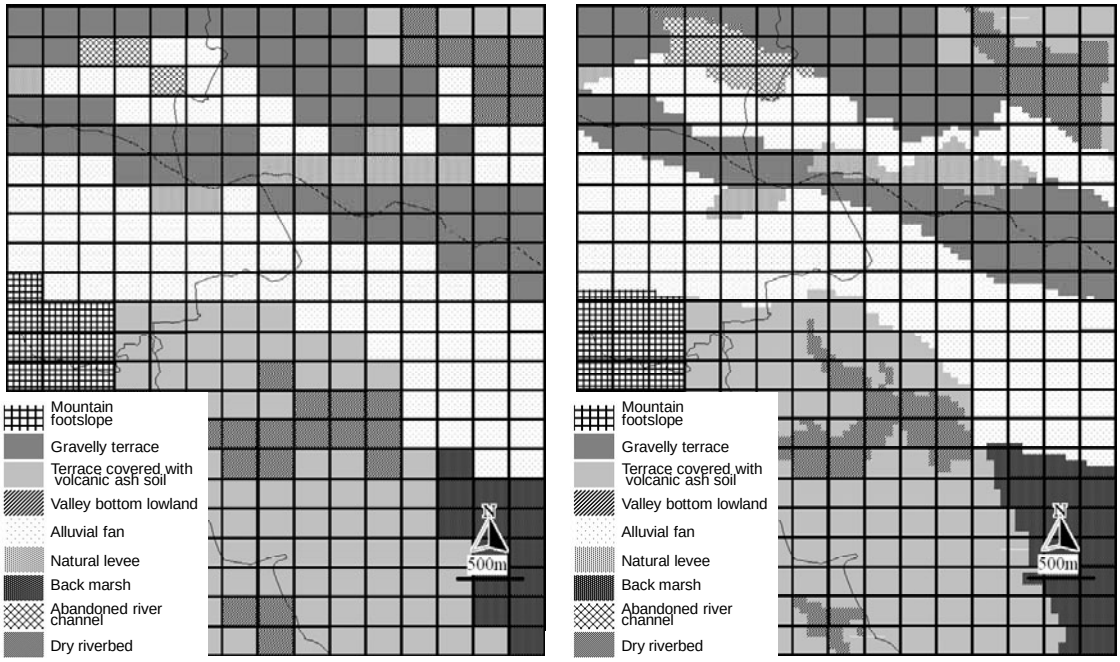

(a) 250m-mesh map (b) Manually classified 50m-mesh map

Figures 6 Geomorphologic Classification Maps in Alluvial Fan Area

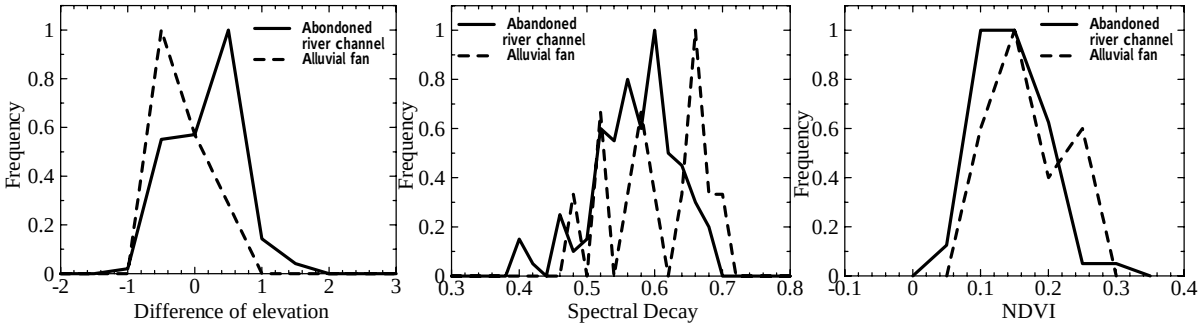

Figures 7 Histogram of Indices in Alluvial Fan Area

mountain, the mountain footslope and the terrace, indicating that the elevation and relief in mountain area are higher than those in the mountain footslope and the terrace. By thresholding of the indices and by considering the continuity of the geomorphology, the detailed map is estimated.

Figures 6(a) and (b) show the comparison of the exiting 250-mesh map and manually classified 50m-mesh map in the boundary of the alluvial fan area. Figures 7 show the histogram of the difference of elevation, spectral decay and NDVI between the each geomorphology such as the natural levee, abandoned river channel and back marsh in alluvial fan area. By thresholding of the indices and by considering the continuity of the geomorphology, the detailed map is estimated.

4. DETAILED MAPPING OF GEOMORPHOLOGIC CLASSIFICATION MAP

4.1 Classification Rules

Based on the results in the previous chapter and the previous studies (Ishii *et al.* 2007 and 2009), classification rules for detailed mapping are constructed. Table 1 shows the classification rules proposed in this study

For the mountain area, valley bottom lowland is classified by using difference of elevation. In the hill area, mountain footslope, terrace and valley bottom lowland are classified by using difference of elevation, relief and slope.

For the filled land, filled land is classified by using elevation because the elevation in the filled land is higher than other lowlands.

For the lowland, the alluvial fan areas and back marsh and delta areas are broadly classified by using the existing 250m-mesh map. For the alluvial fan areas, natural levee, and abandoned river channel is classified by using NDVI, relief, difference of elevation and spectral decay. For the back marsh and delta areas, marine sand and gravel bars, natural levee, and abandoned river channel are classified by using relief, difference of elevation, and spectral decay.

The threshold values of the indices are determined by comparing the histograms of the indices evaluated from the manually classified 50m-mesh map. The continuity of the

Table 1　Classification Rules for Detailed Mapping

Large Classification	Geomorphology		Classificatin rule for detailed mapping
Mountain	Mountain		Elevation110m or higher or relief 28m or higer.
	Vally bottom lowland		① In 250m mesh of Mountain, difference of elevation 0m or smaller. ② In 250m mesh of Vally bottom lowland, difference of elevation -10m or smaller.
hii	Vally bottom lowland		① In 250m mesh of Vally bottom lowland, difference of elevation -2m or smaller. ② In 250m mesh other than Vally bottom lowland, difference of elevation -4m or smaller.
	Boundary of Mountain footslope and Terrace		In 250m mesh of Mountain footslope, relief 20m or lager and slope 4 degree or lager.
	Other lowland area		In other meshes, relief 8m or lager is Terrace. Other meshes are Lowland.
Filled land	Filled land and Reclaimed land		①In 250m mesh, a mesh surrounded by filled land or sea is considered to be filled land ②Elevation 2～3.5m ③After converting 250m mesh into 50m mesh, if there is a mesh which is not clasified as filled land, the land side considered to be lowland.
	Other lowland area		Other meshes
Lowland	Alluvial fan	Dry riverbed	① In 250m mesh of Natural levee, NDVI 0.4 or lager or difference of elevation -2.0m or smaller. ② In 250m mesh of Alluvial fan, NDVI 0.4 or lager or difference of elevation -2.0m or smaller. ③ In 250m mesh of Dry riverbed, NDVI 0.4 or lager or Spectral decay 0.7 or lager.
		Natural levee	① In 250m mesh of Natural levee, relief 1m or smaller or Spectral decay 0.7 or lager. ② In 250m mesh of Alluvial fan, difference of elevation 0m or smaller and NDVI 0.15 or lager.
		Abandoned river channel	① In 250m mesh of Abandoned river channel, difference of elevation -0.2m or lager or Spectral decay 0.64 or smaller or NDVI 0.2 or smaller. ② In 250m mesh of Alluvial fan, relief 1.8m or lager and Spectral decay 0.58 or lager. ③ Other meshes are Alluvial fan.
	Boundary of Alluvial fan and Back marsh - Delta and Coastal lowland		① In 250m mesh of Alluvial fan, relief 1.2m or lager or Spectral decay 0.7 or smaller: Alluvial fan ② In 250m mesh of Back marsh, difference of elevation 0m or smaller and NDVI 0.1 or lager: Alluvial fan ③ Other meshes are Back marsh - Delta and Coastal lowland
	Back marsh-Delta and coastal lowland	Marine sand and gravel bars	① In 250m mesh, In case at least two sides of a certain mesh is adjacent to terrace, a, Relief 0.75m smaller is candidate of Delta and coastal lowland, relief 0.75m or lager and 1.0m smaller is candidate of boundary area, relief 1.0m or lager is candidate of Marine sand and gravel bars. b, Spectral decay 0.64 smaller is candidate of Marine sand and gravel bars, spectral decay 0.64 or lager and 0.7 smaller is candidate of boundary area, spectral decay 0.70 or lager is candidate of Delta and coastal lowland. ② In 250m mesh, In case at least two sides of a certain mesh is not adjacent to terrace, a, Elevation 1.5 smaller is candidate of Delta and coastal lowland, elevation 1.5 or lager and 1.9m smaller is candidate of boundary area, elevation 1.9m or lager is candidate of Marine sand and gravel bars. b, Spectral decay 0.58 smaller is candidate of Marine and gravel bars, spectral decay 0.58 or lager and 0.66 smaller is candidate of boundary area, spectral decay 0.66 or lager is candidate of Delta and coastal lowland. Using a conbination of each candidate site geomorphology, to construct a classification rules, respectively.
		Natural levee	a, Elevation 3.0m smaller is candidate of Natural levee, Elvation 3.0m or lager and 3.4m smaller is candidate of boundary area, elevation 3.4m or lager is candidate of Back marsh - Delta and coastal lowland. b, Spectral decay 0.6 smaller is candidate of Natural levee, spectral decay 0.6 or lager and 0.76 smaller is candidate of boundary area, spectral decay 0.76 or lager is candidate of Back marsh - Delta and coastal lowland. Using a conbination of each candidate site geomorphology, to construct a classification rules, respectively.
		Abandoned river channel	a, Spectral decay 0.7 smaller is candidate of Back marsh - Delta and coastal lowland, spectral decay 0.7 or lager and 0.74 smaller is candidate of boundary area, spectral decay 0.74 or lager is candidate of Abandoned river channel. b, Relief 0.8 or smaller is candidate of boundary area, relief 0.8 lager is candidate of Abandoned river channel. Using a conbination of each candidate site geomorphology, to construct a classification rules, respectively.
		Dry riverbed	In 250m meshes of Dry riverbed, meshes of not exemplified above
		Back marsh-Delta and coastal lowland	Other meshes

geomorphologies is also considered in the classification rules.

4.2 Validation

The 50m-mesh map is estimated by using the classification rules. The accuracy of the classification is computed by comparing the result with the manually classified 50m-mesh maps in the training areas. Table 2 shows the number of manually classified meshes for each geomorphology, the number of correctly classified meshes, and the percentages of correctly classified meshes. The comparison shows that the mountain area, the hill area, the filled area and the alluvial fan in lowland area are correctly classified because the accuracies in the areas are about 90%. As shown in Table 2, the total accuracy of the proposed method is about 88 %.

However, the classification in the back marsh-delta and coastal lowland area does not well corresponds to the manually classified map. Especially, the accuracies in the abandoned river channel and the natural levee lower than 30 %. One of the reasons for these low accuracies in the lowland areas would be that the differences of the indices among the geomorphologies are not significant. Because the difference of the topographic information is small in the lowlands, the land cover information from the satellite image might be necessary to be examined in more detail to improve the accuracies.

4.3 Application to Wide Area

The classification rules are applied to the whole target area. Figure 8 shows the estimated geomorphologic classification 50m-mesh map. Compared to the 250m-mesh map (Fig. 2(a)), the boundaries of the geomorphologies are represented in more detail.

To validate the estimated geomorphologic mesh map, average shear wave velocity in the upper 30m (AVS30) is estimated from the geomorphologic map by the method of Matsuoka et al. (2005).

Table 2 Accuracy of Classification

Geomorphology units		Manually classified (a)	This study (b)	Accuracy rate(%) (b)/(a)
Mountain		2609	2507	96.1
Mountain footslope		764	694	90.8
Terrace		4913	4224	86.0
Valley bottom lowland		1285	612	47.6
Filled land-Reclaimed land		5565	5315	95.5
Alluvial fan	Alluvial fan	365	313	85.8
	Abandoned river channel	148	135	91.2
	Natural levee	195	156	80.0
Back marsh-Delta and coastal lowland	Back marsh-Delta and coastal lowland	3626	3295	90.9
	Abandoned river channel	221	56	25.3
	Marine sand and gravel bars	568	283	49.8
	Natural levee	343	122	35.6
Total		11031	9675	87.7

Figure 9 shows that the distribution of AVS30. In mountain and hill area, AVS30 with 400 to 600m/s is widely distributed. In the lowland area such as the lower valley of the Tama river and Sagami river as shown by arrows in Fig. 9, soft soil area with AVS30 of 200m/s or less is widely distributed, indicating that the area may suffer strong ground shaking due to an earthquake.

5. CONCLUSIONS

A methodology of semi-automated detailed mapping of geomorphologic classification using the existing 250m-mesh map, the DEM and the satellite image is introduced in this study. Firstly, the characteristics of the DEM and the satellite image are examined at different site geomorphologies in the study areas.

The classification rules based on the characteristics in each geomorphology are applied to estimate the detailed 50m-mesh map. In study areas, estimated 50m-mesh map is compared with the manually classified map. The result shows that the 88% of the meshes are correctly classified while the accuracy in the lowland area is relatively low.

Finally, 50m-mesh map is constructed from classification rules in wide area. Compared the 50m-mesh map to the 250m-mesh map, the boundaries of the geomorphologies are represented in more detail. The distribution of AVS30 is estimated from the 50m-mesh map.

Acknowledgements:

This study was done as a part of "Development of Integrated Geo physical and Geological Information Database" supported by Special Coordination Funds Promoting Science and Technology of the Japanese Ministry of Education, Culture, Sports, Science and Technology. This study is also supported by Global COE Program "International Urban Earthquake Engineering Center for Mitigating Seismic Mega Risk" by Ministry of Education, Culture, Sports, Science and Technology (MEXT), Japan.

References:

Ishii, K. Midorikawa, S. Miura, H. (2007), "Detailed Mapping of Engineering Geomorphologic Classification Using Digital Elevation Model and Satellite Image," *Journal of Social Safety Science*, No.9, pp. 121-129 (in Japanese with English Abstract).

Ishii, K. Midorikawa, S. Miura, H. (2009), "Revised Method for Detailed Mapping of Engineering Geomorphologic Classification Using Satellite Image and Digital Elevation Model," *Journal of Social Safety Science*, No.11, pp. 61-68 (in Japanese with English Abstract).

Kitagaki, R. Kanematsu, M. Noguchi, T. (2003), "Evaluation of Features of Color Distribution Related to Visual Impression of Architectural Cladding Surfaces by using 2DFFT," *6th Asian Design International Conference*, pp.24-27.

Matsuoka, M., Wakamatsu, K., Fujimoto, K., and Midorikawa, S.,(2005)"Average Shear-wave Velocity Mapping Using Japan Engineering Geomorphologic Classification Map ", *Journal of Structural Mechanics and Earthquake Engineering*, No.794/ I-72,pp.239-251 (in Japanese with English Abstract).

Wakamatsu, K., and Matsuoka, M. (2009). Development of GIS-Based 7.5-arc-second Japan Engineering Geomorphologic classification map, *Proceedings of the Development of an Integrated Geophysical and Geological Information Databese-3th symposium*, pp.15-20.

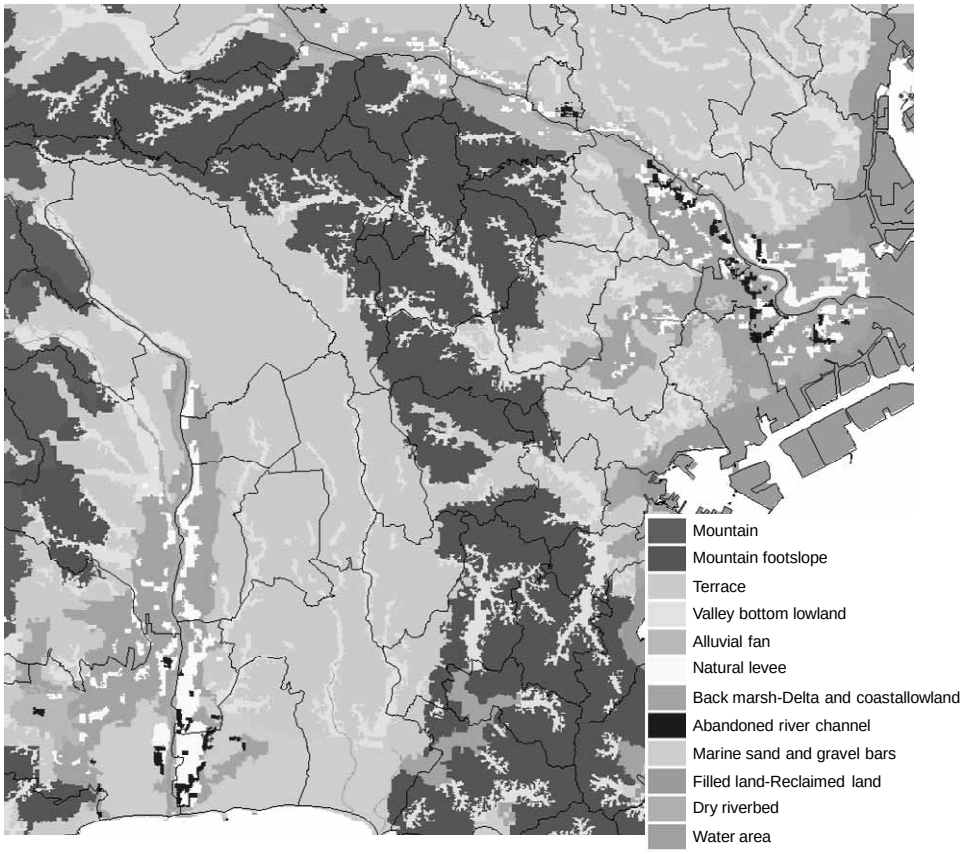

Figure 8 Estimated 50m-Mesh Geomorphologic Classification Map

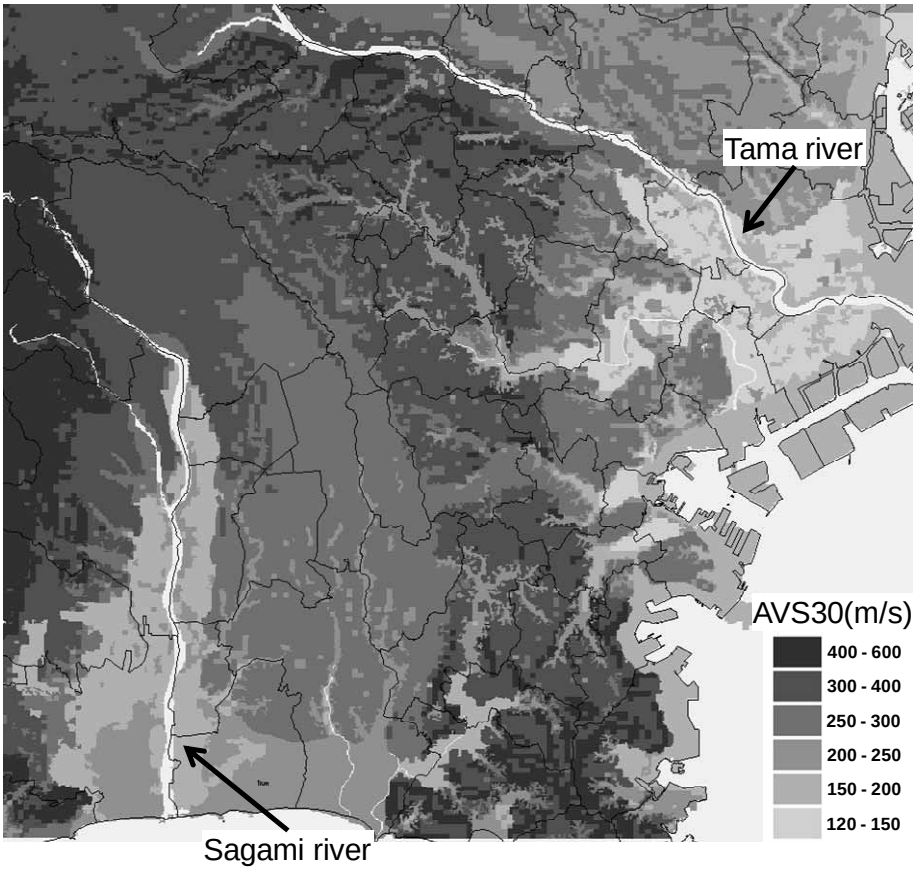

Figure 9 Distribution of AVS30 Estimated from the 50m-Mesh Map

JOINT CONFERENCE PROCEEDINGS
7th International Conference on Urban Earthquake Engineering (7CUEE) &
5th International Conference on Earthquake Engineering (5ICEE)
March 3-5, 2010, Tokyo Institute of Technology, Tokyo, Japan

ANALYSIS OF THE BICEP BOREHOLE ARRAY

Liam Wotherspoon[1)] and Rolando Orense[2)]

1) Research Fellow, Civil & Environmental Engineering Dept., The University of Auckland, New Zealand
2) Senior Lecturer, Civil & Environmental Engineering Dept., The University of Auckland, New Zealand
l.wotherspoon@auckland.ac.nz, r.orense@auckland.ac.nz

Abstract: The Borehole Instrument Centre for Eden Park (BICEP) is a 383 m deep instrumented borehole beneath the new South Stand of Eden Park Sports Stadium in Auckland, New Zealand. The borehole was permanently instrumented using seismographs at the surface, at 26 m and at 383 m depth, providing a three dimensional view of the dynamic characteristics of the strata beneath the highest point of the new stand. Sources of dynamic excitation captured by this array are seismic events and excitation of the overlying stadium from wind and crowd movements. Characteristics of the borehole array and the subsurface conditions are detailed in this paper. At this site 20 m of basalt flows covered sedimentary rock, transitioning from highly weathered to fresh, site conditions commonly encountered as Auckland sits on a volcanic field. Seismometers were able to capture the transition of characteristics through these layers. The borehole array captured multiple seismic events from within New Zealand, providing a good representation of the dynamic response of the strata at the site from depth to the ground surface.

1. INTRODUCTION

The Borehole Instrument Centre for Eden Park (BICEP) is a 383 m deep borehole beneath Eden Park stadium constructed for earth science and engineering research. This is the first borehole site of the "Strata to Structure" project, which aims to develop a better understanding of the seismic and dynamic characteristics of the Auckland region from deep in the ground up to the surface and into overlying structures. Research will also look at the effect of the movement of the stadium on the underlying strata. Data retrieved from the borehole will open the door to new research directions by providing an opportunity for earth scientists and engineers to carry out integrated research projects.

2. BOREHOLE CONSTRUCTION

The BICEP site at Eden Park stadium in Auckland, New Zealand is shown by the arrow and solid circle marker in Figure 1. It is located close to the central business district (open circle) and within the Auckland Volcanic Field, providing an insight into the seismicity of the downtown area. The urban areas of Auckland extend well beyond the range indicated in this figure.

An upgrade of the stadium began in 2008 with the construction of new stands for the Rugby World Cup in 2011. As part of this upgrade, the South West and South stand in Figure 2 were demolished and replaced by a new larger South stand. Construction of the borehole took place prior to the demolition of the South West stand in 2008, and was positioned beneath the footprint of the new South Stand as shown in Figure 3. This placement coincided with the tallest part of the new stadium superstructure, and allowed for easy access to the head of the borehole. The borehole coordinates are 36.88 S, 174.74 E.

2.1 Site Geology

The site consists of approximately 20 m of basalt flows overlying a layer (0.5-4.5 m) of soft Tauranga group alluvium. Rock conditions within the basalt flows ranged from hard, soil rock to scoria layers. Sandstones and mudstone layers of the East Coast Bays or Waitemata formation extend from this point down to the base of the borehole, transitioning from highly weathered to fresh rock with depth. Samples were taken at every metre within the basalt and at every five metres within the underlying material in order to characterise the geology at the site. The harder basalt material overlying softer sedimentary rock is a common occurrence in the Auckland region as a result of its positioning within a volcanic field.

Two projects are underway involving the samples and faculty at the University of Auckland School of Environment: First, the clays are being studied using x-ray diffraction (XRD) analysis in order to test whether samples obtained by this drilling method can be used to determine clay mineralogy and the local sedimentation history. Second, the samples are being prepared for long term storage, as faculty plan to involve students at the Master's and/or PhD level to study the petrology of the samples and decipher past sedimentary processes.



Figure 1 Location of borehole within the Auckland Volcanic Field (Homer et al. 2000)

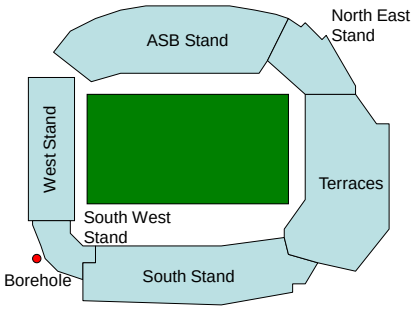

Figure 2 Location of borehole in comparison with the old Eden Park complex

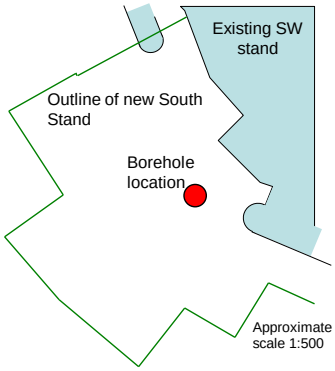

Figure 3 Location of borehole behind old South West Stand with indication of the footprint of the new stand

2.2 Borehole Characteristics

Characteristics of the borehole immediately after construction are presented in Figure 4 and were as follows:

- From the surface to 2.9 m depth a 254 mm (10") ID steel conductor casing was installed and cemented into place
- Through basalt layers a 254 mm (10") diameter bit was used and the hole cased with 203.2 mm (8") ID steel casing, extending down to a depth of 20.3 m
- From 20.3 m to 30 m a 203.2 mm (8") bit was used with 152.4 mm (6") ID PVC casing
- Below this depth the borehole was uncased and a 152.4 mm (6") diameter bit was used to drill the hole to a depth of 393 m

Both at a depth of 309 m and at the base of the borehole (393 m), a single camera shot (using a Reflex EZ-SHOT instrument (Reflex 2008)) was taken in order to determine the inclination of the borehole. At 309 m the inclination of the borehole was 2.2° off vertical, and at the base it was 1.6°.

In order for the sondes to function efficiently they had to be adequately coupled to the surrounding stratum, which was achieved using a grout that filled the borehole volume and eliminated all voids. Prior to grouting, the 20.3 m length of 203.2 mm diameter steel casing was removed, minimising the casing layers between the sondes and the surrounding soil. Thus, grouting was only required within the 152.4 mm diameter PVC casing/open hole and in the annulus between the borehole wall and the PVC casing.

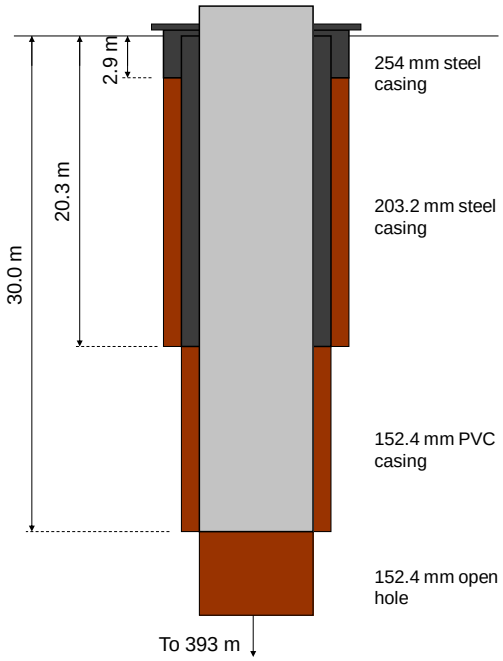

Figure 4 Details of borehole characteristics with depth

3. INSTRUMENTATION

Two borehole seismographs, or sondes, designed and constructed by the Institute of Earth Science and Engineering (IESE) were installed to record the dynamic response down hole in the vertical and two perpendicular horizontal directions. The deepest instrument, defined as the Base sonde, was installed just above the bottom of the borehole at a depth of 382 m. The second, defined as the Waitemata sonde, was installed at a depth of 26 m coinciding with the top of the Waitemata strata. Between construction of the borehole and installation of equipment, material from the side of the uncased borehole partially filled the hole, reducing the depth from 393 m to 383 m.

The Base sonde houses three 2Hz geophones, while the Waitemata sonde contains three 2Hz geophones and a MEMS (Micro-Electro-Mechanical Systems) accelerometer. Within the sonde each geophone was housed in a set of two gimbals to keep each geophone orientated in the correct plane. Both sondes were attached to data cables that run up the length of the borehole for connection to the surface recording equipment. Figure 5 provides a view of the geophones used inside the borehole seismometers prior to the installation of the assembly within a steel outer casing. Moving across the figure from left to right are the geophones oriented within the gimbals for the vertical, horizontal 1, and horizontal 2 directions. The vertical is oriented along the length of the sonde, while the horizontals are perpendicular to the long axis of the sonde, each at 90° to one another.

Two REF TEK 130-01 seismic recorders (Refraction Technologies 2008) were used at the ground surface to digitize and record the data. To record the response at the ground surface, a Geospace HS-1 seismometer (Geospace 2009) was positioned at the head of the borehole. The difference in the conversion of velocity to volts for the surface seismometer was accounted for in comparisons by scaling the counts from the surface recorder to the equivalent counts of the borehole seismographs.

There is a possibility of installing accelerometers throughout the stadium superstructure once construction of the new stand has been completed. Data from this instrumentation can then be combined with the data from the BICEP surface and borehole seismographs. This will also be used for analysis of the dynamics of the superstructure from seismic events, as well as the effect of crowd movements on the dynamics of the stadium and the underlying strata.



Figure 5 Internal view of IESE borehole seismometer indicating gimballed geophones. Top is to the left.

4. BACKGROUND NOISE

Because BICEP reduces city noise by placing seismographs in a quiet downhole environment, the instruments can also record small, local earthquakes and provide insight into the seismicity of the central city. To provide an indication of performance at different depths, the background noise recorded by each seismograph was compared against the internal noise of the REF TEK recorder (defined as digitizer noise). To determine this value the REF TEK units were shorted out and the noise recorded at unity and 32 gain. At both gains the noise levels were comparable, indicating that the recorded signal was internal to the REF TEK unit. As the background noise was recorded at a gain of 32, this was scaled back to compare both signals at a gain of unity.

Noise level comparisons have indicated a significant reduction in noise with depth and changes in the characteristics of seismic signals with changing rock and soil layers. Figure 6 compares the vertical noise and digitizer noise from the Base sonde, the Waitemata sonde, and a surface seismometer. Results have been presented in terms of counts, as it is of interest to look at the comparative response of instruments rather than absolute values. Comparison of Figures 6(a) and (b) indicates that the noise level from the vertical sensor of the Base sonde was approximately equal to the digitizer noise, while the Waitemata sonde noise levels were approximately twice the digitizer noise. In Figure 6(c), noise from the surface seismometer was much larger than the borehole seismometers, with a range 270% of the Waitemata sonde and 640% of the Base sonde. This data clearly indicates the effectiveness of placing the seismometers at depth in terms of reducing background noise.

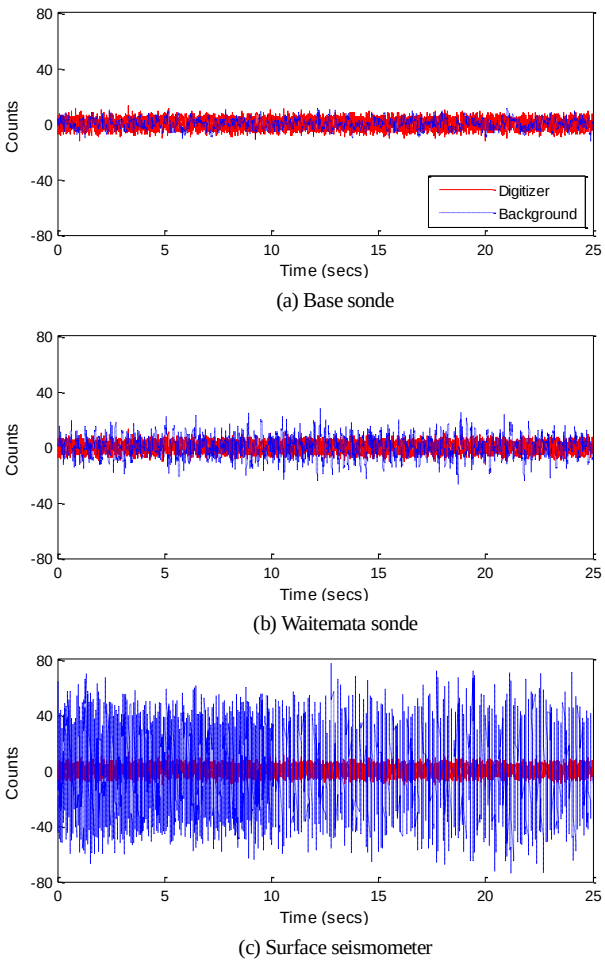

(a) Base sonde

(b) Waitemata sonde

(c) Surface seismometer

Figure 6 Comparison of digitizer noise and background noise

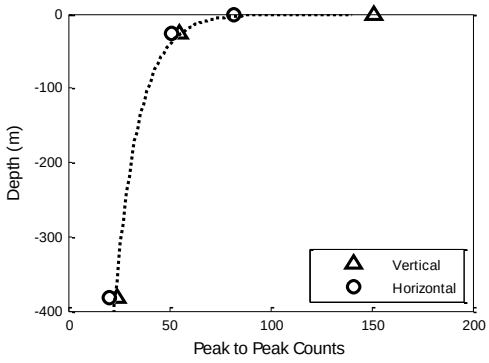

Figure 7 Variation of background noise with depth

Similar reductions in noise characteristics with depth were also evident in the two horizontal directions. These reductions were not as significant at the vertical direction, with the noise range of the surface seismometer 150 – 200% of the Waitemata sonde and 350 – 500% larger than the Base sonde. The peak to peak background noise characteristics with depth are presented in Figure 7, indicating similar noise levels in the horizontal and vertical directions in the sondes, while at the ground surface there is much larger vertical noise compared to horizontal. Using a trend line to fit the horizontal noise data, the variation in noise with depth reduces towards an asymptotic value equal to the noise created by digitizer. This suggests that at greater depths the background noise levels will not experience significant reductions.

5. SONDE ORIENTATION

An issue with the installation of borehole seismometers is that the orientation of the horizontal axes of the instrument in the borehole is not always known. For BICEP, the orientation of both sondes was not known. There are methods that can be used to determine the orientation, such as the cutting of slots in the casing, but as the majority of this borehole was uncased this was not possible.

Instead of constraining the orientation of the seismometers, seismic events that have been located by other seismic stations can be used to determine the orientation of the seismometers downhole. The process used to determine this is as follows:

- Determine co-ordinates of the seismometer site
- Determine co-ordinates of the epicentre of the seismic event
- Use these co-ordinates to define the bearing (θ_1) of line between the seismometer and the epicentre (Figure 8)
- Plot the particle motion of the seismic velocity data in the horizontal direction beginning at the s-wave arrival time using an assumed north direction (Figure 9). If a linear relationship is evident then the direction of the seismic wave can be approximated as a line perpendicular to this. This will give a bearing in the assumed axes (θ_2).
- The difference in the bearing of these two lines (θ_1-θ_2) will be the amount the axes of the seismometer will need to be rotated from north to define the actual orientation

By using the data from multiple events, the orientation of the borehole seismometers can be averaged and refined. Works are currently underway to define the orientations.

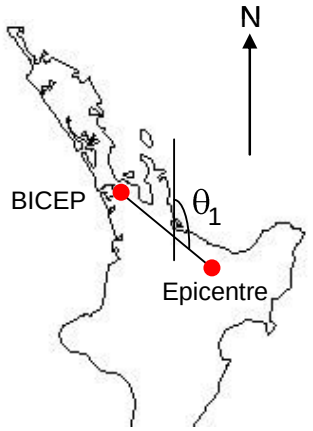

Figure 8 Bearing between seismometer and event epicentre

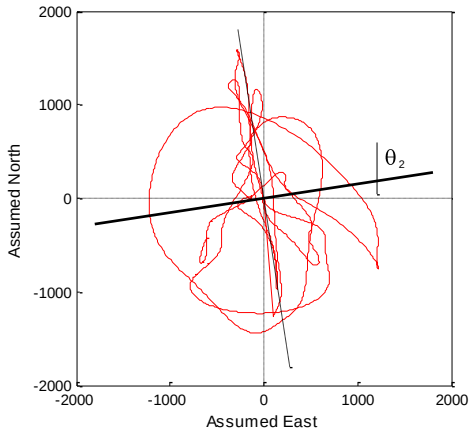

Figure 9 Particle motion of S-wave and wave direction

6. PRELIMINARY DATA

During the preliminary recording period there were no Auckland seismic events captured by the BICEP seismometers. However, four seismic events recorded from within New Zealand were:

1. October 18th 2008, 12.13 pm, 5.6 Richter Magnitude, 38.00 S 176.24 E, 200 km focal depth. (20 km N of Rotorua, NZ)
2. October 19th 2008, 2.05 pm, 4.3 Richter Magnitude, 38.22 S 177.38 E, 50 km focal depth. (40 km SE of Whakatane, NZ)
3. July 15th 2009, 9.22 pm, 7.8 Richter Magnitude, 45.75 S 166.58 E, 12 km focal depth. (100 km NW of Tuatapere, NZ)
4. July 16th 2009, 1.50 am, 5.9 Richter Magnitude, 45.40 S 166.50 E, 5 km focal depth. (120 km NW of Tuatapere, NZ)

As these were events some distance from the BICEP site, the accelerations recorded were very small. To provide an indication of the level of acceleration, the largest signal was recorded from the 7.8 magnitude event, which had a peak acceleration of approximately 0.001 m/s^2. These accelerations are small, but this highlights the sensitivity of the equipment and its ability to capture small levels of excitation. This will be important for the detection of small magnitude local events.

Acceleration characteristics for the October 19th 2008 Rotorua event recorded by the Waitemata and Base sondes are presented in Figure 10 for the vertical and one horizontal component. All data has been presented with the same scale to provide a clear comparison of the characteristics. This data clearly illustrates the amplification of the seismic signal from the Base to the Waitemata sonde in both the vertical and horizontal directions. Although not shown here, the other recorded events also displayed these characteristics.

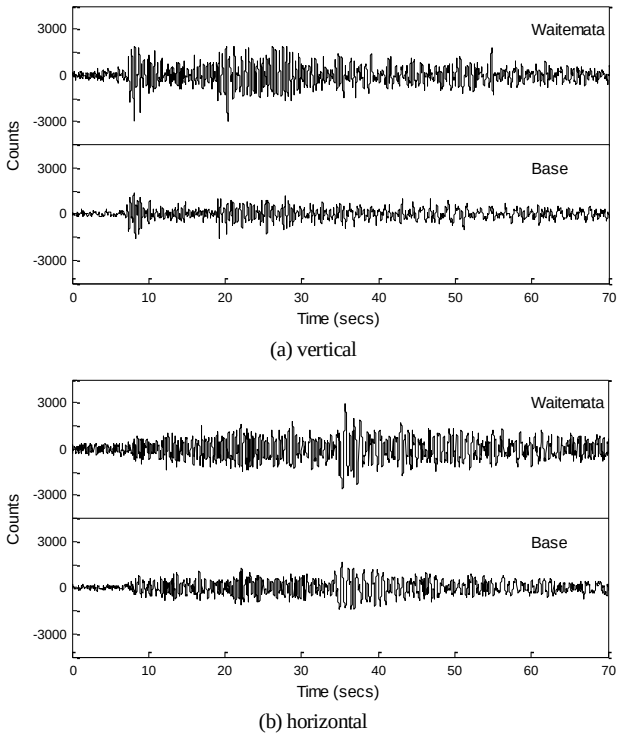

Figure 10 Comparison of traces from Waitemata and Base sonde for the Oct 19th 2008 Rotorua event

6.1 Signal to noise ratio

Using data from the seismic events, it was evident that the peak signal-to-noise amplitude ratio increased when the depth of the seismometer increased. The signal-to-noise ratio ranged from 72 to 2.3 for the Waitemata sonde, and from 140 to 2.9 for the Base sonde. To provide an indication of the effect of depth on response, the signal-to-noise ratio of the Base sonde (SNR_b) was divided by the signal-to-noise ratio of the Waitemata sonde (SNR_w). This gives an indication of the improvement in the signal-to-noise ratio for each earthquake record due to positioning of the sonde at a larger depth. This information is summarized in Table 1, showing that the Base sonde had a signal-to-noise ratio 24-71% higher than Waitemata sonde for the vertical direction, and 40-78% higher in the horizontal direction. Clearly, the placement of the sonde at depth helps to improve the clarity of signals, and reduce the threshold of events that can be detected. Even though the amplitude of the Base sonde seismic signal was smaller than the Waitemata sonde, the signal to noise ratio was larger at the deeper position.

Table 1 Signal to noise ratio characteristics of range of events

	Mag	Distance (km)	SNR_b/SNR_w Vertical	Horizontal
Record 1	5.6	182	1.39	1.43
Record 2	4.3	276	1.24	1.63
Record 3	7.8	1198	1.71	1.40
Record 4	5.9	1171	1.27	1.78

6.2 Amplification characteristics

Using the recordings from these four earthquakes, the amplification of the accelerations from the Base sonde to the Waitemata sonde were defined using the accelerations at these positions, and are presented in Figures 11 and 12 for the horizontal and vertical directions, respectively. Similar amplification characteristics were shown by all the earthquake records in both the vertical and the horizontal directions. This was most likely a result of the small acceleration levels preventing any significant non-linearity of the soil from developing.

Horizontal acceleration amplification showed peaks at approximately 12 and 21 Hz, with the overall trend shown for amplification to increase with frequency. Accelerations were amplified across the entire range shown in the figure. On the other hand, vertical amplifications increased to a peak between 2 and 5 Hz, before reducing down to a value close to 1 at 10 Hz. Beyond this point there was a gradual increase in amplification with frequency.

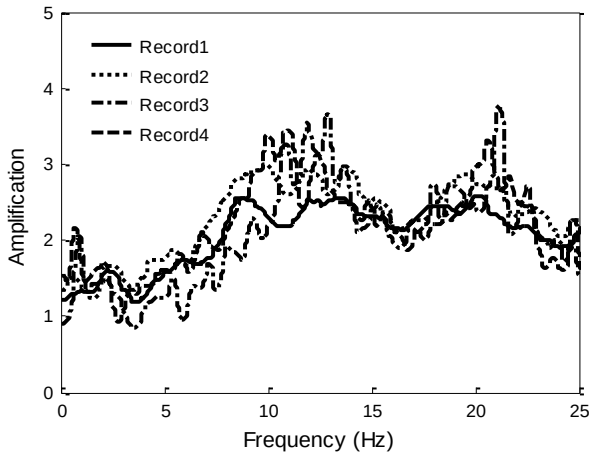

Figure 11 Amplification factor between Base and Waitemata sonde horizontal acceleration for range of distant seismic events

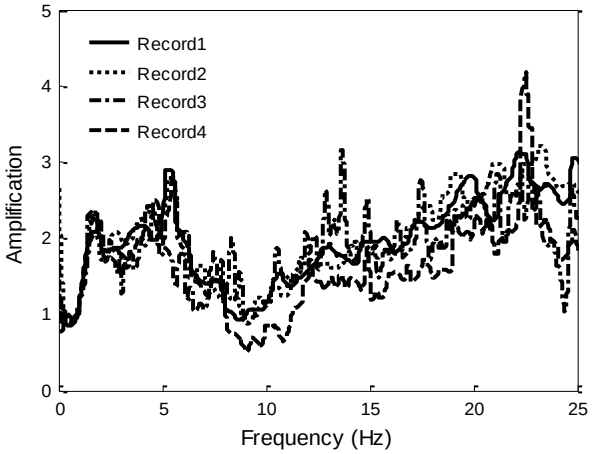

Figure 12 Amplification factor between Base and Waitemata sonde vertical acceleration for range of distant seismic events

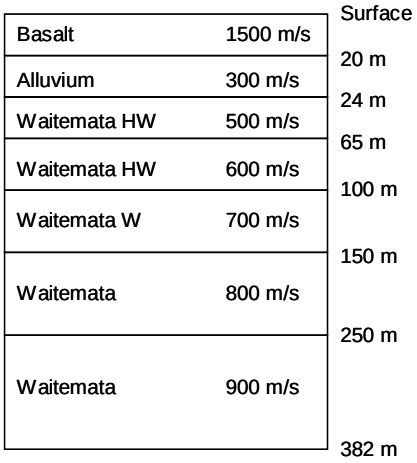

Figure 13 Simplified site soil profile

A simplified representation of the site profile indicated in Figure 13 was used to provide a comparison with the horizontal acceleration experimental results. The depths of the interfaces between each different layer of material are shown on the right, along with the shear wave velocities used for each layer. The soil profile shows 20 m of basalt with a shear wave velocity of 1500 m/s over 4 m of the soft alluvial layer with a shear wave velocity of 300 m/s. To represent the variation of conditions within the Waitemata materials due to weathering, the shear wave velocity was increased from 500 m/s at the top of the layer to 900 m/s at the base. This profile was developed using data from borehole logs and other material testing carried out at the Eden Park site. Due to the small acceleration levels, an elastic site analysis was carried out using DeepSoil (Hashash et al. 2008). It was also assumed that the damping in the soil layers was minimal due to the small accelerations.

Using this profile and the acceleration from the Base sonde as input, the amplification through the soil profile was calculated at the position of the Waitemata sonde (ModelBW) and at the ground surface (ModelBS). These are compared with the mean recorded amplification (ExpBW) in

Figure 14. Although not well matched, both recorded and computed results display similar overall characteristics at the position of the Waitemata sonde. There is a small peak at low frequencies before a reduction in the amplification around 3-4 Hz. This is followed by a gradual increase in the amplification with frequency. In contrast, the computed amplification between the Base sonde and the ground surface indicates a rapid reduction in amplification with increasing frequency. The peak amplification for this model at approximately 1Hz is larger than that which developed between the Base and Waitemata sonde at the same frequency.

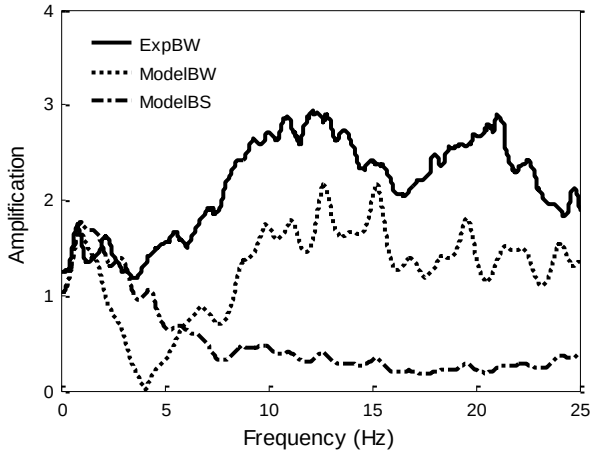

Figure 14 Comparison of experimental and analytical amplification factors for horizontal acceleration

3. CONCLUSIONS

This paper has provided an overview of the characteristics of the Borehole Instrument Centre for Eden Park (BICEP) from the construction process to the details of preliminary data recording. Preliminary recordings presented the background noise conditions characteristics in the area and demonstrated the significant reduction in noise that can be achieved by placing seismometers at depth. Even the placement of the seismometers at a shallow depth of 26 m resulted in a large reduction in background noise.

Comparison of the signal to noise ratio during seismic events indicated that the deeper the recording, the better the signal to noise ratio, even with the amplification of the seismic signal up the strata. These amplifications were consistent across all the earthquake records analysed, with the small accelerations preventing soil non-linearity and reducing the damping in the strata. Amplification of the signals were identified over a large frequency range for both vertical and horizontal accelerations.

This paper has presented preliminary data from the BICEP site, which will continue to record and provide information on Auckland's seismicity, on the characteristics of the strata in the Auckland area, and the effect of crowd-induced stadium motion on the underlying material.

Acknowledgements:

The following parties are recognized by the Institute of Earth Science and Engineering for their assistance with this project: Boart Longyear, Connell Wagner, Counties Readymix, Eden Park Redevelopment Board, Eden Park Trust Board, Earthquake Commission, Fletcher Construction, Golden Bay Cement, HOK Sports Architecture, Humes, and RCP.

References:

Homer, L., Moore, P., and Kermode, L. (2000), "Lava and Strata: A guide to the volcanoes and rock formations of Auckland," Landscape Publications, Wellington, NZ.

Reflex. (2008), "Reflex – Products," Retrieved January 10 2009, from http://www.reflex.se/products.php?ID=1

Refraction Technology, Inc. (2008), "About REF TEK," Retrieved January 10 2009, from http://www.reftek.com/model130-0.html

Geospace, (2009), "Geospace, LP," Retrieved January 10 2009, from http://www.geospacelp.com/

Hashash, Y.M.A., Groholski, D.R., Philips, C.A., and Park D. (2008), "DEEPSOIL v3.5beta, User manual and tutorial," University of Illinois, Urbana-Champaign, USA.

JOINT CONFERENCE PROCEEDINGS
7th International Conference on Urban Earthquake Engineering (7CUEE) &
5th International Conference on Earthquake Engineering (5ICEE)
March 3-5, 2010, Tokyo Institute of Technology, Tokyo, Japan

THREE-DIMENSIONAL SITE RESPONSE AT KiK-NET DOWNHOLE ARRAYS

Eric M. Thompson[1,2], Yasuo Tanaka[2], Laurie G. Baise[1], and Robert E. Kayen[3]

1) Civil and Environmental Engineering Department, Tufts University, USA
2) Research Center for Urban Safety & Security, Kobe University, Japan
3) U. S. Geological Survey, USA
eric.thompson@tufts.edu, ytgeotec@tiger.kobe-u.ac.jp, laurie.baise@tufts.edu, rkayen@usgs.gov

Abstract: Ground motions at two Kiban-Kyoshin Network (KiK-net) strong motion downhole array sites in Hokkaido, Japan (TKCH08 in Taiki and TKCH05 in Honbetsu) illustrate the importance of three-dimensional (3D) site effects. These sites recorded the M8.0 2003 Tokachi-Oki earthquake, with recorded accelerations above 0.4 g at both sites as well as numerous ground motions from smaller events. Weak ground motions indicate that site TKCH08 is well modeled with the assumption of plane SH waves traveling through a 1D medium (SH1D), while TKCH05 is characteristic of a poor fit to the SH1D theoretical response. We hypothesized that the misfit at TKCH05 results from the heterogeneity of the subsurface. To test this hypothesis, we measured four S-wave velocity profiles in the vicinity (< 300 m) of each site with the spectral analysis of surface waves (SASW) method.

This KiK-net site pair is ideal for assessing the relative importance of 3D site effects and nonlinear site effects. The linear ground motions at TKCH05 isolate the 3D site effects, as we hypothesized from the linear ground motions and confirmed with our subsequent SASW surveys. The Tokachi-Oki time history at TKCH08 isolates the effects of nonlinearity from spatial heterogeneity because the 3D effects are negligible. The Tokachi-Oki time history at TKCH05 includes both nonlinear and 3D site effects. Comparisons of the accuracy of the SH1D model predictions of these surface time histories from the downhole time histories indicates that the 3D site effects are at least as important as nonlinear effects in this case. The errors associated with the assumption of a 1D medium and 1D wave propagation will be carried into a nonlinear analysis that relies on these same assumptions. Thus, the presence of 3D effects should be ruled out prior to a 1D nonlinear analysis. The SH1D residuals show that 3D effects can be mistaken for nonlinear effects.

1. INTRODUCTION

Site response is a relative quantity, and thus requires a pair of ground motions, one of which contains the effects of the near-surface soils and one that does not. The record without the effects of the soil is termed the "input" time series and the receiver is either located at some depth below the free surface (i.e., a "downhole" receiver), or on outcropping bedrock. The "output" motion includes the effects of soil, so it is either above a downhole input motion, or seated on soil near the outcrop motion. Thus, site response is often represented as an input/output transfer function, and we refer to estimates of the site response transfer function derived from recordings of ground motions as the empirical transfer function (ETF), which can be compared to theoretical predictions of the transfer function based on in situ estimates of the seismic properties of the soil. The transfer function (empirical or theoretical) shows how the soil amplifies and attenuates seismic waves as a function of frequency. Thus, it is convenient to visualize the transfer function in the frequency domain.

In the analysis of 13 Kiban-Kyoshin Network (KiK-net) strong motion down-hole arrays throughout Japan, Thompson et al. (2009) showed that the largest discrepancies between the ETF and the one-dimensional (1D) plane SH wave solution (SH1D) occurred at sites where the *downgoing-wave effect* is diminished and in some cases nearly absent. The downgoing-wave effect is the interference between the upgoing wave and the downgoing wave at the downhole receiver. It is visible in the spectra of the downhole recording as valleys or "spectral holes." These spectral holes in the downhole receiver are seen as spectral peaks in the transfer function because the downhole response is in the denominator.

Thompson et al. (2009) hypothesized that the idealized downgoing-wave effect is removed where the subsurface geologic materials are particularly heterogeneous. They also demonstrated that representing the medium as a three-dimensional (3D) spatially correlated random field can substantially improve the fit to the ETF at sites where the downgoing-wave effect is diminished. The best fit was achieved with a random field characterized by an exponential covariance model with a range parameter of 100 m and a coefficient of variation (ratio of the standard deviation to the mean) $c_v = 0.25$. The parameters of the covariance model control the frequency-dependent scattering that results from the random field, which diminishes the interference created by the downgoing-wave

effect.

This paper seeks to expand on the analysis of Thompson et al. (2009), where the available field observations were not sufficient to confirm the 3D variations and all ground motions were within the linear range. This meant that (1) the hypothesis that the large misfit between the ETF and SH1D results from unaccounted for 3D heterogeneity could not be confirmed by in situ observations; (2) the random field could only be modeled as a non-conditioned simulation (i.e., the spatial variability was not constrained by observations); and (3) the relative contribution of 3D heterogeneity and soil nonlinearity could not be evaluated.

According to Thompson et al. (2009), 3D heterogeneity described by correlation structure with a range parameter of 100 m was required to improve the accuracy of the seismic simulations. Variability at length scales as large as 100 m can be modeled deterministically rather than stochastically with a conditional simulation of the random field (e.g., Emery and Lantuéjoul 2006). This requires multiple velocity profiles in the vicinity of the strong motion downhole array.

The two sites that we study in this paper were selected by first looking at the linear ETF at locations that recorded large accelerations from the M8.0 2003 Tokachi-Oki earthquake. Based on the linear ETFs, we selected one site that is accurately modeled by the SH1D site response transfer function and one site that is not. Then we measured four S-wave velocity profiles in the vicinity (< 300 m) of each site to test the hypothesis that the misfit of the ETF to SH1D is due to 3D heterogeneity. Ground motions from the 2003 Tokachi-Oki earthquake then allow us to evaluate the relative effect of 3D heterogeneity and nonlinear soil behavior.

Table 1 Earthquakes used to compute the Empirical Transfer function.

ID	Date	Time	M_w	Lat	Lon	Depth(km)
1	2000/10/07	08:19:00	4.6	42.3000	143.0000	60
2	2000/11/15	23:19:00	4.5	42.7400	144.5500	57
3	2001/04/23	09:04:00	4.2	42.4720	143.4170	55
4	2001/07/05	22:12:00	4.9	42.9450	145.2400	61
5	2002/07/28	20:31:00	4.8	42.3180	143.0700	51
6	2002/08/29	18:04:00	4.6	41.9270	142.3230	67
7	2002/10/29	08:26:00	4.2	42.3230	142.9970	54
8	2003/01/07	03:27:00	4.6	42.3450	143.0570	52
9	2003/01/15	18:02:00	4.5	41.9680	142.5580	62
10	2003/02/03	04:25:00	4.3	42.0850	142.5630	67
11	2003/02/24	02:00:00	4.6	41.9350	142.4430	65
12	2003/04/14	12:46:00	4.3	42.3620	143.1220	50
13	2003/05/01	18:11:00	4.0	41.9120	143.0770	40
14	2003/06/18	13:35:00	4.4	42.3420	143.0730	51
15	2003/09/26	04:50:00	8.0	41.7780	144.0780	42
16	2003/09/26	05:25:00	4.5	42.4820	143.8120	59
17	2003/09/26	08:11:00	4.8	42.8080	145.0000	46
18	2003/09/28	09:23:00	5.0	42.2650	143.3230	43
19	2003/09/29	19:35:00	4.2	42.4070	144.0500	61

Table 2 Event IDs that correspond to the events used for the different stations.

Station	1	2	3	4	5	6	7	8	9	10	11
TKCH08	15	14	13	12	11	10	9	8	5	7	6
TKCH05	15	8	5	4	3	2	1	19	18	17	16

2. DATA

2.1 Strong Motion Downhole Arrays

Data from the KiK-net strong-motion network in Japan provides numerous surface-downhole station pairs that have recorded earthquakes over a wide range of magnitudes and peak ground accelerations (Aoi et al. 2001). KiK-net also provides the seismic velocity structure for each station which is derived from surface-source downhole-receiver logging.

The downhole travel-time measurements have been processed to produce a simplified stepped profile prior to being distributed via the KiK-net website. Thus, we cannot test the effect of the limited resolution of these profiles in this paper. But Boore and Thompson (2007) showed that approximating detailed suspension log measurements with 10 m thick homogeneous layers has negligible effects on the predicted amplification factors below approximately 5 Hz. Thus, large residuals between observed and predicted amplifications below 5 Hz cannot be attributed to a lack of precision of the soil profile.

An additional source of bias in the seismic velocity structure is the uncertainty of the individual travel-time measurements. We were given the opportunity to inspect the time-series data from which the downhole travel-time measurements are derived. We found no reason to expect substantial bias to result from the processing of the travel-time measurements for the KiK-net profiles that we use in this paper.

Table 1 summarizes the 19 earthquakes included in our analysis. We include the 2003 Tokachi-Oki earthquake (event ID 15) and 10 weak motion events at each site. Table 2 describes which event is used for each station, and the order corresponds to the event number used in subsequent figures (i.e., event number 1 is the Tokachi-Oki earthquake for both stations; Event number 2 is earthquake 14 from Table 1 for TKCH08, while event number 2 is earthquake 8 from Table 1 for TKCH05).

3. METHODS

3.1 Theoretical Transfer Function

We evaluate the accuracy of site response models by comparing the theoretical amplifications to the ETF. The most common assumptions for computing a theoretical transfer function include: (1) The medium is assumed to consist of laterally-constant layers overlying a non-attenuating halfspace; (2) Wavefronts are assumed to be planar; (3) Only the horizontally-polarized component of the S wave (the SH wave) is modeled. We refer to these collective assumptions as the SH1D site response model. We compute the SH1D site response transfer function with the Thomson-Haskell matrix method (Haskell 1953; Thomson 1950) as implemented by the program Nrattle. Nrattle is

written by C. Mueller with modification by R. Herrmann and included in the Boore (2005) ground motion simulation program SMSIM.

The input parameters of Nrattle include S-wave velocity (V_s), density (ρ), and the intrinsic attenuation of S waves ${}_i Q_s^{-1}$. Since we do not have in situ estimates of ρ, we use the procedure recommended by Boore (2008a) for estimating ρ from V_p, where V_p is reported by the surface-source downhole-receiver survey. We set V_s and ρ of the non-attenuating halfspace to the values of the deepest measured layer to avoid spurious amplifications from an arbitrary impedance contrast at the bottom of the borehole.

3.2 Empirical Transfer Function

We assume that the spectral ratio amplitude a at frequency f, defined as amplitude of the surface spectra divided by the downhole spectra, follow a lognormal distribution. We define $\mu_{\ln(a)}$ as the mean of $\ln[a(f)]$. Thus, the median of $a(f)$ is given by

$$\hat{a}(f) = \exp[\mu_{\ln(a)}]. \qquad (1)$$

We compute the spectra of the surface and downhole recordings from a 20 sec duration time window that begins 1 sec before the onset of the S wave arrival to allow for a 5% cosine taper. We compute the surface and downhole spectra from the two-dimensional (2D) complex time-series of the two orthogonal horizontal time histories following Steidl et al. (1996). We then smooth the spectra with a logarithmic triangular weighting function where the width of the weighting function is one fifth of a decade using the Fortran subroutines in Boore (2008b). At each site we estimate the linear ETF from 10 weak motion earthquakes. The weak events are selected so that the recording has a large signal-to-noise ratio and an easily identifiable S wave arrival.

3.3 Response Spectra

Response spectra are a convenient method for describing a ground motion in a form that is more meaningful from an engineering perspective. The response spectra S_a at oscillator period T is the maximum acceleration of a single-degree-of-freedom system with damping ratio ξ and natural period T (Kramer, 1996).

We compute an orientation-independent S_a termed GMRotI50 by Boore et al. (2006), which is easily computed with the Boore (2008b) Fortran programs. GMRotI50 is derived from the set of geometric means of the two horizontal components rotated to all possible orthogonal rotation angles (see Boore et al., 2006 for further details).

Following Kwok et al. (2008), we define the S_a residuals in terms of natural log units,

$$S_a^R(T) = \ln[S_a^o(T)] - \ln[S_a^p(T)], \qquad (2)$$

where $S_a^o(T)$ is the observed S_a and $S_a^p(T)$ is the predicted S_a. We compute $S_a^p(T)$ from the output time series that results from applying the SH1D site response transfer function to the downhole time series.

3.4 Velocity Characterization by SASW

The S-wave velocity (V_s) profile measurements that we have collected include multiple spectral analysis of surface waves (SASW; Nazarian and Stokoe, 1984) profiles at each site. SASW is a noninvasive method of measuring the V_s profile. The procedure measures the phase velocity of Rayleigh waves at a wide range of wavelengths, which is related to the V_s profile through a nonlinear and nonunique geophysical inversion. Thus, the most direct observations for the SASW test are the dispersion curves. The Rayleigh waves are generated by an electromechanical shaker that vertically loads the ground surface at discrete frequencies.

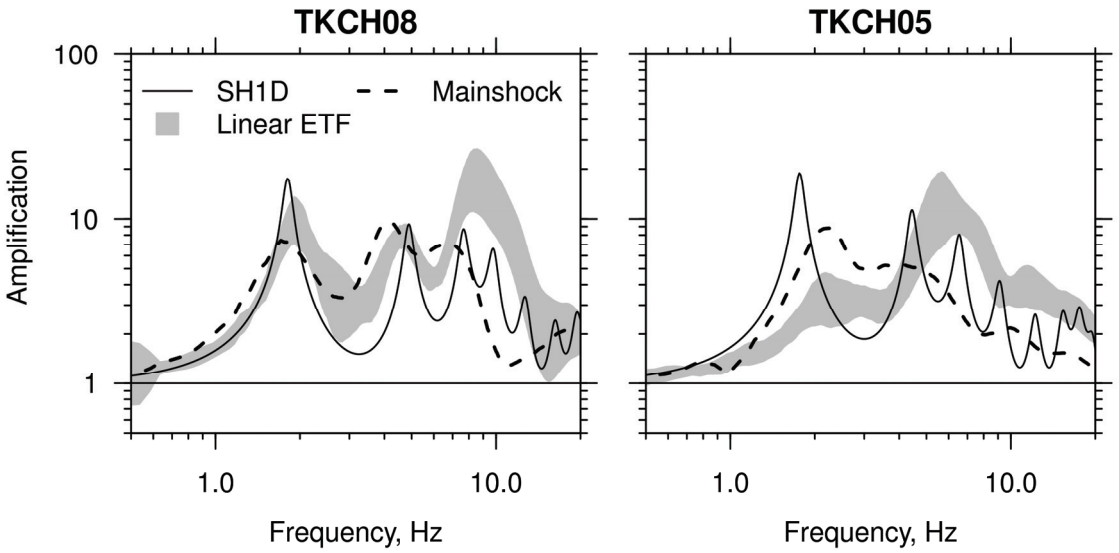

Figure 1 SH1D theoretical amplifications at KiK-net sites TKCH08 and TKCH05 compared to the 95% confidence interval of the linear ETF from 10 earthquakes, and the ETF from the 2003 Tokachi-Oki earthquake.

We employ the Lai and Rix (1998) Fortran subroutines to solve the nonlinear SASW inverse problem. This method uses the Hisada (1994) algorithm to compute the Rayleigh wave phase velocity from the 1D V_s profile (i.e., the forward problem), and the Constable et al. (1987) inverse algorithm to select the smoothest V_s profile that accurately reproduces the empirical dispersion curve.

We use the SASW method to characterize the V_s profiles because the costs of multiple PS suspension logs, which can achieve better resolution, are prohibitive. Note that blind prediction site characterization studies have shown that SASW characterizations are reliable and sufficiently accurate for site response studies (Brown et al., 2002; Boore and Asten, 2008).

The goal for each SASW survey was to measure the Rayleigh wave phase velocity at wavelengths that would characterize the V_s of the upper 40 to 50 m of the subsurface. Although the deeper V_s structure is important for site response analysis, we did not attempt to maximize the depth of exploration because of the inherent lateral averaging of the SASW procedure. Larger depths are sampled by longer wavelength Rayleigh waves, which sample a large volume of the subsurface. This attribute may be advantageous in many circumstances where a site-wide average estimate of the V_s is desirable. But the purpose of these data is to identify lateral variations in the V_s structure, so the lateral averaging of the SASW method obscures our ability to resolve these fluctuations.

4. RESULTS

4.1 Identification of 3D Site Effects

Figure 1 shows the linear ETF from weak motion records, the ETF from the M8.0 2003 Tokachi-Oki earthquake (with accelerations recorded above 0.4 g at both

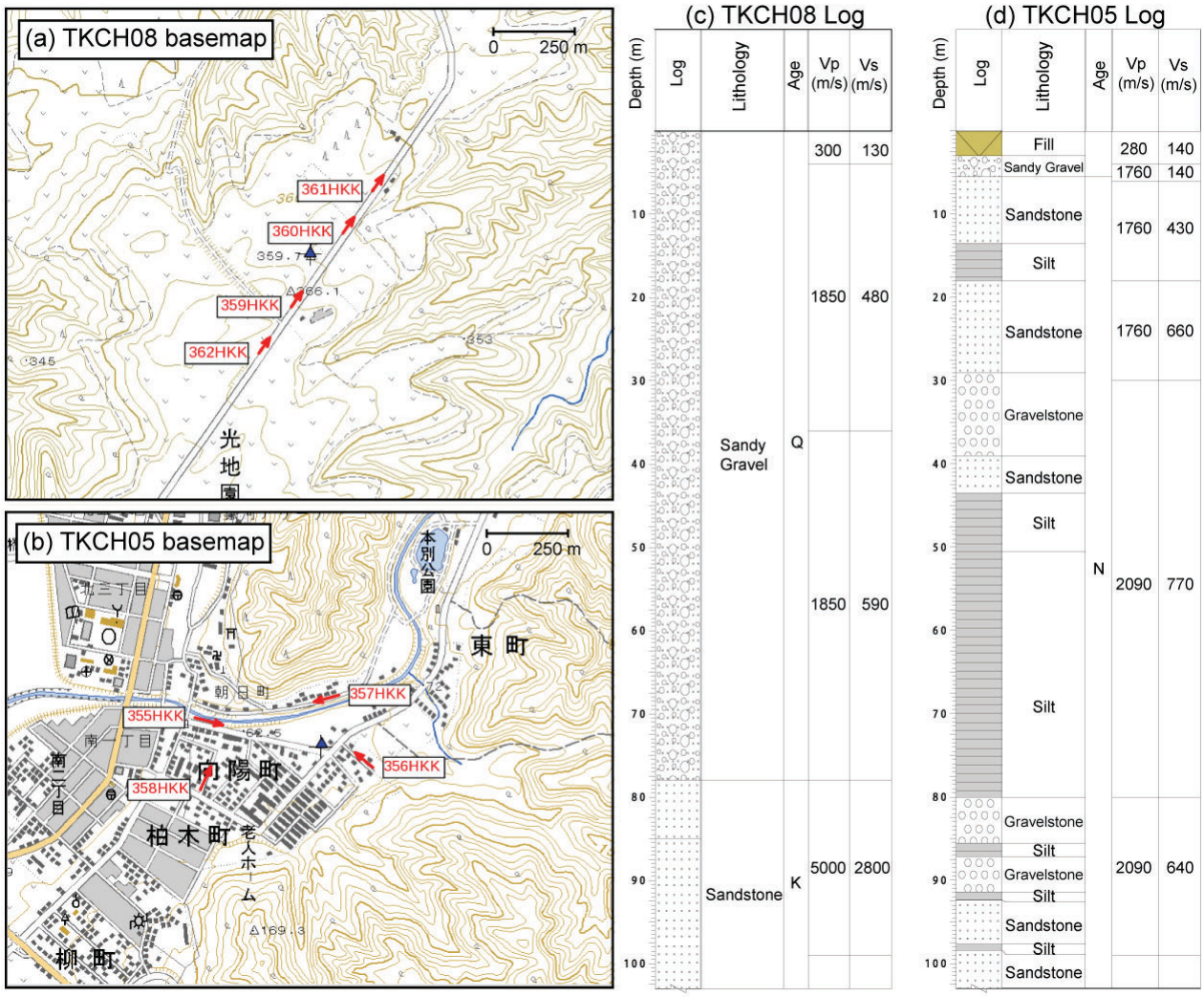

Figure 2 Vicinity maps of KiK-net stations (a) TKCH08 and (b) TKCH05; and boring logs at stations (c) TKCH08 and (d) TKCH05. The Vicinity maps show the location and orientation of the SASW surveys (red arrows) relative to the downhole arrays (blue triangles). The base of the red arrow identifies the location of the SASW seismic source, and the seismometer transect extends in the direction of the arrow. The length of the arrow indicates the distance to the furthest seismometer. The boring logs are modified from those available from the KiK-net website and include lithologic descriptions and the surface-source downhole-receiver velocity estimates.

sites), and SH1D model transfer function. The input velocities for the SH1D model are derived from downhole travel-time measurements taken at the time of the borehole installation. The similarity of SH1D with the ETF at site TKCH08 (Figure 1a) indicates that the SH1D assumptions are reasonable in this case, while the ETF at TKCH05 exhibits poor fit to the SH1D model indicating that one or more assumption is substantially violated at this site. We hypothesized that the misfit at TKCH05 largely results from the assumption of a laterally constant medium where the subsurface exhibits large lateral variations.

We visited each site with the goal of obtaining four SASW velocity profiles to supplement the existing surface-source downhole-receiver velocity profiles. The vicinity maps and boring logs (including the lithologic descriptions and velocity estimates) for both stations are shown in Figure 2. Note that TKCH05 is in the town of Honbetsu while TKCH08 is located on a relatively isolated ridge. Thus, more potential testing locations are available at TKCH05, while access was limited to a single road at TKCH08. Note also that the ambient noise was greater at TKCH05. The spacing between the SASW surveys varied from 159 to 616 m at THCH08, and from 227 to 578 m at TKCH05. The red arrows indicate the layout of the SASW surveys in Figure 2. The base of the arrow identifies the location of the electromechanical seismic source, and the length of the arrow indicates the distance that the receiver array extends away from the source. The KiK-net downhole array is located at the blue triangle.

The descriptions of the lithology provided by the KiK-net website (Figure 2 c and d) provide further evidence that TKCH05 may be more heterogeneous than TKCH08. TKCH08 consists of 78 m of Quaternary sandy gravel over Cretaceous sandstone. In contrast, the top 80 m is mostly sediment and consists of eight layers of Neogene deposits including fill, sandy gravel, sandstone, silt, and gravelstone. The stratigraphy below 80 m is mostly gravelstone and standstone with thin interbeds of silt.

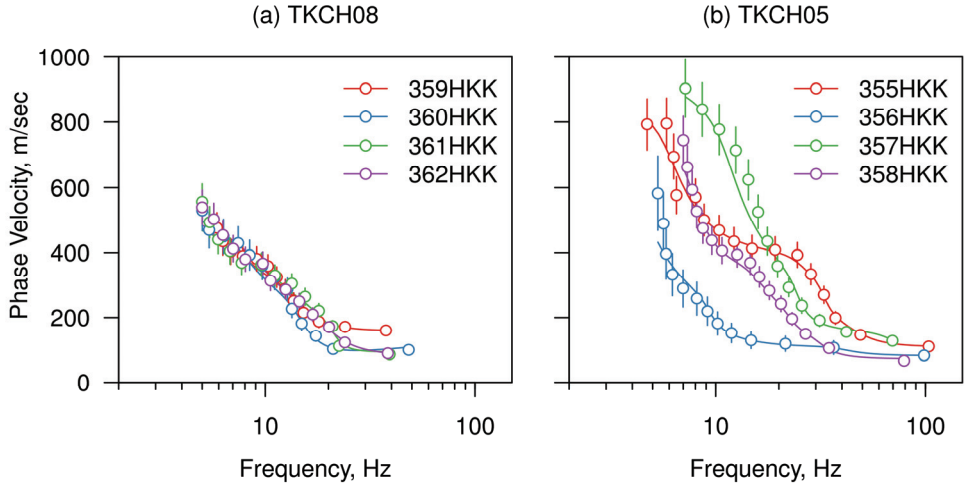

Figure 3 Empirical (points) and theoretical (lines) dispersion curves near KiK-net sites (a) TKCH08 and (b) TKCH05.

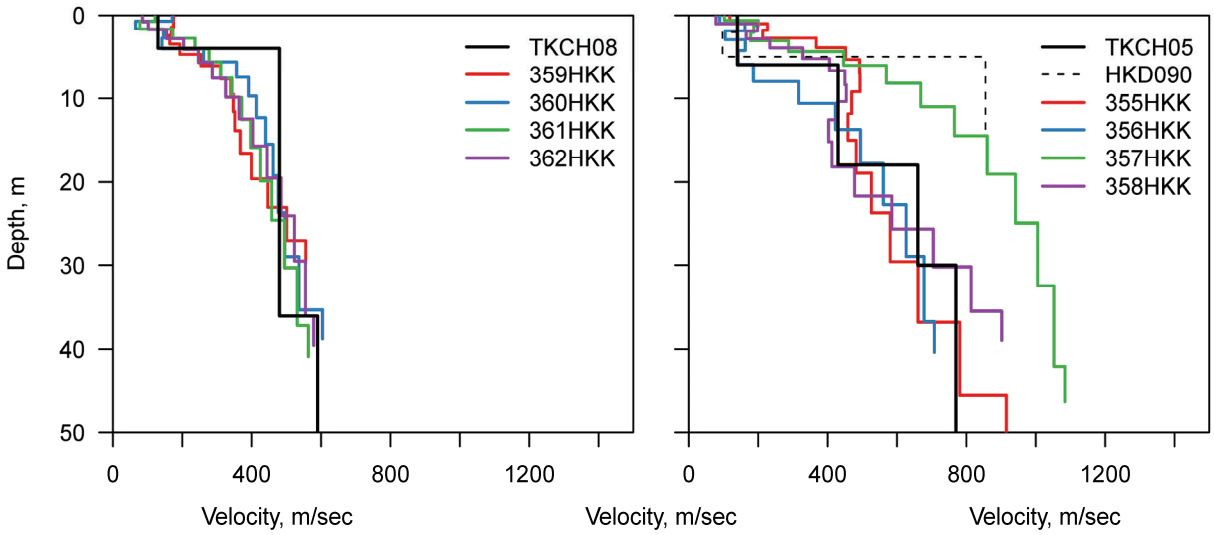

Figure 4 SASW and invasive V_s profiles near KiK-net sites (a) TKCH08 and and (b) TKCH05.

4.2 Quantifying 3D Spatial Variability

The empirical and theoretical dispersion curves for each SASW survey at sites TKCH08 and TKCH05 are summarized in Figure 3. The theoretical dispersion curves in Figure 3 correspond to the V_s profiles in Figure 4. Figure 4 also shows the KiK-net downhole profiles and the K-net profile at HKD090 because it is installed adjacent to TKCH05. The increased lateral variability of the in situ V_s profiles in the vicinity of the TKCH05 relative to TKCH08 supports our hypothesis that the misfit observed at TKCH05 in Figure 1 is caused by 3D spatial variability of the soil properties.

4.3 Example Time Histories

Plots of the predicted and observed time histories are the most direct and intuitive method for assessing the performance of a ground motion model. However, such comparisons can be misleading because there is generally only space for a small subset of the ground motions in a single article. Nevertheless, Figure 5 illustrates the goodness-of-fit of the SH1D model for the East-West (EW) components at sites TKCH08 and TKCH05 for the 2003 Tokachi-Oki earthquake (Figure 5a and b) and a weak motion (Figure 5c and d). For each plot, we show the input downhole motion below the predicted and observed surficial time series.

As expected from Figure 1, we see that the weak ground motion is accurately predicted at the surface at TKCH08 by the SH1D model (Figure 5c) while the weak motion is substantially overpredicted at the surface at TKCH05 (Figure 5d). This results because the SH1D model predicts a strong downgoing-wave effect that is not present in the observed ground motions.

The SH1D model predicts the strong motion from the 2003 Tokachi-Oki earthquake surprisingly well at site TKCH08 (Figure 5a) when compared to the goodness-of-fit observed for the linear event at TKCH05 (Figure 5d). Still, the SH1D model overpredicts the overall amplitude of the ground motion, which is likely due to the fact that the SH1D model does not account for nonlinearity. Because the weak motion is relatively well modeled at TKCH08 (Figure 5c), the misfit in Figure 5a largely represents unaccounted-for nonlinear site response effects. In contrast, the misfit observed at TKCH05 for the weak motion (Figure 5d) represents only the unaccounted-for 3D wave propagation effects because the ground motion is too small to exhibit significant nonlinearity. And the misfit at TKCH05 for the 2003 Tokachi-Oki earthquake includes both accounted-for nonlinear and 3D wave propagation effects.

4.4 Response Spectra

It is important to include both components and all of the ground motions when comparing predictions to observations because the goodness-of-fit varies substantially from one recording to the next and between the different components of the same recording. Thus, the data in Figure 5 are intended to be schematic for the purpose of demonstrating our procedure. Figures 6 and 7 summarize performance of the SH1D model in terms of S_a for sites TKCH08 and TKCH05 respectively. Subfigures (a) through (k) show the observed and predicted S_a at the surface recording for the

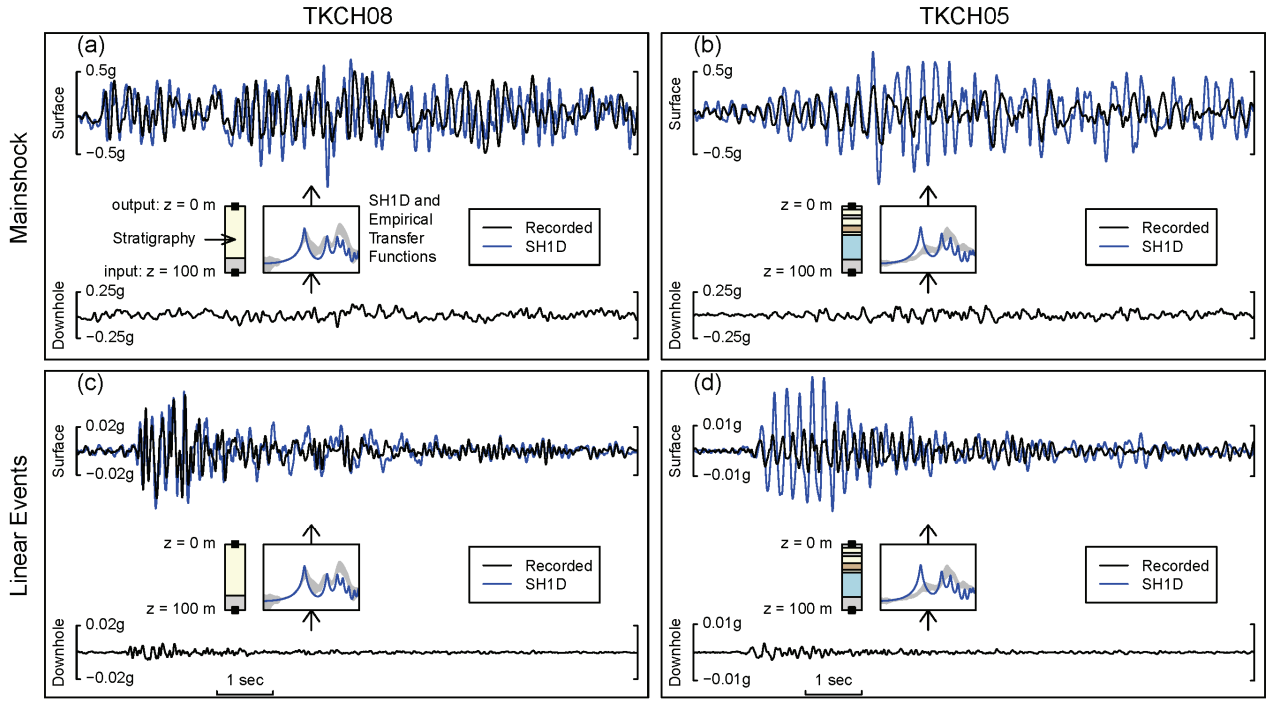

Figure 5 Surface and downhole EW components of the ground motions at sites TKCH08 and TKCH05 for the M8.0 2003 Tokachi-Oki earthquake (a and b) and linear events (c and d). In each diagram, the dowhole record is displayed below the surface record. The surface record shows both the observed record as well as the ground motion that is predicted by the SH1D transfer function.

11 earthquakes at each site as summarized by Tables 1 and 2. Event number 1 in Figures 6 and 7 is the 2003 Tokachi-Oki earthquake. The predicted S_a is computed from the time history that is predicted from the downhole recording by applying the SH1D transfer function based on the KiK-net downhole seismic logging. Subfigure (l) in Figures 6 and 7 plots the S_a residuals S_a^R as defined in equation 2. We plot the 95% confidence interval of the 10 linear events keeping the 2003 Tokachi-Oki earthquake separate.

While it is informative to see the individual response spectra, the comparison of the linear S_a^R 95% confidence interval and the 2003 Tokachi-Oki S_a^R in subfigure (l) of Figures 6 and 7 is most informative. The residuals at TKCH08 show us that there is substantial scatter in the goodness-of-fit of the predicted and observed S_a, but the linear S_a^R 95% confidence interval shows that the bias is relatively small when compared to the bias observed in the linear S_a^R 95% confidence interval at TKCH05.

At TKCH05, there is a clear tendency for the SH1D model to overpredict the S_a at 0.2 sec and above (i.e., 5 Hz and below) with the largest (negative) S_a^R at about 0.5 sec (2 Hz). Note that this closely corresponds to the largest discrepancy between the SH1D transfer function and the linear ETF 95% confidence interval at TKCH05 in Figure 1, which is caused because the observed ground motions do not exhibit the strong downgoing-wave effect that is predicted by the SH1D model. Thus, the largest response spectra residuals for linear events are caused because of the missing downgoing-wave effect at TKCH05.

The plots of S_a^R at both TKCH08 and TKCH05

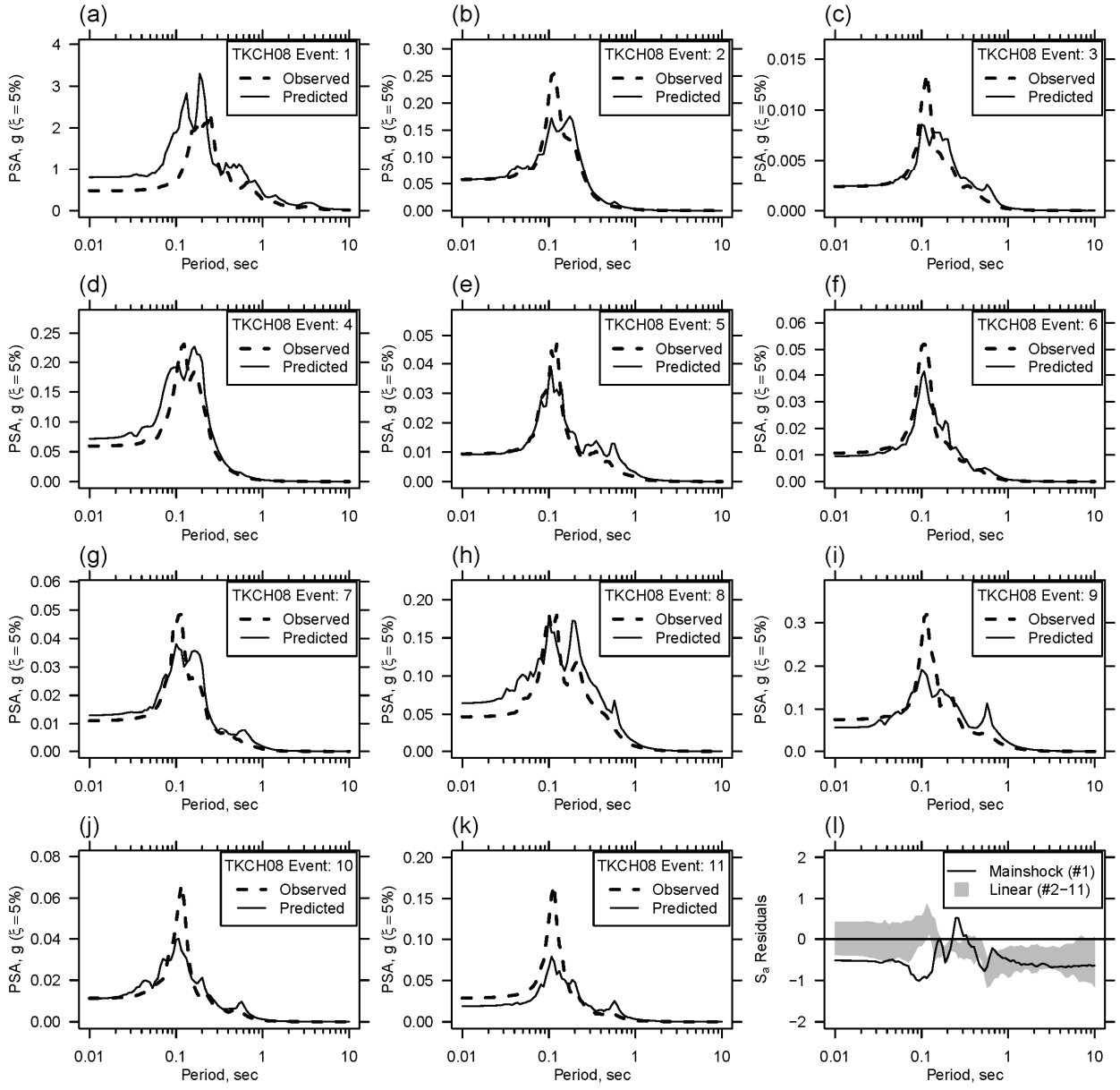

Figure 6 Predicted and observed response spectra at site TKCH08, in including (a) the Tokachi-Oki earthquake, (b)-(k) linear/weak ground motions, and (l) the response spectra residuals.

show that the 2003 Tokachi-Oki earthquake record deviates from the linear S_a^R 95% confidence interval by overpredicting the amplification near 0.1 sec (10 Hz) and underpredicting the amplification at 0.25 to 0.4 sec (2.5 to 4 Hz). Thus, there is increased attenuation due to nonlinear soil response at high frequencies that is not accounted for by the linear SH1D assumption. However, it is interesting to note that the deviation of the strong motion from the linear S_a^R is generally not larger than the amplitude of the linear S_a^R. At periods longer than 2 sec (<0.5 Hz) the strong motion response is within the range of observed linear S_a^R, indicating that nonlinear effects are most important at periods less than 2 sec.

5. CONCLUSIONS

The assumption of plane SH-wave propagation through a 1D medium is severely violated in site response studies at some sites because the subsurface is characterized by substantial 3D heterogeneity. The same assumptions are assumed in standard nonlinear site response analysis codes, including SHAKE (e.g., Schnabel et al., 1972). Thus, we suggest that prior to a 1D nonlinear analysis, the linear ground motions should be rigorously checked to confirm that the SH1D assumptions are valid. If they are violated for the linear ground motions, the same errors will be carried into the nonlinear analysis. These errors can be as large or larger than the errors created by the linear approximation of the nonlinear dynamic soil behavior. Further, the 3D effects

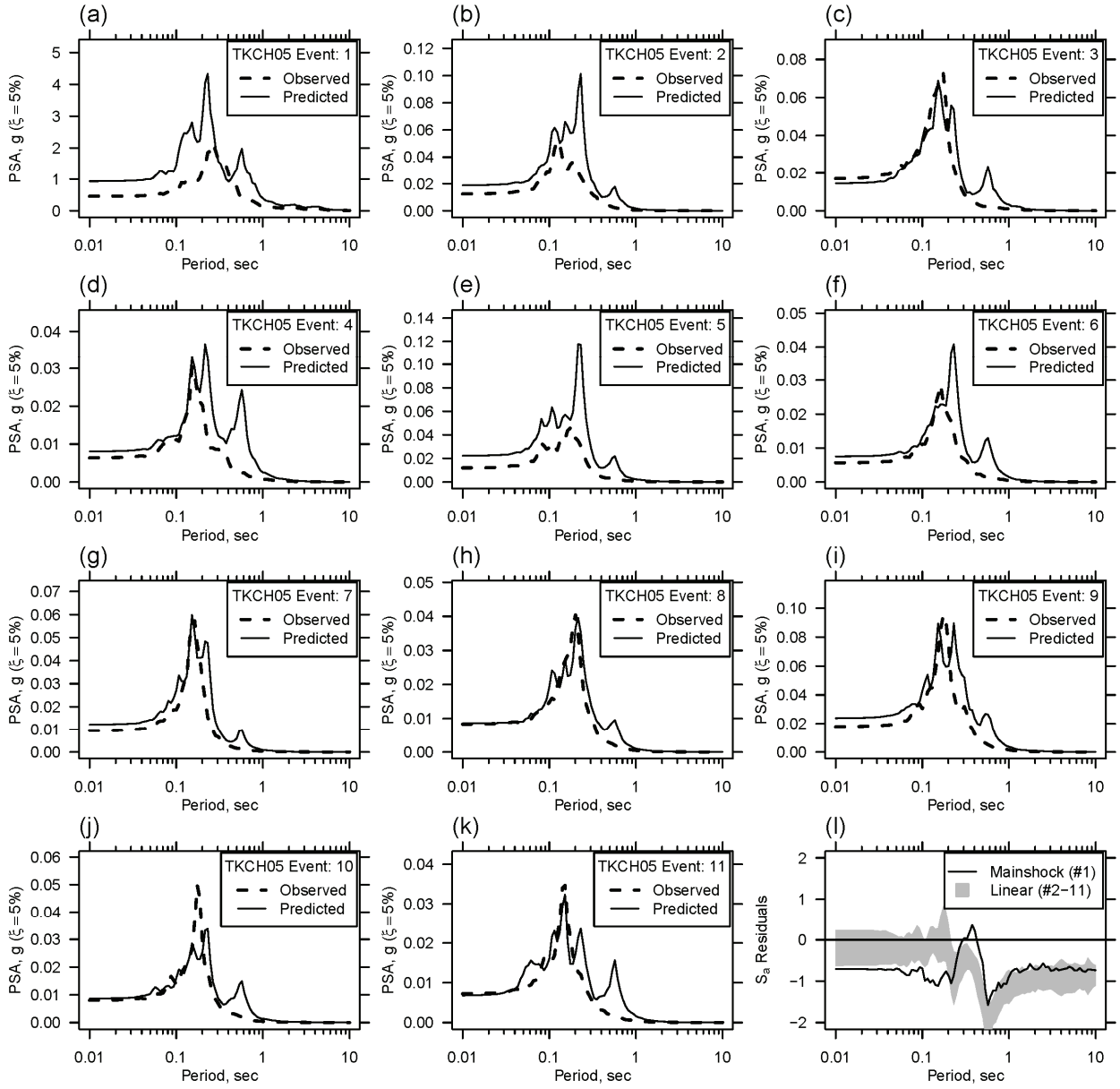

Figure 7 Predicted and observed response spectra at site TKCH08, in including (a) the Tokachi-Oki earthquake, (b)-(k) linear/weak ground motions, and (l) the response spectra residuals.

observed at TKCH08 could be masked by incorrectly adjusting the modulus reduction and damping curves in a 1D nonlinear analysis, thus confounding nonlinear and 3D effects.

Future work will include 3D wave propagation modeling of the ground motions at TKCH08 and TKCH05 where the medium will be represented by a conditionally simulated random field; the medium will be constrained by the SASW measurements and will exhibit a realistic spatial covariance structure for geologic materials. Once the linear events at TKCH05 can be modeled accurately by accounting for realistic 3D structure, then the next step will be to apply a 3D nonlinear constitutive formulation, which can be validated by the 2003 Tokachi-Oki records.

Acknowledgements:

The Research Center for Urban Safety and Security at Kobe University hosted the first author which made this collaboration possible and funded the data collection presented in this article. Hidetaka Koumoto helped prepare the basemaps in Figure 2. We thank Dr. Aoi and Prof. Kagawa for giving us the opportunity to inspect the detailed site investigation reports for each KiK-net site.

References:

Aoi, S., Obara, K., Hori, S., Kasahara, K., and Okada, Y. (2001). "New Japanese uphole-downhole strong-motion observation network: KiKNet," *Seismological Research Letters*, **72**(2)**,** 239.

Boore, D.M. (2005). "SMSIM - Fortran programs for simulating ground motions from earthquakes: version 2.3," A revision of U.S. Geological Survey Open-File-Report 96-80-A, 55 pp.

Boore, D.M. (2008a). "Some thoughts on relating density to velocity," http://quake.usgs.gov/~boore/daves_notes/ (last accessed 24 April 2008).

Boore, D. M. (2008b). "TSPP---A Collection of FORTRAN Programs for Processing and Manipulating Time Series," U.S. Geological Survey Open-File Report 2008-1111.

Boore, D.M., and Asten, M.W. (2008). "Comparisons of shear-wave slowness in the Santa Clara Valley, California, from blind interpretations of data from a comprehensive set of invasive and non-invasive methods using active- and passive-sources," *Bulletin of the Seismological Society of America*, **98**(4), 1983-2003.

Boore, D.M., and Thompson, E.M. (2007). "On using surface-source downhole-receiver logging to determine seismic slownesses." *Soil Dynamics and Earthquake Engineering*, **27**(11), 971-985.

Boore, D.M., Watson-Lamprety, J., and Abrahamson, N.A. (2006). "Orientation-Independent Measures of Ground Motion," *Bulletin of the Seismological Society of America*, **96**(4a), 1502-1511.

Brown, L.T., Boore, D.M., and Stokoe, K.H. II (2002). "Comparison of shear-wave slowness profiles at 10 strong-motion sites from noninvasive SASW measurements and measurements made in boreholes," *Bulletin of the Seismological Society of America*, **92**(8), 3116-3133.

Constable, S.C., Parker, R.L., and Constable, G.G. (1987). "Occam's Inversion: A Practical Algorithm for Generating Smooth Models from Electromagnetic Sounding Data," *Geophysics*, **52**, 289-300.

Emery, X., and C. Lantuéjoul (2006). "TBSIM: A computer program for conditional simulation of three-dimensional Gaussian random fields via the turning bands method," *Computers & Geosciences*. **32**, 1615-1628.

Haskell, N.A. (1953). "The dispersion of surface waves on multilayered media," *Bulletin of the Seismological Society of America*, **72**(1), 17-34.

Hisada, Y. (1994). "An Efficient Method for Computing Green's Functions for a Layered Half-Space with Sources and Receivers at Close Depths," *Bulletin of the Seismological Society of America*, **84**(5), 1456-1472.

Kramer, S.L. (1996). "Geotechnical Earthquake Engineering," Prentice Hall.

Kwok, O.L., Stewart, J.P., and Hashash, Y.M.A. (2008). "Nonlinear ground-response analysis of Turkey Flat shallow stiff-soil site to strong ground motion," *Bulletin of the Seismological Society of America*, **98**(1), 331-343.

Lai, C.G. and Rix, G.J. (1998). "Simultaneous Inversion of Rayleigh Phase Velocity and Attenuation for Near-Surface Site Characterization," *Report No. GIT-CEE/GEO-98-2*, School of Civil and Environmental Engineering, Georgia Institute of Technology, 258 pp.

Nazarian, S. and Stokoe, K.H. II (1984). "In situ shear wave velocities from Spectral Analysis of Surface Waves," in *Proceedings of the Eighth World Conference on Earthquake Engineering*, Prentice-Hall, Inc., Englewood Cliffs, New Jersey, Vol. III, 31–38.

Schnabel, P.B., Lysmer, J., and Seed, H.B. (1972) "SHAKE: A computer program for earthquake response analysis of horizontally layered sites," report *UCB/EERC-72/12*, Earthquake Engineering Research Center, University of California, Berkeley, 102 pp.

Steidl, J.H., Tumarkin, A.G., and Archuleta, R.J. (1996). "What is a reference site?" *Bulletin of the Seismological Society of America*, **86**(6), 1733-1748.

Thompson, E.M., Baise, L.G., Kayen, R.E., and Guzina, B.B. (2009), "Impediments to Predicting Site Response: Seismic Property Estimation and Modeling Simplification," *Bulletin of the Seismological Society of America*, **99**(5), 2927-2949.

Thomson, W.T. (1950). "Transmission of elastic waves through a stratified solid," *Journal of Applied Physics*, **21**, 89-93.

JOINT CONFERENCE PROCEEDINGS
7th International Conference on Urban Earthquake Engineering (7CUEE) &
5th International Conference on Earthquake Engineering (5ICEE)
March 3-5, 2010, Tokyo Institute of Technology, Tokyo, Japan

GROUND MOTION SELECTION AND SCALING FOR SITE RESPONSE ANALYSIS

Gökçe Tönük[1], and Atilla Ansal[2]

1) Dr., Dep. of Earthquake Eng., Kandilli Observatory and Earthquake Research Institute, Bogazici University, Istanbul, Turkey
2) Professor, Dep. of Earthquake Eng., Kandilli Observatory and Earthquake Research Institute, Bogazici University, Istanbul, Turkey
gokce.tonuk@boun.edu.tr, ansal@boun.edu.tr

Abstract: Ground motion records have different characteristics in time and frequency domains and thus using input motions selected randomly may introduce significant scatter in dynamic response. In this study, it is investigated to understand how ground motion selection and scaling with respect to different parameters affect the results of site response analysis allowing selection of a most suitable scaling parameter that minimizes the scatter of the response. Using 1D equivalent-linear model at selected soil profiles with pre-determined levels of earthquake hazard, the resulting response variability was studied under a series of ground motion records selected as compatible with the site specific earthquake hazard in terms of fault type, magnitude and distance and scaled with respect to different intensity measures. The variability introduced by scaling and the effectiveness of scaling parameter were evaluated including the selection of records from different distance – magnitude ranges. The results are given for the parametric study with eight different scaling parameters for three damage parameters (peak ground acceleration, peak ground velocity, maximum spectral acceleration) based on nine bins of magnitude and distance pairs for three soil profiles.

1. INTRODUCTION

The uncertainty in site response analysis can be considered as a result of the uncertainties related to stratification and material properties of the soil layers, definition of the bedrock depth, analysis method, and due to the variability introduced by the selected input acceleration time histories. This study describes the procedures used to select and scale time histories to be used as input for ground response analyses and discusses variability associated with performing ground response calculations at the selected sites concerning these procedures.

Studies carried out on the nonlinear response of structures under input ground motion records selected and scaled to different criteria such as peak ground acceleration, peak ground velocity, Arias intensity, effective peak velocity etc. have shown that for the same structural model there exists a significant response variability (Martinez-Rueda, 1998). The necessity for better assessment of the effects of the input motion characteristics to achieve more realistic evaluation of structural performance requires identification of more suitable ground motion intensity measures for nonlinear structural response analysis (Naeim et al., 2004). Similar response patterns are also observed for natural and man-made geotechnical structures and similar need also exists for evaluating site response analysis.

Nonlinear dynamic analysis of geotechnical structures can be highly sensitive to the selection of input ground motion. It is possible to select time series such that their seismological and geotechnical conditions are consistent with the design earthquake and whose acceleration response spectra match the design spectrum but whose nonlinear response are very different. Selection based on seismological principles may lead to large variability in the results. Ground Motion Selection and Modification (GMSM) Program maintained at the Pacific Earthquake Engineering Research Center (PEER) which has a mission to provide guidance and tools to the engineering community on appropriate GMSM methods for nonlinear dynamic analyses proposes two solutions to this problem: To perform a more sophisticated analysis that uses large number of ground motions and couples regression on the results of the nonlinear dynamic analysis with ground motion prediction equations that gives best estimate of structural response, and to select time series based on record properties that affect nonlinear response which leads to a decrease in variability and better estimates of response (Goulet, 2008).

Acceleration time histories recorded during same or different earthquakes on different soil conditions may be very different which introduces a significant uncertainty in engineering applications and unrealistic estimations of earthquake characteristics. Studies on microzonation with respect to peak spectral accelerations using two different sets of three real (compatible with the earthquake hazard and scaled with respect to the same peak accelerations) and one set of three simulated (compatible with the earthquake hazard spectra) acceleration time histories reveal that independent than the scenario selected, acceleration time histories used in site response analysis, in other words source characteristics are very important (Ansal and Tönük, 2007b).

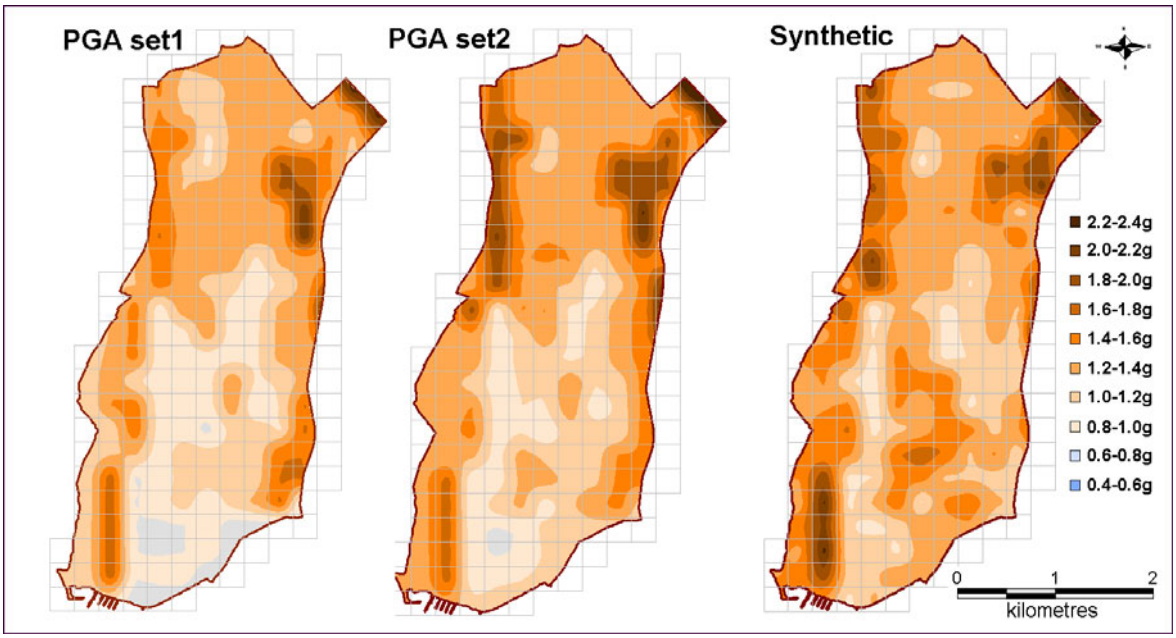

Figure 1 Microzonation of Zeytinburnu with respect short period (T=0.2s) spectral accelerations using two sets of PGA scaled real and one set of synthetic acceleration input motion

As can be observed from Figure 1, even though there is a general agreement among all three options, there are also differences that introduce difficulties to select one option and to estimate the building stock vulnerability based on that selection. Using synthetic acceleration time histories generally yielded higher amplitudes indicating more conservative solution. However, the degree of conservatism cannot be defined and the generated acceleration records may be considered unrealistically demanding. Thus for that case, the use of scaled regional earthquake hazard compatible real acceleration records appears more suitable for microzonation studies.

In this study in order to understand how ground motion selection and scaling affect the results of site response analysis, 1D equivalent linear soil model Shake91 by Idriss and Sun (1992) was used to conduct analyses at selected sites with pre-determined level of earthquake hazard. Resulting response variability was investigated when analyzed under a series of ground motion records selected compatible with the site-specific earthquake hazard. Site specific earthquake hazard is considered as dependent on the fault type, magnitude range, and epicenter distance. The set of input strong ground motion records were scaled to different intensity measures such as peak ground acceleration, peak ground velocity and Arias intensity, and the uncertainty introduced by scaling and the effectiveness of different scaling parameters were evaluated.

2. METHODOLOGY

PEER database was used to select specific time histories representing possible earthquake ground motions that would be expected at the selected sites. The selected time histories were scaled as described later, and then used as input for ground response analyses for the selected sites.

The seismological criteria, by which these rock time histories were selected, where the term "target" refers to a characteristic of the causative earthquake for the subject site, are as follows:

- Magnitude: Selected records must have been triggered by an event with a magnitude within ± 0.5 of the target.
- Distance: For specific cases, records are selected within 10 km range of the expected source distance to the site. For general purposes, records representing near and far field properties are differentiated.
- Fault mechanism (the type or style of faulting): It is preferable to select the records of the same fault mechanism with the subject site. It should be noted that significant differences are observed between reverse and strike-slip earthquake motions such that reverse and thrust faulting causes higher ground motion than strike-slip or normal faulting (Campbell, 1981).
- Amplitude: Time histories were sought that had a PGA within a factor of two to three of the target PGA on rock (evaluation of target PGA on rock is based on the hazard studies for that specific site).
- Site Condition: Time histories were selected from sites underlain by geologic rock or with a thin (< 20 m) layer of soil overlying rock. The site condition corresponds to soft, weathered rock – rock having an average shear wave velocity that has been estimated as $V_{s30} \geq 500$ m/s.

Scaling of input time histories can be carried out in time-domain and in frequency domain. In time-domain scaling involves only the amplitude of the time series whereas in frequency domain scaling the frequency content is changed within a pre-determined frequency window.

Scaling of input time histories was carried out in time-domain that involves only the amplitude of the time series. Linear scaling is preferred in this study since the

main concern was to search the effectiveness of different scaling parameters on the damage parameter predicted at the ground surface. Using a frequency scaling method by means of design spectrum matching was not chosen because the additional variability due to the change in the frequency content of time histories may not so easily be compared for different scaling parameters. Individual time histories are scaled up or down by factor so that their maximum acceleration values matches the target value in an average sense. The scaling factor was determined as the ratio of PGA of time history giving the target scaling parameter value over the PGA of the unscaled time history.

3. PARAMETRIC STUDY

A detailed parametric study was conducted to evaluate the effects of input motion scaling by considering eight scaling parameters (PGA; PGV; Arias Intensity, I_a; Root Mean Square Acceleration, a_{rms}; Cumulative Absolute Velocity, CAV; maximum spectral acceleration, SA_{max}; Spectrum Intensity, SI and Acceleration Spectrum Intensity, ASI) for three different real soil profiles with different depths (182m, 100m and 45m) but similar average shear wave velocities (V_{s30}=267 m/s, 294 m/s, 304 m/s) for three earthquake hazard levels (M=6-6.5, M=6.5-7, and M=7-7.5) and for three distance ranges (R=0-30km, R=30-60km, R=60-90km). Input acceleration time histories were selected from PEER data set which was also used to estimate the attenuation relationships for these parameters.

3.1 Soil Profiles

A very comprehensive site investigation study was carried out as part of the large-scale microzonation project in Istanbul (OYO, 2007). 2912 borings (mostly down to 30m depth with approximately 250m spacing) were conducted within an area of about 182 km^2 to investigate local soil conditions. Standard Penetration Test (SPT), Cone Penetration Test (CPT), PS Logging, Refraction Microtremor (ReMi), seismic reflection and refraction measurements were carried out at each borehole location. Samples collected in the field were tested in the laboratory to determine index and engineering properties of local soils within the investigated area.

The three soil profiles were selected from this microzonation study area. Shear wave velocity profiles were based on in-situ measurements conducted using PS Logging in-hole seismic wave velocity measurements as well as in-situ geophysical seismic wave velocity measurements and based on empirical correlation with respect to SPT blow counts.

In addition to the shear wave velocity measurements in these soil profiles, the types of soil layers were determined based on laboratory index tests and thus site characterization was reliable and sufficiently detailed in assigning modulus reduction and damping curves (Figure 2).

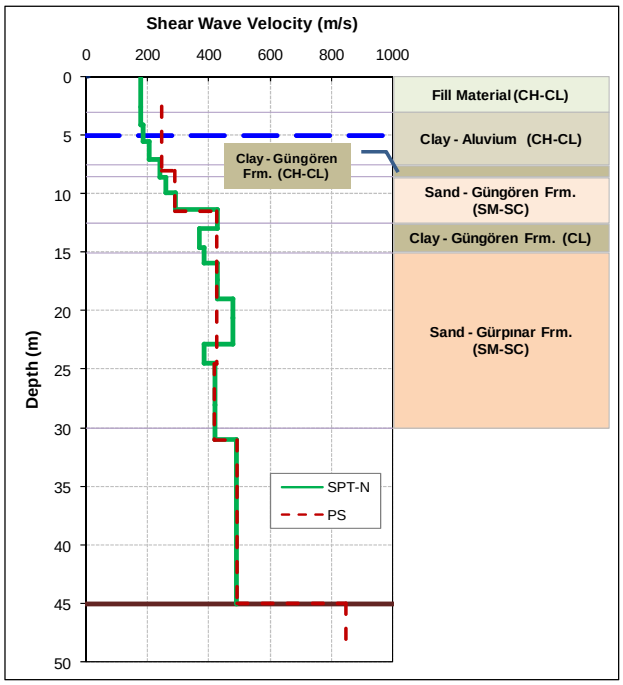

Figure 2 Soil Profile-3 used in the parametric study

In order to evaluate the effect of soil profile depth on scaling analysis, three soil profiles with similar equivalent shear wave velocities (V_{s30}=267 m/s, 294 m/s, 304 m/s) but with different bedrock depths (182 m, 100m, 45m) were selected to conduct the parametric study.

3.2 Time History Database

The strong motion records used in this study are obtained from the NGA database maintained at the Pacific Earthquake Engineering Research Center (PEER) website because of its high quality and availability for the supplied information required and homogeneity due to the same processing procedures used.

Time histories selected for the sites with average shear wave velocity at the upper 30 m, $V_{s30} \geq 500$ m/s are grouped based on magnitude and distance ranges considering the methodology proposed and the reliability of statistical evaluation. Site response analysis were conducted for nine sets corresponding to three magnitude ranges (6.0-6.5, 6.5-7.0, 7.0-7.5) and three distance ranges (0-30km, 30-60km, 60-90km). Number of input motions in each bin is given in Table 1.

3.3 Scaling Parameters

Level of ground shaking for earthquake resistant design and thus damage potential of an earthquake are defined based on different ground motion parameters. The better damage indicators are the parameters that can reflect nearly all of the amplitude, frequency content and duration characteristics of an earthquake ground motion. Some of the engineering ground-motion parameters correlate well with several damage parameters of structural performance, liquefaction, seismic slope stability, vulnerability assessments, microzonation studies etc.

Table 1 Scaling study magnitude and distance bins

Magnitude Range	Distance Range	No. of Records	Bin Name
6.0 – 6.5	0-30 km	45	1A
	30-60 km	92	1B
	60-90 km	64	1C
6.5 – 7.0	0-30 km	34	2A
	30-60 km	31	2B
	60-90 km	26	2C
7.0 – 7.7	0-30 km	49	3A
	30-60 km	49	3B
	60-90 km	31	3C

Examples on the use of these parameters are; generation of shake maps for rapid visualization of the extent of the expected damages to be used for emergency response, loss estimation, and public information (Wald et al., 1999); the development of early warning systems for the reduction of the seismic risk of vital facilities, such as nuclear power plants (EPRI, 1988), pipelines, high-speed trains; and estimation of damage potential due to liquefaction (Kramer and Mitchell, 2005).

For this study, peak ground acceleration (PGA), peak ground velocity (PGV), root-mean-square acceleration (a_{rms}), Arias intensity (I_a), cumulative absolute velocity (CAV), maximum spectral acceleration (SA_{max}), response spectrum intensity (SI) and acceleration spectrum intensity (ASI) are selected as representative ground motion parameters that have the advantage of describing ground-motion damage potential and incorporate in their definition one or more of the effects of amplitude, frequency content, duration, and / or energy of a ground-motion record.

For the prediction of these parameters on rock outcrop, new empirical attenuation relationships were proposed based on Next Generation Attenuation (NGA) database (Tönük, 2009). The need for developing new predictive relations was due to the lack of existing relations for some of the parameters selected and due to the need to use a more homogeneous data set of empirical equations that minimizes the regression variability on the results.

The parameters were determined as rock outcrop values from the proposed predictive equations for the specific site selected. Then all the records were scaled with a factor which was determined as the ratio of PGA of time history giving the target scaling parameter value over the PGA of the unscaled time history.

The variation of maximum accelerations of the input motions scaled with respect to eight different scaling parameters ready to be used in the analysis is given in the Figure 3 for the sub bin 1C (M= 6.0-6.5 and R= 60-90 km). Although the target PGA was selected as 0.25 g, input motion PGAs show variation in the range of 0.1 – 0.5 g.

3.4 Results

Histograms of damage parameters: peak ground acceleration, PGA; peak ground velocity, PGV; and maximum spectral accelerations, SA_{max} for three soil profiles were calculated on the ground surface from the site response analyses that used input time histories scaled with respect to eight scaling parameters for each bin of magnitude and distance.

Then for each bin and for three soil profiles, the effectiveness and suitability of the scaling ground motion parameter were evaluated from the variation of mean, mean±SD and range of damage parameters as shown in the Figure 4 which is the case of bin 1C (M= 6.0-6.5 and R= 60-90 km). Variations of statistical parameters like kurtosis, variance and SD/mean with respect to scaling parameters were also considered in the evaluation (Figure 5).

The results for the three soil profiles as the response spectra for different scaling cases were also studied for nine bins of magnitude and distance pairs to compare the average spectrum of each bin. In Figure 6, the response spectra for PGA scaling case and for soil profile 1 are given as an example. The variations of normalized standard deviation (SD/Mean) for three damage parameters for three soil profiles with respect to scaling parameters were examined with changing magnitude and distance ranges.

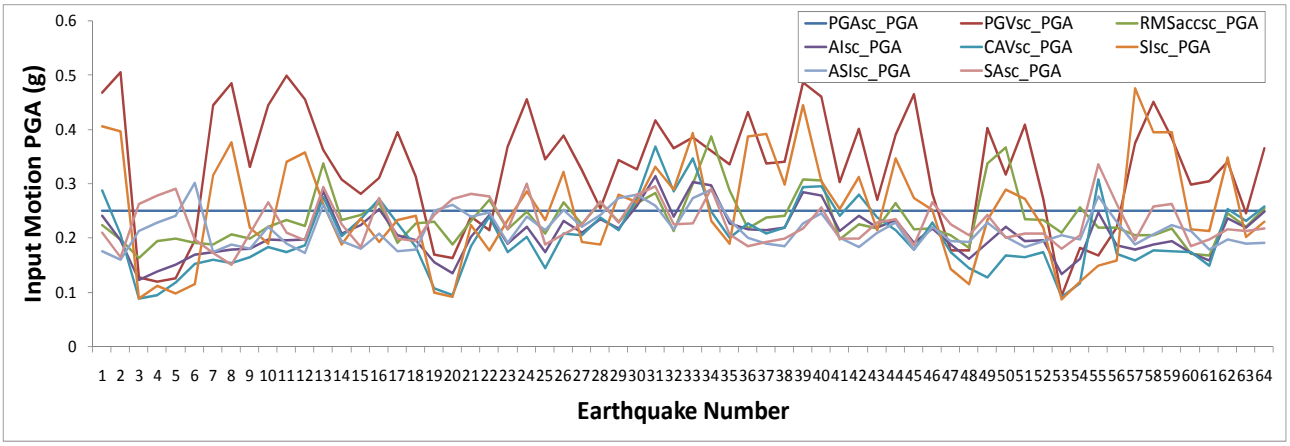

Figure 3 The variation of maximum accelerations of the input motions scaled with respect to eight different scaling parameters for the bin 1C (M= 6.0-6.5 and R= 60-90 km)

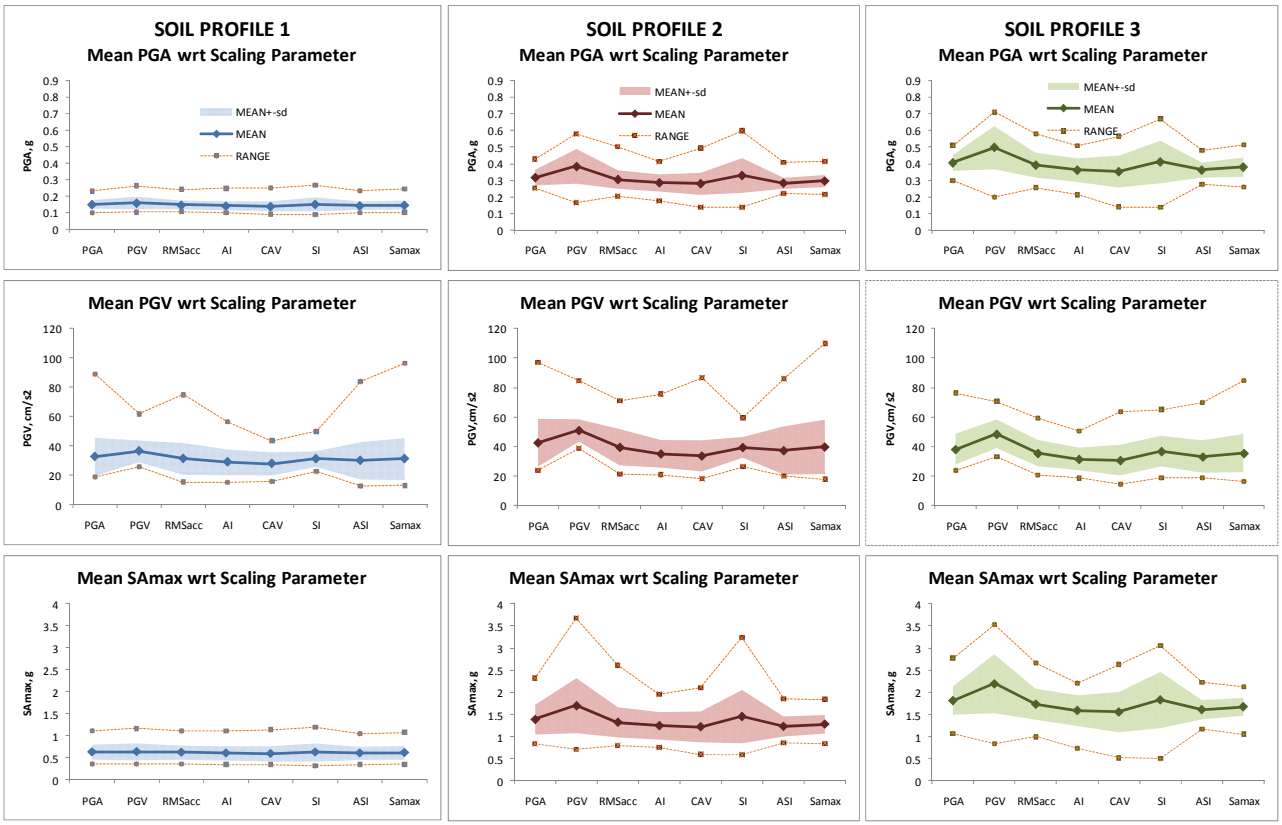

Figure 4 Variation of mean (full line), mean±SD (shaded area) and range (broken lines) of PGA (1st row), PGV (2nd row) and SAmax (3rd row) for three soil profiles (columns) wrt scaling parameters for the bin 1C (M= 6.0-6.5 and R= 60-90 km)

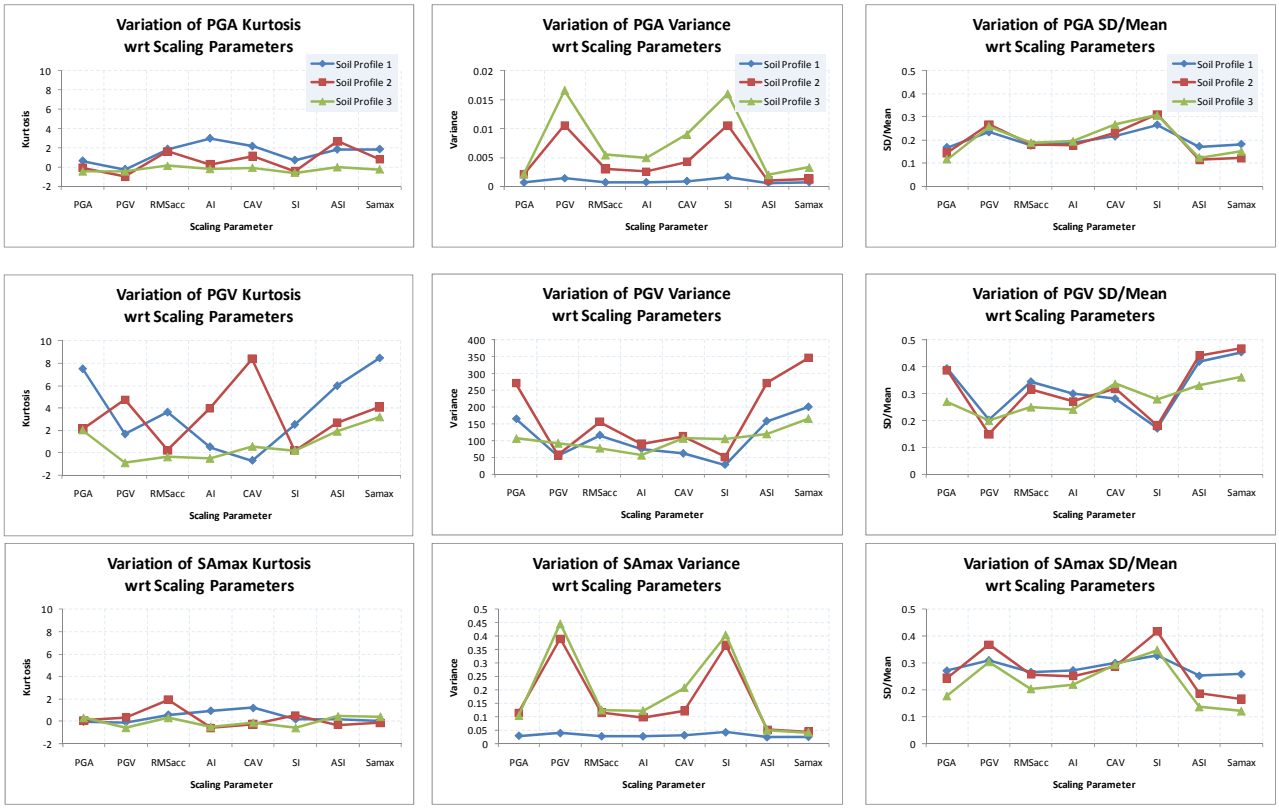

Figure 5 Variation of kurtosis (1st column), variance (2nd column) and SD/mean (3rd column) of PGA (1st row), PGV (2nd row) and SAmax (3rd row) for three soil profiles (soil profile 1 is the deepest profile) with respect to eight scaling parameters for the bin 1C (M= 6.0-6.5 and R= 60-90 km)

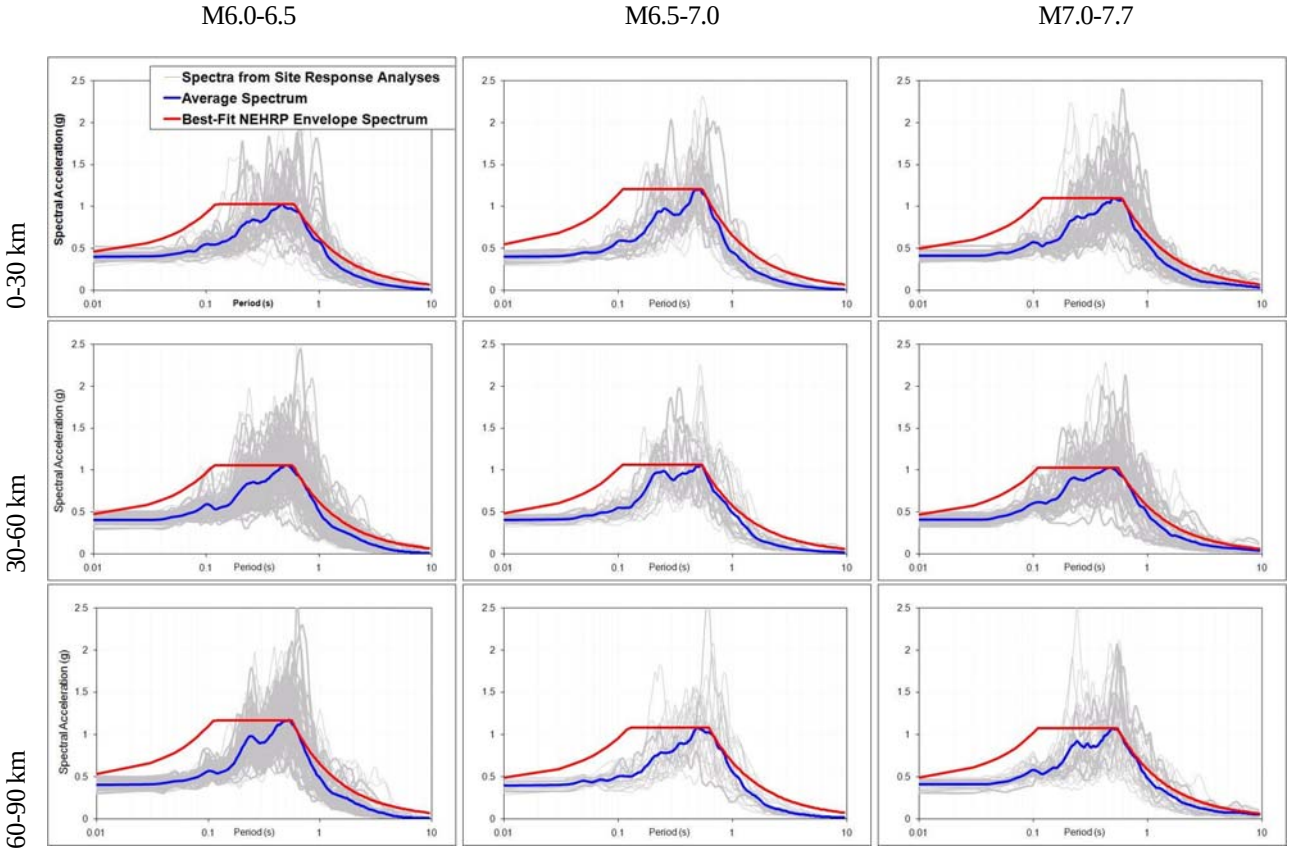

Figure 6 Soil Profile 1 – response spectra for PGA scaling case - for nine bins of magnitude (columns) and distance (rows) pairs

Based on the histograms for the calculated damage parameters for all soil profiles for the eight scaling options using the considered input motions, it seems that among different scaling parameters, taking into consideration all three statistical parameters calculated to determine the variability in each set (variance and normalized standard deviation being minimum, and range being the smallest), the PGA, ASI, SA_{max}, AI, and RMS_{acc} scaling appear to be the most suitable (suitability decreases with the given order) scaling parameters in terms of calculated peak ground accelerations on the ground surface if it is the desired damage parameter (e.g., liquefaction susceptibility analysis or landslide hazard).

In the case of maximum spectral accelerations (which can be taken as spectral acceleration at period T=0.2s), maximum spectral acceleration (SA_{max}) scaling yielded the smallest range and normalized standard deviation for which ASI and PGA scaling parameters can also be used as the suitable solutions with the small variability. If we consider spectral acceleration at 0.2s as the main damage parameter for the geotechnical engineering structures, than it is possible to suggest the use of SA_{max} scaling as the first option when conducting site response at a site to determine the design ground motions for geotechnical engineering structure.

If PGV is required as damage parameter (e.g. vulnerability analysis of lifeline system) then the situation changes significantly. This time, scaling parameters giving the smallest range and minimum variance are PGV and SI scaling methods. Scaling with all other scaling parameters is definitely not appropriate.

Variance and range are observed to be dependent on soil profile depth, and they increase as the profile depth decreases. However the depth dependence is not as significant when the damage parameter is PGV as for PGA or SA_{max}. Kurtosis value changes irregularly, thus it is not a good parameter to evaluate effectiveness of the scaling parameter for this general case.

4. CONCLUSIONS

Using different scaling parameters determined from empirical attenuation relationships regressed using the same thus homogeneous data set; it was possible to study how ground motion selection and scaling affects the site response.

Ground motion scaling is basically emerging as a need following recent developments in the earthquake resistant design philosophy (Kappos and Kyriakakis, 2000) for using the most appropriate set of strong ground motion time series (Bommer and Acevedo, 2004) recorded or simulated to minimize the scatter in response in the dynamic analysis of structures.

Even using records selected in accordance with the site-specific hazard parameters, may not generally solve the problem of large scatter. Scaling the records for

time-domain analysis to values chosen consistent with site-specific hazard parameters is a way to handle this situation. Scaling the input motion according to the most appropriate parameter so that the scatter of the model response is reduced is also important when design is required for different performance levels such as limit, serviceability etc. and also for displacement and acceleration sensitive structures and components (Heuze et al., 2004).

During the selection of input motions, the site specific seismological criteria in terms of magnitude, distance, fault type, amplitude and site conditions should be considered. Site response analyses should be performed using a bin of input motions. The number of time histories in the bin should be large enough to provide a stable estimate of the median and to provide a smaller variation.

The general parametric study on scaling with eight different scaling parameters on three damage parameters (PGA, PGV, SA_{max}) based on nine bins of magnitude and distance pairs for three soil profiles reveal that:

(1) when there are enough large number of input motions, the variation of average damage parameter is not sensitive to selected magnitude – distance bin,

(2) the soil profile depth is a dominating factor on the results, as the profile gets deeper the selection of scaling parameter is not important,

(3) the selection of scaling parameter is closely related with the damage parameter, the variance in the PGA and SA_{max} is smaller when the input motions are scaled with respect to acceleration based parameters like PGA, Arias intensity, acceleration spectrum intensity, and the variance in the PGV is smaller when the input motions are scaled with respect to velocity based parameters like PGV, and spectrum intensity,

(4) Normalized standard deviation (SD/mean) is a preferable comparison parameter, for which the minimum value may indicate the best scaling parameter.

References:

Ansal, A. and Tönük, G. (2007), "Source and Site Effects for Microzonation," *Theme Lecture, Fourth International Conference on Earthquake Geotechnical Engineering*, K.Pitilakis (ed.), Chapter 4, 73-92, Springer.

Bommer, J. J. and Acevedo, A. B. (2004), "The Use of Real Earthquake Accelerograms as Input to Dynamic Analysis," *Journal of Earthquake Engineering*, **8**(1), 43-91.

Campbell, K.W., (1981), "Near-Source Attenuation of Peak Horizontal Acceleration," *Bulletin of the Seismological Society of America*, **71**, 2039–2070.

EPRI, Electrical Power Research Institute, (1988), "A Criterion for Determining Exceedance of the Operating Basis Earthquake, EPRI NP-5930, Electrical Power Research Institute, Palo Alto, California".

Goulet, C. A., (2008), "Ground Motion Parameters That Control Ground Response Analysis Results", *Presentation in 2008 COSMOS Technical Session*, Oakland, CA.

Heuze, F., Archuleta, R., Bonilla, F., Day, S., Doroudian, M., Elgamal, A., Gonzales, S., Hoehler, M., Lai, T., Lavallee, D., Lawrence, B., Liu, P. -C., Martin, A., Matesic, L., Minster, B., Mellors, R., Oglesby, D., Park, S., Riemer, M., Steidl, J., Vernon, F., Vucetic, M., Wagoner, J. and Yang, Z. (2004), "Estimating Site-Specific Strong Earthquake Motions," *Soil Dynamics and Earthquake Engineering*, **24**(3), 199-223.

Idriss, I. M. and Sun, J. I. (1992), "Shake91, A Computer Program for Conducting Equivalent Linear Seismic Response Analysis of Horizontally Layered Soil Deposits, Modified based on the original SHAKE program by Schnabel, Lysmer and Seed, 1972".

Kappos, A. J. and Kyriakakis, P. (2000), "A Re-Evaluation of Scaling Techniques for Natural Records," *Soil Dynamics and Earthquake Engineering*, **20**(1-4), 111-123.

Kramer, S. L. and Mitchell, R. A. (2005), "Ground Motion Intensity Measures for Liquefaction Hazard Evaluation," *Earthquake Spectra*, **22**(2), 413–438.

Martinez-Rueda, J. E., (1998), "Scaling Procedure for Natural Accelerograms Based on a System of Spectrum Intensity Scales," *Earthquake Spectra*, **14**(1), 135-152.

Naeim F., Alimoradi, A. and Pezeshk, S. (2004), "Selection and Scaling of Ground Motion Time Histories for Structural Design Using Genetic Algorithms," *Earthquake Spectra*, **20**(2), 413-426.

OYO Inc., Japan, (2007), "Production of Microzonation Report and Maps on European Side (South), Final Report to Istanbul Metropolitan Municipality".

PEER, Pacific Earthquake Engineering Research Center: Ground Motion Selection and Modification Program, http://peer.berkeley.edu/gmsm/

PEER, Pacific Earthquake Engineering Research Center: NGA Database, http://peer.berkeley.edu/nga/

Tönük, G. (2009), "Factors Affecting Site Response Analysis," Ph. D. Dissertation, Bogazici University.

Wald, D. J., Quitoriano, V., Heaton, T. H. and Kanamori, H. (1999), "Relationships between Peak Ground Acceleration, Peak Ground Velocity, and Modified Mercalli Intensity in California," *Earthquake Spectra*, **15**(3), 557–564.

JOINT CONFERENCE PROCEEDINGS
7th International Conference on Urban Earthquake Engineering (7CUEE) &
5th International Conference on Earthquake Engineering (5ICEE)
March 3-5,2010, Tokyo Institute of Technology, Tokyo, Japan

Imaging Sedimentary Layers of Metro Manila, Philippines from the Joint Inversion of Receiver function and Surface-wave phase velocity

Rhommel Grutas[1] and Hiroaki Yamanaka[2]

1) Graduate Student, Dept. of Environmental Sci. and Tech, Tokyo Institute of Technology, Japan
2) Associate Professor, Dept. of Environmental Sci. and Tech, Tokyo Institute of Technology, Japan
grutas.r.aa@m.titech.ac.jp, yamanaka@depe.titech.ac.jp

Abstract: In this study, genetic algorithm (GA) was applied in the joint inversion of receiver function (RF) and surface-wave phase velocity to determine the shear-wave velocity structure of deep sedimentary layers. Using water-level method of calculating receiver functions in the analysis of 11-year earthquake data of strong motion accelerographs, the observed RF contains seismic phases generated from P-S conversions at velocity discontinuities. The derived shear-wave velocity profiles from RFs inversion at 8 sites and from joint inversion are presented here. Results show the inferred deep sedimentary layers in Metro Manila that can be used for further studies on seismic hazard analysis.

1. INTRODUCTION

Metro Manila, the capital of the Philippines is situated in Luzon Island. Its total population is more than 10 million living in a total land area of 640sq.km, making it the most densely populated area in the Philippines.

Seismotectonic of the Philippines shows that Luzon Island is located between two Plates, the Eurasian Plate to the west and the Philippine Sea Plate to the east. The Eurasian Plate subducts eastward beneath the Luzon Island along the Manila Trench producing high seismicity (Figure 1). Most of the earthquakes that have been felt in Metro Manila came from this trench. Metro Manila is transected by 135 km long right lateral strike slip Valley Fault System (VFS). The estimated earthquake magnitude for the VFS for a single-event fall within the range of magnitude 7.3-7.7 (Rimando and Knuepfer 2006). Moreover, the paleoseismic data of VFS (Nelson et al. 2000) indicated a recurrence interval of 200-400 years for magnitude 6-7 earthquakes over the past 1500 years.

Historical accounts of damaging earthquakes in Metro Manila show that as early as 1599, the city of Manila has experienced devastating effects of large magnitude earthquakes from near to distant events. To mention some of these are the earthquakes in 1863 and 1968. The significant earthquake of 1863 is a near field event that damaged more than 1000 buildings in Manila, with various geologic effects including extensive fissuring, liquefaction and tsunami (SEASEE 1985). Distant event from Metro Manila like the Casiguran earthquake on 02 August 1968 with a magnitude of 7.3 caused the Ruby Tower, a six story building in Binondo Manila to suffer total collapse. Several major buildings near Binondo and Escolta area in Manila also sustained partial to severe damage (Osome et al. 1969).

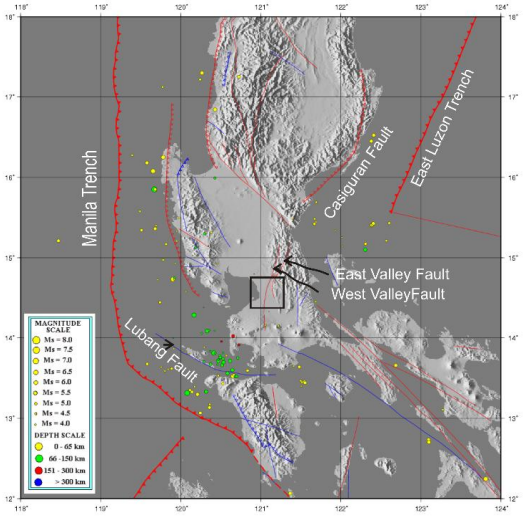

Figure 1 Tectonic setting and recorded earthquakes of strong motion network in Metro Manila.

Receiver function analysis has been applied extensively to determine mainly the interface between the crust and upper mantle by using broadband earthquake records. The method uses seismic phases generated from P-S conversions and multiple reflections at velocity discontinuities. The advancement of this technique is being used to estimate the fine-scale S-wave velocity structure of the lithosphere by inversion of receiver functions (e.g. Owens et al. 1984; Ammon et al. 1990). In view of the increased interest in receiver function studies, the receiver function has also been attracting attention in earthquake engineering as a method of estimating basement depth using arrival time difference between direct P and P-S converted waves (e.g. Kobayashi et al. 1998). However, its applications mainly focus on the use of P-S conversion generated in sediment/basement interface. Recently, in crust and mantle studies, the joint inversion of receiver function and surface-wave group velocities is used to bridge the gaps associated with the two separate methods of receiver functions and surface wave dispersion (eg. Ozalaybey et al. 1997; Du and Foulger 1999; Julia et al. 2000). The receiver functions are sensitive to shear wave velocity contrast and vertical travel times while surface wave dispersions are sensitive to vertical shear wave velocity. In sedimentary layers application, Kurose and Yamanaka (2006) performed the joint inversion of receiver function and surface-wave phase velocity using genetic algorithms to estimate the shear-wave velocity structure of deep sedimentary layers.

In this study the joint inversion method using genetic algorithm was applied to estimate the shear-wave velocity structure of sedimentary layers in Metro Manila. The 11-year records of strong motion for receiver function obtained in this study and the Rayleigh wave phase velocity data obtained through long period microtremor array measurement by Yamanaka et al. 2000 were utilized in the analysis.

2. STRONG MOTION OBSERVATION

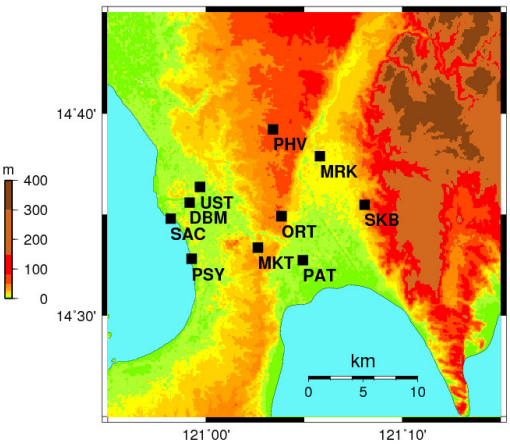

Figure 2 Digital Elevation Map (DEM) showing locations of strong motions accelerographs. The colors represent different elevations.

In 1998, ten Strong Motion (SM) seismometers were installed in different geological setting in Metro Manila. The geomorphologic feature of Metro Manila is divided into three major districts; the Central Plateau, Coastal Lowland and the Marikina River Plain or Flood Plain. The SM at UST, DBM, SAC and PSY are located in Coastal Lowland, while PHV, ORT and MKT are in Central Plateau area (Figure 2). In the Flood Plain, MRK and PAT stations are situated. These strong motion instruments have been operated by Philippine Institute of Volcanology and Seismology (PHIVOLCS) and Tokyo Institute of Technology to observe the strong ground motions and different amplifications from geological conditions (Yamanaka et al. 2002). As of December 2008, a total of 133 earthquake events have been recorded by the strong motion array with magnitudes ranging from 2.3 to 6.8. These earthquake events are mostly coming from Manila Trench and Lubang Fault. With these 11-year strong motion records the receiver function analysis could be performed.

Closely watching the SM records for receiver function analysis, it was observed that in the P-wave part of strong motion acceleration record there are P converted S waves contained in horizontal component of the waveform (Figure 3). For the radial component of strong motion P-SV type of waves are contained in the P wave part of the record which represent the conversion from different interfaces below the station. These interfaces are sedimentary layers, basement/sediment interface, crust/upper mantle interface and others. In order to limit the observation to basement and sedimentary layers a certain time window starting from the first impulse of the P wave should be assessed. In this study the first 10 seconds of P waveform was extracted. P-SH type of wave could also be observed in the tangential component of the strong motion record.

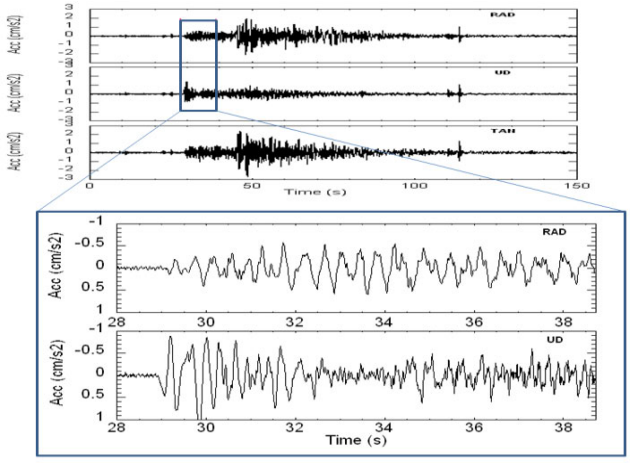

Figure 3 Strong motion acceleration record at PSY station for the Feb. 9, 2005 earthquake, with a magnitude of 5.4, 89km depth, and epicentral distance of 106km. (Top) whole 3-component waveform record. (Bottom) close-up view of radial and vertical component. The first ten seconds is used in receiver function starting from 0.15 sec before the first arrival.

3. RAY TRACING

Earth model is necessary to find the incident angles at the top of the basement using ray-tracing formalism. In determining the parameters for ray tracing, two earth models were tested, one is from Besana et al. (1995) and the other is PHIVOLCS model that is based on IASP91 with some modification to appropriate the Philippine settings (Figure 4). The PHIVOLCS model has been the one being used to locate earthquake hypocenters in the Philippines and it has interface between the crust and upper mantle at the depth of 25km. The Besana's earth model was inferred from the broadband station in Tagaytay seismic station which is about 56 kms SW of Metro Manila. For comparison, the earthquake event in Figure 3 has an incident angle of 29 degrees in PHIVOLCS model that corresponds to 35 degrees in Besana's model. In this study, the PHIVOLCS model is chosen for ray-tracing analysis because it gives incident values for all earthquake events and since it had been used for locating the earthquakes that were analyzed in this study. The earth model that was used for ray-tracing does not have sedimentary layers and the surface was assumed to be basement rock or outcropping basement rock. The incident angles calculated for each event at the depths of 1-20km for a distance of 110-210km are 48.17° and 51.54°. These two incident angles represent the critical angle. For EQ events with depths of 80-95km for an epicentral distance of 100-150km the incident angles ranges from 28° to 33°.

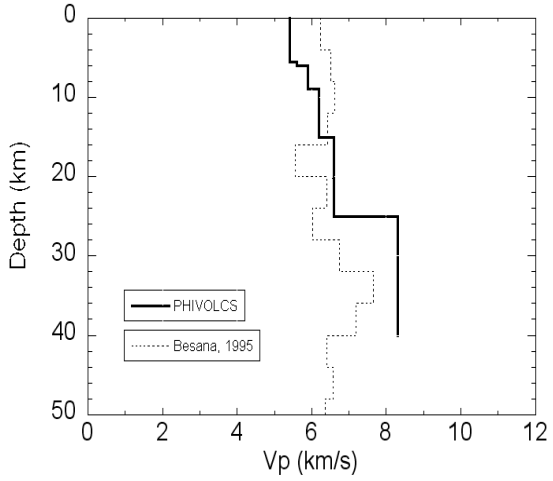

Figure 4 Earth models tested in Ray Tracing

4. OBSERVED RECEIVER FUNCTION

The source equalization method of Langston, 1979, sometimes called the water level method is applied in this study to isolate the response of basement and sedimentary layers beneath a station from the observed strong motion record. The observed spectra of radial components of an incident P-wave can be described as:

$$D_{rad}(\omega) = I(\omega)S(\omega)E_{rad}(\omega) \qquad (1)$$

Here $D_{rad}(\omega)$ is the radial displacement response at the surface, $I(\omega)$ is the instrument response, $S(\omega)$ is the source spectrum, and $E_{rad}(\omega)$ is the radial response of the subsurface structure of the station. By approximation of $S(\omega)$, letting $I(\omega)S(\omega) \cong D_{ver}(\omega)$, where $D_{ver}(\omega)$ is the vertical displacement. The implicit assumption is that $D_{ver}(\omega)$ behaves mostly like one Dirac delta function which contains almost exactly the factors that should be removed from the observed accelerograms. From Eq. (1) gives deconvolution of the vertical component from the radial component:

$$E_{rad}(\omega) = D_{rad}(\omega) / D_{ver}(\omega) \qquad (2)$$

The estimate in Eq. (2) is then multiplied by the transform of a Gaussian to limit the final frequency band by excluding high-frequency signals not obviously present in the original recording, then a water level c is applied to avoid instability caused by a very small denominator. $E_{rad}(\omega)$ is now designated into $R_{rad}(\omega)$ and the inverse Fourier transform gives the receiver function, $R_{rad}(t)$. Langston (1979) formulated this as follows.

$$R_{rad}(\omega) = D_{rad}(\omega)\overline{D}_{ver}(\omega)G(\omega)/\psi(\omega)$$
$$where: \psi(\omega) = \max\left\{D_{ver}(\omega)\overline{D}_{ver}(\omega), c\max\left[D_{ver}(\omega)\overline{D}_{ver}(\omega)\right]\right\} \qquad (3)$$
$$and \quad G(\omega) = e^{-\omega^2/4a^2}$$

The function $\psi(\omega)$ can be thought of as simply being the autocorrelation of $D_{ver}(\omega)$ with any spectral trough filled to a level depending on the parameter c, and the bar over $D_{ver}(\omega)$ denotes the complex conjugate, $G(\omega)$ is a filter in which a controls the width of the Gaussian pulse. In this study, the water-level is fixed at 0.01. To get the absolute amplitude of receiver function the method of Ammon (1991) is applied.

Table 1. List of earthquakes used in the calculation of receiver functions at PSY station

Code	Lat. (deg)	Long. (deg)	Depth (km)	Mag	Epi.Dist. (km)	BAZ (deg)
015PSY	13.707	120.290	66	4.3	119.92	218.78
032PSY	14.748	119.922	72	4.2	116.80	280.89
043PSY	15.420	121.670	5	5	121.57	37.13
069PSY	13.699	120.535	89	5.4	106.16	207.33
072PSY	13.558	120.584	95	5.3	118.25	201.57
086PSY	13.328	120.140	1	4.9	163.44	213.93

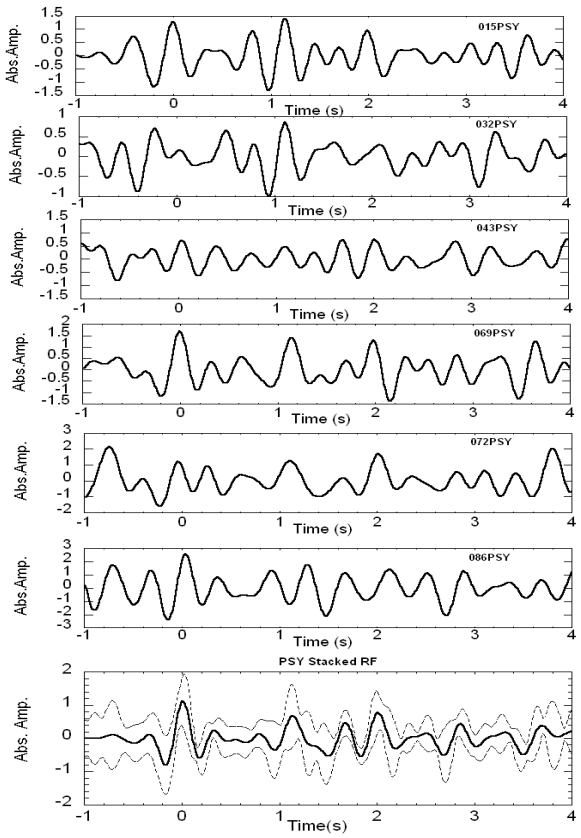

Figure 5 Receiver functions calculated from earthquake records and stacked receiver function with standard deviation indicated by broken line.

Figure 5 displays the observed receiver functions at PSY station and the details of the analyzed earthquake events are listed in Table 1. The epicentral distance of the events ranges from 106 to 168km. In applying the RF method to P waveforms in PSY station, careful selection of earthquake waveforms that exhibit clear records of P wave arrival and with incident angles that satisfy the ray tracing formalism was made. The individual RF was evaluated if it has anomalous troughs and negative polarities before applying the stacking. These irregularities in receiver functions were affected by anisotropic and non-homogenous media. It was clear in the individual RF (Figure 5) that the arrival of direct P wave at zero lag time and followed by the arrival of P converted S (P-S) phases which consequently yielded significant pulses of P-S waves from the stacked of individual receiver functions to have dominant pulses at 1.1 and 2.0 sec. These pulses represent conversions from high velocity contrast at major interfaces below the PSY seismic station. The conversion of P-S wave in sediment/basement and major sedimentary layers interfaces were included in these RF phases. Inversion of whole RF waveform will reveal the major interfaces of substructures at one station.

The incident angle of stacked RF at PSY derived from the average of individual receiver functions is 38°. The conversion of P-S wave in crust/mantle interface was also tested if it has an effect in the RF observations on this study. Using theoretical receiver function analysis the first arrival time of P-S wave for crust/mantle interface were distinguished to be at 3 seconds after the arrival of direct P wave (zero lag time) which means that in the RF waveforms the time window from 0 to 3 seconds is not significantly affected by the mantle/crust interface. The main focus of this study is only within this time window and the RF phases after 3 seconds are considered to be reverberations at the sediments and arrival of P-S wave from crust/mantle interface.

5. RECEIVER FUNCTION INVERSION

To investigate the result of receiver function alone, a receiver function inversion method using genetic algorithms was applied for earthquake records to obtain 1-D S-wave velocity profile. The theoretical RF calculation employed was based on Haskell (1962). The P-wave velocity used was derived using empirical relation of S-wave velocity by Kitsunezaki et al. (1990) with density fixed in the RF inversion. A band-pass filter with a period range of 0.5 to 3.33sec was applied during calculations. The incident angle for stacked RF was the average of individual event.

Out of ten SM sites, eight stations were analyzed for receiver function inversion because two sites did not have vertical component. The RF inversions produced excellent fits on the major phases in the observed receiver function and with only some slight discrepancies in the fittings were affected by structure complexity due to assumed plane layered models (Figure 6).

In GA's formulation, 10 inversions were conducted with 100 generations using seeds of random numbers where good models with smaller misfit survive more in the next generation while bad models are replaced by newly generated models. Details on GA's process can be seen in Yamanaka and Ishida (1996).

The observed RFs at seven stations were inverted assuming a 5-layer model in the search parameters while at SKB a 3-layer model was used (Table 2). In Central Plateau, the top layer S-wave velocities in PHV, ORT and MKT are 1.2, 1.0 and 0.71 km/s, respectively (Figure 7). PHV site corresponds to the Diliman Tuff, a deposit of volcanic origin and part of Guadalupe Formation that covers about 60 percent of Metro Manila (MMEIRS 2003). In coastal lowland where PSY and DBM are situated the Vs values are 0.68 and 0.71km/s. In MRK, a low velocity of 0.2km/s was observed on the top layer that corresponds to the unconsolidated sediments deposited by the Marikina River. The thickness of the sediments and location of the basement in Metro Manila ranges from 1.78 to 2.3km while the basement of SKB is 12m. The identified basement in this study for PSY and PHV are very near to the result of Yamanaka et al. (2000) that was inferred from long period microtremor array.

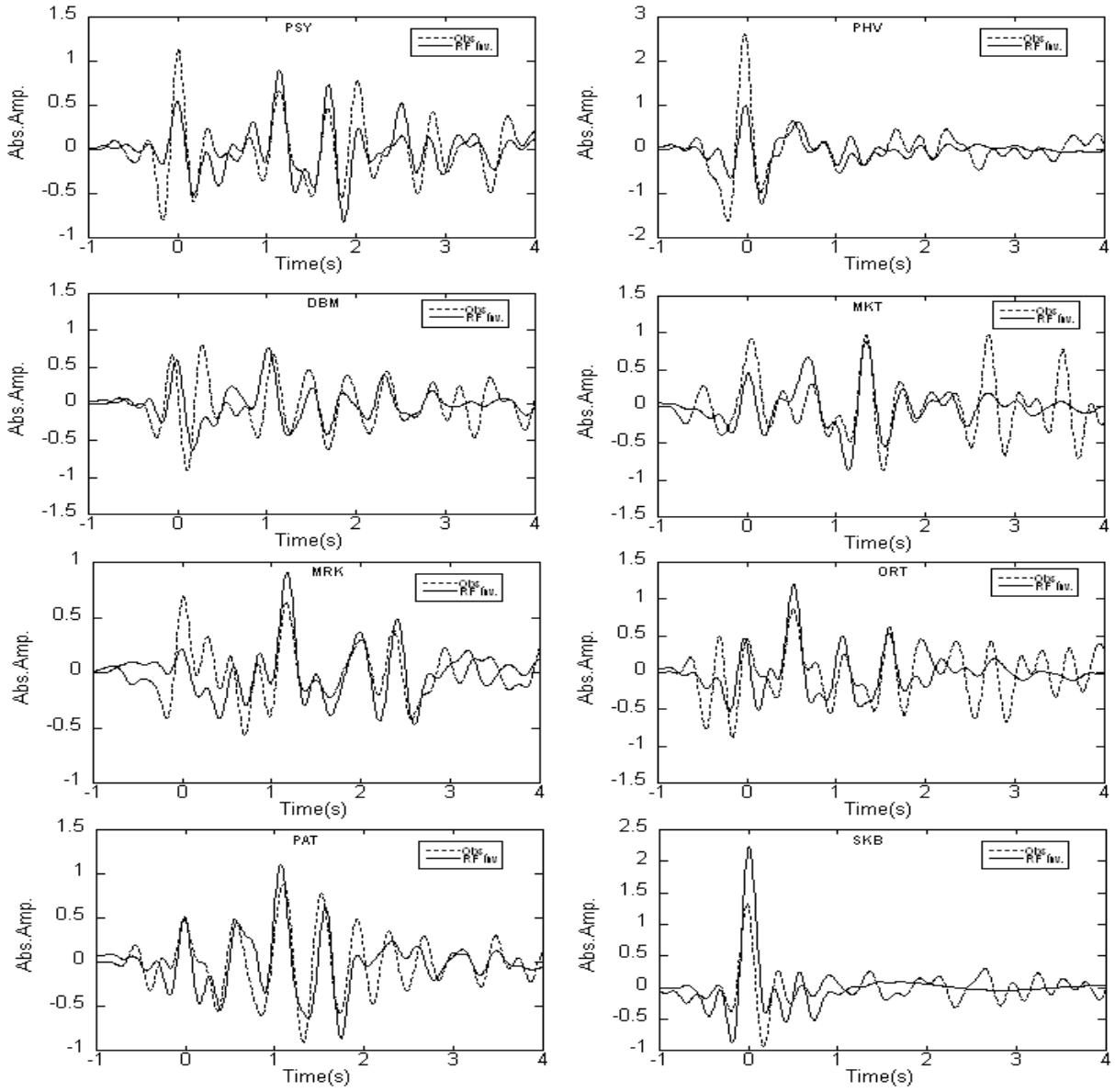

Figure 6 Comparison of observed stacked RF (dashed line) and inverted synthetic data (solid line) obtained from receiver function inversion.

Table 2 Search areas of parameters in the inversion of receiver function

No.	SKB		PHV,ORT,MKT		PSY,MRK,PAT		DBM	
	Vs (km/s)	H(km)	Vs (km/s)	H(km)	Vs(km/s)	H(km)	Vs(km/s)	H(km)
1	0.2~0.9	0.01~0.1	0.5~1.3	0.01~0.2	0.2~0.7	0.01~0.2	0.2~0.8	0.01~0.2
2	0.8~2.9	0.02~1.0	0.5~0.9	0.2~0.5	0.5~1.0	0.2~0.5	0.5~0.9	0.2~0.5
3	2.7~3.6	∞	0.4~1.9	0.2~0.8	0.4~1.9	0.2~0.8	0.4~1.9	0.2~0.8
4			0.8~2.7	0.5~2.0	0.8~2.7	0.5~2.0	0.8~2.7	0.8~1.2
5			2.7~3.9	∞	2.7~3.9	∞	2.7~3.9	∞

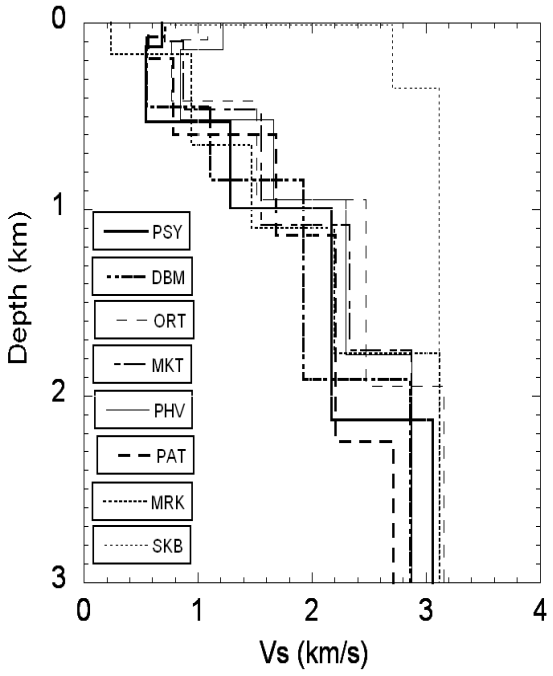

Figure 7 S–wave profile from inversion of receiver functions

6. OBSERVED LONG PERIOD MICROTREMOR

Long-period microtremor array measurements were conducted by Yamanaka et al. (2000) at four sites in Metro Manila in 2000 to know deep S-wave profiles for strong ground motion estimation. The survey set-up was composed of a circular array of 7 stations to measure vertical microtremor at each site. The circular arrays generated from this had a radius of 0.1, 0.5, and 1.5km to better estimate the phase velocities at periods from 0.3 to 4 seconds using frequency-wavenumber spectral analysis. The dispersive features of surface phase velocities from these records exhibit the propagation of Rayleigh waves which will be used in this study for the joint inversion together with the receiver functions.

7. JOINT INVERSION

From the previous results on the Rayleigh wave phase velocity inversion in Metro Manila observed from the long period microtremor array and from the results of inversion of RFs in this study, preliminary idea on the subsurface structures are already imaged which provided a good assumption in the joint inversion modeling.

The GA that was implemented here for the joint inversion is similar to that of Takekoshi and Yamanaka (2009), which is a modified GA of Yamanaka and Ishida (1996). The method adopted a real number coding and introduced an elite selection and dynamic mutation, except for the definition of misfit, which will be minimized in the inversion.

Joint inversion of two independent data sets, arises questions regarding consistency. However, joint inversion usually means refinement of results to obtain the optimum value. In the case of receiver function the dimensions and number of data are different from that of surface wave phase velocity (Figure 8). Thus, the data are reduced to dimensionless form in order to invert them simultaneously. The objective function (goodness of fit) for receiver function ϕ_{RF} and for the phase velocity ϕ_{ph}, are defined as the sum of squared differences between the observations and calculated values, normalized by the standard deviation and divided by the number of data. Kurose and Yamanaka (2006) enumerated this as follows.

$$\begin{aligned} \phi_{RF} &= (1/N_{RF})\sum_i \left[\{R_{obs}(t_i) - R_{cal}(t_i)\}/\sigma_{RF}(t_i)\right]^2 \\ \phi_{ph} &= (1/N_{ph})\sum_j \left[\{C_{obs}(T_j) - C_{cal}(T_j)\}/\sigma_{ph}(T_j)\right]^2 \end{aligned} \quad (4)$$

where N_{RF} and N_{ph} are the number of data while $\sigma_{RF}(t_i)$ and $\sigma_{ph}(T_j)$ are the standard deviations of the observed receiver function $R_{obs}(t_i)$ at time t_i, and the observed phase velocity $C_{obs}(T_j)$ at period T_j, respectively. The objective function ϕ to be minimized in the joint inversion is defined as the average of two misfits ϕ_{RF} and ϕ_{ph}:

$$\phi = (\phi_{ph} + \phi_{RF})/2 \quad (5)$$

Theoretical receiver-function and Rayleigh-wave phase velocity values are calculated using P and S wave velocities, thickness, and density of each layer in a flat-layered model. The theoretical receiver function $R_{cal}(t_i)$, and the theoretical phase velocity, $C_{cal}(T_j)$, in equation (4) are calculated by the methods of Haskell (1962) and Haskell (1960), respectively.

For the GA parameters, the population size and rates of crossover and mutation were set to be 20, 0.7, and 0.01, respectively. Selection was performed according to a roulette rule. The inversion result was evaluated after 10 repetitions of a 100-generation calculation with different seeds of random number generator.

In the S-wave velocity profile, the joint inversion method inferred a 5-layered structure while the result of the inversion of surface-wave by Yamananaka et al. (2000) had 4 layers (Figure 9). In the result of Yamanaka et al. (2000), the 3rd layer has a thickness of 0.4 to 1.85km. Within this layer, one more layer was inferred by joint inversion at a depth of 1.1km with shear wave velocity of 2.0km/s. This variation in the number of layers happens because of difference in the search parameters of the inversion of individual data. The joint inversion finds the optimum model that suits both methods. The basement depth of 1.94km at PSY was also identified by the joint inversion.

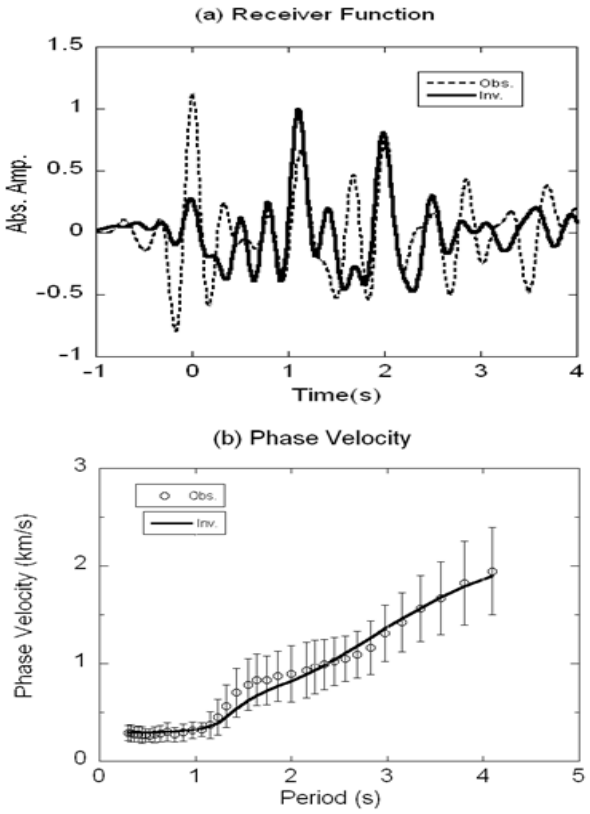

Figure 8 Comparison of observed and inverted synthetic data obtained from the joint inversion. (a) Receiver function and (b) Rayleigh-wave phase velocity.

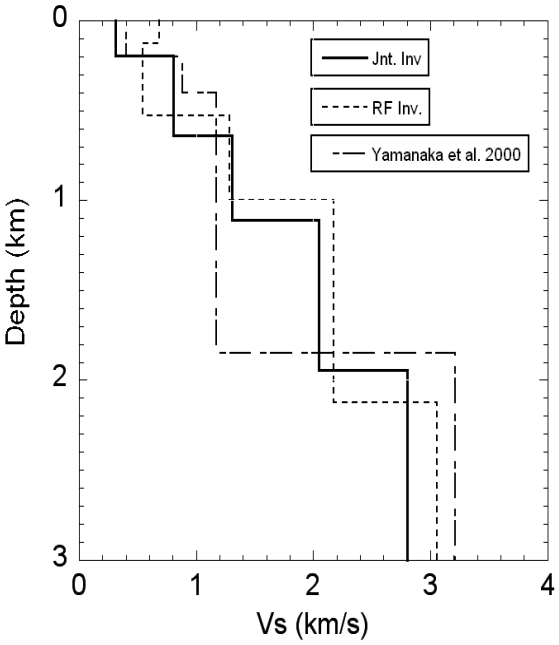

Figure 9 Comparison between S-wave velocity structure obtained by joint inversion (solid line), receiver function inversion and profile estimated from long period microtremor array survey by Yamanaka et al. (2000) at PSY.

Although only one station (PSY) was analyzed here for the joint inversion, the sedimentary layers can still be clearly pictured. The top layer has low velocity corresponding to coastal lowland in PSY area. Differences in velocity could be observed on the top layer of RF inversion (0.68km/s) compared to the result of joint inversion (0.31km/s). These velocities clearly identified in the borehole data at PSY station (Yamanaka et al. 2002) that featured a low velocity on top 30m and a velocity of 0.6km/s at the depth of 40m. The result of joint inversion has low velocity due to the influence of surface wave phase velocity data of Yamanaka et al. (2000). The surface wave phase velocities obtained by Yamanaka et al. (2000) cover a wide area. This wide area is composed of different deposits that may have affected the variations in thickness of low shear-wave velocity in PSY.

8. CONCLUSIONS

This study outlined the implementation of receiver function inversion of eight SM stations in Metro Manila and presented result of one station for the joint inversion.

Inversion of strong motion receiver function alone has provided much general information about the shear velocity structure in Metro Manila. Although some phases of the inverted models have slight discrepancies in the observed data, it was obvious that these features cannot be adequately approximated by flat layered models. Further constraints on the dipping layers could be obtained by receiver function on tangential component. Our model in receiver function inversion for PHV site clearly identified the Guadalupe Formation in Diliman, Quezon City. However, limitations on thicknesses of the top layers could be further improved by joint inversion together with the dispersion of surface-wave from long period and short period microtremor measurements. The SKB basement at 12 m identified by RF inversion will be a good reference for site response evaluation in Metro Manila considering the 1.94 km deep sediments at PSY. The effect of deep sediments could amplify the ground motion of distant earthquakes such as that of the 1968 earthquake generated by Casiguran fault that caused the collapse of Ruby Tower in Manila (Osome et al. 1969). The identified sediment/basement interface in receiver function inversion has been in good agreement with the previous studies using long period microtremor array measurements and been improved by the joint inversion.

It was also pointed out in the joint inversion that the difference of one layer in velocity structure of surface-wave phase velocity inversion of Yamanaka et al. (2000) to that of receiver function inversion was due to the different assumptions of search parameters. The joint inversion could find the suitable layers that fit the two methods.

ACKNOWLEDGEMENTS

The authors acknowledge the financial support of Center for Urban Earthquake Engineering (CUEE) under G-COE program of Tokyo Institute of Technology. We thank Seismological Observation and Earthquake Prediction Division (SOEPD) of PHIVOLCS-DOST for continued operation and maintenance of Strong Motion Network in Metro Manila. The first author gratefully acknowledges Mombukagakusho scholarship from the Japanese government.

REFERENCES

Ammon, C.J. (1991), "The Isolation of Receiver Effects from Teleseismic P Waveforms", *Bulletin of the Seismological Society of America*, **81**(6), 2504-2510.

Ammon, C.J., Randall, G.R., and Zandt, G. (1990), "On the Nonuniqueness of Receiver Function Inversion", *Journal of Geophysical Research*, **95**, 15303-15318.

Besana,G.M., Shibutani,T., Hirano,N., Ando,M., Bautista, B., Narag,I., and Punongbayan,R.S. (1995)," The Shear Wave Velocity Structure of the Crust and Uppermost Mantle beneath Tagaytay, Philippines inferred from receiver function analysis", *Geophysical Research Letters*, **22**(23), 3143-3146.

Du, Z.J., and Foulger, G.R. (1999), "The crustal structure beneath the northwest fjords, Iceland, from receiver functions and surface waves", *Geophysical Journal International*, **139**, 419-432.

Haskell, N.A. (1960), "Crustal Reflection of Plane SH Waves", *Journal of Geophysical Research*, **65**(12), 4147-4150.

Haskell, N.A. (1962), "Crustal Reflection of Plane P and SV Waves", *Journal of Geophysical Research*, **67**(12), 4751-4767.

Julia, J., Ammon, C.J., Herrmann, R.B., and Correig, A.M. (2000), "Joint Inversion of receiver function and surface wave dispersion observation", *Geophysical Journal International*, **143**, 99-112.

Kobayashi, K., Uetake, T., Mashino, M., and Kobayashi, H. (1998), "An investigation on detection method of P to S converted waves for estimating deep underground structures", *Journal of Structural and Construction Engineering, Architectural Institute of Japan*, **505**, 45-52.

Kitsunezaki,C., Goto,N., Kobayashi,Y., Ikawa,T., Horike,M., Saito,T., Kurota,T., Yamabe,K., and Okuzumi,K.(1990), "Estimation of P-and S- wave velocities in Deep Soil Deposits for evaluating Ground Vibrations in Earthquake", *Journal of the Japan Society for Natural Disaster Science*, **9**,1-17.

Kurose, T., and Yamanaka, H. (2006), "Joint inversion of receiver function and surface-wave phase velocity for estimation of shear-wave velocity of sedimentary layers", *Exploration Geophysics*, **37**, 93-101.

Langston, C.A. (1979), "Structure under Mount Rainier, Washington, inferred from teleseismic body waves", Journal of Geophysical Research, **84**, 4749-4762.

Metro Manila Earthquake Impact Reduction Study (MMEIRS) (2003), "Soil Investigation Report", Earthquake Impact Reduction Study for Metro Manila, Republic of the Philippines, Vol. 1, 80 pages.

Nelson,A.R., Personius,S.F., Rimando,R.E., Punongbayan,R.S., Tungol,N., Mirabueno,H., and Rasdas,A. (2000), "Multiple Large Earthquakes in the past 1500 years on a Fault in Metropolitan Manila, the Philippines", *Bulletin of the Seismological Society of America*, **90**, 73-85.

Osome, S., Osawa, Y., Skinner, I., and Yoshima, Y. (1969). "Philippines: Luzon Earthquake of August 02, 1968", *UNESCO*, Serial No. 977/BMS. RD/SCE. NR, Paris.

Owens, T.J., Zandt, G., and Taylor, S.R. (1984), "Seismic evidence for an ancient rift beneath the Cumberland Plateau, Tennessee: A detailed analysis of broadband teleseismic P waveforms", *Journal of Geophysical Research*, **89**, 7783-7795

Ozalaybey, S., Savage, M.K., Sheehan, A.F., Louie, J.N. and Brune, J.N. (1997), "Shear-wave velocity structure in the northern basin and range province from the combined analysis of receiver functions and surface waves", *Bulletin of the Seismological Society of America*, **87,183**-189.

Rimando, R. and Knuepfer, P. (2006), "Neotectonics of the Marikina Valley Fault System (MVFS) and tectonic framework of structures in Northern and Central Luzon, Philippines", *Tectonophysics*, **415**, 17-38.

Southeast Asia Association of Seismology and Earthqauke Engineering (SEASEE). (1985), "Series in Seismology", Volume IV, Philippines.

Takekoshi, M. and Yamanaka, H. (2009), "Waveform inversion of shallow seismic refraction data using hybrid heuristic search method", *Exploration Geophysics*, **40, 99**-104

Yamanaka, H. and Ishida, H. (1996), "Application of genetic algorithms to an inversion of surface-wave dispersion data", *Bulletin of the Seismological Society of America*, **86**, 436-444.

Yamanaka, H., Midorikawa, S., Kinugasa, Y., Bautista, B. and Rimando, R. (2002), "Estimation of Seismic Risk in Metro Manila", *Metro Manila in Search of a Sustainable Future*, *University of the Philippines Press*, 308-326.

Yamanaka, H., Takezono,M., Ogata,Y., Eto, K., Banganan, E., Narag, I., DeOcampo,J., Tiglao, R., Garcia, D., Bautista, B. and Punongbayan, R. (2000), "Estimation of S-wave Velocity profiles in Metro Manila from Long-Period Microtremor Array Measurements", *Proceedings of the International Workshop on the Integration of Data for Seismic Disaster Mitigation in Metro Manila, Nov.2000, PHIVOLCS, Quezon City*, 13-29.

JOINT CONFERENCE PROCEEDINGS
7th International Conference on Urban Earthquake Engineering (7CUEE) &
5th International Conference on Earthquake Engineering (5ICEE)
March 3-5, 2010, Tokyo Institute of Technology, Tokyo, Japan

SITE CHARACTERIZATION USING SPATIAL AUTOCORRELATION METHOD IN LINEAR AND TRIANGULAR ARRAYS BY MEANS OF AMBIENT VIBRATION MEASUREMENTS

Fabio M. Upegui-Botero[1)], Carlos I. Huerta-López[2)], Jorge A. Caro-Cortés[1)] and José A. Martínez-Cruzado[3)]

1) Graduate Student, Department of Civil Engineering and Surveying, University of Puerto Rico at Mayagüez, Puerto Rico- USA
2) Visiting Professor, Department of Civil Engineering and Surveying, University of Puerto Rico at Mayagüez, Puerto Rico- USA – Home Institution: CICESE, Seismology Department, Earth Sciences Division. Ensenada, México
3) Professor, Department of Civil Engineering and Surveying, University of Puerto Rico at Mayagüez, Puerto Rico- USA
fabio.upegui@upr.edu, carlos.huerta@upr.edu, andres.caro@upr.edu, jose.martinez44@upr.edu

Abstract: The SPatial Auto-Correlation method (SPAC) method can be used to estimate the subsoil structure by using Ambient Vibration (AV) measurements. AV measurements were recorded at two different sites within the University of Puerto Rico at Mayagüez campus. Two different seismic arrays were used. The first design was a linear configuration, and the second one in an equaled spaced 120° triangular scheme at radial distances of up to 30-m. Time series of 30 minutes in length were recorded simultaneously at sampling frequency of 100 Hz. The SPAC method uses simultaneous records of ambient vibration measurements at several stations of a designated geometrical array of seismic instruments. In this study, the sub-soil shear wave velocity (*Vs*) model of two sites using the SPAC method was estimated. According to the local geological conditions of the area in which the experiments were conducted, the shear wave velocity profile with low *Vs* values agrees well with soft materials of Quaternary alluvial soil deposits (site A). The site with large *Vs* values agrees well with stiff materials of soil deposits derived from Cretaceous rocks (site B).

1. INTRODUCTION

The SPatial Auto-Correlation method (SPAC) is currently being used by the engineering community (near-surface geophysics, seismology, and geotechnical) for soil shear wave velocity (*Vs*) profiling as an *in-situ* technique for site characterization. The method, then have the potential to contribute in studies for the evaluation of local site effect and ground response up-on seismic loads. The SPAC method was initially proposed by Aki (1957), and is based on the theory of the stationary random functions, in which the ambient vibrations are considered stationary in both time and space. The SPAC method estimates the correlation coefficients between pairs of measurements in an azimuthal array of ground motion sensors from which the dispersion curve of surface Rayleigh wave is estimated.

It has been proved that local site effects depends on the geometry sub-soil structure and the physical properties of the soil at the site. The *Vs* of the subsurface structure and the contrast of the impedance among the layers are considered key parameters for its major influence on local ground motion amplification.

Puerto Rico is located in the Caribbean zone, over and surrounded by tectonic plates capable to cause strong ground motions. The tectonic plates that affect Puerto Rico are the North American Plate and The Caribbean Plate. To the north of Puerto Rico is located the Puerto Rico Trench and to the west the fault known as the *Mona* Canyon. At the south is the *Muertos* through while at the east is the *Anegada* through. There are some faults inside the island but their extent and location are still under investigation. The area chosen for the present study is located in the city of Mayagüez, which is located in the west coast of the island.

The aim of this study was to determine the *Vs* and the geometry of subsoil conditions using the SPAC method in a Linear and a Circular array at two selected sites.

2. THEORETICAL BACKGROUND

2.1 SPATIAL AUTOCORRELATION METHOD (SPAC)

The SPAC method was originally proposed to determine the phase velocity of surface Rayleigh waves using ambient vibration (AV) records. The essence of SPAC is that having AV records from an array of seismic stations

along different azimuths, it is possible to estimate the phase velocity of the waves crossing the array. The phase velocity is determined as a function of frequency. The estimated function of the phase velocity is then inverted to estimate the *Vs* as a function of the depth, which will allow the estimation of the *Vs* profile of the site where the array of sensors was deployed for the AV measurements.

The SPAC method is based on the hypotheses that the noise is an stochastic process; stationary both in time and space, and that the ground motion of vertical component is mostly composed of Rayleigh waves.

The method was proposed for horizontally propagating waves; it uses AV measurements in stations distributed azimuthally. The Spatial Autocorrelation function $\Gamma_{o,j}(r,\theta,\omega)$ is calculated at two stations by computing the auto power spectrum and the cross power spectrum of the stations and between the pair of stations (center-location j), respectively. The SPAC coefficients $\overline{\rho(r,\omega)}$ may be directly calculated from the observed microtremor data in the frequency domain using the Fourier Transform as stated in Eq. (1).

$$\Gamma_{o,j}(r,\theta,\omega) = Re\left(\frac{A_{oj}(r,\theta,\omega)}{\sqrt{A_o(\omega)\cdot A_j(r,\theta,\omega)}}\right) \quad (1)$$

where $A_o(\omega)$ and $A_j(r,\theta,\omega)$ are the auto power spectral densities of the microtremors at two sites, *O(0,0)* and *j(r;θ)*, respectively. $A_{oj}(r,\theta,\omega)$ is the cross power spectrum between *o(0,0,ω)* and *j(r;θ,ω)*. *Re ()* is the real part of complex value and $\Gamma_{o,j}(r,\theta,\omega)$ is the spatial autocorrelation function calculated at two stations. The spatial autocorrelation coefficient of signals recorded at two stations separates by a distance *r* can be written as Eq. (2).

$$\overline{\rho(r,\omega)} = \frac{1}{2\pi\Gamma(r=0,\omega)}\int_0^{2\pi}\Gamma_{o,j}(r,\theta,\omega)d\theta = J_0\left(\frac{\omega r}{c(\omega)}\right) \quad (2)$$

where, $\bar{\rho}$ is the azimuthal average of the correlation ratio, $\Gamma(r=0,\omega)$ is the average autocorrelation function at the center of the array, $\Gamma(r,\theta,\omega)$ is the cross-correlation function between the record at a site coordinates *(r, θ)*, and the record obtained at the station at the origin, $c(\omega)$is the phase velocity at angular frequency ω for the Rayleigh waves with the fundamental mode, and finally, J_0 is the Bessel function of the first kind of zero order.

The SPAC method, although rarely used, can be extended for dealing with the horizontal components of ambient vibration in order to calculate Love wave velocities. The combination of Love and Rayleigh velocities together may contribute to have a better constrain of the *Vs* distribution (García-Jerez et al. 2008).

According to Chávez, et. al, (2006) consistent and similar results are obtained when using measurements of AV recorded along a line, which means it is not mandatory to use a circular array of sensors. The fact to consider is that larger time series are needed for the analysis.

The SPAC coefficients are obtained by averaging the normalized coherence functions with regard to site location θ, where the coherence functions are defined as the real part of cross spectrum $A_{oj}(r,\theta,\omega)$ and normalized by the power spectrum *O(0,0)* (Morikawa et al., 2004).

Four steps are required for completing the process in obtaining the shear wave velocity profile, those are:

(a) The estimation of the spatial autocorrelation coefficients.
(b) The inversion for obtaining the theoretical Bessel function of order zero.
(c) The estimation of the phase velocity curve (from the obtained Bessel function).
(d) The inversion of the shear wave velocity profile from the phase velocity curve.

3. DATA ACQUISITION AND PROCESSING OF AMBIENT VIBRATIONS MEASUREMENTS

AV recordings were carried out at two experimental sites (site A, and B) in an open space inside the campus of the University of Puerto Rico at Mayagüez. The site B is located in the parking lot next to the Biology's building, and site A is located close to the coliseum (Figure 1). The sites were selected taking in to consideration that they have significant differences on surface geological conditions, which are also expected at depth.

The measurements for the linear SPAC array (Site A) were taken using a linear, which consisted of stations placed at 2.5-, 5-, 10-, 15-, 20-, and 30-m, and the radial arrays (Site B) in which the sensors where placed at 5-, 10-, 20-, and 30-m all of them respect to the sensor located at the center. Figure 2, shows an schematic description of both arrays.

Broad-band WR-1 sensors were used for recording the AV on the SPAC arrays. These sensors are configured to have velocity and acceleration (AC-coupled, DC-coupled) output simultaneously. The sensitivities and frequency response characteristics are: (i) ± 2.5 V/± 0.01g, DC to 20 Hz for the acceleration output with DC coupled, (ii) ± 2.5 V/± 0.01g, 0.05 to 20 Hz for the acceleration output with AC coupled, and (iii) 160 V/m/s, 0.05 to 20 Hz in velocity. Figure 3 shows the WR-1 transfer functions. The data was recorded in a 24 bits of analog to digital converter (ADC) dataloger. The time synchronization was obtained with a GPS integrated on the recorder. The sampling rate was 0.01s, and unit gain.



Figure 1 Location of the experimental test sites, at University of Puerto Rico at Mayagüez (UPRM). (Adapted from: Huerta et. al. 2009). Colors represent the surface geology classification. Light green: Cretaceous rocks (Ky), Brown: Quaternary rocks (Qa), Dark green: Jurassic rocks (Jse).

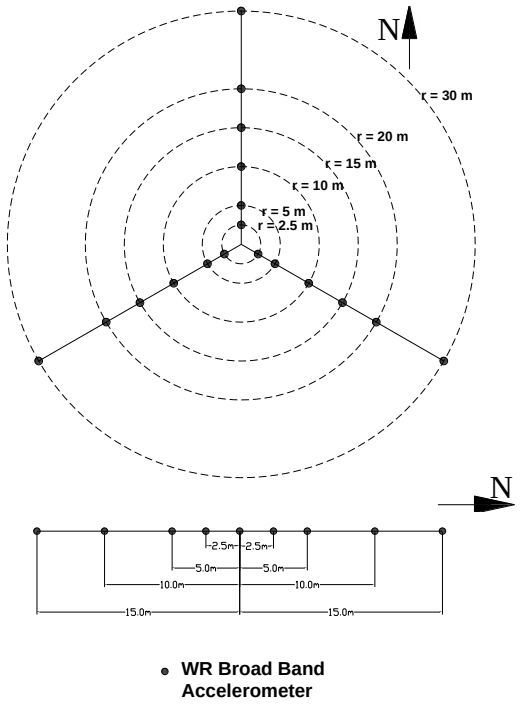

Figure 2 Top: Geometry of the radial stations, bottom Geometry of the linear stations for ambient vibration detection.

The sensors were placed directly on the ground surface properly leveled and coupled to the ground. The record length for each measurement was at least 30 min. At each setting up distance of both arrays. To obtain the most accurate ambient vibration measurements, free of transients due to human activities at small distances from the recording sites, the experimental sites were located as far as possible from anthropogenic sources of noise.

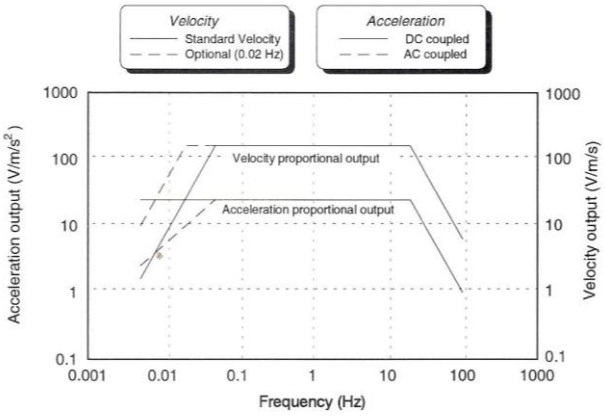

Figure 3 Transfer function velocity and acceleration output. (Adapted from: Kinemetrics Inc, June 1994)

AV measurements were made on the assumption that the SPAC method is applied to determine the phase velocity dispersion curves of Rayleigh surface waves at the site. Only the vertical component of velocity ground motions was used to apply the SPAC method.

Figure 4 shows the time series of 30 minutes of AV recorded simultaneously for the sensors at 5-m (station 1), 20-m (station 2) and 30-m (station3) for the linear array. For each simultaneous time series, the records were baseline corrected.

The entire length signal was divided in time windows segments. An overlap of 75% was applied in order to obtain unbiased estimates (Kanasewich, 1981).

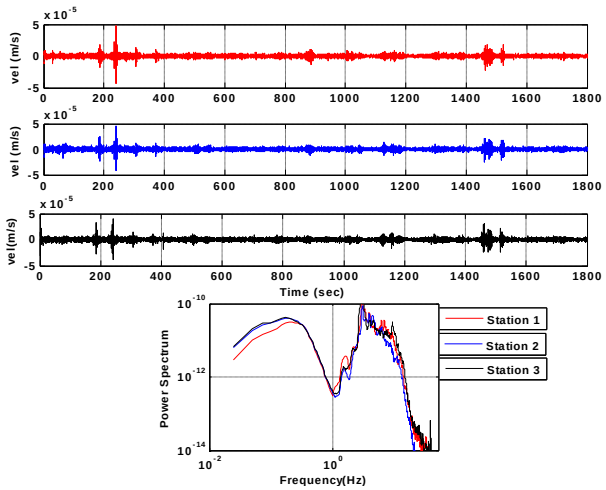

Figure 4 Example of simultaneous ambient vibration records of 30 min duration and their Power Spectra. First, second, and third rows are the vertical-component at the Linear array. Fourth row is the Power Spectral Density Spectra (PSD) of each signal.

4. ANALYSIS OUTLINE

The SPAC method was used to determine the phase velocity of Rayleigh wave from ambient vibration measurements. The first stage of the signal processing was the calculation of the Fourier Spectra and the power spectra of the signals. It was carried out in the same manner for all records. Second, Spatial Autocorrelation coefficients were calculated by averaging, using the Eq. (1). Having the average autocorrelation coefficients function, the third step was to obtain the theoretical Bessel function of the first kind (zero order), which is also shown in Figure 5.

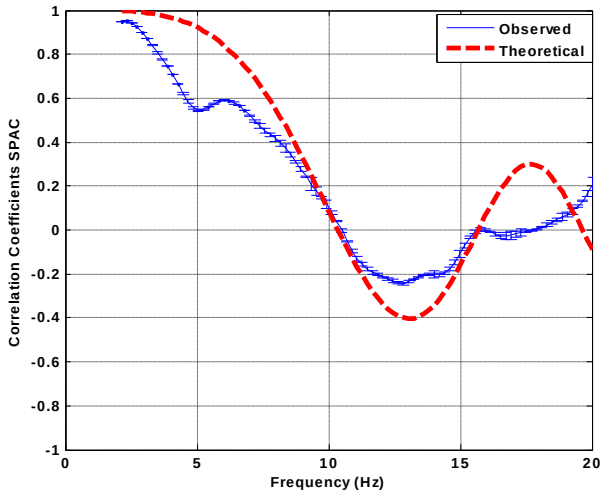

Figure 5 Autocorrelation coefficients averaged observed and their fit to zero order Bessel function.

A typical behavior of the Bessel function is that the first zero crossing (fundamental mode) will be at large frequencies for small separation distance between sensors and at lower frequencies for large distances between observation points.

Finally, the last step to obtain the experimental phase velocity of Rayleigh waves results from the inversion of correlations coefficients obtained from each distance of the array, as stated in Equation 2.

Figure 6 shows results of both: (i) the composed curve (asterisks) and (ii) the smoothed curve (circles) of the experimental dispersion curve of the obtained phase velocity of Rayleigh waves.

For the determination of *Vs*, an initial layered soil model with thickness, Poisson ratio, density and velocities for each layer and the half space is required. The process compares the theoretical dispersion curve computed from an initial model with the experimental phase velocity. A genetic algorithm (adapted from Tapia, 2009) was used, and the procedure iterates until the adopted convergence criteria is reached. When the theoretical dispersion curve matches with the experimental one, it is then assumed that the theoretical model describes well the subsoil stratigraphy and the velocity profile.

4.1 Results for Linear and Circular SPAC

In the Linear SPAC case the parameterization of the subsoil model was achieved from the inversion of the Rayleigh wave dispersion curve, for which a six-layers soil model resting on the half space provided the best match between the theoretical and experimental curves. Figure 7 shows the inversion of phase velocity curve obtained for the linear and circular array (sites A and B).

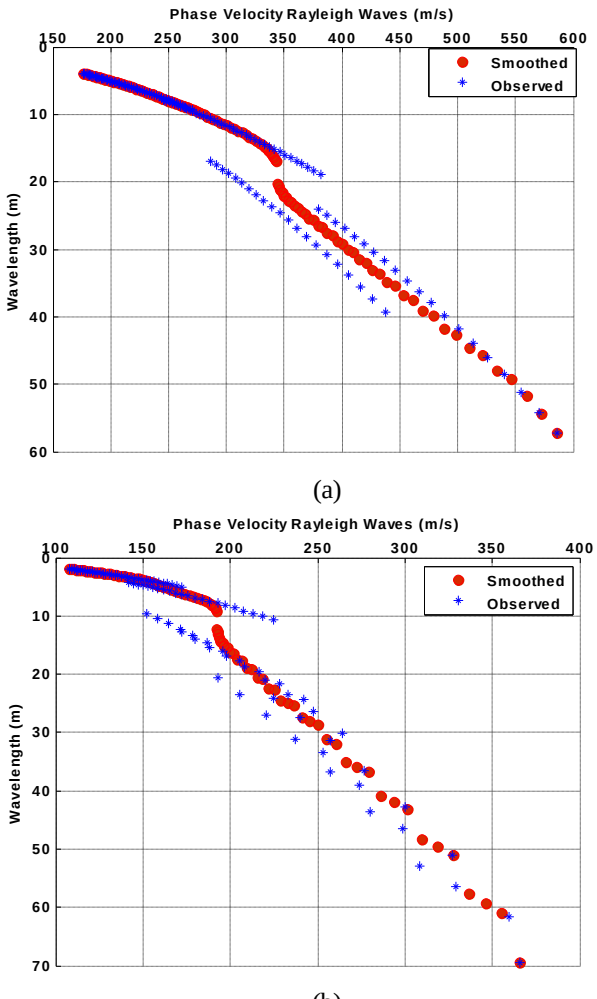

Figure 6 Results from the inversion of the auto correlation function from which the phase velocity of Rayleigh waves was obtained. a) Circular SPAC array, and b) Linear SPAC array.

In the Circular SPAC case the parameterization of the subsoil model corresponded for a five layers soil model resting on the half space. Figure 8 shows the shear velocity model calculated for Linear and Circular Array (sites A and B).

5. DISCUSSION AND CONCLUSIONS

In this study, a genetic algorithm was applied to SPAC data in order to calculate the *Vs* profiles from ambient vibration measurements.

The experimental phase velocity curve showed a gap in frequencies between 5 to 7 Hz in both cases (Linear and Circular SPAC) (see Figure 9). The inability to estimate the phase velocity at frequencies from 5 to 7 Hz is probably due to the fact that the dimensions used in the arrays could not provide enough signals in that wavelength range necessary to describe discrete values at that frequency interval.

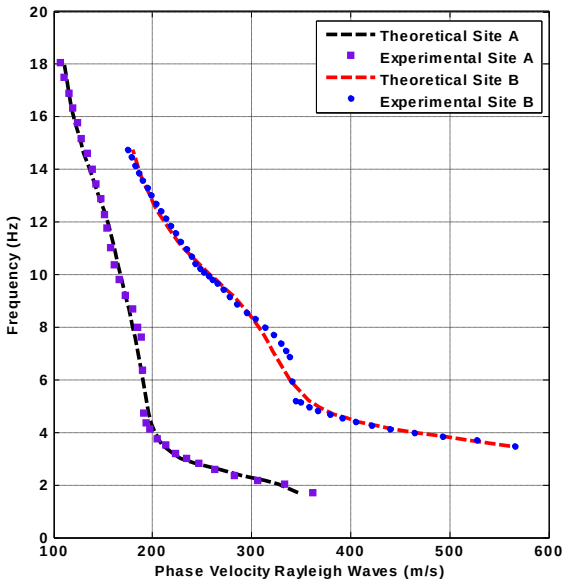

Figure 7 Experimental (dots), and theoretical (dashed line) Phase velocity dispersion curves.

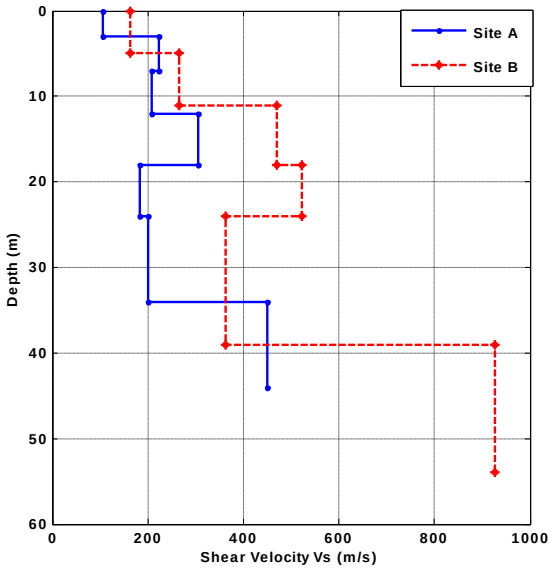

Figure 8 Obtained shear wave velocity model profiles for sites A and B.

The SPAC Linear array clearly shows a weak velocity inversion at the depth of 7- and 18-m. The velocity inversion at depth of 7-m of 15 m/s. probably results by the algorithm artifacts in the fitting process between the theoretical and the experimental curves. A real physical meaning of this velocity inversion, at this depth on the site is dubious. However the velocity inversion at the depth interval of 18- to 24-m is large enough that has non-dubious physical meaning of a change of the materials physical properties.

The Circular SPAC clearly shows a velocity inversion at the depth of 24-m. in this case the inversion is slightly larger than 100 m/s.

Regarding to the frequency content and the wave type of AV measurements, the determination of dispersion curves indicate that surface waves are dominant. Moreover, it is assumed that a single mode is dominant and it may correspond to the fundamental vibration mode.

According to the local geological conditions of the area in which the experiments were conducted, the shear wave velocity profile with low *Vs* values agrees well with soft materials of Quaternary alluvial soil deposits (site A). The site with large *Vs* values agrees well with stiff materials of soil deposits derived from Cretaceous rocks (site B).

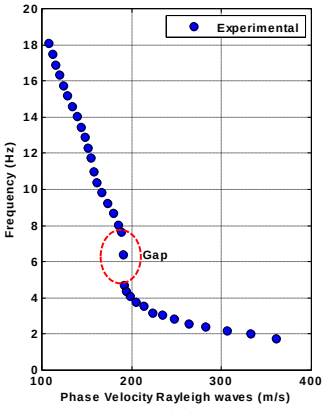

(a)

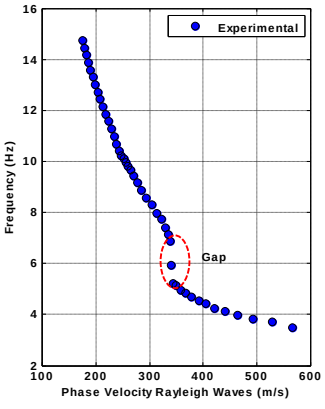

(b)

Figure 9 Experimental Phase Velocity of Rayleigh Waves: a). Linear SPAC – b) Circular SPAC

Acknowledgements:

We express our thanks to Puerto Rico Strong Motion Program. The University of Puerto Rico at Mayagüez, for the computational facilities for the data processing and analysis.

References:

Aki, K. (1957), "Space and time spectra of stationary stochastic waves, with special reference to microtremors", *Bulletin of the Earthquake Research Institute*, vol. 35, pp. 415 – 457.

Chávez-García, F. J., Rodriguez, M., and Stephenson W. R. (2005), "An alternative approach to the SPAC analysis of microtremors: Exploiting stationary of noise", *Bulletin of the Seismological Society of America*, vol. 95, No 1, pp. 277 – 293.

Chávez-García, F. J., Rodriguez, M., and Stephenson W. R. (2006), "Subsoil structure using SPAC measurements along line", *Bulletin of the Seismological Society of America*, vol. 96, No 2, pp. 729 – 736.

García-Jerez, A., Luzon, F., Navarro, M., and Pérez-Ruiz, A. (2008), "Determination of elastic properties of shallow sedimentary deposits applying a spatial autocorrelation method", *Geomorphology*, vol. 93, pp. 74 – 88.

Huerta-López, C. I., Pando, M A., Suárez, L E., Ritta, R., and Martínez-Cruzado, J A. (2009). "Shallow Soil Layers Fundamental Vibration Mode: A Comparison of Estimations Obtained With the Random Decrement Method and H/V Spectral Ratios Using Weak and Moderate Seismic Ground Motions", *Meeting American Geophysical Union, Joint Assembly.* Toronto, Canada, May 24 - 27, Paper: NS23B-01.

Kanasewich, E.R. (1981). "Time series analysis in geophysics", Third Edition. University of Alberta Press, Edmonton, Alberta.

Kinemetric, Inc (1994). "Kinemetrics WR-1 Wide-Band Ranger Seismometer", *Operation Instructions Booklet*, Pasadena, California, USA.

Morikawa, H., Sawada, S., Akamatsu, J.(2004), "A method to estimate phase velocities of Rayleigh waves using microseisms simultaneously observed at two sites", *Bulletin of the Seismological Society of America*, vol. 94, No3, pp. 961 – 976.

Nogoshi, M. and Igarashi, T. (1971). "On the amplitude characteristics of microtremor (part 2)", *Journal of the Seismological Society*, Japan, Vol. 24, 26–40. (In Japanese)

Tapia-Herrera, R. (2009), "*Estudio comparativo de los métodos SASW, SPAC y HV-SPR para la estimación in-situ de propiedades del terreno*", M.Sc Thesis, CICESE, Seismology Department, Earth Sciences Division. Ensenada México.

JOINT CONFERENCE PROCEEDINGS
7th International Conference on Urban Earthquake Engineering (7CUEE) &
5th International Conference on Earthquake Engineering (5ICEE)
March 3-5, 2010, Tokyo Institute of Technology, Tokyo, Japan

TIME-FREQUENCY ENERGY DISTRIBUTION OF WENCHUAN EARTHQUAKE MOTIONS BASED ON MATCHING PURSUIT DECOMPOSTION

Dongwang Tao[1], Hui Li[2]

1) PhD student, School of Civil Engineering, Harbin Institute of Technology, China
2) Professor, School of Civil Engineering, Harbin Institute of Technology, China
taodongwang@hit.edu.cn, lihui@hit.edu.cn

Abstract: In this paper, the matching pursuit decomposition, an adaptive time-frequency transform, combined with the Wigner-Ville distribution is employed to analyze non-stationary strong earthquake acceleration records. The obtained time frequency energy distribution (TFED) captures the temporal evolution of the frequency contents efficiently and it can also indicate earthquake energy release characteristics which are not available from traditional time series or frequency amplitude spectrum (FAS). According to the TFEDs of accelerograms recorded at the surface in Wenchuan earthquake, the energy release styles both in time and frequency at sites along the Longmen Shan fault and sites with different epicenter distance are obtained and their effects on different structures are discussed.

1. INTRODUCTION

In earthquake engineering, a knowledge of the ground motion is essential to an understanding of the earthquake behavior of structures (Housner, 1970). In most cases the basic obtained data are the strong earthquake acceleration records which contain valuable characteristics and information of earthquakes and the corresponding parameters such as peak ground motion values (PGA, PGV and PGD), frequency contents, duration of strong shaking phase and other intensity index (Arias Intensity, Characteristic Intensity, etc.) are defined to measure earthquake intensity or input energy and evaluate structural response in the past decades (Yousef Bozorgnia and Kenneth W. Campbell, 2006). However, due to the non-stationary nature of earthquake, the above mentioned parameters alone can not truly represent the characteristics of strong ground motion, especially its temporal evolution of the frequency contents and energy release style in both time and frequency domain, both of which may make structure behave quite differently and exhibit considerable difference in destructiveness even in apparently similar ground motions (Jun Iyama and Hitoshi Kuwamura, 1999). Therefore, it is indispensable to analyze and interpret strong ground motion in both time and frequency domains so as to help researchers and designers have more understanding of the non-stationarity of earthquake ground motion and its effect on structural behaviors.

Up to now there has been a growing trend to implement time frequency analysis mainly wavelet transform to analyze strong ground motion in earthquake engineering. Iyama and Kuwamura (1999) established energy principles in wavelet analysis and proposed methods to simulate pseudo-ground motions. Later Iyama (2005) developed the energy principle to estimate input energy for elasto-plasto SDOF systems. Basu and Gupta (1997, 1998) presented stochastic analysis of linear SDOF and MDOF under ground motions based on Littlewood-Paley basis and harmonic wavelet basis by Newland (1994). Zhou and Adeli (2003) proposed wavelet energy spectrum to show time-frequency localization using Mexican hat wavelets. Cao and Friswell (2009) demonstrated the effect of energy distribution in time and frequency domain on nonlinear response of RC structures. However, the frequency contents are not the same after translating different series in different scales. As the time frequency localizations of earthquake accelerations vary widely, the decompositions should be flexible and adaptive enough to capture the different local characteristics of ground motions.

In this article, first the adaptive matching algorithm, which was proposed by Mallat and Zhang (1993), Qian and Chen (1993) independently, is implemented to decompose seismic accelerogram and the corresponding time frequency energy distribution (TFED) is obtained by adding the Wigner-Vill distribution of each decomposed atom. Later simple artificial signals with same PGA and frequency contents are generated to demonstrate the significance of TFED. Then several observations in great Wenchuan earthquake are analyzed to obtain the TFED using MPD, and characteristics of energy released are found. Finally the relationship between maximum resonance displacement and maximum atom energy is discussed by analyzing the TFED of EW component of Bajiao station and its artificial earthquake records.

2. TIME-FREQUENCY ENERGY DISTRIBUTION

2.1 Matching Pursuit Decomposition

The matching pursuit decomposition (Mallat and Zhang, 1993) divides any complex signal $x(t)$ into a set of orthogonal components $x(t)$ as follows:

$$x(t) = \sum_{n=0}^{\infty} x_n(t) \tag{1}$$

$$x_n(t) = < R^n x(t), g_{\gamma_n}(t) > g_{\gamma_n}(t) \tag{2}$$

$$R^n x(t) = < R^n x(t), g_{\gamma_n}(t) > g_{\gamma_n}(t) + R^{n+1} x(t) \tag{3}$$

$$g_{\gamma_n}(t) = \frac{1}{\sqrt{s_n}} g(\frac{t-u_n}{s_n}) e^{i2\pi f_n t} \tag{4}$$

Here, $R^n x(t)$ is the n th residual where n is the iteration number, with $R^0 x(t) = x(t)$; $g_{\gamma_n}(t)$ is the optimal time frequency atom which is defined as

$$g_{\gamma_n}(t) = \arg \max_{g_{\gamma_n} \in D} < R^n x(t), g_{\gamma_n}(t) > \tag{5}$$

where $<\bullet>$ stands for inner product; $D = g_{\gamma_n}(t)$ is an extremely redundant dictionary with the norm of each atom equals to 1; $\gamma_n = (s_n, u_n, f_n)$ is the parameters defining an atom, where s_n is the spread in time or scale, u_n is the time delay or translation, f_n is the center cyclic frequency or modulation, $g(t)$ is a normalized window function. In this paper $g(t)$ is chose as a Gaussian window with the form of

$$g(t) = 2^{1/4} e^{-\pi t^2} \tag{6}$$

For the real seismic acceleration, the data has to be decomposed into real components by

$$x(t) = \sum_{n=0}^{\infty} < R^n x(t), g_{(\gamma_n, \varphi_n)}(t) > g_{(\gamma_n, \varphi_n)}(t) \tag{7}$$

with the real atoms given by

$$g_{(\gamma_n, \varphi_n)}(t) = \frac{C_{(\gamma_n, \varphi_n)}}{\sqrt{s_n}} g(\frac{t-u_n}{s_n}) \cos(2\pi f_n t + \varphi_n) \tag{8}$$

where $C_{(\gamma_n, \varphi_n)}$ is a constant coefficient to make the norm of atom equal to 1, and φ_n, a hidden phase in complex atom, now is a parameter defining an atom which best matches the residue of signal together with s_n, u_n, f_n. The transformation from complex atoms to real atoms can also be written by

$$g_{(\gamma_n, \varphi_n)}(t) = \frac{C_{(\gamma_n, \varphi_n)}}{2} (e^{i\varphi_n} g_{\gamma_n}(t) + e^{-i\varphi_n} g_{\gamma_n^-}(t)) \tag{9}$$

where $\gamma_n^- = (s_n, u_n, -f_n)$.

2.2 Wigner-Vill Energy Distribution

The time-frequency energy distribution of real seismic acceleration is obtained by summing the Wigner-Vill distribution of the decomposed atoms on the right side of equation (10).

$$Ex(t) = \frac{1}{2} \sum_{n=0}^{\infty} | < R^n x(t), g_{(\gamma_n, \varphi_n)}(t) > |^2 \cdot (WVg_{(\gamma_n, \varphi_n)}(t, f) + WVg_{(\gamma_n^-, \varphi_n)}(t, f)) \tag{10}$$

where the Wigner-Vill distribution is defined by

$$WVg(t, f) = \int_{-\infty}^{\infty} Hf(t + \frac{\tau}{2}) \overline{Hf}(t - \frac{\tau}{2}) e^{-if\tau} d\tau \tag{11}$$

here Hf is the Hilbert transform of signal f, and $\overline{Hf}$ is the conjugate of Hf.

2.3 Significance of Time-frequency Energy Distribution

In order to demonstrate the significance of time-frequency energy distribution of earthquake, two artificial signals with exactly the same peak absolute value and frequency content are generated. The formula are

$$a_1 = \exp(-2\pi(\frac{t-10}{5})^2) \sin(2\pi f_0 t) + 0.447 \exp(-2\pi(\frac{t-30.48}{5})^2) \sin(4\pi f_0 t) \tag{12}$$

$$a_2 = 0.707 \exp(-2\pi(\frac{t-10}{5})^2) \sin(2\pi f_0 t) + 0.447 \exp(-2\pi(\frac{t-10}{5})^2) \sin(4\pi f_0 t) + 0.707 \exp(-2\pi(\frac{t-30.48}{5})^2) \sin(2\pi f_0 t) \tag{13}$$

with $f_0 = 0.9766$. The signals and their corresponding frequency amplitude spectrums are shown in Figures 1, 2 and 3. But the resonance responses of structure with natural frequency of $f_0 = 0.9766$ under the above artificial signals are quite different as shown in Figure 4. The response under signal a_1 is bigger than that of signal a_2 in the first phase, but in the second phase the response under the former signal is much small than that of the latter one. The PGA and frequency contents can't explain this phenomenon because they are exactly same in above two signals. The time frequency energy distributions by matching pursuit decomposition of the signals are shown in Figure 5 and Figure 6. The maximum displacement in signal a_1 is bigger than that in a_2 is due to that released energy in atom 1 of a_1 is bigger than that in atom 1 of a_2, even though the total released energies are the same in the two signals as shown in frequency amplitude spectrums. This means the time frequency energy distribution should be considered in earthquake characteristics besides the traditional PGA and frequency amplitude spectrums.

3. APPLICATION TO THE GREAT WENCHUAN EARTHQUAKE MOTIONS

3.1 Analyzed Observations in Main Shock of Wenchuan Earthquake

In this paper station records with PGA greater than 300

gal and far-epicenter records are analyzed to obtain time frequency energy distribution using matching pursuit algorithm. The distribution of the observations and corresponding epicenter, nearest surface fault distance are shown in Figure 7 and Table 1. The surface Longmen Shan fault is approximately represented by the line from point 1, 2 and 3 which means Wenchuan epicenter, Yingxiu and Qingping respectively (Li, et. al, 2008). Among the stations, Wolong is closest to the epicenter with distance of 19 km and corresponding PGAs in EW, NS, UD directions are 957gal, 653gal, 948 gal, and Qingping is closet to the surface fault with distance of less than 3 km and corresponding PGAs in EW, NS, UD directions are 824gal, 802gal, 623 gal.

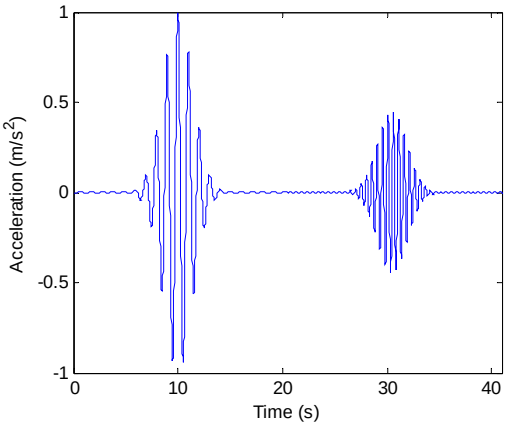

Fig. 1. Signal a_1

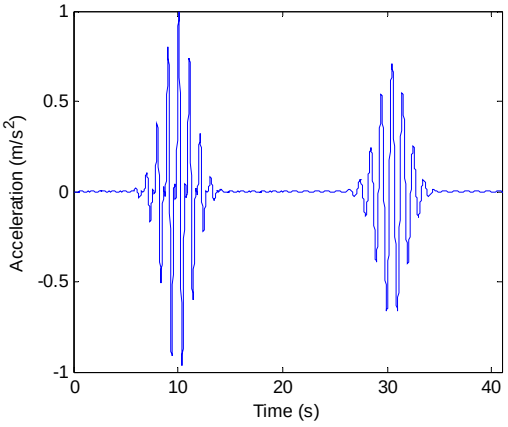

Fig. 2. Signal a_2

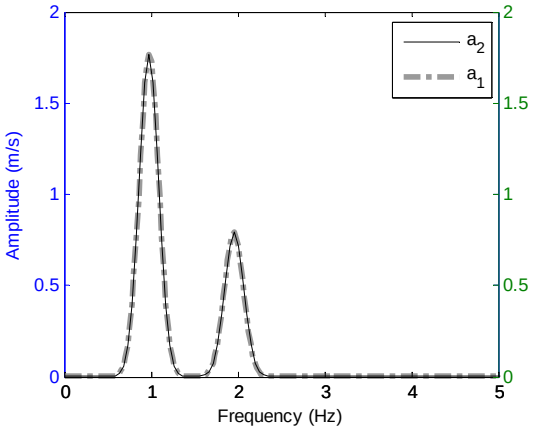

Fig. 3. Frequency Amplitude Spectrums of a_1, a_2

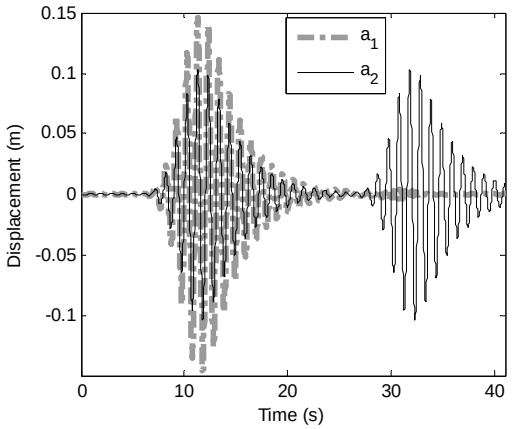

Fig. 4. Resonance Response under a_1, a_2

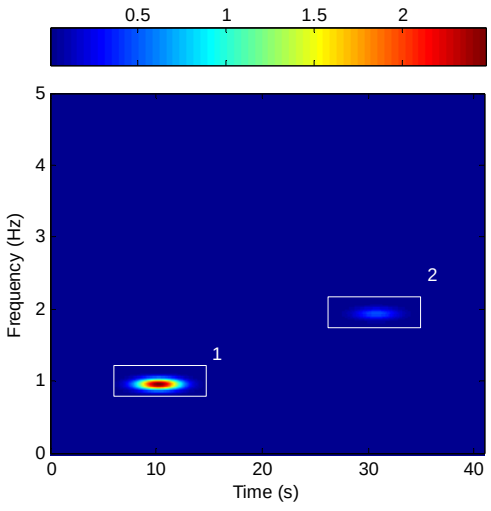

Fig. 5. Time-frequency Energy Distribution of a_1

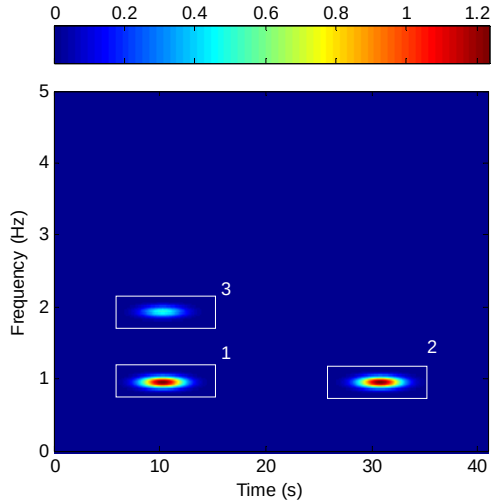

Fig. 6. Time-frequency Energy Distribution of a_2

3.2 Time-frequency Energy Distribution of Analyzed Observations

The recorded duration in each of the above stations is more than 120 seconds with sample frequency of 200Hz, however, in order to make the MPD more efficiently, only strong phase in 89.12 seconds with resampling frequency of 100Hz is analyzed. The frequency contents are not changed due to the resampling, which is shown later. The time-frequency energy distributions of the three components in EW, NS, UD directions of Wolong station are shown in Figures 8, 9 and 10. The corresponding distributions for Qingping station are shown in Figure 11, 12 and 13. In each Figure, the up subplot is the acceleration time history, the left subplot is the fourier amplitude spectrum and the middle one is the time-frequency energy distribution with the colorbars standing for the magnitudes.

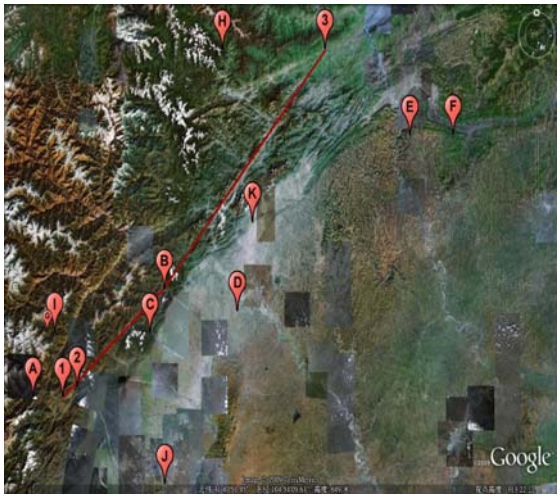

Fig. 7. Distribution of Observation Stations in Main Shock of Wenchuan Earthquake (from Google Earth)

Table 1. Epicenter Distance and Nearest Surface Fault Distance of Stations

Label	Station	Epicenter Distance (km)	Nearest Surface Fault Distance (km)
A	Wolong	19	19
B	Mianzhu Qingping	87	<3
C	Shifang Bajiao	65	11
D	Jiangyou Hanzeng	123	44
E	Guangyuan Shijin	264	69
F	Guangyuan Zengjia	289	95
G	Lixian Muka	34	28
H	Pingwu Muzuo	206	51
I	Maoxian Nanxin	34	32
J	Chengdu Zhonghe	81	76
K	Jiangyou Dizhentai	152	21
L	Enshi	590	590

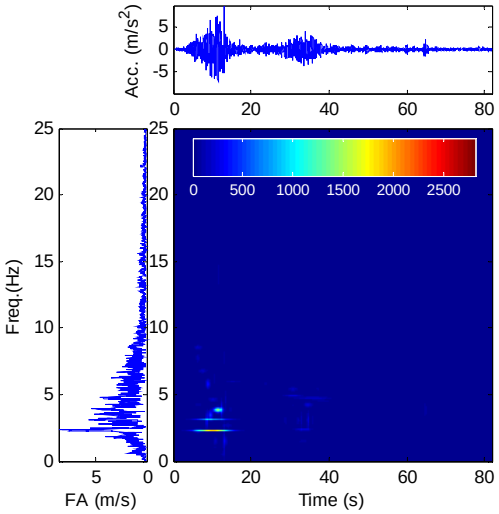

Fig. 8. Time-frequency Energy Distribution of EW Component of Wolong

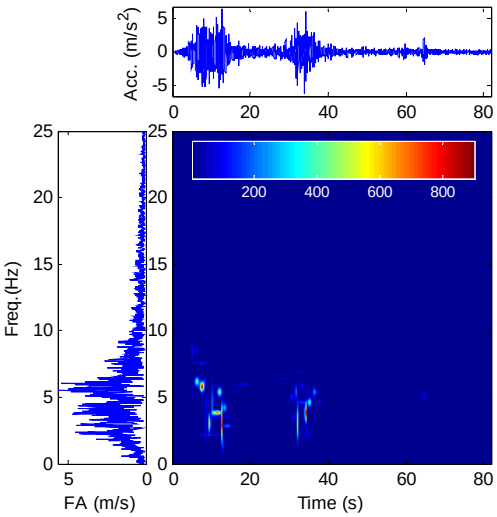

Fig. 9. Time-frequency Energy Distribution of NS Component of Wolong

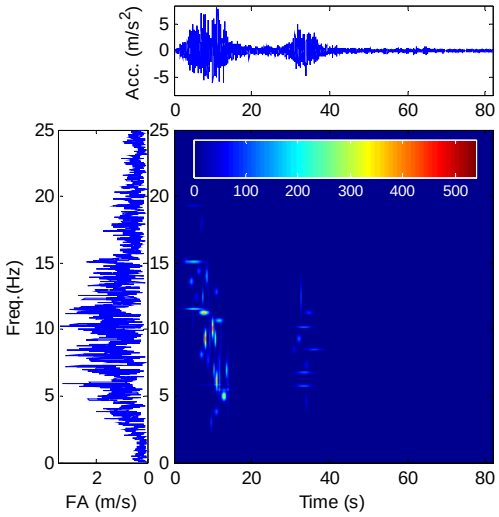

Fig. 10. Time-frequency Energy Distribution of UD Component of Wolong

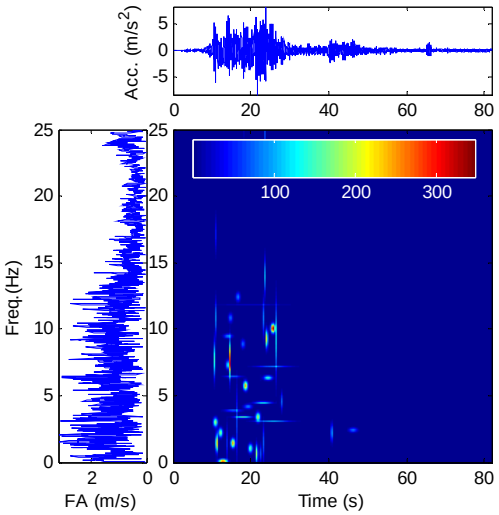

Fig. 11. Time-frequency Energy Distribution of EW Component of Qingping

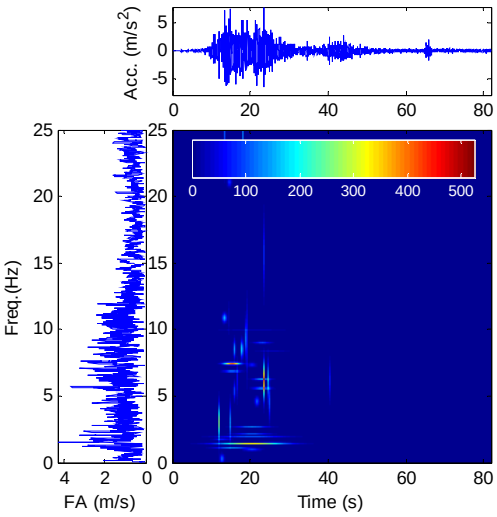

Fig. 12. Time-frequency Energy Distribution of NS Component of Qingping

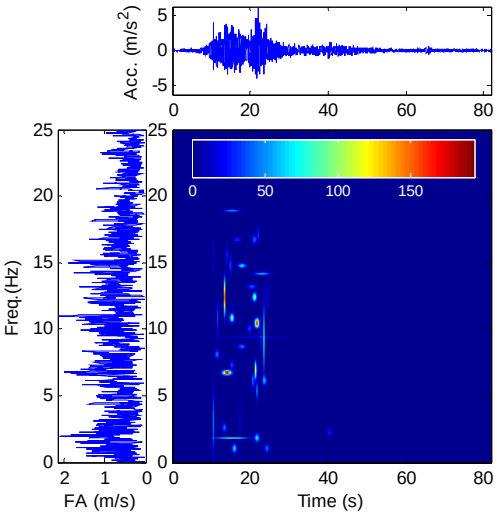

Fig. 13. Time-frequency Energy Distribution of UD Component of Qingping

For simplicity in the following discussion, the frequency below 2Hz is called low frequency, 2 to 5 Hz as medium frequency, above 5 Hz as high frequency. From Figures 8, 9 and 10, it can be seen that the frequency contents in each direction of Wolong are different with low frequency in EW component, medium frequency in NS one and high frequency in UD one. The energy release styles are also different: in EW component, there exists an atom with center frequency of 2Hz and scale time of 10.24 second; however there are only atoms with scale time no more than 5.12 second in the other components. In Qingping, however, energy is evenly distributed in low, medium and high frequencies in each direction. The energy release styles in EW and UD direction are similar in time frequency domain, but in NS component there exists an atom with center frequency of 1.5Hz and scale time of 10.24 second.

The peak ground acceleration (PGA), the maximum time frequency atom energy and the corresponding center time, center frequency, time spread and frequency spread are shown in Table 2, 3, and 4 for EW, NS and UD components respectively. From these figures, it can be seen that the maximum atom energy of EW component is much bigger than that of NS component, which is bigger than UD component for all the stations except Qingping, even though the three component PGAs of these stations may be much of a size. It means that in time-frequency domain the released energy is more concentrated in EW direction followed by NS and UD directions. The EW component PGA of Qingping, 824.1 gal, is much bigger than that of Bajiao, 581.6 gal, but the maximum atom energy of the former one, 174.1 m^2/s^4, is much smaller than the latter one, 1057.6 m^2/s^4. The corresponding time frequency

Table 2. Energy Characteristics of EW Components of Analyzed Stations

Epicenter Distance (km)	19	34	34	65	81	87	123	590
Nearest Surface Distance (km)	19	28	32	11	76	<3	21	590
PGA (gal)	957.7	339.7	409.1	556.2	79.2	824.1	519.5	8.0
Maximum Atom Energy (m^2/s^4)	1404.3	162.8	346.7	1057.6	6.0	174.1	402.4	0.4
Center Time (s)	10.2	12.8	23.0	23.7	35.8	25.6	29.4	43.5
Center Frequency (Hz)	2.3	6.6	1.9	2.3	0.5	10.2	6.8	0.7
Time Spread (s)	10.2	1.3	5.1	1.3	10.2	1.3	2.6	5.1
Frequency Spread (Hz)	0.2	1.6	0.4	1.6	0.2	1.6	0.8	0.4

Table 3. Energy Characteristics of NS Components of Analyzed Stations

Epicenter Distance (km)	19	34	34	65	81	87	123	590
Nearest Surface Distance (km)	19	28	32	11	76	<3	21	590
PGA (gal)	648.6	342.4	318.3	581.6	69.7	797.9	347.1	7.3
Maximum Atom Energy (m^2/s^4)	440.8	97.7	133.2	767.7	3.1	235.8	109.3	0.2
Center Time (s)	7.7	33.9	23.0	24.3	30.7	20.5	29.4	30.7
Center Frequency (Hz)	5.9	8.2	1.9	3.1	1.1	1.5	8.6	0.7
Time Spread (s)	1.3	1.3	5.1	2.6	5.1	20.5	0.6	10.2
Frequency Spread (Hz)	1.6	1.6	0.4	0.8	0.4	0.1	3.1	0.2

Table 4. Energy Characteristics of UD Components of Analyzed Stations

Epicenter Distance (km)	19	34	34	65	81	87	123	590
Nearest Surface Distance (km)	19	28	32	11	76	<3	21	590
PGA (gal)	818.2	368.1	352.5	633.1	45.3	622.9	417.8	5.3
Maximum Atom Energy (m^2/s^4)	258.5	91.9	58.2	182.0	3.0	97.1	49.6	0.3
Center Time (s)	11.5	30.7	19.2	17.0	41.0	14.1	28.2	25.6
Center Frequency (Hz)	6.3	10.1	3.1	6.3	0.5	6.8	17.6	0.5
Time Spread (s)	0.3	20.5	2.6	0.6	41.0	2.6	2.6	10.2
Frequency Spread (Hz)	6.2	0.1	0.8	3.1	0.0	0.8	0.8	0.2

energy distributions are shown in Figures 11 and 14. As mentioned in Section 2.3, the more concentrated energy both in time and frequency will cause larger structural response which was not considered too much by designers and researchers before.

3.3 The Effect of Time-frequency Energy Distribution on Structural Response

To demonstrate the effect of time-frequency energy on the structural response, from EW component of Bajiao station 100 artificial earthquake records are generated based on two restrictions: same PGA and same frequency contents. The TFED of one of the records is shown in Figure 15. As it can be seen the released energy is evenly distributed in the time duration. The maximum displacements of structure with natural frequency of 2.3 Hz, the center frequency of the maximum energy atom, excited by the above records are different due to the different time frequency energy distributions. Among the 101 records, the records where the maximum displacement is mainly caused by the corresponding largest atom energy with center frequency of 2.3 Hz are selected. The relation between them is shown in Figure 16, which shows that the more concentrated energy gives larger displacement. Better relationship can be further researched by taking time spread, frequency spread into consideration.

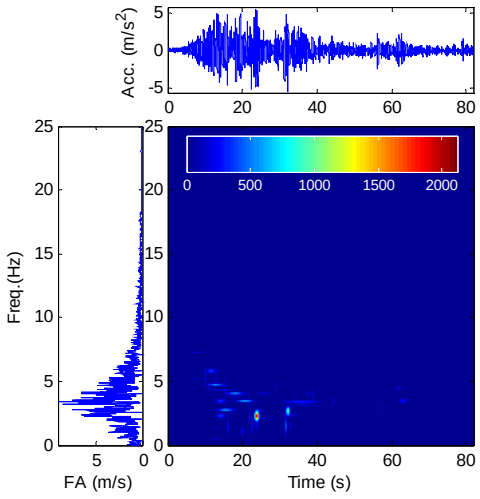

Fig. 14. Time-frequency Energy Distribution of EW Component of Bajiao

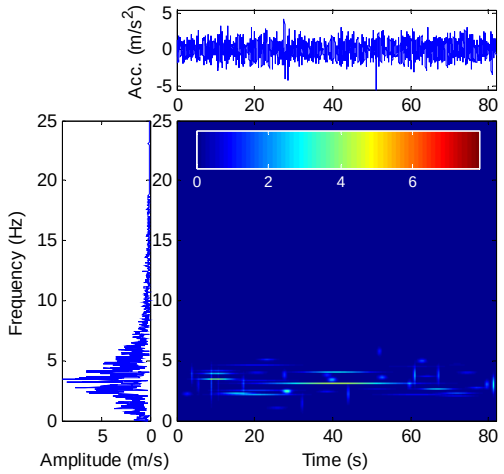

Fig. 15. Time-frequency Energy Distribution of EW component of artificial record

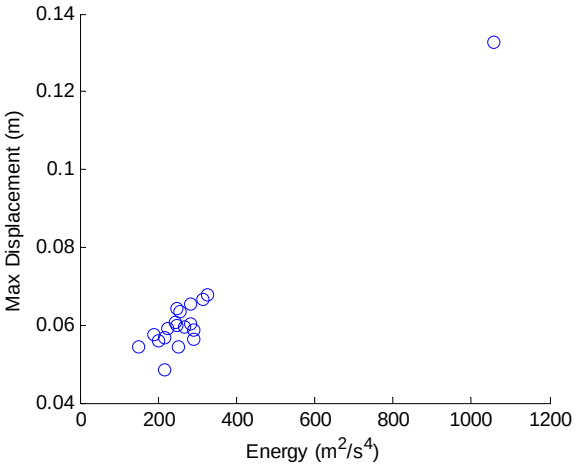

Fig. 16. Scatter of Maximum Displacement and Largest Atom Energy

4. CONCLUSIONS

Matching pursuit decomposition was implemented in this paper to obtain the high resolution time-frequency energy distribution of earthquake accelerogram. The time-frequency energy distribution plot can be used to show the evolution of frequency contents and the local energy concentration.

Based on the analysis of the EW, NS and UD components records in great Wenchuan earthquake, it shows that the energy released characteristics are different with EW component most concentrated followed by NS, UD direction orderly.

From the demonstration examples of synthetic signals and artificial earthquake records, different structural response is due to the different local energy concentration both in time and frequency, even though the records have the same PGA and frequency contents, with more concentrated energy giving larger structural response. It implies that the time-frequency energy distribution could be considered as another characteristic of ground motion.

Acknowledgements:

The authors acknowledge support from the Chinese Ministry of Science and Technology with Grant No. 2007CB714205 and help from China Strong Motion Networks Center for providing the Wenchuan earthquake records. The authors thank E. Bacry for suggestions on implementing LastWave software.

References:

Housner, G.W. (1970), Strong Ground Motion, *Earthquake Engineering*, Edited by Wiegel R.L., Prentice-Hall Inc.

Bozorgnia, Y and Campbell, K.W. (2006), Engineering Characterization of Ground Motion, *Earthquake Engineering from Engineering Seismology to Performance-based Engineering*, Edited by Bozorgnia Y. and Bertero V.V, Taylor & Francis Group.

Iyama, J. and Kuwamura, H. (1999), Application of Wavelets to Analysis and Simulation of Earthquake Motions, *Earthquake Engineering and Structural Dynamics*, **28**(3), 255-272.

Iyama, J. (2005), Estimation of Input Energy for Elasto-plastic SDOF Systems during Earthquakes Based on Discrete Wavelet Coefficients, *Earthquake Engineering and Structural Dynamics*, **34**(15), 1799-1815.

Basu, B. and Gupta V.K. (1997), Non-stationary Seismic Response of MDOF Systems by Wavelet Transform, *Earthquake Engineering and Structural Dynamics*, **26**(12),1243-1258.

Basu, B. and Gupta V.K. (1998), Seismic Response of SDOF Systems by Wavelet Modeling of Non-stationary Process, *Journal of Engineering Mechanics*, American Society of Civil Engineers, **124**(10), 1142-1150.

Newland, D.E. (1994), Wavelet Analysis of Vibration, Part 2: Wavelet Maps, *Journal of Vibration and Acoustics*, Transaction on American Society of Mechanical Engineers, **116**, 417-425.

Zhou, Z. and Adeli, H. (2003), Wavelet Energy Spectrum for Time-frequency Localization of Earthquake Energy, *International Journal of Imaging Systems and Technology*, **13**(2), 133-140.

Cao, H. and Friswell, M.I. (2009), The Effect of Energy Concentration of Earthquake Ground Motions on the Nonlinear Response of RC Structures, *Soil Dynamics and Earthquake Engineering*, **29**(2), 292-297.

Mallat, S.G. and Zhang, Z. (1993), Matching Pursuits with Time-frequency Dictionaries, *IEEE Transactions on signal processing*, **41**(12), 3397-3415.

Qian, S., and Chen, D. (1994), Signal Representation via Adaptive Normalized Gaussian Functions, *Signal Processing*, **36**(1), 1-11

Li, X., et. al. (2008), Strong Motion Observations and Recordings from the Great Wenchuan Earthquake, *Earthquake Engineering and Engineering Vibration*, **7**(3), 235-246.

JOINT CONFERENCE PROCEEDINGS
7th International Conference on Urban Earthquake Engineering (7CUEE) &
5th International Conference on Earthquake Engineering (5ICEE)
March 3-5, 2010, Tokyo Institute of Technology, Tokyo, Japan

A QUANTITATIVE APPROACH TO ESTIMATE COSEISMIC DISPLACEMENTS IN THE NEAR-FIELD FROM STRONG-MOTION ACCELEROGRAPHS: EXAMPLE OF THE 2007 NIIGATA-KEN CHUETSU-OKI EARTHQUAKE, JAPAN.

Emmanuel H. Javelaud[1)], Tatsuo Ohmachi[2)], Yoichiro Murakami[3)] and Shusaku Inoue[4)]

1) Former Research Student, Department of Built Environment, Tokyo Institute of Technology, Japan
2) Professor, Department of Built Environment, Tokyo Institute of Technology, Japan
3) Graduate Student, Department of Built Environment, Tokyo Institute of Technology, Japan
4) Research Associate, Department of Built Environment, Tokyo Institute of Technology, Japan
Emmanuel.Javelaud@ens-lyon.org, ohmachi@enveng.titech.ac.jp, murakami@enveng.titech.ac.jp, shusaku@enveng.titech.ac.jp

Abstract: Zeros pads are added to acceleration time-series recorded in the near-field of the 2007 Niigata-ken Chuetsu earthquake, Japan, in order to improve their visual continuity at long period in the frequency domain. This allows us to observe that the low frequency part of the acceleration records are dominated by noise: simple step function, whose amplitude and starting time can be determined uniquely. Removing these step functions from the acceleration records before carrying out a double integration lead to stable residual displacements. The corrected displacement time-series and residual displacements are checked against 1-Hz GPS data. The displacements obtained by the two methods show interestingly good agreements.

1. INTRODUCTION

The determination of coseismic displacements from strong-motion accelerographs is needed when displacements cannot be measured by methods such as GPS: for instance within structures, boreholes, or for tsunami prediction, the coseismic displacement of the seafloor.

Displacement time-histories can theoretically be obtained by double integration of accelerograms recorded by modern strong-motion seismometers but they usually show drifts larger than expected for the true ground displacement (Figure 1). Various long-period corrections of the acceleration records have been applied since the first attempts: making baseline adjustments such as simple step function, pulse followed by a step function (Iwan 1985, Boore 2001, Wang et al. 2003), parabola or other function removed from accelerograms, filtering (Trifunac 1971, Boore et al. 2002, Graizer et al. 2002, Wang et al. 2003, Boore and Bommer 2005) or a combination of both (Boore et al. 2002, Boore and Bommer 2005).

The processing scheme proposed in this paper is specifically designed to estimate the displacement time-histories in the near-field of large earthquakes from the Japanese K-Net and Kik-Net strong motion seismometers. It is based on the following two issues:

1) the observation of the signal characteristics at very low frequencies (down to 10^{-4}Hz) provides information about the long-period noise of the record. By noise, we mean the long period information contained in the signal that is not the translational acceleration itself. The analysis of the observed shape of the noise is telling us how to remove it from the record, in the time domain.

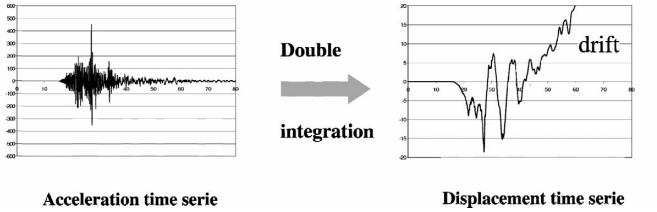

Figure 1 Acceleration and displacement time series derived from a record of the 2007 Niigata-ken Chuetsu-Oki earthquake at K-NET NIG019 station, EW component

2) a detailed study of accelerographs used by the two Japanese nationwide networks (Kinoshita et al. 1997, Kinoshita 1998, NIED 2000, Scherbaum 2001, Javelaud et al, 2005, Murakami 2008).

This paper begins with the description of the proposed processing scheme. The second part shows the comparison of displacements obtained by processing acceleration records with 1-Hz GPS data.

2. PROCESSING SCHEME

The recorded accelerations are processed according to the flow chart detailed in figure 2.

In this section, we used the acceleration record shown in Figure 1 as an example. It is the 300 sec long EW component of the NIG019 station recorded on the 16th of

July 2007: the filename of the acceleration data downloaded from the K-NET homepage (NIED 2009) is NIG0190707161013.EW.

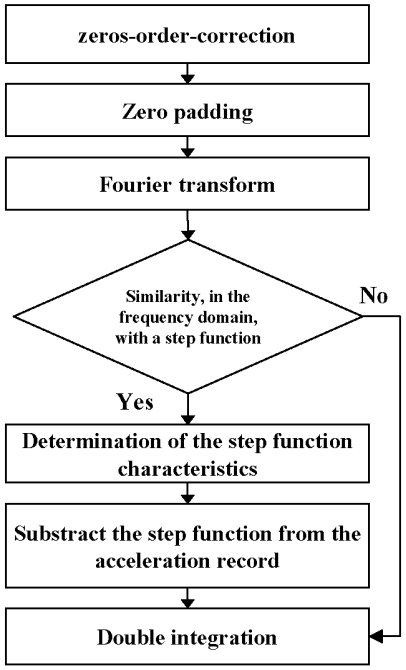

Figure 2 Description of the processing scheme

2.1 Zero order correction

We apply the condition that the acceleration is zero before the earthquake shaking starts: the mean of the pre-event portion of the acceleration record is subtracted from the whole record.

2.2 Zero padding

A long period (low frequency) correction of the acceleration is needed. The nature of the long period noise can be observed by looking carefully at the low frequency content of the signal. By noise, we mean the long period information contained in the record that is not the translational acceleration itself.

In signal processing, the frequency spacing of a Fourier transform is $\Delta f = \frac{1}{N.\Delta t}$ where Δt is the sampling interval and N the number of data. When N increases, Δf decreases and more details of the low frequency part of the acceleration record are revealed. Without increasing the duration of records, adding zeros before and after the acceleration time-series results in a smaller frequency spacing of the Fourier transform. The added zeros do not change the shape of the spectrum (nor add information).

Acceleration time-histories are first padded with zeros. Figure 3 shows the Fourier transform of the acceleration recorded at station NIG019 (EW Component) after adding a variable number of zeros (from 2^{16} to 2^{23}).

The Fourier amplitude spectrum with little zero pads is very jagged at low frequencies due to the small number of sampling defining the curve there. This situation is improved

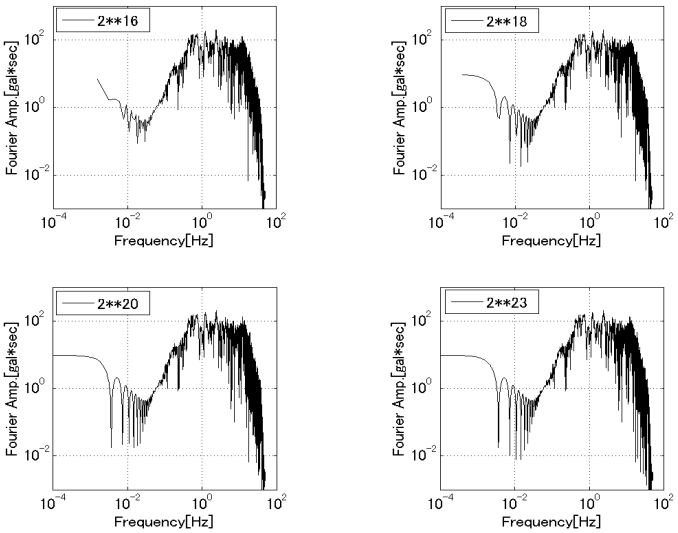

Figure 3 Effect of padding the acceleration history recorded at NIG019 station, EW component

by increasing the number of zeros pads in the acceleration record before taking the discrete Fourier transform. Adding zeros to make the record 2^{23} sample long results in a smaller frequency spacing of the Fourier transform. It provides enough details at low frequency for the purpose of this method, without taking much computing time (one to two seconds with current computers). This tool reveals the characteristics of the long period information contained in acceleration record.

2.3 Comparison of the Fourier transforms of acceleration records and step function

The amplitude A and duration T used to define a step function in the time domain (Fig. 4, top left) can be extracted in the frequency domain from the Fourier transform of the step function (top right): by definition, the Fourier amplitude

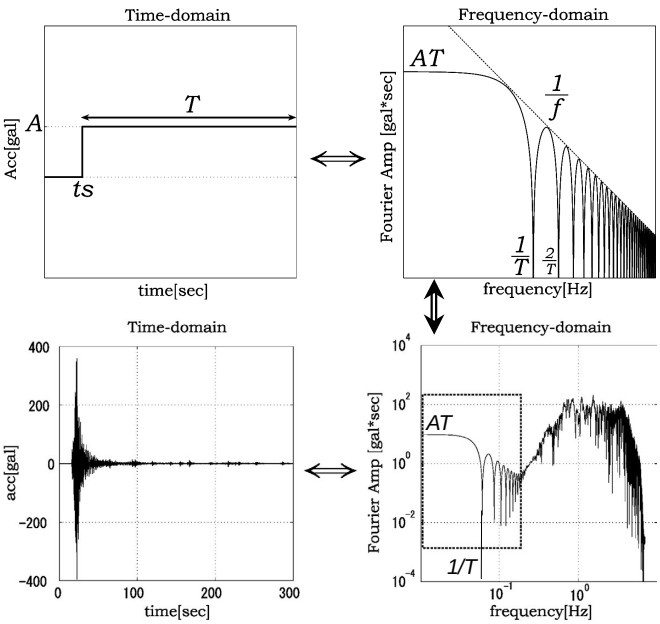

Figure 4 Comparison of acceleration record (below) and step function (top) in both time and Fourier domains

at zero frequency is A.T, and the frequency when the Fourier amplitude is zero for the first time is 1/T. Therefore, A and T of a step function can be uniquely derived from its Fourier transform. It is important to note that A and T are not randomly hand picked up, but really extracted from the Fourier transform.

In figure 4, we compare the acceleration record and its Fourier transform (below), with a simple step function and its Fourier transform (top). It can be seen that in the frequency domain, the low frequency part of the record (bottom right, in the box) is identical to a step function (top right). We therefore observed that the acceleration record (bottom left) is contaminated by a step function, whose amplitude and starting time can be determined.

In this example, we obtained the following values from the Fourier transform of the acceleration record (Fig.4, bottom right): A.T = 11.7177 Gal.sec (Fourier amplitude at zero frequency) and 1/T= 0.0036467 sec^{-1} (frequency when the Fourier amplitude is zero for the first time). Thus T = 1/(1/T) = 274.2186 sec, A = A.T / T = 0.042731 Gal and the starting time of the step function (ts) = duration of the record - T = 300 sec - T = 25.7814 sec. In Figure 5, the superposition in the frequency domain of the acceleration record and the step function of characteristics A and ts shows extremely good match at low frequencies.

2.4 Subtraction of the step function from the acceleration record

Subsequent processing is applied in the time domain. A step function of amplitude A = 0.042731 Gal and of starting time ts = 25.7814 sec is subtracted from the acceleration record (Figure 6, top).

Note that we corrected the acceleration time-series from a step function starting at ts (until the end of the record). While zero pads are added after the acceleration record, it is strictly speaking a rectangular box of amplitude A, starting at ts, until the end of the record (300 sec in K-Net case).

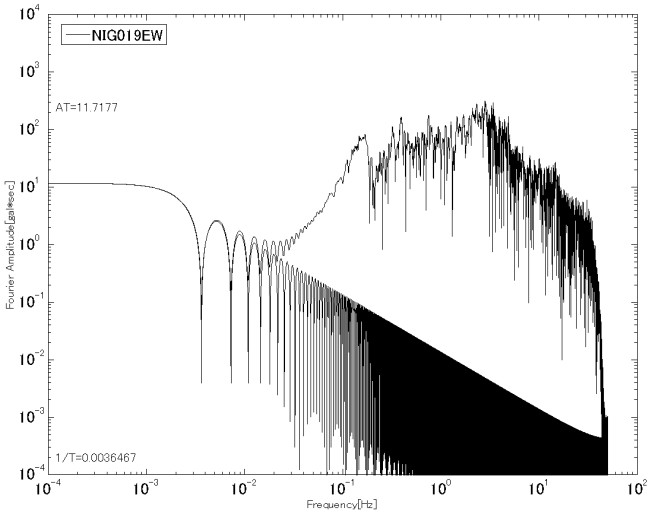

Figure 5 The superposition in the frequency domain of the acceleration record and a step function of amplitude A and starting time ts (determined above) shows extremely good match at low frequency

2.5 Double integration

Double integration of the corrected acceleration time-history shows no more drift: the displacement is perfectly stable after the shaking (Figure 6, bottom). The residual displacement is estimated at -3.2 cm.

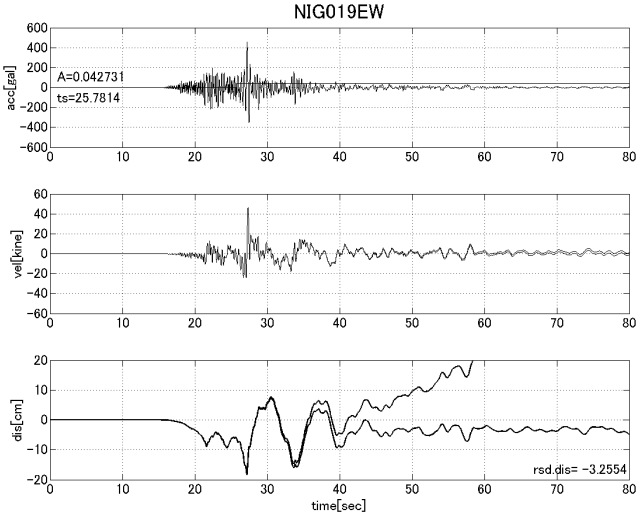

Figure 6 Top, superposition of the acceleration record and the step function of amplitude A (not on scale) and starting time ts used to correct the acceleration record; Below, uncorrected and corrected velocity and displacement time-histories. The corrected displacement time-history is obtained by subtracting the step function from the acceleration record, then double integrating the corrected acceleration time-history. The displacement is stable after the earthquake

3. COMPARISON BETWEEN SEISMIC 1 HZ AND GPS DATA

The 2007 Niigata-ken Chuetsu-Oki earthquake, Japan, produced a large set of strong-motion records including near-field ground motions. All the data used in this study were recorded during that event. The efficiency of the processing scheme described in the above section is tested: displacement time histories obtained by using the proposed scheme are compared with 1-Hz GPS measurements.

3.1. Comparison of displacement time-histories

During the earthquake, the K-NET NIG019 OJIYA station and the 1-Hz GPS OJIYA station recorded the event. Both stations are 600 m distant from each other. Displacement time histories calculated from processed acceleration records were compared with the 1-Hz GPS data (Figure 7). The steps used to obtain the E-W component displacement time-history have been detailed above.

For each component, the seismic displacement and the 1-Hz GPS diplacement time histories show extremely good similitude for both the residual and the dynamic parts of the displacement.

3.2 Comparison of residual displacement plotted on a map

In the near-field of the 2007 Niigata-ken Chuetsu-Oki earthquake, residual displacements calculated as suggested above were compared with displacements measured at surrounding GPS stations (Figure 8).

When GPS and seismometer stations are collocated (a few hundred meters apart from each other), the residual displacements obtained by the two methods are almost identical (Figure 7).

At other locations where accelerometers and GPS stations are a few kilometers distant from each other, residual displacements obtained by processing seismometer records are completely consistent with displacements measured by GPS stations.

Note that at Izumozaki and Kashiwazaki, the displacements obtained by the two methods do not agree well. The reason is the presence of soil deformation, including liquefaction, at Izumozaki and Kashiwazaki GPS stations (Tabuchi et al. 2008), and also at Kashiwazaki NIG018 accelerometer (NIED 2007).

4. DISCUSSION AND CONCLUSION

This paper proposes a simple method to investigate the low frequency content of acceleration records. From the acceleration records that we processed, we observed that in the near field of large earthquakes, they contain baseline offsets: simple step function, whose starting time and amplitude are determined. Removing these step functions as detailed allows to retrieve the displacement time-histories. Collocated seismic and GPS stations were used as a check of the method against measurements.

This processing scheme is efficient in the near-field of earthquakes, because the low frequency components of the acceleration records are dominated by the step functions (of low amplitude but long duration). Other sources of noise (1/f electronic noise, etc.) are completely overshadowed by the step function and by the strong translational acceleration.

Far from the epicenter, the residual displacement decreases. From our experience of processing strong-motion acceleration records, the amplitude of the step function decreases as well. The current method is working up to the point where, at low frequency, the amplitude of the step function is so small that other sources of noise are competing with it.

Another limitation is that this method requires a minimum length of original data: the data used in this study are 300 sec long acceleration time-series recorded at a sample frequency of at least 100 Hz. Also, the method does not work in the case, not observed in this study, when the acceleration data contain more than one event.

From the equation of a seismometer (Graizer 2006, Graizer 2007), the step function observed may be considered as a record of the residual tilt (tectonic & local), its amplitude being proportional to the permanent rotation angle.

The method described provides accurate estimates of the displacement time-histories in the near-field of the studied earthquake. We believed that it can be used to estimate the displacement time-histories at places where GPS stations cannot be installed, such as on the seafloor or within structures.

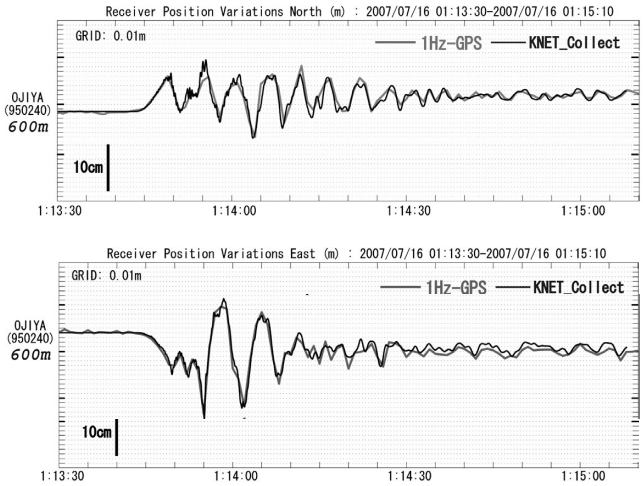

Figure 7 Comparison of displacements at NIG019 OJIYA station between processed acceleration record and 1-Hz GPS data

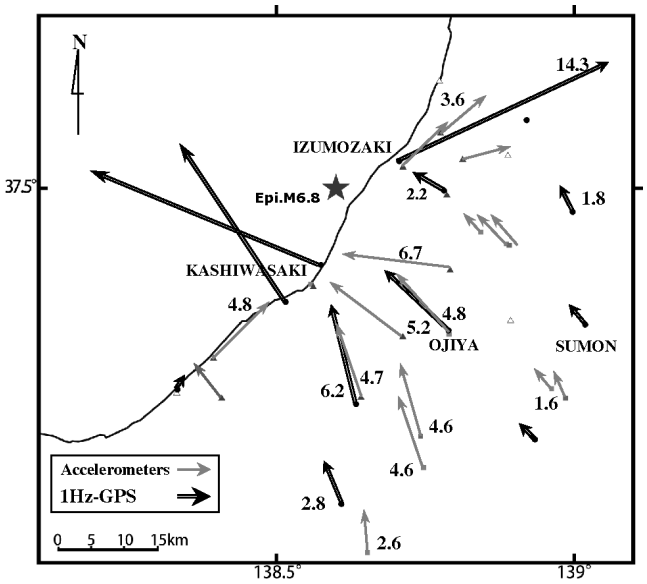

Figure 8 Comparison of coseismic residual displacement obtained from strong-motion seismometers and surrounding GPS stations during the 2007 Niigata-ken Chuetsu-Oki earthquake

Acknowledgements:

The first author wishes to acknowledge the Japanese government for funding his research term through the Monbukagakusho scholarship program. We are indebted to V. Braquet who shared with us his experience of signal processing. His suggestions and comments were deeply appreciated. We also

thanks L. Tabiso for his encouragements. Seismograms were provided by K-NET, KIK-NET (National Research Institute for Earth Science and Disaster Prevention, Tsukuba, Japan) and by the Japanese Meteorological Agency, and GPS measurements by GSI (Geographical Survey Institute, Ministry of Land, Infrastructure and Transport, Ibaraki, Japan).

References:

Boore, D. M. (2001). "Effect of Baseline Corrections on Displacements and Response Spectra for Several Recordings of the 1999 Chi-Chi, Taiwan, earthquake." *Bulletin of the Seismological Society of America*, Vol. 91, 1199-1211.

Boore, D.M. and Bommer, J.J.(2005). "Processing of strong-motion accelerograms: needs, options and consequences." *Soil Dynamics and Earthquake Engineering,* Vol. 25, 93-115.

Boore, D.M., Stephens, C. and Joyner, W. (2002). "Comments on Baseline Correction of Digital Strong-Motion Data: Examples from the 1999 Hector Mine, California, earthquake." *Bulletin of the Seismological Society of America*, Vol.92, 1543-1560.

Graizer, V. (2006). "Theoretical Basis for Rotational Effects in Strong Motion and Some Results" *Presentation at Menlo Park.* February 16.

Graizer, V. (2007). "Tilts in Strong Ground Motion." *Bulletin of the Seismological Society of America*, Vol. 96, 2090-2102.

Graizer, V., Shakal, A., Scrivner, C., Hauksson, E., Polet, J. and Jones, L. (2002). "TriNet Strong-Motion Data from the M7.1 Hector Mine, California, earthquake of 16 October 1999". *Bulletin of the Seismological Society of America*, Vol. 92, 1525-1542.

Iwan, W.D., Moser, M.A. and Peng, C-Y. (1985). "Some observations on strong motion earthquake measurement using a digital accelerograph." *Bulletin of the Seismological Society of America*, Vol. 75, 1225-1246.

Javelaud, E.H., Kubo, G., Ohmachi, T. and Inoue. S. (2005). "Coseismic ground displacement due to the 2004 Niigata-ken Chuetsu earthquake, Japan." *Proc. 4th Annual Meeting of Japan Association for Earthquake Engineering*, 312-313.

Kinoshita, S. (1998). "Kyoshin~Net~(K-NET)." *Seismological Research Letters*, Vol. 69, 309-332.

Kinoshita, S., Uehara, M., Tozawa, T., Wada, Y. and Ogue. Y. (1997). "Recording Characteristics of the K-NET95 Strong-motion Seismograph." *Jishin 2,* Vol. 49, 467-481. (in~Japanese).

Murakami Y. (2008). "Evaluation of near field displacements." *Master thesis, Tokyo Institute of Technology.*

NIED: National Research Institute for Earth Science and Disaster Prevention, Japan. Kyoshin Network. (2009) www.k-net.bosai.go.jp

NIED: National Research Institute for Earth Science and Disaster Prevention, Japan (2000). "Fundamentals of Strong Motion." *CD version.*

NIED: National Research Institute for Earth Science and Disaster Prevention, Japan, Kyoshin Network. (2007). "Topic of seismic activity : the 2007 Niigata-ken Chuestu-Oki earthquake - about the NIG018 Kashiwazaka station." (in japanese)
http://www.k-net.bosai.go.jp/k-net/topics/chuetsuoki20070716/K-NET¥_Kashiwazaki.pdf

Scherbaum F. (2001) "Of Poles and Zeros : fundamentals of Digital Seismology." Kluwer Academic Publishers, Dordrecht, The Netherlands,

Tabuchi, H., Tomoya, H. and Ishibashi, K. (2008). "A southeasterly-dipping static fault model of the 2007 Niigata-ken Chuetsu-oki, Japan, earthquake based on crustal movements, tsunamis, aftershock distribution and neotectonics." *Report of Research Center for Urban Safety and Security*, Kobe University, Vol. 3, 1-10.

Trifunac M. (1971). "Zero baseline correction of strong-motion accelerograms." *Bulletin of the Seismological Society of America*, Vol. 61, 1201-1211.

Wang G.Q., Boore, D.M., Igel, H. and Zhou, X.Y. (2003). "Some Observations on Collocated and Closely Spaced Strong Ground-Motion Records of the 1999 Chi-Chi, Taiwan, earthquake." *Bulletin of the Seismological Society of America*, Vol. 93, 674-693.

JOINT CONFERENCE PROCEEDINGS
7th International Conference on Urban Earthquake Engineering (7CUEE) &
5th International Conference on Earthquake Engineering (5ICEE)
March 3-5, 2010, Tokyo Institute of Technology, Tokyo, Japan

DEVELOPMENT OF A FORWARD-INVERSION CRUST MODELING SCHEME FOR ACCURATE STRONG-GROUND MOTION PREDICTION

Pher Errol B. Quinay[1)], Tsuyoshi Ichimura[2)], and Muneo Hori[3)]

1) PhD Candidate, Department of Civil and Env. Eng'g, Tokyo Institute of Technology, Japan
2) Associate Professor, Earthquake Research Institute, The University of Tokyo, Japan
3) Professor, Earthquake Research Institute, The University of Tokyo, Japan
quinay.p.aa@m.titech.ac.jp, ichimura@eri.u-tokyo.ac.jp, hori@eri.u-tokyo.ac.jp

Abstract: To accurately estimate the long-period component of ground motions, the basin boundary separating the soft and hard layer of the crust must be well-estimated. In this study, a three-dimensional basin boundary shape estimation is proposed using forward-inversion modeling. The inversion uses the Broyden-Fletcher-Goldfarb-Shanno (BFGS) method, a quasi-Newton optimization method. The forward modeling uses the Finite Element Method (FEM) with hybrid mesh modeling. The proposed scheme is tested in a problem with a target frequency of 1.0 Hz. In this problem, hierarchical parameterization approach, starting with few number of parameters and step-wise increase with minimization is employed. A comparison of inversion problem for a model with and without topography is made, to emphasize the importance of obtaining good solution if surface effect is accounted for. Results show that the proposed scheme converges to the desired basin boundary solution and, at the same time, gives an accurate reproduction of the target waveform.

1. INTRODUCTION

Accurate strong ground motion prediction is important for earthquake damage mitigation. For application to civil engineering studies, the information that can be obtained is crucial for design or analysis of structures situated in earthquake-prone regions. One example is the long period component of strong ground motion which is known to have direct effect on large structures. Long-span bridges, high-rise buildings, and oil tanks are very susceptible to damages under this component because of the resulting resonance on the same period range. Several studies (Aoi 2002, Koketsu 2008) mention that the long period component is affected by the nature of the basin boundary separating the soft and hard layer at the crust. Another important aspect is the topography-modeling. Ma et.al. (2007) and Lee et.al. (2009) are among the recent studies that dealt with the effect of irregular topography on the amplifications of ground motions. Therefore, to advance the study of strong ground motion prediction, accurate topography-modeling and basin boundary estimation have to be given significance.

The objective of this paper is to propose a scheme for accurate estimation of the basin boundary shape. This objective is to be solved by utilizing a forward-inversion approach to model the basin shape in three-dimensions. For the forward modeling, the multi-resolution structured and unstructured grid FEM, MCFEM (Ichimura, et.al. 2009) is employed. In comparison with the general FEM implementation, this FEM can accurately and efficiently model the crust's topography, homogeneous regions and their interface by using a hybrid mesh of structured (hexahedra) and unstructured (tetrahedra) elements. Moreover, several methods to reduce memory requirement and computational time were implemented. For the inversion, the quasi-Newton method, Broyden-Fletcher-Goldfarb-Shanno method (BFGS) (Nocedal and Wright, 2006) is employed. This method is widely-used for unconstrained optimization and is known for its good convergence properties.

In this paper, the forward-inversion scheme is first described. Then a verification of applicability is done together with an analysis of surface effect. Based from the results, a discussion is made on the importance of including the topography in modeling. At the end, some points on applicability to realistic data and areas of improvement are briefly mentioned.

2. Methodology

The objective function chosen for minimization is:

$$f(\mathbf{x}) = \sum_{i,n} |\tilde{u}_{in} - u_{in}(\mathbf{x})| \quad , \qquad (1)$$

where, $\tilde{u}$ and u are the displacement components of target and test models, respectively. Subscripts i and n are spatial and temporal counter, and $\mathbf{x}$ is the parameter vector (depth values of the parameterized boundary). Equation (1) is the L1 norm of the difference between the target and

synthetic displacement response per time step.

The BFGS method is used to minimize Equation (1). This method has the advantage of computational-efficiency because it approximates the Hessian by updating and improving a previous estimate with iteration. This updating involves incorporating the curvature information from the sensitivity functions, which are computed in this study using the forward difference expression, as implemented in Aoi (2002),

$$\nabla f(\mathbf{x}) = \frac{\partial f}{\partial x} = \frac{f(\mathbf{x} + \mathbf{\Delta x}_k) - f(\mathbf{x})}{\Delta x_k} \quad , \quad (2)$$

where, $\mathbf{\Delta x}_k$=(0,0,..Δx_k,..,0) and k is a parameter counter. This expression means that the sensitivity with respect to a parameter is computed by perturbing the parameter by a value of Δx while keeping other parameters unperturbed. Minimization in BFGS uses gradient-based line-searching, and search directions are computed using the approximated Hessian. For each search direction, the step length is computed using an initial positive length and successively reduced until the length satisfies the Armijo rule (Nocedal and Wright, 2006).

Determining a value for the objective function or sensitivity function requires forward modeling. This study uses the MCFEM because of its flexibility in modeling regular and irregular regions with structured hexahedral and unstructured tetrahedral elements. This hybrid meshing scheme also allows for multi-resolution by fitting the appropriate dimensions of finite elements based on the material properties of the region being meshed, resulting to significant computational savings. Emphasis is made on the use of unstructured elements for this allows for tailored modeling of the irregular surfaces of the target model. Because this study parameterizes the layer interface which is generally irregular, the continuity of solution for the calculated sensitivity functions can be satisfied. Hence, the limitation of placing inversion values exclusively on structured grid nodes is eliminated.

Moreover, to achieve stability in the solutions and efficient minimization of the objective function, the hierarchical parameterization approach as in Aoi(2002) is implemented. This hierarchical scheme is done by starting the inversion with a few number of parameters and eventually increased step-wise as the desired value of the minimized function is achieved.

3. Application Example

A two-layer problem is considered. The top layer is modeled as a soft sedimentary and the bottom layer is modeled as hard bedrock. The target computational accuracy is 1.0 Hz and 10 elements are used to approximate a wavelength. These settings resolve to a maximum discretization size of 150.0m for the upper layer and 300.0m for the lower layer. The seismic source used is a double couple. To approximate the half-space, viscous absorbing boundaries are implemented. Rayleigh damping is used for material attenuation. The time discretization method is Newmark beta (beta=1/4) method.

Tables 1, 2, and 3, and Figure 1 give the details of the problem settings. To obtain point responses at the surface, 16 receivers are placed to record x-, y-, and z- displacement waveforms. The data from all the 16 receivers are used in the inversion run. The hypothetical target solution is constructed from these settings. It consists of two minima of different depths located on opposite quadrants. The resulting model consists of 527,916 voxels, 342,082 tetrahedra and 607,512 nodes corresponding to 1,822,536 degrees of freedom.

This application example aims to verify the applicability of the method and at the same time perform an analysis of the surface effect. Two cases were considered both having an initial solution located at -2500.0m elevation (with this setting, the maximum difference with the target solution is 1001.6m.). The only difference is that Case 1 includes topography-modeling similar to the hypothetical target model, while Case 2 considers flat surface.

Table 1: Inversion Problem BFGS Settings

Initial B_o	Identity matrix, I
Armijo rule parameter	0.0001
Sensitivity function parameter, Δx	150.0m

Table 2: Forward Modeling Problem Settings

Domain	-9.6km ≤ x ≤ 9.6km	
	-9.6km ≤ y ≤ 9.6km	
	-15.0km ≤ z ≤ 0km (varies)	
Parameterized Area	-8.5km ≤ x ≤ 8.5km	
	-8.5km ≤ y ≤ 8.5km	
	1st Layer(Sedimentary)	2nd Layer(Bedrock)
ρ(kg/m3)	1900	2500
V_p(m/s)	2300	4500
V_s (m/s)	1500	3000
Q	100	300

Table 3: Force Settings

Hypocenter(x,y,z)	(-1200m,-1200m,-7000m)	
Source function	$M_o(2t^2/T_o^2)$	$0 \le t \le T_o/2$
	$M_o(1-2(t-T_o)^2/T_o^2)$	$T_o/2 \le t \le T_o$
	M_o	$t \le T_o$
Magnitude, M_o	1.0×10^{17}N-m	
Strike,Dip,Rake	30°,40°,60°	
Rise Time, T_o	2.0sec	

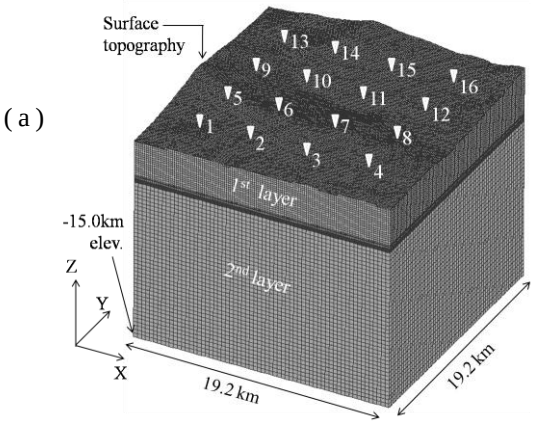

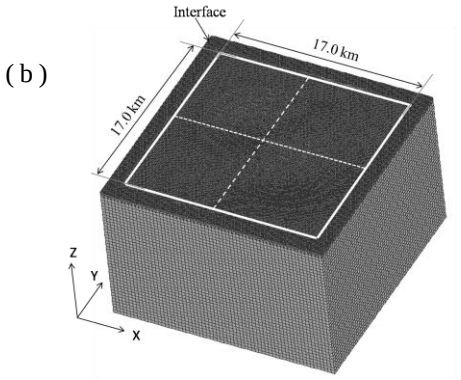

Figure 1. (a) The 3D Finite Element model; (b) The 4-parameterized interface (without the top layer).

4. Results and Discussion

The results at the interface for Case 1 and Case 2 are shown in Figures 2 and 3. In both figures, the inversion is started without initial information about the target model. Selected waveforms recorded at the surface are shown in Figures 4 and 5.

For Case 1 (Figure 2), after the 5th iteration with 4 parameters, it appears that the two locations of the minima have already been located. However, the actual basin shape is still not well-recognizable. This is because with the rough parameterization, the resulting dimensions of the parameters are still larger than the details of the target model. With such constraint, the scheme can only, at-best, result to an average estimate of the parameterized area. Increasing to 16 parameters, the parameter dimensions are then refined. As evident after the 10th iteration, more details have been extracted and the shape of the basin and the locations of the minima are all well-estimated.

For Case 2 (Figure 3), after the 6th iteration, the resulting approximation seems to converge to a different location of a minimum. Then increasing to 16 parameters, after the 12th iteration, the scheme converged to another location. Also, no significant improvement in basin shape estimation had been achieved. Comparing this result with the target model, it can be said that this case is converging to a different basin shape but similar velocity structure.

The resulting velocity waveforms for the two cases (Figures 4 and 5) support these results. The component waveforms for the selected receivers have converged to the target waveform from the initial solution under Case 1. The phase and amplitude differences have been improved at the same time that the basin shape has been constructed (10th iteration). As for Case 2, it can be observed that the initial solution has a larger difference from the target waveform compared to Case 1. After 12 iterations, improvements in phase and amplitude can be seen, but the waveforms are still not well-reproduced.

The performed numerical test both showed the applicability of the proposed scheme (convergence in Case 1), and the importance of modeling the topography to account for surface effect (varied results of Case 1 and Case 2). It is evident from the test that information regarding the interaction of the waves and the irregular surface are lost when flat-surface approximation is done. This is expected especially when considering higher frequencies in numerical simulations. It has been shown in this test the importance of topography modeling in order to obtain good results for basin boundary shape estimation.

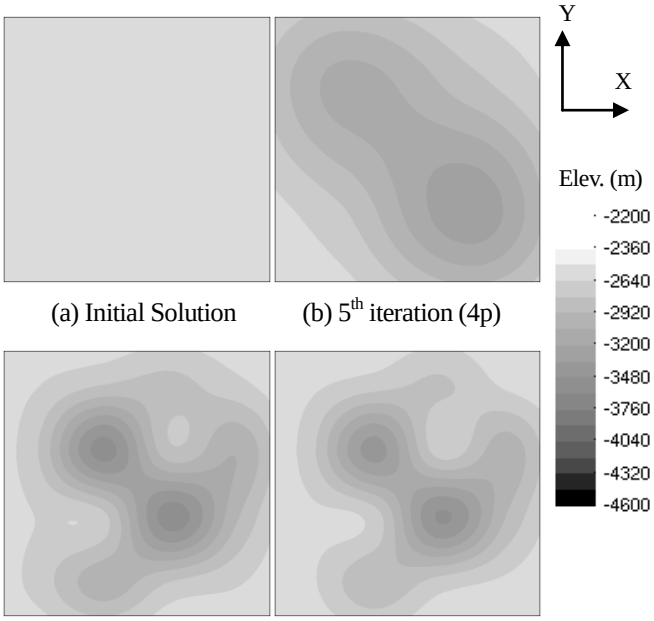

(a) Initial Solution (b) 5th iteration (4p)

(c) 10th iteration (16p) (d) Target solution

Figure 2. Case 1 results at the interface: (a) Initial solution; (b) after 5th iteration; (c) after 10th iteration; (d) Target solution

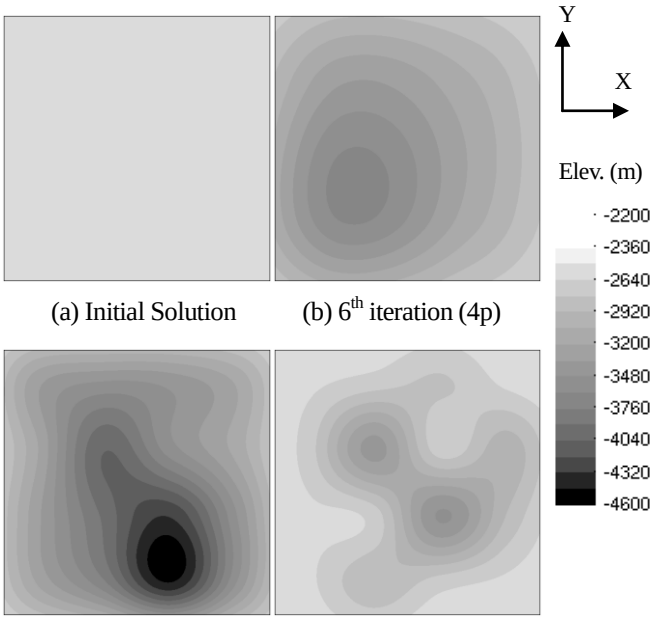

(a) Initial Solution (b) 6th iteration (4p)

(c) 12th iteration (16p) (d) Target solution

Figure 3. Case 2 results at the interface: (a) Initial solution; (b) after 6th iteration; (c) after 12th iteration; (d) Target solution

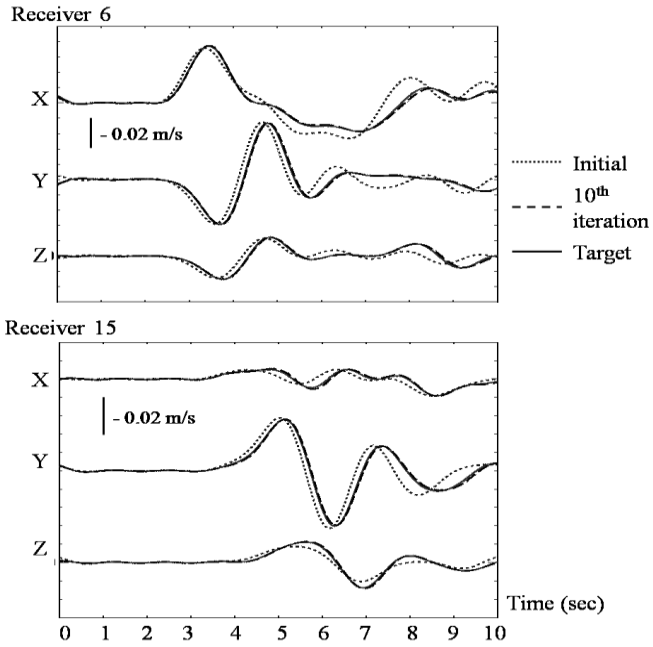

Figure 4. Case 1 and Target solution: Velocity waveforms for Receivers 6 and 15, low-pass filtered at 1.0Hz

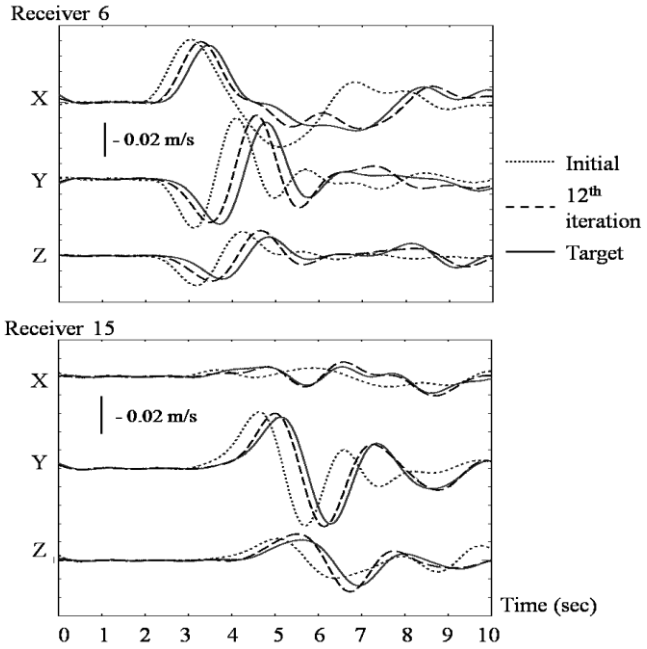

Figure 5. Case 2 and Target solution : Velocity waveforms for Receivers 6 and 15, low-pass filtered at 1.0Hz

For application to realistic data, several points are seen to require further analysis. As examples, (1) crust modeling would have to accommodate problems on multi-layer inversion; (2) study on the effect of random distribution of receivers; and (3) study on the invariance of the chosen objective function with changes in the inverted parameters and noise in the waveforms.

5. CONCLUSIONS

A scheme to estimate the crust's soft and hard layer interface by inversion and forward modeling has been presented. The optimization method uses the Broyden-Fletcher-Goldfarb-Shanno (BFGS), and the forward modeling uses a hybrid mesh implementation of the Finite Element Method (MCFEM). The scheme also employs a hierarchical parameterization approach by starting with few number of parameters and increases step-wise until the desired convergence is achieved.

In the application example, the two cases considered emphasized the importance of modeling the topography. It has been shown that in order to obtain an accurate estimate of the interface, the topography has to be introduced in the analysis. The case which included the topography converged to the target waveform, while the case which did not include the topography resulted to a poor estimation. The example performed is done for a simple two-layer problem with realistic settings. Lastly, it is recognized that for future application to realistic data, further analyses have to be made on several components of this proposed scheme.

Acknowledgements:

The authors acknowledge support from the Japan Ministry of Education, Culture, Sports, Science, and Technology (MEXT). The authors used the computer systems of the following institutions: (1) Earthquake Information Center (EIC), Earthquake Research Institute, The University of Tokyo, and (2) TSUBAME Grid Cluster, Global Scientific and Information Center, Tokyo Institute of Technology.

References:

Aoi, S. (2002), "Boundary Shape Waveform Inversion for Estimating the Depth of Three-Dimensional Basin Structures," *Bulletin of Seismological Society of America*, **92(**6), pp.2410-2418.

Koketsu, K. and Miyake, H. (2008), "A Seismological Overview of Long-period Ground Motion," *J.Seismol*, **12**, pp.133-143.

Ma, S., Archuleta, R. J. and Page, M. T. (2007), "Effects of Large-Scale Surface Topography on Ground Motions, as Demonstrated by a Study of the San Gabriel Mountains, Los Angeles, California," *Bulletin of Seismological Society of America*, **97** (6). pp.2066-2079.

Lee, S-J., Komatitsch, D., Huang, B-S. and Tromp, J. (2009), "Effects of Topography on Seismic-Wave Propagation: An Example from Northern Taiwan," *Bulletin of Seismological Society of America*, **99** (1). pp.314-325.

Ichimura, T., Hori, M. and Bielak, J. (2009). "A Hybrid Multiresolution Meshing Technique for Finite Element Three-Dimensional Earthquake Ground Motion Modelling in Basins Including Topography," *Geophysical Journal International*, **177(**3) 6, pp. 1221-1232.

Nocedal, J. and Wright, S. (2006), "Numerical Optimization 2nd Ed.," Springer.

Ji, C., Helmberger, D.V. and Wald, D.J. (2000), "Basin Structure Estimation by Waveform Modeling: Forward and Inverse Methods," *Bulletin of Seismological Society of America*, **90** (4), pp.964-976

JOINT CONFERENCE PROCEEDINGS
7th International Conference on Urban Earthquake Engineering (7CUEE) &
5th International Conference on Earthquake Engineering (5ICEE)
March 3-5, 2010, Tokyo Institute of Technology, Tokyo, Japan

EFFECTS OF WATER DEPTH VARIATION ON SEISMOGRAM SYNTHESIS IN OCEANIC STRUCTURES BASED ON A HYBRID BOUNDARY ELEMENT METHOD

Zheng-Hua Qian[1], Hiroaki Yamanaka[2], and Sohichi Hirose[3]

1) G-COE PD, Dept. of Mechanical and Environmental Informatics, Tokyo Institute of Technology, Japan
2) Professor, Dept. of Environmental Science and Technology, Tokyo Institute of Technology, Japan
3) Professor, Dept. of Mechanical and Environmental Informatics, Tokyo Institute of Technology, Japan
qian.z.aa@m.titech.ac.jp, yamanaka@depe.titech.ac.jp, shirose@cv.titech.ac.jp

Abstract: In this paper, we study the P-SV wave propagation in an inhomogeneous biphase medium such as oceanic structures by a hybrid boundary element method. The structures are modeled by using a multilayered medium composed of irregular interfaces. The method can be simply understood as a combination of the traditional boundary element method and the global matrix propagator method. Numerical examples are first taken for two simple models including a semi-circular canyon model and a deep basin model to validate our program and the method itself. In each model, the incidence of both plane P and SV waves are considered. And then a model consisting of one water layer and one irregular solid layer is calculated to study the effects of water depth on the synthetic seismograms. Some conclusions are drawn to help use the method to investigate effects of sea water in Tokyo bay on seismic wave propagation in the Kanto basin using a realistic model including sea water in the future.

1. INTRODUCTION

Seismological evidence indicates that the interior of the Earth is inhomogeneous on scales ranging from a few to thousands of kilometers. Seismic wave propagation in inhomogeneous structures is in general complicated, so synthetic seismograms are indeed needed to understand systematically the variability of full waveforms propagating in a set of hypothetical velocity models. This is essential for the further development of the inverse problem in the determination of robust geological structures. Many approaches have been developed to calculate synthetic seismograms. At the early stage of seismology, the reflectivity method (Kennett, 1983) and the generalized ray method (Miklowitz and Achenbach, 1978) were widely used for simulating seismic wave excitation and propagation, where a laterally homogeneous model is considered. The study of seismic wave excitation and propagation in laterally inhomogeneous media has become extensively important in seismology and geophysics in the last three decades, including analytical solutions (Zhao, 2006), high-frequency approximation methods (Cerveny, 2001), plane wave decomposition methods (Chen, 1990 and 1995), and so on.

Nowadays, the major approaches to study a laterally inhomogeneous model mainly rely on numerical methods which include domain methods and boundary methods. The domain numerical methods (such as finite difference (Zhang and Chen, 2006), finite element (Koketsu et al, 2004), pseudo-spectral method (Wang et al, 2001), and spectral element method (Komititsch and Tromp, 2002)) have become the standard tools for seismic wave modeling, however, these methods do not explicitly consider the boundary continuity conditions between different formations. That disables the methods to sufficient accuracy for modeling the reflection/transmission across irregular interfaces. Furthermore, they have difficulties in dealing with the case when the domain needs to be extended to infinity. Boundary element method (BEM) (Fu and Mu, 1994) has emerged as good alternatives to the domain numerical methods in simulating seismic wave excitation and propagation in an infinite continuum model because the radiation condition at infinity is easily fulfilled. However, the computing time needed for the traditional boundary element method increases tremendously as the number of layers increases in a stratified model. Ge and Chen (2007, 2008) proposed a boundary element method combined with global reflection/transmission matrix propagator method which is expected to solve this problem. In this paper, we extend this promising approach to a biphase model (such as a water/crust model) by modeling a transient P-SV wave propagation. The effects of water depth variation on synthetic seismograms are investigated in detail, which is significant to help understand the amplification of seismic wave propagation in gulf or coastal area, or even the tsunami phenomenon due to deep-sea earthquake.

The manuscript is organized as follows: the detailed

mathematical formulation of the hybrid boundary element method is given in Section II, where some formulas are taken from the previous work (Ge and Chen, 2008) and some details concerning programming the new approach is listed, followed by two validation examples in Section III; the synthetic seismogram calculations for a water-solid model are shown in Section IV; some conclusions are drawn in Section V.

2. METHODOLOGY STATEMENT

The problem to be studied is illustrated in Fig. 1. In this model, there are L homogeneous layers $\Omega^{(i)}$ (i=1, 2, …, L) over a half-space, among which the ith layer is bounded by two irregular interfaces $\Gamma_{(i-1)}$ and $\Gamma_{(i)}$ (Throughout the paper, the superscript with round brackets is used for layer index and the subscript with round brackets for interface index). The uppermost interface is a free surface, and an arbitrary source is embedded in the sth layer. Assume each individual layer to be isotropic, linearly elastic material, so the tensor of elastic constants is determined by two independent Lame constants because of the rotational and translational symmetry, i.e., $\lambda^{(i)}$, $\mu^{(i)}$. And the mass density is denoted by $\rho^{(i)}$. Since the method is a combination of the traditional boundary element method (BEM) and the global matrix propagator method, we first introduce BEM in brief.

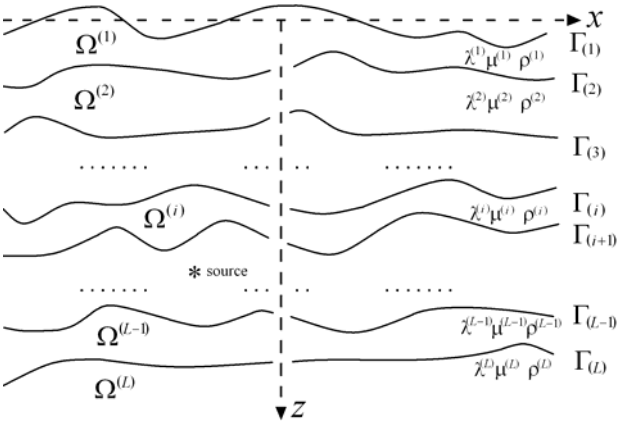

Fig. 1 A multilayered model with irregular interfaces

Consider the boundary element problem in a region Ω, where the elastic wave equation in frequency domain is given by

$$\mu\nabla^2\mathbf{u}+(\lambda+\mu)\nabla\nabla\bullet\mathbf{u}+\rho\omega^2\mathbf{u}=-\mathbf{f} \tag{1}$$

where $\mathbf{u}$ is the seismic displacement response in frequency domain, and $\mathbf{f}$ is the seismic source. Suppose the seismic source distribution consists of a simple point source at a position vector $\mathbf{s}$. With the aid of the free-space Green's function, Eq. (1) can thus be transformed into the following boundary integral equation for the displacement $u_j(\mathbf{r})$ on the boundary Γ of the region Ω (Balas et al, 1989)

$$\begin{aligned}&\Delta(\mathbf{r})u_k(\mathbf{r})+\int_\Gamma u_j(\mathbf{r}')T_{jk}(\mathbf{r},\mathbf{r}')\mathrm{d}\Gamma(\mathbf{r}')\\&\quad=\int_\Gamma t_j(\mathbf{r}')U_{jk}(\mathbf{r},\mathbf{r}')\mathrm{d}\Gamma(\mathbf{r}')+f_jU_{jk}(\mathbf{r},\mathbf{s})\end{aligned} \tag{2}$$

where j and k can be 1, 2. $\mathbf{r}$ and $\mathbf{r}'$ are the position vectors of "field point" and "source point" on the boundary Γ, respectively. The coefficient $\Delta(\mathbf{r})$ generally depends on the local geometry at $\mathbf{r}$, $t_j(\mathbf{r}')$ are the traction components, and $U_{jk}(\mathbf{r}, \mathbf{r}')$ and $T_{jk}(\mathbf{r}, \mathbf{r}')$ are the fundamental solutions for displacements and tractions, respectively, which can be found in Balas et al, (1989). The source exciting direction can be controlled arbitrarily by changing one of two components f_j. Application of Eq. (2) in domain $\Omega^{(i)}$ and discretization of interfaces $\Gamma_{(i)}$ and $\Gamma_{(i+1)}$ each into N elements (for simplicity, we use constant element) give rise to

$$\mathbf{H}^{(i)}\mathbf{u}^{(i)}=\mathbf{G}^{(i)}\mathbf{t}^{(i)}+\mathbf{F}\delta_{is} \tag{3}$$

where $\mathbf{H}^{(i)}$ and $\mathbf{G}^{(i)}$ are the coefficient matrices obtained by integrating over elements at both interfaces $\Gamma_{(i)}$ and $\Gamma_{(i+1)}$, and $\mathbf{u}^{(i)}$ and $\mathbf{t}^{(i)}$ are vectors containing element displacements and tractions at both interfaces $\Gamma_{(i)}$ and $\Gamma_{(i+1)}$, respectively. Obviously, $\mathbf{H}^{(i)}$ and $\mathbf{G}^{(i)}$ are of the dimension $4N\times4N$, and $\mathbf{u}^{(i)}$ and $\mathbf{t}^{(i)}$ are of the dimension $4N\times1$. In the multilayered medium (as shown in Fig. 1), considering the continuity conditions of displacements and tractions at inner interfaces, Eq. (3) needs to be rewritten into

$$\begin{aligned}&\begin{bmatrix}\mathbf{H}_{(i)}^{(i)} & \mathbf{H}_{(i+1)}^{(i)}\end{bmatrix}\begin{bmatrix}\mathbf{u}_{(i)}^{(i)}\\ \mathbf{u}_{(i+1)}^{(i)}\end{bmatrix}\\&\quad=\begin{bmatrix}\mathbf{G}_{(i)}^{(i)} & \mathbf{G}_{(i+1)}^{(i)}\end{bmatrix}\begin{bmatrix}\mathbf{t}_{(i)}^{(i)}\\ \mathbf{t}_{(i+1)}^{(i)}\end{bmatrix}+\mathbf{F}\delta_{si}\end{aligned} \tag{4}$$

where $\mathbf{u}^{(i)}$ and $\mathbf{t}^{(i)}$ with subscripts (i) and (i+1) corresponds separately to the element displacements and tractions at $\Gamma_{(i)}$ and $\Gamma_{(i+1)}$. Similarly, the subscripts (i) and (i+1) in $\mathbf{H}^{(i)}$ and $\mathbf{G}^{(i)}$ indicate the integration over elements at $\Gamma_{(i)}$ and $\Gamma_{(i+1)}$, respectively. Obviously, the matrices $\mathbf{H}^{(i)}$ and $\mathbf{G}^{(i)}$ with subscripts (i) or (i+1) are here of the dimension $4N\times2N$.

To facilitate the application of the matrix propagator method, the upward direction is defined as the positive direction for tractions so that they have unique values at each interface. Following Ge and Chen (2007), Eq. (4) becomes

$$\begin{aligned}&\mathbf{H}_{(i)}^{(i)}\mathbf{u}_{(i)}+\mathbf{H}_{(i+1)}^{(i)}\mathbf{u}_{(i+1)}\\&\quad=\mathbf{G}_{(i)}^{(i)}\mathbf{t}_{(i)}-\mathbf{G}_{(i+1)}^{(i)}\mathbf{t}_{(i+1)}+\mathbf{F}\delta_{si}\end{aligned} \tag{5}$$

where only one subscript index is needed to distinct

displacements and tractions at different interfaces, and the minus sign in front of the matrix $\mathbf{G}^{(i)}$ with the subscript (i+1) is due to the above-defined positive direction for traction.

Up to now, one can form a system of simultaneous equations by the traditional boundary element method using boundary and continuity conditions at free surface and inner interfaces. This is not very efficient, however, especially when the number of layers increases. So a global matrix propagator method is incorporated into the traditional boundary element method, resulting in a hybrid boundary element method adopted in this paper. The detailed procedure refers to Ge and Chen (2007, 2008). Here, the global matrix propagators are directly given as

$$\begin{cases} \mathbf{u}_{(i)} = \mathbf{D}_{uu}^{(i)} \mathbf{u}_{(i+1)} \\ \mathbf{t}_{(i+1)} = \mathbf{D}_{tu}^{(i)} \mathbf{u}_{(i+1)} \end{cases}, i = 1, 2, \cdots, s-1, \tag{6}$$

for the layers above the source, and

$$\begin{cases} \mathbf{u}_{(i+1)} = \mathbf{D}_{uu}^{(i)} \mathbf{u}_{(i)} \\ \mathbf{t}_{(i)} = \mathbf{D}_{tu}^{(i)} \mathbf{u}_{(i)} \end{cases}, i = s+1, s+2, \cdots, L, \tag{7}$$

for the layers below the source.

The explicit expressions for $\mathbf{D}_{uu}$ and $\mathbf{D}_{tu}$ in Eqs. (6) and (7) can be found in Ge and Chen (2008). It can be readily seen from Eqs. (6) and (7) that two global matrix propagators exist in each layer but function in different ways for the layers above and below the source. $\mathbf{D}_{uu}$ transfers the information of element displacements from the upper interface to the lower interface in an arbitrary layer above the source whilst $\mathbf{D}_{tu}$ bridges the element tractions and displacements at the lower interface of the layer. However, for an arbitrary layer below the source, $\mathbf{D}_{uu}$ transfers the information of element displacements from the lower interface to the upper interface whilst $\mathbf{D}_{tu}$ bridges the element tractions and displacements at the upper interface of the layer. That's the main idea of the global matrix propagators which propagate information from "top and bottom" where the boundary conditions are known to "middle" where the source is located. Both of the two matrices $\mathbf{D}_{uu}$ and $\mathbf{D}_{tu}$ are of the dimension $2N \times 2N$ in the case of 2-D P-SV wave propagation.

In order to get the solution of the problem, we need to form a system of equations in the source layer, which can be easily done by setting $i = s$ in Eq. (5) as

$$\begin{aligned} &\mathbf{H}_{(s)}^{(s)} \mathbf{u}_{(s)} + \mathbf{H}_{(s+1)}^{(s)} \mathbf{u}_{(s+1)} \\ &\quad = \mathbf{G}_{(s)}^{(s)} \mathbf{t}_{(s)} - \mathbf{G}_{(s+1)}^{(s)} \mathbf{t}_{(s+1)} + \mathbf{F} \end{aligned} \tag{8}$$

in which both the element displacements and tractions are unknowns and cannot be solved from the present form of Eq. (8) yet. Now, it is the time to apply the aforementioned definitions of the global matrix propagators which give the relationship between the traction and displacement at the sth and (s+1)th interfaces as

$$\begin{aligned} \mathbf{t}_{(s)} &= \mathbf{D}_{tu}^{(s-1)} \mathbf{u}_{(s)}, \\ \mathbf{t}_{(s+1)} &= \mathbf{D}_{tu}^{(s+1)} \mathbf{u}_{(s+1)}. \end{aligned} \tag{9}$$

Substitution of Eq. (9) into Eq. (8) gives rise to

$$\begin{aligned} &\left[\mathbf{H}_{(s)}^{(s)} - \mathbf{G}_{(s)}^{(s)} \mathbf{D}_{tu}^{(s-1)} \right] \mathbf{u}_{(s)} \\ &\quad + \left[\mathbf{H}_{(s+1)}^{(s)} + \mathbf{G}_{(s+1)}^{(s)} \mathbf{D}_{tu}^{(s+1)} \right] \mathbf{u}_{(s+1)} = \mathbf{F} \end{aligned} \tag{10}$$

which has the same number of unknowns and equations.

Once the displacements at the interfaces enclosing the source are solved, the displacements and tractions at all the other interfaces can be easily obtained by

$$\begin{cases} \mathbf{u}_{(i)} = \mathbf{D}_{uu}^{(i)} \mathbf{D}_{uu}^{(i+1)} \cdots \mathbf{D}_{uu}^{(s-1)} \mathbf{u}_{(s)} \\ \mathbf{t}_{(i+1)} = \mathbf{D}_{tu}^{(i)} \mathbf{u}_{(i+1)}, i = 1, 2, \cdots, s-1, \end{cases} \tag{11}$$

$$\begin{cases} \mathbf{u}_{(i+1)} = \mathbf{D}_{uu}^{(i)} \mathbf{D}_{uu}^{(i+1)} \cdots \mathbf{D}_{uu}^{(s+1)} \mathbf{u}_{(s+1)} \\ \mathbf{t}_{(i)} = \mathbf{D}_{tu}^{(i)} \mathbf{u}_{(i)}, i = s+1, s+2, \cdots, L. \end{cases} \tag{12}$$

Then the displacements at any observation points in the whole model can be obtained by the following integral equation applied in the domain

$$\begin{aligned} u_k(\mathbf{r}) = &\int_\Gamma \left[t_j(\mathbf{r}') U_{jk}(\mathbf{r}, \mathbf{r}') - u_j(\mathbf{r}') T_{jk}(\mathbf{r}, \mathbf{r}') \right] \mathrm{d}\Gamma(\mathbf{r}') \\ &+ f_j U_{jk}(\mathbf{r}, \mathbf{s}) \delta_{is}, \quad \mathbf{r} \in \Omega^{(i)} \end{aligned} \tag{13}$$

which can be transformed into a summation of the element displacements and tractions obtained just now without extra effort. Usually, displacements at free surface are of practical interest. By taking the inverse Fourier transform on the above frequency domain solution, one can finally get the solution in time domain, i.e., the synthetic seismogram.

3. VALIDATION EXAMPLES

In order to apply the method to study the effects of water depth variation on synthetic seismograms, we first calculate the wave fields in two simple models for which the existing results calculated by different methods are available

in published papers. The comparison of the calculated results below with published ones can be a validation test to our program and the method itself. Let's show them one by one in this section.

3.1 Semi-circular Canyon Model

As shown in Fig. 2, the model is a semi-circular canyon in an elastic homogenous half-space subject to incident body waves.

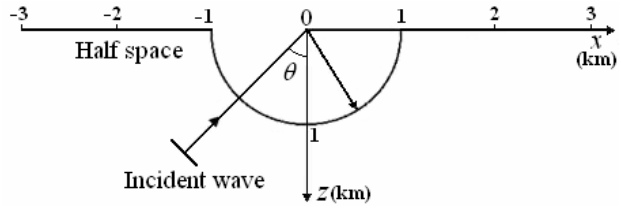

Fig. 2. Semi-circular canyon topography and the surrounding homogeneous half-space

Although the shape is too simple for a realistic canyon, the wave reflection and diffraction due to the topographical irregularity in time domain are quite complex, which can serve for an eligible test to the present method and our computation program. Here, we calculate the time-domain responses of the surface along the semi-circular canyon subject to incident SV and P waves.

In all of the cases shown hereafter, the shape of the incident wave is a Ricker wavelet defined as (Ricker, 1977)

$$u(t) = \left(2\pi^2 f_c^2 t^2 - 1\right)\exp\left(-\pi^2 f_c^2 t^2\right) \qquad (14)$$

where f_c is the characteristic frequency of the wavelet and t is the time. Observation points are set along the surface both inside and outside the canyon. The shear wave velocity is 1000m/s and Poisson's ratio is 1/3.

SV-wave incidence. Figure 3 (a and b) shows the time-domain responses of the semi-circular canyon topography due to a vertically incident SV wave for the horizontal (inplane) and the vertical motions, respectively. It can be seen from Fig. 3 that the direct waves appearing in the horizontal component keep the same amplitude along the surface of the canyon except near the edges, where complicated interference occurs. The vertical component generated by the impact and subsequent reflection of incident wave at the canyon surface grows as the wave propagates upward and reaches its maximum at the edges. The so called creeping P waves generated due to wave diffraction inside the canyon can also be distinguished. Outside the canyon, the later arrivals can be observed to become Rayleigh waves soon after the departure from the edges. This problem was first calculated in the work by Kawase (1988) using DWBEM (Discrete Wavenumber Boundary Element Method). The remarkable agreement can be seen between our calculated results and his results, which shows the validity of the present method and computation program.

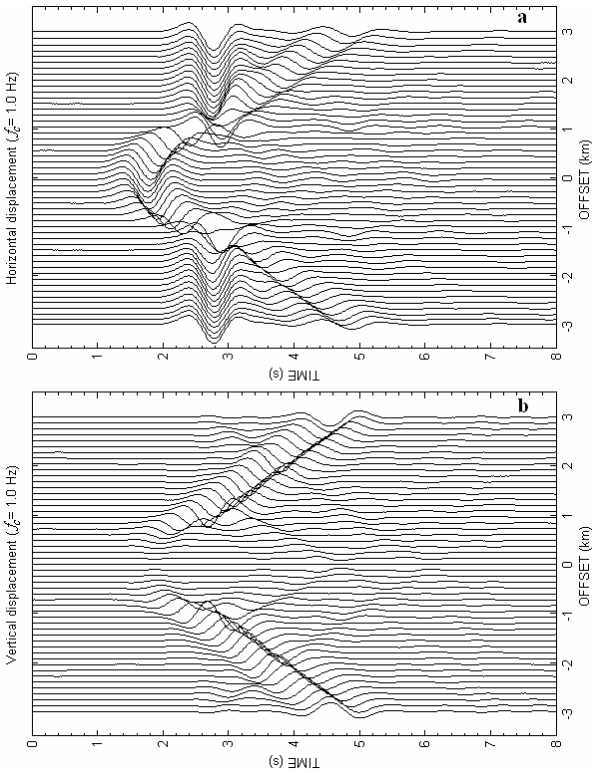

Fig. 3. Time responses along the semi-circular canyon topography due to a vertically incident SV wave: (a) and (b) correspond to the horizontal and vertical components.

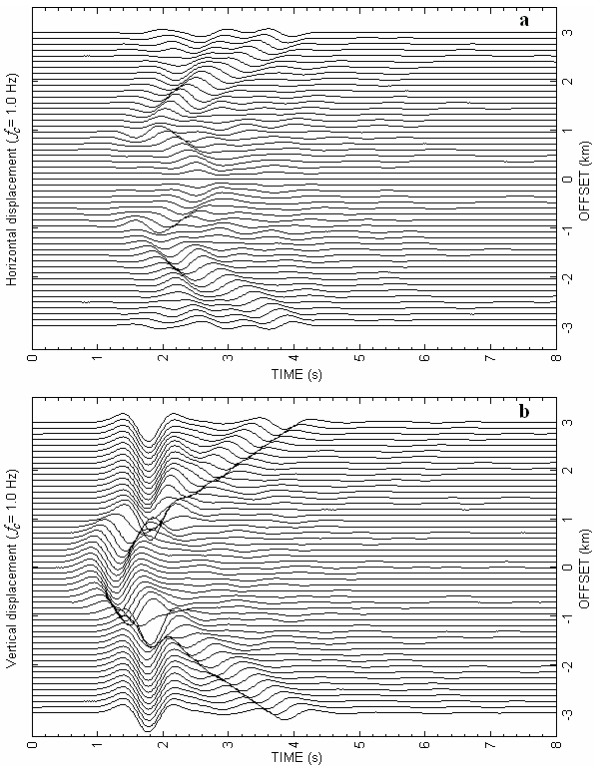

Fig. 4. Time responses along the semi-circular canyon topography due to a vertically incident P wave: (a) and (b) correspond to the horizontal and vertical components.

P-wave incidence. Furthermore, a vertically incident P wave is calculated. The corresponding results are plotted in Fig. 4 (a and b), which also shows perfect agreement with the results by Kawase (1988). Comparing with SV wave incidence, everything in the case of P wave incidence becomes simpler. The amplitudes of the direct arrivals on the vertical component are almost the same along the surface except near the edges, and those of the diffracted waves inside the canyon and Rayleigh waves outside the canyon are relatively small.

3.2 Deep Basin Model

Next, we consider a relatively complex model. Figure 5 shows the model configuration consisting of a deep basin structure. The basin has a trapezoidal shape with 1 km depth and 10 km width at the surface. The shear wave velocity of the basin-filling sediments and the half-space are 2.5 km/s and 1 km/s, respectively, and Poisson's ratio is 1/3, the ratio of mass density is set to 3:4. Although the upper part seems to have a smaller shear wave velocity, it must increase with depth. Therefore 1 km/s is a reasonable estimate for the average shear wave velocity for the sedimentary basin.

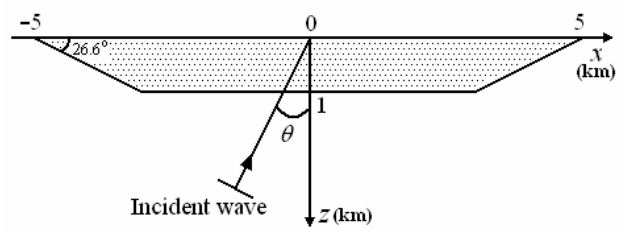

Fig. 5. Deep basin topography and the surrounding homogeneous half-space

This model was first used by Kawase and Aki (1989) to investigate the long duration of strong motions observed in Mexico City during the Michoacan, Mexico earthquake of 1985. Here, we calculate the time-domain responses of the free surface on the top of the deep basin layer subject to incident SV and P waves.

SV-wave incidence. Figure 6 (a and b) gives the horizontal and vertical components of the seismic response to a vertically incident SV-wave with f_c = 0.25 Hz (4 sec) in time domain for the sedimentary basin. It can be readily seen from Fig. 6 that successive wave trains appear in the transition zone (horizontal displacement) and in the flat part (vertical displacement). The remarkable agreement can be seen between our calculated results and their results, which shows the validity of the present method and computation program.

P-wave incidence. Furthermore, a vertically incident P wave is calculated. The corresponding results are plotted in Fig. 7 (a and b), which also shows perfect agreement with the results by Kawase and Aki (1989). It can be seen that the later arrivals in the vertical displacement are very similar to those for SV wave incidence. Although it is of little practical importance to study the responses for P wave incidence, it is worthwhile from a theoretical point of view. Also, the calculation can be used to validate our program.

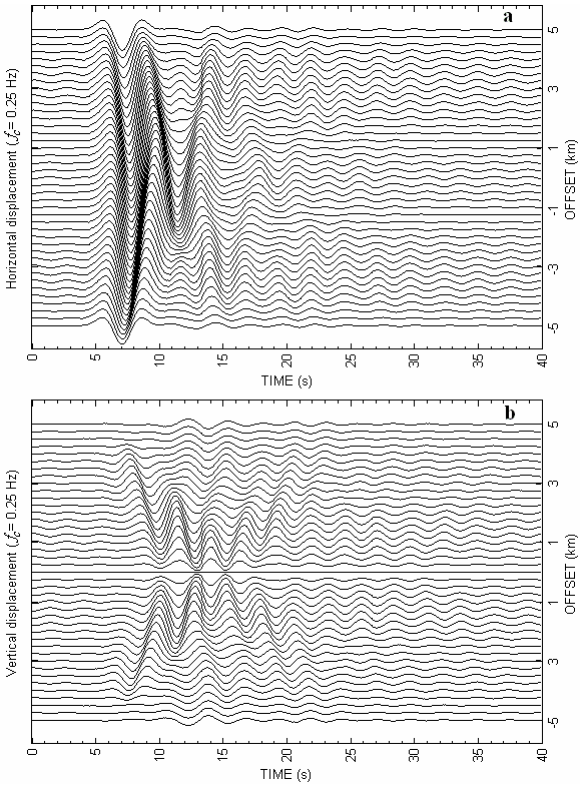

Fig. 6. Time responses along the free surface of the basin due to a vertically incident SV wave: (a) and (b) correspond to the horizontal and vertical components.

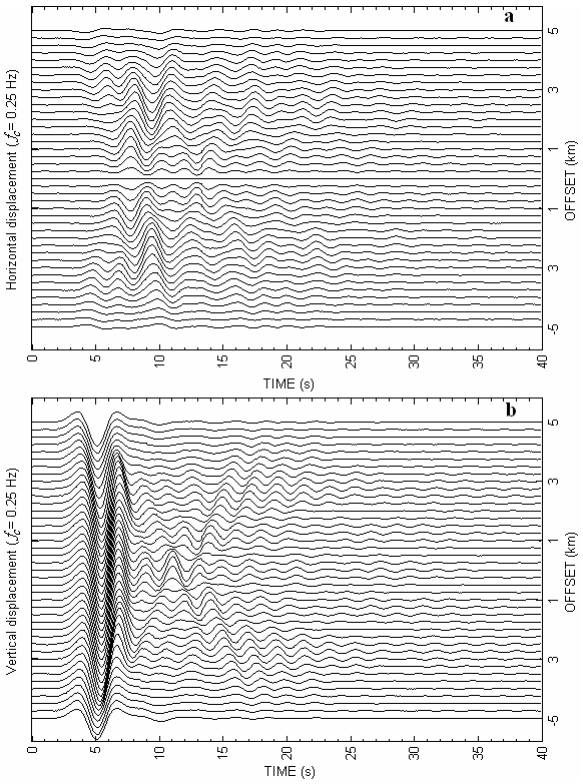

Fig. 7. Time responses along the free surface of the basin due to a vertically incident P wave: (a) and (b) correspond to the horizontal and vertical components.

From the abovementioned validation examples, we can come to the conclusion that our computation program is correct and the method proposed by Ge and Chen (2007, 2008) has proved to be effective. In the next section, we start to use the method to study the effects of water depth variation on synthetic seismograms by using a simple water-solid model consisting of one water layer covering one irregular solid half-space.

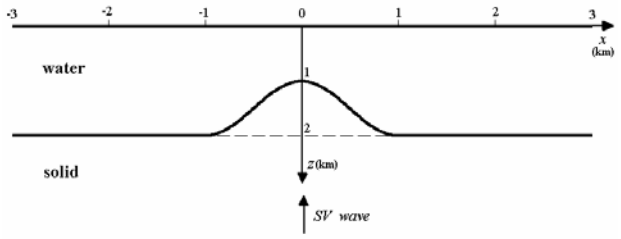

Fig. 8. A schematic model consisting of a hump topography covered by a water layer on the top

4. EFFECTS OF WATER DEPTH VARIATION

As shown in Fig. 8, the model considered in this section consists of a hump half-space covered by a water layer. Here, the water is assumed to be linear, incompressible liquid without viscosity. Therefore, the wave propagation problem in the water layer can be taken as a potential problem, which results in the following BEM matrix equation

$$-\mathbf{H}^{(1)}_{(2)}\mathbf{p}_{(2)} = \mathbf{G}^{(1)}_{(1)}\mathbf{q}_{(1)} + \mathbf{G}^{(1)}_{(2)}\mathbf{q}_{(2)} \tag{15}$$

where $\mathbf{p}$ and $\mathbf{q}$ are the vectors of the dimension $N\times1$ (suppose each interface is discretized into N elements), with water pressure p and its normal derivative q being the element components, the minus sign on the left hand side is due to the positive direction defined for traction in Section 2. And the continuity conditions at the interface between the water layer and the solid half space are as follows based on aforementioned assumption on the water

$$\begin{aligned} &-p = \mathbf{n}\bullet\mathbf{t}, \boldsymbol{\tau}\bullet\mathbf{t} = 0, \\ &-\partial p / \partial \mathbf{n} = \rho_{\mathrm{f}}\mathbf{n}\bullet\partial_t^2\mathbf{u} \end{aligned} \tag{16}$$

where $\mathbf{n}$ and $\boldsymbol{\tau}$ are the normal vector and the inplane tangential vector at the interface, respectively. ρ_{f} is the water mass density, and ∂_t denotes time derivative.

To apply the hybrid boundary element method introduced in Section 2 to the present water-solid model, we first define the global matrix propagators $\mathbf{D}_{qq}$ and $\mathbf{D}_{pq}$ in the water layer as follows

$$\begin{cases} \mathbf{q}_{(1)} = \mathbf{D}^{(1)}_{qq}\mathbf{q}_{(2)} \\ \mathbf{p}_{(2)} = \mathbf{D}^{(1)}_{pq}\mathbf{q}_{(2)} \end{cases} \tag{17}$$

which is similar to Eqs. (6) and (7). The explicit expressions for $\mathbf{D}_{qq}$ and $\mathbf{D}_{pq}$, suppressed for brevity, can be easily obtained following the procedure mentioned by Ge and Chen (2008). One point noted here is that the global matrix propagators defined in Eq. (17) have the dimension $N\times N$ which is different from those in Eqs. (6) and (7). Therefore, we need to extend the global matrix propagators defined for water layer into the same dimension as those defined for solid layer, i.e., from $N\times N$ to $2N\times2N$, by using the continuity conditions between the water and the solid half space, i.e., Eq. (16).

Through the global matrix propagators, we can thus calculate the wave propagation in the bottom layer. The parameters used in our calculation are: the acoustic wave velocity in water is 1.5 km/s, the shear wave velocity in the solid layer is 1 km/s with Poisson's ratio being 1/3, the ratio of mass density is set to 1:2.

Figure 9 (a and b) gives the horizontal and vertical components of the seismic response along the interface between the water layer and the solid half space due to a vertically incident SV-wave with f_c = 1.0 Hz in time domain. It can be seen from Fig. 9 that the direct arrivals keep the same amplitude except in the hump zone where vertical displacement generated by the impact and subsequent reflection of the incident wave along the hump interface grows as the wave propagates upward and reaches its maximum value at the top.

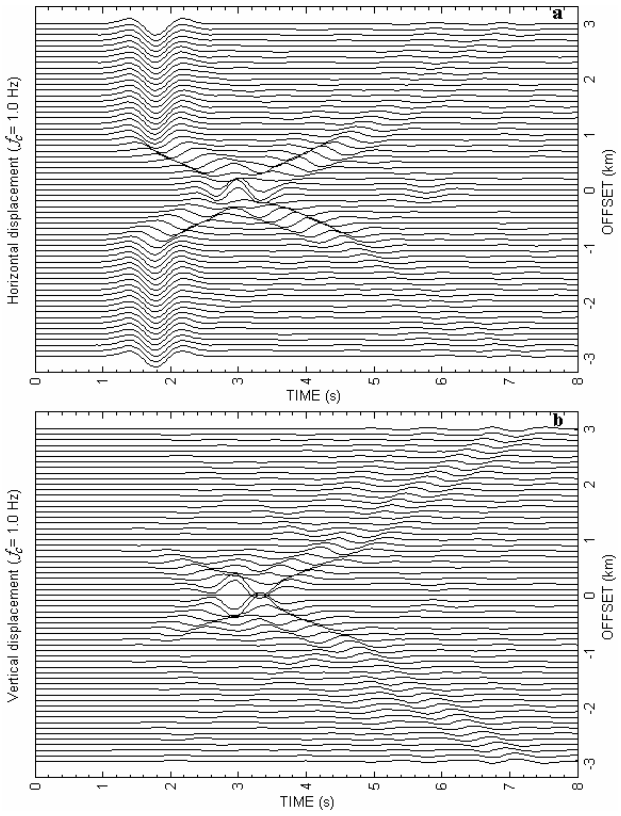

Fig. 9. Time responses along the hump interface in Fig. 8 due to a vertically incident SV wave: (a) and (b) correspond to the horizontal and vertical components.

In order to show the effects of water depth variation on the synthetic seismograms, we also calculate the time-

domain responses of the hump topography without water covering layer due to a vertically incident SV wave for the horizontal (inplane) and the vertical motions, respectively, as shown in Fig. 10 (a and b). The comparison between Figs. 9 and 10 shows that the direct arrivals in both horizontal and vertical displacements are almost exactly the same and the differences between the two figures appear most in the later arrivals, which is very consistent with the two models used in calculation. For horizontal displacement, Fig. 9 (a) shows the same pattern as that in Fig. 10 (a) except the waves at the top of the hump where the stronger constructive interference occurs in the case of the model with water covering layer. While for the vertical displacement, the differences between Figs. 9 and 10 are more obvious. This is reasonable because only P wave is possible in the water layer. The two later arrivals in Fig. 10 (b) becomes only one in Fig. 9 (b), which means part energy of the vertical displacement is transmitted into the water layer. All the observations clearly show the effects of water depth variation on the synthetic seismogram along the interface between the water layer and the solid half space due to a vertically incident SV wave.

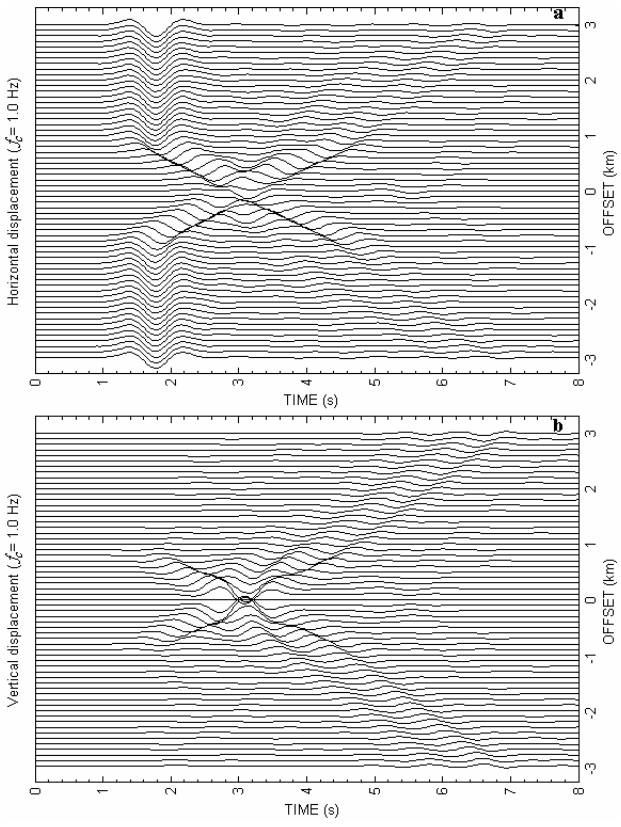

Fig. 10. Time responses along the free surface of a hump topography due to a vertically incident SV wave: (a) and (b) correspond to the horizontal and vertical components

5. CONCLUSIONS

In this paper, we first introduced a hybrid boundary element method which has the potential advantage over other methods in computation time and memory requirement during seismogram synthesis for multi-layered media with irregular interfaces. Then two typical numerical examples were done to show the validity of the method and our computation program. Finally, we extended the method to biphase media and studied the effects of water depth variation on synthetic seismograms by using a simple water-solid model subject to a vertically incident SV wave. The method proves to be effective. In the next step, we will investigate the effects of sea water in Tokyo bay on seismic wave propagation in the Kanto basin using a realistic model including sea water, as shown in Fig. 11.

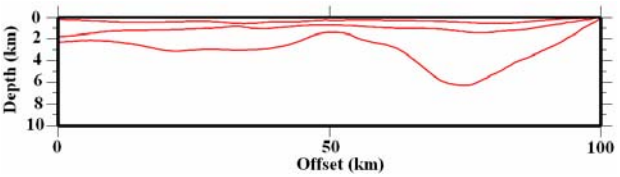

Fig. 11. The 2-D underground profile between Tokyo (139.765827/35.681421) and Simoda (138.89719/34.64911)

Acknowledgements:

The authors are very grateful to Prof. Kohji Tokimatsu, the Leader of the Global COE Program entitled "International Urban Earthquake Engineering Center for Mitigating Seismic Mega Risk", Tokyo Institute of Technology, for his advice and support. Financial support from the Center for Urban Earthquake Engineering (CUEE), Tokyo Institute of Technology, through the project "Seismogram Synthesis for Three-dimensional Multi-layered Media with Irregular Interfaces based on Boundary Element Method", is gratefully acknowledged.

References:

Balas, J., Sladek, J. and Sladek, V. (1989), "Stress Analysis by Boundary Element Methods," Elsevier., New York.

Cerveny, V. (2001), "Seismic Ray Theory," Cambridge University Press, Cambridge.

Chen, X.F. (1990), "Seismogram synthesis for multi-layered media with irregular interfaces by global generalized reflection/ transmission matrices method-I. Theory of 2D SH case," *Bulletin of the Seismological Society of America*, 80, 1696-1724.

Chen, X.F. (1995), "Seismogram synthesis for multi-layered media with irregular interfaces by global generalized reflection/ transmission matrices method-II. Applications for 2D SH case," *Bulletin of the Seismological Society of America*, 85, 1094-1106.

Fu, L.Y. and Mu, Y.G. (1994), "Boundary element method for elastic wave forward modeling," *Acta Geophysica Sinica*, 37, 521-529.

Ge Z.X. and Chen X.F. (2007), "Wave propagation in irregularly layered elastic models: a boundary element approach with a global reflection/transmission matrix propagators," *Bulletin of the Seismological Society of America*, 97, 1025-1031.

Ge Z.X. and Chen X.F. (2008), "An efficient approach for simulating wave propagation with the boundary element method in multilayered media with irregular interfaces," *Bulletin of the Seismological Society of America*, 98, 3007-3016.

Kawase, H. (1988), "Time-domain response of a semi-circular canyon for incident SV, P, and Rayleigh waves calculated by the

discrete wavenumber boundary element method," *Bulletin of the Seismological Society of America*, 78, 1415-1437.

Kawase, H. and Aki, K. (1989), "A study on the response of a soft basin for incident S, P, and Rayleigh waves with special reference to the long duration observed in Mexico City," *Bulletin of the Seismological Society of America*, 79, 1361-1382.

Kennett, BLN. (1983), "Seismic wave propagation in stratified media," Cambridge University Press, New York.

Koketsu, K., Fujiwara, H. and Ikegami, Y. (2004), "Finite-element simulation of seismic ground motion with a voxel mesh," *Pure Applied Geophysics*, 161, 2183-2198.

Komititsch, D. and Tromp, J. (2002), "Spectral-element simulations of global seismic wave propagation-I. Validation," *Geophysical Journal International*, 149, 390-412.

Miklowitz, J. and Achenbach, J.D. (1978), "Modern Problems in Elastic Wave Propagation," Wiley, New York.

Ricker, N.H. (1977), "Transient waves in visco-elastic media," Elsevier, Amsterdam.

Wang, Y.B., Takenaka, H. and Furumura, T. (2001), "Modeling seismic wave propagation in a two-dimensional cylindrical whole-earth model using the pseudo-spectral method," *Geophysical Journal International*, 145, 689-708.

Zhang, W. and Chen, X.F. (2006), "Traction image method for irregular free surface boundaries in finite difference seismic wave simulation," *Geophysical Journal International*, 167, 337-353.

Zhao, C.G., Dong, J., Gao, F.P. and Jeng, D.S. (2006), "Seismic responses of a hemispherical alluvial valley to SV waves: a three-dimensional analytical approximation," *Acta Mechanica Sinica*, 22, 547-557.

JOINT CONFERENCE PROCEEDINGS
7th International Conference on Urban Earthquake Engineering (7CUEE) &
5th International Conference on Earthquake Engineering (5ICEE)
March 3-5, 2010, Tokyo Institute of Technology, Tokyo, Japan

DEVELOPMENT OF EARTHQUAKE EXPERIENCE SYSTEM USING GROUND MOTION SIMULATOR "JISHIN THE VUTON"

Sou Adachi[1], Masayuki Matsudaira[2], Yoshiharu Hirayama[3], Minoru Yoshida[4]
Saburoh Midorikawa[5], Shigeo Hirose[6]

1) Technical Dept, Division of Disaster Prevention System, Hakusan Corporation, Japan
2) Technical Manager, Division of Mechatronics, Hakusan Corporation, Japan
3) Research Director, Division of Disaster Prevention System, Hakusan Corporation, Japan
4) CEO, Hakusan Corporation, Japan
5) Professor, Department of Built Environment, Tokyo Institute of Technology, Japan
6) Professor, Department of Mechanical and Aerospace Engineering, Tokyo Institute of Technology, Japan
adachi@hakusan.co.jp, matsu@hakusan.co.jp, hirayama@hakusan.co.jp,
yoshida@hakusan.co.jp, smidorik@enveng.titech.ac.jp, hirose@mes.titech.ac.jp

Abstract: We developed "Jishin-The-Vuton", the portable earthquake simulator that can reproduce a waveform of a two-dimensional earthquake vibration, and confirmed that it can reproduce a pretty strong earthquake. By combination with a movie projection tool, "Jishin-The-Vuton" can be a powerful demonstration system of earthquake disasters.

1. INTRODUCTION

Devices to simulate and reproduce earthquake motion are installed and used by various research institutions (e.g. E-defence). All of these simulators have a platform driven by an actuator with structures or furniture on it. They are used in various applications such as earthquake resistance test and experience of ground motion to raise the awareness of disaster prevention. Although an existing portable earthquake simulator can reproduce ground motion of Japanese seismic intensity 7, its motion is restricted within rather short distance for large amplitude vibration.

In recent years, long period ground motion by major earthquakes such as Tokai, Tonankai and Nankai earthquake is expected to predominate in sedimentary plains. Damage inside high-rise buildings by the motion is anticipated (Midorikawa et al 2008). To raise public awareness to seismic risks, it is necessary to experience destructive ground motion as well as long period vibration.

In this study, we developed a new system to experience ground motion using a portable earthquake simulator "Jishin The VUTON" (Yamaguchi et al. 2009). The system can accurately reproduces long-period and/or destructive ground motion. For effective recognition of damage in a room by earthquakes, this system uses video pictures taken by using the two dimensional large amplitude vibration platform. This made it possible to develop the experiential earthquake system of accurately simulated ground motion with real scene of a damaged room inside.

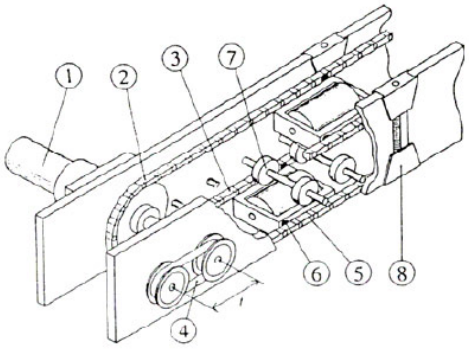

Figure 1 Outline of the VUTON Crawler

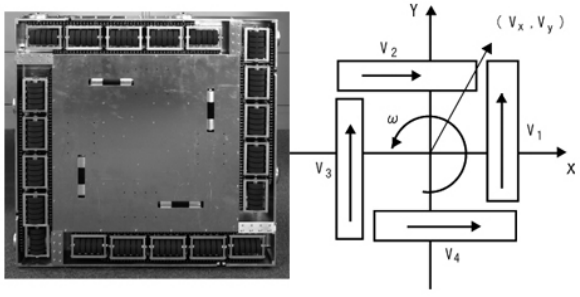

Figure 2 Arrangement of VUTON Crawlers

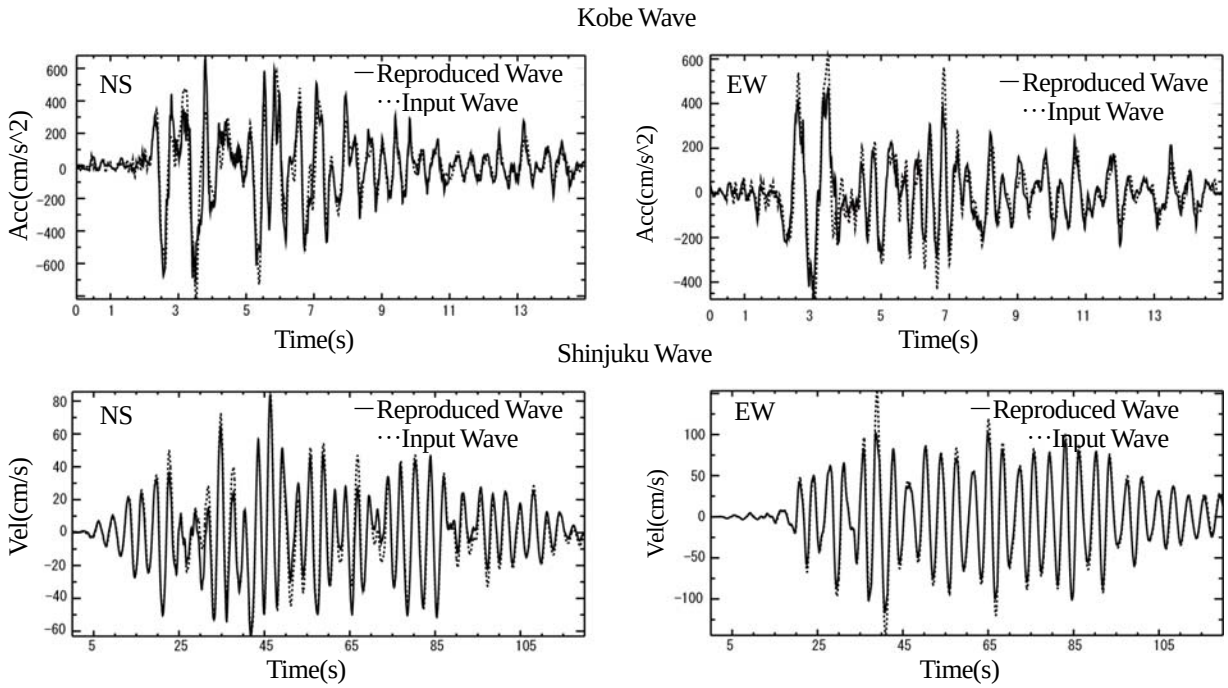

Figure 3 Comparison of the Ground Motion reproduced by Jishin The VUTON (Solid Line) with Ground Motion Input(Dotted Line)

2. CHARACTERISTICS OF GROUND MOTION SIMULATOR

The VUTON crawler (Hirose and Amano 1993) is characterized by the large load capacity because the load is carried by multiple rollers individually, which is the most suitable actuating mechanism for an earthquake simulator reproducing the high acceleration caused by ground motion (see Figure 1). The VUTON crawler is a mechanism where two rows of chains (3) and (5) are driven synchronously by a geared motor (1) and belt (4). Between the two chains, a number of frames (6) with rubber wheels are connected. When the chains move, the rubber wheels in contact with the floor generate an actuating force between the floor and the mechanism in the direction of chain movement by gripping the floor. In the direction perpendicular to the movement of the chains, each rubber wheel can rotate freely and carries the load only from above.

The VUTON crawler works as an actuating mechanism in a direction parallel to the axis of the roller and as the supporting mechanism following in a direction perpendicular to the axis of the roller. The combined movement of these in the oblique direction can also be generated. With four units of VUTON crawlers arranged as shown in Figure 2 and with the appropriate control, an actuating force can be generated in any direction in Jishin The VUTON.

3. PERFORMANCE OF GROUND MOTION SIMULATOR

Characteristics of the ground motion and the associated damage have been examined by Kawase (1998). In his study, a destructive damage zone is defined where maximum acceleration of ground motion is equal to or greater than 800 cm/s^2 and the maximum velocity of the motion is equal to or greater than 100 cm/s. In the gigantic ocean trench earthquake predicted for the near future , long-period ground motion with a structural response of 100cm/s(a period of 5s, h=0.05) or more is expected to predominate in the sedimentary plains(The Headquarters for Earthquake Research Promotion News 2009). Accordingly, a prototype of the ground motion simulator was constructed to reproduce maximum destructive ground motion corresponding to seismic intensity scale 7 with around 1 Hz, and to reproduce a motion of more than 100 cm/s in long-period range as a target.

Performance of this prototype was presented in the meetings of the Robotics Society of Japan (Matsudaira et al. 2009) and in the Japan Association for Earthquake Engineering (Hirayama et al. 2009), which indicated that the motion of the prototype was very close to the acceleration waveform in two horizontal components recorded at JMA Kobe in the Southern-Hyogo Prefecture Earthquake of 1995 (hereinafter referred to as Kobe Wave) and the structural response in two horizontal components to be encountered on 25th floor of a 30-story high-rise building in the predicted Tokai earthquake (hereinafter referred to as the Shinjuku Wave). These waveforms are shown in Figure 3.

4. SPECIFICATION OF GROUND MOTION SIMULATOR

Figure 4 is an outside view of the prototype. The dimensions of the equipment are 744 × 744 × 115 [mm] (excluding the chair), the weight is approximately 65 kg, and the load capacity is for one person.

An external DC power source is used to actuate the equipment. A capacitor circuit for recovery and storage of regenerative power from the motor can be connected externally because reproduction of the ground motion requires actuation of frequent acceleration and damping (deceleration). This enables actuation of high acceleration and velocity.



Figure 4 Outside View of Jishin The VUTON

A Windows PC is used to control the equipment. For control of the motor, velocity command data are transmitted in real time via serial communication using CAN bus with a general purpose servo-amplifier. The velocity command data are recorded in CSV text file format in 0.01-second time steps.

5. THE SYSTEM FOR EXPERIENCING GROUND MOTION

According to a recent questionnaire survey about earthquake damage (Tokyo Fire Department. 2008), about 40 percent of injuries are caused by falling furniture as in the case of the Niigataken Chuetsu-oki earthquake in 2007. And about 30 percent of the causes of personal injury is falling due to ground motion. Accordingly, we considered that experiencing ground motion with a movie showing how furniture will respond to an earthquake is effective in order to expand awareness of seismic risks. For effective recognition of the damage caused by destructive and/or long-period ground motions inside a room, movies showing the damage caused by vibration experiments on the large amplitude two-dimensional vibration platform using the Kobe Wave and Shinjuku Wave were taken. The maximum displacement of the vibration platform is ±100 cm in the transverse direction and ±50 cm in the radial direction. Maximum acceleration of 1000 cm/s^2 and maximum velocity of 150 cm/s can be generated. Dimensions of the platform are 3.2 m × 2.5 m. However in the case of the Shinjuku Wave, half amplitude of the motion is more than one meter, which exceeds the limit of performance of the vibration platform, and the amplitude of the wave input was restricted to 85 percent. A table, chairs, cupboard, and pendant light are arranged inside the room simulating a dining kitchen for the movie of the damage caused by the Kobe Wave and Shinjuku Wave, respectively (Figure 5). As for the structural response to long-period ground motion, an experiment on a high-rise building conducted by E-defense (Nagae et al. 2009) indicates that a copier with a weight of more than 200 kilograms may move around for a long period of time because of the casters. Accordingly, for the Shinjuku Wave experiment where the long-period component of the motion is predominant, articles were arranged so that furniture equipped with casters could move freely (Figure 6) while the movie was recorded.

The system configuration where the movie and the actuation of Jishin The VUTON were synchronized is as shown in Figure 7. In this system, two operators, one for operation of the controller PC for Jishin The VUTON and the other for operation of the movie projector, and another one as an instructor are required. At this moment, synchronization of Jishin The VUTON and the movie projector is not automatic, and two operators are required. We intend to construct a system that enables automatic synchronization of the movie and Jishin The VUTON shortly.



Figure 5 Vibration Platform with Furniture and Articles Arranged in the Simulated Room

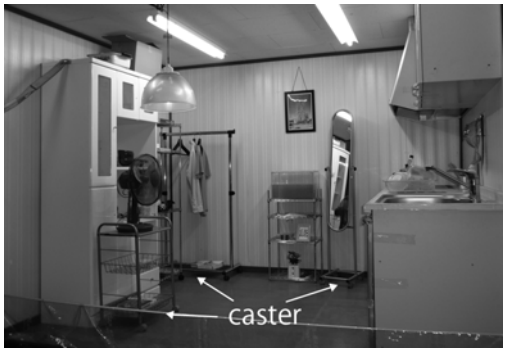

Figure 6 Vibration Platform with Furniture and Articles Arranged in the Simulated Room so that Furniture with Casters can move freely

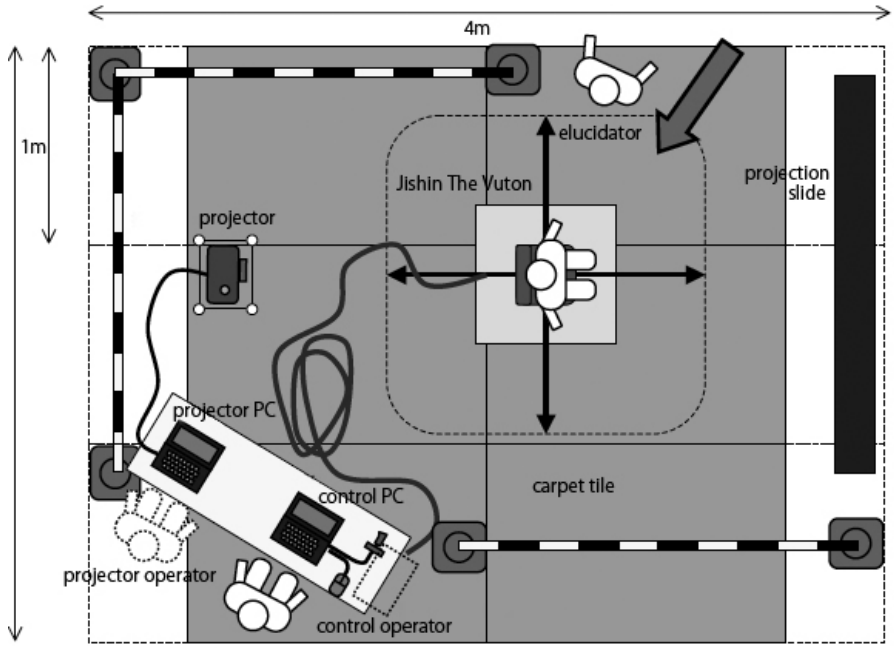

Figure 7 Jishin The VUTON System Configuration



Figure 8 Demonstration of Jishin The VUTON System

6. CONCLUSIONS AND FUTURE TASKS

Effectiveness of Jishin The VUTON as an educational tool for prevention of seismic disaster that accurately reproduces destructive and/or long period ground motion combined with movies depicting damage inside a room was demonstrated. Jishin The VUTON is the only one portable facility providing an opportunity to the general public to experience the earthquake vibration in high-rise building where long period and large amplitude response occur.

Future tasks are as follows.

Enhancement of safety, improvement of strength of the rollers, development of mechanism for reproduction of three dimensional ground motion and development of automatic system for complete synchronization of the movie and Jishin The VUTON.

References:

Midorikawa, S., Masatsuki, T., Ohori, M. and Miura, H. (2008), "Seismic Behavior of Office Furniture in High-Rise Building due to Long Period Ground Motion," Proceedings of 5th International Conference on Urban Earthquake Engineering, pp.73-76.

Yamaguchi, R., Wang, T., Matsudaira, M., Hirayama, Y., Midorikawa, S. and Hirose, S. (2009), "Development of Brand-new Portable Earthquake Simulator Using Holonomic Omni-directional Vehicle," Proceeding of the Sixth International Conference on Urban Earthquake Engineering, pp.171-176.

Hirose and Amano. (1993), "The VUTON: High Payload High Efficiency Holonomic Omni-Directional Vehicle," Proc. ISRR, Hidden Valley, USA, pp. 253-260.

Kawase, H. (1998), "Amplification Process Of Near Fault Strong Ground Motion in Subsurface Structure and Their Damage Impact To Structures." Proceeding Of The 10th Japan Earthquake Engineering Symposium, pp.29- 34.

The Headquarters for Earthquake Research Promotion News, November, (2009) http://www.jishin.go.jp/main/herpnews/2009/nov/index.html

Matsudaira, M., Yamaguchi, R., Hirayama, Y., Wang, M., Yoshida, M., Midorikawa, S., and Hirose, S., (2009), "Development of 'Jishin-The-Vuton', The Portable Earthquake Simulator Using Omni-Directional Platform," 27th Annual Conference of the Robotics Society of Japan, 3Q1-03.

Hirayama, Y., Yamaguchi, R., Matsudaira, M., Wang, M., Yoshida, M., Midorikawa, S., and Hirose, S., (2009), "Development of 'Jishin-The-Vuton', The Earthquake Simulator Reproducing Destructive and Long-period Ground Motions," Proceeding of the 7th Annual Meeting of Japan Association for Earthquake Engineering, pp.116-117.

Tokyo Fire Department, (2008), "Result of discussions in the Committee on Countermeasures for Prevention of Tipping –over and Falling of the Furniture".

Nagae, T., Kajiwara, K., Fukuyama, K., Inoue, T., Nakashima, M., (2009), "Experiments for High-rise Buildings conducted by E-Defense," http://www.bosai.go.jp/hyogo/project/aij-draft.pdf .

JOINT CONFERENCE PROCEEDINGS
7th International Conference on Urban Earthquake Engineering (7CUEE) &
5th International Conference on Earthquake Engineering (5ICEE)
March 3-5, 2010, Tokyo Institute of Technology, Tokyo, Japan

GROUND-MOTION SELECTION FOR PEER TRANSPORTATION RESEARCH PROGRAM

Nirmal Jayaram[1)], and Jack Baker[2)]

1) Ph.D. Candidate, Dept. of Civil and Environmental Engineering, Stanford University, CA, USA
2) Assistant Professor, Dept. of Civil and Environmental Engineering, Stanford University, CA, USA
nirmalj@stanford.edu, bakerjw@stanford.edu

Abstract: Dynamic structural analysis is commonly used in performance-based earthquake engineering to predict the response of a structure subjected to the earthquake ground motions. It is important to select appropriate input ground-motion time histories in order to obtain unbiased estimates of the structural response. The goal of this study is to select a standardized set of ground motions for the Pacific Earthquake Engineering Research (PEER) Transportation Research Program that can be used to analyze a variety of buildings, bridges and geotechnical systems located in different sites in California. Since these goals are neither structure specific nor site specific, ground-motion selection techniques developed in previous PEER projects are not directly applicable here.

In this study, we use a ground-motion selection algorithm proposed by Jayaram et al. (2009) to select a set of ground-motion time histories from the Next Generation Attenuation (NGA) database whose response spectra match a target response spectrum median and variance over a range of periods. The target median and variance are computed using the Boore and Atkinson (2008) ground-motion prediction model for a scenario earthquake of magnitude 7 occurring at a distance of 10km, and ground-motion time histories are selected for both soil and rock sites. This manuscript summarizes a variety of properties of the selected ground motion time histories. These time histories can be used as input ground-motions for the applications described earlier, as well as any other applications requiring the use of strong ground motions typical of high-seismicity regions.

1. INTRODUCTION

Dynamic structural analysis is commonly used in performance-based earthquake engineering to predict the response of a structure subjected to the earthquake ground motions. It is important to select appropriate input ground-motion time histories in order to obtain unbiased estimates of the structural response. Much progress has been made by the Pacific Earthquake Engineering Research (PEER) Center and others in recent decades to understand the properties of earthquake ground motions that affect geotechnical and structural systems (e.g., Haselton et al. 2009, Power et al. 2007). This has led to insights for structure-specific ground-motion selection, which is done to obtain a set of ground motions whose intensity (measured by an intensity measure such as the spectral acceleration) is exceeded with some specified probability at a given site.

This recent progress has focused primarily on cases where the structure and the location of interest are known (so that ground motions can be selected and modified with specific structural properties and seismic hazard information in mind). The goal of this study, in contrast, is to select a standardized set of ground motions for the PEER Transportation Research Program (http://peer.berkeley.edu/transportation/index.html) that can be used to analyze a variety of buildings, bridges and geotechnical systems located at a variety of locations. It is also desired to select a single set of ground motions that can be used with multiple structural systems at a given site in order to facilitate comparisons of different systems, even though structural parameters such as periods of interest might change from system to system. Since these goals are neither structure specific nor site specific, ground-motion selection techniques developed in previous PEER projects are not directly applicable here.

In this study, we use a ground-motion selection algorithm proposed by Jayaram et al. (2009) to select separate sets of ground-motion time histories for soil and rock sites that are usable over a wide range of high-seismicity sites such as California for studying the earthquake structural response of a wide variety of structures. This manuscript describes the selection procedure and summarizes the properties of the selected ground-motion time histories. The selected time histories are available at http://www.stanford.edu/~bakerjw/PEER _gms.html.

2. OBJECTIVES

The general objective of the study is to select site-independent and structure-independent ground motions, but several decisions were made to constrain the scope of the

ground-motion selection:

1. Although the sites of interest will vary, we are generally interested in high-seismicity sites that may experience strong ground motions from mid- to large-magnitude earthquakes at close distances.
2. There are a variety of structures to be studied, some of which are also sensitive to excitation at a wide range of periods. This means that it is not useful to focus on a specific period or a narrow range of periods when selecting ground motions.
3. The primary period range of interest is between 0 and 3 seconds, with secondary interest in periods as long as 5 seconds.
4. The users are willing and able to utilize a relatively large number of ground motions (i.e., dozens to hundreds) in order to identify probability distributions and statistical trends in system responses.
5. Three component ground motions are needed.
6. Separate sets of unscaled ground-motion time histories are needed for rock sites and soil sites.

Site and structure-specific ground-motion selection methods often involve selecting a set of ground motions whose response spectra match a site-specific target median response spectrum (e.g., Haselton et al. 2009, Bazzurro and Luco 2005, Naeim and Lew 1995), without any consideration of the inherent variance in the response spectrum. Estimates of structural response obtained using the ground motions selected only based on the median values will show smaller than 'actual' variance. As a result, there has recently been a bigger focus on selecting ground motions based on not only the target median response, but also a target variance (e.g., Kottke and Rathje 2008). The current work follows a similar approach and focuses on selecting ground motions considering both the median and the variance. Since it is desired to obtain ground motions that can be used at multiple locations, ground motions are selected such that the median and the variance of their response spectra resemble what can be expected from the following 'generic earthquake scenario' typical of high-seismicity sites:

Magnitude = 7.
Closest distance = 10 km.
Earthquake mechanism = strike slip.
V_s30 = 250 m/s for soil sites and 760m/s for rock sites, where V_s30 is the average shear-wave velocity in the top 30m of the soil.

The median and the variance values corresponding to the above scenario are obtained using the Boore and Atkinson (2008) ground-motion model.

3. GROUND-MOTION SELECTION ALGORITHM

Selecting time histories only based on a target median response spectrum is computationally inexpensive since it can be done by choosing time histories whose response spectra individually deviate the least from the target. When matching a target median and a target variance, however, it does not suffice to treat ground motions individually, but rather requires comparisons of the median and variance of *sets* of ground motions to the target values. That is, the suitability of a particular ground motion can only be determined in the context of the complete ground-motion set in which it might be included. There is generally an intractably large number of possible ground-motion sets, and so identifying the best set is a computationally-expensive combinatorial optimization problem (e.g., Kottke and Rathje 2008). The current work uses a ground-motion selection algorithm recently proposed by Jayaram et al. (2009) for this purpose. This algorithm uses the fact that the logarithmic spectral accelerations at multiple periods in a single ground motion follow a multivariate normal distribution (Jayaram and Baker 2008). This distribution can be parameterized using the target mean and the target covariance of the logarithmic response spectrum, which are related to the target median and the target covariance of the response spectrum based on the properties of the multivariate normal distribution. The selection algorithm first probabilistically generates multiple realizations of response spectrum from this distribution, and then selects recorded ground-motion time histories whose response spectra individually match the simulated response spectra. The following subsections briefly highlight the steps involved in the algorithm. A complete description of the algorithm can be found in Jayaram et al. (2009).

3.2.1 Step 1: Parameterization of the target response distribution

The first step is to parameterize the multivariate normal distribution of the logarithmic spectral accelerations at multiple periods (i.e., the distribution of $[\ln S_a(T_1), \ln S_a(T_2), \ldots, \ln S_a(T_n)]$, where $\ln S_a(T_i)$ denotes the logarithmic spectral acceleration at period T_i). The two parameters of the multivariate normal distribution are the mean matrix and the covariance matrix of the logarithmic spectral accelerations. Based on the target earthquake scenario (defined in Section 3.1), the mean value and the standard deviation of each $\ln S_a(T_i)$ can be obtained from an empirical ground-motion model (e.g., Boore and Atkinson 2008) as follows:

$$\ln S_a(T_i) = \overline{\ln S_a}(T_i) + \sigma(T_i)\varepsilon(T_i) \quad (1)$$

where $\overline{\ln S_a}(T_i)$ denotes the predicted (by the ground-motion model) mean logarithmic spectral acceleration at period T_i, which depends on parameters such as magnitude, distance and local-site conditions; $\varepsilon(T_i)$ denotes the normalized (total) residual and $\sigma(T_i)$ denotes the logarithmic standard deviation that is estimated as part of the ground-motion model.

Therefore, the target mean matrix of the vector $[\ln S_a(T_1), \ln S_a(T_2), \ldots, \ln S_a(T_n)]$ can be expressed as follows:

$$\mu = \begin{pmatrix} \overline{\ln S_a}(T_1) \\ \overline{\ln S_a}(T_2) \\ . \\ . \\ \overline{\ln S_a}(T_n) \end{pmatrix} \quad (2)$$

While ground-motion models provide estimates of the standard deviation of a single $\ln S_a(T_i)$ (i.e., $\sigma(T_i)$), they do not provide any information about the correlation $\rho(T_i,T_j)$ between $\ln S_a(T_i)$ and $\ln S_a(T_j)$, which is required for obtaining the covariance matrix of the vector $[\ln S_a(T_1), \ln S_a(T_2), \ldots, \ln S_a(T_n)]$. Therefore, in this study, we used estimates of this correlation provided by Baker and Jayaram (2008). The covariance matrix can then be estimated as follows:

$$\Sigma = \begin{bmatrix} \sigma(T_1)^2 & \rho(T_1,T_2)\sigma(T_1)\sigma(T_2) & \ldots & \rho(T_1,T_n)\sigma(T_1)\sigma(T_n) \\ \rho(T_2,T_1)\sigma(T_2)\sigma(T_1) & \sigma(T_2)^2 & \ldots & \rho(T_2,T_n)\sigma(T_2)\sigma(T_n) \\ . & . & \ldots & . \\ . & . & \ldots & . \\ \rho(T_n,T_1)\sigma(T_n)\sigma(T_1) & \rho(T_n,T_2)\sigma(T_n)\sigma(T_2) & \ldots & \sigma(T_n)^2 \end{bmatrix} \quad (3)$$

The rest of the steps of the algorithm are intended to select ground motions whose logarithmic response spectra have the mean and covariance matrices described by Equations 2 and 3 respectively.

3.2.2 Step 2: Response spectrum simulation

The second step in the ground-motion selection algorithm is to simulate response spectra using the mean and covariance matrices defined in Equations 2 and 3 respectively. This can be done by sampling multiple times from a multivariate normal distribution (for instance, this can be done using the *mvnrnd* command in MATLAB) with the above-mentioned mean and covariance matrices (Law and Kelton 1991). The number of response spectra to be simulated equals the desired number of ground motions.

3.2.3 Step 3: Ground-motion time history selection

In the third step, ground-motion time histories are selected whose response spectra match the response spectra simulated in Step 2. One effective criterion for determining the similarity between a ground-motion response spectrum and a simulated response spectrum is the sum of squared errors (*SSE*) described below:

$$SSE = \sum_{j=1}^{p} \left(\ln S_a(T_j) - \ln S_a^{(s)}(T_j) \right)^2 \quad (4)$$

where $\ln S_a(T_j)$ is the ground-motion logarithmic spectral acceleration at period T_j, $\ln S_a^{(s)}(T_j)$ is the simulated logarithmic spectral acceleration at period T_j. For each simulated response spectrum, the ground motion which minimizes *SSE* is selected. Since the simulated response spectra have the desired mean and covariance structure, the response spectra selected using this approach will also have the desired mean and covariance.

3.2.4 Step 4: Greedy improvement algorithm

When a small number of ground motions are selected using the approach described above, the sample means and variances can deviate slightly from the target values due to the small size. In such cases, a 'greedy' algorithm is used to further improve the match between the sample and the target means and variances. In this approach, each time history selected in Step 3 is replaced one at a time with a time history from the ground-motion database that causes the best improvement in the match between the target and the sample means and variances (diagonals of the covariance matrix in Equation 3). If none of the potential replacements causes an improvement, the original ground-motion time history is retained. The mismatch between the target and the sample means and the variances is estimated as the sum squared difference between the target and the sample values over the period range of interest.

$$SSE_s = \sum_{j=1}^{p} \left[\left(\hat{m}_{\ln S_a(T_j)} - \overline{\ln S_a}(T_j) \right)^2 + w \left(\hat{s}_{\ln S_a(T_j)} - \sigma(T_j) \right)^2 \right] \quad (6)$$

where SSE_s is the sum of squared error of the subset, which

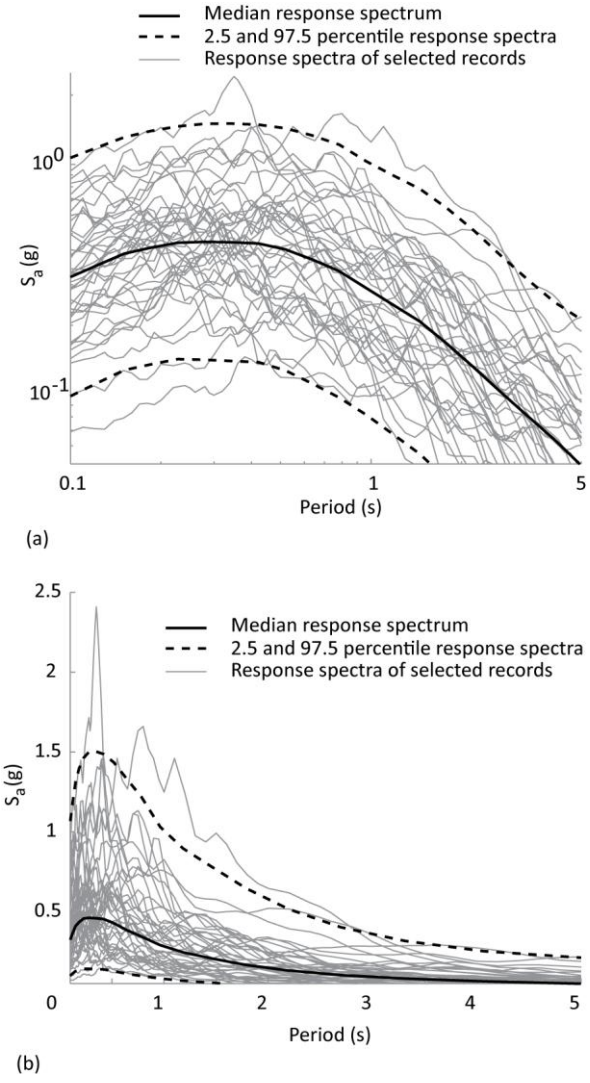

Figure 1 Response spectra of the selected ground motions for soil sites (a) Log-Log plot, and (b) Linear plot.

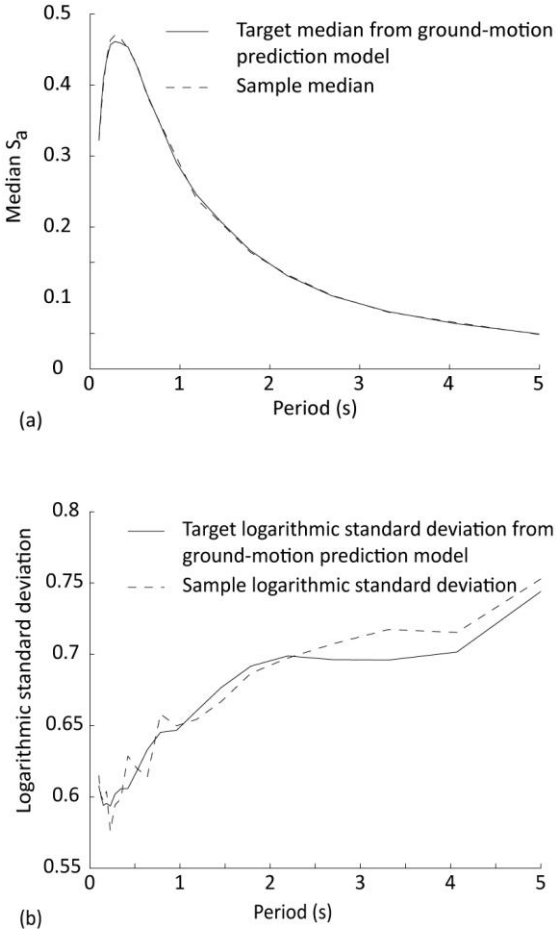

Figure 2 Soil sites: (a) Comparison of the target and the sample medians, and (b) Comparison of the target and the sample logarithmic standard deviations.

is the parameter to be minimized, $\hat{m}_{\ln S_a(T_j)}$ is the subset mean logarithmic spectral acceleration at period T_j, $\hat{s}_{\ln S_a(T_j)}$ is the subset standard deviation of the logarithmic spectral acceleration at period T_j, w is a weighting factor indicating the relative importance of the errors in the standard deviation and the mean (a typical starting value for w equals 1), and p denotes the total number of periods (T_j) at which the error is computed.

4. PROPERTIES OF THE SELECTED GROUND MOTIONS

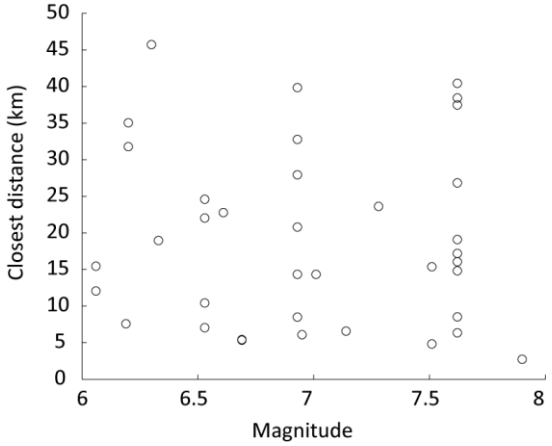

Figure 3 Magnitudes and closest distances for soil site ground-motion records.

This section describes the properties of two sets of forty ground-motion time histories selected for soil and rock sites based on the algorithm described in Section 3. The ground motions are selected from the PEER Next Generation Attenuation (NGA) database (Power et al. 2007). The NGA database time histories are rotated to the strike-normal and the strike-parallel directions before selection.

4.1 Ground motions for soil sites

A set of ground motions was desired that was representative of those observed at site conditions commonly observed in California. In order to ensure that the objectives defined earlier (Section 2) are satisfied, only NGA database records satisfying the following criteria are considered for selection.

1. The magnitude corresponding to the record ranges between 6 and 8.
2. The closest distance between the source and the recording site is less than 50km.
3. The recording site V_s30 ranges between 200m/s and 400m/s.

No restrictions are placed on the number of recordings that can be selected from the same earthquake. A total of 391 records satisfy the above-mentioned criteria and are

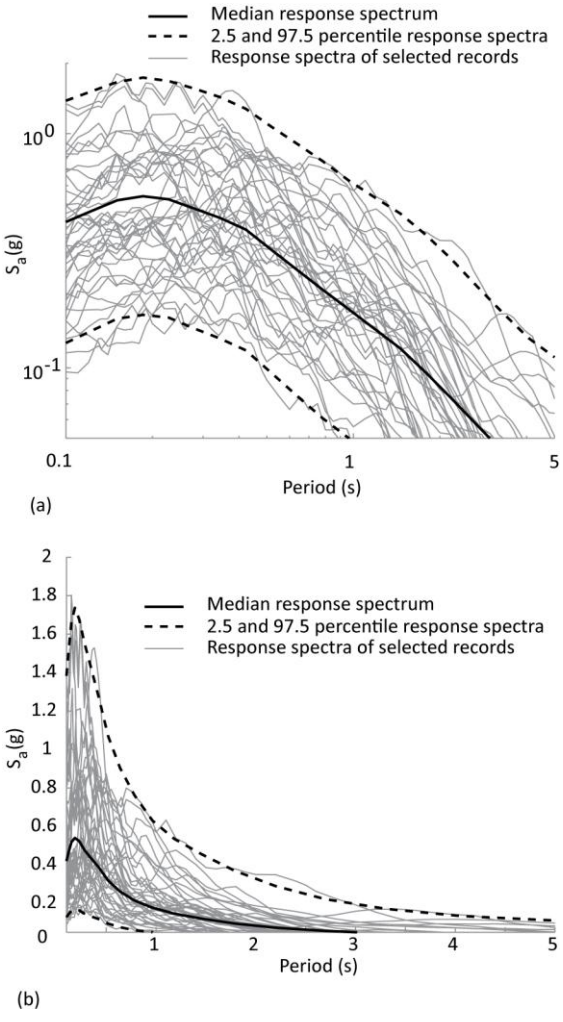

Figure 4 Response spectra of the selected ground motions for rock sites (a) Log-Log plot, and (b) Linear plot.

considered for selection.

Figure 1 shows the response spectra of the forty ground-motion time histories (Table 1) selected for the soil sites. The figure also shows the target median response spectrum (exponential of the target means shown in Equation 2, based on the properties of the normal distribution) and the 95 percentile confidence interval for the response spectrum. These ground-motion response spectra have the desired medians and logarithmic standard deviations (the diagonals in the covariance matrix shown in Equation 3) as indicated by Figure 2. Figure 3 shows the magnitudes and the closest distances of the selected ground-motion records. Note that while some magnitudes and distances differ significantly from the target event's, the properties of the response spectra of the selected ground motions match the target properties as desired.

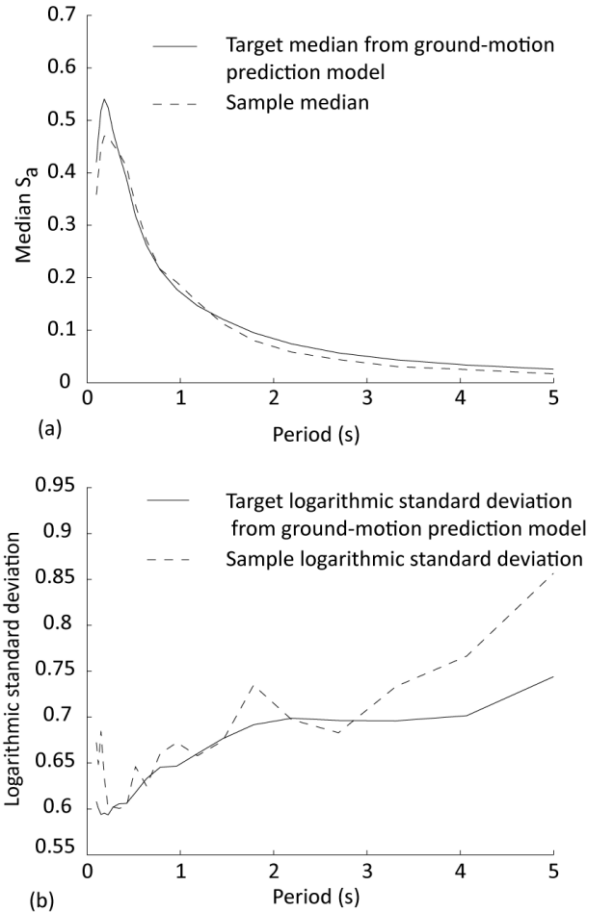

Figure 5 Rock sites: (a) Comparison of the target and the sample medians, and (b) Comparison of the target and the sample logarithmic standard deviations.

4.2 Ground motions for rock sites

A second set of ground motions was desired to be representative of those observed at rock sites (or to be used as bedrock level ground motions for site response analyses). On account of the fewer number of rock-site ground motions in the NGA database, all records at sites with V_s30 values over 625m/s are considered for selection, irrespective of the magnitude corresponding to the record or the distance of the recording site from the earthquake source. A total of 282 NGA database ground-motion records qualify under this criterion for selection.

Figure 4 shows the response spectra of the forty ground motions (Table 2) selected for the rock sites. The figure also shows the target median response spectrum and 95 percentile confidence interval for the response spectrum. Figure 5 shows a very good match between the target and the sample median values and a reasonably good match between the target and the sample logarithmic standard deviations. Figure 6 shows the magnitudes and the closest distances of the selected ground-motion records. It can be seen from this figure that the selected records primarily correspond to magnitudes between 6.5 and 7.5 and source-to-site distances less than 50km.

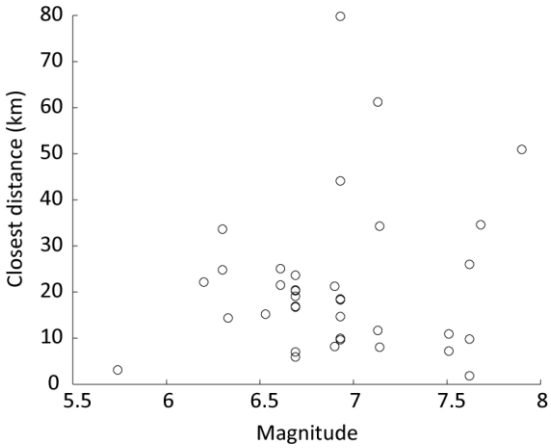

Figure 6 Magnitudes and closest distances for rock site ground-motion records.

5. STRUCTURE-SPECIFIC SCALING OF THE SELECTED GROUND MOTIONS

Often, a structure-specific response analysis is performed using a set of ground-motion time histories whose spectral acceleration at the structure's fundamental period equals a pre-specified value (e.g., Baker 2009). The target conditional mean and variance of the logarithmic response spectrum in such cases can be obtained using the conditional mean spectrum (CMS) method (Baker 2009).

5.1 Target conditional mean and variance

The target mean and variance for a conditional logarithmic response spectrum can be obtained as follows: Define the parameter $\varepsilon(T)$ as follows (rearranging Equation 1):

$$\varepsilon(T) = \frac{\ln S_a(T) - \overline{\ln S_a}(T)}{\sigma(T)} \quad (5)$$

Let S denote the target spectral acceleration at period T^*, the fundamental period of the structure. Note that $\varepsilon(T^*)$ is known since $S_a(T^*)$ equals S (the target).

The target conditional means of logarithmic spectral accelerations (i.e., $\ln S_a(T)$) can then be obtained as

$$E\left[\ln S_a(T_i) \mid \ln S_a(T^*)\right] = \overline{\ln S_a}(T_i) + \rho(T_i, T^*)\varepsilon(T^*)\sigma(T_i) \quad (6)$$

where $E[\ln S_a(T_i)| \ln Sa(T^*)]$ denotes the target conditional mean of $\ln S_a(T_i)$, and $\rho(T_i,T^*)$ denotes the correlation coefficient between $\ln Sa(T_i)$ and $\ln Sa(T^*)$. The target conditional medians of spectral accelerations can be obtained as the exponential of $E[\ln S_a(T_i)| \ln Sa(T^*)]$ (based on the properties of a normal distribution).

The target conditional variance of logarithmic spectral accelerations equals

$$Var\left[\ln S_a(T_i) \mid \ln S_a(T^*)\right] = \sigma(T_i)^2\left[1-\rho(T_i,T^*)^2\right] \quad (7)$$

where $Var[\ln S_a(T_i)| \ln Sa(T^*)]$ denotes the target conditional variance of $\ln S_a(T_i)$.

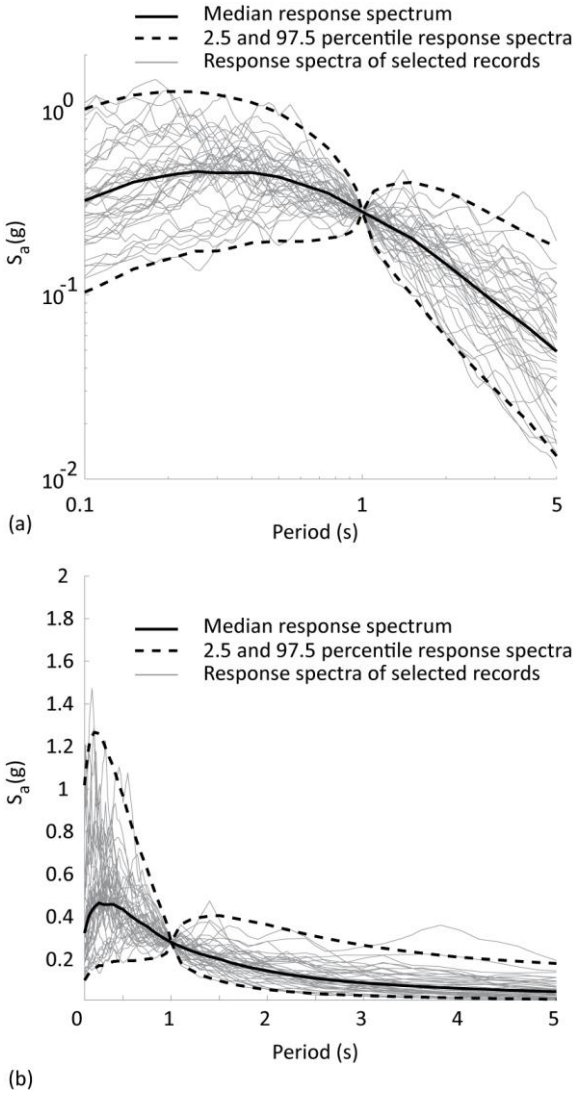

Figure 7 Case 1: Conditional response spectra of the scaled selected ground motions for soil sites (a) Log-Log plot, and (b) Linear plot.

5.1 Obtaining conditional ground motions from the selected unconditional ground motions

Though the ground motions selected in this study are not conditioned on any particular spectral acceleration, they can be scaled so that their spectral accelerations at the fundamental period equal the pre-specified value before being used for any response analysis. This section compares the medians and variances of such scaled ground motions to the corresponding targets defined in Equations 6 and 7.

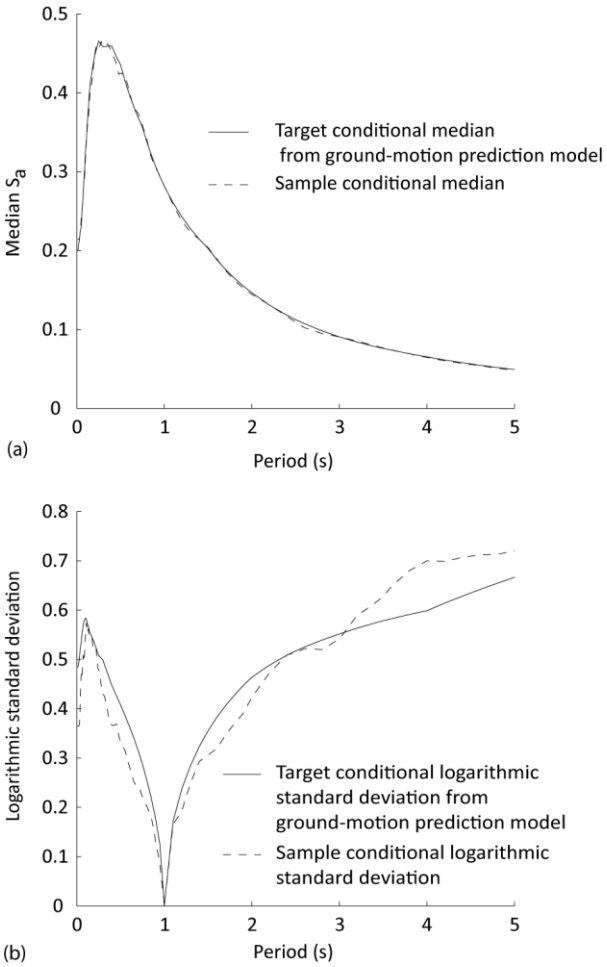

Figure 8 Case 1: (a) Comparison of the conditional target and sample medians, and (b) Comparison of the conditional target and sample logarithmic standard deviations.

5.2.1 Case 1: $\varepsilon(T^*) = 0$

Let the target spectral acceleration at period T^* equal $\overline{\ln S_a}(T^*)$ (from Equation 5 for $\varepsilon(T^*) = 0$). Figure 7 shows the selected soil-site ground motions scaled such that their logarithmic spectral accelerations at 1s (assumed value of T^*) equal this target. The figure also shows the target conditional median spectrum along with the confidence interval obtained using the CMS method. Figure 8a shows that the target median conditional spectrum and the sample median spectrum (median of the scaled selected ground-motion response spectra) match very well. Figure 8b shows a good match between the target and the sample conditional logarithmic standard deviation values at periods

close to 1s (the fundamental period). At periods farther away from 1s, a small mismatch can be seen between the sample and the target values. A theoretical explanation for this mismatch is provided subsequently in the manuscript.

5.2.2 Case 2: $\varepsilon(T^*) = 1$s

Let the target spectral acceleration at period T^* equal $\overline{\ln S_a}(T^*) + \sigma(T^*)$ (from Equation 5 for $\varepsilon(T^*) = 1$). Figure 9 shows the selected soil-site ground motions scaled such that their logarithmic spectral accelerations at 1s equals this target. Figure 10a shows some mismatch between the target median conditional spectrum and the sample median spectrum. (Incidentally, this mismatch also manifests in

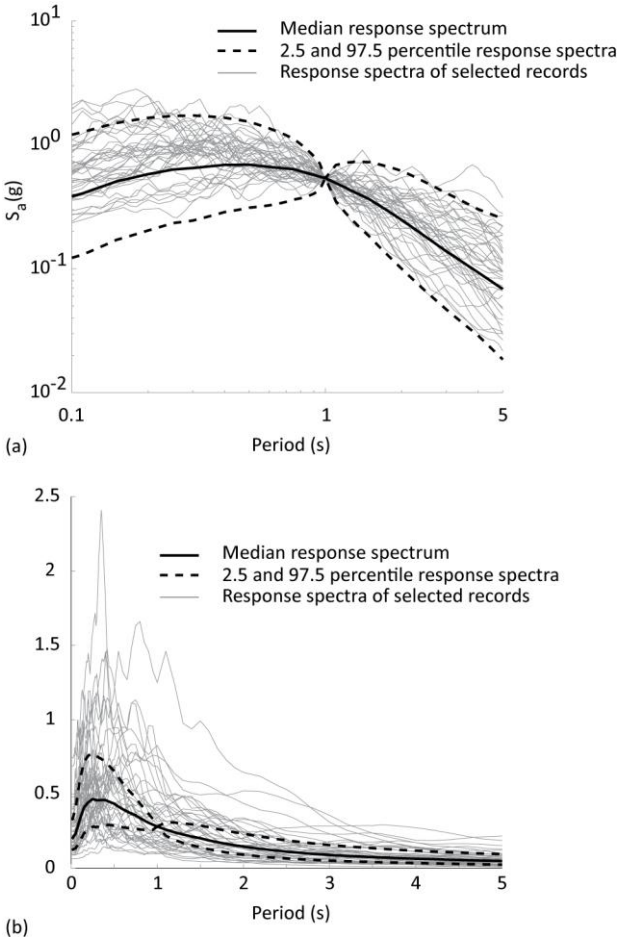

Figure 9 Case 2: Conditional response spectra of the scaled selected ground motions for soil sites (a) Log-Log plot, and (b) Linear plot.

Figure 9.) Figure 10b is identical to Figure 8b since the sample conditional logarithmic variance is independent of $\varepsilon(T^*)$ (subsequently shown theoretically).

5.3 Theoretical explanation for the observed results

Let $S_a(\boldsymbol{T})$ (i.e., $[S_a(T_1), S_a(T_2), \ldots, S_a(T_n)]$) denote the response spectrum of a selected unscaled ground motion record. Let $S'_a(\boldsymbol{T})$ denote the response spectrum of the ground motion after scaling such that the value of $S'_a(T^*)$ equals S. $S'_a(T_i)$ can be obtained in terms of $S_a(T_i)$ as follows:

$$S'_a(T_i) = S_a(T_i)\frac{S}{S_a(T^*)} \tag{8}$$

Therefore,

$$\ln S'_a(T_i) = \ln S_a(T_i) + \ln S - \ln S_a(T^*) \tag{9}$$

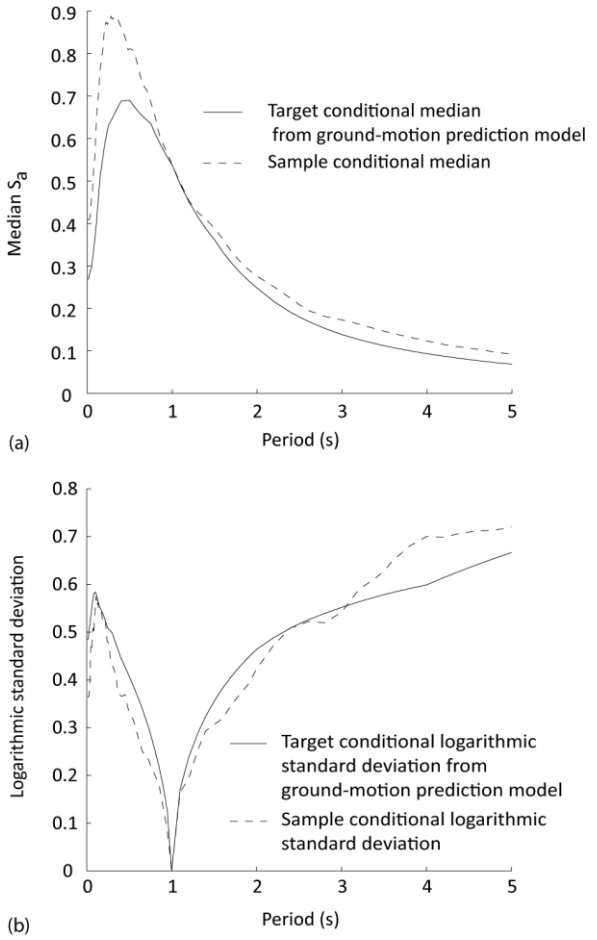

Figure 10 Case 2: (a) Comparison of the conditional target and sample medians, and (b) Comparison of the conditional target and sample logarithmic standard deviations.

Hence,

$$E\left[\ln S'_a(T_i)\right] = \overline{\ln S_a}(T_i) + \left(\overline{\ln S_a}(T^*) + \varepsilon(T^*)\sigma(T^*)\right) - \overline{\ln S_a}(T^*)$$
$$= \overline{\ln S_a}(T_i) + \varepsilon(T^*)\sigma(T^*) \tag{10}$$

$$Var\left[\ln S'_a(T_i)\right] = Var\left[\ln S_a(T_i) - \ln S_a(T^*)\right] \tag{11}$$
$$= \sigma(T_i)^2 + \sigma(T^*)^2 - 2\rho(T_i, T^*)\sigma(T_i)\sigma(T^*)$$

It can be seen that the sample mean in Equation 10 equals the target mean in Equation 6 only when $\varepsilon(T^*) = 0$ (Case 1). For other values of $\varepsilon(T^*)$, the mismatch between the two means is small at periods close to T^* (because

$\rho(T_i,T^*)$ is approximately equal to 1) and increases as the difference between T_i and T^* increases (as $\rho(T_i,T^*)$ decreases). While this discrepancy in mean values cannot be addressed simply by changing the scaling of these ground motions, it can in theory be addressed by post-processing the structural analysis results to account for the impact of this known discrepancy (e.g., Haselton et al., 2010).

The variance of the scaled response spectrum (Equation 11) does not exactly match the target variance obtained using the CMS method (Equation 7) irrespective of the value of $\varepsilon(T^*)$. The two variance terms are, however, similar when $\sigma(T_i)$ approximately equals $\sigma(T^*)$ and $\rho(T_i,T^*)$ equals 1 (i.e., T_i equals T^*) . When T_i differs from T^*, the variance term in Equation 11 is generally larger than that in Equation 7, as seen in Figure 8b at periods longer than 3s. At other periods, the closeness of the expected sample and the target variances along with sample variability obscures this effect.

6. CONCLUSIONS

In this study, two sets of ground-motion time histories were selected for soil and rock sites that are usable at a wide range of high seismicity sites for analyzing a wide variety of structures. The selection was carried out using a ground-motion selection algorithm proposed by Jayaram et al. (2009), which selects time histories whose response spectra match a target response spectrum mean and variability. In order to ensure that the ground motions are usable at multiple sites, they were selected such that the median and the variance of their response spectra resemble what can be expected from a magnitude 7 earthquake at a distance of 10km, which is presumed to be a typical earthquake for high seismicity sites. The manuscript described the properties of the selected ground-motion sets for both the soil and the rock sites. It was seen that the sample mean and variance values closely match the corresponding target values.

Though the ground motions selected in this study were not conditioned on any particular spectral acceleration, they can be scaled so that their spectral accelerations at a particular period (e.g., the fundamental period of a structure) equal a pre-specified value. This enables the use of the selected ground motions for structure-specific earthquake response analysis. The manuscript illustrated this scaling approach, and showed that the properties of these scaled conditional ground motions may reasonably match the target conditional properties in some cases, while in other cases, some post processing of structural analysis results may be needed to account for discrepancies.

Acknowledgements:

This work was supported by the State of California through the Transportation Systems Research Program of the Pacific Earthquake Engineering Research Center (PEER). Any opinions, findings, and conclusion or recommendations expressed in this material are those of the authors and do not necessarily reflect those of the funding agency. The first author also acknowledges the travel grant provided by Tokyo Institute of Technology, Japan.

References:

Baker, J.W. (2009), "The conditional mean spectrum: A tool for ground motion selection," *ASCE Journal of Structural Engineering*, (in press).

Baker, J.W. and Jayaram, N. (2008), "Correlation of spectral acceleration values from NGA ground motion models," *Earthquake Spectra*, **24**(1), 299-317.

Bazzurro, P and Luco, N. (2006), "Do scaled and spectrum-matched near-source records produce biased nonlinear structural responses'?," *Proceedings of 8th National Conference on Earthquake Engineering*, San Francisco, CA.

Boore, D. and Atkinson, G. (2008), "Ground-motion prediction equations for the average horizontal component of PGA, PGV and 5% damped SA at spectral periods between 0.01s and 10.0s," Earthquake Spectra, **24**(1), 99-138.

Haselton, C., Baker, J.W., Bozorgnia, Y., Goulet, C., Kalkan, E., Luco, N., Shantz, T., Shome, N., Stewart, J., Tothong, P., Watson-Lamprey, J. and Zareian, F. (2009), "Evaluation of ground motion selection and modification methods: Predicting median interstory drift response of buildings," *Technical Report*, Pacific Earthquake Engineering Research Center, Report 2009/01.

Haselton, C., Baker, J.W., Liel, A., and Deierlein, G. (2010), "Accounting for ground motion spectral shape characteristics in structural collapse assessment through an adjustment for epsilon," *ASCE Journal of Structural Engineering*, in press.

Jayaram, N. and Baker, J.W. (2008), "Statistical tests of the joint distribution of spectral acceleration values," *Bulletin of the Seismological Society of America*, **98**(5), 2231-2243.

Jayaram, N. and Lin, T. and Baker, J. (2009), "A computationally efficient ground-motion selection algorithm for matching a target response spectrum mean and variability," *Earthquake Spectra*, in preparation.

Kottke, A. and Rathje, E. (2008), "A semi-automated procedure for selecting and scaling recorded earthquake motions for dynamic analysis," *Earthquake Spectra*, **24**(4), 911-932.

Law, A.and Kelton, W.D. (1991), "Simulation Modeling and Analysis," McGraw-Hill, New York.

Naeim, F, Alimoradi, A. and Pezeshk, S. (2004), "Selection and scaling of ground motion time histories for structural design using genetic algorithms," *Earthquake Spectra*, **20**(2), 413-426.

Naeim, F. and Lew, M. (1995), "On the use of design spectrum compatible time histories," *Earthquake Spectra*, **11**(1), 111-127.

Power, M., Youngs, R. and Chin, C. (2007), "Design ground motion library," *Report* of PEER-LL Program Task 1F01.

7. APPENDIX: TABLES OF SELECTED GROUND MOTIONS

The following tables provide basic summary data for the selected ground motions. Additional summary data, along with the time history files for these ground motions, are available at: http://www.stanford.edu/~bakerjw/PEER_gms.html. Complete summary data for these ground motions can be obtained by cross-referenceing the NGA record sequence numbers given here with the corresponding values in the "NGA flatfile" at http://peer.berkeley.edu/nga/documentation.html.

Table 1 Selected ground-motion records for soil sites.

Record number	NGA Record Sequence Number	Earthquake Name	Year	Magnitude	Closest Distance (km)	Preferred Vs30 (m/s)
1	231	Mammoth Lakes-01	1980	6.1	15.5	345
2	1203	Chi-Chi, Taiwan	1999	7.6	16.1	233
3	829	Cape Mendocino	1992	7.0	14.3	312
4	169	Imperial Valley-06	1979	6.5	22.0	275
5	1176	Kocaeli, Turkey	1999	7.5	4.8	297
6	163	Imperial Valley-06	1979	6.5	24.6	206
7	1201	Chi-Chi, Taiwan	1999	7.6	14.8	379
8	1402	Chi-Chi, Taiwan	1999	7.6	38.4	375
9	1158	Kocaeli, Turkey	1999	7.5	15.4	276
10	281	Trinidad	1980	7.2	-	312
11	730	Spitak, Armenia	1988	6.8	-	275
12	768	Loma Prieta	1989	6.9	14.3	222
13	1499	Chi-Chi, Taiwan	1999	7.6	8.5	273
14	266	Victoria, Mexico	1980	6.3	19.0	275
15	761	Loma Prieta	1989	6.9	39.9	285
16	558	Chalfant Valley-02	1986	6.2	7.6	271
17	1543	Chi-Chi, Taiwan	1999	7.6	26.8	215
18	2114	Denali, Alaska	2002	7.9	2.7	329
19	179	Imperial Valley-06	1979	6.5	7.1	209
20	931	Big Bear-01	1992	6.5	-	271
21	900	Landers	1992	7.3	23.6	354
22	1084	Northridge-01	1994	6.7	5.4	251
23	68	San Fernando	1971	6.6	22.8	317
24	527	N. Palm Springs	1986	6.1	12.1	345
25	776	Loma Prieta	1989	6.9	27.9	371
26	1495	Chi-Chi, Taiwan	1999	7.6	6.4	273
27	1194	Chi-Chi, Taiwan	1999	7.6	19.1	278
28	161	Imperial Valley-06	1979	6.5	10.4	209
29	1236	Chi-Chi, Taiwan	1999	7.6	37.5	273
30	1605	Duzce, Turkey	1999	7.1	6.6	276
31	1500	Chi-Chi, Taiwan	1999	7.6	17.2	273
32	802	Loma Prieta	1989	6.9	8.5	371
33	6	Imperial Valley-02	1940	7.0	6.1	213
34	2656	Chi-Chi, Taiwan-03	1999	6.2	31.8	273
35	982	Northridge-01	1994	6.7	5.4	373
36	2509	Chi-Chi, Taiwan-03	1999	6.2	35.1	223
37	800	Loma Prieta	1989	6.9	32.8	271
38	754	Loma Prieta	1989	6.9	20.8	295
39	1183	Chi-Chi, Taiwan	1999	7.6	40.4	211
40	3512	Chi-Chi, Taiwan-06	1999	6.3	45.7	215

Table 2 Selected ground-motion records for rock sites

Record number	NGA Record Sequence Number	Earthquake Name	Year	Magnitude	Closest Distance (km)	Preferred Vs30 (m/s)
1	72	San Fernando	1971	6.6	25.1	822
2	769	Loma Prieta	1989	6.9	18.3	663
3	1165	Kocaeli, Turkey	1999	7.5	7.2	811
4	1011	Northridge-01	1994	6.7	20.3	1223
5	164	Imperial Valley-06	1979	6.5	15.2	660
6	1787	Hector Mine	1999	7.1	11.7	685
7	80	San Fernando	1971	6.6	21.5	969
8	1618	Duzce, Turkey	1999	7.1	8.0	660
9	1786	Hector Mine	1999	7.1	61.2	685
10	1551	Chi-Chi, Taiwan	1999	7.6	9.8	653
11	3507	Chi-Chi, Taiwan-06	1999	6.3	24.8	664
12	150	Coyote Lake	1979	5.7	3.1	663
13	572	Taiwan SMART1(45)	1986	7.3	-	660
14	285	Irpinia, Italy-01	1980	6.9	8.2	1000
15	801	Loma Prieta	1989	6.9	14.7	672
16	286	Irpinia, Italy-01	1980	6.9	21.3	1000
17	1485	Chi-Chi, Taiwan	1999	7.6	26.0	705
18	1161	Kocaeli, Turkey	1999	7.5	10.9	792
19	1050	Northridge-01	1994	6.7	7.0	2016
20	2107	Denali, Alaska	2002	7.9	50.9	964
21	1	Helena, Montana-01	1935	6.0	-	660
22	1091	Northridge-01	1994	6.7	23.6	996
23	1596	Chi-Chi, Taiwan	1999	7.6	1.8	664
24	771	Loma Prieta	1989	6.9	79.8	642
25	809	Loma Prieta	1989	6.9	18.5	714
26	265	Victoria, Mexico	1980	6.3	14.4	660
27	1078	Northridge-01	1994	6.7	16.7	715
28	763	Loma Prieta	1989	6.9	10.0	730
29	1619	Duzce, Turkey	1999	7.1	34.3	660
30	957	Northridge-01	1994	6.7	16.9	822
31	2661	Chi-Chi, Taiwan-03	1999	6.2	22.2	653
32	3509	Chi-Chi, Taiwan-06	1999	6.3	33.6	653
33	810	Loma Prieta	1989	6.9	18.4	714
34	765	Loma Prieta	1989	6.9	9.6	1428
35	1013	Northridge-01	1994	6.7	5.9	629
36	1012	Northridge-01	1994	6.7	19.1	706
37	1626	Sitka, Alaska	1972	7.7	34.6	660
38	989	Northridge-01	1994	6.7	20.5	740
39	748	Loma Prieta	1989	6.9	44.1	628
40	1549	Chi-Chi, Taiwan	1999	7.6	1.8	664

JOINT CONFERENCE PROCEEDINGS
7th International Conference on Urban Earthquake Engineering (7CUEE) &
5th International Conference on Earthquake Engineering (5ICEE)
March 3-5, 2010, Tokyo Institute of Technology, Tokyo, Japan

SEISMIC EARTH PRESSURE ACTING ON CANTILEVERED RETAINING WALLS

Akihiro Takahashi[1)], Shunsuke Tanimoto[2)], and Hideki Sugita[2)]

1) Associate Professor, Dept. of Civil and Environmental Engineering, Tokyo Institute of Technology, Japan
(Formerly, Public Works Research Institute, Japan)
2) Public Works Research Institute, Japan
takihiro@cv.titech.ac.jp, s-tanomo@pwri.go.jp, sugita@pwri.go.jp

Abstract: A series of dynamic centrifuge model tests were conducted to examine seismic loads, especially the load induced by the lateral earth pressure, for evaluating internal stability of externally very stable cantilevered retaining walls. Test results reveal that relatively larger earth pressure acts on the retaining wall when the wall is externally stable. In addition, the damping effects of the backfill soil seem to increase the lateral load acting on the wall and the seismic earth pressure calculated by the Mononobe-Okabe method underestimates the backbone curves of the hysteresis loops in the earth pressure—acceleration diagram. These findings suggest that the current design seismic earth pressure can underestimate the force demand when the internal stability of the retaining wall is assessed using conventional quasi-static methods.

1. INTRODUCTION

External failure of retaining walls under seismic loading can occur either with sliding or rotation, depending on the foundation condition. In addition to these, for cantilevered retaining walls, internal failure involving plastic deformation of the lower part of stem walls is possible, especially when (1) a retaining wall is founded on competent ground or (2) movement of its base is restrained for some reason. Not only for the cases mentioned above but also for older walls with insufficient reinforcement, retaining walls may collapse due to lack of the internal stability against strong earthquakes. The other type of retaining walls and wing walls of abutments were also damaged in the earthquake (Koseki *et al*., 2006, Tatsuoka *et al*., 2006 among others.)

In conventional seismic design of retaining walls, evaluation of the internal stability is made with seismic loads for externally instable retaining walls, i.e., using the seismic earth pressure for the full active failure in the backfill. However, if the retaining wall base is constrained and hardly moves outward, the active failure of the backfill may not be achieved and larger lateral load can act on the retaining wall. In other words, use of such a design earth pressure leads to underestimation of the force demand. In this study a series of dynamic centrifuge model tests were conducted to examine seismic loads, especially the load induced by the lateral earth pressure, for evaluating internal stability of externally very stable cantilevered retaining walls.

2. OUTLINE OF CENTRIFUGE MODEL TESTS

A cantilevered retaining wall rested on a competent ground was modelled. Cross section of the model ground is illustrated in Fig. 1. Using the Dynamic Geotechnical Centrifuge at PWRI (Matsuo *et al*., 1998), shake table tests were conducted at 60g with application of earthquake motions in the direction normal to the retaining wall.

Applied earthquake motions are shown in Fig. 2. The cantilevered wall height is 8.1m (the embedment depth=1.2m, except Case S4) and the length of the base is 5.4m in the prototype scale. The model retaining wall is made of aluminium. Based on the standard design of the retaining walls for road infrastructures in Japan, the dimensions of the model retaining wall were specified so that the flexural rigidity of the members of the model retaining wall approximates to that of the prototype. The flexural rigidity of the stem is 870MN.m^2/m and the natural frequency of the stem in the flexural vibration mode is about 8Hz in the prototype scale. The model retaining wall is instrumented with strain gauges and earth pressure cells so that both the lateral earth pressure acting on the stem and the flexural response of the stem can be measured.

The Toyoura sand was used to create the model ground. Specimens were prepared by the air-pluviation method using air-dried sand. The relative density of the foundation ground was 90%, while that of the backfill was 80%. Three foundation conditions were adopted in this study; one was the case with the retaining wall resting on the horizontally layered ground having the standard embedment depth (Case S1). The other two were the cases with the

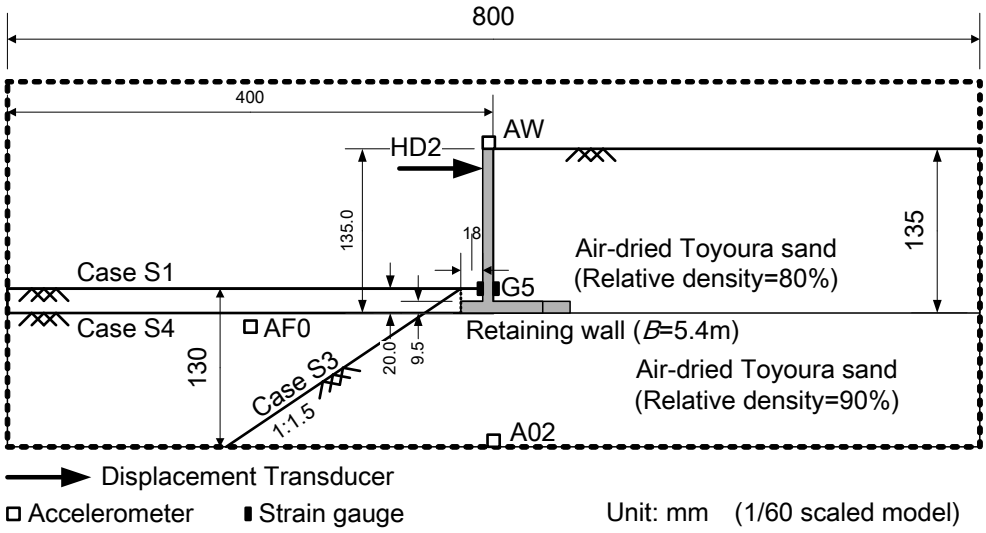

Figure 1 Model set-up

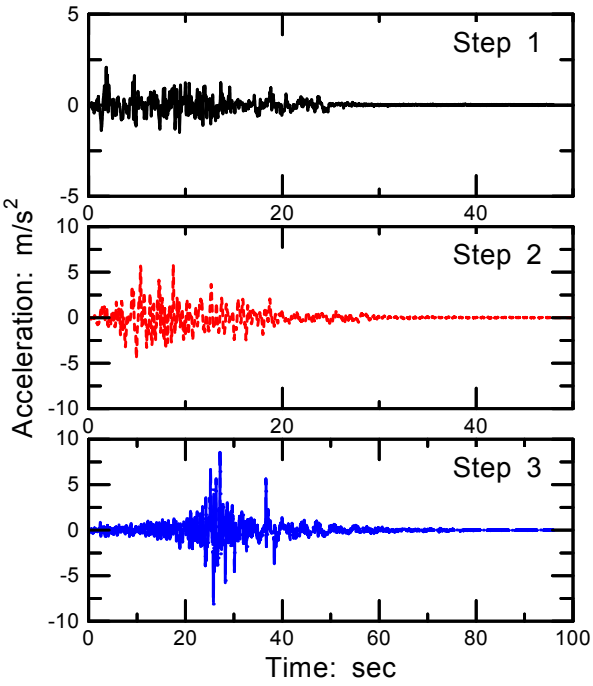

Figure 2 Earthquake motions applied

relatively smaller factor of safety for the external failure; the case without the embedment (Case S4) and the case for the retaining wall on top of the sloping ground (Case S3.) In all the cases, no marked slip surface appeared, i.e., no clear active failure was observed, in the backfill after the application of three earthquake motions shown in Fig. 2.

3. TEST RESULTS AND DISCUSSION

The stem of the retaining wall can fail either by bending fracture or by shear failure. In this paper, the discussion is

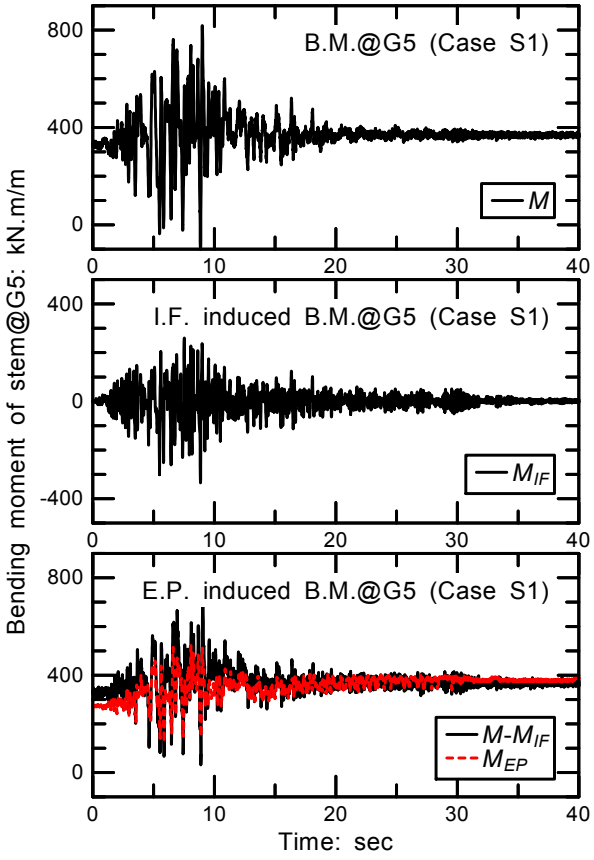

Figure 3 Bending moment changes (Case S1, Step 2)

confined to the bending fracture.

Since the maximum bending moment of the stem appears near the bottom of the stem for the cantilevered retaining walls, attempt was made to decompose the bending moment (M) of the stem near the base (Point G5) to that induced by the inertia force of the stem (M_{IF}) and by the lateral earth pressure acting on the stem (M_{EP}.)

Time histories of the bending moments, M, M_{IF} & M_{EP}, for Case S1 in Step 2 are plotted in Fig. 3. M was

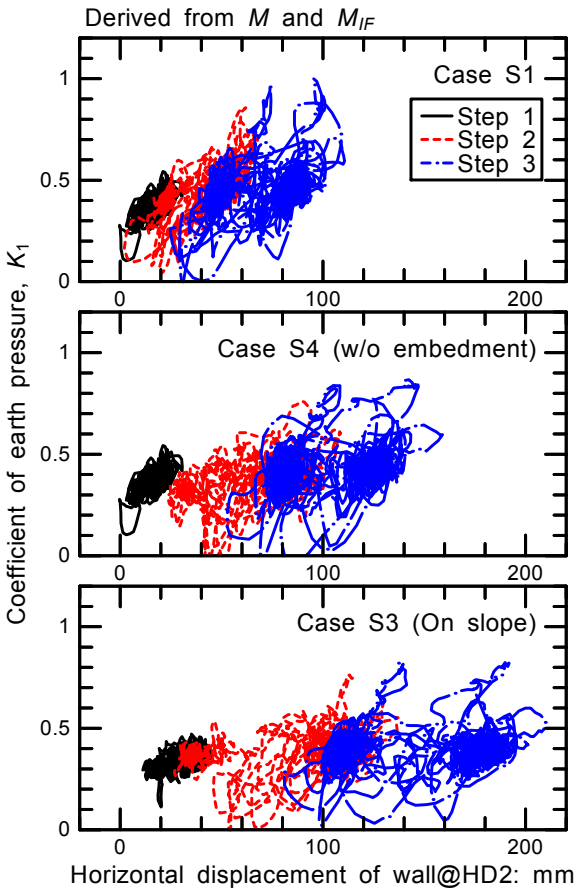

Figure 4 Earth pressure coefficient versus horizontal displacement of wall (Method 1)

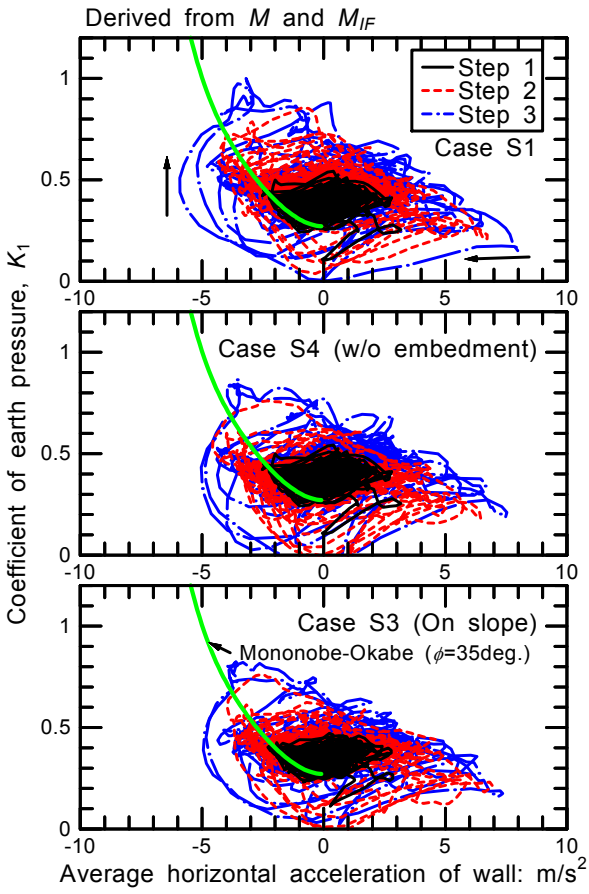

Figure 5 Earth pressure coefficient versus average horizontal acceleration of wall (Method 1)

calculated by strains measured at both side of the stem at Point G5 and M_{IF} was determined from the assumed horizontal acceleration distribution based on the acceleration records at the top and bottom of the stem.

To calculate M_{EP}, two methods were used; one is by subtracting M_{IF} from M by assuming that damping effects are negligible (hereafter this is referred to Method 1). The other is by the lateral earth pressure distribution measured using the earth pressure cells (Method 2). As shown in the bottom chart in Fig. 3, the trend lines for the both methods are almost identical, while the magnitude of fluctuation in the former is relatively large. This difference in the magnitude of fluctuation is considered to be mainly induced by the damping in the backfill.

In any case, contribution of the earth pressure acting on the stem is much larger than that of the inertia force of the stem and hence it can be said that the determination of the magnitude of the seismic earth pressure acting on the stem is more important. In addition, the damping effects of the backfill soil seem to increase the lateral load acting on the wall for cantilevered retaining wall designed in accordance with the standard design of the retaining walls for road infrastructures in Japan.

Figure 4 plots the equivalent coefficient of earth pressure for Method 1 (K_1) versus horizontal displacement of the wall measured at Point HD2 for all the cases. Here

K_1 and K_2 (equivalent coefficient of earth pressure for Method 2) are defined as

$$K_1 \frac{\rho g l^2}{2} \frac{l}{3} = M - M_{IF} \quad (1)$$

$$K_2 \frac{\rho g l^2}{2} \frac{l}{3} = M_{EP} \quad (2)$$

where ρ = density of the backfill, l=depth of Point G5 from the top of the stem. By comparing among the cases it reveals that the externally more stable the retaining wall the larger the coefficient of earth pressure (K_1) as expected. Relationships between the earth pressure coefficient and average horizontal acceleration of wall are plotted for all the cases using the Method 1 (Fig. 5) and Method 2 (Fig. 6.) For reference, the coefficient of earth pressure calculated by the Mononobe-Okabe method is also plotted. In the calculation of the coefficient of earth pressure by the Mononobe-Okabe method, the sharing resistance of the Toyoura sand, ϕ, is assumed to be 35° since the ϕ_{peak}=42° and ϕ_{res}=35° in direct shear box tests. The seismic earth pressure proposed by Koseki *et al.* (1998) considers both the

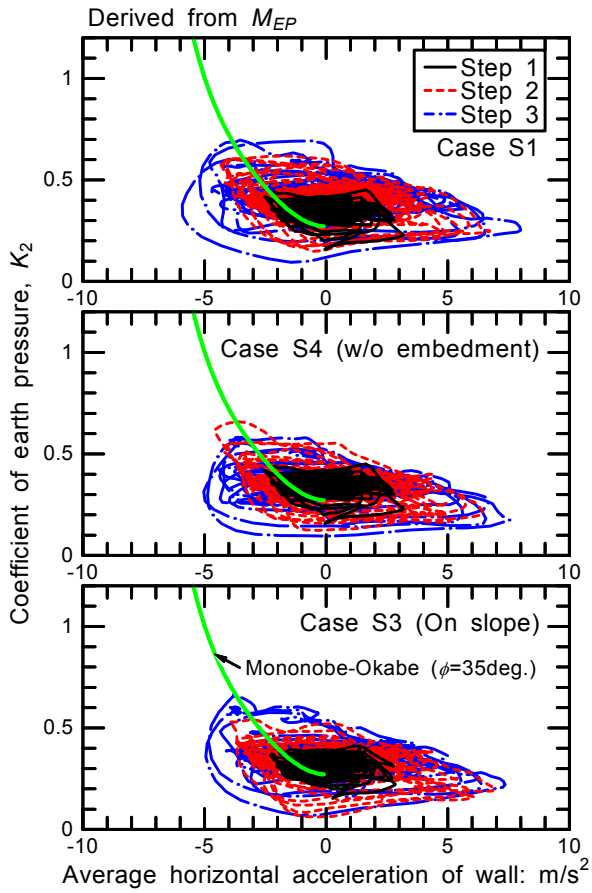

Figure 6 Earth pressure coefficient versus average horizontal acceleration of wall (Method 2)

peak and residual states. Although it is not plotted in the figure, it was located below that calculated in accordance with the Mononobe-Okabe method.

The figures indicate that the Mononobe-Okabe's coefficient approximate backbone curves of the hysteresis loops with Method 2, while it seems to underestimate the backbone curves for Method 1, especially the case where the wall is externally very stable (Case S1.) When we assess the stability of the retaining wall using a quasi-static method, the damping effects should be accommodated as the seismic load applied, i.e., the earth pressure equivalent to that derived using Method 1 may be used. The test results suggest that the current design practice can result in underestimation of the force demand and it is advisable to use the larger K_1 value. The further analysis may be needed to quantitatively evaluate the K_1 value for such a purpose.

3. CONCLUSIONS

A series of dynamic centrifuge model tests were conducted to examine seismic loads, especially the load induced by the lateral earth pressure, for evaluating internal stability of externally very stable cantilevered retaining walls. Test results reveal that (1) contribution of the earth pressure acting on the stem is much larger than that of the inertia force of the stem and (2) relatively larger earth pressure acts on the retaining wall when the wall is externally stable. In addition, the damping effects of the backfill soil seem to increase the lateral load acting on the wall and the seismic earth pressure calculated by the Mononobe-Okabe method underestimates the backbone curves of the hysteresis loops in the earth pressure—acceleration diagram. These findings suggest that the design seismic earth pressure calculated using the Mononobe-Okabe method, widely used in practice, can underestimate the force demand when the internal stability of the retaining wall is assessed using conventional quasi-static methods.

References:

Koseki, J., Sasaki, T., Wada, N., Hida, J., Endo, M. & Tsutsumi Y. 2006. Damage to earth structures for national highways by the 2004 Niigata-ken Chuetsu Earthquake, *Soils and Foundations*, Vol.46, No.6, 739—750.

Koseki, J., Tatsuoka, F., Munuf, Y., Tateyama, M., & Kojima, K. 1998. A modified procedure to evaluate active earthpressure at high seismic load, *Soils and Foundations, Special Issue on Geotechnical Aspects of the Jan. 17, 1995 Hyogoken-Nambu Earthquake*, No.2, 209—216.

Matsuo, O., Tsutsumi, T., Kondoh, K. & Tamoto, S. 1998. The dynamic geotechnical centrifuge at PWRI, *Proc. Centrifuge 98*, Vol.1, 25—30.

Tatsuoka, F., Konagai, K., Kokusho, T., Koseki, J. & Miyajima, M. 2006. Special session on the 2004 Niigata-ken Chuetsu Earthquake, *Proc. 16th Int'l Conf. Soil Mech. Geotech. Eng.*, Vol.5, 3279—3287.

JOINT CONFERENCE PROCEEDINGS
7th International Conference on Urban Earthquake Engineering (7CUEE) &
5th International Conference on Earthquake Engineering (5ICEE)
March 3-5, 2010, Tokyo Institute of Technology, Tokyo, Japan

INVESTIGATION ON THE SEISMIC PERFORMANCE OF UNDER GROUND EFFICIENT TIE-ROD SYSTEM, A NEW EXISTING QUAY REINFORCEMENT METHOD BY THE CENTRIFUGE EXPERIMENT

Takashi Matsuda[1] and Shunichi Higuchi[2]

1) General Manager, Civil Engineering Division, Obayashi Corporation, Japan
2) Senior Researcher, Technical Research Institute, Obayashi Corporation, Japan
matsuda.takasi@obayashi.co.jp, higuchi.shunichi @ obayashi.co.jp

Abstract: Under Ground Efficient Tie-rod System (UGETS, hereafter) is a practical construction method for deepening of the existing sheet-pile type quays during service. Additional ties and support structures are constructed behind the existing quays by utilizing a newly developed construction method of drilling boreholes for ties. Therefore, additional lateral resistance against the seismic force will be expected. Centrifuge experiments were carried out to investigate the performances of the UGETS against the seismic action and the dynamic characteristics of a quay reinforced by this method. Two different conditions of reinforcement systems are chosen, a horizontal tie system and a slanting tie system are chosen. A present quay (no reinforcement) and a UGETS-reinforced quay were tested simultaneously for each case. The experimental results show the reinforcement method is well effective by confirming the reduction of the section forces of the reinforced quay structures, as well as the reduction of the deformations.

1. INTRODUCTION

The demand of earthquake-proof upgrading for harbor facilities such as quays is increasing from the point of view of reservation against marine transportation during post earthquake disaster restoration.

Although seismic retrofitting works of in-service harbor facilities are planed, it is difficult to undertake construction at in-service facilities due to maintain function of cargo handling and storage capability. There are structural reinforcement such as additional piles and soil improvement of backfill for seismic retrofitting of quay-walls. In each existing countermeasures, retrofit construction works affect regular function of harbor.

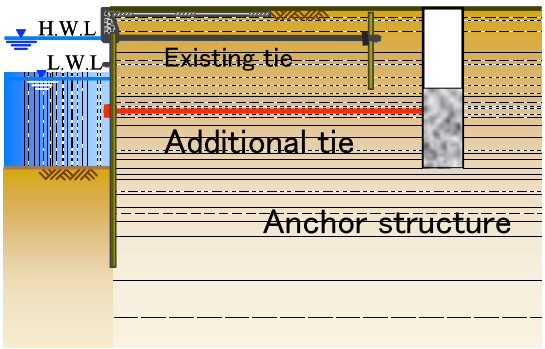

Fig.1 Conceptual layout of UGETS

UGETS (Under Ground Efficient Tie-rod System, see Fig.1) is one of retrofitting construction methods, which is able to reinforce an existing quay-walls without depressing function of harbor. UGETS consists of additional tie rod or tie-rope and high efficiency small caliber drilling method.
The authors performed a large-scale centrifuge dynamic test in order to obtain basic dynamic characteristics of UGETS and its effectiveness. This paper describes major results of the centrifuge test as well as a numerical simulation.

2. CENTRIFUGE TEST MODEL

2.1 Test Conditions

The conceptual members in cross section of UGETS are shown in Fig.1. UGETS consists of additional tie rod or tie rope and vertical pile anchorage as stay structure. The target models of UGETS are shown in Fig.4 and Fig.5. These models consist of sheet pile type quay-wall, front ground with sea and backfill. In the case-1model backfill was assumed as dense sandy ground. In the case-2 backfill was assumed as alternation of strata of lower normal consolidation clay and upper medium dense sand. Fig.1 and Fig.2 indicate retrofitted models using UGETS, although models without any countermeasures were performed simultaneously in each case to comprehend the effective of UGETS.

Dynamic centrifuge test in 50G was conducted using OBAYASHI's large device. Each model (case-1 and case-2) was installed in the rigid soil container. (L=2000mm, Width=700mm, Depth=650mm in model scale) (L=100m, Width=35m, Depth=32.5m in proto type scale). The soil container was divided by two cells in the perspective direction (Width direction). UGETS model and original model (without countermeasures) was installed in each cell. UGETS model and original model were excited simultaneously, so that comparison between UGETS and original was comprehended at sight.

2.2 Case-1 (Horizontal reinforcement tie rod model)

Original model of case-1 was steel pipe sheet pile type quay-wall with vertical pile anchorage. Proto type of this model is shown in Fig.4, and centrifuge model is shown in Fig.2. UGETS model was installed additional horizontal reinforcement tie rod with new vertical pile anchorage. Water depth was 10m in proto type scale, and front ground and backfill was same layer using dense sand. The reason for adoption of unique stratum was to comprehend basic phenomena and effectiveness of UGETS during large earthquake.

The interval of existing and additional tie rod and vertical pile anchorage was 1.5m in proto type scale. All structure models were made by steel works, steel pipe sheet pile and vertical pile anchorage were tuned by equivalent bending stiffness (EI), while tie rod was tuned by equivalent axial stiffness (AI). Profiles of quay wall model are tabulated in Table.3.

2.3 Case-2 (Slanting reinforcement tie rod model)

Original model of case-2 was steel pipe sheet pile type quay-wall with batter piles anchorage. Proto type of this model is shown in Fig.5, and centrifuge model is shown in Fig.3. UGETS model was installed additional slanting reinforcement tie rod with new vertical pile anchorage. In this case, existing soil layers condition in general and ordinary design section of quay-wall was adopted.

The ground model consisted of loose sand in surface layer as land reclamation, marine clay and dense sand layer as bed ground. UGETS was designed with consideration of increasing the quay-wall depth from 10m to 12m. From the final design for UGETS, the connection depth of additional

Table 1 Similarity Rule for Centrifuge Experiment

Item	similitude
Displacement	1/N
Acceleration	N
Density	1
Time	1/N
Bending Rigidity	$1/N^4$

Table 2 Profiles of Model Section for Centrifuge

Case	1	2
Additional Tie	Horizontal Vertical Anchorage	Slanting Batter Anchorage
Ground Model	Dense Sand	Sand & Clay

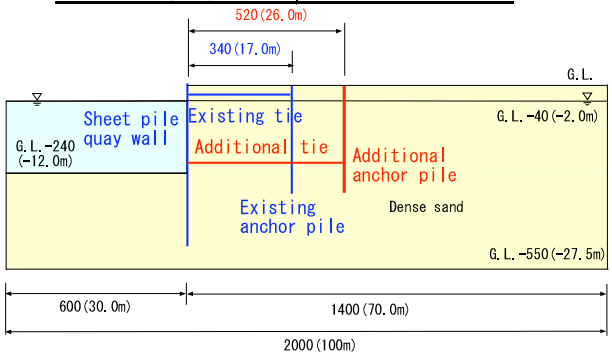

Fig.2 Cross Section of Centrifuge Model （Case-1）
- Reinforced Section -

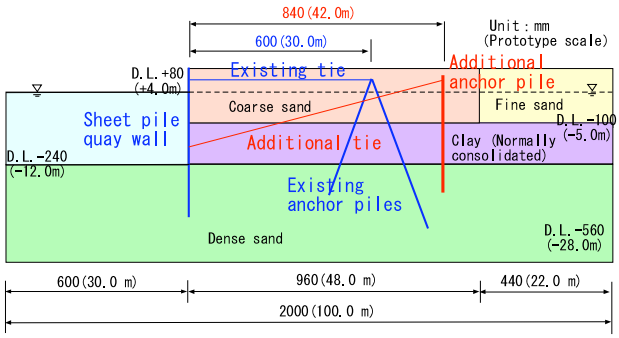

Fig.3 Cross Section of Centrifuge Model（Case-2）
- Reinforced Section -

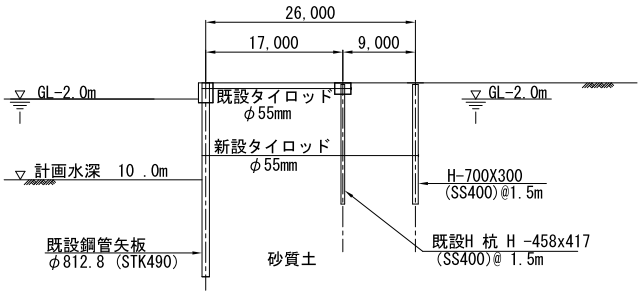

Fig.4 Cross Section of Prototype Quay Walls
(Horizontal Tie System)

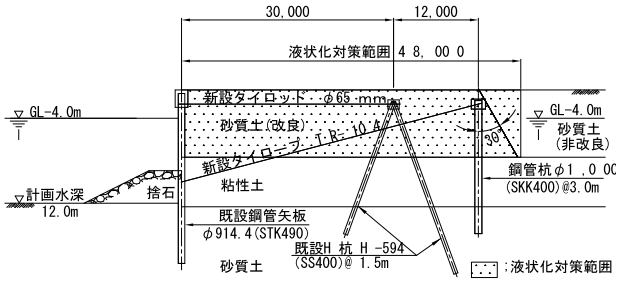

Fig.5 Cross Section of Prototype Quay Walls
(Slanting Tie System)

Table 3 Profiles of Quay Model (Case-1)

Member	Original		UGETS	
	Prototype	Model	Prototype	Model
Quay-Wall	Steel Pipe ϕ 812.8, t=10	Steel Plate t=6		
Anchorage	H Steel H-458x 417x30x50 @1.5m	Steel Plate 8.3x7.6 @30mm	H Steel H-700x 300x13x24 @1.5m	Steel Plate 8.3x7.6 @30mm
Tie	Tie Rod ϕ 55 @1.5m	Rebar ϕ 1@30mm	Tie Rod ϕ 55 @1.5m	Rebar ϕ 1@30mm

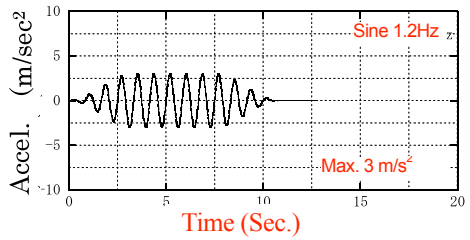

Fig.6 Input Earthquake Motion (Case-1)

Table 4 Profiles of Quay Model (Case-2)

Member	Original		UGETS	
	Prototype	Model	Prototype	Model
Quay-Wall	Steel Pipe ϕ 914.4, t=18	Steel Plate t=8		
Anchorage	H Steel H-594x 302x14x23 @1.5m	Steel Plate 前:13x6 後:9x9	Steel Pipe ϕ 1,000, t=19 @3.0m	Steel Plate 32x9 @60mm
Tie	Tie Rod ϕ 65 @1.5m	Rebar ϕ 1@30mm (ϕ 2@30mm)	Tie RopeTR-104 @3.0m	Rebar ϕ 1@30mm (ϕ 2@30mm)

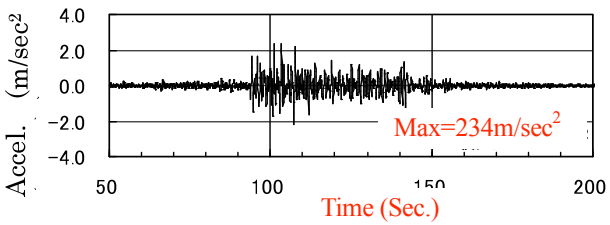

Fig.7 Input Earthquake Motion (Case2)

tie rod was 9m under the sea level, and the interval of additional tie rod and slanting pile anchorage was 3m in proto type scale.

Backfill (From quay-wall to 48m behind) consisted of dense sand layer as soil improvement against soil liquefaction, while the far field (beyond 48m) consisted of liquefiable loose sand layer.

Profiles of quay wall model are tabulated in Table 4.r

3. EXPERIMENTAL METHODS

3.1 Centrifuge test

In centrifuge test, existing tie rod and additional tie rod are subjected reaction forces due to earth pressures, while reaction forces subject only existing tie rod in real structure. The authors adopted following procedures to avoid generation of initial stress along additional tie rod.

1) Centrifugal force was subjected to model ground and structures without connection between additional tie rod and existing sheet pile quay-wall. The model ground and structures were deformed by centrifugal force, and existing tie rod accumulated initial stresses. .
2) Centrifugal force was released to 0G to perform connection between additional tie rod and existing quay-wall. .
3) Centrifugal force was subjected to model ground and structures with additional tie rod. And vibration force was subjected to the model. .

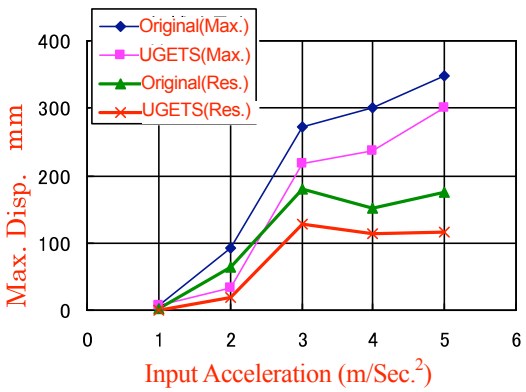

Fig.8 Relation between the Maximum Input Acceleration and Horizontal Displacement of the Quay

3.2 Shaking Table Test

In case-1, step-stage method using sine wave (1.2Hz in proto type with 5 waves) was adopted to comprehend basic phenomena during earthquake. Amplifications of the sine waves were from 100Gal up to 500Gal in proto type scale. Typical input motion of sine waves is shown in Fig.6.

In case-2, considering the effect of realistic conditions, the input ground motion is shown in Fig.7 using artificial seismic waves.

Table 5 Stress of Tie Member (MPa: Tension +)

Model	UGETS		Original
Member	Existing	Additional	Existing
Permanent	33	33	63
Increment (0.1g/0.3g)	35/141	69/298	78/152

4. EXPERIMENTAL RESULTS

4.1 Case-1 (Horizontal reinforcement tie rod model)

The maximum tensile stresses in the tie rod at the stage of centrifugal gravity of 50g (hereafter "permanent condition") as well as during vibration (0.1g: amplitude of input motion is 100Gal in proto type, 0.3g: amplitude of input motion is 300Gal) are tabulated in Table 5. Fig.8 indicates the depth of distribution of maximum bending moments in the sheet pile quay-wall at permanent condition, 0.1g and 0.3g (increment component from permanent

condition during vibration).

Sectional forces at permanent condition

Sectional force in the existing tie rod of UGETS model (159Mpa) has decreased to 3/4 of original model (209Mpa). Sectional force distribution differences in cross-section of sheet pile quay-wall are also observed, the maximum value (at GL-6m) has decreased about 30% of the reduction from original model. The additional tie rod has found that the same level of tensile stress of existing tie rod has generated.

Sectional forces at vibration condition

Incremental stress of existing tie rod in UGETS model (35Mpa) was about half of original model (78Mpa) as well as permanent condition.

Differences in the distribution of bending moment of the quay-wall has observed (see Fig.9 (b)), the largest increment of UGETS (at GL =-6m) is compared to 40 percent of original model, the absolute maximum sectional force (at GL =-6m) of UGETS has reduced to about 60 percent of original model.

Incremental stress in additional tie rod of UGETS model at 0.1g (69MPa) was larger than that of existing tie rod. At 0.3g, incremental stress in additional tie rod (141MPa) is almost equal to original model (152MPa), the effect as reducing sectional force at 0.3g is smaller than that at 0.1g. Stress in additional tie rod is established 331MPa (permanent + earthquake) over the yield stress (320MPa) at 0.3g, so that the possible effect of additional tie rod has reduced distortion. Besides, the reducing effect on bending moment distribution on the quay-wall of UGETS at 0.3g is smaller that at 0.1g, the maximum reduction rate is about 25 percent.

Displacement of quay-wall during earthquake

Fig.11 shows the relationship between amplitudes of input motion and lateral displacement of top of the quay-wall, which indicates the incremental lateral displacement in proportion to the amplitude of input motion. The reduction effect of UGETS can be observed, for example, maximum displacement of UGETS at 0.1g decreases to 1/3 of original model. However, displacement difference between UGETS and original model decreases over case of 0.3g.

4.2 Case-2 (Slanting reinforcement tie rod model)

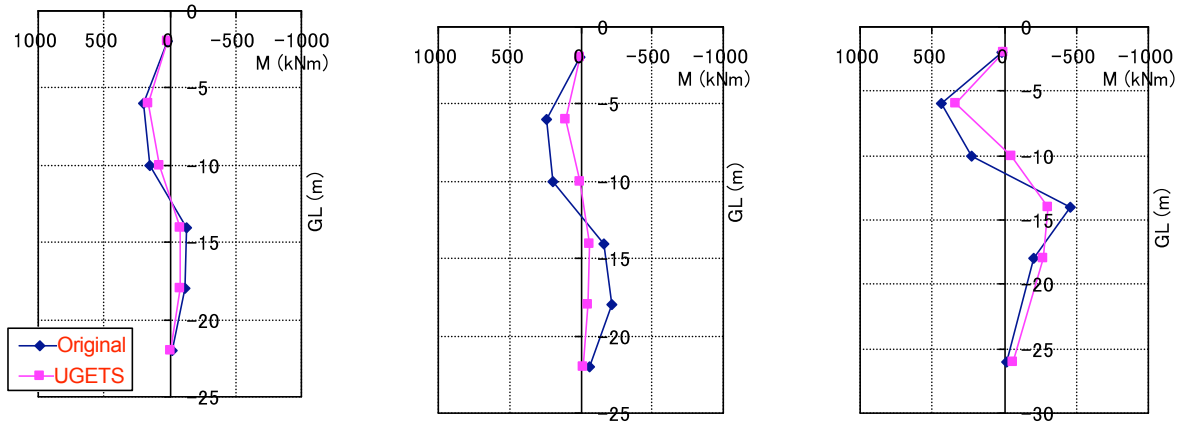

(a) Permanent (b) 0.1g (c) 0.3g

Fig.9 Maximum Bending Moment Distribution throughout the Quay Sheet-piles (Case1)

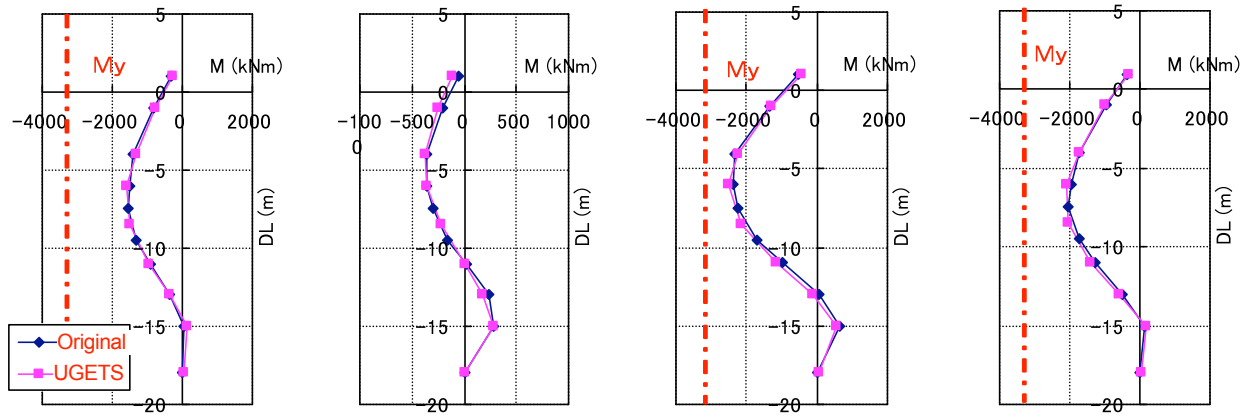

(a) Permanent (b) Increment (c) Maximum (d) Residual

Fig.10 Maximum Bending Moment Distribution throughout the Quay Sheet-piles (Case-2)

The maximum tensile stresses in the tie rod at permanent condition as well as 0.1g and 0.3g are tabulated in Table. 6. Fig.10 indicates the depth of distribution of maximum bending moments in the sheet pile quay-wall at permanent condition, 0.1g and 0.3g.

Table 6 Maximum Stress of Tie Member (MPa: Tension +)

Model	UGETS		Original
Member	Existing	Additional	Existing
Permanent	159	45	209
Increment (T=95s)	83	25	78
Maximum (T=141.2s)	308	63	372
Residual	45	-4	61

Table 7 Displacement of the Quay top (Seaward +)

Model	UGETS	Original
Maximum	208.3	224.7
Residual	159.5	172.0

Sectional forces at permanent condition

Sectional force in the existing tie rod of UGETS model (33Mpa) has decreased compared to about half of original model (63Mpa). Sectional force distribution differences between UGETS and original model in cross-section of sheet pile quay-wall are not observed.

Sectional forces at vibration condition

The increments of the sheet pile quay-wall to seismic bending moment and the axial stresses increment of the tie rod during earthquakes are shown in Fig.10 (b) and Table, respectively. The maximum bending moments of sheet pile quay-wall reached to about 90% of yield moment (My), while the maximum axial force of tie rod in case of original model (372MPa) exceeded yield moment of 320MPa. Fig.10 (d) indicates section force distribution (permanent + earthquake) of sheet pile quay-wall at end of the input motion. Maximum bending moment of the sheet pile quay-wall with UGETS decreased to 90% of original model, and incremental axial force of the tie rod in UGETS model decreased to 80% of original model (see Table.6)

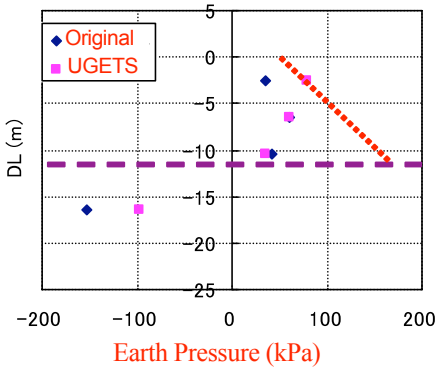

Fig.11 Maximum Dynamic Earth Pressure on the Quay

Earth pressure distribution during earthquakes

Fig.11 shows the distribution of earth pressure during earthquakes measured by earth pressure gauges located behind the quay-wall. Red dotted line shown in the figure is the design value in the seismic coefficient method (dynamic earth pressure + dynamic water pressure). Earth pressure in the underground section of the experiment decreased in proportion to the depth, and experimental earth pressure acting on the quay was found to be different from the design assumptions.

Displacement of quay-wall during earthquake

Lateral displacement of top of the sheet pile quay-wall and time histories are shown in Table 7 and Fig.12, respectively. Lateral displacements of UGETS were smaller than those of original model.

5. NUMERICAL SIMULATION

A dynamic effective stress analysis against the centrifuge test results was conducted using 2-Dimensional FEM code of "FLIP", aimed at the verification of application of UGETS.

5.1 Analysis Conditions

Case-2 model both of UGETS and original model in proto type has been selected as analysis of the target (see Fig.2). Perspective unit length is 1m, so that all of structural rigidity of the cross section is evaluated as unit length of 1m. Table 9 shows analytical condition of each member, and Table 10 shows soil properties for the FEM analysis.

Input ground motion for the analysis wais based on the measured time history waveforms during centrifuge test.

5.2 Analytical results

Bending moments of quay-wall

Maximum bending moment distributions of sheet pile quay-wall during earthquake are shown in Fig.13 (a), however experimental result indicates that the distribution at the time when the maximum value appeared (= distribution at the same time), while analytical result indicates envelop of maximum value of each node.

Analytical bending moments (indicated in solid circle dot) are 20-30% larger than those of experimental bending

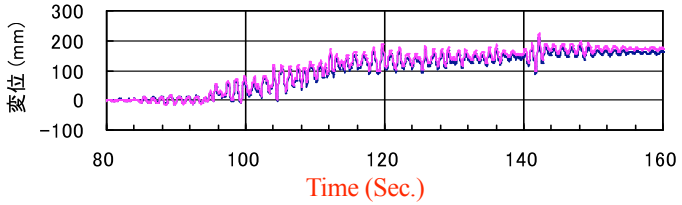

Fig.12 Time History of the Quay-wall top

Table 8 Force Distribution on Reinforced Tie Member

Case	1	2
Permanent	1	0.17
Increment	2 (0.1g) 2 (0.3g)	0.10

＊Existing tie was assumed to be one.

Table 9 Summary of the Numerical Model

Structure	Original quay-wall		UGETS	
	Model	Analysis	Model	Analysis
Sheet Pile	Plat t=8mm	Nonlinear		
Ancorage	Plate @ 30mm Front : 13x6 Rear : 9x9	Nonlinear	Plate B=32, t=9 @ 60mm	Nonlinear Beam
Tie	Rebar φ1 @ 30mm	Linear Spring	Rebarφ1 @ 60mm	Linear Spring

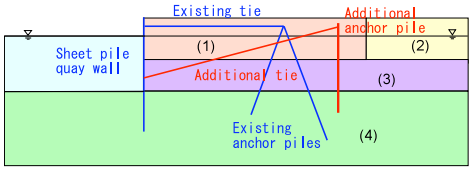

Table 10 Material Properties for the Soil

	Location	Vs (m/s)	φ	C (kN/m^2)	γ (kN/m^3)	
①	Backfill Soil Improvement	200	40		14.0+ 19.0	+ : Upper groundwater level
②	Backfill Rear	150	30		14.0+ 19.0	Liquefiable
③	Alluvial Clay	200	32	30	20.0	σv'=100kN/m^2
④	Diluvial Sand	250	45	*	20.0	

moments (indicated in hollow triangle dot), however the shape of the depth analytical distribution is well simulated to those of experimental distribution.

Axial force of tie rod

Axial force time histories of additional and existing tie rod are shown in Fig14 (a)-(c), while experimental result is the average value of all measurement points on the rod. Both of additional and original tie rods, analytical results are larger than experimental results, however, trend of building up the axial force are consistent. Besides, analytical dynamic amplification and phase lag of axial forces coincide with those of experiment.

Displacement of quay-wall

Displacement time histories of top of the quay-wall are shown in Fig.15. In the experiment, the residual displacement of sheet pile quay crest inhibitory effect was observed due to additional tie, while almost no difference appear in the FEM analysis. The residual displacement in the FEM analysis was smaller than that in the experiment, however the amplitude of displacement time history of analysis and experiment is almost similar. As a result, 2-dimensional FEM analysis is able to adopt to design for UGETS method, and UGETS is found to have a profound effect on seismic reinforcement of the sheet pile quay-wall.

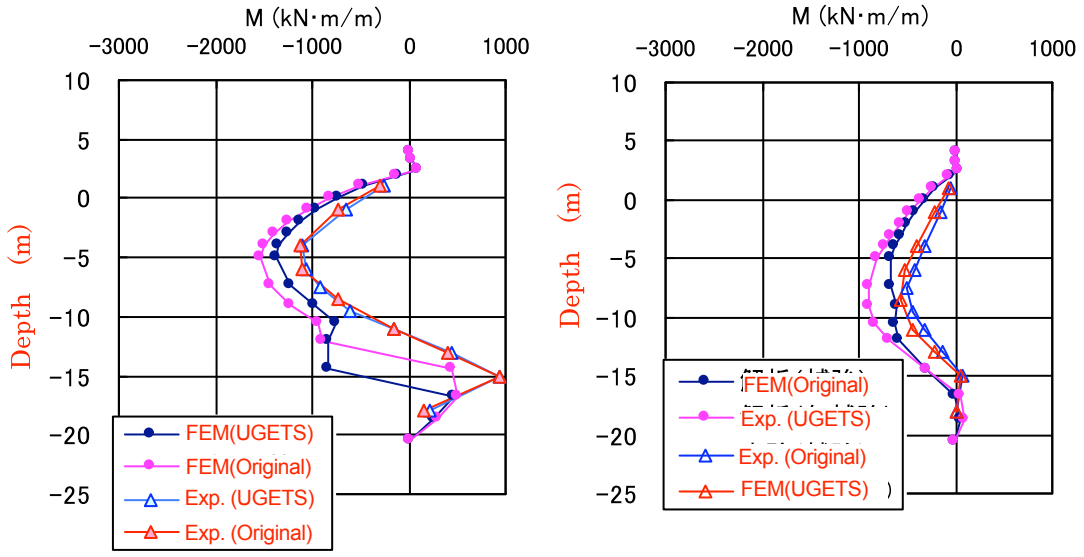

(a) Permanent

(b) Increment

Fig.13 Bending Moment Distribution throughout the Quay Sheet-piles (Tested and Simulated)

6. CONCLUSIONS

1) From results of centrifuge test, an additional tie is able to reduce axial force of existing tie using UGETS method. Result showed that the resulting change in the rate of load sharing existing structures. As a result, it has been understood that the change takes place in the load apportion rate of the existing quay-wall.
2) Due to result from 1), the entire quay-wall system stability level is able to be improved in the reinforcement section, the effect of earthquake-proof reinforcement of additional tie using UGETS method was able to be confirmed.
3) The effect of earthquake-proof reinforcement of additional tie is influenced according to the amplitude of the input earthquake motion. When the input earthquake motion grows, the effect of the load decrease on the existing structures and the lateral displacement reducing effect of the quay become small.
4) Slanting reinforcement tie rod model could not burden large portion of the axial force on the existing tie compared to horizontal reinforcement tie rod model. So that the reduction effect on section force of quay-wall declined, compared to horizontal reinforcement tie rod model. It is thought that the installation position of the additional tie to the sheet pile and flexure of additional tie affect to reduce the load burden effect.
5) It was confirmed not only to conduct the dynamical FEM simulation that used effective stress analysis code FLIP of the centrifuge model test, but also to be able to reproduce the section force increment of the sheet pile quay-wall well during earthquake. The amplitude and the phase were able to be simulated well about the shaft pile stress of the existing and additional ties. Therefore, the applicability to the UGETS of FLIP is able to be verified.

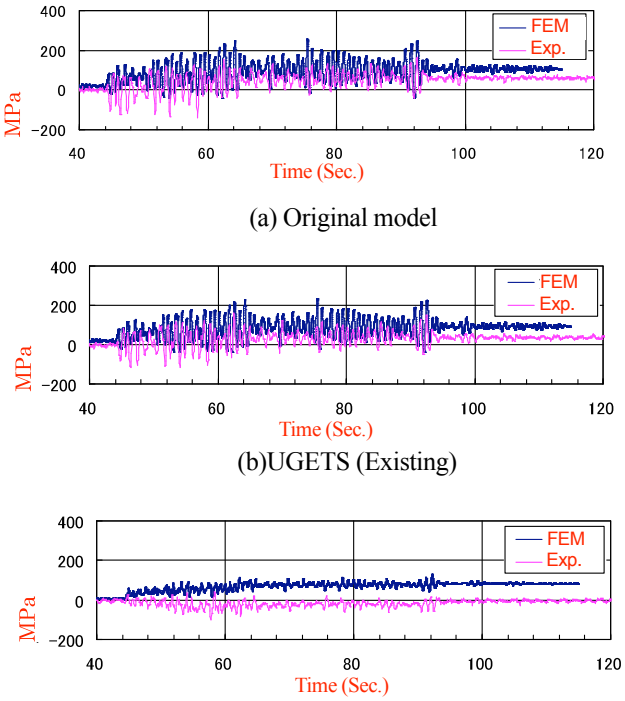

(a) Original model

(b)UGETS (Existing)

c)UGETS (Additional)

Fig.14 Time Histories of the Axial Stress Increment of Tie

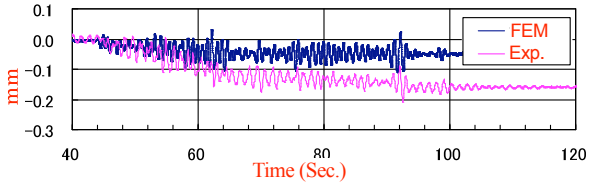

(a) Original model

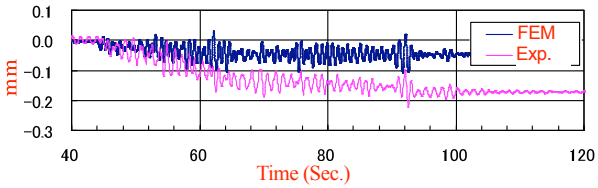

(a) UGETS model

Fig.15 Time Histories of the Lateral Displacement of the Quay Top

References:

Obayashi Corp. centrifugal model experiment group: Use case with centrifugal model experiment device (in Japanese), Annual report of Technical Research Institute of Obayashi Corp, No.66, pp.121-pp.124, 2003

Iai Susumu, Takita Masayoshi, Kozumi Masaru, Tamari Yukio and Yamamoto Yuuji: Analytical examination of influence on initial stress condition of the ground gives to seismic performance of sheet pile quay-wall (in Japanese), No.26 Earthquake engineering research symposium lecture thesis collection, pp.809-812, 2001

Shiozaki Teirou, Sugano Takahiro and Kohama Eiji: Experiment and analysis concerning earthquake resistance of Sheet pile quay-wall (in Japanese), Oceanic development thesis collection, Vol.20, pp.131-136, 2004

JOINT CONFERENCE PROCEEDINGS
7th International Conference on Urban Earthquake Engineering (7CUEE) &
5th International Conference on Earthquake Engineering (5ICEE)
March 3-5, 2010, Tokyo Institute of Technology, Tokyo, Japan

EVALUATION OF DAMAGE IN GEOGRID REINFORCED SOIL WALLS BASED ON WALL DISPLACEMENT

Jun Izawa[1] and Jiro Kuwano[2]

1) Assistant Professor, Department of Civil Engineering, Tokyo Institute of Technology, Japan
2) Professor, Geosphere Research Institute, Saitama University, Japan

Abstract: Geogrid reinforced soil walls (GRSW) have showed high seismic stability with limited deformation in the past earthquakes. GRSWs are often used without considerable repair or reconstruction after simple inspection in many cases even after strong earthquakes. For the proper repair or reconstruction, it is necessary to evaluate damage of GRSWs. As the restoration method of the structure should be decided right after the event, the damage must be evaluated by a simple index such as the wall displacement. Evaluation of damage in GRSWs subjected to earthquake is discussed in this paper based on results of centrifuge tests. The discussion is especially focused on the estimation of slip line formation by surface displacement. As a result, it was found that clear slip line may occur in reinforced area when inclination of the wall reaches to half of maximum shear strain of backfill material. However, the model GRSWs maintained adequate stability due to the pullout resistance of the geogrid even after the slip line generated. In addition, after the formation of the slip line, the sliding displacement along the slip line is getting significant. Such sliding displacement depends on the pullout resistance of the geogrid. Thus, it is necessary to know the appropriate pullout characteristics for evaluating the seismic stability of the GRSW having the slip line.

1. INTRODUCTION

Geogrid reinforced soil walls (GRSW) showed very high seismic stability with limited deformation in past severe earthquakes. GRSWs have been used without considerable repair or reconstruction after simple inspection in many cases even after such earthquakes. For proper repair or reconstruction, it is necessary to evaluate damage of GRSWs properly. Since restoration method for structure should be decided right after earthquake, damage of them must be evaluated with a simple index such as wall displacement, crest settlement and others. Thus, evaluation for damage in GRSWs due to earthquake is discussed in this paper based on results of centrifuge tests. The discussion is especially focused on estimation of slip line formation by wall inclination.

2. CENTRIFUGE TILTING AND SHAKING TABLE TESTS

Authors conducted a series of centrifuge tilting and shaking table tests focusing on effect of tensile stiffness of geogrid and properties of backfill soils on seismic performance of GRSWs (Izawa et al., 2002; 2002; 2004). Test cases are summarized in Table 1. Three silica sands having different particle size were used with relative density of 80%. Model geogrids used were made of polycarbonate plates with 0.5 mm or 1mm thickness. Schematic diagrams of a model GRSW and a geogrid used in both centrifuge tilting and shaking table tests were indicated in Figure 1. Five layers of 90mm long geogrids were laid in the backfill at 30mm interval. Five pieces of aluminium plates were used as a model facing wall and each facing was attached to one geogrid rigidly. Some optical targets were set on the surface of the transparent side wall for visually detailed observation of deformation. All tests were conducted in the centrifugal acceleration of 50G. In the centrifuge tilting table tests, pseudo static horizontal loading usually used in the design could be applied to the models by tilting the model. On the other hand, in the centrifugal shaking table tests, some sinusoidal seismic waves with frequency of 100Hz, which

Table 1 Test cases and properties of the model geogrids and the backfills

Geogrid				Backfill				Pullout characteristics			
Case	Type	Thickness (mm)	Tensile Stiffness (kN/m)	Type	D_{50}	γ_d (kN/m^3)	ϕ(°)	c_p (kN/m^2)	ϕ_p(°)	$\tan\phi_p/\tan\phi$	
CS-T	CS	0.5	197	Toyoura	0.19	15.7	40.4	0.930	21.4	0.451	
CS2-T	CS2	1.0	557	Toyoura	0.19	15.7	40.4	7.90	40.5	0.983	
CS2-S5	CS2	1.0	557	Silica No. 5	0.52	14.5	45.0	16.7	44.5	0.949	
CS2-S3	CS2	1.0	557	Silica No. 3	1.40	14.8	46.0	30.2	46.1	0.903	

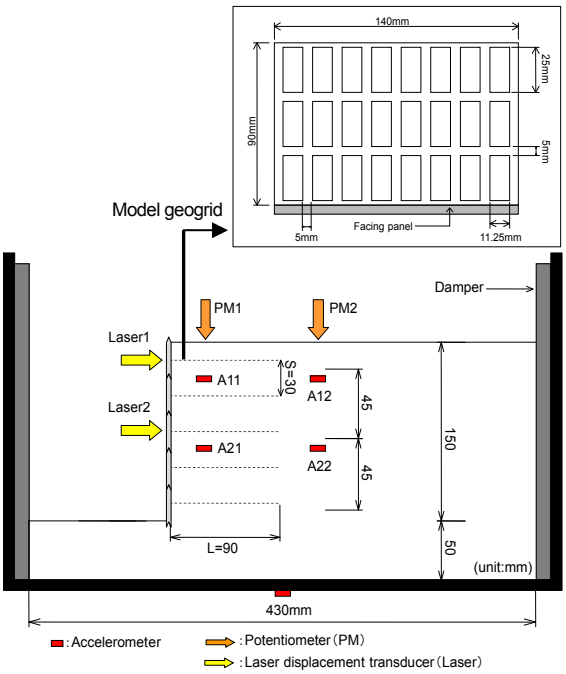

Figure 1 Schematic diagrams of a model GRSW and a geogrid

corresponds to 2Hz in prototype, were applied to the model with gradually increasing amplitude of acceleration.

3. WALL INCLINATION AT FAILURE SUBJECTED TO PSEUDO STATIC LOADING

Figure 2 shows relationships between horizontal displacement at the top of the model GRSWs and horizontal seismic coefficient, kh=tanη, where η indicates tilting angle. In all cases, horizontal displacements increased gradually with tilting and finally the model GRSWs failed suddenly due to sliding. However, overturning failure was observed only in the case of CS2-S3. In addition, effect of tensile stiffness of geogrid and soil properties can be detected in deformation curves. Figure 3 shows vertical distributions of horizontal displacements of the model observed in centrifuge tilting table tests. These were obtained from displacements of the optical targets set on side face of the models. In these figures, horizontal displacement at the bottom target and gradient indicate sliding displacement and shear deformation, respectively. From this point of view, these figures clearly show that shear deformation at lower part of the reinforced area was significant. Thus, inclinations of the bottom facing panel are plotted against horizontal seismic coefficient in Figure 4, together with horizontal seismic coefficients at failure. Here, the inclination of the bottom panel "θ" is defined as $\theta = d_p/H_p$, where dp and Hp indicate the horizontal displacement of the bottom facing panel and the height of the facing panel. This figure clearly shows that the model GRSWs failed when the inclination of the bottom facing panel reached to about 3.0%. Immediately before that time, clear slip lines appeared in the cases of CS-T, CS2-T and CS2-S5 as shown in Figure 5, where distributions of maximum shear strain before failure are

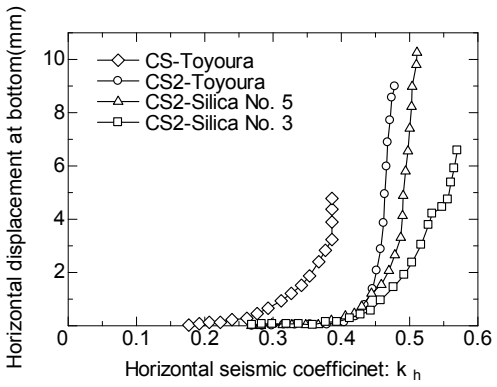

Figure 2 Horizontal displacements at bottom panel vs horizontal seismic coefficient

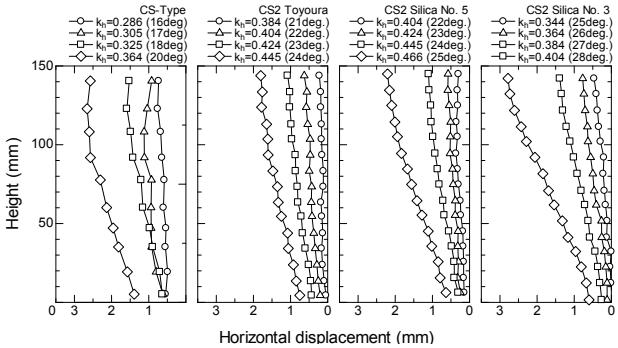

Figure 3 Vertical distributions of horizontal displacements of panels

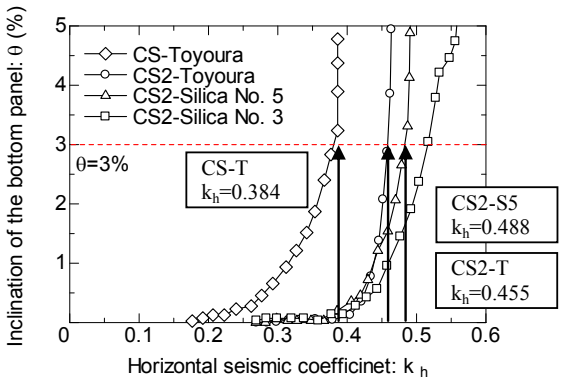

Figure 4 Inclinations of bottom panels vs horizontal seismic coefficient

indicated. On the other hand, the model of CS2-S3 did not show clear slip line and failed due to overturning.

In summary, the model GRSWs subjected to pseudo static loading failed due to sliding immediately after the inclination of the wall at bottom reached to the particular value and slip line generated. Additionally, such critical inclination didn't depend on tensile stiffness of geogrid since sliding failures were observed at almost the same wall inclination in the cases of CS-T and CS2-T, where the same backfill material used but different model geogrids. Thus, it is considered that such slip line generated when backfill itself in reinforced area reaches to failure. Relationship between inclination of facing panel and strain in the backfill is discussed in next chapter.

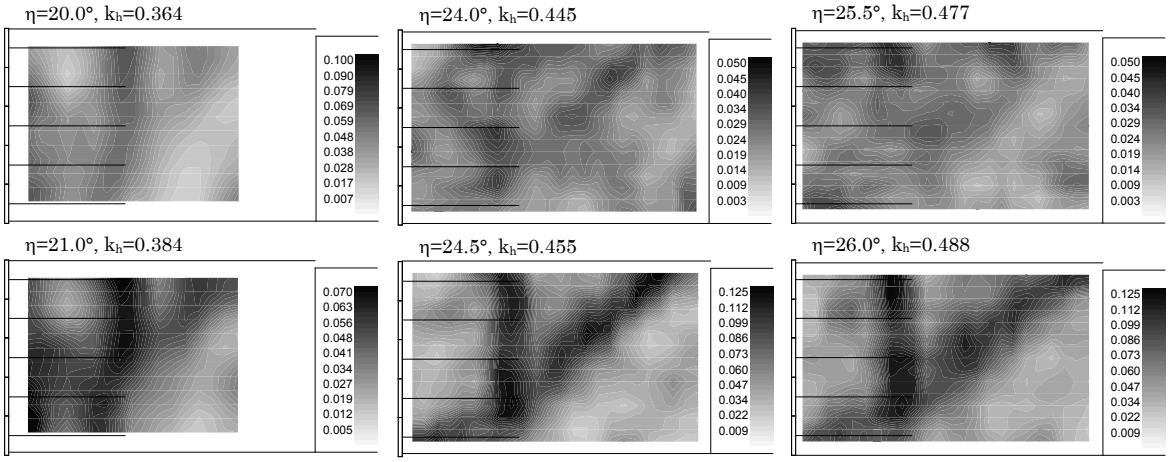

(a) CS-Toyoura (b)CS2-Toyoura (c)CS2-Silica sand No. 5

Figure 5 Distributions of maximum shear strain before failure in CS-T, CS2-T and CS2-S5

4. EVALUATION FOR GENERATION OF SLIP LINE

Bransby et al.(1975) proposed relationship between inclination of sheet pile wall and maximum shear strain occurred in the backfill based on test results as follows.

$$\gamma_{max} = \frac{2\theta}{\cos\varphi} \qquad (1)$$

where, γ_{max}: maximum shear strain occurred in backfill, θ: inclination of sheet pile wall and φ: dilatancy angle. Furthermore, it was reported that the proposed equation could give good agreement with test results. Here, it is not easy to obtain the dilatancy angle. Here, it is difficult to know the dilatancy angle easily. Figure 6 shows relationships between wall inclination and maximum shear strain occurred in the backfill calculated by the proposed equation with different dilatancy angle. This figure clearly shows that the effect of dilatancy angle on maximum shear strain is small enough to be negligible. Thus, the proposed equation can be simplified as follows.

$$\gamma_{max} = 2\theta \qquad (2)$$

Above equation is equivalent to the Bolton's equation (Botlon, 1988), which was derived from test results focused on undrained behaviour of the sheet pile wall. By using equation (2), maximum shear strain occurred in reinforced area can be estimated with wall inclination. As mentioned above, the slip lines generated when the inclination of the facing of the model GRSW reached to about 3.0%. That is to say, it can be estimated that maximum shear strain about 6.0% occurred in the backfill of the model GRSWs.

Figure 7 shows relationships between deviator stress and maximum shear strain of Toyoura sand, Silica sand No. 5 and No. 3 obtained from drained tri axial compression tests at the confining pressure of 98kPa, which is almost the same pressure in the bottom reinforced area of the model GRSWs under the centrifugal acceleration of 50G. Maximum shear strain was calculated assuming that Poisson's ration of all sands is 0.2. As shown in this figure, the peak deviator stress could be obtained at the maximum shear strain of 6.2% and

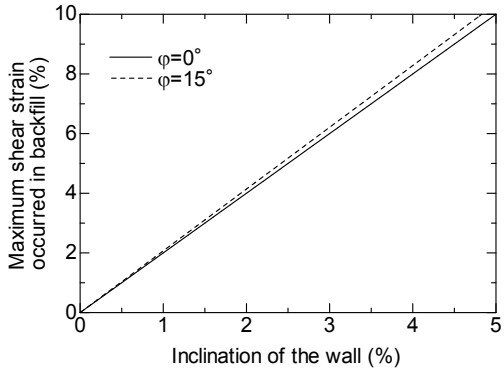

Figure 6 Effect of dilatancy angle on estimated maximum shear strain in backfill calculated by equation(1)

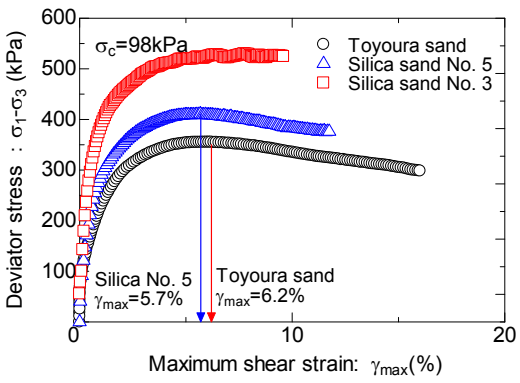

Figure 7 Results of tri axial tests under σ_3=98kPa

5.7% for Toyoura sand and Silica sand No. 5, respectively. That is, the backfill materials in the reinforced reached to their failure value when the wall inclinations reached to about 3.0%. This led to formations of slip line. On the other hand, clear peak value is not shown in tri axial test result of Silica sand No. 3. This resulted in no formation of slip line in CS2-S3 and the model failed due to overturning.

In summary, maximum shear strain in the backfill of GRSWs can be estimated by using equation (2). When the maximum shear strain reached to the peak value, slip line generates in the reinforced area and sliding failure occurred. Based on this relation, generation of the slip line can be evaluated using only horizontal displacement of facing.

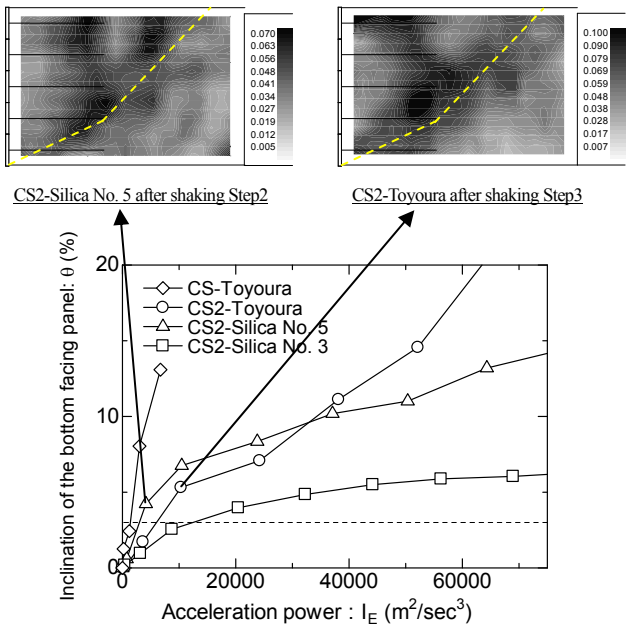

Figure 8 Inclination of the bottom facing panel vs cumulated acceleration power, together with maximum shear strain distributions at failure of CS2-T and CS2-S5

5. VALIDATION WITH RESULTS OF CENTRIFUGE SHAKING TABLE TESTS

In the centrifuge shaking table tests, the models showed almost the same deformation modes with those of the centrifuge tilting table tests. That is to say, shear deformation of lower part in the reinforced area was significant. Figure 8 shows the relationships between the inclination of the bottom facing panel and cumulated acceleration power. Acceleration power can consider both acceleration and duration of shaking wave, and it is calculated by the following equation.

$$I_E = \int_0^T a^2(t)dt \quad (3)$$

where, T: Shaking duration (sec), a: Input acceleration (m/s2). In CS2-T and CS2-S5, the inclinations of the bottom facing panel exceeded 3.0% at the shaking step 3 and 2, respectively. Maximum shear strain distributions are also indicated in Figure 9. As shown in these figures, slip lines generated after the shaking step 3 and 2 although they were not so clear than those in the centrifuge tilting table tests. This result clearly shows that the criteria for evaluating generation of slip line, as indicated in equation (2), can be applied to the GRSWs subjected to earthquake.

On the other hand, the model GRSWs did not collapse even after the slip lines occurred in the centrifuge shaking table tests. Figure 9 shows vertical distributions of horizontal displacement of CS2-T, in which slip line generated at the shaking step 3. As shown in this figure, sliding displacement was much larger than horizontal displacement due to shear deformation at the shaking step 4. This means that sliding displacement was significant after formation of slip line although shear deformation was dominant before formation

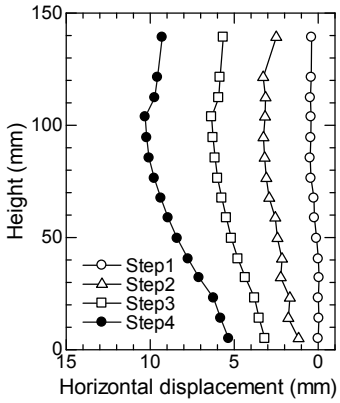

Figure 9 Vertical distributions of the horizontal displacement in the centrifuge shaking table test of CS2-T

of slip line. Amount of such sliding displacement may depend on pullout resistance of the geogrid cutting through the slip line. Thus, the horizontal displacement in CS2-T was larger than that of CS2-S5 after the slip line occurred as shown in Figure, since pullout resistance of CS2-S5 was larger than that of CS2-T as indicated in Table 1.

6. CONCLUSIONS

This paper describes evaluation of damage in geogrid reinforced soil walls based on results of centrifuge tilting and shaking table tests. In particular, authors focused on generation of slip line in the reinforced area was. Slip line generates in the reinforced area when the maximum shear strain of the backfill reaches to their peak value. The maximum shear strain occurred in the backfill can be estimated by the following equation.

Since inclination of bottom facing panel can be calculated by horizontal displacement, formation of slip line in reinforced area can be estimated using only the horizontal displacement of the facing. The GRSW maintains its adequate stability due to the pullout resistance of the geogrid after formation of slip line. However, after formation of slip line, sliding displacement along the slip line is getting significant. Such sliding displacement depends on pullout resistance of the geogrid.

References:

Izawa, J., Kuwano, J. and Ishihama, Y. 2004. Centrifuge Tilting and Shaking Table Tests on the RSW with Different Soils, Proc. of the 3rd Asian Regional Conference on Geosynthetics, pp. 803-810.

Izawa, J., Kuwano, J. and Takahashi, A. 2002. Centrifuge tilting and Shaking table tests on reinforced soil wall, Proc. of 7th International Conference on Geosynthetics, pp. 229-232.

Izawa, J., Kuwano, J. and Takahashi, A. 2002. Befavior of steep geogrid-reinforced embankments in centrifuge tilting tests, Proc. of Physical Modelling in Geotechnics, pp.993- 998.

Bransby, P. L. and Milligan, G. W. E. 1975. Soil deformations near cantilever sheet pile walls, Geotechnique, Vol. 25, No. 2, pp. 175-195.

Bolton, M. D. and Powrie, W. 1988. Behaviour of diaphragm walls in clay prior to collapse, Geotechnique, Vol 38, No. 2, pp. 167-189.

JOINT CONFERENCE PROCEEDINGS
7th International Conference on Urban Earthquake Engineering (7CUEE) &
5th International Conference on Earthquake Engineering (5ICEE)
March 3-5, 2010, Tokyo Institute of Technology, Tokyo, Japan

THE STUDY OF RELATIONSHIP BETWEEN LANDSLIDE GEOMETRY AND RUN-OUT DISTANCE OF LANDSLIDE MASS

Muneyoshi Numada[1] and Kazuo Konagai[2]

1) Research Associate, International Center for Urban Safety Engineering, Institute of Industrial Science, University of Tokyo, Japan
2) Professor, Institute of Industrial Science, University of Tokyo, Japan
numa@iis.u-tokyo.ac.jp, konagai@iis.u-tokyo.ac.jp

Abstract: The parameters that control the run out-distance of landslides mass are geometry, physical property and frictional coefficients to observe the contribution to run out-distance. For different lengths of the landslide mass, the mass movement is examined in the time-marching calculation of MPM. Lengths of the landslide mass segments L_1 and L_2 on the flat and inclined sliding surfaces are obtained respectively at every time step. Also analyze the effect of width of a landslide mass are carry out. As the width increases, the curve converges on the plane-strain solution. The ultimate load capacity would be more crucial in determining its distal reach. This research introduced some results for extracting important pieces of information for landslide risk assessment from numerical model and real landslide masses. For coherent mass movements, numerical simulation of landslide mass movements using MPM did hint an idea for extracting parameters from real landslide masses. This knowledge will provide a good perspective for landslide risk assessments.

1. INTRODUCTION

Landslide dangerous area, where are a debris flow, a steep slope collapse and slope failure and so on exist, are found more than 200,000 places in the whole Japan. Landslides can range in size from small movements of loose debris to massive collapses of entire summits. For short to medium-length slopes, installing preventive drainage works, anchoring and/or reinforcing slopes will be effective for assessing and mitigating landslide hazards. However for extremely large slope failures, it is very difficult to mitigate and thus the importance of run out analysis emerges. Many landslides with limited internal deformation will move as coherent masses on thin mobile basal layers. However, others will become flow-like in character after running some long distances, though exhibiting some solid features at their early stages of failure. It is important to forecast the run out distance of landslides mass to reduce the landslide disaster.

This research is aim to analyze the key parameter that control the run out distance of landslides mass. The numerical analysis is an effective approach to analyze the dynamic mechanism of the landslide. For numerical analysis, Material Point Method (MPM) is used in this research.

2. LANDSLIDE PARAMETERS AND MODELING

2.1 Landslide parameters

The type of landslide can be described by the point of various different kinds of sliding mass material and the movement mode. According to the USGS publication, a classification system based on these parameters is shown in Figure 1. In addition to that, other parameters such as form of landslide mass and coefficient of friction are also important to deal with landslide movement. The form of landslide is one of the important measurable parameter and can describe its scale and size. The movement of landslide mass can be different from its initial form or scale.

In this research, the relationships between the different forms such as initial length, width of landslide mass and landslide movement are examined.

2.2 Modeling of landslide mass

The MPM is categorized as one of the mesh-less methods formulated in an arbitrary Lagrangian-Eulerian description of motion (Sulky 1994). In MPM, a body is to be analyzed as a cluster of material points. Material Point has information of physical properties on a peculiar position and the stress, etc. The material points, which carry all Lagrangian parameters, can move freely across cell boundaries of a stationary Eulerian lattice, and the information is distributed to each node of belonging cells. This mesh is called as computational mesh, should cover the virtual position of the analyzed body. The computational mesh can remain constant for the entire computation, thus the main disadvantage of the conventional finite element method related to the problem of mesh distortions is eliminated for large deformation of soils (Figure 2).

All Lagrangian parameters for the entire landslide mass are hardly obtained. For example, it is often that the plants

LANDSLIDE CAUSES (USGS)
1. Geological causes
a. Weak or sensitive materials
b. Weathered materials
c. Sheared, jointed, or fissured materials
d. Adversely oriented discontinuity (bedding, schistosity, fault, unconformity, contact, and so forth)
e. Contrast in permeability and/or stiffness of materials
2. Morphological causes
a. Tectonic or volcanic uplift
b. Glacial rebound
c. Fluvial, wave, or glacial erosion of slope toe or lateral margins
d. Subterranean erosion (solution, piping)
e. Deposition loading slope or its crest
f. Vegetation removal (by fire, drought)
g. Thawing
h. Freeze-and-thaw weathering
i. Shrink-and-swell weathering
3. Human causes
a. Excavation of slope or its toe
b. Loading of slope or its crest
c. Drawdown (of reservoirs)
d. Deforestation
e. Irrigation
f. Mining
g. Artificial vibration
h. Water leakage from utilities

Figure 1 Landslide parameters (USGS)

growing on a landslide mass shoot their roots all through the soil mass. In such a way that overall characteristics of the soil mass is largely different from those obtained through test of soil samples taken point-wise from the landslide mass.

The condition requested for the numerical analysis includes two following elements: 1. Large deformation of soil; and 2. Input parameters composed of information which can be measured. Input parameters applied in MPM model are slope form (geographical features and slide surface), physical properties of deformation of sliding mass (geological features) and physical properties of sliding surface.

A lot of parameters that constitute physical properties of landslide are taken into real landslide phenomenon, but the pseudo-three dimensional model can reduce the number of complex parameters as much as possible (Hungr 1995). The landslide mass is considered to be equivalent fluid in this model and modeling it as assemble of soil columns. In such a model, complex landslide model can be expressed by the interactive force between soil columns, basal force and reducing necessary parameters. Therefore, there is an advantage that the computational complexity can be decreased at the computing lead time (Konagai 2002, Numada 2003, Abe 2004).

3. NUMERICAL SIMULATION

3.1 Length of landslide mass and run-out distance

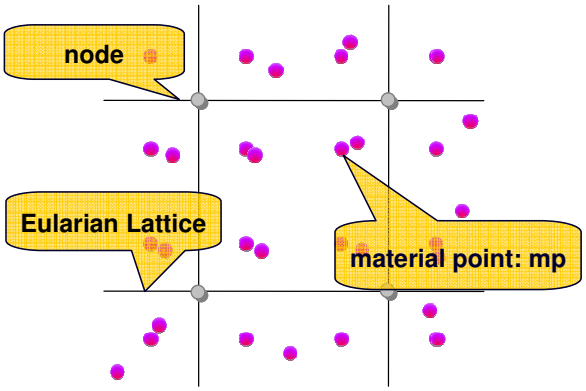

Figure 2 Eularian lattice and material points

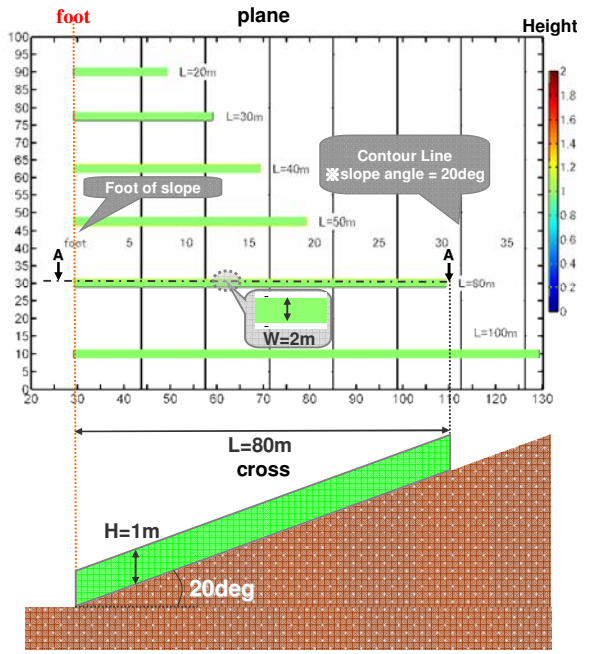

Figure 3 MPM model for different length of landslide mass (upper: plane view, lower: cross)

For landslide mass is modeled in MPM, width of the landslide W and depth H are made constant, the landslide length is set different six pattern from 20 to 100m length (Figure 3). The initial thickness H of the landslide mass is set to 1m. A rectangular-planner soil mass of 1m thick is assumed to be resting on a flat slope dipping to a level ground, which spreads in immediately front of the toe of the landslide mass.

The slope angle of MPM model is set uniformly to 20 degrees. The coefficient of friction is set separately on the slope side and flat surface side, and the coefficient of flat surface side μ_1 and slope side μ_2 are 0.8 and 0.2 respectively (Table 1).

Table. 1 parameter of landslide mass and MPM setting

Parameter	Value
Sliding surface dip	20 deg
μ_1 (flat surface)	0.8
μ_2 (slope surface)	0.2
ϕ (soil mass)	30 deg
Young's modulus	2×10^6 Pa
Possson's ratio	0.3
Density	1600 kg/m^3
Cell size	0.2m × 0.2m
Initial arrangement of particles in a cell	2 × 2
Time increment	5 × 10-4

The Young's modulus of the landslide mass E is taken as 2×10^6 Pa, poisson's ratio is 0.3, internal frictional angle ϕ is set to 30 degrees, cohesion C is derived from Rankin's earth pressure model to stand upright 1m height in the gravity. Drager-Prager model is used as the constitutive law of landslide mass in this research. The initial material point for one cell arranges to be 2×2 for 0.2m×0.2m size cell.

For different lengths of the landslide mass L, the mass movement is examined in the time-marching calculation of MPM (Figure 4). The run out-distance L_1 is defined as the distance from boundary of slope-flat surface zone to head of the landslide mass, and L_2 is the distance of the landslide mass that remains of a slope side. These are obtained at every time step. The average stress σ_a is the average value of the stress that acts upon the boundary on a slope and flat side. The average stress σ_a is calculated the average value of the stress of node on the boundary between a slope and a flat surface side. Initially landslide mass keeps $L_1 + L_2$ to be completely identical to the entire length of the landslide mass L. To be exact, the entire length is kept unchanged (Figure 5).

However, as the landslide mass runs further forward over the level ground (deposition zone), its movement slows down due to larger frictional coefficient and with no driving force induced on the level ground. Eventually the following segment of the landslide mass pushes the soil from behind, and immediately after the ultimate load capacity F, the average stress σ_a reaches peak strength σ_p, that the limit landslide mass can sustain is reached and $L_1 + L_2$ value is starts shrinking ($L_1 + L_2 < L$). For long landslide masses, L_1 converges on a constant value, ultimate L_{1y}, suggesting that the entire length of the landslide mass has little or nothing to do with the ultimate load capacity (Figure 6). In the other word, there is the upper bound of distal reach of the landslide mass. It will be also a matter of course that L_2 can converge likewise on a particular value, ultimate L_{2y}, with the presence of the ultimate load F.

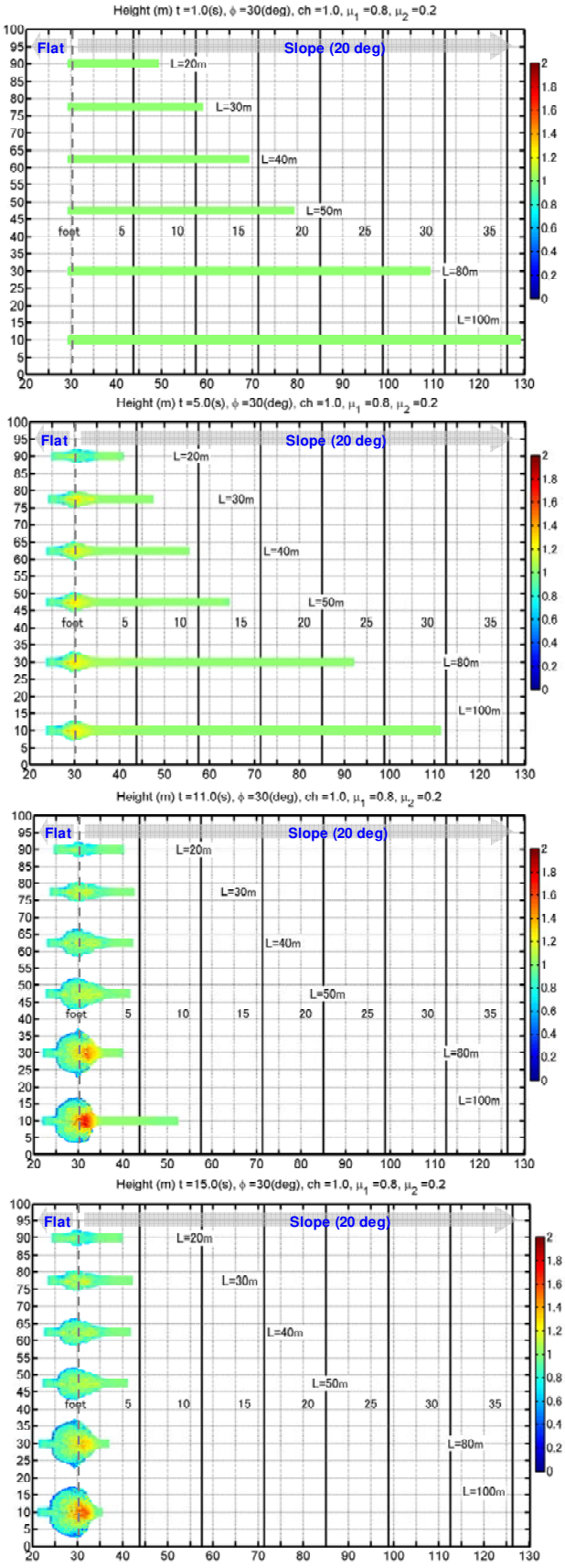

Figure 4 Plane view of numerical result for different length of landslide mass (time 1s-15s)

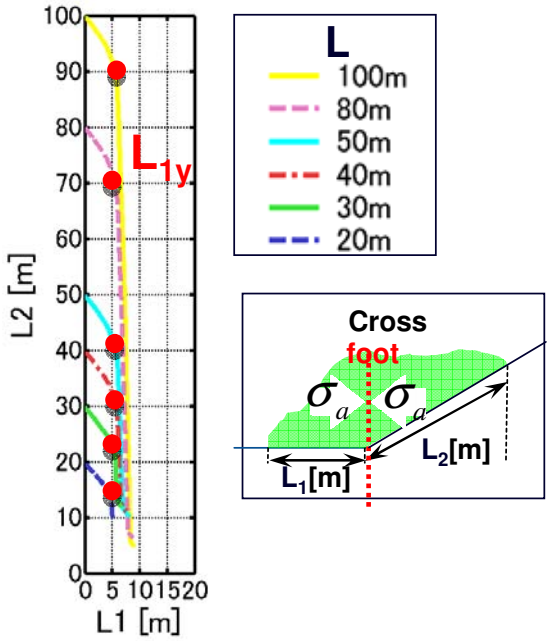

Figure 5 Relationship between L1 and L2 for different length of landslide mass

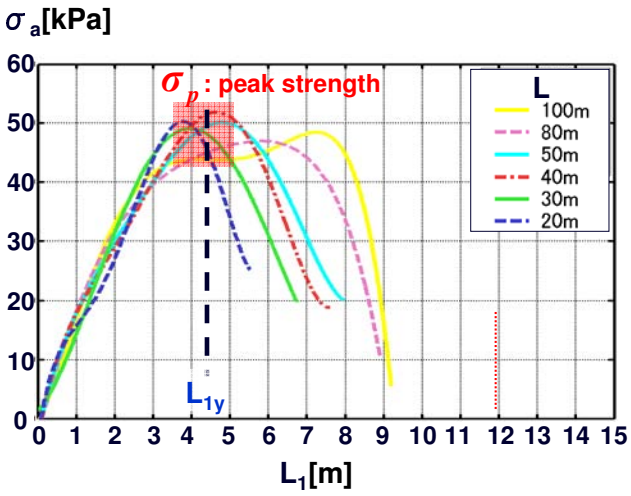

Figure 6 Relationship between L1 and the average stress σ_a for different length of landslide mass

3.2 Width of landslide mass and run-out distance

Width of a landslide mass can also affect F and therefore L_{1y} and L_{2y}, as the width increases, the curve converges on the plane-stress solution for thinner soil cases (Figure 7). In Figure 8, after the landslide mass starts yielding, dL_2/dL_1 becomes less steep for wider soil masses. This can be explained as follows: This dL_2/dL_1, when multiplied by the cross-sectional area of the landslide mass, is identical to $-dV_2/dV_1$, where dV_2 and dV_1 are soil volumes which pass through the cross section per unit time for segments L_1 and L_2, respectively.

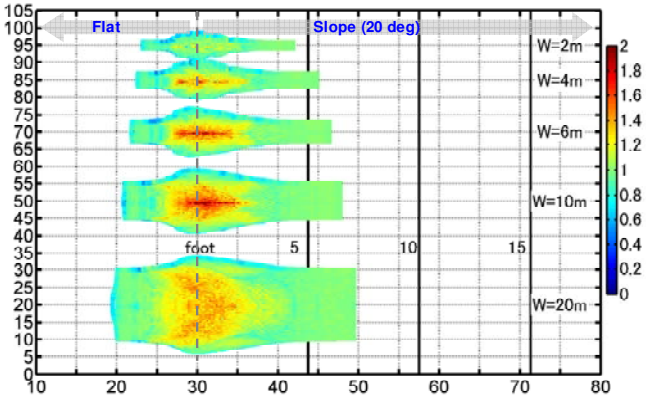

Figure 7 Plane view of numerical result for different width of landslide mass (time 10s)

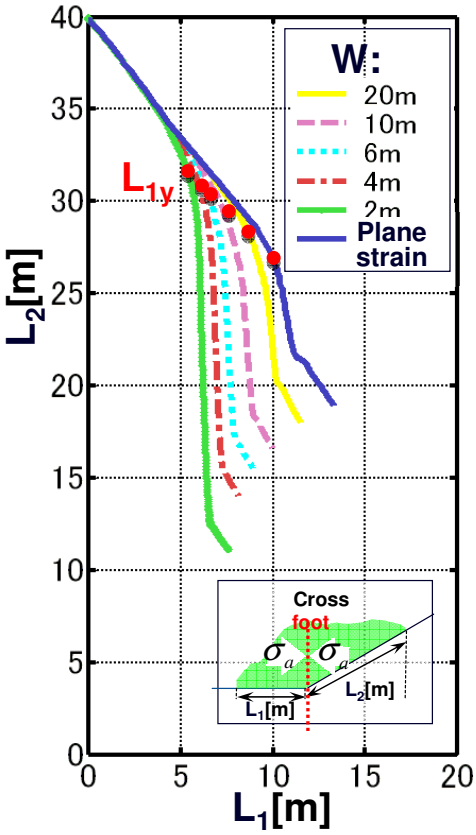

Figure 8 Relationship between L1 and L2 for different width of landslide mass

The soil volume dV_1 will be pushed forward over the deposition zone by the following soil volume dV_1, while the volume of $dV_2 - dV_1$ is pushed up and/or sideways making a bulge at around the toe of the slope. It is clear that, less steep dV_2/dV_1 indicates larger confinement of $dV_2 - dV_1$ causing slight increase of the average stress σ_a even after the initial ultimate capacity σ_p was reached (Figure 9). In other words, the effect of confinement can be quantitatively estimated from geometry of the deformed landslide mass.

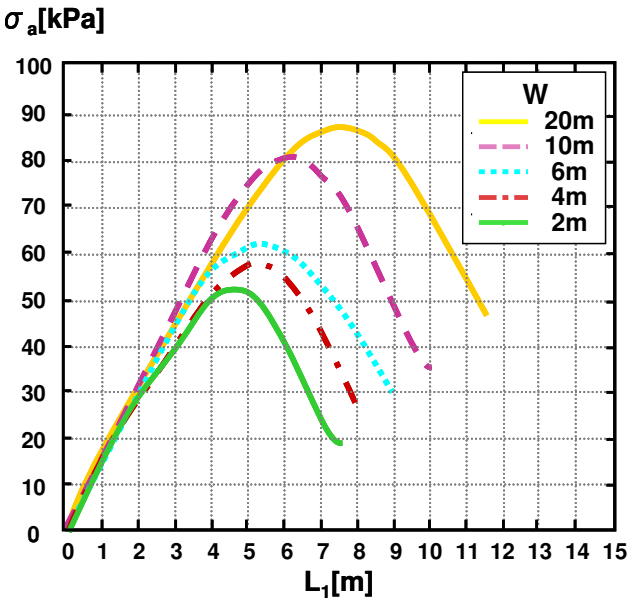

Figure 9 Relationship between L_1 and the average stress σ_a for different width of landslide mass

Width of a landslide mass can also affect *F*. As the width increases, the curve converges on the plane-strain solution, while it is rather closer to plane-stress solution for thinner soil cases. The ultimate load capacity *F* would be more crucial in determining its distal reach. In this research, by analysis on different width of the landslide, as the confining pressure is increasing, peak stress is increasing; it becomes a phenomenon similar to tri-axial compression tests.

5. CONCLUSIONS

This research introduced some results for extracting important pieces of information for landslide risk assessment from numerical model and real landslide masses. For coherent mass movements, numerical simulation of landslide mass movements using Material Point Method (MPM) gave an idea for extracting parameters from real land slide masses. A real cohesive landslide can be viewed as a large-scale specimen of a monotonic loading test for obtaining its ultimate load capacity, which can be greatly responsible for distal reach of the landslide mass. And also, the coefficient of sliding surface that is one of the important parameter to define run-out distance on the deposit zone is difficult to be evaluated from real site. For that one possible approach is proposed in this research. This knowledge will provide a good perspective for landslide risk assessments.

References:

U.S. Geological Survey: Landslide Types and Processes, http://pubs.usgs.gov/fs/2004/3072/pdf/fs2004-3072.pdf

Sulky, D., Chen, Z. and Schreyer, H.L. (1994), "A particle method for history dependent materials," Computer methods in applied mechanics and engineering, 118, pp. 179-196.

Hungr, O. (1995): A model for the run out analysis of rapid flow slides, debris flows, and avalanches, Canadian Geotechnical Journal, 32, pp. 610-623.

Konagai, K. and Numada, M. (2002): Pseudo-three dimensional lagrangian particle finite difference method for modeling long-traveling soil flows, Journal of Dam enginnering, 12(2), pp. 123-128.

Numada, M., Konagai, K., Ito, H. and Johansson, J. (2003): Material point method for run out analysis of earthquake-induced long-traveling soil flows, Journal of Earthquake Engineering, 27.

Keita Abe, Muneyoshi Numada and Kazuo Konagai (2004): A method and its problems for numerical analysis of rapid and long traveling soil flows, Seisan kenkyu, University of Tokyo, IIS, Vol. 56, No. 6, pp. 487-491.

JOINT CONFERENCE PROCEEDINGS
7th International Conference on Urban Earthquake Engineering (7CUEE) &
5th International Conference on Earthquake Engineering (5ICEE)
March 3-5, 2010, Tokyo Institute of Technology, Tokyo, Japan

MECHANISM AND SLIDING DISTANCE OF EARTHQUAKE-INDUCED AMAYACHI LANDSLIDE ESTIMATED BY MODIFIED NEWMARK METHOD

Atsuo Onoue[1] and Junichi Onda[2]

1) Professor, Civil Engineering Department, Nagaoka National College of Technology, Japan
2) Engineer, Hokuriku Gas Co. Ltd., Japan
onoue@nagaoka-ct.ac.jp, jonda@hokurikugas.co.jp

Abstract: A large scale landslide occurred in the Amayachi area in Old Yamakoshi Village, Niigata, Japan during the 2004 Mid Niigata Prefecture Earthquake. A part of mountain slope slid about 40 m in horizontally converted distance. Undisturbed samples taken from the site were tested mainly through the cyclic simple shear test under the constant volume condition and it was confirmed that the strength of soil at a sliding plane decreases with increasing shear displacement due to cyclic loading. A modified Newmark Method which took into consideration the decrease of undrained shear strength, was applied to this landslide. As a result, it was estimated that the slope lost limit equilibrium during seismic motion when accumulated displacement reached 3.8 cm, and kept sliding until the sliding block traveled such distance as it was due to gravity.

1. INTRODUCTION

The Mid-Niigata Earthquake (M_{JMA}6.8) shook the Chuetsu region, Niigata Prefecture, Japan at 17:56 on October 24, 2004, and more than 4,000 slope failures occurred due to strong motion of a seismic intensity of 7, the largest ever recorded in the seismological observation history of Japan. Many studies have been carried out on the sliding mechanism of the Chuetsu earthquake-induced large scale landslides on dip slopes with relatively gentle slants including interpretation of long sliding distance common to slope failures occurred in this region. This paper describes the sliding distance estimation of the Amayachi landslide, one such landslides occurring in an active fold area in the Chuetsu district, using a modified Newmark Method considering decrease of soil strength due to cyclic loading.

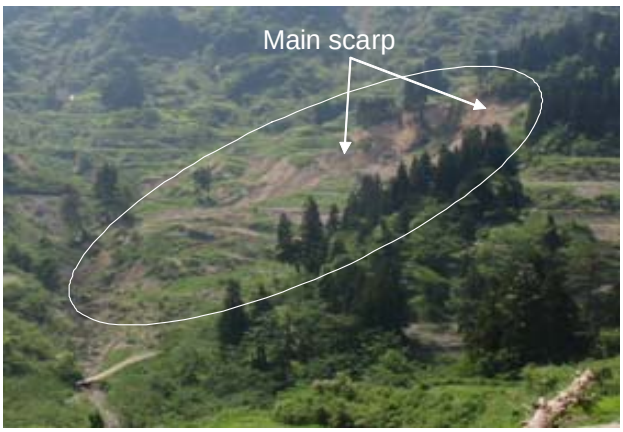

Figure 1 Whole view of Amayachi Landslide

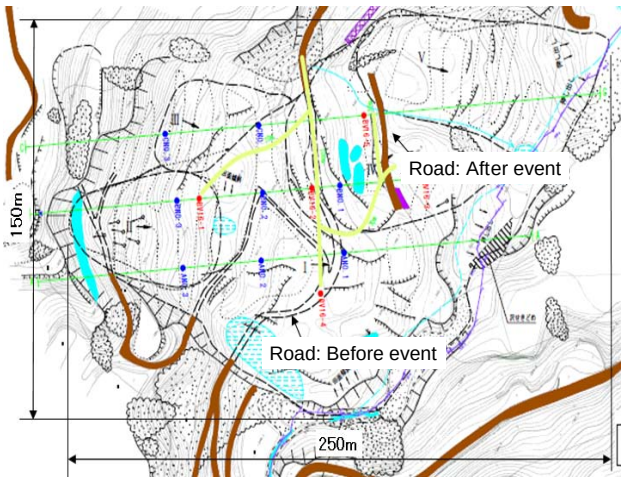

Figure 2 Plans before and after Earthquake

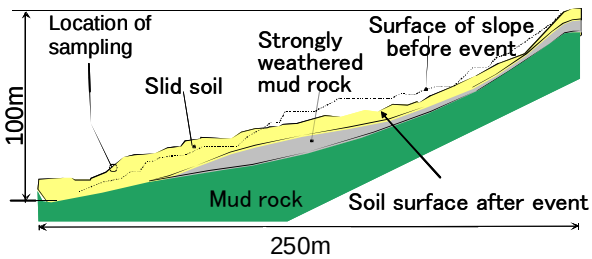

Figure 3 Cross Section at Center Line of Slid Soil

2. AMAYACHI LANDSLIDE

The Amayachi landslide is located near the north end of Old Yamakoshi Village in the Chuetsu district,and 9 km northeast of the epicenter of the earthquake. The elevation varies from 300 m – 400 m with an slope angle of 15° -20° . The sliding block with a length, a width and a maximum depth of 250 m, 150 m and 25 m, respectively, moved to a S20 – 30E direction for approximately 40 m in a horizontally converted distance.

According to Hasbaator et. al.'s study (2006), this is a landslide of reoccurrence type because it occurred almost along the pre-existing landslide area of the 1980 and 1981 landslides due to heavy rainfall. They investigated geological components of the site in detail and concluded the low possibility of liquefaction because the ruptured surface consists of mainly massive mudstone. On the other hand, Ugai et. al. (2007) estimated, based on the results of an undrained cyclic triaxial compression test, that the pore water pressure of the strongly weathered mudstone composed of sandy clay and/or clayey silt with sand must have increased to a certain degree during the main- and after-shocks. Wakai et. al. (2008) simulated the long distance sliding of the Amayachi landslide by dynamic elasto-plastic FEM where the decrease of shear strength with increasing accumulated plastic strain due to cyclic loading was taken into consideration.

The authors conducted a series of constant volume direct shear tests to confirm the decrease of shear strength due to cyclic loading and estimated the time history of sliding amount of the Amayachi landslide using a modified Newmark method taking the strength decrease into consideration.

3. SAMPLED SOIL

Two kinds of undisturbed samples, ① and ② were taken from natural ground near the lower end of the sliding block shown in Figure 3. Lots of samples were extracted for each kind by driving short thin-wall samplers with an outer radius of 7.8 cm and a length of 19.8 cm into the intact soil. The soils sampled were strongly weathered mud rock with plenty of cracks and considered to be colluvium deposits resulted from past landslides. The soil properties were tabulated in Table 1. According to the grain size analysis, the soils were classified to be clayey silt with sand.

4. CONSTANT VOLUME DIRECT SHEAR TEST

Three specimens from each sample were subjected to a constant volume cyclic direct shear test following JGS standard after consolidation under a pressure of 50 or 100 or 200 kN/m^2. The maximum shear displacement of one direction loading, 5 mm, was repeatedly loaded 10 times, hence the accumulated shear displacement was 100 mm. Figure 4 exemplifies a cyclic relationship between shear

Table 1 Soil Properties of Undisturbed Samples

No. of sample		①	②
Wet density	ρ_t [g/cm^3]	1.788	1.793
Dry density	ρ_d [g/cm^3]	1.364	1.366
Density of soil	ρ_s [g/cm^3]	2.716	2.690
Moisture content	w [%]	31.3	31.2
Void ratio	e	0.980	0.970
Degree of saturation	Sr [%]	85.9	86.8
Liquid limit	W_L [%]	63.9	64.2
Plasticity limit	W_p [%]	25.1	25.9
Soil classification	Clay (%)	30.6	25.6
	Silt (%)	37.3	44.5
	Sand (%)	32.1	29.9
	Gravel (%)	0.0	0.0

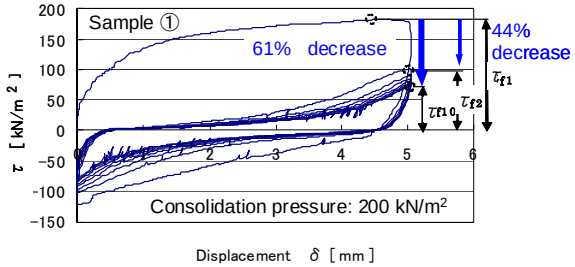

Figure 4 Example of Shear Displacement vs. Shear Stress

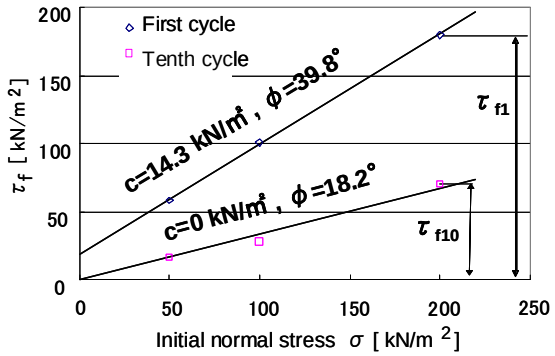

Figure 5 Decrease of Strength Parameters due to Loading Cycle (Sample ①)

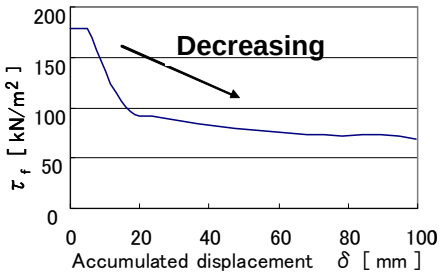

Figure 6 Accumulated Shear Displacement vs. Shear Strength

displacement and shear stress. Peak shear strengths of the second and 10th cycle decreased by 44% and 61%, respectively, comparing to that of the first cycle for this sample.

The strength parameters of sample ① expressed in the total stress method were shown in Figure 5 for the peak strength at the first and the 10th cycles. The values are; c=14.3 kN/m^2 and ϕ=39.8° at the first cycle and c=0.0 kN/m^2 and ϕ=18.2° at the 10th cycle for this sample case. There are little discrepancies in the value of strength parameters between the two samples. Estimated mean depth of sliding plane was 18 m and that of the ground water table was 5.5 m. Since the effective vertical stress at the sliding plane was about 200 kN/m^2, the shear strengths at the first and the 10th cycles were denoted using symbols τ_{fl} and τ_{fl0} for this stress level in Figure 5. Decrease of strength from τ_{fl} to τ_{fl0} with increasing accumulated shear displacement is shown in Figure 6.

5. ASSUMPTION OF SLIDE TYPE

Figure 7 shows a schematic cross section of an infinite slope with water flow in the soil subjected to seismic motion (ONOUE et.al. 2006). Although the Amayachi landslide was composed of multi sliding planes and could be divided into five units in terms of the deformation and movement of soil masses (Hasbaator et. al. 2006), it was assumed to be the slide of infinite straight slope having an inclination of β, a depth of imaginary sliding plane of Z and a depth of ground water table of z for simplify the problem. The forces E1, E2 acting on the vertical sides of the element are assumed to exactly balance each other. In Figure 7, (W, W_1) = weight of soil slice (below, above) the water table, (H, H_1) =k_h*(W, W_1), (V, V_1) = k_v*(W, W_1), T= shear force, N' = effective normal force and U = the total water force, where (k_h, k_v) = horizontal and vertical seismic intensity. The values of soil and geometric parameters here are γ_t= 17.5 kN/m^3, γ_{sat} = 18.3 kN/m^3, Z = 18 m, z = 5.5 m and β = 15.5° . The safe factor, Fs, for stationary condition was revealed to be 2.0 for the above strength parameters at the first loading cycle.

6. CALCULATION METHOD

6.1 Newmark Method

When the parallelogram soil block in Figure 8 is accelerated by upslope acceleration, Ag, in a direction parallel to the slope, the shear force between the block and the slope must differ from the shear force required for static equilibrium. Note the acceleration the block can experience is the yield acceleration, A'g, where A'= τ_f /(W_1+W). The soil block moves together with the slope if Ag≦A'g . On the other hand, if Ag>A'g, the shear failure occurs between the block and the slope, then relative displacement develops between them as the double integral result of the relative acceleration, Ag-A'g with respect to time. The total sliding amount can be obtained by summing the relative downhill displacement through out the entire seismic motion under the assumption that the shear strength of soil is constant (Newmark 1964).

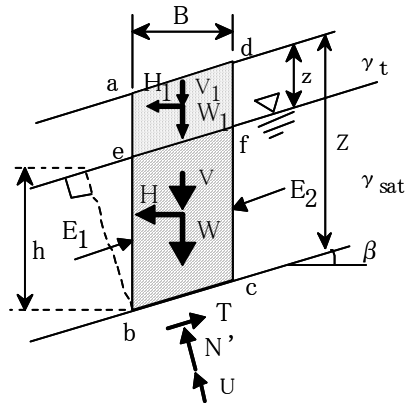

Figure 7 Schematic Picture of Infinite Slope

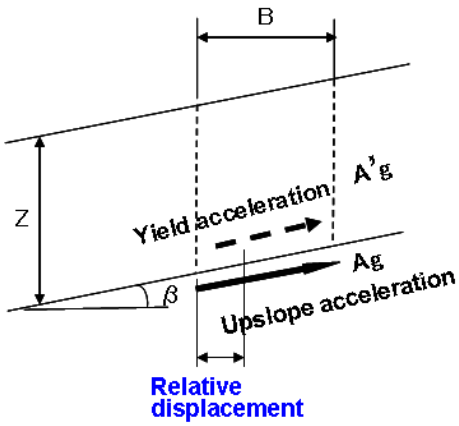

Figure 8 Yield Acceleration and Upslope Acceleration

6.2 Modified Newmark Method

Newmark method is not satisfactory for problems in which there is a major loss of shear strength as a result of cyclic loading like the Amayachi case. In order to incorporate strain softening characteristics of soil, many studies have been conducted by modifying conventional Newmark method (for example, Satoh et.al. (2001)). Since excess pore water buildup was confirmed in an undrained cyclic triaxial compression test (Ugai et. al. 2007) and the vertical effective stress markedly decreased in the constant volume cyclic direct shear test for the strongly weathered mud rock at Amayachi as aforementioned, the shear strength decrease on the way to liquefaction was taken into consideration. In this paper, the shear strength decrease with increasing accumulated shear displacement, δ, shown in Figure 6 was applied to Newmark method.

Since the yield acceleration, A'g, is limited by the shear strength, τ_f, of δ which is calculated every moment, A'g is denoted as A'g(δ(t)). During the time when Ag(t)> A'g(δ(t)), relative velocity can be obtained by integral of the excess acceleration, Ag(t)- A'g(δ(t)), which is shown by shadowed portion in Figure 9. Since relative acceleration is zero during the time when Ag(t)≦ A'g(δ(t)), the soil block continues to keep uniform motion until relative velocity becomes to zero. The accumulate displacement is thus obtained by integrating relative velocity.

6.3 Seismic Wave

The time histories of seismic acceleration in horizontal EW, NS and vertical UD directions observed by the Japan Meteorological Agency at Takezawa in Old Yamakoshi village were used in this calculation. Horizontal accelerations in EW and NS directions were at first converted to the direction of sliding, S25E, and overlapped. The seismic wave parallel to the slope surface, Ag, was next obtained by overlapping the horizontal wave in S25E direction and the vertical one, and it was shown in Figure 9 together with the yield acceleration, A'g. Acceleration in upslope direction is positive in the figure.

7. CALCURATION RESULTS

As seen in Figure 10, upslope seismic acceleration exceeded the yield acceleration four times during the earthquake. The first strong acceleration at 3 seconds after the start of earthquake was large but too short to cause relative displacement, and the following three intensive accelerations created large displacements. According to Figure 11, while the sliding amount was only 8.6 mm by the end of earthquake in the constant strength case, it accumulated 3.9 mm by 6.45 seconds after the start of earthquake and the slope lost static equilibrium to start infinite sliding in the decreasing strength case. The soil block slid down 15.2 m by the time 10 sec had passed, provided the constant acceleration motion could be assumed after loosing static equilibrium.

8. CONCLUDING REMARKS

The long distance sliding of Amayachi landslide during the 2004 Mid-Niigata Earthquake was successfully simulated by the modified Mewmark method considering the strength decrease due to cyclic loading. The cause of the decrease can be attributed to the excess pore water pressure generation in the strongly weathered mud rock along the sliding plane.

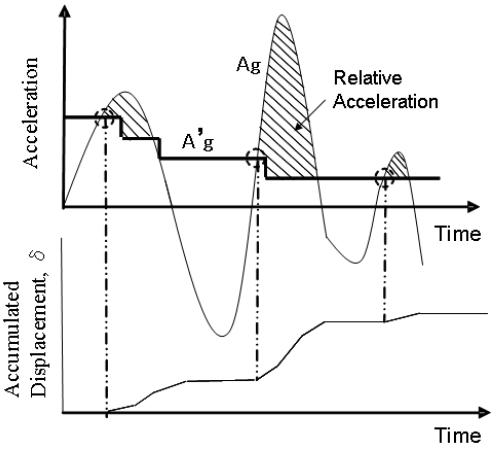

Figure 9 Schematic Picture of Relationship between Relative Acceleration and Accumulated displacement

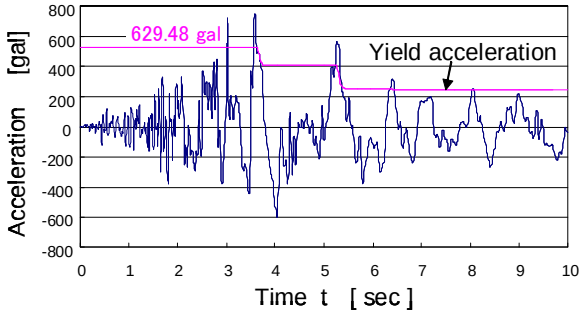

Figure 10 Yield Acceleration and Time history of Seismic Wave Converted to Direction and Inclination of Slope

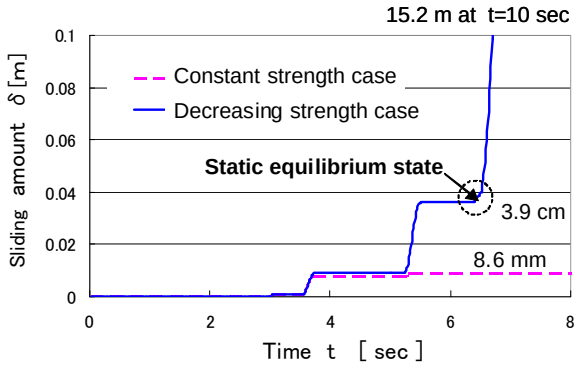

Figure 11 Time History of Estimated Sliding Amount

References:

Hasbaator, Hanaoka, M., Nozawa, E., Momose, A. and Sasaki, K. (2006), "Behavior and Mechanism of Earthquake-Induced Landslides within Pre-Existing Landslide Topography: the Case of the 2004 Mid-Niigata Prefecture Earthquake," *Proceedings of the Conference on Disaster Mitigation of Debris Flows Slope Failures and Landslides (Vol.1)*, 35-46.

Ugai K., Wakai, A., Onoue A., Kuroda S. and Higuchi K. (2007), "Mechanism of a Large Slope Failure Composed of Strongly Weathered Mudstone Induced by the 2004 Mid Niigata Prefecture Earthquake," *Proceedings of the 47th Conference of Japan Landslide Society*, 87-90. (In Japanese)

Wakai, A., Ugai K., Onoue A., Kuroda S. and Higuchi K. (2008), "Numerical Simulation for a Landslide Induced by Cyclic Shearing," *Proceedings of the 12th International Conference of International Association for Computer Methods and Advances in Geomechanics (IACMAG)*, 4606-4613.

Onoue, A., Wakai, A., Ugai, K., Higuchi, K., Fukutake, K., Hotta, H., Kuroda, S. and Nagai H. (2006), "Slope Failures at Yokowatashi and Nagaoka College of Technology due to the 2004 Niigata-ken Chuetsu Earthquake and their Analytical Considerations", *Soils and Foundations, Vol.46, No.6*, 751-764.

Newmark, N.M.(1964), "Effects of Earthquakes on Dams and Embankments," *Geotechnique*, *Vol.15*, 139-160.

Satoh, N., Banda, K., Horii, K., Tatsuoka, H. and Koseki, J. (2001), "Residual Deformation Analysis of Rockfill Dam due to Strong Earthquake by the Modified Newmark Method considering Strain Softening and Particle Size Effects," *Proceedings of 36th JGS Conference*, 1337-1338. (In Japanese)

JOINT CONFERENCE PROCEEDINGS
7th International Conference on Urban Earthquake Engineering (7CUEE) &
5th International Conference on Earthquake Engineering (5ICEE)
March 3-5, 2010, Tokyo Institute of Technology, Tokyo, Japan

CENTRIFUGE MODEL TESTS AND DEFORMATION ANALYSES ON SEISMIC BEHAVIORS OF EMBANKMENTS IN MOUNTAINOUS AREAS

Susumu Nakajima[1)], Tadao Enomoto[2)], and Tetsuya Sasaki[3)]

1) Researcher, Soil Mechanics and Dynamics Research Team, Public Works Research Institute, Japan
2) Researcher, Ditto
3) Team Leader, Ditto
s-nakaji55@pwri.go. jp, enomoto@pwri.go.jp,t-sasaki@pwri.go.jp

Abstract: The series of the dynamic centrifuge model tests were conducted so as to investigate into the seismic behaviors of the embankment constructed in mountainous area whose damages are highlighted during recent large earthquakes in Japan. In the presented paper, the effects of the degree of compaction of the embankment, ground water level within the embankment and height of the embankment on the seismic behaviors of the mountainside embankment were discussed based on the series of the model tests. The deformation analyses using Newmark's method on the model tests were also carried out so as to examine its applicability as a methodology to evaluate earthquake-induced deformations of the embankment. It was found from the series of the analyses that Newmark's method could be applicable to evaluate earthquake-induced residual deformations of the embankment while the further development are found to be necessary in considering the effects of the amplification of the response acceleration of the embankment and fluidal deformation of the embankment, which significantly affect the seismic behavior of the mountainside embankment in the shaking table model tests.

1. BACKGROUND

The 2004 Niigataken-Chuetsu earthquake and 2007 Noto Peninsula earthquake caused considerable damage to the embankments in mountainous areas (e.g. Koseki et al. 2007, Ohkubo et al. 2009). Aerial photo of the damaged embankment used for the toll road during the 2007 Noto peninsula earthquake is shown in Fig. 1, and the cross section of the damaged site is also indicated in Fig. 2. At the damaged site, the embankment with the height of about 30 m was constructed on the sloped bedrock. These figures show that the embankment moved largely to the downward along the sloped bedrock.

It is usual for the construction of the mountainous road that embankment is constructed on the sloped bedrock as typically illustrated in Fig. 2. It is usually observed during the post earthquake survey on the damaged mountainous embankment that the soils at the toe of the embankment had high water contents whose water was mostly came from the upward of the mountain. As a result, it is also generally observed that high ground water level within the embankment was kept as usual especially at the toe of the embankment.

It is considered that partial failure at the toe of the

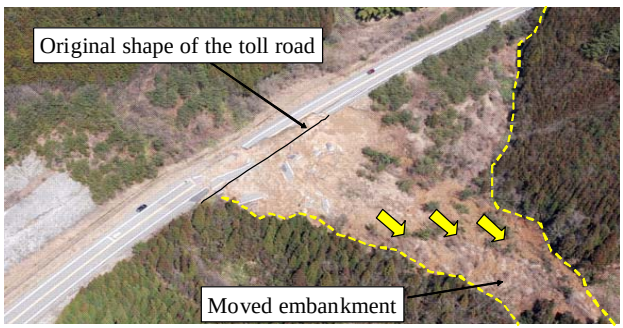

Fig. 1 Aerial photo of the damaged mountainous embankment during the 2007 Noto peninsula earthquake

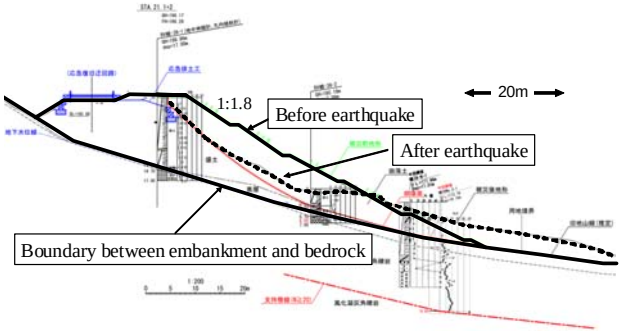

Fig. 2 Cross section of the damaged mountainous embankment

embankment due to the seismic loading could be trigger of the large deformation of the embankment as typically shown in Figs. 1 and 2. This local failure is thought to be caused because of lower effective stress at the toe of the mountainous embankment as compared with the ordinary embankment, which is possibly due to the high ground water level at the toe of the mountainous embankment.

On the other hand, the mountainous road has rarely alternative road although they tend to be constructed as the high embankment. Therefore, the mountainous road shall be designed with considering the effects of the earthquake so as not to deform catastrophically even during the large earthquakes.

Based on the background above, the authors have conducted the series of the centrifuge model tests on the seismic behaviors of the mountainous embankments so as to investigate into the effects of 1) the degree of the compaction of the embankment, 2) height of the embankment, 3) subsoil condition and 4) ground water level within the embankment on the seismic behavior of the mountainous embankment.

Results of the relevant deformation analyses using the Newmark's method (Newmark, 1965) on the model test results are also presented in the later part of this paper.

2. OUTLINE OF MODEL TESTS PROCEDURE

The series of the model tests were conducted using the Geotechnical Centrifuge Mk3 in Public Works Research Institute, Japan. Typical cross section of the model is illustrated in Fig. 3. The models of bedrock and embankment were prepared in the soil container with the height of 0.5 m, length of 1.5m and width of 0.3 m.

The model of the bedrock was prepared so as to simulate the embankment in the mountainous area by using the gypsum before conducting the series of the shaking table model tests and sand paper was pasted at the surface of the bedrock model to achieve the frictional resistance between the bedrock and embankment in the actual field. Acrylic pipes, which were connected to the water supply tanks, were also installed in advance within the model bedrock so as to control the ground water level within the embankment before the shaking.

Model embankment was prepared by compacting the Edosaki sand (e_{max}=1.16, e_{min}= 0.654, d_{50}=0.277 mm and G_s=2.731) with the target degrees of compaction were set equal to 82, 85 and 90%. The grain size distribution and compaction curve of Edosaki sand are shown in Figs 4a and b. The grain size distribution of the soils obtained from the

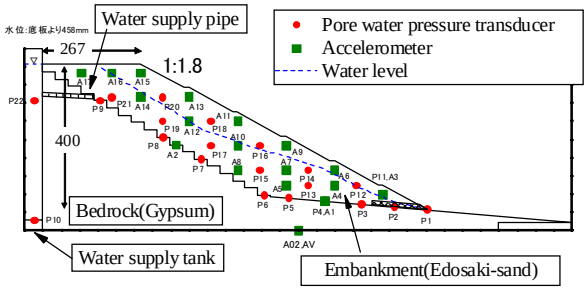

Fig. 3 Typical cross section of the model (test 07_2, model scale unit in mm)

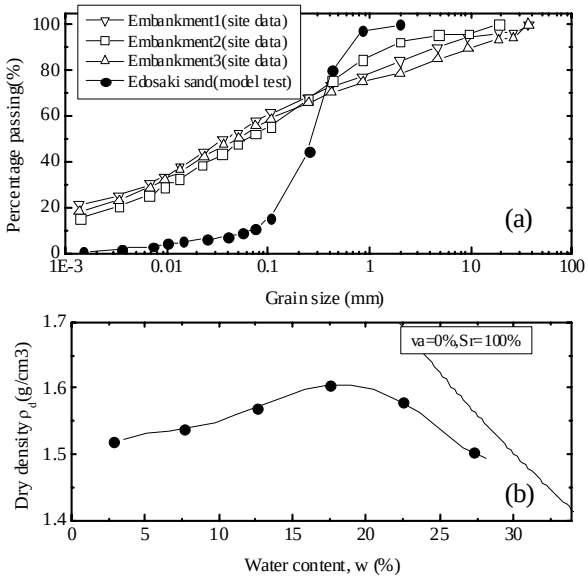

Fig. 4a Grain size distributions of model embankment and soil samples taken from the damaged site, 4b Compaction curve of Edosaki-sand

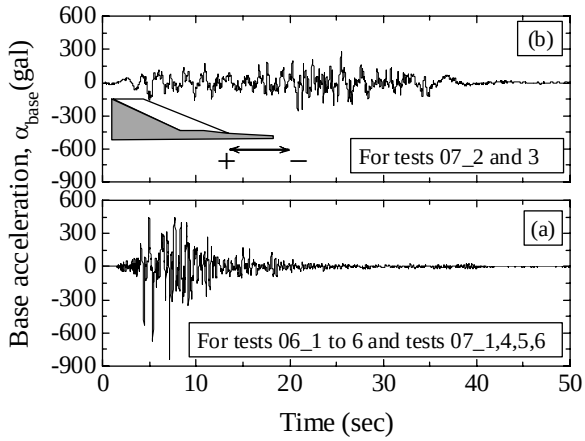

Fig. 5a; Irregular excitation simulating a near field earthquake, 5b; Irregular excitation simulating a plate boundary earthquake

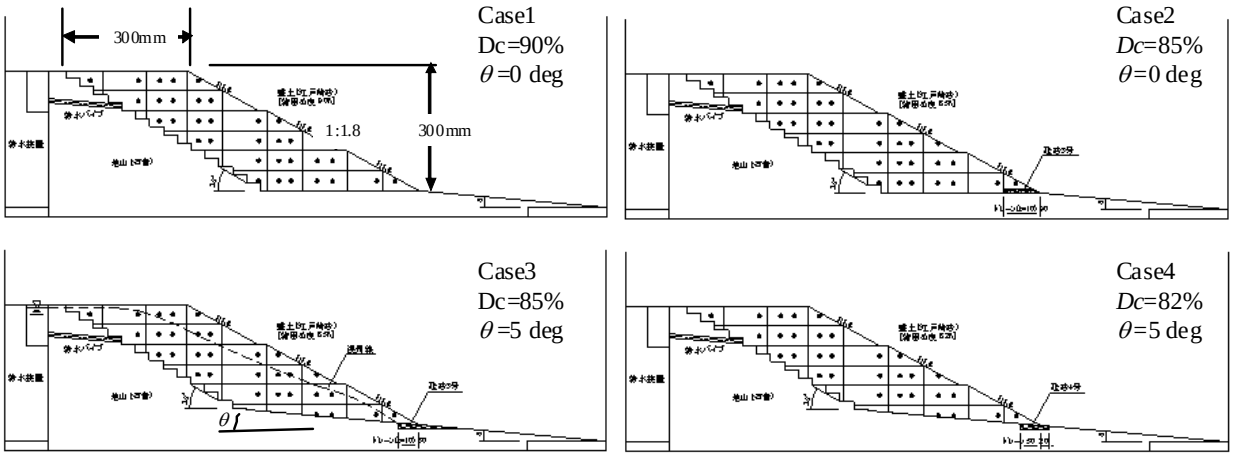

Fig. 6 Cross section of the model tests in the series A (unit in mm and shown in model scale)

Table 1 Summary of test condition in the series A

Case	Applied centrifugal acceleration (G)	Height of embankment in prototype scale (m)	Degree of compaction; *D*c (%)	Inclination of bedrock; θ (degree)	Length of the drainage layer in prototype scale(m)
Case 1	50	15	90	0	
Case 2	50	15	82	5	
Case 3	50	15	85	5	
Case 4	50	15	82	5	

damaged site shown in Figs 1 and 2 are also indicated in Fig. 4a as a reference. It is clearly shown that the embankment was constructed using the soils including fine contents of about 40%.

After the centrifugal acceleration was increased up to 50 or 75 G, the ground water level within the embankment was controlled by changing the water level in the water supply tank so as to achieve the target level. In controlling the ground water level before applying the shaking, the ground water level in the model embankment was precisely evaluated based on the measurement from the pore water pressure transducers, which were installed at the surface of the bedrock as schematically illustrated in Fig. 3.

After achieving the target ground water level, seismic load was applied by shaking the soil container horizontally using the irregular excitation as shown in Figs. 5a and 5b, which simulated the near field earthquake and plate boundary earthquake, respectively (JRA, 2002).

Detailed test conditions will be explained later in discussing the model test results.

3. RESULTS AND DISCUSSIONS

3.1 Effects of compaction and bedrock inclination

Two series of the model tests are conducted while the former one was conducted to investigate into the effect of the degree of compaction D_c of the embankment, which will be called as series A, hereafter. The latter series of the model tests are conducted to investigate into the effects of ground water level within the embankment, height of the embankment and subsoil conditions, while which will be discussed later.

The cross sections of the model and test conditions in the series A are shown in Fig. 6 and Table 1, respectively. These models were subjected to the shaking using the irregular excitation in Fig. 5a under the centrifugal acceleration of about 50G, thus the embankment height in the prototype scale was 15m. The drainage layers consisting of silica sand were prepared at the toe of the embankment as indicated in Fig. 6 and Table 1.

The drainage layers were prepared at the toe of the embankments so that the embankments would not deform largely in increasing the centrifugal acceleration and controlling the ground water level within the embankment. The ground water level within the embankments were kept at the same level among the series of the model tests based on the pore water pressure measurement, while the measured ground water level in Case 3 immediately before the shaking

is typically illustrated in Fig. 6.

Time histories of the settlement d_v measured at the top of the slope during the shaking are shown in Fig. 7. Importance of the degree of compaction D_c of the embankment was confirmed in comparing the test results from Cases 1 to 4. Even though the same excitation was used for the shaking in these tests, the residual value of d_v in Case 1, where the degree of compaction D_c of embankment was equal to 90 %, was smaller than those of Cases 2, 3 (D_c=85%) and 4 (D_c=82%).

Effect of the bedrock inclination θ is also observed in Cases 2 and 3. Although the bedrock inclination was not so large, the settlement of Case 3 (θ = 5 degree) was larger than the one of the Case 2 (θ= 0 degree). This behavior indicates that the inclination of the bed rock shall be properly removed by conducting foundation treatments.

The largest settlement was observed in Case 4 although the residual settlement could not be properly measured due to the over scaling of the displacement transducer. In Case 4, the settlement of the embankment continued to increase even after the shaking, although such behavior was not observed in the other cases. The continuous deformations after the shaking observed in Case 4 was possibly triggered by the local increase of the excess pore water pressure at the toe of the embankment as indicated in Fig. 8.

Time histories of the excess pore water pressure at the toe of the embankment in Cases 1 to 4 are compared in Fig. 8. Generated excess pore water pressure did not dissipate even after the end of shaking in Case 4, while such behaviors were not observed in the other cases. Even though the maximum amplitude of the excess pore water pressure in Case 4 was about 75 % as compared to the effective overburden pressure (i.e. far from the occurrence of the liquefaction), the embankment showed fluidal deformation which is usually observed in the liquefied soils.

The other series of the model tests were also conducted so as to investigate into the effect of the ground water level in the embankment, which was also highlighted as the important factor in investigating the earthquake-induced damage of the mountainous embankment during the recent large earthquakes.

3.2 Model tests on the effect of water level within the embankment

The other series of the model test was conducted so as to investigate into the effects of the water level within the embankment and drainage layers on the seismic behavior of the mountainside embankment. The cross sections of the model and test conditions are summarized in Figs. 9 and

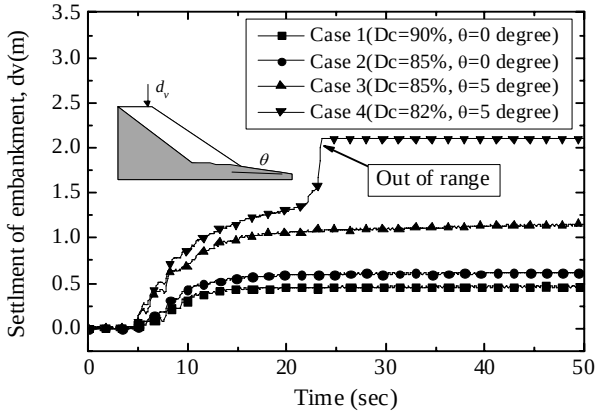

Fig.7 Time histories of settlement at the top of slope

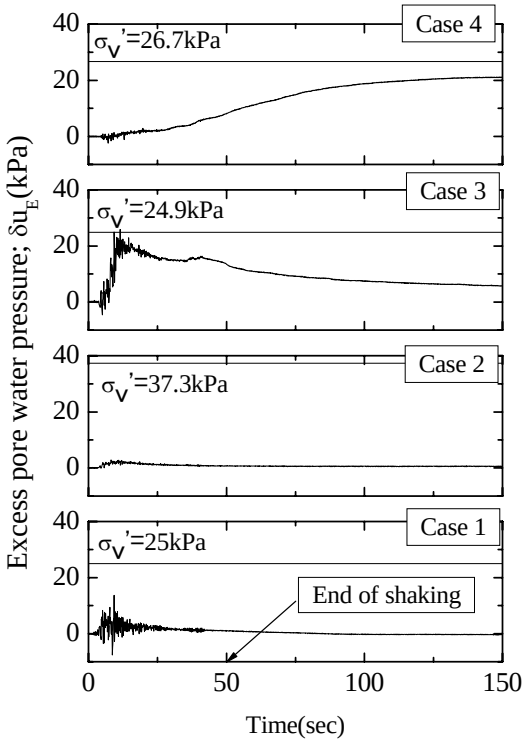

Fig.8 Time history of excess pore water pressure at the toe of the slope

Table 2, respectively. The height of the embankment, ground water level within the embankment and length of the drainage layer were highlighted in the series of the model tests.

In Cases 07_2 and 3, the value of the centrifugal acceleration was increased up to 75 G before the shaking whose test condition simulated that the embankment with the height of 30 m in the prototype scale was subjected to large earthquake. The heights of the model embankment were set equal to 15 m by applying the centrifugal

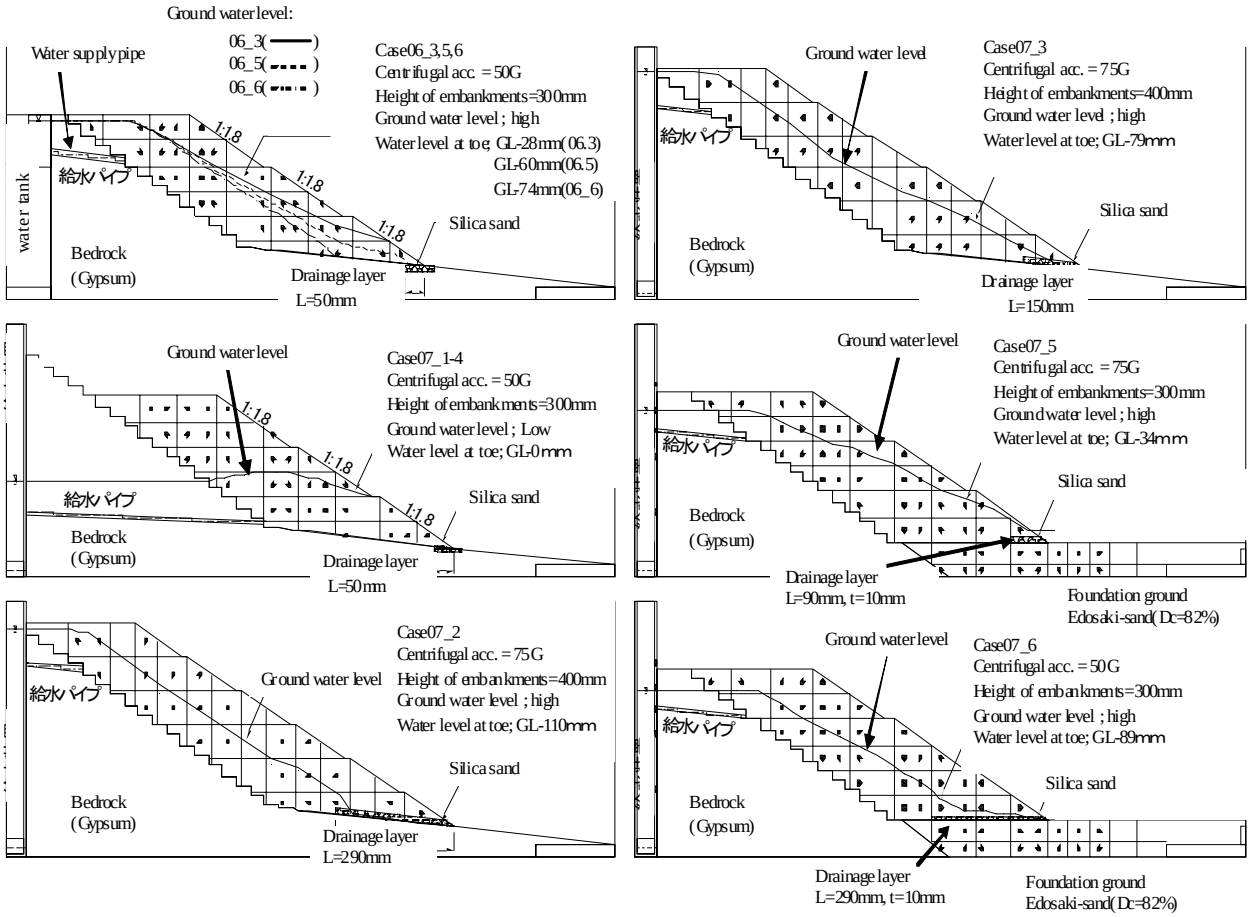

Fig. 9 Cross sections of the model tests (unit in mm and model scale)

Table 2 Summary of the model test conditions

Case	Centrifugal acceleration	Embankment Height	Foundation ground	Seepage water level		Drainage layer	Maximum base acceleration
				embankments	Toe of the slope		
06_3	50G	300mm* (15m)**	Gypsum (Bedrock)	High	GL-28mm (1.4m)	Silica sand L=50mm(2.5m)	47.4G
06_5					GL-60mm (3.0m)	Silica sand L=50mm(14.5m)	47.8G
06_6					GL-74mm (3.7m)	Silica sand L=50mm(14.5m)	45.3G
07_1-4				Low	GL-0mm (0.0m)	Silica sand L=50mm(2.5m)	41.5G
07_2	75G	400mm (30m)		High	GL-110mm (8.3m)	Silica sand L=50mm(21.8m)	21.5G
07_3					GL-79mm (5.9m)	Silica sand L=50mm(11.3m)	21.5G
07_5	50G	300mm (15m)	Edosaki sand (D_c=82%)		GL-34mm (1.7m)	Silica sand L=50mm(4.5m)	42.7G
07_6					GL-89mm (4.5m)	Silica sand L=50mm(14.5m)	43.2G

*model scale
**value in gravitational field

acceleration of 30 G. in the other cases.

In Cases 07_5 and 6, the foundation of the model embankment was prepared by loosely compacted Edosaki sand so as to investigate into the effect of liquefaction occurrence in the foundation layer on the seismic behavior of the embankment.

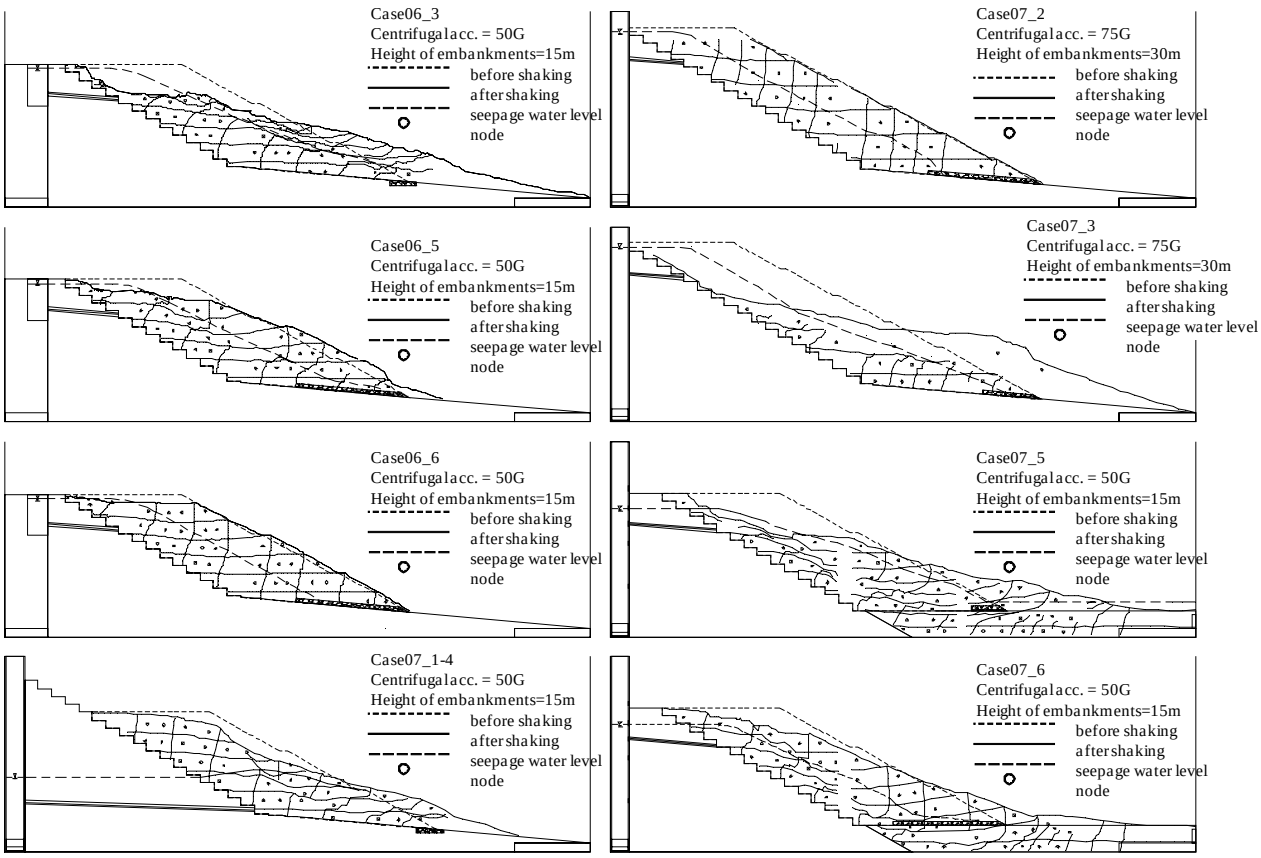

Fig. 10 Cross sections of the model embankments after shaking

The ground water level within the embankment was controlled by changing the length and materials of the drainage layer installed at the toe of the embankment and the height of the water supply pipes as schematically illustrated in Figs. 9. The ground water level in Case 07_1-4 was controlled to be low at the middle height of the embankment while although the high level was kept at the toe of the embankment as schematically illustrated in Figs. 9.

Seismic excitations were applied using the irregular shaking as shown in Figs. 5 after the ground water level became the steady state under the target centrifugal acceleration.

The model embankments after the shaking are schematically illustrated in Figs. 10. It should be emphasized that the model embankment in Case 06_3, where the ground water level at the toe of the embankment was high, deformed in the same manner with the observation in the actual site as schematically illustrated in Fig. 2. It should be also noted that the deformations of the model embankment became more significant in the cases where the ground water level within the embankment especially at the toe of the embankment located at higher level.

Relationships between the residual settlement of the embankment and normalized water level within the embankment are summarized in Fig. 11. All the values shown in Fig. 11 are in the prototype scale. As also schematically illustrated in Fig. 11, the normalized water level is an index to show the water level at the toe of the embankment.

The effect of the normalized water level on the deformation of the embankment was typically observed by referring to Cases 06_3, 5 and 6, where the ground water levels were controlled by changing the length and materials of the drainage layer at the toe of the embankment. In these tests, the residual settlements increased with the increase of the values of normalized water level.

The similar tendency with Cases 06_3, 5 and 6 was also observed in the Cases 07_2 and 3 where the height of the embankment was 30 m, while the settlement of the embankment increased more significantly with the increase of the normalized ground water level as compared with the cases where the embankment height was 15 m.

On the other hand, the residual settlement in Case 07_1-4 was smaller regardless of the high water level at the toe of the embankment because the ground water level at the upper part of the embankment was lowered in this test.

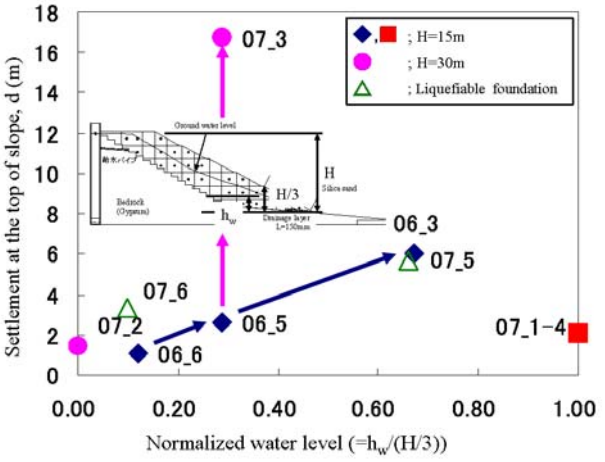

Fig. 11 Relationships between settlement and water level

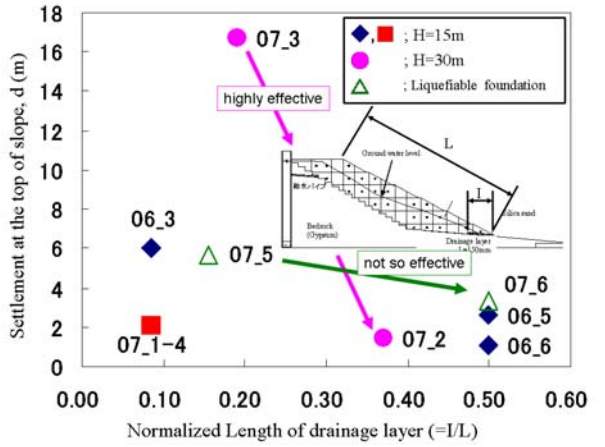

Fig. 12 Relationships between settlement and drainage layer

The above discussion indicates that the lowering of the water level within the embankment will be highly effective in improving the seismic performance of the mountainous embankment.

The effect of the liquefaction in the foundation layer of the embankment is also observed in Cases 07_5 and 6. As schematically illustrated in Fig. 10, the deformations of the model embankment in these tests seemed to be more catastrophic due to the deformation of the subsoil as compared with the other cases. It should be also emphasized that the lowering of the ground water level (Case 07_6) was not so effective in reducing the settlement of the embankment as compared with the other cases because the embankment was subjected to the settlement due to the liquefaction induced deformation in the foundation layer.

Length of the drainage layer is highly important in the practical design as a countermeasure for improving the

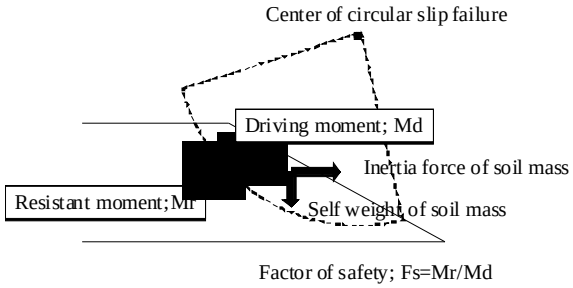

Fig. 13 Schematic diagram of the circular slip analysis

seismic performance of the embankment. Relationships between the normalized length of the drainage layer and settlement of the embankment are summarized in Fig. 12. Normalized length of the drainage layer is evaluated by normalizing the length of the drainage layer with the slope length as schematically illustrated in Fig. 12. The settlement of the embankment reduced with the increase of the drainage layer. In the tested condition, it was found that the settlement of the embankment can be effectively reduced by installing the drainage layer with the normalized length of about 0.4 except for cases 07_3 and 4 where the foundation layers were liquefied

Based on the results from the series of the centrifuge model tests, it was found that the seismic performance of the mountainous embankment is highly dependant on the degree of compaction, height of the embankment, ground water level and subsoil conditions. Therefore, the effects of these factors shall be properly taken into account in the design methodology. In this paper, it is also attempted to examine the applicability of the Newmark's method to evaluate earthquake induced deformation of the embankment for the further introduction to the practical design.

4. DEFORMATION ANALYSES

Pseudo static limit equilibrium procedure based on the circular slip analysis is usually adopted for the seismic design in the current design guideline of Japanese road embankment (JRA, 1999) as schematically illustrated in Fig. 13. This procedure is highly convenient as the practical design methodology because of the simplicity, while the result of the analyses is achieved as the factor of safety whose definition is also indicated in Fig. 13. As defined in Fig. 13, the factor of safety is evaluated as the ratio of the resistant moment to the driving moment. Therefore, it is difficult to evaluate the residual state of the embankment from the current design methodology because the factor of safety is not directly linked to the deformation of the

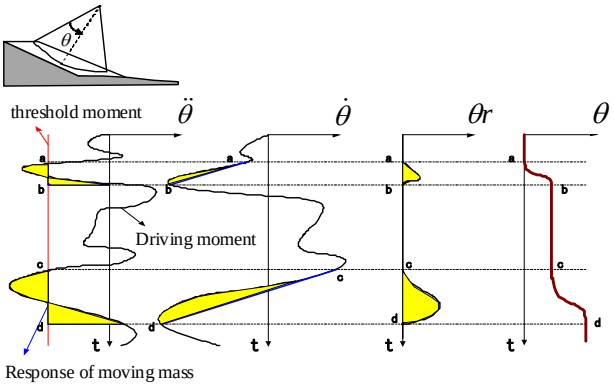

Fig. 14 Concept of Newmark's deformation analyses

Table 3 Summary of the input parameters

Input acceleration	Base acceleration
Gs (g/cm^3)	2.657
Maximum dry density, ρ_{dmax} (g/cm^3)	1.604
Fine contents; *Fc*(%)	6.9
Mobilized angle of internal friction, ϕ (degree)	32.8
Cohesion, *c* (kPa)	6.9

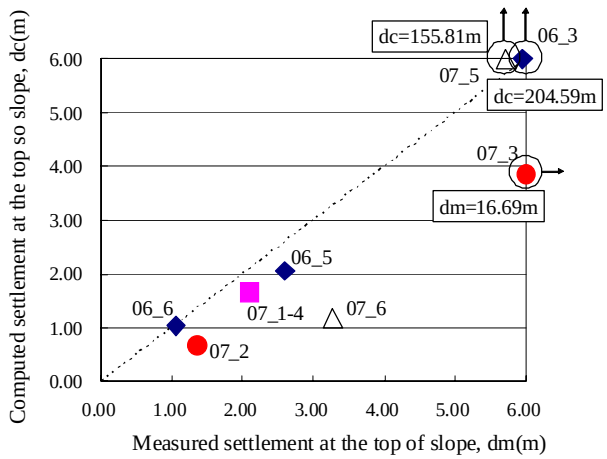

Fig. 15 Result of simulation

embankment after the earthquake.

On the other hand, there is the apparent trend to shift the design procedure to performance based design from the conventional factor of safety-based procedure in Japan. In the performance based design of the embankment, the seismic performance of the embankment will be typically evaluated by comparing the residual deformations with the allowable ones whose values are different depending of the required performances of the embankment (RTRI, 2007).

Based on the above background, it is also important to develop a methodology to evaluate the earthquake-induced deformation of the embankment. Therefore, it is also attempted in this study to apply Newmark's method in evaluating the residual deformation of the embankment in the series of the model tests.

The basic concept of Newmark's method is schematically illustrated in Fig. 14. Residual deformation of the embankment can be evaluated by the double integration of the difference between the driving moment and threshold moment. The values of threshold moment in the following simulation are evaluated as the resistant moment when the factor of safety became unity (i.e. resistant moment and driving moment are equal to each other) in the conventional circular slip method as shown in Fig. 13.

In the following simulation, the ground water level within the embankment was set to the steady state, which can be evaluated from the pore pressure measurement immediately before the shaking. The parameters showing the soil strength of the embankment are evaluated from the relevant soil testing as summarized in Table 3. It should be emphasized that the measured base acceleration is used as the input acceleration in the following analysis.

Results of the analyses and comparisons of the evaluated displacement with the measured ones are summarized in Fig. 15. Calculated settlements increased with the increase of the measured ones in general, which means that the Newmark's method can be applicable to evaluate the seismic performance of the embankment in terms of the residual deformations. Especially in Cases 06_6, 07_1-4 and 06_5 where the ground water at the toe or within the embankment were lowered, the calculated settlements corresponded well with the measured ones even in the quantitative comparisons.

On the other hand, the calculated settlements were much larger than the measured ones in Cases 06_3 and 07_5 where the ground water levels at the toe of the embankment were higher than the other cases. In the presented Newmark's deformation analyses, it was assumed for the simplicity that the deformation of the embankment can be modeled as the relative displacement between the two rigid mass (i.e. relative displacement between the moving soil mass and the embankment as schematically illustrated in Fig. 13). However, the actual deformations of the model embankments in Cases 06_3 and 07_5 were not like the relative displacement between the two rigid mass but fluidal deformations as schematically illustrated in Fig. 10. The neglect for the effect of fluidal deformation properties of the

embankment is thought to be the reason for large discrepancy between the calculated and measured settlements.

It should be also noted that the effect of the possible liquefaction at the foundation layer in Cases 07_5 and 07_6 were not also taken into account in this analyses, which would be the reason for the underestimation of the deformation in the simulation on Case 07_6.

In contrast with Case 07_6, the calculated settlement in Case 07_5 was greatly overestimated as compared with the measured one. This is possibly because the effect of the high ground water level on the result of the Newmark's deformation analyses was more significant than the effect of the un-conservative assumption on neglecting the occurrence of liquefaction in the foundation layer.

The calculated settlements in Cases 07_2 and 07_3, where the height of the embankment was 30 m, were smaller than the measured ones possibly because the effect of the response amplification was neglected by using the base acceleration as the input acceleration for the deformation analyses.

Two aspects should be emphasized based on the above discussions. First, the result of the Newmark's deformation analyses was highly sensitive to the ground water level within the embankment. Second, the effect of the amplification seems to be considered especially in cases of the high embankment.

5. SUMMARY

Knowledge achieved from the series of the dynamic centrifuge model tests and relevant deformation analyses using Newmark's method can be summarized as follows.

1. High degree of compaction, which could be achieved by the good compaction, would be highly effective in improving the seismic performance of the embankment.
2. High ground water level within the embankment caused large earthquake-induced deformation because of the occurrences of fluidal deformation, which seemed to be triggered by the local deformation at the toe of the embankment.
3. Lowering the ground water level at the toe of the embankment by installing the drainage layer was also effective in reducing the settlement of the embankment.
4. Calculated displacements using Newmark's method agreed well with the measured ones in case the ground water level within the embankment was lowered.
5. Calculated displacement obtained from Newmark's deformation analyses in the presented procedure did not correspond well with the measured ones in the cases of high ground water level or the high embankment.
6. Above discrepancies between the model test results and simulations are possibly because the effects of the amplification and the fluidal deformation were not taken into account in the presented simulation, which were found to be significant based on the model test results.

References:

Japan Road Association (1999), Road Earthworks –Design guideline for retaining walls– (in Japanese)

Japan Road Association (2002), Design specifications of highway bridge part 5, Seismic division

Koseki, J., Watanabe, K., Tateyama, M. and Nakajima, S.(2007), Stability of earth structures of against high seismic load, Keynote lectures for 13th Asian Regional Conference on Soil Mechanics and Geotechnical Engineering, India, Proc. of the 13th Asian Regional Conference on Soil Mechanics and Geotechnical Engineering, Vol.2, pp. 222-241.

Newmark, N.M. (1965), Effects of earthquake on dams and embankments, Geotechnique, Vol.15, No.2, pp.139-159.

Ohkubo, K., Fujioka, K. and Yasuda, S. (2009) , Slump failure of highway embankments during the 2004 Niigataken Chuetsu earthquake in Japan, Proc. of International Conference on Performance-Based Design in Earthquake Geotechnical Engineering - from case history to practice -, Tsukuba, pp.71-82.

Railway Technical Research Institute (2007), Design standard for railway earth structures (in Japanese), Railway Technical Research Institute (ed), Maruzen.

JOINT CONFERENCE PROCEEDINGS
7th International Conference on Urban Earthquake Engineering (7CUEE) &
5th International Conference on Earthquake Engineering (5ICEE)
March 3-5, 2010, Tokyo Institute of Technology, Tokyo, Japan

DIFFERENCE BETWEEN VISCOUS DAMPING AND HYSTERESIS DAMPING IN EARTHQUAKE RESPONSE ANALYSIS OF GROUND

Nozomu Yoshida[1)]

1) Professor, Department of Civil and Environmental Engineering, Tohoku Gakuin University, Japan

Abstract: A common sense that hysteresis damping can be treated same as viscous damping characteristics if they are expressed by the same definition as damping constant is shown not to hold under large earthquakes. A stress-strain model that can control damping characteristics arbitrary is used in a case study. It is found that hyperbolic model which shows much larger damping than that of Hardin-Drnevich model causes larger response spectrum at a frequency range important in the geotechnical engineering, because high frequency behavior becomes more frequent in the case with larger damping constant than that in the smaller damping constant or less stiffness. On the other hand, peak acceleration at the ground surface under a large earthquake is controlled by the weakest shear strength regardless of damping constant.

1. INTRODUCTION

Nonlinear characteristics of soil under earthquake loads is expressed as shear modulus and damping ratio as functions with respect to shear strain amplitude or, so called, G-γ and h-γ relationships, where G, h and γ denote secant shear modulus, damping constant (will be called the hysteretic damping constant in the following) and shear strain amplitude, respectively. Here, hysteretic damping constant h is defined as a ratio of the energy absorbed in a hysteresis loop to the strain energy, by dividing 4π. This definition means that the hysteretic damping constant can be treated same as the damping constant which is evaluated from viscous damping (it will be called viscous damping constant in the followings in order to distinguish the hysteretic damping constant).

In the field of the earthquake response of grounds, both stiffness and damping characteristics have been believed to be important factors. However, it seems not to be well understood the difference between the hysteretic and viscous damping constants related with the nature of the input motion. If input motion is a sinusoidal wave and steady state response is of interested, both hysteretic and viscous damping may show the same response. However, we are dealing with earthquake motion, a random type wave.

Theoretically, a hysteretic damping constant can take a value up to $2/\pi$, whereas the viscous damping constant can take arbitrary value. This difference comes from the definition of the damping constant as described at the beginning. It indicates that hysteretic damping and shape of the hysteresis loop or stress-strain curve is strongly related. It is well known that shape of the stress-strain curve affects the whole behavior of the ground. Therefore, hysteretic damping characteristics affect not only to decrease ground shaking but alto whole behavior of the ground.

As discussed in this paper later, the hyperbolic stress-strain model shows the hysteretic damping constant much larger than that of actual soils. It is also frequently observed that acceleration of the ground calculated by using the hyperbolic model is smaller than the case by using another stress-strain model such as the Ramberg-Osgood model. Therefore, it is frequently concluded that the hyperbolic model shows much larger damping constant, resulting in smaller acceleration or deamplification because of the larger damping ratio that the hyperbolic model has.

On this deamplification, the authors showed another possibility through the earthquake response analysis during the 1995 Hyogoken-nambu (Kobe) earthquake (Suetomi and Yoshida, 1998); deamplification of the earthquake motion occurs if there are soft soils such as Holocene clay. It succeeded to explain why the damage ratio of wooden residential houses is smaller near the shore and why south (shore side) boundary of the seismic belt zone with severe earthquake motion of seismic intensity I_{JMA}=7 (maximum intensity) existed north from theoretically expected boundary. After that Suetomi et al. (2000) confirmed that the peak acceleration at the ground surface and seismic intensity have upper boundary associated by the shear strength of the weakest layer. It indicates that amplification of the ground is determined regardless to the damping characteristics. In other words, effect of the hysteretic damping constant is not the one we knew from the vibration characteristics of a single-degree of freedom system with the viscous damping constants. It is, however, difficult to confirm it by numerical analyses because of the reasons described in the next

section.

If effect of stress-strain curve on the response of the ground is discussed, shape of the hysteresis loop is also to be discussed. This rule this paper, difference of the stiffness at unload will also be discussed.

2. MODELING OF HYSTERESIS CURVE

Hysteresis curves are calculated from the skeleton curve by applying the Masing's rule in many constitutive models. It is a convenient rule to handle or to develop computer codes because no other information except the skeleton curve is necessary in order to develop hysteresis curves. On the other hand, the Masing's rule does not hold in the actual soil. It can be easy recognized by considering the model proposed by Hardin and Drnevich (1972), for example. Damping characteristics obtained by applying the Masing's rule to a hyperbolic model shows quite different characteristics compared with the damping characteristics proposed by them. In spite of this clear fact, many computer codes used Masing's rule. It seems to come from the difficulty to control damping characteristics keeping the skeleton curve identical, which is the difficulty described in the previous section.

In order to overcome this shortage, the author had proposed a new hysteresis rule by which one can obtain damping characteristics that completely coincide with test result (Ishihara et al., 1985). This concept has been employed in several models (e.g., Iai et al., 1999; Railway Technical Research Institute, 1999). This model was extended by expressing a skeleton curve as an assemblage of piecewise linear or Lagrangean interpolated segments, by which one can obtain stress-strain model that perfectly agrees with arbitrary defined G-γ and h-γ relationships (Yoshida et al., 1990).

Figure 1 schematically shows the method to build a hysteresis curve that has arbitrary defined damping characteristics (Ishihara et al., 1985), where τ denotes shear stiffness, and the subscript R indicates unloading. Here, hysteresis curve should satisfy two requirements. The one is that if unload occurs at (τ_R γ_R), then it should pass axial symmetric point (-τ_R -γ_R). The other is that the hysteresis damping constant is to be equals to the specified value. A fictitious skeleton curve is introduced by which above two conditions are satisfied if Masing's rule is applied to this fictitious skeleton curve. Since there is two conditions, mathematical equation that has more than two parameters can be used as a the fictitious skeleton curve.

The simplest model that satisfy this condition is a hyperbolic model expressed as

$$\tau = \frac{G_0 \gamma}{1 + \gamma / \gamma_r} \tag{1}$$

where G_0 is a shear modulus at unload and γ_r is a parameter. It is noted that when this model is used for a skeleton curve, then G_0 indicates an elastic shear modulus G_{max}, and γ_r is a reference strain evaluated from shear strength τ_f as $\gamma_r = \tau_f / G_{max}$. However, in the hysteresis curve, they are mere parameters although G_0 has mechanical meaning that it is stiffness at the unload.; they are determined automatically under two conditions described above.

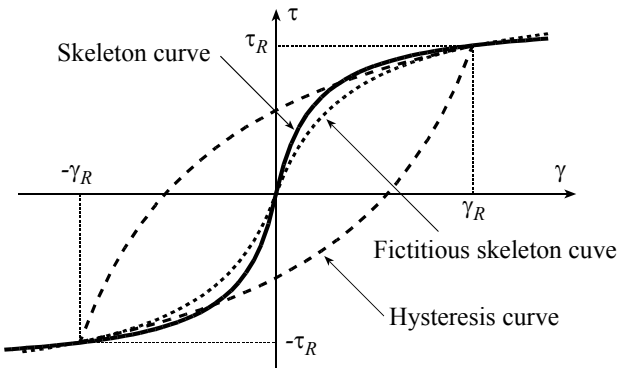

Figure 1. Hysteresis curve that developed from fictitious skeleton curve.

Since the hysteresis damping constant varies from zero to $2/\pi$, the theoretically maximum value, this model can be used under any damping ratio. In this sense, it is one of the most convenient and easy handling model although it has shortage that G_0 is also used as a parameter. If one wants to add an additional condition such that, for example, the shear modulus at unloads is equal to the elastic shear modulus G_{max}, he needs a model that uses more than two parameters.

In this paper, shear modulus at unload is also controlled in addition to strain dependent shear modulus and damping ratio, a model that has three parameters is required at minimum. The Ramberg-Osgood model is one of the relevant models, and frequently used model in the practice. This model is expressed as

$$\gamma = \frac{\tau}{G_0}\left\{1 + \alpha \tau^{\beta - 1}\right\} \tag{2}$$

where α and β are parameters. If Masing's rule is applied, damping ratio yields

$$h = h_{max}\left(1 - G / G_0\right) \tag{3}$$

where h_{max} is a maximum damping constant. Note that this equation is same with that proposed by Hardin & Drnevich (1972), which is the reason why the R-O model has been used in practice as well as a hyperbolic model. The maximum damping ratio h_{max} is calculated from a model parameters β as

$$h_{max} = \frac{2}{\pi}\frac{1 - \beta}{1 + \beta} \tag{4}$$

This equation can also be used to evaluate the value of β from test result.

Since values of h, G and G_0 are known at the unloading point, h_{max} is evaluated from Eq. (3). The value of β is evaluated by substituting h_{max} into Eq. (4). Finally the

value of α is computed from Eq. (2) by substituting these quantities. It is necessary to solve nonlinear equation in order to calculate parameters if the hyperbolic model is used for hysteresis curve, but they are sequentially obtained in the Ramberg-Osgood model.

3. MODELING OF STIFFNESS AT UNLOAD

In many constitutive models, stiffness at unload is defined to be same as initial or elastic modulus, but it may change. In order to grasp strain dependency of stiffness at unload, it is read from stress-strain curve of the Toyoura sand with relative density D_r = 50 and 80 % and Holocene clay sampled at Tokyo. Here, the stiffness is evaluated by using several data points just after the unload with respect to shear strain amplitude γ. They are shown in Figure 2 as solid circles and G_0 with ordinary secant modulus G (hollow circle). The solid line in the figure is a hyperbolic model

$$\frac{G}{G_{max}} = \frac{1}{1+\gamma/\gamma_r} \tag{5}$$

whose coefficient is chosen to fit the experiment; agreement with test result is good. Here, it is noted that both Eq. (5) and Eq. (1) are equivalent. The evaluated values are summarized in Table 1.

It is clearly seen that modulus at unload is not constant but depends on shear strain. These relationships are

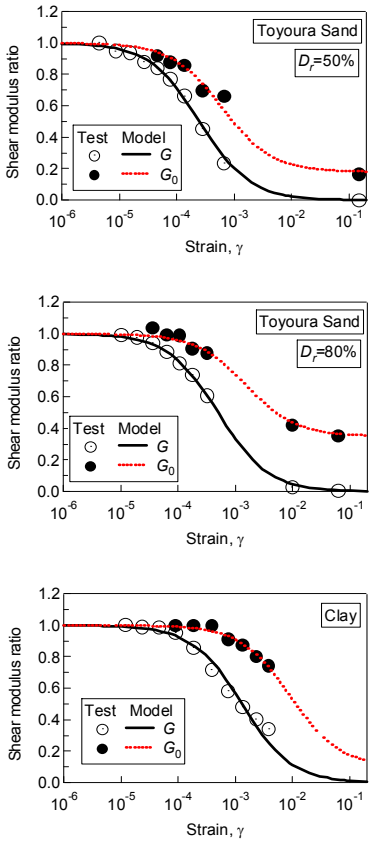

Figure 2. Shear modulus and stiffness at unload as a function with respect to strain

modeled into another hyperbolic model defined as

$$\frac{G_0}{G_{max}} = \frac{1-G_{min}/G_{max}}{1+\gamma/\gamma_{r0}} + \frac{G_{min}}{G_{max}} \tag{6}$$

where G_{min} is the minimum stiffness at unload, and γ_{r0} is reference strain for stiffness at unload. Dotted line in Figure 2 is a fitted curve and agreement with test result is as good as ordinary G-γ curves. The evaluated values are shown in Table 1, too. General tendencies of the curves are as follows:

1) γ_{r0} becomes greater as γ_r increases
2) G_{min}/G_{max} is larger for sand than that of clay

In the case of sand, two characteristics, i.e. decrease of stiffness as excess porewater pressure generates and increase of stiffness by cyclic mobility, seems key factors affecting the stiffness at unload. Since decrease of stiffness occurs at small strain where excess porewater generation is not expected, another factor, possibly a mere nonlinear behavior, also affects these characteristics.

Table 1 Evaluated model parameters

Material	γ_r	γ_{r0}	G_{min}/G_{max}
Sand (D_r=50%)	0.00025	0.0006	0.18
Sand (D_r=80%)	0.0005	0.0015	0.35
Clay	0.0013	0.013	0.1

4. A CASE STUDY

The effects of hysteretic damping and stiffness at unload is examined through a numerical study. A ground in Tokyo city area (Sato et al., 1998) shown in Figure 3 is used in this case study.

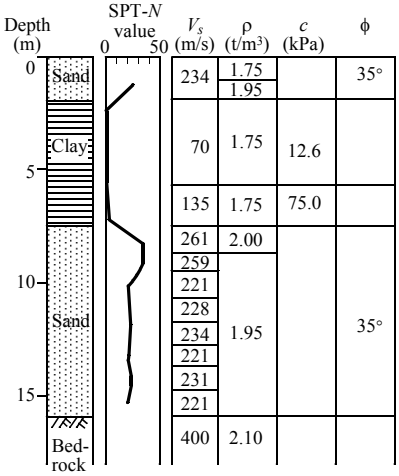

Figure 3. Soil profiles

4.1 Soil profiles and material

Dynamic deformation characteristics of this site are modeled into Hardin-Drnevich model by Sato et al. (1998). Model parameters are summarized in Table 2 and dynamic deformation characteristics are shown in Figure 6 as the H-D model (dashed line).

Three stress-strain models are used in this case study. All models have the same hyperbolic skeleton curve expressed as Eq. (1), but hysteresis curves are differently defined.

1) Hyperbolic model: ordinary hyperbolic model whose hysteresis loop is made by applying the Masing's rule to a skeleton curve. This model is referred as "Hyperbolic."
2) H-D model: damping characteristics is evaluated from Eq. (3). This model gives the same strain dependent shear modulus and damping characteristics proposed by Hardin and Drnevich (1972). Since the hyperbolic model is used for hysteresis curve, stiffness at unload cannot be controlled, but determined automatically. This model is referred as "H-D"
3) Same as "H-D", but hysteresis curve is made by means of R-O model. Therefore, stiffness at unload can also be controlled, and Eq. (6) is used to evaluate it. This model is referred as "H-D /w E". Note that both "H-D" and "H-D /w E" gives the same damping characteristics shown as H-D in Figure 6, and will be call H-D type model in the discussion, especially to compare with the hyperbolic model which shows much larger damping.

Damping characteristics of the hyperbolic model is also shown in Figure 6. As well known, the hyperbolic model shows much larger damping at large strain than that of the H-D model, but damping at small strain is nearly the same for both models. Figure 4 compares stress-strain curve of three models for shear strain amplitude of 0.6 % and 4 %, respectively. Curves are quite different between the hyperbolic model and two H-D type models, but that those by two H-D type models are similar to each other, which indicates that stiffness at unload may not be a key factor. There is not much allowance for stress-strain model to take variety shapes because the shape of the hysteresis loop is to be spindle shape and the area is defined.

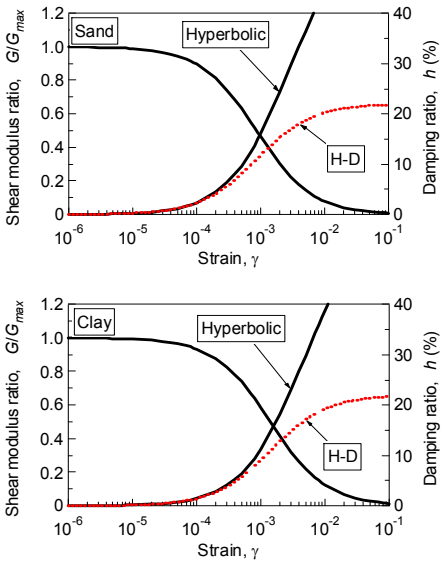

Figure 6. Dynamic deformation characteristics of sand and clay

Table 2. Model parameters

Material	γ_r	h_{max}	γ_{r0}	G_{min}/G_{max}
Sand	8.63×10^{-4}	0.22	0.002	0.4
Clay	1.42×10^{-3}	0.22	0.013	0.1

4.2 Earthquake motions

Two earthquake motions are chosen among the earthquake motions shown by Sato et al. (1998), which is shown in Figure 5. The one has limited number of large amplitude wave and the other large number of large amplitude wave, and are called shock wave and vibration wave, respectively. Since difference of damping characteristics appears at large strains, input earthquake motion is to be large enough to cause strong motion. Therefore, the waves are scaled so that peak acceleration becomes 8 m/s^2 at the outcrop base layer.

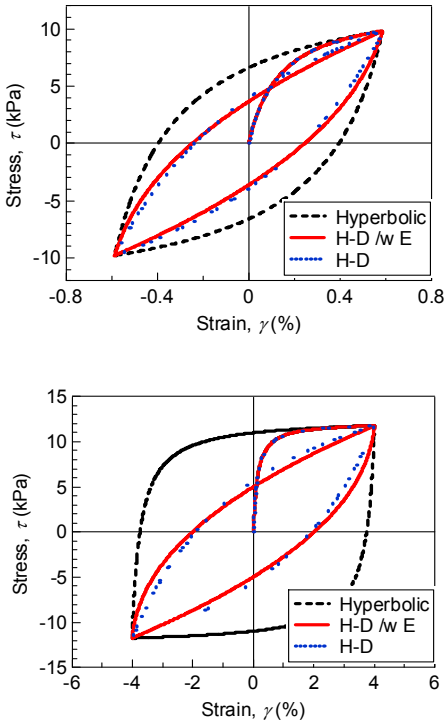

Figure 4. Stress-strain curve of clay

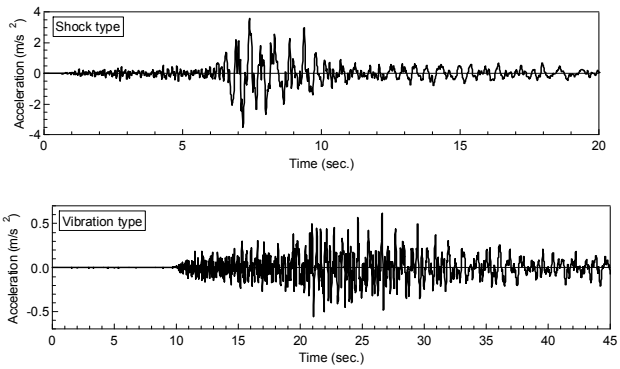

Figure 5. Earthquake motions to the engineering seismic base layer

4.3 Response under shock wave and discussion

Maximum response is shown in Figure 7. The maximum acceleration decreases rapidly at GL-5.8 m, resulting in about 2 m/s^2 at the ground surface. Since the layer between GL-3.8 and 5.8 m (clay layer) shows large strains of several percent, shear stress in these layer reaches shear strength, which can be confirmed through the chained line (shear strength) in Figure 7. If a layer reaches shear strength, acceleration above this layer reaches limit acceleration (Suetomi et al., 2000) because of the equilibrium condition of shear stress in this layer and inertia force above this layer. There is slight difference between the hyperbolic model and the H-D type models in the layer between GL-5.8 and 11.8 m; the hyperbolic model shows smaller acceleration. However, the difference is very small that we can say the response is identical in the engineering practice.

Comparison of acceleration time history at the ground surface is shown in Figure 8. Although there is less difference in peak response, there are significant differences between the hyperbolic model and the H-D type model in the waveform; the hyperbolic model show large number of large acceleration wave whereas the H-D type models show small amplitude waves after the peak acceleration.

As discussed by Suetomi et al. (2000) and in the preceding, acceleration at the ground surface is strongly affected by the nonlinear behavior of the weakest layer. In order to see the differences more clear, stress-strain curve of the 6th layer where shear strength is the smallest and maximum shear strain is the largest is shown in Figure 9 and time history of strain is shown in Figure 10.

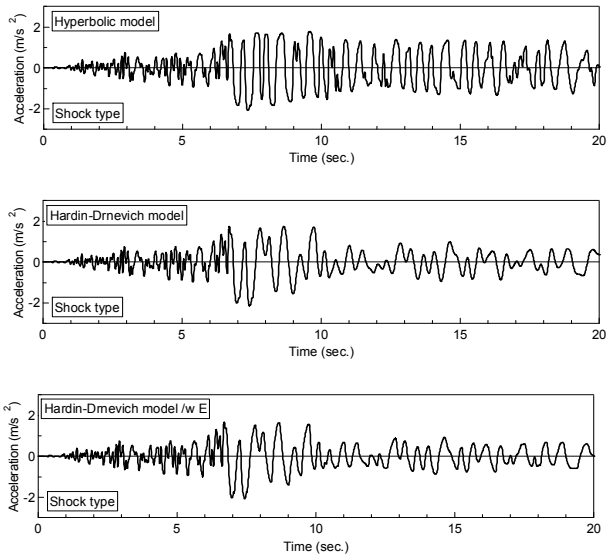

Figure 8. Acceleration time history at ground surface under shock wave

Maximum strain of several percents occurs at about 7.5 s following a relatively large spike at about 6.5 seconds with shear strain of about 1%. Shear strain is the largest in the hyperbolic model in both positive and negative sides. This is against the common sense that hysteresis curve with larger damping constant suppress the amplification resulting in smaller response (e. g., Railway Technical Research Institute, 1999). If, let suppose, earthquake motion is a mere pulse, then it is clear that only skeleton curve affects the maximum response and hysteresis loop does not affect it because maximum response occurs on the skeleton curve. Therefore, difference comes from the hysteretic behavior.

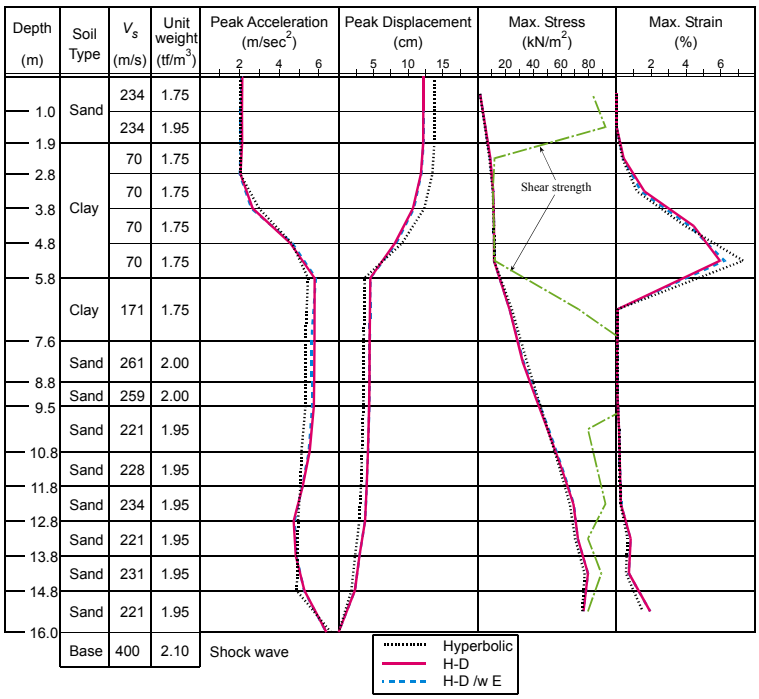

Figure 7. Maximum response under shock wave

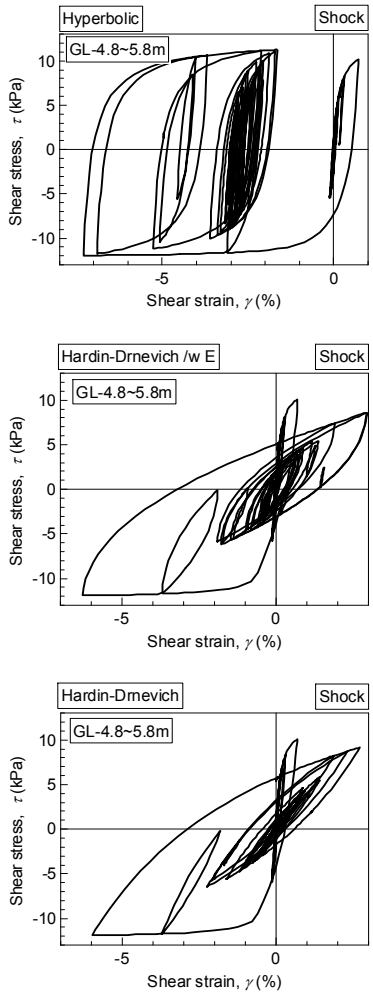

Figure 9. Stress-strain curves at 6th layer under shock wave

Since the hyperbolic model has large damping, stiffness after unload becomes larger than that of the H-D type model, which can be seen clearly in Figure 4 and Figure 9. Therefore, shear stress increase more rapidly than that of the H-D type models, which indicates that the hyperbolic model comes to large strain quickly. On the other hand, since the stiffness is smaller after unload in the H-D type models, larger strain is required to cause the same shear stress as the hyperbolic model. However, generating a larger strain requires more time. If unload occurs before it, shear stress at the cycle becomes smaller. This is the reason why the H-D type models show smaller shear stress amplitude after the maximum stress. This again explains why acceleration is smaller in the H-D type models than that in the hyperbolic model.

Finally acceleration response spectrum is shown in Figure 11. Acceleration is nearly identical in all models at period larger than 0.5 s, but that by the hyperbolic model is much larger than that by the H-D type models. This frequency range is important in the engineering practice. Therefore effect of shape of hysteresis loop is important in the earthquake response. It is also emphasized that model with larger damping ratio shows larger response acceleration.

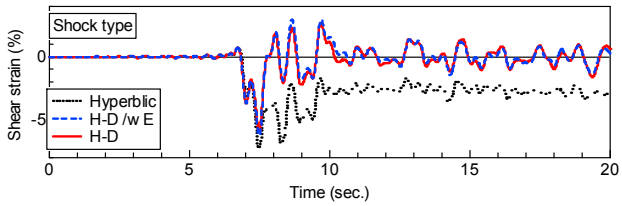

Figure 10. Stress-strain curve under shock wave

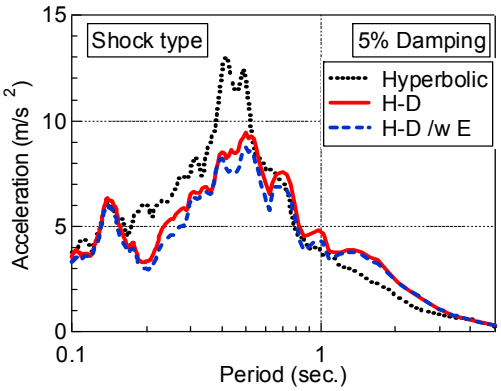

Figure 11. Response spectrum under shock wave

Differences between two H-D type models, that have same stiffness and damping characteristics but stiffness at unload is taken into account only in the proposed model in this paper, is not large; the behavior is quite similar. Regardless of the models, shape of the hysteresis loop must be in spindle shape. Therefore, if their areas are same, then the possible shape is limited. Actually the shapes of both models is quite similar as can be seen in Figure 4 and Figure 9. This is the reason why two H-D type models show similar behavior.

4.4 Response under vibration wave and discussion

Same as shock wave case, maximum response is shown in Figure 12, acceleration time history at the ground surface is shown in Figure 13, stress-strain curves are shown in Figure 14, time history of shear strain is shown in Figure 15, and acceleration response spectrum is shown in Figure 16.

The difference with shock wave can be clearly seen in Figure 14. Under the shock wave input, shear stress close to shear strength appears only a few times as can be seen in Figure 9, whereas it appears many times under the vibration wave. As discussed in the preceding, stiffness at unload is larger in the hyperbolic model than in the H-D type models. Therefore, it looks that average or representative stiffness is larger in the hyperbolic model compared with that in the H-D type models.

The maximum acceleration has the same nature as the case of shock wave, but differences from the case of shock wave becomes larger. In addition, decrease of acceleration is seen in GL-2.6 to 5.8 m, which is caused by the large strain

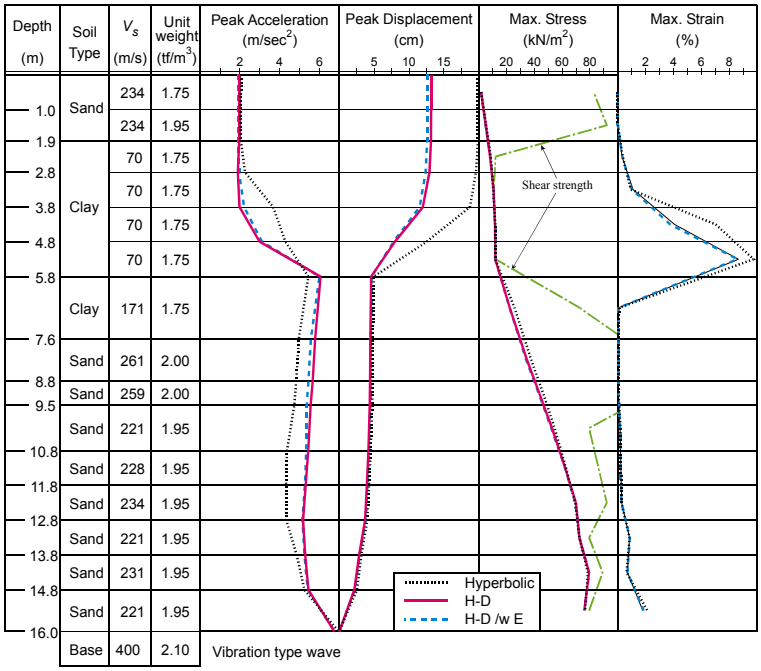

Figure 12. Maximum response under vibration wave

in this layer. Correspondingly, maximum displacement is larger in the hyperbolic model.

Looking at the acceleration time history at the ground surface, acceleration is smaller at the latter half in the H-D type models than that in the hyperbolic model, which is similar nature observed in the shock wave calculation. In addition, longer period wave seems to include more in the H-D type model than in the hyperbolic model. This can be explained easily by looking at Figure 14; stiffness is smaller in the H-D type models than in the hyperbolic model. Again, larger damping requires large stiffness at unload, resulting in small period wave.

Shear strain drifts in positive side at about 26 s in the hyperbolic model as can be seen in Figure 15, which is the

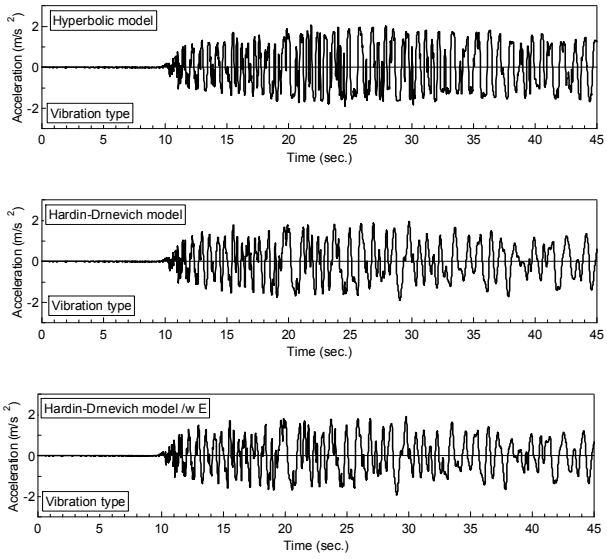

Figure 13. Acceleration time history at ground surface under vibration wave

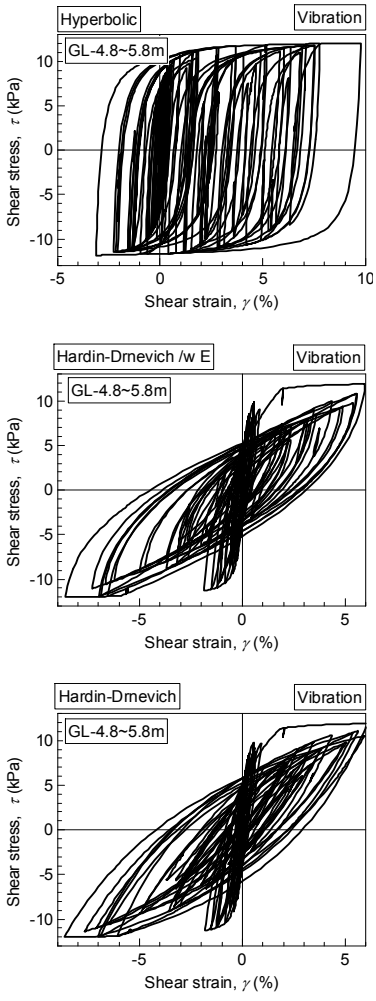

Figure 14. Stress-strain curve at 6th layer under vibration wave

reason why the hyperbolic model shows larger strain than the H-D models.

Finally, response spectrum shows smaller amplification at period longer than 1 s in the hyperbolic model, whereas is larger in the period shorter than 1 s. This behavior again can be recognized by looking at Figure 14. The difference between the hyperbolic model and H-D type models are larger under the vibration wave input than under the shock wave input.

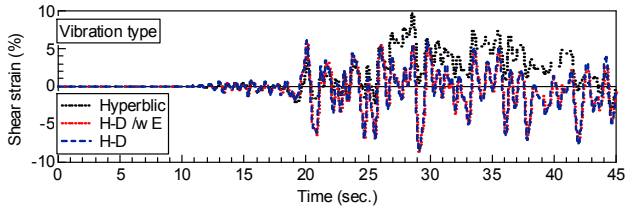

Figure 15. Strain time history at 6th layer under vibration wave

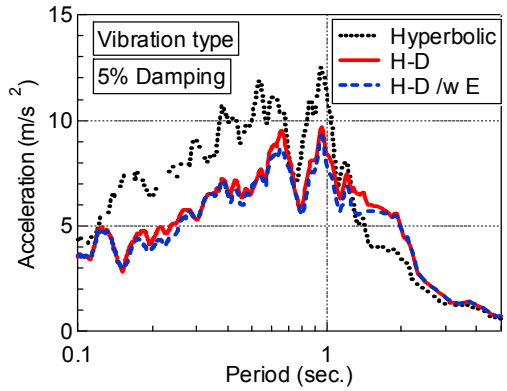

Figure 16. Response spectrum under vibration wave

5. CONCLUDING REMARKS

Difference of hysteresis damping from the viscous damping is discussed.

At first, it is emphasized that maximum acceleration at the ground surface is determined from the shear strength of the weakest layer, and it is not related to the damping characteristics. The hyperbolic model has a tendency to reach shear strength quickly compared with the other models, which is the reason why maximum acceleration is smaller in the case of the hyperbolic model than the case when other stress-strain models are used.

As for the effect of the hysteresis damping, the function of the hysteresis damping is not so simple as that of the viscous damping, because hysteresis damping strongly related to the stress-strain curve after unload. If hysteretic damping is larger, therefore, stiffness at unload becomes larger. As a result, change of shear stress becomes larger, because it takes less time than the case with smaller stiffness. Considering these, ground shaking includes more high frequency, but important frequency range in the engineering practice, component in the case with large hysteretic damping than that with smaller hysteretic damping.

Other findings are as follows:

1) Stiffness at unload decreases with strain, and it can be modeled by a hyperbolic equation with minimum stiffness.
2) Difference of hysteresis loop does not affect the maximum response significantly under large earthquakes. On the contrary, they affect hysteretic behavior after unload.
3) Effect to consider stiffness at unload is not large probably because shape of hysteresis loop is essentially similar if area of the hysteresis loop is the same.
4) Effect of damping characteristics is lager under vibration type earthquake than shock type earthquake.

References:

Hardin, B. O. & Drnevich, V. P (1972) Shear modulus and damping in soils: design equations and curves, *Proc. of the American Society of civil engineers*, 98 (SM7),.667-692

Ishihara, K., Yoshida, N. & Tsujino, S. (1985): Modelling of stress-strain relations of soils in cyclic loading, *Proc. 5th International Conference for Numerical Method in Geomechanics*, 1: 373-380

Iai, S., Matsunaga, Y. & Kameoka, T. (1999): Strain space plasticity model for cyclic mobility, *Soils and Foundations*, 32 (2): 1-15

Railway Technical Research Institute (1999): Design standard of railway facilities and commentary, *Maruzen*, Tokyo

Yoshida, N., Tsujino, S. & Ishihara, K. (1990): Stress-strain model for nonlinear analysis of horizontally layered deposit, *Summaries of the Technical Papers of Annual Meeting of AIJ*, Chugoku. B (Structure I), 1639-1640 (in Japanese)

Sato, M., Yasuda, S., Yoshida, N. & Masuda, T. (1998): Simplified method for estimating maximum shear stress in the ground during earthquakes, *J. of Geotechnical Engineering, Proc. JSCE*, 610/III-45: 83-96 (in Japanese)

Suetomi, I., Sawada, S., Yoshida, N. and Toki, K. 2000. Relation between shear strength of soil and upper limit of earthquake ground motion, *J. of Structural Mechanics and Earthquake Engineering, Proc. JSCE*, 654/I-52: 195-206 (in Japanese)

Suetomi, I. and Yoshida, N. (1998): Nonlinear behavior of surface deposit during the 1995 Hyogoken-nambu earthquake, Soils and Foundations, *Special Issue on Geotechnical Aspects of the January 17 1995 Hyogoken-Nambu earthquake*, 2, 11-22

JOINT CONFERENCE PROCEEDINGS
7th International Conference on Urban Earthquake Engineering (7CUEE) &
5th International Conference on Earthquake Engineering (5ICEE)
March 3-5, 2010, Tokyo Institute of Technology, Tokyo, Japan

SEISMIC DAMAGES OF MOUNTAIN TUNNELS IN JAPAN AND CASE STUDIES

Kazuhide Yashiro[1], Jun Saito[2], Tomomi Iura[3] and Jiro Takemura[4]

1) Assistant Senior Researcher, Railway Technical Research Institute, Japan
2) Assistant Professor, Department of Civil and Earth Resorses Engineering, Kyoto University, Japan
3) Chief, Japan Railway Construction, Transport and Technology Agency, Japan
4) Associate Professor, Department of Civil Engineering, Tokyo Institute of Technology, Japan
kyashiro@rtri.or.jp, saito-j@mbox.kudpc.kyoto-u.ac.jp, t.iura@jrtt.go.jp, jtakemur@cv.titech.ac.jp

Abstract: Since mountain tunnels are mainly surrounded by stable ground and its displacement upon seismicity is less, they are considered susceptible to seismic damage. However, many mountain tunnels have suffered damage from the 1923 Kanto Earthquake to the 2007 Niigataken-Chuetsu-Oki Earthquake. This paper shows an outline of the historical damage of mountain tunnels in Japan and result of case studies of damage to mountain tunnels.

1. INTRODUCTION

Since mountain tunnels are mainly surrounded by stable ground, its displacement upon seismicity is less, therefore, they are structures less susceptible to seismic damage to compare with other structures such as bridges and foundations. (Figure 1) However, earthquake-resistant tunnels are highly noted since the 2004 Niigataken-Chuetsu Earthquake occurred. Upon the foregoing earthquake, some tunnels located at disaster area were heavily damaged and have been impediment to reopening of Shinkansen and conventional lines. Especially, a concrete lining of the Uonuma Tunnel of the Jyoetsu Shinkansen located adjacent to the epicenter was heavily damaged and two- month time required for restoration. (Asakura et al. 1996, Shimizu et al. 2005 and Saito et al. 2007)

Owing to the progress of construction technology, more and more structures are being constructed by the tunneling method, and even tunnels need to have sufficient earthquake resistance. In this paper, we introduce case studies on the historical damage of mountain tunnels, an outline and assumed causes of damage by the foregoing earthquake.

2. HISTORICAL DAMAGE OF MOUNTAIN TUNNELS BY EARTHQUAKE

2.1 Outline of damage

Figure 2 summarizes the large-scale earthquakes which caused damage to mountain tunnels in Japan. There are five major earthquakes: the 1923 Kanto Earthquake, the 1978 Izu-Oshima-kinkai Earthquake, the 1995 Hyogoken-nanbu Earthquake, the 2004 Niigataken-Chuetsu Earthquake and the 2007 Niigataken-Chuetsu-oki Earthquake. The outline of damage of mountain tunnels will be respectively described below.

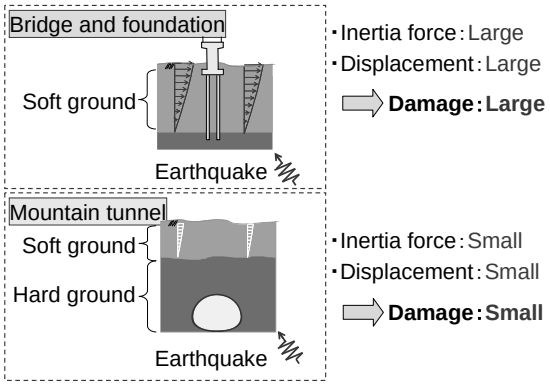

Figure 1 Difference of Behavior during Earthquake Between Bridges and Foundations and Mountain Tunnels

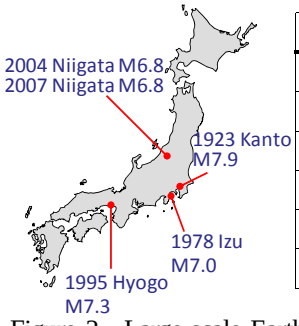

Earthquake	Total	Damaged
1923 Kanto	148	93
1978 Izu-Oshima-kinkai	31	9
1995 Hyogoken-nanbu	110	30
2004 Niigataken-Chuetsu	138	49
2007 Niigataken-Chuetsu-oki	20	6
TOTAL	447	187

Figure 2 Large-scale Earthquakes which Caused Damage to Mountain Tunnels in Japan

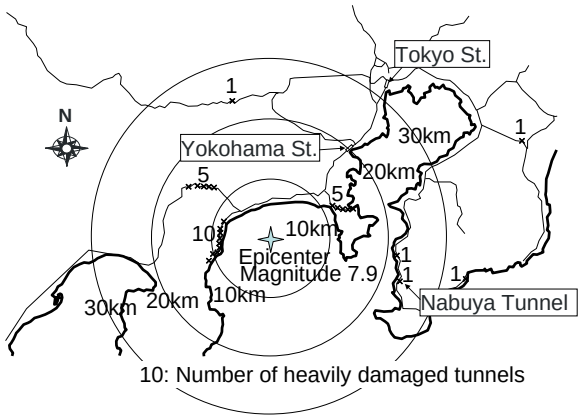

Figure 3 Distribution of Heavily Damaged Railway Tunnels upon the 1923 Kanto Earthquake

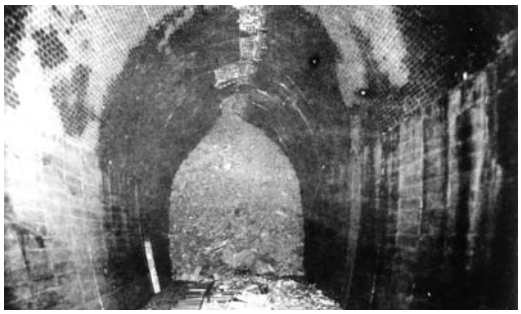

Figure 4 Collapse of the Nabuya Tunnel

2.2 1923 Kanto Earthquake

The 1923 Kanto Earthquake is the earthquake, which caused the largest damage to mountain tunnels. There were 148 railway tunnels located within a range of a 120-km radius area from the epicenter at the time, and 93 tunnels among them were damaged to be reinforced, and 25 tunnels to be reconstructed due to collapse of linings. (Figure 3) As an example of the heavily damaged tunnels, Figure 4 shows collapse of the Nabuya Tunnel. It is conceivable that a slide of an earthquake fault or a landslide caused the ground move to the tunnel and destructed a tunnel lining.

2.3 1978 Izu-Oshima-kinkai Earthquake

Upon the 1978 Izu-Oshima-kinkai Earthquake, nine railway tunnels suffered from damage. The largest damage is that of the Inatori Tunnel. (Figure 5) A fault crossing the tunnel slid upon the earthquake, a lining of the tunnel collapsed and the track alignment longitudinally displaced. A relative displacement of the fault was 70-cm horizontally and 20-cm vertically according to the results of surveying.

2.4 1995 Hyogoken-nanbu Earthquake

Upon the 1995 Hyogoken-nanbu Earthquake, 12 tunnels among 110 mountain tunnels located within a disaster area suffered serious damage and required repair and reinforcement. Figure 6 shows a distribution of heavily damaged railway tunnels. As a typical example, Figure 7 shows the damaged conditions observed at the Rokko Tunnel. Several damage patterns observed at various

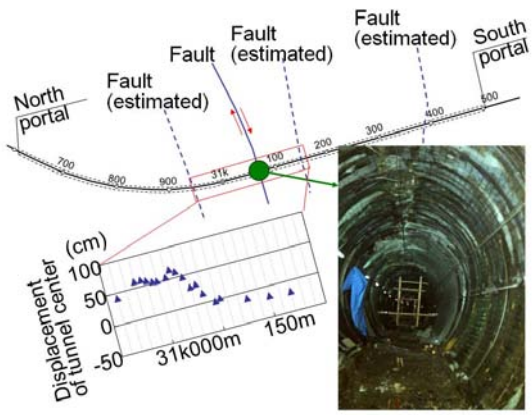

Figure 5 Damage of the Inatori Tunnel

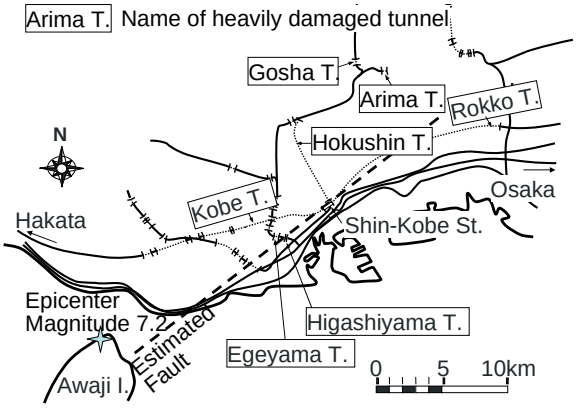

Figure 6 Distribution of Heavily Damaged Railway Tunnels upon the 1995 Hyogoken-nanbu Earthquake

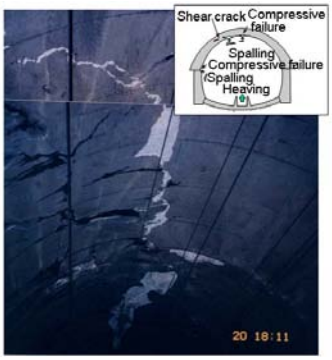

Figure 7 Damage of the Rokko Tunnel (Asakura et al. 1996)

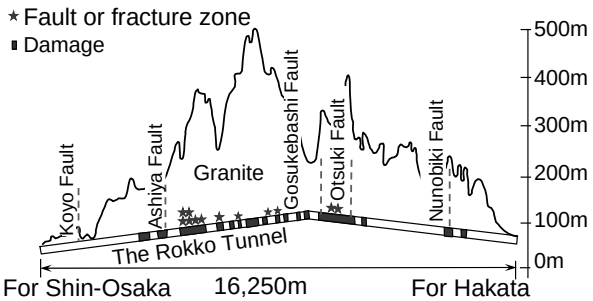

Figure 8 Longitudinal Profile and Damaged Locations of the Rokko Tunnel (Asakura et al. 1996)



Figure 9 Damage of the Higashiyama Tunnel (Asakura et al. 1996)

locations are superimposed in one figure. Typical damage was of compressive and shear failures at the arch of a lining and compressive failures with spalling at joints between the arch and sidewall, and it took two months until reopening. Figure 8 shows a longitudinal profile and damaged locations of the Rokko Tunnel. Almost all the damaged locations coincide with faults or fractured zones. Figure 9 shows a damage situation of the Higashiyama Tunnel. Typical damage was of crack on the shoulder of the tunnel portal.

2.5 2004 Niigataken-Chuetsu Earthquake

On October 23, 2004, a large earthquake of magnitude 6.8 occurred at latitude 37°17' N. and longitude 138°52' E., depth 13-km of Niigata prefecture in Japan. Due to this earthquake, a running Shinkansen train derailed and some mountain tunnels suffered from severe damage. Eleven tunnels had serious damage, and 25 tunnels required repair and reinforcement of linings. Figure 10 shows distribution of heavily damaged railway tunnels. It is obvious that heavily damaged tunnels concentrated at a limited area of approximately within a 10-km radius area from the epicenter. The most heavily damaged tunnel was the Uonuma Tunnel, which runs nearby the epicenter. The Uonuma Tunnel is a long railway tunnel driven in Neogene's mudstone with a length of 8,625-m. There were three heavily damaged sections in this tunnel. (Figure 11)

Figure 12 shows a damage situation of the most heavily damaged section. A concrete lining was broken to fall off to a track. The largest concrete block amounted to approximately $2m^2$ (5ton). Other observed damage consisted of reduction of a tunnel diameter, heaving of a roadbed concrete and cracking of an invert. This is the largest disaster among the Shinkansen tunnels after inauguration. The locations were restored by rock bolting, removal of the concrete by breakers, shotcreting, and reinforcement by mortal precast boards, however it became a critical path and took two months until reopening. There was another damage of the Myoken Tunnel of the Jyoetsu Shinkansen. This tunnel had a compressive failure at a crown (Figure 13) and an invert also heaved like the Uonuma Tunnel. At the Wanatsu Tunnel of the conventional line, there was a compressive failure at a crown and large brocks fell off a lining and steel supports of the tunnel were exposed. At the Tenno and Shin-Enoki Tunnel, bedrock collapsed and slid above the tunnel and cracks occurred on a lining.

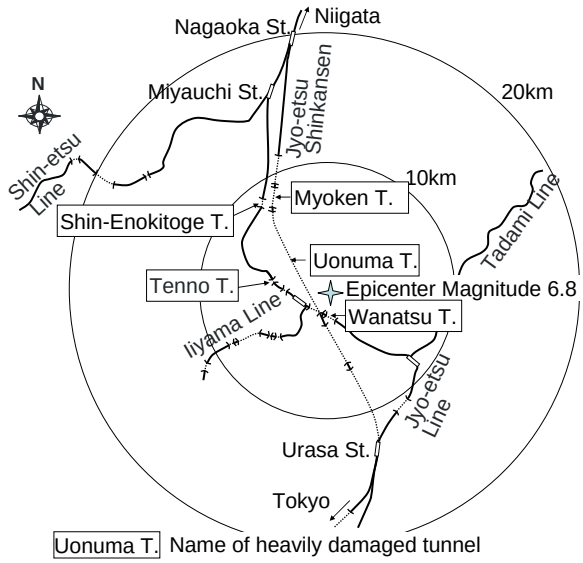

Figure 10 Distribution of Heavily Damaged Railway Tunnels upon the 2004 Niigataken-Chuetsu Earthquake

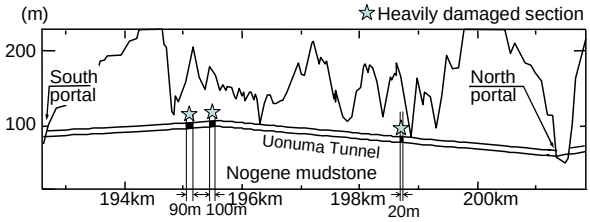

Figure 11 Longitudinal Profile and Damaged Locations of the Uonuma Tunnel



Figure 12 Damage of the Uonuma Tunnel

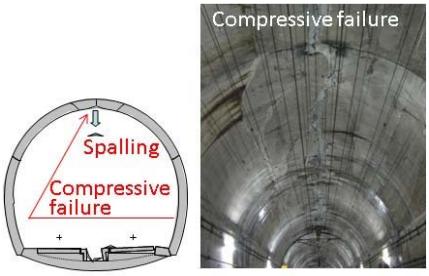

Figure 13 Damage of the Myoken Tunnel (Shimizu et al. 2005)

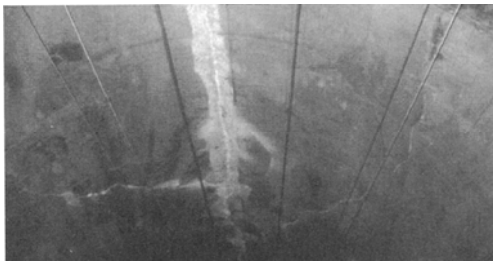

Figure 14 Damage of the Yoneyama 1 Tunnel (Saito et al. 2007)



Figure 15 Damage of the Yoneyama 2 Tunnel (Saito et al. 2007)

2.6 2007 Niigataken-Chuetsu-oki Earthquake

Upon the 2007 Niigataken-Chuetsu-oki Earthqake, four tunnels among 20 mountain tunnels located within a disaster area suffered serious damage, and five tunnels required repair and reinforcement. As a typical example, Figure 14 shows the damaged conditions observed at the Yoneyama 1 Tunnel and Figure 15 shows the damaged conditions observed at the Yoneyama 2 Tunnel. Typical damage was of compressive failures at the arch of a lining and compressive failures with spalling at joints between the arch and sidewall, and took two months until reopening.

3. CASE STUDIES ON DAMAGE OF EARTHQUAKE

3.1 Damage level

Table 1 shows the large-scale earthquake which caused damage to mountain tunnels in Japan. Figure 16 shows the composition of damage levels, that is "None", "Slight", "Medium" and "Large" according to the necessity of reinforcements and repair works. (Table 2) Approximately 20% of the damaged tunnels are classified into "Medium" or "Large", which needed reinforcements of repair woks. From such case studies, it is evident that even mountain tunnels suffered damage by an earthquake.

3.2 Conditions of damage

Susceptible conditions under which tunnels suffered from damage are provided that:

1. A great magnitude of an earthquake
2. Tunnels located adjacent to an epicenter or an earthquake fault.

Table 1 Large-scale Earthquake which Caused Damage to Mountain Tunnels in Japan

Name of earthquake	Magni -tude	Seismic intensity	Number of damaged tunnels					Note
			Large	Medium	Slight	None	Total	
Kanto	7.9	6	25	12	56	55	148	Only Railway
Izu	7.0	5	2	4	3	22	31	
Hyogo	7.2	7	12	-	18	80	110	
Chuetsu	6.8	7	11	14	24	89	138	
Chuetsu-oki	6.8	6+	4	1	1	14	20	
Total			54	31	102	260	447	

Table 2 Definition of Damage Level

Damage	Damage level
None	(No damage)
Slight	Needed neither reinforcements nor repair works
Medium	Needed reinforcements or repair works
Large	Needed serious reinforcements or repair works

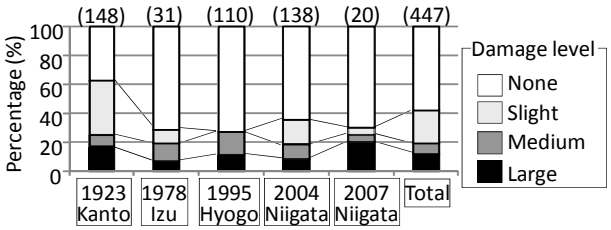

Figure 16 Composition of Damage Levels

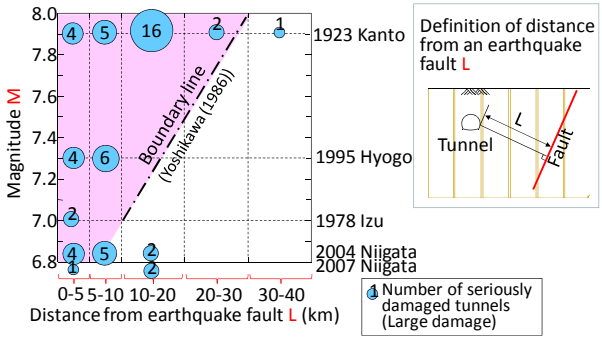

Figure 17 Relation of Distance from an Earthquake Fault, Magnitude of an Earthquake and Number of Heavily Damaged Tunnels

Figure 17 shows relation of distance from an earthquake fault, magnitude of an earthquake and number of seriously damaged tunnels ("Large" damage.) From this figure, we find that a risk of earthquake damage becomes large under on the condition of both 1 and 2. Roughly speaking, tunnels suffered serious damages at areas within 10km from an earthquake fault in the case of M7, and areas within 30km in the case of M8. Figure 18 shows relation between a distance from an earthquake fault and a percentage of damaged tunnels in the 1995 Hyogoken-nanbu Earthquake, the 2004 Niigataken-Chuetu Earthquake and the 2007 Niigataken-Chuetsu-oki Earthquake. From this figure, we find that damage that requires reinforcement occurred approximately within 10km from an earthquake fault. However, these figures have entirely not considered the conditions proper to tunnels such as the ground adjacent

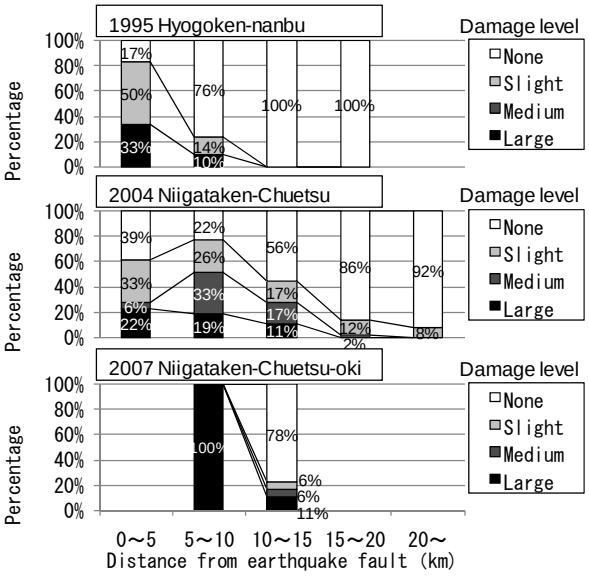

Figure 18 Relation between a Distance from an Earthquake Fault and a Percentage of Heavily Damaged Tunnels

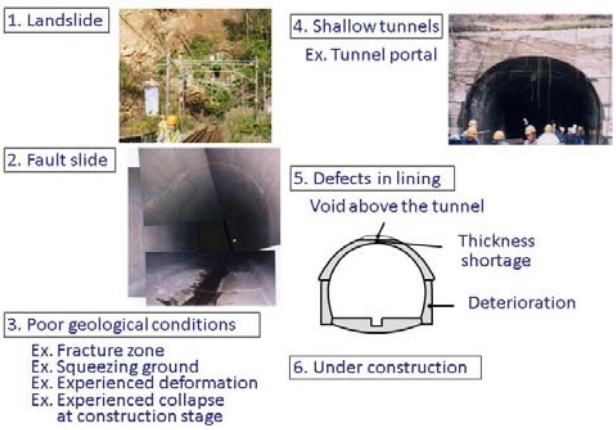

Figure 19 Definition of " Special Conditions" (Yoshikawa 1986)

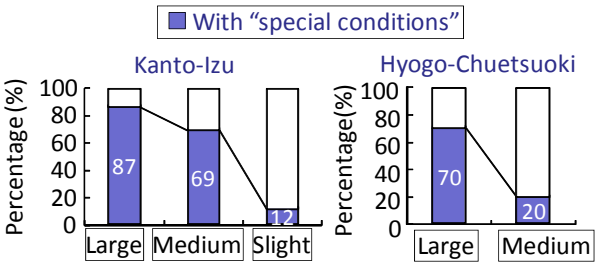

Figure 20 Number of Damaged Tunnels with the Special Conditions (from the 1923 Kanto Earthquake to 2007 Niigataken-Chuetsu-oki Earthquake)

to the tunnel and a tunnel structure and some tunnels even located farther than the boundary line defined by Yoshikawa(1986) have damaged seriously. This indicates that beside the magnitude and distance, there are some other factors or conditions which effect the damage of tunnel. Such factors or conditions are called "special conditions." According to Yoshikawa(1986), there are six "special

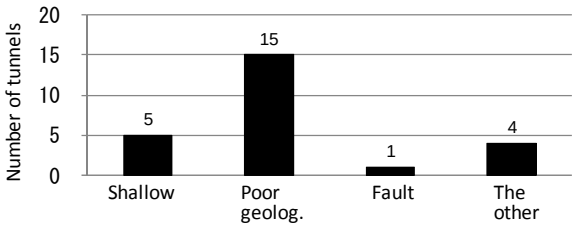

Figure 21 Number of Damaged Tunnel (Respective Types)

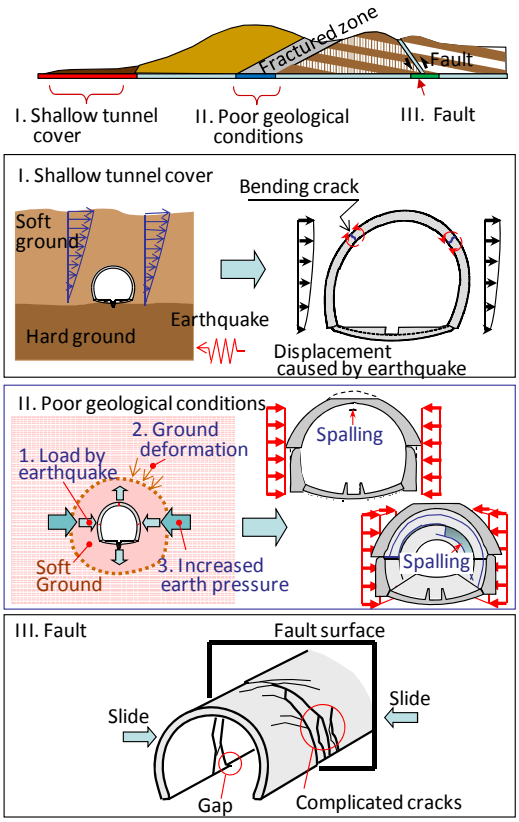

Figure 22 Classification of Damage Patterns and Supposed Damage Mechanism (Asakura et al. 2000 and Yashiro et al.2009)

conditions" as shown in Figure 19.

Figure 20 shows the ratio of the tunnels with special conditions according to damage level in the past 5 large earthquakes (from 1923 Kanto to 2007 Niigata.) From this figure, it is conceivable that tunnels with "Large" seismic damage have the special conditions more than tunnels with "Medium" and "Slight" damages, and when the tunnel has the special conditions, the special care is required for the seismic design.

3.3 Classification of damage patterns

From case studies, heavily damaged tunnels are able to be classified according to geological conditions into three patterns "Shallow tunnel cover", "Poor geological conditions" and "Fault". Figure 21 shows result of classified damage patterns on the earthquakes from the 1995 Hyogoken-nanbu Earthquake to the 2007 Niigataken-Chuetsu-oki Earthquake, for which various

valuable information and data remained. Figure 22 shows the classification of damage patterns and supposed damage mechanism.

Type 1: Shallow tunnel cover

This type is visible on tunnels with shallow cover. Typical example of this type is the damage of the Higashiyama tunnel (Figure 9.) In general, tunnels with shallow cover are likely to suffer from earthquake, as they often constructed in the loose ground where a seismic activity is amplified and the ground deforms largely. Cracks in the arch of the lining are characteristic of this type. It is conceivable that tunnels deform like shearing deformation by displacement of the earthquake and cracks occur at a shoulder part of an arch by bending moment.

Type 2: Damage of tunnels of poor geological condition

This type is visible on tunnels in the soft ground like a fractured zone, sometimes on tunnels of large earth covering. Typical example of this type is the damage of the Rokko tunnel (Figure 7.) If tunnels are constructed in the poor geological conditions, the ground around the tunnel is soft. So, it is conceivable that when the load is acted on the tunnel by the large earthquake, the ground deformation becomes large, and earth pressure to the tunnel increases and tunnel is damaged.

From the model tests and numerical analysis (Yashiro et al. 2009), following conclusions are derived;

1. Damage with spalling in the crown such as damage of the Myoken tunnel (Figure 14) occurs when the horizontal uniform load is added.
2. Damage with spalling in the spring line such as damage of the Yoneyama 2 tunnel (Figure 15) occurs when the vertical uniform load is added.
3. Damage with transversal cracks and large spalling such as the Uonuma Tunnel (Figure 12) occurs when the local load is acted.

Type 3: Damage of tunnels by a slide of a fault

Type 3 is a type that an earthquake fault is crossing a tunnel. A slide of the earthquake fault makes various stress such as shear stress, tensile stress and compressive stress on a lining and cause complicated cracks like shear cracks and cracks in round slices.

4. CONCLUSIONS

In this paper, an outline of the historical damage of mountain tunnels in Japan and result of case studies of damage to mountain tunnels is described. A classification of damage patterns and conditions of damage are also described based on the result of the case studies. However, there are many unknown factors on the damaging mechanism of tunnels under an earthquake. It is very important to establish the way to evaluate earthquake resistance of tunnels. We are planning model tests and numerical analyses to evaluate deformation behavior of tunnels under an earthquake and we are going to use the outcome for maintenance of railway tunnels.

Acknowledgements:

The research introduced in this paper is part of a series of studies on the mechanism of seismic damage and improvement of the earthquake resistance of mountain tunnels, jointly conducted by Kyoto University, the Railway Technical Research Institute (RTRI) and the Japan Railway Construction, Transport and Technology Agency (JRTT) under "Program for Promoting Fundamental Transport Technology Research" from the Japan Railway Construction, Transport and Technology Agency (JRTT).

References:

Asakura, T., Shiba, Y., Sato, Y. and Iwatate, T. (1996), "Mountain tunnels performance in the 1995 Hyogoken Nanbu Earthquake", *Special report of the 1995 Hyogoken-Nanbu Earthquake*, JSCE, 265-276.

Shimizu, M., Saito, T., Suzuki, T. and Asakura, T. (2005), "Damages of railway tunnels by the Mid Niigata Prefecture Earthquakes" (in Japanese), *Tunnels and underground*, Japan tunneling association, 36(5), 421-428.

Saito, T., Mukoyama, M., and Taguchi, Y. (2007), "Damages to railway tunnels in the Niigataken Chuetsu-oki Earthquake" (in Japanese), *Tunnels and underground*, Japan tunneling association, 38(12), 47-56.

Yoshikawa, K. (1981), "Investigations about past earthquake disasters of railway tunnels", *Quarterly report of RTRI*, Railway technical research institute, 22(3), 103-107.

Asakura, T., Shiba, Y., Matsuoka, S., Oya, T. and Yashiro, K. (2000), "Damage to mountain tunnels by earthquake and its mechanism (in Japanese)," *Journals of the Japan society of civil engineers*, JSCE, 659(52), 27-38.

Yashiro, K., Kojima, Y., Fukazawa, N., Asakura, T., and Takemura, J. (2009), "Seismic damage mechanism of mountain tunnels in poor geological conditions" (in Japanese), *Journals of the Japan society of civil engineers*, JSCE, C-65(4), 1045-1061.

JOINT CONFERENCE PROCEEDINGS
7th International Conference on Urban Earthquake Engineering (7CUEE) &
5th International Conference on Earthquake Engineering (5ICEE)
March 3-5, 2010, Tokyo Institute of Technology, Tokyo, Japan

ISOLATION METHOD FOR EXISTING CUT AND COVER TUNNEL USING POLYMER MATERIAL

Satoshi Kiryu[1)], Yoshitaka Murono[2)], and Hitoshi Morikawa[3)]

1) Senior seismic engineer, Structure Engineering Division, JR East Consultants Company, Tokyo, Japan
2) Senior Researcher, Earthquake and Structural Engineering, Railway Technical Research Institute, Tokyo, Japan
3) Associate professor, Dept. of Built Environment, Tokyo Institute of Technology, Tokyo, Japan
kiryu@jrc.jregroup.ne.jp, murono@rtri.or.jp, morika@enveng.titech.ac.jp

Abstract: An effective method for the seismic retrofitting of the sidewalls of cut and cover tunnels has not yet been established. Thus, a new method of seismic retrofitting for cut and cover tunnels, called the "polymer isolation method", is developed here. In this method, thin walls made of polymer material, called "isolation walls", are inserted between the ground and the sidewalls of a tunnel. We demonstrate the effectiveness of the proposed method in reducing the seismic response of tunnels by employing some numerical simulations. It is found that the proposed method depends on the thickness of the soil cover over the tunnel and the ratio of the stiffness between the soil and the structure. Furthermore, a simple chart is proposed for convenience to represent the applicability of the polymer isolation method to the design of seismic retrofits for cut and cover tunnels. Although this particular chart has been obtained through a limited case, some other typical cases in which the chart can also be implemented for special conditions are addressed, and the applicability and the limitations of this chart are suggested for possible conditions of the ground and of tunnel structures.

1. INTRODUCTION

After the 1995 Hyogoken-Nanbu Earthquake (The Great Kobe Earthquake), two different types of earthquakeground motion, namely, Level I and Level II, were introduced into a new design code in Japan for civil engineering structures. The Level II motion, in particular, is used to describe the severest ground motion that can affect specific structures. It is imperative that structures do not collapse from Level II motion. This concept is applied to the design of newly constructed structures, including cut and cover tunnels. The seismic performance of existing tunnels, designed according to the conventional codes determined before 1995, is also investigated to determine whether these tunnels are safe against Level II motion. Unfortunately, we sometimes find an insufficient seismic performance at the pillar and/or the sidewalls of cut and cover tunnels. Generally speaking, it is impossible to replace such inadequate tunnels with new ones, due to the lack of space for new structures and so on. Thus, it is necessary to retrofit the existing tunnels and to improve their seismic performance.

For structures constructed above ground level, such as bridge piers, viaduct columns, and so on, effective methods have been proposed to improve their seismic performance [Kobayashi et al. 2001]. Some researchers have proposed techniques to retrofit cut and cover tunnels which do not satisfy the present design codes, for example, a method to improve the shear strength by inserting many bolts in the sidewalls, a method to isolate the tunnel by wrapping the structure with a soft material, and so on. However, we can find very few applications of these techniques to real structures at the present time. Since time and space for construction are limited, due to the need to avoid traffic inside tunnels, it is difficult to work from inside tunnels. Thus, we should consider a method to retrofit tunnels from the outside. It was reported by the Public Works Research Institute of Japan [1995] that isolation techniques are powerful methods which can be applied from the outside of the tunnel. For these techniques, a soft material, whose shear strength is less than 1/100 of that of the soil around the tunnel, can work effectively as an isolation layer. However, the isolation methods proposed previously required the complete wrapping of the outside of the tunnel, including its bottom, with a soft material. In actuality, it is impossible to apply these isolation methods to existing tunnels.

Generally speaking, the seismic response of cut and cover tunnels depends on the deformations of the ground around the tunnel. This means that we may improve the seismic performance of a tunnel by employing an isolation technique between the tunnel and the soil. We have developed a new method for the seismic retrofitting of cut and cover tunnels under the concept of creating isolation between the tunnel and the soil. A thin wall made of polymer material, whose shear strength is extremely small, is inserted between the ground and each sidewall of the tunnel. We call

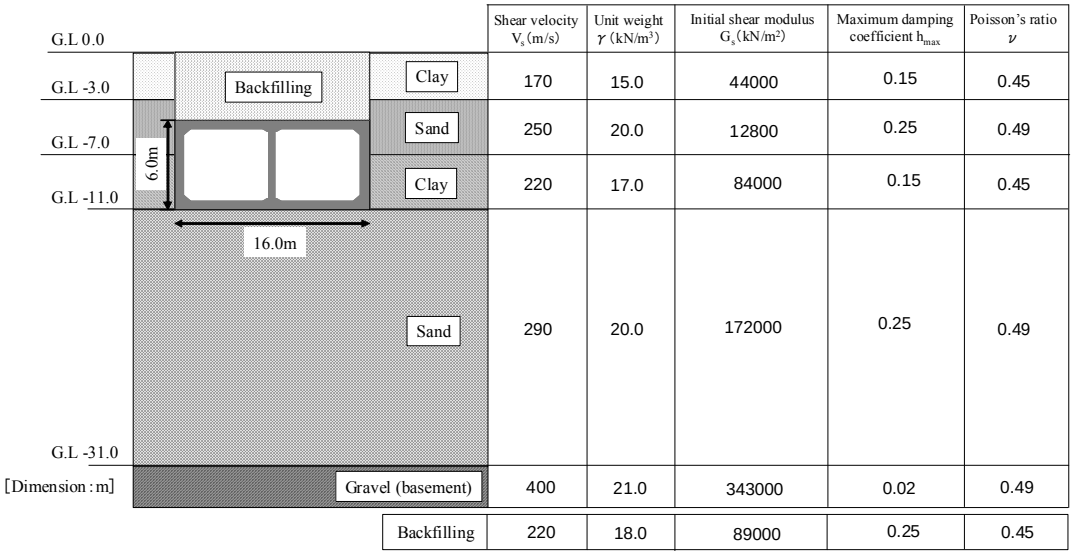

	Shear velocity V_s (m/s)	Unit weight γ (kN/m^3)	Initial shear modulus G_s (kN/m^2)	Maximum damping coefficient h_{max}	Poisson's ratio ν
Clay	170	15.0	44000	0.15	0.45
Sand	250	20.0	12800	0.25	0.49
Clay	220	17.0	84000	0.15	0.45
Sand	290	20.0	172000	0.25	0.49
Gravel (basement)	400	21.0	343000	0.02	0.49
Backfilling	220	18.0	89000	0.25	0.45

Figure 1 Conditions of the ground and the tunnel

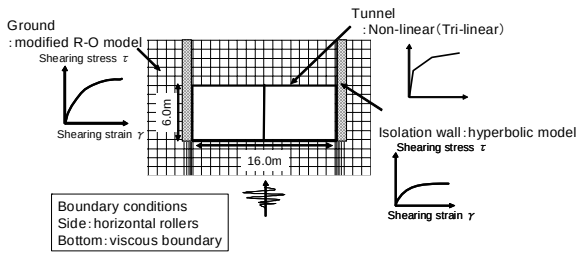

Figure 2 Model for the numerical analysis

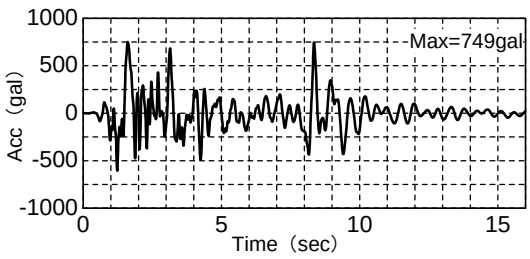

Figure 3 Input seismic wave

this technique the "polymer isolation method" and the inserted thin wall an "isolation wall." It is expected that these isolation walls will reduce the seismic load conducted from the ground and the deformations of the tunnel. We introduce an outline of the polymer isolation method, and demonstrate the effectiveness of the proposed technique. To design the seismic retrofit of cut and cover tunnels, the approximate effectiveness of the polymer isolation method must be determined before a detailed design process is carried out. For this purpose, we propose a simple chart to represent the seismic performance of the isolation walls. This chart is obtained through a limited case. Thus, we also discuss whether the chart can be applied to some other special or extreme conditions of the ground and the tunnel structure, as well as the generality and the applicability of the proposed method.

2. SETTINGS FOR THE NUMERICAL ANALYSIS

2.1 Conditions of the tunnel and the ground

Figure 1 shows a cross section view of the tunnel with which we deal in this study and the parameters of the ground. We consider the most typical case of a cut and cover tunnel for a Japanese railway structure and the ground conditions in an urbanized area of Japan with soft soil sediment, namely, a one-layer, two-span tunnel, 6 m in height and 16 m in width, buried in a layered medium which consists of soft soil, clay, and sand. For the numerical analysis, the two-dimensional non-linear finite element method (FEM) is adopted. Figure 2 presents a schematic figure of the model used for the tunnel analysis. We apply solid elements to the soil and the polymer material, and beam elements to the tunnel. Some non-linear characteristics are introduced into the soil, the polymer material, and the tunnel. The characteristics of the soil are modeled by the modified Ramberg-Osgood model [Idriss et al. 1978], the polymer material by the hyperbolic model, and the tunnel by the tri-linear model [Murono et al. 2006]. The shear strength of the polymer material is only about 1/100 of that of the soil. Each isolation wall has a width of 800 mm and is inserted from the ground surface to the bottom of the tunnel, as shown in Figure 2. Horizontal roller elements are used for the vertical boundaries of the calculation area, and a viscous boundary is used for the horizontal boundary at the bottom of the area.

2.2 Input Seismic Motion

For the numerical analysis, we use the time history shown in Figure 3, which is one of the time series provided in the seismic design codes for Japanese railway structures [Railway Technical Research Institute 1999].

Newmark's β method is applied to the time integration ($\beta = 1/4$), and a time increment of 1/1000 seconds is used. The duration of the analysis is 16 seconds. The

Table 1 Settings for the analysis

Case	Soil cover	Stiffness of the structure	With friction and Without isolation	With friction and With isolation	Without friction and With isolation	Without friction and With isolation
			a	b	c	d
A	Without	Rigid				
B	With					
C	With	Soft				

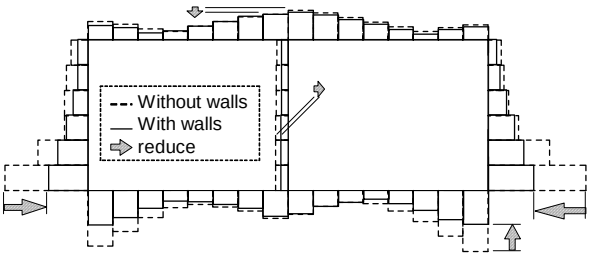

(a) Case A

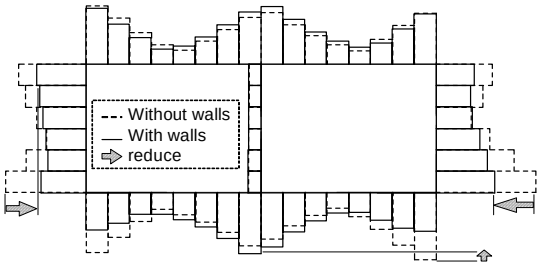

(b) Case B

Figure 4 Comparison of the maximum shear forces by the static condition and by the earthquake ground motion

damping constants for the soil and the structure are considered to be those of Rayleigh damping, namely, 5%.

2.3 Analytical Settings

Table 1 lists the settings for the different conditions in the analysis. Each case is examined with and without isolation walls. In Case A, the thickness of the soil cover over the tunnel is 0 m. In Cases B and C, the tunnel is covered with 5 m of soil. The stiffness of the structure in Case C is different from that in the other cases. In Case B, the friction between the upper slab and the soil over the tunnel is removed in order to discuss the influence of the soil cover. This can be realized by a kind of friction-free sheet, and joint elements are applied in the numerical model to represent this friction-free sheet.

3. RESULTS AND DISCUSSION

3.1 Effectiveness of the Polymer Isolation Method

Next, we consider the performance of the tunnel during

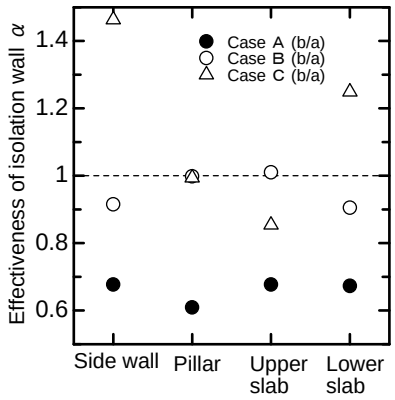

Figure 5 Effectiveness of the polymer isolation method

earthquake ground motion, as shown in Figure 3. Figure 4 shows the distribution of the maximum shear forces occurring due to the ground motion for Cases A and B. The dashed and the solid lines show the section forces without and with isolation walls, respectively. These distributions show similar shapes to those of the shear forces by the static condition. From this figure, it is observed that the shear forces of the sidewalls and the lower slab are noticeably reduced. It is recognized that the maximum section forces during ground motion depend on those brought about by the static condition. This means that it is not practical to use the absolute values of the maximum section forces to evaluate the effectiveness of isolation walls. Thus, we introduce normalized parameter α, namely,

$$\alpha = \frac{(Q_{\max})_{with_isolation} - (Q_{\mathrm{int}})_{with_isolation}}{(Q_{\max})_{without_isolation} - (Q_{\mathrm{int}})_{without_isolation}}, \quad (1)$$

where α denotes the ratio of the maximum section forces with and without isolation walls during ground motion, Q is the shear force, and subscripts "max" and "int" stand for the maximum value during ground motion and the value by the static condition, respectively. From the definition for index α, we can say that the polymer isolation method works effectively in reducing the seismic load when $\alpha < 1$. The value of index α is shown in Figure 5 for three different cases at different members, namely, the sidewalls, the upper and the lower slabs, and the pillar. From a comparison between Cases A and B in Figure

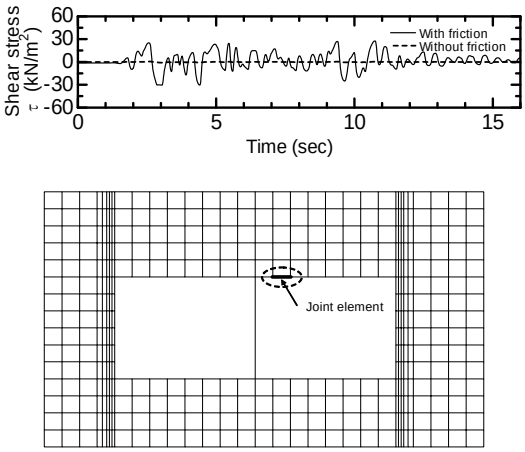

Figure 6 Time history of the shear stress

5, a lower level of effectiveness of the isolation walls is recognized for the soil cover with a larger thickness. On the other hand, it is suggested from a comparison between Cases B and C that the contrast in shear strength between the soil and the tunnel must play an important role in the polymer isolation method. Thus, the key issues in evaluating the effectiveness of the polymer isolation method are as follows:

1) the behavior of the soil cover during earthquake ground motion, and
2) the difference in shear strength between a structure and the soil around the structure

3.2 Contribution of the Soil Cover to the Effectiveness of the Isolation Walls

To discuss the effect of the soil cover on the shear forces, we make a comparison between the tunnel with and without friction between the upper slab and the soil cover. Figure 6 shows the time history of the shear stress for the case with isolation walls. From this figure, it is seen that the shear stress fluctuates less than between the upper slab and the soil cover. On the other hand, it is observed that the shear stress vanished by installing the friction-free sheet. This means that the numerical calculation, which includes the friction-free sheet, works appropriately. From this analysis, we obtain the distribution of the maximum shear forces, as shown in Figure 7. In this figure, two different conditions are presented, namely, one without isolation walls (Panel (a), Cases B-a and B-c) and the other with isolation walls (Panel (b), Cases B-b and B-d). For each case, the results with and without friction are drawn by dashed and solid lines, respectively. From Figure 7(a), which shows the cases without isolation walls, the shear forces decrease slightly around the upper corners for the case without friction. From Figure 7(b), which shows the cases with isolation walls, we can recognize that the shear forces are reduced significantly along the sidewalls and around the upper corners when the friction-free sheet is inserted. To discuss the effectiveness of isolation walls and the friction-free sheet, we introduce the following index for the cases without friction, as shown Figure 8:

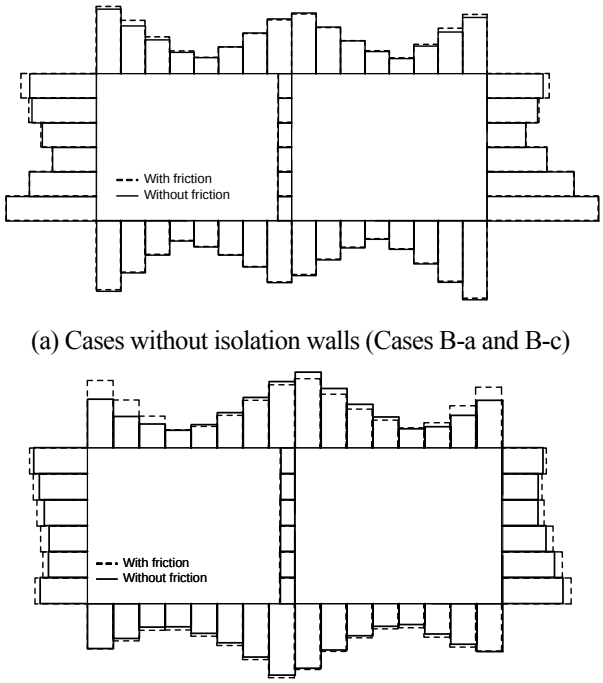

(a) Cases without isolation walls (Cases B-a and B-c)

(b) Cases with isolation walls (Cases B-b and B-d)

Figure 7 Comparison of the shear forces with and without friction

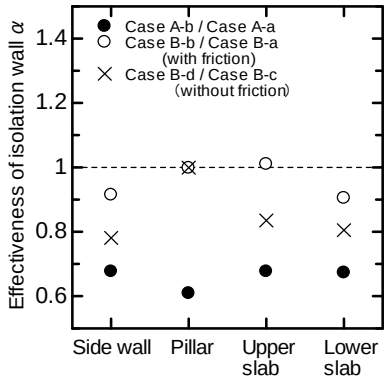

Figure 8 Effectiveness of the polymer isolation method for the cases without friction

$$\alpha = \frac{(Q_{\max})_{without_friction+with_isolation} - (Q_{\mathrm{int}})_{without_friction+with_isolation}}{(Q_{\max})_{without_friction+without_isolation} - (Q_{\mathrm{int}})_{without_friction+without_isolation}} \quad ,(2)$$

We use the same index, α, as in Equation (1) because of their common concepts. The subscripts "without friction + without isolation" and "without friction + with isolation" denote Cases B-c and B-d, respectively. It is noted that Case B-d shows a greater effectiveness of the isolation walls than Case B-b, namely, α for Case B-d is smaller than that for Case B-b. This means that α depends on the friction between the upper slab and the ground. α for Case B-d, however, is larger than that for Case A, which is a case without a soil cover over the tunnel. This suggests that the difference in shear strength between the structure and the

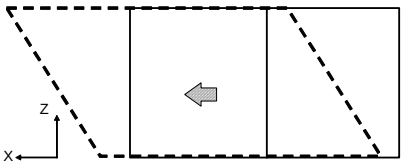

Figure 9 Structural deformation in a case where the stress distribution of the ground is discussed

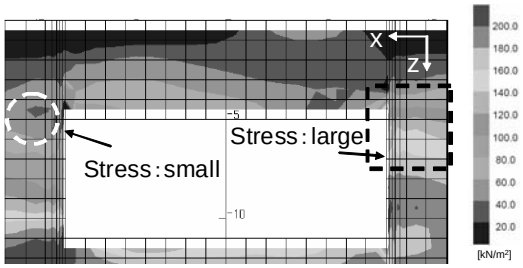

(a) Case B

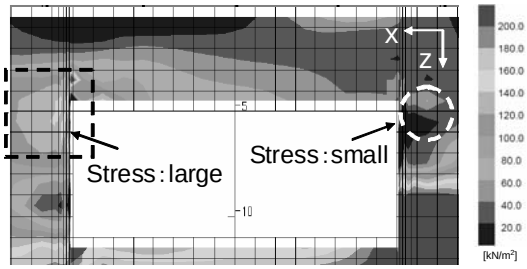

(b) Case C

Figure 10 Distribution of compressive stress in the ground (in the X direction)

soil contributes to the difference in α between Cases B-d and A.

3.3 Different Types of Stress Conditions

To discuss the effect of the difference in shear strength between the structure and the ground, we calculate the stress distribution of the ground without isolation walls. Although we can analyze the stress distribution of the ground with isolation walls, the parameters for the isolation walls can vary infinitely. Thus, for our purpose in this section, it is not very suitable to consider the ground with isolation walls. The ratio of shear strength between the structure and the ground is introduced as an appropriate index, which is independent of the properties of the isolation walls. We discuss the stress distribution of the ground under specific conditions, namely, that the structure and the ground are deformed in the +X direction, as shown in Figure 9, and that the maximum shear forces are provided at the sidewalls. Figure 10 shows the distributions of stress in the ground in the X direction. In this figure, the compressive stress is colored with a warm color, such as red, and the tensile stress, set at 0 N/mm^2, is shown with the color blue. It is observed from Figure 10(a) that the compressive stress of the ground is very small around the outside of the upper-left corner of the tunnel for Case B, while it is large around the upper-right corner. In this case, it seems that the ground pushes the structure in the X direction. On the other hand, the compressive stress is large around the upper-left corner and small around the upper-right corner for Case C, as shown in Figure 10(b). In this case, it seems that the ground supports the structural deformation on the left side. Thus, two different types of stress distribution are possible for a specific situation of ground deformation. Since only the shear strength of the structure is different between Cases B and C, it is expected that the difference in stress distribution is caused by the difference in the ratio of shear strength between the structure and the soil. Remembering that the polymer isolation method performs more efficiently for Case B than for Case C, the ratio of shear strength can be a very important parameter when considering the effectiveness of the polymer isolation method.

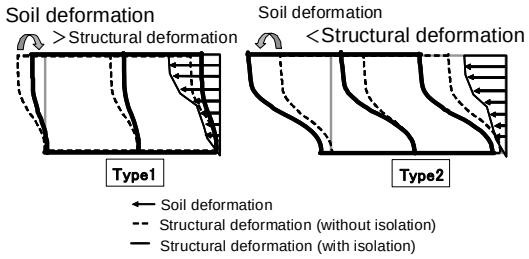

Figure 11 Different types of deformations and their stress distributions

Figure 11 shows a schematic concept for representing the different types of conditions for stress and deformation during ground motion. In a case where the shear strength of the soil is significantly smaller than that of the structure, the deformation of the soil is larger than that of the structure (Type 1 in Figure 11). Then, the ground pushes the tunnel in the X direction. Type 2 in Figure 11 denotes that the deformation of the structure is larger than that of the soil; thus, the structure pushes the ground in the X direction. From this discussion, we can conclude that the shear forces are reduced by isolation walls for Type1, but that the shear forces are increased for Type 2 in the case where isolation walls are is inserted. Therefore, isolation walls are very effective for Type 1.

From the aforementioned discussion, we may estimate qualitatively whether the polymer isolation method works effectively or not, using the distribution of compressive stress of the ground without isolation walls. Furthermore, it is suggested that the ratio of shear strength between the soil and the structure can be used as a simple index for obtaining a rough evaluation of the effectiveness of the polymer isolation method.

4. REPRESENTATION OF THE APPLICABILITY OF THE POLYMER ISOLATION METHOD

To design the seismic retrofitting of existing tunnels, we have to choose an appropriate method from the various methods available. For this purpose, a simple index to represent the effectiveness of the polymer isolation method would surely be useful to many designers. From the discussion in the previous sections, it is suggested that the

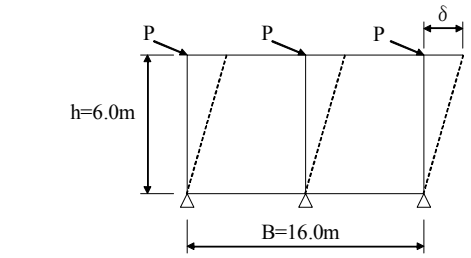

Stiffness of the structure : $G_s = \tau / \gamma$

$\tau = 3P / B$ P: unit horizontal force

$\gamma = \delta / h$ δ : displacement

Figure 12 Schematic figure to define the stiffness of the structure

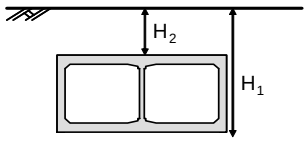

Figure 13 Parameters to define index β

ratio of shear strength between the ground and the structure, and the thickness of the soil cover over the tunnel are key issues. Using these two parameters, a chart is proposed from which we can obtain a rough estimate of the effectiveness of isolation walls, and the validity of the chart is discussed.

4.1 Chart to represent the effectiveness of isolation walls

The proposed chart is expected to be used to acquire a rough estimate of the effectiveness of isolation walls at the initial stage of the design. Thus, the control parameters are limited to only two, namely, the ratio of shear strength between the structure and the ground, and the thickness of the soil cover. These parameters can be readily determined by the conditions of the existing tunnel. Index α, which represents the effectiveness of the isolation walls, is calculated for various values of parameters under the conditions shown in Figures 1, 2, and 3. In these calculations, it is assumed that the beam elements of the tunnel are elastic, because the chart is used for only a rough estimation of the effectiveness of the isolation walls. To obtain the effective results of the isolation, we have to install isolation walls with a thickness of at least 450 mm [Kiryu, et. al. 2008]. Thus, the thickness of the isolation walls is set at 450 mm for the calculations. The shear strength of the structure, G_s, is defined from the displacement determined by the horizontal unit force shown in Figure 12, and the shear strength of the soil, G_g, is defined as the average value of the soil stiffness between the upper and the lower slabs. To represent the thickness of the soil cover, index β is introduced:

$$\beta = 1.0 + H_2 / H_1, \qquad (3)$$

where H_1 and H_2 are defined as shown in Figure 13. β is 1.0 m in the case where the thickness of the soil cover is 0 m,

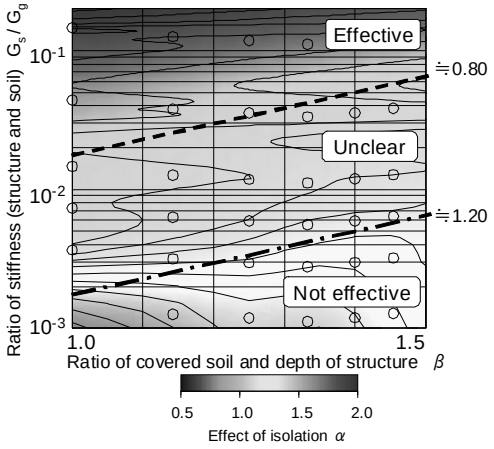

Figure 14 Chart of index α for designing the seismic retrofit

like in Case A in Table 1, and the maximum value for β is usually 1.5 for cut and cover tunnels. We apply the values of 1/10 to 1/1000 for the ratio of stiffness, G_s / G_g, and 1.0 to 1.5 for the index of the soil cover, β. In Figure 14, the values used for the calculations are shown by open circles. The distribution of the values for α is drawn by colored contour lines using a simple linear interpolation technique. From this figure, the aforementioned qualitative properties of α can be recognized, namely, the polymer isolation method is more effective for tunnels with larger shear strength and a thinner soil cover, which is located more around the upper-left area of the chart. The upper area of the chart corresponds to Type 1 in Figure 11, and the lower area to Type 2. Therefore, we would like to propose the use of Figure 14 for estimating the effectiveness of the polymer isolation method, where the isolation wall is not effective if $1.2<\alpha$, its effectiveness is unclear if $0.8<\alpha<1.2$, and it is clearly effective if $\alpha<0.8$. We can divide the state into two classes, namely, "effective" and "not effective" for the numerical calculations, because there are no uncertainties in the calculations. However, definite classifications for real phenomena are usually difficult. Thus, "unclear" is introduced as a safety buffer with a range of around 20% or $\alpha=1.0$. In a case where a designer obtains the results of "unclear" for an existing tunnel, he/she may apply some detailed analyses. It is useful that the chart can provide the following instructions from only two parameters, β and G_s / G_g.

-whether or not the polymer isolation method is effective, and

-whether or not a detailed analysis is required to choose an appropriate method for the retrofitting of an existing tunnel.

4.2 Applicability for different ground conditions

Figure 14 is obtained from specific conditions of the structure and the ground. Although it is not practical to examine all the possible conditions to confirm the generality of the proposed chart, it is very important to discuss the applicability of the chart to different conditions. Thus, we discuss the applicability of the chart to a few extreme

Table 2　Ground conditions for the analysis

	Ground［1］ (Soft ground)	Ground［2］ (Hard ground)	Ground［3］ (Soft and hard grounds)	
Soil cover (m)	0.0	5.0	3.0	
Initial shear modulus G_g(kN/m²) (Side of tunnel)	45700	144000	(Upper) 44000	(Lower) 172000
Maximum damping coefficient h_{max}	0.15	0.25	0.15	0.25
Poisson's ratio ν	0.45	0.49	0.45	0.49

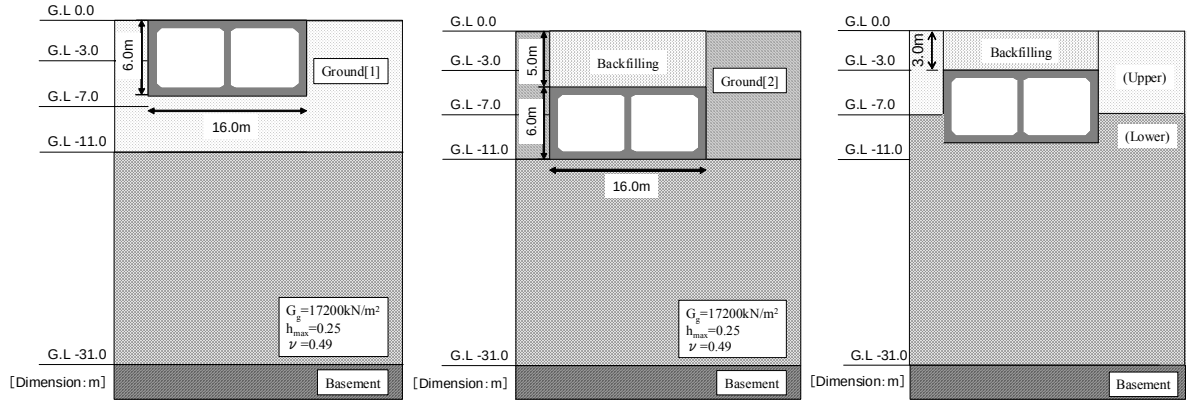

(a) Ground［1］　(b) Ground［2］　(c) Ground［3］

Figure 15　Conditions of the ground

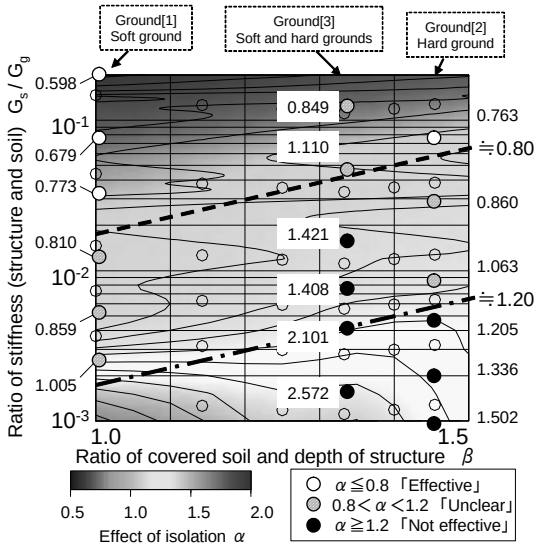

Figure 16　Chart of index α for designing the seismic retrofit　(different ground conditions)

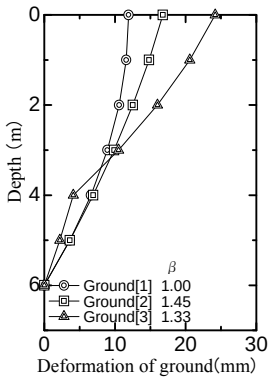

Figure 17. Relative deformations of the ground for Grounds [1], [2], and [3]

conditions. Firstly, three special conditions of the ground are discussed in this section. Secondly, the non-linear properties of the structure are introduced in the following section. The setting of the ground conditions are listed in Table 2 and shown in Figure 15, namely, "Ground［1］" with small shear strength, "Ground［2］" with large shear strength, and "Ground［3］", which consists of two layers with a distinct contrast in acoustic impedance. The boundary for the layers of Ground［3］ is located in the middle of the sidewalls of the tunnel. The soft and the hard grounds consist of one layer on the basement. The characteristics of the other soil, the polymer, and the structure are the same as those described in Section 2.

Figure 16 is obtained by overlapping the results of the three different ground conditions in Figure 14. From this figure, it is observed that the proposed chart is applicable to extreme conditions of the ground, that is, both Ground［1］ and Ground［2］. For Ground［3］, however, the values for index α differ from the values in Figure 14. This may be caused by the distribution of the soil deformations. The distribution of the soil deformations is shown in Figure 17 for various conditions of the ground, including the typical ground conditions shown in Figure 15, that is, Ground［1］, Ground［2］, and Ground［3］. In Figure 17, the relative values for the maximum displacement are drawn using the maximum displacement at the level of the lower slab as reference, and the relative displacements are shown between the upper and the lower slabs. The level of the upper slab is depth = 4.0 m and the level of the lower slab is depth = 6.0

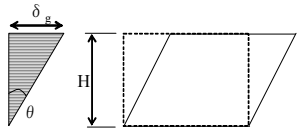

Relative story distortion angle $\theta = \delta_g/H$	～ 1/150	～ 1/100	～
Equivalent shear modulus of the tunnel G_s'	$0.2G_s$	$0.15G_s$	$0.1G_s$

δ_g: Relative story displacement of the ground (between upper and lower slabs)
H: Height of the tunnel
G_s: Initial shear modulus of the tunnel

Figure 18. Schematic figure of the equivalent stiffness of the a structure

Table 3. Analysis cases

	Case		
	A	B	C
α (Fig 6)	0.620	0.831	1.463
$\beta = 1+H_2/H_1$	1.00	1.45	1.45
Relative story distortion angle $\theta = \delta_g/H$	1/600 (≦1/150)	1/230 (≦1/150)	1/230 (≦1/150)
Equivalent shear modulus of the tunnel G_s' (kN/m²)	$0.2G_s$ =12640	$0.2G_s$ =12640	$0.2G_s$ =2528
Shear modulus of the ground G_g (kN/m²)	86000	98667	98667
G_s'/G_g	0.1470	0.1281	0.0256

m. From this figure, it is observed that the shapes for the distributions of soil deformations are very close to a quarter of a sinusoidal curve, except for the case of Ground [3]. For Ground [3], the shape of the soil deformations is not smooth at a depth of 4.0 m, which corresponds to the boundary of the layers with large differences in acoustic impedance. This suggests that the proposed chart can be applied only to grounds whose soil deformations are distributed sinusoidally. In cases where there is a boundary of layers with a large contrast in acoustic impedance in the middle of the sidewalls, the chart in Figure 14 cannot be used to evaluate the effectiveness of the isolation walls. However, the above results suggest that the chart can be applied to many of the conventional conditions of the ground.

4.3 Applicability to non-linear structures

Figure 16 is obtained under the assumption that the structure consists of linear elements, because the simple chart used to represent the effectiveness of the polymer isolation method must be convenient for many designers. However, a structure may show plasticity behavior due to strong ground motion. To consider the critical behavior of the ground-structure system during strong motion, it is important to investigate the non-linear performance of the system. We examine whether or not the proposed chart can be applied to a structure with non-linear elements.

We have already finished the detailed calculations of the responses for tunnel structures with non-linear elements in Section 3, namely, Cases A, B, and C listed in Table 1.To overlap the results, including the non-linear structure on the proposed chart in Figure 14, we have to introduce a typical value of stiffness to represent the non-linear structure. For this purpose, we adopt a simple method to determine the

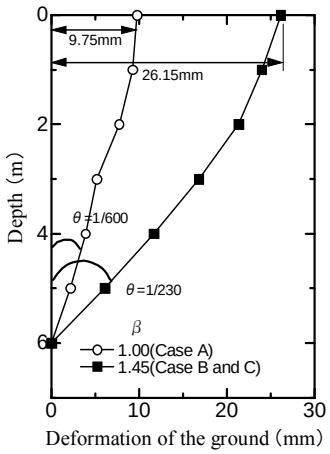

Figure 19 Relative story displacement of the ground

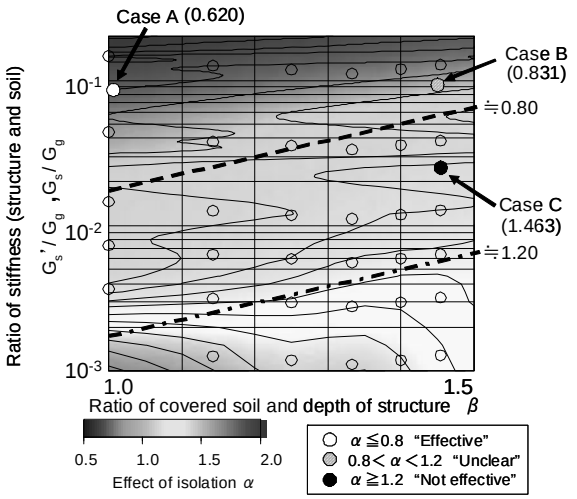

Figure 20 Chart of index α for designing the seismic retrofit (non-linear)

equivalent stiffness of a non-linear structure [Railway Technical Research Institute 1999]. The Railway Technical Research Institute (1999) proposed the table shown in Figure 18 to determine the equivalent stiffness of a structure, G_s, from values of a relative story distortion angle, θ, and the initial shear modulus of a tunnel, G_s: G_s is determined at three levels as $0.2\,G_s$, $0.15\,G_s$, and $0.1\,G_s$ for θ <1/150, 1/150< θ <1/100, θ >1/100, respectively. θ is defined as

$$\theta = \delta_g / H, \qquad (4)$$

where δ_g stands for the relative story displacement of the ground and H for the height of the tunnel (see Figure 18). Table 3 shows the effectiveness of the isolation walls, α, and the ratio of the soil cover and the depth of the structure, β, for Cases A, B, and C in Table 1. These values correspond to Figure 5. The relative story distortion angles, θ, are determined as 1/600 for Case A and 1/230 for Cases B and C from Figure 19, which shows the distributions of the relative story displacement of the ground. From this, the equivalent stiffness of the structure, G_s, is determined as $0.2\,G_s$ using the table in Figure 18.

The effectiveness of isolation walls for Cases A, B, and C are plotted in Figure 14, as shown in Figure 20. In this figure, the vertical axis is G_s / G_g for non-linear structures instead of G_s / G_g given in the original chart. The values of α for the non-linear structures are slightly different from the values in the chart for the linear cases. Figure 20 suggests that we can roughly say that a condition in the "effective" zone may be also effective for non-linear structures and that the conditions outside of the "effective" zone are definitely unclear. However, we conclude that the proposed chart can work well for its own purpose, that is, to act as an aide in the preliminary decision making regarding the employment of isolation walls.

5. CONCLUSIONS

The conclusions of this study are as follows:

1. If we employ polymer isolation walls, we should verify the safety of the structure under the static condition.
2. The effectiveness of polymer isolation walls depends on the thickness of the soil cover over the tunnel and the ratio of shear strength between the soil and the structure.
3. A simple chart is proposed to represent the applicability of the polymer isolation method. Although the proposed chart has been obtained from specific ground conditions and for a structure with a linear response, the chart has the potential to be generalized for conventional ground conditions and non-linear structures for its purpose, namely, to aide in the preliminary decision making regarding the employment of the polymer isolation method.

References:

Idriss, I. M., Dobry, R. and Singh, R. M. (1978). Nonlinear behavior of soft clays during cyclic loading, J. GED, Proc. ASCE, Vol. 104, No. GT12, pp. 1427~1447.

Kiryu, S., Murono, Y. and Morikawa, H. (2008). Mechanism and Applicability of the Isolation Method for Cut and Cover Tunnel, JSCE, Vol. 64, No. 4, pp. 905~914.

Kobayashi, K. and Ishibashi, T. (2001). An Experimentally Study on Effect of Retrofitting of Existing Reinforced Concrete Columns by Steel Plate on One Face after Constructed Seismic Retrofitting Method, JSCE , Vol. 52, pp. 75-89 (in Japanese).

Murono, Y., Kiryu, S. and Tateyama, M. (2006). First European Conference on Earthquake Engineering and Seismology, Geneva, Switzerland.

Public Works Research Institute, (1998). Cooperative Research Reports of PWRI, Joint Research on Development of Isolation Material for Underground (in Japanese).

Railway Technical Research Institute (1999). Design Standards for Railway Structures and Commentary (Seismic Design), Maruzen (in Japanese).

JOINT CONFERENCE PROCEEDINGS
7th International Conference on Urban Earthquake Engineering (7CUEE) &
5th International Conference on Earthquake Engineering (5ICEE)
March 3-5, 2010, Tokyo Institute of Technology, Tokyo, Japan

INITIAL SHEAR MODULUS OF AUCKLAND RESIDUAL SOIL FROM FIELD AND LABORATORY TESTS

Norazzlina M.Sa'don[1], Anas Ibrahim[1], Rolando Orense[2], Michael Pender[3] and Naotaka Kikkawa[4]

1) PhD Student, Department of Civil & Environmental Engineering, University of Auckland, New Zealand
2) Senior Lecturer, Department of Civil & Environmental Engineering, University of Auckland, New Zealand
3) Professor, Department of Civil & Environmental Engineering, University of Auckland, New Zealand
4) Researcher, National Institute of Occupational Safety and Health, Tokyo, Japan
nmsa001@aucklanduni.ac.nz, aibr008@aucklanduni.ac.nz, r.orense@auckland.ac.nz, m.pender@auckland.ac.nz, kikkawa@s.jniosh.go.jp

Abstract: This paper describes the experiments performed to investigate the initial shear modulus of Auckland residual soil. Firstly, WAK (wave-activated stiffness) tests and spectral analysis of surface waves (SASW) tests were conducted at a residual soil site by applying impact and harmonic loads on a circular steel plate in vertical direction. A sledgehammer equipped with a dynamic force transducer was used to produce the impact load while harmonic loading was applied using an eccentric mass shaker to generate steady-state excitations. The initial shear modulus of soil was obtained by considering the soil to be vibrating as a single degree of freedom (SDOF) system. Next, undisturbed soil samples from the site were subjected to consolidated undrained tests with three submersible miniature linear variable differential transducers (LVDTs) mounted on the sides of the specimen to measure the small strain stiffness. The LVDTs were capable of resolving displacements of less than 1 μm and measuring axial strains ranging from less then 0.001% to 2.5%. The small strain stiffness obtained from laboratory tests compared very well with those determined from geophysical tests.

1. INTRODUCTION

The initial shear modulus is an important parameter used in solving dynamic problems, such as ground response analysis and soil-structure interaction problems. Several researchers have investigated the initial shear modulus of sand and clay and proposed relationships based on void ratio and confining pressure (e.g., Hardin and Richart, 1963; Hardin and Black, 1966; Kokusho, 1980) However, these relationships were developed and calibrated based on normally consolidated Northern Hemisphere sedimentary soils. As a result, their applicability for analyses in residually weathered soils in sub-tropical climates is unclear.

Most of the present Auckland region is underlain by Waitemata sandstones and siltstones. The in-situ chemical weathering of Waitemata sediment group produced a highly variable material referred to as Auckland residual soil. The depth of the weathering profile ranges from a few metres to a few tens of metres at the very maximum. In designing structures to be built over this formation, characterisation of the foundation ground is very important. Toward this end, research efforts are currently underway to investigate the properties of Auckland residual soil, including its initial shear modulus.

This paper focused on the results of both field and laboratory testing which were conducted to investigate the initial shear modulus of Auckland residual soil. For field testing, WAK (wave-activated stiffness [K]) test and spectral analysis of surface waves (SASW) method were employed to investigate the small-strain stiffness of the ground consisting of residual soils. Next, undisturbed samples were obtained from the same site, and the samples were subjected to undrained triaxial tests with three linear variable displacement transducers (LVDTs) attached to the specimen to measure the axial strain. The results of the field and laboratory tests were then compared.

2. SITE DESCRIPTION

The selected site is located in a sloping ground in Orewa, north of Auckland City, within an area being developed for residential purposes. The site consists of residual clay of yellow reddish in colour and was excavated to about 1.3 m depth from the actual ground surface. WAK test and SASW method were then performed at the leveled site.

Next, undisturbed samples were obtained from the

same site by pushing 200 mm diameter and 200 mm long sampling tubes which were fitted with a low angle cutting shoe into the ground at the desired depth using a hydraulic jack. Sample ends were leveled and sealed with thin rubber disks between the soil and caps to preserve the natural water content. The soil samples were then transported to the laboratory for testing.

The physical properties of the Auckland residual soil are tabulated below:

Table 1 Index properties of Auckland residual clay

Particle density, G_s	2.59
Liquid limit, w_{LL} (%)	65.4
Plastic limit, w_{PL} (%)	42.3
Plasticity index, I_p	23.1
Natural water content, w_N (%)	37.8
Bulk unit weight of specimen, γ(kN/m^3)	17.6

3. FIELD TESTS

3.1 Background

The analysis of surface wave propagation in soils for characterization purposes has gained great popularity in the past decades because of the intrinsic advantages of such testing techniques. In particular the non-invasive nature of these methods makes them less costly and time effective when compared to borehole methods, such as cross-hole or down-hole tests (Foti et al., 2001).

The WAK (wave-activated stiffness [K]) test, developed by Briaud and Lepert (1990), is a dynamic load test performed by hitting a spread footing with sledgehammer in the vertical direction to measure the stiffness of the soil underlying the footing. The force-time signal from the hammer dynamic load cell (input) and the velocity-time signal from the geophones on the spread footing (output) are recorded during the impact. The stiffness of the soil is obtained by considering the soil to be vibrating as a single degree of freedom (SDOF) system. The most important feature of this test for the design of foundation is that, although essentially a dynamic test, the excitation and the free-body response are of such low frequency that the output may be used to predict the static-output relationship and the transfer function will be independent of the magnitude of the input (Merrifield and Davies, 2000). Moreover, Briaud and Lepert (1990) showed that an analysis of the force and velocity signals using the fast Fourier transform provides a good estimate of the stiffness of the footing-soil assembly. The idea of WAK test comes from the non-destructive techniques (NDT) developed by Paquet (1968) and Stokoe et al. (1987) for foundation control and also finds its basis and background in the work of several leading researchers in soil dynamics (Briaud and Ballouz, 1996).

The SASW method is a seismic technique used for in-situ evaluation to determine shear wave velocity and shear modulus profiles of target sites. The method has been introduced by Nazarian and Stokoe (1984) as an extension of a steady-state Rayleigh wave technique by Richart et al. (1970). The tests consists generally of three steps: (a) field testing; (b) evaluation of dispersion curve by phase unwrapping method to compute the variation of Rayleigh wave velocity with frequency; and (c) determination of shear wave velocity profile by inversion curve. In the SASW method, both the source and receivers are placed on the ground surface. Impulsive, harmonic or random-noise load was used to apply vertical excitation to generate Rayleigh waves. Propagation of the waves is monitored with the surface receivers located at known distances apart. The SASW method is based on dispersive characteristic of surface waves because it allows different materials to be sampled by using different wavelengths. Most of the wave energy exists within one wavelength of the surface and in layered media, the propagation velocity of surface waves become dependent on the frequency or wavelength; thus, different frequencies will propagate with different velocities. This velocity is termed phase velocity or apparent Rayleigh wave velocity (Stokoe and Nazarian, 1985). In this paper, both WAK test analysis SASW method were used to evaluate the initial shear modulus of the soil.

3.2 Instrumentation and test procedure

A circular steel plate of 50 cm in diameter with 2.54 cm thickness was placed on top of leveled ground surface as shown in Figure 1(a). It can be seen from Figure 1(b) that a layer of sand was laid between the steel plate and the ground surface to ensure good contact between them. By applying the principles of the WAK and SASW tests, two types of dynamic loading were used. Sledgehammer (Dytran model 5803A) and electro-dynamic linear mass shaker (APS Dynamic Model 400) were utilised to produce impact and harmonic loadings, respectively. Impact loading tests were initially performed followed by application of harmonic loadings.

Figure 2 shows the 16-bit data acquisition box connected to a computer for recording the output and input signals during the tests. MATLAB 2007 software was used to control the shaker and data acquisition operations. The



(a) (b)

Figure 1 Types of dynamic loadings applied in the tests: (a) sledgehammer; and (b) electro-dynamic shaker



Figure 2 Data acquisition system for field test

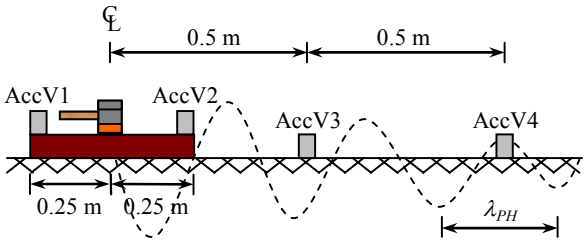

Figure 3 Experimental setup for WAK and SASW tests

sample rate used in all tests was 500 data per second. Instead of geophones, four vertical accelerometers with sensitivity of ±2g were used to record the acceleration produced by the impact loads. This was recommended by Merrifield and Davies (2000), who indicated that the geophones were not appropriate for detecting the change in stiffness due to the high accelerations generated by impulsive forces.

Two vertical accelerometers (AccV1 & AccV2) were screwed on top of the circular steel plate for soil stiffness determination (WAK tests). The remaining two accelerometers, labeled as AccV3 and AccV4, were securely placed on the ground at 50 cm and 100 cm, respectively, from the centre of the steel plate to measure the shear wave velocity produced by dynamic loading (SASW tests). By applying the experimental setup shown in Figure 3, WAK and SASW tests were implemented one after the other.

For the impact loading, two sets of impact tests were carried out with four blows for each set of test. All tests were performed by hitting the centre of the circular steel plate using the sledgehammer equipped with a dynamic force transducer. A rubber tip was attached to the sledgehammer to focus the energy of the impact in the lower frequencies. It was suggested by Briaud and Lepert (1990) that the frequency content of the impact should be as low as possible in order to get the best match between the static test and impact test. In all cases, the operator attempted to produce a similar magnitude of force and the response was recorded for 120 seconds. Typical load signal obtained from the impact loading is illustrated in Figure 4.

In the harmonic loading tests, an electro-dynamic

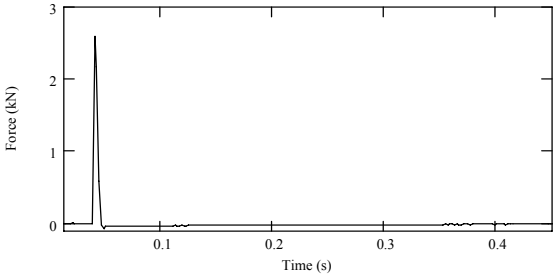

Figure 4 Recorded signals for impact Test 1

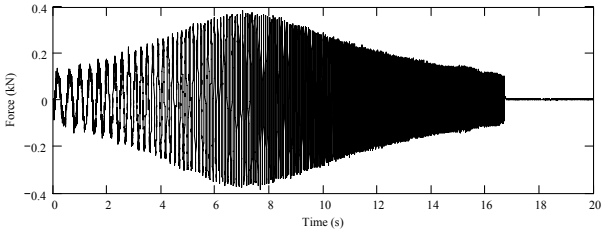

Figure 5 Recorded signals during harmonic loading Test 1

shaker was used to generate vibration on the plate in the vertical direction. Two harmonic loading tests were conducted using sweeping-sine input motion with frequency range from 2 Hz to 100 Hz. Figure 5 shows the recorded load signal obtained from the harmonic loading test. From the vibration record, the frequency corresponding to the peak vibration amplitudes was then determined.

3.3 Results and Discussion

Wave-activated stiffness (WAK) test results

The force-time signal from the impact loading (input) and the acceleration-time signal obtained from the vertical accelerometers (output) were analysed. For WAK tests, only accelerometers attached to the steel plate were considered in the analysis. The coherence values between the input and output were initially determined as shown in Figure 6. These coherence values were used as an indicator of data quality in a given frequency range and only information corresponding to high values of such function were considered. The result shows that the output recorded was over 95% at frequency

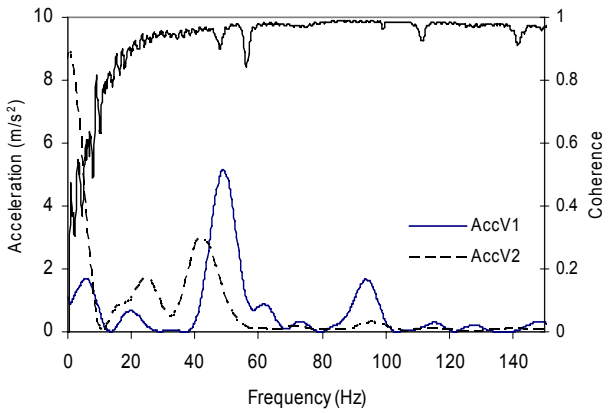

Figure 6 Power spectrum readings from two accelerometers and coherence functions for impact loading

ranging from 20 Hz to 250 Hz. This indicates perfect correlation between the two signals and that the signals are not contaminated with random background noise. Thus, only the responses corresponding to 20 Hz and above were considered for further analyses. An average of four blows was used to produce the power spectrum for both vertical accelerometers (AccV1 and AccV2) attached to the steel plate, as shown in Figure 6.

Figure 7 shows two modes of vibrations that were found in the range of 0 – 100 Hz: (a) rocking mode and (b) punching mode. Punching mode was determined by averaging both the AccV1 and AccV2 signals. This punching mode is the mode of interest in determining the stiffness of the soil against vertical motion (K_v). Therefore, the average of the signals from the two accelerometers was used to obtain the acceleration of the footing for all other tests. Meanwhile, the rocking mode was also found by calculating the differences between the two signals. The two peak frequencies indicate punching and rocking modes occurred at 48 Hz and 50 Hz, respectively (see Figure 7).

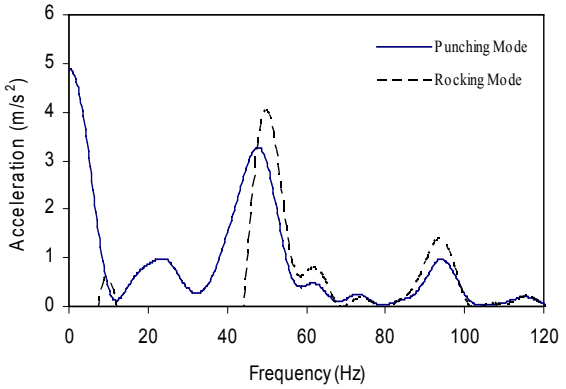

Figure 7 Punching and rocking modes for impact loading

Next, harmonic loading was considered. Figure 8 shows that coherence values between the shaker excitation and vertical accelerometers were over 95% for frequencies greater than 10 Hz, and the power spectrum calculated for both signals. Similar analyses were performed as in impact loading to determine the punching and rocking modes. The frequencies for punching and rocking modes were taken at

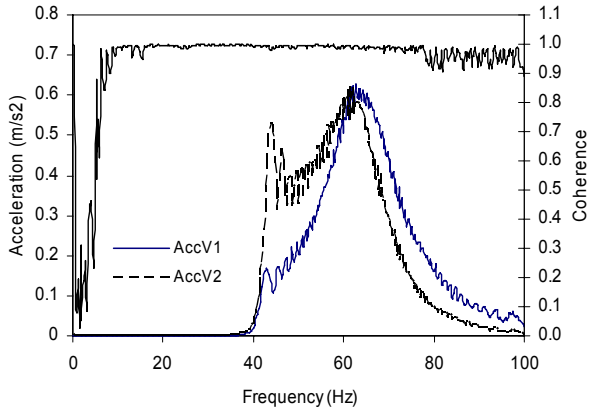

Figure 8 Power spectrum and coherence function of two signals for harmonic loading

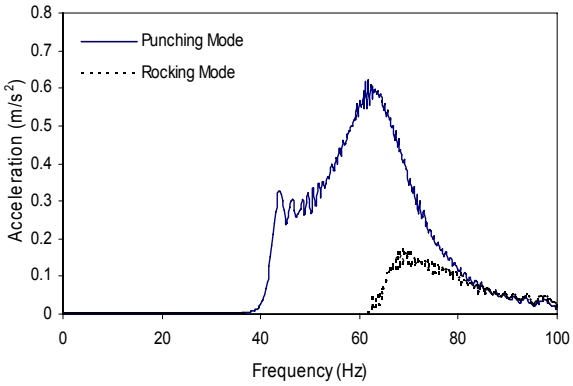

Figure 9 Punching and rocking modes for harmonic loading

the highest peak of resonance, as shown in Figure 9. The peak frequency of the punching mode (averaging two signals) was obtained at 62 Hz and the rocking mode (difference between two signals) at 44 Hz.

The vertical stiffness (K_v) of the soil was then calculated by using Eq. (1):

$$K_v = 2\pi\left(\frac{\text{Frequency}}{\text{Velocity}/\text{Force}}\right) \tag{1}$$

while the shear modulus (G) and Young's modulus (E) of Orewa soil were determined by using the equation for elastic stratum on rigid base of surface circular foundation as stated below:

$$G = \frac{K_v(1-\nu)}{2R} \tag{2}$$

$$E = 2G(1+\nu) \tag{3}$$

The shear wave velocity (V_s) which is related to the dynamic elastic constants of the soil is calculated by using Eq. (4):

$$V_s = \sqrt{G/\rho} \tag{4}$$

In the above equations, R = radius of circular plate; ν = Poisson ratio of 0.4 and ρ = 1800 kg/m^3.

The vertical stiffness (K_v) and the shear modulus (G) of the soil determined from dynamic load were calculated and summarized in Table 2. The table shows a marked difference in dynamic stiffness obtained by two different types of loading used. This may be due to the uneven contact area between the steel plate and the ground surface during the testing. It was observed that a layer of sand seemed to disperse outward after several applied impact loading.

Table 2 Summary for Orewa clay - WAK test analysis

Type of Loading	Vertical Stiffness, K_v (kN/mm)	Shear Modulus, G (MPa)	Shear Wave Velocity, V_s (m/s)
Impact	47.25	56.70	177.48
Harmonic	32.70	39.24	147.65

Spectral Analysis of Surface Waves (SASW) Tests

For the SASW tests, only the two vertical accelerometers (V3 and V4) that were placed on the ground surface were used. Figures 10 and 11 show the results of typical signal processing in SASW testing obtained for both impact and harmonic loading tests, respectively. According to Stokoe and Nazarian (1984), the cross power spectrum is a good tool to determine the relative phase difference between two signals caused by time delays, propagation delays or varying paths between receivers.

Also, the coherence function shows the frequency range at which most of energy is concentrated and indicates that the signals recorded are not contaminated with random background noise (i.e. high response-to-noise ratio). Thus, from the coherence function, only frequency ranges for which coherence was greater than 0.9 were considered and further analysed to determine the shear modulus and shear wave velocity.

By knowing the distance between the receivers (x) and the phase shift ($\Delta\theta$) for each frequency (f) determined from the cross power spectrum of the two signals, the phase velocity, (V_{PH}), and wavelength, (λ_{PH}), associated with a given frequency can be calculated by the following formulas:

Phase velocity, $$V_{PH} = \frac{360xf}{\Delta\theta} \quad (5)$$

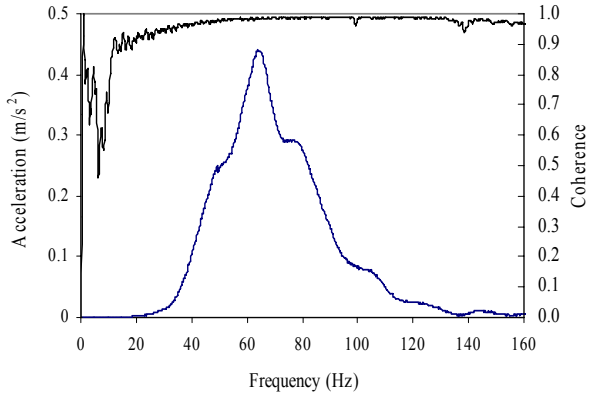

(a) Coherence functions and accelerations amplitude of cross power spectrum

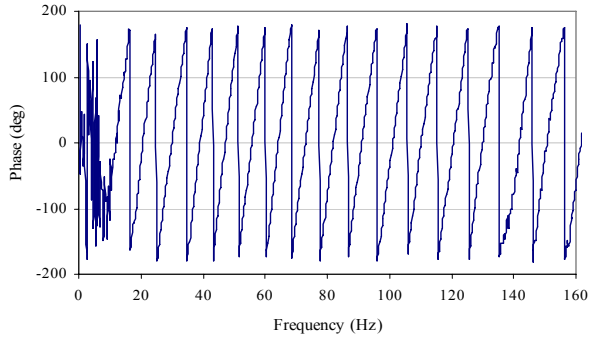

(b) Phase components of cross power spectrum

Figure 10 Typical signal processing in SASW testing for impact loading

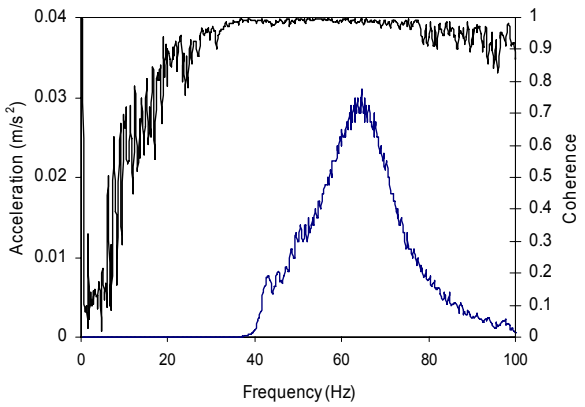

(a) Coherence functions and accelerations amplitude of cross power spectrum

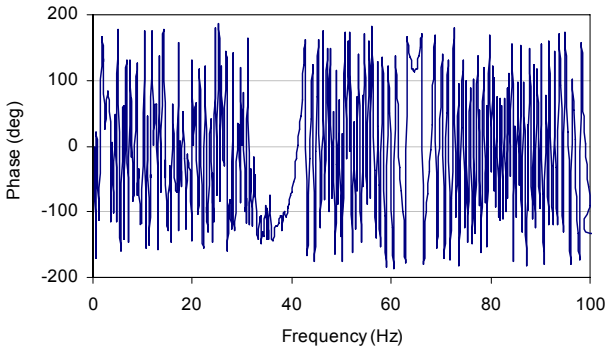

(b) The phase of cross power spectrum

Figure 11 Typical signal processing in SASW testing for harmonic loadings

Wavelength, $$\lambda_{PH} = \frac{V_{PH}}{f} \quad (6)$$

These calculations yielded an experimental dispersion curve (V_{PH} vs. λ_{PH}) for the receiver spacing. Once all experimental dispersion curves for a set of receiver spacing were constructed, they were combined together and a composite experimental dispersion curve of a site was developed. The dispersion curve may be disturbed in the low frequency range because of the near field effect which occurred due to limitation of recording equipment and attenuation properties of soil media. To overcome near field effect, a filtering criterion is commonly applied to the information extracted from a single testing setup. Many

Table 3 Filtering criteria for SASW test (adopted from Ganji et al., 1998)

Source	First receiver	Receiver spacing
Lysmer	$2.5\lambda < x$	–
Heisey et al.	$x = \Delta x$	$0.333\lambda < \Delta x < 2\lambda$
Sanchez-Salinero et al.	$x = \Delta x$	$2\lambda < \Delta x$
Roesset et al.	$0.5\ \lambda < x < 2\lambda$	$0.5x < \Delta x < x$
Gucunski and Woods	–	$0.5\lambda < \Delta x < 4\lambda$
Tokimatsu et al.	$0.25\lambda < x + \Delta x/2$	$0.0625\lambda < \Delta x < \lambda$

Note: x indicates near receiver distance from source; Δx is receiver spacing; and λ is wavelength

filtering criteria are proposed, as shown in Table 3. In this study, Heisey et al. (1982) criterion was chosen as it is widely used in SASW method.

Table 4 shows typical calculations for Rayleigh wave velocity V_R, which gives phase differences, $\Delta\theta$, against distance, x (0.5m), at peak frequencies recorded. Richart et al. (1970) stated that in linear elastic homogeneous medium, Rayleigh wave velocity of propagation is dependent on frequency and its value is about 10 percent less than that of the shear waves velocity, V_s (i.e., $V_s \approx 1.1 V_R$).

Table 4 Typical calculation for Rayleigh wave velocities for impact tests

f (Hz)	$\Delta\theta$ (deg)	λ (m)	Z = $\lambda/2$ (m)	$V_{PH} = V_R$ (m/s)	$V_s = 1.1\ V_R$ (m/s)
94.5	120.26	1.497	0.75	141.44	155.6
129.5	150.86	1.193	0.60	154.51	170.0

Thus, by employing an approximate straightforward inversion technique, the initial shear modulus of Orewa clay, G, was calculated from the shear wave velocity by using $G = \rho V_s^2$. The Young's modulus, E, was then determined using Eq. (3). The results obtained from SASW are summarised in Table 5.

Table 5 Summary for Orewa clay - SASW test analysis

Type of Loading	Shear Waves Velocity, V_s (m/s)	Shear Modulus, G_s (MPa)	Young's Modulus, E (MPa)
Impact	170.89	52.57	147.19
Harmonic	130.70	30.75	86.10

Comparing the results of WAK test and SASW method, summarized in Tables 2 and 5, respectively, it can be observed that the values agree well, although the moduli obtained by impact loading were consistently higher than those from harmonic loading. This may be due to the difference in loading used, which could represent different depths of soil profile, Z (i.e. for impact loads, Z ≈ 0.65 m and harmonic loads, Z ≈ 0.35 m). Note that the effective sampling depth for each wavelength is considered here to be equal to a fraction of the wavelength obtained. It has been recommended by several authors that 1/2 – 1/3 of the wavelength is representative of the effective depth of sampling (Stokoe and Nazarian, 1985).

4. LABORATORY TESTS

4.1 Background

It has long been established that the measurement of small strain stiffness in triaxial testing requires that sensitive instrumentation be attached directly to the soil specimen so that errors caused by bedding and other effects at the top and bottom platens are eliminated (Brown et al., 1980; Burland and Symes, 1982; Costa Filho, 1985; Goto et al., 1991; Cuccovillo and Coop, 1997; and DaRe et al., 2001). The technique used and discussed in this paper was based on the work of DaRe et al (2001) and employed LVDTs with a linear range of about ±1.27 to ±2.54 mm (Schaevitz 050 MHR, 100 MHR). In conjunction with a 16 bit AD converter, these were found to be able to resolve displacements smaller than 1 micron, i.e., an axial strain of less than 0.001% over a 100 mm gauge length. The aim of the work was to develop a method capable of measuring the full stress-strain curve for undisturbed soil specimens, so that the relationship between the shear modulus (tangent or secant) and axial strain could be established.

We encountered several difficulties in achieving our aim. The difficulties revolved around the preparation and mounting of the specimen in the triaxial cell. Initially, it was found that the top loading cap needed to be restrained against rotation. Previous experience in testing residual soils from around Auckland had alerted us to the fact that the material is variable, even in a volume of soil as small as that for a 75 mm diameter and 150 mm high specimen. This meant that an unrestrained loading cap tends to rotate at even very small axial strains with the consequence that the LVDTs on one side of the specimen indicate compressive axial strain whilst on the other side the strains are extensional. The first step in improving things was to restrain the top cap against rotation and a great improvement ensued but we then became aware that our specimen trimming procedures were not achieving end faces of the specimen that were flat and parallel. This was remedied by developing a special three-part trimming mould which resulted in much better end conditions. Finally, for specimens that were difficult to trim with smooth ends, we used a thin layer of plaster. Details of the results are presented below.

4.2 Experimental procedure

The soil samples obtained from Orewa site were brought to the laboratory where they were removed using a laboratory hydraulic extruder and cut into quarters through the cross-section using a woodworking band-saw. Each quarter of material was then trimmed to 75 mm diameter and 150 mm long using a hand-operated soil lathe, thereby minimising the disturbance to the specimen.

To ensure flat and square ends of the specimen, a special three-part split mould was used to cut the soil surplus, as mentioned above. Top and bottom retaining rings assisted in holding the mould when the trimming of specimen's ends was performed. Thin layer of quick-setting plaster was applied on the ends if necessary, to ensure flat and parallel ends.

Compared to a conventional triaxial testing machine, the apparatus used in this study employed a stepper motor to raise the pedestal during the shearing stage. The stepper motor can perform 200 steps per revolution and each step moved the working surface by 0.39 μm. The use of a 16 bit A/D converter in the system produced a resolution better than 1μm over a 100 mm gauge length. Moreover, it enabled

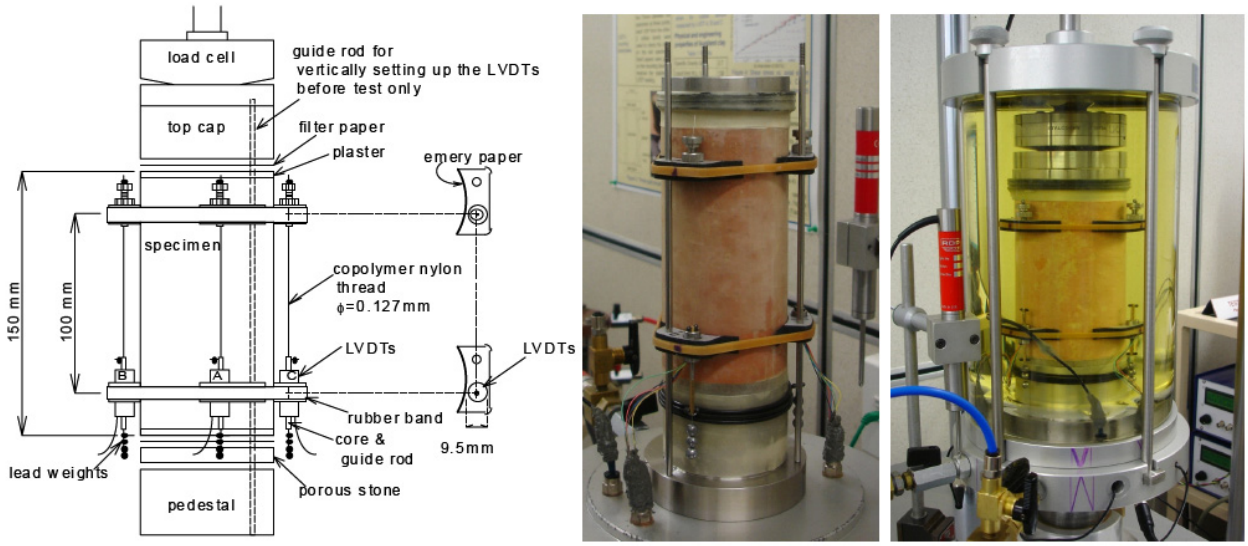

Figure 12 Experimental set up for small strain triaxial test

the data acquisition system to record 1520 data/sec at this setting. However, the rate of data acquisition can be adjusted depending on the rate of shearing applied.

Three submersible miniature linear variable differential transducers (LVDTs) were used in the tests. Each transducer was 16.8 mm long and only 5g in mass. The principle of displacement measurement was based on changes in the movement of the LVDT core which triggered changes in voltage signal. To supplement the measurement at levels of strain up to more than 10%, an external transducer attached to the base of the apparatus was also used.

Figure 12 shows the experimental set up used in this study. Three sets of mounting blocks were clamped individually into the 75mm diameter soil specimen at three points, each 120° from the other. Each LVDT block had an inner surface lined with emery paper and held against the specimen using rubber bands. The top and bottom blocks were positioned during setting-up using an alignment pin and the gauge length set to 100 mm. This method of mounting the LVDTs was simpler than the usual approach of having a pair of spring-loaded cradles attached to the specimen. It also has the advantage that specimens of different diameters can be accommodated easily.

The LVDTs can resolve distances less than 1 micron, or an axial strain of 0.001% for a 100 mm gauge length. Moreover, the load cell can resolve forces of less than 0.4 N, that is, an axial stress of less than 0.1 kPa on a specimen 75 mm in diameter. Therefore, the small strain stiffness can be discussed within an accuracy of 0.1 MPa.

The system required non-conductive cell fluid for unsealed electronic devices. Thus, Dow-Corning #200 silicone oil was used as cell fluid instead of normal water. The oil used has extremely low viscosity under a wide range of temperature and is optically transparent (see right side of Figure 12), thus ideal for observation purposes during the test. The oil also does not degrade the O-ring seals or the latex membrane which enclosed the specimen. In addition, its large molecular structure helps prevent cell fluid penetration through the membrane and eliminates osmotic pressure gradient across it.

4.3 Test results

Calibration with rubber specimen

Rubber specimen with 75 mm in diameter and 150 mm high was used to calibrate the performance of the system. The same specimen set-up discussed earlier was used in preparing the rubber specimen. Figure 13 shows the results of calibration test, indicating an excellent agreement between the three LVDTs (A, B and C), from very small strain levels up to 2.5%.

For axial strains less than about 0.3%, the displacements measured by external transducer gave displacements much larger than those obtained by on-specimen transducers. This observation is fairly common and therefore transducers attached directly to the specimen are required to obtain more accurate measurements of soil stiffness at small strains.

Test results on Auckland soils

The soil specimens were saturated by applying 700 kPa back-pressure, and then consolidated to an effective confining pressure ranging from 60 to 769 kPa. During consolidation, a small axial load was maintained to ensure that no rotation of the top cap occurred at the top of the specimen. Undrained shearing was done at a displacement rate of 0.1 mm/sec and the data logging system took 150 sets of readings every second.

Figure 14 illustrates the shear stress – axial strain relation observed for Orewa residual soil within a small range of strains (i.e. up to 0.01%) for effective confining pressure of 60 kPa. Similar to the trend seen in the rubber specimen, the readings obtained by the three LVDTs are

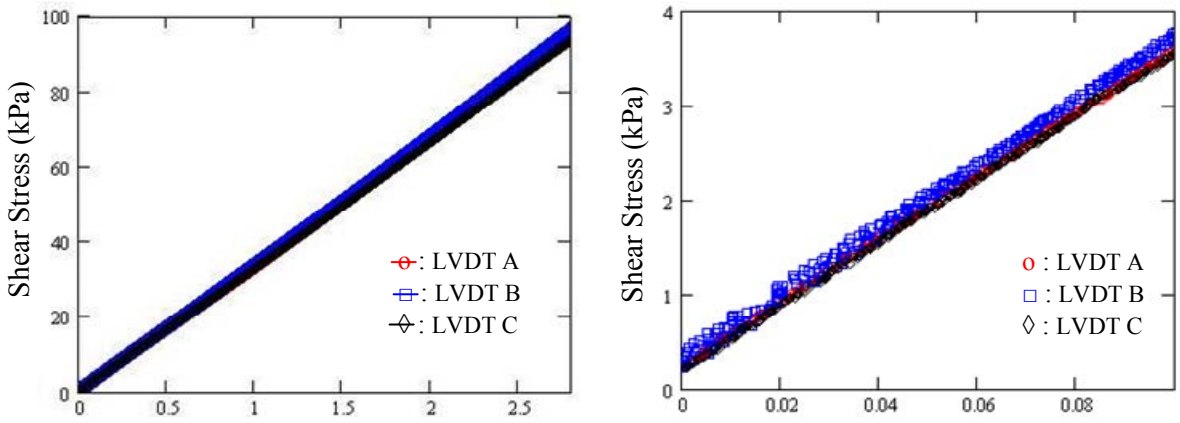

(a) Axial strain (up to 2.5%) (b) Axial strain (up to 0.1%)

Figure 13 Shear stress vs. axial strain measured by LVDT A, B and C for the rubber specimen

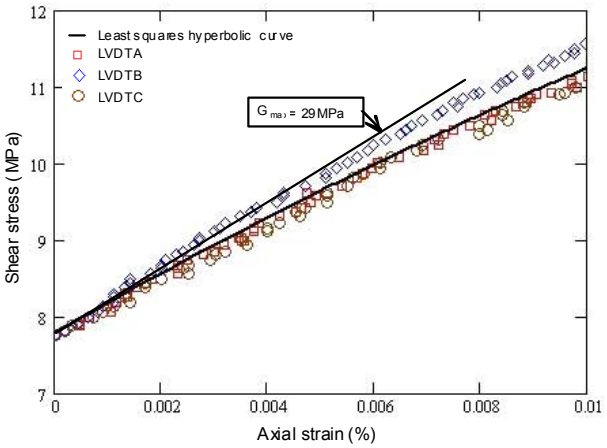

Figure 14 Shear stress-axial relation for Orewa residual clay at σ_c'=60 kPa up to an axial strain of 0.01% obtained by the three LVDTs and by least-squares fitting

fairly close to each other. The minor difference can be due to the natural variability within the clay specimen. Looking closely, the plots show an initial linear portion at strains up to about 0.002%, indicating the quasi-elastic property of the soil. As the strain level increases beyond this threshold value, a continuous decrease in stiffness is observed.

For the purposes of data representation, a hyperbolic model was used to idealise the nonlinear stress-strain behaviour of soil (e.g., Tatsuoka , 1987; Ishihara, 1995):

$$q - q_0 = \frac{1}{\frac{1}{(\varepsilon_a - \varepsilon_{a0})E_{\max}} + \frac{1}{a}} \qquad (7)$$

where, q is the deviator stress, q_0 is the initial deviator stress, ε_a is the axial strain, ε_{a0} is the initial axial strain, $E_{\max}$ is the Young's modulus, and a is a constant.

Firstly, the Young's modulus, $E_{\max}$, of each specimen was determined from the slope of the quasi-elastic portion of the deviator stress-axial strain curve (up to 0.002% axial strain) using the method of least squares. Then, the constant value, a, which gives the minimum root mean square error, was computed using the $E_{\max}$ determined earlier and the average of the data points up to about 0.1% axial strain. The initial shear modulus (or shear modulus at small strain), $G_{\max}$ is related to $E_{\max}$ using a Poisson's ratio ν=0.5. The hyperbolic curve obtained from least-squares fitting is also shown in Figure 14, where it is clear that the curve represents the trend in the data very well. Similar procedure of fitting a hyperbola was adopted in assessing the test results for specimens under different confining pressures. From the fitted hyperbola, the secant shear modulus of the soil for a wide range of axial strain can be easily obtained.

Figure 15 presents the secant modulus-axial strain relationship obtained for Orewa samples for strains up to 2.5%. The average of the data obtained by the three LVDTs was plotted (for axial strains ranging from 0.1% to 2.5%) and the trend was extrapolated through a hyperbolic curve using least-squares fitting as described above. For each sample, the plots indicate an initial linear portion for strains up to about 0.002%, indicating the initial shear modulus, $G_{\max}$, of each specimen. With increasing strain level, degradation of stiffness is observed.

The results shown in Figure 15 indicate that the initial shear modulus is dependent on the effective confining pressure, with the relation given by

$$G_{\max} = 3380(\sigma_c')^{0.54} \qquad (8)$$

where $G_{\max}$ and σ_c' are in kPa. The subscript of 0.54 is close to the value of 0.5 typically used for natural sedimentary soils. Note that residual soils are generally thought to behave quite differently from natural soils because the former are products of weathering from underlying parent rocks and have undergone different formation process; however, Eq. (8) seems to indicate that existing correlations used for natural soils may be applicable for residual soils. Further tests are planned in the future to confirm this.

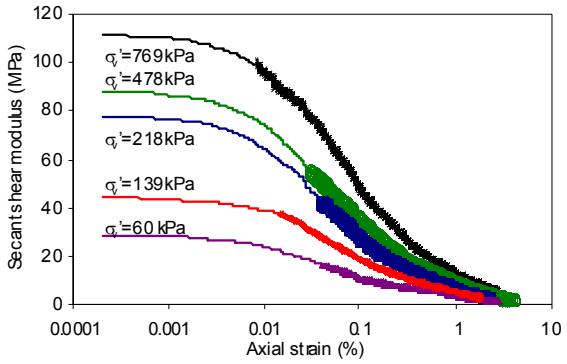

Figure 15 Shear modulus and axial strain relationship for Orewa soil under different confining pressures

5 COMPARISON BETWEEN FIELD AND LABORATORY RESULTS

The geophysical methods (WAK and SASW tests) presented in Section 3 typically give shear wave velocities (and initial shear moduli) for shallow portions of the deposit where the waves are propagated. Based on comparison with the results of seismic cone penetration tests (sCPT), good correlations are obtained up to a depth of 2-3m (Algie et al., 2010). For this depth, the magnitude of initial shear modulus using Eq. (8) is in the range of 18-30 MPa, which is slightly lower than those obtained from the geophysical tests as indicated in Tables 2 and 5. However, it should be mentioned that the laboratory tests were performed under fully saturated condition (B-value > 0.96) while the WAK and SASW tests were done on partially saturated ground where the effect of suction is significant. Considering this difference, it can be said that there is a good correlation between the field- and laboratory-obtained initial shear modulus.

6 CONCLUDING REMARKS

WAK and SASW tests are non-invasive seismic approach used for determining in-situ dynamic stiffness of the soil using the surface wave energy. This paper discussed the WAK and SASW test techniques for determining the shear wave velocity, V_s and shear modulus, G of the soil. Field testing involved the generation and measurement of surface waves which permitted all testing to be performed on the ground surface. Both methods showed good correlation for the shear modulus and the shear wave velocity which were in the range of 30 – 56 MPa and 130 – 178 m/s, respectively.

Moreover, test results showed that the experimental apparatus developed was capable of measuring the soil stiffness at very small strain. The LVDTs used showed the possibility of obtaining shear modulus – axial strain relationship for large range of strains. The objective of developing a low-cost system with simple installation and operation appeared to be successful.

ACKNOWLEDGMENTS

The authors would like to express gratitude to the Ministry of Higher Education (MOHE) Malaysia, and Universiti Malaysia Sarawak (UNIMAS) and the Universiti Teknologi MARA (UTiM), for the financial support granted for the doctoral studies of the first two authors.

REFERENCES

Algie, T.B., Pender, M.J. and Orense, R.P. (2010). Dynamic field testing of shallow foundations subjected to rocking, *Proc. 7th International Conference on Urban Earthquake Engineering and 8th International Conference on Earthquake Engineering*, Tokyo (to appear).

Briaud, J.-L., and Ballouz, M. (1996). LATWAK: impact test to obtain pile lateral static stiffness, *Journal of Geotechnical Engineering*, 122(6), 437-443.

Briaud, J.-L., and Lepert, P. (1990). WAK test to find spread footing stiffness, *Journal of Geotechnical Engineering*, 116(3), 415-431.

Brown, S. F., Austin, G. & Overy, R. F. (1980). An instrumented triaxial cell for cyclic loading of clays, *Geotechnical Testing Journal, GTJODJ*, Vol. 3, No.4, pp. 145-152.

Burland, J. B. & Symes, M. J. (1982). A simple axial displacement gauge for use in the triaxial apparatus, *Géotechnique*, 32 (1), 62-65.

Costa Filho, L. de M. (1985). Measurement of axial strains in triaxial tests on London clay, *Geotechnical Testing Journal, GTJODJ*, 8 (1), 3-13.

Cuccovillo, T. & Coop, M. R. (1997). The measurement of local axial strains in triaxial tests using LVDTs, *Géotechnique*, 1 (47), No. 1, pp. 167-171.

DaRe, G., Santagata, M. & Germaine, J.T. (2001). LVDT-based system for the measurement of the pre-failure behavior of geomaterials, *Geotechnical Testing Journal, ASTM*, 24(3), 288-298.

Foti, S., Lancellotta, R., Socco, L. V., and Sambuelli, L. (2001). Application of fk analysis of surface waves for geotechnical characterization, *Proc. 4th International Conference on Recent Advances in Geotechnical Earthquake Engineering and Soil Dynamics and Symposium in Honour of Professor W.D. Liam Finn*, San Diego, California, Paper No: 1.14.

Ganji, V., Gucunski, N. and Nazarian, S. (1998). Automated inversion procedure for spectral analysis of surface waves, *Journal of Geotechnical and Geoenvironmental Engineering*, 124, 757-770.

Goto, S., Tatsuoka, F., Shibuya, S., Kim, Y.S. and Sato, T. (1991). A simple gauge for local small strain measurements in the laboratory, *Soils and Foundations*, 31, 169–180.

Hardin, B.O. and Richart, F.E. Jr. (1963). Elastic wave velocities in granular soils, *J. Soil Mechanics and Foundations Division, ASCE*, 89 (1), 33-65.

Hardin B.O. and Black, W.L. (1966). Sand stiffness under various triaxial stresses, *J. Soil Mechanics and Foundations Division, ASCE*, 92(2), 27-42.

Heisey, J. S., Stokoe, K. H. II, and Meyer, A. H. (1982). Moduli of pavement systems from spectral analysis of surface waves,

Research Record No. 852, Transportation Research Board, 22-31.

Ishihara, K. (1996). *Soil Behaviour in Earthquake Geotechnics*. Oxford.

Kokusho, T. (1980). Cyclic triaxial test of dynamic soil properties for wide strain range, *Soils and Foundations*, 22 (4), 1-18.

Merrifield, C. M., and Davies, M. C. R. (2000). A study of low-energy dynamic compaction: field trials and centrifuge modeling, *Geotechnique*, 50(6), 657-681.

Nazarian, S. and Stokoe, K. H. II (1984). In situ shear wave velocities from spectral analysis of surface waves, *Proc. of the Eighth World Conference on Earthquake Engineering,* San Francisco, California, Vol. III, July 21-28, 31-38.

Paquet, J. (1968). Study vibratory concrete piles; harmonic and transient response; application control, *Annals of the Institute of Technical Building and Public Works*, 245, 789-803 (in French).

Richart, F. E. Jr., Wood, R. D. and Hall, J. R. Jr. (1970). *Vibration of soils and foundations*, Prentice-Hall, New Jersey.

Stokoe, K. H. II and Nazarian, S. (1985). Use of Rayleigh waves in liquefaction studies, *Measurement and Use of Shear Wave velocity for Evaluating Dynamic Soil Properties, Proceedings of a Geotechnical Engineering Division Session, ASCE Convention*, Denver, Colorado, May 1, 1-17.

Stokoe, K. H., Olson, L. D. and Reese, L. D. (1987). Integrity testing of drilled shaft, *Geotech. Engineering. Faculty Workshop Proc.*, Int. Assoc. of Drilled Shaft Contractors, Fort Collins, Colo., Jul.

Tatsuoka, F. (1987). *Handbook of the strength of soils and failure in ground, Handbook Series 13*, Japanese Geotechnical Society, 76-78 (in Japanese).

JOINT CONFERENCE PROCEEDINGS
7th International Conference on Urban Earthquake Engineering (7CUEE) &
5th International Conference on Earthquake Engineering (5ICEE)
March 3-5, 2010, Tokyo Institute of Technology, Tokyo, Japan

LIQUEFACTION POTENTIAL AT PADANG CITY: COMPARISON OF PREDICTED AND OBSERVED SOIL LIQUEFACTION DURING THE PADANG EARTHQUAKE

Adrin Tohari[1)], and Eko Soebowo[1)]

1) Reseacher, Research Center for Geotechnology, Indonesian Institute of Science, Indonesia
adrin@geotek.lipi.g.id, eko.soebowo@geotek.lipi.go.id

Abstract: The 2009 Padang earthquake has resulted in damages to infrastructures and building and a death toll of 383 in Padang City. Numerous liquefaction and ground deformations caused by the earthquake were particularly evidence in the areas few kilometers from the coast. The paper presents the results of a previous field geotechnical investigation of liquefaction potential and the recent liquefaction observation in Padang City. A microzonation map was created using the data from liquefaction susceptibility analyses and a liquefaction index. The predicted liquefaction zones showed good agreement with site observations. The assessment suggests that the susceptibility decreases to the northeast away from the coastal line.

1. INTRODUCTION

The 2009 Padang earthquake in West Sumatera (Mw = 7.6) resulted in significant loss of life and structural damage. The earthquake resulted in 383 deaths as well as significant damage in Padang (Satkorlak, 2009). The casualties were mostly due to building collapse. It also triggered liquefaction in numerous inland alluvial areas as well along the coast. Lateral spreading, sand boiling and ground settlement were widely observed in the City of Padang, and along the northern coast of Padang Bay. However, a few investigations of the occurrences of liquefaction and associated ground failures have been conducted after the earthquake (e.g., EERI, 2009).

Liquefaction potential of the northern part of Padang City has been studied by the authors after the 2004 Banda Aceh earthquake, for the purpose of government and public awareness on earthquake collateral hazard (Tohari and Daryono, 2007). A subsequent investigation was then conducted to cover the southern part of the city in 2008 (Tohari et al, 2008). The objectives of this paper are to presents the result of previous investigations of liquefaction potential in Padang City and to compare the results with the observed liquefaction phenomena occurred during the 2009 Padang earthquake.

2. GEOLOGICAL AND TECTONIC SETTING

2.1 Geological Setting

As seen from the geological map in Figure 1, Padang City is made up of three different geological units. The oldest units are the Tertiary volcanic rock, which present in the hill to the southeast. They are composed of altered and mineralized andesitic to basaltic tuff, breccia and lava. They are overlain by the Plio-Plistocene volcanic rocks, that are composed of rhyolitic, dacitic and andesitic tuff, breccia and lava. They are present in the hill to the northeast. The youngest units are the quarternary deposits that consist of alluvial, lacustrine and marine deposits. Borehole data indicate sand and silt layers susceptible to liquefaction present in the alluvial deposits. The depth of groundwater generally ranges between 0.5 and 5.0 m; the mean groundwater depth near the shoreline is about 1.5 m.

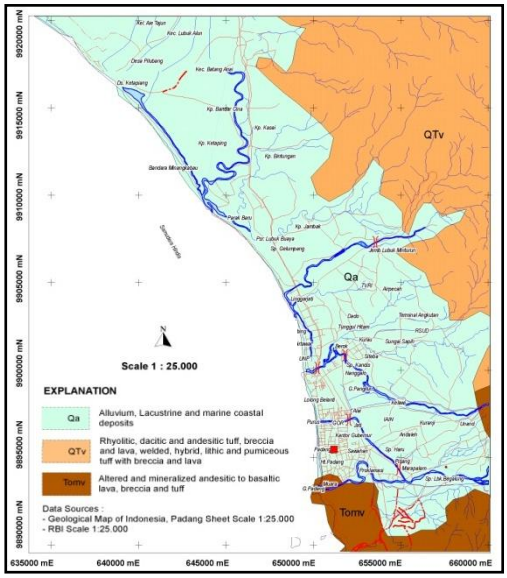

Figure 1 Geological Map of Padang City region

2.2 Tectonic Setting

The island of Sumatra sits atop the Southeast Asian plate, which overrides the subducting Indian and Australian oceanic plates that converges obliquely at about 50 to 60 mm/yr (Prawirodirdjo et al., 2000). The oblique convergence is partitioned into two components: the dip slip is accommodated on the subduction interface, and the strike-slip component is accommodated largely by the Sumatran fault (McCaffrey, 1992; Sieh and Natawidjaja, 2000). The 1900-km long Sumatran fault zone (SFZ) runs along the back-bone of Sumatra, within or near the active-volcanic arc. The SFZ is highly segmented, and hence consists of 19 major segments ranging in length from 35 km to 200 km. These fault segments are separated by more than a dozen discontinuities, ranging in width from less than 4 to 12 km, mostly are dilatational stepovers (Sieh and Natawidjaja, 2000) The SFZ pose major hazards, particularly to people live on and near the active fault trace. Since 1890, about 21 major earthquakes ruptured the segments of the SFZ with magnitudes ranges from 6.5 to 7.7.

3. MAIN CHARACTERSITICS OF THE PADANG EARTHQUAKE

The Padang earthquake, with a magnitude of 7.6 (Mw) occurred on Wednesday September 30, 2009, at 5:16 p.m., affecting an area with a population of about 1.2 M people, including 900,000 in Padang and 80,000 in Pariaman. The epicenter of the earthquake was located offshore about 60 km WNW of Padang, at a depth of about 80 km within the oceanic slab of the Indo-Australian plate (Figure 2). The earthquake produced a compact rupture zone, with a nearly circular shape with a radius of only 15 km (EERI, 2009).

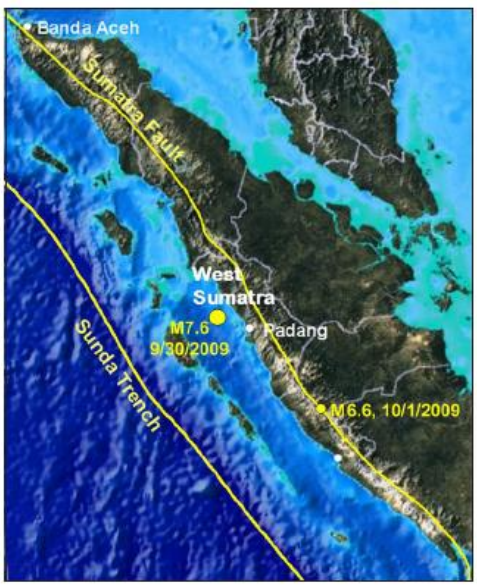

Figure 2 Location of the September 30 earthquake epicenter on the Sunda thrust fault (Sieh, 2009).

During the earthquake, a peak ground acceleration (PGA) of 0.3g was recorded at the strong ground motion station in Padang (PDSI). Since the station is located at the base of the mountains, the ground motions in the center of Padang, on softer deeper soil deposits, are likely to have been larger (EERI, 2009).

4. LIQUEFACTION DAMAGE IN PADANG CITY

Figure 3 show the location of ground settlement, sand boiling and lateral spreading due to the earthquake. The ground settlement and lateral spreading generally occurred in the populated areas up to 5 km from the coastal line, with a significant damage to the city infrastructures (roads and bridges), residential housing and buildings. Many buildings, located near the river front experienced foundation movement due to ground settlement. One example of foundation movement was shown by four-story public work building, located near the river front (Figure 4). The building configuration concentrated lateral deformations and residual drift in the first story. In the vicinity of the building, fine sand were commonly ejected out of the ground crack. Ground settlement also caused the foundation of many residential housing to settle up to 1.0 m (Figure 5). These phenomena were well observed in the northern part of Padang City, especially in the Koto Tangah Sub-District.

Lateral spreading mainly occurred in the areas along the swamps and rivers, usually in the road embankments and river dikes. One good example of lateral spreading was evident in Samudera road which is an embankment road located along the Padang Beach (Figure 6).

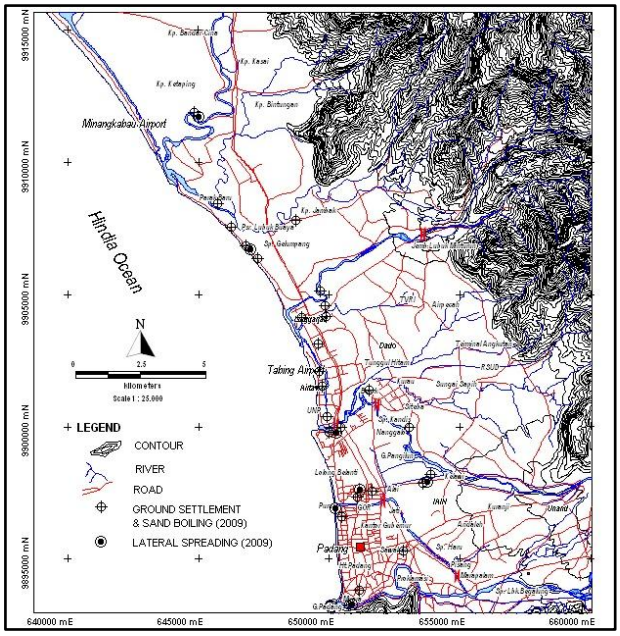

Figure 3 Locations of ground deformation associated with liquefaction due to the September 30 earthquake event



Figure 4 First-story column damage in the public work building due to ground settlement



Figure 5 Foundation settlement in brick masonry house building due to liquefaction in Koto Tangah Sub-District, Padang. The total settlement was about 1.0 m.



Figure 6 Ground cracking at an embankment road in the Padang Bay due to lateral spreading

5. EVALUATION OF LIQUEFACTION POTENTIAL PRIOR THE 2009 EARTHQUAKE

5.1. Location and Methodology

In 2006 and 2008, a series of geotechnical investigations was conducted to evaluate and assess the liquefaction potential in Padang City. Figure 7 shows the location of the field geotechnical investigation. The investigations comprised of geotechnical drilling up to 30 m deep at 6 locations, standard penetration tests at every 1.5 m at each borehole, cone penetration tests at 40 locations up to 30 m deep, mapping of the depth of groundwater table, and laboratory determination of grain size distribution and soil unit weight.

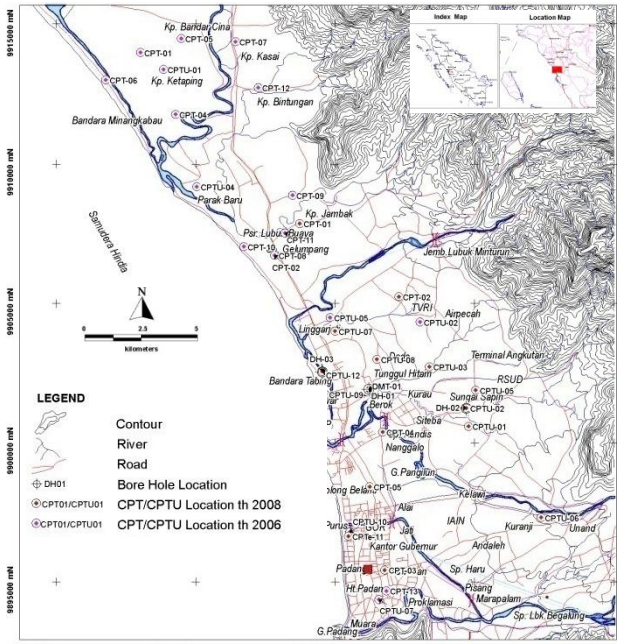

Figure 7 Locations of the sub-surface geotechnical investigation

Liquefaction potential analyses were then carried out using the SPT- and CPT-based methods which requires the calculation of two variables: the seismic demand placed on a soil layer, expressed in terms of cyclic stress ratio (CSR), and the capacity of the soil to resist liquefaction, expressed in terms of cyclic resistance ratio (CRR).

The cyclic stress ratio (CSR) is defined by Seed and Idriss (1971) as:

$$CSR = 0.65(a_{\max}/g)\times(\sigma_{vo}/\sigma'_{vo})r_d \qquad (1)$$

where a_{max} is the peak horizontal acceleration at the later interest, g is the acceleration of gravity, σ_{vo} and σ'_{vo} are total and effective vertical overburden stresses, respectively, and r_d is stress reduction factor.

The simplified procedure proposed by Seed and Idriss (1971) and Seed et al. (1985) was employed to evaluate the liquefaction resistance (CRR) based on the SPT data. Meanwhile, the procedure by Robertson and Wride (1998)

were employed to analyze the liquefaction potential based on the CPT data. The 7.6 (Mw) magnitude measured for the Padang earthquake and the average PHGA of 0.40 g estimated from the attenuation relationship (Youngs et al. 1997; Atkinson et al. 2003) were used for all the analyses.

In order to quantify the potential risk of liquefaction, the liquefaction potential index proposed by Iwasaki et al. (1984) is used. The liquefaction potential index (I_L) is calculated by the following equation:

$$I_L = \int_0^{20} F w(z) dz, \quad (2)$$

which F=1-F_s for F_s <1.0 and F= 0 for $F_s \geq$1.0 and:

$$w(z) = 10 - 0.5z, \quad (3)$$

where $w(z)$ is the function for accounting for soil liquefaction with respect to depth and z is the depth (in meters).

Three potential risk categories are discussed:

0 – 5 : liquefaction risk is low
5 – 15 : liquefaction risk is high and
> 15 : liquefaction risk is very high

5.3. Results of Liquefaction Potential Analysis

The results obtained from SPT- and CPT-based empirical methods are presented in graphical form to show the depth and the thickness of potentially liquefiable soil layers for the NW-SE cross sections to represent the coastal and inland areas (Figures 8 and 9). The potentially liquefiable layers are shown in dashed line on these sections. All the liquefiable zones correspond to layers of sand to silty and a mixture of gravel and sand. The liquefiable zone is likely to become deeper and thinner southeastward. Moreover, the liquefaction potential becomes less pronounced toward the northeast due to the presence of finer grained soils and thicker cap soils.

5.4. Microzonation of Liquefaction Potential

As seen in Figure 10, the study area was divided into three zones from low liquefaction to very high liquefaction potential. The very high potential risk areas concentrate along the shoreline. The extent of these areas is larger in the northwestern part than in the southeastern part of the city. The potential risk decreases towards the northeast away from the coastal line

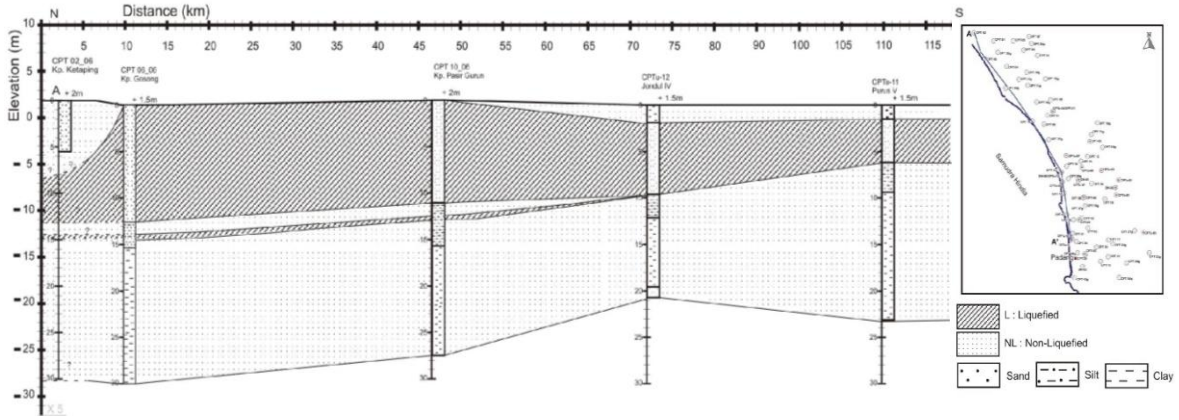

Figure 8 Cross section of potentially liquefiable soil layers across the line A-A'

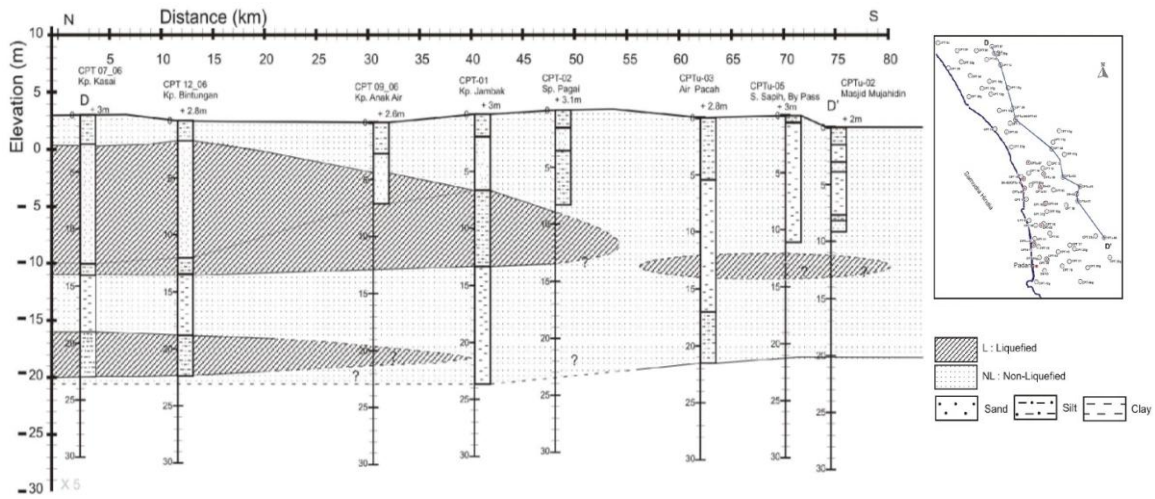

Figure 9 Cross section of potentially liquefiable soil layers across the line D-D'

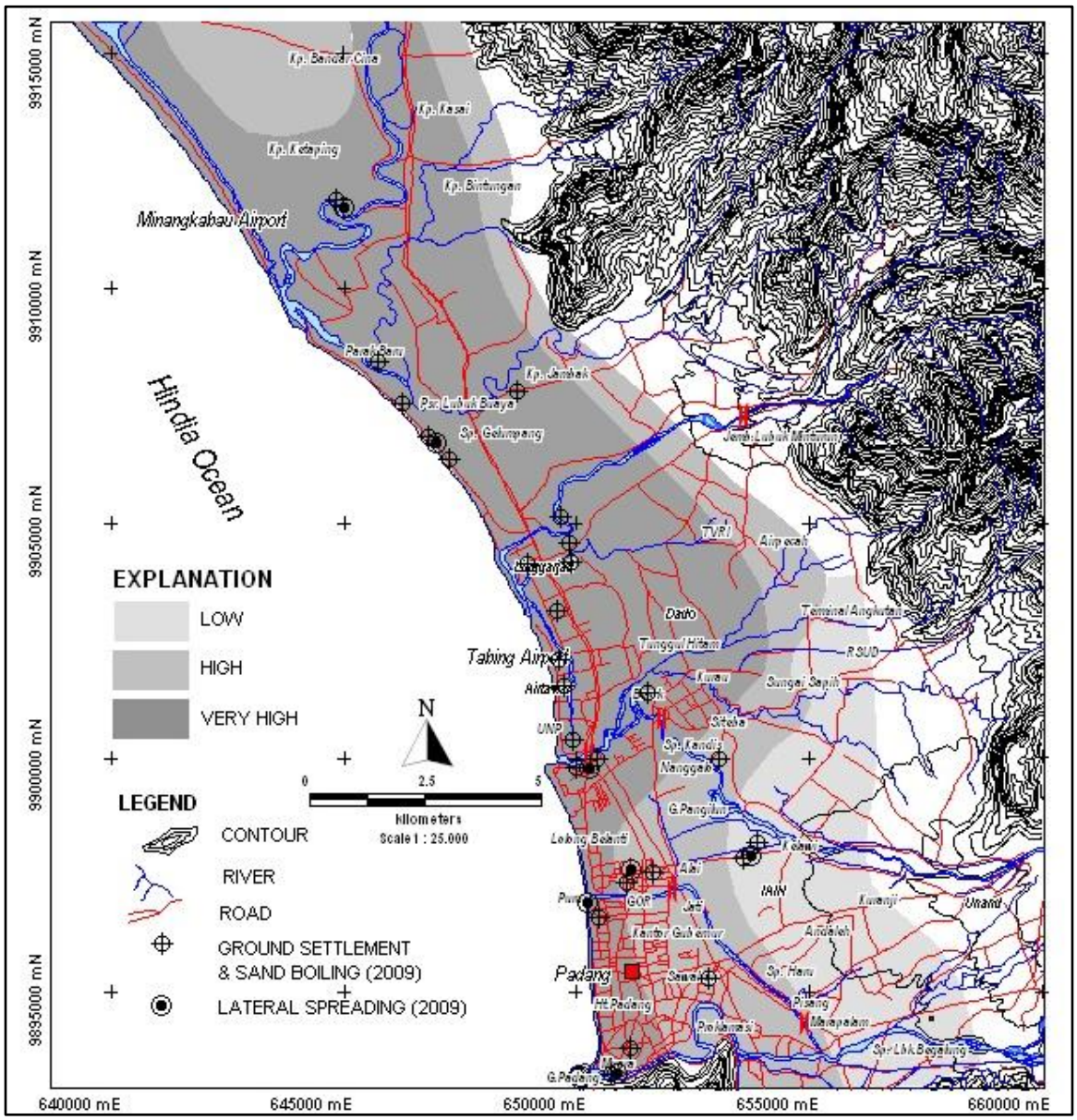

Figure 10 Liquefaction potential map of the Padang City region

Figure 10 also presents the plot of all the sites of observable liquefactions (i.e., ground settlement, lateral spreading) due to the 2009 Padang earthquake. It is clear that there is a generally good agreement between the predicted zones and the sites observed after the earthquake. In particular, Koto Tangah, Padang Utara, Padang Timur dan Padang Selatan Sub-Districts where sand boiling, ground settlement and lateral spreading were observed, fall into the very high to high liquefaction potential risk zones.

6. CONCLUSIONS

Based on the available geotechnical and information available from the site observation following the 2009 Padang earthquake, the liquefaction potential of the Padang City was evaluated. The liquefaction potential risk map established was compared to the liquefaction-affected areas. The main conclusions drawn are:

a. Liquefaction in the Padang City appears to have occurred primarily within the Quarternary deposit at shallow depth. The major regions of liquefaction and associated ground deformations are mainly located along the shoreline and associated with alluvial deposits.
b. A microzonation map of liquefaction potential risk for the Padang City was prepared. The zones representing the different degree of risk show good agreement with the field observations conducted after the 2009 earthquake event. Toward the southeast and the northeast,

the liquefaction potential of the soil layers becomes very low, probably due to the presence of finer grained soils and thicker cap soils.

Acknowledgements:

The authors acknowledge support from the Research Center for Geotechnology-Indonesian Institute of Sciences. This support makes possible the field investigations of the liquefaction potential in 2006 and 2008, and field observation of liquefaction phenomena in Padang after the earthquake.

References:

Atkinson, G.M., and D.M. Boore. (2003), "Empirical Ground Motion Relations for Subduction-Zone Earthquakes and Their Application to Cascadia and Other Regions", *Bulletin SSA*, v. **93**, 1703-1729.

EERI (2009), "The Mw 7.6 Western Sumatra Earthquake of September 30, 2009", Special Earthquake Report — December 2009.

McCaffrey, R. (1992), "Oblique Plate Convergence, Slip Vectors, and Forearc Deformation", *J. Geophys. Res*., **97**, 8905-8915.

Prawirodirdjo, L., Y. Bock, J.F. Genrich, S. S. O Puntodewo, J. Rais, C. Subarya, S. Sutisna. (2000), "One Century of Tectonic Deformation Along the Sumatran Fault From Triangulation and Global Positioning System Surveys", *J. Geophys. Res*., **105**, 28,343-28,363.

Robertson, P.K. and Wride, C.E. (1998). "Evaluating Cyclic Liquefaction Potential Using the Cone Penetration Test", *Canadian Geotechnical Journal*, **35** (3), 442-459.

Sakorlak (2009). "Recapitulation of West Sumatra EQ Impacts —Friday, October 23", circulated by UN OCHA, Sumatra.

Seed, H.B., Idriss, I.M. (1971), "Simplified Procedure for Evaluating Soil Liquefaction Potential," *J. Soil. Mech. Foundat. Div., ASCE* , **97**, no. SM9, 1249-1273.

Seed, H.B., Tokimatsu, K., Harder, L.F., and Chung, R.M. (1985), "Influence of SPT Procedures in Soil Liquefaction Resistance Evaluations", *J. Geotech. Engrg.*, **111**, 1425-1445.

Sieh, K. (2009), "Padang Earthquake Struck at Edge of Zone Where Much Bigger Quake is Expected", http://www.earthobservatory.sg/news/2009/.

Sieh, K., and Natawidjaja, D. (2000), "Neotectonics of the Sumatran Fault, Indonesia", *J.Geophys. Res*., **105**, 28,295-28,326.

Tohari, A., Soebowo, E., Daryono, M. D., Anwar, H. Z., Kumoro, Y., Wibowo, S., Galih, D. R., and Rahardjo, P. P. (2006), "Assessment of Liquefaction Potential Due To Earthquake for Padang City", *Research Report*, Research Center for Geotechnology, Bandung, 41 p (*in Indonesian*).

Tohari, A., Damayanti, M., Sugianti, K. (2008), "Engineering Geological Survey in Coastal Area of Padang City: Liquefaction potential and susceptibility, and quality of water resources", *Research Report*, Research Center for Oceanography, Bandung, 67 p (*in Indonesian*).

Youngs, R. R. et al. (1997), "Strong Ground Motion Attenuation Relationships for Subduction Zone Earthquakes," *Seismological Research Letters*, **68**, 58-73.

JOINT CONFERENCE PROCEEDINGS
7th International Conference on Urban Earthquake Engineering (7CUEE) &
5th International Conference on Earthquake Engineering (5ICEE)
March 3-5, 2010, Tokyo Institute of Technology, Tokyo, Japan

PERFORMANCE-BASED EARTHQUAKE EVALUATION OF A SINGLE COLUMN BRIDGE SYSTEM

Jinchi Lu[1], Kevin Mackie[2], and Ahmed Elgamal[3]

1) Assistant Project Scientist, Dept. of Structural Engineering, University of California, San Diego, CA 92093-0085, USA
2) Assistant Professor, Dept. of Civil and Env. Engineering, University of Central Florida, Orlando, FL 32816-2450, USA
3) Professor, Dept. of Structural Engineering, University of California, San Diego, CA 92093-0085, USA
jinlu@ucsd.edu, kmackie@mail.ucf.edu, elgamal@ucsd.edu

Abstract: A graphical user interface is under development to combine nonlinear dynamic time history analysis of coupled soil-structure systems with an implementation of performance-based earthquake engineering (PBEE). This user interface builds upon previous code that allowed for analysis of piles in a soil domain under nonlinear static and nonlinear dynamic loads (OpenSeesPL). Functionality was extended for analysis of multiple suites of ground motions and combination of results probabilistically using the performance-based earthquake engineering framework developed by the Pacific Earthquake Engineering Research (PEER) Center. Definition of the bridge and underlying ground configuration and material properties is greatly facilitated using this new interface. In addition, all stages of the involved analyses are conveniently executed in a systematic fashion, allowing the end user to investigate parametric or what-if scenarios on typical simple bridge configurations. In this paper, the main elements of this numerical framework are presented including the graphical user interface elements and the underlying theoretical framework. A pilot study of a simple bridge-ground model using this tool is also demonstrated.

1. INTRODUCTION

Performance-Based earthquake engineering (PBEE) emerged in recent years as a desirable approach towards the design of earthquake-resistant structures. PBEE aims to quantify the seismic performance and risk of engineered facilities using metrics that are of immediate use to both engineers and stakeholders. The Pacific Earthquake Engineering Research (PEER) Center, based at University of California at Berkeley, has been a major proponent for both the theoretical development of a PBEE methodology as well as deployment of the concepts into academia and industry, including incorporation of precepts into the next generation of building/design codes. PBEE as applied to buildings has seen rapid development and adoption recently (e.g., ATC-58 and ATC-63); however, in the bridge and infrastructure arena, there have been relatively few attempts at rigorous development of the data necessary for PBEE or packaging the tools in a form that allows rapid PBEE-based evaluation and assessment such as PACT. This is the motivation behind development of OpenSeesPL (*Bridge PBEE*), a graphical environment for finite element modeling of coupled soil-structure systems as well as complete PBEE assessment. The user interface builds upon previous code that allowed for analysis of piles in a three-dimensional soil domain under nonlinear static and nonlinear dynamic loads (Lu, 2006; Lu et al., 2006).

Specifically, the efforts to develop the OpenSeesPL (*Bridge PBEE*) user interface include (Mackie et al. 2010): i) build on the PEER PBEE framework by implementing all details within the graphical user-interface, ii) build a module for handling the needed input ground motion ensemble and computing the corresponding intensity measures (IMs), iii) modify the graphical interface to automatically generate user-defined bridge-ground FE models, and iv) build the post-processing capability to display the seismic response ensembles, and to display the PBEE outcomes. Elements of this framework are presented in this paper. A pilot investigation of a single-bent bridge that makes use of the graphical user-interface environment is presented.

2. PBEE ANALYSIS FRAMEWORK

PBEE considers seismic hazard, structural response, resulting damage, and repair costs associated with restoring a structure to its original function, using a fully consistent, probabilistic analysis of the associated parts of the problem (Cornell and Krawinkler, 2000). The uncertainty surrounding the PBEE framework components necessitates a probabilistic approach and acceptance criteria based on levels of confidence that probabilities of failure are acceptably small. Adoption of

such PBEE methodology in practice requires abandonment of prescriptive seismic safety specifications and acceptance of performance objectives defined in terms of quantities familiar to engineers, owners, managers, and stakeholders alike. This approach to earthquake engineering is, above all, sustainable because the underlying framework is independent of the performance objectives selected for the particular evaluation or design project, thus allowing for seamless adaptation to specific project needs, new design methods, and innovative structural systems.

A rigorous yet practical implementation of the PEER PBEE methodology was adapted for use in the developed graphical user interface. The methodology is subdivided to achieve performance objectives stated in terms of the probability of exceeding threshold values of socio-economic decision variables (DVs) in the seismic hazard environment under consideration. The PEER PBEE framework utilizes the total probability theorem to disaggregate the problem into several intermediate probabilistic models. This disaggregation of the decision-making framework outcome involves the following intermediate variables: repair quantities (Q), damage measures (DMs), engineering demand parameters (EDPs), and seismic hazard intensity measures (IMs). Consequently, engineers may choose to scrutinize probabilities of exceeding an EDP, such as strain, while an owner may choose to scrutinize probabilities of exceeding a DV, such as repair cost. An important step enabling effective aggregation of decision data is the association of structural elements and assemblies into performance groups (PGs) based on commonly used repair methods. The numerical implementation of the methodology is described in Mackie et al. (2009).

The EDPs are computed directly from the ensemble of time history analyses performed. These are automatically associated with the PGs and the damage states DSs for each. For example, additional bridge bents will automatically generate additional drift recorders and the distribution of maxima from multiple ground motion records will be compared to a set of damage fragility curves computed for each column PG. The data used to populate the relationships that associate EDPs to DMs and DMs to Qs were previously described in Mackie et al. (2007). There exist default values for all of the built-in repair quantities, including the unit costs and production rates for each one of these items. However, the user has the ability to modify these if more state-specific or site-specific information is available.

3. BRIDGE PBEE USER INTERFACE

The major components of a PBEE analysis in OpenSeesPL (*Bridge PBEE*) (Figure 1) are: specification of ground motions, mesh and soil constitutive model determination, bridge superstructure model and constitutive model determination, specification of PGs and the associated PBEE quantities, and the myriad of post-processing capabilities.

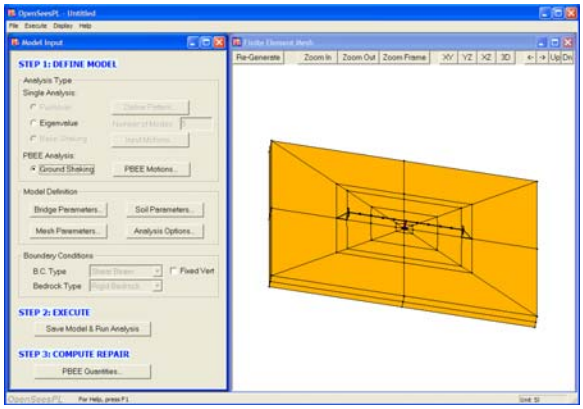

Figure 1 OpenSeesPL (*Bridge PBEE*) user interface

3.1 Specification of Ground Motion Input

The framework allows selection of individual ground motions, suites of ground motions, and bins of ground motions. At the current time, all motions are obtained from the PEER NGA database (http://peer.berkeley.edu/nga/) with a future option of importing arbitrary delimited text files or to search the NGA database interactively through a socket. An ensemble of 100 selected ground motions is employed in the PBEE analysis illustrated in this paper. Each motion is composed of 3 perpendicular acceleration time history components (two lateral and one vertical). These motions were selected through earlier efforts (Gupta and Krawinkler, 2000; Mackie et al., 2007) and were selected to be representative of seismicity in typical regions of California. The motions are divided into 5 bins of 20 motions each with characteristics: i) moment magnitude (Mw) 6.5-7.2 and closest distance (R) 15-30 km, ii) Mw 6.5-7.2 and R 30-60 km, iii) Mw 5.8-6.5 and R 15-30 km, iv) Mw 5.8-6.5 and R 30-60 km, and v) Mw 5.8-7.2 and R 0-15 km. The user selects this motion ensemble by specifying the folder where the motion time histories have been stored in text files (Figure 2).

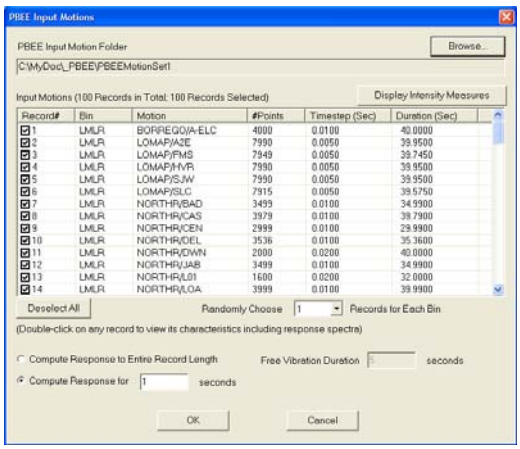

Figure 2 Ground motion selection screen

For each set of 3 orthogonal acceleration time histories, a large number of IMs are calculated, including peak ground acceleration (PGA), peak ground velocity (PGV), peak ground displacement (PGD), Arias intensity, strong motion duration (D5-95), and cumulative absolute velocity (CAV). The IMs are calculated and displayed as a vector (one value for each shaking direction), and also in the form of the square root-sum-of-squares (SRSS) in the two horizontal directions (Figure 3). In addition, for each ground motion component, time histories and frequency domain (spectral) displays are provided for acceleration, velocity, and displacement (Figure 4). The user can obtain this information by selecting an individual motion (Figure 2).

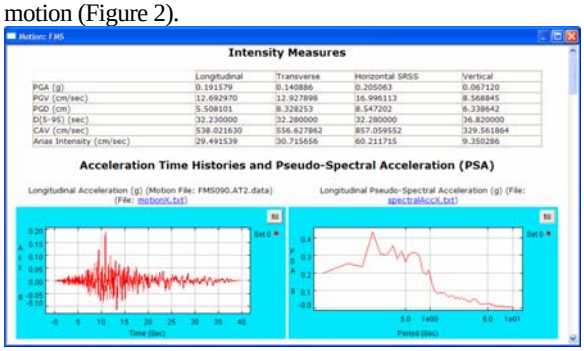

Figure 3 IMs computed for FMS090 record (Loma Prieta 1989 Federal Medical Station)

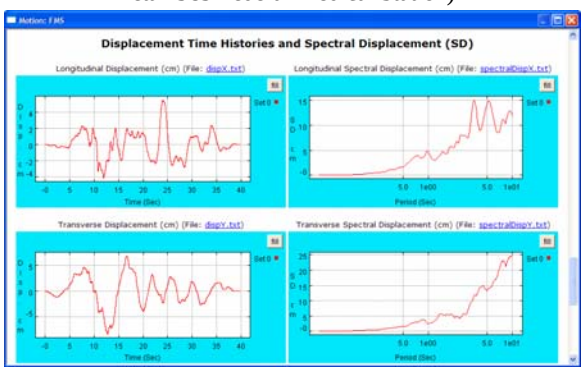

Figure 4 Displacement time history and spectral displacement for FMS record

While the ability to scrutinize individual records has numerous benefits, the use of PBEE necessitates the inclusion of multiple ground motions. Once these motions have been selected and/or binned, it is of interest to see what the salient characteristics (IMs) are of the group or bin of ground motions. These characteristics for the entire ground motion ensemble are automatically generated and displayed in the form of histograms and cumulative distribution functions (CDF) for each of the IMs calculated. For example, the distribution of PGA values (Figure 5) shows the majority of records utilized have less than or equal 0.25 g PGA; however, the suite contains motions with PGAs as large as 1g.

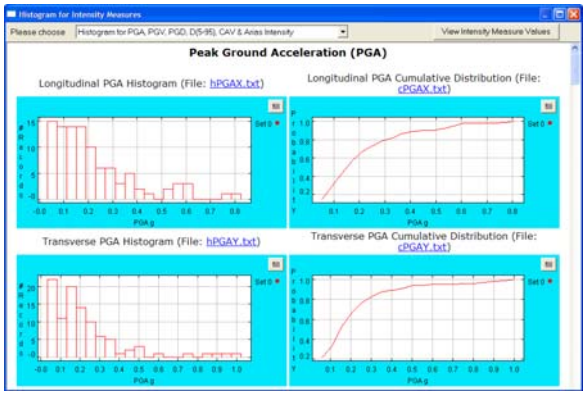

Figure 5 100 motion PGA distribution

3.2 Bridge-Ground Finite Element Model

The bridge-ground configurations available for construction in the user interface are currently based on single column bents extending into integral Type 1 pile shafts below grade. Mesh refinement is performed automatically surrounding each pile shaft in the ground. The columns are modeled as nonlinear beam-column elements with fiber cross sections. The user has the ability to configure the cross-sectional properties, shape, and materials. The current user interface supports reinforced concrete columns only. The deck is also modeled using two-noded beam-column elements discretized into five separate elements along each clear span. The deck is assumed to be capacity designed so that it responds in the elastic range. The gross or cracked section properties can be specified by the user. At the current stage of development, the approach ramp model connects the bridge longitudinal boundaries to the ground motion as specified by motion of the soil domain below the abutments (Figure 6).

Several abutment models are currently available and provide the interface between the approach ramps and the bridge ends. These abutment options include roller, elastic, simplified, and spring as described below.

The roller abutment model consists of a simple boundary condition module that applies single-point constraints for displacement in the vertical direction and rotation about the bridge longitudinal axis. The elastic abutment model is similar, except it has explicit user-configurable elastic stiffness values in all six degrees-of-freedom between the approach ramp and deck. The simplified abutment model consists of a rigid element of the same length as the superstructure width, connected through a rigid joint to the superstructure centerline, with defined longitudinal, transverse, and vertical nonlinear response at each end. The longitudinal response accounts only for the gap and the embankment fill response, where passive pressures are produced by the abutment back wall pushing into the fill. The corresponding elastic-perfectly-plastic (EPP) backbone curve is assigned properties obtained from the Caltrans SDC (2004). Shear resistance of the bearing pads is

ignored. In the transverse direction, a zero-length element is defined at each end of the rigid link with an assigned EPP backbone curve representing the backfill, wing wall, and pile system response. Resistance of the brittle shear keys and distributed bearing pads is ignored in this model for simplicity. In the vertical direction, an elastic spring is defined at each end of the rigid link, with a stiffness corresponding to the bearing pads stiffness. Stiffness of the pads in compression and tension is assumed to be identical.

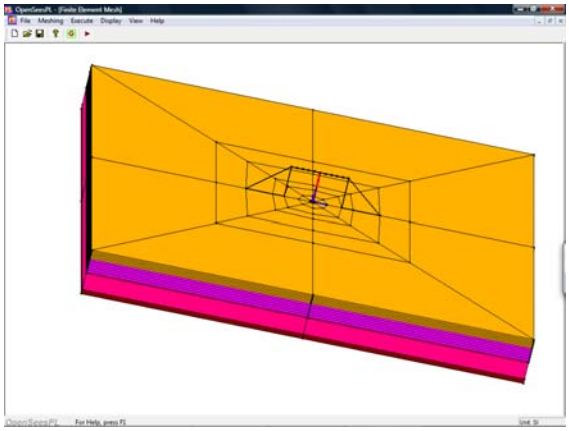

Figure 6 Perspective view of 3D bridge-ground domain with different soil layers.

The spring abutment model also includes longitudinal, transverse, and vertical nonlinear response. The longitudinal response is based on the system response of the elastomeric bearing pads, gap, abutment back wall, abutment piles, and soil backfill material. Prior to impact or gap closure, the superstructure forces are transmitted through the elastomeric bearing pads to the stem wall, and subsequently to the piles and backfill, in a series configuration. After gap closure, the superstructure bears directly on the abutment back wall and mobilizes the full passive backfill pressure. A system of zero-length elements is distributed along two rigid elements oriented in the transverse bridge direction, connected together by bearing pads. The transverse response is based on the system response of the elastomeric bearing pads, exterior concrete shear keys, abutment piles, wing walls, and backfill material. Transverse stiffness and strength of the backfill, wing wall, and pile system is calculated using the same modification of the SDC (2004) procedure for the longitudinal direction as defined for the simplified abutment model. Stiffness and strength are distributed equally to the two extreme zero-length elements of the second rigid element. Vertical response of the abutment model includes the vertical stiffness of the bearing pads in series with the vertical stiffness of the trapezoidal embankment. The abutment is assumed to have a nominal mass proportional to the superstructure dead load at the abutment, including a contribution from structural concrete as well as the participating soil mass. More details on the abutment models can be found in Aviram et al. (2008).

Finally, the ground domain is specified by: i) definition of the zone occupied by the pile in terms of its diameter, ii) definition of ground below the bridge, iii) definition of the domain to support the approach ramp and abutment zones, iv) definition of the outer free-field lateral extent, and v) definition of the ground layer depth. Along the depth, the thickness of laterally uniform soil layers may be specified in order to capture the site stratification characteristics. Properties of each layer are defined by selection from an available set of soil models and model properties. A shear-beam type boundary condition is employed for the soil domain, i.e., at any given depth, displacement degrees of freedom of both sides of the longitudinal (and transverse) boundaries are tied together (both horizontally and vertically) to reproduce a 1D shear wave propagation mechanism effect.

3.3 Performance-based Earthquake Engineering Quantities

During transient analysis for each ground motion (either as a single ground motion analysis or as part of the ensemble of PBEE motions), response quantities are tracked at each time step. The response quantities of interest are tied directly the PGs that are used in the PBEE analysis for assessing damage and repair. Each major bridge component is grouped into a PG. Each PG contains a collection of components that reflect global-level indicators of structural performance and that contribute significantly to repair-level decisions. The notion of a PG allows grouping several components for related repair work; therefore PGs are not necessarily the same as the individual load-resisting structural components. The PGs (and associated EDP) used in this pilot study are: PG1 - maximum column drift ratio, PG2 - residual column drift ratio, PG3 - maximum relative left deck-end/abutment displacement, PG4 - maximum relative right deck-end/abutment displacement, PG5 - maximum absolute bearing displacement (left abutment), PG6 - maximum absolute bearing displacement (right abutment), PG7 - approach residual vertical displacement (left abutment), PG8 - approach residual vertical displacement (right abutment), PG9 – left abutment residual pile cap displacement, PG10 – right abutment residual pile cap displacement, and PG11 - column residual pile cap displacement.

Discrete damage states (DS) are defined for each performance group. Each damage state has an associated repair method that also has a subset of different repair quantities (Qs). Once the Qs have been established for a given scenario (damage to different PGs), the total repair costs can be generated through a unit cost function. In addition, an estimate of the repair effort can be obtained through a production rate for each Q. The user has the ability to modify the default values specified for all of the repair quantities per damage state, unit costs, and

production rates. More information on the derivation of the default DSs, Qs, unit costs, and production rates can be found in Mackie et al. (2007). For the purposes of the user interface, an estimate of the replacement cost of the bridge is automatically generated based on the square footage of the deck and the Caltrans Comparative Bridge Costs (CBC) data, corrected to be consistent with the year 2007 cost data used in the calibration of the unit costs. The CBC includes a 10% mobilization cost but does not include any costs for demolition or removal of existing infrastructure.

4. PILOT SINGLE-BENT BRIDGE CASE STUDY

Earlier, the most prevalent ordinary construction types for new California bridges were selected for a study on the relationship between bridge construction cost and design ground motion level (Ketchum et al., 2004). Of the eleven typical types and configurations, two continuous, five-span, straight, post-tensioned, cast-in-place, box girder bridges on monolithic piers were selected for previous PEER studies (Mackie et al., 2007). Common to both of the bridge types selected are 3 internal spans of 45.7m (150 ft) and 2 end spans of 36.6m (120 ft). The decks are 1.83m (6 ft) deep cast-in-place CIP post-tensioned box girders that accommodate 2 lanes of traffic plus shoulders and barriers on both sides. All bents contain a single monolithic column. The bridge designated as Type I has 6.7m (22 ft) clear column heights. The abutments at both ends of the bridge are of a seat type. For the pilot investigation using OpenSeesPL (*Bridge PBEE*), the same dimensions were selected, but using only a single bent (two spans of 45m).

The finite element mesh for bridge model is shown in Figure 7. Eight nonlinear beam-column elements are used for the bridge column and 416 brick elements used for the soil domain in this pilot study. A 10 m cohesive soil layer (Cohesion = 43 kPa) is assumed.

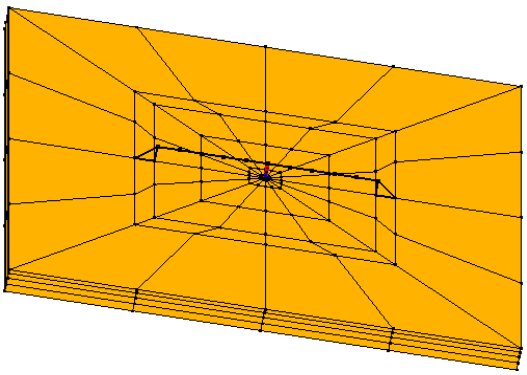

Figure 7 Finite element mesh employed in the pilot study

5. PBEE STUDY RESULTS

The salient PBEE response outcomes are listed in Table 1. The disaggregation of cost by performance group is performed at the maximum value of the SRSS of the two horizontal PGVs (167 m/sec). Note that PGs 7 and 8 do not contribute in this study because no nonlinearities are included in the approach ramp. Contribution to expected repair cost ($) from each performance group against PGV is shown in Figure 8.

One benefit of the PBEE method utilized in the user interface is that the intensity-dependent repair cost or repair time response can be obtained for each simulation. One convenient method of expressing cost is in terms of the repair cost ratio (RCR), or the repair cost normalized by the replacement cost. The mean and ±1 standard deviation RCR values are shown in Figure 9. The user has the ability to specify three intensity hazard levels at a selected site (e.g., 2% probability of exceedance in 50 years). The derivative of a fitted power-law hazard curve is then integrated with the RCR-IM probabilistic relationship to obtain a loss hazard curve, as shown in Figure 10.

Table 1 PBEE outcomes at PGV = 167 cm/sec (see Section 3.3 for PG descriptions)

Total repair cost	$877,933
Contribution from PG 1	$35,516
Contribution from PG 2	$39,259
Contribution from PG 3	$182,223
Contribution from PG 4	$182,223
Contribution from PG 5	$90,488
Contribution from PG 6	$90,488
Contribution from PG 9	$5
Contribution from PG 10	$4
Contribution from PG 11	$257,727

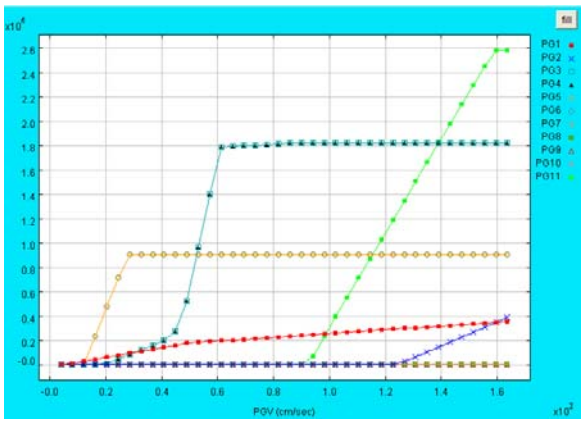

Figure 8 Contribution to expected repair cost ($) from each performance group

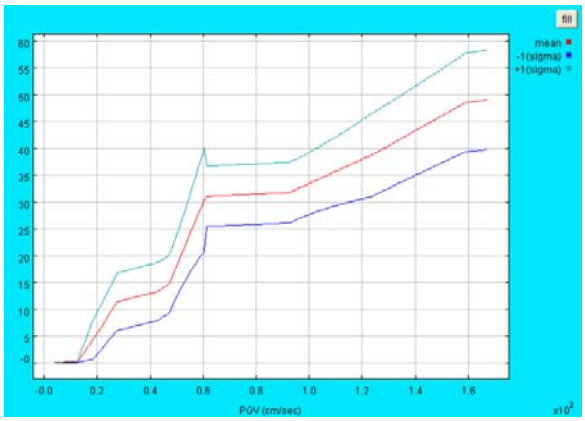

Figure 9 Intensity-dependent RCR (in percent)

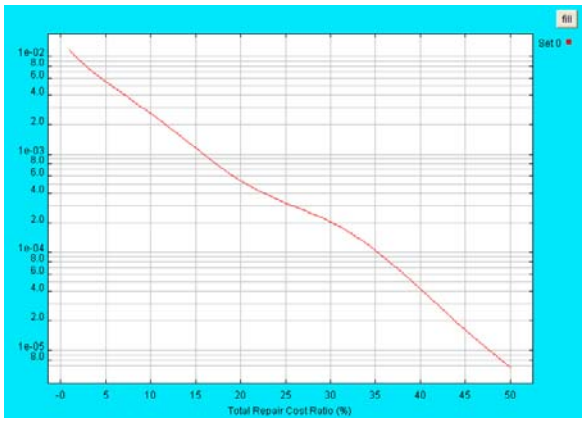

Figure 10 RCR hazard curves (vertical axis: mean annual frequency of exceedance)

5. CONCLUSIONS

By coupling a refined graphical user interface for modeling of bridge-ground FE models with a PBEE framework, OpenSeesPL (*Bridge PBEE*) has enabled more transparent access to performance-based assessment for typical highway bridges. The elements of this framework were presented in this paper along with a pilot investigation of a single-bent bridge model. The pilot study is one illustration of the parametric studies that are possible with the user interface. Sufficient flexibility is provided in the interface that the users can select their own ground motion suites, bridge geometry and configuration, constitutive models, unit costs, and production rates. The interface allows the user, be it a researcher or a practitioner, to focus on the PBEE outcomes and decision variable drivers rather than becoming inundated with the details of ground motion selection, FE modeling, constitutive model parameter calibration, and damage and repair data selection.

Acknowledgements:

This work was supported primarily by the Pacific Earthquake Engineering Research Center (PEER). Contributions, guidance, and feedback from PEER researchers working within the PEER Bridge Group, led by Professors Ross Boulanger and Stephen Mahin, are gratefully acknowledged. The data for this PBEE user interface draws heavily from previous PEER projects and would not have been possible without collaboration with the California Department of Transportation. In particular, Mike Keever, Steve Sahs, Tom Shantz, and Richard Porter contributed the data needed to complete the simulations and to establish the repair cost and repair time databases.

References:

Aviram, A, Mackie, K.R., and Stojadinovic, B., 2008. Effect of abutment modeling on the seismic response of bridge structures. *Earthquake Engineering and Engineering Vibration* 7(4), 395-402.

Caltrans SDC, 2004. Caltrans Seismic Design Criteria version 1.3, California Department of Transportation, Sacramento, California.

Cornell, C. A. and Krawinkler, H., 2000. Progress and challenges in seismic performance assessment. *PEER Center News* 3(2).

Gupta, A., and Krawinkler, H., 2000. Behavior of ductile SMRFs at various hazard levels. *Journal of Structural Engineering*, 126(ST1), 98-107.

Ketchum, M., Chang, V., and Shantz, T., 2004. Influence of Design Ground Motion Level on Highway Bridge Costs. *Report No. Lifelines 6D01*, University of California, Pacific Earthquake Engineering Research Center, Berkeley CA.

Lu J., 2006. Parallel finite element modeling of earthquake site response and liquefaction, *PhD Thesis*, Department of Structural Engineering, University of California, San Diego, La Jolla, CA.

Lu, J., Yang, Z., and Elgamal, A., 2006. OpenSeesPL three-dimensional lateral pile-ground interaction version 1.00 user's manual. *Report No. SSRP-06/03*, Department of Structural Engineering, University of California, San Diego.

Mackie, K.R., Lu, J., and Elgamal, A., 2010. User Interface For Performance-Based Earthquake Engineering: A Single Bent Bridge Pilot Investigation. Proceedings of the Ninth US National and Tenth Canadian Conference on Earthquake Engineering: Reaching Beyond Borders, Toronto, Canada, July 25-29 (in review).

Mackie, K.R., Wong, J-M., and Stojadinovic, B., 2010. Post-earthquake bridge repair cost and repair time estimation methodology. *Earthquake Engineering & Structural Dynamics*, in press.

Mackie, K.R., Wong, J-M., and Stojadinovic, B., 2007. Integrated Probabilistic Performance-Based Evaluation of Benchmark Reinforced Concrete Bridges, *Report No. 2007/09*, Pacific Earthquake Engineering Research Center, University of California, Berkeley.

JOINT CONFERENCE PROCEEDINGS
7th International Conference on Urban Earthquake Engineering (7CUEE) &
5th International Conference on Earthquake Engineering (5ICEE)
March 3-5, 2010, Tokyo Institute of Technology, Tokyo, Japan

EFFECTS OF ROUGHNESS OF SHALLOW FOUNDATION SURFACE ON SUPERSTRUCTURE RESPONSE DURING A STRONG EARTHQUAKE

Shuji Tamura[1], Keisuke Adachi[2], Kohji Tokimatsu[3]

1) Associate Professor, DPRI, Kyoto University, Japan
2) Graduate Student, Kyoto University, Japan
3) Professor, Tokyo Institute Technology, Japan
tamura@sds.dpri.kyoto-u.ac.jp

Abstract: Dynamic centrifuge tests were performed on a soil-footing-superstructure model to investigate effects of the footing surface roughness on the superstructure response during a strong earthquake. The footing model with smooth or rough surfaces was either placed on the soil or embedded into the sand. The following conclusions were drawn. (1) A smooth footing surface on the soil reduces the superstructure's horizontal acceleration and rocking motion of the footing. (2) A smooth surface of the embedded footing in the dry sand does not markedly affect the superstructure horizontal acceleration but does increase the rocking motion of the footing. (3) The footing with a smooth surface on the soil apparently slid, but the embedded footing with smooth surface slid only slightly because the earth pressure, of which the amplitude was about half of the base friction, restricted the footing.

1. INTRODUCTION

Extremely high peak ground acceleration and velocities more than 1700 cm/s^2 and 140 cm/s, respectively, have been observed during recent earthquakes in Japan. Despite the extremely strong motions that were recorded, structural damage, especially to low-rise buildings, was slight. Apparently, the unexpectedly minor structural damage was the result of nonlinear soil–structure interaction.

The soil–structure interaction of a shallow foundation depends mainly on the friction force acting on a footing base and the earth pressure acting on active/passive sides. Friction amplitude between sand and a structure is affected by the roughness of the structure (Uesugi et al.). The seismic passive earth pressure amplitude also depends on the wall friction angle, based on the Mononobe–Okabe theory, indicating that earth pressure is also affected by the roughness of active/passive side walls. This idea suggests that the foundation surface roughness can affect the superstructure response. However, knowledge of the effects of the shallow foundation surface roughness on the superstructure response remains limited.

This study is intended 1) to investigate the effects of footing surface roughness on the superstructure response during a large earthquake, 2) to evaluate the base friction and earth pressure acting on a footing with surfaces of different roughness. Dynamic centrifuge tests on a superstructure–footing model with smooth and rough surfaces were performed, in which the footing was either placed on the ground surface or embedded in the sand layer.

2. CENTRIFUGE TESTS PERFORMED

2.1 Test cases

Centrifuge tests were performed at 40 × *g* centrifugal acceleration using the geotechnical centrifuge at the Disaster Prevention Research Institute, Kyoto University. A footing–superstructure model was prepared in a laminar shear box with inner dimensions of 450 mm (length) × 150 mm (width) × 200 mm (height). Four cases of the performed tests are presented in Fig. 1 and Table 1. The soil model used for the dry sand deposit was Toyoura sand (D_{50}=0.21 mm) with Dr=90%. The sand was air pluviated. The soil model heights were 148 mm. A superstructure–footing model was set on the ground surface for Cases 1 and 2. The soil model heights were 198 mm; the footing was embedded 50 mm into the dry sand layer for Cases 3 and 4. The distance from the footing base to the shear box bottom is 148 mm, which is equal to that for Cases 1 and 2. Table 2 presents weights and dimensions of the footing–superstructure model in the model and prototype. The footing was modeled with aluminum alloy

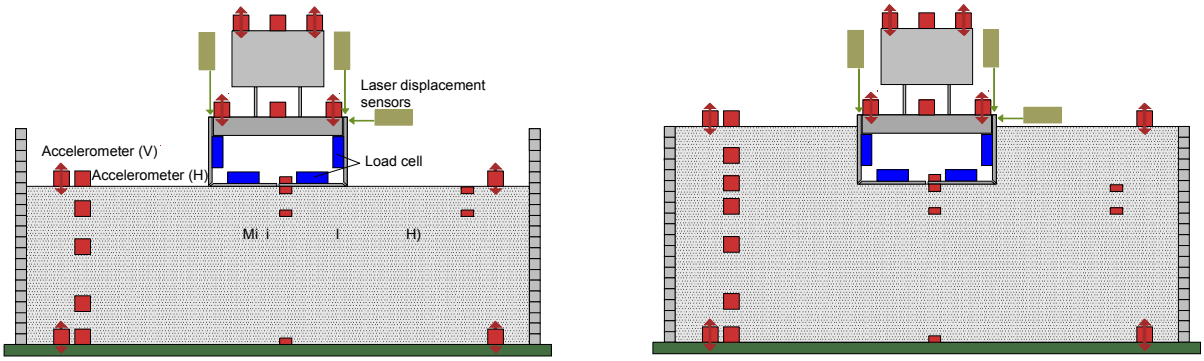

(a) Cases 1 and 2 (b) Cases 3 and 4

Figure 1 Test cases and sensor locations

of 124 mm (shaking direction) × 64 mm (width) × 52 mm (height). Toyoura sand was pasted on the footing surface for Cases 2 and 4. The superstructure, 2.0 kg, was modeled with rigid brass and supported by two plate springs. The footing was 1.0 kg. The natural frequency of the superstructure and damping constant under the fixed footing condition were about 105 Hz and 0.5%.

To evaluate the friction between the footing base and the soil underneath accurately, the base of the footing was made of two separate plates of equal size, each supported by small load cells, as presented in Fig. 1. The load cells were capable of separate measurements from the horizontal shearing and vertical compressive forces, which act orthogonally on the base plates. Two plates supported by load cells were also set up on the active and passive sides of the footing to evaluate the earth pressure. The load cells were available for measurement of horizontal compressive and vertical shear forces, acting orthogonally on active and passive sides. The baselines of the base friction and earth thrust were set to zero before the shaking tests.

During the shaking table test, the horizontal accelerations of the superstructure, footing, and soil, the vertical accelerations of the footing, ground surface and shear box bottom, and the horizontal and vertical displacements of the footing were measured along with the forces acting on the base, and active and passive sides of the footing.

The excitation used for the test was Rinkai92, which is a synthesized ground motion for the Tokyo Bay area. The maximum acceleration of the shaking table was scaled to about 800 cm/s^2. All data presented herein are of prototype scale.

3. CENTRIFUGE TEST RESULTS

3.1 Soil–structure responses for Cases 1 and 2

Figures 2 and 3 respectively depict the time histories of the horizontal acceleration of the input, ground surface,

Table 1 Test cases

Case	Foundation embedment	Footing surface roughness
Case 1	No	Smooth
Case 2	No	Rough
Case 3	Yes	Smooth
Case 4	Yes	Rough

Table 2 Conditions of footing-superstructure model in prototype and model scale

		Unit	Prototype	Model
Footing	Mass	kg	64,000	1.0
	Length (L×B×H)	m	4.96×2.56×2.08	0.124×0.064×0.052
Structure	Mass	kg	128,000	2.0
	Natural frequency	Hz	3.8	105

footing and superstructure, the displacement of ground surface and footing, and the footing rotation for Cases 1 and 2. The displacement, measured by laser displacement sensors, was interrupted during the tests because the footing moved considerably and the laser beams missed the targets. The displacements were calculated according to the double integration of the accelerometer recordings. Therefore, the displacement data presented in this paper correspond to those of the dynamic component. The footing rotations were evaluated by the vertical displacement of left and right side of the footing, which were also calculated by the double integration of the acceleration.

The maximum horizontal acceleration of the ground surface is less than that of the input motion in both cases, suggesting that the sand layer shows strong nonlinearity. The maximum horizontal accelerations of the superstructure for Cases 1 and 2 are, respectively, 533 cm/s^2 and 714 cm/s^2. The superstructure acceleration peaks for Case 1 tend to be smaller than those for Case 2. The

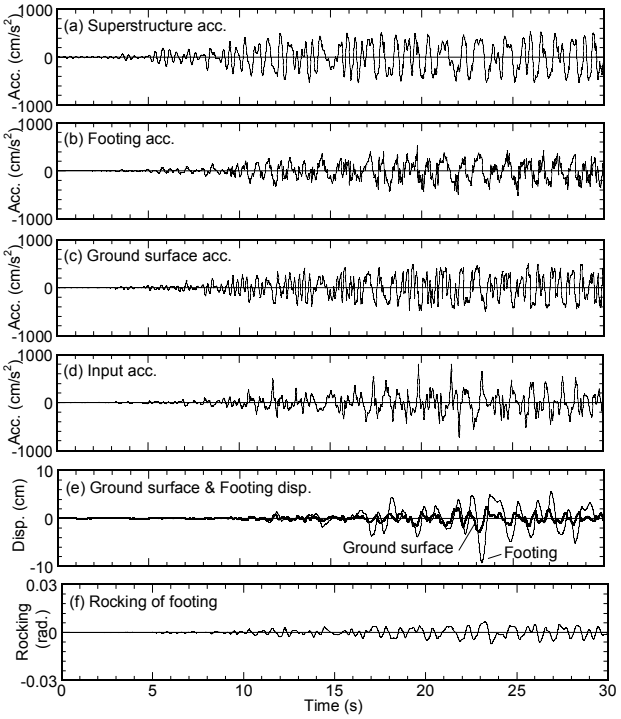

Figure 2 Time histories of acceleration, displacement and footing rotation (Case 1)

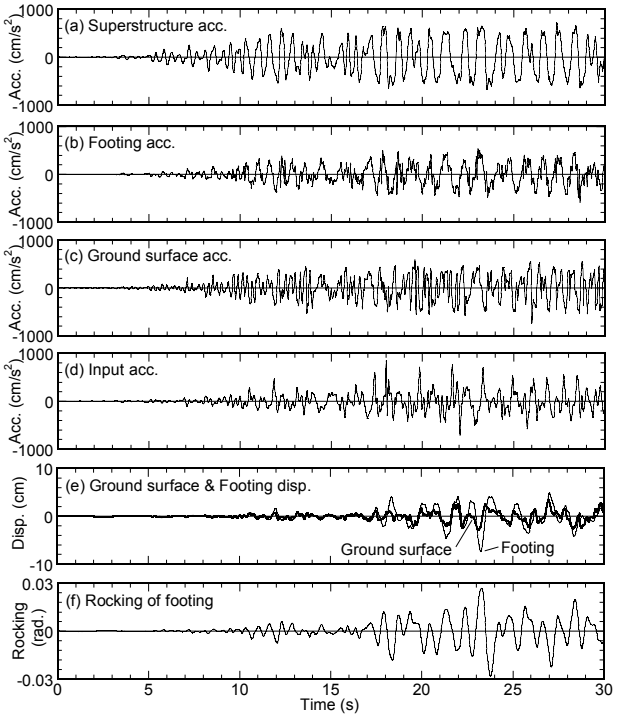

Figure 3 Time histories of acceleration, displacement and footing rotation (Case 2)

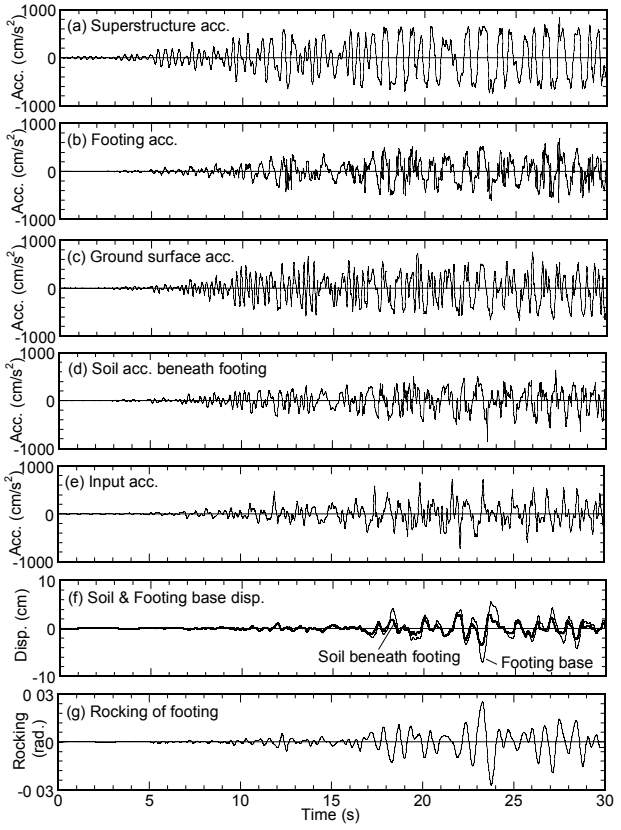

Figure 4 Time histories of acceleration, displacement and footing rotation (Case 3)

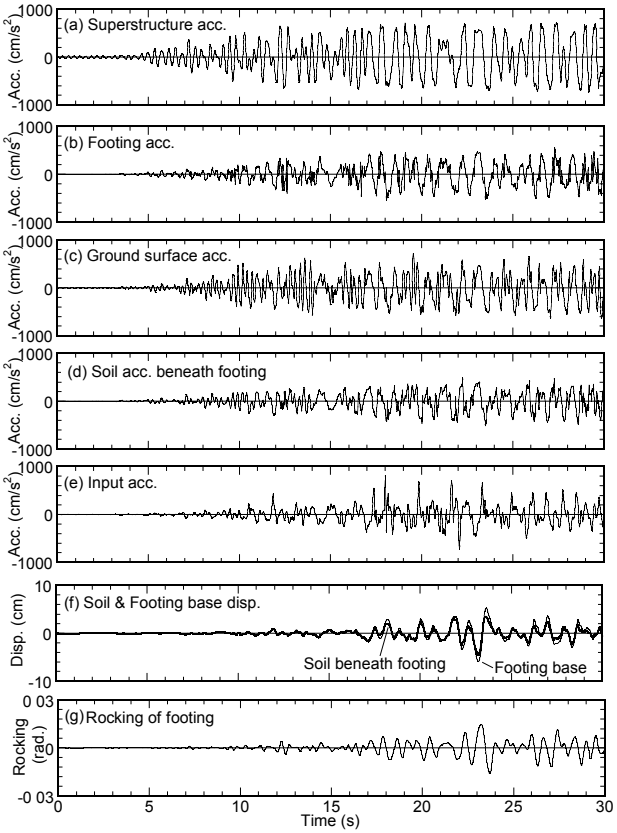

Figure 5 Time histories of acceleration, displacement and footing rotation (Case 4)

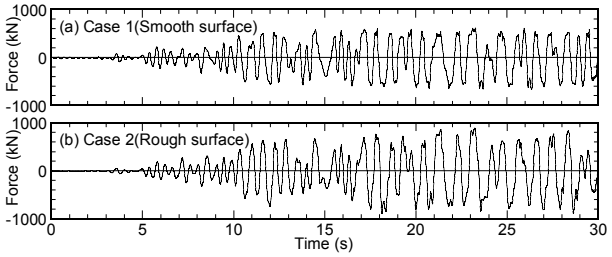

Figure 6 Time histories of base friction of the footing on ground surface (Cases 1 and 2)

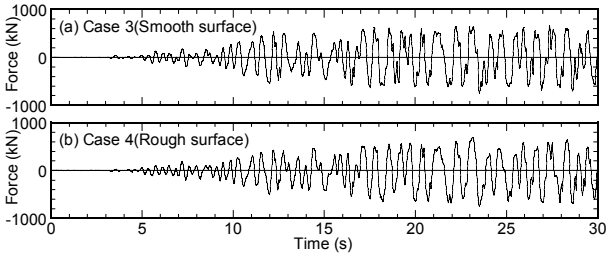

Figure 7 Time histories of base friction of the embedded footing in sand layer (Cases 3 and 4)

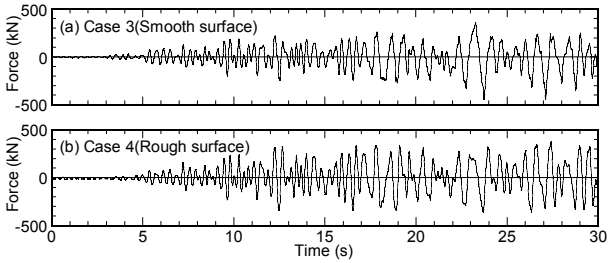

Figure 8 Time histories of total earth thrust (Cases 3 and 4)

ground surface displacements in both cases are almost identical. The footing displacement for Case 1 is apparently larger than that for Case 2. The footing rotation for Case 1 is less than that for Case 2. The description above indicates that the smooth surface of the footing base on the soil reduces the superstructure acceleration and the footing rotation, but it increases the footing displacement.

3.2 Soil–structure responses for Cases 3 and 4

Figures 4 and 5 respectively depict the time histories of the horizontal acceleration of input, soil beneath the footing, ground surface, footing and superstructure, the displacement of footing and soil beneath the footing, and the footing rotation for Cases 3 and 4. The maximum accelerations of the ground surface were, respectively, 748 cm/s^2 and 714 cm/s^2 for Cases 3 and 4. The acceleration amplitudes of the soil beneath the footing were apparently less than those of the ground surface in both cases. The superstructure acceleration peaks for Case 3 resemble those for Case 4. The footing displacement for Case 3 is greater than that for Case 4. The footing rotation for Case 3 is greater than that for Case 4. Taken together, these indicate that the smooth footing surface does not significantly affect the horizontal superstructure acceleration, but it increases the footing rocking motion. These tendencies differ from data recorded for Cases 1 and 2.

3.3 Base friction and earth pressure acting on the footing

The time histories of the horizontal base friction acting on the footing for Cases 1 and 2 are shown in Fig. 6. The base friction amplitude for Case 1 tends to be about 75% of that for Case 2, indicating that the smooth surface base reduced the base friction. The structure inertia defined by the sum of the superstructure and footing inertial forces is equivalent to the base friction force because the base friction is the only reaction force to the structure inertia. Therefore, the smooth surface of the base reduced the structure inertial force, suggesting that the horizontal acceleration of the superstructure also decreased, as shown in Figs. 2(a).

Figure 7 depicts time histories of the horizontal base friction acting on the embedded footing for Cases 3 and 4. The amplitudes of the base friction for Cases 3 and 4 were almost identical, indicating that the footing base roughness does not markedly affect the base friction. This tendency differs from that for Cases 1 and 2.

Figure 8 shows time histories of the total earth thrust acting on the embedded footing for Cases 3 and 4. The total earth thrust $E_{H(\text{total})}$ is

$$E_{H(\text{total})} = E_{H(\text{right})} + E_{H(\text{left})} \quad (1)$$

Therein, $E_{H(\text{right})}$ and $E_{H(\text{left})}$ respectively signify the earth thrust at the right and left sides of the footing. The maximum amplitude of the total earth thrust peaks for Case 3 was larger than that for Case 4. Most total earth thrust peaks for Case 3, however, are less than that for Case 4.

4. DISCUSSION

4.1 Footing roughness and superstructure response

To investigate the base friction effects on the superstructure response, the relation between relative displacement and the base friction of the footing on the soil for Cases 1 and 2 are shown in Figs. 9. The relative displacements reflect the differences between the footing base plate and the soil displacement beneath the footing. The friction–displacement loop for Case 1 differs greatly from that for Case 2. The base friction for Case 1 reached the maximum amplitude—about 500 kN at small displacement—and tended to remain constant, indicating that the footing with a smooth surface slid on the soil. Therefore, the base friction, i.e. the structure inertia amplitude, was limited. Additionally, sway motion was dominant and rocking

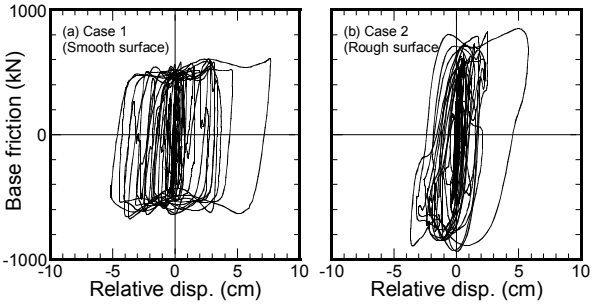

Figure 9 Relation between relative displacement and base friction of the footing on ground surface (Cases 1 and 2)

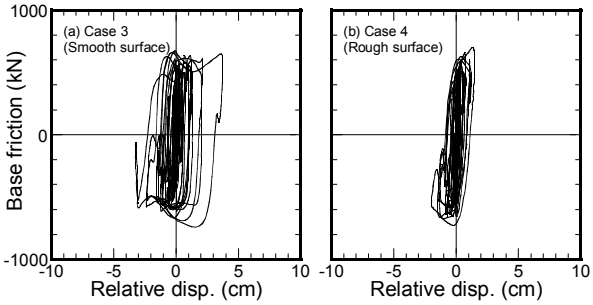

Figure 10 Relation between relative displacement and base friction of the embedded footing (Cases 3 and 4)

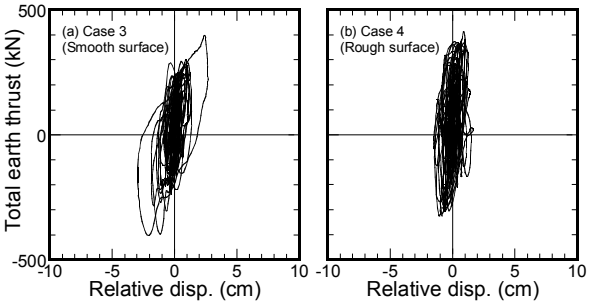

Figure 11 Relation between relative displacement and total earth thrust (Cases 3 and 4)

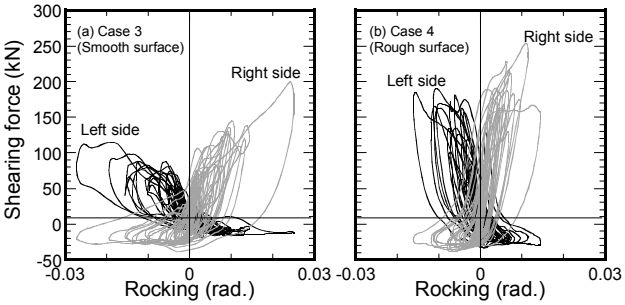

Figure 12 Relation between footing rotation and vertical shearing force acting on active/passive sides (Cases 3 and 4)

motion became extremely small for Case 1, as presented in Fig. 2. In contrast, the base friction amplitude for Case 2 tended to increase concomitantly with increasing relative displacement and was apparently larger than that for Case 1, indicating that the footing did not slide on the soil.

Figure 10 shows the relation between the relative displacement and the base friction of the embedded footing for Cases 3 and 4. The friction–displacement loop for Case 3 is similar to that for Case 4, except the most outside loop. The relative displacement for Case 3 was much less than that for Case 1, suggesting the embedded footing slides only slightly.

Figure 11 portrays the relation between the relative displacement and the total earth thrust for Cases 3 and 4. The relative displacement is the difference between the surface soil layer and the footing. The total earth thrust amplitudes for Case 4 tend to be larger at small relative displacement than those for Case 3, which is consistent with that the passive earth pressure depends on the wall friction angle. The maximum amplitude of the total earth thrust for Case 3 was larger than that for Case 4 because the maximum relative displacement for Case 3 was larger than that for Case 4.

The friction–displacement loop for Case 1 differs greatly from that for Case 2. In contrast, the friction–displacement loop for Case 3 is similar to that for Case 4. The difference resulted from the fact that the footing for Case 1 apparently slides, but the embedded footing for Case 3 slides only slightly because the earth pressure, of which the amplitude was about half of the base friction, restricted the footing. The relation between the earth pressure and the relative displacement for Case 3 also resembled that for Case 4, indicating that the soil–structure interaction for Cases 3 and 4 was almost identical. Consequently, the superstructure response for Case 3 tended to be similar to that for Case 4, as shown in Figs. 4(a) and 5(a).

4.2 Footing roughness and rocking motion

To investigate the mechanism that the rough surface of the embedded footing reduced the rocking motion of the footing, the relation between the footing rotation and vertical shearing force acting on the active and passive sides for Cases 3 and 4 are presented in Fig. 12. The shearing force tends to increase concomitantly with increasing footing rotation in both cases, suggesting that the shear force resists the footing rotation. The shearing force amplitude of the rough surface tends to be greater than that of the smooth surface in spite of the small footing rotation. Consequently, the rough surface reduced the footing rocking motion.

CONCLUSION

Dynamic centrifuge tests were performed using this soil-footing–superstructure model to investigate the effects of

footing surface roughness on superstructure response during a large earthquake. The footing model with smooth or rough surfaces was either placed on the soil or was embedded in the sand. The following conclusions were drawn.

1) A smooth footing surface on the soil reduces the horizontal superstructure acceleration because the base friction force of a smooth surface is much less than that of a rough surface.
2) Roughness of an embedded footing in the dry sand does not markedly affect the superstructure horizontal acceleration because the friction–displacement loop and the relation between the earth pressure and displacement of the footing with a smooth surface are similar to those of a footing with rough surface.
3) The footing with a smooth surface on the soil apparently slid, but the embedded footing with smooth surface slid only slightly because the earth pressure, of which the amplitude was about half of the base friction, restricted the footing.
4) A smooth surface of the footing on the soil reduces the rocking motion of the footing because the footing slides on the soil.
5) A smooth surface of the embedded footing in the dry sand increases the rocking motion of the footing slightly because the vertical shear force acting on the active/passive side with a smooth surface is less than that with a rough surface.

Acknowledgements:
This study was conducted with the financial support of a Grant-in-Aid for Scientific Research from the Ministry of Education, Culture, Sports, Science and Technology of Japan.

References:

Uesugi, M. and Kishida H. (1986), "Influential factors of friction between steel and dry sands," *Soils and Foundations*, **26** (2), 33-46.

JOINT CONFERENCE PROCEEDINGS
7th International Conference on Urban Earthquake Engineering (7CUEE) &
5th International Conference on Earthquake Engineering (5ICEE)
March 3-5, 2010, Tokyo Institute of Technology, Tokyo, Japan

CENTRIFUGAL MODELING OF ROAD EMBANKMENTS ENGULFED BY TSUNAMI FOR ITS DAMAGE PREDICTION

Akihiko Hiro-oka[1)], Hiroshi Fujii[2)], Kousuke Tanaka[2)], and Hideo Nagase[3)]

1) Associate Professor, Department of Civil Engineering, Kyushu Institute of Technology, Japan
2) Research Student, Graduate School of Civil Engineering, Kyushu Institute of Technology, Japan
3) Professor, Department of Civil Engineering, Kyushu Institute of Technology, Japan
ahirooka@civil.kyutech.ac.jp, hfujii@geo.civil.kyutech.ac.jp, ktanaka@ geo.civil.kyutech.ac.jp, nagase@civil.kyutech.ac.jp

Abstract: This study aims to examine judging the extent of Tsunami damage that is caused in road embankments and comparing between the existing method for judging the extent of Tsunami damage and model test results. To evaluate these, we carried out a series centrifuge model tests. It is found that the existing method for judging the extent of Tsunami damage is useful as one means of a damage judging for a simple embankment on which we conducted model tests in centrifuge.

1. INTRODUCTION

Massive underwater earthquake often triggers Tsunami. Since Japan is surrounded by sea and frequently has large earthquakes around, we may be hit by large Tsunamis in a wide range of coastal areas. The 2004 Tsunami disaster in the Indian Ocean has taught us that we must be alert to the dangers of Tsunamis. Relative to the earthquake itself, the Tsunami caused much heavier damage. Overall, the natural disaster took the lives of more than 220,000 people and an estimated five million people were affected by this Tsunami damage. Tsunami damages were still spotted in 2008 around Sumatra. Figure 1 shows outflow of the bridge girder and Figure 2 shows the collapsed road embankment behind a bridge abutment. Therefore, preparation for large Tsunamis is necessary to realize "Construction of a secure and safe society".

In the aftermath of large Tsunami, the roadway network is expected as one of important infrastructures to support emergency activities. It means that the accurate damage prediction of the road in the coastal area is needed. It is necessary to obtain basic information about the damaged road embankments by Tsunami which help in the accurate prediction.

Paying attention to road embankments, existing method for judging the extent of Tsunami damage is suggested to apply the past examples of the damaged embankments and the method is shown in Figure 3. The damaged road embankments are divided into total demolished, major damage, minor damage, and slight damage by the extent of



Figure 1 The outflow of the bridge girder by Tsunami



Figure 2 The collapsed road embankment behind a bridge abutment

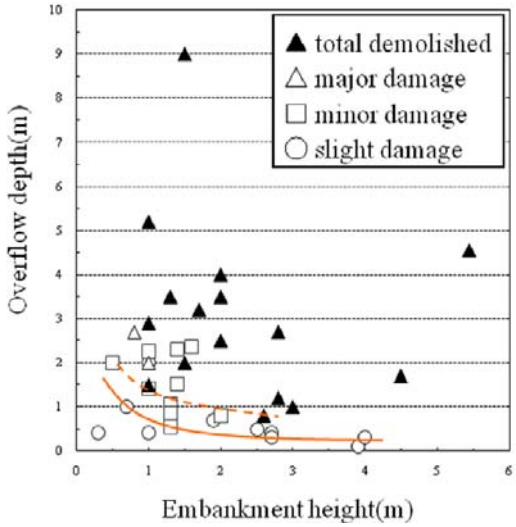

Figure 3 The criterion of embankment damage due to Tsunami suggested by Shoto (1999)



Figure 4 An example of the sampling sites; the damaged road embankment

Tsunami damage and the figure shows the relationship between embankment height and overflow depth. The broken line means lower limit where the extent of Tsunami damage is judged "total demolished" or "major damage" and the solid line means upper limit where the extent of Tsunami damage is judged "slight damage" or "no damage". This study aims to examine judging the extent of Tsunami damage that is caused in road embankments and comparing between the existing method for judging the extent of Tsunami damage and model test results. To evaluate these, we carried out a series centrifuge model tests.

2. CENTRIFUGE MODEL TEST

2.1 The Testing Material and Model Embankment

We examined the soil samples, which are obtained from the damaged road embankments by Tsunami in Sumatra as shown in Figure 4, by method of classification of geomaterials for engineering purposes. Testing material that composes the model embankments was determined to be the mixture of Toyoura sand and silt by referring result of the classification. Its grading curve is shown in Figure 5 and the result of box shear test on this testing material is shown Figure 6 and the physical and mechanical properties are summarized in Table 1. Model embankments are made of

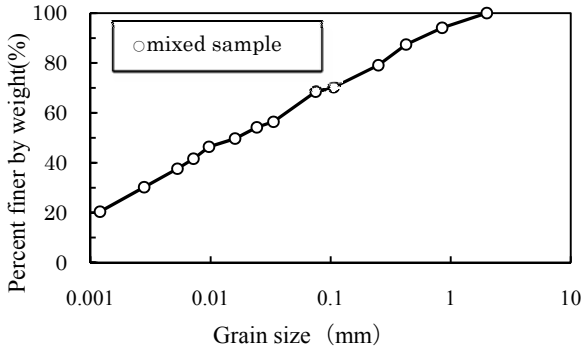

Figure 5 The grading curve of the testing material

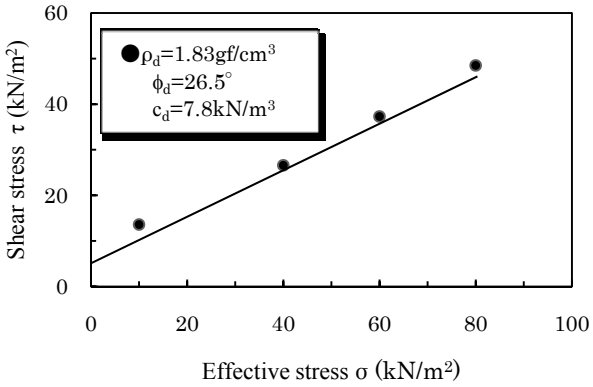

Figure 6 The result of the box shear test on the testing material

Table 1 The physical and mechanical properties of the testing material

natural water content w_n(%)		9.28
mean grain size(mm)		0.15
optimum moisture content w_{opt}(%)		13.63
maximum dry density γ_d(g/cm^3)		1.83
strength parameters	c_d(kN/m^3)	7.8
	ϕ_d (degree)	26.5

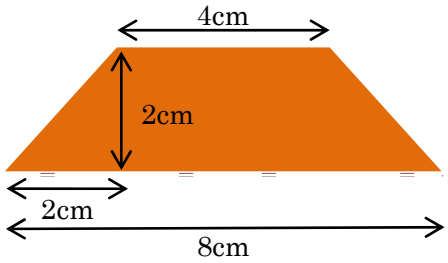

Figure 7 The model embankment

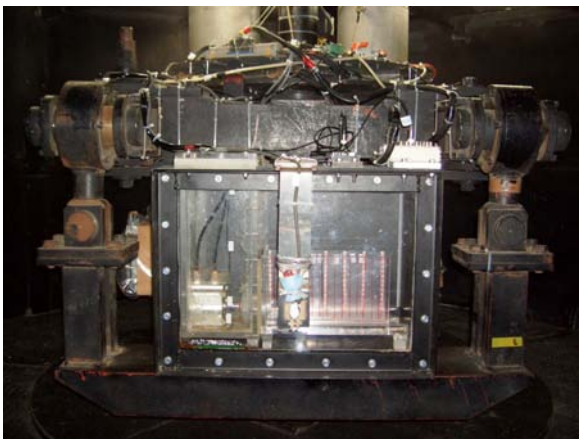

Figure 8 The test system loaded on the K.I.T. Centrifuge

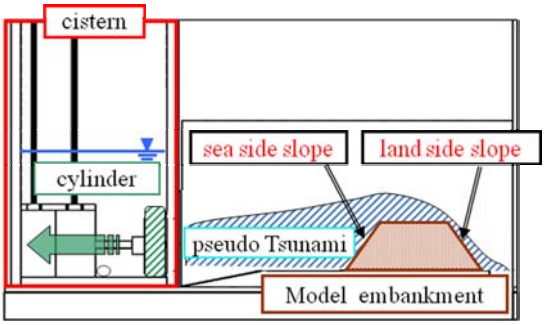

Figure 9 Overview of model apparatus setup

Table 2 Test condiotions

model embankment height(cm)	centrifugal acceleration(G)	Prototype embankment height(m)
2.0	50	1.0
	70	1.4
	100	2.0

testing material with the optimum moisture content by compaction. All model embankments height is 2cm and gradient of embankment slope is 1:1 as shown in Figure 7.

2.2 Test System and Test Conditions

Figures 8 and 9 show the test system and the overview of model apparatus setup. We tried to simulate Tsunami that overflows the road embankments in a series of model test. While the centrifuge is in flight at the constant configured centrifugal acceleration, air cylinder moves backward to open the water gate of the cistern for creating pseudo Tsunami. With the test method described above, we conducted experiments of 13 cases by changing the centrifuge acceleration as shown in Table 2 and the quantity of water. The photographs of the model embankment before Tsunami and engulfed by pseudo Tsunami are shown in Figure 10. After the pseudo Tsunami passes model embankment, we observed the extent of Tsunami damage

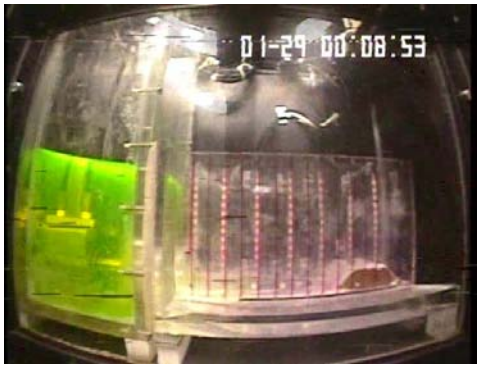

Before Tsunami



Engulfed by Tsunami

Figure 10 The photographs of the model embankment before Tsunami and engulfed by pseudo Tsunami

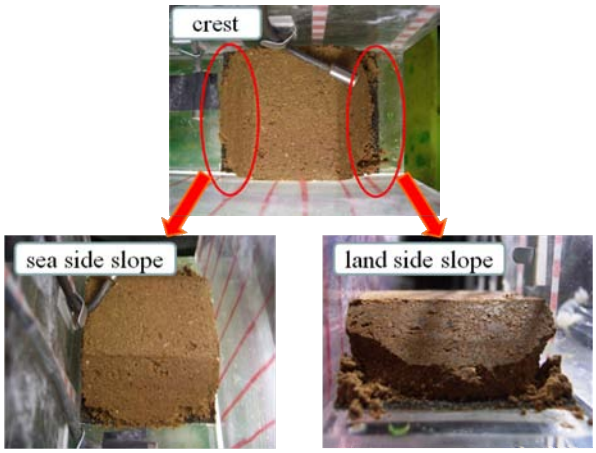

Figure 11 The photos of a model embankment after the model test

that is caused in model embankments. We defined embankment slope that is near the cistern as “sea side slope” and the other side as “land side slope”.

3. TEST RESULTS AND DISCUSSIONS

3.1 Model Embankment after the Experiment

These photos in Figure 11 show model embankment

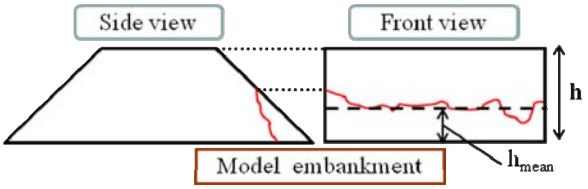

Figure 12 The definition of the average height of sliding of the model slope h_{mean}

Table 3 The relationship between the value of P and the Tsunami damage

Value of P	Extent of Tsunami damage
50≦P＜100	major damage
30≦P＜50	minor damage
0≦P＜30	slight damage

Table 4 The results of a series of model tests

Extent of Tsunami damage	Prototype embankment height(m)	Prototype overflow depth(m)
slight damage	1.0	1.4
	1.4	0.7
		2.5
	2.0	0.4
		1.1
minor damage	1.0	0.6
		1.6
	1.4	1.4
		1.7
	2.0	1.2
major damage	1.0	1.8
	2.0	2.7
		3.3

after the experiment. Conspicuous Tsunami damage of model embankment in crest was not observed in all the cases while the Tsunami damage was observed in both sides of embankment slope. Therefore, we determined to judge the extent of Tsunami damage by paying attention to embankment slope. The severer Tsunami damage was observed especially in the land side slope than in the sea side slope.

3.2 Tsunami Damage

In this section, we would like to explain about Tsunami damage judging of model embankment. In order to judge the damage quantitatively, we suggested the formula (1) by the model embankment height h and the average height of sliding of the model slope h_{mean} (see Figure 12).

$$P = \frac{h_{mean}}{h} \times 100\ (\%) \qquad (1)$$

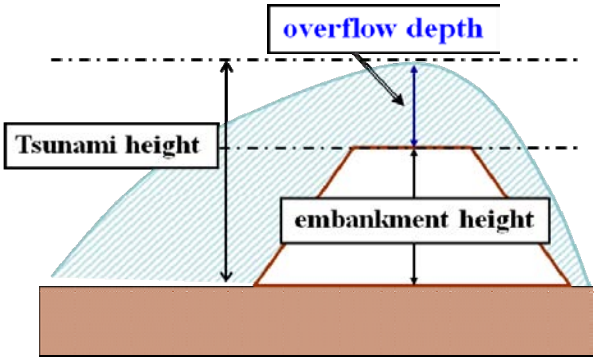

Figure 13 The definition of the overflow depth

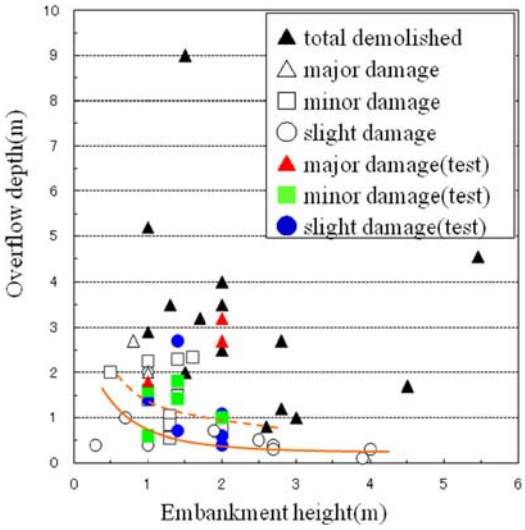

Figure 14 The comparison between the existing criterion of embankment damage due to Tsunami and the results of model tests

The extent of Tsunami damage is divided into major damage, minor damage, and slight damage by the value of P as shown in Table 3. The values of P are calculated on the both sides of the embankment slope and the extent of Tsunami damage of the embankment is determined by the larger value of P.

When the extent of Tsunami damage was judged in each cases and that is shown together with prototype embankment height and prototype overflow depth, the results are shown in Table 4. The overflow depth in this table means the difference between Tsunami height and embankment height as shown in Figure 13.

3.3 Comparison between the Test Results and the Existing Criterion for Judging the Extent of Tsunami Damage

A series of model tests results are directly compared

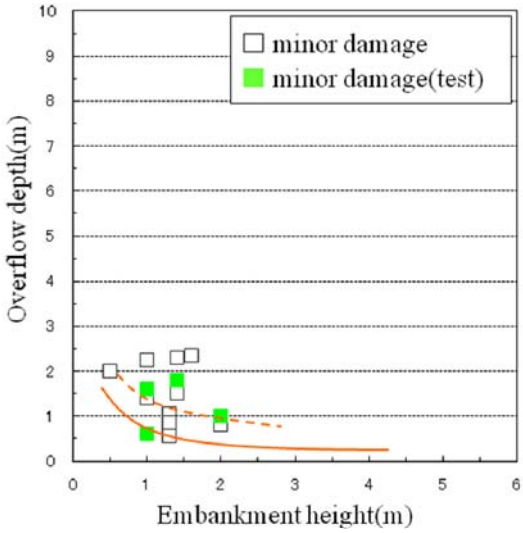

Figure 15 The comparison between the existing criterion of embankment damage due to Tsunami and the results of model tests (especially on minor damage)

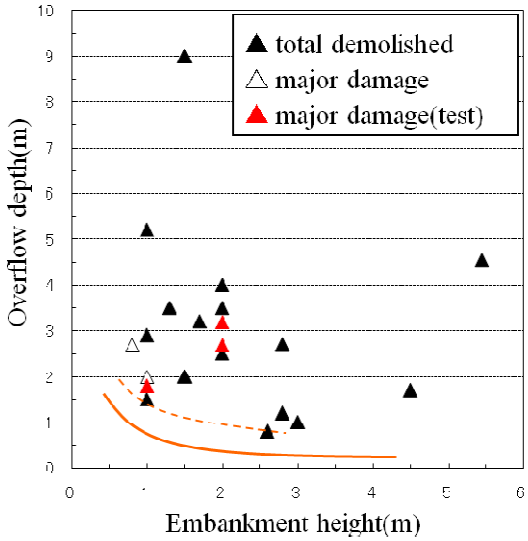

Figure 16 The comparison between the existing criterion of embankment damage due to Tsunami and the results of model tests (especially on major damage)

with the criterion of embankment damage due to Tsunami by plotting together in Figure 14 to evaluate the existing method for judging the extent of Tsunami damage. According to this figure, the test results seem to be close to the plot of past examples of the damaged embankment. Therefore, it is meaningful to compare between the existing method for judging the extent of Tsunami damage and model test results in more detail.

Figure 15 shows the comparison the existing method for judging the extent of Tsunami damage and minor damage of the test results. The test results are plotted near the line drawn on the basis of the past examples and almost plots are in the upper range of the solid line. Supposed the overflow depth and the embankment height in the range below the solid line, the extent of Tsunami damage in the same type of model embankment is considered to be slight damage.

Figure 16 shows the comparison the existing method for judging the extent of Tsunami damage and major damage of the test results. The test results are plotted near the line drawn on the basis of the past examples and almost plots are in the upper range of the broken line. If we have the same type embankment as models and Tsunami with the overflow depth in the range above the broken line, the extent of Tsunami damage is considered to be major damage As mentioned above, the existing method for judging the extent of Tsunami damage can be used at least as one means of a damage judging for a simple embankment on which we conducted model tests in this study.

4. CONCLUSIONS

The conclusions derived from this study are below.

1. When the Tsunami overflow the road embankment, Tsunami damage was observed in both sides of embankment slope and the severer Tsunami damage was observed especially in the land side slope.
2. As a result of the comparison between the past examples of the damaged embankment and the test results, each of these plots indicate a good agreement for the each extent of damage. Therefore, the damage judging by the average slide quantity rate **P** is considered to be effective.
3. The existing method for judging the extent of Tsunami damage is effective as a means of damage judging for a simple embankment on which we conducted model tests in this study.

Acknowledgements:

This research was funded by the National Institute for Land and Infrastructure Management as part of "The study on the damage prediction of the road structure due to Tsunami and its measures to reduce the damage". This support is gratefully acknowledged by the authors.

References:

Fujima, K., Shigihara, Y., Shimamora, C., Matsutomi, H., Sakakiyama, T., Tatsumi, D., Miyajima, M., Hakuno, M., Tekeuchi, M., Ono, Y., Kosa, K., SHOJI, G. and TASAKI, K.(2007), "Trace Height Distribution of 2004 Indian Ocean Tsunami along the Northwest Coast of Sumatra Island," (in Japanese) *JSCE Journal of Earthquake Engineering*, 29, 874-880,

Kataoka, M., Turuta, M., Nagao, K., and Kusakabe, T. and Shoji, Y. (2007), "Development of an Earthquake-Tsunami Disaster Scenario and a Policy of its Application to Planning Measures," (in Japanese) *JSCE Journal of Earthquake Engineering*, 29, 918-925,

Shuto, N. (1997), "Road Traffic Disorder just after being hit by

Tsunami," (in Japanese) *Tsunami engineering technical report* 14, 1-31.
Shuto, N. (1999), "The Damages of Embankment due to Tsunami," (in Japanese) *Tsunami engineering technical report* 16, 1-37.

JOINT CONFERENCE PROCEEDINGS
7th International Conference on Urban Earthquake Engineering (7CUEE) &
5th International Conference on Earthquake Engineering (5ICEE)
March 3-5, 2010, Tokyo Institute of Technology, Tokyo, Japan

BOUNDARY EFFECTS OF LAMINAR CONTAINER IN CENTRIFUGE SHAKING TABLE TEST

Chung-Jung Lee[1], Yu-Chieh Kuo[2], and Yu-Chen Wei[2]

1) Professor, Dept. of Civil Engineering, National Central University, Jhongli, Taiwan
2) Graduate student, Dept. of Civil Engineering, National Central University, Jhongli, Taiwan
cjleeciv@cc.ncu.edu.tw ,jk731231@gmail.com, u0116000@cc.ncu.edu.tw

Abstract: Two dynamic centrifuge model tests are conducted to simulate dry and saturated sandy soil deposit subjected to base shaking. The aim of this study is to investigate the boundary effects of laminar container on the test data acquired from the accelerometers and the pore pressure transducers embedded at different depths and located at different distances away from the end wall. The test results show that the percent changes in the maximum amplitude of acceleration and maximum Fourier amplitude away from the distance of 18 cm is less than 10% and no significant discrepancies in the time histories of excess pore water pressure ratio are observed. The observed phase lags at the depths of 9.6 m and 19.2 m are insignificant in the cases of both measured at 4 cm and 18 cm away from the end wall. It proves that the change in the seismic behavior towards the end wall is minimal and the laminar container used in the study functions appropriately for simulating a one dimensional shear wave propagation problem.

1. INTRODUCTION

Geotechnical centrifuge shaking table tests has been used for many years to investigate the seismic behavior of various soil-structure systems. The artificial boundary of a model container may cause distortion in the stress and strain field in the model compared with those in the prototype modeled. Accurate boundary conditions in the model boundary are absolutely necessary to create the same behavior as the semi-infinite soil layers in the field.

Various types of containers have been used for geotechnical centrifuge shaking table tests. The rigid-wall container was used to hold the soil model in the early period of earthquake centrifuge model experiments. In a rigid end wall container, soil cannot deform, as it would do in the field, and that results in the strain dissimilarity between the model and the prototype. If the end walls are smooth, stress dissimilarity will also arise owing to lack of complementary shear stress. To solve the problem of end effects of the rigid container energy adsorbing materials such as Duxseal was proposed as an attempt to create an ideal end wall condition. However, the compressibility and friction characteristics of Duxseal are not easy to determine, therefore, the use of Duxseal still can not achieve the ideal end wall conditions.

The end walls of the container would have to have the same deflection and natural frequency as the soil in the model container. Teymur and Madabhush (2003) designed an equivalent shear beam (ESB) container, which was built from rectangular frames of dual separated by rubber layers, to obtain the same dynamic response during base shaking. To sustain the complementary shear stress induced by base-shaking, a flexible and in-extensive friction sheet was attached to the end walls. This design appears to satisfy the most of the requirements for a model container. However, different boxes with different shear stiffness are needed for the different types of soil tested at different g levels. The box stiffness must match to that of the soil column modelled. Besides, the ESB container still can not satisfy the requirements for a model container when the occasion of gross changes in soil stiffness due to occurrence of liquefaction during shaking.

The design concept of laminar container is that the container should play little part in the response of the soil system. Laminar containers are constructed of light-weight ring stacked with bearings in between, permitting relative free movement of the soil and ring during shaking. This is to reduce the friction so as to mirror the stiffness of a liquefied soil column. Complementary shear stresses induced by base shaking are not considered and that would cause non-uniform vertical stresses along the base and overturning moment. The boundary effects of the laminar container may be inevitable; therefore, the assessment of boundary effects for the laminar container is essential for performing shaking table tests to study the seismic response of soil deposit.

Two centrifuge 1-D shaking table tests involving dry and saturated sands of horizontal layers were conducted to simulate sandy soil deposits subjected to different magnitudes of base shaking. The time histories of acceleration and excess pore water pressure ratio measured at various depths and at the locations of different distances away from the end wall were taken to assess and quantify the effects of the end wall of laminar container on the seismic response behavior.

2. EXPERIMENTAL METHOD AND APPARTUS

2.1 Testing Equipments

This experiment work was undertaken in the Centrifuge at the National Central University (NCU) Taiwan (Lee & Chiang 2007). The NCU Centrifuge has a nominal radius of 3 m and equips a 1-D servo-hydraulically controlled shaker integrated within a swing basket. The shaker is used to apply 1-D horizontal base input accelerations to geotechnical centrifuge model containers in response to an applied input voltage signal. The shaker has maximum nominal shaking force 53.4 kN with maximum table displacement of ±6.4 mm and operates at up to 80 g centrifugal acceleration. The nominal operating frequency range is 0 - 250 Hz. The table payload mounting area is 1000 mm x 546 mm x 500mm.

A laminar container with inside dimensions of 711 mm x 356 mm x 353 mm is constructed from 38 light-weight aluminum alloy rectangular frames arranged in a stack. Each frame is 8.9 mm in height and is separated from those adjacent to it by roller bearings, specially designed to permit translation in the longitudinal direction with minimal frictional resistance. The laminar container is designed specifically for use with centrifuge shakers to facilitate accurate and efficient dynamic centrifuge modeling of geotechnical soil-structure systems subjected to horizontal one-dimensional earthquake excitation at the base of a soil deposit. The container is designed for dry or saturated soil models and permits development of stresses and strains associated with one dimensional wave propagation. A flexible 0.3 mm thick latex membrane is used for containment of soil and pore fluid. Approximate net sliding friction coefficient of each frame and the frame-to-soil mass ratio are as low as 0.01 and 0.24, respectively.

2.2 Tested Sand and Preparation of Sand Bed

A fine quartz sand was used to prepare the sand deposit. The characteristics of the quartz sand are summarized in Table 1. The quartz sand was pluviated with a regular path into the container from a hopper at various falling heights and at a constant flow rate for preparing fairly uniform sand deposits having various relative densities. The pluviation process was interrupted as needed for embedding the accelerometers and pore water pressure transducers (PPT) at specified elevations and locations. After completion of the sand bed preparation, the package was mounted on the shaker. An acrylic plate was used to tightly cover the container. Air was simultaneously and continuously vacuumed out from both the container and the outside of container and at the same time de-aired water (or a water-metulos solution with a viscosity of 80 times the viscosity of water for simulating a deposit of fine sand in the field) was carefully dripped into the container to saturate the sand bed until the water level rose to 2 mm above the sand surface. About 48-72 hours was required for completion of the saturation process.

The arrays of accelerometer and PPT were placed at the middle of the container and the distances of 4 cm and 18 cm away from the end wall. Figure 1 presents a typical sketch of laminar container, soil profile and instrumentation used in the study. The thickness of model sand bed is 30 cm, simulating a 24 m thick sand deposit at a centrifuge acceleration of 80 g. Two tests were conducted: the dry sand model with the relative density of 43% and the saturated sand model with pore water pressure measurement. The models were subjected to a sequence of shaking, from small to large amplitude of acceleration. The dry sand model was instrumented three arrays of accelerometer, one at the middle of container, the others 4 cm and 18 cm away from the end wall, respectively. Each array consisted of vertical spaced accelerometers (A#) to record the time histories of acceleration at various depths when the shear wave propagating to the ground surface. The saturated sand model was instrumented three arrays of accelerometer and two arrays of PPT. The center accelerometer array consisted of six vertical spaced accelerometers; the other two arrays consisted of three accelerometers embedded at various depths, respectively. Two arrays of PPT (P#) were placed at the middle of the container and the location of 180 mm away from the end wall. These arrangements and measurements are important to understand the seismic response of the sand layer at different elevations and at different distances away from the end walls and the associated excess pore water pressure generation during shaking. Two LVDTs were installed at the top of the container to measure the surface settlements. Figure 2 shows the test package on the shaker.

Table 1. Characteristics of fine quartz sand

	G_s	D_{50} in (mm)	D_{10} in (mm)	[1]ρ_{max} (g/cm^3)	[1]ρ_{min} (g/cm^3)
Quartz sand	2.65	0.193	0.147	1.66	1.44

[1]The maximum and minimum densities of the sand were measured in the dry state, according to the method (JSF T 161-1990) specified by the Japanese Geotechnical Society.

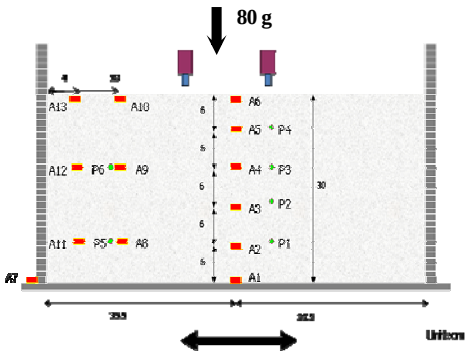

Figure 1 Instrumentation layout (in model scale) of dry sand model and saturated sand model used in the study (A# : accelerometer; P# : pore pressure transducer,)

Table 2. Test conditions

Test No	Sequence of input motion (g)	Dr (%)	Pore fluid
C1	0.07/0.2/0.3/0.4	43	-
C2	0.07/0.2/0.3/0.4	46	water

The analysis of the measured accelerations and pore pressures for the models with the test conditions as listed in Table 2 are reported and discussed in the following section. For easily reading all the physical quantities are expressed in the prototype scales except that the distances away from the end wall are expressed in the model scale.

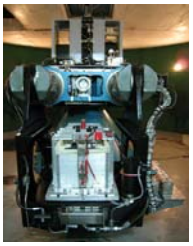

Figure 2. Test package and instrumentation on the shaker.

3. TEST RESULTS AND DISCUSSION

3.1 Comparision of Time histories of Acceleration For Dry Sand During Shaking

The input acceleration propagates vertically through the soil layer will be amplified or attenuated depending on the soil dynamic properties and the input motion. Figure 3(a) – 3(c) and Figure 3(d) – 3(f) show the time histories of acceleration for the center array of acceleration and those near the end walls as shown in Figure 1 for Model C1 subjected to small shaking (0.07 g) and large shaking (0.2 g), respectively. Figures 4 and 5 display their Fourier spectra for comparison.

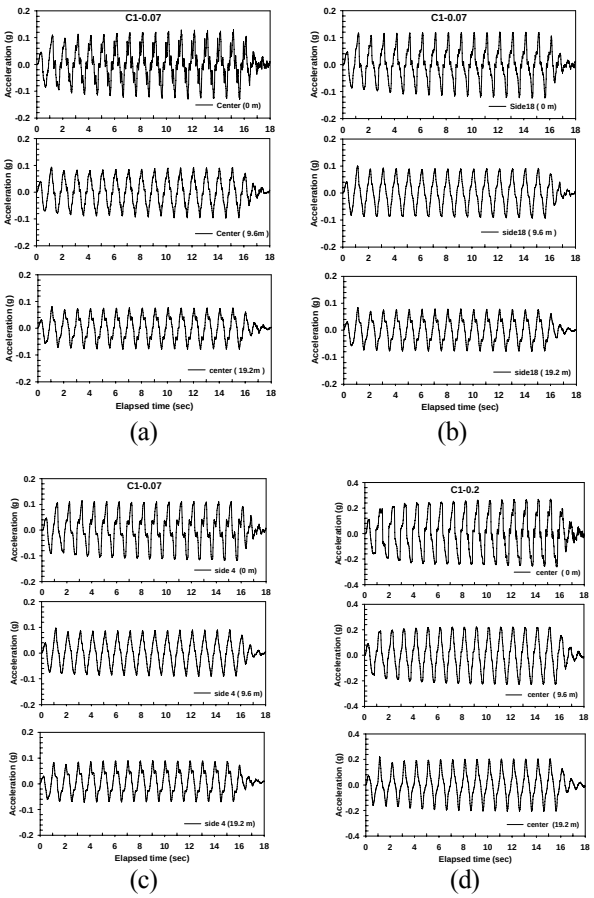

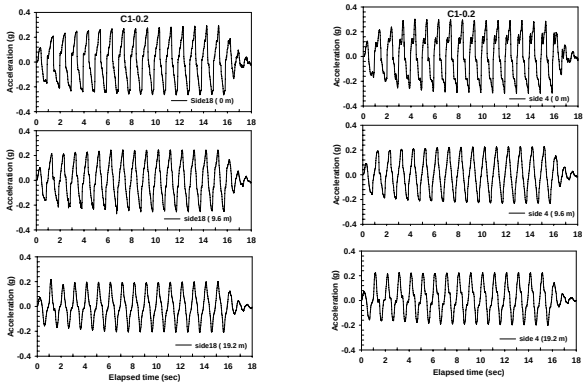

Figure 3 Time histories of acceleration recorded at different depths and various distances from end wall and at 0.07g and 0.2 g input motion for Model C1: (a) center (0.07 g); (b) 18 cm from end wall (0.07 g); (c) 4 cm from end wall (0.07 g); (d) center (0.2 g); (e) 18 cm from end wall (0.2 g); (f) 4 cm from end wall (0.2 g)

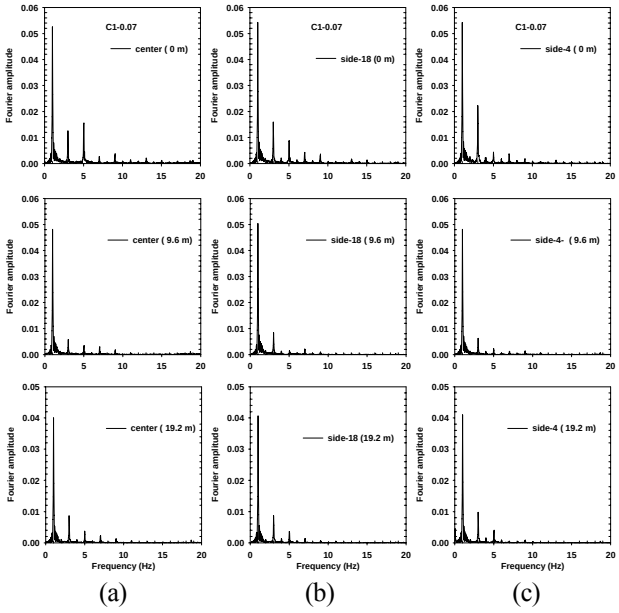

Figure 4 Fourier spectra of measured accelerations for Model C1 subjected to small shaking (0.07 g) at: (a) center array; (b) 18 cm from end wall; (c) 4 cm from end wall

Although no big differences in the acceleration time histories after comparisons of Figures 3(a) to 3(f), the percent of changes in the maximum amplitude of, maximum Fourier amplitude of, and phase lag of the acceleration among the time history of accelerations measured at the same elevations but at different distances away from the end walls are used to examine the boundary effects of laminar container. Influence factors D_A *(%)* and D_F *(%)* are first defined to investigate the boundary effects on the maximum amplitude of the acceleration and the maximum Fourier amplitude, respectively. The formulae are given below:

$$D_A(\%) = \left(\frac{a_e - a_c}{a_c} \right) \times 100 \qquad (1)$$

$$D_F(\%) = \left(\frac{Fa_e - Fa_c}{Fa_c} \right) \times 100 \qquad (2)$$

in which a_e = the maximum accelerations in the time history of acceleration at 4 cm or 18 cm from the end walls; a_c = the maximum acceleration in the time history of acceleration at the center array; Fa_e = the maximum Fourier amplitudes of Fourier spectrum for the time histories of acceleration measured at 4 cm or 18 cm from the end wall; Fa_c = the maximum Fourier amplitude in the Fourier spectrum for the time histories of acceleration measured at the center array. Tables 3 and 4 summarize the percent changes in the maximum acceleration amplitude and in the maximum Fourier amplitude, those which calculated at the depths of 0, 9.6 m, and 19.2 m, towards the end wall for Model C1 experienced to small shaking to large shaking. It is observed that the percent of changes in both the maximum amplitudes of maximum acceleration and maximum Fourier amplitude become larger when the embedment depths of accelerometer are shallower and are nearer the end wall. The variation in the percent changes becomes more obvious in larger shaking. It could be concluded that the percent changes in the maximum amplitude of acceleration and maximum Fourier amplitude away from the distance of 18 cm is less than 10% .

Table 3. Percent changes in the maximum acceleration amplitude, calculated at the depths of 0, 9.6 m, and 19.2 m, towards the end wall for Model C1 during different magnitudes of shaking

Depth (m)	Percent changes (%) in maximum acceleration amplitude					
	0.07 g		0.2 g		0.4 g	
	18 cm	4 cm	18 cm	4 cm	18cm	4 cm
0	-7	-11	10	12	17	29
9.6	8	5	10	2	6	-4
19.2	5	13	-2	2	-8	-14

Table 4. Percent changes in the maximum Fourier amplitude, calculated at the depths of 0, 9.6 m, and 19.2 m, towards the end wall for Model C1 during different magnitudes of shaking

Depth (m)	Percent changes (%) in maximum Fourier magnitude					
	0.07 g		0.2 g		0.4 g	
	18 cm	4 cm	18 cm	4 cm	18cm	4 cm
0	2	2	4	10	3	2
9.6	4	0	6	0	7	0
19.2	3	3	2	10	1	8

To investigate the phase lags between the acceleration time histories measured at the same elevation but at the different distances away from the end wall for Model C1, we assign the acceleration time history measured at the center array to the horizontal axis, and that measured at the distance of 18 cm to the vertical axis. The same coordinates are also used to investigate the phase lag of the acceleration time history measured at center and at the distance of 4 cm away from the end wall. In this way, the phase lags between the center array and the side arrays for Models C1 subjected to small shaking (0.07 g) and large shaking (0.4 g) are demonstrated in Figures 6 and 7. If the traces of the acceleration all lie in the lines with the slope of 1 as shown in Figures 6 and 7 there will be no phase lag at all. If the traces of acceleration deviated more from the lines there will be the larger phase lags between the accelerations measured at the center array and at the side arrays. We draw the following observations from these two figures. The phase lags are obvious on the surface and become more in the large shaking. The observed phase lags at the depths of 9.6 m and 19.2 m become insignificant in the cases of both measured at 4 cm and 18 cm away from the end wall. This agrees with the conclusions we made in the last section.

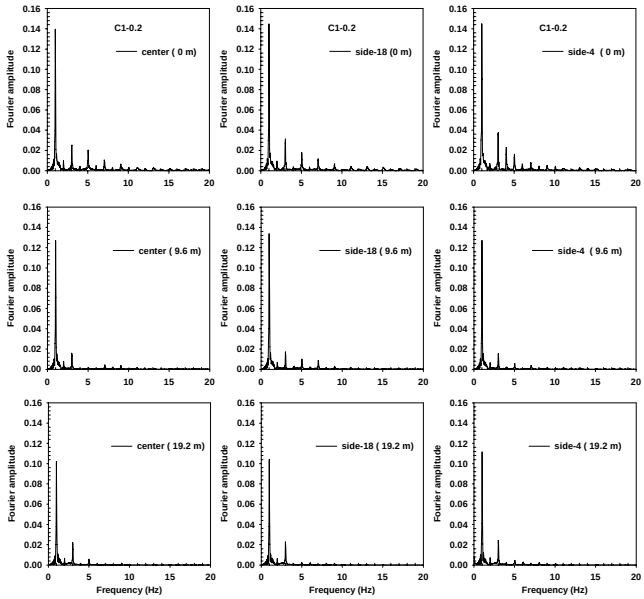

(a) (b) (c)

Figure 5 Fourier spectra of measured accelerations for Model C1 subjected to large shaking (0.2 g) at : (a) center array; (b) 18 cm from end wall; (c) 4 cm from end wall

3.2 Comparision of Time histories of Acceleration For Saturated Sand During Shaking

Figure 8(a) – 3(c) and Figure 8(d) – 3(f) show the time histories of acceleration for the center array of acceleration and those near the end wall for Model C2 subjected to small shaking (0.07 g) and large shakingr (0.2 g), respectively. Figures 9 and 10 display their Fourier spectra for comparison. Figures 8, 9 and 10 show that the amplification of acceleration appears during the shear wave propagate to the ground surface in the case of small shaking (0.07 g) but attenuation in the case of large shaking (0.2 g) because of larger pore water pressure generation.

Tables 5 and 6 summarize the percent changes in the maximum acceleration amplitude and in the maximum Fourier amplitude, those which calculated at the depths of 0, 9.6 m, and 19.2 m, towards the end wall for Model C2

experienced to small shaking to large shaking. The same conclusions as those obtained from Model C1 that the percent of changes in both the maximum amplitudes of maximum acceleration and maximum Fourier amplitude become larger when the embedment depths of accelerometer are shallower and are nearer the end wall.

The use of the same method as the last section, the phase lags between the center array and the side arrays for Models C2 subjected to small shaking (0.07 g) and large shaking (0.2 g) are demonstrated in Figures 11 and 12. The phase lags are obvious on the surface and become more significant in the large shaking and in the case of higher excess pore water pressure generation. The observed phase lags at the depths of 9.6 m and 19.2 m become insignificant in the cases of both measured at 4 cm and 18 cm away from the end wall. This agrees with the conclusions we made in the last section.

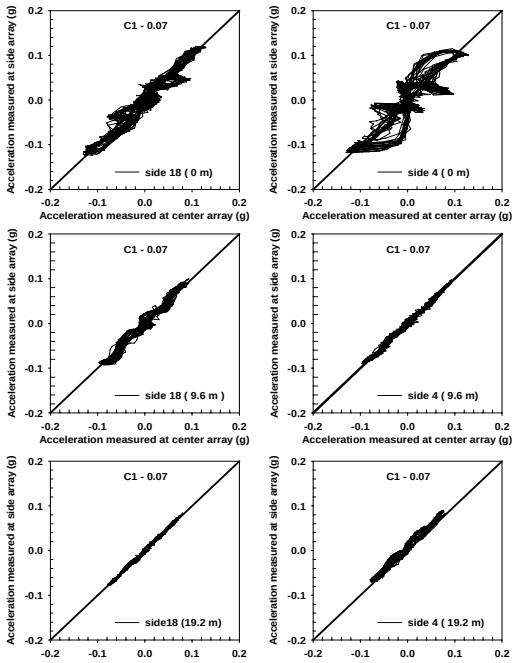

(a) (b)

Figure 6 Phase relations between the center array and the side arrays (18 cm and 4 cm) at different depths for Model C1 subjected to small shaking (0.07 g): (a) center – 18 cm from end wall; (b) center - 4 cm from end wall

Table 5. Percent changes in the maximum acceleration amplitude, calculated at the depths of 0, 9.6 m, and 19.2 m, towards the end wall for Model C2 during different magnitudes of shaking

Depth (m)	Percent changes (%) in maximum acceleration amplitude					
	0.07 g		0.2 g		0.4 g	
	18 cm	4 cm	18 cm	4 cm	18cm	4 cm
0	-7	-4	18	-9	-1	-31
9.6	8	3	2	17	-9	24
19.2	5	-	-10	11	-8	-14

Table 6. Percent changes in the maximum Fourier amplitude, calculated at the depths of 0, 9.6 m, and 19.2 m, towards the end wall for Model C2 during different magnitudes of shaking

Depth (m)	Percent changes (%) in maximum Fourier magnitude					
	0.07 g		0.2 g		0.4 g	
	18 cm	4 cm	18 cm	4 cm	18cm	4 cm
0	2	-3	-14	-26	-7	-17
9.6	-2	6	-2	2	-1	4
19.2	0	-	0	15	0	11

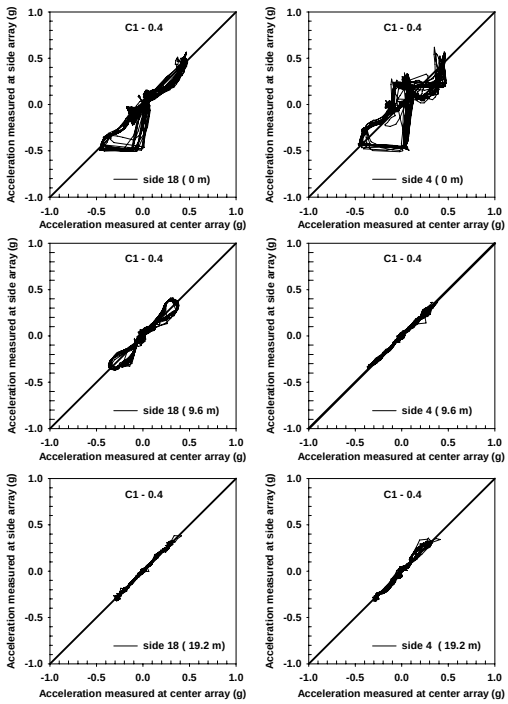

(a) (b)

Figure 7 Phase relations between the center array and the side arrays (18 cm and 4 cm) at different depths for Model C1 subjected to large shaking (0.4 g): (a) center – 18 cm from end walls; (b) center - 4 cm from end walls.

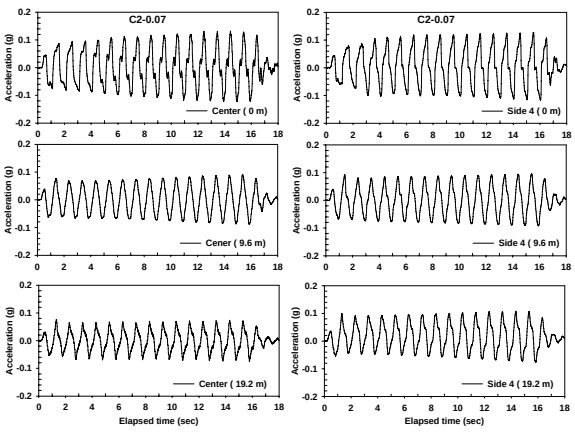

(a) (b)

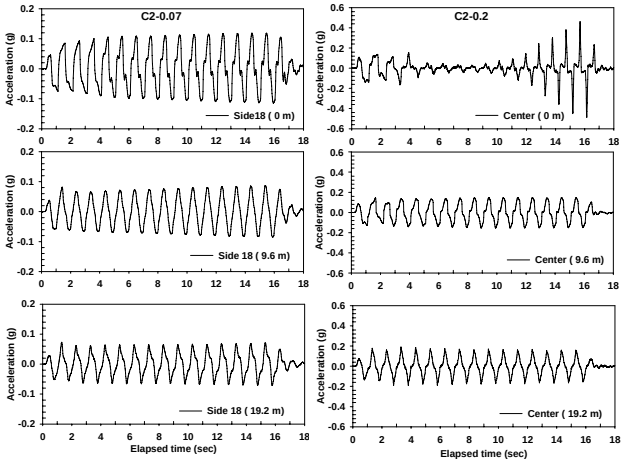

(c) (d)

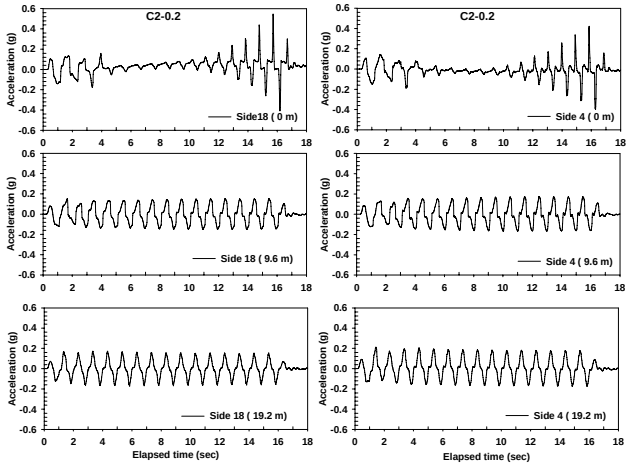

(e) (f)

Figure 8 Time histories of acceleration recorded at different depths and various distances from end wall and at 0.07g and 0.2 g input motion for Model C2: (a) center (0.07 g); (b) 18 cm from end wall (0.07 g); (c) 4 cm from end wall (0.07 g); (d) center (0.2 g); (e) 18 cm from end wall (0.2 g); (f) 4 cm from end wall (0.2 g)

3.3 Comparision of Time histories of Excess Pore Water Pressure For Saturated Sand During Shaking

The pore water pressure transducers as shown in Figure 1 can record the time histories of pore water pressure at two soil columns and at the depths of 9.6 m and 19.2 m. One was located at the center of container the other was instrumented at the distance of 18 cm away from the end wall. Figure 13 displays the time histories of the ratio of the excess pore water pressure measured at the center array and the array which is 18 cm distant from the end wall in the large shaking (0.2 g) for Model C2. The ratio of the excess pore water pressure is defined as the ratio of the excess pore pressure developed to the initial effective vertical stress. As shown in Figure 13 no significant discrepancies in the time histories of excess pore water pressure ratio are observed. This also proves that no significant boundary effect would arise.

4. CONCLUSIONS

Two dynamic centrifuge model tests are conducted to investigate the boundary effects of laminar box on the test data acquired from the accelerometers and the pore pressure transducers those which were instrumented at different depths and located at different distances away from the end wall for the dry and saturated sand model. The test results show that the percent changes in the maximum amplitude of acceleration and maximum Fourier amplitude away from the distance of 18 cm is less than 10% and no significant discrepancies in the time histories of excess pore water pressure ratio are observed. The observed phase lags at the depths of 9.6 m and 19.2 m become insignificant in the cases of both measured at 4 cm and 18 cm away from the end wall. It proves that the change in the seismic behavior towards the end wall is minimal except that the behavior measured on the surface. The obvious boundary effects on the ground surface can be attributed that the bond between the accelerometer equipped on the ground surface and the surrounding soil was bad owing to the lower overburden pressure on it. Therefore we conclude that the laminar container used in the study can function appropriately.

References:

Teymur B. and Madabhush, S.P.G. (2003), "Experimental Study of Boundary Effects in Dynamic Centrifuge Modeling," Geotechnique 53(7), 655-663.

Lee, C.J., and Chiang, K. H. (2007), "Response of single piles to tunnel-induced soil movements in sandy ground," Candian Geotecnical Journal, 44(10), 1224-1241.

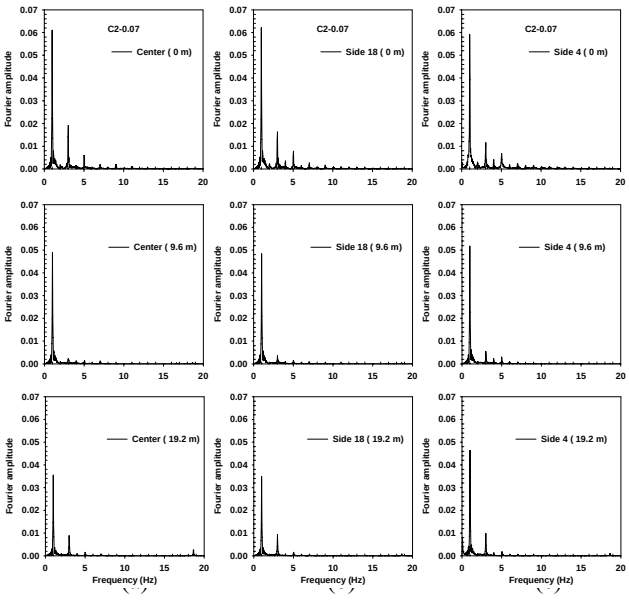

Figure 9 Fourier spectra of measured accelerations for Model C2 subjected to small shaking (0.07 g) at: (a) center array; (b) 18 cm from end wall; (c) 4 cm from end wall

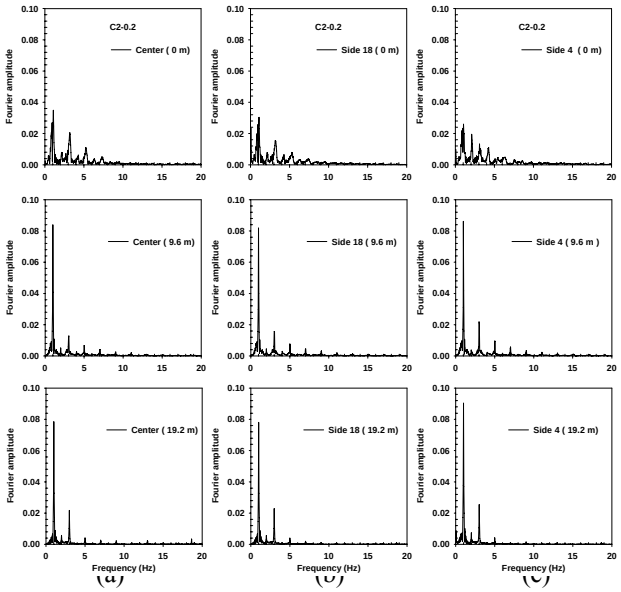

Figure 10 Fourier spectra of measured accelerations for Model C2 subjected to large shaking (0.2 g) at: (a) center array; (b) 18 cm from end wall; (c) 4 cm from end wall

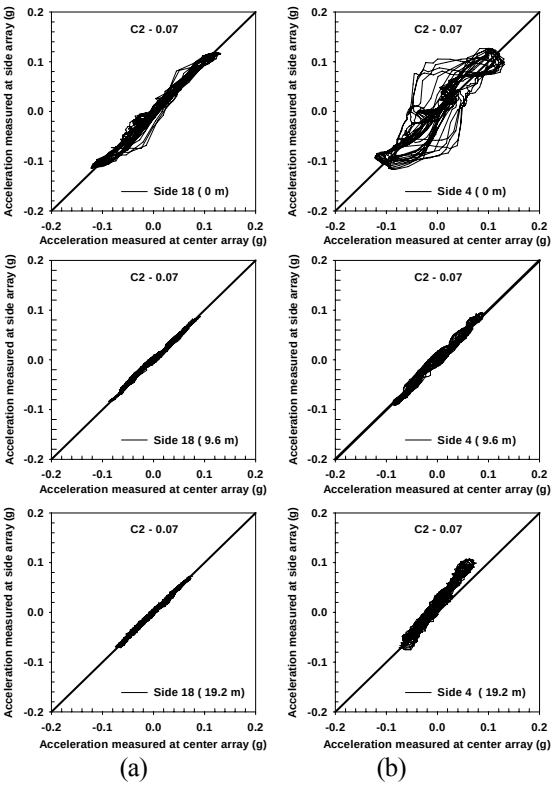

Figure 11 Phase relations between the center array and the side arrays (18 cm and 4 cm) at different depths for Model C2 subjected to small shaking (0.07 g): (a) center – 18 cm from end wall; (b) center - 4 cm from end wall

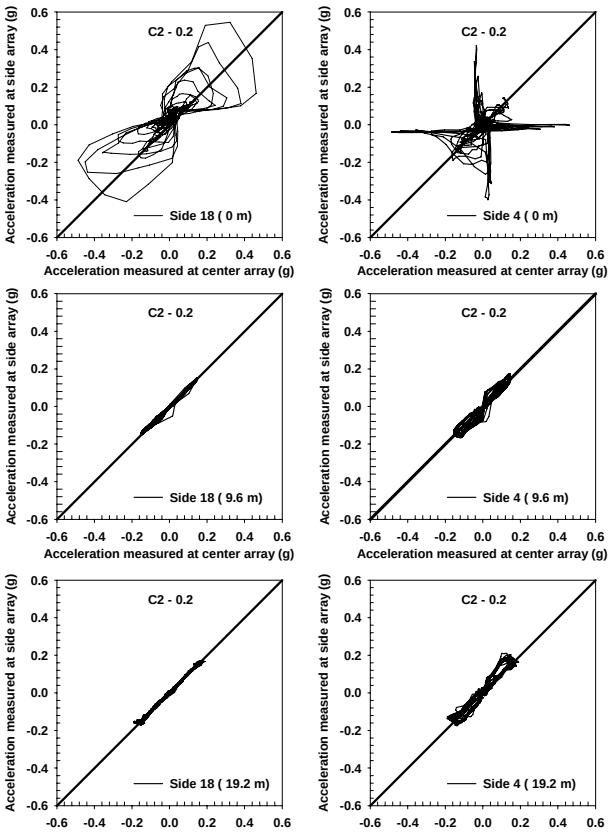

Figure 12 Phase relations between the center array and the side arrays (18 cm and 4 cm) at different depths for Model C2 subjected to small shaking (0.2 g): (a) center – 18 cm from end wall; (b) center - 4 cm from end wall

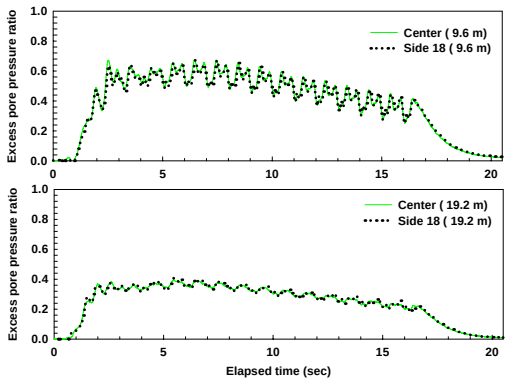

Figure 13 Time histories of the excess pore water pressure ratio recorded at the different depths for Model C2

JOINT CONFERENCE PROCEEDINGS
7th International Conference on Urban Earthquake Engineering (7CUEE) &
5th International Conference on Earthquake Engineering (5ICEE)
March 3-5, 2010, Tokyo Institute of Technology, Tokyo, Japan

DISTINCT ELEMENT ANALYSIS ON UPLIFT RESISTANCE OF BELLED PILES AND MULTI-BELLED PILES

Tsuyoshi Honda[1] and Yoshio Hirai[2]

1) Dr., Research & Development Institute, Takenaka Corporation, Japan
2) Dr., Research & Development Institute, Takenaka Corporation, Japan
honda.tsuyoshi@takenaka.co.jp, hirai.yoshio@takenaka.co.jp

Abstract: Uplift force acts on piles under a high-rise building during earthquake. Belled piles and multi-belled piles that have enlarged projections have been used to increase uplift capacity of a foundation. However, mechanism of uplift resistance in the piles with one or plural projection has not been clearly shown. This study aimed to investigate the mechanism of uplift resistance in belled piles and multi-belled piles from distinct element analysis on axial tensile load tests of a pile. Uplift resistance in four kinds of pile (: a strait pile, a belled pile and two multi-belled piles) was compared. It was found that the multi-belled piles had largest resistance and stiffness in the early stage of uplift displacement, and that the belled pile had larger resistance and stiffness than the strait pile. Additionally, a theoretical solution to estimate ultimate uplift resistance was derived from the upper bound limit analysis based on soil movements in DE analysis.

1. INTRODUCTION

Uplift force acts on piles under a high-rise building during earthquake. Belled piles and multi-belled piles have been used to increase uplift capacity of a foundation. The multi-belled pile is cast in place concrete pile with enlarged projections built in middle hard layers and bearing stratum as well as the belled pile (See Figure 1). It has higher performance in uplift capacity than strait piles and belled piles. However, mechanism of uplift resistance in belled piles and multi-belled piles has not been clearly shown. Uplift resistance in a belled pile has been studied by many researchers (Tsutsui et al. 1995, Hirai et al. 2002 and Chatani et al. 2008), and several methods to *practically* predict uplift resistance of a belled pile were proposed. Most of them are for a design to calculate the lowest value of uplift resistance that was measured in several axial tensile load tests. They frequently underestimate uplift capacity of a foundation. In contrast, uplift resistance of an anchor plate has been *theoretically* studied by Meyerhof & Adams (1968) and so on. Murray & Geddes (1987) showed that the theoretical solutions obtained from equilibrium analysis, lower and upper bound limit analysis could give good agreements with experimental results of pullout tests of an anchor plate in dense sand. Kumar (2003) proposed a theoretical solution of uplift resistance of an anchor plate in a two-layered sand by upper bound limit analysis. However, these theoretical solutions can not be directly applied to uplift resistance in belled piles and multi-belled piles, since the anchor plates is horizontal plate and used in a shallow foundation, while the belled piles and the multi-belled piles have sloping surfaces and are used in a deep foundation.

This paper aimed to investigate mechanism of uplift resistance in belled piles and multi-belled piles. Distinct element analysis was carried out to examine soil movements and stress-strain behavior around a pile which was buried as a deep foundation. Distinct element method (Cundall, 1971) is a powerful tool to simulate large and discontinuous deformation of soil. DE analysis can easily reproduce the interaction between soil and structures, which is often difficult problem in finite element methods. In this paper, axial tensile load tests using four kinds of pile (: a strait pile, a belled pile and two multi-belled piles) were simulated. Additionally, a theoretical solution to predict ultimate uplift resistance was obtained from the upper bound limit analysis based on soil movements in DE analysis.

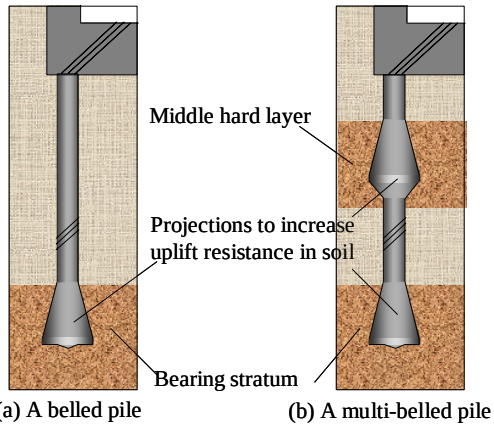

Figure 1. Schematic diagrams of a belled pile and a multi-belled pile

2. DISTINCT ELEMENT ANALYSIS

2.1 Mechanical Property of Aggregates Used in DE Analysis

Figure 2 illustrates a shape of the cluster disks used in DE analysis. The cluster disks were formed from two circular particles with the diameter of "b", and had the size of "a" in long axis. The ratio of length in short and long axis was constant (b/a = 0.7). Figure 3 shows the grain size distribution curve of the cluster disks. Table 1 shows the numerical parameters used in DE analysis.

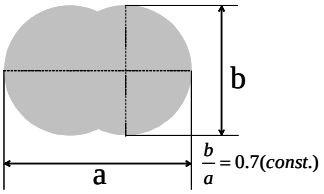

Figure 2. A shape of the cluster disks used in DE analysis.

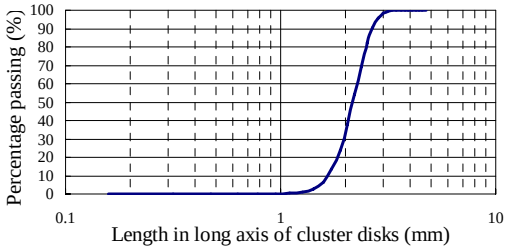

Figure 3. Grain size distribution curve of the cluster disks.

Table 1. Numerical parameters used in DE analysis.

Density of particles	1.8E+03 kg/m^3
Normal stiffness (k_n)	1.5E+08 N/m
Shear stiffness (k_s)	3.8E+07 N/m
Normal damping (η_n)	3.8E+01 Ns/m
Shear damping (η_s)	9.6E+00 Ns/m
Cohesion (c')	0.0 N
Friction angle (ϕ')	40.0 degrees

Before starting the simulation of axial tensile load tests of a pile, direct shear tests and simple shear tests under constant pressures were carried out to evaluate mechanical property of aggregates that consisted of the cluster disks in Figure 2. Schematic diagrams of the direct shear tests and the simple shear test are illustrated in Figure 4. The result in direct shear tests gives mechanical property of soil in shear band, and mechanical property in simple shear tests is useful to evaluate the interaction between soil and pile's surface.

Simulated results in the direct shear tests are shown in Figure 5. The peak strength increased in proportion to the vertical constant pressure. Strain softening was observed after the peak in all the tests. Figure 6 shows the vertical displacements due to dilatancy of soil with the shear displacements. All the tests showed a similar curve. The vertical displacement slightly decreased with the increase of the constant vertical pressure. The results in the simple shear test are shown in Figures 7 and 8. The strength in the simple shear tests was lower than in the direct shear tests. Strain softening was hardly observed in the lowest constant pressure. Vertical displacements in the early stage of shear displacement were remarkably lower than in the direct shear tests. The reason for this is that the disks easily slipped on the boundaries' surface. Mechanical property obtained from the simulation of the direct shear tests and simple shear tests is summarized in Table 2.

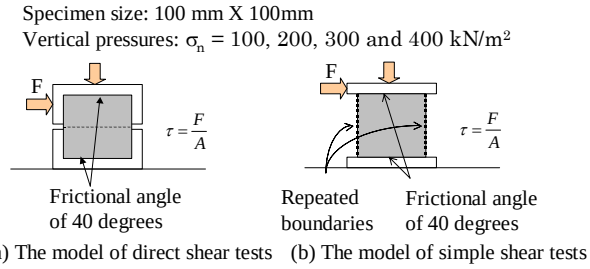

Figure 4. Schematic diagrams of the direct shear tests and the simple shear tests.

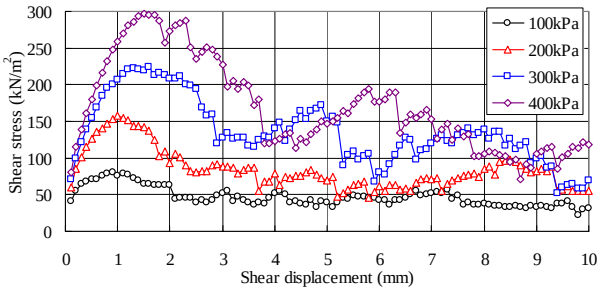

Figure 5. Simulated results on the direct shear tests under the constant vertical pressure of 100, 200, 300 and 400 kN/m^2.

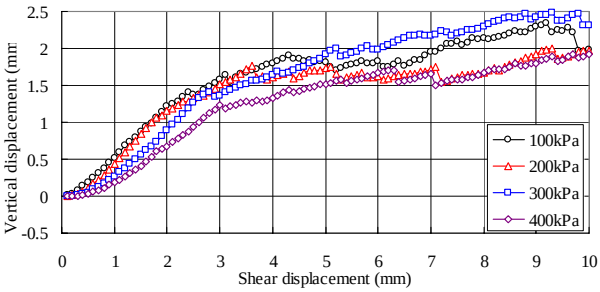

Figure 6. Vertical displacement in the direct shear tests under the constant vertical pressure of 100, 200, 300 and 400 kN/m^2.

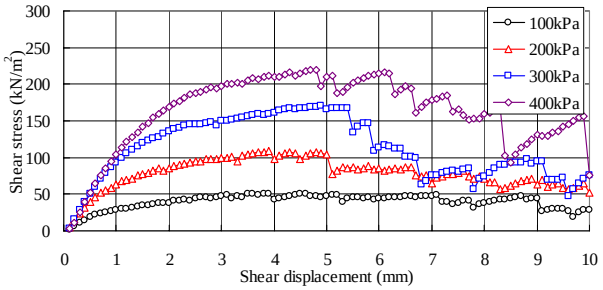

Figure 7. Simulated results on the simple shear tests under the constant vertical pressures of 100, 200, 300 and 400 kN/m^2.

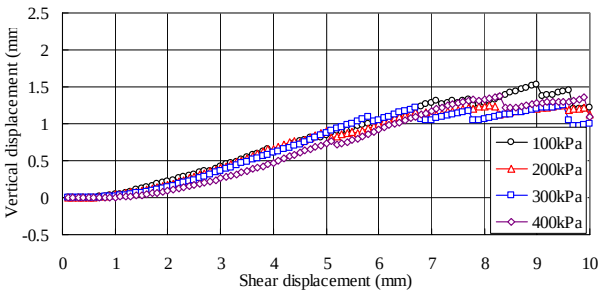

Figure 8. Vertical displacements in the simple shear tests under the constant vertical pressure of 100, 200, 300 and 400 kN/m^2.

Table 2. Summarized mechanical property of aggregates obtained from the simulation of the direct shear tests and simple shear tests.

Soil in shear zone	
Friction angle	37 degrees
Dilatancy angle	45 degrees
Interaction between soil and pile's surface	
Friction angle	27 degrees
Dilatancy angle	12 degrees
Unit weight of aggregates	15.5 kN/m^3

2.2 Simulation on Axial Tensile Load Test of A Pile

Figure 9 illustrates schematic diagrams of the piles used in DE analysis. The four kinds of piles were tested; Case 1 was the strait pile with the diameter of 1.7 m, Case 2 was the belled pile with the diameter of 1.7m in the shaft and 2.5 m at the base, Case 3 and 4 were the multi-belled piles the diameter of 1.7m in the shaft and 2.5 m at the projections. All the inclination of upper surface in the projections was 12 degrees. The lower surface in the middle projections was inclined at the angle of 45 degrees.

DE analysis on the axial tensile load tests of the pile was conducted by using the miniature models with the scale of 1/50 in the 50 times gravity field. Figure 10 shows the numerical model of Case 4 as an example, which has half a cross section. The reason for this is to use the same cluster disks as used in Section 2.1 and reduce the number of the cluster disks for minimizing the calculation time. The same similarity rule was adopted in DE analysis as the one used in centrifuge model tests.

The simulation of axial tensile load tests of the pile was carried out as the following process,

(i) All the disks were randomly arranged in the area,
(ii) The acceleration of 50 G was applied in all the disks,
(iii) The disks in the pile's area were removed, and then the pile with self-weight was inserted,
(iv) The piles were pulled out at the constant rate of 5 mm/sec. up to 500 mm in prototype scale.

Figure 11 shows the relationship between pullout resistance and vertical displacement. It was observed from Figure 11 that the multi-belled piles in the early stage of the vertical displacement had larger resistance and stiffness than the others, and that uplift resistance in Case2 and Case 4 where the belled pile and the multi-belled pile with longer distance between the two projections were used gradually increased after the yielding. Uplift resistance in Case4 was larger than in Case 3. In addition, it was also found that the belled pile had the higher performance in the uplift resistance and stiffness than the strait pile.

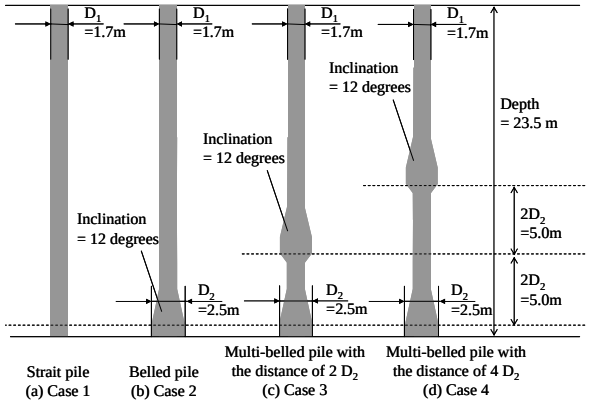

Figure 9. Schematic diagrams of the piles used in DE analysis (the sizes of piles are expressed in prototype scale).

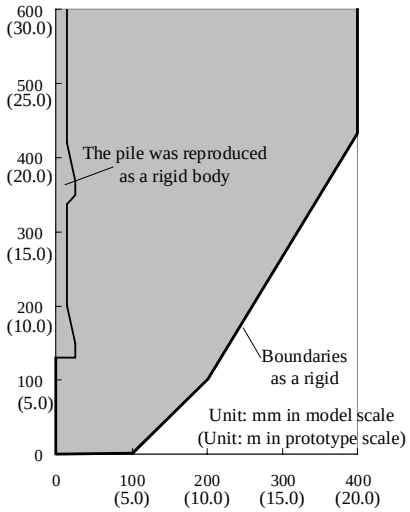

Figure 10. The numerical model in Case 4 (the dimensions of the model are expressed in model and prototype scale).

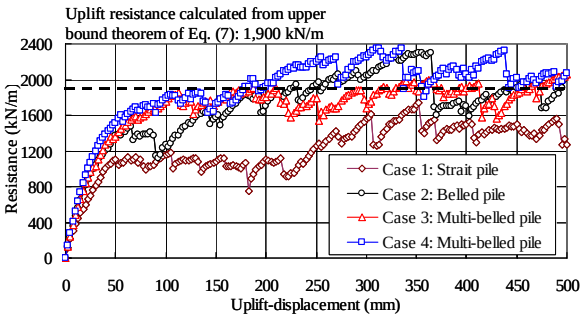

Figure 11. Pullout resistance of the piles against vertical displacement.

The final ground deformation at the vertical displacement of 500 mm ($0.2D_2$) was shown in Figure 12. No remarkable failure line was observed. The ground deformation was limited only around the pile. Additionally, loci of soil movements at the vertical displacement of 250 mm ($0.1D_2$) were illustrated in Figure 13. The circles in Figure 13 indicate the initial points, and the curves showed 10 times displacement vectors of soil movements. It was found from Figure 13 that the soil movements were very small in the strait pile of Case 1, which had the lowest resistance. The soil movements around the projections became larger than around the shaft in all the cases. Soil adjacent to the projections moved in an upward direction at first, and then the direction gradually inclined to a horizontal direction with the increase of vertical displacement. It was also observed that soil mass with the shape of reverse triangle moved as a body in the area adjacent to the projections, and that the soil movements in the area were not fully transmitted to the upper layer.

Figure 14 and 15 show the distribution of vertical and horizontal stress at the vertical displacement of 250 mm ($0.1D_2$). The concentration of the vertical and horizontal stress due to the effect of bearing load was seen in the area adjacent to the projections. The area where the stress concentrated was limited in the outer side of the projections.

Figure 16 shows the distribution of the maximum shear strain at the vertical displacement of 250 mm ($0.1D_2$). It was found from this figure that large shear deformation was induced only around the shaft in the lower and upper area of the projections. Large shear deformation was hardly observed in the area adjacent to the projections, which is consistent with the phenomenon that the soil mass with the shape of reverse triangle moved as a body in the area adjacent to the projections in Figure 13.

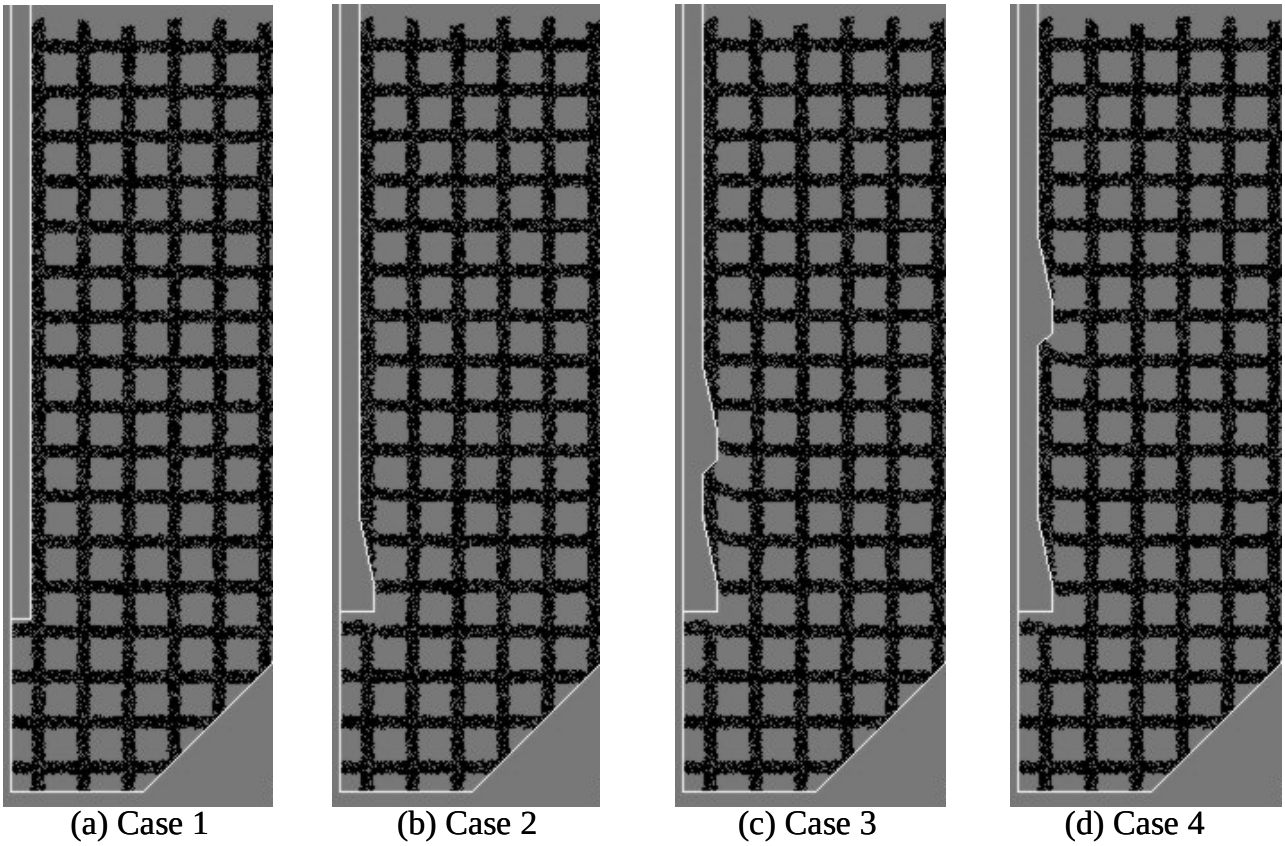

Figure 12. Ground deformation at the vertical displacement of 500 mm ($0.2D_2$).

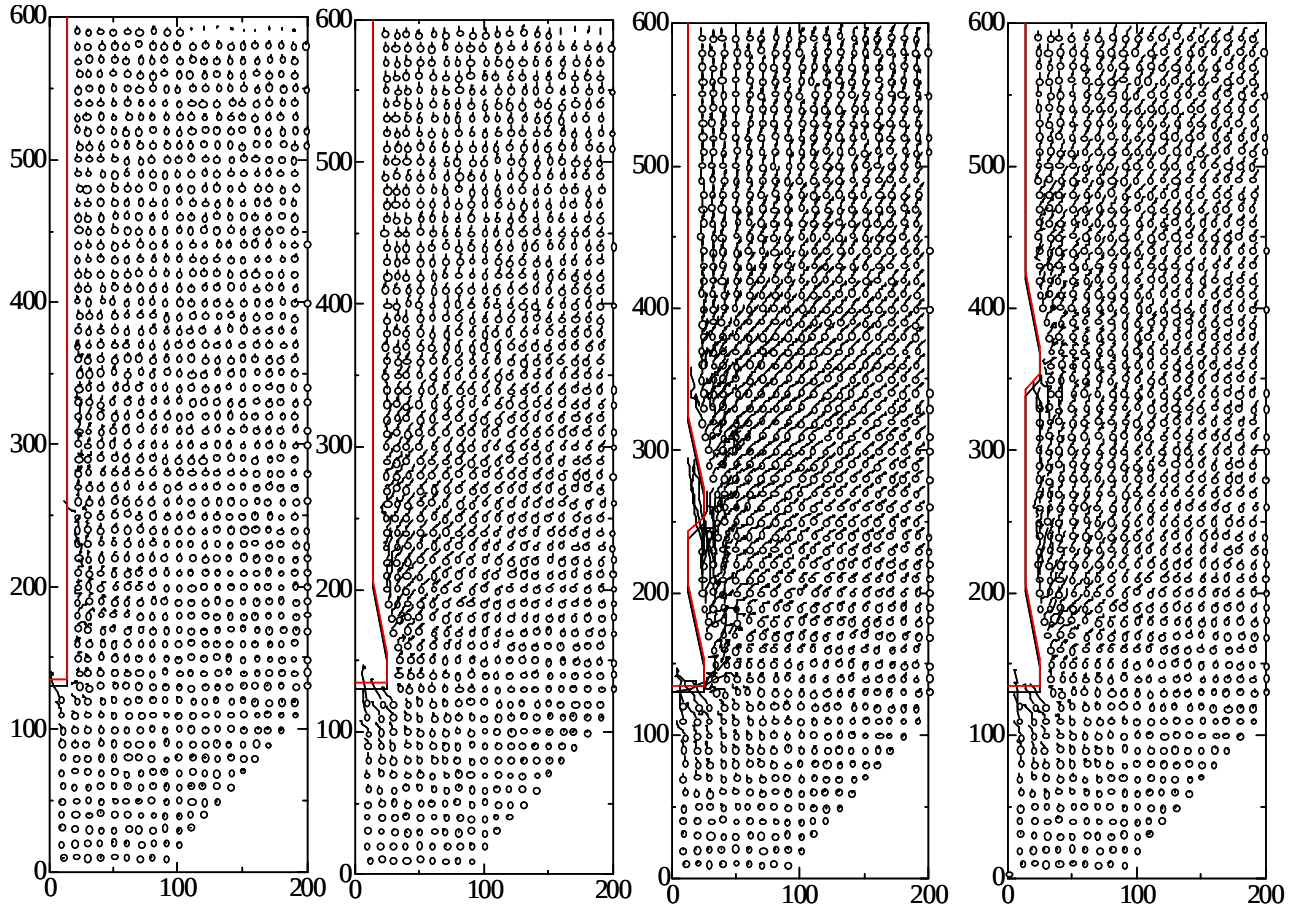

Figure 13. Loci of soil movements at the vertical displacement of 250 mm ($0.1D_2$)

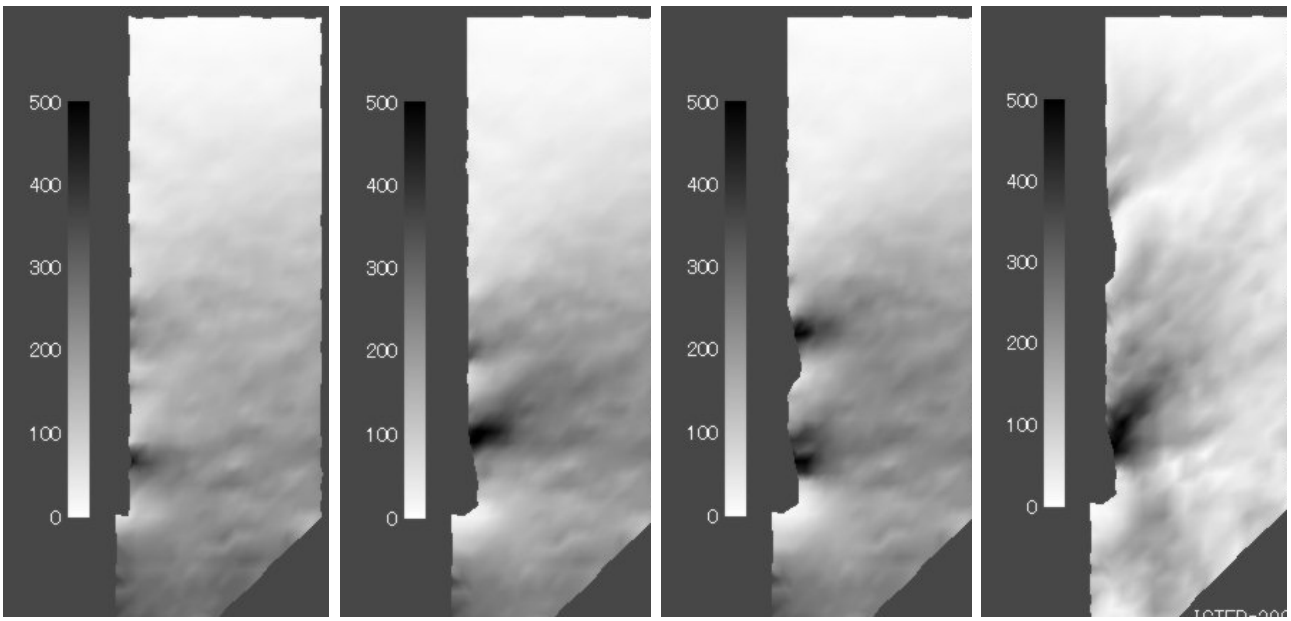

Figure 14. Distribution of the vertical stress at the vertical displacement of 250 mm ($0.1D_2$).

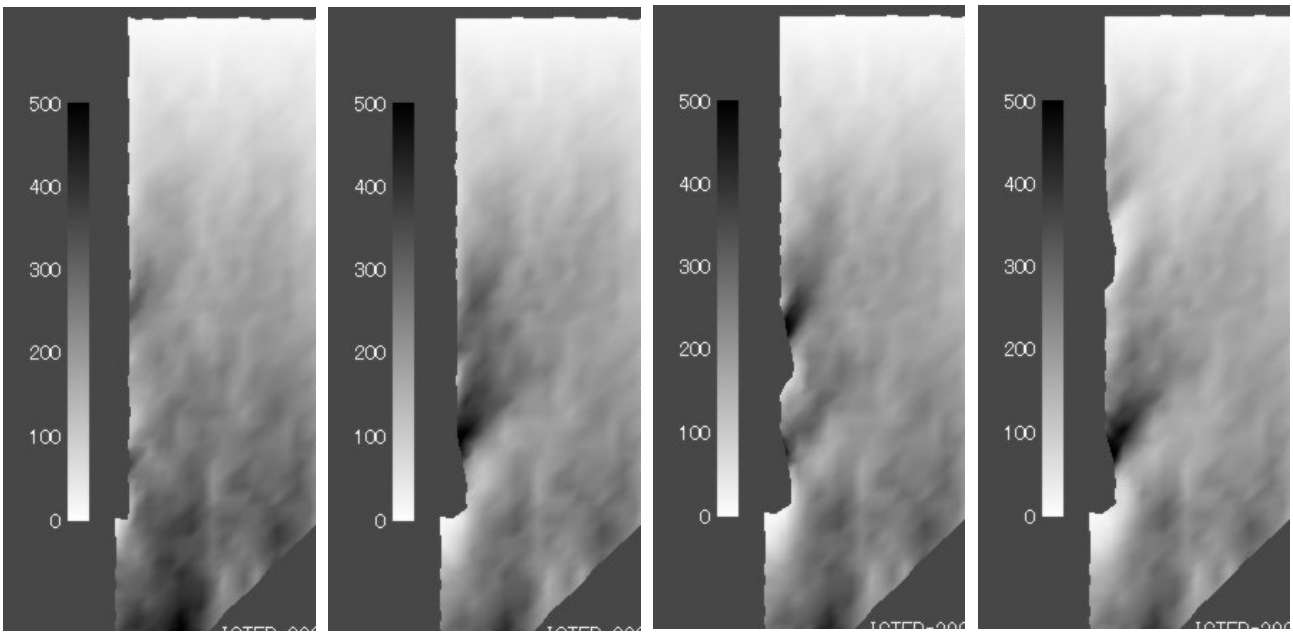

Unit: kN/m^2 Unit: kN/m^2 Unit: kN/m^2 Unit: kN/m^2

(a) Case 1 (b) Case 2 (c) Case 3 (d) Case 4

Figure 15. Distribution of the horizontal stress at the vertical displacement of 250 mm ($0.1D_2$).

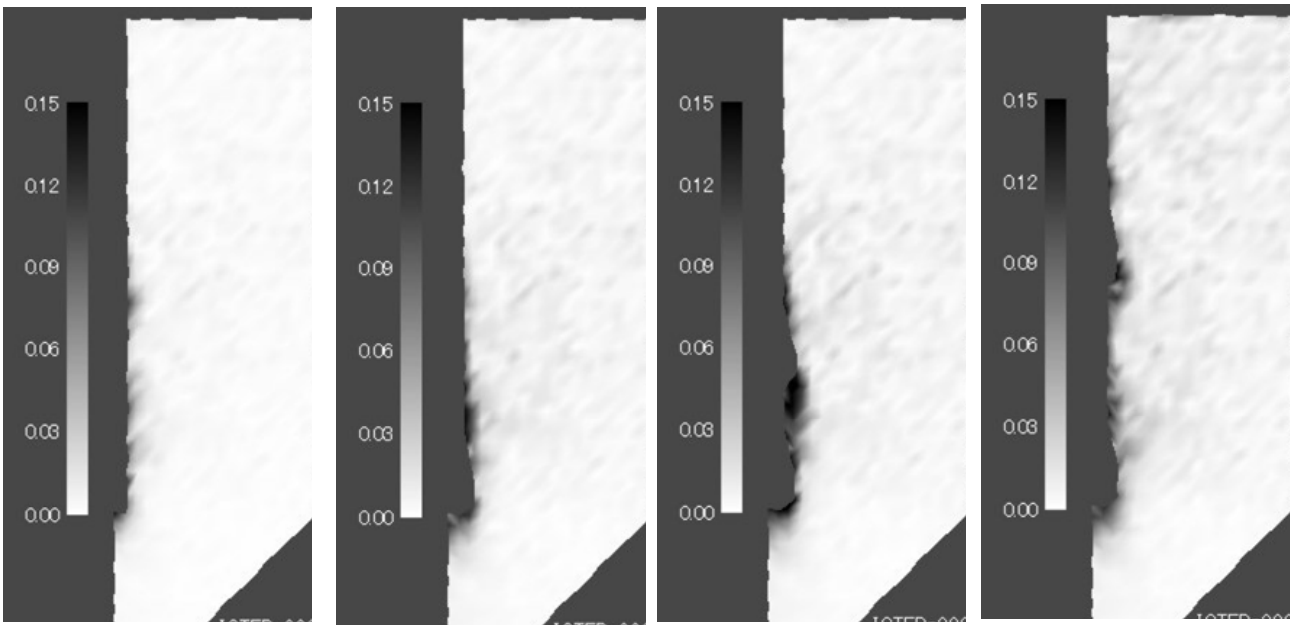

Unit: --- Unit: --- Unit: --- Unit: ---

(a) Case 1 (b) Case 2 (c) Case 3 (d) Case 4

Figure 16. Distribution of the maximum shear strain at the vertical displacement of 250 mm ($0.1D_2$).

3. ULTIMATE UPLIFT RESISTANCE OF BELLED PILES AND MULTI-BELLED PILES

In this section, the ultimate uplift resistance of belled piles and multi-belled piles is evaluated by the upper bound limit analysis based on the soil movements in DE analysis. Figure 17 shows a mechanism of plastic collapse around the projection in belled piles and multi-belled piles. The plastic collapse can reproduce the phenomenon in Figure 13 that soil adjacent to the projection moves vertically as a body and the soil movements are not fully transmitted to the upper layer. In Figure 17, P is the ultimate uplift resistance, p_a and p_b is overburden pressure on the lines of AD and DC. D_1 and D_2 are the diameter at the shaft and the projection. H and θ are the height and gradient of the inclined upper surface of the projection. α is the direction of the soil movements in the blocks of ABD and BCD. c and ϕ are cohesion and friction angle of soil. ψ is the dilatancy angle which is assumed to equal the friction angle, ϕ. δ is the friction angle of the projection's surface, which depends on the roughness of the pile surface and loosening during excavation. δv_0, δw_a and δw_b are the displacement vectors of the pile, the blocks of ABD and BCD. δw_{a0} is the relative displacement vector on the line of AB.

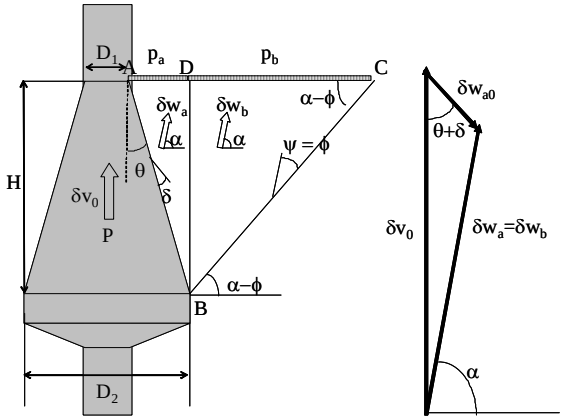

(a) Failure mechanism (b) Displacement vector diagram

Figure 17. A mechanism of plastic collapse of the soil adjacent to the projection in the belled piles and multi-belled piles.

The displacement vectors in Figure 17(b) must satisfy the following equations,

$$\delta v_0 = \delta w_a \sin\alpha + \delta w_a \cos\alpha / \tan(\theta+\delta), \quad (1a)$$

$$\delta w_b = \delta w_a, \quad (1b)$$

$$\delta w_{ba} = 0, \quad (1c)$$

$$\delta w_{a0} = \delta w_a \cos\alpha / \sin(\theta+\delta). \quad (1d)$$

External loads in Figure 17(a) are the gravity acting on the blocks of ABD and BCD, and the overburden pressure on the lines of AD and DC. Each of them is calculated by Eq. (2) and (3).

$$W_a = \frac{1}{2}\gamma H^2 \tan\theta, \quad W_b = \frac{1}{2}\gamma H^2 / \tan(\alpha-\phi), \quad (2)$$

$$P_A = p_a H \tan\theta, \quad P_B = p_b H / \tan(\alpha-\phi), \quad (3)$$

where W_a and W_b are the self-weight in the blocks of ABD and BCD, γ is the unit weight of soil, P_a and P_b are the overburden forces, which are calculated by integrating the overburden pressure on the lines of AD and DC. The increment of work done by external loads is expressed as Eq. (4).

$$\Delta W = P \cdot \delta v_0 - (P_a + W_a)\cdot \delta w_a \sin\alpha - (P_b + W_b)\cdot \delta w_b \sin\alpha \quad (4)$$

The work done by internal stress is calculated on the lines of AB and BC. Now, the dilatancy angle is assumed to equal the friction angle. The increment of work done by internal stress is due to cohesion, and is expressed as following,

$$\Delta E = c \cdot H/\cos\theta \cdot \delta w_{a0} \cos\delta + c \cdot H/\sin(\alpha-\phi)\cdot \delta w_b \cos\phi. \quad (5)$$

From the principle of virtual work, the increment of work done by external load equal that by internal stress as following,

$$\Delta W = \Delta E \quad (6)$$

The ultimate uplift resistance is calculated by substituting Eqs. (1a) – (1d) to Eq. (6) and is expressed as Eq. (7)

$$P = \frac{1}{\sin\alpha + \cos\alpha/\tan(\theta+\delta)}\left[(P_a + W_a)\cdot\sin\alpha + (P_b + W_b)\cdot\sin\alpha + c\cdot H/\cos\theta\cdot\cos\alpha/\sin(\theta+\delta)\cdot\cos\delta + c\cdot H/\sin(\alpha-\phi)\cdot\cos\phi \right] \quad (7)$$

The uplift resistance is obtained by searching for the angle of α to minimize the uplift resistance. Using the mechanical property in Table 2 and the unit weight of 15.5 kN/m^3 in the aggregates, the uplift capacity of the belled pile in Figure 9 is about 1900 kN/m which includes the piles' self-weight of about 425 kN/m, where the angle of α to minimize the uplift resistance is about 84 degrees. Incidentally, skin friction on the shaft above the projection can be ignored, because uplift resistance due to the skin friction cause the reduction of the overburden force on the lines of AD and DC in Figure 17.

The uplift resistance in the multi-belled pile is obtained as the summation of uplift resistance in each projection. If the multi-belled pile which has the same dimension in both of the middle and bottom projection is constructed in a homogeneous layer, the ultimate uplift resistance almost

equal that of the belled pile without the middle projection. This uplift capacity of the belled pile and the multi-belled piles is shown in Figure 11.

It was found from Figure 11 that the proposed equation of Eq. (7) has good agreement with the results in DE analysis. But, the belled pile (Case 2) and the multi-belled pile with longer distance between two projections (Case 4) exceeded the upper limit value of Eq. (7) after the vertical displacement of 10 % in the diameter of D_2. The reason for this might be that soil movements in Figure 13(b) and (d) were induced in the outer area of the block of ABC in Figure 17.

4. CONCLUSIONS

Distinct element analysis was carried out to investigate mechanism of uplift capacity of belled piles and multi-belled piles. Additionally, the upper bound limit analysis based on soil movements in DE analysis was conducted to estimate the ultimate uplift resistance. The followings were obtained from DE analysis and the upper bound limit analysis,

1. The multi-belled piles showed the largest uplift resistance and stiffness in the early stage of the vertical displacement.
2. The belled pile has lower uplift resistance in the early stage of the vertical displacement than multi-belled piles. However, it finally showed the almost same ultimate resistance as in the multi-belled pile.
3. No remarkable failure line was observed in the ground deformation of DE analysis.
4. It was observed from soil behavior in DE analysis that soil mass with the shape of reverse triangle adjacent to the projections moved vertically, and that such soil movements did not fully transmit to the upper layer.
5. The theoretical solution to estimate the ultimate uplift capacity of the belled pile and multi-belled pile was obtained from the upper bound limit analysis. It could reproduce the ultimate uplift resistance of the piles in DE analysis.

Acknowledgements:

The authors are thankful Mr. Tamai, Mr. Wakai and Dr. Koumura (Research & Development Institute, Takenaka Corporation) to give valuable suggestions about mechanism of uplift resistance and soil behavior around a belled pile and a multi-belled pile.

References:

Tsutsui, M., Takagi, T., Katoh, K. and Shimatani, Y. (1995), "Experimental Study on Pulling Resistance of Cast-in-Place Belled Pile,-Part 2-," *Annual Meeting Architectural Institute of Japan*, 933-934, (in Japanese).

Hirai, Y., Wakai, S., Aoki, M. and Maruoka, M. (2002), "Cetrifuge Model Test on Pull-out Resistance of Belled Pile in Sand,-Part 1-," *Annual Meeting Architectural Institute of Japan*, 507-508, (in Japanese).

Chatani, F., Suzuki, N., Nishimura K. and Wada Y. (2008), "Static Axial Reciprocal and Tensile Load Tests of Single Cast-in-Place Concrete Nodular Piles, -Part 5-," *Annual Meeting Architectural Institute of Japan*, 575-576, (in Japanese).

Meyerhof, G.. C. and Adams, J. L. (1968), "The Ultimate Uplift Capacity of Foundations," *Canadian Geotechnical Journal*, Vol. 5, No. 4, 225-245.

Murray, E. J. and Geddes, J. D. (1987), "Uplift of Ancor Plates in Sand," *Journal of Geotechnical Engineering*, ASCE, Vol. 113, No.3, 202-215.

Kumar, J. (2003), "Uplift Resistance of Strip and Circular Aanchors in a Two Layered Sand," *Soils and Foundations*, Japanaese Geotechnical Society, Vol. 43, No.1, 101-107.

Cundall, P. A. (1971), "A Computer Model for Simulating Progressive Large Scale Movements in Blocky Rock System," *Symposium, ISRM*, Nancy, France, Proc. Vol. 2, 129-136.

JOINT CONFERENCE PROCEEDINGS
7th International Conference on Urban Earthquake Engineering (7CUEE) &
5th International Conference on Earthquake Engineering (5ICEE)
March 3-5, 2010, Tokyo Institute of Technology, Tokyo, Japan

SITE AMPLIFICATION FORMULA FROM BEDROCK TO SURFACE USING AVERAGE VS IN EQUIVALENT SURFACE LAYER BASED ON VERTICAL ARRAY RECORDS

Takaji Kokusho[1)]

1) Professor, Civil & Environmental Engineering Department., Chuo-University, Tokyo, Japan

Abstract: Site amplification essential for seismic zonation between ground surface and bedrock was investigated using surface and base accelerations recorded in a number of KiK-net downhole arrays in Japan during recent destructive earthquakes. Based on soil investigation data available for individual arrays, theoretical amplifications for surface arrays consistent with the vertical array records were calculated. A good and unique correlation was found between the peak amplification thus obtained and a newly proposed S-wave velocity ratio, which is defined as S-wave velocity in a base layer divided by average S-wave velocity, $\overline{Vs}$ for different sites and different earthquakes. The value of $\overline{Vs}$ was evaluated from fundamental mode frequency and a thickness of equivalent surface layer in which peak amplification was exerted. The conventional parameter Vs_{30}, often used in current practice, showed poorer correlation than $\overline{Vs}$ with the obtained amplifications. It is suggested that $\overline{Vs}$ may be readily determined from microtremor measurements.

1. INTRODUCTION

Site amplification defined here between ground surface and bedrock depends on several factors; the composition of soil layers, S-wave velocities, soil densities, internal damping of the individual layers. Furthermore, strain-dependent nonlinear properties may affect site response in soft soils during strong earthquakes.

Among the influencing factors, a ratio of S-wave velocity between base layer and surface soil is of utmost importance. Shima (1978) found that the analytically calculated site amplification is almost linearly related to S-wave velocity ratio between base layer and top layer irrespective of intermediate layers.

In order to evaluate site amplification from a base layer to ground surface, NIED (National Research Institute for Earth Science and Disaster Prevention, Japan) deployed several hundreds of vertical array strong motion recording systems called KiK-net all over Japan, which comprises a pair of 3D accelerometers at ground surface and base layer. The observed records together with associated geotechnical data are easily accessible by international researchers at the web site; http://www.kik.bosai.go.jp/kik/.

In general, there can be two different seismic array systems to measure the site amplification between ground surface and base layer as illustrated in Figs. 1(a) and (b). One is a surface array (a) consisting of a set of surface seismometers on different surface geologies in a relatively small area with a common base layer. Seismic records $2A_s$ on a surface soft soil and $2A_b$ on outcropping base layer allow to directly evaluate site amplification between the two different geologies $2A_s$ /$2A_b$ if incident seismic wave A_b is assumed basically the same in that area. The other is a vertical array (b) consisting of surface and down-hole seismometers at the same place. This can evaluate site amplification exactly at the same location, though some modification is necessary to extract the outcrop motion $2A_b$ from observed base motion (A_b+B_b) which is more or less contaminated by downward wave B_b from overlying layers.

In this context, Kokusho and Sato (2008) evaluated spectrum amplifications from strong motion records obtained by the KiK-net vertical arrays during 3 strong earthquakes occurred in recent years in Japan. The Fourier spectrum ratio $2A_s/(A_b+B_b)$ between the two measured motions at surface and base first calculated was used to modify the theoretical transfer function $2A_s$ /$2A_b$ based on multiple

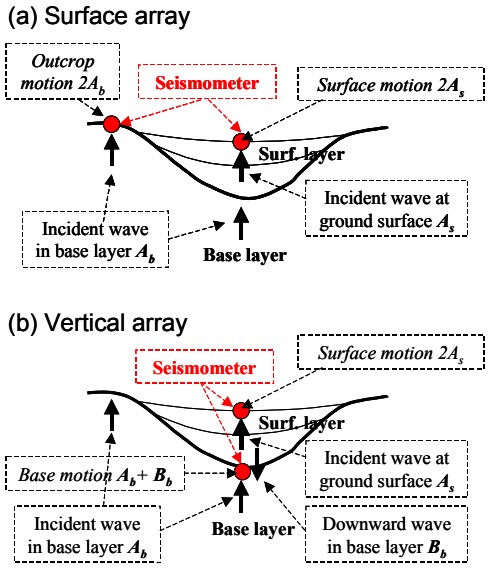

Figure 1 Two seismic array systems (a) & (b) to measure site amplification between ground surface and base layer.

reflection theory of 1-dimensional SH waves by removing the effect of downward wave B_b on the measured motion at the base layer. The peak amplifications of the modified transfer functions $2A_s$ /$2A_b$ were then correlated with S-wave velocity ratios between base and surface which was newly proposed in the research. In this paper, the number of earthquakes is increased from 3 to 8 to investigate if their spectrum amplifications are correlated in the similar manner with the S-wave velocity ratios.

2 EARTHQUAKE RECORDS AND AVERAGE Vs

In addition to three earthquakes (EQ1: the 2003 Tokachi-Oki earthquake (M_J=8.0), EQ2: the 2004 Niigataken-Chuetsu earthquake (M_J=6.8), EQ3: the 2005 Fukuokaken-Seihou-Oki earthquake (M_J=7.0)), five new earthquakes are used here; EQ4: the 2000 Tottoriken-Seibu earthquake (M_J=7.3), EQ5: the 2001 Geiyo earthquake (M_J=6.4), EQ6: the 2007 Niigataken-Chuetsu-Oki earthquake (M_J=6.8), EQ7: the 2007 Noto-Hanto earthquake (M_J=6.9) and EQ8: the 2008 Iwate-Miyagi-Nairiku earthquake (M_J=7.2). Here, M_J is the earthquake magnitude on the Japanese Meteorological Agency scale and nearly equivalent to the Richter Magnitude. Strong motion records at 20 sites with peak ground acceleration (*PGA*) higher than 200 cm/s^2 in EQ1, at 15 sites with *PGA* >100 cm/s^2 in EQ2, at 11 sites with *PGA* >100 cm/s^2 in EQ3, at 20 sites with *PGA* >100 cm/s^2 in EQ4, at 17 sites with *PGA* >100 cm/s^2 in EQ5, at 10 sites with *PGA* >100 cm/s^2 in EQ6, at 5 sites with *PGA* >100 cm/s^2 in EQ7, and at 17 sites with *PGA* >150 cm/s^2 in EQ8 are used in this research. Fig. 2 indicates peak measured accelerations at surface and base of all the sites used in this research. The PGA-values in the vertical axis span from 100 to 2500 cm/s^2, while maximum accelerations at the base in the horizontal axis are less than 2000 cm/s^2, showing approximately 2-10 times amplification of the peak horizontal accelerations.

The depths of the down-hole seismometers in the vertical arrays used here vary from 100 m to 330 m except for 1 site (800 m). S-wave velocities at the surface and base levels of all the vertical arrays are plotted in the vertical and horizontal axes, respectively, in Fig. 3. S-wave velocity in the depth Vs_b is normally stable in each site and does not drastically change in neighboring layers. However, the Vs_b-values among different sites diverge from Vs_b =400 m/s to 3000 m/s for the eight earthquakes as plotted in Fig. 3. In a good contrast, the surface velocities *Vs* are around 200 m/s on average for most of the recording sites used here.

Fourier spectrum ratio was computed between ground surface and base layer. Typical results for main shock and several aftershocks of EQ1 at 2 sites are exemplified for the EW direction in Figs. 4(a) and (b). There is a clear difference in the spectrum ratio between main shock and aftershocks in both sites reflecting the effects of the

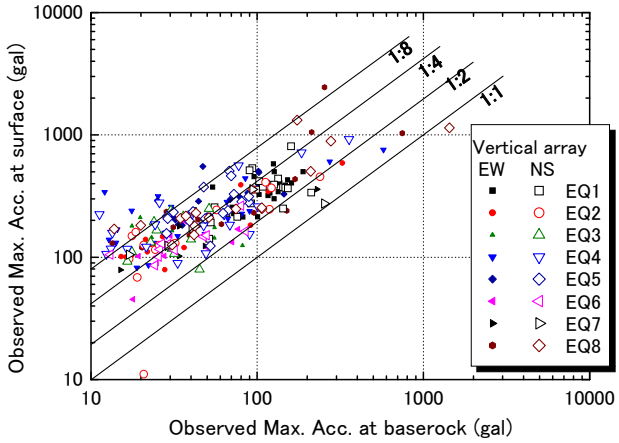

Figure 2 Maximum accelerations at surface and base for all vertical array records of 8 earthquakes.

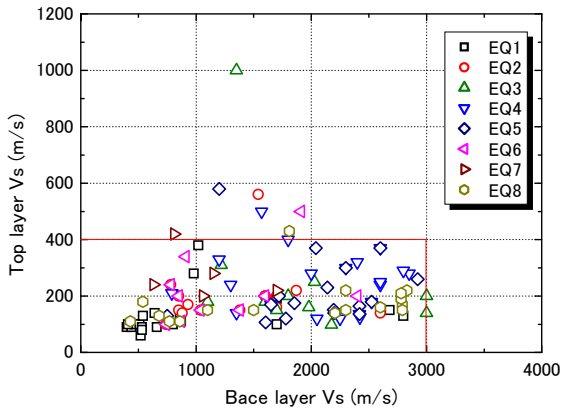

Figure 3 S-wave velocities in surface and base layers for all vertical array sites of 8 earthquakes.

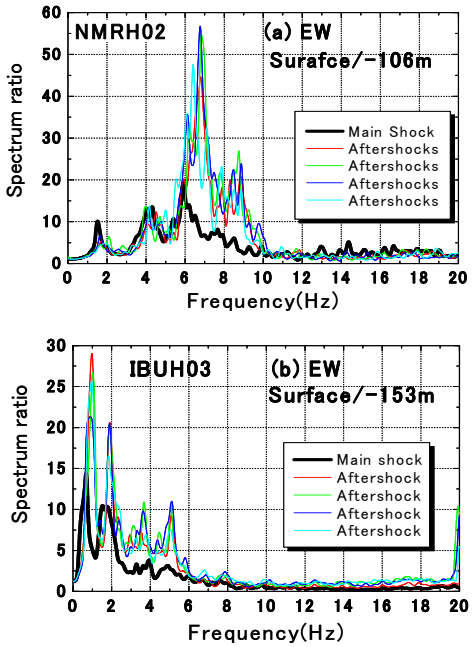

Figure 4 Spectrum ratios versus frequency in EW directions for main shock and aftershocks at 2 sites in EQ1.

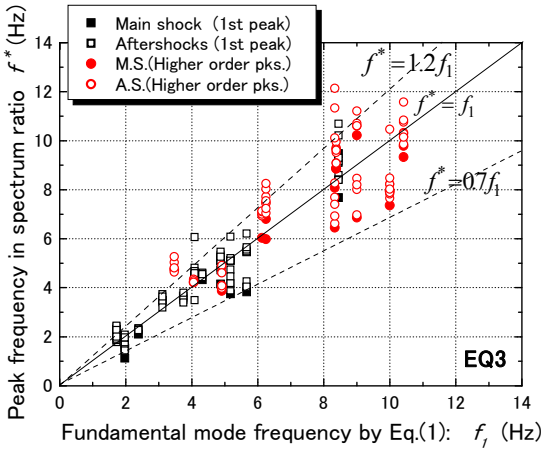

Figure 5 Peak frequencies calculated by Eq.(1) based on soil data compared with identified frequencies in observed spectrum ratios for main shock and aftershocks for all sites in EQ3.

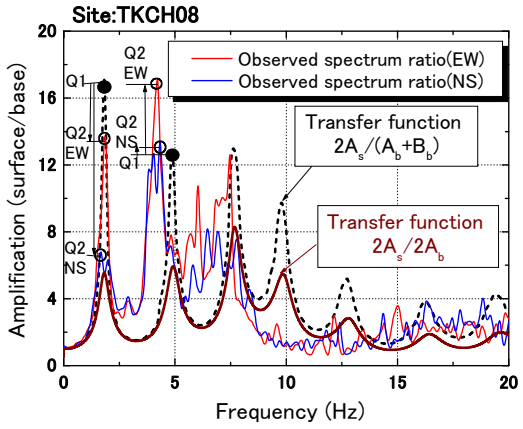

Figure 6 Comparison of transfer functions, $2A_s/(A_b+B_b)$ and spectrum ratio of observed motions at the same site.

strain-dependent soil properties which result in nonlinear site response to strong shaking. In order to specify soil layers generating peak frequencies in the spectrum ratios, fundamental mode frequencies of layered soil systems f_1 were calculated by the following formula based on soil logging data along with S-wave velocities of individual layers.

$$f_1 = 1\Big/\left[4\sum_{i=1}\left(H_i/Vs_i\right)\right] \tag{1}$$

Here, H_i and Vs_i are the thickness and the S-wave velocity of the *i*-th layer numbered from the top, and the summation is implemented layer by layer down to the base. This frequency corresponds to a wave length which is equal to 4 times the layer thickness. The calculated frequency was compared one by one with the peak frequency in the spectrum ratio of observed motions such as in Figs. 4(a) and (b) to identify equivalent surface layers of thickness $H_s=\sum H_i$ consisting of one or more layers, generating the fundamental mode frequency calculated by Eq.(1). Note that there can be multiple equivalent surface layers in the same site corresponding to individual peak frequencies.

In Fig. 5, the peak frequencies f_1 calculated by Eq.(1) based on given soil data are taken in the horizontal axis to compare with the frequencies f^* identified in the observed spectrum ratios for the main shock and aftershocks in the vertical axis for the recording sites of EQ3. It indicates that there exists a satisfactory correspondence between the fundamental mode frequency of soil models f_1 based on Eq.(1) and the peak frequency f^* observed in spectrum ratios irrespective of the order of peaks. The average S-wave velocity $\overline{Vs}$ for each equivalent surface layer can be calculated from the fundamental mode frequency f_1 and its thickness $H_s=\sum H_i$ as

$$\overline{Vs}=4H_s f_1 \tag{2}$$

3 SURFACE TO BASE SPECTRUM RATIO

In seismic zonation of an area resting on a common base layer, a transfer function between ground surface and an outcropping base layer $2A_s/2A_b$ is needed, while in vertical array records another transfer function $2A_s/(A_b+B_b)$ is obtained. Hence, the problem is how to evaluate $2A_s/2A_b$ based on measured motions in the vertical arrays. A procedure chosen here is as follows (Kokusho and Sato 2008).

1) A theoretical transfer function, $2A_s/(A_b+B_b)$ is calculated for each site using given soil properties with frequency-independent damping ratio, *D*, tentatively assumed as 2.5% in all layers.
2) The theoretical transfer function $2A_s/(A_b+B_b)$ is compared with measured spectrum ratio as exemplified in Fig. 6. If a peak in the transfer function can be found at about the same frequency in the spectrum ratio of observed motions, it is identified as the corresponding peak, and the damping ratio, assumed as *D*=2.5% previously, is modified by $D=Q_1/Q_2\times 2.5$ (%) to have the same peak value, where Q_1 is the peak amplitude of the theoretical transfer function, and Q_2 is that of spectrum ratio based on the actual records. The calculation in EW and NS directions are carried out, and their average is taken.
3) Another theoretical transfer function $2A_s/2A_b$ is computed using the modified damping ratio *D* based on the same soil layers model. When the two functions are not so similar as in the case in Fig. 6, peak frequencies of $2A_s/2A_b$ are compared with fundamental mode frequencies calculated by Eq.(1) and equivalent surface layers, and associated average S-wave velocities by Eq.(2) are determined again. The peak values of $2A_s/2A_b$ are adjusted using *D*-values determined from the nearest peaks of $2A_s/(A_b+B_b)$. In cases where such peaks are not found at all, that particular data is omitted.

4 Vs-RATIO VERSUS PEAK AMPLIFICATION

At the top of Fig. 7, the peak amplifications for $2A_s/2A_b$ computed by the methodology mentioned above for vertical array sites of EQ1 are plotted versus average S-wave velocity ratios $Vs_b/\overline{Vs}$ for the main shock with solid symbols. The velocity ratio $Vs_b/\overline{Vs}$ is defined here as a division of the S-wave velocity at a base layer Vs_b by the velocity $\overline{Vs}$ evaluated by Eq.(2) from the fundamental mode frequencies of Eq.(1) based on S-wave logging data at each site. A clear correlation can be recognized between the peak amplification and the velocity ratio both for 1st and higher order peaks. Four aftershock records of EQ1 are also analyzed in the same way and the results are plotted in the same graph with open symbols. A similar chart of the peak amplification for $2A_s/(A_b+B_b)$ plotted versus the same velocity ratio $Vs_b/\overline{Vs}$ is shown at the bottom of Fig. 7. The difference in amplification for $2A_s/(A_b+B_b)$ between main shock and aftershocks is evidently larger than that for $2A_s/2A_b$.

A simple 2-layers system of a surface layer (Impedance= $\rho_1 Vs_1$, Damping ratio=D_1) and an infinitely thick base layer (Impedance= $\rho_2 Vs_2$, Damping ratio=D_2) shown in Fig. 8(a) was basically studied to explain this difference (Kokusho and Sato 2008), assuming the impedance ratio for small strain properties as $\alpha = \rho_1 Vs_1/\rho_2 Vs_2$ =0.3. The transfer functions $2A_s/(A_b+B_b)$ and $2A_s/2A_b$ can be expressed by the following equations, respectively (Kokusho et al. 2008);

$$2A_s/(A_b+B_b) = 2/\left(e^{ik_1^*H}+e^{-ik_1^*H}\right) \quad (3)$$

$$2A_s/2A_b = 2/\left[\left(1+\alpha^*\right)e^{ik_1^*H}+\left(1-\alpha^*\right)e^{-ik_1^*H}\right] \quad (4)$$

where,

$k_1^* = \omega/\left(Vs_1\sqrt{1+2iD_1}\right)$, $\alpha^* = \alpha\sqrt{(1+2iD_1)/(1+2iD_2)}$, $i=\sqrt{-1}$.

In taking account the effect of strain-dependent soil properties on the amplification, shear modulus ratio and damping ratio in the surface layer are parametrically changed;

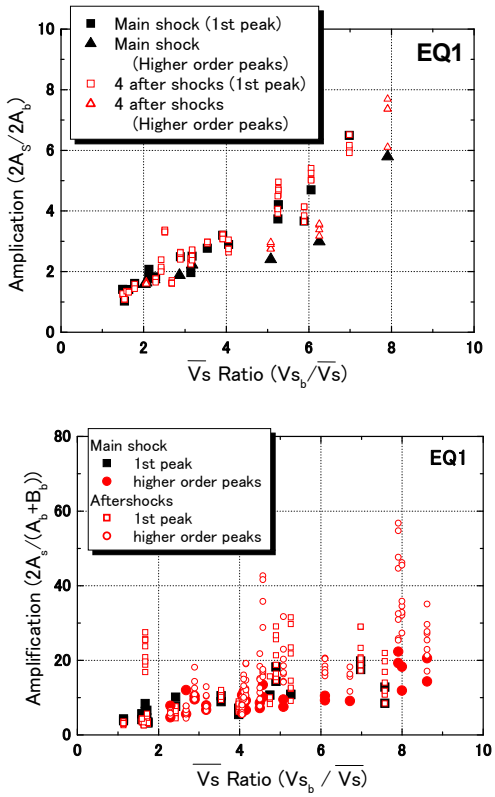

Figure 7 Peak amplitudes of $2A_s/A_b$ (top) and $2A_s/(A_b+B_b)$ (bottom) for main shock and aftershocks of EQ1 versus average S-wave velocity ratios.

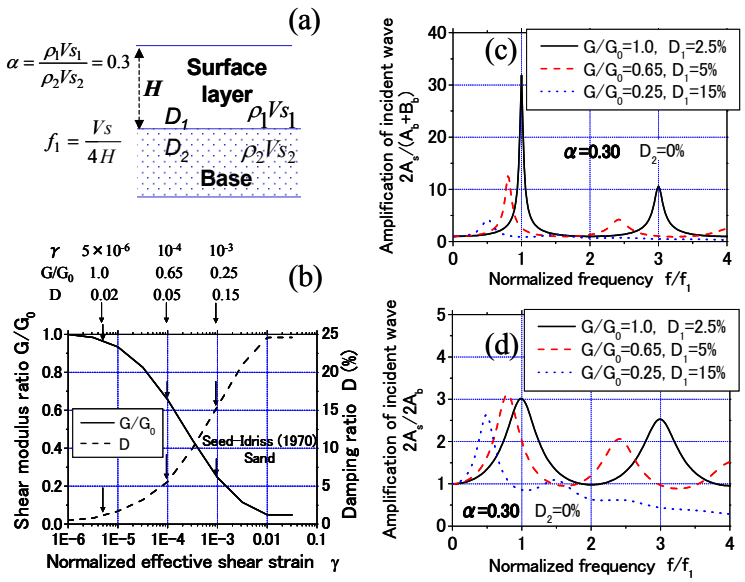

Figure 8 Two-layers system (a), Strain-dependent properties of surface layer (b), $2A_s/(A_b+B_b)$ (c) and $2A_s/2A_b$ (d); for different strain levels in surface layer.

G/G_0 =1.0, 0.65, 0.25 and D_1=2.5, 5 and 15% correspondingly, for strain level of 5 x 10^{-6}, 1 x 10^{-4}, 1 x 10^{-3}; respectively, assuming a typical degradation curve for sand (Seed and Idriss 1970) as indicated in Fig.8(b), while in the base layer, the shear modulus is linear and D_2=0. The calculated results of $2A_s/(A_b+B_b)$ and $2A_s/2A_b$ are shown in Figs. 8(c) and (d), respectively, in which the amplification between surface and base is taken versus normalized frequency, f/f_1, where f_1 =fundamental mode frequency of the surface layer for small strain properties (G/G_0 =1.0).

Obviously, the soil nonlinear properties have great effects on the peak frequencies and the amplifications. However, the difference in the peak amplifications is less pronounced in $2A_s/2A_b$ than in $2A_s/(A_b+B_b)$ for the 1st peak in particular, because radiation damping effect represented by impedance ratio α^* affects $2A_s/2A_b$ in Eq.(4), whereas no effect of impedance ratio α^* is involved in $2A_s/(A_b+B_b)$ as indicated in Eq.(3). Under the paramount effect of radiation damping, the difference in the amplification $2A_s/2A_b$ due to strain-dependent properties becomes less conspicuous. Furthermore, the impedance ratio $\alpha=\rho_1 Vs_1/\rho_2 Vs_2$, which becomes smaller with degraded modulus or degraded S-wave velocity in the surface layer, tends to give larger amplification compensating the effect of increased damping ratio during strong earthquakes. Thus, the difference in soil nonlinearity between strong motions and weak ones tends to have smaller influence on the amplification in $2A_s/2A_b$ than in $2A_s/(A_b+B_b)$ as indicated from the comparison of Fig.7.

Fig. 9 shows the relationship between the peak amplitude corresponding to $2A_s/2A_b$ and the velocity ratio $Vs_b/\overline{Vs}$ plotted for main shocks of the eight strong earthquakes incorporated here. Totally 133 data points (95 for the 1st peak and 38 for the higher order peaks) from 37 recording sites are included in this chart (14 data points in which $Vs_b/\overline{Vs}\geq 12.0$ are excluded here), and a large number of plots are overlapping in the zone of $Vs_b/\overline{Vs}\leq 4.0$. Quite remarkably, the plots show a fairly good correlation including both 1st and higher order peaks despite differences in various influencing factors associated with the eight earthquakes; namely, dominant frequency, shaking duration, regional geological difference, etc.

In the current practice of seismic zonation, the S-wave velocity Vs_{30} = averaged S-wave velocity over top 30 m from ground surface is sometimes used (Joyner and Fumal 1984, Midorikawa 1987) instead of $\overline{Vs}$ proposed here. In Fig. 10, the same peak amplitudes corresponding to $2A_s/2A_b$ are plotted versus the velocity ratio, Vs_b/Vs_{30}. Here, Vs_{30} (m/s) is calculated by the equation; $Vs_{30}=30/T_{30}$ in which T_{30} (s) is the traveling time of S-wave in the top 30 m based on soil logging data. Obviously, the correlation becomes poorer than in Fig. 9. Inconsistency in plots between 1st and higher order peaks is also evident. This indicates the importance to define the average S-wave velocity properly by identifying site by site the equivalent surface layer in which individual peak amplifications are exerted.

In the previous research (Kokusho and Sato 2008), a simple linear function;

$$2A_s/2A_b=0.175+0.685\left(Vs_b/\overline{Vs}\right) \qquad (5)$$

was proposed for the condition of $Vs_b/\overline{Vs}\leq 10.0$, which also seems quite consistent with the data of the eight earthquakes as obviously seen in Fig. 9. If the constants in Eq.(5) is newly computed from the data points in this paper, they slightly shift from 0.175 to 0.345 and 0.685 to 0.634.

Eq.(5) may be conveniently used because of its applicability to a wide variety of base layers with Vs_b =400 m/s to 3000 m/s as indicated in Fig. 3. The relative amplification for the same seismic motion in an area overlying a common base layer is readily evaluated. The procedure is as follows (Kokusho and Sato 2008);

1) Based on microtremor measurements, decide fundamental frequency f_1 of a site using H/V spectrum ratios (Nakamura 1989). Estimate the thickness of a soft soil or Holocene layer H where the fundamental fre-

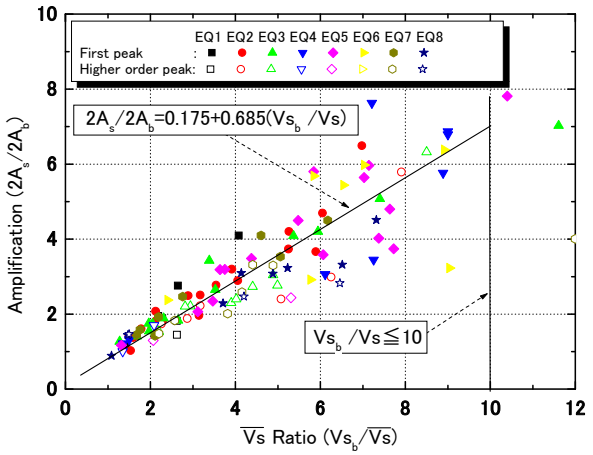

Figure 9 Peak amplitudes of $2A_s/2A_b$ for main shocks of 8 earthquakes versus average S-wave velocity ratios $Vs_b/\overline{Vs}$ proposed here and approximation by empirical equation.

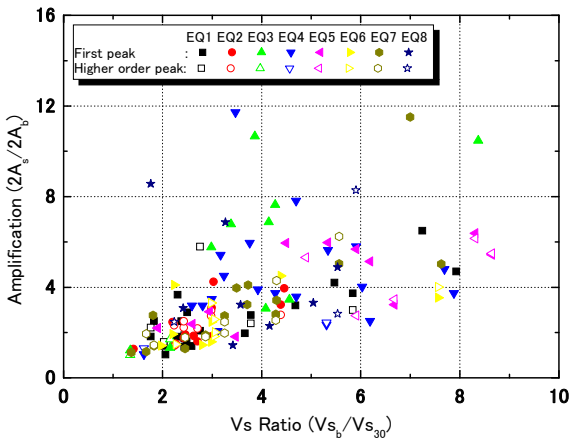

Figure 10 Peak amplitudes of $2A_s/2A_b$ for main shocks of 8 earthquakes versus average S-wave velocity ratios Vs_b/Vs_{30} using Vs_{30} of top 30m surface soils.

quency is exerted, which is sometimes possible referring to geological maps or high-density soil logging data available in city areas. Then, the average S-wave velocity can be calculated by $\overline{Vs} = 4Hf_1$.

2) Calculate the S-wave velocity ratio $Vs_b/\overline{Vs}$ from Vs_b of the common base layer and $\overline{Vs}$ obtained above for individual site conditions.
3) Comparing the amplifications by Eq.(5) at two different sites gives the relative amplification between them. To be precise, the amplification by Eq.(5) is slightly changeable depending on the value of Vs_b to be chosen among different base layers in the two sites, though its effect is ignorable for design purposes.

In the above, seismic response of ground is evaluated based on linear transfer function assuming that soil nonlinearity exerted during earthquakes is not so considerable. This assumption may not hold in those sites, such as Port Island during the 1995 Kobe earthquake (Kokusho et al. 2005). Strong soil nonlinearity by extensive liquefaction occurred there may have completely changed the soil system not to be able to justify the methodology employed here.

5 CONCLUSIONS

In studying seismic amplification between ground surface and base layer using KiK-net records of recent 8 strong earthquakes occurred in Japan, average S-wave velocity $\overline{Vs}$ for equivalent surface layer corresponding to each peak of a Fourier spectrum ratio was introduced from S-wave logging data. Then, a velocity ratio $Vs_b/\overline{Vs}$ was defined by dividing S-wave velocity at a base layer Vs_b by the average velocity $\overline{Vs}$ in the equivalent surface layer. Peak amplifications of spectrum ratios in terms of outcrop motions, computed from 1D multi-layered systems using soil investigation data, were adjusted to be consistent with the peak amplifications of the array record, read off and correlated with the velocity ratio.

The major findings in this series of research using 3 earthquakes and 8 earthquakes are;

1) The spectrum peak amplifications of $2A_s/2A_b$ for outcrop motions plotted versus the velocity ratios $Vs_b/\overline{Vs}$ show a good correlation with between the peak amplification and the velocity ratio both for 1st and higher order peaks, despite differences in influencing factors of individual earthquakes.
2) Strain-dependent soil nonlinearity tends to have a minimal effect on the peak amplifications of $2A_s/2A_b$ for surface arrays compared to those of $2A_s/(A_b + B_b)$ for vertical arrays for the strong motion records investigated here.
3) The correlation mentioned above obtained by utilizing 8 strong earthquakes coincides well with Eq.(5), which was previously proposed. Eq.(5) or its modified version with slightly changed constants may be conveniently used for evaluating relative amplification in seismic zonation study covering an area sharing a common base layer with S-wave velocity, Vs_b.
4) If the same peak amplifications are plotted versus velocity ratios conventionally defined as Vs_b/Vs_{30} (Vs_{30} = average velocity for top 30m sometimes used in the current seismic zonation practice), the correlation becomes poorer, indicating the importance to define the average S-wave velocity adequately by identifying a site-specific equivalent surface layer in which peak amplifications are exerted.
5) The velocity $\overline{Vs}$ of the equivalent surface layer can be readily decided from fundamental mode frequency f_1 of a site using H/V spectrum ratios in micro-tremor measurements together with the thickness of soft soil or Holocene layer H, where f_1 if generated, by $\overline{Vs} = 4Hf_1$.

Acknowledgments

NIED (National Research Institute for Earth Science and Disaster Prevention) in Tsukuba, Japan, who generously provided KiK-net data through the Internet, is gratefully acknowledged. The great efforts in data reduction of voluminous KiK-net records by graduate and undergraduate students of Civil Engineering Department in Chuo University are also very much appreciated.

References

Joyner, W. B. and Fumal, T. E. (1984), "Use of measured shear-wave velocity for predicting geologic site effects on strong ground motion", Proc. of 8th World Conference on Earthquake Engineering, Vol.2, pp.777-783.

Kokusho, T., Aoyagi, T. and Wakunami, A. (2005), "In situ soil-specific nonlinear properties back-calculated from vertical array records during 1995 Kobe Earthquake", *Journal of Geotechnical and Geoenvironmental Engineering*, ASCE, Vol.131, No.12, 1509-1521.

Kokusho, T. and Sato, K. (2008), "Surface-to-base amplification evaluated from KiK-net vertical array strong motion records", *Soil Dynamics and Earthquake Engineering, Elsevier*, 707-716.

Midorikawa, S. (1987), "Prediction of iso-seismal map in the Kanto Plain due to hypothetical earthquake". *Journal of Structural Engineering*, Vol.33B, 43-48, (in Japanese).

Nakamura, Y. (1989), "A method for dynamic characteristics estimation of subsurface using microtremor on the ground surface", *QR of Railway Technical Research Institute*, Vol.30, 25-33.

Shima, E. (1978),: "Seismic Microzoning map of Tokyo". *Proc. Second Inter. Conf. on Microzonation* (1), 433-443.

WHERE TOPOGRAPHIC EFFECTS RESPONSIBLE FOR BUILDING COLLAPSES IN THE 2001 SOUTHERN PERU EARTHQUAKE?

Joseph Wartman[1)] and Nicholas E. Malasavage[2)]

1) Associate Professor, Dept.of Civil, Arch., & Env. Engineering, Drexel University, Philadelphia, U.S.A.
2) Research Assistant, Dept.of Civil, Arch., & Env. Engineering, Drexel University, Philadelphia, U.S.A.
jw64@drexel.edu, nem23@drexel.edu

Abstract: Significant damage occurred to residential buildings in the City of Moquegua, Peru during the 2001 M_w 8.4 Southern Peru Earthquake. This article examines the role of topography in the distribution of building collapse locations in the San Francisco neighborhood of Moquegua. A local indicators of spatial association (LISA) analysis of a building damage inventory from the earthquake indicate that in contrast to preliminary studies that suggested damage concentrations were a consequence of topographic amplification, clusters of collapsed buildings are generally correlated with flatter ground in the study area. This suggests that topographic effects did not play a significant role in the distribution of building collapse.

1. INTRODUCTION

During the 2001 M_w 8.4 Southern Peru Earthquake, significant damage occurred to residential buildings in the San Francisco neighborhood of the City of Moquegua. In contrast to most of parts of this city, which is relatively flat, the neighborhood of San Francisco is distinguished by its variation in topography. Several preliminary post-earthquake investigation reports (e.g. Kosaka-Masuno et al., 2001; Kusunoki, 2002; Rodriguez-Marek et al., 2003) hypothesized that the high levels of damage to were due to topographic effects, resulting in localized strong ground shaking. This phenomenon, whereby topographic features (e.g. hills and ridges) alter and amplify local ground shaking, has been observed in past earthquakes and is most pronounced near ridge tops. Given the topography of San Francisco, this was a plausible explanation; however, later published data suggested damage clusters were located away from ridge tops, indicating other factors may have governed localized ground motion intensity in the neighborhood. In this paper we consider the question of what role, if any, did topography play in the distribution of building collapses in San Francisco? More specifically, we present the results of spatial point pattern analyses to determine if building damage in San Francisco was clustered and if so, to see if the cluster locations coincide with areas of relief as would be expected with topographic amplification.

2. DAMAGE DISTRIBUTION

The 23 June 2001 moment magnitude (Mw) 8.4 Southern Peru earthquake affected a widespread area that included several important population centers in southern Peru and northern Chile, including Moquegua (Figure 1). The earthquake occurred along the active subduction boundary of the Nazca and the South American plates resulting in widespread damage throughout the region. In general, adobe buildings and older structures were most susceptible to damage, though a significant number of modern engineered structures were also impacted by the earthquake. Rodriguez-Marek and Edwards (2003) present a comprehensive overview of the damage caused by the earthquake. Only a limited number of strong motion instruments recorded the main shock, with the largest peak ground acceleration of 0.33 g being measured in the northern Chilean city of Arica. The only ground motion station in Peru, coincidently located in the city of Moquegua, registered a moderately high peak ground acceleration of 0.30 g.

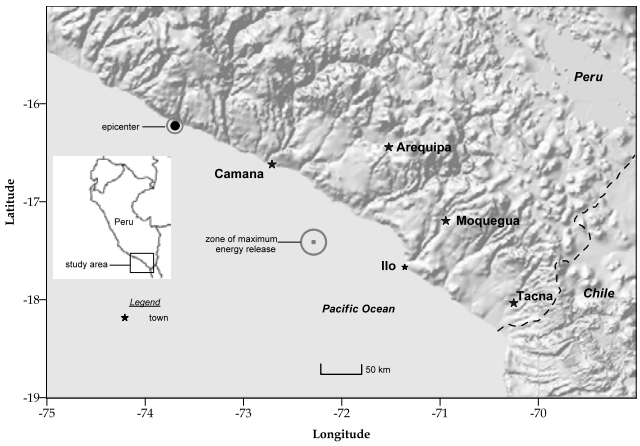

Figure 1. Regional map showing the location of urban centers impacted by the 2001 Southern Peru earthquake

The city of Moquegua is situated in an alluvial valley at the base of the Andes Mountains. The city is located approximately 55 km east of the Pacific coast at an elevation of 1400 meters. San Francisco, an approximately 1 km^2 neighborhood located in the southwestern part of Moquegua, was one of the most damaged areas in the city. San Francisco is situated on a geologic outcrop that includes three ridges rising roughly 100 m above the surrounding portions of the city (Figure 2). This outcrop, which daylights in the upper half of each ridge, consists of stiff conglomerate of the Moquegua geologic formation. This outcrop is also the primary source of the alluvium and colluvium that forms a soil mantle that generally thickens with decreasing elevation. Soil thickness ranges from 0 m on the hillside, to approximately 6 m in valley and flatland areas. Buildings in Moquegua are primarily of masonry or similar construction, with a lesser number of older adobe structures. The absence of earthquake-induced ground failure (i.e., soil liquefaction and landslides) in San Francisco suggested that the high levels of building damage were a result of strong localized shaking.

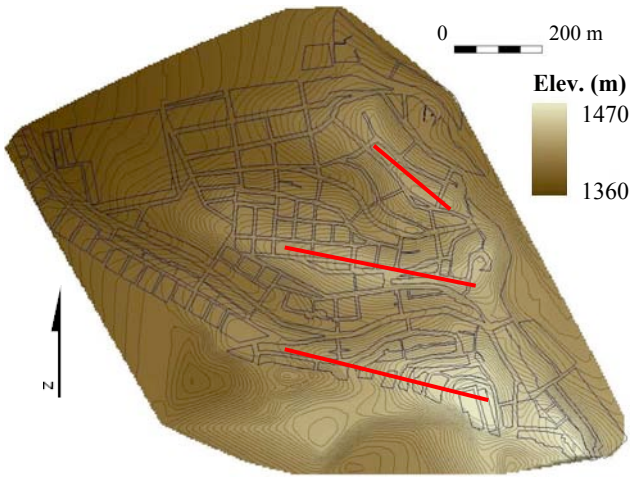

Figure 2 Street map and topography of San Francisco. The red lines indicate the locations of ridgetops.

2.1 PREDES Damage Inventory

Several earthquake damage inventories for the region have been published, including a high quality, comprehensive account produced by Peru's Center for the Study and Prevention of Disasters (PREDES 2003). The PREDES survey was based on individual inspections of close to 1900 buildings whose seismic performance was rated as good, moderate or poor, corresponding to buildings that exhibited no significant damage, significant cracks to loading bearing members, and collapse, respectively. The survey also categorized each building according to its typology (masonry, mixed, or adobe), as this is known to be an important factor governing the seismic performance of structures. Buildings comprised of masonry and "mixed" construction (i.e., combined masonry and adobe materials) are widely recognized to be of higher construction quality (and seismic resistance) than adobe dwellings.

Figure 3 shows the locations of buildings in San Francisco and their respective typologies. The open areas in the northwest corner of the study area are the locations of two undeveloped land parcels. The study zone was defined to include only the areas where complete data was available for all buildings. With some minor exceptions pertaining to a concentration of mixed dwellings located in the south-central portion of San Francisco, the building types appear to be generally well distributed throughout the neighborhood.

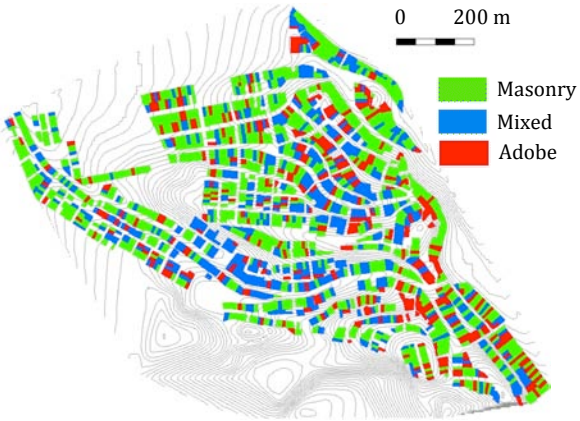

Figure 3 Building locations and typologies in San Francisco (after PREDES 2003).

The combination of different building types and performance levels make the damage inventory quite complex when considered in aggregate. Point pattern analysis techniques are quantitative methods that describe the pattern of point locations and their degree of clustering. These techniques require consistency in the database and thus the PREDES data inventory was modified to ensure uniform building construction quality. Specifically, adobe buildings, which have significantly lower seismic resistance than masonry and mixed structures, were not considered. As these comprised only a small fraction of the total building inventory, this did not significantly reduce the total number of buildings in the inventory. The performance of the remaining 1513 buildings in the inventory (i.e., masonry and mixed structures) was re-categorized in a binary manner as "no damage/moderate damage" and "collapse." As collapsed buildings (rather than partially damaged) were responsible for most of the injuries and fatalities in the earthquake, the clustering analysis was focused specifically on this damage category. Based on these refinements to the original PREDES database, the point

events for the analysis was thus defined as masonry and mixed construction buildings (i.e., higher quality structures) that collapsed in the earthquake. The locations of these damaged buildings are shown in Figure 4.



Figure 4 Collapsed masonry and mixed buildings (shown in red) in San Francisco.

2.2 Local Indicators of Spatial Association

Local indicators of spatial association, or LISA (Anselin, 1995), are a class of point pattern analysis techniques. The LISA approach is based on the concept of autocorrelation, meaning that correlations or relationships exist among spatially distributed data. The most popular of the LISA approaches was developed by Getis and Ord (1992), and later modified by Ord and Getis (1995) to what has is commonly known as the Gi* statistic. This approach computes the spatial autocorrelation structure over defined sampling windows and compares this to the global autocorrelation structure for the study region. Significant differences between local and global autocorrelation structures imply localized deviations from the global norm, implying localized clustering of events. The Gi* statistic is computed as:

$$G_i^* = \frac{\sum_j w_d^*(i,j) z(j)}{\sum_j z(j)} \qquad (1)$$

Where z(*j*) are known attribute values at all known point (i.e. low/moderate damage = 1, collapse = 2) and $w_d^*(i,j)$ is a matrix of spatial weights describing the influence of other known points up to a defined threshold distance (i.e. points within *d* are assigned a weight of 1, while those beyond *d* are assigned a weight of 0).

The Gi* statistic is most meaningfully interpreted within a larger statistical framework. In this case, a *Z-score* [Z(Gi*)] can be computed for each point by subtracting the expected Gi* value from the observed value, and dividing this by the square root of the variance for all points in the defined region of study:

$$Z(G_i^*) = \frac{G_i^* - E(G_i^*)}{\sqrt{Var(G_i^*)}} \qquad (2)$$

A Z-score of 0 implies no clustering, while increasingly positive or negative values suggest point concentrations. The statistical significances of clustering can be determined by comparing the computed Z-score with a range of values for a given confidence level (Mitchell, 2005). Figure 5 shows the results from this type of analysis for a 100 m sampling window. The filled contours correspond to collapsed building clusters associated with statistical confidence levels of 86 % (light red) and 95 % (dark red). A useful aspect of a LISA analysis is that extremes at both ends of parameter spectrum can be identified (i.e., "hot" and "cold" spots). For example, included on Figure 5 are blue-toned contours corresponding to local clusters of buildings with a low level of damage (i.e., "cold spots" of low damage caused to mixed and masonry buildings).

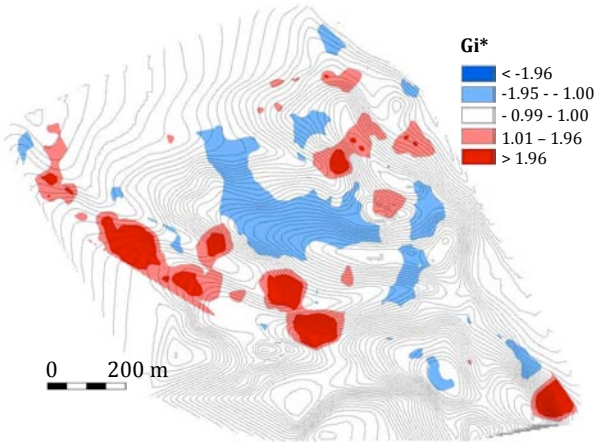

Figure 5 Gi* value contours for a 100 m diameter sample window.

Review of Figure 5 reveals two main trends:

1. The locations of the collapsed buildings in San Francisco are locally clustered, with the highest degree of clustering occurring for point (i.e., collapsed building) spacing in the range of approximately 25 to 100 m.

2. Collapsed buildings are clustered along a northwest-southeast trending valley. This cluster extends further into an adjacent flatland area in the western portion of the neighborhood. A second and more highly localized cluster of collapsed buildings is found along a hillslope located in the northeast portion of the neighborhood.

3. CONCLUSIONS

The point pattern analysis results clearly indicate that the largest cluster of collapsed buildings is correlated with flatter ground over the study area, which contrasts with preliminary studies that suggested concentrations of high building damage were localized at ridge tops. This suggests that topographic effects were not primarily responsabile for the collapse of buildings in San Francisco. Moreover, damage cold spots identified from the Gi* analysis generally overlie areas of topographic relief, which further discredits the topographic amplification hypothesis. The clusters in this study are associated with a high degree of statistical confidence, and thus it is unlikely that the observed concentrations of collapsed buildings were a result of natural background variation. These findings by themselves do not fully disqualify the hypothesis that topographic amplification played a role in damage distribution; however, they suggest that at a minimum these effects were less significant then originally thought. It is possible that the damage distribution was more closely related to "site effects" (Kramer, 1996) whereby earthquake ground motion is amplified by surficial soils and sediments such as those that underlie the small valleys and flatlands of San Francisco. Note that the scale of clustering of collapsed buildings (i.e., 25 to 100 m) corresponds closely with the dimensions of the valleys in the study area, leading further credibility to the site effects hypothesis.

References:

Anselin, L. (1995). "Local indicators of spatial association – LISA," *Geographical Analysis*, **27**, 93-115.

Center for the Study and Prevention of Disasters (PREDES). (2003), Study of the physical environment, social economics and evaluation of the risk in the neighborhood of San Francisco with reference to the District of Moquegua and Mariscal Nieto Province. Center for the Study and Prevention of Disasters, 261p.

Getis, A. & Ord, J.K. (1992). "The analysis of spatial association by use of distance statistics," *Geographical Analysis*, **24**, 189-206.

Ord, J.K. & Getis, A. (1995). "Local spatial autocorrelation statistics : distributional isssues and an application," *Geographical Analysis*, **27**, 286-306.

Kosaka-Masuno, M., Gonzales-Zenteno, E., Arias-Barahona, H., Minaya-Lizarraga, A., Faran-Bazan, E., Ticona-Paucara, J. (2001). Seismic Hazard Evaluation in the city of Moquegua. Convenio UNSA-INDECI. Proyect PER 98/018 PNUDINDECI, San Agustin de Arequipa National University, Arequipa, Peru.

Kramer, S.L. (1996). "Geotechnical Earthquake Engineering", Prentice Hall Inc.

Kusunoki, K. (2002). "Report on the damage investigation of the 2001 Atico Earthquake in Peru," Building Research Institute of Japan. 27 p.

Mitchell, A. (2005). "The ESRI Guide to GIS Analysis, Volume 2 : Spatial Measurements & Statistics", ESRI Press.

Rodriguez-Marek, A & Edwards, C. (2003). "Southen Peru earthquake of 23 June 2001 reconnaissance report," *Earthquake Spectra*, **19**(S1), pp. 165.

Rodriguez-Marek, A., Williams, J.L., Wartman, J., Repetto, P.C. (2003), "Ground motion and site response," *Earthquake Spectra*, **19**(S1), 11-34.

JOINT CONFERENCE PROCEEDINGS
7th International Conference on Urban Earthquake Engineering (7CUEE) &
5th International Conference on Earthquake Engineering (5ICEE)
March 3-5, 2010, Tokyo Institute of Technology, Tokyo, Japan

H/V METHOD USED TO QUALIFY THE MODIFICATION OF DYNAMIC SOIL CHARACTERISTICS DUE TO GROUND IMPROVEMENT WORK BY MEANS OF HEAVY COMPACTION PROCESS. A CASE STUDY : THE FORMER GIVORS'S GLASS FACTORY

S. Brûlé[1)], E. H. Javelaud[1)], T. Ohmachi[2)], Y. Nakamura[3)] and S. Inoue[4)]

1) Civil Engineer, Menard, France
2) Professor, Department of Built Environment, Tokyo Institute of Technology, Japan
3) President, System and Data Research, Tokyo, Japan
4) Research Associate, Department of Built Environment, Tokyo Institute of Technology, Japan
Stephane.Brule@menard-mail.com, Emmanuel.Javelaud@menard-mail.com, ohmachi@enveng.titech.ac.jp, shusaku@enveng.titech.ac.jp, yutaka@sdr.co.jp

Abstract: The H/V method put into relief its efficiency for geotechnical site classification according to the Eurocode 8: "Design of structures for earthquake resistance" (2005). The main classification criteria V_{s30}, average velocity of shear waves in first 30 meters, is obtained from the natural period of soil, knowing the soft and superficial soil thickness. In particular cases, the H/V method clearly shows the difference between the "geotechnical" bedrock and the "seismic" bedrock. At Givors' site, the H/V method is transposed as a ground improvement control method to appreciate the soil densification after an outstanding heavy dynamic compaction works. Compared with geotechnical and other geophysical in situ investigations, H/V measurements bring arguments for a more accurate seismic soil response characterization before and after treatment.

1. INTRODUCTION

Heavy dynamic compaction work (Mayne et al., 1984; FHWA, 1995) was performed at the Givors' former glass factory area (France) to improve 7 to 15 m of well graded gravel backfills laying on the geotechnical bedrock, to increase the bearing capacity and to regulate the total and differential settlements.

The H/V method was tested as a non destructive, convenient and cost-effective method to evaluate the soil dynamic properties before and after the ground improvement.

2. SCOPE OF WORK AND OBJECTIVES

Unlike ground improvement with addition of material (stone columns, lime or mortar columns, etc.), dynamic compaction tends towards an improved soil with more homogeneous properties. Therefore, for this 85 000 m² building project, the heavy compaction work (E > 400 t.m) increased the density of the soil by means of energy applied by ponder free-dropped on the soil surface from various height with a 5.0 x 5.0 print grid. It leaded to a large-scale ground modification.

Our objective is to quantify the evolution of the dynamic properties of the soils, characterized by its shear wave velocity *Vs*. In this paper, the properties of the soils are discussed in term of :

1) **Nature of the bedrock: engineering bedrock vs seismic bedrock.** Can the H/V method be used to obtain information about the nature of the bedrock in the usual geotechnical contexts of soil improvement sites ? (Figure 7)

2) **Soil characterization and evolution of the soil classification.** The ground improvement and the increase of the static Young modulus are well known due to numerous and usual geotechnical site investigation (SPT, CPT, Ménard pressuremeter test PMT, etc.). However, the new dynamic soil characteristics resulting of the compaction work are not usually determined and taken into account for the seismic design of the structures. Knowing the lithology and the thickness of the compacted backfills, the *Vs* is determined by the site investigations, and the results from mechanical (derived by correlation from CPT) and geophysical methods (MASW & H/V method) are compared.

3) **H/V practical application in civil engineering.**

According to the European seismic building code Eurocode 8 (2005) – "Design of structures for earthquake resistance", the average velocity of shear waves in the first 30 meters (Vs_{30}) is a main parameter of the seismic soil classification. The additional information provided by the H/V measurements at soil improvement sites is evaluated in term of a better comprehension of the soil dynamic response.

3. PROJECT SITUATION AND GEOLOGICAL CROSS-SECTION

The site (Figure 1) had been used for more than one hundred years by a glass company to manufacture its products. The old factory had been dismantled recently and new constructions are now being built. Heavy dynamic compaction is applied because it offers a solution to both remediation of brownfield sites and geotechnical issues. The dynamic compaction program was designed to improve the 7 to 15 m of well graded gravel backfill, which is covering the sand and gravels from the nearby Gier river. Below is the granite (Figure 2). The water level is about 5 to 6 meters below the ground surface.

The sedimentary depositional environment is suitable for seismic site amplification.

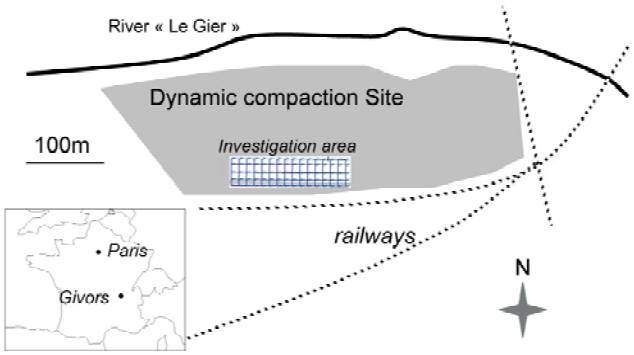

Figure 1 Project situation, showing the specific investigation area where denser geotechnical investigations have been were carried out

4. INVESTIGATIONS AND RESULTS

4.1 Investigation area

We defined a specific investigation area (80 regularly spaced points) in the southern part of the site (Figures 1&3, 5 lines, 16 columns), and carried out twice the following geotechnical investigations at exactly the same positions, before and after the dynamic compaction work :

- H/V measurements (80 points) at each intersection of the grid;
- MASW (4 profiles along the lines of the grid);

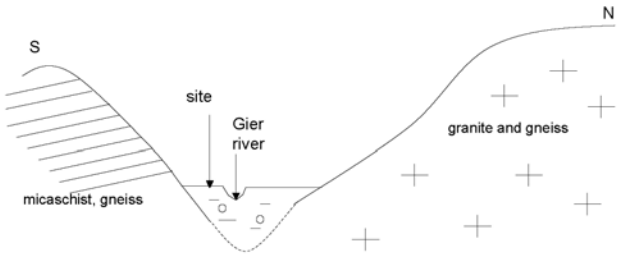

Figure 2 Schematic geological cross-section of the area and project location.

- Cone Penetration Tests (CPT) at 5 points (β3, β15, γ8, δ3 and δ15);
- Backfill material laboratory tests (5 samples);
- A topographic survey (altitude) at each point of the grid.

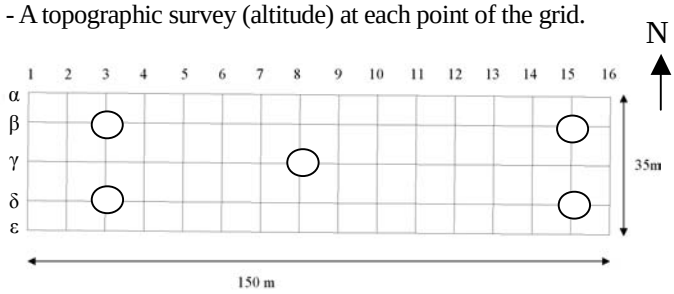

Figure 3 Detailed plan view of the specific investigation area grid. The five circles show the positions where CPT have been carried out.

4.2 Topographic survey

The topographic surveys recorded a settlement due to the dynamic compaction work ranging from 80 to 100 cm.

4.3 Backfill material laboratory identification

The particle size distribution of the compacted material had been determined on 5 samples. The results are given in the table below.

Table 1 USCS laboratory identification of the backfill material
USCS - Unified Soil Classification System

N° of sample	Depth (m)	W_n (%)	Laboratory classification criteria
Pit sample n°1 - β3	2.0	5	GW
Pit sample n°2 - β15	2.0	8	GW
Pit sample n°3 - γ8	2.0	5.7	GW
Pit sample n°4 - δ3	2.0	7.4	GW
Pit sample n°5 - δ15	2.0	7.4	GW

Wn : natural water content (%)
GW : well graded gravel

4.4 Cone Penetration Test (CPT)

The cone penetration test involves the hydraulic push of a steel probe in the soil to obtain a continuous vertical profile of the resistance at the conic tip of the probe.

The position of the five CPT is shown in Figure 3. The tip resistance (qc) curves are averaged over one meter (Figure 4). CPT values after dynamic compaction are compared with values before dynamic compaction. The initial soil shows an overall values of $q_c < 3.0$ MPa, and after the soil improvement work, $q_c > 3.0$ MPa. By correlation to Standard Penetration Test values (Robertson et al, 1982), the initial values of $N < 15$ although after the dynamic compaction work $N > 15$. According to the soil classification of the Eurocode 8, the site classification changes from the D to the C ground type.

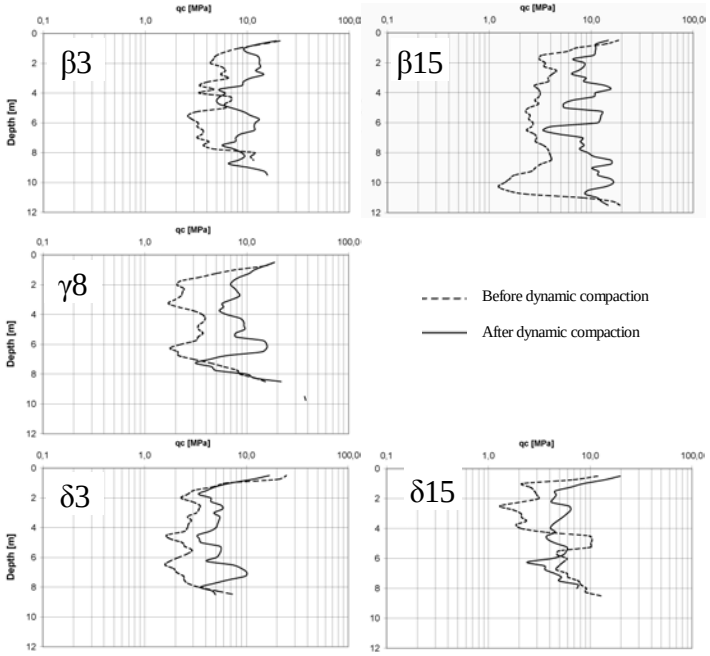

Figure 4 CPT carried out before and after the dynamic compaction work.

4.5 Multichannel Analysis of Surface Waves (MASW)

Multichannel Analysis of Surface Waves (MASW) is one of the non-intrusive geophysical technique used primary for evaluating subsurface shear wave velocity profiles. The shear wave velocity has been determined along four profiles (lines α, β, γ and δ) before and after the dynamic compaction work. A clear shift of the shear wave velocity of the first top six meters of soil is observed. It varies from 150 to 200 m/s. From the measurements alone and according to the soil classification of the Eurocode 8, we would say that the site changes from the D to the C ground type.

4.6 H/V measurements

Microtremors have been measured at 80 points before and after the soil improvement, and the natural frequency of the ground Fo determined by application of the H/V method (Nakamura 1989). The H/V spectra at five points is shown in Figure 5. For each H/V measurement, Fo is stable before and after the dynamic compaction work, which is confirmed by a statistical analysis of the 80 measurements (Figure 6 and Table 2).

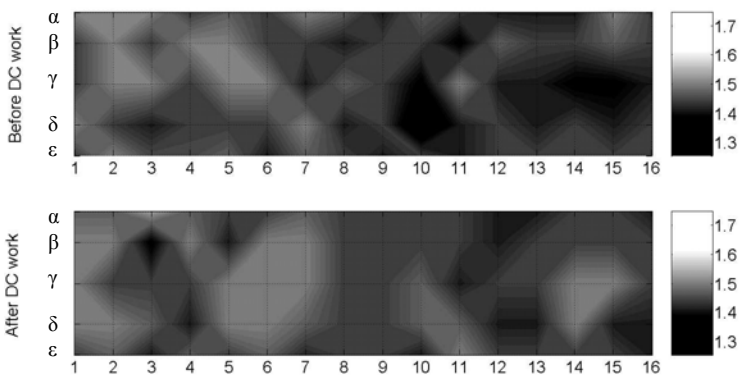

Figure 6 Isovalues of the measured natural frequency of the site by the H/V method. Each grid intersection is identified by its row and column numbers.

We analyzed the microtremors measurements recorded at 11 positions and processed uniformly (Konno et Ohmachi, 1998) filter, b parameter = 40) to investigate the evolution of the H/V amplitude Ao (Table 3).

Table 2 Statistical analysis of the natural frequency of the site before and after the dynamic compaction work

Fo (Hz)	Average	Standard-deviation
Before DC work	1,44	0,03
After DC work	1,45	0,03

Table 3 Statistical analysis of the H/V amplitude Ao, before and after the dynamic compaction work

Ao	Average	Standard-deviation
Before DC work	5,38	0,89
After DC work	5,78	1,04

Assuming that a homogeneous soft layer is lying on the granite, we can use Nakamura (2000) formula :

$$Ao = \frac{\rho_b . V_b}{\rho_s . V_s} = 5{,}4 \pm 0{,}9 \qquad (1)$$

where V_b is the shear wave velocity in the weathered granite (taken as 2000 m/s), ρ_b the density of the granite (taken as

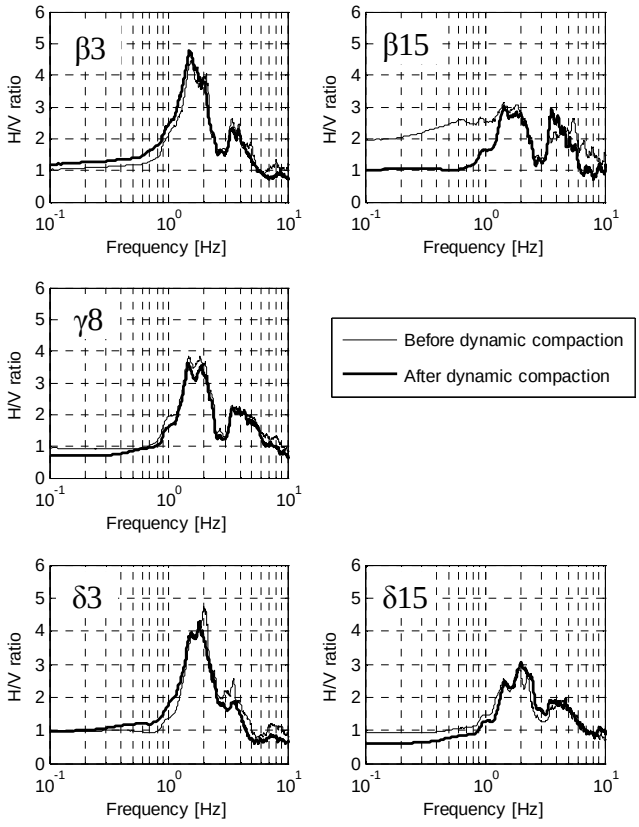

Figure 5 Comparison of H/V spectra recorded at the same position before and after the dynamic compaction work.

2600 kg/m3), and ρ_s the density of the superficial layers (taken as 2000 kg/m3). Therefore Vs~410-580 m/s

The depth H (m) of the geological substratum can be estimated as follow:

$$H = \frac{V_S}{4.Fo} = 71\,to\,100\ m \qquad (2)$$

where Fo ~1,445 Hz, and Vs~410-580m/s. This is consistent with the geological bibliography that shows that the geological substratum is deeper than 30 m.

In the present geotechnical and geological context, the main result of the survey is that there is no modification of the natural period of the soil due to the dynamic compaction work. According to the soil classification of the Eurocode 8, the site was and remains a B ground type site.

5. DISCUSSION

5.1 Nature of the bedrock

H/V measurements are providing us with an important information about the nature of the bedrock: engineering bedrock vs seismic bedrock. For standard civil engineering projects requiring soil improvement techniques, the site investigation usually identifies a deep geotechnical bedrock. It is important to know the relative positions of the geotechnical and the seismic bedrocks. In this Givors case and following the microtremor analysis, we had to requalify the depth of the seismic bedrock: it is actually deeper than expected.

In term of methodology to determine the Vs_{30}, two cases can be distinguished (Figure 7):
Note that the ground types given for the case 1 (Ground type A and E) and case 2 (Ground types B and C) are taken from the Eurocode 8, and that our analysis does not include the Eurocode 8 specific ground types S1 and S2.

- Case 1: a soft layer underlained by a hard bedrock (Figure 7a)

The relation $Vs_{soft\ layer} = \frac{4\,h}{To}$ can be used, where To (s) is determined by microtremor measurements, h (m) known and reliable from the numerous geotechnical investigation, and Vs the shear wave velocity of the superficial layer (m/s). Therefore, $Vs_{bedrock}$ can be estimated from the formula (1),

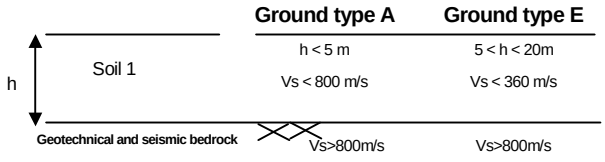

Figure 7a Case 1: a soft layer underlained by a hard bedrock (Eurocode 8 ground types A and E).

Vs_{30} can then be computed and the soil classed according to the Eurocode 8. An example of case 1 site is detailed in Brule et al (2009).

- Case 2: soil layers without clear impedance (ρ.V) contrast (Figure 7b)

In that case, the seismic and the geotechnical bedrock are distinct. An approximate value of Vs obtained under the assumption that a single soft layer is above the seismic bedrock is given in §4.6. However, an another but recommended method when the Eurocode 8 is the seismic code of the project, is to consider the Eurocode 8 depth of interest, H=30m. The average shear wave velocity Vs_{30} of the site to be considered for the design is $Vs_{30} = \frac{4\times 30}{To} = \frac{120}{To}$ (=170 m/s; a D ground type).

5.2 Soil characterization, soil classification and its evolution

The example detailed here shows that the Eurocode 8 ground type may vary according to the method of investigation used. The utilization of a combination of techniques is therefore recommended. It allows us to precisely class the initial site as a D ground type.
The dynamic properties of the soil and the ground type of a site may also be modified by the dynamic compaction work: a small change in SPT value or Vs_{30} may be enough to imply a ground type change, especially if the initial soil characteristic are near the upper limit of a ground type. In this example of a case 2 site (§5.1), CPT and MASW measurements are indicating an increase of Vs in the first few meters of the ground, which is however not confirmed by the H/V method that is providing information about a deeper volume of soil.

5.3 H/V practical application in civil engineering

The additional information provided by the H/V method is proving its usefulness to estimate the Vs_{30} (cases 1 & 2) and to class the constructions sites with soil improvement according to the Eurocode 8. The civil engineering community in countries such as France would benefit from systematic site classification over large areas (city, prefectures) instead of project by project site classification. The H/V method is believed to be a interesting tool for such mapping.

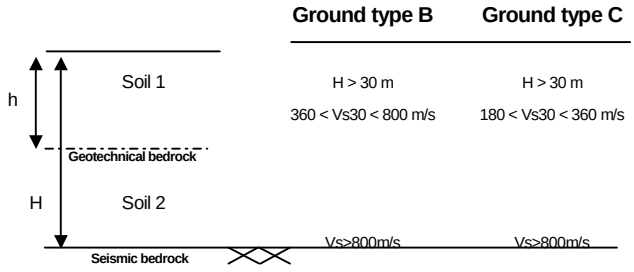

Figure 7b Case 2: soil layers without clear impedance (ρ.V) contrast (Eurocode 8 ground types B and C).

6. CONCLUSIONS

The H/V method proved its usefulness for civil engineering applications. The soil investigation results at hand as early as for the pre-design of structures usually contain enough information to fully use the H/V results. This clearly make it an efficient method to estimate the Vs_{30}, and categorized the site according to the Eurocode 8.

The H/V method is also believed to be a promising tool (especially in clear impedance contrast case study -- 5<H<20m-- , as case 1) to estimate the overall benefic change of dynamic soil properties due to soil improvement works at dynamic compaction sites, vibroflotation sites, but also probably at sites with rigid inclusion.

Acknowledgements:

The authors are grateful to the Center for Urban Earthquake Engineering (CUEE) in Tokyo Institute of Technology.

References:

Brule S., Javelaud E., Pal O., Rizzo A.V. et E. Brunet-Manquat (2009). Le nouveau centre hospitalier d'Annemasse et Bonneville (CHIAB) en Haute-Savoie : un projet de renforcement de sol hors norme. Revue Travaux (866). *In french.*

Eurocode 8 (2005). "Design of Structures for Earthquake Resistance – Part 1 : General rules, seismic actions and rules for buildings –," *Comité Européen de Normalisation – European Committee for Standardization*.

Federal Highway Administration – US Department of Transportation. (1995). "Dynamic compaction", Publication No. FHWA-SA-95-037.

Federal Highway Administration – US Department of Transportation. 2002)-" Geotechnical Engineering Circular n°5", Publication No FHWA-IF-02-034.

Konno K. and T. Ohmachi (1998), "Ground motion characteristics estimated from spectral ratio between horizontal and vertical component of microtremor, " *Bulletin of the Seismological Society of America*, **88** (1), 228-241.

Mayne P.W., Jones J.S., and Dumas J.C. (1984), "Ground response to dynamic compaction", *Journal of Geotechnical Engineering*, 110(6), 757-774.

Nakamura Y. (1989), "A method for dynamic characteristics estimation of subsurface using microtremor on the ground surface", *Quaterly Report of Railway Technical Research Institute (RTRI)*, 30 (1).

Nakamura Y. (2000), "Clear Identification of Fundamental Idea of Nakamura's Technique and its Applications", *12WCEE*, 1256.

Robertson P.K., Campanella R.G. and Wightman A. (1982), "SPT-CPT Correlations", University of British Columbia, Vancouver, Civil Engineering Department, Soil Mechanics Series N_0 62.

JOINT CONFERENCE PROCEEDINGS
7th International Conference on Urban Earthquake Engineering (7CUEE) &
5th International Conference on Earthquake Engineering (5ICEE)
March 3-5, 2010, Tokyo Institute of Technology, Tokyo, Japan

SIMULATION OF STRONG GROUND MOTIONS AT K-NET KASHIWAZAKI DURING THE 2007 NIIGATA-KEN CHUETSU-OKI EARTHQUAKE

Kohji Tokimatsu[1)], Kota Katsumata[2)], and Hiroshi Arai[3)]

1) Professor, Center for Urban Earthquake Engineering, Tokyo Institute of Technology, Japan
2) Undergraduate Student, Tokyo Institute of Technology, Japan
3) Senior Research Engineer, Building Research Institute, Japan
kohji@o.cc.titech.ac.jp, katsumata.k.aa@m.titech.ac.jp , arai@genken.go.jp

Abstract: The strong ground motions recorded at K-NET Kashiwazaki had spiky acceleration time history, suggesting liquefaction or cyclic mobility of the ground, while those at nearby JR Kashiwazaki did not show such spiky waves. A preliminary attempt was made to examine why such spiky waves were induced during the main shock and, for this purpose, to propose and employ a method for searching reasonable rock outcrop motion that could simulate the ground surface motions recorded at the two sites during the main shock. It has been shown that: (1) Conventional deconvolution and convolution analysis using strong motion recording at the JR station as reference for estimating that at the K-NET station has been proven effective for this particular pair of stations subjected to a moderate-intensity earthquake, whereas it was ineffective for a strong-intensity shaking which would induce liquefaction of soil deposits under consideration; and (2) The proposed method can reproduce reasonably well the spiky waves observed in the ground surface motion at the K-NET station and thus could show promise in estimating reasonable rock outcrop motion from ground surface motions recorded during strong-intensity shaking which would induce liquefaction of soil deposits under consideration.

1. INTRODUCTION

The Niigata-ken Chuetsu-oki earthquake (Mj=6.8) occurred on July 16, 2007, with an epicenter off the Niigata prefecture. The quake affected the coastal areas of the southwestern Niigata prefecture, including Kashiwazaki city and Kariwa village as well as the Kashiwazaki-Kariwa nuclear power plant of Tokyo Electric Power Company (TEPCO), most of which were located on or near the sand dunes that run parallel to the coastline (Tokimatsu, 2008).

The earthquake claimed a death toll of fifteen, with more than 2,340 injuries, as of December 28, 2007. More than forty-one thousand residential houses were either totally collapsed or partially damaged. The strong ground motions recorded at the K-NET (NIG018) station near the Kashiwazaki municipal building had spiky acceleration time history recording with a peak acceleration of 6.7 m/s^2 , whereas those at the JR Kashiwazaki station about 1.2 km apart did not show such spiky waves with a peak value of 3.2 m/s^2 (Yoshida et al, 2007; Tokimatsu, 2008).

The objective of this paper is to examine why such spiky waves were induced during the main shock and, for this purpose, to propose and employ a method for searching reasonable rock outcrop motion that could simulate the ground surface motions recorded at the two sites during the main shock, based on numerical analyses using dynamic soil properties obtained from field investigation made after the quake.

2. GEOLOGICAL SETTING

Figure 1 shows a geomorphological map of the central part of Kashiwazaki city (Kashiwazaki city, 1983). The city has been developed in the Kashiwazaki plain that faces the Sea of Japan on the northwest. The Kashiwazaki plain consists mainly of the Holocene alluvial deposit formed by the U and Sabaishi rivers and their tributaries. Running in parallel with and between the coastline of the Sea of Japan and the alluvial deposit is the Arahama sand dune that is trisected by the U and Sabaishi rivers where they flow into

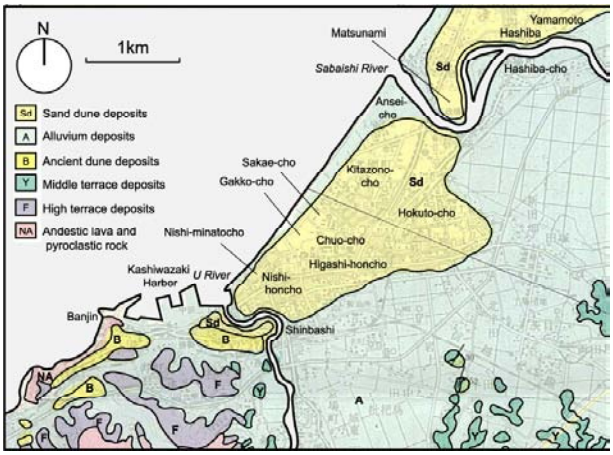

Figure 1 Geomorphological map of Central Kashiwazaki city (Kashiwazaki city, 1983)

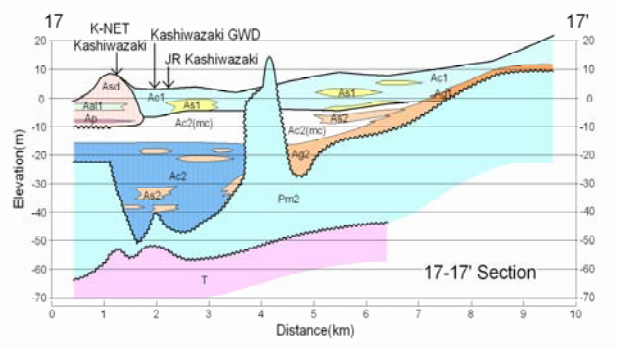

Figure 2 Geological sections of Kashiwazaki city (Association of Subsurface Exploration in Niigata Prefecture, 2002)

the Sea of Japan. It extends from the southwest of the city towards the northeast, with its plateau altitude of about 10 m in the central city of Kashiwazaki.

Figure 2 shows a NS geologic section across the city. The Holocene deposit in the lowland consists of the Top, Upper and Lower Kashiwazaki Formations (Ac1/As1, Ac2/As2, and Ac3/As3), with thicknesses varying from 40-70 m along the lower courses of the two rivers, that overlie the Pleistocene and Tertiary Formations (Pm2 and T). The Arahama sand dune about 2 km in width consists of the New Holocene sand dune (Asd) and Pleistocene sand dune called Banjin Formation (Psd) that is underlain by the Kashiwazaki Formations on the south of the Sabaishi River. Typical shear wave velocities of the New Sand Dune, Banjin Formation, Kashiwazaki Formation, Yasuda Formation, and Nishiyama Formation are 100-200, 200-350, 100-200, 350, and 500-600 m/s, respectively.

3. STRONG GROUND MOTIONS AND SITE CONDITIONS

The Niigata-ken Chuetsu-oki earthquake (Mj=6.8) occurred at 10:13 a.m. on July 16, 2007, with an epicenter off the Niigata Prefecture and with a focal depth of about 12 km. The Kyoshin strong motion network (K-NET) recorded the main shock at 20 stations within 50 km from the epicenter. Tokyo Electric Power Company (TEPCO) recorded time histories of the main shock at 33 locations within the Kashiwazaki-Kariwa nuclear power plant. In addition, several strong ground motions were recorded in Kashiwazaki city by several organizations including East Japan Railway Company (JR East), East Nippon Expressway Company Limited (E-NEXCO), Kashiwazaki City and Niigata Prefecture. Among the strong motion stations in the central city, only the K-NET station is located on the sand dune while other stations including JR Kashiwazaki, Kashiwazaki Gas and Water, and E-NEXCO Kashiwazaki are on the alluvial plain.

Figure 3 shows acceleration time histories at the K-NET and JR stations during the main shock. The accelerograms

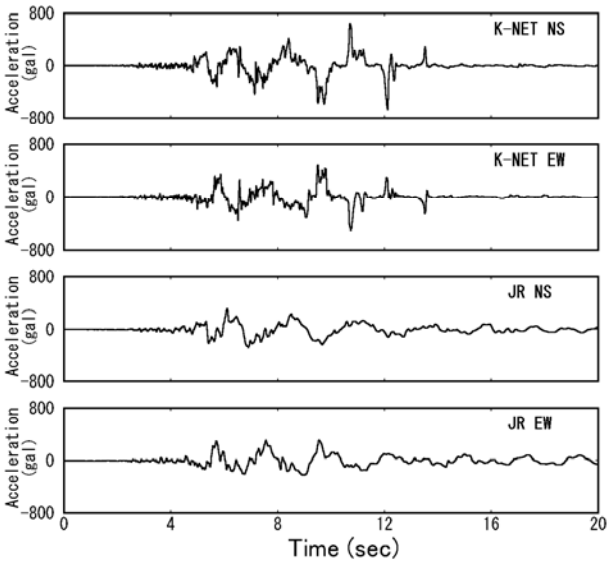

Figure 3 Acceleration time histories at K-NET and JR Kashiwazaki during the 2007 Niigaka-ken Chuetsu-oki earthquake

at both stations have long period components, probably reflecting the thick alluvial deposit underlying the sites. It is interesting to note that the accelerogram at K-NET Kashiwazaki on the sand dune shows spiky waves, associated with liquefaction or cyclic mobility of sand, and rapidly decreasing its amplitude with time due probably to cyclic degradation of the sand. Similar spiky waves are, however, not observed at JR Kashiwazaki on the alluvial deposit about 1.2 km south.

Some of the strong ground motions recorded at both sites during other earthquakes are also available. Figure 4 shows such acceleration time histories during the aftershock

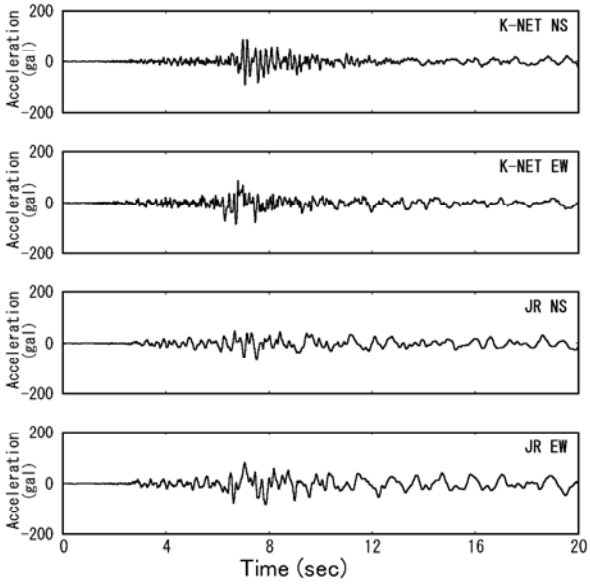

Figure 4 Acceleration time histories at K-NET and JR Kashiwazaki during the aftershock of the Niigata-ken Chuetsu Earthquake on October 23, 2004

of the Niigata-ken Chuetsu Earthquake that occurred at 18:12 on October 23, 2004. Neither spiky waves nor long period component can be seen in any of the records, highlighting the strong nonlinear soil behavior including soil liquefaction at the K-NET station during the main event as shown in Figure 3.

Geological and geophysical field investigation was made at both stations after the earthquake as well as laboratory tests to determine dynamic soil properties of the sites. Figure 5 shows the geological boring logs and shear wave velocity logs for the two sites. The groundwater table was located at a depth of about 5.0 m and 0.8 m, respectively. The surface soil at K-NET station to a depth of 13 m is dense sand with SPT N-values ranging from 10 to 40 and Vs from 110-250 m/s, which is underlain by a thick clayey soil with Vs 200-290 m/s. Mudstone with Vs over 500 m/s occurs at a depth of about 65 m. The surface soil at JR station to a depth of 18 m, in contrast, consists of soft silty clay and sandy silt with N-Values of 0-1 and VS of 70-100 m/s, which overlays alternate sand and clayey silt with N-values of 3-20 and Vs of 190-450 m/s. Mudstone with Vs over 500 m/s occurs at a depth of about 66 m. It seems that the sandy soils at depths between 5-10 m at K-NET might have undergone cyclic mobility and/or liquefaction, although no evidence of soil liquefaction was identified nearby.

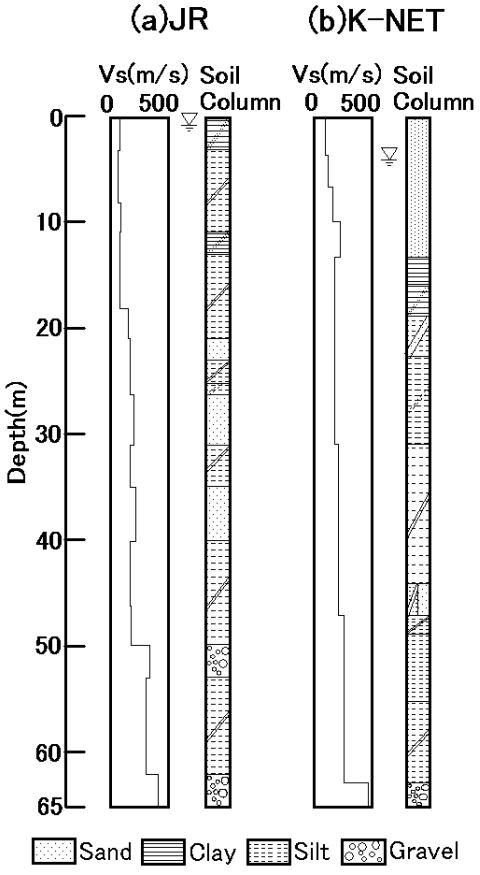

Figure 5 Geological and geophysical logs at K-NET and JR Kashiwazaki

4. ANALYTICAL SIMULATION OF STRONG GROUND MOTIONS AT K-NET KASHIWAZAKI

4.1 Ground Motions during a Moderate-Intensity Earthquake

Figure 6 shows a flowchart to estimate the ground motion recorded at the K-NET from one at the JR station. It was assumed that the rock occurring at a depth of about 65 m is the equivalent rock for the two sites. First, the rock outcrop motion was estimated, based on the deconvolution analysis using the observed ground motions and soil profile at JR Kashiwazaki. The ground surface motion at the K-NET site was then estimated, with the back-calculated rock outcrop motion as input to the soil column of the K-NET station. The programs used for this deconvolution and convolution analyses including the following:

(1) A one-dimensional equivalent-linear response analysis of a deposit subjected to a vertically incident SH waves in which damping ratios of soil depend only on shear strain developed in the soil (hereby call SHAKE 1);

(2) An extended version of the equivalent linear response analysis in which the damping ratios of the deposit are assumed to be dependent on the Fourier amplitude of shear strain in the frequency domain (e.g., Sugito et al, 1993), which has been developed to improve over-damping nature of the original SHAKE (Schnabel et al, 1972) in the short period range during strong shaking (hereby call SHAKE 2); and

(3) A nonlinear effective response analysis (Shamoto et al, 1992, hereby call ESA).

The same program was used for both deconvolution and convolution analyses, except for the convolution analysis of ESA for which SHAKE 2 was used for deconvolution analysis.

To confirm the applicability of the deconvolution and convolution analyses shown in Fig. 6 for this particular pair of stations and for a moderate-intensity earthquake, strong motions recorded at both stations during the aftershock of the Niigata-ken Chuetsu Earthquake that occurred at 18:12 on October 23, 2004 was used.

Figure 7 shows the time histories computed by the three methods, compared with the recorded ones. There is a good agreement between the observed and computed values, confirming the applicability of any of the deconvolution and convolution analysis for this particular pair of stations and for a moderate-intensity earthquake.

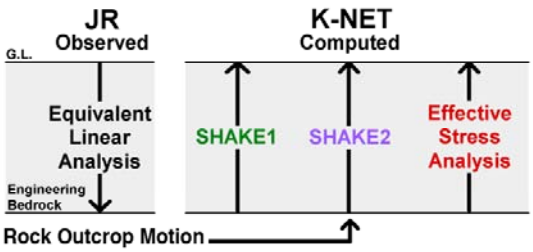

Figure 6 Flowchart to estimate ground surface motion at K-NET from recorded motion at JR station

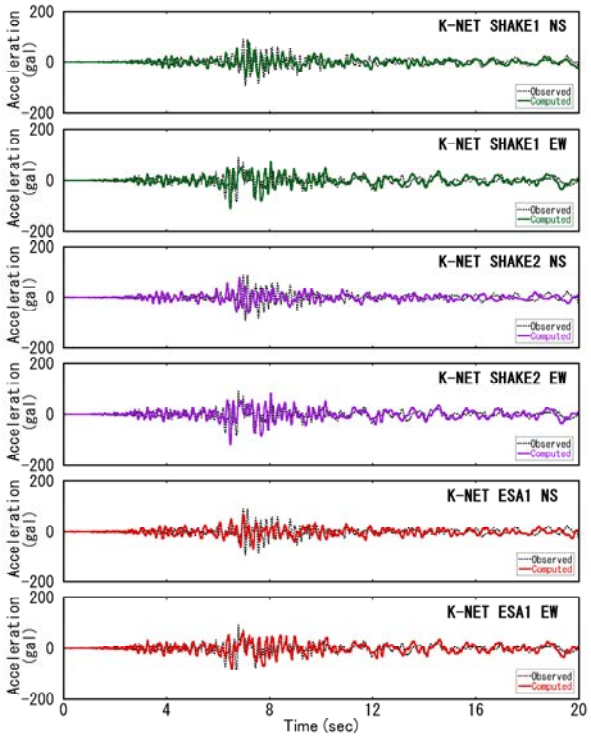

Figure 7 Acceleration time histories of computed ground surface motions, compared with those recorded at K-NET during a moderate-intensity earthquake

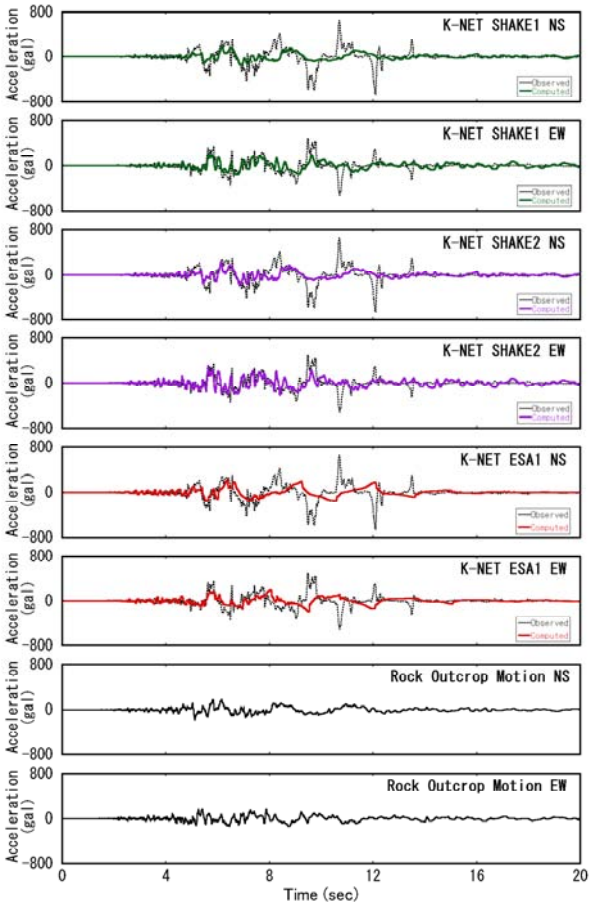

Figure 8 Acceleration time histories of computed rock outcrop and ground surface motions, compared with those recorded at K-NET during the 2007 Niigata-ken Chuetsu-oki earthquakes

4.2 Ground Motions during a Strong-Intensity Earthquake

To study further the applicability and limitation of the three deconvolution and convolution methods for estimating site response during strong-intensity shaking and the cause of spiky waves observed in the K-NET Kashiwazaki, similar analysis was made with the strong ground motions recorded during the 2007 Niigata-ken Chuetsu-oki Earthquake.

Figure 8 shows the acceleration time histories of the deconvoluted rock outcrop motions and the ground surface motions computed from the three methods, compared with those of the recorded motions. It seems that the computed results from any of the three methods are inconsistent with the recorded motions and unable to reproduce spiky waves observed in the recorded motions.

A close examination further suggests that the computed ground motion in the later phase is smaller in amplitude and more delayed than the observed one. This suggests that the actual rock outcrop motion in the later phase might have been larger and more behind than the one deconvoluted by the equivalent linear method.

Based on the above discussions, a preliminary attempt was made to search more reasonable rock outcrop motion that could show a better agreement with the ground motions recorded at the two sites during the main shock. This was made by a try-and-error method as shown in the flowchart of Figure 9 in which the rock outcrop motion is updated so that the difference between observed and computed ground surface motions can be minimized.

The rock outcrop motion initially assumed is one determined as deconvolution analysis of the modified SHAKE using the observed ground surface motion at the JR station. The effective stress analysis was then employed to determine the ground surface motions at the two sites using the rock outcrop motion. The rock outcrop motion was modified in terms of amplitude and phase so that the difference between the computed and observed ground surface motions at the two sites becomes small. This convolution analysis and modification of rock outcrop motion was repeated until the observed and computed ground surface motions become compatible with each other.

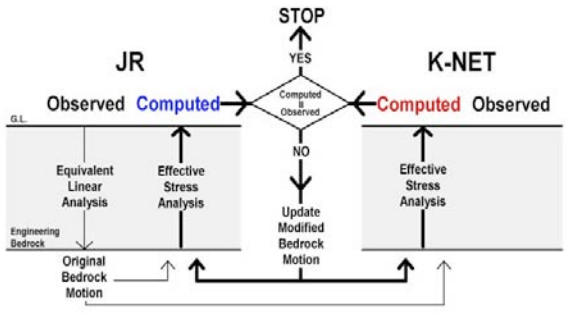

Figure 9 Flowchart to estimate rock outcrop motion from recorded ground motions at K-NET and JR stations

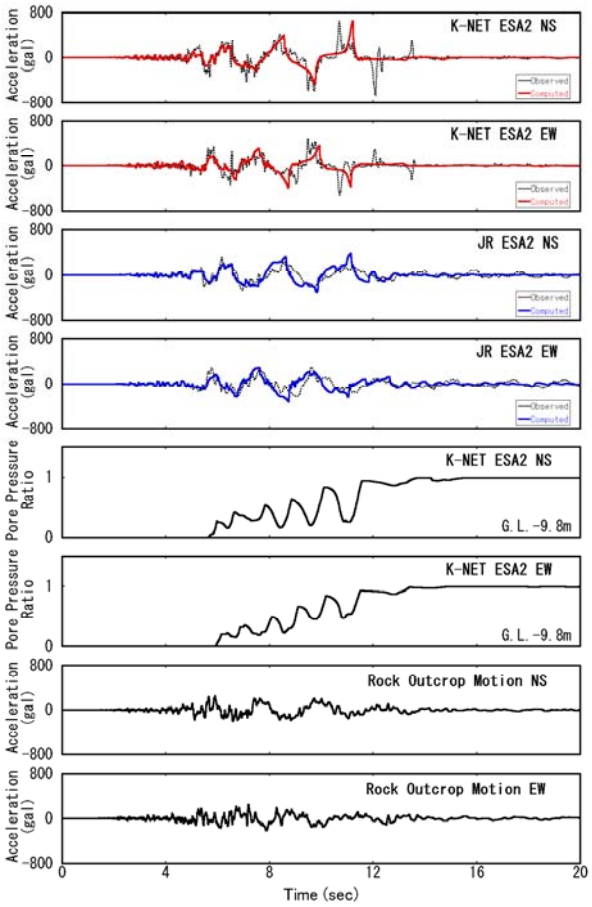

Figure 10 Time histories of computed rock outcrop motion, ground surface motion and pore pressure ratio, compared with those recorded at K-NET and JR Kashiwazaki during the 2007 Niigata-ken Chuetsu-oki earthquake

Figure 10 shows the acceleration time histories of the ground surface motions computed with the most updated rock outcrop motion, compared with the recorded ones. Also shown in the figure are those of pore pressure ratio in a critical layer. There is a good agreement between the observed and computed values. A comparison of the back-caluculated rock outcrop motions shown in Figs. 8 and 10 confirms that the actual rock outcrop motion in the later phase might have been larger and more behind than the one deconvoluted by the equivalent linear method. The computed pore pressure ratio in the dense near-surface layer at a depth of about 10 m reaches to unity, suggesting that soil liquefaction might have occurred in this layer and contributed to the spiky acceleration waves observed in the strong motion recording observed at K-NET Kashiwazaki. The above discussions suggest that the rock outcrop motion may be estimated based on the method presented in this study, although more refinement is definitely needed.

3. CONCLUSIONS

The strong ground motions recorded at K-NET Kashiwazaki had spiky acceleration time history recording with a peak acceleration of 6.7 m/s^2, suggesting liquefaction or cyclic mobility of the ground, while those at nearby JR Kashiwazaki did not show such spiky waves with a peak value of 3.2 m/s^2. A preliminary attempt has been made to examine why such spiky waves were induced during the main shock and, for this purpose, to propose and employ the method for searching reasonable rock outcrop motion that could simulate the ground surface motions recorded at the two sites during the main shock. On the basis of the analysis and discussions, the following conclusions have been made:

(1) Conventional deconvolution and convolution analysis using strong motion recording at one site as reference for estimating that at nearby other station has been proven effective for this particular pair of stations subjected to a moderate-intensity earthquake, whereas it was ineffective for a strong-intensity shaking which would induce liquefaction of soil deposits under consideration.

(2) The proposed method can reproduce reasonably well the spiky waves observed in the recorded motion at K-NET Kashiwazaki and thus could show promise in estimating reasonable rock outcrop motion from strong ground motions recorded during strong-intensity shaking which would induce liquefaction of soil deposits under consideration.

(3) The actual rock outcrop motion in the later phase at a liquefied site would be larger and more behind than the one deconvoluted by the equivalent linear method.

Acknowledgements:

The authors acknowledge support from the Japan Ministry of Education, Culture, Sport, Science, and Technology (MEXT) for establishing the Center for Urban Earthquake Engineering (CUEE) in Tokyo Institute of Technology. This support makes possible the forthcoming international conference, as well as international joint research projects and exchange programs with overseas universities.

References:

ASENP (2002): Geotechnical Engineering Map of Niigata prefecture, Editorial Committee for geological map of Niigata prefecture, Association of Subsurface Exploration in Niigata Prefecture (ASENP), (in Japanese).

Kashiwazaki city (1983): Historical records of Kashiwazaki city (in Japanese).

Schnabel, P.B., J. Lysmer, and H.B. Seed (1972): SHAKE – A computer program for earthquake response analysis of horizontally layered sites, EERC Report, No. 72-12.

Sugito, M., Goda, H., Masuda, T. and Etsunada, K. (1993): Equi-linearlized method with frequency-dependent shear modulus and damping, Proc., 28th Japan National Conference on SMFE, pp. 1129-1132 (in Japanese).

Shamoto, Y., Tokimatsu, K., and Ariizumi, K. (1992): Applicability of A One-Dimensional Effective Stress analysis to An Existing Soil Deposit, J. Struct. Constr. Eng., AIJ, 433, 113-119. (in Japanese)

Tokimatsu, K. (2008): Geotechnical Problems in the 2007 Niigata-ken Chuetsu-oki Earthquake, Geotechnical Earthquake Engineering and Soil Dynamics (GSP 181), ASCE, Proceedings of the Geotechnical Earthquake Engineering and Soil Dynamics IV Congress 2008, 30pp.

Yoshida, N. et al. (2007): Investigation on Record at K-NET Kashiwazaki during the 2007 Niigatakeb-chuetsu-oki earthquake.

JOINT CONFERENCE PROCEEDINGS
7th International Conference on Urban Earthquake Engineering (7CUEE) &
5th International Conference on Earthquake Engineering (5ICEE)
March 3-5, 2010, Tokyo Institute of Technology, Tokyo, Japan

NON-LINEAR DYNAMIC MODELING OF BRIDGE EMBANKMENTS UNDERLAIN BY LIQUEFIED SOIL

R. J. Armstrong[1)], R. W. Boulanger[2)], and M. H. Beaty[3)]

1) Water Resource Engineer, Calif. Dept. of Water Resources, Division of Safety of Dams, Sacramento, CA, USA
2) Professor, Department of Civil & Environmental Engineering, University of California, Davis, CA, USA
3) Consulting Engineer, Beaty Engineering LLC, Beaverton, OR, USA
rarmstro@water.ca.gov, rwboulanger@ucdavis.edu, mhb@beatyeng.com

Abstract: Non-linear dynamic numerical analyses are presented of dynamic centrifuge model tests involving bridge approach embankments underlain by liquefied soil. Each of the three centrifuge tests considered two identical approach embankments of dry sand, each 7.2 m high, separated by a channel. One embankment had a pile group at the crest. The piles extended through the dry embankment and the underlying 5.4 m of saturated loose sand into a saturated dense sand layer. The embankment, loose sand, and dense sand units were separated by thin silt layers. The numerical simulation procedures are described. The patterns of deformation predicted by the numerical simulations were similar to that observed from each of the three centrifuge tests. Representative results are presented and discussed in this paper.

1. INTRODUCTION

This paper presents results from nonlinear dynamic numerical analyses of dynamic centrifuge model tests involving embankments underlain by liquefied soil. Three centrifuge tests are described that each modeled two identical bridge approach embankments underlain by liquefied soil, such that a total of six embankments were modeled. The embankments were constructed of dry sand and were underlain by saturated loose sand that liquefied during shaking. Each centrifuge test included one embankment with a pile group at its crest and one without. The development of the non-linear simulation is given after a brief description of the centrifuge test program, test measurement, and data processing. Results are then presented from the non-linear dynamic simulations and compared to those measured in the centrifuge tests. The ability of these non-linear numerical simulations to approximate the observed behaviors and their utility for understanding key mechanical behaviors are discussed.

2. CENTRIFUGE EXPERIMENTS

The centrifuge program consisted of three highly-instrumented dynamic centrifuge tests. Each centrifuge model comprised two identical approach embankments of dry sand separated by a river channel. One embankment had a pile group that extended through the underlying saturated loose sand layer and into saturated dense sand. All three centrifuge tests had essentially the same soil properties and soil geometry but had different pile group configurations or input motions (see Table 1 for a comparison of the three tests). A representative photograph of the embankments at the end of construction is shown in Figure 1a for the Kobe_2X4 model and a representative photograph of the post-testing excavation for the Kobe_1X6 model is presented in Figure 1b (additional photographs of each model during post-testing excavation can be found in Armstrong et al. 2008). The cross-section of the models is illustrated by the mesh shown in Figure 2.

All centrifuge tests were performed on the 9-m radius centrifuge at the University of California at Davis in a flexible shear beam container with centrifugal accelerations of 60 g. Results are presented in prototype units unless otherwise noted.

The pile group used in the Kobe_1X6 model was a row of 6 individual piles with outer diameters of approximately 0.72 m prototype.

The pile group used in the Kobe_2X4 and Sine_2X4 models was a 2x4 pile group. The piles had outer diameters of approximately 1.22 m prototype, and were spaced at three diameters center-to-center. The pile groups were connected by an epoxy pile cap that was 13.2 m by 6.0 m by 2.4 m.

The geometry and soil properties were essentially the same for all three centrifuge tests (section shown in Figure 2). Embankments were 7.2 m high at the crest and 11.4 m high at the model container wall, and were comprised of dry, coarse, medium-dense to dense Monterey sand. All soils were placed by dry pluviation. Silt layers were also statically compacted after pluviation. The model was saturated from the bottom of the container upwards until the channel between the two embankments was partially



(a) Embankments at end of construction



(b) Excavation of a model after testing

Figure 1. Photographs of two centrifuge models

Table 1. Centrifuge test details.

Model code	Kobe_1X6	Kobe_2X4	Sine_2X4
Report name	DDC03	UGU01	UGU02
Type of pile group	Row of 6 piles; outer diameter of pile 0.72 m	2x4 pile group; outer diameter of pile 1.22 m; pile-cap dimension 13.2 x 6.0 x 2.4 m	2x4 pile group; outer diameter of pile 1.22 m; pile-cap dimension 13.2 x 6.0 x 2.4 m
Input motion	Scaled Port Island motion	Scaled Port Island motion	Sine waves
Peak base acc.	0.8 g	0.7 g	0.5 g and 0.7 g

filled with fluid. The pore fluid was a methylcellulose solution with a viscosity about 20 times that of water.

Shaking motions were in the longitudinal direction for the centrifuge models. Models Kobe_1X6 and Kobe_2X4 were subjected to a motion that is a modified and scaled version of the ground motion recorded at a depth of 83 meters at Port Island in the 1995 Kobe earthquake. Model Sine_2X4 was subjected to two shaking events consisting of a series of varying-amplitude sine waves.

Instrument recordings acquired from each of the centrifuge tests were processed and archived for public distribution through NEES archives (Chang et al. 2007, Gulerce et al. 2007, and Gulerce et al. 2007).

3. NUMERICAL MODEL

The numerical simulations were conducted using the commercial program FLAC (Itasca 2009). The mesh used in the simulation is shown in Figure. 2. The mesh was discretized so that the smallest zone would pass 1/10th the

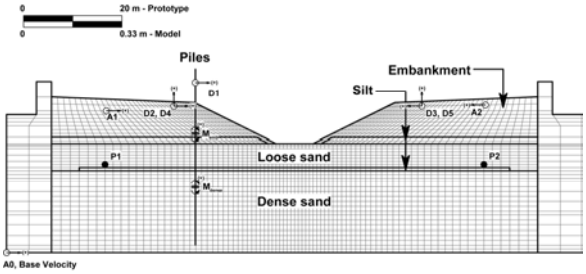

Figure 2. Mesh for first centrifuge tests

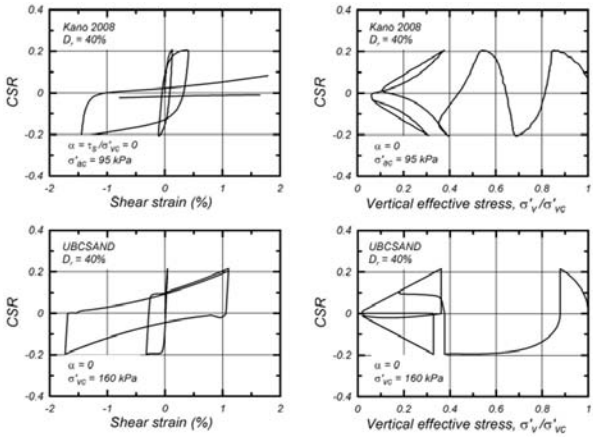

Figure 3. Measured and computed undrained cyclic response of loose Nevada

minimum wavelength of 20 m or 2 m. The piles and pile cap were modeled with pile elements (essentially beam elements) and were connected to the zones using elastic-plastic coupling springs.

The centrifuge container was modeled in the simulation as two elastic "container walls" with the stiffness and mass for the simulations chosen to match both: (1) the natural frequency of the centrifuge container, and (2) the ratio of the centrifuge container mass to the enclosed soil mass.

The UBCSAND model was used for all soils in the centrifuge models. As described by Byrne et al. (2004), the UBCSAND model is an incremental effective stress model with plastic shear strains accumulated with changes in stress ratio. Plastic volumetric strains are contractive for stress ratios less than $\sin(\phi'_{cv})$ and dilative for stress ratios greater than $\sin(\phi'_{cv})$. Hence in undrained shear loading the model can capture the increase and decrease of effective stress due to volumetric strains resulting from contraction or dilation.

Calibration of the UBCSAND model for the liquefiable soils was based on data for Nevada sand from a variety of sources. Maximum shear modulus was set by shear wave velocity data. Calibration for cyclic response included using a single element in simple shear loading to run a series of analysis until a reasonable match between the model predictions and the laboratory data was obtained for liquefaction triggering. An example comparison of

laboratory test behavior of loose Nevada sand measured from Kano (personal communication) and computed using UBCSAND is shown in Figure 3.

The piles were modeled using linear elastic beam elements (note that the piles did not yield in each of the centrifuge tests). Converting the 3-D foundation to 2-D was accomplished by multiplying the stiffness and density of the piles by the number of out-of-plane piles divided by the equivalent crest width. A normal coupling spring and a shear coupling spring were defined to model relative lateral and shear movement between the soil mesh and piles, respectively.

The numerical model was constructed in stages similar to that of the actual centrifuge test. To ensure a realistic static earth pressure K_0 value prior to shaking, the K_0 was periodically checked throughout the construction of the numerical model and the horizontal stresses were reinitialized if the K_0 was outside the range of 0.3 to 0.8.

During the dynamic analysis, ½-percent of Rayleigh stiffness and mass proportional damping was assigned at the predominant frequency of the model of 1.5 Hz.

4. NUMERICAL MODEL RESULTS

Measured and computed time histories for the Kobe_1X6 model are shown in Figure 4 and correspond to the instrument locations shown in Figure 2. These plots include (1) measured horizontal and vertical displacements at the embankment crest, (2) pile bending moments at two locations, (3) excess pore water pressure ratios (defined as $r_u = \Delta u/\sigma_{vo}'$) for points in the loose sand beneath the two embankments, (4) horizontal accelerations at the base of the container and in the two embankments, and (5) the input horizontal base velocity of the simulation. The sign convention used in Figure 4 is shown in Figure 2 (horizontal displacement, velocity, and acceleration are positive to the right and vertical displacement is positive upwards).

The final horizontal displacement of the nonpiled embankment crest in the simulation was 2.1 m, which is more than the 1.7 m measured in the test, and the final horizontal displacement of the piled embankment crest in the simulation was about 1.7 m, which is also more than the 1.2 m measured in the test. These over-predictions of displacement may be attributed to several factors. One of the most significant may be the computed excess pore water pressures were generally higher during shaking in the loose and dense sand layers in the simulation as compared to the centrifuge test, resulting in more shear strain.

Settlement of the crest was slightly under-predicted in the simulation as compared to the test (e.g., 1.1 m versus 1.3 m for the nonpiled embankment). This may be attributed to crest settlements in the centrifuge being affected by transverse embankment displacements (note that the embankment had side slopes of about 2 to 1 in three directions, see Figure 1a). These transverse displacements were measure in the centrifuge tests to be up to 50% of the horizontal longitudinal embankment displacements. This three-dimensional effect was not modeled in the simulation.

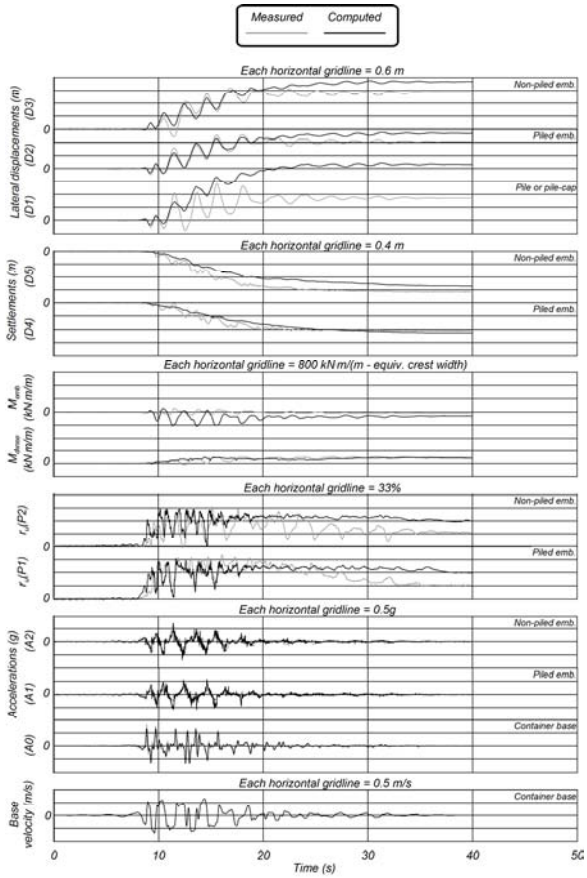

Figure 4. Measured and computed responses for the Kobe_1X6 model

Pore water pressure ratios in the simulation were similar to those measured in the test at the bottom of the loose sand layer but differed more in the dense sand and in the top of the loose sand layer. Since the triggering of liquefaction for the dense sand in the laboratory was captured well with the UBCSAND model, the over-prediction of pore water pressure in the centrifuge model may be due to a number of factors, including possible differences in the properties of the Nevada sand in the laboratory test and the centrifuge simulations. The significant deviation in measured and simulated pore pressures at the top of the loose sand layer is somewhat unclear but could be due to out-plane shear stresses that would reduce the pore water pressure ratio due to transverse embankment displacement, to imperfect saturation in the sand, or to three-dimensional water flow considerations that are not addressed in the two-dimensional plane strain simulation.

The accelerations in the dense and loose sand layers were similar in both amplitude and period content for the test and simulation. Embankment accelerations showed greater differences between the test and simulations, but were still reasonable.

The computed final deformed shape with contours of

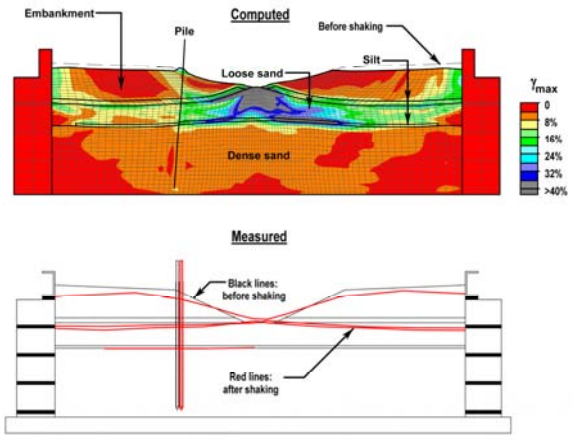

Figure 5. Contours of computed maximum shear strain and final computed and measured deformed shapes.

the maximum shear strain for the simulation and the measured final deformed shape of the centrifuge test are shown in Figure 5. The simulation captured the overall deformed shape of the test with vertical compression of the loose sand layer near the container wall and the vertical expansion (heave) at the channel. For the embankment without piles a deep failure plane in Figure 5 starts in the embankment near the container wall and extends along the bottom of the loose sand layer and in the bottom silt layer. For the embankment with piles there are two failure planes; a shallow failure plane near the crest of the embankment and extending into the top of the loose sand layer and top silt layer and a deeper failure plane starting in the embankment near the container wall and extending along the bottom of the loose sand layer and bottom silt layer.

Results of the non-linear simulations and their comparisons to the recorded responses for the other two centrifuge model tests are presented in detail in Armstrong (2010, in preparation). In general, the comparisons for the Kobe_1X6 and Kobe_2X4 models were of comparable quality, whereas the simulations for the Sine_2X4 model tended to over-predict deformations by a greater amount. Sensitivity of the simulations to variations in the major input parameters is also presented.

5. CONCLUSIONS

A non-linear numerical modeling procedure using the program FLAC and the constitutive model UBCSAND was evaluated against the results of three dynamic centrifuge model tests which included piled and non-piled approach embankments underlain by liquefied soil. The numerical simulation results presented in this paper focused on results from one of the three centrifuge tests. Additional details regarding the centrifuge tests and the numerical simulations are available in Armstrong (2008, 2010).

The numerical simulations were generally capable of reproducing the primary features of the observed responses across the set of six embankments, including the patterns of deformation and the relative differences between deformations in the piled and non-piled embankments. The simulations did tend to conservatively over-predict the magnitude of the embankment deformations for the set of calibration protocols and numerical modeling details that were used in this study. Some of the differences between measurement and prediction were likely due to three-dimensional effects in the centrifuge model.

Acknowledgements:

Funding was provided by Pacific Earthquake Engineering Research (PEER) Center and the PEER Lifelines program, under contract 65A0058. The contents of this paper do not necessarily represent a policy or an endorsement by the state or federal government. The authors appreciate the contributions of Seiji Kano for providing the results of his laboratory testing of Nevada sand. The authors acknowledge support from the Japan Ministry of Education, Culture, Sport, Science, and Technology (MEXT) for establishing the Center for Urban Earthquake Engineering (CUEE) in Tokyo Institute of Technology and making attendance at this conference possible.

References:

Armstrong, R. J. 2010. Performance of piled bridge abutments to liquefy induced ground deformations through centrifuge tests and numerical analysis tools. Ph. D. Thesis, University of California, Davis, CA, in preparation.

Armstrong, R. J., Boulanger, R. W., Gulerce, U., Kutter, B. L., and Wilson, D. W. 2008. Centrifuge modeling of pile pinning effects. Geotechnical Earthquake Engineering and Soil Dynamics IV, Geotechnical special publication, (181).

Byrne, P. M., Park, S. S., Beaty, M., Sharp, M., Gonzalez, L., Abdoun, T. 2004. Numerical modeling of liquefaction and comparison with centrifuge tests. Canadian Geotechnical Journal. 41 (2): 193-211.

Chang, D., Gulerce, U., Armstrong, R. J., Khosravifar, A., Boulanger, R. W., and Kutter, B. L. 2007. Pile pinning effects on a bridge abutment in laterally spreading ground during earthquakes: centrifuge data report for DDC03, Report no. UCD-CGMDR-06-01. Center for Geotechnical Modeling, Department of Civil & Environmental Engineering, University of California, Davis, 53.

Gulerce, U., Armstrong, R. J., Khosravifar, A., Boulanger, R. W., and Kutter, B. L. 2007. Pile pinning effects on a bridge abutment in laterally spreading ground during earthquakes: centrifuge data report for UGU01. Report no. UCD-CGMDR-06-02. Center for Geotechnical Modeling, Department of Civil & Environmental Engineering, University of California, Davis, 51.

Gulerce, U., Armstrong, R. J., Brandenberg, S. J., Khosravifar, A., Boulanger, R. W., and Kutter, B. L. 2007. Pile pinning effects on a bridge abutment in laterally spreading ground during earthquakes: centrifuge data report for UGU02. Report no. UCD-CGMDR-06-03. Center for Geotechnical Modeling, Department of Civil & Environmental Engineering, University of California, Davis, 79.

Itasca. 2008. FLAC, fast lagrangian analysis of continua, user's guide, version 6.0, Itasca Consulting Group, Inc., Minneapolis.

JOINT CONFERENCE PROCEEDINGS
7th International Conference on Urban Earthquake Engineering (7CUEE) &
5th International Conference on Earthquake Engineering (5ICEE)
March 3-5, 2010, Tokyo Institute of Technology, Tokyo, Japan

SEISMIC STABILITY OF GRAVITY TYPE QUAY WALL ON DESATURATED LOOSE SAND

Jiro Takemura[1)], Komatsumoto Naomi[2)], Seki Sakae[3)] and Jun Izawa[4)]

1) Associate Professor, Dept. Civil and Environmental Engineering, Tokyo Institute of Technology, Japan
2) Graduate Student, Dept. Civil and Environmental Engineering, Tokyo Institute of Technology, Japan
3) Technical Staff , School of Engineering, Tokyo Institute of Technology, Japan
4) Assistant Professor, Dept. Civil and Environmental Engineering, Tokyo Institute of Technology, Japan
jtakemur@cv.titech.ac.jp, komatsumoto.n.aa@m.titech.ac.jp, seki@cv.titech.ac.jp, jizawa@cv.titech.ac.jp

Abstract: Entrapped air in the pore of sand increases the compressibility of pore fluid and has an effect of preventing the excess pore pressure generation due to cyclic shearing. In this study, an attempt was made to prepare partially saturated sand with ground water table (GWT) at the ground surface by the desaturation process of lowering and raising GWT in a centrifuge. Shaking table tests of the submerged partially saturated sand with a gravity type caisson quay wall were conducted under centrifugal acceleration of 50g to study the applicability of soil desaturation as a liquefaction countermeasure. With the conditions adopted in the study, the residual degree of saturation, S_{rw}, was about 90%. The pore water pressure generation was effectively reduced both beneath the caisson and at the backfill by the S_{rw} attained after the desaturation process. Horizontal displacement, settlements and rotation of the caisson for the cases with the desaturated sand were much smaller than those of the fully saturated sand.

1. INTRODUCTION

Entrapped air in the pore of sand increases the compressibility of pore fluid and has an effect of preventing the excess pore pressure generation due to cyclic shearing. This positive effect of partial saturation on the liquefaction resistance of sand is considered to utilize for an economical countermeasure against liquefaction, if the entrapped air in the pore of soil introduced by the desaturation process can be sustained below the ground water table.

The positive effects of partial saturation on the liquefaction resistance have been investigated to discuss the applicability of soil desaturation as a liquefaction countermeasure by many researchers (e.g., Yoshimi et al., 1989; Tsukamoto et al., 2002; Okamura and Soga, 2006, Unno et al., 2008; Takemura et al., 2009). Okamura and Soga (2006) found a unique relationship between the liquefaction resistance ratio (R_u/R_s, where R_u and R_s are liquefaction resistance of unsaturated and saturated soils respectively) and the potential volumetric strain ε_v^* defined by the following equation.

$$\varepsilon_v^* = \frac{\sigma_c'}{p_0 + \sigma_c'}(1 - S_r)\frac{e}{1+e} \quad (1)$$

where σ_c', p_0, S_r and e denote effective confining pressure, absolute pressure of the fluid, degree of saturation and void ratio of soil respectively.

As measures for reducing degree of saturation of soils, two desaturation methods are practically applicable, namely lowering the ground water table (GWT) and injecting air as shown in Figs. 1. The ground water lowering technique (Fig. 1(a)) has been already applied as a liquefaction countermeasure, which normally requires the ground water table kept below the liquefiable layer by pumping ground water. This leads to relatively high operational cost and may cause ground subsidence due to the compression of less permeable underlying soft layer. Therefore, this technique will be more feasible, if the air in the pore of soils introduced in the ground water lowering process can be retained to the extent enough to enhance the liquefaction resistance after the ground water table rises to the natural depth. Air injection or air sparging (Fig.1 (b)) has been successfully developed as a technique for the cleanup of contaminated aquifers (USEPA, 1994). Although the main concern in the air sparging for the geoenvironmental problems is not the residual degree of saturation, S_{rw}, but the flow pattern, the injection of air is expected as a very economical remedial method against liquefaction if the air retained in the pore after the injection can be sustained for a reasonably long duration.

Centrifuge modeling has been used as a useful approach in the study of soil liquefaction, especially for verification of countermeasures against liquefaction (e.g., Kimura et al, 1997). Equation (1) implies that that effect of the degree of saturation cannot be well represented in small scale models at 1g but in the centrifuge models. Furthermore, the capillary rise can be well scaled in the centrifuge model, which is crucial in the simulation of lowering the ground water table.

In the centrifuge model test of this study, an attempt was made to prepare partially saturated sand with ground water table (GWT) at the ground surface by the desaturation

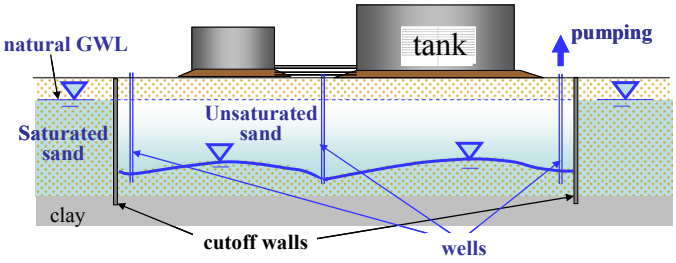

Figure 1(a) Desaturation of liquefiable soils by groundwater lowering.

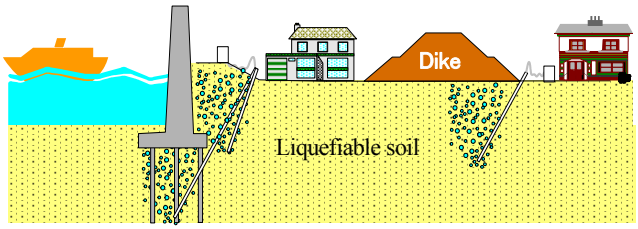

Figure 1(b) Desaturation of liquefiable soils by air injection.

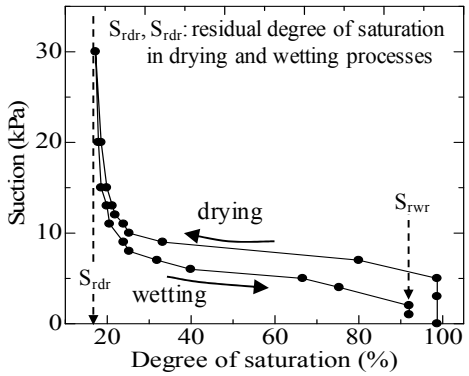

Figure 2 Capillary pressure and degree of saturation curve : Silica sand No.8.

process of lowering and regaining GWT in a centrifuge. Shaking table tests of the submerged partially saturated sand with a gravity caisson type quay wall were conducted under centrifugal acceleration of 50g to study the applicability of soil desaturation as a liquefaction countermeasure.

2. CENTRIFUGE MODEL TESTS

2.1 Soils used for tests

Two types of silica sand with properties shown in Table 1 were used for the tests. In centrifuge modeling, viscous liquids are often used as pore-fluid to overcome a mismatch in the similitude concerning seepage and dynamic events. However, to avoid uncertainty in the mechanical behavior of unsaturated sand with such viscous liquids, fine silica sand (No.8) and coarse silica sand (No.3) were used as the materials for the liquefiable sand and the bottom drainage layer respectively with water as the pore-fluid in this study. In the centrifugal field of 50 g, the permeability coefficients of the two silica sands in a prototype scale are 50 times those in 1 g as shown in Table 1. Capillary pressure - Sr curve of Silica sand No.8 is shown in Figure 2. Air entry value of the

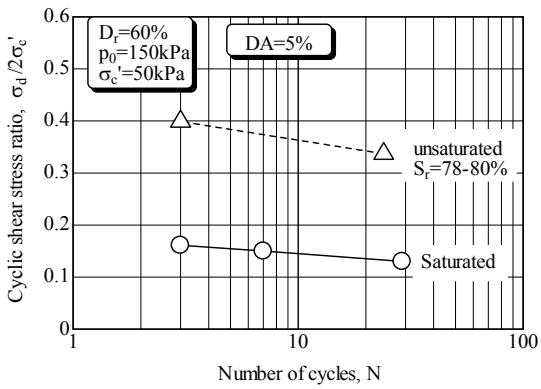

Figure 3 Relationship between cyclic shear stress ratio and number of cycles obtained from cyclic triaxial tests: Silica sand No.8.

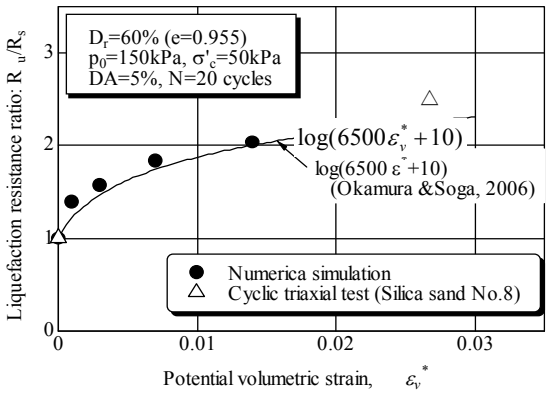

Figure 4 Relationship between potential volumetric stain and liquefaction resistance ratio.

Table 1 Properties of silica sands used

	No.8	No.3
Specific gravity: G_s	2.65	2.56
Mean particle size: D_{50} (mm)	0.100	1.47
Particle size: D_{10} (mm)	0.041	1.21
Coefficient of uniformity: U_c	2.93	1.26
Max. void ratio: e_{max}	1.333	0.971
Min. void ratio: e_{min}	0.703	0.702
Permeability coef.: k (m/sec)	2.0×10^{-5}	4.6×10^{-3}
(k in prototype scale with 50 g)	(1.0×10^{-3})	(2.3×10^{-1})

silica sand is about 10kPa and the residual S_r in wetting process is about 90%.

Figure 3 shows liquefaction curves obtained from cyclic triaxial tests on Silica sand No.8 with Dr=60% for Sr=100 % and about 80 %. Figure 4 depicts the relationship between the potential volumetric strain and the liquefaction resistance and the relationship proposed by Okamura and Soga (2006).

2.2 Model preparation and test procedures

A rigid model container made of aluminum with inner sizes of 450 mm in width, 150 mm in breadth and 270 mm in height was used for the tests. Silica sand No.3 was first placed as the bottom drainage layer by compacting with a wooden rod and a dry layer of Silica sand No.8 with

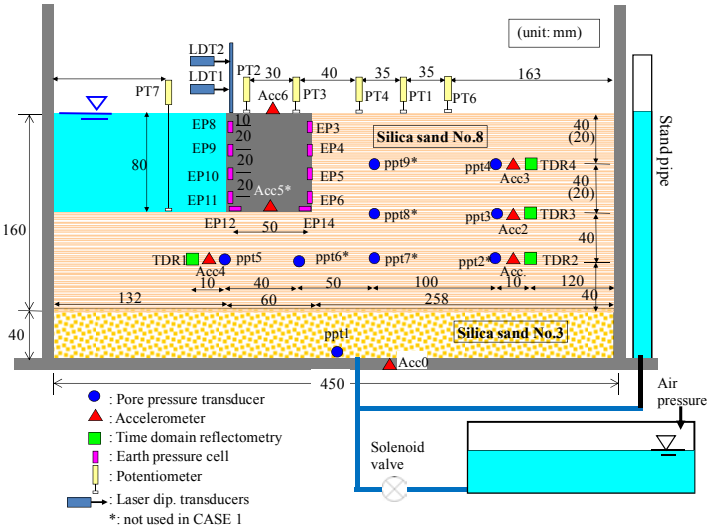

Figure 5 Test setup and location of sensors

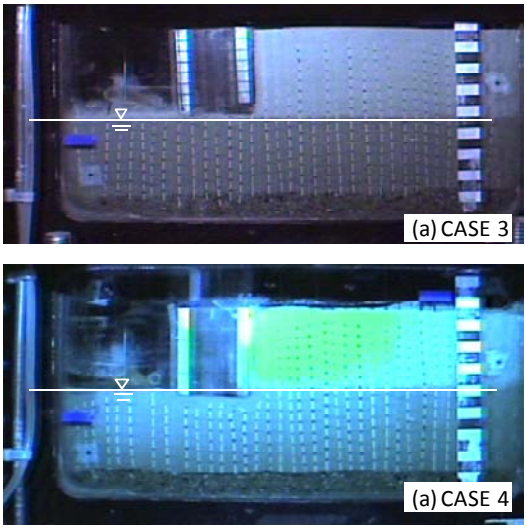

Figure 6 Minimum ground water level in CASE 3 and 4.

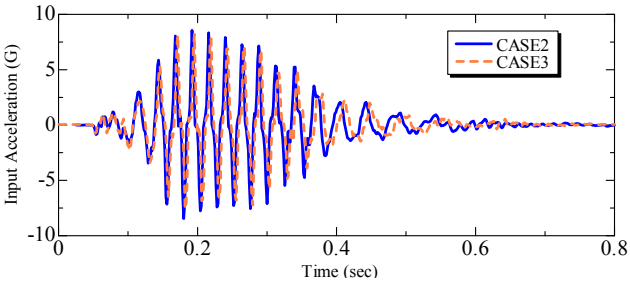

Figure 7 Input base acceleration measured by Acc0.

Table 2 Test condition

Test code	CASE1	CASE2	CASE3	CASE4
Relative density Dr (%)	60	60	60	60
Minimum water level in GWT lowering (mm)	-160	0	-90	-70

Dr=60 %was made by air pluviation. When the thickness of the sand became 80 mm, a model caisson (80 mm height, 60 mm width and 149 mm breadth) was placed on the surface. The mass of the caisson is 1.6kg, giving the base contact pressure, p_c =87 kPa in 50 g. Sand papers were glued on the bottom and back sides of the caisson to create rough surface condition. The sand was then further poured to make the backfill. During the sand preparation, various sensors were placed at the locations shown in Figure 5. The model ground was saturated in a vacuum tank by introducing deaired water from the bottom of the box. After saturating the sand, the model was then taken to Tokyo Tech Mark III Centrifuge and mounted on the mechanical shaker (Kimura et al., 1988). Potentiometers were installed at the position shown in Figure 5 and the centrifugal acceleration was increased up to 50g.

After confirming the equilibrium condition in the model, the water was drained from the bottom to the water tack by opening the solenoid valve (Figure 5). The valve was closed when the ground water level (GWL) in the standpipe lowered to the targeted depth (Figures 6). Achieving stationary reading of TDR sensors, the water was recharged from the bottom by applying air pressure to the water tank and opening the valve. Although air injection is a practically feasible desaturation method for the quay wall, the ground water lowering technique was employed in this study to create uniform and clear ground conditions in the model.

Confirming no change in the reading of TDR sensors and PPTs after the water table recovered to the original level, a shaking test was conducted by applying an input sinusoidal motion using the mechanical shaker. The input motion was generated by rotating the mechanical motor of the shaker in 0.2 second with the frequency of 40 Hz. Although the input motion did not have a constant amplitude because of the short shaking period, very good repeatability was confirmed in the input motions applied in the tests as shown in Figure 7. Four tests were conducted in this study with the condition shown in Table2.

3. TEST RESULTS AND DISCUSSIONS

3.1 Desaturation process

Figures 8 show the pore water pressures and volumetric water contents observed with PPTs and TDR sensors during the desaturation process of CASE1. Depth profiles of the minimum S_r and the residual S_r, which were observed during and after desaturation process, are depicted in Figure 9. The S_rs in the desaturation process were calculated from the water volumetric content assuming full saturation before lowering the water table. Due to some inevitable errors in the TDR measurement of volumetric water contents and the initial S_rs less than 100%, the estimated S_rs had some inconsistency. However, the variation of S_r during desaturation process and the residual S_r after raising GWT can be reasonably monitored by the TDRs. By lowering the GWL, S_r decreased to about 20 % and recovered to 85 to 90 % at the original GWT. The potential volumetric strain for S_r =90% for the depth of 40, 80 and 120mm are 0.0071, 0.012 and 0.016, and the liquefaction resistance ratio, R_u/R_s

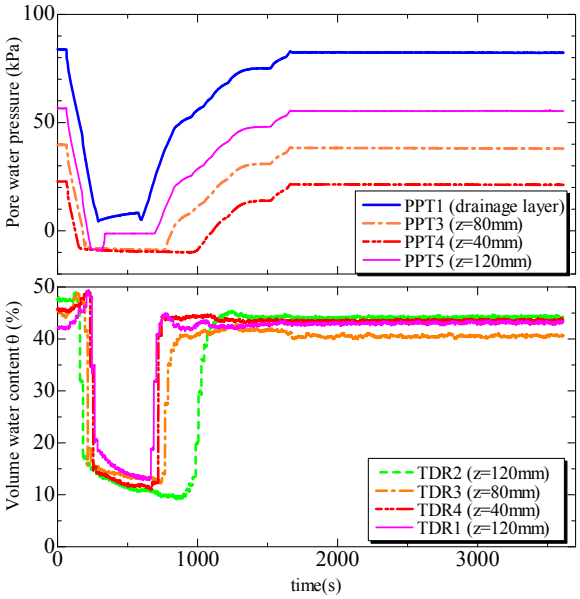

Figure 8 Variation of pore pressures and volumetric water contents estimated by TDRs : CASE1.

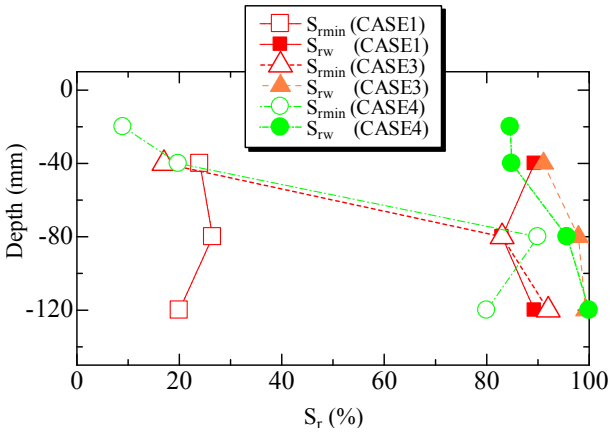

Figure 9 Depth profile of minimum degree of saturation (S_{rmin}) and residual degree of saturation below GWT (S_{rw}) estimated by TRDs

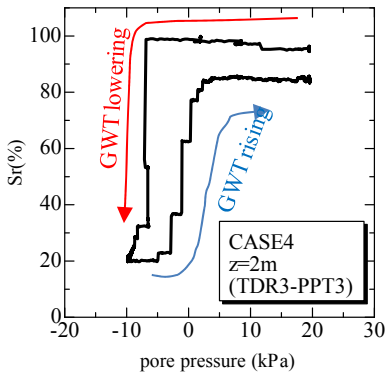

Figure 10 Relationships between the degrees of saturation and pore pressure.

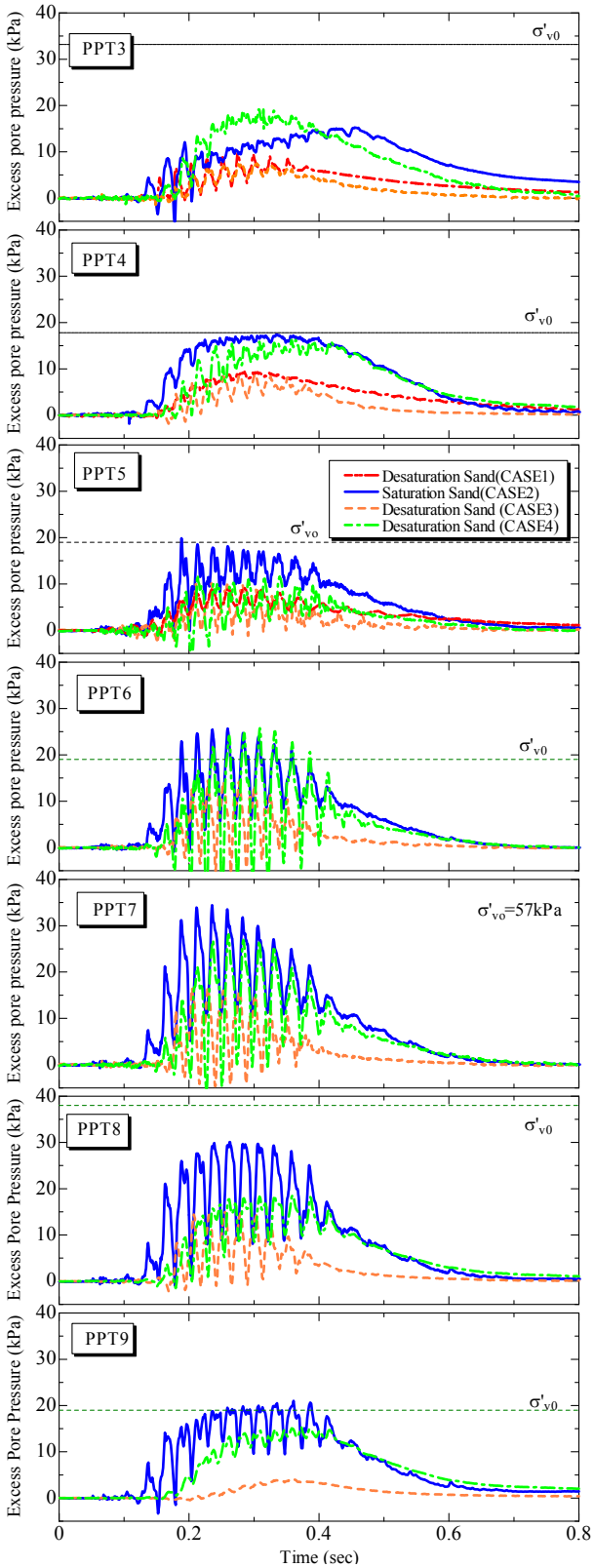

Figure 11 Variation of excess pore pressure in the model ground during shaking.

estimated by the equation given in Figure 4 is 1.8, 2.0 and 2.1 respectively. An example of the variation of pore pressure with S_r is shown in Figure 10. From this figure, it can be inferred that the capillary rise in the sand is slightly over than 0.5m in a prototype, which indicates that the same size of 1g model could be fully saturated by the capillary rise if the GWL is at the bottom of the sand..

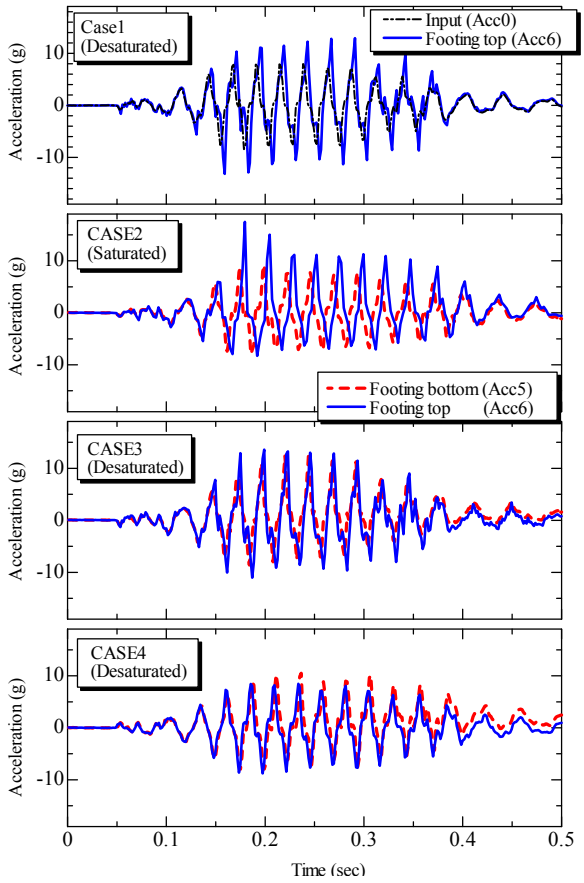

Figure 12 Observed accelerations of caisson

3.2 Shaking tests

(1) Pore water pressure behavior

Excess pore water pressures (EPWP) observed during the shaking are shown in Figure 11. In the CASE1, PPT 2 and PPTs 6 to 9 were not embedded in the ground (Figure 5). The effective overburden stress, σ'_{v0}, is shown in the figure. At the shallow depth behind the caissons (PPTs 4 and 9), the EPWPs in the saturated case (CASE1) reached to σ'_{v0} in the early stage of shaking, implying the clear liquefaction. While for the desaturated cases (CASE1, CASE3 and CASE4), the generations of EPWP were more gradual, confirming the effect of partial saturation on the liquefaction resistance. The EPWP generations of CASE 4 with shallower desaturated depth were faster than those of the cases with deeper desaturated depths (CASE1 and CASE3) even for the location with desaturation (PPT4 and PPT9). Large cyclic variations of the EPWP near the caisson are attributed to the cyclic load from the caisson. These amplitudes of EPWP are larger for the locations without desaturation than those with desaturation, which also showed the effect of entrapped air in the pore on the pore water generation due to the increase of total stress under an undrained condition. The amplitudes near the back toe of the caisson (PPTs 6 and 7) in CASE4 are the largest among all cases.

(2) Acceleration response

Horizontal accelerations observed at the top and bottom of the caisson are shown in Figure 12. The rightward direction was taken as positive in the acceleration

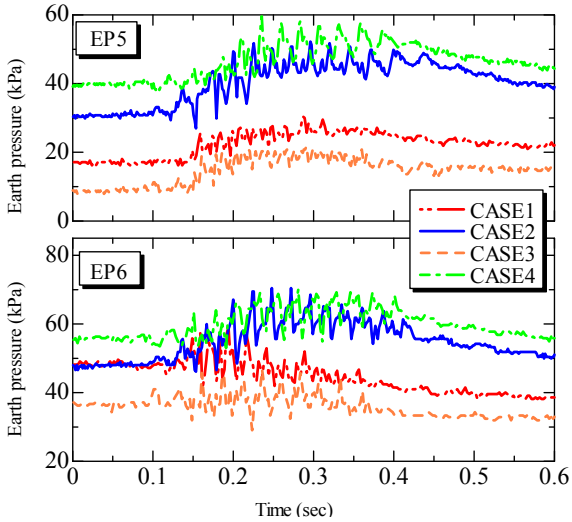

Figure13 Observed earth pressures behind caisson.

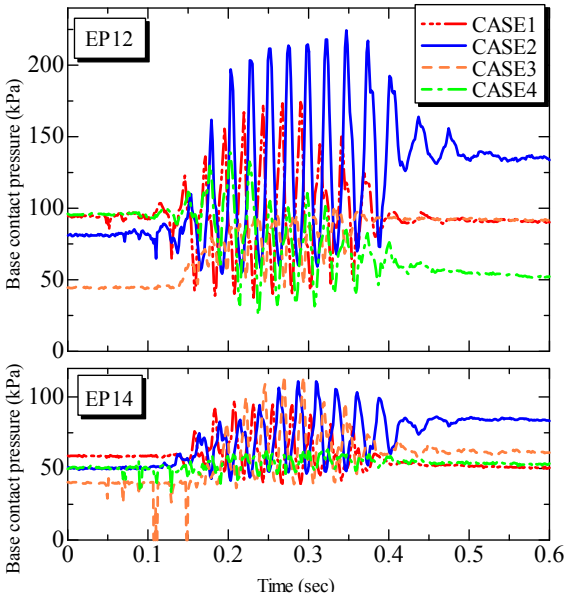

Figure14 Observed caisson base contact pressures.

measurement. In CASE1, the acceleration was not measured at the bottom of the caisson. The acceleration of caisson bottom was similar to the input motion and there was some amplification in the acceleration at the top of the caisson especially for the saturated case (CASE2). Clear phase lags in the acceleration responses can been seen between the bottom and top of the caisson in the saturated case, but not in the desaturated cases, which implying that rocking motion of the caisson took place more in the former than the latter.

(3) Pressures acting on the caisson

Earth pressures observed at the backside of the caisson and the contact pressures at the caisson base are shown in Figures 13 and 14. It is not easy to measure total stresses accurately using small pressure cells due to stress concentration or reduction by bedding error between the cell and soil. Because of this difficulty, the pressures before the shaking were different each other and also different from the calculated earth pressures. The initial horizontal earth

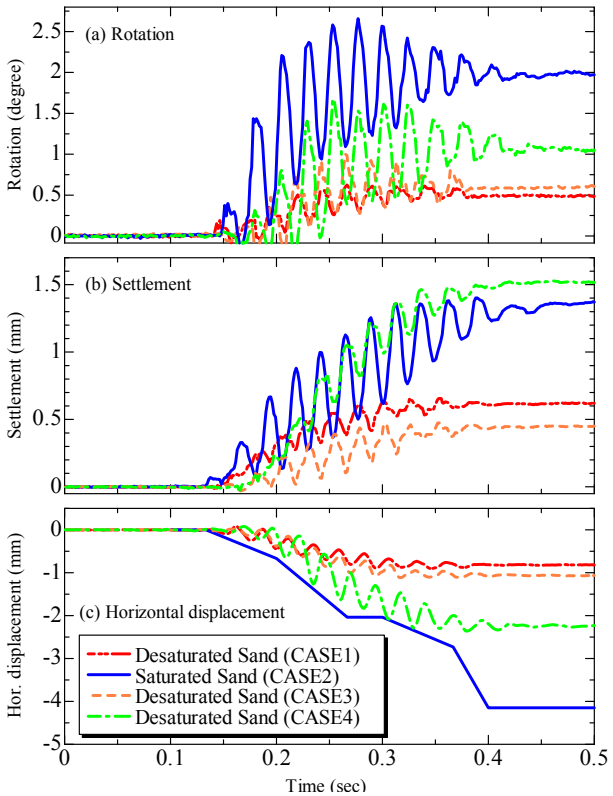

Figure15 Observed displacements of caisson .

pressures σ_h are 36 kPa and 51 kPa for EP5 and EP6, which are calculated assuming K_0=0.5, and the average base contact pressure by the caisson dead weight is 87 kPa. However, clear trends can be seen in the figure. For examples, larger pressure amplitude at the front toe (EP12) of the caisson than the back toe (EP14) and the increase of earth pressure behind the caisson during shaking.

(4) Caisson displacements

Observed displacements of the caisson, i.e., rotation, settlement and horizontal displacement at the center of gravity, during the shaking tests are shown in Figures 15. These displacements are calculated from the measurements by the potentiometers and laser displacement transducers (LDTs) shown in Figure 5. As the LDTs did not work in CASE2 and the horizontal displacement was measured from the video images, the data point of the horizontal displacement is sporadic (Figure 15 (c)). Form the figures, marked efficiencies of desaturation in preventing the displacement can be confirmed especially for CASE 1 and CASE3, in which the desaturation was done to the depth below the caisson base. The rotations, settlements, and horizontal displacements of CASE 1 and CASE4 were about one third, one half and one fifth for the saturated case (CASE2) respectively. While in CASE4 where the desaturation was made only behind the caisson, the rotation and horizontal displacement are about one half of those in CASE2 and the settlement is almost the same as that of CASE2. As can be seen in the excess pore water pressure responses of PPT6 and PPT7 (Figure 11) , EPWPs near the caisson base are very similar in CASE2 and CASE4, and the EPWP amplitudes are even greater for the latter than the former. From the displacement behavior discussed above, it can be said that the desaturation beneath the caisson is very critical in preventing the displacements of the caisson due to soil liquefaction. All displacements primarily occurred during the shaking and very minute residual displacements were observed after the shaking for all the cases.

4. CONCLUSIONS

The following conclusions can be drawn in this study.

1) Centrifuge modeling is a useful tool to create the desaturated sand. By lowering and raising the ground water table in the sand with the conditions adopted in the study, the residual degree of saturation was about 90%.
2) Accumulated and amplitude of pore water pressure can be effectively prevented both beneath and behind the caisson by the desaturation process with the residual S_r attained.
3) Rotation, seent, and horizontal displacement of the caisson can be also prevented by the desaturation. The desaturation of the sand beneath the caisson is very critical for the displacement prevention.

Acknowledgements:

The authors acknowledge the support to this research by the DaiDaiToku Project from the Ministry of Education, Culture, Sport, Science, and Technology (MEXT) .

References:

Kimura, T., Takemura, J., Hirooka, H. and Okamura, M. (1997): Countermeasures against liquefaction of sand deposits with structures, *Proc. Intn. Conf. Earthquake Geotechnical Engineering, IS Tokyo 95*, Vol.3, 1203-1224.

Kimura, T., Takemura, J. Saitoh, K. (1988): Development of a simple mechanical shaker using a cam shaft, *Proc. Centrifuge 88*, Paris, 107-110.

Okamura, M. and Soga, Y. (2006): Effects of pore fluid compression on liquefaction resistance of partially saturated sand, *Soils and Foundations*, 46(5), 695-700.

Takemura, J. Igarashi, R., Izawa, J, Okamura, M. and Masuda, M.(2009): Centrifuge model tests on soil desaturation as a liquefaction countermeasure, *Proc. 17th ICSMGE,* Alexandria, Vol. 1, 502-505.

Tsukamoto, Y., Ishihara, K. Nakazawa, H., Kamada, K. and Huang, Y. (2002): Resistance of partially saturated sand to liquefaction with reference to longitudinal and shear wave velocities, *Soils and Foundations*, 42(6), 93-104.

Unno, T., Kazama, M., Uzuoka, R. and Sento, N. 2008. Liquefaction of unsaturated sand considering the pore air pressure and volume compressibility of the soil particle keleton. *Soils and Foundations* 48(1): 87-99.

USEPA (1994): Air Sparging, Chapter 7, How To Evaluate Alternative Cleanup Technologies For Underground Storage Tank Sites: *A Guide For Corrective Action Plan Reviewers* (EPA 510-B-94-003).

Yoshimi, Y., Tanaka, K. and Tokimatsu, K.(1989): Liquefaction resistance of a partially saturated sand, *Soils and Foundations*, 29(3), 157-162.

JOINT CONFERENCE PROCEEDINGS
7th International Conference on Urban Earthquake Engineering (7CUEE) &
5th International Conference on Earthquake Engineering (5ICEE)
March 3-5, 2010, Tokyo Institute of Technology, Tokyo, Japan

CENTRIFUGE MODEL TESTS ON EFFECT OF DEEP MIXING WALL SPACING ON LIQUEFACTION MITIGATION

Masaki Kitazume[1] and Hidenori Takahashi[2]

1) Distinguished Researcher, Port and Airport Research Institute, Japan
2) Senior Researcher, Port and Airport Research Institute, Japan
kitazume@pari.go.jp, takahashi-h@pari.go.jp

Abstract: Liquefaction often takes place in saturated loose sand deposits, and causes structure loss. Many ground improvement techniques to mitigate liquefaction have been developed and applied to a range of construction projects, and the deep mixing method (DMM) has been applied for many projects aimed at such improvement. In the grid type DMM, rigid treated soil walls are expected to mitigate excess pore water pressure generation by confining soil movement during earthquakes. The applicability and improvement effect of this technique were demonstrated in the Hanshin-Awaji earthquake of 1995. Experimental and numerical studies have been carried out to investigate the effect of grid spacing on pore water pressure generation and liquefaction mitigation. Based on the results, a relatively simple design guideline was established. However, this guideline needs to be modified by incorporating various levels of seismic response at different depths in order to make it more applicable to a wider variety of ground types and earthquake conditions. In this study, a series of centrifuge model tests was conducted to investigate the effects of grid spacing on pore water pressure generation and seismic response in homogeneous sand layer. In this article, the centrifuge model tests and modified design criteria are briefly described.

1. INTRODUCTION

Large earthquakes near major cities may be rare, but the potential devastation resulting from the societal and economic impact they can cause makes them a matter of serious national concern. Recent examples include earthquake disasters in Los Angeles, USA, in 1994; Kobe, Japan, in 1995; Kocaeli, Turkey in 1999; Athens, Greece, in 1999; and Sumatera, Indonesia, in 2004. Accordingly, mitigating earthquake disasters is a matter of worldwide concern. As part of efforts to minimize earthquake-related hazards and losses, seismic design methodologies and ground improvement techniques have been developed and implemented in design practice in many regions. Liquefaction often takes place in saturated loose sand deposits, causing huge structural and human loss. Table 1 shows damage to port facilities caused by strong earthquake conditions (Noda, 1991), and demonstrates the large difference between with and without liquefaction. According to the table, the amount of damage when liquefaction takes place is about 20 to 50 times greater than that without liquefaction. This highlights the importance of liquefaction mitigation to minimize the effects of earthquake disasters.

Many ground improvement techniques for liquefaction

Table 1 Comparison of amount of damage

Earthquake	Magnitude	Port	Ground condition	Max. accel. (gal)	liquefaction	Damage (million yen)
Niigata, 1964	7.9	Hachiohe	Sand	233	No	1,980*
Tokachi Oki, 1968	7.5	Niigata	Sand	159	yes	49,700*
Miyagiken Oki, 1978	7.4	Shiogama	Clay	273	No	160*
	7.4	Ishinomaki	Sand	195-210	Yes	3,008*
Urakawa Oki, 1982	7.3	Muroran	Sand	164	No	120
Nihonkai Chubu, 1983	7.7	Akita	Sand	205	Yes	6,400

* converted into 1978 prices

mitigation have been developed and applied to a range of construction projects. The techniques are categorized as (a) densification, (b) stabilization, (c) replacement, (d) de-saturation, (e) enhancement of effective stress, (f) dissipation of excess pore water pressure, (g) mitigation of excess pore water pressure propagation, and (i) mitigation of shear deformation.

The deep mixing method (DMM), an in-situ admixture stabilization technique using cement and/or lime as a binder, has been adopted in many construction projects for various improvement purposes (CDIT, 2002). The special machine used to stabilize soft soil is basically composed of several mixing shafts and blades, and a binder-supplying system. In one operation, a column of treated soil is constructed in a ground. Through a series of construction steps, any arbitrary shape of improved mass (such as block, wall and grid types) can be formed in the ground. For liquefaction mitigation, the block and grid types of DMM have been applied as methods of (b) stabilization and (i) mitigation of shear deformation, respectively. In the grid type DMM, rigid grid walls consisting of overlapped stabilized columns are expected to mitigate excess pore water pressure generation by confining soil particle movement during earthquakes. The applicability and improvement effects of this technique were demonstrated in the Hanshin-Awaji earthquake of 1995, where a large hotel on improved ground demonstrated negligible damage despite huge earthquake motion (Suzuki et al., 1996).

The effects of ground improvement with the grid type DMM are highly dependent upon the grid spacing. Experimental and numerical studies have been carried out to investigate the effects of this spacing on pore water pressure generation and liquefaction mitigation (Koga et al., 1988, Suzuki et al., 1991). Based on these studies, a relatively simple design guideline was established in which the ratio of grid spacing and the thickness of the liquefiable sand layer, *L/H* (*L*: grid spacing, *H*: thickness of sand layer), should be less than 0.2 - 0.33 to prevent liquefaction in the event of an earthquake with an amplitude of 200 gal (Public Works Research Institute, 1992). However, this guideline does not consider various levels of seismic response seen at different depths, instead evaluating the possibility of liquefaction only at mid-depth. Kodaka et al. (2002) pointed out a limitation of the guideline that the grid spacing needs to be quite fine for liquefiable sand layer with small thickness. The guideline therefore needs to be modified by incorporating various levels of seismic response at different depths in order to make it a wider variety of ground and earthquake conditions.

In the present study, a series of centrifuge model tests was conducted to investigate the effects of grid spacing on pore water pressure generation and seismic response in homogeneous sand layer. Based on the test results, a modified design criteria is proposed. Some of the research results have been reported elsewhere (Takahashi et al., 2006a, 2006c), and are cited in the modified design (Architectural Institute of Japan, 2006). In this article, the centrifuge model tests as well as modified design criteria are introduced.

2. CENTRIFUGE MODEL TESTS

2.1 Model Test Apparatus

All the tests in this study were carried out in the PARI centrifuge, which has a radius of 3.8 m, a maximum payload of 2.7 tons and a maximum acceleration of 113 g. The details of the centrifuge were described by Kitazume and Miyajima (1995). A typical model ground is schematically shown in Fig. 1, where two grids with spacing sizes are prepared in a specimen box for the implementation of various model tests within a limited period. The model grid was made of Bakelite panels with a thickness of 2 cm which were glued in the parallel crosses, as shown in Fig. 2. The model grid was fixed to the specimen box with several bolts. Model grids with various grid spacing sizes (6, 8, 10, 12 and 24 cm) were prepared to enable parametric tests, while the depth and length were kept constant throughout the tests as 14 cm and 7 cm, respectively. On the bottom plate to which the grid panels were glued, a series of small holes measuring 6 mm in diameter was drilled to allow smooth percolation of pore fluid from its bottom.

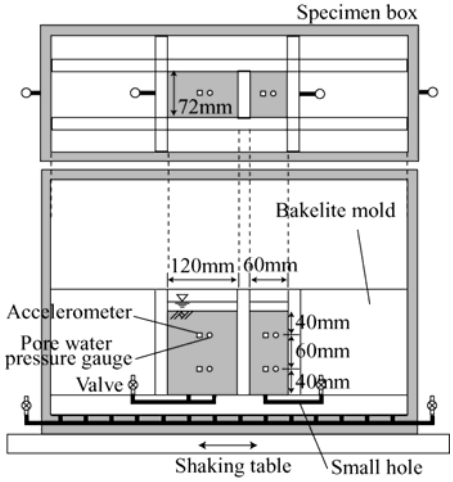

Figure 1 Schematic view of model ground

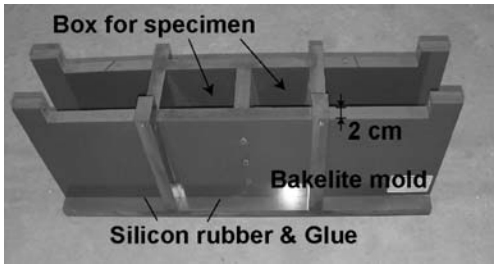

Figure 2 Bakelite panels

2.2 Preparation of Model Ground

The sand material used in this study was Soma sand excavated in Fukushima Prefecture, Japan. The major properties of this material are summarized in Table 2. Before depositing the sand into the model grids, several accelerometers and pore pressure gauges were fixed precisely at depths of 4 cm and 10 cm from the ground surface with the help of fine fishing lines, rubber bands and

acrylic plates, as shown in Fig. 3. The faces of the gauges were oriented perpendicularly to the shaking direction so that measurement would not be influenced by the induced impact of pore fluid during excitation.

The model sand ground was made using the sand raining technique with a sand hopper, a sand tank with an inside diameter of 30 cm, a flexible hose and a set of three stacks of sieves, as shown in Fig. 4. At the bottom of the sand tank, a steel plate containing holes with a specific diameter was placed so that the prescribed ground density could be achieved by controlling the flow rate of the raining sand. The sand tank was placed high enough so that the ground density would not be influenced by the decreasing fall height of the sand. After the grid had been filled with sand, the ground surface was carefully flattened out using a vacuum, and the fishing lines used to suspend the accelerometers and pore pressure gauges were cut.

Table 2 Major property of Soma sand

Property	Value
Specific gravity, G_s	2.64
Maximum void ratio, e_{max}	1.10
Minimum void ratio, e_{min}	0.70
Grain size distribution, D_{60}	0.34
Grain size distribution, D_{30}	0.27
Grain size distribution, D_{10}	0.20
Uniformity coefficient, D_{60}/D_{10}	1.7

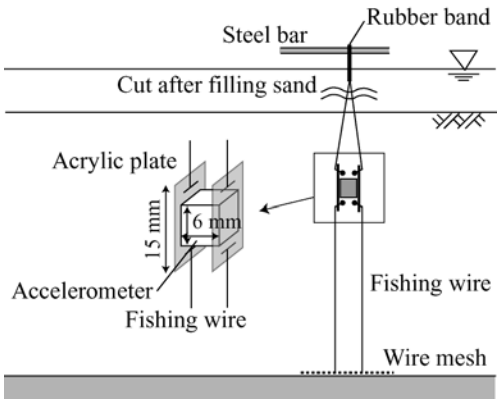

Figure 3 Sensors set in ground

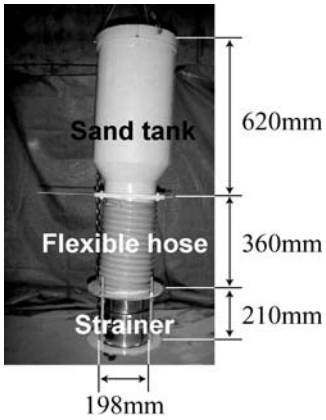

Figure 4 Sand hopper

The dry sand layer thus prepared was fully saturated using the percolation technique with carbon dioxide gas (CO_2) and a vacuum (see Fig. 5). By the method, CO_2 gas was gradually percolated into the sand layer through the holes in the bottom plate to displace air left between the soil particles. The model ground and fluid were placed in a vacuum chamber for de-airing more than 12 hours. The de-aired fluid was then percolated into the sand layer under a vacuum condition to create fully saturated ground. The fluid head difference between the storage tank and the model ground was kept within a relatively small range of 2 cm to 5 cm to enable the fluid to percolate very slowly and uniformly through the ground, which took about a whole day to complete. The degree of saturation was estimated by measuring the P-wave velocity in propagation through the ground. A measured P-wave velocity in high range of 1300 to 1600 m/s indicated that the sand ground prepared using the above technique could be almost fully saturated (Takahashi et al., 2006b).

The fluid used in this study was an aqueous solution of hydroxypropyl methylcellulose manufactured by Shin-Etsu Chemical Co., Ltd, Japan. Its viscosity was controlled to be 25 m^2/s for the 25 g centrifuge test by changing its concentrations for the temperature in the test.

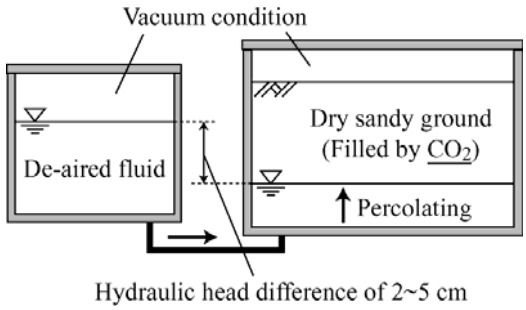

Figure 5 Illustration of saturation technique

Table 3 List of model tests

Case	Wall spacing m	Relative density %	Viscosity m^2/s
E1-1	1.5	49.7	23.6
E1-2	1.5	44.0	15.2
E2-1	2.0	44.0	21.5
E2-2	2.0	41.7	13.0
E3-1	2.5	44.0	21.5
E3-2	2.5	41.7	13.0
E4-1	3.0	49.7	23.6
E4-2	3.0	44.0	15.2
M25-5	6.0	33.7	18.3
M25-6	6.0	53.0	20.9
M25-7	6.0	50.0	24.2

2.2 Test Procedure

Soon after reaching a centrifugal acceleration of 25 g, the model ground was subjected to several seismic excitations of 50 sinusoidal waves of 4 Hz in the prototype scale. After confirming the complete dissipation of excess pore pressure generated in the previous excitation, the excitation level increased stepwise to 75, 150, 250, 400 and 500 gal in the prototype scale until the model ground was liquefied. A total of 11 model tests were carried out with different grid spacing values, as summarized in Table 3. In the table, the viscosity of fluid as reference was measured and tabulated. As viscosity is easily influenced by temperature, a significant scatter is seen among the measured viscosity values of the fluid despite the best efforts during preparation.

3. TEST RESULTS

3.1 Induced Acceleration

The relationships between the induced acceleration and the input excitation at depth of 1.0 m and 2.5 m in the prototype scale are plotted in Figs. 6 (a) and 6 (b), respectively. As shown in Fig. 6 (a), at a depth of 1.0 m, the

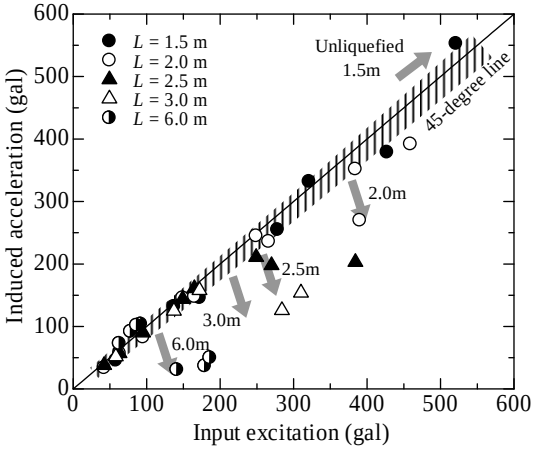

(a) at a depth of 1.0 m

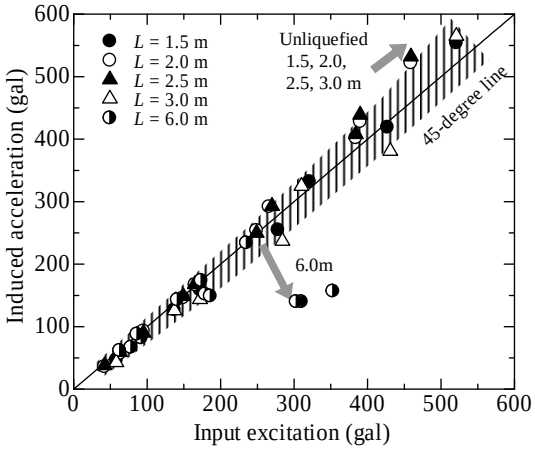

(b) at a depth of 2.5 m

Figure 6 Relationship between induced acceleration and input excitation

induced acceleration measured with the various grid spacing values increased at almost the same rate as the input acceleration while this excitation was in a relatively low range. The measured induced acceleration for an L value of 6.0 m showed a sharp decrease at an input excitation level of about 120 gal. A sharp decrease phenomenon was also seen in the other test cases as the input excitation increased. The input acceleration seen at the point of sharp decrease in the induced acceleration increased with smaller values of grid spacing: 100, 170 - 280, 250, and 380 gal for grid spacing values of 6.0, 3.0, 2.5, and 2.0 m, respectively.

In Fig. 6 (b), the induced acceleration at a depth of 2.5 m also increased at almost the same rate as the input acceleration. No sharp decrease in the induced acceleration was seen here even after the input acceleration exceeded about 500 gal except in the test case with an L value of 6.0 m. The induced acceleration for this L value decreased sharply at an input acceleration of about 250 gal.

3.2 Excess Pore Water Pressure Generation

The relationships between the maximum excess pore pressure ratio $(\Delta u/\sigma')_{max}$ and the input excitation are shown in Figs. 7 (a) and 7 (b) for depths of 1.0 m and 2.5 m, respectively. The $(\Delta u/\sigma')_{max}$ was defined as the maximum of the ratio of the residual component of excess pore water pressure during earthquake excitation against the effective overburden pressure at depth. In the figures, the measured data for various grid spacing values are plotted together with approximate lines for each spacing interval for ease of comparison. As the input excitation increased, the $(\Delta u/\sigma')_{max}$ value gradually increased irrespective of the measured depth and grid spacing.

For a depth of 1.0 m, as shown in Fig. 7 (a), $(\Delta u/\sigma')_{max}$ value increased to unity with increasing the input excitation in the cases where the grid spacing L was equal to or larger than 2.0 m, and the magnitude of input acceleration $(\Delta u/\sigma')_{max}$ being unity with increasing the value of L. In ground with an L value of 1.5 m, $(\Delta u/\sigma')_{max}$ also increased with the higher input excitation, but didn't reach unity even when the input acceleration exceeded about 500 gal.

At a depth of 2.5 m, as shown in Fig. 7 (b), $(\Delta u/\sigma')_{max}$ increased to unity with increasing the input excitation at an L value of 6.0 m. The input excitation at $(\Delta u/\sigma')_{max}$ being unity was about 250 gal, which was larger than that at a depth of 1.0 m. However, in the other cases, $(\Delta u/\sigma')_{max}$ increased with increasing the input excitation but did not reach unity.

From the induced acceleration measurements in Fig. 6 and the excess pore water pressure measurements in Fig. 7, it was found that the input excitation at the point of sharp decrease in the induced acceleration were close to those at the excess pore water ratio, $(\Delta u/\sigma')_{max}$ being unity, in the case of measurement at a depth of 1.0 m. This indicated that the sand layer was liquefied at this point of the input excitation; part of the ground being liquefied caused loss of stiffness due to the absence of effective stress and the input excitation at the ground bottom did not propagate through the liquefied portion to the ground surface. It was also found that the improvement effect in terms of liquefaction

mitigation was highly dependent upon the grid spacing, and the degree of improvement effect should be evaluated by incorporating the depth and input excitation concerned.

According to the discussion above, the model ground with an L value of 1.5 m did not show a sharp decrease in acceleration nor $(\Delta u/\sigma')_{max}$ increase to unity, even when the input acceleration exceeded about 500 gal, which indicated that no part of the ground was liquefied.

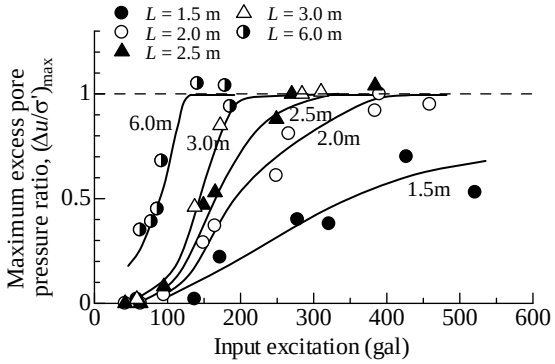

(a) at a depth of 1.0 m

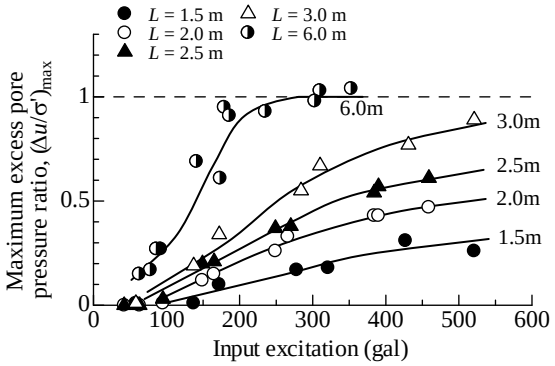

(b) at a depth of 2.5 m

Figure 7 Relationship between maximum ratio of excess pore pressure and input excitation

4. DISCUSSIONS

4.1 Liquefaction Phenomena with Grid Ratio

Figure 8 shows the relationship between the maximum excess pore pressure ratio, $(\Delta u/\sigma')_{max}$, and the grid ratio, L/H. In the figure, the measured data at two depths for two input acceleration levels are plotted together. As shown in the figure, $(\Delta u/\sigma')_{max}$ increased with higher L/H values irrespective of d/H, where d and H were the depth concerned and the thickness of the sand layer, respectively. The $(\Delta u/\sigma')_{max}$ value for a d/H of 0.3 and an input acceleration of 150 - 180 gal increased rapidly to unity when L/H became about 0.9. A similar phenomenon was seen in the case of an input acceleration of 250 - 280 gal, but the L/H value when $(\Delta u/\sigma')_{max}$ was unity was about 0.7, which was smaller than that in the case of input excitation of 150 - 180 gal. This indicated that the required L/H ratio for liquefaction mitigation depended upon the magnitude of earthquake concerned and the value should be smaller for larger earthquakes.

For a d/H of 0.7, $(\Delta u/\sigma')_{max}$ increased with higher L/H values to unity for the input excitations of 150 - 180 gal and 250 - 280 gal. The L/H value with $(\Delta u/\sigma')_{max}$ at unity in this case was larger than that for ad/H value of 0.3. This showed that liquefaction could be seen at shallow depths first even in relatively small earthquakes. The required L/H ratio for liquefaction mitigation was also dependent upon the d/H value.

According to these discussions, the required grid spacing ratio, L/H should be precisely determined by incorporating the magnitude of earthquake and the depth concerned, and the current guideline for grid design should be modified by incorporating these factors.

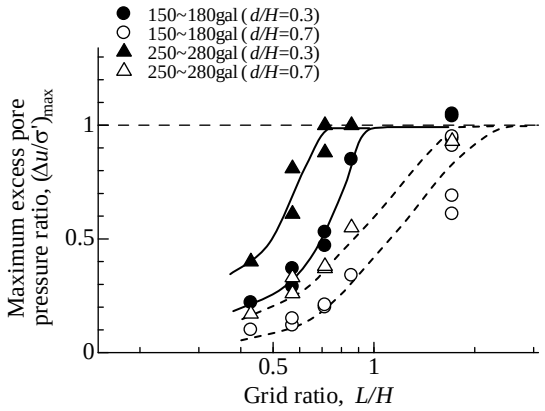

Figure 8 Relationship between maximum excess pore pressure ratio and grid ratio L/H

4.2 Liquefaction Phenomena with Grid Spacing

Figure 9 shows the relationship between the ratio of the grid spacing to the depth concerned, L/d, and the input excitation. In the figure, the measured data from all the test cases are plotted with different markers depending upon whether liquefaction occurred or not. The test case in which $(\Delta u/\sigma')_{max}$ increased to almost unity and a sharp decrease in the induced acceleration was observed (see Fig. 6) is classified as "fully liquefied", while that in which $(\Delta u/\sigma')_{max}$ didn't increase to unity and no sharp decrease in induced acceleration was observed is classified as "not liquefied". The test case in which $(\Delta u/\sigma')_{max}$ increased to almost unity and no sharp decrease in the induced acceleration was observed is classified as "liquefied". The data for the three categories are plotted as black, open, and gray circles respectively.

Based on the test data plotted in the figure, there are two parts associated with liquefaction and a sort of boundary could be drawn as a hatched portion. The figure shows that the boundary increased gradually with decreasing the L/d value as long as they were larger than around 2, but increased very rapidly when L/d became less than around 2.

This figure confirmed that a significant liquefaction mitigation effect could be expected when the L/d ratio fell below about 2. However, it also indicates that liquefaction could be induced in the shallow part of ground (i.e. areas

with a small *d* value) by relatively small earthquake motion even if the grid spacing, *L*, was small. This suggests limitation in the application of grid type improvement for liquefaction mitigation at shallow depths, and that grid spacing should be small in shallow depths of ground for liquefaction mitigation.

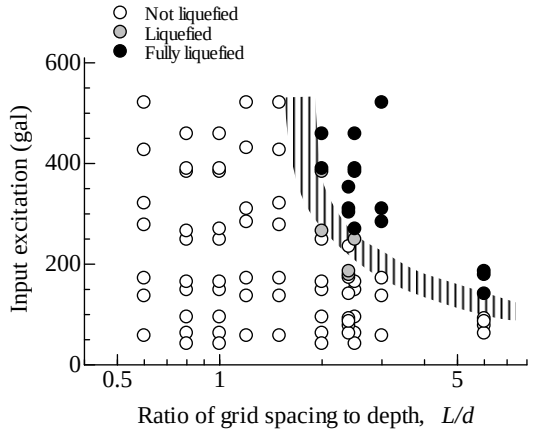

Figure 9 Relationship between input excitation and ratio of grid spacing to depth

5. CONCLUSIONS

In this study, the effects of grid spacing on liquefaction mitigation were investigated and assessed by a new factor *L/d* in order to enable rational design for grid spacing, where *L* and *d* are the grid spacing and the depth concerned respectively. The major findings of the study can be summarized as follows:

(1) Based on the input acceleration and pore water pressure values measured in the model ground, it was confirmed that the improvement effect on liquefaction mitigation was influenced not only by the grid spacing but also by the magnitude of input excitation and depth.

(2) The current guideline for grid design should be modified by incorporating the effects of the magnitude of input excitation and the depth concerned. In the present study, the test data were assessed by the ratio of grid spacing to depth, *L/d*, and a rational design guideline using *L/d* was proposed.

References:

Architectural Institute of Japan. (2006), "Recommendations for design of ground improvement for building foundations," 450 (in Japanese).

Coastal Development Institute of Technology. (2002), "The Deep Mixing Method -principle, design and construction-," Balkema, 123.

Kitazume, M. and Miyajima, S. (1995), "Development of PHRI Mark II geotechnical centrifuge," *Technical Note of Port and Harbour Research Institute*, Port and Harbour Research Institute, **817**, 33.

Kodaka, T., Oka, F. and Tanaka, K. (2002), "Evaluation of stability of grid-shaped improved ground using a 3-D liquefaction analysis," *Proceedings of the 57th JSCE annual conference*, Japan Society of Civil Engineers, 1109-1110 (in Japanese).

Koga, Y., Matsuo, O., Enokida, M., Ito, K. & Suzuki, K. (1988), "Shaking table tests on DMM method as a countermeasure against liquefaction of sandy ground (Part 2)," *Proceedings of the 23rd JGS annual meeting*, Japanese Geotechnical Society, 1019-1020 (in Japanese).

Noda, S. (1991), "Waterfront development and liquefaction," *Journal of the Japanese Society of Soil Mechanics and Foundation Engineering, 'Tsuchi-to-Kiso'*, Japanese Geotechnical Society, 39(2), 1-4 (in Japanese).

Public Works Research Institute (1992), "Cooperative research report on seismic resistant ground improvement methods (Part 6)," *Cooperative Research Report*, **68**, Public Works Research Institute (in Japanese).

Suzuki, K., Babasaki, R. and Suzuki, Y. (1991), "Centrifuge tests on liquefaction-proof foundation," *Proceedings of Centrifuge 91*, Balkema, 409-415.

Suzuki, Y., Saitoh, S., Onimaru, S., Kimura, G., Uchida, A. and Okumura, R. (1996), "Grid-shaped stabilized ground improved by deep cement mixing method against liquefaction for a building foundation," *Journal of the Japanese Society of Soil Mechanics and Foundation Engineering, 'Tsuchi-to-Kiso'*, Japanese Geotechnical Society, **44**(3), 46-48 (in Japanese).

Takahashi, H., Kitazume, M. and Ishibashi, S. (2006a), "Effect of deep mixing wall spacing on liquefaction mitigation," *Proceedings of the 6th International Conference on Physical Modelling in Geotechnics*, **1**, 585-590.

Takahashi, H., Kitazume, M., Ishibashi, S. and Yamawaki, S. (2006b), "Evaluating the saturation of model ground by P-wave velocity and modeling of models for a liquefaction study," *Proceedings of the International Journal of Physical Modelling in Geotechnics*, **6**(1), 13-25.

Takahashi, H., Yamawaki, S., Kitazume, M. and Ishibashi, S. (2006c), "Effects of deep mixing method on liquefaction prevention and proposal on new arrangement of grid-type improvement," *Report of the Port and Airport Research Institute*, **45**(2), 135-167 (in Japanese).

JOINT CONFERENCE PROCEEDINGS
7th International Conference on Urban Earthquake Engineering (7CUEE) &
5th International Conference on Earthquake Engineering (5ICEE)
March 3-5, 2010, Tokyo Institute of Technology, Tokyo, Japan

IN-SITU AIR INJECTION AS LIQUEFACTION COUNTERMEASURE AND ITS EVALUATION BY MULTIPHASE FLOW SIMULATION

Mitsu Okamura[1], Hideaki Yasuhara[2] and Emiko Nakagawa[3]

1) Professor, Graduate School of Science and Engineering, Ehime University, Japan
2) Associate Professor, Graduate School of Science and Engineering, Ehime University, Japan
3) Takamatsu Research and engineering office for port and Airport, Shikoku Regional Development Bureau, MLIT, Japan
okamura@cee.ehime-u.ac.jp, hide@dpc.ehime-u.ac.jp, nakagawa-e88s3@ pa.skr.mlit.go.jp

Abstract: Desaturation of ground by air injection attracts considerable attention in resent years as an innovative technique for liquefaction countermeasure. This paper describes an in-situ air injection test which aimed to confirm the effectiveness of the air injection to desaturate ground and validity of numerical simulation to predict the evolution of unsaturated zone. Comparison results between the predictions and 3-D tomography imaged by the electric resistivity measurements are qualitatively compatible with respect to likely-desaturated magnitude, and degree of saturation predicted are in relatively, quantitatively agreement.

1. INTRODUCTION

Although soil liquefaction during earthquakes has repeatedly caused serious damages to engineering structures, large number of existing structures which is prone to be damaged by foundation soil liquefaction, remains untreated. This is largely due to the fact that liquefaction countermeasures are generally very costly.

Natural soil deposits below ground water table are usually fully or nearly saturated with water. Recent investigations revealed, however, that injection of air into ground could lower the degree of saturation of subsoil substantially (Tokimatsu et al., 1990; Okamura et al., 2003) and the unsaturated condition of the desaturated soil lasted for a long time, typically more than tens of years (Okamura et al., 2006). Effects of saturation on the liquefaction resistance of sand have been well recognized: even a small amount of decrease in the degree of saturation, ca. several percent, doubled the liquefaction resistances.

These facts strongly suggest a possibility that desaturation of soils could be an effective and inexpensive way to enhance the resistance of soil to liquefaction in the field (Yegian, et al., 2007; Nishigaki et al., 2008). Some small scale model tests and centrifuge tests have been carried out to develop methods to desaturate liquefiable sand (Okamura and Teraoka, 2005; Takemura et al., 2009).

On October 2007, the authors conducted a field test on ground-desaturation by means of air injection. An attempt was made to detect the area of desaturation around the air injection point by using the 3-dimensional electric resistivity tomography technique. Numerical analyses via a gas-liquid two-phase flow simulator were also conducted to examine the evolution of degree of saturation mediated by the in-situ air injection, and predicted results were compared qualitatively to the tomographic images

2. AIR INJECTION AND MONITORING OF DEGREE OF SATURATION

2.1 Test site

The in-situ air injection test was carried out at reclaimed land in Kochi prefecture, Japan. The test site was level with altitude of 3.5m above mean sea level and about 20m from quay wall as shown in Fig. 1(a).

A total of seven boreholes were excavated to investigate the soil condition. Soil profile of the section passing through the boreholes A and C is illustrated in Fig. 1(b). Above the silt layer at about 6m from the ground surface, sandy gravel and sand layers are deposited. Gravel content decreases and fines content increases with an increase in the depth in these layers. The soil in the layer below ground water table (approx. GL. -3.5m) has lower SPT *N* values and judged liquefiable. In this study, fine sand and sandy gravel layers below the ground water table were set to be the target layer to desaturate.

2.2 Air injector

Air injector used in the test was a 20mm diameter and 100mm long plastic pipe with many small drilled holes (1mm diameter). A flexible tube for air pressure supply was connected to the injector. The injector was set in the borehole at a depth of GL. -6.6m and the borehole around the injector was refilled with coarse sand to the depth of GL.

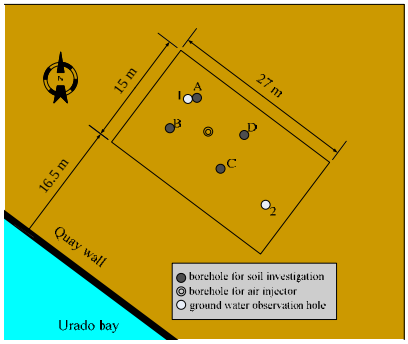

(a) Plan view of the site

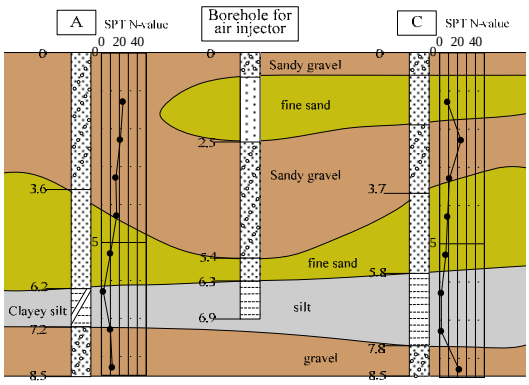

(b) Soil profile

Figure 1 General view of test site and locations of borehole for soil investigation

-6.15m as shown in Fig. 2. In order to prevent the borehole from being a preferential pathway for injected air, the borehole was refilled carefully.

A hydrophilic polymer which swells water and expands significantly to fill up the hole was pored into the borehole followed by mortar to close the hole.

2.3 Air injection

Flow of injected air through saturated soils will occur when the air entry pressure at the injection point is exceeded. The injection pressure needs to overcome the sum of hydrostatic pressure at the injection point, P_{hyd}, and capillary pressure arising from the presence of the soil (Marulanda et al., 2000). The minimum injection pressure is given by

$$\left(P_{inj}\right)_{\min} = P_{hyd} + P_{aev} \qquad (1)$$

where P_{ave} is air entry value of the soil.

In addition, air injection pressures must be lower than the in situ effective stress in order to avoid unwanted soil cracking or fissuring at around injection point. For a granular material with no tensile strength, the upper bound to the injection pressure may be given by:

$$\left(P_{inj}\right)_{\max} = \min\left(\sigma'_{vertical}, \sigma'_{horizontal}\right) \qquad (2)$$

where $\sigma'_{vertical}$ and $\sigma'_{horizontal}$ denote effective vertical and horizontal stress, respectively. This has been experimentally verified by Ogata and Okamura (2006) that the injection pressure at which cracking started to develop was approximately 0.8 times the vertical effective stress in addition to the hydrostatic pressure.

Air injection in the field was conducted four times as shown in Table 1. In the first injection test (I-1), injection air pressure was increased very gradually until injected air started flowing into soil. The pressure was found to be 35kPa which is almost identical to that derived from eq.(1). At the injection point, the effective vertical stress and the hydrostatic pressure were approximately 94kPa and 32kPa, respectively. The injection pressure was increased stepwise from 44kPa in the I-2 injection to 92kPa in I-4 injection, which is sum of P_{hyd} and two thirds of $\sigma'_{vertical}$. Ample time of at least 24 hours was taken between injection tests to dissipate excess pore pressure.

2.4 Electric Resistivity tomography

Electric resistivity of a soil depends on several parameters including water content, void ratio, temperature, ionic content, resistivity of solid phase, particle size and pressure. The influences of these factors on the resistivity are

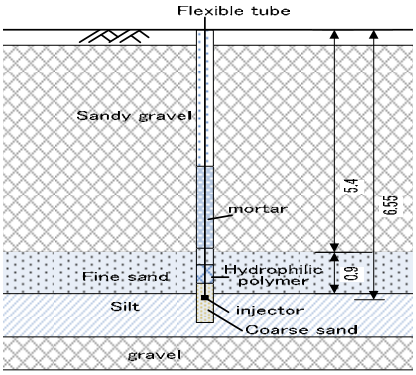

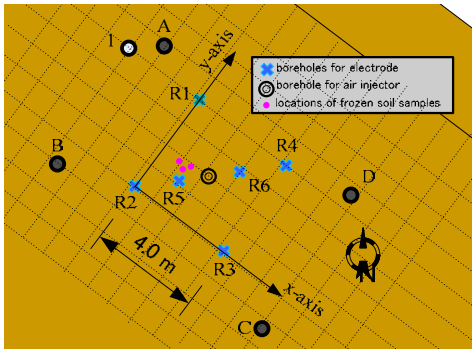

Figure 2 Arrangement of the boreholes for air injection and electrodes

Table 1. Summary of air injection test condition.

Injection #	Duration (hour)	Injection air pressure (kPa)	Maximum flow rate (10^{-3}m^3/min)	Integrated air volume (m^3)
I-1	2	34.7	0.71	0.028
I-2	24	43.9	1.81	1.8
I-3	7	47.4	47.4	0.87
I-4	7	92.0	92.0	3.4

different for different soil, however, desaturation technique by the air injection does not alter these parameters with an exception of volumetric water content (degree of saturation). Equation (3) indicates the relationship between electric resistivity and degree of saturation, which is known as Archie's law,

$$\rho = a\rho_w n^{-m} S_r^{-p} \tag{3}$$

where ρ is resistivity, n is void ratio, S_r is degree of saturation, ρ_w is resistivity of pore fluid and a, m and p are soil constant. Since it is reasonable to assume S_r = 1.0 for soil below ground water table, the ratio of resistivity after air injection to that before injection can be uniquely correlated with degree of saturation,

$$\frac{\rho_a}{\rho_b} = S_r^{-p} \tag{4}$$

where, ρ_a *and* ρ_b denote resistivity before and after air injection, respectively. The constant, p, is often assumed to be 2.0.

In the field test, 21 electrodes were set on the ground surface at an interval of 0.5m and 63 electrodes were set in six boreholes, R1 – R6. The arrangement of the boreholes is depicted in Fig. 2. oreholes R1 – R4 were excavated to the depth of GL. -8m at a 4m square arrangement. Five electrodes were set in each borehole at an interval of 0.5m from GL. -4m to -8m. While in the boreholes R5 an R6, which were excavated at locations 1m from the air injection borehole to the depth of GL. -6m, nine electrodes were set at an interval of 0.25m from GL. -4m to -6m. These boreholes were refilled with bentonite slurry to prevent injected air from exiting through the boreholes.

2.5 Test results

Evolutions of air injection pressure, flow rate and cumulative air volume during the injection I-2 are shown in Fig. 3. The air started to flow at the air pressure reached 36kPa which was consistent with the pressure obtained from eq. (1). The flow rate increased with increasing the air pressure.

The electric resistivity was observed using 3D array of electrodes before and after the I-2 injection. Figure 4 depicts 3D view of variations of the interpreted electric resistivity change $(\rho_a-\rho_b)/\rho_b$.The yellow and red zone corresponds to resistivity increase due to the decrease in degree of saturation by the air injection. The coordinates of the injection point in this figure is x=2m, y=2m and z=6m. The desaturated zone seems to have extended upwards from the injection point with the radius of the zone being increased with decreasing depth. At the depth of injection point, the radius of influenced zone is very limited, while the zone with radius of some 3m around injection borehole was influenced at the depth of GL. -5m and -4m. Figure 6 illustrates the interpreted resistivity change on the horizontal section at the depth of GL. -4.5m. The open circles indicate locations of the borehole for electrodes which were buried with bentonite. The borehole for the injection is at the center of the figure. Except for the location near the electrode boreholes where injected air can not flow due to very high air entry value of the bentonite, the resistivity change is more than 20%, which corresponding to the degree of saturation lower than 90%. The electric resistivity measured after the I-3 injection test was very close to that after I-2 injection.

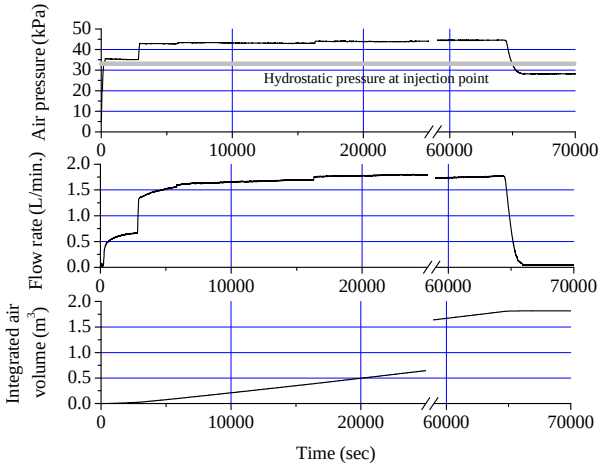

Figure 3 Air pressure, flow rate and integrated air volume during the injection I-2

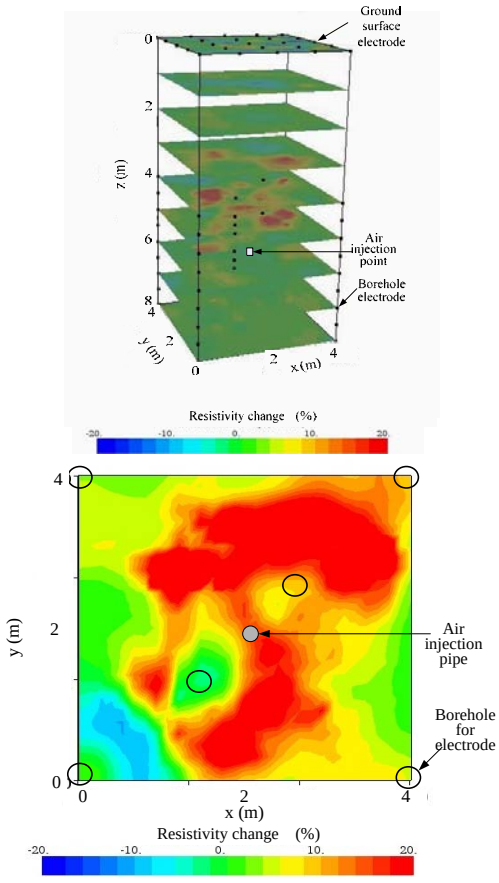

Figure 4 3D image of variation of resistivity change and resistivity change on GL. -4.5m (z = 4.5m)

3. PREDICTIONS BY GAS--LIQUID TWO-PHASE FLOW SIMULATION

During the air injection, simultaneous flow of water and air occurs, and thus the effects of capillary pressures and the mutual flow interaction between the two phases should be addressed in a computational manner. In this study, a gas-liquid two-phase simulator of TOUGH2 (Pruess et al. 1999) that accounts for the above requisites is utilized to examine the consistent desaturation process observed in the in-situ test field. In this chapter, firstly a suite of the mathematical equations is presented and then the parameters for predictions are identified through replicating the laboratory tests for determining soil-water retention characteristics. Finally, the comparison results between the experimental measurements and the predictions are shown in detail.

3.1 Mathematical formation

In TOUGH2, a mass balance may be expressed in integral form for arbitrary sub-volume, V_n, bounded by a surface area of Γ_n, given as,

$$\frac{d}{dt}\int_{V_n} M^\kappa dV_n = \int_{\Gamma_n} \mathbf{F}^\kappa \cdot \mathbf{n}\, d\Gamma_n + \int_{V_n} q^\kappa dV_n \tag{4}$$

where κ denotes the component, M^κ is the amount of component κ with a dimension of mass per volume, $\mathbf{F}^\kappa$ is the flux of component κ, $\mathbf{n}$ is the outward unit vector normal to the volume surface, q^κ is the rate of generation of component κ within the volume.

The mass accumulation term for air and water is given by,

$$M^\kappa = \phi \sum_\beta S_\beta \rho_\beta X_\beta \tag{5}$$

where S_β, ρ_β, and X_β denote the degree of saturation, density, and mass fraction of phase β (liquid or gaseous phase), respectively. The advective mass flux terms sum over the liquid and gaseous phases, as,

$$\mathbf{F}^\kappa = \sum_\beta X_\beta^\kappa \mathbf{F}_\beta \tag{6}$$

Advective flow for each phase β is defined by considering the driving forces of pressure and gravity according to a multiphase extension of Darcy's low, given as,

$$\mathbf{F}_\beta = \rho_\beta \mathbf{u}_\beta = -k \frac{k_{r\beta}\rho_\beta}{\mu_\beta}\left(\nabla P_\beta - \rho_\beta \mathbf{g}\right) \tag{7}$$

where $\mathbf{u}_\beta$ is the β phase Darcy velocity, k is the intrinsic permeability, $k_{r\beta}$ is the β phase relative permeability, μ_β is the β phase dynamic viscosity, P_β is the β phase pressure, and $\mathbf{g}$ is the gravitational acceleration vector. The hydraulic conductivity, K, is evaluated through a simple laboratory test, and the intrinsic permeability, k, is obtained by the following relation between K and k, given as,

$$k = \frac{\nu_w}{g} K \tag{8}$$

The Mualem-van Genuchten model (Mualem, 1976; van Genuchten, 1980) is used to describe the relation between degree of saturation and β phase relative permeability, as,

$$k_{rl} = \begin{cases} \sqrt{S^*}\left\{1-\left(1-[S^*]^{1/\lambda}\right)^\lambda\right\}^2 & \text{if } S_l < S_{ls} \\ 1 & \text{if } S_l < S_{ls} \end{cases} \tag{9}$$

$$k_{rg} = \begin{cases} 1-k_{rl} & \text{if } S_l < S_{ls} \\ \left(1-\hat{S}\right)^2\left(1-\hat{S}^2\right) & \text{if } S_l < S_{ls} \end{cases}, \tag{10}$$

where,

$$S^* = \left(S_l - S_{lr}\right)/\left(S_{ls} - S_{lr}\right) \tag{11}$$

$$\hat{S} = \left(S_l - S_{lr}\right)/\left(1 - S_{lr} - S_{gr}\right). \tag{12}$$

Here, S_{ls} is the maximum liquid degree of saturation, and λ is the constant. S_{lr} and S_{gr} denote the residual liquid and gaseous degree of saturation, respectively.

The relation between liquid (l) and gaseous (g) pressures is defined, via the capillary pressure, P_{cap}, as,

$$P_l = P_g + P_{cap} \tag{13}$$

The relation between the capillary pressure and degree of saturation (i.e., water retention curve) may be described by the van Genuchten equation (van Gennuchten, 1980), as,

$$P_{cap} = -P_0\left([S^*]^{-1/\lambda} - 1\right)^{1-\lambda} \tag{14}$$

where P_0 is the constant that may be related to an air entry value.

The continuum equations (Eq. (4)) are discretized in space to numerically solve multiphase flow processes. After discretized as a first-order finite difference, the flux and sink and source terms are evaluated at the next time step. An iterative procedure is adopted to solve in time until a prescribed time.

Table 1. Parameters used to in the analyis .

Soil type	K_V and K_H (cm/sec)	λ^*	P_0 (kPa)*	$S_{lr}{}^*$	$S_{ls}{}^*$	$S_{gr}{}^*$
Gravel	1.00	0.900	2.00	0.170	1.00	0.01
	1.00	0.900	2.00	0.170	0.90	0.01
Sandy gravel	2.48×10^{-4}	0.745	7.02	0.150	1.00	0.13
	3.48×10^{-4}	0.717	3.74	0.130	0.91	0.10
Fine sand	1.23×10^{-3}	0.738	35.0	0.286	1.00	0.09
	2.24×10^{-3}	0.556	6.33	0.212	0.91	0.09
Silt	4.16×10^{-5}	0.669	16.3	0.308	1.00	0.15
	6.09×10^{-5}	0.535	5.62	0.308	0.85	0.15

*The upper and lower values denote those used for drainage and imbibition processes, respectively.

3.2 Constraining calculation domain and flow parameters

A 3-D calculation domain is constructed utilizing the boring data revealed from the five boreholes A-D and one for air injection (see, Figure 1). The simulated domain with a dimension of 9m in width, 9m in depth, and 8m in height has no-flow boundaries for both water and air except a top surface boundary open for flow, and has the five different layers as shown in Fig. 5, compatible to Fig. 1. Air pressure exerted at the top elements is fixed to be 101.3 kPa of an atmospheric pressure. The vertical and horizontal hydraulic conductivities for each layer were evaluated by a typical constant-head permeability test using the boring samples. Likewise, the relation between the capillary pressure and degree of saturation (Eq. (14)) for each layer was determined through soil water retention experiments measured in this study as shown in Figure 6, together with the well-fitted predictions by Eq. (14). The parameters used for the fitting is tabulated in Table 2. The parameters of λ, S_{lr}, and S_{ls} for relative permeability function (Eqs. (9) – (12)) are assumed equivalent to those determined from fitting the water retention curve for drainage. The residual gaseous degree of saturation of S_{gr} is obtained from trapped air saturation at the end of the water retention experiment for imbibition.

3.3 Comparison between measurements and predictions

Predictions of the evolution in degree of saturation utilizing the ground model and parameters constrained in the previous section are shown in

Figure 7. A desaturated bulb augments as the prediction proceeds. This is apparently interpreted as the horizontal permeabilities used in the prediction, being superior to the vertical. Close to a water table at G.L. -3.3m, the domain horizontally within a radius of roughly 3m is desaturated as reaching a steady state (i.e., >9700min). After halting the air injection, evolution in the desaturated zone is subsequently predicted (**Figure 8**8). As apparent, the whole magnitude of the desaturated zone little evolves even after 1 week, although the degree of saturation at well-desaturated area around G.L. -4m (S_r ~60% when the air injection is halted) decrease down to roughly 85%. Ultimately, those in the desaturated zone range from 85 to 95%.

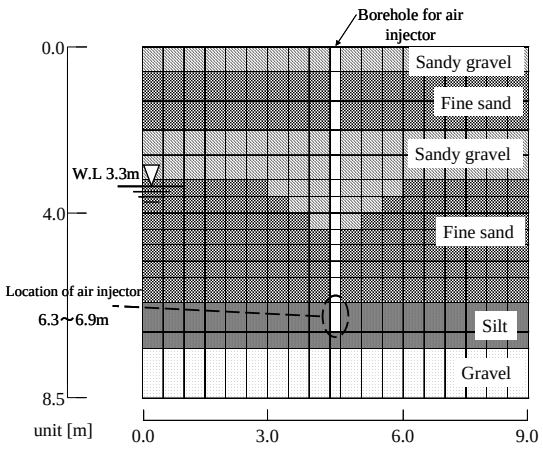

Figure 5 2-D representation of calculation domain

Qualitative comparison between degree of saturation predicted and in-situ electric resistivity tomography observed is conducted for the horizontal sections at G.L. -4.5, -5.0, and -5.5m as shown in **Figure 9**. Although distributions of desaturated zone at all sections are different between the predictions and observations, magnitudes of degree of saturation predicted may be comparable to the observations. This indicates that the model may be capable of predicting desaturation processes mediated by air injection under arbitrary conditions, and be applicable to field problems as flow characteristics are identified, *a priori*.

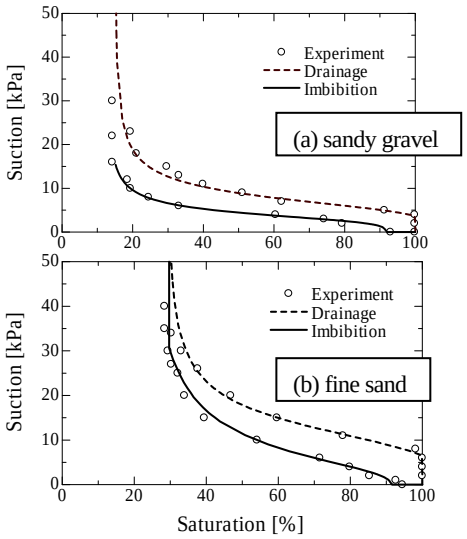

Figure 6 Replicating experimental measurements of water retention curves for drainage and imbibition processes

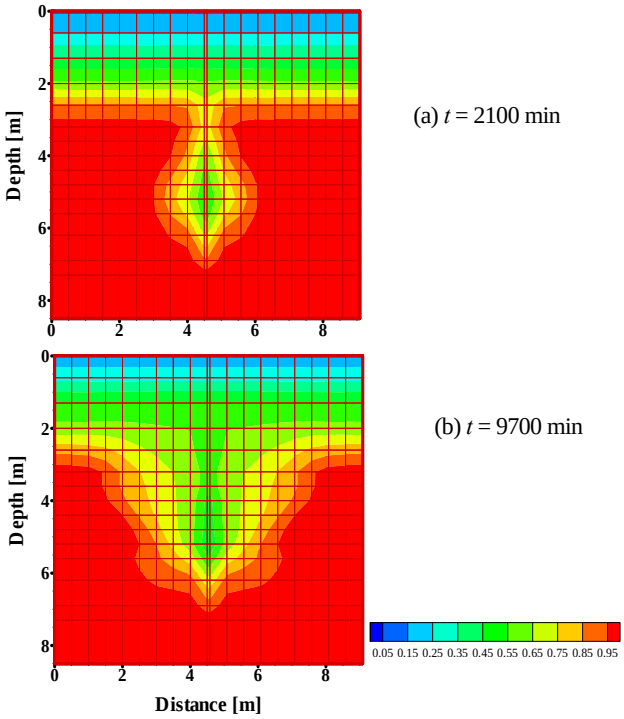

Figure 7 Temporal change in degree of saturation induced by air injection (2-D representation of vertical section including air injection point)

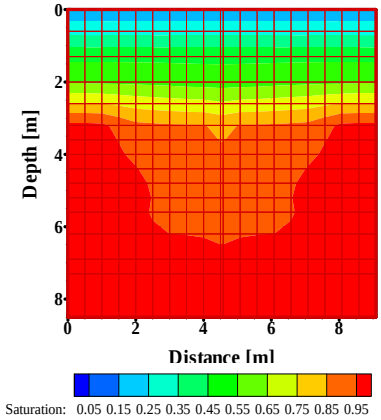

Figure 8 Temporal change in degree of saturation after air injection halted (2-D representation of vertical section including air injection point)

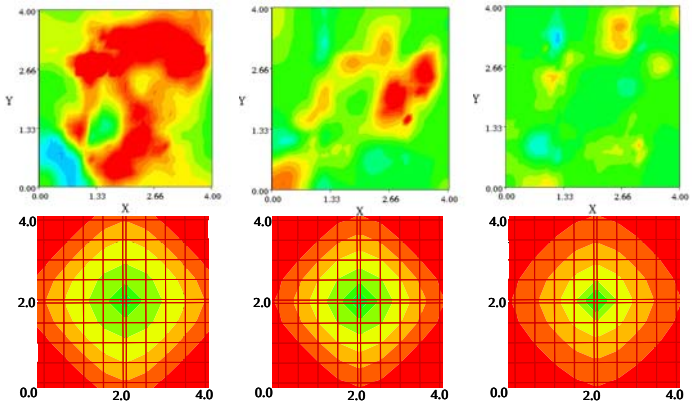

Figure 9 Qualitative comparison between predictions 7 days after air injection halted and in-situ electric resistivity tomography

4. CONCLUSIONS

An in-situ desaturation by air injection was conducted at a reclaimed quay, susceptible to liquefaction. Desaturated soil should strengthen liquefaction resistance, and this study was aimed to examine the validity and usefulness of simple anti-liquefaction technique of the air injection. Electric resistivity pre- and post-air injection has been successfully monitored and showed us a change in the resistivity, viz., induced degree of saturation. The 3-D tomography revealed that the desaturated domain may be generated within 4m from the injection point. After halting air injection, frozen soil samples were recovered so as to measure the in-situ degree of saturation evaluated in the laboratory, resulting in those ranging between 88.4% and 98.4% in the silty sand layer, and between 65% and 88% in the gravel mixed fine sand layer.

Simulating rates and magnitudes of desaturation mediated by air injecting at the test site, a gas-liquid two-phase flow calculation was conducted using a commercial simulator of TOUGH2. Parameters utilized in the predictions were carefully identified by performing flow-through tests and soil water retention tests for horizontal and vertical hydraulic conductivities and the relation between the capillary pressure and degree of saturation, respectively. Comparison results between the predictions and 3-D tomography imaged by the electric resistivity measurements are qualitatively compatible with respect to likely-desaturated magnitude, and degree of saturation predicted are in relatively, quantitatively agreement.

References:

Marulanda, C., Culligan, P. J., and Germaine, J. T. (2000). "Centrifuge modeling of air sparging – a study of air flow through saturated porous media." *J. Hazardous Materials,* 72, 179-215.

Mualem, Y. (1976). "A new model for predicting the hydraulic conductivity of unsaturated porous media." *Water Resour. Res.*, 12, 512-522.

Nishigaki, M., Komatsu, M., Fujii, N., and Ohuchi, M. (2008). "Experimental study on unsaturating soil using proposed method of injecting air into the ground to increase liquefaction strength." *Proc. JSCE, Div. C* 64(2), 340-352 (in Japanese).

Okamura, M., Ishihara, M., and Oshita, T. (2003): Liquefaction resistance of sand improved with sand compaction piles. *Soils and Foundations,* 43(5), 175-187.

Ogata, H. and Okamura, M. (2006). "Experimental study on air behavior in saturated soil under air injection." *Proc. Symposium on Natural Disaster Prevention*, Shikoku Branch, JSCE, 89-90 (in Japanse).

Okamura, M., Ishihara, M., and Tamura, K. (2006). "Degree of Saturation and Liquefaction Resistances of Sand Improved with sand compaction piles." *J. Geotech. Geoenviron. Eng., ASCE*, 132(2), 258-264.

Okamura, M. and Noguchi, K. (2009). "Liquefaction resistance of unsaturated non-plastic silt. " *Soils and Foundations*, 49(2), 221-229.

Okamura, M. and Soga, Y. (2006). "Effects of pore fluid compressibility on liquefaction resistance of partially saturated sand." *Soils and Foundations*, 46(5), 93-104.

Okamura, M. and Teraoka, T. (2005). "Shaking table tests to investigate soil desaturation as a liquefaction countermeasure", *Geotechnical Special Publication, ASCE*, 145, 282-293.

Pruess, K., C. Oldenburg, and G. Moridis (1999). *TOUGH2 User's Guide Version 2.0*, Rep. LBNL-43134, Berkeley, CA, 197pp.

Takemura, J., Okamura, M., Igarashi, R., Masuda, M., and Izawa, J. (2009). "Centrifuge model tests on soil desaturation as a liquefaction countermeasure." *Proc. XVII ICSMGE*, (in print).

Tokimatsu, K., Yoshimi, Y. and Ariizumi, K.(1990): Evaluation of liquefaction resistance of sand improved by deep vibratory compaction, Soils and Foundations, 30(3), 153-158.

van Genuchten, M. Th. (1980). "A closed-form equation for predicting the hydraulic conductivity of unsaturated soils." *Soil Sci. Soc.*, 44, 892-898.

Yegian, M. K., Eseller-Bayat, E., Alshawabkeh, A., Ali, S. (2007). "Induced Partial Saturation for Liquefaction Mitigation: Experimental Investigation." *J. Geotech. Geoenviron. Eng., ASCE*, 133(4), 372-380.

JOINT CONFERENCE PROCEEDINGS
7th International Conference on Urban Earthquake Engineering (7CUEE) &
5th International Conference on Earthquake Engineering (5ICEE)
March 3-5, 2010, Tokyo Institute of Technology, Tokyo, Japan

EFFECTS OF CALCITE PRECIPITATION ON LIQUEFACTION RESISTANCE OF SAND

Kazuyuki Hayashi[1)], Hideaki Yasuhara[2)], and Mitsu Okamura[3)]

1) Graduate Student, Graduate School of Science and Engineering, Ehime University, Japan
2) Associate Professor, Graduate School of Science and Engineering, Ehime University, Japan
3) Professor, Graduate School of Science and Engineering, Ehime University, Japan
Hayashi.kazuyuki.08@cee.ehime-u.ac.jp, hide@dpc.ehime-u.ac.jp, okamura@cee.ehime-u.ac.jp

Abstract: In this study, an attempt was made to solidify sands with the calcite of an ionic crystal which is precipitated through the ionic solution injection with a small viscosity. A suite of undrained cyclic triaxial tests was performed to study the effects of calcite precipitation on liquefaction strength of sand. It was found that the calcite precipitation of 1 or 3 wt. % of sand increased the liquefaction resistance two to four times. The stiffness of the sand was also significantly improved. Detailed observation using SEM (Scanning Electron Microscopy) and XRD (X-Ray Diffractometer) revealed that the calcite adheres to the surface of the sand particles and the calcite-bridges formed bridges between sand particles.

1. INTRODUCTION

Chemical grouting has occasionally been addressed as liquefaction countermeasure, but the conventional methods may be costly because many injections are required, due to the high viscosity, to improve the targeted ground. Alternatively, other chemical grouting methods with low viscosity of permeant are recently applied for it (e.g., Oka, et al., 2008; Hayashi et al., 2001).

Specifically, the particular ones of biogrouting utilizing microbial metabolism are also developed and extensively studied to examine its applicability to the countermeasure techniques. Biogrouting is that minerals precipitated within void spaces, induced by microbial metabolism, are used as cementation materials, and may be much kinder to geo-environment than the conventional methods.

Dejong et al. (2006) adopted calcite, generated by microbially urea hydrolysis, as a cementation mineral and evaluated the effects on mechanical properties of loose sand through triaxial tests under consolidated and undrained conditions – yield stress improved by ranging 50 to 200kPa was observed, which is in line with that of gypsum cemented soils. Kuwano et al. (2009) also reported the improved effects of microbially induced calcite that shear wave velocity in the sand increased two times greater than the pre-experimental specimens. The effects of the calcite precipitation on permeability of sand were also studied (Kawasaki et al. (2006), Hata et al.(2005), and Nemati et al.(2000)). They observed a decrease of permeability in the sands by roughly one order of magnitude.

Evidences obtained by mechanical and hydraulic experiments indicate that calcite biogrouting (i.e., using calcite as a cementation material) may be viable and applicable to an effective liquefaction countermeasure. However, it is difficult to prescribe the rates and amounts of calcite precipitation even under well-controlled laboratory conditions because activities of microbes are significantly susceptible to changes in their surrounding environments.

Alternatively, Hayashi et al. (2010) made an attempt to precipitate calcite with an inorganic method, and studied the effects of amount of calcite precipitation on mechanical properties of sand. Results of the CD-tests for specimens with approximately 1 or 3 wt.% calcite, revealed an increase in shear strength by 10-35% and in Young's modulus 2-2.5 times, and showed that negative dilation were restrained. These ensemble outcomes implicate that the method improves liquefaction properties.

As mentioned above, static mechanical tests have been conducted for calcite-precipitated sand. However, dynamic tests should be also done to examine the liquefaction properties for the sand. Thus, in this study we have performed a suite of undrained cyclic triaxial tests using calcite-precipitated sand that was prepared by the method proposed by Hayashi et al. (2010). Post-experiments, changes in geometry of sand particles resulted from calcite precipitation were observed by SEM and secondary minerals precipitated within specimens were identified by XRD.

2. EXPERIMENT

2.1 Method of Calcite Precipitation in Sand Specimens

A careful sample preparation was conducted for the experiments. We attained calcite precipitated in sand specimens by injecting a calcium chloride solution into the specimens that were premixed with sodium carbonate

Table 1 Chemical properties of reactants and products

chemical species	formula mass (g/mol)	solubility (at 20℃)
Calcium chloride($CaCl_2$)	110.98	42.7g/water100g
Sodium carbonate(Na_2CO_3)	105.99	18.1g/ water 100g
Calcium carbonate($CaCO_3$)	100.09	0.091g/ water 100g
Sodium chloride(NaCl)	58.44	26.4g/ water 100g

Table 2 Physical properties of Toyoura Sand

Soil particle density ρ_s (g/cm^3)	2.64
Maximum void ratio e_{max}	0.973
Minimum void ratio e_{min}	0.609
Mean grain size D_{50} (mm)	0.17
10% grain size D_{10} (mm)	0.11
Fine fraction content F_c (%)	0

Table 3 Test conditions

test name	D_r (%)	R_{Ca} [1)] (%)	σ_0' (kPa)	$\sigma_d/2\sigma_0'$
N	47.0~51.5	0.0	100	0.13, 0.14, 0.15, 0.17, 0.18
P_L	47.6~52.2	1.17~1.44	100	0.20, 0.25, 0.40, 0.50
P_L'	48.1~52.6	1.17~1.44	100	0.13, 0.15, 0.20, 0.25
P	49.3~52.2	3.12~3.59	100	0.40, 0.45
P'	48.3~50.5	3.12~3.59	100	0.15, 0.20

1) Mass ratio of calcite precipitated to sand

powder (details in Hayashi et al. (2010)).

Sodium carbonate in the sand specimen is dissociated into a sodium ion (Na^+) and carbonate ion (CO_3^{2-}) after injecting the calcium chloride solution, given by,

$$Na_2CO_3 \rightarrow 2Na^+ + CO_3^{2-} \quad (1)$$

Subsequently, a calcium ion (Ca^{2+}) included in the calcium chloride solution (Eq. (2)) reacts with carbonate ion, and a calcite($CaCO_3$) precipitates on the sand particle surface (Eq. (3)), as,

$$CaCl_2 \rightarrow Ca^{2+} + 2Cl^- \quad (2)$$

$$Ca^{2+} + CO_3^{2-} \leftrightarrow CaCO_3 \downarrow \quad (3)$$

Eq. (4) indicates the overall chemical equations.

$$CaCl_2 + Na_2CO_3 \rightarrow CaCO_3 \downarrow + 2NaCl \quad (4)$$

A sodium chloride (NaCl) generated as a by-product in the process of the reaction was well-excluded by injecting distilled water. This is assured because of its 300 times higher solubility than calcite. Consequently specimens

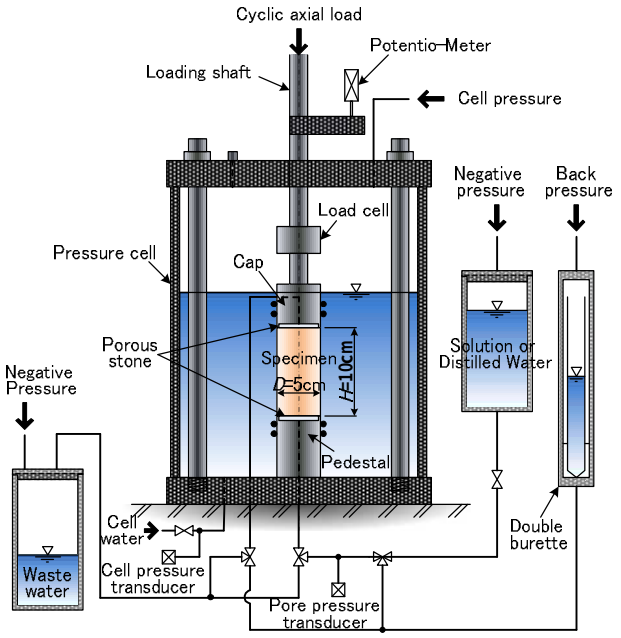

Figure 1 Schematic diagram of test equipment

consist of the sand, water, and calcite precipitated.

The amounts of sodium carbonate powder and calcium chloride solution were adjusted so that those of calcium ions and carbonate ions were equivalent. Therefore, the resulting amount of calcite precipitated should be equivalent to the same moles of calcium and carbonate ions prescribed. Table 1 shows the chemical properties of reactants and products in Eq. (4).

2.2 Sample Preparation

Sodium carbonate passing through the 75μm mesh screen was mixed into Toyoura Sand. Table 2 shows the physical properties of Toyoura Sand. The samples for test specimens are as follows,

(1) Toyoura Sand (N)
(2) Sand including sodium carbonate 2 wt. % of sand (P_L)
(3) Sand including sodium carbonate 5 wt. % of sand (P)
(4) Sand disturbed by screening with 425μm mesh and reconstituted after calcite precipitation of P_L (P_L')
(5) Sand disturbed by screening with 425μm mesh and reconstituted after calcite precipitation of P (P')

2.3 Test Procedures

Figure 1 shows a schematic diagram for undrained cyclic triaxial tests. Firstly, sand specimens 5cm in diameter and 10cm in height, were prepared by air-pluviation method – in all cases, desired relative density was D_r=50%. Secondary, the confining pressure was applied and the calcium chloride solution was injected into dry specimen from a lower inlet. Throughout the tests, effective confining pressure of σ_c' was maintained at 100kPa.

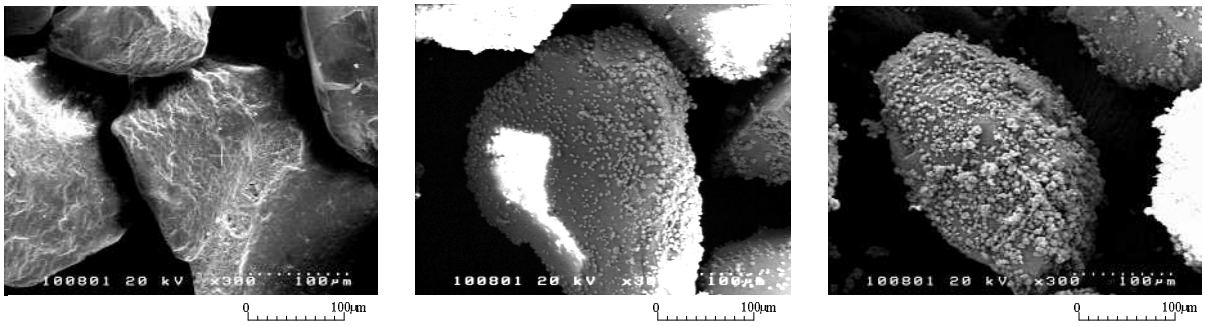

(a)N50 (b) P_L50 (c)P50

Figure 2 Scanning electron microscopy image for (a) non-precipitated sand (Toyoura Sand); (b) calcite precipitated sand P_L; (c) calcite precipitated sand P

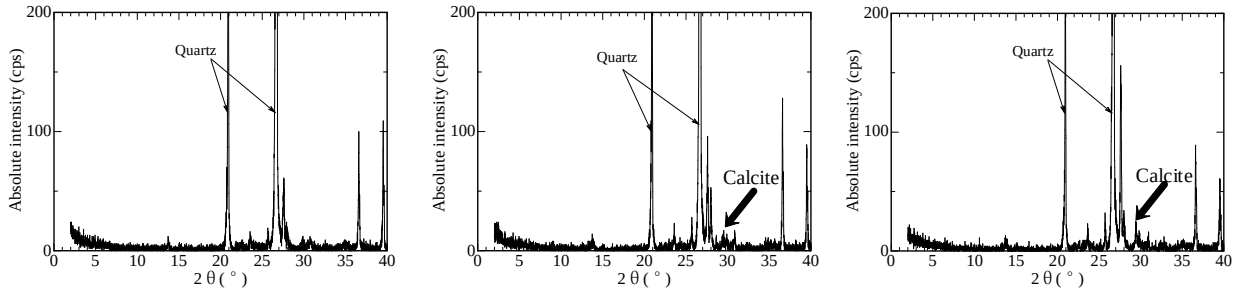

(a)N50 (b) P_L50 (c)P50

Figure 3 X-ray diffraction for (a) non-precipitated sand (Toyoura Sand); (b) calcite precipitated sand P_L; (c) calcite precipitated sand P

After ceasing the injection of the calcium chloride solution, the specimens were cured for 24hours. Then, distilled water of 150ml was injected into the specimens to remove sodium chloride with maintaining the effective confining pressure.

Finally, undrained cyclic triaxial tests at the constant amplitude and the different frequency of 0.05Hz and 1.0Hz were performed at back pressures ranging100 to 300kPa. The B-values for all the specimens measured right before cyclic tests were greater than 0.95. In the tests using reconstituted samples (i.e., P_L' and P'), curing was not performed to avoid further solidification induced by calcite. Those test conditions are listed in Table 3.

2.4 Evaluation of Amount of Calcite Precipitated

The mass of calcite precipitated was evaluated by a nominal difference between the dried specimens recovered carefully from the cyclic tests and pre-experimental dry sand.

2.5 Observation of Calcite on Sand Particle Surface

Calcite precipitated on sand particle surfaces was observed by SEM (Scanning Electron Microscopy) using samples dried after tests. The sample surfaces were coated with gold to avoid electrical discharge.

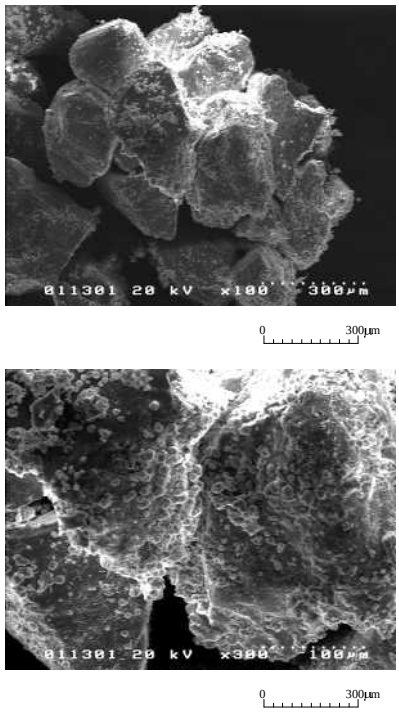

Figure 4 The bridge formed by calcite precipitated between sand particles

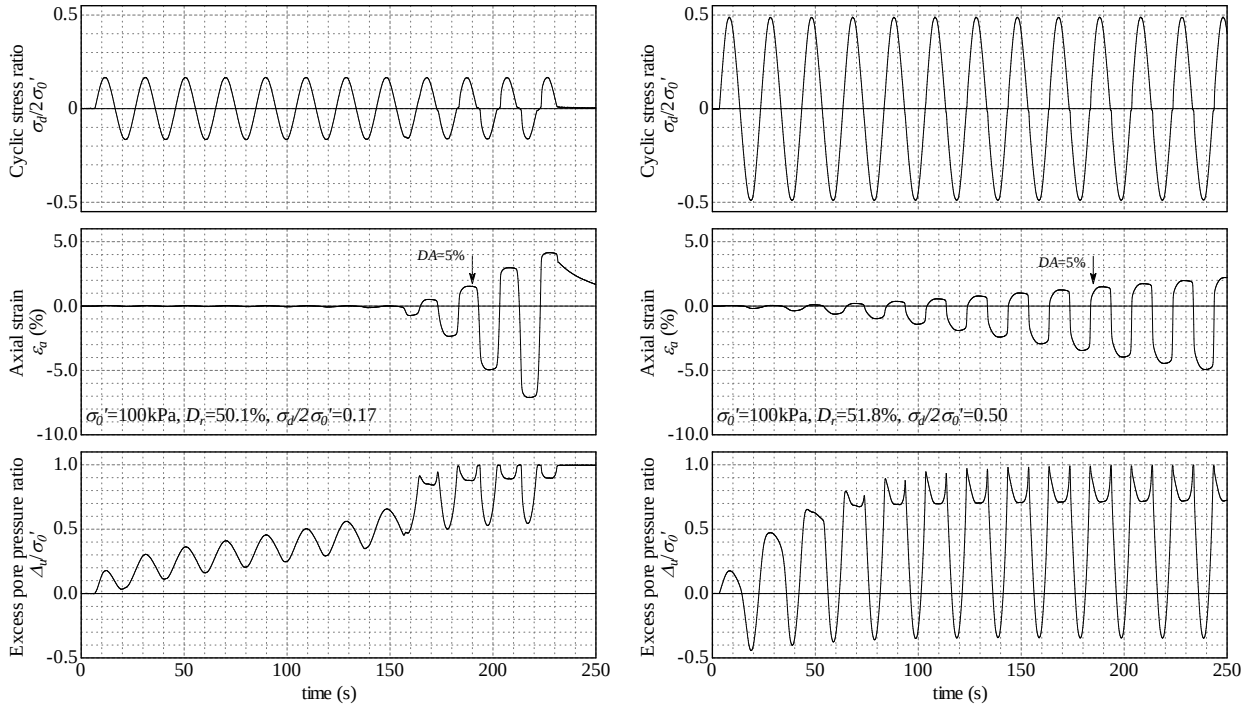

(a)N (Toyoura Sand) (b) P_L

Figure 5 Time history of cyclic stress ratio, axial strain, and excess pore water pressure ratio(N, P_L)

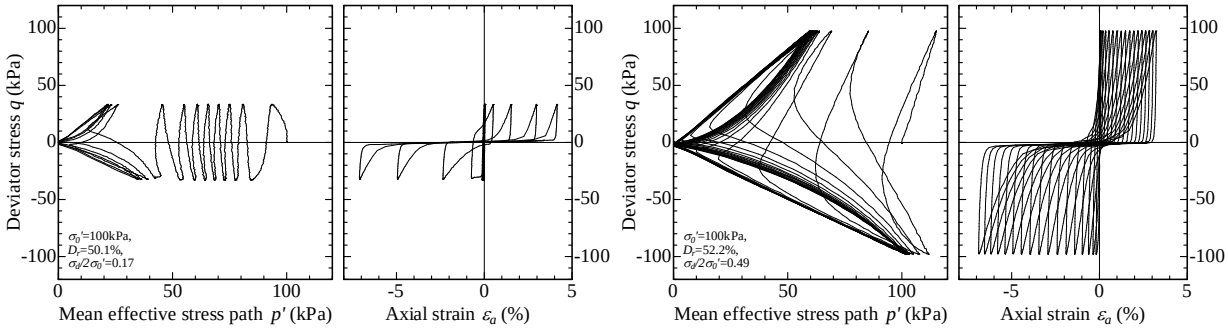

(a)N (Toyoura Sand) (b) P_L

Figure 6 Effective stress path and stress-strain curved line (N and P_L)

2.6 Identification of Secondary Minerals

Minerals precipitated on sand particle surfaces were identified by powder X-ray diffraction (XRD) using the samples dried after the cyclic tests.

3. RESULTS AND DISCUSSION

3.1 SEM and XRD

Micro-scale investigations were performed to observe calcite adhesion and calcite bridges formed between sand particles. Surface of the sand particles are shown in Figure 2. The surface of Toyoura Sand (N) is relatively smooth (Figure 2(a)), while for sand particles of P_L and P specimens (Figure 2(b), (c)) the crystal precipitated on the surface provides roughness.

XRD analyses were performed to identify the minerals precipitated on sand surface (Figure 3). While there is no calcite precipitation in N, there is the precipitation in P_L and P. It can be said that the minerals precipitated on sand surfaces are calcite.

Figure 4 shows the bridge formed by calcite precipitated between sand particles. Bridges are formed by small crystal particles. Therefore, an aggregate of sand particle with calcite in the range from 1 to 3 wt. % of bulk sand may be easy to break.

3.2 Undrained Cyclic Triaxial Tests

Time histories of cyclic stress ratio, axial strain, and excess pore water pressure ratio for N and P_L tests are depicted in Figure 5. Although cyclic stress ratios for the two tests were considerably different, both specimens reached 5% double amplitude axial strain at about the same number

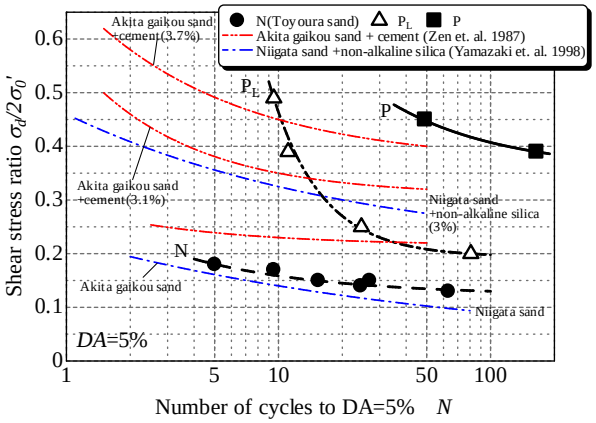

Figure 7 The relation between the number of cycles until *DA*=5% and the shear stress ratio

of cycles. Excess pore water pressure and the axial strain of the N specimen started to increase quickly at around 170 seconds, and the axial strain reached double amplitude of axial strain *DA*=5% just after the excess pore pressure ratio reached unity (Figure 5 (a)). On the other hand, axial strain of P_L specimen increased at significantly lower rate than N.

Effective stress path and stress-strain curves of the tests are shown in Figure 6. A decline of mean effective principle stress in an early loading stage of P_L is clearly restrained compared with N.

The relationship between the number of cycles to cause *DA* of 5% and the shear stress ratio is shown in Figure 7. In this figure, test results on the sands improved by cement mixing and non-alkaline silica grouting conducted by Zen et. al. (1987) and Yamazaki et. al. (1998) are also shown for comparisons. In these cases, liquefaction strength (shear stress ratio at *N*=20) increase roughly 2 times greater than untreated sand. Similarly, in the case of P_L and P, liquefaction resistance increases roughly 2 or 4times greater than N. Thus, it seems that the effects of calcite precipitation on liquefaction strength are at the same level or greater than conventional method such as cement mixing.

As apparent in Figure 7, the liquefaction strength of P_L increases compared with N. Specifically, it should be noticed that a gradient of the liquefaction strength curve for P_L increases abruptly in the number of cycles smaller than 20, whereas those for the cement-mixed (the red line in Figure 7) and silica grouted sand (the blue line) changes slightly throughout the number of cycles. This prominent result obvious for P_L concludes that loose sand improved by calcite precipitation acquires more tenacious resistance between sand particles, that should result in the sand being less susceptible to liquefaction.

3.3 Liquefaction Properties of Reconstituted Specimens

Figure 8 shows the time history of cyclic stress ratio, axial strain, and excess pore water pressure ratio observed for tests on P_L' and P' specimens, both of which were subjected to the same cyclic stress ratios of 0.20. In P_L and P, several cycles were needed to reach *DA*=5% after excess

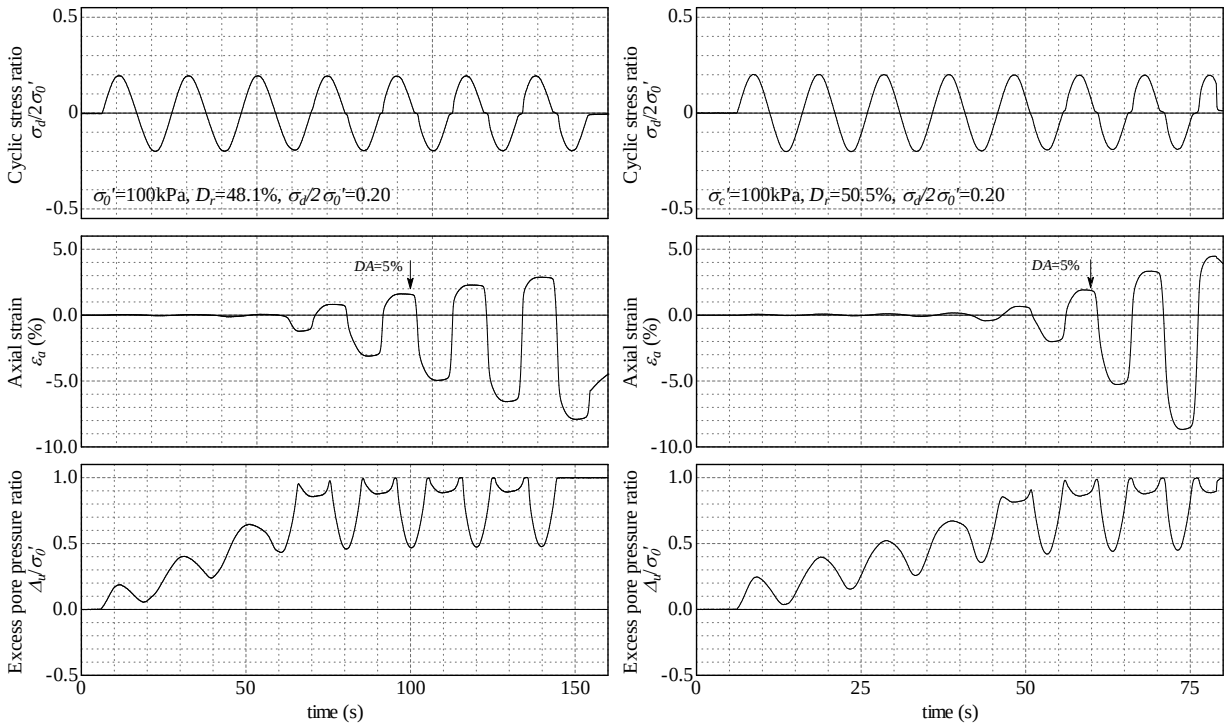

(a)P_L' (b) P'

Figure 8 The time history of cyclic stress ratio, axial strain, and excess pore water pressure ratio(P_L', P')

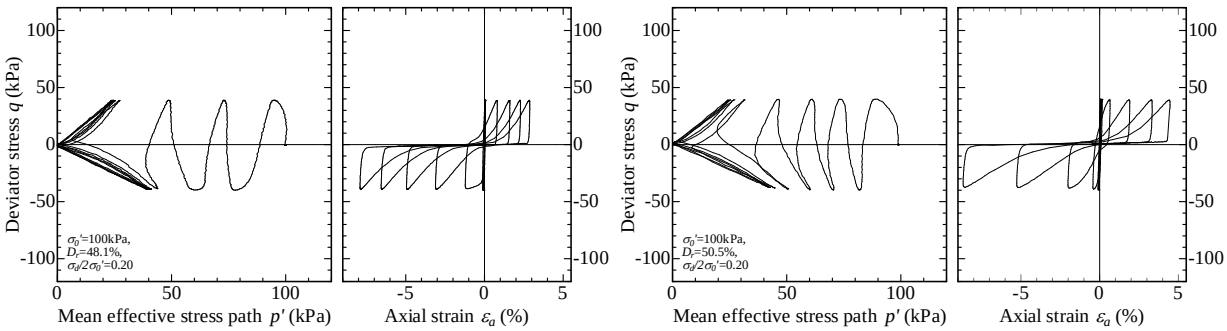

(a)P_L' (b) P'

Figure 9 Effective stress path and stress-strain curved line (P_L' and P')

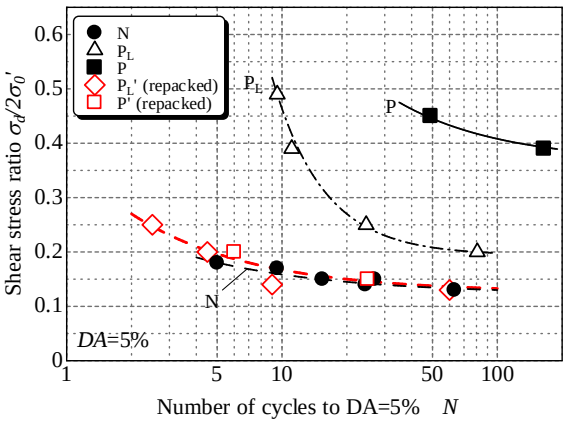

Figure 10 The relation between the number of cycles until *DA*=5% and the shear stress ratio (repacked specimens)

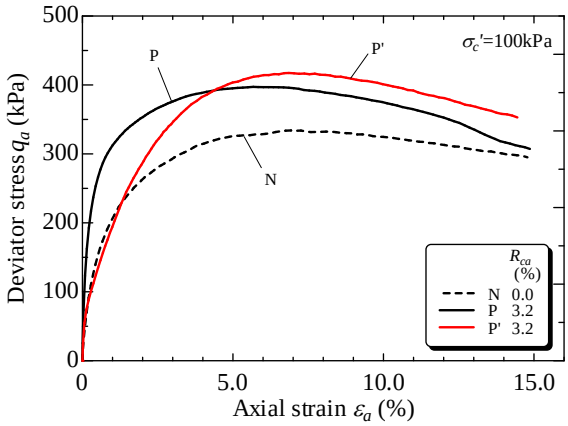

Figure 11 Difference of stress strain relations due to presence of bridge formed between sand particles (Hayashi et al. 2010)

pore water pressure became 1.0, indicating more ductile behavior as compared to P_L' and P'.

Effective stress paths and stress-strain curves of P_L' and P' are shown in Figure 9, which are more or less similar to those of N specimen (Fig. 3(a)).

The relationships between the number of cycles to cause *DA* of 5% and the shear stress ratio of P_L' and P' are indicated in Figure 10. The amount of calcite for P_L' and P' are the same as those for P_L and P, respectively. Observation of the particles using SEM revealed that roughness induced by precipitated calcite on sand particle did not change by reconstituting the sand. However, liquefaction strength ratios (defined as a stress ratio to cause *DA*=5% in 20 cycles) of reconstituted specimens (P_L' and P') are the same as that of N. This fact strongly suggests that calcite which connects sand particles plays a important role to increase the liquefaction strength.

Stress strain relations obtained form CD-tests are shown in Figure 11 (Hayashi et al. 2010). The peak deviator stress of P and P' are almost the same. On the other hand, the initial gradient of the reconstituted specimens of P' is apparently lower than that of P specimen. This is also the case in the range of small axial strain as depicted in Figure 12. Initial Young's modulus of reconstituted specimen, P'

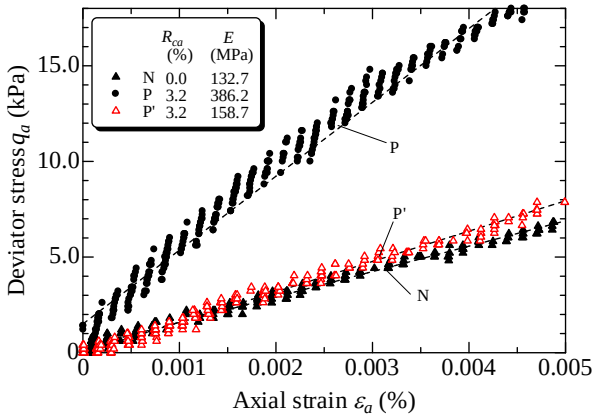

Figure 12 Difference of Young's modulus due to presence of bridge formed between sand particles (Hayashi et. al 2010)

which has precipitated calcite, is almost the same as that of N specimen.

It can be concluded that calcite bridges connecting sand particles increases Young's modulus as well as liquefaction

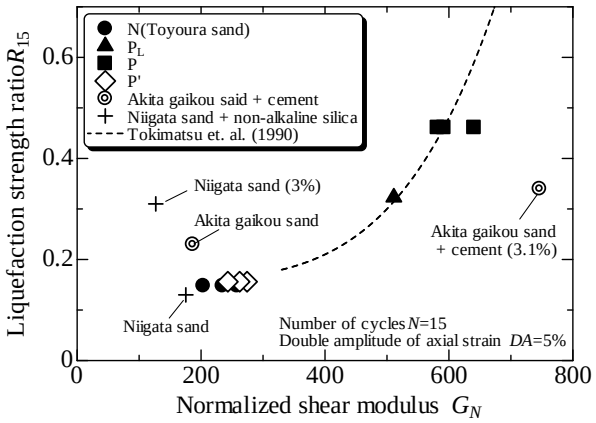

Figure 13 Relations between the normalization shearing modulus and liquefaction strength

strength.

3.4 Relations Between Stiffness and Liquefaction Strength

Tokimatsu et al. (1990) showed that there is a unique relation between the normalized shear modulus G_N and the liquefaction strength. G_N is expressed as follows:

$$G_N = G_0 / [F(e_{\min})(\sigma_m')^{2/3}] \quad (5)$$

$$F(e_{\min}) = (2.17 - e_{\min})^2 / (1 + e_{\min}) \quad (6)$$

where G_0 is the elastic shear modulus, σ_m' is the mean effective confining pressure and e_{min} is minimum void ratio of the sand. Figure 13 shows a relation between normalized shear modulus and liquefaction strength. Results indicated by Tokimatsu et al., Zen et al. (1987) for the cement mixed sand as well as Yamazeki et al. (1998) for the non alkali silica grouted sand are also plotted in the figure It should be noted that a deformation characteristics test was not performed in this study, the shear modulus G_0 was evaluated from Young's modulus measured at CD test (Hayashi et. al.)

Results of cement mix sand and non-alkaline silica improvement sand are plotted well far from the curve suggested by Tokimatsu et al. In contrast, results of the calcite precipitated sand lies along with the curve. This fact indicates that increase in liquefaction strength by the calcite precipitated may be estimated base on the shear modulus.

3. CONCLUSIONS

A suite of undrained cyclic triaxial tests were performed to investigate the influence of calcite precipitated on liquefaction properties of Toyoura Sand. The results can be summarized as follows:

(1) Calcite precipitation in sand restrains the growth of both excess pore water pressure and axial strain in the cyclic shear.

(2) Under the presence of calcite-bridges between sand particles due to calcite precipitation, the larger amount of calcite precipitation is, the larger liquefaction strength become. Liquefaction resistance increases 2 or 4 times with approximately 1 or 3 wt. % calcite precipitation for sand.

(3) The increase of liquefaction strength by calcite precipitation derives from improvement of deformation characteristic due to calcite-bridges between sand particles.

(4) Increase in liquefaction strength by the calcite precipitated may be estimated base on the shear modulus.

References:

Dejong, J. T., Fritzges, M. B. and Nusslein and K. (2006), "Microbially Induced Cementation to Control Sand Response to Undrained Shear," *Journal of Geotechnical and Geoenvironmental Engineering*, American Society of Civil Engineers, **132**(11), 1381-1392.

Hata, T., Kuwano, R. and Abe, H. "Fundamental Study of In-Situ Permeability Control Technique Using Microbial Function," *Journal of the Japan Society of Environmental System and Engineering*, Japan Society of Engineering Geology, **64**(2), 168-176 (in Japanese).

Hayashi, K., Tadanobu, S., Yasuhara, H., and Okamura, M. (2010) , "Identification of Mechanical Properties in Sand Improved by Calcium Carbonate Precipitated," *Journal of Geotechnical Engineering*, Japan Society of Civil Engineers, **66**(1), 31-42 (in Japanese).

Hayashi, K., Zen, K., Yamazaki, H. and Hayashi, N. (2001), "A Large Soil Stratum Test on the Permeability and the Improved Strength of New Solution Type Chemical Grout," *Journal of Geotechnical Engineering*, Japan Society of Civil Engineers, **694**(57), 221-228 (in Japanese).

Kawasaki, S., Murao, A., Hiroyoshi, N., Tsunekawa, M. and Kaneko, K. (2006), "Fundamental Study on Novel Grout Cementing Due to Microbial Metabolism," *Journal of the Japan Society of Engineering Geology*, Japan Society of Engineering Geology, **47**(1), 2-12 (in Japanese).

Kuwano, R. and Sugimoto, D.(2009), "Trial Tests and Evaluation of Microbially Induced Cementation in Sand," *Seisan Kenkyu*, Institute of Industrial Science the University of Tokyo, **61** (4), 682-685(in Japanese).

Nemati, M., Greene, E. A., and Voordouw, G. (2005), "Permeability profile modification using bacterially formed calcium carbonate: comparison with enzymic option, "Process *Biochemistry*, **40**, 925-933

Oka, F., Kodaka, T. and Ohno, Y.(2008), "Applicability of Permeation Grouting Method Using Colloidal Silica for Coral Sand," *Journal of the Japan Society of Engineering Geology*, Japan Society of Engineering Geology, **64**(3), 571-584 (in Japanese).

Tokimatsu, K. and Uchida, A. (1990), "Correlation between Liquefaction Resistance and Shear Wave Velocity," Soils and Foundations, Japanese Geotechnical Society, **30**(2), 33-42.

Yamazaki, H., Maeda. K., Takahashi, K., Zen, K. and Hayashi, K. (1998), "Development of Counter-measure against Liquefaction by using Solution Type Grout, " Technical Note of the Port and Harbor Research Institute Ministry of Transport, **905**, 10-12(in Japanese).

Zen, K., Yamazaki, H., Watanabe, A., Yoshizawa, H. and Tamai, A. (1987), "Study on a Reclamation Method with Cement-mixed Sandy Soils - Fundamental Characteristics of Treated Soils and Model Tests on the Mixing and Reclamation," Technical Note of the Port and Harbor Research Institute Ministry of Transport, **579**, 4-15(in Japanese).

JOINT CONFERENCE PROCEEDINGS
7th International Conference on Urban Earthquake Engineering (7CUEE) &
5th International Conference on Earthquake Engineering (5ICEE)
March 3-5, 2010, Tokyo Institute of Technology, Tokyo, Japan

A 3D SOIL-STRUCTURE INTERACTION COMPUTATIONAL FRAMEWORK

Ahmed Elgamal[1], Jinchi Lu[2], Zhaohui Yang[3], and Thomas Shantz[4]

1) Professor, Dept. of Structural Engineering, University of California, San Diego, CA 92093-0085, USA
2) Asst. Project Scientist, Dept. of Structural Engineering, University of California, San Diego, CA 92093-0085, USA
3) California Department of Transportation, Oakland, California, USA
4) California Department of Transportation, Sacramento, California, USA
elgamal@ucsd.edu, jinlu@ucsd.edu, sunny_yang@dot.ca.gov, tom_shantz@dot.ca.gov

Abstract: Three-dimensional (3D) nonlinear finite element (FE) simulations are becoming increasingly feasible for geotechnical earthquake engineering applications. This paper presents a framework that helps streamline the adoption of such simulations for analyses of soil and soil-structure systems. For that purpose, a Windows-based graphical-user-interface OpenSeesPL is developed for footing/pile-ground interaction studies. The open-source computational platform OpenSees (http://opensees.berkeley.edu) is employed as the FE analysis engine. On this basis, OpenSeesPL allows convenient modeling of three-dimensional seismic (earthquake) and/or push-over scenarios. Various ground modification situations may be also addressed by appropriate specification of the material within the pile zone. The presented analysis scenarios aim to highlight the framework capabilities and range of potential applications.

1. INTRODUCTION

Soil-Foundation-Structure Interaction (SFSI) may result in important mechanisms that affects the performance of buildings and bridges. With the recent developments in numerical modeling techniques and high-speed efficient computers, linear and nonlinear three-dimensional (3D) finite-element (FE) methods are becoming a viable technique for understanding the involved SFSI mechanisms. Particularly suited to seismic applications, the open-source computational platform OpenSees (Mazzoni et al. 2006) provides such 3D simulation capabilities for the ground, foundation, and super- structure.

In conducting 3D numerical simulations, preparation of the FE data file is a step that is typically laborious and time consuming. In this regard, a user-friendly graphical interface can significantly simplify this task, and allow for high efficiency and much increased confidence.

In order to address this issue, a graphical user-interface "OpenSeesPL" is under development (Figures 1 and 2), to allow for the execution of push-over and seismic footing/pile-ground simulations (Lu et al. 2006, https://neesforge.nees.org/ projects/openseespl/). In addition, ground modification scenarios may be studied by appropriate specification of the pile zone material.

In the following sections, a brief overview of OpenSeesPL capabilities is presented, followed by a set of illustrative simulation scenarios. The aim is to highlight the analysis framework capabilities and range of potential applications.

2. COMPUTATIONAL FRAMEWORK

The open-source platform OpenSees (http://opensees.berkeley.edu, Mazzoni et al. 2006) is employed throughout. OpenSees is a software framework for developing applications to simulate the performance of structural and geotechnical systems subjected to earthquakes. As such, OpenSees can be used to study the performance of infrastructure facilities (bridges, buildings, etc.) under static loads, and during earthquake events.

In the OpenSees platform, a wide range of linear and nonlinear soil and structural elements is available. The pre- and post-processing capabilitiess presented below are generated by the user interface OpenSeesPL (http://cyclic.ucsd.edu/openseespl) which allows for: i) convenient generation of the mesh, associated boundary conditions, and loading parameters (FE input file), ii) execution of the computations using the OpenSees platform, and iii) graphical display of the results for the footing/pile and the ground system.

3. MODELING CONFIGURATIONS

The OpenSeesPL graphical interface (pre- and post-processor) is focused on facilitating a wide class of 3D studies (with additional capabilities yet under development). The basic default configuration is in the form of a 3-dimensional soil island with the possibility of including a footing/pile/pile-group model. Full-mesh, half-mesh, or quarter mesh configurations may be

analyzed, as dictated by symmetry considerations (Figures 2-4).

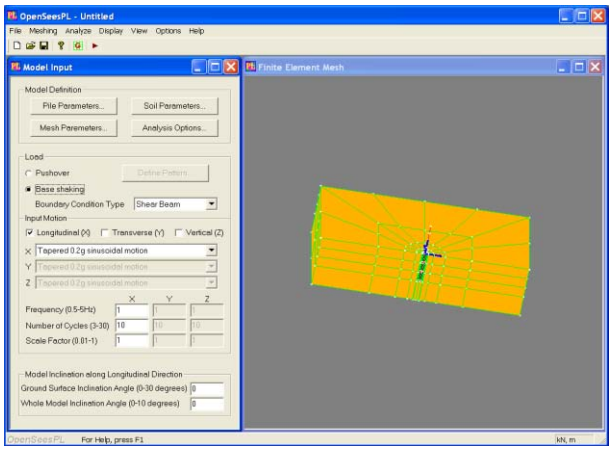

Figure 1. OpenSeesPL user interface with mesh showing a circular pile in level ground (Lu 2006, Lu et al. 2006).

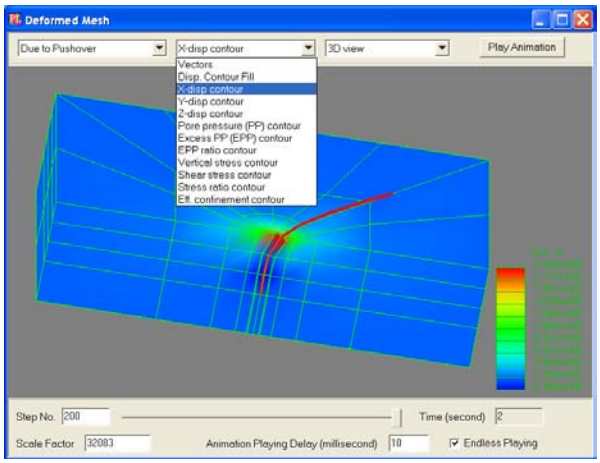

Figure 2. Longitudinal push-over analysis and deformed mesh (1/2 mesh configuration due to symmetry) window in OpenSeesPL (Lu et al. 2006).

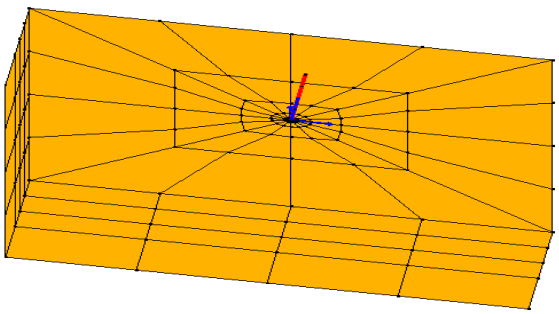

Figure 3. Full 3D mesh-pile configuration.

In OpenSeesPL, the mesh configuration may be easily modified to: i) change the pile diameter, depth of embedment, height above ground surface, and number of pile beam-column elements, and ii) refine the ground mesh domain in the lateral and vertical directions (Figure 5).

Square or circular pile cross-sections may be specified. As such, the pile model may be employed to study the response of a tall building that can be modeled as a bending beam. Shallow foundations (rigid) in square or circular configurations may be also conveniently analyzed (Figure 6).

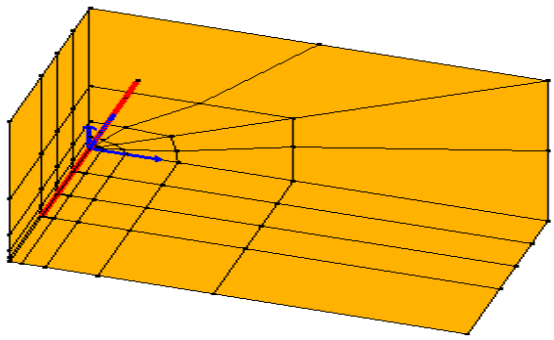

Figure 4. Quarter 3D mesh-pile configuration.

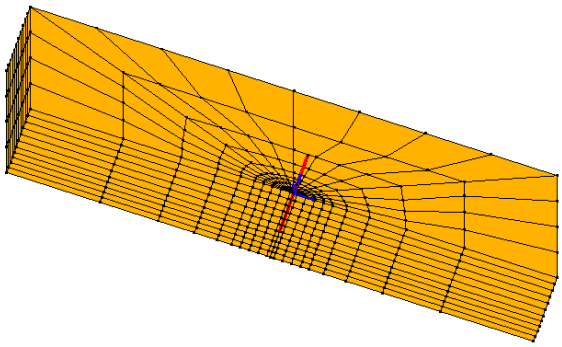

Figure 5. Mesh refinement in OpenSeesPL.

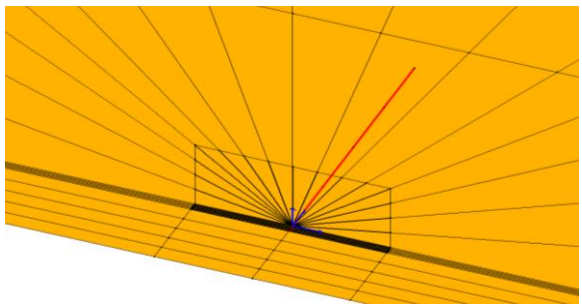

Figure 6. Building modeled as a bending beam on a shallow foundation embedded in the ground.

Independent control over the pile zone material may be exercised, allowing for a wide range of ground modification studies (Figure 7). Of particular importance and significance in these scenarios is the ability to simulate the presence of a mild infinite-slope configuration, allowing estimates of accumulated ground deformation, efficacy of a deployed liquefaction countermeasure, pile-pinning effects, and liquefaction-induced lateral pile loads and resulting moments/stresses.

Material for the pile-soil interfacing zone may be also specified by the user, permitting scenarios such as analysis of pipe-shaped foundations, and/or control over pile-soil friction and potential no-tension interaction during lateral deformation. In addition to the footing and single pile configurations, pile groups may be also represented in the free head or fixed head configurations.

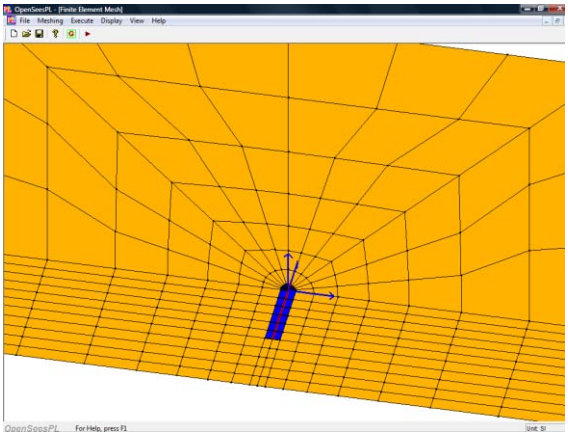

Figure 7. Control over specification of soil inside the pile zone.

4. LOAD APPLICATION

Static and dynamic loads may be applied. For static loading, push-over type analyses may be conducted where the loads/moments are directly applied to the pile top or footing surface, in force or in displacement modes. Capabilities are provided for monotonic loading, cyclic loading, and for user-defined load patterns to be uploaded as text file. Push-over along the finite element mesh boundary may be also specified, for instance to explore loads on pile foundations due to lateral ground displacement.

Dynamic and earthquake shaking may be also imparted along the soil lower boundary (base). Shaking is allowed in 3D with a small set of available motions, and a capability to upload user specified base shaking excitation (Figure 8).

5. SOIL MESH BOUNDARY CONDITIONS

For static loading on the pile or footing system, a fixed boundary condition may be specified along the base and lateral boundaries of the soil mesh. For dynamic/earthquake excitation, ground motion is specified uniformly along the soil model base as mentioned earlier. Along the lateral boundaries, users can choose between fixed, shear beam, or periodic boundary conditions.

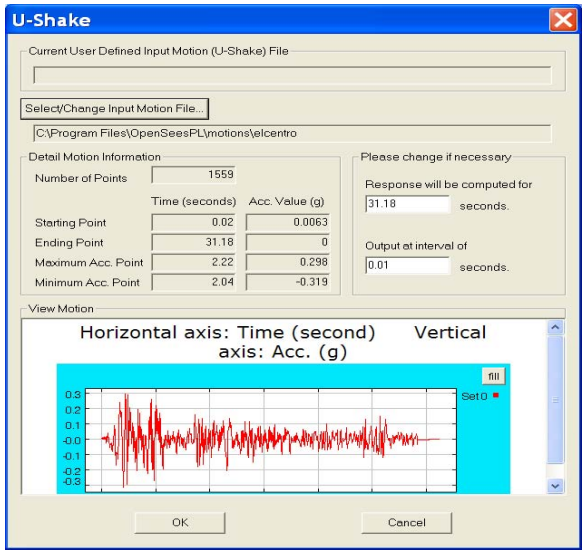

Figure 8. User-uploaded earthquake base excitation.

6. SOIL PROPERTIES

Linear and nonlinear elasto-plastic cyclic soil modeling capabilities are available. For nonlinear soil response, pressure independent (Mises or J2) plasticity and pressure dependent (Drucker-Prager cone yield surface) models are available (Elgamal et al. 2003, Yang et al. 2003). The available solid-fluid coupled formulation allows for conducting liquefaction-type analyses (Yang et al. 2003). Selection may be made from a set of available soil model properties, or by user-defined input modeling parameters (Figure 9).

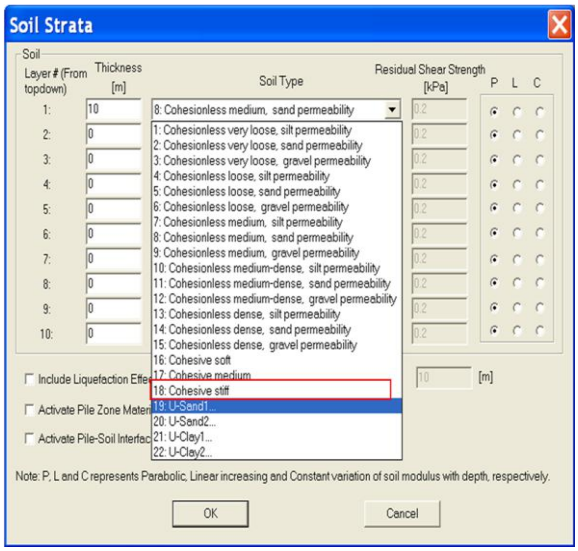

Figure 9. Menu of soil properties, and user-defined parameters.

7. BEAM-COLUMN ELEMENTS

OpenSeesPL employs state-of-the-are beam-column element formulations through the FE analysis engine OpenSees (Mazzoni et. al 2006). In addition to static analysis, these elements allow for dynamic/cyclic earthquake-type simulations. Linear, bilinear hysteretic, and nonlinear fiber element formulations are available (Mazzoni et al. 2006), based on steel and concrete cyclic constitutive models. Using OpenSeesPL, such beam column modeling properties may be specified, and a display of the resulting moment-curvature relationship can be generated as shown in Figure 10.

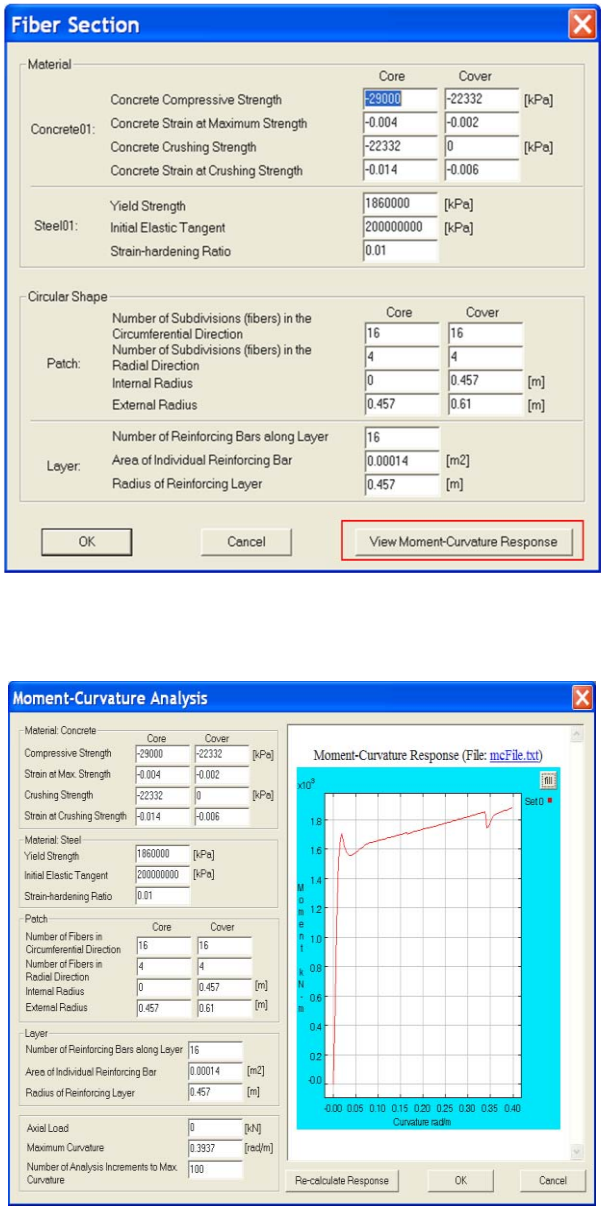

Figure 10. Fiber section and moment-curvature relationship.

8. VISCOUS DAMPING

For dynamic computations, viscous damping at the level of the entire model may be specified conveniently. A dedicated interface allows users to define damping ratios at two different frequencies, according to the Rayleigh mass-stiffness damping logic. Conversely, the mass and stiffness matrix viscous damping multipliers may be specified directly.

9. POST-PROCESSING

Upon specification of the model parameters, the interface accesses the FE OpenSees platform to conduct the computations. If needed, own weight is applied first (soil domain followed by super-structure), nonlinear material properties are activated, and the specified loading scenario is finally executed (static or dynamic/earthquake loading).

Upon completion of the computational phase, display of the results is initiated by OpenSeesPL. Structural response may be viewed as time histories and/or as spatial profiles at various levels of the applied static load. The deformed mesh may be also viewed (Figure 2), with capabilities for animation and display of conditions after application of own weight only, and after execution of the static/dynamic load computations. Contour quantities such as displacement, strain, stress, pore pressure, and stress-ratio (stress-state relative to failure condition) may be also viewed.

10. ILLUSTRATIVE SIMULATIONS

I. Elgamal and Lu (2009a) conducted a pilot study of lateral loading on a 3x3 pile group. A single-pile FE model was first calibrated in the linear range based on the 3D analytical solution of Abedzadeh and Pak (2004). Response of this linear pile in an idealized nonlinear undrained-clay material was then computed and compared to the linear solution. The corresponding 3x3 pile group response was also addressed, as a function of pile-spacing for the above linear and nonlinear soil cases (Figures 11 and 12).

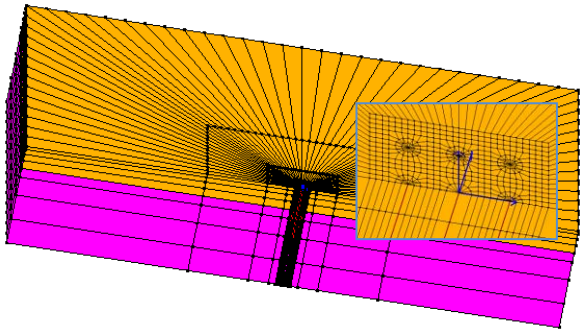

Figure 11. Pile group (3x3, 1/2 mesh due to symmetry).

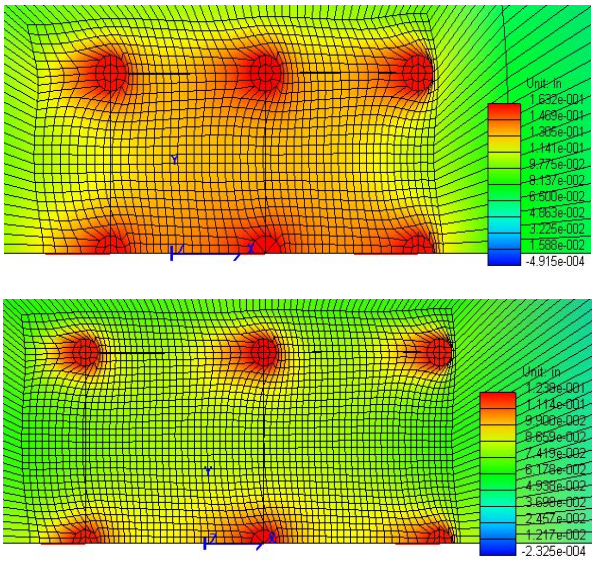

Figure 12. Plan view of displacement around piles for 5 (above) and 7 (below) pile-diameter spacing (1/2 mesh configuration, with red color denoting the large displacement zones).

II. In a remediated area of large spatial extent (Figure 13), the periodic boundary technique offers an effective approach for conducting 3D analyses (i.e., symmetry allows the investigation of a representative remediated "cell"). On this basis, Elgamal et al. (2009b) conducted a 3D FE ground modification parametric study, to evaluate mitigation of liquefaction-induced lateral soil deformation by the stone column and the pile pinning approaches. An effective-stress plasticity-based formulation was employed. Using OpenSeesPL, a half-mesh was studied due to symmetry (Figure 13). A 10 m depth mildly-inclined (4 degrees) saturated layer was analyzed, with the remediated zone diameter maintained at 0.6 m throughout. Liquefaction-induced lateral deformation and remediation procedures for mildly sloping sand and silt strata were investigated under the action of an applied earthquake excitation. The extent of deployed remediation (area replacement ratio) and effect of the installed stone column permeability were analyzed. Effect of lateral spreading on the pile response was also investigated.

III. Lateral response of large pile groups due to seismic excitation is often an important consideration for bridge foundation analysis. Lu et al. (2010) initiated a study to explore the response of such systems, by conducting a push-over analysis of a 32 pile-group bridge foundation (Figure 14). After application of own weight, the pile cap was subjected to lateral translation, with the overall lateral resistance approaching the tributary bridge vertical own weight force. Distribution of axial and lateral load among the piles was explored. Corner piles were observed to shoulder the highest loads, followed by the perimeter piles, with the internal piles carrying relatively little of the imposed overall forces.

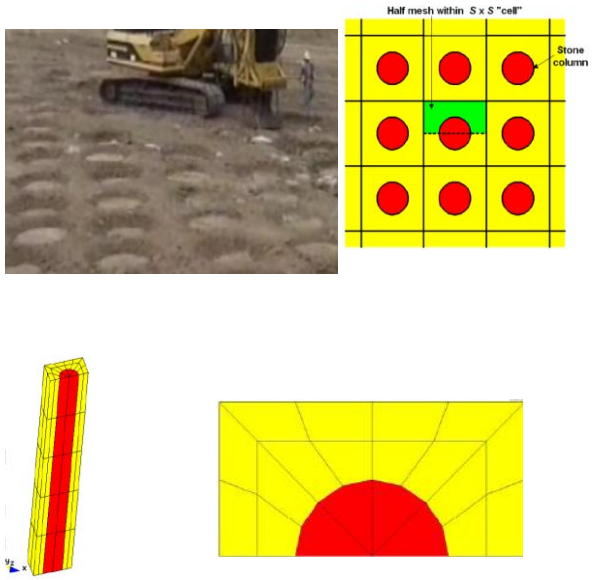

Figure 13. Ground modification study showing pattern of stone column construction and periodic boundary logic (above), and plan and side-views of FE mesh below (1/2 mesh due to symmetry).

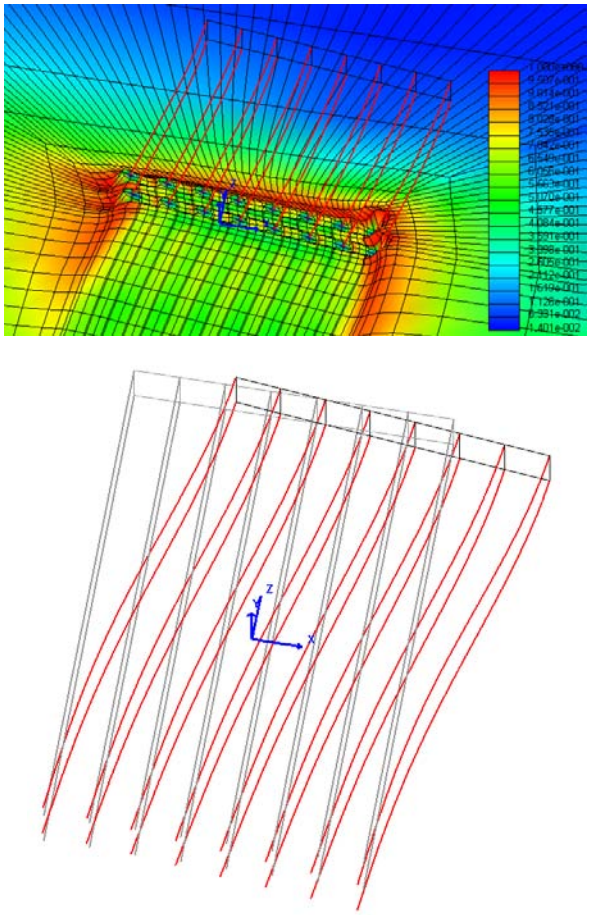

Figure 14. Longitudinal push-over of bridge 32-pile group (1/2 mesh configuration).

11. CONCLUSIONS

A robust and versatile framework for computational analysis of pile-ground systems was presented. The open-source platform OpenSees is employed throughout. For illustration, scenarios of lateral response of pile groups, as well as ground remediation against liquefaction-induced lateral spreading were discussed. The conducted investigations aim to highlight the analysis framework capabilities and range of potential applications.

Acknowledgements:

Funding for this research is provided by the Pacific Earthquake Engineering Research (PEER) Center under NSF Award Number EEC-9701568, the PEER Lifelines program, and the NSF grant No. OCI-0749227.

References:

Abedzadeh, F., and Pak, Y.S. 2004. "Continuum Mechanics of Lateral Soil–Pile Interaction." Journal of Engineering Mechanics, Vol. 130 (11): 1309-1318.

Elgamal, A., Yang, Z., Parra, E., and Ragheb, A. 2003. Modeling of cyclic mobility in saturated cohesionless soils. International Journal of Plasticity, 19(6), 883-905.

Elgamal, A., and Lu, J. 2009a. A Framework for 3D finite element analysis of lateral pile system response, Proceedings of the 2009 International Foundation Congress and Equipment Expo, Contemporary Topics in In Situ Testing, Analysis, and Reliability of Foundations, ASCE GSP 186, M. Iskander, D. F. Laefer, and M. H. Hussein, Editors, Orlando, Florida, March 15–19, pp. 616-623.

Elgamal, A., Jinchi Lu, J., and Forcellini, D. 2009b. Mitigation of liquefaction-induced lateral deformation in a sloping stratum: 3D numerical simulation, Journal of geotechnical and geoenvironmental engineering, ASCE, Vol. 135, No. 11, November, 1672-1682.

Lu J., 2006. Parallel finite element modeling of earthquake site response and liquefaction, *PhD Thesis*, Department of Structural Engineering, University of California, San Diego, La Jolla, CA.

Lu, J., Yang, Z., and Elgamal, A. 2006. Openseespl three-dimensional lateral pile-ground interaction version 1.00 user's manual, Report No. SSRP-06/03, Department of Structural Engineering, University of California, San Diego, La Jolla, CA.

Lu, J., Elgamal, A., Sikorsky, C., and Shantz, T. 2010. Computational modeling of a large pile group under lateral load, Proc. Intl. Conf. on Recent Advances in Geotechnical Earthquake Engineering and Soil Dynamics, May 24-29, San Diego, CA (to appear).

Mazzoni, S., McKenna, F., and Fenves, G. L. 2006. Open system for earthquake engineering simulation user manual, Pacific Earthquake Engineering Research Center, University of California, Berkeley (http://opensees.berkeley.edu/).

Yang, Z., Elgamal, A., and Parra, E. 2003. A computational model for cyclic mobility and associated shear deformation, Journal of Geotechnical and Geoenvironmental Engineering, 129 (12), 1119-1127.

JOINT CONFERENCE PROCEEDINGS
7th International Conference on Urban Earthquake Engineering (7CUEE) &
5th International Conference on Earthquake Engineering (5ICEE)
March 3-5, 2010, Tokyo Institute of Technology, Tokyo, Japan

RESPONSE CHARACTERISTICS AND FAILURE MECHANISMS OF PILE FOUNDATIONS IN LIQUEFIABLE SOIL

Sumanta Haldar[1)], and G.L. Sivakumar Babu[2)]

1) Assistant Professor, School of Infrastructure, IIT Bhubaneswar, India
2) Professor, Department of Civil Engineering, IISc Bangalore, India
sumanta @iitbbs.ac.in, gls@iisc.ernet.in

Abstract: The shear strength of a saturated loose cohesionless soil decreases due to increase of pore water pressure under seismic excitation and it behaves like a liquid. The failure mechanisms of pile in liquefied soil are predominantly due to bending failure because of lateral flow of soil, or because of lateral instability for slender piles. This paper examines the response of a single end bearing pile in a liquefied soil. The objective of the study is to identify the pile failure mechanisms for different types of soil, earthquake predominant frequency, pile diameters and pile materials as they alter the pile response in liquefiable soil. A parametric study on the pile failure mechanisms is performed for different relative densities of soil, earthquake intensities, earthquake predominant frequencies, pile diameters and pile strength properties. It is observed that the potential failure modes of piles are influenced by the above factors.

1. INTRODUCTION

The seismic response of pile foundation in a liquefiable soil is a complex phenomenon. Design of pile foundations under these circumstances involves difficulties in understanding the appropriate failure mechanisms. Analysis and design of pile foundations in liquefiable soil has drawn considerable attention in the recent years (e.g. Finn and Fujita 2002; Abdoun and Dobry 2002; Bhattacharya 2003; Boulanger and Tokimatsu 2005; Tazoh 2007). Several guidelines for pile design are developed, such as Japanese Code of Practice (JRA 1996), Eurocode 8: Part 5 (1998), NEHRP (2000), IS: 1893: Part 1 (2002) from time to time. Pile behaviour in liquefiable soil deals with understanding of pile-soil interaction, failure mechanisms and pile response. Different types of pile failure mechanisms such as bending failure, buckling instability, shear failure, settlement failure are observed in liquefied soil (e.g. Tokimatsu et al. 1996, JRA 1996, Bhattacharya 2003). Among the different failure modes, failure may happen predominantly due to bending because of lateral flow of soil, or due to lateral instability for slender piles (Bhattacharya 2003). Previous studies reveal that dynamic behaviour of soil may affects by the earthquake frequency content, peak acceleration and soil type (Kostadinov and Towhata 2002). Hence pile failure mechanisms in a liquefied soil not only dependent on pile dimension & pile material strength, but also dependent on earthquake intensity & earthquake predominant frequency.

This paper examines the effects of soil, pile and earthquake parameters on the response & failure mechanisms of pile in a liquefied soil. A single end bearing pile is considered for this study. Three different ranges of soil relative density values, five earthquake time history data with different predominant frequency values and, concrete and steel tube piles with two different pile diameters with fixed pile length are considered for the analysis. The original earthquake time-history data are scaled to 0.1g, 0.2g & 0.3g peak acceleration values. Two plausible failure mechanisms namely bending failure and lateral instability (or, buckling failure) of pile in liquefied soil are considered. The response of the pile is obtained using two-dimensional plain strain finite difference program (*FLAC*^{2D}, Itasca 2006). Initially the validation of the analysis procedure is conducted with reference to the centrifuge data pertaining to two layered soil reported in Wilson et al. (2000). A non-linear constitutive model (Byrne 1991) is utilized for the liquefied soil. The liquefaction behaviour of a single layer of soil and the pile response are studied and failure mechanisms are identified.

2. PILE FAILURE IN LIQUEFIABLE SOIL

Different types of failure mechanisms of pile foundations are observed in liquefied soil. Some of the failure mechanisms are: (i) bending failure: when the developed maximum bending moment in the pile section due to inertial and kinematic force exceeds the yielding moment capacity; (ii) lateral/buckling instability: when slender piles in liquefied soil loses its lateral support, it may unstable laterally due to presence of axial load and lateral inertial force; (iii) shear failure: when developed shear force due to high lateral inertial and kinematic force exceeds the shear capacity of pile section. In general, piles with low shear capacity, such as hollow concrete piles often fail in shear; (iv) settlement failure: when pile undergoes excessive settlement due to the soil liquefaction. Amongst different failure modes, two plausible failure mechanisms, namely bending and buckling

mechanisms are explained in the following sections.

2.1 Bending Mechanism

Lateral loads due to inertia of the superstructure and/or kinematic loads due to lateral spreading of the soil induce bending failure in the pile. Lateral flow of soil may possible at a particular depth due to flow liquefaction. Hence, the bending moment in the pile is developed due to the inertia and kinematic loads. At the end of the earthquake shaking, the lateral flow of soil continues till the pore pressure fully not dissipated. The bending moment is generated only due to kinematic flow. In terms of pile-soil interaction, the mechanism of failure assumes that soil pushes the pile.

2.2 Lateral / Buckling Instability

It considers the piles as laterally unsupported slender columns in liquefied zone and therefore prone to buckling instability. During earthquake-induced liquefaction, the soil surrounding the pile loses its effective stress and can no longer offer sufficient support to it. Stability of a pile foundation in liquefied soil can be estimated using the Euler's critical buckling load (P_{cr}) of the pile, which is defined by,

$$P_{cr} = \pi^2 E_P I_P / L_{eff}^2 \quad (1)$$

where L_{eff} is the effective length of the column (i.e. unsupported length of pile), which depends on the boundary conditions of the column ends. The critical buckling load (P_{cr}) of an axially loaded structure is defined as the minimum axial load at which the structure becomes unstable and the transverse deflection becomes indefinitely large. The value of critical buckling load for an axially loaded pile in liquefied soil can be computed as,

$$P_{cr} = \pi^2 E_P I_P / \{\alpha_l (h_L + L_h)\}^2 \quad (2)$$

where L_h is the length of pile in free air/water, h_L is the depth of liquefied soil, α_l is the effective length multiplier which is a function of the boundary condition of the pile at the top and bottom of the liquefiable layer. E.g. for fixed-free cantilever, α_l = 2. If δ_0 is the displacement of a cantilever column due to lateral loads alone, the final displacement (δ) gets amplified in the presence of axial load (P) by the following expression (Timoshenko and Gere 1961),

$$\delta/\delta_0 = 1/(1 - P/P_{cr}) \quad (3)$$

where δ/δ_0 is defined as buckling amplification factor. The amplification of lateral displacement of a pile is almost 1.5 times static lateral displacement due to the applied axial load P acting on the pile for $P/P_{cr} = 0.33$. This lateral displacement gives rise to the additional moment which eventually leads to plastic collapse.

3. NUMERICAL MODEL

Since, pile response and failure mechanisms depend on depth of liquefied soil layer, correct estimation of the depth of liquefiable layer is essential. The depth of liquefied soil not only influences the drag forces in the pile for bending calculations but also, determines the length of the unsupported pile leading to lateral instability. Hence, coupled analysis (Itasca 2006) incorporating pile-soil interaction is conducted to understand the behaviour of the piles under earthquake loading.

3.1 Constitutive Model

In loose sand pore pressure may build up considerably due to cyclic shear loading. Eventually effective stress approaches to zero. A built-in constitutive model proposed by Byrne (1991) is used for liquefaction analysis. The constitutive model uses a few soil parameters and is related to the SPT-N value of the soil. The model is given by,

$$\Delta\varepsilon_{vd}/\gamma = C_1 exp\left(-C_2(\varepsilon_{vd}/\gamma)\right) \quad (4)$$

where $\Delta\varepsilon_{vd}$ is the incremental volumetric strain, ε_{vd} is accumulated volumetric strain, γ is the cyclic shear strain amplitude and C_1, C_2 are constants. Where $C_2 = 0.4/C_1$ and C_1 can be represented with other parameters as follows,

$$C_1 = 8.7\left(N_{1(60)}\right)^{-1.25} \quad (5)$$

$N_{1(60)}$ is the normalized SPT-N value with respect to overburden pressure of 100 kPa and corrected to a ratio of 60%.

Variation in shear modulus and hysteretic damping with cyclic strain is represented by Hardin and Drnevich (1972) model. The $N_{1(60)}$ values are obtained from corrected N-values, using the relationship given by Kramer (2003),

$$(N_1)_{60} = N C_N E_m / 0.6 E_{ff} \quad (6)$$

where N is measured penetration resistance, C_N is overburden correction factor, E_m is actual hammer energy and E_{ff} is theoretical free-fall hammer energy. E_m can be considered as $0.72E_{ff}$. The value of C_N is given as,

$$C_N = \sqrt{1/\sigma'_{v0}} \quad (7)$$

where σ'_{v0} is vertical effective overburden pressure in tons/ft^2. The other soil parameters namely small strain shear modulus (G_{max}), bulk modulus (K) and the friction angle (ϕ) are established on the basis of correlation with $(N_1)_{60}$.

The soil medium is discretised into a number of 4-noded quadrilateral finite difference grids. The dynamic loading is applied as a horizontal acceleration history at the model base. Wave reflections at model boundaries are minimized by specifying free-field boundary conditions at the two sides. The pile is modeled using linearly elastic beam elements with interface properties (termed as pile element). Each element has three-degrees-of freedom (two displacements and one rotation) at each node. The analysis of pile is basically a 3-D problem. In the present case, plain strain analysis is conducted. For the pile element elastic modulus, soil-pile stiffness of the interface springs and pile perimeter are given.

4. VALIDATION OF NUMERICAL MODEL

The finite difference model is validated using centrifuge test data reported in Wilson et al. (2000) to observe soil and pile responses in liquefied sand. Wilson et al. (2000) used a two horizontal layered soil profile using saturated, fine and uniformly graded Nevada sand prepared for the centrifuge test. At prototype scale the lower layer was of 11.4 m thick with 80% relative density (D_r) and the upper layer was 9.1 m thick with 55% relative density. A steel pipe pile with outer diameter 0.67 m and 0.019 m wall thickness was considered to simulate the structural model. The pile was extended up to 3.8 m above the ground surface with a superstructure load of 480 kN. The pile was embedded up to 15 m below ground surface. The fundamental period of the pile was about 1sec at small strain levels. The properties of Nevada sand are presented in Table 1. The shear modulus of the soil deposit was computed using the following equation given by Popescu and Prevost (1993),

$$G = G_{max}\left(\frac{1+2K_0}{3}\sigma'_{v0}/p_0\right) \quad (8)$$

where K_0 is the coefficient of lateral earth pressure at rest, p_0 is the reference normal stress (100 kPa). The 1995 Kobe earthquake time history data with scaling of peak acceleration value to 0.22g was used for the centrifuge test.

The centrifuge model test is simulated using finite difference program to validate the constitutive model used for the analysis. The soil medium is divided into two soil layers with the same depth and properties as adopted in the centrifuge test (Table 1). The lateral dimension is adopted as 40 m for the analysis. Total soil medium is discretised into 750 finite difference grids in 30 rows and 25 columns. The pile is divided into 20 equal segments. Figure 1 illustrates the schematic diagram of the finite difference model.

Table 1 Properties of Nevada sand (Popescu and Prevost 1993).

Properties	Naveda Sand	
	D_r = 55%	D_r = 80%
Density (kg/m^3)	2670	2670
Porosity	0.406	0.373
G_{max} (kPa)	28×10^3	41.46×10^3
p_0 (kPa)	100	100
Friction angle, ϕ (°)	34.15	39.5
Permeability, k (m/s)	6.05×10^{-5}	3.7×10^{-5}
K_0	0.5	0.5
G (kPa)	4.19×10^4	3.02×10^4

The parameters for the dynamic analysis are shear modulus, bulk modulus, normalised SPT-N value $N_{1(60)}$, friction angle of soul and permeability of the soil, bulk modulus of water. The value of $N_{1(60)}$ is quantified using the relationship given by Itasca (2006),

$$(N_1)_{60} = (D_r/15)^2 \quad (9)$$

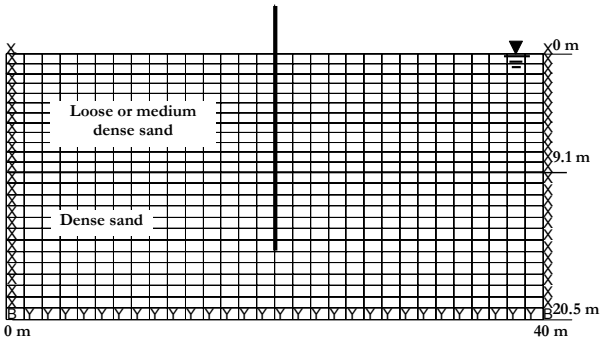

Figure 1 Schematic diagram of finite difference model.

Pile and soil parameters are given in Table 2. The input horizontal acceleration is applied at the base of the model as a uniform acceleration boundary condition. A linear baseline correction is adopted for the acceleration time history.

Table 2 Soil and pile properties for the validation of numerical model.

Properties	D_r = 55%	D_r = 80%
Poisson's ratio	0.45	0.45
Bulk modulus	4.05×10^5	2.92×10^5
$(N_1)_{60}$	13	28
Bulk modulus of water (kPa)	3.74×10^6	2.47×10^6
Pile elasticity modulus (kPa)	2×10^9	2×10^9
Moment of inertia of pile (m^4)	2.06×10^{-3}	2.06×10^{-3}

4.1 Comparison of Results

Numerical analysis results are compared with available results from the centrifuge test. Comparison of pore water pressure & acceleration time history at different depth of soil, pile head displacement and bending moment in pile are observed. Typical results of comparison are shown in Figure 2. It is observed that the results from 2-dimensional plain strain finite difference model and centrifuge test results match reasonably well. Hence, the above finite difference model is used in obtaining the response of a pile in liquefied soil for the following parametric study.

5. PARAMETRIC STUDY

A schematic diagram of a numerical model is presented in Figure 3. A parametric study is conducted considering various soil, pile and earthquake parameters.

5.1 Soil Parameters

Three different soil relative densities, namely, 40%, 55% and 80% are considered, which represent loose, medium and dense sand deposits respectively. The soil parameters used for the analysis are given in Table 3. A 20m soil depth and 2670 kg/m^3 soil density are considered. A 40 m Lateral dimension of soil media is adopted. The entire soil medium is discretised into 600 finite difference grids in 30 rows and 20 columns. The water table is considered to be present at the ground level.

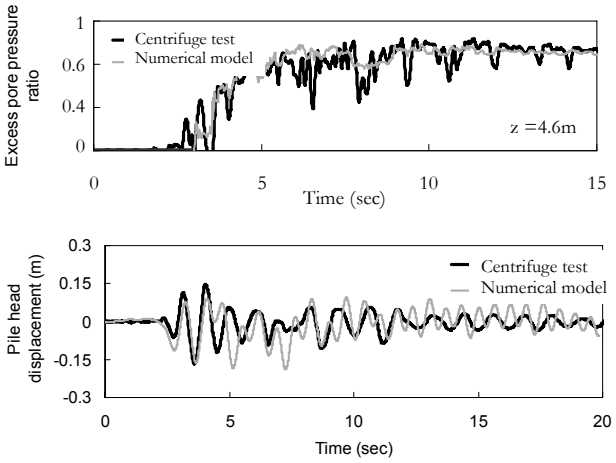

Figure 2 Comparison of time history of pore water pressure ratio at the 4.6 m depth from soil surface and comparison of time history of pile head displacement.

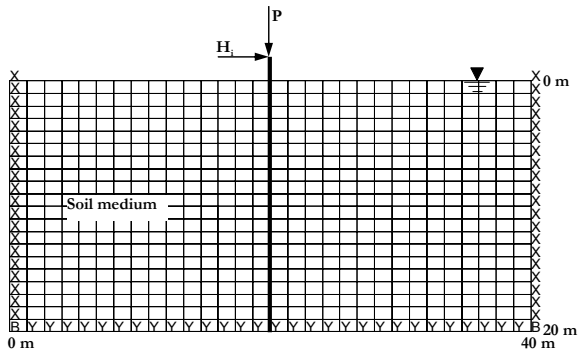

Figure 3 Schematic diagram of the numerical model used for the parametric study.

5.2 Pile Parameters

A 21m length single pile is considered. The pile is embedded in the ground by 20 m and 1 m above the soil surface. The embedded length of pile and the soil depth are considered same to simulate an end bearing pile. The pile is discretised into 21 equal segments. Two different pile materials, concrete and steel piles and two different pile diameters, 0.6 m and 1.0 m are considered for analysis. Different pile parameters are given in Table 4. A vertical load of 1000 kN is applied on the pile head. A pseudo-static lateral inertial load of 10% of the axial load (i.e. 100 kN), (which is typically valid for bridges) is also applied at the pile head. A rotational restraint is applied at the pile head so that it cannot rotate but can laterally deflect. It is assumed that, when the liquefaction starts the resistance offered at the pile head minimizes due to severe displacement, and hence the pile acts as a fixed-free cantilever. Hence, at the onset of liquefaction, a free head boundary condition is imposed.

Table 3 Soil properties for the parametric analysis.

Properties	D_r (%)		
	40	55	80
Soil Depth (m)	20	20	20
Poisson's ratio	0.45	0.45	0.45
σ'_{v0} (kPa)	167	167	167
p_0 (kPa)	100	100	100
K_0	0.5	0.5	0.5
Shear modulus (kPa)	2.7×10^4	3.02×10^4	4.47×10^4
Bulk modulus (kPa)	2.16×10^5	2.92×10^5	4.32×10^5
$(N_1)_{60}$	7.2	14	30
Porosity	0.424	0.406	0.373
Permeability (m/s)	6.6×10^{-5}	6.05×10^{-5}	3.7×10^{-5}
ϕ	33	34.2	39.5
Bulk modulus of water (kPa)	2.51×10^6	2.7×10^6	3.67×10^6

Table 4 Pile properties for the parametric analysis.

Properties	Concrete pile		0.016m thick steel pipe pile	
	Pile diameter D_P (m)		Pile diameter D_P (m)	
	0.6	1.0	0.6	1.0
Pile length below ground (m)	20	20	20	20
Pile length above ground (m)	1.0	1.0	1.0	1.0
Density (kg/m^3)	2500	2500	7800	7800
Flexural strength (kPa)	1.12×10^4	1.12×10^4	5×10^5	5×10^5
Yield moment of pile (kNm)	237	1099	2087	5987
Moment of inertia (m^4)	0.006	0.049	0.0013	0.006
Pile cross-sectional area	0.283	0.785	0.029	0.049

5.3 Earthquake Parameters

Five different earthquake time history data with different predominant frequencies are considered for the analysis. Each earthquake time acceleration data is scaled to 0.1g, 0.2g and 0.3g peak acceleration values. Table 5 presents the details of earthquake records. Linear base line corrected scaled earthquake data are used for all combinations of soil and pile parameters. The depth of liquefiable soil, maximum shear strain level, pile lateral displacement and maximum bending moment are obtained from the analysis. Based on the analysis results, the potential failure modes of the pile foundation are identified.

Table 5 Earthquake date for the parametric analysis.

Earthquake record	Predominant frequency (Hz)
Loma Prieta (USA) earthquake of October 18, 1989; Emeryville recording station	0.85
El-Centro (1940)	2.00
Friuli (Italy) earthquake of May 6, 1976; Unknown recording station	3.85
Kocaeli (Turkey) earthquake of August 17, 1999; Sakaria recording station	6.25
Parkfield earthquake June 28, 1966, CHOLAME #5, DWN (CDMG station 1014)	12.5

6. RESULTS AND DISCUSSION

Soil and pile response are obtained for all soil, pile & earthquake properties from numerical analysis.

6.1 Effects on Maximum Shear Strain in Soil

When a liquefiable soil layer subjects to an earthquake loading, the soil layer experiences a high value of shear strain and that leads to soil liquefaction (Kramer 1993). The shear strain values are obtained at different soil depths from the analysis. The maximum shear strains values for different soil relative densities (D_r) and peak acceleration values (a_{max}) with respect to earthquake predominant frequencies are presented in Figure 4. It can be noted that the maximum shear strain values in the liquefied layer are significantly influenced by the soil relative densities or $(N_1)_{60}$ and a_{max} values. Figure 4 shows that the maximum shear strain decreases with the increase in soil relative density.

The effect of peak acceleration is also evident from the above figures. It is observed that the increase in the a_{max} increases the maximum shear strain in the soil. The figures also indicate that the maximum shear strain is significant at the different earthquake predominant frequency values. The maximum shear strain value decreases when the predominant earthquake frequency value increases for a given a_{max} value. The explanation of the above phenomena can be described with respect to the fundamental frequency of the non-liquefied and liquefied soil. Fundamental frequencies of the non-liquefied (without water table) soil are obtained 2.5Hz, 3Hz and 3.8Hz for D_r = 40%, 55% and 80%, respectively. After the liquefaction, the fundamental frequencies reduced to 0.67 Hz, 0.68 Hz and 0.71 Hz; which is close to the low predominant frequency of the earthquake and that yields high shear strain values in the soil.

6.2 Effects on Depth of Liquefied Soil Layer

Due to seismic excitation, pore water pressure develops at different soil depths. Excess-pore water pressure ratios (EPWPR) at different times of excitation at different depths of soil are obtained. The soil is said to be completely liquefied when EPWPR reaches 1.0. The depth of liquefied soil layer (h_L) is obtained where EPWPR is greater than or equal to 1.0 over the entire soil layer. Figure 5 shows a typical plot of depth of liquefied layer observed for different soil and earthquake parameters. It can be noted that the depth of liquefied layer decreases with the increase in D_r and decrease in the a_{max} values. The h_L value decreases with the increase in earthquake predominant frequency values. At low earthquake predominant frequency value the value of increases as the fundamental frequency of the liquefied soil significantly reduces.

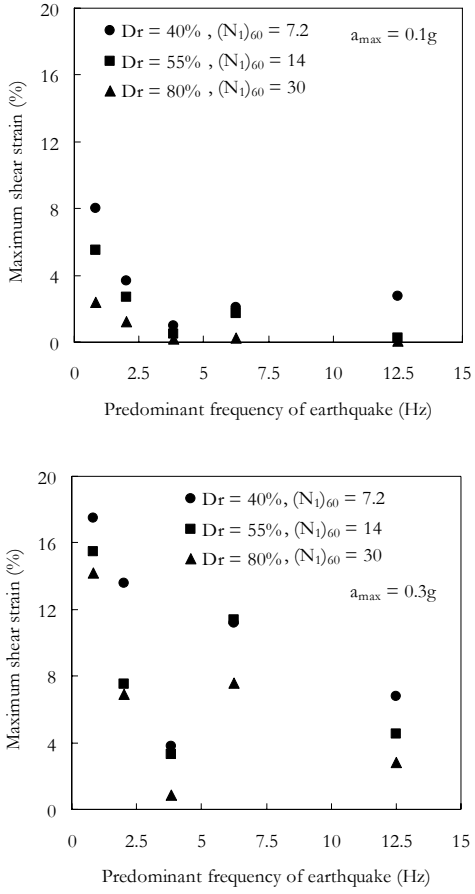

Figure 4 Effect on maximum shear strain for different predominant frequencies of earthquake.

6.3 Pile Failure Modes

Based on the results from the previous sections, it can be noted that the pile response is also significantly influenced by the soil relative density and earthquake characteristics. The bending moment developed in the pile section is observed over the pile length and the value of maximum bending moment over the pile length is considered at different times of excitation. The maximum bending moment and lateral displacement value are observed before starting the liquefaction and after the complete liquefaction. It can be stated that the pile is said to have failed due to bending if the maximum bending moment value in the pile exceeds the yield moment value of the pile

section. The other failure mechanism as mentioned in the earlier section is due to the buckling instability of pile. It can be noted that the buckling mechanism is directly related to the depth of liquefied soil layer. Theoretically, a pile is prone to buckle when the value of vertical load from the superstructure exceeds the value of critical buckling load (P_{cr}) from equation (1). A pile becomes laterally unstable when the vertical applied load value is much less than the critical buckling load of the pile section. It is observed that the pile starts to deflect abruptly when critical buckling load is almost 3 times the applied load i.e. at $P/P_{cr} = 0.33$. Hence, the pile is considered to be susceptible to buckle, when the P/P_{cr} value exceeds 0.33. Bending failure of pile occurs when the ratio of developed maximum bending moment value (M_{max}) and yield moment value of the pile section (M_y), i.e. M_{max}/M_y value exceeds 1.0.

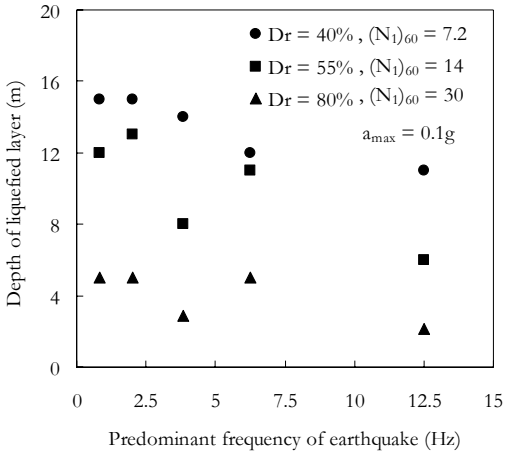

Figure 5 Effect on depth of liquefied soil layer for different predominant frequency of earthquake at a_{max} = 0.1g.

The M_{max}/M_y and P/P_{cr} values are computed for different soil, earthquake and pile data. The state can be divided into four zones depending on the limiting values of M_{max}/M_y and P/P_{cr}. It can be stated that if P/P_{cr} < 0.33 and M_{max}/M_y < 1.0, the pile is safe against bending and buckling. When $P/P_{cr} \geq 0.33$, but M_{max}/M_y < 1.0, pile fails due to buckling instability. If P/P_{cr} < 0.33 and $M_{max}/M_y \geq 1.0$, the pile fails in bending. When $P/P_{cr} \geq$ 0.33 and $M_{max}/M_y \geq 1.0$, the combined failure mode can be represented as bending-buckling interaction, and at this stage identification of the governing failure mode is difficult. In general, the pile acts as a cantilever column in liquefied soil and when P/P_{cr} exceeds 0.33, the application of a lateral inertial load made the pile more laterally unstable, whereby an additional moment is added due to the lateral displacement of pile. Hence, bending moment in the pile increases just after the liquefaction and when the developed moment in the pile section exceeds the yield moment capacity, the pile fails. If at this stage the maximum bending moment does not exceed the yield moment capacity, the pile fails due to excessive lateral displacement or buckling instability. This failure mechanism is experienced in the case of the bending-buckling interaction region.

The effects of soil, earthquake and pile parameters on failure modes are presented in Figure 6. Fig. 6(a) and 6(b) present the possible failure modes due to different D_r and a_{max} values for concrete and steel piles. Fig. 6(a) shows that soil with low D_r (e.g. 40%) and low a_{max} values (e.g. 0.1g), the concrete pile is susceptible to buckling instability. At high a_{max} value, with low D_r value, a bending-buckling interaction failure mode is identified for the concrete pile. Fig. 6(b) shows that the steel pile is susceptible to buckling failure at low D_r and high a_{max} values. The yielding moment capacity of a steel pile is greater than a concrete pile section with the same diameter and hence a steel piles performance is good against bending. However, because of the large depth of liquefied layer at high a_{max} values, the steel pile becomes laterally unstable. At the low a_{max} and high D_r value, the piles are safe against bending and buckling.

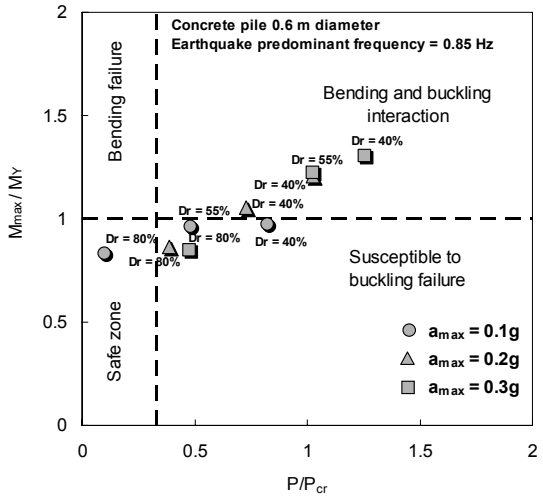

Figure 6(a) Pile failure modes for different earthquake peak acceleration values for 0.6 m diameter concrete pile.

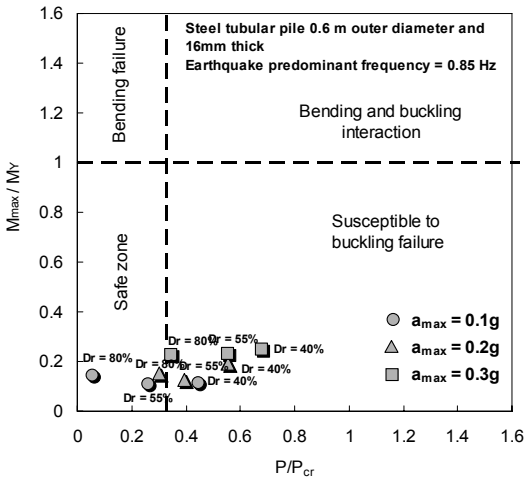

Figure 6(b) Pile failure modes for different earthquake peak acceleration values for 0.6 m outer diameter 0.016 m thick steel pile.

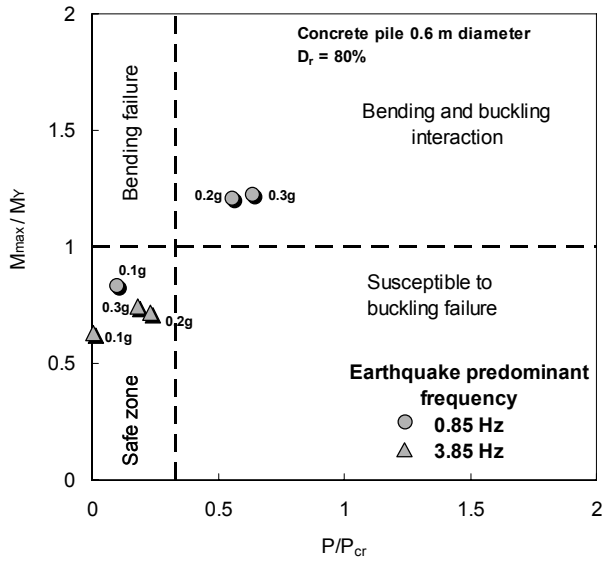

Figure 6(c) Pile failure modes for different earthquake predominant frequencies for 0.6 m diameter concrete pile.

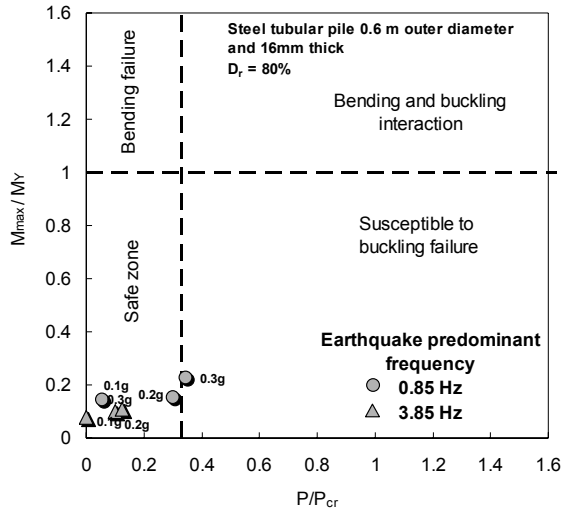

Figure 6(d) Pile failure modes for different earthquake predominant frequencies for 0.6 m outer diameter 0.016 m thick steel pile.

Fig. 6(c) and 6(d) present the effects on pile failure modes due to different earthquake predominant frequency for 0.6m diameter concrete and steel piles. Fig. 6(c) shows concrete pile failure modes at two different predominant frequencies (0.85 Hz and 3.85 Hz) and a_{max} = 0.1g, 0.2g and 0.3g for D_r = 80%. It is observed that a concrete pile is susceptible to bending-buckling interaction at low earthquake predominant frequency value due to the large depth of liquefied soil layer. At high predominant frequency and low a_{max} values, the depth of liquefied layer is less and hence the concrete pile is safe against bending and buckling. A steel pile of 0.6 m diameter with 0.016 m wall thickness is prone to be laterally unstable at low earthquake predominant frequency (0.85 Hz) and at high a_{max} value (i.e. 0.3g) as shown in Fig. 6(d). The concrete and steel piles are observed to be safe in bending and buckling at high earthquake predominant frequency values.

The effect of pile diameter on concrete and steel pile failure modes is also evident from Figs. 6(e) and 6(f). Two different pile diameters namely 0.6m and 1m are considered. It is observed from Fig. 6(e) that a concrete pile with lower diameter (e.g. 0.6 m) is generally subjected to bending-buckling interaction at high a_{max} values (e.g. 0.2g, 0.3g). A higher diameter concrete pile (e.g. 1.0 m) is observed to be safe against bending and buckling even at higher a_{max} values (e.g. 0.2g and 0.3g). Fig. 6(f) shows that a steel pile is prone to buckle at a lower pile diameter and high a_{max} values, whereas the steel piles with large diameter are safe against bending and buckling.

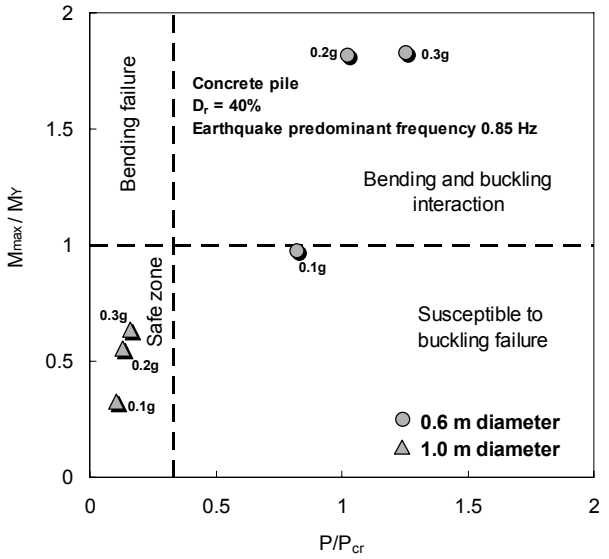

Figure 6(e) Pile failure modes for different concrete pile diameters.

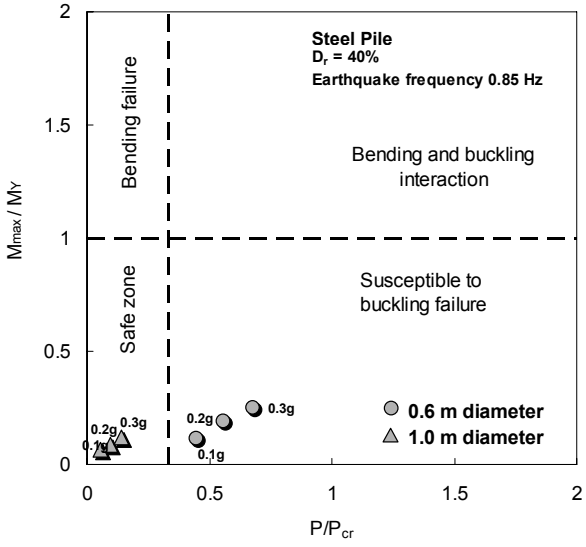

Figure 6(f) Pile failure modes for different steel pile diameters.

7. CONCLUSIONS

The effects of soil relative density, earthquake predominant frequency, earthquake intensity, pile material and pile diameter on the pile response in liquefiable soil are examined. It is observed that the failure modes of pile significantly depend on the depth of the liquefied soil layer. However it may vary due to different soil relative density, earthquake predominant frequencies and peak acceleration values. Pile material and pile diameter also influence pile failure mechanisms significantly. Therefore potential failure mechanisms of a pile need to be identified considering the soil, pile and earthquake parameters for seismic pile design in liquefied soil.

References:

Abdoun, T., Dobry, R. (2002). "Evaluation of pile foundation response to lateral spreading." *Soil Dynamics and Earthquake Engineering*, 22, 1051-1058.

Bhattacharya, S. (2003). Pile instability during earthquake liquefaction. Ph.D. Thesis, University of Cambridge, U.K.

Boulanger, R.W., and Tokimatsu, K. (2005). Editors of the *Proceedings of the workshop on Simulation and Seismic Performance of Pile Foundations in Liquefied and Laterally Spreading Ground, ASCE* Geotechnical Special Publication No. 145.

Byrne, P. (1991). "A cyclic shear-volume coupling and pore-pressure model for sand." In *Proceedings of Second International Conference on Recent Advances in Geotechnical Earthquake Engineering and Soil Dynamics* (St. Louis, Missouri, March), Paper No. 1. 24, 47-55.

Eurocode 8 (1998). Design provisions for earthquake resistance of structures. Part 5: Foundations, retaining structures and geotechnical aspects. Brussels: European Committee for Standardization.

Finn, W.D.L., and Fujita, N. (2002). "Piles in liquefiable soils: seismic analysis and design issues." *Soil Dynamics and Earthquake Engineering*, 22, 731-742.

Hardin, B.O., and Drnevich, V.P. (1972). "Shear modulus and damping in soils: Design equations and curves." *Journal of Soil Mechanics and Foundation Engineering Division, ASCE*, 98 (7), 667-692.

IS 1893: part 1. (2002). Criteria for earthquake resistant design of structures: General provisions and structures. 5th Revision, Bureau of Indian Standards.

Itasca Consulting Group Inc. (2006). FLAC, Fast Lagrangian analysis of continua. User's manual, version 5.0. Minneapolis, USA.

JRA (1996) Specification for Highway Bridges. Part V, Seismic Design. Japanese Road Association.

Kostadinov, M.V. and Towhata, I. (2002). "Assessment of liquefaction-inducing peak ground velocity and frequency of horizontal ground shaking at onset of phenomenon." *Soil Dynamics and Earthquake Engineering*, 22, 309-322.

Kramer, S.L. (2003). Geotechnical Earthquake Engineering. Pearson Education, Inc.

NEHRP. (2000). Commentary (Federal FEMA 369 USA) on seismic regulations for new buildings and other structures, National Earthquake Hazards Reduction Program.

Popescu, R., and Prevost, J.H. (1993). "Centrifuge validation of a numerical model for dynamic soil liquefaction." *Soil Dynamics and Earthquake Engineering*, 12, 73-90.

Tazoh, T. (2007). "Earthquake engineering research on pile foundations with emphasis on pile foundations subjected to large ground deformations." Chapter 6 on Design of Foundations in seismic areas: Principles and Application (Bhattacharya Ed), NICEE Publication, 2007.

Timoshenko, S.P and Gere, J.M. (1961). Theory of elastic stability, McGraw-Hill Book Company, New York.

Tokimatsu, K., Mizuno, H., and Kakurai, M. (1996). "Building damage associated with geotechnical problems." *Soils and Foundations*, special issue (Jan), 219–234.

Wilson, D.W., Boulanger, R.W., and Kutter, B.L. (2000). "Observed seismic lateral resistance of liquefying sand." *Journal of Geotechnical and Geoenvironmental Engineering, ASCE*, 126 (10), 898-906.

JOINT CONFERENCE PROCEEDINGS
7th International Conference on Urban Earthquake Engineering (7CUEE) &
5th International Conference on Earthquake Engineering (5ICEE)
March 3-5, 2010, Tokyo Institute of Technology, Tokyo, Japan

EFFECTS OF SPATIAL VARIATION OF LATERALLY SPREADING GROUND ON STRESS DISTRIBUTIONS WITHIN PILE GROUPS

Hiroko Suzuki[1)] and Kohji Tokimatsu[2)]

1) Assistant Professor, Dept. of Architecture and Building Engineering, Tokyo Institute of Technology, Japan
2) Professor, Dept. of Architecture and Building Engineering, Tokyo Institute of Technology, Japan
hsuzuki@arch.titech.ac.jp, kohji@o.cc.titech.ac.jp

Abstract: To investigate stress distributions within pile groups during liquefaction-induced laterally spreading, physical model tests were conducted using a large shaking table at E-Defense and a centrifuge shaker at UC Davis. In test models, 2x3 or 2x2 pile groups were constructed near quay walls in liquefiable sand deposits in containers. Both the E-Defense and centrifuge tests were conducted with the ground motion recorded in the 1995 Kobe earthquake as input motions. Extensive soil liquefaction occurred in a few seconds after the start of shaking, causing seaward displacement of the quay wall, ground and piles. The ground displacement increased with decreasing the distance to the quay walls. Damage to piles was significant on the landside of the pile group in the E-Defense test but on the seaside in the centrifuge test. Since the pile displacement was larger than the ground displacement in the E-Defense test but smaller than the ground displacement in the centrifuge test, spatial variation of ground displacement created large relative displacement of piles with the ground of the landside in the E-Defense test but of the seaside in the centrifuge test. This made the landside soil of the pie group stiff in the E-Defense test but the seaside soil stiff in the centrifuge test due to dilatancy of soil subjected to a large shear strain.

1. INTRODUCTION

Recent earthquakes have demonstrated that lateral spread induced by soil liquefaction could have a significant effect on damage to pile foundations (BTL, 1998). It was also observed that failure and deformation modes of piles were different within a building located near the waterfront, probably due to spatial variation of lateral spreading (e.g. Oh-oka et al. 1996). To estimate influential factors affecting failure and deformation modes of piles during lateral ground spreading, many studies have been made through physical model tests (e.g., Abdoun et al. 2003, Boulanger et al. 2003).

To investigate failure and deformation mode of piles during liquefaction-induced lateral spreading, a physical test on a soil-pile-structure model was conducted (MEXT and NIED 2006, Sato and Tabata 2009) using E-Defense at the National Research Institute for Earth Science and Disaster Prevention (NIED). E-Defense was one of the largest shaking table facilities in the world and could simulate nearly full-scale phenomena during earthquakes; however, the number of tests to be performed at E-Defense facilities with a brief period was limited because of costs and labors involved. To compensate this deficit, centrifuge shaking table tests were conducted using NEES facilities at UC Davis (Suzuki et al. 2009).

The objective of this study is to investigate factors influencing stress distribution within pile groups during liquefaction-induced lateral spreading based on shaking table tests conducted using E-Defense facilities as well as UC Davis centrifuge facilities.

2. LIQUEFACTION-INDUCED LATERAL SPREADING TEST

Figs. 1 and 2 show test models used for liquefaction-induced lateral spreading tests. A model for the E-Defense test had a 2x3 pile group (Fig. 1) and that for the centrifuge test had two 2x2 pile groups (Fig. 2). Pile groups in both test models were placed in saturated sand deposits near quay walls facing waterfront.

The E-Defense test model was constructed in a rigid rectangular box, with a height of 5 m, a length of 16 m and a width of 4 m (Fig. 1). Albany sand (D_{50}=0.310 mm, U_c=2.02), imported from Australia, was used for preparing a sand deposit. After setting a pile group in the rigid box, the sand was air-pluviated and compacted to designated densities. The relative density was 70 % for an underlying dense sand layer with a thickness of 0.75 m and 60 % for an overlying sand layer. A quay wall penetrated the sand deposit. The sand deposit behind the quay wall had a thickness of 4.5 m, while that in front of the quay wall had a thickness of 3.2 m. The model ground was infiltrated and

then saturated under vacuum by water. The groundwater table was 0.5 m below the landside ground surface.

A 3x2 steel pile group was placed behind the quay wall. Each pile had a diameter of 152.4 mm and a wall thickness of 2.0 mm. The tips of the piles were jointed to the rigid box base with pins and their heads were fixed to a foundation of a weight of 10 tons with a superstructure of 12 tons supported by four steel columns.

Many strain gauges, accelerometers, earth pressure transducers, pore water pressure transducers, displacement transducers and load cells, about 900 sensors in total, were placed in the sand deposit as well as on the pile-structure system and the quay wall. In addition, inclinometers were placed at points A, B and C indicated in Fig. 1(a) for measuring ground displacement distributions with depth. Further detail of instruments and sensor layout is described elsewhere (MEXT and NIED 2006).

The centrifuge test model was constructed in a flexible beam container (Fig. 2). The dimensions of the container were 1.6 m in length, 0.8 m in width and 0.6 m in height. The test was performed at a centrifugal acceleration of 30 g. So, the test model was on a scale of 1:30 in length. Values in parentheses in Fig. 2 stand for length in the prototype scale. The soil profile in the centrifuge model consisted of three layers including a top gravel layer 100 mm thick, a liquefiable loose fine sand layer 300 mm thick and a bottom coarse sand layer 150 mm thick. Silica #2 gravel (D_{50}=3.22 mm, U_c=1.43) was used for the top layer, Albany sand for the liquefiable fine sand layer and Silica #4 coarse sand (D_{50}=1.42 mm, U_c=1.45) for the non-liquefiable bottom layer. After constructing pile models in the flexible container base, the coarse and fine sands were in turn air-pluviated to form a bottom layer and a liquefiable layer. The model ground was infiltrated and then saturated under vacuum by methylcellulose with a viscosity of about ten times that of water (Stewart et al., 1998). After saturation, gravel was further placed on the loose saturated sand to form the top layer. The groundwater table was set 100 mm below the final ground surface. The quay wall penetrated into the bottom dense sand layer.

Two 2x2 pile groups were placed in the model. One of the two had aluminum pipes with a diameter of 16 mm and a wall thickness of 1 mm and the other had stainless steel pipes with a diameter of 15.9 mm and a wall thickness of 0.3 mm. The aluminum and stainless steel pipes had the same stiffness but difference strength. All the pile tips were fixed to the container base and the pile heads were fixed to a pile cap. In this paper, results of the aluminum pile group are described.

In the test, strain of piles, pore water pressures, and accelerations and displacements of ground and footing were observed. The observed values in the test are, hereafter, presented in the prototype scale corresponding to the centrifugal acceleration of 30 g.

In the two tests, a ground motion recorded at Takatori in the 1995 Kobe earthquake was used as an input motion (Fig. 3). The NS and UD components were applied to the longer direction of the rigid box and the vertical direction, respectively in the E-Defense test. The maximum accelerations were adjusted to 6.0 m/s^2 in the horizontal direction and to 2.0 m/s^2 in the vertical direction. In the centrifuge test, only the horizontal NS component was used as an input motion with a maximum acceleration of about 0.4 g in the prototype scale. To investigate variation of pile stresses within pile groups, piles located close to the quay wall or far from the quay wall are, hereafter, called the seaside piles or the landside piles, respectively.

3. RESIDUAL DEFORMATION OF PILES

During the shaking event in both the tests, the quay wall moved seaward, inducing seaward movements and settlements of the ground behind. This caused seaward displacement of the pile-structures. In the E-Defense test, residual deformation of the pile heads was 1.3 m with inclinations of the superstructure and footing up to 14 degrees. In the case of the centrifuge test, the residual displacement of the pile heads was about 0.8 m.

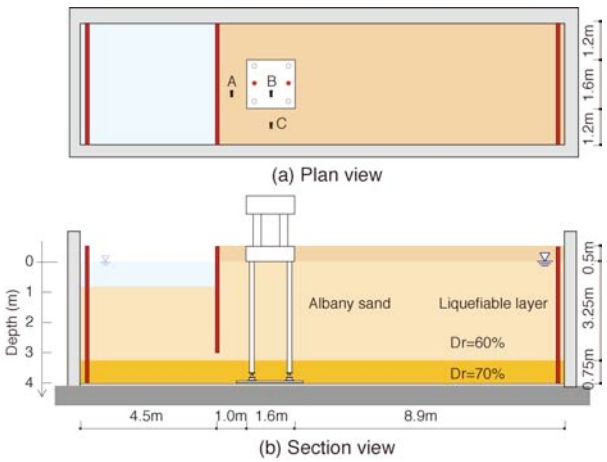

Figure 1 E-Defense test model

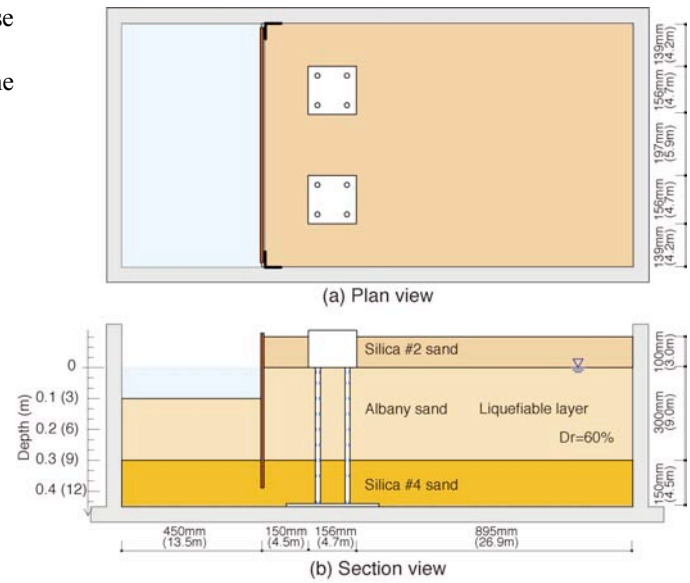

Figure 2 Centrifuge test model

Figs. 4 and 5 show time histories of accelerations of shaking table, footing and superstructure, displacements of ground surface and footing, bending strains of piles and pore water pressures observed in the seaside and landside of the pile groups for the E-Defense and centrifuge tests. The positive values in the figures stand for the landward displacement or acceleration and clockwise moment, while the negative values stand for the opposites. The footing displacement and bending strain in the E-Defense test are ranged out at 5-10 s after the start of shaking in Fig. 4(a)(g).

The pore water pressure rises up to the initial effective stress at about 3 s after the start of shaking in both the tests, leading to liquefaction of the soil (Figs. 4 and 5(e)(f)). The pore water pressure after reaching the initial effective stress changes with cyclic loading. This trend in pore water pressure is more significant in the landside soil of the pile group in the E-Defense test (Fig. 4(f)) but in the seaside soil of the pile group in the centrifuge test (Fig. 5(e)). The displacements of the footing and ground surface increase with time (Figs. 4 and 5(a)(b)). The bending strain also increases with increasing ground displacement (Figs. 4 and 5(g)(h)). In the case of the E-Defense test, the bending strain at a depth of 0.1 m is larger of the seaside pile than of the landside pile but that at a depth of 1.5 m is larger of the landside pile than of the seaside pile (Fig. 4(g)(h)). In the case of the centrifuge test, the bending strains at both depths of 0.15 and 9.0 m are larger of the seaside pile than of the landside pile (Fig. 5(g)(h)).

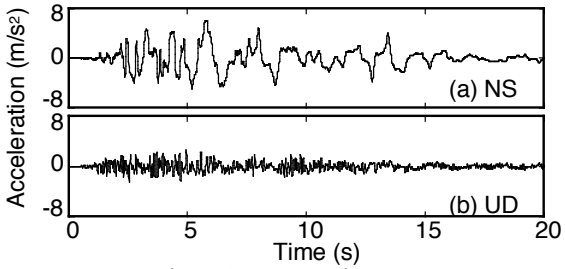

Figure 3 Input motion

4. FACTORS INFLUENCING DEFORMATION MODES OF PILES

4.1 Variation in bending strains of piles in E-Defense test

To investigate factors influencing pile deformation,

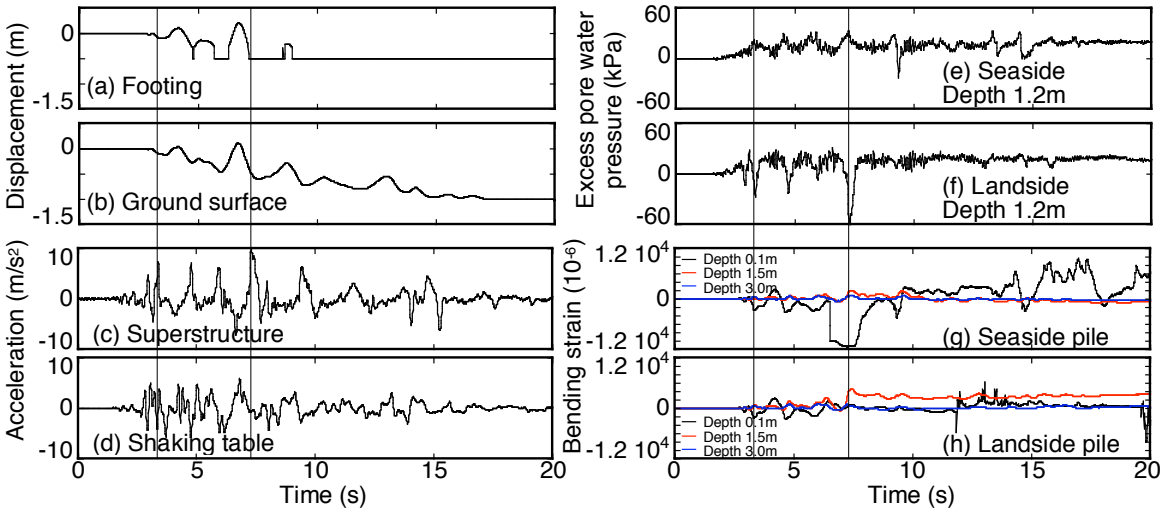

Figure 4 Time histories of major values in E-Defense test

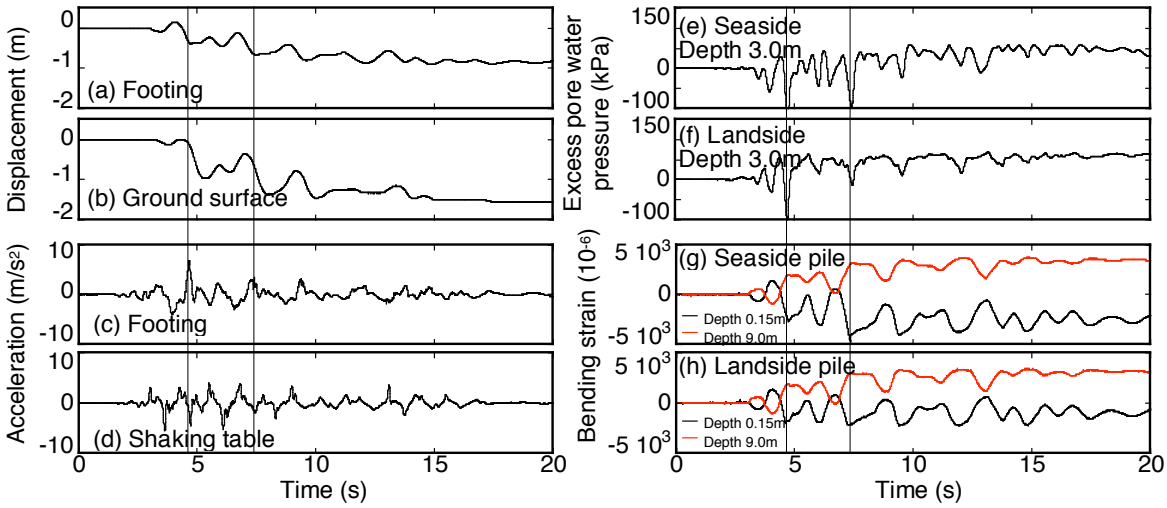

Figure 5 time histories of major values in centrifuge test

Fig. 6 shows a relation of the inertial force with the earth pressure acting on the footing. The inertial force is computed by accelerations of the superstructure and footing. The earth pressure acting on the footing is estimated using outputs from earth pressure sensors attached on the footing surface. Symbols of a circle and a triangle stand for instants of 3 and 7 s after the start of shaking, corresponding to those presented with lines in Fig. 4. With increasing inertial force, the earth pressure also becomes large but acts against the inertial force. This is probably because the footing displacement is larger than the ground displacement, due to a larger inertial force induced by a superstructure.

Fig. 7 shows bending strain distributions with depth for the seaside and landside piles at about 3 s and 7 s, corresponding to the instants marked in Figs. 4 and 6. At these instants both the inertial force and ground displacement increase seaward (Figs. 4(b) and 6). The bending strain of both the piles at 3 s becomes large at their heads (Fig. 7(a)) due to the seaward inertial force (Fig. 6), inducing yielding of the pile heads. The magnitude of the bending strain at the pile heads is larger of the seaside pile than of the landside pile. This is probably because the seaside pile suffers large compression stress when the inertial force increases seaward. As a result, yielding of piles might have progressed on the seaside of the pile group. It is interesting to note that a depth at which the bending strain takes the peak other than the pile head is shallower in the landside pile than in the seaside pile. This suggests that the shear force at the pile head of the landside pile is reduced more at shallow depths, while that of the seaside pile is transmitted to much deeper depths. At 7 s, the bending strains of both the landside and seaside piles become large at a depth of 1.5-2.0 m (Fig. 7(b)). The magnitude of bending strain in the seaside pile is, however, much smaller than that in the landside pile.

To estimate the difference in bending strains between the seaside and landside piles, Fig. 8 shows relations of the bending strain at a depth of 1.5 m of the seaside pile or the landside piles with the pore water pressure at a depth of 1.2 m either in the seaside or landside of the pile group. The pore water pressure in the landside of the pile group decreases, with increasing bending strains of the landside pile (Fig. 8(b)). Such a trend is unclear in the case of the seaside pile and pore water pressure in the seaside of the pile group (Fig. 8(a)). This suggests that the dilatancy characteristics of the soil are more significant on the landside of the pile group than in the seaside.

To further investigate the difference between the seaside and landside piles, Fig. 9 shows distributions of the ground and pile displacements and pore water pressures on the seaside and landside of both the seaside and landside piles at instants of 3 and 7 s. The ground displacement presented in Fig. 9(a)(e) corresponds to the average of the observed ones at points A and B shown in Fig. 1(a) and that in Fig. 9(b)(f) corresponds to the one at point B. The pile displacement is computed by the integration of bending strains in pile with depth (Fig. 9(a)(b)(e)(f)).

At 3 s, the pore water pressure decreases both the landside and seaside of the landside pile (Fig. 9(d)). The reduction in pore water pressures is more significant on the landside. This indicates that the compression stress state develops on the seaside with the extension stress state on the landside. Namely, the pore pressure reduction on the extension side (landside) becomes significant due to the combined effects of the extension stress and the soil dilation caused by the shear stress. In contrast, the pore pressure reduction on the compression side (seaside) becomes insignificant due to the adverse effects of the compression stress and the soil dilation. As a result, the landside pile is pushed to the extension side, as presented in the previous study (Tokimatsu and Suzuki 2004). The bending strain at a depth of about 1.5 m becomes large (Fig. 7(a)), related to the pore water pressure reduction at the same depth. Such a trend, in contrast, is insignificant in the pore water pressures observed on the seaside pile (Fig. 9(c)).

The difference in pore water pressures between the landside and seaside piles is probably due to spatial variation of ground displacement and dilatancy of soil subjected to large shear strain. As shown in Fig. 9(a)(b), the ground displacement becomes larger with decreasing distance to the quay wall. Since the pile displacement is larger than the ground displacement (Fig. 9(a)(b)), the

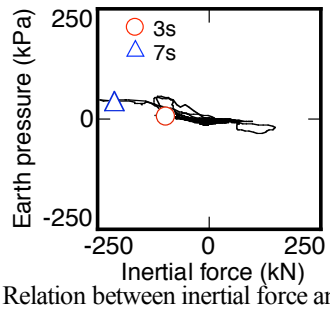

Figure 6 Relation between inertial force and earth pressure

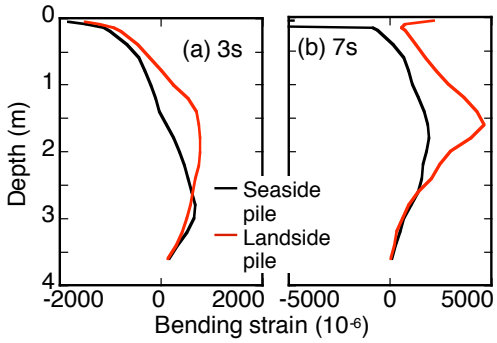

Figure 7 Distributions of bending strain

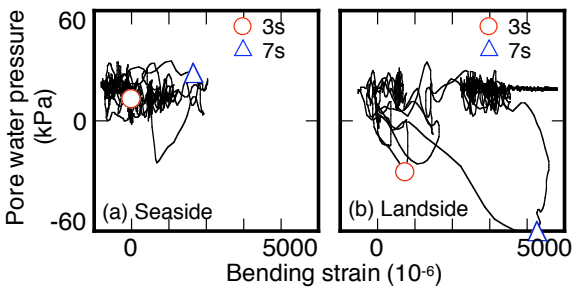

Figure 8 Relations of pore water pressures and bending strains

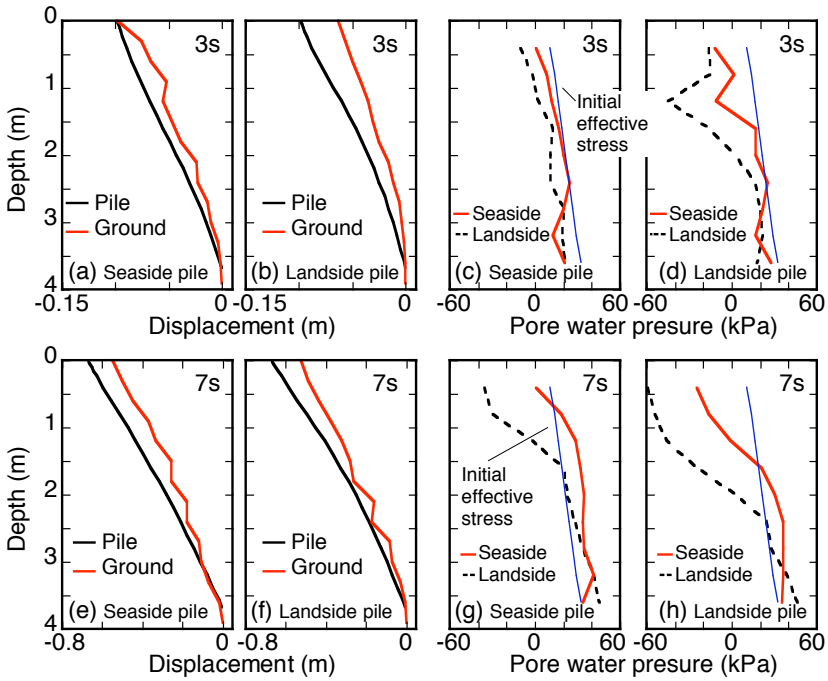

Figure 9 Distributions of pile and ground displacements and pore water pressures observed on piles

relative displacement with respect to the ground of the landside pile becomes larger than that of the seaside pile. This could have created larger pore pressure reduction, thereby making the soil around the landside pile stiffer than that around the seaside pile.

At 7 s, the pore water pressure decreases on the landside of both the landside and seaside piles (Fig. 9(g)(h)). As a result, the seaside pile as well as the landside pile is pushed landward at a depth of 1.0-2.0m (Fig. 7(b)). This is probably because, with increasing seaward movement, the relative displacements of both seaside and landside piles with the ground could have become large, making the soil around both piles stiff. Due to the yielding at the heads and an increase in kinematic force in liquefied layer, the bending strains of both the seaside and landside piles become large at a depth of about 1.5-2.0 m.

4.2 Centrifuge test

To investigate factors affecting stresses in piles, the earth pressure acting on a pile cap is estimated as the difference between the inertial force and shear force at pile heads (Tamura et al. 2002). The shear force is computed from the differentiation of observed bending moment. Fig. 10 shows the relations of the inertial force and the earth pressure. Fig. 10 suggests that the inertial force and earth pressure act with in the same direction, indicating that the pile cap displacement is smaller that the ground displacement. This is different from the trends in the E-Defense test, in which the pile cap displacement larger than the ground displacement due to a large inertial force (Fig. 6).

Fig. 11 shows the distributions of bending strains at instants of 4 and 7 s, which are marked with lines and symbols of a circle and a triangle in Figs. 5 and 10. The bending strain becomes large at the pile heads and at the bottom of the liquefied layer at both 4 s and 7 s. It is interesting to note that the bending strain at the pile heads is larger in the seaside pile than in the landside pile. Additionally, only the seaside pile yield near the head with a bending strain of 4000 μ at 7 s (Fig. 11(b)).

Fig. 12 shows relations of bending strains of the seaside and landside piles and pore water pressures in the seaside or landside of the pile group at a depth of 3 m below. Symbols of circles and triangles correspond to the two instants in Fig. 11, respectively. The pore water pressure decreases with increasing bending strain. The reduction of pore water pressure is more significant in the seaside (Fig. 12(a)) than in the landside (Fig. 12(b)). Since the ground displacement, which increases with decreasing the distance to the quay wall, is larger than the pile displacement, the relative displacement between pile and soil becomes larger on the seaside than the on the landside. This creates larger pore pressure reduction and makes the soil around the seaside pile stiffer than that around the landside pile. The seaside piles might therefore have attracted more kinematic force than the landside piles. This is different from the trend in the E-Defense test, in which the pore water pressure reduction is significant in the landside of the pile group since the relative displacement with the ground is larger in the landside than in the seaside.

5. CONCLUSIONS

To investigate stress distributions within pile groups during liquefaction-induced laterally spreading, physical model tests were conducted using E-Defense, NIED, and the centrifuge system, UC Davis. The test results and

discussions have led to the following:

Extensive soil liquefaction occurred in a few seconds after the start of shaking, causing laterally spreading. Quay walls had large residual deformation, inducing seaward movements and settlements of the ground behind. Piles moved seaward with increasing the quay wall and ground displacement.

In the case of the E-Defense test, the bending strain at pile heads is larger of the seaside pile than of the landside due to the seaward inertial force. In contrast, the bending strain in the ground (at depths of about 1.5-3.0 m) becomes larger of the landside pile than of the seaside pile. This is probably due to the spatial variation of ground displacement and dilatancy of soil subjected to a large shear strain. Since the pile displacement is larger than the ground displacement that becomes larger with decreasing distance to the quay wall, the relative displacement with respect to the ground becomes larger in the landside pile than in the seaside pile. This creates larger pore pressure reduction and thus makes the soil around the landside pile stiffer than that around the seaside pile, inducing a larger kinematic force on the landside pile.

In the case of the centrifuge test, the bending strains of piles are greater on the seaside than on the landside. This is probably because the ground displacement is larger than the pile displacement. Thus, the relative displacement between pile and soil becomes larger in the seaside than in the landside, creating larger pore pressure reduction and making the soil around the seaside pile stiffer than that around the landside pile. The seaside piles might therefore have attracted more kinematic force than the landside piles.

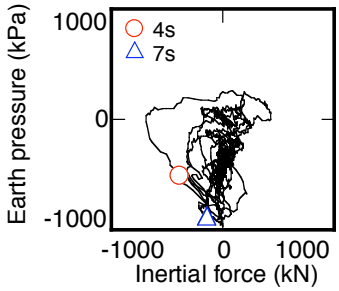

Figure 10 Relation of inertial force and earth pressure

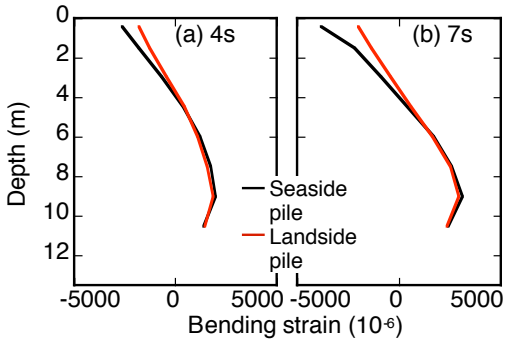

Figure 11 distributions of bending strains

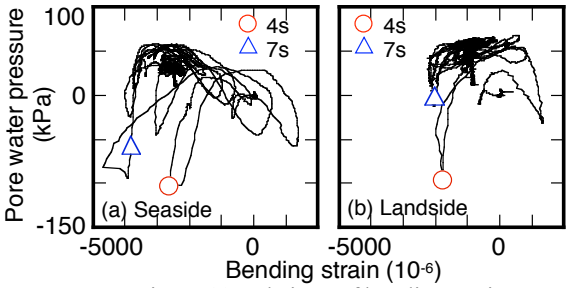

Figure 12 Relations of bending strains and pore water pressures

Acknowledgments:

The study described herein was made possible through Special Project for Earthquake Disaster Mitigation in Urban Areas, supported by the Ministry of Education, Culture, Sports, Science and Technology (MEXT) and E-Defense and NEES collaboration research. Faculties at Center for Geotechnical modeling at UC Davis, from Prof. Ross Boulanger, Prof. Bruce Kutter and Dr. Dan Wilson assisted in conducting the lateral spreading test. The authors express their sincere thanks to the above organizations and persons.

References:

Abdoun, T., Dobry, R., O'Rourke, T. D. and Goh, S. H. (2003), "Pile response to lateral spreads: centrifuge modeling", *Journal of Geotechnical and Geoenvironmental Engineering*, **129**(10), 869-878.

BTL Committee (1998), *Research Report on liquefaction and lateral spreading in the Hyogoken-Nambu earthquake* (in Japanese).

Boulanger, R. W., Kutter, B. L., Brandenberg, S. J., Sihgh, P. and Chang, D. (2003), "Pile foundations in liquefied and laterally spreading ground during earthquakes: Centrifuge experiments & analyses", *Report No. UCD/CGM-03/01*, Center for Geotechnical modeling, University of California, Davis.

Ministry of Education, Culture, Sports, Science and Technology (MEXT) and National Research Institute for Earth Science and Disaster Prevention (NIED) (2006), *Research Theme No. 2 Annual Report of the fiscal year 2005, Special project for earthquake disaster mitigation in urban area*, 831p (in Japanese).

Oh-oka, H., Iiba, M., Abe, A. and Tokimatsu, K. (1996), "Investigation of earthquake-induced damage to pile foundation using televiewer observation and integrity sonic tests", *Tsuchi-to-Kiso*, **44**(3), 23-30 (in Japanese).

Sato, M. and Tabata, K. (2009), "Shaking table test of a large-size model on failure mechanism of sheet-pile quay wall and pile foundation due to lateral spreading", *Japanese Geotechnical Journal*, **4**(4), 259-271 (in Japanese).

Stewart, D. P., Chen, Y.-R. and Kutter, B. L. (1998), "Experience with the use of methylcellulose as viscous pore fluid in centrifuge models", *Geotechnical Testing Journal*, 365-369.

Suzuki, H., Tokimatsu, K. and Boulanger, R. W. (2009), "Effects of ground displacement on piles with different strength during laterally spreading in centrifuge test", *Proceedings of International Conference on Performance-Based Design in Earthquake Geotechnical Engineering*, 8pp.

Tamura, S., Tokimatsu, K., Uchida, A., Funahara, H. and Abe, A. (2002), "Relation between seismic earth pressure acting on embedded footing and inertial force based on liquefaction test using large scale shear box", *Journal of Structural and Construction Engineering*, 559, 129-134 (in Japanese).

Tokimatsu, K. and Suzuki, H. (2004), "Pore water pressure response around pile and its effects on p-y behavior during soil liquefaction", *Soils and Foundations*, **44**(6), 101-110.

JOINT CONFERENCE PROCEEDINGS
7th International Conference on Urban Earthquake Engineering (7CUEE) &
5th International Conference on Earthquake Engineering (5ICEE)
March 3-5, 2010, Tokyo Institute of Technology, Tokyo, Japan

KINEMATIC BENDING MOMENTS IN PILES: AN EXPERIMENTAL STUDY

S.Bhattacharya[1], L.Dihoru[2], C.A.Taylor[3], D.Muir Wood[4], G.Mylonakis [5], F.Moccia[6] and A.L.Simonelli[7]

1) University Lecturer, Department of Civil Engineering, University of Bristol, UK
2) Research Associate, Dept. of Civil Engineering, University of Bristol, UK
3) Professor, Department of Civil Engineering, University of Bristol, UK
4) Professor, Department of Civil Engineering, University of Dundee, UK
5) Professor, Dept. of Civil Engineering, University of Patras, Greece
6) Research Student, Department of Civil Engineering, University of Sannio, Italy
7) Professor, Department of Civil Engineering, University of Sannio ,Italy
S.Bhattacharya@bristol.ac.uk, Luiza.Dihoru@bristol.ac.uk, Colin.Taylor@bristol.ac.uk, d.muirwood@dundee.ac.uk, mylo@upatras.gr, flaviana.moccia@unina.it, alsimone@unisannio.it

Abstract: Eurocode 8 advises designers to consider the kinematic bending moment in piles arising from the soil deformations from the passage of seismic waves which impose curvatures and thereby strains on the piles. A recent seismic Italian normative specify that kinematic effects should be taken into account when seismicity of the area is moderate or high, subsoil type is C or worse and consecutive soil layers with sharply different shear moduli are present. However, the code of practice does not suggest methods for calculating these kinematic moments. While various methods can be found in the literature to predict these bending moments based on certain assumptions and simplifications, experimental data to validate the methods are limited in the public domain. A shaking table study was conducted to verify some of the assumptions behind the proposed methods of kinematic bending moment estimation. This paper summarizes some aspects of the experimental study carried out the BLADE [Bristol Laboratory for Advanced Dynamics Engineering].

1. INTRODUCTION

Piles are one of the most commonly used foundations in seismic areas where the soil is inadequate to carry the load on its own. In these seismic areas, piles often pass through (penetrate) shallow loose and/or soft soil deposits and rests on competent end bearing soils. Post-earthquake reconnaissance work (Mexico City 1985, Kobe 1995, 2001 Bhuj earthquake) has shown that a large number of pile-supported buildings built in layered soils suffered significant settlement and tilting and that in several cases pile damage has occurred close to interfaces separating layers with very different shear moduli. It is widely acknowledged that piles are affected by both the movement of the superstructure, i.e. inertial forces, and the kinematic bending moments induced by the surrounding soil. Recent building codes (Eurocode 8) include pile design provisions that account for the combined effect of both mechanisms. One of the challenges faced by the engineers is the prediction of the maximum bending moment in the pile at the interface having a sharp stiffness contrast.

It is of interest to discuss the relevant clauses from Eurocode 8 (EN 1998-5): The code prescribes that kinematic effects should be taken into account when all the following conditions simultaneously exist:

(1) Seismicity of the area is moderate to high. It is being characterized by a *normalized Peak Ground Acceleration* $a_gS>0.1g$, where a_g is the design ground acceleration on type A subsoil (essentially rock) and S is the soil factor.

(2) Subsoil type is D or worse, characterized by sharply different shear moduli between consecutive layers;

(3) The importance of the superstructure is of III or IV class.

The above factors have been echoed in the recent Italian building code normatives (OPCM 3274/2003). A research program (funded by Department of Civil Protection, Italian Government) was carried out to evaluate the various methods available for computing the bending moments of piles at the interface of contrasting stiffness. This paper presents some of the findings from the experimental program. The aims of the paper are as follows:

1) Provide a brief review of the available methods of analysis for prediction of the bending moments at the interface. Emphasis is given on the methods where simple hand calculations can predict the bending moments.

2) Describe the series of experiments carried out at BLADE [Bristol Laboratory for Advanced Dynamics Engineering, University of Bristol] to investigate the validity behind the assumptions in the various methods. Other details related to the experiments can be found in Dihoru et al (2009, 2010a, 2010b).

2.0 METHODS OF ANALYSIS

Kinematic pile-soil interaction has been studied by many researchers, see for example Margason & Holloway (1977), Kuhlemeyer (1979), Krishnan et al (1983), Gazetas et al. (1992), Kaynia & Mahzooni (1996), Wu & Finn (1997), Zhang et al (2000), Padron et al (2008), Chau et el (2008), , Mylonakis (2001), Nikolaou et al. (2001), Saitoh (2005), Cairo and Dente (2007), Sica et al. (2007). The main issues that need to be investigated are:

(1) Under what conditions (i.e. ratio of the soil stiffness, earthquake magnitude and frequencies) kinematic interactions may govern the pile design. Conversely, when these effects can be neglected.

(2) The method of analysis of kinematic interactions.

Essentially, there are three classes of analysis as discussed in Table 1.

Table 1: Methods of Analysis

Method and references	Main Analytical Features
Simplified Methods Examples: NEHRP (1997), Margason & Holloway (1977)	(1) Pile follows the free-field motion. (2) Kinematic bending moments derived from peak curvature of the pile. (3) Soil-pile interaction neglected (4) Pile-soil relative stiffness neglected (5) Pile slenderness neglected (6) Radiation damping neglected
Beam on Winkler approach Penzien (1970), Matlock & Foo (1979), Novak (1979), Kavvadas & Gazettas (1993), Mylonakis et al (1997), Tahghighi & Kanagai (2007)	(1) They may include linear, equivalent linear or non-linear analyses. (2) Soil-pile kinematic interaction catered for. (3) Several models account for soil non-linearity and stiffness degradation.
Finite Element and Boundary Element Analyses Kuhlemeyer (1979), Krishnan et al (1983), Kaynia & Mahzooni (1996), Wu & Finn (1997), Zhang et al (2000), Padron et al (2008), Chau et el (2008)	Based on continuum mechanics models – (1) Pile and surrounding soil simulated by axisymmetric elements and energy transmitting boundaries. (2) Soil-pile kinematic interaction catered for. (3) Soil non-linearity and stiffness degradation accounted for.

3.0 EXPERIMENTAL METHODOLOGY

A series of dynamic pile tests were carried out on the earthquake simulator at Bristol University (BLADE laboratory). The research was carried out within the framework of the RELUIS (Rete di Laboratori Universitari Ingegneria Sismica) project. A small scale model pile was installed in a shear stack containing several granular material configurations. The shear stack (see Figure 1) was subjected to real seismic inputs while the free-field motion and the bending response of the pile were measured.

The small scale model employed in this study was based on a reference numerical prototype (Figure 2) used in a number of previous parametric studies (Mylonakis et al (1997), Sica et al (2007)).

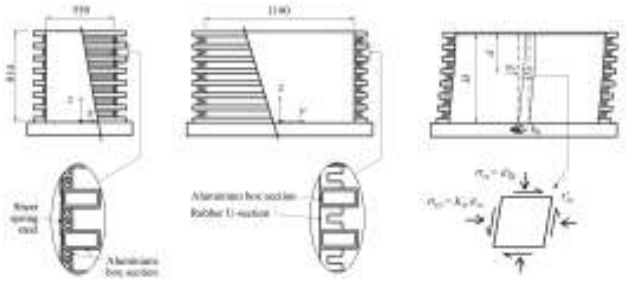

Figure 1: Shear stack at BLADE [University of Bristol], Dietz (2006)

The prototype is a simplified two-layered profile with a total thickness of 30 m, containing a concrete pile of diameter d=600 mm, length L=20 m and Young's modulus E_p=25 GPa. Each soil layer is characterized by its thickness, density, shear wave velocity, Poisson's ratio and damping ratio. The prototype shear wave velocities are v_{s1}=100 m/s and v_{s2}=400 m/s.

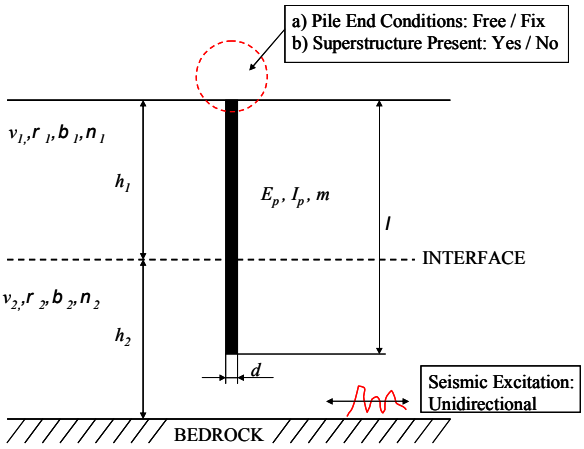

Figure 2: Prototype structure

The experimental work made use of an existing shear stack of length 1190 mm, width 550 mm and height 818 mm. The ratio between the prototype soil depth (30 m) and the shear stack height (0.8 m) gave the fundamental scale factor for length (n = 37.5) which governed all the compliance laws employed in modeling. The details regarding the physical and geometrical similitude between the model and the prototype have already been described in Dihoru et al (2009), Dihoru et al (2010a, 2010b). A strain-gauged 6063-T6 HE9TF aluminum alloy model pile (E_{Al} = 70 GPa, outer diameter D_0 = 22.23 mm, length L = 0.75 m, thickness t = 0.71 mm) was installed in the centre of the stack and the model soil was deposited by dry pluviation from a drum suspended above the shear stack. Figure 3 shows the different soil configuration used in the study. Mainly three configurations were studied: only Fraction E sand (fine grained sand- Case I), Fraction E and Fraction B+E (Case II) and finally Rubber and Fraction E. In order to have a high contrast between layers, fine graded rubber granules were

used (Rubber CT0515). Different boundary conditions were used

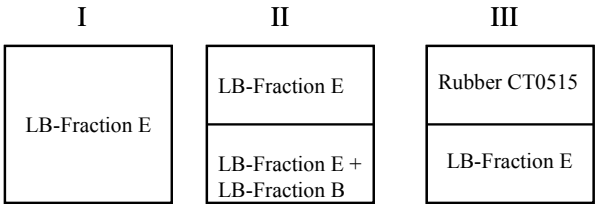

Figure 3 Soil configurations employed in testing.

Real acceleration records of three Italian earthquakes (Friuli (1976), Irpinia (1980) and Norcia (1998)) were employed in testing. Different boundary conditions used fo the top and bottom of the pile, see Figures 4, 5, 6 and 7.

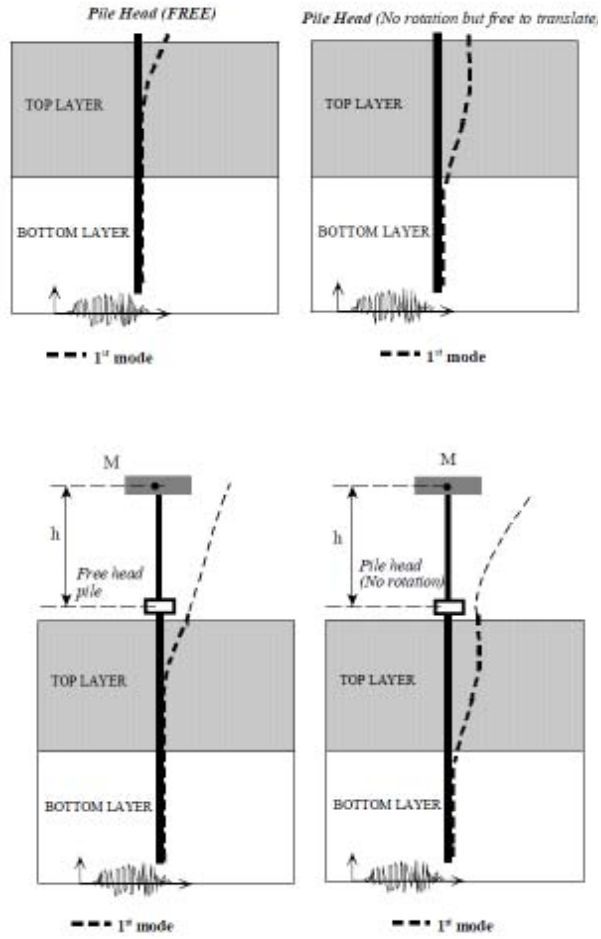

Figure 4 Different boundary conditions used for the pile

4.0 COMPARISON BETWEEN EXPERIMENTAL AND THEORETICAL

Three classic theoretical models of soil-pile interaction: Dobry and O'Rourke (1983), Nikolaou et al 1995 and Mylonakis et al 1997) were employed in evaluating the soil-pile kinematic interaction. A comparison is made between the experimental and the numerical simulation results of pile bending.

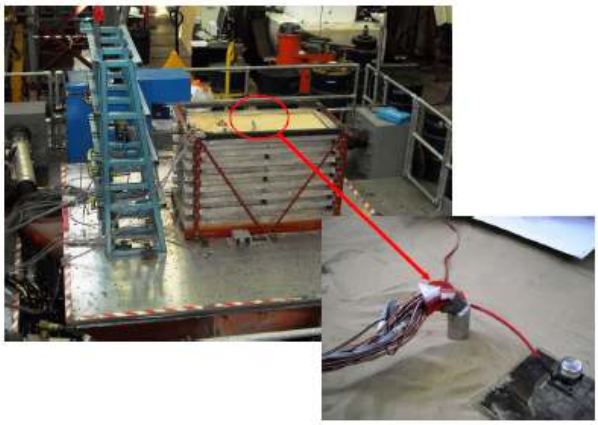

Figure 5: Free headed pile

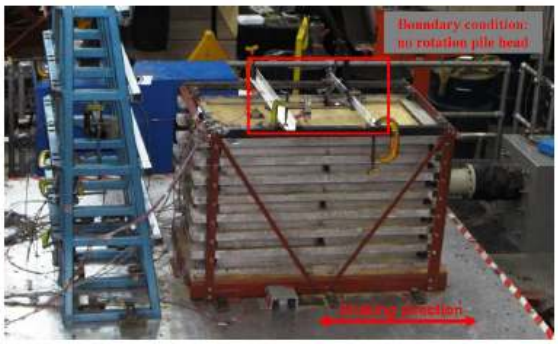

Figure 6: Rotation restrained at the pile head

Verification based on Dobry and O'Rourke (1983)

Based on homogenous, isotropic, linear elastic soil and uniform static stress field assumptions, the moment at the interface is given by:

$$M \cong 1.86\left(E_P I_P\right)^{\frac{3}{4}}\left(G_1\right)^{\frac{1}{4}}\gamma_1 F \qquad (1),$$

where

E_PI_P = Bending rigidity of the piles

G_1 = Shear Modulus of the top layer

γ_1 = Peak uniform soil strain in Layer 1 which may be obtained from any simplified approach

F = Dimensionless factor depending on the stiffness contrast at the interface (G_2/G_1) where G_2 is the shear modulus of the bottom layer. F is a function of c where c is given by equation 2.

$$F = \frac{(1-c^{-4})(1+c^3)}{(1+c)(c^{-1}+1+c+c^2)} \qquad (2)$$

$$\text{Where } c = \left(\frac{G_2}{G_1}\right)^{\frac{1}{4}} \qquad (3)$$

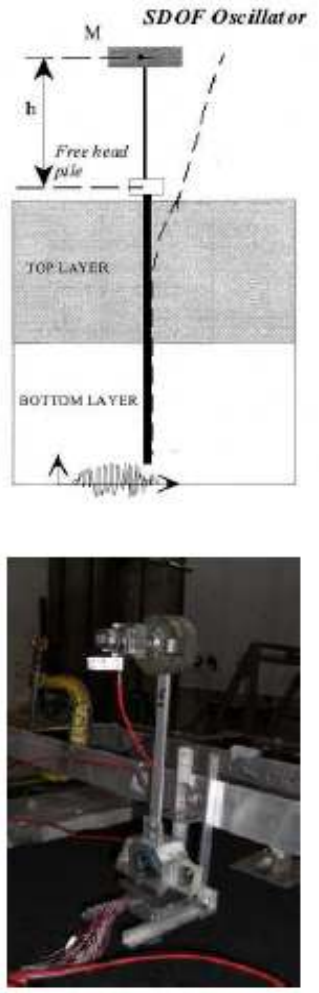

Figure 7: SDOF structure

An improvement of the Dobry and O'Rourke (1983) solution has been achieved by Mylonakis (2001). Using more suitable dynamic parameters, the following expression has been derived:

$$M = 2\frac{E_p I_p}{d}\left(\frac{\varepsilon_p}{\gamma_1}\right)\gamma_1\phi \qquad (4)$$

Where ε_P indicates the pile peak bending strain

and γ_1 denotes the soil shear strain at the layer interface.

The ratio of these parameters represents a sort of "*strain transmissibility*" function, which is strongly frequency-dependent. The effect of frequency may be introduced in terms of the ratio:

$$\Phi = \left(\frac{\varepsilon_p}{\gamma_1}\right) \Big/ \left(\frac{\varepsilon_p}{\gamma_1}\right)_{\omega=0} \qquad (5)$$

which is a function of H_1/d, G_1/G_2, E_p/E_1. Nevertheless, in the range of frequencies of interest ϕ is generally less than 1.25.

In this paper, the experimental results are compared with two types of analysis: (a) Linear Elastic; (b) Non-linear analysis using equivalent linear procedure. Some details of the method of analysis are discussed below:

Linear analysis: In this type of analysis, the pile and the soil is assumed to be in linear elastic region. Under the strong earthquakes used in this study, soil will no longer be in linear elastic response. However, this type of analysis is carried out to compare with the experimental results in order to understand under what condition non-linear analysis is more appropriate. This has been carried out using the SPIAB code.

Non-linear analysis: In this type of analysis, non linear behavior of the soil is represented by the equivalent linear procedure, which provides soil stiffness and damping ratio consistent to the earthquake-induced level of shear strains. This is still a crude representation of the actual soil response under earthquakes but certainly more realistic than the linear elastic model, widely adopted in the literature studies. Equivalent linear site-response analyses of the subsoil depicted has been carried out using EERA and the equivalent stiffness and damping parameters thus obtained is compares used in the SPIAB code. The next section the results obtained from analytical methods and experiments.

Figure 8 and 9 shows typical results from the test and its comparison with the other methods. Figure 8 shows a typical test result for free headed pile while Figure 9 shows for fixed headed pile.

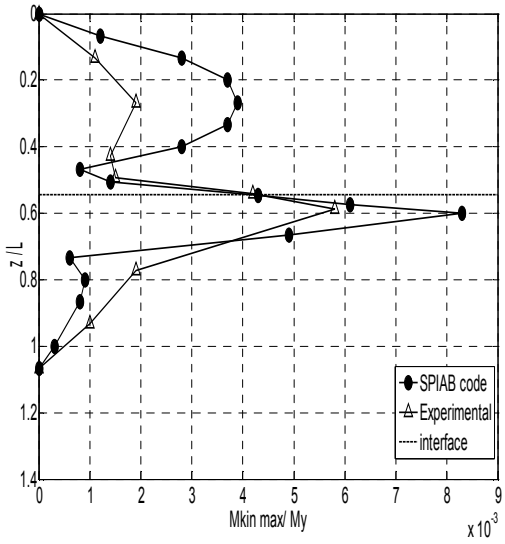

Figure 8: Typical result from a Free headed piles

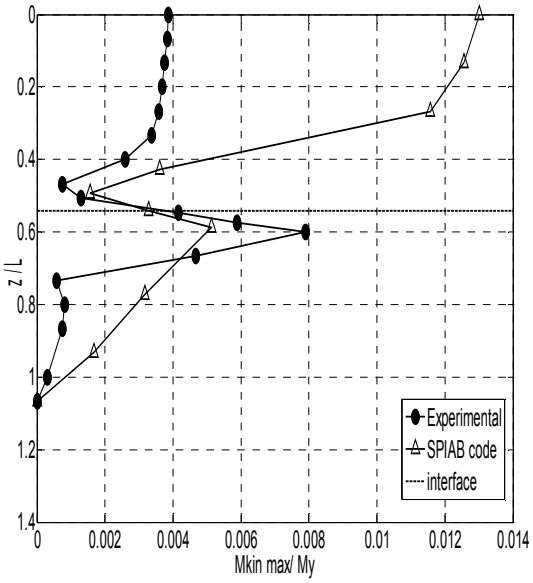

Figure 8: Typical result from a Fixed headed piles

5.0 CONCLUSIONS

From the results of this study, the following remarks may be made:

(1) The maximum kinematic bending moment generally occurs at the soil layer interface. The kinematic bending moment dramatically increases when the shear wave velocity contrast between the bottom and top layer increases.

(2) Complex seismic pile-soil interaction can be modeled in a shaking table for better understanding of their behavior leading to efficient design. The stiffness contrast of granular materials can be replicated by innovative ways, such as mixing Fraction B and E sand to obtain greater packing density.

(3) Bending moments were measured using strain gauges and this shows the influence of boundary condition of the pile head, stiffness ratio between the layers and the input motion.

(4) Linear elastic analysis could predict the kinematic bending moment for many cases but it underestimated for strong motions. However, equivalent linear analysis better predicted the kinematic bending moments.

(5) The predicted bending moments were found to be strongly influenced by the type of analyses (linear or equivalent linear) and the set of preliminary assumptions regarding the soil stiffness.

Acknowledgements:

The research is in the main frame of RELUIS [Rete dei Laboratory universtari di Iiggengrie Seismica] funded by DPC [Italy]. The support from RELUIS for conducting this research is gratefully acknowledged. The research is a joint research amongst the University of Sannio (Italy), University of Bristol (United Kingdom) and University of Patras (Greece) on soil-pile interaction. The experimental part is developed at University of Bristol. The authors would like to thank Eleonora Iannacce and Domenico Lombardi for their valuable contribution to the experimental work.

References:

API (2003): American Petroleum Institute Code of Practice.

Banerjee, P.K., 1995, The boundary element methods in engineering, McGraw-Hill, New York.

Chau, K.T., Shen, C.Y., Guo, X., 2008, Non-linear seismic soil-pile-structure interaction: Shaking table tests and FEM analyses, Soil Dynamics and Earthquake Engineering, Article in press.

Dihoru, L., Bhattacharya, S., Taylor, C.A, Muir Wood, D. Moccia, F., Simonelli. A.L., Mylonakis, G (2009): Experimental modeling of kinematic bending moments of piles in layered soils, IS-Tokyo.

Dihoru, L., Bhattacharya, S., Taylor, C.A, Muir Wood, D. Moccia, F., Simonelli. A.L., Mylonakis, G (2010a): Physical and Numerical Modelling of kinematic pile-soil interaction under seismic conditions, Physical Modelling Conference, Zurich.

Dihoru, L., Bhattacharya, S., Taylor, C.A, Muir Wood, D. Moccia, F., Simonelli. A.L., Mylonakis, G (2010b): Stiffness design for granular materials- theoretical and experimental considerations, Physical Modelling Conference, Zurich.

Dietz, M, 2006,Test Method Statement - Physical Modelling of Pile-Soil Interaction within a Layered Deposit, EERC, University of Bristol.

DnV (1992): Det Norske Veritas – Foundation code.

Dobry R. and O'Rourke M.J., 1983, Discussion on 'Seismic response of end-bearing piles' by Flores-Berrones R.,Whit-man R.V.', J. Geotech. Engng. Div., ASCE, 109, 778-781.

Eurocode 8: Design of Structures for Earthquake Resistance Part 5: Foundations, Retaining Structures and Geotechnical Aspects.

German,R.,1989, Particle Packing Characteristics, Metal Powder Industries Federation, New Jersey.

Hardin, B.O., Black, W.L.,1969, Vibration modulus of nor- mally consolidated clay, ASCE, SM6, 95.

Kaynia, A.M., Mahzooni, S.,1996, Forces in pile founda- tions under seismic loading, J. Engng. Mech., ASCE, 122, 46-53.

Kavvadas, M., Gazetas, G., 1993, Kinematic seismic response and bending of free-head piles in layeres soil, Geotechnique, 43, 207-222.

Krishnan, R., Gazetas, G., Velez, A., 1983, Static and dynamic lateral deflection of piles in non-homogeneous soil stratum, Geotechnique, 33, 307-326.

Kuhlemeyer, R.L., 1979, Static and dynamic laterally loaded floating piles, J. Geotechn. Eng. Div., ASCE, 105, 289-304.

Matlock, H. and Fo, S.H.C., 1979, Axial analysis of piles using a hysteretic and degrading soil model, Numerical Methods in Offshore Piling, Institution of Civil Engineers, London, May, 127-34.

Mylonakis G, Nikolaou A., Gazetas G, 1997, Soil-pile-bridge seismic interaction: kinematic and inertial effects. Part I: soft soil, Earthquake engineering and structural dynamics, 26, 337-359.

Mylonakis G, 2001, Simplified model for seismic pile bending at soil layer interfaces, Soils and Foundations, 41, 47-58.

Muir Wood, D., Crewe, A., Taylor, C.A., 2002, Shaking Table Testing of Geotechnical Models, UPMG- International Journal of Physical Modelling in Geotechnics, 2,1-13.

Novak, M.,1979, Soil-pile interaction under seismic loads, Proc. Int. Symp. Num. Meth. Offshore Piling, London, 41- 50.

Novak, M., 1987, Experimental studies of the dynamic behaveiour of piles and pile groups, Banerjee and Butterfield (eds), Dynamic behaviour of foundations and buried structures, 135-165.

Padron, L.A., Aznarez, J. J., Maero, O.,2008, Dynamic analysis of

piled foundations in stratified soils by a BEM-FEM model, Soil Dynamics and Earthquake Engineering, 5, 333-346.
Penzien, J., 1970, Soil-pile foundation interaction, Earthquake Engineering, ed. R.L. Wiegel, Prentice-Hall, Englewood Cliffs, New Jersey.
Randolph, M.F., 1981, The response of flexible piles to lateral loading, Geotechnique, 31, 247-259.
Sica, S., Mylonakis, G., Simonelli, A.L., 2007, Kinematic bending of piles: analysis vs. code provisions', Proc. of the 4th International Conference on Earthquake Geotechnical Engineering, Thessaloniki, Greece.
Tahghighi, H., Kanagai, K., 2007, Numerical analysis of non- linear soil-pile group interaction under lateral loads, Soil Dynamics and Earthquake Engineering, 5, 463-474.
Tan, F.S.C., 1990, Centrifuge and theoretical modelling of conical footings on sand, PhD Thesis, University of Cam-bridge, U.K..
Wu G., Finn W., 1997, Dynamic elastic analysis of pile foundations using finite element method in the time domain, Can. Geotech. J., 34, 44-52.

JOINT CONFERENCE PROCEEDINGS
7th International Conference on Urban Earthquake Engineering (7CUEE) &
5th International Conference on Earthquake Engineering (5ICEE)
March 3-5, 2010, Tokyo Institute of Technology, Tokyo, Japan

SIMULATION OF SOIL-PILE-STRUCTURE INTERACTION THROUGH MULTI-DIMENSIONAL SHAKING TABLE TESTS USING E-DEFENSE FACILITY

Hiroyuki Yoshida[1] , Youhao Zhou[2], Hiroko Suzuki[3], Yasushi Nukui[4] , Kohji Tokimatsu[5]

1) Chief, Arch. & Struct. Eng. Operation Center, Tokyo Electric Power Services Co., Ltd., Japan (TITECH)
2) Master Student, Dept. Architecture and Building Engineering, Tokyo Institute of Technology, Japan
3) Assistant Professor, Dept. Architecture and Building Engineering, Tokyo Institute of Technology, Japan
4) Group Manager, R&D Center, Tokyo Electric Power Company, Japan
5) Professor, Dept. Architecture and Building Engineering, Tokyo Institute of Technology, Japan
yoshida@tepsco.co.jp, shiyuu.y.aa@m.titech.ac.jp, hsuzuki@arch.titech.ac.jp, nukui.y@tepco.co.jp, kohji@o.cc.titech.ac.jp

Abstract: Geotechnical shaking table tests were conducted using the E-Defense facility to investigate the response and failure of a nearly full-scale pile-structure system to multi-dimensional loading. We executed a numeric simulation analysis by the three-dimensional nonlinear finite element method for these examinations. As a result, the three-dimensional behavior including a perpendicular movement was able to be reproduced well.

1. INTRODUCTION

Most of Japanese metropolises lie on soft ground near seas and large rivers. For this reason, pile foundations are commonly applied for substructures, representing 70~80% of all buildings. Pile foundation is, however, weak in horizontal direction, thus soil and structures are easily damaged by both inertial force from superstructures and kinematic force from ground displacement during earthquakes with large-scale horizontal shaking. Despite of this fact, mechanism of those damages is, due to the lack of data since no observation has ever been made, not fully understood.

In order to gain sufficient data to establish a design method for pile foundation with failure of piles taken into account, a series of shaking table tests using soil-pile-structure models was performed. The E-Defense shaking table platform and a cylindrical laminar shear box were used for the tests, and a full-scale pile-structure system was subjected to a series of single- or multi-dimensional loading. In cases where large scale loading was applied, subsidence and residual displacement of footing were observed, and data including pile damage process were obtained.

By performing numerical analysis of abovementioned shaking table tests using three-dimensional finite element method, this paper verifies the validity of the evaluation method on dynamical behavior of pile foundation structures when soil shows strong nonlinearity.

2. SHAKING TABLE TESTS

The E-Defense shaking table platform has a dimension of 15 m long and 20 m wide. Figure 1 and Photo 1 show a test model constructed in a cylindrical laminar box 6.5 m high with an outside diameter of 8.0 m. It consists of forty-one stacked ring flames, enabling two-dimensional shear deformation of the inside soil.

A 3x3 steel pile group was used for the test. The piles were labeled A1 to C3 according to their locations within the pile group, as shown in Figure 1. Each pile had a diameter of 152.4 mm and a wall thickness of 2.0 mm. The piles were set up with a horizontal space of four-pile diameters center to center. Their tips were jointed to the laminar box base with pins and their heads were fixed to the footing of a weight of 10 tons.

Dry Albany sand from Australia was used for preparing the sand deposit. Figure 2 shows the grain size distribution of the sand. The sand had a mean grain size D50 of 0.31 mm and a coefficient of uniformity U_c of 2.0. After setting a pile group in the laminar box, the dry sand was air-pluviated and compacted at every 0.275m to a relative density of about 70% to form a uniform sand deposit with a thickness of 6.3m.

A total of five test series named A to E was conducted, in which the presence of foundation embedment and superstructure, and the natural period of superstructure, as well as the type of input motions, and their component and maximum accelerations were varied. In test series E, which this paper focuses on, natural frequencies of the soil and the superstructure, obtained from microtremor observation, were about 7.9 Hz and

6.0 Hz, respectively.

Table 1 shows the list of shaking conditions of test series. In order to clarify the effect of natural period of superstructure on dynamic behavior of test model, the tests were conducted under one-, two- or three-dimensional shaking with three types of ground motions, which dominate in different period ranges, with maximum horizontal accelerations adjusted to 30 cm/s^2 and 90 cm/s^2 (and 110 cm/s^2 in selected cases). Pile strains were within elastic range in all test series. In addition, in order to investigate the pile destruction process induced by ground motion, additional tests were conducted for series E, under three-dimensional shaking with maximum accelerations at levels in actual earthquakes. JR Takatori wave was used, with maximum horizontal accelerations at 300 cm/s^2 and 600 cm/s^2.

Among the cases conducted with three-dimensional JR Takatori wave, this paper focuses on the one in test series E with maximum acceleration adjusted to 110 cm/s^2 (as underlined in Table 1), in which the soil showed strong nonlinearity, and reports the results of numerical analysis.



Photo 1 Test Model on Large Shaking Table

	Superstructure	Embedment
A	Rigid	Yes
B	Long period	Yes
C	No	Yes
D	Short period	Yes
E	Short period	No

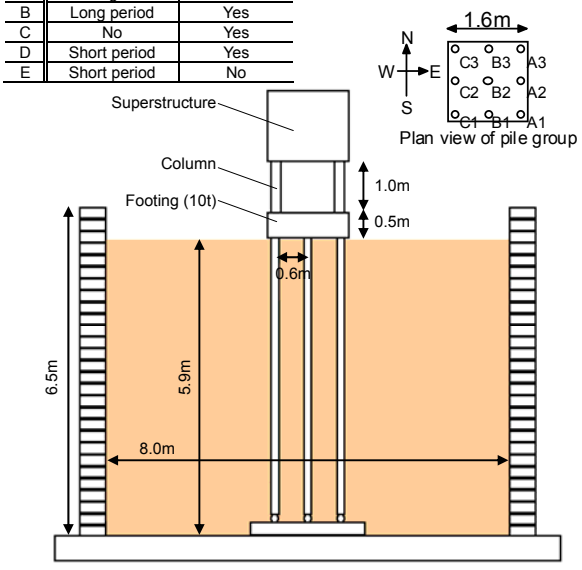

Figure 1 Soil-Pile-Structure Model (Series E)

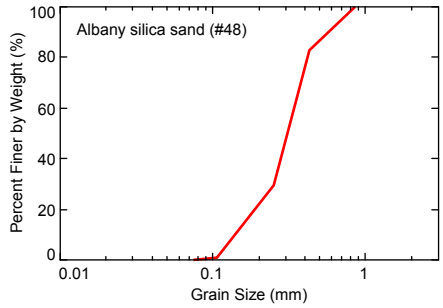

Figure 2 Grain Size Distribution of Albany Sand

Table 1 Shaking Conditions of Test Series

	Maximum input acceleration (cm/s^2)			
	JR Takatori		Taft and Tottori	
	XYZ	XY, X, Y	XYZ	XY, X, Y
A, B	30, 90		30, 90	-
C	30, 90, 110		30, 90, 110	-
D	30, 90		30, 90	
E	30, 90 110 300, 600	30, 90	30, 90 (Taft only)	-

3. NUMERICAL ANALYSIS

3.1 ANALYTICAL MODEL

A numerical analysis was conducted with a three-dimensional FEM model using analysis code EENA3D developed by TEPCO (Yoshida et al., 2006).Figure 3 and Figure 4 illustrate the model.

The laminar shear box is modeled as solid elements with equivalent mass and adequately small stiffness. Degree of freedom is restrained, so that each ring frame of the shear box may maintain its plane during shear deformation. To take the effect of rocking behavior of the shaking table into account, additional vertical springs are placed at eight points at bottom of the box.

Specifications and dynamic strain dependency of the soil are explained in Table 2 and Figure 5, respectively. Velocities of P and S waves, V_P and V_S, are obtained by regressing results of PS logging depending on overburden pressure σ'_z. Poisson's ratio ν is calculated from V_P and V_S. As shown in Figure 6, in order not to include engineering judgments in parameter setting, discrete data of G/G_0-γ regression curve shown in Figure 5 are directly inputted to simulate soil's nonlinearity. τ-γ relation is obtained from inputted data, also as discrete data. The discrete τ-γ relation is linearly interpolated to define skeleton curve. Cohesion c is set to zero. Internal friction angle φ is obtained from Equation 1;

$$\tau_{\max} = \sigma_c \cdot \tan\phi \qquad (1)$$

where σ_c is consolidation stress; and shear strength τ_{max} is defined by the maximum value of τ-γ skeleton curve, which can be obtained from G-γ dynamic strain dependency curve. Obtained internal friction angle is used to define the strength of joint elements.

In addition, in this study, the nonlinear model of soil concerning its shear deformation component is defined by the second constant J_2 of deviatoric stress q, based on von Mises' failure criterion. Relation of equivalent stress $\sigma_e(=\sqrt{1/2\times s_{ij}s_{ij}})$ and equivalent strain $e(=\sqrt{2\times\varepsilon_{ij}\varepsilon_{ij}})$, which are expressed by root of deviatoric stress q and deviatoric strain ε_s respectively, is defined by stress-strain relation given by Equation 2.

$$\sigma_e = G \cdot e \tag{2}$$

Dynamic strain dependencies (G/G_0-γ, h-γ) are considered in Equation 2. However, since equivalent stress σ_e and equivalent strain e both only take positive values, it is impossible to identify whether it is pulsating or alternating. In order to draw hysteresis curve, the radius of yield surface in π plain is given as deviatoric strain e (Yoshida et al, 1993).

Input motion, as shown in Figure 7, is calculated by averaging each component of four observed records obtained at bottom of the shear box. All three components of the input motion are applied simultaneously to the bottom center of the box.

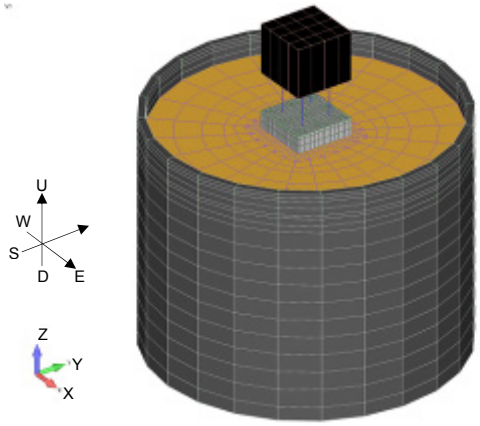

Figure 3 Analysis Model (Overview)

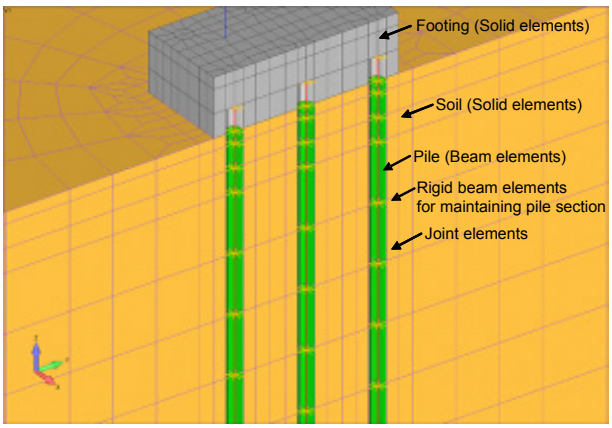

Figure 4 Details on Pile and Footing

Table 2 Specification of Soil

Parameter	Value
Density ρ (t/m^3)	1.709
S wave velocity V_S (m/s)	$86\sigma_v^{0.25}$
P wave velocity V_P (m/s)	$146\sigma_v^{0.25}$
Poisson's ratio v	0.234
Cohesion c (kPa)	0
Internal friction φ (°)	29.5

* σ_v : Overburden pressure (kN/m^2)

3.2 NUMERICAL ANALYSIS RESULTS

Among the numerical analysis results, distribution of the maximum shear strain in soil is shown in Figure 8. The level of strain is approximately 2~10% at ground surface and near piles, which indicates that the soil was at strong nonlinear state.

Figure 9 shows maximum acceleration distribution in soil. The estimated maximum accelerations are in good agreement with observed records in X, Y and Z directions, which proves the validity of the suggested three-dimensional nonlinear model of soil. However, as seen from maximum bending strain distribution shown in Figure 10, the strains are overestimated at pile heads, and the depths of inflection point tend to be deeper than observed ones.

Figure 11~Figure 13 show time histories of acceleration at selected points. Estimated accelerations are in good

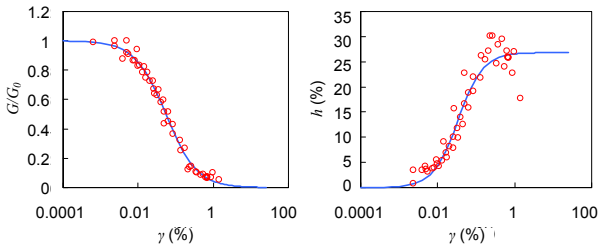

Figure 5 G/G_0-γ, h-γ Relation

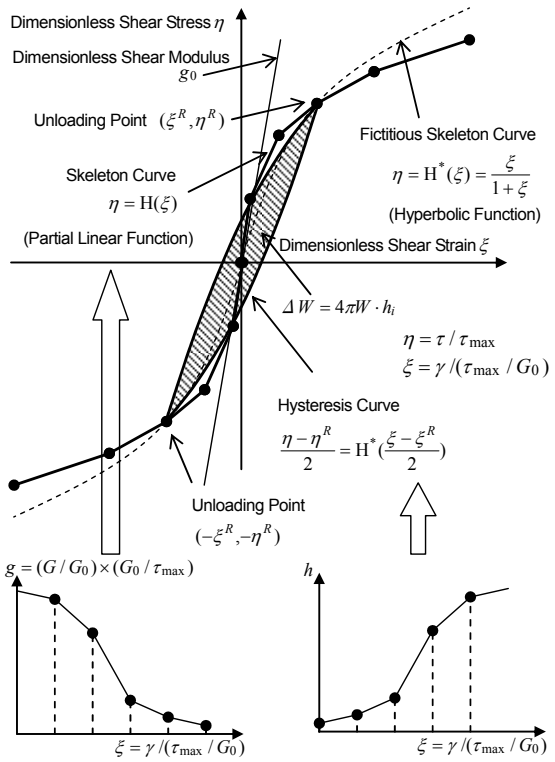

Figure 6 Modeling of Nonlinearity for Shear Strain

agreement with observed ones, not only in Y direction which is the strong axis of the seismic wave, but also in X direction which is the weak axis. In addition, accelerations in vertical direction are also reproduced with reasonable accuracy. It therefore suggests that, for the overall behavior, the obtained response is appropriate. On the other hand, as seen from time histories of bending strain of selected corner pile A1 shown in Figure 14 and Figure 15, the estimated strains are larger than observed ones at pile heads. This suggests that the details of pile head joints in the analysis model might be slightly different from that in the test model.

In the test model, steel pipe piles and steel footing were rigidly fixed together by injecting non-shrinkage cement into gaps between them. However, it is possible that the cement had been broken in previous tests, and rigidity at pile heads had decreased. In order to simulate the fracturing of cement and the decreasing of pile head rigidity, additional analysis was conducted with joint elements connecting piles and footing bottom removed, so that piles and footing bottom may move independently. Parts of pile heads that penetrate the footing, however, are still completely fixed with the footing in this case.

Maximum acceleration distribution in soil is shown in Figure 16. Similar to the first analysis with piles and footing rigidly fixed together, estimated results are in good agreement with observed ones, which indicates that rigidity of pile head seldom affect soil response. In addition, as seen from maximum strain distribution of

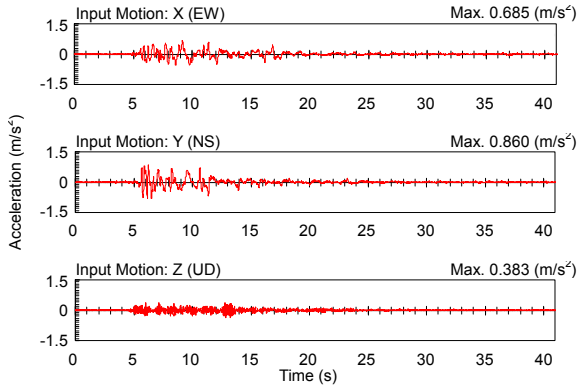

Figure 7 Time Histories of Input Motion

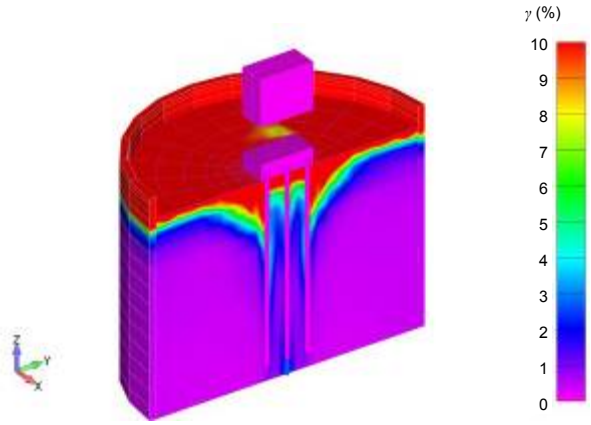

Figure 8 Maximum Strain Distribution

piles shown in Figure 17, both strain at pile heads and depth of inflection point are in good agreement with the observed ones as well. This indicates that the assumption of decrease in pile head rigidity is appropriate.

Time histories of acceleration at selected points are shown in Figure 18~Figure 20, and time histories of bending strain of selected corner pile A1 are shown in Figure 21 and Figure 22, in compare with observed ones. Estimated results and observed records are in good agreement, which reconfirms the validity of assumption that pile head rigidity had decreased.

4. CONCLUSIONS

In order to confirm the validity of the evaluation method of pile foundation behavior while soil shows strong nonlinearity, numerical analysis of full-scale shaking table test was conducted using three-dimensional finite element method. As a result, the behavior of soil including its vertical component, along with the behavior of piles, was reproduced with a degree of accuracy. In addition, it was suggested that in the test model, pile head rigidity might have decreased during test cases prior to the one discussed in this paper.

Acknowledgments:

The study described herein was made possible through Special Project for Earthquake Disaster Mitigation in Urban Areas, supported by the Ministry of Education, Culture, Sports, Science and Technology (MEXT). The authors express their sincere thanks to the above organization.

References:

MEXT and NIED (2006), Research Theme No. 2 Annual Report of the fiscal year 2005, Special project for earthquake disaster mitigation in urban area, 831p (in Japanese).

H. Suzuki, K. Tokimatsu et al. (2008), "Stress distribution within pile group during failure process in large shaking table tests," *JGS*, pp. 1161-1162, 2008

K. Tokimatsu, H. Suzuki et al. (2007), "Three-dimensional shaking table tests on soil-pile structure models using E-Defense facility," *Proc. of 4th International Conference on Earthquake Geotechnical Engineering*, 11 pp.

H. Yoshida, K. Tokimatsu et al. (2008), "Practical Three-Dimensional Effective Stress Analysis Considering Cyclic Mobility Behavior," *The 14th World Conference on Earthquake Engineering*, Paper_ID 04-01-0061.

H. Yoshida, Y. Ohmiya, K. Tokimatsu et al. (2006) "Study on Practicable 3-Dimensional Effective Stress Analysis Using the Ground Survey Result., *Summaries of technical papers of Annual Meeting AIJ*, p623-626, B-1

N. Yoshida, S. Tsujino et al. (1993), "A Simplified Practical Stress-Strain Model for the Multi-Dimensional Analysis under Repeated Loading Part2 Consideration of Dilatancy" *Proc. of Annual Conference of the Japan Society of Civil Engineers*, pp.1221-1224

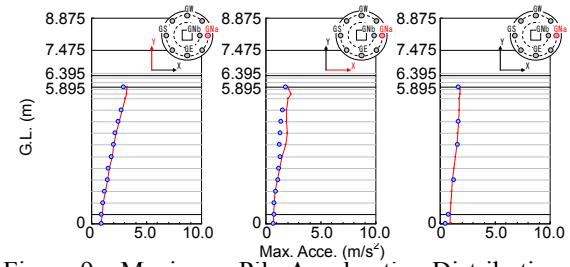

Figure 9 Maximum Pile Acceleration Distribution (Pile Heads Attached)

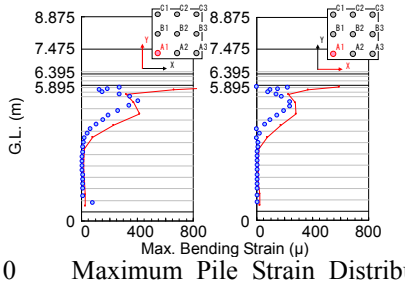

Figure 10 Maximum Pile Strain Distribution (Pile Heads Attached)

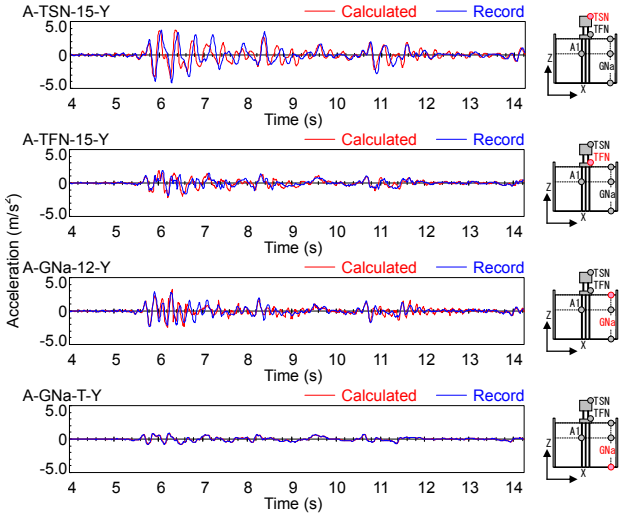

Figure 12 Time Histories of Acceleration on Y Direction (Pile Heads Attached)

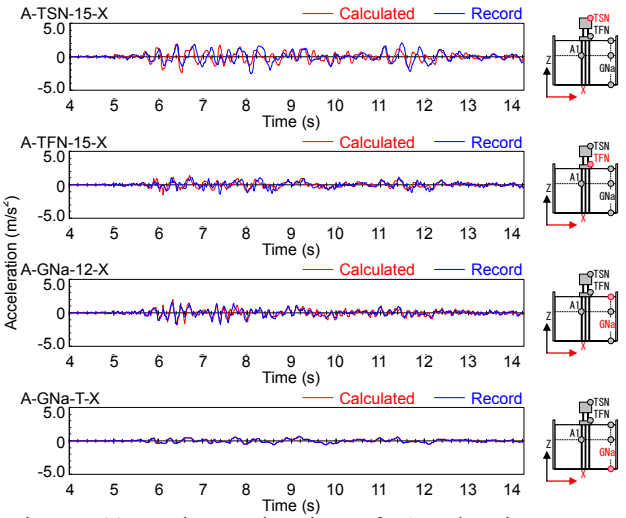

Figure 11 Time Histories of Acceleration on X Direction (Pile Heads Attached)

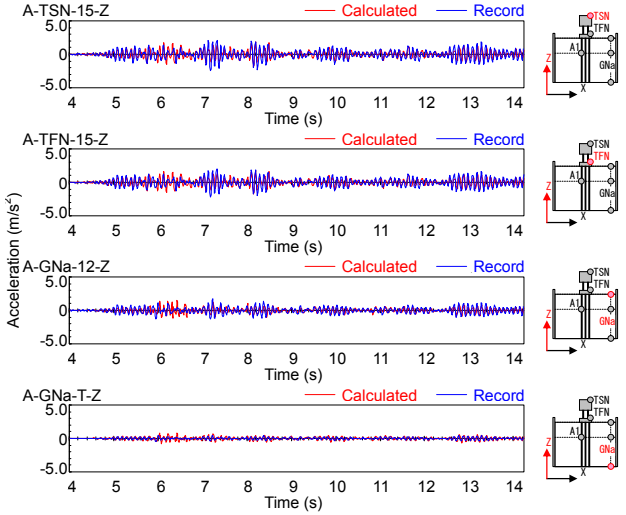

Figure 13 Time Histories of Acceleration on Z Direction (Pile Heads Attached)

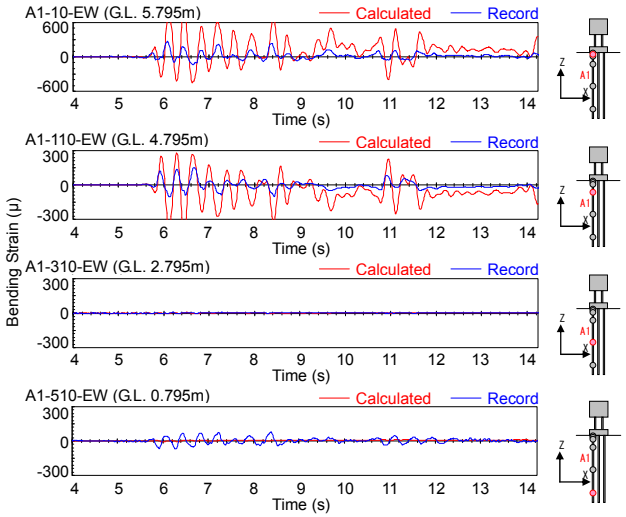

Figure 14 Time Histories of Bending Strains about X Axis of Pile A1 (Pile Heads Attached)

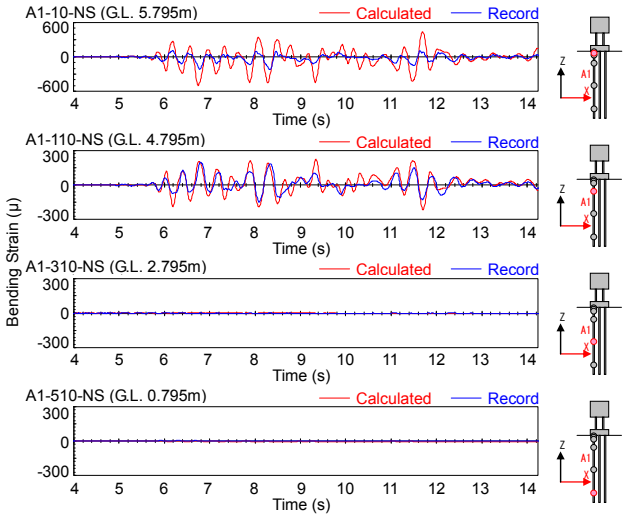

Figure 15 Time Histories of Bending Strains about Y Axis of Pile A1 (Pile Heads Attached)

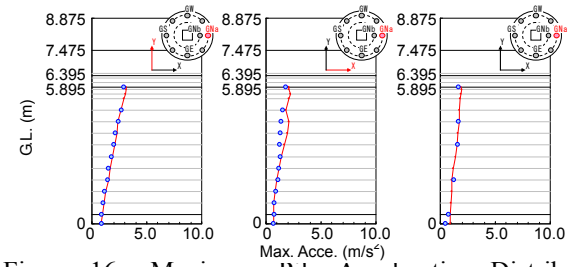

Figure 16 Maximum Pile Acceleration Distribution (Pile Heads Detached)

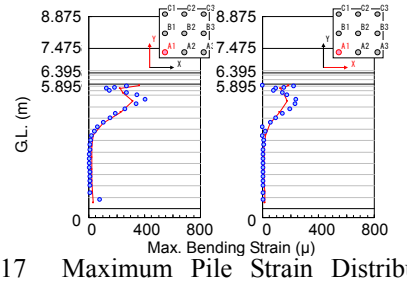

Figure 17 Maximum Pile Strain Distribution (Pile Heads Detached)

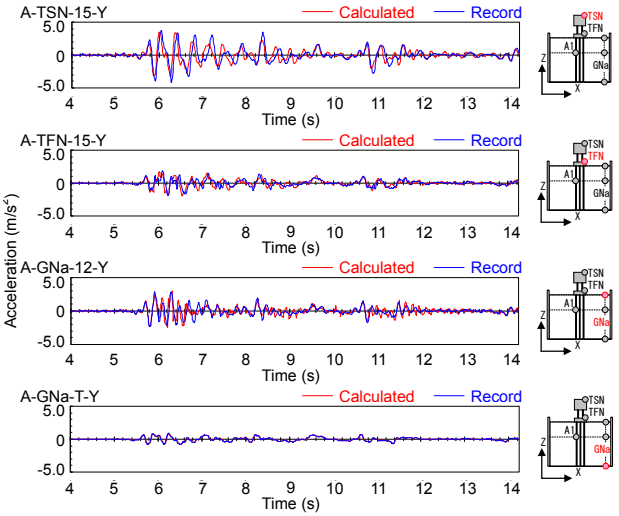

Figure 19 Time Histories of Acceleration on Y Direction (Pile Heads Detached)

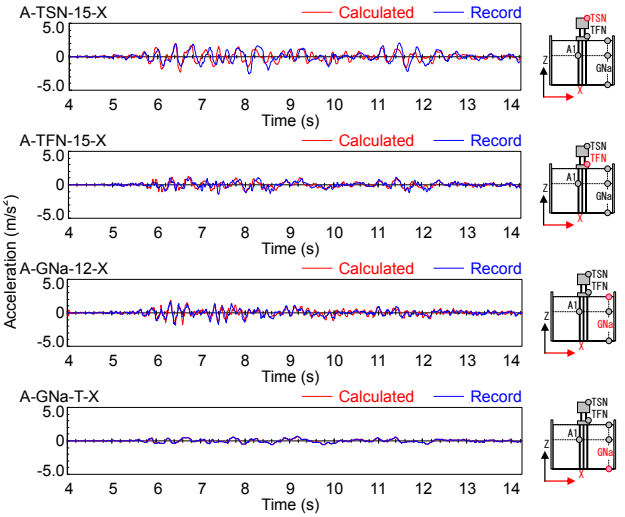

Figure 18 Time Histories of Acceleration on X Direction (Pile Heads Detached)

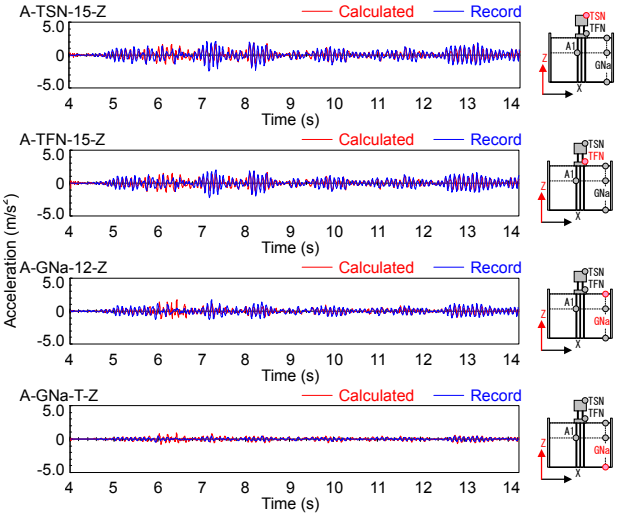

Figure 20 Time Histories of Acceleration on Z Direction (Pile Heads Detached)

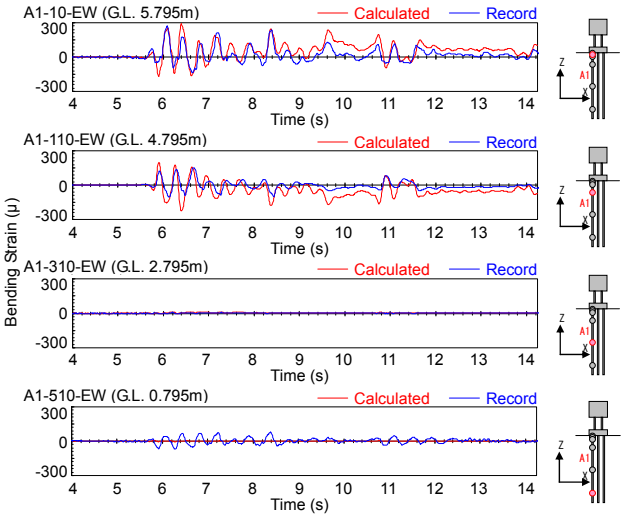

Figure 21 Time Histories of Bending Strains about X Axis of Pile A1 (Pile Heads Detached)

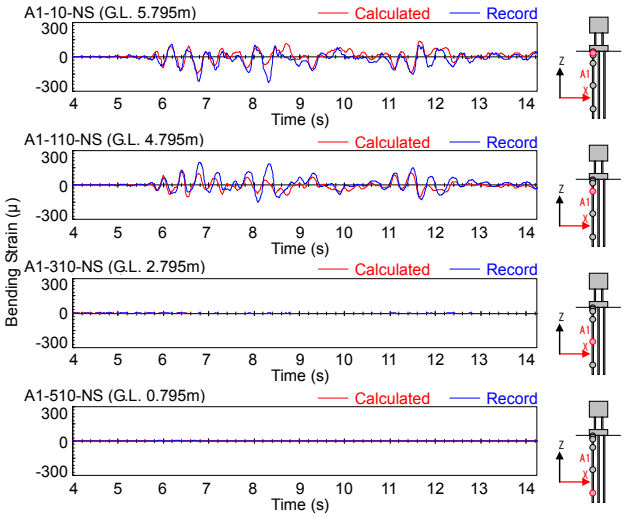

Figure 22 Time Histories of Bending Strains about Y Axis of Pile A1 (Pile Heads Detached)

JOINT CONFERENCE PROCEEDINGS
7th International Conference on Urban Earthquake Engineering (7CUEE) &
5th International Conference on Earthquake Engineering (5ICEE)
March 3-5, 2010, Tokyo Institute of Technology, Tokyo, Japan

SIMULATION ANALYSIS OF SHAKING TABLE TEST ON SOIL-PILE-STRUCTURE MODEL WITH SEMI-RIGID PILE HEAD CONNECTIONS

Sadayuki Ishizaki[1)], Hideki Funahara[2)], Toshiaki Nagao[2)]

1) Research Engineer, Technology Center, Taisei Corp., Japan
2) Senior Research Engineer, Technology Center, Taisei Corp., Japan
sada.ishizaki@sakura.taisei.co.jp, hideki.funahara@sakura.taisei.co.jp, toshiaki.nagao@sakura.taisei.co.jp

Abstract: A simulation analysis of a shaking table test on a soil-pile-structure model with semi-rigid pile head connections is performed using 2D-FEM. The analysis takes into consideration the effects of varying axial force at semi-rigid pile head connections at each time step. Comparisons between simulation results and test results reveal that (1) this simulation analysis is able to successfully predict the test result on the behavior of the superstructure; and (2) this simulation analysis can accurately estimate the difference between the bending moment of pile heads subjected to compression and that of pile heads subjected to pullout force.

1. INTRODUCTION

Several semi-rigid pile head connection methods were developed that permit the rotation of pile heads as more effective pile design methods (for example, Hara et all. 2002). In the previous study by authors (Ishizaki et al. 2009), shaking table tests on soil-pile-structure models were conducted to investigate the seismic behaviour of buildings with semi-rigid pile head connection method. The dynamic test results show that (1) The semi-rigid pile head connection is effective to reduce bending moment of piles and footing beams; (2) In case of semi-rigid pile head connections, the shear force of pile head at the end of building tend to increase, when axial force increase; and (3) The maximum acceleration of superstructure with semi-rigid pile head connections is slightly smaller than that of rigid one. Therefore, it's necessary to take into consideration the dynamic soil-pile-structure interaction and the effects of varying axial force at semi-rigid pile head connections to predict the seismic behavior of building with semi-rigid pile head connection method.

In this study, the simulation analysis of the test is performed using 2D-FEM in which the relationship between the bending moment and the angle of rotation at pile head is expressed as nonlinear elastic rotational spring which varies according to the axial force. And it is investigated how the simulation analysis predict the seismic behavior of the building with semi-rigid pile head connection method.

2. TEST OUTLINE AND TEST RESULTS

2.1 Test Models and Measurement Items

The building, piles and soil assumed in the test (Ishizaki et al. 2009) are listed in Table 1.

The semi-rigid connection model with higher aspect ratio is selected as an analysis object, because it is necessary to estimate the effects of varying axial forces on the behavior of the semi-rigid pile head connection.

The model is outlined in Figure 1. The laminar shear box measured 2.7 m in the direction of shaking, 1.2 m transverse to the direction of shaking and had a depth of 1.5 m. The soil model was created using silica sand No. 5. The target relative density was set at 90% to minimize the variations of soil properties due to soil compaction at each round of shaking. Aluminum pipes with an outer diameter of 70 mm and a thickness of 1.5 mm were used as piles. Two spans constituted the foundation in the direction of shaking and a single span in the direction perpendicular to the direction of shaking. Pile tips were connected using pins to the bottom of the laminar shear box. Pile heads were connected semi-rigidly to the pile cap.

The building model was composed of a weight (steel plates) and plate springs. The total of weights above the plate springs was 5000 N. The own natural period of the superstructure was 0.065s, it was calculated by a transfer function between the top of the building and the pile cap.

The cross section of the semi-rigid pile head connection is shown in Figure 2. At first, a pile cap was placed on the pile head as in the actual structure (Hara et al. 2002). The semi-rigid pile head connection method is designed to have

varying rigidity according to the axial force at the pile head. Some of pile heads were unlikely to contact the pile cap when the frame of the building was assembled. Bolts were therefore installed to connect the pile heads to the pile cap before conducting the test, then applied an axial force of approximately 300 N to 500 N. The rotation characteristics at the pile head connection were identified in preliminary static tests. A cantilever beam composed of a pile cap and a pile was used as a model. Piles were subjected to loading and unloading in a direction perpendicular to the axis, and the bending moment and the angle of rotation at pile head were measured. Several initial axial forces were applied to the semi-rigid connection model. The relationships between bending moment and angle of rotation are shown in Figure 3. In the tests, the angle of rotation increased drastically as the bending moment increased. The relationship between the bending moment and the angle of rotation were represented by nearly the same curve either in loading or unloading. Thus, the model exhibited nonlinear elastic behavior. The bending moment was found to correspond to the initial axial force.

Measurement items are shown in Figure 1. Measured were the horizontal and vertical accelerations of soil and structure; lateral displacements of pile cap and building; strains of piles and footing beams; angles of rotation of pile heads; and strain of bolt for applying axial forces to the semi-rigid connection models.

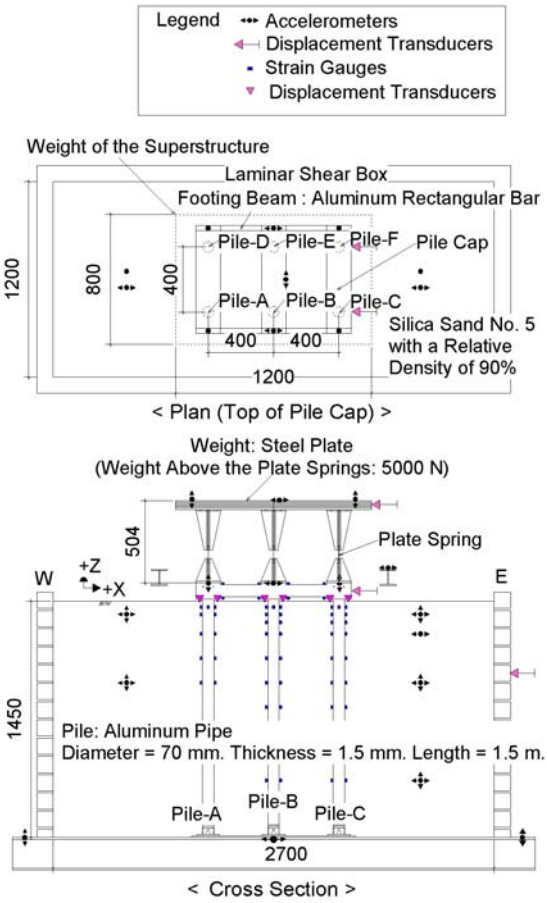

Figure 1 Outline of Model and Measurement Items

The pile head axial force varied slightly from pile to pile. On the other hand, the rigidity against pile head rotation was also considered to vary according to the axial force. In the following discussions, therefore, the bending moments in the piles were evaluated using a mean value for two piles perpendicular to the direction of excitation. For example, a mean value was obtained between Piles-A and -D, and represented as Pile-AD.

The N-S component of the Hachinohe record was used as an input motion for excitation. The amplitude was adjusted to obtain a maximum horizontal velocity of 50 cm/sec for Level 2 ground motion in prototype scale. The distributions of axial forces just before excitation are shown in Table 2.

Table 1 Building, Piles and Soil Assumed in This Study

Building	Eleven-storied Reinforced Concrete Rigid-frame Structure with a Period of 0.8 Second
Piles	Cast-in-place Reinforced Concrete Pile with an Axial Diameter of 1200 mm
Soil	Surface Soil Depth: 25 m. γ = 16 kN/m^3. N-value: 10. Vs = Approximately 150 m/sec

Table 2 Axial Force Before Excitation

Pile-AD	Pile-BE	Pile-CF
1700N	1100N	1400N

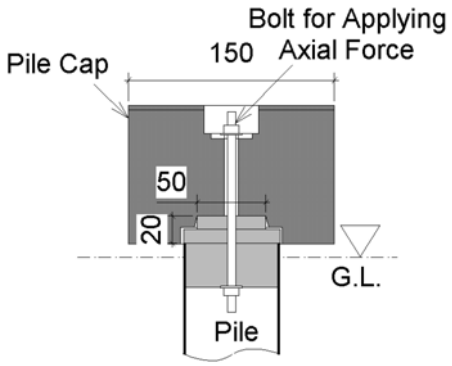

Figure 2 Cross Section of Semi-Rigid Pile Head Connection

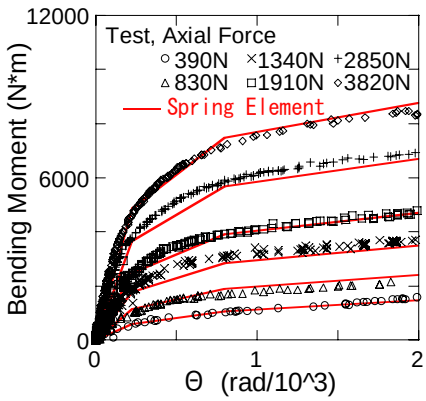

Figure 3 Results of Preliminary Test at Pile Head and Spring Element in Simulation Analysis

2.2 Test Results

Some representative results are described below. Figure 4 shows distributions of bending moments along the piles and footing beams nearly at the second when a maximum inertia force acted from the building. And Figure 5 shows the distributions of shear force along the piles at the same timing. The bending moment in the pile subjected to compression due to overturning moment (Pile-CF) are higher than that in the pile subjected to pullout force due to overturning moment (Pile-AD). And the shear force concentrated at the end pile subjected to compression (front piles) because of the variation of axial force and the positioning of piles (Pile-CF).

3. SIMULATION MODELS

Two dimensional finite element analysis is employed to simulate the shaking table test on the soil-pile-structure model with semi-rigid pile head connections. The finite element model is shown in Figure 6.

The soil is modeled using plane strain elements. The nonlinearity of the shear stiffness is represented by Ramberg-Osgood model. Model parameters of the soil are based on the torsional shear tests on hollow cylindrical specimens under low confining pressure. The piles, the footing beams, and the building are modeled using linear beam elements. Rayleigh damping is adopted, and the damping factors of the soil-pile-structure system are assumed as 1% at first and second eigen periods.

It is important to take into account the effects of varying axial forces on the behavior of the semi-rigid pile head connection model. In this study, the relationship between the bending moment and the angle of rotation at the pile heads is modeled using a spring element, which exhibits nonlinear elastic behavior and takes into consideration the effects of varying axial force. The skeleton curve of this spring element is tri-linear, and the bending moment at the yield points changes in proportion to the axial force, but rotation angle at the yield points doesn't change. The relationship between bending moment and angle of rotation at the pile head of the spring element is compared with the test result (Figure 3). The skeleton curve obtained from the spring element agrees well with the test results. In this dynamic analysis, the skeleton curve varies according to the axial force at each time step (Figure 7).

The observed acceleration at the bottom of the laminar box is used as an input motion in this simulation analysis.

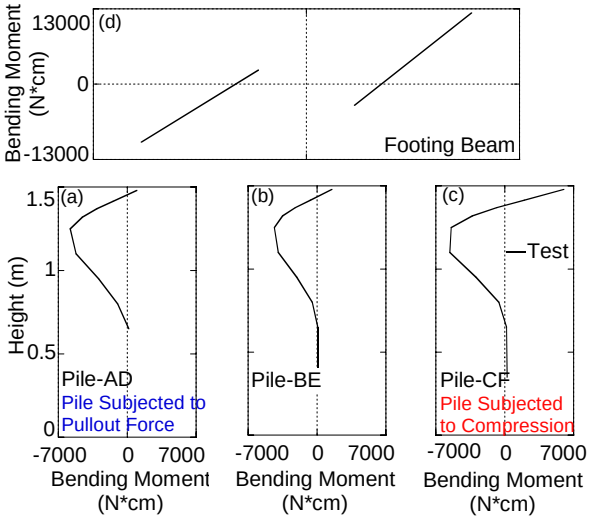

Figure 4 Distributions of Bending Moments of Pile and Footing Beams (Nearly at T = 1.24 Seconds)

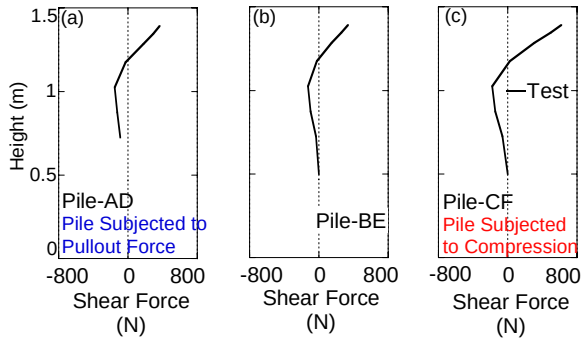

Figure 5 Distributions of Pile Shear Forces (Nearly at T = 1.24 Seconds)

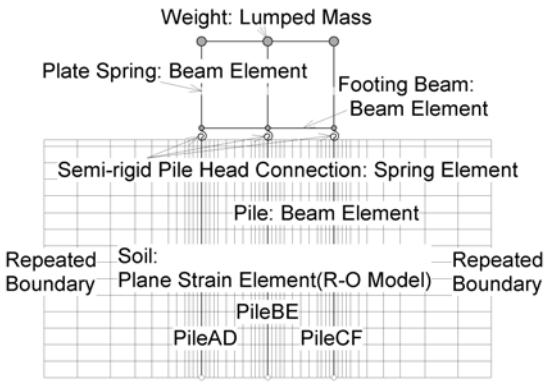

Figure 6 Finite Element Model

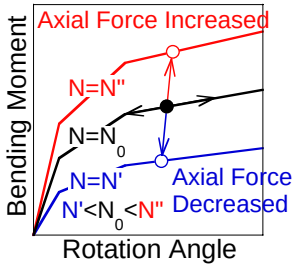

Figure 7 Spring Element Under Varying Axial Force

4. COMPARISONS BETWEEN TEST RESULTS AND SIMULATION RESULTS

The observed and calculated time histories are compared in Figure 8. The simulation results show good agreement with test results of the acceleration of the building, the displacement of the footing, and the bending moment of pile head. But the shear force at pile head tends to be higher in the simulation than that in the test when the pile is subjected to pullout force.

The observed and calculated distributions of bending moment along piles and footing beam nearly at T = 1.24 seconds when the maximum inertia force acts from the building are compared in Figure 9. And the observed and calculated distributions of shear force along piles at the same timing are compared in Figure 10. The observed and calculated distributions show a following similar tendency. As seen in the test result, simulation results show that the pile head bending moment in pile subjected to compression is higher than that in pile subjected to pullout force, and large shear force occurs on the pile head subjected to compression.

The observed and calculated relationships between bending moment and angle of rotation at pile head, and those between axial force and angle of rotation at pile head are shown in Figure 11. In the test result of Pile-AD, the bending moment once increases in the first quadrant. But it decreases with increasing rotation angle because the axial force decreases. The simulation result shows nearly the same characteristic curve, because the spring element takes into account the effects of axial force at each time step. But a drastic increase of the rotation angle nearly at T = 1.24 seconds in the test isn't simulated accurately. At this timing, the observed and calculated displacements of footing are positive. On the other hand, the observed displacement of the ground is negative but the calculated displacement of the ground is positive(Figures 8 (b) and (c)). In other words, this two dimensional finite element analysis doesn't represent the relative displacement between piles and the surrounding soil at this timing. Two reasons are supposable for this simulation result. First, the extreme nonlinearity of the soil near the pile isn't estimated in this simulation. Second, the rear soil elements of the pile in direction of the relative displacement don't loose but pull the pile. Therefore soil reactions could be overestimated on the pile near the ground level.

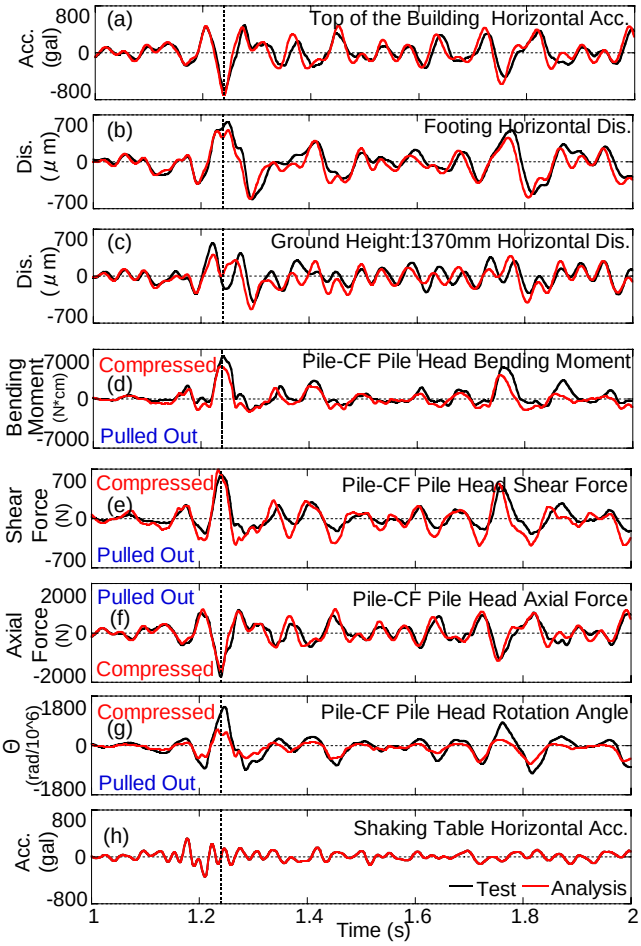

Figure 8 Major Time Histories

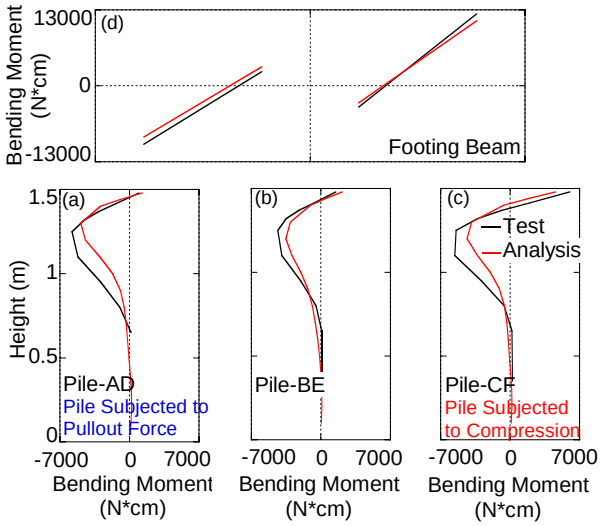

Figure 9 Distributions of Bending Moments Along Piles and Footing Beams (Nearly at T = 1.24 Seconds)

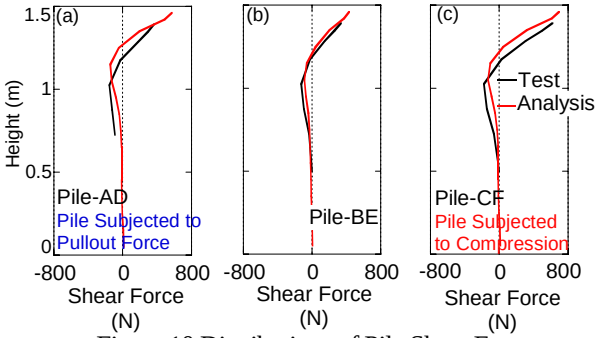

Figure 10 Distributions of Pile Shear Forces (Nearly at T = 1.24 Seconds)

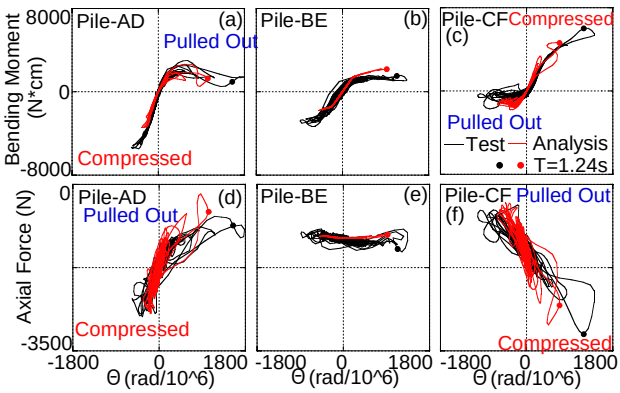

Figure 11 Bending Moment and Angle of Rotation at Pile Head, and Axial Force and Angle of Rotation at Pile Head

5. CONCLUSIONS

The simulation analysis of the shaking table test on the soil-pile-structure model with semi-rigid pile head connections is performed using 2D-FEM. In the analysis, the relationship between the bending moment and the angle of rotation at the pile head is expressed as nonlinear elastic rotational spring which vary according to the axial force at each time step. The simulation results are compared to the test results. The conclusions are described below.

1) This simulation analysis which takes into consideration the effects of varying axial force at semi-rigid pile head connections is able to successfully predict the test results on the behavior of the superstructure: acceleration of the superstructure and displacement of the basement.

2) This simulation analysis can estimate the characteristic distributions of bending moment and shear force along the piles as seen in the test. That is, the simulation analysis shows that the bending moment of the pile head subjected to compression is higher than that of pile head subjected to pullout force, and the large shear force occurs on the pile head subjected to compression.

This study was conducted as a part of the special project for earthquake disaster mitigation in urban areas (theme II significant improvement of seismic performance of structures) launched by the Ministry of Education, Culture, Sports, Science and Technology.

References:

Hara, T. Yasuda, S. Kawabata, I. Komuro, T. Korenaga, T. Tatsuno, S. (2002), "Development of Pile Head-Foundation Joint without Anchorage of Pile Rebar," Summaries of Technical Papers of Annual Meeting, AIJ, C-2, 187-190.

Ishizaki, S. Majima, M. Nagao, T. Funahara, H. Aoshima, K. (2009), "Shaking Table Tests on Soil-Pile-Structure Models with Semi-Rigid Pile Head Connections," *Proceedings of the 6th International Conference on Urban Earthquake Engineering*, 555-560.

JOINT CONFERENCE PROCEEDINGS
7th International Conference on Urban Earthquake Engineering (7CUEE) &
5th International Conference on Earthquake Engineering (5ICEE)
March 3-5, 2010, Tokyo Institute of Technology, Tokyo, Japan

CHARACTERISATION OF ERT AS A NEW NON-INVASIVE MONITORING METHOD OF LIQUEFACTION PROCESS

Suresh R. Dash[1)], Suresh Kumar N. K.[2)], Subhamoy Bhattacharya[3)] and Anthony Blakeborough[4)]

1) DPhil Scholar, Department of Engineering Science, University of Oxford, UK
2) MSc Scholar, Department of Engineering Science, University of Oxford, UK
3) University Lecturer, Department of Civil Engineering, University of Bristol, UK
4) Professor, Department of Engineering Science, University of Oxford, UK

Suresh.Dash@eng.ox.ac.uk, suresh@robots.ox.ac.uk, S.Bhattacharya@bristol.ac.uk, Tony.Blakeborough@eng.ox.ac.uk,

Abstract: Often, while studying liquefaction at micro level in saturated sandy soils in laboratory environment, placing Pore-Pressure-Transducer (PPT) to measure the degree of liquefaction becomes undesirable. This situation mainly arises where the local disturbances to the soil sample is significant due to the placement of PPT. The present study looks at another way of measuring liquefaction by using Electrical Resistance Tomography (ERT). The major benefit of ERT method is derived from its non-invasive technique of measurement. In this paper we attempt to study how ERT can be used to measure liquefaction in laboratory environment. To achieve that, as a first step, three small scale experimental setups are prepared to characterize the soil sample. This paper presents the background theory of ERT, its suitability and limitations with respect to its usability in monitoring liquefaction.

1. INTRODUCTION

Miniature Pore-Pressure-Transducers (PPTs) having sizes 6mm-12mm diameter and about 10mm long are most often used in small scale experiments to monitor liquefaction. However, using these sensors for soil-structure interaction model may be problematic as they may disturb the soil sample locally around it. This makes the measurements, thus obtained, difficult to interpret as they may not reflect the actual free field condition. This situation becomes more undesirable when the purpose of the experiment is to study liquefaction behaviour at micro level. Thus, a non-invasive method of liquefaction monitoring is often sought.

Electrical Resistance Tomography (ERT) is a non-invasive technique that is widely used in geophysical explorations (Milson 2003). In ERT, the electrical resistivity measurements are taken at the surface to image subsurface structures. While much research has been carried out to characterize ERT methods and its configuration in the field, relatively little has been done on its applicability at laboratory scale with validation. To use ERT technique to monitor liquefaction during the laboratory tests requires an intensive set of tests to calibrate the saturated sand.

This paper aims to investigate the background theory of ERT, its calibration technique and suitability for implementing in the experimental studies involving liquefaction.

2. HOW DOES ERT WORK?

2.1 ERT theory

The Electrical Resistivity Tomography (ERT) employed in geophysical exploration normally involves making a dipole configuration on the earth surface by placing the current electrodes at a defined spacing. The electric field potential is then measured at different locations of known electrode configuration. Figure 1 shows a schematic of the Wenner's configuration, which is one of the widely used electrode arrangement in geophysical study (Milson 2003).

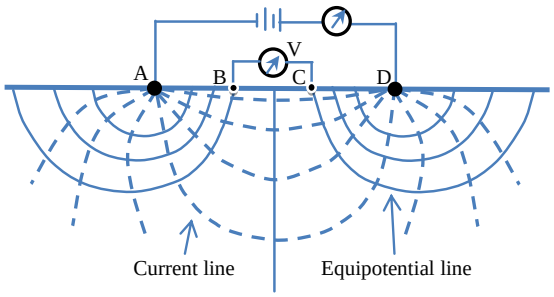

Figure 1 Wenner's Electrode configuration for ERT

Wenner's configuration consists of four electrodes (A, B, C and D as in Figure 1) in a line separated by equal intervals, 'a'. The apparent resistivity in the soil (ρ_a) is calculated by measuring the potential difference between the two middle electrodes as:

$$\rho_a = 2 \pi a (V/I) \quad \text{(Eq. 1)}$$

where
V = Potential difference between two mid electrodes
I = Current flowing through the circuit

Here, the term apparent resistivity (ρ_a) should not be confused with the actual resistivity (ρ) of the material at a particular position. The resistivity calculated by Eq.1 is the average resistivity of the material between the electrodes considering the material to be homogeneous, even if the measurements are made over heterogeneous earth. Hence, ρ (resistivity) is normally denoted by ρ_a (apparent resistivity) in ERT systems (Eq.1).

2.2 ERT for liquefiable soil

Experimentally, it has been shown by numerous researchers (Archie 1942, Arulmoli et al. 1985, Jinguuji et al. 2007 and Dikjastra et al. 2008) that a non-dimensional parameter, the formation factor (F), can fairly characterize the particle shape, orientation, size distribution, degree of saturation, anisotropy and porosity of soil as a lumped parameter. The formation factor for a particular soil can be calculated using Archie's law (Archie 1942) as given in Eq. (2).

$$F = an^{-m} \quad \text{(Eq.2)}$$

Where
F = Formation factor
n = Porosity of soil
a, m = Constants depending on geometry of soil pores

The quantities 'a' and 'm' have been reported to vary widely for different formations. Typical values of 'a' range from 0.47 to 2.3 and the value of 'm' generally varies between 1 for uncemented soil (sand) to 3 for fully cemented soil (clay) (Sammis and Henyey 1987).

The process of liquefaction is unarguably a complex physical phenomenon where the saturated sandy soil changes its state from solid to fluid due to development of excess pore fluid pressure. During the process of liquefaction in saturated sandy soil the arrangement of pore fluid in the soil skeleton changes. This affects the porosity of the soil-fluid medium, which may change the formation factor of the soil. If this formation factor can be related to the degree of liquefaction, then the electrical resistivity measurement of the soil can be used to calculate the degree of liquefaction. If this is valid, it can be employed during the test to monitor the degree of liquefaction in the soil continuously and non-invasively.

Though this method seems very promising, it is necessary to understand that the electrical resistance of soil is not a simple and straight forward parameter like other geotechnical parameters such as water-content, liquid limit, plastic limit, etc. (Gio et al 2003). There are many factors that affect the electrical resistivity of saturated sand. The major ones can be grouped into three categories such as:

a) Bulk soil and the volumetric fractions occupied by the two phases (soil and water) which can be described as porosity.
b) Relatively time-invariable solid quantifiers which can be described with the particle shape and orientation, particle-size distribution and its ion exchange capacity.
c) Soil solution (pore fluid) which can be a time varying quantity due to the restructuring of the ion exchange path.

These factors may be considered as constant in field measurements; but, this is not true in laboratory tests. Also, it is extremely difficult to control all these parameters in repeating the sample preparation in the laboratory and there is not much guidance available in the literature for the same. This study attempts to see if the formation factor (F, as in equation 2) can be treated as a major governing parameter to quantify liquefaction. Using this parameter as a tool, liquefaction can be monitored continuously during the tests. In this study, experimental procedures are designed (i.e. setup-1 and setup 2) to quantify porosity (n) with respect to the electrical resistivity of sand, considering 'a' and 'm' (Eq.2) are constants.

3. TEST SETUP

The test setup has been carried out in three stages.

3.1 Setup-1 (To calibrate ERT configuration of test Setup-2)

The first test setup (Figure 2) is to measure the resistivity of a homogeneous fluid solution by conventional Ohm's law. The solution is prepared from De-Ionised (DI) water by adding 0.1% NaCl since the resistivity of deionised water is very high. The same solution is used in the first part of the following test setup (Setup-2 A). The resistivity value obtained in Setup-1 is compared with the values obtained from Setup-2A for the same solution. The aim of the Setup-1 is to confirm the applicability of the ERT configuration in Setup-2 (Four node Wenner configuration) for further experimental study.

In Setup-1, the solution is kept in an insulated cylinder of known volume (Figure 2). Two copper plates are connected on both the sides of the tube to act like a conductive plane and a known resistor and a voltmeter are connected to measure the current and voltage in the circuit. The resistivity of the solution is calculated from the

measured values of *V* and *I* by using Eq.3 as 8 Ohm-m.

$$\rho = \frac{RA}{L} = \frac{V}{I} \times \frac{\pi / 4D^2}{L} \qquad \text{(Eq.3)}$$

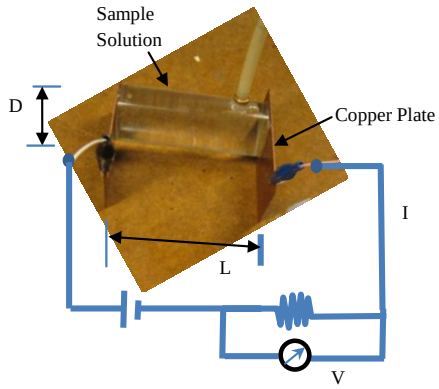

Figure 2 Test setup for measuring resistivity of a homogenous fluid solution (**Setup 1**)

3.2 Setup-2 (To calibrate porosity *versus* resistivity)

This setup calibrates the saturated sand with the ERT type of configuration (Figure 3). The setup is prepared with a Perspex® box of internal dimension 10cm×10cm×20cm. Nine electrodes are fixed 1cm apart on one of the box's inner surfaces. Only the four middle electrodes are used in the present study, which create a Wenner configuration with an inter-electrode spacing of 1cm. The remaining electrodes are provided for further investigation of the electrical resistivity profiling in 2D, beyond the scope of this paper.

There are two types of experiments with this test setup:
A: The solution alone
B: the solution with oven dried sand at a known porosity.

A: This part of the test is primarily meant to characterise Wenner's 4 node configuration. The same solution used in the Setup-1 is placed in the box. The resistivity of the solution is computed using equation 1. The above test is repeated for several times with different values for electric currents at different frequencies (Table 1). The results are presented in Figure 4. The resistivity values obtained from both setup-1 and setup-2 match quite well. It is worth noting that in setup-2 the results are sensitive to the amplitude and frequency of the current source (AC Sinusoidal). The next stage of the study (Clause 4) has been carried out to characterise the test and measurement procedure that will be followed in further tests.

B: Once Wenner's configuration of the ERT is verified, oven dried sand is added to the box and saturated with the same solution (DI water + 0.1% NaCl). The sample is prepared at a known porosity and its electrical resistivity is measured (Figure 5). The details of this test and results will be discussed in section 5.2.

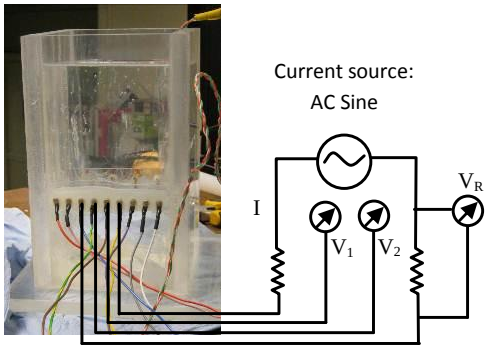

Figure 3 Test setup for calibrating ERT configuration by using a homogeneous solution as the conductive medium (Setup-2A)

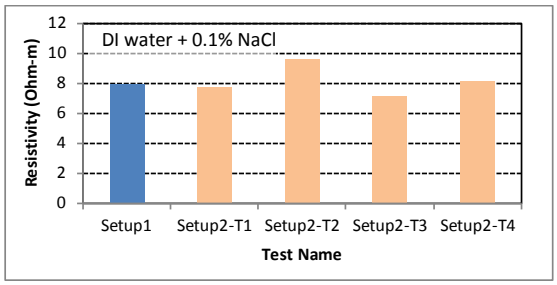

Figure 4 Comparison of resistivity obtained from test setup 1 and test setup 2 for the solution (DI water + 0.1% NaCl).

Table 1 Electrical sources for the tests in Setup-1 &2

Test Name	Input Type	Frequency
Setup 1	DC	--
Setup 2-T1	DC	--
Setup 2-T2	AC	5Hz
Setup 2-T3	AC	10Hz
Setup 2-T4	AC	20Hz

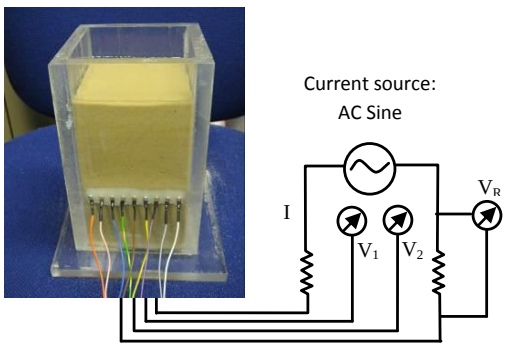

Figure 5 Test setup for calibrating electrical resistivity of saturated sandy soil (Setup-2B)

3.3 Setup-3 (To calibrate pore water pressure *versus* resistivity)

This setup (Figure 6) performs continuous measurement of electrical resistance during liquefaction. The same Wenner's electrode configuration validated in the earlier test Setup-2 is used. The test box measures 24cm×45cm×40cm internally. It is filled with saturated sand and fitted with 4 Pore Pressure Transducers (PPTs). Four electrodes in Wenner's configuration are fixed on the front inner surface of the box. The box is shaken at base to cause liquefaction. Readings of PPTs and ERT electrodes are recorded continuously. The results from this test will be described in section 5.3.

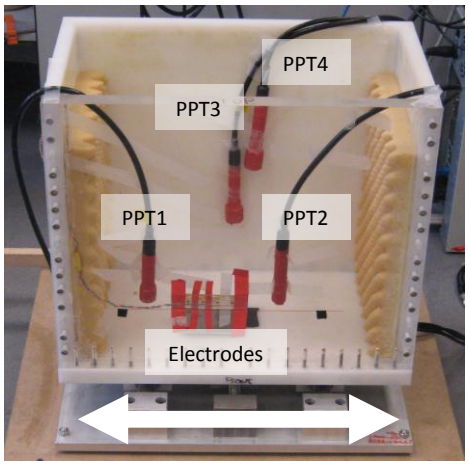

Figure 6 Test box for continuous measurement of electrical resistivity of saturated sandy soil during liquefaction (**Setup -3**).

4. CHRACTERISATION OF TEST SETUP

4.1 Input current, AC or DC

Normally, field electrical resistivity surveys use a DC source. This is better than AC in two ways.

(1) It allows greater depth of investigation, and

(2) it avoids the complexities that may arise in AC supply, such as: ground inductance and ground capacitance.

However, using the electrical resistivity method in the laboratory using DC has the following shortcomings:

1) The electrodes produce polarized ionization fields in the electrolytes around them. This is due to running the tests for long time with the same soil sample.
2) Also, these polarized ionization fields produce additional voltage that may cause the potential distribution in the soil to be different from those measured by the electrodes.

The above shortcomings of DC can be reduced by using AC, but special care needs to be taken to avoid the adverse effect of AC. This can be achieved by using a low frequency AC (typically below 20 Hz) for a very short time. In the present study, the input current used is an AC Sine wave with a frequency of 20 Hz, which gives more consistent results.

4.2 Measurement of resistance in AC circuit

Ohm's law, $V = IR$, also applies to resistors in an AC circuit in the same way as in DC circuit. In AC circuit, instead of instantaneous V and I values, RMS values are to be used in equation 1 while estimating the electrical resistivity of soil.

4.3 Tools and instruments

The main components of the test setup are detailed below.

- Power Source: AC analog voltage source obtained from dSpace® board (± 10V) with a current capacity of about 5mA.
- Data Logging: dSpace® data logger with 16 bit A/D connections.
- Electrode: 4 electrodes in Wenner configuration. each are spaced 1cm apart.
- Resistor: A known resistor of 250 Ω is used in the circuit to measure the current.

5. CHARACTERIZATION OF SAND

5.1 Basic properties of the sand

The sand sample taken for this test is Red Hill amber sand. The friction angle is 32.9˚, evaluated from the dry slope test. However, the static shear box test showed that the friction angle varied from 32.1˚ to 29.1˚ for the unit weight of 17.6 kN/m^3 to 15.7 kN/m^3 respectively.

5.2 Relationship between porosity and electrical resistance

The concept of electrical resistance tomography for liquefaction is based on the assumption that the grain material has far higher resistance as compared to the pore fluid. The ERT method, hence, tries to observe the changes in the arrangement of the pore fluid in the soil skeleton. To characterize this, tests are carried out to establish the relationship between porosity and the electrical resistivity. For this purpose, the test Setup 2B (Figure 5) is used.

This is one of the most important parts of ERT calibration and it needs special care while preparing sand sample at desired porosity. It is also necessary to change the porosity of the same sample and repeat the resistivity measurement. Setup 2B allows us to prepare a fully saturated loose soil sample initially. The density of the sample is changed by tapping and shaking the box. Figure 7 shows the plot for a range of porosity obtained in the tests. As expected, the figure shows a decreasing electrical resistivity with increasing porosity. With this box it is difficult to prepare fully saturated soil sample with a bigger

range of porosities. More porosity conditions in fully saturated soil are needed to establish a better relationship for the apparent electrical resistivity of the soil. This relationship can then be represented as formation factor versus resistivity for the sand, if Archie's constants (*a,m* in Eq.2) are not much affected during the liquefaction test.

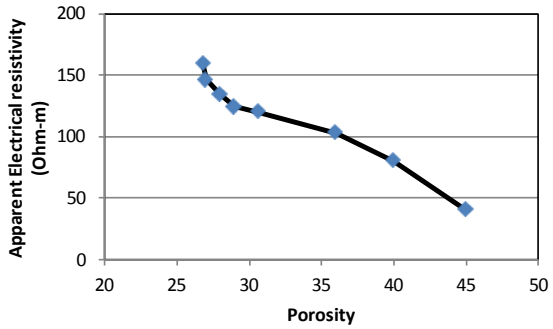

Figure 7 Porosity *versus* electrical resistivity of the soil.

5.3 Relationship between pore water pressure and electrical resistance

The relationship between pore water pressure and electrical resistivity of the sand is studied with test setup 3 (Figure 6). The box is filled with saturated sand placed on a shaking table. The electrical resistivity and the pore water pressure are monitored continuously throughout the shaking. The PPTs placed inside the box are electrically insulated to avoid any effect on the ERT readings. The resistivity is calculated for the whole length of test by using RMS value of the recorded ERT reading. Results from one test during the shaking are shown in Figure 8. The figure plots pore pressure ratio (from PPT1) and apparent resistivity of soil with respect to time. The pore pressure ratio is defined as the ratio between excess pore pressure (developed during shaking) and initial vertical effective stress in the soil at the considered location.

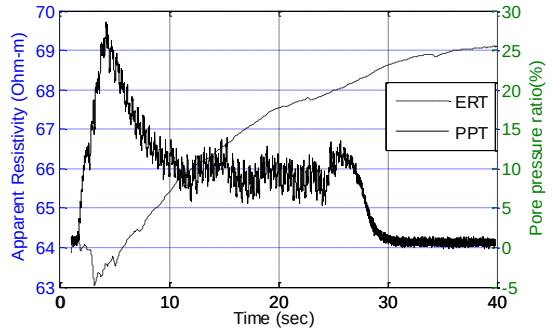

Figure 8 Pore pressure ratio versus apparent electrical resistivity during 1g shaking test in saturated sand.

Figure 8 shows that the change in pore pressure causes the rearrangement of the pore fluid and consequently changes the electrical resistivity. The dilation during pore pressure generation and the densification during pore pressure dissipation are being reflected in the resistivity readings. The figure also shows that the density of the sand increases during post liquefaction stage. Though these observations are very promising, they are still qualitative. To make a quantitative judgement from ERT test alone requires rigorous characterisation procedure, which is the scope of further research.

6. CONCLUSIONS

The present study shows that electrical resistivity tomography (ERT) can be a useful tool to monitor liquefaction during experiments non-invasively. However, the difficulty lies in characterising the formation factor of the soil that can be used as a benchmark to define the degree of liquefaction. This work sets the test and measurement procedure as the base for future research. This will be useful to establish the relationship between apparent electrical resistivity with respect to formation factor (*F*) and the degree of liquefaction for the particular sand.

References:

Archie, G.E. (1942), "The electrical resistivity log as an aid in determining some reservoir characteristics," *AIME transaction*, Vol-**146**, 54–61.

Arulmoli, K., Arulanandan, K. and Seed, H.B. (1985), "New method for evaluating liquefaction potential," *Journal of Geotechnical Engineering*. **111** (1), 95–114.

Jinguuji, M., Toprak, S. and Kunimatsu, S. (2007), "Visualization technique for liquefaction process in chamber experiments by using electrical resistivity monitoring," *Soil Dynamics and Earthquake Engineering*, **27**(3), 191-199.

Dikjastra, J., Broere, W., Bezuijen, A. and Van Tol, A.F. (2008), "Density changes near an advancing displacement pile in sand," *Proc. 2nd BGA Intl. Conf. on Foundations*, Brown M.J., Bransby M.F., Brennan A.J, and Knappett J.A. (Editors). 545-554.

Giao, P.H., Chung, S.G., Kim, D.Y. and Tanaka, H. (2003), "Electrical imaging and laboratory resistivity testing for geotechnical investigation of Pusan clay deposits," Journal of Applied Geophysics, **52**, 157-175.

Milson, J. (2003) *Field Geophysics*, 3rd Edition, Wiley Press.

Sammis C.G. and Henyey, T.L. (1987) *Methods of experimental physics, Vol-24, Geophysics: Field measurements*. Academic Press Inc (London) Ltd.

JOINT CONFERENCE PROCEEDINGS
7th International Conference on Urban Earthquake Engineering (7CUEE) &
5th International Conference on Earthquake Engineering (5ICEE)
March 3-5, 2010, Tokyo Institute of Technology, Tokyo, Japan

LARGE DEFORMATION ANALYSIS OF DYNAMIC BEHAVIOR OF EMBANKMENT ON LIQUEFIABLE SAND DEPOSIT USING A STRAIN SPACE MULTIPLE MECHANISM MODEL

Kyohei Ueda[1], Susumu Iai[2], and Tetsuo Tobita[3]

1) Graduate Student, Department of Civil and Earth Resources Engineering, Kyoto University, Japan
2) Professor, Disaster Prevention Research Institute, Kyoto University, Japan
3) Assistant Professor, Disaster Prevention Research Institute, Kyoto University, Japan
ueda@geotech.dpri.kyoto-u.ac.jp, iai@geotech.dpri.kyoto-u.ac.jp, tobita@geotech.dpri.kyoto-u.ac.jp

Abstract: In order to verify the applicability of an effective stress model, infinitesimal and large deformation analyses are performed on the dynamic behavior of a sand embankment on liquefiable sand deposit in geotechnical centrifuge experiments. The model used in the analysis is a strain space multiple mechanism model, which has been extended based on finite strain formulation (both total and updated Lagrangian formulations) to take into account the effect of geometrical nonlinearity. Comparison between the experimental and analytical results indicates that the infinitesimal deformation analysis overestimates the amount of the crest settlement approximately as three times as that measured, while the large deformation analyses give close agreements with that measured. The results obtained in total and updated Lagrangian formulations are consistent with each other, and thereby demonstrating the validity of the computer programming for large deformation analysis. In order to predict the amount of deformation of embankments during earthquake accurately, it is necessary to carry out a finite element analysis by taking into account the effect of not only material nonlinearity but also geometrical nonlinearity with total or updated Lagrangian formulations.

1. INTRODUCTION

Seismic design of embankments has been conventionally performed by using the circular arc method based on the pseudo-static limit equilibrium method. With an appropriately assigned safety factor, the design provides an acceptable degree of seismic resistance for the embankments which are founded on firm foundation soils. However, the conventional pseudo-static method has no capability to take into account the characteristics of earthquake motion and the variation in behavior of soils due to liquefaction. Therefore serious problems arise in seismic design in terms of accuracy when the method is applied to the embankments which are constructed on liquefiable deposits.

In order to estimate the degree of liquefaction-induced deformation of embankments, many studies have been performed by using numerical methods as represented by the finite element method. Ozutsumi et al. (2002) carried out a series of effective stress analyses on the seismic performance of river dikes based on the case histories of the Hokkaido -Nansei-oki earthquake (1993) and Hyogoken-Nambu earthquake (1995) in Japan. Tobita et al. (2006) performed centrifuge model tests to study dynamic behavior of a sand embankment on saturated sand deposits with a variety of relative densities, and carried out effective stress analyses to verify the applicability to the liquefaction-induced behavior in the experiments.

The effective stress model used in these two studies was a strain space multiple mechanism model (Iai et al., 1992a). This model can take into account the effect of rotation of principal stress axis directions, the effect of which is known to play an important role in the cyclic behavior of the anisotropically consolidated sand (Iai et al., 1992b). However, the formulation of the model has been carried out based on the infinitesimal strain theory, and thereby the model has difficulty in analyzing large deformation and rotation. In other words, beyond a strain level of about 10 % the model is unable to take into account the effect of geometrical nonlinearity (Ueda, 2009).

In the Hyogoken-Nambu earthquake (1995) in Japan, it is reported that the seismic wave induced large crest settlements (up to 3.0 m) of embankments (JICE, 2002). In the next 30 years, it is predicted that Japan will be hit by some major earthquakes (e.g., Tokai and Tonankai earthquakes), which are likely to cause serious damage to earth structures such as embankments. Therefore it is necessary to take into account geometrical nonlinearity in numerical simulations for dynamic behavior of the geotechnical structures. For these reasons, the strain space multiple mechanism model has been extended based on two types of finite strain formulations (total and updated Lagrangian) for large deformation analyses (Iai et al., 2009a).

In this research, performance of the model which takes into account the effect of geometrical nonlinearity is studied for its capability to simulate the dynamic behavior of embankments on liquefiable sand deposits during shaking. The target of the simulation is the centrifuge model test performed in the P.W.R.I. (2000). In what follows, units are in prototype if not otherwise specified.

2. SUMMARY OF CENTRIFUGE MODEL TEST

To study the dynamic behavior of an embankment on a liquefiable sand deposit, a series of centrifuge model tests was performed in the P.W.R.I (2000). The applied centrifugal acceleration was 50 G. In the experiments, various sorts of countermeasures were adopted. In this research, the target of the simulation is the result of the test case with no countermeasures.

A model configuration shown in Fig. 1 is a cross section of an embankment on the sand deposit with 13.0 m depth. The crest height is 5.0 m, and lateral length at the top and bottom are 3.0 m and 23.0 m, respectively. Groundwater level is at 1.8 m below the surface of the ground. The relative density of the upper and lower layer of the saturated sand deposit is approximately 60 % and 90 %, respectively. Table 1 shows the physical properties of the Edosaki sand, which was used for the upper deposit and embankment, and the silica sand No.7, which was used for the lower deposit. Aggregates were placed at the bottom of the embankment with the aim of preventing the embankment from soaking up pore water by suction.

Figure 2 shows the input motion, which is composed of seven sinusoidal waves (main shock) with a peak acceleration of approximately 0.4 g and subsequent aftershocks with acceleration amplitudes less than 0.1 g. The induced crest settlement was 2.04 m at the end of the main shocks, and 2.30 m at the end of the aftershocks.

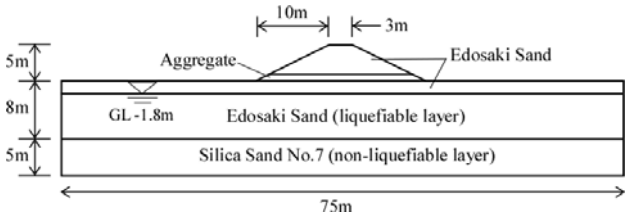

Figure 1 Cross-section diagram in centrifuge model test (Modified after P.W.R.I. (2000))

Table 1 Physical properties of sands (P.W.R.I. (2000))

	Edosaki Sand	Silica Sand (No.7)
density of sand (g/cm^3)	2.684	2.642
fines content Fc (%)	10.8	0.7
average grain size/diameter D_{50} (mm)	0.181	0.169
relative density Dr (%)	60.7	90.8

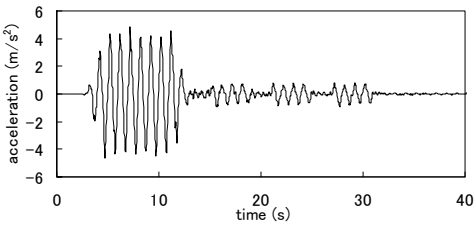

Figure 2 Input acceleration (P.W.R.I. (2000))

3. CONSTITUTIVE MODEL OF SOILS

3.1 Generalized Multiple Mechanism Model Based on Infinitesimal Deformation Theory

The effective stress model of sands to be used in this study is a strain space multiple mechanism model (Iai et al., 1992a; Iai and Ozutsumi, 2005). This model has been extended as a generalized form by introducing a new stress-dilatancy relationship proposed by Iai et al. (2008).

With the effective stress and strain vectors in plane strain condition expressed as

$$\boldsymbol{\sigma}' = \left\{ \sigma'_x \quad \sigma'_y \quad \tau_{xy} \right\}^{\mathrm{T}} \tag{1}$$

$$\boldsymbol{\varepsilon} = \left\{ \varepsilon_x \quad \varepsilon_y \quad \gamma_{xy} \right\}^{\mathrm{T}} \tag{2}$$

the integrated form of the constitutive relation is given by

$$\boldsymbol{\sigma}' = -p\mathbf{I} + \sum_{i=1}^{I} q^{(i)} \left\langle \mathbf{t}^{(i)} \otimes \mathbf{n}^{(i)} \right\rangle \Delta\omega \tag{3}$$

$$\left\langle \mathbf{t}^{(i)} \otimes \mathbf{n}^{(i)} \right\rangle = \mathbf{t}^{(i)} \otimes \mathbf{n}^{(i)} + \mathbf{n}^{(i)} \otimes \mathbf{t}^{(i)} \tag{4}$$

where $p = p(\varepsilon')$ denotes effective confining pressure (isotropic stress), $\mathbf{I}$ denotes second order identity tensor, $q = q(\gamma,\ \varepsilon',\ \varepsilon'')$ denotes virtual simple shear stress, $\mathbf{n}$ denotes a unit vector along the direction of the branch between the particles in contact with each other, $\mathbf{t}$ denotes a unit vector normal to $\mathbf{n}$.

The volumetric strain ε and the virtual simple shear strain γ are defined as follows:

$$\varepsilon = \mathbf{I} : \boldsymbol{\varepsilon} \tag{5}$$

$$\gamma^{(i)} = \left\langle \mathbf{t}^{(i)} \otimes \mathbf{n}^{(i)} \right\rangle : \boldsymbol{\varepsilon} \tag{6}$$

where the double dot symbol defines double contraction. In order to take into account the effect of volumetric strain due to dilatancy ε_{d}, effective volumetric strain ε' is introduced by

$$\varepsilon' = \varepsilon - \varepsilon_{\mathrm{d}} \tag{7}$$

According to Iai et al. (2008), dilatancy in Equation (7) is decomposed into contractive component $\varepsilon_{\mathrm{d}}^{\mathrm{c}}$ and dilative component $\varepsilon_{\mathrm{d}}^{\mathrm{d}}$ as

$$\varepsilon_{\mathrm{d}} = \varepsilon_{\mathrm{d}}^{\mathrm{c}} + \varepsilon_{\mathrm{d}}^{\mathrm{d}} \tag{8}$$

By using the contractive component, virtual effective

volumetric strain ε'' is defined as

$$\varepsilon'' = \varepsilon - \varepsilon_{\mathrm{d}}^{\mathrm{c}} \tag{9}$$

The time derivative of both sides of Equation (3) yields the incremental constitutive equation as follows:

$$\dot{\boldsymbol{\sigma}}' = \mathbb{C} : \dot{\boldsymbol{\varepsilon}} \tag{10}$$

where

$$\begin{aligned}\mathbb{C} = {} & K_{\mathrm{L/U}}\mathbf{I}\otimes\mathbf{I} + \sum_{i=1}^{I} G_{\mathrm{L/U}}^{(i)} \left\langle \mathbf{t}^{(i)}\otimes\mathbf{n}^{(i)} \right\rangle \otimes \left\langle \mathbf{t}^{(i)}\otimes\mathbf{n}^{(i)} \right\rangle \Delta\omega \\ & - K_{\mathrm{L/U}}\mathbf{I}\otimes\mathbf{I}_{\mathrm{d}} + \sum_{i=1}^{I} \left(H_{\mathrm{L/U}}^{(i)} + L_{\mathrm{L/U}}^{(i)} \right) \left\langle \mathbf{t}^{(i)}\otimes\mathbf{n}^{(i)} \right\rangle \otimes \mathbf{I}\Delta\omega \\ & - \sum_{i=1}^{I} \left\langle \mathbf{t}^{(i)}\otimes\mathbf{n}^{(i)} \right\rangle \otimes \left(H_{\mathrm{L/U}}^{(i)}\mathbf{I}_{\mathrm{d}} + L_{\mathrm{L/U}}^{(i)}\mathbf{I}_{\mathrm{d}}^{\mathrm{c}} \right) \Delta\omega \end{aligned} \tag{11}$$

$$\mathbf{I}_{\mathrm{d}} = \mathbf{I}_{\mathrm{d}}^{\mathrm{c}} + \mathbf{I}_{\mathrm{d}}^{\mathrm{d}} \tag{12}$$

Following the classic postulate of interlocking that is defined as the energy less component of deformation by Taylor (1948), the increment of the dilative component of dilatancy is given as follows:

$$\dot{\varepsilon}_{\mathrm{d}}^{\mathrm{d}} = \mathbf{I}_{\mathrm{d}}^{\mathrm{d}} : \dot{\boldsymbol{\varepsilon}} \tag{13}$$

$$\mathbf{I}_{\mathrm{d}}^{\mathrm{d}} = \sum_{i=1}^{I} \frac{\gamma^{(i)} / \gamma_{\mathrm{v}}}{1 + \left| \gamma^{(i)} / \gamma_{\mathrm{v}} \right|} \mathrm{M}_{\mathrm{fv}} \left\langle \mathbf{t}^{(i)}\otimes\mathbf{n}^{(i)} \right\rangle \Delta\omega \tag{14}$$

where

$$\mathrm{M}_{\mathrm{fv}} = \frac{q_{\mathrm{v}}}{p} \tag{15}$$

The parameters q_{v} and γ_{v} are the shear strength and the reference strain of the virtual shear mechanism, respectively.

The increment of the contractive component of dilatancy is given by the hypothesis in which the macroscopic component is given from the microscopic counterparts associated with the virtual simple shear strain as follows:

$$\dot{\varepsilon}_{\mathrm{d}}^{\mathrm{c}} = \mathbf{I}_{\mathrm{d}}^{\mathrm{c}} : \dot{\boldsymbol{\varepsilon}} \tag{16}$$

$$\mathbf{I}_{\mathrm{d}}^{\mathrm{c}} = -\sum_{i=1}^{I} \mathrm{M}_{\mathrm{v}} \left(1 - \left(\frac{G_{\mathrm{L/U}}^{(i)}}{G_{\mathrm{L0}}} \right) \right) \left| \left\langle \mathbf{t}^{(i)}\otimes\mathbf{n}^{(i)} \right\rangle \right|^{*} \Delta\omega \tag{17}$$

where, if $\left\langle \mathbf{t}^{(i)}\otimes\mathbf{n}^{(i)} \right\rangle : \dot{\boldsymbol{\varepsilon}} \geq 0$, then

$$\left| \left\langle \mathbf{t}^{(i)}\otimes\mathbf{n}^{(i)} \right\rangle \right|^{*} = \left\langle \mathbf{t}^{(i)}\otimes\mathbf{n}^{(i)} \right\rangle \tag{18}$$

and, if $\left\langle \mathbf{t}^{(i)}\otimes\mathbf{n}^{(i)} \right\rangle : \dot{\boldsymbol{\varepsilon}} < 0$, then

$$\left| \left\langle \mathbf{t}^{(i)}\otimes\mathbf{n}^{(i)} \right\rangle \right|^{*} = -\left\langle \mathbf{t}^{(i)}\otimes\mathbf{n}^{(i)} \right\rangle \tag{19}$$

For more details, refer to Iai et al. (2008).

3.2 Finite Strain Formulation of Generalized Multiple Mechanism Model in Reference Configuration

The generalized multiple mechanism model described in the previous section has been extended based on finite strain (large deformation) formulation (Iai et al., 2009a). In the finite strain formulation of the model, the unit vector $\mathbf{N}$ along the direction of the branch and the unit vector $\mathbf{T}$ normal to $\mathbf{N}$ are defined in the reference configuration of the material. These vectors are assumed to change their direction and magnitude into $\mathbf{n}$ and $\mathbf{t}$ in the current configuration through the deformation gradient $\mathbf{F}$ as follows:

$$\mathbf{n} = \mathbf{F}\mathbf{N} \tag{20}$$

$$\mathbf{t} = \mathbf{F}\mathbf{T} \tag{21}$$

$$\mathbf{F} = \frac{\partial \mathbf{x}}{\partial \mathbf{X}} \tag{22}$$

where the motion of the material transforms the initial position vector $\mathbf{X}$ defined in the reference configuration to the current position vector $\mathbf{x}$ defined in the current configuration.

The material description of integrated form of the strain space multiple mechanism model in the reference configuration is given as follows:

$$\mathbf{S}' = \mathbf{S}'_{p} + \mathbf{S}'_{q} = -Jp\mathbf{C}^{-1} + J^{-1}\mathbb{Q} : \overline{\mathbf{S}} \tag{23}$$

where $\mathbf{S}'$ denotes the second Piola-Kirchhoff effective stress and

$$\mathbf{C} = \mathbf{F}^{\mathrm{T}}\mathbf{F} \tag{24}$$

$$J = \det \mathbf{F} \tag{25}$$

The fourth-order tensor $\mathbb{Q}$ and the second-order tensor $\overline{\mathbf{S}}$ in Equation (23) are respectively defined by

$$\mathbb{Q} = \mathbb{N} - \frac{1}{2}\mathbf{C}^{-1}\otimes\mathbf{C} \tag{26}$$

$$\overline{\mathbf{S}} = \sum_{i=1}^{I} Jq^{(i)} \left\langle \mathbf{T}^{(i)}\otimes\mathbf{N}^{(i)} \right\rangle \Delta\omega \tag{27}$$

Incremental form of the constitutive equation in the reference configuration is derived by taking the material time derivative of both sides of Equation (23) as

$$\dot{\mathbf{S}}' = \mathbb{C} : \dot{\mathbf{E}} \tag{28}$$

where

$$\mathbb{C} = \mathbb{C}_{p} + \mathbb{C}_{q} \tag{29}$$

$$\begin{aligned}\mathbb{C}_{p} = {} & J\left(K_{\mathrm{L/U}} - p\right)\mathbf{C}^{-1}\otimes\mathbf{C}^{-1} \\ & + 2Jp\mathbf{C}^{-1}\odot\mathbf{C}^{-1} - JK_{\mathrm{L/U}}\mathbf{C}^{-1}\otimes\mathbf{C}_{\mathbf{d}}^{-1}\end{aligned} \tag{30}$$

$$\begin{aligned}\mathbb{C}_{q} = {} & J^{-1}\left[\mathbb{Q} : \overline{\mathbb{C}}_{q} + \left(\mathbf{C} : \overline{\mathbf{S}} \right)\tilde{\mathbb{Q}} \right] \\ & - \left(\mathbf{C}^{-1}\otimes\mathbf{S}'_{q} + \mathbf{S}'_{q}\otimes\mathbf{C}^{-1} \right)\end{aligned} \tag{31}$$

$$\overline{\mathbb{C}}_{q} = \sum_{i=1}^{I} J \left\langle \mathbf{T}^{(i)}\otimes\mathbf{N}^{(i)} \right\rangle \otimes \mathbf{C}_{q}^{(i)-1}\Delta\omega \tag{32}$$

$$\begin{aligned}\mathbf{C}_{q}^{(i)-1} = {} & q^{(i)}\mathbf{C}^{-1} + G_{\mathrm{L/U}}^{(i)} \left\langle \mathbf{T}^{(i)}\otimes\mathbf{N}^{(i)} \right\rangle \\ & + H_{\mathrm{L/U}}^{(i)} \left(\mathbf{C}^{-1} - \mathbf{C}_{\mathbf{d}}^{-1} \right) + L_{\mathrm{L/U}}^{(i)} \left(\mathbf{C}^{-1} - \mathbf{C}_{\mathbf{dc}}^{-1} \right)\end{aligned} \tag{33}$$

$$\tilde{\mathbb{Q}} = \mathbf{C}^{-1}\odot\mathbf{C}^{-1} - \frac{1}{2}\mathbf{C}^{-1}\otimes\mathbf{C}^{-1} \tag{34}$$

The dilative component of dilatancy in the reference

configuration is given through a derivation analogous to that in the infinitesimal strain formulation as follows:

$$\dot{\varepsilon}_{\mathrm{d}}^{\mathrm{d}} = \mathbf{C}_{\mathrm{dd}}^{-1} : \dot{\mathbf{E}} \tag{35}$$

$$\mathbf{C}_{\mathrm{dd}}^{-1} = J^{-1} \sum_{i=1}^{I} \left(\frac{\gamma^{(i)} / \gamma_{\mathrm{v}}}{1 + \left| \gamma^{(i)} / \gamma_{\mathrm{v}} \right|} \right) \mathrm{M}_{\mathrm{fv}} \times \left(\left\langle \mathbf{T}^{(i)} \otimes \mathbf{N}^{(i)} \right\rangle - \frac{1}{2} \gamma^{(i)} \mathbf{C}^{-1} \right) \Delta\omega \tag{36}$$

The contractive component of dilatancy in the reference configuration is given as follows:

$$\dot{\varepsilon}_{\mathrm{d}}^{\mathrm{c}} = \mathbf{C}_{\mathrm{dc}}^{-1} : \dot{\mathbf{E}} \tag{37}$$

$$\mathbf{C}_{\mathrm{dc}}^{-1} = -\sum_{i=1}^{I} \mathrm{M}_{\mathrm{v}} \left(1 - c_1 \left(\frac{G_{\mathrm{L/U}}^{(i)}}{G_{\mathrm{L0}}} \right) \right) \left| \left\langle \mathbf{T}^{(i)} \otimes \mathbf{N}^{(i)} \right\rangle \right|^{*} \Delta\omega \tag{38}$$

where, if $\left\langle \mathbf{T}^{(i)} \otimes \mathbf{N}^{(i)} \right\rangle : \dot{\mathbf{E}} \geq 0$, then

$$\left| \left\langle \mathbf{T}^{(i)} \otimes \mathbf{N}^{(i)} \right\rangle \right|^{*} = \left\langle \mathbf{T}^{(i)} \otimes \mathbf{N}^{(i)} \right\rangle \tag{39}$$

and, if $\left\langle \mathbf{T}^{(i)} \otimes \mathbf{N}^{(i)} \right\rangle : \dot{\mathbf{E}} < 0$, then

$$\left| \left\langle \mathbf{T}^{(i)} \otimes \mathbf{N}^{(i)} \right\rangle \right|^{*} = -\left\langle \mathbf{T}^{(i)} \otimes \mathbf{N}^{(i)} \right\rangle \tag{40}$$

3.3 Finite Strain Formulation of Generalized Multiple Mechanism Model in Current Configuration

The spatial description of integrated form in the current configuration is obtained through the push-forward operation (Holzapfel, 2001) of the material description in Equation (23) as follows:

$$\boldsymbol{\sigma}' = \boldsymbol{\sigma}'_{p} + \boldsymbol{\sigma}'_{q} = -p\mathbf{I} + J^{-1}\mathbb{Z} : \overline{\boldsymbol{\sigma}} \tag{41}$$

where $\boldsymbol{\sigma}'$ denotes the Cauchy effective stress and

$$\mathbb{Z} = \mathbb{N} - \frac{1}{2}\mathbf{I} \otimes \mathbf{I} \tag{42}$$

$$\overline{\boldsymbol{\sigma}} = \sum_{i=1}^{I} q^{(i)} \left\langle \mathbf{t}^{(i)} \otimes \mathbf{n}^{(i)} \right\rangle \Delta\omega \tag{43}$$

With the Oldroyd stress rate of the Kirchhoff effective stress (Holzapfel, 2001), incremental form of the strain space multiple mechanism model in the current configuration is given as follows:

$$\mathrm{Oldr}\left(J\boldsymbol{\sigma}' \right) = J\mathbb{C} : \mathbf{d} \tag{44}$$

where $\mathbf{d}$ denotes the rate of deformation tensor and

$$\mathbb{C} = \mathbb{C}_{p} + \mathbb{C}_{q} \tag{45}$$

$$\mathbb{C}_{p} = \left(K_{\mathrm{L/U}} - p \right) \mathbf{I} \otimes \mathbf{I} + 2p\mathbb{N} - K_{\mathrm{L/U}} \mathbf{I} \otimes \mathbf{I}_{\mathrm{d}} \tag{46}$$

$$\mathbb{C}_{q} = J^{-1} \left[\mathbb{Z} : \overline{\mathbb{C}}_{q} + \mathrm{tr}\overline{\boldsymbol{\sigma}}\mathbb{Z} \right] - \left(\mathbf{I} \otimes \boldsymbol{\sigma}'_{q} + \boldsymbol{\sigma}'_{q} \otimes \mathbf{I} \right) \tag{47}$$

$$\overline{\mathbb{C}}_{q} = \sum_{i=1}^{I} \left\langle \mathbf{t}^{(i)} \otimes \mathbf{n}^{(i)} \right\rangle \otimes \mathbf{I}_{q}^{(i)} \Delta\omega \tag{48}$$

$$\mathbf{I}_{q}^{(i)} = q^{(i)}\mathbf{I} + G_{\mathrm{L/U}}^{(i)} \left\langle \mathbf{t}^{(i)} \otimes \mathbf{n}^{(i)} \right\rangle + H_{\mathrm{L/U}}^{(i)} \left(\mathbf{I} - \mathbf{I}_{\mathrm{d}} \right) + L_{\mathrm{L/U}}^{(i)} \left(\mathbf{I} - \mathbf{I}_{\mathrm{d}}^{\mathrm{c}} \right) \tag{49}$$

The dilative component of dilatancy in the current configuration is defined as follows:

$$\dot{\varepsilon}_{\mathrm{d}}^{\mathrm{d}} = \mathbf{I}_{\mathrm{d}}^{\mathrm{d}} : \mathbf{d} \tag{50}$$

$$\mathbf{I}_{\mathrm{d}}^{\mathrm{d}} = J^{-1} \sum_{i=1}^{I} \left(\frac{\gamma^{(i)} / \gamma_{\mathrm{v}}}{1 + \left| \gamma^{(i)} / \gamma_{\mathrm{v}} \right|} \right) \mathrm{M}_{\mathrm{fv}} \times \left(\left\langle \mathbf{t}^{(i)} \otimes \mathbf{n}^{(i)} \right\rangle - \frac{1}{2} \gamma^{(i)} \mathbf{I} \right) \Delta\omega \tag{51}$$

The contractive component of dilatancy in the current configuration is given as follows:

$$\dot{\varepsilon}_{\mathrm{d}}^{\mathrm{c}} = \mathbf{I}_{\mathrm{d}}^{\mathrm{c}} : \mathbf{d} \tag{52}$$

$$\mathbf{I}_{\mathrm{d}}^{\mathrm{c}} = -\sum_{i=1}^{I} \mathrm{M}_{\mathrm{v}} \left(1 - c_1 \left(\frac{G_{\mathrm{L/U}}^{(i)}}{G_{\mathrm{L0}}} \right) \right) \left| \left\langle \mathbf{t}^{(i)} \otimes \mathbf{n}^{(i)} \right\rangle \right|^{*} \Delta\omega \tag{53}$$

where, if $\left\langle \mathbf{t}^{(i)} \otimes \mathbf{n}^{(i)} \right\rangle : \mathbf{d} \geq 0$, then

$$\left| \left\langle \mathbf{t}^{(i)} \otimes \mathbf{n}^{(i)} \right\rangle \right|^{*} = \left\langle \mathbf{t}^{(i)} \otimes \mathbf{n}^{(i)} \right\rangle \tag{54}$$

and, if $\left\langle \mathbf{t}^{(i)} \otimes \mathbf{n}^{(i)} \right\rangle : \mathbf{d} < 0$, then

$$\left| \left\langle \mathbf{t}^{(i)} \otimes \mathbf{n}^{(i)} \right\rangle \right|^{*} = -\left\langle \mathbf{t}^{(i)} \otimes \mathbf{n}^{(i)} \right\rangle \tag{55}$$

For more details, refer to Iai et al. (2009a).

4. OUTLINE OF FINITE ELEMENT ANALYSIS

4.1 Determination of Model Parameters

The strain space multiple mechanism model described in the previous chapter has 15 parameters for the analysis of liquefaction; three specify volumetric mechanism, three specify shear mechanism, and the rest control liquefaction and dilatancy.

The parameters for defining the characteristics of volumetric and shear deformation are shown in Table 2. These parameters were obtained from the past analytical study (Hyodo et al., 2008). In Table 2, the parameters r_K and l_K, which control the bulk modulus for liquefaction analysis, are defined only for the saturated sand deposits.

Table 2 Model parameters for deformation characteristics

Soil Type			Parameters for deformation characteristics					
			volumetric mechanism			shear mechanism		
	ρ (t/m^3)	n	K_{ma} (kPa)	r_K	l_K	G_{ma} (kPa)	φ_{f} (°)	$h_{\max}$
Edosaki Sand (embankment)	1.70	0.49	218000	-	-	84000	34.0	0.26
Edosaki Sand (dry)	1.68	0.49	107000	-	-	41000	34.0	0.26
Edosaki Sand (saturated)	1.86	0.49	107000	0.5	2.0	41000	34.0	0.26
Silica Sand No.7 (saturated)	1.98	0.40	224000	0.5	2.0	86000	48.0	0.24

(σ_{ma}'=98.0kPa)

The rest of 15 parameters, which specify the characteristics of liquefaction and dilatancy, are shown in Table 3. These parameters were determined by referring to the liquefaction resistance curves which were obtained from the cyclic triaxial tests under the undrained condition. Figure 3 shows measured and computed liquefaction resistance curves. The parameter q_{us} in Table 3, which is the undrained shear strength for describing the steady state of sand (e.g., Yoshimine and Ishihara (1998)), was determined from the void ratio and fines content following Motoshima et al. (2008). This parameter is defined only for the Edosaki sand layer, which is considered to have major effects on the deformation of the embankment.

Table 3 Model parameters for dilatancy

Soil Type	Parameters for dilatancy								
	φ_p (°)	ε_d^{cm}	$r_{\varepsilon_d^c}$	r_{ε_d}	q_1	q_2	S_1	c_1	q_{us} (kPa)
Edosaki Sand (saturated)	28.0	0.10	18.00	0.20	1.00	2.50	0.005	1.00	17.0
Silica Sand No.7 (saturated)	33.0	0.10	5.00	0.10	1.00	3.50	0.005	1.00	-

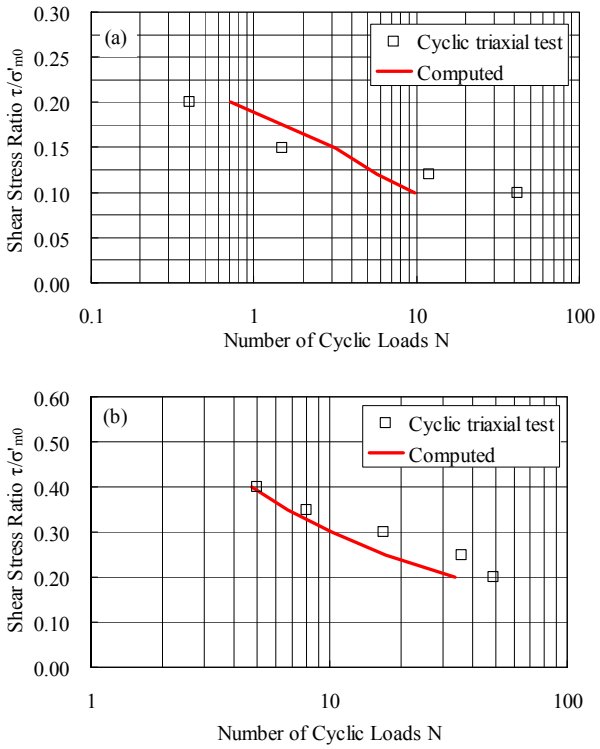

Figure 3 Liquefaction resistance curves: (a) Edosaki sand; (b) Silica sand No.7

4.2 Initial and boundary conditions and input motion

The numerical analysis was carried out with the same prototype dimension of the centrifuge model test. Figure 4 shows the finite element mesh for numerical analysis. In order to approximate the boundary conditions of the rigid container in the centrifuge model test, degrees of freedom of displacements at the base were fixed both horizontally and vertically, and only horizontal displacements were fixed at the side boundaries.

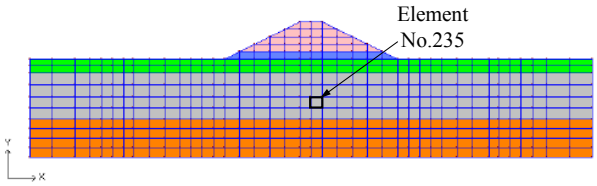

Figure 4 Finite element mesh for numerical analysis

With these boundary conditions, a seismic response analysis was performed for 11 s under the undrained condition. The main shock from 2.6 s to 13.6 s in the recorded motion (Fig. 2) at the bottom of the container in the centrifuge model test was used as an input motion. The numerical time integration was done by the Wilson-θ method (θ=1.4) using a time step of 0.01 seconds. Rayleigh damping (α =0.0 and β =0.0002), which was proportionally decreasing with the degree of cyclic mobility, was used to ensure stability of the numerical solution process. Selective reduced integration was adopted for Gauss integration using four nodes isoparametric elements.

Before the dynamic response analysis, a static analysis was performed with gravity in order to simulate the initial stress condition in the centrifuge model test before shaking. The same constitutive model was used as in the dynamic response analysis but under the drained condition.

In computation, both an infinitesimal deformation analysis and large deformation (finite strain) analyses were performed to compare the differences in the results due to the effect of geometrical nonlinearity. In the large deformation analyses, we employed both total Lagrangian (TL) formulation with material description based on reference configuration (see Section 3.2) and updated Lagrangian (UL) formulation with spatial description based on current configuration (see Section 3.3).

5. RESULTS OF THE ANALYSIS

5.1 Computed deformation of the embankment

Figure 5 shows measured and computed deformations of the embankment after shaking. The deformations are shown by deformed meshes in solid lines with reference to the original configuration in broken lines. While the computed deformations were obtained at the end of the main shock, the measured one was obtained after the aftershocks shown in Fig. 2. Therefore, at the end of the main shock the amount of deformed configuration in the centrifuge model test is expected to be less than the observed one shown in Fig. 5(d). However, the crest settlement due to the aftershocks is small with 0.26 m, so that by using the deformed configuration shown in Fig. 5(d) it seems possible to verify the applicability of the analysis about the deformed configuration of the embankment.

Figure 5(a) indicates that the deformed configuration obtained in the infinitesimal deformation analysis differs widely from the measured shown in Fig. 5(d). The deformation shown in Fig. 5(a) is unrealistic, in that most part of the embankment sinks down into the liquefiable

deposit. Figure 5(a) also shows that the infinitesimal deformation analysis overestimates the amount of the crest settlement (5.95 m) approximately as three times as the measurement (2.04 m) at the end of the main shock.

Figure 5(b) and (c) indicate that the results obtained in the large deformation analyses are in good agreement with the measurement shown in Fig. 5(d). In both the measurement and computation, soils near toes of the embankment are laterally expanded in the direction opposite to the embankment, while soils under the embankment are compressed vertically and sheared. The computed deformation mode is characterized by a crest settlement associated with lateral spread in foundation soils as the measured one is. The computed deformed configurations show that no significant difference exists between the total and updated Lagrangian formulation. The measured amount of the crest settlement was 2.04 m, while the computed ones obtained by using total and updated Lagrangian formulation were 2.14 m and 2.07 m, respectively. The computed crest settlements in the large deformation analyses gave close agreement with the measured one. As mentioned earlier about the deformations, both formulations, which are the total and updated Lagrangian formulations, are equivalent to each other about the settlement. The multiple mechanism model which has been extended based on the finite strain formulation, in which the total or updated Lagrangian formulation is arbitrarily chosen, shows a reasonable capability to reproduce the deformation and settlement of the embankment.

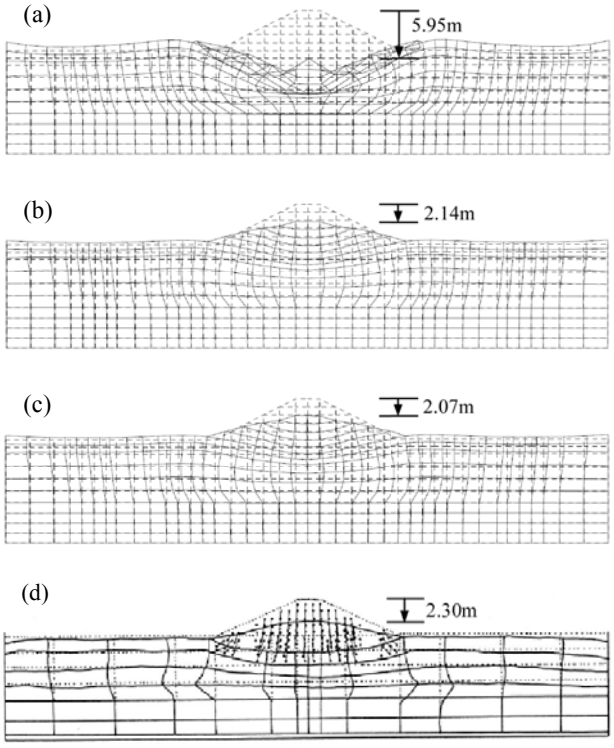

Figure 5 Computed and measured deformation: (a) Infinitesimal deformation analysis; (b) Large deformation analysis (TL formulation); (c) Large deformation analysis (UL formulation); (d) Centrifuge model test

5.2 Variation of peak acceleration with depth

Vertical arrays of the peak amplitude of horizontal acceleration are shown in Fig. 6 to compare the variation in the liquefiable and non-liquefiable deposits. Measured and computed ones are indicated solid and hollow squares, respectively.

In the centrifuge model test, the accelerations in the liquefiable deposit are more or less attenuated and not amplified due to partial liquefaction. The variation at the center axis of the embankment indicates that the strong attenuation of the acceleration amplitude in a shallow layer prevents the wave propagation to the embankment. Meanwhile, the accelerations in the non-liquefiable dense deposit are amplified up to as 1.3 times as the amplitude of the input wave.

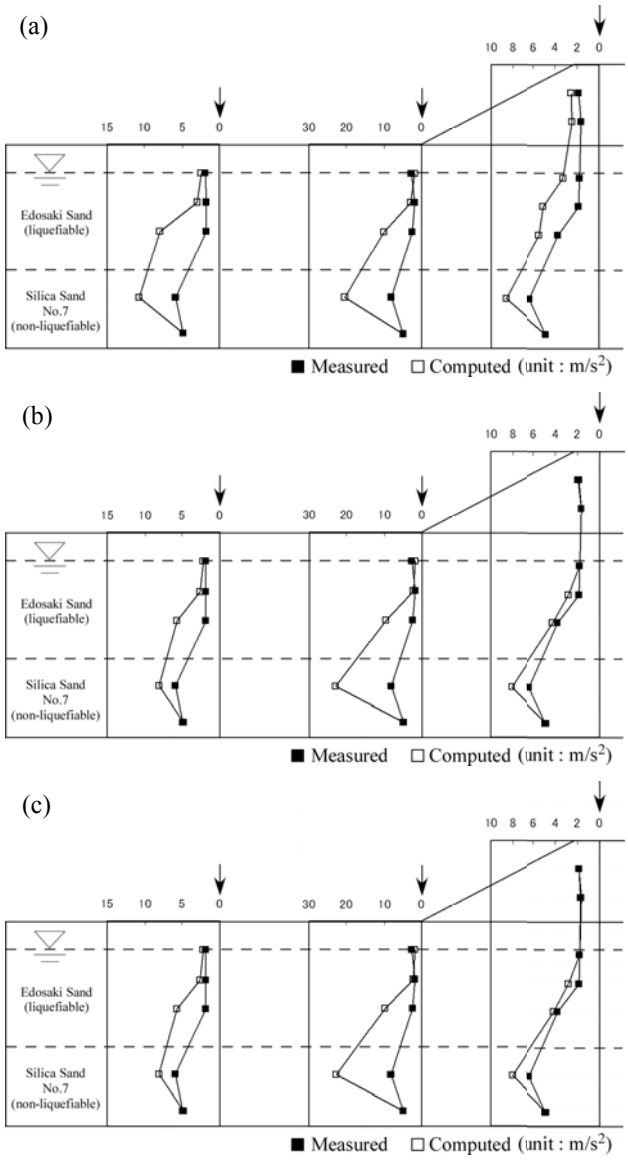

Figure 6 Variation of peak amplitude of acceleration in depth: (a) Infinitesimal deformation analysis; (b) Large deformation analysis (TL formulation); (c) Large deformation analysis (UL formulation)

Figure 6(a) indicates that the variations of the peak amplitude obtained in the infinitesimal deformation analysis overestimate the measured ones except for the shallow layer besides the embankment. In the large deformation analysis, as shown in Fig. 6(b) and (c) the computed variations generally get closer to the measured ones, in particular at the center axis of the embankment. As mentioned in the previous section, the total and updated Lagrangian formulations give the same results about the variation of peak acceleration with depth, too. This consequence indicates that these two formulations are not only theoretically but also numerically equivalent to each other, and thereby demonstrates the validity of the computer programming for large deformation analysis.

5.3 Distribution of excess pore water pressure ratio

Figure 7 shows the computed distribution of excess pore water pressure ratio ($=1-\sigma'_m/\sigma'_{m0}$) at the end of the main shock. In the infinitesimal deformation analysis, the excess pore water pressure ratio rises only up to 0.6 in most parts of the saturated deposit as shown in Fig. 7(a). Particularly in an upper layer of the non-liquefiable deposit beneath the embankment, the excess pore water pressure ratio remains unchanged at zero. In the large deformation analyses, we can see the fully liquefied zones (i.e. excess pore water pressure ratio is higher than 0.9) of the liquefiable deposit in the vicinity of the side boundaries and in the shallow layer beneath the toes of the embankment as shown in Fig. 7(b) and (c). These figures indicate that the excess pore water pressure ratio in the central zones beneath the embankment rises only up to 0.6. This is because soils in the zones constantly undergo the deviator stresses due to overburden stresses from the embankment. These soils tend to undergo shear failure rather than liquefaction. Comparison between Fig. 7(b) and (c) shows that the total and updated Lagrangian formulations are equivalent to each other in terms of the distribution of excess pore water pressure ratio.

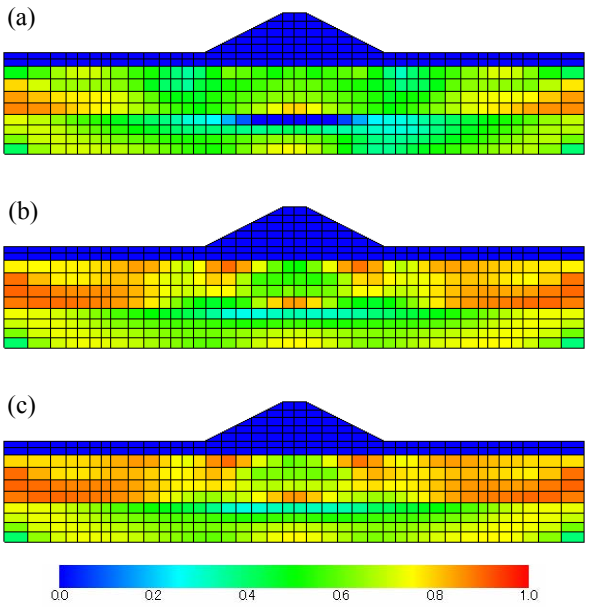

Figure 7 Computed distribution of excess pore water pressure ratio ($=1-\sigma'_m/\sigma'_{m0}$) after shaking: (a) Infinitesimal deformation analysis; (b) Large deformation analysis (TL formulation); (c) Large deformation analysis (UL formulation)

5.4 Effective stress path and stress-strain relationship

Figure 8 shows computed effective stress paths in an element, which is shown in Fig. 4, beneath the embankment in the liquefiable deposit. In the large deformation analyses (both the total and updated Lagrangian formulations), maximum shear stress τ and mean effective stress σ'_m are given as follows:

$$\tau=\sqrt{\left(\left(\sigma'_{11}-\sigma'_{22}\right)/2\right)^2+\left(\sigma'_{12}\right)^2} \tag{56}$$

$$\sigma'_m=\left(\sigma'_{11}+\sigma'_{22}\right)/2 \tag{57}$$

in which $\sigma'_{11},\sigma'_{12},\sigma'_{22}$ are the components of Cauchy effective stress. Figure 8 indicates that in the large deformation analyses the effective stress paths with respect to the maximum shear stress are almost consistent with the result in the infinitesimal deformation analysis. This consequence denotes the same tendency of the results obtained in simulation for monotonic loading (Iai et al., 2009b) and cyclic loading (Ueda, 2009). In Fig. 8, the effective stress paths move toward the steady state defined by undrained shear strength (17 kPa in this study) from an initial point, in which a stress condition is largely anisotropic due to the overburden pressure of the embankment, with the progress of shaking and following deformation.

Computed relationship between shear stress and shear strain for the element indicated in Fig. 4 is shown in Fig. 9. In the large deformation analyses, shear stress and shear strain are expressed in terms of the Cauchy (effective) stress σ'_{12} and Euler-Almansi strain $2e_{12}$, respectively. The curves for the total and updated Lagrangian formulations are almost consistent with each other. While the maximum shear strains in the large deformation analyses are about 10 %, the one in the infinitesimal deformation analysis is 30 %. The infinitesimal deformation analysis overestimates shear strain up to as three times as those in the large deformation analyses. Figure 9 indicates that at the range of shear strain more than 10 % we need to adopt the large deformation analysis to take into account the effect of geometrical nonlinearity in seismic response analyses.

Figure 10 shows computed relationship between deviator stress and deviator strain for the element indicated in Fig. 4. In the large deformation analyses, deviator stress and deviator strain are expressed as $\left(\sigma'_{11}-\sigma'_{22}\right)/2$ by the Cauchy effective stress and $e_{11}-e_{22}$ by the Euler-Almansi strain, respectively. As mentioned earlier in Fig. 9, the curve in the total Lagrangian formulation gives close agreement with the one in the updated Lagrangian formulation. Figure 10 indicates that the infinitesimal deformation analysis overestimates the residual deviator strain approximately as twice as those in the large deformation analyses. So, when

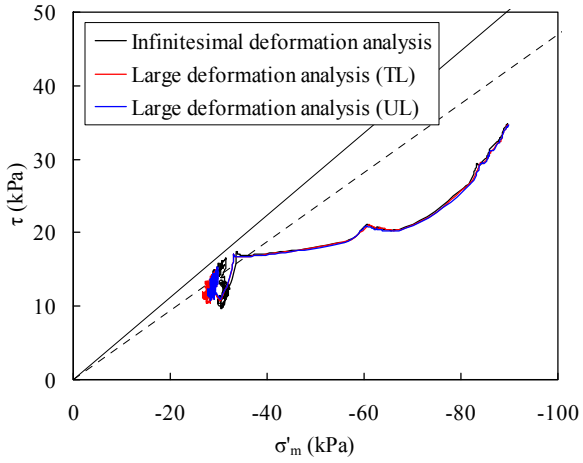

Figure 8 Computed effective stress path (Element No.235)

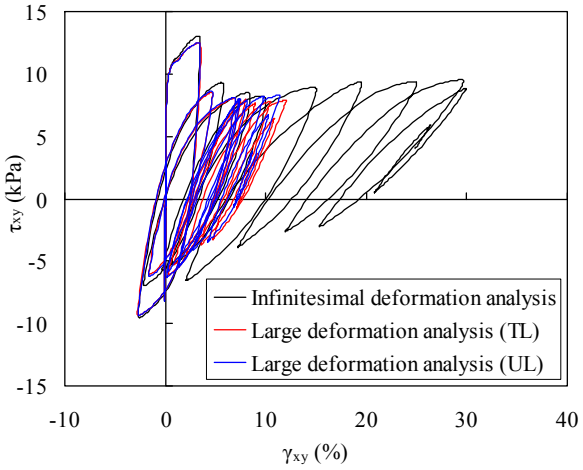

Figure 9 Computed relationship between shear stress and shear strain (Element No.235)

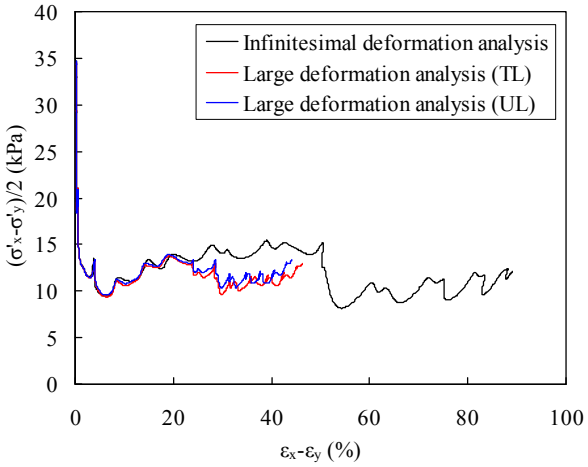

Figure 10 Computed relationship between deviator stress and deviator strain (Element No.235)

the range of large strain as shown in Fig. 10 is targeted, it is necessary to perform the analysis based on the finite strain formulation.

6. CONCLUSIONS

In this study, infinitesimal and large deformation analyses are performed on the dynamic behavior of an embankment on liquefiable sand deposit in geotechnical centrifuge experiments in order to verify the applicability of an effective stress model. The model used in the analysis is a strain space multiple mechanism model, which has been extended based on finite strain formulation to take into account the effect of geometrical nonlinearity (Iai et al., 2009a). In the large deformation analyses, both total and updated Lagrangian formulations are adopted. Primary conclusions of this study are summarized as follows:

The infinitesimal deformation analysis overestimates the amount of the crest settlement of the embankment after shaking approximately as three times as that measured, while the computed crest settlements in the large deformation analyses give close agreement with the measured one. In the infinitesimal deformation analysis, the deformed configuration, in which most parts of the embankment sink down into the liquefiable deposit, is widely different from the observed deformation. On the contrary, the large deformation analyses well simulate the observed deformed configuration.

Variations of the peak amplitude of horizontal acceleration with depth in the infinitesimal deformation analysis overestimate the measured ones, while the computed ones in the large deformation analyses mostly get closer to the measurements, in particular at the center axis of the embankment.

All of the computed results (e.g., crest settlement, peak acceleration, excess pore water pressure, and stress-strain relationship) indicate that the total and updated Lagrangian formulations are not only theoretically but also numerically equivalent to each other, and thereby demonstrate the validity of the computer programming for large deformation analysis. In order to predict the amount of deformation of embankments during earthquake accurately, it is necessary to carry out a finite element analysis by taking into account the effect of not only material nonlinearity but also geometrical nonlinearity with total or updated Lagrangian formulations.

References:

Holzapfel, G.A. (2001), "Nonlinear Solid Mechanics," John Wiley&Sons.

Hyodo, J., Iai, S., Yokoyama, N., Ozutsumi, O., and Yoshikawa, S. (2008), "Effective Stress Analysis Considering Steady State of Sandy Soil on Centrifuge Model Test," The 43rd Japan National Conference on Geotechnical Engineering, Hiroshima, 1807 -1808 (in Japanese).

Iai, S., Matsunaga, Y., and Kameoka, T. (1992a), "Strain Space Plasticity Model for Cyclic Mobility," Soils and Foundations, **32**(2), 1-15.

Iai, S., Matsunaga, Y., and Kameoka, T. (1992b), "Analysis of Undrained Cyclic Behavior of Sand under Anisotropic Consolidation," Soils and Foundations, **32**(2), 16-20.

Iai, S., and Ozutsumi, O. (2005), "Yield and Cyclic Behaviour of a Strain Space Multiple Mechanism Model for Granular Materials," International Journal for Numerical and Analytical Methods in Geomechanics, **29** (4), 211-240.

Iai, S., Tobita, T., and Ozutsumi, O. (2008), "Stress Dilatancy Relation in Strain Space Multiple Mechanism Model for Cyclic Behavior of Sand," Annuals of Disaster Prevention Research Institute, Kyoto University, **51**(B), 291-303 (in Japanese).

Iai, S., Ueda, K., Tobita, T., and Ozutsumi, O. (2009a), "Finite Strain (Large Deformation) Formulation of Sand Based on Multiple Mechanism Model," Annuals of Disaster Prevention Research Institute, Kyoto University, **52**(B), 323-343 (in Japanese).

Iai, S., Ueda, K., Tobita, T., and Ozutsumi, O. (2009b), "Finite Strain Formulation of a Strain Space Multiple Mechanism Model for Granular Materials," International Journal for Numerical and Analytical Methods in Geomechanics (submitted).

Japan Institute of Construction Engineering (2002), "Analytical Methods to Predict the Deformation of River Dike during Earthquake," JICE, No.102001 (in Japanese).

Motoshima, K., Iai, S., Yokoyama, N., and Sawada, S. (2008), "Influence of Fine Fraction Content, Void Ratio, etc. to the Steady State of Sandy Soil," The 43rd Japan National Conference on Geotechnical Engineering, Hiroshima, 1799 -1800 (in Japanese).

Ozutsumi, O., Sawada, S., Iai, S., Takeshima, Y., Sugiyama, W., and Shimazu, T. (2002), "Effective Stress Analyses of Liquefaction –induced Deformation in River Dikes," Soil Dynamics and Earthquake Engineering, **22**, 1075-1082.

Public Works Research Institute (2000), "An Experimental Study on the Effects of Remedial Measure for Embankment Failure due to Earthquake-induced Foundation Liquefaction," Technical Note of P.W.R.I.., No.3688 (in Japanese).

Taylor, D.W. (1948), "Fundamentals of Soil Mechanics," John Wiley&Sons.

Tobita, T., Iai, S., and Ueda, K. (2006), "Dynamic Behavior of Sand Levee on Saturated Sand Deposits - Centrifuge and Numerical studies -," 100th Anniversary Earthquake Conference Commemorating the 1906 San Francisco Earthquake, San Francisco, U.S.A., paper No.1114.

Ueda, K. (2009), "Finite Strain Formulation of a Strain Space Multiple Mechanism Model for Granular Materials and its application," Doctoral Thesis, Kyoto University, Japan (in Japanese).

Yoshimine, M., and Ishihara, K. (1998), "Flow Potential of Sand during Liquefaction," Soils and Foundations, **38**(3), 189-198.

JOINT CONFERENCE PROCEEDINGS
7th International Conference on Urban Earthquake Engineering (7CUEE) &
5th International Conference on Earthquake Engineering (5ICEE)
March 3-5, 2010, Tokyo Institute of Technology, Tokyo, Japan

ADDITIONAL ANCHOR INFLUENCE ON DYNAMIC BEHAVIOR OF ANCHORED RETAINING WALL

Ali Derakhshani [1], Mohammad Sajjad Fayyazi [2], and Khosrow Bargi [3]

1) Ph.D. Student, Department of Civil Engineering, University of Tokyo, Japan
2) M.Sc. Student, Faculty of Civil Engineering, University of Tehran, Iran
3) Professor, Faculty of Civil Engineering, University of Tehran, Iran
aderakhshani@ut.ac.ir, sfayyazi@ut.ac.ir, kbargi@ut.ac.ir

Abstract: Anchored retaining wall is one of the common geotechnical structures. Penetration depth, maximum bending moment and lateral displacement of wall will be reduced in design due to anchoring the wall. Also, utilizing an additional tie rod can improve the design in longer walls. In this research, using "Finite Difference Method", effect of additional tie rod behind walls in seismic condition is considered. Dynamic response of different cases (various tie rod depths) is provided. Practical history curves of "maximum positive and negative moments" and "lateral displacements" are obtained by means of "FDM". Evaluating these charts, influence of additional tie rod position in anchored retaining wall is investigated in order to seismic assessment and rehabilitation of the structure. Adding new tie rod appropriately causes better serviceability and lower construction cost.

1. INTRODUCTION

Dynamic behavior of flexible long "Bored/Continuous pile walls" including retaining diaphragm walls is considerable. It is common to use an anchorage system, when their height from the dredge line is more than about 6 meters. Utilizing such systems leads to improvement in design due to decrease of penetration depth, maximum bending moment and lateral displacement. Also, using additional tie rod in walls with more than about 11 meters free height can improve the design and serviceability of structure and results in more economical construction. The effect of additional tie rod position in anchored concrete retaining walls placed in sand is evaluated for seismic assessment and rehabilitation. There is no classic method (using equilibrium equations) to analyze and design anchorage system with two tie rods. Therefore, it will be necessary to utilize the numerical methods to find more accurate results. This will help the designer to evaluate the response of the structure in case of earthquake.

2. MODELING

2.1 Features of Models

Analyses of this research are primarily done by modeling retaining diaphragm walls with tie rods in three different depths (4, 8 and 12 meters under the ground surface). Then, some other models with two tie rods in different pairs of positions mentioned above are analyzed. Variations of different design items are illustrated with respect to deepening tie rod position in first step of this research; then different position of couple of tie rods is investigated.

2.2 Details of Models

Soil and model parts' properties are showed in tables 1 and 2 respectively. Table 2 shows the characteristics of retaining wall, anchor wall and tie rod.

Table 1 Soil properties

	Y (KN/m3)	Ysat (KN/m3)	φ (Degree)	C (KN/m2)
Sand	21	25	38	0

Table 2 Model parts' properties

	E (N/m2)	A (m2/m)	P (m/m)	I (m4/m)
Quay wall	3.20E+10	1.44	4	2.01
wall	3.20E+10	1	2	0.083
Cable	2.00E+11	0.00277	-	-

Free height of the wall is 22 meters and water depth in front of wall is 18 meters. Wall profile shape and dimensions are illustrated in figure 1.

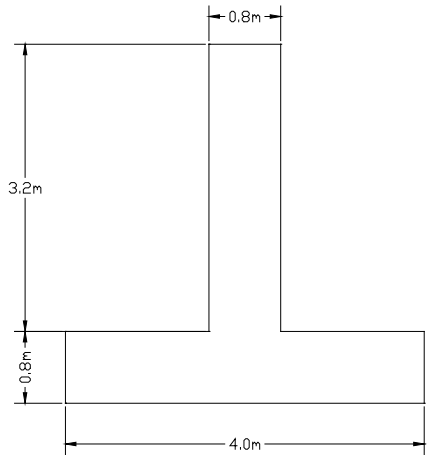

Figure 1 Concrete wall profile

3. "FINITE DIFFERENCE METHOD" ANALYSES

Powerful, accurate and fast numerical method is needed in order to modeling and seismic evaluation of the structure. In this research "Finite Difference Method" is used for sensitivity analyses; the structure is modeled by means of "FLAC 2D" software in both static and dynamic conditions.

3.1 "FLAC 2D" Software Introduction

"FLAC2D" is a two-dimensional finite difference program for engineering soil mechanics computation. This program simulates the behavior of structures built of soil or other materials that may undergo plastic flow when their yield limits are reached. Materials are represented by elements, or zones, which form a grid that is adjusted by the user to fit the shape of the object to be modeled. In this research the effect of tie rod position in anchored concrete wall is mentioned to rehabilitate the structure in Seismic condition and complicated soil behavior is considered by means of Mohr-Coulomb plastic soil model.

3.2 Stages of Problem Solving with "FLAC 2D"

Problem geometry is created via Finite Difference elements firstly; then Mohr-Coulomb behavior model is selected and material properties are assigned. Also, it is necessary to determine boundary and initial conditions.

Modeling and loading procedure are summarized below:

1. Modeling soil considering initial stress in soil mass.
2. Installing main and anchorage walls in soil.
3. Positioning tie rod between two walls.
4. Excavating front of main wall to final dredging level.
5. Applying water pressure.
6. Solving problem in static condition.

After evaluating wall behavior in static condition, sinusoidal acceleration wave is applied to the lower model boundary with maximum amplitude of 0.15g in four seconds duration and calculation is continued for four more seconds. The view of model is shown in figure 2.

Dynamic loading procedure is summarized below:

1. Changing boundary condition.
2. Applying seismic load.
3. Dynamic analysis of the problem.

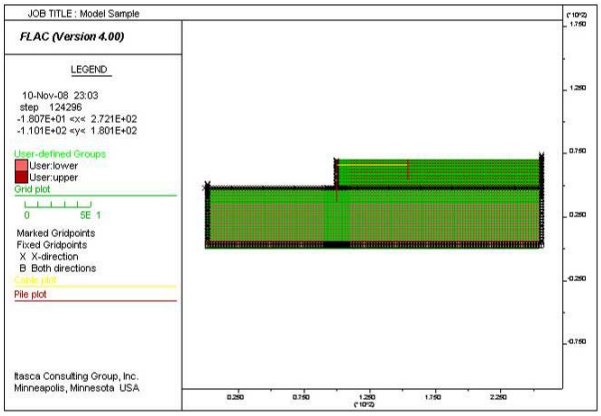

(a)Quay wall with One Tie rod

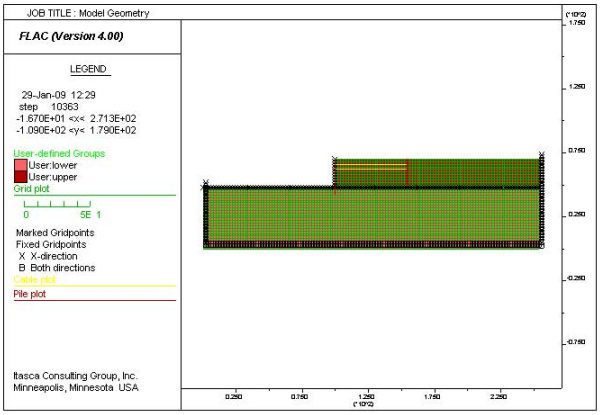

(b)Quay wall with Two Tie rods

Figure 2 Sample views of "Finite Difference Method" models.

4. ANALYSES RESULTS

4.1 Walls with One Anchor

Dynamic analyses Results are illustrated in figures 3 and 4. Lateral displacements are shown in figure 6. Charts based on different tie rod depths, show that maximum lateral displacement in bottom of the wall is less than middle point displacement and the latter is less than top point drift during time history. It means that in this research tilting shape mode of displacement is happened. Also, free vibration is obvious after the end of dynamic loading.

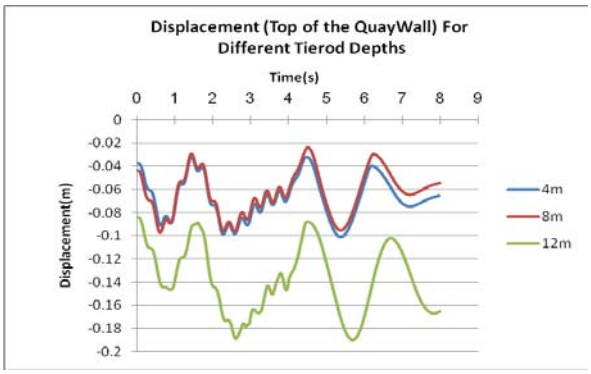

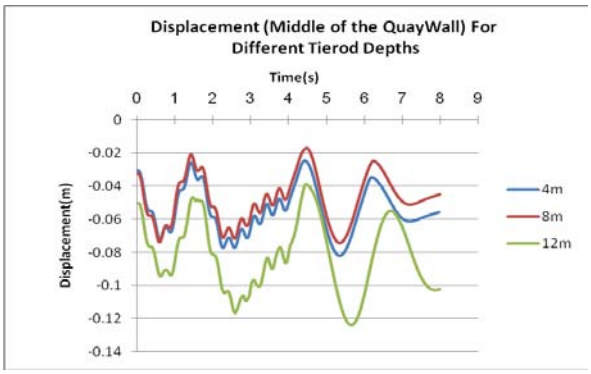

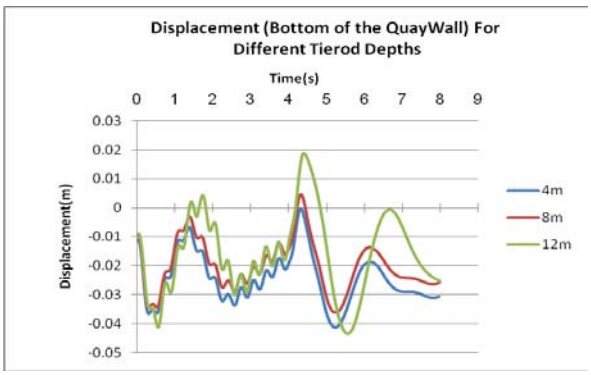

Figure 3 Lateral Displacements of Wall for Different Tie rod Depths

Note that all lateral quay wall top displacements are limited to allowable displacement of 0.3 meter due to "OCDI".

Maximum positive moment in wall (Figure 4) increases with deepening tie rod position in all history duration.

Moreover, Absolute value of maximum negative moment in wall during time history decreases with lowering tie rod position.

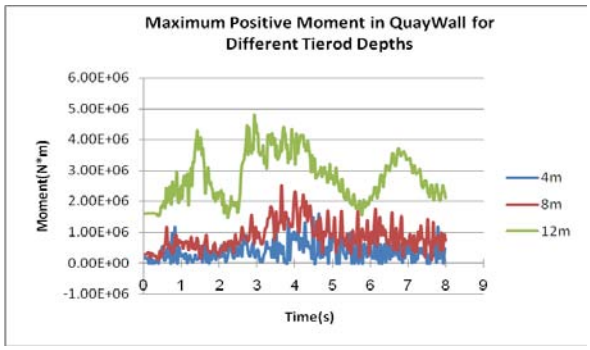

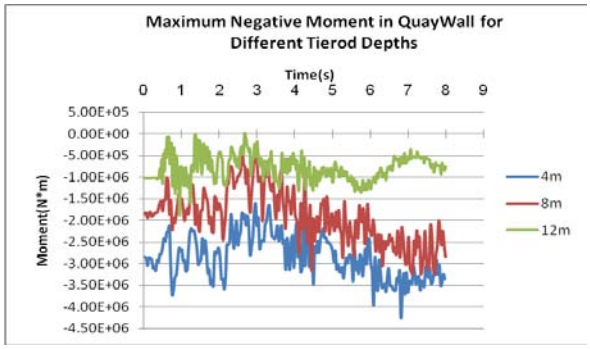

Figure 4 Maximum Moments of Wall for Different Tie rod Depths

Changes of the main criterion of serviceability -maximum displacement of wall top- and main design parameters -maximum bending moment of wall and maximum tie rod axial force- are shown in table 3 with deepening tie rod position during assessment time.

Table 3 Maximum Moment of Quay wall & Tie rod Axial Force & Displacement in Sand (One Tie rod)

Tie rod Depth (m)	Quay wall Length (m)	Tie rod Depth Ratio	M+ (KN*m)	M- (KN*m)	f1 (KN)	d (m)
4	28	0.14	1613.5	-4261.2	560.7	-0.101
8	28	0.28	2529.4	-3236.5	583.2	-0.097
12	27	0.44	4783.9	-1881.6	1416	-0.19

Considering the results discussed above, during dynamic calculations, the maximum moment in anchored diaphragm wall is the least when tie rod is put in depth ratio of about (r =) 0.26. This is found through comparing values of maximum positive and negative moments demonstrated in Table 3. The tie rod axial force regarding depth ratio of about (r =) 0.26 is between axial forces for two other depths allover history duration.

It is inferred that an appropriate serviceability is obtained due to various tie rod positions and all cases satisfy the quay wall horizontal top displacement limit (based on “OCDI").

Furthermore, it is obvious that utilizing an anchor in depth ratio of about (r =) 0.26 leads to less lateral displacement.

In order to rehabilitate the structure in seismic condition economically, it is logical to select a tie rod position which gives lower maximum moment and axial force (which cause more economical wall profile and anchorage system). Achieving to better serviceability is also important in the structure design. It is possible to select a suitable tie rod position by means of analyses and curves that are illustrated in this research.

4.2 Walls with Two Anchors

Lateral displacements curves of top, middle and bottom of walls during calculation time with different tie rod positions are shown in figure 5.Retaining walls are anchored in variety of depths such as: 4&8m, 4&12m and 8&12m. This figure shows that how additional tie rod affects the wall drift.

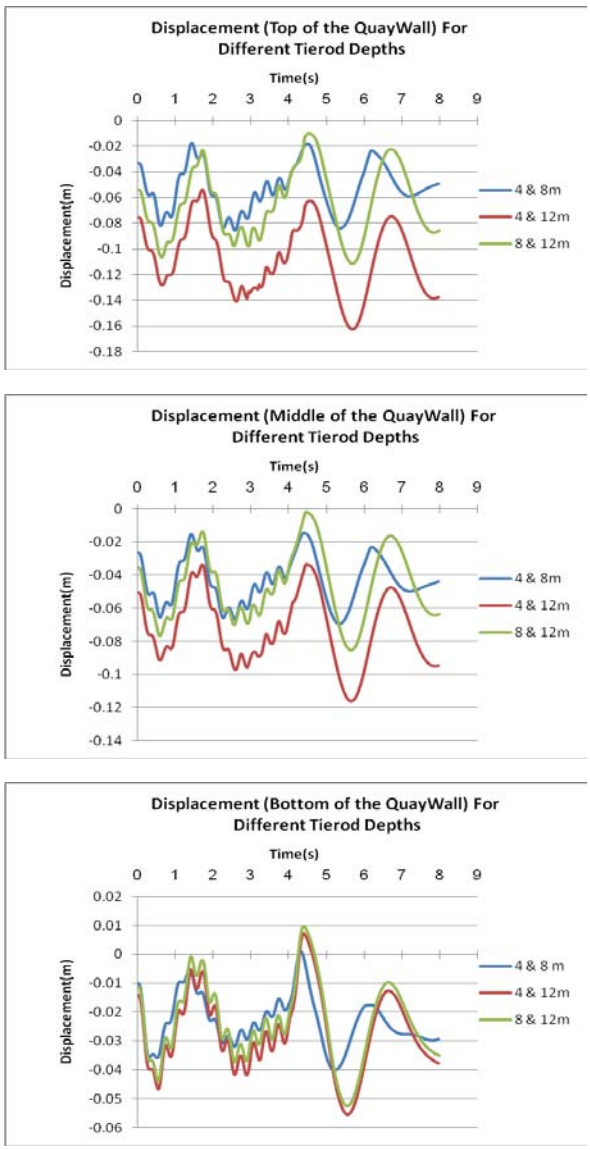

Figure 5 Lateral Displacements of Wall for Different Tie rod Depths (Two Tie rods)

Time histories of Maximum positive and negative Moments of Wall for different positions of Tie rods are illustrated in figure 6.

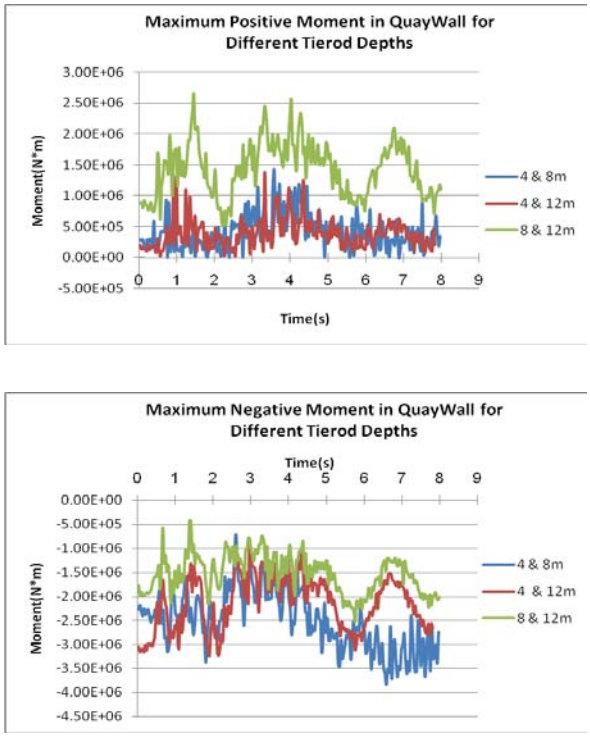

Figure 6 Maximum Moments of Wall for Different Tie rod Depths (Two Tie rods)

Changes in maximum displacement of wall top and main design parameters -maximum bending moment of wall and maximum tie rod axial force- are shown in table 4 with respect to tie rod position in analyses time duration.

Table 4 Maximum Moment of Quay wall & Tie rod Axial Force & Displacement in Sand (Two Tie rod)

Tie rod Depth (m)	Quay wall Length (m)	Tie rod Depth Ratio	M^+ (KN*m)	M^- (KN*m)	f1 (KN)	f2 (KN)	d (m)
4&8	28	.14&.28	1435.1	-3836.8	355	380	-0.085
4&12	27	.15&.44	1376.7	-3227.3	590	542	-0.162
8&12	27	.30&.44	2648.8	-2521.4	772	589	-0.111

Upper tie rod maximum axial force is comparable with lower tie rod force. In the first and second case the absolutevalue of maximum negative moment is more than maximum positive moment.

5. CONCLUSIONS

First, approximate suitable position of a tie rod

anchoring the long retaining wall is investigated in this research. Then, the influence of positioning another tie rod is investigated.

When free height of the anchored retaining wall is more than about 11 meters using another anchor can improve the design. It results in reducing maximum moment and total length of wall, wall drift and tie rod axial force (in comparison with walls anchored by just one tie rod). Using information provided above change of these parameters by adding a new anchor in different positions is clear.

Through the results of this research it is inferred that using both tie rods in upper parts of wall will decrease the lateral displacement more considerably. Therefore, serviceability will increase.

Reduce in axial force and consequently diameter of tie rods as a result of utilizing another tie rod will prevent using extraordinary tie rod prestressing equipment. So, construction cost will be reduced.

Utilizing two tie rods especially in lower part of investigation interval is more effective to reduce maximum moment and then wall profile. Also, via decrease in wall penetration depth by placement of second tie rod in appropriate location, construction cost will become less again.

Due to very complicated changes based on each tie rod position and selected penetration depth of retaining wall, it seems that more evaluation is useful in every particular case of design.

Acknowledgements:

The authors acknowledge support from the Japan Ministry of Education, Culture, Sport, Science, and Technology (MEXT) for establishing the Center for Urban Earthquake Engineering (CUEE) in Tokyo Institute of Technology.

References:

Kristian Krabbenhoft, Lars Damkilde, Sven Krabbenhoft, 2005, "Ultimate limit state design of sheet pile walls by finite elements and nonlinear programming "www.elsevier.com/locate/compstruc

Itasca consulting group, 2002, Inc,"FLAC Manual", version 4.0

Technical Standards and Commentaries for Port and Harbor Facilities in Japan,"OCDI, 2002, The Overseas Coastal Area Development Institute of Japan"

ARCELOR RPS,"Piling Handbook", 2005, 8TH EDITION

U. S. Department of Transportation /FHWA, 1984, "USSteel, Steel Sheet Piling Design Manual"

Bowles. J. E, 1996 "Foundation Analysis and Design", McGraw Hill

Das. B. M., 1990, "Principles of Geotechnical Engineering", 2nd Ed., PWS-KENT

Department of the Army U.S. Army Corps of Engineers Washington, 1994, DC 20314-1000" DESIGN OF SHEET PILE WALLS"

JOINT CONFERENCE PROCEEDINGS
7th International Conference on Urban Earthquake Engineering (7CUEE) &
5th International Conference on Earthquake Engineering (5ICEE)
March 3-5, 2010, Tokyo Institute of Technology, Tokyo, Japan

EFFECT OF STRESS STATE AROUND TUNNEL ON PSEUDO-STATIC RESPONSE OF URBAN MOUNTAIN TUNNEL IN SAND

Shuhei Shibayama[1], Jun Izawa[2], Akihiro Takahashi[3] and Osamu Kusakabe[4]

1) Doctoral student, Dept. of Civil Engineering, Tokyo Institute of Technology, Japan
2) Assistant Professor, Department of Civil Engineering, Tokyo Institute of Technology, Japan
3) Associate Professor, Department of Civil Engineering, Tokyo Institute of Technology, Japan
3) Professor, Department of Civil Engineering, Tokyo Institute of Technology, Japan
sh4880@cv.titech.ac.jp, jizawa@cv.titech.ac.jp, takihiro@cv.titech.ac.jp, kusakabe@cv.titech.ac.jp

Abstract: It is widely accepted that underground structures have high seismic stability because of confining effects from the surrounding ground. However, tunnel structures have experienced serious damages. Although the need for seismic performance of tunnels is emphasized in specifications for tunnels, it is required to understand detailed mechanisms on the interaction between the structure and soil. There are many uncertain factors which affect the soil-structure interaction, e.g., arch action of ground, deformation of ground together with tunnel and tunnel cover depths. The arch action of the ground is expected to occur due to tunnel and ground deformation during the construction process of the mountain tunnel, and it might be changed by the earthquake-induced ground deformation. In order to investigate the pseudo-static response of the urban mountain tunnel in sandy ground and effect of stress state around the tunnel, centrifuge model tests were carried out in this study. In conclusion, following results were obtained. Firstly, the deterioration of the arch action takes place due to shear deformation of ground. Secondly, the pseudo-static response before and after deterioration of the arch action are significantly different. Thirdly, the tunnel cover depth has a significant effect on the pseudo-static response of the tunnel structure.

1. INTRODUCTION

Recently, the number of construction of urban tunnels has been increasing because of intensive use of urban areas. In order to reduce construction cost of the urban tunnels, mountain tunnels have extended its application to urban area in sandy ground at relatively shallow depth.

Underground structures were considered having high seismic stability because of a confining effect from tunnel surroundings (Kawashima 1994). However, tunnel structures have experienced serious damages in the 1995 Hyogoken-Nanbu Earthquake (Asakura et al. 1996), and consequently the design codes for tunnels were revised (JSCE 1996 and JSCE 2001). The revised specifications recommend taking into account the soil-structure interactions by proper methods, such as the seismic displacement method. This method is a kind of pseudo-static approach in which seismically induced ground motion is applied to the tunnel structure through the soil springs. This soil-structure interaction is affected by many factors, e.g., stress conditions of soil, tunnel cover depths, deformation of ground together with tunnel structure, surface condition of tunnel and lining structures, thus, there are many uncertainties in the application of the seismic displacement method. Although the need for seismic performance of the urban tunnels is emphasized in JSCE standard specifications for tunnels, it is required to understand detailed mechanisms on the soil-structure interaction under various conditions. Arch action of the ground above the mountain tunnel is expected to occur due to tunnel and ground deformation during tunnel construction, i.e. stress releasing of the ground is generated, and the earth pressure acting on the tunnel lining is much smaller than that by the shield tunneling method. According to previous studies (Kusakabe et al. 2008), the experimental results showed that the earth pressure changes due to deterioration of the arch action which is caused by the shear deformation of the ground, however an effect on the structural response have not been investigated.

In this study, active type shear tests in a centrifuge were carried out to understand the pseudo-static seismic response of the urban mountain tunnel in sandy ground, and the effect of the stress state around the tunnel. In particular, difference of the pseudo-static response of the tunnel structure before and after deterioration of the arch action and an effect of the tunnel cover depths are discussed.

2. CENTRIFUGE MODEL TESTS

2.1 Introduction

Seismic stability of a tunnel structure is usually evaluated by the seismic displacement method. This method evaluates structural forces exerted on the tunnel by applying the shear deformation of surrounding ground to the tunnel in a pseudo-static approach, because the effect of inertia force acting to the underground structure can be neglected as compared with super structures. Figure 1 shows an active type shear box used in this study. The seismic displacement method was experimentally reproduced by using this shear box. Validity of the experimental method for a rectangular tunnel and its countermeasures in sand has been confirmed by the previous study (Izawa et al. 2006). In this study, pseudo-static response of the tunnel structure was investigated by the experimental simulation of the seismic displacement method using the active type shear box in a centrifuge.

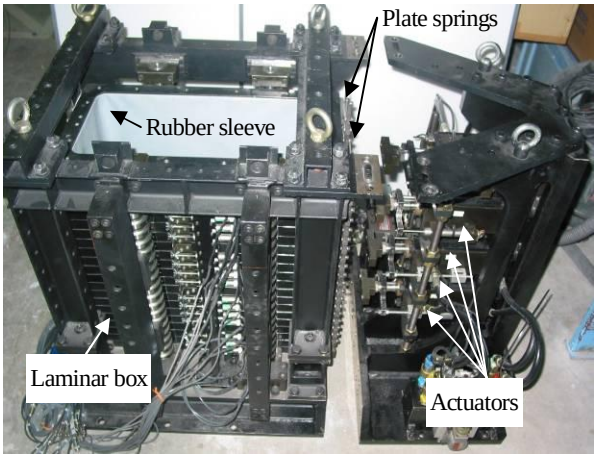

Figure 1 Active type shear box

Table 1 Specifications of shear box

Maximum centrifuge acceleration		100g
Actuator	Number	4
	Stroke	±20mm
	Force capacity (20.5MPa oil pressure)	25.8kN (outward) 18.0kN(inward)
	Peak velocity	133mm/sec
Laminar box	Dimensions (inner)	W 452mm B 202mm H 524mm
	Number of laminae	20+fixed one

2.2 Test and model description

The active type shear box comprises two parts; a laminar box and actuators. The laminar box consists of 20 stacked 24mm laminae with a roller bearing support and one fixed lamina at the base of the box. The shear deformation of the box was imposed by four hydraulic actuators connected to the four laminae at specific elevations. Lateral displacements of the other laminae were created by transmitting forces from the actuators to them through four linked sets of 0.6mm plate springs. A rectangular shape rubber sleeve was placed on the inner wall of the box to prevent the soil particles from getting into the gaps of the laminae. Thin stainless vertical sheets and a horizontal sheet of 0.2mm thickness with rough surface were fixed to both the inner end walls and the base of the box, respectively. These sheets are used for mobilizing the shear stresses on the inner boundary when the box is sheared. The specifications of the shear box are summarized in Table 1.

Assuming horseshoe-shaped mountain tunnel in sandy ground, a horseshoe-shaped aluminium model tunnel was used as is shown in Figure 2. The model lining has a diameter of 100mm, a height of 75mm and a thickness of 2mm with smooth surface, which approximately corresponds to a 5m diameter tunnel with a RC lining of 300mm thickness in the prototype scale under centrifugal acceleration of 50g.

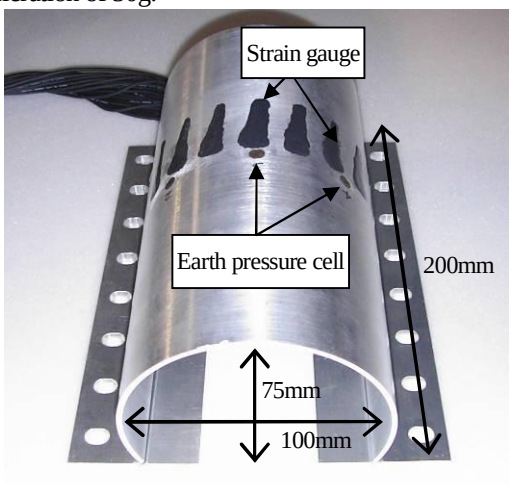

Figure 2 Horseshoe-shaped model tunnel

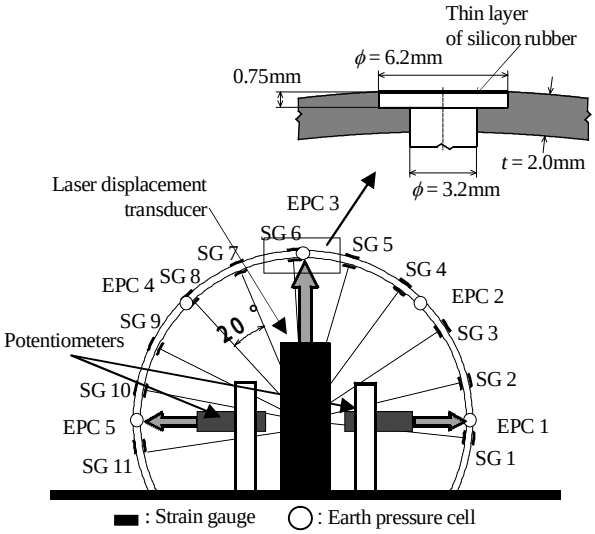

Figure 3 Positions of sensors

In total, 22 strain gages were attached on both outer and inner sides of the two models in pairs to obtain bending moment and axial force distributions of the tunnel lining. Five earth pressure cells of 6.2mm diameter and 0.75mm

thick were embedded to measure the earth pressures acting on the outer surface of the lining. Measurement points of the earth pressures were at tunnel crown, spring lines and midpoints between the crown and the spring lines. A thin layer of silicon rubber coated over the surface of the earth pressure cells. In addition, to measure vertical and horizontal convergences, a laser displacement transducer and two potentiometers were placed inside the tunnels model. Figure 3 illustrates the positions of these sensors attached to the model tunnel.

Figure 4 illustrates the schematic diagram of model setups for the tests. Dry silica sand No.6 (G_s=2.64, D_{50}=0.51mm, Uc=1.74, e_{max}=0.922, e_{min}=0.565) was used for the model ground. After the model tunnel was placed on the base of the laminar box, the model ground was constructed by the air pluviation method to achieve a relative density of 80% (γ_d=15.8kN/m^3, ϕ=41deg.). In order to investigate the effect of the tunnel cover depths, the covers of the model ground, *C*, were selected to be 100mm (i.e. *C=1D* case) and 300mm (i.e. *C=3D* case) which corresponds to a tunnel cover-diameter ratio, *C/D* of 1 and 3.

Figure 5 shows a typical example of the input horizontal displacement distributions of the laminar rings measured by potentiometers at nominal 1%, 2% and 4% shear strains both on the positive and negative side, for the *C=1D* and *C=3D* cases. The measured distributions for the both *C=1D* and *C=3D* cases are almost the same, in particular, at the depth of the tunnel, although there are some different parts between the Actuator 2 and 3, in which, the case of the *C=1D* has no ground material.

The input nominal shear strain time histories are shown by a thin dashed curve in Figure 6. The input nominal shear strain is defined by the gradient of the intended distribution of the input horizontal displacements, as shown in Figure 5. The two cycles sinusoidal nominal shear strain for the amplitudes of 1%, 2% and 4% respectively, were imposed on the model ground continuously in the centrifugal acceleration of 50g. An each cycle of shear strain was applied in 100sec. In Figure 6, the sinusoidal waves shown by broken and solid lines indicate nominal shear strain histories at the ground center for the case of *C=1D* and *C=3D*, respectively. The values of the shear strain were calculated from the measured horizontal displacement at the center of ground surface divided by the height of model ground (i.e. tunnel cover, *C* + height, *h*, 175mm for the *C=1D* case and 375mm for the *C=3D*). The nominal shear strains at the center are consistently about 30% for the *C=1D* and 60% for the *C=3D* case of the input shear strain throughout the shearing histories. The previous studies with the active type shear box reported the similar results, Takahashi et al. (2001) used the original shear box and reported 70-80% of the input nominal shear strain under the conditions of 325mm deep Toyoura sand of relative density of 80% under 25g. They also reported a numerical result for the case with an aspect ratio of the ground, Width/Height=3, in which 30% of input horizontal displacement were obtained. The aspect ratio of the *C=1D* case is about 2.6. Yamada et al. (2002) also used the

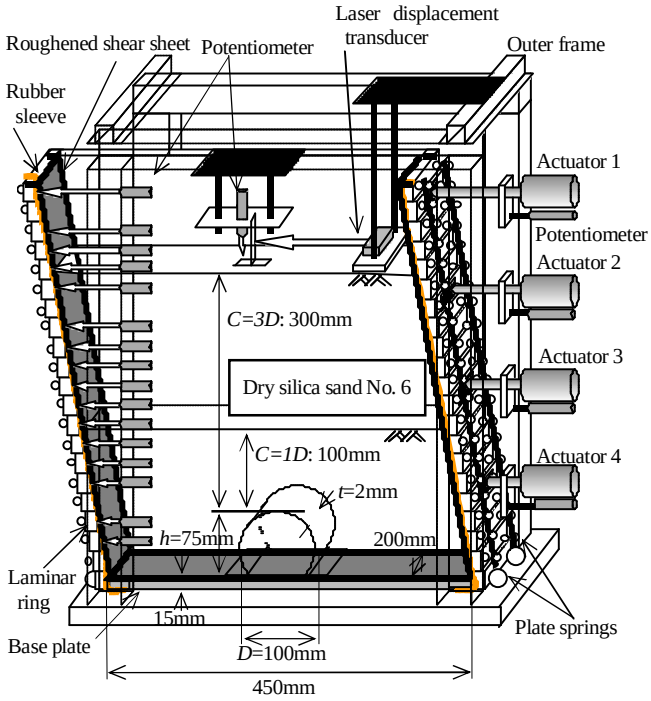

Figure 4 Model setup

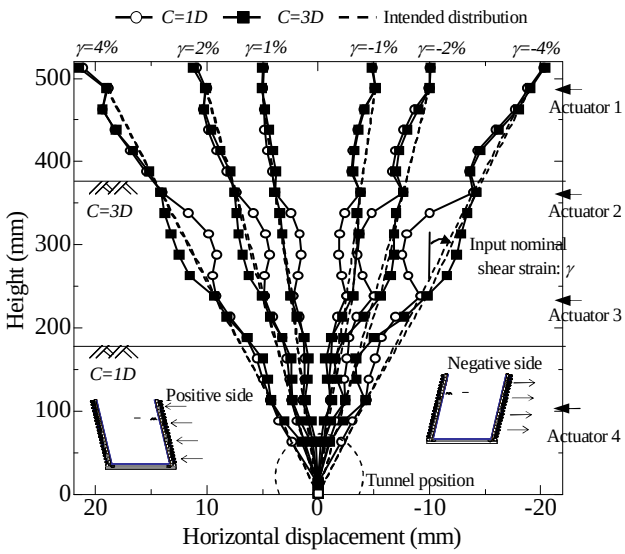

Figure 5 Distributions of horizontal displacement

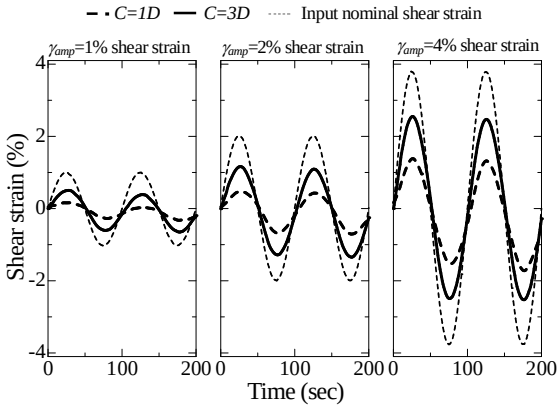

Figure 6 Shear strain history

shear box and reported 70% under the conditions of 300mm deep Toyoura sand of relative density of 90% under 50g. Although the test conditions and material properties are different in these tests, the general trend is similar to the previous observations. However, in both the tests, even though the magnitude of the horizontal displacement was smaller than that at the side boundaries, the horizontal displacement profile at the center of the box was similar to that at the side boundaries. These suggest that the shear strain around the center of the box can be evaluated by the nominal shear strain at the side boundaries. Thus, it can be said that the prescribed shear strain can be imposed on the tunnel structure and the active type shear test can be regarded as the seismic displacement method.

2.3 Results and discussion

Figure 7 shows the time histories of the measured radial earth pressures at the tunnel crown (EPC3), the right shoulder (EPC2) and the right spring line (EPC1), during the shearing processes of three different amplitudes (γ_{amp}), separately for the both cases of the *C=1D* and *C=3D*. Hear, the measured earth pressures are normalized by the full overburden pressure at the tunnel crown, $\gamma_d C$ (i.e. 79.3kPa for the case of *C=1D*, 237.8kPa for the *C=3D*). The input nominal shear strain is indicated as the dashed wavy lines in the figure. Before the first shearing (γ_{amp}=1%), the normalized earth pressure of the all cases are smaller than unity, which means the earth pressures are smaller than the full overburden pressures acting on the tunnel crown. This is probably due to the formation of the arch action above the tunnel during the period of increasing centrifugal acceleration up to 50g, as reported by Shibayama et al. (2007). It is shown in Figure 7 (a) that after shearing, the normalized earth pressure at the tunnel crown for the both cases *C=1D* and *C=3D* increase and approach to the unity (i.e. the full overburden pressure). For the case of the *C=3D* shown by a solid line in Figure 7 (a), the earth pressure at the crown significantly increased by the positive 1% shear strain application and then slightly decreased,

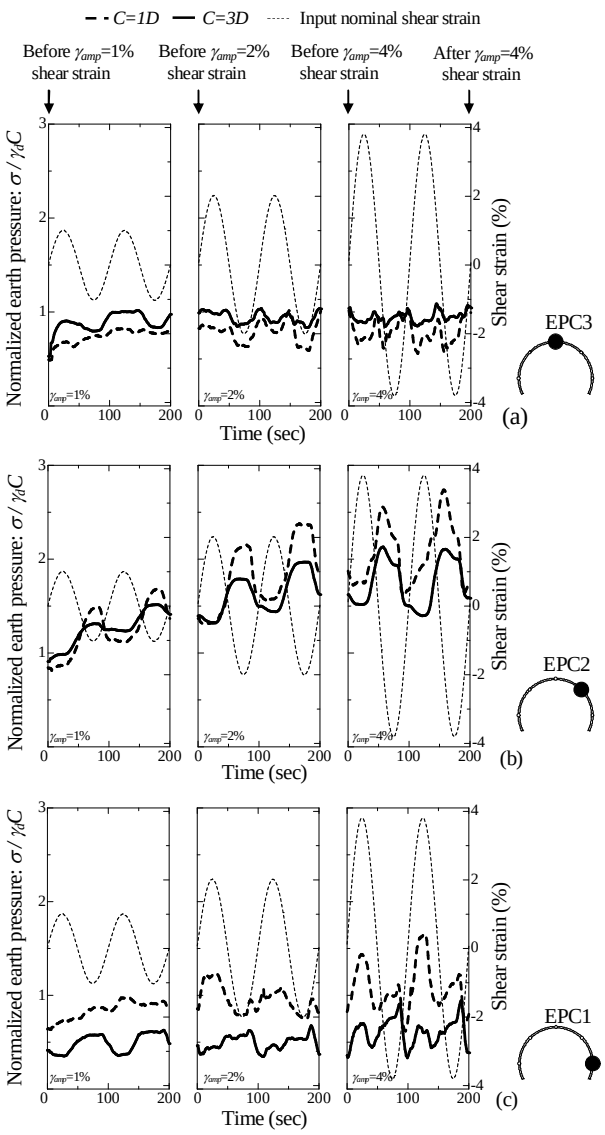

Figure 7 Time histories of normalized earth pressure
(a) Tunnel crown, (b) Right shoulder and (c) Right spring line

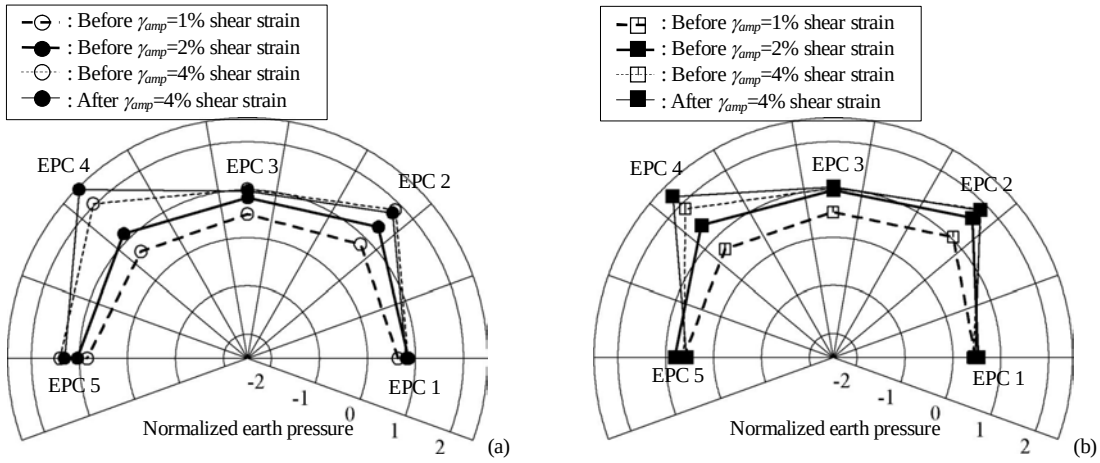

Figure 8 Distributions of normalized earth pressure before and after γ_{amp}=1, 2 and 4% shearing
(a) *C=1D* and (b) *C=3D*

associated with the negative 1% shear strain application during the first cycle. In the second cycle, the earth pressure further increased up to the full overburden pressure and then decreased, as the negative shearing process proceeded. For the case of the *C=1D* shown in a broken line, the earth pressure progressively increased regardless of sign convention of the shear strain until the end of the first cycle of the 2% shear strain application. Once the normalized earth pressures at the crown reach to the unity and vary within certain ranges. The variation of the earth pressure for the case of *C=3D* (about 20% of the normalized earth pressure) is smaller than that for the *C=1D* case (about 50%). It is observed from Figures 7 (b) and (c) that the earth pressures not only at the crown but also at spring line and at shoulder increased with the application of shear deformation, although the data at shoulder exhibit considerable fluctuation. Figure 8 shows the distributions of the normalized earth pressure ($\sigma/\gamma_d C$) measured before two cycles of shear deformation for the γ_{amp}=1, 2 and 4% shear strain and after γ_{amp}=4% shear strain for the both *C=1D* shown in Figure 8 (a) and *C=3D* shown in Figure 8 (b). The terms "before" and "after" in the figure correspond to the test elapsed time of 0 and 200sec in each shearing event as is indicated in Figure 7 (a). It is shown in Figure 8 that the normalized earth pressures acting on the tunnel lining, especially the upper part of the lining, increased after experience shearing events for the both cases. As mentioned before, this observation must be associated with the deterioration of the arch action. This experimental fact implies that the initial stress states for the each shearing event changed and the earth pressure distribution reached to a certain distribution in which the earth pressures at the tunnel shoulders were the largest.

In order to understand the effect of the initial stress change on the structural response due to the shear deformation of the ground, the distributions of the absolute and incremental value of the structural forces for the *C=3D* case were compared. Figure 9 (a) shows the distributions of the absolute earth pressures measured at the input nominal shear strain γ=1% in the first cycle of the γ_{amp}=1%, 2% and 4% shearing event for the case of *C=3D*. Through the all cases, the absolute values of the earth pressures acting on the tunnel crown, right and left spring lines show no applicable changes. On the other hand, the earth pressure acting on the tunnel shoulders show considerable change, even though the same value of shear strains γ=1% are imposing on the model. The values of the earth pressures acting on the tunnel shoulders increase, as experience the shear strain histories (i.e. the value of shear strain amplitude of the event, γ_{amp}, increase). Figure 9 (b) shows the distributions of the incremental value of the earth pressures measured from the beginning of the each shearing events to the same point of Figure 9 (a). As compare with the absolute values shown in Figure 9 (a), the incremental values of earth pressures are small. The only distribution in theγ_{amp}=1% event is considerable different from the others, which has the maximum value at the tunnel crown. It might be related to deterioration of arch action at tunnel crown. Figures 10 and 11 show the absolute and incremental distributions of the bending moments and the axial forces, respectively, measured at the same point shown in Figure 9. The previous experiments (Yamada et al. 2002 and Izawa et al. 2006) indicated that sectional forces at the tunnel corners are remarkable when the pseudo-static shear deformation of the ground was imposed on the model tunnel. The present data shown in Figures 10 and 11 also support the previous experimental observations. As shown in Figures 10, the bending moment distributions of the absolute and incremental values of γ_{amp}=2% and 4% shearing events are almost the same, however, the distributions of γ_{amp}=1% (shown by open circles and a solid line) are slightly different, especially SG8 for the absolute values and SG10 for the incremental values. It can be said that the structural force responses of the γ_{amp}=1% event are regarded as before earthquake responses, on the other hand for the γ_{amp}=2% and 4% events, these are regarded as post-earthquake responses. The term of "before earthquake" and "post- earthquake" has a meaning of the response before (or during) and after the deterioration of the arch action of the ground above the tunnel, respectively. The absolute distributions for the all cases shown in Figure 10 (b) has the peak values at left shoulder (i.e. SG9) and the values are almost the same. Similarly, the peak values for the distributions of incremental bending moment are also the same at SG8 as shown in Figure 10 (b). It is shown in Figure 11 that the absolute and the incremental distributions of the axial force for the γ_{amp}=1% event differ from these for the other events, as well as in the bending moment distributions shown in Figure 10. Especially, the distribution of the incremental values significantly differs from the others, that for the γ_{amp}=1% has the peak value at the left spring line (SG10), while the others (for the γ_{amp}=2% and 4%) has the left shoulder (SG8). As shown in Figure 10 (a), the absolute value of the axial force distributions for the all events show the maximum value at SG8, and the value of the γ_{amp}=2% and 4% events 50% larger than that of the γ_{amp}=1%. These experimental results suggest that the structural response before earthquake (i.e. γ_{amp}=1% shearing event) and the post-earthquake response (i.e. γ_{amp}=2% and 4% shearing events) are different, even though the same value of the input nominal shear strain were imposed. In particular, the peak values of the axial force for the post-earthquake responses are larger than that before earthquake, although the peak bending moment at tunnel shoulder for the both cases are almost the same.

In order to investigate the effect of the tunnel cover depths, direct comparisons of the structural responses between the *C=1D* and the *C=3D* cases were conducted when the same value of the nominal shear strain imposed on the model tunnels in the γ_{amp}=1% and 4% shearing event. These comparisons in the γ_{amp}=1% and 4% shearing events means that the structural response of the before earthquake and the post-earthquake, respectively. Figures 12 (a) and (b) show the comparisons for the distributions of the absolute value of the earth pressure when the same value of the nominal shear strain at ground center were imposed on the models in γ_{amp}=1% and 4% shearing event, respectively.

For the *C=1D* case, the comparisons were conducted when the first maximum shear strains were applied in the γ_{amp}=1% and 4% event, while for the *C=3D*, when the same values of the shear strain at ground center for the *C=1D* case were imposed, as shown in Figure 12. According to Figure 12, the earth pressures acting on the tunnel lining for the *C=3D* case are about 3 times larger than that for the *C=1D*, thus the absolute values of the structural forces are quite different between the *C=1D* and the *C=3D* cases. Hereafter, only the incremental values of the structural forces are discussed. Figures 13 and 14 show the incremental values of the bending moment and the axial force distributions measured from the beginning of the each shearing event to the same points shown in Figure 12. As shown in Figure 13 (a), the both distributions of bending moment for the *C=1D* and *C=3D* are the almost the same, except at left spring line (i.e. SG10). The incremental value of the bending moment at SG 10 for the *C=3D* case is 4 times larger than that for the *C=1D* case. It is shown in Figure13 (b) that the both distributions has the negative and positive peaks at the left and right shoulders (i.e. SG8 and SG4), as mentioned before it is following previous results. The peak values at the SG4 and SG8 for the *C=3D* case are about 30% larger than that for the *C=1D*. Compared with the bending moment distributions, the axial force distributions are quite different between the *C=1D* and the *C=3D* cases. The *C=1D* case has the peak value at the right shoulder (SG4), while the *C=3D* case has the peak in the left hand side (at SG10 in γ_{amp}=1% event, SG4 in γ_{amp}=4% event), as shown in Figure 14. It is indicated that the axial force-generating mechanisms due to the seismically induced ground shear deformation are different between the *C=1D* and the *C=3D* cases. According to these comparisons, it can be said that the pseudo-static responses of the tunnel structure are significantly affected by the tunnel cover depth. As compared with the case of shallow tunnel (*C=1D*), the deeper tunnel (*C=3D*) show larger peak response of the bending moment when the same values of the nominal shear strain were imposed on the tunnel structure. Between the cases of the deeper and shallow cover depths, the mechanisms of the axial force response are different. The shallow case has the peak value at the right shoulder, while the deeper case has the peak in the left hand side.

3. CONCLUSIONS

This paper presented some results of the active type shear box tests in a centrifuge by modeling the horse-shaped aluminum tunnel in sand to understand the pseudo-static seismic response of the urban mountain tunnel in sandy ground, especially the effect of stress state around tunnel on the structural response due to the earthquake-induced ground deformation. According to the results, the following findings were obtained.

1. Deteriorations of the arch action of tunnel surroundings for both shallow (tunnel cover-diameter ratio, *C/D*=1) and deeper (*C/D*=3) tunnel take place by seismically induced pseudo-static shear deformation of surrounding ground. According to the deterioration of the arch action, earth pressures acting on tunnel structure before and after experience of the ground shear deformation change.
2. Pseudo-static responses of the tunnel structural before and after experience the ground shear deformation are different. In particular, larger peak axial force response is exerted on the tunnel shoulder after experience the ground shear deformation, compared with that before experience.
3. Tunnel cover depth has significant effect on the pseudo-static responses of the tunnel structural. As compared with the shallow tunnel (*C/D*=1), the deeper tunnel (*C/D*=3) shows larger peak pseudo-static response of the bending moment at the tunnel shoulders when the same value of the nominal shear strain are imposed on the tunnel structure. Between the shallow and deeper tunnels, the incremental values of the axial force response are significantly different.

Acknowledgements:

This research was partially supported by Grant-in-Aid for Scientific Research (A), 2005-2007, No. 17206050, "Seismic stability of the large cross-section urban tunnel with located in relatively shallow depth". The authors gratefully acknowledge the funding for this research from the 21st Century Centre of Excellence (COE) program entitled "Evolution of Urban Earthquake Engineering".

References:

Kawashima, K. (1994), "Seismic Design of Underground Structures," Kajima Publishing Co. Ltd., (In Japanese)

Asakura, T. and Sato, Y. (1996), "Damage to Mountain Tunnels in Hazard Area," *Soils and Foundations Special Issue on Geotechnical Aspects of the January 17 1995 Hyogoken-Nanbu Earthquake*, 301-310.

Japan Society of Civil Engineers (1996), "Standard Specifications for Cut and Cover Tunnels," (in Japanese)

Japan Society of Civil Engineers (2001), "Japanese Standard for Shield Tunneling -1996- The Third Edition,"

Kusakabe, O., Takemura, J., Takahashi, A., Izawa, J. and Shibayama, S. (2008), "Physical Modeling of Seismic Responses of Underground Structures, "*Proc. 12th Int'l Conf. of Int'l Association for Computer Methods and Advances in Geomechanics*, 1459-1474.

Izawa, J., Kusakabe, O., Nagatani, H., Yamada, T. and Ohbo, N. (2006), "Centrifuge Modeling on Seismic Behavior of Rectangular Tunnels," *Physical Modeling in Geotechnics 6th ICPMG*, 1163-1169.

Terzaghi, K. (1948), "Theoretical Soil Mechanics," John Wiley and Sons, 66-76.

Yamada, T., Nagatani, H., Igarashi, H. and Takahashi, A. (2002), "Centrifuge Model Tests on Circular and Rectangular Tunnels Subjected to Large Earthquake-induced Deformation," *Proc. of the 3rd Int'l Symp. on Geotechnical Aspects of Underground Construction in Soft Ground*, 673-678.

Shibayama, S., Izawa, J., Takahashi, A., Takemura, J. and Kusakabe, O. (2009), "Pseudo-static Seismic Response of Urban Mountain Tunnel in Sand," *Proc. of the 6th Int'l Conf. on Urban Earthquake Engineering*, 561-566.

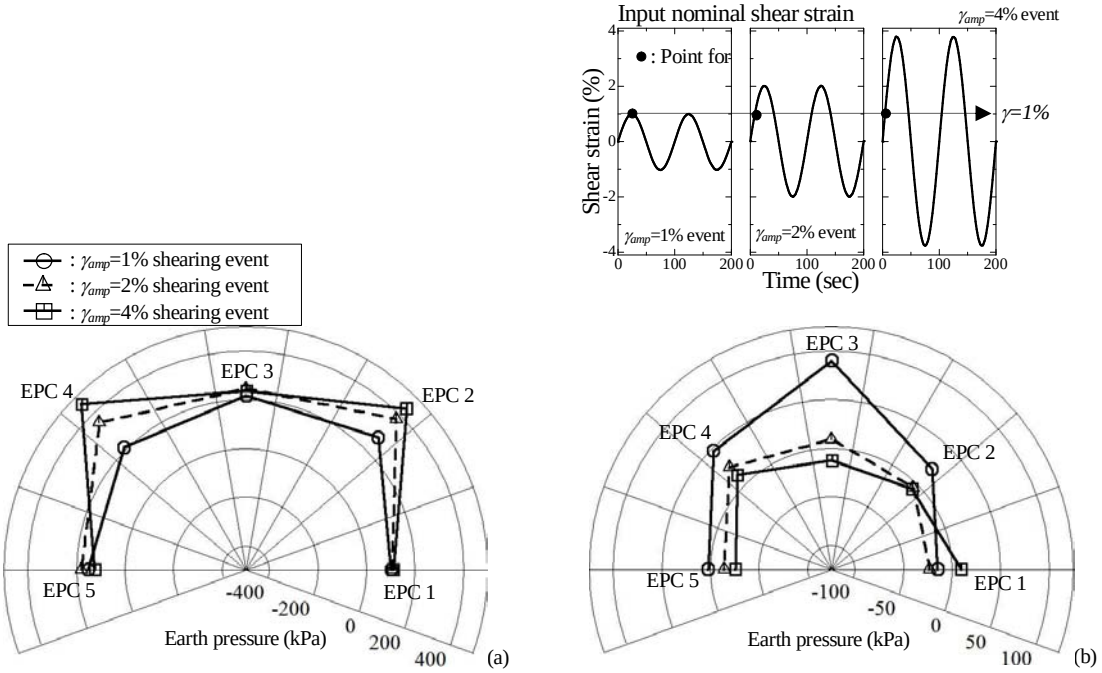

Figure 9 Distributions of normalized earth pressure for *C=3D* when γ=1% shear strains imposed
(a) Absolute values and (b) Incremental values from

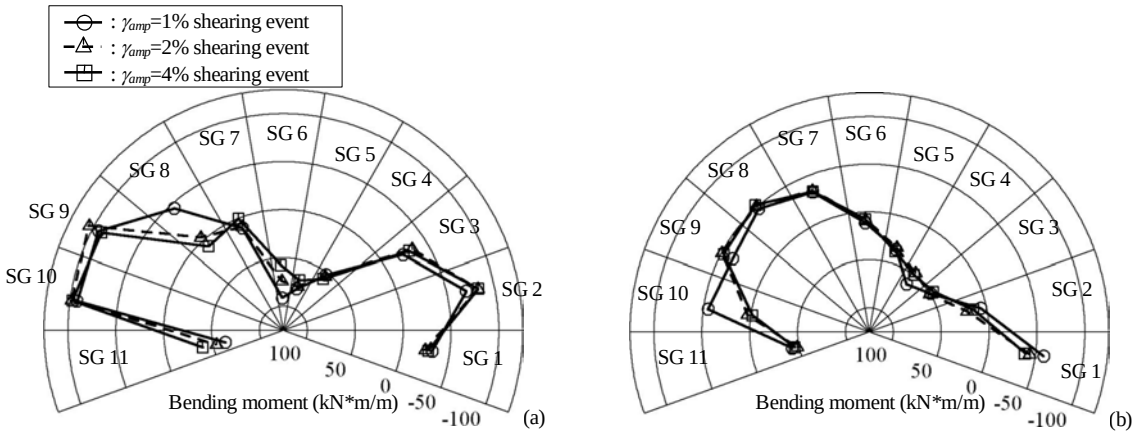

Figure 10 Distributions of bending moment for *C=3D* when γ=1% shear strains imposed
(a) Absolute values and (b) Incremental values

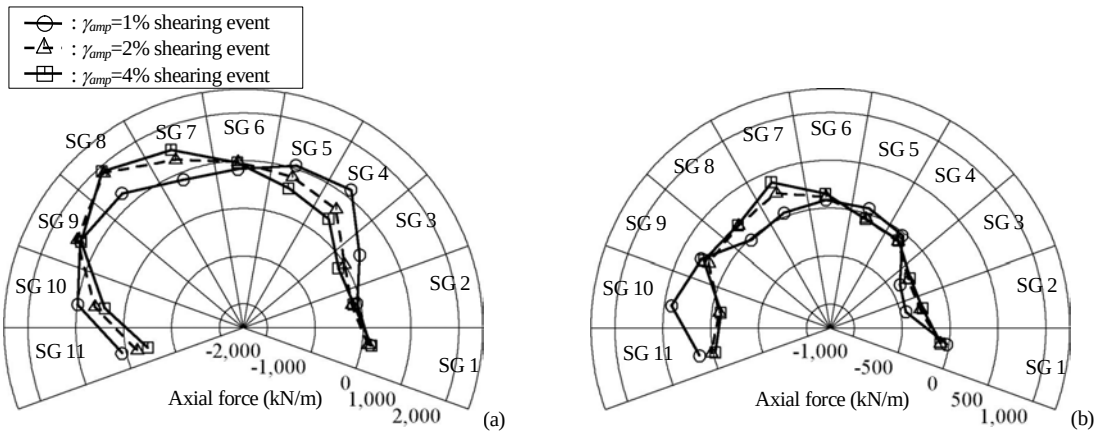

Figure 11 Distributions of axial force for *C=3D* when γ=1% shear strains imposed
(a) Absolute values and (b) Incremental values

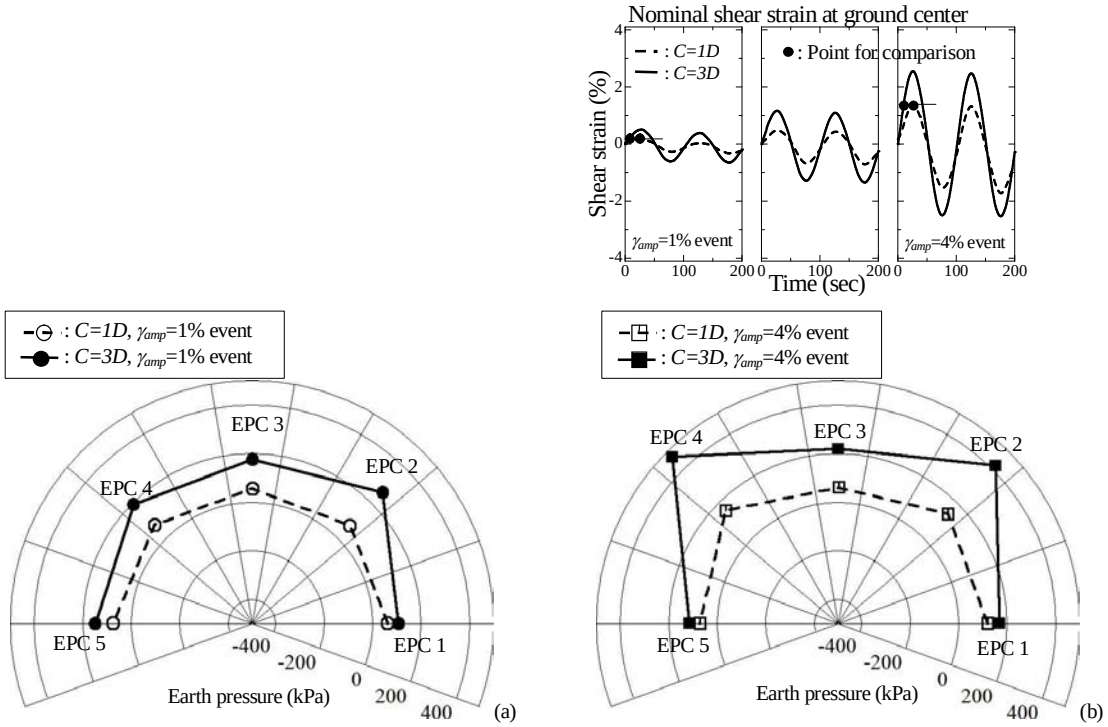

Figure 12 Distributions absolute value of normalized earth pressure compared *C=1D* with *C=3D*
(a) γ_{amp}=1% event and (b) γ_{amp}=4% event

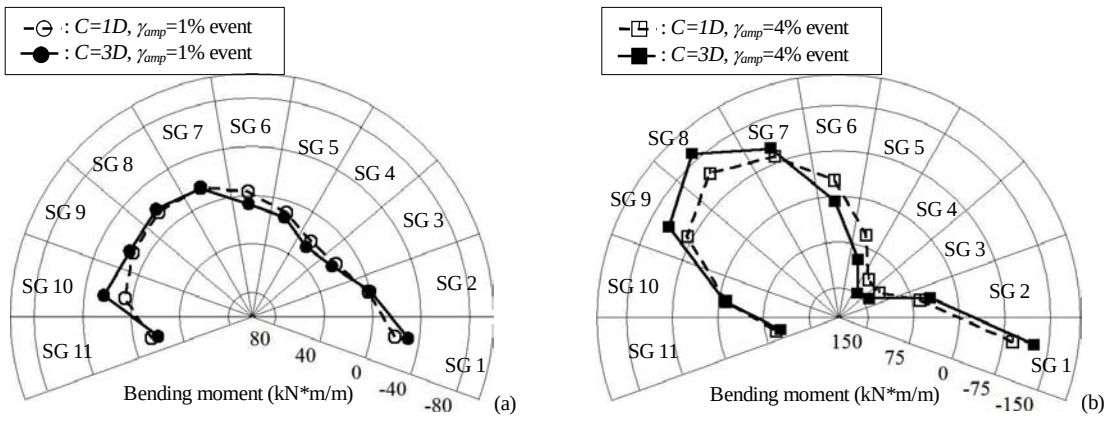

Figure 13 Distributions incremental value of bending moment compared *C=1D* with *C=3D*
(a) γ_{amp}=1% event and (b) γ_{amp}=4% event

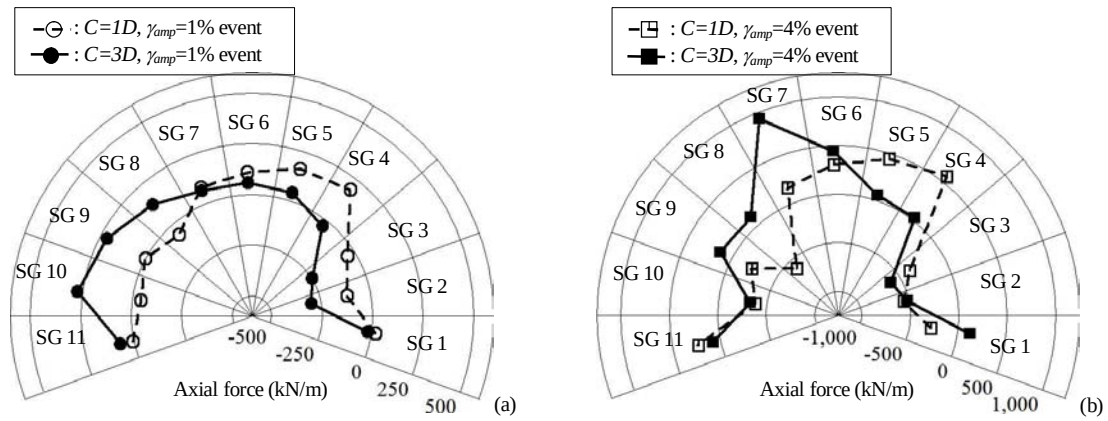

Figure 14 Distributions incremental value of axial force compared *C=1D* with *C=3D*
(a) γ_{amp}=1% event and (b) γ_{amp}=4% event

JOINT CONFERENCE PROCEEDINGS
7th International Conference on Urban Earthquake Engineering (7CUEE) &
5th International Conference on Earthquake Engineering (5ICEE)
March 3-5, 2010, Tokyo Institute of Technology, Tokyo, Japan

DYNAMIC FIELD TESTING OF SHALLOW FOUNDATIONS SUBJECTED TO ROCKING

Thomas B. Algie[1)], Michael J. Pender[2)], and Rolando P. Orense [3)]

1) Ph.D. Candidate, Dept. of Civil and Environmental Engineering, University of Auckland, New Zealand
2) Professor of Geotechnical Engineering, Dept. of Civil and Environmental Engineering, University of Auckland, New Zealand
3) Senior lecturer, Dept. of Civil and Environmental Engineering, University of Auckland, New Zealand
talg001@aucklanduni.ac.nz, m.pender@auckland.ac.nz, r.orense@auckland.ac.nz

Abstract: Nonlinear soil-foundation-structure interaction (SFSI) of shallow foundations may be beneficial during a strong seismic event. This paper details two tracks of research being carried out at the University of Auckland on the seismic response of shallow foundations. The research is both experimental and numerical. Large scale field tests on shallow foundations were carried out. In addition a spring bed model was developed and used to predict the experimental behaviour. Prior to the experiments a full geotechnical investigation was carried out to determine soil conditions. A test structure, made from structural steel, was designed and fabricated specifically for this testing. Road construction plates were attached to the structure to create realistic vertical loads and achieve different static factors of safety in bearing. Tests were carried out with estimated static factors of safety of 49 and 8. The development of a numerical model, done using OpenSees, is outlined. Nonlinear behaviour of the foundations and underlying soil was evident and comparison between the experimental and numerical results is encouraging. The measured response of the foundations indicate good energy dissipation during the rocking cycles.

1. INTRODUCTION

Nonlinear soil-foundation-structure interaction (SFSI) of shallow foundations may be beneficial during a strong seismic event. Uplift reduces the contact area between soil and foundation and induces nonlinearity from local bearing capacity failure at the edges. This can potentially reduce forces exerted on the super-structure, protecting structural beams and columns. Adversely, permanent settlement and rotation of a foundation may occur during the rocking motion.

In New Zealand, some buildings do not have sufficient weight to resist the overturning moment (Kelly, 2009). To prevent rocking in these cases tension piles may be included, adding considerable cost to the structure. In the older version of the New Zealand design and loadings standard, there was a provision for rocking foundations (Standards, 1992), this stated:

"Where dissipation of energy is primarily through rocking of foundations, the structure shall be subject to a special study, provided that this need not apply if the structural ductility factor is equal to or less than 2.0."

The understanding of this clause was that engineers could design a foundation for the reduced forces from a ductility factor (μ) of 2 without any extra analysis. Thus the foundation could be sized such that at design forces for $\mu = 2$, the overturning moment is equal to the restoring moment and rocking occurs.

This provision for rocking foundations was removed in the newer New Zealand design and loadings standard (Standards, 2004), which stated:

"Where energy dissipation is through rocking of structures or structural sub-assemblies… the actions on the structures and parts being supported by the structures shall be determined by special study."

This new clause states that all rocking foundation designs have to be done as a special study. In New Zealand a special study would require the development of a computer model with time history analysis being undertaken. Often design offices will not have the time or resources to carry out such an extensive study (Kelly, 2009).

However, the fact still remains that rocking foundations can have a positive influence on earthquake performance of a structure. Our research is focused on experimental and numerical investigation of rocking foundations. In particular we have been developing numerical models and carrying out large scale experiments to validate them.

1.1 Background

The rocking foundation concept, was first researched by Housner (1963). In his paper Housner gave equations of motion of an inverted pendulum rocking on a rigid surface and calculated energy dissipation resulting from the impacts (radiation damping). Since that time numerous studies on

rocking foundations have been carried out both experimentally and numerically.

Experimentally, there have been both centrifuge experiments and 1g model tests done. At the University of Auckland, slow cyclic tests of shallow foundations on clay and sand were conducted (Bartlett, 1976; Taylor et al., 1981; Wiessing, 1979). From those experiments, it was suggested that spread footings may be intentionally designed to yield during high intensity earthquakes.

Gajan et al. (2005) carried out centrifuge tests on rocking shear walls sitting on moderately dense sand. He concluded that foundations produce a well defined moment capacity. He found that for foundations to maintain stability, a critical contact length (L_c) must remain between the soil and foundation. The moment capacity (M_{max}) can be calculated by the equation:

$$M_{\max} = \frac{V \cdot L}{2}\left[1 - \frac{L_c}{L}\right] \quad (1)$$

where; V = vertical load (kN) & L = foundation length (m).

In addition, Gajan developed a numerical model, called a Contact Interface Model (CIM), for predicting shallow foundation behavior (Gajan, 2006).

Ugalde et al. (2007) conducted similar centrifuge experiments, however testing single degree of freedom structures; modelling bridge columns with square footings.

Algie et al. (2008) expanded on the rocking bridge foundation concept to include yielding columns coupled with yielding foundations and this was carried out on both single degree of freedom structures and holistic bridge systems.

Substantial research has also been undertaken numerically. Several different types of numerical models are currently available. A spring bed model, which uses springs to represent soil behaviour is perhaps the most common approach to modelling the soil-structure interaction.

Pender et al. (2009) compare three such models to centrifuge tests conducted on clay (Rosebrook & Kutter, 2001). In the paper, they compared the Contact Interface Model, developed by Gajan, a spring bed model developed by Wotherspoon (2007) and a bearing strength surface model developed by Toh (Toh & Pender, 2008). They reached a satisfactory comparison of all three models with the centrifuge data.

One potential issue of modelling foundations as a bed of discrete springs is that it under-predicts the rotational stiffness of the system (Pender et al., 2006). This however is accommodated in the FEMA 356 guidelines; where it specifies a zone of stiffer springs at the ends of the footing (FEMA-356, 2000). An example of modelling shallow foundations using this technique can be found in (Raychowdhury & Hutchinson, 2009). This technique of placing stiffer springs to the side is adopted for the numerical model predictions in this paper.

1.2 Content of this Paper

This paper outlines large scale experiments conducted in New Zealand on shallow foundations. It also details numerical model development and prediction, carried out in OpenSees, an open source finite element platform (PEER, 2009). The model is similar to that described in (Raychowdhury & Hutchinson, 2009).

The experiments were done onsite to test insitu geotechnical properties rather than assumed idealised. A full geotechnical investigation was conducted before the testing begun, and results from this were used in numerical analyses. Reinforced concrete foundations were cast into the ground and a large scale structure, made from structural steel, was constructed and fixed to the foundations. This structure was subsequently excited with an eccentric mass shaker capable of delivering a sinusoidal forcing function.

This paper goes through the concept, design and construction of the experiments. It details the fundamentals of the numerical model developed. It gives comparisons between the experimental data and the numerical model for moment-rotation and settlement-rotation plots. In addition, moment capacities, calculation from Equation 1 are given. The effect of embedment of the foundation is considered.

2. CONCEPT

The concept of the experiments conducted was to test shallow foundations that, in practice, could be implemented into a design solution. In New Zealand, many shear wall foundations have been designed to rock under the NZS 4203 standard because they have insufficient weight to prevent rocking during a large earthquake. To conduct large scale tests on these types of shear walls would be ideal. However, remembering that these foundations were to be tested dynamically, to construct and test realistic concrete shear walls onsite provided some technical issues, such as;

1. Testing dynamically could damage the concrete making a wall usable for one test only.

2. Loading the wall vertically with enough mass to be realistic and at the same time maintain stability.

3. Mounting the shaker on top because this has a footprint of around 1 metre square.

The idea of this research was to design and build a structure that would be versatile enough to conduct these experiments, yet remain realistic enough to be deemed useful for realistic applications.

Firstly it had to be and reusable and transportable, making it possible to test on different soils around New Zealand. The structure had to be built to allow rocking foundations but remain essentially elastic, a yielding structure would create difficulties in data analysis and would prove very costly. Lastly, it had to be large enough to

accommodate vertical mass, used to achieve realistic soil pressures, and the earthquake shaker placed on top of it. It was decided to design and construct a steel frame because this can accommodate all the requirements. Figure 1 shows a sketch of the structure designed.

The foundations were to be reinforced concrete and cast into the ground. As Figure 1 shows, there are two foundations per test; one at each end of the structure. A total of 4 test positions were constructed (8 foundations total). The tests are currently still in progress however and this paper will only look at results from two foundation locations. From those two foundation locations, only one foundation from each will be given; this will be Foundation 3 from Test 1 and Foundation 4 from Test 2. Table 1 gives the parameters of the two tests that are given in this paper.



Figure 1. An image of the steel frame and foundations

2.1 Design

The design of the frame was in three pieces; two end pieces that were identical and represented the 'shear walls' that we were trying to replicate and a top piece which held the vertical mass and the shaker. A full design was performed on the proposed structure and this was fabricated by professional steel fabricators. Two universal column sections were used in the design; 200 UC 42.6 and 100 UC 14.8. Structurally it was designed to handle a 100 kN horizontal load as a fixed base system.

A large steel plate was welded onto the middle of the top frame and the shaker was bolted to this using eight M24 8.8 structural bolts. The three pieces were bolted together using M20 8.8 structural bolts. Out of plane bracing was used to make the structure as rigid as possible. A 100 circular hollow section (CHS) ran horizontally between the two end frames close to the ground surface. In addition Reid Braces were fixed diagonally across the structure. The out of plane bracing can be seen in the photo of the structure in Figure 4.

2.2 Addition Vertical Mass

The structure by itself was relatively light; weighing around 4800 kg and thus putting minimal stresses in the soil when sitting on the foundations. It was desired to conduct tests with varying vertical load to achieve different static factors of safety in bearing. Traditionally a factor of safety (FoS) of 3 is typically used for the lower bound in shallow foundation design.

Additional vertical mass came in the form of steel road construction plates. These were hired, lifted up on the structure and then 'sandwiched' into place using channel sections. Each plate weighed 1200 kg and there were 6 plates each side of the shaker. This made the additional mass 14,400 kg and the total mass of the system around 19,200 kg.

3. SOIL PROPERTIES

Previous to any construction onsite, a full geotechnical investigation was undertaken to determine accurately the properties of the soil. Because the experiments are on a residual soil it is necessary to develop a good understanding, or else anomalies in results may be difficult to describe. The various field tests performed onsite were; cone penetration tests (CPT's), seismic cone penetrations tests (SCPT's), hand shear vanes and wave activated stiffness tests (WAK tests). In addition, laboratory tests are to be carried out at the University of Auckland.

3.1 CPT Data

In total 16 CPT's were carried out onsite over a two day period with two CPT's at each foundation location. They were done with a target depth of 10 m however many of them only reached 5 m. As is mentioned above, for this paper, only data from two foundations are compared. The cone resistance plots for each foundation are given in Figures 2 and 3.

The plots show that the ground is very similar beneath each foundation. The two cone resistance plots given were taken from the ends of each foundation. Foundation 3 has a spike in the cone resistance (around 4.5 MPa) at around 1.6 m deep. The rest of the data lies between 1 and 3 MPa. Foundation 4 has a similar shape; a spike of around 6.6 MPa at around 1.5 m deep and the rest of the data lying between 1 and 3 MPa.

From the CPT data, a description of the soil was also given. The upper layers, which are applicable to shallow foundations, were mostly very stiff and fine grained. The lower layers were clay to silty clay or clayey silt to silty clay.

The CPT pore pressure response puts the water table at 5.1 m below the ground surface, but the soil was saturated to near the surface because the tests were being conducted near the end of the wet season.

Table 1. Properties of the foundations and soil for the two tests conducted

Test no.	*Foundations*	s_u *(kPa)*	*Vertical Load (kN)*	*FoS*	*Footing dimensions (m)*	V_s *(m/s)*	G_{max} *(MPa)*
1	1 & **3**	185	48	49	2 x 0.4 x 0.4	147	38
2	2 & **4**	175	190	8	2 x 0.4 x 0.4	141	35

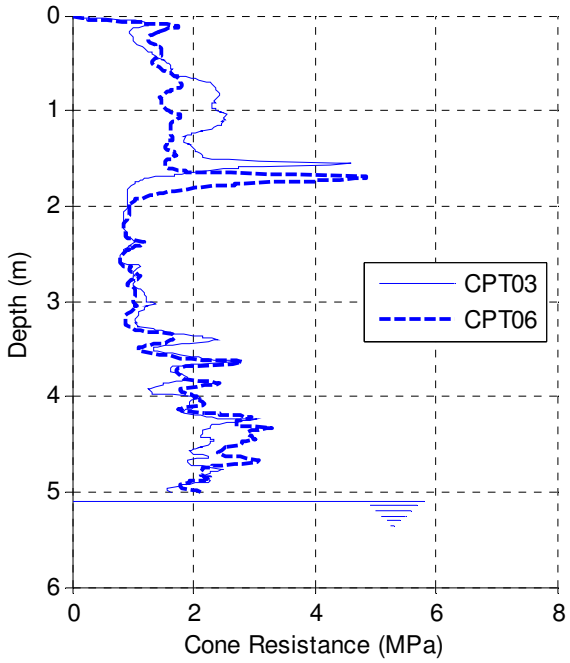

Figure 2. Cone resistance plots for Foundation 3

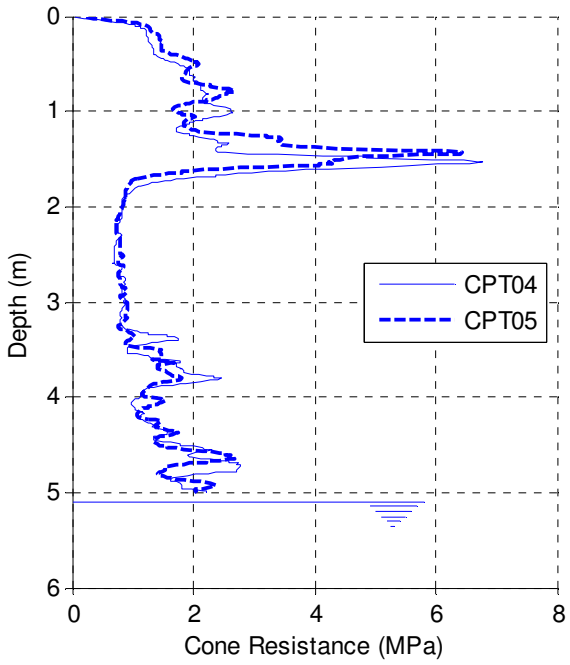

Figure 3. Cone resistance plots for Foundation 4

3.2 SCPT Data

Seismic Cone Penetration tests (SCPT's) were performed in parallel to every CPT conducted. They are a simple test to measure the shear wave velocity (V_s) of the soil. The CPT operator strikes a plate on the ground with an instrumented hammer. The ground accelerations are measured by an accelerometer on the CPT tip. This is done at different depths to obtain an accurate estimate of V_s.

The SCPT's were conducted at every CPT location between the depths of 2-3 m. Foundation 3 had V_s readings of 150 and 144 m/s and Foundation 4 had V_s readings of 152 and 135 m/s. The corresponding G_{max} values are given in Table 1.

3.3 WAK Test Data

Wave activated stiffness tests, WAK tests, were first described by Briaud and Lepert (Briaud & Lepert, 1990). A WAK test is a simple test conducted to determine the small strain shear modulus near the ground surface. A 500 mm diameter plate is rested on the ground surface with accelerometers each side of it. An instrumented hammer strikes the middle of the plate and acceleration readings obtained. The modulus is obtained as explained by Briaud and Lepert.

A WAK test was done at each foundation location, the calculated G_{max} values obtained from Foundation 3 and 4 were 38 MPa and 35 MPa respectively. As Table 1 shows, there is good correlation between the small strain shear moduli (G_{max}) obtained from the SCPT and WAK tests.

3.4 Hand Shear Vane Data

Between the foundations being excavated and the concrete of the foundation poured, hand shear vane tests were performed along the bottom of the foundations. In total, 5 ultimate and 2 remoulded undrained shear strength readings were taken for each foundation.

From the shear strength values (s_u), the ultimate bearing pressure a foundation, sitting on a cohesive soil, can sustain can be described by:

$$q_u = N_c \cdot s_u \cdot \gamma_s \cdot \gamma_d \cdot \gamma_i \qquad (2)$$

where; q_u = ultimate bearing capacity; N_c = bearing capacity factor (5.14); s_u = undrained shear strength of the soil; γ_s = shape factor; γ_d = depth factor; and γ_i = inclination factor.

The undrained shear strengths for each foundation was between 100 to 200 kPa. According to the New Zealand guideline for the classification and description of soil and rock for engineering purposes (NZGS, 2005), the soil at both foundations was very stiff to hard; indicating that it is very competent material.

4. EXPERIMENTAL PROGRAM

4.1 Excitation

The dynamic excitation of the structure was by an eccentric mass shaker attached to the top middle of the structure. This shaker has two counter-rotating fly wheels, with various numbers of masses attached to one half of each of them. As they rotate, the inertia force from the masses adds in one direction but cancel each other in the perpendicular direction, delivering a unidirectional sinusoidal forcing function.

The force that the shaker delivers is dependent on the frequency and how many masses are attached. At full capacity the shaker can deliver 98.1 kN dynamic force at a frequency of 7.1 Hz.

Low capacity tests were conducted before and after the stronger shake, to determine the response when the small strain soil properties of the soil are mobilised and to get a feel of the structural response of the system. The stronger shake was carried out at maximum capacity.

4.2 Instrumentation

Pressure Sensors

Pressure sensors are paper thin instruments that can record change of pressure of a defined bearing area. They were placed at intervals on the underside of the foundation. Under constant loads the readings from these sensors tend to drift, making calibration nearly impossible because they were sitting under the concrete foundations. However the main purpose of the sensors was to achieve a 'before and after' picture of what was happening to the soil underneath the footing. By recording before, during and after the excitation one would be able to achieve an idea of how much soil is still in contact with the foundation and what the length of any gap between the foundation and underlying soil is.

Strain Gauges

It was determined that the best way to record the forces going into the foundations was through strain gauges attached to the steel columns. Recording the axial and bending strain in the members, the axial force and bending moment can be accurately obtained. The strains recorded were then converted into forces through elastic strain principles.

The strain gauges were calibrated prior to any of the field tests conducted. A simple push over test, done on each end frame individually, was carried out with a hydraulic actuator. The strains recorded were converted into forces and the gauges calibrated.

Accelerometers

Accelerometers were placed on the foundation and the structure, these measured the acceleration in all three directions; vertical, longitudinal and transverse. The accelerometers used had a range of +/- 2g and gave a good check on forces and moments calculated by the strain gauge data.

Linear Variable Differential Transformers

Linear Variable Differential Transformers (LVDT's) were attached to the foundation to measure vertical and horizontal movement. The vertical movement was used to calculate settlement and rotation of the foundation and the horizontal movement was used to calculate sliding.

These LVDT's were in turn attached to a 6 m long 5" by 2" piece of timber that was anchored to the ground at each end but remained off the ground along its length. This was done to ensure minimal vibrations from the foundations rocking were transferred into the LVDT recordings. It was determined the span of the beam (6 m) was far enough away from the foundations for the readings not to be impaired.

4.3 Construction

Foundations

To reduce the impact of drying and cracking in hot sunny weather or alternatively flooding due to heavy rain, the foundation excavation and construction was completed in one day. The foundation dimensions were 0.4 m by 0.4 m by 2 m in length. They acted as strip footings underneath each end of the frame and were embedded to 0.4 m, with the top of the concrete at the ground surface.

An excavator cut the foundation trenches to the required width; any parts that needed extra work were done using a spade. Following the holes being excavated, the pressure sensors were placed along the ground surface. A layer of geotextile was laid on top of the pressure sensors to give them extra protection from the concrete and the reinforcing steel cages were placed.

The anchor bolts for the structure were located within the reinforcing steel using templates made from plywood to make sure the bolt pattern would align with the structures base plates. The distance between the two foundations, specifically the foundation bolts were carefully measured to ensure there was no issue with the structure connecting to the foundations.

Once all the steel was placed and the anchor bolts carefully positioned, concrete was poured from a concrete truck until it rose to the underside of the plywood templates; or the ground surface. Once all the foundations were cast, the concrete was left to cure for 28 days before the testing began.

Structural Frame

The set up of the frame onsite was done piece by piece. Firstly, mortar was placed on the foundations to ensure the end pieces were level. Each end piece was carefully lowered using a crane and bolted into place. The top frame was placed on top of the end pieces and bolted down. Lastly, the tubes and braces were added which stiffened the frame and made the structure complete.



Figure 4. The structure, with road plates and shaker attached to it, setup in Test 2

5. NUMERICAL MODEL

In parallel to the large scale experiments, numerical modelling of shallow foundation behavior was undertaken. The numerical model used for predicting the soil-foundation-structure interaction was a spring bed model developed in OpenSees; an open source finite element platform (PEER, 2009)

The model consisted of uncoupled vertical and horizontal non-linear springs. There are some disadvantages to have the vertical springs and the horizontal springs not 'interacting' with each other due to the uncoupling effect. When the foundation uplifts, there is a reduced contact area and consequently a reduction in vertical stiffness. However because the springs are uncoupled the horizontal springs do not decrease in stiffness along with the vertical because of this reduction in bearing area.

The springs used vertically were q-z element *(QzSimple1)* springs that were originally developed by Boulanger et al. (1999) for the OpenSees platform. The model was subsequently updated by Raychowdhury (2008) for shallow foundations *(QzSimple2)*.

The q-z element (and indeed all the nonlinear spring elements in OpenSees) has three parts to the spring behavior connected in series. These are far-field elastic, near field plastic and gap effects ($q\text{-}z^e$, $q\text{-}z^p$ and $q\text{-}z^g$ respectively):

1. The far field $q\text{-}z^e$ part consists of a dashpot and a spring connected in parallel and can account for radiation damping effects based on the displacement rate (velocity).

2. The near field, $q\text{-}z^p$ component consists of a non-linear spring. This has an initial elastic–range followed by yielding up to the ultimate limit (q_{ult}).

3. The gap component comprises of a closure effect and a drag effect which are two springs in parallel. The gap spring is a simple bi-linear elastic spring which is rigid in compression and very flexible in tension. The drag effect accounts for any tensile (suction) behavior between the foundation and soil.

Figure 5 shows a schematic of what the *QZSimple2* comprises of and Figure 6 gives the backbone curve used by Boulanger et al. (1999) in his development of the elements.

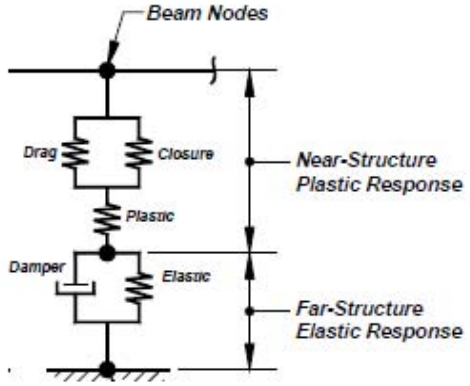

Figure 5. Spring element setup in OpenSees

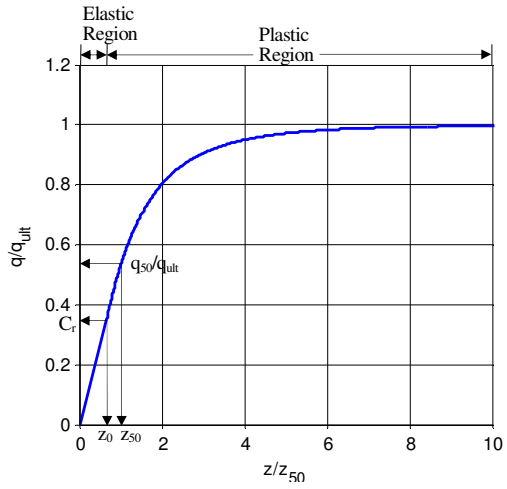

Figure 6. Backbone curve of the *QzSimple2* material

In the horizontal direction, t-x and p-x springs *(TzSimple1 and PySimple1)* were used to account for horizontal resistance from friction and passive earth pressure respectively. The springs work the same way and have the same inputs as the QzSimple2.

The model developed is very similar to the model described in (Raychowdhury & Hutchinson, 2009) and uses FEMA 356 guidelines for spring stiffness's (FEMA-356, 2000). It has outer zone (approximately 1/6 of the foundation length at each end) with increased stiffness to account for a lack of rotational stiffness that a spring bed model can potentially have. Thus in the vertical direction, two spring stiffnesses were used. The stiffness per unit length of foundation, for each zone, are given in equations 3 and 4 below.

The shear modulus used was not the small strain shear modulus (G_{max}) but a reduced 'secant' modulus and Poisson's ratio (υ) was assumed to be undrained and was 0.5.

$$k_{end} = \frac{6.83 \cdot G}{1-\nu} \quad (3)$$

$$k_{mid} = \frac{0.73 \cdot G}{1-\nu} \quad (4)$$

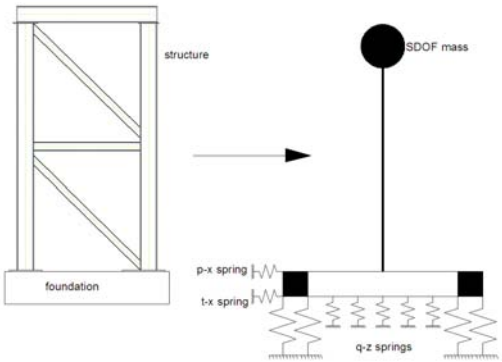

Figure 7. Setup of the numerical model

Figure 7 shows how the structure was represented by a single degree of freedom (SDOF) structure sitting on the spring bed model. Most of the behaviour of the system during the experiments came from the non-linear action of the soil, the structure itself remaining linear, therefore a simple 'lollipop' structure was deemed appropriate.

6. RESULTS

6.1 Moment-Rotations and Settlement-Rotations Results

The next page gives plots of the results of the experiments and the numerical model respectively. On the left is moment-rotation and on the right are settlement-rotation plots. The first row is experimental data from Test 1, the second from the numerical prediction of Test 1. The third row is experimental data from Test 2 and the fourth from the numerical prediction of Test 2. For the experimental plots, not all the time history is shown as this would clutter the graphs because the tests are long (around 20 minutes per test)

The experimental results of Test 1 (row 1) show nonlinear behavior of the foundation; the rotation increases with each cycle while the moment does not. The moment-rotation shows a moment capacity of around 62 kNm, The maximum rotation is around 0.007 radians.

The settlement during the test was minimal; 0.85 mm. This could be due to the small amount of vertical load. The vertical factor of safety for this test was predicted at 49, very large for a shallow foundation. The yielding that is shown in the moment-rotation plot will lead to deformation at the edges, not effecting the overall foundation settlement.

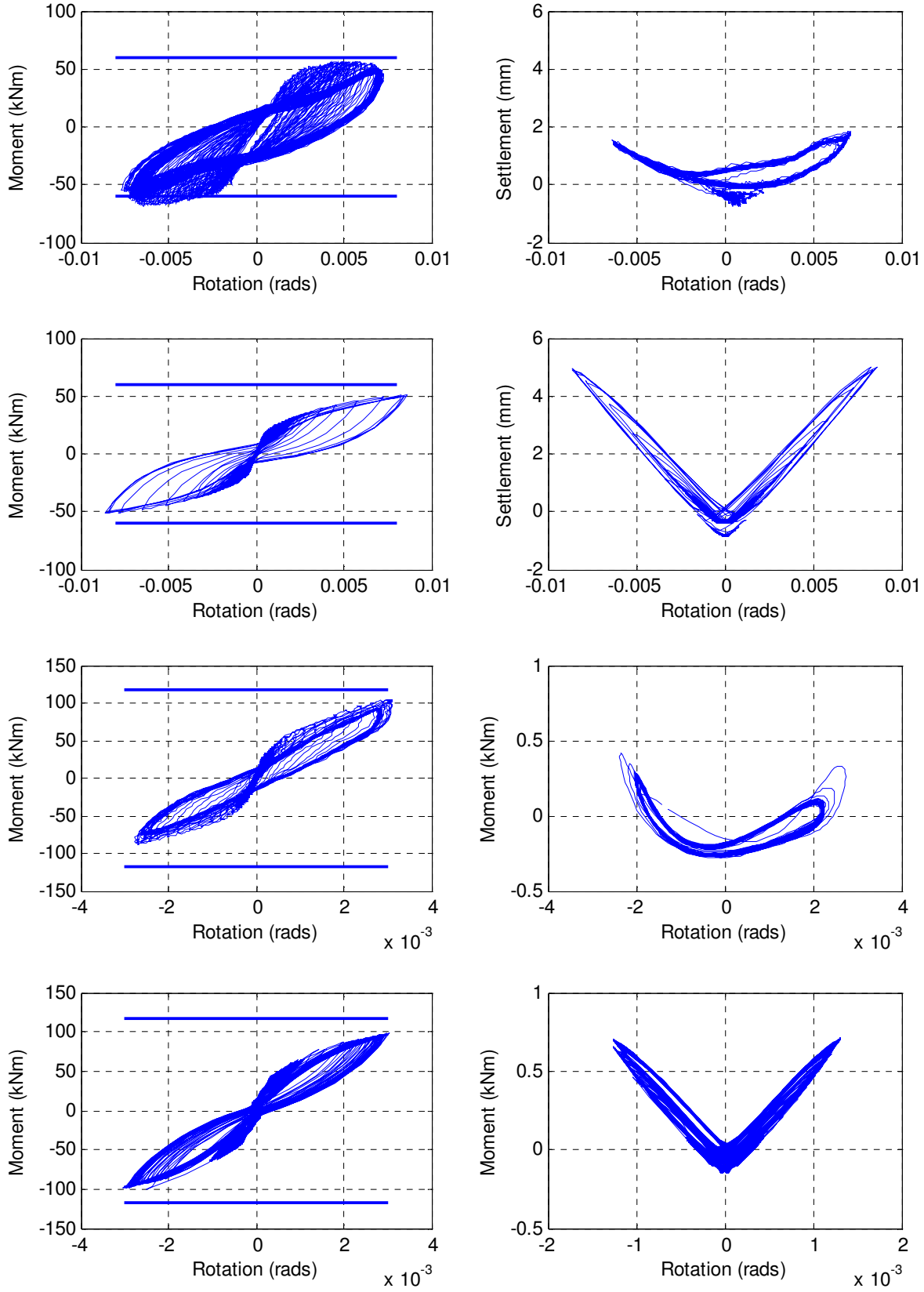

Figure 8. The results from both tests and model predictions; row 1 = experimental Test 1, row 2 = numerical result for Test 1, row 3 = Experimental Test 2 and row 4 = numerical result for Test 2

The model prediction of the foundation behavior (row 2) for Test 1 is encouraging. The model does not show the same style of yielding as the experiment; nevertheless the moment capacity and maximum rotations are within 10%. In addition, the settlement prediction of the model is 0.9 mm; very close to the experimental settlement obtained.

The behavior of the foundation in Test 2 is somewhat different than in Test 1. During the test, it was observed that the foundation went from no rocking to rocking in a very small amount of time. The moment-rotation plot of Test 2 (row 3) shows this transition. The initial no rocking zone can be seen by the more or less straight line, then the rocking cycles, which are increasing with every cycle can be seen to follow. The moment-rotation plot does not show the same amount of yielding as Test 1. This could be due to the moment capacity not being reached yet; the maximum moment recorded in the test was around 100 kNm. The maximum rotations recorded during the test were around 0.003 radians. This is less than in Test 1 because of the extra vertical weight from the road plates. To move this extra mass requires much more energy and therefore with the same force being delivered, the rotations are much less.

The settlement during Test 2 is less than that of Test 1; around 0.3 mm. This could be from the fact that vertical settlement occurred statically, increasing the stiffness of the ground. The static settlement measured was 10 mm; far greater than the settlement recorded during the dynamic shaking.

The model prediction of Test 2 is very accurate. The shape of the moment-rotation plot is within 5% and gives a very similar shape to the experiment. The settlement predicted in the model was around 0.2 mm, which is still an encouraging outcome compared to the experiment.

5.2 Effect of Foundation Embedment

Because the foundations were embedded when constructed, the effects due to side friction and passive and active earth pressures need to be taken into account. In effect, the moment capacity is increasing due to friction on the side walls between the concrete and soil, and additional passive earth pressure is mobilised at the toe of the foundation. This effect was studied by Gajan et al. (2005). The moment capacity from Equation 1 is changed to include these effects:

$$M_{\max} = \frac{L \cdot V}{2}\left(1 - \frac{1}{FoS}\right) + P_p \frac{D}{3} - P_a \frac{D}{3} \qquad (5)$$

where; P_p, P_o and P_a = passive, and active earth thrusts at the ends of the foundation; D = depth of foundation..

The moment capacities predicted by Equation 6 are shown as the bolder straight lines in the moment-rotation plots in Figure 8. For Test 1 the calculated moment is well matched to the experimental results. Test 2 shows the experiment being lower than the moment capacity. This is consistent with the moment capacity not being reached during the test (as mentioned above).

Overall the moment capacity predictions from the simple static equation are accurate when compared to the experimental results.

7. CONCLUSIONS

From the results, several conclusions were obtained;

Test 1 shows nonlinear behaviour of the foundation. This was evident in the moment-rotation plot where the rotation increased, to a maximum of 0.007 radians, with each cycle and the moment capacity (62 kNm) did not. The lower factor of safety associated with Test 2 produced more moment but less rotation. The increase in moment was due to an increase in vertical weight from the road plates. The reduction in rotation was due to the extra energy required by the shaker to move this extra mass.

The settlement in Test 1 was minimal (only 0.85 mm), most likely due to the factor of safety being very high for that particular test. The settlement of test 2 was very small, only around 0.3 mm. Most of the settlement of that foundation occurred statically when the road plates were added (10 mm), not dynamically during the test. Therefore, from these tests, settlement from a rocking foundation is not a large issue and may be less than static settlement.

The hysteresis of each test was positive; showing good energy dissipation. Test 1 had more hysteresis because it displayed more nonlinearity than Test 2. More energy dissipation is beneficial because it reduces the forces on the super-structure, protecting the structural elements more.

Although still ongoing at the University of Auckland, the model predictions of both tests were very encouraging with the general shape of the moment-rotation plots being captured by the model. In addition, maximum moments and settlements were within 10% of experimental results.

The static equation for calculating the moment capacity was consistent with the experimental results. For Test 1 the prediction was very accurate. For Test 2, the prediction was greater than the experimental moment, however this shows that, for this test, the moment capacity was not reached.

Acknowledgements:

Due to the large scale nature of this experiment, several people and businesses gave time and resources to help the tests take place. The authors would like to thank CDL Investments for allowing the use of their land for this experiment, and also their engineering representative Coffey Geotechnics for their involvement. Associate Professor Dr Charles Clifton, of the University of Auckland Department of Civil and Environmental Engineering, and Mr. Craig Stevenson, of Aurecon, for their assistance and guidance in designing the frame. Hicks Bros. for creating an access way onsite. Fletcher Reinforcing and Pacific Steel for supplying the concrete reinforcement and the Reid Brace bars respectively. Firth for supplying the concrete for the foundations. Perry drilling for carrying out the extensive CPT testing; and finally BHP piling for providing a crane on site.

References:

Algie, T.B., Deng, L., Erduran, E., Kutter, B.L. & Kunnath, S. (2008). Centrifuge Modeling of Innovative Foundation Systems to Optimize Seismic Behavior of Bridge Structures. *14th World Conference on Earthquake Engineering (14 WCEE)*.

Bartlett, P.E. (1976). *Foundation Rocking on a Clay Soil.* Master's thesis, University of Auckland, New Zealand.

Boulanger, R.W., Curras, C.J., Kutter, B.L., Wilson, D.W. & Abghari, A. (1999). Seismic soil-pile-structure interaction experiments and analyses. *Journal of Geotechnical and Geoenvironmental Engineering, 125*(9), 750-759.

Briaud, J.L. & Lepert, L. (1990). WAK Test to Find Spread Footing Stiffness. *116*, 415-432.

FEMA-356. (2000). *Prestandard and Commentary for the Seismic Rehabilitation of Buildings*. D.C., USA: Federal Emergency Management Agency.

Gajan, S. (2006). *Physical and numerical modeling of nonlinear cyclic load-deformation behavior of shallow foundations supporting rocking shear walls.* Ph.D. dissertation, University of California, Davis, U.S.A.

Gajan, S., Kutter, B.L., Phalen, J.D., Hutchinson, T.C. & Martin, G.R. (2005). Centrifuge modeling of load-deformation behavior of rocking shallow foundations. *Soil Dynamics and Earthquake Engineering, 25*(7-10), 773-783.

Housner, G.W. (1963). Behavior of inverted pendulum structures during earthquakes. *Seismological Society of America -- Bulletin, 53*(2), 403-417.

Kelly, T.E. (2009). Tentative Seismic Design Guidelines for Rocking Structures. *Bulletin of the New Zealand National Society for Earthquake Engineering, 42*(4), 239-274.

NZGS. (2005). *Field Description of Soil and Rock: Guidelines for the field classification and description of soil and rock for engineering purposes*: New Zealand Geotechnical Society.

PEER. (2009). OpenSees - Open System for Earthquake Engineering Simulation: http://opensees.berkeley.edu/.

Pender, M.J., Toh, J.C.W., Wotherspoon, L.M., Algie, T.B. & Davies, M.C.R. (2009). Earthquake induced permanent displacements of shallow foundations – performance based design. *IS Tokyo*, Tokyo, Japan.

Pender, M.J., Wotherspoon, L.M., Ingham, J.M. & Carr, C.J. (2006). Shallow foundation stiffness: continuous soil and discrete spring models compared. *New Zealand Society of Earthquake Engineering Conference*.

Raychowdhury, P. (2008). *Nonlinear Winkler-based Shallow Foundation Model for Performance Assessment of Seismically Loaded Structures.* Ph.D. Dissertation, University of California, San Diego, U.S.A.

Raychowdhury, P. & Hutchinson, T.C. (2009). Performance evaluation of a nonlinear Winkler-based shallow foundation model using centrifuge test results. *Earthquake Engineering and Structural Dynamics, 38*(5), 679-698.

Rosebrook, K.R. & Kutter, B.L. (2001). *Soil-foundation-structure interaction: shallow foundations. Centrifuge Data Report for test series KRR03* (No. Report No. UCD/CGMDR-01/11): University of California, Davis.

Standards, N.Z. (1992). *Code of practice for General Structural Design and Loadings for Buildings, NZS 4203:1992*: Standards, New Zealand.

Standards, N.Z. (2004). *Structural Design Actions Part 5 : Earthquake actions New Zealand*. Retrieved. from.

Taylor, P.W., Bartlett, P.E. & Wiessing, P.R. (1981). Foundation Rocking Under Earthquake Loading. *Proceedings of the International Conference on Soil Mechanics and Foundation Engineering, 3*, 313-322.

Toh, J.C.W. & Pender, M.J. (2008). Earthquake performance and permanent displacements of shallow foundations. *New Zealand Society of Earthquake Engineering Conference*, Wairakei, New Zealand.

Ugalde, J.A., Kutter, B.L., Jeremic, B. & Gajan, S. (2007). Centrifuge Modeling of Rocking Behavior of Structures on Shallow Foundations. *Fourth International Conference on Earthquake Geotechnical Engineering*.

Wiessing, P.R. (1979). *Foundation Rocking on Sand.* Master's thesis, Univeristy of Auckland, New Zealand.

Wotherspoon, L.M. (2007). *Integrated modeling of Structure-Foundation systems.* Ph.D. thesis, University of Auckland, New Zealand.

JOINT CONFERENCE PROCEEDINGS
7th International Conference on Urban Earthquake Engineering (7CUEE) &
5th International Conference on Earthquake Engineering (5ICEE)
March 3-5, 2010, Tokyo Institute of Technology, Tokyo, Japan

MECHANICAL BEHAVIOR OF PILED RAFT FOUNDATION IN SAND SUBJECTED TO STATIC HORIZONTAL LOAD

Kouhei Sawada[1)], Jiro Takemura[2)], Jun Izawa[3)], and Sakae Seki[4)]

1) Graduate student, Department of Civil Engineering, Tokyo Institute of Technology, Japan
2) Associate Professor, Department of Civil Engineering, Tokyo Institute of Technology, Japan
3) Assistant Professor, Department of Civil Engineering, Tokyo Institute of Technology, Japan
4) Technician, Tokyo Institute of Technology, Japan
sawada.k.ab@m.titech.ac.jp, jtakemur@cv.titech.ac.jp, jizawa@cv.titech.ac.jp, seki@cv.titech.ac.jp

Abstract: Piled raft foundation has been recognized as an economical foundation system with the combined effects of raft and piles. However, the proportion of the vertical load carried by the raft and piles, and these effects on the behavior of foundations subjected to horizontal load have not been well understood. In order to discuss the effect of the proportion of the vertical load carried by the raft and piles, and the moment loads on the behavior of horizontally loaded piled raft foundations, vertical and horizontal loading tests were carried out on piled raft models and their components (pile group and raft models) in dry Toyoura sand by using a geotechnical centrifuge.

1. INTRODUCTION

Piled raft foundation has been recognized as an economical and rational foundation system since Burland et al. (1977) presented the concept of settlement reducers. Some design concepts and their applications have been reported (Randolph, 1994; Horikoshi and Randolph, 1998). However, the behavior of the piled raft foundation is complex especially when the foundation is horizontally loaded, because the contact condition between the raft base and the ground varies during the loading, resulting in complicated soil structure interaction.

Design concepts of piled raft foundations are to take advantage of the bearing load of the raft and to reduce the settlement of foundations to an acceptable level by piles. Piles in the piled raft foundations play roles in reducing the settlement and transferring a part of the load to the deep ground. Although considerable researches on the piled raft foundations subjected to the vertical load have been carried out, it seems that a number of researches on the behavior of horizontally loaded piled raft foundations are limited. However, it is very important to clarify the behavior of piled raft foundations in highly seismic areas such as Japan.

Physical modeling studies on the behavior of piled raft model subjected to static or dynamic horizontal loads are reported. In the static and dynamic 1g model tests conducted by Matsumoto et al. (2004a, 2004b), the influences of moment loads and pile head connection conditions on the behavior of the piled raft were discussed. In the static and dynamic centrifuge model tests conducted by Horikoshi et al. (2003a, 2003b), the proportion of the horizontal load carried by raft and pile were investigated for the different pile head connection conditions. However, in above researches, the influences of moment load relative to horizontal load applied to the foundations and the proportion of the vertical load carried by the raft (raft load proportion, RLP, Figure 1) were not taken as a parameter. It is important to consider the influence of moment load especially on the foundation of tall superstructure, such as, bridge pier, high rise building, and tower.

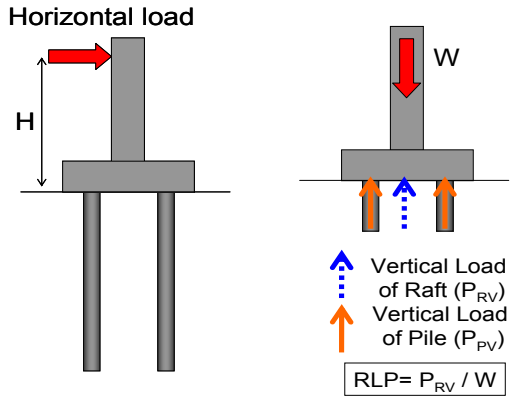

RLP (Raft load proportion)

Figure 1. Definition of horizontal loading height and RLP

In this research, centrifuge model tests were conducted to investigate the influence of the moment load and RLP for three types of foundation models, raft, pile group and piled raft.

2. MODEL FOUNDATION AND TEST PROCEDURES

2.1 Model Foundations

Static vertical and horizontal loading tests were conducted on the piled raft, the pile group and the raft foundation in this study. Figure 2 shows the raft and pile models used in this study. Stainless steel raft with 80mm*80mm*20mm is divided into three parts and the model piles were clutched between the parts.

Sandpaper was pasted on the raft base to make rough base condition. On top of the raft, stainless steel thick plate with 80mm height and 20mm or 32mm thickness was fixed as the superstructure, to which horizontal load was applied at different height, and by which vertical load was applied to foundation in horizontal loading tests. Total mass of the raft and the plate are 1.8kg (20mm thickness) or 2.7kg (32mm thickness), which are equivalent to W_L=882 N and W_H=1332 N of vertical dead load under 50g centrifugal acceleration, respectively. In this paper, the result of

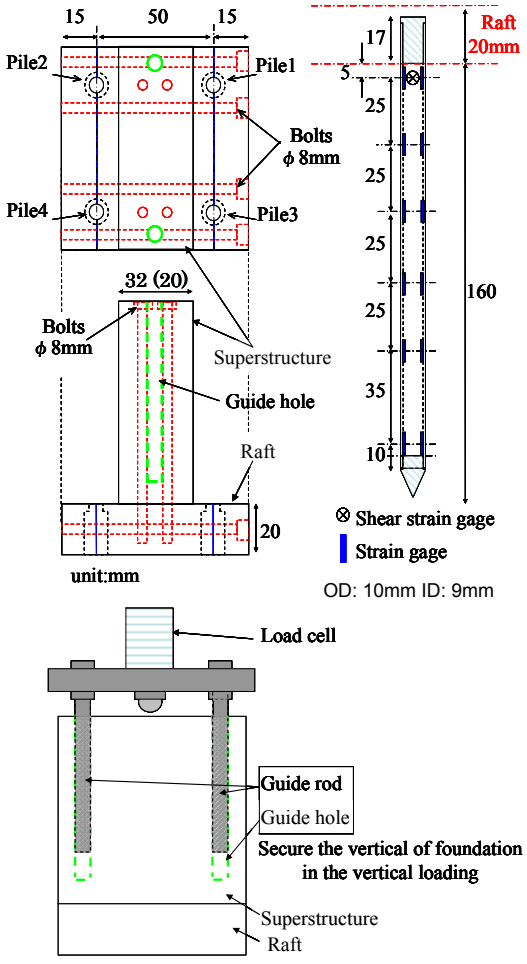

Figure 2. Model raft, pile, superstructure and guide rod

Table 1 Properties of model pile

Properties	Model	Prototype
Material	Stainless steel	Concrete
Diameter	10mm	500mm
Thickness	0.5mm	Solid
Embedment depth	160mm (piled raft) 155mm (pile)	8mm 7.75m
Longitudinal rigidity EA	2.98×10^{-3}GN	7.46GN
Bending rigidity EI	3.37×10^{-8}GNm^2	0.211GNm^2

Table 2 Physical properties of Toyoura sand

Specific gravity (G_s)	2.65
Mean particle diameter (D_{50})	0.162
Maximum void ratio (e_{max})	0.973
Minimum void ratio (e_{min})	0.609

W_H=1332 N is showed. The superstructure has guide holes to secure the vertical of foundation in the penetrating piles and the vertical loading tests by inserting the guide rods in these holes as shown Figure 2.

The model pile is stainless steel made with 10mm of outer diameter and 0.5mm of thickness. Strain gages were attached inside the piles to measure the bending moments and the axial forces acting on piles. A set of strain gages was also attached at the outer surface of pile head to measure the shear forces. Table 1 shows the properties of the model pile. Four piles were rigidly fixed to the raft in the square arrangement of 50mm spacing (s). This model was used for both tests of the piled raft and the pile group foundation. In the pile group model, 5mm gape between the raft base and the ground surface was provided to avoid the interaction between them.

2.2 Model Ground and Container

Air-pluviated dry Toyoura sand was used throughout the present study. The physical properties of the Toyoura sand are summarized in Table 2. The target relative density is 50 %.

The model container is made of aluminum with inner dimension of 800mm in length, 250mm in breadth and 400mm in depth.

2.3 Model Preparation

The procedures of the model preparation are as follows:

1) The model ground was made by air pluviation.
2) In 1g, the piles were penetrated into the ground by deadweight with a guide to secure the verticality of the piles.
3) Centrifugal acceleration was increased up to 50g and the piles were further penetrated by the deadweight.
4) Penetrate piles by the two way actuator until the raft base contacted to the ground for the piled raft model or reached 5mm above the ground for the pile group model in 50g. The pile tip resistance was measured during the penetration.
5) Centrifugal acceleration was down to 1g, for setting all instrumentations, such as potentiometers and laser displacement transducers. For the horizontal loading tests, remove the guide rod and set the horizontal loading device.

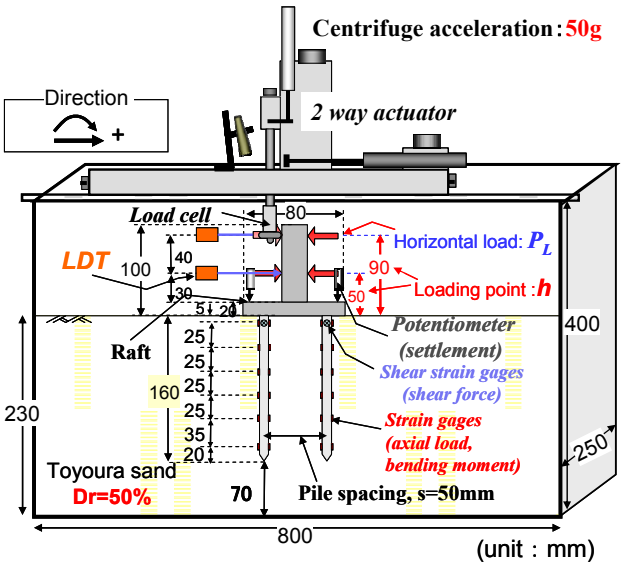

Figure 3. Model setup and location of sensors

6) After centrifugal acceleration was increased up to 50g again, vertical load applied to the foundation with the guide rod for the vertical loading tests. For the horizontal loading tests, vertical load was applied to the foundation before horizontally loaded without the guide rod.

Displacement of the model foundation was measured by potentiometers and laser displacement transducers. Shear force, bending moment and axial force acting on the piles were measured by the strain gages. Applied vertical and horizontal load were measured by two directional load cell attached to the two way actuator. The locations of the instrumentations are shown in Figure 3.

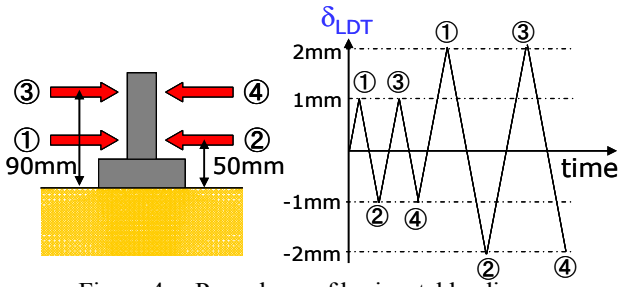

Figure 4. Procedures of horizontal loading

2.3 Loading Test Procedures

Having completed the model setup, the centrifugal acceleration was increased to 50g for both vertical and horizontal loading tests. Horizontal displacement with two amplitudes, 1mm and 2mm were applied by the two way actuator from right side and then left side at two different heights from the raft base, h=50mm and 90mm, as shown in Figure 4. Rightwards horizontal load, displacement and clockwise moment are taken positive in this study. This loading cycle was repeated until the displacement measured at lower LDT, δ_{LDT}, was prescribed value shown in Table 3. Vertical and Horizontal loading tests were conducted by displacement control, with loading rate of 0.0162 mm/s and 0.155 mm/s respectively.

By the instrumentations shown in Figure 3, measured are the horizontal displacements of the raft base, δ, the rotation of the foundation, θ, and the shear force, the bending moment and the axial force of the piles. The moment load applied to the foundation, M_L is estimated by

Table 3 Test cases

Case	Details of Test	Vertical load of superstructure, W	Horizontal displacement at h=50mm, δ_{LDT}	Relative Density
R1	Raft	882 N	Vertical loading	50.3%
R2	Raft	882 N	±1mm (h/s=1) , +5mm (h/s=1)	50.3%
R3	Raft	882 N	±1mm (h/s=1), +5mm (h/s=1.8)	46.0%
R4	Raft	1332 N	Vertical loading	52.4%
R5	Raft	1332 N	±1mm(h/s=1,1.8) +5mm(h/s=1)	52.4%
R6	Raft	1332 N	±1mm(h/s=1,1.8) +4mm(h/s=1.8)	51.1%
P1	Pile group	882 N	±1mm (h/s=1,1.8), ±2mm (h/s=1,1.8)	49.6%
P2	Pile group	1332 N	±1mm、 ±2mm(h/s=1,1.8)	53.0%
PR1	Piled raft	882 N	±1mm (h/s=1,1.8) , ±2mm (h/s=1,1.8)	53.0%
PR2	Piled raft	882 N	±2mm (h/s=1)	53.0%
PR3	Piled raft	1332 N	Vertical loading	50.9%
PR4	Piled raft	1332 N	±1mm (h/s=1,1.8)、 ±2mm(h/s=1,1.8)	52.8%
PR5	Piled raft	1332 N	±1mm (h/s=1,1.8)、 ±2mm(h/s=1,1.8)	49.4%

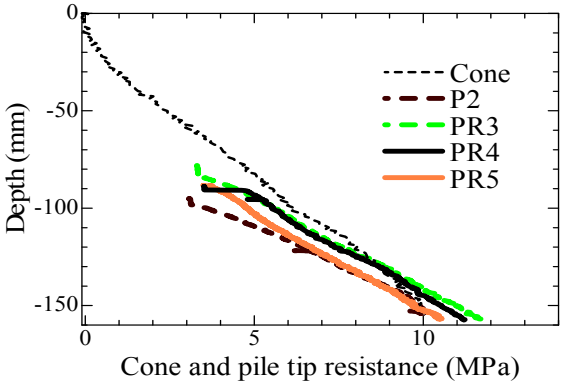

Figure 5 Profiles of cone and pile tip resistance

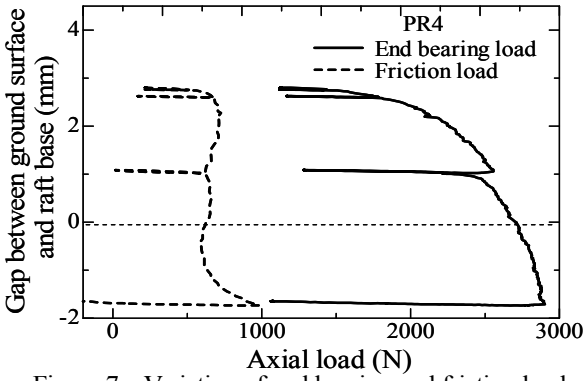

Figure 7 Variation of end bearing and friction load with gap between ground and raft base

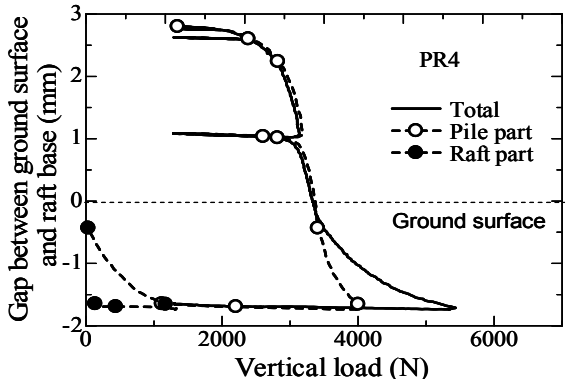

Figure 6 Vertical load - gap between ground and raft base relationship

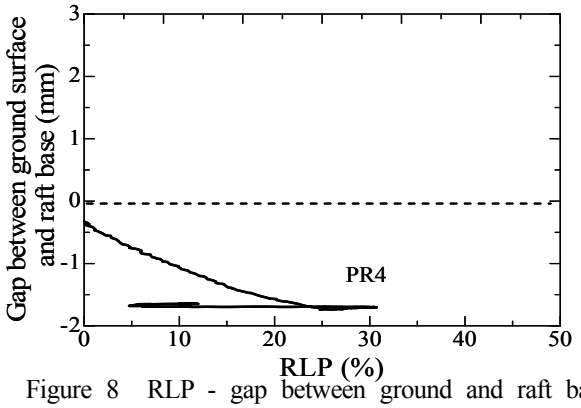

Figure 8 RLP - gap between ground and raft base relationship

multiplying horizontal load, P_L, by the loading height h. The vertical and horizontal resistances of piles are calculated by the sum of the total axial load at pile head, P_{PV}, and the total shear force, P_{PH}, respectively. Although the vertical and horizontal resistances carried by the raft are not measured, vertical resistance carried by the raft, P_{RV} is estimated by subtracting P_{PV} from the total vertical load, W, and horizontal load carried by the raft, P_{RH} is estimated by subtracting P_{PH} from the applied horizontal load P_L.

3. TEST RESULTS AND DISCUSSIONS

3.1 Cone Penetration Test and Pile Penetration

The distribution of the soil strength and its repeatability were examined by the cone penetration test and the pile penetration. The measured tip resistances are summarized in Figure 5. The figure shows that the strength increases linearly with depth, and the repeatability of the strength between the different cases was excellent.

3.2 Vertical Loading Tests

Figure 6 shows the relationship between the vertical load and the gap between the ground and the raft base for the piled raft foundation. The vertical load carried by pile part and the raft part in the piled raft foundation are also shown in this figure. The broken line shows the ground surface, implying above this line, the raft base was not in contact to the ground (behaved as the pile group foundation), and the raft base attached to the ground under this line (behaved as the piled raft foundation). The vertical loads carried by the raft part and the pile part increased shapely after the raft base touched to the ground. The reason why the vertical load carried by pile part increased is the increase of the friction load of piles under the raft base. The vertical load of piles can be divided into two parts, the friction load and the end bearing load. Figure 7 shows the variation of the friction load and the end bearing load against the gap between the raft base and the ground. Although there was no difference between before and after the raft base was in contact to the ground for the end bearing load, the friction load rapidly increased with the settlement after the raft base touched to the ground. This was probably due to the increase of the soil stiffness and the strength beneath the raft base related to the increase of the confining stress around the piles.

Figure 8 shows the relationship between the RLP (raft load proportion, see Figure 1) and the gap between the raft base and the ground. From this figure, it can be said that RLP increased with the settlement after the raft base touched to the ground. Therefore RLP can be controlled by this pre-vertical loading process before the horizontal loading tests.

3.3 Horizontal Resistance

Figure 9 (a) and (b) shows the δ - P_L relationships of three foundation models for the normalized loading height h/s=1.0 and 1.8 respectively. The horizontal resistance of the piled raft foundation was largest. Although the horizontal displacement can be restrained in the raft foundation in the small δ range, it increased rapidly with the increase of δ,

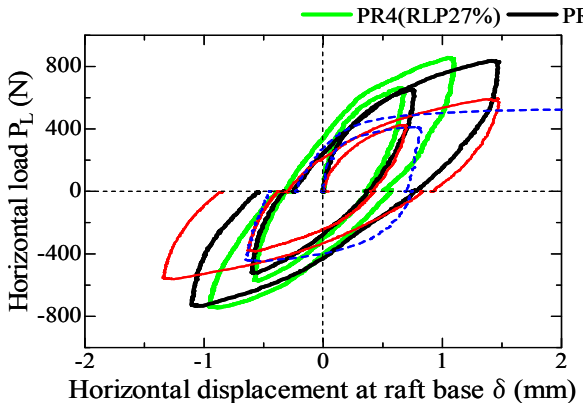

Figure 9 (a) Relationship between δ and P_L (h/s=1)

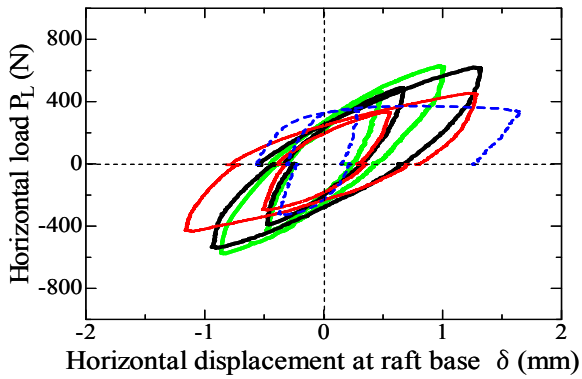

Figure 9 (b) Relationship between δ and P_L (h/s=1.8)

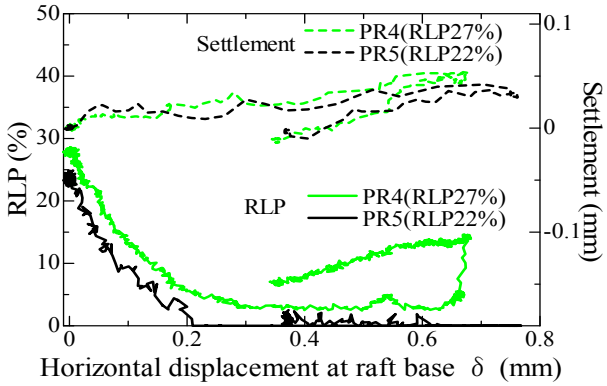

Figure 10 Variation of RLP and settlement with δ

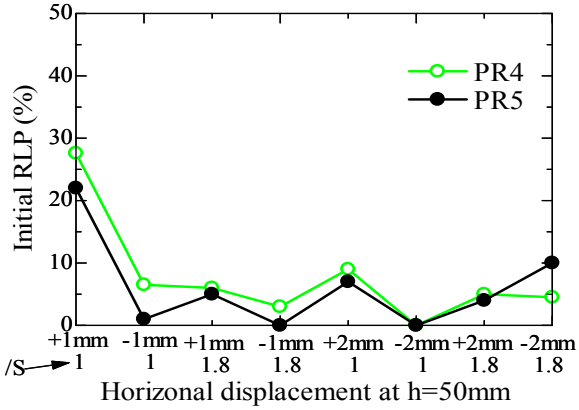

Figure 11 Initial RLP of each loading step

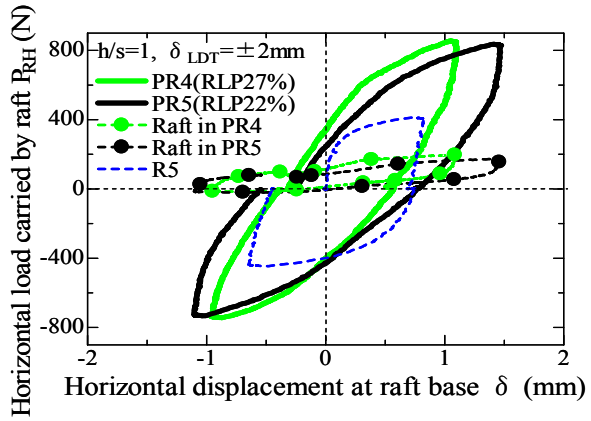

Figure 12 P_{RH}, P_L-δ relationship of piled raft and raft

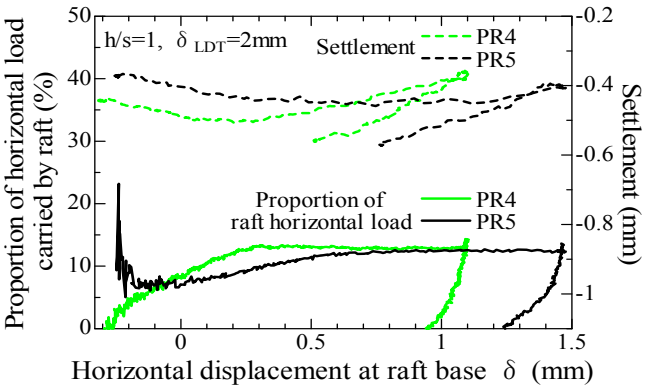

Figure 13 Variation of raft horizontal load proportion and settlement with δ

implying clear failure of the foundation. On the other hand, the horizontal resistance of the pile group foundation was smaller than that of the raft foundation in the small δ range, but it increased with displacement showing the higher horizontal resistance in the large δ than the raft foundation.

The variation of RLP and settlement for the case with PR4 and PR5 are shown in Figure 10. RLP decreased during the horizontal loading because foundations moved upward. Therefore RLP reached to the different value before the horizontal loading, by which the initial RLP in each loading cycle were different as shown in Figure 11.

Figure 12 shows the δ - P_{RH} relationships of PR4 and PR5, which had different RLP, for h/s=1.0 and δ_{LDT} = ±2mm. δ- P_L relationships of PR4, PR5 and R5 also shown in this figure. Figure 13 shows the variation of the proportion of the horizontal load carried by the raft against δ in the same loading step as Figure 12. The variation of settlement is also added in this figure. From Figure 12, it can be said that horizontal resistance of PR4 with larger RLP was larger than that of PR5. P_{RH} was much smaller than horizontal resistance of the raft foundation, and the horizontal load carried by raft part was about 10% of the total horizontal resistance as shown Figure 13. Proportion of the horizontal load carried by the raft increased during the piled raft foundation settled down; on the other hand it decreased or remained constant during the piled raft moved upward, implying settlement of foundation affected to the horizontal load carried by the raft part.

Figure 14 (a) and (b) show the P_{PH} – δ relationships of left piles and right piles respectively. The horizontal resistance of piles can be divided into two parts, push-in side and pull-out side. In the push-in side, P_{PH} of the piled raft

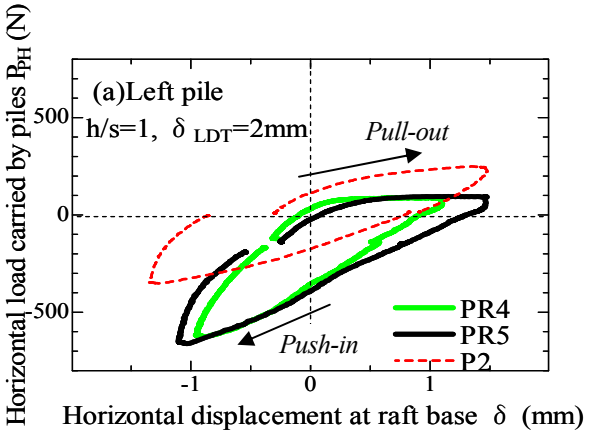

Figure 14 (a) P_{PH}-δ relationship of left pile

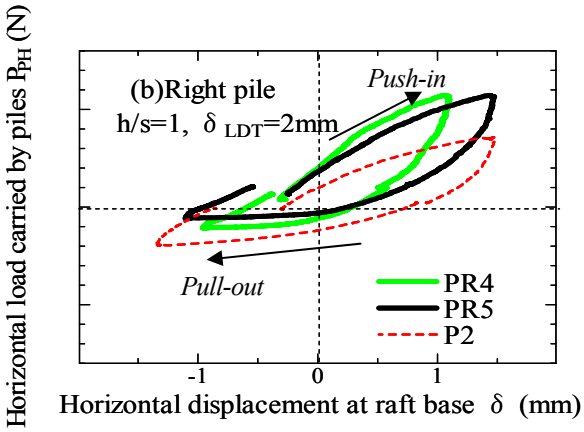

Figure 14 (b) P_{PH}-δ relationship of right pile

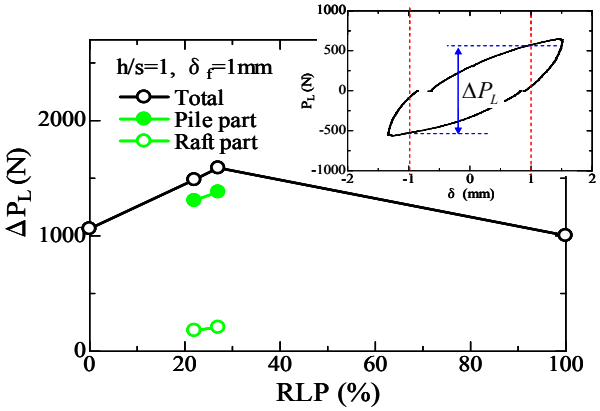

Figure 15 RLP- ΔP_L relationship

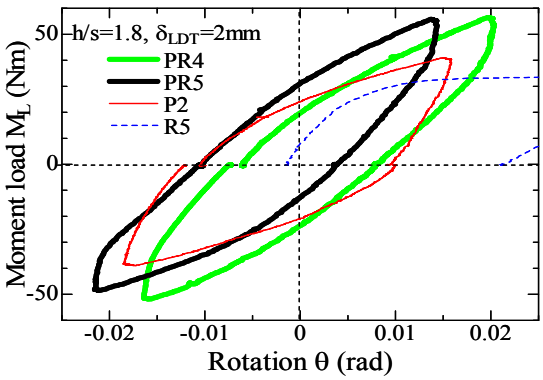

Figure 16 Relationship between θ and M_L (h/s=1.8)

was larger than that of the pile group foundation. The reason for this behavior was considered to be the increase of confining stress around the piles as explained in the vertical pile response (Figure 7). On the other hand, P_{PH} of the piled raft foundation was smaller than that of the pile group foundation in the pull-out side. This behavior was thought to be due to two possible causes. One is the residual shear force. In the pile group foundation, P_{PH} became to be zero after the horizontal loading, which means the residual shear force did not occur. In contrast, P_{PH} of the piled raft foundation had the residual shear force after the horizontal loading, which attributed the smaller P_{PH} of the piled raft foundation than the pile group foundation. Another cause is the soil movement beneath the raft base. In the piled raft foundation, soil moved together with the raft base during the horizontal loading because the raft base touched to the ground. Therefore the relative displacement of piles to soil was smaller in the piled raft foundation compared to the pile group foundation, implying P_{PH} of the piled raft was smaller than that of the pile group foundation.

Figure 15 shows RLP-ΔP_L relationships of three types of foundations for h/s=1 and δ=±1mm, where ΔP_L is defined in Figure 15 and it can be considered as the horizontal resistance. ΔP_L of the raft part and pile part in the piled raft foundation are also shown in this figure. RLP 0 % and 100 % represent the pile group foundation and the raft foundation respectively. The horizontal resistance in the push-in and the pull-out side are larger and smaller for the piled raft than the pile group foundation respectively as explained Figure 14. However, the increase of the horizontal resistance in the push-in side was larger than the decrease of that in the pull-out piles. As a result, the horizontal resistance of the pile part in the piled raft foundation was larger than that of the pile group foundation as shown in Figure 15. In addition to the increase of the horizontal resistance of the pile part, mobilized horizontal resistance of the raft part contribute the higher horizontal resistance of the piled raft than that of the pile group foundation.

3.4 Moment Resistance

The relationships between θ and M_L of three types of foundations for h/s=1.8 are shown in Figure 16. The moment resistance of the piled raft foundation was highest. The rotation of the raft foundation was smaller than that of the pile group foundation in the small rotation range. By contrast, the pile group foundation can restrain the rotation in the large rotation range compared to the raft foundation. Similar trends can be observed in δ - P_L relationships. Figure 17 shows the relationship between θ_f and normalized moment resistance, $\Delta M_{Lf}/\Delta M_{Lf(PILE)}$, where θ_f and ΔM_{LF} are defined in Figure 17, and $\Delta M_{Lf(PILE)}$ is ΔM_{Lf} of the pile group foundation, which means the broken line represents the result of the pile group foundation. From this figure it can be clearly seen that the moment resistance of the piled raft foundation was larger than that of the pile group foundation, and that of the raft foundation was smaller than that of the

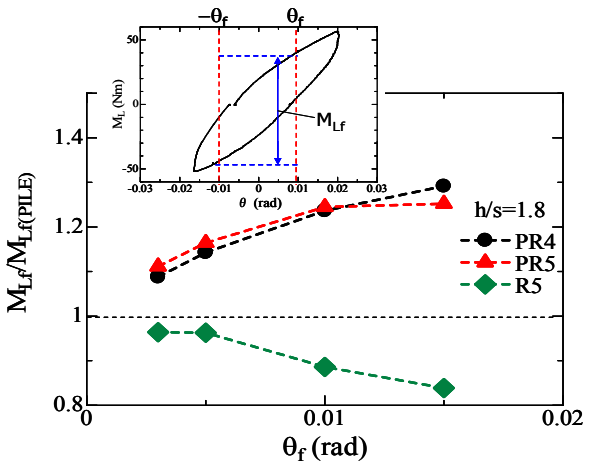

Figure 17 Relationship between θ_f and normalized moment resistance

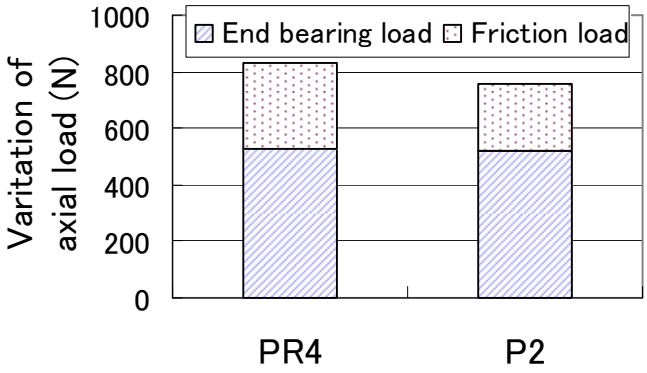

Figure 18 Variation of axial load during loading step with h/s=1.8 and δ_{LDT} = ±2mm

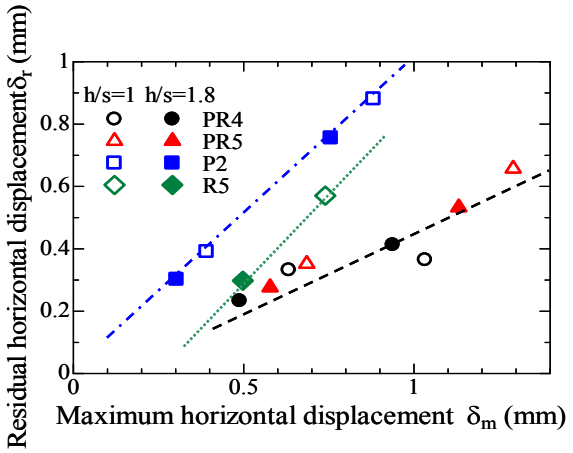

Figure 19 Relationship between δ_m and δ_r

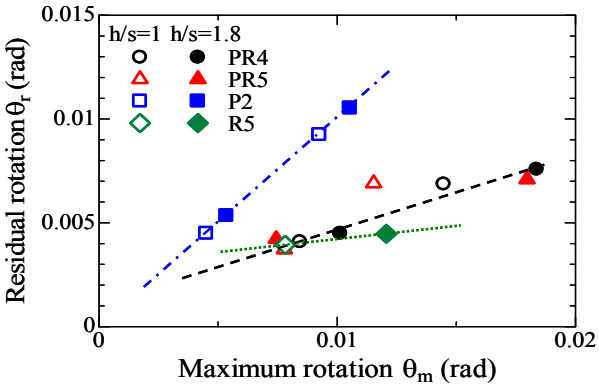

Figure 20 Relationship between θ_m and θ_r

pile group foundation. These trends developed as the rotation increased. The reason why the moment resistance of the piled raft foundation is higher than that of the pile group foundation is the increase of the axial load at pile head. Figure 18 shows the variation of the axial load at pile head in the loading step with h/s=1.8 and δ_{LDT} = ±2mm. The variation of the axial load can be divided into two components, the friction load and the end bearing load. There was not much difference between the piled raft and the pile group foundation in the variation of the end bearing load. On the other hand, the variation of the friction load of the piled raft foundation was larger than that of the pile group foundation. This is probably due to the increase of the confining stress under the raft base in the piled raft foundation as explained in the vertical loading test (Figure 7).

3.5 Residual Displacement and Rotation

Figure 19 shows the relationship between the maximum horizontal displacement, δ_m and the residual horizontal displacement, δ_r for all foundation types, where δ_m is the maximum horizontal displacement of each loading step and δ_r is the horizontal displacement after the each loading step. Regardless of the loading height, it can be said that the piled raft foundation can restrain the residual horizontal displacement.

Figure 20 shows the relationship between the maximum rotation, θ_m and the residual rotation, θ_r, where θ_m and θ_r are the maximum rotation and the residual rotation of each loading step respectively. The residual rotation of the raft foundation was smallest. Compared to the piled raft and the pile group foundation, the residual rotation can be restrained in the piled raft foundation.

3.6 Settlement and Bending Moment of Piles

Observed settlements are plotted against the horizontal displacement at raft base, δ in Figure 21. From this figure, it can be confirmed that the settlements of the piled raft foundation were much smaller than those of the pile group foundation. The piled raft foundation moved up as the horizontal displacement increased because the raft base touched to the ground.

Figure 22 shows the bending moment profiles of right pile in the loading step of h/s=1.0 and δ=±1mm. Maximum bending moment in compression side was larger than tension side. The bending moment of the piled raft foundation was nearly equals to that of the pile group foundation in the tension side. However that of the piled raft

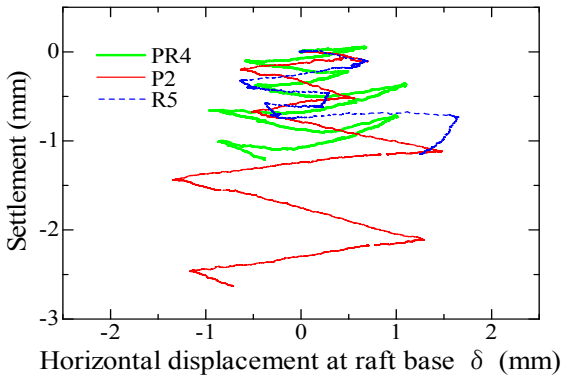

Figure 21 Observed settlements of the foundation caused by cyclic loading

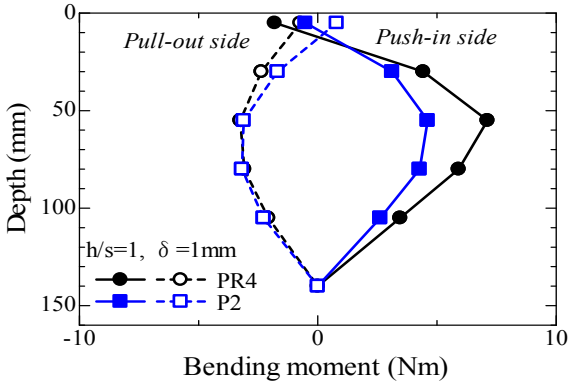

Figure 22 Bending moment profile of right pile (h/s=1, δ=1mm

foundation was larger than that of the pile group foundation in the compression side. This is due to the confining stress around the piles was larger in the piled raft than the pile group.

4. COUCLUSIONS

Vertical and horizontal loading tests were conducted on the piled raft, the pile group and the raft foundation models by using a geotechnical centrifuge. The following conclusions were derived from this study.

1) Vertical load of the piled raft foundation is larger than that of the pile group foundation. This is due to the increase of the friction load of piles, which is caused by the increase of the confining stress around the piles in the piled raft foundation.
2) Horizontal resistance of push-in pile is larger for the piled raft than pile group. This is due to the increase of confined stress around the piles. On the other hand, that of pull-out pile is smaller for the piled raft than the pile group, but the increase of the horizontal resistance of push-in piles is larger than decrease of that of the pull-out piles. In addition to the increase of the horizontal resistance of the pile part, mobilized horizontal resistance of the raft part contribute the higher horizontal resistance of the piled raft than that of the pile group foundation.
3) Variation of the pile head axial load of the piled raft foundation is larger than that of the pile group foundation during horizontal loading. Therefore, the moment resistance of the piled raft foundation is higher than the pile group foundation.
4) The piled raft foundation can restrained the residual horizontal displacement and the residual rotation compared to the pile group foundation.
5) The settlement caused by the cyclic loading of the piled raft foundation is smaller than that of the pile group foundation. The bending moment of the piled raft foundation is larger than the pile group foundation.

References:

Burland, J. B., Broms, B. B. and De Mello, V. F. B. 1977. Behaviour of foundations and structures. Proc.of 9th ICSMFE, Tokyo, 2: 496-546

Randolph, M. F. 1994. Design methods for pile groups and piled rafts. Proc.of 13th ICSMGE, Vol.5, New Delhi, pp.61-82.

Horikoshi, K. and Randolph, M. F. 1998. A contribution to optimum design of piled rafts. Geotechnique Vol. 48, No.3, 301-317.

Matsumoto, T., Fukumura, K., Kitiyodom, P., Horikoshi, K., Oki, A. (2004a) "Experimental and analytical study on behaviour of model piled rafts in sand subjected to horizontal and moment loading" Int. Jour. of Physical Modelling in Geotechnics, Vol. 4, No. 3, pp.1-19.

Matsumoto, T., Fukumura, K., Kitiyodom, P., Horikoshi, K., Oki, A. (2004a) "Experimental and analytical study on behaviour of model piled rafts in sand subjected to horizontal and moment loading" Int. Jour. of Physical Modelling in Geotechnics, Vol. 4, No. 3, pp.1-19.

Horikoshi, K., Matsumoto, T., Hashizume, Y., Watanabe, T. and Fukuyama, H. 2003a. Performance of piled raft foundations subjected to static horizontal loads. *Intl. Jour. of Physical Modelling in Geotechnics*, Vol. 3, No. 2, 37-50.

Horikoshi, K., Matsumoto, T., Hashizume, Y. and Watanabe, T. 2003b. Performance of piled raft foundations subjected to dynamic loading. *Int. Jour. of Physical Modelling in Geotechnics*, Vol. 3, No.2, 51-62.

JOINT CONFERENCE PROCEEDINGS
7th International Conference on Urban Earthquake Engineering (7CUEE) &
5th International Conference on Earthquake Engineering (5ICEE)
March 3-5, 2010, Tokyo Institute of Technology, Tokyo, Japan

SIMPLIFIED DYNAMIC ANALYSIS OF PILE SUPPORTED STRUCTURES IN LIQUEFIABLE SOILS

Domenico Lombardi[1], Suresh R. Dash [2], and Subhamoy Bhattacharya[3]

1) Postgraduate Student, Department of Civil Engineering, University of Bristol, Bristol, United Kingdom
2) Postgraduate Student, Department of Engineering Science, University of Oxford, United Kingdom
3) University Lecturer, Department of Civil Engineering, University of Bristol, Bristol, United Kingdom
Domenico.Lombardi@bristol.ac.uk, Suresh.Dash@eng.ox.ac.uk, S.Bhattacharya@ bristol.ac.uk

Abstract: This paper explores the possibility of simplified analysis of pile supported structures in liquefied soils using Winkler spring approach. The main aim is to model the degradation effects of soil stiffness due to liquefaction. Two aspects are studied: (a) Lowering of depth of fixity of piles during (transient phase) and after liquefaction (post-liquefaction). (b) Change in time period of the pile supported system. It will be shown that the time period of the pile supported system will increase and the depth of fixity of the pile goes down. The practical design implications of these aspects will be highlighted.

1. INTRODUCTION

Buildings and bridges on loose to medium dense sands are often built on piles to limit settlements because the sand is not stiff enough to support the structure on its own. In an earthquake, if these loose sands are saturated they lose strength as excess pore water pressure is generated and the soil tends to liquefy. This means that if the soil is on a slope it will flow downslope, which is often termed as "Lateral, spreading".

Collapse or severe tilting of buildings and bridges founded in liquefiable soils still are observed after most major earthquakes. Figure 1 shows the Kandla Port Tower Building following the 2001 Bhuj Earthquake (India).



Figure 1 Pile-supported building that tilted during the 2001 Bhuj Earthquake

1.1 Structural damage of piles as observed following excavation

As earthquakes are very rapid events and as much of the damage to piles occurs beneath the ground, it is hard to ascertain the failure mechanism unless deep excavation is carried out. Twenty years after the 1964 Niigata earthquake and also following the 1995 Kobe earthquake, investigation has been carried out to find the failure pattern of the piles, see Yoshida and Hamada (1990), BTL Committee (2000) and Fig. 2. Piles were excavated or extracted from the subsoil, borehole cameras were used to take photographs, and pile integrity tests were carried out. These studies hinted the location of the cracks and damage patterns for the piles.

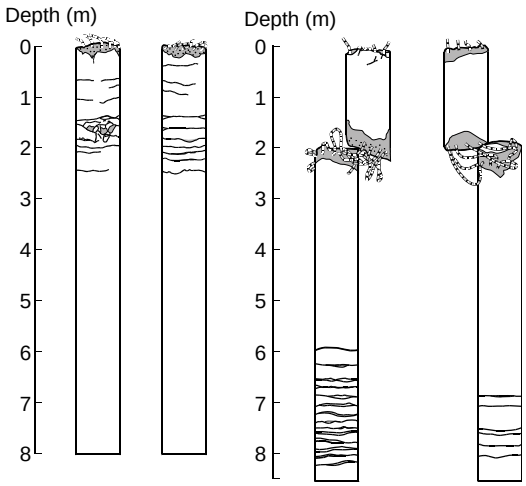

Figure 2 Interpreted pile damage of a building in Niigata City (Yoshida and Hamada, 1990)

Of particular interest is the formation of plastic hinges in the piles, see Figure 2. This indicates that the stresses in the pile during the earthquakes exceeded the yield stress of the material of the pile. As a result, design of pile foundation in seismically liquefiable areas still remains a constant source of attention to the earthquake geotechnical engineering community. A good review of the failure theories can be found in Bhattacharya and Madabhushi (2008). There are two competing theories of pile failure:

1. Bending theory: In this theory, piles are treated as beams. The lateral loads on the piles are due to inertial effects from the superstructure and kinematic effects due to ground movement. This theory is explained in more details in Ishihara (1997) and Tokimatsu et al. (1998).

2. Buckling instability theory: Bhattacharya (2003) and Bhattacharya et al. (2004) proposed a new theory in which piles are treated as beams-columns, i.e. axially loaded slender columns carrying lateral loads. Essentially piles are treated as unsupported columns in the liquefiable zone. This has been verified further by Kimura and Tokimatsu (2005), Knappett and Madabhushi (2009), Shanker et al. (2006), Lin et al (2005).

While the two competing theories of pile failure can explain many observations, uncertainties still exists with respect to locations of hinge formations in the pile and are summarized below:

1. The failure of foundations not only occurred in laterally spreading grounds but also was observed in level grounds where no lateral spreading would be anticipated.
2. The failure patterns of the buildings in level ground and in laterally spreading ground are similar i.e. the buildings tilt considerably, as shown in Fig. 1.
3. Cracks were observed near the bottom and top boundaries between liquefied and non-liquefied layers. Often cracks were observed at the pile head (see Fig.2).
4. Plastic hinges also formed not only at the boundaries of the liquefiable and non-liquefiable layers but also at various depths, see Bhattacharya and Madabhushi (2008).
5. There are few cases where plastic hinges formed at the middle of the liquefied layer, see Bhattacharya and Madabhushi (2008).

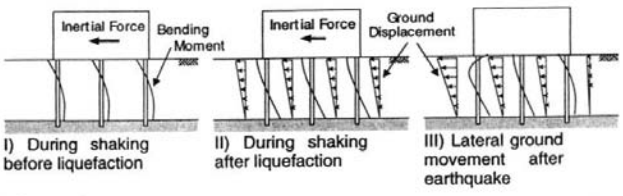

Figure 3 Schematic diagram showing the pile failure based on the bending theory (after Tokimatsu et al., 1998)

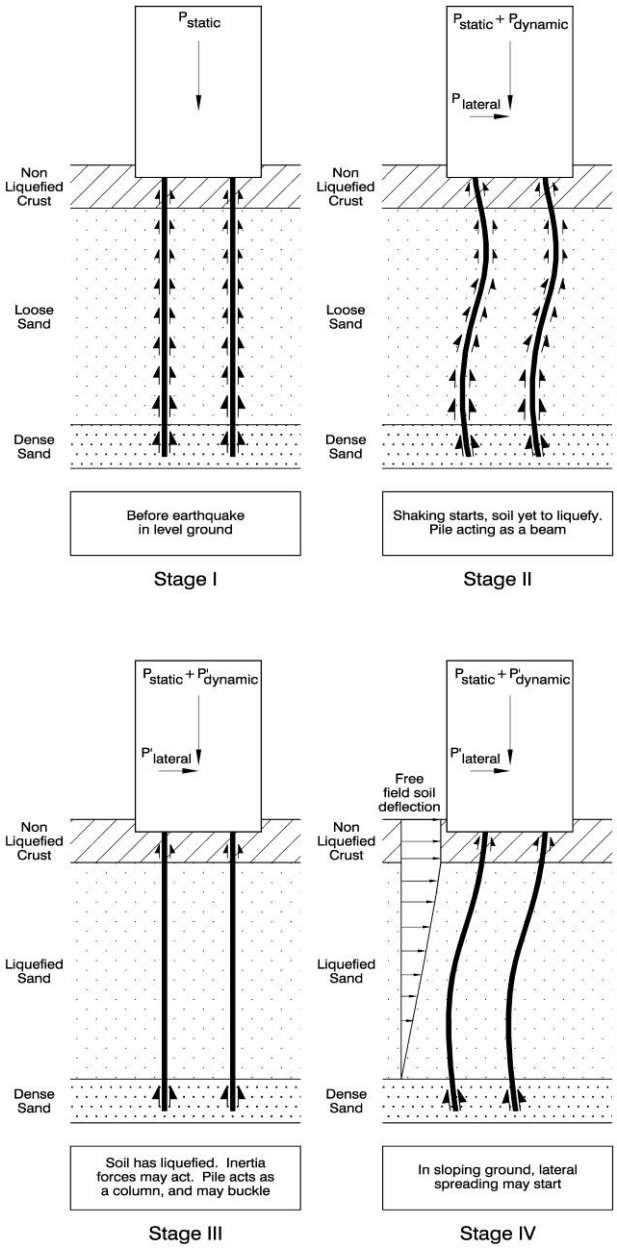

Figure 4 Explanation of the buckling theory

1.2 Aim of this paper

As structural failure of piles (by the formation of plastic hinges) are observed, bending moments or shear forces that are experienced by the piles must have exceeded the bending or shear carrying capacity of the pile section. The aim of this study is to explore two possible mechanisms by which the bending moment in the pile may exceed owing to liquefaction.

1. Lowering of the depth of fixity of the pile during liquefaction: In a simplified structural analysis, a pile can be considered as fixed at a certain depth below the ground level depending of the relative pile-soil stiffness. As soil liquefies, the relative pile-soil increases and as a result the point of fixity goes down. This is schematically shown in Figure 5 and 6. In these

figures, a typical pile-supported building is considered. The pile passes through two layers (numbered 1 and 2, out of which layer 2 is liquefiable, see Fig. 6) and is resting on non-liquefiable (dense sand denoted by 3 in Fig. 6). As soil liquefies, the depth of fixity goes down to layer 3. The effect will change the bending moment in the pile. The change in bending moment is predominantly a function of the time period of the structure considering the new unsupported length of the pile, damping of the liquefied soil-structure. This paper shows a simple way to compute the depth of fixity of the piles based on the Winkler Approach.

2. The increase in depth of fixity will make the structure more flexible. This would also result in increase in time period resulting in decrease in frequency.

2. DEPTH OF FIXITY CONCEPT

The stability analysis of fully and partially embedded piles is highly indeterminate and intractable unless some simplifying conditions are imposed. As proposed by Davisson and Robinson (1965), the most desirable simplification is to consider the lower end of the pile as fixed at some depth below the ground surface, termed as depth of fixity, L'_S. Figure 5 shows a free-head pile with an unsupported length L_U and an embedded length L_S. Considering the depth of fixity concept, the pile can be considered as simple cantilever of an equivalent total length L_E:

$$L_E = L_U + L'_S \tag{1}$$

L_E represents the equivalent length of the cantilever, which is presumed to behave in the same manner of the freestanding pile.

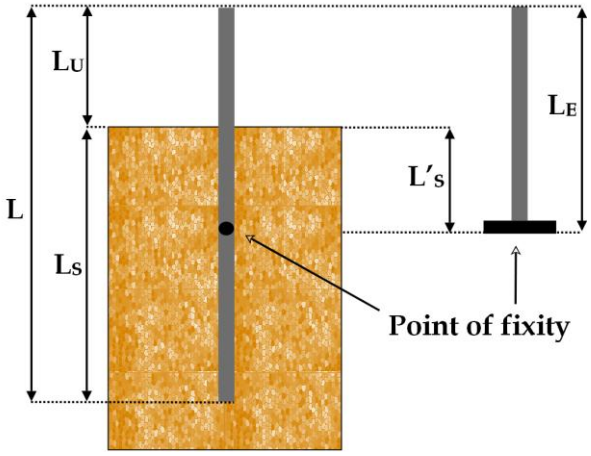

Figure 5 Partially embedded pile and definition of the depth of fixity using the equivalent cantilever concept.

While Davisson and Robinson (1965), evaluated the depth of fixity L'_S, based on considering both bending and buckling approach, in this paper, the authors have considered only the buckling theory, in which, at full liquefaction the pile behaves as a long unsupported *cantilever column*. The depth of fixity, can be simply evaluated from the expression of the buckling load valid for a cantilever:

$$P_C = \frac{\pi^2 EI}{4L_E^2} \tag{2}$$

EI is represents flexural rigidity of the pile while L_E is the equivalent length as described in Fig. 6. Combining equation (1) with equation (2), the depth of fixity L'_S, is given by:

$$L'_S = \sqrt{\frac{\pi^2 EI}{4P_C}} - L_U \tag{3}$$

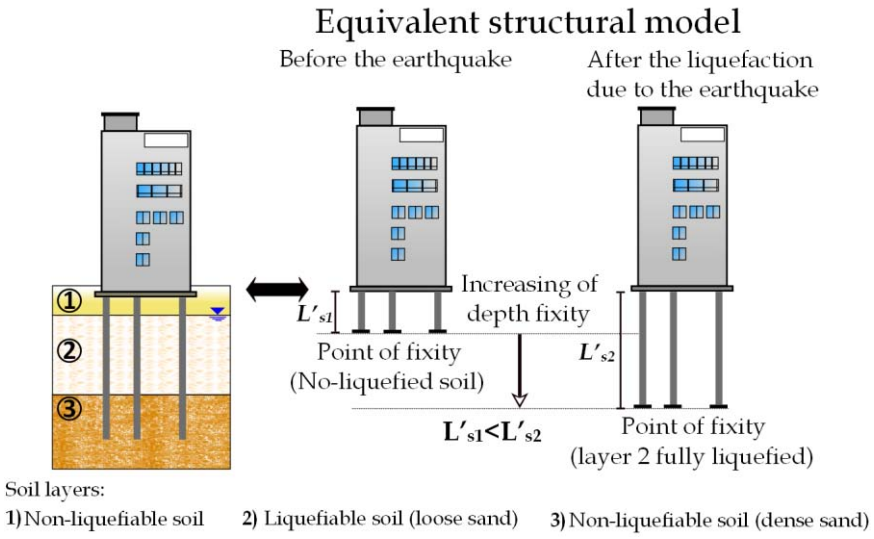

Figure 6 Equivalent structural model using the concept of depth of fixity in the case of non-liquefied soil and fully liquefied layer (layer 2).

2.1 Numerical analysis

Many authors, such as Davisson and Robinson (1965), Fleming et al. (1992), Heelis et al. (2004) have been studied the problem of the buckling load of fully and partially embedded piles and have suggested analytical expression to calculate P_C. In this paper, the buckling load of the pile shown in Fig. 4, has been evaluated using a numerical analysis carried out by SAP2000 V12 (CSI, 2008). The soil has been modelled using the Winkler approach (see Fig. 7), which models the lateral restraining effect of the soil on the pile as a set of discrete one-dimensional springs distributed.

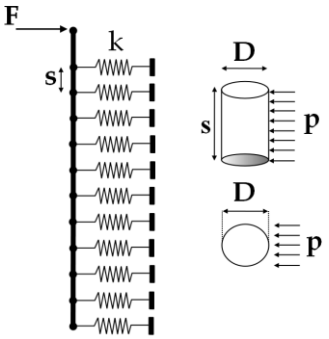

Figure 7 Illustration of the Winkler approach (1867)

Each spring is characterized by a constant value, called coefficient of subgrade reaction, k [N/m^3], which represents the ratio between the horizontal pressure, p [kN/m^2], at a certain point along the beam and the horizontal displacement, y [m], at that point. (Eq. 4). Many authors refer to the modulus of subgrade reaction K [kN/m^2], which takes in to account the width of the pile, see Eq. 5:

$$p = k \cdot y \tag{4}$$

$$K = k \cdot D \tag{5}$$

2.2. Non-dimensional variables

In order to compare and validate the results obtained in the numerical analysis carried out in SAP2000 with the results obtained from previous analysis the introduction of non-dimensional variables is required. In Table 1 the main non-dimensional groups governing the buckling problem of partially and fully embedded pile are presented.

Table 1 Definition of non-dimensional variables (see also Fig. 5)

Non-dimensional variable	Symbol	Expression
Non-dimensional stiffness parameter	λ	$\sqrt{\frac{kL^4}{EI}}$
Embedment ratio	δ	$\frac{L_S}{L}$
Non-dimensional unsupported length	J_R	$\frac{L_U}{R}$
Non-dimensional depth of liquefaction	H_R	$\frac{h}{R}$
Non-dimensional depth of fixity	S_R	$\frac{L'_S}{R}$
Non-dimensional equivalent length of cantilever	E_R	$\frac{L_E}{R}$
Non dimensional buckling load	N	$\frac{P_C}{P_E}$

A comparison of the results obtained from the simplified analysis presented in this paper is compared in terms of normalized buckling load, N, and non-dimensional stiffness parameter λ with other authors: Davisson and Robinson (1965), Fleming et al. (1992), Heelis et al. (2004), and Kerciku (2007), Kerciku et al (2008),

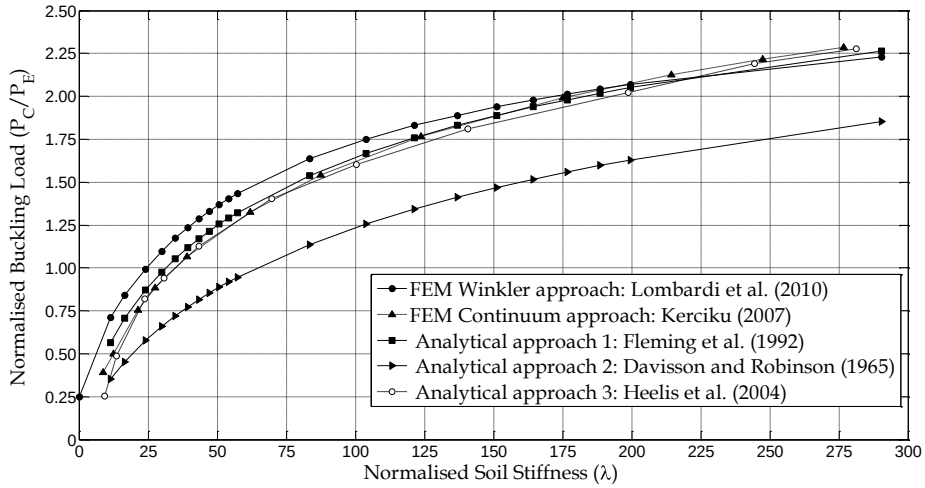

Figure 8 Comparison of the results obtained from different authors in terms of non-dimensional buckling load, N and non dimensional stiffness parameter, λ.

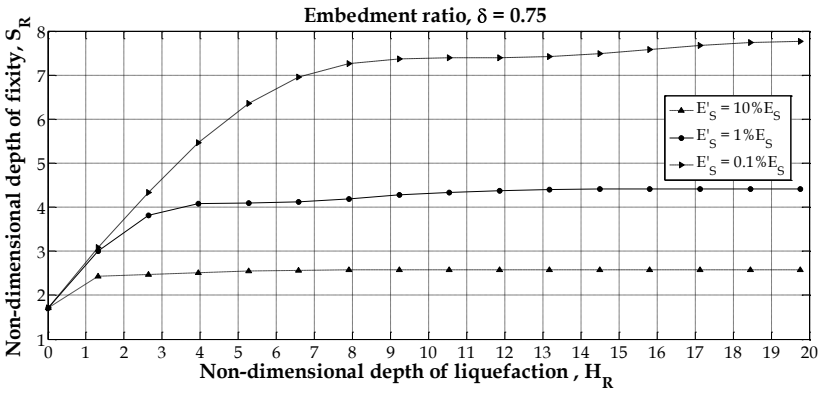

Figure 9 Results of partially embedded pile, δ=0.75, in terms of non-dimensional depth of liquefaction H_R and non-dimensional depth of fixity, S_R.

The parameter R, introduced in Table 1, represents the ratio between the flexural rigidity of the pile, EI [kNm^2] and the modulus of subgrade reaction, K [kN/m^2]:

$$R = \sqrt[4]{\frac{EI}{K}} \tag{6}$$

From a dimensional analysis can be seen that R has the dimension of a length [m]. The depth of liquefaction, h [m] is introduced, as well as the Euler buckling load, P_E [kN], for a hinged-end bar of length L and flexural rigidity EI [kNm2] with no elastic support along its span.

$$P_E = \frac{\pi^2 EI}{L^2} \tag{7}$$

Typical results, of the numerical analysis proposed in this paper, show that the depth of fixity of partially or fully embedded piles increases when the depth of liquefaction increases.

3. CHANGE IN TIME PERIOD

It has been shown by Bhattacharya and Adhikari (2007) that the frequency of a pile-supported structure changes with the stiffness degradation of the soil surrounding the pile. Usually, the time period of vibration of a pile-supported structure is estimated based on formulas which are derived from internationally calibrated data; see Chopra and Goel (2000), IS: 1893 (2002). This time period depends on the dimension of the superstructure without any consideration to the foundation. However, during and after liquefaction, as the pile loses its lateral confinement, it becomes an integral part of the superstructure. Fig. 10 (a) and 10 (b) show a typical variation of the structural configuration of the pile-supported structure during the transition of soil from being "solid" to "liquid-like-medium". Increase in fundamental time period of the structure will increase its flexibility and it may experience more lateral deformation.

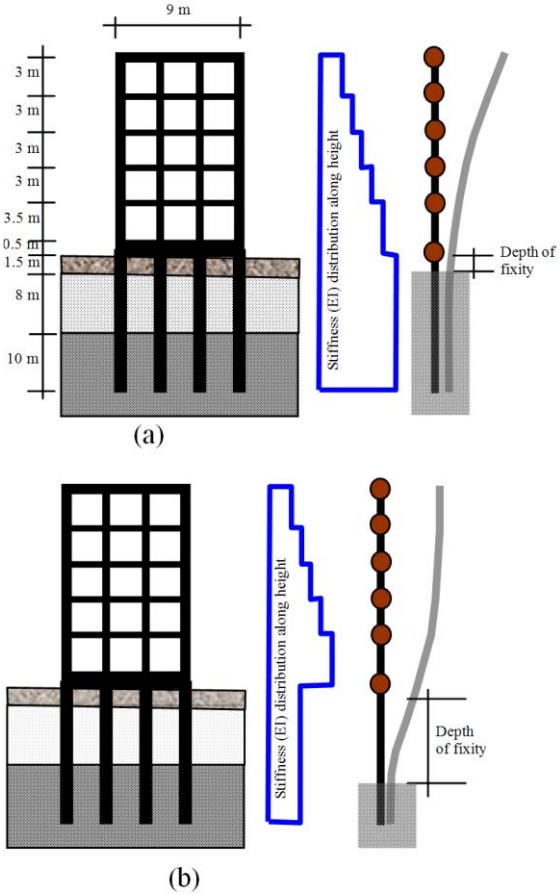

Figure 10 (a) Structural configuration before liquefaction and (b) after liquefaction

Also, the designers must ensure that the frequency of the structure at full liquefaction should not come close to the driving frequency of the earthquake to avoid resonance effect. For more details see Dash and Bhattacharya (2007).

4. APPLICATIONS

4.1 Example 1: An example of evaluation of the depth of fixity

In this section a practical application of the simplified method presented in the previous sections is illustrated.

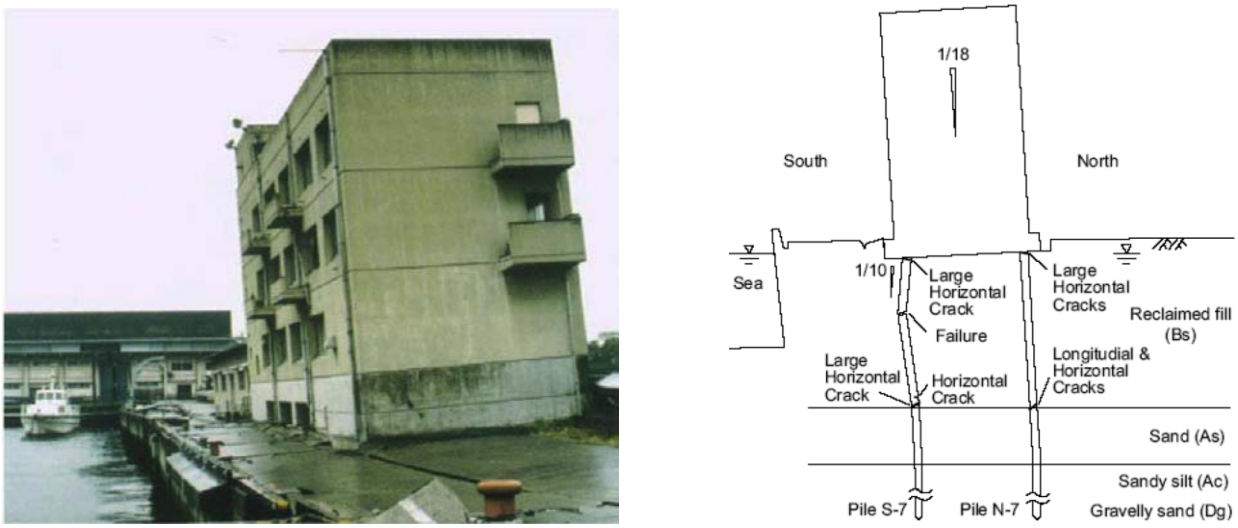

(a) **(b)**

Figure 11 (a) Pile supported building in Kobe, the building tilted of 3 degrees after the Kobe 1995 earthquake, (b) Post-earthquake failure investigation of the building, Uzuoka et al (2002).

Figure 11(a) shows a building located in the Higashinada-ku area of Kobe City. The building was built on a piled foundation as shown in Fig. 12. Following the 1995 Kobe earthquake, the building tilted by 3 degrees. Table 2 summarizes the design data of the building and while Table 3 shows the main properties of the piles foundation.

Table 2 Design data of the building (Uzuoka et al., 2002)

Building Height	14.5m above the ground
Foundation type	Precast driven pile
Number of stories	5
Axial load on each pile	412 kN
Dead load of the building	15656 kN

Table 3 Design data of pile (Uzuoka et al., 2002)

Length	20 m
External diameter	400 mm
Internal diameter	240 mm
Material	Pressed concrete
Young's modulus	30 GPa
EI	32.35 MNm^2

The depth of fixity can be estimated from the curves plotted in Fig 9 and 13. From the soil profile (see Fig. 12) , it is possible to assume that the depth of liquefaction is approximately 10m. The value of the non-dimensional depth of liquefaction, H_R, is required in order to estimate the non-dimensional depth of fixity, S_R, (see Table 1). Empirical calculations considering the results from a SPT test and the effective vertical stress (Meyerhof, 1957), allow us to evaluate the relative density of the soil. From the relative density, it is possible to estimate the modulus of subgrade reaction, see for example the charts given by such codes as API and DNV. In this example, authors considered a subgrade reaction equals to 3.2 MN/m^2.

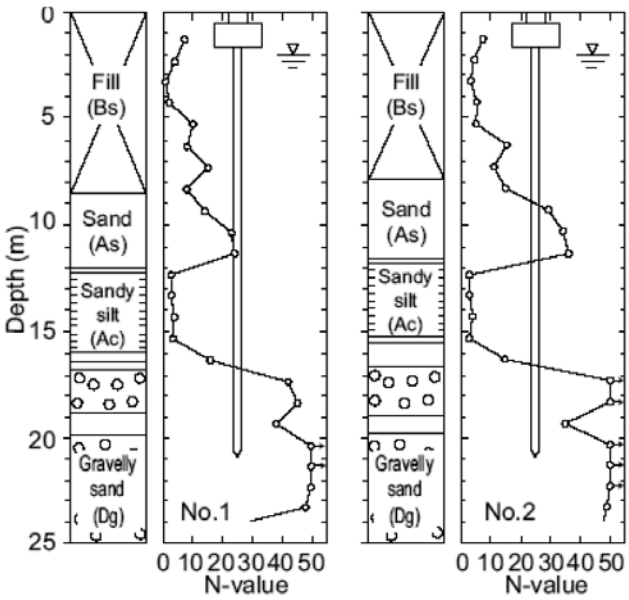

Figure 12 Profile of the N value estimated from a Standard penetration test at two different locations (from Uzuoka, 2002).

Step by step procedure

- Calculation of R:

$$R = \sqrt[4]{\frac{EI}{K}} = \sqrt[4]{\frac{32.35 MNm^2 m^2}{3.2 MN}} = 1.78m$$

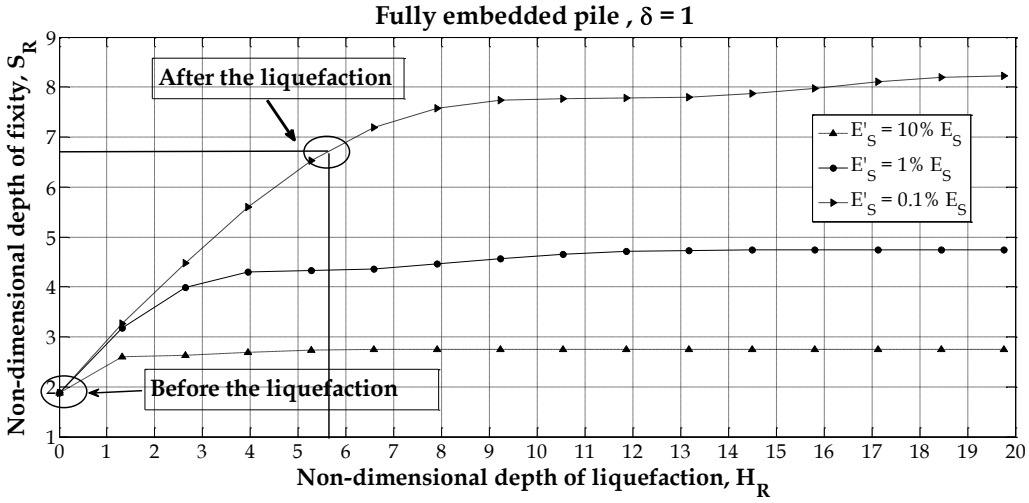

Figure 13 Analytical results for a fully embedded pile, δ=1, in terms of non-dimensional depth of liquefaction H_R and non-dimensional depth of fixity S_R

- Calculation of H_R:

$$H_R = \frac{h}{R} = \frac{10m}{1.78m} = 5.62$$

- Calculation of L'_S:
  S_R can be estimated from Fig. 13

  Before the liquefaction:

$$L'_S = S_R \cdot R = 1.90 \cdot 1.78m = 3.38m$$

  After the liquefaction:

$$L'_S = S_R \cdot R = 6.75 \cdot 1.78m = 12.02m$$

- Calculation of the buckling load capacity of a single pile, P_C:

  Before the liquefaction:

$$P_C = \frac{\pi^2 EI}{4L'^2_S} = \frac{\pi^2 \cdot 32.35MNm^2}{4 \cdot (3.38m)^2} = 7.0MN$$

  After the liquefaction:

$$P_C = \frac{\pi^2 EI}{4L'^2_S} = \frac{\pi^2 \cdot 32.35MNm^2}{4 \cdot (12.02m)^2} = 0.55MN$$

Remarks:

When the soil liquefied the depth of fixity increases from 3.38m to 12.02 while the buckling load capacity of the single pile reduces from 7.0 MN to 0.55MN. Considering the simplified analysis presented in this paper, the dynamic axial load (which is from 10 to 50% more than the axial load due to the inertial action of the dead load of the building) acting on the single pile is exceeded the buckling capacity of the pile.

4.2 Example 2: Modal analysis of the Kandla port and customs tower building

The dynamic behaviour of soil-pile-structure interaction during liquefaction has been further investigated using the case history of building failure in liquefiable soil from 2001 Bhuj earthquake, India. The considered building was the Port and Customs Tower situated at the Kandla Port area, Gujarat, India (see Fig. 1). This building had tilted during the 2001 Bhuj Earthquake and liquefaction have been observed around the building. Hence the building is chosen to study if there is any possibility of dynamic amplification in the building response as liquefaction progresses during the earthquake. This behaviour is studied considering the change in fundamental time period. The building, foundation and soil data used can be seen in Dash et al (2009) and Figure 14. Further to Dash et al. (2009), the model in this example incorporates both foundation as well as superstructure in the analysis.

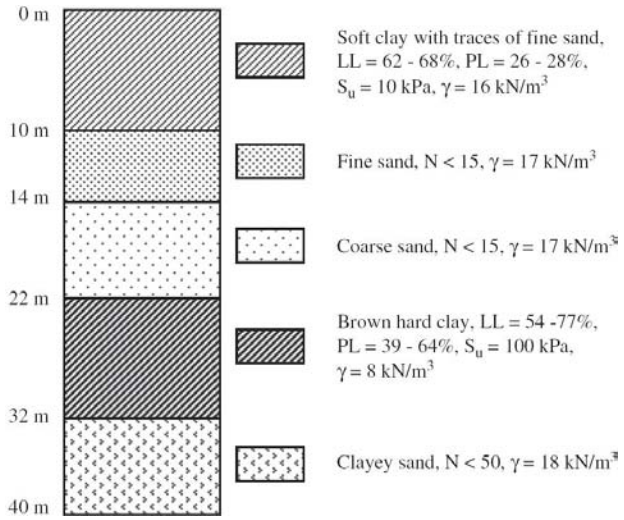

Figure 14 Typical soil profile in the vicinity of tower of the Port and Customs office

The superstructure is modelled as an equivalent SDOF system which gives the same fundamental period of the actual building. The top 10m soil is clayey soil over a saturated sandy bed which has been evaluated to have liquefied during the earthquake (Dash et al 2009). The model used in this example is presented in Fig. 15. The analysis is carried out for both service condition and seismic condition. The service condition is modelled without any strength degradation of the soil around the pile foundation. In the seismic condition the effect of liquefaction is incorporated in the analysis in stages. For example seismic condition 1 (denoted by seismic cond1) represents sandy soil has been liquefied fully for a depth of 1m, starting from 10m depth. Service condition 2 represents 2m of soil liquefied and so on. The top 10m clayey layer is degraded as per the shear strain induced during the earthquake as given in the figure 7 of Dash et al. (2009). The depth of liquefaction has been increased in different analysis and the fundamental time period of the soil-pile-structure system is recorded. Figure 16 shows the change in time period during the process of liquefaction.

It may be observed that the during the transition from service period to the seismic period the fundamental time period did not change much and therefore progressive liquefaction at deeper depth has very little effect on the structure. Mostly of this change is attributed to the degradation in the top 10m clayey layer. Hence, this building's foundation with a significantly thick clayey layer at top zone has avoided the fundamental time period change during the progression of liquefaction. The above analysis signifies that as the top part of the foundation is embedded on a clay layer over sandy liquefiable soil, the dynamic amplification due to fundamental period change of the structure during liquefaction has very little influence. However the significance of the liquefaction process can be very high where the foundation is fully embedded in liquefiable soil. To study this, the above soil-pile-structure system has been re-analysed considering the embedded soil as fully saturated sandy soil, and is described in the next paragraph.

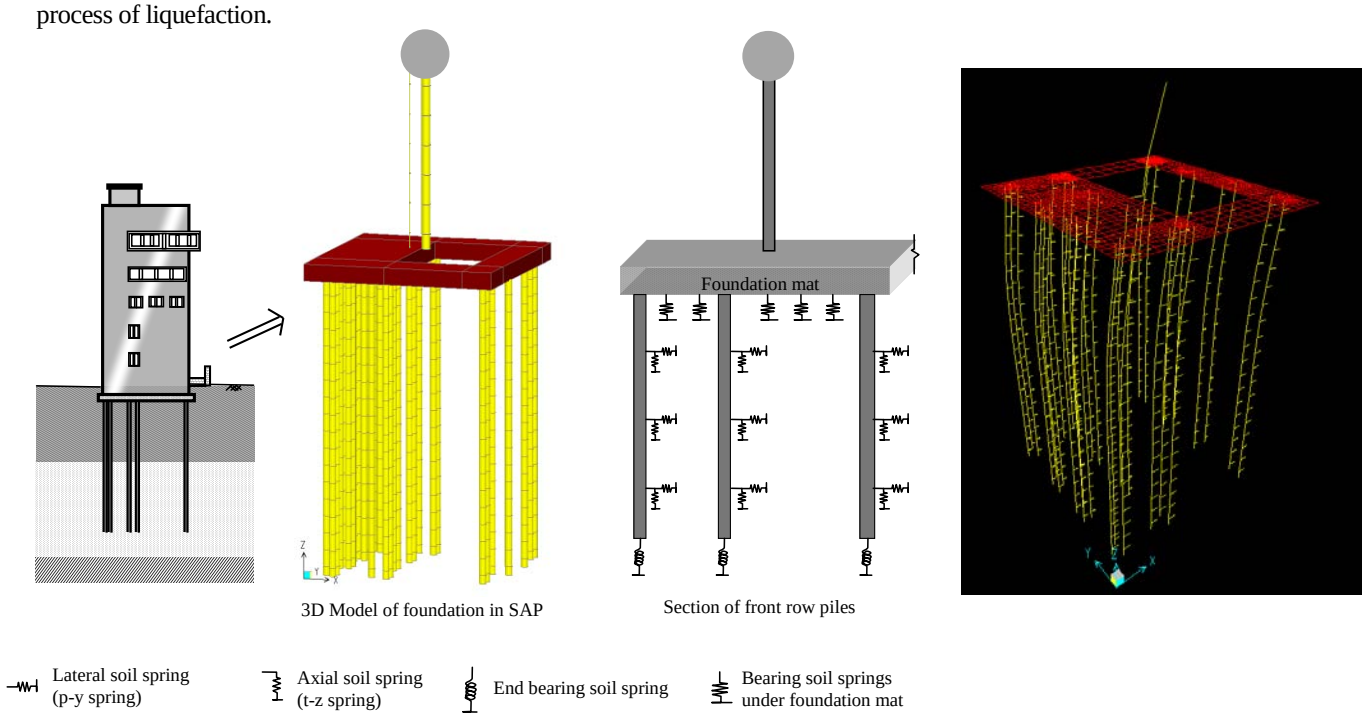

Figure 15 Modelling building shown in Fig. 1 using Winkler approach in SAP2000

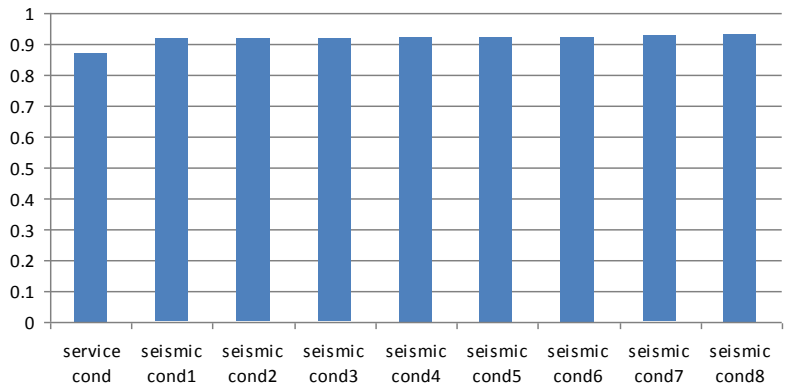

Figure 16 Change in time period of the building due to liquefaction

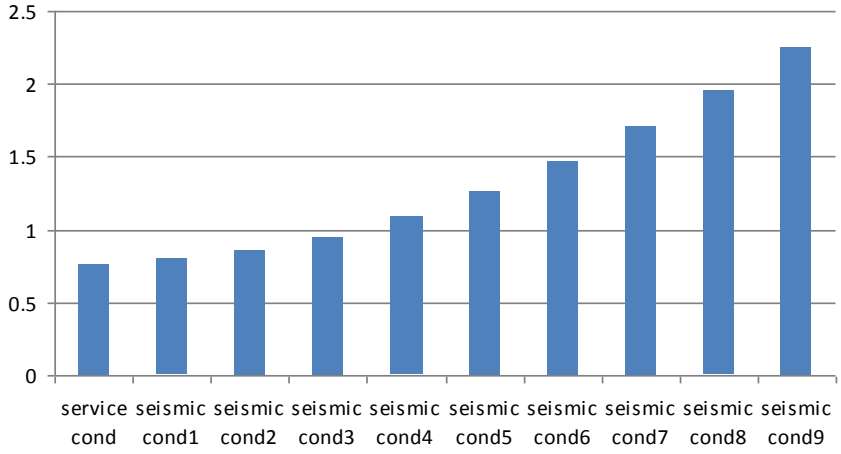

Figure 17 Example 2 re-analysed assuming the top soil is loose to medium dense liquefiable

Considering a fully saturated sandy soil:

The above analysis of Kandla Port and Customs Tower building is repeated to study the significance of progressing liquefaction on the dynamic behaviour of the soil-foundation-structure interaction. This model considers a single sand profile throughout the foundation depth that may liquefy during the earthquake. The SPT value for soil considered is 15. The liquefaction is considered to happen from top down and the linear spring stiffness is calculated according to the API guidelines for different seismic conditions. Figure 17 shows the change in fundamental frequency as the liquefaction initiates from top down. The building has 0.78 sec of fundamental period and it increases gradually as liquefaction progresses. The worst scenario may arise if the soil-pile-structure system's fundamental frequency hit the dominant frequency of the earthquake. In this case of resonance, the structure may observe very high level of bending moment and may sometimes lead to failure.

4. CONCLUSION

Two plausible failure mechanisms of piles in liquefiable soils due to liquefaction have been studied. Owing to liquefaction, the support provided by soil will reduce to near zero value and a pile may become unstable. This paper shows a simple method to compute the depth of fixity of piles for carrying out simplified buckling calculations. Another aspect that is studied is the change in fundamental frequency of the structure-foundation system. During liquefaction, the structure-foundation system becomes more flexible. Detailed study is required to compute the bending stresses in the pile during the transition from no-liquefaction to full liquefaction.

References:

API (1993), American Petroleum Institute, "Recommended Practice for planning designing and constructing Fixed offshore platforms – Load and Resistance Factor design". First edition, July 1, 1993.

Bhattacharya, S. (2003), "Pile instability During Earthquake Liquefaction", PhD Thesis, University of Cambridge, UK.

Bhattacharya, S., Madabhushi S.P.G. and Bolton M.D. (2004), "An Alternative Mechanism of Pile Failure in Liquefiable Deposits during Earthquake", *Géotechnique*, No.3, pp 203-213.

Bhattacharya, S. and Adhikari, S. (2007), "Dynamic behavior of piled foundations in liquefiable soils during strong earthquakes", Design of Foundations in seismic areas: Principles and Applications, NICEE Publications (IIT Kanpur).

Bhattacharya, S. and Madabhushi, S. P. G. (2008), "A critical review of methods for pile design in seismically liquefiable soil" *Bulletin of Earthquake Engineering*, No.6, pp 407-446.

BTL Committee (2000), "Study on liquefaction and lateral spreading in 1995 Kobe earthquake", Building Research Report, 138.

Chopra, A.K and Goel, R.K. (2000), "Building Period Formulas for estimating seismic displacements", *Earthquake Spectra*, Vol 16, No 2, EERI. Publication.

CSI. SAP2000 V12, Computer and Structures Inc. (2008). "Analysis Reference Manual", Berkeley, CA, USA.

Davisson M.T. and Robinson K. E. (1965), "Bending and buckling of partially embedded piles" *Proc. 6th Int. Conf. SoilMech. Found. Eng*., Vol.2, pp 243-246.

DnV (1992), "Foundation Design code".

Dash, S.R., Govindaraju, L. and Bhattacharya, S (2009), "A case study of damages of the Kandla Port and Customs Office Tower supported on a mat-pile foundation in liquefied soils under the 2001 Bhuj earthquake", *Journal of Soil Dynamics and Earthquake Engineering*, Vol 29, Number 2, pp 333-346.

Fleming, W. G. K., Weltman, A., Randolph, M.F. and Elson, K. (1992), "Piling Engineering", Blackie Academic and Professional, London.

Heelis, M.E., Pavlovic, M.N. and West, R.P. (2004), "The analytical prediction of the buckling loads of fully and partially embedded pile", *Géotechnique*, No.54, pp 363-373.

Ishihara, K (1997), Terzaghi oration: "Geotechnical aspects of the 1995 Kobe earthquake", *Proceedings of ICSMFE*, Hamburg, pp 2047-2073.

IS 1893 (2002), Indian Code of Practice for Seismic Design.

Kimura, Y. and Tokimatsu, K. (2007), "Buckling stress of slender pile with lateral displacement at the pile head in liquefied soils", *Journal of Structural and Construction Engineering*, AIJ (Architectural Institute of Japan) No 617, pp 169-175, July 2007.

Kerciku, A. A., Bhattacharya, S., Burd, H.J. and Lubkowski, Z.A. (2008), "Fixity of pile foundations in seismically liquefied soils for buckling calculation-an eigenvalue analysis", *Proc. 14th World Conf. on Earthquake Engineering*, Beijing, China.

Kerciku, A.A (2007), "Stability of pile foundations in liquefiable soils", Masters Thesis, University of Oxford (U.K).

Knappett, J.A. and Madabhushi, S.P.G. (2009), "Influence of axial load on lateral pile response in liquefiable soils", *Geotechnique*, Vol. 59, pp. 571-581.

Lin et al (2005), "Damage of piles caused by lateral spreading – Back study of three cases", *ASCE Geotechnical Special Publication*, No. 145 on Seismic Performance and Simulation of Pile Foundations in Liquefied and Laterally Spreading Ground, (Boulanger and Tokimatsu ed.),

Meyerhof, G.G (1957), "Discussion on research on determing the density of sands by spoon penetration testing", *Proc. 4th ICSMFE*.

Shanker, K., Basudhar, P.K. and Patra, N.R. (2007), "Buckling of piles under liquefied soil condition", *Geotechnical and Geological Engineering* , Volume 25, pp 303-313.

Tokimatsu K., Oh-oka Hiroshi, Satake, K., Shamoto Y. and Asaka Y (1998), "Effects of Lateral ground movements on failure patterns of piles in the 1995 Hyogoken-Nambu earthquake", *Proceedings of a speciality conference, Geotechnical Earthquake Engineering and Soil Dynamics III, ASCE Geotechnical Special publication*, No 75, pp 1175-1186.

Uzuko, R., Sento, N., Yashima, A. and Zhang, F (2002), "3 Dimensional effectice stress analysis of a damaged group pile foundation adjacent to a quay wall". *Journal of Japan Association Earthquake Engineering*, Vol 2, No 2, pp1-14.

Yoshida and Hamada (1990), "Damage to foundation piles and deformation pattern of ground due to liquefaction induced permanent ground deformation". *Proc. 3rd Japan-US Workshop on Earthquake Resistant design of lifeline facilities and counter measures for soil liquefaction*, pp 147-161.

JOINT CONFERENCE PROCEEDINGS
7th International Conference on Urban Earthquake Engineering (7CUEE) &
5th International Conference on Earthquake Engineering (5ICEE)
March 3-5, 2010, Tokyo Institute of Technology, Tokyo, Japan

EVALUATION OF PILE DIAMETER EFFECT ON P-Y METHOD PRECISION, IN SEISMIC ANALYSIS OF PILE SUPPORTED WHARVES

Mohammad Sajjad Fayyazi[1)], Ali Derakhshani[2)], and Khosrow Bargi[3)]

1) M.Sc Student, Department of Civil Engineering, University of Tehran, Iran
2) PhD Student, Dept. of Civil Engineering, University of Tokyo, Japan
3) Professor, Department of Civil Engineering, University of Tehran, Iran
sfayyazi@ut.ac.ir, aderakhshani@ut.ac.ir, kbargi@ut.ac.ir

Abstract: Pile supported wharf is one of the most common marine structures. One of the greatest challenges for designing of these giant and expensive marine structures is their foundations. They always contain pile group regarding soil and sea conditions .Hence, the method in which soil pile interaction is considered, is so important in foundation designing and analysis. There are several methods in codes for analyzing and designing of this interaction. Codes' methods are applicable and rather simple .In most cases this simplicity and applicability causes a reduction in accuracy. P-y method is one of the most common methods for soil pile interaction which is recommended in many codes such as API. In this paper the accuracy of P-y method for pile groups is examined versus one of its main structural characteristics of pile (pile diameter) in order to seismic evaluation of the pile groups. Finite Difference Method (FDM) and P-y method are used for evaluating piles maximum head displacement, maximum bending moment, lateral displacement and shear forces in different models with different piles' diameter in pile group in seismic conditions.

1. INTRODUCTION

In offshore structures, where cyclic wave loading applies lateral loads to pile-supported marine structures, a limited series of field and model tests has established the empirically-based and widely accepted "p-y" method of laterally loaded pile analysis. This static loading analysis method has been modified and extended to cyclic loading conditions, and is also routinely applied to dynamic or earthquake loading cases. the soil-pile contact is discretized to a number of points where combinations of springs represent the soil-pile stiffness at each particular layer. These soil-pile springs may be linear elastic or nonlinear; p-y curves typically used to model nonlinear soil-pile stiffness have been empirically derived from field tests, and have the advantage of implicitly including pile installation effects on the surrounding soil, unlike other methods. [3]

P-y method accuracy depends on many variables, one of its most effective parameters is pile diameter.

2. ANALYSIS METHODS

2.1 P-y method using SAP2000

The offshore oil industry has been a driving force behind the development of analysis methods for the response of pile foundations under lateral cyclic loading. The API Recommended Practice 2A-WSD (API, 2000)[2] codifies the p-y type analysis method, which is directly based on field tests conducted by Reese and Matlock in sands and clays .

In this method, the soil-pile contact is discredited to a number of points where springs represent the soil-pile stiffness at each particular layer. There are three types of springs:

(1)Lateral Springs(P-y)
(2) Frictional Springs (t-z)
(3)Tip Load Springs (Q-z)

These soil-pile springs may be linear elastic or nonlinear; these curves typically used to model nonlinear soil-pile stiffness have been empirically derived from field tests. Figure 1 describes a p-y curves for a single pile in depth of 6m in sand , p-y curves get normally stiffer with depth. The lateral soil resistance-deflection (p-y) and Tip Load-Displacement (t-z) and Axial Load Transfer (t-z) relationships for sand are non-linear and in the absence of more definitive information may be approximated at any specific depth H as it is illustrated in API. [2]

SAP2000 is used for p-y model because it has features for modeling nonlinear springs and running

nonlinear time history analysis. A sample p-y model which is constructed via SAP2000 is shown in Figure 3.

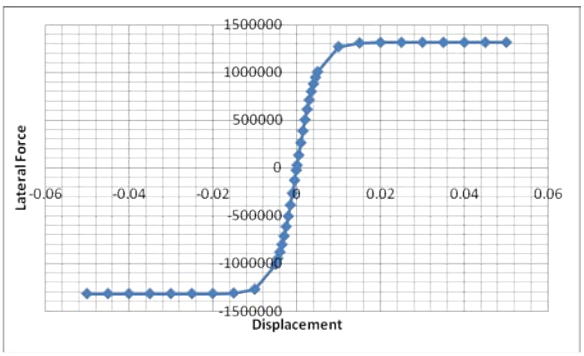

Figure 1- P-y curve in depth of 6m in sand

2.2 Finite Difference Method using FLAC 2D

FLAC is a two-dimensional explicit finite difference program for engineering mechanics computation.

The finite difference method is perhaps the oldest numerical technique used for the solution of sets of differential equations, given initial values and/or boundary values. In the finite difference method, every derivative in the set of governing equations is replaced directly by an algebraic expression written in terms of the field variables (e.g., stress or displacement) at discrete points in space; these variables are undefined within elements.

This program simulates the behavior of structures built of soil, rock or other materials that may undergo plastic flow when their yield limits are reached. Materials are represented by elements, or zones, which form a grid that is adjusted by the user to fit the shape of the object to be modeled. Each element behaves according to a prescribed linear or nonlinear stress/strain law in response to the applied forces

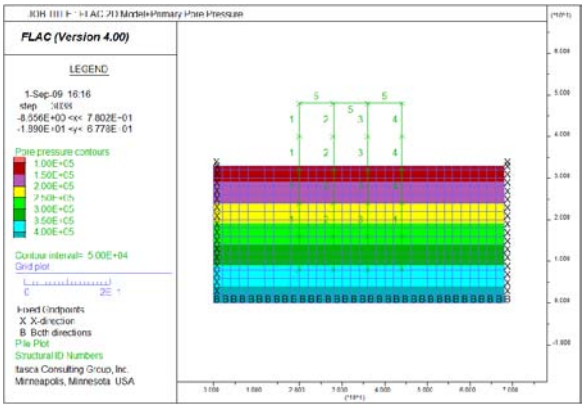

Figure 2 – Model preview and pore pressure in FLAC2D

or boundary restraints. The material can yield and flow, and the grid can deform (in large-strain mode) and move with the material that is represented. The explicit, Lagrangian calculation scheme and the mixed-discretization zoning technique used in FLAC ensure that plastic collapse and flow are modeled very accurately. Because no matrices are formed, large two-dimensional calculations can be made without excessive memory requirements. Figure 2 illustrate a FLAC 2D model.

3. Model definition

FLAC 2D works with the assumption of equal length and numerous spans perpendicular to the model page(like plain strain conditions) therefore if the model has enough longitudinal spans then the assumption for 2D analyzing is provided and its results in more accurate response in FLAC 2D .

For determination of proper number of longitudinal spans, different models with various number of spans range from 4 to 12 longitudinal spans using p-y method were analyzed in SAP2000 , according to analysis's results the model response is approximately constant and similar in the wharves with more than 8 longitudinal spans. As a result, for more certainty ,12 spans is used.

The number of cross sectional spans is 3, because with adding each one span the analyze time in FLAC 2D will increase dramatically. Pile spacing in both direction (longitudinal and cross sectional) is 8 meter.

Models with the different pile diameters (0.6 , 0.7 , 0.8 and 1 meter) are used for this research. Soil parameters are shown in table 1 and pile parameters which are used in models are shown in table 2.All piles are 15m above seabed and 4m above sea water level. Total length of each pile is 40m.

Applied acceleration to all models is a sinusoidal wave with maximum amplitude of 0.15g in five seconds duration. The general preview of model is shown in Fig 2 (FlAC Model) and Fig 3 (SAP2000).

Table 1 Soil Parameters

	γ	E	ν	Dr	φ
Sand	(kN/m3)	(MPa)		(%)	(Deg)
	20	110	0.38	80	40

Table 2 Pile Properties

	t	Length	Dr	φ
Pile	(m)	(m)	(%)	(Deg)
	0.01	40	80	40

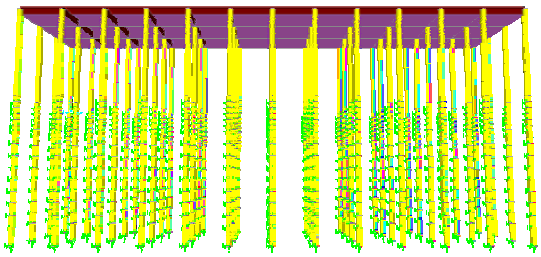

Figure 3 – Model and p-y springs preview in SAP2000

4. Analysis results

Table 3 and table 4 shows that most of parameters which obtained with p-y method are lower than their obtained value with Finite Difference method. The reason of this general difference is that for a specific soil ,p-y curves should be calculated with site investigations and experiments but here they are obtained with general data based on API [2] so they are not so accurate for this soil. Another reason is that in p-y method soil is modeled with discrete springs which these springs have not any influence on each other but in fact soil is continued along pile length.

But it should be noticed that here the influence of variation of pile diameter in p-y method accuracy is important ,not total accuracy of p-y method.

Table 3 Flac Analysis Results

Diameter (m)	Axial (kN)	Max Moment (kN.m)	Max Shear (kN)	Max Head Displacement (m)
0.6	184446	17996	15643	0.154
0.7	182296	15911	15372	0.147
0.8	183221	20659	18374	0.129
1	176383	23869	10298	0.094

Table4 SAP2000 Analysis Results

Diameter (m)	Axial (kN)	Max Moment (kN.m)	Max Shear (kN)	Max Head Displacement (m)
0.6	141346	22330	6670	0.0863
0.7	168640	28318	6959	0.071
0.8	167198	29620	6999	0.0586
1	167779	37859	7698	0.0421

As the main criteria of serviceability, different pile head displacements which are shown in Figure 4, error increases with growth of diameter . This error will be approximately constant after 0.1L (0.8m) where L means pile spacing. As it can be seen in this figure with decrease of pile diameter, error will decrease ,the reason for this event is

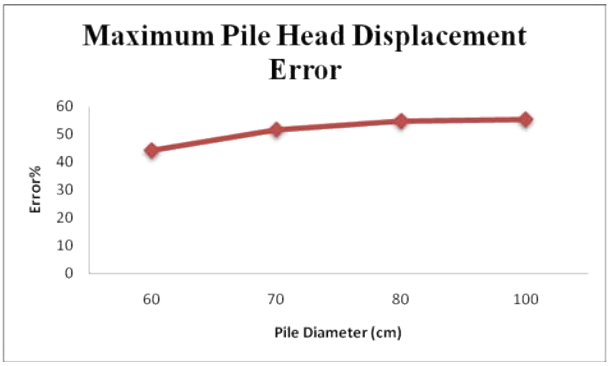

Figure 4 – Max Pile Head Displacement

the assumption of p-y method in which springs are separate and have not any effect on each other it means that each layer of soil responds independently to adjacent layers ignores the shear transfer between layers of soil, this assumption have less contrast with smaller diameters.

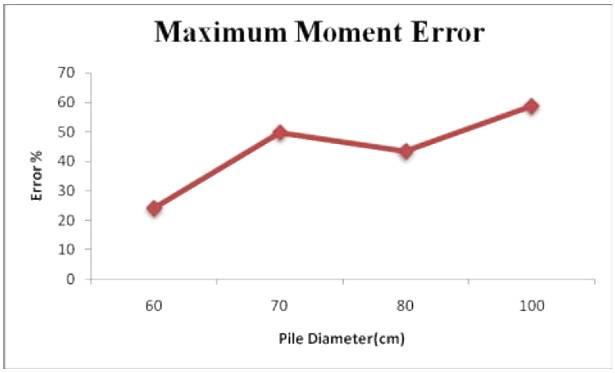

Figure 5 – Max Moment Error

It is obtained from figure 5 and table 5 that with increase of pile diameter maximum moment error along pile length during earthquake will increase generally. This is because of separate soil springs .

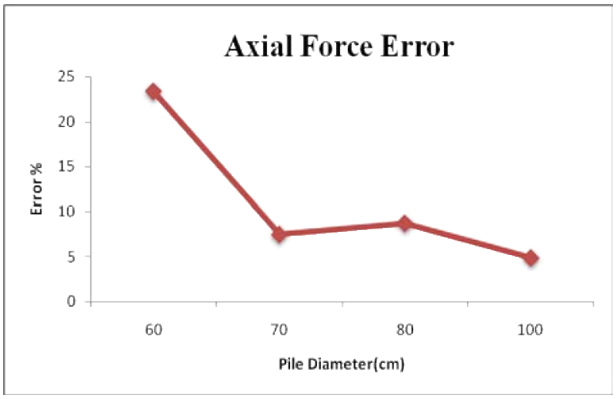

Figure 6 – Max Axial Force Error

Axial force and shear force are two parameter with less importance in designing in comparing with displacement and moment, maximum axial force error during earthquake is illustrated in Figure 6 and table 5 ,chart shows that error decreases intensively with increase of pile diameter from 0.6m to 0.7m.

In Figure 7 the same reduction is presented in Shear force error curve. The reason is t-z springs(frictional springs) and Q-z spring (pile end springs) Which are obtained according to some simple assumptions which are presented and discussed in API code[2].

These figures show that major reduction is occurred between (L/13 to L/10). where L is pile spacing.

Table5 Errors

Diameter (m)	Axial (%)	Max Moment (%)	Max Shear (%)	Max Head Displacement (%)
0.6	23.38	24.07	57.36	44.12
0.7	7.49	77.97	54.73	51.67
0.8	8.74	43.37	61.90	54.77
1	4.88	58.61	25.24	55.27

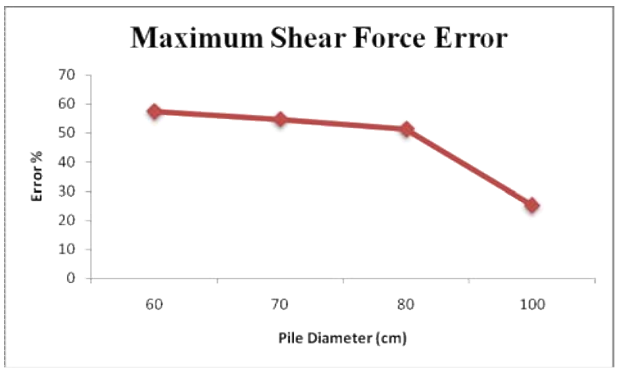

Figure 7 – Max Shear Force Error

4. CONCLUSIONS

Considering charts and results discussed above, major forces and displacement errors' increases with increase of pile diameter in seismic conditions.

The main reason is that In P-y method effect of piles on each other in a pile group is not considered. Adjacent piles reduce soil strength but in p-y method each spring is determined independently. As it is said before another reason is p-y assumption that each layer of soil responds independently to adjacent layers ignores the shear transfer between layers of soil.

It should be noticed that p-y model is the two-dimensional simplification of the soil-pile contact, which ignores the radial and three dimensional components of interaction and this causes inaccuracy too.

API suggests using p-y method for pile groups with at least L/6 to L/8 pile diameter for static condition. Here it is obtained that in seismic condition the best and efficient diameter for using p-y method for analysis is at least L/12 to L/10.

References:

[1] American Petroleum Institute (API). Recommended Practice for Planning, Designing and Constructing Fixed Offshore Platforms

[2] American Petroleum Institute (API). Recommended Practice for Planning, Designing and Constructing Fixed Offshore Platforms – Working Stress Design, API Recommended Practice 2AWSD (RP 2A-WSD), 21th edition, 2000, p60-p65

[3] Shaking Table Scale Model Tests of Nonlinear Soil-Pile-Superstructure Interaction In Soft Clay, Philip James Meymand,1998

[4] FLAC 2D Manual, Itasca Consulting Group, Second Revision April 2002

JOINT CONFERENCE PROCEEDINGS
7th International Conference on Urban Earthquake Engineering (7CUEE) &
5th International Conference on Earthquake Engineering (5ICEE)
March 3-5, 2010, Tokyo Institute of Technology, Tokyo, Japan

LATERAL RESISTANCE REDUCTION FOR STATIC ANALYSIS OF LATERAL SPREADING

Christopher R. McGann[1)], Pedro Arduino[2)], and Peter Mackenzie-Helnwein[3)]

1) Ph.D. Candidate, Dept. of Civil & Environmental Engineering, University of Washington, Seattle, WA
2) Associate Professor, Dept. of Civil & Environmental Engineering, University of Washington, Seattle, WA
3) Research Assistant Professor, Dept. of Civil & Environmental Engineering, University of Washington, Seattle, WA
mcganncr@u.washington.edu,parduino@u.washington.edu,pmackenz@u.washington.edu

Abstract: This paper presents the basis for a procedure to estimate an appropriate reduction in lateral resistance for use in static beam on nonlinear Winkler foundation (BNWF) analysis of piles subject to lateral spreading. Three–dimensional finite element (FE) models are created in the OpenSees FE analysis platform. These models consider a single pile embedded in a soil continuum. The soil profile is layered, with a liquefied layer located between two unliquefied layers. The FE model is used to compute representative force density–displacement ($p-y$) curves for a set of soil profiles in which the thickness and depth of the liquefied layer are varied. Through comparison with $p-y$ curves resulting from a homogenous soil profile, the reductions in ultimate lateral resistance, p_u, and initial stiffness, k_T, of the unliquefied curves due to the presence of the liquefied layer are characterized. It is observed that the influence on lateral resistance of a liquefied layer of a given thickness decreases with increasing vertical effective stress (layer depth). At a constant depth, increasing reductions are observed with increasing liquefied layer thickness. An exponential decay function is proposed as a means of implementing appropriate lateral resistance reductions in practice.

1 INTRODUCTION

Pile foundations are commonly used to support bridges and wharves in locations where there is the potential for lateral spreading during or after a seismic event. Due to the complexity of the kinematic demands placed upon an embedded pile during a lateral spreading event, it is difficult to obtain a reasonable estimate of the pile bending moment and shear force demands. Design of piles for this load case must therefore rely upon conservative analysis in order to ensure compliance with specified failure criteria. As a result of this conservatism, current simplified analysis methods often lead to overly expensive solutions in which the capacity far exceeds the demand.

In current geotechnical practice, it is common to conduct numerical analysis of piles under lateral loads using the $p-y$ method (McClelland and Focht 1958; Matlock and Reese 1960; Reese and Van Impe 2001). This method uses a beam on nonlinear Winkler foundation (BNWF) approach in which uncoupled one-dimensional (1D) nonlinear springs are used to model the three–dimensional (3D) soil–pile interaction. Procedures have been developed to extend the $p-y$ method for use in layered soil profiles (Georgiadis 1983) and liquefied soils (Wang and Reese 1998). Brandenberg et al. (2007) identified design guidelines for use in static $p-y$ analysis of the lateral spreading problem which produce results which are reasonably similar to centrifuge test data. Despite known shortcomings, the $p-y$ method can be used successfully in many lateral pile analysis applications, though the force density–displacement behavior of the $p-y$ curves must be chosen carefully for each particular case.

There are two factors to consider when selecting $p-y$ curves for use in a static BNWF analysis of lateral spreading: (1) the dependence of computed $p-y$ curves on pile kinematics, and (2) the effective reduction in the available lateral resistance of the unliquefied layers due to proximity to the liquefied interface. The kinematics of the pile significantly affects the $p-y$ curves computed using 3D FEA. Curves obtained from one type of pile deformation are not necessarily applicable to a different deformation pattern (McGann et al. 2010). The liquefied layer acts like a free surface, allowing the unliquefied layers to be pushed into the liquefied layer during the lateral displacement of the pile. This effective reduction in resistance occurs in both the upper and lower unliquefied layers and has been shown to vary in severity according to the vertical effective stress at the layer interface (McGann et al. 2010).

This paper further explores the lateral resistance reduction that can be mobilized in the unliquefied layers upon liquefaction of the middle soil layer. To this purpose, 3D FEA for a single pile embedded in a soil continuum are used to compute representative $p-y$ curves for a variety of

soil profiles in which the vertical location and thickness of the liquefied layer are varied. An exponential decay function is proposed to model the zone of reduction and the dependence of the reduction on vertical effective stress, depth, and liquefied layer thickness is explored. A plan for a comprehensive characterization of an appropriate resistance reduction for any depth and thickness of liquefied layer is outlined.

2 FINITE ELEMENT MODEL

A 3D FE model is created for the case of a single circular pile embedded in a soil continuum using the open–source FE framework OpenSees (`http://opensees.berkeley.edu`) developed through the Pacific Earthquake Engineering Research (PEER) Center. Figure 1 shows the undeformed configuration of the FE mesh used for one of the analysis cases. The commercial program GiD (CIMNE, 2008) is used as a graphical pre– and post–processor for OpenSees. Symmetry conditions are utilized as shown. Displacement–based beam–column elements are used to model the pile, eight–node brick elements are used to model the soil, and beam–solid contact elements are used to define the soil–pile interface (Petek 2006; Lam et al. 2009).

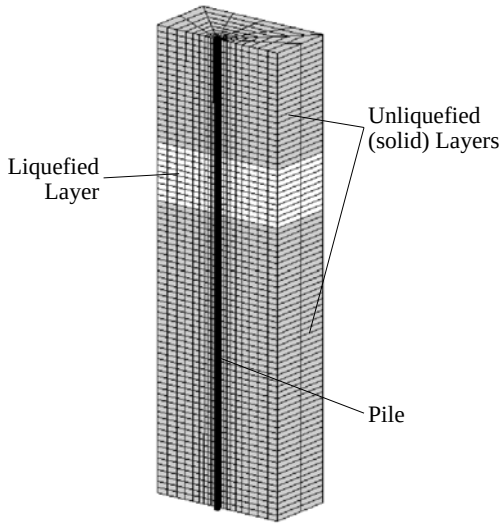

Figure 1: Typical layered soil 3D FE mesh.

The model considers a 0.61 m diameter pile and has a height of 40 m. Using past findings with 3D FEA of laterally loaded piles by Yang and Jeremic (2005) and Brown and Shie (1990), a lateral extent of 10 pile diameters from the pile centerline is selected for the FE model. Preliminary work with this model has shown that at moderate levels of lateral pile deformation, this distance sufficiently limits the influence of boundary effects.

Beam–solid contact elements (Petek 2006) are used to model the soil–pile interface. The contact elements provide a link between the line elements (pile) and brick elements (soil), creating a frictional interface allowing for sticking, frictional slip, and soil–pile separation.

The soil and pile nodes on the base of the model are fixed against displacements parallel to the pile axis. All of the nodes on the symmetry plane are fixed against translation normal to this plane. The pile is held fixed against all rotations. All outer surfaces of the soil continuum are held fixed against lateral in–plane translation and translation normal to their surface for stability.

Gravity loads are applied using a soil unit weight of $\gamma = 17$ kN/m^3, creating an appropriate distribution of vertical stress in the model, critical to defining the shear strength and contact resistance of the soil. The self–weight of the pile is neglected. Rigid pile displacement is used to mobilize the soil response evenly at all depths. This displacement is achieved by gradually imposing lateral displacement equally at all pile nodes. The maximum displacement considered is one pile diameter.

3 CONSTITUTIVE MODELING

Material nonlinearity in the soil is considered through a Drucker–Prager constitutive model which considers pressure–dependent shear strength, tension cutoff, and non–associative plasticity (McGann 2009). Written in terms of stress–type variables, the yield condition for the Drucker–Prager model can be expressed as

$$f(\boldsymbol{\sigma}) = \sqrt{\mathbf{s} : \mathbf{s}} + \rho \operatorname{tr} \boldsymbol{\sigma} - \sqrt{\frac{2}{3}}\, \sigma_Y \leq 0 \qquad (1)$$

in which $\mathbf{s} = \operatorname{dev} \boldsymbol{\sigma} = \boldsymbol{\sigma} - (\operatorname{tr} \boldsymbol{\sigma}/3)\, \mathbf{1}$ is the deviatoric stress tensor, ρ and σ_Y are positive material parameters which define the yield surface and can be computed from the Mohr–Coulomb cohesion, c, and internal friction angle, ϕ, using Equations 2 and 3 (Chen and Saleeb 1994). A non-associative plastic flow rule is defined by a positive parameter $\overline{\rho} \leq \rho$. An intermediate case where $\overline{\rho} = 0.150$ is used in the unliquefied layers.

$$\rho = \frac{2\sqrt{2} \sin \phi}{\sqrt{3}\,(3 - \sin \phi)} \qquad (2)$$

$$\sigma_Y = \frac{6c \cos \phi}{\sqrt{2}\,(3 - \sin \phi)} \qquad (3)$$

Variation in the soil elastic modulus, E, with depth is accounted for using

$$E = E_0 \sqrt{1 + \frac{|\sigma_m|}{|\sigma_a|}} \qquad (4)$$

where E_0 is the elastic tangent modulus at atmospheric pressure, σ_a, and $\sigma_m = \operatorname{tr} \boldsymbol{\sigma}/3$ is the mean stress. The upper and lower unliquefied layers are defined with matching material parameters. The liquefied layer, when used, has a separate set of parameters which reflect a liquefied state. All material parameters are summarized in Table 1.

Table 1: Material parameters in soil constitutive model.

Soil Layer	E_0 (kPa)	ν	ϕ (°)	σ_Y (kPa)	γ (kN/m^3)	ρ	$\overline{\rho}$
Unliquefied Sand	25000	0.350	36	5	17	0.398	0.150
Liquefied Sand	25000	0.485	0	5	17	0.000	0.000

4 COMPUTATION OF $p-y$ CURVES

The $p-y$ curves most commonly used for cohesionless soils, those developed by Reese et al. (1974) and later adopted by the American Petroleum Institute (API) (1987) in a slightly modified form, are based upon the results of lateral load tests. In these tests, large pile deflections occur near the ground surface while little or no pile deflection occurs at increased depths. For this reason, the response of the soil at shallower depths is captured fairly accurately, however, there is insufficient data available to characterize the response at depth. This is relatively inconsequential for numerical analyses which mirror the physical tests, but becomes problematic when large pile displacements occur below the near–surface zone.

In addition to the bias created by the load test, the $p-y$ curves recommended by the API (1987) are based upon the interpretation of experimental evidence using a simplified analytical model (BNWF) that is not applicable to all types of pile deformation. In 3D FEA, the kinematics of the pile significantly affect the $p-y$ curves which result for a particular load case (McGann et al. 2010). To eliminate the kinematic bias from $p-y$ curves obtained using 3D FEA, a kinematic case in which a rigid pile undergoes a uniform lateral displacement into the soil is used. This case returns $p-y$ curves which are representative of the soil–pile interaction independent of any pile kinematics. A schematic of this kinematic case and the procedure used to compute $p-y$ curves from the 3D model is shown in Figure 2.

Computing a set $p-y$ curves from the 3D model requires both the force and displacement at each pile node in the direction of loading. The forces exerted on the pile are determined directly from the beam–solid contact elements (Petek 2006), eliminating the need for back–calculating pile forces from the moment diagram. The contact elements resolve the interface forces applied by the soil to the outer surface of the pile into a vector with three orthogonal components acting at each pile node (two lateral, one axial), though only the lateral component in the direction of loading is needed. The forces obtained from the contact elements are distributed over the tributary length of the pile associated with each respective pile node to obtain mesh–independent $p-y$ curves. The lateral displacements of each pile node relative to the surrounding soil are determined directly from the model.

To obtain a smooth continuous function for the $p-y$ curves at each pile node, a hyperbolic tangent function of the form

$$p(y) = p_u \tanh\left(\frac{k_T}{p_u}\, y\right) \tag{5}$$

is fit to the force density–displacement data using least squares. This function defines the two characteristic curve parameters used to compare sets of $p-y$ curves: (1) the ultimate lateral resistance p_u, and (2) the initial tangent stiffness $k_T = dp(y)/dy|_{y=0}$. Together, these two parameters uniquely define each of the computed $p-y$ curves.

4.1 Considered Soil Profiles

To obtain a set $p-y$ curves which is representative of many different field conditions, a set of 21 soil profiles (17 primary, 4 supplementary) are created in the 3D FE model. Four liquefied layer thicknesses are considered to study the effect of layer thickness on the soil response. To capture the effects of depth and vertical effective stress at the

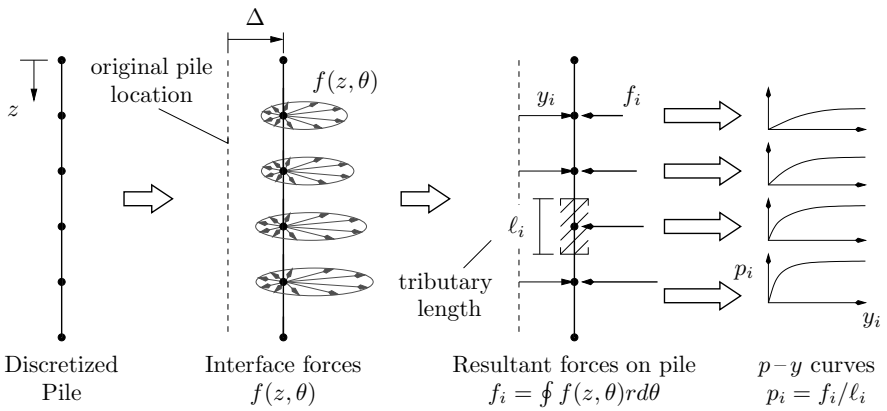

Figure 2: Computation of $p-y$ curves from the 3D FE model using rigid pile displacement.

Table 2: Primary analysis cases.

		Thickness (m)			
		1	2	5	10
Depth (m)	5	x	x		
	10	x	x	x	
	15	x	x	x	x
	20	x	x	x	x
	25	x	x	x	x

layer interface, nine liquefied layer depths are considered. Layer depths are referenced with respect to the bottom of the liquefied layer. Table 2 summarizes the 17 primary analysis cases with respect to liquefied layer thickness and depth. The four supplementary cases are considered in order to obtain additional data for the upper unliquefied layer. In the primary set, there are no combinations of depth and thickness such that the top of the liquefied layer is at depths of 10 m and 15 m for the 1 m and 2 m thick liquefied layers. The supplementary cases supply this data.

5 CHARACTERIZATION OF COMPUTED $p-y$ CURVES

The $p-y$ curves computed from the 3D FE model differ significantly from the $p-y$ curves recommended by the API (1987), especially at increased depth (McGann et al. 2010). This difference is apparent in each of the two characteristic $p-y$ curve parameters (p_u and k_T). Figure 3 shows the distribution of ultimate lateral resistance with depth computed using the 3D model alongside the API (1987) recommended distribution and several other distributions proposed in the literature (Broms 1964; Fleming et al. 1985; Brinch Hansen 1961). The differences in the cited p_u distributions have been previously noted (Kulhawy and Chen 1995; Zhang et al. 2005), however, Figure 3 shows that the FE results also differ from the established distributions. In the case of the API (1987) distribution, which is commonly used for cohesionless soils, the difference is very significant. There is some similarity near the ground surface, however, at depths beyond the first few pile diameters the variation becomes marked, with the FE results first exceeding and then becoming significantly less that the API distribution. Overall, the FE results compare favorably with the distributions cited in Figure 3 and other similar distributions, such as that of Zhang et al. (2005). Use of one of these methods is recommended over the API (1987) distribution for a static BNWF analysis of lateral spreading in order to obtain reasonable pile shear and moment demands.

The distribution of initial stiffness recommended by the API (1987) also differs from that obtained from the computed $p-y$ curves, as shown in Figure 4. Where the API initial stiffness distribution increases linearly with depth, the computed curves show a bi–linear distribution

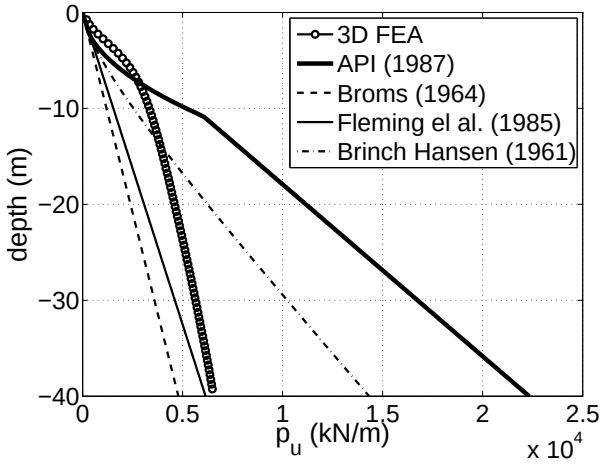

Figure 3: Variation of ultimate lateral resistance, p_u, with depth.

with depth having a curved transition zone between the two linear portions (McGann et al. 2010). As with ultimate lateral resistance, the values of k_T at shallow depths correspond fairly well between the two methods, however, the API (1987) recommendations significantly overestimate the initial stiffness at deeper locations. The computed k_T distribution correlates well with the work of Lam and Cheang (1995) and Brandenberg et al. (2007), who both used a parabolic variation of initial stiffness in BNWF analyses and produced results which corresponded well with experimental data.

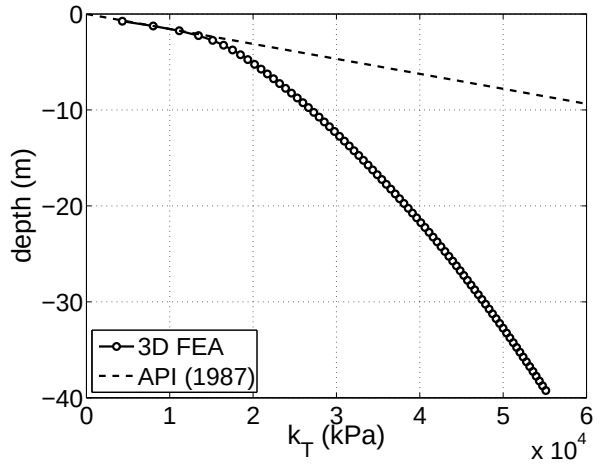

Figure 4: Variation of initial stiffness, k_T, with depth.

6 INFLUENCE OF LIQUEFACTION

In a liquefaction–induced lateral spread, once the middle layer has liquefied, its shear strength is reduced significantly. During the application of lateral loads to the soil by an embedded pile, the unliquefied soil at the layer interfaces is now able to move into the liquefied layer, effec-

tively reducing the available lateral resistance to the passage of the pile in the unliquefied layers. This effect is most intense at layer interfaces and lessens in magnitude with increasing distance from the liquefied layer. This resistance reduction mechanism is explored in terms of p_u and k_T values for $p-y$ curves computed from 3D FEA. Comparisons are made between cases which consider homogenous and liquefied soil profiles.

Figure 5 shows the p_u and k_T distributions resulting from the homogenous and liquefied profile analyses for three combinations of liquefied layer depth and thickness. The reduction in the $p-y$ curve parameters is related to both the depth of the liquefied interface and the thickness of the liquefied layer, though the lateral resistance is more sensitive to changes in these soil profile variables. In all considered cases, the reduction in p_u encompasses a larger zone of soil than the reduction in k_T, which is isolated to those areas in the immediate vicinity of the liquefied layer.

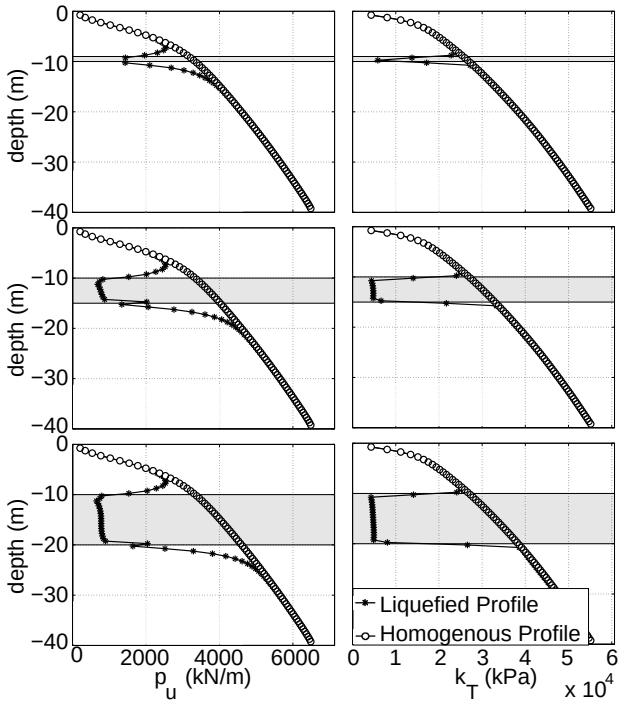

Figure 5: Comparison of p_u and k_T in homogenous and liquefied soil profiles.

To better characterize the observed reductions in the characteristic $p-y$ curve parameters, the ratios of p_u and k_T in the liquefied cases are taken with respect to the homogenous case. The computed p_u and k_T ratios in the upper and lower unliquefied layers are computed for all analysis cases.

6.1 Reduction in Ultimate Lateral Resistance

The computed ultimate lateral resistance ratios, shown for the upper and lower unliquefied layers in Figures 6 and 7, respectively, show that the presence of the liquefied layer

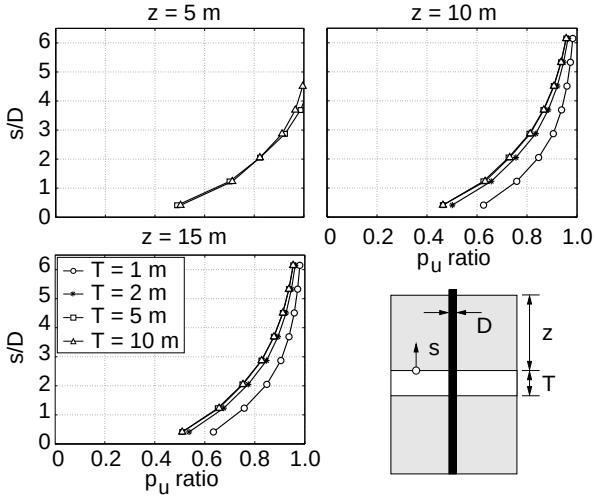

Figure 6: Reduction of p_u in upper unliquefied layer for various combinations of liquefied layer thickness, T, and interface depth, z.

reduces the resistance of a zone of unliquefied soil which becomes smaller with increasing distance from the layer interface. Several trends are observed from Figures 6 and 7. For a constant depth, the reduction in p_u tends to increase with increasing liquefied layer thickness, T. There appears to be a limit to this effect, however, as the p_u ratios for $T = 5$ m and $T = 10$ m are essentially identical.

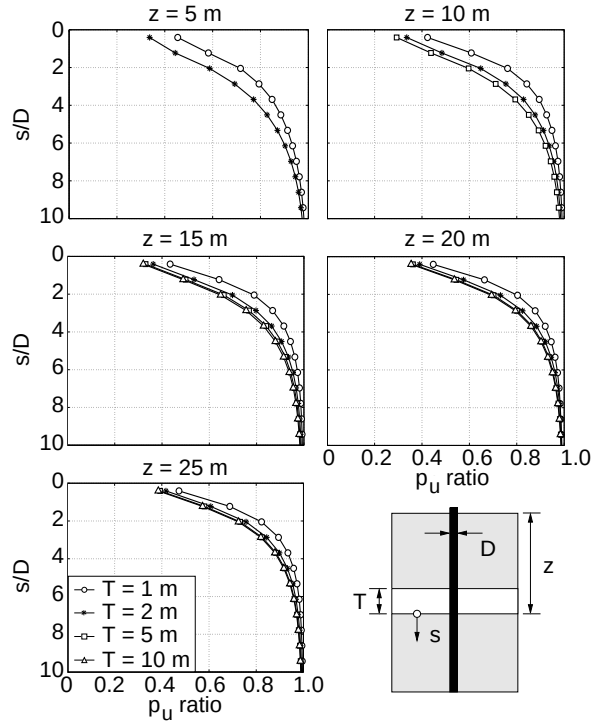

Figure 7: Reduction of p_u in lower unliquefied layer for various combinations of liquefied layer thickness, T, and interface depth, z.

The observed lateral resistance reduction depends on the depth of the liquefied layer in two ways. At shallow depths, the proximity of the ground surface is apparent in the response of the upper unliquefied layer. Away from this near–surface zone it is evident that for a constant distance from the layer interface, s, increasing vertical effective stress decreases the reduction in lateral resistance. This results in a reduced zone of influence at greater levels of effective stress.

To establish a procedure which can be used in practice to estimate the lateral resistance reduction, p_{ur}, suitable for use in a static BNWF lateral spreading analysis for any soil profile, it is necessary to have a general way in which to represent the reduction which occurs. The shape of the zone of reduction shown in Figures 6 and 7 suggests an exponential decay function of the form

$$p_{ur}(s) = 1 - a \exp\left(-\frac{s}{s_c}\right) \tag{6}$$

in which s is the distance from the liquefied layer interface, the reduction coefficient a defines the magnitude of the reduction at the interface, and s_c characterizes the point at which the reduction becomes negligible.

Using least squares, the exponential decay function of Equation 6 is fit to the p_u ratio data for the upper and lower unliquefied layers. This procedure defines the parameters a and s_c for each of the considered analysis cases, establishing a database of reduction information that is representative of a variety of soil profiles. Example fitted decay functions are plotted with the computed data for the upper unliquefied layer in Figures 8 and 9. As shown, the chosen exponential decay function represents the data well in both layers.

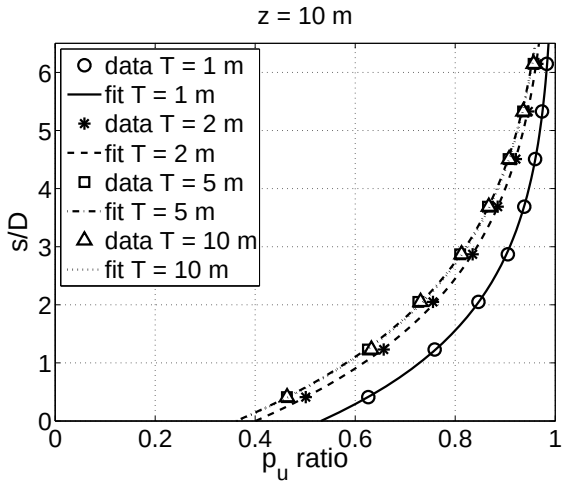

Figure 8: Computed p_u data and fitted exponential decay curves for upper unliquefied layer.

The terms of Equation 6 can be manipulated to provide physical meaning to the decay function. As shown in Figure 10, the distance at which the lateral resistance reduction is considered to become negligible is defined as s_u. This point is chosen to occur when $p_{ur} = 5\%$, resulting in $s_u = 3s_c$. A characteristic length s_{50} is defined as the distance s corresponding to a resistance reduction of $p_{ur} = a/2$. The value of the characteristic length can be determined as $s_{50} = s_c \cdot \ln 2$. The decay function can thus be defined in an alternative form

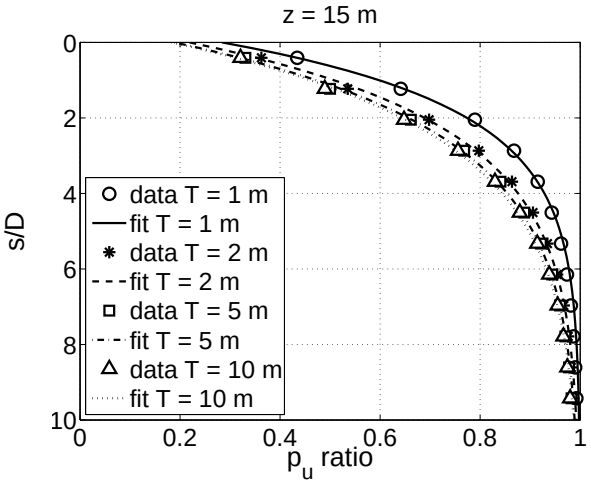

Figure 9: Computed p_u data and fitted exponential decay curves for lower unliquefied layer.

$$p_{ur}(s) = 1 - a \cdot 2^{-s/s_{50}} \tag{7}$$

which is in terms of the characteristic length, s_{50}, and the reduction coefficient a. This form of the function is useful in that each of the two parameters, s_{50} and a, are physically meaningful variables, whereas the form expressed in Equation 6 is written in terms of the not directly physical variable s_c.

The results presented here are for only one pile diameter and one set of soil parameters. To fully capture the general response of the problem, a parametric study, consisting of additional numerical simulations in which these parameters are varied, is necessary. Once this paramet-

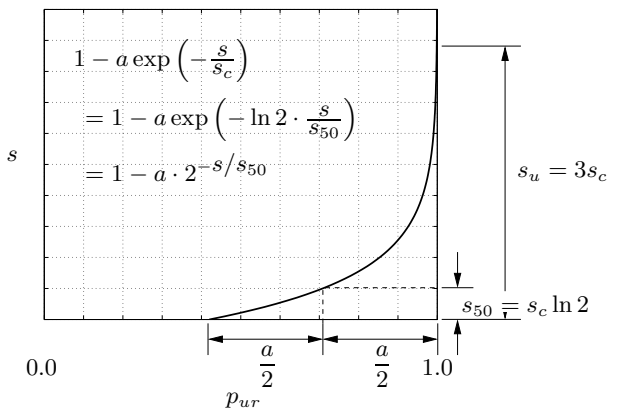

Figure 10: Physical meaning of terms in exponential decay resistance reduction function.

ric study has been completed, a dimensional analysis of the data will be performed in order to obtain a method which can be used to predict reasonable values of the reduction coefficient a and the characteristic length, s_{50}, for a given set of input parameters. Using this procedure, a reduction in ultimate lateral resistance suitable for use in a static BNWF lateral spreading analysis for any combination of pile diameter, soil strength and stiffness, and liquefied layer thickness and depth can be computed.

6.2 Reduction in Initial Stiffness

In both the upper and lower liquefied layers, the initial stiffness observed in the liquefied cases is essentially identical to that in the homogenous case with the exception of the pile nodes immediately adjacent to the liquefied layer (Figures 11, 12). It is unclear whether this is representative of a true response or if it is a mesh–based effect. Further analysis is necessary to definitively characterize the reduction in k_T. Due to the localized nature of the observed reduction, it is hypothesized that the initial stiffness of the $p-y$ curves in a static BNWF lateral spreading analysis may be left unreduced. Therefore, no curve fitting procedure is undertaken for the initial stiffness data.

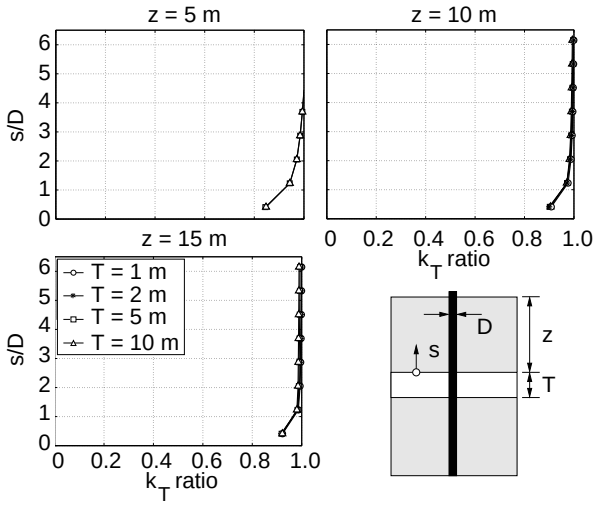

Figure 11: Reduction of k_T in upper unliquefied layer for various combinations of liquefied layer thickness, T, and interface depth, z.

7 SUMMARY AND CONCLUSIONS

Analysis of pile foundations subject to liquefaction–induced lateral spreads is difficult due to the complexity of the problem. A kinematic demand is placed on the pile by the lateral displacement of the upper soil layer and the response of the pile is governed by fundamentally 3D soil–pile interaction. In order to design a pile for such an event, simplified static BNWF analyses using

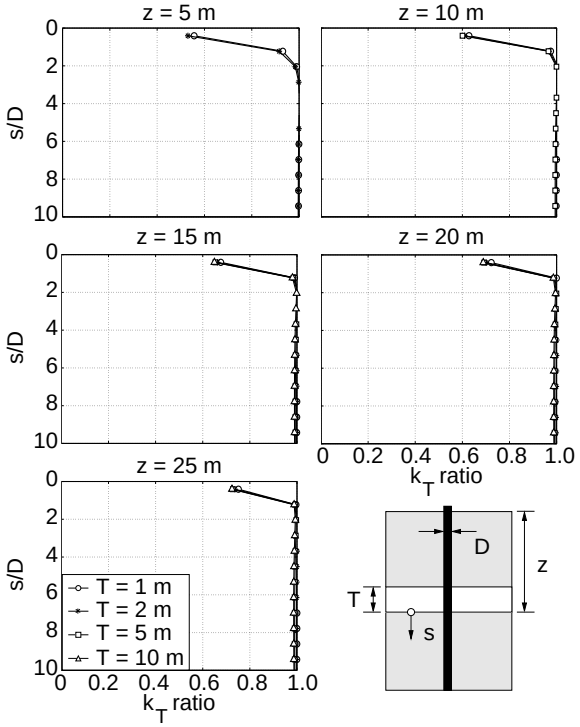

Figure 12: Reduction of k_T in lower unliquefied layer for various combinations of liquefied layer thickness, T, and interface depth, z.

$p-y$ curves are often used to obtain design parameters. Inherent conservatism in many simplified analyses leads to over–designed solutions. Careful and informed selection of the $p-y$ curves for a particular analysis, as defined by the characteristic $p-y$ curve parameters of ultimate lateral resistance, p_u, and initial stiffness, k_T, can increase the effectiveness of the $p-y$ method as an analysis tool.

Problems associated with commonly used $p-y$ curves for sand (API 1987), such as the tendency for values of p_u and k_T to be too large at increased depth, and the kinematic dependence observed in $p-y$ curves computed from 3D FEA have been briefly discussed. In both cases, no significant problem is posed in an analysis of a pile with a lateral loading applied at or above the ground surface. However, in the case of lateral spreading, in which large pile deflections can occur at depth and the pile kinematics differ from those used to define the API $p-y$ curves, use of these curves becomes problematic.

3D FE analysis has been used to compute a set of $p-y$ curves for a single pile diameter and a variety of layered soil profiles. These curves have been used to evaluate the effective reductions in p_u and k_T which occur in the upper and lower unliquefied layers upon liquefaction of the middle layer. It is observed that for a constant distance away from the liquefied layer interface, the computed reduction in resistance decreases with decreasing liquefied layer thickness and increasing depth (effective stress). An exponential decay function is fit to the reduced resistance

data in order to obtain a means of characterizing this reduction in a general sense. Continuing numerical analyses which consider additional pile diameters and soil parameters will allow a simplified procedure for estimating the magnitude and spatial extents of the effective resistance reduction. Using this procedure, a set of $p-y$ curves suitable for use in a static BNWF analysis of lateral spreading can be obtained for any combination of pile, soil strength, and liquefied layer thickness and depth.

Acknowledgements

This work was supported by the Pacific Earthquake Engineering Research (PEER) Center under Sub-Agreement No. 00006405, which is gratefully acknowledged.

References

American Petroleum Institute (API) (1987). *Recommended Practice for Planning, Designing and Constructing Fixed Offshore Platforms*. API Recommended Practice 2A(RP–2A), Washington, D.C., 17th edition.

Brandenberg, S. J., Boulanger, R. W., Kutter, B. L., and Chang, D. (2007). "Static pushover analyses of pile groups in liquefied and laterally spreading ground in centrifuge tests." *Journal of Geotechnical and Geoenvironmental Engineering, ASCE*, 133(9), 1055–1066.

Brinch Hansen, J. (1961). "The ultimate resistance of rigid piles against transversal forces." *Bulletin No. 12*, Geoteknisk Institute, Copenhagen, 5–9.

Broms, B. B. (1964). "Lateral resistance of piles in cohesionless soils." *Journal of the Soil Mechanics and Foundations Division, ASCE*, 90(SM3), 123–156.

Brown, D. A. and Shie, C. F. (1990). "Three dimensional finite element model of laterally loaded piles." *Computers and Geotechnics*, 10(1), 59–79.

Chen, W. F. and Saleeb, A. F. (1994). *Constitutive Equations for Engineering Materials Volume I: Elasticity and Modeling*. Elsevier Science B.V., Amsterdam.

Fleming, W. G. K., Weltman, A. J., Randolph, M. F., and Elson, W. K. (1985). *Piling Engineering*. Surrey University Press, London.

Georgiadis, M. (1983). "Development of p–y curves for layered soils." *Geotechnical Practice in Offshore Engineering*, Reston, VA. ASCE, 536–545.

International Center for Numerical Methods in Engineering (CIMNE) (2008). *GiD User Manual*. `http://gid.cimne.upc.es/`.

Kulhawy, F. H. and Chen, Y. J. (1995). "A thirty year perspective of Broms' lateral loading models, as applied to drilled shafts." *Bengt B. Broms Symposium on Geotechnical Engineering*, Singapore. 225–240.

Lam, I. P., Arduino, P., and Mackenzie-Helnwein, P. (2009). "Opensees soil–pile interaction study under lateral spread loading." *International Foundation Congress & Equipment Expo*, Orlando, FL.

Lam, I. P. and Cheang, L. (1995). "Dynamic soil–pile interaction behavior in submerged sands." *Earthquake–Induced Movements and Seismic Remediation of Existing Foundations and Abutments*, S. L. Kramer and R. Siddharthan, eds., Geotechnical Special Publication No. 55. ASCE, 110–135.

Matlock, H. and Reese, L. C. (1960). "Generalized solutions for laterally loaded piles." *Journal of the Soil Mechanics and Foundations Division, ASCE*, 86(SM5), 63–91.

McClelland, B. and Focht, J. (1958). "Soil modulus for laterally loaded piles." *Transactions, ASCE*, 123, 1049–1086.

McGann, C. R. (2009). "Analysis and evaluation of single piles in laterally spreading soil," Master's thesis, University of Washington.

McGann, C. R., Arduino, P., and Mackenzie-Helnwein, P. (2010). "Applicability of the $p-y$ method to the analysis of piles in laterally spreading soil." *Journal of Geotechnical and Geoenvironmental Engineering, ASCE*, Under review.

OpenSees. *Open System for Earthquake Engineering Simulation*. `http://opensees.berkeley.edu`. Pacific Earthquake Engineering Research Center, University of California, Berkeley.

Petek, K. A. (2006). "Development and application of mixed beam–solid models for analysis of soil–pile interaction problems," Ph.d. thesis, University of Washington.

Reese, L. C., Cox, W. R., and Koop, F. D. (1974). "Analysis of laterally loaded piles in sand." *Proceedings of the 6th Offshore Technology Conference*, Vol. 2, Houston. 473–483.

Reese, L. C. and Van Impe, W. F. (2001). *Single Piles and Pile Groups Under Lateral Loading*. A.A. Balkema, Rotterdam, Netherlands.

Wang, S. T. and Reese, L. C. (1998). "Design of pile foundations in liquefied soils." *Geotechnical Earthquake Engineering and Soil Dynamics III*. ASCE, 1331–1343.

Yang, Z. and Jeremic, B. (2005). "Study of soil layering effects on lateral loading behavior of piles." *Journal of Geotechnical and Geoenvironmental Engineering*, 131(6), 762–770.

Zhang, L., Silva, F., and Grismala, R. (2005). "Ultimate lateral resistance to piles in cohesionless soils." *Journal of Geotechnical and Geoenvironmental Engineering*, 131(1), 78–83.

JOINT CONFERENCE PROCEEDINGS
7th International Conference on Urban Earthquake Engineering (7CUEE) &
5th International Conference on Earthquake Engineering (5ICEE)
March 3-5, 2010, Tokyo Institute of Technology, Tokyo, Japan

VERTICAL LOADS EFFECT ON LATERAL PILE GROUP RESPONSE ON THE BASIS OF SOIL-PILE-CAP INTERACTIONS

Mahmoud N. Hussien[1], Tetsuo Tobita[2], Susumu Iai[3], and Kyle M. Rollins[4]

1) PhD student, Department of Civil and Earth Resources Eng., Kyoto University, Japan
2) Assistant professor, Disaster Prevention Research Institute, Kyoto University, Japan
3) Professor, Disaster Prevention Research Institute, Kyoto University, Japan
4) Professor, Department of Civil and Environmental Eng., Brigham Young University, USA
mnasser2002002@geotech.dpri.kyoto–u.ac.jp, tobita@geotech.dpri.kyoto–u.ac.jp, iai@geotech.dpri.kyoto–u.ac.jp, rollinsk@byu.edu

Abstract: This paper presents the results of a numerical investigation conducted to study the effect of vertical loads on lateral response of free head and capped pile groups in sand. A coupled soil-pile system is idealized through 2-D finite elements with soil models idealized by a hyperbolic type multiple shear mechanism. The analysis focuses on the five piles in the middle row of a 3x5 pile group spaced at 3.92 pile diameters. The interaction between a pile and the surrounding soil in the 3-D type is idealized in the 2-D analysis using soil-pile interaction springs with a hysteretic non-linear load displacement relationship. The presence of vertical loads on free head piles increases the confining pressures in the sand deposit confined by the piles but the rate of increase in those outside the group is relatively small, resulting in the difference in a balance of lateral soil pressures acting at the back of and in front of individual piles. A vertical load applied to a group pile with a uniform vertical displacement of 0.1 pile diameter decreases the lateral resistance of the leading pile (pile 1) by 10 % and increases the lateral resistance of piles 3 and 5 by 14 and 35 %, respectively. The same trend with higher percentages of increase or decrease is observed in the capped pile group case

1. INTRODUCTION

Pile groups connected by concrete caps are used in building and bridge structures to support a combination of both vertical and lateral loads which result from the weight of the structure and any acting sea wave or seismic forces. All methods of analysis consider that axial and lateral loads act independently, assuming that there is no interaction. However, recent studies on single piles suggested a significant increase in the lateral resistance of piles in the presence of vertical loads. In particular, Karthigeyan and Ramakrishna (2005) and Karthigeyan et al. (2006, 2007) showed through a series of finite-element analyses on single piles that the presence of vertical loads increases the lateral load capacity of piles in sandy soils by as much as 40 %. In fact, the scopes of these recent studies were limited to the behavior of single piles. Yet, little work has been devoted to the behavior of pile groups subject to the combined action of vertical and lateral loads. Moreover, the effect of the inclusion of pile caps on the interaction between vertical and lateral load was not fully examined.

The objective of this study was to help quantify the effect of vertical loads on the lateral resistance of pile groups not only for free head piles, but also for capped piles. A two-dimensional finite element analysis based on a multi-shear mechanism constitutive relationship, **FLIP** (**F**inite element analysis program for **LI**quefaction **P**rocess) (Iai et al. 1992), was used to this end. In addition, the applicability of the computer code FLIP to the analysis of pile groups under lateral loads has been confirmed through a study based on a full scale test of a 3 by 5 pile group at the Salt Lake City International Airport (Snyder 2004).

After the description of the finite element model used in this study, a brief review was given to the applicability of the model to the full scale test of a pile group. This paper then presented the initial part of the study that analyses the effect of vertical loads on the lateral resistance of a single pile with and without a pile cap, to be followed by the main part of the study with respect to the behavior of free head and capped pile groups. The primary findings from this study were summarized as conclusions.

2. FINITE ELEMENT MODELING

The two-dimensional finite element program FLIP was employed to analyze the behavior of pile groups under pure lateral loads and a combination of vertical and lateral loads. The analysis focused on the five piles in the middle row of a 3x5 pile group spaced at 3.92 pile diameters (pile diameter =324 mm). Prior to the analysis of pile group behavior, analysis of single piles was performed as a reference in order to discuss the specific behavior of the pile group under combined loads. Two type of pile cap conditions were considered in the

analysis: no cap condition, in which the top and bottom of the piles were set as displacement and rotation free, and capped pile conditions in which a concrete cap with 0.495 m thickness and attached to the ground surface was considered. Figure 1 shows the general layout and meshing of the FE model with a concrete cap attached to the ground surface. The same meshing of the soil profile was used to analyze the single pile. Side boundary displacements were fixed in the horizontal direction, while those at the bottom boundary were fixed in both the horizontal and vertical directions.

A total of 8 cases were considered in the analysis. Pure lateral loads were considered in half of these cases while a combination of vertical and lateral loads were considered in the others. In the analysis, a vertical displacement (V) of 0.1D (D = pile diameter) was applied at the pile head (0.495 m above the ground surface) prior to the application of lateral loads for both the single and grouped piles then lateral loads were statically applied at the same points until a target lateral displacement of 60 mm was achieved. The maximum vertical applied displacement at the pile head was kept constant during the application of the lateral displacement.

2.1 Soil Model

The soil model used in this study consists of a multiple shear mechanism (Iai et al. 1992) with the basic form of the constitutive relation given by:

$$\{d\sigma'\} = [D](\{d\varepsilon\} - \{d\varepsilon_p\}) \quad (1)$$

where σ' is effective stress. ε and ε_p are the strain and the plastic volumetric strain generated by the transient and cyclic loads, respectively. More details about the soil model could be found in Iai et al. (1992). In the analysis, a uniform layer of sand was used. Model parameters of the sand layer are shown shaded in Table 1.

2.2 Pile Model

Bilinear one-dimensional beam elements with three degrees of freedom per node were used to model the piles. Normal force, shear force, and bending moment of each element were obtained directly from the finite element program. Table 2 defines the model parameters of pile elements. The parameters for piles were from the industrial standard (Tobita et al. 2006).

2.3 Pile Cap Model

Linear plan elements with two degrees of freedom per node were used to model the concrete pile caps. The Elastic modulus (E), Possion's ratio (υ), and density (ρ) were set to be 40 GPa, 0.18, and 2.5 t/m^3, respectively.

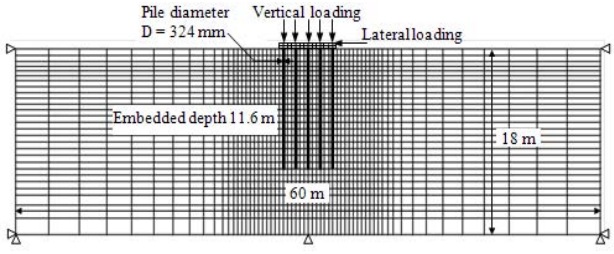

Figure 1. General layout and meshing of the FE model.

2.4 Soil-Structure Interface

Joint elements were used at the soil-pile and soil-cap interfaces to represent sliding and separation mechanisms between them. Figure 2 indicates that sliding will be initiated when the shear stress at the interface exceeds a certain value of τ_f given by the equation:

$$\tau_f = c_J + \sigma tan\phi_J \quad (2)$$

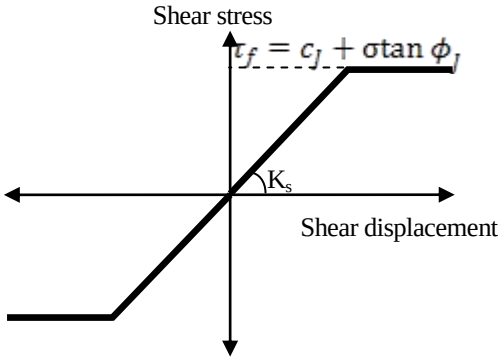

Figure 2. Sliding mechanisms at soil-pile interface

Table 1. Idealized soil layers at the Salt Lake City test site and model parameters for soil elements.

Soil layer	Depth (m)	γ_{sat} (t/m^3)	G_{ma} (kPa)	υ	K_a (kPa)	ϕ_f (degrees)	c (kPa)
Soft clay	0-1.22		12,200		31,720		27
Soft clay	1.22-2.14	1.92	18,000		46,800		40
Soft clay	2.14-3.06		15,800		41,080		35
Sand	3.06-4.80	1.83	161,000		418,600	38	
Soft clay	4.80-5.33		34,100	0.33	88,660		56.9
Soft clay	5.33-5.87	1.92	15,000		39,000		25
Soft clay	5.87-6.48		32,400		84,240		54
Sand	6.48-11.6	1.83	127,000		330,200	33	
Sand	11.6-18.00		40,600		105,560	31	

Table 2. Model parameters for pile elements.

Gs (kPa)	υ	ρ (t/m^3)	Initial flexural rigidity (kPa)	Flexural rigidity after yield (kPa)
77,500,000	0.29	7.9	108,67	65,200

Table 3. Model parameters for joint elements.

Angle of friction (ϕ_J)	Cohesion(c_J)	Normal stiffness (kN/m^3)	Tangential stiffness (kN/m^3)
2/3 ϕ_f	c	1,000,000	1,000,000

where c_J and ϕ_J are shear strength parameters of the soil at the interface. A separation-contact model was used to idealize the separation between the pile and the surrounding soil where the normal compression at the interface was modeled using a high rigidity spring (Kn) between the pile and the soil elements to avoid the overlapping of elements during compression. In the tension side, no stress will transfer between the pile and the soil at any tension stress value. Model parameters for joints element are defined in Table 3.

2.5 End Bearing Spring

The axial soil reactions at pile tips were simulated using nonlinear spring elements (Q-z curve). The nonlinear spring at the pile tip can be represented according to Zhang et al. (1999) as:

$$z = \frac{Q_b(1-\upsilon)}{4r_o G_{ma}(1-\frac{Q_b}{Q_f})} \qquad (3)$$

where Q_f is ultimate tip resistance (force). G_i and υ are initial shear modulus and Poisson's ratio of the soil at the pile tip, respectively. r_o is pile radius and Q_b is mobilized tip resistance (force) for a given displacement z.

2.6 Pile-soil Interaction Spring

The interaction between a pile and the surrounding soil in 3-D was idealized using a 2-D analysis as follows. The nonlinear-spring element in Fig. 3 was used to represent the soil-pile interaction. The underlying concept of this spring was to analyze soil deformation between the piles in a row perpendicular to the direction of load. Parameters of the spring element were determined by parametric studies on the soil-pile interaction in a 2-D horizontal plane as shown in Fig. 4. Figure 4a shows a single row of equally spaced piles deployed perpendicular to the direction of load, while Fig. 4b shows a simplified model for one pile in a group with boundaries parallel to the load direction that pass through the centers of the pile spacing. These boundaries were periodic and shared the same displacements at the boundary nodes with the same x-coordinate where the x-axis is towards the right. At the right and left side boundaries, displacements were fixed (Iai et al. 2006).

Figure 5 shows the load-relative displacement relationship under cyclic loading where the relative displacement is defined as the difference in horizontal displacement between the center point of the pile and a point located at the pile boundary at y = 0. Figure 6 depicts the shear stress and shear strain relationship of a saturated clay model under cyclic loading. The relationship between the load and relative displacement of a pile (Fig. 5) and the relationship between shear stress and shear strain of one element of saturated clay (Fig. 6) were similar. Based on such similarities, the relationships between the relative displacement of a pile and the shear strain in an element test

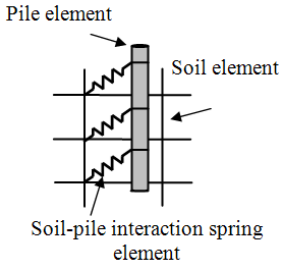

Figure 3. Concept of the soil-pile interaction spring element.

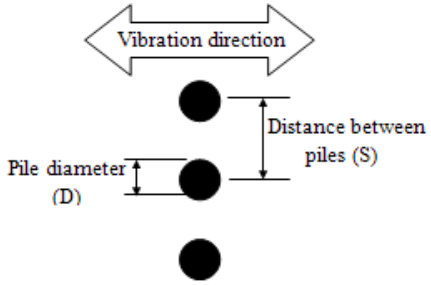

(a) Single row of equally spaced pile group.

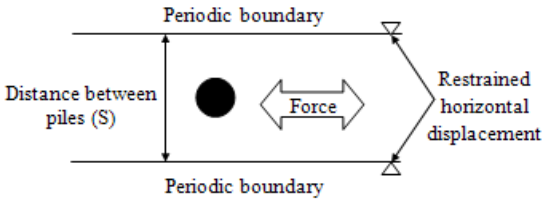

(b) Analysis domain for one pile in the group.

Figure 4. 2-D analysis of the soil-pile system in a horizontal plane

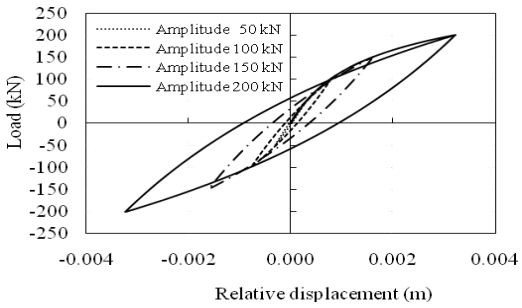

Figure 5. the load-relative displacement relationship under cyclic loading.

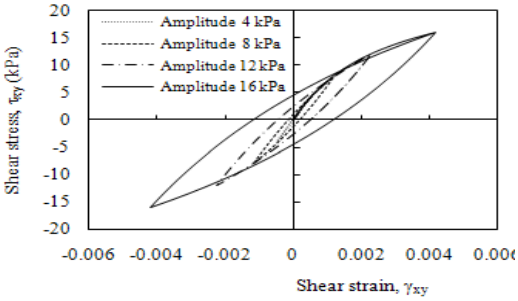

Figure 6. Undrained cyclic shear test simulation of a single soil element.

of the soil can be calibrated (more detail can be found in Ozutsumi, et al (2003)).

3. APPLICABILITY OF THE FINITE ELEMENT MODEL TO THE ANALYSIS OF PILE GROUPS: A REVIEW

Before describing the results of the analyses of single piles and pile groups, a brief review was given to discuss the applicability of the analysis model used in this study to the behavior of pile groups under pure lateral loads. A full scale lateral load test of a 3 x 5 pile group was performed at the Salt Lake City Airport. The idealized soil layers at the test site and model parameters for soil elements used in the analysis are defined in Table 1. Soil properties were obtained from geotechnical investigation data at the site, including standard laboratory tests, unconsolidated-undrained (UU) traixial tests, consolidation tests, and in-situ tests such as cone penetration test, pressure meter test, and standard penetration test.

For the full scale model tests, steel pipe piles were driven closed end to an embedment depth of 11.6 m. The test pile has a 0.324 m outside diameter with a 9.5 mm wall thickness. The piles in the group were driven in a 3 x 5 pattern with a nominal spacing of 3.92 pile diameters center to center in the loading direction and of 3.29 pile diameters perpendicular to the loading direction. The lateral load was applied 495 mm above the ground surface. The piles and the load frame are pin-connected so that the rotation is free at the pile head.

In the FE analysis of the full scale group pile test, lateral load was statically applied at piles heads (0.495 m above the ground surface) until the displacement of 90 mm at the loading point was achieved. Computed and measured average load per pile versus deflection for piles 1 (leading pile), 3 (middle pile), and 5 (trailing pile) are shown in Fig. 7. Both of the measured and the computed results indicate that the load distribution in the pile group is not uniform but is a function of the pile position. The computed results slightly overestimate the load carrying capacity of the leading pile while the computed loads of other piles are in good agreement with the measured ones. The comparison can be considered as good for all practical design purposes. Consequently, the analysis model used for this study has a reasonable applicability to capture the essential behavior of pile group under pure lateral loads. More details on the analyses reviewed above could be found in Hussien et al. [Submitted for possible publication in Canadian Geotechnical Journal].

4. SINGLE PILE RESPONSE UNDER COMBINED LOADS

The soil profile and material parameters described in Section 2 were used for the analysis of single piles. Results of the analysis on free head and capped pile responses under both pure lateral and combined loads are shown in Fig. 8. Figure 8a indicates that a vertical load inducing a vertical

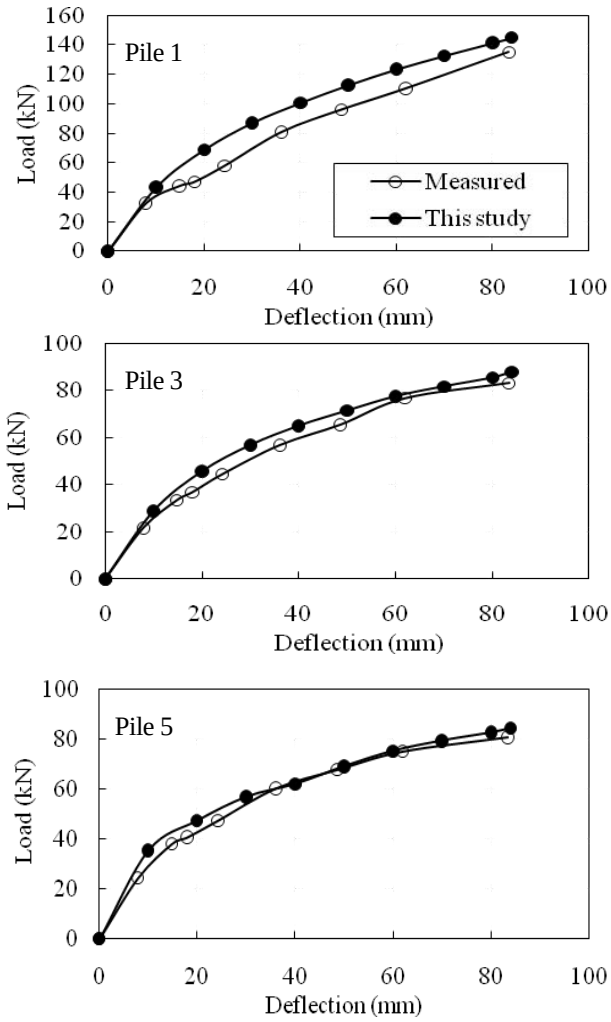

Figure 7. Computed and measured average load per pile versus deflection for piles 1, 3, and 5.

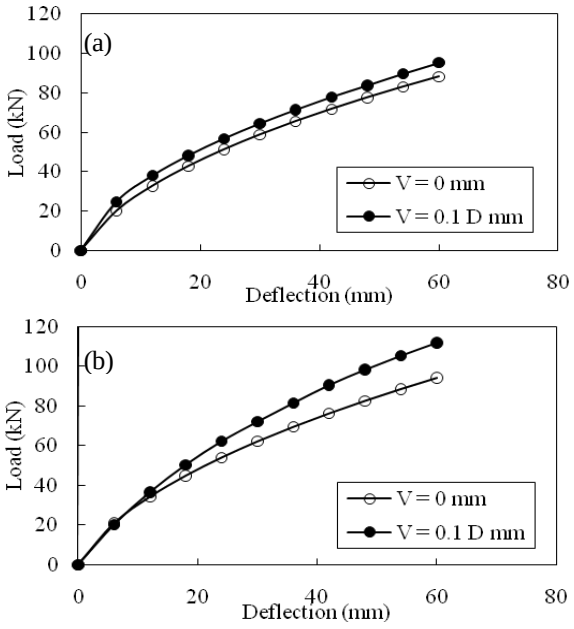

Figure 8. Load-deflection curve of single piles: (a) free head pile, and (b) capped pile.

displacement (V = 0.1D) of the pile head increases the lateral load-carrying capacity of a free head pile by 8 % at a maximum lateral deflection of 60 mm. A similar trend with a higher percentage of 19 % at the maximum lateral deflection was observed in the capped pile case as shown in Fig. 8 b.

An attempt to identify the mechanism of the increase in the lateral resistance of the single pile subject to a vertical load was made by plotting the horizontal soil stress along the upper part of the pile (the upper portion of the subsurface (5 to 10 pile diameter) is of predominant importance in pile-soil interaction due to lateral loading as suggested by Reese and Van Impe (2002)). These horizontal stresses induced before and after the application of the vertical load for both analyses with and without a pile cap as shown in Fig. 9. Figure 9 declares that the inclusion of vertical loads prior to lateral loads increases the horizontal stress of soil elements along the upper part of the pile depth (4 m) for both cases with and without a pile cap but the shape and nature of these increases differ. The horizontal stress profile induced after the application of the vertical load on the free head case is affected only by the relative movement between the pile and the soil (soil-pile interaction), while the corresponding profile of the capped pile case is affected by the movements of both the pile and cap relative to the soil movement (soil-pile and soil-cap interactions). As shown in Fig. 9, the free head stress profile starts at the ground surface (where the stress levels are smaller and the soil response exhibits a higher degree of softening) and propagates downwards as the vertical stress transfer from the pile to the surrounding soil. In contrast the capped pile stress profile starts at the ground surface with a high stress value due to the confinement condition of the soil comes from the downward movement of the cap then the horizontal stress gradually decreases with the depth and approaches the stress profile of the free head case when the effect of soil-cap interaction vanishes. The difference between the confining pressure in capped pile case and the corresponding curve of the free head case may explain the difference in the percentages of lateral load capacity increase in the two cases.

5. BEHAVIOR OF PILE GROUPS UNDER COMBINED LOADS

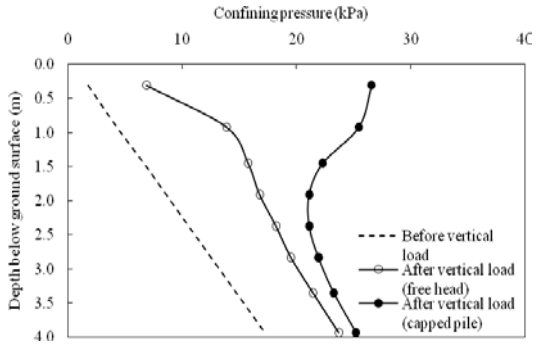

Figure 9. Horizontal soil stresses along the upper part of the pile.

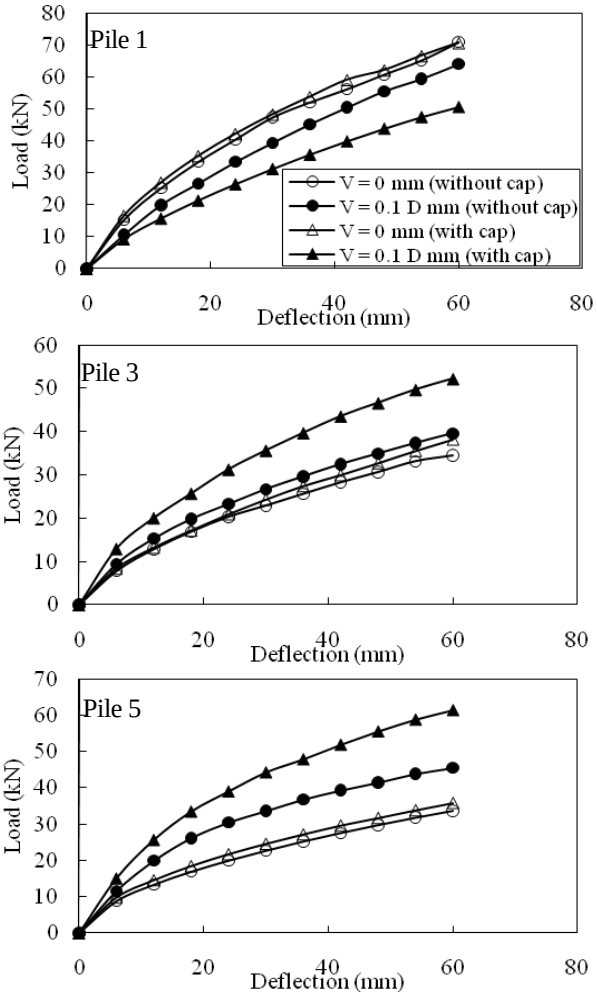

Figure 10. Load-deflection curves for piles 1, 3, and 5.

Loads were statically applied in the same manner as for the single pile. The same model parameters as those for the single pile were used. Figure 10 shows the load versus pile head deflection of piles 1, 3, and 5 in the free head group compared to the corresponding curves in the capped pile group. These curves were computed with and without the presence of vertical loads. As shown in Fig. 10, the effect of vertical loads on the response of each pile in the free head pile group is not the same but is a function of the pile position. In the presence of vertical loads, the lateral load of the leading pile (pile 1) at all deflections is less than the corresponding load developed under pure lateral loads. The percentage reduction reached to a 10% at a 60 mm lateral deflection. For piles 3 and 5, the vertical loads increases the subsequent lateral loads at all deflections. The percentages of increase reached to 14 and 35% for piles 3 and 5, respectively.

The lateral load-carrying capacity of each pile in the group (for pure lateral load) was slightly increased in the presence of the pile cap. The effect of vertical loads on the lateral load carrying capacity of each pile in the capped group is similar to the free head case but with higher percentages of decrease or increase. The percentage of decrease of the lateral load carrying capacity of pile 1 at the

maximum lateral deflection was 28 % while the percentages of increase for piles 3 and 5 were 37 and 71 %, respectively. The inclusion of the pile cap maximizes the effect of vertical loads on the subsequent lateral load response of piles.

In order to discuss the effect of vertical loads on the load distribution among piles in the group for both analyses with and without a pile cap, the ratios of the lateral load of each pile relative to the corresponding load of the single pile at the maximum deflection of 60 mm were plotted in Figure 11. In particular, the free head pile group results are shown in Fig. 11a whereas those of the capped pile group are shown in Fig. 11b. Figure 11a and 11b show, for pure lateral load, that the leading pile carried the greatest load while the other piles including the trailing pile carried loads significantly less than the leading pile. As shown in this Fig. 11a, the presence of vertical loads on free head piles reduces the difference in pile loads especially for the leading piles but keep the shape of the load distribution curve (i.e. the leading pile carried the greatest load while the other piles carried loads less than the leading pile). Fig. 11b shows that the presence of vertical loads on capped group piles reverses the load distribution curve (i.e. the trailing pile carried the greatest load while other piles including the leading pile carried loads less than the trailing pile).

In order to discuss the mechanism of the change in the lateral response of each pile in the group due to vertical loads, the horizontal soil stresses along the first four meters on piles. 1, 3, and 5 in the group are shown in Figures 12a, and 12b for the free head group and capped pile group, respectively. The stresses at the back of and in front of the piles were separately plotted. Figure 12a shows that, for pile 3, the increases in horizontal soil stress along the pile depth due to the presence of vertical loads are the same for both sides of the pile. For pile 1, the increase in the horizontal stress at the back of the pile is larger than that in front of it due to the effect of the interaction of the next row of piles behind the leading pile (pile-pile interaction). For Pile 5, opposite trend with the same magnitude is observed. For middle pile (pile 3), there is no net lateral stress induced by vertical loads. This means that pile 3 behaves approximately the same as the single pile (see Figure 11a). For the leading pile (pile 1), the net horizontal stress due to vertical loads acts in the same direction with the prospective lateral load, leading to a decrease in the pile resistance to the subsequent lateral load. For the trailing pile (pile 5), the net horizontal stress acts against the prospective lateral load, leading to an increase in the pile resistance to the subsequent lateral load.

On the other hand, the horizontal stress profiles induced in the capped pile group case are shown in Fig. 12b. Figure 12b declares a highly uniform increase in the horizontal stresses of soil surrounding the piles after the application of vertical loads. With the application of lateral loads, the horizontal stresses stored in soil elements due to vertical loads in front of the leading pile may release while those stresses stored in the inner soil elements back to this pile will have little change due to the confinement of soil elements by piles and the cap and the difference between soil stresses (the net horizontal stress) due to vertical loads will act in the same direction with the prospective lateral load, leading to a decrease in the pile resistance to the subsequent lateral load. For the trailing pile, the net horizontal stress will act against the prospective lateral load, leading to an increase in the pile resistance to the subsequent lateral load.

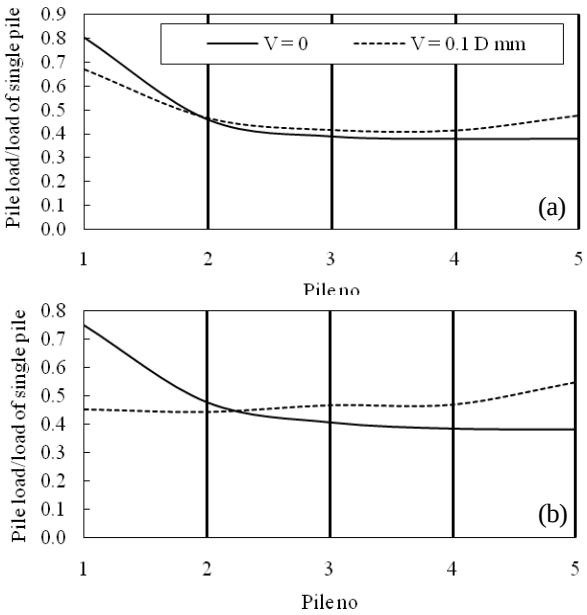

Figure 11. Ratio of lateral load of each pile relative to the load of the corresponding single pile; deflection = 60 mm

6. CONCLUSIONS

The effect of vertical loads on the lateral response of free head and capped pile groups embedded in sandy soil has been studied in this paper through a series of 2-D finite element analyses. The interaction between a pile and the surrounding soil in 3-D type is idealized in the 2-D analysis using soil-pile interaction spring with a hysteretic non-linear load displacement relationship. Of the findings of this study, the following conclusions can be drawn:

(1) The influence of vertical load is to increase the confining pressure in the sand deposit surrounding the pile, leading to an increase in the lateral pile resistance. A vertical load applied to a free head single pile with a vertical displacement of 0.1 pile diameter (D = 324 mm) leads to an 8 % increase in the lateral pile resistance at a 60 mm lateral deflection.

(2) The effect on individual piles in a free head pile group spaced at 3.92 pile diameters depends on the pile position. The vertical load leads to a 10 % decrease in the lateral resistance of the leading pile (pile 1) and 14 and 35 % increases in the lateral resistances of piles 3 and 5, respectively.

(3) The inclusion of the pile cap maximizes the effect of vertical loads on the subsequent lateral load response of piles.

References:

Karthigeyan S, Ramakrishna VVGST. (2005), “Interaction between

vertical and lateral loads on the response of piles in soft clays," *Proceeding of the 16th International Conference on Soil Mechanics and Geotechnical Engineerin*g, Osaka, 1997–2000.
Karthigeyan S, Ramakrishna VVGST, Rajagopal K. (2006), "Influence of vertical load on the lateral response of piles in sand,". *Computers and Geotechnics*, **33**(2): 121–131.
Karthigeyan S, Ramakrishna VVGST, Rajagopal K. (2007), "Numerical investigation of the effect of vertical load on the lateral response of piles," *Journal of Geotechnical and Geoenvironmental Engineering* (ASCE), **133**(5): 512–521.
Iai S, Matsunaga Y, Kameoka T. (1992), "Strain space plasticity model for cyclic mobility," *Soils and Foundations*, **32**(2): 1–15.
Snyder JL. (2004), "Full–scale lateral–load tests of a 3x5 pile group in soft clays and silts," M.Sc. thesis, Brigham Young University, Provo, Utah, United States.
Tobita T, Iai S, Rollins KM. (2006), "Numerical analysis of full–scale lateral–load tests of a 3 × 5 pile group," *Proceeding of the first European Conference on Earthquake Engineering and Seismology*, Geneva, Switzerland.
Zhang L, McVay MC, Lai P. (1999), "Numerical analysis of laterally loaded 3×3 to 7×3 pile groups in sands," *Journal of Geotechnical and Geoenvironmental Engineering* (ASCE) 1999; **125**(11): 936–946.
Iai S, Tobita T, Donahue M, Nakamichi M, Kaneko H. (2006), "Soil–pile interaction in horizontal plane: Seismic Performance and Simulation of Pile Foundations in Liquefied and Laterally Spreading Ground". Geotechnical Special Publication (ASCE), **145**: 38–49.
Ozutsumi O, Tamari Y, Oka Y, Ichii K, Iai S, Umeki Y. (2003), "Modeling of soil–pile interaction subjected to soil liquefaction in plane strain analysis," *Proceeding of the 38th Japan National Conference on Geotechnical Engineering*, Akita, Japan, 1899–1900. (In Japanese).
Reese L.C, Van Impe W.F. (2001), "Single piles and pile groups under lateral loading" A.A. Balkama, Rotterdam, Netherlands.

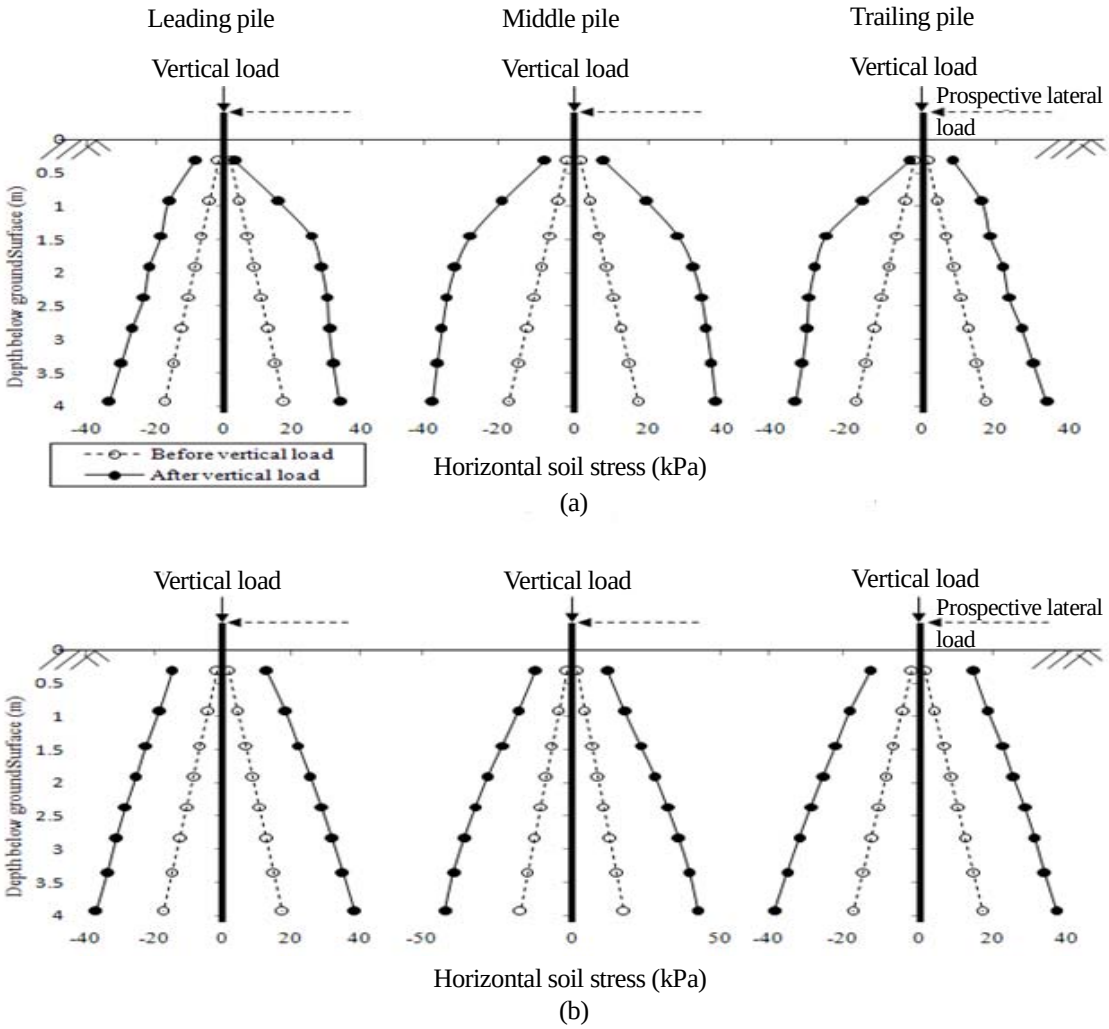

Figure 12. Horizontal soil stresses before and after the application of vertical loads along the upper part of the pile depth just at the back of and in front of piles 1, 3, and 5; free head pile group (a), capped pile group (b).

JOINT CONFERENCE PROCEEDINGS
7th International Conference on Urban Earthquake Engineering (7CUEE) &
5th International Conference on Earthquake Engineering (5ICEE)
March 3-5, 2010, Tokyo Institute of Technology, Tokyo, Japan

EARTHQUAKE DAMAGE ASSESSMENT OF MULTIPLE LIFELINES FOR SYSTEM INTERACTION ANALYSIS

Nobuoto Nojima[1)]

1) Professor, Dept. of Civil Engineering, Gifu University, Japan
nojima@gifu-u.ac.jp

Abstract: Earthquake damages to collocated lifeline facilities cause damage spread as well as conflicts in repair works. In this study, a probabilistic model has been developed to assess coincidence of damage to collocated facilities. First, occurrence rate of coincidence of damage to two different systems is derived assuming uniform rate of damage occurrence. Next, the basic model is extended to deal with non-uniform damage rate depending on spatial distributions of seismic intensities and vulnerability of facilities. Numerical examples are shown for simple representative systems.

1. INTRODUCTION

Lifeline systems collectively support people's daily lives and socioeconomic activities in modern cities. In spite of recent development of earthquake countermeasures, lifeline systems are still prone to suffer damage in an earthquake, resulting in subsequent loss of urban functions that causes significant societal impacts. One of the critical issues in lifeline earthquake disaster is system interactions. Compound, cascade and/or feedback effects among lifeline damage exacerbate the extent and significance of loss of functions and also interrupt the recovery process. Such problems were clearly demonstrated in an unprecedented scale in The Hanshin-Awaji (Kobe) earthquake disaster, 1995, Japan (Nojima and Kameda, 1996). Rinaldi et al. (2001) categorized critical infrastructure interdependencies into physical, cyber, geographic and logical ones. Chang et al. (2009) categorized societal impacts of infrastructure failure interdependencies (IFIs) into economic, environmental, health, safety and social ones.

Among various aspects of lifeline system interactions, this study focuses on problems arising from geographical proximity of underground pipelines. Since large part of pipelines of water delivery, city gas supply and sewer systems are buried under roads or streets, those facilities are collocated (i.e., closely located from each other). When elements of multiple infrastructures are in close spatial proximity, a geographic interdependency occurs (Rinaldi et al., 2001). For example, leak of wager can wash out a road, gas leak can cause gas explosion, resulting in damage to neighboring facilities; leak of wastewater can contaminate water (Edwards, 2008). Conflicts among multiple lifeline service providers in recovery work are also serious concerns associated with pipe damages that coincidently occurred to the collocated facilities. Organizational coordination across those involved providers may be required so as to avoid such conflicts, making recovery plans less effective than unrestricted ones. However, little attention has been paid to quantitative assessment of such situations.

In this view of the problem, a probabilistic model is developed in this study for assessment of coincidence of damage to collocated facilities which may cause system interactions in earthquake disasters. The main idea is simple: combining individual damage assessment for involved systems in a probabilistic manner. The occurrence rate of coincidence of damage to two different systems is derived assuming uniform and non-uniform rate of damage occurrence.

2. OCCURRENCE RATE OF COINCIDENT DAMAGE TO TWO LINEAR SYSTEMS WITH UNIFORM DAMAGE RATES

2.1 Modeling and Formulation

Consider two lifeline systems (System 1 and 2) within a certain region. In reality, these systems are geographically distributed networks. In this section, for simplification, these systems are modeled as one-dimensional linear facilities closely collocated as shown in Figure 1. Assume that occurrence of damages is mutually independent and random over the entire length of L with uniform rate of damage occurrence (= expected number of damage in a unit length) of ν_1 and ν_2, respectively. Occurrence of damage to the two systems

is mutually independent.

In each system, the expected number of damage within a distance of x from an arbitrary location is νx ($\nu=\nu_1$ for System 1, $\nu=\nu_2$ for System 2). The probability distribution of the number, k, of damage to the system follows Poisson distribution with a parameter of νx. The probability mass function is represented by:

$$\mathrm{P}(k)=\frac{(\nu x)^k e^{-\nu x}}{k!} \tag{1}$$

Therefore, the probability of non-occurrence of damage within a distance of x from an arbitrary location is obtained as:

$$\mathrm{P}(0)=e^{-\nu x} \tag{2}$$

The cumulative distribution function $F(x)$ and the probability density function $f(x)$ of the nearest distance, x, to damage from an arbitrary location are represented by

$$F(x)=1-\mathrm{P}(0)=1-e^{-\nu x} \tag{3}$$

$$f(x)=\frac{dF(x)}{dx}=\nu e^{-\nu x} \tag{4}$$

which are known as exponential distributions. The expected value μ_X, standard deviation σ_X and coefficient of variation δ_X are given by:

$$\mu_X=\frac{1}{\nu},\quad \sigma_X=\frac{1}{\nu} \tag{5}$$

$$\delta_X=\frac{\sigma_X}{\mu_X}=1 \tag{6}$$

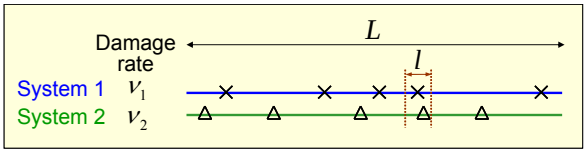

(a) Infinitesimal length of l

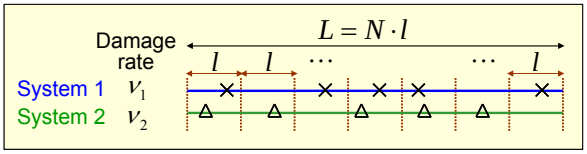

(b) Segment of length of l

Figure 1 Models for coincident damage to two lifeline systems with the entire length L

2.2 Coincidence of Damage within an Infinitesimal Length of *l*

Consider coincident damage (i.e., a situation where damages occur to both System 1 and 2) within an infinitesimal length of l as shown in Figure 1(a). The occurrence rate of coincident damage per unit length is obtained as follows under the condition that $\nu_1 l$ and $\nu_2 l$ are small enough.

$$\begin{cases}\nu_1(1-e^{-\nu_2 l})\approx\nu_1\nu_2 l\\ \nu_2(1-e^{-\nu_1 l})\approx\nu_1\nu_2 l\end{cases} \tag{7}$$

Since the occurrence rate of coincident damage is given by the product of the damage rates of the two systems and the prescribed length l, it can be said that there is a multiplier effect. Especially, in catastrophic disaster, lifeline interactions such as damage spread and recovery interruption may be exacerbated, because both ν_1 and ν_2 take on high value.

From the discussion above, the probability distribution of the number, k, of coincident damage to two systems over the entire length L follows Poisson distribution with parameter $\nu_1\nu_2 lL$. The probability mass function is represented by:

$$\mathrm{P}(k)=\frac{(\nu_1\nu_2 lL)^k e^{-\nu_1\nu_2 lL}}{k!} \tag{8}$$

The expected number of coincident damage and its standard deviation are given by $\mu_k=\nu_1\nu_2 lL$ and $\sigma_k=\sqrt{\nu_1\nu_2 lL}$, respectively.

2.3 Coincidence of Damage within a Segmented Length of *l*

In the previous subsection, the prescribed length l is assumed to be infinitesimal so that $\nu_1 l$ and $\nu_2 l$ are small enough. In actual situations, however, system interactions can be induced even though two damages occur with a certain distance as far as they are closely located. For this reason, segmented systems composed by N segments with length of l ($=L/N$) are considered as shown in Figure 1(b). Assuming that occurrence of damages is random and mutually independent with uniform rates of ν_1 and ν_2 over the entire length, the probability of occurrence of coincident damage to each segment is identically represented by the product of damage probability of System 1 and that of System 2. As shown in Eq. (3), the multiplier effect similar to Eq. (1) is observed herein.

$$p_S=\left(1-e^{-\nu_1 l}\right)\left(1-e^{-\nu_2 l}\right) \tag{9}$$

From the assumption, the sequence of occurrence and non-occurrence of coincident damage in each section constitutes Bernoulli sequence of N trials with the probability represented by Eq. (4). Therefore, the probability distribution of the number, N_S, of segments where coincident damage occurs follows binomial distribution with parameter p_S. The probability mass function is represented by:

$$\mathrm{P}(N_S) = \binom{N}{N_S} {p_S}^{N_S} (1-p_S)^{N-N_S} \qquad (10)$$

The expected number of segments where coincident damage occurs and its standard deviation are given by $\mu_{N_S} = N \cdot p_S$ and $\sigma_{N_S} = \sqrt{N(1-p_S)p_S}$, respectively.

3. OCCURRENCE RATE OF COINCIDENT DAMAGE TO TWO DISTRIBUTED SYSTEMS WITH UNIFORM DAMAGE RATES

3.1 Modeling and Formulation

Consider a geographically distributed network over an infinite area. For simplification, assume that the network facility is uniformly distributed and its extended length per unit area is given by ρ [km/km^2]. Thus, the extended length of network facility within a radius of x from an arbitrary site is $\pi x^2 \rho$ [km]. Assume random occurrence of damage with occurrence rate of ν[damage/km] as shown in Figure 2. Then, the expected number of damage within a radius of x from an arbitrary site is $\pi x^2 \rho \nu$. The probability distribution of the number, k, of damage to the system follows Poisson distribution with a parameter of $\pi x^2 \rho \nu$. The probability mass function is represented by:

$$\mathrm{P}(k) = \frac{(\pi x^2 \rho \nu)^k e^{-\pi x^2 \rho \nu}}{k!} \qquad (11)$$

Therefore, the probability of non-occurrence of damage within a radius of x from an arbitrary site is obtained as:

$$\mathrm{P}(0) = e^{-\pi x^2 \rho \nu} \qquad (12)$$

The cumulative distribution function $F(x)$ and the probability density function $f(x)$ of the nearest distance, x, to damage from an arbitrary site are represented by:

$$F(x) = 1 - \mathrm{P}(0) = 1 - e^{-\pi x^2 \rho \nu} \qquad (13)$$

$$f(x) = \frac{dF(x)}{dx} = 2\pi\rho\nu x e^{-\pi x^2 \rho \nu} \qquad (14)$$

which are known as Rayleigh distributions. The expected value μ_X, standard deviation σ_X and coefficient of variation δ_X are given by:

$$\mu_X = \frac{1}{\sqrt{4\rho\nu}}, \quad \sigma_X = \sqrt{\frac{4-\pi}{4\pi\rho\nu}} \qquad (15)$$

$$\delta_X = \frac{\sigma_X}{\mu_X} = \sqrt{\frac{4}{\pi} - 1} \approx 0.52 \qquad (16)$$

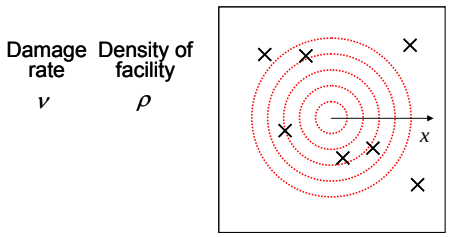

Figure 2 A model for geographically distributed network system

3.2 Coincidence of Damage within an Infinitesimal Radius of *r*

Consider coincident damage (i.e., a situation where damages occur to both System 1 and 2) within an infinitesimal radius of r as shown in Figures 3 and 4(a). The occurrence rate of coincident damage per unit area is obtained as follows under the condition that $\nu_1\rho_1$ and $\nu_2\rho_2$ are small enough.

$$\begin{cases} \nu_1\rho_1(1-e^{-\pi r^2\nu_2\rho_2}) \approx \pi r^2 \nu_1\nu_2\rho_1\rho_2 = \beta\pi r^2 \\ \nu_2\rho_2(1-e^{-\pi r^2\nu_1\rho_1}) \approx \pi r^2 \nu_1\nu_2\rho_1\rho_2 = \beta\pi r^2 \end{cases} \qquad (17)$$

where $\beta = \nu_1\nu_2\rho_1\rho_2$. The probability distribution of the number, k, of coincident damage to two systems over the entire area A follows Poisson distribution with parameter $\beta\pi r^2 A$. The probability mass function is represented by:

$$\mathrm{P}(k) = \frac{(\beta\pi r^2 A)^k e^{-\beta\pi r^2 A}}{k!} \qquad (18)$$

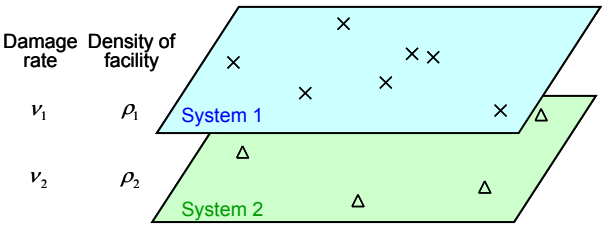

Figure 3 Models for coincident damage to two geographically distributed lifeline systems

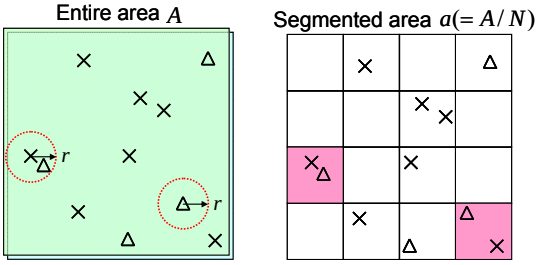

(a) Infinitesimal length of r (b) Segmented area of a

Figure 4 Models for coincident damage to two lifeline systems

The expected number of coincident damage and its standard deviation are given by $\mu_k = \beta\pi r^2 A$ and $\sigma_k = \sqrt{\beta\pi r^2 A}$, respectively.

3.3 Coincidence of Damage within a Segmented area of *a*

Segmented systems composed by *N* segments with length of *a* (=*A*/*N*) are considered as shown in Figure4(b). Following the discussion in the subsection 2.3, the probability of occurrence of coincident damage to each segment is identically represented by:

$$p_S = \left(1 - e^{-\nu_1 \rho_1 a}\right)\left(1 - e^{-\nu_2 \rho_2 a}\right) \tag{19}$$

The probability distribution of the number, N_S, of segments where coincident damage occurs follows binomial distribution with parameter p_S shown in Eq.(19). See Eq.(10) for the probability mass function.

4. NUMERICAL EXAMPLES

4.1 Linear system

Numerical examples of probability distributions derived in Section 2 are shown for two linear systems with the entire length *L*=100 (unit). Table 1 compiles the occurrence rates of damage to System 1 and 2 for four cases (a)-(d) studied herein. Case (a) is the base case with ν_1=ν_2=0.1; the damage rates are one fifth in Case (b) and fivefold in Case (c). Different values of damage rates for System 1 and 2 are assumed in Case (d), keeping their product to be 0.01.

Table 1 Parameters for example systems

Case	ν_1	ν_2	$\nu_1\nu_2 lL$	$\beta\pi r^2 A$
(a)	0.1	0.1	1	π
(b)	0.02	0.02	0.04	0.04π
(c)	0.5	0.5	25	25π
(d)	0.5	0.02	1	π

Figure 5 shows exponential distributions of nearest distance to damage from an arbitrary location represented by Eqs.(4) and (3). Figure 6 compares Poisson distributions represented by Eq.(8) for the number of coincident damage *k*. In this case study, infinitesimal length is set as *l*=1. The expected numbers of coincident damage, $\nu_1\nu_2 lL$, are shown in Table 1. Case (a) resulted in zero to four coincident damages. In Cases (b) and (c), multiplier effects are clearly observed where less/more coincident damages than in Case (a) occur, respectively. Case (d) gives exactly identical result with the base Case (a) because of the same parameters.

Figure 7 compares binomial distributions represented by Eqs.(9) and (10) for the number of segments N_S where coincident damage occurs. The

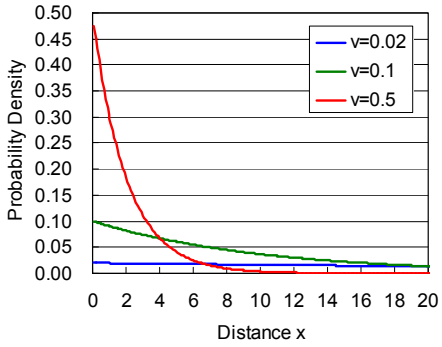

(a) Probability density function

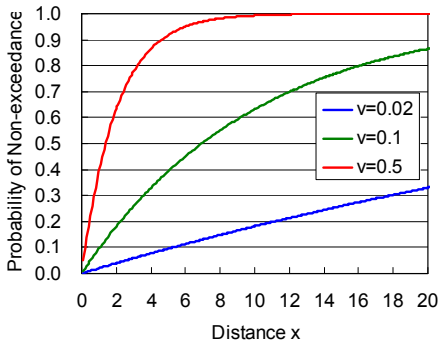

(b) Cumulative distribution function

Figure 5 Exponential distribution of nearest distance to damage from an arbitrary location for linear system

vertical axis represents N_S, and the horizontal axis represents the number of segments *N* (=*L*/*l*) ranging from 1 to 50 (the entire length *L*=100, the segment length *l* (=*L*/*N*) ranging from 100 to 2).

In the base Case (a), almost all the segments suffer coincident damages when the number of segments is small, because the segment length *l* is long enough to be almost certainly damaged. Although N_S increases with increasing *N*, the variance increases as well. As a result, $\mu_{N_S} = 4$ peaks at *N*=8. In Case (b), the probability distribution shifts downward, and $\mu_{N_S} = 0.8$ peaks at *N*=2. In Case (c), on the contrary, the probability distribution shifts upward, and $\mu_{N_S} = 20$ peaks at *N*=40. The probability distribution shifts downward also in Case (d), and $\mu_{N_S} = 1.8$ peaks at *N*=12. In binomial distributions, unlike in Poisson distributions which are dependent on the product of the two damage rates, results of Cases (a) and (d) are not identical; the difference of two damage rates also affects the chance of coincident damage. However, binomial distributions asymptotically approach to Poisson distributions with large *N* (=short *l*), and μ_{N_S} approaches μ_k.

$$\mu_{N_S} \approx N \cdot \nu_1 l \cdot \nu_2 l = \nu_1 \nu_2 lL = \mu_k \tag{20}$$

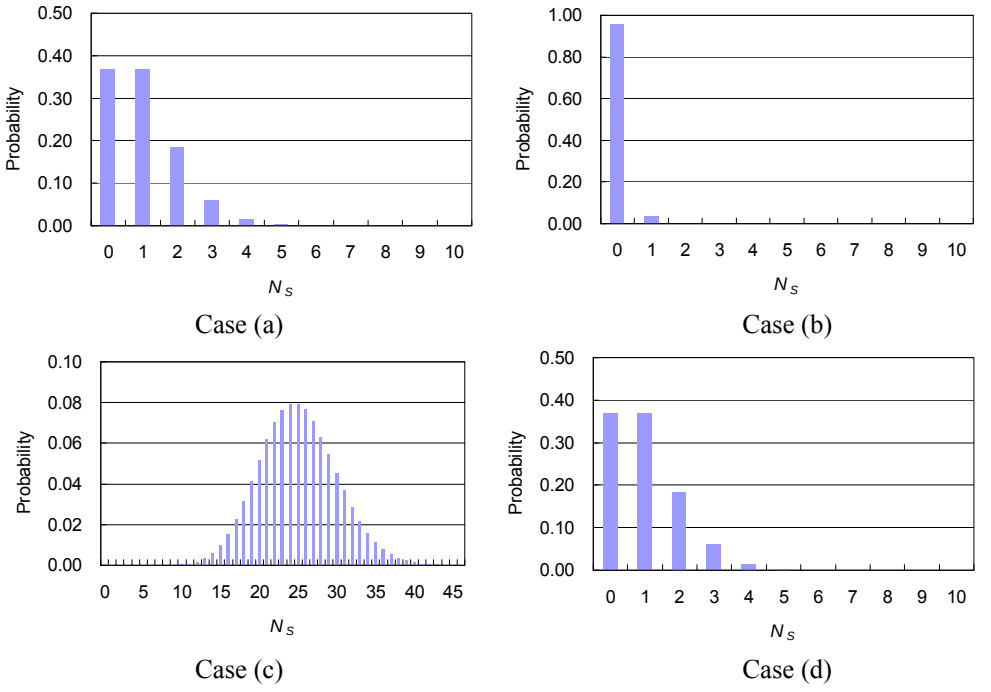

Figure 6 Poisson distributions for the number of coincident damage (Values sum up to unity.)

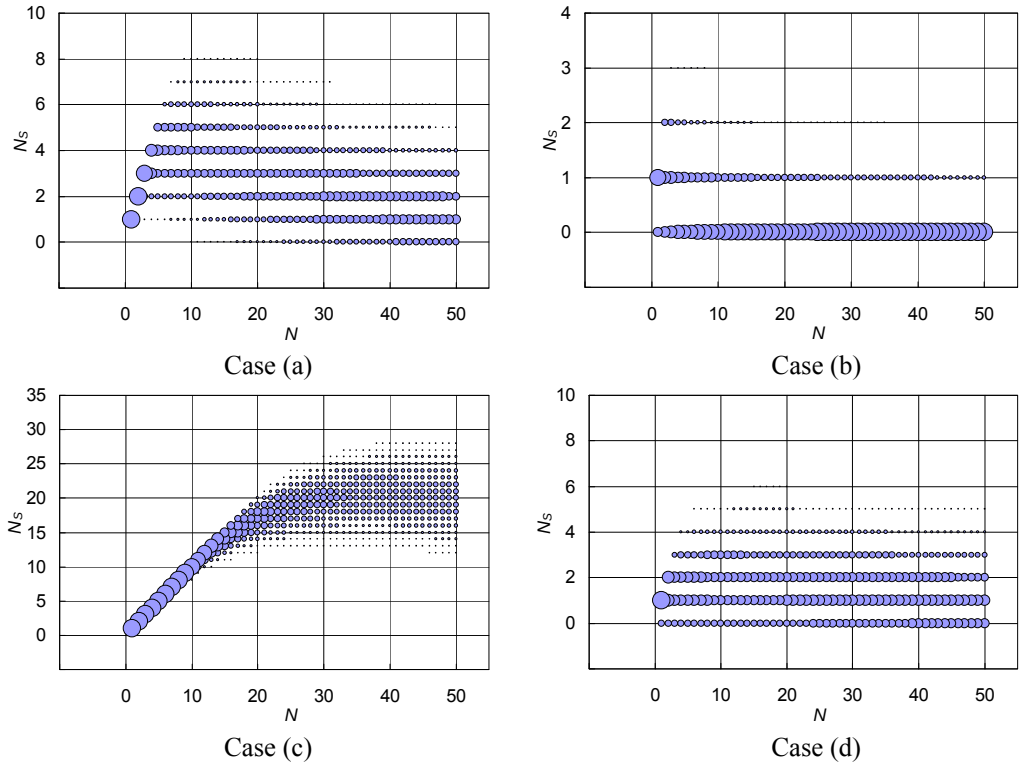

Figure 7 Binomial distributions for the number of segments where coincident damage occurs (Circle symbols represent the values of probability mass whose summation in the vertical direction sum up to unity.)

4.2 Distributed system

Numerical examples of probability distributions derived in Section 3 are shown for two distributed systems with the entire area A=100 km^2. The same pairs of occurrence rates for four cases shown in Table 1 are used. The extended lengths per unit area are set as ρ_1= ρ_2=1 [km/km^2].

Figure 8 shows Rayleigh distributions of nearest distance to damage from an arbitrary location represented by Eqs.(14) and (13). Figure 9 compares Poisson distributions represented by Eq.(18) for the number of coincident damage k. In this case study, infinitesimal radius is set as r=1. The expected numbers of coincident damage, $\beta\pi r^2 A$, shown in Table 1 indicate the values are π–fold of those for linear systems.

Binomial distributions represented by Eqs.(19) and (10) for the number of segments N_S are mathematically in the same form as those for linear systems. Therefore, given that $\rho_1 a = \rho_2 a = l$, exactly same results are obtained as Figure 7.

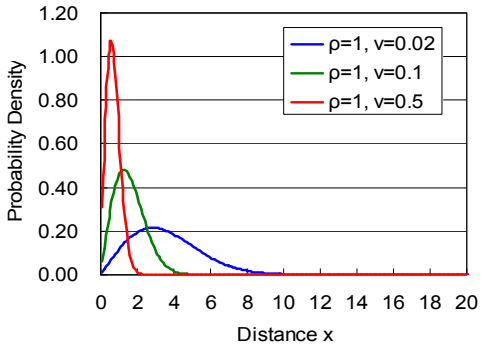

(a) Probability density function

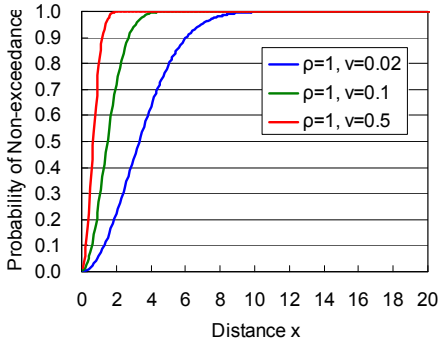

(b) Cumulative distribution function

Figure 8 Rayleigh distribution of nearest distance to damage from an arbitrary location for distributed system

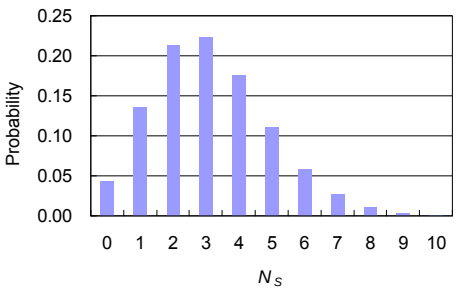

Case (a)

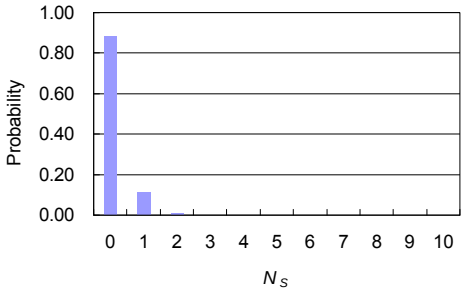

Case (b)

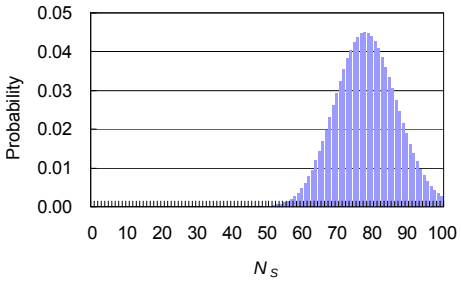

Case (c)

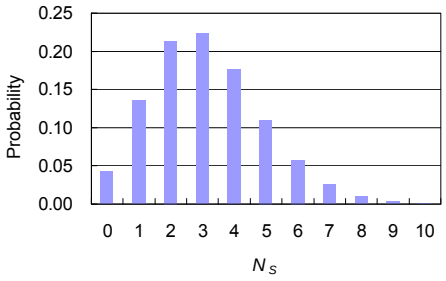

Case (d)

Figure 9 Poisson distributions for the number of coincident damage (Values sum up to unity.)

5. OCCURRENCE RATE OF COINCIDENT DAMAGE TO TWO LINEAR SYSTEMS WITH NON-UNIFORM DAMAGE RATES

In previous sections, damage rates are assumed to be uniform over the entire system. However, in reality, damage rates of lifelines vary location to location across the service area covered by the extended networks according to spatial distributions of seismic intensity, soil (or ground) condition and seismic vulnerability of facilities. Let $I(x)$, $S(x)$ and $V(x)$ denote the three main factors (*I*ntensity, *S*oil and *V*ulnerability) to the non-uniform damage rates, respectively, as functions of location x. Widely-used formula for estimation of the number of damage to pipelines are in the form of the following expression.

$$\begin{cases} \nu_1(x) = R_1(I(x), S(x)) \cdot V_1(x) \\ \nu_2(x) = R_2(I(x), S(x)) \cdot V_2(x) \end{cases} \tag{21}$$

where $R(\ )$ represents standard damage rate function for specified pipe material and pipe diameter, and subscripts 1 and 2 corresponds to System 1 and 2, respectively. The two systems have their own characteristic damage standard damage rate function $R(\ )$ and vulnerability factor $V(x)$. On the other hand, seismic intensity $I(x)$ and soil condition $S(x)$ are common to the two systems, because they are closely located and little difference is expected between them in terms of $I(x)$ and $S(x)$. Therefore, two damage rates $\nu_1(x)$ and $\nu_2(x)$ are spatially correlated due to the common factors. At a particular site x with strong ground motion and/or bad ground condition, both $\nu_1(x)$ and $\nu_2(x)$ take on high values, so both systems tend to suffer damage.

Now let $E_1(x)$ and $E_2(x)$ represent the events of damage occurrence to System 1 and 2 at the site x. Even though there exists spatial correlation in damage distribution of the two systems, it can be assumed that the two events, $E_1(x)$ and $E_2(x)$, are statistically independent. Since the correlation between $\nu_1(x)$ and $\nu_2(x)$ does not stem from causal relationships but from the common factors mentioned above, damage occurrence in one system does not influence that in the other system. In probabilistic terms, $P(E_1|E_2) = P(E_1)$ and $P(E_2|E_1) = P(E_2)$ hold at arbitrary site, which means statistical independence between the two events. Therefore, $P(E_1E_2) = P(E_1|E_2)P(E_2) = P(E_2|E_1)P(E_1) = P(E_1)P(E_2)$ holds from location to location.

Based on the discussion above, the results derived in the previous chapter can be extended for dealing with the general case with non-uniform damage rates. As shown in Figure 10, spatially distributed occurrence rate of coincident damage can be defined as $\nu_1(x)\nu_2(x)l$, which is a general form of Eq. (1). By piecewise application of non-stationary Poisson process, the number of coincident damage can be evaluated using Eq. (8). When dealing with segmented systems, the probability of coincident damage at a site x is obtained by Eq. (22).

$$p_S(x) = \left\{1 - e^{-\nu_1(x)l}\right\}\left\{1 - e^{-\nu_2(x)l}\right\} \tag{22}$$

The spatial contrast in distribution of coincident damages should become more apparent, potentially bringing about significant local system interactions especially in a catastrophic disaster.

Obviously, similar extension can be done for geographically distributed systems as shown in Eq.(23).

$$p_S(x) = \left\{1 - e^{-\nu_1(x)\rho_1(x)a}\right\}\left\{1 - e^{-\nu_2(x)\rho_2(x)a}\right\} \tag{23}$$

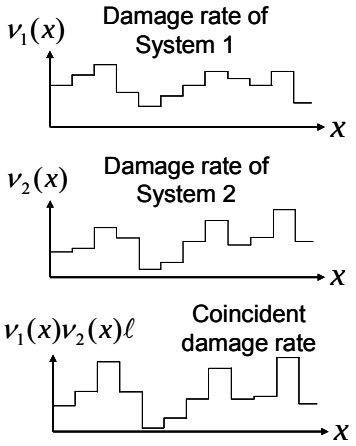

Figure 10 Spatially varying damage rates of two systems and their coincident damage rate

6. CONCLUSIONS

A probabilistic model has been proposed for assessment of coincidence of earthquake damage to collocated lifelines. For the fundamental case with assumptions of uniform damage rate, the occurrence rate is represented by the product of the damage rates of the two systems concerned and the infinitesimal length within which coincident damage occurs.

For practical applications, the fundamental model has been extended for non-uniform damage rate and arbitrary segment length defining coincident damage. Even though there exists spatial correlation between the damage rates of the two systems, the proposed model is applicable by piecewise applying non-stationary Poisson process.

Acknowledgements:

This study was supported by the Grant-in-Aid for "Special Project for Disaster Prevention and Mitigation of Tokyo Metropolitan Regions" by Ministry of Education, Culture, Sports, Science and Technology, Japan.

References:

Chang, S.E., McDaniels T. and Beaubien C.(2009), "Infrastructure failure interdependencies: Societal Impacts of Infrastructure Failure Interdependencies: Building an Empirical Knowledge Base," *Proc. of the 2009 ASCE Technical Council on Lifeline Earthquake Engineering (TCLEE)*, *Lifeline Earthquake Engineering in a Multihazard Environment*, ASCE, 693-702.

Edwards, C.L. (2008), "Infrastructure interactions – Response and recovery time," *Proc. of the 14th World Conference on Earthquake Engineering*, Beijing, China, Paper No.S30-010. (on CD-ROM)

MLIT (Ministry of Land, Infrastructure, Transport and Tourism), Sewerage and Wastewater Management Department, City and Regional Development Bureau (2005), "On seismic damage assessment method for sewer pipelines, Committee Material." (in Japanese)

Nojima, N. and Kameda, H. (1996), "Lifeline interactions in the Hanshin-Awaji Earthquake Disaster," *The 1995 Hyogoken-Nanbu Earthquake Investigation into Damage to Civil Engineering Structures*, Committee of Earthquake Engineering, JSCE, 253-264.

Rinaldi, S. M., Peerenboom, J.P., and Kelly, T.K. (2001), "Identifying, understanding, and analyzing critical infrastructure interdependencies," *IEEE Control Systems Magazine*, December, 11–25.

JOINT CONFERENCE PROCEEDINGS
7th International Conference on Urban Earthquake Engineering (7CUEE) &
5th International Conference on Earthquake Engineering (5ICEE)
March 3-5, 2010, Tokyo Institute of Technology, Tokyo, Japan

EARTHQUAKE DISASTER RESTORATION SUPPORT TECHNOLOGIES FOR ELECTRIC POWER DISTRIBUTION EQUIPMENT

Yoshihharu Shumuta[1)]

1) *Senior Research Engineer, Central Research Institute of Electric Power Industry, Japan*
shumuta@criepi.denken.or.jp

Abstract: This paper reviews recent studies related to disaster restoration support technologies for electric power distribution equipment. In general, since electric power distribution equipment has been installed in many electric power supply areas, it is difficult to completely avoid the damage due to a large scale earthquake. Therefore, the restoration countermeasures against an earthquake are a very important issue for the Power Company. In this paper, a sequential damage estimation system of electric power distribution equipment is proposed. The proposed system enables us to estimate the damage on the basis of the seismic intensity, power outage and inspection information just after an earthquake occurs.

1. INTRODUCTION

When a large scale earthquake occurs, a lot of components of an electric power distribution system are simultaneously damaged. However, if an electric power distribution system is seismically damaged, it usually takes a long time to collect accurate damage detection information because it consists of a huge number of components and is installed in many electric power supply regions. It is also difficult to estimate the damage because the equipment is installed on various uncertain local conditions. Therefore, in order to realize its effective and quick functional recovery against an earthquake, it is important to develop the technologies associated with its damage detection, collection and estimation.

This paper reviews recent studies related to disaster restoration support technologies for electric power distribution equipment. The typical and dominant seismic damage modes for electric power distribution equipment are illustrated in order to discuss the difficulties in the damage estimation. On the basis of this discussion, a sequential updated damage estimation system is proposed to overcome these difficulties. The proposed system mainly focuses on the damage estimation issues for electric power distribution equipment. As numerical examples, the proposed system is applied to a hypothetical electric power distribution system to clarify its effectiveness.

2. TYPICAL SEISMIC DAMAGE MODE OF ELECTRIC POWER DISTRIBUTION EQUIPMENT

Fig.1 shows the typical seismic damage modes of electric power distribution equipment. The inclination of transformers, inclination of poles, snapping of wires and landslides are the typical damages caused by an earthquake. Moreover, if the equipment is installed on poor ground conditions including soft ground and steep slopes, the damages are often caused by liquefaction or landslides.

Fig.2 shows the causes of damage due to the 1995 Hyogo-Ken Nanbu Earthquake as reported by the Agency for Natural Resources and Energy (1996). About 80 percent of the total number of distribution pole damage was caused by building collapses on the JMA Seismic Intensity Scale of 7. Similarly, the breaking of distribution lines due to the 2004 Niigata-Ken Chuetsu earthquake were often caused by indirect factors such as tree and residential home collapses reported by the Niigata-Ken Chuetsu Earthquake Investigation Committee (2004). These facts indicate that the seismic damage of the distribution poles is caused by not only a direct seismic force, but also indirect factors such as surrounding building seismic damage. These characteristics suggest that in order to accurately estimate the damage degree of electric power distribution equipment, it is necessary to consider not only the earthquake intensity, ground hazard conditions, and the dynamic characteristics of the equipment, but also the dynamic characteristics of the surrounding facilities including trees, residential homes, commercial buildings and other infrastructures. However, it is usually difficult to collect the multiple and precise dynamic characteristics for surrounding facilities existing in the many electric power supply regions. As a result, since it is difficult to realize a highly accurate seismic damage estimation before the occurrence of an earthquake within limited data conditions, new damage estimation concepts

and technologies are needed.



Inclination of transformer



Inclination of pole



Snapping of wires



Landslide

Figure 1 Typical damage modes of electric power distribution equipment

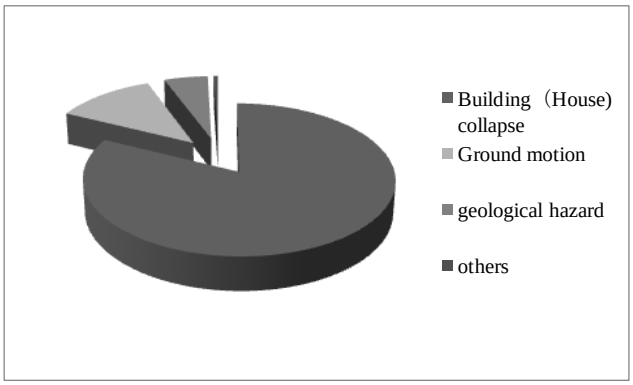

Figure 2 Causes of the damage to electric power distribution poles during the 1995 Hyogo-Ken Nanbu Earthquake (Agency for Natural Resources and Energy, 1996)

3. SEISMIC DAMAGE ESTIMATION SYSTEM FOR ELECTRIC POWER DISTRIBUTION EQUIPMENT

CRIEPI has started a new project associated with damage estimation for electric power distribution equipment by considering the correlation the damage between the equipment and surrounding facilities during a seismic event.

Fig.3 shows the concept of a sequential updated damage estimation system called RAMP-Er (Shumuta and Ishikawa, 2008). RAMP-Er stands for "***R**isk **A**ssessment and **M**anagement system for **P**ower Lifeline-**E**arthquake **r**eal time*". The updated information indicates the earthquake intensity information, electric power system online and offline information including power outage and damage inspection information. The updated disaster information is integrated using a Bayesian network (Russell,S. and Norvig,p.,1995) to improve the estimation accuracy. RAMP-Er focuses on the equipment damage estimation from the time just after the occurrence of an earthquake to the completion of the emergent restoration. On the basis of a precise database associated with equipment dynamic characteristics, local conditions and collected offline disaster information, the damage estimation is sequentially updated.

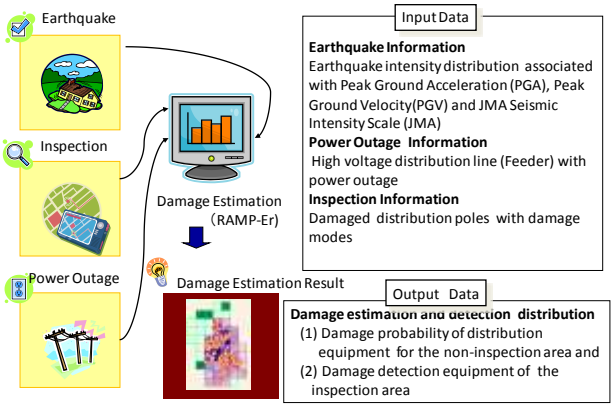

Figure 3 Concept of the proposed sequential updated damage estimation system (RAMP-Er)

Fig.4 shows a flow chart of the sequential damage estimation process of RAMP-Er. RAMP-Er consists of five steps.

STEP1 is a damage estimation process just after an earthquake occurs. When an earthquake occurs, RAMP-Er tries to collect the earthquake and power outage information. The earthquake information includes the distribution (1km×1km) of the Peak Ground Acceleration (PGA), Peak Ground Velocity (PGV) and Japan Meteorological Agency Seismic Intensity Scale (JMASIS) and Response Spectrum (SE). RAMP-Er receives the earthquake information from a sequential updated Seismic Intensity Evaluation System (SEIS) that we developed as an associated system for RAMP-Er.. SEIS is supposed to automatically receive earthquake early warning information associated with the epicenter and the magnitude from the Japan Metrological Agency whenever an earthquake occurs. On the basis of the received earthquake early warning information, SEIS evaluates the seismic intensity distribution within several minutes just after the earthquake occurs. SEIS also evaluates the updated seismic intensity distribution using actual seismic ground motion records distributed by F-net (NIED,2008) and K-net (NIED,2008) to improve the evaluation accuracy.

On the other hand, the power outage information is collected for every high voltage distribution line (feeder) with a power outage obtained from an online monitoring system operated by a power company. RAMP-Er uses this

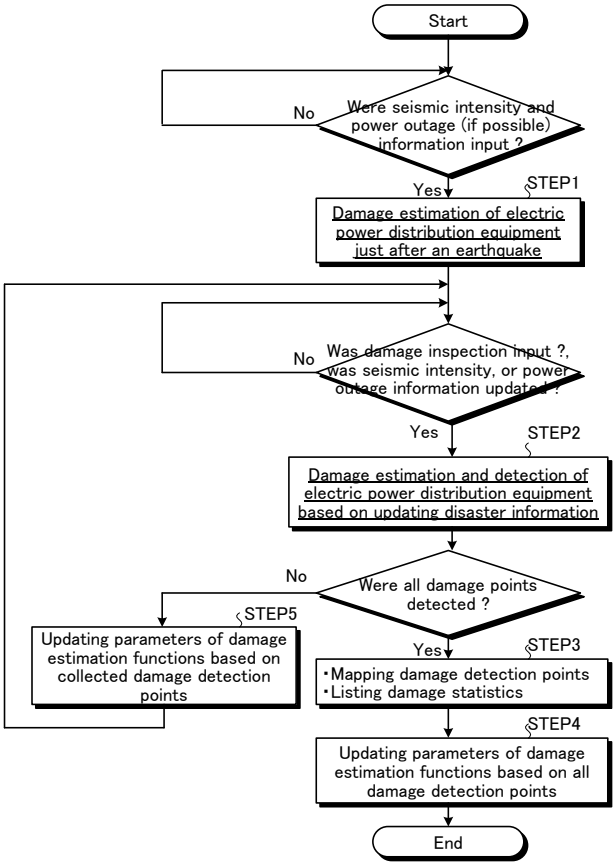

Figure 4 Flowchart of the proposed sequential updated damage estimation in RAMP-Er

power outage information to improve the accuracy of the damage estimation using the Bayesian Network modeling process.

Fig.5 shows the conceptual damage estimation process based on the Bayesian Network just after the earthquake occurrence. In RAMP-Er, the distribution of the seismic intensity is first collected for every third mesh (1km×1km) as shown in Fig.5(A). Secondly, the power outage information for every high voltage distribution line (Feeder) is also collected and converted into every third mesh to clarify the power outage area as shown in Fig.5 (B). On the basis of the seismic intensity and power outage information, the damage ratio of every electric power distribution equipment is estimated using the Bayesian Network model. The Bayesian Network is a probabilistic graphical model that represents a set of variables and their probabilistic independencies. It could represent the probabilistic relationships between the equipment damage and its causes. The damage ratio is converted into the expected damage ratio for every third mesh as shown in Fig.5(C). The details of the Bayesian network modeling process are referred to (Shumuta and Ishikawa, 2008).

STEP2 is an updated process of the damage estimation based on inspection information. The inspection information is collected by a power company using mobile phones and PDAs as offline information. When the damage detection information is collected by the inspection, the

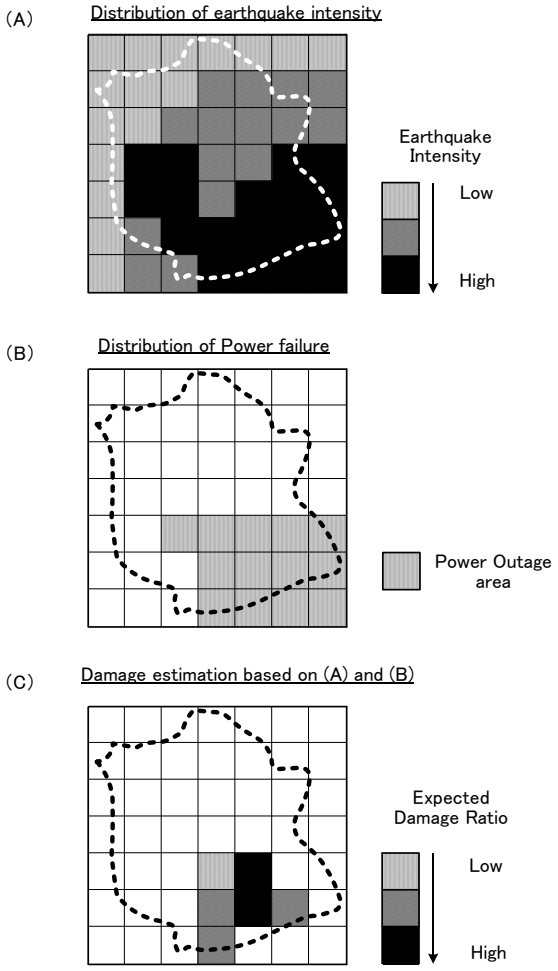

Figure 5 Damage estimation process in RAMP-Er just after the earthquake occurrence

damage estimation for the non-inspected area is executed and updated. The damage estimation result is replaced by the damage detection information one by one as the affected area are inspected.

STEP3 is a process to integrate and report all damage detection information. Using the required reporting format, the damage detection statistics are displayed and electrically stored.

STEP4 is a parameter improvement process of the damage estimation functions based on all the collected damage records. STEP 4 is an offline process during a typical maintenance process of RAMP-Er.

STEP5 is also a parameter improvement process of the damage estimation functions based on the collectable damage record during an emergency restoration period. It sometimes takes a long time for emergency restoration because of unscheduled events such as blocked roads. In this case, the parameters of the damage estimation functions are improved to more accurately estimate the damage of uninspected regions during the emergency restoration. RAMP-Er applies a Bayesian Network modeling process to improve the accuracy of the damage estimation based on not only the seismic intensity, but also the power outage and

damage inspection information. Therefore, compared with existing damage estimation systems, RAMP-Er enables us to more accurately estimate the damage on the basis of the above sequential updated multiple disaster information.

4. BASIC FUNCTION OF THE SEISMIC DAMAGE ESTIMATION OF ELECTRIC POWER DISTRIBUTION EQUIPMENT

Eq.(1) is a basic function of the seismic damage ratio of the electric power distribution equipment ($F_{mijklc}(z(a))$).

$$F_{mijklc}(z(a)) = L_m \cdot C_i \cdot B_j \cdot T_k \cdot S_l \cdot f_c(z(a)) \quad (1)$$

where, $f_c(z(a))$ is the seismic damage ratio of equipment with seismic countermeasures C and seismic performance $z(a)$ assuming that the seismic intensity a affects the surface ground supporting the target equipment. The seismic countermeasure C indicates with or without pole anchor installation and transformer bracket type (Unit bracket, Wood and steel bracket, or Hanger bracket). For example, Fig.6 shows the transformer damage ratio caused by the 2007 Niigata-Ken Chuetsu-Oki Earthquake. The transformer damage ratios with and without pole anchors are compared for every measured seismic intensity (JMA). Fig.6 suggests that the pole anchor effectively mitigates the seismic damage of a transformer. RAMP-Er enables us to estimate the damage ratio of four equipment components including the distribution pole, electric wire, transformer and switch using an equipment database related to the detailed dynamic characteristics of the seismic countermeasures.

The seismic performance $z(a)$ indicates the seismic safety margin evaluated by the bending moment of the ground surface of electric power distribution poles caused by the seismic intensity a defined by (Shumuta and Ishikawa, 2008).

S_l is the correction coefficient evaluated by the line connected type l. Fig.7 shows the line connectivity types of electric power distribution poles. It includes an edge pole, line pole, cross pole and T junction pole. T_k is the correction coefficient of the land use condition k, B_j is the correction coefficient of the micro-topography division j, C_i is the correction coefficient of the seismic countermeasure of equipment I, L_m is the correction coefficient of local region m. RAMP-Er produces a database associated with the surface ground condition of each distribution pole defined by the micro-topography division, the land use condition correlated with the seismic damage of surrounding facilities, and the line connectivity type. On the basis of this database, the correction coefficients are evaluated in order to improve the seismic damage estimation of the electric power distribution equipment.

Whenever the seismic intensity distribution is updated, RAMP-Er estimates the damage ratio of the equipment based on *Eq.*(1). The Bayesian Network is then applied to improve the seismic damage ratio evaluated by *Eq.*(1) based on the power outage and inspection information as follows.

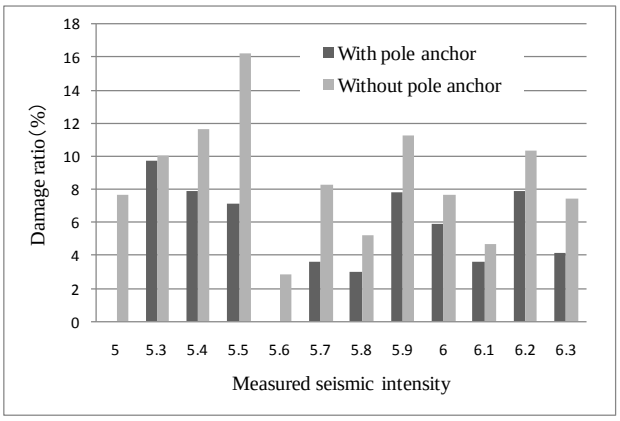

Figure 6 Relationship between the damage ratios of transformers with and without pole anchors for every measured seismic intensity

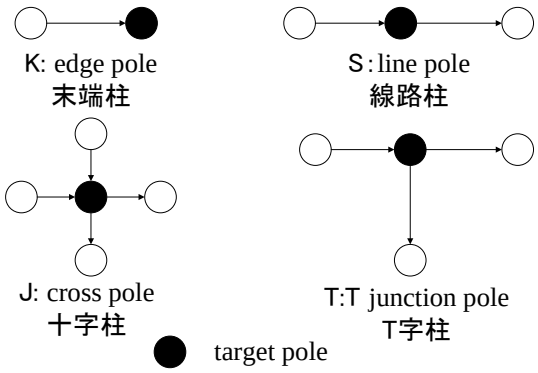

Figure 7 Line connectivity types of electric power distribution poles

5. DAMGE ESTIMATION BASED ON A BAYESIAN NETWORK

Fig.8 illustrates a Bayesian network and its conditional probability tables (CPT) used to update the seismic damage estimation of electric power distribution equipment. The Bayesian network is applied to the RAMP-Er as a disaster information integration model. Fig.6 describes the relationships among the Earthquake Ground Motion ($EGM(a)$) as a parent node, the Electric Power Distribution Equipment damage ($EPDE$), and power outage (PO).

$EGM(a) = 1$ indicates the occurrence of the earthquake intensity a. On the other hand, $EGM(a)=0$ indicates that no earthquake intensity a occurs. P_α ($EPDE=1/EGM(a)=1$) in CPT (A), which represents the conditional probability of $EPDE$ assuming that an earthquake has occurred, which is estimated by Eq.(1) as $F_\alpha(z(a))$. $F_\alpha(z(a))$ indicates the damage ratio of equipment α due to the seismic intensity a. a represents equipment condition $mijklc$ defined by *Eq.*(1). When an earthquake occurs, $EGM(a)$ is given by a sequential updated Seismic Intensity Evaluation System (SEIS) mentioned in Chapter 3. On the other hand, P_α ($EPDE=0$), which indicates the non-damage probability, becomes 1- $F_\alpha(z(a))$. If no

earthquake occurs, $P_\alpha(EPDE=1)$ becomes 0 and $P_\alpha(EPDE=0)$ becomes 1 as shown in CPT (A).

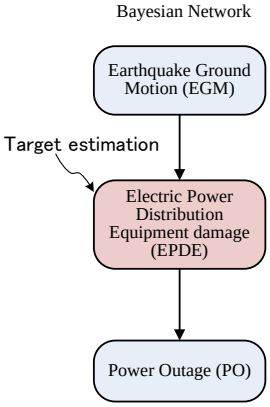

CPT (A)

	$P_\alpha(EPDE/EGM(a))$	
$EGM(a)$	$EPDE$=0: no damage	$EPDE$=1: damage
0:False	1	0
1:True	1-$F_\alpha(Z(a))$	$F_\alpha(Z(a))$

CPT (B)

	$Pa(EPDE/EGM(a))$	
$EPDE$	PO=0: no power outage	PO=1: power outage
0	$\prod_{i=1}^{N-1}(1-F_i(z(a)))$	$1-\prod_{i=1}^{N-1}(1-F_i(z(a)))$
1	0	1

Figure 8 A Bayesian network representing the dependencies among earthquake disaster events

When an earthquake occurs, $P_\alpha(EGM(a))$ is given as Table 1.

Table 1 $P_\alpha(EGM(a))$

$P_\alpha(EGM(a))$	
$EGM(a)=0$	$EGM(a)=1$
0	1

When equipment α is damaged, $P_\alpha(PF=0/EPDE=1)$ in CPT (B), which indicates the conditional non-power outage probability, is assumed to be 0. $P_\alpha(PF=1/EPDE=1)$, which indicates the conditional power outage probability, is also assumed to be 1.

Table 2 Combination of the joint probability distributions

Combination No	$EGM(s)$	$EPDM$	PO	$P_\alpha(PO/EPDE)P_\alpha(EPDE/EGM(s))P_\alpha(EGM(s))$
[1]	0	0	0	0
[2]	0	0	1	0
[3]	0	1	0	0
[4]	0	1	1	0
[5]	1	0	0	$1\cdot(1-F_\alpha(z(s)))\cdot\prod_{\alpha=1}^{C-1}(1-F_\alpha(z(s)))$
[6]	1	0	1	$1\cdot(1-F_\alpha(z(a)))\cdot\left\{1-\prod_{\alpha=1}^{C-1}(1-F_\alpha(z(a)))\right\}$
[7]	1	1	0	0
[8]	1	1	1	$1\cdot F_\alpha(z(a))\cdot 1$

On the other hand, when equipment α is not damaged, the conditional power outage probability $P_\alpha(PF=0/EPDE=0)$ and non-power outage probability $P_\alpha(PF=1/EPDE=0)$ are respectively estimated as

$$P_\alpha(PO=0/EPDE=0)=\prod_{i=1}^{N-1}(1-F_i(z(a))) \quad (2)$$

$$P_\alpha(PF=1/EPDE=0)=1-\prod_{i=1}^{N-1}(1-F_i(z(a))) \quad (3)$$

where N indicates the total number of equipment connected to the same distribution line (same feeder). *Eq.*(2) and *Eq.*(3) assume that if any equipment is damaged, a power outage occurs to all equipment connected to the same distribution line of the damaged equipment.

The combination of all joint probability distributions of the Bayesian network in Fig.6 is shown in Table 2.

For example, based on the marginalization shown in Eq. (1) and Table 2, when the observed information ($EGM(a)=1$) is given, the conditional damage probability of equipment α becomes

$$P_\alpha(EPDE=1/EGM(a)=1)=\frac{[7]+[8]}{[5]+[6]+[7]+[8]}=F_\alpha(z(a)) \quad (4)$$

Furthermore, when the observed information ($PF=1$; power outage occurs to equipment α) is given, the conditional damage probability of equipment α becomes

$$P_\alpha(EPDE=1/PF=1,EGM(a)=1)=\frac{[8]}{[6]+[8]}=\frac{F_\alpha(z(a))}{(1-F_\alpha(z(a)))(1-\prod_{i=1}^{N-1}(1-F_i(z(a))))+F_\alpha(z(a))} \quad (5)$$

Comparing Eq.(4) with Eq.(5), it is understood that the power outage information can significantly contribute to the improvement of the damage probability of equipment α.

6. NUMERICAL EXAMPLES

In order to demonstrate the effectiveness of RAMP-Er, a numerical example was performed on the basis of a hypothetical electric power distribution system. The following numerical example is based on Shumuta(2009). The hypothetical system is assumed to have the following conditions

(1) Hypothetical electric power distribution system

Total number of distribution poles: 27,000

Total number of high voltage distribution lines (feeders): 84

(2) Observed Earthquake Ground motion ($EGM(a)$)

$EGM(a)$ is evaluated on the basis of the epicenter and earthquake magnitude.

The earthquake magnitude is assumed as M8.0

(3)Conditional damage probability of equipment α ($P_\alpha(PEDE=1/EGM(a)=1)$)

Table 3 shows the assumed conditional damage probability of equipment i by considering seismic intensity a and liquefaction risk g evaluated by the micro-topography division. The other local conditions defined by *Eq.*(1) are assumed to be 1.0.

(4) Assumed seismic damaged poles

Fig. 9 shows the assumed damaged poles and damage ratio for every third mesh. The damage points were generated by one trial of a Monte Carlo simulation based on

Table 3. In order to clarify the estimation accuracy, the damage points and damage ratio in Fig.9 are assumed as the observed equipment damage due to the earthquake scenario.

Table 3 Damage probability of equipment

g : Ground Condition Liquefaction risk	*a* : Peak Ground Acceleration			
	lower that 200	200gal-250gal	251gal-400gal	401ga-
Large	1.1×10^{-6}	8.8×10^{-5}	2.9×10^{-3}	8.6×10^{-3}
Medium	0.0	6.5×10^{-5}	2.0×10^{-3}	5.9×10^{-3}
No Liquefaction	0.0	1.7×10^{-4}	5.2×10^{-3}	1.5×10^{-2}

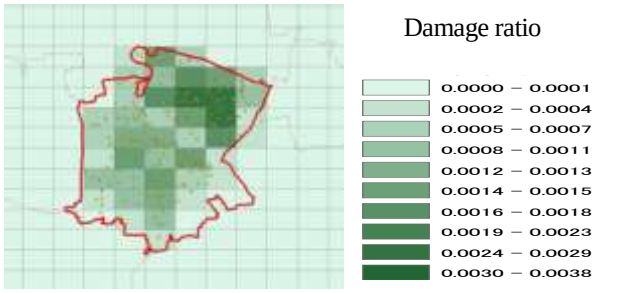

Figure 9 Assumed damaged points and damage ratio distribution

(5) Observed power outage information (*PO*)

Fig.10 shows the observed feeders with power outage due to the damaged equipment assumed by Fig.9. Fig.10 shows that the power outage occurs in about 80 % of the feeders due to the earthquake scenario.



Figure 10 Observed power outage information

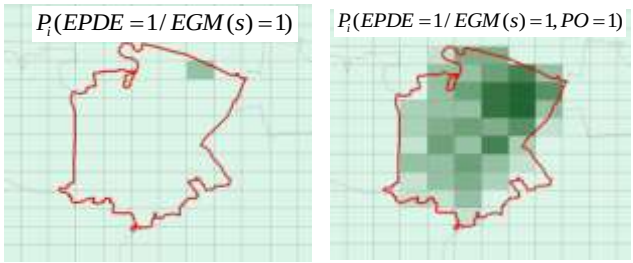

(a) Observed information
1) Seismic Intensity

(b) Observed information
1) Seismic Intensity
2) Power Outage

Figure 11 Comparison of estimated results

Fig.11 shows a comparison of the damage estimation results between $P_\alpha(PEDE=1/EGM(a)=1)$ and $P_\alpha(EPDE=1/EGM(a)=1,PO=1)$. By comparing Fig.9 with Fig.10, it is understood that the damage ratio due to $P_\alpha(PEDE=1/EGM(a)=1)$ shown in Fig.11 (a) under estimates the observed one in Fig.8.

On the other hand, the damage ratio due to $P_\alpha(PEDE=1/EGM(a)=1,PO=1)$ shown in Fig.11 (b) is similar to the one observed in Fig.9. This result suggests that the power outage information can effectively improve the damage estimation of the electric power distribution equipment.

7. CONCLUSION

This paper reviewed CRIEPI's recent studies associated with a sequential updated damage estimation system for electric power distribution equipment called RAMP-Er. RAMP-Er applied a Bayesian network which enables us to improve the accuracy of the damage estimation based on sequential updated multiple disaster information associated with not only the seismic intensity, but also the power outage and damage inspection. In this study, a Bayesian network modeling process is illustrated to emphasize the difference between the proposed model and the existing damage estimation model. As a numerical example, RAMP-Er is applied to a hypothetical system. As a result, it is demonstrated that the proposed model with power outage information is very useful for improving the accuracy of the seismic damage estimation.

References:

Agency for Natural Resources and Energy (1996) "To realize the high performance of electric power facilities against earthquake", Denryoku-Shinpo-Sha (in Japanese).

The Niigata-Ken Chuetsu Earthquake Investigation Committee (2004) "Report of the 2004 Niigata-Ken Chuetsu-Oki earthquake damage investigation report" , Japan Society of Civil Engineering (in Japanese).

Shumuta, Y. and Ishikawa, T. (2008) "Basic model for the damage estimation of electric power distribution facilities based on a sequential processing of the disaster information after the earthquake", Technical Report N07027 (in Japanese).

Shumuta, Y., Takahashi, K., and Matsumoto, T. (2009) Development of a damage estimation system for electric power distribution equipment using the Bayesian network, Proceedings of Technical Council of Lifeline Earthquake Engineering, pp197-208.

Russell, S. and Norvig, p.(1995) *Artificial intelligence: A modern approach*,. Prentice Hall.

NIED F-net, (2008) http://www.fnet.bosai.go.jp, National Research Institute for Earth and Disaster Prevention (in Japanese).

NIED-K-net,(2008)http://www.k-net.bosai.go.jp, National Research Institute for Earth and Disaster Prevention (in Japanese).

JOINT CONFERENCE PROCEEDINGS
7th International Conference on Urban Earthquake Engineering (7CUEE) &
5th International Conference on Earthquake Engineering (5ICEE)
March 3-5, 2010, Tokyo Institute of Technology, Tokyo, Japan

MODELING OF RESTORATION PROCESS ASSOCIATED WITH CRITICAL INFRASTRUCTURES AND THE INTERDEPENDENCY DUE TO A SEISMIC DISASTER

Gaku Shoji[1] and Ayumi Toyota[2]

1) Associate Professor, Dept. of Engineering Mechanics and Energy, Graduate School of Systems and Information Engineering, University of Tsukuba, Japan
2) Graduate Student, Dept. of Risk Engineering, Graduate School of Systems and Information Engineering, University of Tsukuba, Japan
gshoji@kz.tsukuba.ac.jp, toyota@risk.tsukuba.ac.jp

Abstract: Anticipated scenarios of the restoration process during about 72 hours after an event associated with critical infrastructures such as electric power supply systems, gas supply systems, water treatments, and communication networks due to a seismic disaster are modeled. To clarify the structure of the scenarios, current operational plans for disaster prevention provided by stakeholders associated with the infrastructures distributed in the Tokyo metropolitan area, are analyzed based on the graph theory. And the related interdependency in the restoration process is modeled by idealizing the relations between the restoration activities as the network. From sensitivity analysis to the derived model, it was found that strong and weak connectivity of the relations associated with the information, human resources and materials in the restoration process between various stakeholders involved in the management of critical infrastructures is quantitatively shown.

1. INTRODUCTION

Economical and societal activities in a mega city strongly depend on the function of critical infrastructures such as electric power supply systems, gas supply systems, communication networks, water treatments, transportation facilities and so forth. Hence, physical failures and functional impairment induced in the infrastructures due to a seismic disaster cause severe damage to above activities. In order to reduce the damage, improvement of the efficiency of the related restoration activities as well as physical strengthening of the facilities, is important.

The restoration activities associated with critical infrastructures during a seismic disaster have been discussed among many researchers. Most of them (Hoshiya, 1981, Shinozuka, 1981, Kozin and Zhou, 1990, Nojima and Kameda, 1992, Chang *et al*., 1999, Cagnan *et al*., 2006) aim to clarify the effectiveness of restoration strategy on shortening the restoration periods based on reliability engineering methodologies, since the strategy is utilized for preparing the restoration plans before an anticipated event occurs. In the activities, it is well known that the function of an infrastructure could be affected by that of other infrastructures. Nojima and Kameda (1995) clarify the issue as interdependency associated with seismic damage of infrastructures, which is classified into six categories: physical damage effect, functional damage effect, recovery interruption, interconnected functional damage, joint damage and customers' inconvenience. The relations associated with the related information, human resources and materials (hereinafter collectively called as restoration resources) in the restoration process are affected due to the interdependency. For instance, from the point of view of recovery interruption, the stakeholders associated with electric power supply systems and communication networks need to adjust their restoration plans in the case that they share utility poles in a managing area. We realize the interdependency on the restoration activities from previous disasters such as the 1995 Kobe earthquake and 2004 Niigata Chuetsu earthquake. Hada and Meguro (2000) verify the relation between the restoration process of water supply systems and that of gas pipelines by assessing the data in the 1995 Kobe earthquake. In recent research, Ünen *et al*. (2009) propose a tool to analyze the effect of the interdependency on the reduction of service level by electric power supply systems and water supply systems.

Above previous studies mainly intend to examine various restoration strategies in view of efficiently allocating restoration resources. However less study has been done to clarify the interacted structure of whole restoration process with respect to the flow of the restoration resources, which depends on the physical and organizational features of infrastructures.

From the reasons above, this paper analyzes scenarios of the restoration process associated with critical infrastructures and the structures of the scenarios in the process are modeled as the networks. Five systems of critical infrastructures are selected: electric power supply systems

(EPSS), gas supply systems (GSS), communication networks (CN), water supply systems (WSS) and sewerage systems (SS). Developed network models can be available of the related infrastructure managers and local government officers to understand whole restoration process and to revise their operational plans to effective ones

2. ANTICIPATED SEISMIC DISASTER AND ITS DAMAGE OF CRITICAL INFRASTRUCTURES

For analysis, we select the scenarios due to the seismic damage by the North Tokyo Bay earthquake *M*7.3, which Central Disaster Prevention Council (2005) and Tokyo metropolitan government (2006) assume as one of the severe seismic events in Tokyo metropolitan area. In terms of the damage of subject infrastructures in the Tokyo metropolitan area, the rate of power failures reaches 16.9% and 6 days are required to repair temporarily after the event. The outage rates of GSS and WSS, the damage rate of sewerage pipelines and the interrupted rate of CN become 17.9%, 34.8%, 22.3% and 10.1% immediately after the anticipated event, respectively. 53 days, 30 days, 30days and 14 days are required to repair GSS, WSS, SS and CN. In the light of these assessments, suppliers and managers of above infrastructures revise their operational plans for disaster prevention, which we analyze to clarify the scenarios of the restoration process in the following sections.

3. ANALYSIS OF RESTORATION PROCESS OF SUBJECT CRITICAL INFRASTRUCTURES

3.1 Analytical Framework

For analysis, emergency response phase and temporary restoration phase after an event are focused on. These phases correspond to ones from the immediately after an event to 72 hours after an event. The disaster prevention plans offered by Tokyo metropolitan government (2007) and the operational plans for disaster prevention by infrastructure suppliers and managers are referred (Tokyo Electric Power Company, Inc., 2006, Tokyo Gas Company, Ltd., 2008, Bureau of Waterworks, Tokyo Metropolitan Government, 2006, Bureau of Sewerage, Tokyo Metropolitan Government, 1998, and Nippon Telegraph and Telephone Corporation Group, 2007). By analyzing these operational plans, all sectors associated with the restoration process of the infrastructures are detected and the relations among their activities in the process are clarified qualitatively. Figure 1 shows a frame of scenarios. A column denotes a series of restoration activities which a sector is involved in, and a cell shows a restoration activity. We can see the relations among the activities with respect to the flow of the restoration resources. The relations are clarified into three types: relation of the related information, relation of the human resources and relation of the materials associated with the restoration activities.

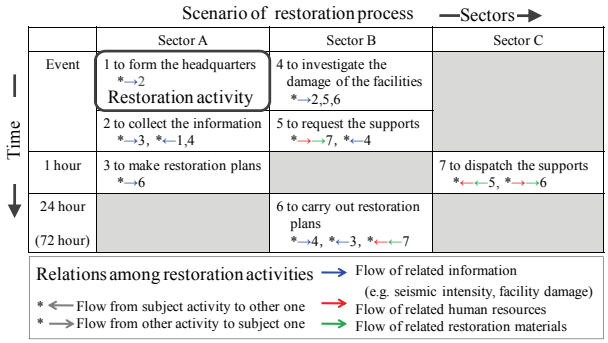

Figure 1 Frame of Scenarios

3.2 Scenarios of Restoration Process

Figure 2 shows the part of the scenario of the restoration process on EPSS. We must pass the results associated with the scenarios of the restoration process on other subject infrastructures, owing to the limitation of this paper length.

In the case that seismic intensity becomes 6 lower, the third emergency operation system is formed automatically and all staffs (about 40,000 people at 2006) gather to their own responsible sections. In the period when the staffs are gathering, 24 hours-working operators in nuclear power stations, thermal power stations, transmission offices and load dispatching offices start the emergency responses. In this process, automatic restoration system begins to work and the operators check the damage of the facilities, switch over normal modes of the equipments to emergency modes and shutdown the equipments to be suffered. At the same phase, central load dispatching office starts the systematic emergency response such as to collect the information of the damage of the related facilities and to instruct the operators in the facilities how to respond. Corresponding to these activities, the headquarters is formed in the head office and all other offices, and the sections of the head office make the decision and play central roles in the restoration process. In order to start these activities quickly, about 20 staffs live nearby head office and some of the staffs work in night duty.

In 1 hour from the event, branch offices start to check the damage of their facilities, confirm the stock of the related materials and the safety of staffs. The information associated with damage of facilities and induced blackouts is informed from all offices to the restoration section and the information section in the headquarters of disaster countermeasures in the head office. These two sections inform the related information to other sections of the head office. The power operational section and the restoration section check the efficiency of the restoration process and make the temporary restoration plans for the affected facilities such as the load dispatching centers, the power plants, the transmission offices and the branch offices. The information associated with the shortage of the related materials and human resources with the restoration process is reported from the offices to the restoration section in the head office. The

	Tokyo Electric Power Company, Inc												
	Head office								Branch Office (B.Office)	Nuclear Power Station (N.P. Sta.)	Thermal Power Station (T.P. Sta.)	Transmission Office (Trans. Office)	Central Load Dispatching Center (CLDC)
	Chairman	Information Section (Info. Sec.)	Public Info. Section (Pub. Info. Sec)	Restoration Section (Rest. Sec.)	Power Operational Section (P.O. Sec.)	Logistics Section (Logis. Sec.)	Welfare Section (Wel. Sec.)	General Affairs Section					
Event	◂Form the 3rd emergency operation												
	◂Move to specified place												
	◂Form disaster headquarters												
										◂Activate automatic recovery system			
										◂Investigate damage of facilities *→CLDC	◂Investigate damage of facilities *→CLDC	◂Investigate damage of facilities *→LDO	◂Investigate damage of facilities *←N.P.Sta., T.P.Sta., LDO
										◂Emergency response (shutdown damaged equip. & switch over to normal one) *→CLDC	◂Emergency response (shutdown damaged equip. & switch over to normal one) *→CLDC	◂Emergency response (shutdown damaged equip. & switch over to normal one) *→LDO	◂Emergency response *←N.P.Sta., T.P.Sta., LDO
													◂Monitor load factor *→Electric Power System Council
1hour	◂Collect info on disaster *←Info.Sec. Press	◂Collect info on disaster *←Cabinet Office, Tokyo gov, METI, TFD, MPD, Press, JMA, B.Office *→all Sec., Chairman	◂Collect info on disaster *←Info.Sec, Press	◂Collect info on disaster *←Info.Sec. Press	◂Collect info on disaster *←Info.Sec., Press, CDLC *→CDLC	◂Collect info on disaster *←Info.Sec., Press	◂Collect info on disaster *←Info.Sec, Press	◂Collect info on disaster *←Info.Sec, Press	◂Collect info on disaster *←Local gov., Press, TFD, MPD *→Info.Sec.	◂Collect info on disaster *←Info.Sec, Press	◂Collect info on disaster *←T.P. Office, Press	◂Collect info on disaster *←Info.Sec, Press	◂Collect info on disaster *←P.O.Sec, Press *→P.O.Sec.
	◂Collect info on damage of facilities *→Info.Sec.	◂Collect info on damage of facilities *←all Sec. *→Cabinet Office, Tokyo gov., METI, TFD, MPD, Press, JMA, B.Office	◂Collect info on damage of facilities *→Info.Sec.	◂Collect info on damage of facilities *←N.P.Sta., B.Office, Trans. Office *→Info. Sec.	◂Collect info on damage of facilities *←CDLC, LDO *→Info. Sec., Rest. Sec.	◂Collect info on damage of facilities *←Info. Sec. *→Info. Sec.	◂Collect info on damage of facilities *←Info.Sec. *→Info.Sec.	◂Collect info on damage of facilities *←Info.Sec. *→Info.Sec.	◂Collect info on damage of facilities *←LDO, Trans.Office *→Rest. Sec.	◂Collect info on damage of facilities *→CLDC, Rest.Sec.	◂Collect info on damage of facilities *→CLDC, T.P. Office	◂Collect info on damage of facilities *→LDO, B.Office, Res.Sec.	◂Collect info on damage of facilities *←N.P.Sta., T.P. Office, *→P.O.Sec.
	◂Collect info on safety of staffs *→Wel.Sec.	◂Collect info on safety of staffs *→Wel.Sec.	◂Collect info on safety of staffs *→Wel.Sec.	◂Collect info on safety of staffs *→Wel.Sec.	◂Collect info on safety of staffs *→Wel.Sec. *←CLDC	◂Collect info on safety of staffs *→Wel.Sec.	◂Collect info on safety of staffs *→Wel.Sec.	◂Collect info on safety of staffs *→Wel.Sec.	◂Collect info on safety of staffs *→Wel.Sec., *←Trans.Office	◂Collect info on safety of staffs *→Wel.Sec.	◂Collect info on safety of staffs *→T.P. Office	◂Collect info on safety of staffs *→B.Office	◂Collect info on safety of staffs *→P.O .Sec.
				◂Collect info on rest. materials *←B.Office, N.P.Sta., P.O.Sec.	◂Collect info on rest. materials *→Rest.Sec.				◂Collect info on rest. materials *→Rest.Sec. *←Trans.Office	◂Collect info on rest. materials *→Rest.Sec.	◂Collect info on rest. materials *→T.P.Sta.	◂Collect info on rest. materials *→B.Office	◂Collect info on rest. materials *→P.O.Sec.
24hours	◂Send staff *→→ Tokyo gov. *→Info.Sec. *←Info.Sec.	◂Communicate with the staffs in Tokyo gov. *←Chairman *→Chairman	◂Implement public relations *→Press, Info. Sec.	◂Make restoration plan *←P.O. Sec. *→P.O. Sec., N.P.Sta., Trans. Office, B.Office	◂Make power supply strategy *←Rest. Sec. *→CLDC, LDO, Rest. Sec.	◂Manage restoration materials *←Rest. Sec. *→Conf. of Electric Power Supply, Electric Power System Council of Japan, Group companies	◂Confirm safety of staffs *←all Sec.	◂Control telephone communic-ation	◂Implement public relations *←Info.Sec. Pub. Info.Sec. *→Press, Local gov., TFD, MPD	◂Carry out restoration plans of facilities *←Rest.Sec. P.O.Sec.	◂Carry out restoration plans of facilities *←Rest.Sec. P.O.Sec. *→T.P.Sta.	◂Carry out restoration plans of facilities *←Rest.Sec. B.Ofiice, LDO	◂Switch the modes systematic-ally *←P.O.Sec. LDO
	◂Request the support by SDF *→Tokyo gov.	◂Collect info. on customer service		◂Request for supports *→→ Logis. Sec., Groupe companies	◂Request temporary power supply *→other electric power companies				◂Carry out restoration plans of power cables *←Rest. Sec				

T.P.Office: Thermal Power Office, LDO: Load Dispatching Office, JMA: Japan Meteorological Agency, METI: Ministry of Economy, Trade and Industry, TFD: Tokyo Fire Department
MPD: Metropolitan Police Department, SDF: Self Defense Forces

Figure 2 Part of the Scenario of the Restoration Process of Electric Power Supply Systems

logistics section, the welfare section and the general affairs section request the related materials, human resources and spaces to be used in the restoration activities from the headquarters of disaster countermeasures in the Tokyo metropolitan government, related industry associations, other electric power companies and group companies. They also request the support by the Self Defense Forces immediately after the event from Tokyo metropolitan government. They request the ways of transporting the related materials from contracted companies and other electric power companies. In 24 hours from the event, temporary restoration activities are carried out in the power stations, transmission offices, power system offices and remote control offices. In the activities, operators in the load dispatching offices switch the damaged systems over to safety ones. After 24 hours, the restoration of damaged distribution facilities such as cables and utility poles starts in the branch offices and the operators in the load dispatching offices systematically switch over the transmission lines to alternative ones up to the temporary restoration process. Estimated number of staffs and workers involved in the restoration process of EPSS in a unit day is about 12,000 people.

4. QUANTITATIVE MODELING OF SCENARIOS

4.1 Quantitative Modeling

We model the structure of the scenarios of restoration process as the network, assuming the restoration activity as a node and the relation of the activities as a link, shown in Figure 3. Consequently, the structure of the scenarios on EPSS is modeled as a network composed by 73 nodes and 236 links. Detailed description of all nodes is shown in Table 1. Those of GSS, CN, WSS and SS are modeled as the networks of 66 nodes and 187 links, 63 nodes and 149 links, 82 nodes and 240 links, and 56 nodes and 123 links, respectively.

These network models can be numerically represented by adjacent matrixes used in the graph theory. In the case that there is a relation from the restoration activity *i* to *j*, the number of 1 is set in the (*i*,*j*) component on the adjacent matrix, and in the case that there is no relation from *i* to *j*, the number of 0 is set on that matrix.

Next, by referring the method based on Decision Making Trial & Evaluation Laboratory (DEMATEL) method (Fontela and Gabus, 1974), the sum of components in row *i* on the adjacent matrix is set as X_i and the sum of those in column *i* as Y_i. X_i means the total number of relations from the restoration activity *i* to others (total number of active relations), and Y_i means the total number of relations that the restoration activity *i* has from others (total number of passive relations). Hence, (X_i+Y_i) shows the sum of active and passive relations with respect to the activity *i*. That is, (X_i+Y_i) indicates the degree of importance that the activity *i* plays in the entire structure. We define it as related level R_i (*RL*) of the activity *i*. On the contrary, (X_i-Y_i) shows

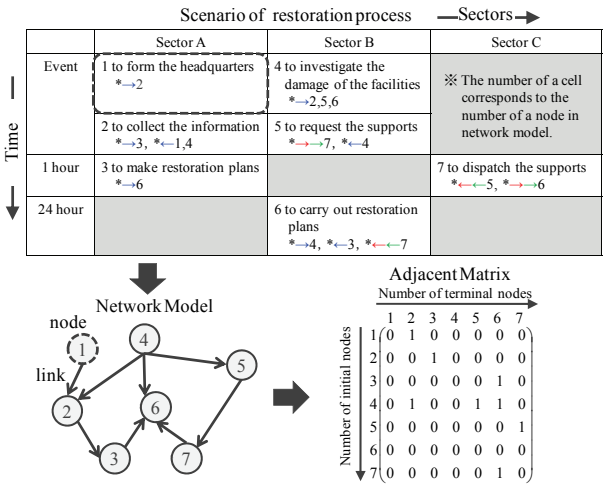

Figure 3 Quantitative Modeling of Scenarios

the difference between the number of active relations and that of passive ones. We define it as influence level I_i (*IL*). Now, the coordinates (R_i, I_i) is defined to visualize the network structure. When a restoration activity is highly related with other ones, the coordinates of the activity is in the region at high *RL*. Positive value of *IL* means that an activity has more active relations with other activities than passive ones. Negative value of *IL* indicates the meanings that an activity has more passive relations than active ones. In order to compare the structure of scenarios, R_i and I_i are normalized by the maximum values as shown below.

$$NR_i = (X_i + Y_i)/2(n-1) \quad (1)$$

$$NI_i = (X_i - Y_i)/(n-1) \quad (2)$$

Table 1 Node Number of the Network on Electric Power Supply Systems

No.	Sectors		Activities
1	Head Office	Chairman	to instruct restoration activities
2			to dispatch the officers to Tokyo metropolitan gov.
3			to request the support by Self Defense Forces
4		Information Section	to confirm safety of the staffs
5			to collect information
6			to collect information on customers service
7		Public Information Section	to confirm safety of the staffs
8			to implement public relations
9		Restoration Section	to confirm safety of the staffs
10			to make restration plans
11			to manage human resources and materials associated with restoration
12		Power Operational Section	to confirm safety of the staffs
13			to make power supply strategy
14			to request temporary electoric power supply
15		Logistics Section	to confirm safety of the staffs
16			to request and divide the materials associated with restoration
17		Welfare Section	to confirm safety of the staffs in the related sector
18			to confirm safety of all staffs
19			to request and divide the necessaries
20		General Affairs Section	to confirm safety of the staffs
21			to manage headquarters
22			to check damage of buildings
23			to control telephone communication
24	Branch Office		to confirm safety of the staffs
25			to collect information
26			to implement public relations
27			to carry out restoration plans of distribution facilities
28	Nuclear Power Station		to investigate damage & to do emergency response by operators
29			to confirm safety of the staffs
30			to carry out restoration plans of nuclear power plants
31	Thermal Power Office		to confirm safety of the staffs
32			to carry out restoration plans of thermal power plants
33	Construction Office		to confirm safety of the staffs
34			to carry out restoration plans of facilities
35	Thermal Power Plant		to investigate damage & to do emergency response by operators
36			to confirm safety of the staffs
37			to carry out restoration plans of thermal power plants

No.	Sectors	Activities
38	Transmission Office	to investigate damage & to do emergency renponse by operators
39		to confirm safety of the staffs
40		to carry out restoration plans of transmission offices
41	Remote Control & Maintenance Office	to investigate damage & to do emergency renponse by operators
42		to confirm safety of the staffs
43		to carry out restoration plans of remote control offices
44	Sub Office	to confirm safety of the staffs
45		to carry out customer services
46		to carry out restoration plans of distribution facilities
47	Customers Center	to confirm safety of the staffs
48		to carry out customer services
49		to carry out restoration plans of distribution facilities
50	Central Load Dispatching Office	to collect info. & to do emergency renponse by operators
51		to confirm safety of the staffs
52		to switch the modes systematically
53	System Load Dispatching Office	to investigate damage & to do emergency renponse by operators
54		to confirm safety of the staffs
55		to carry out systematic switching
56	Branch Office of the Load Dispatching	to investigate damage & to do emergency renponse by operators
57		to confirm safety of the staffs
58		to carry out systematic switching
59	Electric Power systems Council	to confirm load factor on power supply
60	Central Power systems Council	to request supports by the electoric companies
61	Conference of the Electric Power Supply	to request supports by the electoric companies
62	Other Electric Power Companies	to support restoration activities
63	Group Companies	to support restoration activities
64	Self Defense Forces	to support restoration activities
65	Headquarters for Disaster	to collect information
66	Countermeasures of Tokyo Metropolitan	to request supports by Self Defense Forces
67	Government	to supply the open spaces
68	Tokyo Fire Department	to collect information
69	Metropolitan Police	to collect information
70	Local Government	to collect information
71	Cabinet Office, Government of JAPAN	to collect information
72	Ministry of Economy, Trade and Industry	to collect information
73	Japan Meteorological Agency	to collect information

where, n is the total number of nodes.

Figure 4 shows the structures of the scenarios in the restoration process associated with subject infrastructures. Node numbers denoted in Figure 4 (a) are the same as those of Table 1. Horizontal and vertical axes denote the normalized related level NR_i (*NRL*) and influence level NI_i (*NIL*).

4.2 Network Structures of Scenarios

The central load dispatching office on EPSS, the supply control center on GSS, the network control center on CN and the water supply operation center on WSS play substantial roles in collecting the related information immediately after the event since the sectors are engaged in the activities associated with monitoring the networks for 24 hours. *NRL*s of the corresponding activities are 0.05-0.10 and the *NIL*s are 0.01-0.04. After the headquarters is formed in the offices of all infrastructures, the information sections on EPSS, CN and WSS, the disaster prevention section on GSS and the management and construction sections on SS play substantial roles. These related activities locate in the region at high *NRL*s of 0.04-0.21, whereas those locate in the region near zero *NIL*s of -0.02-0.11. The reason of showing the negative *NIL*s is that the sectors involved in the activities receive the related information frequently from the related outer sectors in the restoration process. In addition, the headquarters meetings in which the sectors on WSS and SS share the information and adjust their restoration plans, are set up in the restoration process of WSS and SS commonly. The values of those *NRL*s are high at 0.10-0.15.

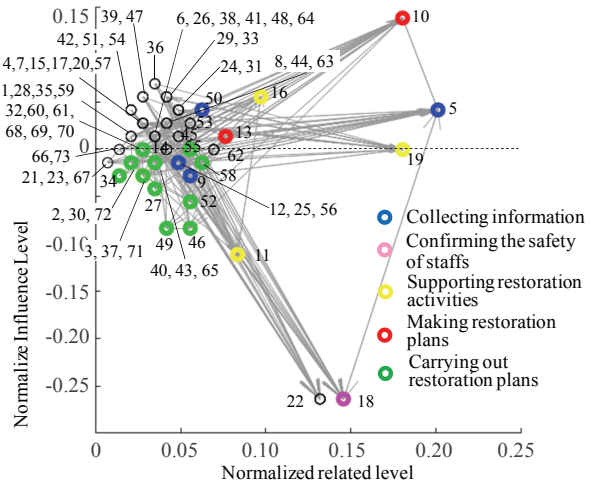

(a) Electric Power Supply Systems

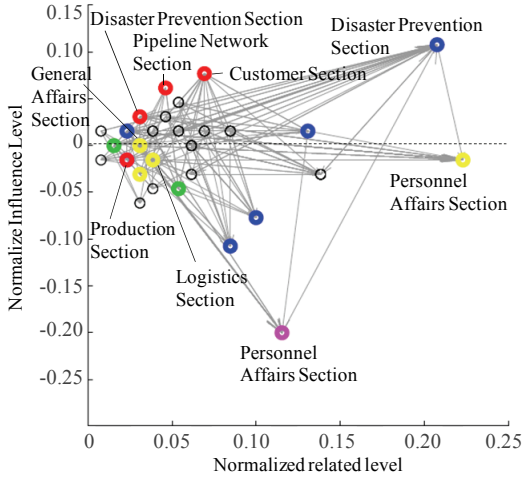

(b) Gas Supply Systems

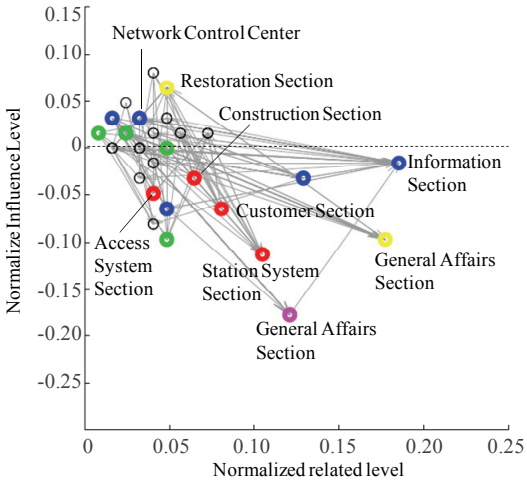

(c) Communication Networks

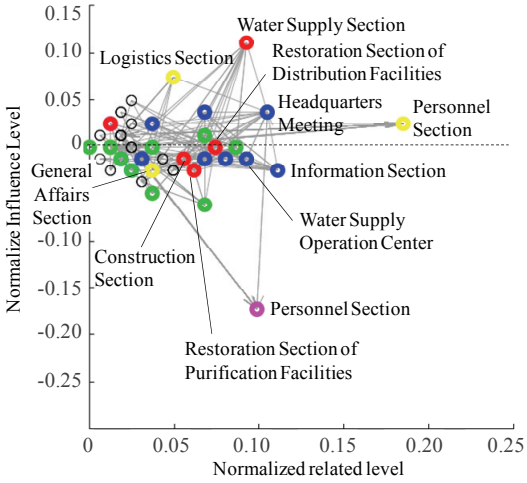

(d) Water Supply Systems

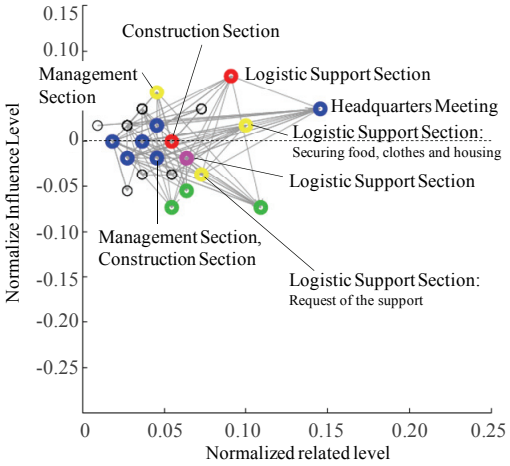

(e) Sewerage Systems

Figure 4 Network Models of Restoration Process

The values of *NRL*s of the activities associated with confirming the safety of staffs are 0.06-0.15 and those of *NILs* indicate all negative ones. The reason of showing the negative *NIL*s is that the sectors involved in these activities need to gather much related information from other sectors. The welfare section on EPSS, the personnel affairs section on GSS, the general affairs section on CN, the personnel section on WSS and the logistics support section on SS are involved in the activities.

The activities associated with supporting the restoration activities are classified into two types: activities associated with the management of food, clothing and housing, and those of the related human resources and materials. The welfare section on EPSS, the personnel affairs section on GSS, the general affairs section on CN, the personnel section on WSS and the logistics support section on SS are involved in the former activities. Even though the structures of the restoration activities of the infrastructures are different as shown in Figure 4, the values of *NRL*s of those activities show high at 0.10-0.22 and those of *NIL*s are near zero at -0.09-0.02. In terms of the latter activities, the values of *NRL*s are 0.03-0.09 and those of *NIL*s have wide variation. We examine the trends since the logistics of the related human resources and materials is a key in the restoration process.

The value of *NIL* of the restoration section on EPSS is negative at -0.11 whereas that of the logistics section is positive at 0.06. The restoration section dominantly manages the human resources and materials. It means the section needs to collect considerable related information from other sectors and has more passive relations with others. On the other hand, the logistics section follows the management of the human resources and materials, and requests them from the related outer associations by dealing with the summarized information by the restoration section. It means the section has more active relations with others. The related sectors on GSS with the activities of the related human resources and materials are the general affairs section and the logistics section. The *NIL*s of the activities by the sectors show 0 and -0.01. In the structure, the number of active and passive relations associated with the activities on the sectors is almost same. The related sector on CN with the activities of the related human resources and materials is the restoration section. The *NIL* of the related activity is positive at 0.06 and it means the activity has more active relations with others than passive ones. The section collects the information associated with the lack of the human resources and materials from the access system section, the station system section and the construction section on CN. After collecting the information, the section adjusts the resources with the branch offices and asks those for the group companies and the logistics companies. The related sectors on WSS with the activities of the related human resources and materials are the logistics section and the general affairs section. The value of *NIL* on the logistics section shows positive at 0.07 and that of the general affairs section shows negative at -0.02. The reason of this is that the logistics section requests the resources from various sectors such as water suppliers in other cities and the contractors, whereas the general affairs section asks only for the headquarters of Tokyo metropolitan government. The restoration structure on SS has the same trend as above WSS structure.

The activities associated with making the restoration plans have wide variation on the *NIL*s. We also examine the details of these characteristics.

The related sectors on EPSS are the power operational section and the restoration section. The *NIL*s of the corresponding activities show positive at 0.01 and 0.14, respectively. It means these sections have more active relations than passive ones. The power operational section makes the corresponding power supply strategies to control load dispatching centers, and the restoration section makes the restoration plans for power plants and distribution facilities. Both sections communicate each other to optimize the plans. The related sectors on GSS are the customer section, the pipeline network section, the disaster prevention section and the production section. The *NIL*s of the related activities of former three sections are positive at 0.08, 0.06 and 0.03, whereas that of the production section is negative at -0.02. The reason of showing the negative *NIL* is that the production section needs to collect the related information from former three sections since the gas production plan depends on the restoration progress of pipelines. Similarly, the related sectors on SS are the management section and the construction section. The management section manages the pipelines and water reclamation plants, and the construction section manages the construction sites and buildings. The *NIL* of the activity by the management section is positive at 0.07 and that by the construction section is 0. The reason of lower *NIL* on the construction section is that passive relations on the construction section become more dominant than active ones since the restoration plan is up to the restoration progress of the pipelines and water reclamation plants managed by the management section. The related sectors on CN are the access system section, the station system section, the construction section and the customer section. All these *NIL*s indicate negative values. The reason of this is that making the restoration plans by each section is strongly dependent on that by other sections, even though each section manages the corresponding different facilities. In the same way, the *NIL*s of the activities by the related sectors on WSS such as the restoration section of purification facilities, the distribution facilities and the construction section are negative at -0.02, 0 and -0.01.

The *NIL*s of most of the activities associated with carrying out the restoration plans indicate the negative values since these involved sectors get the related information and instruction on the restoration plans from the head offices.

4.3 Connectivity of Networks

To clarify robustness and weakness of the connectivity of the networks, first, all combinations of the relations (links) from the restoration activity (node) *i* to *j* are detected, second, the minimum path sets are computed for the combinations (node pairs). After carrying out the procedures

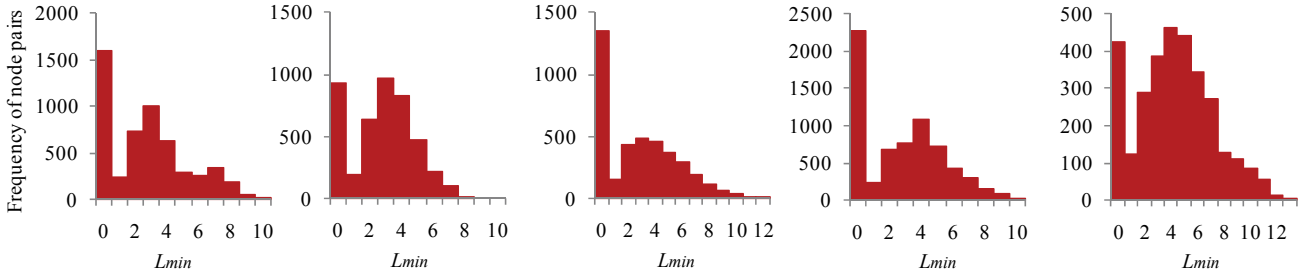

(a) EPSS (N_p=5329) (b) GSS (N_p=4356) (c) CN (N_p=3969) (d) WSS (N_p=6729) (e) SS (N_p=3136)

Figure 5 Frequency of Node Pairs with respect to the Minimum Path *Lmin* (N_p: Sum of All Node Pairs)

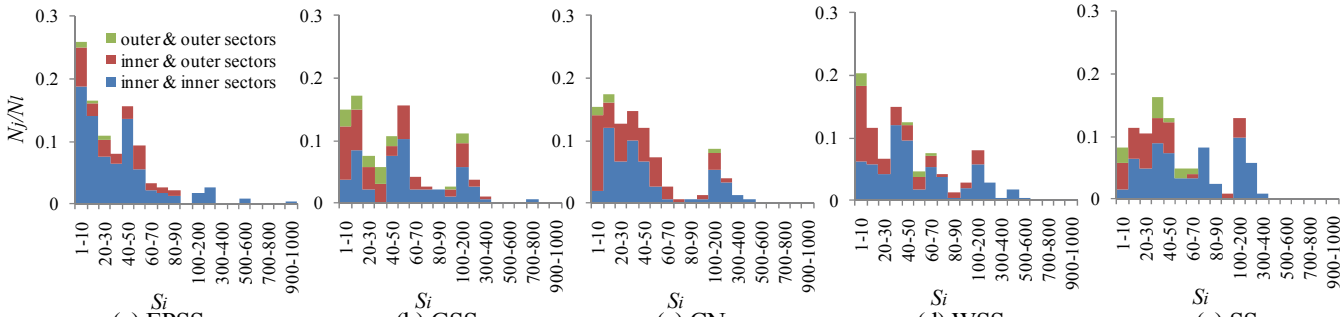

(a) EPSS (N_l=236, m_{Si}=27.8) (b) GSS (N_l=187, m_{Si} =48.0) (c) CN (N_l=149, m_{Si} =32.5) (d) WSS (N_l=240, m_{Si} =36.1) (e) SS (N_l=127, m_{Si} =42.1)

Figure 6 Relative Frequency of Cumulative number as Minimum Path Sets Obtained between Any Node Pairs (N_j: Frequency of Links, N_l: Sum of All Links, m_{Si}: Median)

for all node pairs of the activities, the frequency that the relation on the pair becomes the minimum path sets is computed for all node pairs. Figure 5 shows the frequency of node pairs with respect to minimum path *Lmin*.

In addition, cumulative number S_i that the relation on the pair is selected as minimum path sets from the point of view of a link, is computed for all links shown in Figure 6. In computing S_i, we compute 1/*Lmin* and sum up the value for all node pairs, in order to consider the participation of each minimum path *Lmin* on the frequency.

From Figure 5, we can find unconnected node pairs in all node pairs. The proportions of the pairs with all pairs are 30% for EPSS, 21% for GSS, 34% for CN, 14% for WSS and 19% for SS. The reason is that the restoration activities associated with these node pairs occur simultaneously.

Except the frequency of *Lmin* of 0, *Lmin* of 3-4 is frequent for each structure. Therefore we focus on the relations between the activities on *Lmin* of 3-4. The types of the relations are classified as follows: 1) relation between collecting information on the damage and making restoration plans, 2) relation between confirming the safety of staffs and making restoration plans, 3) relation between collecting information and carrying out the restoration plans, and 4) relation between investigating the system damage and supporting restoration activities. An examples of first type is the relation from the branch offices (to collect information on damage of facilities) to the power system section (to make electric power supply strategy) by way of the restoration section (to collect information on damage of facilities and to make restoration plans) on EPSS. An example of second type is the relation from the construction office (to check the safety of staffs) to the management section (to make the restoration plans) by way of the construction section (to collect information on the safety of staffs), the logistics support section (to collect information on the safety of staffs) and the secretariat (to make reallocation plan of the staffs) on SS. An example of third type is the relation from the water supply operation center (to monitor the network flow) to the branch offices (to carry out temporary water supply activities) by way of the restoration section of purification facilities (to collect information on damage of the facilities), the headquarters meeting and the emergency water supply section (to devise temporary water supply strategy) on WSS. An example of forth type is the relation from the pipeline management section (to collect information on damage of pipelines) to the group companies of gas supplier (to support restoration activities) by way of the pipeline network section (to collect information on damage of pipelines) and the logistics section (to request restoration materials) on GSS.

Figure 6 shows the relative frequency on S_i. In driving Figure 6, we compute S_i with *Lmin* in the range under 6, since the cumulative frequency of the links reaches more than 75 % with respect to all links. The blue bar in Figure 6 denotes the relations among the sectors in subject infrastructure suppliers and managers (inner sectors). The red bar denotes the relations between the inner sectors and the related outer sectors with the restoration activities (outer sectors), and green one denotes those among the outer sectors.

From Figure 6, the medians of S_i are 27.8, 48.0, 32.5, 36.1and 42.1 for EPSS, GSS, CN, WSS and SS. Focusing on the distribution profiles, these of EPSS and WSS show the declined trends at almost same rate. The frequency in the

class of 1-10 with respect to S_i is commonly high in both cases. On the other hand, obvious declining tendency is not found in those of GSS, CN and SS. The frequencies are high in the class of 10-20, around median and more than 100 on GSS, CN and SS.

We focus on the relations between the inner sectors in subject infrastructures. The relations of high S_i are classified into three types: 1) relation of the information on system damage, 2) relation of the information on the safety of the staffs and 3) relation of the information on the human resources and materials. An example of first type is the relation from the information section (to collect the information on the system damage) to the restoration section (to make the restoration plans) on EPSS (S_i=529). The same relation is found on GSS (S_i=129). An example of second type is the relation from the general affairs section (to confirm the safety of the staffs) to the restoration section (to check the human resources and materials) on CN (S_i=201). Also the same relation is found on SS (S_i=348). And an example of third type is the relation from the personnel section (to confirm the safety of the staffs) to the headquarters meeting on WSS (S_i=576).

The frequency with respect to S_i on the relations connected with the activities of the headquarters meeting is also high. The examples of related relations are the relation from the restoration section of purification facilities (to collect the information on the system damage) to the headquarters meeting on WSS (S_i=236), that from the headquarters meeting to the water supply section (to devise temporary water supply strategy) on WSS (S_i=149). The same relations are found on SS such as the relation from the construction section (to collect the information on the damage of facilities and construction sites) to the headquarters meeting on SS (S_i=233) and that from the headquarters meeting to the logistics support section (to request the human resources and materials) on SS (S_i=138).

In addition, the frequency with respect to S_i on the relations connected with the sectors monitoring and controlling the networks are high such as the relation from the central load dispatching center (to switch the power supply systematically) to the system load dispatching office (to switch the power supply systematically) on EPSS (S_i=211), that from the branch offices (to investigate the damage of facilities) to the network control center (to collect the information on the system damage) on CN (S_i=415), that from the purification administration office (to investigate the damage of purification plants) to the water supply operation center (to collect the information on the damage of facilities) on WSS (S_i=196).

5. INTERDEPENDENCY IN THE RESTORATION PROCESS

Based on the modeling of scenarios on the restoration process associated with subject infrastructures, the interdependency is modeled quantitatively as the network shown in Figure 7. In modeling, the connectivity between the activities on the restoration process is measured by the following normalized index.

$$NS_i = \frac{S_i - \mu_{S_i}}{\sigma_{S_i}} \tag{3}$$

where, μ_{S_i} is the mean of S_i and σ_{S_i} is the standard deviation. The values of NS_i are divided into seven classes from the range of -1.1 to 3.1 at a 0.6 interval.

From Figure 7, in terms of the flow of the related information with the restoration process, the restoration activities by the inner sectors have strong relations with the headquarters of Tokyo metropolitan government: the relations from the headquarters to the corresponding information sections on EPSS (NS_i=0.53), on CN (NS_i=2.28) and on WSS (NS_i=1.42), the relation from the headquarters to the disaster prevention section on GSS (NS_i=3.06) and that from the headquarters to the chairman on SS (to collect the related information) (NS_i=0.98). In addition, the information on the damage and restoration process of road networks is important for the restoration process of subject infrastructures. Hence, the meeting on road restoration is held in the headquarters of Tokyo metropolitan government.

The relations of the activities between the inner sectors and related ministries are important since the infrastructure supplier and manager should report the damage of their own facilities and get the information on the overview of the seismic damage: the relation from the Ministry of Economy, Trade and Industry to the information section on EPSS (NS_i=0.34) and that from the Cabinet Office to the disaster prevention section on GSS (NS_i=0.52). The relations of the inner sectors with the police, fire departments and road managers are also important to collect the information of the damaged facilities such as power cables and pipelines: the relation from the Tokyo Fire Department to the information section on EPSS (NS_i=0.13), that from the pipeline management section on GSS to the Tokyo Metropolitan Police Department (NS_i=2.10) and that from the branch offices on GSS to the Bureau of Construction in the Tokyo metropolitan government (NS_i=2.10).

In terms of the relations associated with the human resources and materials on the restoration process, all suppliers and managers of subject infrastructures have the relations with the outer sectors: the relation from the restoration section on EPSS to other electric power companies (to support the restoration activities) (NS_i=0.15), that from the gas associations (to support the restoration activities) to the IT section on GSS (to repair the communication systems) (NS_i=0.89), that from the access system section on CN (to request the supports) to the telecommunication conductors (to support the restoration activities) (NS_i=0.03), that from the restoration section of distribution facilities on WSS (to request the supports) to local water suppliers contracted with subject sector (to support the restoration activities) (NS_i=0.30), and that from the logistics support section on SS (to request the supports) to the headquarters of Tokyo metropolitan government (NS_i=1.03). Both gas supplier and communication network manager secure the stockyard of the materials and the bases

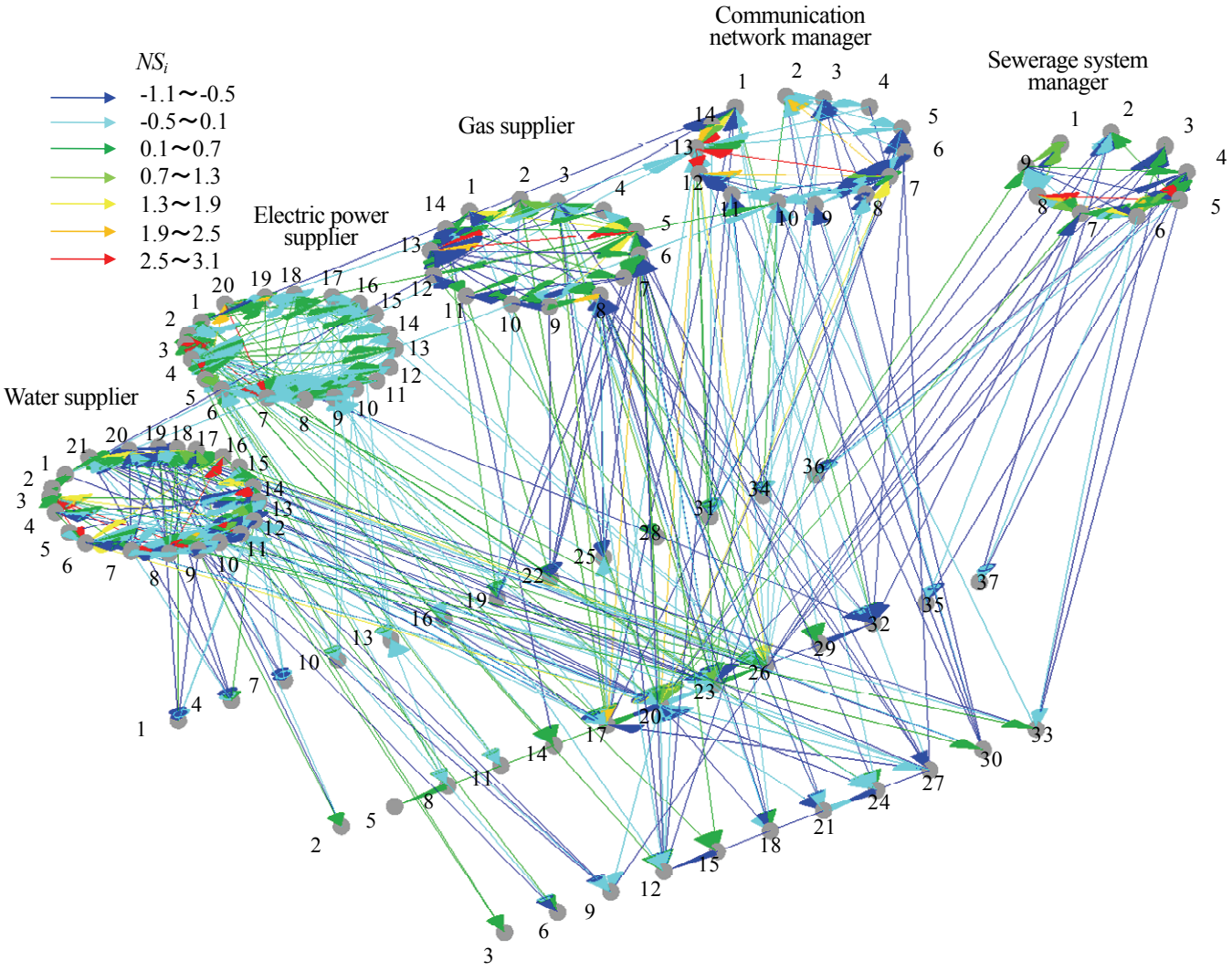

Electric Power Supply System	
1	Headquarters (Chairman)
2	Information Section
3	Public Information Section
4	Operational Section
5	Power System Section
6	Logistics Section
7	Welfare Section
8	General Affairs Section
9	Branch Offices
10	Nuclear Power Station
11	Thermal Power Office
12	Construction Office
13	Thermal Power Plant
14	Transmission Office
15	Remote Control & Maintenance Office
16	Sub Office
17	Customer Center
18	Central Load Dispatching Center
19	System Load Dispatching Center
20	Branch Office of Load Dispatching

Gas Supply System	
1	Public Information Section
2	General Affairs Section
3	Personnel Affairs Section
4	Accounting Section
5	Logistics Section
6	Local Administration Section
7	Customer Section
8	Branch Office
9	Pipeline Network Section
10	Pipeline Management Section
11	Disaster Prevention Section
12	Energy Resources & Production Section
13	Plant
14	Information Technology Section

Communication Network		
1	Head Office	
2	Network Control Center	
3	Branch Office	Information Section
4		Restoration Section
5		Access System Section
6		Station System Section
7		Construction Section
8		Customer Section
9		General Affairs Section
10		Public Information Section
11	Sub Office	Information Section
12		Customer Section for repais
13		Mass User Section
14		General Affairs Section

Water Supply System	
1	Headquarters (Chairman)
2	Headquarters (Sub Chairman)
3	Headquarters Meeting
4	Emergency Measure Meeting
5	Emergency Personnel
6	Information Section
7	General Affairs Section
8	Personnel Section
9	Logistics Section
10	Emergency Water Supply Section
11	Restoration Section of Purification Facilities
12	Restoration Section of Distribution Facilities
13	Construction Section
14	Water Supply Operation Center
15	Water Quality Management Center
16	Emergency Water Service Squad
17	Water Resources Administration Office
18	Branch Office
19	Service Station
20	Purification Administration Office
21	Construction Office

Sewerage System	
1	Headquarters (Chairman)
2	Secretariat
3	Headquarters Meeting
4	Logistics Support Section
5	Management Section
6	Construction Section
7	Sewerage Office
8	Water Reclamation Center
9	Construction Office

Other Related Sectors	
1	River Administrators
2	Material Manufactures for Water Pipelines
3	Japan Water Works Association
4	The Associated General Contractors of Tokyo
5	Ministry of Health, Labour and Welfare
6	Water Suppliers of Contracted Cities
7	Water Works Contractors
8	Conference of the Electric Power Supply in East Area
9	Group Companies of Electric Power Supplier
10	Volunteer
11	The Central Electric Power Council
12	Other Electric Power Companies
13	Tokyo Fire Department
14	Ministry of Economy, Trade and Industry
15	Electric Power System Council of Japan
16	Japan Meteorological Agency
17	Metropolitan Police Department
18	The Japan Gas Association
19	Japan Coast Guard
20	Headquarters for Disaster Countermeasures of Tokyo Metropolitan Government
21	Group Companies of Gas Supplier
22	Ministry of Land, Infrastructure, Transport and Tourism
23	Local Government
24	Tokyo Metropolitan Government Bureau of Port and Harbor
25	Cabinet Office
26	Self Defense Forces
27	Tokyo Metropolitan Government Bureau of Construction
28	Ministry of Internal Affairs and Communications
29	Financial Sectors
30	Transporters
31	Press
32	Group Companies of Telecommunication Supplier
33	Fuel Companies
34	Sewerage Managers of Disaster Contract Cities
35	Telecommunication Contractors
36	Japan Sewerage Works Association
37	Construction Companies contracted with Sewerage Supplier

Figure 7　Model of Interdependency among All Sectors associated with the Restoration Process of Critical Infrastructures

for the restoration activities with the supports of the headquarters of Tokyo metropolitan government: the relation from the local administration section on GSS (to secure the stockyard and bases) to the headquarters (NS_i=0.41) and that from the general affairs section on CN (to secure the stockyard and bases) to the headquarters (NS_i=1.25). The communication network manager cooperates with electric power supplier and water supplier to maintain the power backup systems in the facilities: the relation from the chairman on EPSS to the station system section on CN (NS_i=0.21) and that from the head office on CN to chairman on WSS (NS_i=0.15).

From the point of view of the logistics, it is necessary to achieve the efficiency of transporting the human resources and materials. To do that, the inner sectors of subject infrastructures should have strong supports from the outer sectors with allocating their own vehicles: the relation from the information section on CN to the Self Defense Forces (NS_i=1.25) and that from the headquarters of Tokyo metropolitan government to the logistics support section on SS (NS_i=0.48).

6. CONCLUSIONS

In this study, the scenarios of the restoration process associated with critical infrastructures and its interdependency due to a seismic disaster is quantitatively modeled. Five systems of critical infrastructures distributed in a mega city such as the Tokyo metropolitan area are selected: electric power supply systems, gas supply systems, communication networks and water treatments. Current operational plans for disaster prevention offered by the suppliers and managers associated with subject infrastructures are analyzed.

First we clarify the structure of restoration processes qualitatively and summarize as scenarios. Second such scenarios are numerically modeled as a directed network based on graph theory and the characteristics of the restoration activities are clarified with respect to the related and influence levels between the activities. From sensitivity analysis to the derived model it was found that strong and weak connectivity associated with the relations of information, human, and material resources regarding the restoration process between various sectors involved in the management of critical infrastructures is shown. In addition, based on these numerical analyses the interdependency of the restoration process associated with subject infrastructures is revealed from the point of view of the relations on the related information, human resources and materials in the restoration activities.

Acknowledgements:

This research was sponsored by the Ministry of Education, Culture, Sports, Science and Technology (MEXT) under a grant as Special Funds for Disaster Prevention and Reduction associated with the anticipated Tokyo Metropolitan earthquake (leader, Professor H. Hayashi at DPRI, Kyoto University and F. Yamazaki at Chiba University).

References:

Bureau of Sewerage, Tokyo Metropolitan Government (1998), *Operational Plans for Seismic Disaster Prevention (Chapter of Emergency Policy).*

Bureau of Sewerage, Tokyo Metropolitan Government (1998), *Operational Plans for Seismic Disaster Prevention (Chapter of Prevention Policy)*.

Bureau of Waterworks, Tokyo Metropolitan Government (2006), *Operational Plans for Seismic Disaster Prevention*, http://www.waterworks.metro.tokyo.jp/press/h18/press060825.pdf.

Central Disaster Prevention Council (2005), *Report of Special Investigation Committee*, http://www.bousai.go.jp/jishin/chubou/shutochokka/houkoku.pdf.

Cagnan, Z., Davidson, R.A. and Guikema, S.D. (2006), "Post-Earthquake Restoration Planning Los Angeles Electric Power," *Earthquake Spectra*, **22**(3), 1-20.

Chang S.E., Shinozuka, M. and Svekla, W. (1999), "Modeling Post-Disaster Urban Lifeline Restoration." in Elliott, W.E. and McDonough, P. eds. *Optimizing Post Earthquake Lifeline System Reliability: Proceedings of the fifth U.S. Conference on Lifeline Earthquake Engineering*. ASCE Technical Council on Lifeline Earthquake Engineering Monograph (16), 602-611.

Disaster Prevention Conference of Tokyo Metropolitan Government (2006), *Publication of Tokyo Regional Disaster Prevention Measures*, http://www.bo-usai.metro.tokyo.jp/japanese/knowledge/materialh.html.

Disaster Prevention Conference of Tokyo Metropolitan Government (2007), *Local Plans for Disaster Prevention of Tokyo Metropolitan*.

Fontela, E. and Gabus, A. (1974), *DEMATEL Structural Analysis of the World Programatique*, Battelle Report, Geneva.

Hada, Y. and Meguro, K. (2000), "Optimum Restoration Model Considering Interactions among Lifeline Systems - Interactions among Restoration Activities of Lifeline Utilities., *Proceedings of 12th World Conference on Earthquake Engineering,* 8p(CD-ROM), Auckland, New Zealand.

Hoshiya, M. (1981), "Seismic Damage Restoration of Underground Water Pipeline," *Proceedings of U.S.-Japan Cooperation Research Seismic Analysis and Its Application to Lifeline System*, Honolulu, USA.

Kozin, F., Zhou H. (1990), "System Study of Urban Response and Reconstruction due to Earthquake." *Journal of Engineering Mechanics,* ASCE, 116, 1959-1972.

Nippon Telegraph and Telephone Corporation Group (2007), http://www.ntt-east.co.jp/saigai/taisaku/bousai.pdf.

Nojima, N. and Kameda, H. (1992), "Optimal Strategy by use of Tree Structure for Post-Earthquake Restoration of Lifeline Network Systems." *Proceedings of the 10th World Conference on Earthquake Engineering,* 5541-5546, Madrid, Spain.

Nojima, N. and Kameda, H. (1995), "Seismic Risk Assessment of Urban Lifelines under System Interactions," *Journal of Structural Mechanics and Earthquake Engineering*, JSCE, **507**(I-30), 231-241.

Shinozuka, M. (1981). "Estimation and Optimization of the Serviceability of Underground Water Transmission Network System under Seismic Risk," *Proceedings of U.S.-Japan Cooperation Research Seismic Analysis and Its Application to Lifeline System*, Honolulu, USA.

Tokyo Electric Power Company, Inc. (2006), *Operational Plans for Disaster Prevention*, http://www.tepco.co.jp/cc/pressroom/bousai.pdf.

Tokyo Gas Company, Ltd. (2008), *Operational Plans for Disaster Prevention*, http://www.tokyo-gas.co.jp/safety/bousai.pdf.

Ünen, H.C., Elnashai, A.S. and Sahin, M. (2009), "Seismic Performance Assessment of Interdependent Utility Network Systems," TCLEE2009 Lifeline Earthquake Engineering in a Multihazard Environment, ASCE, Oakland, California, **357**(62), 659-669.

JOINT CONFERENCE PROCEEDINGS
7th International Conference on Urban Earthquake Engineering (7CUEE) &
5th International Conference on Earthquake Engineering (5ICEE)
March 3-5, 2010, Tokyo Institute of Technology, Tokyo, Japan

Multi-Hazard Resilient Bridges: Facts and Challenges

George C. Lee[1], and Zach Liang[2]

1) Professor, Department of Civil, Structural and Environmental Engineering, MCEER, University at Buffalo, Buffalo, NY 14260
2) Research Professor, Dept. of Mechanical and Aerospace Engineering, MCEER, University at Buffalo, Buffalo, NY 14260
gclee@buffalo.edu, zliang@buffalo.edu

Abstract: Bridge engineering typically deals with loads whose occurrence and magnitude, to various degrees, are probabilitistic in nature. Bridge loads may simply be classified into two categories: those that are always present or occurring regularly and frequently (i.e. dead loud and traffic loads); and those extreme hazard load effects with long return periods. There are no probability-based bridge design guidelines including both categories of load effects. A current MCEER research project sponsored by the Federal Highway Administration is to explore principles and approaches to establish multi-hazard LRFD guidelines. This paper is a progress report of the project where a research framework is presented together with selected case studies.

1. INTRODUCTION

The first edition of the AASHTO LRFD bridge design specifications was published in 1994 (AASHTO, 1994) after an intensive period of study between 1988 and 1993 (Kulicki, 1933; Kulicki, Mertz, and Wassef, 1955; Nowak, 1993; Novak, 1999). The advantages and design philosophy have been well articulated (Kulicki, 1999; Lwin, 1999). Since 1994, a number of states have begun their design for new bridges based on the LRFD specifications. As of 2009 the LRFD specifications has already undergone two revisions (2008 and 2009) to its 4th edition published in 2007.

From a historical perspective of bridge design methodology, LRFD specifications is the result of a logical progression evolved from the allowable stress design approach which only had a single strength limit state. LRFD has a more logical consideration of the safety margins using the reliability-based approach. Such a distributed consideration of the safety factors for different aspects of demand and capacity resulted in many design "strength limit states" in LRFD. This reliability-based approach is a major milestone in the progression of formulating bridge design guidelines.

There is a substantial difference in concept and approach between ASD and LRFD. The formal considers the load intensity in establishing the limit state while the latter considers both the load intensity and its occurrence probability in establishing the limit states.

During the first decade of the 21st century, the structural engineering community has been faced with a new challenge to design structures for multiple extreme hazard load effects, ignited by the World Trade Center disaster in 2001. This new challenge to the structural engineering community includes the need for design principles and guidelines for multi-hazard resilient systems including bridges.

From the viewpoint of a bridge designer, one must ask the question of how important is it to consider those extreme events with long return periods (e.g. 1,000 years earthquakes) for a bridge with a design life of 75 years? We will not know the answer until a comprehensive probability-based methodology is established and occurrences of extreme events properly considered together with the frequent, non-extreme event loads. The current AASHTO LRFD specifications have already provided the foundation of probability-based approach in terms of its rationale and acceptance by the bridge engineering community. The challenge now is to extend it to multi-hazard LRFD specifications that includes all non-extreme event load effects and extreme event load effects and calibrated through reliability considerations (Ghosn and Wang, 2003). This is the research challenge facing the bridge engineering R and D community.

The current LRFD specifications for bridges, in which the safety margins are established by the probability-based approach, is only calibrated by using the dead load (DL) and vehicular load or live load (LL). For extreme events, current bridge design considers them individually by using either the force-based or displacement-based criterion, not calibrated through failure probability (or bridge structure reliability) considerations.

The most advanced and comprehensive specifications for extreme event, The Guide Specifications (AASHTO, 2009a),

which continues to use limit state based on load intensity and displacement measure that are not reliability based. Similarly, recent design guidelines for vessel collision (AASHTO, 2009b and others have all adopted the load intensity or force-based approach as a "checking" measure for bridges designed based on the DL and LL calibrated LRFD. In each case, the formulation is reasonable from the viewpoint of a single hazard. However, further developments in the same direction will not necessarily provide useful input for establishing multi-hazard (MH) LRFD guidelines for bridges. What is needed is to have a framework for bridge reliability-based design approach against all hazards. Then studies of individual hazards (by different disciplinary experts) will have a total perspective to gradually direct their efforts towards the eventual establishment of an MH-LRFD specifications for highway bridges, which is expected to be philosophically sound because safety is more ensured through equal failure probability considerations with reasonable cost.

The load intensity based considerations lead to load intensity combinations for design which is essentially the load factors design approach. LRFD is reliability-based design which needs the probability of load combinations, and the failure probability of bridges due to the load combinations. One of the fundamental questions in probability-based design is the chance that a long-return-period-extreme-load (and/or a combination of such extreme load with other extreme and non-extreme loads) can cause unwanted damage of a bridge during its limited service life span?

In earthquake engineering design, a load with a 1,000 year return period may cause damages to a bridge (whose design life is only 75 years) with an unacceptable probability. The return period itself is not directly important in bridge design. How bad the return period, whether its 100 years or 1,000 years, can cause unacceptable damage to a given bridge is a more important consideration.

This important issue underlines the development efforts for MH-LRFD specifications currently being carried out at MCEER, sponsored by FHWA.

2. CHALLENGES FOR MH-LRFD DEVELOPMENT

There are significant challenges involved in the development of a comprehensive MH-LRFD. Some of the basic difficulties are related to the lack of sufficient historical data on the various types of natural extreme events. Furthermore, for certain man-made extreme hazards such as the World Trade Center disaster, it would be impractical to consider them in formulating the MH-LRFD for bridges at the present time. In this paper, the multiple extreme hazards considered tentatively include earthquakes, wind gusts, vessel collision, vehicle impacts, storm surge, scour and possibly fire. These several extreme hazards are either natural hazards or accidental hazards and concern the bridge owners and designers.

Having defined the extreme hazards, the next general issue to be defined in the current FHWA research project is the reliability of the bridge as a system. In current design practice, component failures due to extreme events control the design of a bridge. This is acceptable because extreme event load effect is checked individually. For MH-LRFD, it is necessary to establish the probability of the design reliability which should involve all possible combinations of the dead loads, vehicular loads and the several extreme hazard loads effects. For multiple hazards, failure may occur at different components due to different extreme hazards (i.e. earthquake damage to the columns base and vehicle impact cause damage to the superstructure). Hence, design based on probability of component failure will not be sufficient to describe bridge reliability as a structural system. This issue is further complicated if cascading effects are to be considered. In order to define a manageable scope of the research project, it was decided that the formulation of MH-LRFD framework be divided into two stages. The first stage, to be covered by the current contract, is to only consider bridge reliability based on probability of failure of components, and that cascading effects (except for the scouring effects) be considered later in the second stage. With this scope, the developed framework can be quantitatively illustrated by real world examples using the "regional" concept. For example, a set of strength limit states for the mid-Atlantic region can involve combinations of dead load, live load, vessel collision and scour, and those for the west coast can include dead load, live load, earthquakes and vessel collision, etc.

Within the above defined scope, some specific challenges to develop the first phase of MH-LRFD are given below:

2.1 Insufficient Data on Extreme Hazard Loads

Comparing with the availability of data for dead load and live load, extreme hazard loads have very limited information with respect to their intensity, variation and return periods. As a results, the standard deviation (assume normal distribution) can be very large which may predict comparatively large failure probability for a bridge than its actual failure probability. Furthermore, estimation of random distribution for the extreme hazards would be less accurate which will also contributed to inaccurate estimation of the failure probability.

2.2. Complexity of Load Combinations

For dead load and live load only, the limit state or performance function, g_o, can be written in general as

$$g_o = \varphi R - (\alpha_D L_D + \alpha_L D_L) \qquad (1)$$

where φ is the resistance factor

R is the nominal resistance

α_D and α_L are respectively the load factor of the nominal dead load L_D and live load L_L. When R, L_D and L_L are normally distributed random variables the performance function g also has normal distribution. Its mean value μ is given by

$$\mu_{g_o} = \varphi\mu_R - (\alpha_D\mu_D + \alpha_L\ \mu_L) \qquad (2)$$

and the standard deviation of g_o is

$$\sigma_{g_o} = \left(\sigma_p^2 + \sigma_D^2 + \sigma_L^2\right)^{1/2} \qquad (3)$$

For the extreme hazard loads, the random distributions of them are not necessarily normal. Certainly there are insufficient data to substantiate it. In general, if the performance function g , assumed linear, includes extreme hazard loads may be written as

$$g_n = \varphi R - (\alpha_D L_D + \alpha_L\ L_L + \sum_i \alpha_i L_i \qquad (4)$$

If earthquake load effect is considered, Eq. (4) can be written as

$$g_E = \varphi R - (\alpha_D L_D + \alpha_L\ L_L + \alpha_E\ L_E) \qquad (5)$$

Expanding this formulation to include two extreme hazard loads, earthquake and wind, the failure probability can be written as (Wen, Hwang, Shinozuka, 1994)

$$\begin{aligned} P_f &= P[g_0 < 0 | (\alpha_D L_D + \alpha_L\ L_L]\, P(\alpha_D L_D + \alpha_L\ L_L)] \\ &+ P[g_E < 0 | (\alpha_D L_D + \alpha_L\ L_L + \alpha_E\ L_E)]\, P(\alpha_D L_D + \alpha_L\ L_L + \alpha_E\ L_E)] \\ &+ P[g_W < 0 | (\alpha_D L_D + \alpha_L\ L_L + \alpha_W\ L_W)] \\ &\quad P(\alpha_D L_D + \alpha_L\ L_L + \alpha_W\ L_W)] \\ &+ P[g_{EW} < 0 | (\alpha_D L_D + \alpha_L\ L_L + \alpha_E\ L_E + \alpha_W\ L_W)] \\ &\quad P(\alpha_D L_D + \alpha_L\ L_L + \alpha_E\ L_E + \alpha_W\ L_W)] \end{aligned} \qquad (6)$$

where

$$g_W = \varphi R - (\alpha_D L_D + \alpha_L\ L_L + \alpha_W\ L_W) \qquad (7)$$

And

$$g_{EW} = \varphi R - (\alpha_D L_D + \alpha_L\ L_L + \alpha_E\ L_E + \alpha_W\ L_W) \qquad (8)$$

Two observations may be made from Eq. (6). First, the failure probability by combining the extreme loads and non-extreme loads can be quite different from that due to non-extreme loads only. Second, there are no convenient methods for the computation of failure probability involving multiple extreme loads other than Monte Carlo simulations. This suggests that we may use the regional approach mentioned earlier, so that for each region only a few extreme loads need to be considered.

2.3. The Assumption of Extreme Hazard Loads as Random Variables

The performance function, g, in the equation of failure probability is a function of random variable, x. In the current LRFD specification, x represents generalized forces such as bending moments or shear forces. Treating x events, certain random variables are time invariant. That means, the events of bridge capacity being less than demands cannot necessarily be described by random variables but by random processes. A common notation of the latter is to use the variable "t" so that the mean value is given by:

$$\mu_x = \mu_x(t) \qquad (9)$$

And the standard deviation is described by:

$$\sigma_x = \sigma_x(t) \qquad (10)$$

In Eqs. (9) and (10) t is a generic value. It may be the independent variable time as we normally use, or it can represent a "time period" such as the exposure time period (or service time period) of a bridge to extreme events. For deadload and the vehicular loads the mean values of both should remain pretty much the same regardless of the bridge service period but for extreme hazard loads, longer service period of a bridge will have a greater chance to experience them. This means the mean values of extreme hazard loads will be greater than that for the non-extreme loads, and they are a function of the service period of bridges.

At the present time, the concept of "return period" is commonly used to quantify the chance of seeing certain level of extreme hazard loads. However, the distributions of those levels affected by the service period (or exposure period) remains to be a challenge. For lack of historical data on intensity and frequency of occurrences as mentioned earlier, we need to establish the rationale for the assumption that random processes may be approximated as random variables, or the distributions of extreme hazard loads are normal (or symmetric) or treated as lognormal with virtually identical confidence level.

2.4. Nonlinear Dynamic Responses

A major research challenge in structural dynamics is to determine the structural response after the structure reaches the material inelastic range. This is an existing challenge for non-extreme loads and an even greater challenge for extreme hazard loads. Obviously it is also true for structures subjected to time-dependent multiple extreme hazard loads. In other words, when a structure is yielded the order of load applications will affect the responses of the structure. How to approximate this effect for engineering design against multiple extreme hazards is a significant challenge that has to be somehow addressed in formulating MH-LRFD guidelines.

Furthermore, for a bridge designed to resist different probabilities of various extreme hazard loads, the design guidelines must be formulated to include the cascading effects due to multiple hazards. In this situation, one possibility is to modify the resistance factor. That is, instead of defining the resistance factor by using Eq. (6), the

performance function, g_1, should include the extreme load L_j. We thus have

$$g_1 = \varphi_1 R_1 - (\alpha_D L_D + \alpha_L L_L + \sum_{i \neq j} \alpha_i L_i + \alpha_j L_j) \quad (11a)$$

$$g_2 = \varphi_2 R_2 - (\alpha_D L_D + \alpha_L L_L + \sum_{i \neq k} \alpha_i L_i + \alpha_k L_k) \quad (11b)$$

In Eq. (11) L_j is assumed to occur before the second extreme hazard load L_k. R_1 is the designed resistance without L_k. After the load L_j, the bridge is damaged or weakened, which may be not serious or even may not be visible by routine inspection, and its resistance is reduced to R_2. In this case the second performance function, g_2, should be used to consider the cascading effect.

Equation (11) suggests that for more than one extreme hazard load, consideration of their cascading effect requires more than a single performance function.

3. OVERCOME THE CHALLENGES

In recent years, many individuals and organizations have articulated nicely the need to establish design principles and MH-LRFD guidelines for bridges as well for buildings and the infrastructure systems. However, successful results have been very limited. This is to be expected because of the difficulties mentioned above. These difficulties can be overcome, certainly from the viewpoint of establishing acceptable guidelines for structural engineering applications, but will require time. The time required would be longer than the process of formulation of the AASHTO LRFD specifications (1994) or the Guide Specifications for Seismic Design (2009a), not only due to the challenges mentioned above, but also the multi-disciplinary nature of the research project. Each of the extreme hazard areas has its own research and professional constituency to address the demand (or hazard load effects) and/or the capacity (or structural design approaches) related to the specific hazard. Each constituency has been, to different degrees, devoting significant effort to improve its own single hazard design guidelines and approaches, which have their own traditions and culture, and are challenging pursuits by themselves. It will take certain time for the traditions to be interconnected for serious joint efforts. In this regard, the traditional funding approach used by NCHRP and other agencies (such as NSF) emphasizes individual PI or several collaborating Co-PIs with limited funding and time period may not be the most efficient approach. A major and long term (say, ten years) research thrust with interconnected tasks (each with specific objectives and goals) and full cooperation of selected AASHTO technical committees will be a more desirable approach to establish the MH-LRFD.

Although there are many difficulties, the basic idea is to first establish proper limit states considering non-extreme and extreme loads and their possible combinations and to formulate practice/friendly design guideline with acceptable accuracy.

The current MCEER project began at the fundamental level to establish a roadmap for the development of MH-LRFD specifications, with a detailed framework and recommended approaches. A certain example will be given in detail to illustrate the approach by choosing only two extreme hazards (the regional approach concept mentioned earlier). These examples will show possible approaches to address the issues of (1) a limited database for extreme hazard distributions, (2) bridge reliability from component failure probability, (3) establishing limit states and the corresponding load and resistance factors, and if possible, (4) simplified format for practical applications.

The MCEER project deliverables are intended to be a clear roadmap and a framework for MH-LRFD development with clear examples to illustrate the challenges and their possible solutions. Complete draft of the project report is expected to be available in 2011 for review and comments. Continued efforts are necessary.

4. SUMMARY

Development of MH-LRFD specifications for highway bridges is a challenging and very desirable goal that will require a sustained effort for a long period of time. This paper briefly defines the objectives and approaches of the a current MCEER research project towards establishing MH-LRFD Guidelines for highway bridges. Due to the complexity of the problem, cooperation from international partners are most welcome.

Acknowledgement:

This work is an MCEER project funded by FHWA, #DTFH61-08-C-00012. It is a five year study to define the problems and challenges with a roadmap to develop MH-LRFD with illustrative examples. The authors express their sincere appreciation to Dr. Phillip Wen-Hui Yen for his valuable input, and continued support, and to John Kulicki Masanobu Shinozuka, Tom Murphy, and Harry Capers for their contribution to this research project.

References:

AASHTO (1994). "LRFD Bridge Design Specifications," First Ed.

Kulicki, J. M. (1933). "Development of Comprehensive Bridge Specifications and Commentary," Final Report, NCHRP 12-33.

Kulicki, J. M., Mertz, D. R. and Wassef, W. G. (1955). "Load and resistance factor design for highway bridges," FHWA HI-95-0017.

Nowak, A. S. (1993). "Calibration of LRFD Bridge Design Code." Department of Civil and Environmental Engineering Report, UMIE 92-25, University of Michigan.

Novak, A. S. (1999). "Calibration of LRFD Bridge Design Code," NCHRP 368.

Kulicki, J. M. (1999). "Design Philosophy of Highway Bridges," *Bridge Engineering Handbook*.

Lwin, M. M. (1999). "Why the AASHTO Load and Resistance Factor Design Specifications?" Transportation Research Record Paper No. 99-0935.

AASHTO (2009a). "Guide Specifications for LRFD Seismic

Bridge Design."
AASHTO (2009b). "Guide Specifications and Commentary for Vessel Collision Design of Highway Bridges," 2nd Ed.
AASHTO (2008). "Guide Specifications for Bridge Vulnerable to Coastal Storms.
Wen, Y. K. Hwang, H. and Shinozuka, M. (1994). "Development of Reliability-Based Design Criteria for Buildings Under Seismic Load," NCEER-94-0023.
Ghosn, M. and Wang, Jian (2003). "Design of Highway Bridges for Extreme Events," NCHRP Report 489.

JOINT CONFERENCE PROCEEDINGS
7th International Conference on Urban Earthquake Engineering (7CUEE) &
5th International Conference on Earthquake Engineering (5ICEE)
March 3-5, 2010, Tokyo Institute of Technology, Tokyo, Japan

APPLICATION OF DISASTER CHAIN PRINCIPLE IN THE EARTHQUAKE DISASTER MITIGATION

Yu Shizhou[1], Zhao Zhendong[2] and Li Tianqi[3]

1) Associate professor, Institute of Engineering Mechanic, China Earthquake Administration, China
2) Professor, Institute of Engineering Mechanic, China Earthquake Administration, China
3) Ph.D., Institute of Engineering Mechanic, China Earthquake Administration, China
zhxszy@126.com, zhaozd@iem.net.cn, ltq_tiger15@sohu.com

Abstract: Sometimes, the destructive earthquake disaster is more than just an isolated incident, often be accompanied by some secondary disasters occurrence, such as flood, mud-rock flow, fire, explosion, and diffusion of poison gas, and so on. These disasters have certain relevance to each other. Earthquake disaster supplies the occurrence conditions to the secondary disaster, at the same time, the secondary disaster extends the earthquake losses in further, even brings great difficulties to post-earthquake emergency rescue.

In recent years, the concept of earthquake disaster chain has gradually been used to the actual working in earthquake disaster mitigation. And it is of momentous current significance by using the chain-cutting disaster mitigation from gestation source to avoid or reduce the secondary disasters.

In this paper, the concept of earthquake disaster chain and the chain-cutting disaster mitigation from gestation source method are introduced in brief. For some typical earthquake secondary disasters, analysis of occurrence mechanism have been given and mathematical models have been established based on the earthquake disaster chain principle. Final, some appropriate analysis examples are used to verify these principle and method.

1. INTRODUCTION

After a destructive earthquake, the earth's surface damage, building collapses and function failure often have been observed. Under certain conditions, it could also cause the secondary disasters, which not only increase the earthquake loss, but also offer great difficulties to post-earthquake emergency rescue. With the development of society, the sources of secondary disaster are increase more and more, especially in the energy supply system, and it's a serious threat to the surrounding people and property.

For example, on June 16, 1964, Japan Niigata M7.4 earthquake has occurred. Due to vibration, the oil tank burst into flames, and then causes the adjacent tank and refinery explosion, soon, which raises a larger fire. The fire burned for a whole two weeks. Niigata refinery had been ruin throughout, more than 80 oil tanks were damaged, 500 people were killed, and 75% of the gas pipelines and 11 transformer substations were damaged.

The earthquake-induced disasters are diversity and relevancy, which do not occur in isolation; they interact and relate to each other. The former disaster will create the necessary conditions for the occurrence of the next disaster, and the latter can aggravate existing disaster. In this process, we are aware of these disasters do not occur at the same time, and they generally follows a sequence. The former disaster will create the necessary conditions, as "chain", arrange and connect the disasters by the time order. The role of the "chain" is very important, as long as the proper and timely cutting off or control of chain will prevent the formation and development of disaster chain. By this method, the probability of the occurrence of secondary disaster can be minimized, which is named Chain-Cutting Disaster Mitigation from Gestation Source.

2. MECHANISM PROCESS OF DISASTER CHAIN FORMATION

Due to disaster chain principle can clearly describe the relationship between the various disasters, so, in this paper, it has been quoted to study the secondary disasters of earthquake. In the disaster chain of earthquake, as the first event, earthquake appears in the chain. With the necessary conditions and secondary disaster sources, they all form the disaster chain together. For the fire, a simple sketch of disaster chain is showed in the Figure 1.

According to the action of earthquake, source of secondary disaster leaks, and when leak source meet the fire source, the fire disaster will be caused. In this chain, as the necessary conditions of the fire, the leak source of secondary disaster and fire source are caused by the earthquake. When

the fire disaster occurs, it will increase more conditions and strengthen the disaster chain in further.

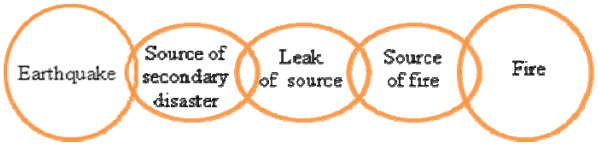

Figure 1 Earthquake & fire link in disaster chain

In the same way, we can get the others chain between the difference disasters. In the Figure 2, shows the simple sketch of fire & explosion link in disaster chain, and in the Figure 3, shows the simple sketch of the link among fire, explosion and poison gas pollution in disaster chain.

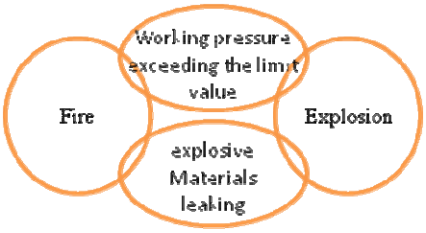

Figure 2 Fire & explosion link in disaster chain

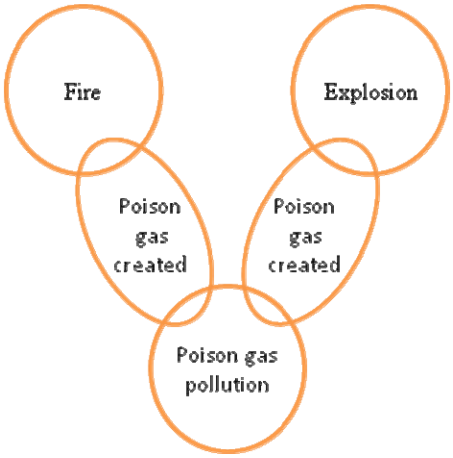

Figure 3 Link among fire, explosion and poison gas pollution in disaster chain

Because the formation of earthquake disaster chain has an important relationship with secondary disaster source and its surrounding environment, the component parts of disaster chain are also complex. So in order to ensure the accuracy and feasibility of the method, it must be possible to identify all links among the variety disasters. At the same time, unimportant links would be rejected, therefore, the relationship between the disasters could be described accurately and the purpose of simplifying the analysis would be achieved.

The above sketches just give some parts of whole disaster chain, and in fact, the disaster chain is complex. In Figure 4, as an example, sketch of a complete chain formed in petrochemical industry system is given.

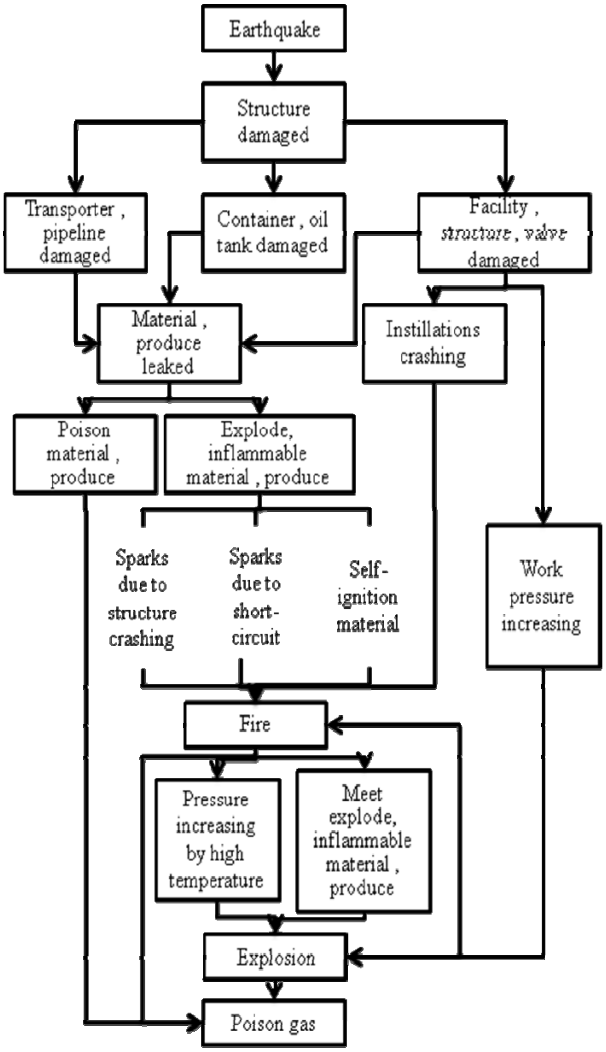

Figure 4 Sketch of complete earthquake disaster chain of petrochemical industry system

Although the equipments and structures in petrochemical industry system are very different comparing each other, but in general we can divide them into three categories by the function: transportation equipments, storage devices and production equipments. Under the earthquake action, seismic response and failure types of these devices are different, which may form different chains.

1. Disaster chain formed due to the transportation equipments damaged by earthquake

Because transportation equipments are mainly various style of oil and gas pipelines, the major damages due to earthquake are pipelines fracture or broken, then the materials or product in these pipelines leak. If the materials or products are harmful, the environment would be polluted, and ecological disasters will be caused. If the materials and products are inflammable, special performances contribute to fire, explosion, and poison smog or gas will be created

further which causes the environment pollution.

2. Disaster chain formed due to the storage devices damaged by earthquake

Earthquakes also can cause damage or capsizing to the oil and gas tank, which make it possible for materials and product leaking. At the same time, due to impact and friction between devices by earthquake vibrations, it easily causes spark and raises the fire, explosions and producing poison gases.

3. Disaster chain formed due to the production equipments damaged by earthquake

The mainly style of production equipments are high rise structures, the earthquake damage of these devices usually are local crack failure, lean and collapses. Which will threaten adjacent devices, then causes the secondary disaster. In addition, for the working production equipments, working pressure will increase due to some structural components damaged by earthquake, which will cause the explosion, fire easily.

3. CHAIN-CUTTING DISASTER MITIGATTION FROM GESTATION SOURCE

The formation and development of disaster chain will create a huge casualties and property loss. According to requirement of earthquake disaster mitigation, it's necessary and important to cut off the disaster chain and prevent its continuation. In this way, we could minimize the loss of disaster possibly. In order to prevent the formation of complete disaster chain effectively, the measurement should be carried out in the initial stage of the disaster chain formation.

As the component part of disaster chain, earthquake is the major disaster, and also is the main reason causing the occurrence of other disasters. At present, there is no way to control the earthquake, so more preventive measures are necessary in the earthquake mitigation. Major frameworks are showed in the following:

1. The safety evaluation of earthquake should be carried out according to law, possibly avoid seismic regions and active fault in the vicinity.
2. For existing disaster source, the study should be focus on the probability of attacking by strong earthquake, early warning system and the emergency program against great earthquake. Anti-seismic evaluation should be carried out for the important facilities.
3. It is necessary to carry out strict seismic design and construction for these relative constructions, storage devices and industrial equipments.
4. Especially, for the important links with impact probability in the disaster chain, which would be paid more attention to, and more relative measurements would be carried out to reduce the possibility of secondary disaster.

4. EXAMPLE

As an example, earthquake & fire link in disaster chain of petrochemical industry system is used, and the sketch of disaster chain is given in the Figure 5.

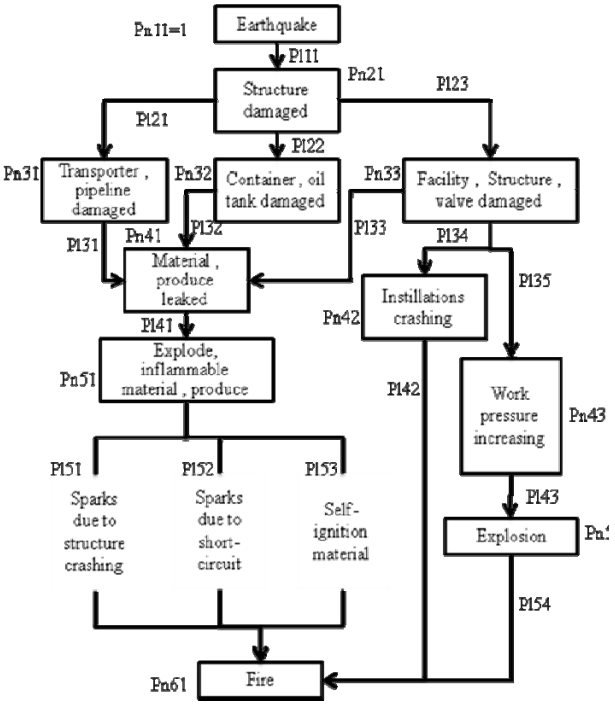

Figure 5 Earthquake & fire link in disaster chain of petrochemical industry system

In this disaster chain, the events are looked as nodes and the conditions are looked as the links. Refer to the exiting safety evaluation methods, such as the event tree analysis method, the probability of the links can be got, here, we assume their values given in Table 1. And then the probability of the nodes will be calculated by the Eq. (1) below:

$$Pn_{i+1} = 1 - \prod_{j=1}^{n} (1 - Pl_{ij} \times Pn_{ij}) \tag{1}$$

Here, Pn is the probability of node; Pl is the probability of link; i is the i-th stage of chain j is the j-th link in the i-th stage of chain; and n is the link number in the i-th stage. The results are showed in Table 2.

Table 1 The assumed probability values of the links Pl_{ij}

i \ j	1	2	3	4	5
1	0.500	-	-	-	-
2	0.700	0.500	0.300	-	-
3	0.800	0.800	0.600	0.200	0.200
4	0.700	0.600	0.700	-	-
5	0.200	0.200	0.100	0.800	-

Table 2 The calculated probability values of the nodes Pn_{ij}

i \ j	1	2	3	4	5
1	1.000	-	-	-	-
2	0.200	-	-	-	-
3	0.350	0.250	0.150	-	-
4	0.480	0.030	0.030	-	-
5	0.336	0.021	-	-	-
6	0.190	-	-	-	-

Compared with the probability of links in the i-th stage, the Max one will be looked as the main condition in the i-th stage, and compared with the probability of nodes in the i-th stage, the Max one will be looked as the main event in the i-th stage. The measurement directed against these events and conditions will reduce the probability of secondary disaster occurrence effectively. That is the main idea of the Chain-Cutting Disaster Mitigation from Gestation Source Method.

5. CONCLUSIONS

Based on the above contents, some major points of this paper are given in the following.

1. Secondary disasters of earthquake have complex diversity, according to comprehensive study of earthquake-induced disasters clearly, disaster chain theory has been used in this paper. Based on this method, it's easy to take effective measures to prevent and mitigate secondary disasters of earthquake.
2. The formation process of earthquake disaster chain has been analyzed, and as an example, a sketch of complete disaster chain based on the petrochemical industry system has been given.
3. The method, Chain-Cutting Disaster Mitigation from Gestation Source, has been used in this paper. According to reduce disaster hazard, it's necessary and important to cut off the disaster chain initial stage of its formation, in further, prevent the whole disaster chain formed effectively.
4. Based on the disaster chain principle, a probability analysis method of earthquake-induced disaster occurrence has been established, and as an example, preliminary analysis of this method is given.

Acknowledgements:

The authors acknowledge support from the bellow fund projects of China Earthquake Administration, Institute Fund Project (0418002) and Profession Fund Project (200708036).

References:

Li Tianqi and Zhao Zhendong. (2006), "Research on earthquake disaster chain of energy supply systems," *Journal of Natural Disaster*, **15**(5), 148-153.

Li Tianqi and Zhao Zhendong. (2007), "The earthquake disaster interaction research of the energy supply systems," *World Earthquake Engineering*, **23**(1), 21-25.

Corr R B, Tan V H Y. (1992), "Interim Guidance Note for the Design and Protection of Topside structure Against Explosion and Fire," *Joint Industry Project on Blast and Fire Engineering for Topside Structures.*

Corr R B, Tan V H Y. and Snell R O, Frieze P A. (1999), "Development of the limit state approach for design of offshore Platforms," *Era Conference 'Safety on Offshore Installations'. London : 8th International Conference Safety Oil offshore Installations*.

Walker S, Ta han N. (1991), "Behavior of Oil and Gas Fires in the Presence of Confinement and Obstacles," *Blast and Fire Engineering Joint Industry for Topside structure*.

JOINT CONFERENCE PROCEEDINGS
7th International Conference on Urban Earthquake Engineering (7CUEE) &
5th International Conference on Earthquake Engineering (5ICEE)
March 3-5, 2010, Tokyo Institute of Technology, Tokyo, Japan

SEISMIC PERFORMANCE AND COMMUNICATION FAILURE OF CELL PHONE TOWERS IN IRAN'S SEISMIC ZONES, CASE STUDY: DEVELOPING STRUCTURAL AND COMMUNICATIONAL FRAGILITY CURVES FOR 24M MONOPOLE TOWER

Mehdi Sadeghi[1)], Farzad Mohajeri[2)] and Erfan Khalaghi[1)]

1) M.Sc. Student, Department of Civil Engineering, Science and Research Branch of Islamic Azad University of Tehran, Iran
2) Assistant Professor, Department of Electronic and communication, Shiraz University, Shiraz, Iran
3) M.Sc. Student, Department of Civil Engineering, Science and Research Branch of Islamic Azad University of Tehran, Iran

Mehdisadeghi84@gmail.com, Mohajeri@shirazu.ac.ir,erfan.khalaghi@gmail.com

Abstract: Cell phone towers are among the most important parts in the communication systems and play a vital role in the stability, controllability and serviceability of the communication systems after the earthquake .it is obvious that correct operation of such communicating systems deeply affects better risk management in earthquake conditions. In this paper the seismic performance and failure conditions in cell phone operating mechanism with emphasize on Iran's seismicity are discussed by probabilistic approach. Fragility function of structures is the major requirement of seismic loss estimation which is widely used in the seismic risk management. In this paper, firstly, method is presented on brief for development of analytical fragility functions. Secondly, by performing a sets of nonlinear incremental dynamics analyzes (IDA) on convenient communicational tower (24m height monopole) tries to derived fragility curve for structural and communicational performance separately. At the end; results are discussed .this research shows the high reliability for communicational and structural performance of this specific structure.

1. INTRODUCTION

Iran is located in region with high level of seismicity. During the past 20 years great earthquake with high fatality and losses have struck different parts of the country. Earthquake cause extensive direct and indirect losses in which the damages to lifelines play an important role. Communications and its sensitive components are a key element among all other group of lifelines such as Electric power networks, transportation networks, pipelines, etc. According to vast usage of cell phone and its vital rule in controllability and serviceability of the risk management after an earthquake could prevent extensive direct and indirect losses, such as physical vulnerability and severe damages of communication facilities which are very expensive or connection failures due to cell phone tower's damage. On the other hand, it has been learned from the past earthquake that the existence of communication especially cell phones could facilitate the rescue and relief operation and this leads to saving more lives which is very important.

Several researchers have studied the effects of past earthquake on cell phone towers since early 80s to recent years. Gerstoft and Devenport (1986), Gantes, Khoury, Connor and Pouangare(1993), Khedr and McClure (1999,2000), Meshmesha, Sennah and Kennedy(2006) have developed an equations as simplified methods for seismic analysis of latticed telecommunication towers. Amiri(2007) has studies empirical equations for finding the time period of first three modes. But none of these mentioned researches haven't any risk management horizon as a part of urban lifelines. This paper try to construct a probabilistic approach to use on post earthquakes risk management by developing fragility functions, in addition for the first time in this paper import a non-structural damage index for developing fragility curves.

2. CELL PHONE TOWERS

A cell phone tower consists of multiple parts, most of which are owned by different companies. Typically a cell phone tower is built either by a tower company or a wireless carrier looking to expand their network coverage.

A cell phone tower consists of the following parts:

2.1 Tower

There are four different types of towers:

-Lattice Tower: also referred to as a self-support tower or SST, the lattice tower affords the greatest flexibility and is often used in heavy loading conditions. A lattice tower is typically three sided and has a triangular base; however there are some four sided lattice towers.

-Monopole Tower: A monopole tower is a single tube tower. It requires one foundation and typically don't exceed 200'. The antennas are mounted on the exterior of the tower.

-Guyed Tower: Guyed towers used to be the cheapest tower to construct, but require the greatest amount of land. For taller heights (300' and greater) it is much cheaper to build a guyed tower. Most radio and television towers are guyed towers. A guyed tower is a straight tower supported by guy wires to the ground which anchor the tower.

-Stealth Tower: Typically required by zoning. They are always more expensive than the other types of towers. More often than not they require additional material to "Stealth" their appearance and typically don't provide the same amount of capacity for tenants.

2.2 Equipment

Each of the tenants who mount their antenna on the cell phone tower uses transmitters installed in cabinets or in shelters. Different wireless carriers use different means of protecting their equipment. Many place outdoor cabinets on concrete pads, while others use premanufactured equipment shelters. This equipment is also called the "Base Transmitter Station" or "BTS".

2.3 Antennas

Each carrier will typically use multiple antennas on the tower. Sometimes there are as few as three antennas, sometimes as many as eighteen antennas per carrier. As additional subscribers come onto the carriers system the carriers need additional antennas to handle the added capacity.

2.4 Utilities

Almost every cell phone tower site has utilities installed at the site for use by the carriers. Typically each carrier has power run to the site as well as phone service. On some cell sites, each carrier will use up to 10 T-1 lines.

3. MONOPOLE TOWERS

The most common cell phone towers in Iran's urban area are Monopole 24meter height. Its consist of four main parts:

1-body's and flanges
2-ladder
3-lightening system
4-V or X pole antenna
5- Parabolic Reflector antenna

The body has four parts which connected with flanges. The ladder that lay through the tower's body. Lightening system, parabolic reflector and V or X pole are set on rooftop.

The Antenna's type is differential in assemblage and depending on its coverage area.

4. AN OVERVIEW ON DEFINITION OF FRAGILITY FUNCTION AND ESTIMATION METHOD

Due to practical reasons, continuous damage in structures is divided into several discrete damage states. Fragility function estimates the conditional exceeding probability of damage from a damage state at given ground motion intensity:

$$F_i(\mathrm{im}) = P(D > d_i \,|\, IM = \mathrm{im}) \qquad (1)$$

Where, *Fi (im)* is the probability of exceeding damage "D" from damage state "d*i"* at given ground motion "*IM=im"*. Ground motion intensity parameters denote the magnitude of ground motion which is measured by Peak Ground Acceleration (PGA), Peak Ground Velocity (PGV) or Spectral Displacement (SD). Damage states "*i"* are defined from the non-damage state (*i*=0) to the *n*th damage state (*i*=n) by qualitative and analytical definitions .Since damage in structures, in this study, is measured by Damage Index (DI), Eq. (1) is changed to:

$$F_i(\mathrm{im}) = P(DI > di_t \,|\, IM = \mathrm{im}) \qquad (2)$$

Where, *dit* is the damage index at the threshold of damage states. Having the Probability Density function(PDF) of "*DI"* or its cumulative distribution function(CDF) at every *"im"* (f_{im} (*di*) and (*t*) F_{im}*(dit)*), Eq. 3 is evaluated from probabilistic theorem:

$$F_i(\mathrm{im}) = P(DI > di_t \,|\, IM = \mathrm{im}) = 1 - F_{im}(di_t) \Rightarrow \qquad (3)$$
$$= 1 - \int_{-\infty}^{di_t} f_{im}(di)\,d(di)$$

In this paper, PDF of DI is evaluated by multi-stripe analysis. Here, tower is analyzed subjected to several real ground motion records that are all scaled to specific *IM (*here PGA*)* level and distribution of structural response in the particular *IM*(for two separated case: structural & communicational) is estimated from the results of the nonlinear analysis set. Based on these assumptions, procedure of fragility curve development for real structure(s) is summarized in five major steps shown in flowchart of methodology given in Figure 1:

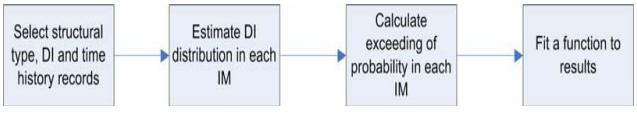

Figure 1 Procedure of estimating analytical fragility function

5. CASE STUDY

In this section case study monopole tower 24m height which is more common in Iran, is discuss. It is apparent that these cell phone tower plays vital role to make proper connection after an earthquake. The analyses are performed by advanced finite element software; for investigating structural performance transient translational and for Communicational performance permanent rotational displacement at the antenna location are derived. Then importing rotational displacement data into communicational software called, HFSS which can calculate the reduction of antenna's radiation magnitude that depend on the angular position of the top of tower. This is the most important communication parameter which can describe the condition of connection between tower and main center. Finally From two sets data for two different criteria (structural & Communicational) the fragility curves are developed and discussed.

5.1 Structural modeling

Refer to the technical documents, material of tower members is ST-37 steel grade with modulus elasticity of E=2.1E6 Kg/cm² , passion ratio of ν=0.3 and yielding stress F_y=2400 kg/cm². The material stress-strain curve is presented on fig.2 According to structural details fixed support is assigned in modeling. Gravitational forces considered in analysis are: weight of tower itself, antenna and the ladder. Specification of this tower and its antenna is illustrated in table 1& 2.

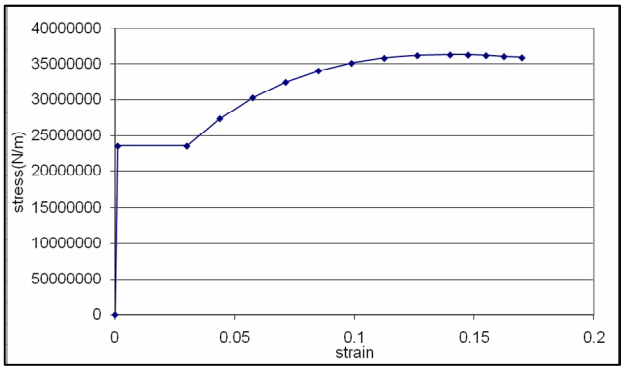

Figure 2 ST-37 stress-strain diagram

Table 1 Monopole (24m) detailing

part	Height(mm)	Thickness(mm)	Initial Diameter(mm)	End Diameter(mm)
1st	5970	5	940	839.5
2nd	5967	4	837.5	601
3rd	5981	4	601	400
4th	6000	4	400	400

Table 2 Antenna specification

Type	Parbolic Reflector
Diameter	40-45 cm
Frequency Range	1.5-2.5 GHz
Gain	20-35 dB

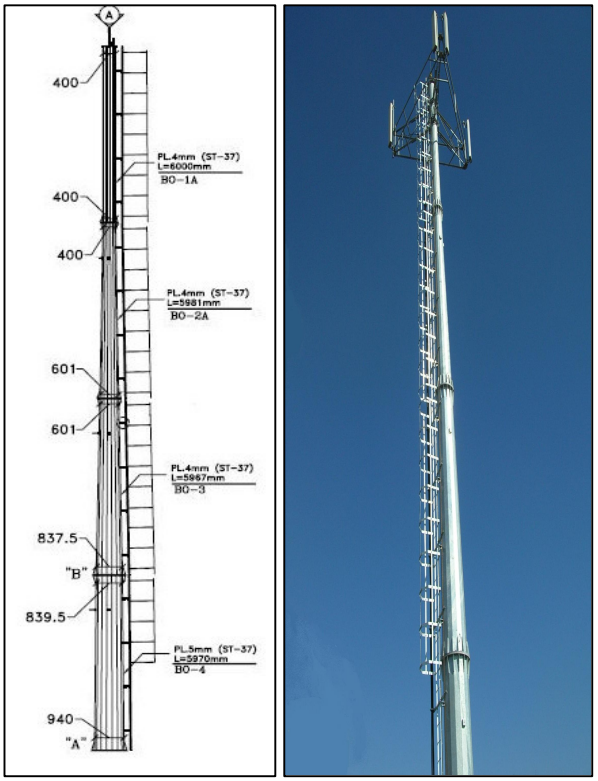

Figure 3 Structural detail and real monopole tower

5.2 Seismic input

Seven earthquake records are selected to be employed as the tower base excitations. All the records normalized to a maximum ground excitations as series of [0.1G, 0.2G, 0.3G, 0.35G, 0.45G, 0.5G, 0.6G, 0.7G, 0.8G, 0.9G, 1G] and all of them would be baseline corrected. Because of risk management bases of this project, authors prefer to select PGA for intensity measure criteria on developing fragility curve. Selected records along with their characteristics are describing on table3:

Table 3 earthquake detail

Earthquake	PGA(g)	Location	Moment magnitude	Year
Naghan	0.73	Iran	5.9	1977
Tabas	0.85	Iran	7.8	1978
Bam	0.81	Iran	6.5	2003
El centro	0.3	USA	7.1	1940
Hollister	0.279	USA	5.9	1989
Kobe	0.5	Japan	6.9	1995
Cape mendocino	0.8	USA	7.1	1992

5.3 Analysis Method

FEM Nonlinear dynamic approach has been employed for tower analysis. For this purpose, time history acceleration records are import to software; totally 77 analysis are performed, maximum transient translational and permanent rotational displacement at the antenna location are derived. The damping ratio used in all analysis is equal to 5 percent witch assumed is proportional to the mass and stiffness matrix.

$$\alpha[M]+\beta[K]=C \tag{4}$$

In this equation alpha and beta are RILEY linear coefficients and there relation between ζ is calculated from Eq2 for two different vibration modes:

$$\xi_i=\frac{\alpha_R}{2\omega_i}+\frac{\beta_R\omega_i}{2} \tag{5}$$

Geometric nonlinear (P-Δ effect) option is activated on the all situation.

6. DEFINITION OF LIMIT STATES

the authors didn't access any predefined structural limit state of damage index for this special structure, so perform an nonlinear pushover analyze with a uniform pattern loading along the tower height . From combination of this analyze and engineering judgment, defined 3 level limit sates. For Communicational performance 3 level limit states from experts opinions would be defined.(table4)

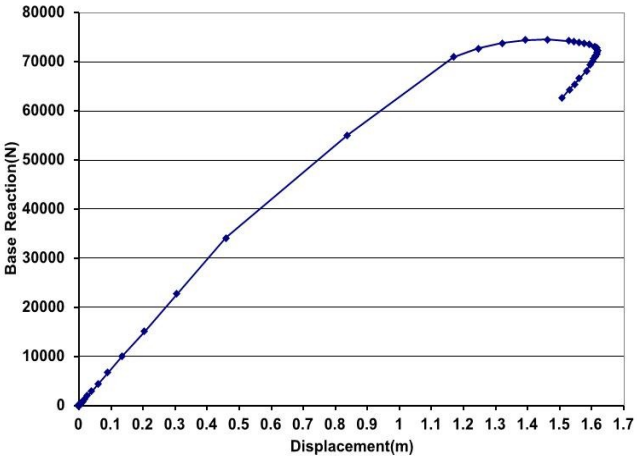

Figure 4 capacity curve from pushover analyze

Table 4 Final Limit States Definition

Structural Limit state		
level	**Description**	**limite state**
Low	first yeilding point	45cm
Medium	70% elastic stiffness	125cm
Sever	ultimate capacity curve point	161cm
Communicational Limit state		
level	**Description**	**limite state**
Full connection	continuse connection	4.5 deg
Medium connection	connection with some trouble	9 deg
NO connection	any connection	12 deg

7. NUMERICAL RESULT AND DEVELOPING FRAGILITY CURVES

The distribution of maximum top displacement and reduction of antenna radiation which is estimated from the analyses are shown in Figures 5 and 6. The solid line represent of mean value of results. To find appropriate distribution function for results, normal and log-normal distribution functions were tested. Although lognormal distribution was better fitted to results distributions in general.

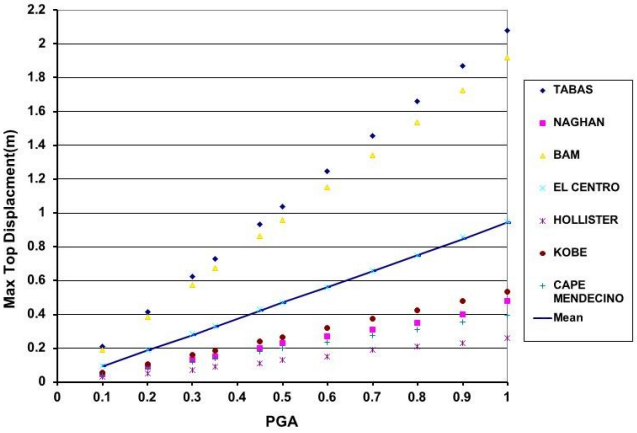

Figure 5 Maximum Top displacement of tower

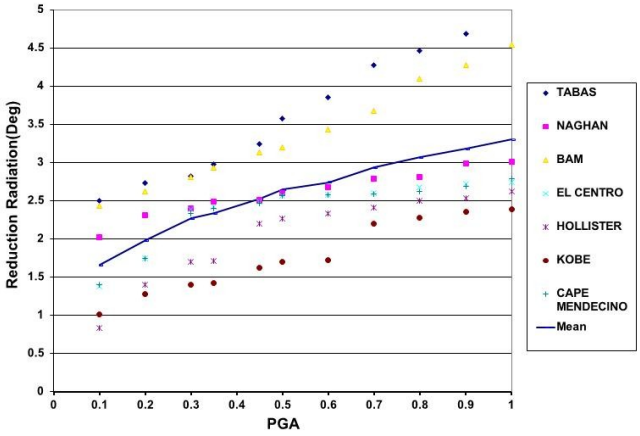

Figure 6 Maximum reduction of radiation of antenna

The fragility value at each *PGA* ($F\,i\,(PGA)$) is estimated by changing the notation of Eq. 3 and replacing the distribution of damage index ($f\,(di)\,im$) by lognormal distribution of results :

$$f(isd) = \varphi\left[\ln(ISD), \beta_{sd}\right] \tag{6}$$

$$\begin{aligned} F_i(sd) &= P(D > d_i \,|SD = sd) \Rightarrow \\ &= 1 - P(D \le d_i \,|SD = sd) \Rightarrow \\ &= 1 - \Phi(1/\beta_{sd}.\ln(ISD_i / \hat{ISD})) \end{aligned} \tag{7}$$

Where, *ISD i* is the mean ISD(result) threshold of damage states (e.g. Table 4). The results are shown in Figures 6 and 7 by dots. Fragility functions shown in the figures are estimated by fitting a log-normal cumulative distribution function:

$$F_i(sd) = P(D > d_i \,|SD = sd) = \Phi\left(\frac{1}{\beta_i}\ln\left(\frac{sd}{SD_i}\right)\right) \tag{8}$$

Where *SDi* and βi are mean and deviation of the function respectively.

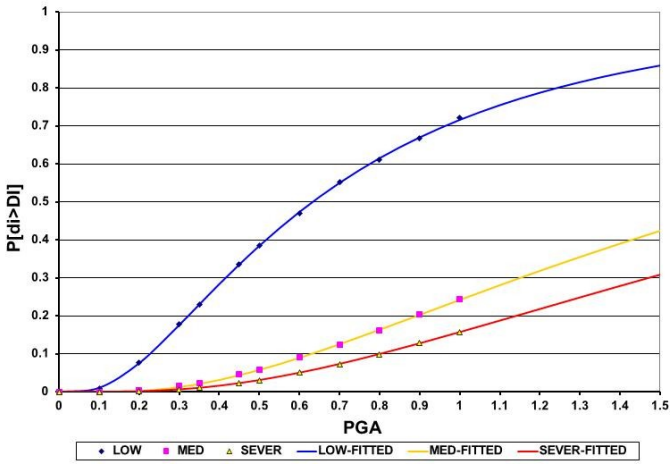

Figure 7 Fragility values and functions for structural performance

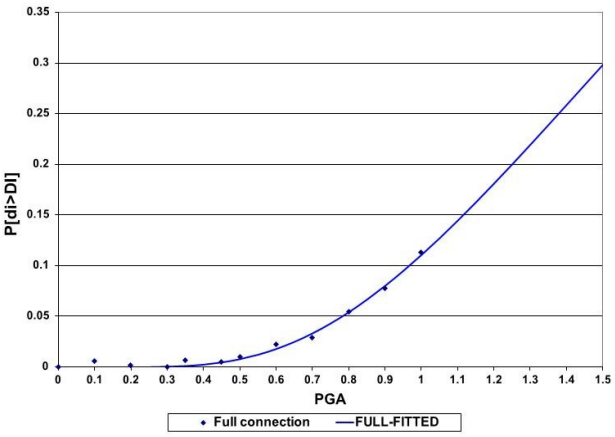

Figure 8 Fragility value and function for Communicational performance

Because of negligible amount of probability of exceedance of other limit states on fragility curves with Communicational criteria, just first limit state of these curves are plotted. By reviewing the results witch represent on figure 6 this condition could be predictable, because none of the results did not being on communicational limit state range.

At this step by knowing the hazard risk of each seismic zone, we can derived the exceeding probability of each limit state on any seismic zone. According to Iranian seismic code (2800 code) Iran is divided into four seismic zones. Figure 9.

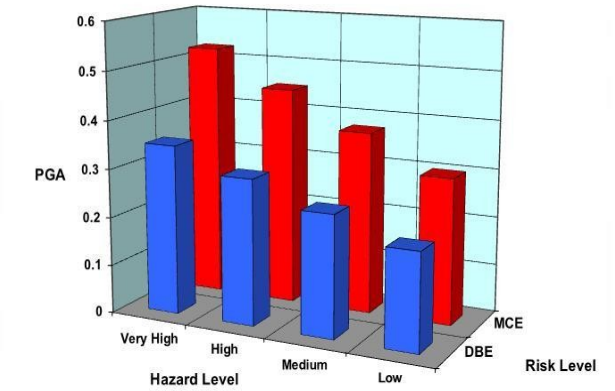

	Very High	High	Medium	Low
DBE	0.35	0.3	0.25	0.2
MCE	0.525	0.45	0.375	0.3

Figure 9 Iran's seismic zone and PGA hazard Levels

Corresponding to each seismic zone and by studying on fragility curve, we can access to simplified fragility matrixes according to figure 10 &11. Although as reason mentioned above this result illustrated just for structural performance. This result could be use directly on urban post earthquakes scenario based management procedure.

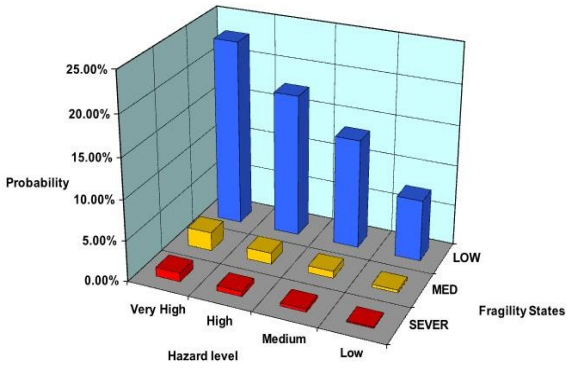

	Very High	High	Medium	Low
SEVER	1.10%	0.61%	0.37%	0.13%
MED	2.30%	1.39%	0.87%	0.34%
LOW	23.00%	17.62%	13.50%	7.55%

Figure 10 Fragility matrix for DBE risk level

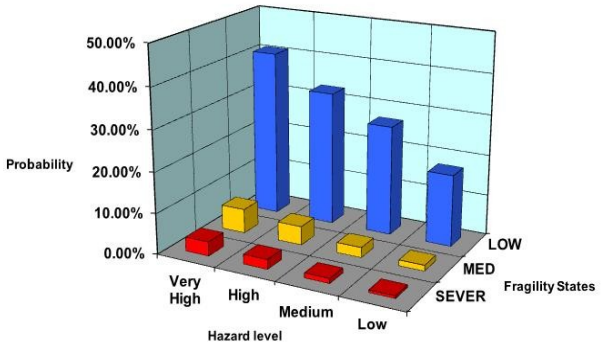

	Very High	High	Medium	Low
SEVER	3.50%	2.40%	1.20%	0.61%
MED	6.00%	4.60%	2.50%	1.40%
LOW	41.00%	33.00%	27.00%	17.62%

Figure 11 Fragility matrix for MCE risk level

8. CONCLUSIONS AND PROPOSALS FOR FUTURE WORK

By studying fragility curves and matrixes witch presented on figure 7 to 11; the following conclusions could be stated:

1. at the acceleration more than 0.65g, the probability of structural fragility at the low damage level has exceeded more than 50 percent.

2. even at the very high level of acceleration in order to pass medium and Sever condition level, the tower structure has a fragility probability less than 50 percent.

3. The communicational performance of a system is very reliable even at a high level of acceleration. Also it has shown that it has less dependent on levels of structural damages.

4. on general conclusion, this system in both communicational and structural performance has a high reliability even at very high peak ground accelerations.

The authors propose future works conduct on some additional field, for example: effect of tower beneath soil (SSI), derived better intensity measure for fragility curve, nonstructural equipment of communicational system…

References:

K. Nasserasadi,M. Ghafory-Ashtiany, S. Eshghi and M.R. Zolfaghari , DEVELOPING SEISMIC FRAGILITY FUNCTION OF STRUCTURES BY STOCHASTIC APPROACH , ASIAN JOURNAL OF CIVIL ENGINEERING (BUILDING AND HOUSING) VOL. 10, NO. 2 (2009)

Porter, K.A. "An overview of PEER's performance-based earthquake engineering methodology." Proc.Ninth International Conference on Applications of Statistics and Probability in Civil Engineering (ICASP9*)*, Volume 2, pp. 973-980, San Francisco, CA, USA, July 6-9, 2003.

Cornell, C. A., Krawinkler, H. "Progress and challenges in seismic performance assessment." PEER Center News 2000; 3(2).

Khedr, M. A. and McClure, G., (1999) "Earthquake amplification factors for self-supporting telecommunication towers", Canadian Journal of Civil Engineering, Vol. 26, No. 2, pp.208-215.

Khedr, M.A., and G. McClure, (2000). A simplified method for seismic analysis of lattice telecommunication towers. Canadian Journal f Civil Engineering, Vol. 27, pp. 533-542

Gerstoft, P.; and Devenport, A. G., (1986). A simplified method for dynamic analysis of a guyed mast. Journal of Wind Engineering and Industrial Aerodynamics, Vol.23, No.1, pp. 487-499.

Gantes, CH.; Khoury, R.; Connor, J. J.; and Pouangare, C. (1993) Modeling, loading, and preliminary design considerations for tall guyed towers. Computers and Structures, 1993, Vol. 49, No.5, pp. 797-805.

Meshmesha, H.; Sennah, K.; and Kennedy, J. B., (2006) Simple method for static and dynamic analyses of guyed towers. Structural Engineering and Mechanics, 2006, Vol.23, No.6, pp. 635-649.

Amiri, G.G., Massah, S. R., and Boostan, A., (2007) Seismic Response of 4- Legged Self-Supporting Telecommunication towers, IJE Transactions B: Applications, Vol. 20, No. 2, August, pp.107-126.

Clough, Ray W, and Penzien Joseph, (1993),"Dynamics of structures"2nd edition.

Chopra, Anil K.(1980) "Dynamics of structures a primer"

Subramanian, N., "A simplified method for seismic analysis of Legged lattice telecommunication towers" www.Google.com, -2009

Iranian earthquake code (2800 standard),2001,building and housing research center.

Steel in the air. " Cell phone tower types and information " www.Google.com, -2009

Jalayer F. Direct probabilistic seismic analysis: implementing non-linear dynamic assessments, PhD thesis Civil and Environmental Engineering Department, University Stanford, California, 2003.

JOINT CONFERENCE PROCEEDINGS
7th International Conference on Urban Earthquake Engineering (7CUEE) &
5th International Conference on Earthquake Engineering (5ICEE)
March 3-5, 2010, Tokyo Institute of Technology, Tokyo, Japan

BAYESIAN NETWORK FOR INFRASTRUCTURE SEISMIC RISK ASSESSMENT: CHALLENGES AND OPPORTUNITIES

Michelle T. Bensi[1)], Armen Der Kiureghian[2)], and Daniel Straub[3)]

1) Doctoral Candidate, Department of Civil & Environmental Engineering, University of California, Berkeley, USA
2) Taisei Professor of Civil Engineering, Department of Civil & Environmental Engineering, University of California, Berkeley, USA
3) Associate Professor, Engineering Risk Analysis Group, Technical University Munich, Germany
mbensi@berkeley.edu, adk@ce.berkeley.edu, straub@era.bv.tum.de

Abstract: An overview of recent efforts directed at developing a probabilistic decision-support system (DSS) for seismic infrastructure risk assessment and management is presented. The DSS is based on a Bayesian network (BN) framework which is particularly well-suited for the proposed application. BNs are graphical and intuitive, facilitate information updating, can be used for identification of critical components within a system, and can be extended by decision and utility nodes to solve decision problems. In particular, the facility for information updating renders the BN an ideal tool for post-event infrastructure risk assessment and decision support. However, BNs have several limitations that must be addressed to make them a viable tool in the suggested context. Some of these challenges and proposed solutions are described in this paper.

1. INTRODUCTION

Civil infrastructure systems are the backbones of modern societies yet they remain vulnerable to a wide-variety of natural and man-made hazards. In many regions of the world earthquakes pose the dominant risk to infrastructure systems. However, through sound engineering and decision-making it is possible to mitigate these risks. There are three distinct phases during which seismic risk assessment and management decisions must be made: (1) pre-event, (2) immediate post-event, and (3) longer-term post-event. In the phase prior to the occurrence of an earthquake, it is necessary to assess risks by identifying critical components and bottlenecks in the system, and then take actions to minimize the risk exposure, e.g. retrofit/replace components, implement an optimal inspection/maintenance schedule, modify system configuration. In the phase immediately following an earthquake, decisions must be made to reduce the severity of post-event consequences. Often, at this stage, emphasis is placed on life safety and restoration of critical services. Post-event decisions include the dispatching of rescue, inspection, and repair crews as well as decisions to open or close facilities. These decisions are made under the competing demands to maintain operability (to prevent revenue loss) while not sacrificing safety (to avoid deaths and injury, as well as liability). This decision-phase is characterized by an environment in which information is both uncertain and quickly evolving in time. Sources of information at this phase may include ground motion (GM) intensity measurements, structural health monitoring sensors, inspection results, and even observations reported by citizens and facility employees. Finally, in the longer-term post-earthquake recovery phase, it is necessary to take actions to minimize long-term economic consequences from the event, e.g. optimal prioritization of replacement and retrofitting of damaged facilities. Additionally, hazard and system models must be updated based on knowledge gained from the earthquake.

With the above motivation in mind, we are working toward the development of a probabilistic decision-support system (DSS) for seismic infrastructure risk assessment and management. Ultimately, the DSS will aid decision-making during each of the aforementioned phases. To date, our efforts have focused primarily on a post-earthquake DSS able to incorporate uncertain and time-evolving information from a variety of sources. We utilize a Bayesian Network (BN) framework for the DSS because it is particularly well-suited for the proposed application. This paper provides an overview of the BN models developed for this purpose.

The paper begins with a brief introduction to BNs. Next, an overview of recent work towards the development of the DSS is presented. Components of the proposed BN framework include: (1) a seismic demand model of ground motion intensity as a spatially distributed random field accounting for finite fault rupture and directivity effects, (2) models of performance for both point-site and distributed components, (3) models of system performance, and (4) the extension of the BN to include decision and utility nodes to aid post-earthquake decision-making. Like other computational methods, BNs are not without shortcomings. In particular, calculations in BNs can be highly demanding of computer memory. Throughout the paper, work done to address this limitation is described.

2. BRIEF ON BAYESIAN NETWORKS

2.1 Motivation for using Bayesian networks

A BN is a probabilistic graphical model that represents a set of random variables and their probabilistic dependencies. The variables may represent demand or capacity values, or the states of components and systems. BNs are graphical and intuitive, facilitate information updating, can be used for identification of critical components within a system, and can be extended by decision and utility nodes to solve decision problems. In particular, the facility for information updating renders the BN an ideal tool for infrastructure risk assessment and decision support. Evidence on one or more variables (e.g. observed component capacities, demands, or component/system states) is entered into the BN and this information propagates throughout the network to provide an up-to-date probabilistic characterization of the performance of the infrastructure system in light of the new observations. This dynamic system representation is particularly critical for post-event, near-real time applications when the available information is uncertain and rapidly evolves with time.

2.2 Brief Introduction to Bayesian Networks

A BN is a directed acyclic graphical model consisting of a set of nodes representing random variables and a set of links representing probabilistic dependencies. Typically, links represent causal relationships. Consider the simple BN shown in Figure 1 modeling five random variables $\mathbf{X} = \{X_1, \dots X_5\}$ and their probabilistic relationships. For example, the random variable X_3 is probabilistically dependent on variables X_1 and X_2, as represented by arrows going from nodes X_1 and X_2 to node X_3. In the BN terminology, X_3 is a *child* of X_1 and X_2, while X_1 and X_2 are the *parents* of X_3. Additionally, X_4 is defined conditionally on its parent node X_1 and X_5 is defined conditionally on X_4. Each node is associated with a set of mutually exclusive collectively exhaustive states. To be able to utilize exact inference algorithms, it is generally necessary to discretize all continuous random variables in the BN (with the exception of continuous Gaussian nodes without discrete children). We will not address BNs with continuous nodes in this paper, but additional details can be found in Lauritzen (1992), Lauritzen & Jensen (2001), and Langseth (2009). For discrete nodes, probabilistic dependencies are encoded by attaching to each node a *conditional probability table* (CPT) providing the conditional probability mass function (PMF) of the random variable given each of the mutually exclusive states of its parents. . For random variables without parents (e.g. X_1 and X_2), a marginal probability table is assigned.

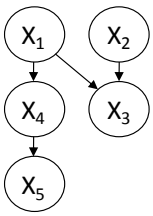

Figure 1: A simple BN

The ability to model a problem using conditional distributions is convenient in civil engineering applications, where often only conditional relationships are available, e.g. typically we may know the probability of a load exceeding a specific value *given* an event of a certain size, or the probability of damage *given* a particular demand value. The joint distribution of all random variables in the BN, **X**, is constructed as a product of the conditional distributions as

$$p(\mathbf{X}) = \prod_{i=1}^{n} p(x_i | pa(x_i)) \tag{1}$$

where $pa(x_i)$ is the set of parents of node X_i, $p(x_i | pa(x_i))$ is the CPT of X_i and n is the number of random variables (nodes) in the BN. Thus, for the BN in Figure 1, the joint PMF is

$$p(x_1, x_2, x_3, x_4, x_5) = \\ = p(x_5|x_4)p(x_4|x_1)p(x_3|x_1, x_2)p(x_1)p(x_2) \tag{2}$$

BNs are useful for answering probabilistic queries when one or more variables are observed. That is, BNs efficiently compute the conditional distribution of any subset $\mathbf{X}'$ of the variables in the BN given observations (or evidence) on any other subset $\mathbf{X}^e$ of the variables . The ease with which BNs facilitate the calculation of the conditional distribution $p(\mathbf{X}'|\mathbf{X}^e)$ is the main feature that makes the BN framework ideally suited for the proposed application. For example, suppose observations have been made on nodes X_3 and X_5 in Figure 1 and we are interested in computing the conditional distribution $p(X_2|X_3 = x_3, X_5 = x_5)$. This quantity can be computed by first marginalizing the joint distribution in (2) to obtain the joint distributions over the subsets of the variables:

$$p(x_2, x_3, x_5) = \sum_{x_1, x_4} p(x_1, \dots, x_5) \\ p(x_3, x_5) = \sum_{x_1, x_2, x_4} p(x_1, \dots, x_5) \tag{3}$$

The desired conditional distribution is then obtained as

$$p(x_2|x_3, x_5) = \frac{p(x_2, x_3, x_5)}{p(x_3, x_5)} \tag{4}$$

There are more efficient ways to do this calculation. Specifically, there are algorithms that facilitate probabilistic updating in BNs without repeated calculations over the joint distribution as demonstrated above. The reader is referred to Jensen & Nielson (2007) for additional details on probabilistic inference algorithms.

3. SEISMIC DEMAND MODEL

Infrastructure systems are typically distributed over a geographic region. As a result, they have a higher rate of exposure to hazard than single-site facilities and are subject to a wider range of hazards (e.g. ground shaking, ground deformation due to liquefaction and fault rupture). Furthermore, the ground motion intensity must be modeled as a spatially distributed random field to account for the statistical dependence between the seismic demand values at the locations of different components of the system.

In this section we introduce a BN model of the GM intensity as a spatially distributed random field. We focus here on hazard due to ground-shaking, but the framework is easily extended to other hazards. Models for predicting liquefaction-

induced ground deformation (lateral spreading, settlement) are currently under development.

Consider a system of n sites distributed over a geographic region in the vicinity of multiple faults. We now construct a BN predicting the distribution of GM intensity at each site for an earthquake occurring randomly on one of the faults. For each earthquake fault, there is a source-dependent distribution of magnitude and earthquake epicenter location. Furthermore, the rupture length on a fault is a function of earthquake magnitude and source characteristics (Wells & Coppersmith 1994). Figure 2 shows a BN model of these relationships. The node representing magnitude (M) is specified as a child of the source node (S_C), indicating that the probability of experiencing an earthquake of a certain magnitude differs based on the source. Similarly, S_c is a parent of the node modeling epicenter location (X_e). Node R_L, representing the rupture length, is a child of node M and node S_C.

To define the geometry of the geographic region of the infrastructure system, we use a fault specific local coordinate system. Consider an idealization of a fault as a straight line. A source-specific local coordinate system with the fault oriented along the x-axis and its left end located at the origin is shown in Figure 3. In this local coordinate system, the location of the epicenter (shown as a star in Figure 3) is defined by a point on the x-axis between 0 and F_L, where F_L is the length of the fault. The location of the rupture within the fault is defined as a function of the epicenter location and the rupture length. Let X_r denote the coordinate of the left end of the rupture. Assuming the length of the segment of the rupture to the left of the epicenter is uniformly distributed over the interval $[0, R_L]$, one can show that X_r is uniformly distributed within the interval

$$\left[X_e - \min(R_L, X_e)\,, X_e - \max\left(0, R_L - (F_L - X_e)\right)\right] \quad (5)$$

Thus, node X_r is a child of S_c, R_L, and X_e.

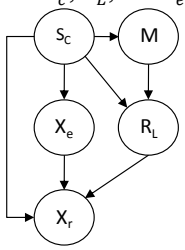

Figure 2: BN modeling rupture length and location as a function of earthquake source, epicenter location, and magnitude

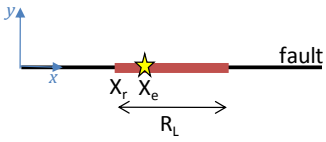

Figure 3: Fault-specific local coordinate system

For a given rupture length, the source-to-site distance (the shortest distance between the site and the rupture) is defined for each site within the source-specific coordinate system (see Figure 4). Suppose that there are J faults (indexed by $j = 1, \ldots, J$) in the region of the infrastructure system. Using the line-source idealization for all faults, the distance between the ith site and a rupture on the jth fault, is computed as

$$R_i = \sqrt{\left(X_{d,i}^j\right)^2 + \left(y_{s,i}^j\right)^2 + \left(z_{s,i}^j\right)^2} \quad (6)$$

where $y_{s,i}^j$ and $z_{s,i}^j$ are the coordinates of site i in the coordinate system defined by source j, and $X_{d,i}^j$ is the x-direction distance between site i and the nearest point on the rupture on source j. For the straight-line idealization of a fault, $X_{d,i}^j$ is expressed using simple geometry as:

$$X_{d,i}^j = \max\left[X_r^j - x_{s,i}^j, x_{s,i}^j - min\left(X_r^j + R_L, F_L^j\right), 0\right] \quad (7)$$

where $x_{s,i}^j$ is the x-direction coordinate of site i and X_r^j is the left end of the rupture, both in the coordinate system defined by source j. The term $\min\left(X_r^j + R_L, F_L^j\right)$ specifies the coordinate of the right end of the rupture. Due to finite fault dimensions, this coordinate is physically constrained to be less than the fault length. For more general geometric configurations, i.e., faults that are not idealized as straight lines, similar expressions can be derived, though they are typically more complicated.

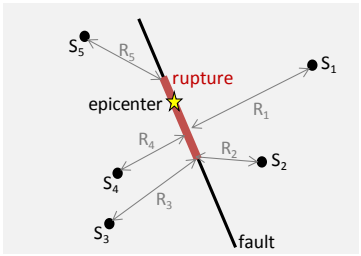

Figure 4: Geographically distributed sites in vicinity of a fault

The BN corresponding to the above description is shown in Figure 5. Node R_i is a child of nodes S_C, R_L, and X_r and is a function of the site coordinates as well. The site coordinates need not be represented in the BN as nodes because they are considered deterministic.

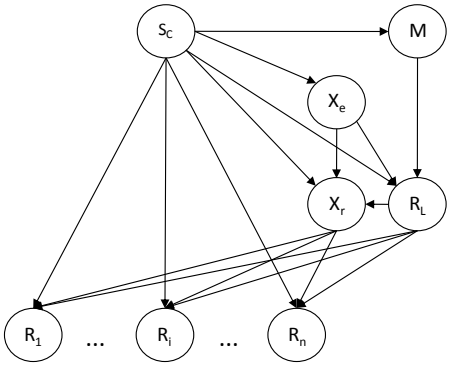

Figure 5: BN modeling source-to-site distance as a function of earthquake source and rupture length and location

Prediction models based on regressions of observed data relate GM intensity at a site to earthquake source and site characteristics, e.g., see Abrahamson et al. (2008). GM prediction equations (also known as attenuation laws) typically have the form

$$\ln S_i = \ln \overline{S}_i + \epsilon_m + \epsilon_{r,i} \quad (8)$$

where $\ln \overline{S}_i = f(M, R_i, \boldsymbol{\theta}_i)$ is the natural logarithm of the median GM intensity at site i expressed as a function of the site-

to-source distance, the earthquake magnitude, and a vector of site/source properties, $\boldsymbol{\theta}_i$, (e.g. faulting mechanism, shear wave velocity, depth to significant impedance contrast). Thus, a node $\ln \overline{S_i}$ is added as a child of nodes M, R_i and S_C. As long as the site properties are taken to be deterministic (or stochastic but unobservable), there is no need to explicitly model them as nodes in the BN. In the above expression, ϵ_m is an inter-event error term and $\epsilon_{r,i}$ is an intra-event error term, both describing variabilities in the logarithmic intensity value relative to the median. Both error terms are zero-mean and normally distributed. The inter-event deviations arise from inaccuracy or idealization in the characterization of the source and represent the variability in GM intensity from earthquake to earthquake. The intra-event deviations arise from uncertain wave propagation and site effects. For a particular earthquake, intra-event deviations represent the variability in the GM intensity from site to site. For a given earthquake, ϵ_m is the same for all sites. As a result, a single node ϵ_m is introduced that is a parent of all site-specific GM intensity nodes. The intra-event errors are site-specific but are spatially correlated. The correlation arises because, for a given earthquake, the magnitude of the difference between the actual and predicted median GM intensity is similar for sites in close proximity to one another but can be less similar as the distance between the sites increases. A node representing $\epsilon_{r,i}$ is added to the BN for each site. The correlation among $\epsilon_{r,i}$'s is modeled with links between all pairs of the corresponding nodes. This is illustrated in Figure 6.

Directivity effects are included in the BN through the addition of a node $f_{d,i}$ representing an amplification factor on GM intensity at site i. In Abrahamson (2000), an amplification factor is added to the natural logarithm of the spectral acceleration from the GM prediction equation. The factor is specified as a function of the amount of the rupture that propagates toward the site and the angle between the direction of the rupture and the site. For this reason, node $f_{d,i}$ is a child of nodes defining the site and source geometry. Additionally, $f_{d,i}$ is affected by the earthquake magnitude and so is a child of node M. Figure 6 shows the complete BN model, including the spatial correlation as well as directivity effects. We refer to the sites for which GM intensity nodes are included in the BN as *ground motion prediction points* (GMPPs).

Monte Carlo simulation is used to compute the CPTs for R_L, X_r, R_i, S_i and other nodes described in the paper, for which the functional dependence between the nodes is known.

4. BN MODELING OF RANDOM FIELDS

Modeling RFs in BNs is computationally demanding. This is because BNs with broadly dependent random variables (densely connected nodes) result in exponential increases in computational demands. This is the case with the nodes representing the intra-event error terms $\epsilon_{r,i}$ in the BN in Figure 6. The increase in computational demand can quickly render the BN computationally intractable for infrastructures with many sites. For this reason we have developed a procedure for modeling the GM intensity RF within the BN framework in a computationally tractable manner.

Define $\epsilon_{r,i} = \epsilon_r(\mathbf{x}_i)$, $i = 1, \dots, n$ as a set of discrete points in the zero-mean Gaussian RF $\epsilon_r(\mathbf{x})$ describing the spatial distribution of the intra-event error term. This field is defined by a standard deviation function $\sigma_r(\mathbf{x})$ and an autocorrelation function $\rho(\mathbf{x}_i, \mathbf{x}_j)$. Thus the Gaussian vector $\boldsymbol{\epsilon}_r = [\epsilon_{r,1}, \epsilon_{r,2}, \dots, \epsilon_{r,n}]^T$ has a zero mean vector, standard deviation matrix $\mathbf{D} = diag[\sigma_{r,i}]$ and correlation matrix $\mathbf{R} = [\rho_{ij}]$, where $\sigma_{r,i} = \sigma_r(\mathbf{x}_i)$ and $\rho_{ij} = \rho(\mathbf{x}_i, \mathbf{x}_j)$. The BN representing $\boldsymbol{\epsilon}_r$ is shown in Figure 7. The CPTs in this BN require the specification of the distributions $p(\epsilon_{r,i} | \epsilon_{r,1}, \dots, \epsilon_{r,i-1}), i = 1, \dots, n$.

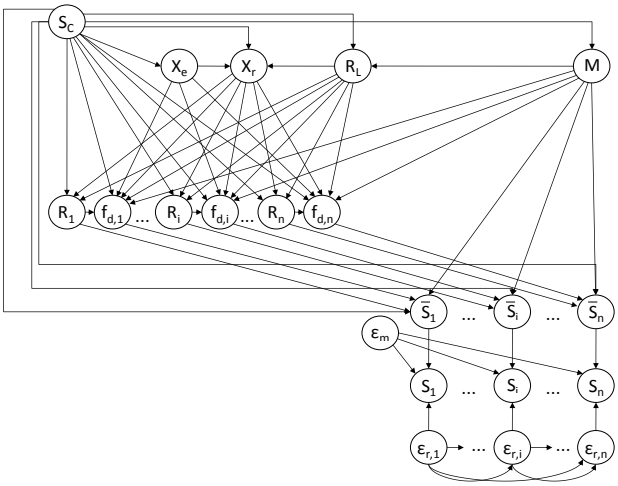

Figure 6: BN modeling GM intensity at each site across a geographically distributed system

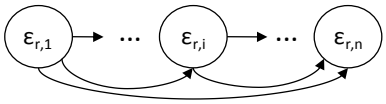

Figure 7: BN modeling points in Gaussian RF

The vector $\boldsymbol{\epsilon}_r$ can be decomposed as a product of an $n \times n$ transformation matrix $\mathbf{T}$ and a $n \times 1$ vector of statistically independent standard normal random variables (RVs) $\mathbf{U}$ as

$$\boldsymbol{\epsilon}_r = \mathbf{TU} = \begin{pmatrix} t_{11} & \cdots & t_{1n} \\ \vdots & \ddots & \vdots \\ t_{n1} & \cdots & t_{nn} \end{pmatrix} \begin{bmatrix} U_1 \\ \vdots \\ U_n \end{bmatrix} \quad (9)$$

The BN corresponding to this transformation is shown in Figure 8. An element of the transformation matrix, t_{ij}, is interpreted as a factor on the link between U_j and $\epsilon_{r,i}$. The covariance matrix is computed as a product of the transformation matrix and its transpose: $\boldsymbol{\Sigma} = \mathbf{TT}'$. It is easy to specify the CPTs required by the BN in Figure 8 because each $\epsilon_{r,i}$ is a deterministic function of the U_i's.

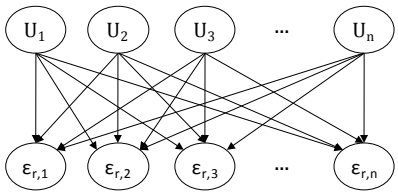

Figure 8: BN showing the transformation $\boldsymbol{\epsilon} = \mathbf{TU}$

The transformation matrix can be determined using the Cholesky factorization, an Eigenvalue (Karhunen–Loève) expansion, or other decomposition methods. The values of the transformation matrix can also be determined approximately via numerical optimization methods, as described later.

While the aforementioned decomposition results in CPTs that are easier to specify than the formulation in Figure 7, it does not decrease computational demand. A reduction in computational demand can be achieved by: (1) reducing the density of links in the BN in Figure 8 and/or (2) reducing the number of states associated with each node (which results in a reduction in CPT sizes, but at the cost of loss of accuracy) We focus here on the reduction of links required to model the random field, which results in the approximation of the spatial error correlation structure. While discretization is not addressed specifically here, the reader is referred to Straub (2009) for additional details on this subject.

Removing a link in the BN corresponds to setting the associated element of the transformation matrix equal to zero. Setting $t_{ij} = 0$ implies removal of the link connecting U_j and $\epsilon_{r,i}$. Define $\hat{\mathbf{T}} = [\hat{t}_{ij}]$ as the matrix $\mathbf{T}$ with some of its elements set to zero. If column i of the transformation matrix has all zero entries, then this implies node U_i has no children and it can be eliminated from the BN. The reduction of nodes/links in the BN results in an approximation of the covariance matrix of $\boldsymbol{\epsilon}_r$. By introducing an additional $n\times1$ vector of statistically independent standard normal RVs $\mathbf{V}$, the approximation in the variances can be eliminated without affecting the covariance (off-diagonal) terms. The addition of these correction terms does not affect the computational efficiency gained through link reduction. Incorporating these correction terms, $\boldsymbol{\epsilon}_r$ is approximated using the transformation

$$\widehat{\boldsymbol{\epsilon}_r} = \mathbf{SV} + \hat{\mathbf{T}}\mathbf{U} = \begin{pmatrix} s_1 & \cdots & 0 \\ \vdots & \ddots & \vdots \\ 0 & \cdots & s_n \end{pmatrix}\begin{bmatrix} V_1 \\ \vdots \\ V_n \end{bmatrix} + \begin{pmatrix} \hat{t}_{11} & \cdots & \hat{t}_{1m} \\ \vdots & \ddots & \vdots \\ \hat{t}_{n1} & \cdots & \hat{t}_{nm} \end{pmatrix}\begin{bmatrix} U_1 \\ \vdots \\ U_m \end{bmatrix} \quad (10)$$

where $\hat{\mathbf{T}}$ is an $n\times m$ $(m \le n)$ transformation matrix, $\mathbf{U}$ and $\mathbf{V}$ are respectively $m \times 1$ and $n\times1$ vectors of statistically independent standard normal RVs, and $\mathbf{S}$ is a diagonal matrix having the elements

$$s_i = \sqrt{\sigma_{r,i}^2 - \sum_{k=1}^{m\le n} \hat{t}_{ik}^2} \quad (11)$$

This formulation ensures that $\hat{\epsilon}_{r,i}$ has the same variance as $\epsilon_{r,i}$. The corresponding BN is shown in Figure 9.

A review of a procedure for determining $\hat{\mathbf{T}}$ is presented here; more details can be found in Bensi et al. (2010a). As described above, setting the elements in the transformation matrix to zero corresponds to a reduction of links. Link reduction may be accomplished by: (1) removing U-nodes and all associated links by setting an entire column of the transformation matrix to zero, (2) selectively removing links while keeping the full number of U-nodes, or (3) first reducing the number of U-nodes and then selectively removing links from the remaining U-nodes. When eliminating nodes and links, the goal is to properly balance computational efficiency and accuracy, i.e., removing as many nodes/links as possible without significantly reducing the accuracy of representing the correlation structure of the RF.

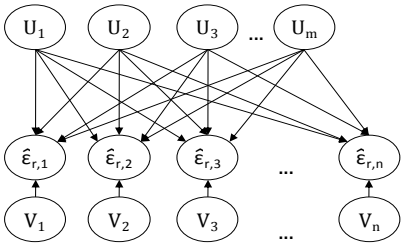

Figure 9: BN corresponding to $\widehat{\boldsymbol{\epsilon}_r} = \mathbf{SV} + \hat{\mathbf{T}}\mathbf{U}$

When using transformation matrices obtained by decomposition methods (e.g. eigenvalue expansion, Cholesky factorization), nodes and links are eliminated as a function of node and link importance measures. The node importance measure (NIM) is defined as

$$M_i = \sum_{k=1}^{n}\sum_{l=k}^{n} |\Delta_i(k,l)| \quad (12)$$

where M_i is the NIM associated with node U_i and $\Delta_i(k,l)$ is the $(k,l)^{th}$ element of the matrix Δ_i, computed as

$$\Delta_i = T_i T_i' \quad (13)$$

where T_i is the ith column of the transformation matrix $\mathbf{T}$ and the prime indicates matrix transpose. Δ_i quantifies the contribution of U_i to the covariance matrix. Thus M_i is a measure of how much of the information contained in the covariance matrix is lost by eliminating U_i. It follows that eliminating the U-node associated with the smallest NIM results in the least loss in accuracy. Similarly, a link importance measure (LIM) associated with each t_{ij} is defined as

$$m_{ij} = \sum_{k=1}^{n}\sum_{l=k}^{n} |\delta_i(k,l)| \quad (14)$$

where m_{ij} is the NIM associated with link t_{ij}, $\delta_{ij}(k,l)$ is the $(k,l)^{th}$ element of the matrix δ_{ij} computed as:

$$\delta_{ij} = T_i T_i' - T_{j,i} T_{j,i}' \quad (15)$$

where T_i is the ith column of the transformation matrix $\mathbf{T}$ and $T_{j,i}$ is i^{th} column of the transformation matrix with the jth element set equal to zero. The links in the BN are ordered by LIM and elimination of the link with the smallest importance measure results in the least loss in accuracy. The node- and link-based approaches can be combined, with U-nodes first eliminated based on NIMs followed by the elimination of links based on LIMs.

Alternatively, the approximate transformation matrix can be defined through an optimization scheme. A node-based elimination approach is defined by first specifying the number of U-nodes to include (m) and then solving the optimization problem

$$\min \sum_{i=1}^{n-1}\sum_{j=i+1}^{n}\left[\rho_{ij} - \frac{\sum_{k=1}^{m\le n} \hat{t}_{ik} * \hat{t}_{jk}}{\sigma_{r,i}\sigma_{r,j}}\right]^2 \quad \text{subject to:} \quad \sum_{k=1}^{m\le n} \hat{t}_{ik}^2 < \sigma_{r,i}^2, \ \forall i \quad (16)$$

where the objective is to minimize the sum of squared

deviations between the actual and approximated correlation coefficients. The use of non-linear constrained optimization to determine the terms of the approximate transformation matrix was suggested by Song & Ok (2009) and Song & Kang (2009).

Analogously, a link-based optimization problem can be formulated in which the number of links is specified rather than the number of nodes. The result is a mixed-integer non-linear constrained optimization problem. It was found that such a formulation performs poorly in practice. Instead, an iterative procedure for link elimination has been developed. First, the optimization described in (16) is performed. Then links are eliminated individually according to their LIM. The values of the remaining links are then re-optimized. The full iterative procedure is described in Figure 10. The iterative procedure can be adapted so that links are eliminated based on magnitude of LIM, i.e. all links with LIMs below a specified threshold are eliminated.

INITIALIZE

1. Specify:
   m = maximum number of U-nodes to include
   N_e = the number of links to eliminate (N_e)
2. Determine the $n \times m$ matrix $\mathbf{T}_0$ with elements obtained by solving the optimization problem in (16)

ELIMINATE LINKS

for $p = 1, \ldots, N_e$

1. Calculate LIMs for all elements of $\hat{\mathbf{T}}_{p-1}$
2. Identify indices for the elements in $\hat{\mathbf{T}}_{p-1}$ with the smallest p LIM values
3. Determine the $n \times m$ matrix $\mathbf{T}_p$ by setting all elements corresponding to the indices identified in step 2 equal to zero and solving for the remaining elements using (16)

end

Figure 10: Iterative numerical procedure for determining approximate transformation matrix through link elimination

A numerical study was performed in which a large number of standard infrastructure configurations were considered and different analytical and numerical approaches used to compute the approximate transformation matrix. Configurations were analyzed in which the GMPPs were arranged in a line, circle, grid or cluster formation with different inter-site distances. It was found that the numerical optimization procedures achieved the best trade-off between efficiency and accuracy.

5. COMPONENT PERFORMANCE

Typically, the GMPPs selected in the random field model correspond to locations of components in the infrastructure system. For point-site components, such as relatively short span highway bridges and individual facilities, their performance is predicted as a function of the site-specific GM intensity using fragility functions.

Define a damage index set $k = \{0,1,,\ldots,K\}$ such that $k = 0$ corresponds to the intact (no damage) state and $k = K$ corresponds to the most severe damage state considered. A seismic fragility function provides the conditional probability of meeting or exceeding a particular component damage state (DS) k given the GM intensity. Define the fragility of component i for state k as

$$F_k^i(s_i) = \Pr(\text{meeting or exceeding DS } k | S_i = s_i) \quad (17)$$

Note that $F_0^i(s_i) = 1$. The probability that the component is in damage state k is then computed as

$$p_k^i(s_i) = F_k^i(s_i) - F_{k+1}^i(s_i) \quad (18)$$

A node is introduced into the BN representing the state of point-site component i and is labeled C_i. Node C_i has mutually exclusive collectively exhaustive states corresponding to the damage index set. The corresponding BN is shown in Figure 11. The BN shown in this figure makes use of objects represented by rectangles with rounded corners. Behind this object there is a BN modeling seismic demands (as in Figure 6) that is hidden to reduce graphical clutter.

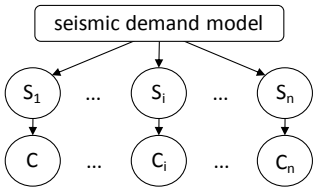

Figure 11: BN modeling performance of point-site components

For distributed components, such as pipelines and rail segments, it is not adequate to model the performance at a single point. Typically, performance functions (analogous to fragility functions) of these linear components are expressed as a mean number of damages of state k or greater per unit length, given a level of GM intensity. The failures along a distributed component are often assumed to follow a Poisson process. One or more failures along the length constitutes failure of the entire component (Adachi & Ellingwood 2008).

While a distributed component may be continuous, the BN requires discretization of the random field and thus distributions of GM intensity are only available at the discrete GMPPs represented by nodes S_i, $i = 1, \ldots, n$. As a result, it is necessary to discretize the distributed component into segments. GMPPs modeled in the BN are then selected to correspond with the ends of each segment. Each discretized segment is considered a "component" in the system. Define $C_{i,i+1}$ as the segment between GMPPs represented by nodes S_i and S_{i+1}.

Let $\eta_i^k(s_i)$ be the mean rate of damage points of state k or greater along the component when GM intensity $S_i = s_i$. Associated with the component segment $C_{i,i+1}$ there are two mean damage rates: $\eta_i^k(s_i)$ and $\eta_{i+1}^k(s_{i+1})$. Interpolating linearly between these two values gives the mean damage rate as a function of the coordinate along the component. Assuming damages occur randomly, the probability that the component experiences damage of state k (i.e. the probability of at least one incident of damage of state k) is computed by treating the occurrence of damages as a non-homogenous Poisson process. The mean number of damages of state k or greater for the entire component $C_{i,i+1}$ is then

$$\mu^{\mathrm{k}}_{i,i+1}(s_i, s_{i+1}) = \frac{L_{i,i+1}}{2}\left(\eta^{\mathrm{k}}_{i}(s_i) + \eta^{\mathrm{k}}_{i+1}(s_{i+1})\right) \quad (19)$$

where $L_{i,i+1}$ is the length of $C_{i,i+1}$. The probability that $C_{i,i+1}$ is in damage state k given GM intensity s_i and $s_{i,i+1}$ (expressed $p^k_{i,i+1}(s_i, s_{i,i+1})$) is then be computed as

$$\begin{aligned} p^k_{i,i+1}(s_i, s_{i+1}) &= \exp\left(-\mu^1_{i,i+1}(s_i, s_{i+1})\right) \quad \text{for } k = 0 \\ &= \exp\left(-\mu^{k+1}_{i,i+1}(s_i, s_{i+1})\right) - \exp\left(-\mu^k_{i,i+1}(s_i, s_{i+1})\right), \\ &\quad \text{for } k = 1, \ldots, K-1 \\ &= 1 - \exp\left(-\mu^{\mathrm{K}}_{i,i+1}(s_i, s_{i+1})\right), \text{ for } k = K \end{aligned} \quad (20)$$

The BN corresponding to the above description is shown in Figure 12. The node representing the damage state of component segment $C_{i,i+1}$ is modeled as a child of GM intensity nodes at either end of the segment: S_i and S_{i+1}.

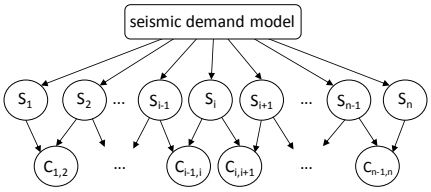

Figure 12: BN modeling performance of discretized segments of a continuous component

6. SYSTEM PERFORMANCE

6.1 Performance of series and parallel systems

The performance of the system is defined as a function of the component damage states. For brevity and simplicity, we focus here on series and parallel systems with binary components. However, BN formulations for more complex system configurations (e.g. general systems with multi-state components) have been developed with an emphasis on computational efficiency and readability (Bensi et al. 2009; Bensi et al. 2010b). Additionally a simple illustrative example is presented to demonstrate how descriptions provided in this paper can be extrapolated to more complex systems. One option for characterizing system performance is to define a single node S_{sys}, which gives the state of the system as a child of all nodes representing the states of the components (a converging structure). For a system with n binary components, node S_{sys} would have a CPT of size 2^n. The exponential growth in the size of the CPT associated with S_{sys} as n increases can quickly render a BN computationally intractable. A more efficient system performance formulation is achieved by constructing chain-like structures that we term failure path sequences (FPSs) and survival path sequences (SPSs). We describe this below for a system with binary component states.

Define a FPS as a chain containing a minimum set of failure events whose joint realization constitutes failure of the system. It is noted that the terms "sequence" and "chain of events" do not have any time-based implications. For a parallel system, there is only one FPS (i.e. all components must fail for the system to fail). For a series system with n components, there are n FPSs (i.e. if any component fails, the system fails). Conversely, a SPS is a chain containing a minimum set of survival events whose joint realization constitutes system survival. A series system has one SPS while a parallel system as n SPSs. Readers familiar with classical systems analysis will recognize the connection between FPSs and minimum cuts sets as well as SPSs and minimum link sets.

A FPS is comprised of a chain of failure path events (FPEs), each of which gives the state of the chain up to that event. Let $E_{f,i}$ be a node representing the FPE associated with component i. Node $E_{f,i}$ has two states: failure (state 0) and survival (state 1). The state of $E_{f,i}$ is as a function of the states of associated component i and the previous FPE in the FPS. The state of $E_{f,i}$ is expressed as

$$\begin{aligned} E_{f,i} &= 0 \text{ if } E_{f,i-1} = 0 \text{ and } C_i \text{ has failed} \\ &= 1 \text{ otherwise} \end{aligned} \quad (21)$$

Thus, for a parallel system, the BN system formulation takes the form shown in Figure 13. The state of node $E_{f,1}$ is equal to the state of node C_1. $E_{f,2}$ is in failed state only if the previous FPE $E_{f,1}$ is in failed state and C_2 is in failed state. This pattern continues such that $E_{f,n}$ is in failed state only if both $E_{f,n-1}$ and C_n are in failed state. Thus, the state of $E_{f,n}$ gives the state of the system, which is shown by node S_{sys} being a child of $E_{f,n}$.

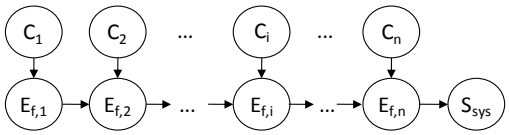

Figure 13: BN using FPEs to define a parallel system

For a series system, the BN formulation using FPSs is shown in Figure 14. As can be seen, there are n FPSs, each of which is defined by one FPE. Thus, the size of the CPT associated with the S_{sys} is 2^n and there is no computational advantage to this approach. As shown below, a more efficient formulation is achieved by using SPSs.

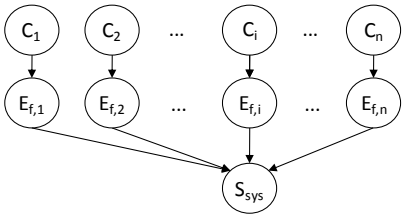

Figure 14: BN using FPEs to define a series system

A SPS is comprised of a chain of survival path events (SPEs), each of which gives the state of the chain up to that event. The state of each SPE is defined as a function of an associated component and the previous SPE in the SPS. Thus, the state of $E_{s,i}$ is defined as

$$\begin{aligned} E_{s,i} &= 1 \text{ if } E_{s,i-1} = 1 \text{ and } C_i \text{ has survied} \\ &= 0 \text{ otherwise} \end{aligned} \quad (22)$$

Where $E_{s,i} = 1$ indicates that node $E_{s,i}$ is in survival state and $E_{s,i} = 0$ indicates failure. Thus, for a series system, the BN system formulation takes the form shown in Figure 15. The state of node $E_{s,1}$ is equal to the state of node C_1. $E_{s,2}$ is in survival state only if $E_{s,1}$ is in survival state and C_2 is in survival state. This pattern continues such that $E_{s,n}$ is in survival state only if both $E_{s,n-1}$ and C_n are in survival state. Consequently, the state of $E_{s,n}$ gives the state of the system.

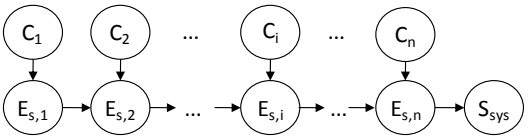

Figure 15: BN formulation using SPEs to define a series system

For more complex systems, a more sophisticated approach has been developed but is not detailed in this paper (see Bensi et al. 2009; Bensi et al. 2010b).

6.2 Example Application

Consider the simple infrastructure system in Figure 16 located parallel to a 120km long fault and consisting of distributed components (lines) and point-site components (squares). The coordinates of the GMPPs (represented by numbered circles) in the fault-specific coordinate system are indicated on the figure. System survival is defined as the event in which there is connectivity between the source and sink. The direction of flow through the network is indicated by arrows.

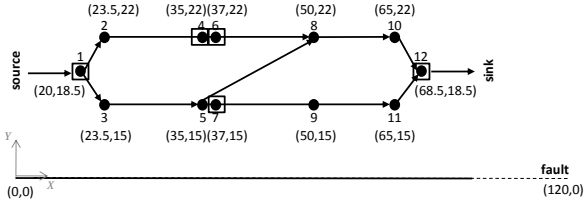

Figure 16: Example infrastructure system

Seismic demands on the system are modeled using the previously described GM intensity RF BN using the Campbell & Bozorgnia (2006) GM prediction equation. The magnitude distribution is based on a characteristic earthquake model. Wells and Coppersmith (1994) defines the magnitude-rupture length relationship. The spatial error correlation model is taken from Park et al. (2007). The performance of the point-site (PGA-sensitive) and distributed (PGV-sensitive) components is modeled as described in section 5 using damage functions adapted from HAZUS-MH. The performance of the system is modeled by extension of the previously described parallel and series system formulations. This example is presented for illustrative purposes to demonstrate the development of a systems analysis BN for non-parallel/series systems and to show the power of using the BN for information updating. The model assumptions are not restrictive and can easily be changed based on the knowledge and preferences of the modeler.

Let $C_{d,i,j}$ represent the distributed component between GMPPs i and j. Let $C_{p,k}$ be the point-site component located at GMPP k. There are three survival path sequences (minimum link sets) for this system. The components associated with the SPEs in the SPSs are:
$\{C_{p,1}, C_{d,1,2}, C_{d,2,4}, C_{p,4}, C_{d,4,6}, C_{p,6}, C_{d,6,8}, C_{d,8,10}, C_{d,10,12}, C_{p,12}\}$, $\{C_{p,1}, C_{d,1,3}, C_{d,3,5}, C_{d,5,8}, C_{d,8,10}, C_{d,10,12}, C_{p,12}\}$, $\{C_{p,1}, C_{d,1,3}, C_{d,3,5}, C_{d,5,7}, C_{p,7}, C_{d,7,9}, C_{d,9,11}, C_{d,11,12}, C_{p,12}\}$.

There are many ways to formulate a system analysis BN for this example using different orderings of the SPEs/FPEs of SPSs/FPSs. Figure 17 presents a BN formulation in which SPE nodes are arranged in three distinct chains, each corresponding to one SPS. Because multiple SPEs are associated with some of the components, an additional superscript index is added to the SPE nodes. In Figure 17, the performance of the overall system is represented by node S_{sys} with its state defined as

$$S_{sys} = \bigcup_{i=1}^{3} E_{S,12}^{(i)} \tag{23}$$

where S_{sys} is the event in which the system survives and $E_{s,12}^{(i)}$ represents the ith SPE associated with component 12.

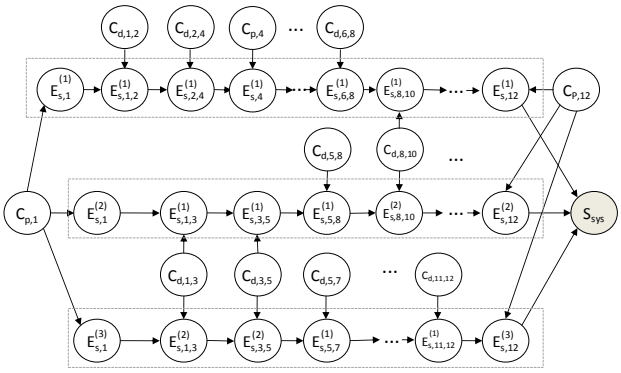

Figure 17: BN model for example system

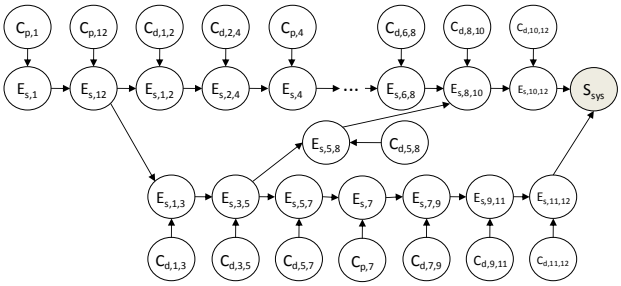

Figure 18: Improved BN model for example system

The number of SPE nodes in the BN can be reduced through careful structuring. The order in which SPE nodes are chained together to create SPSs must be optimized to minimize computational demand. The optimization is subject to the requirement that all SPSs are included and no artificial SPS is introduced that is not present in the actual system. Additional details on optimizing the arrangement of SPEs/FPEs to create SPSs/FPSs in system analysis BNs can be found in Bensi et al (2010b). For this example, Figure 18 presents an improved system analysis BN in which the order of SPE nodes is such that there is only one SPE associated with each component.

To illustrate the value of the BN framework for information updating, we show the effect of different post-earthquake evidence scenarios on the system and component failure probabilities. The following post-earthquake evidence cases (ECs) are considered:
(1) A magnitude 6.8 earthquake has occurred with epicenter located 30km from left end of the fault
(2) EC (1) + PGV at GMPP 3 is measured to be 23cm/sec.
(3) EC (2) + component $C_{d,6,8}$ is observed to have failed.
(4) EC (2) + component $C_{d,6,8}$ is observed to have survived.

Table 1 contains component and system failure probabilities for each EC. Note that the probabilities change with different ECs. Particularly, observe that evidence on the

intensity at a GMPP or the performance of a component has the greatest impact on the failure probabilities of near-by components due to RF effects. Evidence on the performance of a component propagates through the BN by updating the distribution of the GM intensity at the location of the component. This in turn updates the full GM intensity RF model and provides revised distributions of GM intensities at other locations. The updated GM distributions then change the failure probabilities of associated components. As more observations become available, the model "infers" the true value of unobservable parameters (e.g. the values of the inter- and intra-event deviations or the location of the rupture, which is not commonly known immediately following an earthquake) with increasing accuracy. Thus, we have a probabilistic framework that combines observations and physical models to provide an up-to-date characterization of the system.

Table 1: Failure probabilities (%) for example system

	EC(1)	**EC(2)**	**EC(3)**	**EC(4)**
$C_{p,1}$	4.5	8.1	9.0	8.0
$C_{d,1,2}$	2.7	4.3	4.7	4.3
$C_{d,1,3}$	3.8	7.9	8.1	7.9
$C_{d,2,4}$	5.0	6.5	8.1	6.4
$C_{d,3,5}$	9.7	17.0	18.3	16.9
$C_{d,4,6}$	0.9	1.0	1.6	1.0
$C_{p,4}$	3.2	3.9	6.2	3.7
$C_{d,5,7}$	1.8	2.1	2.7	2.1
$C_{d,5,8}$	10.2	11.5	15.8	11.3
$C_{p,6}$	2.6	3.1	5.9	2.9
$C_{d,6,8}$	5.4	6.2	100	0.00
$C_{p,7}$	6.6	7.8	10.3	7.6
$C_{d,7,9}$	10.4	11.8	14.7	11.6
$C_{d,8,10}$	5.5	6.2	8.9	6.1
$C_{d,9,11}$	9.6	10.9	13.1	10.7
$C_{d,10,12}$	1.8	2.1	2.4	2.1
$C_{d,11,12}$	2.4	2.7	3.1	2.7
$C_{p,12}$	2.2	2.7	3.2	2.6
System	**12.05**	**18.91**	**39.82**	**17.53**

7. SOLVING DECISION PROBLEMS

To solve decision problems, a BN can be extended by decision and utility nodes. Once these nodes have been added to a BN, the new graph is called an *influence diagram* (ID). An ID encodes both the probability model and the decision problem structure. A decision node is represented by a rectangle and is defined by a finite set of states corresponding to decision alternatives. Links going into a decision node, referred to as *information links*, indicate that the states of the parent nodes are known prior to deciding. A utility node is represented by a diamond. Utility nodes have no states; instead they are assigned a utility value (e.g. monetary units) as a function of the states of their parents. The optimal decision alternative is the one that maximizes expected utility. Additional details on influence diagrams can be found in Jensen & Nielson (2007).

For simplicity, in this paper, we explain IDs by an example. Consider a post-earthquake scenario in which an earthquake has occurred and placed a seismic demand on a facility. The owner must decide whether to inspect the facility (for which a cost will be incurred) and then decide whether to shut it down (with or without first making an inspection). The decision to shut down the facility must be made under competing objectives: the owner does not want to incur a liability by making an unsafe decision (i.e. keep the facility open when it is damaged) nor lose revenue by unnecessarily shutting down the facility. The ID modeling this decision problem is shown in Figure 19. Different IDs can be constructed for this simple problem based on the preferences and practices of the decision-maker. The following notation is used: S= seismic demand, D_{true} = true damage state of the facility (e.g. heavily damaged, slightly damaged, no damage), D_{obs} = observed component damage state based on an inspection, C_I = inspection cost, L = liability for making an unsafe decision to continue operation of the facility when it is damaged, R = lost revenue due to shutting down the facility, $Inspect?$= the inspection decision (e.g. no inspection, visual inspection, extensive inspection), $Shut\text{-}down?$= decision to shut-down the facility.

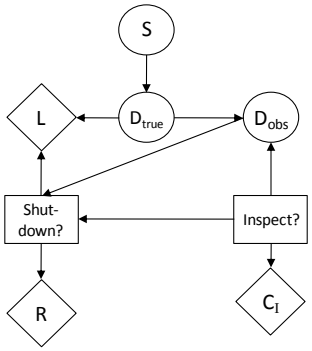

Figure 19: ID corresponding to inspection/close decision

In Figure 19, the true damage state of the component is a function of the seismic demand. The true component damage state is assumed to be a latent variable but it can be known with less uncertainty depending on the inspection type selected, e.g. the true damage state of the component may be known with (near) perfect certainty if an extensive inspection is performed, but with less certainty if only a visual inspection is performed. Of course, no information is gained if an inspection is not performed. Node D_{obs} represents the damage state observed during the inspection. The "inspection-quality" relationship between observed and actual damage is encoded in the ID with node D_{obs} being a child of node D_{true} and the inspection decision. Observations are entered in node D_{obs} and based on the inspection type, this evidence probabilistically updates the damage probabilities for node D_{true}. Associated with the inspection choice is a cost, which will increase as the inspection quality improves. This is modeled by a utility node that is functionally dependent on the inspection decision node. It is assumed that the inspection decision and associated outcome (if an inspection is made) are known before a decision is made regarding facility shut-down. This is indicated by information links between nodes $Inspect?$ and D_{obs} and node $Shut\text{-}down?$. When working with IDs, defining the order of

decisions is important. Defining this order encodes the value of information obtained by performing the inspection. As a function of the closure decision and the true damage state of the facility, there is a utility node that represents the liability incurred when making an unsafe decision. Note that this liability is a function of the true damage state, not the observed damage state. There is an additional utility node dependent on the shut-down decision node, which represents the loss incurred when the facility is not operating. Thus, the two utility nodes represent the competing objectives to maintain operability and not incur a liability.

For more complex decision problems relating to geographically distributed infrastructure systems, the GM demands are modeled as a spatially distributed RF with component specific intensity nodes. Component performance is modeled as described in section 5. System performance is modeled consistent with the procedure outlined in section 6. Typically, the utility node representing lost revenue is associated with system failure rather than component failure. Thus, we take into account the importance of a component to the entire system and its likelihood of damage when deciding whether to shut it down.

As information evolves in near-real time following an earthquake, observations of GM intensity, component performance, and system response are entered into the BN. As decisions are made, the choices are also entered into the BN. This information propagates through the BN to provide an up-to-date characterization of the probability model and decision structure. Thus, the ID provides the decision-maker with guidance on optimal decisions at any point in time, based on all the available information.

8. CONCLUSIONS

A broad overview of a BN-based framework for aiding near-real time post-earthquake decision-making is presented. It is shown that BNs are particularly well-suited for the proposed application, but like other computational tools, they are not without limitations. We have detailed some of our efforts to address these limitations and make BNs a viable tool for infrastructure risk assessment and management. It has also been shown that the facility of information updating makes BNs an excellent tool for near-real time risk management and decision-support.

Acknowledgements:

The authors acknowledge research support from the Pacific Earthquake Engineering Research (PEER) center Transportation Systems Research Program.

References:

Abrahamson, N.A., 2000. Effects of rupture directivity on probabilistic seismic hazard analysis. In *Proceedings of the 6th International Conference on Seismic Zonation, Palm Springs, Earthquake Engineering Research Institute*.

Abrahamson, N. et al., 2008. Comparisons of the NGA Ground-Motion Relations. *Earthquake Spectra*, 24(1), 45-66.

Adachi, T. & Ellingwood, B.R., 2008. Serviceability of earthquake-damaged water systems: Effects of electrical power availability and power backup systems on system vulnerability. *Reliability Engineering & System Safety*, 93(1), 78-88.

Bensi, M., Straub, D. & Der Kiureghian, A., 2010a. Bayesian network modeling of correlated random variables drawn from a Gaussian random field. *Article in Preparation*.

Bensi, M., Straub, D. & Der Kiureghian, A., 2010b. Efficient Bayesian network formulations for modeling system performance (forthcoming). In *Proceedings of IFIP working group 7.5 on Reliability and Optimization of Structural Systems*. Munich, Germany.

Bensi, M., Straub, D., Friis-Hansen, P. & Der Kiureghian, A., 2009. Modeling infrastructure system performance using BN. In *Proceedings of the 10th International Conference on Structural Safety and Reliability*. Osaka, Japan.

Campbell, K. & Bozorgnia, Y., 2007. *Campbell-Bozorgnia NGA Ground Motion Relations for the Geometric Mean Horizontal Component of Peak and Spectral Ground Motion Parameters*, University of California, Berkeley: Pacific Earthquake Engineering Research Center.

Department of Homeland Security, Emergency Preparedness and Response Directorate, *HAZUS-MH MR4 Technical Manual*, Washington D.C.: FEMA, Mitigation Division.

Hugin Expert, *Hugin Ressearcher*, Denmark. Available at: www.hugin.com.

Jensen, F.V. & Nielson, T.D., 2007. *Bayesian Networks and Decision Graphs* second., New York: Springer Science Business Media|Springer.

Langseth, H. et al., 2009. Inference in hybrid Bayesian networks. *Reliability Engineering & System Safety*, 94(10), 1499-1509.

Lauritzen, S., 1992. Propagation of probabilities, means and variances in mixed graphical association models. *Journal of the American Statistical Association*, 87, 1098-1108.

Lauritzen, S.L. & Jensen, F., 2001. Stable local computation with conditional Gaussian distributions. *Statistics and Computing*, 11(2), 191-203.

Lauritzen, S.L. & Nilsson, D., 2001. Representing and Solving Decision Problems with Limited Information. *Management Science*, 47(9), 1235-1251.

Park, J., Bazzurro, P. & Baker, J.W., 2007. Modeling spatial correlation of ground motion Intensity Measures for regional seismic hazard and portfolio loss estimation. In T. Kanda, ed. *Applications of Statistics and Probability in Civil Engineering*. Tokyo, Japan: Taylor & Francis Group.

Song, J. & Kang, W., 2009. System reliability and sensitivity under statistical dependence by matrix-based system reliability method. *Structural Safety*, 31(2), 148-156.

Song, J. & Ok, S., 2009. Multi-scale system reliability analysis of lifeline networks under earthquake hazards. *Earthquake Engineering & Structural Dynamics*. Available at: http://dx.doi.org/10.1002/eqe.938 [Accessed January 6, 2010].

Straub, D., 2009. Stochastic Modeling of Deterioration Processes through Dynamic Bayesian Networks. *Journal of Engineering Mechanics*, 135(10), 1089-1099.

Wells, D. & Coppersmith, K., 1994. New Empirical Relationships among Magnitude, Rupture Length, Rupture Width, Rupture Area, and Surface Displacement. *Bulletin of the Seismological Society of America*, 84(4), 974-1002.

JOINT CONFERENCE PROCEEDINGS
7th International Conference on Urban Earthquake Engineering (7CUEE) &
5th International Conference on Earthquake Engineering (5ICEE)
March 3-5, 2010, Tokyo Institute of Technology, Tokyo, Japan

AN OVERLOOKED FAILURE MECHANISM OF REINFORCED CONCRETE BEAM-COLUMN JOINTS – AN EXPERIMENTAL VERIFICATION –

Hitoshi Shiohara[1)] and Fumio Kusuhara[2)]

[1]Associate Professor, Dept. of Architectural Engineering, The University of Tokyo; Tokyo, Japan
[2]Assistant Professor, Dept. of Architectural Engineering, The University of Tokyo; Tokyo, Japan
shiohara@arch.t.u-tokyo.ac.jp, kusuhara@arch.t.u.-tokyo.ac.jp

Abstract: Tests on one third scale, reinforced concrete interior beam-column joint subassemblages are reported. The effects of the design parameters of joints on lateral capacity and post yielding behavior are investigated. Three major parameters of the test program are (1) amount of longitudinal reinforcement, (2) ratio of the flexural strength of the beams to the flexural strength of the columns framing into a joint, and (3) ratio of the depth of the beam to the depth of the column. Maximum story shear of some specimens fell 5% to 30% short of the story shear calculated by the flexural strength of the beam or the column, although the joints have enough margin of the nominal joint shear strength by 0% to 50% compared to the calculated value by a current seismic provision. The extent of insufficiency in the story shear strength is larger if the flexural strength ratio is equal or nearer to unit, and if the depth of the column is larger than that of the beam. This type of beam-column joint design parameters is allowed by current seismic codes and seen in huge stock of existing buildings in the world. So serious attention should be addressed to this experimental results.

1. INTRODUCTION

The current building codes for high seismic zone have special provisions for reinforced concrete beam-column joints to preclude joint shear failure. They are based on a concept that such failure occurs before yielding of the beams or columns, if excessive tensile force in longitudinal reinforcing bars passing through a joint is developed in too small horizontal section of a column. Joint shear capacity equations are provided for the design of joints in the provisions. The equations of joint shear strength have been empirical and derived from database of beam-column joints which are with heavily reinforced beams as well as columns to assess a potential of joint shear resistance. So the test parameters of beam-column joint have been biassed due to the hypothesis on the joint failure.

Figure 1 shows the distribution of column-to-beam strength ratio of 288 interior RC beam-column joint specimens tested and reported in Japan in these three decades. A clear tendency is seen that the most of the joints showed beam-hinging mechanism (B) have values of column-to-beam strength ratio of larger than 1.8. It means specimens that showed beam hinging mechanism have very strong column relative to beam. It is also seen that number of the specimenss are very few by which

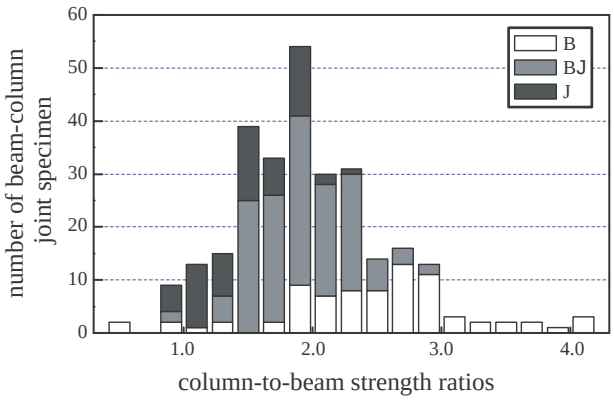

Figure 1. Beam-column joint tests in Japan

they were intended to verify the actual strength and post-yielding behavior of more common beam-column joints with moderate amount of longitudinal reinforcement and in particular with low column-to-beam strength ratio in the range of 1.0 to 1.5. Actually they are more commonly constructed in practice. However there is very limited number of tests for this type of beam-column joints.

Author revealed recently that the flexural strength of beam nor column may not be achieved if the column-to-beam strength ratio are unit or close to unit, despite of the ratio of joint shear demand to joint shear capacity with a

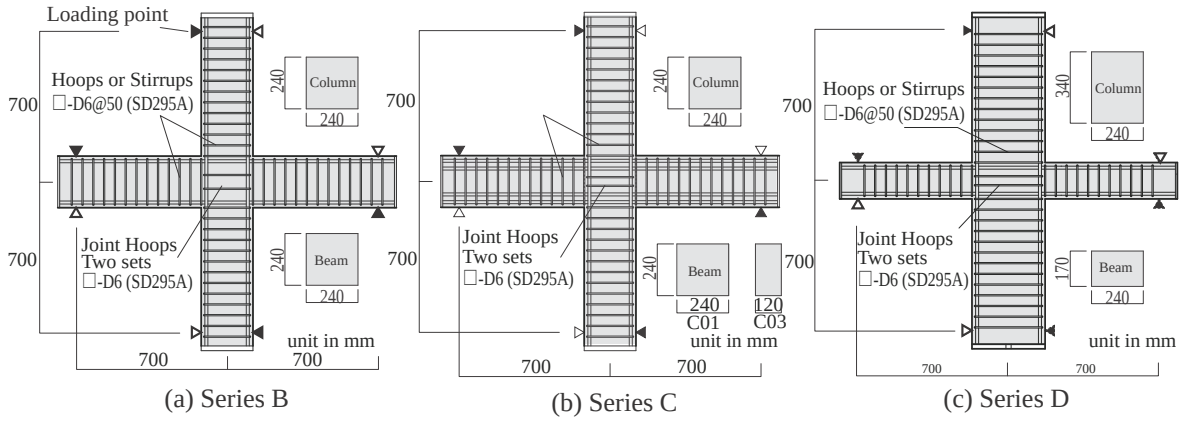

Figure 2. Geometry of Specimens

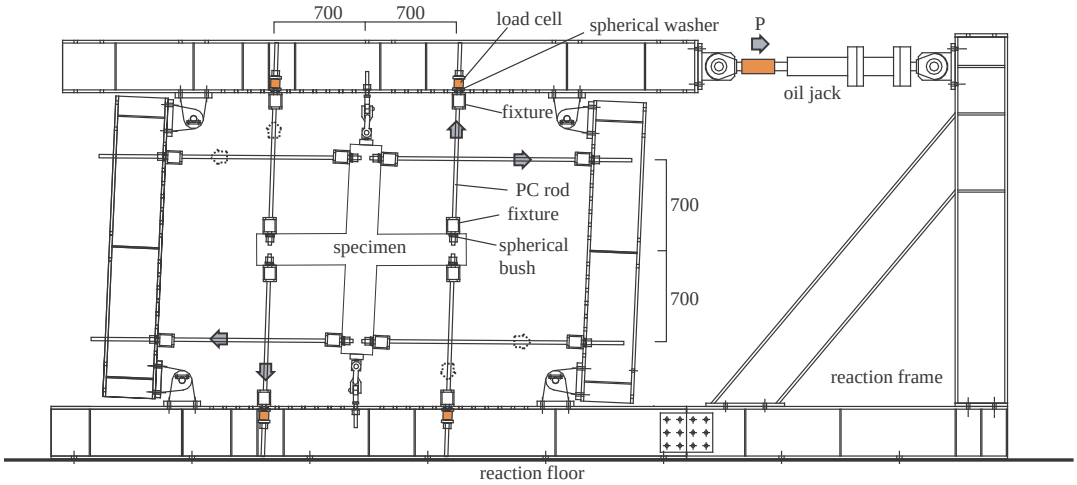

Figure 3. Loading Setup

introduction of a theoretical model (Shiohara 2008). But there were few tests for a validation. Hence, an experimental program was planed. This is a report of the test program. It focuses on the investigation of the effects of the three major design parameters, including (1) longitudinal reinforcement ratio in beams, (2) ratio of the flexural strength of the beams to the flexural strength of the columns framing into a joint, and (3) ratio of the depth of the beam to the depth of the column. The current codes are evaluated and the validity of the model are discussed with respect to maximum story shear.

2. TEST PROGRAM

Test result of twenty specimens are reported here. The specimens are 1/3 scale beam-column joint subassemblages of crucial form. Table. 1 summarizes the arrangement of the reinforcements and other properties of the specimens. The depth of the columns and the beams are 240 mm in common for Series B and Series C, whereas the depths of column and beam are 340 mm and 170 mm for Series D. The width of all the beams and the columns is 240 mm in common. Figure 2 shows the geometry and dimensions of the specimens. The hoops and the stirrups of all the specimen are of rectangular shape of D6 deformed bars at spacing of 50 mm. Two sets of rectangular hoops of D6 deformed bars are provided in horizontal direction in a joint of all the specimen. The joint shear reinforcement ratio is approximately 0.3% and satisfies the minimum requirement of the AIJ Guidelines (1999).

2.1 Test Parameters

Four test parameters are included in the specimens selected in this report. They are (1) ratio of joint shear demand to joint shear capacity; 0.55-1.50, where joint shear capacity is calculated by the AIJ Guidelines (1999), (2) ratio of flexural strength of beam and column evaluated at the center of a joint; 0.72-2.24, (3) ratio of column depth to beam depth; 1.0 or 2.0, and (4) longitudinal reinforcing bar distant ratio; 0.5-0.8, which is the ratio of distance of tensile and compressive reinforcements to the full depth of a cross section.

2.2 Material Properties

The specimens are made of normal concrete and normal strength deformed steel bars. Concrete

compressive strengths were tested by a 100 mm by 200 mm cylinder. They are 29.0 MPa, 31.0 MPa and 32.4 MPa for Series A, B and C respectively. The yield points by tensile tests of reinforcing steel are 399 MPa, 378 MPa, and 425 MPa for D6, D13 and D16 deformed bars respectively.

2.3 Loading setups

The loading setup are shown in Figure 3. The upper horizontal loading beam is supported with two vertical loading columns with a pinned joint at the both ends. The vertical loading columns are connected to a lower horizontal loading beam with a pinned joint. The lower loading beam is fixed to a testing floor. A specimen is connected to a loading steel frame with a set of horizontal and vertical PC rods. The distance of the loading points at the end of the beams and the ends of columns is 1400 mm in common. By applying a horizontal displacement by a oil jack to the upper loading beam, a beam-column joint specimen is forced to deform like in a moment resisting frame.

Table 1. Properties of Specimens

(a) Series B

Specimens		B01	B02	B03	B04	B05	B06	B07	B08	B09	B10
concrete compressive strength in MPa		29.0									
longitudinal reinforcing bar distant ratio		0.8						0.65	0.5	0.65	0.5
beam	section in mm	240 × 240									
	longitudinal reinforcing bars	4-D13	5-D13	5-D16	4-D13	5-D13		4-D13		5-D16	
		SD345	SD345	SD390	SD345	SD345		SD345		SD390	
	tensile reinforcement ratio %	0.98	1.22	1.92	0.98	1.22	1.22	1.07	1.18	2.09	2.30
column	section in mm	240 × 240									
	longitudinal reinforcing bars	4-D13	5-D13	5-D16	6-D13	5-D13 2-D13	5-D13 5-D13	4-D13		5-D16	
		SD345	SD345	SD390	SD345	SD345		SD345		SD390	
	tensile reinforcement ratio %	0.98	1.22	1.92	1.47	1.80	2.67	1.07	1.18	2.09	2.30
joint	joint hoops	□-D6(SD295) 2 sets									
joint shear capacity margin		1.29	1.03	0.57	1.29	1.03	1.03	1.26	1.24	0.56	0.55
column-to-beam strength ratio ΣMuc / ΣMub		1.00	1.00	1.00	1.48	1.35	1.78	1.00	1.00	1.00	1.00

(b) Series C & D

Specimens		C01	C03	D01	D02	D03	D04	D05	D06	D07	D08
concrete compressive strength in MPa		31.0		32.4							
beam	width in mm	120	240	240							
	depth in mm	240	240	170							
	longitudinal reinforcing bar distant ratio	0.5 & 0.8		0.72							
	longitudinal reinforcing bars	3-D13+2-D13		5-D13			7-D13				7-D16
		SD345		SD345							
	tensile reinforcement ratio %	1.31	2.62	1.81			2.54				3.98
column	width in mm	240		240							
	depth in mm	240		340							
	longitudinal reinforcing bar distant ratio	0.8	0.8	0.86							
	longitudinal reinforcing bars	5-D13		2-D13	3-D13	5-D13	2-D13	3-D13	4-D13	6-D13	3-D16
		SD345		SD345							
	tensile reinforcement ratio %	1.22		0.33	0.50	0.84	0.33	0.50	0.67	1.04	0.79
joint	joint hoops	□-D6(SD295) 2 sets									
joint shear capacity margin		1.10	0.80	1.50			1.06				0.68
column-to-beam strength ratio ΣMuc / ΣMub		1.03	1.10	0.99	1.42	2.24	0.72	1.03	1.34	1.72	1.01

2.4 Loading Cycles and Measurements

Statically cyclic lateral load reversals with an increasing amplitude were applied to the specimen to get load-deformation relationships. The first cycle is load controlled before cracking. Then two reversals with displacement control are applied at each story drift ratio of 0.25%, 0.5%, 1.0%, 1.5%, 2.0% and 3.0%. In Series D, loading cycles with 4.0% story drift ratio are added. No axial force in the columns and beams are applied during the test in all specimens. Shear story is measured from the force reading by load cells which are installed at the end of vertical PC rods. Story drift ratio is measured as the difference of lateral displacement at the two inflection points in the column divided by the distance of the inflection points (=1400 mm). The strain on the longitudinal reinforcing bars in beams and columns as well as in joints are measured by strain gauges. The strain at the column face as well as in the joint on the point of diagonal of the joint are measured.

3. TEST RESULTS

3.1 Overall Behavior

Photo 1 shows typical appearance at story drift ratio of 3%. In all the specimen, diagonal cracks at the corner started at story shear around 5 kN in loading cycles to both directions. Diagonal cracks at the center of the joint appeared at story shear around 30 kN. As the number of loading cycles increases, the number of cracks increased and the width of the diagonal cracks increased. At the load cycles with story drift ratio of 2.0%, concrete crush at the center of the joint initiated and cover concrete spalled off at the load cycle with story drift ratio of 3.0% or more. In all the specimens, significant cracks are observed on the beam-column joints but on beams nor columns. While the flexural cracks in the beam or column ends are observed, their crack width remained small compared to the cracks in the beam-column joints.

3.2 Yielding of Reinforcement

The story shear-story drift ratio relation of each specimen is shown in Figure 4. The marks are put in the figures to show the sequence of the yielding of reinforcing bars. Table 2 lists the location of strain gauges and the story shear at which yielding of the reinforcing bars are observed. In all specimens except specimen D08, yielding of longitudinal bars in beams occurred before the specimens attained its maximum story shears. In all specimens except specimens B06, yielding of longitudinal bars in columns occurred. The story shear at first yielding and attained maximum story shear and the story drift ratio are also listed in Table 2. It should be noted that yielding of beam bars was observed in most of the specimen with joint shear demand higher than code specified and the yielding of column bars was observed in most of the specimen with stronger column than beams framing into a joint with margin less than 2.0. The joint hoops yielded before the first yielding of longitudinal reinforcement in all the specimen in Series B and C. On the contrary, the yielding of joint hoops in Series D is not necessary observed in all the specimens.

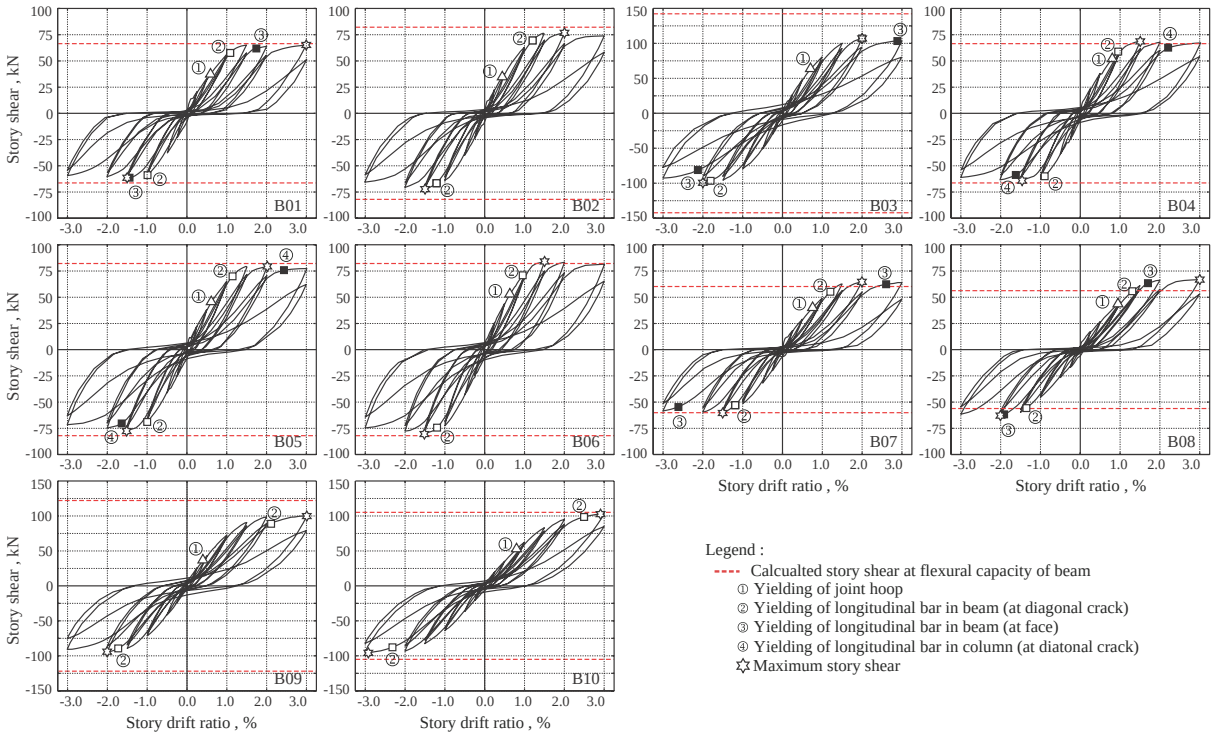

(a) Series B

Figure 4. Story shear-story drift relations (Continued)

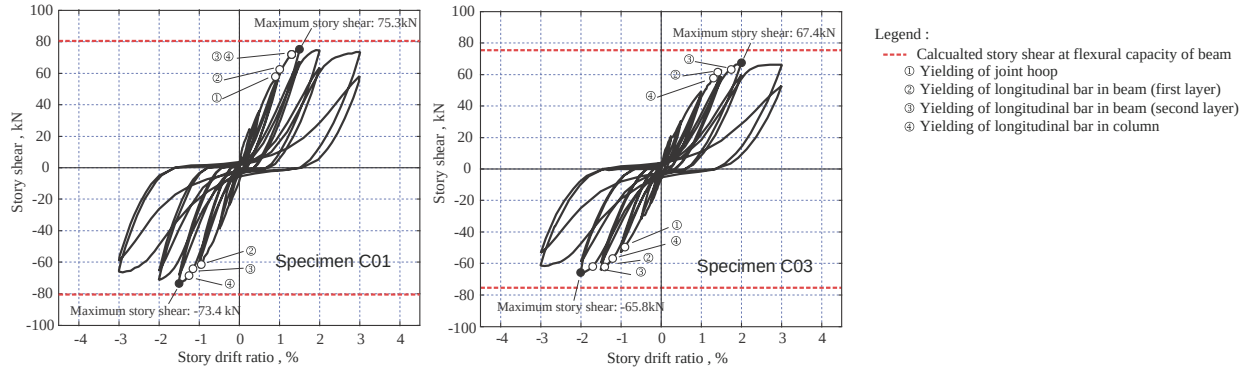

(b) Series C

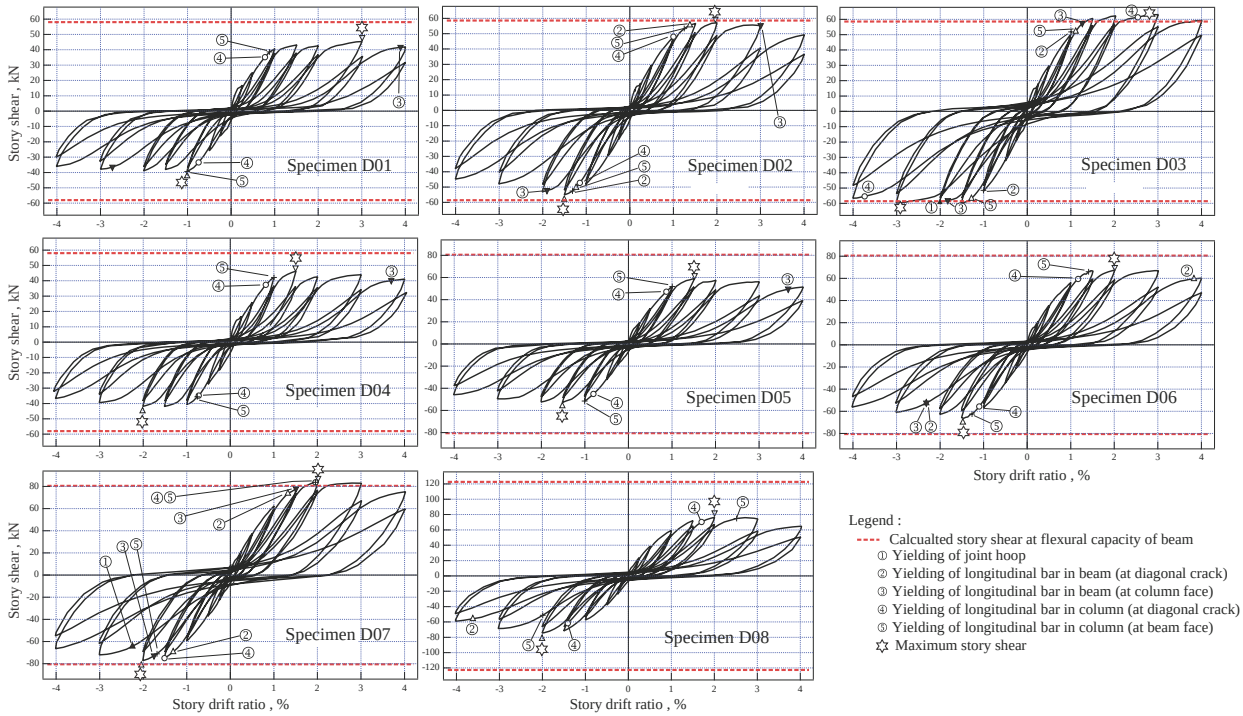

(b) Series D

Figure 4. Story shear-story drift relations

3.3 Maximum Story Shear

Calculated story shear by the flexural theory is shown as horizontal dotted line in Figure 3. The values are also listed in Table 3. Results of material test are used for the calculation. The maximum story shear are not be attained in the tests except a few specimens. In some specimens, the calculated maximum story shear overestimate 5% to 30% the test results. The exceptions in Series B are specimen B04, B05, and B06, which have columns the flexural strength of which are larger than that of beam by 48%, 35% and 78%, and specimen B07 and B08, in which the distance ratio of reinforcement of beams is 0.65 and 0.5 which is smaller than ordinary reinforced concrete beams in practice. The exception in Series D are Specimens D03 and D07, the flexural strength of the column of which are larger than that of the beams by 124% and 72%. So it is concluded that for ordinary beam-column joint, the story shear calculated based of flexural theory of the section overestimate, if the flexural strength of beams and columns are identical or near.

3.4 Post-yielding Behavior

Post-yielding hysteresis relation of beam-column joint subassemblages are compared in Figure 4. All the specimens show poor hysteresis curves with little energy dissipation and severe slip shape. No significant strength degradation are observed within the range of displacement reversals. No sudden strength degradation are observed instead the some of the specimen are judged to joint shear failure type by current seismic design codes. Strength degradation ratio due to cyclic loading of same amplitude are estimated 20-30% in most of the specimens within the story drift ratio less than 3.0%.

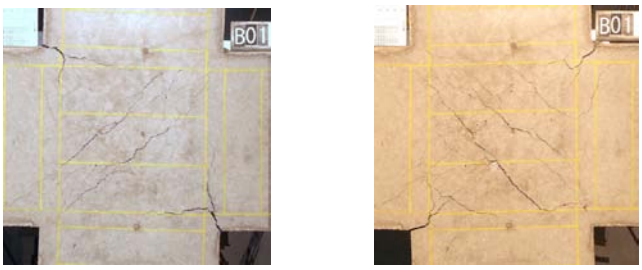

(a) Specimen B01 at story drift ratio of 3.0%



(b) Specimen D02 at story drift ratio of 3.0%
Photo 1. Typical damage of beam-column joints

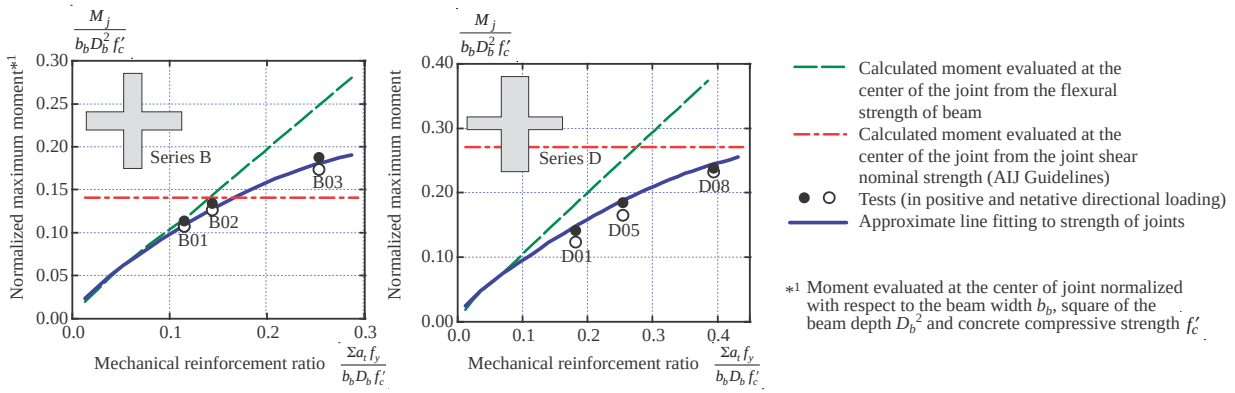

Figure 5. Effect of mechanical reinforcement ratio on strength

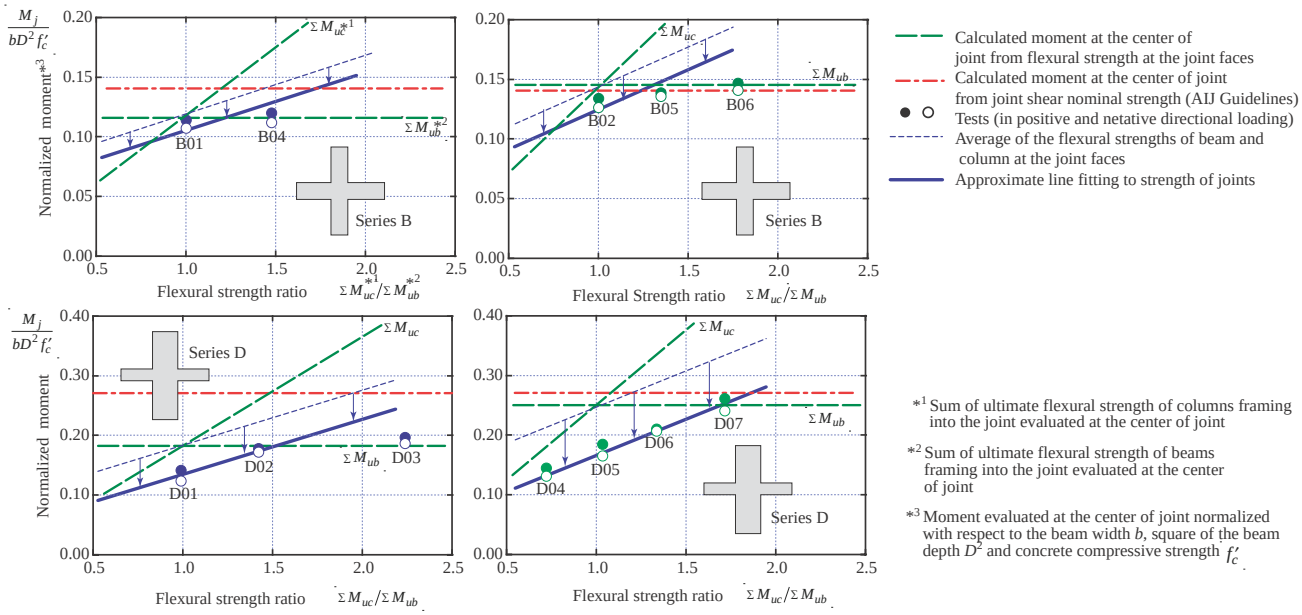

Figure 6. Effect of ratio of flexural capacity of column to flexural capacity of beam

Table 2. Strengths at yielding and maximum strength

(a) Series B

Specimen			B01	B02	B03	B04	B05	B06	B07	B08	B09	B10
Yielding of longitudinal bars in beams	at diagonal cracks in joint		57.6 1.09	69.5 1.20	107.1 2.20	58.8 0.95	69.9 1.14	70.9 0.95	57.0 1.25	55.7 1.31	88.8 2.11	98.5 2.50
	at column face		61.8 1.74	–	NY	–	–	–	63.1 2.80	66.4 2.80	NY	NY
Yielding of longitudinal bars in columns	at diagonal cracks in joint		57.6 1.09	69.5 1.20	101.5 2.62	62.6 2.21	75.8 2.44	NY	55.2 1.20	59.5 1.45	93.6 2.32	98.5 2.50
	at beam face		63.0 1.88	–	103.3 2.89	–	–	–	62.3 2.60	63.3 1.70	NY	NY
Yielding of horizontal joint hoops			37.3 0.59	34.2 0.44	63.1 0.70	52.0 0.80	45.2 0.61	52.5 0.63	40.0 0.76	43.5 0.95	36.1 0.40	52.1 0.80
At attained maximum story shear		+	65.2	76.7	107.1	68.6	79.3	84.0	64.6	66.7	99.8	102.6
		–	-61.5	-72.3	-99.4	-64.2	-77.7	-80.5	-60.4	-63.0	-94.2	-95.8

Upper low：story shear in , Lower low：story drift ratio in %, N/A : data not available, NY : no yielding

(b) Series C & D

Specimen			C01	C03	D01	D02	D03	D04	D05	D06	D07	D08
Yielding of longitudinal bars in beams	at diagonal cracks in joint		62.5 1.00	61.4 1.41	NY	55.5 1.38	52.1 1.11	NY	NY	59.6 3.83	73.7 1.32	NY
	at column face		–	–	41.6 3.89	55.3 3.00	57.4 1.26	40.1 3.70	49.6 3.67	NY	77.8 1.51	NY
Yielding of longitudinal bars in columns	at diagonal cracks in joint		72.0 1.30	57.7 1.30	35.2 0.78	48.0 1.00	61.3 2.54	37.4 0.82	47.2 0.87	59.4 1.17	83.7 1.96	70.3 1.70
	at beam face		–	–	38.6 0.88	53.4 1.25	55.2 3.01	42.2 1.00	51.8 1.01	65.9 1.41	83.7 1.96	74.9 2.52
Yielding of horizontal joint hoops			57.8 0.90	-49.4 -0.90	NY	NY	-59.0 -2.00	NY	NY	–	-63.5 -2.21	NY
At attained maximum story shear		+	75.3	67.4	45.4	57.1	63.1	46.3	59.3	67.4	83.8	76.4
		–	-73.4	-65.8	-39.4	-55.1	-59.8	-41.9	-52.8	-66.3	-77.3	-74.4

Upper low：story shear in , Lower low：story drift ratio in % , N/A : data not available, NY : no yielding

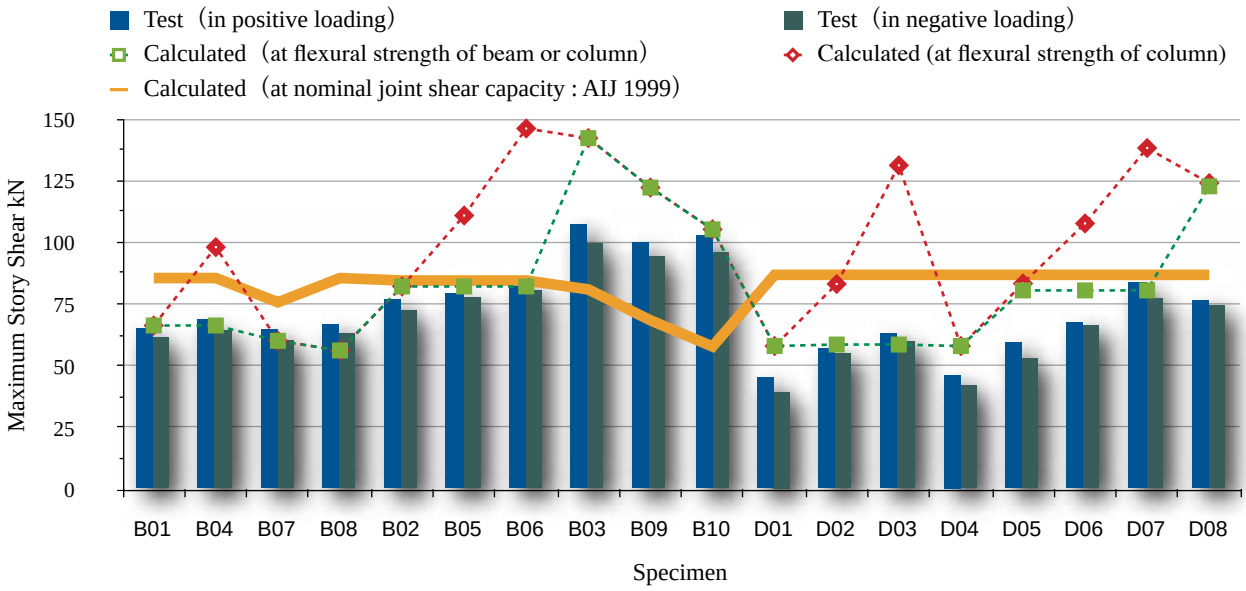

Figure 7. Comparison of test and calculation for maximum story shear

4. DISCUSSION

4.1 Mechanical Reinforcement Ratio in Beam

The maximum moment at the center of the joint normalized by the width of the beam section *b*, square of beam depth D^2 and concrete compressive strength f'_c are plotted against the mechanical reinforcement ration of beam for the specimens at which the flexural strength of beams are identical to that of the columns in Figure 5. Lines drawn in the figure are the prediction by the current design equations for comparison. They correspond to the calculated moment at flexural strength of beams and calculated moment at joint shear nominal strength based on the equations adopted in the AIJ Guidelines (1999). In Series B, the both current design equations for flexural failure and joint shear failure overestimate the test results of specimen B01 and B02, while the joint shear strength of specimen B03 is underestimated. In series D, the current design equations both for flexural strength and joint shear strength overestimate the test results. Therefore, it is concluded that the current design equations underestimate lateral capacity of beam-column joint subassemblages with moderately reinforced beam-column joint. In particular, the deficiency of strength of beam-column joints is significant if the depth of beam is smaller than that of column. An approximate line fitting is shown for each series in Figure 5. The approximate lines for Series B and D seems to coincide.

4.2 Ratio of Flexural Strength of Column to Flexural Strength of Beam

The attained maximum moment normalized by the beam width *b*, square of beam depth D^2 and concrete compressive strength f'_c are plotted against the ratio of the flexural strength of the column to the flexural strength of the beam in Figure 6. The lines representing flexural strength of the columns and the beams are also shown in the same figure. The plot of test results are not on the calculated lines but locates beneath the lines. In Series B, the test valued is smaller when the ratio of the flexural strength the column is equal to the flexural strength of the beam framing into the joint. The strength of the specimens the flexural strength of the column of which is much larger than the flexural strength of the beam is well predicted by the flexural theory. In Series D, the deficiency in strength is more evident than Series B. In all these specimen in Series B and D, the line fitting to the test results seems to be on the straight line which has the slope equal to the average slope of the flexural strength of beam and the strength of the column.

4.3 Evaluation of Current Code

Figure 7 compares the values of maximum story shear for test and calculation. The story shear calculated by the flexural theory of the section of beams and columns are not conservative for the specimens B01 B05 D01 D02 D04 D05 and D06, the column-to-beam strength ratio of which are in range of 1.0 and 1.4. The joint shear demand of these specimens are below nominal joint shear capacity in the code. So the current code for beam-column joint is not conservative in predicting the lateral capacity of moment resisting frame structure. Also the one of the predictions by the theory (Shiohara 2008) has been experimentally verified.

5. CONCLUSIONS

Results of seismic test on twenty interior reinforced concrete beam-column joint were reported. Story shear capacity of some specimens fell 5% to 30% short of the story shear predicted by the flexural strength of the beam or the column, although the joints have enough margin for nominal joint shear capacity by 0% to 50% based on current seismic provisions. In such specimens, the calculated flexural strength of the column are found to be fallen in the range of 70% to 140% of the flexural strength of the beam. The extent of insufficiency in the story shear is larger if the flexural strength of the column is equal or nearer to the flexural strength of the beam, and if the depth of the column is larger than that of the column. This kind of combination of design parameters is not a rare feature but is rather seen frequently in existing reinforced concrete buildings. This means that current seismic provisions for RC beam-column joints are deficient and can not secure the lateral strength of moment resisting frames predicted by the flexural theory of RC sections. So serious attention should be addressed to this experimental results.

ACKNOWLEDGMENTS

The authors acknowledge the supports of the Grant-in-aid for researches on the building codes improvement by the Ministry of Land, Infrastructure, Transport and Tourism, Japan, to a research program entitled “Research on design parameters of RC reinforced concrete beam-column joint necessary for ductile behavior of building structures (PI: Hitoshi Shiohara),” FY2008.

REFERENCES

Architectural Institute of Japan. 1999. “Guidelines for Earthquake Resistant Reinforced Concrete Building Based on Inelastic Displacement Concept.” AIJ. (in Japanese)

Shiohara, H.. 2009. “Reinforced Concrete Beam-column Joint: An Overlooked Failure Mechanism.” *Proc. 6CUEE*, Tokyo Institute of Technology, March 3-4, 2009, Tokyo, pp. 209-218.

JOINT CONFERENCE PROCEEDINGS
7th International Conference on Urban Earthquake Engineering (7CUEE) &
5th International Conference on Earthquake Engineering (5ICEE)
March 3-5, 2010, Tokyo Institute of Technology, Tokyo, Japan

STUDY ON COMPRESSIVE STRENGTH OF R/C COLUMN BY USING THE UPPER BOUND THEOREM

Koshiro Nishimura[1], Hisato Hotta[2], and Katsuki Takiguchi[3]

1) Assistant Professor, Dept. of Architectural and Building Engineering, Tokyo Institute of Technology, Japan
2) Associate Professor, Dept. of Architectural and Building Engineering, Tokyo Institute of Technology, Japan
3) Professor, Dept. of Mechanical and Environmental Informatics, Tokyo Institute of Technology, Japan
nishimura.k.ac@m.titech.ac.jp, hotta@arch.titech.ac.jp, ktakiguc@tm.mei.titech.ac.jp

Abstract: It is well known a compressive strength of reinforced concrete column rises by arranging transverse reinforcements. There are many experimental and analytical studies regarding to the compressive strength of reinforced concrete columns. In order to consider the effect of transverse reinforcements in reinforced concrete columns from the other point of view, a theoretical solution of compressive strength based on the upper bound theorem was shown in this study. A bi-axial failure criterion for concrete in plane strain was assumed with two parameters in this solution. The two parameters of the failure criterion were considered by comparing with experimental results of compressive tests of reinforced concrete column specimens, which conducted by one of the authors.

1. INTRODUCTION

It is well known a compressive strength of reinforced concrete column rises by arranging transverse reinforcements. There are many experimental and analytical studies regarding to the compressive strength of reinforced concrete columns. In order to consider the effect of transverse reinforcements in reinforced concrete columns from the other point of view, a theoretical solution of compressive strength based on the upper bound theorem was shown in this study. A bi-axial failure criterion for concrete in plane strain was assumed with two parameters in this solution. The two parameters of the failure criterion were considered by comparing with experimental results of compressive tests of reinforced concrete column specimens, which conducted by one of the authors (Yanagi et al. 1996).

2. THEORETICAL SOLUTION OF COMPRESSIVE STRENGTH OF R/C COLUMNS

2.1 Solution of Diagonal Failure Mechanism

As shown in Figure 1, a failure mechanism in pure compression of reinforced concrete column is considered. The column has a uniform rectangular section which dimension is width b and depth j. The failure mechanism has a yield plane at the angle β with the axis, and an infinitesimal thickness of the element δ. A total compressive force N is acted on the column. The upper part of column is assumed to move virtual displacement u in the axis and at the angle α with the axis. The yield plane is assumed to deform with uniform strain. The ranges of β and α are considered from zero to $\pi/2$. A coordinate on the yield plane is considered as shown in Figure 1.

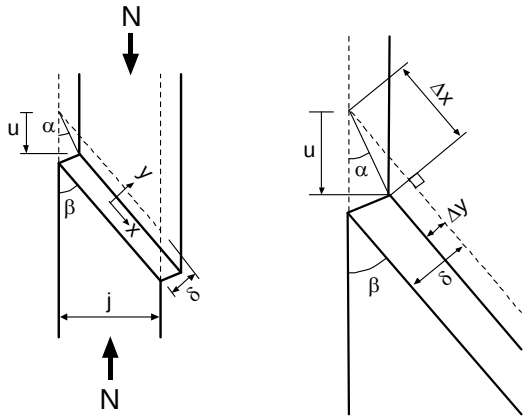

Figure 1 Failure Mechanism of R/C Column

The strains in the yield plane are

$$\varepsilon_{xx} = 0 \tag{1}$$

$$\varepsilon_{yy} = \frac{\Delta y}{\delta} = -\frac{u}{\delta \cos\alpha}\sin(\beta - \alpha) \tag{2}$$

$$\gamma_{xy} = \frac{\Delta x}{\delta} = \frac{u}{\delta \cos\alpha}\cos(\beta - \alpha) \tag{3}$$

Therefore the principal strains are obtained as follows.

$$\varepsilon_1 = \frac{u}{2\delta \cos\alpha}\left\{ 1 - \sin(\beta - \alpha) \right\} \tag{4}$$

$$\varepsilon_2 = -\frac{u}{2\delta \cos\alpha}\left\{ 1 + \sin(\beta - \alpha) \right\} \tag{5}$$

Mohr's circle of strain can be written as shown in Figure 2, and the axis of the principal strain is equal to the angle θ with the yield plane.

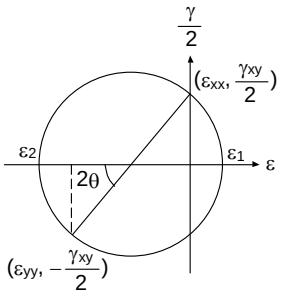

Figure 2 Mohr's Circle of Strain

The failure criterion for concrete is assumed as shown in Figure 3. A solid line in Figure 3 is under bi-axial compressive condition. σ_B and ν are compressive strength of concrete cylinder and effectiveness factor of its strength, respectively.

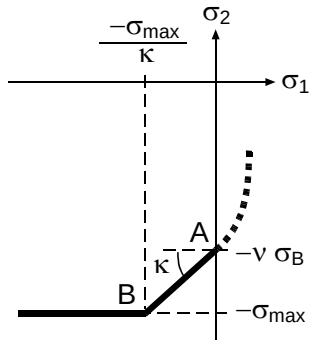

Figure 3 Failure Criterion for Concrete

When a stress is on the line ranged from A to B in Figure 3, σ_2 is equal to $\kappa\sigma_1 - \nu\sigma_B$. An internal virtual work of concrete is written as follows from an assumption that axis of principal stress is corresponded to axis of principal strain.

$$W_{iconc} = \frac{bj\delta}{\sin\beta}\left(\varepsilon_1\sigma_1 + \varepsilon_2\sigma_2\right)$$

$$= \frac{bju}{2\sin\beta\cos\alpha}\left\{\nu\sigma_B\left(1 + \sin(\beta - \alpha)\right)\right.$$

$$\left. + \sigma_1\left(1 - \kappa - (1 + \kappa)\sin(\beta - \alpha)\right)\right) \tag{6}$$

Internal virtual works of longitudinal and transverse reinforcements, W_{ilong} and W_{itrans}, respectively, are

$$W_{ilong} = bjp_g\sigma_y u \tag{7}$$

$$W_{itrans} = bjp_{ww}\sigma_y u \cot\beta \tan\alpha \tag{8}$$

In above equation, p_g and σ_y are ratio and yield strength of longitudinal reinforcements, and p_w and ${}_w\sigma_y$ are ratio and yield strength of transverse reinforcements, respectively.

External virtual work W_e is equal to Nu. Therefore, because of equilibrium between internal and external virtual works, the following equation can be given, where σ_o is equal to $N/(bj)$.

$$\sigma_o = \frac{\left(1 + \sin(\beta - \alpha)\right)\nu\sigma_B + \left(1 - \kappa - (1 + \kappa)\sin(\beta - \alpha)\right)\sigma_1}{2\sin\beta\cos\alpha}$$

$$+ p_g\sigma_y + p_{ww}\sigma_y \cot\beta \tan\alpha \tag{9}$$

The minimum of σ_o is the solution of compressive strength from the upper bound theorem.

The following equation can be given on condition that $\partial\sigma_o / \partial\sigma_1 = 0$.

$$(1 - \kappa) - (1 + \kappa)\sin(\beta - \alpha) = 0 \tag{10}$$

It can be confirmed from Eq. (4), (5), and (10) that this model satisfies the flow rule of the theory of plasticity. Eq. (9) is written by substituting Eq. (10) as follows.

$$\sigma_o = p_{ww}\sigma_y + p_g\sigma_y + \frac{\nu\sigma_B + (\kappa - 1)p_{ww}\sigma_y}{(1 + \kappa)\sin\beta\cos\alpha} \tag{11}$$

The following relationships are given when σ_o agrees with the local minimum.

$$\beta + \alpha = \pi/2 \tag{12}$$

$$\cos 2\beta = \frac{\kappa - 1}{1 + \kappa}, \text{ or } \cot\beta = \sqrt{\kappa} \tag{13}$$

Eq. (13) shows that the angle β in Figure 1 is related to the parameter κ of failure criteria shown in Figure 3. The compressive strength of reinforced concrete column is given as follows from Eq. (11), (12), and (13).

$$N = bj\left(p_g\sigma_y + \nu\sigma_B + \kappa p_{ww}\sigma_y\right) \tag{14}$$

2.2 Relationship between Three-axial Failure Criterion and Plane Strain

The yield plane shown in Figure 1 must be at plane strain field because the column is assumed as rigid body except the yield plane. On the other hand, failure criterion for concrete must be considered in three-dimensional space. If the failure criterion is regarded as yield surface and the associated flow rule is assumed, plastic strain must be normal to the failure criterion. Here we consider about relationship between three-axial failure criterion and plane strain.

A part of surface in Figure 3 ranged from A to B is cut off line by a plane parallel to σ_3 axis. σ_3 is not always equal to zero, and its normal direction satisfies the condition that ε_3=0. Regarding left side from the point B of surface in Figure 3, two interpretations can be considered as follows.

One is to regard as that this part is cut off line by a plane parallel to σ_1 axis. It can be considered as plane strain problem under a condition that ε_1=0. In this case, virtual displacement directs to perpendicular to Figure 1. The failure direction is the same as a direction of lower $\kappa p_{ww}\sigma_y$, which is shown in Eq. (14) and is stress caused by transverse reinforcements. If $\kappa p_{ww}\sigma_y$ is equal in all direction perpendicular to the axis of column, the failure direction cannot be decided and the compressive strength of column is given by point B of concrete stress shown in Figure 3. In case of rectangular section, if total section area of transverse reinforcement in short side direction is identical with that in long side direction, the failure direction is the same as short side direction. And the compressive strength of column is given by concrete stress in the range from A to B in Figure 3 if σ_1 axis is directed to short side direction.

The other is to regard as that this part is cut off line by a plane parallel to both σ_1 and σ_3 axes. It is the same as assumption that the compressive strength of column can be decided when the minimum principal stress gets to $-\sigma_{max}$. This assumption can express a behavior that a column deforms in the direction of force without yield of transverse reinforcements, and has benefit of giving limit of concrete strength. However, this assumption means that yield surface of concrete forms triangle on deviatoric planes. It contradicts properties of concrete that its shape is close to circle under hydrostatic compression.

3. COMPARISON WITH TEST RESULTS

3.1 Outline of Experiments

Outline of experiments in previous study by one of the authors (Yanagi et al. 1996) is explained here. The parameters of the experiments were concrete strength σ_B and ratio of transverse reinforcement p_w. As shown in Figure 4, all the specimens have 200 x 200 mm of square section and 375 mm of clear span. Table 1 and 2 are list of specimens and material properties of reinforcements. Concrete strength was about 30 or 60 N/mm^2. Deformed bars D13 and 6ϕ of round bars are used for longitudinal and transverse reinforcements, respectively. The ratio of transverse reinforcement p_w was 1.5 % or 0.3 %. All the specimens were subjected to monotonic compressive loading at the centre of the column as shown in Figure 4. Two rods were set on top and bottom of the specimen to work as pins. Strain gages were pasted on both longitudinal and transverse reinforcements.

Figure 5 and 6 show pictures of the specimens after the tests. Both longitudinal and transverse reinforcements yielded in all the specimens according to measurement with strain gages.

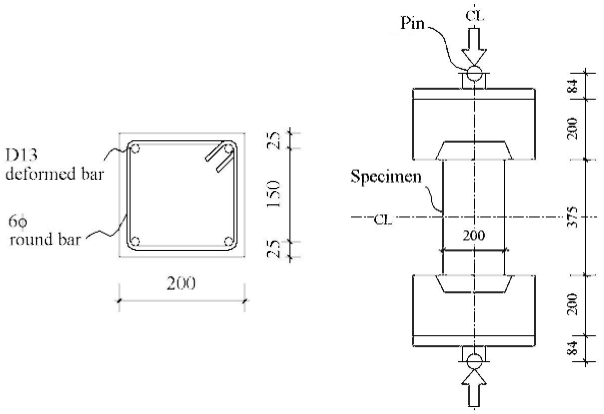

Figure 4 Section and Loading Setup of Specimen

Table 1 List of specimens

Name of specimen	Hoop reinf. Pw [%]	Main reinf.	Concrete	
			Age at test [days]	σ_B [N/mm^2]
CN-375-20	6ϕ-@20	4-D13	41	32.5
CH-375-20	1.50		42	68.5
CN-375-100	6ϕ-@100		42	31.0
CH-375-100	0.30		43	68.0

σ_B: Compressive strength of concrete cylinder

Table 2 Material Properties of reinforcements

	Deformed bar D13	Round bar 6ϕ
Nominal diameter [mm]	12.7	6
Yield strength [N/mm^2]	471	393
Young's modulous [kN/mm^2]	203	205

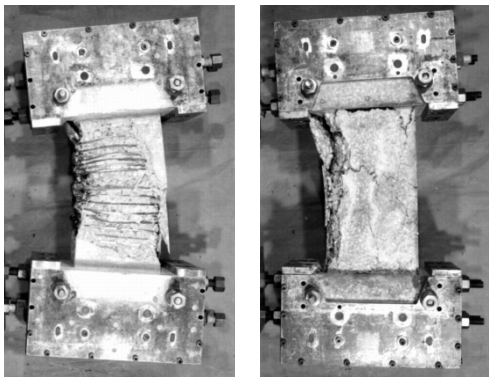

CN-375-20 CN-375-100

Figure 5 Pictures of Normal Strength Specimens

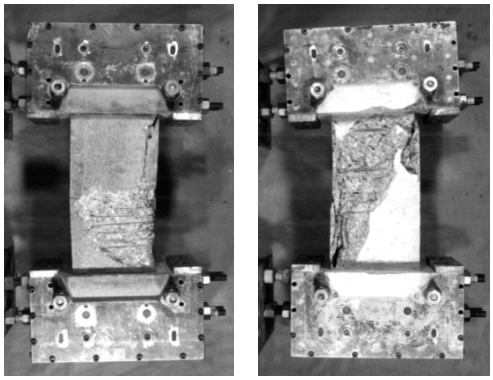

CH-375-20 CH-375-100

Figure 6 Pictures of High Strength Specimens

3.2 Consideration of Failure Criterion for Concrete in Reinforced Concrete

Here the two parameters of failure criterion for concrete in reinforced concrete column, ν and κ shown in Figure 3, are considered by comparing with the test results. The test results are compared with calculations given by Eq. (14) in four cases those are ν=0.85 and κ=1.0, ν=0.85 and κ=4.0, ν=0.85−σ_B/340 and κ=1.0, and ν=0.85−σ_B/340 and κ=4.0. ν=0.85 is often used in calculation for flexural strength of reinforced concrete member section, and ν=0.85−σ_B/340 is a effectiveness factor for stress transferred diagonally in reinforced concrete member that was proposed by Takiguchi and Nishimura (2000). κ=1.0 means Tresca yield criterion, and κ=4.0 is similar to angle of friction for concrete in Mohr-Coulomb failure criterion (Chen 1982).

The comparisons between test results and calculations in four cases were shown in Figure 7, 8, 9, and 10, respectively. The horizontal axis is ratios of test result to calculation. Characters N and H in the name of specimens mean normal strength and high strength of concrete, respectively. Numbers 20 and 100 in the name of specimens express space of transverse reinforcements.

As shown in these four Figures, the calculation in case of ν=0.85 and κ=1.0 shows good agreement with the test results. As shown in Figure 8, κ=4.0 is too large for dense transverse reinforcement which CN-375-20 and CH-375-20 have. This tendency can be seen in Figure 10 by comparing CN-375-20 and CN-375-100, or comparing CH-375-20 and CH-375-100. Regarding ν, a constant value showed good estimation in this study. ν=0.85−σ_B/340 gave under estimation against high strength concrete specimens as shown in Figure 9.

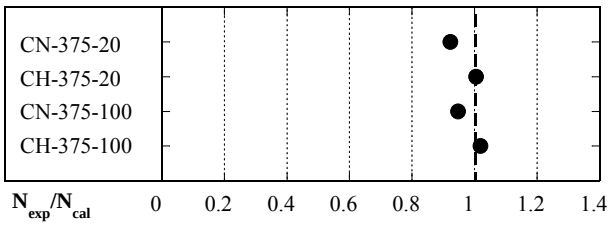

Figure 7 Ratio of Test Result to Calculation with ν=0.85 and κ=1.0.

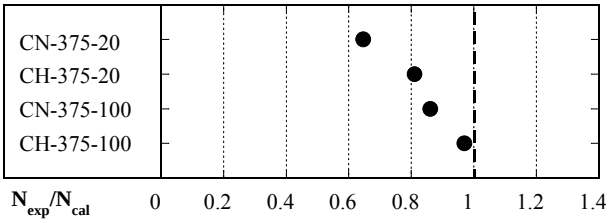

Figure 8 Ratio of Test Result to Calculation with ν=0.85 and κ=4.0.

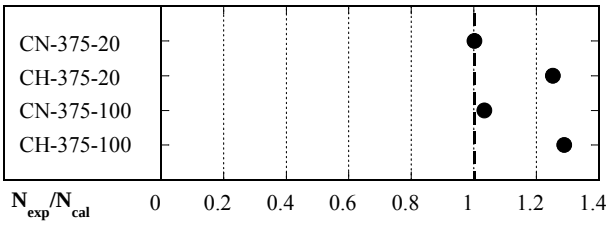

Figure 9 Ratio of Test Result to Calculation with ν=0.85−σ_B/340 and κ=1.0.

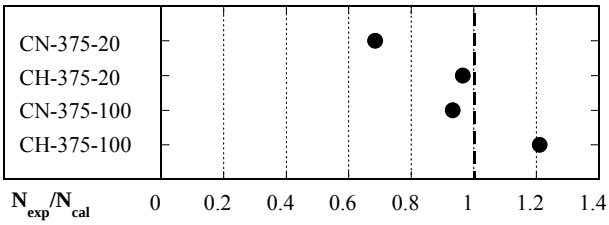

Figure 10 Ratio of Testl Result to Calculation with ν=0.85−σ_B/340 and κ=4.0.

4. CONCLUSIONS

A theoretical solution of compressive strength of reinforced concrete column subjected to pure compression was shown in this paper, which was based on the upper bound theorem. The solution can express effect of raising the strength by transverse reinforcements, and has two parameters of failure criterion for concrete. The two parameters of failure criterion, which were ν and κ shown in Figure 3, were considered by comparing with the test results of four specimens. As results, ν=0.85 and κ=1.0 shows good estimation in this study.

References:

Chen, W.F. (1982), "Plasticity in Reinforced Concrete," Mc-Graw Hill.

Nielsen, M.P. (1999), "Limit Analysis and Concrete Plasticity, Second Edition," CRC press.

Takiguchi, K. and Nishimura, K. (2000), "Diagonal Transfer Capacity of Compressive Force in R/C Columns without Shear Reinforcement," *Journal of Structural and Construction Engineering*, Architectural Institute of Japan, No.534, 113-119, (in Japanese).

Yanagi, K., Takiguchi, K., and Inada, T. (1996), "A Study of the Compressive Strength of R/C Columns," *Summaries of Technical Papers of Annual Meeting*, Architectural Institute of Japan, Structures IV, 41-42, (in Japanese).

JOINT CONFERENCE PROCEEDINGS
7th International Conference on Urban Earthquake Engineering (7CUEE) &
5th International Conference on Earthquake Engineering (5ICEE)
March 3-5, 2010, Tokyo Institute of Technology, Tokyo, Japan

LARGE-SCALE TESTING OF HIGH-PERFORMANCE FIBER-REINFORCED CONCRETE COUPLED WALLS

Rémy D. Lequesne[1)], James K. Wight[2)], and Gustavo J. Parra-Montesinos[3)]

1) PhD Candidate, Department of Civil and Environmental Engineering, University of Michigan, Ann Arbor, USA
2) Professor, Department of Civil and Environmental Engineering, University of Michigan, Ann Arbor, USA
3) Associate Professor, Department of Civil and Environmental Engineering, University of Michigan, Ann Arbor, USA
remyl@umich.edu, jwight@umich.edu, gjpm@umich.edu

Abstract: Two large-scale, four-story, coupled-wall specimens were tested under lateral displacement reversals to investigate the impact that the use of high-performance fiber-reinforced concrete (HPFRC) has on the design, construction and behavior of coupled-wall systems. Each coupled-wall specimen consisted of four precast coupling beams linking two T-shaped reinforced concrete structural walls. The designs of the individual precast beams, which were based on a previously completed series of component tests, were slightly varied. This allowed a comparison of the response of different detailing schemes when integrated into a coupled-wall system. HPFRC was shown to contribute to the shear resistance, energy dissipation and damage tolerance of the coupling beams.

The second coupled-wall specimen also incorporated fiber reinforcement in the plastic hinge region at the base of the walls. This use of HPFRC allowed for a reduction in transverse reinforcement for boundary element confinement and a higher contribution from concrete to the wall shear strength. The responses of the coupled-wall systems showed good strength and stiffness retention, and energy dissipation up to drifts as large as 3%. The complement of reduced reinforcement and HPFRC provided adequate shear resistance and confinement of longitudinal reinforcement in both coupling beams and wall plastic hinge regions.

1. INTRODUCTION

Coupled walls constitute the primary lateral force resisting system of many reinforced concrete structures and often require cumbersome detailing to ensure adequate behavior during earthquakes. With the use of tensile strain hardening, high-performance fiber reinforced concrete (HPFRC), it is possible to relax the detailing requirements, thus simplifying both design and construction.

For satisfactory performance of a coupled-wall system during a seismic event, the short coupling beams must retain a significant strength and stiffness through large displacement reversals. To ensure that adequate coupling beam ductility is achieved, the ACI Building Code (ACI 318-08) requires the use of diagonal reinforcement to resist all of the shear demand in short and highly stressed coupling beams. This reinforcement detail has been shown by many researchers to provide a stable behavior under earthquake-type displacement reversals, but can be difficult and time consuming to construct. Results from recent coupling beam component tests (Canbolat, Parra-Montesinos and Wight 2005, Wight, Parra-Montesinos and Lequesne 2009) have demonstrated that precasting coupling beams with strain-hardening HPFRC can simplify the construction process without sacrificing overall performance under large displacement reversals. In addition to relaxing the reinforcement requirements for coupling beams, it is believed that HPFRC can allow a simplification of the detailing in the critical lower stories of structural walls because of its large compression ductility and contribution to shear resistance and confinement of the longitudinal reinforcement

2. RESEARCH SIGNIFICANCE

An experimental investigation of the impact of using precast HPFRC coupling beams on the design, constructability, and seismic performance of coupled walls is presented. More specifically, this project seeks to: 1) demonstrate the ease with which precast coupling beams can be connected to cast-in-place structural wall systems, 2) evaluate the effectiveness of combining HPFRC and reduced boundary element confinement in plastic hinge regions of structural walls, 3) compare the behavior of coupling beams with various details when subjected to similar deformation demands, and 4) study the interaction between HPFRC coupling beams, slabs, and structural walls.

3. MATERIAL PROPERTIES

The HPFRC mix design used for this study is shown in Table 1. Details on the development of this mixture are reported by Liao et al. (2006). This HPFRC includes a 1.5% volume fraction of high-strength hooked steel fibers (described in Table 2), and coarse aggregate with a maximum nominal size of 0.5 in. (13 mm). The conventional concrete used throughout this study was either mixed in the laboratory or delivered by local suppliers, and had a specified compressive strength ($f_c^{'}$) of 6 ksi (41 MPa).

Results from compressive tests of 4 in. by 8 in. (100 mm by 200 mm) cylinders and of bending tests performed in accordance with ASTM C1609–05, are shown in Table 3. The results from these bending tests showed pronounced deflection hardening behavior, with peak bending stresses that exceeded the first cracking stress by more than 30% near deflections of L/800, where L is the beam span length (18 in. or 450 mm). Results from tests on representative coupons of the reinforcing steel used in this study are listed in Table 4.

4. COUPLED-WALL SYSTEM TESTS

Two four-story coupled wall specimens were built at approximately one-third scale and subjected to earthquake-type lateral displacement reversals. A completed specimen and testing setup is shown in Fig. 1. Each of the coupling beams had a slightly different reinforcement detail, allowing for a comparison of various reinforcement layouts. Slabs were built at the second and fourth levels to facilitate lateral load application. Slab reinforcement placed perpendicular to the loading direction was continuous through the structural walls, but not the precast coupling beams. The slabs provided an opportunity to observe the interaction between precast coupling beams and the adjacent slab, and to evaluate the need for design modifications to minimize damage at this connection.



Figure 1 Photo of test setup

For design of the specimen, the base of each wall was assumed to be fixed, which was achieved experimentally through the use of deep reinforced concrete foundation elements bolted directly to the laboratory strong floor. A vertical force, equivalent to an axial stress of 7% of the specified $f_c^{'}$, based on the gross area of the walls, was applied at the second story through external prestressing tendons anchored at the bottom of the foundation. Steel tube sections embedded through each wall above the second story slab transferred force from the external tendons into the walls. Hydraulic jacks were used to apply this vertical force before any lateral displacement was applied, and held it constant throughout the duration of the test. This level of gravity load is consistent with current design practice for structural walls and was sufficient to offset a majority of the uplift force resulting from the coupling of the walls.

Lateral displacements were pseudo-statically applied through the slabs cast at the second and fourth levels. The actuator mounted on the fourth level applied a predetermined sequence of reversing lateral displacements, while the actuator at the second level applied a force equivalent to 60% of the force applied by the top actuator. These lateral forces were transferred to the coupled walls through a yolk and four channel sections that were attached to the top and bottom of the outer edges of the slabs. This was intended to allow for a distribution of lateral force to each of the structural walls that is similar to the load transfer mechanism that develops in a real building system.

4.1 HPFRC Coupling Beams

The design approach for the HPFRC coupling beams used in the coupled-wall tests was developed through two series of tests on HPFRC coupling beam components (Canbolat, Parra-Montesinos, and Wight 2005, Wight, Parra-Montesinos, and Lequesne 2009). The most recent series of tests involved three large-scale, precast HPFRC coupling beams with a span-to-depth ratio (l_n/h) of 1.75. A sample result from this series of tests is shown in Fig. 2. The results indicate that HPFRC contributes appreciably to the shear capacity of the coupling beam, provides

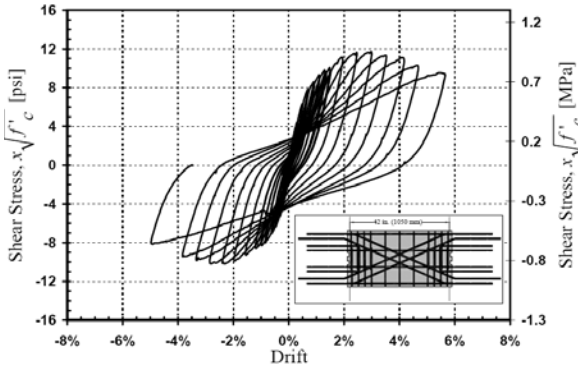

Figure 2 Shear stress vs. drift for coupling beam

Table 1 Mix proportions by weight

Cement (Type III)	Fly Ash	Sand	Aggregate	Water	Superplasticizer	Viscosity Modifying Agent	Steel Fiber	Fiber V_f (%)
1	0.88	2.2	1.2	0.8	0.005	0.038	0.32	1.5%

Table 2 Fiber properties

Length (in./mm)		Diameter (in./mm)		L/d	Specified Tensile Strength (ksi/MPa)	
1.2	30	0.015	0.38	80	333	2300

Table 3 Concrete properties

Specimen	Portion of Specimen	Fibers Y/N	28-Day Tests										Test Day	
					ASTM 1609 Flexural Tests									
			f'_c (ksi/MPa)		σ_{fc} [a] (psi/MPa)		σ_{peak} [b] (psi/MPa)		$\sigma_{(\delta=L/600)}$ [c] (psi/MPa)		$\sigma_{(\delta=L/150)}$ [d] (psi/MPa)		f'_c (ksi/MPa)	
Coupled Wall #1	CB-1	Y	5.5	38	710	4.9	1030	7.1	970	6.7	520	3.6	10.3	71
	CB-2	N	5.3	37									9.8	68
	CB-3	Y	5.5	38	710	4.9	1030	7.1	970	6.7	520	3.6	10.3	71
	CB-4	Y	6.0	41	830	5.7	1120	7.7	1050	7.2	600	4.1	10.8	74
	Foundation	N	5.0	34									7.7	53
	Wall 1st lift	N	5.3	37									7.0	48
	Wall 2nd lift	N	4.1	28									6.7	46
	Slab #1	N	3.6	25									5.3	37
	Wall 3rd lift	N	5.5	38									6.6	45
	Wall 4th lift	N	6.9	48									9.5	65
	Slab #2	N	7.4	51									9.5	65
	Wall 5th lift	N	6.6	46									8.9	61
Coupled Wall #2	CB-1	Y	6.0	41	830	5.7	1120	7.7	1050	7.2	600	4.1	10.4	72
	CB-2	N	6.6	46									9.2	63
	CB-3	Y	5.5	38	710	4.9	1030	7.1	970	6.7	520	3.6	10.4	72
	CB-4	Y	6.0	41	830	5.7	1120	7.7	1050	7.2	600	4.1	10.4	72
	Foundation	N	7.2	50									7.6	52
	Wall 1st lift (a)	Y	2.7	19									2.7	19
	Wall 1st lift (b)	Y	7.2	50	800	5.5	1170	8.1	1040	7.2	740	5.1	7.4	51
	Wall 2nd lift	Y	6.7	46	835	5.8	1050	7.2	1010	7.0	570	3.9	7.3	50
	Slab #1	N	5.9	41									6.6	46
	Wall 3rd lift	N	7.9	54									8.3	57
	Wall 4th lift	N	6.5	45									7.0	48
	Slab #2	N	7.3	50									7.7	53
	Wall 5th lift	N	7.7	53									8.1	56

[a] Bending stress at first cracking
[b] Equivalent bending stress at peak stress
[c] Equivalent bending stress at a deflection of L/600
[d] Equivalent bending stress at a deflection of L/150

Table 4 Reinforcing steel properties

Specimen	Bar Size		Yield Stress (ksi/MPa)		Ultimate Stress (ksi/MPa)	
Coupled Wall #1	#6	19	64.2	440	108	745
	#5	16	67.2	465	109	750
	#3	10	71.8	495	112	770
	#2	6	64.1	440	73.3	505
Coupled Wall #2	#6	19	64.2	440	108	745
	#5	16	67.2	465	109	750
	#4	13	60.1	415	97.0	670
	#3	10	67.3	465	117	805
	#2	6	64.1	440	73.3	505
Coupling Beams	#4	13	75.7	520	116	800
	#3	10	71.1	490	114	785
	#2	6	64.1	440	73.3	505

confinement to diagonal reinforcement, and results in improved damage tolerance evidenced by reduced crack widths and wide shear force vs. member drift hysteresis loops. Furthermore, two different connection details were shown to successfully transfer moment and shear between the precast section and the adjacent structural walls without interfering with wall boundary reinforcement. The connection details were successful at forcing flexural rotations to localize away from the beam-wall interface. This permitted the precast HPFRC section to penetrate into the wall face only as deeply as the cover, thus allowing wall boundary reinforcement to continue, uninterrupted. A close-up photo of the proposed connection design, taken during construction, is shown in Fig. 3.

Based on these component tests, a design approach for HPFRC coupling beams has been proposed that represents a major change from the current state of the art. This new approach accounts for the improved damage tolerance exhibited by HPFRC elements by assuming the full coupling beam section maintains its integrity and remains active in resisting shear and moment through large displacement reversals, reducing the need for diagonal and transverse reinforcement for resisting applied shear. This is in contrast to the current approach which assumes the full beam capacity is uniquely controlled by two intersecting diagonal reinforcement cages.

Accordingly, the following approach for HPFRC coupling beam design was adopted for the beams used in the coupled-wall systems, given an expected beam shear demand, V_u, and a corresponding moment demand, M_u ($M_u = V_u \cdot L/2$, where L is the clear span of the beam).

1) Select cross-sectional beam dimensions that satisfy architectural requirements while ensuring that $V_u \le 10\sqrt{f_c'}A_{cw}, [\text{psi}] (0.83\sqrt{f_c'}A_{cw}, [\text{MPa}])$, where f_c' is the specified concrete compressive strength and A_{cw} is the cross-sectional area of the coupling beam.
2) Assume diagonal reinforcement resists approximately 30-40% of the expected shear demand, V_u, and select appropriate diagonal bar orientation angle and bar sizes.
3) From Step 2, the contribution of the diagonal reinforcement to the beam probable moment strength, M_{pr}, is determined. Select flexural reinforcement, A_s, to ensure $\phi M_{pr} \ge M_u$. This procedure is a capacity-based approach, so $\phi = 1.0$ is recommended.
4) Place a reasonable fraction of this longitudinal flexural reinforcement as short dowel bars to ensure failure will not localize at the precast beam-wall interface.
   - Based on the beam components tested, "reasonable fraction" corresponds to:
     -30-40% of A_s for coupling beams with an aspect ratio less than 2
     -15-20% of A_s for more slender coupling beams
5) In this project, a moment-curvature analysis performed at the precast beam-wall interface was used to verify that $M_{pr} \ge M_u$, and the flexural design was modified if required.
6) Shear design: Use the probable coupling beam moment capacity, M_{pr}, to determine the expected shear demand, V_{pr} and check that $V_{pr} \le 10\sqrt{f_c'}A_{cw}, [\text{psi}] \left(0.83\sqrt{f_c'}A_{cw}, [\text{MPa}]\right)$. The HPFRC coupling beam shear capacity, V_n, should be designed to satisfy $\phi V_n \ge V_{pr}$, where $\phi = 0.85$. For HPFRC coupling beams, $V_n = V_d + V_s + V_c$, where V_d is the contribution from the diagonal reinforcement, V_s is the contribution from the stirrups, which is suggested to be 30-40% of V_{pr}, and V_c is the contribution from the HPFRC. $V_c \le 5\sqrt{f_c'}A_{cw}, [psi] (0.42\sqrt{f_c'}A_{cw}, [MPa])$ appears to be appropriate, based on test results.
7) Detailing: Provide column-type seismic confinement to the ends of the coupling beam, extending approximately $h/2$ away from the face of the walls, where h is the coupling beam height. Due to the confinement provided by the HPFRC, no special confinement reinforcement is required for the remaining portion of the span.

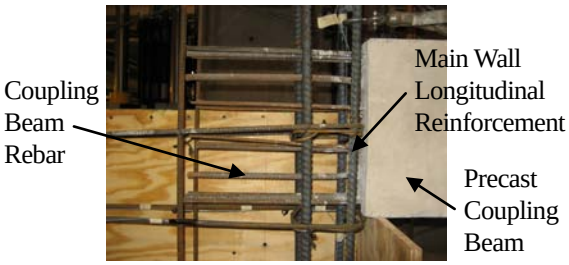

Figure 3 Precast coupling beam embedment detail

Typical reinforcement details used in the coupling beams of the test specimens are shown in Fig. 3. The first, third, and fourth story coupling beams were constructed with HPFRC, and the second story beam in both specimens was cast with conventional concrete. The flexural and diagonal reinforcement were identical for the HPFRC and RC coupling beams to provide similar stiffnesses and flexural capacities. However, the transverse reinforcement ratio was increased from 0.55% for the HPFRC coupling beams to 1.5% to provide additional shear resistance and confinement to the RC beam.

The flexural reinforcement of the coupling beams used in the first coupled-wall system was terminated 3 in. (75 mm) into the wall to be more consistent with current design requirements. This resulted in an undesirable localization of damage along the interface between the structural wall and precast coupling beam section, and is therefore not recommended. All of the coupling beam reinforcement was fully developed in the second coupled-wall system, which resulted in damage occurring within the precast section and full development of the coupling beam capacity.

4.2 Coupled Wall Design

The coupling beam dimensions and detailing were of special interest in this project, and thus, they were the initial focus of the coupled wall design. The structural walls in the first coupled-wall specimen were subsequently designed in accordance with the seismic provisions of the ACI Building

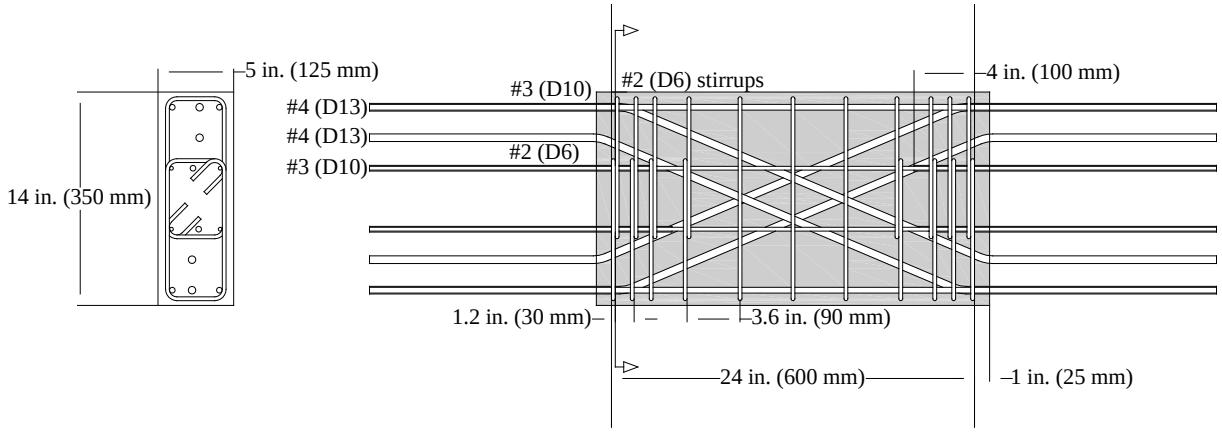

Beam 1, 3, 4: HPFRC

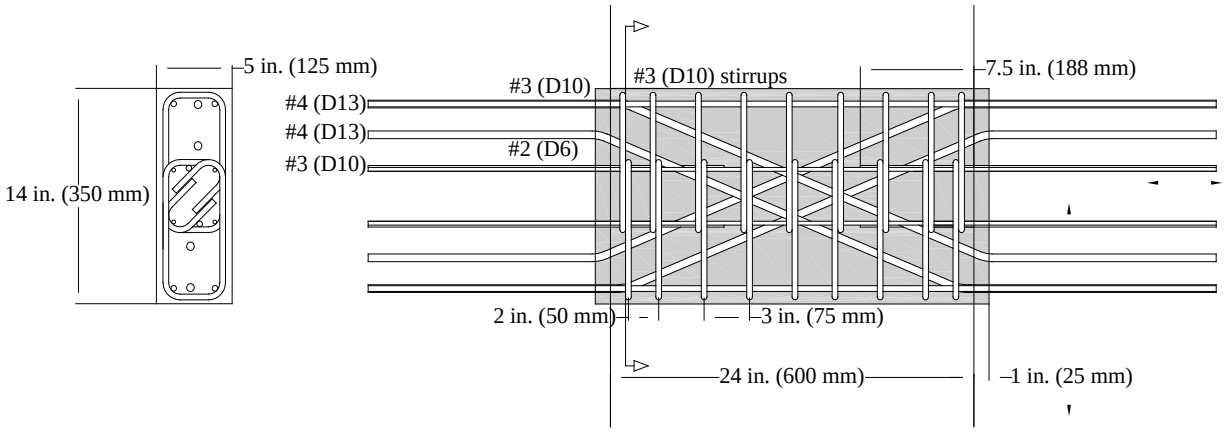

Beam 2: RC

Figure 4 Coupling beam reinforcement

Code (ACI 318-08) to provide the required overturning moment capacity, shear strength, and ductility for the coupled-wall system to behave realistically. Fiber reinforcement was used in the first two stories of the second coupled-wall system, as shown in Fig. 5. The compression ductility of HPFRC, and the confinement it provides to the wall boundary reinforcement, allowed for an increase in the spacing of the hoops from $b_w/3$. Stirrups were spaced at $b_w/2$ in one HPFRC wall, and at b_w in the other.

The wall shear design was based on the expected ultimate capacity of the system, assuming that a mechanism controlled by flexural hinging at the base of both walls and in each of the beams would develop. To resist the expected shear demand, the wall concrete in the first coupled-wall system was assumed to carry a shear stress of $2\sqrt{f_c'}, [psi] (0.17\sqrt{f_c'}, [MPa])$, and wall transverse (horizontal) reinforcement, anchored by alternating 90- and 135-degree hooks, was provided to resist the remaining shear. For the reinforced concrete walls the transverse reinforcement ratio was 0.45%. The concrete in the second coupled-wall system, which was fiber reinforced, was assumed to carry a shear stress of $4\sqrt{f_c'}, [psi] (0.34\sqrt{f_c'}, [MPa])$, resulting in the same wall transverse reinforcement ratio, despite an increased shear stress demand. This higher shear demand was a result of the higher overturning moment capacity of the second specimen caused by full development of the coupling beam reinforcement.

5. PRELIMINARY COUPLED-WALL TEST-RESULTS

A plot of the overturning moment vs. drift responses of the coupled-wall specimens is shown in Fig. 6. Both specimens exhibited the high strength and stiffness characteristic of coupled-walls, with excellent strength retention. The first specimen maintained more than 80% of the peak overturning moment capacity to beyond 2.5% drift in both loading directions. The second specimen did even better, retaining more than 80% of the peak capacity to beyond 3% drift. Furthermore, the hysteresis loops show no appreciable pinching in either test, because the responses were governed by flexural hinging in the bases of the walls and at the ends of the coupling beams, as intended in design.

Assuming this flexurally-dominated plastic mechanism developed, and accounting for the measured concrete and reinforcing steel properties, the system overturning moment capacity for the first specimen was under-predicted by only approximately 5%. This capacity was largely maintained until the test was terminated when the integrity of the structure had been compromised by the fracturing of

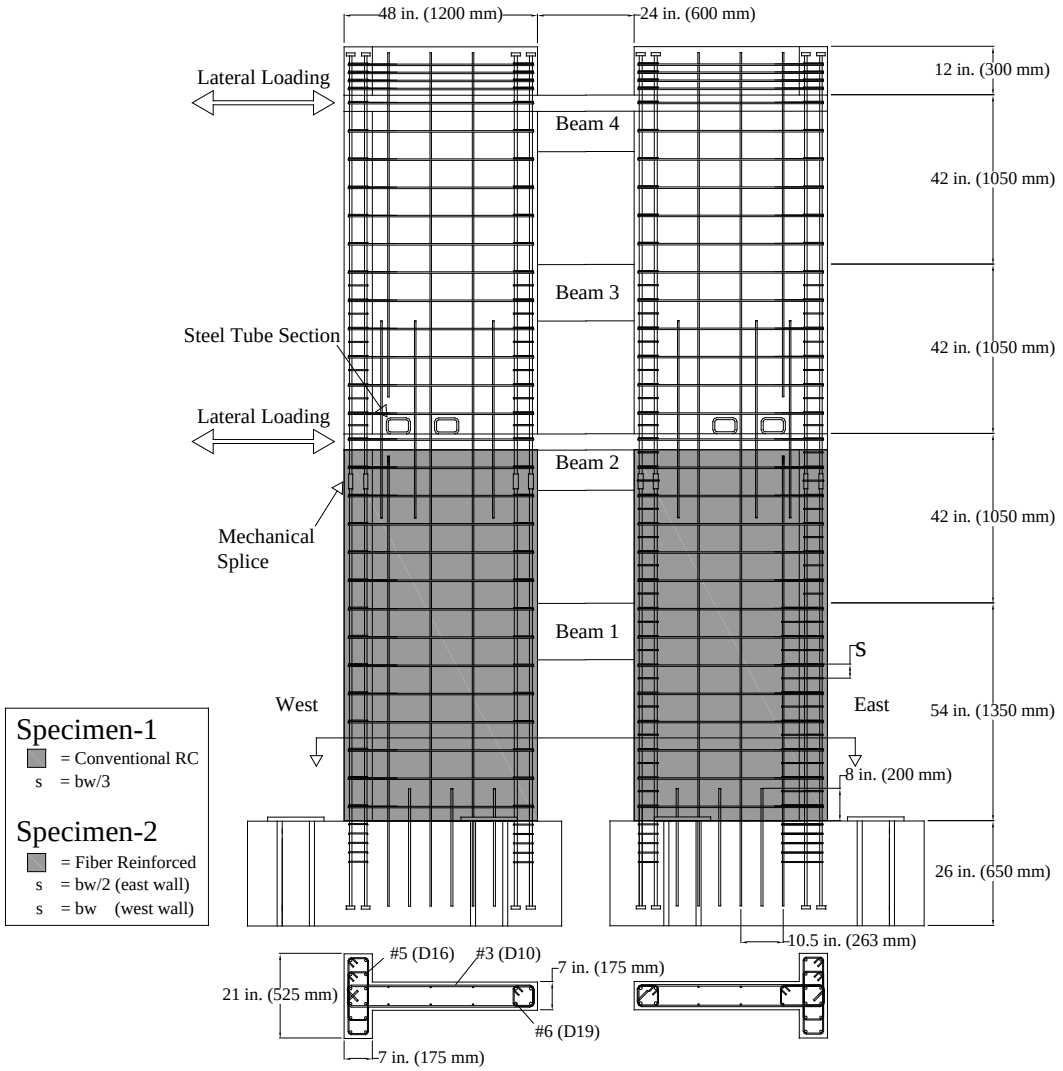

Figure 5 Coupled-wall system reinforcement

diagonal reinforcement in the coupling beams and flexural reinforcement in the walls. Similar predictability was exhibited by the second coupled system. The second test was terminated once the compression wall failed in shear-compression at a system drift of 3%, and the opposing wall exhibited a flexural failure upon load reversal at a drift of 3.3%. Throughout this paper, "compression" wall is used to refer to the wall that, due to the coupling action of the beams, was subjected to increased compression within a particular loading half-cycle.

Both specimens exhibited predominantly diagonal-shear cracking in the base of the walls in early cycles, with flexural cracking becoming more prevalent at larger drifts. This indicates that the ACI Building Code requirements for structural wall design provided adequate shear resistance and confinement of longitudinal reinforcement to accommodate a ductile flexural mechanism in the first specimen. Likewise, the stable response of the second specimen indicates that the combination of reduced reinforcement and HPFRC also provided adequate shear resistance and confinement of longitudinal reinforcement.

5.1 Coupled wall cracking

The coupled walls exhibited predominantly diagonal-shear cracking at their base in early cycles, with flexural cracking becoming more prevalent at larger drifts beyond approximately 0.75%. Although the overall response of the HPFRC wall system was very similar to the companion RC specimen, the extent and severity of cracking differed. The HPFRC specimen exhibited a much higher number of narrower cracks when compared to the reinforced concrete wall system, as shown in Fig. 7. The HPFRC walls developed diagonal cracks spaced at approximately 2 in. (50 mm), less than half of the typical diagonal crack spacing of the first specimen. The individual crack widths were consistently less than half those observed in the first specimen. This is typical of HPFRC members, and results in greater damage tolerance.

5.2 Coupling beam performance

In both specimens, diagonal-shear cracking was first observed in all four coupling beams near system drifts of 0.5%. As drifts increased in the first coupled-wall system, damage began to localize near the precast beam-wall interface due to the

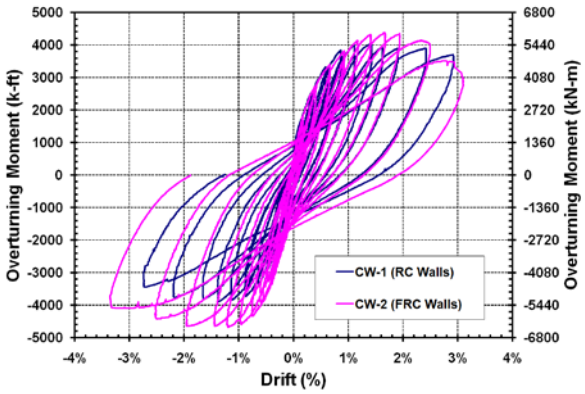

Figure 6 Overturning moment vs. drift for coupled-wall specimens

termination of coupling beam flexural reinforcement only 3 in. (75 mm) into the wall. The result was crushing and spalling of the wall concrete near the interface at system drifts exceeding 2.5%, which precluded the development of a more desirable damage pattern within the precast beams.

The second specimen, with the fully developed coupling beam reinforcement, showed coupling beam damage localizing within the precast beam away from the wall connection. This allowed for a better comparison of HPFRC coupling beam reinforcement details. At a system drift of 1.5%, initiation of spalling was first noted in the reinforced concrete (RC) beam at the second level. When the system drift reached 2%, significant loss of cover had exposed much of the transverse reinforcement in the RC beam. The other beams, constructed with HPFRC, also began to exhibit wider cracks, but they remained less than 0.04 in. (1 mm) in width. It was not until the system had reached drifts of 2.5% that the HPFRC beams exhibited unsightly damage consisting of wider cracks and superficial flaking. However, at this same drift, the RC beam had spalled extensively, exposing nearly all of the reinforcement. Significant damage to the core of the RC coupling beam was evident. Further loading led to nearly complete destruction of the RC beam which left gaping holes through the critical core of the member. Fig. 8 shows a photo of the first two coupling beams at a system drift of 3.3%, and illustrates the substantial improvement in damage tolerance exhibited by HPFRC beams relative to the RC coupling beam.

5.2.1 Coupling beam chord rotations

For typical coupled-wall systems, the chord rotation expected in coupling beams (as defined in ASCE/SEI 41/06), can be roughly predicted as the coupled-wall rotation times the ratio of the distance between the wall centroidal axes to the effective length of the coupling beam (2.1 for the test specimen). The effective coupling beam length, L_{eff}, was defined as $L_{eff} = L + h$, where L is the clear span and h is the height of the beam. The experimentally observed relationship between coupling beam chord rotations and inter-story wall rotations are shown in Fig. 9, plotted along with the predicted value. When the system drift exceeded 2.5%, nearly all of the coupling beams were subjected to chord rotations exceeding 4.0% (ratio = 1.6). Although these large deformation demands emphasize the need for highly ductile coupling beams, the observed ratio is lower than the calculated value of 2.1. This indicates that this rough predictor may over-estimate coupling beam chord rotation demands.

5.2.2 Coupling beam elongations

When reinforced concrete members are subjected to cyclic displacements large enough to cause significant cracking and yielding of the reinforcement, the members have a tendency to expand longitudinally. In most design cases, the resulting axial strain is either too small or the members are insufficiently restrained to cause significant axial forces to develop. However, the large drift demands placed on short coupling beams result in a strong tendency to expand longitudinally, and the adjacent structural walls and surrounding slab should provide non-negligible resistance to this expansion, as identified by Teshigawara et al. (1998a).

In component tests, few researchers have addressed longitudinal expansion of coupling beams and the possible axial forces that may develop as a result. Most experimental work has allowed for unlimited axial elongation, which has been reported to be as high as 4.0% of the beam length (Kwan and Zhao 2002,

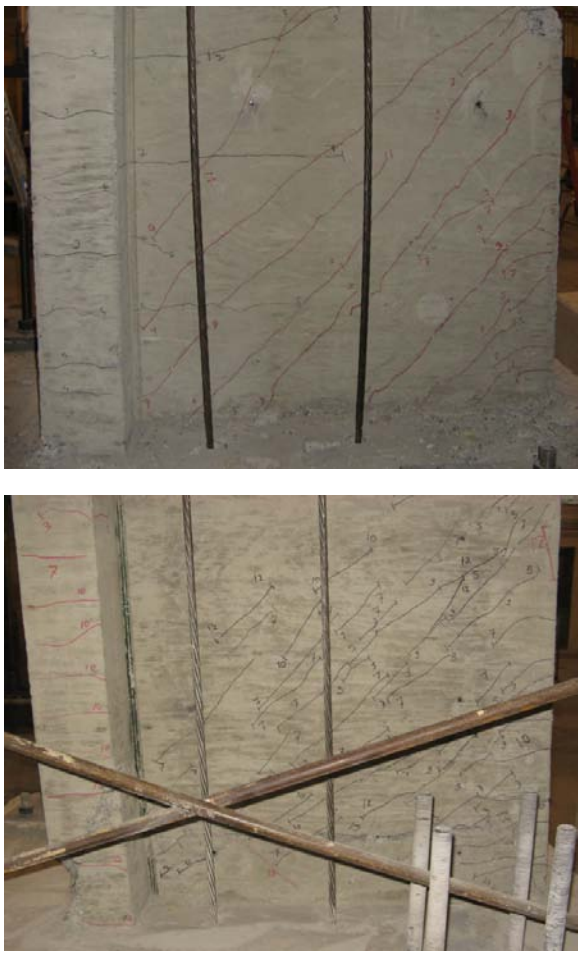

Figure 7 Structural wall crack patterns after test termination (top to bottom, conventional and high-performance fiber-reinforced concrete)

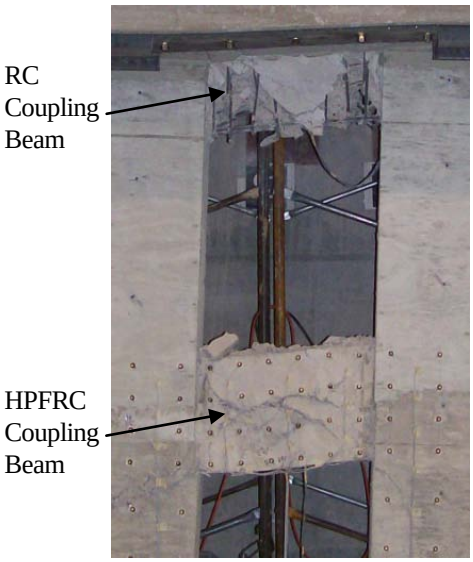

Figure 8 CW-2 beam damage

Zhao and Kwan 2003). In recent tests of coupling beam components with aspect ratios of 1.75 (Lequesne et al. 2009b), longitudinal expansion was partially restrained, which led to maximum average axial strains between 0.5-1.0%. The result was the development of axial forces within the coupling beams as high as 55% of the applied transverse shear force at coupling beam drifts over 4%.

The coupled-wall tests described herein provided an opportunity to observe the magnitude of longitudinal beam strains developed in a realistic coupled-wall system. Fig. 10 shows the measured average axial strains of the coupling beams at all four levels at various interstory-drift levels. The small axial strain observed in the coupling beam at the first level suggests a significant axial restraint and/or compression force acting on this member throughout the test. This axial force would result in a shifting of base shear towards the compression side of the system consistent with previously tested coupled-wall systems (Aktan and Bertero 1984, Teshigawara et al. 1998b).

Positive (tension) axial strains were observed in the other beams, with a general trend towards larger axial strains further from the foundation. If correlated with the component tests cited previously, axial strains of the magnitudes observed indicate significant restraint from the adjacent walls, and thus, the development of significant axial compression forces that will affect the capacity and ductility of the coupling beams. The extent to which these observations apply to taller and monolithically cast coupled-wall systems will need to be investigated further.

6. SUMMARY AND CONCLUSIONS

Two large-scale four-story coupled-wall specimens were tested to investigate the impact that precast HPFRC coupling beams have on the design, construction, and behavior of coupled-wall systems. The design of the HPFRC coupling beams was based on results from a series of coupling-beam-component tests that demonstrated the utility of

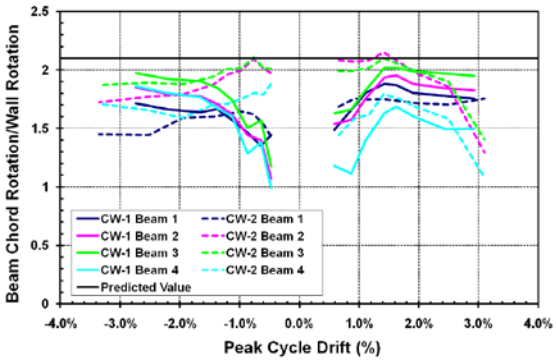

Figure 9 Coupling beam chord rotations

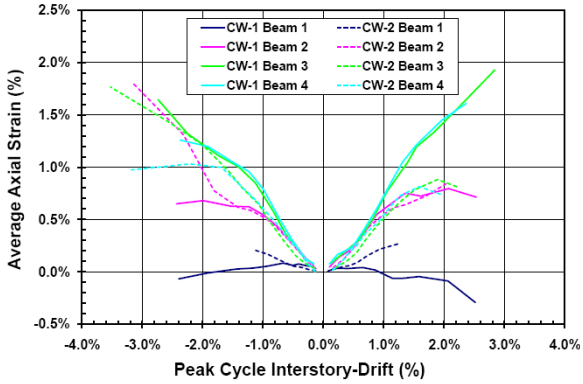

Figure 10 Coupling beam elongations

HPFRC in coupling beam design. HPFRC used in the base of the walls allowed for a reduction of transverse reinforcement for confinement of the boundary elements and a higher shear stress contribution from the concrete in design. The following conclusions can be made regarding the performance of the systems tested.

- The coupled-wall specimens exhibited the high strength and stiffness characteristic of coupled-walls, with excellent strength retention up to system drifts as large as 3.0%. The HPFRC regions exhibited narrower crack spacing and significantly improved damage tolerance, despite simplified reinforcement detailing.
- Placing the precast coupling beams, with beam reinforcement threading through adjacent wall reinforcement, proved to be simple and is believed to be a viable alternative method for assembling a coupled-wall system.
- Terminating longitudinal reinforcement within the wall near the coupling beam-wall interface is not recommended. This detail caused a concentration of damage along the coupling beam-wall interface in the first specimen, a damage pattern that was not observed in the second system with fully developed longitudinal beam reinforcement.
- Spacing the ties in the wall boundary element at $b_w/2$ or b_w, as compared to $b_w/3$ for the RC walls, did not lead to premature failure in the HPFRC walls, indicating that effective confinement was achieved.
- A design value of $4\sqrt{f_c'}, [psi] (0.34\sqrt{f_c'}, [MPa])$ for the contribution of HPFRC to the nominal shear stress capacity of structural walls seems appropriate.

- Coupling beam chord rotations, relative to the inter-story wall rotations, were generally less than predicted. This implies that coupling beam chord rotations may be over-estimated by the commonly used procedure that amplifies beam rotations based on the ratio of the distance between the wall centroids and the coupling beam span.
- Measurements indicate the tendency for coupling beams to elongate when subjected to reversing displacements is restrained by the adjacent structural walls and floor slabs. When correlated to component tests of coupling beams, the axial elongations permitted by the walls imply the development of significant axial forces that will impact both their strength and ductility.
- Although not a focus of the current study, the ACI Building Code seismic requirements for structural wall design provided adequate shear resistance and confinement, which led to the development of a stable flexural mechanism.

Acknowledgements:

The tests reported herein were funded by the National Science Foundation through the NEES research program under Grant No. CMS 0530383 and Bekaert Corp. Special thanks go to Erico Corp. for donation of materials used in construction of the specimens described herein. The ideas and conclusions are those of the writers and do not necessarily represent the views of the sponsors.

References:

ACI Committee 318 (2008), *Building Code Requirements for Structural Concrete (ACI 318-08) and Commentary*, American Concrete Institute, Farmington Hills, MI, 465 pp.

Aktan, A. E., Bertero, V. V. (1984), "Seismic Response of R/C Frame-Wall Structures," *ASCE Journal of Structural Engineering*, V. 110, No. 8, pp. 1803-1821.

ASCE/SEI 41/06 (2007), *Seismic Rehabilitation of Existing Buildings*, American Society of Civil Engineers, Reston, Virginia.

ASTM C 1609/C 1609M – 05 (2005), "Standard Test Method for Flexural Performance of Fiber-Reinforced Concrete (Using Beam With Third-Point Loading)," West Conshohocken, PA.

Canbolat, B. A., Parra-Montesinos, G. J., and Wight, J. K. (2005), "Experimental Study on Seismic Behavior of High-Performance Fiber-Reinforced Cement Composite Coupling Beams," *ACI Structural Journal*, V. 102, No. 1, pp. 159-166.

Kwan, A. K. H., and Zhao, Z. Z. (2002), "Cyclic Behaviour of Deep Reinforced Concrete Coupling Beams." *Structures and Buildings*, V. 152, No. 3, pp. 283-293.

Lequesne, R. D., Parra-Montesinos, G. J., and Wight, J. K. (2009a), "Test of a Coupled Wall with High Performance Fiber Reinforced Concrete Coupling Beams," *Thomas T. C. Hsu Symposium: Shear and Torsion of Concrete Structures*, SP-265, American Concrete Institute, Farmington Hills, MI, 16 pp.

Lequesne, R.D., Setkit, M., Parra-Montesinos, G. J., and Wight, J. K. (2009b), "Seismic Detailing and Behavior of Coupling Beams with High-Performance Fiber Reinforced Concrete," *Antoine E. Naaman Symposium – Four decades of progress in prestressed concrete, fiber reinforced concrete, and thin laminate composites*, ACI Special Publication – *In Press*.

Liao, W. C., Chao, S. H., Park, S. Y. and Naaman, A. E. (2006), "Self-Consolidating High Performance Fiber Reinforced Concrete (SCHPFRC) – Preliminary Investigation," *Report No. UMCEE 06-02*, University of Michigan, Ann Arbor, MI, 68 pp.

Teshigawara, M., Kato, M., Sugaya, K. and Matsushima, Y. (1998a), "Energy Absorption Mechanism and the Fluctuation of Shear Force in the Coupled Shear Walls," *Structural Engineers World Congress 1998*, Paper Number T-186-5, Elsevier Science Ltd.

Teshigawara, M., Sugaya, K., Kato, M. and Matsushima, Y. (1998b), "Seismic Test on 12-Story Coupled Shear Wall with Flange Walls," *Structural Engineers World Congress 1998*, Paper Number T-186-4, Elsevier Science Ltd.

Wight, J. K., Parra-Montesinos, G. J. and Lequesne, R. D. (2009), "The Design of Coupled Wall Systems for Earthquake Motions with High-Performance Fiber Reinforced Concrete." *Proceedings of WCCE-ECCE-TCCE Joint Conference Earthquake & Tsunami*, Istanbul, Turkey, June 22-24, 13 pp.

Zhao, Z. Z. and Kwan, A. K. H. (2003) "Nonlinear Behavior of Deep Reinforced Concrete Coupling Beams." *Structural Engineering and Mechanics*, V. 15, No. 2, pp. 181-198.

JOINT CONFERENCE PROCEEDINGS
7th International Conference on Urban Earthquake Engineering (7CUEE) &
5th International Conference on Earthquake Engineering (5ICEE)
March 3-5, 2010, Tokyo Institute of Technology, Tokyo, Japan

ANALYTICAL STUDY OF SHEAR STUD BEHAVIOR IN HIGH STRENGTH CONCRETE

Shim Hak Bo[1], Jang Sung Hoon[2], Park Soon Jeon[3] and Lee Joo Ho[4]

1) Researcher, Lotte Research & Development Institute, Korea
2) Chief Researcher, Lotte Research & Development Institute, Korea
3) Principal Researcher, Lotte Research & Development Institute, Korea
4) Principal Researcher, Lotte Research & Development Institute, Korea
hbshim@lottenc.com, classic4@lottenc.com, soon1026@lottenc.com, joo7777@lottenc.com

Abstract: Current design code methods of the shear studs are based on studs embedded in normal strength concrete and on studs of normal diameter. It also appeared that the diameter of connector and the concrete strength are the main factors affecting the behavior of shear connections. So it is necessary to evaluate the shear strength of studs by concrete strength change and stud diameter change with the current design code. In this paper, It was evaluated the results of design codes by concrete of various strength and stud of various diameter. And It was studied to estimate accurately the finite element model with material properties. The results of the finite element model are also verified with results of push-out test.

1. INTRODUCTION

Steel-concrete composite members have seen widespread use in high-rise building. Shear Studs are commonly used to transfer longitudinal shear forces across steel-concrete interface in composite member design.

Several researchers performed push-out tests to evaluate the capacity of the shear stud and the load-slip behavior of the stud. Gattesco et al(1996) carried out experimental study on stud shear connectors subjected to cyclic loading of simple beam. Li An(1996) carried out push-out tests on studs in high strength of 100MPa and normal strength concrete of 30MPa. Sameh S. Badie, P.E(2002) studied 31.8mm large shear studs for composite action in steel bridge girders. A. Nakajima et al(2003) studied Cyclic shear force-slip behavior of studs under alternating and pulsating load condition. Scott A. Civjan (2003) analysis behavior of shear studs subjected to fully reversed cyclic loading. S. Bullo et al(2004) suggested a simplified method for assessing the ductile behaviour of stud connectors in composite beams with high strength concrete slab. Chang-Su Shim(2004) evaluated static behavior of 25, 27, 30mm large stud shear connectors. Cem Topkaya(2004) studied composite shear studs strength at early concrete ages. Gerhard Hanswille(2006) studied resistance of headed studs subjected to fatigue loading Part I : Experimental study, Part Ⅱ : Analytical study. Shervin Maleki(2008) studied behavior of channel shear connectors, Part Ⅰ: Experimental study, Part Ⅱ: Analytical study. Weichen Xue (2008) studied static behavior and theoretical model of stud shear connectors with stud diameter, length, concrete strength and stud welding technique. Huu Thanh Nguyen(2009) carried out finite element modeling of push-out tests for large stud shear connectors of 22, 25, 27 and 30mm.

Almost study evaluated the capacity of shear stud in high strength concrete and large shear connector. But it is necessary to compare with the shear strength of studs by concrete strength change and stud diameter change with the current design code. It is important to find the accurate design code or to make new design code for various parameter. And It need to estimate accurately the finite element model with material properties because it is impossible to perform push-out test for all cases with various change. In this paper, It was evaluated the results of design codes by concrete of various strength and stud of various diameter. And It was studied to estimate accurately the finite element model with material properties. The results of the finite element model are also verified with results of push-out test.

2. ULTIMATE STRENGTH OF SHEAR STUD IN DESIGN CODE

2.1 Ollgaard et al.(1971)

A calculation model was presented as Eq(1) by Ollgaard et al. at Lehigh University based on push-out tests, and the model became the basis of present design methods in the codes

$$Pu = 0.5As\sqrt{f'cEc} \quad (1)$$

2.2 Oehlers and Johnson(1987)

Oehlers and Johnson proposed one formula to include contributions from both studs and concrete. The mean strength of stud connectors in the push-out specimens could be determined by

$$Pu = KAs(\frac{E_c}{E_s})^{0.4}(\frac{f_{cu}}{f_u})^{0.35} \quad (2)$$

Where the units are N, mm; Ec = modulus of elasticity of concrete, Es = modulus of elasticity of concrete, Fcu = compressive strength of concrete cube; Fu = ultimate tensile strength of stud ; As=cross-sectional area of a stud shear connector; $K=4.1\text{-}n^{-1/2}$; and n=number of studs.

2.3 Korea building code(2005)

In the Koea building code(KBC), the stud shear bearing capacity is determined by

$$Pu = 0.5RaAs\sqrt{f'cEc} \le AsFu \quad (3)$$

Ra=1.0 for reinforced concrete flat slab of the fixed thickness (resistance factor of shear stud connectors) ; As=cross-sectional area of a stud shear connector(mm2) ; f'c = compressive strength of concrete cylinders ; Ec = elastic modulus of concrete

f'c ≤29.4N/ mm^2 : $Ec= 4{,}700\sqrt{f'c}$

f'c > 29.4N/ mm^2 : $Ec= 3{,}300\sqrt{f'c} + 6{,}900$

Fu = ultimate tensile strength of stud(≤440N/mm^2)

2.4 Eurocode4

In the latest proposal of Eurocode 4, the shear resistance of a headed stud is determined by

$$Pu = \frac{0.8Fu\pi\alpha^2/4}{\gamma_v}, Pu = \frac{0.29\alpha^2\sqrt{f'cEc}}{\gamma_v} \quad (4)$$

Whichever is smaller

Where the units are N, mm; d=diameter of the studs ; Fu = ultimate tensile strength of stud ; f'c = compressive strength of concrete cylinders ; Ec = elastic modulus of concrete ; The partial safety factor rv should be taken as 1.25 ; α=0.2(H/d+1)≤1; and H=height of the studs.

2.5 Comparison of shear stud strength by design code

Shear stud strength was compared by above design code. Material properties was like this. Modulus of elasticity of concrete is 41000MPa, modulus of elasticity of stud is 218000MPa, compressive strength of concrete is 60, 80, 100Mpa, ultimate tensile strength of stud is 440MPa, stud length is 135mm and stud diameter is 19, 22, 25mm

Table 1. Ultimate strength comparison of shear stud by compressive strength of concrete

Design code	Ultimate strength of shear stud (stud diameter : D19)			note
	60MPa	80MPa	100Mpa	
Ollgaard et al	222.7kN	257.2kN	287.5kN	
Oehlers and Johnson	224.7kN	248.5kN	268.7kN	
Korea building code	125kN	125kN	125kN	
Eurocode4	79.8kN	79.8kN	79.8kN	

Table 2. Ultimate strength comparison of shear stud by stud diameter

Design code	Ultimate strength of shear stud (compressive strength of concrete : 80MPa)			note
	D19	D22	D25	
Ollgaard et al	257.2kN	344.1kN	444.6kN	
Oehlers and Johnson	248.5kN	332.5kN	429.6kN	
Korea building code	125kN	167.2kN	216kN	
Eurocode4	79.8kN	107kN	138.2kN	

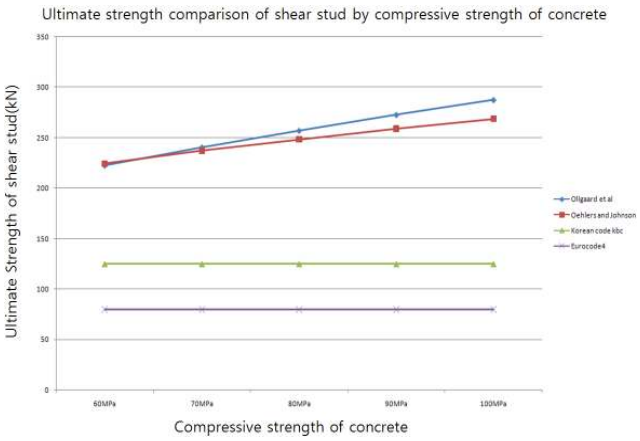

Figure 1. Ultimate strength comparison of shear stud by compressive strength of concrete

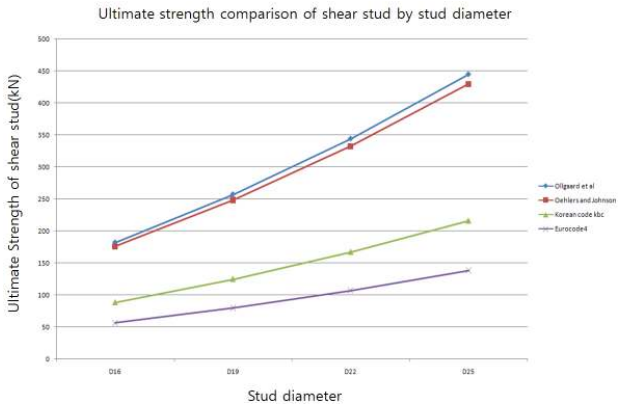

Figure 2. Ultimate strength comparison of shear stud by stud diameter

As compared with the maximum shear resistance result by design code, difference is appeared. If concrete strength become high, the resistance difference of shear stud by design code become large. If stud diameter become large, the resistance difference of shear stud by design code also become large. It is important to find the accurate design code or to make new design code for various parameter.

3. FINITE ELEMENT MODELING

3.1 Finite element mesh and boundary condition

It is capable of conducting three-dimensional finite element analysis considering both geometric and nonlinearity in ANSYS program. It includes contact elements and boundary conditions for modeling complex systems. The separation of concrete from the shear stud occurred not in physical contact. The each element consisting model is capable of supporting only the load compression direction and shear in the tangential direction. And the effect of steel beam is insignificant in the push-out test in this case. Its effect is to allow for transmission of the applied load to the shear studs. Contact part of the concrete slab and stud to the flange of the steel beam are bonded to restrict from moving to the rotation-direction. The finite element mesh of studs, H-beam and welding part separated for accurate calculation and convergence of calculation result. All concrete nodes and plate nodes of bottom part are bonded to restrict from moving in the Z-direction because of symmetry. The contact area of H-beam and concrete considered no friction effect.

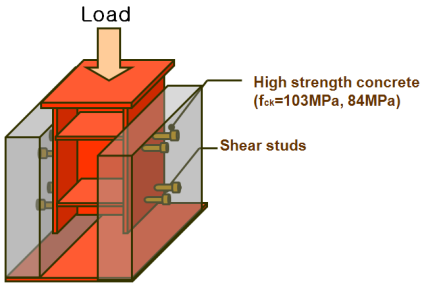

Figure 3. Detailing of push-off test specimen

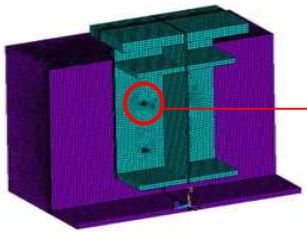

Figure 4. Finite element modeling

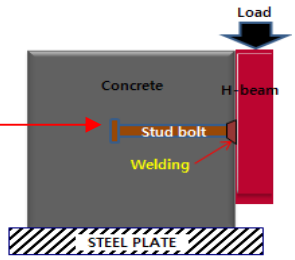

Figure 5. Sectional view

3.2 Material modeling of steel stud and concrete

It is applied test results of material experiment as input values of modeling. In the mechanical properties of studs, ultimate tensile strength is 509.2MPa, elastic modulus is 218GPa and Ultimate elongation is 29.1%. Compressive strength of concrete is 84MPa, 103MPa. And Elastic modulus is 36.9GPa in the case of 84MPa compressive strength and 44.8GPa in the case of 103MPa compressive strength. Material properties of H-beam is SS400.

3.3 Application of load

The form of displacement in all nodes of the stud is considered the nonlinear behavior of the model. The load application during the test was also displacement controlled. At each substep, the program will perform a number of equilibrium iterations to obtain a converged solution. The load at each substep can be obtained. At that time, the stress of welding part can be also obtained. Therefore ultimate capacity of shear studs can be determined.

3.4 Numerical verification

Experimental test results used to the accurate analysis of the finite element model. In the case of finite element model, maximum shear resistance was 1552kN and maximum slip at failure was 3.2mm in case of D16-84MPa. And the kind of failure was stud failure. In the case of experimental test, maximum shear resistance was 1869kN. Maximum slip at failure was 6.03mm in case of D16-84MPa. And the kind of failure also was stud failure. And maximum shear resistance was 2760kN and maximum slip at failure was 8.0mm in case of D22-84MPa. And the kind of failure was stud failure. In the case of experimental test, maximum shear resistance was 2753kN. Maximum slip at failure was 8.2mm in case of D22-84MPa. And the kind of failure also was stud failure. So results of modeling was appeared with a reliability.

3.5 Comparison of design code and ANSYS modeling

The result compared with design codes and ANSYS modeling was shown in Table 3. It appeared that Ollgaard et al method is similar to the finite element model results. But the interaction between the two materials has not been applied in equations. So new design code is proposed for applying to high strength concrete and large stud. In the future, it is necessary to analysis shear stress distribution of stud welded all around and high strength concrete from finite element model.

Table 3. Comparisons of maximum shear resistance(kN)

Specimen	ANSYS modeling	Ollgaard et al	Oehlers and Johnson	KBC	Eurocode4
D16-84MPa	1552	1415.5	1305.9	818.8	516.4
D22-84MPa	2760	2676.1	2468.9	1548	976.3

D16-84MPa	1552	1415.5	1305.9	818.8	516.4
D16-103MPa	1853	1727.1	1400.2	818.8	516.4

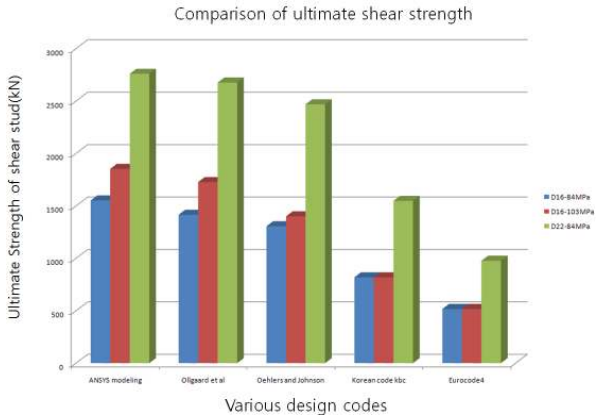

Figure 6. Comparison of ultimate shear strength

4. CONCLUSIONS

As compared with the maximum shear resistance result by design code, difference is appeared by concrete strength and stud diameter. If concrete strength become high, the resistance difference of shear stud become large. If stud diameter become large, the resistance difference of shear stud also become large. It is important to make new design code for various parameter.

The FE results were compared with results obtained from push-out tests. The finite element modeling result was appeared with a reliability. As compared maximum shear resistance result by design code, it appeared that the FE results is similar to Ollgaard et al method. But the interaction between the two materials has not been applied in equations. So new design code is proposed for applying to high strength concrete and large stud. In the future, it is necessary to analysis shear stress distribution of stud welded all around and high strength concrete from finite element model.

Acknowledgements:

This research supported by a grant from High-Tech Urban Development Program funded by the Ministry of land, transport and maritime affairs.

References:

N. Gattesco & E. Giuriani(1996) "Experimental study on stud shear connectors subjected to cyclic loading", Elsevier Science, No. 1, 1-21

Li An & Krister Cederwall(1996). "Push-out Tests on Studs in High Strength and Normal Strength Concrete", Engineering structure, vol 36, No. 1, 15-29

Sameh S. Badie, P.E. Maher K. Tadros, P.E., M.ASCE, Hussam F. Kakish, P.E. Darin L. Splittgerber, P.E. and Mantu C. Baishya, P.E.(2002). "Large Shear Studs for Composite Action in Steel Bridge Girders ", Journal of Bridge Engineering, Vol. 7, No. 3, May 1, 195-203

A. Nakajima, I. Saiki M. Kokai, K. Doi, Y. Takabayashi, H. Ooe(2003) "Cyclic shear force-slip behavior of studs under alternating and pulsating load condition", Engineering structure, No. 25, 537-545

Scott A. Civjan, M.ASCE, Prabhjeet Singh(2003). "Behavior of Shear Studs Subjected to Fully Reversed Cyclic Loading". ASCE , Vol. 129, No. 11, November 1.

S. Bullo , R. Di Marco(2004). "A simplified method for assessing the ductile behaviour of stud connectors in composite beams with high strength concrete slab", Engineering structure, No. 64, 2004, 1387-1408

Chang-Su Shim, Pil-Goo Lee, Tae-Yang Yoon(2004)"Static behavior of large stud shear connectors" Engineering structure, No. 26, 1853-1860

Cem Topkaya, Joseph A. Yura, Eric B. Williamson(2004). "Composite Shear Stud Strength at Early Concrete Ages" ASCE Vol. 130, No. 6, June 1.

Gerjard Hanswille, Markus Porsch, Cenk Ustundag(2007) "Resistance of headed studs subjected to fatigue loading Part Ⅱ : Analytical study", Elsevier Science, No. 63, 485-493

Shervin Maleki, Saman Bagheri(2008). "Behavior of channel shear connectors, Part II: Analytical study", Engineering structure, No. 60, 1341-1348

Weichen Xue, Min Ding, Hua Wang, and Ziwen Luo(2008)."Static Behavior and Theoretical Model of Stud Shear Connectors" ASCE ,Vol. 13, No. 6, November 1

Huu Thanh Nguyen, Seung Eock Kim(2009). "Finite element modeling of push-out tests for large stud shear connectors", Elsevier Science, No. 65, 1909-1920

JOINT CONFERENCE PROCEEDINGS
7th International Conference on Urban Earthquake Engineering (7CUEE) &
5th International Conference on Earthquake Engineering (5ICEE)
March 3-5, 2010, Tokyo Institute of Technology, Tokyo, Japan

STRENGTHENING OF MASONRY INFILL PANELS WITH GRP FABRIC FOR OUT-OF-PLANE SEISMIC LOADS

Luiza Dihoru[1], Adam Crewe[2], Olafur Oddbjornsson[3], and Colin Taylor[4]

1) Research Associate, Earthquake Engineering Research Centre, University of Bristol, UK
2) Senior Lecturer, Earthquake Engineering Research Centre, University of Bristol, UK
3) Postdoctoral Student, Earthquake Engineering Research Centre, University of Bristol, UK
3) Professor, Earthquake Engineering Research Centre, University of Bristol, UK
Luiza.Dihoru@bristol.ac.uk, A.J.Crewe@bristol.ac.uk, O.Oddbjornsson@bristol.ac.uk , Colin.Taylor@bristol.ac.uk

Abstract: The seismic behaviour of masonry structures strengthened with fibre-reinforced polymer (FRP) materials has received very little attention experimentally and theoretically. This paper outlines an experimental investigation of the potential for FRP strengthening of unreinforced masonry (URM) infill panels. Various options for FRP strengthening of masonry infill panels are compared, and results from a series of full scale push-over and seismic tests conducted at Bristol University are presented. The test results are compared with estimates of their vulnerability produced by a simplified analytical model. This research therefore aimed at developing a methodology for modelling the behaviour of infill panels taking account of the FRP reinforcement of the infill panels.

The strengthening methodology finally adopted involved the removal of excess mortar from the masonry surface using a wire brush followed by roller application of a primer. Pre-cut GRP (Glass fibre Reinforced Polymer) fabric strips were saturated with a laminating resin while lying on a horizontal surface. The GRP strips were then rolled onto the walls followed by the roller application of a resin top coat to bond the fabric to the wall. In all cases both sides of the masonry panels were treated in the same manner. It was discovered that it was important to lap the GRP fabric at least 75mm over boundaries to secure panel into the structural frame. Using this methodology the experimental tests showed that the GRP reinforcement significantly increased the lateral load capacity, the ductility and stiffness of the panels. There were also noticeable changes in crack patterns, strain distributions and the failure mechanisms of the panels. The change in the stiffness of the panels was probably the most important consequence of the GRP application as this had the effect of increasing the natural frequency of the panels, effectively "detuning" them from earthquake spectral content. In fact the strength and stiffness increases recorded were so great that engineering calculations are arguably not necessary if it is possible to ensure proper specification and quality of application for the GRP. Because the application procedure was very simple and also relatively cheap GRP strengthening of masonry infill panels is a realistic retrofitting technique.

However some caution must be exercised if GRP is to be used to strengthen masonry infill panels. For example, although the panel itself is significantly stronger, this strengthened panel may act in in-plane shear with frame and generate adverse forces in frame. This may have the effect of moving a potential failure from the panels into the structural frame. Also fire resistance and other environmental factors must be considered before FRP strengthening of unreinforced masonry infill panels could be widely adopted.

1. INTRODUCTION

Many of the existing buildings in Europe today are unreinforced masonry (URM) buildings and have features that could threaten lives under extreme events like high-winds or earthquakes. There has been an unprecedented growth in research in the area of composites in the last 30 years (Bakis et al. 2002), resulting in a wide range of high-strength, light-weight and environmentally resistant materials available at low costs. Numerous investigators have explored the potential use of FRP on concrete and on masonry structures under in-plane or out-of-plane monotonic loading. Previous experimental studies have shown increases in capacity and ductility of the FRP reinforced structures (Tikalsky et al. 1995, Velasquez-Dimas et. al. I 2000, Tumialan et al. 2003, Krevaikas and Triantafillou 2005). However their behaviour under seismic loading has been addressed very little by the experimentalists with most testing being 'simulated earthquake loading' (large number of cyclic tests) e.g. Ehsani et al. 1999. Simple analytical methods to assess the out-of-plane behaviour of URM or FRP-reinforced panels were developed based on the flexural theory of masonry present in the building codes (Velasquez-Dimas et. al., II, 2000, Hamilton and Dolan, 2001). The general trend has been to adapt the monotonic loading assessment methods for seismic loading as well, but the developed analytical models have not been validated through dynamic experimentation. A need to evaluate the mechanical behaviour under truly seismic conditions has emerged. This study was meant to fill

the gap in the existing knowledge on the dynamic behaviour of FRP reinforced masonry. Four full-scale quasi-static tests and four full-scale shaking table tests on both unreinforced and reinforced specimens were performed. The experimental observations on pre-cracking and post-cracking behaviour provided more understanding on the reinforcement requirements associated with a seismically-sound system. A software tool capable of predicting the mechanical response of masonry walls was employed and the results from the simulation were compared with the experimental ones.

2. PREVIOUS WORK IN THE FIELD

The rationale for using FRP reinforcement on masonry structures has been investigated by many researchers in relation to the advantages and the disadvantages of the materials employed and their application methods. Factors like cost, functionality during and after retrofit, seismic risk and aesthetics were part of the evaluation criteria. The cost of strengthening, the possible alteration of functionality of the building, the increase of inertia and seismic forces by the addition of mass and the possible overloading of the existing foundation have been topical issues since the early '70s, when the FRPs started to spread beyond the niche applications in the aerospace and defence areas to become an increasingly cheaper option in the construction industry (Bakis et al. 2002). In practice, the choice of a particular FRP material, the reinforcement ratio, the location and the orientation of reinforcement have been dictated by the orientation and the intensity of the principal stress field and by crude approximations of the ultimate strength conditions.

The preferred method of reinforcement has been with FRP strips or continuous jackets applied on the masonry surface using a layer of epoxy-based resin. Detailed concepts on the effectiveness of the method were first developed by Triantafillou and Fardis (1993, 1997). In 1994, Schwegler (1994) reported the first results of a full-scale in-plane and out-of-plane cyclic testing of masonry walls reinforced with carbon fibre polymers. A large number of studies have since focused on the in-plane and/or the out-of-plane monotonic loading of reinforced masonry. Results from walls subjected to monotonic (Albert et al. 2001, Hamilton and Dolan 2001) and cyclic (Ehsani et al.1999, Kuzic et al. 2003) tests have demonstrated that the presence of the FRP increases the capacity of panels and changes the crack patterns and failure modes. It has been shown that when out-of-plane bending dominates, horizontally applied strips of FRP may offer a considerable strength increase, while in the case of in-plane bending, high reinforcement ratios placed near the highly stressed zones could offer the solution. The use of anchorage and clamping of the FRP strips to prevent end-peeling has also been addressed and many researchers have focused on special strengthening techniques which result in a more economical use of materials (Triantafillou et al 1992, Lamanna et al. 2001).

The main mechanisms of failure have been identified as being the FRP delamination in flexure, FRP delamination in shear, brick crushing and FRP rupture. The occurrence of these events has been shown to be largely dependent on the type of loading, the panel boundary conditions and the reinforcement layout. Ehsani et al (1999) reported on half-scale masonry walls reinforced with glass fibre fabrics and subjected to cyclic out-of-plane loading. Their findings show that the mode of failure is controlled by tensile failure when wider and lighter composite fabrics are used and by delamination when stronger ones are used. The specimens were capable of supporting a lateral load of 32 times the weight of the wall and deflected as much as 2% of the wall height. Arching of the panels was observed when low reinforcement ratios were used and then the reinforced panel cracking patterns more closely resembled the ones exhibited by the URM walls. Arching is reported as a main resistance mechanism in URM panels subjected to out-of-plane loads. Taylor (1998) carried out shaking table tests on 13 URM specimens with various boundary conditions. The panels showed a highly non-linear and chaotic behaviour dependent on the boundary conditions and the input motion. A frequency response shift followed the panel's stiffness degradation under dynamic loading. The top and bottom supported panels cracked at table accelerations ranging between 0.33-1.89 g. A need to address these issues for FRP-reinforced masonry emerged. This study presents data and observations from full-scale seismic tests (LessLoss 2006) of URM control specimens and FRP-reinforced walls that were performed at Bristol under the European funded LESSLOSS framework (Risk Mitigation for Earthquakes and Slides Project no. GOCE -CT-2003-505488). The aim of the research was to establish the true response of the FRP-reinforced structures and to supply experimental data for the development of modelling tools.

3. OBJECTIVES AND TEST STRATEGY

The research programme at Bristol University investigated the quasi-static and the seismic behaviour of FRP-reinforced masonry panels of various strengthening ratios. The strengthening ratio represents the ratio between the reinforced area and the total area of the wall surface, Qualitative and quantitative data of dynamic response were gathered. The experimental results were compared with simulated dynamic results obtained via CRAMP (Cracked Response Analysis of Masonry Panels, Taylor 1998), a simplified analytical model whose features are described in Section 8. The specific experimental layouts and the objectives associated with each of the tests are listed below.

STU1 (unreinforced, 3 cycles monotonic loading):

1. Control specimen for static tests
2. Investigate cracking mechanisms and compare data with Taylor(1998) results and CRAMP simulations
3. Load, deflection, arching force data

STU2 (unreinforced, 3 cycles monotonic loading):

1. Improvement of boundary conditions

2. Compare with STU1 results and CRAMP simulations
3. Load, deflection, arching force data

STR1 (100% reinforced, continuous jacket on tensile face, 3 cycles monotonic loading):

1. Investigate quasi-static response
2. Compare response with URM response
3. Inspiration for future FRP layout design
4. Comparison with CRAMP simulations
5. Load, deflection, strain, arching force data

STR2 (100% reinforced, continuous jacket on tensile face. FRP fabric attached to the soffit of the top and bottom beams to prevent sliding, 3 cycles monotonic. loading):

1. Improvement of boundary conditions
2. Investigate quasi-static response and reproducibility
3. Compare response with URM and STR1 response
4. Inspiration for future FRP layout design
5. Comparison with CRAMP simulations
6. Load, deflection, strain, arching force data

SEU1 (unreinforced, exploratory tests, seismic tests):

1. Investigate the modal parameters of URM
2. Investigate seismic response of URM
3. Compare with Taylor (1998) and CRAMP simulations
4. Load, deflection, arching force data

SER1 (100% reinforced, continuous jacket on both faces, exploratory tests, seismic tests):

1. Investigate the modal parameters of FRP-URM
2. Investigate seismic response
3. Compare data with SEU1 and CRAMP simulations
4. Load, deflection, strain, arching force, frequency response data
5. Inspiration for future FRP layout design

SER2 (60% reinforced, vertical strips on both faces, exploratory tests, seismic tests):

1. Lower the stiffness to achieve cracking and better cost / strength ratio
2. Investigate the modal parameters
3. Investigate cracking mechanisms & seismic response
4. Compare data with SER1, SEU1 and CRAMP simulations
5. Load, deflection, arching force, frequency response data
6. Inspiration for future FRP layout design

SER3 (40%, reinforced, vertical strips on both faces, exploratory tests, seismic tests):

1. Lower the stiffness to achieve cracking and better cost / strength ratio
2. Investigate the modal parameters
3. Investigate cracking mechanisms & seismic response
4. Compare data with SER1, SER2, SEU1 and CRAMP simulations
5. Load, deflection, arching force, frequency response data
6. Conclusions and recommendations for FRP layout design

Although both the masonry and the FRP exhibit a brittle type of failure, their combination was expected to show increased load-carrying capacity and ductility caused by the elastic deformation of fibres and the shear transfer in the resin connection layer. Beside the strength benefits, the intention was to investigate reinforcement patterns that would lead to slowly-progressing modes of failure. The typical sudden collapse of unreinforced masonry or the explosive failure of the FRP needed to be replaced with a slow and energy dissipative process e.g. FRP delamination. It was believed that the layout of the FRP and the reinforcement ratios could be used as control factors in triggering the failure mechanisms.

Four full-scale quasi-static tests and four full-scale seismic tests were performed. The research concentrated on the simplest case of a panel supported top and bottom only, with the vertical sides being unrestrained. All specimens were single-wythe, top and bottom supported panels (size 3000 x 2000 x 100 mm) aimed at providing information on the following aspects of mechanical response:

- mechanisms of the failure modes
- crack patterns and strain profiles
- influence of the FRP lay-out and reinforcement ratio on the mechanical response
- influence of the loading characteristics on the mechanical response
- evolution of panel stiffness and modal parameters under seismic loading

4. EXPERIMENTAL PROGRAMME

4.1 Material tests

Material tests were performed according to BS EN 1052-1:1999 'Methods of test for masonry' using a standard cube test machine. The following material properties were investigated prior to the masonry panel construction:

- brickwork density
- brick units compression capacity
- mortar compression capacity
- compressive strength of the brick mortar assemblage (tests on three brick prisms)
- modulus of rupture of the brick-mortar assemblage
- stress-strain behaviour of the brick-mortar assemblage (see figure 1)

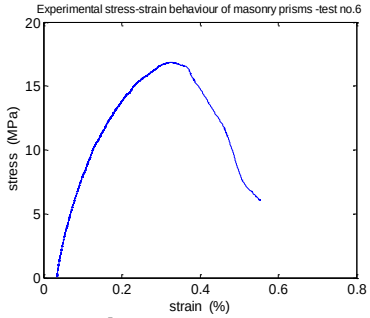

Figure 1. Material tests on masonry prisms, prior to STR1

4.2 Masonry Panels

The masonry panels were built within a pin-jointed steel frame fabricated from 254x254 universal column sections. The sections were stiffened by thick plates welded longitudinally between the flanges on both sides of the beams in order to prevent the flange flexure. The specimens for the pseudo-static tests were located parallel to the laboratory reaction wall where the hydraulic actuator was mounted. A load distribution beam consisting of a steel square plate and two steel rollers was employed to distribute the load onto the central area of the wall.

The specimens for the seismic tests were built off the shaking table and left to cure using standard practices. Each masonry wall was built in two lifts. Mortar was packed on the top side of the wall to fill the gap caused by shrinkage. The walls were left for 21 days to cure. When the specimens were cured, they were bolted onto the shaking table and instrumented.

4.3 FRP Materials

When selecting the FRP materials for reinforcement of panels, the main parameters that are generally taken into account are the specific strength (tensile strength/specific gravity) or the specific stiffness (modulus of elasticity/specific gravity). The carbon fibre composites (CF) exhibit better specific strength and specific stiffness values than their competitors. However, when the seismic behaviour of the retrofitted system comes into play, the systems' ductility and capacity of energy absorption become important. Fibre ductility increases from carbon to aramid and further to glass. For this reason a glass-fibre fabric system was selected for reinforcement (manufacturer: EXCHEM LTD-UK).

Discrete strips or continuous jackets of FRP fabric were used. Samples using various reinforcement ratios were tested. Preliminary observations on the first tests were meant to lead to the selection of reinforcement ratios in further experiments. The lay-out of the FRP was chosen in relation to the boundary conditions of the panel. The URM panels (STU1, STU2) failed with a horizontal cracking line at the midheight of the panel. In order to prevent this failure caused by arching in vertical plane, the FRP fabric was applied with its fibres running in the vertical direction.

The FRP application procedure started with the preparation of masonry surface for primer application. Particular attention was paid to cleaning the joints and to removal of excessive mortar from the wall surface. The surface was cleaned with a wire brush and checked for tool marks and other surface variation problems. A dual system that could be used as a primer and as a laminating resin was employed (Selfix MPA 22 Laminating Resin, Exchem Ltd.) A foam roller was used to apply a thin layer of primer on the wall surface (average primer consumption 1 kg/ 5 m2). The primer was used to minimise the porosity of the wall surface and to provide a good bonding substrate for the resin. Pre-cut FRP strips of 300 mm by 1960 mm were saturated with resin (average resin consumption: 1 kg/3 m2) while lying on a horizontal surface. They were then applied to the wall surface using a foam roller and by applying hand-pressure. The change of fabric colour from white to transparent yellow was used as an indication that saturation was reached. A final layer of laminating resin was applied on the FRP fabric for full saturation, protection and instrumentation purposes. The FRP layouts are shown in Figures 2 to 4. The FRP fabric was applied 21 days after the building of the wall. The testing took place at min. 10 days after the FRP installation. A photo of the SER2 panel (60% reinforcement) is shown in Figure 5.

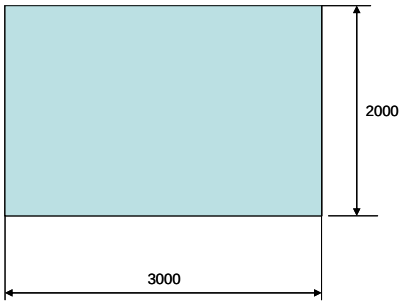

Figure 2. Layout of FRP fabric for masonry panels STR1, STR2, and SER1

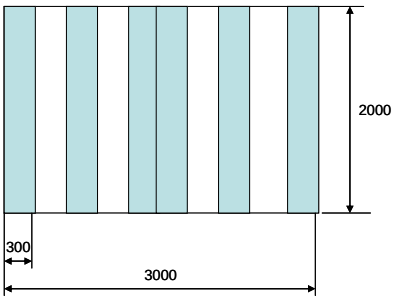

Figure 3. Layout of FRP fabric for masonry panel SER2

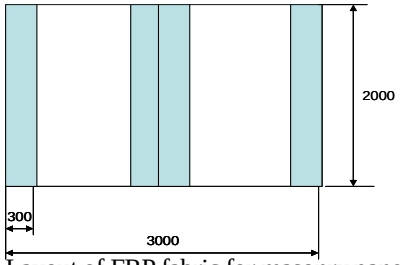

Figure 4. Layout of FRP fabric for masonry panel SER3



Figure 5. SER2 panel ready for testing (60% reinforcement)

4.4 Instrumentation

CELESCO type PT101 cable-extension position transducers were employed to measure out-of-plane deflections. The transducers were placed at midheight and at

positions symmetrically-located about the centerline. The bodies of the transducers were fixed to a rigid frame standing parallel to the wall surface, and for the static tests on wooden plates bolted on the laboratory wall (parallel to the masonry panel).

Four load cells were incorporated in the four bolts attaching the top beam to the frame columns to measure the panel arching forces. The load cells measured the arching forces on the wall. The top beam was separated from the top of the column by washers around the instrumented bolts.

Vishay type CEA-06-250UW-350 strain gauges were used to record the FRP tensile strain at midheight and at locations symmetrically located about the centerline. The strain gauges were mounted on the FRP fabric in areas located on top of a brick unit. All the strain gauges employed had uniaxial wiring and 350 ohm resistors. They were quarter-bridge type, therefore a strain gauge amplifier (RDP 628-type) was used to complete the bridge.

One 200 kN load cell was mounted on the same axis with the hydraulic actuator to measure the applied out-of-plane force during the monotonic tests.

SETRA type 141A accelerometers were used to measure wall accelerations and the table accelerations. The accelerometers had a calibrated range of +/-8g. Three accelerometers were installed on the shaking table (X, Y, Z directions) while other three were installed on the panel. A seventh accelerometer was installed on the frame's top beam.

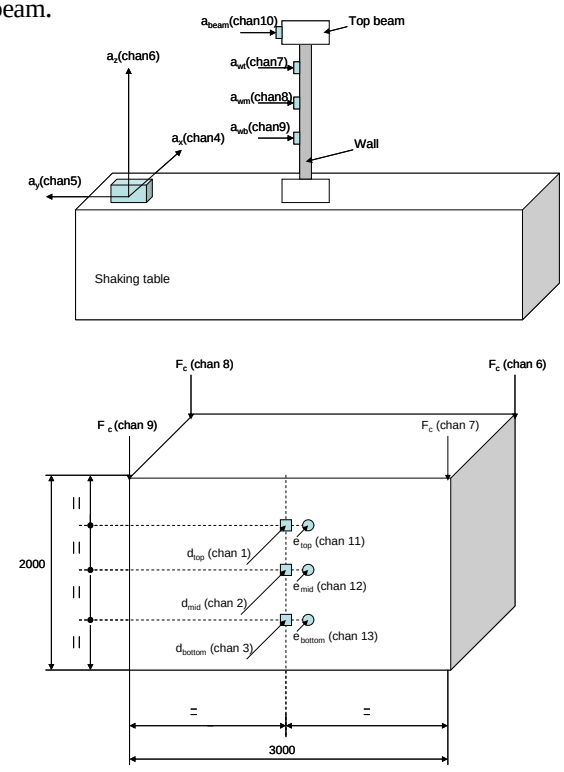

Figure 6. Instrumentation lay-out

An RDP 600-type modular electronics system supplied the excitation voltage for the displacement transducers and the load cells. The completion of the bridge and the excitation voltage for the strain gauges was made via an RDP 628-type strain gauge amplifier module. Four other RDP 628-type strain gauge amplifiers were used for the load cells in the columns and for the load cell on the actuator axis. For the seismic tests, the SETRA accelerometer signals were amplified by a set of three Fylde 245GA mini-amplifiers. The amplified acceleration signals were supplied to a FERN EF6 multi-channel programmable filter. A common cut-off frequency of 80 Hz was set for all the channels. Diagrams slowing locations of the key instrumentation are shown in figure 6.

4.5 Input Motions

Exploratory tests were used to determine the modal parameters of the specimens. The resonant frequency of the first mode of vibration and the viscous damping of the specimen were the main parameters of interest. The exploratory tests used broadband (0-100 Hz) random noise applied on the out-of-plane axis only (Y axis). The driving signal was generated by an Advantest 9211C FFT Servo Analyzer and had 'RMS' (Root Mean Square) voltage values ranging from 35 mV to 150 mV, which in acceleration terms corresponded to 0.035-0.150g. The signal amplitude was increased from one exploratory test to another, in order to observe the dependency of wall frequency response on the driving input.

An elastic response spectrum for soil type B acc. to Eurocode 8 was used in the seismic tests. Acceleration, velocity and displacement time histories were generated to match the Eurocode 8 response spectrum. The displacement time history was used to drive the shaking table.

5. QUASI-STATIC TESTS

STU1 and STU2 (quasi-static tests on unreinforced panels): The URM wall cracked along an horizontal line situated at the midheight of the wall (Figure 7a) This cracking pattern was observed by other researchers and it is considered typical for top-and-bottom-supported masonry panels. The main resistance mechanism was arching of the panel with increasing of contact forces between panel and top and bottom supports.

STR1 and STR2 (quasi-static tests on reinforced panels): The presence of the FRP brought changes to the following aspects of mechanical response:

- sequence of occurrence of the failure mechanisms
- masonry cracking pattern
- lateral deflection profile
- distribution of strains in the masonry substrate
- mechanical parameters: loading capacity, stiffness, 'pseudo-ductility'

The FRP was a unidirectional fabric with vertical glass fibres oriented perpendicular to the wall supports. The orientation of fibres (which have very high tensile strength: 1090 N/mm^2) prevented the initiation of vertical strains in the masonry, therefore no horizontal crack was formed in the

initial stage of loading. The low compressive strength of masonry (approx. 18 N/mm^2 – as measured in the material tests) caused an early vertical crack to occur at the mid-width of the panel. The interlaminar resin gave way and caused the fabric to tear in the vertical direction (Figure 7b). The strain gauge situated at midheight was damaged following the propagation of rupture in the FRP along the vertical direction.

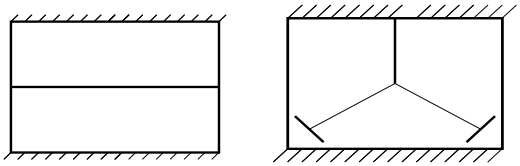

(a) (b)

Figure 7. Failure modes for a) unreinforced panel, b) 100% reinforcement

An important experimental observation was that the vertical FRP strips changed the way the panel arched. Wall flexure in the vertical plane was no longer possible and the panel therefore started arching in the horizontal plane.

The main failure modes identified during the STR1 and STR2 tests were: flexural failure, shear failure and FRP debonding. Flexural failure was triggered by the crushing of the masonry in compression and by the rupture of the FRP in tension. Initial cracking occurred at the interface of mortar and masonry. The initial cracking was delayed by the presence of the FRP. Since the tensile strength of the masonry was lower than that of the epoxy resin (55 MPa), the failure line appeared first in the masonry. The vertical crack in the masonry caused the wall to slide while a differential displacement in the shear plane developed. The shear failure mechanism resulted in the FRP debonding alongside the masonry crack. The FRP fabric situated above the opening crack of the masonry started to deform and broke in tension vertically. Debonding of the FRP laminate from the masonry substrate was triggered by the central vertical crack in the masonry and propagated at first vertically, then multiaxially towards the final stages of loading. It was noticed that part of the concrete brick faceshell remained attached to the laminate. This showed that the resin-masonry connection was stronger than the tensile strength of the masonry. End-debonding of the FRP was expected as a main failure mode, but this did not occur. The strength and stiffness of the STR walls increased dramatically in comparison to the STU specimens. A 2.6 times increase in maximum strength was recorded (see figure 8).

The elastic behaviour of the FRP under loading was obvious. The first loading cycle (R1) was almost a straight line. There was very little degradation of stiffness due to repeated loading, again because the FRP behaved elastically up to failure. Overall, the FRP presence caused an increase in capacity (from 13.5 kN to 35 kN) with confinement of the lateral deflections from 30 mm (STU1) to 24 mm (STR1).

In the STR2 test the FRP fabric was folded and glued to the soffit of the top and bottom beams in order to prevent sliding. Arching took place in the horizontal plane. Cracking occurred at midwidth in the vertical direction. The FRP broke at the interface between the wall and the top beam due to wall sliding. The cracking pattern was a vertical line situated at the middle of the panel. The main observation coming out of this test was that by attaching the FRP jacket to the soffit of the top beam the sliding of the wall could be prevented. This created uniform boundary conditions for the top and bottom interfaces which lead to a vertical failure line situated at the midwidth of the panel.

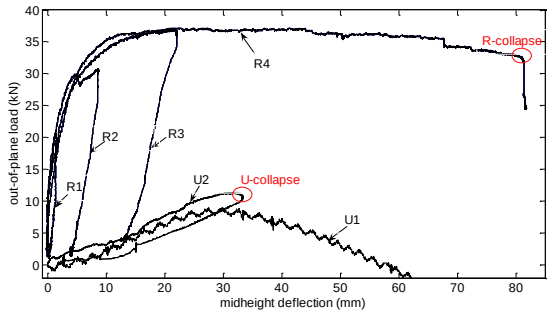

Figure 8. Loading curves during static testing (STU1 -unreinforced wall, STR1 reinforced wall)

The slenderness ratio (height/thickness) is an important factor of influence for the out-of-plane behaviour of masonry walls. This ratio accounts for the ability of the masonry wall to be controlled by the flexural capacity rather than the shear capacity. The larger the slenderness ratio, the smaller the maximum out-of-plane load becomes. The STU and STR walls had a slenderness ratio of 20. When h/t > 30 the arching mechanism becomes insignificant.

6. SEISMIC TESTS

6.1 Exploratory tests

The dynamic properties of a structure are defined by its mode shape, damped natural frequency and damping for each mode of vibration over some frequency range of interest. The exploratory tests carried out prior and during the seismic testing revealed information about these parameters for URM and reinforced panels in intact or cracked form. The driving signal (0-100 Hz random noise) was generated by an Advantest 9211C FFT Servo Analyzer, which was also employed to acquire the signals from the accelerometer on the shaking table (Y direction) and the accelerometers situated at midheight and at quarter heights on the wall. The analyser computed the frequency response function (FRF) between the input and the output signals at the points of interest on the wall (figure 9). The frequency response function was calculated using windowed signal data using a rectangular window function. The rectangular window function chosen was zero-valued outside the chosen frequency interval. A rectangular window function has proved to work well in the low dynamic range, when the signals have comparable strengths and frequencies. The FRF measurements were processed using curve-fitting algorithms that take the experimentally measured FRFs and fit to them an analytical function using a least squared error technique.

The poles of the transfer function were used to compute the viscous damping for various modes of vibration. The damping values for the URM wall (SEU1) were 0.3% to 4.3% while for a reinforced wall (SER1) damping values varied from 4.8% to 22%. In both these cases panels were intact when the measurements were taken. Other panels had similar damping values.

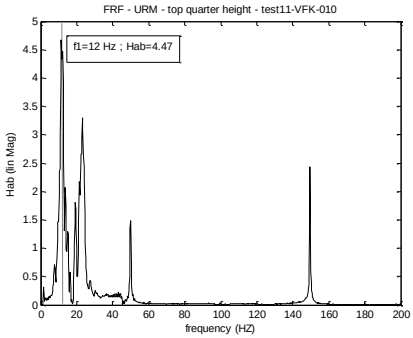

Figure 9. FRF - SEU1 test (intact wall)

Table 1 shows how the natural frequency of vibration increased from 12 Hz for the URM panel (SEU1) up to 30.3 Hz for the reinforced panel with maximum reinforcement ratio (SER1). Lowering the reinforcement ratio from 100% to 40% lead to a shift in the natural frequency from 30.3 Hz to 15 Hz. The evolution of panel stiffness during testing occurred in parallel with a measurable shift in panel's natural frequency .

Table 1. Evolution of panel's natural freq. during seismic testing

Test	**Reinf.**	**Uncracked natural frequency (Hz)**	**Cracked natural frequency (Hz)**	**Cracking table acceleration or max. table acceleration**
SEU1	None	12.0	7.5	cracking: 1.18g (SEU1_60), collapse: 2.4g
SER1	100% reinf.	30.3	uncracked	max : 3.53g (SER1_130)
SER2	60% reinf.	28.6	uncracked	max : 2.28g (SER2_120)
SER3	40% reinf.	15.0	8.2	cracking: 2.44g (SEU3_80)

6.2 Seismic tests and CRAMP simulations - URM

Particular attention was given to tests SEU1_65 that lead to the URM wall cracking and SEU1_110 that lead to its collapse. The table acceleration reached 2.44g in SEU1_110 (Figure 10).

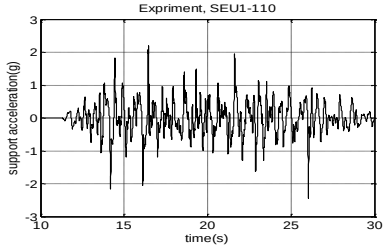

Figure 10. Shaking table acceleration in test SEU1_110

The lateral deflections recorded midheight on the panel are shown in figure 11 and in detail in figure 12.

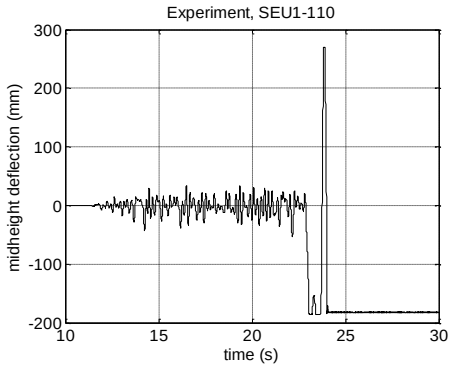

Figure 11. Midheight deflection measured in test SEU1_110

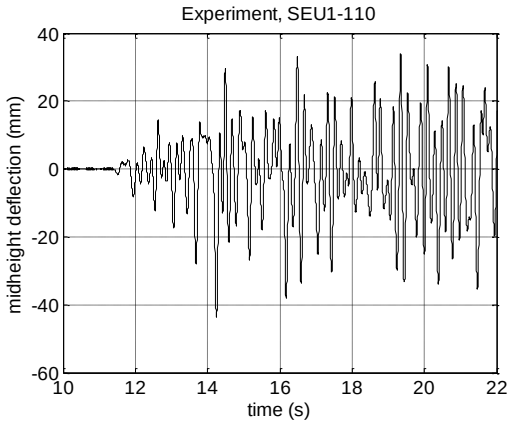

Figure 12. Midheight deflection measured in test SEU1_110 – detailed view

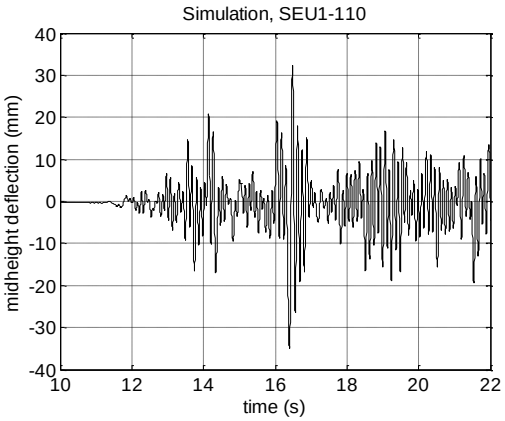

Figure 13. Simulated midheight deflection in test SEU1_110

A simulated evolution of wall displacement with time is presented in figure 13. The equivalent velocity data was also calculated using CRAMP. The dynamic response of the wall could then be uniquely defined at any point in time by its instant velocity and displacement. The displacement-velocity plot, called the 'phase-space diagram' can reveal interesting information about system's stability and about the dynamic parameter values that cause the wall to collapse (figure 14).

Under seismic excitation, the wall response follows a constantly changing path in the phase-space diagram. The

path resembles an ellipse that changes size within an envelope that borders the domain of the wall's stability. When the dynamic path escapes the borders, the wall becomes unstable and will collapse.

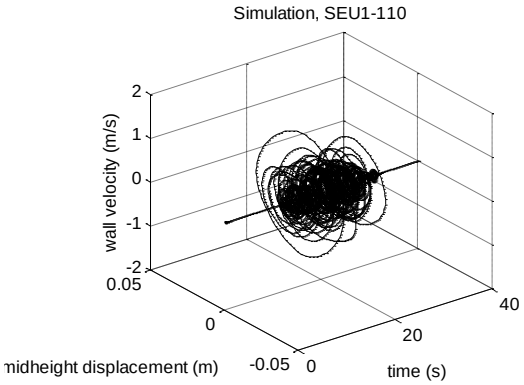

Figure 14. Simulated phase space diagram with time coordinates for test SEU1_110

An interesting part of the SEU1 test was shake SEU1_65, when the imposed seismic input lead to cracking. The input motion lasted for 40 s and accelerations up to 1.175 g were recorded by the Y-axis accelerometer mounted on the shaking table. After this particular test, the wall accelerometers were removed for protection.

The experimental results were compared to simulated data obtained from CRAMP. The simulations used the same table motion input used in the experiments. The main features of CRAMP simulation: wall parameters: height: 2 m, thickness: 0.1 m, width: 3 m, mass density: 2200 kg/m^3, compressive strength: 4.8 MPa, max strain: 0.006, ultimate strain: 0.0065, damping ratio: 4.3 %. Top and bottom supports of very high stiffness, no sliding allowed.

Displacement, acceleration and force data for the wall were obtained through direct measurement (e.g. figures 15-17).

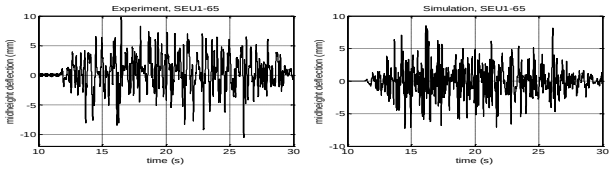

Figure 15. Midheight deflection in test SEU1_65 (left-measured, right-simulated)

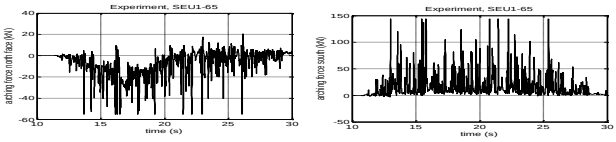

Figure 16. Measured arching forces in test SEU1_65 (left - north, right - south)

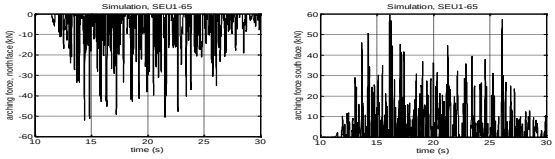

Figure 17. Simulated arching force in test SEU1_65 (left – north, right - south)

The wall velocity, which could provide information on the wall's kinetic energy in addition to its total energy, was also considered a parameter of interest. The wall velocity was not measured directly but it could be approximated by integrating the measured acceleration data. However, the simple integration of the acceleration data is in general a process that generates bias and drift in the output, unless suitable safeguarding measures are taken through filtering. A more sophisticated method of approximation was proposed by Stoten (2001) and it involves the use of both acceleration and displacement data. The displacement data are only reliable in the lower frequency range (typically 0-30 Hz) because of the problem of resolving small-amplitude high frequency deflections even with high accuracy LVDT systems. However, acceleration data are reliable in the medium-high frequency range, i.e. up to 50 Hz on the shaking table. Hence, the two types of signals could be combined for the velocity prediction over the entire frequency range. A composite filter was used which consisted of a low-pass Butterworth filter for displacement data and a high-pass Butterworth filter for acceleration data. The filtered velocity components (figure 18) were combined to yield the velocity history over the full frequency range.

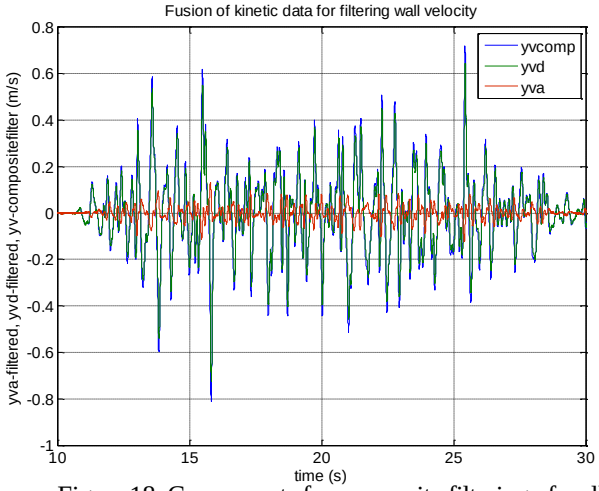

Figure 18. Components for composite filtering of wall velocity (SEU1_65)

6.3 Seismic tests and simulations - reinforced panels (SER1, SER2, SER3)

The 100% reinforced SER1 panel withstood accelerations of up to 3.53g without cracking. The panel behaved like a highly-stiff rigid block and no significant lateral deflections or arching forces were recorded. The imposed shaking table displacement history was increased from 2% up to 130%, the performance limit of the shaking table.

The 60% reinforced SER2 panel also withstood accelerations of up to 2.28g without cracking. It is worth mentioning that the URM panel collapsed at 2.4g. Therefore, the presence of the FRP lead to a significant capacity increase. The SER2 test did not lead to any cracks in the panel and it was stopped at a table displacement amplification factor of 120%. Minor deflections with the

average ranging from +2 to -2 mm and max peak of 8.4 mm were recorded. Arching was limited by the vertical strips of the FRP and low arching forces were recorded.

The first cracks in the 40% reinforced SER3 panel appeared at accelerations of around 2.44g in the unreinforced areas of the panel as step-like lines propagating diagonally from the corners of the FRP strips. Table displacement amplification factors ranging from 2% to 80% were used. The lateral deflections recorded during the 80% test are shown in figure 19. At this point the top and bottom connections became loose and the test was stopped in order to protect the shaking table.

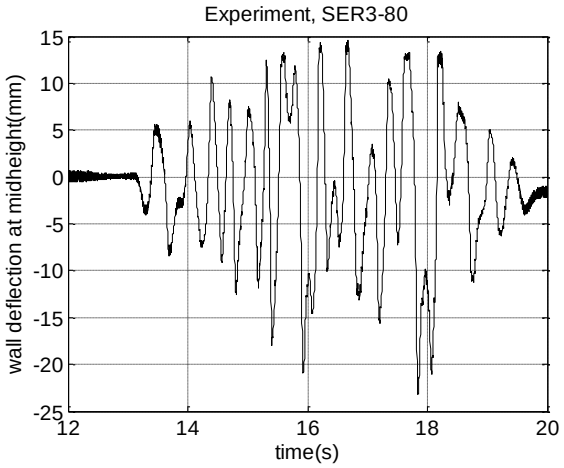

Figure 19. Wall deflection in test SER3_80

7. CONCLUSIONS - EXPERIMENTAL TESTS

The URM walls cracked along a horizontal fracture line, typical for their boundary conditions. The crack pattern for the URM walls was the same in both the static and the seismic tests. Arching in vertical plane was the main resistance mechanism in the URM walls.

The FRP application procedure proved to be a simple one, which did not require highly-skilled personnel to accomplish. The entire reinforcement activity took on average 5 hrs for each panel.

The FRP reinforced panel subjected to monotonic out-of-plane loading withstood forces that were 2.7 times larger than the maximum load taken by the URM walls.

A summary of relevant data from seismic testing is presented in Table 2. The reinforced panels exhibited increased load-carrying capacity. A layout of vertical FRP strips limited the panel arching in the vertical plane. A relatively low reinforcement ratio of 40% was sufficient to bring sufficient strength and ductility to the reinforced wall (SER3_80, a = 2.44 g, first cracks) in order to cope with seismic forces that previously caused the collapse of the URM wall (SEU1_110, a = 2.4 g).

Higher reinforcement ratios (60% and 100%) lead to a dramatic increase of the panel's stiffness and natural frequency of vibration. Panel flexure was completely prevented and the walls systems behaved like rigid blocks exhibiting very small lateral deflections.

Table 2. Summary of relevant results from seismic testing

Test	**Reinf.**	**Cracking table acceleration or max/col. table acceleration**	**Cracking**	**Max. mid-height deflection**
SEU1	None	cracking: 1.175g (SEU1_65), collapse: 2.4g (SEU1_110)	cracked brought to collapse	8 mm (SEU1_65) 42 mm (SEU1_110)
SER1	100%	max : 3.53g (SER1_130)	un-cracked	7.1 mm (SER1_130)
SER2	60%.	max : 2.28g (SER2_120)	un-cracked	8.1 mm (SER2_120)
SER3	40%.	cracking: 2.44g (SEU3_80)	cracked	26 mm (SER3_80)

8. ANALYTICAL WORK

The modelling of the masonry panels built upon an existing model for predicting the seismic behaviour of URM panels (Taylor 1998). The URM model is embedded in the CRAMP program (Cracked Response Analysis of Masonry Panels) available in both Ryan-Macfarland FORTRAN v2.43 and MATLAB 6.5. The main features of the CRAMP model are given below:

- The masonry panel is considered as a SDOF system which exhibits residual strength due to arching action (simple case: rigid top and bottom supports, horizontal crack along the wall length)
- Strip analysis technique (each vertical strip consists of two segments that join at the location of the crack)
- Non-linear dynamic analysis. Equation of motion solved using a step-by-step formulation
- Seismic behaviour depicted in a velocity-displacement diagram ('phase-space-diagram')
- Capacity assessment method based on spectral velocity and spectral displacement

The FRP panel consists of an URM panel with two purely-elastic FRP membranes attached on its faces (figure 20). Its mechanical behaviour changes its nature if the FRP delamination is to be considered.

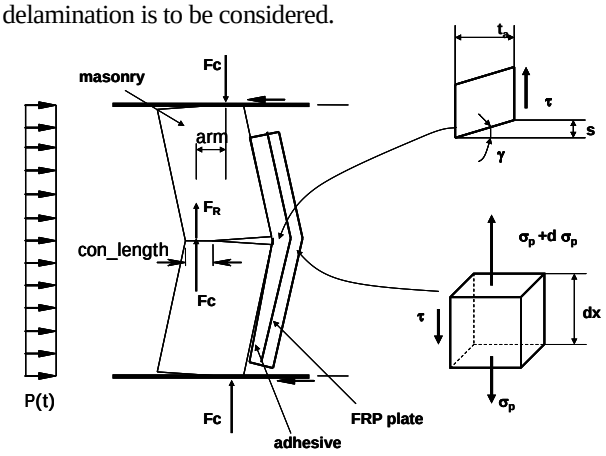

Figure 20. Modelling of top and bottom FRP reinforced panels within CRAMP

Main assumptions in pre-debonding analysis:

- homogeneous layers, no slip between layers, composite action between layers
- tensile resistance of the FRP is transmitted through shear in the adhesive
- longitudinal stresses uniformly distributed over the layer thickness
- stresses normal to the interface are ignored
- conditions of instantaneous equilibrium apply
- equal curvature of the masonry and the FRP
- crack in masonry occurs when: $\varepsilon_{masonry} = \varepsilon_{ult\ masonry}$

Main assumptions in debonding analysis:

- FRP layer elastically deformed (Hookian)
- sharply-defined boundary at the end of the FRP and adhesive layers
- longitudinal stresses uniformly distributed over the layer thickness
- both normal and tangential interfacial stresses considered
- debonding: steady-state process caused by normal interfacial stresses
- conditions of instantaneous equilibrium apply
- equal curvature of the masonry and the undetached FRP wrap
- debonding starts when: $\tau_{adhesive} = \tau_{max\ adhesive}$

Since the FRP material will never reach its max tensile strength (1099 N/mm2), it is fair to say that the FRP membranes behave hookian during testing and that no rupture of fibres takes place.

9. CONCLUSIONS

This study has shown the efficacy of a relatively simple method of reinforcing unreinforced masonry infill panels with glass fibre FRP laminates. Provided the reinforcement covers at least 60% of the surface area of the panel (preferably 100%), and the reinforcement overlaps the surrounding frame by at least 75mm, the reinforced panel gains a significant amount of strength to out-of-plane seismic loads. So great are the strength and stiffness increases that, for typical panel configurations, it appears unlikely that a strengthened panel would suffer significant distress during an earthquake due to out-of-plane loads. (Note, however, that this study has not considered combined in-plane and out-of-plane loading.) The evidence derived from this study suggests that this kind of FRP strengthening can simply be specified, rather than requiring detailed engineering calculations for its justification.

The method of application of the FRP reinforcement is very simple, requiring minimal training. It is within the ability of a semi-skilled builder, subject to appropriate supervision. The chosen glass fibre based materials are relatively cheap.

Acknowledgements:

This research was part of the LESSLOSS (Risk Mitigation for Earthquakes and Slides) project, funded by the European Union under grant no. GOCE -CT-2003-505488. Their financial support is gratefully appreciated.

References:

Albert M.L., Elwi A.E., Cheng J.J.R.. (2001) "Strengthening of unreinforced masonry walls using FRPs", *J. Compos. for Constr.*, Vol. 5, No. 2, pp. 76-84.

Bakis C.E., Bank L.C., Brown V.L., Cosenza E., Davalos J.F., Lesko J.J., Machida A., Rizkalla S.H., Triantafillou T.C. (2002) "Fiber-Reinforced Polymer Composites for Construction – State-of-the-Art Review", *J. Compos. for Constr*., Vol. 6, No. 2, pp. 73-87.

Ehsani M.R., Saadatmanesh H, Velasquez-Dimas, J.I. (1999) "Behaviour of retrofitted URM walls under simulated earthquake loading", *J. Compos. for Constr*., Vol. 3, No.3, pp. 134-142.

Hamilton H.R. , Dolan C.W. (2001) "Flexural Capacity of Glass FRP Strengthened Concrete Masonry Walls", *J. Compos. for Constr*., Vol. 5, No. 3, pp. 170-178.

Krevaikas T.D. and Triantafillou T.C. (2005) "Masonry Confinement with Fiber-Reinforced Polymers", *J. Compos. for Constr.*, Vol. 9, No. 2, pp. 128-135.

Kuzic M.D., Elwi A.E., Cheng J.J.R. (2003) "Cyclic flexure tests of masonry walls reinforced with glass fiber reinforced polymer sheets", *J. Compos. for Constr*., Vol. 7, No. 1, pp. 20-30.

Lamanna A.J., Bank L.C., Scott D.W. (2001) "Flexural strengthening of reinforced concrete beams using fasteners and fiber reinforced polymer strips", *ACI Struct. J*., Vol. 98, No. 3, pp. 368-376.

LessLoss (2006) Deliverable 50 "Technical report on the design of FRP reinforcement of masonry infill walls against transverse movement", Subproject 7, "Techniques and methods for vulnerability reduction". Lessloss Project - Risk mitigation for earthquake and landslides integrated project – EU Project No.: GOCE-CT-2003-505488.

Schwegler G. (1994) "Masonry construction strengthened with fiber composites in seismically endangered zones", *Proceedings of the 10th European Conf. on Earthquake Engineering*, Rotterdam, The Netherlands.

Stoten D.P. (2001) 'Fusion of kinetic data using composite filters', *Proc. Inst. Mech. Engrs*, Vol. 215(I), pp. 483-497.

Taylor C. (1998) "Seismic performance of masonry panels for Nuclear Electric plc", *EERC Project Report* NE395/RP/6, Bristol, United Kingdom.

Tikalsky P.J., Atkinson R.H, Hammons M.I. (1995) *Journal of Structural Engineering*, Vol. 121, No.2, pp. 283-289.

Triantafillou T.C., Deskovic N., Deuring M. (1992] "Strengthening of concrete structures with prestressed FRP sheets", *ACI Struct. J*., Vol. 89, No. 3, pp. 235-244.

Triantafillou T.C., Fardis M.N. (1993) "Advanced composites as strengthening materials of historic structures", *IABSE Symp. on Structural Preservation of the Architectural Heritage, International Association for Bridge and Structural Engineering*, Lisbon, Portugal.

Tumialan J.G., Galati N., Nanni A. (2003) "Field Assessment of Unreinforced Masonry Walls Strengthened with Fiber Reinforced Polymer Laminates", *Journal of Structural Engineering*, Vol. 129, No. 8, pp. 1047-1056.

Velasquez-Dimas J.I., Ehsani M.R., Saadatmanesh H. (2000) "Out of plane behaviour of brick masonry walls strengthened with fiber composites", *ACI Struct. J*., Vol. 97, No. 5, pp. 377-387.

Velasquez-Dimas J.I., Ehsani M.R., II. (2000) "Modelling Out-of-Plane Behaviour of URM Walls Retrofitted with Fiber composites", *J. Compos. for Constr*., Vol. 4, No.4, pp. 172-18.

JOINT CONFERENCE PROCEEDINGS
7th International Conference on Urban Earthquake Engineering (7CUEE) &
5th International Conference on Earthquake Engineering (5ICEE)
March 3-5, 2010, Tokyo Institute of Technology, Tokyo, Japan

VERIFICATION OF PUSHOVER ANALYSIS WITH CHI-CHI EARTHQUAKE DAMAGE DATABASE OF SCHOOL BUILDINGS

Fu-Pei Hsiao[1], Yeong-Kae Yeh[2], Lap-Loi Chung[2], and Shyh-Jiann Hwang[3]

1) Associate Research Fellow, National Center for Research on Earthquake Engineering, Taiwan
2) Research Fellow, National Center for Research on Earthquake Engineering, Taiwan
3) Professor, Department of Civil Engineering, National Taiwan University, Taiwan
fphsiao@ncree.org.tw, ykyeh@ncree.org.tw, chung@ncree.org.tw, sjhwang@ntu.edu.tw

Abstract: Based on the observations made after the Chi-Chi earthquakes occurred in Taiwan, school building has been found most seriously damaged among all building types. Although the seismic design force for school buildings has been 25% higher than the ordinary buildings, serious casualties and losses may be resulted from the collapse of school buildings under strong earthquake. Seismic evaluation and retrofit of these numerous vulnerable school buildings is an important societal issue to be resolved. A method of seismic evaluation for existing buildings needs to be confirmed. Base on the capacity spectrum method proposed by ATC-40, this study has developed a seismic evaluation method by using pushover analysis. The properties of nonlinear hinges for nonlinear pushover analysis with low-rise RC structure have been determined. However, different definitions of nonlinear hinges will cause different solutions. The verifications with 35 typical school buildings damage by the Chi-Chi earthquake are discussed in this paper. In the conclusion, the proposed pushover analysis is beneficial for seismic evaluation with existing school buildings.

1. INTRODUCTION

Taiwan is in the region of the circum-pacific seismic zone. Earthquakes are common experiences for people in Taiwan. People are used to earthquakes and even ignore them. In the morning of September 21, 1999, the Chi-Chi earthquake awoke the people of Taiwan with its huge destructiveness. It told us the importance of the seismic capacities of structures. The Chi-Chi Earthquake caused nearly half of the school buildings in the central area of Taiwan to collapse or damage seriously. 656 primary and secondary school buildings were damaged in that earthquake. This disaster told us the seismic capacities of existing school buildings in Taiwan are probably not sufficient. Due to the existence of windowsill in traditional school buildings, the short-column effect caused the weak seismic capacity along the direction of the passage. Serious casualties and losses may result from the collapse of school buildings under strong earthquakes. To avoid casualties in the future earthquakes is the most important job in Taiwan. To retrofit these bad seismic performance school buildings is one solution to reduce the probable casualties. Before the retrofitting the seismic capacity of school buildings should be evaluated with a reliable method.

Based on the damage statistics, a lack of seismic resistance appears to be a common problem in the existing primary and secondary school buildings in Taiwan. Significant casualties and property losses could be resulted from the collapse of these school buildings under strong earthquakes. Furthermore, school buildings might have to be assigned as emergency shelters immediately after a severe earthquake. For the purposes of conducting seismic performance evaluation and retrofit of these noted structures, a rather simple template has been developed in NCREE for preliminary seismic evaluation of typical school buildings. The proposed template is to evaluate the structural types, apparent seismic weaknesses, potential failure modes and the available experimental data. The complete strategy for seismic evaluation and retrofit of school buildings is introduced later in this paper. Some key factors, among many items, responsible for the poor seismic performance of school buildings are discussed hereafter.

According the capacity spectrum method proposed by ATC-40 (ATC 1996), the pushover analysis is used to get the nonlinear base-shear to roof-displacement relationship of school buildings which is named as the capacity curve. The seismic capacity of buildings can be specified with the damage peak ground acceleration which can be determined from the pushover curve and the corresponding performance point. The accuracy of the pushover analysis is dependent on the well-defined properties of nonlinear hinges in structure elements. The load-deformation relationships of nonlinear hinges in beams, columns, brick walls and RC walls are discussed in this paper. The seismic retrofits with RC jackets, steel plate jackets, composite columns and shear walls are commonly used in existing low-rise school buildings in

Taiwan. The designs of all the mentioned retrofit methods are also introduced in this paper.

2. PUSHOVER ANALYSIS

The capacity curve from the pushover analysis is the foundation of the purposed detailed seismic evaluation method in this paper. Many commercial programs like ETABS and SAP2000 can process nonlinear static analyses which are also called pushover analyses. The nonlinear response of a structure is restricted to nonlinear hinges which are assigned on the structural elements of that structure. These nonlinear hinges can be divided to three types, moment hinges, shear hinges and axial hinges. As shown in Figure 1, the mechanic parameters of a nonlinear hinge are constructed from the nonlinear part of the load-deformation curve of a structural member. For moment hinges, load *Q* is moment *M* at the location of the moment hinge, and deformation Δ is associate rotation angle of the moment hinge. For shear hinges, load *Q* is lateral force *V* of the structural member, and deformation Δ is associate lateral displacement of the structural member. For axial hinges, load *Q* is axial force *P* of the structural member, and deformation Δ is associate axial displacement of the structural member.

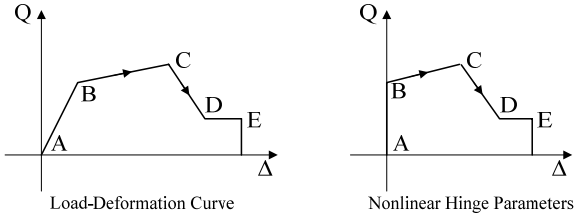

Figure 1 Nonlinear Hinge Parameters

In the pushover analysis, the flexural rigidity of reinforced concrete beams is assumed as $0.35E_cI_g$ and the flexural rigidity of reinforced concrete columns is assumed as $0.35E_cI_g$, where E_c is Young's modulus for concrete; and I_g is moment of inertia of gross concrete section. In the following the constructions of nonlinear hinges for columns will be presented.

3. NONLINEAR HINGES FOR COLUMNS

3.1 Behavior of Columns

The deformation of beams or columns in structure frames can be simulated as double curvature deformation of columns as shown in Figure 2. According to the research works of Elwood and Moehle (2005a; 2005b), for the double curvature reinforced concrete columns with light transverse reinforcement, under the axial load *P* and lateral load *V*, as the lateral displacement δ reaches yield displacement δ_y, the main reinforcement of columns is yielding, as the lateral displacement δ reaches flexure-shear failure displacement δ_s, large shear cracks will be observed at the regions of plastic hinges and lateral strength will be degraded, and as the lateral displacement δ reaches axial failure displacement δ_a, the columns will lose their axial capacity and their collapse will occur.

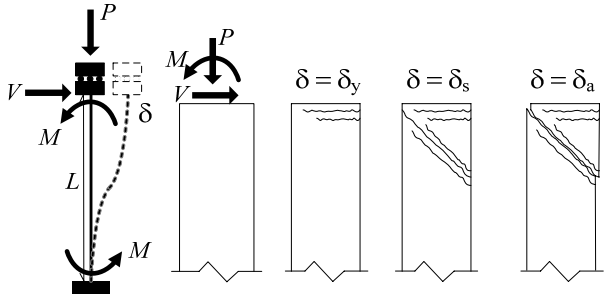

Figure 2 Double Curvature Deformation of Columns

The flexure-shear failure displacement can be calculated as (Elwood and Moehle 2005a)

$$\frac{\delta_s}{L} = \frac{3}{100} + 4\rho'' - \frac{1}{40}\frac{\upsilon}{\sqrt{f_c'}} - \frac{1}{40}\frac{P}{A_g f_c'} \geq \frac{1}{100} \qquad (1)$$

where *L* is the length of the column; ρ'' is the transverse reinforcement ratio as A_{st}/bs; A_{st} is the area of the transverse reinforcement; *b* is the column section width; *s* is the spacing of the transverse reinforcement; υ is the maximum nominal shear stress in MPa as V/bd; *d* is the depth to centerline of tension reinforcement; f_c' is the concrete compressive strength in MPa; and A_g is the gross cross-sectional area of the column.

The axial failure displacement δ_a can be calculated as (Elwood and Moehle 2005b)

$$\frac{\delta_a}{L} = \frac{4}{100}\frac{1+(\tan\theta)^2}{\tan\theta + P\dfrac{s}{A_{st} f_{yt} d_c \tan\theta}} \qquad (2)$$

where θ is the angle from horizontal of critical shear-failure plane, and can be assumed to be 65 degrees; f_{yt} is the yield strength of the transverse reinforcement; and d_c is the depth of the column core from centerline to centerline of the ties.

3.2 Nonlinear Moment Hinge

At the both ends of a beam or column, nonlinear moment hinges are assigned to represent the flexure-shear or flexure failure mode. According to the lateral force-displacement relationship of the element, the parameters of the nonlinear moment hinge are shown in Figure 3 and Table 1. The moment SF is the nominal moment strength M_n and the rotation SF is 1. The parameters are

$$a = \frac{\delta_s}{H} - \frac{\delta_y}{H} \qquad (3)$$

$$b = \max\left(\frac{\delta_a}{H}, \frac{\delta_s}{H}\right) \quad (3)$$

$$\delta_y = \frac{V_b}{k} = \frac{V_b H^3}{12(EI)_c} \quad (4)$$

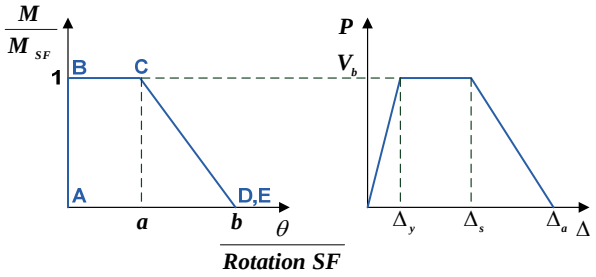

Figure 3 Moment-rotation Relationship of Nonlinear Moment Hinge

Table 1 Parameters of the Nonlinear Moment Hinge (M3 type)

Points	Moment/SF	Rotation/SF
A	0	0
B	1	0
C	1	a
D	0	b
E	0	b

3.3 Nonlinear Shear Hinge

At the center of a beam or column, a nonlinear shear hinge is assigned to represent the shear failure mode. According to the lateral force-displacement relationship of the element, the parameters of the nonlinear shear hinge are shown in Figure 4 and Table 2. The shear SF is the nominal shear strength V_n and the displacement SF is L. The parameter is

$$c = \min\left(\frac{\delta_a}{H}, 0.04\right) \quad (5)$$

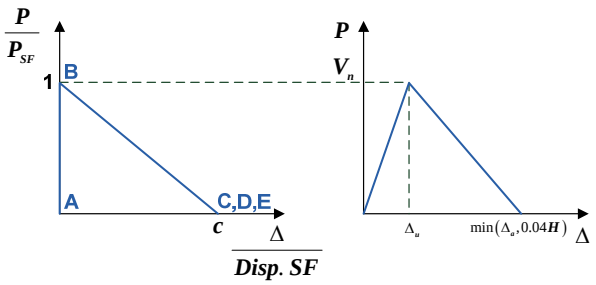

Figure 4 Shear-displacement relationship of nonlinear shear hinge

Table 2 Parameters of the nonlinear shear hinge (V2 type)

Points	Shear/SF	Disp./SF
A	0	0
B	1	0
C	0	c
D	0	c
E	0	c

4. VERIFICATION

A method of seismic evaluation for existing buildings needs to be confirmed. However, different definitions of nonlinear hinges will cause different solutions. The in-situ test is the best way to verify our assumptions for pushover analysis. NCREE preceded a series of in-situ pushover experiments for school buildings (Chiou et al. 2008, Jaung et al. 2008, Jiang et al. 2008, Weng et al. 2008). In the past, four in-situ tests of school buildings have been carried out. The experimental results are valuable to our research. In this paper, the ETABS pushover analysis results are compared with the experimental results to verify the accuracy of the present study. The experimental and analytical curves are compared in order to verify the seismic detailed evaluation method, as shown in Figure 5. The compared results indicate that the proposed analytical method can simulate the strength and the actual seismic behavior of low-rise school buildings accurately. Then, the seismic detailed evaluation method which suggested by this paper can provide the engineers a way to perform precise seismic evaluation. The proposed seismic evaluation method is beneficial for engineers in doing seismic evaluation for low-rise buildings.

Typical school buildings in the midland of Taiwan suffered severe damage by the Chi-Chi earthquake due to their common architecture plan and structural defects. Numerous damage records were left but without systematically arrangement. By collecting damage and structural data, such like original design drawings, acceleration records, and earthquake damage records of the school buildings in the midland of Taiwan, a digital databank is established. Structural variable statistics of 157 samples of the school buildings shows that the buildings have similarity in story, span, depth, and corridor type (Tu et al. 2007). The relationships between ratios of total column area to floor area, PGA of the site and damage level, show approximately reasonable result. The buildings with lower ratio of column area usually had severer damage, but for those had slight damage, the ratio of columns area distributes widely since the site PGA spreads. However, there is no obvious correlation between ratio of columns area and PGA of the site. The detailed evaluation method proposed by this paper is verified with 35 typical school buildings of the databank, as shown in Table 3. In the table, $0.4S_{DS}$ is the code-required seismic capacities, and CDR is the capacity-demand ration. The comparison with the detailed evaluation method shows accurate prediction results. The method also underestimates collapse PGA of most buildings, but it's still acceptable for

seismic assessment.

All of the results from simply survey, preliminary and detail evaluation have been submitted to the databank of the computer server in NCREE through internet. The accuracy of simply survey, preliminary and detail evaluation can be compared by the databank. Then the parameters of those evaluation methods can be adjusted to make them more accurately. Furthermore, the valuable experience can be used in other types of buildings like street-front residential buildings or governmental buildings.

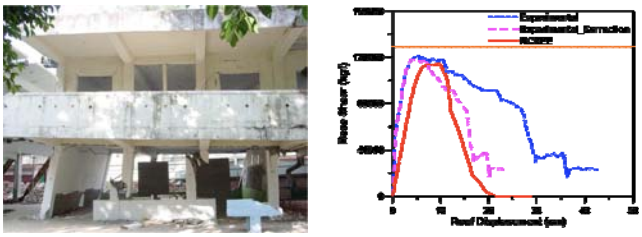

(a) Reui-Pu Elementary School

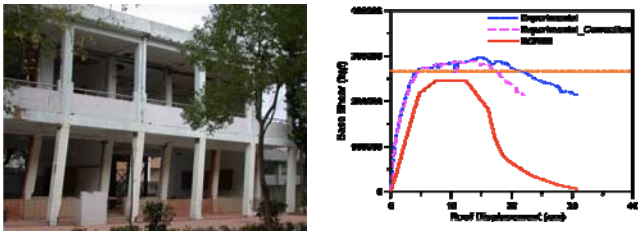

(b) Sin-Chen Junior High School

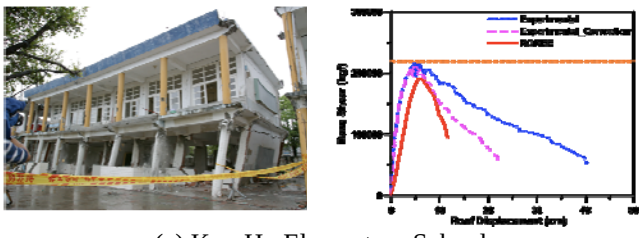

(c) Kao-Hu Elementary School

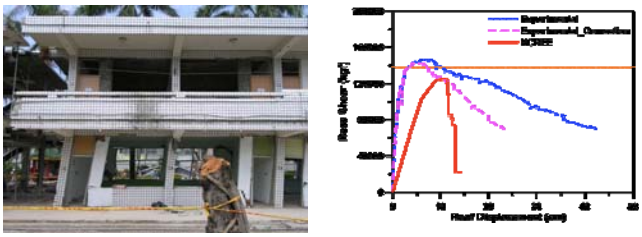

(d) Guan-Miao Elementary School

Figure 5 Photos of Specimens and Verifications of Pushover Curves with In-situ Tests

5. CONCLUSIONS

Among many type of governmental buildings, primary and middle schools have been found the most spacious and uniformly distributed according to the distribution of populations. Therefore, school buildings are likely to play a very important role for emergency response purposes immediately after a natural disaster. Hence, the structural safety of school buildings is evident. This explains why the seismic design force for school building structures has always been 25% higher than ordinary buildings. However, according to the observation made from the Chi-Chi earthquakes, damages of school building have been the most serious one among all building types. The specific features of the school building structures noted above should help to explain why it had suffered the most during a severe earthquake. Based on the NCREE proposed seismic evaluation method of school buildings noted in this paper, the Taiwan Ministry of Education has implemented an extensive program for improving the seismic performance of elementary and secondary schools. A significant number of school buildings are being retrofitted for a higher seismic resistance. Based on the verification with chi-chi earthquake damage database of school buildings, the detailed seismic evaluation method proposed in this paper can reasonably provide a measure to determine the seismic capacity of buildings.

References:

ATC (1996), Seismic Evaluation and Retrofit of Concrete Buildings, ATC-40 Report, Applied Technology Council, Redwood City, California, USA.

Elwood, K. J., and Moehle, J. P. (2005a), "Drift Capacity of Reinforced Concrete Columns with Light Transverse Reinforcement," Earthquake Spectra, Vol. 21, No. 1, pp. 71-89.

Elwood, K. J., and Moehle, J. P. (2005b), "Axial Capacity Model for Shear-Damaged Columns," ACI Structural Journal, Vol. 102, No. 4, pp. 578-587.

Tu, Y. S., Yeh, P. L. and Liu, T. W. (2007), "Chi-Chi Earthquake Damage Database of School Buildings in the Midland of Taiwan," NCREE Report, NCREE-07-023. (In Chinese)

Chiou, Y. J., Hwang, S. J. and Tsai K. C. (2008), "Proceedings of the conference on in-situ pushover test of RC school buildings with seismic retrofitting in Guanmiao," NCREE Report, NCREE-08-001. (In Chinese)

Jaung, W. C., Chiou, T. C., Hsiao, F. P., Tu, Y. H., Chien, W. Y., Yeh, Y. K., Chung, L. L. and Hwang, S. J. (2008), "In-Situ pushover test of school building structure in Sin-Chen junior high school," NCREE Report, NCREE-08-008. (In Chinese)

Jiang, W. G., Chiou, T. C., Hsiao, F. P., Tu, Y. H., Chien, W. Y., Yeh, Y. K., Chung, L. L. and Hwang, S. J. (2008), "In-Situ Pushover Test of School Building Structure in Kao-Hu Elementary School," NCREE Report, NCREE-08-044. (In Chinese)

Weng, Y. T., Lin, K. C., Hwang, S. J. and Chiou, T. C. (2008), "In situ pseudo-dynamic test and cyclic pushover test of existing school buildings," NCREE Report, NCREE-08-004. (In Chinese)

Table 3 Verification of Detail Evaluation and 35 Typical School Buildings Damaged in Chi-Chi Earthquake

Name	Damage Status	Actual PGA (g)	Evaluation PGA (g)	$0.4S_{DS}$ (g)	CDR	Evaluation Result
She-Liao Elementary School B	Collapse	0.470	0.220	0.394	0.558	Need Retrofitting
Yong-Chang Elementary School A	Collapse	0.742	0.223	0.330	0.676	Need Retrofitting
Yan-He Junior High School C	Collapse	0.244	0.206	0.394	0.523	Need Retrofitting
Yan-He Junior High School D	Collapse	0.244	0.162	0.394	0.411	Need Retrofitting
Zhu-Shan Junior High School D	Collapse	0.259	0.139	0.394	0.353	Need Retrofitting
Dong-Guang Elementary School A	Heavy	0.841	0.226	0.308	0.734	Need Retrofitting
Ji-Ji Junior High School A	Heavy	0.619	0.214	0.330	0.648	Need Retrofitting
Zhu-Shan Elementary School A	Heavy	0.240	0.207	0.394	0.525	Need Retrofitting
Nan-Guang Elementary School A	Heavy	0.597	0.215	0.308	0.698	Need Retrofitting
Pu-Li Junior High School E	Heavy	0.590	0.196	0.308	0.636	Need Retrofitting
Ji-Ji Elementary School A	Heavy	0.570	0.212	0.330	0.642	Need Retrofitting
E-Liao Elementary School A	Heavy	0.742	0.205	0.371	0.553	Need Retrofitting
Zhong-Shan Elementary School A	Medium	0.714	0.243	0.371	0.655	Need Retrofitting
Rui-Zhu Elementary School A	Medium	0.430	0.207	0.394	0.525	Need Retrofitting
Qiao-Xing Elementary School C	Medium	0.821	0.232	0.394	0.589	Need Retrofitting
Zhong-Shan Elementary School B	Small	0.714	0.257	0.371	0.693	Need Retrofitting
Tai-Ping Elementary School A	Small	0.575	0.411	0.308	1.334	To be Safe
Tai-Ping Elementary School B	Small	0.575	0.437	0.308	1.419	To be Safe
Tai-Ping Elementary School C	Small	0.575	0.489	0.308	1.588	To be Safe
Yong-He Elementary School A	Small	0.690	0.502	0.371	1.353	To be Safe
Nan-Fong Elementary School A	Small	0.519	0.317	0.308	1.029	To be Safe
Ming-Jian Elementary School B	Small	0.674	0.214	0.394	0.543	Need Retrofitting
Yan-He Junior High School B	Small	0.244	0.393	0.394	0.997	Need Retrofitting
E-Liao Elementary School B	Small	0.742	0.299	0.371	0.806	Need Retrofitting
She-Liao Elementary School A	Slight	0.470	0.501	0.394	1.272	To be Safe
She-Liao Elementary School C	Slight	0.470	0.502	0.394	1.274	To be Safe
Tou-She Elementary School A	Slight	0.590	0.485	0.308	1.575	To be Safe
Dong-Guang Elementary School B	Slight	0.841	0.495	0.308	1.607	To be Safe
Yong-Chang Elementary School B	Slight	0.742	0.503	0.330	1.524	To be Safe
Ming-Gang Elementary School A	Slight	0.580	0.229	0.342	0.670	Need Retrofitting
Ming-Gang Elementary School C	Slight	0.580	0.426	0.342	1.246	To be Safe
Xi-Ling Elementary School A	Slight	0.292	0.671	0.342	1.962	To be Safe
Xi-Ling Elementary School B	Slight	0.292	0.441	0.342	1.289	To be Safe
He-Ping Elementary School B	Slight	0.578	0.257	0.342	0.751	Need Retrofitting
He-Ping Elementary School A	Slight	0.578	0.279	0.342	0.816	Need Retrofitting

JOINT CONFERENCE PROCEEDINGS
7th International Conference on Urban Earthquake Engineering (7CUEE) &
5th International Conference on Earthquake Engineering (5ICEE)
March 3-5, 2010, Tokyo Institute of Technology, Tokyo, Japan

SEISMIC PERFORMANCE EVALUATION OF INDUSTRIAL BUILDING STRUCTURES IN TURKEY USING CAPACITY SPECTRUM METHOD

Baki Ozturk[1], and Melih Sadak[2]

1) Asst.Professor, Department of Civil Engineering, Nigde University, Turkey
2) Graduate Student, Department of Civil Engineering, Nigde University, Turkey
bakiozturk@nigde.edu.tr, bakiozturk1@gmail.com

Abstract: Precast concrete building structures constitute the main type of construction in industrial areas in Turkey. Several major destructive earthquakes occurred sequentially in Turkey since early 1990's. Two of these major earthquakes are namely Marmara Earthquake (August 17th, 1999) and Duzce Earthquake (November 12th, 1999) both of which occurred in a highly industrialized part of Turkey. Excessive levels of damage were observed at precast concrete structures after these earthquakes. The observed damage was mainly destruction at column-girder connections or column failures. Investigation of seismic behaviour of precast concrete structures located at this highly earthquake-prone region in Turkey is inevitable. Therefore, seismic performance of precast concrete industrial building structures representative of the current design practice in Turkey are examined. These buildings are designed according to the current seismic code in Turkey and are subjected to several ground motions from recent earthquakes. The capacity spectrum method is applied in order to assess the seismic performance of investigated precast concrete buildings subjected to selected earthquake excitations. The results of capacity spectrum method application for two sample industrial building structures are provided and discussed in this study.

1. INTRODUCTION

Several major destructive earthquakes occurred sequentially in Turkey since early 1990's. Two of these earthquakes are namely Marmara Earthquake (August 17th, 1999) and Duzce Earthquake (November 12th, 1999). As a consequence of two earthquakes named above, both of which occurred at a highly industrialized part of the country, excessive levels of damage were observed at precast concrete structures. It is obvious that there is a need for investigation of seismic behaviour of precast concrete structures since the observed damage was mainly in the form of destruction at column-girder connections or column failures. In this study, the results of application of capacity spectrum method on precast concrete building structures representative of the current construction practice for industrial buildings in Turkey are provided. The investigated buildings are designed considering the current seismic code in Turkey.

Performance based design is becoming more popular in earthquake engineering. In recent decades extensive scientific research has been conducted regarding the investigation of behavior of reinforced concrete building structures located at regions of high seismicity (Shibata and Sozen 1976, Shimazaki and Sozen 1984, Lepage 1997, Ozturk 2003, Ozturk 2006). Ozturk (2003) considered the effect of ground velocity, base shear strength of the structure and initial period of the structure on its seismic behavior.

In addition, recently there has been research (Ozturk and Demiralan 2007, Ozturk et al. 2008, Demiralan 2009, Ozturk 2009, Sadak 2009) aiming at determination of seismic behavior of precast concrete building structures. In this study, a perspective regarding investigation of seismic behavior of precast concrete structures considering the capacity spectrum method (CSM) will be introduced.

The CSM was provided in ATC-40 (1996) for estimating the peak inelastic responses. It is a performance-based seismic analysis technique which compares the capacity of the structure (i.e. pushover curve) with the demands on the structure (i.e. response spectra) (Chopra and Goel 1999, Fajfar 1999, Fajfar 2000, Kim et al. 2005). It is a nonlinear static analysis procedure which provides a graphical representation of the expected seismic performance of the existing or retrofitted structure by the intersection of the structure's capacity spectrum with a response spectrum representing the displacement demand on the structure due to earthquake. The intersection point refers to the performance point which is the intersection of both the spectral response curve and the nonlinear demand curve. In order to account for non-linear inelastic behavior of the structural system, effective viscous damping values are applied to linear-elastic response spectra similar to inelastic response spectra. Currently, the CSM and its applications is being used to solve various earthquake engineering problems (Guyader and Iwan 2006, Casarotti and Pinho 2007, Zhao and Zhang 2007, Gencturk and Elnashai 2008, Barbat et al. 2008).

In this study, the capacity spectrum method is applied in order to assess the seismic behavior of two prefabricated industrial buildings (Building 1 and Buiding 2) subjected to different earthquake excitations. Building 1 is located at a region of high seismicity (seismic zone 1) while Building 2 is located in seismic zone 2. Both of the investigated buildings are constructed considering the current earthquake design practice. In design of these buildings and evaluation of their seismic behavior, principles provided in TS 498 (1987), TS 9967 (1992), TS 500 (2000) and Regulation for Buildings to be Constructed at Earthquake-Prone Regions (2007) are applied. These buildings are subjected to different ground motions which were obtained during recent earthquakes in Turkey (i.e. Ceyhan 1998, Marmara 1999, Duzce 1999).

The application of capacity spectrum method provides the capacity of both of the investigated precast concrete buildings regarding the principles of performance-based design. As an outcome of this study, the capacity spectrum diagrams are obtained for both of the investigated buildings.

2. INFORMATION ABOUT THE INVESTIGATED BUILDINGS

In this study, two industrial structures one of which is designed to be built at seismic zone 1 while the other one is designed to be built in seismic zone 2 are investigated considering the application of the capacity spectrum method (Figures 1&2). In the design of the structures current seismic codes in Turkey (TS 498 1987, TS 9967 1992, TS 500 2000) and Regulation for Buildings to be Constructed at Earthquake-Prone Regions (2007) are used.

Building 1 has a length of 40 m in X direction and 56 m in Y direction. The columns are 7 m in height. In X direction there are six spans with a span length of 6.65 m each, and in Y direction there are seven spans with a span length of 8 m each. Total weight of the structure is around 5300 kN.

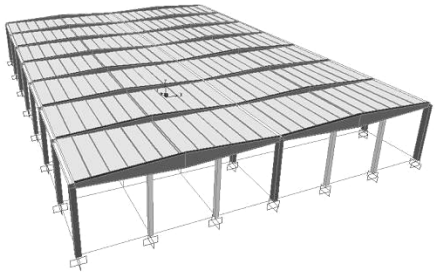

Figure 1 Structural System of Building 1 (Demiralan 2009)

Building 2 has a length of 40 m in X direction and 60 m in Y direction. Its columns are 7.5 m in height. In the X direction there are two spans with a span length of 20 m each, and in Y direction there are eight spans with a span length of 7.5 m each. The weight of the structure is around 7250 kN.

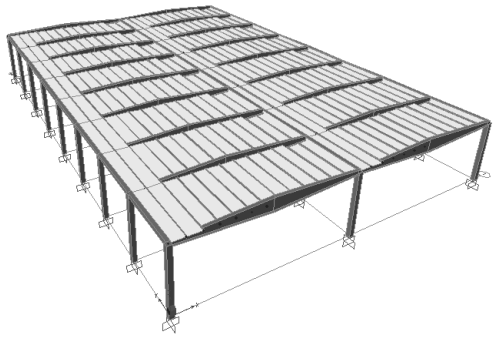

Figure 2 Structural System of Building 2 (Demiralan 2009)

3. MODAL AND RESPONSE SPECTRUM ANALYSIS OF THE STRUCTURES

For the analyses of the structures, SAP2000 Program (2000) is used. First four structural periods obtained as a result of modal analyses are provided in Tables 1&2. An additional response spectrum analysis is applied for the structures. In the analyses, a damping ratio of 5 % is considered. The periods of first two modes of Building 1 are 1.05 sec in the short direction (Mode 1) while 0.88 sec in the long direction (Mode 2). For Building 2 the periods of first two modes are 1.03 sec both in short and long directions (Modes 1 & 2).

Table 1 Structural Periods of Building 1 (Demiralan 2009)

Mode	Period (sec)	Mode	Period (sec)
1	1.05	2	0.88
3	0.77	4	0.53

Table 2 Structural Periods of Building 2 (Demiralan 2009)

Mode	Period (sec)	Mode	Period (sec)
1	1.03	2	1.03
3	0.91	4	0.34

The soil type on which Building 1 is constructed is defined as Z3 with T_A= 0.15 sec and T_B= 0.6 sec, respectively. The corresponding spectrum function is given in Figure 3 and spectrum constant, K is evaluated using Equation 1. In the analysis, effective ground acceleration constant, A_O value is 0.4g, building importance constant, I value is 1.0 and building ductility constant, R value is taken as 3. K value is evaluated as 1.31 m/sec^2, accordingly.

Building 2 is also constructed on Z3 soil type. The effective ground acceleration constant, A_O value is 0.3g, building importance constant, I value is 1.0 and building ductility constant, R value is 3. Upon application of Equation 1, K value is evaluated as 0.98 m/sec^2.

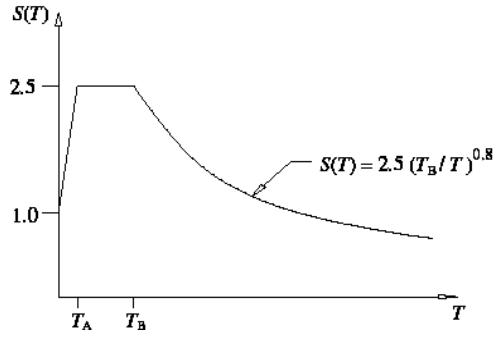

Figure 3 Spectrum Function

$$K = \frac{A_O \cdot I \cdot g}{R} \quad (1)$$

Spectrum constant, *S(T)* is calculated to be 1.6 for Building 1 and 1.62 for Building 2 using Equation 2 .

$$S(T) = 2.5(\frac{T_B}{T})^{0.8} \quad (2)$$

4. DETERMINATION OF PERFORMANCE POINT USING CAPACITY SPECTRUM METHOD

Nonlinear deformations occur under increasing earthquake loads. These deformations increase the structural damping and decrease the displacement demand. In capacity spectrum method, due to the occurrence of nonlinear structural deformations, elastic demand spectrum is reduced. The equilibrium point of capacity and demand is defined afterwards. At this certain point, named the performance point, the realization of performance target which is desired for the structure is controlled. In capacity spectrum method, determination of three essential parameters are required. These parameters are capacity (Figures 4-5), displacement and acceleration demand (Figures 6-7), and performance point (Figure 8).

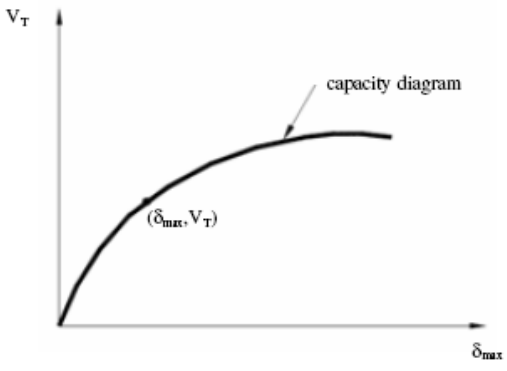

Figure 4. Capacity diagram

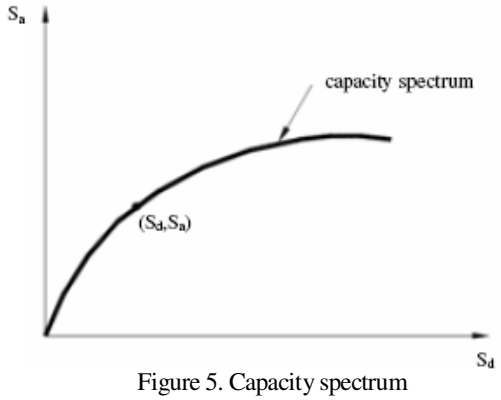

Figure 5. Capacity spectrum

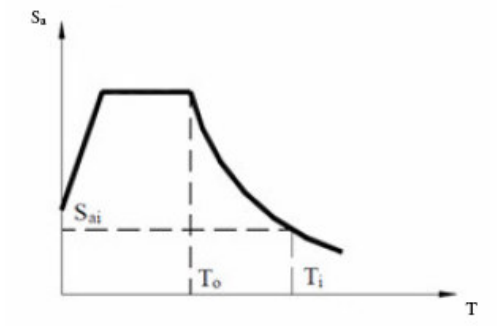

Figure 6. Elastic demand spectrum

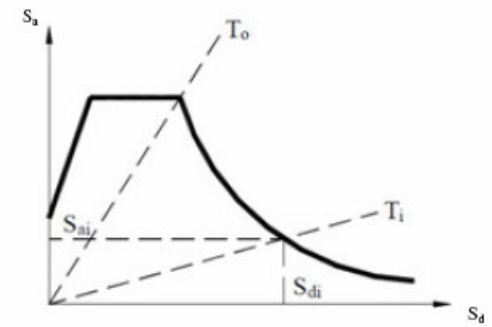

Figure 7. Spectral acceleration – spectral displacement demand spectrum

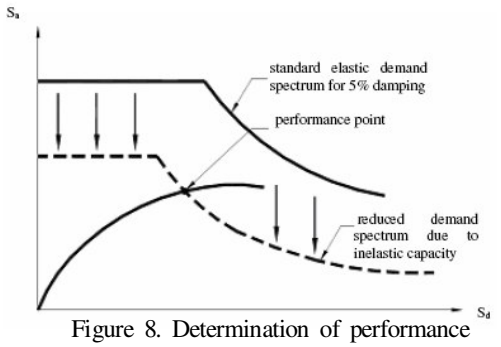

Figure 8. Determination of performance point using capacity spectrum method

In order to compare the capacity curve with the demand spectrum, there is a need for its conversion to spectral format which is composed of spectral acceleration, S_a and spectral displacement, S_d. However, since the demand spectrum is for a

single-degree-of-freedom system there is a need for transformation of capacity curve for multi-degree-of-freedom system into an equivalent single-degree-of-freedom system. This operation is applied for modal mass constant, α_1 and modal participation factor, PF_1 using Equations 3-5 given below.

$$\alpha_1 = \frac{\left[\sum_{i=1}^{N} \frac{w_i \phi_{i,1}}{g}\right]^2}{\left[\sum_{i=1}^{N} \frac{w_i}{g}\right]\left[\sum_{i=1}^{N} \frac{w_i \phi_{i,1}^2}{g}\right]} \qquad (3)$$

$$S_a = \frac{V_T}{W\alpha_1} \quad , \quad S_d = \frac{\delta_{max}}{PF_1 \phi_{top,1}} \qquad (4)$$

$$PF_1 = \frac{\left[\sum_{i=1}^{N} \frac{w_i \phi_{i,1}}{g}\right]}{\left[\sum_{i=1}^{N} \frac{w_i \phi_{i,1}^2}{g}\right]} \qquad (5)$$

where the parameters are:

S_a	: Spectral acceleration
S_d	: Spectral displacement
V_T	: Total base shear force
δ_{max}	: Maximum displacement at the top of the structure
W	: Total weight of the structure
$\Phi_{top,1}$	: Maximum displacement at top level due to first mode of the structure
$\Phi_{i,1}$	: Maximum displacement at story number (i) due to first mode of the structure
N	: Story number
W_i/g	: Mass of story number (i)
α_1	: Modal mass constant for the first mode
PF_1	: Modal participation factor

Using the building, soil and seismic region properties of the industrial buildings explained above analyses are conducted both in X and Y directions of the investigated buildings for the ground motion records provided in Table 3. The maximum ground acceleration values (PGA) of these 20 ground motions are ranging in between 0.12g for Izmir EW record which was recorded during 1977 Izmir earthquake, and 0.82g for Bolu EW record which was recorded during 1999 Duzce earthquake. For the given earthquake data maximum ground acceleration values (PGA) are given in Table 3.

Table 3 Ground motion records and maximum ground acceleration (PGA) values (Sadak 2009)

Ground Motion Record	Maximum Ground Acceleration (PGA)
Ceyhan EW (Ceyhan1998)	0.23 g
Ceyhan NS (Ceyhan1998)	0.28 g
Bingol EW (Bingol 2003)	0.28g
Bingol NS (Bingol 2003)	0.55g
Bolu EW (Duzce 1999)	0.82 g
Bolu NS (Duzce 1999)	0.75 g
Denizli EW (Denizli 1976)	0.29g
Denizli NS (Denizli 1976)	0.35g
Dinar EW (Dinar 1995)	0.33g
Dinar NS (Dinar 1995)	0.28g
Duzce EW (Duzce 1999)	0.41g
Duzce NS (Duzce 1999)	0.52g
Erzincan EW(Erzincan 1992)	0.48g
Erzincan NS (Erzincan 1992)	0.41g
Izmir EW (Izmir 1977)	0.12g
Izmir NS (Izmir 1977)	0.39g
Izmit EW (Marmara 1999)	0.23 g
Izmit NS (Marmara 1999)	0.17 g
Sakarya EW (Marmara 1999)	0.35g
Sakarya NS (Marmara 1999)	0.21g

The capacity spectrum curves and the corresponding performance points for both Building 1 and Building 2 are shown in Figures 9 & 10. The coordinate values of performance points are tabulated in Tables 4 & 5. The performance point of Building 1 has a spectral displacement value of 0,13 m and a spectral acceleration value of 0,14g for a base shear force, V of 4970 kN and displacement of 0,15 m (Table 4) while the performance point of Building 2 has a spectral displacement value of 0,12 m and a spectral acceleration value of 0,12g for a base shear force, V of 1150 kN and displacement of 0,14 m (Table 5).

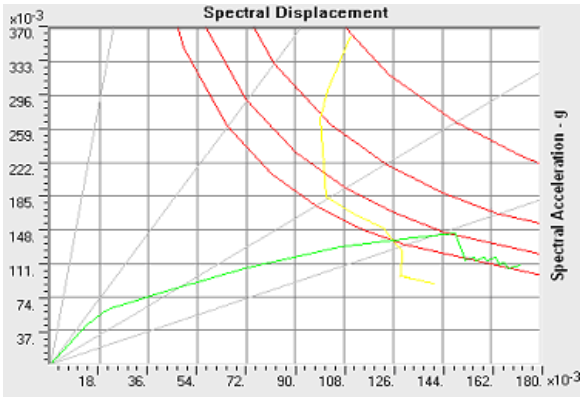

Figure 9. Determination of performance point using capacity spectrum method for Building 1(Sadak 2009)

Table 4 Performance point coordinate values for Building 1 (Sadak 2009)

Parameter	V, kN	D, m	S_a, g	S_d, m
Value	4970	0.15	0.14	0.13

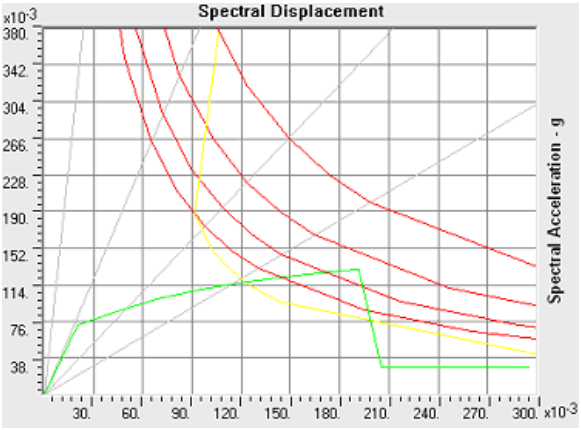

Figure 10. Determination of performance point using capacity spectrum method for Building 2(Sadak 2009)

Table 5 Performance point coordinate values for Building 2 (Sadak 2009)

Parameter	V, kN	D, m	S_a, g	S_d, m
Value	1150	0.14	0.12	0.12

5. CONCLUSIONS

In this study, seismic behavior of two prefabricated industrial buildings, one of which is designed for seismic zone 1 while the other is designed for seismic zone 2, is evaluated and discussed using the capacity spectrum method (CSM). Both of these buildings are designed according to the current design codes in Turkey and are subjected to 20 different earthquake excitations in order to investigate their seismic behavior.. The maximum ground acceleration values (PGA) of these 20 ground motions are ranging in between 0.12g (for Izmir EW record which was recorded during 1977 Izmir earthquake) and 0.82g (for Bolu EW record which was recorded during 1999 Duzce earthquake).

The application of capacity spectrum method provides the performance point which has a spectral displacement value of 0,13 m and a spectral acceleration value of 0,14g for a base shear force, V of 4970 kN and displacement of 0,15 m for Building 1 while the performance point has a spectral displacement value of 0,12 m and a spectral acceleration value of 0,12g for a base shear force, V of 1150 kN and displacement of 0,14 m for Building 2. Regarding the comparison of base shear force values at performance points for both of the investigated buildings, it is examined that Building 1 has a higher base shear force capacity compared to Building 2 (Tables 4 & 5).

It has to be noted that the capacity spectrum method provides an efficient tool in evaluation of the performance point for prefabricated industrial building structures and assessment of their seismic performance.

Acknowledgements:

The authors acknowledge support from the Japan Ministry of Education, Culture, Sport, Science, and Technology (MEXT) for establishing the Center for Urban Earthquake Engineering (CUEE) in Tokyo Institute of Technology. This support makes possible the forthcoming international conference, as well as international joint research projects and exchange programs with other international universities.

References:

Shibata, A. and Sozen, M.A. (1976), "Substitute-Structure Method for Seismic Design in Reinforced Concrete," *Journal of Structural Division*, American Society of Civil Engineers, **102**(3), 1-18.

Shimazaki, K. and Sozen, M.A. (1984), "Seismic Drift of Reinforced Concrete Structures," Technical Research Report of Hazama-Gumi Ltd., 145-166.

Lepage, A. (1997), "A Method for Drift Control in Earthquake Resistant Design of RC Building Structures," Ph.D. Dissertation, University of Illinois, Urbana-Champaign, Illinois, U.S.A.

Ozturk, B. (2003), "Seismic Drift Response of Building Structures in Seismically Active and Near-Fault Regions," Ph.D. Dissertation, Purdue University, W. Lafayette, Indiana, U.S.A.

Ozturk, B. (2006), "Dynamic Analysis and The Resulting Nonlinear Response of Building Structures Located in Seismically Active Regions in Turkey," *Proceedings of the 4th International Conference on Earthquake Engineering*, Paper No.078, Taipei, Taiwan.

Ozturk, B. and Demiralan, F. (2007), "Investigation of Seismic Behavior of a Prefabricated Building Located at a Seismically Active Region Using Various Ground Motion Records," *Sixth National Conference on Earthquake Engineering,* Istanbul, Turkey.

Ozturk, B., Demiralan, F., and Civalek, O. (2008), "Seismic Drift Response of Precast Concrete Building Structures Located in Earthquake-Prone Regions in Turkey Considering Nonlinear Analysis Procedures," *14th World Conference on Earthquake Engineering*, Beijing, China.

Demiralan, F. (2009), "Investigation of Seismic Behavior of Prefabricated Buildings Designed According to Current Standards in Turkey by Using Different Analysis Methods," Master Thesis, Nigde University, Nigde, Turkey.

Ozturk, B. (2009), "Seismic risk assessment studies of prefabricated buildings located in highly seismic regions of Turkey," *Turkish-Japanese Earthquake Workshop*, TUBITAK, Gebze, Turkey.

Sadak, M. (2009), "Investigation of Damage Risks during Earthquakes by Using Capacity Spectrum Method for Prefabricated Buildings Designed According to Current Standards in Turkey," Master Thesis, Nigde University, Nigde, Turkey.

Applied Technical Council (1996), "Seismic evaluation and retrofit of concrete buildings," ATC-40, Redwood City, U.S.A.

Chopra, A.K. and Goel, R.K. (1999), "Capacity-demand-diagram methods based on inelastic design spectrum," *Earthquake Spectra*, **15**(4), 637–656.

Fajfar, P. (1999), "Capacity spectrum method based on inelastic demand spectra," *Earthquake Engineering and Structural Dynamics*, **28**(9), 979-993.

Fajfar, P. (2000), "A Nonlinear Analysis Method for Performance Based Seismic Design," *Earthquake Spectra*, **16**(3), 573-592.

Kim, H., Min, K., Lan, C., Park, M., and Lee, S.H. (2005), "Evaluation of capacity spectrum method for estimating the peak inelastic responses," *Journal of Earthquake Engineering*, **9**(5), 695-718.

Guyader, A.C. and Iwan, W. (2006), "Determining Equivalent Linear Parameters for Use in a Capacity Spectrum Method of Analysis," *Journal of Structural Engineering*, American Society of Civil Engineers, **132**(1), 59-67**.**

Casarotti, C. and Pinho, R. (2007), "An adaptive capacity spectrum method for assessment of bridges subjected to earthquake action," *Bulletin of Earthquake Engineering*, **5**(3), 377-390.

Zhao, J. and Zhang, J. (2007), "Inelastic Demand Spectra of Bi-Linear Models for Capacity Spectrum Method and Response of Simple Structures under Near-Source Records," *Journal of Earthquake Engineering*, **11**(4), 631-652.

Gencturk, B. and Elnashai, A. (2008), "Development and application of an advanced capacity spectrum method," *Engineering Structures*, **30**(11), 3345-3354.

Barbat, A.H., Pujades, L.G., and Lantada, N. (2008), "Seismic damage evaluation in urban areas using the capacity spectrum method: Application to Barcelona," *Soil Dynamics and Earthquake Engineering*, **28**(10-11), 851-865.

TS 498 (1987), "Calculation Values of Loads to be Applied in Dimensioning Structural Elements," Turkish Standards Institute, Ankara, Turkey.

TS 9967 (1992), "Design, Construction and Erection Methods for Precast, Reinforced and Prestressed Concrete Elements, Structures and Buildings," Turkish Standards Institute, Ankara, Turkey.

TS 500 (2000), "Principles of Design and Construction of Reinforced Concrete Structures," Turkish Standards Institute, Ankara, Turkey.

RBCEPR (2007), "Regulation for Buildings to be Constructed at Earthquake-Prone Regions," Ankara, Turkey.

SAP2000 Analysis Reference (2000), Structural Analysis Program, Computers and Structures Inc. (CSI), Berkeley, California, U.S.A.

JOINT CONFERENCE PROCEEDINGS
7th International Conference on Urban Earthquake Engineering (7CUEE) &
5th International Conference on Earthquake Engineering (5ICEE)
March 3-5, 2010, Tokyo Institute of Technology, Tokyo, Japan

SYSTEM IDENTIFICATION AND DAMAGE DETECTION OF DEGRADING HYSTERESIS OF REINFORCED CONCRETE FRAMES

Chin-Hsiung Loh[1], Chien-Hong Mao[2], and Jhih-Ren Huang[2]

1) Professor, Department of Civil Engineering, National Taiwan University, Taipei 10617, Taiwan
2) Graduate student, Department of Civil Engineering, National Taiwan University, Taipei 10617, Taiwan
lohc0220@ccms.ntu.edu.tw, r96521207@ntu.edu.tw, r96521208@ntu.edu.tw

Abstract: Vibration-based damage detection approaches assume that changes in a structure's integrity influence the measured vibration signals, enabling damage of the modal parameters to be detected independently. In this study, seismic response data of a total of six reinforced concrete frames, designed with same dimensions and same seismic design code, subject to different level of ground excitation individually from shaking table test, are used to study the damage pattern of reinforced concrete structure and to identify the degrading hysteretic behavior of the test RC structure. Both model-based and signal-based damage identification methods are applied to identify the damage features of the structure. From model-based identification, the general Bouc-Wen hysteretic model was used to identify the physical parameters such as stiffness degradation, strength deterioration and hysteresis behavior of the reinforced concrete frame. From signal-based identification, damage features in relating to the change of Hilbert marginal spectrum, the change of instantaneous frequency and phase difference, the change of Holder exponent, and the change of wavelet component correlation are identified from the response measurements. Finally, the relationship between the change of model properties (stiffness degradation and strength deterioration), the global damage index and the identified damage features are investigated. The results can be used as a safety assessment index for the seismic assessment of reinforced concrete structure.

1. INTRODUCTION

Most civil engineering structures exhibit hysteresis behaviour accompanied by stiffness degradation, strength deterioration or pinching phenomenon when undergoing significant deformations induced by severe external excitations. In any assessment of the damage to a reinforced concrete structure, nonlinear hysteretic behavior of each member must be considered. The Bouc-Wen model of smooth hysteresis [1] is receiving increasing attention as a means of specifying analytically a range of shapes of hysteretic cycles. To quantify the damage, this physical model can be employed to determine the load-displacement relationship between the model and the measurements so as to elucidate the degradation of stiffness and strength behavior of the inelastic hysteretic relationship to the severity of damage and the effect of nonlinearity. Unlike a theoretical model, a damage identification system using vibration measurements is an effective means of detecting damage to whole structures without considering the theoretical model. Vibration-based damage detection approaches assume that changes in a structure's integrity influence the measured vibration signals, enabling damage to be detected independently of the modal parameters. In many cases damage causes a structure that initially behaves in a predominantly linear manner to exhibit nonlinear response when subject to its operating environment. One important issue in global vibration-based damage assessment approaches concerns the choice of damage indices. Doebling *et al.* [3] summarized the historic development of damage assessment approaches. Summary and comparing overview of techniques for the detection of nonlinear distortions had been presented [3]. In this study, nonlinear system identification and feature extraction processes are used to investigate the physical parameters in the degrading hysteretic model of a reinforced concrete frame and the severity of damage thereto. Six reinforced concrete frame test data collected in response to various degrees of seismic excitation, including seismic response data, ambient test data and cyclic loading test data, are used to study the severity of damage. The proposed methods identify physical parameters such as stiffness degradation, strength deterioration and the pinching behavior of the reinforced concrete structure, as well as the feature extraction using nonlinear indices to determine the severity of damage. Finally, the global damage index is studied in relation to both stiffness degradation and the damage severity.

2. DESCRIPTION OF TEST FRAMES

Six reinforced single-story two-bay reinforced concrete frames were constructed and designed with the same dimensions and the design details. *Figure 1* presents the test frame. The height of each frame structure is 2.0 m and the length of each span is 2.0 m. The designed compressive strength of the concrete is 210kg/cm^2 and the designed strength of the steel is 4200 kg/cm^2. The frame comprised a T-beam, with a floor dimension of the first story of 4.7 m $\times$ 0.7 m, and three columns with cross-sectional dimensions

of 20 cm × 20 cm. The total mass of each frame is 8490 kg (which includes 4000 kg of lead ballast). Both a shaking table test and a cyclic loading test are performed on the structure following the approaches for each frame that are presented in *Table 1*. Accelerometers and LVDT are installed in the basement and on top of the floor. Damage is caused to each frame in the shaking table test in which various intensities of base input excitations are used. Chi-Chi earthquake ground motion data from station TCU082 (NS-direction with duration of 98 sec) is adopted as an input excitation. Damage is determined from seismic response data for the following four specimens; Specimen RCF6 (with input PGA=649gal), Specimen RCF2 (with input PGA=840gal), Specimen RCF4 (with input PGA= 1186gal) and Specimen RCF3 (with input PGA=1310gal).

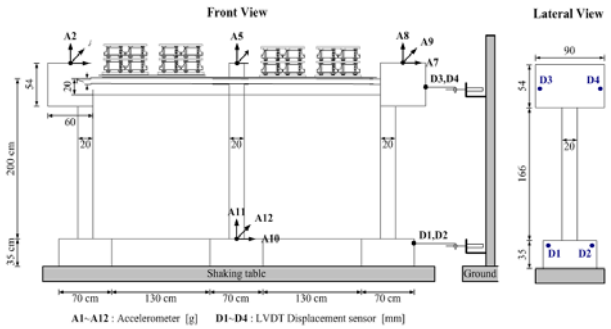

Figure 1: Front view and side view of the test specimen.

Table 1: Test procedures on six reinforced concrete frames.

Test Cases	*Shaking Table Test (Input Level)*	*Ambient Test (before shaking table test)*	*Cyclic Loading Test*	*Ambient Test (after shaking table test*
RCF1	None	Acceleration Velocity	5% Drift Ratio	Acceleration Velocity
RCF2	840gal	Acceleration Velocity	5% Drift Ratio	Acceleration Velocity
RCF3	1310gal	Acceleration Velocity	5% Drift Ratio	Acceleration Velocity
RCF4	(a) 1186gal (b) 668gal	Acceleration Velocity	5% Drift Ratio	Acceleration Velocity
RCF5 (with additional dead load)	1249gal	Acceleration Velocity	5% Drift Ratio	Acceleration Velocity
RCF6	649gal	Acceleration Velocity	5% Drift Ratio	Acceleration Velocity

The maximum inter-story drift ratio and the peak floor acceleration can be determined directly from the response measurements of these frame structures made during the shaking table tests, as presented in *Table 2*. For the RCF3 specimen, the peak floor acceleration achieved using the shaking table was 1287 gal, which induced a maximum inter-story drift ratio of the structure of the structure of 4.46%, while for the RCF6 specimen, it induced a maximum inter-story drift ratio of 1.35%. Table 3 clearly indicates that these four specimens experienced different degrees of damage, and provides important information for determining the different degrees of damage to the RC frame in response to various degrees of ground excitation. *Figure 2* plots the load-displacement hysteresis of these four specimens based on the displacement and acceleration measurements made in the shaking table tests. Hysteresis is important in determining the nonlinear response of reinforced concrete structures as well as the damage. Variations in the load-displacement relationship among these four tests are obvious. The following section will discusses the stiffness and strength degradation of these specimens.

Table 2: Physical parameters measured or identified from the shake table tests

Specimen NO.	Excitation	PGA (gal)	Max. Absolute Acceleration (gal)	Max. Inter-Story Drift Ratio (%)	Reduction of Dominant Frequency	
					Starting Freq. (Hz)	Ending Freq. (Hz)
RCF6	White Noise	29	24	0.06	5.81	5.8
	TCU082	**622**	**750**	**1.35**	**5.87**	**2.87**
	White Noise	30	15	0.04	3.24	3.14
RCF2	White Noise	27	41	0.02	6.2	6.02
	TCU082	**815**	**1241**	**2.43**	**6.05**	**2.72**
	White Noise	30	28	0.05	3.06	2.85
RCF4	White Noise	29	46	0.03	5.68	5.68
	TCU082	**1157**	**1305**	**3.29**	**5.6**	**2.49**
	White Noise	32	25	0.06	2.67	2.61
RCF3	White Noise	24	40	0.04	5.83	5.78
	TCU082	**1287**	**1216**	**4.46**	**5.68**	**2.06**
	White Noise	35	25	0.06	2.24	2.32

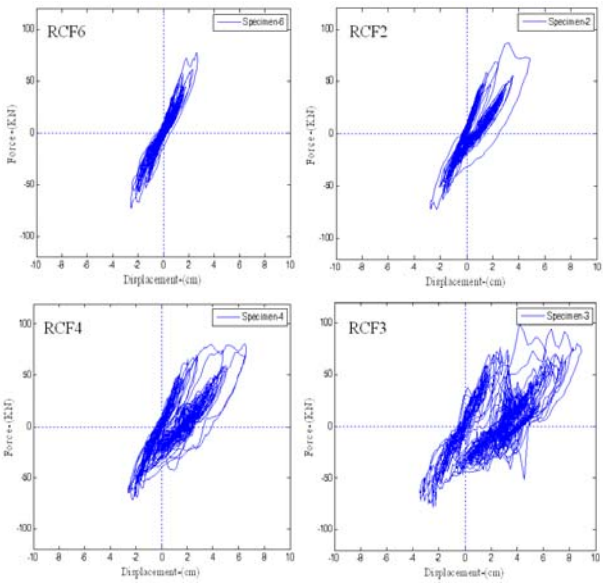

Figure 3: Inter-story load-displacement hysteretic diagram of the four frame structures under different excitation level.

3. SIGNAL-BASED NONLINEAR IDENTIFICATION

The observed load-displacement hysteresis curves and the maximum inter-story drift ratios of the four test specimens clearly show the structural nonlinearity that is caused by the decrease in stiffness of the structures, and the consequent change in their dynamic responses (inter-story drift). To detect damage to the RC frame, signal-based identification can be conducted. Besides, the benefit of the nonlinear effect is that it amplifies the damage-sensitive features of the measured data. Therefore, damage-related features can also be identified. In this section, several nonlinear indices are extracted from the response measurements. The degree of nonlinearity that is induced in these specimens by various levels of base excitation will be identified.

3.1 Linearity Check

Observing the time-varying natural frequency of the system and damping ratio of the equivalent linear single-degree-of-freedom dynamic system yields the nonlinearity

of the system. The identified time-varying system dominant frequency can provide information of the system linearity. *Figure 4* plots the fundamental natural frequency of the identified time-varying system. *Table 2* also presents the changes of the estimated natural frequency of the system estimated using the equivalent linear system before and after the significant excitation (at t=28.0 s and t=95.0 s) for each specimen. The variations in the natural frequency with time and the level of excitation are obvious. It shows that all these structural systems behave nonlinear during ground excitation.

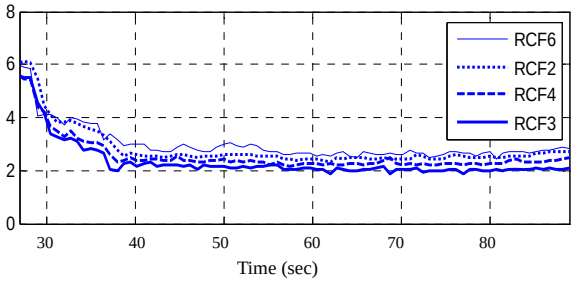

Figure 4: Identified time-varying model frequency of the four frames using equivalent linear model.

3.2 Estimation of Residual Deformation

Yielding of a reinforced concrete structure can cause a structure to behave in a nonlinear manner, and yielding is accompanied by permanent deformation. Singular spectrum analysis (SSA) is applied to the recorded displacement data of the specimen under an earthquake excitation to estimate the residual and the permanent deformations of the specimen from the seismic response data of the frame structure [4]. SSA is employed as an alternative to traditional digital filtering. SSA is a novel non-parametric approach that is based on the principles of multivariate statistics. The original time series is decomposed into various additive time series, each of which can be easily identified as being part of either the modulated signal or the random noise. The method begins by generating a Hankel matrix from the original time series by sliding a window that is shorter than the original series. This matrix is decomposed by SVD into many elementary matrices with decreasing norm. *Figure 5* presents the estimated time-dependent residual deformation of the four tested frames. Significant residual deformation is observed under strong ground excitation such as exhibited by the RCF3 specimen.

3.3 Estimation of Instantaneous Frequency

Estimation of the instantaneous frequency from the acceleration response data of these four specimens is listed as follows:

a. Apply the wavelet packet transform on the response data where the decomposition level equals to 9 and the mother wavelet is using 'bior6.8'. Extract the components whose energy ratios are lager than 0.1% for further analysis.
b. Apply Hilbert transform to each of the extracted component and derive the instantaneous modulus $A_{j,t}$ and instantaneous phase (unwrapped).
c. Introduce the numerical differentiation technique to the component instantaneous phase to derive the component instantaneous frequency $\omega_{j,t}$.
d. The instantaneous frequency can be estimated from the following equation:

$$f(k)/2\pi = \sum_{j=1}^{J_0} A_{j,k}^2 \omega_{j,k} / \sum_{j=1}^{J_0} A_{j,k}^2 \qquad (1)$$

e. To eliminate the fluctuations, one can apply the simple

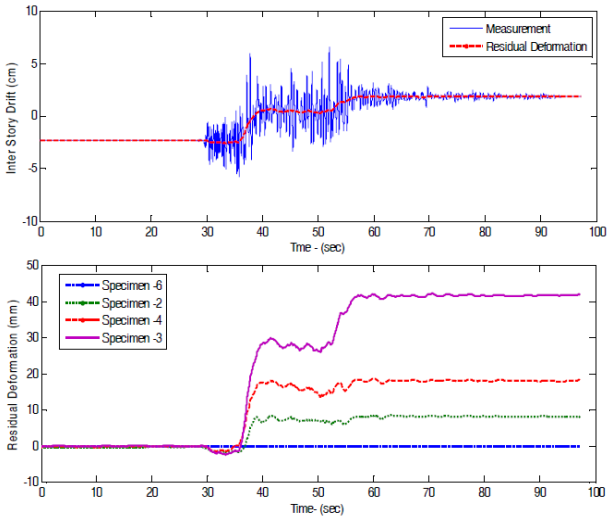

Figure 5: Identified residual deformation from the displacement response of the four specimens (RCF6, RCF2, RCF4, and RCF3).

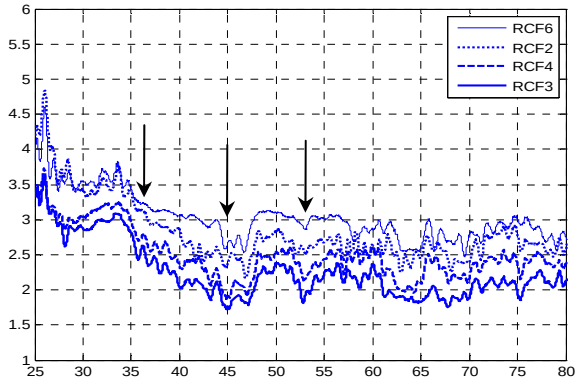

Figure 6: Estimated instantaneous frequency from the seismic acceleration response data of four specimens.

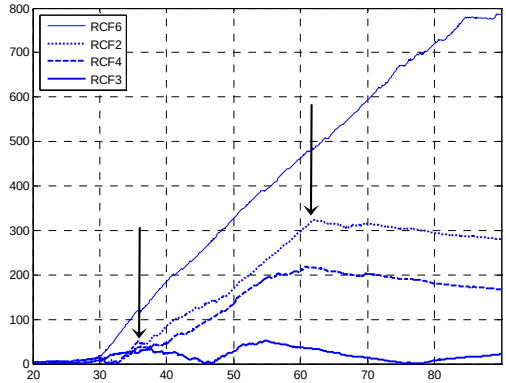

Figure 7: Estimated instantaneous phase difference between input and response displacement records.

moving average smoothing algorithm. Here the window length of 0.5 second is used.

From the plot of instantaneous frequency, as shown in *Figure 6*, it is evident that there is a descending of frequency during 30 to 40 second for all four specimens which indicate obvious stiffness degradation. It is also noted that some drops occur at 45 second and 53 second for all specimens. These drops coincide with the peaks in inter-story drift ratio which may be related to the occurrence of strength

deterioration. Similar approach was also applied to the recorded displacement data. The unwrapped instantaneous phase of input (i.e. base displacement) and output (i.e. relative displacement) of all four specimens is shown in *Figure 7*. The figure shows that the phase difference of RCF3 is the lowest, which is the specimen subjected to severest damage. The more severe damage the more stiffness degradation and cracks may occur in the structural member, which may cause the reflection and refraction of propagation waves between the base excitations and the response.

3.4 Distribution of WPT Component Energy

Since using the wavelet packet analysis of the signal can be regarded as a sifting bank with adjustable time and frequency resolution, a sifting process that is based on wavelet packet decomposition (WPT) to analyze a non-stationary signal can be formulated and used for monitoring structural health. In the j-th level WPT decomposition, the distribution of component energy of each decomposed signal can be generated with respect to its central frequency. The distribution of the wavelet packet component energy of the decomposed response data can be taken as the distribution of energy that is stored in the frequency band that is determined by the wavelet function. The time-frequency characteristics of the response signals can be used to study the effect of system nonlinearity of the system. The distribution of component energy obtained from the acceleration response data of the four specimens can be used not only to extract the dominant frequency component of the response signal but also to determine the distribution of component energy in the frequency domain. Based on the wavelet decomposition of the acceleration responses of these four specimens, *Figure 8* plots the percentage distribution of wavelet component energy. According to the date, the distribution of the dominant energy of the wavelet components from the specimen subjected to a stronger excitation level is shifted to lower frequency.

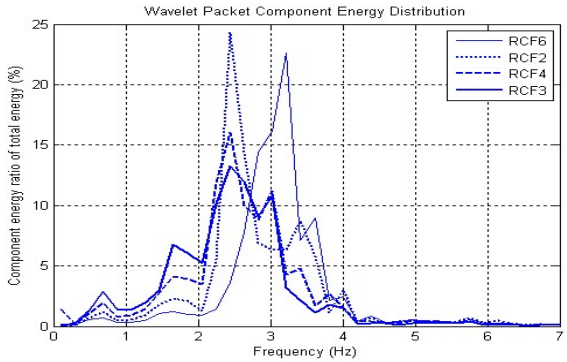

Figure 8: Distribution of component energy from wavelet packet transform of the acceleration response of the four specimens.

4. MODEL-BASED NONLINEAR IDENTIFICATION

To quantify the damage of the structural system, a physical model was employed to determine the load-displacement relationship, to elucidate the degradation of stiffness and strength behavior, the relationship to the severity of damage and the effect of nonlinearity. In this work, the Bouc-Wen hysteretic model is adopted to capture analytically a range of shapes of hysteretic cycles that match the behavior of a wide range of nonlinear systems [5]. The single-story reinforced concrete frame, as shown in Figure 9, is modeled as a single degree-of-freedom system with viscous damping and a hysteretic restoring force that is given by Bouc-Wen model, and is governed by the following equation;

$$\ddot{u} + 2\xi\omega_o\dot{u} + \alpha\omega_o^{\,2}u + (1-\alpha)\omega_o^{\,2}z = f(t) \qquad (2)$$

where u is the displacement; ξ is the damping ratio, and ω_o is the natural frequency that is associated with small, non-yielding displacements. The external excitation $f(t)$ is mass-normalized. The rigidity ratio α is employed to separate the restoring force into a linear component and a hysteretic component. The hysteretic component exhibits a hysteretic displacement z, which is related to the displacement u by a constitutive law of the form:

$$\dot{z} = h(z)\frac{\dot{u} - \nu(\beta|\dot{u}||z|^{n-1}z + \gamma\dot{u}|z|^n}{\eta} \qquad (3)$$

where the unspecified parameters $\beta, \gamma, n, \nu, and\ \eta$ are called loop parameters, and $h(z)$ is the pinching function, which specifies the pinching hysteretic loop. These loop parameters govern the shape and the magnitude of a hysteresis loop. Generally, β and γ affect the size, while n influences the smoothness of the hysteresis loops. Strength and stiffness degradation can be modeled by allowing the parameters ν and η to vary as a function of the duration and the amplitude of the response. A convenient measure of the combined effect of the duration and response amplitude is the total energy that is dissipated via hysteresis as the system evolves. As explained by Baber and Wen [6], two physically realistic functions, the stiffness degradation function $\eta(\varepsilon)$ and the strength degradation function $\nu(\varepsilon)$, can be obtained by setting

$$\begin{aligned} \eta(\varepsilon) &= 1.0 + \delta_\eta\varepsilon \\ \nu(\varepsilon) &= 1.0 + \delta_\nu\varepsilon \end{aligned} \qquad (4)$$

where δ_η and δ_ν are non-negative parameters that are known as stiffness and strength degradation ratios, respectively. The pinching function is expressed as

$$h(z) = 1.0 - \xi_1 \exp[-z\cdot\mathrm{sgn}(\dot{u}) - q\cdot z_u)^2 / \xi_2^2] \qquad (5)$$

and

$$\xi_1(\varepsilon) = \xi_s\left[1 - e^{(-p\varepsilon)}\right]$$

$$\xi_2(\varepsilon) = (\psi + \delta_\psi\varepsilon)(\lambda + \xi_1)$$

A total of 13 parameters are employed to control the hysteretic model:

$$\{A,\ \alpha,\ \beta,\ \gamma,\ n,\ \delta_\eta,\ \delta_\nu,\ \xi_\xi,\ p,\ q,\ \psi,\ \delta_\psi,\ \lambda\}$$

In this model, four parameters $\{\alpha, \beta, \gamma, and\ n\}$ determine the shape of the hysteretic model; two parameters $\{\delta_\eta\ and\ \delta_\nu\}$ control the system degradation, and six parameters $\{\xi_\xi,\ p,\ q,\ \psi, \chi_\psi\ and\ \lambda\}$ control the pinching phenomenon.

In this study, the differential evolutionary method, proposed by Storn and Pierce [7] and Kyprianou *et al.* [8], was employed to evaluate time-dependent model parameters. The advantage of using the differential evolutionary method is that it allows a direct search over a continuous parameter space without the need to estimate any derivative. Based on the sensitivity study, a two-stage parameter evaluation scheme was proposed. In the first stage, the non-sensitive parameters, such as $\{p, \delta_\psi, \delta_\theta\}$, are assumed to be fixed, and then the remaining parameters $\{\alpha, \beta, \gamma, n, \delta_\eta, \xi_s, q, \psi, \lambda\}$ are evaluated. In this study, parameter A is set to A=1.0 without affecting the estimates of the other parameters [9]. The second stage uses all of the parameters as an initial guess, including parameters estimated from stage one, to evaluate the optimal value of all 12 parameters.

To quantify the damage to these four RC frames, the hysteretic model parameters were evaluated from the

load-displacement data of the RC frame. The original rough data were not used; rather, the SSA method was applied to filter out the high-frequency components (>20.0Hz) of the recorded acceleration response, to yield a smooth load-displacement hysteretic loop. The smoothed load-displacement curve is used to evaluate the hysteretic model parameters. Based on the shaking table test data for the four specimens, *Figure 9* plots the time varying strength factor $\eta(\varepsilon)$, the stiffness factor $\nu(\varepsilon)$) and the pinching factor ζ_1. Notably, the stiffness and strength parameters, δ_η and δ_ν, respectively, are not plotted: rather, the stiffness factor and the strength factor that are functions of the hysteretic energy **ε,** are plotted. Figure 9 indicates that the times when the stiffness factor began to increase (at t=30.0 s) and at its maximum value (t=37.5 s).

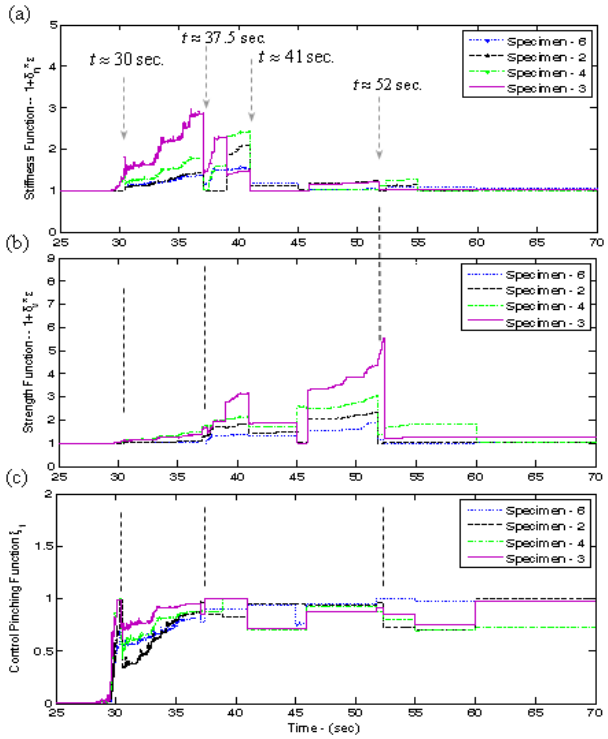

Figure 9: Estimated time-varying damage index, stiffness and strength factors, and pinching factor from four specimens (a) Park & Ang damage index; (b) Stiffness function $\eta(\varepsilon)$; (c) Strength function $\nu(\varepsilon)$; (d) Pinching factor ξ_1.

5. DAMAGE EVALUATION

To evaluate the damage severity of these four specimens under different intensity level of ground excitation from shaking table, first, the inter-story drift ratio of these four specimens are plotted, as shown in Figure 10. This figure will serve as the reference to discuss the damage evaluation using different nonlinear indicators.

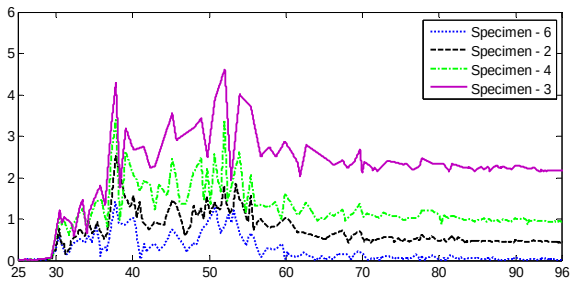

Figure 10: Inter-story drift ratio of the four specimens.

First, comparison between the inter-story drift and the damage index is made. The damage index of Park and Ang is used. The Park and Ang damage index DI_g is defined as [10, 11]:

$$DI_g = \frac{\delta}{\delta_u} + \beta \frac{E_H}{\delta_u F_y} \qquad (6)$$

where δ_u is the ultimate displacement; F_y is the yield force; E_H is the hysteretic energy of the structural element and β is a parameter. Both δ_u and F_y are estimated by performing cyclic loading test of specimen RCF1 (the reference specimen). *Figure 11* plots the damage index of these four specimens subjected to different level of ground excitation. Comparison the damage index and the inter-story drift ratio, at $t = 30.0$ sec, $t = 37.5$ sec and $t = 52$ sec, considerable increases in the damage index occurred which consistent with a large inter-story drift ratio.

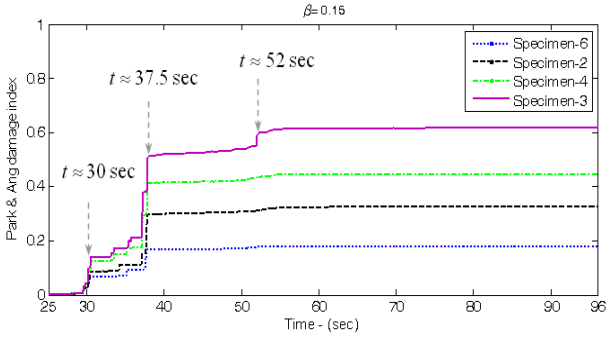

Figure 11: Estimated time-dependent damage index.

To identify changes some nonlinear index functions can be employed to identify changes that are indicative of the onset of nonlinear system response, directly from only the response measurements without the input data. The following two feature extraction methods are applied to the floor acceleration response data of the four test structures: the Level-1 detail component of Discrete Wavelet Transform (DWT) and the instantaneous phase and phase change. Comparison with the inter-story drift ratio and the identified stiffness function and strength function was made, as shown in *Figure 12*. It is observed that the spikes in the DWT are in consistent with the rate of change of stiffness and strength functions where large inter-story drift ratio was observed. Figure 12 indicates that the times when the stiffness factor began to increase (at t=30.0 s) and at its maximum value (t=37.5 s) both match the times of the singularities that were revealed by the Level-1 detail component of DWT. Importantly, the first significant inter-story drift (at t=37.5 sec) occurred at when the stiffness factor was at its maximum. After the stiffness factor reached its maximum, the second significant inter-story drift (at t=51.5 s) reduced the strength of the structural system. *Figure 13* plots the relationship among the rate of change in the stiffness functions (ϕ) in the first stage of excitation (from t=30.0 s to t=37.5 s) for the four structures, which correspond to various inter-story drift ratios. This figure reveals that a larger value of the stiffness function corresponds to cases of severe base excitation such as experienced by specimen RCF3. *Figure 14* plot the relationship of frequency degradation ratio and the rate of change of stiffness factor in relating to the damage index. The rate of change of stiffness factor is from 0.05 to 0.25 and the frequency degrading ratio is from 0.18 to 0.24 were observed for excitation level from 0.622 g to 1.287 g.

6. CONCLUSIONS

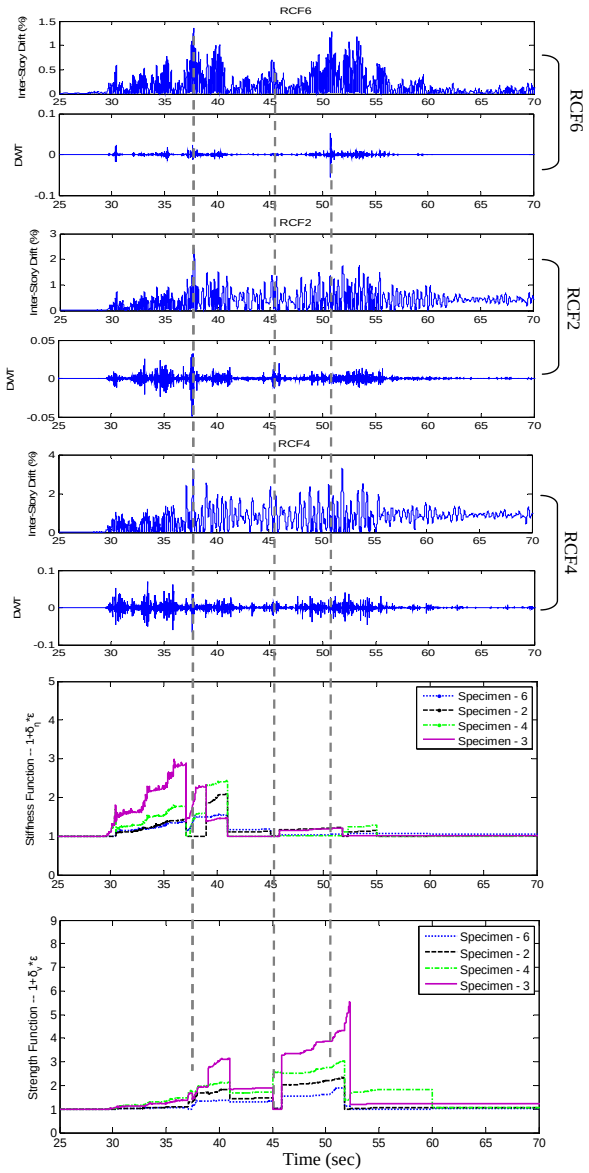

Figure 12: Comparison on Inter-story drift ratio, Level-1 detail component and identified strength and stiffness function using seismic response data from specimens RCF6, RCF2 and RCF3.

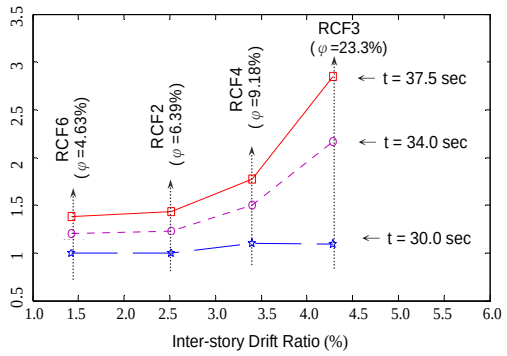

Figure 13: Plot of stiffness function with respect to the inter-story drift ratio for the four specimens at time t=30.0 s, t=34.0 s and t=37.5 s.

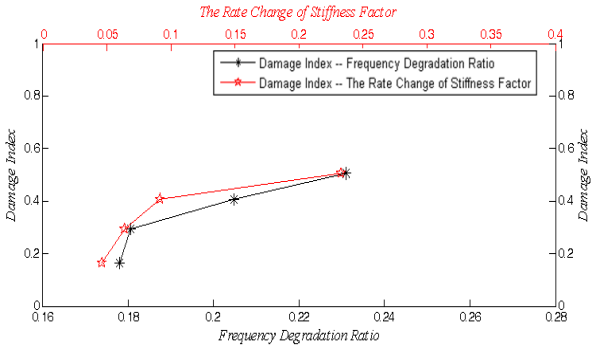

Figure 14: The relationship between frequency degradation ratio and the rate of change of stiffness factor in relating the damage index (from the shaking table test of four specimens).

The performance and safety of reinforced concrete structures under severe earthquake loading depend on their nonlinear hysteretic behavior. Such a structural system exhibits significant energy dissipation and tends to exhibit a large hysteresis loop with strength and stiffness degradation as well as pinching. In this study a total of four reinforced concrete frames, designed with the same dimensions and the same seismic design code, are individually subjected to different degrees of ground excitation in shaking table tests. Their response data are used to determine the pattern of damage to a reinforced concrete structure with respect to the degree of ground shaking. Both identification of system nonlinearities and feature extraction are developed to investigate the physical parameters that govern the degradation of hysteretic behavior and the severity of damage of a reinforced concrete structure. First, the nonlinearity of the system under earthquake excitation is studied by examining the time-varying dominant frequency of the equivalent linear system and the component energy distribution of the response. Then, nonlinear indices, such as the instantaneous phase and phase change and singular spectral analysis on residual deformation are also calculated to enable the time of significant damage. To quantify the degree of nonlinearity or severity of damage, the general Bouc-Wen hysteretic model is employed to evaluate the physical parameters, including stiffness degradation, strength deterioration and hysteresis behavior of the reinforced concrete frame. The relationship among the damage index, the inter-story drift ratio, the singularities of the nonlinear indices and the evaluated stiffness and strength degradation function is examined.

The seismic response data of these specimens support the following conclusions.

1. The distribution of the wavelet component energy in the response, and the time-varying dominant frequency of the equivalent linear system can be employed to detect the nonlinearity of the system. The permanent deformation of the structure can be estimated by singular spectrum analysis.
2. To determine the time of significant inter-story drift from only acceleration response data, the Holder exponent and Level-1 detail component of DWT can be adopted.
3. To quantify the degree of stiffness degradation, a theoretical model, such as the modified Bouc-Wen hysteretic model with stiffness and strength degradation, must be used, and the system identification approach must be utilized to evaluate the model parameters.
4. The analysis of the shaking table test data for the four RC specimens reveals that under the earthquake excitation, the stiffness of the structure was degraded first, and then the strength deteriorated. Experimental results indicate that the characteristics of the model are consistent with the singularities determined from the nonlinear indices.

Acknowledgements:

The authors would like to thank the National Science Council of the Republic of China, Taiwan (Contract No. NSC96-2221-E-002-121-MY3) and the Research Program of Excellency of National Taiwan University (Contract No. 97R0066-06) for financially supporting of this research. Experimental support from National Center for Research on Earthquake Engineering (Taiwan) was also acknowledged.

References:

1. Wen, Y.K., "Method of random vibration of hysteretic systems,", J. Eng. Mech. ASCE 102 (2), 1976, p. 249–263.
2. Doebling, S.W., Farrrar, C.R. and Prime, M.B, "A summary Review of Vibration-based Damage Identification Methods," shock Vibration digest, 30(2), 1998, p:91-105.
3. Charles R. Farrar, *et al.*, "Nonlinear system identification for damage detection," Los Alamos National Laboratory, Technical Report, LA-14355, November 2007.
4. Alonso, F.J., J.M. Del Castillo, and P. Pintado, "Application of singular spectrum analysis to the smoothing of raw kinematic signals," Journal of Biomechanics, 2005. **38**(5): p. 1085-1092.
5. Kunnath, Shashi K., J. B. Mander and L. Fang, "Parameter Identification for Degrading and Pinched Hysteretic Structural Concrete System," J. of Structures, ASCE, Vol. 19, No. 3, 1997, p.224-232.
6. Baber, T. T. and Y. K. Wen, "Random Vibration Hysteretic, Degrading Systems," , J Eng Mech Div, ASCE, 107:6 (1981), 1069-1087.
7. Storn, R. and K. Price, "Differential Evolution - A Simple and Efficient Heuristic for Global Optimization over Continuous Spaces," Journal of Global Optimization, 11:4 1997, p.341-359.
8. Kyprianou, A. and K. Worden, "Identification of Hysteretic Systems Using the Differential Evolution Algorithm,", J. of Sound & Vibration, 248(2), 2001, p: 289-314
9. Ma, F., H. Zhang, A. Bockstedte, G. C. Foliente, and P. Paevere, "Parameter analysis of the differential model of hysteresis," Journal of Applied Mechanics, Transactions ASME, 71:3, 2004,p: 342-349.
10. Park, Y.-J. and A. H. S. Ang, "Mechanistic seismic damage model for reinforced concrete," Journal of Structural Engineering, 111:4 (1985), 722-739.
11. Park, Y.-J., A. H. S. Ang, and Y. K. Wen, "Seismic damage analysis of reinforced concrete buildings," Journal of Structural Engineering, 111:4 (1985), 740-757.

JOINT CONFERENCE PROCEEDINGS
7th International Conference on Urban Earthquake Engineering (7CUEE) &
5th International Conference on Earthquake Engineering (5ICEE)
March 3-5, 2010, Tokyo Institute of Technology, Tokyo, Japan

EARTHQUAKE RESPONSE EVALUATION USING EQUIVALENT SDOF SYSTEM FOR SINGLE-STORY ASYMMETRIC BUILDINGS

Hiroshi Kutamoto[1)]

1) Professor, Department of Architectural Engineering, Osaka University, Japan
kuramoto@arch.eng.osaka-u.ac.jp

Abstract: This paper shows two methods of reducing from a single-story asymmetric building under uni-directional earthquake motion to the equivalent single degree of freedom (ESDOF) system to improve the capacity spectrum method used in the Calculation of Response and Limit Strength provided in the Building Standard Law Enforcement Order of Japan. One is the static reduction method with mode-adaptive pushover analysis and the other is the dynamic reduction method using modal decomposition procedure together with earthquake response analysis. Applying both methods to four types of single-story RC buildings with different eccentricities, the validity of the methods and the earthquake response characteristics of the ESDOF systems are examined.

1. INTRODUCTION

Most seismic provisions concerning torsional vibrations of buildings at home and abroad, including the Building Standard Law Enforcement Order of Japan (the ultimate strength design method) enforced in 1981 (BCJ 1994, Kuramoto 2006a), are based on elastic torsional vibrations caused by eccentricities in the stiffness of members. Even when the Calculation for Response and Limit Strength (CRLS; Kuramoto 2006a) has been adopted, which was enforced in 2000 as a performance-based structural calculation procedure and wherein a procedure that also takes into account the elasto-plastic response in evaluating the maximum earthquake response via reduction of the building structure into an equivalent single degree of freedom (ESDOF) system, this issue for eccentric buildings has been dealt with by multiplying the load applied within the pushover analysis by the eccentricity factor F_e which has been used in the ultimate strength design method (BCJ 1994) for the convenience of structural calculations. With such a method, it would be hard to say that a reduction to a proper ESDOF system is possible for cases such as those involving yielding in the building. Viewed in this light, therefore, the earthquake response evaluation procedure is still not properly established for eccentric buildings

On the other hand, with the revision of the Building Standard Law in 1981, studies on nonlinear torsional response of buildings with the aim of improving these eccentricity provisions has been conducted by numerous researchers from the mid-1980s until the early 1990s in Japan (for example, Ozaki et al. 1986, Yamasaki 1986, Azuhata et al.1991). And more recently, researches on earthquake response evaluation methods for eccentric buildings have also been undertaken, with the application to a seismic evaluation method that is performance-based, in the same manner as that of the CRLS (Fujii et al. 2003 and 2005, Kabeyasawa 2005,).

The author has also continuously undertaken studies for the past several years to improve the performance-based seismic evaluation procedure in the CRLS (Kuramoto et al. 2000, Kuramoto and Matsumoto 2002 and 2004, Kuramoto 2006b and 2007, Kuramoto and Akita 2008, Akita and Kuramoto 2008). In these studies, two ESDOF system reducing methods have been proposed for multi-story buildings with no eccentricities. One is the static reduction method using pushover analysis and another is the dynamic reduction method using time history earthquake response analysis and modal decomposition procedure. Moreover, the author has suggested not only the static and dynamic reduction methods but also a nonlinear mode-adaptive pushover analysis method (hereafter referred to as MAP analysis), which allows for the application of an elasto-plastic first-mode loading pattern that corresponds to the degree of plastic yielding of the building.

In this study, the static and dynamic reduction methods and MAP analysis method are proposed for single-story asymmetric buildings, as a fundamental research aimed to the improvement of the seismic performance evaluation method based on the CRLS for asymmetric buildings. In addition, the proposed method of analysis and response evaluation procedure will be compared to the time history earthquake response analysis results of four types of single-story reinforced concrete (RC) buildings with uniaxial or biaxial eccentricities, in order to verify their validity and to investigate the earthquake response characteristics of ESDOF systems for single-story asymmetric buildings.

2. *ESDOF* SYSTEM REDUCTION

2.1 Static Reduction

For a single-story biaxially asymmetric building subjected to an earthquake motion input in one direction, the three oscillations in the x-direction, y-direction and z-rotation axis are coupled as shown in Fig. 1(a). Here, the counterclockwise direction is positive for the z-rotation axis since the figure was drawn following the right-handed coordinate system. If the seismic input is in the x-direction alone, then the equation of vibration for the coupled x-direction, y-direction and z-rotation is expressed by the following equation.

$$[M]\{\ddot{\delta}\}+[C]\{\dot{\delta}\}+[K]\{\delta\}=-[M]\{1\}\ddot{x}_0 \tag{1}$$

where, $\{\delta\}$ =displacement vector (= $\{\delta_x,\ \delta_y,\ \delta_z\}^T$), $[M]$ =mass matrix, $[C]$ =damping matrix, $[K]$ =stiffness matrix, $\ddot{x}_0$ =ground acceleration in the x-direction and $\{1\}$ =ground motion distribution vector ($=\{1,\ 0,\ 0\}^T$). Moreover, the displacement δ_z expresses the displacement taken radius of gyration i away from the center of gravity, as shown in Fig. 1, and has a relationship with rotation angle θ given by the following equation.

$$\delta_z = i\theta \tag{2}$$

Now, the solution to Eq. (1) may be written as follows through modal superposition.

$$\{\delta\}=\sum_{s=1}^{3} {}_s\beta\{{}_s u\}\,{}_s S_d \tag{3}$$

where, ${}_s\beta$, $\{{}_s u\}$ and ${}_s S_d$ are the modal participation factor, mode vector and displacement response corresponding to the s-th mode, and in which ${}_s\beta$ and $\{{}_s u\}$ are defined by Eqs. (4) and (5), respectively.

$${}_s\beta=\frac{\{{}_s u\}^T[M]\{1\}}{\{{}_s u\}^T[M]\{{}_s u\}}=\frac{{}_s u_x}{{}_s u_x^2+{}_s u_y^2+{}_s u_z^2} \tag{4}$$

$$\{{}_s u\}=\{{}_s u_x,\ {}_s u_y,\ {}_s u_z\}^T \tag{5}$$

From Eq. (3), the first-mode component of the displacement vector $\{{}_1\delta\}$ may be given as

$$\{{}_1\delta\}={}_1\beta\{{}_1 u\}\,{}_1 S_d \tag{6}$$

Hence, the first-mode vector $\{{}_1 u\}$ becomes

$$\{{}_1 u\}=\frac{\{{}_1\delta\}}{{}_1\beta\cdot{}_1 S_d} \tag{7}$$

and considering that $\{{}_1\delta\}=\{{}_1\delta_x,\ {}_1\delta_y,\ {}_1\delta_z\}^T$ and $\{{}_1 u\}=\{{}_1 u_x,\ {}_1 u_y,\ {}_1 u_z\}^T$, the displacement response of the ESDOF system ${}_1 S_d$ may be given by Eq. (8), based on Eq. (4).

$${}_1 S_d=\frac{{}_1\delta_x^{\,2}+{}_1\delta_y^{\,2}+{}_1\delta_z^{\,2}}{{}_1\delta_x} \tag{8}$$

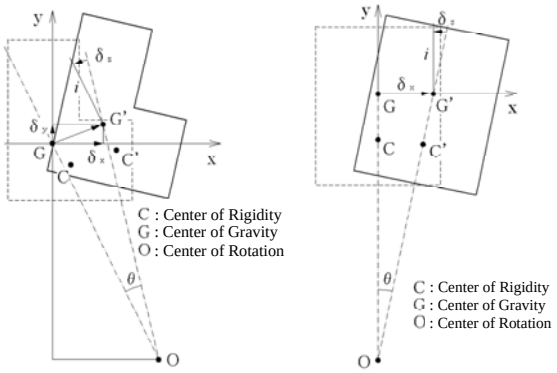

(a) Biaxial Asymmetry **(b) Uniaxial Asymmetry**

Figure 1 Schematic View of Torsional Behavior

Meanwhile, if the restoring force vector $\{R\}$ is

$$\{R\}=[C]\{\dot{\delta}\}+[K]\{\delta\} \tag{9}$$

then Eq. (1) can be rewritten as

$$[M]\{\ddot{\delta}\}+\{R\}=-[M]\{1\}\ddot{x}_0 \tag{10}$$

and if Eq. (3) is substituted into Eq. (10), ${}_1\beta\{{}_1 u\}^T$ is multiplied beforehand and modal orthogonality is considered, then the following equation is obtained as the equation of vibration for the ESDOF system.

$${}_1\overline{M}\cdot{}_1\ddot{S}_d+{}_1 R_{eq}=-{}_1\overline{M}\cdot\ddot{x}_0 \tag{11}$$

where, ${}_1\overline{M}$ is the first-mode equivalent mass which, if the mass of the single-story asymmetric building is given as m , may be obtained by the following equation from Eqs. (4) and (7).

$${}_1\overline{M}=m\cdot{}_1\beta\cdot{}_1 u_x=\frac{m\cdot{}_1\delta_x^{\,2}}{{}_1\delta_x^{\,2}+{}_1\delta_y^{\,2}+{}_1\delta_z^{\,2}} \tag{12}$$

In addition, ${}_1 R_{eq}$ is the equivalent restoring force for the first-mode of vibration, which has the following relationship if the orthogonality of the modal vector is considered.

$${}_1 R_{eq}={}_1\beta\{{}_1 u\}^T\{R\}={}_1\beta\{{}_1 u\}^T\{Q\}={}_1\beta\{{}_1 u\}^T\{{}_1 Q\}\quad\left(={}_1\overline{Q}\right) \tag{13}$$

where, $\{Q\}=\{Q_x,\ Q_y,\ Q_z\}^T$ and is the shear force vector corresponding to the displacement vector $\{\delta\}$. At the same time, $\{{}_1 Q\}=\{{}_1 Q_x,\ {}_1 Q_y,\ {}_1 Q_z\}^T$ and expresses the first-mode component of $\{Q\}$. Moreover, ${}_1\overline{Q}$ is the first-mode equivalent shear force (i.e. representative shear force). Using the acceleration response of the ESDOF system ${}_1 S_a$, Eq. (11) becomes

$${}_1 R_{eq}=-{}_1\overline{M}\left({}_1\ddot{S}_d+\ddot{x}_0\right)={}_1\overline{M}\cdot{}_1 S_a \tag{14}$$

Thus, from Eqs. (12) to (14), the acceleration response of the ESDOF system ${}_1 S_a$ may be given by the following equation.

$$ {}_1S_a = \frac{{}_1R_{eq}}{{}_1\overline{M}} = \frac{{}_1\beta\{{}_1u\}^T\{{}_1Q\}}{m\cdot{}_1\beta\cdot{}_1u_x} \tag{15} $$

Meanwhile, if M_z is the moment about the center of gravity, then the relationship in the following equation is true.

$$ M_z = -I\ddot{\theta} \tag{16} $$

where, I is the rotational inertia given by the relationship in Eq. (17).

$$ I = m\cdot i^2 \tag{17} $$

Furthermore, the following can be obtained from Eqs. (2), (16) and (17).

$$ M_z = -m\cdot\ddot{\delta}_z\cdot i \tag{18} $$

where, $m\cdot\ddot{\delta}_z$ is the load due to rotational inertia and is related to Q_z as follows.

$$ m\cdot\ddot{\delta}_z = -Q_z \tag{19} $$

Thus, if the first-mode component of M_z is ${}_1M_z$, and Eqs. (18) and (19) are considered, then

$$ {}_1Q_z = {}_1M_z/i \tag{20} $$

and the following expression may be obtained from Eqs. (7), (15) and (20).

$$ {}_1S_a = \frac{{}_1\delta_x\cdot{}_1Q_x + {}_1\delta_y\cdot{}_1Q_y + {}_1\delta_z\cdot{}_1M_z/i}{m\cdot{}_1\delta_x} \quad \left(= \frac{{}_1\overline{Q}}{{}_1\overline{M}}\right) \tag{21} $$

By using Eqs. (8) and (21), the capacity spectrum (${}_1S_a - {}_1S_d$ curve) can be plotted using the shear force and displacement in the x- and y-directions, ${}_1Q_x$, ${}_1\delta_x$ and ${}_1Q_y$, ${}_1\delta_y$, as well as the displacement in the z-rotation axis ${}_1\delta_z$ and moment about the center of gravity ${}_1M_z$, all of which were obtained at every step of the three-dimensional pushover analysis of the single-story biaxially asymmetric building.

For uniaxial asymmetry, the ${}_1S_d$ and ${}_1S_a$ of the ESDOF system may be obtained by the following equations, in which the y-component is omitted from Eqs. (8) and (21), since the y-direction vibrates independently as shown in Fig. 1(b).

$$ {}_1S_d = \frac{{}_1\delta_x{}^2 + {}_1\delta_z{}^2}{{}_1\delta_x} \tag{22} $$

$$ {}_1S_a = \frac{{}_1\delta_x\cdot{}_1Q_x + {}_1\delta_z\cdot{}_1M_z/i}{m\cdot{}_1\delta_x} \quad \left(= \frac{{}_1\overline{Q}}{{}_1\overline{M}}\right) \tag{23} $$

2.2 Dynamic Reduction

Dynamic reduction for a single-story biaxially asymmetric building subjected to a uni-directional earthquake motion input may be performed by assigning a reference modal system, similar to that for multi-story buildings described in Refs. (Kuramoto 2006b and 2007). Specifically, using the MAP analysis to be discussed later in Section 3, the load step in the pushover analysis results that corresponds to the maximum displacement response of the ESDOF system is determined, of which the ESDOF system is reduced by means of the to-be-discussed Eqs. (27) and (28 are the results of earthquake response analysis. The reference modal system is then obtained by evaluating the first-mode participation function at this step through Eq. (24).

$$ {}_1\beta\{{}_1u\} = \frac{{}_1\delta_{x\max}}{{}_1\delta_{x\max}{}^2 + {}_1\delta_{y\max}{}^2 + {}_1\delta_{z\max}{}^2}\{{}_1\delta_{\max}\} \tag{24} $$

where, $\{{}_1\delta_{\max}\}$ $(=\{{}_1\delta_{x\max}, {}_1\delta_{y\max}, {}_1\delta_{z\max}\}^T)$ expresses each of the displacement at the load step of the MAP analysis wherein ${}_1\beta\{{}_1u\}$ is adopted. Hence, since the ESDOF system has not been determined yet initially, the ${}_1\beta\{{}_1u\}$ is assumed from the load step in the MAP analysis results corresponding to the maximum displacement response of the single-story asymmetric system, reduction is performed, and the same steps are repeated once or twice to determine the actual ${}_1\beta\{{}_1u\}$ (Kuramoto 2006b).

Meanwhile, similar to Eq. (6), the following relationship holds between the first-mode component of the displacement vector at time t $\{{}_1\delta(t)\}$ and the representative displacement response ${}_1S_d(t)$.

$$ \{{}_1\delta(t)\} = {}_1\beta\{{}_1u\}\,{}_1S_d(t) \tag{25} $$

Multiplying both sides of Eq. (25) by ${}_1\beta\{{}_1u\}^T[M]$ from the left and transposing,

$$ {}_1S_d(t) = \frac{{}_1\beta\{{}_1u\}^T[M]\{{}_1\delta(t)\}}{{}_1\beta\{{}_1u\}^T[M]\,{}_1\beta\{{}_1u\}} = \frac{{}_1\beta\{{}_1u\}^T\{{}_1\delta(t)\}}{{}_1\beta\cdot{}_1u_x} \tag{26} $$

is obtained. Here, if orthogonality is taken into account, then ${}_1\beta\{{}_1u\}^T\{{}_1\delta(t)\} = {}_1\beta\{{}_1u\}^T\{\delta(t)\}$ and the following equation is obtained.

$$ {}_1S_d(t) = \frac{{}_1\beta\{{}_1u\}^T\{\delta(t)\}}{{}_1\beta\cdot{}_1u_x} \tag{27} $$

Moreover, the acceleration response ${}_1S_a(t)$ for the ESDOF system may be given by the following equation if the relationship in Eq. (15) and ${}_1\beta\{{}_1u\}^T\{{}_1Q(t)\} = {}_1\beta\{{}_1u\}^T\{Q(t)\}$ is considered.

$$ {}_1S_a(t) = \frac{{}_1\beta\{{}_1u\}^T\{Q(t)\}}{m\cdot{}_1\beta\cdot{}_1u_x} \tag{28} $$

where $\{Q(t)\} = \{Q_x(t),\ Q_y(t),\ Q_z(t)\}^T$. Therefore, dynamic reduction may be performed by means of Eqs. (27) and (28), using the modal participation function obtained from Eq. (24) and the $\{Q(t)\}$ and $\{\delta(t)\}$ which can be obtained from time history earthquake response analysis.

For uni-axial asymmetry systems, use Eq. (29), in which the y component is omitted from Eq. (24), as the reference modal system.

$$ {}_1\beta\{{}_1u\} = \frac{{}_1\delta_{x\max}}{{}_1\delta_{x\max}{}^2 + {}_1\delta_{z\max}{}^2}\{{}_1\delta_{\max}\} \tag{29} $$

3. MODE-ADAPTIVE PUSHOVER ANALYSIS

In the static reduction method described in Section 2.1, it is assumed that the mode-adaptive pushover analysis (MAP analysis) is performed using a load distribution that is always proportional to the first mode of vibration, regardless of whether the asymmetric building is in an elastic state or a plastic state (Kuramoto and Matsumoto 2004). For such type of analysis, methods proposed in recent years (Bracci et al. 1997, Chopra and Goel 2002) are intended for multi-story buildings with no eccentricities and involve performing the eigenvalue analysis at each load step of the pushover analysis, while studies looking into asymmetric buildings have not been found with the exception of Fujii et al. (2003). Fujii et al. implemented a MAP analysis for asymmetric buildings by carrying out the eigenvalue analysis based on the equivalent stiffness at each displacement step of the pushover analysis. At the same time, the authors have also proposed a method (Kuramoto and Matsumoto 2004) for multi-story buildings without eccentricities, which assigns a load distribution that is proportional to the elasto-plastic first-mode through the incremental load pattern at each load step of the pushover analysis. Hereinafter, this method proposed by the authors is extended to the MAP analysis for asymmetric buildings.

The first-mode load vector for a single-story biaxially asymmetric model $\{{}_1P\}$ ($=\{{}_1P_x,\ {}_1P_y,\ {}_1P_z\}^T$) may be given by the following equation.

$$ \{{}_1P\} = m\cdot{}_1\beta\{{}_1u\}_1S_a \tag{30} $$

If Eqs. (13) and (15) are taken into account, Eq. (30) may be expressed by the following equation.

$$ \{{}_1P\} = {}_1\beta\{{}_1u\}\frac{{}_1\overline{Q}}{{}_1\beta\cdot{}_1u_x} \tag{31} $$

In addition, if Eq. (7) is substituted into Eq. (31), then the following relationship is obtained.

$$ \{{}_1P\} = \{{}_1\delta\}\frac{{}_1\overline{Q}}{{}_1\delta_x} \tag{32} $$

Based on Eq. (32), if the load at k -th step of the pushover analysis is set using the following equation, the MAP analysis applicable to single-story biaxially eccentric buildings is made possible.

$$ \{{}_1P_k\} = \{{}_1\delta_{k-1}\}\frac{{}_1\overline{Q}_{k-1} + d\,{}_1\overline{Q}_k}{{}_1\delta_{x,k-1}} \tag{33} $$

And considering that the load about the z-rotation axis ${}_1P_z$ and the moment about the center of gravity ${}_1M_z$ have the relationship ${}_1M_z = {}_1P_z\cdot i$, it may also be expressed as follows.

$$ {}_1M_{z,k} = i\cdot{}_1\delta_{z,k-1}\frac{{}_1\overline{Q}_{k-1} + d\,{}_1\overline{Q}_k}{{}_1\delta_{x,k-1}} \tag{34} $$

Since $\{{}_1\delta_{k-1}\}$ in Eq. (33) has not been obtained on the first step, the load distribution is obtained by substituting the elastic first-mode participation function ${}_1\beta\{{}_1u\}$, derived from modal analysis, into Eq. (31). As for the uniaxially asymmetric case, Eq. (33) may be used with the y-direction component omitted.

4. OVERVIEW OF ANALYSES

In order to verify the validity of the static and dynamic reduction methods shown in Section 2, the conventionally practiced three-dimensional pushover analysis with the load made to act in the x-direction alone (Conventional analysis), the MAP analysis described in Section 3, and the time history earthquake response analysis were performed.

The plan view of the analytical models is shown in Fig. 2. There are four types of analytical models, possessing identical plan sections but different locations of the center of rigidity: two uniaxially eccentric models (E1-A and E1-B) and two biaxially eccentric models (E2-A and E2-B). Each analytical model is a single-story RC building with identical longitudinal and transverse lengths of 6.0m x 2 spans, a height of 3m, and the weight, center of gravity (x_g , y_g), center of rigidity (x_c , y_c), eccentricity factor (R_x , R_y) and elastic radius ratio (j_x , j_y) set as shown in Table 1. The model name E1 stands for uniaxial eccentricity and E2 is for biaxial eccentricity, whereas A stands for the models with the shorter eccentric distance while B is for the models with the longer eccentric distance. Column cross-section details and layouts for each analytical model are given in Tables 2 and 3 respectively. Beam cross-sections are identical for all models, with details as shown in Table 4.

Mode diagrams for E1-B and E2-B are shown in Fig. 3. It can be seen that there is torsion at each mode caused by eccentricity. Note that although there is actually a third mode for the uniaxially eccentric model, it is omitted here since the

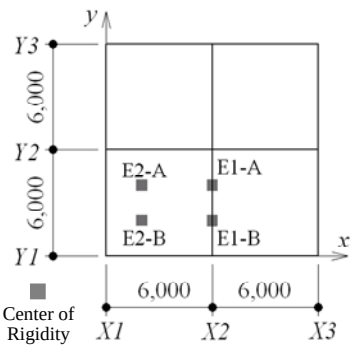

Figure 2 Plan View of Analytical Models

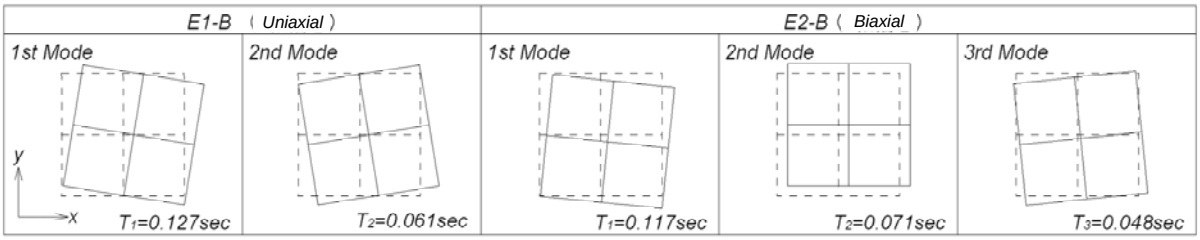

Figure 3 Vibration Modes for Models E1-B and E2-B

Table 1 Summary of Analytical Models

	Analytical Model	Weight (kN)	Cent. of Gravity (cm)		Cent. of Rigidity (cm)		Eccentricity Factor		Elasticity Radius Ratio	
			x_g	y_g	x_c	y_c	R_x	R_y	j_x'	j_y'
Uniaxial Eccentricity	E1-A	1909	600.0	597.8	600.0	400.0	0.307	0	1.042	1.217
	E1-B	1926	600.0	592.6	600.0	200.0	0.768	0	0.824	1.266
Biaxial Eccentricity	E2-A	1943	589.7	595.0	200.9	400.7	0.270	0.711	1.155	0.878
	E2-B	1990	581.9	581.9	201.6	201.6	0.670	0.670	0.904	0.904

Table 2 Column Section

Column Type	$D_x \times D_y$	Tensile Reinf.		Trans. Reinf.
		x-Dir.	y-Dir.	
A	400×400	2-D19	2-D19	2-D13@100
B	640×400	2-D19	2-D19	2-D13@100
C	1220×400	2-D19	2-D19	2-D13@100
D	400×1260	2-D19	2-D19	2-D13@100
E	670×1260	2-D19	2-D19	2-D13@100
F	670×400	2-D19	2-D19	2-D13@100
G	400×1350	2-D19	2-D19	2-D13@100
H	1350×400	2-D19	2-D19	2-D13@100
I	1350×1350	2-D19	2-D19	2-D13@100

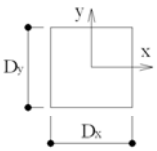

Table 3 Column Arrangement

Analytical Model	Column Type								
	X1-Frame			X2-Frame			X3-Frame		
	Y1	Y2	Y3	Y1	Y2	Y3	Y1	Y2	Y3
E1-A	B	A	A	B	A	A	B	A	A
E1-B	C	A	A	C	A	A	C	A	A
E2-A	E	D	D	F	A	A	F	A	A
E2-B	I	G	G	H	A	A	H	A	A

Table 4 Beam Section

	B×D	Upper Reinf.		Lower Reinf.		Trans. Reinf.
		1st Ln.	2nd Ln.	1st Ln.	2nd Ln.	
Beam	370×600	5-D32	-	5-D32	-	2-D13@150
Foundation	800×1300	8-D35	8-D35	8-D35	8-D35	2-D13@150

y-direction mode is independent. For both time history earthquake response analysis and nonlinear static pushover analysis, the beams and columns were modeled with end-member spring models using the Takeda model for hysteresis characteristics. Note that for single-story buildings, the effect of axial load fluctuations are considered small and are thus neglected in the analysis.

For the input earthquake used in the time history earthquake response analysis, only the El Centro NS (1940) wave motion, standardized to a maximum velocity of 50cm/sec, was used. Moreover, only the main 10sec duration of the earthquake wave motion was used as the seismic input duration. Also, viscous damping was considered as instantaneous-stiffness- proportional damping, with the damping coefficient assumed as 5% for the elastic first mode. For the numerical integration, the Newmark-β method (β =1/4) was used at 0.0001 integration time intervals.

5. ANALYTICAL RESULTS

The time history earthquake response analysis results of the analytical models are shown in Fig. 4. In the figure, results are grouped as x-direction responses ($Q_x - \delta_x$ relationship: top), y-direction responses ($Q_y - \delta_y$ relationship: center) and z-rotation responses ($Q_z - \delta_z$ relationship: bottom). Thus, for the uniaxially asymmetric models E1-A and E1-B, there are no y-direction responses.

In models with small eccentricities, E1-A and E2-A, responses in the x-direction are predominant and exhibiting stable hysteretic properties. Moreover, in the biaxially asymmetric model E2-A, it can be seen that response in the z-rotation axis is smaller than that of the uniaxially asymmetric model E1-A, since there is also a response in the y-direction.

In contrast to models with small eccentricities, responses in the x-direction are quite unstable in models with large eccentricities, E1-B and E2-B. Moreover, the

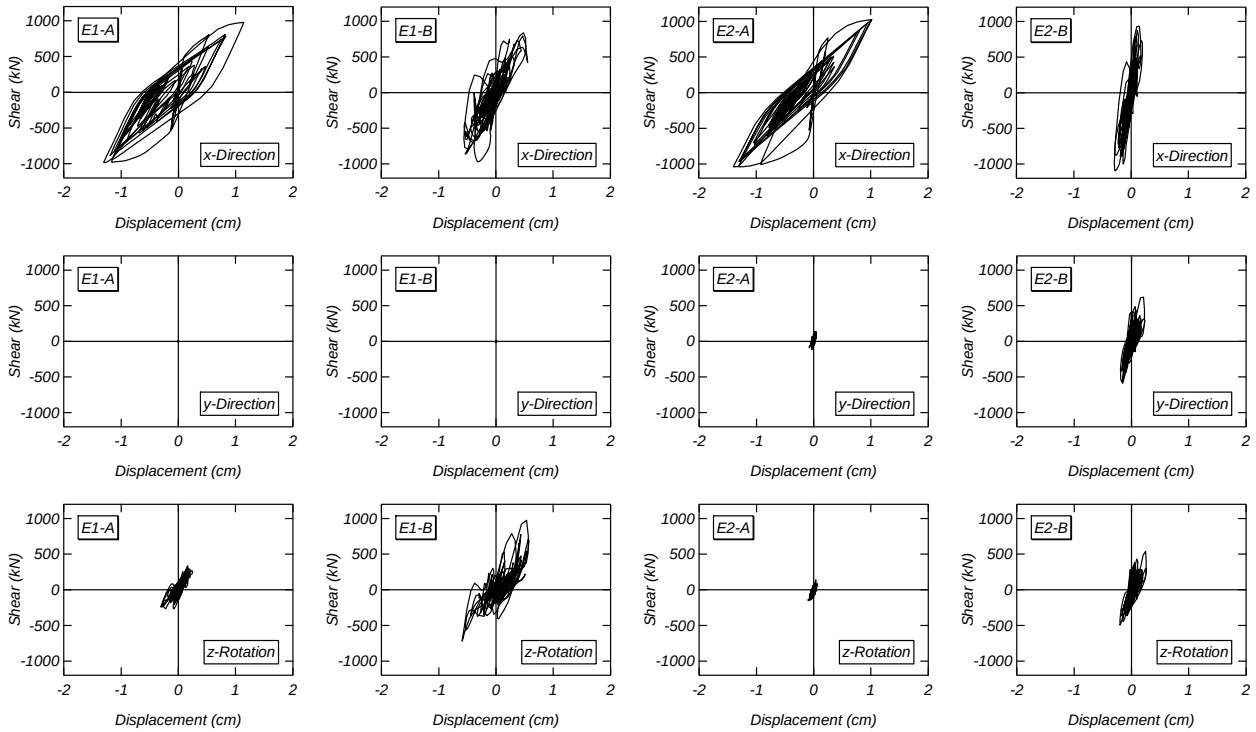

Figure 4 Results of Time History Earthquake Response Analysis

magnitude of the peak deformation response is quite small compared to models with small eccentricities, with such trend becoming more evident for the biaxial model. Similar to the x-direction response, responses in the y-direction and z-rotation axis are also unstable. Similar to models with small eccentricities, another notable feature is that the z-rotation response in the biaxially asymmetric model E2-B is smaller than that in the uniaxially asymmetric model E1-B, since there is a response in the y-direction as well.

For the ESDOF systems of the analytical models, comparison of the static reduction result, calculated from Eqs. (8) and (21) with the use of Conventional analysis results, and the dynamic reduction result, obtained via Eqs. (27) and (28) using time history earthquake response analysis results, are shown in Fig. 5. For E1-A and E2-A with small eccentricities, the static reduction and dynamic reduction envelope curves show good correspondence and are similar to the results obtained for multi-story buildings without eccentricities described in Ref. (Kuramoto 2006b) that *in the response history of the ESDOF system before the maximum response, the deformation response peaks experienced up until certain points in time closely agree with the first-mode pushover analysis results*. However, for E1-B and E2-B with large eccentricities, observation of the figures suggests that strength deteriorates more at the maximum deformation response in dynamic reduction than in the static reduction result.

On the other hand, looking at the results in Fig. 6, which is a comparison of the static reduction result, calculated from Eqs. (8) and (21) with the use of MAP analysis results described in Section 3, and the dynamic reduction result, static and dynamic reductions show very good correspondence. Namely, the results are similar to that shown in Fig. 5 for small eccentricity models E1-A and E2-A, and even for large eccentricity models E1-B and E2-B, the strength deterioration seen in Fig. 5 improved.

Note that for the Conventional and MAP analyses, the displacement vectors $\{{}_1\delta\}$ for the same load step differ as the load increases; hence during dynamic reduction, the value of the first-mode participation function (Eq. (24)) referred also differs. Therefore, the accuracy of pushover analysis becomes important since the difference in static analysis methods affect not only the static reduction result but also the dynamic reduction result. However, in the discussion of the ESDOF systems given above, although obvious differences were found in static and dynamic reductions of both Conventional and MAP analyses for large eccentricity models, similar results were obtained for small eccentricity models. Further consideration of this matter is given below.

Figure 7 is a comparison of the variation between participation functions from dynamic reduction and from static reduction using Conventional analysis for biaxially asymmetric models E2-A and E2-B. In the figures dotted lines represent the participation function ${}_1\beta\{{}_1u\}_{St}$ evaluated from Eqs. (24) and (29) using the results from Conventional analysis while solid lines represent the participation function ${}_1\beta\{{}_1u\}_{Dy}$ evaluated via eigenvalue analysis using the secant stiffness of each element during the peak response up to the point in time concerned of the dynamic reduction. The dashed-dotted lines in the figure represent the maximum deformation response point in dynamic reduction. For E2-A, in which good correspondence between static and dynamic reductions are seen in Fig. 5, ${}_1\beta\{{}_1u\}_{St}$ and ${}_1\beta\{{}_1u\}_{Dy}$ are

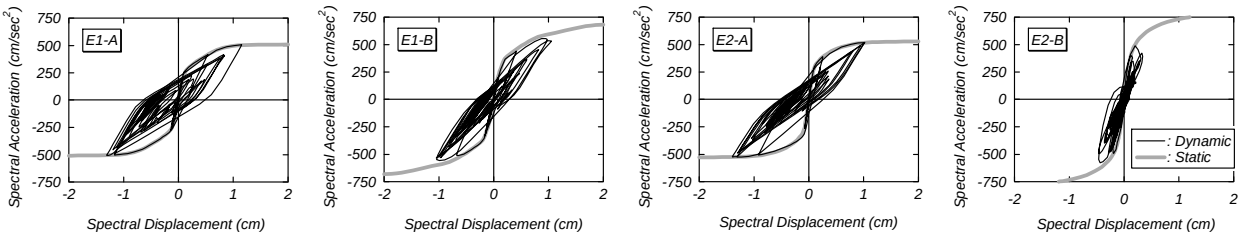

Figure 5 Static and Dynamic Reduction Results Using Conventional Analysis

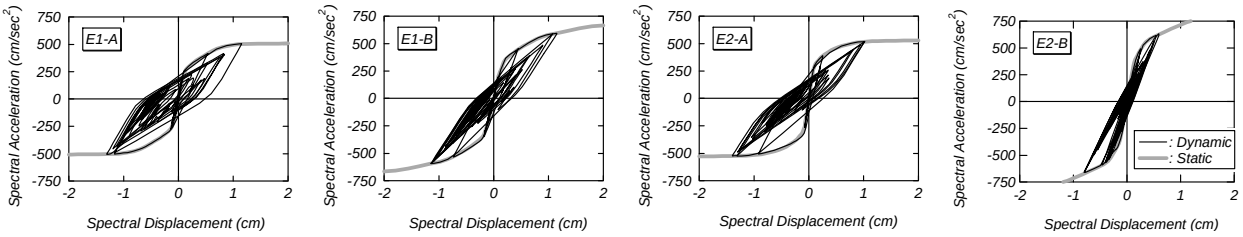

Figure 6 Static and Dynamic Reduction Results Using MAP Analysis

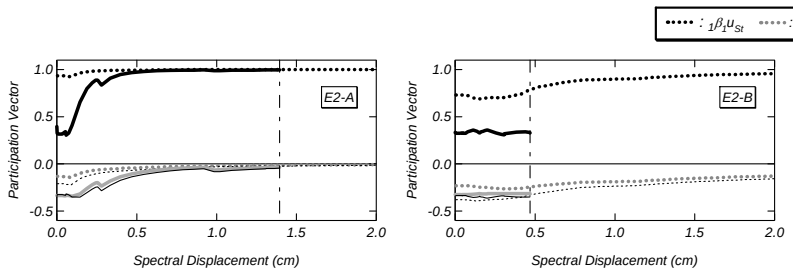

Figure 7 Variation of Participation Functions by Conventional Analysis

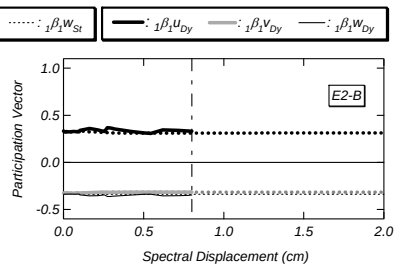

Figure 8 Variation of Participation Functions by MAP Analysis

Table 5 Participation Vectors at Elastic and Elasto-plastic Responses

Elastic	E1-A			E1-B			E2-A			E2-B		
	1st	2nd	3rd	1st	2nd	3rd	1st	2nd	3rd	1st	2nd	3rd
${}_s\beta \cdot {}_su_x$	0.633	0.367		0.530	0.470		0.312	0.674	0.014	0.326	0.500	0.174
${}_s\beta \cdot {}_su_y$	0.000	0.000		0.000	0.000		-0.333	0.407	-0.075	-0.326	0.500	-0.174
${}_s\beta \cdot {}_su_z$	-0.482	0.482		-0.499	0.499		-0.323	0.232	0.091	-0.337	0.000	0.337

Elasto-Plastic (at Max. Response)	E1-A			E1-B			E2-A			E2-B		
	1st	2nd	3rd	1st	2nd	3rd	1st	2nd	3rd	1st	2nd	3rd
${}_s\beta \cdot {}_su_x$	0.997	0.003		0.491	0.509		0.999	0.001	0.000	0.310	0.493	0.197
${}_s\beta \cdot {}_su_y$	0.000	0.000		0.000	0.000		-0.017	0.020	-0.003	-0.315	0.500	-0.184
${}_s\beta \cdot {}_su_z$	-0.054	0.054		-0.500	0.500		-0.025	0.023	0.003	-0.338	-0.014	0.352

shown to be roughly coinciding at the maximum deformation response point in dynamic reduction. However for E2-B, in which the correspondence between static and dynamic reductions is not good, rather large differences are seen between ${}_1\beta\{{}_1u\}_{St}$ and ${}_1\beta\{{}_1u\}_{Dy}$ values at the maximum deformation response point in dynamic reduction.

On the other hand, Figure 8 is a comparison of the variation between participation functions from dynamic reduction and from static reduction using MAP analysis for E2-B. When MAP analysis is used, it can be seen that ${}_1\beta\{{}_1u\}_{St}$ and ${}_1\beta\{{}_1u\}_{Dy}$ values have a good corresponding relationship over the whole of the dynamic deformation response (up to about 0.8cm). In addition, in the dynamic response of E2-A shown in Fig. 7, although a value close to the participation function during elastic stage is shown in the beginning, the participation function changes suddenly between the maximum deformation response values of 0.2 to 0.5cm. This implies that the vibration mode shifted from a mode accompanied by torsion to a translational mode (${}_1\beta\{{}_1u\} = \{1,\ 0,\ 0\}^T$). In contrast, for the large eccentricity E2-B, the participation function generally maintains its elastic-stage value, from the initial stage up to the maximum response stage of the dynamic response. This can be interpreted to mean that a torsional mode is included in the vibration mode at all times.

As shown above, the reason why reduction to an ESDOF system can be performed successfully for small eccentricity models even if conventional analysis is used is

because translational mode dominates during maximum deformation of the ESDOF system. As a result, the first-mode proportional load after the frame yields is nearly the same as the one used in Conventional analysis. On the other hand, since a post-yield first-mode proportional load could suitably be applied on the frame with the use of MAP analysis, as shown in Fig. 8, it is confirmed that the reduction to an ESDOF system can be performed successfully regardless of the degree of eccentricity. Therefore, the static and dynamic reduction methods for single-story asymmetric buildings described in Section 2, as well as the MAP analysis described in Section 3, are confirmed as valid. The modal participation functions during elastic stage and those obtained using equivalent stiffness during peak deformation response in the dynamic reduction based on MAP analysis are shown respectively for each model in Table 5, which serves to substantiate the validity of study given above.

6. CONCLUSIONS

In this paper, two methods of reduction to an ESDOF system (static and dynamic reduction methods) for asymmetric buildings were proposed as a fundamental research aimed towards the improvement of the seismic performance evaluation procedure based on the Calculation for Response and Limit Strength (CRLS). Their validity was also verified through comparison with time history earthquake response analysis results.

The findings obtained from this research can be summarized as follows.

1) The representative displacement response ${}_1S_d$ and representative acceleration response ${}_1S_a$ of the ESDOF system based on static reduction method may be obtained by Eqs. (8) and (21) for biaxial eccentricity and Eqs. (22) and (23) for uniaxial eccentricity, respectively.
2) The representative displacement response ${}_1S_d(t)$ and representative acceleration response ${}_1S_a(t)$ of the ESDOF system based on dynamic reduction method may be obtained by Eqs. (27) and (28).
3) For a building with a relatively small eccentricity, all frames in the direction of seismic input yield with increase in response and shift from a mode accompanied by torsion to a translational mode. In contrast, for a building with a relatively large eccentricity, there is a strong tendency to maintain the vibration mode accompanied by torsion because highly stiff frames do not yield easily even if yielding develops at the weak frames in the direction of seismic input.

References:

Akita T. and Kuramoto H. (2008), "Time History Response Prediction for Multi-story Buildings Consisting of Mixed Soft and Rigid Stories under Earthquake Motions," *Proceedings of Fourteenth World Conference on Earthquake Engineering*, Beijing, China, Paper ID: S15-020.

Azuhata T., Takahashi T., Hu M. and Ozaki M. (1991), "Study on Damage Evaluation of Single Story Structures with One Axis Eccentricity Subjected to Strong Earthquakes," *Journal of Structural and Construction Engineering, AIJ*, No.426, 59-66. (in Japanese)

Building Center of Japan (BCJ: 1994), *The Building Standard Law of Japan*. (English version)

Bracci J.M., Kunnath S.K. and Reinhorn A.M. (1997), "Seismic Performance and Retrofit Evaluation of Reinforced Concrete Structures," *Journal of Structural Engineering*, ACI, Vol. 123, No. 1, 3-10

Chopra A.K. and Goel R.K. (2002), "A Modal Pushover Analysis Procedure for Estimating Seismic Demands for Buildings," *Earthquake Engineering & Structural Dynamics*, Vol.31, 561-582

Fujii K. Nakano Y. and Sanada Y. (2003), "Nonlinear Response of Single-Story Asymmetric Buildings Considering Stiffness Degradation in Transverse Frames," *Journal of Structural Engineering, AIJ*, Vol. 49B, 221-234. (in Japanese)

Fujii K., Nakano Y., Sanada Y., Sakata H. and Wada A. (2005), "Prediction of Seismic Response of Single Story Unsymmetric buildings Using Equivalent SDOF Model and Its Applicability," *Journal of Structural and Construction Engineering, AIJ*, No.596, 101-108. (in Japanese)

Kabeyasawa T. and Kabeyasawa T. (2005), "A Method of Estimating Earthquake Responses of Asymmetric Reinforced Concrete Structures Based on Nonlinear Deformation Modes," *Journal of Structural and Construction Engineering, AIJ*, No.596, 87-94. (in Japanese)

Kuramoto H., Teshigawara M., Okuzono T., Koshika N., Takayama M. and Hori T. (2000), "Predicting the Earthquake Response of Buildings Using Equivalent Single Degree of Freedom System," *Proceedings of Twelfth World Conference on Earthquake Engineering*, Auckland, New Zealand, Paper No. 1039.

Kuramoto H. and Matsumoto K. (2002), "Comparison between US and Japan on Performance Based Seismic Evaluation Method for RC Buildings," *Proceedings of Structural Engineers World Congress (SEWC2002)*, Yokohama, CD-ROM No. T1-6-b-3.

Kuramoto H. and Matsumoto K. (2004), "Mode-Adoptive Pushover Analysis for Multi-Story RC Buildings," *Proceedings of Thirteenth World Conference on Earthquake Engineering*, Vancouver, Canada, Paper No. 2500 (CD-ROM).

Kuramoto H. (2006a), "Seismic Design Code for Buildings in Japan," *Journal of Disaster Research*, Vol.1, No.3, 341-356.

Kuramoto H. (2006b), "Prediction of Higher Mode Shear Response for Multi-Story Buildings under Earthquake Motions," *Proceedings of the 8th U.S. National Conference on Earthquake Engineering (8NCEE)*, San Francisco, California, USA, Paper No. 1289.

Kuramoto H. (2007), "Prediction of Higher Mode Story Drift Response for Multi-story Buildings under Earthquake Motions," *Proceedings of 8th Pacific Conference on Earthquake Engineering*, Singapore, Paper No. 2A134 (CD-ROM).

Kuramoto H. and Akita T. (2008), "Prediction of Shear Contribution of Walls in RC Wall-Frame Buildings under Earthquake Motions," *Proceedings of Fourteenth World Conference on Earthquake Engineering*, Beijing, China, Paper ID: S15-003

Ozaki M., Sota S., Yasuda S. and Namikawa T. (1986), "A Study on Maximum Lateral Shear Strength and Plastic Deformation of Torsionally Coupled Single Story Structures," *Journal of Structural and Construction Engineering, AIJ*, No.364, 53-60. (in Japanese)

Yamasaki Y. (1986), "Lateral Torsional Response of Buildings During Earthquake," *Proceedings of Ninth World Conference on Earthquake Engineering*, Vol V, 73-78.

JOINT CONFERENCE PROCEEDINGS
7th International Conference on Urban Earthquake Engineering (7CUEE) &
5th International Conference on Earthquake Engineering (5ICEE)
March 3-5, 2010, Tokyo Institute of Technology, Tokyo, Japan

SEISMIC PERFORMANCE OF RC BUILDING BY CYCLIC PUSHOVER ANALYSIS

Phaiboon Panyakapo

Associate Professor, Faculty of Engineering, Sripatum University, Thailand.
phaiboon.pa@spu.ac.th

Abstract: Nonlinear static analysis based on Pushover method has been widely employed as a procedure to evaluate the seismic performance of structures. The lateral loads applied to the structures may be a single mode or multi-modes lateral force distribution. However, this procedure is primarily based on a monotonic pushover load. The results may not be used to predict the cumulative damage of structure under cyclic loading. Therefore, this paper presents an alternative approach to evaluate the seismic performance of structures taking cumulative damage into account by Cyclic Pushover Analysis (CPA). In this method, the seismic performance of structure is analyzed by applying a set of cyclic lateral load with a prescribed cyclic-displacement pattern. The seismic capacity spectrum can be presented as a relationship of base shear and top displacement including the levels of seismic damage (in term of damage index) along the curve. A 14-stories reinforced concrete building was analyzed by CPA with a set of prescribed cyclic-displacement patterns. These patterns include, for examples, laboratory-test-like displacement history and sequential phased displacement history. The analysis results reveal that the seismic capacity of CPA is lower than those of conventional Pushover Analysis (PA) and Modal Pushover Analysis (MPA). In addition, the average seismic damage indices due to CPA are greater than those of PA and MPA. It was found that cumulative damage plays an important role to contribute the level of seismic damage due to the significant absorbed hysteretic energy during cyclic loading.

1. INTRODUCTION

Nonlinear static analysis based on Pushover method has been widely employed as a procedure to evaluate the seismic performance of structures. In the pushover method, the building is subjected to a pattern of lateral force distribution which is monotonically increased to push the building laterally. These include single-mode load vector and multi-mode pushover procedures. The single-mode load vector as described in FEMA-440 consists of concentrated load, uniform load, triangular load, Code distribution load, first mode load, adaptive load, and SRSS load. The static pushover procedure has been improved by adopting adaptive pushover method (Antoniou and Pinho, 2004; Papanikolaou, Elnashai, Pareja, 2006) to capture the changes that occur in the vibration properties of a structure. For each step of an adaptive pushover analysis, the lateral force distribution is evaluated and adjusted based on the nonlinear behavior of the structure. Although this approach can provide good estimates of the displacement demands, however, the method has not considered the effect of higher mode of vibration. For the multi-mode pushover method, the Modal Pushover Analysis has been proposed by Chopra and Goel (2002, 2004, 2005) to allow for the influence of higher modes. This method uses invariant modal lateral force distribution to push the structure for each mode, and the results in each mode are combined with SRSS by assuming linear elastic behavior. The method is widely used; however, some limitations have been reported (Chopra and Goel, 2005) regarding the reversal in the pushover curve under higher mode lateral force distribution, and the location of plastic hinges may not accurately predicted.

One important seismic performance is that seismic damage of structures resulting from these pushover procedures does not reflect cumulative damage resulting from earthquake cyclic loading because the approaches are based on monotonic loading. This paper presents an alternative approach to capture this characteristic. Cyclic Pushover Analysis is proposed by introducing a set of cyclic lateral load with a prescribed cyclic-displacement pattern. Seismic damage of structures resulting from cyclic reversal can be considered by adopting some damage models that taking cumulative damage into account. Hysteretic behavior under cyclic loading also plays an important role in the determination of cumulative damage. The resulting pushover curve is appropriate for predicting seismic damage under nonlinear behavior in performance based seismic design.

2. BASIC CONCEPT

The differential equation governing the response of a multi-degree-of-freedom (MDOF) system subjected to earthquake ground motion is as follows:

$$[m]\{\ddot{u}\}+[c]\{\dot{u}\}+\{f_s\}\left(\{u\},sign\{\dot{u}\}\right)=P_{eff}(t) \quad (1)$$

Where $[m],[c]$ are the mass and damping matrices of the structure, $\{f_s\}$ is the internal resisting force vector, and $\{u\},\{\dot{u}\}$ are roof relative lateral displacement and velocity vectors, respectively.

The effective earthquake forces $P_{eff}(t)$ can be written as

$$P_{eff}(t)=-[m]\{i\}\ddot{u}_g(t) \quad (2)$$

Where $\{i\}$ is the unit vector, and $\ddot{u}_g(t)$ is acceleration of ground motion.

The term $[m]\{i\}$ represents the spatial distribution of the effective earthquake forces over the height of the building, and can be expressed as $\{s\}$ which can be expanded as a summation of modal inertia force distribution as follows:

$$[m]\{i\}=\{s\}=\sum_{n=1}^{N}s_n=\sum_{n=1}^{N}\Gamma_n[m]\{\phi_n\} \quad (3)$$

Where Γ_n is the modal participation factor of the nth mode and it can be determined from

$$\Gamma_n=\frac{L_n}{M_n}=\frac{\{\phi_n\}^T[m]\{i\}}{\{\phi_n\}^T[m]\{\phi_n\}} \quad (4)$$

And $\{\phi_n\}$ is the corresponding mode shape.

The governing equation of motion for the structure can then be written as :

$$[m]\{\ddot{u}\}+[c]\{\dot{u}\}+\{f_s\}\left(\{u\},sign\{\dot{u}\}\right)=-\sum_{n=1}^{N}\{s_n\}\ddot{u}_g(t) \quad (5)$$

Eq.(5) can be uncoupled to the equivalent governing equation of motion for a SDOF system by introducing the lateral displacement vector, $\{u\}$ in the form

$$\{u\}=\sum_{n=1}^{N}\{u_n\}=\sum_{n=1}^{N}\{\phi_n\}q_n \quad (6)$$

Where q_n are the modal amplitudes.

Substituting Eq.(6) and its derivatives into Eq. (5), and using the mass and damping orthogonality of the mode shapes, the governing equation of motion for a SDOF system becomes

$$\ddot{D}_n+2\xi_n\omega_n\dot{D}_n+\frac{F_{sn}}{L_n}=-\ddot{u}_g(t) \quad (7)$$

Where $F_{sn}=\{\phi_n\}^T\left\{f_s\left(D_n,sign\,\dot{D}_n\right)\right\}$ is the modal internal resisting force, $D_n,\dot{D}_n,\ddot{D}_n$ are the modal displacement, velocity and acceleration, respectively, and ξ_n and ω_n are the modal damping and frequency, respectively.

Eq.(7) can be solved either by conducting a nonlinear SDOF dynamic time-history analysis or by using a nonlinear SDOF displacement response spectrum. To solve Eq.(7), the relationship between F_{sn} and D_n need to be determined using pushover analysis. Applying Eq.(3) for cyclic pushover analysis, the force distribution in each mode is proposed as follows:

$$f_n=\lambda_i\Gamma_n[m]\{\phi_n\}A_n \quad (8)$$

where f_n is the lateral force distribution in each mode, and $A_n=\omega_n^2D_n$. λ_i is a variable factor which defines the direction of force, i is the number of cycles for the specified displacement history, for i =1,3,5,…, λ_i = 1 , and for i = 2,4,6,….., λ_i = -1.

For the response of structures that are primarily governed by the first mode, Eq.(8) can be simplified to

$$f_1=\lambda_i\Gamma_1[m]\{\phi_1\}A_1 \quad (9)$$

Where Γ_1 is the Participation factor of the first mode,

A_1 is the acceleration in the first mode $=\omega_1^2D_1$, ω_1,D_1 is the angular frequency and displacement in the first mode.

The base shear force and roof displacement relationship obtained from the cyclic pushover analysis of the structure is converted to an equivalent SDOF pseudo-acceleration and displacement relationship using the relationship as shown in Fig.1.

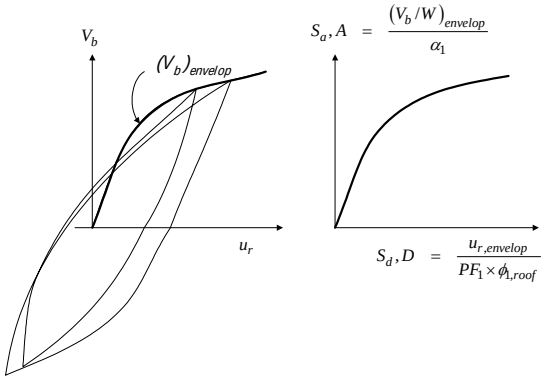

a) Cyclic pushover curve b) Pseudo-acceleration and displacement

Figure 1 Conversion from cyclic pushover curve to pseudo-acceleration and displacement relation (Capacity spectrum)

The pushover base shear force, V_b is converted to SDOF pseudo-acceleration, S_a or A by using the relation

$$S_a, A = \frac{(V_b / W)_{envelop}}{\alpha_1} \quad (10)$$

The pseudo-displacement, S_d or D is given by

$$S_d, D = \frac{u_{r,envelop}}{\Gamma_1 \times \phi_{1,roof}} \quad (11)$$

Where α_1 is the modal mass coefficient for the first mode, and W is building weight .

3. CYCLIC PUSHOVER PROCEDURE

In this study, the lateral force distribution according to Eq.(9) was adopted in the procedure of cyclic pushover analysis which can be summarized as follows:

a) Compute the lateral force distribution corresponding to the first mode shape, Eq.(9).
b) Define the displacement history which is the relationship between displacement and number of cycles to control the displacement pattern.
c) Perform nonlinear static analysis using the above specified force distribution and displacement history. The results are plotted for the relationship between base shear and top displacement.
d) Determine the envelop curve for the relationship between base shear and top displacement to obtain the Pushover Curve $(V_b - u_r)$.
e) Compute the seismic damage of structure, in this study, the Park-Ang damage index (Pak and Ang, 1985) was adopted, and plot the values of damage index along the pushover curve.

3.1 Displacement History

A number of displacement histories have been developed for cyclic load test in the laboratory. These are adopted to control the displacement pattern in cyclic pushover analysis. In this study, four types of displacement histories were selected. One of the well-known displacement histories is the Laboratory-Test-like-Displacement History that is shown Fig. 2, which is typically employed in the laboratory. In this displacement pattern, each cycle is dependent on the displacement ductility ratio, μ .

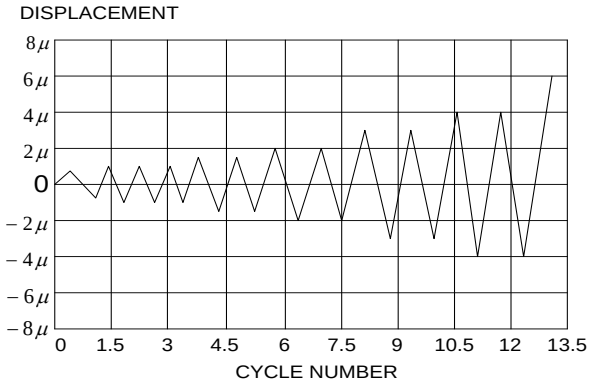

Figure 2 Laboratory-Test-like-Displacement History

The ISO Displacement History was adopted from ISO Protocol which was prepared by the ISO Technical Committee on Timber Structures, originally for joint testing, it was later considered appropriate for testing wood-framed shear wall. The loading history is based on the displacement at ultimate load, D_m .

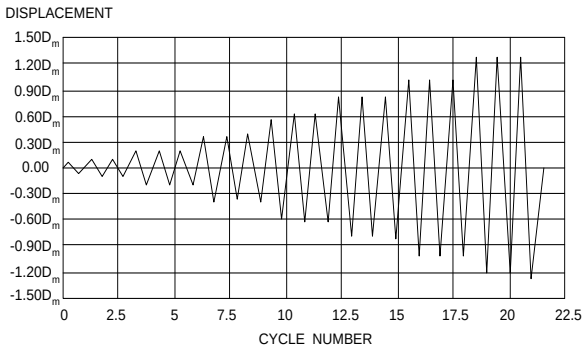

Figure 3 ISO Displacement History

The SPD (Sequential Phased Displacement) protocol was developed in 1987 by the Technical Coordinating Committee on Masonry Research (TCCMAR). This displacement history has been modified and accepted by the Structural Engineers Association of Southern California (SEAOSC). The protocol is based on what is called the First Major Event (FME) which can generally be considered as the displacement corresponding to the yield state of the specimen, D_y .

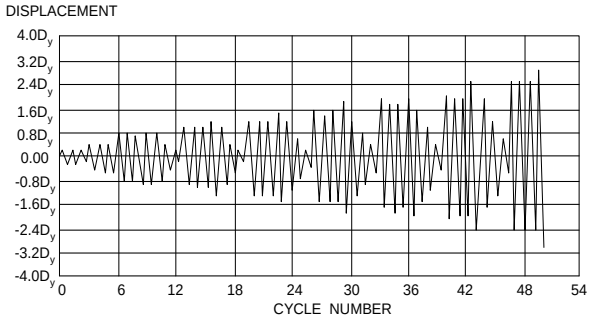

Figure 4 SPD Displacement History

The ATC-24 Protocol was developed by Krawinkler (1992) for the testing of steel components. The displacement history is controlled by the yield displacement of the specimen, D_y.

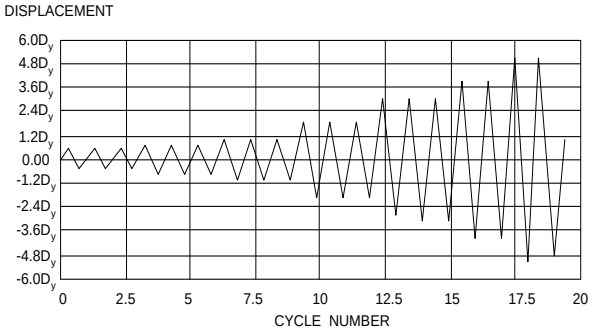

Figure 5 ATC-24 Displacement History

4. ANALYSIS OF 14-STORY RC BUILDING

In this study, a 14-storey reinforced concrete building with 2-story basement was employed in the cyclic pushover analysis as shown in Fig.6. The details of building can be summarized as follows: a) The floor plan is 29.0x110.70 meters with overall height 50.50 meters, b) the floor systems are flat plates with reinforced concrete and post-tensioned concrete, c) columns are 0.8x0.80 meters, d) compressive strength of concrete is 320 ksc, and the tensile strength of reinforcing steel is 4,000 ksc. The reinforced concrete structure was designed according to EIT (2000). Since this is an old building, it had not been designed for seismic loading. The slab-column frame was modeled as effective beam width model. The modified Takeda model was assumed as the hysteretic behavior of structure, as shown in Fig. 7. The model was applied for the behavior of column and beam by using the appropriate values of α and β. For column member, $\alpha = 0.23, \beta = 0.60$, and for an equivalent beam member, $\alpha = 0.35, \beta = 0.43$. The strength degradation of each inelastic cycle was assumed to be based on cycle numbers of inelastic excursion. The cyclic pushover analysis was performed by the computer program RUAUMOKO (Carr, 2006) to generate the pushover curve.

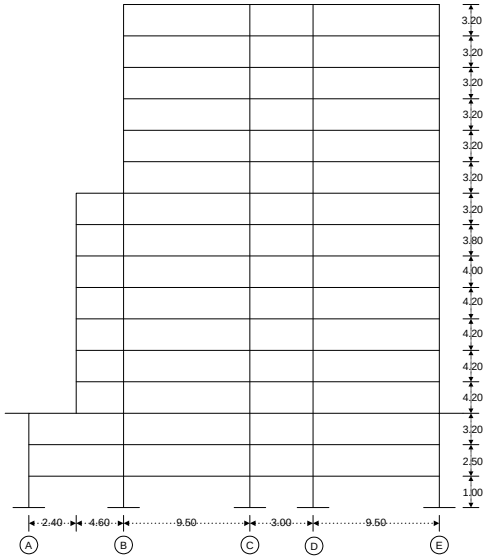

Figure 6 Two-Dimension model frame

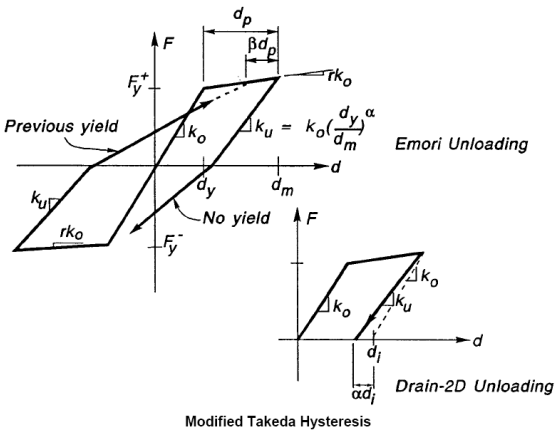

Figure 7 Modified Takeda hysteretic model

The pushover curves for cyclic pushover analysis (CPA) with four sets of displacement histories are compared with those of conventional pushover (PA) and modal pushover analyses (MPA) shown in Figure 8. It should be noted that each pushover curve of CPA was plotted from the cyclic envelop of base shear and top displacement relation. The seismic damages of structures were computed based on Park-Ang (1985) damage model. The values of Damage Index (DI) were plotted along the pushover curves for each analysis.

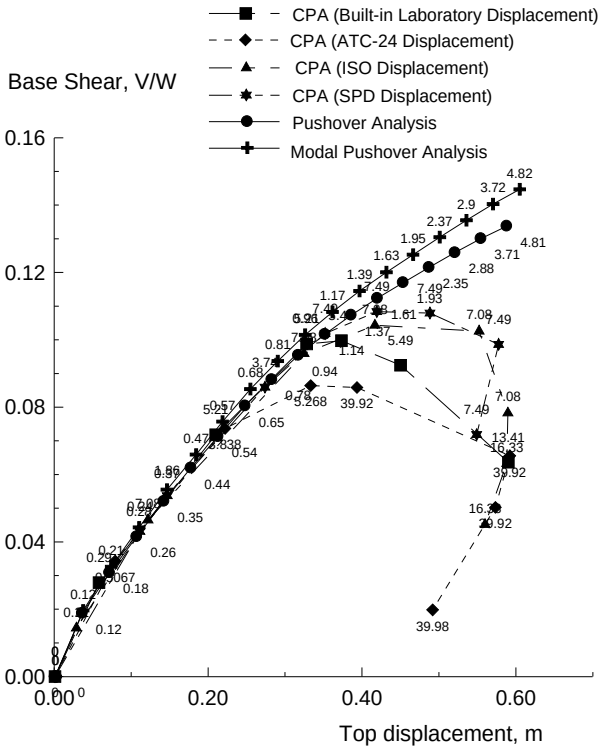

Figure 8 Pushover curves for CPA, PA and MPA.

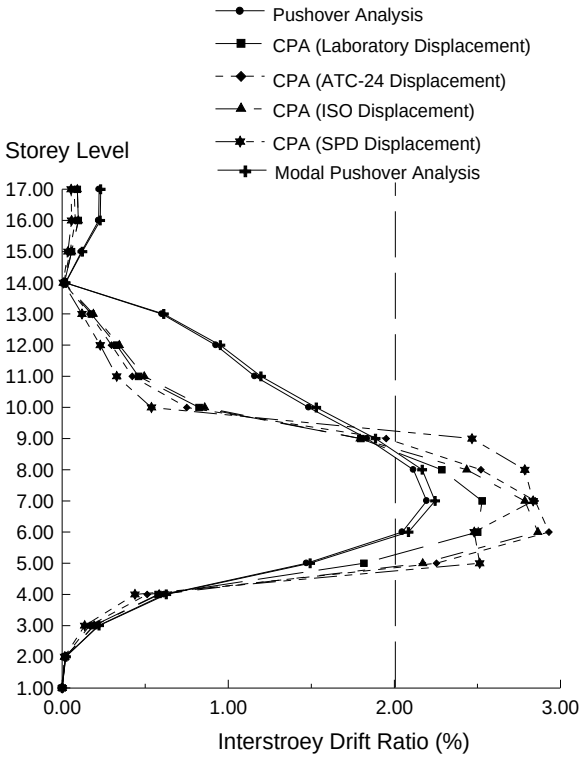

Figure 9 Inter-story drift ratio

The seismic damage of structures indicated by DI for each curve show that significant damages occur when the top displacement go beyond linear elastic displacement. The values of DI for cyclic pushover (CPA) are greater than those of PA and MPA. This characteristic is consistent with the strength degradation of structures caused by cyclic pushover.

It can be observed that the strengths of structure due to cyclic pushover are significantly reduced for each set of cyclic pushover. This is due to the characteristic of strength degradation of hysteretic behavior under inelastic cyclic excursion. The pattern of displacement history also plays an important role on strength degradation. The strength is significantly reduced when cyclic displacement is repeated at large amplitude and several numbers of cycles. This is particularly observed for ATC-24 displacement history, which shows many repeated cycles at larger amplitude than other patterns.

The inter-story drift ratio for each pushover analysis was plotted as shown in Fig. 9. It is noted that the inter-story drift ratios for CPA are greater than those of PA and MPA, especially for the lower floor between 5th and 8th floor. The inter-story drift ratios for these floor levels go beyond 2% which is normally used for the limit of building regulation (Kappos, 1991). This indicates that the P-δ effect is significant reducing the lateral force resistance and the stiffness of the vertical structural members and precipitating failure.

To investigate the seismic damage in more details, the DI of beams which are located between axis B and C were plotted against the story levels. The DI for CPA and PA were compared as shown in Fig.10.

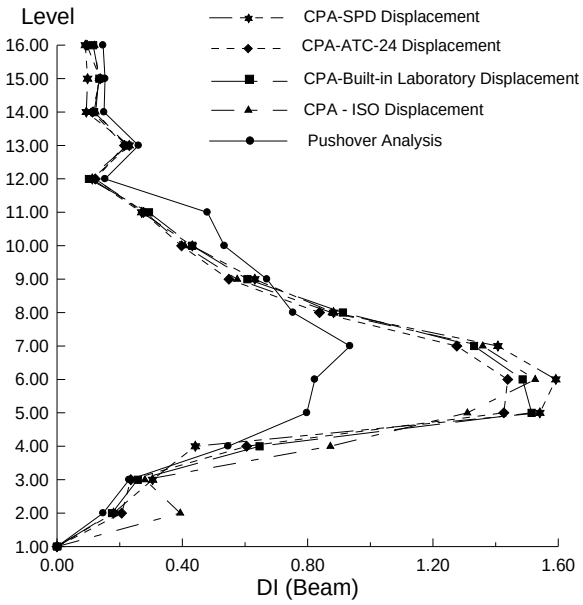

Figure 10 Damage Index of beams in axis B-C for each story

These values of DI were computed from the average DI occurred at the plastic hinges forming at the end of beams. It is clear that the DI for CPA are

greater than those of PA, especially for the lower floor between 5th and 8th floor, similar to the case of inter-story drift ratio.

To investigate the cause of seismic damage, the DI was separated into two components, i.e., damage caused by maximum deformation and cumulative damage. These values of DI were plotted for PA and CPA as shown in Fig. 11(a), (b), respectively. It is shown that seismic damage due to PA is governed by the maximum deformation. On the other hand, cumulative damage due to CPA is significantly increased, and it affected the total seismic damage.

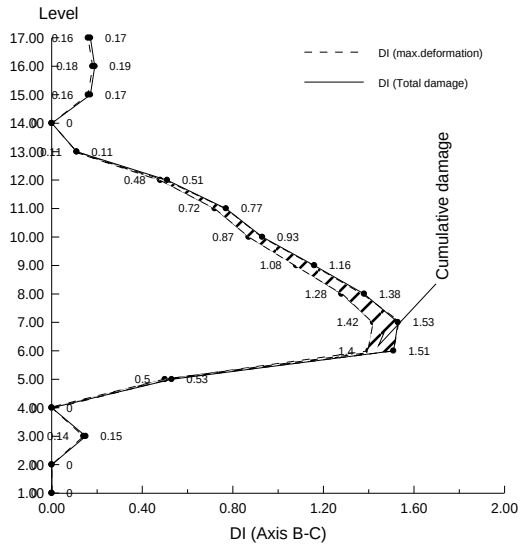

(a) Pushover Analysis

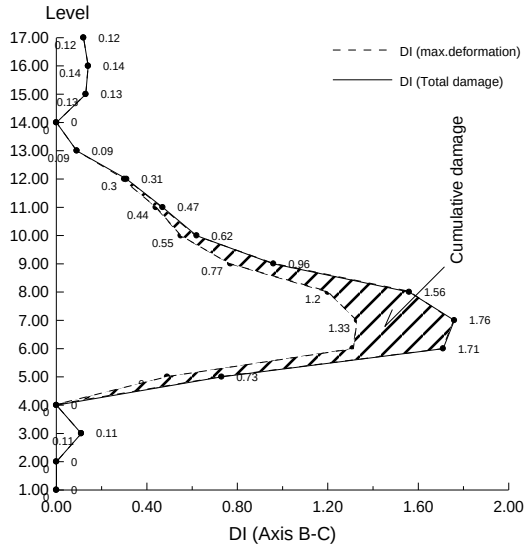

(b) Cyclic Pushover (ATC 24-Displacement)

Figure 11 Cumulative Damage of beam for
(a) Pushover Analysis (PA) and
(b) Cyclic Pushover Analysis

5. CONCLUSIONS

Based on the above results, the following conclusions can be drawn.

a) Cyclic pushover analysis may be used to determine the seismic performance of building under cyclic load reversal. This is due to the effect of cumulative damage, which cannot be account by monotonic pushover analysis, can be incorporated in the pushover analysis.

b) Seismic damage of structures may be evaluated based on some selected damage models, which are reasonable to measure cumulative damage under cyclic loading.

c) Further investigations are still required to evaluate the validity of cyclic pushover analysis. These include, for example, the comparison of displacement demands between nonlinear time-history analysis and cyclic pushover analysis.

References:

Antoniou S., Pinho, R. (2004), "Development and verification of a displacement-based adaptive pushover procedure," *Journal of Earthquake Engineering*; **8**(5), 643-661.

Carr A.J. (2006), "RUAUMOKO computer program,"*University of Canterbury*, Christchurch, New Zealand.

Chopra, A.K., Goel, R.K. (2002), "A modal pushover analysis procedure for estimating seismic demand of buildings," *Earthquake Engineering and Structural Dynamics*, **31**:561-582.

Chopra, A.K., Goel, R.K. (2004), "A modal pushover analysis procedure to estimate seismic demands for unsymmetrical-plan buildings," *Earthquake Engineering and Structural Dynamics*, **33**(8):903-927.

Chopra, A.K., Goel, R.K. (2005), "Role of higher mode pushover analyses in seismic analysis of buildings," *Earthquake Spectra*; **21**(4):1027-1041.

Engineering Institute of Thailand (2000). "Standard for Reinforced Concrete Building (Strength Design Method)," *EIT Standard 1008-38*, Bangkok, Thailand.

FEMA (2005). "Improvement of Nonlinear Static Seismic Analysis Procedures," *Federal Emergence Management Agency, FEMA 440*, Washington D.C.

Kappos, A.J. (1991), "Analytical prediction of the collapse earthquake for R/C buildings: suggested methodology," *Earthquake Engineering and Structural Dynamics*, **20**: 167-176.

Krawinkler, H. (1992), "Guidelines for cyclic seismic testing of components of steel structures," *ATC-24*, Redwood city, California.

Papanikolaou, V.K. Elnashai, A.S., Pareja, J.F. (2006), "Evaluation of conventional and adaptive pushover analysis II: Comparative results, *Journal of Earthquake Engineering*; **10**(1), 127-151.

Park, Y. J. and Ang, A. H. (1985). Mechanistic seismic damage model for reinforced concrete. *Journal of Structural Engineering. ASCE*, **111**(4): 722-739.

JOINT CONFERENCE PROCEEDINGS
7th International Conference on Urban Earthquake Engineering (7CUEE) &
5th International Conference on Earthquake Engineering (5ICEE)
March 3-5, 2010, Tokyo Institute of Technology, Tokyo, Japan

EFFECTS OF ASPECT RATIOS ON SEISMIC BEHAVIOUR OF CONCRETE-FILLED RECTANGULAR STEEL TUBULAR COLUMNS UNDER LOW CYCLE REVERSED LOADING

Wang Lai[1)], Li Wensheng[2)], Liu Ming[3)]

1) Professor, Shandong Provincial Key Laboratory of Civil Engineering Disaster Prevention and Mitigation (Shandong University of Science and Technology) , Qingdao, China;
2) Engineer, Manager, Shanxi Yuan Fang Road Bridge Group Co., Ltd., Datong, China;
3) Master of philosophy, College of Civil Engineering and Architecture, Shandong University of Science and Technology, Qingdao, China

wlkdtjxy@sina.com, tumuliuming@126.com

Abstract: With the increasing use of concrete-filled rectangular steel tube (CFRST) in actual projects, it is important to make further study of seismic behavior of CFRST. Considering the main parameter, i.e. aspect ratios, five concrete-filled rectangular steel tube members with different aspect ratios, say 1, 1.25, 1.5, 1.75 and 2 respectively are tested. Failure modes, bearing capacity, deformability, ductility, hysteretic model, and energy-dissipating capacity, retrogression of strength and rigidity degeneration under low cycle reversed loading are investigated in the experiments. The influence of the aspect ratio of a column on the anti-seismic behavior of the concrete-filled rectangular steel tube member is also studied.

The results obtained from the experiments show that: (1) The load-displacement hysteretic curves are plump in shape and no significant pinch occurs. (2) Members have a good capacity for energy-dissipating. It trends to increase beyond the plastic state of the members. However, capacity for energy-dissipating decreases with the increments of the aspect ratios. (3) Aspect ratio has an influence on shapes and values of the hysteretic curves. Hysteretic curves of members with small aspect ratio are plump in fusiform shape. Therefore, that means the members have a good anti-seismic behavior. (4)The elastic stiffness based on the load-displacement hysteretic curves increases with the increments of aspect ratios, thus the lateral bearing capacity increases obviously. However, ductility, deformability and energy-dissipating capacity of the members decrease. Accordingly, retrogression of strength and rigidity degeneration becomes much more obvious.

1. INTRODUCTION

Concrete-filled rectangular steel tube has some advantages as follows: high bearing capacity, good seismic behavior, excellent fire–resistant behavior and convenient construction. So CFRST is more widely used in columns of single and multi-story workshop, equipment-upright of frame, bearer, trestle type column, column of platform in subway, transmission tower, compression members of truss, piles, high and ultra-high-rise buildings, spatial structures and bridges. CFRST has achieved good economic and styles of buildings. Though bounding force on core concrete of CFRST is not as big as steel tubes, it is easier to tackle with connected nodes with beams and can effectively improve the ductility of components. Thus, CFRST is widely used in Europe, America, Japan and Australia. There have been lots of researches on steel pipe and square concrete column. However, study on seismic behavior of CFRST is still insufficient. China is a country suffered from earthquakes. So it's necessary to study the seismic behavior of CFRST.

In this paper, five concrete-filled rectangular steel tube members with different aspect ratios, say 1, 1.25, 1.5, 1.75 and 2 respectively are tested. Failure modes, bearing capacity, deformability, ductility, hysteretic model, energy-dissipating capacity, retrogression of strength and rigidity degeneration under low cycle reversed loading are investigated in the experiments.

2. INTRODUCTION OF TEST

In order to study the seismic behavior of concrete-filled rectangular steel tubular columns under low cycle reversed loading, 5 frame columns are tested in Shandong

Provincial Key Laboratory of Civil Engineering Disaster Prevention and Mitigation.

2.1 Experimental design and characteristics of material

Table1 Parameter of specimens

1. No.	serial number	$B\times D$(mm×mm)	Thickness t/mm	Effective length L/mm	Steel ratio α	Confining factor	Ratio of axial compression stress to strength	Axial force /kN
1	R2020-4	200×200	4	1040	0.085	0.93	0.35	649.1
2	R2025-4	200×250	4	1040	0.076	0.83	0.35	776.7
3	R2030-4	200×300	4	1040	0.070	0.76	0.35	904.2
4	R2035-4	200×350	4	1040	0.066	0.72	0.35	1031.8
5	R2040-4	200×400	4	1040	0.063	0.69	0.35	1159.3

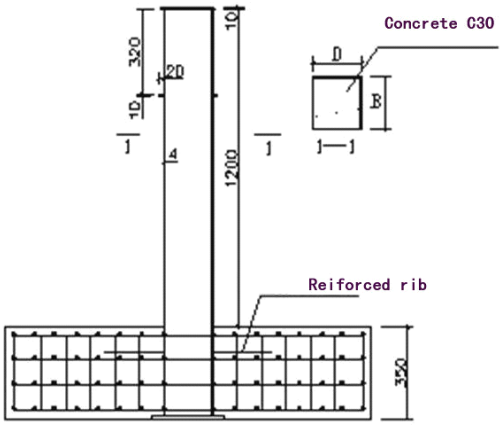

Fig.1 Dimension of specimen

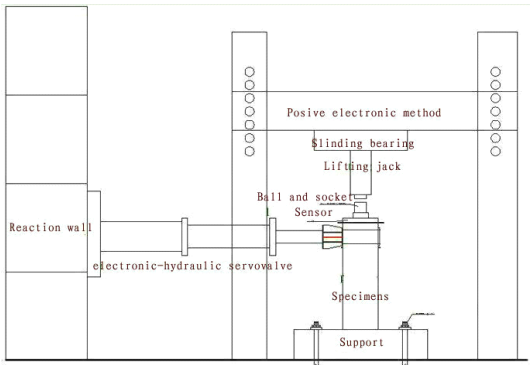

Fig.2 Test loading device sketch

Note: R in RBD-t stand for that the shape of the cross-section is rectangular, B indicates the dimension of the short side of the cross section (cm), t stands for the thickness of the steel plate. L=1200-160(1200 is the height of the cross section, 160 is half of the height of the loaded plate), cross-sectional area of steel is $A_s = 2t(D+B-2t)$ and cross-sectional area of concrete is $A_c = (D-2t)(B-2t)$, steel ratio: $\alpha = A_s / A_c$.

N indicates the Ratio of axial compression stress to strength. $n = N / N_0$. $N_0 = A_c f_{ck} + A_s f_y$, N_0 is the nominal axial stress.

Taking the main parameter, such as depth-width ratio of section, five concrete-filled rectangular steel tube members with different depth-width ratios are tested. The depth-width ratios of sections are 1, 1.25, 1.5, 1.75 and 2. Parameters of specimens are written in table 1.

Q235-B steel plate is used in the experiment. The steel pipe is made by four welding steel plate. Welded seam is designed according to the Code for Design of Steel Structures. Welded blanks adopt sweated straight welded joint.

According to the code Metallic Materials--Tensile Testing at Ambient Temperature(GB/T228-2002), yield strength of the steel plates with the thickness of 4 mm is 284.6MPa, ultimate strength is 390.5MPa, elastic modulus = 1.97e5 MPa.Steel pipe is filled with C30 commercial concrete with water reducing admixture and expansion admixture. Material of the foundation structure is C30 concrete consisted of ordinary Portland cement, limestone gravel, intermediate sand. According to the Standard for Test Method of Mechanical Properties on Ordinary Concrete (GB/T50081-2002), 9 specimens of 150mmX150mmX300mm standard concrete prism specimens and 9 specimens of 150mmX150mmX150mm standard concrete are made .Two groups are cured under the same circumstances. After 28 days, test of the cubic compression strength experiment and the prismy compression strength are made. The cubic compression strength f_{cu} =39.0MPa, f_c =29.8MPa; Characteristic value of the prismy compression strength is f_{ck} =0.88×0.76×1.00× f_{cu} =26.1MPa.

2.2 Loading units and loading system

2.2.1 Loading units

In this experiment, vertical pressure is exerted by a 3000 k N lifting jack. Lifting jack is fixed on a horizontal sliding bearing. The horizontal sliding bearing is fixed on a cross beam through two U-shaped steel bars. There are ball-and-socket and sensor on the top of the column. Relief valve is used to control the desired oil pressure in order to keep the applied axial force constant. Lateral force is applied by electronic-hydraulic servovalve fixed on the reaction wall. Vertical load is transmitted to the base and horizontal load is supported by the reaction wall. Loading units are shown in Figure 2.

2.2.2 Measuring equipment

It's very important to study the strain distribution on surface of steel pipes under cyclic loading .In this experiment; strain near the surface of steel columns is mainly studied. 24 strain gauges are pasted on the steel tubes.6 strain gauges are pasted on each side of tubes. Four pieces are pasted on the vertical position and two pieces are pasted on the horizontal position. Strain gauges are divided into two groups. The first group is 50mm far from the bottom, and the second group is 70mm far from the bottom. The strain cell used in the experiment is BX120-5AA. Strain in different stages is measured by DH-3815N, which is produced by Donghua Test Company in Jiangsu Province.

2.2.3 Loading system

During the experiment, axial force is first applied and the pre-loading takes 50 percent of the axial force. The non-uniform nature of the specimen is eliminated by pre-loading method, and then load is applied step by step until applied to the full load. Then full load has been maintained to the end of the experiment. Value of axial pressure is determined by the designed ratio of axial compression stress to strength. Value of axial pressure should be noticed and the changes of axial pressure should be controlled within 5%.Loading system of the experiment is shown in Fig.3.Force control loading system is adopted before the steel plate yields. Load is applied step by step. The steps are $0.25\,P_c$, $0.5\,P_c$, $0.7\,P_c$, P_c stands for failure load. One cycle of every stage. P_c is determined according to reference 1. Displacement control loading system is adopted after the steel plate yields. Taking the maximum displacement of the yielding specimen, load is applied step by step and controlled according to multiples of the displacement, three cycles of every stage until horizontal reaction dropped to 85% below the peak value of it. The yield point is determined by the coming up of inflection point of the hysteretic curve or the yield strain of steel.

2.3 Analysis of the results of experiment

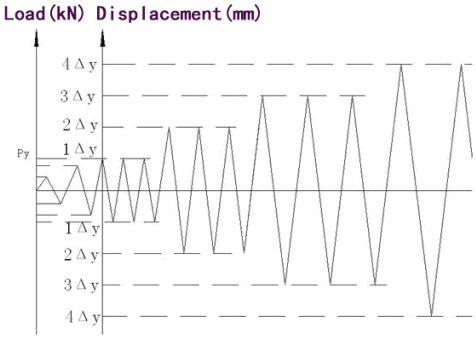

Fig.3 Loading system of the experiment

2.3.1 Failure mode

Failure modes of the four specimens are nearly the same and press-bending damages. With the increment of the horizontal displacement, buckling at the plate of column comes up after the load comes to the yielding load. In the process of unloading and loading, the buckling part is tensioned again and micro-buckling comes up at the other side of the plates. Buckling range is increasing and finally developed to lantern-like failure mode. The lower corners of the weld of R2035-4 and R2040-4 are ripped. Powder of concrete drops from the cracked welded seam. This indicates the internal concrete has been crushed and the quality of weld should increase with aspect ratios. Buckling part of the column lies 5-7cm above the column foot. Strain gauges lies nearly the same location. This indicates the locations of strain gauges are appropriate enough to capture the changes of the strain gauges. Sound of fragmentation of concrete can be heard in the loading process. The buckling specimen is still of great rigidity. This shows the good plasticity of the steel. Horizontal load doesn't increase until the buckling becomes very serious. So experiment shows the CFRST has good characteristics: high bearing capacity and good ductility. After the experiment, the steel plates are moved in order to observe the core concrete near the buckling plate.

2.3.2 Hysteretic curves

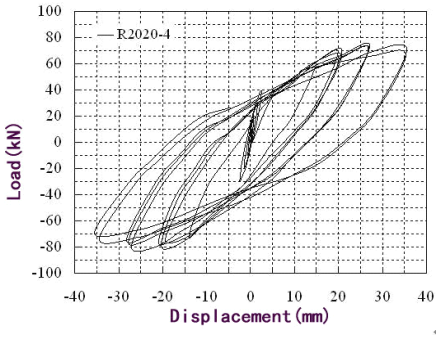

(a)

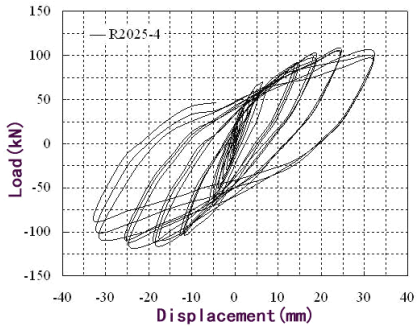

（b）

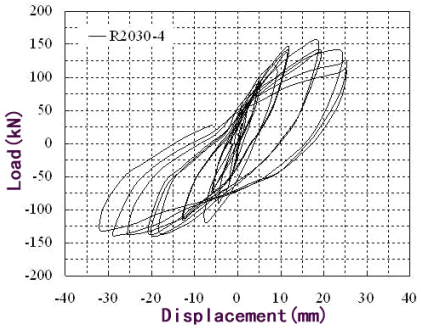

（c）

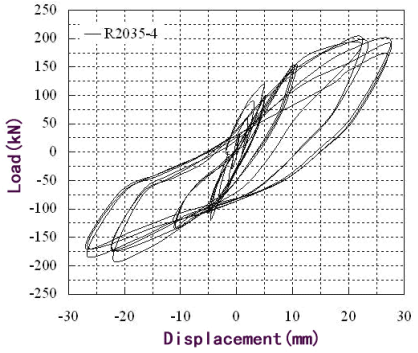

（d）

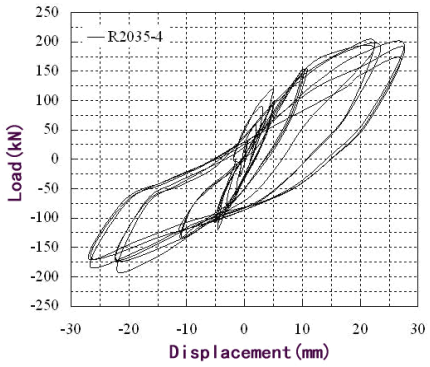

（e）

Fig.4 Hysteretic curve of specimens

（a）R2020-4 （b）R2025-4（c）R2030-4

（d）R2035-4 （e）R2040-4

Collusions can be achieved from the hysteretic curve of specimens: No matter what changes the parameters of components are, the load-displacement hysteretic curves are plump in shape and no significant pinch occurs. Hysteretic curves of R2020-4 and R2025-4 are most plump. Retrogression of strength and rigidity degeneration becomes not very obvious. A slight pinch contraction comes up in hysteretic curves of R2020-4 and R2025-4. Pinch contraction of the specimen R2040-4 is more obvious. This indicates effects of shear force and slip on big cross-section aspect ratio can't be neglected in process of the experiment.

2.3.3 Ductility and deformability

Ductility is a kind of deformability that structures (components, cross section, material) can still maintain its bearing capacity after the structure reach the elastic limit. Ductility can be evaluated by ductility parameter. Ductility parameter is the ratio between the maximum deformation Δ_u and elastic ultimate Δ_y. According to the code for seismic design of building, limit value of elastic story drift rotation $[\theta_e] = 1/300 = 0.0033$, limit value of elasto-plastic story drift $[\theta_u] = 1/50 = 0.02$. Value of elasto-plastic story drift rotation and limit value of elasto-plastic story drift are shown in Table 2. Limit value of elastic story drift rotation θ_y=0.0046～0.0069=(1.39～2.09) $[\theta_e]$, θ_u=0.023～0.034=(1.15～1.7) $[\theta_u]$, so structure comply with requirements according to the code for seismic design of building. With the increments of aspect ratios, deformability of specimen becomes weaker. So regulations should be made in order to ensure that columns of CFRST have sufficient deformability capacity.

Table2 Deformation and ductility factor of specimens

Serial number	NO.	Effective length	λ	Δ_y	Δ_u	μ	θ_y	θ_u
1	R2020-4	1040	18.01	7.2	35.48	4.93	0.0069	0.034
2	R2025-4	1040	14.41	6.5	32.8	5.05	0.0063	0.032
3	R2030-4	1040	12.01	6.06	27.27	4.5	0.0058	0.026
4	R2035-4	1040	10.29	5.46	27.07	4.96	0.0053	0.026
5	R2040-4	1040	9.01	4.8	24.81	5.17	0.0046	0.023

2.3.4Skeleton curves

Skeleton curves(P-△) of different CFRST specimens with different aspect ratios as shown in Figure 5.Figure 5 shows that the decline part of skeleton curves of the CFRST specimens with small aspect ratio is not obvious, this indicates the constraints of CFRST on the core concrete is obvious. However, the constraints becomes weaker with the increasement of the aspect ratio.

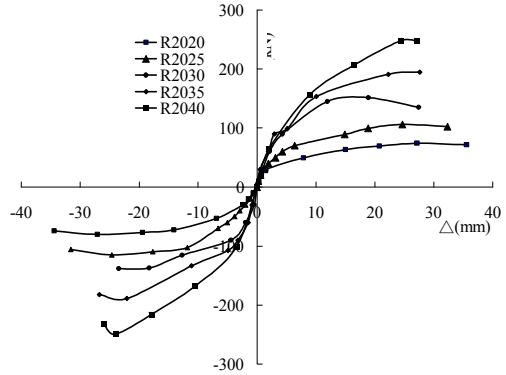

Fig.5 Impact of depth-to width ratio of section to skeleton curve

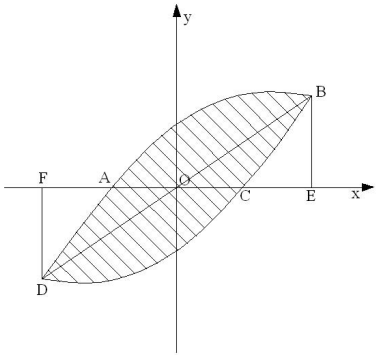

Fig.6 Diagrammatic sketch of calculation of energy P-△dissipated coefficient

2.3.4 Capacity of energy dissipation

Table3 The chart of the energy dissipative coefficients in different stages

Loading stages		1△	2△	3△	4△	5△
R2020-4	E	0.73	0.85	1.07	1.21	1.49
	β	0.12	0.14	0.17	0.19	0.24
R2025-4	E	0.68	0.93	1.02	1.22	1.52
	β	0.11	0.15	0.16	0.19	0.24
R2030-4	E	0.57	0.81	0.95	1.12	1.38
	β	0.09	0.13	0.15	0.18	0.22
R2035-4	E	0.61	0.76	0.81	1.05	1.13
	β	0.10	0.12	0.13	0.17	0.18
R2040-4	E	0.68	0.82	0.88	0.95	1.04
	β	0.11	0.13	0.14	0.15	0.17

By the role of alternate load applied on the columns, columns absorb energy when is loaded and release energy when is unloaded. Energy consumption in a loop is the difference between the absorbed and released energy. According to the Specification of Test Methods for Earthquake Resistant Building (JGJ101-96), energy dissipative coefficients E and equivalent viscous damping coefficients is used to evaluate the seismic performance of specimen.

$$E = \frac{S_{(ABC+CDA)}}{S_{(OBE+ODF)}} \qquad (1)$$

$$\beta = E/2\pi \qquad (2)$$

With the increasement of displacement, specimens gradually come into plastic stage. Energy dissipative coefficients E and equivalent viscous damping coefficients become bigger. However, capacity for energy-dissipating decreases with the increasement of aspect ratio.

3. CLOUSIONS

Five concrete-filled rectangular steel tube members with different aspect ratios are tested under low cycle reversed loading. The experiment indicates that: (1) The load-displacement hysteretic curves are plump in shape and no significant pinch occurs; (2) Members have a good capacity for energy-dissipating. It trends to increase beyond the plastic state of the members. However, the capacity for energy-dissipating decreases with the increments of the aspect ratios; (3) Aspect ratio has an influence on shapes and values of the hysteretic curves. Hysteretic curves of members with small aspect ratio are plump in fusiform shape. Therefore, that means the members have a good anti-seismic behavior. The elastic stiffness based on the load-displacement hysteretic curves increases with the increments of aspect ratios, thus the lateral bearing capacity increases obviously.

Acknowledgements:

This paper is supported by special subsidies construction of Shandong province “ Taishan Scholars ” programme. This support is gratefully acknowledged.

Reference:

Han L.H(2000), Concrete Filled Steel Tubular Structure.Beijing: Science press.

Li X.P, Lv X.L, Guo S.C (2005),"Seismic Behavior of CFRT Columns under Cyclic Loading I: experimental Study” Earthquake Engineering and Engineering Vibration, **25**(5): 95-103.

Zhu B.L(1989). Seismic experiment on structure.Beijing: Earthquake press.

You J.T(2002). Study for Dynamical Behaviors of Concrete Filled Rectangular Steel Tubes, FuZhou: FuZhou University.

JOINT CONFERENCE PROCEEDINGS
7th International Conference on Urban Earthquake Engineering (7CUEE) &
5th International Conference on Earthquake Engineering (5ICEE)
March 3-5, 2010, Tokyo Institute of Technology, Tokyo, Japan

SEISMIC RETROFIT OF RC OR SRC BUILDINGS WITH PRESTRESSED BRACES

Susumu Kono[1)], Takeshi Katayama[2)] and Fumio Watanabe[3)]

1) Associate Professor, Dept. of Architecture and Architectural Engineering, Kyoto University, Japan
2) Structural Engineer, Takenaka Co., Japan
3) Professor Emeritus, Dept. of Architecture and Architectural Engineering, Kyoto University, Japan
kono@archi.kyoto-u.ac.jp, katayama.takeshi@takenaka.co.jp, watanabe.fumio@takenaka.co.jp

Abstract: A seismic retrofit scheme using a prestressed concrete brace system was first proposed in 2001 to dramatically simplify seismic strengthening procedures by not using steel bar anchorage. The new system is quick to construct and economical compared to conventional retrofit methods. The system has been revised in terms of its aesthetics, materials, and construction methods from the first proposal. This paper introduces a series of prestressed concrete brace system and discusses their interesting features.

1. 1. INTRODUCTION

1.1 Background

The seismic upgrading of existing buildings has been attracting more attention than ever after major cities in the world experienced earthquakes last 20 years. The Japanese engineering society have made efforts to address problems related to the seismic rehabilitation of existing building structures. As a consequence, the standard and guidelines for seismic evaluation and retrofit methods were summarized (The Japan Building Disaster Prevention Association, 2005) and some codes were translated to English (Japan Concrete Institute, 2007).

Seismic retrofit is normally achieved by increasing strength, or ductility, or combining both of them. When a ductility enhancement retrofit method is taken, the retrofit cost is lower but the response displacement under seismic excitation becomes large resulting in serious damage of structural components. When a strength enhancement retrofit method is taken, the retrofit cost is higher but the damage tends to be minor since the retrofitted buildings tend to stay elastic. In addition to the structural performance, some other factors play important roles to determine the retrofit method. They involve aesthetics, construction period, construction cost, and etc.

Many existing buildings in Japan have not had seismic upgrading with any methods since construction is costly due to intensive labor work and long suspension of service no matter what retrofit scheme is taken. A research project started to develop a simple seismic strengthening system which decreases construction period and construction cost by employing no bolt anchorage. Based on this concept, a prestressed precast concrete brace system was initially proposed (Watanabe et al., 2004). The system has been revised to refine the configuration, materials and construction procedures. This paper introduces a series of prestressed brace system and their interesting features with experimental results.

1.2 Basic concept of prestressed brace system

Figure 1(a) shows schematic view of a prestressed brace system in an existing frame with some design issues. The diagonal members are ordinary precast concrete, fiber reinforced concrete, concrete filled tube, or steel. When the diagonal member experiences shortening, the horizontal component of the axial force resists the external lateral force. When the diagonal member experiences elongation, it is possible to freely come out of the surrounding frame since there is no bolt anchorage. To avoid this phenomenon, a special device with a flat spring and steel pipe (FSSP) in Figure 1(b) is installed at the bottom end of each diagonal member. FSSP maintains a certain amount of compressive force in the diagonal member even if the diagonal brace elongates.

The axial compression force – shortening relation of a brace is shown in Figure 1(c). First, the diagonal member and FSSP are assembled and prestressing force is introduced to the assemblage. After placing the assemblage in the frame and releasing the prestressing force, the force - shortening relation comes to Point C. As time goes by, the prestressing force decreases to Point D due to creep and shrinkage of concrete and Point D represents the ordinary service condition. The amount of creep and shrinkage is evaluated from empirical equation to predict Point D. When the assemblage experiences the seismic force, the force –

shortening relation of the brace is designed to stay between Point F and Point B. Then the brace does not fail due to excessive shortening and does not come out of the existing frame under elongation. In this manner, the brace resists the lateral load while it is in the first quadrant of Figure 1(c). In other words, due to the initial prestressing force, the brace resists the lateral force mainly when it is subjected to compression but to some extent when it is subjected to minor tension. If it experiences a large amount of tension, the brace no longer carries lateral force. Major design issues related to the prestressed brace system can be seen in Figure 1(a). These design issues are again discussed using the design flow chart later.

2. Evolution of presressed brace system

The proposed prestressed brace system is explained in three different stages of development. Authors had specific intensions to develop each generation of the system in terms materials, seismic performance, aesthetics, ease of construction, and etc. This does not mean that the most recent generation is superior to the other two in all aspects. However, each generation has different characteristics and all of them can be used in practice. As a matter of fact, the first generation is still being used after the second and third generations have been proposed. This chapter discusses the characteristic features of each generation.

2.1 First generation: X-shape precast prestressed concrete brace with a circular center core

The first generation of prestressed concrete brace consists of four precast elements as shown in Figure 2(a) and the detail information is seen in References (Watanabe et al. 2004, Kono et al. 2005). Precast Element C has a circular core which works as a hub of the diagonal braces. After assembling four elements at a construction site, prestressing force is introduced to two lower legs. Gaps between element ends and frame corners are filled with high strength no-shrinkage mortar. After hardening of mortar, the prestressing force is released. Then the X-shape brace extends and fixed to the boundary frame by itself. When a frame with the brace experiences lateral load, one of diagonal members works effectively in compression and the other diagonal member carries a little or no load. Figure 3 shows lateral load – drift relations of tested specimens shown in Figure 2(b). Two figures showed the results of two specimens with different axial buckling strengths of braces: the brace of No. 2 had higher buckling strength than that of No. 1. Both No. 1 and No. 2 failed with crushing of the brace concrete. The maximum capacity of No.1 was +397 kN and -410 kN, that of No. 2 was +726 kN. The initial stiffness was 122 kN/mm for No. 1 and 162 kN/mm for No. 2. Both specimens showed elastic response with small energy dissipation till failure. The hysteresis curves show minor slips near the origin. As mentioned earlier the axial stiffness of a brace changes at the point E in Figure 1(c), that is, the brace shows relatively low stiffness until the re-contact of the steel bearing plate and the steel pipe of FSSP device. Observed slip is mainly due to this abrupt stiffness change. The amount of slip depends on several variables such as the initial prestressing force and the stiffness of FSSP device. The slip does not seem to affect the seismic performance very much. Figure 3 also shows the lateral load carried by frame. The contribution of the original frame was obtained by deducting the lateral component of measured brace compressive force from total lateral force where the brace compressive force was calculated by concrete strain measurements. At the peak load, 64 % was sustained by the brace in No.1 and 79 % in No.2, respectively. However, the post-peak behavior for both specimens is brittle since the failure is caused by the compressive failure of the brace as shown in Figure 4 although the damage of surrounding frame was limited to flexural cracks of beams and columns since the enforced displacement was not very large. Hence, it is not appropriate to anticipate any energy dissipation after the peak and the design should count solely on the strength enhancement. Due to its low cost and ease of construction, the first generation brace system has been used at many school buildings and some office buildings as shown in Figure 5. For example, it is quite attractive to be able to finish the retrofit work during a two-week winter or spring vacation if the prestressed brace system is employed.

For the first generation brace system, prestressing force was applied with prestressing rods embedded in the X-shape assemblage. Since the one end of the rod was anchored at the central hollow circle as shown in Figure 2(a), prestressing force was not very efficiently introduced and it was not possible to take out prestressing rods after the construction. Hence removing the installed prestressed braces was not possible without damaging them. However, the circular central part of the brace system, the hub of the brace, is sometimes preferred to other generations and still be used in practice. The seismic performance is equivalent to that of the second generation.

2.2 Second generation: X-shape precast prestressed concrete brace without a circular center core

The second generation of prestressed brace system does not have a circular central core as shown in Figure 6 (Kono and Watanabe, 2006a and 2006b). The brace system consists of four legs and one central unit. Five units are assembled at a construction site and prestressing force is applied along both diagonal directions with external cables as shown in Figure 7. The gaps between the brace ends and frame corners are filled with high strength and no-shrinkage mortar as the first generation brace system. After the grout mortar hardens, the prestressing force is released so that the brace diagonals extend and securely fit into the existing frame. From this generation, the prestressing force is applied to the whole length of the brace with external rods and the efficiency of introduction of prestressing force was greatly

improved. Rods can be reused and the brace can be taken out by reapplying the prestressing force if necessary, making it possible to relocate the brace. The relocation capability is appealing to warehouse structures which occasionally change the live load configurations.

Two-story braced specimens in Figure 6(b) were built and tested to see the behavior under cyclic lateral load when the multi-story frame with the second generation bracing system experiences overall cantilever type deformation. Details of experiment can be seen in References (Kono and Watanabe, 2006a and 2006b). The ultimate failure was caused by the tensile yielding of the first story column and the load-drift relation after the yielding was greatly enhanced as shown in Figure 8. Specimen E1 had much larger deformation capacity after the peak. This large deformation capability was made possible by tensile yielding of the first story columns. Stiffness of the frame decreased first when the flexural cracking started at drift angle (R), R=±0.05 %, then again when longitudinal bars of columns started to yield at R= ±0.4 %. The maximum lateral load in positive direction, +324 kN, was recorded at R= +1.5 %. The force in the diagonal brace at the first floor was computed from the mean strain measured with strain gages on all four brace surfaces and the stress-strain relationship obtained from a cylinder compression test. The horizontal component was subtracted from the total lateral load to obtain the contribution due to the two columns of the original frame. The portion of the lateral load carried by the original frame is compared to the total load carried by the braced frame. The lateral load carrying capacity of braced frames was nearly three times larger than that of the original bare frame as Specimens No. 1 and 2. Specimen E1 also shows some slip near the origin due to the loose contact of FSSP device as Specimens No.1 and 2 but a small amount of slip is considered permissible. The ductility of Specimen E1 is much greater than the first generation brace system. An example of the second generation is shown in Figure 9. Since the volume of concrete decreases, the brace blocks out less view and more light can pass the retrofitted span.

The second generation does not have a circular central hub which exists in the first generation, and it is slender and takes more light than the first generation. Since the prestressing is carried out with the external tendons, the brace can be taken out by applying the prestressing later. This makes it possible to relocate the brace when it is necessary. These features are preferred to the first generation.

2.3 Third generation: Single line prestressed brace using concrete filled tube or fiber reinforced concrete

The third generation of prestressed brace system is a single line element as shown in Figure 10 (Kono and Watanabe, 2007a and 2007b)). Materials of the brace were either concrete filled tube (CFT) or fiber reinforced concrete (FRC) to increase the deformation capability so that the brace does not exhibit sudden drop of load after the peak load. The details of experiment are shown in References (Kono and Watanabe, 2006a and 2006b). Loading system is shown in Figure 11. Figure 12 shows the lateral load – drift relations for CFT (CFT-S60) and FRC (FRC-L30) braced frames. For CFT-S60, the initial stiffness changed when cracking was observed at the left (left in Figure 10 and Figure 11) column-beam joint and the beam ends at R=0.2%. The load carrying capacity still increased until the yielding of the beam at R=0.6%. The number of cracks increased from R=0.4% at the left column-beam joint but the maximum crack width was less than 0.1 mm. The axial force of the brace reached the maximum value at R=0.4% and started to buckle resulting in the second stiffness change. Total lateral load reached the peak at R=0.6% when buckling deformation of the brace was visually observed. Load carrying capacity decreased gradually after buckling but brittle failure did not happen. On the other hand, the load – drift relation of FRC-L30 was stiffer than that of CFT-S60 because of the larger section size of the brace. The reinforced concrete portal frame of FRC-L30 showed the first cracks at the left column-beam joint at R=0.2%. The load carrying capacity increased up to R=0.6%. After that, drift angle increased with keeping the load carrying capacity almost constant. At this stage, large diagonal bearing and shear cracks were observed at the left column-beam joint and the brace started to penetrate the left column-beam joint. Minor cracks parallel to the axial direction were observed in the brace at R=0.8%. The brace of FRC-L30 was so strong that it penetrated the left column-beam joint by 20 to 30 mm. FRC-L30 failed due to the shear or bearing failure of the left beam-column joint.

CFT-S60 showed gradual degradation of load after the buckling occurred at the spliced mid span. FRC-L30 reaches the peak load at drift angle of 0.8%, whereas Specimens No. 1 and No. 2, which employ the ordinary precast concrete as shown in Figure 3, reached the peak at drift angel less than 0.6%, and the effect of fiber can be seen. However, FRC-L30 shows the rapid degradation after the compressive failure has occurred at the mid span.

The configuration of the third generation was changed to a line element so that the brace aesthetically looks better and an opening can be made at the braced span if necessary. Since a line element can resist against force in a single direction and does not work in opposite direction, it is necessary to place braces for the opposite direction at some other spans. However, placing simple line elements instead of X-shape elements saves construction time and labor. In addition, CFT has more advantages in construction. The steel tube of CFT may be divided into several pieces, brought to the construction site using existing elevators, assembled at site, and placed in the existing frame, then the inside of the steel tube is filled with grout mortar. In this way, CFT necessitates the minimum amount of construction materials and excludes heavy construction equipment.

3. design and construction

3.1 Design procedures

The proposed design procedure (Kono and Watanabe, 2008) is shown in Figure 13. The possible ultimate failure modes of braced frame include five modes: (1) buckling of diagonal members, (2) joint shear failure, (3) tensile failure of beams, (4) tensile or compression failure of the first story column when the multiple-story brace system, and (5) the rocking mode of the foundation. The buckling of diagonal members is designed to precede the other failure modes to avoid the damage to the structural components in the existing buildings. The buckling strength needs to take into account the initial imperfections of the diagonal members. All possible failure modes are sequentially checked based on the design flow in Figure 13. After the determination of the ultimate failure mode, the initial prestressing force of the brace is determined considering the prestressing loss due to the shrinkage and creep. The number and location of braces and the structural type of existing buildings also influence the initial prestressing force. Main consideration at design is the determination of the ultimate failure mode, computation of the lateral load carrying capacity and displacement capacity, determination of the initial prestressing force, and determination of the mechanical properties of FSSP (flat spring-steel tube).

3.2 Construction methods

There are two ways to introduce prestressing force to braces: pre-tensioning and post-tensioning. For a pre-tensioning system, the prestressing force is introduced to the assembled braces with external cables, the assemblage is placed inside the frame, the gap between the assemblage and the surrounding frame is grouted, and the external cables are released and taken out. On the other hand, the post-tensioning system, the assemblage of brace is placed inside the frame, the gap is grouted, and the hydraulic jack is used to introduce prestressing to the assemblage. The threaded steel tube is extended to fill the gap made after the introduction of prestressing force. It is possible to relocate both pre-tension and post-tension systems. By re-applying the prestressing force to the brace assemblage, the assemblage shortens and can be removed form the position. The same procedure may be taken to put the assemblage in a new location.

4. CONCLUSIONS

Prestressed brace system was proposed to retrofit existing buildings vulnerable to seismic damage by basically increasing the strength. The system is recognized as a quick, easy and economical retrofit method since it employs no bolt anchorage. The system has been frequently used at school buildings for its short-term and economical construction. The paper introduces the evolution of the system since 2001. The current system has ductility, re-location ability and short-term and economical construction capability using advanced materials. The good seismic performance of the system has been proved through experiment and analysis from their first introduction. The authors hope that the proposed system is widely used for the seismic upgrade of existing structures.

Acknowledgements:

A part of this research was financially supported by Japanese Ministry of Land, Infrastructure and Transport (PI, F. Watanabe) and Kajima Research Fund (PI, S. Kono). The authors acknowledge S. Miyazaki, Y. Okuno, M. Tani, Y. Ichioka, K. Takao, T. Matsuda, M. Oda, Y. Kimura and H. Hasegawa, who are former students at Kyoto University, for their contribution to experimental and analytical works from 2001 through 2008. Special thanks are extended to Takenaka Co., Daiwa Co. and Nagai Design Office for their valuable technical suggestions.

References:

Japan Concrete Institute (2007) “Seismic Rehabilitation of Concrete Structures.” Editor Shunsuke Sugano.

Kono S. and Watanabe F. (2005). “Seismic retrofit using precast prestressed concrete braces” Advanced Materials for Construction of Bridges Buildings and other Structures, August 14-19, Maui, Hawaii.

Kono S. and Watanabe F. (2006a). “Seismic Performance of RC Structures Strengthened with Precast Prestressed Concrete Braces.” 2nd International fib Congress, June 5-8, Naples, Italy, Paper 9-36.

Kono S. and Watanabe F. (2006b). “Seismic retrofit using precast prestressed concrete braces.” 8th US National Conference on Earthquake Engineering, Disc1, Paper 8NCEE-00063.

Kono S., Oda M., Watanabe F. (2007a). “Seismic retrofit of RC structures with prestressed CFT and FRC braces.” Eighth Pacific Conference on Earthquake Engineering, Dec 5-7, Singapore, Paper 8PCEE/109.

Kono S., Oda M., Watanabe F. (2007b). “Proposal of a new RC structure seismic retrofit method using prestressed concrete braces.” Structural Engineering World Congress - 2007, Nov 2-7, 2007, Bangalore, India, Paper 123.

Kono S. and Watanabe F. (2008). “Seismic Retrofit of RC Buildings with Prestressed Braces.” Fumio Watanabe Symposium, October 24-25, 2008, Kyoto, Japan, pp. 233-240.

The Japan Building Disaster Prevention Association (2005). “English version 1st, Standard for Seismic Evaluation of Existing Reinforced Concrete Buildings, 2001, Guidelines for Seismic Retrofit of Existing Reinforced Concrete Buildings, 2001, and Technical Manual for Seismic Evaluation and Seismic Retrofit of Existing Reinforced Concrete Buildings, 2001” Translated by Building Research Institute.

Watanabe, F., Miyazaki, S., Tani, M. and Kono, S. (2004). “Seismic Strengthening Using Precast Prestressed Concrete Braces.” The 13th World Conference on Earthquake Engineering, Vancouver, August, Paper 3406.

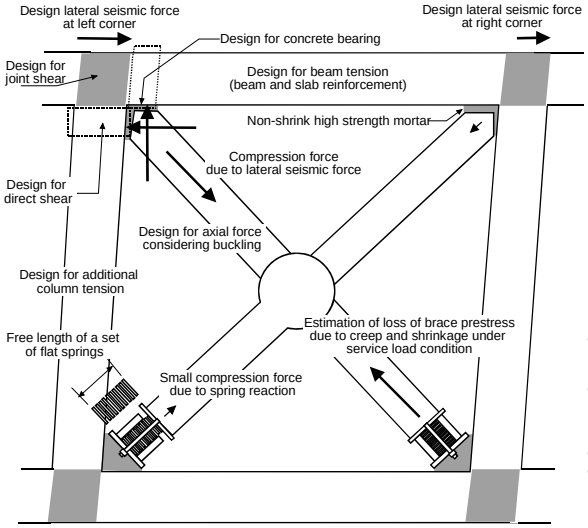

(a) Brace system and its major design issues

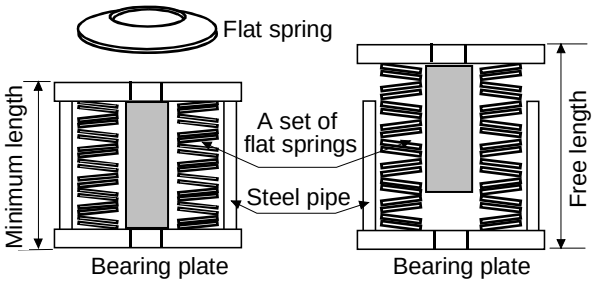

(b) Assemblage of flat springs and steel tube

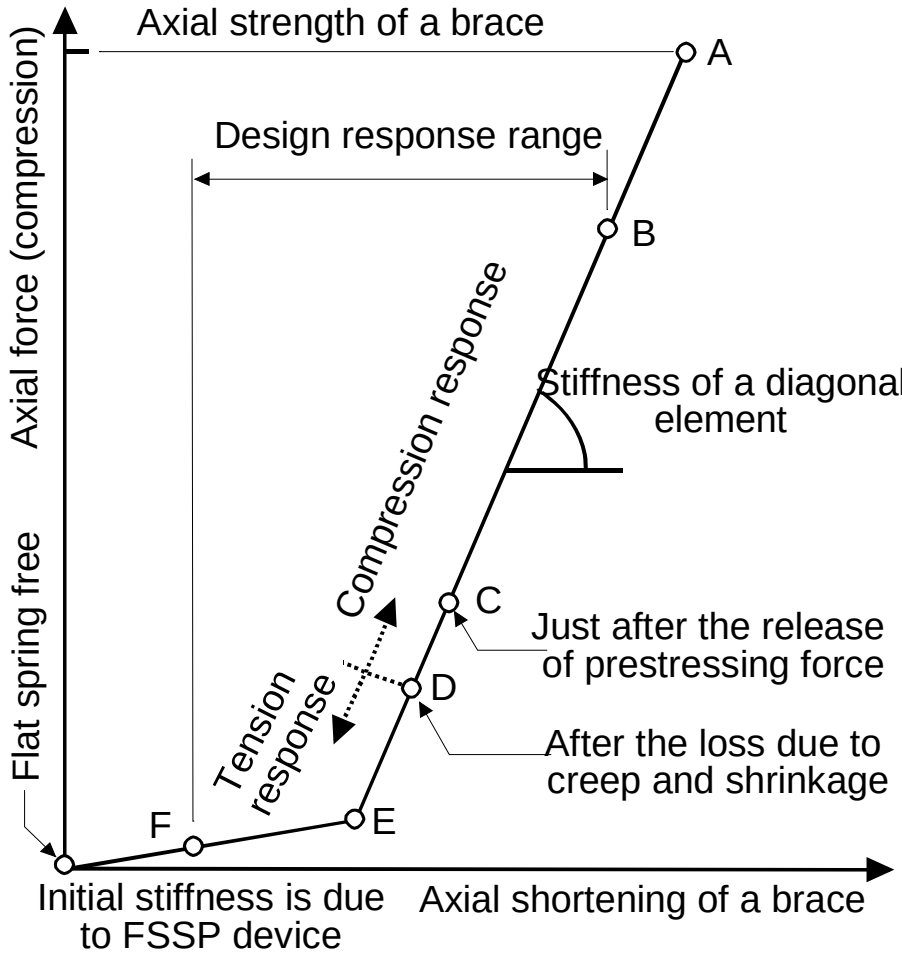

(c) Axial force-displacement relation of brace

Figure 1. Prestressed brace system and its resisting mechanism

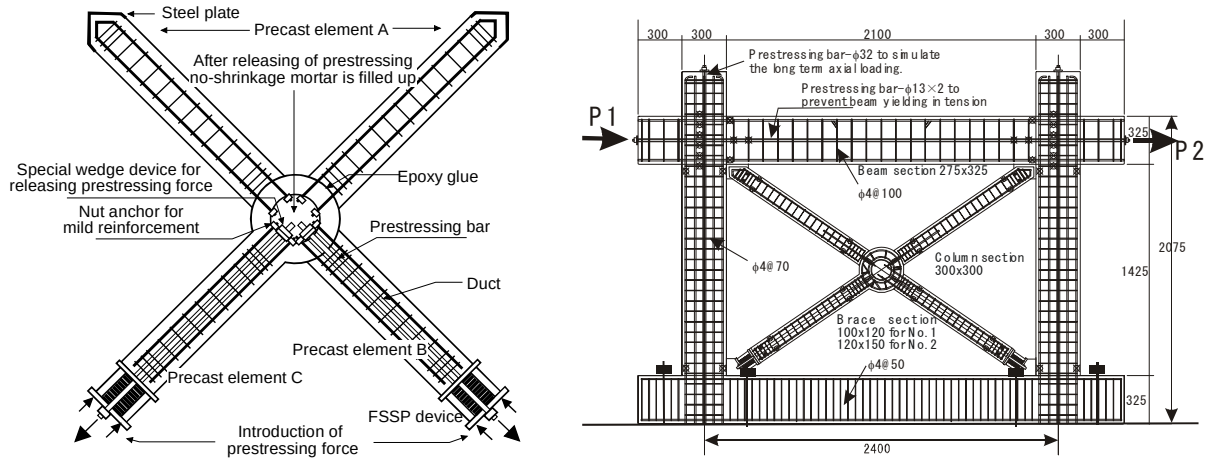

(a) Four-piece precast brace unit (b) Specimen configuration (Unit: mm)

Figure 2. The first generation prestressed brace system (Watanabe et al., 2004)

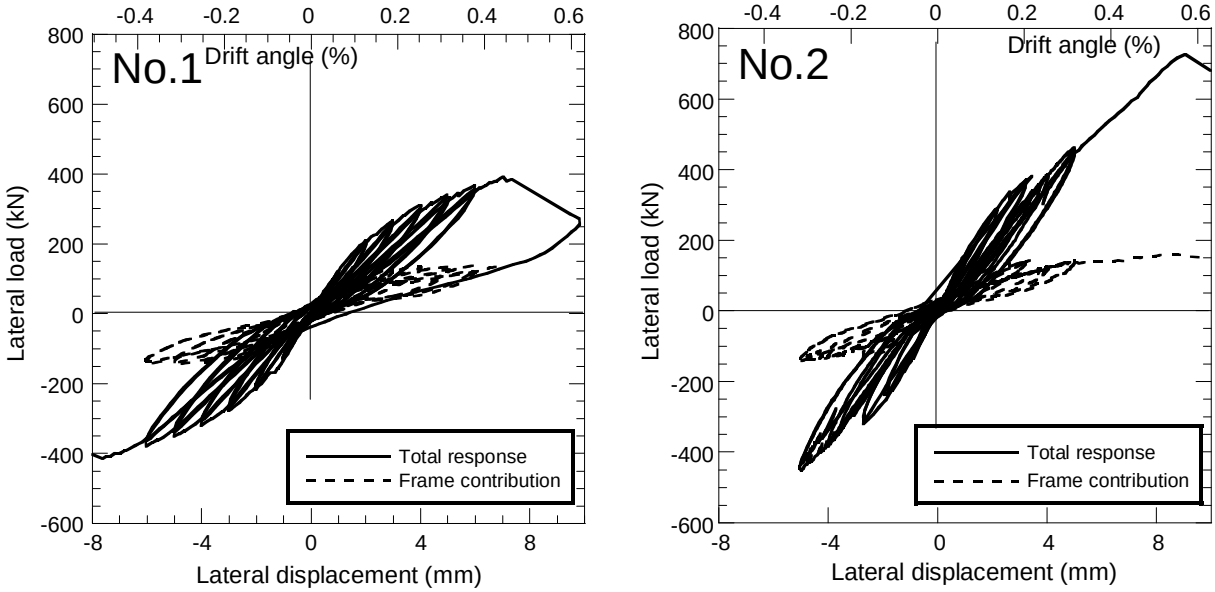

(a) Specimen No. 1 (b) Specimen No. 2

Figure 3. Lateral load – drift relation of the prestressed brace system (Watanabe et al., 2004)

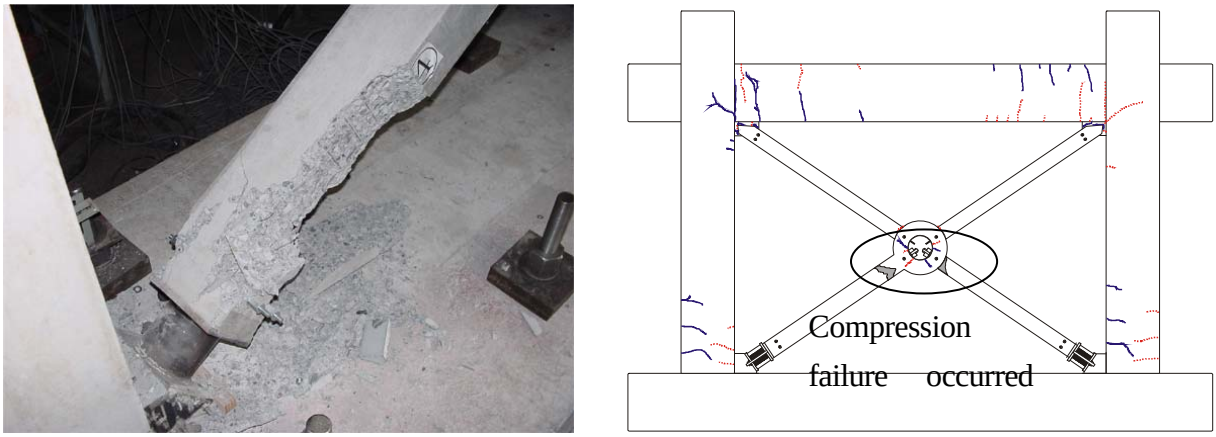

(a) Compression failure at the foot of brace No. 1 (b) Failure modes of No. 2

Figure 4. Failure modes of the first generation brace system



(a) Office building



(b) High school building



(c) University building A



(c) University building B

Figure 5. Examples of the first generation brace system (Courtesy of Daiwa Co.)

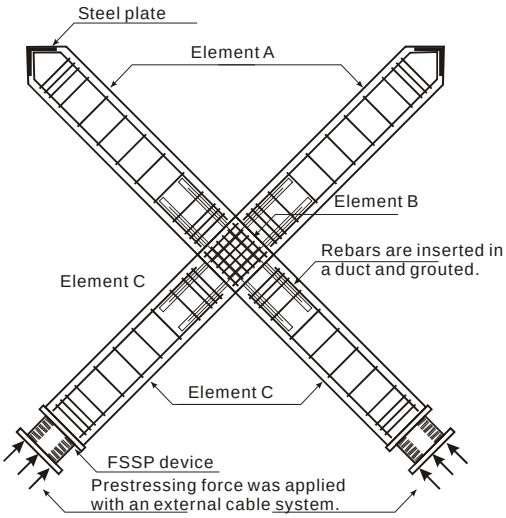

(a) Assembled brace

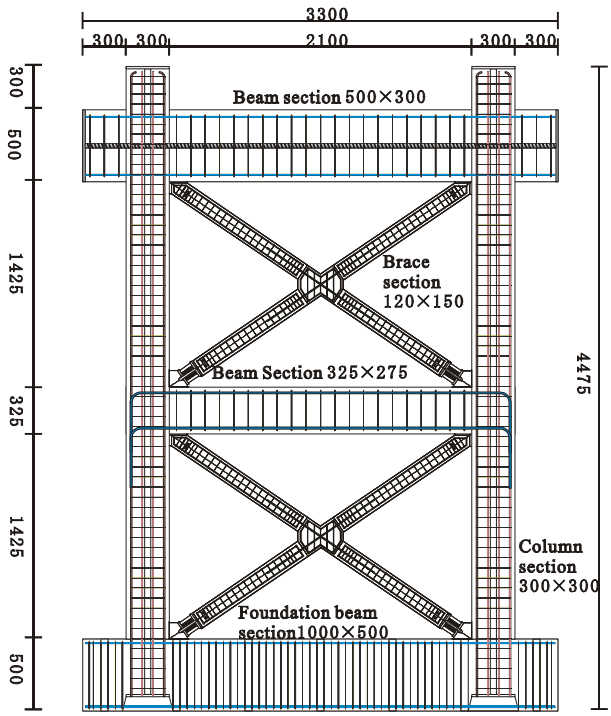

(b) Two-story specimen (E1)

Figure 6. The second generation prestressed brace system (Kono and Watanabe, 2006a)



Figure 7. Introduction of prestressing force by external cable (Courtesy of Daiwa Co.)

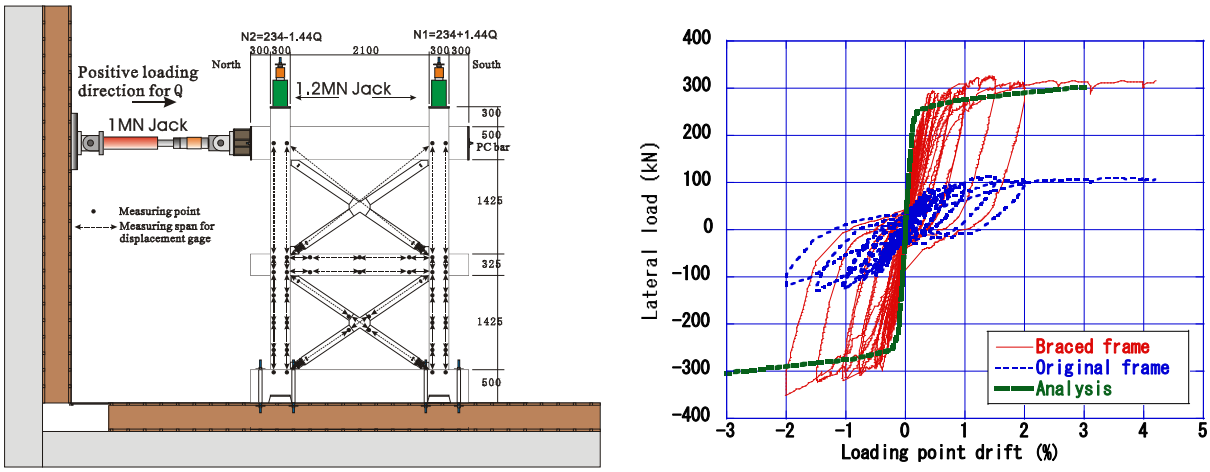

(a) Loading system (b) Lateral load – drift relation

Figure 8. Test setups and results for Specimen E1 in Figure 6 (Kono and Watanabe, 2006a)



Figure 9. Use of the second generation brace system at the first story of a company dormitory building (Courtesy of Daiwa Co.)

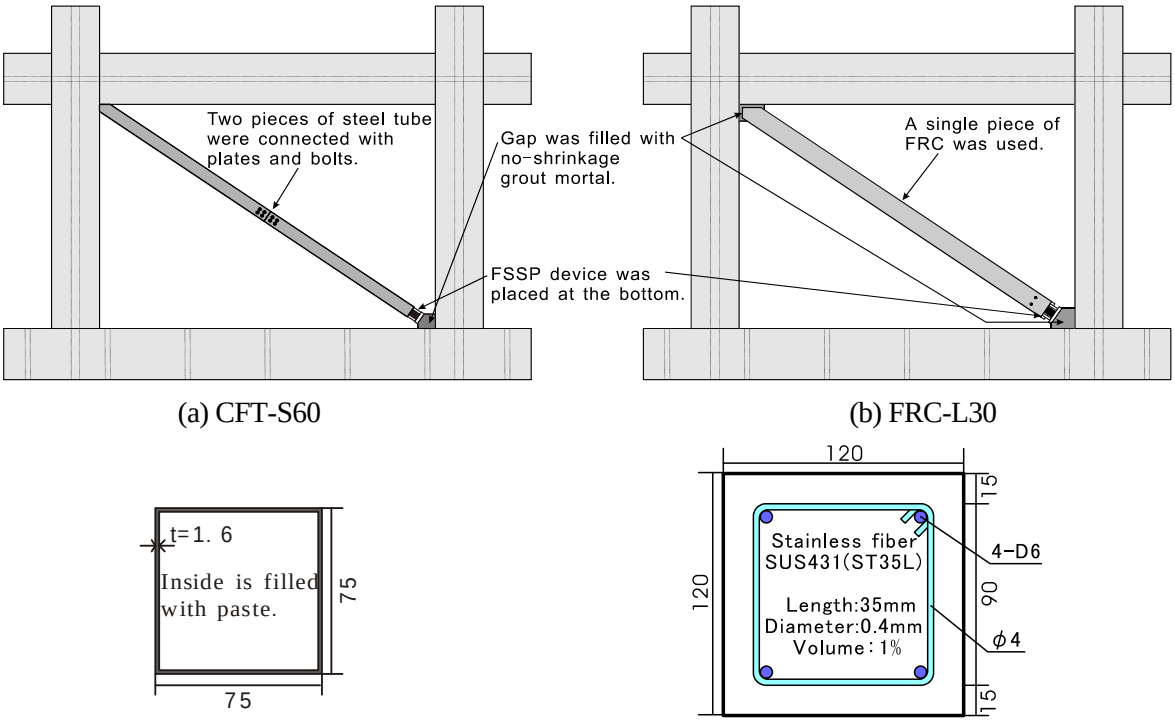

Figure 10. Third generation bracing system with CFT and FRC braces (Kono and Watanabe, 2007a)



Figure 11. Loading system in 2007

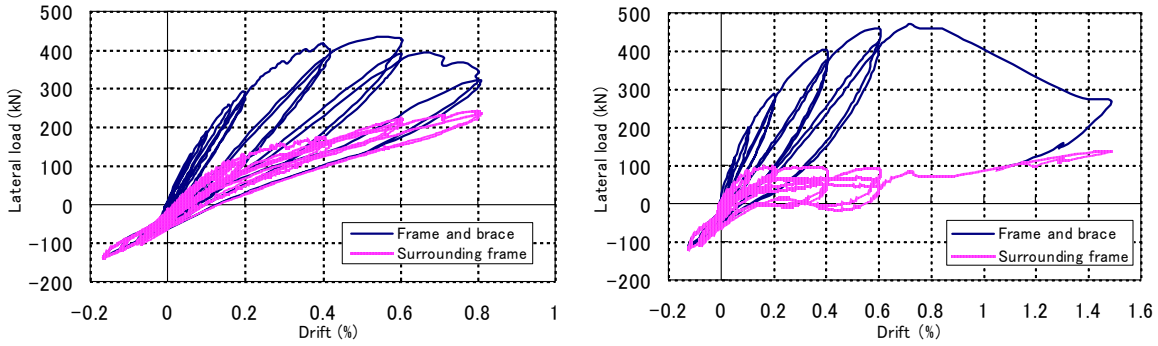

(a) CFT-S60 (b) FRC-L30

Figure 12. Lateral load – drift relations for specimens in Figure 10 (Kono and Watanabe, 2007a)

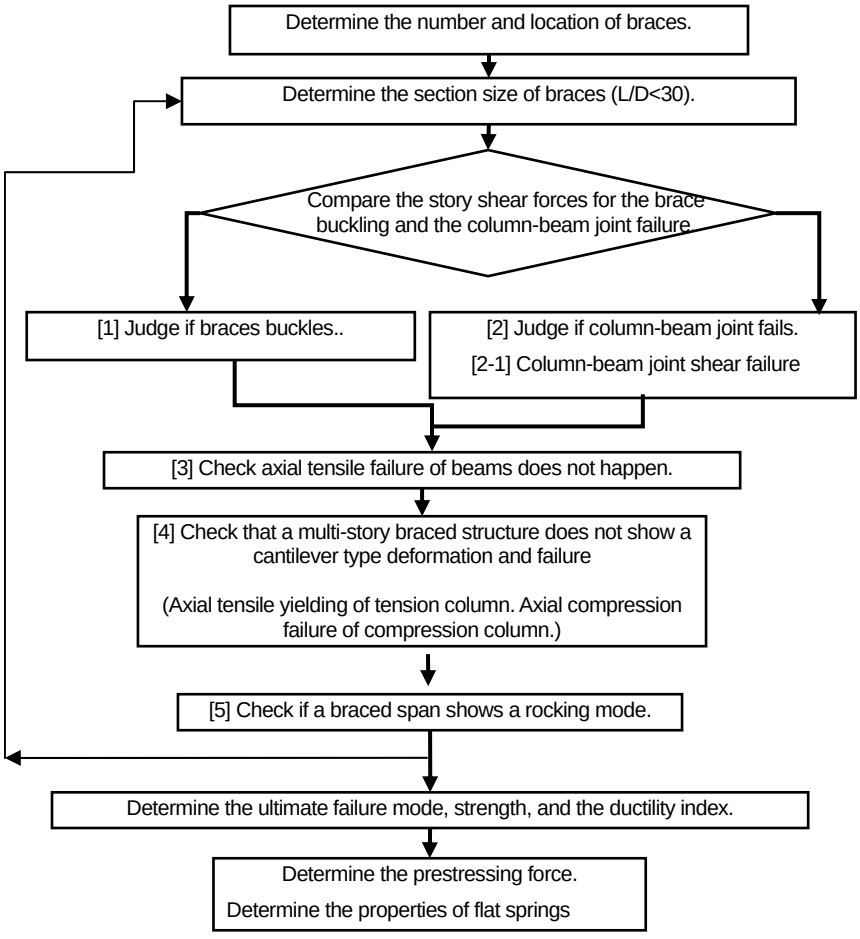

Figure 13. Design flow of prestressed braces

JOINT CONFERENCE PROCEEDINGS
7th International Conference on Urban Earthquake Engineering (7CUEE) &
5th International Conference on Earthquake Engineering (5ICEE)
March 3-5, 2010, Tokyo Institute of Technology, Tokyo, Japan

SEISMIC EVALUATION AND RETROFIT OF RC BUILDINGS BY USING STRUCTURAL WALLS

Chao-Lin Huang, Yeou-Fong Li* and Chih-Tsung Lin
Department of Civil Engineering
National Taipei University of Technology
yfli@ntut.edu.tw

Abstract : In this paper, two types of innovative web reinforcement configuration based on the concept of maximum principal stress trajectories are presented. One is the concentric circles reinforcement, and the other is spiral reinforcement with the placement of the conventional type (horizontal and vertical reinforcement). Analytical and experimental results show that structural walls with that reinforcement perpendicular to the inclined cracks have greater ductility than that of the conventional structural walls. The SDOF model with a bilinear force-displacement relationship and an "equivalent column" model are used to define the suitable parameters of plastic hinges of walls, and apply it to perform nonlinear static pushover analysis for seismic evaluation and retrofit of existing RC buildings with inadequate lateral force resisting systems

1. INTRODUCTION

The RC structural wall is an effective earthquake resistance element and it is widely used by structural engineers in designing new structures as well as in rehabilitating existing RC buildings. However, the conventional RC walls failed due to web crushing and diagonal cracking with a sudden and brittle fracture. Therefore, to improve the seismic performance of structural walls, the innovative web reinforcement configuration based on the maximum tensile principal stress and the compressive stress trajectories is presented, which combines the concentric circles reinforcement (or spiral reinforcement) with the placement of the conventional type (horizontal and vertical reinforcement), as shown in Fig. 1and Fig. 2, respectively. Because it is clear to predict the cracking patterns and failure modes in the RC walls by using the maximum principal trajectories, it can help engineers decide where to reinforce and how to increase the ductility for the wall.

In the past few decades, most researches focused the experimental investigations on the failure mechanism, strength, stiffness, ductility, and the hysteretic loop of RC shear walls under lateral loading. For instance, Hwang et al. [1] presented a softened strut-and-tie model to determine the shear strength and load deflection responses of short walls. Li et al. [2] proposed an equivalent column model to analyze the RC frames with RC walls and compared with the experimental results. The results show that the equivalent column model can simulate the pushover analysis of RC frames with structural walls with a good accuracy. Mo et al. [3] performed a series of experimental tests on RC framed shear walls subjected to reversed cyclic lateral loading by the large-scale specimens. The experimental results show that structural walls with reinforcement oriented close to the principal tensile direction of applied stresses have greater ductility than that of the conventional structural walls.

The purpose of this paper is to improve the ductility of RC structural walls under lateral seismic forces. To achieve this goal, the wall structure should be able to dissipate energy during an earthquake and brittle shear failure should be prevented. This basis implies that micro-cracks gradually and uniformly distributed along the wall web. The SDOF model with a bilinear force-displacement relationship is used to determine the elastic-plastic seismic responses of structural walls. Also, the RC structural wall is modeled as an "equivalent column" to define the suitable parameters of plastic hinges of walls, and perform nonlinear static pushover analysis for seismic evaluation and retrofitting of existing RC buildings.

2. MAXIMUM PRINCIPAL AND SHEAR STRESSES

It is important to determine the orientation of the planes that causes the maximum principal and shear stresses in engineering practice; therefore, the cracking patterns and failure modes can be predicted.

2.1 Principal Stress Trajectories

The elements in Fig. 3e are subjected to combined normal stresses due to flexural stress τ_{yy} , and shear

stress τ_{xy}. The maximum and minimum normal stresses acting on such an element are called principal stresses (σ_1, σ_2), and the corresponding planes are called the principal planes of stress as shown in Fig. 3f. In order to find the magnitudes of principal stress for this element can be applied by either the stress-transformation equation or Mohr's circle, due to τ_{xx}, that is

$$\sigma_{1,2} = \frac{\tau_{yy}}{2} \pm \sqrt{\left(\frac{\tau_{yy}}{2}\right)^2 + \tau_{xy}{}^2} \tag{1}$$

The magnitude of the maximum shear stress can be determined as follows:

$$\tau_{\max} = \sqrt{\left(\frac{\tau_{xx} - \tau_{yy}}{2}\right)^2 + \tau_{xy}{}^2} = \frac{\sigma_1 - \sigma_2}{2} \tag{2}$$

The directions of principal stresses σ_1 and σ_2 can be determined as following

$$\tan 2\phi = -\frac{2\tau_{xy}}{\tau_{yy}} \tag{3}$$

Applying Eq. (1) and Eq. (3), the principal stresses and their corresponding principal directions at each element can be obtained. For element 1 or 5 in Fig. 4b, we have $\tau_{xy} = 0$ and obtain $\tan 2\phi = 0$, yielding $\phi_1 = 0^0$ and $\phi_2 = 90^0$. For the element 3 at the neutral surface, due to shear stress only, so that the $\phi = \pm 45^0$. The results of shear stress, bending stress, and principal stress are shown in Fig. 3c ~ Fig. 3f. Besides, by calculating ϕ from Eq. (3) for a number of points defined by coordinates x and y, it is possible to construct two families of orthogonal curves whose tangents at each point coincide with the directions of principal stress trajectories as shown in Fig. 4a. Here the solid lines represent the direction of the maximum tensile principal stresses and the dashed lines represent the direction of the compressive principal stresses (in Fig. 4a). As expected, the lines intersect the neutral axis at 45^0, and the solid and dashed lines always intersect at 90^0. It should be noted that knowing the direction of principal stress trajectories can help structural engineers decide where to reinforce a structural wall to prevent diagonal tension cracks from extending and brittle crushing of the wall.

3. INELASTIC FORCE-DISPLACEMENT RELATIONSHIPS

The plastic behavior of structural walls can be analyzed and designed using the theory of flexure when subjected to lateral loads.

3.1 SDOF Model

A RC structural wall can be modeled as an SDOF spring-mass system, and the illustration figure is shown in Fig. 5a. The bilinear force-displacement relationship of the SDOF spring-mass system is shown in Fig. 5b. In Fig. 5b, the ultimate spring force, P_u, for the maximum displacement of the spring can be expressed as follows.

$$P_u = P_y + P_{iy} = k_e u^*{}_y + k_p u_i \tag{4}$$

where P_y is the yield force, P_{iy} is the force after yielding, k_e is the elastic stiffness and k_p is the post-yield stiffness, $u^*{}_y$ is the displacement of the SDOF spring-mass system at the beginning of yielding, and u_i is the displacement that occurs after yielding. The maximum displacement of the SDOF system, u_m, can be expressed as

$$u_m = u^*{}_y + u_i \tag{5}$$

Therefore, Eq. (4) becomes

$$P_u = k_e u^*{}_y + k_p \left(u_m - u^*{}_y\right) \tag{6}$$

If the u_m is greater than the yield displacement, then P_u becomes

$$P_u = P_y + k_p \left(u_m - u^*{}_y\right) \tag{7}$$

3.2 The Curvature and Curvature Ductility

As seen in Fig. 6, the point at the yielding point ($\phi^*{}_y$, M_y) defines a straight line from the origin, whose intersection with the horizontal line at the ultimate flexural strength M_u may be considered the nominal yield curvature ϕ_y. The yield curvatures of walls are calculated here.

$$\phi^*{}_y = \frac{M_y}{E_c I_{zz}} = \frac{\varepsilon_y}{d - c} = \frac{\varepsilon_y}{(1 - k_y)d} \tag{8}$$

$$\phi_y = \frac{4}{3}\phi^*{}_y \tag{9}$$

Next, the ultimate curvature can be calculated as follows:

$$\phi_u = \frac{\varepsilon_{su}}{(d - c)} = \frac{\varepsilon_{su}}{(1 - k_{su})d} \tag{10}$$

The curvature ductility is defined as follow.

$$\mu_\phi = \frac{\phi_u}{\phi^*_y} \tag{11}$$

3.3 Yield Displacements and Displacement Ductility

Consider the MDOF system shown in Fig. 7a. The flexural yield displacement can be calculated with the elastic bending moment-curvature relationship, and the resulting equation can be expressed as:

$$u_y = C\phi_y H^2 \tag{12a}$$

where *C* can be derived by using the unit force method and expressed as follows

$$C = \frac{2n^4 + \sum_{i=1}^{n}(n-i)^3(2n+i)}{2n^2(n!)(2n+1)} \tag{12b}$$

where *n* is the number of degree-of-freedom.

Finally, the displacement ductility is determined from the equation proposed by Priestley and Park [4]:

$$\mu_u = 1 + 3(\mu_\phi - 1)\frac{L_p}{H}\left(1 - 0.5\frac{L_p}{H}\right) = \frac{u_m}{u_y} \tag{13}$$

where L_p is the plastic hinge length, and L_p=0.5$L_w$is generally a good estimate for RC structural walls (Wallace and Moehle 1992) [5]:

Once the values of u_y and displacement ductilityμ_u are obtained, the maximum displacement u_m can be determined directly from Eq. (13).

4. NONLINEAR STATIC PUSHOVER ANALYSIS

In this section, the nonlinear static pushover analysis of RC structural walls is used to verify the effectiveness of the proposed methodology. In order to perform nonlinear static pushover analysis with ETABS Version 9.0 program to determine the force-displacement capacity curve of walls, the RC structural wall can be modeled as an "equivalent column" shown in Fig. 8.

In addition, it is assumed that the entire vertical loads are supported by both boundary columns and RC wall, but all the lateral loads are resisted by the wall only.

4.1 Analytical Model

Fig. 9a shows the analytical model of framed RC walls. As seen from Fig. 9b, the boundary columns are modeled to be axially rigid as two-force members, and the RC wall is modeled by an "equivalent column" located at the wall centerline. It also indicates that the boundary column uses an axial spring to represent the axial stiffness and strength of the boundary column. Meanwhile, the wall uses two rotational springs, one axial spring and one shear spring to represent the flexural, axial and shear stiffnesses and strengths of the wall, as shown in Fig. 9a. Please note that the structural wall is regarded as an equivalent column, and it must resist the moments, shears, and axial loads acting on it.

4.2 Define Plastic Hinge Properties

The RC wall is modeled as two rotational springs shown in Fig. 9a; the nonlinear moment hinge corresponding to the rotational spring is shown in Fig. 9, and the parameters of moment hinge are listed in Table 1. Please note that the points D and E are the residual strength of the wall where $P_r = 0.4P_u$. In Table 1, "Moment/SF" is defined as $M_u = P_u \times H$, and the "Rotation/SF" is defined as $\left(u_m - \frac{P_u}{P_y}u_y^*\right)\frac{1}{H}$. Also, the nonlinear shear hinge corresponding to the shear spring is shown in Fig. 9, and the parameters of shear hinge are listed in Table 2. The "Force/ SF" is defined as P_u; and the "Displacement /SF" $=\left(u_m - \frac{P_u}{P_y}u_y^*\right)$, where the maximum lateral force P_u is determined as follows:

$$P_u = \min.(P_{fu}, P_{su}) \tag{14}$$

where the maximum flexural strength $P_{fu} = M_u / H$, and the maximum shear strength $P_{su} = V_u = (V_c + V_s)$, as according to ACI code.

5. CONCLUSIONS

1. Analytical and experimental results show that structural walls with the proposed Concentric circles reinforcement, or spiral reinforcement perpendicular to the inclined cracks have greater ductility than that of the conventional RC walls.
2. Experimental results show that micro-cracks will occur gradually and uniformly distributed along the wall web, which implies that will be able to dissipate energy during an earthquake and brittle shear failure can be avoided.
3. The proposed analytical procedures for bilinear force-displacement curves can predict the nonlinear seismic behavior of structural walls. In addition, the RC wall can be easily implemented by using suitable parameters of plastic hinges of "equivalent column model" obtained from the bilinear force-displacement curve to perform nonlinear static pushover analysis. It will be very helpful for the seismic evaluation of existing RC structural wall buildings.

REFERENCES

[1] Hwang, S.J., Fang, W.H., Lee, H.J. and Yu, H.W., 2001, "Analytical model for predicting shear strength of squat walls." ASCE Journal of Structural Engineering, Vol.2, pp. 43-50.

[2] Li, Y. F., Lin, Y. J., Chen, C. W., and Lin, C. T., 2007, "Theoretical and Experimental Studies on the As-built and Repaired Rehabilitated RC Frames," Canadian Journal of Civil Engineering, Vol. 34, No. 8, pp. 923-933.

[3] Mo, Y.L., Liao, W.I. and Loh, C.H., 2005, "Studies of high seismic performance shear walls-test and simulation." In 7th Japan-Taiwan-Korea joint seminar on earthquake engineering for building structures, Seoul, Korea.

[4] Priestley, M.J.N., and Park, R., 1987, "Strength and ductility of concrete bridge columns under seismic loading." ACI Structural Journal, Vol. 84, pp. 61-76.

[5] Wallace, J.W. and Moehle, J.P., 1992, "Ductility and detailing requirements of bearing wall buildings," Journal of Structural Engineering, ASCE, Vol. 118, No. 6, pp. 1625-1644.

.

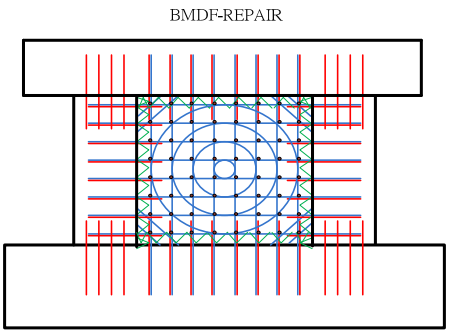

Fig. 1 The Concentric Circles Reinforcement Configuration

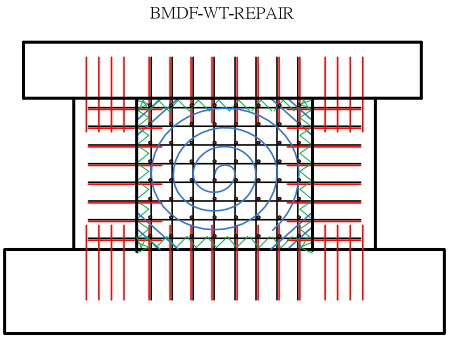

Fig. 2 The Spiral Reinforcement Configuration

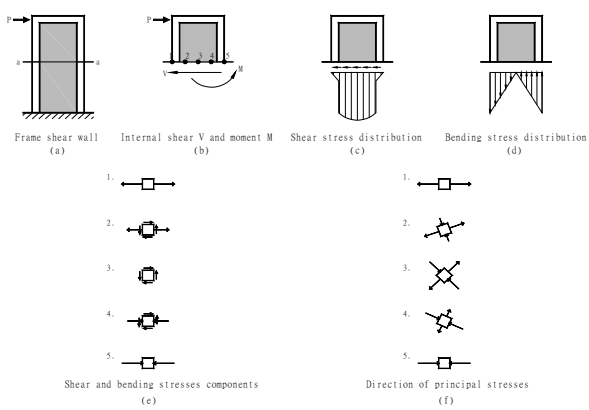

Fig. 3 Stress Variations Throughout a Framed Shear Wall

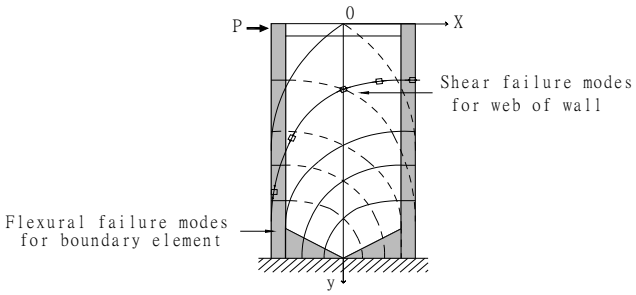

Fig. 4 Principal Stress Trajectories and Failure Modes In framed Shear Wall

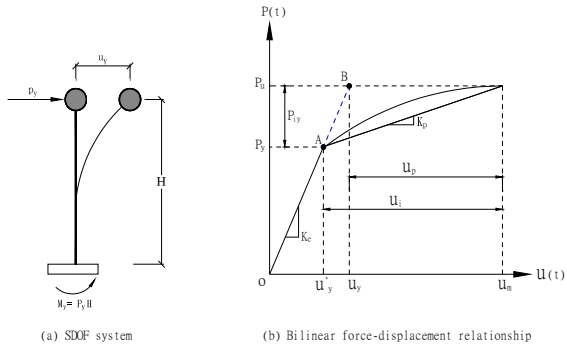

Fig. 5 The Illustration Figures of the Bbilinear Force-Displacement Relationship of a SDOF System

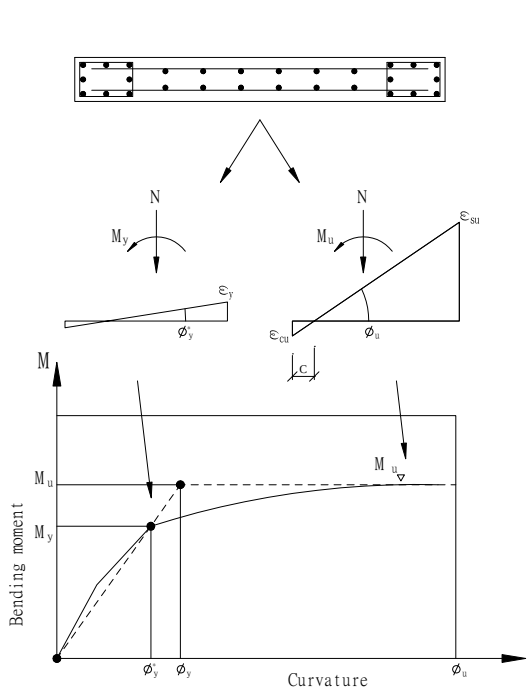

Fig. 6 The Illustration Figures of the Moment-Curvature Relationship at the Yield and Ultimate Points

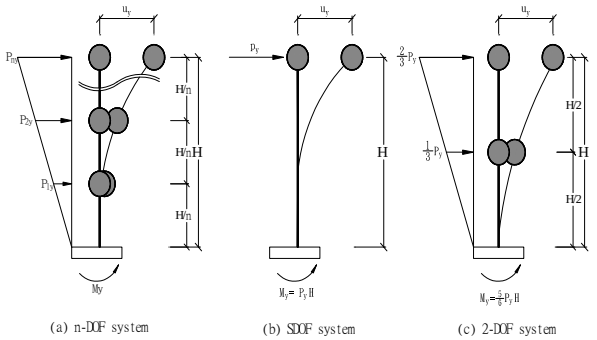

Fig. 7 Yield Displacement Determination for SDOF and MDOF Systems With a Triangular Force Distribution

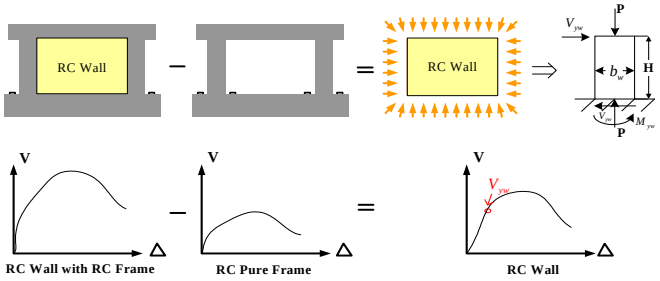

Fig. 8 The Illustration Figures of the Equivalent Column Model for a RC Structural Wall

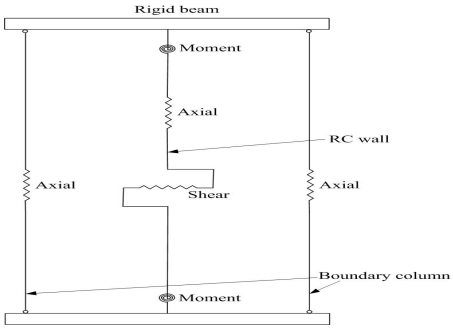

(a)

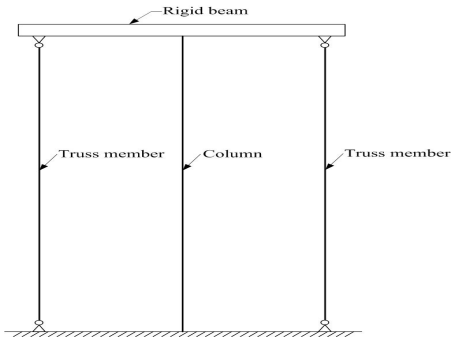

(b)

Fig. 9 The Analytical Model for RC Framed Walls: (a) Force Expression; (b) Member Expression

Table 1 The parameters of moment hinge of RC structural walls

Points	Moment/SF	Rotation/SF
A	0	0
B	$\frac{M_y}{M_u}$	0
C	1	1
D	0.4	$\frac{\left(u_p - \frac{0.4P_u}{P_y}u_y^*\right)\frac{1}{H}}{Rotation/SF}$
E	0.4	$\frac{\left(u_p - \frac{0.4P_u}{P_y}u_y^*\right)\frac{1}{H}}{Rotation/SF}$

Table 2 The parameters of shear hinge of slender RC walls

Points	Force/SF	Displacement/SF
A	0	0
B	$\frac{P_y}{P_u}$	0
C	1	1
D	0.4	$\frac{\left(u_p - \frac{0.4P_u}{P_y}u_y^*\right)}{Displacement/SF}$
E	0.4	$\frac{\left(u_p - \frac{0.4P_u}{P_y}u_y^*\right)}{Displacement/SF}$

JOINT CONFERENCE PROCEEDINGS
7th International Conference on Urban Earthquake Engineering (7CUEE) &
5th International Conference on Earthquake Engineering (5ICEE)
March 3-5, 2010, Tokyo Institute of Technology, Tokyo, Japan

STRUCTURAL RETROFIT FOR DEPTH REDUCED BEAM IN MID-RISE EXISTING REINFORCED CONCRETE BOXED WALL-BUILDINGS

Yo Hibino[1], Hiroki Tauchi[2], Masaomi Teshigawara[3], Hiroshi Fukuyama[4] and Yoshio Inoue[5]

1) Assistant Professor, Materials and Structures Laboratory, Tokyo Institute of Technology, Japan
2) Graduate Student, Department of Environmental Engineering and Architecture, Nagoya University, Japan
3) Professor, Department of Environmental Engineering and Architecture, Nagoya University, Japan
4) Chief Researcher, Department of Structural Engineering, Building Research Institute, Japan
5) Managing Officer, Urban Renaissance Linkage Co., Ltd.
hibino@serc.titech.ac.jp, tauchi@dali.nuac.nagoya-u.ac.jp, teshi@corot.nuac.nagoya-u.ac.jp, fukuyama@kenken.go.jp, inoue-y@urlk.co.jp

Abstract: This paper presents structural techniques to retrofit the depth reduced beam in existing reinforced concrete boxed wall-building. The experimental tests using two types specimen assuming retrofitted beam and whose end joint were carried out. The strengths and bending stiffness of the retrofitted beams were verified; and methods to predict the rotation capacity of the connection were presented by considering combinations of shear and moment or using an equation based on the concept of torsional moment with applicable coefficient of friction.

1. INTRODUCTION

The old existing reinforced concrete (RC) buildings which were built about 30 years ago have a low-ceiling space and the rooms with short under beam height. The small spaces are not comfortable for people live in contemporary society and next generation. Especially, the narrowness of the room and a low-ceiling can be seen in RC boxed wall-building which are rest many. The destruction of such buildings and rebuilding of new one is a simple solution to provide comfortable dwellings; however, the environmental problems may be caused by conventional renewal method. The alternative way to satisfy the needs without reconstruction has been required.

Recently, some ideas have been discussed to reuse the old existing buildings without rebuilding by using structural techniques (Building Research Institute 2004). For the narrowness of the spaces, an idea which expands the residential spaces was presented, which were reduction of the depth of beam, relocation of two rooms into one, and. But to realize the idea, specific techniques are not developed. Thus, the standard for the structural retrofitting for reuse the structure is not given, either.

Then, it is important to accumulate knowledge to establish the basis for retrofitting techniques. The objective of this paper is to present the structural techniques for the reduction of depth of beam and evaluate the structural performance by experimental tests.

2. METHOD OF RETROFITTING

The target of the beam to reduce was the beam whose span and cross-section area were large in old existing 5-story RC residential boxed wall-building whose type named 65-5N-3K-3 built in 1955 by Japan Housing Corporation (presently named as Urban Renaissance Agency).

The section and side elevation of the original beam are shown in Figure 1. The beam is casted with the slab. The original heights of the slab and beam are 110 mm and 500

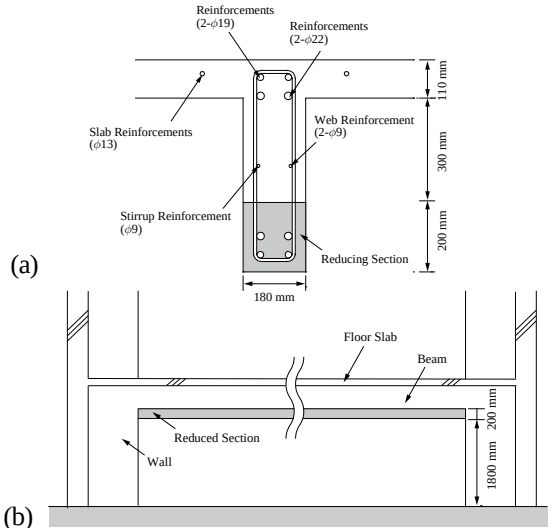

Figure 1 Section and Side Elevation of Existing Beam: (a) Section, and (b) Side Elevation

mm, respectively (see Figure 1(a)). Two longitudinal reinforcements which are rounded bars: ϕ19 and ϕ22, are placed at the top and bottom of the section, and the reinforcement (ϕ13) for the slab is also placed. The beam is connected with walls (see Figure 1(b)) at the both ends. The under beam height is 1800 mm which is not comfortable for modern people. Therefore, we presented the reduction of the beam of 300 mm from 500 mm to expand the space of the room to ensure enough under beam height more than 2000 mm. The concept of the retrofitting we presented after the reduction of the height of the beam is to keep the strengths and bending stiffness of the beam between before and after the retrofitting.

There are two kinds of techniques we presented for retrofitting after the reduction of the beam height. A method is to retrofit the beam with additional reinforcements and concrete (see Figure 2(a)) and another method is retrofitting with parallel flange channels (PFC) (see Figure 2(d)).

Additional reinforcement bars were located at the bottom of the reinforced beam, which were determined so that the bending moment is equal to that before retrofitting using the existing reinforcements (see Figure 2(a)). The width of retrofitted area was determined to ensure the moment of inertia, which was three times wider than the original beam. The additional stirrup reinforcements are hungered with the slab reinforcement through drilled holes (ϕ19) in the slab. The additional stirrup reinforcements are spliced on the middle height of the beam shown in Figure 2(a). At the bottom of the beam, additional stirrup reinforcements and existing reinforcements are spliced with/without weld. The ends of the beam are connected with the walls (see Figure 1(b)) with post-installed anchors (see Figure 2(b)) or PC steel bars (see Figure 2(d)).

As shown in Figure 2(c), PFC casted with existing slab and beam using headed anchors, steel plate and post-installed anchors. The steel plate is connected existing beam by high-strength bolts to ensure the stiffness and integrate the plate and the beams (shown in Figure 2(c)). The end of the beam is joined wall by PC steel bars (see Figure 2(d)).

In this paper, we carried out two series of experimental tests assuming the retrofitted beam to investigate the structural performance of the beam. The the method to design the connection at the end of the beam.

3. EXPERIMENTAL TESTS FOR BEAM SERIES

3.1 Specimens

The properties of specimens are shown in Table 1. The specimens were fabricated at approximately original scale and the shear span ratio was assumed to 1.5 to investigate the shear failure mainly. There are two identically designed groups, named series B-R and B-S. The series B-R are the specimens which retrofitted with concrete and reinforcements. The series B-S are the specimens retrofitted with PFC., which elevation and sectional properties are shown in Figure 3.

The identical properties for the series B-R are the design strength of concrete. The concrete strength of 18 N/mm^2 and 24 N/mm^2 were used for the existing beam and retrofitted beam, respectively. The grey area shown in Figure 2 means the section of retrofitting. The specimen B-R-1 is the prototype which is designed to be failed in flexural yielding. The other specimens are designed to be failed in shear failure before flexural yielding by arranging the reinforcement ratio. The main bars at the existing beam consist of 2-D19 and 2-D22 and high-strength steel bars were used in retrofitted area to be failed in shear before flexural yielding. The stirrup reinforcement ratio was determined in accordance with the shear strength calculated by guidelines of Architectural Institute of Japan (AIJ 1999) and American Concrete Institute (ACI 2008). The existing reinforcement and additional reinforcement were welded for the specimen B-R-3 only (see Figure 4). The length of

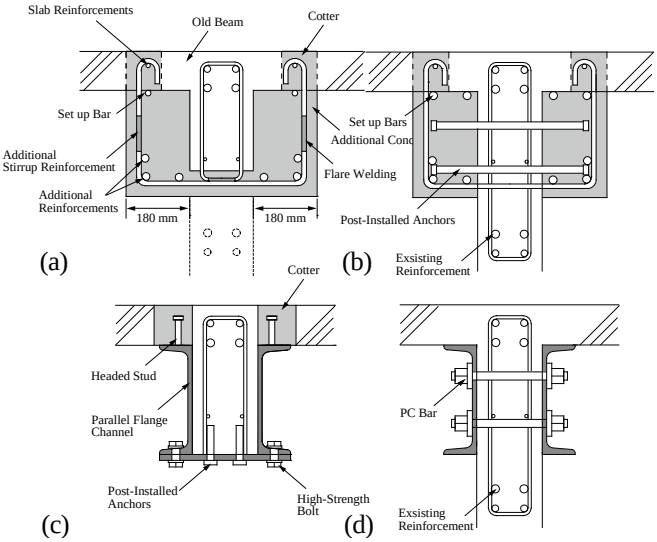

Figure 2 Shape of Retrofitted Beam: (a) Retrofitted with RC, (b) Joint with Post-installed Anchors, (c) Retrofitted with PFC, and (d) Joint with PC Steel Bars

Table 1 Properties of Specimens

Name	Method	Width (mm)	Depth (mm)	Main Bar	Stirrup Reinforcement	Welded	Stirrup Reinforcement Ratio (%)
B-R-1	RC	540	410	6-D22(SD345)	D10@250 and D13@250(SD295A)	No	0.29
B-R-2				6-D22 (USD685)			
B-R-3						Yes	0.58*
B-R-4					D13@83(SD295A)	No	0.57
B-S	Parallel Flange Channels ([-300×90×12×16])	360	426	-	-	-	-
B-S-H		270		-	-	-	-

* Sum of existing and additional reinforcements.

welded part was assured to almost 70 mm (6 times diameter). The welded old reinforcements were taken account for the calculation of the stirrup reinforcement ratio to investigate the effect of existing reinforcement on shear strength. Hence, the reinforcement ratio of the specimen B-R-3 listed in Table 1 is larger than that of the specimen B-R-2.

In the series B-S, there are two specimens, named B-S and B-S-H. The specimen B-S is constructed with two PFC

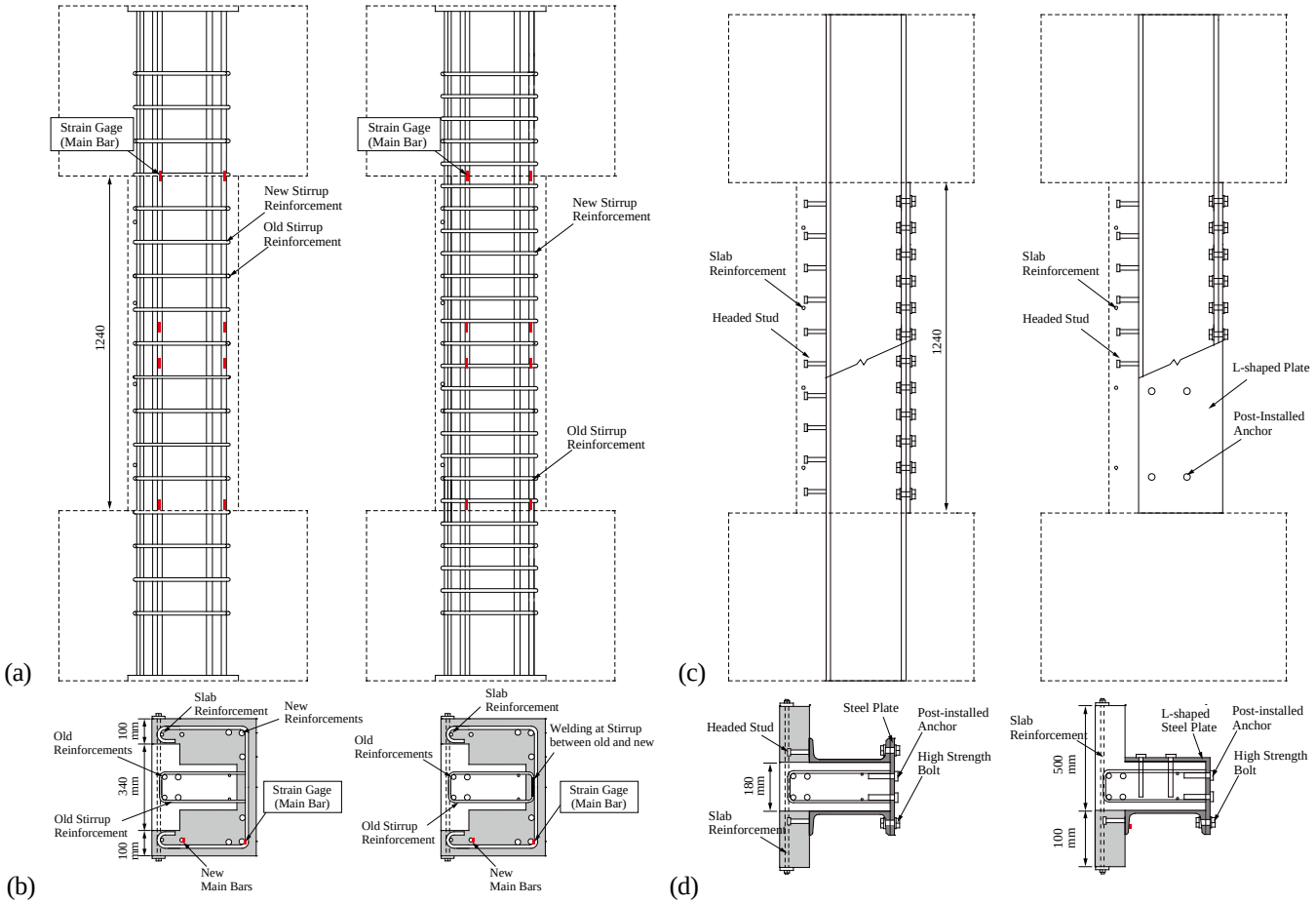

Figure 3 Test Specimen: (a) Front Elevation (Series B-R), (b) Plane View (Series B-R), (c) Front elevation (Series B-S), and (d) Plane View (Series B-S)

Table 2 Material Properties of Steel Bars

Section	Name	Specimen	Yield Strength (N/mm^2)	Tensile Strength (N/mm^2)	Elastic Modulus ($\times 10^5$ N/mm^2)
Existing	Stirrup Reinforcement (ϕ9)	B-R-1, B-R-2, B-R-3, B-R-4, B-S, B-S-H	330.1	447.9	2.00
	Slab Reinforcement (ϕ13)		297.5	424.9	2.05
	Main Bar (ϕ19)		316.3	448.0	2.04
	Main Bar (ϕ22)		301.5	452.2	2.06
Retrofitting	Stirrup Reinforcement (D10)	B-R-1, B-R-2, B-R-3	395.3	549.9	1.93
	Stirrup Reinforcement (D13)	B-R-1, B-R-2, B-R-3, B-R-4	398.6	528.6	1.94
	Main Bar (D16)	B-R-1	372.6	570.3	1.85
	Main Bar (D22)	B-R-2, B-R-3, B-R-4	390.1	559.1	1.87
			706.6	896.3	1.92
	Steel Plate (PL-16)	B-S, B-S-H	289.2	434.0	1.89

Table 3 Material Properties of Concrete

Section	Compressive Strength (N/mm^2)	Tensile Strength (N/mm^2)	Elastic Modulus ($\times 10^4$ N/mm^2)
Existing	20.6	2.16	2.26
Retrofitting	26.8	2.40	2.48

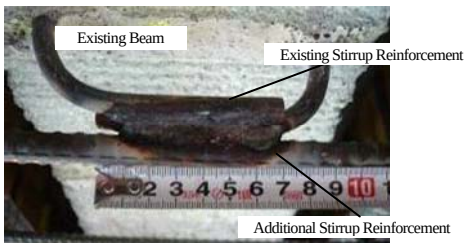

Figure 4 Welding at Stirrup Reinforcement

in accordance with JIS standard size of 300×90×12×16 (SS400). The specimen B-S-H is constructed with single PFC. But the opposite side of which, L-shaped steel plate are connected PFC and RC beam, with the high-strength bolts and the post-installed anchors, respectively. Both specimens were designed to be failed in flexural yielding. The steel plate was not connected the stab, which not affect the flexural strength of the specimen.

The material properties of steel bars and concrete are listed in Table 2 and 3, respectively. In the existing beam and the retrofitted beam, rounded steel bars and deformed bars were used, respectively.

3.2 Test setup for specimen series B-R

The bi-directional cyclic loading tests were conducted using the test rig shown in Figure 5. The specimen was set on the test rig vertically. The left side of the specimen is the surface of the slab and the opposite side is under the beam. The specimen was loaded with double bending moment. The two jacks were used for controlling axial force and shear force. The tests were controlled by the deflection angle obtained by the horizontal displacement divided by the shear span which is 1240 mm (see Figure 3), with keeping their axial load to zero. The loading history was as follows: ±1/800, ±1/400 × 2, ±1/200 × 2, ±1/100 × 2, and ±1/50 × 2. The direction of the loading was displayed on Figure 5.

3.3 Test results of specimen series B-R

The observed cracks after the failure are shown in Figure 6. The left side of the specimen is the surface of the slab and the opposite side is under the beam. The bending cracks were observed for the specimen B-R-1. Many fine cracks along the main bars were observed for the specimens B-R-3 and B-R-4, which indicate the bond splitting. On the other hand, for the specimen B-R-2, the cracks were less than the other specimens.

The lateral load-overall deflection ratio relations of the specimen B-R tested are shown in Figure 7. Circles are drawn at the points where the specimen was yielded. The lines on the figures indicate the predictions by the guidelines: ACI and AIJ. The cyclic loading of the specimen B-R-1 showed small strength degradation before the deflection ratio was 0.04 rad. Otherwise, the cyclic loading of the specimens B-R-2, B-R-3 and B-R-4 shown in Figure 7(b), (c), and (d), caused large strength degradation when the deflection was 0.02 rad. Especially, the cyclic loading of the specimen B-R-3 shows large stiffness degradation and the delamination crack was observed at the lower surface of the slab, which affected by compression force, when the deflection was 0.02 rad. Furthermore, the predictions were agreed with the yielded point except the specimen B-R-3. We assumed the delamination crack was caused by following mechanisms under positive direction loading: (1) compression strut in core concrete resist tension force of the existing and additional stirrup reinforcement, (2) the welded existing reinforcements were pushed out by the compression strut because of lack of longitudinal reinforcements, which make the tension side weaker than compression side, and (3) the delamination of concrete of the tension side was caused.

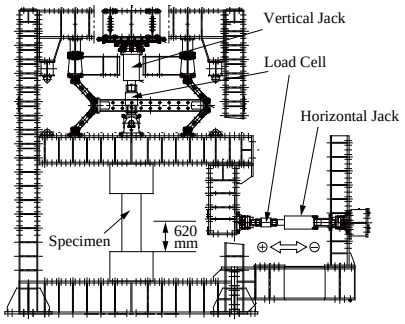

Figure 5 Test Setup for Beam Series Specimen

The elastic modulus K_e was compared between the calculation and experiment. The elastic modulus is expressed by Equation 1 using the equivalent values (E_e, A_e) were obtained by according to the allocation of the area of the existing and new concrete area.

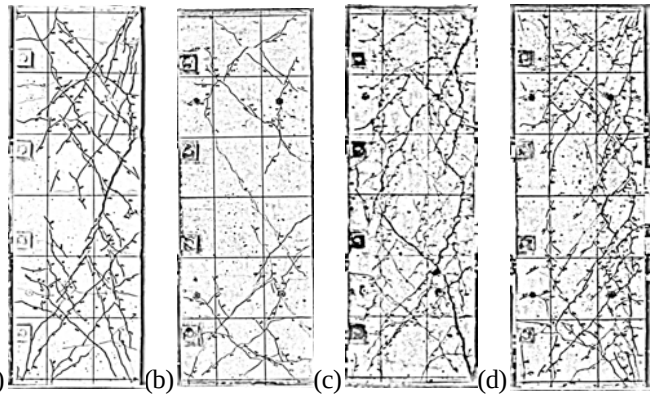

Figure 6 Cracks Schematics after Failure (1/50 rad.): (a) B-R-1, (b) B-R-2, (c) B-R-3, and (d) B-R-4

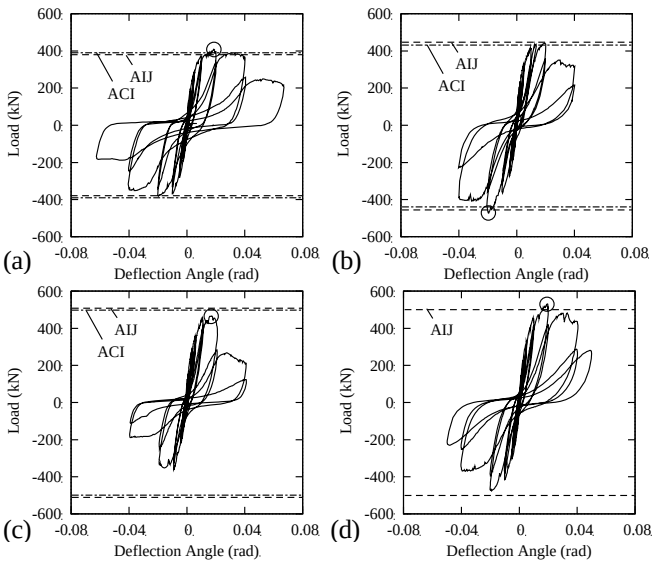

Figure 7 Shear Forces verses Deflection Angle Relationships: (a) B-R-1, (b) B-R-2, (c) B-R-3, and (d) B-R-4

Table 4 Elastic Modulus

Specimen	Calculation ($\times 10^5$ N/mm)	Experiment ($\times 10^5$ N/mm)	Calculation / Experiment
B-R-1	2.79	2.79	1.0
B-R-2	2.80	1.96	0.7
B-R-3		2.24	0.8
B-R-4		1.51	0.5

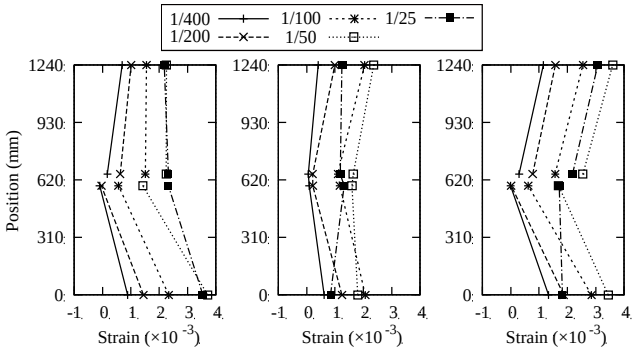

Figure 8 Strain of Main Bars: (a) B-R-2, (b) B-R-3, and (c) B-R-4

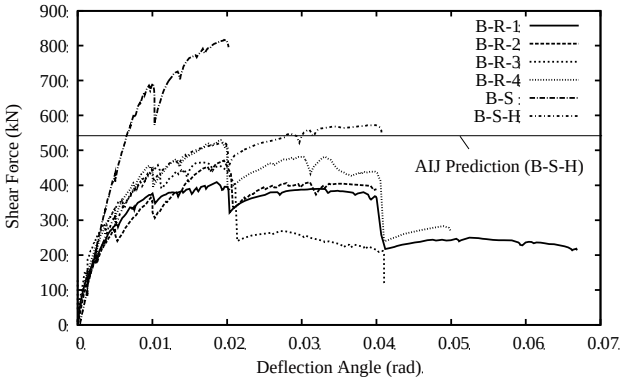

Figure 9 Envelope Curve for Shear Force versus Deflection Angle Relationship

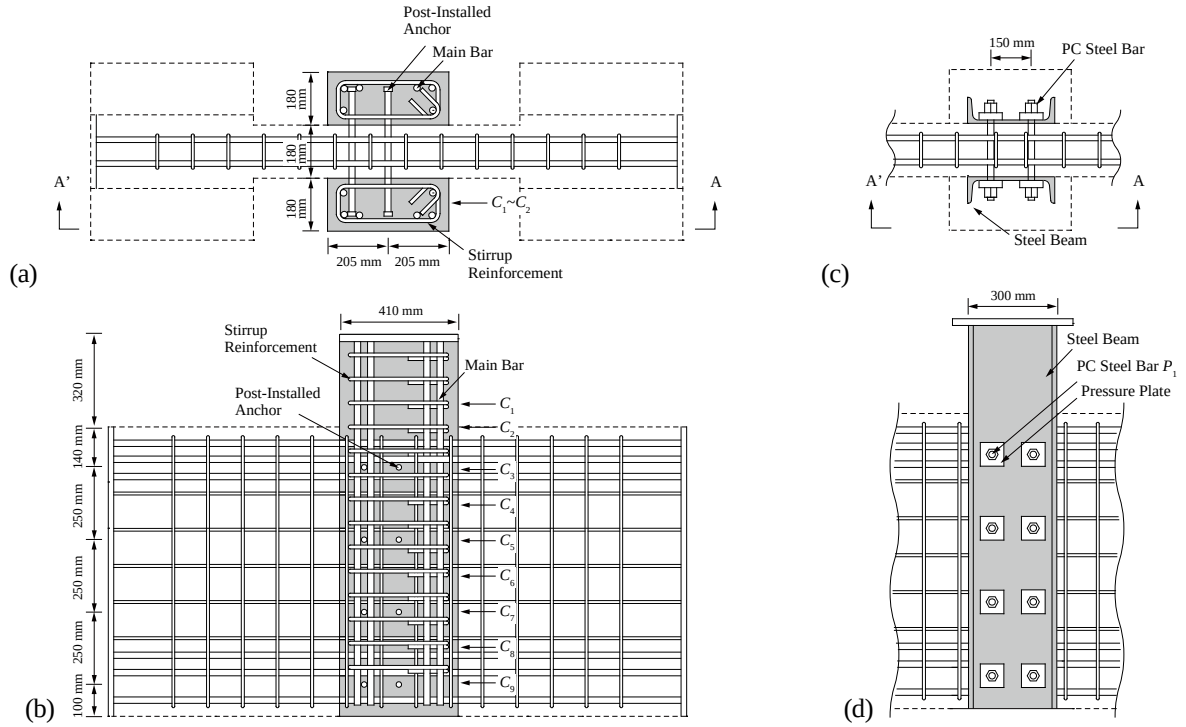

Figure 10 Test Specimen (a) Side View (J-A), (b) A-A' Elevation (J-A), (c) Side View (J-P), and (d) A-A' Elevation (J-P)

$$\frac{1}{K_e}=\frac{1}{K_b}+\frac{1}{K_g}=\frac{1}{\left(\frac{12E_eI}{h_0^3}\right)}+\frac{1}{\left(\frac{GA_e}{\kappa h_0}\right)} \quad (1)$$

where E_e=equivalent elastic modulus; G_e=shear modulus; I=second moment of the cross section of the beam; h_0=effective height obtained by sum of the beam length and the length of quarter of stabs (1240+410/4×2=1445 mm); κ=shape index; and A_e= area of cross section of the beam.

The experimental results were close to the calculation except the specimen B-R-4 listed in Table 4. However, the elastic modulus, when the strain of the main bars was 1000 μ, was agreed with all the specimens, which was about 40 % of elastic modulus.

Figure 8 shows that the strain of main bars at each height for 1/400 rad., 1/200 rad., 1/100 rad., 1/50 rad. and 1/25 rad. The strain was measured by strain gage patched on the beam at hinge positions and the center of the beam shown in Figure 3(a) and (b). The strain at both hinges of all the specimens: B-R-4, and B-R-3; when the deflection ratio was 1/25 rad. were reduced less than whose when the deflection ratio was 1/50 rad. because we assumed the bonds of main bars were lost. For the specimen B-R-2, the strain shows small decrease when the deflection was 1/50 rad., which means that the specimen B-R-2 was assumed failed in shear before yielding.

3.4 Test results of B-S series specimen

The specimen series B-S were designed to be failed in flexural yielding. The envelope curves of shear force versus deflection angle relationship of the specimen series B-S are shown in Figure 9 with the other specimens: B-R-1 to B-R-4. The prediction by AIJ for the specimen B-S was drawn as a line. We note that the experimental test of B-S specimen was not exceeded larger than 1/100 rad. because of the collapse of the anchor at the stub. Then, the maximum yield strength of the specimen B-S could not confirm. But the maximum yield strength of the specimen B-S-H which was failed in shear was agreed with the design strength calculated based

Table 5 Properties of Specimens for Joint

Name	Beam					Wall		
	Material	Depth (mm)	Width (mm)	Main Bar	Stirrup Reinforcement	Depth (mm)	Vertical Reinforcement	Horizontal Reinforcement
J-A	RC	410	180	3-D22 (USD685)	D13@80 (SD295A)	180	D10@120 (SD295A) (p_w=0.66 %)	D10@125 (SD295A) (p_w=0.64 %)
J-P	Steel	300	90	-	-			

Table 6 Properties of Joint

Name	Beam	Joint		
		Method	Horizontal Spacing (mm)	Vertical Spacing (mm)
J-A	RC	Post-Installed Anchor (M20, SS400)×8	123	250
J-P	PFC	PC Steel Bars	150	

Table 7 Properties of Concrete for Series J Specimens

Cast Section	Compressive Strength (N/mm^2)	Tensile Strength (×10^5 N/mm^2)	Young's Modulus (×10^5 N/mm^2)
Wall	23.8	3.21	2.23
Beam	30.5	3.62	2.42

Table 8 Strength of Post-installed Anchor in Shear

Steel Strength of Anchors in Shear, V_{sa}(kN)		Concrete Breakout Strength of Anchors in Shear, V_{cb} (kN)
Used Yield Strength	Used Tensile Strength	
57.1	76.5	71.5

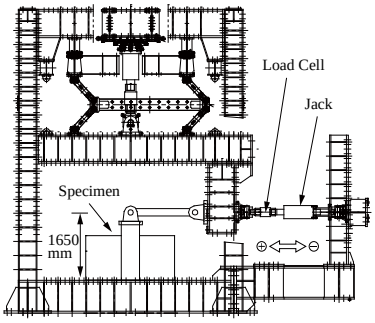

Figure 11 Test Setup for Specimen of Joint

on the equations using the idea of full-plastic moment provided by Design Recommendation for Composite Constructions (AIJ 1985) considering the existing beam as compression area.

We note that the specimen B-R-1 and B-S-H was ductile due to the failure in flexural yielding; however, about 55 % deterioration was observed in the specimen B-R-3.

4. EXPERIMENTAL TESTS FOR JOINT SERIES

4.1 Specimens

We assumed the joints of the connection at the end of retrofitted beam between the beam and wall (see Figure 1(b)) were post-installed anchors or PC steel bars like as Figure 2(c) and (d). To investigate a method to design the joints, the experimental tests were conducted using two specimens, shown in Figure 10 and listed in Table 5. The arrow symbols on the figures show positions of measurement. The C_1 is at the level of 90 mm above the wall and the C_2 is at the same level of the wall. Each position of the other measurements is either at the level of joints or the midway in those. The properties of joint are shown in Table 6. The arrangements of the anchors and PC steel bars are determined in accordance with the code by Japan Building Disaster Prevention Association (JBDPA). The span between the highest position (C_3) and lowest position (C_9) is 750 mm. The depth and width of the beam of the specimen J-A is the same as the specimen series B-R. Similarly, the properties of the wall are the same in all specimens. On the other hand, for the specimen J-P, the properties of PFC is the same as the one used in the specimen series B-S. The properties of concrete used are shown in Table 7. The shear strengths of the post-installed anchor were also calculated by below equations (JBDPA):

$$V_{sa} = 0.7 \times \sigma_s \times {}_s a_e \tag{2}$$

$$V_{cb} = 0.4 \times \sqrt{E_c \times \sigma_B} \times {}_s a_e \tag{3}$$

where V_{sa}=steel strength of anchor in shear; σ_s=strength of anchor; ${}_s a_e$=area of the anchor; V_{cb}=concrete breakout strength of anchor in shear; E_c=elastic stiffness of concrete; σ_B=compression strength of concrete.

Table 8 shows that the strength of the post-installed anchor in shear of whose steel strength was calculated by yield and tensile strength using Equations 2 and 3. Typically, the yield strength is used for steel strength of anchor in shear; however, the tensile strength was used as reference.

4.2 Test setup for joint series specimen

The specimens were setup at the rig shown in Figure 11. The jack loads the beam of the specimen horizontally and the specimen and the jack were linked by the beam with the pinned at the both ends. The cyclic loading was controlled by shear force as follow: ±50 kN, ±100 kN, ±200 kN, and ±300 kN. To simplify the explanation, the shear force was described as a half of the load below after.

4.3 Test results of J-A specimen

The crack figure of the specimen J-A is shown in Figure 12. The cracks when the loads, V are +25 kN, +150 kN and after the loading are drawn. The cracks increased as the loads increased. The observed cracks when the load was 150 kN were placed evenly spaced apart at the level of the post-installed anchors. The vertical crack observed was assumed to be due to the lost bond of man bar was on the left side of the beam. The shear cracks which were extended from the bending cracks observed when the load was +150 kN.

The relationship between moment and rotation angle is shown in Figure 13. The circle symbol means the maximum

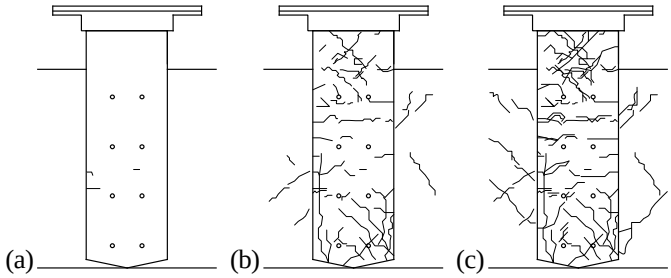

Figure 12 Crack Drawing (J-A): (a) +25 kN, (b) +150 kN, and (c) After Loading

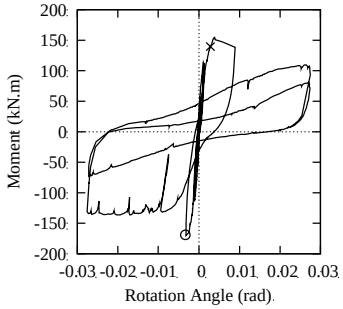

Figure 13 Moment versus Rotation Angle Relationship (J-A)

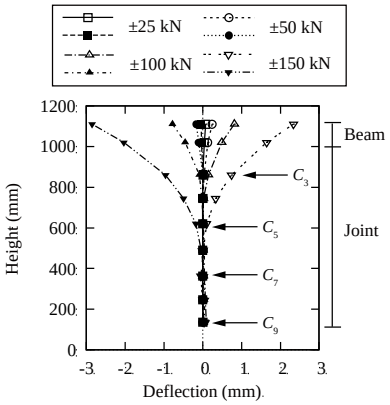

Figure 14 Height versus Deflection Relationship (J-A)



Figure 15 Gap Between Beam and Wall (J-A)

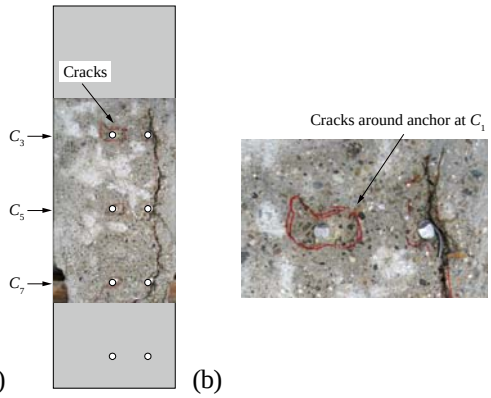

Figure 16 Cracks at Boundary Face Between Beam and Wall: (a) Cracks at the levels of C_3, C_5 and C_7, and (b) Zoom around Anchor at the level of C_3

moment, which was 170 kN·m (V=153 kN). The relatively rotation angle was calculated by the deflection at the levels of C_1 and C_9 using the span length of those. The moment was obtained from the load multiplied the length (1115 mm) between the loading point and the center of the wall. The cyclic loading shows that small stiffness deterioration when the moment was 139 kN·m (illustrated by x symbol in Figure 13). Therefore we assumed that the point was the beginning of the rotation of the beam. Note that the load of the point was 125 kN.

The deflection of the beam when the load were ±25 kN, ±50 kN, ±100 kN, and ±150 kN are shown in Figure 14. The arrow symbols are the level of the post-installed anchors. Outside of the figure, the parts of specimen are displayed. The deflection was observed only when the load was small. The deflection at the level of C_3 was increased after the load was 100 kN, then the deflection at the level of C_5 was increased when the load equals maximum load of 153 kN. The deflection at the level of C_9 was 0.034 mm, which was much smaller than that at the level of C_5. This means that the beam did not rotate. Note that the gap between the beam and the wall after the loading test was about 1.6 mm (see Figure 15).

Figure 16 depicts cracks at boundary face between the beam and wall around the anchors at the level of C_3, C_5 and C_7. The cracks were closed round by red lines to mark the positions. The red circle of the crack at the level of C_3 is larger than that at the level of C_7. This means that the anchor was failed in shear by concrete breakout. Then, we presented a method to predict the anchors' capacity strength against the

Table 9 Shear Strength and Moment of Post-installed Anchors

	Assumption		Prediction
	Shear (kN)	Moment (kN·m)	Moment (kN·m)
Experiment	125	139	
Equation 2 (V_{sa}=57.1 kN)	228 (+103)	85.7 (-53.3)	98.5
Equation 3 (V_{sa}=71.5 kN)	286 (+161)	107 (-32)	127.4

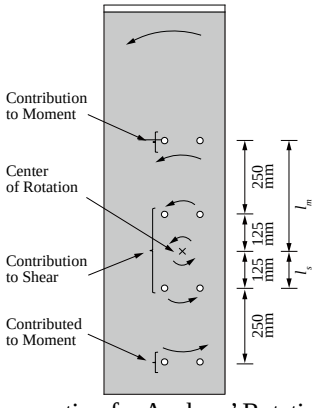

Figure 17 Assumption for Anchors' Rotation Capacity

rotation of the beam, which made by the combination of shear and moment, based on an assumption shown in Figure 17 the anchors studded outside contribute to moment and the anchors studded inside contribute shear force.

The shear and moment we calculated based on the assumption using Equations 2 and 3 is listed in Table 9. The numbers between parentheses in cells are the differences

from the experiment. The moment of experiment is larger than that of equations 2 and 3 whereas the shear of experiment is larger than that of equations. The redundant shear, V_r obtained by subtracting the shear of experiment from that of experiment shall be work for moments, which are 103 kN and 161 kN. Hereby, the moments, M_p considering redundant strength were calculated by following equation.

$$M_p = V_{sa} \times n_m \times l_m + V_r / n_m \times n_s \times l_s \quad (4)$$

where n_m is the number of anchors contribute to moment; l_m is length due to moment; n_s is number of anchors contribute to shear; l_s is length due to shear.

The moment predicted, using Equation 3 and redundant shear, listed in Table 9 is agreed with the experiment. Therefore, the anchors mainly worked for moment rather than shear under loading and the capacity of joints against the rotation was evaluated safety by the assumption shown in Figure 17considering the redundant strength of anchors

Furthermore, we assumed the capacity against the rotation of the anchors by considering the bearing strength yielded by anchor's tensile strength and torsional moment, which idea is provided by following equations (AIJ 1999). If the bearing strength does not reach the capacity, the Equation 6 which expressed by the combination of shear and moment must be less than one.

$$\frac{V_u}{V_0} + \frac{M_u}{M_0} \le 1 \quad (5)$$

$$M_0 = \frac{a^2}{2} \times \left(b - \frac{a}{3} \right) \times \tau_u \quad (6)$$

$$V_0 = \tau_u \times a \times b \quad (7)$$

$$V_0 = \mu \times N \quad (8)$$

where V_u=shear force works; V_0=shear strength when shear force works only; M_u=designed torsional moment; M_0=torsional moment when torsional moment works only; a=narrow side of beam; b=longitudinal side of beam; τ_u=ultimate shear strength; μ=coefficient of friction; N=tensile strength.

The beginning of the rotation of the beam was assumed when the load was 125 kN (M_u=139 kN·m). The coefficient of friction was assumed as 1.0 referring ACI. The tensile strength, N of the post-installed anchor was $\sigma_s \times A_s \times 8$=912 kN using the post-installed anchors' tensile strength Then, the following equation is given by substituting N to Equation 5 like below.

$$\frac{V_u}{V_0} + \frac{M_u}{M_0} = \frac{125}{912} + \frac{139}{161.5} = 0.99 \approx 1.0 \quad (9)$$

Equation 9 represents that the anchors reached the capacity of the rotation when the load we assumed.

4.4 Test results of specimen J-P

The specimen was the connection of PFC and wall using PC steel bars. Prestressed force of 132 kN was used for the PC steel bars, which were in accordance with an allowable stress of compression for concrete, 1/3 for compressive strength defined by AIJ (1999).

The cracks on the wall observed when the load were

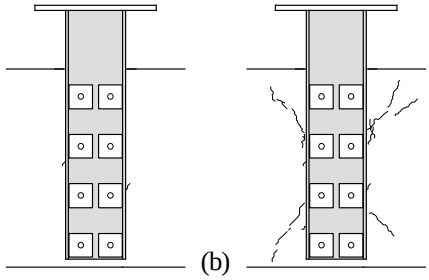

Figure 18 Crack Drawing (J-P): (a) +25 kN, and (b) -112 kN

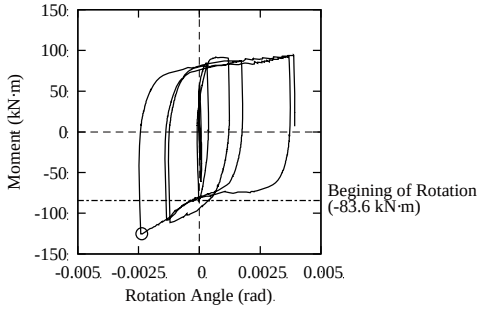

Figure 19 Moment versus Rotation Angle Rlationship (J-P)

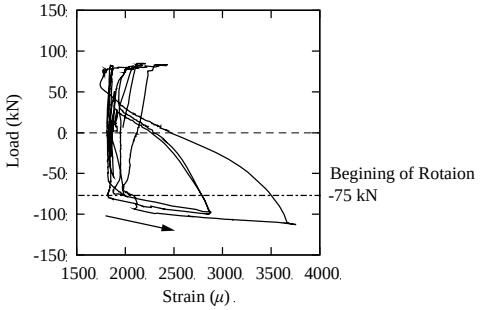

Figure 20 Load versus Strain Relationship of PC Steel Bar at P_1 (J-P)

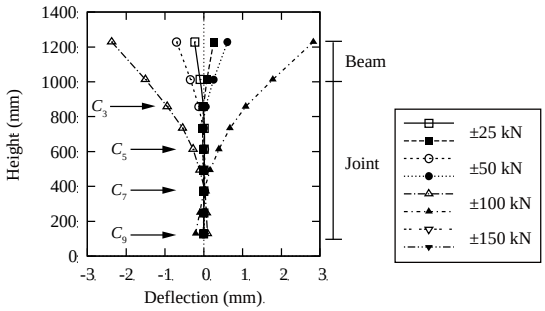

Figure 21 Moment versus Rotation Angle Relationship (J-P)



Figure 22 Gap Between Beam and Wall (J-P)

+25kN and -112 kN were drawn in Figure 19. The many cracks were observed when the load was -112 kN, which assumed to be due to moment transmitted from the beam.

The moment versus rotation angle are shown in Figure 19 whose maximum moment was 125 kN·m. The cyclic loading shows that the large stiffness upgrade after the point we assumed as the beginning of rotation. The load versus strain of PC steel bar at P_1 is shown in Figure 20. The stain was dramatically increased when the load was -75 kN where agreed with the beginning of the rotation we assumed, which moment was 83.6 kN·m.

The deflection of the beam was shown in Figure 21. The deflection began when the load was ±100 kN and negative deflection caused by rotation was observed at the level of C_9. We note that the maximum gap between beam and wall is about 5.6 mm (shown in Figure 22).

We again examined Equation 5 for the specimen J-P to verify our assumption using the coefficient of friction of 0.75. From the beginning of the rotation, shear and moment shall be obtained as V_u of 75 kN and M_u of 83.6 kN·m, respectively. The tension force of the PC steel bars was estimated at 117 kN by measured strain of the PC steel bars. The V_0 and M_0 were obtained as 700 kN and 94.5 kN, respectively. Using the former values, the following equation was given.

$$\frac{V_u}{V_0}+\frac{M_u}{M_0}=\frac{75}{700}+\frac{83.6}{94.5}=0.99\approx 1.0 \qquad (10)$$

The right term is agreed with 1.0, which means the beginning of the rotation whose load of 75 kN can be predicted by Equation 5.

Moreover, we adopted the method shown in Figure 17 to predict the capacity of the rotation using the redundant shear force. The predicted moment was agreed with that of the experimental result of 83.6 kN·m. Hence, the capacity of the rotation can be predicted by the method depicted in Figure 17 as well as Equation 5.

5. CONCLUSIONS

This paper presents structural techniques for the reduction of beam height in existing RC boxed wall-building. The experimental tests using two types specimen assuming retrofitted beam and whose end joint were carried out. The structural technique we presented is to make integrated beam using reinforced concrete or PFC. The end of the beam joined wall by post-installed anchors or PC steel bars. The experimental tests were examined for two parts of the beam: shear span and joint. The following collusions were obtained:

1. The structural performance: binding stiffness, flexural strength, and shear strength, of the retrofitted beam using reinforced concrete and PFC was verified.
2. The flexural strength and shear strength was predicted by equations provided by AIJ and ACI guidelines.
3. In case of the structural retrofit using reinforced concrete, to weld stirrup reinforcement with no longitudinal reinforcement may cause a brittle failure by crashing concrete.
4. The rotation capacity of joints was verified by the method considering the combinations of shear and moment as shown in Figure 17. Alternatively, the rotation capacity was verified by the equation evaluate torsional moment using applicable coefficient of frictions.

Acknowledgements:

This work was sponsored by the Japan Association for Building Research Promotion as a part of Research Project on Urban Renaissance Agency, entitled “the retrofit technique for structure of existing housings”. This work was supported by Grants-in-Aid for Young Scientists (A) from the Ministry of Education, Culture, Sports, Science and Technology.

References:

American Concrete Institute (2008). Building Code Requirements for Structural Concrete (ACI 318-08) and Commentary, Michigan, USA.

Architectural Institute of Japan (1999). *AIJ Standard for Structural Calculation of Reinforce Concrete Structures –Based on Allowable Stress Concept-* , Tokyo, Japan. (in Japanese)

Architectural Institute of Japan (1999). *Design Guidelines for Earthquake Resistant Reinforced Concrete Buildings Based on Inelastic Displacement Concept*, Tokyo, Japan. (in Japanese)

Architectural Institute of Japan (1985). *Design Recommendation for Composite Construction*, Tokyo, Japan. (in Japanese)

Building Research Institute (2004). “Feasibility study on upgrading existing buildings suitable for next-generation”, *Building Research Data*. (in Japanese)

Japan Building Disaster Prevention Association (2001). *Seismic Evaluation and Retrofit*, Tokyo, Japan.

JOINT CONFERENCE PROCEEDINGS
7th International Conference on Urban Earthquake Engineering (7CUEE) &
5th International Conference on Earthquake Engineering (5ICEE)
March 3-5, 2010, Tokyo Institute of Technology, Tokyo, Japan

A BRIEF INTRODUCTION TO THE NEW STANDARD FOR SEISMIC APPRAISAL OF EXISTING BUILDINGS IN CHINA

Cheng Shaoge[1)], Shi Tiehua[2)], and Bai Xueshuang[3)]

1) Professor, Institute of Earthquake Engineering, China Academy of Building Research, China
2) Senior Engineer, Institute of Earthquake Engineering, China Academy of Building Research, China
3) Ph. D, Institute of Earthquake Engineering, China Academy of Building Research, China
chengshaoge@163.com, cabrsth@126.com,

Abstract: After Wenchuan Earthquake, the revision of "Standard for seismic appraisal of buildings GB50023-95" has been carried out. The new standard GB50023-2009 was put into effect on July 1st this year. In this paper, the main issues in the revision of GB50023-2009 were introduced, include: (a) clarification of seismic fortification level of existing buildings, (b) introduction of continuous seismic service life of existing buildings, (c) classification of existing buildings according to construction age or corresponding design code series, called category A, B and C, (d) seismic appraisal methods of buildings with different continuous seismic service life, (e) improvement of seismic fortification criterion for those buildings of major fortification category, such as school or hospital buildings.

1. INTRODUCTION

After Wenchuan Earthquake, the seismic appraisal for all the buildings in disaster zone had been carried out. In 2009, the central government impel safety project for school buildings all over china, every building need be appraised, if it can not satisfied the seismic requirement, strengthening must be adopted. The former "standard for seismic appraisal of buildings GB50023-95" had been used for over 10 years, it can not meet current requirement and should be revised, so the revision of standard must be carried out. The new standard GB50023-2009 was put into effect on July 1st 2009, in this paper, the main revision was introduced briefly.

2. MAIN PROBLEMS IN GB50023-95

2.1 Scope of Application of GB50023-95

The former standard was only suitable for those buildings which built early than 1990 or designed according to TJ11-78 or even early more. But now lots of buildings were constructed after 1990 and seismic designed according GBJ11-89 or GB50011 (new Chinese seismic code), the problem how to deal with these buildings must be solved.

2.2 Seismic Fortification Level of Existing Buildings

According to current Chinese seismic design code, the seismic fortification level of buildings is, no or slightly damage with continued service without repair under frequently earthquake influence, damaged with continued service after ordinary repair or without repair subjected to local fortification intensity earthquake influence, not collapse nor suffer damage that would endanger human lives subjected to rarely earthquake influence which intensity is expected to higher than the local fortification intensity.

But in GB50023-95, buildings only not collapse nor suffer damage that would endanger human lives or equipment subjected local fortification intensity was mentioned. So we don't know the performance if it is subjected to rarely earthquake influence. It also means that it is different between existing buildings and new design buildings.

2.3 Seismic Appraisal for Major Fortification Category Buildings

After Wenchuan Earthquake, buildings such as school buildings and hospital buildings were changed from standard fortification to major fortification according to new "standard for classification of seismic protection of building constructions GB50223-2008". The seismic measures for these buildings advanced obviously in the new seismic design code of buildings GB50011-2001(2008), but in the standard GB50023-95, these requirements are not listed completely.

3. MAIN ISSUES IN THE REVISION OF GB50023

3.1 Continuous Seismic Service Life for Existing Buildings

The definition of continuous seismic service life is duration of a building which can serve normally without any seismic appraisal or strengthening. For new buildings, the design reference period of 50 years is compulsory required, but it is unnecessary for existing building which had used for several decade years. In ISO 2394, the reduction of live load according to real service life was also allowed for the reason of economy.

The classification of continuous seismic service life mainly depends on the construction age of buildings. Considering the adoption time variance of code in different district in china, so the design code is also one of the factor in classification. The stipulation of seismic service life in new standard GB50023-2009 as follows:

1. Buildings which built before 1970's and can satisfy normal service after safety appraisal (not include seismic appraisal), 30 years of service life is compulsory needed. Buildings which constructed in 1980's, 40 years or more is needed, but never less than 30 years. In this period, the current Chinese seismic code is TJ11-74/78.
2. Buildings which built in 1990's, the current Chinese seismic code is GBJ11-89, 40 years of service life could be adopted, sure 50 years could be also selected under the permission of economy.
3. Buildings which built in this century, the current Chinese seismic code is GB50011, the service life is same to the design reference period of new design buildings.

3.2 Seismic Fortification Level of Existing Buildings

In GB50023-2009, the seismic fortification level gives different performance subjected to frequent , local fortification intensity, and rarely earthquake influence. It is a little different to the new design buildings. The fortification level of existing buildings which have 50 year's service life should be same with new design buildings, but buildings which less than 50 year's service life have lower fortification level the those of 50 years. That is to mean, when subjected to frequently earthquake influence, the building maybe slightly damaged with continued service after ordinary repair, when subjected to local fortification intensity earthquake influence, the building maybe damaged severely and need much more money to repair it, anyway the building can not collapse nor suffer damage that would endanger human lives subjected to rarely earthquake influence.

The fortification level of existing building was based on the assumption of equal probability during corresponding continuous seismic service life. Recent studies[1] shown that not only seismic action but also seismic measures is related to the service life (see in Table 1,Table 2, Figure 1 and Figure 2).

It shown that the earthquake action was mainly depended on the seismic service life, and has a little relationship with fortification intensity, while the seismic measures were not only related to service life but also related to fortification intensity. In high seismic zone, the curve is rather smooth, but in lower seismic zone, it is cliff compare to high zone.

Table 1 Variation of Seismic Factor With Seismic Service Life (Year)

Seismic service life	10	20	30	40	50
Seismic action factor	0.37	0.59	0.75	0.88	1.00
Seismic service life	60	70	80	90	100
Seismic action factor	1.10	1.20	1.28	1.36	1.43

Table 2 Variation of Seismic Measures With Seismic Service Life (Year)

Seismic service life		20	30	40
Seismic Intensity	6	0.57	0.76	0.90
	7	0.47	0.71	0.87
	8	0.34	0.63	0.84
	9	0.27	0.57	0.81
Seismic service life		50	60	70
Seismic Intensity	6	1.0	1.08	1.15
	7		1.11	1.20
	8		1.13	1.25
	9		1.17	1.32
Seismic service life		80	90	100
Seismic Intensity	6	1.21	1.26	1.30
	7	1.28	1.35	1.41
	8	1.35	1.43	1.51
	9	1.45	1.54	1.61

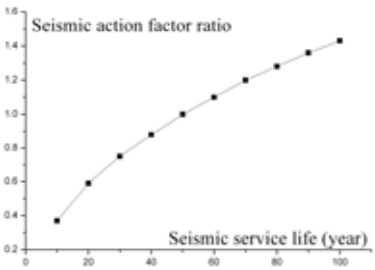

Figure 1 Seismic Action Factor Ratio Curve

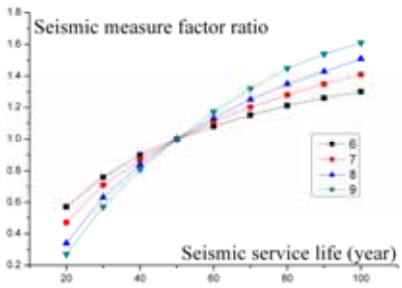

Figure 2 Seismic Measure Factor Ratio Curve

3.3 Seismic Appraisal of Buildings With Different Seismic Service life

In the new standard GB50023-2009, buildings with different continuous seismic service life should be appraised according to different methods. Those building with 30 year's service life should be appraised using category A method specified in the standard which is similar to GB50023-95. Those buildings with 40 year's service life should be appraised using category B methods specified in standard which is basically equal to the former seismic design code GBJ11-89. Buildings with 50 year's service called category C should be appraised according to the current seismic design code GB50011.

Seismic appraisal emphasize the structure seismic capacity called compound seismic capacity not for each structure members. Building with higher seismic capacity can decrease seismic ductility measures, on the other hand, if building has good ductility measures, the seismic capacity could be lower.

No matter what kind of structures, the seismic appraisal of buildings could be divided into two steps, the first is called seismic measures checking, including the real strength of material, rationality of structure system, structure entirety and special members which would be damaged easily in earthquake. The second is seismic calculation, it can be calculated using seismic code method or simplified method specified in the standard. Generally speaking, simplified method was recommended in category A buildings, seismic design code method was suggested in category B and C buildings.

The appraisal method or process was illustrated in Figure 3.

3.4 Improvement of Major Fortification Category Buildings

After Wenchuan Earthquake, the fortification criterion of school or hospital buildings was improved[2]. In the revision of GB50023, the requirement for those buildings were also increased.

1. For major fortification category buildings, the seismic fortification measure should be checked according to the intensity that high than local fortification intensity, the seismic action should be calculated based on the intensity that not less than local fortification intensity.
2. The story and height of multi-story masonry buildings was strictly controlled. For school or hospital buildings with rare transverse wall, the story number would decrease one, height limitation would decrease 3m, buildings with single side corridor would decrease another one story or 3m. If buildings exceed the limitation, it must be strengthened using special method to change masonry structure to R.C. shear wall structure. Additionally, the tie column checking was added in category A buildings in GB50023-2009, the arrangement and numbers of tie column in category B buildings was also increased.
3. For R.C. frame, utilizing the lessons from Wenchuan Earthquake, the single bay frame structures is forbidden used in major fortification category buildings because of its lack of seismic redundancy, it should be strengthened to multi-bay frame or frame-shear wall system. Checking of "strong column and weak beam" should be carried out for all R.C. frames and seismic deformation must be analyzed for category B frames.
4. Because of the poor seismic performance of multi-story brick buildings with bottom-frame or inner-frame, these kind of structure can not be used in school or hospital buildings which specified as major fortification category buildings.

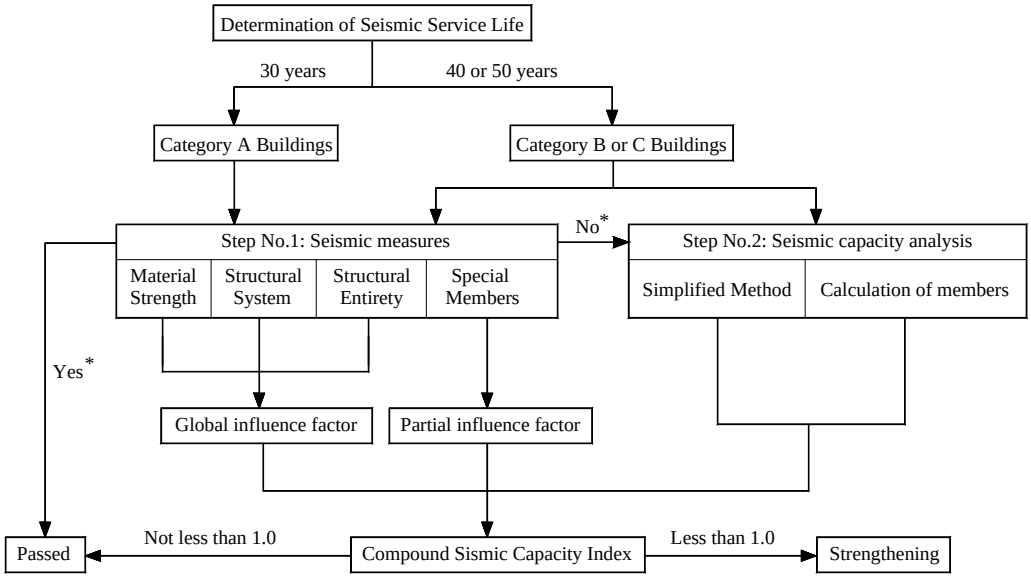

Note: * only for category A buildings

Figure 3 Seismic Appraisal Chart of Existing Buildings

4. BRIEF INTRODUCTION OF SEISMIC APPRAISAL FOR EXISTING BUILDINGS

4.1 Seismic Appraisal of Category A Buildings

For category A buildings, building meet the requirement specified in the first step can be regard as accepted, and the second step is unnecessary. If it can not satisfy the requirement of seismic measures, the influence factor less than 1.0 would be given, and seismic calculation must be taken with considering influence factor. The compound seismic capacity can be expressed using an index as follows.

For multi-story masonry

$$\beta = \psi_1 \psi_2 A / (A_b \xi_o \lambda) \tag{1}$$

For R.C. frame

$$\beta = \psi_1 \psi_2 V_y / V_e \tag{2}$$

Where, β —story compound seismic capacity index.

A, A_b —brick wall section area and story area of story respectively.

ξ_o —story characteristic ratio of seismic wall.

λ —seismic factor of fortification zone.

V_y, V_e —available capacity and seismic action of *i* story respectively.

ψ_1, ψ_2 —global and partial seismic measure factor respectively.

If $\beta \le 1.0$, the building should be strengthened.

4.2 Seismic Appraisal of Category B Buildings

The seismic appraisal of category B buildings is also divided into two parts, seismic fortification measures checking and seismic capacity analysis. Different with category A buildings, the two parts should be done simultaneously. That is to say if the building meet the requirement of seismic measures, the seismic analysis should also be done. Similar to category A buildings, the influence factor of seismic measures could be considered in the capacity analysis. The compound seismic capacity could be meet the requirement as follows.

$$S \le \psi_1 \psi_2 R / \gamma_{Ra} \tag{3}$$

Here, S is the base combination of seismic effect and other load effects, R is the resistant capacity of structural member. While γ_{Ra} is called seismic appraisal adjusting factor for bearing capacity of member, it reflected the seismic action variation with different seismic service life.

So the compound seismic capacity index could be written as:

$$\beta = \psi_1 \psi_2 R / S \gamma_{Ra} \tag{4}$$

If $\beta \le 1.0$, the building should be strengthened.

5. EXAMPLES

5.1 Seismic appraisal of a masonry building

A classroom of 4-story masonry structure used as school classroom, the height of story is 3m and overall height of building is 12.5m. The strength grade of mortar is M2.5 in 1 to 2 story and M1 in 3 to 4 story, the floor lab is concrete cast in site. The width of door and window is 1m and 1.8m respectively, width of wall is 240mm. This building was built in 1970's and the fortification intensity is 7 degree according to Chinese code. Figure 4 is plan of the building.

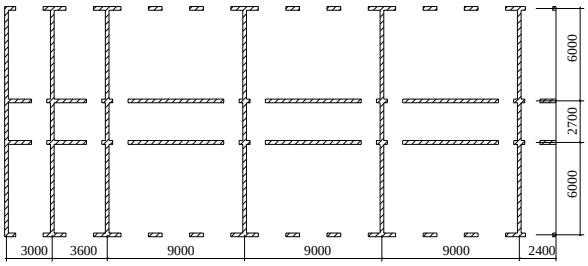

Figure 4 Plan View of the 4-story Masonry Structure

Table 3 Main Results of Seismic Measure Appraisal

Items		Requirement	Reality	Conclusion
Structural system	Story numbers	4	4	Passed
	Overall height	13m	12.5m	Passed
	Story height	4m	3m	Passed
	Height/width of building	2.2	0.85	Passed
	Max space of seismic brick wall	15m	9.0m	Passed
Material	Strength grade of mortar	M1	M2.5, M1	Passed
Structural entirety	Connection of walls	/	/	Passed
	Arrangement of tie R.C. beams	No needed	None	Passed
	Arrangement of tie columns	Needed	None	Unqualified
Partial dimension	Width of bearing wall (m)	1.00	0.90	Unqualified
	Width of wall at the end (m)	1.00	0.87	Unqualified

Table 4 Calculation of Compound Seismic Capacity Index

Direction	Story	A (m^2)	A_b (m^2)	ξ_o	Ψ_1	Ψ_2	λ	β
Transverse	1~2	37.12	1079.27	0.0335	0.8	1.0	1.0	0.821
	3			0.0414				0.665
	4			0.0286				0.962
Longitudinal	1~2	40.07		0.0283		0.9		0.945
	3			0.0354				0.755
	4			0.0253				1.066

The key points of seismic appraisal of this building are as follows. First, the continuous seismic service life for this building is 30 years and could be appraised according to category A building. Second, it is belong to major fortification category because it is a school classroom. Third, it is a rare transverse wall masonry structure.

The first stage appraisal results listed in Table 3.

The second stage appraisal is seismic capacity calculation. Considering the appraisal results of seismic measures, the entirety seismic influence factor $\psi_1 = 0.8$ (None tie column is set), partial seismic influence factor $\psi_2 = 0.9$. The compound seismic capacity index β was calculated as in Table 4. It shown that the story compound seismic capacity index were less then 1.0 except the 4th story in longitudinal, so the building need be strengthened. But if the building used as an ordinary office not as classroom, the seismic influence factor ψ_1, ψ_2 were equal to 1.0, thus the compound seismic capacity of all story were great than 1.0, so the strengthening was not needed.

5.2 Seismic Appraisal of a R.C. Frame

A 4-story concrete frame building which was built in 1950's located in seismic zone of 9 degree. The story height is 4.5m at the first story and 3.6m at the other stories. the longitudinal bar of column is 8φ16, and the hoop bar at the end of column or beam is φ6@200. Figure 5 shows the plan view of the structure.

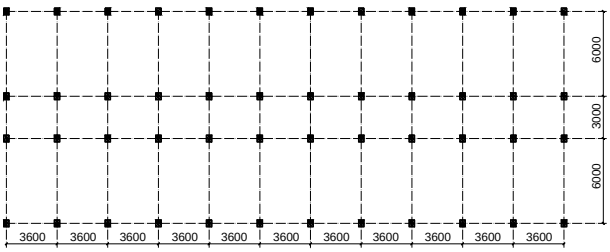

Figure 5 Plan View of the 4-story R.C. Frame

In the first stage appraisal, the strength grade of concrete is only C13 less than C18, the hoop of column and beam can not satisfy the requirement (φ8@150) of category B buildings specified in GB50023. So compound seismic capacity should be analyzed with entirety influence factor $\psi_2 = 0.8$, Table 5 shown the results (only transverse results listed). The compound seismic capacity index of all stories is less than 1.0, and the building need be strengthened.

Acknowledgements:

This project was funded by National Key Technology Program (2006BAJ13B01).

References:

[1] Standard for Seismic Appraisal of Buildings GB 50023-2009 (In Chinese). *China Architecture & Building Press*, 2009.

[2] Dai guoying, Li Dehu. Several Problems in Seismic Appraisal & strengthening of Existing Buildings. *The 5th Conference of China Earthquake Engineering*, 1998.

[3] Zhang Xiguang, Wang Junsun, Liu Huishan. Manual of Seismic Appraisal & Strengthening of Existing Buildings. *China Architecture & Building Press*, 2001.

JOINT CONFERENCE PROCEEDINGS
7th International Conference on Urban Earthquake Engineering (7CUEE) &
5th International Conference on Earthquake Engineering (5ICEE)
March 3-5, 2010, Tokyo Institute of Technology, Tokyo, Japan

SEISMIC EVALUATION OF EXISTING FACILITIES OF PRIMARY AND SECONDARY SCHOOLS IN SHANGHAI, CHINA

Haibei XIONG[1)], Wei ZHANG[2)], Xilin LU[1)], Xiaone WEI[3)]

1) Professor, Research Institute of Structure Engineering and Disaster Mitigation, Tongji University, China
2)Master of science, department of construction engineering quality & safety supervision, Ministry of Housing and Urban-Rural Development of the People's Republic of China
3)Student，College of Civil Engineering, Tongji University, China
xionghaibei@tongji.edu.cn, zrr.zhang@gmail.com, lxlst@tongji.edu.cn,weixiaona259@126.com

ABSTRACT

"5.12"Wenchuan Earthquake (occurred at 14:28 May 12, 2008, magnitude 8.0, the epicenter is located at Wenchuan, Sichuan Province, China at N31.0°, E103.4°) caused a large number of casualties and severe damages to buildings, for which the collapsed school buildings received most attention from media and authorities. The earthquake exposed vulnerability of school buildings disproportionately compared to the other infrastructures. Learnt from this disaster, Chinese government quickly required all local authorities to conduct earthquake resistance inspection to facilities in all primary, secondary schools and kindergartens.

In this paper, some general information, which including the construction time, the type of structure, the construction materials and the lever of earthquake resistance of facilities are briefly introduced and analyzed based on the seismic inspections of buildings of almost two hundred schools in Shanghai, China. Some treatments and suggestions of seismic upgrading, strengthening and retrofitting of buildings which not satisfied with the new standard are brought forward.

1. Introduction

The violent Wenchuan Earthquake with a magnitude of 8.0 occurred in China. And following it, government officials decided to make an entire survey about the resistance of school buildings and tried to make sure about the seismic safety of children. A lot of problems have been revealed during the catastrophe and the need for assessing and upgrading existing school buildings is urgent. Some possible reasons for disproportionate rate of school collapse are listed below: 1) school buildings have large space which lack of sufficient lateral resistance. 2) Many school buildings are old and poor constructed with no seismic design. 3) Some buildings have been altered to accommodate increased pupil numbers without standard design and with poor construction. 4) Pre-cast concrete slabs were used with poor continuity at joints. 5) Standards for school building were not higher than ones for normal business or residence buildings.

A feasible, cost-effective solution should be conducted all over the country and identify the most vulnerable buildings for retrofitting and strengthening. To make up the defects of school facilities' insufficient resistance under earthquake, retrofitting should be at low cost and completed faster. Relatively small numbers compared should be demolished and reconstructed to provide for greater long-term safety.

2. INVESTIGATION OVERVIEW

We gathered data from investigations of a part of school buildings which were listed in first period seismic evaluation in Shanghai. 195 primary and junior high schools with 736 buildings are surveyed by engineers and experts of Tongji University. And the data are classified according to structural type, construction time and seismic detailing etc. The distribution of schools is showed in Table 1 below. Functions of the building varied from classroom, laboratory to canteen, dormitory, etc.

3. STATISTICS AND ANALYSIS

3.1 Date of Construction

According to the new issued code, Standard for Seismic Appraisal of Buildings (GB 50023-2009) and

Table 1 Distribution of the school buildings

Locating district	numbers	scale
Jiading	5	2.6%
Changning	5	2.6%
Qingpu	5	2.6%
Nanhui	8	4.1%
Putuo	30	15.4%
Hongkou	51	26.2%
Chongming	82	42.1%
others	9	4.6%

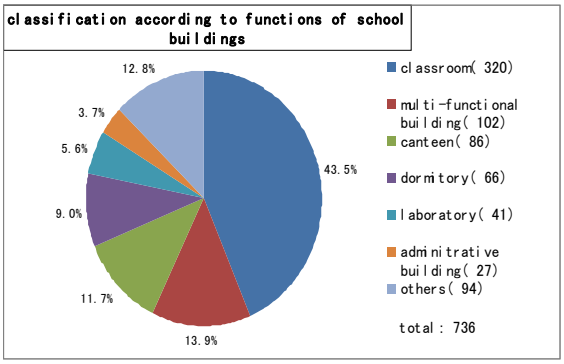

Figure 1 Numbers and scales of buildings with different functions

Technical Specification for Seismic Strengthening of Buildings (JGJ 116-2009), the continued service life and the requirements of buildings for seismic evaluation and strengthening are classified to three types, which based on different construction time of buildings.

In this investigation, buildings built between 1970s and 1980s were mostly masonry structures and characterized by no seismic design and poor quality of construction and materials. Most of the masonry buildings built after 1980 are of reinforced concrete confined brick masonry construction. Reinforced concrete frame constructions with infill masonry walls are also popular during and after 1980's in the investigated area. The poor construction quality of some building structures still existed which did not conform to the current Chinese Seismic Design Code in terms of materials and some detailing. The statistics about the construction time of the school buildings is showed in Table 2.

Table 2 Construction time of the school buildings

Construction Time	Numbers	Scales
1901~1980	112	11.8%
1981~1990	208	28.3%
1991~2000	249	33.8%
2001~2005	167	22.7%

3.2 Structural Type

From the data we got, we can observe that the masonry structures and reinforced concrete structures mixed with masonry buildings occupy 67.6% in all the school buildings. According to investigations of building disaster of Wenchuan Earthquake, the seismic capacities of buildings with different structure types can be concluded as the following sequence from poor to good: masonry structure, RC frame-masonry hybrid structure, RC frame structure.

Table 3 Structural types of school buildings

Structural Type	Numbers	Scales
Masonry Structures	441	59.9%
RC Frame	224	30.4%
RC Frame mixed with Masonry Structures	57	7.7%
Others	14	1.9%

The large stock of unconfined and unreinforced masonry buildings, as well as of reinforced concrete confined masonry buildings, which in the presence of irregular geometries, poor materials and inadequate detailing, offer low margins of safety with brittle modes of failure in masonry structure, resulted in responsible of most of the full and partial collapses observed in the affected areas in Wenchuan Earthquake. The large number of window openings and open space with the deficient arrangement in masonry structures were led to extensive cracking and out-of-plane failure of the clay brick walls. And the pre-cast floor slabs fell down due to large lateral displacement and short support area.

Reinforced concrete frame performs well than masonry structure and slight number of them is reported collapse in the Wenchuan earthquake. But many of them have been largely damaged due to various reasons. And most of the reinforced concrete building frames did not perform as intended by the current Chinese code. Most failures developed at the columns rather than at the beam. Damage of beam-column joints happened (see Figure 2) due to insufficient confinement and shear reinforcement at the joint as well as of the irregular geometry in plan and the absence of capacity design principles. The masonry infill walls between the ground and the upper storey would provide the change in relative stiffness. Many short column failures develop due to inappropriate structural arrangements or to continuous openings at the top of infill walls not foreseen in the design of columns.



Figure 2 Joint failure Mode of RC Frame

The main part of RC frame and masonry mixed structure is the one or multi-story RC frame with one or two storey attached. In order to obtain more room, they usually have an ancillary masonry structure attached to main building. In severe earthquakes, stiffness centers and mass centers usually do not coincide and distortion of the structure would occur. The observed damage often occurs in ends of the RC frame or the attached masonry structure in earthquake area.

3.3 Numbers of Stories

With more numbers of stories and larger height, the demands of seismic design value become bigger. Among the seismic summary of Wenchuan earthquake, considering building height, multistory buildings sustained more severe damage than high-rise buildings and two and three story buildings. Figure 3 shows the classification of school buildings by story numbers in this investigation.

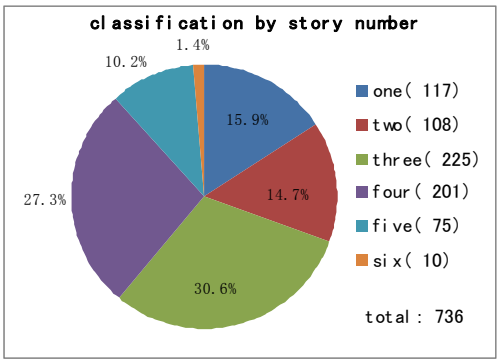

Figure 3 Classification of school buildings by story numbers

3.4 Location of Stairwells

To multi-story buildings, stairwells serve as an important part in the escape routes. Stairwells, compared to the other part of the building, lack the confinement of the floor slab and have relatively low special stiffness. Attentions should be paid, so we examined the location of the stairwells of 170 school buildings. The number of school buildings which have stairwells located at only one side is 59(34.7%). 85 buildings with a percentage of 50% have stairwells located in the middle. The rest 26(15.3%) have stairwells located at both sides.

The locations of stairwells greatly affect the distribution of stiffness and mass of buildings. The shear force induced by the stair structure can shear off the first-story column at mid-height due to short column, and less lateral support by stair slab on the top floor, which result soft story. And the stair beam should be recognized as a main structural member and be fully retrofitted to avoid destruction.

3.5 Corridor

Corridors, same to the stairwells, are essential to people who want to get out the buildings in an earthquake. Among all the 208 buildings in the survey of corridor location, 95 buildings with the ratio of 45.7% have exterior corridors. Corridors that have cantilevered beam supported by below columns are 89 with the ratio of 42.8%. Interior corridors located between classrooms have the least number of 24, which has the ratio of 11.5%.

Damages can often be seen in exterior cantilevered corridors with brick parapet (see Figure 4), because of relative larger vibration of cantilevered parapet contributing the vertical and horizontal shake of corridors and resulting to collapsed during sever earthquake. Although the collapse of the parapets in non-structural and did not compromise the stability of the structure, it posed a great threat to the school children in the court yard as well as to those evacuating the building from the corridor.



Figure 4 Parapet of Corridor collapsed

3.6 Seismic Detailing

The seismic fortification intensity for Shanghai is 7, set by the code for seismic design of buildings GB50011-2001. In 224 reinforced concrete frame buildings, 38 (30.8%) are designed to satisfy this regulation, while the numbers of reinforced concrete frame building designed under the seismic fortification intensity of 6 are 56 with the ratio of 25%. Adequate detailing assures the weak-beam and

strong-column systems with beam-column joints capable of ensuring the formation of plastic hinges.

Most masonry structures have concrete ring beam to increase the integrity. Among 441 masonry structures surveyed, 83 (18.8%) of them have both concrete confined columns and the ring beam. They can help form an integral framework that provides sufficient confinement to brick walls. They are very important to increase the system robustness, stability and firmness although they don't carry much load during normal service.

In Hongkou District, buildings of 51 schools were examined as to the function of seismic gaps. 47% (24) of those evaluated have seismic gaps. Lacking integral planning in advance, new classrooms were added to the existing ones to solve the problems of under-supply of classroom. The two structures may possess different fundamental vibration periods. When an earthquake occurred, the old and new classrooms would vibrate not in-phase. Under this circumstance, if the adjacent seismic gaps were not designed or not wide enough due to blocking, those classrooms could have pounded each other.

3.7 Need of Seismic Retrofit

buildings used for education, dormitories and canteens of kindergarten, primary schools and middle schools are classified as "Special Protection" for seismic fortification in Seismic Protection of Building Construction (GB50223-2008) after the grate shake. The standard of seismic detailing of those buildings shall be taken according to one grade higher than that of the local region fortification. That means, almost all those buildings should be strengthened or retrofitted for seismic upgrading in Shanghai.

More than 95.3 percent of the investigated structures need to be retrofitted to meet the demand of the current code for seismic design of buildings GB50011-2001(2008 version). The structures that are evaluated to perform well in the earthquake have the ratio of 4.3%. But 3 of the school buildings can not be retrofitted and should be demolished and should be reconstructed.

4. METHODS OF RETROFITTING

Lots of new techniques and materials can be used in retrofitting of exist buildings. But some methods with feasible, effective, fast constructed and lower cost are listed below.

4.1 Masonry Structure

4.1.1 Reinforcing integral seismic performance

In the case of seismic strengthening and retrofitting of masonry structure, the integrity of building should be improved. RC bond-beams should be provided under the floor slab, and casting tie-columns should be confined at corners, wall intersections and on both sides of large openings. In order to be effective, tie columns should connect with a tie beam along the walls at floors levels. The confinement prevents disintegration and improves ductility and energy dissipation of unreinforced masonry buildings.

4.1.2 Reinforcing pre-cast RC slabs

The toweling layer on the floor slabs should be removed and cleaned it up firstly. Then reinforcement of φ6@200 should be installed and anchored into the adjacent vertical wall before the in-situ concrete is pumped. The new layer depth is around 40mm, which will effect on the ultimate load resistance in limited range. But, it is normally can be supported by subsoil, because these buildings are used more than twenty years, and the strength of these buildings' subsoil can be improved by 20% than design value.

4.1.3 Reinforcing masonry walls

Construction of reinforced cement or reinforced concrete jacket on one or both sides of walls is mostly used in the instances where strengthening of the wall is necessary for rehabilitation purposes or when the wall was severely cracked and damaged in the event of an earthquake. This method is applicable to most types of masonry walls and consists of applying reinforced cement or concrete coatings onto one or both faces of a wall. However application of coating on both sides is strongly recommended. Cement or mortar spray at one face or both faces of the wall form a coating up to 35~40mm thick with reinforcement of φ6@200. Once dry, the coating can enhance the shear capacity of the masonry wall significantly.

4.2 Reinforced Concrete Frame Structure

4.2.1 Damper System

The use of supplemental damping devices such as viscous dampers shows substantial promise for improving the seismic resistance of these rather flexible structures. The energy dissipated by a damper reduces the energy demand on the structure and damps the structural response.

4.2.2 Increase of Redundancy

To single-span RC frame structure, such as canteens and stadiums in school, the beams and columns are sparse and very important, which will result in total structural collapse triggered by only these few members. There is an inadequate provisioning of lateral-load resisting members. So, the additional shear walls or special moment-resisting frames shall be strengthen to the lateral frames and increase its redundancy in severe earthquakes.

4.2.3 Improvement of Deformation Capacity

The RC frame buildings have deficiencies with insufficient strength and/or ductility to behave

satisfactorily during earthquakes. These deficiencies can be corrected by one of the following techniques: increasing the effectiveness of the existing walls using external coatings, filling existing windows or doors, constructing new shear walls or new steel braced frames inside or outside of the building. Strong-column, weak-beam joints should be formed by retrofitting. But we should avoid the appearance of new weak part after the retrofit.

4.3 RC frame mixed with masonry system

4.3.1 The setting of seismic gaps

The two parts of buildings can be separated by seismic gaps to avoid large torsion of irregular configuration. And the seismic force can be resisted by each of them separately. But with separated two parts, the additional wall should be erected and the new foundation should be set.

4.3.2 Retrofit by adding new parts

The destruction during the earthquake is mainly induced by the no coincidence of stiffness and mass center. Additional stiffness and/or mass can be imparted into another part to making the mass center close to the stiffness center.

4.3.3 Demolishment of the masonry part

After the calculation of lateral resistant strength and deformation of the two aforementioned methods, if the structure still can not meet the demands, we should tear down the attached masonry structure at the end.

5. SUMMARIES AND RECOMMENDATIONS

1) We should formulate a comprehensive plan for assessing and retrofitting public facilities and infrastructure such as schools and use them to instruct our work. Government should guarantee whether they are implemented in order to ensure the quality of retrofit of buildings, particularly public facilities. The various choices provided should incorporate the economical factor. With the least investment and least time, we can make sure that all school can go through those terrible earthquakes.

2) Except for structural difference, building quality management is another important issue influencing the seismic capacities of buildings with different structural types. The degradation of material strength and insufficient seismic detailing should be carefully examined which deviate from the design and affect the performance of structures in earthquakes.

3) The interaction of masonry infill walls with the concrete frame should be carefully studied and adequate connection must be included in the retrofit to ensure its performance. The strengthening of nonstructural components should be paid more attention since the damage would also cause injuries and death.

4) The improvement of seismic performance should be the focus of the retrofit of the structures. And there needs to be an emphasis on either side as to different buildings. The integrity of the building should be considered and we should avoid the appearance of new weak part after the retrofit.

6. ACKNOWLEDGEMENT

This research project is funded by department of construction engineering quality & safety supervision, Ministry of Housing and Urban-Rural Development of the People's Republic of China (MOHURD). And some statistics data are support from Committee on Seismic Evaluation of Building Construction of Tongji University. The research groups did the statistical work on classifying all the data. All of these are really appreciated by authors.

References

[1] GB 50011-2001, Code for seismic design of buildings[S], Beijing: China Building Industry Press, 2001

[2] GB 50367-2006, Code for retrofit of concrete buildings[S], Beijing: China Building Industry Press, 2006

[3] GB 50223-2008, Seismic Protection of Building Construction[S], Beijing: China Building Industry Press, 2008

[4] GB 50023-2009, Standard for Seismic Appraisal of Buildings[S], Beijing: China Building Industry Press, 2009

[5] JGJ 116-2009, Technical Specification for Seismic Strengthening of Buildings[S], Beijing: China Building Industry Press, 2009

JOINT CONFERENCE PROCEEDINGS
7th International Conference on Urban Earthquake Engineering (7CUEE) &
5th International Conference on Earthquake Engineering (5ICEE)
March 3-5, 2010, Tokyo Institute of Technology, Tokyo, Japan

STRUCTURAL RETROFIT OF THE TAIPEI CAMPHOR FACTORY

Chao-Hsun Huang[1], Sheng-Feng Zeng[2], and Cheng-Guan Lin[2]

1) Associate Professor, Dept. of Civil Engineering, National Taipei University of Technology, Taipei, Taiwan
2) Graduate Students, Dept. of Civil Engineering, National Taipei University of Technology, Taipei, Taiwan
steve@ntut.edu.tw, starwalker1920@yahoo.com.tw, qoosue7106@yahoo.com.tw

Abstract: To renovate the historical Taipei Camphor Factory, a seismic retrofit plan using steel frames was proposed by a local structural engineer. To verify the effectiveness of this plan, a structural investigation and analysis was conducted. It was found that even though the steel frame could improve the seismic resistance of the building, it would not meet the seismic requirements under the current building code. For comparison purposes, an alternative retrofit scheme using concrete shear walls was also studied, and it happens to have better seismic performance and would satisfy the most current seismic code.

1. INTRODUCTION

The Taipei Camphor Factory was found in 1902 by Japanese as the main base of camphor production in northern Taiwan. After the War, the Factory was transferred to the Taiwanese government and then converted into a distribution center of the Taiwan Tobacco and Liquor Corporation (TTL). Recognizing the significance of this facility in the development of modern Taiwanese economy, the Council for Cultural Affairs (CCA) assigned the old site and the remaining building, the Camphor Warehouse (see Figure 1), at the Factory as National Heritage in 1998 and set out a renovation project at the same time. The content presented in this paper is a structural assessment sponsored by the current owner of the facility, National Taiwan Museum (, to evaluate the structural safety of the Camphor Warehouse as well as the effectiveness of a retrofit plan proposed by local engineers.



Figure 1 The Camphor Warehouse of the Taipei Camphor Factory

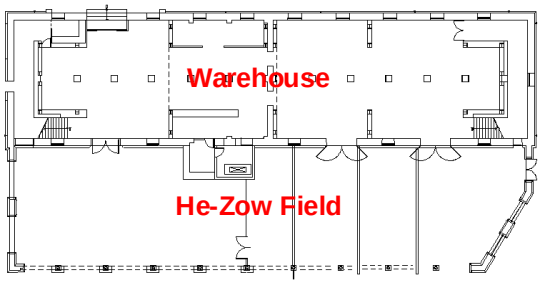

Figure 2 First floor plan of the Camphor Warehouse

2. DESCRIPTION OF THE BUILDING

2.1 Building Structural System

The Camphor Warehouse consists of two parts: the Warehouse and the He-Zow Field, as shown in Figures 2 and 3. The Warehouse is a two-story building constructed of reinforced concrete diaphragm supported by a row of concrete columns along the centerline of the building in the longitudinal direction and (unreinforced) brick walls around the perimeter. The He-Zow Field is an extended work area attached on the east side of the Warehouse, which is a one-story addition constructed of plywood roof sheathing, light steel trusses, and brick walls. Dimensions of the above structural elements are given in Table 1.

2.2 Material Properties

To calculate the strength of the structure, both field and laboratory investigations were conducted on structural components. To verify the number and locations of steel reinforcement, an ultrasonic scan was performed on reinforced concrete members using a BOSCH D-TECT 100 scanner; and to identify the diameters of reinforcing bars the

concrete cover was removed at selected areas. Since a destructive test on existing rebars is not permitted, the yield strength of steel reinforcement is assumed as 280 MPa. Eleven cylindrical samples of concrete were drilled from beams, columns, and both the roof and floor slabs before tested in the laboratory. Result of the concrete compressive test is given in Table 2.

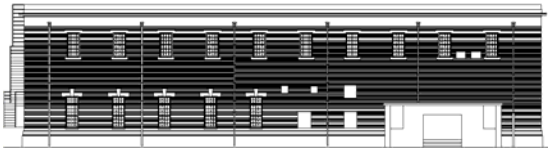

(a) West elevation

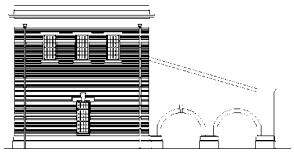

(b) South elevation

Figure 3 Elevations of the Camphor Warehouse

Table 1 Dimensions of structural components in the Camphor Warehouse

Component	Location		Dimension[1]
Slab	All		100
Beam	2F		360 x 970
	RF		300 x 400
Column	1F		540 x 540
	2F		360 x 360
Wall[2]	Warehouse	N and S	500
		E and W	610
	He-Zow Field		250

1. All dimensions are given in millimeters
2. Dimension of walls is represented by thickness

Table 2 Compressive strength[1] of concrete specimens

Element	Beams	columns	Slabs	
			2F	RF
f'_{c_avg}	8.04	9.57	1.16	1.69

1. All strengths are given in MPa

Samples of the brick walls are also taken from removed pieces of the exterior walls for compression and direct shear tests. The average compressive strength of the brick prisms and average shear strength of the joints were obtained as 28.2 MPa and 1.33 MPa, respectively. The out-of-plan tensile (flexural) strength of the walls is assumed as 0.12 MPa as described in a CCA report (CCA 2001).

3. STRUCTURAL ANALYSIS

A finite-element computer model (see Figure 4) was constructed using the SAP 2000 Program based on current configuration of the Camphor Warehouse (see Figure 5). Load combinations corresponding to strength design and allowable-stress design were applied for the analysis of concrete, steel, and brick wall components respectively according to applicable codes (ASCE 2006). The strengths of the structural members were calculated based on the dimensions and strengths obtained from field investigations as well as assumptions described in Section 2.

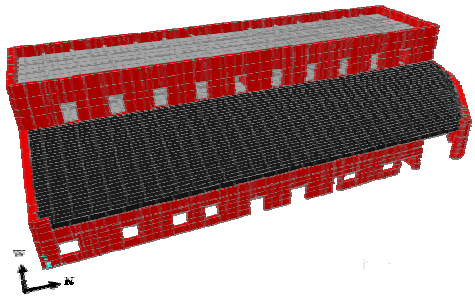

(a) Complete Building

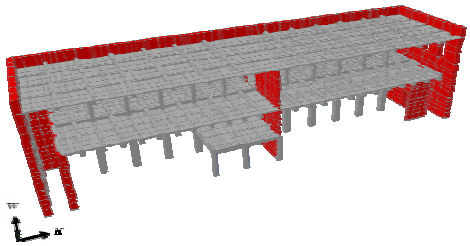

(b) Interior concrete floor system

Figure 4 Finite-element model of the Camphor Warehouse

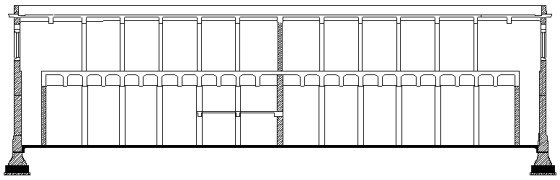

(a) Longitudinal section of the Warehouse

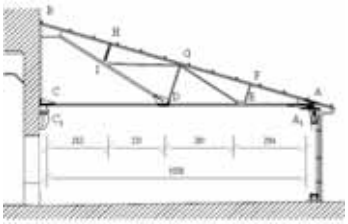

(b) Roof truss system at the He-Zow Field

Figure 5 Interior configuration of the Camphor Warehouse

Figure 6 shows the bending moments on the roof slab of the Warehouse in both longitudinal and transverse directions. It was found that the flexural strength of the roof slab is inadequate under factored gravity load near the mid-span of the first and second girders from both longitudinal ends of the building. This is because that a second column is missing at these locations, as shown in Figure 5(a), without any structural compensation. The second floor slab, in which a one-way slab system is used, has a better performance due to shorter spans and structural regularity. (See Figure 7)

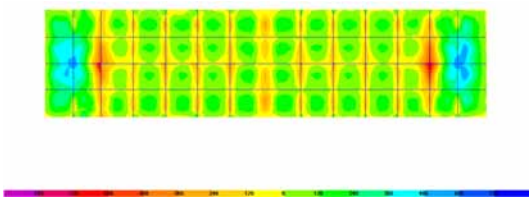

(a) Longitudinal bending moment

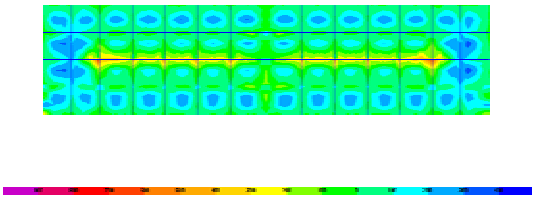

(b) Transverse bending moment

Figure 6 Bending moment on the roof slab of the Warehouse ($U = 1.2D + 1.6L + 1.2L_r$)

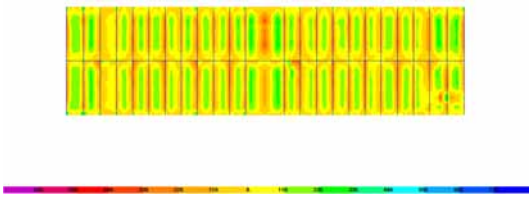

Figure 7 Bending moment on the second floor slab of the Warehouse ($U = 1.2D + 1.6L + 1.2L_r$)

For the roof and second floor beams, both shear and flexural strengths were examined. It was found that the structural capacities of existing members are adequate to carry the factored load (see Table 3) since lateral deformation is restricted by the perimeter and partition walls. For both first and second floor columns, the demand and capacity relationship is represented by comparing the highest flexural and axial load demands corresponding to respective load combinations with the interaction diagrams of the columns, as shown in Figure 8. It was found that the columns are able to sustain the factored load as long as most of the lateral (seismic) load is resisted by the brick walls.

Table 3 Flexural and shear demands and capacities for floor beams ($U = 1.2D + 1.6L + 1.2L_r$)

FL.	Direction of Beams	M_{u+max} (kN-m)	ϕM_{n+} (kN-m)	M_{u-max} (kN-m)	ϕM_{n-} (kN-m)	$V_{u\,max}$ (kN)	ϕV_n (kN)
RF	long.	49	74	51	50[1]	49	178
	trans.	73	296	113	167	88	221
2F	long.	126	402	127	243	135	282
	trans.	68	349	131	243	90	264

[1]The strength is considered adequate based on engineering judgment. (The flexural capacity is only 2% below demand.)

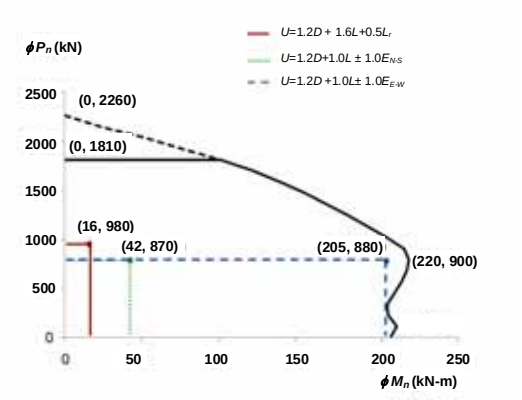

(a) First floor columns

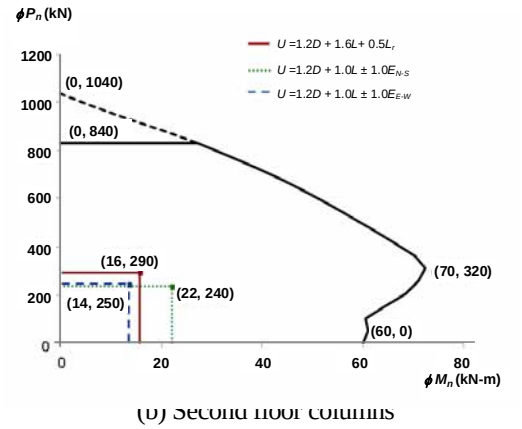

(b) Second floor columns

Figure 8 Interaction diagrams of concrete columns in the Warehouse

For the brick walls, both the (in-plane) shear and (out-of-plane) flexural strengths were examined using allowable-stress design (ASD) provisions. With a considerable number and total horizontal area, the existing brick walls (and wall piers) in the Camphor Warehouse should be able to resist the in-plane shear forces. (See Table 4) Nevertheless, due to the lack of flexural resistance, these walls will not be able to sustain the out-of-plane bending induced mainly by earthquake load (see Table 5), as encountered by most unreinforced masonry structures. Should these walls fail during an earthquake, they will no longer provide vertical supports for the floor slabs and beams and result in a catastrophic collapse of the building. Therefore, a seismic retrofit is strongly desired.

Table 4 In-plane shear demands and capacities for the brick walls ($U = 0.6D \pm 0.7E$)

Wall Location		Maximum shear stress (MPa)	Allowable stress (Mpa)
Warehouse	East	0.43	0.67
	West	0.51	
	South	0.64	
	North	0.55	
He-Zow Field		0.10	

Table 6 Out-of-plane flexural demands and capacities for the brick walls with the proposed retrofit ($U = 0.6D \pm 0.7E$)

Wall Location		Maximum flexural stress (MPa)	Allowable stress (Mpa)
Warehouse	East	0.27	0.12
	West	0.33	
	South	0.25	
	North	0.19	
He-Zow Field		0.29	

4. THE TENTATIVE RETROFIT PLAN

A tentative retrofit plan is proposed by local engineers using a braced steel frame, as shown in Figure 9. It is found that with the strength and stiffness provided by the frame, the capacity of the structure will be significantly improved. Unfortunately, the out-of-plane bending stresses in the brick walls still exceed the allowable stress. (See Table 6) One way to solve this problem is to reinforce these walls with steel bars or meshes, which has been proved effective by laboratory tests (ElGawady et al. 2004, Abrams and Lynch 2001). However, with a concern that the existing brick walls could be permanently damaged, the Museum does not seem to appreciate this idea, and the final decision is yet to be made.

5. CONCLUDING REMARKS

The result of a finite element analysis shows that both the brick walls and the roof slab of the Camphor Warehouse do not have sufficient flexural strength to support the specified factored load. While the current retrofit plan would enhance the structural capacity of the existing building, it cannot protect the brick walls against out-of-plane failure. It is hereby recommended that the building owner should consider providing steel reinforcement to the existing brick walls to improve the flexural capacity of these walls.

Table 5 Out-of-plane flexural demands and capacities for the brick walls ($U = 0.6D \pm 0.7E$)

Wall Location		Maximum flexural stress (MPa)	Allowable stress (Mpa)
Warehouse	East	0.51	
	West	1.05	
	South	0.26	
	North	0.29	
He-Zow Field		0.17	

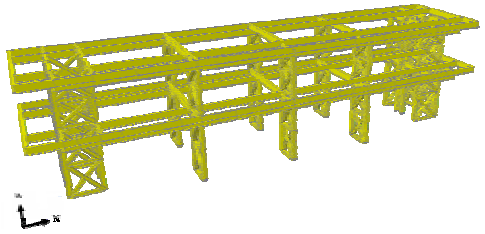

(a) The braced steel frame to be added

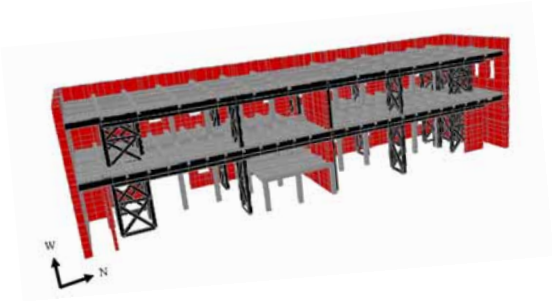

(b) The floor system with an added braced steel frame

Figure 9 The tentative retrofit plan proposes for the Camphor Warehouse

Acknowledgements:

The authors acknowledge the supports from National Taiwan Museum and National Science Council (Project ID. NSC 98-2625-M-027 004) for sponsoring this study and making the authors' participation in the conference possible. The authors also owe special thanks to the architect I. Z. Chan and structural engineer S. H. Liu for providing valuable drawings as well as other assists in the preparation of the final report.

References:

Abrams, D. P. and Lynch, J. M. (2001), "Flexural behavior of retrofitted masonry piers," *KEERC-MAE Joint Seminar on Risk*

Mitigation for Regions of Moderate Seismicity, Illinois, USA.
ElGawady M., Lestuzzi P., and Badoux M. (2004), "A review of conventional seismic retrofitting techniques for URM," *Proceedings of 13th International Brick and Block Masonry Conference*. Paper No. 89.
CCA (2001), "Repair and Retrofit on Historical Brick Buildings Constructed during the Japanese Colonial Period in Taiwan," Council of Cultural Affairs (in Chinese).
ASCE (2006), "Minimum Design Loads for Buildings and Other Structures," ASCE 7-05, American Society of Civil Engineers.

JOINT CONFERENCE PROCEEDINGS
7th International Conference on Urban Earthquake Engineering (7CUEE) &
5th International Conference on Earthquake Engineering (5ICEE)
March 3-5, 2010, Tokyo Institute of Technology, Tokyo, Japan

MODELING OF DIAGONALLY REINFORCED CONCRETE COUPLING BEAMS

David Naish[1)], John Wallace[2)], J. Andrew Fry[3)], and Ron Klemencic[4)]

1) Student, Dept of Civil and Environmental Engineering, University of California, Los Angeles, USA
2) Professor, Dept of Civil and Environmental Engineering, University of California, Los Angeles, USA
3) Senior Associate, Magnusson Klemencic Associates Inc., Seattle, USA
4) President, Magnusson Klemencic Associates Inc., Seattle, USA
dnaish@ucla.edu, wallacej@ucla.edu, afry@mka.com, rklemencic@mka.com

Abstract: An efficient structural system for tall building construction to resist earthquake loads consists of RC shear walls connected by reinforced concrete coupling beams. Understanding of the load-deformation characteristics is essential to modeling the overall system response to seismic loading. Modeling studies are performed to evaluate the effectiveness of current modeling approaches with respect to key performance parameters, including effective elastic stiffness, ductility, and residual strength. As well, most of the experimental work that has been performed on coupling beams has been on specimens at less than full-scale. The impact of this scaling effect on the full-scale models is presented and shown to be potentially significant on the expected ductility of the member. A brief summary of simplified modeling techniques using commercially available software is presented to provide practical applications for design engineers. Results indicate that these simple modeling approaches reasonably capture measured force versus deformation behavior.

1. INTRODUCTION

Tall building construction is common in metropolitan areas and it has become increasingly important to provide methods of construction that improve both seismic performance and constructability. Reinforced concrete core walls, with coupling beams above openings to accommodate doorways, are an efficient lateral-force-resisting system for tall buildings. When subjected to strong shaking, coupling beams act as fuses and typically undergo large inelastic rotations. Various testing programs have been carried out to assess the load – deformation behavior of coupling beams. Based on investigation of prior studies [(Paulay 1974), (Tassios 1996), (Galano 2000)], the following parameters were deemed particularly important for study: aspect ratio, residual capacity/failure, slab inclusion (RC and PT), and detailing of confinement steel.

Use of diagonal reinforcement in coupling beams with clear length to total depth less than four was introduced into ACI 318-95. Providing transverse reinforcement around the diagonal bar bundles, to suppress diagonal bar buckling, as detailed in ACI 318-05 S21.7.7 is difficult where the diagonal groups intersect at the beam mid-span, particularly for shallow beams, as well as at the beam-wall interface due to interference with the wall boundary vertical reinforcement. ACI 318-08 S21.9.7 introduced an alternative detailing option, where transverse reinforcement is placed around the beam cross section to provide confinement and suppress buckling, with no transverse reinforcement provided directly around the diagonal bar bundles.

Nonlinear modeling of coupling beams has received increased attention as the use of performance-based design for tall core wall buildings has become more common (Wallace 2007). Modeling parameters for diagonally-reinforced coupling beams were introduced into Table 6-18 of FEMA 356. Of particular interest is the selection of the effective secant bending stiffness at yield E_cI_{eff} and the allowable plastic rotation prior to significant lateral strength degradation. The value used for coupling beam bending stiffness has a significant impact on the system behavior.

2. MODELING RESULTS

2.1 Effective Stiffness

Elastic analysis approaches require estimation of the effective elastic bending and shear stiffness values. In FEMA 356, stiffness values of $0.5E_cI_g$ and $0.4E_cA_{cw}$ are recommended for bending and shear, respectively. ASCE 41-06 including Supplement #1 incorporates a lower value for effective stiffness of $0.3E_cI_g$, with a mean value obtained from tests of $0.2E_cI_g$. The New Zealand Code (NZS-3101 1995) includes an equation to estimate the effective bending stiffness that depends on the expected ductility demand as:

$$E_cI_{eff} = \frac{A \times E_cI_g}{B + C \times (h/l_n)^2} \quad (1)$$

where A, B, and C vary with ductility [A=1.0 and 0.40; B=1.7 and 1.7; C=1.3 and 2.7; for ductility=1.25 and 6.0]. For beams with aspect ratio l_n/h = 2.4, Equation 1 yields a beam with effective elastic stiffness of around fifty percent

of the gross section stiffness, $0.5E_cI_g$, whereas for a ductility ratio of 6, the effective (secant) stiffness drops to eighteen percent of the gross section properties, $0.18E_cI_g$.

Test results (Naish 2009) indicate that for beams with aspect ratio l_n/h = 2.4, the initial stiffness of each residential beam is approximately $0.25E_cI_g$, with an effective stiffness at the yield rotation (~1.0% rotation) of $0.12E_cI_g$. Of the various approaches noted above for estimating the effective stiffness at yield, only ASCE 41-06 (2007) addresses the impact of slip/extension on the effective stiffness at yield [it is noted that median effective stiffness reported by Elwood et al (2007) is actually $0.3E_cI_g$ at low axial load, the value of is used as a compromise to address issues associated with deformation compatibility checks for gravity columns].

The contribution of slip/extension to the yield rotation is estimated for the beams tested using the approach recommended by Alsiwat and Saatcioglu, where the crack width that develops at the beam-wall interface depends on bar slip and bar extension (strain). Using a coupling beam effective stiffness derived from a moment-curvature analysis of the beam cross-section at the beam-wall interface $0.5E_cI_g$ and the slip/extension model noted above, the effective stiffness at yield reduces to $0.12E_cI_g$, which is consistent with the effective stiffness at the yield rotation (approximately 1.0% for all beams) derived for the tests.

Table 1 Effective stiffness values

	Test Results	FEMA 356	ASCE 41	ASCE 41 S1, w/slip	NZS-3101 95 (μ=1)
EI_{eff} [% EI_g]	14.0 12.5*	50.0	30.0	16.5 13.0*	50.0
θ_y [% drift]	0.70 1.00*	0.23	0.39	0.75 0.95*	0.23

*modifications for ½-scale

2.2 Slip Extension Calculations

Slip and extension of the flexural reinforcement contributes a large portion (40-50%) of the beam deformations prior to yield. The approach developed by Alsiwat and Saatcioglu is used to model this contribution to the yield rotation. The calculations are provided here for the case of determining the slip/extension rotations at the yield point of the flexural reinforcement. If adequate embedment of the flexural reinforcement is provided, then the slip contribution is negligible. However, this calculation is also included for the sake of completeness. The parameters that are required for this calculation are d_b, A, l_d, f'_c, f_y, M_y, and f_s.

Preliminary calculations:

$$u_e = \frac{f_y \times d_b}{4 \times l_d} \quad [MPa] \tag{2}$$

$$L_e = \frac{f_s \times d_b}{4 \times u_e} \quad [mm] \tag{3}$$

$$u_u = \left(20 - \frac{d_b}{4}\right) \times \sqrt{\frac{f'_c}{30}} \quad [MPa] \tag{4}$$

$$\delta_{s1} = \sqrt{\frac{30}{f'_c}} \quad [mm] \tag{5}$$

In these calculations, u_e represents the elastic bond stress, L_e represents the elastic region length, u_u represents the peak bond stress, and δ_{s1} represents the local slip at the peak bond stress.

Calculations for $f_s = f_y$:

$$\delta_s = \delta_{s1} \times \left(\frac{u_e}{u_u}\right)^{2.5} \quad [mm] \tag{6}$$

$$\delta_{ext} = 1.25 \times \varepsilon_y \times \frac{L_e}{2} \quad [mm] \tag{7}$$

$$\delta_{tot} = \delta_s + \delta_{ext} \quad [mm] \tag{8}$$

$$\theta_{@\,\delta tot} = \frac{\delta_{tot}}{d - x} \quad [rad] \tag{9}$$

$$K = \frac{M_y}{\theta_{@\,\delta tot}} \quad [mm - MPa] \tag{10}$$

In these calculations, δ_s represents the slip of the reinforcement, δ_{ext} represents the extension of the bar due to accumulation of strain along its length, δ_{tot} represents the total displacement of the bar at the beam-wall interface, $\theta_{@\delta tot}$ represents the angle of the crack that opens at the beam-wall interface due to the slip/extension of the bar, and K represents the stiffness of the corresponding moment-rotation hinge that can be implemented in a structural model.

2.3 Scale Effects

It is important to understand the potential impact of scale on the effective yield stiffness as well as the overall load-deformation behavior. The relative contribution of flexural deformations (curvature) and slip/extension to the yield rotation of the test beams at full scale (i.e. prototype beams) is assessed using the same approach as noted in the previous section for the one-half scale beams. The study is extended to consider coupling beam aspect ratios beyond those tested, by varying the beam length. Results are reported in Figure 1, where the effective yield rotation is plotted against beam aspect ratio (l_n/h) for various scale factors.

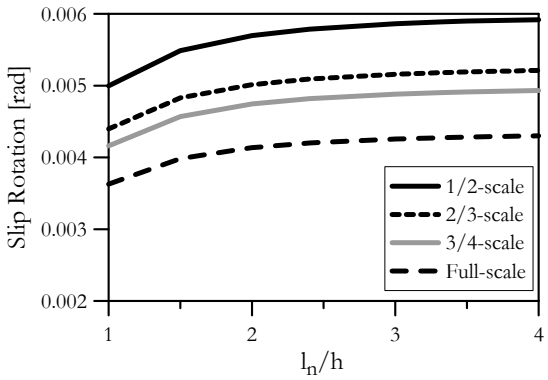

Figure 1 Yield rotation due to slip/extension for various aspect ratios and testing scales.

For a given aspect ratio, slip rotation at yield is significantly impacted by scale, with a 35 to 40% reduction for beams at one-half versus full scale. The effective bending stiffness at yield for the one-half scale tests of $0.12E_cI_g$ increases to $0.14E_cI_g$ for the full-scale prototypes due to the reduction in the relative contribution of slip rotation. Based on these results, we recommend use of an effective yield stiffness value of $0.15E_cI_g$ for full-scale coupling beams (l_n/h=2.4).

2.4 Backbone Relations

Linearized backbone relations for normalized shear strength versus rotation are plotted in Figure 2. The dotted lines represent recorded test results, and the solid lines represent relations modified for full-scale beams. Including the slab provides a nominal increase to the shear strength (~25%).

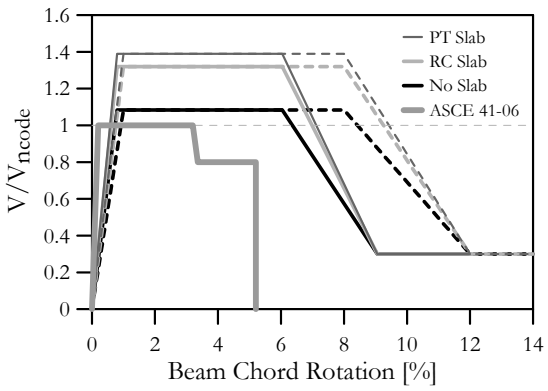

Figure 2 Backbone load-deformation for full-scale beam models and ASCE 41-06 model (1/2-scale test results are dotted lines).

ASCE 41-06 with Supplement #1 modeling parameters also are plotted on Figure 2 and indicate that the test beams are more flexible at yield and that they attain substantially higher deformation capacity prior to lateral strength degradation than the standard backbone relation. The elastic stiffness of the ASCE 41 relation is based on a bending stiffness of $0.3E_cI_g$, or about double that derived for full-scale beams from the test data. The plastic rotation capacity given by ASCE 41-06 Table 6-18 is limited to 3%, whereas the backbone relations for the full-scale beams derived from the test data yield at approximately 0.7% rotation and reach 6.0% rotation prior to strength degradation, or a plastic rotation of 5.3%. Therefore, relative to ASCE 41-06, the relations derived for the full-scale beams have a lower effective yield stiffness ($0.14E_cI_g/0.3E_cI_g$ = 0.47) and substantially greater deformation capacity (5.3%/3.0% = 1.77).

It is noted that the ASCE 41-06 relation applies to all diagonally-reinforced coupling beams, including beams with aspect ratios significantly less than the values of 2.4 and 3.33 investigated in this test program. Results presented in Figure 2 apply for the beam aspect ratios tested (2.4 and 3.33), as well as to beams between these ratios. It is reasonable to assume these values can be extrapolated modestly to apply to beams with $2.0 < l_n/h < 4.0$.

2.5 Test vs. Model Results

Nonlinear modeling approaches commonly used by practicing engineers were investigated to assess how well they were able to represent the measured test results. Two models were considered, one utilizing a rotational spring at the ends of the beam to account for both nonlinear flexural and slip/extension deformations (M_n hinge) and one utilizing a nonlinear shear spring at beam mid-span to account for both shear and slip/extension deformations (V_n hinge).

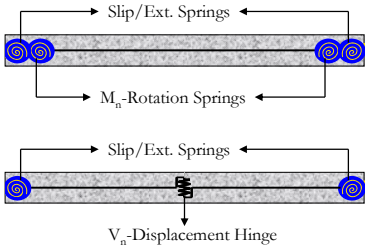

Figure 3 Modeling components: (a) Mn-hinge model, and (b) Vn-hinge model

The M_n-hinge model consists of an elastic beam cross-section with E_cI_{eff} = $0.5E_cI_g$, elastic-rotation springs (hinges) at each beam-end to simulate the effects of slip/extension deformations, and rigid plastic rotational springs (hinges) at each beam-end to simulate the effects of nonlinear deformations. The stiffness of the slip/extension hinges are defined using the Alsiwat and Saatcioglu model discussed above, whereas the plastic rotations of the nonlinear flexural hinges are modeled using the backbone relations derived from test results (Fig. 2, excluding the elastic portion) and the capacity is defined using ACI 318-08 eqn. 21-9. The V_n-hinge model also consists of an elastic beam cross-section and slip/extension hinges. However, instead of using flexural hinges at the beam ends, a shear

force versus displacement hinge (spring) is used at the beam mid-span to simulate the effects of nonlinear deformations. The shear hinge properties are defined using the backbone relations derived from the test results.

Figure 4 shows cyclic load-deformation plots for the two models and the test results for CB24F. Both models accurately capture the overall load-displacement response of the member; however, the M_n-hinge model (Fig. 4(a)) captures the unloading characteristics better than the V_n-hinge model (Fig. 4(b)), due to the fact that unloading stiffness modeling parameters, which help to adjust the slope of the unloading curve, are available for the flexural hinges in the commercial computer program used, but not for the shear hinges (see Naish et al, 2009). For the beam test aspect ratios (2.4 and 3.33), flexural and slip/extension deformations account for approximately 80-85% of total deformation whereas shear deformations generally account for only l5-20% of total deformation. Therefore, in both models, the flexural and shear hinges are used to represent flexural deformations, with shear deformations not considered. Therefore, depending on the computer program used, similar modeling studies should be conducted to calibrate available model parameters with test results.

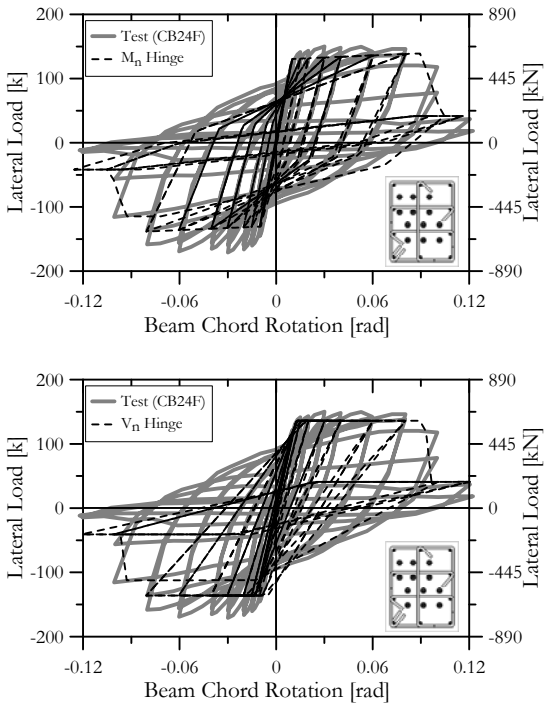

Figure 4 Cyclic load-deformation modeling results (ln/h = 2.4): (a) Test vs. moment hinge model; and (b) Test vs. shear hinge model.

3. CONCLUSIONS

Effective elastic stiffness values for test beams are determined to be ~10-15% of the gross section stiffness, values that are much less than FEMA and ASCE 41 prescribed values of 50% and 30%, respectively. Designers should therefore utilize the slip/extension hinge model detailed in Supplement 1 to ASCE 41 to better approximate the elastic stiffness of the coupling beam.

While flexural and shear deformation contributions are equivalent regardless of the scale of the specimen, deformations due to slip and extension of the flexural reinforcement at the beam-wall interface must be modified to account for the scale of the given specimen.

Simple nonlinear models, either moment-hinge or shear-hinge, accurately represent the load-deformation behavior of test beams. The flexural hinge model better matches the test results in the unloading and reloading range, due to the specific modeling parameters available in the computer software used (unloading stiffness modeling parameters), although both models produce acceptable results up to 3% total rotation for beams with ln/h between 2.0 and 4.0.

Acknowledgements:

The research has been funded by the Charles Pankow Foundation, with significant in-kind support provided by Webcor Concrete; this support is gratefully acknowledged. As well, material contributions from Catalina Pacific Concrete, SureLock, and Hanson Pacific are appreciated. Thanks are extended to laboratory assistants Joy Park, Nolan Lenahan, and Cameron Sanford, as well as UCLA laboratory technicians Steve Keowen, Alberto Salamanca, Steve Kang, and Harold Kasper, for help in test preparation and completion.

References:

ACI Committee 318, 1995, *Building Code Requirements for Structural Concrete (ACI 318-95) and Commentary (318R-95)*, American Concrete Institute, Farmington Hills, Michigan.

ACI Committee 318, 2005, *Building Code Requirements for Structural Concrete (ACI 318-05) and Commentary (318R-05)*, American Concrete Institute, Farmington Hills, Michigan.

ACI Committee 318, 2008, *Building Code Requirements for Structural Concrete (ACI 318-08) and Commentary (318R-08)*, American Concrete Institute, Farmington Hills, Michigan.

Alsiwat, J., and Saatcioglu, M., 1992. Reinforcement Anchorage Slip under Monotonic Loading, *Journal of Structural Engineering*, ASCE, Vol. 118, No. 9, pp. 2421-2438.

American Society of Civil Engineers, 2007, *ASCE/SEI Standard 41-06, Seismic Rehabilitation of Existing Buildings*, Reston, VA.

Elwood, K.J., et al. (2007), Update to ASCE/SEI 41 Concrete Provisions, *Earthquake Spectra*, EERI, Vol. 23, Issue 3, pp. 493-523.

Federal Emergency Management Agency, 2000, *Prestandard and Commentary for the Seismic Rehabilitation of Buildings (FEMA-356)*, Washington DC.

Galano, L., and Vignoli, A., 2000, Seismic Behavior of Short Coupling Beams with Different Reinforcement Layouts, *ACI Structural Journal*, V. 97, No. 6, Nov.-Dec., pp. 876-885.

Naish, D., Fry, A., Klemencic, R., and Wallace, J., 2009,

Experimental Evaluation and Analytical Modeling of ACI 318-05/08 Reinforced Concrete Coupling Beams Subjected to Reversed Cyclic Loading, *UCLA-SGEL Report 2009/06*.

New Zealand Standards Association (NZS), 1995, *NZS 3101:1995 Concrete Structures Standard*, Wellington, New Zealand, 256 pp.

Paulay, T., and Binney, J. R., 1974, Diagonally Reinforced Coupling Beams of Shear Walls, *Shear in Reinforced Concrete, SP-42*, American Concrete Institute, Farmington Hills, Mich., pp. 579-598.

Tassios, T. P.; Moretti, M.; and Bezas, A., 1996, On the Coupling Behavior and Ductility of Reinforced Concrete Coupling Beams of Shear Walls, *ACI Structural Journal*, V. 93, No. 6, Nov.-Dec., pp. 711-720.

Wallace, J. W., 2007, Modeling issues for tall reinforced core wall buildings, *The Structural Design of Tall and Special Buildings*, V. 16, No. 5, pp. 615-632.

JOINT CONFERENCE PROCEEDINGS
7th International Conference on Urban Earthquake Engineering (7CUEE) &
5th International Conference on Earthquake Engineering (5ICEE)
March 3-5, 2010, Tokyo Institute of Technology, Tokyo, Japan

The effect of angle`s crack on the Debonding of the reinforced beams By polymer`s fiber of the FRP (experimental and modeling)

Zaniar Salimi[1)], Hassan Afshin[2)]

1) MS Student in Civil - Structural course in Technology University in Sahand Tabriz
2) Assistant Professor of Civil Engineering Faculty, Sahand University in Tabriz
zaniarsalimi@yahoo.com, hassanafshin@yahoo.com

Abstract: In this study, using laboratory and numerical analysis, the effect of the angle of crack on the Debonding of the reinforced concrete curved beam with FRP sheets is analyzed. In numerical analysis is used of plastic damaged concrete model for simulating non-linear behavior of concrete and its softening strain. In laboratory department have been made 15 numbers of the reinforced concrete beam and tested. Analyzing the effect of angle of crack on the Debonding of the reinforced_beams was performed with using the limited components of ABAQUS software. With comparison of the results that based on the numerical analysis and experimental results can state that there is a good convergence between numerical and laboratory results and chart Load-deflection, maximum load, distribution of strain in the mode of concrete beams` fracture.
Key words**:** Angle of crack, reinforced concrete, Debonding, damaged model, FRP, failure mechanic

1. INTRODUCTION

Today strengthen the reinforced concrete with helping the reinforced polymer sheets with FRP fiber is used as a new method. Using the FRP for retrofitting than the traditional methods includes advantages such as increased resistance and high hardness, lightness of weight, resistance against crushing, low thickness and easy transportation and easy installation. After the cementation the FRP sheet to the concrete beam, structural response is different in cases such as plasticity, resistance, and failure`s type with not reinforcement structural behavior.

Therefore, experimental tests and founding analytical and numerical methods to predict the behavior of reinforced structures seems necessary. So far many studies on the reinforced structures have been done. According to experimental tests that have done various failures strain reinforced concrete beams with FRP sheets are:

1 - yield longitudinal steel with rupture FRP sheets .
2 - crush concrete in the pressure before rupture FRP sheets .
3 - Separate the end of FRP sheets at the concrete surface with cover of concrete on the longitudinal bar.
4 - Separate the end of FRP sheets to concrete surface along part of the concrete cover .
5 - Separate FRP sheets to concrete surface along part of the concrete cover.

2. Laboratory samples

Laboratory samples are used for comparing with numerical analysis of two series of laboratory work that are done. 15 tested samples of beams with 100 mm width of section, height 200 mm and length is 1200 mm. (Figure 1) Eleven samples of reinforced concrete beams nclude FRP with 1400 mm development length that has gone up 200 mm in each side of height in the beam and two samples of reinforced concrete beams include FRP with 1120 mm development length and an instance of reinforced concrete beams include FRP with 880 mm development length. In all samples were used a three segments hinge in the middle of the beam that connect to it four reinforcements with 8 mm diameter and 300 mm length. Reinforcement networks are according to figure one. Longitudinal reinforcement was cut in the down. And a 2 mm thick plastic paper was used to create crack. And also the details of laboratory samples and failure mode in each of them is presented in table one.

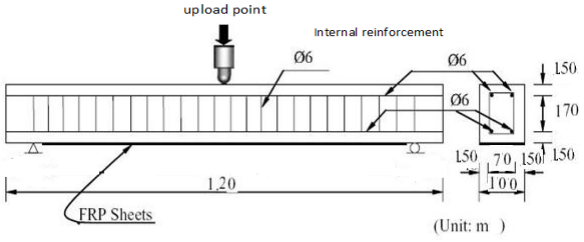

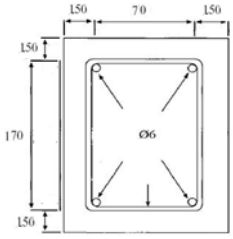

Figure (1): geometric dimensions and arrangement of transverse and longitudinal bars of samples



Figure (2): Experimental setup

3. The model of the simulation in numerical analysis

3-1 Concrete

Damaged concrete model is used to simulate its behavior that in this model is used the real behavior of concrete and stress - strain steel both in the compressive mode and tensile mode. The compressive and tensile damages also apply to the model.

3-2 Behavior of concrete in uniaxial compressive loads (Monotonic):

relationship of stress - strain in the main switch of the stress i is obtained with using strains of Nadly uniaxial. Here, a main Conservative rule is used by Saynz:

$$\sigma_i = \frac{\varepsilon_{iu} E_0}{1 + \left[\frac{E_0}{E_S} - 2\right]\frac{\varepsilon_{iu}}{\varepsilon_{ic}} + \left[\frac{\varepsilon_{iu}}{\varepsilon_{ic}}\right]^2}, \quad 0 \geqslant \varepsilon_{iu} \geqslant \varepsilon_{ic},$$

in this relationship ε_{ic} , equivalent axial strain is at the point of two linear resistance of Sic which can also depend on axial compressive strength f_c and main stresses ratio is $a=S_1/S_2$. E_0 is Young's modulus in the $\varepsilon_{iu}=0$ and E_s placed for the tangent modulus in the ε_{ic}. The softening strain section starts as the straight line from S_{ic} and ends in the 0.2 S_{ic} in the strain $\varepsilon_{iu}=(1+n)\varepsilon_{ic}$:

$$\{\varepsilon_{ic}, \sigma_{ic}\} \Rightarrow \{(1+n)\varepsilon_{ic}, 0.20\sigma_{ic}\}$$

In the following conditions, Darwin and the Pknold considered the value of n equals 3:

$$E_0 / E_S \geqslant 2.0$$

in this model, mechanic characters of the concrete are:

1 - Concrete elasticity model Ec

2 - Poisson Coefficient υ

3 - density

4 - Charts of the stress - compressive strain of concrete for the case of non-elastic strain

5 - damage graphs of compressive concrete to non-elastic strain

6 - Charts of stress - tensile of concrete strain for the case corrosion strain.

7 - Graphs of tensile damage of the concrete to the strains of corrosion concrete.

3-3. Steel

Method Isotopic - hardening is used for behavior simulation of the steel that its mechanic characters is:

1 - Concrete elasticity model Ec

2 - Poisson Coefficient υ

3 - density

4 - Chart of steel tension according to plastic strain

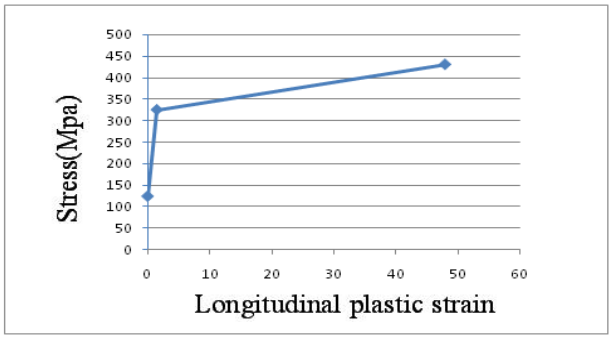

Figure (3): Strain-stress curve of reinforcement

3-4. CFRP behavior simulation

For modeling the CFRP fiber in software is used Membrane and Lamyna Theory for its introduction., thus the its mechanic characters is:

1 - elasticity model of fiber

2 - general thickness of layers

3 - Mode of orientation on the fiber line

4 - tensile strength of the fiber on the layers

5 - density of the layers

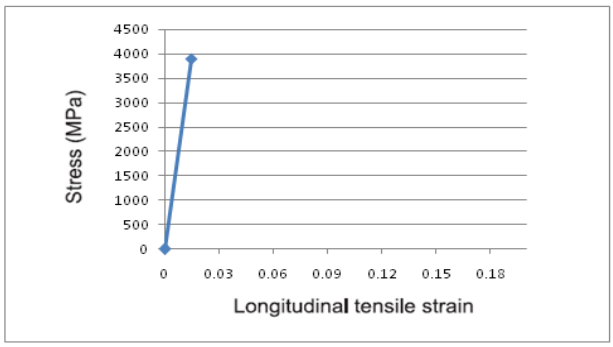

Figure (4): Strain-stress curve of CFRP

4-4. Glue modeling

in this section, FRP sheets and the Glue as like as page strain (CPE4R) are modeling. Connection in the components of Glue with the concrete are conducted with useful contacts.

In this simulation has been used the useful contact to stick FRP sheets to cross section of the beam. This type of contact makes it possible, sticking two levels with different lattice work. Also the definition of this type of contact between the two levels causes that in each level point with lattice, displacement, temperature and pressure equal to the nearest point on the surface with coarse reticulation is more.
This method provides the possibility of modeling in vertical and shear stress during the total stuck thickness. The definition of this type of contact between the two levels that each of the points level with fine netting, more displacement, temperature and pressure equal to the nearest point on the surface with coarse reticulation is more.

4. Comparison of numerical and experimental results

graphs of load - shift in the center of opening for samples with laboratory results are presented. As can be seen, there are very good coordination between the results.

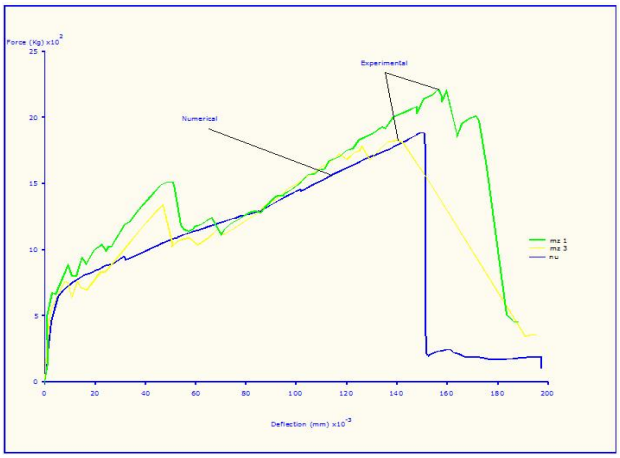

Figure (5): Load-deflection curves of beam(MZ13)

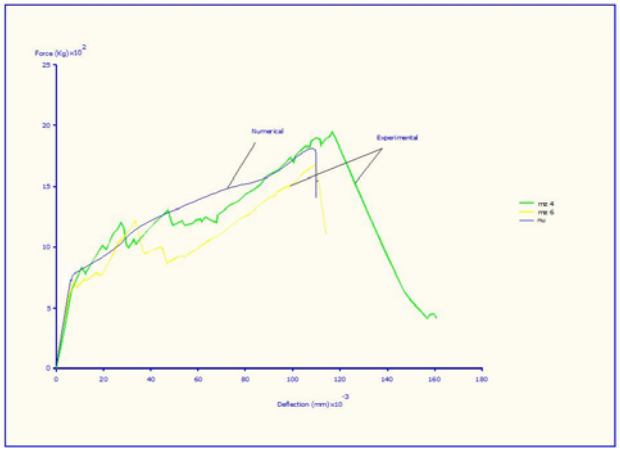

Figure (6): Load-deflection curves of beam(MZ46)

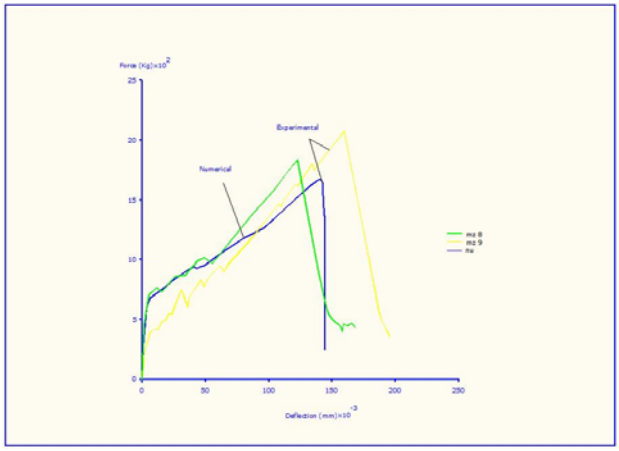

Figure (7): Load-deflection curves of beam(MZ89)

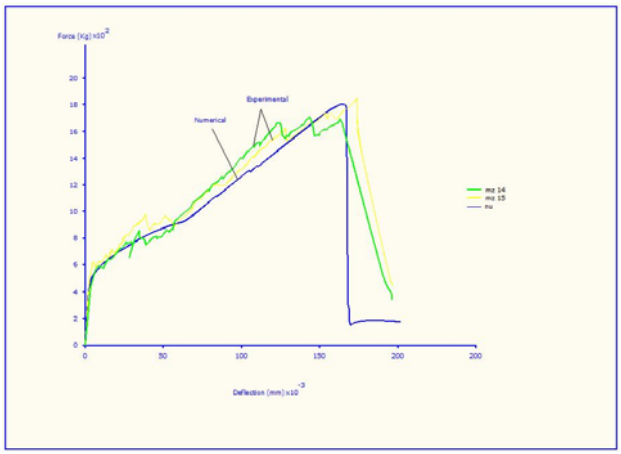

Figure (8): Load-deflection curves of beam(MZ1415)

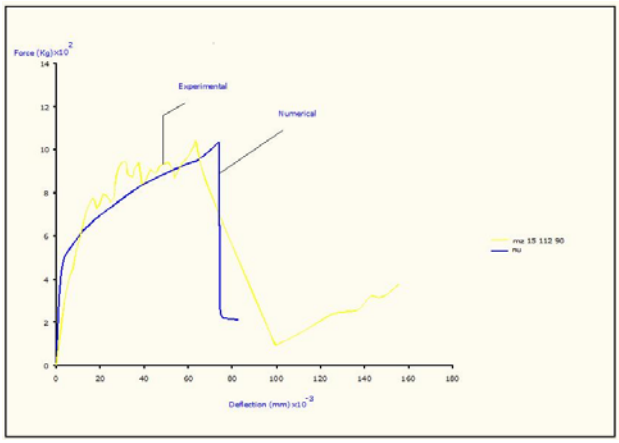

Figure (9): Load-deflection curves of beam(MZ 15 112 90)

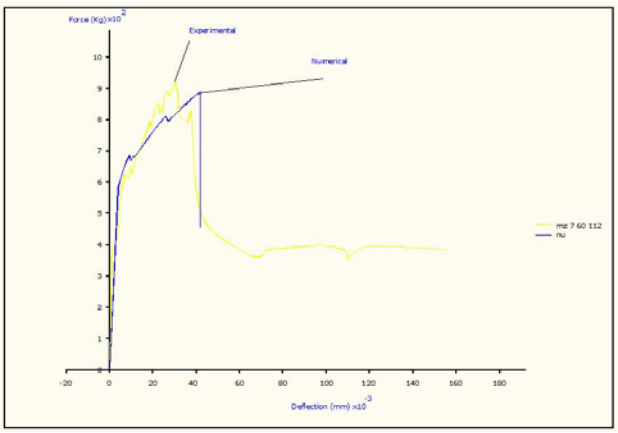

Figure (10): Load-deflection curves of beam(MZ 7 60 112)

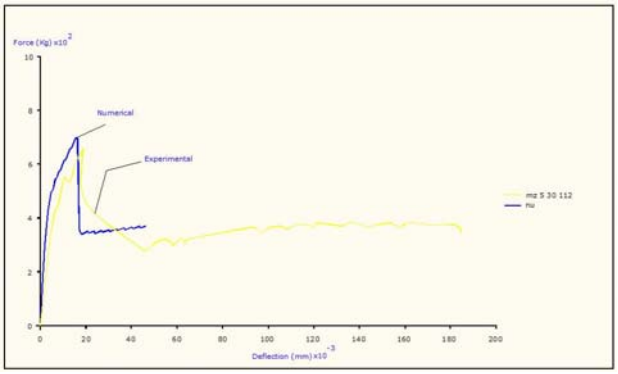

Figure (11): Load-deflection curves of beam(MZ 5 30 112)

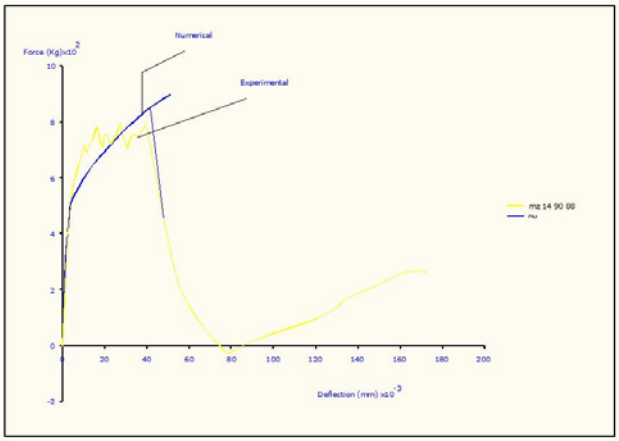

Figure (12): Load-deflection curves of beam(MZ 14 90 88)

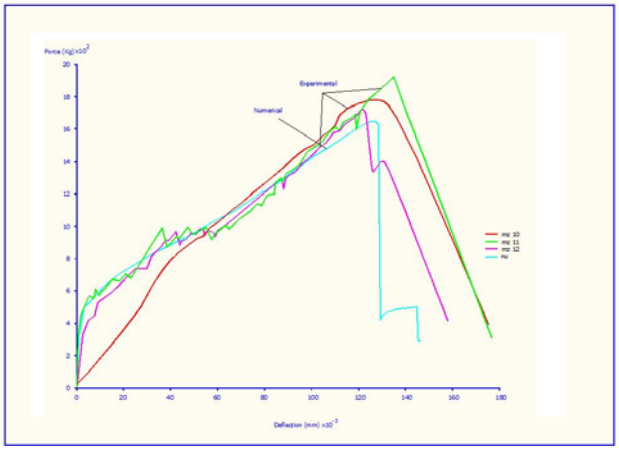

Figure (13):Load-deflection curves of beam(MZ 101112 75)

5. Conclusion

in this research the effect of crack' angle on the Debonding of reinforced concrete beams by fiber polymer FRP with testing and use of numerical analysis has examined that following results were obtained:

1 - FRP plays an important effect in increasing the capacity of the ultimate load and ultimate pitch on the samples.

2 - What we increase value of the development length, we have taken higher level of the ultimate load

3 - Matching the the results of laboratory with results of ABAQUES, the created model was acceptable, but for more accurate studies, it needs to develop.

4 - As the regard of the lab results and the ABAQUES results, the samples which were 140 cm in development length, angle of 60 degrees has carried the most loads and angle of 45 degree has carried the minimum load.

5 - As the regard of the lab and the ABAQUES results, the samples which were 140 cm in development length, angle of 90 degrees has most shifts and Angle of 30 degrees has the minimum shift.

6 - As the regard of the lab results and the ABAQUES results, the samples which were 112 cm in development length, angle of 90 degrees has carried the most loads and angle of 30 degree has carried the minimum load.

7 - As the regard of the lab results and the ABAQUES results, the samples which were 112 cm in development length, angle of 90 degrees has most shifts and Angle of 30 degrees has the minimum shift.

References:

Yao, J.Teng, J.G., "Plate and debonding in FRP-plated RC beams –I:experiments," Engineering Structures 2007,PP. 2457-2471.

Teng, J.G., Yao, J., "Plate and debonding in FRP-plated RC beams –II:strength model ," Engineering Structures29, 2007,PP. 2472-2486.

C. Faella, E. Martinelli, E. Nigro ,"Formulation and validation of a theoretical model for intermediate debonding in FRP-strengthened RC beams ,"Composites: Part B ,2007.

Sam-Young Noh.,Kratzig,W.B.,Meskouris,K.,2003."Numerical simulation of serviceability, damage evolution and failure of reinforced concrete shells".Ruhr-university Bochum,Germany.

H. K. Lee, S. K. Ha and M. “Afzal Finite element analysis of shear-deficient RC beams strengthened with CFRP strips/sheets”, Structural Engineering and Mechanics, Vol. 30, No. 2 (2008) 247-261.

Kasidit Chansawat, Tanarat Potisuk, Thomas H.Miller, Solomon C. Yim, and Damian I. Kachlakev . “FEM models of GFRP and CFRP Strengthening of Reinforced Concrete Beams”, Hindawi Publishing Corporation Advances in Civil Engineering Volume 2009, Article ID 152196.

Mohammad Reza Aram, Christoph Czaderski, Masoud Motavalli. “Debonding failure modes of flexural FRP-strengthened RC beams,” Part B 39 (2008) 826–841.

ABAQUES Help [6.8.1], Theory, Element manual & Analises Guides.

JOINT CONFERENCE PROCEEDINGS
7th International Conference on Urban Earthquake Engineering (7CUEE) &
5th International Conference on Earthquake Engineering (5ICEE)
March 3-5, 2010, Tokyo Institute of Technology, Tokyo, Japan

EFFECT ON NONLINEAR PERFORMANCE OF TALL BUILDINGS UNDER THE EARTHQUAKE DUE TO THE SIMPLIFICATION TO STRUCTURAL SYSTEMS

Du Wenxue[1, 2], andZhang Lingxin [3]

1) PhD candidate. Institute of Engineering Mechanics, China Earthquake Administration, Harbin, China
2) Lecturer, Heilongjiang Science & Technology Institute, Harbin, China
3) Professor, Institute of Engineering Mechanics, China Earthquake Administration, Harbin, China
Dwx621@126.com, Zhang _ Lingxin@163.com

Abstract: In order to obtain correct nonlinear performance of tall building at seismic zone, several typical planar and elevation irregular tall buildings with different structural system are mainly discussed in the paper. Effect on the seismic response of structures due to the hazard bearing structure simplification are analyzed so as to obtain nonlinear performance accurately of structures for the seismic risk analysis, important influencing factors are also discussed followed. The results show that it is efficient to forecast the performance of tall buildings for the seismic risk analysis at seismic zone after Wen-Chuan Earthquake in China cities.

1. INTRODUCTION

The significant earthquake which hit 8.0 on the Richter scale and astonished all over the world, had happened at May 12 in 2008 at Wen-chuan city in the Si-Chuan province of China. Focal depth is 12km, rocks mass fractured two time within 100 seconds by the main shock and Doppler Effect of seismic source made more damages followed. Energy of earthquake was 6.3×1016J, nearly 100 thousands people lost their lives and huge property loss due to the earthquake.

According to the investigation at seismic zone, we found that the damage and collapse of buildings made much more loss than shock itself. Without considering effect of human factor, it is conclude that human-beings could not grasp the essential response of earthquake and underestimate the effect of ground motion. So, the paper mainly discusses types of earthquake damage of buildings and obtains important conclusions in order to design structures and assess the seismic hazard correctly!

2. EFFECT ANALYSIS ON THE SEISMIC RESPONSE DUE TO THE SIMPLIFICATION TO STURCTURE SYSTEM

2.1 Effect of local outstanding on the top of buildings on the dynamical response to structure subject

It is common to find that there are a few outstanding parts, which are considered as small sized towers on the top of buildings for some performance or facilities reasons. Due to the Whiplash Effect, the design of this parts should be paid much attention to in order to attach their good reliability for the earthquake. Most parts of towers, however, are easy to damage due to these or others reasons. But , why? In our opinions, most of these kinds of damages occurred on the connections between towers and structures. The tower itself has the resistance to earthquake generally, because structural designers always amplify the seismic action on the towers while the connections performance is generally neglected unfortunately. So, damages of connections have adverse effect commonly on the dynamical response of structures subject, which is further analyzed in the paper in order to reduce the loss of such kind of buildings due to the further earthquake in China cities.

Example: Project of a star hotel building in Guangdong province of China.

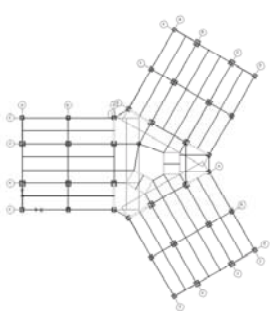

Fig.1 plane layout



Fig.2 Three-dimension layout

Relative information: 19 floors with local 4 stories, frame and shear wall structural system, Y plan shape. seismic fortification intensity of 7 degree, third type of site, first type of architecture. Plane and elevation show as Figure1-2. The results of considering tower or not are showing as firgure3-8.

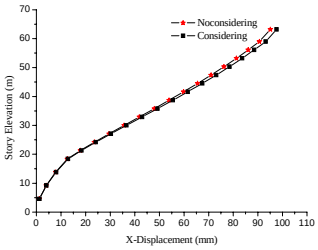

Fig.3 X-Displacement at seismic fortification intensity

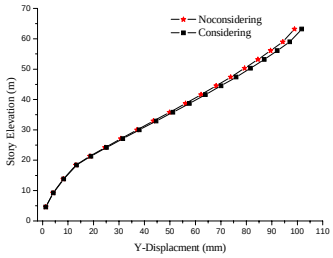

Fig.4 Y-Displacement at seismic fortification intensity

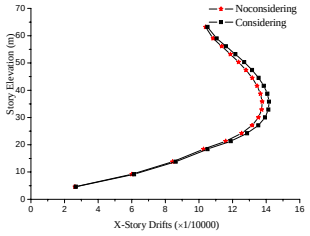

Fig.5 X-Story drift angle at seismic fortification intensity

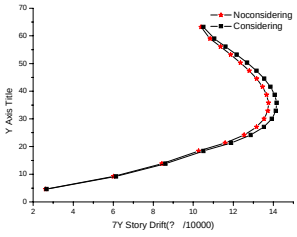

Fig.6 Y-Story drift angle at seismic fortification intensity

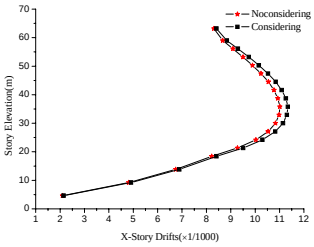

Fig.7 X-Story drift angle under rare earthquake

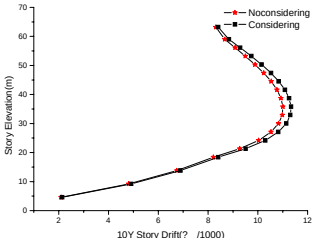

Fig.8 Y-Story drift angle under rare earthquake

From mentioned above, We can find that the whole structure is nearly elastic at the seismic fortification intensity and the Whiplash Effect of towers is so small that it can be neglected. Results show that maximum relative error of displacement is nearly 3 percent, which can be accepted in engineering. The Maximum relative error of maximum story drift in two orthogonal layouts are also within 3 percent and happened at 11th story, difference of story drift at 7th-14th are obvious relatively. Results at the rare shock are the same as above.

So, it can be concluded that, for the high rise buildings, the Whiplash Effect on structure subject has little influence so that we can neglect local outstanding parts on the top of buildings when analysis of seismic hazards evaluation and fragility analysis of hazard bearing system is carried out. Construction method and concept design of connections between towers and structure system, however, should be paid much attention and need to discuss further, in order to design this kind of system correctly and improve the whole connected performance.

2.2 Effect analysis of podium structure on the structure subject

Generally, tall buildings are multifunctional with several stories podium structure for commercial use. Frame system is commonly used for this part of buildings. However, the existence of podium has the influence on structure subject and the connection between both is also very importance for the anti-seismic of whole structure. So, the paper also discusses this kind of interaction.

Earthquake is very different from other kinds of load which may act on the buildings during their service period. There are three types of connections between podium and structure subject. One is releasing, which permit two parts of the whole buildings settle freely in order to avoid uneven settlement. So the interaction between both may be neglected and analyzed each other separately. Another kind of method is absolute resistance, which overcomes the uneven settlement by use of one rigid foundation for two parts. The voids between both should be filled with other filler. Last method is harmony, which overcome uneven settlement by subsequent construction. i.e. late poured band is often used to connect two parts of building. It could be concluded that construction with the first two methods may separately analyze two different parts of structures without considering interaction each other. So, connections with late poured band should consider the adverse influence of podium structure on structure subject at seismic action. The paper discusses followed the connection between two parts with late poured band by an actual project and gives some useful advise to the design of this kind of structures.

Example: Project of a communication building in Guangdong province in China. Total building area is 12000m2, 15 stories for structure subject with two stories podium structure for staff restaurant. The total height is 75.95m. Reinforced concrete frame and shear walls system for structure subject and frame system for podium structure.

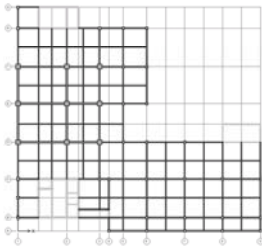

Fig.9 plane layout



Fig.10 Three-dimension layout

The plane and elevation layout shows as Fig.9-10 relatively. Results of finite element analyses show as Fig.11 -16.

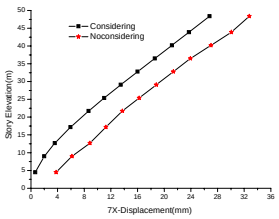

Fig.11 X-Displacement at seismic fortification intensity

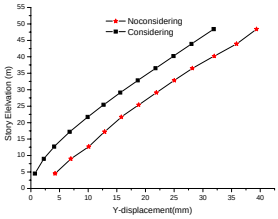

Fig.12Y-Displacement at seismic fortification intensity

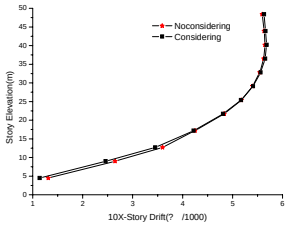

Fig.13 X-Story drift angle at seismic fortification intensity

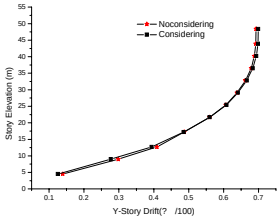

Fig.14 Y-Story drift angle at seismic fortification intensity

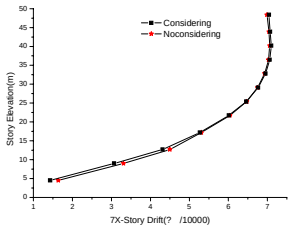

Fig.15 X-Story drift angle under rare earthquake

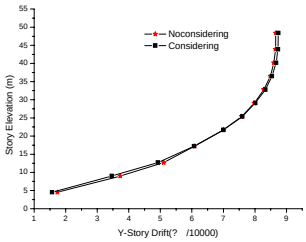

Fig.16 Y-Story drift angle under rare earthquake

According to the results above mentioned, the whole structure is in elastic stage and the information about story displacement of two orthogonal directions are showed as as fig.11-16. It can be seen that there are no obious weak floors, however, the existence of podium structrucres haver influence on a certain stories of sturcture subject within height of podium structure, such as displacements of the third floors are greater than others. So, we can conclude that the influence of podium sturctures should be paid much attention to druing the analyse on seismic hazards evaluation of buildings, i.e. errors of story displacement may be great without considering podium structure, parameters of fragility may be incorrect and risk of earthquake should be increased.

2.3. Effect analysis of stairs interaction on the structure subject

At Wenchuan earthqake in 2008 in China, stairs in different structure systems were distroied with different degree. Investigation of seismic samage showed that the damage of office and teahcing buildings are much more serious than that of other types. Typical damage is as followed: supporting damage of platform beam;.shearing damage of bench in cranked slab stairs and cracks horizontally; connection damage between cranked slab stairs and frame beam, concrete were crushed and reinforcemests were outbursed ,etc. So,the damage of stairs due to the seismic could be sumarized as the destory of connections, element and the global. As we all know that , however, as the safety zone tall buildings, stairs are so important for humanbeings to excape from the destoried buildings when earthquake happens, so as to need the ability to resist the earthquake without seriouse destory and collapse. So ,the paper also discusses the interectirion of stairs to the structure response of seismic and gives some advices to avoid serious damage of stairs from the view of design during earthquake.

Example: Project of a municipal party committee building in Guangdong province in China.

Total building area is 33148.84m^2, 16 stories for structure subject with two stories underground for commercial use. The total height is 130.15m. Reinforced concrete frame and shear walls system for structure subject and farm system for podium structure. The elevation layout shows as Fig.17. Results of finite element analyses show as Fig.18 -22.

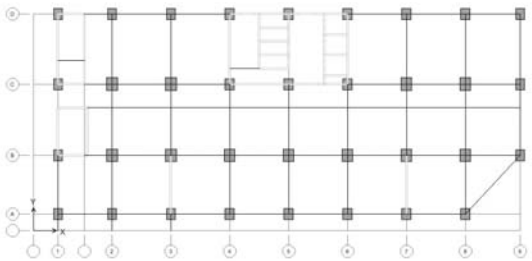

Fig.17 Three-dimension layout

Results show that both story displacement and story drift are much greater than that of non-considering the interaction between structure subject and stairs. The taller the floor is, the greater the difference is. The maximum error of story displacement is 2.85% and 4.73% at two principal axis directions relatively, which are all permitted in

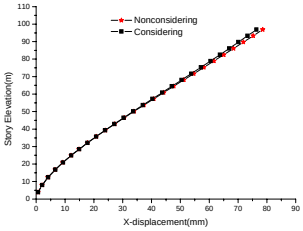

Fig.18 X-Displacement at seismic fortification intensity

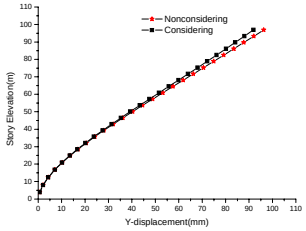

Fig.19 Y-Displacement at seismic fortification intensity

engineering at fortification intensity. Unfortunately, however, the maximum error of story drift is also nearly 10% at rare earthquake, which could not be accepted!

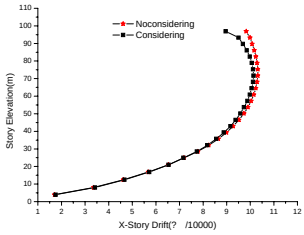

Fig.20 X-Story drift angle at seismic fortification intensity

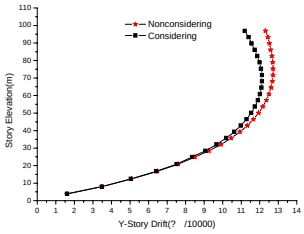

Fig.21 Y-Story drift angle at seismic fortification intensity

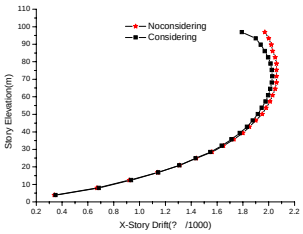

Fig.21 X-Story drift angle under rare earthquake

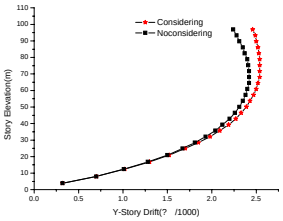

Fig.22 X-Story drift angle under rare earthquake

As a part of the whole structure system, stairs are so rigid that the displacement considering stairs is smaller than that of without stairs, which has been validated above. Stairs, however, would resist much seismic action for their rigid so that stairs would destroy firstly and lose their function of safety zone, which had been validated at 5.12 Wenchuan earthquake in China. After the earthquake, Code for seismic design buildings in China has revised some specifications about the role of stairs on structure subject.

The interaction between both are considered emphatically in the code, however, no measurement has been taken to strengthen the designing of stairs themselves. As the safety zone of building at crisis, stairs are the key parts of structural system in order to ensure human beings escape from destroyed building without serious damage. At present in China, stairs are designed elastically, elements and connections of stairs are generally neglected so that it is easy to damage and collap at seismic. Especially to the stairs in large space structure system, such as frame and frame-shear wall structural system. Generally, stairs occupy local areas in one structural element and the 3-dimesional characteristically make them very difficult to be one rigid body to resist the seismic action. All these reasons make the stairs themselves are destroied sooner than other structural elements when earthquake happens. So, In authors' opinion, good connections and anti-seismic performance of stairs themselves are the key to prevent stairs from destroy firstly at seismic.

3. CONCLUSIONS

Based on the characteristic of building damage due to the Wenchuan earthquake, the paper mainly discusses influence of analyzing simplification to the structure system for the seismic hazards evaluation. Effect of three kinds of simplification to structural system on the whole structure seismic response is analyzed with the finite element method in order to pre-cast the response of structure due to the seismic action correctly. Finally, good advice on structure design is obtained. It is help to offer the correct analyzing method for the seismic risk evaluation and seismic vulnerability analysis on the building, which may bear the seismic action in further in order to ensure the reliability of buildings and reduce the life and property loss as possible.

Acknowledgements:

The authors acknowledge support from the Cooperative Fund of Earthquake Science (China Earthquake Administration). This support makes possible the continuous research on the dynamical response of buildings due to the seismic action. Thanks also for all the information from our colleagues who helped me much during the earthquake relief at Wen Chuan earthqake.

References:

Sathish K. Ramamoorthy, Paolo Gardoni and Joseph M.Bracci. "Probabilistic Demand Models and Fragility Curves for reinforced Concrete Frames,"(2006), *Journal of Structural Engineering*. 1563-1572

Anil K. Chopra, Rakesh K. Goel, and Chatpan Chintanapakdee. (2003), "Statistics of Single-Degree-of-Freedom Estimate of Displacement for Pushover Analysis of Buildings," *Journal of structure engineering*. **129**(4), 459-469

Anil K. Chopra. Dynamics of structures:Theoryand ApplicationstoEarthquakerEngineering(Third Edition)

Alemdar, B. N., Taylor, J., White, D. W., and Leon, R. T. (1999), "Nonlinearanalysis of buildings with partially-restrained composite(PRC)connections." Proc., 1999 Structures Congress "Structural Engineeringin the 21st Century," ASCE, Reston, Va., 402–405.

Ray Clough, Penzien. Dynamics of structures.

Bolander, J., and Wight, J. K,(1991). "Finite element modeling of shearwall-dominant buildings." *J. Struct. Eng.*, **117**(6) 1719–1739.

Hu Yuxian. (2006) "Earthquake Engineering," Earthquake publishing house..

"Seismic damage investigation of buildings & Research report of reconstruction at Wenchuan Earthquake"(2006), China Building Industry Publishing House.

Li Chuangfeng,Hanxue. (2002)_ "Analysis on the whiplash effect at seismic action,"*Journal of Heilongjiang Institute of Science and Technology.***12**(1)39-42

"Code for seismic design buildings in China "(2008)8-9

Lincy Pyl , Geert Degrande and Geert Lombaert. (2002) *"Numeerical Modeling of Traffic Induced Vibrations in Buildings Based on a Dynamic Soil-Structure Interection Formulation.15th ASCE Engineering Mechanics Conference.June2-5,2002,Columbia University, New York,NY*

LU Dagang ,LI Xiaopeing, WANG Guangyuan.(2006), "Global seismic fragility analysis of structures based on reliability and performance," Journal of Natural Disasters, **15**(2)107-114

Emrah Erduran,Ph.D. and Ahmet Yakut.(2007), "Vulnerability Assessment of Reinforced Concrete Moment Resisting Frame Buildings," *J. Struct. Eng.*, **133**(4) 576-586

Chatpan Chintanapakdee and.Anil K. Chopra, (2004), “Seismic Response of Vertically Irregular Frames: Response History and Modal Pushover Analyses,” *Journal of structure engineering.* 130(8), 1177-1185

William T. Holmes ,Charles Kircher, William Petak, and Nabih Youssef,(2008), “Seismic Performance Objectives for Tall Buildings,” PEER Report 2008/01

JOINT CONFERENCE PROCEEDINGS
7th International Conference on Urban Earthquake Engineering (7CUEE) &
5th International Conference on Earthquake Engineering (5ICEE)
March 3-5, 2010, Tokyo Institute of Technology, Tokyo, Japan

AN EVALUATION OF VIBRATION COMPORT ON REACTION MASS FOUNDATION WITH SHAKE TABLE SYSTEM

DaJung Jung [1], JungWoo Kim[2] ,HyoungSuk Choi[3], and JinHwan Cheung [4]

1) M. D student, Civil Engineering, Pusan National University, Pusan, Korea
2) M. D student, Civil Engineering, Pusan National University, Pusan, Korea
3) Ph. D student, Civil Engineering, Pusan National University, Pusan, Korea
4) Professor, Civil Engineering, Pusan National University, Pusan, Korea
dajung20b@pusan.ac.kr, civilkjw@pusan.ac.kr, engineer@pusan.ac.kr, cheung@pusan.ac.kr

Abstract: Machine vibration has bad effects not only on the building structure but also inside resident and equipments such as expensive measuring instrument and operating system in laboratory. These vibrations are generally checked by calculating acceleration values like RMS (root mean square), RMQ (root mean quad) and VDV (vibration dose value) from dynamic structural analysis during the building design. BS 6841 and ISO 2631 standards advice to use the values for investigating comfort limit. However, it is difficult to determine adequate mass ratio that is the proportion of vibrating mass to foundation mass for reducing the vibration, and also analyzing structure is usually done by FEM analysis with great delicacy and it takes engineers a long time to compute system dynamics because building and its foundation is very complex. This study is comparing complicated FEM analysis results with simple model analysis that is a one-degree-of-freedom system of seismic testing facility which has concrete foundation with steel piles. From comparing two methods, the simple analysis method shows good effectiveness and so variable simulations were performed with sinusoidal and earthquake waves to determine adequate mass ratio.

1. INTRODUCTION

In case of designing machine foundation, the building should be structurally safe and also people in the building be secured from the machine generating vibration that may have a bad effect to human and measurements. The vibration effect is generally depended on the mass ratio which is the proportion of foundation system and vibrating machine. Therefore, determination of mass ratio is the most important and difficult problem in laboratory building design. Low mass ratio can make system resonance and it makes operator hard to control the machine such as shaker and shaking table which are impossible to install isolator. Designing with high mass ratio to prevent resonance of foundation system, however, makes construction costs increased in case of big research center. Most of the research work done so far has been focused on the system produced to analysis and check vibration issues and the results could not be helpful to designers.

The evaluation method of whole-body vibration has been widely investigated and reported in previous studies and ISO 2631(Mechanical Vibration and shock of human exposure to whole-body vibration) is commonly used of estimation criteria in vibration effect evaluating. The standard defines measurement method of periodic, random and excessive whole-body vibration and whether how many vibration exposure can allowable and acceptable. ISO 2631 is divided into 5 sections that general requirements and evaluation method (ISO 2631-1), the evaluation of vibration and shock about frequency range from 1 Hz to 80 Hz in the building (ISO 2631-2), evaluation of exposure to whole-body z-axis vertical vibration in the frequency range 0.1 to 0.63 Hz (ISO 2631-3), the evaluation of the effects of vibration and rotational motion on passenger and crew comfort in fixed guide way transport systems (ISO 2361-4), method for evaluation of vibration containing multiple shocks(ISO 2631-5).

The purpose of this paper is to analyze and evaluate a vibrating foundation example that is a large shaking table laboratory using complicated model by FEM and simple single degree of freedom mathematical model. The first part of the paper presents a comparison on simulation response results of two methods in case that the massive concrete foundation inflicts only horizontal motion and people in the lab has the standing position. In the second part, the optimum mass ratio between foundation and vibrating machine is discussed from the simple model simulation. The acceleration response was analyzed with the effect factor by applying the evaluation method of the ISO 2631-1. These analyzed results was suggested the method that can evaluate about the usability of vibrating foundation.

2. THE VIBRATION EVALUATION OF MACHINE FOUNDATION

In case that the building structure is used to vibration foundation of the machine such as shaker and shaking table, ISO 2631 part 1 and 2 can be applied to evaluate the effects of human-body. ISO 2631-1 and 2 are applicable to transmitted vibration to the human body as a whole through the supporting surfaces that the feet of a standing person, the buttocks, back and feet of a seated person or the supporting area of a recumbent person. Part 1 of the standard is for the vibration evaluation transmitted to human-body of general position and part 2 is intended to encourage the uniform collection of data on human response to building vibration. If the posture of the occupant is defined in the ISO 2631-2, however, the frequency weighting given in ISO 2631-1 can be used. The evaluation method and flow of ISO 2631-1 is shown in Fig 1. In order to evaluate machine foundation by ISO 2631, human model is firstly confirmed about boundary condition as seated and standing position and then acceleration is measured in accordance with the boundary condition. The acceleration value is estimated by various estimating methods such as RMS(Root-mean-square) value, MTVV (Maximum Transient Vibration Value), VDV (Vibration Dose Value). Finally the estimated value can be compared with the perception limit value by ISO 2631.

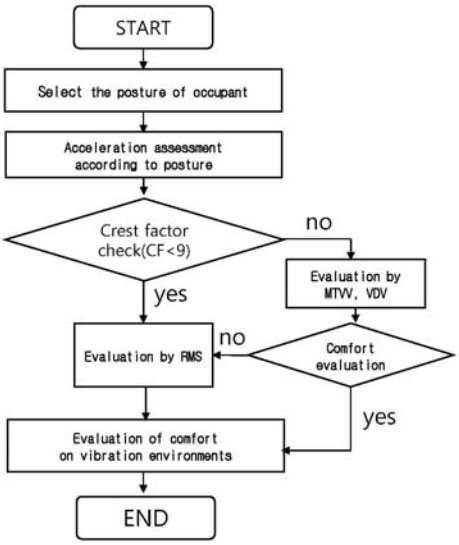

Fig 1 Evaluation method of vibration in ISO 2631-1

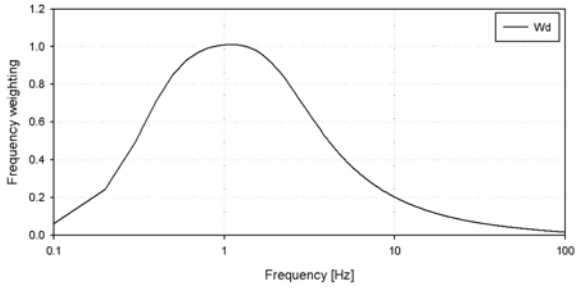

Fig 2 Frequency weighted curve for Wd, standing position

Table 1 Vibration perception limit

State	Not uncomfortable	A little uncomfortable	uncomfortable	Extremely uncomfortable
Magnitude (m/sec^2)	Less than 0.315	0.315 to 0.630	0.8 to 1.6	Greater than 2.0

Table 2 Weighted function parameters in frequency

weighting	Band-limiting		Acceleration-velocity transition		
	f1(Hz)	f2(Hz)	f3(Hz)	f4(Hz)	Q4
Wd	0.4	100	2.0	2.0	0.63

$$|H_h(s)| = \left| \frac{1}{1+\sqrt{2}\omega_1 / s + (\omega_1 / s)^2} \right| = \sqrt{\frac{f^4}{f^4 + f_1^4}} \quad (1)$$

$$|H_l(s)| = \left| \frac{1}{1+\sqrt{2}s / \omega_2 + (s / \omega_2)^2} \right| = \sqrt{\frac{f_2^4}{f^4 + f_2^4}} \quad (2)$$

$$|H_t(s)| = \left| \frac{1+s/\omega_3}{1+s/(Q_4\omega_4) + (s/\omega_4)^2} \right| = \sqrt{\frac{f^4 + f_3^4}{f_3^4}} \sqrt{\frac{f_4^2 Q_4^2}{f^4 Q_4^2 + f^2 f_4^2 (1-2Q_4^2) + f_4^2 Q_4^2}} \quad (3)$$

$$H(s) = H_h(s) * H_l(s) * H_t(s) \quad (4)$$

Frequency domain component of the vibration effects health, comfort, perception and motion sickness of person. Especially, the low-frequency has significant effects to the human-body and therefore it is necessary that low frequency component of measured vibration values should be weighted and estimated with adequate weighting functions. In ISO 2631, the weighted value of the different frequency in accordance with the transmission direction and the position is used for the vibration of human-body. Butter worth filter which has a slope of -12dB/decade is performed by low-pass and high-pass filter (respectively, 2-pole). The specific of the filter is shown in the equation (1), (2) and (3) which are the transfer functions of the high-pass, low-pass filter and acceleration-velocity respectively and function (4) is the whole weighted function.

Where, s is a variable of Laplace transform and the each parameter of transfer function is shown in Table2. Fig 2 illustrates the weighted value in the frequency domain.

3. THE MODEL OF FOUNDATION TYPE

Machine foundation of the building has various types in accordance with the depth of support base, the magnitude of top load, geological structure and surroundings as shown in Fig 3. However, if vibrating points where the machine is are determined and the excitation can be presented in time series equations which are not affected about the torsion and moment of foundation according to the mass center by the load, the foundation could be idealized and presented as Fig

4 and the system can be simulated as a spring-damper model. The way that is using simple SDOF (Single Degrees of Freedom) model approach is a very efficient method for the response calculation and simulating the vibration foundation by using the fewer DOF in terms of effort and time. In order to evaluate the usability of the vibration foundation using this model, it is necessary to prove the application in comparison with the result of the acceleration response by the detailed and more accuracy analysis method. In this paper, The SDOF model is compared with the result of the 3-D FEM model analysis result about the concrete foundation with steel files. FEM model is shown in Fig 5.

The SDOF model is expressed by the equation of motion as function (5) and forcing function (6) that is the load transmitted directly from fixed vibration source in the foundation.

$$m_1\ddot{x}(t) + c_1\dot{x}(t) + k_1 x(t) = F(t) \quad (5)$$

$$F(t) = M\sin(\bar{\omega}t) \quad (6)$$

Where, m_1, c_1, k_1 is the mass, stiffness, viscous damping of foundation and M is the magnitude of vibration that is expressed by the excitation mass and gravity acceleration and $\bar{\omega}$ is excitation frequencies. If the vibration load is large scale, generally the machine installs spring or rubber dampers to isolate the vibration source and secure the safety of structure but testing instrument such as shaker and shaking table, which are directly connected to the foundation, could not be isolated because of the control issues.

In this paper, large scale seismic simulation testing lab is selected as comparing example that is KOCED Multi-platform Seismic Simulation Test Center in Korea. The testing center has three shaking tables that can be operated from 0.5Hz to 60Hz with maximum 600kN weights at the same time. The facility has a 66meters long and 24meters width concrete foundation with 178 steel piles that is for preventing settlements because the facility is located on the soft ground. The mass of the concrete foundation is up to 14,340 ton and the excitation mass is almost 190ton in case of full payload condition. In designing process of the lab, it was necessary to time and efforts to check vibration serviceability of the facility by FEM model which is difficult to construct and analyze. Fig 5 is a designed FEM model using 3D solid elements to concrete foundation and beam elements to steel piles. According to the result of ground investigation, calculated reaction factors of the horizontal direction are applied to steel piles and in addition, the concrete and pile damping is assumed 5%, 2% each respectively.

The vibration is occurred from the hydraulic actuators connected to the shaking tables and the load transmitted to the foundation. If vibration loading is assumed that transmitted directly to the structure, the system can be simulated as SDOF model.

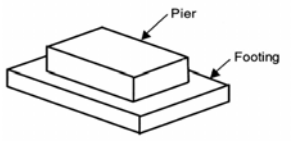

a) Block-type foundation

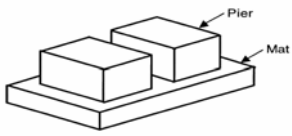

b) Combined block foundation

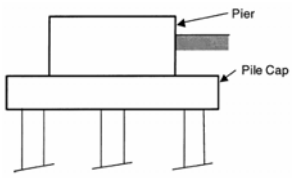

c) Pipe-supported foundation

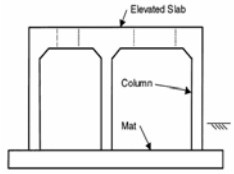

d) Tabletop-type foundation

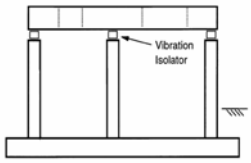

e) Tabletop with isolators

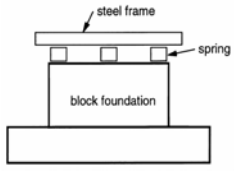

f) Spring-mounted block formation

Fig 3. Foundation types (ACI 315.3R-04)

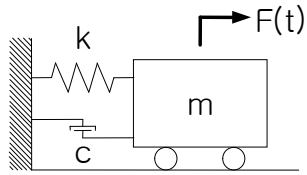

Fig 4. Spring-Damper Model

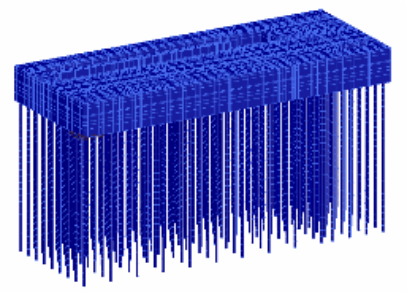

Fig 5. FEM Model

Comparison plot of FEM model and SDOF model analysis result are shown as fig 6 and fig 7. FEM model is solved by modal analysis method and SDOF model used Newmark beta method. In part of the transient response by the initial excitation force, the acceleration response was not well corresponded with SDOF results. This case is because the damping of simulated model is underestimated. In the result of steady-state, however, the response agrees very well with precision measurement in FEM model because the actuator and frame are stiff enough. For this reason, the loading affected concrete foundation without divergence of energy. If the concrete of vibration foundation is considered of elastic behavior, the result can be judged that the concrete of vibration foundation which has steel piles can simulate to SDOF spring-damper model in the steady-state.

4. EVALUATION OF VIBRATION SERVICEABILITY

Comparison result of complicated FEM analysis and SDOF analysis is presented in the previous section. From the result, SDOF analysis shows good performance to evaluate machine foundation system and so this paper simulates vibrating foundation by changing mass ratio, which is relationship between excitation and foundation mass, to determine appropriate mass ratio according to ISO 2631-1. The vibration level evaluated by ISO 2631-1 uses values of weighted acceleration. From the Laplace Transform of equation (5) and (6) with filter properties (equation (4)), weighted acceleration could be calculated as equation (7). In this study, vibration was evaluated by RMS value (equation (8)).

Where s is a Laplace parameter and R is the ratio (m_2 / m_1) of foundation mass about excitation mass and g, ζ, ω present the gravity acceleration, damping and natural frequency of foundation respectively.

$$a_\omega(t) = s^2 X(s) = R \frac{\bar{\omega} g s^2}{(s^2 + 2\varsigma\omega s + \omega^2)(s^2 + \bar{\omega}^2)} H(s) \quad (7)$$

$$a_\omega = \left[\frac{1}{T} \int_0^T a_\omega{}^2(t) dt \right]^{1/2} \quad (8)$$

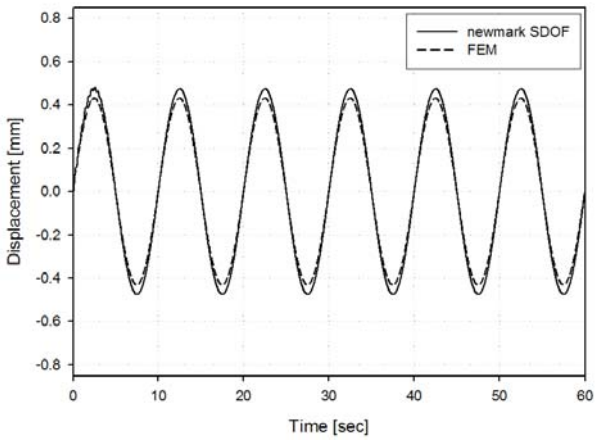

Fig 6. Displacement in case of SDOF

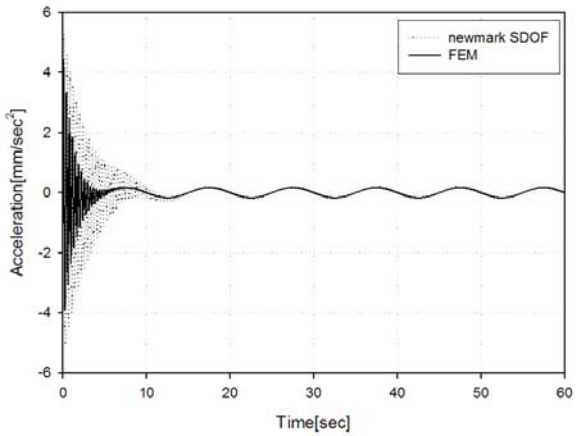

Fig 7. Acceleration in case of SDOF

Equation (7) is the function of damping factor and natural frequency, excitation frequency and the equation is shown that the acceleration response proportionate to mass ratio and also total exposure time could be important because effect of vibration is evaluated by weighted acceleration which is related to exposure time. The excitation force can regulate to sine function which has consistent amplitude.

Fig 8 and fig 9 is shown RMS acceleration change. fr is the frequency ratio(excitation frequency / natural frequency). In the Fig 8, when the mass ratio is a value of 0.5, 1, 2 it is shown that RMS acceleration changed. Fig 8 is shown that RMS can be predicted through mass ratio. Fig 9 is shown acceleration change in perception limit as 0.315 to 1.0 m/s^2 magnitude. Also the adequate mass ratio is obtained

by perception limit magnitude. When the frequency ratio is 1, RMS was presented relatively large value. In other words RMS value was amplified when the frequency vibration is similar to excitation frequency.

The comfort of vibration foundation should be ensured about the vibration during the experiment time of structure and the contacted body should be offered safe semi-permanently. The evaluation limit of comfort regulates $0.315m/\sec^2$ in ISO 2631-1. Therefore the vibration of foundation should be designed within this magnitude.

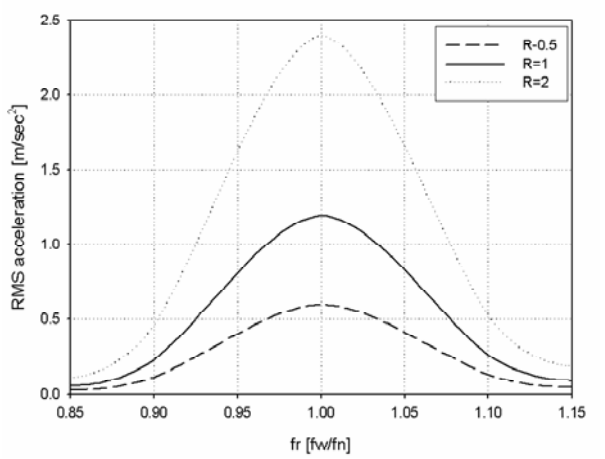

Fig 8 Acceleration change according to mass ratio

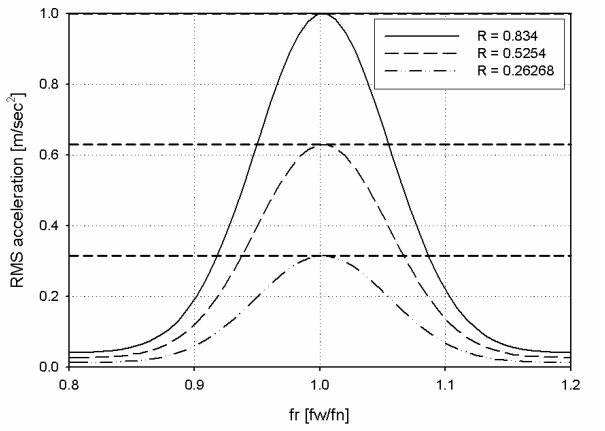

Fig 9 Acceleration change in adequate perception limit

Table 3 Mass ratio according to the perception limit magnitude

State	Not uncomfortable	A little uncomfortable	Fairly uncomfortable
Magnitude (m/sec^2)	0.315	0.630	1.0
R(m_2/m_1)	0.26268	0.5254	0.834

$$0.834 \geq 0.0411 + 0.9596 \times e^{\left(-0.5\times\left(\frac{x-1.0024}{0.0532}\right)^2\right)} \quad (9)$$

$$0.5254 \geq 0.0267 + 0.6037 \times e^{\left(-0.5\times\left(\frac{x-1.0024}{0.0531}\right)^2\right)} \quad (10)$$

$$0.26268 \geq 0.0129 + 0.3202 \times e^{\left(-0.5\times\left(\frac{x-1.0024}{0.0532}\right)^2\right)} \quad (11)$$

The natural frequency of foundation is 2.76Hz. In addition, the excitation frequency should be satisfied to value over natural frequency of foundation. This resonance phenomenon is difficult to occur. For this reason the result judged that the using for experiment satisfied in the maximum load, if we can endure a little uncomfortable about the occuring vibration during the vibration experiment. Even though the human-body feels a little uncomfortable during the experiment, the minimum perception limit magnitude is $1.0m/sec^2$. In this case, R was obtained 0.834 m/sec^2. Thus various equation is presented by using linear regression analysis as Fig 9. This equation was obtained regression of mass ratio according to perception limit magnitude.

5. CONCLUSIONS

This study compares complicated FEM model analysis method with simple dynamic model that is a 1DOF mass-damper system of seismic testing facility which has concrete foundation with steel piles. Sine functions are considered for the machine vibration during the exposure time and the foundation materials are assumed to be linear behavior. The weighted acceleration values are used for the effect factor of the vibration serviceability.

1. The steady-states analysis of the concrete foundation has no significant different between the result of FEM model analysis method and 1DOF the simple dynamic model analysis. 2. When the vibration is transmitted directly to the foundation, there are no influences according to the materials damping and exposure duration time in the analysis results of the evaluation but the weighted acceleration was presented by increasing mass ratio and changing frequency ratio that relationships between forcing frequency and natural frequency of the foundation system. The weighted acceleration was amplified by the change of the system resonance. 3. The method of adequate mass ratio determination is proposed by applying the evaluation limit in ISO 2631-1 standard and the used frequency and mass ratio of example structure are satisfied with proposed equation and complicated FEM analysis results. The occupant of the facility, therefore, will feel a little uncomfortable. In addition, the mass of foundation of facility (KOCED Multi-platform Seismic Simulation Test Center) by the proposed equation judged that this facility has the enough comfort of the excitation mass.

Acknowledgements:

This work was supported by KOCED seismic simulation test center at Pusan National University and the Second stage of Brain Korea 21 Project in 2009.

References:

International Organization for Standardization (2003), "ISO 2731 Mechanical Vibration and Shock"

M.Z. Asik, C.V.G. Vallabhan (2001), "A simplified model for the analysis of machine foundations on a nonsaturated, elastic and linear soil layer, Computers and Structures 79, 2717-2726.

Shi-Shuenn Chen, Jun-Yang Shi (2007), "Simplified model for torsional foundation vibrations", Soil Dynamics and Earthquake Engineering, 27, 250-258

R. Venugopala Rao, N. S. V. (1999), "Dynamic analysis of pile foundations in time domain using Lanczos vectors", Computers and Geotechnics , 24, 297-322

R.O. Curadelli, R. D. Ambrosini, R.F. Danesi(2004), "Vibration control by attaching masses to a plate excited by rotating machinery", Journal of Sound and Vibration, 273, 1087-1100

Chen SS, Shi JY. (2006), "A Simplified model for vertical vibrations of surface foundations", ASCE J Geotech Geoenviron Eng, 115(4), 491-503.

JOINT CONFERENCE PROCEEDINGS
7th International Conference on Urban Earthquake Engineering (7CUEE) &
5th International Conference on Earthquake Engineering (5ICEE)
March 3-5, 2010, Tokyo Institute of Technology, Tokyo, Japan

ANALYTICAL AND EXPERIMENTAL STUDY ON RC EXTERIOR BEAM-COLUMN JOINTS WITHOUT TRANSVERSE REINFORCEMENT

Sangjoon Park[1] and Khald M. Mosalam[2]

1) PhD Candidate, Dept. of Civil and Environmental Engineering, University of California, Berkeley
2) Professor, Dept. of Civil and Environmental Engineering, University of California, Berkeley
sangjoon@berkeley.edu, mosalam@ce.berkeley.edu

Abstract: This study presents a semi-empirical strength model to predict the shear strength of reinforced concrete (RC) exterior beam-column joints without transverse reinforcement (denoted as unreinforced) in the joint region. The strength model includes the effect of joint aspect ratio and beam longitudinal reinforcement ratio, both of which are found to be key parameters to affect the shear strength of unreinforced exterior joints from a parametric study. To investigate the effect of these two parameters, four full-scale RC corner beam-column joints without transverse reinforcement were constructed. This paper reports the experimental results of the first two specimens having different beam reinforcement ratio with the same joint aspect ratio (1:1). The obtained shear strength of these two tested specimens is compared with the predictions by the joint shear strength model.

1. INTRODUCTION

There have been efforts to assess the shear strength of unreinforced beam-column joints. Several empirical and analytical models have been developed based on test data and mechanistic concepts. However, a robust shear strength model of unreinforced beam-column joints is still lacking. In the existing empirical models, inappropriate parameters are used or some parameters are obtained from insufficient data without an attempt to mechanistically address the significance of these parameters. In the existing analytical models that are typically developed for reinforced joints and then specialized to unreinforced joints, some conceptual limitations may negatively affect the accuracy of these models for unreinforced beam-column joints. On the other hand, a large number of tests have been conducted with different joint geometries, beam reinforcement ratios, and column axial load ratios. Tests from literature showed that ASCE 41 may underestimate the shear strength of unreinforced exterior joints. However, the majority of tests from literature were conducted with two dimensional exterior joints under constant column axial load.

In this study, a semi-empirical strength model for unreinforced joints is presented. Moreover, test results of two full-scale unreinforced corner beam-column joints are reported.

2. PARAMETRIC STUDY

Past laboratory test data were collected from the literature for unreinforced exterior and corner joints with no lateral beams or with a lateral beam on one side only. Two failure modes were mainly reported for the laboratory tests, namely joint shear failure without beam reinforcement yielding (J) and joint shear failure with beam reinforcement yielding (BJ).

2.1 Joint Aspect Ratio

Using a single strut mechanism, the equilibrium equation is derived as follows,

$$V_{jh} = c_0 D\cos\theta,\ \theta = h_b/h_c,\ D = \sigma_d b_j h_s \tag{1}$$

where c_0 is a constant to be determined from experimental data, D is the compressive force in the diagonal strut with σ_d as its average compressive stress, h_b and h_c are beam and column cross section height, respectively, b_j is effective joint width, and h_s is the width of the diagonal strut, refer to Figure 1. The softening concrete model suggested by Vollum (1998) is adopted to develop a relevant model for the concrete panel of unreinforced joints, i.e.

$$\sigma_d = \frac{a_1\sqrt{f_c'}}{0.8+170\varepsilon_1} \tag{2}$$

where a_1=5.92 [MPa units] and ε_1 is the principal tensile strain of the concrete panel. The width of the diagonal strut, h_s, is replaced by the column cross section height, h_c, from the C-C-T node as,

$$h_s\sin\theta = kh_c,\ \sin\theta = \frac{1}{\sqrt{1+(h_b/h_c)^2}} \tag{3}$$

where k is a constant.

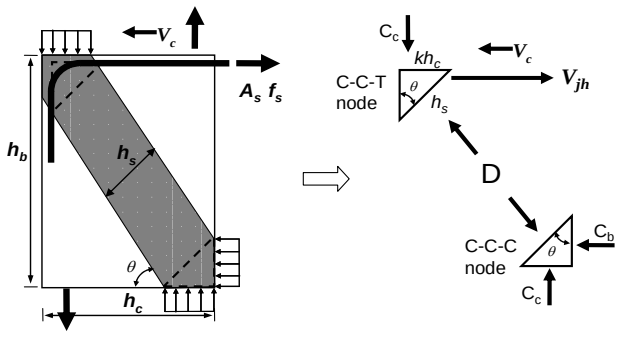

Figure 1 Single diagonal strut mechanism

Substituting Eqs. (2) and (3) into Eq. (1) and normalizing, the equilibrium equation becomes

$$\frac{V_{jh}}{b_j h_c \sqrt{f_c'}} = c_1 \left\{ \frac{a_1}{(0.8+170\varepsilon_1)\sin\theta} \right\} \cos\theta \tag{4}$$

where $c_1=c_0k$ is a constant to be determined from the experimental data. The denominator in the braces is simplified as discussed in (Park and Mosalam 2009) to the following,

$$\begin{aligned}(0.8+170\varepsilon_1)\sin\theta &\approx 0.8+170\left\{0.0035+0.0005\left(\frac{h_b}{h_c}-1\right)\right\} \\ &= 1.31+0.085\frac{h_b}{h_c}\end{aligned} \tag{5}$$

Substituting Eq. (5) into Eq. (4) and combining the two constants a_1 and c_1, Eq. (4) becomes

$$\frac{V_{jh}}{b_j h_c \sqrt{f_c'}} = \frac{a_2}{1.31+0.085 h_b/h_c} \cos\theta \tag{6}$$

where a_2=1.91 as an upper limit and a_2 =0.83 as a lower limit from the database, as shown in Figure 2.

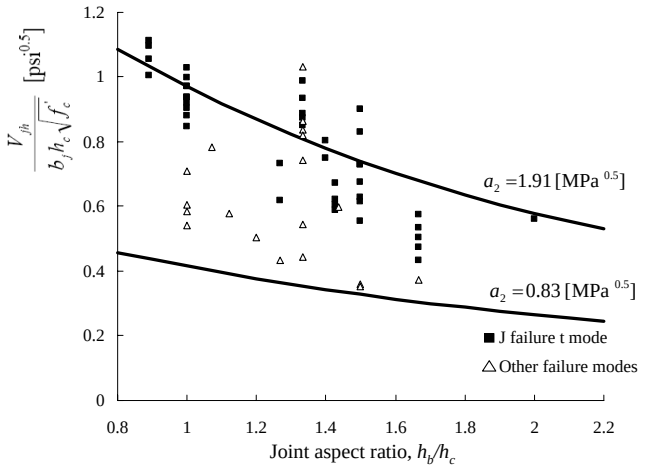

Figure 2 Effect of joint aspect ratio

2.2 Beam Longitudinal Reinforcement

A beam reinforcement index is derived considering the free body diagram in Figure 3. The horizontal joint shear is expressed as

$$V_{jh} = A_s f_s - V_c = A_s f_s - \frac{L+h_c/2}{H} V_b = A_s f_s \left(1 - \frac{L+h_c/2}{H}\frac{jd}{L}\right) \tag{7}$$

where A_s and f_s are the total cross-sectional area and stress of tension beam reinforcement, V_c and V_b are the column and beam shear forces, H is the height between the upper and lower column inflection points, L is the length from the beam inflection point to the column face, and jd_b is the internal moment arm of the beam cross section. To simplify Eq. (7), the following approximation is made,

$$jd = 0.8h_b \Rightarrow \frac{L+h_c/2}{H}\frac{jd}{L} = \frac{L+h_c/2}{L}\frac{0.8h_b}{H} \approx 0.85\frac{h_b}{H} \tag{8}$$

If beam reinforcement is yielding, f_s=f_y can be used in Eq. (7) assuming that the material of the beam reinforcement is elastic-perfectly-plastic. Normalizing Eq. (7) and using Eq. (8), the beam reinforcement index is expressed in Eq. (9) and plotted on the horizontal axis of Figure (4).

$$\frac{V_{jh}}{b_j h_c \sqrt{f_c'}} = \frac{A_s f_y}{b_j h_c \sqrt{f_c'}} \left(1 - 0.85\frac{h_b}{H}\right) \tag{9}$$

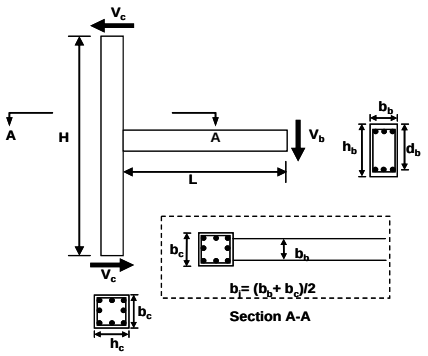

Figure 3 Global equilibrium of exterior joint

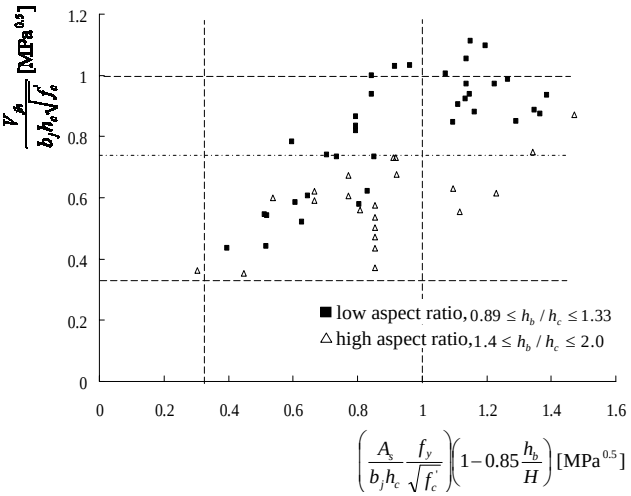

Figure 4 Effect of beam reinforcement

3. STRENGTH MODEL

Two basic assumptions are made: (1) maximum and minimum joint shear strengths are affected by the joint aspect ratio with no influence of the beam reinforcement index based on Figure 2, and (2) joint shear strength is linearly proportional to beam reinforcement index within upper and lower bounds of the joint shear strengths based on Figure 4. Finally, the joint strength equation is proposed as,

$$\frac{V_{jh}}{b_j h_c \sqrt{f_c'}} = \Phi\left[\left(\frac{A_s f_y}{b_j h_c \sqrt{f_c'}}\right)\left(1-0.85\frac{h_b}{H}\right)\right] \geq 0.83\frac{\cos\theta}{1.31+0.085\frac{h_b}{h_c}} \quad (10)$$

$$\leq 1.91\frac{\cos\theta}{1.31+0.085\frac{h_b}{h_c}}$$

The procedure to predict the joint shear strength by the proposed model is summarized as follows:

(1) Input the joint geometry, concrete strength, and joint aspect ratio.

(2) Determine the minimum, Y_{min}, and maximum, Y_{max}, joint shear strengths as shown in Figure 5.

(3) Calculate the beam reinforcement index by Eq. (9).

(4) Check if the calculated beam reinforcement index is located between X_1 and X_2. If so, interpolate the corresponding over-strength factor, Φ, from 1 to 1.25 as shown in Figure 5.

(5) Calculate the joint shear strength by Eq. (10).

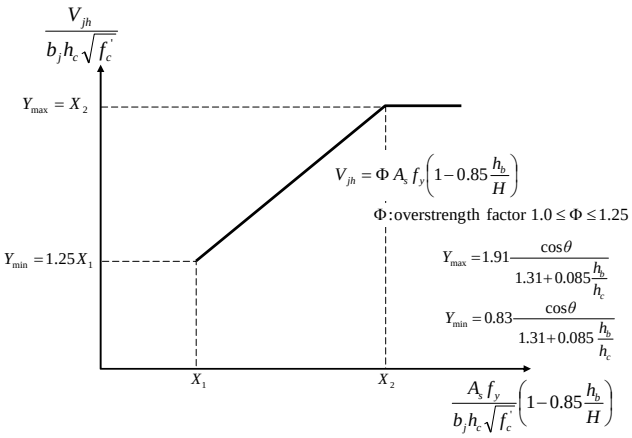

Figure 5 Semi-empirical Model

4. Experimental Program

4.1 Specimen Configuration

Four full-scale corner beam-column joint specimens were constructed with RC slabs. Test matrix addressed two parameters: (1) joint aspect ratio, and (2) beam longitudinal reinforcement ratio. The configuration of the specimens and their design details are summarized in Figure 6. Two specimens, SP1 and SP2, were recently tested, while testing of specimens SP3 and SP4 is in progress. The material properties of specimens SP1 and SP2 are presented in Table 1 where f'_c is the concrete compressive strength, and f_y and f_{yu} are the reinforcing steel yield and ultimate strength. The two orthogonal beam cross sections had different effective depth at the column face because the reinforcing bars of the East-West (EW) direction beam were placed under those of the North-South (NS) beam, as shown Figure 7.

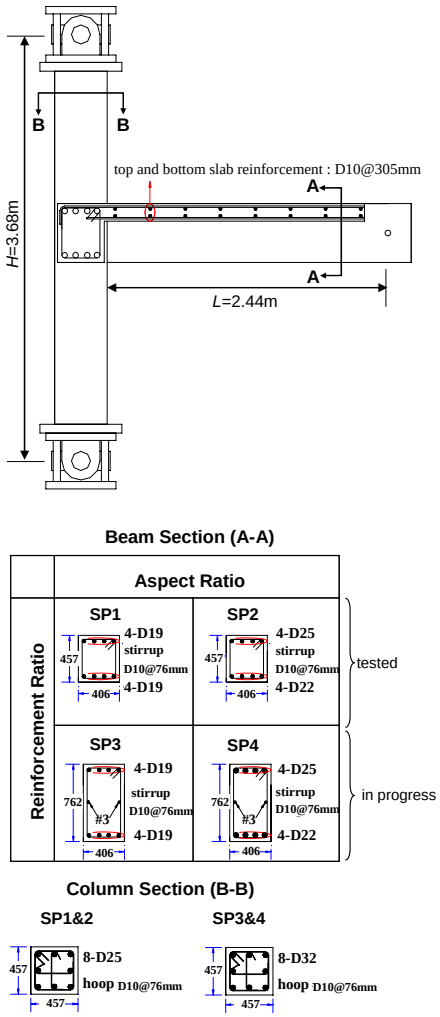

Figure 6 Configuration and details of specimens

Table 1 Material properties of SP1 and SP2

Concrete (MPa)	Reinforcement Strength (MPa)							
	D25mm		D22mm		D19mm		D10mm	
f_c	f_y	f_u	f_y	f_u	f_y	f_u	f_y	f_u
24.5	498	708	506	711	542	721	507	793



Figure 7 Placement of beam reinforcement at corner

4.2 Loading Protocol

The lateral load was applied in a quasi-static (0.5 mm/sec) manner through displacement control at the end of each beam. The applied displacement alternated between the two beams, i.e. one beam remained at a reference point during the loading of the other orthogonal beam. Both beams were pulled down to one quarter of the estimated yield displacement (Δ_y=31.5 mm for specimens SP1 and SP2) to simulate gravity load prior to the cyclic testing and this displacement was defined as the reference point, Δ_0. The number of peak displacement levels was limited to three values prior to yielding to reduce unnecessary effect of low-cycle fatigue on the joint strength. Upon yielding, the peak displacement (applied in two cycles for each beam) of the next level was determined as 1.5 times the previous displacement level. In the inelastic loading range, a single low-level cycle, being equal to 1/3 of the previous displacement level, was added after each group of cycles to quantify the stiffness degradation. The protocol of the displacement-controlled loading is depicted in Figure 8.

The beam shear forces for the EW and NS directions, $V_{b,EW}$ and $V_{b,NS}$, respectively, corresponding to each applied tip displacement were recorded in real time and these forces directly determined the applied column axial load by a predefined linear equation based on pre-test analyses of a selected prototype structure. The axial load varied from 369 kN in tension to 512 kN (0.10 f'_cA_g) in compression in SP1 and from 100 kN in tension to 1157 kN (0.23 f'_cA_g) in compression in SP2. The variation of column axial load during test is shown in Figure 9. The difference in the column axial load variation between SP1 and SP2 is due to an error in experimental procedure of SP1.

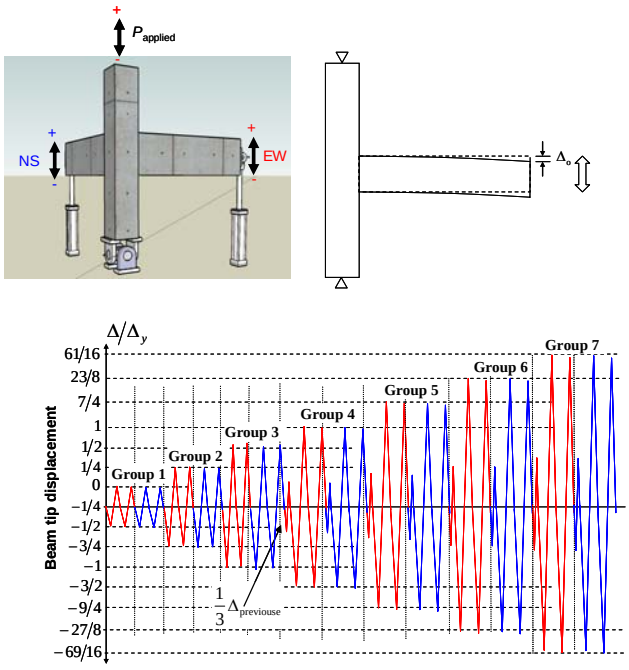

Figure 8 Displacement history

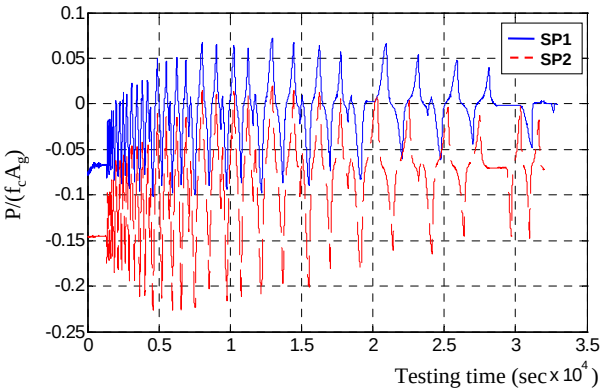

Figure 9 Variation of column axial loading during test

4.3 Test Setup

The test setup consisted of a lateral restraining frame and two 3D swivels, Figure 10. The lateral restraining frame allows vertical movement to achieve variable column axial loading but prevents horizontal displacement at the top end of column to satisfy the boundary conditions represented by inflection points in both directions (EW and NS) assumed to be located in the middle of both top and bottom columns and EW and NS beams of the prototype 3D building frame. Top and bottom ends of the column were artificially confined to prevent local failure during testing. In the test setup, no P-delta effect was taken into consideration.

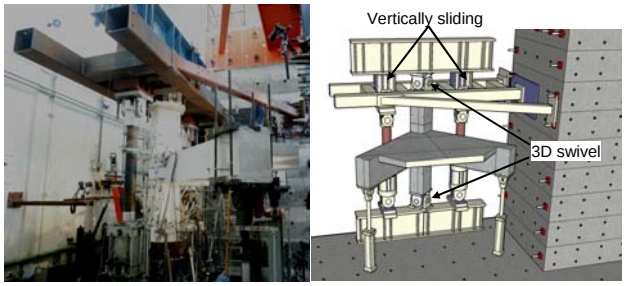

Figure 10 Test setup

5. Test Results

5.1 Hysteretic Behavior

Hysteresis curves of the applied beam shear versus the drift of SP1 and SP2 are shown in Figure 11 and exact values are given in Table 2. Loading group numbers are shown in Fig. 8. In addition to the seven loading group, tip displacement was manually applied up to 203.2mm (8 inches) with single cycle, which is referred to as the eighth loading group in Table 2. It is noted that the drift is defined as the applied beam vertical displacement normalized by the length L+0.5b_c where L is defined in Figure 1 and b_c=457 mm is the column width, Figure 6.

The drift levels at yielding and strength degradation starting point in SP1 and SP2 were similar as shown in Figure 11. First, yielding of beam reinforcements occurred at the fourth group of loading, i.e. downward drift of 1.75%, and the fifth group of loading, i.e. upward drift of 2.06%, for SP1 and SP2, respectively.

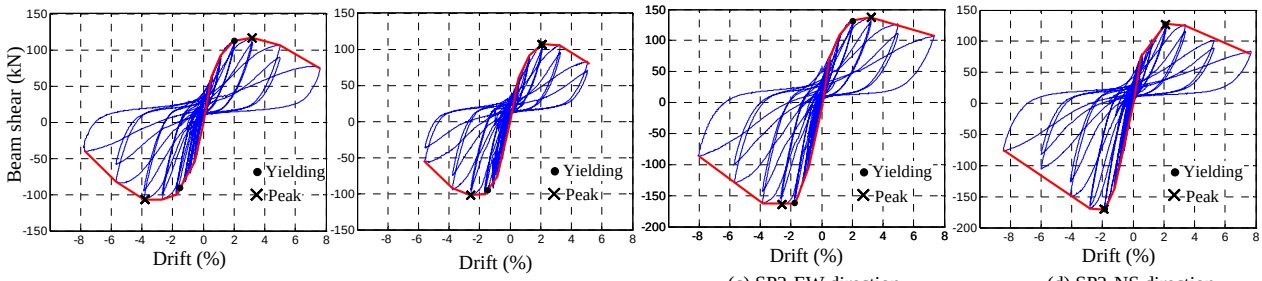

(a) SP1-EW direction (b) SP1-NS direction (c) SP2-EW direction (d) SP2-NS direction

Figure 11 Beam shear versus drift curves

Table 2 Measured drift, Δ (%) and beam shear, V_b (kN) at each loading cycle

Group No.	SP1								SP2							
	EW				NS				EW				NS			
	Down		Up		Down		Up		Down		Up		Down		Up	
	Δ	V_b	Δ	V_b	Δ	V_b	Δ	V_b	Δ	V_b	Δ	V_b	Δ	V_b	Δ	V_b
1	-0.57	-55.1	-0.02	31.7	-0.56	-53.5	-0.01	33.6	-0.57	-73.4	-0.02	18.5	-0.57	-76.5	-0.01	29.0
2	-0.87	-70.2	0.27	45.9	-0.85	-77.0	0.28	43.9	-0.87	-101.9	0.27	55.2	-0.88	-107.2	0.28	61.8
3	-1.17	-82.3	0.55	63.2	-1.14	-85.5	0.61	61.3	-1.17	-126.3	0.56	68.5	-1.16	-137.9	0.57	79.6
4	-1.77	-99.6*	1.15	91.7	-1.67	-101.1*	1.25	91.5	-1.75	-160.1*	1.15	108.1	-1.76	-170.4*#	1.18	102.8
5	-2.66	-106.7	2.03	113.0*	-2.57	-102.0#	2.11	107.6*#	-2.66	-163.7#	2.04	131.7*	-2.66	-169.5	2.06	129.0*#
6	-3.86	-107.2#	3.21	117.5#	-3.77	-94.0	3.29	105.8	-3.86	-162.8	3.22	137.9#	-3.88	-150.4	3.24	126.3
7	-5.36	-84.5	4.99	106.8	-5.31	-56.1	5.05	82.7	-5.68	-129.4	4.99	126.8	-5.70	-105.0	5.01	101.9
8	-7.71	-41.4	7.27	77.4	-	-	-	-	-8.06	-86.7	7.30	106.8	-8.05	-77.0	7.31	83.6

*: beam reinforcement yielding , #: peak loading

These drifts (marked with filled circles in Figure 11 were greater than the yield drift of 1.2% estimated by conventional rigid joint analysis.

In SP1, the peak load of the EW direction increased by 7.6% and 4.0% from the yield load due to the strain hardening in downward and upward loadings, respectively. In SP2, the peak load of the EW direction increased by 2.2% and 4.7% from the yield load in downward and upward loadings, respectively. For the NW direction, the peak loads in downward and upward loadings were observed at the next group of loading to the EW peak loadings in both specimens because the joint was already damaged during the EW loadings. Note that the peak loads are marked with × symbols in Figure 11. For both SP1 and SP2, the applied beam downward shear was sharply reduced after the sixth group of cyclic loading, while the reduction in the upward loading was less severe.

5.2 Joint Behavior and Shear Strength

The diagonal cracking in the joint region occurred with "X" shape pattern in both SP1 and SP2. The cover concrete on the open side of joint spalled off and column and beam reinforcement were exposed. The concrete in the joint was severely damaged by crushing. Based on the above observations, the lateral load-carrying capacity of both SP1 and SP2 deteriorated due to the joint failure instead of beam hinging mechanism as shown in Figure 12.



(a) SP1 (b) SP2

Figure 12 Damaged specimens at the end of test

The diagonal crack pattern of SP1 and SP2 differed as shown in Figure 13. In SP1, a single diagonal crack in each direction was dominant except for the NS direction in the upward loading. However, multiple diagonal cracks formed in SP2 except for a single diagonal crack dominating the EW direction in the upward loading.

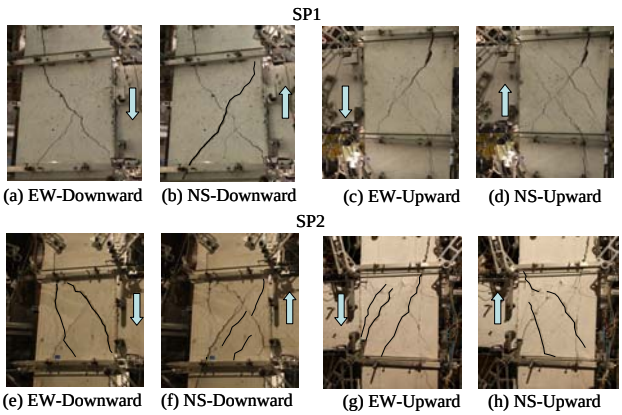

(a) EW-Downward (b) NS-Downward (c) EW-Upward (d) NS-Upward

(e) EW-Downward (f) NS-Downward (g) EW-Upward (h) NS-Upward

Figure 13 Crack patterns of specimens

Joint shear strain was smaller when slab was in tension than when slab was in compression. At the point of shear strength degradation, joint shear strain in downward loading, i.e. slab in tension, ranged from 0.002 rad. to 0.007 rad., while it ranged from 0.008 rad. to 0.012 rad. in upward loading. This difference resulted from the effect of slab which is discussed later in this paper.

Joint shear strength of SP1 was obviously less than that of SP2 because of low beam reinforcement ratio, refer to Figure 14 where the joint shear stress-strain relationships are presented with the shear stress normalized by $f'_c{}^{0.5}$. However, the joint shear strength of the two specimens was greater than that predicted by the ASCE 41 provisions for shear strength of unreinforced (nonconforming transverse reinforcement) exterior joint. According to ASCE 41, nominal joint shear stresses are limited to $0.5f'_c{}^{0.5}$ MPa ($6\,f'_c{}^{0.5}$ psi). The joint shear strength of the two specimens at peak and prediction by the aforementioned model are compared in Table 3

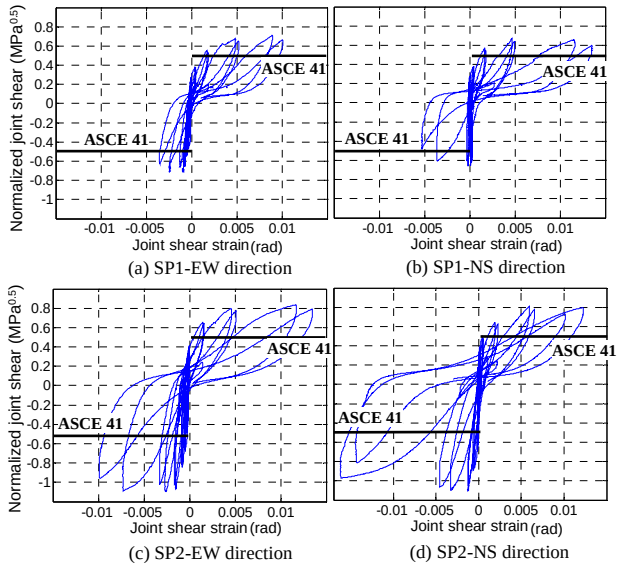

Figure 14 Joint shear response

Table 3 Comparison of normalized joint shear strength test results and predictions by model

*( ) the ratio of the joint shear strength prediction to the test

	Loading		d_b (mm)	Test ($MPa^{0.5}$)	Semi-empirical ($MPa^{0.5}$)
SP1	EW	Up (+)	409.6	0.71	0.64 (0.90)*
		Down (-)	375.0†	0.71	0.71 (1.00)*
	NS	Up (+)	396.9	0.67	0.64 (0.96)*
		Down (-)	384.9†	0.66	0.71 (1.08)*
SP2	EW	Up (+)	408.0	0.80	0.79 (0.99)*
		Down (-)	373.5†	1.09	0.97 (0.89)*
	NS	Up (+)	395.3	0.81	0.79 (0.98)*
		Down (-)	384.6†	1.10	0.97 (0.88)*

†effective depth includes contribution of top 2-D10 slab reinforcement

5.3 Effect of Beam Reinforcement Ratio

Comparing the increase of load from yielding point to peak point in SP1 and SP2, the increase was greater in SP1 having low beam reinforcement as shown in Table 2. This is attributed to the strain hardening of the beam reinforcement beyond yield which was more pronounced in SP1 than SP2. This is coincident with the variation of beam reinforcement strain as shown in Figure 15. In this figure, all strain values of beam reinforcement in SP1 were greater than that in SP2 at the same drift level. In particular, the increase of the strain at location "2" for EW loading of top reinforcement shows that beam reinforcement yielding penetrated more severely into the joint of SP1 than SP2. It is also shown that the rate of yield penetration with distance was slower in specimen with high beam reinforcement ratio, i.e. SP2. Thus, it is expected that the bond strength deteriorated less in SP2 due to low tensile stress of beam reinforcement in the joint region.

The peak load at joint failure, i.e. joint shear strength, increased proportional to the increase of beam reinforcement ratio. This increase in specimen with high beam reinforcement

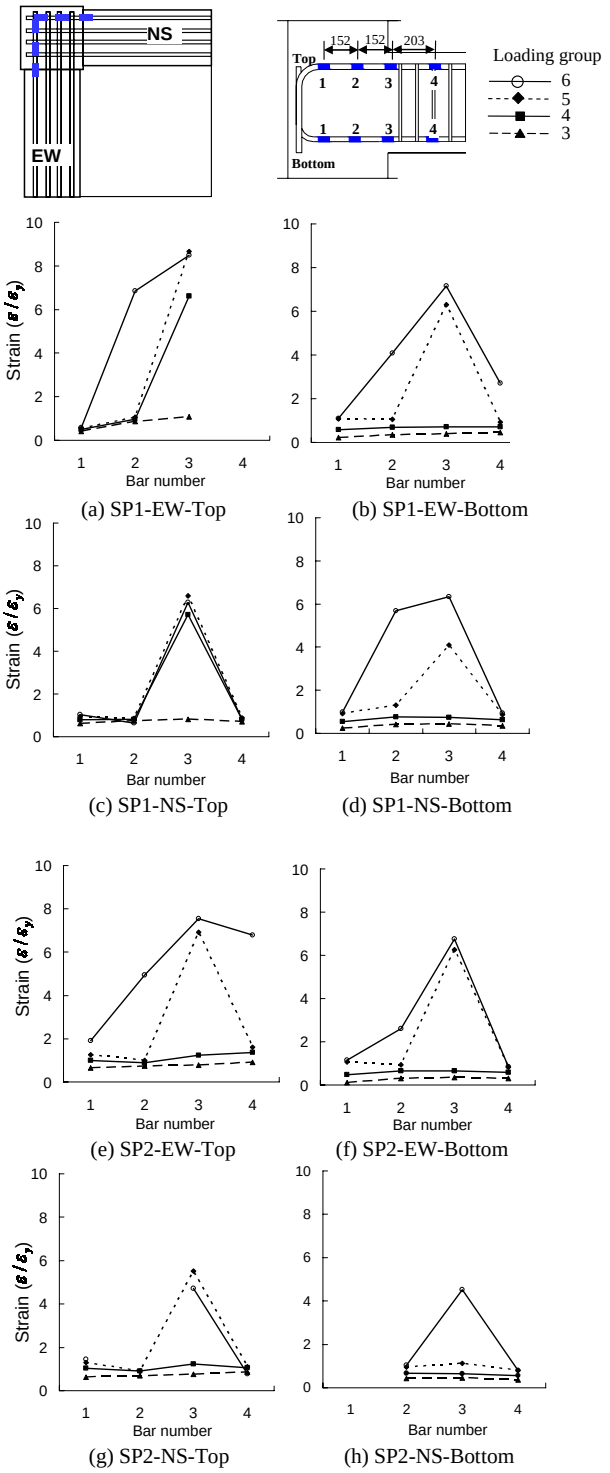

Figure 15 Strain gage data of beam reinforcement

ratio can be explained as follows: an increase of beam reinforcement ratio must cause an increase of the compression force in the diagonal strut with less loss of bond resistance. This more stable bond resistance induces multiple diagonal cracks in the joint region as shown in SP2, refer to Figure 13. In other words, multiple inclined struts are formed in the joint region for SP2 and can carry more horizontal joint shear stress. On the same basis, an analytical strength model using two inclined struts mechanism was recently developed by Park and Mosalam (2009).

5.5 Effect of Intermediate Column Bar

The strain variation of intermediate column bar along joint cross section height is shown in Figure 16 for SP2. The tensile strain of mid-height location was less than or very close to the lower values of the top and bottom of joint cross section. The same trend was observed in SP1. From this result, it is concluded that the intermediate column bar did not function as a tension tie in joint shear resisting mechanism for joint regions without transverse reinforcement as those tested in SP1 and SP2. This conclusion is different from the observation of reinforced exterior joints reported by Hwang et el. (2005).

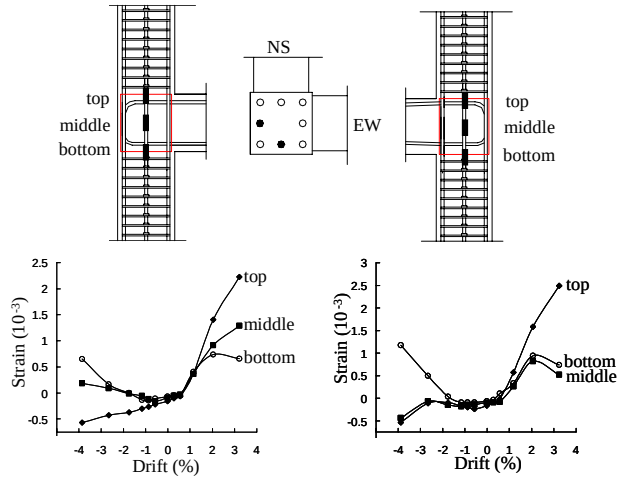

(a) EW direction (b) NS direction

Figure 16 Measured strain of intermediate column bar in SP2

5.4 Effect of Slab

The contribution of slab reinforcement to the horizontal joint shear strength is investigated from the strain distribution and cracking due to twisting moments. It was observed that flexural and torsional cracks took place in both beam and slab and they were widely open at the peak loads. Torsional cracks in the slab circled from the column face with 305 mm diameter as shown in Figure 17 for SP2. Based on these observations, it is concluded that the top slab reinforcing bars placed within a distance equals the beam depth from column face (top two D-10 reinforcing bars, refer to Figure 6) participated in resisting the horizontal joint shear force. The strain distribution of slab reinforcing bars is illustrated in Figure 18. The slab top reinforcement closest to the column face yielded under the same loading when beam reinforcement yielded. At the sixth group of cyclic loading, three and two top reinforcing bars have yielded in the EW and NS directions, respectively for both SP1 and SP2. However, the slab bottom reinforcing bars did not yield during test and bar slippage of these bottom bars was observed at the sixth group of cyclic loading for both specimens. In addition, the location of slab bottom reinforcing bars in the L-shape beam and slab cross section is close to its neutral axis considering the ratio of beam

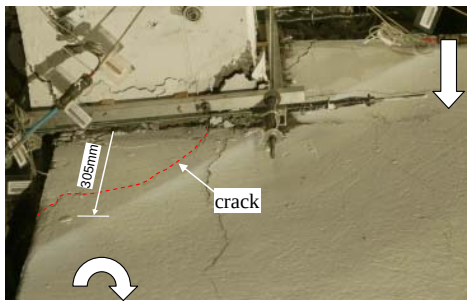

Figure 17 Torsional crack during orthogonal beam loading in SP2

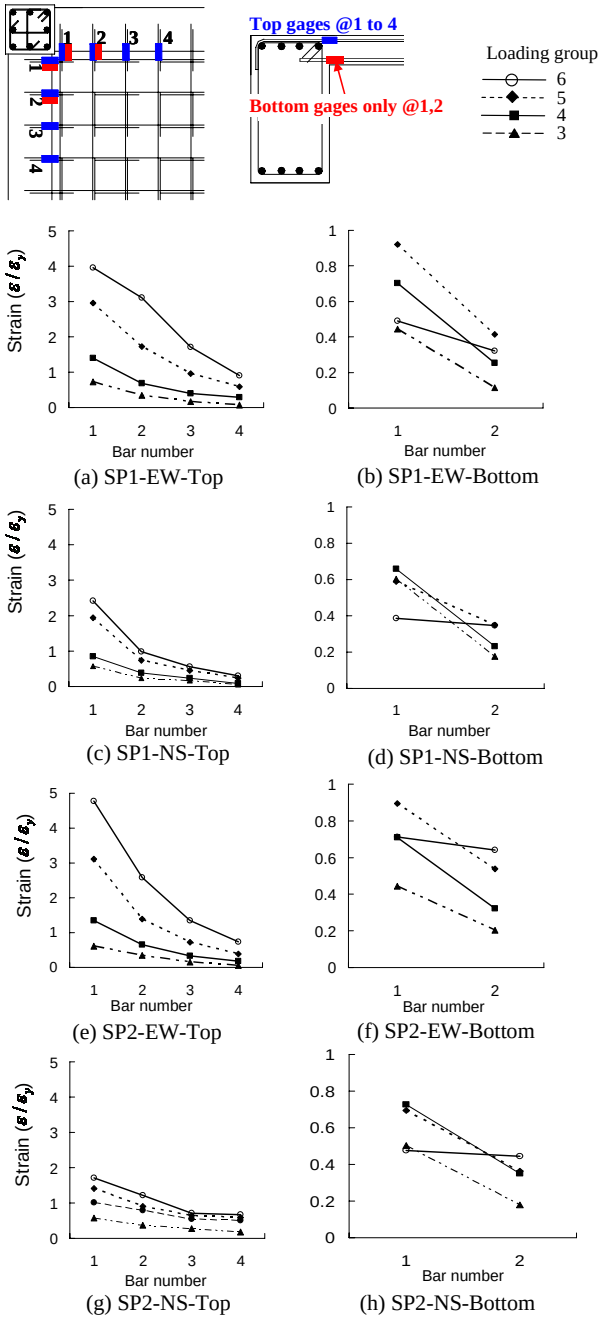

(a) SP1-EW-Top (b) SP1-EW-Bottom

(c) SP1-NS-Top (d) SP1-NS-Bottom

(e) SP2-EW-Top (f) SP2-EW-Bottom

(g) SP2-NS-Top (h) SP2-NS-Bottom

Figure 18 Strain gage data of slab reinforcement

depth (457 mm) to slab thickness (152 mm). Therefore, it is concluded that the contribution of slab bottom reinforcement to joint shear strength is negligible.

When one beam was subjected to upward loading, a horizontal crack took place in the joint face orthogonal to loading direction and torsional crack did not appear in the other orthogonal beam in SP1, Figure 19 (a). In contrast, torsional cracks occurred and widely opened in the orthogonal beam without horizontal crack in the joint face in downward loading in SP1, Figure 19 (b). This behavior was the same in SP2. This behavior conforms with the joint shear strain results in the preceding section and the variation of the twisting angle along the orthogonal beam which is shown in Figures 19 (c) and (d). The twisting angle is computed from two vertical measurements for each of the sections at "A", "B", and "C" as shown in Figure 19. Twisting angle was significantly increasing between section "A" and "B" in the downward loading, while the variation of twisting angle from "A" to "C" was small in the upward loading. Moreover, twisting angle at section "A", which is closest to the join, was greater under upward loading than downward loading at the similar drift level. Therefore, between sections "A" and "B" where torsional cracks in the beam took place as shown in Figure 19 (b), less twisting moment was transferred to the joint region under downward loading. On the other hand, in the upward loading, both NS and EW beams were twisted for the entire beam length and consequently the joint distortion was more affected by the transferred twisting moment due to the slab effect.

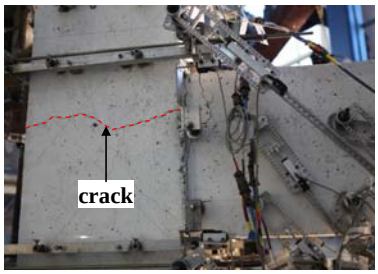

(a) Horizontal crack during NS upward loading

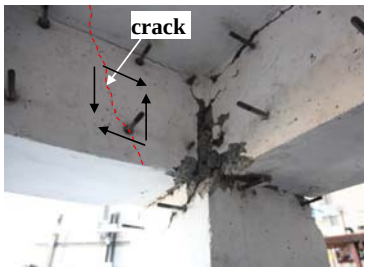

(b) Torsional crack during NS downward loading

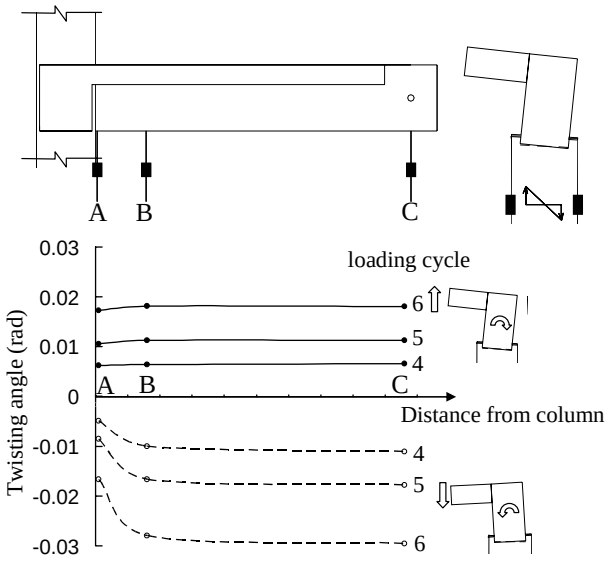

(c) Twisting of NS beam during EW loading

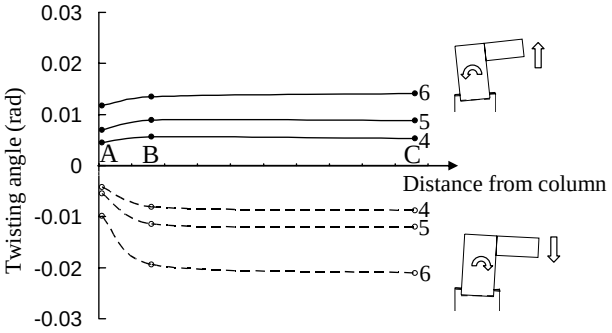

(d) Twisting of EW beam during NS loading

Figure 19 Torsional effect of slab in SP1

6. Conclusion

Survey of experiments on unreinforced exterior beam-column joints was performed and a semi-empirical strength model was developed based on the collected database from this survey. To investigate the effect of beam longitudinal reinforcement ratio on the shear strength of unreinforced corner joints, two specimens having different beam reinforcement ratio but same joint aspect ratio were tested. From the results of the analytical and experimental study, the following conclusions can be made:

1. Shear strength of unreinforced exterior joints is strongly affected by joint aspect ratio and beam longitudinal reinforcement ratio which is related to the joint shear demand. The joint strength model introduced in this paper incorporates these effects and accurately (with $\leq$ 12% error) predicts the strengths of specimens SP1 and SP2.

2. The loss of load-carrying capacity was caused by joint shear failure with beam reinforcement yielding in both SP1 and SP2 due to the absence of transverse reinforcement in the joint region. The joint shear strength of SP1 was measured to be $0.69\,f'_c{}^{0.5}$ MPa ($8.3\,f'_c{}^{0.5}$ psi) for both upward and downward loading. In SP2, the joint shear strength was measured to be $0.81\,f'_c{}^{0.5}$ MPa ($9.7\,f'_c{}^{0.5}$ psi) and $1.10\,f'_c{}^{0.5}$ MPa ($13.2\,f'_c{}^{0.5}$ psi) on average for upward and downward loading, respectively. These joint shear strengths of SP1 and SP2 are greater than that of unreinforced exterior joint from ASCE 41, i.e. $0.5\,f'_c{}^{0.5}$ MPa ($6.0\,f'_c{}^{0.5}$ psi).

3. The increase of beam longitudinal reinforcement leads to higher joint shear strength from the comparison the joint shear strength of SP1 and SP2. In contrast, the yield penetration of beam reinforcement into the joint made more progression in the specimen with low beam reinforcement ratio, i.e. SP1. The

different rate of yield penetration resulted in different joint crack patterns, i.e. either single diagonal crack for SP1 or multiple diagonal cracks for SP2.

4. The intermediate column bars did not play the role of a tension tie in shear resisting mechanism of unreinforced exterior joints.

5. Based on the observation of strain gage data and cracks, the slab top reinforcing bars placed within the beam depth from the column face appeared to have participation in the joint shear strength. In other words, the slab contribution to the load input into the beam-column joint can be estimated by considering an effective slab width measured from the column face and equal to the beam depth.

6. The joint distortion was greater when slab is in compression than in tension. This is attributed to the fact that torsional cracks formed in the orthogonal beam in relation to the loading direction reduced the torsional moment transferred to the joint region during downward loading, i.e. when the slab is in tension.

Acknowledgements:

This study is supported by the NSF (National Science Foundation) award #0618804 through PEER, University of California, Berkeley. NSF financial support is gratefully acknowledged. Opinions, findings or recommendations expressed in this paper are those of the authors and do not necessarily reflect those of NSF. The authors acknowledge the technical contributions of Prof. J.P. Moehle and Mr. W. Hassan. The laboratory assistance of nees@berkeley staff was essential for the experimental part of the study.

References:

ASCE/SEI Seismic Rehabilitation Standards Committee, (2007), *Seismic Rehabilitation of Existing Buildings* (ASCE/SEI 41-06), American Society of Civil Engineers, Reston, VA, US.

Hwang, S. J., Lee, H. J., Liao, T. F., Wang, K. C., and Tsai, H.H. (2005)," Role of Hoops on Shear Strength of RC Beam-Column Joints," *Journal of Structural Engineering*, American Concrete Institute, **102**(3), 445-453.

Park, S. and Mosalam, K.M. (2009), "Shear Strength Models of Exterior Beam-Column Joints without Transverse Reinforcement," *PEER Report 2009/106*, University of California, Berkeley.

Vollum, R.L. (1998), "Design and Analysis of Exterior Beam Column Connections," *PhD thesis*, Imperial College of Science Technology and Medicine-University of London.

JOINT CONFERENCE PROCEEDINGS
7th International Conference on Urban Earthquake Engineering (7CUEE) &
5th International Conference on Earthquake Engineering (5ICEE)
March 3-5, 2010, Tokyo Institute of Technology, Tokyo, Japan

DISTRIBUTION OF BUILDING DAMAGE IN ISTANBUL DURING THE 1894 MARMARA SEA, TURKEY, EARTHQUAKE

Masashi Morita[1] and Saburoh Midorikawa[2]

1) Post-Doctoral Research Fellow, Center for Urban Earthquake Engineering, Tokyo Institute of Technology, Japan
2) Professor, Dept. of Built Environment, Tokyo Institute of Technology, Japan
mmorita@enveng.titech.ac.jp, smidorik@enveng.titech.ac.jp

Abstract: Istanbul is designated a World Heritage Site because of many historical monuments and cityscape. It has been repeatedly struck by destructive earthquakes. It is important for earthquake disaster prevention of human lives and those monuments to investigate building damages caused by past earthquakes. From this view point, this paper examines building damages and its distribution caused by the 1894 Marmara Sea Earthquake based on the records of the day as a case study. The distribution maps of building damage in the old city area of Istanbul were created. It was confirmed that the building damage was heavier in the middle of southern part of the city. Then, the distribution of building damage was compared with the geology and soil conditions in Istanbul. As the result, correlation between damage degrees and soil conditions was found

1. INTRODUCTION

Istanbul, which is one of the mega cities in the world, has been repeatedly struck by destructive earthquakes because it is located at the west end of the North Anatolian Fault Zone. At the same time, it is designated a World Heritage Site because of many historical monuments and cityscape. Therefore it is important for the earthquake disaster prevention of human lives and those monuments to investigate building damages caused by past earthquakes. Findings obtained from such historical facts and lessons contribute to develop a better disaster protection and reduction countermeasure.

From this view point, this paper examines building damages and its distribution in Istanbul during the 1894 Marmara Sea Earthquake (Ms=7.3), which is the latest earthquake causing severe damage to Istanbul, as a case study.

Concerning to casualties and building damages, books and articles are published by several researchers. Ambraseys (2001) and Ürekli (1999) summarized damages of buildings with collecting records from many newspapers and journals of the day. Çalık (2003) introduced a diary-like record of earthquake at that time with a translation. Ansal *et al.* (1990) examined the distribution of building damage and the influence of local soil condition. However, the damage distribution was grossly compiled, and the discussion was limited to the damage of several important buildings.

Among of them, Öztin (1994) also collected a lot of records from newspapers and journals of the day and provided original texts to give detail information. In this study, this report is used as a main source to examine damages of individual buildings on the 1894 earthquake in detail. Based on descriptions of building damages, damage degrees of buildings are classified into four levels in accordance with their descriptions at first. Next, the locations of damaged buildings are identified and plotted on a map according to building types and damage levels. Then, a damage distribution is compared with the geology and soil condition in Istanbul to consider a reason resulted in such distribution.

2. OUTLINE OF BUILDING DAMAGES CAUSED BY THE 1894 EARTHQUAKE

One technical report of the day by the director of the Athens Observatory, Eginitis, tells the general outline of this earthquake in 1894 (Sezer 1996). According to this report, the earthquake occurred on 10 July 1894 at 12:24 local time with three strong shakings. This ground motion was observed over a large region. Although no figure was mentioned, not only many houses but also mosques and churches were heavily damaged or collapsed in many villages located on the islands and the sea sides of Marmara Sea.

The report by Öztin (1994) contains records of building damages in the area corresponding to Istanbul province at present (Fig.1). A damage on each building was mainly described by use of the words, "*yıkılmak (yıkılmıştır)*" which means to collapse or to fall down and "*çatlamak*

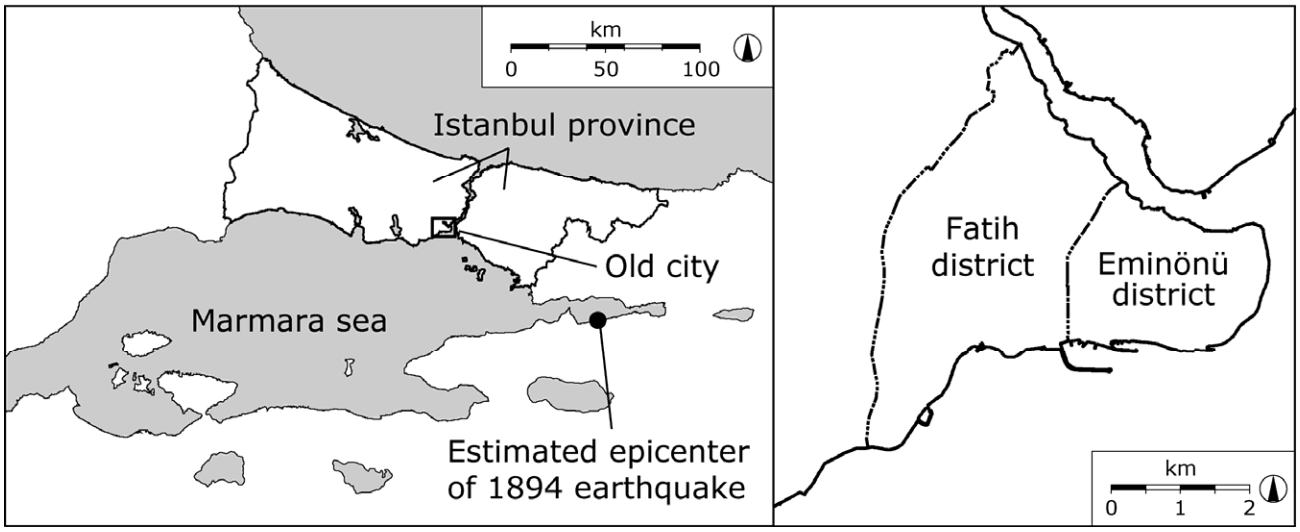

Figure 1 Istanbul Province and the Old City Area

Table 1 Number of Damaged Buildings in accordance with Building Types

Damage Level \ Building Type	Mosque	Minaret	Church	Commercial Building (Han)	Public Bath (Hamam)	Muslim Seminary (Medrese)	School (Mekteb)	Mausoleum (Türbe)	Sufi Lodge (Tekke)	Station	Hospital	Factory	Covered Market (Çarşı)	Police Station	Hotel	Villa	City Wall	Fountain/Well	Dock/Pier	Other	Total
DL4	18	9	10	6	2	4	8	1	2	1	0	0	1	3	0	0	1	1	3	1	71
	23.1%	14.5%	32.3%	14.3%	10.0%	14.8%	23.5%	12.5%	25.0%	33.3%	0.0%	0.0%	20.0%	16.7%	0.0%	0.0%	8.3%	8.3%	30.0%	5.9%	17.2%
DL3	18	15	7	10	7	6	9	1	1	1	0	0	3	4	3	1	2	2	2	5	97
	23.1%	24.2%	22.6%	23.8%	35.0%	22.2%	26.5%	12.5%	12.5%	33.3%	0.0%	0.0%	60.0%	22.2%	42.9%	14.3%	16.7%	16.7%	20.0%	29.4%	23.5%
DL2	38	13	7	17	8	15	9	3	3	1	1	5	1	7	2	3	3	4	3	9	152
	48.7%	21.0%	22.6%	40.5%	40.0%	55.6%	26.5%	37.5%	37.5%	33.3%	33.3%	55.6%	20.0%	38.9%	28.6%	42.9%	25.0%	33.3%	30.0%	52.9%	36.8%
DL1	4	25	7	9	3	2	8	3	2	0	2	4	0	4	2	3	6	5	2	2	93
	5.1%	40.3%	22.6%	21.4%	15.0%	7.4%	23.5%	37.5%	25.0%	0.0%	66.7%	44.4%	0.0%	22.2%	28.6%	42.9%	50.0%	41.7%	20.0%	11.8%	22.5%
Total	78	62	31	42	20	27	34	8	8	3	3	9	5	18	7	7	12	12	10	17	413

(çatlamıştır)" which means to be cracked. When those words are solely used to describe a damage condition of building, it is difficult to determine which part and how degree a damage was caused. In cases that damaged parts such as a dome or a wall are clearly written and damage degrees are explained with the words, whole (*tümüyle*), most part (*ekseri yerleri*), half (*yarsı*), some parts (*bazı yerleri*) and so on, it is possible to estimate a damage degree. Taking how to describe damage conditions of buildings into consideration, damage degrees of buildings are classified into four levels. DL4, DL3 and DL2 are totally collapsed, half collapsed or heavy damage and partly collapsed or light damage respectively. DL1 is that damage level is not determined because of no description about a damage degree.

Table 1 shows the number and the ratio of damaged buildings with respect to its damage degree for each building type. The total number of buildings, whose damages were recorded, is 413. The number of buildings classified into DL4 is 71 (17.2%), DL3 is 97 (23.5%), DL2 is 152 (36.8%) and DL1 is 93 (22.5%). In more than 75% of the total number, damage degrees can be identified. As for building types, the numbers of records about major historical buildings such as mosques, churches, large commercial buildings (*han*), and public bathes (*hamam*) are large, and their ratio of DL4 and DL3 are also high. From this fact, it is reconfirmed vulnerability of historical buildings to earthquakes.

3. DISTRIBUTION OF BUILDING DAMAGE IN THE OLD ISTANBUL

Most of historical buildings in Istanbul are located in the old city area, Eminönü and Fatih districts (Fig.1). Regarding this area, there is the old map edited by Ayverdi (1978). Although the author and the drawn date of this map are unknown, it is thought that this map was drawn between 1875 and 1882 judging from buildings on the map (Konagaya 2000). It is possible to identify the locations of damaged buildings including defunct buildings from this map because the names of major buildings and streets are also written. Here, eight important building types are selected and the locations of damaged buildings are identified.

Table 2 shows the number of damaged buildings in Eminönü and Fatih districts. There are some unmapped buildings even though their damages are recorded. The

number of buildings, whose locations were identified and the number of buildings, whose locations were not identified, are counted separately. The ratios of identified buildings in each building type except large commercial buildings (*han*) are around 90%. Moreover, the total numbers of identified and unidentified buildings are 191 and 24 respectively, so that it can be said that the locations of buildings, whose damages were recorded, were mostly identified.

Next, damage distributions in each building type are examined (Figs.2 to 9). In those figures, locations of the same type of buildings, whose damages were not recorded, are also indicated for considering overall distribution of buildings in the old city at that time.

Figure 2 shows the damage distribution of mosques. Since mosques were already built in the whole city area at that time, damaged mosques can be identified at any places. However, the numbers of damaged mosques in the western part of the city and at the middle of the northern coastal area were relatively few. While all collapsed mosques were located from the central to the western part of the city, the damage degrees of mosques located in the eastern part of the city are light. In the case of minarets annexed to a mosque (Fig.3), damaged minarets concentrate somewhat from the northwestern to the eastern part of the city in comparison with mosques. As the different point from mosques, several minarets located in the eastern part were heavily damaged or collapsed.

Figure 4 shows the damage distribution of churches. All of damaged churches were located in the coastal area. Above all, the two churches located in the northwestern part of the city were damaged heavily. However, it is difficult to say that damage degrees of churches were heavy in a specific area since churches themselves were located on the very limited area and the number of records in this area was relatively few. On the other hand, most of large commercial buildings (*han*) concentrated on the eastern part of the city (Fig.5). Among them, partly damaged ones were located on the northern coastal area and heavily damaged ones were located on the inland area.

Public bathes (*hamam*), Muslim seminaries (*medrese*) and schools (*mekteb*) were randomly located on the whole city except the western part (Figs.6 to 8). In contrast to mosques, damaged public bathes and Muslim seminaries were not scattered. In addition, most of heavily damaged ones concentrated on the middle of southern part of the city. In the case of schools (*mekteb*), a specific pattern of distribution as for both location and damage degree can't be found. In the case of mausoleums (*türbe*) (Fig.9), the number of identified buildings is not enough to consider its damage distribution.

Figure 10 shows the distribution of all buildings. Damaged buildings mostly stood from the eastern to northwestern part of the city except at the middle of the northern coastal area. Along the southwestern coastal area, somewhat concentration of damaged buildings is also identified. With respect to damage degree, heavy damages occurred in the middle of southern part of the city.

Table 2 Number of Damaged Buildings in Eminönü and Fatih Districts

Building Type	Location	DL4	DL3	DL2	DL1	N/A
Mosque	Identified	10	13	27	1	311
	Unidentified	3	0	3	0	
Minaret	Identified	8	10	6	18	320
	Unidentified	0	0	1	1	
Church	Identified	1	2	2	2	22
	Unidentified	0	0	0	0	
Commercial building (Han)	Identified	4	8	11	4	33
	Unidentified	2	2	3	4	
Public bath (Hamam)	Identified	1	6	5	2	47
	Unidentified	0	0	2	0	
Muslim Seminary (Medrese)	Identified	4	5	14	2	61
	Unidentified	0	0	1	0	
School (Mekteb)	Identified	2	3	8	5	53
	Unidentified	0	0	0	1	
Mausoleum (Türbe)	Identified	1	1	3	2	49
	Unidentified	0	0	0	1	
Total	Identified	31	48	76	36	896
	Unidentified	5	2	10	7	

Identified: Number of damaged buildings, whose location are identified

Unidentified: Number of damaged buildings, whose location are not identified

N/A: Number of buildings, which are drawn on the map but damages were not recorded

4. RELATION BETWEEN DISTRIBUTION OF BUILDING DAMAGE AND SOIL CONDITION

For the risk assessment of future earthquakes, several geological maps and site classification maps in Istanbul were recently conducted by JICA and Istanbul Metropolitan Municipality (IMM) based on the result of soil surveying. The distributions of building damage discussed above are compared with those maps to grasp a relation between damage degree and soil condition. Fig.11 to 13 show the maps overlaid the distribution of all damaged buildings on the geological map (JICA *et al.* 2002) and the site classification maps (JICA *et al.* 2000, IMM 2007). Fig.14 to 16 show the ratio of damaged buildings together with the damage degrees and the classification criteria in each map.

As shown in Fig.11, Trakya formation of Lower Carboniferous age, which is composed of sandstone and siltstone, is widespread from the eastern to northwestern part of peninsula. Bakırköy and Güngören formations of Upper Miocene, which are mainly composed of loose clay and sand, occupy in the western part. In the coastal area, Kuşdili formation of the youngest sediment and artificial fills mainly cover. The ratio of total damaged buildings in Kuşdili formation exceeds 20% (Fig.14). The ratios in Trakya and Güngören formations are a little less than 20%, and less than 15% in Bakırköy formation. As for DL4, their ratios in Bakırköy and Güngören formations are higher than the ratio in Trakya formation, which is the oldest formation. A distinctive relation between distribution of building damage and geological feature is not clearly shown due to the big difference of occupied area in each formation. However, a

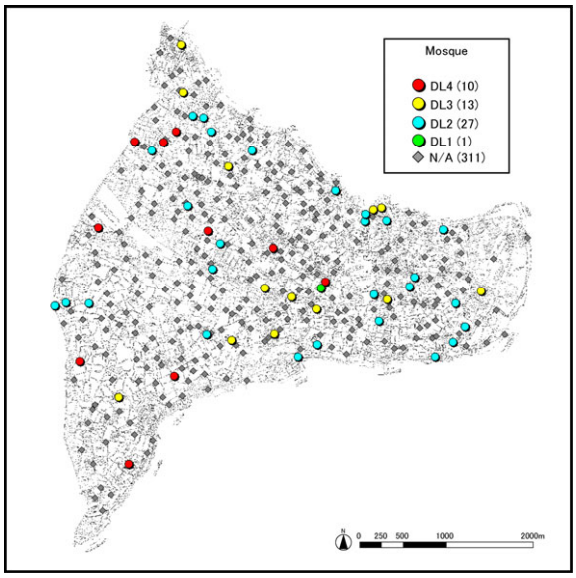

Figure 2 Distribution of Damaged Mosques

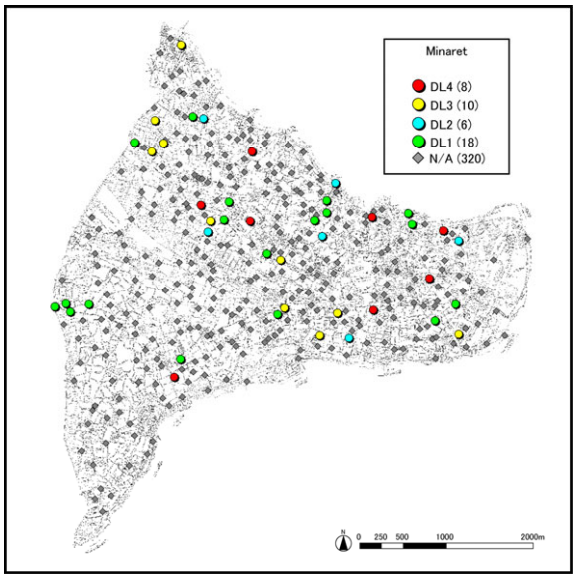

Figure 3 Distribution of Damaged Minarets

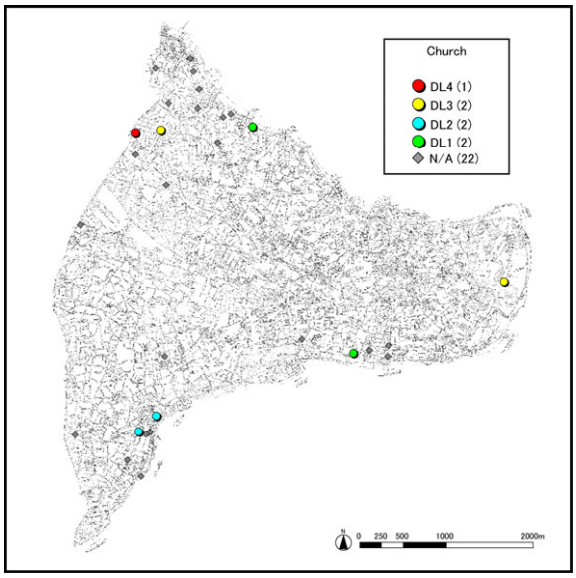

Figure 4 Distribution of Damaged Churches

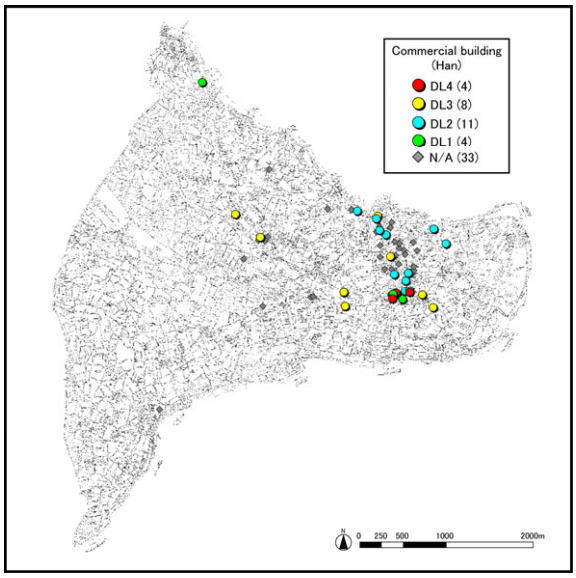

Figure 5 Distribution of Damaged *Han*s

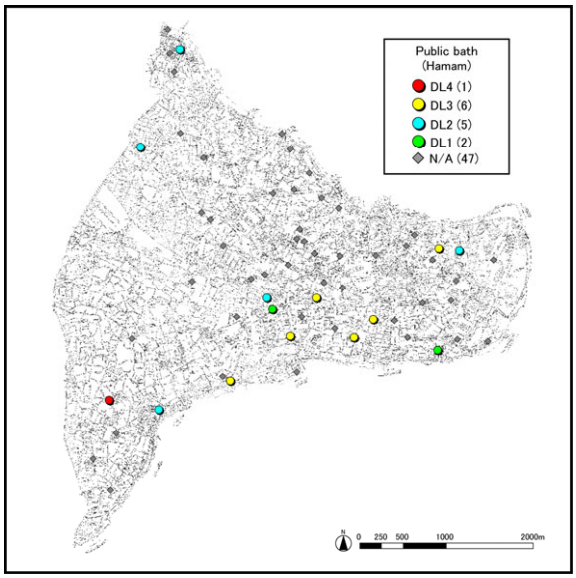

Figure 6 Distribution of Damaged Public Bathes

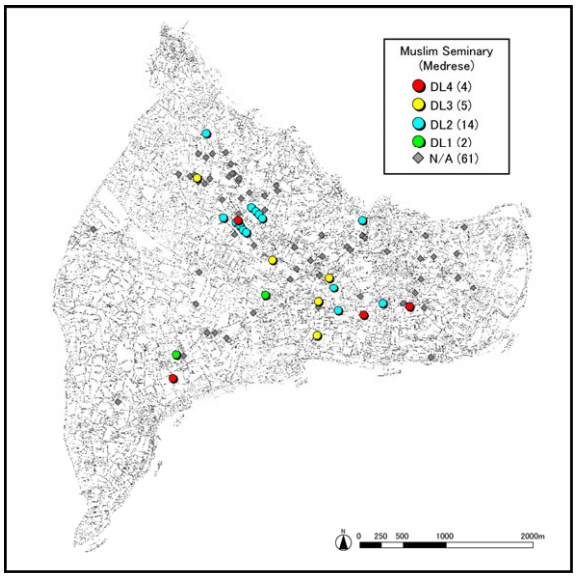

Figure 7 Distribution of Damaged Muslim Seminaries

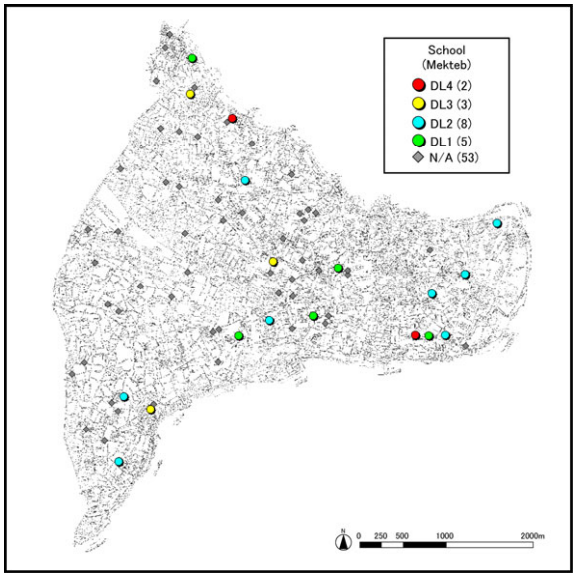

Figure 8 Distribution of Damaged Schools

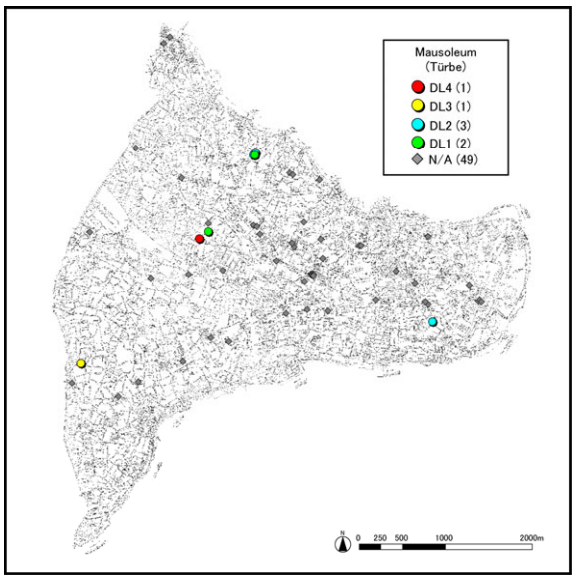

Figure 9 Distribution of Damaged Mausoleums

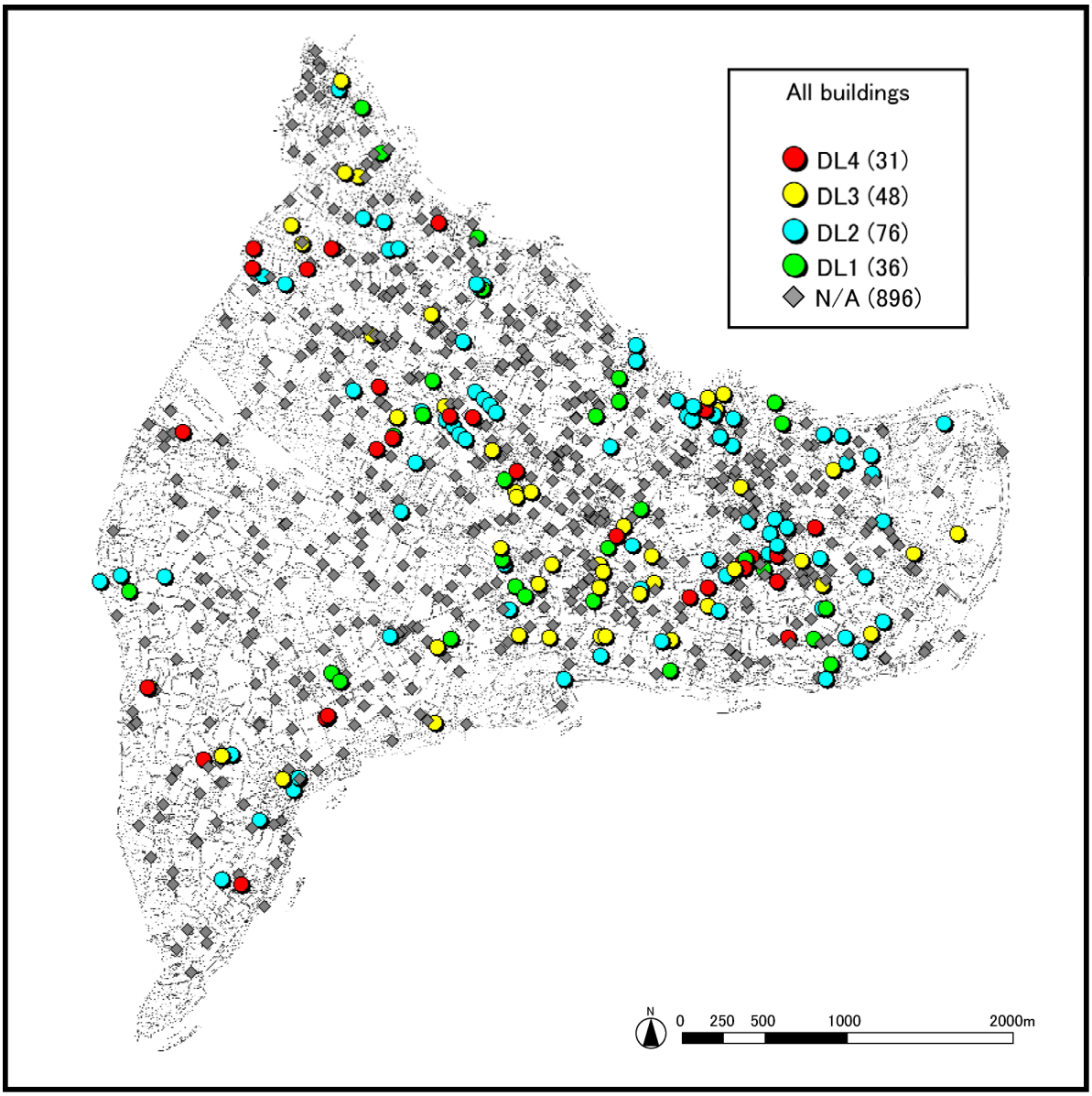

Figure 10 Distribution of All Damaged Buildings

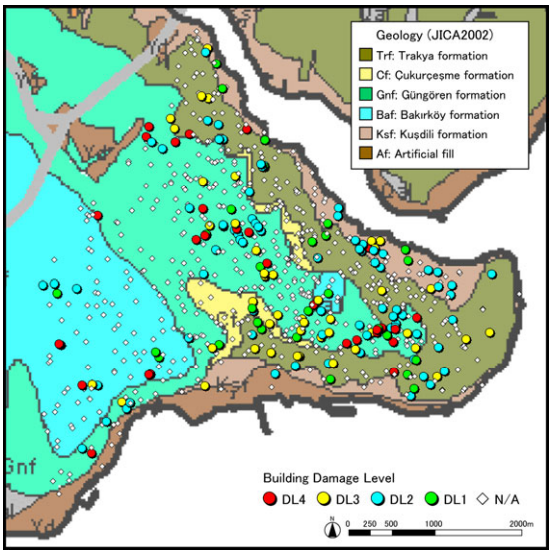

Figure 11 Distribution of All Damaged Buildings Overlaid on the Geology Map (JICA 2002)

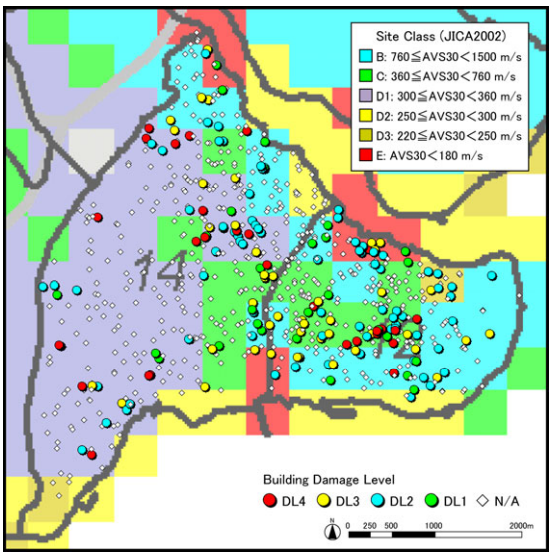

Figure 12 Distribution of All Damaged Buildings Overlaid on the Site Class Map (JICA 2002)

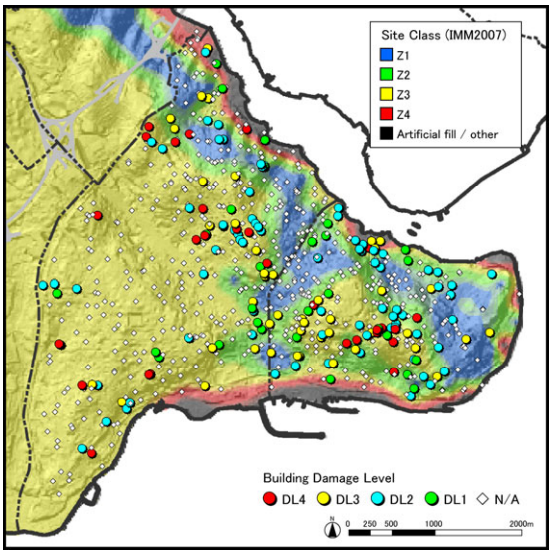

Figure 13 Distribution of All Damaged Buildings Overlaid on the Site Class Map (IMM 2007)

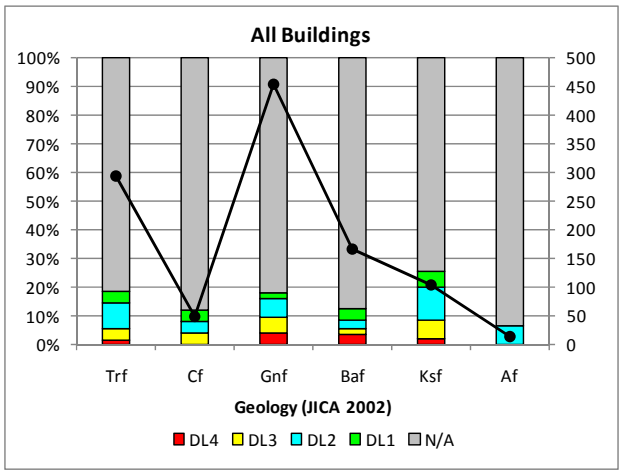

Figure 14 Number and Ratio of All Damaged Building in accordance with Geology (JICA 2002)

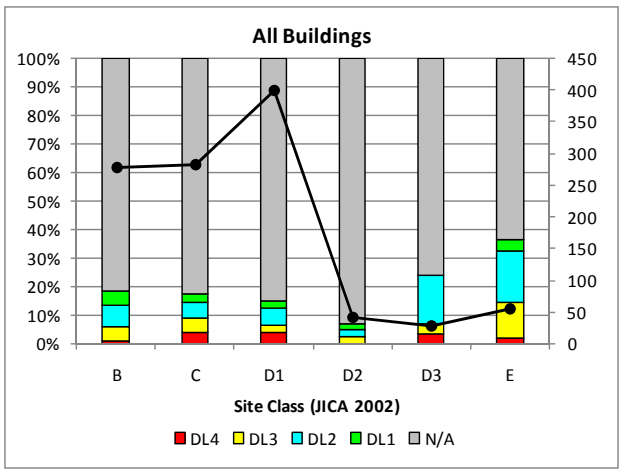

Figure 15 Number and Ratio of All damaged Bbuilding in accordance with the Site Class (JICA 2002)

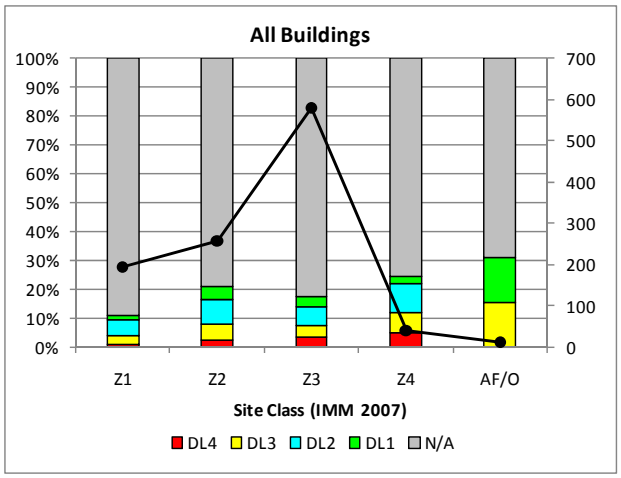

Figure 16 Number and Ratio of All Damaged Building in accordance with the Site Class (IMM2007)

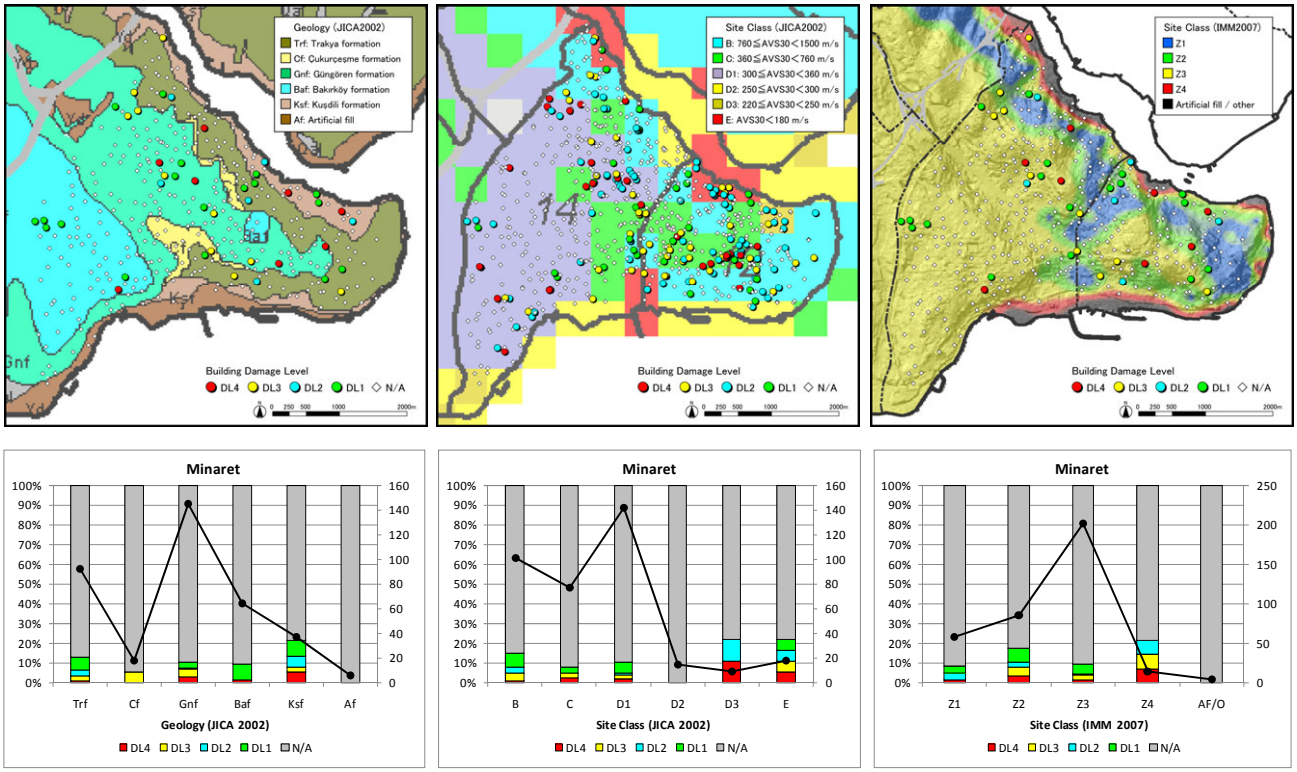

Geology (JICA 2002)　　Site Class (JICA 2002)　　Site Class (IMM 2007)

Figure 17　Comparison of Damage Distribution and Soil Conditions in Minaret

damage degree seems to be heavy as a formation age becomes young.

In the study by JICA (2002) (Fig.12), each site class at 500m grids is determined according to the average S wave velocity over the upper 30 m of the surface soil (AVS30) based on the criteria of the NEHRP. The range from 180 to 360 m/sec is subdivided into five ranges. As shown in Fig.15, the ratios of DL4 in C and D1 are around 4.0% and higher than the ones in other site classes. While the ratio of DL3 in E is the highest (12.7%), the ones in B and C are also relatively high (around 5.0%). However, the ratio of total damaged buildings in D3 exceeds 20%, and the ratio in E, where AVS30 is the lowest, exceeds 30%. When subdivisions of D1 to D3 are thought as a same group, it can be said that the ratio of heavily damaged buildings becomes high as AVS30 becomes low.

The site class by IMM (2007) (Fig.13) is determined by combination of standard penetration test, relative density, S-wave velocity and thickness of topmost soil in accordance with the Turkish Regulation (Ministry of Public Works and Settlement 1997). In this criterion, Z1 means the hardest soil, Z4 means the softest soil and AF/O means artificial soil or other soils not defined by the regulation. As shown in Fig.16, the ratios of DL4 are about 1.0%, 2.7%, 3.5% and 4.9% in Z1 to Z4 respectively. In regard to total damaged building, the ratio in Z1 is about 10% and the ratios in Z2 to Z4 are about 20%. The ratio in AF/O exceeds 30%. Comparing to the site classification by JICA, it is clearly shown that damage degrees become heavy when soils are soft.

The distributions of the damage in each building type are compared with the geology and the soil condition. Figure 17 shows the result in minarets. Their results also show that damage degrees seem to be heavy as soil conditions become bad. This correlation is the same as what discussed in all damaged buildings. Especially, the relation of damage degree and soil condition corresponds well to the newest result of soil conditions by IMM.

5. CONCLUDING REMARKS

As a case study, building damage caused by the 1894 Marmara Sea Earthquake was examined based on the records of the day. The distribution maps of building damage in the old city area in Istanbul were created. As the result, the distributions in each building type were different. However, the number of damaged buildings and their damage degrees tended to be large and heavy in the middle of southern part of the city area as a whole.

The distribution of building damage was preliminary compared with the geology and the soil condition in Istanbul. It was reconfirmed that the distribution of building damage agreed with a general relation as damage of building standing on soft soils tends to be serious.

Acknowledgements:

This study is supported by the Global COE Program "International Urban Earthquake Engineering Center for Mitigating Seismic Mega Risk" in Tokyo Institute of Technology supported by Japan Ministry of Education, Culture, Sport, Science, and Technology (MEXT).

References:

Ambraseys, N.N. (2001), "The Earthquake of 10 July 1894 in the Gulf of Izmit (Turkey) and Its Relation to the Earthquake of 17 August 1999", *Journal of Seismology*, Vol. 5, pp.117-128

Ansal, A. and Güneş, A.M. (1990), "The 1894 Earthquake of Istanbul", *3rd International Workshop on Historical Earthquakes in Europe*, Prague, Czechoslovakia, pp.263-271

Çalık, S. (2003), *An Anonymous Diary about the Destructive Earthquake of 1894 in Istanbul*, Istanbul (in Turkish)

IMM (2007), *Microzonation Maps and Reports (South Section of European Side)*, http://www.ibb.gov.tr/tr-TR/SubSites/IstanbulVeDeprem/Calismalarimiz/Pages/AnaSayfa.aspxJICA and IMM

JICA and IMM (2002), *The Study on a Disaster Prevention / Mitigation Basic Plan in Istanbul Including Seismic Microzonation in the Republic of Turkey*.

Konagaya, K. (2000) "An Old Map of Istanbul and Historical Geography", *Maps and Historical Geography*, pp.436-449 (in Japanese)

Ministry of Public Works and Settlement, Republic of Turkey (1997), "*Regulation on Construction in Disaster Areas*", R*esmi Gazete*, No.23098 (in Turkish)

Öztin, F., (1994), *The Report of the 10 July 1894 Istanbul Earthquake*, Ankara (in Turkish)

Sezer, H. (1996), "*A Study on the Report of the 1894 Istanbul Earthquake*", *Tarih Araştırmaları Dergisi*, Cilt18, Sayı29, pp.169-197 (in Turkish)

Ürekli, F. (1999), *The 1894 Earthquake in Istanbul*, Ankara (in Turkish)

JOINT CONFERENCE PROCEEDINGS
7th International Conference on Urban Earthquake Engineering (7CUEE) &
5th International Conference on Earthquake Engineering (5ICEE)
March 3-5, 2010, Tokyo Institute of Technology, Tokyo, Japan

THE ANALYSIS OF NON-LINEAR SEISMIC RESPONSE BETWEEN A COLLAPSED AND A SERIOUS DAMAGE INFILLED FRAME STRUCTURE IN YINGXIU TOWN–THE HEAVY DISASTER AREAS OF WENCHUAN 8.0 EARTHQUAKE

YAN Peilei [1], SUN Baitao [2], and CHEN Hongfu [2]

1) Doctor, College of Aerospace and Civil Engineering, Harbin Engineering University, China
2) Professor, Institute of Engineering Mechanics, China Earthquake Administration, China
3) Doctor, Institute of Engineering Mechanics, China Earthquake Administration, China
yanpeilei325@sohu.com, sunbt@iem.net.cn, chen-hongfu@163.com

Abstract: On 12 May 2008, a magnitude 8.0 earthquake happened in Wenchuan, Sichuan province, China .It was the most serious earthquake in china since 1949, causing very huge casualties and economic loss. The complex building and the office building of the Yingxiu secondary school in Yingxiu town were designed by the Code for Seismic Design of Buildings of China (GB50011-2001), the seismic fortification intensity of the buildings were both 7 degree. In the earthquake, the complex building collapsed completely, the adjacent office building was serious damaged, but didn't collapse. In the paper, the properties of material nonlinearity were considered ,the nonlinear analysis model of infilled frame structure was established, the time history analysis was used, the main cause of structural destruction was obtained, the influence of the infill wall on the structure was discussed.Therefore ,the results can provide valuable reference for the seismic design of infilled frame structure.

1. INTRODUCTION

On May 12 2008, a magnitude 8.0 earthquake occurred in Wenchuan County, Sichuan Province, China. It was the most serious earthquake in china since 1949, causing very huge casualties and engineering damages to the buildings. The complex building and the office building of the Xuankou secondary school in Yingxiu town were both built in 2005, designed by the Code for Seismic Design of Buildings of China (GB50011-2001); the seismic fortification intensity of the buildings was 7 degree. In the earthquake, the complex building collapsed completely, while the office building was destroyed most seriously, but didn't collapse. It is important to the investigation on theory and engineering

In the paper, the property of material nonlinearity was considered, the nonlinear analysis model of infilled frame structure was established, the time history analysis and nonlinear static analysis were used during inelastic stage, the main cause of structural destruction was obtained, and the influence of the infill wall on the structure was discussed. Therefore, the results can provide valuable reference for the seismic design of infilled frame structure.

2. DESCRIPTION OF THE BUILDING AND THE ENGINEERING SEISMIC DAMAGE

The complex building and the office building were built in 2005. The concrete grade is: column C30; beam C30; plate C30, the reinforced grade: I-reinforced HPB235, II-class steel HRB335, the floor pillar size is 400 × 400 *mm* ,the filling wall is construct by MU10 hollow block and M5 Mortar. The thickness of the walls is 200 *mm* ; the roof and floor are cast-in-place. The basis is individual footing of column; the foundation depth is 3 m^2 . The complex building is the six-storey building with level roof. The area of the complex building is 3618.3 m^2 . The height of the first floor is 4.05 m^2 , the other is 3.60 m^2 . The office building is the four-storey building with level roof. The area of the office building is 1180.44 m^2 . The height of the first floor is 4.05 m^2 , the height of the second floor and the fourth floor is 3.60 m^2 , and the height of the third floor is 3.9 m^2 .

In Fig.1, the complex building is composed by 1-18 axis and K-G axis; there is a seismic joint between 6 axes and 7 axes. In Fig.3 and Fig.4, the part of 1-6 axis inclined eastwardly, the first story disappeared. In Fig.2, the part of 7-18 axis collapsed completely. [1]

The office building is composed by 19-23 axis and A-J axis. In Fig.5, the main structure of the framework is basically undamaged; the local part of the office building is serious damage by the collision with the complex building that collapsed.[1]

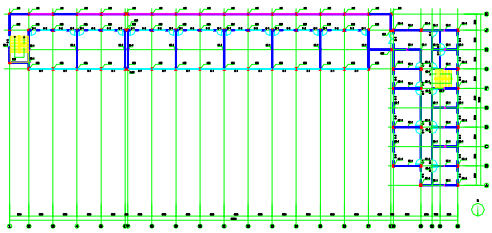

Fig.1 The planar graph of the structure



Fig2.The complex building of the Xuankou secondary school(Global)



Fig3.The complex building of the Xuankou secondary school(Local1)



Fig4.The complex building of the Xuankou secondary school(Local 2)



Fig5. the office building of the Xuankou secondary school

3. ESTABLISHMENT OF FINITE ELEMEMT MODEL

In the paper, the space finite element model is established by ANSYS. Beam and column is simulated by beam188 element, the filling wall is simulated by link10 element, and the floor slab is simulated by shell63 element. There are 13461 nodes in the model, and the element type and the element quantity are in table1.

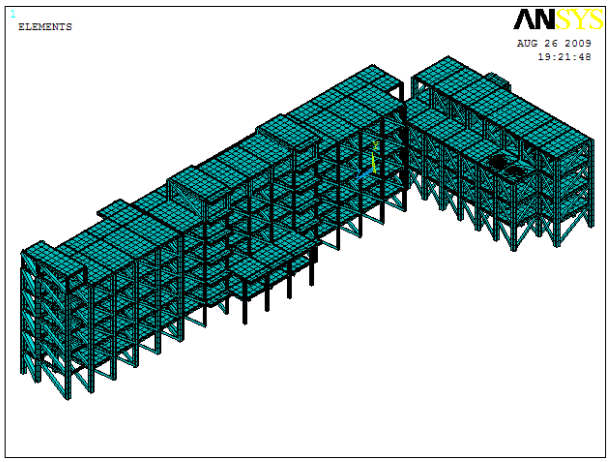

Fig6.Finite element model

Table1 classifications of finite element

Component	Element type	Element No.
Beam,Column	beam188	4827
Floor	shell63	6121
Infilled Wall	link10	993

3.1 Treatment of reinforced concrete

In the paper, the four-line stiffness degradation model is used for the simplification of the restoring force characteristics according to Fig.7. [2] In the model, the

restoring force skeleton curve is represent by four lines, the stiffness degradation of reinforce concrete members is considered. The model could reflect the mechanical properties of reinforced concrete members under the action of the periodic reciprocating load.

3.2 Treatment of filling wall

The filling wall is considered as a slant beam which hinged in the frame. The thickness of the slant beam is 200mm.The width is between 1/10 and 1/7 of the length of diagonal of filling wall according to Fig.8. [3] The slant beam only bears pressure.

3.3 Treatment of floor slab

In the paper, the stiffness of floor slab is huge in its own plane, and the stiffness which out of its own plane is very small, could be neglected. [4] Horizontal displacement of vertical members in each floor is transfer by the horizontal rigid motion of the floor slab.

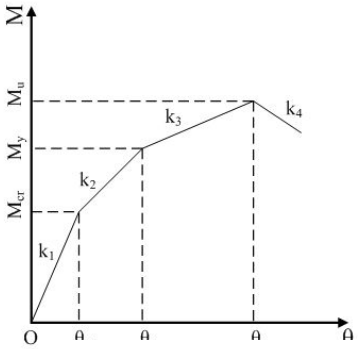

Fig7. The curve of $M-\theta$

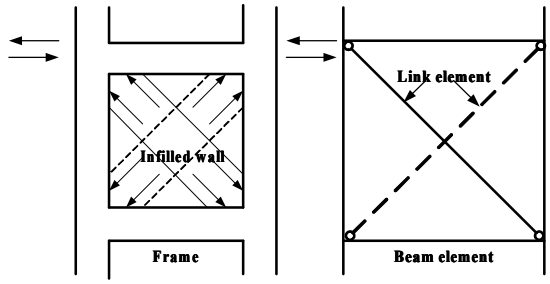

Fig8.Finite element model of infilled wall

4、STRONG MOTION DATA

In the paper, the strong motion data of Wolong station（31.04N ， 103.18E） is used for the time history analysis. The result will be obtained by input the finite element model with the ground motion parameter from ns-trending, we-trending, vertical- trending.

5、RESULT ANALYSIS

5.1、The Story Drift Angle

The story drift angle is adopted for judging the collapse of the structure. [5]The calculation formula is as follow:

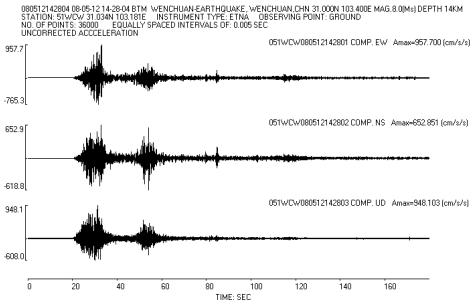

Fig9. Strong motion data of WoLong

$$\left[\theta_{\mathrm{p}}\right] \leq \frac{\Delta u_p}{h}$$

Δu_p -elastic-plastic inter-story displacement (1)

h -height of the story

(1)In Fig.10, the first story drift angle of the 1-6 axis part of the complex building is 0.020587 at 32.310s, exceed the limit value of the elastic-plastic inter-story displacement angle of RC frame structure (1/50) [5],the maximum value is 0.0210024.So the first story collapsed at 32.310s in the earthquake(as Fig.3 and Fig.4);

(2)In Fig.11, the first story drift angle of the 7-18 axis part of the complex building is 0.0201153 at 32.310s, the maximum value is 0.04398; In Fig.12, the second story drift angle of the 7-18 axis part of the complex building is 0.203989 at 33.010s, the maximum value is 0.04004; In Fig.13, the third story drift angle of the 7-18 axis part of the complex building is 0.0200684 at 33.240s, the maximum value is 0.03033; In Fig.14, the fourth story drift angle of the 7-18 axis part of the complex building is 0.0202572 at 33.280s, the maximum value is 0.02355;so the first to the fourth story collapsed in the earthquake(as Fig.1);

(3)In Fig.15, the first story drift angle of the office building is 0.0211061 at 33.27s, and the other time is less than 0.02.Compare with Fig.5, the office building didn't collapse. So the limit value of the elastic-plastic inter-story displacement angle of RC frame structure which is defined by the Code for Seismic Design of Buildings of China (GB50011-2001) maybe relatively small. From Fig.16 to Fig.18, the story drift angles of the second、the third and the fourth story did not exceed the limit value of the elastic-plastic inter-story displacement angle of RC frame structure. So the office building did not collapse in the earthquake (as Fig.5).

5.2 、 The Reason of the Collision between Complex Building and Office Building

The nodal displacement of the third story of the office building at the place of 19 axes -J axes is defined as δ_{b} . The nodal displacement of the third story of the complex

building at the place of 18 axes -J axes is defined as δ_c .The width of the seismic joint between 18 axes and 19 axes is 0.1m. If the collision between the complex building and the office building happened, the condition $\Delta\delta = \delta_b - \delta_c > 0.1$ must be satisfied. In Fig.19, the condition $\Delta\delta = \delta_b - \delta_c > 0.1$ happened at 29.19s, the maximum value is 0.20139m.So the complex building and the office building impacts each other at 29.19s (as Fig.4). If the width of the seismic joint is more than 0.20139, the collision will not happen in the earthquake.

5.3、The Internal Force at the time of Collapse

In Fig.20 and Fig.21, the internal force of the 7-18 axis part of the complex building is more than the 1-6 axis part of the complex building and the office building .In X--direction, the maximum value of the internal force is 3400MPa. In Z--direction, the maximum value of the internal force is 5030MPa.

5.4、The Story Drift

In Fig.22 and Fig.23, the story drifts of the complex building and office building are reasonable and with a uniform variation along the height. The variation of the stiffness of each story is uniform. So under strong seismic action, the first story will be the weak story of the two buildings. The maximum value of the complex building's top story is 0.103122m. The maximum value of the office building's top story is 0.0331m.

6、CONCLUSION

In the paper, the collapse mechanism of the infilled frame structure under the strong seismic action is discussed. Firstly, the story drift angle is adopted for judging the collapse of the structure. The reason of the collapse of the complex building and the office building is given, and the internal force at the time of collapse is given. Secondly, the reason of the collision between complex building and office building is discussed. The reasonable width of the seismic joint is given.

Acknowledgements:

This Work was supported by the National natural science foundation (50938006), National 973 planning topics (2007CB714205) and Special research in Chinese seismological industry (200708041).

References:

[1]. Sun Baitao. The Overview of Seismic Damage and the Analysis of the Reasons of Different Structure in Yingxiu Town –the Heavy Disaster Areas of Wenchuan 8.0 Earthquake [J]. Earthquake engineering and engineering vibration. 2008, 28(5):1-9.

[2]. Zhang Peixin. The Nonlinear Analysis of Reinforced Concrete Seismic Structures[M].Beijing, Science press,2003:30-32.

[3]. Zhao Xin.Elasto-Plastic Seismic Responses Analysis of Steel Frame Considering the Contributions of Concrete Floor Slabs and Masonry Infilled Walls [D]. Doctoral dissertation of Tungchi University, 2005:96-97.

[4]. Wei Lian. The seismic design handbook of multistory and tall reinforced concrete structure [M]. Beijing, Earthquake press, 1990:50-51.

[5]. People's Republic of China National Standard, Code for seismic design of buildings GB 50011-2001 [S]. Beijing, china building industry press, 2001: 44-49.

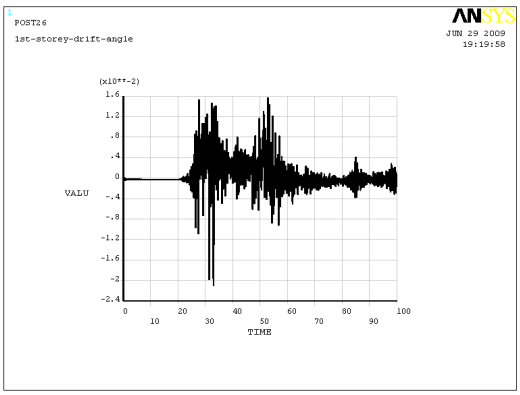

Fig10.The 1st story drift angle of the complex building（1-6axis1-6axis）

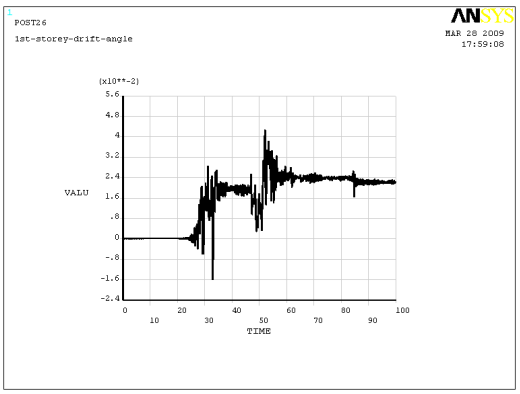

Fig11. The 1st story angle of the complex building (7-18 axis)

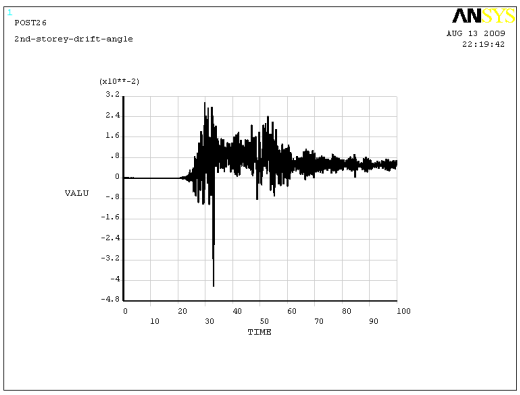

Fig12. The 2nd story angle of the complex building (7-18 axis)

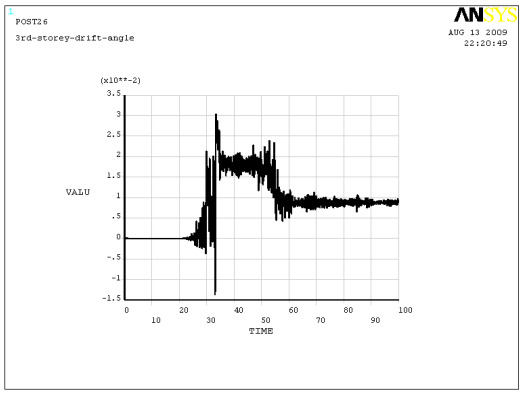

Fig13. The 3rd story angle of the complex building (7-18 axis)

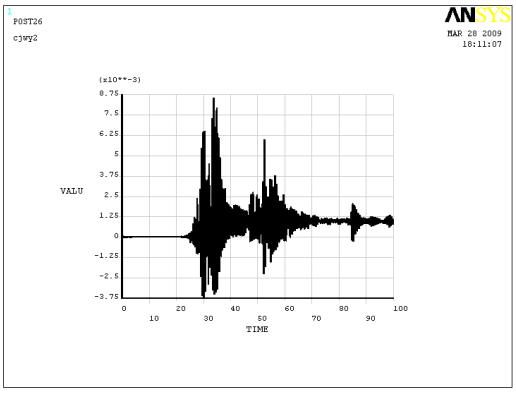

Fig16. The 2nd story angle of the office building

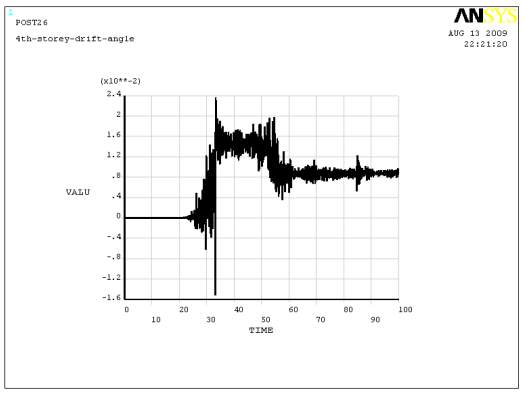

Fig14. The 4th story angle of the complex building (7-18 axis)

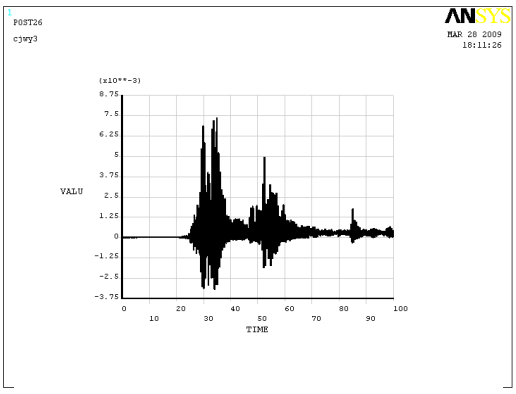

Fig17. The 3rd story angle of the office building

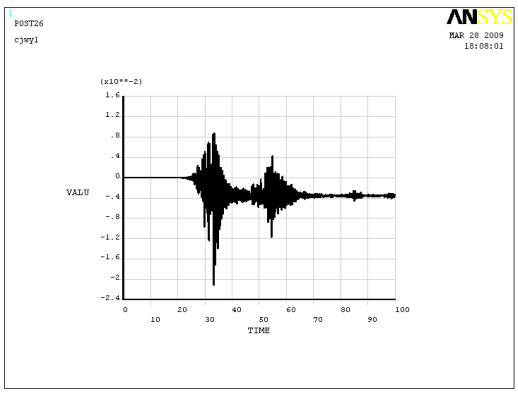

Fig15. The 1st story angle of the office building

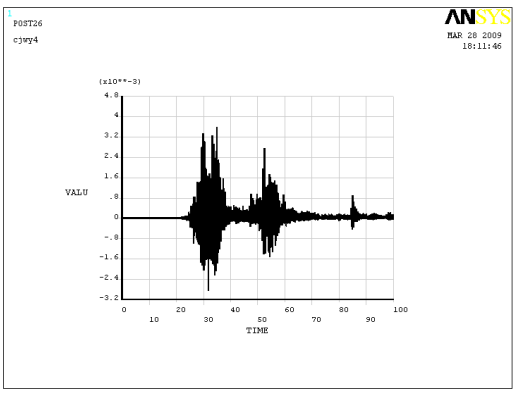

Fig18. The 4th story angle of the office building

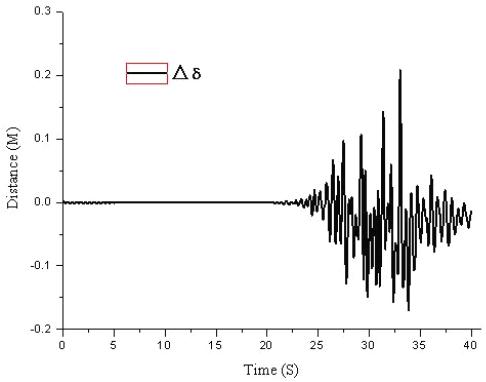

Fig.19 The distance between the office building and the office building

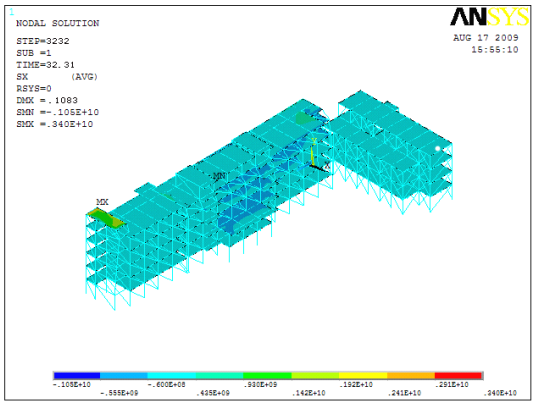

Fig20. The internal force distribution of the structure in X-direction

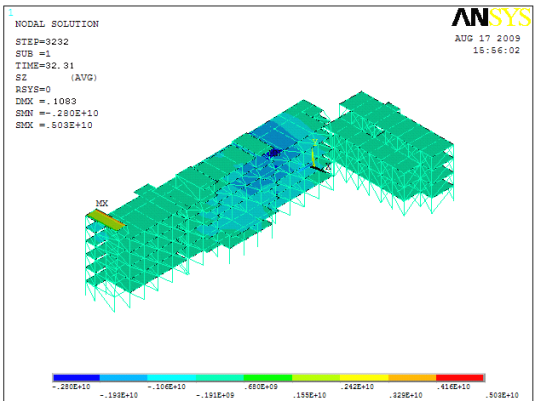

Fig21. The internal force distribution of the structure in Z-direction

JOINT CONFERENCE PROCEEDINGS
7th International Conference on Urban Earthquake Engineering (7CUEE) &
5th International Conference on Earthquake Engineering (5ICEE)
March 3-5, 2010, Tokyo Institute of Technology, Tokyo, Japan

HYSTERESIS MODEL OF SQUARE REINFORCED CONCRETE COLUMNS WITH NON-SEISMIC DETAILING

Wilson Y.M. Chung [1], Eddie S.S. Lam [2], Bo Wu [3], and Ivy F.Y. Ho[4]

1) PhD student, Dept. of Civil & Structural Engineering, The Hong Kong Polytechnic University, Hong Kong
2) Associate Professor, Dept. of Civil & Structural Engineering, The Hong Kong Polytechnic University, Hong Kong
3) Professor, School of Architectural and Civil Engineering, South China University of Technology, Guangzhou, China
4) MPhil student, Dept. of Civil & Structural Engineering, The Hong Kong Polytechnic University, Hong Kong
wilchung123@netvigator.com, cesslam@inet.polyu.edu.hk, ivyhofy08@gmail.com, bowu@scut.edu.cn

Abstract: In this study, cyclic loading tests were carried out on twelve 0.4-scale column specimens having two types of non-seismic reinforcement detail. Parameters being considered include use of long crossties or short crossties as the transverse reinforcement; volumetric transverse reinforcement ratio at 0.15%, 0.66% or 1.15%; and axial load ratio at 0.3, 0.45 or 0.6. Shear span depth ratio of the specimens is about 2.09, typical for columns below transfer plates or for stocky columns at the façade or under spandrel beams. Modes of failure of specimens with high to medium and low volumetric transverse reinforcement ratio are characterized by fully developed flexural-shear cracks and shear failure respectively. Specimens with short crossties have smaller lateral load carrying capacity and are less ductile. Short crossties are not recommended to be used at high volumetric transverse reinforcement ratio as they will lead to 50-60% reduction in the total energy dissipation. With everything else being equal, ultimate drift ratio achieved by a specimen with short crossties is about 85% of that obtained by a specimen with long crossties. Hysteresis model is proposed to represent the cyclic response of columns with this type of non-seismic reinforcement detail. Predictions by the proposed hysteresis model are in very good agreement with the test data.

1. INTRODUCTION

Recent earthquakes have raised concerns on the seismic resistance of existing buildings in areas with moderate seismic risk but without seismic provisions, for instance Hong Kong, China (Lam et al 2002). In fact, studies by various researchers have consistently indicated that Hong Kong is an area with moderate seismic risk (e.g. Lee et al 1996, Chau et al 1998, Chandler and Lam 2002). It is necessary to assess the seismic resistance of existing buildings. As key structural members, columns should have sufficient seismic resistance to prevent collapse of structures when subjected to seismic action. Unfortunately, reinforced concrete columns designed without seismic provisions are characterized by some undesirable factors that are not permitted in seismic resistant design. These include, *inter alia*, high axial load ratio, high main reinforcement ratio and low volumetric transverse reinforcement ratio. For instance, the volumetric transverse reinforcement ratio is only a fraction of that specified in severe seismic zone (Wehbe et al 1999).

In recent years, a few studies were carried out to assess the hysteresis behaviour of columns with non-seismic detailing, for instance Kunnath et al (1995), Pam and Ho (2001), Kuang and Wong (2005), and Ranf et al (2006). Among others, Lam et al (2003) and Elwood and Moehle (2005a-b) have demonstrated that if 90º hooks are used in the hoops and/or large transverse reinforcement spacing are specified, drift capacity of a column will be substantially reduced. To assess the seismic resistance, it is necessary to develop new hysteresis model for columns with non-seismic detailing so that numerical analysis (e.g. push-over analysis) can be carried out.

It is the objective of this study to develop a hysteresis model for one particular type of non-seismic reinforcement detail which has been traditionally allowed in areas without seismic provisions, e.g. Hong Kong, China. Figure 1 shows the reinforcement detail. It provides space at the concrete core to facilitate compaction by poker vibrators. However, it has obvious drawbacks if seismic provisions are to be considered. Firstly, end hooks of the hoops are at 90º instead of 135º. Secondly, short crossties are allowed. They are not tied to the main reinforcement, but to other long crossties being perpendicular to them.

In the past 40 years, many researchers, e.g. Takeda et al (1970), Saiidi (1982), Chung et al (1987), Umemura et al (1998), Phan et al (2007), etc., proposed different hysteresis models to predict the cyclic response of reinforced concrete columns. As the hysteresis models were developed based on testing of columns with seismic detailing, a hysteresis model has to be proposed for the type of non-seismic reinforcement detail considered in this study. In order to do so, twelve

specimens were prepared and tested under cyclic loading.

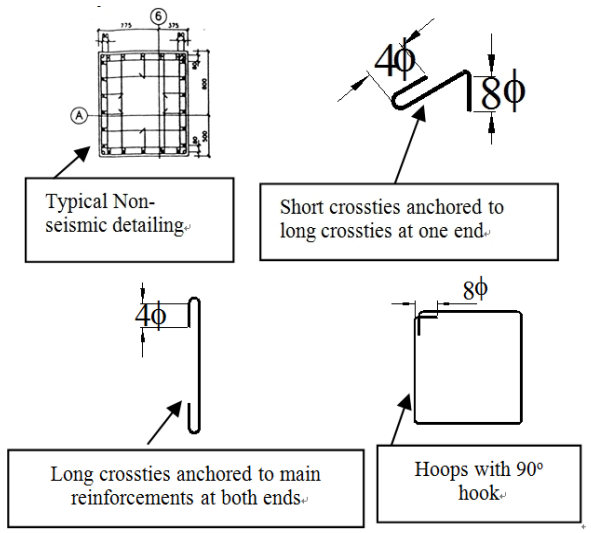

Figure 1 Non-seismic reinforcement detail

2. THE SPECIMENS AND TEST SETUP

The specimens are in 0.4-scale of 320mm by 320mm cross-section and 1120mm height. Concrete cover is 40mm in full-scale or 16mm for the specimens. In the absence of seismic provisions, 20T16 (or 4% main reinforcement ratio) are used as the main reinforcement. Two types of transverse reinforcement detail are considered as shown in Figure 2(a). In type L detailing, long crossties are provided in both directions and are tied to the main reinforcement. In type M detailing, both long crossties and short crossties are used. It represents the non-seismic detailing considered in this study. Basic properties of the specimens are given in Table 1.

Table 1 Basic properties of specimens

Label	Batch	n	Transverse reinforcement		
			Arrangement	Type	ρ_s
T6L35A	1	0.60	T6@35	L	1.15%
T6L35C	1	0.30	T6@35	L	1.15%
T6M35A	2	0.60	T6@35	M	1.15%
T6M35C	2	0.30	T6@35	M	1.15%
T6L61B	2	0.45	T6@61	L	0.66%
T6L61C	2	0.30	T6@61	L	0.66%
T6M61A	2	0.60	T6@61	M	0.66%
T6M61B	2	0.45	T6@61	M	0.66%
T4L120A	1	0.60	T4@120	L	0.15%
T4L120C	1	0.30	T4@120	L	0.15%
T4M120A	1	0.60	T4@120	M	0.15%
T4M120C	1	0.30	T4@120	M	0.15%

Axial load ratio (n) is the ratio of axial load to $f_c'A_g$ and includes 0.3, 0.45 and 0.6. f_c' and A_g are the cylinder strength of concrete and gross cross-sectional area respectively. Volumetric transverse reinforcement ratio (ρ_s) is defined as $A_{sh}/s_t h_c$. A_{sh} is the total area of transverse reinforcement in the lateral direction, s_t is spacing of transverse reinforcement and h_c is the depth of transverse reinforcement measured along centerlines of hoops. ρ_s ranges from 0.15% to 1.15%. Low ρ_s at 0.15% (based on T10@300 in full-scale) and high ρ_s at 1.15% (based on T16@100 in full-scale) are the respective non-seismic detailing according to the Code of Practice (1987) and seismic detailing specified in a severe seismic zone.

Typical elevation of a specimen is shown in Figure 2(b), representing a half-column. Bottom stub of 1700mm by 2200mm and 500mm thick is used to secure the specimen to the strong floor. Shear span depth ratio of the specimens is 2.09. It is defined as the ratio of half column height to depth of column. The specimens represent columns below transfer plates, or stocky columns at the façade or under spandrel beams.

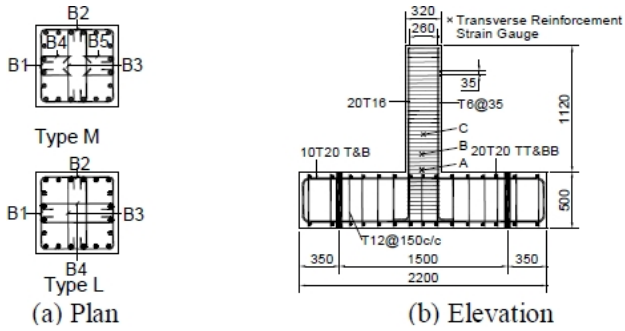

Figure 2 Specimen detail

The specimens were prepared from two batches of ready mix concrete. Averaged cube strengths of concrete are 44.5N/mm^2 and 42.4N/mm^2 for batch 1 and batch 2 respectively (estimated from 150mm test cubes and at the time of testing). Cylinder strength is assumed to be equal to 0.78 of the cube strength.

Measured properties of the reinforcement are given in Table 2.

Table 2 Measured properties of the reinforcement

Diameter (mm)	Yield Strength (N/mm^2)	Ultimate Strength (N/mm^2)
4	745.2	752.1
6	529.3	553.2
12	362.2	523.4
16	509.3	635.3
20	394.4	602.2

Figure 3 shows the test setup. Axial load and lateral force are applied through a hydraulic jack installed on a reaction frame and an actuator mounted on a reaction wall respectively. In the first loading cycle, lateral force at $0.75F\Delta_y$ is applied (Paulay and Priestley 1992). Afterwards, progressive increase in the lateral displacement is applied at two cycles per increment, i.e. $0.75\Delta_y$, $0.75\Delta_y$, Δ_y, Δ_y, $2\Delta_y$, $2\Delta_y$, $3\Delta_y$, $3\Delta_y$, etc., where Δ_y is the yield displacement, until the lateral force is reduced to 80% from its maximum. Yield displacement is estimated by the energy balanced method according to BS EN 1998-3. Moment arm is considered to be the distance from the bottom of the fixing plate attached to the actuator to the base of specimen.

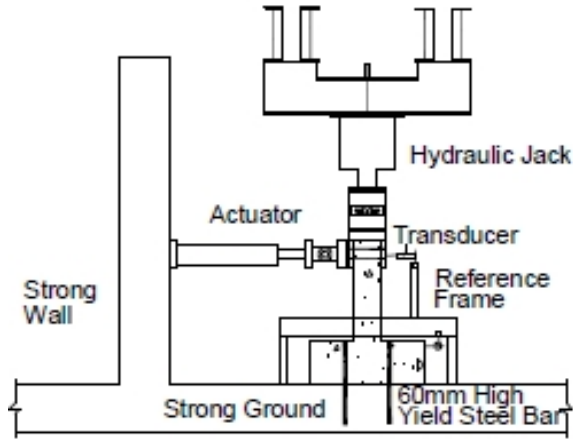

Figure 3 Test setup

Instrumentations include transducers and strain gauges. A transducer is used to measure the lateral displacement. Six pairs of transducers at 80mm spacing are installed along the length of the specimens to estimate the curvature. Strain gauges are installed on the main reinforcement and transverse reinforcement (including hoops, long crossties and short crossties), see Figure 2.

3. TEST RESULTS

Figure 4 shows typical modes of failure. Two distinct modes of failure were observed.

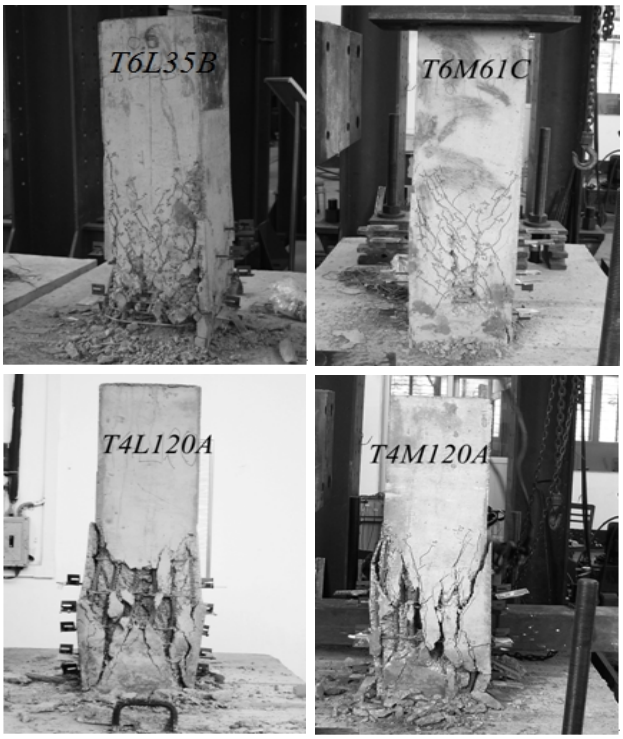

Figure 4 Typical modes of failure

For specimens with high to medium volumetric transverse reinforcement ratio (ρ_s=1.15% and 0.66%), failure was accomplished with opening of some 90º hooks, fracture of the second and third hoops from the base and buckling of the main reinforcement. Modes of failure were characterized by fully developed flexural-shear cracks. For specimens with low volumetric transverse reinforcement ratio (ρ_s=0.15%), failure was observed with propagation of one fully developed diagonal crack, i.e. shear failure. Afterwards, the main reinforcement buckled and the second and third hoops from the base fractured.

Figure 5 shows typical hysteresis loops of lateral load against displacement. Figure 6 plots the lateral load against displacement envelopes.

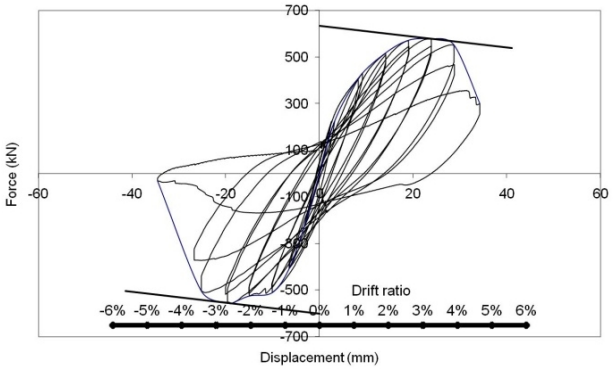

Specimen T6L35A

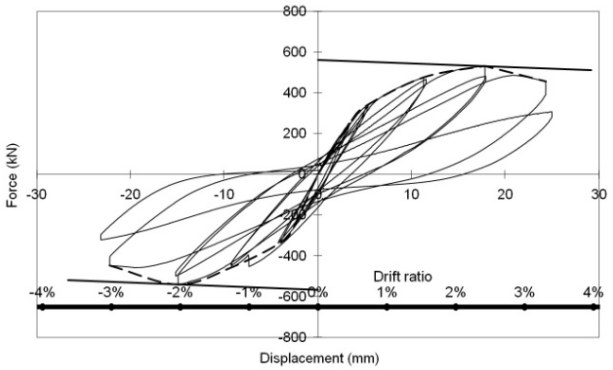

Specimen T6L61B

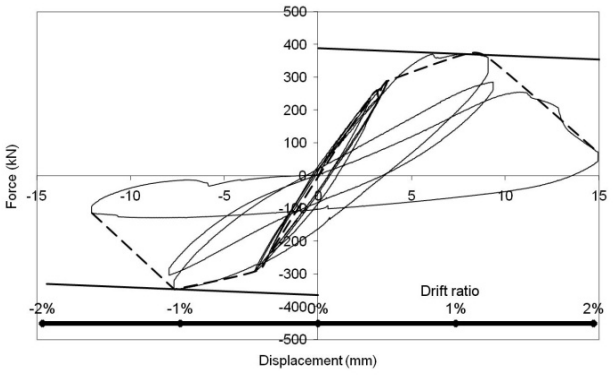

Specimen T4M120A

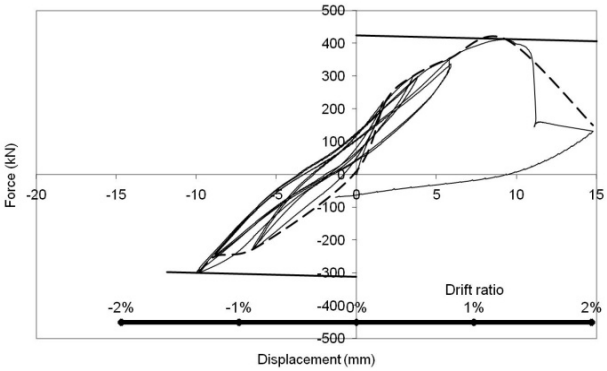

Specimen T4L120C

Figure 5 Typical hysteresis loops

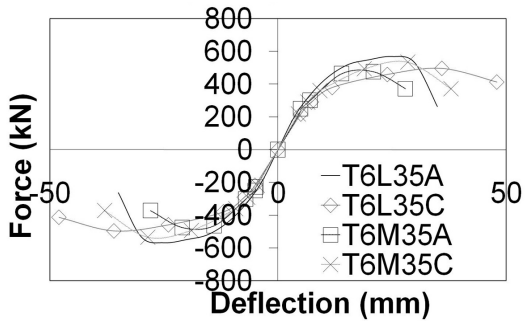

ρ_s=1.15%

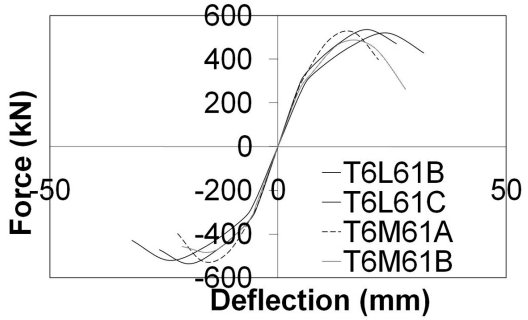

ρ_s=0.66%

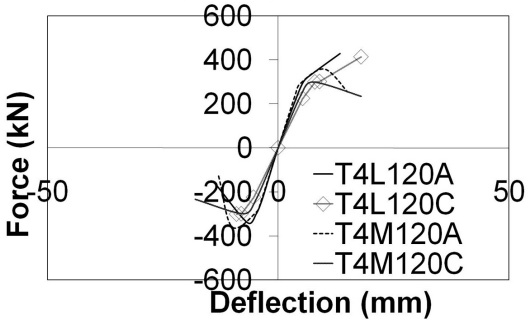

ρ_s=0.15%

Figure 6 Lateral load against displacement envelops

Hysteresis behaviour of specimens with low volumetric transverse reinforcement ratio (i.e. ρ_s=0.15%) is generally unsatisfactory as evidenced by (a) substantial decrease in lateral load carrying capacity after passing the maximum; (b) limited energy dissipation per hysteresis cycle and (c) limited ultimate displacement. This coincides with the observation that specimens with low volumetric transverse reinforcement ratio failed by shear with limited ductility.

Table 3 summarizes the hysteresis responses based on averaging the positive and negative values obtained from the cyclic loading tests. Here, Δ_y, Δ_u, μ_Δ, F_u and θ_u are yield displacement, ultimate displacement, displacement ductility, lateral load carrying capacity and ultimate drift ratio respectively. Ultimate displacement is defined as the displacement when the lateral force is reduced to 80% from its maximum in the post-peak region.

Table 3 Summary of the test results

Label	Δ_y (mm)	Δ_u (mm)	μ_Δ	F_u (kN)	θ_u
T6L35A	10.43	28.71	2.75	452.01	4.10
T6L35C	12.75	33.18	2.60	435.39	4.74
T6M35A	9.70	25.32	2.61	380.76	3.62
T6M35C	11.56	29.09	2.52	429.69	4.16
T6L61B	8.99	25.00	2.78	429.17	3.57
T6L61C	10.77	26.16	2.43	415.31	3.74
T6M61A	7.65	18.08	2.36	421.61	2.58
T6M61B	7.91	20.23	2.56	381.88	2.89
T4L120A	4.17	12.18	2.92	342.30	1.74
T4L120C	6.67	14.20	2.13	307.51	2.03
T4M120A	3.86	10.99	2.85	290.47	1.57
T4M120C	4.70	12.70	2.70	243.85	1.81

To compare the performance of type M and type L detailing, empirical equations of the ultimate drift ratio θ_{ult} are formulated by carrying out non-linear regression analysis on the test data. The results are given in Equations (1a) and (1b) as follows:-

$$\frac{q_{ult}}{100} = 8.087n^{-0.213}\frac{r_s f_y^{0.494}}{f_c'} \quad (1a)$$

$$\frac{q_{ult}}{100} = 8.087n^{-0.213}\frac{r_s f_y^{0.494}}{f_c'} \quad (1b)$$

Accordingly, the ultimate drift ratio achieved by specimens with type M detailing is about (8.087/9.448) or 85% of that obtained by type L detailing for different values of ρ_s and n.

4. ENERGY DISSIPATION

Performance of the specimens under cyclic loading can also be assessed using the concept of energy dissipation. Total energy dissipation is expressed as the sum of energy dissipation in each loading cycle, i.e. the enclosed area (A1)

of a hysteresis loop in each cycle (see Figure 7).

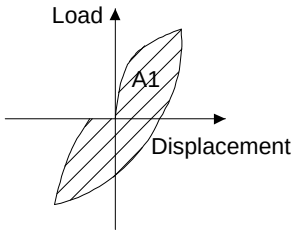

Figure 7 Example of energy dissipation (shaded area)

Table 4 lists out the total energy dissipation achieved by the specimens. At high volumetric transverse reinforcement ratio, total energy dissipation by type L detailing is twice than that of type M detailing. It follows that short crossties are not recommended to be used at high volumetric transverse reinforcement ratio as they will lead to 50-60% reduction in the total energy dissipation. However, the difference in total energy dissipation between the two types of detailing reduces with reducing volumetric transverse reinforcement ratio and becomes insignificant at low volumetric transverse reinforcement ratio. In fact, specimens with low volumetric transverse reinforcement ratio have limited total energy dissipation. This is probably due to shear failure of those specimens after several cycles of loading.

Table 4 Total energy dissipation (∫dE)

Label	∫dE (Nm)	Label	∫dE (Nm)
T6L35A	88599	T6M35A	36050
T6L35B	82791	T6M35B	40212
T6L61B	27102	T6M61A	28379
T6L61C	36588	T6M61C	26611
T4L120A	6116	T4M120A	7824
T4L120B	7238	T4M120B	6451

5. HYSTERESIS MODEL

Figure 8 shows the proposed hysteresis model. Based on the observations on the cyclic loading tests and analysis of the test data (Chung 2009), the proposed hysteresis model is developed by modifying the existing hysteresis models proposed earlier by, for instance, Takeda et al (1970), Saiidi (1982), Chung et al (1987), Umemura et al (1998).

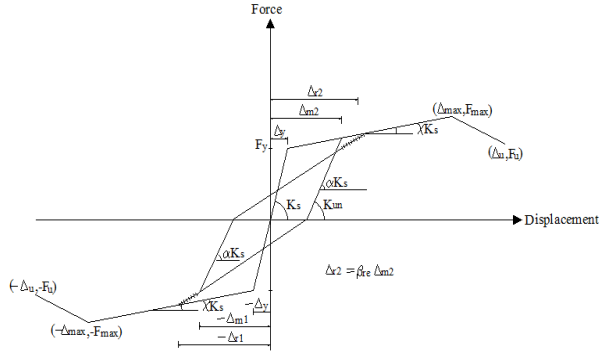

Figure 8 Proposed hysteresis model

The proposed hysteresis model is defined by seven parameters including the following:-

- initial stiffness (K_s)
- yield displacement (Δ_y)
- strain hardening ratio (χ)
- displacement at maximum force (Δ_{max})
- unloading stiffness ratio (α_{un})
- reloading displacement factor (β_{re})
- ultimate displacement (Δ_u)

Ultimate displacement Δ_u is estimated from Equations (1a) or (1b) by considering $\Delta_u=\theta_{ult}*L$, where L is the half column height.

By performing nonlinear regression analysis on the test data, empirical formulae are developed to estimate the parameters used in defining the proposed hysteresis model and these are in the form of:-

Initial stiffness (K_s):

$$K_s = \frac{3E_c I}{L^3}\frac{1}{6.23*(1-0.742n)*(1+6.98*C_{type}\frac{r_s f_y}{f_c})} \quad (2)$$

Yield displacement (Δ_y):

$$\Delta_y = \frac{e_{y,main}L^2}{3d*\left(5.24-4.958n+36.782C_{type}\frac{r_s f_y}{f_c}\right)} \quad (3)$$

Strain hardening ratio (χ):

$$c = 0.270(1+1.185n)\left(1-1.319C_{type}\frac{r_s f_y}{f_c}\right) \quad (4)$$

Displacement at maximum force (Δ_{max}):

$$\Delta_{max} = 6.866n^{-0.460}\left(\frac{r_s f_y}{f_c}\right)^{0.586} C_{type}\frac{L}{100} \quad (5)$$

Unloading stiffness ratio (α_{un}):

$$a_{un} = 1.978n^{-0.254}(C_{type}\frac{r_s f_y}{f_c})^{0.123}\left(\frac{dy}{dm}\right)^{0.568} \quad (6)$$

Reloading displacement factor (b_{re}):

$$b_{re} = 0.58\left(C_{type}\frac{r_s f_y}{f_c}\right)^{-0.138}\left(\frac{dy}{dm}\right)^{-0.342} cycle^{0.371} \quad (7)$$

E_c; I; f_y; f_c; $\varepsilon_{y,main}$; d; dy; dm and *cycle* are the Modulus of Elasticity of confined concrete; second moment of area; yield strength of transverse reinforcement; unconfined concrete strength; yield strain of main reinforcement (assumed to be 0.255%); yield displacement; maximum displacement of the loading cycle and number of cycles respectively. C_{type} is a reduction factor reflecting the effect of

detailing. It is equal to 1.00 for type L detailing. For type M detailing, it is 0.80 in Equations (2) to (6), and 0.75 in Equation (7).

Figures 9 and 10 compare the predictions obtained from the empirical formulae with the test data for the unloading stiffness ratio (α_{un}) and the reloading displacement factor (β_{re}). As shown, the empirical formulae provide reasonable estimation on the hysteresis behaviour.

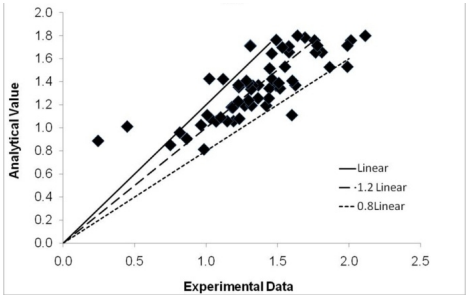

Type L detailing

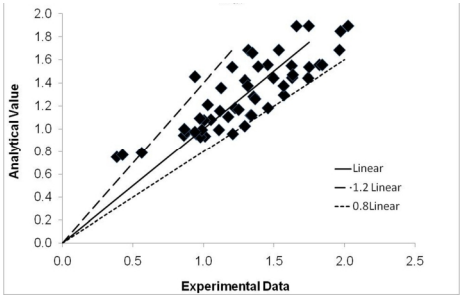

Type M detailing

Figure 9 Unloading stiffness ratio (α_{un})

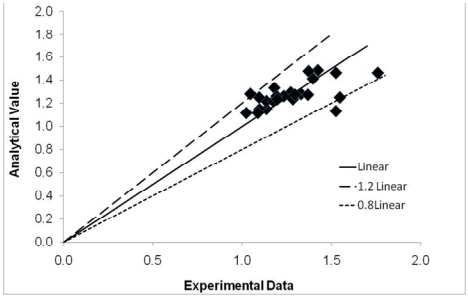

Type L detailing

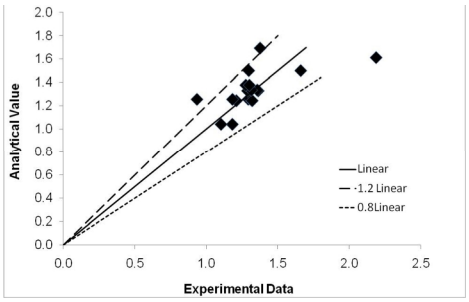

Type M detailing

Figure 10 Reloading displacement factor (β_{re})

For easy reference, Figure 11 formulates the proposed hysteresis model using flow diagrams. The proposed hysteresis model can be easily programmed and integrated with analytical software for non-linear analysis. In this study, the hysteresis model was codified using MATLAB. Source code of the hysteresis model is referred to Chung (2009).

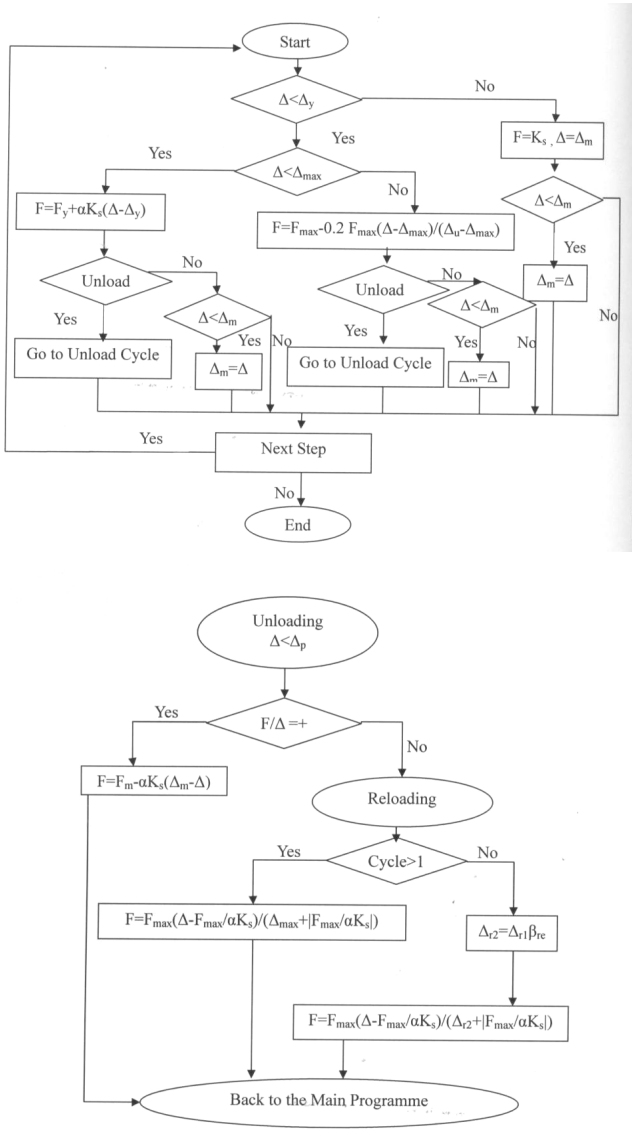

Figure 11 Flow diagrams of the proposed hysteresis model

Figure 12 compares the test data with the predictions by the proposed hysteresis model for some of the specimens. Relatively better correlations are obtained for specimens with low or high volumetric transverse reinforcement ratio (ρ_s = 0.15% or 1.15%). It is well demonstrated that the hysteresis model provides very good simulation of the behavior of columns with non-seismic detailing and in a wide range of volumetric transverse reinforcement ratio and axial load ratio.

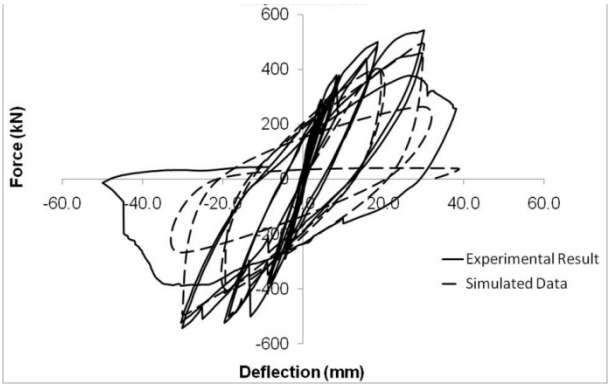

Specimen T6L35C

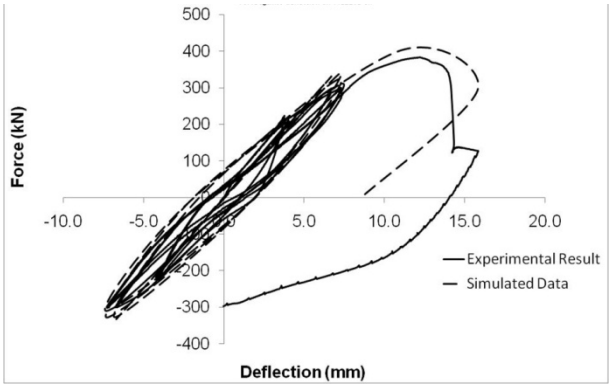

Specimen T4L120C

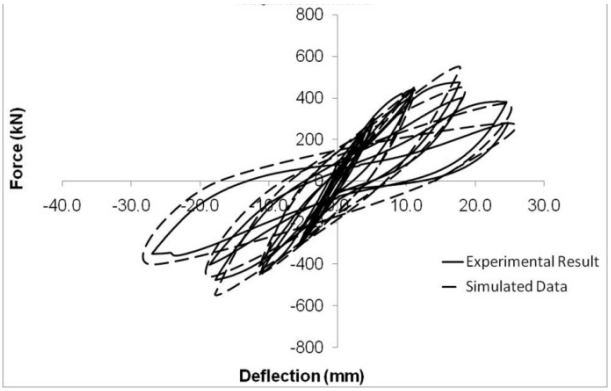

Specimen T6M35A

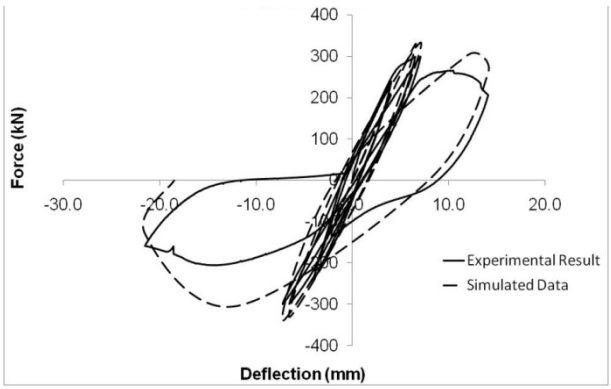

Specimen T4M120C

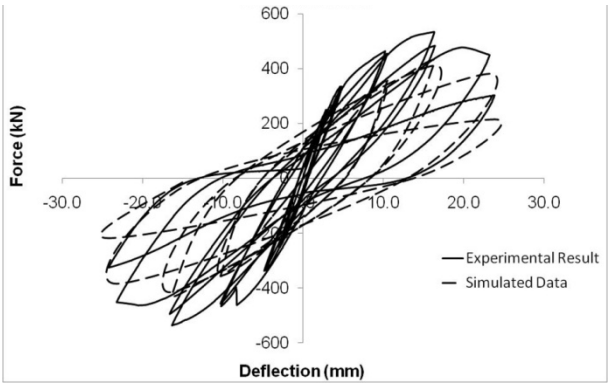

Specimen T6L61C

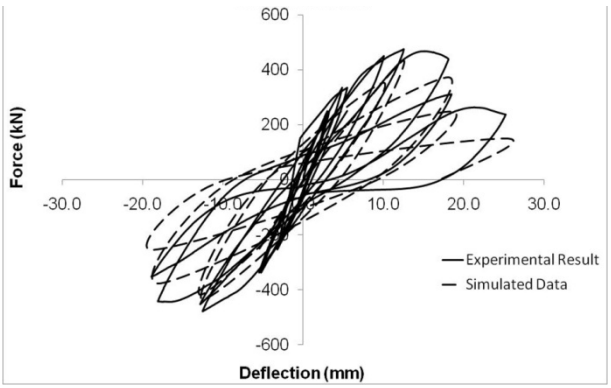

Specimen T6M61B

Figure 12 Comparison of hysteresis behaviour

6. CONCLUSIONS

In this study, twelve 0.4-scale specimens with non-seismic detailing were subjected to cyclic loading. Mode of failure of specimens with high to medium volumetric transverse reinforcement ratio is characterized by fully developed flexural-shear cracks whereas shear failure was observed from specimens with low volumetric transverse reinforcement ratio. Short crossties are less effective as compared with long crossties in confining the core concrete and are not recommended to be used at high volumetric transverse reinforcement ratio as they will lead to 50-60% reduction in the total energy dissipation. With everything else being equal, ultimate drift ratio achieved by type M detailing is about 85% of that obtained by type L detailing. Hysteresis model is proposed to predict the cyclic response of square columns with this type of non-seismic reinforcement detail. Predictions by the proposed hysteresis model are in very good agreement with the test data.

Acknowledgements:

The authors are grateful to the financial support from The Hong Kong Polytechnic University and the Research Grants Council of Hong Kong (RGC No: PolyU 5206/08E).

The authors would like to thank for the technical

assistance provided by the Civil Engineering Department of the South China University of Technology and the Heavy Structural Laboratory of the Hong Kong Polytechnic University.

References:

BS EN 1998-3, *Eurocode 8 - Design of Structures of Earthquake Resistance - Part 3: Assessment and Retrofitting of Buildings,* British Standard Institute

Code of Practice (1987), *Code of Practice for the Structural Use of Concrete 1987*, Building Authority, Hong Kong

Chandler A.M. and Lam N.T.K. (2002), "Scenario Predictions for Potential Near-Field and Far-Field Earthquakes Affecting Hong Kong: Soil Sites", *Journal of Soil Dynamics & Earthquake Engineering*, 22(6): 419-440

Chau K.T., Wong Y.L., Lam S.S.E. and Lee C.M. (1998), *Seismic Risk Assessment for Hong Kong*. CIDARC, Hong Kong Polytechnic University, Hong Kong

Chung W.Y.M (2009), *Confinement of Rectangular Reinforced Concrete Column with Non-seismic Detailing*. PhD thesis, Department of Civil and Structural Engineering, The Hong Kong Polytechnic University, Hong Kong

Chung Y.S., Meyer C. and Shinozuka M. (1987), *Seismic Damage Assessment of Reinforced Concrete Members*. Department of Civil and Engineering Mechanics, Columbia University, New York, NCEER 87-0022

Elwood K.J and Moehle J.P. (2005a), "Drift Capacity of Reinforced Concrete Columns with Light Transverse Reinforcement", *Earthquake Spectra,* (21): 71-89

Elwood K.J and Moehle J.P. (2005b), "Axial Capacity Model for Shear-Damaged Columns", *ACI Structural Journal*, 102(4): 578-587

Kuang J.S. and Wong H.F. (2005), "Ductility Enhancement of Non-seismically Designed Reinforced Concrete Columns for Low to Moderate Seismicity", *Journal of Structures and Buildings*, ICE, 158(1): 13-20

Kunnath S.K., Hoffmann G., Reinhorn A.N. and Mander J.B. (1995), "Gravity-loaded Designed Reinforced Concrete Buildings I: Seismic Evaluation of Existing Construction", *ACI Structural Journal*, 92(3): 343-355

Lam S.S.E, Xu Y.L., Chau K.T., Wong Y.L. and Ko J.M. (2002), "Progress in earthquake resistant design of buildings in Hong Kong". *Proceedings of Structural Engineering World Congress*, October 9-12, 2002, Yokohama, Japan

Lam S.S.E., Wu B., Wong Y.L., Wang Z.Y., Liu Z.Q. and Li C.S. (2003), "Drift Capacity of Rectangular Concrete Columns with Low Lateral Confinement and High Axial Load." *Journal of Structural Engineering*, ASCE, 129 (6): 733-742

Lee C.F., Ding Y.Z., Huang R.H., Yu Y.B., Guo G.A., Chen P.L. and Huang X.H. (1996), *Seismic Hazard Analysis of the Hong Kong Region*. Publication No 65, Geotechnical Engineering Office of Hong Kong

Pam H.J. and Ho J.C.M. (2001), "Flexural Strength Enhancement of Confined Reinforced Concrete Columns", *Journal of Structures and Buildings*, ICE, 146(4): 363-370

Paulay T. and Priestley M.J.N. (1992), *Seismic Design of Reinforced Concrete and Masonry Buildings*. Wiley Inter-Science

Phan V., Saiidi M.S., Anderson J. and Ghasemi H. (2007), "Near-Fault Ground Motion Effects on Reinforced Concrete Bridge Columns", *Journal of Structural Engineering*, ASCE, 133(7): 982-989

Ranf R.T., Nelson J.M., Price Z., Eberhard M.O. and Stanton J.F. (2006), *Damage Accumulation in Lightly Confined Reinforced Concrete Bridge Columns*, Report No. 2005/08, Pacific Earthquake Engineering Research Center

Saiidi M. (1982), "Hysteresis Models for Reinforced Concrete", *Journal of the Structural Division,* ASCE, 108(5): 1077-1087

Takeda T., Sozen M.A. and Nielsen N.N. (1970), "Reinforced Concrete Response to Simulated Earthquake", *Journal of the Structural Division,* ASCE, 96(12): 2557-2573

Wehbe N., Saiidi M. and Sanders D. (1999), "Seismic Performance of Rectangular Columns with Moderate Confinement", *ACI Journal*, 96(2): 248-258

Umemura H., Sakai Y., Minami T. and Kabetasa T. (1998), "Modeling of Reinforced Concrete Member Hysteresis Characteristics Considering Strength Degradation Caused by Cyclic Loading", *Transaction of the Japan Concrete Institute*, 20: 137-142

JOINT CONFERENCE PROCEEDINGS
7th International Conference on Urban Earthquake Engineering (7CUEE) &
5th International Conference on Earthquake Engineering (5ICEE)
March 3-5, 2010, Tokyo Institute of Technology, Tokyo, Japan

SEISMIC ANALYSIS OF RC FRAME STRUCTURE WITH PASSIVE ENERGY DISSIPATION DEVICES USING MODAL PUSHOVER ANALYSIS

Gao Ma[1)], Hui Li[2)], and Jinping Ou[2,3)]

1) PhD Candidate, School of Civil Engineering, Harbin Institute of Technology, Harbin 150090, China
2) Professor, School of Civil Engineering, Harbin Institute of Technology, Harbin 150090, China
3) Professor, School of Civil Engineering and Hydraulic Engineering, Dalian University of Technology, Dalian, 116024, China
magao@foxmail.com

Abstract: In this paper, seismic response of a RC frame structure installed with different passive energy dissipation devices: buckling-restrained brace (BRB) dampers and linear viscous dampers was studied using modal pushover analysis (MPA) based on capacity spectrum method and the effectiveness of these passive control devices under near-fault ground motions was investigated. The influence of parameter variations was studied, such as stiffness、yielding displacement of the buckling-restrained brace (BRB) damper and additional damping ratio afforded by linear viscous damper. The accuracy of MPA method was validated with non-linear response history analysis (RHA). The results show that the story drifts decrease while the story shears increase when BRB dampers are installed. For structure installed with linear viscous dampers, both the story drifts and shears decrease. The study also finds that these passive control devices are still effective under near-fault ground motions and the structural seismic damage indices decrease when installed with BRB dampers or linear viscous dampers.

1. INTRODUCTION

Passive energy dissipation devices can improve seismic behavior of structures significantly (Soong and Dargush 1997, Soong and Spencer 2002) and have been under development and implemented in practical application since 1990s in China. In 2001 Chinese Seismic Code (Chinese Ministry of Construction 2001), requirements for the design of passive energy dissipation devices are provided. However, these provisions are simple and lack an efficient calculation principle for practical application.

This research aims to provide a simple but still efficient procedure for estimating seismic demand of RC frame structure installed with BRB dampers or linear viscous dampers. On this basis, the influence of parameter variations of these dampers on control effect was investigated. MPA method is utilized to estimate seismic demand for its accuracy and simplicity (Chopra and Goel 2002, Chintanapakdee and Chopra 2003).

An universal 12-storey RC frame structure was utilized to install BRB dampers or linear viscous dampers. The influence of parameter variations of these dampers was studied. The results obtained from MPA results were validate with that obtained from non-linear response history analysis (RHA). The performance of these dampers under near-fault ground motions was also investigated based on non-linear RHA and Park & Ang seismic damage model.

2. MODAL PUSHOVER ANALYSIS

2.1 MPA Introduction

Pushover analysis (POA) developed for the seismic analysis of inelastic structure has played an important role in the seismic analysis for low and medium-rise buildings. For the higher mode contribution is not taken into account and the mode shape remains constant during the analysis, POA is not appropriate for high-rise buildings.

Modal pushover analysis (MPA) proposed by Chopra and Geol (2002) is an improved pushover analysis procedure and is gaining ground in building seismic evaluation and design due to its simplicity and accuracy. The derivation of MPA procedure was based on structural dynamic theory and several modes of vibration were included during the analysis. For the MPA method can include the contributions of higher modes, MPA provides a better estimation of seismic demands than POA. The accuracy of MPA was systematically evaluated using six buildings of different heights (Chintanapakdee and Chopra 2003). The results show that the height-wise distribution of responses estimated by MPA is generally similar to the results from nonlinear response history analysis (RHA).

2.2 MPA Procedure for Structure Installed with Passive Energy Dissipation Devices

In this study, MPA method was used to estimate

seismic demand of a RC frame structure installed with passive energy dissipation devices, such as BRB dampers and linear viscous dampers. The first three modes were used in the MPA procedure and were adequate to achieve credible results. For a structure installed with dampers, the effective damping ratio consists of three parts: the inherent damping ratio ξ_0 , usually equal to 5% for RC structures, the supplemental damping ratio provided by the passive energy dissipation devices (ξ_s) and the hysteretic damping ratio induced by the non-linear hysteretic behavior of the structure. The effective damping ratio is used to reduce the elastic 5% demand spectrum to obtain the performance point (ATC-40 1996). Before calculating the effective damping ratio, pushover curve obtained for each mode should be replaced with a bilinear curve according to FEMA 273 (FEMA 273 1997). For the supplemental damping ratio and hysteretic damping ratio is related to the maximum story drift of the structure, so an iterative procedure is needed.

3. PASSIVE DISSIPATION DEVIECES

3.1 Buckling-Restrained Brace Damper

A buckling-restrained brace (BRB) damper consists of a steel core surrounded by a steel tube. Since bulking is prevented, BRB dampers have nearly the same yielding stress and ultimate strength under tension and compression. BRB damps can resist lateral and vertical loads during normal use and absorb seismic input energy significantly through hysteretic deformation of steel core during an earthquake.

According to 2001 Chinese Seismic Code, the arrangement of BRB dampers should meet the following requirements in order to achieve a satisfactory effect.

$$\begin{aligned} &\Delta u_{\mathrm{py}} / \Delta u_{\mathrm{sy}} \le 2/3 \\ &\left(K_{\mathrm{p}} / K_{\mathrm{s}}\right)\left(\Delta u_{\mathrm{py}} / \Delta u_{\mathrm{sy}}\right) \ge 0.8 \end{aligned} \tag{1}$$

In which K_{p} = initial stiffness of energy dissipation device in horizontal direction. Δu_{py} = yield displacement of energy dissipation device. K_{s} = story stiffness where energy dissipation device is installed and Δu_{sy} = story yield drift.

In order to carry out parameter analysis, four different values were considered for $\Delta u_{\mathrm{py}} / \Delta u_{\mathrm{sy}}$: 0.3, 0.4 ,0.5and 0.6; and four $K_{\mathrm{p}} / K_{\mathrm{s}}$ values were considered: 2, 4, 6 and 8 in this study. The BRB dampers were concentrically installed in the RC frame structure to avoid imposing vertical force on the beams during the earthquake and both ends of the damper are hinged to the structure. The layout of BRB dampers is depicted in Figure 1 (b).

The supplemental damping ratio for a MDF system installed with BRB dampers is obtained as follows:

$$\xi_s = \frac{\sum_j W_j}{2\pi \sum_i F_i u_i} \tag{2}$$

Where W_j = the energy dissipated by device j in one complete cycle; F_i = the inertia force at floor i and u_i = the horizontal displacement of floor i ;

3.2 Linear Viscous Damper

Fluid viscous dampers are commonly used as passive energy absorbers in the seismic protection of buildings and can reduce acceleration and displacement response without increasing frequency of the structure. The mathematical model for fluid viscous dampers is given as follows:

$$F(t) = C\dot{x}(t)^{\alpha} \tag{3}$$

Where $x(t)$ = displacement across the damper; C = damping coefficient; α = exponent ranges between 0.1 and 1. Linear viscous damper is used in this article when the exponent equals to 1.

For a MDF system with linear viscous dampers, the supplemental damping ratio for the first mode can be written as follows:

$$\xi_{\mathrm{s}} = \frac{T\sum_j C_j \cos^2\theta_j \Delta u_j^2}{4\pi \sum_i \left(\frac{w_i}{g}\right) u_i^2} \tag{4}$$

Where $F(t)$ = force developed by the damper; T = the fundamental period of the structure including dampers; C_j = the damping constant for device j ; θ_j = the angle of inclination of device to the horizontal; Δu_j = the relative horizontal displacement between the ends of device j ; w_i = weight of floor i ; u_i = the horizontal displacement of floor i . The actual story drift is needed to calculate the supplement damping ratio in Eq. (4).

In this study three different values were considered for ξ_{s} : 10%, 20% and 30%. For the actual story drift is unknown before MPA procedure, the damping constant of viscous device is obtained through Eq. (5):

$$\xi_{\mathrm{s}} = \frac{T\sum_j C_j \cos^2\theta_j \phi_{rj}^2}{4\pi \sum_i \left(\frac{w_i}{g}\right) \phi_i^2} \tag{5}$$

Where ϕ_{rj} = the relative horizontal displacement between the ends of device j for the first mode; ϕ_i = the first mode displacement at floor level i , and other terms are defined above. In this study the damping constant for each device take the same value for simplicity, so the damping constant C is 2.73×10^3 kN/(ms)$^{-1}$, 5.47×10^3 kN/(ms)$^{-1}$, 8.20×10^3 kN/(ms)$^{-1}$ for ξ_{s} = 10%, 20% and 30% respectively. The layout of linear viscous dampers is depicted in Figure 1(b). The arrangements for BRB dampers and linear viscous dampers are the same in this paper just for simplicity.

4. RC FRAME STRUCTURE

4.1 Structure Design

In order to validate the MPA procedure, a mid-rise RC frame structure is utilized in this study. So, a 3-bay and 12-storey RC frame structure shown in Figure 1 (a) was designed according to 2001 Chinese Seismic Code with fortification intensity $I_d = 8$. The story height is 4.2m for the first story and 3.6m for 2nd~12th story. For 1st~5th story, the column section is 700mm× 700mm and the section is 600mm× 600mm for 6th~12th story. The beam section is 400mm× 600mm.The concrete strength grade for all the columns is C45 and C40 for the beams. The total floor mass is 73110kg for 1st~11th story and 75189kg for 12th story. Detailed information of the structure is given in Table 1.

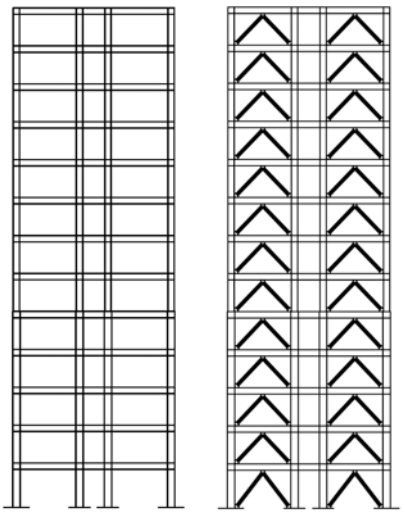

(a) (b)

Figure 1 Elevation View of the RC frame Structure: (a) without Dampers, and (b) Installed with BRB or Linear Viscous Dampers

Table 1 Dimensions and Reinforcement of the RC Frame Structure

Story Number	Reinforcement Areas of Columns (mm^2)		Reinforcement Areas of Beams (mm^2)	
	External Span	Internal Span	External Span	Internal Span
1st~5th	7854	7854	5140	5852
6th~9th	5891	5891	3963	3963
10th~12th	5891	5891	3361	3361

4.2 FEM Model

The open-source platform OpenSees (Mazzoni, McKenna et al. 2006) was utilized to carry out non-linear response history analysis and MPA analysis. Beams and columns were modeled using force-based nonlinear beam column elements with $P-\Delta$ effect considered. Concrete was modeled using a uniaxial concrete material with tensile strength and linear tension softening (Concrete02 Material). Steel was modeled using a uniaxial Giuffre-Menegotto-Pinto material (Steel02 Material) with 1% strain hardening. Detailed material properties are listed in Table 2.

Table 2 Material Parameters of Concrete and Steel

Concrete		E_c (GPa)	f_c(MPa)	f_{cu}(MPa)	ε_c	ε_{cu}
C45	Confined concrete	35.47	40.57	8.12	0.0021	0.01
	Common concrete	35.47	36.88	7.38	0.0019	0.004
C40	Confined concrete	34.53	36.73	7.35	0.0023	0.01
	Common concrete	34.53	33.39	6.68	0.0021	0.004
Steel		E (GPa)	f_y (MPa)	E' (GPa)		
HRB335		200	388.27	2		

5. RESULTS ANALYSIS

5.1 MPA Results of Structure with BRB Dampers

Results for the case of $\Delta u_{py}/\Delta u_{sy} = 0.3$, $K_p/K_s = 2, 4, 6, 8$ are shown in Figure 2 and 3. The story drifts are decreased when the structure installed with BRB dampers and the control effect of displacement increases with the increasing of K_p/K_s. However, each story shear is increased and the increment increases with the increasing of K_p/K_s, this indicates proper values for K_p/K_s is required for practical application for large story shear is adverse for the seismic performance of structure. It should be noted that the control effect decreases for 8th~12th story with the increasing of K_p/K_s.Non-linear RHA results from 6.3 section show the same trends.

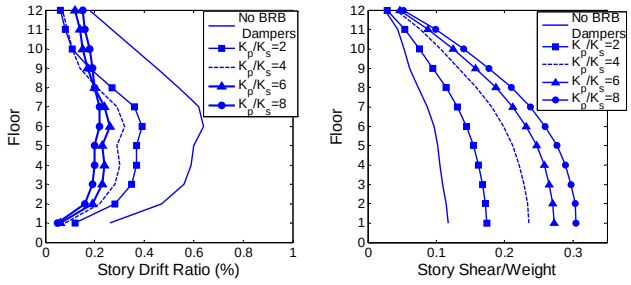

(a) (b)

Figure 2 MPA Results of the Structure Equipped with BRB Dampers: (a) Story Drift Ratio, and (b) Story Shear

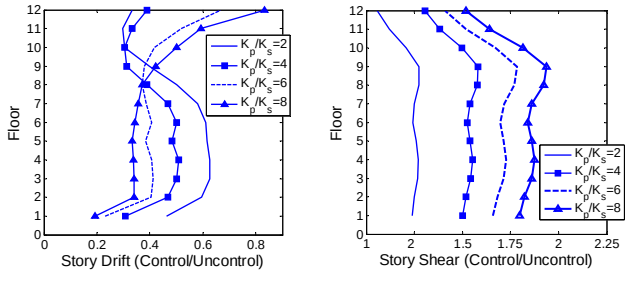

(a) (b)

Figure 3 Control Effect of the Structure Equipped with BRB Dampers: (a) Story Drift Ratio, and (b) Story Shear

For other cases: $\Delta u_{py}/\Delta u_{sy} = 0.4, 0.5$, $K_p/K_s = 2, 4, 6, 8$, the conclusions are similar and the results are not presented.

Figure 4 shows the results for the case of $K_p/K_s = 2$, $\Delta u_{py}/\Delta u_{sy} = 0.3, 0.4, 0.5, 0.6$. It can be found that the story drifts decrease and story shear increase with the increasing of $\Delta u_{py}/\Delta u_{sy}$. It can be qualitative interpreted as the story will yield earlier when $\Delta u_{py}/\Delta u_{sy}$ equal to a smaller value, so the story drifts increase.

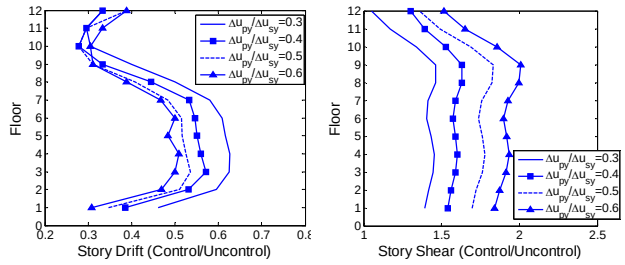

(a) (b)

Figure 4 The Influence of $\Delta u_{py}/\Delta u_{sy}$ on Control Effect: (a) Story Drift Ratio, and (b) Story Shear

5.2 MPA Results of Structure with Linear Viscous Dampers

Figure 5 is the results for $\xi_s = 10\%$, 20% and 30%. Both story shears and story drifts are decreased when the structure installed with linear viscous dampers and the control effect increases with the increasing of ξ_s. This kind of performance is different from the structure installed with BRB dampers.

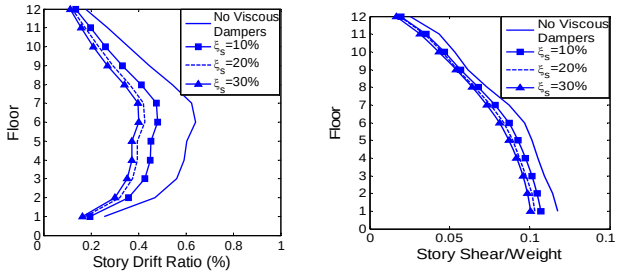

(a) (b)

Figure 5 MPA Results of the Structure Equipped with Linear Viscous Dampers: (a) Story Drift Ratio, and (b) Story Shear

5.3 Verification with Non-Linear Response History Analysis (RHA)

To evaluate the accuracy of MPA method, four ground motions used in the structure control benchmark problem were utilized in non-linear RHA. Newmark integration method was carried out to solve the equations of motion. The defaults values $\beta = 0.25$ and $\gamma = 0.5$ were used. Detailed information of the motions is listed in Table 3.

Table 3 Information of Ground Motions

Recorder Name	Earthquake	Data	Station	Component	PGA (m/s^2)
El Centro	Imperial Valley-02	1940/5/19	117 El Centro Array #9	N-S	3.417
Hachinohe	Tokachi-oki	1968/5/16	Hachinohe City	N-S	2.25
Northridge	Northridge-01	1994/1/17	24514 Sylmar-Olive Med FF	N-S	8.268
Kobe	Kobe	1995/1/16	KJMA	N-S	8.178

During the non-linear response history analysis under major earthquake, the PGA is adjusted to 4 m/s^2 for zones with fortification intensity $I_d = 8$ according to the seismic code. The mean values of the floor drifts and shears obtained from non-linear response history analysis using these four ground motions were used to compare with the floor drifts and shears from MPA analysis.

Partial results are shown in Figure 6 and 7. It is demonstrated that the results obtained from MPA coincide with that from non-linear RHA and the accuracy of MPA method for estimating seismic response for RC frame structure retrofitted with BRB dampers or linear viscous dampers is verified.

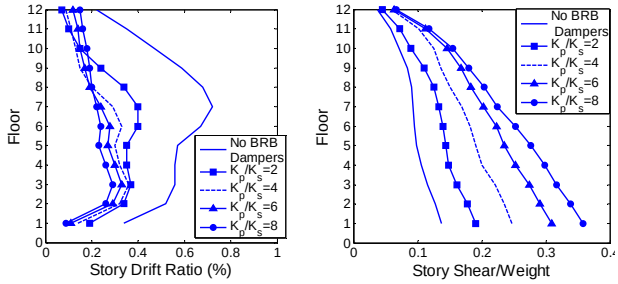

(a) (b)

Figure 6 Non-Linear RHA Results of the Structure Equipped with BRB Dampers: (a) Story Drift Ratio, and (b) Story Shear

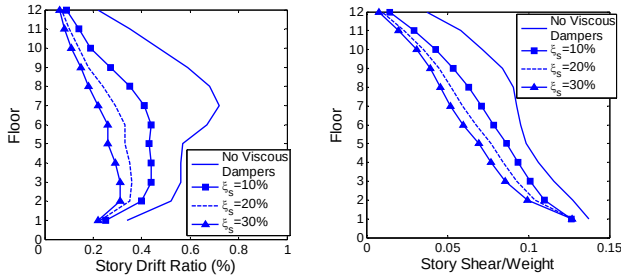

(a) (b)

Figure 7 Non-Linear RHA Results of the Structure Equipped with Linear Viscous Dampers: (a) Story Drift Ratio, and (b) Story Shear

6. RESPONSE UNDER NEAR-FAULT GROUND MOTIONS

6.1 Near-Fault Ground Motions

After the 1994 Northridge, the 1995 Kobe earthquake and the 1999 Chichi earthquake, the severe destructive potential of the near-fault ground motions on structures was recognized and near-fault ground motions have received much attention and become a significant concern in the seismic design. It has been known from the above study that the response of RC frame structure is decreased effectively when equipped with BRB dampers or linear viscous dampers. The effectiveness of BRB dampers and viscous dampers under near-fault ground motions has to be studied. The TCU068 record from Chichi earthquake was selected in the non-linear response analysis.

6.2 Damage Model

During strong ground motions, structures will undergo damage for large deformation and hysteretic energy dissipation. In order to analyze the influence of near-fault ground motions on the RC frame structure equipped with BRB dampers or linear viscous dampers, Park and Ang seismic damage model is utilized. The Park-Ang model proposed by Park and Ang (1985) is a double parameters damage model that the damage index is calculated as a linear combination of excessive deformation and accumulated hysteretic dissipated energy. The model is as follows:

$$DM = \frac{x_m}{x_{cu}} + \beta \frac{E_{hs}}{F_y x_{cu}} \tag{6}$$

Where DM is the damage index; x_{cu} = ultimate displacement of the component under monotonic loading; F_y = calculated yield strength of the component; x_m = actual maximum displacement response under earthquake; E_{hs} = hysteretic energy dissipated by the component during the earthquake; β is the coefficient for cyclic loading effect and is calculated as follows:

$$\beta = \left(-0.447 + 0.073\lambda + 0.24 n_0 + 0.314\rho_t\right) 0.7^{100\rho_w} \tag{7}$$

In witch λ = shear span ratio; n_0 = axial compression ratio; ρ_w = volume-stirrup ratio; ρ_t = longitudinal reinforcement ratio.

The classification of damage levels (shown in Table 4) proposed by Park, Ang and Wen (1985) was utilized to judge the damage level of the structure base on the calculated damage index.

Table 4 Park-Ang Damage Level Classifications

Damage level	Damage Index	Damage Measure
Slight	$DI < 0.1$	No damage; localized minor cracking
Minor	$0.1 \le DI < 0.25$	Minor damage; light cracking throughout
Moderate	$0.25 \le DI < 0.4$	Moderate damage; severe cracking, localized spalling
Severe	$0.4 \le DI < 1.0$	Severe damage; crushing of cracking, reinforcement exposed
Collapse	$DI \ge 1.0$	Loss of element load resistance

6.3 Seismic Damage Analysis

The seismic damage is obtained from damage analysis of the RC frame structure equipped with BRB dampers or linear viscous dampers. Partial results are show in Figure 8 and 9 (Figure 8 is for the case of $\Delta u_{py}/\Delta u_{sy} = 0.3$). The seismic failure modes are concluded.

(1) For the RC structure without BRB dampers, the damage is serious. The damage indices for 1st~5th story are greater than 1 indicating that the service ability of the 1st~5th story is lost and the structure will collapse.

(2) For the RC structure installed with BRB dampers, the damage is decreased largely due to the employ of BRB dampers. The damage indices are less that 0.4 when $\Delta u_{py}/\Delta u_{sy} = 0.3$ and $K_p/K_s = 4$、6 and 8, this indicates that the structure damage is moderate with the feasibility of restoration.

(3) For the RC structure installed with linear viscous dampers, the damage is also decreased. Structure collapse is prevented for $\xi_s = 20\%$ and 30% though the seismic damage is still significant in this case.

It must be noted that the supplemental damping ratio ξ_s = 10%, 20% and 30% in Figure 9 is calculated by Eq. (5) and the actual supplemental damping ratio provide by linear viscous dampers under TCU068 excitation is 9.2%、18.8% and 28.4% respectively. The actual supplemental damping ratio is calculated using the maximum story drift of each story.

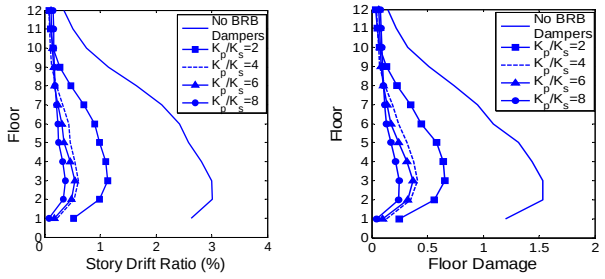

(a) (b)

Figure 8 Non-Linear RHA and Damage Results of the Structure Equipped with BRB Dampers: (a) Story Drift Ratio, and (b) Story Damage

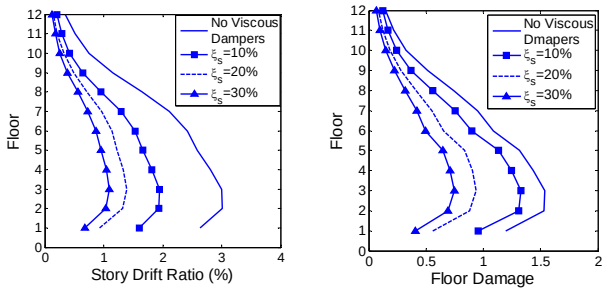

(a) (b)

Figure 9 Non-Linear RHA and Damage Results of the Structure Equipped with Linear Viscous Dampers: (a) Story Drift Ratio, and (b) Story Damage

8. CONCLUSIONS

In this paper, the accuracy and simplicity of MPA procedure for estimating seismic response of RC frame structure installed with BRB dampers or linear viscous dampers is validated through comparison with non-linear RHA method. Due to its accuracy and simplicity, MPA method is an attractive choice for practical application.

For the RC frame structure installed with BRB dampers, the story drifts decrease while the story shears increase. For a determinate $K_p / K_s = 2$, the story drifts decrease and story shear increase with the increasing of $\Delta u_{py} / \Delta u_{sy}$ .For the RC structure equipped with linear viscous dampers, both the story drifts and story shears decrease and the control effect increases with the increasing of ξ_s. The efficiency of BRB dampers or linear viscous dampers under near-fault ground motions is demonstrated. The structural seismic damage decreases effectively when the structure installed with BRB dampers or linear viscous dampers.

Acknowledgements:

This study is financial supported by the Ministry of Science and Technology with Grant No. 2007CB714205.

References:

Soong, T. T. and Dargush, G. F. (1997), "Passive Energy Dissipation Systems in Structural Engineering", John Wiley and Sons, New York, USA.

Soong, T. T., and Spencer, Jr. B. F. (2002), "Supplemental energy dissipation: State-of-the-art and state-of-the-practice", *Engineering Structures*, 24(3), 243-259.

Ministry of Construction. (2001), "Code for Seismic Design of Buildings GB50011-2001", Beijing, China.

Chopra, A. K. and Goel, R. K. (2002), "A modal pushover analysis procedure for estimating seismic demands for buildings", *Earthquake Engineering & Structure Dynamics*, 31(3), 561 -582.

Chintanapakdee, C. and Chopra, A. K. (2003), "Evaluation of modal pushover analysis using generic frames", *Earthquake Engineering & Structure Dynamics*, 32(11), 417-442.

Applied Technology Council (ATC). (1996), "Seismic Evaluation and Retrofit of Concrete Buildings", Redwood City, California, USA.

Federal Emergency Management Agency (FEMA). (1997), "Nehrp Guidelines for the Seismic Rehabilitation of Buildings", FEMA 273, Washington, D. C., USA.

Mazzoni, S., McKenna, F., Scott, M. H., Fenves, G. L., et al.(2006), "OpenSees user manual", Berkeley: PEER Center, University of California at Berkeley, USA.

Park, Y. J. and Ang, A. H - S. (1985), "Mechanistic seismic damage model for reinforced concrete", *Journal of Structural Engineering*, American Society of Civil Engineers, 111(4), 722-739.

Park, Y. J., Ang, A. H – S. and Wen, Y. K. (1985), "Seismic damage analysis of reinforced concrete buildings", *Journal of Structural Engineering*, American Society of Civil Engineers, 111(4), 740-757.

JOINT CONFERENCE PROCEEDINGS
7th International Conference on Urban Earthquake Engineering (7CUEE) &
5th International Conference on Earthquake Engineering (5ICEE)
March 3-5, 2010, Tokyo Institute of Technology, Tokyo, Japan

Experimental Study of Unreinforced Masonry Pier Sub-Structures

Charlotte Knox[1)], Alistair Russell[2)], and Jason Ingham[3)]

1) PhD Student, Department of Civil Engineering, University of Auckland, New Zealand
2) PhD Student, Department of Civil Engineering, University of Auckland, New Zealand
3) Associate Professor, Department of Civil Engineering, University of Auckland, New Zealand
ckno015@aucklanduni.ac.nz, arus033@aucklanduni.ac.nz, j.ingham@auckland.ac.nz

Abstract: Accurate assessment of the structural response of unreinforced masonry buildings when subjected to earthquake loading is essential for the design of efficient and effective seismic retrofit interventions. This study focused on determining the in-plane seismic performance of unreinforced masonry perforated shear walls in order to implement controlled rocking response as a hybrid retrofit solution. The experimental programme and the findings from a series of pseudo-static push-over tests performed on coupled unreinforced masonry pier sub-structures is presented. These sub-structures consisted of two piers with varying aspect ratio and absolute size and were subjected to different levels of vertical overburden. The walls were constructed in the common American bond formation using solid clay bricks and a 1:2:9 composition lime mortar, consistent with historical New Zealand unreinforced masonry buildings. The specimen geometries were chosen to not only replicate typical New Zealand unreinforced masonry perforated shear wall geometries but to also provide data on the three possible failure mechanisms – diagonal shear failure, sliding shear failure and rocking flexural response. When subjected to horizontal load the piers in both sub-structures exhibited a rocking response, with no diagonal shear cracking visible. The damage was concentrated in the spandrel section that spanned across the opening and this was attributed to both flexure and shear forces within the spandrel.

1. INTRODUCTION

All New Zealand unreinforced masonry (URM) buildings have openings for windows or doors on one or more sides. These openings define the geometric configuration of an unreinforced masonry perforated shear wall, by delineating a wall into vertical piers and horizontal spandrels. Inspection of URM buildings after earthquakes has provided evidence that the piers of these perforated walls rock to dissipate seismic energy (Thurston and Beattie 2009; Bothara et al. 2010). The overarching aim of the current research program is to utilize the natural behaviour of rocking to minimize the need for supplementary retrofit interventions, and it is therefore critical to investigate whether rocking behaviour is a likely deformation mode in New Zealand URM buildings.

Guidelines have been developed in New Zealand to determine the structural integrity of unreinforced masonry structures based on research developed overseas (NZSEE 2006). For perforated walls these analysis tools are based on the recognised failure modes for walls and piers, with key variables that determine the failure modes identified as geometry, axial load, material properties and boundary conditions (Yi et al. 2006; Augenti and Romano 2008; Chen et al. 2008). The geometric configuration of New Zealand's URM buildings was studied by Russell and Ingham (2008) which has subsequently let to a set of facade typologies being developed to describe common geometric configurations of piers and spandrels prevalent in New Zealand URM buildings. The experimental programme reported herein was designed to evaluate the accuracy of current New Zealand assessment tools for unreinforced masonry perforated shear walls constructed with the geometry and materials that characterise New Zealand URM buildings.

2. BACKGROUND

On the 3rd of February 1931, a magnitude 7.8 earthquake struck Napier, New Zealand, causing the total collapse of most URM buildings within the city's central business district (Dowrick 1994). This event highlighted the poor seismic performance of URM construction. Reinforced concrete was primarily used for reconstruction of the town and the practice of using steel reinforcement to add ductility

translated into the development of reinforced concrete masonry, in turn leading to the rapid decline of URM in New Zealand (Ingham 2008). Unreinforced masonry construction was eventually prohibited in New Zealand in 1965 due to the propensity for earthquake activity and the recognized vulnerability of URM buildings to seismic loading.

Few URM buildings were constructed in New Zealand after 1931, meaning that the approximately 3500 URM buildings that remain throughout New Zealand are over eighty years old (Russell and Ingham 2008). When compared to the vast history of URM construction in Europe, this narrow time period of only fifty five years during which unreinforced masonry (URM) construction was popular in New Zealand translates into a relatively homogeneous nature of the URM building stock found in New Zealand, allowing experimental results to be applicable to URM buildings nationwide.

2.1. New Zealand's Earthquake Hazard

New Zealand is located along a zone of contact between the Pacific and Australian tectonic plates. The major faults which run along the plate boundaries are responsible for the over 14,000 earthquakes that occur in and around New Zealand each year (GNS Science 2008). New Zealand is positioned on the Pacific 'Ring of Fire' which defines an area of frequent seismic activity. Ninety percent of the world's earthquakes and eighty percent of the world's largest earthquakes occur along the Ring of Fire, which is shown in Figure 1.

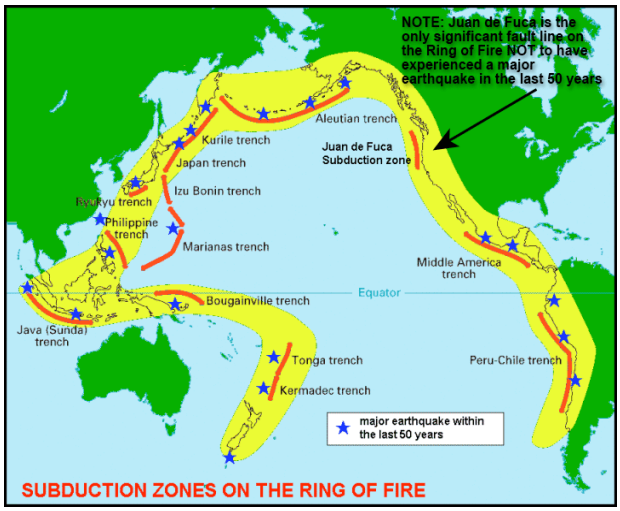

Figure 1: Extent of 'Ring of Fire'

Reproduced from (Westernpower 2008)

2.2. Motivation for research

The Building Act 2004 expresses the New Zealand Government's objective for earthquake-prone buildings to be strengthened to the appropriate seismic standards, or to be demolished. This policy has an underlying objective to reduce the risk of injury or death to occupants or damage to other property that may result from the effects of an earthquake on buildings.

> "A building is earthquake prone for the purposes of The Building Act 2004 if, having regard to its condition and to the ground on which it is built, and because of its construction, the building — (a) will have its ultimate capacity exceeded in a moderate earthquake (as defined in the regulations); and (b) would be likely to collapse causing — (i) injury or death to persons in the building or to persons on any other property; or (ii) damage to any other property,"
>
> Furthermore,
>
> "a moderate earthquake is legally defined as: in relation to a building, an earthquake that would generate shaking at the site of the building that is of the same duration as, but that is one-third as strong as, the earthquake shaking (determined by normal measures of acceleration, velocity and displacement) that would be used to design a new building at the site" (DBH 2007).

As many URM buildings form part of the country's heritage architecture, demolition in order to mitigate their seismic hazard is an unfavourable option. Thus for retrofit solutions to be viable, they must be cost-effective, and to facilitate this, accurate assessment of the structures' expected seismic behaviour that eliminates excessive conservatism is important.

3. PERFORATED WALL TYPOLOGIES

A perforated wall is a wall which is pierced with windows and doors, leaving a series of piers and spandrels to provide the lateral and gravity load resisting system. Five base typologies that are representative of one, two and three and greater storey URM buildings as well as isolated and row type buildings are detailed in Table 1. These typologies describe the geometric properties for which a study on the in-plane seismic response of URM perforated shear walls was organized. As the study is part of a larger project currently being undertaken in New Zealand, the perforated wall types are based on the typologies that have been used to characterize the New Zealand URM building stock. Figure 2 shows the facade of a representative Typology A building and Figure 3 shows the comparative typology A perforated shear wall geometries. Figure 4 shows the typology C perforated shear wall geometries that are representative of two storey row type URM buildings in New Zealand. Figure 5 shows the facade of a four storey URM building in downtown Wellington, and Figure 6 is the typology E perforated shear wall that is representative of three or greater storey isolated buildings.

Table 1. URM Perforated Shear Wall Typologies

Type	Footprint	Prevalence	Description	Lower storey pier aspect ratio	Upper storey aspect ratio
A	One storey, isolated buildings	4	Large openings characterize the facade, allowing for shop display windows and doorways. For buildings with an internal dividing wall, the facade will have a pier in the middle, splitting the front into two openings.	Internal pier - 1.55 External pier - 4.7	N/A
B	One storey, row buildings	3	Essentially a row of facade type A buildings, each sharing an adjoining wall. Most commonly the overall height of the facade is consistent along the length of the row to retain some consistency in appearance.	All piers - 6.75	N/A
C	Two storey, isolated buildings	2	The lower level of the facade can resemble a type A perforated shear wall, with dominant openings, or it can be more closed in with just a door and slender rectangular window openings. The upper level of the facade consists of three or five piers constructed either side of two or four windows respectively.	All piers - 7.5	All piers - 1.4
D	Two storey, row buildings	1	Type D can exhibit two different character profiles. One is of uniform geometry, equal roof height, equal floor height and windows all in the same horizontal line, so that the row appears to be identical buildings joined together. The other gives the appearance of individual and distinct buildings joined together.	All piers - 6.0	All piers - 1.5
E	Three + storey, isolated buildings	5	Include any isolated buildings of three or more storeys. These buildings are different from the other types, not only in number of storeys, but in number of perforated walls. Typology E buildings will often have two or more perforated walls. The facade is homogeneous with high regularity in size and positioning of windows.	Internal pier - 5.0 External pier - 1.25	Identical over all levels



Figure 2: Facade of a Typology A building, located in Auckland

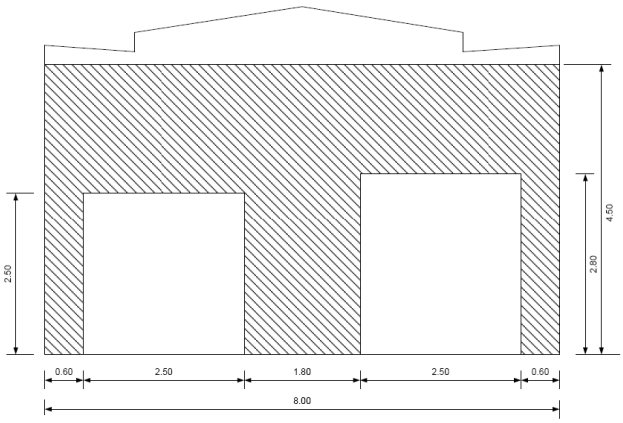

Figure 3: Typology A perforated shear wall

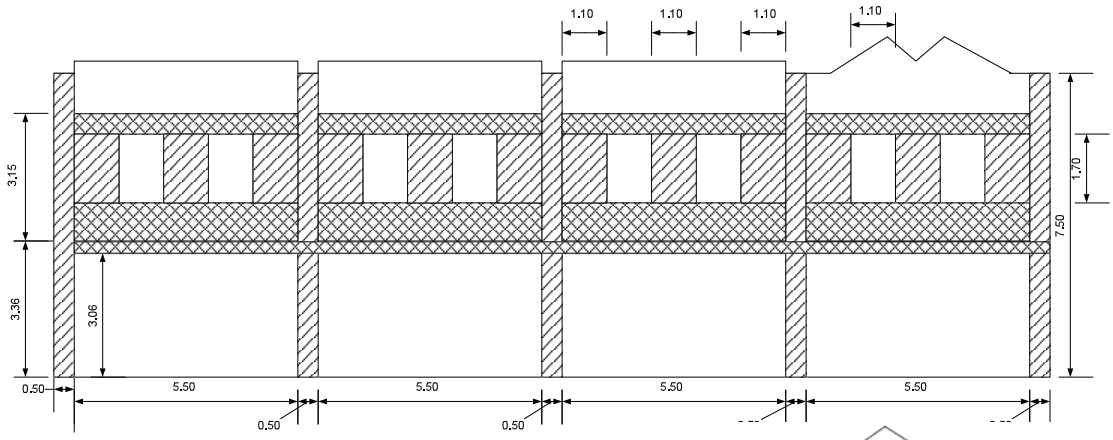

Figure 4: Typology D perforated shear wall



Figure 5: Typology E facade of a downtown Wellington URM building

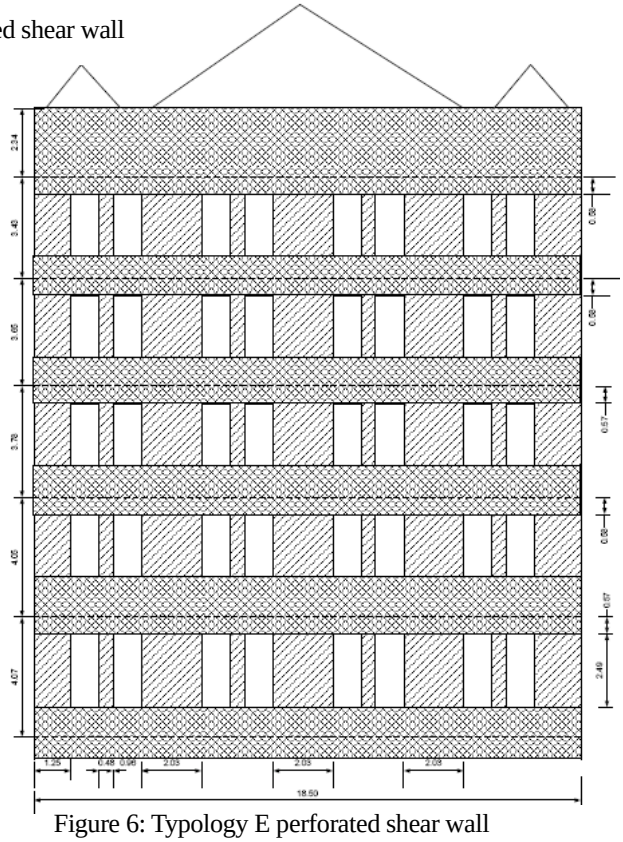

Figure 6: Typology E perforated shear wall

4. EXPERIMENTAL TESTING

4.1. Test Objectives

A number of researchers have conducted tests on isolated URM piers (Drysdale et al. 1979; Magenes and Calvi 1992; Calderini et al. 2009). From these studies it is generally accepted that piers have failure modes that are similar to those of shear walls, and will fail in the weakest mode of: sliding shear, rocking, diagonal shear, or toe crushing. The primary objective of the experimental testing reported here was to determine the failure mode of piers with aspect ratios, material properties and axial loads common to New Zealand URM facades. The secondary objective was to gather experimental data on the influence of the spandrel on the behaviour of piers. A 'strong spandrel' introduces a fixed-fixed boundary condition on the piers, preventing them from behaving as a cantilever and therefore limiting their effective height to the inter-storey height. A 'weak spandrel' results in the piers having an effective height equal to the building height. Adopting a 'strong spandrel' approach in the assessment of a perforated shear wall, rather than a 'weak spandrel' approach, reduces the effective height of the piers and this in turn reduces the aspect ratio(Cattari and Lagomarsino 2009). Two sub-structures were constructed with the first having two piers of the same length and height measured from the bottom course of bricks to the top of the opening, and the second having two piers of different lengths. In both sub-structures the piers were laterally connected by a 590 mm deep spandrel,

spanning between the top of the two piers which were separated by an opening.

4.2. Test Structure

Two-leaf walls are considered the most commonly occurring thickness in New Zealand at the bottom storey of two storey and three storey URM structures, consequently, two two-leaf thick (wythe) sub-structures were constructed, with the Common (American) bond formation to simulate a section from the front face of a multi-storey URM structure. Common bond employs header bricks in every 4th course, and has been found to be the most prevalent bond pattern used in New Zealand (Russell and Ingham 2008). The sub-structures were intentionally constructed in a way that replicated the observed, and often deteriorated, finish quality of walls in real buildings.

4.3. PS1Sub-structure

PS1sub-structure measured 4420 mm long × 2310 mm tall × 230 mm thick (two leaves) and was constructed with two identical piers, having dimensions of 1190 mm long × 1720 mm tall × 230 mm thick each. The piers had an aspect ratio of 1.5. A spandrel connected the two piers together, leaving an opening of 1250 mm between the two piers. The spandrel had a depth of 590 mm and a length of 4420 mm. The geometric configuration of PS1 is shown in Figure 7.

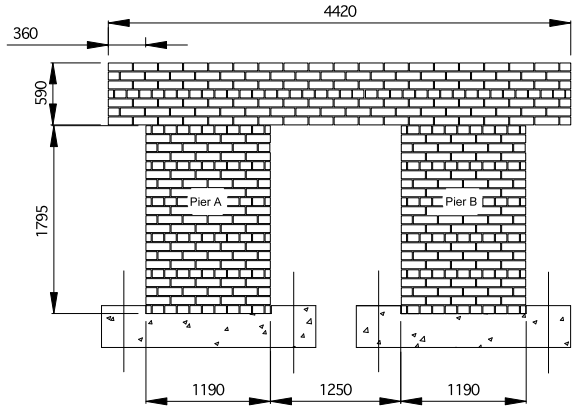

Figure 7: Geometry of PS1 (mm)

A large axial load of 130 kN was applied to the top of the spandrel, over the centerline of each pier. This axial load simulated an overburden pressure of 0.5 MPa at the base of each pier, which is representative of the axial load experienced at the base of the front wall of a characteristic New Zealand typology C building, and is comprised of components due to the weight of the front parapet, loading from the diaphragms (depending on the direction of the joists), a small roof load and the self-weight of the masonry for levels two and three.

4.4. PS2 Sub-structure

PS2 sub-structure had the same overall dimensions as PS1sub-structure so that the testing rig could be ulitized in both tests without any modifications. The two piers in PS2 sub-structure had different lengths of 1190 mm and 710 mm, corresponding to Pier A and B having aspect ratios of 1.5 and 2.5 respectively. The spandrel length, as defined by the opening width, was 1740 mm. Axial load was applied on the top of the spandrel in two locations, directly above the centre of the pier. An axial load of 85.5 kN was applied over Pier A and 82 kN was applied over Pier B. This resulted in stress levels of approximately 0.3 MPa in Pier A and 0.5 MPa in Pier B.

4.5. Materials

Both sub-structures were constructed using recycled vintage clay bricks from a demolished building. The original mortar was removed and the surfaces of the bricks were prepared for new mortar before being reused in the test sub-structure. The bricks were estimated to be 80 years old as the demolished building had been constructed in the 1930's. These vintage bricks were used because the manufacturing processes for making new bricks are sufficiently different to substantially alter the properties and characteristics of the bricks. In particular the difference in porosity between currently manufactured bricks and old bricks means that the bond at the brick-mortar interface is much weaker in new bricks using the mortar required for this test. It is believed that within a building there is significant variability in brick properties, and that reusing vintage bricks also introduced realistic material variability into the test.

Random samples of bricks were taken during construction and tested in compression (ASTM 2001b). Prisms were also built during construction of the wall using randomly selected bricks, and tested in compression and flexural tension. The results of these tests are shown in Table 2. A weak mortar mix, ASTM type 'O' (1:2:9 cement/lime/sand by volume) was selected to simulate weather deteriorated mortar in old URM structures. Standard Portland cement, hydrated lime (Calcium Hydroxide) and river sand were used in the mortar. Portland cement was becoming more widely available at the time when URM was the building material of choice in New Zealand in the early part of the 20th Century, as was hydrated lime. Results of tests conducted on mortar samples are summarized in Table 2. All material tests were conducted according to ASTM standards (ASTM 2001a; ASTM 2001c; ASTM 2002; ASTM 2003). A high coefficient of variation for each property indicates a large variability in the materials used, but this is considered acceptable because of the real variation in material properties in existing URM structures.

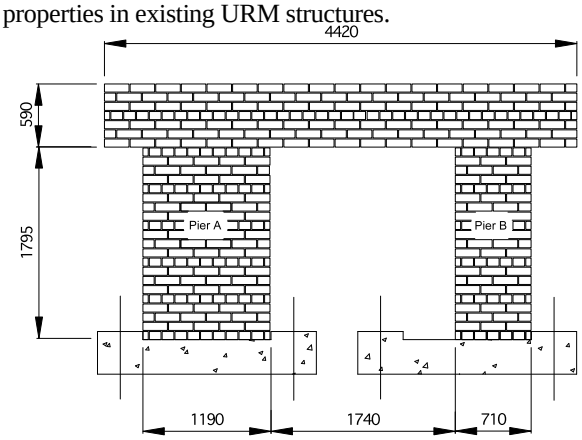

Figure 8: Geometry of PS2 (mm)

Table 2: Average masonry material properties

Parameter	Mortar compressive strength	Brick compressive strength	Masonry compressive strength	Masonry bond strength	Cohesion	Coefficient of friction
	f_{mc}	f_{bc}	f_m	f_t	C	μ
Strength (MPa)	2.1	39.5	23.1	0.147	0.05	1.02
COV (%)	41	19	32	29	15	16
Method of Test	ASTM C109/C109M-02	ASTM C67-03a	ASTM C1314-03b	ASTM 1072-05	NZSEE guidelines	NZSEE guidelines

4.6. Predicted Strength

NZSEE (2006) provides guidelines for predicting wall strength. The strength limits based on sliding shear (V_s), damage to mortar in joints near points of contraflexure (V_j), diagonal tension failure (V_b) and flexural resistance (rocking, V_r) are given in Table 3, with the equations for each described in equations 1-4 respectively. These values are derived using material data as shown in Table 2. A list of symbols is provided in section 8.

(1)

(2)

(3)

(4)

Table 3: Prediction of pier shear strengths

5. Failure mode	PS1 Pier A & B	PS2 Pier A	PS2 Pier B
V_s (kN)	93.4	56.3	6. 35.0
V_j (kN)	67.3	49.0	7. 33.2
V_b (kN)	262.2	257.6	8. 184.2
9. V_r (kN)	39.3	27.1	15.0

10. TEST SET-UP AND LOADING

Both sub-structures were tested as shown in Figure 9. The bottom course of masonry of each pier was seated one course down into the large concrete bases, which were bolted onto the strong floor. Setting the piers into the concrete bases prevented sliding along the artificially smooth strong floor when horizontal load was applied to the sub-structure, but allowed for a sliding shear failure to occur in the bed joint between the first and second course of bricks. The horizontal shear force was applied evenly over the vertical end of the spandrel through a hydraulic-powered actuator, which used the laboratory strong wall as the reaction point. Flat steel plates measuring 10 mm thick × 230 mm wide × 500 mm long were positioned on the top of the spandrel at the centerline of the piers, to provide a smooth horizontal rolling surface for a set of rollers which were then placed on top of the steel plates. The rollers were positioned to reduce any friction transfer of the horizontal load between the steel channel and the spandrel. A steel loading beam was seated on the rollers. A 20 mm thick steel plate was welded on each end of the steel channel so that the horizontal load could be transferred from the actuator into the spandrel directly, with the flybraces mounted on the steel channel to strengthen the connection between the endplate and the I-beam so that it did not deform, ensuring

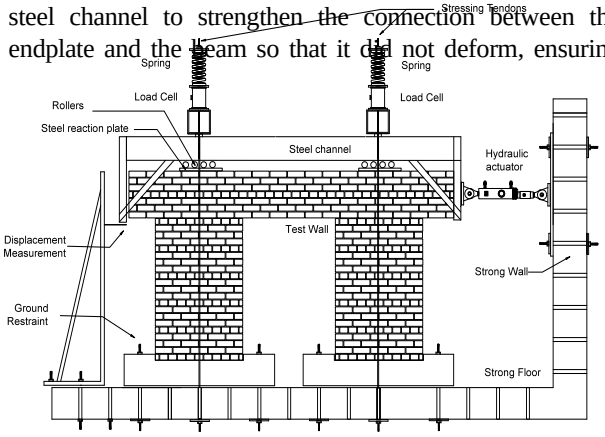

Figure 9: Test rig details

that all the horizontal load was transferred into the test sub-structure. Unbonded post-tensioning tendons on the outside of the wall were used to apply the axial load to the top of the wall, and an independent frame was positioned at one end of the wall against which displacement of the spandrel in the horizontal direction was measured, which eliminated any effects from flexing of the strong-wall.

10.1. Loading History

The loading history is shown in Figure 10. This displacement-controlled pseudo-static procedure was employed to capture the non-uniformly accumulated damage in the wall, and to enable observations of damage and failure mechanisms. The wall was subjected to displacements of 1 mm (0.05% drift) in each direction and then the displacements were increased by increments of 1 mm each cycle until 10 mm (0.5% drift) was reached, after which the increments were increased to 2 mm (0.1% drift) each cycle.

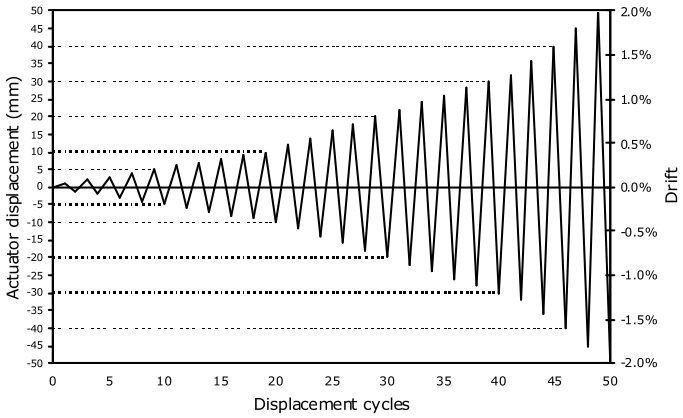

Figure 10: Pseudo-static displacement-controlled loading history employed in sub-structrues PS1 and PS2

11. DATA AQUISITION

Horizontal force was measured from a load cell connected in parallel to the hydraulic pump. Displacement gauges were placed at locations that measured the overall lateral displacement and vertical displacement of the spandrel and the piers, in order to plot the force-displacement behaviour of the test sub-structure and determine the rotations of individual components within the test sub-structure, such as the piers. Small scale plaster modelling was utilized to identify possible locations of cracking in the post-elastic phase. The plaster models were constructed at a 1:9 scale. Dental plaster was used as the construction material, which idealised the masonry as a homogeneous isotropic material. Figure 12 shows the testing rig for the plaster models. Crack patterns evidenced from the plaster models allowed additional gauges to be placed in the spandrel to measure crack widths.

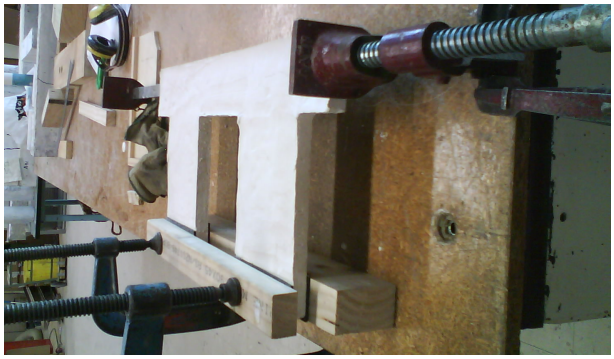

Figure 12: Test rig for plaster models

12. TEST RESULTS

12.1. PS1 Sub-structure

Initial cracking was observed at a drift of 0.05% (displacement 0.95 mm) for PS1 at a base shear of 34.5 kN. This crack propagated vertically up the head joint located in the spandrel above the top right hand corner of the opening. An equivalent crack initiated during the following pull cycle above the left hand corner of the opening. During subsequent loading cycles, both cracks extended vertically up and horizontally towards the centre of the pier, cracking along the brick-mortar interface as shown in Figure 13a. At a drift of 0.15% a vertical crack was visible, initiating from the top of the spandrel directly above the top left hand corner of the opening. This crack was mimicked on Pier B. The push crack extending up is shown in blue and the pull crack extending down is shown in red in Figure 13b.



Figure 13: a – Sub-structure PS1, Crack at top right hand corner of opening, b- Cracking over Pier B.

A total base shear of 88 kN triggered a long horizontal crack spreading through the bed joints in the spandrel, with cracking through the header joints in three courses joining the cracks between the different courses finally linking the vertical cracks over Pier B to the vertical cracks over Pier A. Figure 14a shows the spandrel crack after a push cycle to



Figure 14: a- Push to 12.5 mm, horizontal crack extending across spandrel, b- Push to 17.3 mm, twisting at base of Pier B.

12.5 mm (drift of 0.69%). Horizontal cracking along the base of Pier A and B was evident at 0.35% drift andthe corresponding base shear was 73.7 kN. Testing was terminated at 17.34 mm displacement (0.97% drift) due to out of plane twisting of the test wall as shown in Figure 14b.

12.2. PS2 Sub-structure

The initial crack location observed during loading of PS2 was identical to that of PS1 (vertical cracks developing at the top right hand corner of the opening and extending into the spandrel). PS2 had an increased stiffness compared to PS1 as the onset of the initial cracks occurred at a drift of 0.12%. No crack eventuated from the left hand corner as occurred in PS1. The vertical crack on the Bier B side extended vertically up and across the spandrel towards Pier A. At a drift of 0.25% the overhanging spandrel bricks at the Pier B end broke off. This was due to uneven stress distribution due to the loading position. In the subsequent loading cycles the original crack extended across the entire length of the spandrel and was evidenced in all bed joints as shown in Figure 15a. It was observed that the spandrel was visibly sagging between the piers. Cracking through the bed joints at the base of the piers occurred at a drift of 0.42%, corresponding to a base shear of 41.4 kN. The crack along the base of Pier B stepped down one course of bricks at approximately half the width of the pier. Rocking of Pier B produced an opening in the base crack of 8 mm, as shown in Figure 15b. Loading of PS2 was terminated at a drift of 1.40%, with a corresponding total base shear of 53.9 kN, due to the spandrel becoming unstable.



Figure 15: a- Spandrel cracking in all bed joints, b- Rocking at base of Pier B

12.3. Failure Modes

The piers in both PS1 and PS2 sub-structures exhibited a rocking response. No diagonal shear cracking occurred within the piers, and only minimal sliding along the horizontal crack at the base of the piers was evident. The failure was concentrated in the spandrel with both shear and flexural cracking in both tests.

12.4. Crack Patterns - Small scale comparison

The small scale plaster models that replicated the geometry of sub-structure PS1 were subjected to monotonic displacement controlled horizontal loading and produced crack patterns as shown in Figure 18. Initial crack location and propagation in the plaster model was identical to that observed for the push cycle of sub-structure PS1testing. Figure 19 shows the final crack patterns observed after PS1 testing. It was concluded that the plaster models gave an accurate representation of post-elastic crack locations in the large scale test sub-structure.

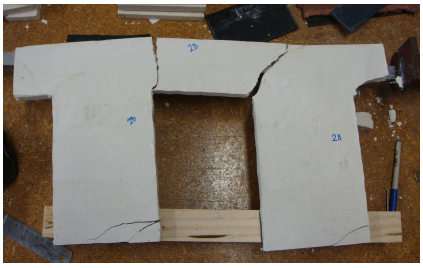

Figure 18: Crack locations plaster model test

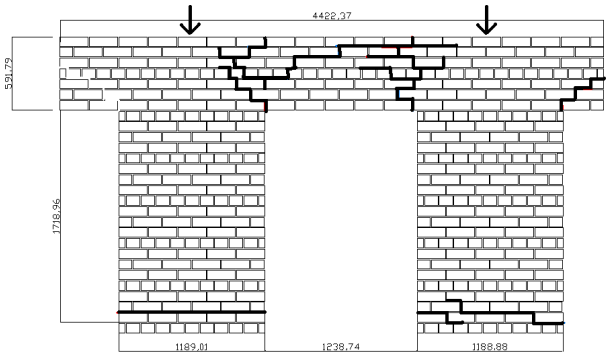

Figure 19: Crack locations from sub-structure PS1 testing

12.5. NZSEE shear strength assessment comparison

The NZSEE prediction for the individual piers of PS1 indicated that they would fail due to rocking at a base shear

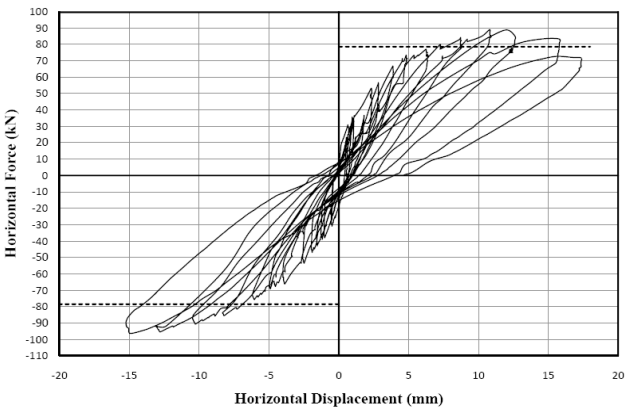

Figure 16: Force-displacement curve for PS1 with NZSEE prediction for rocking

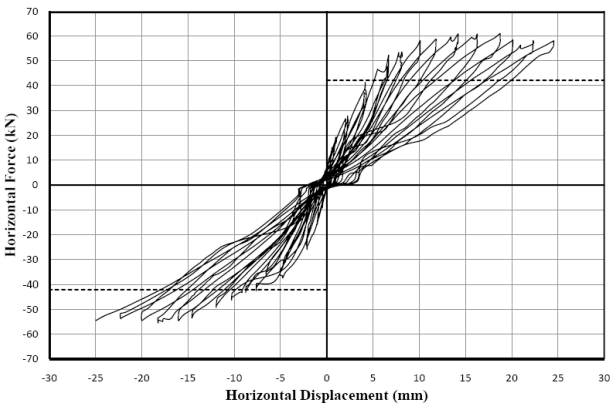

Figure 17: Force-displacement curve for PS2 with NZSEE prediction for rocking

of 39.3 kN, and a simple addition of the two piers strengths gave a predicted shear strength of 78.5 kN. Sub-structure PS1 reached a maximum base shear of 88.8 kN as shown in the force-displacement plot in Figure 16. For Sub-structure 2 NZSEE's predicted strength was 42. kN due to a rocking failure, and in the experimental testing Sub-structure PS2 reached a maximum of 60.9 kN,. Figure 17 shows the force-displacement plot for PS2. The measured axial load applied on each sub-structure increased due to the rocking behaviour and this explains the apparent strain hardening effect.

13. LIST OF SYMBOLS

c	Cohesion	α	Effective aspect ratio
d	Effective height	μ	Coefficient of friction
t	Thickness	f_{bt}	Direct tensile strength of bricks
N	Distance	f_m	Compressive strength of Masonry
z	Distance from the compression edge to the section to the line of action of N	l	Length of section

14. CONCLUSIONS

A clear and accurate assessment of the geometric properties of URM buildings in New Zealand allowed test specimens to be constructed that were representative of the buildings prevalent in New Zealand.

A test rig that simulates the loading characteristics of the bottom floor in a three storey URM building was used to investigate the seismic behaviour of piers coupled by a spandrel. Small scale plaster models were constructed to determine the post-elastic crack pattern for the geometric configuration of the large scale masonry sub-structures. It was determined that the large scale sub-structures replicated the crack pattern of the small scale models, justifying their use in determining locations of displacement gauges for the large scale testing.

Both sub-structures exhibited rocking as the dominant behaviour, with no diagonal tension cracking visible. Energy dissipation was concentrated in damage of the spandrel. Further experimental work is planned to investigate the effect that spandrel depth and spanning distances have on the lateral resistance and coupling strengths of the spandrel.

15. ACKNOWLEDGEMENTS:

The authors acknowledges financial support received for this project from The Foundation for Research Science and Technology, and The University of Auckland. Materials associated with the testing of masonry walls was provided by Firth and Fletcher Reinforcing. The writes also wish to acknowledge contributions by Tony Daligan and Jeffery Ang, who were responsible for the practical aspects in relation to the testing of the sub-structures in the Civil Test Hall of the University of Auckland.

16. REFERENCES

ASTM (2001a). "Standard test method for compressive strength of hyraulic cement mortars (using2-in or 50-mm cube specimens)." *Masonry test methos and specifications for the buildings industry, ASTM C 109/C 109M-99, Philidelphia, American Society for Testing and Materials.*

ASTM (2001b). "Standard test method for compressive strength of masonry prisms." *Masonry test methos and specifications for the buildings industry, ASTM C1314-00a, Philidelphia, American Society for Testing and Materials.*

ASTM (2001c). "Standard test methods for sampling and testing brick and structural clay tile." *Masonry test methos and specifications for the buildings industry, ASTM C67-00, Philidelphia, American Society for Testing and Materials.*

ASTM (2002). "Standard Test Method for Diagonal Tension (Shear) in Masonry Assemblages." *ASTM E-519-02, American Society for Testing and Materials.*

ASTM (2003). "Standard Test Methods for In-situ Measurement of Masonry Mortar Joint Shear Strength Index." *ASTM C1531-03, Philadelphia, American Society for Testing and Materials.*

Augenti, N. and A. Romano (2008). Seismic design of masonry buildings through macro-elements. *14IBMAC Conference*, Bondi, Australia, 17-20 February 2008.

Bothara, J. K., R. P. Dhakal and J. B. Mander (2010). "Seismic perforamnce of an unreinforced masonry building: An experimental investigation." *Earthquake Engineering and Structural Dynamics* **39**(1): 45-68.

Calderini, C., S. Cattari and S. Lagomarsino (2009). "In-plane strength of unreinforced masonry piers." *Earthquake Engineering and Structural Dynamics* **38**(2): 243-267.

Cattari, S. and S. Lagomarsino (2009) Modelling the seismic response of unreinforced existing masonry buildings: A critical review of some models proposed by codes *11th Canadian Masonry Symposium*, Toronto, Canada, 31st May - 3rd June, 2009

Chen, S. Y., F. L. Moon and T. Yi (2008). "A macroelement for the nonlinear analysis of in-plane unreinforced masonry

piers." *Engineering Structures* **30**: 2242-2252.

DBH. (2007). "Department of Building and Housing: Earthquake-prone buildings." Retrieved 6th January 2008, from http://www.dbh.govt.nz/bomd-earthquake-prone-buildings.

Dowrick, D. J. (1994). "Damage and intensities in the magnitude 7.8 1929 Murchison, New Zealand earthquake." *Bulletin of the New Zealand National Society for Earthquake Engineering* **27**(3): 190-204.

Drysdale, R. G., A. A. Hamid and A. C. Heidebrecht (1979). "Tensile strength of concrete masonry." *Journal of Structural Division, ASCE* **105**(ST7): 1261-1276.

GNS Science. (2008). "GNS Science Earthquake information." Retrieved 9 December 2008, from http://www.gns.cri.nz/what/earthact/earthquakes/index.html.

Ingham, J. M. (2008) The influence of earthquakes on New Zealand masonry construction practice *14IBMAC Conference*, Bondi, Australia, 17-20th February 2008, 17-20th February, 2008

Magenes, G. and G. M. Calvi (1992). Cyclic behaviour of brick masonry walls. *Proceedings of the Tenth World Conference on Earthquake Engineering*, Madrid, Spain, 19-24th July, 1992.

NZSEE (2006) Assessment and Improvement of the Structural Performance of Buildings in Earthquakes, Recommendateions of a NZSEE Study Group on Earthquake Risk Buildings

Russell, A. P. and J. M. Ingham (2008) Trends in the architectural characterisation of unreinforced masonry in New Zealand *14IBMAC Conference*, Bondi, Australia, 17-20th February, 2008, 17-20th February, 2008

Thurston, S. J. and G. J. Beattie (2009) Seismic performance of New Zealand two-storey brick veneer houses *NZSEE conference - Why do we still tolerate buildings that are unsafe in earthquakes*, Christchurch, NZ,

Westernpower. (2008). "World of Energy." Retrieved 12/12/08, from http://www.worldofenergy.com.au.

Yi, T., F. L. Moon, R. T. Leon and L. F. Kahn (2006). "Lateral Load Tests on a Two-Storey Unreinforced Masonry Building." *Journal of Structural Engineering* **132**(5): 643-652.

JOINT CONFERENCE PROCEEDINGS
7th International Conference on Urban Earthquake Engineering (7CUEE) &
5th International Conference on Earthquake Engineering (5ICEE)
March 3-5, 2010, Tokyo Institute of Technology, Tokyo, Japan

STRENGTH DETERIORATION MODEL BASED ON EFFECTIVE HYSTERETIC ENERGY DISSIPATION FOR RC MEMBERS UNDER CYCLIC LOADING

Zhe Qu[1], and Lieping Ye[2]

1) PhD Candidate, Department of Civil Engineering, Tsinghua University, Bejing,China
2) Professor, Department of Civil Engineering, Tsinghua University, Bejing,China
qz@mails.tsinghua.edu.cn, ylp@tsinghua.edu.cn

Abstract: In simulating the nonlinear seismic behavior of RC structures subjected to strong earthquake ground motions, it's necessary to take into account the effects of accumulative damage of structural members, of which the strength deterioration is one of the most important aspects. By examining the influence of loading histories on the strength deterioration, it is shown that the extent of damage caused by a certain amount of hysteretic energy is dependent on the displacement amplitude at which the energy is dissipated. The effective hysteretic energy dissipation is defined through combining the hysteretic energy dissipation with its corresponding displacement amplitude. It is proved by calibrating with existing test data that the effective hysteretic energy dissipation shows good correlation with the extent of strength deterioration, and that the proposed strength deterioration model is effective in simulating the hysteretic behavior of reinforced concrete members subjected to various cyclic loading histories.

1. INTRODUCTION

It is of crucial importance to accurately estimate the seismic performance of building structures in performance based seismic design. Observations in structural experiments as well as earthquake reconnaissance implied significant influences of loading histories on the dynamic behavior of structures. Structural members are subjected to various deteriorations during earthquake ground motions, to which the failure of individual members or even the whole structure can be attributed, especially when subjected to long-duration ground shakings with many large-amplitude load reverses. An adequate model to simulate the structural nonlinear dynamic responses should be capable of capturing these features. The present paper will focus on the strength deterioration of reinforced concrete (RC) members.

The mechanism of strength deterioration of RC members is commonly interpreted by concrete spalling and interface bond slip between the concrete and embedded reinforcements. In the celebrated damage model for RC members proposed by Park and Ang (1985), cumulative damage is dependent on a linear combination of the maximum displacement and the cumulative hysteretic energy dissipation. However, only one of the two factors is generally incorporated in existing strength deterioration models in the literature, say some models are based solely on the maximum displacement, such as models in Lai *et al* (1984), Roufaiel and Meyer (1987), Chung *et al* (1989) and Yousseef and Ghobarah (1999), while others on the cumulative energy dissipation, such as in Kunnath *et al* (1990), Mork (1991), Rahnama and Krawinkler (1993) and Sucuoglu and Erberik (2004).

The bilinear peak oriented hysteretic model as shown in Figure 1 provides a common basis for all the existing strength deterioration models. The strength deterioration can be expressed either by softening the skeleton curves (Figure 1a) or moving the reloading oriented points (Figure 1b). In Figure 1, F_{yi} refers to the yield strength at the ith loading cycle; Δu_o and ΔF_o refer to the change of displacement and force of the oriented point, respectively. Triangles and circles indicate the maximum displacement point and the reloading oriented point in a loading cycle, respectively.

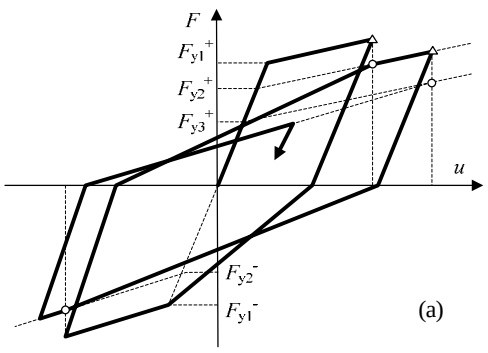

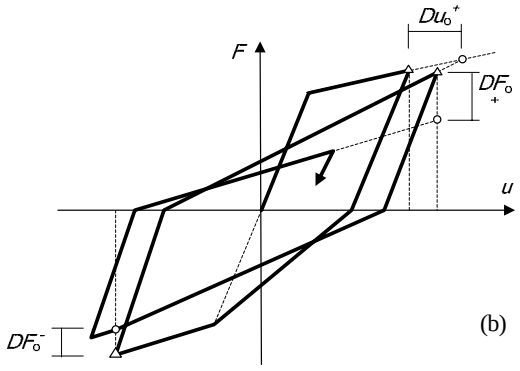

Figure 1 Strength deterioration in peak oriented hysteretic model: (a) Soften the skeleton curve, and (b) Move the reloading oriented point

2. INFLUENCE OF LOADING HISTORIES ON STRENGTH DETERIORATION

To better understand the influences of the maximum displacement or the cumulative hysteretic energy dissipation on the strength deterioration, existing experimental data are re-examined focusing on the influence of various loading histories.

Displacement loading with monotonically increased amplitude is the most commonly used loading scheme in studying the cyclic behavior of structural members while constant amplitude loading is another important scheme especially when the low cycle fatigue performance is of major concern. The structures are however subjected to neither a monotonically increased-amplitude nor a constant amplitude loading during a ground shaking. Large uncertainties exist in the loading histories, which may have significant influence on the deterioration behavior of structural memberes.

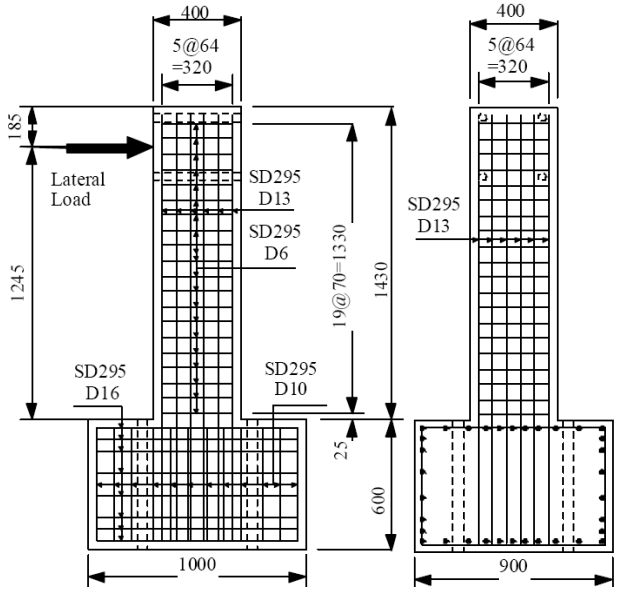

Figure 2 Dimension and reinforcement of the specimen (Figure 1 in Takemura 1997)

Such an influence on the seismic performance of RC bridge piers were studied by Kawashima and Koyama (1988) through large-scale high-speed loading tests. Results showed that severer damage could be expected if the specimens are loaded with monotonically decreasing, rather than increasing, displacement amplitudes. The influence of loading histories on the plastic deformability of bridge piers was further studied by Takemura and Kawashima (1997). In their test, six identical specimens, as seen in Figure 2, were subjected to cyclic loadings with different loading histories. The specimen was a cantilever column with a height of 1245mm from the surface of foundation to the loading point and a cross section of 400mm square. The effective depth of the cross section was 360mm leading to a nominal shear span-to-depth ratio of 3.46. The average concrete strength was about 35MPa. D13 rebars with yield strength of 363MPa were adopted for the longitudinal reinforcement and D6 rebars with yield strength of 368MPa and 70mm spacing for stirrups. Longitudinal reinforcement ratio was 1.66% and stirrup ratio about 0.2%. A constant axial compression of 157kN, about 3% of the column's maximum compressive strength, was applied at the top. Specimens identified as TP001~TP006 were then subjected to lateral load with 6 different histories as shown in Figure 3.

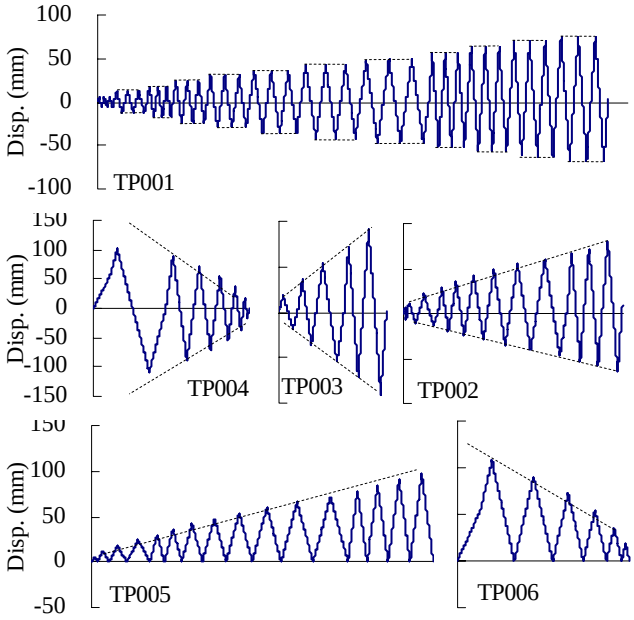

Figure 3 Loading hysteresis in Takemura test (rearranged from Figure 2 in Takemura 1997)

Compared with the yield strength of the skeleton curve (i.e. F_{yi} in Figure 1a) or the change in displacement of oriented point (i.e. Δu_o in Figure 2b), the force of the oriented point in subsequent loading cycles, denoted as F_{oi} in Figure 4, can be readily obtained from the test data without too much idealization of the experimental hysteretic curves. Take TP003 and TP004 for examples. For specimens subjected to displacement cycles with increasing amplitudes, such as TP003, F_{oi} is simply the force achieved at the maximum displacement of the last loading cycle in the same

direction (See Figure 4a). For specimens subjected to loadings with decreasing amplitudes, such as TP004, F_{oi} can be taken as the force on the tangent of the hysteretic curve when it reaches the maximum displacement of the last loading cycle in the same direction (Figure 4b).

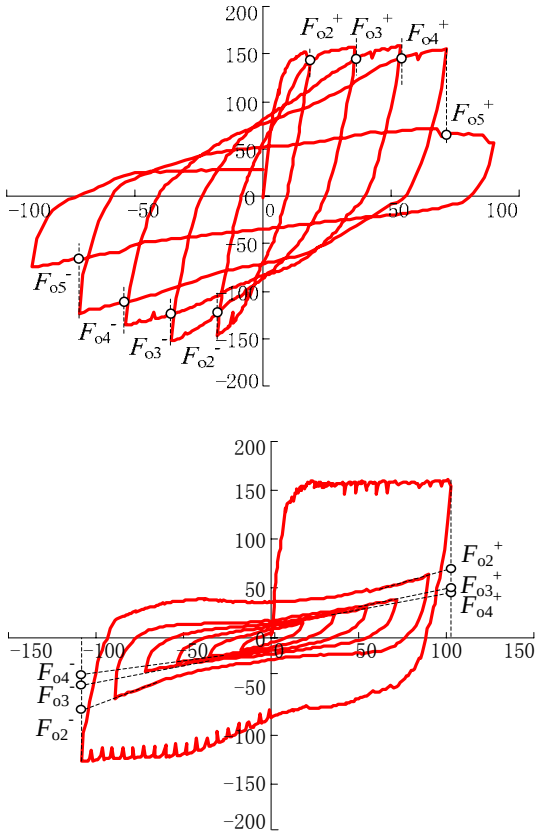

Figure 4 Determination of the forces of oriented points: (a) TP003-Monotonically increasing amplitude, and (b) TP004- Monotonically decreasing amplitude

Through such a manner, forces of the oriented points F_{oi} are obtained for all the six specimens in both loading directions. The dependencies of F_{oi} on the maximum displacement in the last cycle u_{i-1} and the cumulative hysteretic energy ΣE_i for the six specimens are compared in Figure 5. A general trend for specimens with increasing loading amplitudes (TP001, 2, 3 and 5) can be observed that the force of the oriented point F_{oi} drops with the increase of u_{i-1} or ΣE_i. But the story is somehow different for other specimens (TP004 and 6) in that their forces of the oriented points F_{oi} drop with the decrease of u_{i-1} (Figure 5a). This implies that u_{i-1} is not an adequate index to describe the strength deterioration. In addition, large scattering of the relations between forces of the oriented points and cumulative energy dissipations is observed in Figure 5b for specimens subjected to different loading histories despite that their forces of the oriented points perform similar decreasing trends with the increase of cumulative energy dissipation. This further indicates that the cumulative energy dissipation doesn't well represent the strength deterioration either.

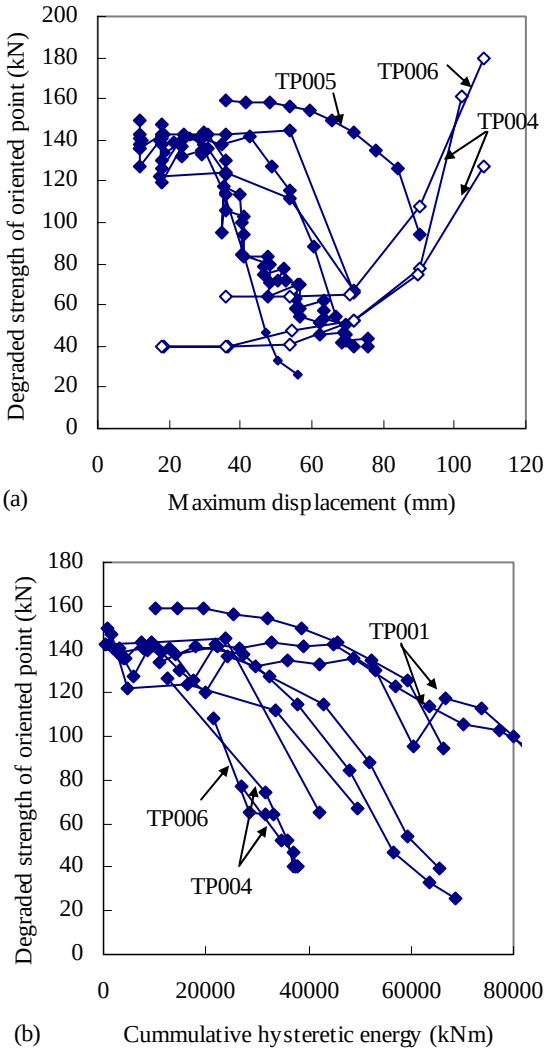

Figure 5 Dependency of the force of oriented points on (a) maximum displacement and (b) cumulative energy dissipation

3. EFFECTIVE HYSTERETIC ENERGY DISSIPATION

Liu *et al* (1998) obtained the relationship between the loading displacement amplitude and the low-cycle fatigue life of RC members through a series of constant-amplitude cyclic loading test. Results showed that the low-cycle fatigue life of an RC member became dramatically shorter and the cumulative energy dissipation needed to cause the failure of the member was smaller when the constant-amplitude loading was carried out at larger amplitude. These results confirm the observations made in Figure 5(b), where, for example, the cumulative energy dissipations to reduce the forces of the oriented points to the same level are much smaller for TP004 and TP006, which were loaded at first with large displacement amplitudes followed by decreasing amplitudes, than for TP001, which was loaded with increasing amplitudes. It can be therefore concluded that the strength deterioration of an RC member subjected to cyclic loading at smaller amplitude can be expected less severe

than that at large amplitude provided the cumulative hysteretic energy dissipations are the same. Based on these findings, the so called "effective hysteretic energy dissipation" is proposed as in Equation 1.

$$E_{\text{eff},i} = \sum_{j=1}^{i} \left[E_j \cdot \left(\frac{u_j}{u_f} \right)^2 \right] \tag{1}$$

where $E_{\text{eff},i}$ is the effective hysteretic energy dissipation up to the ith loading cycle; u_j is the displacement amplitude of the jth cycle; u_f is the ultimate displacement of the member; E_j is the hysteretic energy dissipation in the jth cycle.

It is clearly seen from Equation 1 that the energy dissipation at large displacement amplitude will contribute more to the effective hysteretic energy dissipation.

Figure 6 depicts the relationship between the forces of the oriented points F_o and the effective energy dissipation E_{eff} (Equation 1) for the six specimens in the previous discussion, where F_o and E_{eff} are normalized by the initial yielding strength F_{y1} and the product of F_{y1} and u_f, respectively. It is seen that the large scattering in Figure 5 is significantly reduced, indicating that the content of strength deterioration is strongly correlated with E_{eff}.

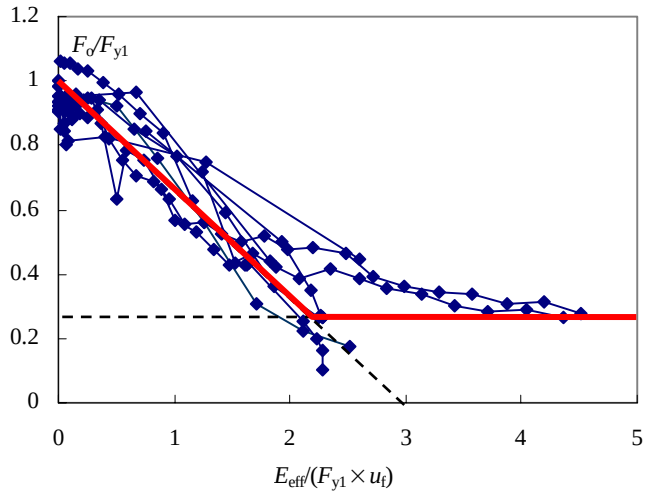

Figure 6 Dependence of the forces of oriented points on effective hysteretic energy dissipation

The bilinear relation in Equation 2 (shown as the bold line in Figure 6) is suggested to idealize the experimental results.

$$\frac{F_{oi}}{F_{y1}} = 1 - \frac{E_{\text{eff},i}}{\lambda F_{y1} u_f} \geq cF_{y1} \tag{2}$$

where F_{oi} is the force of the oriented point for the ith loading cycle; λ and c are parameters determined from the test. For Takemura (1997) test, it is suggested that λ=3.0 and c=0.3 as shown in Figure 6. It is worth noting that these values are determined from test results of RC bridge piers subjected to very small axial compressions. This is generally not realistic for columns in building structures. Besides, other factors such as the amount of confinement and the concrete grades may also have major effects on the strength deterioration behavior of RC members. Hence the evaluation of λ and c deserves further research based on extensive experimental data.

For a hysteretic model with bilinear skeleton curve as in Figure 1(a), a quantitative relationship between the change in forces of oriented points ΔF_{oi} and the change in yield strengths ΔF_{yi} can be readily obtained as in Equation 3.

$$\Delta F_{oi} = \frac{\Delta F_{yi}}{1-\alpha} \tag{3}$$

where α is the ratio of post-yield to initial stiffness.

Substituting Equation 3 into 2 yields the following strength deterioration model in terms of the yield strength of bilinear skeleton curve (Equation 4).

$$F_{yi} = F_{y1}\left(1 - \frac{E_{\text{eff},i}}{\lambda F_{y1} u_f (1-\alpha)}\right) \geq cF_{y1} \tag{4}$$

In this model, the yield strength in the ith cycle F_{yi} is reduced in proportion to the current effective energy dissipation $E_{\text{eff},i}$.

4. MODELING OF STRENGTH DETERIORATION OF RC MEMBERS

For its capability of simulating the bending and axial force interaction and applicability of modeling members with various cross-section profiles and reinforcements, beam elements with fiber section are widely used in simulations of structural seismic behavior, in which the cross section of the element is divided into many segments (fibers) to which various mechanical properties can be assigned. With some modifications, the above-proposed deterioration model for the yield strength of skeleton curve (Equation 4) can be applied in fiber beam elements.

As mentioned before, the macro phenomenon of strength deterioration of RC members is a consequence of the meso-scale behavior including the bond-slip between rebar and concrete as well as the spalling of concrete cover. In studying their effects on the strength deterioration, Youssef (1999) adopted a four-rebar model as described in Lai (1984) and modified the hysteretic behavior of the rebar to simulate the strength deterioration, leaving the concrete hysteresis unchanged as that in non-deteriorating models. Comparisons between the analysis and test results showed that such a manner was effective in simulating the strength deterioration of RC members. This is not surprising since the modeling of rebar is predominant in simulating the behavior of RC members especially when significant plastic deformation is sustained. It is hence suggested that the above-mentioned strength deterioration model based on the effective energy dissipation can also be applied to fiber beam elements by simply replacing the force and displacement in Equation 1 and 4 by stress and strain of the rebar fibers as in Equation 5. In this manner, the strength deterioration of the beam element is taken into account by reducing the yield

strength of the rebar in accordance with its "effective dissipated energy density" as defined in Equation 5(b). Note that this reduction is not the deterioration of the rebar itself, but represents the overall effect of interface bond-slip and the concrete spalling.

$$\sigma_{yi} = \sigma_{y1}\left(1 - \frac{E_{\text{eff},i}}{\lambda\sigma_{y1}\varepsilon_f(1-\alpha)}\right) \geq c\sigma_{y1} \qquad (5a)$$

$$E_{\text{eff},i} = \sum\left[E_i \cdot \left(\frac{\varepsilon_i}{\varepsilon_f}\right)^2\right] \qquad (5b)$$

where ε_f can be taken as the maximum strain of the rebar when the member is monotonically loaded to its maximum displacement u_f.

The deterioration model in Equation 5 is built into an in-house user-material package based on the general purpose program ABAQUS 6.7-1, by which the cyclic responses of the six specimens in Takemura (1997) test are simulated. The non-deteriorating hysteresis of steel rebars and concrete in the package is depicted in Figure 7. The yield strength of the steel rebar will be updated during the analysis in accordance with Equation 5 when the strength deterioration is taken into account.

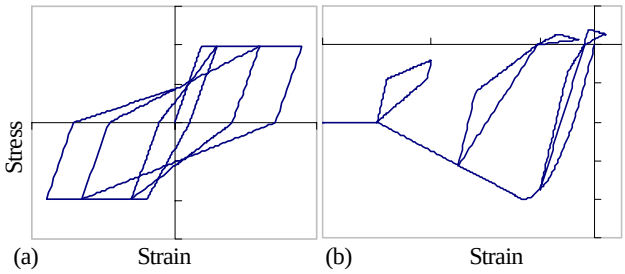

Figure7 Hysteretic models of (a) steel rebar and (b) concrete

The analysis results are compared with the test in Figure 8 for each of the six specimens. It is shown that the strength deterioration revealed by the analysis generally agrees well with the test results for most cases no matter the cyclic loadings are applied with increasing or decreasing amplitude. An exception is however observed for test TP005 where the estimated strength deterioration by the analysis is much severer than in the test. Note that the strength deterioration of TP005 was much delayed in the test as compared to its counterpart TP002, which was also loaded with increasing amplitude but in both directions. It is doubtful whether the strength deterioration could be so dramatically different between members subjected to one-way and two-way cyclic loadings before more experimental results are examined.

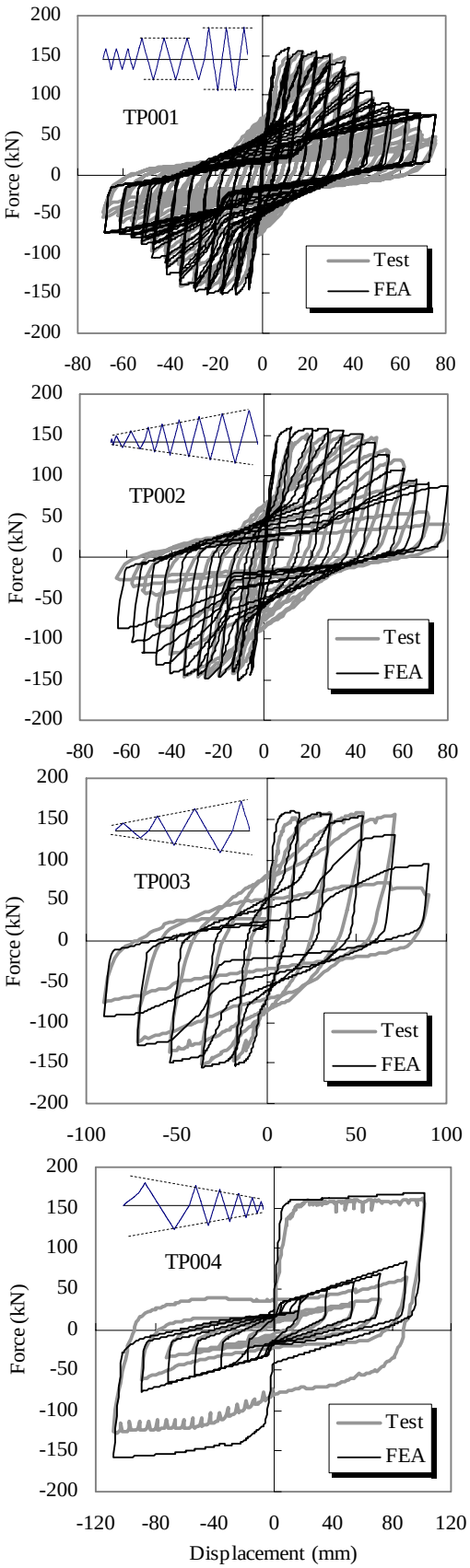

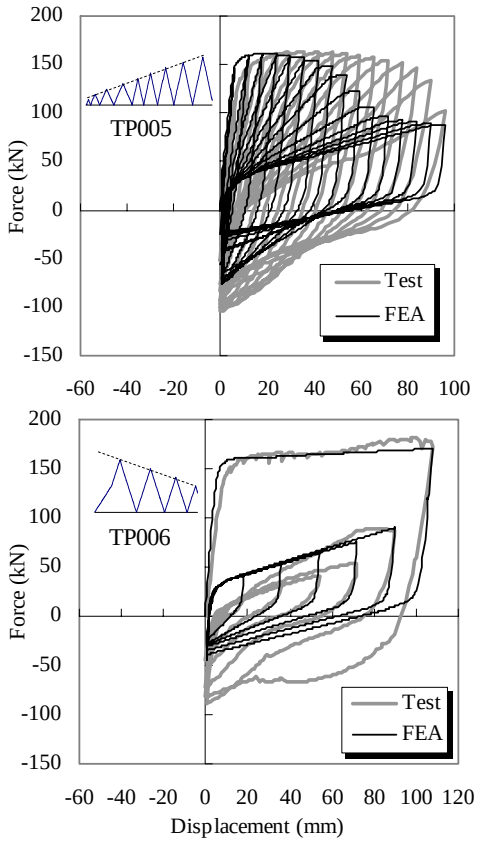

Figure 8 Comparison between the analysis and experimental results of Takemura 1997 test

5. CONCLUSIONS

The influence of loading histories on the strength deterioration of RC members is studied and the "effective hysteretic energy dissipation" is proposed as the controlling quantity influencing the content of strength deterioration, based on which a strength deterioration model is established. Through the above discussions, the following conclusions can be drawn:

(1) Loading histories have major effects on the strength deterioration of RC members. Cyclic loadings with decreasing amplitude are likely to cause severer strength deterioration than those with increasing amplitude.

(2) The proposed "effective hysteretic energy dissipation" integrates the hysteretic energy and maximum displacement in a concise form and well describes the dependency of strength deterioration on loading histories, as is evident from the fact that the effective hysteretic energy dissipation is strongly correlated with the content of strength deterioration for a series of tests with various loading schemes.

(3) It is effective to model the strength deterioration with fiber beam elements by adapting the proposed strength deterioration model and introducing it into the hysteresis of rebar fibers.

It is however worth noting that the evaluation of key parameters in the proposed strength deterioration model, say λ and c, still needs more experimental calibration in order to make it widely applicable to various types of structural members.

Acknowledgements:

The present research is sponsored by the Ph.D Foundation of Education Ministry of China (No. 200800030001) and the key project of National Natural Science Foundation of China (No. 90815025). The financial support is gratefully acknowledged. The authors would also like to appreciate Prof. K. Kawashima in Tokyo Institute of Technology for his kind offer of the experimental data and related documentations. The findings in the present paper would be impossible without these valuable materials.

References:

Chung, Y.S., Meyer, C. and Masanobu, S. (1989), "Modeling of Concrete Damage", *ACI Structural Journal*, **86**(3), 259-271.

Ibarra, L.F. (2005), "Global Collapse of Frame Structures under Seismic Excitations", *PEER Report - 2005/06*

Kawashima, K. and Koyama, T. (1988) "Effects of Cyclic Loading Hysteresis on Dynamic Behavior of Reinforced Concrete Bridge Piers", *Structural Engineering and Earthquake Engineering, JSCE*, **5**(2), 343-350.

Kunnath, S.K., Reinhorn, A.M. and Park, Y.J. (1990), "Analytical Modeling of Inelastic Seismic Response of R/C Structures", *Journal of Structural Engineering, ASCE*, **116**(4), 996-1017.

Lai, S.S., Will, G.T. and Otani, S. (1984), "Model for Inelastic Biaxial Bending of Concrete Members. *Journal of Structural Engineering, ASCE*, **110**(11), 2563-2584.

Liu, B.Q., Bai, S.L, Xu, Y.Z. and Huang, Z.M. (1998), "Experimental Study of Low-cycle Behavior of Concrete Columns", *Earthquake Engineering and Engineering Vibration*, **18**(4): 82-89 (in Chinese)

Mork, K.J. (1991), "Response Analysis of Reinforced Concrete Structures under Seismic Excitation", *Earthquake Engineering and Structural Dynamics*, **23**(1), 33-48.

Park, Y.J. and Ang, A.H.S. (1985), "Mechanistic Seismic Damage Model for Reinforced Concrete", *Journal of Structural Engineering, ASCE*, **111**(4), 722-739.

Rahnama, M. and Krawinkler, H. (1993), "Effect of Soft Soils and Hysteresis Models on Seismic Design Spectra", *John A. Blume Earthquake Engineering Research Center Report No. 108*, Department of Civil Engineering, Stanford University.

Roufaiel, M.S.L. and Meyer, C. (1987), "Analytical Modeling of Hysteretic Behavior of R/C Frames", *Journal of Structural Engineering*, **113**(3), 429-444.

Sucuoglu, H. and Erberik, A. (2004), "Energy-based Hysteresis and Damage Models for Deteriorating Systems", *Earthquake Engineering and Structural Dynamics*, **33**(1), 69-88.

Takemura, H. and Kawashima, K. (1997), "Effect of Loading Hysteresis on Ductility Capacity of Reinforced Concrete Bridge Pier", *Journal of Structural Engineering, Japan*, **43A**, 849-858.

Youssef, M. and Ghobarah, A. (1999), "Strength Deterioration due to Bond Slip and Concrete Crushing in Modeling of Reinforced Concrete Members", *ACI Structural Journal*, **96**(6), 956-968.

JOINT CONFERENCE PROCEEDINGS
7th International Conference on Urban Earthquake Engineering (7CUEE) &
5th International Conference on Earthquake Engineering (5ICEE)
March 3-5, 2010, Tokyo Institute of Technology, Tokyo, Japan

SIMULATION-BASED FRAGILITY RELATIONSHIPS FOR UNREINFORCED MASONRY BUILDINGS

Thomas M. Frankie[1] and Amr S. Elnashai[2]

1) Graduate Research Assistant, M.S. candidate, University of Illinois, Urbana-Champaign
2) William J. and Elaine F. Hall Endowed Professor, Civil and Environmental Engineering, University of Illinois, Urbana-Champaign
frankie2@illinois.edu, aelnash@illinois.edu

Abstract: Unreinforced masonry (URM) structures represent a significant portion of the residential building stock of the Central and Eastern United States (CEUSA), accounting for 15% of homes in the 8-state region impacted by the New-Madrid Seismic Zone and an even greater portion of the building stock in most other regions of the world. In addition to significant population, the brittle nature of URM buildings further supports a thorough consideration of seismic response given the susceptibility to severe failure modes. Currently, there is a pressing need for analytically based fragility curves for URM buildings. In order to improve the estimation of damage state probabilities through the development of simulation-based masonry fragilities, an extensive literature survey is conducted on pushover analysis of URM structures. Using this data, capacity curves are generated, from which damage exceedance limit states are defined. Demand is simulated using synthetically derived accelerograms representative of the CEUSA. Structural response is evaluated using an advanced capacity spectrum method developed at the Mid-America Earthquake Center. Capacity, demand, and response are thus derived analytically and used to generate an improved and uniform set of fragility curves for use in loss-assessment software via a framework amenable to rapid expansion of pushover database and variation of ground motion records. The curves are expressed in multiple forms for wide range of use in loss-assessment applications.

1. INTRODUCTION AND MOTIVATION

Earthquakes pose one of the greatest threats and challenges to mankind due to the potential to cause great devastation in terms of loss of life and livelihood to communities, regions, and entire countries. An average of 10,000 lives and tens of billions of dollars are lost annually due to direct and indirect effects. The importance of understanding vulnerability of structural systems has been underscored by recent events such as the earthquakes of Loma Prieta, CA (1989), Northridge, CA (1994), Kobe, Japan (1995), Kocaeli, Turkey (1999), Chi-Chi, Taiwan (1999), Bhuj, India (2001), Bam, Iran (2003), Sumatra, Indonesia (2004), Kashmir, Pakistan (2005), Jakarta, Indonesia (2006), Sichuan, China (2008), and Port-au-Prince, Haiti (2010). The devastation caused by these events highlight the importance of improving the capabilities of researchers to estimate the impact of future events, and suggest methods for mitigation of potential consequences.

The New Madrid Seismic Zone (NMSZ) is a significant seismic zone composed of three parallel fault segments located in the Central Eastern United States (CEUS). Geologists estimate that the NMSZ has the capability of producing earthquakes with massive destructive capability every 300-500 years as exhibited in a series of powerful earthquakes occurring in 1811 and 1812 estimated to have exceeded magnitude 8.0. In the past 20 years, thousands of smaller earthquakes have been recorded in the region, providing evidence that the NMSZ still remains active. The region clearly poses a low probability, high consequence risk scenario.

The main purpose of the Mid-America Earthquake Center (MAEC) is to minimize the consequences of future seismic disasters for vulnerable populations living in regions including, but not limited to, the CEUS. The MAEC has developed and employs the method of consequence-based risk management (CRM) as a means of handling impact assessment, mitigation, response, and recovery. CRM allows researchers to estimate the possible consequences of earthquakes by performing loss assessment studies for different regions and cities around the world, including those in the CEUS.

The three components of these loss assessment studies are hazard, inventory, and vulnerability. Hazard is best described as ground shaking in the instance of earthquake loss assessment. Inventory is the data necessary to characterize the infrastructure of the region, and includes building type, design level, and quantity. Vulnerability, or fragility, is the component that links the hazard and inventory described above by determining the probability that a certain hazard will exceed specific damage limit states of the building inventory of the region. This component

outputs the consequences such as fatalities and economic losses that are expected to result from the building stock experiencing the various proposed levels of damage limit states. These initial consequences are then used to model the social and economic consequences of experiencing this level of physical damage.

It is this final component of loss assessment, fragility relationships, that is addressed in this study. A framework for relating ground motion intensity to the probability of reaching discrete structural damage levels is proposed as a method of improved fragility analysis, focusing on unreinforced masonry buildings. This study of building fragilities can be subdivided into four parts: building capacity, seismic demand, methodology for structural assessment, and methodology for fragility curve generation. These topics form the structure of this paper.

2. STATEMENT OF PURPOSE

It is the purpose of this study to employ a new framework for developing fragility relationships for URM buildings for use in seismic loss assessment studies. The overall framework was originally introduced by Gencturk (2007) and applied to timber buildings with notes on other building categories. It is the objective of this study to provide a methodology and set of best practices for each step in the procedure, including selection and use of experimental and analytical data, input ground motions, analysis of structural capacity, seismic design categories and groupings, and probabilistic analysis. A framework is therefore developed that can be applied to any building system for any set of earthquake hazards in the world.

Special focus in this study is placed on unreinforced masonry (URM) building typology due to the specific concerns of significant residential building stock both in the CEUS and globally, along with the well known susceptibility to brittle and severe failure modes under seismic demands. The building category is significant from a perspective of performance based design.

In the absence of natural records from large NMSZ events, synthetically derived accelerograms (Fernandez, 2007) are employed to depict the characteristics of the tectonic environment of the CEUS. Due to the regionally specific characterizations of these synthetic time histories, the fragility relationships generated though this study are recommended for use in earthquake loss assessments for regions within the CEUS. However, the methodology and framework of this study may be applied to any set of available ground motions or differently derived synthetic time histories in order to develop fragility relationships for other seismic zones.

3. CAPACITY OF BUILDINGS

The first component of fragility analysis, the capacity of buildings, is investigated through an advanced method of analysis performed on a database of pushover curves. Building capacity is one of the two inputs necessary to perform structural assessment, the results of which are used to derive the fragility relationships used in loss assessment. Uncertainties in the fragilities are due to inaccuracies and variability within the two constituents used to develop them. Therefore, the accuracy of the fragility curves depends in part on making the best possible assessment of the true capacity of the buildings examined.

3.1 Pushover Curves

There are several ways to represent the capacity of a building, but this study uses pushover curves to represent lateral force resisting capacity. A pushover curve, although generated by static loading, can be equated to the envelope of the hysteretic loop that would define the cyclic response of the building. This is a powerful concept because it indicates the limiting boundaries of the global force-displacement relationship of the building. As it is the aim of this study to obtain fragility relationships for a population of buildings with many varying parameters, a relatively simple method is necessary to perform analysis efficiently while still accurately representing behavior due to lateral loading.

There are potential shortcomings to the method, due to its simplicity, including the inability to predict behavior of irregular buildings and to capture local responses such as soft story effects, buckling and pullout of rebar, and higher mode effects. The latter issues are not of significant concern to URM buildings as they are void of reinforcement, and are not built tall enough or ductile enough for a significant portion of the mass to be associated with higher order vibrations. There have been significant research efforts addressing these shortcomings which have demonstrated that pushover analysis can provide a reasonable nonlinear force-displacement relationship for regular structures with negligible higher order effects, confirming the role of non-linear equivalent static pushover analyses as a practical tool for the evaluation of the seismic response of a structure (Magenes, 2000). Pushover analysis also caters to the methodology of structural assessment to be employed in this study.

Therefore, as long as the URM database is comprised of structures that conform to the above criteria, pushover analysis is an adequate method of representing the global response of buildings under lateral demands. These considerations, along with several others explained in the following section, are taken into account in developing the database. The procedures and considerations made in selecting the appropriate curves for deriving fragilities are explained below and subsequently followed by a brief overview of the final database.

3.2 Selection of Sources

In developing the database for use in the URM application of the fragility generation framework, some pushover data available in the literature was excluded from the database due to limitations or incompatibility with the

methodology being implemented in this study. The results from these sources were neglected for a variety of reasons including:

- Lack of available data to convert to capacity diagrams
- Specimen differs significantly from target building stock
- Unique, abnormal, or special performance buildings tested
- Convergence error in analytical models
- Failure mode in small-scale experimental test that is un-scalable

Data necessary to determine the capacity of a building includes mass (weight), loading methods, and testing procedure. It is critical that buildings tested are accurate representations of the types of structures present in the target region of the loss assessment study. Unrepresentative curves can be due to regional design and construction procedures, but differences are often due to the tendency for studies to examine unique or abnormal buildings unlike much of the building stock population. Some results simply lacked accuracy or completeness due to convergence error, typically of post-peak response, in certain analytical software programs used. In other cases, the incompatibility was due to the procedure of the fragility development itself, because the failure mode reached in the lab or analysis could not be scaled or adjusted to fit into the framework. This occurred most often in instances where the data was the result of small scale experimental testing. Small-scale structures exhibiting a failure mode that was entirely shear dominated could not have force values accurately scaled to the height or weight of the building stock.

With these considerations taken into account, the database described below helps to eliminate as best as possible the uncertainties inherent in the use of probabilistic models for loss assessment of the region under consideration by providing accurate force and displacement capacities that represent true behavior based on analytical and experimental results as opposed to empirical relationships.

3.3 URM Database

The final database is composed of nearly 50 curves from six studies that have been verified to be representative of URM behavior. The pushover curves were compiled from notable previous studies available in the literature. Many of the studies listed are cited in FEMA 307 where the results from these tests are used to evaluate the accuracy of the methods of FEMA 273 and ATC-43 in predicting URM seismic behavior. The structural configurations assessed analytically and experimentally span from 1-3 stories with a variety of sizes of floor plan, strength of materials, and size of masonry spandrels and piers. They provide an adequate representation of the diverse configurations of URM buildings present in the building stock.

The six different studies from which structural capacities were selected for use in the database are:

i. RISK-UE Project (Penelis et al. 2002)
ii. Full Scale Seismic Testing of 2-story URM building in Pavia, Italy (Magenes et al. 1995)
iii. Comparative Inelastic Pushover Analysis of Masonry Frames (Salonikios et al. 2003)
iv. Dynamic Response of Masonry Structures (Costley and Abrams, 1995)
v. NDT Confirmation Testing (Epperson and Abrams, 1989)
vi. Cyclic Load Testing of Masonry Walls (Abrams and Shah, 1992)

3.4 Capacity Diagrams

In order to perform the structural assessment, a conversion of the capacity curves is required. Pushover curves are expressed in terms of base shear versus top roof displacement of a structure. However, the advanced CSM used in this study requires that the capacity of buildings be represented in Acceleration-Displacement (AD) format as described in Mahaney et al. (1993). AD format is a plot of spectral acceleration versus spectral displacement, unlike typical spectra which commonly plot one of these values as a function of period. The pushover capacity curves expressed in AD format are referred to as capacity diagrams in this paper. The method for development of equations for use in converting to capacity diagrams follows the same notation and procedure as described by Fajfar (2000). Examples of resulting curves are provided in Figure 1.

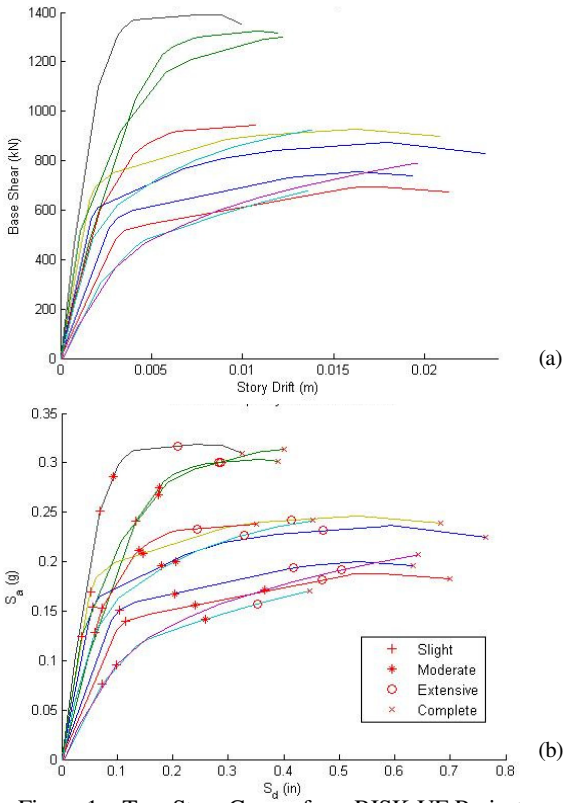

Figure 1 Two-Story Curves from RISK-UE Project: (a) Pushover Curves, and (b) Capacity Diagrams

3.5 Performance Limit States

Limit states are defined according to drift values, but are selected in accordance with both drift and strength values

upon examining the behavior of the structure. There are four structural damage (performance) limit states determined for each building category, which are quantified by slight, moderate, extensive, and complete threshold values. In determining these points, the relationships for yield and ultimate point as defined by Park (1988) are utilized. The slight, moderate, extensive, and complete limit states threshold values are obtained from first yield, yield point of equivalent elasto-plastic system with equal energy absorption, median point of peak plateau, and reduced post-peak load capacity, respectively.

Once these have been determined for each capacity curve, the values for each building category are averaged and stored as the threshold values. Fragility curves are organized into different regions of damage by comparing these values to the displacements resulting from the methodology for structural assessment. An example of the capacity diagrams with limit states for 2-story buildings from the database are given in Figure 2. The parameters for the four damage limit states obtained by this procedure are given in Table 1 for the medium code design category of two story URM buildings.

Table 1 Example Limit State Threshold Values

Spectral Displacement Limit State Thresholds				
Building Category	**Slight**	**Moderate**	**Extensive**	**Complete**
URM2 - Moderate Code	0.0758	0.1920	0.4081	0.6243

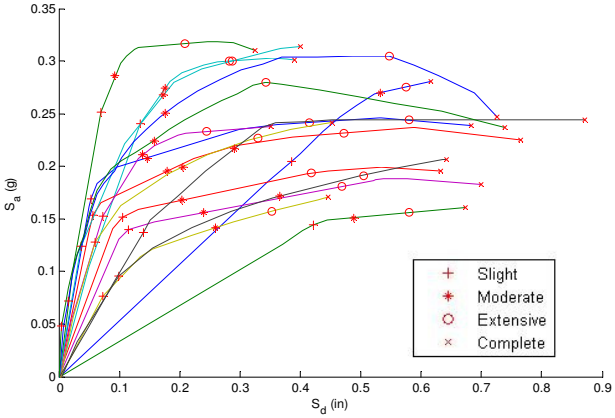

Figure 2 Two-Story Capacity Diagrams with Limit States

These four points result in the classification of five regions of damage realized by the structure under inspection. The first region is that of no damage, for behavior occurring prior to first yielding and stiffness reduction of the building, and the following four regions correspond to achieving a state beyond that of the performance point defined for that region, and are given the same name as the limit state threshold the defines that point. This results in regions classified as none, slight, moderate, extensive, or complete damage. Input parameters from the seismic event being simulated will drive the structure into one of the damage states dependent on where the maximum displacement of the structure falls according to these pre-defined limit states.

3.6 Seismic Design Level

It was determined that there is not a strong enough delineation found in the limit state definitions for URM buildings to justify separating the buildings into more than three categories in terms of seismic design level as is done for many building types (National Institute of Building Sciences, 2003). Therefore, in this paper they are classified in relation to the performance of other URM buildings, and not compared to uniquely different categories of structures composed of materials and configurations not employed by URM buildings. Therefore, according to the description below, URM buildings were categorized relative to one another into the three simple categories of low, moderate, and high seismic use groups as follows.

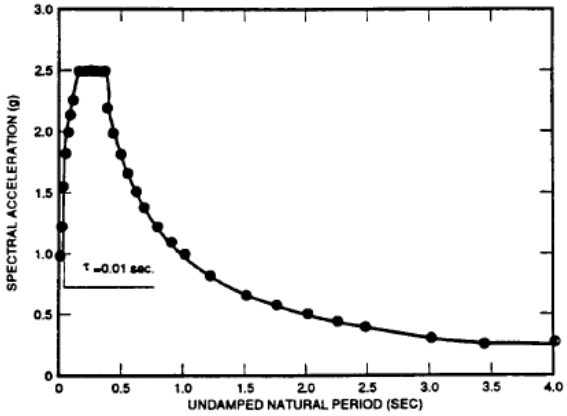

Figure 3 Standard Design Response Spectra (ATC-3-06)

The proposed method for categorizing the structures into appropriate seismic groups involves a combination of force demand and force resistance of the URM buildings. In order to determine seismic force demand, periods were determined for each individual building according to the International Building Code (IBC) equation for estimating the natural period of a structure based on material, type of structural system, and height. The equations referred to in the IBC come from ASCE-7 Section 9.5.2.8

$$T = C_t \left(h_n\right)^x \qquad (1)$$

where x is 0.75, h is the height of the top level of the structure, and C_t is 0.055 for URM structures when h is given in meters. Using a standard design response spectra with 5% damping (Figure 3), spectral accelerations are obtained and then used in determining force demand. In order to estimate force resistance, the formulation for design elastic response acceleration at short periods, S_{DS}, as given in section 1615.1.3 of the IBC must be examined,

$$V_b = \frac{1.2 S_{DS}}{R} W \qquad (2)$$

where V_b is base shear, W is weight of the structure, and R is the force reduction factor. R can be assumed to be

the appropriate constant listed in IBC 1.13.2.2 (ACI 530). Subsequently, Eq. (2) can be solved for S_{DS} which is used to obtain force supplied. This yields the following expression used in this paper to determine seismic use groups:

$$Coeff = \frac{Supply}{Demand} = \left(\frac{V_b}{W} * \frac{R}{1.2}\right) \Big/ S_{a_{(5\%)}} \qquad (3)$$

The resulting coefficients are split uniformly by defining cutoff coefficient levels for each building height category. It becomes clear that beyond building height, the next most controlling factors of seismic design level are dimensions of masonry piers, or effectively the amount of openings in masonry walls. There is a clear correlation as expected between buildings with different known material strengths. It can therefore be concluded that the method developed in this study provides an accurate means for assessing seismic design level of URM buildings.

4. EARTHQUAKE DEMAND

The second component of fragility analysis is the demand imposed on the building stock by the earthquake. There are several methods of representing the lateral forces imposed on structures due to the seismic motion of the ground. The most accurate and rigorous of these methods uses accelerograms, which are chosen for implementation in this study. These ground motion time histories are used because they are capable of reflecting many features of earthquakes such as source distance, depth, site condition, type of fault rupture, and other useful parameters. These characteristics allow for an accurate representation of earthquake demand to be made with the use of a manageable number of records with specified attributes.

Variability in ground motion representation will introduce large levels of uncertainty into the method for fragility analysis when compared to variations in determining capacity and modeling techniques. It is therefore critical to the accuracy of the loss-assessment that the outcome of the fragility analysis is based on selection of appropriate ground motion records. The more precisely that the set of records can match the expected event, the more reliable the resulting analysis and assessment will be.

In this study, source characteristics of the CEUSA take into account the intra-plate region with low levels of attenuation and ground motions that affect large areas. In addition, due to the low probability nature of the region, there are no natural earthquake records that represent a large magnitude event. As a result, synthetically derived accelerograms developed by Fernandez (2007) and based on the stochastic method by Boore (2003) are utilized to represent the strong ground motion to be used in loss assessment for the CEUS.

In the study composed by Fernandez, probabilistic ground motion records were synthetically generated for the seven cities located within the Upper Mississippi Embayment, including Memphis, TN. The motions developed for this city are employed in this study, and contain ground motion records corresponding to two different classifications of site condition. The soil properties that characterize "lowlands" and "uplands" site conditions represent soft soils and competent rock, respectively. A map of the seven cities treated in this study, along with the regions characterized by each soil site classification, can be seen in Figure 4.

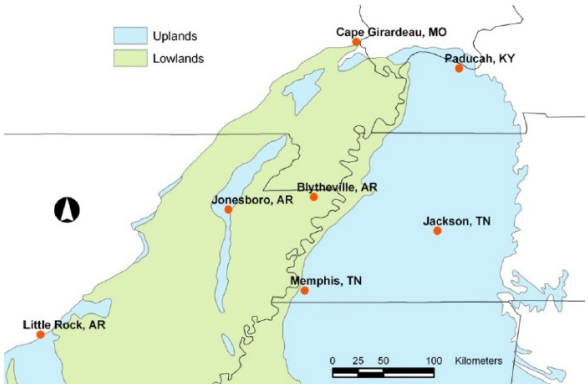

Figure 4 Map of Soil Profiles (Fernandez, 2007)

In this study, the authors incorporated the effects of uncertainties in the source, site, and path characteristics, along with the effect of nonlinear soil behavior in developing ground motion attenuation relationships. These relationships were derived using regression analysis of the spectral accelerations from a point-source based ground motion model, though directivity effects are not accounted for. The uncertainties considered were both epistemic, due to lack of knowledge, missing information, and errors in modeling, and aleatory, due to the fact at many of the factors that affect the resulting relationships are inherently random. This process includes the weighted average of three attenuation relationships, Atkinson and Boore (1995), Frankel et al. (2000) and Silva et al. (2003). An example synthetic record is provided in Figure 5.

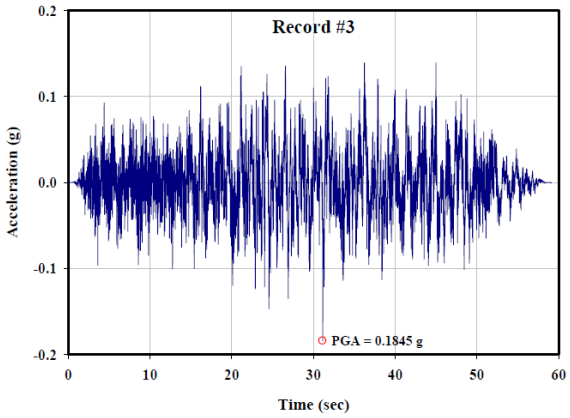

Figure 5 Example of Synthetic Record

The probabilistic ground motions developed in the study are based on hazard levels with 10%, 5%, and 2%

probability of exceedance in 50 years. These probably levels correspond to return periods of 475, 975, and 2475 years. Each set of ground motions contains ten acceleration time histories each for lowlands and uplands soil profiles. The set of synthetically derived accelerograms representing an event with a 975 year return period are selected for use in this study.

The ground motion records are initially scaled such that the peak PGA value is equal to unity, and are subsequently scaled at steps of 0.05 up to the maximum structural resistance of the most resilient buildings in the database. These scaled records are applied in the methodology for structural assessment as described in the following section.

5. STRUCTURAL ASSESSMENT METHODOLOGY

Now that we have developed a database to accurately represent the structural capacity of URM buildings and have also introduced a set of input motions that adequately characterize the ground motion and attenuation relationships relevant to the CEUS, we can use a methodology for structural assessment to obtain an accurate prediction of displacement response data. The intersection of capacity of buildings (supply) and earthquake input (demand) are used to obtain the results which are later statistically evaluated in order to generate the desired fragility relationships.

As building capacity has been represented initially by pushover curves and then converted to equivalent capacity diagrams, a method similar to Capacity Spectrum Method (CSM) is necessary for the assessment of structural responses. CSM was first proposed by Freeman (1978). After appearing in ATC-40 (Applied Technology Council, 1996) it had generated enough interest to spark several additional studies and a variety of proposed improvements.

An overview of four previously developed versions of CSM was conducted and an advanced CSM method developed at the MAE Center, which incorporates the use of nonlinear time history analysis, was compared to other available versions of the CSM and found to be more desirable for use in this type of study (Gencturk, 2007). Updating of bilinear representations of capacity diagrams is also adopted for increased accuracy in assessment. Finally, the Advanced CSM procedure for deriving performance points is chosen because it ensures convergence.

6. FRAGILITY CURVE GENERATION

Fragility curve generation is a statistical analysis performed on the results obtained from the structural response assessment discussed above. The data is a representation of the variance in building capacity under numerous ground motions as assessed using the Advanced CSM method. This procedure is the final component of the proposed framework for fragility analysis and the results yield the desired relationship between damage probability and ground input.

It is the objective of this study to provide parameters that lead to an improved method for generating fragility relationships of URM building stock in a format that can be universally applied to future earthquake hazard and loss assessment studies. The most common form of expressing fragility relationships is to display the exceedance probabilities of certain damage thresholds as a function of the ground input demand. This ground input is most often in terms of parameters such as PGA, PGV, or PGD at a certain period. This will be referred to as the "conventional" format for fragilities presented in this paper. A second and less prominent format of representing vulnerability relationships is considered due to its use in HAZUS (National Institute of Building Sciences, 2003), where the exceedance probabilities are plotted as a function of the structural response of the building.

Conventional fragility curves aim to calculate closed-form equations that will relate seismic excitation parameters at a certain period to a damage state of a building. In this study, the ground motion records are scaled according to PGA, due to the influence of PGA on the behavior of short period structures such as URM buildings. Therefore, PGA is selected as the parameter for use in defining the hazard input in this study. The methodology presented by Wen et al. (2004) is adopted for fragility curve derivation in conventional format.

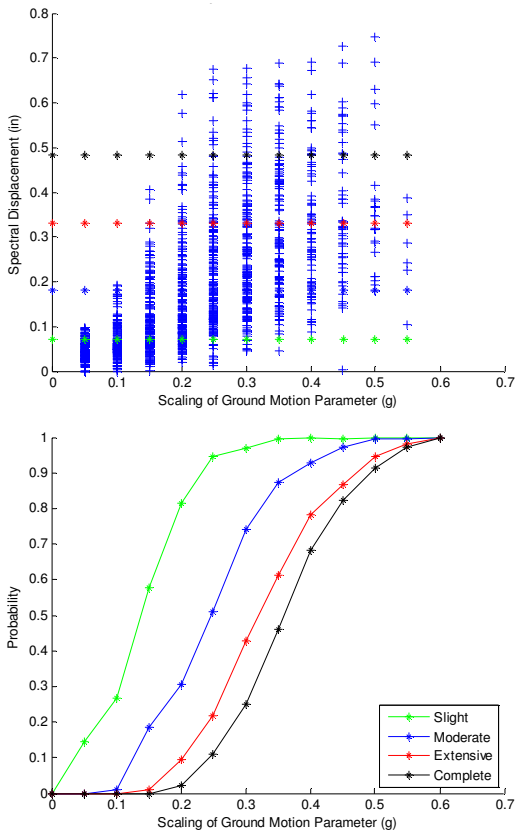

Figure 6 Two-Story Fragility Curve Derivation: (a) Structural Response Data, and (b) Fragility Curve Points

Structural response data is obtained from analysis of the range of demands considered for the varying capacities of structures in the database via structural assessment methods. Probabilistic assessment of this structural response data (Figure 6a) results in the fragilities displayed in Figure 6b.

In is important to note that for most conventional fragility relationships, there are only three limit state threshold values defined, as opposed to the four used in HAZUS compatible fragility relationships. The method with three values is common in that they represent the three society-level consequences that result from earthquake hazards. The definitions are thus directly correlated to the socio-economic concerns regarding serviceability and continued use of facilities, limited economic loss, and life loss prevention. As a result, if the fragility relationships developed in conventional format should demand the use of three limit states for application to specific studies or loss assessment software packages, three appropriate limit states out of the four defined in this study could be chosen. It is natural to combine them in order to represent the final socio-economic limit state of life loss prevention. The impact assessment software platform used at the MAE Center, MAEviz, utilizes three limit states in correlation with the socio-economic situations described above to define four damage regions; i.e. minor, moderate, severe, and collapse.

7. RESULTS

The results that follow from integrating the improved analytical methodologies for assessing building capacity, representing seismic demand, performing structural assessment, and generating fragility curves as laid out in this paper are now presented. This set of improved fragility relationships for URM buildings provides insight into the true behavior of the structures. Both conventional and HAZUS compatible fragility relationships are displayed for each of the two soil site conditions. Curves have been smoothed using lognormal distribution with two parameters.

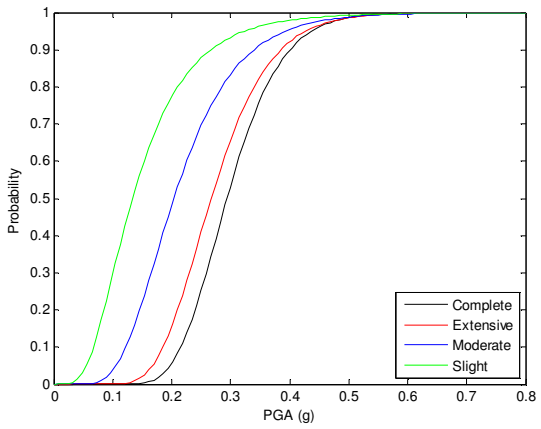

(a)

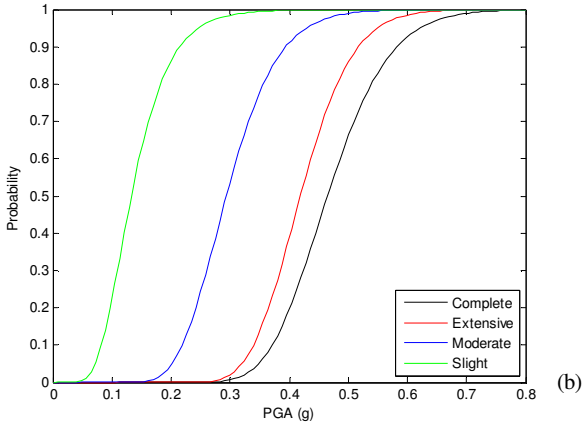

(b)

Figure 7 Two-Storey Conventional Fragility Curves: (a) Low Code, and (b) High Code

Conventional fragility relationships are shown in Figure 7 for low (a) and high (b) code. The probability of reaching limit state thresholds is plotted against the seismic input characteristics in terms of PGA. Results are as anticipated, with higher seismic design levels requiring more intense ground shaking to reach a specific limit state when compared to buildings of lower seismic design levels. HAZUS compatible relationships are shown in Figure 8, where probability is plotted in relation to the structural response in terms of spectral displacement. The HAZUS compatible curves appear counterintuitive because an increase in design level does not increase the limit state parameter reached when plotted in terms of displacement. This is due to the fact that the seismic design level of URM buildings is defined by strength parameters and not in terms of ductility as is common with most other building types.

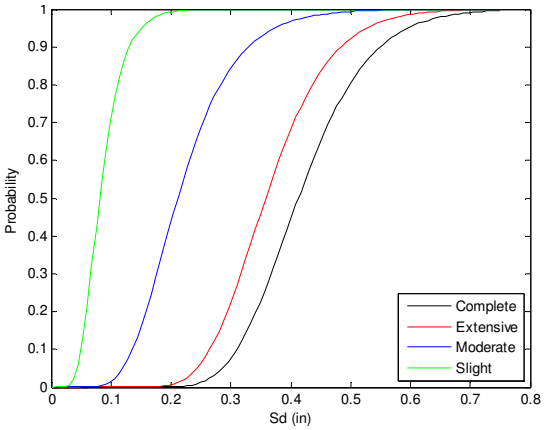

Figure 8 HAZUS Compatible Fragility Relationship for Two-Story URM Buildings

Finally, the fragility curves can be separated according to soil site, and plotted together. This results in the generation of nine sets of fragility curves, one for each building height class and seismic design category. An example of one of these sets is displayed in Figure 9.

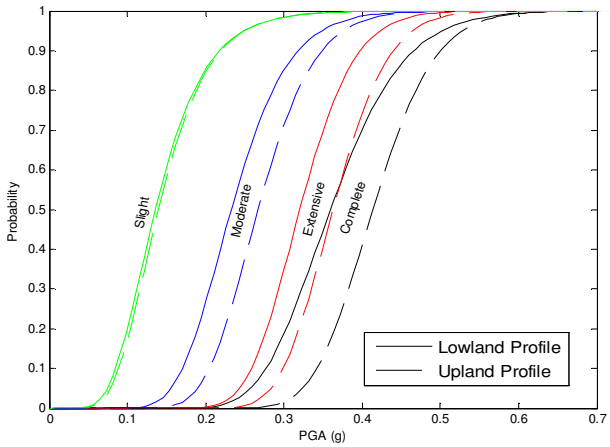

Figure 9 Fragility Curves for Medium Code Two-Story URM Buildings

8. CONCLUSIONS

An improved simulation-based framework for relating ground motion intensity to the probability of reaching discrete structural damage levels has been developed for unreinforced masonry buildings. Specific focus is due to the prevalence of this building class in the CEUS and globally, along with the brittle nature of URM structures. The framework for developing these relationships is composed of careful selection, definition, and execution of building capacity, seismic demand, methodology for structural assessment, and methodology for fragility curve generation in order to represent the true behavior of URM buildings.

The building capacities are represented by a database of simulation-based pushover curves available in the literature. A comprehensive set of best practices are developed for this data selection process. Pushover curves are separated by building heights of 1-3 stories, representing a wide variety of URM building parameters including material strength, pier and spandrel geometry, and construction techniques. Curves are converted to capacity diagrams in A-D format and performance limit states and thresholds are defined based on pre-established and widely accepted criteria. In order to provide a comprehensive set of fragilities, building types are classified according to three seismic design levels: low, medium and high. Differentiation in terms of seismic design levels is based on a simple seismic coefficient developed for this study, specific to URM application and comprised of base shear capacity over seismic demand.

Demand is represented by synthetically generated ground motion records developed by Fernandez (2007) to be representative of the seismic characteristics of the NMSZ with two soil profiles within the CEUS considered, lowlands (soft soils) and uplands (competent rock).

Shortcomings in the ability of traditional CSM approaches to predict displacement demands were observed in Gencturk (2007) and a previously verified advanced CSM that incorporates inelastic dynamic analysis was used in this study.

Fragility curves were generated by integrating the improved analytical methodologies for assessing building capacity and representing seismic demand by performing structural assessment and probabilistic analysis as have been laid out in this paper. The resulting fragility curves are presented in conventional and HAZUS-compatible formats, and the characteristics and implications of these results have been discussed. Conventional fragility curves plot probability of exceedance against ground input motion, while the HAZUS-compatible curves compare the probability of exceedance against structural response. Each set of curves is shown to accurately represent the real behavior of the buildings analyzed. The results are a set of improved fragility relationships for URM buildings that are in a format suitable for application in various loss assessment software packages.

The framework proposed in this paper is amenable to rapid and efficient updating with additional pushover curves and ground motion records as necessary. The outcome of the work presented herein is a set of simulation-based fragility relationships that is more reliable than those generated by empirical methods. Owing to the rigorous models, limit state definitions and input motion used, the relationships are recommended for use in HAZUS and other impact assessment software for use in earthquake loss assessment studies for regions within the CEUS. The new fragility curves are of interest to researchers, due to the new derivation approach presented, and to risk modelers and managers, due to the reliability of impact assessments obtained from their use. The importance of the work presented in this study is emphasized by the brittle and severe failure modes of URM buildings and the high building stock population of URM structures present in many regions of the world, for which this advanced analysis-based fragility generation method can be applied.

Acknowledgements:

The authors acknowledge the support of the Federal Emergency Management Agency (FEMA) for funding of the New Madrid Catastrophic Planning Initiative and the National Science Foundation (NSF) for establishing the Mid-America Earthquake Center (MAEC) at the University of Illinois, Urbana-Champaign.

References:

Abrams, D. P. and Shah, N. (1992). “Cyclic Load Testing of Unreinforced Masonry Walls,” Advanced Construction Technology Center, Department of Civil Engineering, University of Illinois at Urbana-Champaign, Urbana, IL.

Applied Technology Council (1996). Seismic Evaluation and Retrofit of Concrete Buildings, Report ATC-40.

Applied Technology Council ATC-3-06 Tentative Provisions, 1984

Atkinson, G. M. and Boore, D. M. (1995). "Ground-motion relations for eastern North America," Bulletin of the Seismological Society of America, 85(1), 17-30.

Boore, D. M. (2003). "Simulation of Ground Motion Using the Stochastic Method," Pure and Applied Geophysics, 160(3), 635-676.

Costley, A. C. and Abrams, D. P. (1995). “Dynamic Response of Unreinforced Masonry Buildings with Flexible Diaphragms,”

PhD Thesis, Department of Civil Engineering, Unviersity of Illinois at Urbana-Champaign, Urbana, IL.

Epperson, G. S. and Abrams, D. P. (1989). "Nondestructive Evaluation of Masonry Buildings," Advanced Construction Technology Center, Department of Civil Engineering, University of Illinois at Urbana-Champaign, Urbana, IL.

Fajfar, P. (2000). "A Nonlinear Analysis Method for Performance-Based Seismic Design," Earthquake Spectra, 16(3), 573-592.

Fernandez, A. (2007). "Numerical Simulation of Earthquake Ground Motions in the Upper Mississippi Embayment," School of Civil and Environmental Engineering, Georgia Institute of Technology, Atlanta, GA.

Frankel, A. D., Mueller, C. S., Barnhard, T. P., Leyendecker, E. V., Wesson, R. L., Harmsen, S. C., Klein, F. W., Perkins, D. M., Dickman, N. C., Hanson, S. L. and Hopper, M. G. (2000). "USGS National Seismic Hazard Maps," Earthquake Spectra, 16(1), 1-19.

Freeman, S. A. (1978). "Prediction of Response of Concrete Buildings to Severe Earthquake Motion," American Concrete Institute, Publication SP-55, 589-605.

Gencturk, B. E. (2007). "Fragility Relationships for Populations of Buildings Based on Inelastic Response," MS Thesis, Department of Civil and Environmental Engineering, University of Illinois at Urbana-Champaign, Urbana, IL.

HAZUS Technical Manual (National Institute of Building Sciences, 2003).

Kim, H., Min, K.-W., Chung, L., Park, M. and Lee, S.H. (2005). "Evaluation of Capacity Spectrum Method for Estimating the Peak Inelastic Responses," Journal of Earthquake Engineering, 9(5), 695-718.

Magenes, G., Calvi, G. M., and Kingsley, G.R. (1995). "Seismic Testing of a Full-Scale, Two-Story Masonry Building: Test Procedure and Measured Experimental Response," Experimental and Numerical Investigation on a brick Masonry Building Prototype – Numerical Prediction of the Experiment, Report 3.0. University of Pavia, Department of Structural Mechanics, Pavia, Italy.

Magenes, G. (2000). "A Method for Pushover Analysis in Seismic Assessment of Masonry Buildings," *Twelfth World Conference on Earthquake Engineering,* Auckland, New Zealand.

National Institute of Building Sciences, 2003

Park, R. (1988). "Ductility Evaluation from Laboratory and Analytical Testing." *Proc. of the 9th World Conference on Earthquake Engineering*, VIII, Tokyo-Kyoto, Japan, 605-616.

Park, J., Towashiraporn, P., Craig, J. I. and Goodno, B. J. (2009). "Seismic fragility analysis of low-rise unreinforced masonry structures," Engineering Structures, 31, 125-137.

Penelis, Gr. G., Kappos, A. J., Stylianidis, K. C. and Lagomarsino, S. (2002). "Statistical Assessment of the Vulnerability of Unreinforced Masonry Buildings," Lab of R/C Structures, Dept. of Civil Engineering, Aristotle University of Thessaloniki, Thessaloniki and Department of Structural and Geotechnical Engineering, University of Genoa, Genoa.

Salonikios, T., Karakostas, C., Lekidis, V. and Anthoine, A. (2003). "Comparative inelastic pushover analysis of masonry frames," Engineering Structures, 25, 1515-1523.

Silva, W., Gregor, N. and Darragh, R. (2003). Development of Regional Hard Rock Attenuation Relations for Central and Eastern North America, Mid-Continent and Gulf Coast Areas, Pacific Engineering and Analysis, El Cerrito, California.

Wen, Y. K., Ellingwood, B. R. and Bracci, J. M. (2004). *Vulnerability Function Framework for Consequence-Based Engineering,* Project DS-4 Report, Mid-America Earthquake (MAE) Center, Urbana, IL.

JOINT CONFERENCE PROCEEDINGS
7th International Conference on Urban Earthquake Engineering (7CUEE) &
5th International Conference on Earthquake Engineering (5ICEE)
March 3-5, 2010, Tokyo Institute of Technology, Tokyo, Japan

FULL SCALE SHAKING TABLE COLLAPSE EXPERIMENT ON4-STORY STEEL MOMENT FRAME: PART 1 OUTLINE OF THE EXPERIMENT

Satoshi Yamada[1], Keiichro Suita[2], Yuichi Matsuoka[3] , Yuko Shimada[4] , Motohide Tada[5] , and Kazuhiko Kasai[6]

1) Associate Professor, Structural Engineering Research Center, Tokyo Institute of Technology, Japan
2) Professor, Dept. of Architecture and Architectural Eng., Kyoto Univ., Japan
3) Nippon Steel Engineering Co., LTD., Japan
4) Graduate Student, Tokyo Institute of Technology, Japan
5) Professor, Division of Global Architecture, Osaka Univ.,
6) Professor, Structural Engineering Research Center, Tokyo Institute of Technology, Japan
naniwa@serc.titech.ac.jp, suita@archi.kyoto-u.ac.jp, matsuoka.yuuichi@nsc-eng.co.jp
shimada.y.ab@m.titech.ac.jp, tada@arch.eng.osaka-u.ac.jp, kasai@serc.titech.ac.jp

Abstract: Shaking table test of full-scale 4-story building was carried out at E-defense. The objectives of this experiment are to evaluate structural and functional performance of the steel building under design-level ground motions, and to determine the safety margin against collapse under exceedingly large ground motions. In this part, protocols of the excitation and out line of the result are reported.

1. INTRODUCTION

1.1 General

In order to evaluate structural and functional performance of the steel moment frame under design-level ground motions, and to determine the safety margin against collapse under exceedingly large ground motions, full-scale shaking table test of 4-story steel building was carried out at E-defense. This test is a part of the experimental project on steel buildings conducted at the E-Defense shake-table facility. The overview of the project is presented in Kasai et al. (2007). The building specimen was designed current Japanese specifications and practices. In this test, not only seismic performance of structural system, but also seismic performances of non-structural components are examined. In this part, out line of the specimen, out line of the experimental method, and elastic behavior of the specimen are reported. The detail of elasto-plastic behaviors and collapse behaviors of the specimen building are shown in the companion paper by K. Suita et al. (2010)

1.2 Scenario for Complete Collapse

A seismic-resistant steel moment frame aims to contain plastic deformation in beams (and other energy dissipating elements), to limit yielding of the columns, and thereby, to maintain the gravity sustaining capacity and avoid collapse. The current seismic regulations ensure ductile deformation capacity of beams by specifying width-to-thickness ratio limits for the beam cross-section. As long as the story shear strength is sufficient to resist the P-Δ moment produced by gravity loads, the moment frame will not collapse [Figure 1(a)]. On the other hand, as observed in the Northridge and Kobe earth-quakes, fracture of welded moment connections causes deterioration of beam strength, and hence reduces story shear strength [Figure 1(b)], thereby making the building more vulnerable to collapse. There is another possible scenario for collapse. Due to recently adopted improvements, there is little likelihood that moment connections would fracture even under exceedingly large ground motions. However, strain hardening in the plastic hinges could increase story shear forces, which in turn, would increase the forces developed in the columns. If the columns are not designed for the increased forces, i.e., if the width-to-thickness ratio of the cross-section is not small enough to develop the increased forces, then local buckling could occur in the columns. Strength deterioration in the lower-story columns could shift the controlling mechanism of the frame from the overall sway mechanism [Figure 1(a), (b)] to a weak story collapse mechanism [Figure 1(c)]. Based on detailed examination, weak story collapse mechanism due to deterioration in column strength was identified to be the most likely scenario for collapse of a moment frame constructed according to the cur-rent Japanese code.

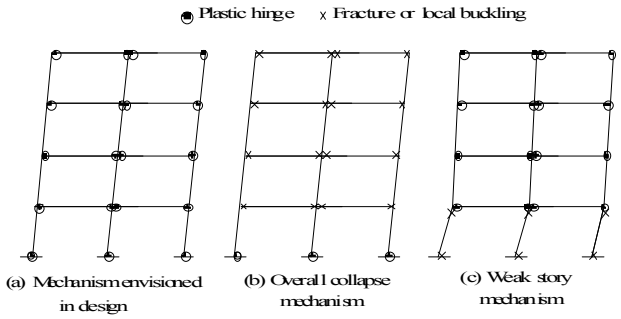

Figure 1 Collapse mechanism of steel moment frame

2. SPECIMEN

2.1 Design Consideration

The building specimen was designed within the following conditions and constraints.

1. Due to the loading capacity of the shaking table and safety considerations, a four-story, two-bay by one-bay steel moment frame was deemed the optimal configuration.
2. The structure was designed following the most common design considerations exercised in Japan for post-Kobe steel moment frames.
3. Welding details with no weld access hole, which are recommended after the Kobe earthquake [JASS6 1996], are adopted for the beam-to-column connections. This is a premium detail to ensure ductile deformation capacity and strain hardening of the beam. And sections with relatively large width-to-thickness ratio were selected for columns.. Those increase the applied forces in columns, and increase the likelihood that local buckling and the consequent strength degradation occur in the columns.
4. The frame should remain elastic and the story drift should be less than 1/200 for Level-1 design earthquake load (computed with a base shear coefficient of 0.2). At the ultimate state (plastic collapse of the frame), the base shear coefficient should be greater than 0.3 (to meet the requirements of Level-2 design).
5. The strong column-weak beam philosophy is employed. Specifically, at each story, the sum of design column strength is more than 1.5 times greater than the sum of the design strength of the beams and 1.3 times greater than the sum of the design strength of the panel zone.
6. Exposed base plate connection with enough rigidity is adopted for the column bases. The design strength of the column base connection, which is controlled by the yield strength of anchor bolts, is between 1.3 and 1.8 times greater than the design strength of columns. The rigid column base connection is expected to increase the likelihood that local buckling and the consequent strength degradation occur at the column base.

2.2 Framing System and Conformance to Code Requirements

The building has plan dimensions of 10 m in the longitudinal direction (Y) and 6.0 m in the transverse direction (X). Each story is 3.5 m high, making the overall story height equal to 14 m. Table 1 shows a list of sections and Table 2 shows the specified and measured material properties of steel members. The wide flange beams ranged from 340 to 400 mm deep, and columns were of square hollow sections of 300 mm wide. The nominal steel strength is 235 and 295 N/mm^2 for the beam and column, respectively. The measured yield strength of columns was rather lower than average actual strength of this type of materials. On the other hand, the yield strength of wide-flanges for beams are fairly larger than specified values. Therefore, the actual strength ratios of columns to beams of the specimen frame are lower than expected in design. Metal decks are connected to the beams through studs which are welded to the beam top flanges through the metal decks. Wire-meshes are placed above the metal deck sheets, and concrete is placed on site. Fully composite action is expected between the steel beams and concrete slab.

The story shear versus story drift relationships at each story, obtained from pushover analyses of the test specimen are shown in Figure 3. In these analyses, the earthquake load distribution specified in the code pro-visions was used. Solid lines are analytical results based on the measured yield strength of material, and the broken lines are analytical results based on the nominal strength of material. The story drift at the Level-1 design earthquake load is indicated by open circles. At this load level, the frame was elastic, and the story drift at each story was less than 1/200. The story drift when the maximum story drift was equal to 1/50 is indicated by filled circles. At this stage, the base shear coefficient was 0.46 in the Y-direction and 0.47 in the X-direction. Therefore, the analysis shows that the structure satisfies essential code requirements. The natural periods of the specimen in Y-direction calculated from these analysis models are 0.90s in 1st mode and 0.29s in 2nd mode, respectively. The total weight of specimen is 2113kN.

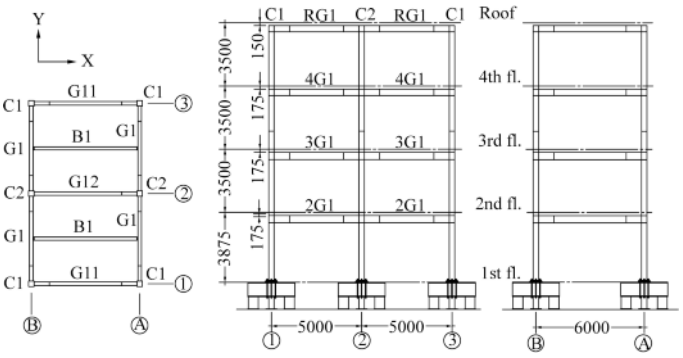

(a) plan (b) Y-elevation (c) X-elevation

Figure 2 Specimen (4-Story Steel Moment Frame)

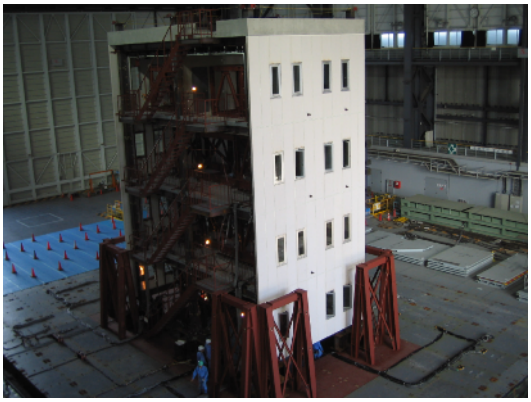

Photo 1 Specimen Building

Table 1 List of member sections

Floor	beam* G1 (SN400B)	G11 (SN400B)	G12 (SN400B)
R	H-346×174×6×9	H-346×174×6×9	H-346×174×6×9
4	H-350×175×7×11	H-350×175×7×11	H-340×175×9×14
3	H-396×199×7×11	H-400×200×8×13	H-400×200×8×13
2	H-400×200×8×13	H-400×200×8×13	H-390×200×10×16

Story	column** C1,C2 (BCR295)
4	SHS-300×300×9
3	SHS-300×300×9
2	SHS-300×300×9
1	SHS-300×300×9

* wide flange section
height x width x web thickness
x flange thickness

** square hollow section
height x width x thickness

Table 2 Material properties

	section	element	Specified Properties sy *	su *	Measured Properties sy *	su *
Beam	H-340×175×9×14	flange	235	400	309	443
		web	-	-	355	468
	H-346x174x6x9	flange	235	400	333	461
		web	-	-	382	483
	H-350x175x7x11	flange	235	400	302	441
		web	-	-	357	466
	H-390x200x10x16	flange	235	400	297	451
		web	-	-	317	458
	H-396x199x7x11	flange	235	400	311	460
		web	-	-	369	486
	H-400x200x8x13	flange	235	400	326	454
		web	-	-	373	482
column	SHS-300x300x9	2nd-4th story	295	400	332	419
		1st story	295	400	330	426

* Unit N/mm^2

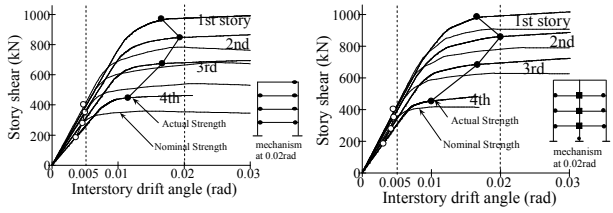

(a) x-direction (transverse) (b) y-direction (longitudinal)

Figure 3 Story shear versus story drift relationships obtained from pushover analyses

3. EXPERIMENTAL METHOD

3.1 Set-up

Specimen building was set on the center of the shaking table. Each column base is connected to steel foundation beams which are tied down to the shaking table. A safeguard system consists of the three safety features to protect the shaking table from damage during the collapse test was designed as shown in Figure 4. (1) Diagonal wires attached to the first and second stories and each span of the perimeter frame to prevent inter-story drift beyond 1/3.5 rad. (2) Tables placed on the floor slab of each story to arrest the floor slab dropping from the upper story. (3) A fence surrounding the specimen which prevents exceedingly large story drift at the first story.

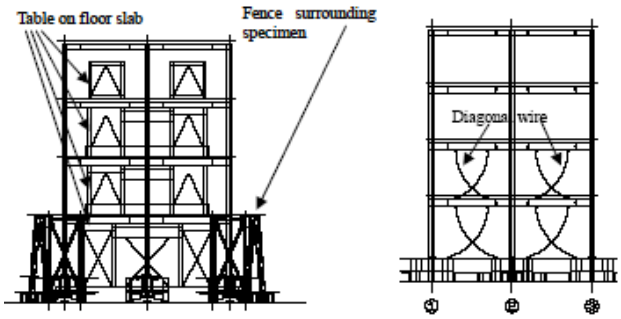

Figure 4 Safe guard system protect shaking table

3.2 Excitation

At first, free vibration test was carried out to exam-ine the fundamental natural period and damping co-efficient of the specimen. Then, several seismic excitations with different input level were applied to the specimen. In the seismic excitation, JR Takatori station Record [Nakamura et al. 1995] was used as in-put wave. NS, EW, and UD components were considered for the Y, X, and Z directions. The positive direction of each coordinate corresponded to South, West, and Up direction, respectively. Response velocity spectrum is shown in Figure 5. Input wave has strong peak at slightly longer period than the pre-dicted fundamental natural period of the specimen. So, large amount of energy input can be expected along with the yielding of the specimen. List of the main excitation is shown in Table 3. The excitation level is expressed as the amplification factor which is multiplied to the original record.

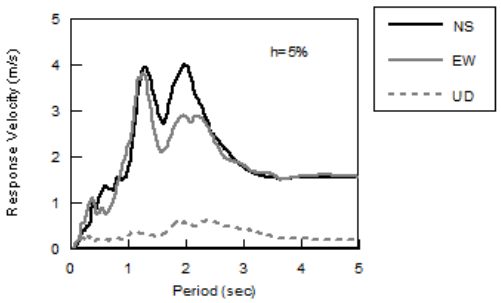

Figure 5 Response velocity spectrum of the JR Takatori station record

Table 3 List of the excitation

Number of the excitation	Amplification factor	State of the specimen	
1	0.05	elastic	
2	0.1	elastic	
3	0.125	elastic	
4	0.2	elastic	corresponding to the design earthquake level-1
5	0.4	elasto-plastic	corresponding to the design earthquake level-2
6	0.6	elasto-plastic	
7	1.0	collapse	

3.3 Measurement

To measure 3-dimensional dynamic behavior of the specimen building, a total of 945 instrumentations are used.

Main measurement items are followings; In order to measure acceleration, three dimensional servo type accelerometers were set up in the center and the four corners of the upper surface of the shaking table and each floor as shown in Figure 6. Inertial force in each direction was obtained by multiplying acceleration to mass of the story. Both laser-type and potentiometer-type displacement transducer were set to directly measure story drift and rotation as shown in Figure 6. These displacement sensors are accurate but not able to measure large displacement because of those capacities. So, in the collapse excitation, three dimension behavior of the 1st and 2nd story were measured by other potentiometer type displacement transducers with large capacity. Rotation angle of beams and columns and deformation of panel zones are also measured by displacement transducers as shown in Figure 7. Restoring forces were measured by strain gauges located at the elastic portion of beams and columns as shown in Figure 8. Besides these, displacement transducers to measure the behavior of non-structural components were in-stalled.

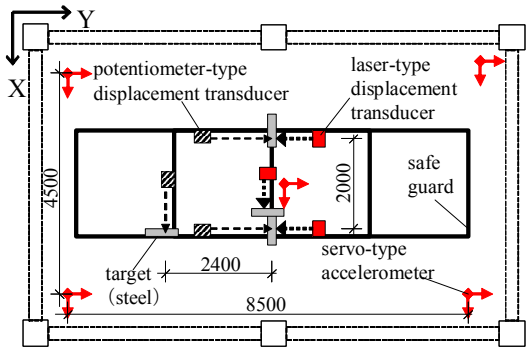

Figure 6 Accelerometers and displacement transducers in each story

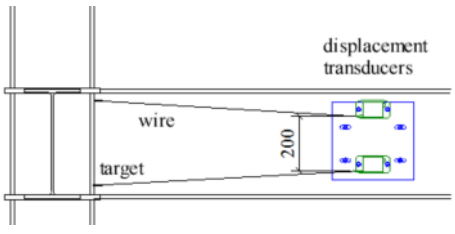

Figure 7 Measurement of rotation angle of beam

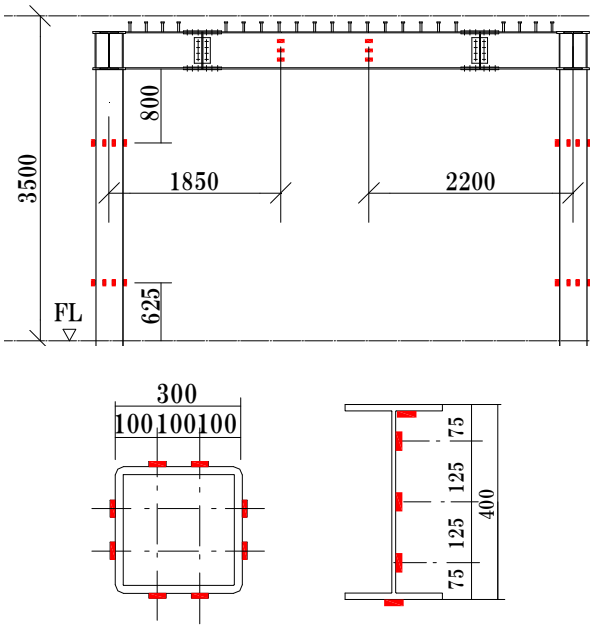

Figure 8 Strain gauges

4. EXPERIMENTAL RESULTS IN ELASTIC RANGE

4.1 Fundamental Natural Period and Damping Factor of the Specimen Building

Before main excitation, free vibration test was carried out to examine the fundamental natural period and damping factor of the specimen building. Time histories of strain gauges are shown in Figure 9 as test results. Fundamental natural period of X and Y direction are 0.80 sec and 0.76 sec, and damping factor of X and Y direction are 2.1% and 2.3% respectively.

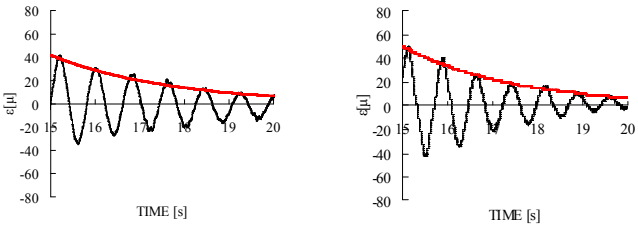

(a)X-Direction (b) Y-Direction

Figure 9 Results of the free vibration tests

4.2 Response under Level 1 excitation

Story shear and story drift angle relationships in X and Y directions at the 1st and 2nd stories are shown in Figure 10. Under Level-1 excitation, maximum story drift angle at each story reached around 1/200 of the design criteria. Slight non-linearity is observed in the Figure10. But each member kept in elastic range under this excitation. That is because story shear in those relationships are calculated by the inertial force obtained from the acceleration record on each floor times mass of the story. It is sum of restoring forces and damping forces related to the whole structural and non-structural components of the specimen building. So, non-linearity in the story shear and story drift angle relationships are thought to be caused by damping.

4.3 Elastic stiffness

Elastic stiffness of each story obtained from story shear and story drift relationship by the least square method are shown in Table 4. In the table, Kbu is the elastic stiffness of whole building including non-structural components. *Kbu* is calculated from story shear which is obtained by inertial force. *Kfr* is the elastic stiffness of framing system. *Kfr* is calculated from story shear which is obtained by restoring force of column measured by strain gauges. *Ka′* is elastic stiffness of the framing system obtained from pushover analysis. Comparing *Kbu* with *Kfr*, *Kbu* is larger than *Kfr* because of the contribution of the stiffness of non-structure components. Comparing *Kfr* and *Ka′*, *Kfr* are larger than *Ka′* in 1st and 4-th story. In 4-th story, stiffness of the parapet is thought to be affected to the elastic stiffness of the story. And in the 1st story, rigidity of the column base is thought to be affected to the elastic stiffness of the story.

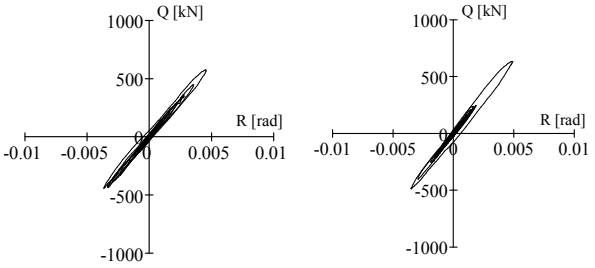

(a)X-direction of 1st Story (b) Y-direction of 1st Story

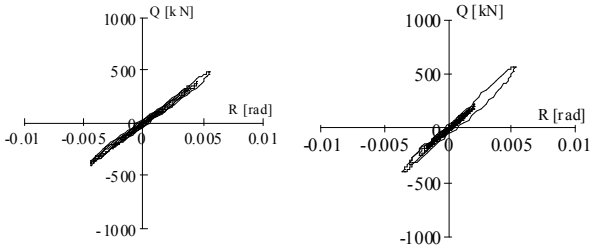

(c)X-direction of 2nd Story (d) Y-direction of 2nd Story

Figure10 Story shear and story drift angle relationship under Level 1 excitation

Table 4 Elastic stiffness

Story	X-direction			Y-Direction		
	Kbu (MN/m)	Kfr (MN/m)	Ka' (MN/m)	Kbu (MN/m)	Kfr (MN/m)	Ka' (MN/m)
4	25.2	18.9	14.7	25.6	20.7	17.4
3	22.7	18.2	17.3	27.4	20.9	19.2
2	24.5	20.1	20.2	28.7	22.3	22.1
1	32.6	27.8	21.9	33.4	29.6	22.3

5. CONCLUSION

In this paper, outline of the specimen building, out-line of the experimental method and experimental results of elastic excitation of the full-scale shaking table test of 4 story steel building were reported. Under level-1 excitation, specimen building remains elastic and generated maximum story drift almost corresponds to the design criteria.

ACKNOWLEDGEMENT

This study is a part of “NEES/E-Defense collabora-tive research program on steel structures”, and was pursued by the Building Collapse Simulation Work-ing Group (WG). The Japan team leader for the overall program is Kazuhiko Kasai, Tokyo Institute of Technology, and the WG leader is Keiichiro Suita, Kyoto University. The writers acknowledge National Research Institute for Earth Science and Disaster Prevention. Special thanks are given to many WG members for their significant efforts on analysis, design, and experiments.

REFERENCES

Japanese architectural standard specification JASS 6 steel work, 7th Ed., The Architecture Institute of Japan, 1996 (in Japanese).

Kasai, K., Ooki, Y., Motoyui, S., Takeuchi, T. and Sato, E. (2007). E-Defense Tests on Full-Scale Steel Buildings : Part 1 ¬ Experiments Using Dampers and Iso-lators, Proc. Structural Congress 2007, ASCE, Long Beach.

Nakamura, Y., Uehan, F. and Inoue, H. (1995), Wave-form and its analysis of the 1995 Hyogo-Ken-Nanbu earthquake information, Railway Technical Research In-stitute, No. 23d (in Japanese).

Suita, K., Yamada, S., Tada, M., Kasai, K., Matsuoka, Y. and Shimada, Y. (2010). Full Scale Shaking Table Collapse Experiment on 4-Story Steel Moment Frame: Part 2 Detail of Collapse Behavior, 7CUEE&5ICEE, Yokohama, Japan.

JOINT CONFERENCE PROCEEDINGS
7th International Conference on Urban Earthquake Engineering (7CUEE) &
5th International Conference on Earthquake Engineering (5ICEE)
March 3-5, 2010, Tokyo Institute of Technology, Tokyo, Japan

FULL SCALE SHAKING TABLE COLLAPSE EXPERIMENT ON 4-STORY STEEL MOMENT FRAME: PART 2 DETAIL OF COLLAPSE BEHAVIOR

Keiichiro Suita[1)], Satoshi Yamada[2)], Yuichi Matsuoka[3)], Yuko Shimada[4)], Motohide Tada[5)], and Kazuhiko Kasai[6)]

1) Professor, Department of Architecture and Architectural Engineering, Graduate School of Engineering, Kyoto University, Japan
2) Associate Professor, Structural Engineering Research Center, Tokyo Institute of Technology, Japan
3) 5Reseacher, Hyogo Earthquake Engineering Research Center, NIED, Japan
4)Graduate Student, Structural Engineering Research Center, Tokyo Institute of Technology, Japan
5) Professor, Division of Global Architecture, Graduate School of Engineering, Osaka University, Japan
6) Professor, Structural Engineering Research Center, Tokyo Institute of Technology, Japan
suita@archi.kyoto-u.ac.jp, naniwa@serc.titech.ac.jp, matsuoka.yuuichi@nsc-eng.co.jp, shimada.y.ab@m.titech.ac.jp, tada@arch.eng.osaka-u.ac.jp, kasai@serc.titech.ac.jp

Abstract: A shaking table test on a full-scale steel building was conducted at the E-Defense shake table facility to evaluate structural and functional performance of the building under design-level ground motions and the safety margin against collapse under exceedingly large ground motions. This paper presents detailed results concerning the nonlinear response of the specimen by 0.4, 0.6 and 1.0 times Takatori records of 1995 Hyogoken-Nanbu earthquake. The detailed behavior of the deteriorated structural members and the process to the complete collapse of a steel moment frame designed in current seismic code are discussed.

1. INTRODUCTION

This study is a part of a shaking table test on a full-scale steel building conducted at the E-Defense shake table facility to evaluate structural and functional performance of the steel building under design level ground motions and the safety margin against collapse under exceedingly large ground motions. The overview of the project is presented by Kasai et al. (2007).

The specimen is a 4-story moment resisting frame designed and constructed according to the current design specifications and practice as shown in Figure 1. The lateral resistance of each story satisfies strength and stiffness requirements of seismic codes and the overall sway mechanism at the ultimate state was verified by static pushover elasto-plastic analysis as shown in Figure 2 in which the thin lines show results based on the nominal

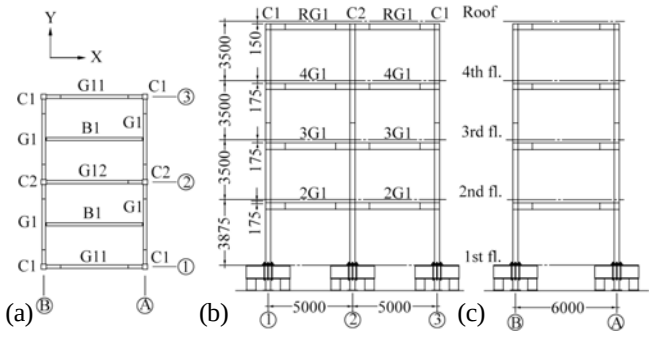

Figure 1 Framing and elevation of specimen (unit: mm): (a) plan, (b) Y-elevation, (c) X-elevation

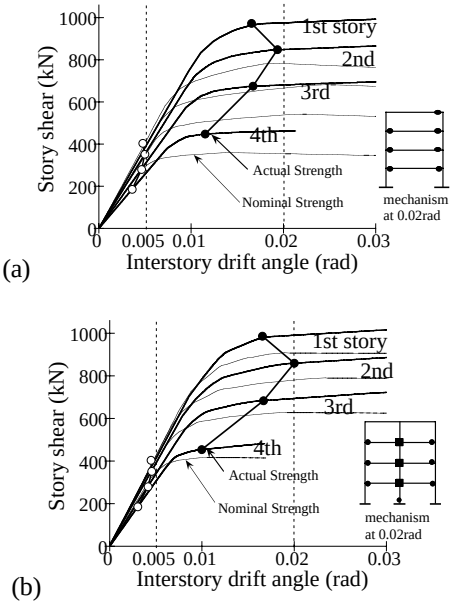

Figure 2 Story shear and interstory drift angle relationships obtained from pushover analyses: (a) X-direction, (b) Y-direction

material strength and thick lines show results from the actual material strength obtained from coupon tests. However, strain hardening in the beam plastic hinges could increase story shear forces, which in turn, would increase the forces developed in the columns. If the columns are not designed for the increased forces, i.e., if the width-to-thickness ratio of the cross section is not small enough to develop the increased forces, then local buckling could occur in the columns. Strength deterioration in the lower-story columns could shift the controlling mechanism of the frame from the overall sway mechanism to a weak story collapse mechanism. Based on these and detailed analytical investigations by Tada et al. (2007), weak story collapse mechanism due to deterioration in column strength was identified to be the most likely scenario for collapse of a moment frame constructed according to the current Japanese seismic code. Therefore, the building specimen was expected to show this type of collapse mechanism. The details of the specimen, plan of experiment, instrumentations and excitation are described in the companion paper by Yamada et al. (2010).

The specimen was subjected to motions as recorded during the 1995 Kobe earthquake at the JR Takatori station. The test consisted of repeated application of the records with progressively increasing scale factors from 0.05 to 1.0. In the response under 0.2 times Takatori, the peak story drift angle is less than 0.005 and no yielding is observed in structural elements. The detail of elastic response and dynamic characteristics of the specimen are shown in the companion paper by Yamada et al. (2009). This pa-per focuses on test results by 0.4 to 1.0 times Takatori records. The test earthquake scale factors and responses are summarized in Table 1

Table 1 Earthquake Scale Factor and Summary of Response

Factor	Response of specimen
0.2	No yielding in steel structural elements. Peak story drift angle less than 0.005 rad. Equivalent to Level 1 design earthquake (PGV=0.25 m/s).
0.4	Slight yielding. Peak story drift angle about 0.01 rad. Equivalent to a Level 2 earthquake (PGV=0.5m/s).
0.6	Yielding. Peak story drift angle about 0.02 rad with residual drift ratio about 0.003 rad.
1.0	Collapse at the 1st story.

2. INELASTIC RESPONSE BY LEVEL 2 EARTHQUAKE

2.1 Response of story

As the records equivalent to a Level 2 design earthquake (peak ground velocity is 0.5m/s), 0.4 times Takatori records are used. The shear force and story drift angle relationships in X and Y direction at the 1st and 2nd story are shown in Figure 3. The story shear force is estimated as the inertial force obtained from the acceleration record on each floor times mass of the story. Therefore, it

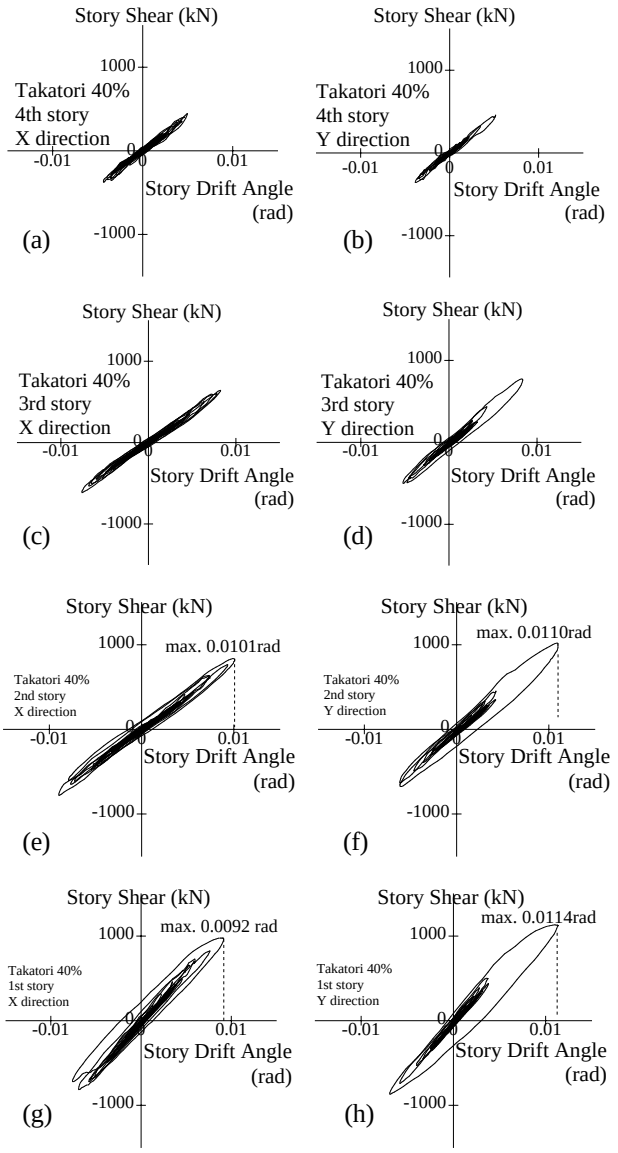

Figure 3 Story shear force and interstory drift relationships by 0.4 Takatori records : (a) 4th story, X-direction, (b) 4th story, Y-direction, (c) 3rd story, X-direction, (d) 3rd story, Y-direction, (e) 2nd story, X-direction, (f) 2nd story, Y-direction, (g) 1st story, X-direction, (h) 1st story, Y-direction

equivalents to the sum of restoring forces and damping forces relate to the whole structural and non-structural components of the story. The peak story drift angle is 0.0114rad at the 1st story and obviously yielded at 1st and 2nd story. The largest inelastic behaviors were observed at panel zones.

2.2 Behavior of structural members

Figure 4 shows response of primary structural members in Y-direction at the 1st and 2nd story. In these figures, the rotation is defined between the inflection point and the end of the member, and the panel moment is defined as shear force of the panel multiplied by the depth. All columns of the first story are slightly yielded (Figure 4a) at the base and

remained in elastic at the top side. All beams behaved in elastic manner because of composite action with concrete slabs and remarkably large actual yield strength of beams compared with other structural members. The primary plastic deformation is observed in the panels of the center columns at the 2nd and 3rd floor level (Figure 4b). At the side columns, panels are also yielded but panel moments are slightly less than the full plastic strength. Both in X and Y direction, the frame behaved in a overall sway mechanism as intended in the design.

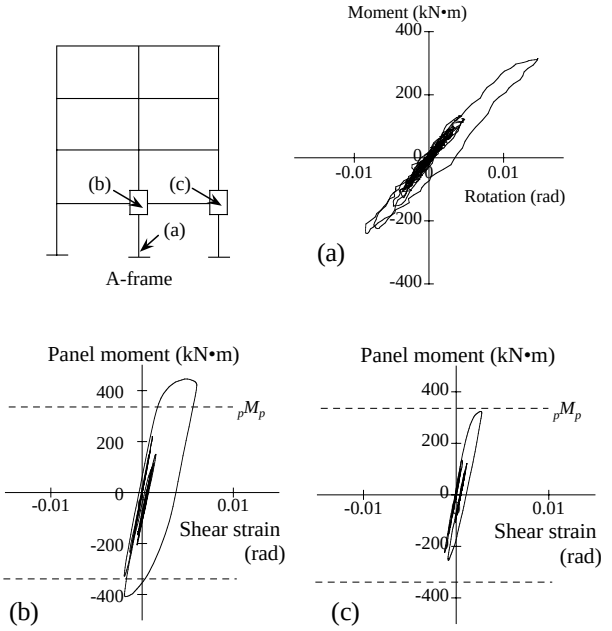

Figure 4 Hysteresis behavior of column and panel by 0.4 Takatori records : (a) Column at the base, (b) Panel of center column, (c) Panel of side column

3. INELASTIC RESPONSE BY OVER LEVEL 2 EARTHQUAKE

3.1 Response of story

Figure 5 shows the story shear force and interstory drift relationships by 0.6 times Takatori records. The peak ground velocity was 0.75m/s, 1.5 times larger than the Level 2 earthquakes. The peak story drift angle increased to 0.019 at 1st story in Y-direction and inelastic hysteresis relationships were observed in the 1st to 3rd stories, which means that the overall sway mechanism proceeded. However, from the comparison between Figure 3(h) and Figure 5(h), the peak story shear at the 1st story in-creased about 1.25 times larger than the response by the 0.4 times Takatori.

Figure 6 shows peak story shear forces by 0.6 times Takatori. The open circles show story shear forces carried by the steel frame only and these values correspond to the results obtained from push-over analysis at 0.02 radian drift angle. The solid circles indicate the inertial forces which correspond to the shear forces carried by a whole building including non-structural components. The peak story shear

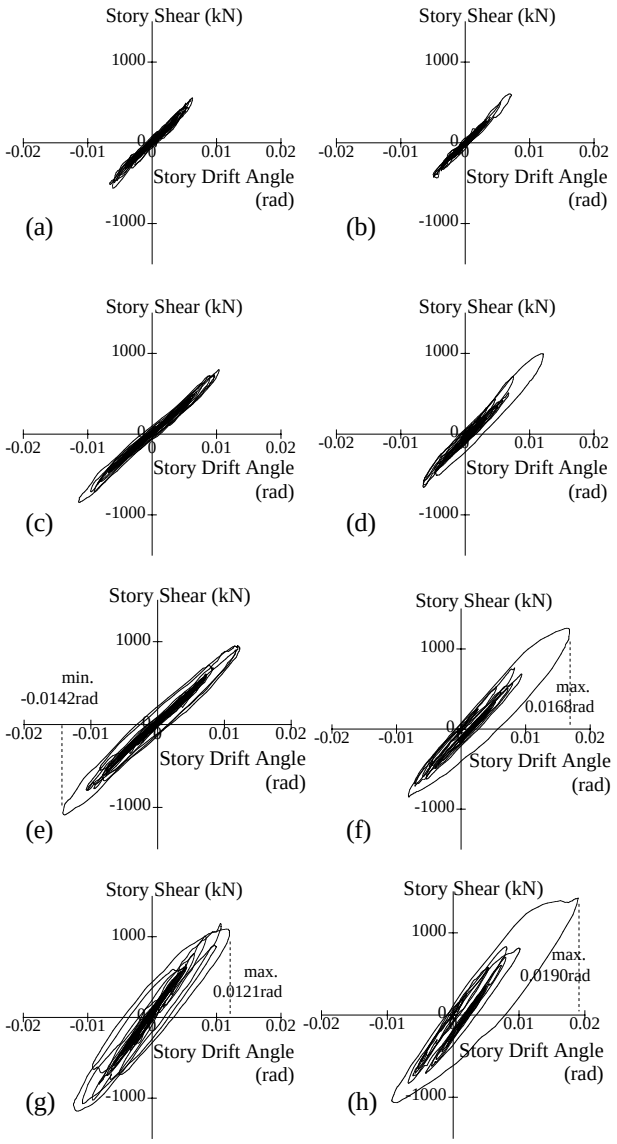

Figure 5 Story shear force and interstory drift relationships by 0.6 Takatori records : (a) 4th story, X-direction, (b) 4th story, Y-direction, (c) 3rd story, X-direction, (d) 3rd story, Y-direction, (e) 2nd story, X-direction, (f) 2nd story, Y-direction, (g) 1st story, X-direction, (h) 1st story, Y-direction

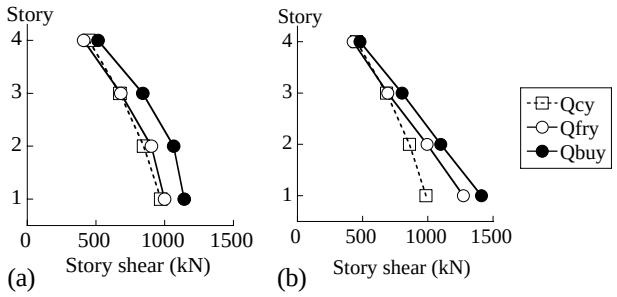

Figure 6 Maximum story shear force of each story by 0.6 Takatori records : (a) X-direction, (b) Y-direction

force at the 1st story increased about 1.25 times larger than the response by 0.4 Takatori records in Y direction. The lateral strength of the 1st story reaches its maximum limit and small degradation of the strength is observed as shown in Figure 4(h). These results indicate that the frame attained its ultimate strength level by the overall sway mechanism.

3.2 Behavior of structural members

Figure 7 shows response of primary members at the 1st and 2nd stories. The inelastic behavior observed not only in panel zones but also in columns. In the center column, yielding occurred at the both of top and bottom ends and the

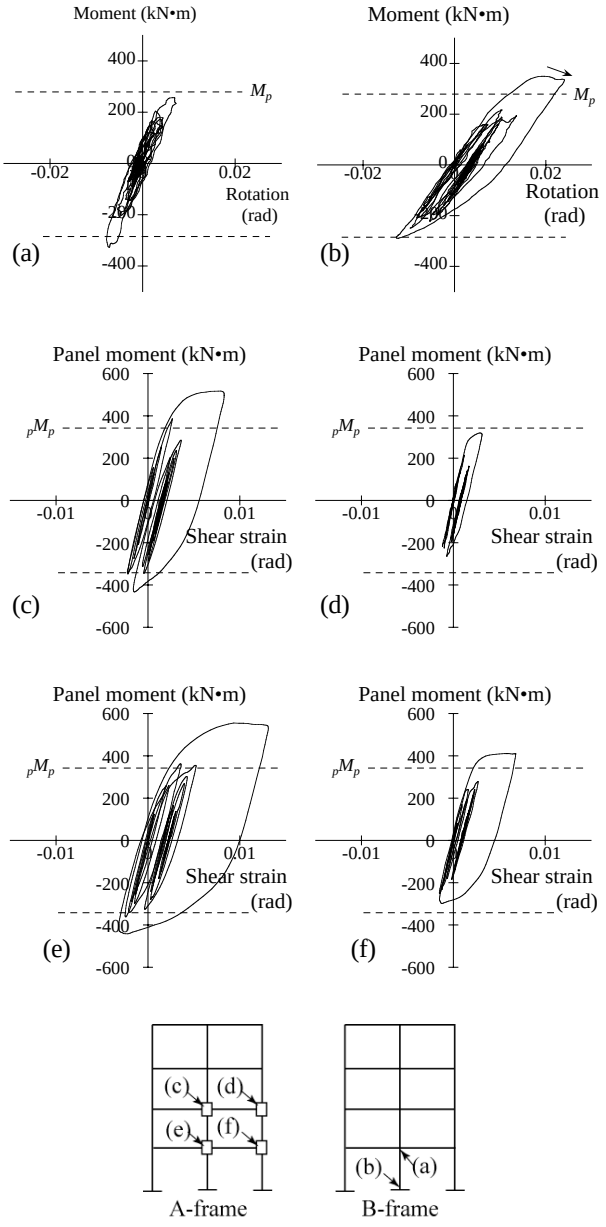

Figure 7 Hysteresis behavior of column and panel by 0.6 Takatori records : (a) Column top (1F), (b) Column base (1F), (c)Panel of center column (3F), (d) Panel of side column (3F), (e) Panel of center column (2F), (f) Panel of side column (2F)

obvious deterioration of the strength is observed in Figure 7(b). From visual observation after the test, residual out-of-plane deformation of the square hollow section was found in the vicinity of the column base. The primary plastic deformation is exhibited in the panels of the 2nd and 3rd stories. The panels, which experienced large plastic strain, were extended to side columns of the 2nd floor and the center column of the 3rd floor compared with the response by 0.4 Takatori records. Therefore, during the response by 0.6 Takatori, a collapse mechanism by yielding of panels in the 2nd and 3rd floor and the column bases at the 1st story is developed.

After the 0.6 times Takatori records shake test, several damage to non-structural components are also observed. The cracks at the corner were observed in some ALC panels of exterior walls. Damage to gypsum boards of partition walls and steel frame of doors are also observed. The details of behavior and damage of non-structural components are presented in the companion paper by Y. Matsuoka et al. (2008).

4. COLLAPSE BEHAVIOR BY TAKATORI RECORD

4.1 Behavior of frame and story

The collapse occurred by 1.0 times Takatori records, peak ground velocity is 1.28m/s, i.e., 2.5 times larger than the level 2 earthquake. The collapse mode was a side-sway with a mechanism in the first story as shown in Figure 8(a,c). Plastic hinging and local buckling occurred at both the top and base of the columns as shown in Figure 8(b). There was yielding in other members (columns above first story, beams, panel zones), but these did not govern the collapse.

Figure 9 shows the story shear force and inter-story drift relationship during 1.0 times Takatori records. The peak story drift angle at 1st story were 0.08 and 0.19 in X and Y direction respectively. On the other hand, the peak story drift angle above the 2nd stories were about 0.01 to 0.02 rad and

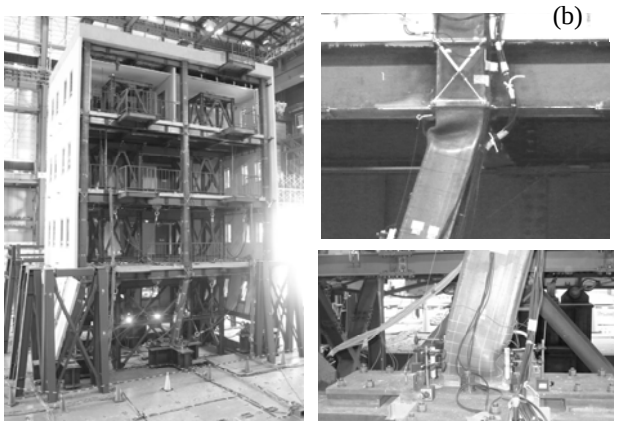

Figure 8 Collapse of specimen after test by 1.0 Takatori re-cords : (a) Overall of A-frame, (b) Center column of 1st story, (c) Collapse of 1st story

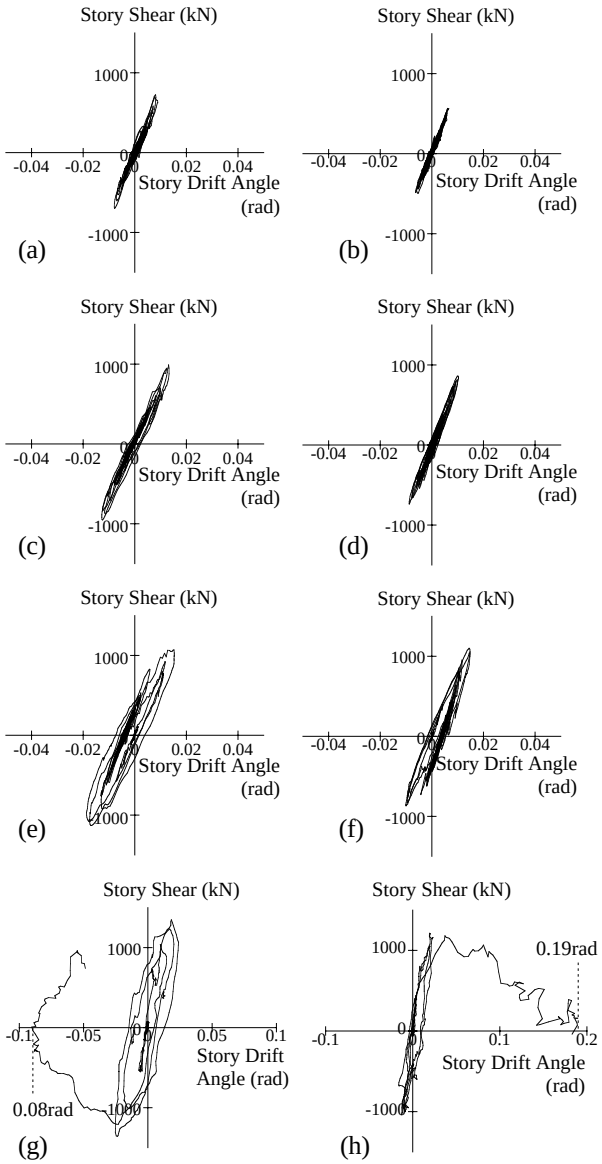

Figure 9 Story shear force and interstory drift relationships by 1.0 Takatori records : (a) 4th story, X-direction, (b) 4th story, Y-direction, (c) 3rd story, X-direction, (d) 3rd story, Y-direction, (e) 2nd story, X-direction, (f) 2nd story, Y-direction, (g) 1st story, X-direction, (h) 1st story, Y-direction

increase of drift angle from previous test were small. The increase of story drift is concentrated at the first story.

The change of the peak story drift during all tests are shown in Figure 10. In the X-direction, the maximum drift occurred at the 2nd story until 0.6 Takatori records, and in the Y-direction, the maximum drift of 1st story increased larger than above stories by 0.2 Takatori. These change of the maximum drift profile indicates that the transition of controlling mechanism of the specimen frame occurred during 0.6 to 1.0 Takatori records.

4.2 Behavior of structural members and transition of collapse mechanism

The transition of the mechanism of the frame from a overall

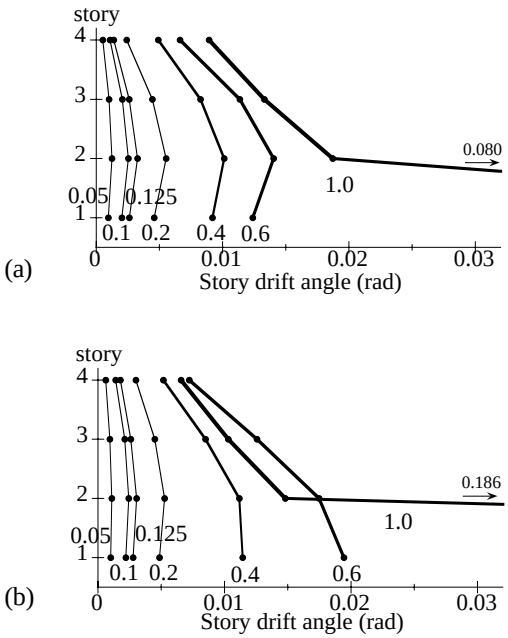

Figure 10 Profile of maximum story drift angle at each excitation level by Takatori records : (a) X-direction, (b) Y-direction

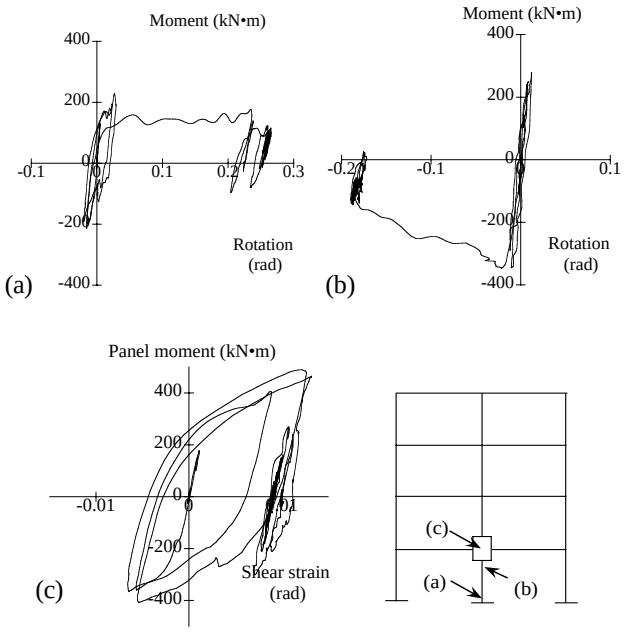

Figure11 Hysteresis behavior of column and panel by 1.0 Takatori records : (a) Column at the base, (b) Column at the top, (c) Panel of center column

sway mechanism to a weak story mechanism is verified from the behavior of structural members. Figure 11 shows the response of primary members at the 1st and 2nd stories by 1.0 Takatori records. At the base of the center column of the 1st story, the peak moment of the column shown in Figure 11(a) is less than the results of the previous test by 0.6 Takatori records shown in Figure 7(b) due to

deterioration. At the top side of the column, the bending moment remarkably deteriorated as shown in Figure 11(b). On the other hand, the panel showed stable hysteresis behavior, but soon after the deterioration of the column strength, unloading of the panel moment occurred as shown in Figure 11(c) and the base shear of the frame decreased fatally. From these hysteresis relationships, the instance at the failure of the primary members are detected.

Figure 12 shows the orbit of story drift at the 1st story by 1.0 Takatori records. The instances of the degradation of the column strength and the unload of the panel are marked by circles on the line of the orbit. The change of the mechanism initiated by the deterioration of the center column at 5.89s elapsed from the start of Takatori records, and a weak story mechanism is completed at 5.97s by the degradation of the side column. As shown in Figure 11, the shift of mechanism occurred in mere 0.08 seconds and the specimen completely collapsed and settled on the safe guard frame in the 1st story at 6.57s elapsed from the start of Takatori records. Thus, the deterioration of the column due to local buckling after several cyclic plastic deformation in large amplitude is likely one of the scenarios for collapse of a steel moment frame designed in current seismic codes. The excitation level of ground motion to collapse was twice and half larger than the level 2 design level.

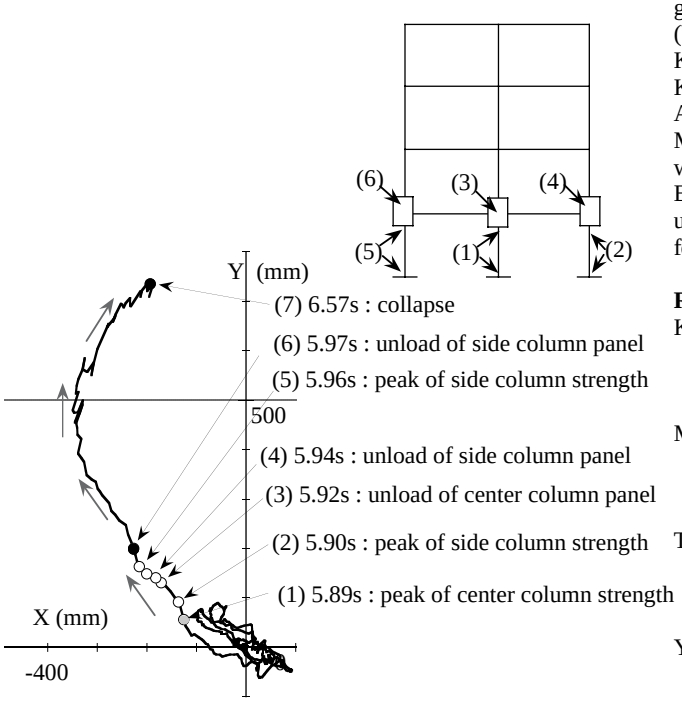

Figure 12 Interstory drift orbit of 1st story and process of collapse by 1.0 Takatori records

5. CONCLUSION

A full-scale shake table test on a four-story steel building was conducted to evaluate structural and functional performance of the steel building under design-level ground motions and under exceedingly large ground motions.

1) From the shake test by level-2 design earthquake, the specimen exhibited stable response behavior and a overall sway mechanism of the moment frame corresponded to the form intended in the seismic design.

2) At the 1.5 times over level-2 excitation test, the primary plastification of the frame extended and a mechanism by yielding of panels in 2nd and 3rd floors and the column base at the 1st story is developed. The frame behaved stably showing increased story shear resistances.

3) By the 2.5 times over level-2 excitation test, the specimen completely collapsed and the deterioration of the column due to local buckling after several cycles of large plastic deformation caused the change of the mechanism to a weak story collapse mechanism. This is a possible scenario of collapse for steel frames designed by current design codes under over design level earthquakes.

Acknowledgements:

This study is a part of "NEES/E-Defense collaborative research program on steel structures", and was pursued by the sub-working group under the Build-ing Collapse Simulation Working Group (WG). The Japan team leader for the overall program is Kazuhiko Kasai, Tokyo Institute of Technology, and the WG leader is Keiichiro Suita, Kyoto University. The writers acknowledge Analysis Method and Verification Working Group (leader is Motohide Tada, Osaka University) for their collaboration. And the writers acknowledge financial support provided by the Ministry of Education, Culture, Sports, Sciences and Technology of Japan under Grant No. 18360266, and by the National Research Institute for Earth Science and Disaster Prevention.

References:

Kasai, K., Ooki, Y., Motoyui, S., Takeuchi, T. and Sato, E. 2007. E-Defense Tests on Full-Scale Steel Buildings: Part 1 - Experiments Using Dampers and Isolators, Proc. Struc-tural Congress 2007, ASCE, Long Beach, No.247-17.

Matsuoka, Y., Suita, K., Yamada, S., Shimada, Y. and Akazawa, M. 2008. Non-Structural Component Performance in 4-Story Frame Tested to Collapse, Proceedings of the 14th World Conference on Earthquake Engineering Beijing, China, No. S17-01-014,.

Tada, M., Ohsaki, M., Yamada, S., Motoyui, S. and Kasai, K. 2007. E-Defense Tests on Full-Scale Steel Buildings, Part 3 - Analytical Simulation of Collapse, Proc. Structural Congress 2007, ASCE, Long Beach, No.247-19.

Yamada, S., Suita, K., Matsuoka, Y., Shimada, Tada, M., Kasai, K, 2010. Full Scale Shaking Table Collapse Experiment on 4-Story Steel Moment Frame: Part 1 Outline of the Experiment, 7CUEE&5ICEE, Yokohama, Japan.

JOINT CONFERENCE PROCEEDINGS
7th International Conference on Urban Earthquake Engineering (7CUEE) &
5th International Conference on Earthquake Engineering (5ICEE)
March 3-5, 2010, Tokyo Institute of Technology, Tokyo, Japan

NUMERICAL SIMULATION OF COLLAPSE USING COLLABORATIVE STRUCTURAL ANALYSIS SYSTEM

Motohide Tada[1] , Akinobu Horimoto[2] , Atsushi Mitani[3] , Seiji Mukaide[4] , Kazuhiko Kasai[5] , Keiichiro Suita[6], and Satoshi Yamada[7]

1) Professor, Division of Global Architecture, Graduate School of Engineering, Osaka University, Japan
2) Structural Engineer, Nikken Sekkei ltd., Japan
3) Graduate Student, Division of Global Architecture, Graduate School of Engineering, Osaka University, Japan
4) Assistant Professor, Division of Global Architecture, Graduate School of Engineering, Osaka University, Japan
5) Professor, Structural Engineering Research Center, Tokyo Institute of Technology, Japan
6) Professor, Department of Architecture and Architectural Engineering, Graduate School of Engineering, Kyoto University, Japan
7) Associate Professor, Structural Engineering Research Center, Tokyo Institute of Technology, Japan
tada@arch.eng.osaka-u.ac.jp, horimoto.akinobu@nikken.co.jp, mitani_atsushi@arch.eng.osaka-u.ac.jp, mukaide@arch.eng.osaka-u.ac.jp, kasai@serc.titech.ac.jp, suita@archi.kyoto-u.ac.jp, naniwa@serc.titech.ac.jp

Abstract: Numerical simulation of collapsing behavior for complete collapse specimen at E-defense are presented. The collaborative structural analysis system was utilized. The analytical results were compared with shaking table test results to show the reliability of analysis. The earthquake response by additional four recorded seismic motions, El Centro, Taft, Hachinohe, and JMA Kobe, were shown. The amplitude of seismic motion was normalized as the maximum velocity being 100 cm/s for first three motions, and non-scaled for JMA Kobe. The specimen collapsed as same as shaking table test by Hachinohe motion, while it did not collapse by El Centro, Taft, and JMA Kobe motions.

1. INTRODUCTION

A full-scale experiment to simulate collapse of a 4-story steel building was conducted using E-Defense shake table facility. The specimen consists of beams of wide-flange sections, columns of rectangular hollow sections, concrete slabs with deck plates, and column bases with anchor bolts. The collapsing of the specimen was characterized by deteriorating behavior caused by local buckling of column at the first story. This paper deals with the analytical simulation of the specimen based on the collaborative structural analysis (CSA) system. Through the comparison of analytical and test results, the reliability of CSA system will be shown. The additional numerical simulations for three other recorded ground motions will be conducted. The seismic performance on the complete collapse for ordinary steel buildings in Japan will be discussed.

2. FULL-SCALE BUILDING SPECIMEN FOR ANALYSIS

The specimen shown in Figure 1 was so designed to conform to Japanese Building Standard law. The building has plan of 10 m in the longitudinal direction (Y) and 6 m in the transverse direction (X). Each story is 3.5 m high, making the overall story height equal to 14 m. Table 1 shows a list of sections and Table 2 shows the material properties obtained by coupon tests. Ribbed metal decks of 75 mm high are connected to the beams through studs that are welded to the beam top flanges on the second to fourth floor. Wire-meshes are placed above the metal deck sheets, and concrete of 100 mm thick is placed on site. Flat metal decks are used on the roof floor, and reinforced concrete slab of 150 mm thick is placed on site. Fully composite action is expected between the steel beams and concrete slab. The column bases are the exposed type with base plate of 50 mm thick and eight anchor bolts of M36-diameter. The anchor bolts are so designed that he bending strength of column base is higher than that of connecting column.

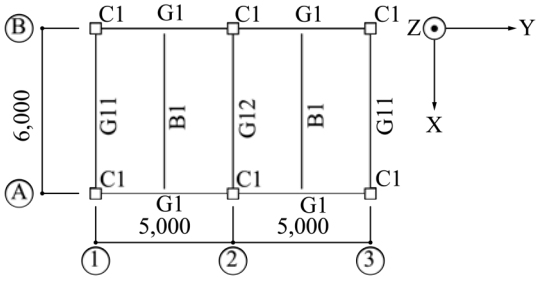

(a)

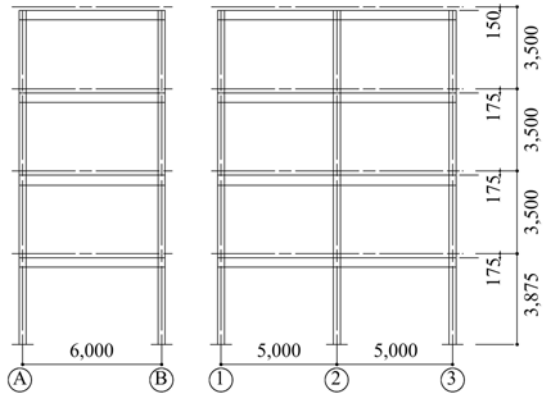

(b)

Figure 1 Framing Plan and Elevation of the Specimen: (a) Plan(1st story) and (b) X- and Y-Elevation

Table 1 Member Schedule

Floor	G1 (SN400B)	G11 (SN400B)	G12 (SN400B)
R	H-346x174x6x9	H-346x174x6x9	H-346x174x6x9
4	H-350x175x7x11	H-350x175x7x11	H-340x175x9x14
3	H-396x199x7x11	H-400x200x8x13	H-400x200x8x13
2	H-400x200x8x13	H-400x200x8x13	H-390x200x10x16

Floor	B1 (SS400)	Story	C1,C2 (BCR295)
R	H-346x174x6x9	4	SHS-300x300x9
4	H-350x175x7x11	3	SHS-300x300x9
3	H-350x175x7x11	2	SHS-300x300x9
2	H-350x175x7x11	1	SHS-300x300x9

*wide flange: height x width x web thickness x flange thickness

**square hollow section: height x width x thickness

Table 2 Material Properties by Coupon Tests

		Yield stress (MPa)		Tensile strength(MPa)	
	Section	Flange	Web	Flange	Web
Beam	H-340x175x9x14	309	355	443	468
	H-346x174x6x9	333	382	461	483
	H-350x175x7x11	302	357	441	466
	H-390x200x10x16	297	317	451	458
	H-396x199x7x11	311	369	460	486
	H-400x200x8x13	326	373	454	482
Column	SHS-300x300x9	2~4 story	1,4 story	2~4 story	1,4 story
		332	330	419	426
Base plate (PL-50)		378		501	
Anchor bolt (M36)		336		507	

3. COLLABORATIVE STRUCTURAL ANALYSIS SYSTEM

A collaborative structural analysis system is proposed by Tada et al (2004), which is capable of performing highly sophisticated structural analysis by utilizing the beneficial features of existing individual structural analysis programs developed by individual researchers. In the system, the simulated structure is divided into multiple substructures, and each substructure is analyzed by an individual program. Specifically, the host program formulates and solves the equations of motion for the entire structure, and sends boundary displacements to the corresponding station programs. The station programs run detailed analyses, and return forces associated with the degrees of freedom at the boundaries through a condensation procedure. The procedure is conducted step by step, and the data are exchanged through Internet.

The program, NETLYS, is used as a host program. It deals with the global equation of motion, to which numerical information of all sub-structures is involved. For the purpose of general combination of various programs, the explicit integration scheme of operator splitting (OS) method (Nakashima 1990) is used. It requires only restoring forces of sub-structures, and does not require tangential stiffness of sub-structures. Thus, general-purpose program, such as MARC, can be used as a station program. Here, a modified OS method (Tada and Pan 2007) is used for the numerical stability in geometrical high nonlinear analyses.

All frames of 1 to 3 in X-direction and A and B in Y-direction are modeled in the same plane as shown in Figure 2. By postulating "rigid slab (in-plane) hypothesis", every horizontal displacement in the same floor is numerically related by the linear combination of horizontal displacements in X- and Y-directions and rotation at the center of the floor. Vertical displacements at the conjunction nodes of orthogonal frames are equalized. Columns are modeled and analyzed in 3D manner, bi-axial bending and longitudinal axial force are considered. While, beams and beam-to-column panels are modeled and analyzed in 2D manner. Thus, 3D analyses are conducted.

Figure 3 shows the formation of sub-structures and program names for each sub-structure. The program, COMPO, is used for analyzing composite beams that consist of steel beam and concrete slab. It can consider the composite action in plus bending, and the crack-opening of concrete slab in minus bending. It can simulate the complex cyclic behavior of composite beams. The general-purpose program, MARC, is used for analyzing columns of rectangular hollow sections in the first story. Shell elements are used to consider the local buckling due to axial force and bending moment. It can simulate the deteriorating post-buckling behavior in detail. As we know that the collapsing of the specimen is mainly characterized by deteriorating behavior at the first story-columns in the pre-analyses (Tada, Ohsaki et al 2007), the column ends at the second to fourth stories are simply modeled using rotational springs which demonstrate deteriorating behavior of local buckling and were used in the pre-analyses (Tada, Ohsaki et al 2007).

Beam-to-column panels are analyzed in detail using subroutines which are installed in NETLYS. Exposed column bases are modeled by elastic rotational springs whose stiffness corresponds to the state that the base plate perfectly touches to the foundation.

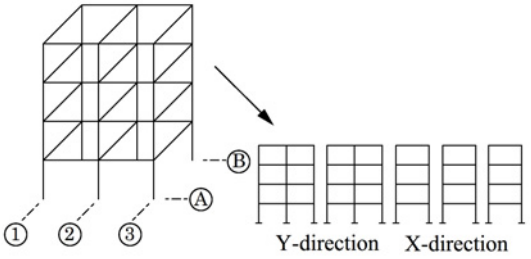

Figure 2 3D Model Consists of Plane Frames

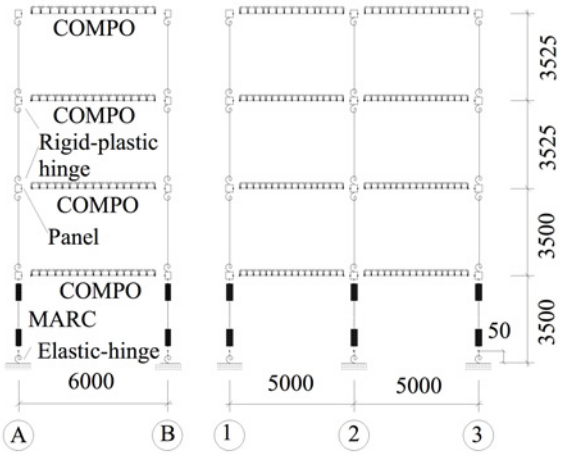

Figure 3 Formation of Sub-structures

4. PUSHOVER ANALYSIS

The results of pushover analysis for plane frames in respective directions are shown in Figures 4 and 5. Figure 4 is for X-direction, and figure 5 is for Y-direction. The constant vertical load and varying horizontal forces proportional to seismic design forces are applied. Story shear (Q) -drift angle (r) relation for each story is shown in Figure (a). The distributions of plasticized sections are shown in Figures (b) and (c). Figure (b) represents the case where horizontal forces reach the maximum value, and Figure (c) represents the case where the analysis reaches the end. Solid circle represents the plastic hinges at beam and column, and solid square represents shear yield at beam-to-column panel. The plasticized sections spread all over the structure as the horizontal forces increase until they reach the maximum value. The horizontal forces deteriorate after the local buckling occurs at the columns of the first story. As the horizontal strength deteriorates, the plasticized sections are localized at the first story. The final collapsing mechanism is column-yield type with local buckling at both ends of the first story-columns.

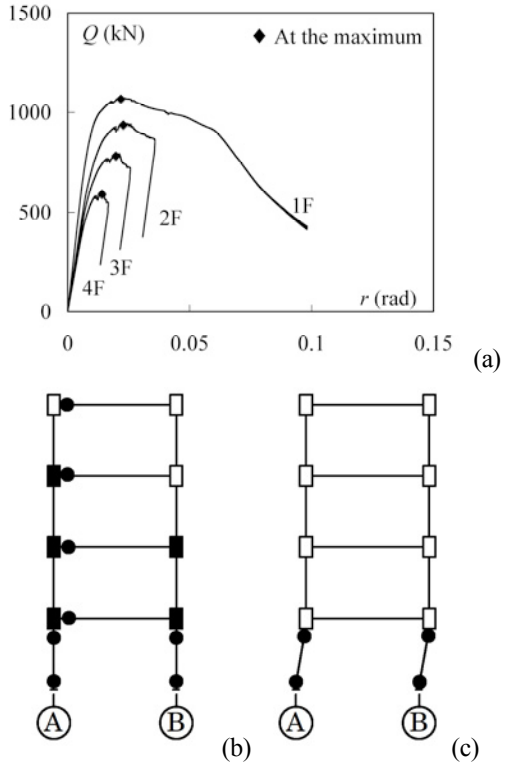

Figure 4 Results for X-direction: (a) Story Shear-drift Angle Relation, (b) At the Maximum, and (c) At the End

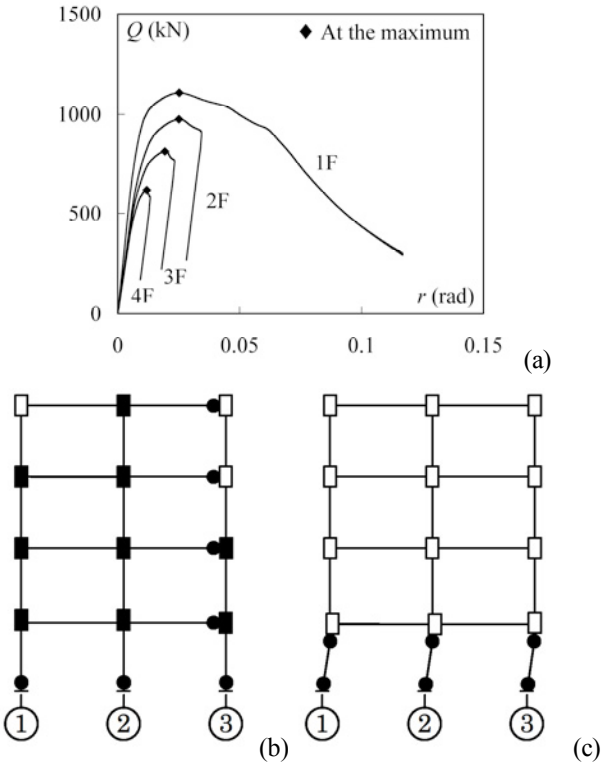

Figure 5 Results for Y-direction: (a) Story Shear-drift Angle Relation, (b) At the Maximum, and (c) At the End

5. COMPARISON OF RESULTS BY SHAKING TABLE TEST AND NUMERICAL ANALYSIS

Time history analyses are conducted to compare with the results of shake table tests. The earthquake ground motion recorded in Hyogoken-Nanbu earthquake, Takatori (Nakamura et al 1995, FD Serial No. T065), was adopted in the tests, and the table motion recorded in the tests are used for the analyses. EW, NS, and UD components are used for the X-, Y-, and Z-directions, respectively. Rayleigh damping is considered, and damping ratio of 2% is assigned to the first and second vibration modes in X-direction. Fundamental and the second periods are 0.81 and 0.26 s in X-direction, 0.78 and 0.25 s in Y-direction. The preliminary tests were conducted under the small excitations in the elastic range. The main excitation levels were 0.2, 0.4, 0.6, and 1.0 of the original record of Takatori in this order. The specimen was plasticized in the excitation levels of 0.4 and 0.6. The following analytical results are those obtained by the excitation level of 1.0 for virgin structure. The effects of residual deformation caused by former excitations are not included. We have confirmed that its effect is negligible by conducting the continuous analysis for the levels of 0.6 and 1.0.

The analytical and test results are shown below. Here, solid lines show the analytical results, and gray lines show the test results reported by the Building Collapse Simulation Working Group. Figure 6 shows the time history of story drift angle (r) at the first story, where Figures (a) and (b) show the cases in X- and Y- directions, respectively. Figure 7 shows the orbit of story drift angles at the first story, where ordinate and abscissa represent drift angles in X- and Y-directions, respectively. Both analytical and test results show that the specimen collapses in minus X-direction and plus Y-direction. Figure 8 shows the story shear (Q) - drift angle (r) relation at the first story. The deterioration of story shear can be observed. Figure 9 shows the distribution of plasticized sections at the end of analysis. The plasticized sections are localized at the column-ends at the first story as observed in the pushover analysis. In Figures 6 to 9, the analytical results can express well the test results obtained by the shake table test.

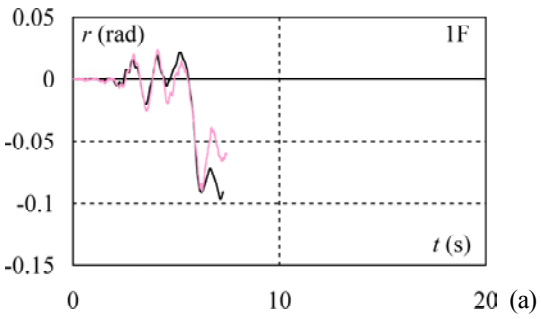

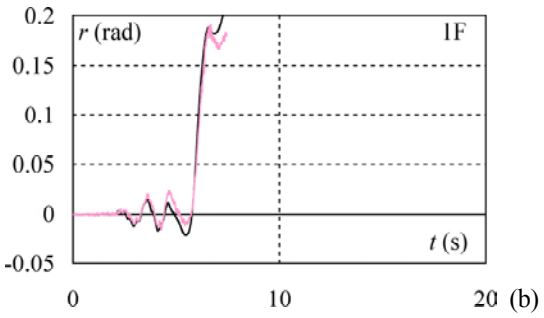

Figure 6 Time History of Story Drift Angle at the First Story: (a) X-direction, and (b) Y-direction

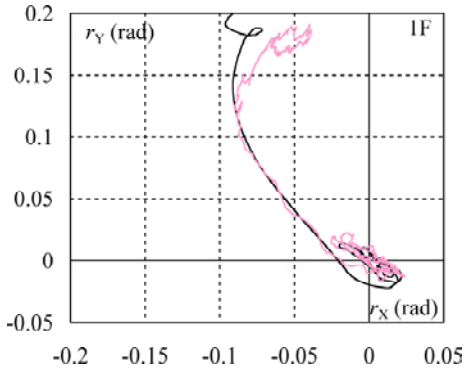

Figure 7 Orbit of Drift Angle

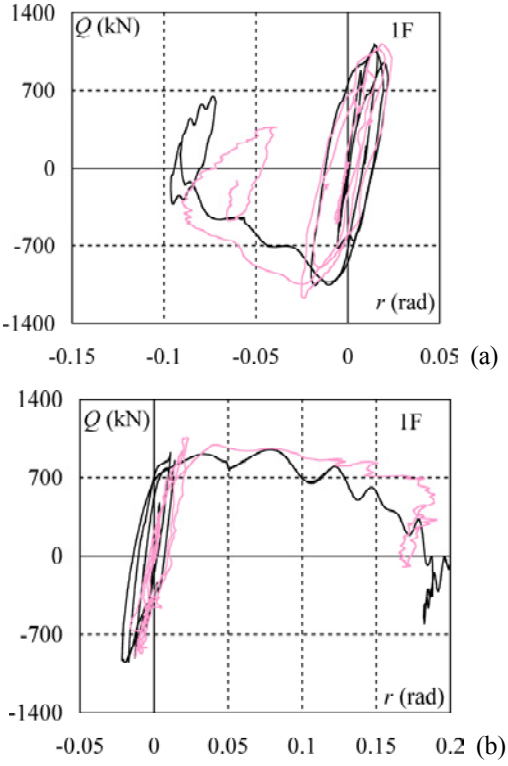

Figure 8 Story Shear-drift Angle Relation at the First Story: (a) X-direction, and (b) Y-direction

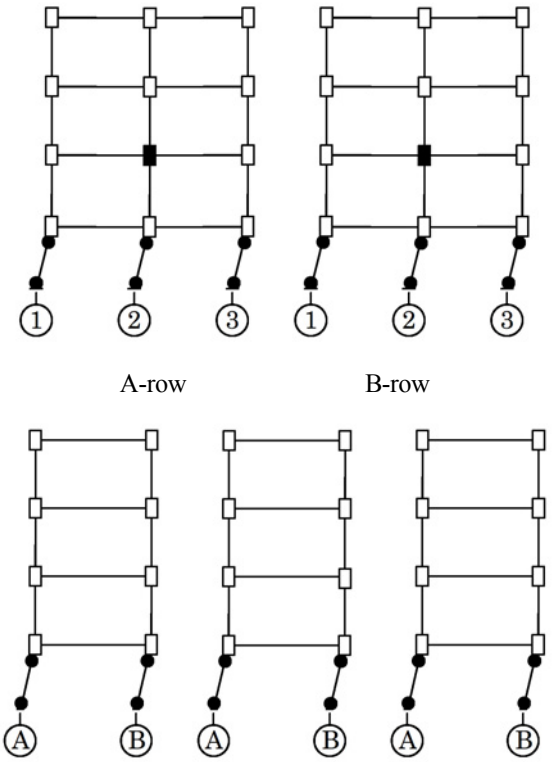

Figure 9 Final Collapse Mechanism

6. NUMERICAL SIMULATION FOR VARIOUS RECORDED GROUND MOTIONS

The merit of numerical simulations, compared to shake table tests, is the capability of parametric simulations in many cases. Here, time history analyses for El Centro (California 1940), Taft (California 1952), Hachinohe (Aomori, Japan 1968), and JMA Kobe are conducted. The amplitudes of the ground motions are specified as the maximum velocity is 100 cm/s for El Centro, Taft, and Hachinohe. Resultant amplified factor to original record is 2.99 for El Centro, 5.65 for Taft, and 2.79 for Hachinohe. On the other hand, non-scaled original excitation is adopted in JMA Kobe. According to the design practice of high-rise buildings in Japan, the ground motion of level 2 is specified by 50 cm/s. Thus, the ground motions considered here are the twice the level 2 of earthquake.

Pseudo velocity response spectrums of all ground motions are shown in Figures 10 and 11. Figure 10 corresponds to X-direction of the specimen, and Figure 11 to Y-direction. The ground motion of Takatori and JMA Kobe are non scaled, and other three motions are amplified and scaled as the maximum velocity be 100 cm/s.

Time history of story drift angle (r) at the first story and distribution of plasticized sections for three ground motions are shown in Figures 12 to 17. Figure 12 corresponds to El Centro, Figures 13 corresponds to Taft, Figure 14 corresponds to Hachinohe, and Figure 15 corresponds to JMA Kobe. The specimen does not collapse for El Centro, Taft, and JMA Kobe, though large story drift angle, as much as 1/40 rad for El Centro, 1/28 rad for Taft, and 1/33 rad for JMA Kobe, experiences. On the other hand, the specimen collapses for Hachinohe. The collapse mechanism is the column-yield type of the first story as same as Takatori.

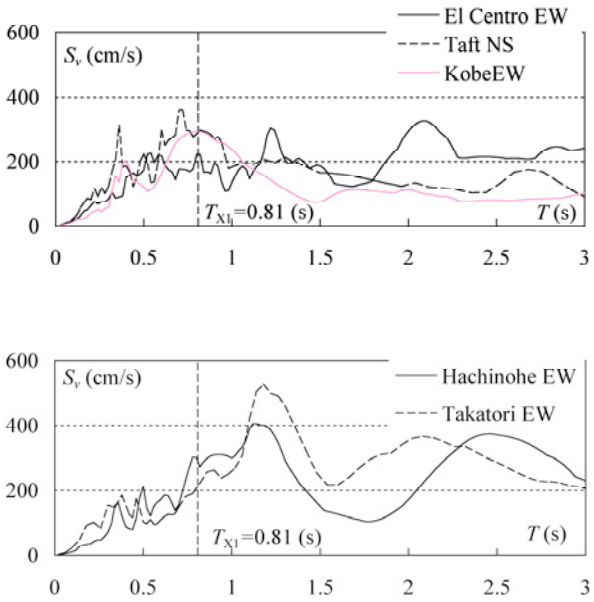

Figure 10 Pseudo Velocity Response Spectrum of Ground Motions for X-direction (El Centro x 2.99, Taft x 5.65, Hachinohe x 2.79, and Kobe x 1.00)

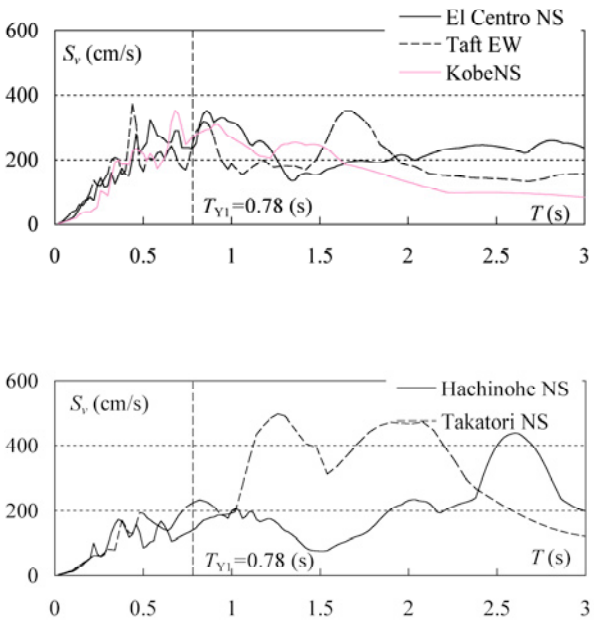

Figure 11 Pseudo Velocity Response Spectrum of Ground Motions for Y-direction (El Centro x 2.99, Taft x 5.65, Hachinohe x 2.79, and Kobe x 1.00)

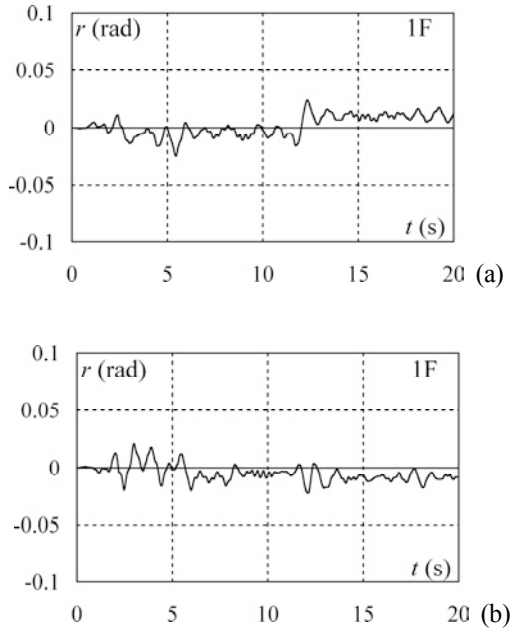

Figure 12 Time History of Story Drift Angle (El Centro x 2.99): (a) X-direction and (b) Y-direction

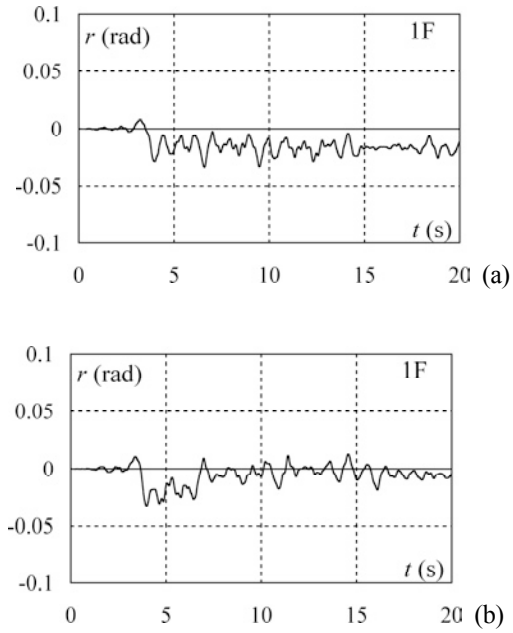

Figure 13 Time History of Story Drift Angle (Taft x 5.65): (a) X-direction and (b) Y-direction

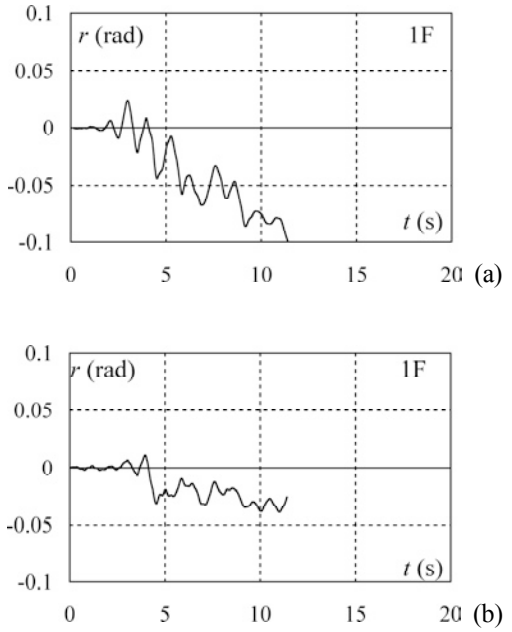

Figure 14 Time History of Story Drift Angle (Hachinohe x 2.79): (a) X-direction and (b) Y-direction

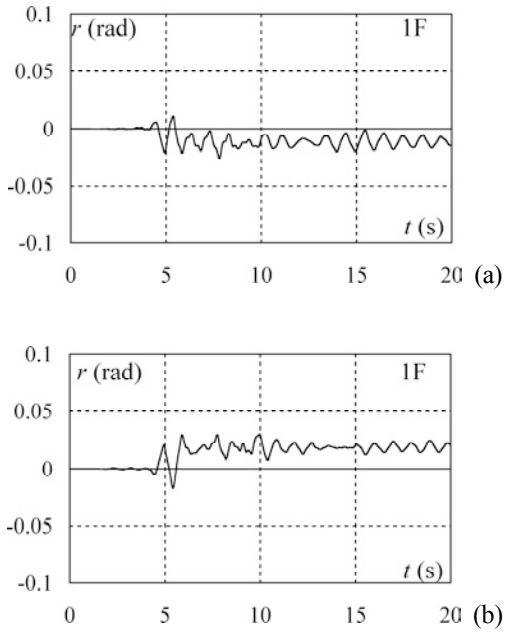

Figure 15 Time History of Story Drift Angle (JMA Kobe x 1.00): (a) X-direction and (b) Y-direction

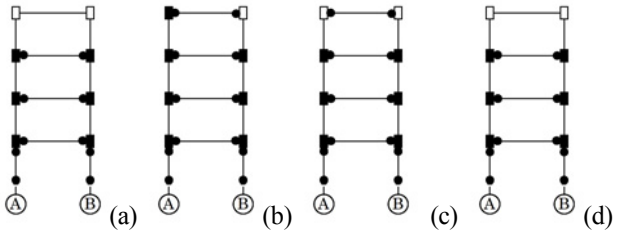

Figure 16 Experienced Plasticized Sections:
(a) El Centro, (b) Taft, (c) Hachinohe, and (d) JMA Kobe

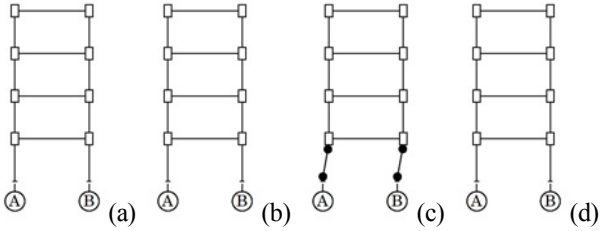

Figure 17 Final Plasticized Sections:
(a) El Centro, (b) Taft, (c) Hachinohe, and (d) JMA Kobe

7. CONCLUSIONS

This paper has discussed analytical simulation of collapsing behavior of 4-story steel building which was tested using E-Defense shake table facility. The specimen conforms to the Japanese Building Standard law. Analytical simulations have been conducted using Collaborative Structural Analysis (CSA) system. In case of non-scaled Takatori, the numerical simulation well express the test results. The plasticized sections spread all over the structure, and then the damage was localized at the first story. As the localization proceeded, the bending strength of columns at the first story heavily deteriorated due to local buckling, and finally it lead the specimen to collapse.

The numerical simulations for other ground motions have also been conducted. The scale of El Centro, Taft, and Hachinohe was specified as the maximum ground velocity is 100 cm/s, which is twice the level 2 of earthquake in Japanese design practice, while non-scaled original record was used for JMA Kobe. The specimen collapsed for Hachinohe (x2.79), while it did not for El Centro (x2.99), Taft (x5.65), and JMA Kobe (x1.00).

Acknowledgments:

This study is a part of "NEES/E-Defense collaborative research program on steel structures", and was pursued by the sub-working group under the Analysis Method and Verification Working Group (WG leader is Motohide Tada, Osaka University), and Building Collapse Simulation Working Group (WG leader is Keiichiro Suita, Kyoto University). The Japan team leader for the overall program is Kazuhiko Kasai, Tokyo Institute of Technology. The writers acknowledge financial support provided by the Ministry of Education, Culture, Sports, Sciences and Technology of Japan under Grant No. 18360266, and by the National Research Institute for Earth Science and Disaster Prevention.

References:

Tada, M., and Kuwahara, S., (2004), "Fundamental Study on Unified Tool for Structural Analysis using Network," *Proceedings of 13th World Conference on Earthquake Engineering*, Paper No. 650.

Tada, M., and Pan, P., (2007), "A Modified Operator Splitting (OS) Method for Collaborative Structural Analysis (CSA)," *International Journal for Numerical Methods in Engineering* 72, 379-396.

Nakamura, Y., Uehan, F., and Inoue, H., (1995), "Waveform and its analysis of the 1995 Hyogo-Ken-Nanbu Earthquake Information," Railway Technical Research Institute, No. 23d (in Japanese).

Nakashima, M., Kaminosono, T., Ishida, M., and Ando, K., (1990), "Integration Techniques for Substructure Pseudo-Dynamic Test," *Proceedings of 4th US National Conference on Earthquake Engineering.*

Tada, M., Ohsaki, M., Yamada, S., Motoyui, S., and Kasai, K., (2007), "E-Defense Tests on Full-Scale Steel Buildings, Part 3 - Analytical Simulation of Collapse," *Proceedings of ASCE Structures Congress*, CD-ROM.

JOINT CONFERENCE PROCEEDINGS
7th International Conference on Urban Earthquake Engineering (7CUEE) &
5th International Conference on Earthquake Engineering (5ICEE)
March 3-5, 2010, Tokyo Institute of Technology, Tokyo, Japan

PARALLEL FE-ANALYSIS FOR COLLAPSE SIMULATION OF 4-STORY STEEL BUILDING FRAME

Tomoshi Miyamura[1], Makoto Ohsaki[2], Masayoshi Kohiyama[3], Kunizo Onda[4], Daigoro Isobe[5], Hiroshi Akiba[6], Muneo Hori[7], Koichi Kajiwara[8], Tatsuhiko Ine[9]

1) Lecturer, Dept. of Computer Science, College of Eng., Nihon University, Japan
2) Associate Professor, Dept. of Architecture and Architectural Eng., Kyoto University, Japan
3) Associate Professor, Dept. of System Design Eng., Keio University, Japan
4) Technical Advisor, Allied Engineering Corporation, Japan
5) Dept. of Engineering Mechanics and Energy, University of Tsukuba
6) President, Allied Engineering Corporation, Japan
7) Professor, Earthquake Research Institute, The University of Tokyo, Japan
8) Senior Researcher, Hyogo Earthquake Engineering Research Center, National Research Institute for Earth Science and Disaster Prevention, Japan
9) Invited Research Fellow, Hyogo Earthquake Engineering Research Center, National Research Institute for Earth Science and Disaster Prevention, Japan
ohsaki@archi.kyoto-u.ac.jp, miyamura@cs.ce.nihon-u.ac.jp, kohiyama@sd.keio.ac.jp, onda@alde.co.jp, isobe@kz.tsukuba.ac.jp, akiba@alde.co.jp, hori@eri.u-tokyo.ac.jp, kaji@bosai.go.jp, ine@bosai.go.jp

Abstract: The results of high-precision FE-analysis is presented for simulation of collapse behavior of the 4-story steel building frame that is the specimen of the full-scale total collapse shaking-table test conducted in September 2007 at E-Defense. The computation is carried out using the E-Simulator, which is under development at Hyogo Earthquake Engineering Research Center (E-Defense) of National Research Institute of Earth Science and Disaster Prevention (NIED), Japan. The E-Simulator uses the parallel finite element (FE) analysis software package called ADVENTYRECluster (ADVC) as a platform. It is shown through numerical examples that elastoplastic dynamic responses can be estimated with good accuracy using a high-precision FE-analysis without resort to macro models such as plastic hinge and composite beam effect.

1. INTRODUCTION

In the framework of performance-based design of steel frames, it is very important to evaluate accurately the collapse behavior of the frame under maximum credible seismic motions. However, in the conventional process of seismic response evaluation of a low-rise steel building frame, dynamic time-history analysis or static pushover analysis is carried out for the frame model using an empirically defined plastic hinge or fiber model. Macro models are also used for representing the properties of column base and composite beam effects. Therefore, the seismic responses obtained using the macro models strongly depend on the assumption incorporated in the building code and the intuition made by an engineer.

The project of E-Simulator is under way at Hyogo Earthquake Engineering Research Center (E-Defense) of National Research Institute of Earth Science and Disaster Prevention (NIED), Japan, which facilitates the world's largest shaking table (Hori *et al*. 2007, E-Defense 2009). The E-Simulator uses ADVENTYRECluster (ADVC) as a platform (Akiba *et al*. 2006, Ogino *et al*. 2005). ADVC is a commercial software package of parallel finite element (FE) analysis that uses domain decomposition technique for parallel implementation. It can solve dynamic nonlinear problems with more than 10 million DOFs for a structure discretized by three-dimensional solid elements. The authors carried out elastoplastic dynamic analysis of a 31-story high-rise steel building model using ADVC (Ohsaki *et al*. 2009). The E-Simulator is conceived as a virtual shaking table, and its final form is a software environment to simulate global and local seismic responses of a city, as assemblage of buildings and infrastructures, by fully taking advantage of recent development of computer science and high-performance computing in computational mechanics.

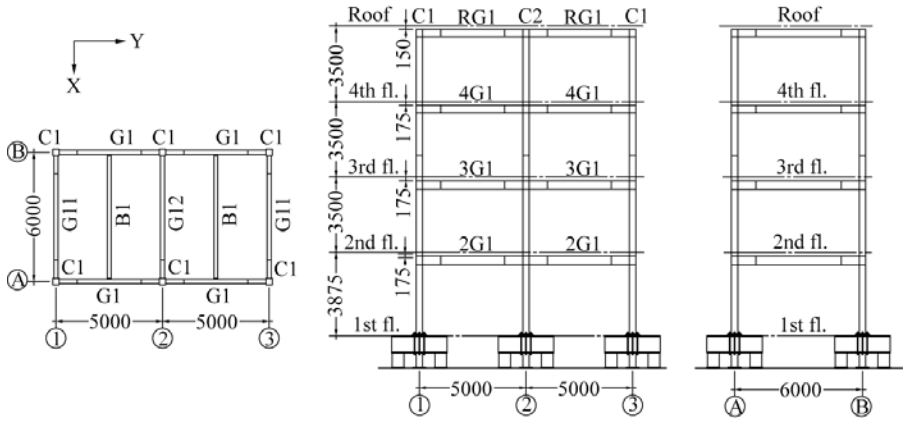

(a) Plan (1st Floor) (b) Y-elevation (longitudinal) (c) X-elevation (transverse)

Figure 1 4-Story Steel Frame Model (Tada *et al*. 2007)

As a part of this project, the purpose of this study is to show that the global and local elastoplastic behaviors of a steel frame under severe seismic motions can be simultaneously simulated by a high-precision FE-analysis software, ADVC. Elastoplastic dynamic analysis is carried out for the 4-story frame model as the specimen of full-scale shaking-table test (Suita *et al*. 2007) conducted in September 2007 at E-Defense shaking-table facility. The test is one of the series of experimental studies on moment-resisting frames, innovative methods for new or existing buildings, protective systems, and nonstructural elements (Kasai *et al*. 2007).

In this study, elastoplastic time-history analysis is carried out for the 4-story steel frame to show that the local and global collapse behaviors of a steel frame consisting of thin plates can be accurately simulated by discretizing the whole structure using hexagonal solid elements without resort to macro models such as plastic hinge and composite beam effect. Shear spring model is presented for simulation of damages of exterior walls, and a spring model and finite element mode are developed for column bases.

2. FOUR-STORY STEEL FRAME MODEL

The FE-model of the 4-story frame, as shown in Fig. 1 (Tada *et al*. 2007), is generated using the data and documents distributed for the blind analysis contest (Ohsaki *et al*. 2008, Hikino *et al*. 2009). All the members as well as the floor slabs are modeled by 8-node hexahedral solid elements that use conventional first-order shape functions, i.e., the DOFs of each node are three translational displacements.

The FE-mesh generated by Noguchi Laboratory at Keio University, Japan, is used as the prototype, where the total numbers of elements, nodes, and DOFs are 651,662, 1,207,902, and 3,623,706, respectively. In order to improve the accuracy, each element is divided twice in the three directions into eight elements, using the conversion program *uvmesh*, to result in 5,181,880 elements, 523,295 nodes, and 22,569,885 DOFs. Figs. 2(a) and (b) show the meshes around the connections before and after subdivision, respectively. Consequently, the plates such as flanges and webs of beams are divided into two layers of solid elements. The slab of each floor is also divided into the solid elements with two layers. The studs connecting the flange and the slab are omitted in the model, and the lower surface along the boundary of the slab is directly connected to the upper layer of the flange.

A piecewise linear isotropic hardening is used for the constitutive model of the steel material, and its parameters are identified from the uniaxial test results, which were distributed for the blind analysis contest. A bilinear relation is used for that of the concrete of the floor slab. The self weight of the steel is computed from the mass density 7.86×10^3 kg/m^3. By contrast, the mass density 2.3×10^3 kg/m^3 of the slab is increased appropriately to include the weights of the nonstructural components and the anti-collapse frames used in the experimental model, etc.

Elastoplastic dynamic collapse analysis is carried out for Cases 1, 2a, and 2b, which are defined as shown in Table 1. Fig. 3 depicts FE-models of these three cases. Case 1 ignores the stiffness of the exterior wall, whereas it is modeled by a shear spring connecting the flanges of the beams in the upper and lower floors. The three types of column bases are considered; i.e., fixed, rotational spring, and solid model. In Case 2a, the rotational stiffness around Z-axis of the column base is 10 times as large as those around X- and Y-axes. Since most of the damping of a steel frame is related to the friction and plastification of the nonstructural components, the ambiguous equivalent linear damping is expected to be replaced by more accurate model of nonstructural components. In the present study, however, the Rayleigh damping is used in all cases.

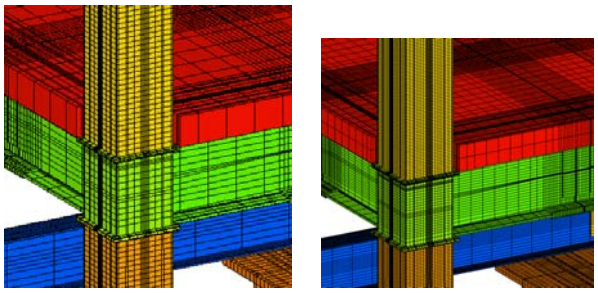

(a) Before subdivision (b) After subdivision

Figure 2 FE-Meshes Near the Connections

Table 1 Model Types of Column Bases and Exterior Walls.

Case	Column base	Stiffness of exterior wall
Case 1	Fixed.	Ignored.
Case 2a	Rotational spring based on the recommendation by Architectural Institute of Japan (1990).	Shear spring (truss element) connecting the flanges of the beams in the upper and lower floors. Parameters are identified from the experimental results (Matsuoka *et al.* 2007).
Case 2b	Solid model. Beam element for the anchor bolt with pretension. Contact with small friction between the lower face of base plate and the upper face of base.	

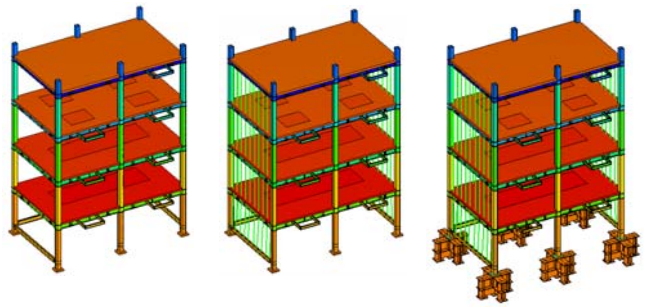

(a) Case 1 (b) Case 2a (c) Case 2b

Figure 3 FE-Models of the Three Cases (Drawn without Mesh).

3. RESULTS OF NUMERICAL ANALYSIS

3.1 Eigenvalue Analysis

The four lowest natural periods obtained by eigenvalue analysis for Cases 1, 2a, and 2b are listed in Table 2. The 1st and 4th modes correspond to translation in X-direction defined in Fig. 1; the 2nd mode is in Y-direction; and the 3rd mode is a torsional mode. Note that Case 2a with stiffness of exterior walls does not always have smaller periods than Case 1 because Case 2a has smaller stiffness at the column bases. The contact state is maintained at the column base in the process of eigenvalue analysis of Case 2b, which leads to the smaller periods than Case 1 or 2a. The shapes of the first and second modes of Case 2b are shown in Fig. 4. Note that the 1st and 2nd periods identified in experiments are 0.82 s and 0.74 s, respectively; i.e., the 2nd period by analysis is larger than that obtained by the experiment. The CPU time for eigenvalue analysis is 5,471.6 s using 16 cores of HP ProLiant BL465 2.6 GHz Dual Core Cluster.

Table 2. Four lowest natural periods (s) for Cases 1, 2a, and 2b

Case	Natural period			
	1st	2nd	3rd	4th
Case 1	0.8389	0.8144	0.5700	0.2702
Case 2a	0.8303	0.8203	0.5555	0.2700
Case 2b	0.7947	0.7833	0.5372	0.2578

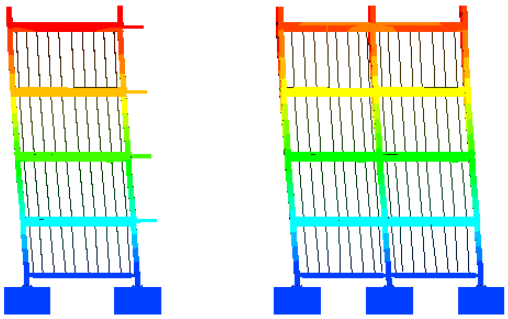

(a) 1st mode (b) 2nd mode

Figure 4 Two Lowest Eigenmodes of Case 2b

3.2 Time-History Analysis

Next, time-history analysis is carried out for Cases 1 and 2a for the three dimensional input motions of the JR-Takatori wave of the 1995 Hyogo-ken Nanbu Earthquake that is scale by 0.6. The acceleration record measured on the shaking table of the full-scale test is used rather than the numerically scaled ground motion record of the earthquake. Note that EW, NS, and UD components correspond to X-, Y-, and Z-directions, respectively. The duration of the motion is 20 s. The Rayleigh damping is used, where the damping factors are 0.02 for the 1st and 4th modes, which are the two lowest modes in X-direction. The Hilber-Hughes-Taylor method is used for time integration with parameters α = –0.05, $\beta = (1 - \alpha)^2/4 = 0.275625$. In this analysis, the 256 cores of one node of SGI Altix 4700 with Intel Itanium 1.66 GHz processors in NIED was used for computation. The elapsed time is 2,414 s for static analysis for self-weight, and average of the elapsed time for one step (Δt = 0.01 s) of the time-history analysis is 1,106 s.

The time histories of interstory drift angles and shear forces of the 1st story are plotted in Figs. 5 and 6, respectively. In Case 2a, better correlation with the experiment result is observed than in Case 1. The maximum and minimum values of the interstory drift angles are 0.01089 rad and –0.01357 rad in X-direction, and 0.02300 rad and –0.007942 rad in Y-direction, whereas the experimental results are 0.0121 rad and –0.0122 rad in X-direction, and 0.0190 rad and –0.00933 rad in Y-direction. Therefore, moderately accurate values are obtained by numerical analysis. Note that a residual deformation exists in Y-direction.

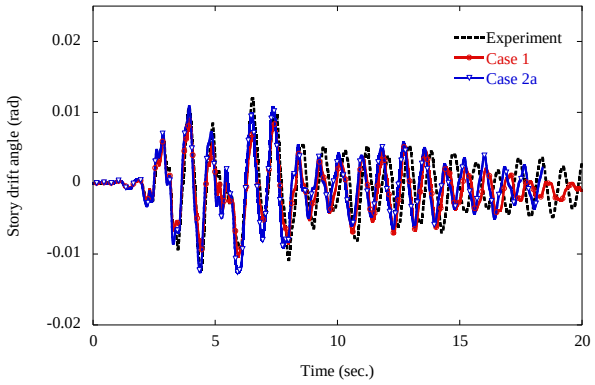

(a) X-direction

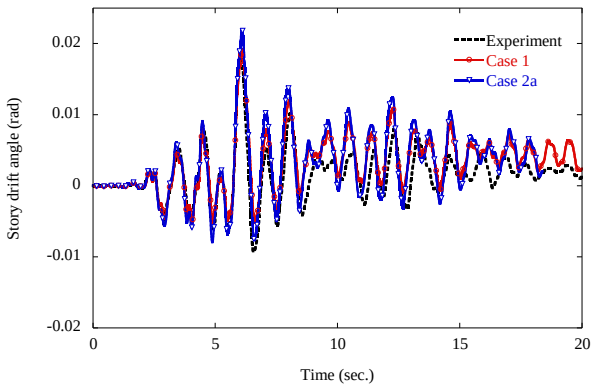

(b) Y-direction

Figure 5 Time-History of Interstory Drift Angle of the 1st Story

The story shear forces are calculated by the summation of the products of concentrated mass of each layer and the acceleration at the center of gravity of each layer. The maximum and minimum values of the shear forces in X-direction are 1142 kN and –1153 kN, respectively, and those in Y-direction are 1385 kN and –1229 kN, respectively. The measured values in the experiment are 1169 kN and –1173 kN in X-direction, and 1423 kN and –1058 kN in Y-direction. Therefore, the shear forces are estimated with good accuracy.

Figuress 7 and 8 respectively depict deformation of Cases 1 and 2a at 6 second, at which the input motion causes nearly the maximum deformation of the specimen. The deformation is magnified 10 times and the colors stand for the distribution of equivalent stress. In Case 2a, rotational response around Z-axis is observed and this is because the model of Case 2a considers exterior walls, which leads to the uniaxial eccentricity. The distribution of equivalent stress at the maximum deformation in Case 1 is shown in Fig. 9. As is seen, large stress is observed around the column base and beam-to-column connections.

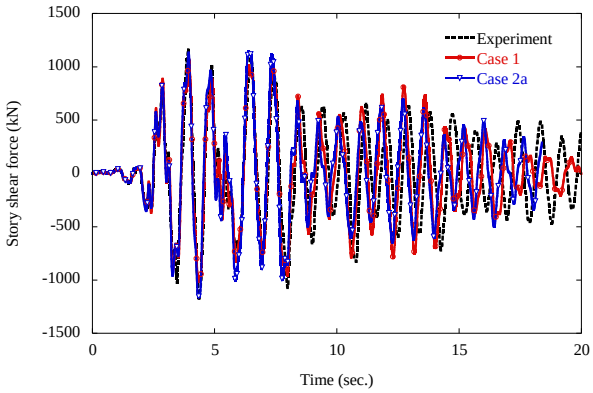

(a) X-direction

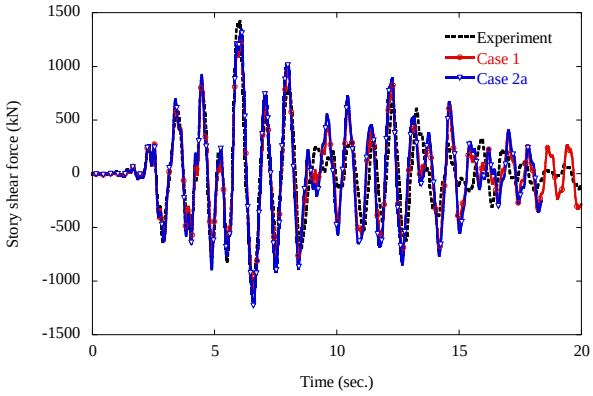

(b) Y-direction

Figure 6 Time-History of Shear Force of the 1st Story

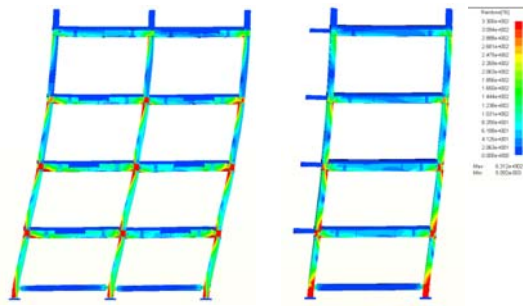

(a) X-axis (b) Y-axis

Figure 7 Case 1: Deformation (Magnified 10 Times) with Distribution of Equivalent Stress at 6 s

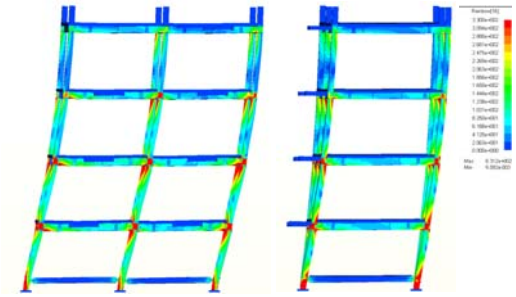

(a) X-axis (b) Y-axis

Figure 8 Case 2a: Deformation (Magnified 10 Times) with Distribution of Equivalent Stress at 6 s

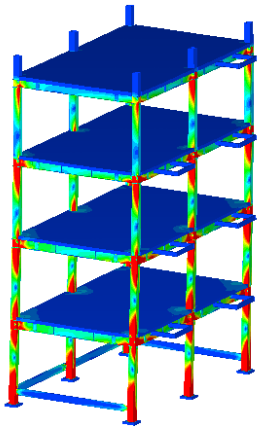

(a) Whole frame

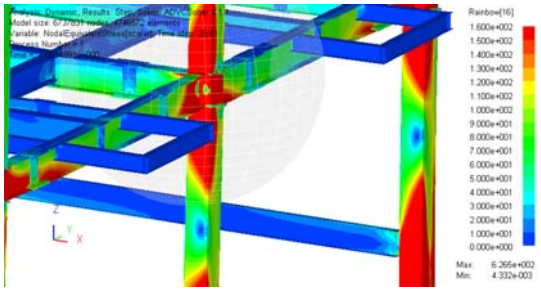

(b) Close view around the 2nd floor and the 1st story

Figure 9 Distribution of Equivalent Stress at the Maximum Deformation (Case 1)

4. CONCLUSIONS

A virtual shaking-table test has been carried out using the prototype of the E-Simulator for investigation of elastoplastic dynamic behavior of the 4-story frame model as the specimen of full-scale shaking-table test conducted in September 2007 at E-Defense. It has been shown that the large-strain elastoplastic dynamic behaviors can be estimated globally and locally with good accuracy by using the fine mesh with the solid elements and the constitutive relations of the steel material without resort to macro models and empirical parameters such as plastic hinge and stiffness amplification factor of the composite beam.

A shear spring that is applicable to large-deformation analysis has been implemented to the E-Simulator, to incorporate the stiffness and strength of the exterior walls. Hence, the use of ambiguous equivalent damping factor due to the friction and plastic deformation of the nonstructural components will be avoided by elaborating the model. This spring model will be further replaced by a solid model that is under development.

Acknowledgements:

This study is a part of E-Defense Seismic Experimental Study and Simulation System Construction Project conducted by E-Simulator Production Committee (Leader: Prof. Muneo Hori, The University of Tokyo). The authors acknowledge the valuable contribution from the committee members, and the financial support by NIED. The contribution by Dr. Yuyama of Allied Engineering Corporation for computation and mesh generation is also acknowledged.

The authors also acknowledge the valuable information from the NEES/E-Defense collaborative research program on steel structures (Leader: Prof. Kazuhiko Kasai, Tokyo Institute of Technology), which was pursued by the Analysis Method and Verification Working Group (Leader: Prof. Motohide Tada, Osaka University) and Building Collapse Simulation Working Group (Leader: Prof. Keiichiro Suita, Kyoto University).

References:

Akiba, H. *et al*. (2006). "Large scale drop impact analysis of mobile phone using ADVC on Blue Gene/L," *Proc. International Conference for High Performance Computing Networking and Storage (SC06)*, Tampa.

Architectural Institute of Japan (AIJ). (1990). "Recommendations for the Design and Fabrication of Tubular Structures in Steel," AIJ. (in Japanese)

E-Defense. (2009). "Hyogo Earthquake Engineering Research Center (E-Defense), National Research Institute of Earth Science and Disaster Prevention (NIED), Japan", http://www.bosai.go.jp/hyogo/ehyogo/index.html, as of 28 October 2009

Hikino, T., Ohsaki, M., Kasai, K. and Nakashima, M. (2009). "Simulation of E-Defense full-scale shake-table test results of moment-resisting steel frame," *Proc. Behavior of Steel Structures in Seismic Areas, STESSA 2009*, Philadelphia, Taylor & Francis, 137-143.

Hori, M., Noguchi, H., and Ine, T. (2007). "Project report of development of numerical shaking table coping with E-Defense," *JSCE Journal of Earthquake Engineering* 29, 1420-1425. (in Japanese)

Kasai, K., Ooki, Y., Motoyui, S., Takeuchi, T. and Sato, E. (2007). "E-Defense tests on full-scale steel buildings: Part 1 – Experiments using dampers and isolators," *Proc. Structural Congress 2007*, ASCE, Long Beach.

Matsuoka, Y., Matsumiya, T., Suita, K., and Nakashima, M. (2007). "Test on seismic performance evaluation of exterior ALC walls with opening: E-Defense experimental projects for steel buildings – Part 14," *Summaries of technical papers of Annual Meeting Architectural Institute of Japan*, **C-1**, 1081-1082. (in Japanese)

Ogino, M., Shioya, R., Kawai, H., and Yoshimura, S. (2005). "Seismic response analysis of nuclear pressure vessel model with ADVENTRUE System on the Earth Simulator," *Journal of The Earth Simulator*, **2**, 41-54.

Ohsaki, M., Kasai, K., Matsuoka, Y., and Zhang, J. Y. (2008). "Results of recent E-Defense tests on full-scale steel buildings: Part 2 – Collapse simulation and blind analysis

contest," *Proc. Structures Congress 2008*, ASCE, Vancouver.

Ohsaki, M., Miyamura, T., Kohiyama, M., Hori, M., Noguchi, H., Akiba, H., Kajiwara K., and Ine, T. (2009). "High-precision finite element analysis of elastoplastic dynamic responses of super-highrise steel frames," *Earthquake Engineering and Structural Dynamics* **38**(5), 635-654.

Suita, K., Yamada, S., Tada, M., Kasai, K., Matsuoka, Y. and Sato, E. (2007). "E-Defense tests on full-scale steel buildings: Part 2 – Collapse experiments on moment frames," *Proc. Structural Congress 2007*, ASCE, Long Beach.

Tada, M., Ohsaki, M., Yamada, S., Motoyui, S., and Kasai, K. (2007). "E-Defense tests on full-scale steel buildings: Part 3 – Analytical simulation of collapse," *Proc. Structures Congress 2007*, ASCE, Long Beach.

Newmark, N.M. and Rosenblueth, E. (1971), "Fundamentals of Earthquake Engineering," Prentice-Hall Inc.

Trifunac, M.D. and Brady, A.G. (1975), "A Study on Duration of Strong Earthquake Ground Motion," *Bulletin of the Seismological Society of America*, **65**(3), 581-626.

Kasai, K., Fu, Y., and Watanabe, A. (1998), "Passive Control Systems for Seismic Damage Mitigation," *Journal of Structural Engineering*, American Society of Civil Engineers, **124**(5), 501-512.

MacRae, G. A. and Kawashima, K. (2001), "Seismic Behavior of Hollowed Stiffened Steel Bridge Columns," *Journal of Bridge Engineering*, American Society of Civil Engineers, **6**(2), 110-119.

Fujimoto, K. and Midorikawa, S. (2000), "Simplified Method for Predicting Ground Motion Intensity Map Considering Effect of Irregular Deep Underground Structure," *Proceedings of the 6th International Conference on Seismic Zonation*, Paper No. 2-23B.

JOINT CONFERENCE PROCEEDINGS
7th International Conference on Urban Earthquake Engineering (7CUEE) &
5th International Conference on Earthquake Engineering (5ICEE)
March 3-5, 2010, Tokyo Institute of Technology, Tokyo, Japan

A STEEL DATABASE FOR COMPONENT DETERIORATION OF TUBULAR HOLLOW SQUARE STEEL COLUMNS UNDER VARYING AXIAL LOAD FOR COLLAPSE ASSESSMENT OF STEEL STRUCTURES UNDER EARTHQUAKES

Dimitrios G. Lignos[1)], Helmut Krawinkler[2)]

1) JSPS Post Doctoral Fellow, Disaster Prevention Research Institute (DPRI), Kyoto University, Japan
2) Professor Emeritus, Dept. of Civil Engineering, Stanford University, Stanford, CA, USA
d.lignos@kt2.ecs.kyoto-u.ac.jp, Krawinkler@stanford.edu

Abstract: Collapse assessment of structural systems under earthquake excitations requires analytical models that are capable to simulate deterioration of structural components. Reliability of analytical predictions to collapse depends on available experimental data that serve for validation and improvement of component deterioration models. This paper summarizes the development of a database that includes more than 120 tubular hollow square steel columns subjected to combined axial load and cyclic moments. The database serves for deterioration modeling of tubular steel columns. Based on extensive calibration of the simulated hysteretic response using a deterioration model with available digitized moment rotation data, relationships are proposed that associate analytical model parameters with criteria that control deterioration of tubular hollow square steel columns. The relationships are developed based on multivariate regression analysis. It is shown that the pre and post capping rotation and cyclic deterioration of tubular hollow square steel columns strongly depend on the axial load and the depth to thickness ratio of the column section.

1. INTRODUCTION

Recent earthquakes around the world (Northridge 1994, Kobe, 1995, Taiwan, 1999, China, 2009) demonstrated that structural systems may collapse when they are subjected to extreme seismic events. In order to assess the collapse potential of structural systems under earthquakes within a confidence level, state-of-the art analytical models that are able to simulate important component deterioration modes should be used together with advanced numerical analysis tools. Reliability of analytical simulations based on these models is based on extensive calibration of the deterioration model parameters with available experimental data from steel and reinforced concrete component tests. This experimental data needs to be available in a consistent format, and most important, the digitized load deformation (deduced moment rotation) diagrams should also be provided. Hence the development of component databases is necessary for calibration and improvement of available deterioration models and statistical assessment of their parameters.

So far, few databases are available that provide partial information on steel and reinforced concrete (RC) component hysteresis, setup and configurations (SAC, 1998, http://www.sacsteel.org/connections/, Berry et al. 2004, Panagiotakos and Fardis, 2001, Fardis and Biskinis, 2003). Hajjar (2000) and Tort and Hajjar (2004) developed a database of rectangular concrete – filled steel tubes (CFT) for performance – based design and evaluation of distributed and concentrated plasticity analytical models for cyclic analysis of CFT columns (Hajjar et al. 1997, 1998).

Recently, Lignos and Krawinkler (2007, 2009) developed a database of more than 300 steel beams. This database provides complete information on metadata, results and fully digitized load - deformation (deduced moment - rotation) data and serves for modeling of component deterioration of steel beams with different connection types. This database can be also used for modeling of component deterioration of steel columns, but with caution due to limited experimental data that is available. The steel beam database is available through George E. Brown, Jr. Network for Earthquake Engineering Simulation (NEES) central repository(https://central.nees.org/?action=DisplayExperimentMain&projid=84&expid=1590).

This paper summarizes the development of a steel database for modeling of component deterioration of tubular hollow square steel columns under varying axial load and cyclic or monotonic bending moments. Based on the available information from this database and a recently developed deterioration model, relationships are proposed that associate deterioration model parameters with geometric and material properties of the tubular hollow square steel columns.

2. COMPONENT DETERIORATION

Many analytical models that simulate component deterioration in strength and stiffness are available in the

literature, such as the one presented by Sivaselvan and Reinhorn (1999, 2000). A detailed summary of the available deterioration models is presented in Lignos and Krawinkler, (2009). In the present paper a modified version of the Ibarra-Krawinkler deterioration model (Ibarra et al. 2005, Lignos and Krawinkler, 2009) with bilinear hysteretic response is used to simulate component deterioration of steel columns. This model is a concentrated plasticity spring that can simulate up to four modes of deterioration (strength, stiffness, post-capping strength and reloading stiffness deterioration) by using a reference backbone curve and an energy-based rule that controls deterioration (Rahnama and Krawinkler, 1993). Figure 1a illustrates an example of calibration of the elastic stiffness K_e, pre and post capping rotation θ_p, θ_{pc} of the component deterioration model to match the monotonic test of a tubular steel section tested by Sugiyama and Igarashi (1986). In the same figure (see Figure 1b) we have also included an example of calibration of the cyclic deterioration parameter Λ of the modified IK model to match the hysteretic response of a tubular square hollow section tested by Tsuji and Nakatsura (1986). Specifics about the deterioration model can be found in Lignos and Krawinkler, (2009).

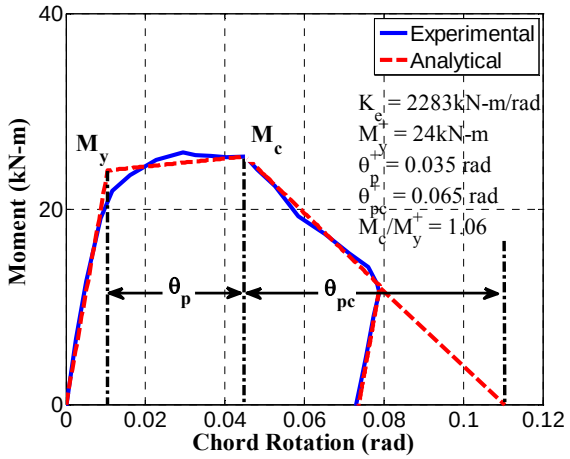

(a) Monotonic response (data from Sugiyama and Igarashi, 1986)

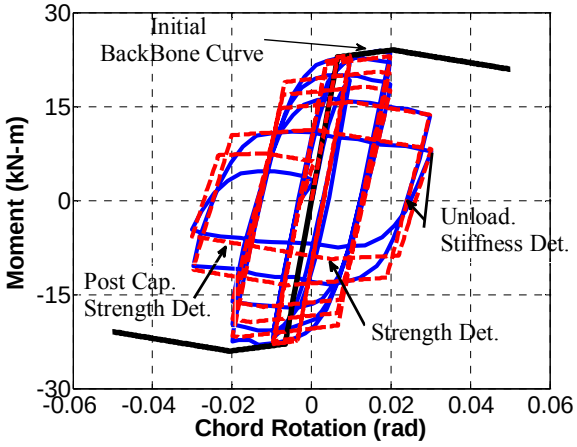

(b) cyclic response (data from Tsuji and Nakatsura, 1986)

Figure 1 Modified Ibarra Krawinkler deterioration model

3. TUBULAR HOLLOW SQUARE STEEL COLUMN DATABASE

A common design practice in Japan for steel moment resisting frames is to use tubular hollow square sections (HSS) as columns. To assess the deterioration properties of HSS columns under varying axial load and cyclic or monotonic bending more than 120 experimental data of HSS columns were collected from the Japanese literature and were categorized in a systematic way. The data set contains 44 monotonic tests and the rest are all cyclic. The axial load ratio N/N_y (expressed by the ratio of applied axial load N to yield axial load N_y) in the data set varies from 0 to 0.60 and column depth D to thickness t ratio D/t varies from 18 to 100. The main configurations in the database are (1) cantilever beams and (2) columns fixed at their both ends. The steel HSS column database is organized in metadata and reported experimental results. Metadata contain information about specimen configuration, column section, geometric and material properties of the steel column, test setup and a summary report excerpt based on the available report from the primary research investigators. Reported experimental results include digitized data of load - displacement curves and cumulative energy dissipation per excursion of the HSS column. All the digitized load- displacement data from the experiments gathered in the HSS database were digitized using an object-oriented software called *Digitizer* developed by Lignos and Krawinkler (2009). Depending on the configuration type of each specimen a moment - rotation diagram is deduced based on the available load - displacement data of the individual tests. Since axial load was applied to most of the tests, the P-delta effect, which depends on the test configuration, is accounted for explicitly by taking into account a second order moment.

3.1 Calibration of Component Deterioration Parameters

The digitized data stored in the HSS column database is utilized to calibrate the cyclic moment - rotation behavior of plastic hinge regions of the HSS columns using the modified Ibarra Krawinkler (IK) model discussed in Section 2 of this paper. The objective is to develop "complete" moment - rotation relationships that incorporate experimental evidence to quantify cyclic deterioration and phenomena that are insufficiently described by engineering mechanics models.

Since the goal is to use the deterioration models for prediction of collapse of structural systems the emphasis during the calibration process is at large inelastic cycles. The calibration process is based on a combination of visual observations and concepts of mechanics. After defining manually the backbone curve and cyclic input deterioration parameters of the model, using a Matlab-based (Mathworks, 2006, http://www.mathworks.com/access/helpdesk/help) interactive software named *Calibrator* (Lignos and Krawinkler, 2009) we are able to simulate the cyclic or monotonic response and the history of peak deformations of each experiment. After displaying the simulated hysteretic response together with the experimental one,, we judge if the

match is satisfactory based on visual inspection. If unsatisfactory, improved backbone and deterioration parameters can be input and the prescribed process is repeated until a satisfactory match is achieved. Figure 2 illustrates an example of a satisfactory match between simulated and experimental hysteretic response for a HSS column tested by Tsuji and Nakatsura (1986).

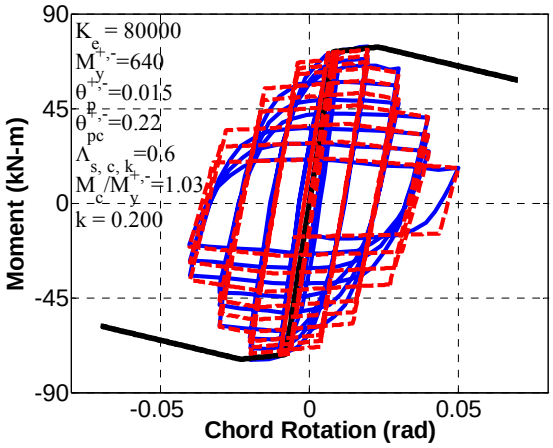

Figure 2 Example of satisfactory match between simulated and experimental hysteretic response of HSS column with N/N_y = 0.40, D/t = 28.6 (data from Tsuji and Nakatsura, 1986)

The calibration process discussed in the previous paragraph was applied to all the available experimental data from the HSS column database. Findings related to deterioration of HSS columns are presented in the subsequent sections.

3.2 Trends on Component Deterioration Parameters

Deterioration modeling parameters θ_p, θ_{pc} and Λ mostly depend on the D/t and N/N_y ratios. Figure 3 illustrates the sensitivity of pre-capping plastic rotation θ_p to those ratios for the complete set (monotonic and cyclic) of the available experimental data. The general trend for all the deterioration parameters is that for D/t ratios larger than 33 and N/N_y ratios above 0.30, the HSS columns deteriorate relatively fast. This observation is also confirmed by a recent earthquake simulator collapse test of a full scale 4-story steel structure with HSS columns that took place at the E-Defense facility in Japan (Suita et al. 2008). The HSS columns of the 4-story steel structure had a D/t ratio equal to 33. The structure collapsed with a first story mechanism primarily because of early strength deterioration of the first story columns.

For about 20 specimens included in the HSS column database the rate of deterioration becomes small enough at large cycles to be neglected in analytical modeling, i.e. strength stabilization occurs. This stabilization occurs at a residual strength that is a fraction of the yield strength. Based on detailed information summarized in Lignos and Krawinkler (2009) there is no clear dependence of the residual strength ratio on D/t and N/N_y ratios, but this may be due to the small number of specimens that reached the stabilization path since the loading program of the associated tests was terminated before the residual strength was attained. Based on the data subset of 20 specimens a residual strength ratio κ = 0.25 appears to be a reasonable estimate for analytical modeling of HSS columns. Kecman (1983) after evaluating experimentally the monotonic behavior of 27 different types of rectangular and steel tubes subjected to pure bending, showed that the residual strength ratio is between 20 to 30% of the yield strength of the column section for a similar D/t range and $N/N_y = 0$.

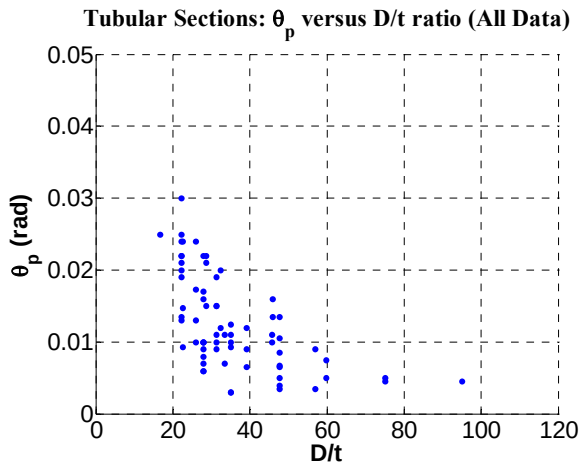

(a) Effect of D/t on θ_p

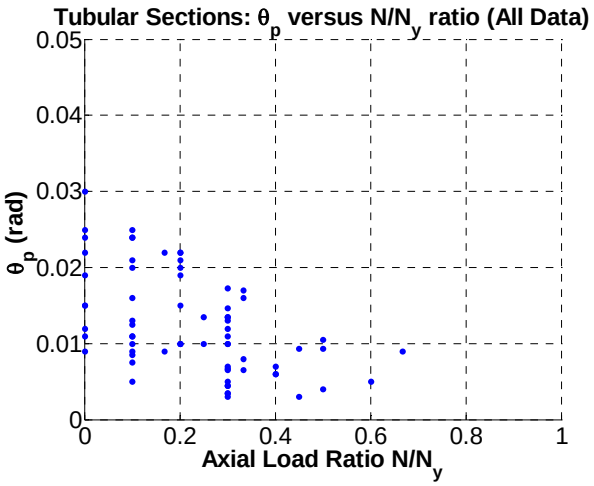

(b) Effect of N/N_y on θ_p

Figure 3 Dependence of pre-capping plastic rotation θ_p on D/t and N/N_y ratios for the complete set of HSS columns

4. RELATIONSHIPS FOR COMPONENT DETERIORATION MODELING OF TUBULAR HOLLOW SQUARE STEEL COLUMNS

Based on the available experimental data included in the HSS column database and after the calibration of the simulated hysteretic response with the individual tests, empirical relationships are proposed to predict the deterioration parameters of HSS columns with the use of stepwise multivariate regression analysis (see Chatterjee et al. 2000). A general function form is used to determine the

response parameter *RP*,

$$RP = a_1\left(\frac{D}{t}\right)^{a_2}\left(1-\frac{N}{N_y}\right)^{a_3}\left(\frac{c\cdot F_y}{380}\right)^{a_4} \quad (1)$$

in which F_y is the expected yield strength of the HSS column in *MPa* and *c* is a coefficient equal to 1.0 when F_y is in MPa and equal to 6.895 when F_y is in *ksi*. The expected yield strength in Eq. (1) is normalized with respect to 380MPa since this is the nominal yield strength of typical Japanese steel BCR295 used in steel construction of tubular sections. The multivariate regression is always performed in the natural log domain of the model parameter since Lignos and Krawinkler (2009) showed that the regression variables D/t and N/N_y follow a lognormal distribution based on a Kolmogorov-Smirnov test (Benjamin and Cornell, 1970). The proposed equations for predicting deterioration parameters of HSS columns are valid for the following D/t, N/N_y and F_y range, $20 \le D/t \le 60$, $0 \le N/N_y \le 0.50$, $276\text{MPa} \le F_y \le 500\text{MPa}$

4.1 Pre-capping plastic rotation θ_p

The proposed relationship to predict pre-capping plastic rotation θ_p is,

$$\theta_p = 0.614\left(\frac{D}{t}\right)^{-1.05}\left(1-\frac{N}{N_y}\right)^{1.18}\left(\frac{c\cdot F_y}{380}\right)^{-0.11} \quad (2)$$

The coefficient of determination R^2 of Eq. (2) is R^2=0.70. A plot of predicted versus calibrated θ_p values based on Eq. (2) is shown in Figure 4. The data exhibits some scatter but the agreement between predicted versus calibrated θ_p values is satisfactory.

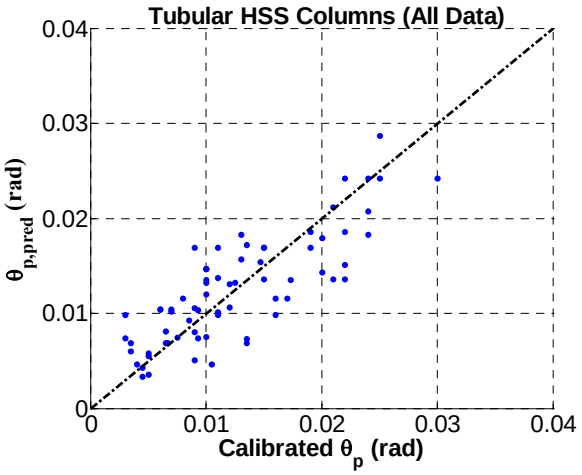

Figure 4 Predicted versus calibrated θ_p values for tubular HSS steel columns

4.2 Post-capping plastic rotation θ_{pc}

In order to propose an empirical relationship for the post-capping rotation θ_{pc} of tubular HSS columns, only specimens with a clear indication of θ_{pc} in their monotonic or hysteretic response have been included in the statistical evaluation using a stepwise regression analysis. The proposed equation is,

$$\theta_{pc} = 13.82\left(\frac{D}{t}\right)^{-1.22}\left(1-\frac{N}{N_y}\right)^{3.04}\left(\frac{c\cdot F_y}{380}\right)^{-0.15} \quad (3)$$

Equation (3) has a coefficient of determination R^2=0.825 indicating a satisfactory match with the experimental data. This can seen also in Figure 5, which shows the predicted versus the calibrated θ_{pc} values.

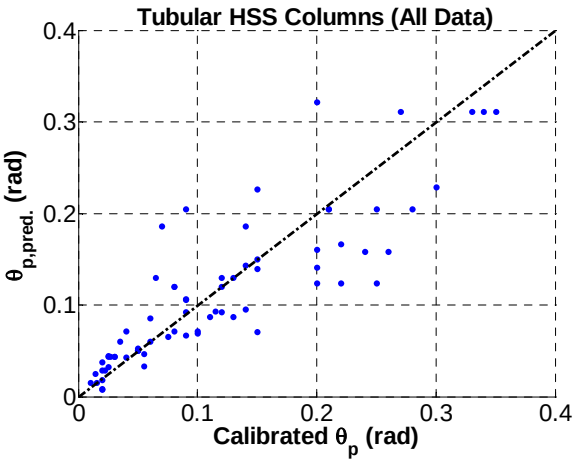

Figure 5 Predicted versus calibrated θ_{pc} values for tubular HSS columns

Kecman (1983) and Gioncu and Petsu (1995) evaluated both experimentally and analytically the sidesway collapse behavior due to pure bending (absence of axial load) of rectangular and square section tubes. They proposed moment - rotation relationships based on the yield line theory to predict the descending portion of the monotonic curve (after buckling occurred) of individual tests. Their equivalent suggested θ_{pc} values for a range of $20 \le D/t \le 60$ are similar to the ones proposed by Eq. (3) for N/N_y=0.

4.3 Cyclic Deterioration Parameter Λ

Cumulative rotation capacity Λ is predicted with an empirical equation that is based on a subset of 40 data points of the HSS column database, since only these specimens show clear strength deterioration under cyclic loading. Specimens that fail in a brittle manner (i.e., rapid deterioration due to brittle failure) are not included in the equation development. Cyclic deterioration parameters for strength Λ_s post-capping strength Λ_c and unloading stiffness Λ_k deterioration are set to be equal in the calibration process for the sake of simplicity. The proposed equation for Λ is,

$$\Lambda = 3012\left(\frac{D}{t}\right)^{-2.49}\left(1-\frac{N}{N_y}\right)^{3.51}\left(\frac{c\cdot F_y}{380}\right)^{-0.20} \quad (4)$$

Equation (4) has an R^2 of 0.838. Predicted versus calibrated Λ values are illustrated in Figure 6 based on the data subset of 40 specimens. Specimens with D/t = 30 and N/N_y=0.30 (typical values for mid-rise Japanese steel structures) have severe strength deterioration mainly due to early occurrence of local buckling. Kawaguchi and Morino (2001) concluded the same based on an extensive experimental program they conducted. They suggested that one way to improve both post-buckling behavior and energy dissipation capacity of HSS columns is the use of concrete infill.

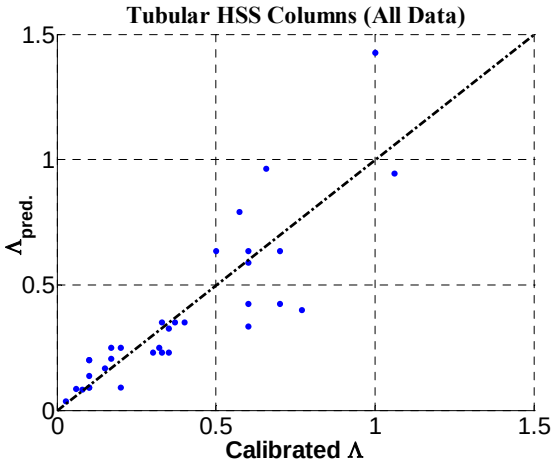

Figure 6 Predicted versus calibrated Λ values for tubular HSS columns

4.4 General Observations on Deterioration Parameters of Tubular Hollow Square Steel Columns Based on Regression Equations

Looking at the combined effect of axial load ratio N/N_y and depth to thickness ratio D/t on deterioration properties of hollow square steel columns from Eq. (2) and (3) that consider the correlation of the two parameters it can be seen that the N/N_y ratio has a larger effect on post-capping rotation θ_{pc} of HSS columns. The reason is that once the HSS column has buckled locally it is the axial force that controls how fast the component will deteriorate. The same observation is made from Table 1, which summarizes the predicted values of θ_{pc} for three different HSS columns and for three different axial load ratios. The cumulative deformation capacity parameter Λ is more detrimental compared to D/t ratio since cyclic deterioration will occur after the column section has buckled. The N/N_y ratio determines the rate of cyclic deterioration after first buckling. Similar observations can be made from Table 1 for the Λ values. The effect of yield strength F_y of the steel material on deterioration parameters is not significant compared to D/t and N/N_y ratios. The non-negligible exponents in Eqs. (2) to (4) likely are due to the material variability in the HSS column data set.

Table 1 Deterioration model parameters based on predictive equations for various tubular column sections and different N/N_y ratios (expected yield strength F_y=380MPa)

Section Size	θ_p (rad)	θ_{pc} (rad)	Λ	N/N_y	D/t
HSS200x200x12	0.032	na	2.73	0	16.67
HSS300x300x9	0.015	0.19	0.49		33.33
HSS175x175x4.5	0.013	0.16	0.33		38.89
HSS200x200x12	0.023	na	1.00	0.25	16.67
HSS300x300x9	0.015	0.19	0.49		33.33
HSS175x175x4.5	0.013	0.16	0.33		38.89
HSS200x200x12	0.018	na	0.45	0.4	16.67
HSS300x300x9	0.015	0.19	0.49		33.33
HSS175x175x4.5	0.013	0.16	0.33		38.89

5. CONCLUSIONS

This paper summarizes a recently developed database of tubular hollow square steel (HSS) columns subjected to combined axial load and bending moments for deterioration modeling of HSS columns. The HSS column database is available through the George E. Brown, Jr. Network for Earthquake Engineering Simulation (NEES) central repository(https://central.nees.org/?action=DisplayExperimentMain&projid=84&expid=1590). The database contains comprehensive information of metadata, results and deduced moment - rotation diagrams of more than 120 specimens. The simulated hysteretic response of these specimens based on a widely used deterioration model for collapse assessment of structural systems is calibrated to match the experimental moment - rotation diagrams.

Deterioration modeling parameters θ_p, θ_{pc} and Λ mostly depend on the depth to thickness D/t and axial load N/N_y ratios. The general trend for all deterioration parameters is that for D/t ratios larger than 33 and N/N_y ratios above 0.30, the HSS columns deteriorate relatively fast. These trends are also confirmed by proposed empirical relationships that predict θ_p, θ_{pc} and Λ with the use of stepwise multivariate regression analysis based on the available experimental data from the HSS column database.

Acknowledgements:
This study is based on work supported by the United States National Science Foundation (NSF) under Grant No. CMS-0421551 within the George E. Brown, Jr. Network for Earthquake Engineering Simulation Consortium Operations and a CUREE-Kajima Phase VI research program. The financial support is gratefully acknowledged. Any opinions, findings, and conclusions or recommendations expressed in this paper are those of the authors and do not necessarily reflect the views of NSF.

References:

Berry, M., Parrish, M., and Eberhard, M. (2004), "PEER structural performance database user's manual," *Report Pacific Engineering Research Center*, University of California, Berkeley, California, 38 pp.

Benjamin, J. R. and Cornell, C. A. (1970), "Probability, statistics, and decision for civil engineers," McGraw Hill, Inc. New York.

Chatterjee, S., Hadi, A.S., and Price, B. (2000), "Regression

Analysis by Example," 3rd Edition, John Wiley and Sons Inc., New York.

Fardis, M. N. and Biskinis, D. E. (2003), "Deformation capacity of RC members, as controlled by flexure or shear," *Otani Symposium*, 511-530.

Gioncu, V, and Petcu D. (1995), "Numerical investigations on the rotation capacity of beams and columns," *In Stability of Steel Structures, (ed. M. Ivayi), SSRC Colloquium, Budapest, 21-23 September 1995*, Akamemiai Kiado Budapest, **1**, 163-174.

Panagiotakos, T. B. and Fardis, M. N. (2001), "Deformations of reinforced concrete members at yielding and ultimate," *ACI Structural Journal*, **98**(2), 135-148.

Tort, C., and Hajjar, J. F. (2004), "Damage assessment of rectangular concrete-filled steel tubes for prerformance-based design", *Earthquake Spectra*, **20** (4), 1317-1348.

Hajjar, J. F., Gourley, B. C., and Olson, M. M. (1997), "A cyclic nonlinear model for concrete-filled tubes, I formulation. II verification," *Journal of Structural Engineering,* American Society of Civil Engineers, **123** (6), 736-757.

Hajjar J. F., Molodan, A., and Schiller, P. H. (1998), "A distributed plasticity model for cyclic analysis of concrete-filled steel tube beam-columns and composite frames," *Engineering Structures*, **20** (4-6), 398-412.

Hajjar, J. F., (2000), "Concrete-Filled steel tube columns under earthquake loads," *Progress in Structural Engineering and Materials*, **2** (1),72-82.

Kecman, D., (1983), "Bending collapse of rectangular and square section tubes," *International Journal of Mechanical Science*, **25**(9-10), 623-636.

Lignos, D. G., and Krawinkler, H. (2007), "A database in support of modeling of component deterioration for collapse prediction of steel frame structures," *Structures Congress*, American Society of Civil Engineers, Long Beach CA, SEI institute.

Lignos, D. G., and Krawinkler, H. (2009), "Sidesway collapse of deteriorating structural systems under earthquake excitations," *Report No. TB 172*, *John A. Blume Earthquake Engineering Center*, Stanford University, Stanford CA.

Sivaselvan MV, and Reinhorn AM. (1999), "Hysteretic models for cyclic behavior of deteriorating inelastic structures," *Report MCEER-99-0018*, Department of Civil, Structural and Environmental Engineering, State University of New York at Buffalo.

Sivaselvan M., and Reinhorn, A.M. (2000), "Hysteretic models for deteriorating inelastic structures," *Journal of Engineering Mechanics*, American Society of Civil Engineers, **126**(6), 633-640.

Suita, K., Yamada, S., Tada, M., Kasai, K., Matsuoka, Y., and Shimada, Y. (2008), "Collapse experiment on 4-story steel moment frame: Part 2 detail of collapse behavior," *Proc. 14th World Conference on Earthquake Engineering 2008, October 12-17, 2008,* China.

Ibarra L. F., Medina R. A., and Krawinkler H. (2005), "Hysteretic models that incorporate strength and stiffness deterioration," *Earthquake Engineering and Structural Dynamics*, **34**(12), 1489-1511.

Rahnama, M., and Krawinkler, H. (1993), "Effect of soft soils and hysteresis models on seismic design spectra," *Report No. 108*, *John A. Blume Earthquake Engineering Research Center*, Department of Civil Engineering, Stanford University, Stanford CA.

Tsuji, B., and Nakatsura, T. (1986), "Safety criteria in design of tubular structures," *Proceedings of the International Meeting held in Tokyo*, Japan.

Sugiyama S., and Igarashi, Y. (1986), "Experimental investigation of inelastic behavior of cold - formed rectangular hollow structural sections under bending and constant axial force," *Journal of Structural and Construction Engineering*, Architectural Institute of Japan.

COLLAPSE MECHANISM FOR STEEL MOMENT RESISTING FRAMES WITH DIFFERENT COLUMN BASES

Katsunori Kaneda [1], Yoshihiro Kimura[2], Shinichi Hamasaki[3] and Akira Wada[4]

1) Professor, Shibaura Institute of Technology, Structural Design PLUS ONE Co., Ltd, Japan
2) Professor, Dept. of Structural Engineering, Nagasaki University, Japan
3) Graduated Student, Graduated School of Science and Technology, Nagasaki University, Japan
4) Professor, Structural Engineering Research Center, Tokyo Institute of Technology, Japan
k-kaneda@sp-plusone.co.jp, ykimura@nagasaki-u.ac.jp, d708185l@cc.nagasaki-u.ac.jp, wada@serc.titech.ac.jp

Abstract: In general, the column bases are allowed to be plastic hinges when the steel moment resisting frames are designed in the seismic design. For the frames with fixed column bases, the soft story mechanism may occur when the frames are subjected to unexpected seismic force. This paper proposes the new support systems on the first story. The first story columns consist of the reinforced concrete downside column and the steel topside column, and their joints with the anchor bolts and the shear plates are supposed to be pinned. This paper clarifies the damage distribution and the collapse deformation capacity of the steel moment resisting frames with these support conditions.

1. INTRODUCTION

The steel moment resisting frames have the column bases such as the exposed type column base or the embedded type column base. In general, the exposed type column base has a small rotational stiffness and small rotational strength. The bending moment at the top of columns on the bottom story becomes larger than that at the base, when the frame is subjected to the seismic forces. So the column should be designed to be fixed with the steel members such as angle section embedded into the joint of the reinforced concrete ground beam, or the column section should be larger. In the former case, the construction become complicate, and in the latter case, the steel weights of the frame become heavier.

On the other hand, the column base with the embedded type column base is designed to be fixed, and then the column must be embedded into the reinforced concrete ground beam. So the reinforced concrete ground beam should have haunches or its section should be larger. For fixed column base, the column moment at the base become largest in all columns, so the column base must yield as early as the beam on the second story yields.

In general, the column bases are allowed to be plastic hinges when the steel moment resisting frames are designed in the seismic design.

The plastic deformation capacities for columns with box section are shown to be smaller than those for beams with H section as shown the references (Kato, Akiyama and Obi, 1977) (Kato., Akiyama and Kitazawa, 1978), so that for the frames with fixed column bases, the soft story mechanism may occur when the frames are subjected to unexpected seismic force.

This paper proposes the new support systems on the first story such as Fig.1. These systems consist of the reinforced concrete downside column and the steel topside column, and their joints with the anchor bolts and the shear plates are supposed to the pinned. For this proposal column support system, the rotational stiffness of the column joints is not required at all, because the joints are closely located on the point of contrary flexure. Applying this system, the column moment at the top and base on the first story become equal. So that the columns can keep elastic until the rotational demand of the beam archives its deformation capacity, which is called as the collapse of the member.

This paper clarifies the damage distribution and the collapse deformation capacity of the steel moment resisting frames with these support systems.

2. COLLAPSE MECHANISM FOR STEEL MOMENT RESISTING FRAMES SUBJECTED TO STATIC LATERAL FORCE

2.1 Outline of Static Analysis

Figure 1 shows the plan and the elevation of the proposed column support system in this paper. Figure 2 shows the analytical models for 6 story frames. The column-to-beam connections for the frames are assumed to be rigid except the joints at the center on the first story. The first story columns consist of the reinforced concrete downside and the steel topside columns. These columns are jointed by the base plate and the anchor bolts. In the analyzed frames, these are assumed to be

Table 1 Member Sections in 3 Story Frames and 6 Story Frames (*mm*)

	3-1.4-A		3-1.4-B		3-1.4-C		3-2.1		3-1.2	
Story/Floor	Column	Girder	Column	Girder	Column	Girder	Column	Girder	Column	Girder
1/2～3/4	□-500×15	BH-650×250 ×12×16	□-430×21	BH-650×250 ×12×16	□-400×25	BH-650×250 ×12×16	□-500×21	BH-600×250 ×12×16	□-430×19	H-600×250 ×12×22
Base	800×800	1200×800	800×800	1200×800	800×800	1200×800	800×800	1200×800	800×800	1200×800

	6-1.4-A		6-1.4-B				6-2.1		6-1.2	
Story/Floor	Column	Girder	Column	Girder			Column	Girder	Column	Girder
4/5～6/7	□-550×17	H-700×300 ×12×19	□-500×22	H-700×300 ×12×19			□-580×21	H-700×300 ×12×17	□-550×17	H-700×300 ×12×22
1/2～3/4	□-550×20	H-700×300 ×12×22	□-500×25	H-700×300 ×12×22			□-600×22	H-700×300 ×12×20	□-550×19	BH-700×300 ×12×25
Base	800×800	1200×800	800×800	1200×800			800×800	1200×800	800×800	1200×800

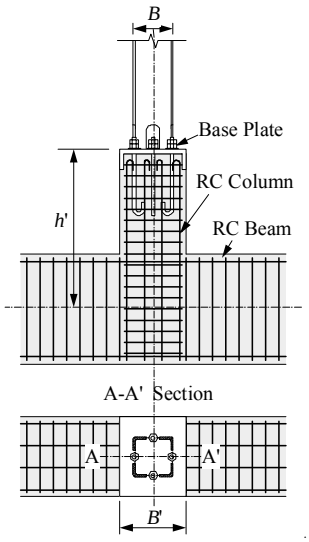

Figure 1 New Column Support System

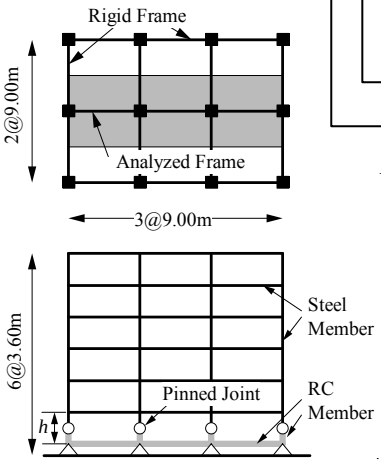

Figure 2 Model of 6 Story Frame

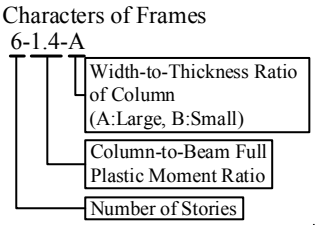

Table 2 Yield Stress and Young's Modulus (N/mm^2)

E_{steel}	205.8×10^3
$\sigma_{y\text{-}steel}$	235.0
$E_{concrete}$	27.3×10^3
$\sigma_{y\text{-}concrete}$	37.0

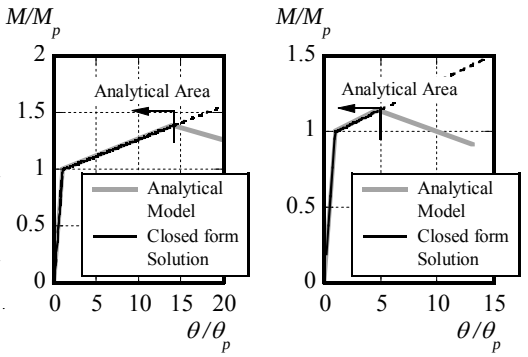

Figure 3 Relationship between Moment and Rotation Angle of Member in 6-1.2 : (a) Beam, (b) Column

pinned. ABAQUS version 6.4.2 is used for the numerical analyses.

Table 1 shows the member sections for 3 story frames and 6 story frames. The underside of Table 1 shows the characters of frames. Where, the first, second numbers and third character represent the number of stories, the column-to-beam full plastic moment ratio, M_{pc}/M_{pb}, and the width-to-thickness ratio of column, B/t, respectively. For the character of the frames with the embedded type column base (ECB), the "-fix" is given. The members of the frames are designed as the initial stiffness and the yield strength of the frames are almost equal. The member sections of the beams and the columns on every three stories are different. When the base shear coefficient, C_0 is 0.2, the maximum story drifts of the frames designed in this paper become below 1/200.

Table 2 shows the material properties. The young's modulus of the steel members is 205.8×10^3 N/mm^2, the yield stress of the steel members is 235.0 N/mm^2, the young's modulus of the concrete members is 27.3×10^3 N/mm^2 and the yield stress of the concrete members is 37.0 N/mm^2.

Figure 3 shows the relationship between the moment and the rotational angle of the beam and the column on first story in the frames with $M_{pc}/M_{pb}=1.2$. The closed form solutions in this figure are suggested from the experimental results (Kato, Akiyama and Obi, 1977) (Kato., Akiyama and Kitazawa, 1978), and the analytical models in this figure are calculated by fitting the lines of closed form solutions. In this paper, it can be assumed that the members possess their strength until the moment reaches the maximum strength. Then it is defined as the collapse of the members.

2.2 Results of static analyses

Figure 4 shows the relationship between the lateral load, Q_1/R_tW_1 and the maximum story drift, δ_{max}/h for 6 story

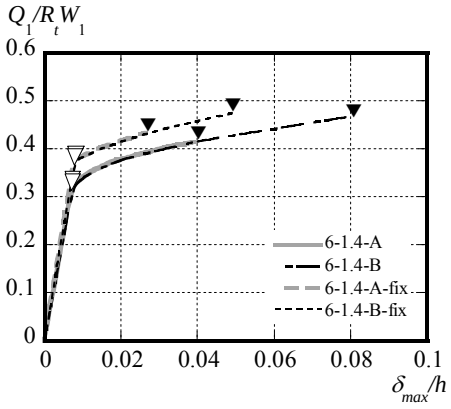

Figure 4 Relationship between Base Shear Strength and Story Drift

frames with the different width-to-thickness ratios of column, B/t. Where, Q_1 is the base shear force, W_1 is the total weight of the frame and R_t is the vibration property coefficient. ∇ in figure shows the point when a member in the frame first yields. This point is defined as the initial yield of the frame. ▼ in figure shows the point when the moment of the member in the frame first arrives at the maximum strength. This point is defined as collapse of the member. The initial stiffness of the frames is almost equal not to depend on the column support system. The yield strength of the frame with the new type column base (NCB) is smaller than that of the frame with the embedded type column base (ECB). When a member in the frames collapses, the story drift of the frame with NCB is greater than that of the frame with ECB. This is because the column with the small plastic deformation capacity collapses for the frames with ECB. When a member in the frame collapses, the story drift of the frame with the small width-to-thickness ratio of column (type A) is greater than that of the frame with the large width-to-thickness ratio of column (type B).

Figure 5 (a) shows the story drift distribution for 6 story frames at δ_{max}/h=0.02. Figure 5 (b) shows the story drift distribution for 6 story frames when a member in the frame first collapses. The large story drift concentrates at second story for all frames. In figure 5 (a), the story drift distributions for all frames are almost same. In figure 5 (b), the maximum story drift of the frames with NCB is greater than that with ECB. The maximum story drift of the frames with the small width-to-thickness ratio of column is greater than that with the large width-to-thickness ratio of column for the frames.

Figure 6 shows the relationship between the lateral load, Q_1/R_tW_1 and the maximum story drift, δ_{max}/h for 6 story frames with the different column-to-beam full plastic moment ratios. The initial stiffness of frames is almost equal not to depend on the column-to-beam full plastic moment ratio. The yield strength for the frames is almost equal except that of the frame with M_{pc}/M_{pb}=1.2. When a member in the frames collapse, the maximum story drift of the frame with M_{pc}/M_{pb}=1.2 is smaller than that of other frames. This is the reason why for the frame with M_{pc}/M_{pb}=1.2, the column with the small plastic deformation capacity collapses and, for the frames with M_{pc}/M_{pb}=1.4 and M_{pc}/M_{pb}=2.1, the beam with the large plastic deformation capacity collapses.

In figure 7 (a), the drift distributions of all frames are almost same at δ_{max}/h=0.02. Figure 7 (b) shows the story drift distribution for 6 story frames when the member in the frame first collapses. The large story drift concentrates at second story in all frames. In figure 7 (a), the story drift distributions for all frames are almost same not to depend on the column-to-beam full plastic moment ratio. In figure 7 (b), the maximum story drift of the frame with M_{pc}/M_{pb}=1.4 is the greatest in frames. This is because the plastic deformation capacity of beam in the frame with M_{pc}/M_{pb}=1.4 is greater than that in the frame with M_{pc}/M_{pb}=2.1.

Figure 8 shows the sequence of the plastic hinges in 6 story frames with the different column-to-beam full plastic moment ratio. The number in this figure represents the sequence when the member yields until δ_{max}/h=1/50. And ▼ in this figure

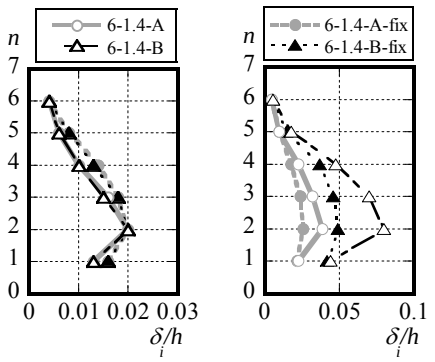

Figure 5 Story Drift Distribution: (a) δ_{max}/h=0.02, (b) Members collapse

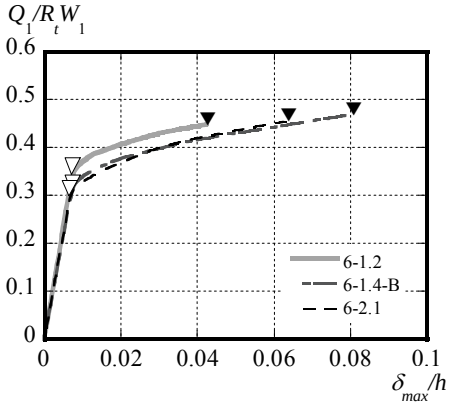

Figure 6 Relationship between Base Shear Strength and Story Drift

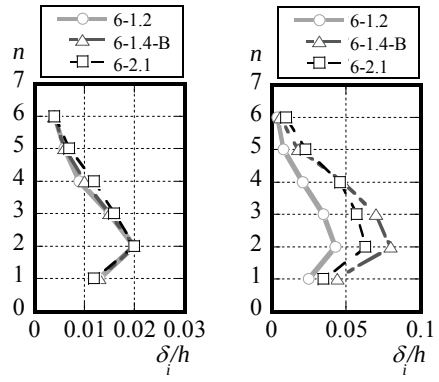

Figure 7 Story Drift Distribution: (a) δ_{max}/h=0.02, (b) Member collapse

represents the collapse member. In the case of ECB, the initial yield occurs at the beam on the first and the second stories and the collapse occurs at the column base on the first story. So that, for ECB, the soft story mechanism may occur when the frames are subjected to unexpected seismic force. In the case of NCB, the initial yield occurs at the beam on the first story. For the frames of 6-1.2 and 6-1.4-A, the column tops on the second, the third and the fourth stories yield until δ_{max}/h=1/50. And the collapse occurs at the column top on the fourth story. For the frame of 6-1.4-B, the column top on the

third story yields until δ_{max}/h=1/50. And the collapse is the beam on the first story. For the frame of 6-2.1, the columns never yield until δ_{max}/h=1/50. Finally, the collapse occurs at the beam on the first story.

3. COLLAPSE MECHANISM FOR STEEL MOMENT RESISTING FRAMES SUBJECTED TO EARTHQUAKE

3.1 Outline of Seismic Response Analysis

The frame models for the seismic response analyses are same as those for the static analyses. Damping was applied as 2% of critical in the first and second mode using a Rayleigh damping model. The kinematic hardening law is applied to hysteresis loop of the members. The mass per story in the frame is 188.3 *tonf*.

Table 3 shows the natural periods of the first and the second mode for 3 story and 6 story frames.

The earthquake records were used with *EL Centro 1940 NS/EW*, *Hachinohe 1968 NS/EW*, *Taft 1952 NS/EW*, *Kobe 1995 NS/EW* and *BCJ L1/ L2* whose maximum value of velocity was 30 to 75 *kine*.

Figure 9 shows the elastic response spectra for observed five earthquake records, *EL Centro 1940 NS*, *Hachinohe 1968 NS*, *Taft 1952 NS*, *Kobe 1995 NS* and *BCJ L1*.

3.2 Results of seismic response analyses.

Figure 10 compares the ratio of the maximum hysteresis energy of the column, E_{Dc} to the sum value of the hysteresis energies of the beams and the columns, ΣE_D and the ratio of the maximum hysteresis energy of the beam, E_{Db} to the sum value of the hysteresis energies of the beams and the columns, ΣE_D. In the case of NCB, the ratio of the energies for columns with the large column-to-beam full plastic moment ratio is lower than that with the small column-to-beam full plastic moment ratio. And the ratios of the energies for beams with NCB reach about 13%. In the case of 3 story frames with ECB, the ratios of the energies for columns are higher than those for beams. And the ratios of the energies for columns for 3 story frames with NCB reach about 13%. In the case of 6 story frames with ECB, the ratios of the energies for columns are almost equal to the ratios of the energies for beams. And the ratios of the energies for columns and beams for 6 story frames with NCB reach at about 6%, respectively.

Figure 11 shows the cumulative plastic ductility, η of the columns in the frames with M_{pc}/M_{pb}=1.4. Figure 11 (a) and

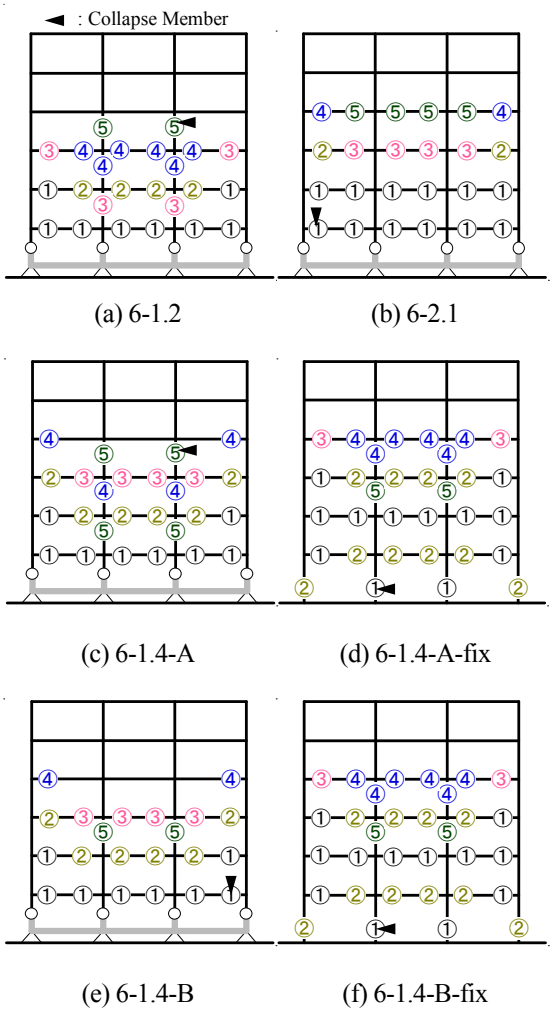

Figure 8 Sequence of Plastic Hinge in 6 Story frames: (a)6-1.2, (b) 6-2.1, (c)6-1.4-A, (d)6-1.4-A-fix, (e) 6-1.4-B, (f) 6-1.4-B-fix

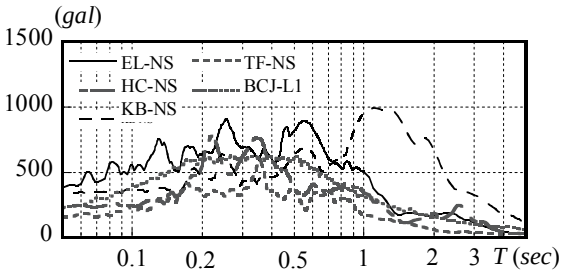

Figure 9 Seismic Response Spectrums for Single Degree of Freedom Model

Table 3 Natural Periods of 3 Story Frames and 6 Story Frames (*sec*)

Frame Type	3-1.2	3-1.4-A	3-1.4-B	3-1.4-C	3-2.1	3-1.4-A-fix	3-1.4-B-fix	3-1.4-C-fix
Mode 1	0.755	0.740	0.757	0.766	0.764	0.701	0.728	0.742
Mode 2	0.219	0.207	0.216	0.221	0.200	0.205	0.216	0.222

Frame Type	6-1.2	6-1.4-A	6-1.4-B		6-2.1	6-1.4-A-fix	6-1.4-B-fix	
Mode 1	1.127	1.162	1.174		1.151	1.111	1.128	
Mode 2	0.361	0.371	0.376		0.358	0.357	0.363	

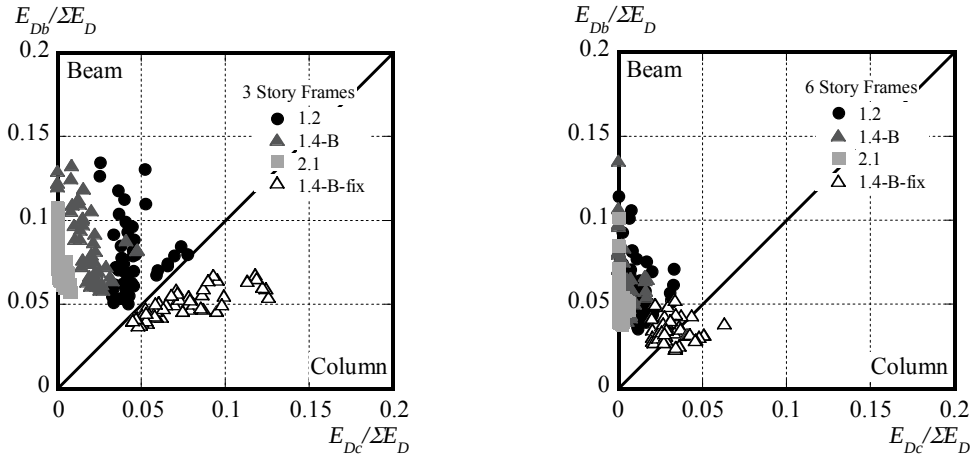

Figure 10 Comparison between Maximum Hysteresis Energy of Column and Maximum Hysteresis Energy of Beam: (a) 3 Story Frames, (b) 6 Story Frames

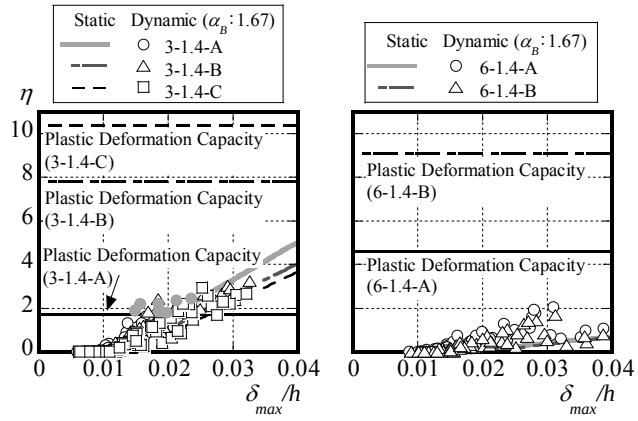

Figure 11 Cumulative Plastic Deformations of Columns in Frames: (a) 3 Story Frames, (b) 6 Story Frames

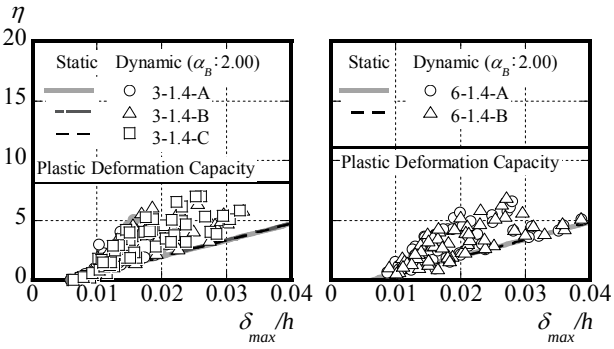

Figure 12 Cumulative Plastic Deformations of Beams in Frames: (a) 3 Story Frames, (b) 6 Story Frames

(b) are the results of the column for 3 story frames and 6 story frames, respectively. The horizontal lines in this figure show the plastic deformation capacities of the column. The curves are the results of the static analyses and the plots are the results of the seismic response analyses. And the plots become gray when η of the columns or η of the beams becomes greater than the plastic deformation capacity. The cumulative plastic ductility, η for the seismic response analyses are given in the following.

1) The hysteresis energies, E_D are calculated from the cumulative hysteresis curves in the plus side and the minus side for the columns and the beams in frames, respectively.
2) The values of E_D are divided by the amplification factor for the bauschinger effect, α_B, and the values in the plus side, η^+ and the values in the minus side, η^- are calculated, respectively.
3) The greater value between η^+ and η^- is defined as η.

The values of α_B are adopted for the designed values from (AIJ, 1990). Where, the values of α_B for the column and the beam are 1.67 and 2.0, respectively. The result of static analyses becomes the lower bound of the result of seismic response analyses. In the case of 3-1.4-A frames with the largest width-to-thickness ratio of column, the cumulative plastic ductility of the columns is over the plastic deformation capacity of column.

Figure 12 shows the cumulative plastic ductility, η of the beams in the frames with M_{pc}/M_{pb}=1.4. Figure 12 (a) and (b) are the results of beams for 3 story frames and 6 story frames, respectively. In case of 3 story frames, the cumulative plastic ductility, η of beams approach the plastic deformation capacity as the maximum value of velocity is 75 *kine*. For the results of analyses in this paper, the cumulative plastic ductility, η of beams doesn't reach the plastic deformation capacity of the beams.

4. CONCLUSIONS

1) For the static analyses, the columns collapse in the case of the frames with the embedded type column base (ECB), and the beams collapse in the case of the frames with the new type column base (NCB) with M_{pc}/M_{pb}=1.4 and M_{pc}/M_{pb}=2.1.
2) In case of the frames with the new type column base (NCB), the 6 story frame with M_{pc}/M_{pb}=2.1 performs the complete beam collapse mechanism, when the frame is

subjected to the seismic forces.

3) For the seismic response analyses, the columns in the frames of 3-1.4-A collapse by the earthquake records with the maximum velocity of 50 to 75 *kine*.
4) The largest hysteresis energies occur at the ends of beams or the columns in the case of the frames with the embedded type column base (ECB). On the other hand, in the case of the frames with the new type column base (NCB), the largest hysteresis energies occur only at the ends of beams except the frame with M_{pc}/M_{pb}=1.2.

Acknowledgements :

References :

Kato B., Akiyama H. and Obi Y. (1977), "Deformation Characteristics of H-Shaped Steel Members Influenced by Local Buckling," *Journal of Structural Construction Engineering*, AIJ, 257, 49-58.

Kato B., Akiyama H. and Kitazawa S. (1978), "Deformation Characteristics of Box-Shaped Steel Members Influenced by Local Buckling," *Journal of Structural Construction Engineering*, AIJ, 268, 71-76.

Architectural Institute of Japan (1990), "Ultimate Strength and Deformation Capacity of Building in Seismic Design"

Building Center of Japan (2001), "The Building Standard Low of Japan"

ABAQUS 6.4.2/Standard User's Manual

JOINT CONFERENCE PROCEEDINGS
7th International Conference on Urban Earthquake Engineering (7CUEE) &
5th International Conference on Earthquake Engineering (5ICEE)
March 3-5, 2010, Tokyo Institute of Technology, Tokyo, Japan

PERFORMANCE OF STEEL FRAME STRUCTURES WITH CONTROLLED BUCKLING MECHANISM IN THE KNEE BRACES

H.-L. Hsu[1] and C.-H. Peng[2]

1) Professor, Dept. of Civil Engineering, National Central University, Taiwan
2) M.S., formerly Graduate student., Dept. of Civil Engineering, National Central University, Taiwan
t3200178@ncu.edu.tw

Abstract: This study focused on the performance evaluation of knee braced moment resisting frames (KBRF) with controlled buckling mechanism. A series of cyclic loading tests were conducted on the special moment resisting frame (SMRF) and KBRF frames with various knee brace arrangements. It was found from the tests that the strength and energy dissipation capacities of the knee-braced frames were larger than those of the moment resisting frames. Test results also showed that the structural responses were closely related to the dimensions of the knee braces. It is suggested that excessively strong knee braces should be avoided in the KBRF designs so that structural integrity could be effectively sustained.

1. INTRODUCTION

Steel moment resisting structures (SMRF), as shown in Figure 1(a), are commonly used for constructions in urban areas with earthquake-resistant concerns. Major benefits in using such designs include the lower structural weight and the significant ductility. However, for medium to high-rise steel structures, excessive structural drifts caused by earthquake loads might limit the application of such designs, because structural members with larger dimensions and higher demand in beam-to-column connection details will be required so that the deformation criteria could be satisfied [Tsai and Popov 1990, Kim et al. 2002, Uang and Fan 2001]. In order to improve the applicability of such designs, brace members are usually added to the structural systems, forming brace-framed systems, as shown in Figure 1(b), to reduce the excessive deformation [Remennikov and Walpole 1997]. Although significant enhancement in structural stiffness could be achieved in the brace-framed system, adequate ductility is still a concern in the construction of the structures.

It has been found in the author's previous study [Hsu and Jean 2003] that the structural performance, both strength and ductility, of the framed systems could be effectively improved by placing the brace members at the corner regions of the beams and columns. The modification in the structural member placements incurred efficient structural form, namely knee-braced moment resisting frame or KBRF. Also indicated in the previous study [Hsu et al. 2009], the structural responses of the KBRF systems were closely related to the strength ratios between the beams and the braces. For example, if strong knee braces with high compressive strength were used in the construction, yielding and subsequent plastic hinges, or possible lateral buckling would occur at the beams. In such cases, replacements of the structural members were inevitable. However, if knee braces with insufficient strength were adopted in the frame constructions, the enhancement in structural performance would be minor. In order to optimize the efficiency of the KBRF system, a modified knee brace member design was considered in this study.

In this design, the knee brace members were fabricated with prescribed reduced section regions. In such cases, the buckling strength as well as the tensile strength of the knee brace could be controlled and the desired structural performance could be achieved by selecting brace members with adequate controlled buckling mechanisms.

This study focused on the performance evaluation of KBRF structures with the proposed knee braces. A series of cyclic loading tests were conducted on the SMRF and KBRF with various knee brace arrangements. Test results were used to validate the effectiveness of KBRF with buckling controlled knee braces and to establish the design references for such systems.

2. EXPERIMENTAL PROGRAM

Six steel frames, including one SMRF and five KBRFs, were fabricated for testing. The SMRF and the KBRFs were composed of identical structural members and connection details. ASTM A-36 H175x175x7.5x11 and H244x175x7x11 were used for beam and column of the frame. The two ends of each beam were welded to a pair of 30-mm-thick end plates. The beam was then attached to a pair of columns by high strength bolts. The knee brace members used to fabricate the KBRF frames were composed of a pair of A-36 C75x40x5x7 channels. The cross section of two prescribed regions located at the two ends of the knee brace members were reduced to form a buckling controlled mechanism. Major differences among the KBRF frames included the effective width and the effective length of the reduced sections. Desired compressive and tensile strengths could be achieved and controlled by adjusting the dimensions of the reduced sections. Figure 2 shows the composition of a KBRF frame and the details of the proposed knee brace members. Table 1 also describes the placement details of the test frames. Performance of the test frames was evaluated by the cyclic loading tests. For this purpose, each frame was subjected to a series of increasing cyclic displacement commands until the frame reached the failure stage. The loading history of the tests was shown in Figure 3. Responses of the structure was measured by the installed strain gages, tiltmeters and LVDTs. The test information was collected using data acquisition systems and was saved for later analyses.

3. FAILURE PATTERNS

Failure of SMRF was initiated by the yielding of the beam at the two ends of the member. Significant inelastic deformation leading to the formation of plastic hinges was observed when the frame was subjected to large drift. It was found from the test that increasing relative deformation between the beam and column was exhibited when the lateral drift was increased. Performance of the structure was closely related to the integrity of the beam-to-column joint. This phenomenon indicated that high demand in joint detailing was a necessity, which might result in significant construction cost, if rigid joint requirements were desired.

Failure modes of KBRFs subjected to lateral loads could be divided into two groups. For KBRF equipped with strong knee braces, yielding of beam was first observed at the location where knee brace and beam intersected, though reduced section mechanism was adopted on the braces. Although the structural strength was sustained, lateral buckling of the beam was observed when the drift was increased. For KBRF designed with knee braces of adequate strength, buckling of the brace occurred at the desired deformation stages. Since the effective length of the reduced section region was small, the behavior of the knee brace was similar to that of a brace with medium slenderness ratio, the post-buckling strength of the brace was stable, therefore, the structural performance could be effectively sustained. Figure 4 shows the failure pattern of the buckling controlled knee brace.

4. COMPARISONS AND INTERPRETATION OF TEST RESULTS

4.1 Strength

Figure 5 shows the hysteretic relationships for the SMRF and KBRF frames with various knee brace placements. It can be found from the figure that the steel moment resisting frame exhibited significant inelastic behavior during the excitation. Similar phenomenon was found in the KBRF frames, except that the strength of the KBRF was higher and a strength drop was exhibited when the knee brace reached the buckling state. Figure 6 compares the structural responses of KBRF frames with various buckling controlled knee braces. It can be observed from further investigation that the drift associated with the strength drop changed when the effective cross section of the brace varied.

For example, when the KBRF was equipped with weak knee braces, such as KB05-2D, the structure experienced strength loss at early stage of load excitation. Although the ultimate strength of this structure was approximately 50% higher than that of the SMRF, strength enhancement was limited when the structure was subjected to drift at service stage. For KBRF with stronger buckling controlled braces, such as KB20-3D, the structural strength as well as the drift at which strength drop occurred was both increased. This phenomenon indicated that better service state and higher strength could be expected in the structure. Figure 7 shows the structural responses of KBRF frames with unbuckled knee braces. Although the structures exhibited higher strength than the above-mentioned KBRF frames, lateral buckling of the beams was observed during the testing. This phenomenon indicated that excessively strong knee braces should be avoided to maintain the integrity of the structure.

4.2 Energy Dissipation

Figure 8 shows the energy dissipation of SMRF and KBRF frames. Energy dissipation was evaluated by the area bounded by the hysteretic loops. It can be found from the comparisons that the dissipated energy of KBRF's was higher that that of a SMRF with identical beam, column and connection details. For example, the energy dissipation of KB05-2D at 2.5% drift is approximately 80% higher than that of the SMRF at the same drift. It is also observed from the figure that further enhancement in energy dissipation could be achieved in KBRF with stronger buckling controlled knee braces. The significant energy dissipating capability in conjunction with the higher strength of KBRF validated the effectiveness of the proposed KBRF designs.

5. CONCLUSIONS

This paper focused on the performance evaluation of KBRF structures subjected to cyclic loads. A series of loading tests were conducted on the SMRF and KBRF with various knee brace arrangements. It was found from the test results that the strength and energy dissipation capacity of KBRF frames were higher than those of SMRF with identical structural members and joint details. It is also suggested that excessively strong knee braces should be avoided in the design of KBRF structures, so that structural integrity could be sustained.

Table 1 Details of the Test Frames

Test Frame	Knee Braces	be (mm)	Le (mm)
SMRF	N.A	N.A	N.A
KB05-2D	2C75x40x5x7	5	150
KB10-2D	2C75x40x5x7	10	150
KB30-2D	2C75x40x5x7	30	150
KB20-2D	2C75x40x5x7	20	150
KB20-3D	2C75x40x5x7	20	225

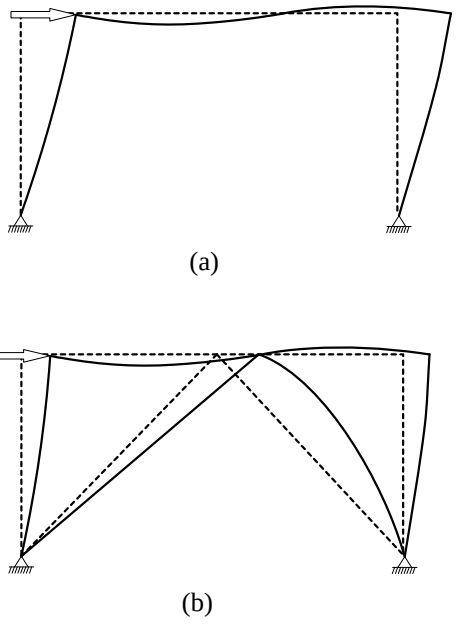

Figure 1 Description of Frame Structures Subjected to Lateral Load: (a) Steel Special Moment Resisting Frame; (b) Braced Frame

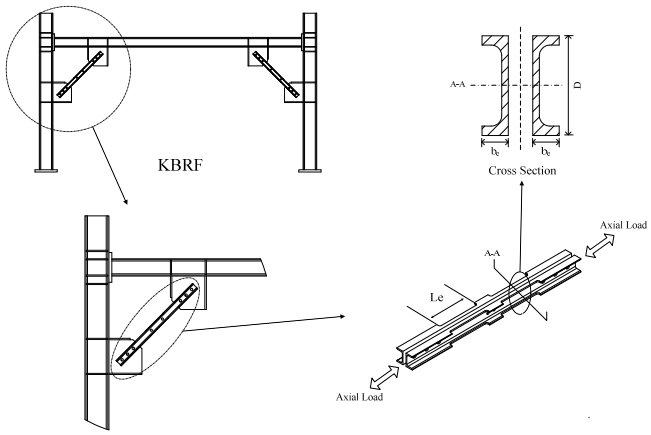

Figure 2 Description of the Test Frame

Acknowledgements:

The test specimens were supported by the National Center for Research on Earthquake Engineering (NCREE), Taiwan, which is gratefully acknowledged. The authors also wish to extend their appreciation to Professor K. C. Tsai and the staff of NCREE for their advice and assistance.

References:

Tsai, K. C. and Popov, E. P. (1990), "Seismic panel zone on elastic story drift in steel moment resistance frames," *Journal of Structural Engineering*, American Society of Civil Engineers, **116**(12), 3285-3301.

Kim, T., Whittaker, A. S., Gilani, A. S., Bertero, V. V. and Takhirov, S. M. (2002), "Cover-plate and flange-plate steel moment-resisting connections," *Journal of Structural Engineering*, American Society of Civil Engineers, **128**(4), 474-482.

Uang, C. M. and Fan, C. C. (2001), "Cyclic stability criteria for steel moment connections with reduced beam section," *Journal of Structural Engineering*, American Society of Civil Engineers, **127**(9), 1021-1027.

Remennikov A. M. and Walpole W. R. (1997), "Analytical prediction of seismic behavior for concentrically braced steel systems," *Earthquake Engineering & Structural Dynamics*, **26**(8), 859-874.

Hsu H. L. and Jean S. Y. (2003), "Improving seismic design efficiency of petrochemical facilities," *Practice Periodical on Structural Design and Construction*, American Society of Civil Engineers, **8**(2), 107-117.

Hsu, H. L., Juang, J. L., and Chou, C. H. (2009), "Seismic performance of steel knee braced frame structures," *Proc. Sixth International Conference on Urban Earthquake Engineering*, Tokyo, Japan, March 3-4.

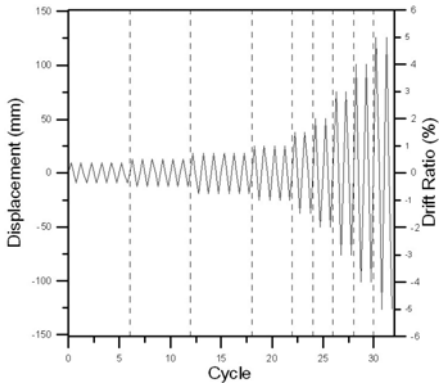

Figure 3 Loading History



Figure 4 Buckling Mode of the Proposed Knee Brace

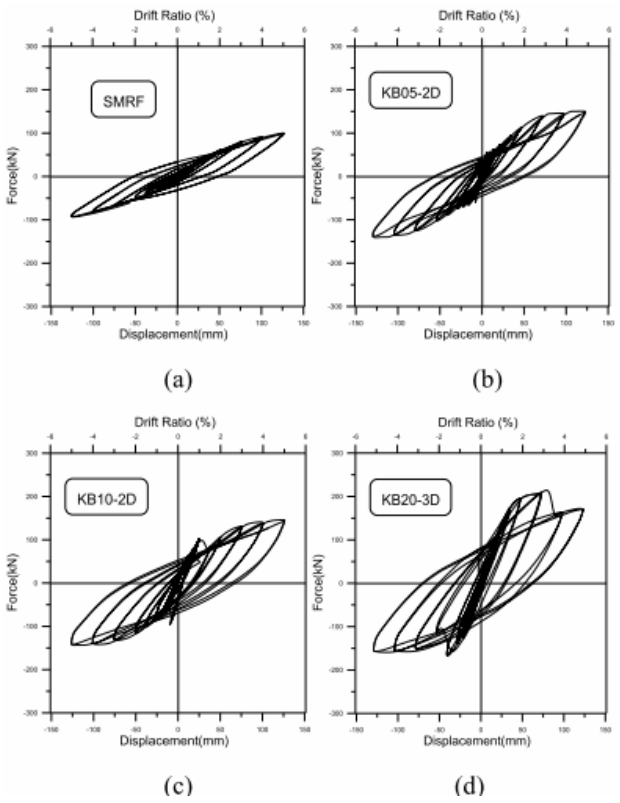

Figure 5 Hysteresis Loops: (a)SMRF; (b)KBRF05-2D; (c)KBRF10-2D; (d)KBRF20-3D

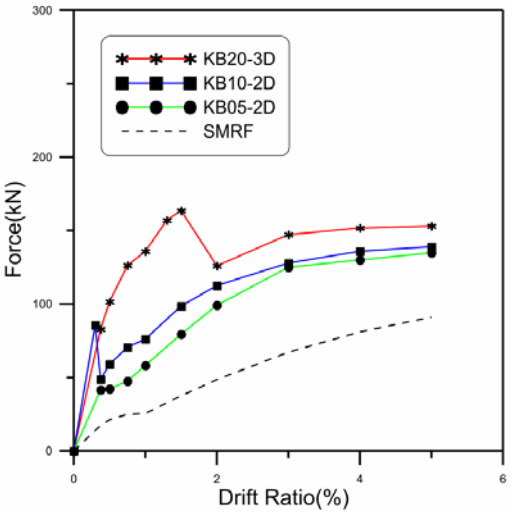

Figure 6 Comparisons of Responses for KBRF Frames with Various Knee Braces

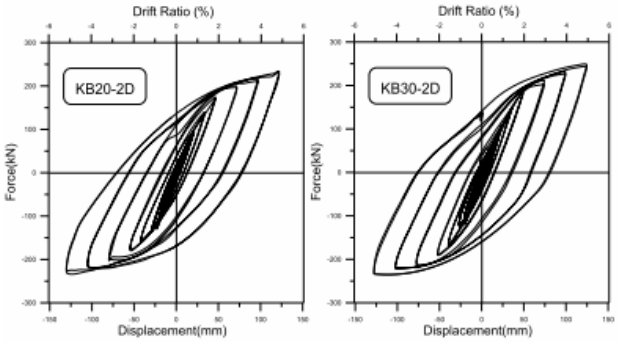

Figure 7 Responses of KBRF Frames with Unbuckled Braces

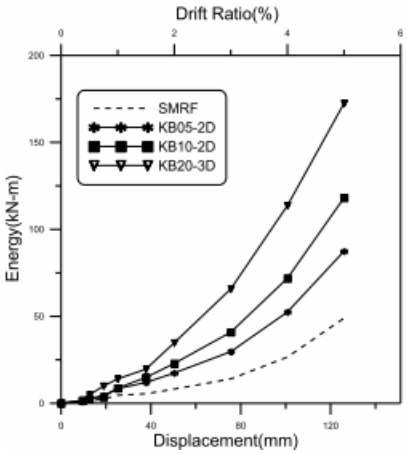

Figure 8 Comparisons of Energy Dissipation for SMRF and KBRF with Various Knee Braces

JOINT CONFERENCE PROCEEDINGS
7th International Conference on Urban Earthquake Engineering (7CUEE) &
5th International Conference on Earthquake Engineering (5ICEE)
March 3-5, 2010, Tokyo Institute of Technology, Tokyo, Japan

SHAKE TABLE STUDY OF DYNAMIC FRICTION BETWEEN STEEL AND MORTAR FOR SEISMIC APPLICATIONS IN STRUCTURES

Jason McCormick[1)], Masahiro Ikenaga[2)], Takuya Nagae[3)] and Masayoshi Nakashima[4)]

1) Assistant Professor, Dept. of Civil & Environmental Engineering, University of Michigan, U.S.A
2) Assistant Professor, Dept. of Civil Engineering and Architecture, Tohoku University, Japan
3) Researcher, National Research Institute for Earth Science and Disaster Prevention, Japan
3) Professor, Disaster Prevention Research Institute, Kyoto University, Japan
jpmccorm@umich.edu, ikenaga@archi.tohoku.ac.jp, nagae@bosai.go.jp, nakashima@archi.kyoto-u.ac.jp

Abstract: Steel structural systems are widely used in seismically active regions around the world. Often, these systems will have both steel and mortar materials present and in contact with each other, particularly at a column base or where the floor slab is supported by beams. During an earthquake, these materials may slide with respect to each other making it necessary to better understand this dynamic behavior. A shake table study is conducted with two frame specimens that contain steel friction elements which rest on mortar surfaces connected to the shake table. Horizontal sinusoidal acceleration inputs of varying magnitudes and frequencies are considered along with non-stationary earthquake ground motions. The results suggest that a repeatable friction behavior can be obtained. However, larger velocities cause a decrease in the friction coefficient during sliding from its initial maximum value. The non-stationary input motions further provide a means of exploring the consistency of the friction coefficient and relating system response measurements to spectral acceleration values for sliding systems. In general, the study provides knowledge of the dynamic sliding behavior of steel on mortar and suggests that a consistent and reliable friction coefficient can be obtained between these materials under seismic loads.

1. INTRODUCTION

The advent of performance-based design combined with a significant amount of research into understanding the behavior of steel moment connections and concentrically braced frame systems after the 1994 Northridge Earthquake and 1995 Hyogoken-Nanbu (Kobe) Earthquake has resulted in the continued use of steel structural systems in seismically active regions around the world. Within these systems, steel and mortar are often present and in contact at a column base or where the floor slab is supported by beams, which can result in sliding with respect to one another during an earthquake. However, the friction resistance associated with the sliding of steel on mortar is often underutilized or ignored in design. For both ease of construction and economic efficiency, exposed base plate type column bases (or standard base plate connections) are often designed as fixed connections where the base plate is connected to the foundation through an anchor bolt to provide the required shear resistance (Wang et al. 2008, Kurata et al. 2005, Nakashima and Liu 2005, Galambos 1998). In the United States, building codes do not allow for consideration of friction in determining the shear resistance of a column base under code specified earthquake loads (AISC 2006). Meanwhile in Japan, both the shear resistance of the anchor bolt and friction resistance between the steel and mortar are considered, but only the smallest of these values dictates the design ignoring the combined effect (AIJ 2004).

The underutilization of the friction resistance obtained from steel sliding against mortar/concrete in the design of steel structural systems and development of new steel-mortar damping systems for seismic response reduction can in part be associated with a lack of information in regards to the sliding behavior under dynamic earthquake-type motions. The majority of studies which have considered friction behavior within structural engineering have typically focused on base isolation systems (Tsai et al. 2006, Roussis and Constantinou 2006, Iemura et al. 2005, and Bondonet and Filiatrault 1997) or energy dissipation devices (Ng and Xu 2006, Pall et al. 1980) where non-traditional structural materials are considered. A study by Nagae et al. (2005) explored the static friction coefficient between more traditional structural materials such as steel on steel or steel on mortar. The findings suggested that the obtained friction coefficients are both large enough and stable enough to use for seismic design applications. However, consistency of the friction coefficient and sliding behavior under cyclic dynamic loading is also necessary to better incorporate it into current seismic design provisions for steel structures.

For this reason, a shake table study is carried out to address the lack of knowledge with respect to the dynamic sliding behavior of steel on mortar. Horizontal motions are used in the form of sinusoidal waves and non-stationary

ground motions. Two frames supported by steel friction elements are considered where the first frame consists of a rigid mass and the second frame consists of four stacked rigid steel frames connected by rubber isolators to better simulate the stories of an actual structure and allow higher velocity levels to be achieved. The dynamic sliding behavior of both systems is analyzed to gain a better understanding of the friction coefficient resulting from steel sliding on mortar and possible parameters affecting this behavior. The non-stationary motions further provide a means of exploring the consistency of the friction coefficient under unequal loading cycles. System response parameters are also considered with respect to spectral acceleration in order to better understand the influence of base sliding (steel on mortar) on the behavior of an actual structure.

2. SHAKE TABLE TEST

2.1 Test Specimens and Setup

A shake table study using the 3 m by 5 m shake table at the Disaster Prevention Research Institute of Kyoto University in Japan is conducted to evaluate the dynamic sliding behavior between steel and mortar. The six degree of freedom shake table can provide a maximum acceleration and velocity of 1.0*g* and 1.5 m/s in each direction, respectively. Only horizontal motion applied parallel to the long direction of the table is considered for this set of tests. Along with the shake table, the test setup consisted of mortar sliding surfaces, steel friction elements, and two separate frames (rigid and flexible). In order to simulate four column bases of a building and provide stability to the system, the two test frames had four points of contact where sliding occurred as can be seen in Figure 1.

The four mortar sliding surfaces are cast directly on top of a Japanese H-section (similar to a U.S. W-shape) using a commercial mortar. A smooth and level surface is obtained by placing a polished steel plate on top of the wet mortar and allowing the mortar to cure. Embedded steel studs attached to the H-section also ensure that the mortar surface will not slide with respect to the H-section during testing. The length of the mortar surface parallel to the loading direction is 1020 mm which allows for approximately 300 mm of sliding in either direction assuming that the steel friction element starts at the center. Each of the four H-sections supporting the mortar surfaces is attached to the shake table providing the only direct connection between the test setup and the shake table. The same four mortar surfaces were used throughout the duration of the study with only removal of accumulated debris with subsequent tests.

The friction elements are fabricated from 250 mm by 250 mm by 60 mm blocks of steel which are tapered on one side down to a 75 mm by 75 mm square. This smaller surface area is placed on the mortar sliding surface and represents the contact area on which the specimen slides. No physical connection besides direct contact is made between the mortar surface and steel friction element. The surface of the steel friction element has the mill-scale removed and is polished to represent an unpainted steel member in a structure. As can be seen if Figure 1, the steel friction element is attached to the bottom of the frame using set bolts which allow for an equal distribution of the gravity load between the four friction elements.

Two separate frames are used to evaluate the dynamic sliding behavior of steel on mortar. The first frame will be called the “rigid” frame for the remainder of the paper and consists of a 68.6 kN concrete block placed on top of a 9.2 kN horizontal steel frame. The block is attached to the steel frame through post-tensioning rods to resist relative motion between the two. The overall weight of the rigid frame specimen including instrumentation is 82.0 kN resulting in a pressure of 14.6 MPa on each of the mortar surfaces at the contact points. The rigid frame is used to provide a better understanding of the fundamental sliding behavior of steel on mortar. Meanwhile, the second frame, which will be called the “flexible” frame for the remainder of the paper, provides a means of more closely simulating the behavior of a sliding building structure and allows for larger velocities to be imparted to the system. The flexible frame consists of four layers of 9.2 kN horizontal steel frames which are connected to one another by rubber isolation bearings. The overall weight of the flexible frame specimen including instrumentation is 43.0 kN resulting in a smaller pressure of 7.6 MPa on each of the mortar surfaces at the contact points. The complete test setup for the rigid and flexible frame specimens can be seen in Figure 1.

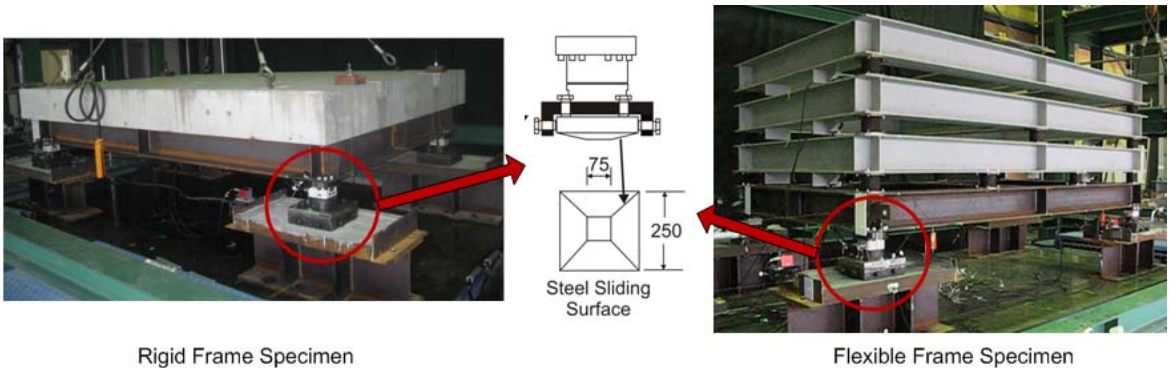

Figure 1 Photograph of the rigid frame and flexible frame test specimens along with details of the steel friction element.

Tri-axial load cells are connected between the steel friction elements and frame to measure the vertical load at each contact point and the shear forces generated by the contact between the steel and mortar. Laser displacement transducers are used to measure absolute displacements of both the mortar surface and frame. Strain potentiometers are used to directly measure the relative sliding between the mortar surface and steel friction element along with the relative displacements between the horizontal steel frames in the flexible frame specimen. For the rigid frame specimen, accelerometers are installed on the shake table and on the surface of the concrete mass to obtain both relative and absolute acceleration values. For the flexible frame specimen, the accelerometers are installed on each of the horizontal steel frames and on the surface of the shake table. The choice of instrumentation allows for a thorough analysis of the dynamic sliding behavior of steel on mortar given the two specimens being studied.

2.2 Loading Protocol

For all of the loadings, the shake table is run in acceleration control using only horizontal inputs parallel to the long direction of the test specimen. Two sets of loading protocols are considered for each frame specimen. The first set uses a sinusoidal input wave which gradually ramps up to its intended maximum input acceleration during the first couple of cycles and then oscillates at this level for a total duration of 10 s. Maximum input accelerations ranged between 5 and 9 m/s^2 at loading frequencies of either 1 or 2 Hz. These acceleration magnitudes and the input frequencies are used throughout the remainder of the paper to specify each individual test. It should be noted that the actual maximum acceleration recorded on the shake table tended to vary from this value due to control difficulties associated with the large mass of the test specimen and high acceleration values. Table I shows the horizontal-sinusoidal input wave loading protocol test matrix for each specimen. Limitations of the shake table prevented some of the larger acceleration magnitudes for the flexible frame specimen to be run.

Table 1 Test matrix for the horizontal sinusoidal input wave loadings. X indicates tested parameters.

Max Acceleration (m/s^2)	Frequency (Hz)	
	1	2
Rigid Frame		
6	X	X
7	X	X
8	X	X
9	X	X
Flexible Frame		
5	–	X
6	X	X
7	X	–
8	X	–
9	–	–

The second set of shake table tests is conducted to evaluate the effects of non-stationary motion on the dynamic sliding behavior and friction coefficient. The JMA Kobe ground motion and JMA Takatori ground motion are considered at increasing magnitudes up to the capacity of the shake table. Four tests are run using the rigid frame specimen (60%, 80%, 100% JMA Kobe and 60% JMA Takatori) and eight tests are run using the flexible frame specimen (20%, 40%, 60%, 80%, 100% JMA Kobe and 20%, 40%, 60% JMA Takatori).

3. SINUSOIDAL LOADING RESULTS

3.1 Rigid Frame Specimen

A summary of the sliding behavior of the rigid frame specimen is provided below. Further details in regards to this portion of the study and the sliding behavior of rigid specimens under a number of loadings can be found in McCormick et al. (2009). For the sinusoidal loading, no sliding of the rigid frame specimen is observed for acceleration magnitudes less than 7 m/s^2 regardless of the loading frequency. At acceleration magnitudes great enough to induce sliding, an overall increase in the relative displacement is observed in one direction due to uneven sliding back and forth along the mortar surface. Figure 2 and 3 provide the relative displacement time histories for the rigid frame specimen undergoing the 8 m/s^2 and 9 m/s^2 sinusoidal input motion at 2 Hz, respectively. The displacement results shown are obtained by averaging the relative displacements for all four friction elements. Since the specimen was rigid, there was very little difference between the relative displacements at the four contact points. The initial cycles in the figures are inconsistent due to the loading protocol which ramps up to the maximum specified acceleration level. This behavior stabilizes after the first 5 s. Thus, the last 5 s of the time histories are used to further analyze the results.

From Figures 2 and 3, it is evident that an increase in acceleration magnitude results in larger relative displacements during the back and forth motion for a given cycle. On average, the largest relative displacement per cycle is 1.4 mm for the 8 m/s^2 loading and 9.8 mm for the 9 m/s^2 loading. No specific trends are present for the overall relative displacement (final position) with respect to loading magnitude. The effect of loading frequency can also be considered by comparing Figure 2 to Figure 4 which contains the relative displacement time history for the 8 m/s^2 sinusoidal input cycled at 1 Hz. In general, the 1 Hz loading frequencies resulted in larger overall relative displacements. The relative displacements associated with a single cycle decreased with an increase in loading frequency. Under all of the sinusoidal loading protocols, the rigid specimen showed a stable and consistent sliding behavior suggesting further consideration of the friction behavior between steel and mortar in design and development of new systems is warranted.

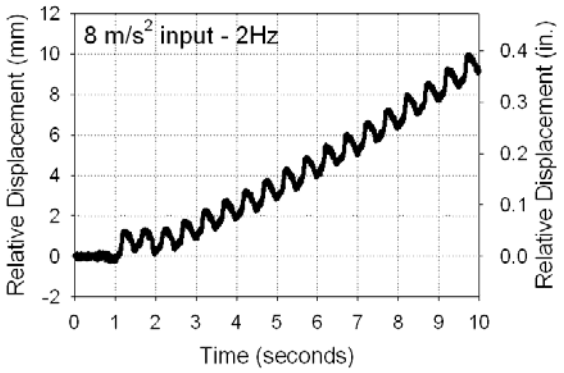

Figure 2 Relative displacement time history for the 8 m/s^2 loading run at 2 Hz.

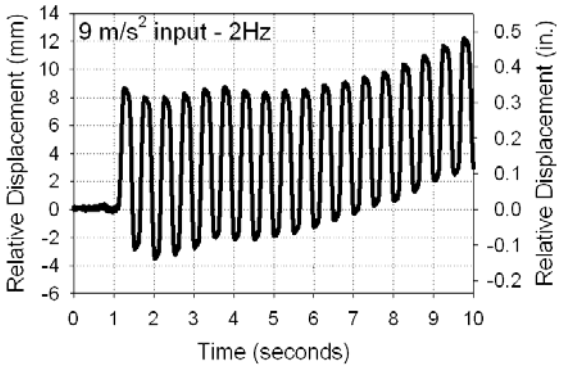

Figure 3 Relative displacement time history for the 9 m/s^2 sinusoidal loading run at 2 Hz (modified from McCormick et al 2009).

Figure 4 Relative displacement time history for the 8 m/s^2 sinusoidal loading run at 1 Hz.

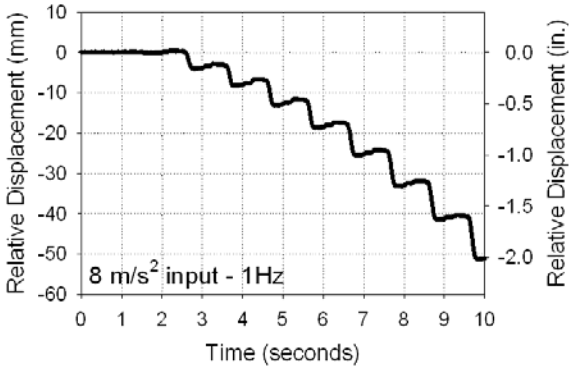

A friction coefficient versus relative displacement plot is provided in Figure 5 for the 8 m/s^2 sinusoidal input loading at 2 Hz where the average maximum friction coefficient per a cycle is 0.75. The friction coefficient is calculated by summing the shear force measured by all four load cells and dividing this value by the sum of the normal force measured by all four load cells. For all of the rigid frame tests, the maximum friction coefficient remained between 0.76 and 0.82 suggesting stability of the sliding behavior.

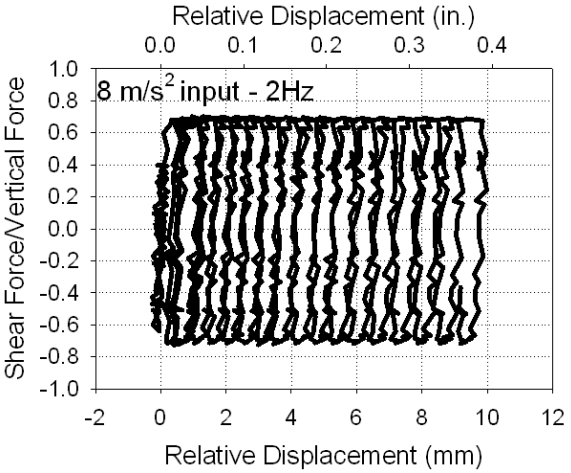

Figure 5 Friction coefficient versus relative displacement results for the 8 m/s^2 sinusoidal loading run at 2 Hz.

3.2 Flexible Frame Specimen

The flexible frame specimen allows for further consideration of the sliding behavior between steel and mortar when a flexible superstructure is present. The first mode of the flexible frame has a period of 0.53 s. In general, the relative displacement results between the steel friction element and mortar surface show a similar behavior to those obtained from the rigid specimen with a back and forth motion but continual progression in a single direction. The relative displacements overall tend to be larger with the flexible frame specimen for a given acceleration magnitude which can be attributed to the smaller mass of the flexible frame specimen compared to the rigid frame.

Figure 6 and 7 provide the relative displacement time histories for the 6 m/s^2 and 8 m/s^2 sinusoidal loadings, respectively, at a loading frequency of 1 Hz. It is clear that the flexible superstructure contributes to increased instability of the early cycles where large relative displacements occur over a single cycle. The maximum sliding distance during these early cycles is 2.3 mm and 265 mm for the 6 m/s^2 and 8 m/s^2 sinusoidal loading cases. The results also show that increasing acceleration amplitude causes larger relative sliding per a cycle once the behavior stabilizes. The average maximum values of sliding per cycle are 1.03 mm, 98.3 mm, and 157 mm for the 6 m/s^2, 7 m/s^2, and 8 m/s^2 loadings at 1 Hz. A similar trend is also seen for the overall maximum relative displacement.

A comparison of Figure 6 and Figure 8 also provides insight into the effect of loading frequency on the behavior of the flexible frame. The larger loading frequency, 2 Hz, results in a longer duration of unstable cycling and a larger overall relative displacement. The trends shown in these results are opposite those obtained from the rigid frame test. This is most likely associated with the fact that the 6 m/s^2 loading is only able to initiate very small sliding at 2Hz in the flexible frame specimen. Even considering these differences, stable behavior is achieved for all of the load cases.

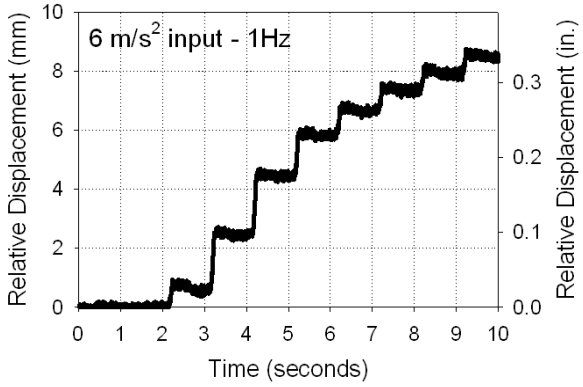

Figure 6 Relative displacement time history between the mortar surface and steel plate of the flexible frame specimen for the 6 m/s^2 sinusoidal loading run at 1 Hz.

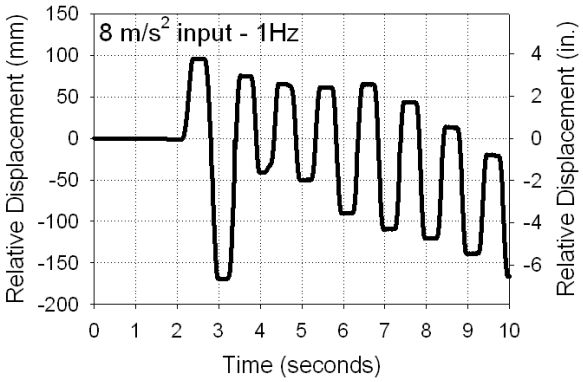

Figure 7 Relative displacement time history between the mortar surface and steel plate of the flexible frame specimen for the 8 m/s^2 sinusoidal loading run at 1 Hz.

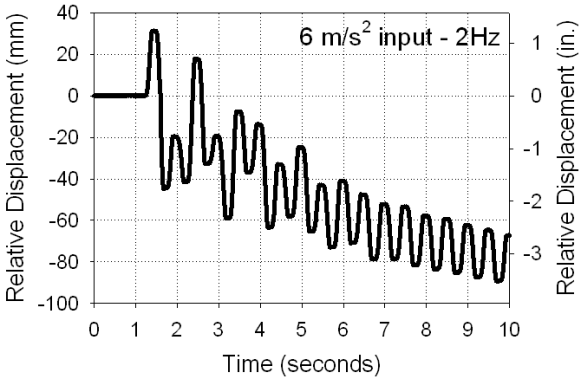

Figure 8 Relative displacement time history between the mortar surface and steel plate of the flexible frame specimen for the 6 m/s^2 sinusoidal loading run at 2 Hz.

For all of the flexible frame tests, the maximum measured friction coefficient remained between 0.61 and 0.71 which is a slightly larger margin than that which was observed for the rigid frame tests. The maximum friction coefficients also are smaller than those measured during the rigid frame tests. The lowest maximum friction coefficient was obtained from the 6 m/s^2 sinusoidal loading at a frequency of 1 Hz. However, it should be noted that this specimen only underwent minimal sliding which may partially account for the lower friction coefficient (Figure 6). In general, the maximum friction coefficient did remain constant during cycling for all of the input loadings.

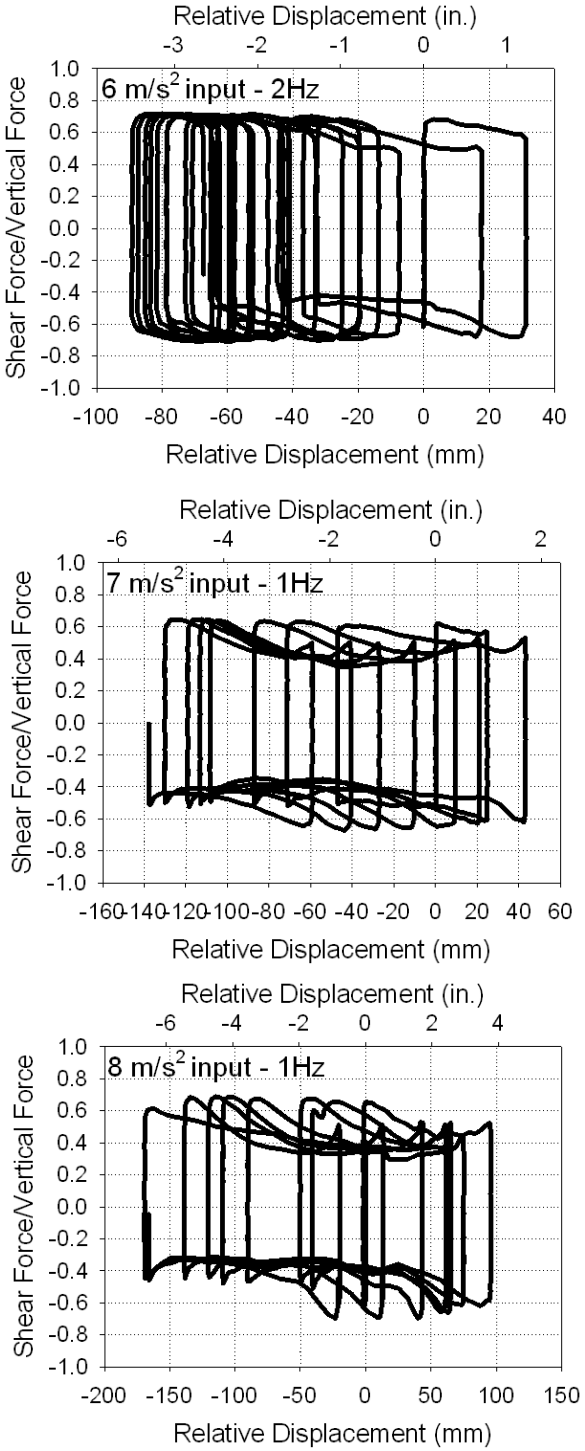

Figure 9 Friction coefficient versus relative displacement plots for the flexible frame specimen run under the 6 m/s^2 – 2 Hz, 7 m/s^2 – 1 Hz, and 8 m/s^2 – 1 Hz sinusoidal loadings.

Figure 9 provides plots of the friction coefficient versus relative displacement associated with the flexible frame for the 6 m/s^2 – 2 Hz, 7 m/s^2 – 1 Hz, and 8 m/s^2 – 1 Hz sinusoidal loadings. As the acceleration magnitude increases, the plots begin to show a decrease in the friction coefficient during sliding which is not observed with the rigid specimens that underwent the same magnitude acceleration. For the 6 m/s^2 input wave cycled at 2 Hz, this decrease is only minor where the maximum friction coefficient dropped from 0.71 to approximately 0.5 during sliding. The decrease becomes substantial at the highest acceleration magnitude where the friction coefficient decreased by just over half from 0.68 to 0.33. This decrease in the friction coefficient can be attributed to an increase in the maximum sliding velocity imparted by the flexible frame specimen. For all of the rigid specimens, the maximum sliding velocity was below 140 mm/s. For the loadings shown in Figure 9, the maximum sliding velocities are 400 mm/s, 850 mm/s, and 1700 mm/s where the larger velocity corresponds to the larger acceleration magnitude test. These results suggest that a threshold sliding velocity exists between 140 mm/s and 400 mm/s at which the friction coefficient will no longer remain constant during sliding.

4. NON-STATIONARY INPUT RESULTS

To better utilize the friction developed between steel sliding on mortar for the design of structural systems or energy dissipation devices, the sliding behavior and friction coefficient must also be studied under non-stationary loadings, such as earthquake ground motions. The horizontal component of two ground motions, JMA Kobe and JMA Takatori recorded during the 1995 Hyogoken-Nanbu Earthquake in Japan are chosen as the input motions (Yamaguchi and Yamazaki 2001). These ground motions are scaled to between 20 and 100% of the recorded motion and applied to both the rigid frame specimen and flexible frame specimen.

As with the sinusoidal input motions, the relative sliding of the steel with respect to the mortar surface and friction coefficient with respect to relative displacement can be considered. Figure 10 provides these values for the JMA Kobe input motion scaled to 60% and applied to the flexible frame specimen. The spectral acceleration associated with the first mode of the flexible frame specimen for this non-stationary motion is approximately 1.7*g*. The relative displacement plot shows that the frame slid only in the positive direction with a residual displacement of 26 mm. At 12.2 s into the ground motion, the frame initiated its longest continuous slide of approximately 28.2 mm. Shorter length sliding occurred just after 9 s into the ground motion and immediately after the maximum slide. The friction coefficient versus relative displacement plot clearly shows the occurrence of sliding. The maximum friction coefficient associated with this sliding was measured to be 0.66 which is consistent with the findings of the sinusoidal input study of the flexible frame specimen. A decrease in the friction coefficient is also apparent, particularly during the longest positive slide where it decreased by 0.10. Based on the previous findings, this decrease suggests that the sliding velocity reached at least 140 mm/s at this point of the loading. The results also suggests that slip distance may play a critical role in the decrease of the friction coefficient during sliding as a much smaller decrease is seen for the smaller slip lengths. In general, all of the non-stationary input tests produced results consistent with the previous sinusoidal input tests.

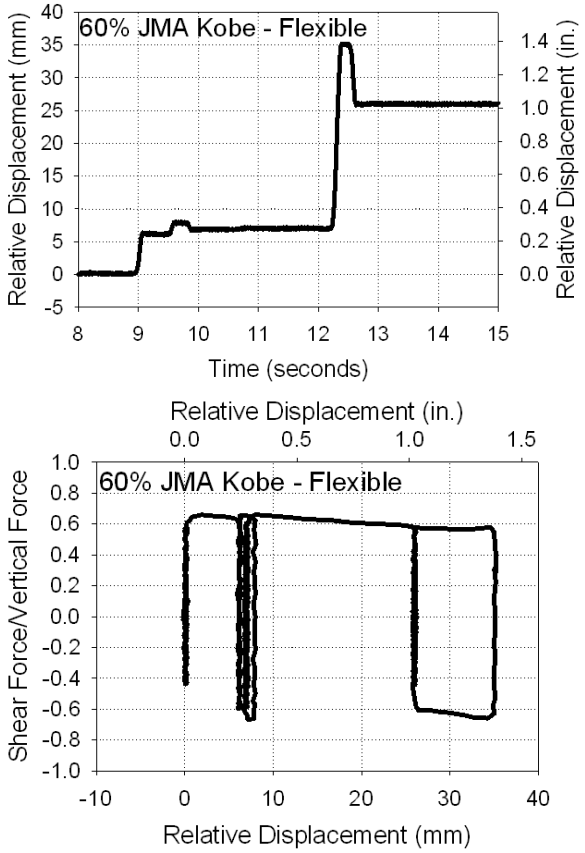

Figure 10 Non-stationary 60% JMA Kobe input motion for the flexible frame specimen: (a) relative displacement time history and (b) friction coefficient versus relative displacement.

The non-stationary input study can be used to gain further insight into the behavior of a structure if its column bases are allowed to slide freely on their mortar surfaces. The plot in Figure 11 provides the total slip that can be expected for a given spectral acceleration. The total slip is obtained by subtracting the maximum overall positive displacement from the maximum overall negative displacement. The plot suggests that only minor slipping will occur up to a spectral acceleration of approximately 1*g*. As the spectral acceleration increases above this value the amount of total slip sustained by the specimen (or structure) will increase quickly. The maximum viable spectral acceleration that the system can withstand can thus be identified based on available slip distance.

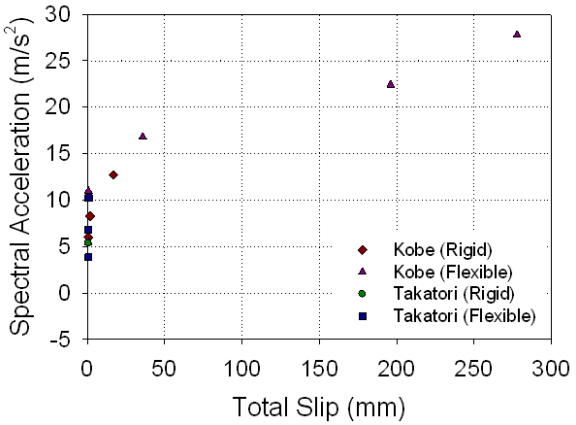

Figure 11 Spectral acceleration versus total slip considering all of the non-stationary input motion results.

To consider the effect of sliding on the response of an actual structure, the maximum relative displacement between the floors of the flexible frame specimen is measured with respect to spectral acceleration. Because the rigid frame only had a single layer consisting of the concrete block, it is not considered here. Figure 12 shows the plot of the spectral acceleration versus maximum relative displacement. The results suggest a fairly linear relationship between maximum relative displacement and spectral acceleration up to values of around 1*g*. For spectral accelerations larger than this value, the effect on the relative maximum displacement tends to dissipate. Although these results suggest a trend, it is difficult to make an overarching assumption since only eight data points are being considered. It should also be noted that the maximum relative displacement occurred between the same floors for all of the loading cases considered.

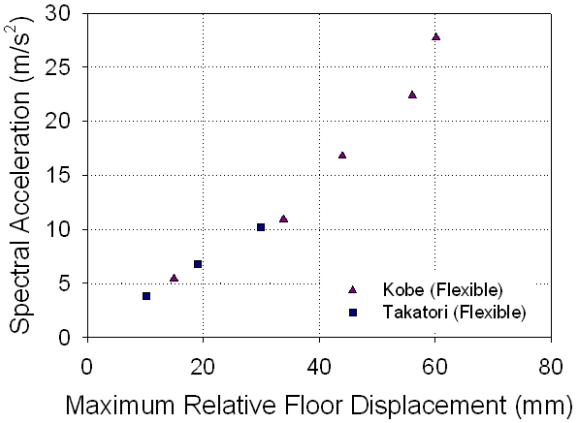

Figure 12 Spectral acceleration versus maximum relative floor displacement between layers of the flexible steel frame.

5. CONCLUSIONS

An experimental shake table study is used to explore the sliding behavior between steel and mortar under both sinusoidal input accelerations and non-stationary input accelerations. A rigid frame specimen, which represents a rigid mass, and a flexible frame specimen, which represents the behavior of a flexible building that may be sliding on its column bases, are used. The stability of the sliding behavior is explored along with the consistency of the dynamic friction coefficient over various loading magnitudes, loading frequencies, and sliding lengths. The major findings from this study are detailed below.

- The sinusoidal input study using the rigid frame specimen resulted in an average friction coefficient of 0.78 with deviations of only 0.02 from this value. Meanwhile, the flexible frame specimen tests under sinusoidal input produced friction coefficients slightly smaller and ranging between 0.61 and 0.71. In general, the sliding behavior remained stable and suggests that further consideration of the friction between steel and mortar is possible for seismic design or for the development of new energy dissipation-type devices.
- The sinusoidal input study of the flexible frame specimen showed a decrease in the friction coefficient during sliding. This is in part attribute to the larger sliding velocities imparted to the system by the flexible frame. Based on the findings, the threshold sliding velocity above which this phenomenon is observed lies between 140 mm/s and 400 mm/s.
- The sliding behavior under non-stationary motion was similar to that observed for the sinusoidal loading. A small decrease in the friction coefficient was observed during longer sliding duration suggesting a further parameter that may affect the consistency of the friction coefficient value.
- In general, the maximum friction coefficient value was maintained between 0.61 and 0.78 even during many repeated cycles using the same steel and mortar surfaces. The results suggest that this behavior can be durable and predictable over time.

Acknowledgements:

This study was conducted as part of a research project supported by Grant-in-Aid for Scientific Research (Basic Research Category YB, 18760419) and administered by the Japan Society for the Promotion of Science. T. Nagae was the principal investigator on that project. J. McCormick was supported by the Japan Society for the Promotion of Science Postdoctoral Fellowship for Foreign Researchers Program.

References:

American Institute of Steel Construction (AISC). (2006), *Seismic Design Manual 13th ed.*, American Institute of Steel Construction: Chicago.

Architectural Institute of Japan (AIJ). (2004), *Design Guidelines for Connections of Steel Building Structures*, Architectural Institute of Japan: Japan.

Bondonet, G. and Filiatrault, A. (1997), "Frictional Response of PTFE Sliding Bearing at High Frequencies," *Journal of Bridge Engineering*, American Society of Civil Engineers, **2**(4), 139-148.

Galambos, T.V. (1998). *Guide to Stability Design Criteria for Metal Structures 5th ed.* Wiley: New York.

Iemura, H., Taghikhany, T., Takahashi, Y., and Jain, S.K. (2005).

"Effect of Variation of Normal Force on Seismic Performance of Resilient Sliding Isolation Systems in Highway Bridges," *Earthquake Engineering and Structural Dynamics*, **34**, 1777-1797.

Kurata, M., Nakashima, M., and Suita, K. (2005). "Effect of Column Base Behavior on the Seismic Response of Steel Moment Frames," *Journal of Earthquake Engineering*, **9**, 415-438.

McCormick, J., Nagae, T., Ikenaga, M., Zhang, P.-C., Katsuo, M., and Nakashima, M. (2009). "Investigation of the Sliding Behavior between Steel and Mortar for Seismic Applications in Structures," *Earthquake Engineering and Structural Dynamics*, **38**, 1401-1419.

Nagae, T., Ikenaga, M., Nakashima, M., and Suita, K. (2005). "Shear Friction between Base Plate and Mortar in Exposed Steel Column Base," *Transactions of AIJ Journal of Structural and Construction Engineering*, **606**(8), 217-223. (in Japanese).

Nakashima, M. and Liu, D. (2005). "Instability and Complete Failure of Steel Columns Subjected to Cyclic Loading," *Journal of Engineering Mechanics*, American Society of Civil Engineers, **131**(6), 559-567.

Ng, C.-L and Xu, Y.-L. (2006). "Seismic Response Control of a Building Complex Utilizing Passive Friction Damper: Experimental Investigation," *Earthquake Engineering and Structural Dynamics*, **35**, 657-677.

Pall, A.S., Marsh, C., and Fazio, P. (1980). "Friction Joints for Seismic Control of Large Panel Structures," *Journal of Prestressed Concrete Institute*, **25**(6), 38-61.

Roussis, P.C. and Constantinou, M.C. (2006). "Experimental and Analytical Studies of Structures Seismically Isolated with an Uplift-Restraining Friction Pendulum System," *Earthquake Engineering and Structural Dynamics*, **35**, 595-611.

Tsai, C.S., Chen, W.-S., Chiang, T.-C., and Chen, B.-J. (2006). "Component and Shaking Table Tests for Full-Scale Multiple Friction Pendulum System," *Earthquake Engineering and Structural Dynamics*, **35**, 1653-1675.

Wang, T., McCormick, J., Yoshitake, N., Pan, P., Murata, Y., and Nakashima, M. (2008). "Collapse Simulation of a Four-Story Steel Moment Frame by a Distributed Online Hybrid Test," *Earthquake Engineering and Structural Dynamics*, **37**, 955-974.

Yamaguchi, N. and Yamazaki, F. (2001). "Estimation of Strong Motion Distribution in the 1995 Kobe Earthquake Based on Building Damage Data," *Earthquake Engineering and Structural Dynamics*, **30**, 787-801.

JOINT CONFERENCE PROCEEDINGS
7th International Conference on Urban Earthquake Engineering (7CUEE) &
5th International Conference on Earthquake Engineering (5ICEE)
March 3-5, 2010, Tokyo Institute of Technology, Tokyo, Japan

EFFECT OF VERTICAL NON-UNIFORM GROUND MOTION ON SEISMIC RESPONSE OF LARGE SPAN STRUCTURES

Feng **Liu**[1], Xilin Lu[2]

1) Assistant Professor, College of Civil Engineering & Architecture, Shandong University of Science & Technology, China
2) Professor, State Key Laboratory for Disaster Reduction in Civil Engineering, Tongji University, China
tjfliu@yahoo.com.cn, lxlst@mail.tonji.edu.cn

Abstract: The objective of this paper is to study the effects of multiple vertical excitations on the large span structures by means of time history analyses. The spatial variation of ground motions are represented as the combined effect of wave-passage and incoherency. They are simulated by the method of conditional simulation based on the selected four series of typical recorded ground motions. Some important responses such as internal force, displacement are monitored and compared between different cases. Finally, the conclusions are drawn concerning whether the multiple vertical components can be safely neglected in determining the seismic actions on critical elements of structures. These analytical simulations provide a tentative work for investigating destructive effects of the multiple vertical excitations which can be solidified by further study and post-earthquake survey.

1. INTRODUCTION

During the past two decades, the effect of the spatial variability of earthquake ground motions on the response of extended structures has been investigated extensively: Bogdanoff [1] investigated traveling wave effects on the seismic response of structures; Zerva [2] and Harichandran [3] examined the effect of spatial variability on the response of bridge models; Zerva [4] studied the quasistatic and dynamic response of bridge models using different coherency expressions; Harichandran [5] analyzed the response of long-span bridges to spatially varying excitations; Monti [6] conducted nonlinear seismic analysis of bridges subjected to multiple support excitations; Price [7] studied an idealized two-span symmetric beam bridge model to non-uniform excitation; and Lou [8] analyzed the effects of spatially variable ground motions on the seismic response of a skewed, multi-span, reinforced concrete highway bridge.

All aforementioned studies indicated that the effects of spatial as well as temporal variation of earthquake ground motion to be a potentially destructive factor for large size structures or spatial structures. The multi-support excitation or non-synchronous input can induce a seismic response very different from that calculated considering the same ground motion at each support, which are the current practices of seismic structure analysis.

It should be noted that in the past, only the effect of spatially horizontal ground motion were taken into account in almost all studies, and the spatially vertical ground motions are hitherto ignored or inadequately taken into account for most spatial structures. The argument in support of ignoring vertical motion lies in the assumption that the vertical acceleration is usually significantly low than the horizontal one. However, in contradiction with the above, several recent earthquakes, especially in Northridge and Kobe, have produced an unexpectedly high level of structural damage in regions where advanced earthquake resistant practice has been adopted. Field observations following these events have repeatedly identified forms of severe structural damage which may be attributed to significant shaking arising from vertical strong-motion.

Notwithstanding with the increase of near-field earthquake records obtained and the associated destruction of structures observed, the extensive research [9, 10, 11] carried out over the last 10 years in the effects of vertical ground motion on the seismic response of structures. However, limited number of studies exists involving a comprehensive analysis for the spatially vertical excitation on the seismic response of spatial structures. Different from the horizontal component of ground motion, the vertical one is associated with higher frequencies, as observed in most strong-motion record. So the conclusion learn from the spatially horizontal excitation is deemed as the same as the vertical one on the response of structure is irrational.

As a tentative work, the present paper sought to answer the question: does the multiple vertical component of ground motion constitute a significant proportion of the loading that has to be resisted by a building or by its foundations. It concentrates on ground motion in near-filed where the

influence of vertical acceleration is greatest. The effect of multiple vertical excitations on the dynamic response of the structure buildings will be investigated by evaluating response of an idealized buildings model to strong ground shaking from a suit of simulated accelerations. Support ground motion time histories were generated corresponding to coherent, wave passage, and coherency loss models of spatially variable earthquake shaking. Two different empirical model of spatial coherency decay were adopted for the generated time histories of horizontal and vertical ground motion using the conditional simulation procedure postulated by Heredia-Zavoni [12]. In addition, due to the particularity of the vertical motion, the power spectra density is achieved by ARMA model from the original ground motions. Support reactions of the buildings were then computed via time history analysis. The change in response relative to various case of ground motion was calculated and compared. Finally, the effect of multiple vertical ground motion on the structure buildings is highlighted.

2. IDEALIZED MODEL OF THE MULTI-SUPPORT SPATIAL STRUCTURE

In this research, a large span multi-support reinforced concrete arch as shown in Fig.1 is selected as the idealized model of the study. To investigate the effect of length of the arch, the span of this model considered in present paper is selected to 50, 100, 200, and 400 meters.

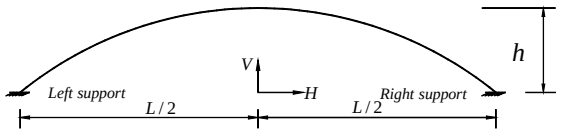

Fig.1 The idealized model of multiple-support structure

It should be noted that this model is relative simple compared to the reality engineering structures, while it can represent some typical member of spatial structures and furthermore, the result of the analysis can provide some fundamental insight of the seismic response induced by the spatially vertical excitations.

3. GENERATION OF SPATIALLY VARIABLE GROUND MOTION

3.1 Selection of the original ground motion

Up to now, as many scholars have examined in their research, The spatial variation of seismic ground motion can be attributed to the following three mechanisms:(1) the difference in arrival times of the seismic waves at different locations, generally known as the “wave passage effect”, (2) the change in shape of the propagating wave form due to multiple scatterings of the seismic waves in the highly inhomogeneous soil medium, referred to as the “incoherence effect”, and (3) the change in amplitude and frequency content of ground motion at different locations on the ground surface due to different local soil conditions known as the “local site effect”.

In this paper, a conditional simulation algorithm has been used to generate different horizontal and vertical component of acceleration time histories at several prescribed locations as shown in Fig.1 on the ground surface.

As shown in Table 1～2, four sets of original ground motions [13] have been selected in present paper for investigate the effect of the multiple vertical excitations. The ratio of V/H of Kobe and Northridge are 0.17, 1.86, respectively, represent the typical horizontal and vertical records. On the other hand, the ratio of V/H of Imperial Valley is 0.67, obeys the rule of the 2/3. Furthermore, V/H of Loma prieta is 0.94, represent the horizontal and vertical ground motion are almost equivalent.

Table 1 Selection of typical recorded motions

Records	Date	Site	Distance(km)	PGA (g)	Acceleration spectra (g)	V/H
Kobe	1995, 01, 16	Shin-Osaka	15.5	0.243 (H)/0.059 (V)	0.896 (H)/0.155 (V)	**0.17**
Imperial valley	1979, 10, 15	El-Centro Array	4.2	0.485 (H)/0.248 (V)	1.081 (H)/0.724 (V)	**0.67**
Loma prieta	1989, 10, 18	47125 Capitola	14.5	0.529 (H)/0.541 (V)	2.113 (H)/1.982 (V)	**0.94**
Northridge	1994, 01, 17	Arleta-Nordhoff	9.2	0.344 (H)/0.552 (V)	0.951 (H)/1.770 (V)	**1.86**

Note: H, V represent the horizontal and vertical component of the recorded motions； 5 % is selected as damping ratio.

Table 2 Information of recorded and simulated motions

Records	Kobe	Imperial Valley	Loma Prieta	Northridge
Number of data	4096	7800	7991	2000
Time interval (s)	0.01	0.005	0.005	0.02
Number of simulated data	4096	7808	8064	2048
Duration (s)	40.96	39.04	40.32	40.96

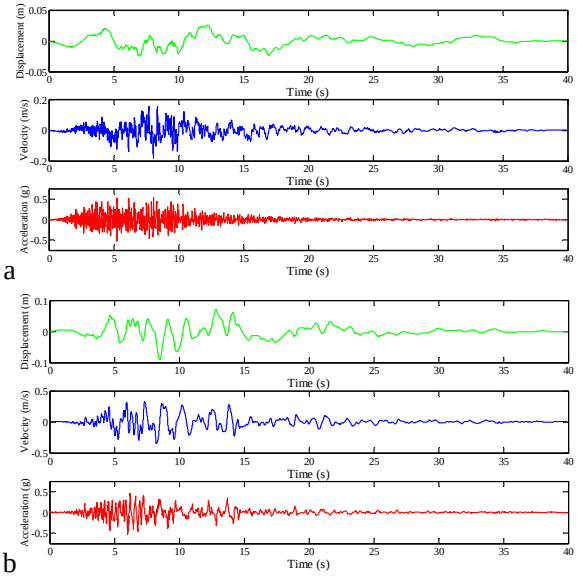

Fig 2: Loma prieta earthquake records at the ground level of station 47125 Capitola (a) horizontal; (b) vertical

3.2 Evaluation of the power spectrum

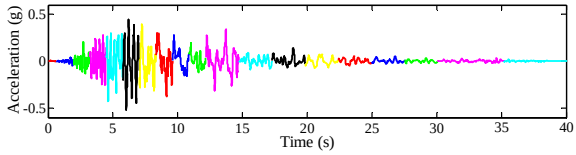

Fig 3. The partition of the vertical component of Loma prieta record

When each segment of the acceleration is supposed as a stationary stochastic process with a zero mean, it can be described accurately by its power spectra density. The significance of the power spectra density lies in the fact that it illustrates how the variance of the stochastic process is distributed with frequency. Some of the methods that have been developed in the past for the simulation of spatially correlated synthetic accelerations, such as the Clough-Penzien acceleration spectrum, and theoretical time envelope functions to account for the non-stationarity characteristics of the generated motions. Studies by Shama[14] showed that introducing time envelope functions might disturb the phase properties of the simulated accelerations and hence alter the correlation characteristics of the developed ground motions. Therefore, this class of method is considered to be inadequate from a practical perspective.

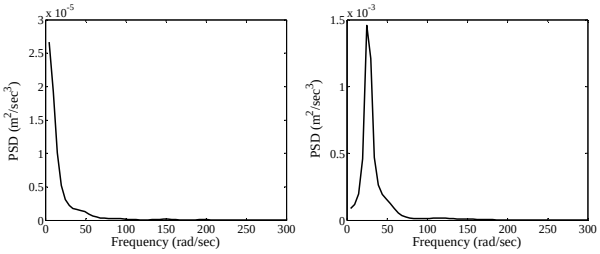

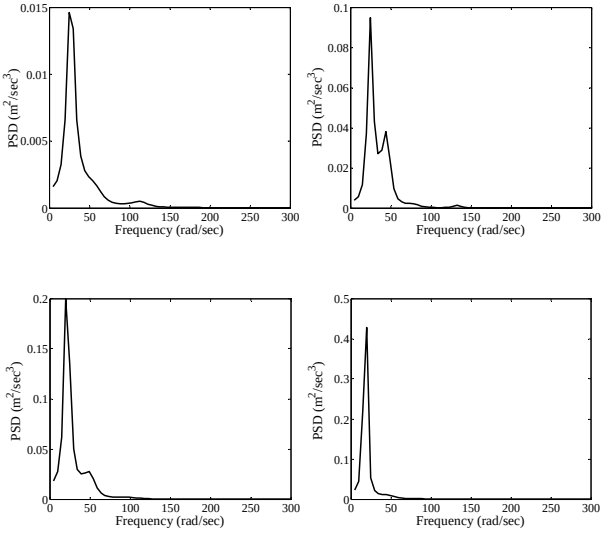

Fig 4. Estimated power spectra density for the first 6 window of the vertical component of Loma prieta record

Consequently, the power spectra density was determined in the present study by the autoregressive moving average (ARMA) models. To represent the evolutionary nature of the recorded ground motion accurately, the original horizontal and vertical accelerations were subdivided into 19 successive windows with 44 additional time steps padded as trailing zeros, to satisfy the Fast Fourier Transform requirements. Fig.4 summarizes the first 6 estimated power spectra density of vertical component of ground motion for each window.

3.3 Coherency models

Spatially variable ground motion measured at discrete location is often described using the coherency function. For observations at two stations denoted by i and j, the frequency dependent coherency function can be written as

$$\gamma_{ij}(\omega) = \left[\frac{|S_{ij}|}{\sqrt{S_{ii}S_{jj}}}\right]\exp(iv_{ij}) \tag{1}$$

Where, S_{ij} is cross-spectra density, and S_{ii}, S_{jj} are power spectral densities for observations i and j. The v_{ij} term is a deterministic factor that accounts for wave passage between stations i and j and is a function of frequency, station separation distance, and apparent propagation velocity of the seismic disturbance.

In this study, the empirical model developed by Harichandran [15] was used as a predicator of the lagged coherency in the generation of horizontal component of ground motion

$$\left|\gamma_{ij}(\omega,\xi)\right| = A\exp[-\frac{2\xi}{\alpha\theta(\omega)}(1-\mathrm{A}+\alpha\mathrm{A})] + (1-\mathrm{A})\exp[-\frac{2\xi}{\theta(\omega)}(1-\mathrm{A}+\alpha\mathrm{A})] \tag{2}$$

Where, ξ is distance between two stations; A and α are constants having values of 0.636 and 0.0186, respectively; and θ is a function of frequency given by

$$\theta(\omega) = k[1+(\frac{\omega}{\omega_0})^{\beta}]^{-1/2} \tag{3}$$

Where, k, ω_0 and β are constants having values of 31200, 9.49 and 2.95, respectively.

Compared to the horizontal component of ground motion, the empirical model developed by Abrahamson [16] was adopted in simulating the vertical earthquake shaking

$$|\gamma(w,\xi)| = \tan\left[\frac{c_1(\xi)}{1+c_2(\xi)w} + (4.65-c_1(\xi)) \right] \tag{4}$$
$$\exp(c_3(\xi)w) + 0.35$$

Where,

$$\begin{aligned} c_1(\xi) &= 3.5 - 0.37\ln(\xi+0.4), \\ c_2(\xi) &= 0.65\left[1-\frac{1}{1+\xi/4}\right], \\ c_3(\xi) &= 3(\exp(-0.05\xi)-1) - 0.0018\xi. \end{aligned} \tag{5}$$

Where, ξ and w are distance and frequency, respectively.

Furthermore, to be consistent with studies by previous researchers, an apparent propagation velocity of $1000m/s$ and $1700m/s$ were used in the simulation of horizontal and vertical components.

3.4 Simulated ground motions

Each support acceleration time histories were simulated according to the above theory. The time histories of horizontal and vertical ground motion at support B were selected as illustration and shown in Fig. 5 and 6.

The comparison of the acceleration spectra between the original and the simulation was shown in Fig. 7. The result shown that they agree quite well each other.

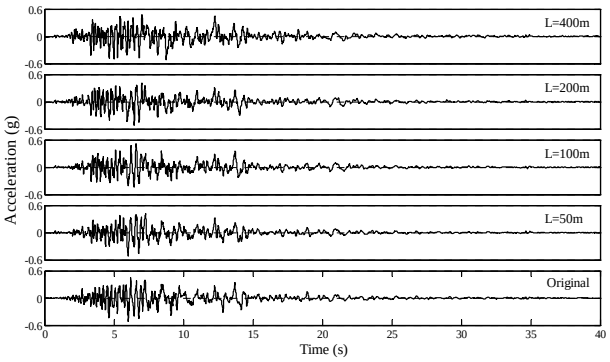

Fig. 5 Simulated horizontal ground motions based on the original Loma prieta accord

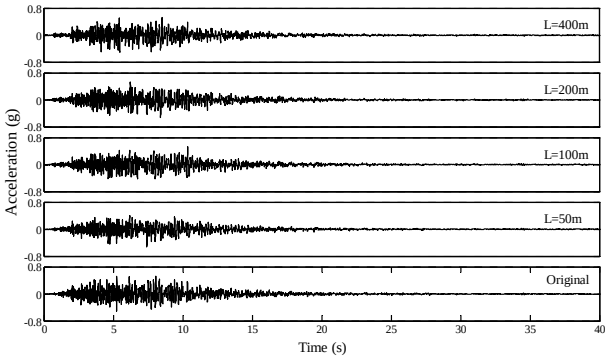

Fig. 6 Simulated vertical ground motions based on the Loma prieta accord

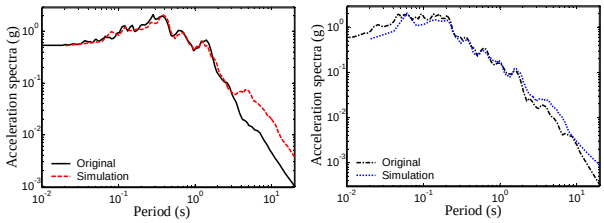

Fig. 7 Comparison of the acceleration spectra between the original and simulated ground motion (200m)

4. ANALYSIS FOR THE SEISMIC RESPONSE OF IDEALIZED LARGE SPAN STRUCTURE

4.1 FE model of the large span structure

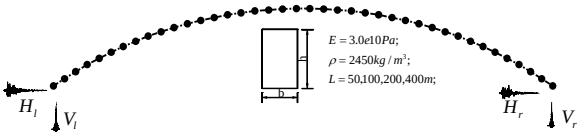

Fig. 8 The idealized FE model of the large span arch

Table 3 The first period of the given structure

Span (m)	50	100	200	400
Period (s)	0.36	1.43	5.88	23.26

The linear elastic models of the multi-support arch as shown in Fig. 8 was created using the finite element code ABAQUS [17]. The technique of composite section was adopted here to simulate reinforced concrete section of critical structural component. The whole arch is represented by 40 beam31 elements totally. The table 3 summary the first period of the arch for each span.

4.2 The cases of excitation and strategy of the comparison of the seismic response

Among all possible seismic motion correlation patterns, four cases of ground motions were considered in present paper and described hereafter:

(1) Uniform excitations;
(2) Only coherency effect was considered.
(3) Only wave-passage effect was considered.
(4) Both coherency and wave-passage were taking into account simultaneously.

It should be noted that the case 1 is a general procedure in almost all current codes. Comparing the seismic response induced by case 2 and 3 with the case 1, the effects of coherency and wave passage can be assessed, respectively. In addition, comparing the seismic response by case 4 with the case 1, the question of whether the multiple vertical excitations can be omitted safely should be answered.

$$\mathbf{N}_i = \max(N_i^j)\big|_{i=1,2,\ldots,40;\, j=1,2,\ldots,T/\Delta t}$$
$$\mathbf{M}_i = \max(M_i^j)\big|_{i=1,2,\ldots,40;\, j=1,2,\ldots,T/\Delta t} \quad (6)$$

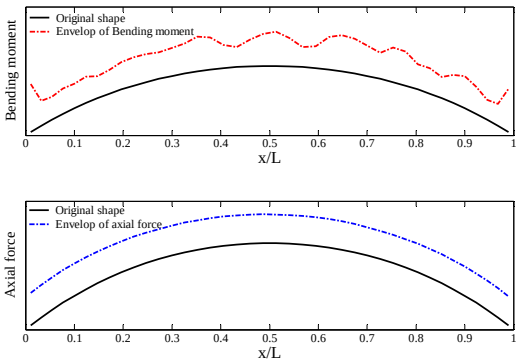

Fig. 9 The envelop of internal force along the span of arch

The Fig 9 plot the envelop of internal force along the whole span of arch. The formulation (7) shows the ratio of internal force and displacement between the non-uniform excitation and uniform excitation. It is evident that the ratio ϕ denotes the effects of the multiple excitations.

$$\phi = \frac{\textit{Maximum value induced by non-uniform excitation}}{\textit{Maximum value induced by uniform excitation}} \quad (7)$$

4.3 Case 1: only the effect of coherency is considered

In this case, only the effect of coherency is considered when generation the non-uniform excitations for the right support using the theory as illustrated in section 3. The ratios ϕ of internal forces are illustrated in Fig.10. It is shown that the data is quite diverse. The minimum and maximum of ratio is 1.38, 0.61, respectively.

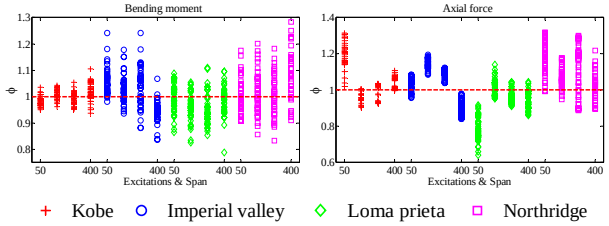

Fig. 10 The ratio of internal force in the case of 1

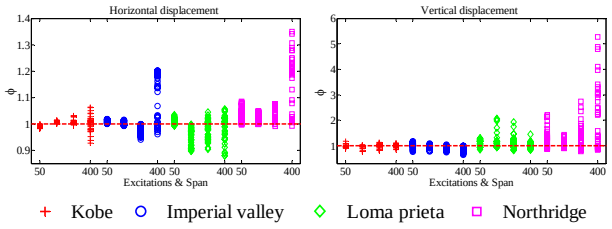

Fig. 11 The ratio of displacement in the case of 1

The ratio ϕ of displacements are identified in Fig.11. It is shown that the data is quite diverse. The minimum and maximum ratio of horizontal displacement is 1.38, 0.87. However, the ratio of vertical displacement is quite different from the horizontal one. These results shown that the multiple vertical excitations when only take the effect of coherency into account may induce bigger vertical displacements.

4.4 Case 2: only the effect of wave passage is considered

Similar to the section 4.3, in this case, only the effect of coherency is considered when generation the non-uniform excitations for the right support. The ratios ϕ of internal forces are illustrated in Fig.12. It is shown that the data is also quite diverse. The minimum and maximum of bending moment ratio is 1.28, 0.55, respectively. For the axial force, more ratio data is below the number 1.0, shown that the effect of multiple vertical excitation when only take the wave passage effect may induce the smaller internal forces.

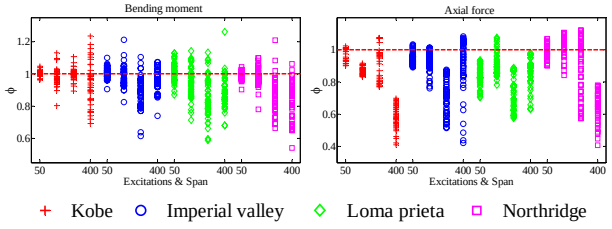

Fig. 12 The ratio of internal force in the case of 2

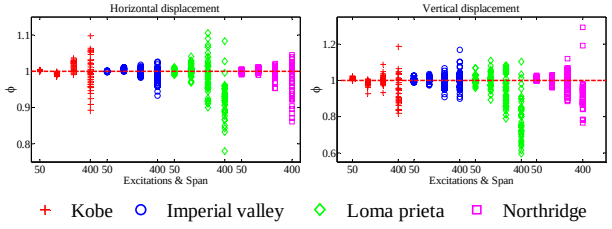

Fig. 13 The ratio of displacement in the case of 2

The ratios ϕ of displacements are identified in Fig.13. It is shown that the data is quite diverse. Compared to the case 1, the results is relative small.

4.5 Case 3: all the effect of coherency and wave passage were considered

The effects of coherency and wave passage are taken into

account simultaneously when generation the ground motion in the right support, the ratios of internal forces and displacements are plotted in Fig. 14～15. Comparatively, the values lie in the scope of case 1 and case 2.

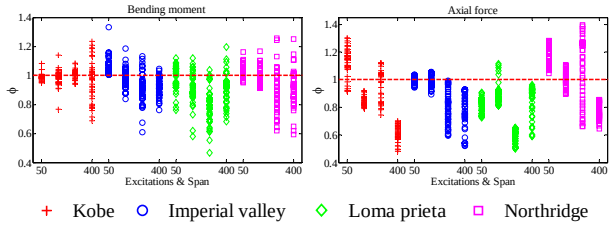

Fig. 14 The ratio of internal force in the case of 3

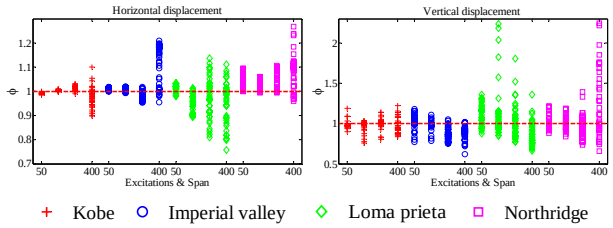

Fig. 15 The ratio of displacement in the case of 3

4.6 Discussion

The average values of the ratio ϕ for all cases are plotted in Fig.16～17. The character shown in X label is explained as following:

(1) K: Kobe; I: Imperial valley; L: Loma prieta; N: Northridge.

(2) C: Coherency; W: Wave passage; F: Full of Coherency and Wave passage.

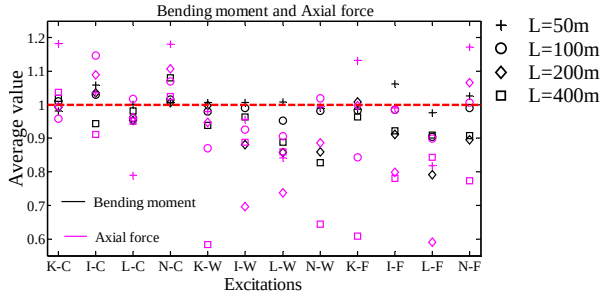

Fig. 16 The average ratio of internal force for all cases

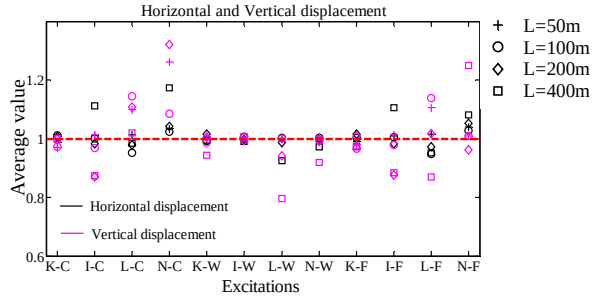

Fig. 17 The average ratio of displacement for all cases

As the results illustrated in the Figures, the following conclusions can be drawn:

1) The coherency effect is the dominant factor for the multiple vertical excitations. In some cases, the effect of wave passage is beneficial.

2) Compared to the large span, the multiple vertical excitations exert the big harmful influence on the short one.

3) Compared to the bending moment and horizontal displacement, the vertical non-uniform imposes bigger effect on the axial force and vertical displacement.

5. CONCLUSIONS

In present paper, computations were performed to examine the effects of spatially variable vertical ground motion on the spatial structures. Sets of support acceleration time histories were generated using a suite of accelerations in conjunction with coherent, wave passage, and coherency loss models. Seismic response were computed for each excitation and compared between each other. The main findings of the study can be summarizes as follows:

1) The maximum of the axial force and bending moment increases, because of the multiple vertical earthquake shaking.

2) The maximum of the horizontal and vertical displacement increases due to the non-uniform vertical excitation.

3) Compared to the effect of wave passage, the effect of coherency may be the controlling factor for the non-uniform vertical ground motions

4) It would be prudent to consider the effect of multiple vertical excitations by using the uniform vertical ground motion applied on the structures.

It should be noted, as a tentative work, the effects of spatially vertical excitations on the seismic response were assessed in the first step, many factors such as geometry and material nonlinear and more sophisticated ground motion generating methods are need in the following study.

Acknowledgements:

The first author acknowledge support from the Taishan scholar award scheme specially in Shandong province, and the funding from the Chunlei project in Shandong University of Science & Technology, China.

References:

[1] Bogdanoff J.L., Goldberg J.E and Schiff A.J. (1965), "The effect of ground transmission time on the response of long structures," *Bulletin of the Seismological Society of America*, 55(5), 627–640.

[2] Zerva, A. (1990), "Response of multi-span beams to spatially incoherent seismic ground motions," *Earthquake Engineering & Structural Dynamics*, 19(6), 819–832.

[3] Harichandran R.S., Wang W. (1990), "Response of indeterminate two-span beam to spatially varying earthquake excitation," *Earthquake Engineering & Structural Dynamics*, 19(2), 173–187.

[4] Zerva, A. (1994), "On the spatial variation of seismic ground motions and its effects on lifelines," *Engineering Structures*,

16(7), 534–546.
[5] Harichandran, R.S. Hawwari, A., and Sweidan, B.N. (1996) "Response of long-span bridges to spatially varying ground motion," *Journal of Structural Engineering*, ASCE, 122(5), 476–484.
[6] Monti, G., Nuti, C., and Pinto, P.E. (1996), "Nonlinear response of bridges under multi-support excitation," *Journal of Structural Engineering*, ASCE, 122(10), 1147–1159.
[7] Price, T.E., Eberhard, M.O. (1998), "Effects of varying ground motions on short bridges," *Journal of Structural Engineering*, ASCE, 124(8), 948–955.
[8] Lou, L., Zerva, A. (2005) "Effects of spatially variable ground motions on the seismic response of a skewed, multi-span, RC highway bridge," *Soil Dynamics and Earthquake Engineering*, 25(7-10), 729-740.
[9] Elnashai, A.S., Papazoglou, A.J. (1997), "Procedure and spectra for analysis of RC structures subjected to strong vertical earthquake loads," *Journal of Earthquake Engineering*, 1(1), 121-155.
[10] Button, M.R., Cronin, C.J., and Mayes, R.L. (2002), Effect of vertical motions on seismic response of highway bridges," *Journal of Structural Engineering*, ASCE, 128(12), 1551-1564.
[11] Ambraseys, N.N., Douglas, J. (2003), "Near-field horizontal and vertical earthquake ground motions," *Soil Dynamics and Earthquake Engineering*, 23(1), 1-18.
[12] Heredia-Zavoni, E., Santa-Cruz, S. (2000), "Conditional simulation of a class of nonstationary space-time random fields," *Journal of Engineering Mechanics*, 126(4), 398-404.
[13] http://peer.berkeley.edu/nga/
[14] Shama, A.A. (2007), "Simplified procedure for simulating spatially correlated earthquake ground motions," *Engineering Structures*, 29(2), 248-258.
[15] Harichandran, R.S., Vanmarcke, E.H. (1986), "Stochastic variation of earthquake ground motion in space and time," *Journal of Engineering Mechanics*, 112(2), 154-174.
[16] Abrahamson, N.A., Schneier, J.F., and Stepp, C. (1991), "Empirical spatial coherency functions for applications to soil-structures interaction analyses," *Earthquake Spectra*, 7(1), 1-27.
[17] ABAQUS, http://www.abaqus.com/.

JOINT CONFERENCE PROCEEDINGS
7th International Conference on Urban Earthquake Engineering (7CUEE) &
5th International Conference on Earthquake Engineering (5ICEE)
March 3-5, 2010, Tokyo Institute of Technology, Tokyo, Japan

CYCLIC BEHAVIOR AND COLLAPSE MODE OF HIGH STRENGTH STEEL H-SECTION BEAMS

Kikuo Ikarashi[1)], Ryota Suekuni[2)] and Tao Wang[3)]

1) Assoc. Professor, Dept. of Arch. and Building Eng., Tokyo Institute of Technology, Japan
2) Graduate Student, Tokyo Institute of Technology, Japan
3) GCOE Postdoctoral Fellowship, CUEE, Tokyo Institute of Technology, Japan
ikarashi.k.aa@titech.ac.jp, suekuni.r.aa@m.titech.ac.jp, wang.t.aa@m.titech.ac.jp

Abstract: This study shows possibility of using high strength steel for H-section beams with large depth-thickness ratio, within elastic range. Especially, influence of cyclic loading and the boundary conditions are examined by loading tests. It is shown that these beams are useful as seismic design beams, although the depth-thickness ratio of these beams is larger than the limit of current standard. So in this study, the new limit value of plate slenderness are proposed. And the redundancy and the stability of these beams within plastic range are investigated. The beams with large depth-thickness ratio gained the upper hand.

1. INTRODUCTION

Nowadays design method for keeping the stress of main structure elastic is discussed, and high strength steel of that yield stress is over 700N/mm^2 is put to practical use. This study shows possibility of using high strength steel for H-section beams within elastic range. Especially, influence of cyclic loading and the boundary conditions are examined by loading test.

In case of using high strength steel, the web plate can be thinner. But it is difficult to cope with the demand of using H-section beams with large depth-thickness ratio as long as we follow the limit value of current standard, and it means that high strength steel isn't made its advantage. The possibility of using H-section beams with large depth-thickness ratio is already shown in the Ref. [3] by monotonic loading. This study propose a new limit value of plate slenderness which rests on the premise that it is used only within elastic range, and examine the possibility of making thinner the web plate.

Besides, we also examined the behavior of H-section beams within not only elastic range but also plastic range so that it is important to grasp their behavior when they are deformed largely. Especially, redundancy and stability of these beams within plastic range are investigated.

2. CYCLIC LOADING TEST OF H-SECTION BEAMS WITH HIGH STRENGTH STEEL

The experiments are cyclic loading test and

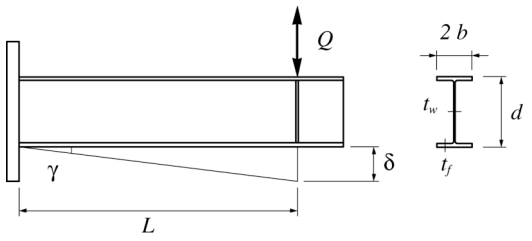

Fig.1: Specimen

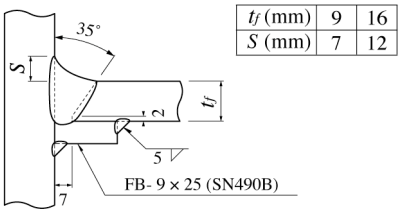

t_f (mm)	9	16
S (mm)	7	12

Fig.2: Weld Detail

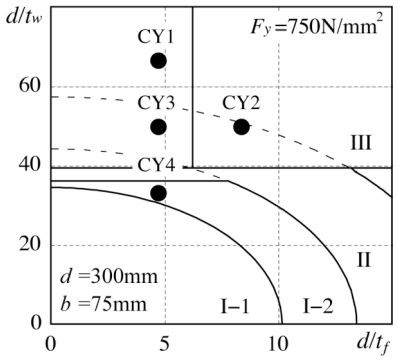

Fig.3: Depth-Thickness Ratio Relationship of Specimens

Table1: Properties of Specimens

Specimen	Section	d/t_w	b/t_f	Q_F (kN)	Q_y (kN)	Q_p (kN)	Q_u (kN)	L (mm)
CY1	H-300×150×4.5×16	66.7	4.69	348	438	481	518	1200
CY2	H-300×150× 6× 9	50.0	8.33	230	303	341	369	1200
CY3	H-300×150× 6×16	50.0	4.69	355	447	498	535	1200
CY4	H-300×150× 9×16	33.3	4.69	373	470	534	574	1200

d/t_w: Web Depth-Thickness ratio b/t_f : Flange Depth-Thickness Ratio $Q_F=ZF/L$ $Q_y=Z\sigma_y/L$ $Q_p=Z\sigma_p/L$ $Q_u=Z_p\sigma_u/L$ Z: Section Modulus Z_p: Plastic Section Modulus F=600N/mm^2

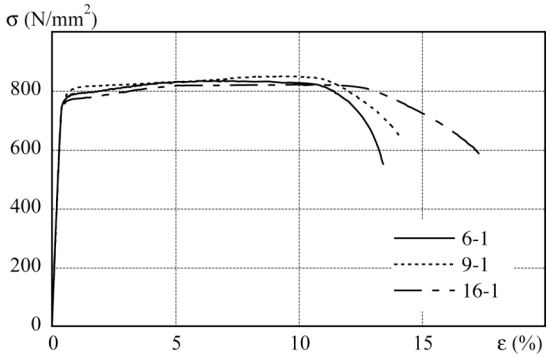

Fig.4: Stress-Strain Relationship of Steels

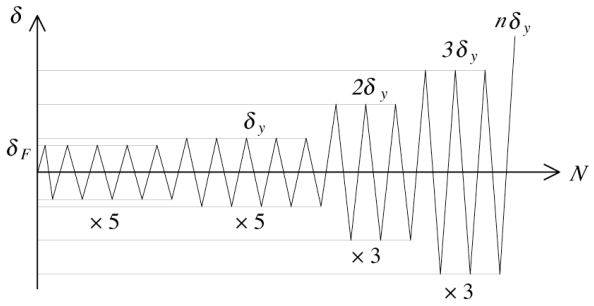

Fig.5: Loading Program

Table2: Mechanical Properties

Specimen	t (mm)	σ_y (N/mm^2)	σ_u (N/mm^2)	E (kN/mm^2)	ν	*Elng* (%)	Y.R.
6-1	6.17	775	834	199	0.30	11.7	0.93
6-2	6.22	776	832	189	0.30	10.5	0.93
9-1	9.23	788	849	198	0.30	12.1	0.93
9-2	9.08	794	861	199	0.30	11.9	0.92
16-1	15.9	762	821	203	0.30	14.1	0.93
16-2	15.9	749	805	201	0.30	13.4	0.93

t: Thickness σ_y: Yield Stress σ_y: Tensile Strength E: Young Modulus ν: Poisson's Ratio *Elng*: Elongation Y.R.: Yield Ratio

monotonic loading test. All specimens are build-up H-section. Their web and flanges are welded by fillet weld both side. Each cyclic specimen is welded to the endplate, flanges are by complete penetration weld and web is by fillet weld. Monotonic specimens are continuous beams to eliminate the influence of welded edge. Figure 1 shows a cyclic loading specimen. Figure 2 shows a detail drawing of a welded flange edge. Mechanical properties of welding consumable are bellow, 0.2% offset strength is 686kN/mm^2, tensile strength is 780kN/mm^2, elongation is 21%, absorbed energy is 108J. The strength of this welding consumable is lower than the steel used in this experiment.

Figure 3 is depth-thickness ratio relationship of specimens. They have large depth-thickness ratio comparatively. The classification in Fig.3 is derived from ref.[2] and F_y is 750N/mm^2, refer the minimal value of σ_y , yield point. Table 1 is properties of specimens. Figure 4 shows an example of strain-stress relationship obtained through the tension test of JIS1A specimens. Table 2 shows mechanical properties. The yield point in it is 0.2% offset strength. All of them have unclear plastic flow and high yield ratio.

Cyclic loading is controlled by the displacement, as the loading program (Fig.5) indicates, and the displacement increases by loading steps. The basis displacement is δ_y , that is the elastic displacement of each specimen when the moment at their edge come to yield moment. Besides, they are also loaded by δ_F corresponding to referenced strength. Now allowable stress is 600N/mm^2. Cyclic loading is repeated 5 times each δ_y and δ_F , so that the behavior within elastic range must be examined especially. After that, similarly $2\delta_y$, $3\delta_y$,and $4\delta_y$ until the strength falls remarkably. δ_F and δ_y

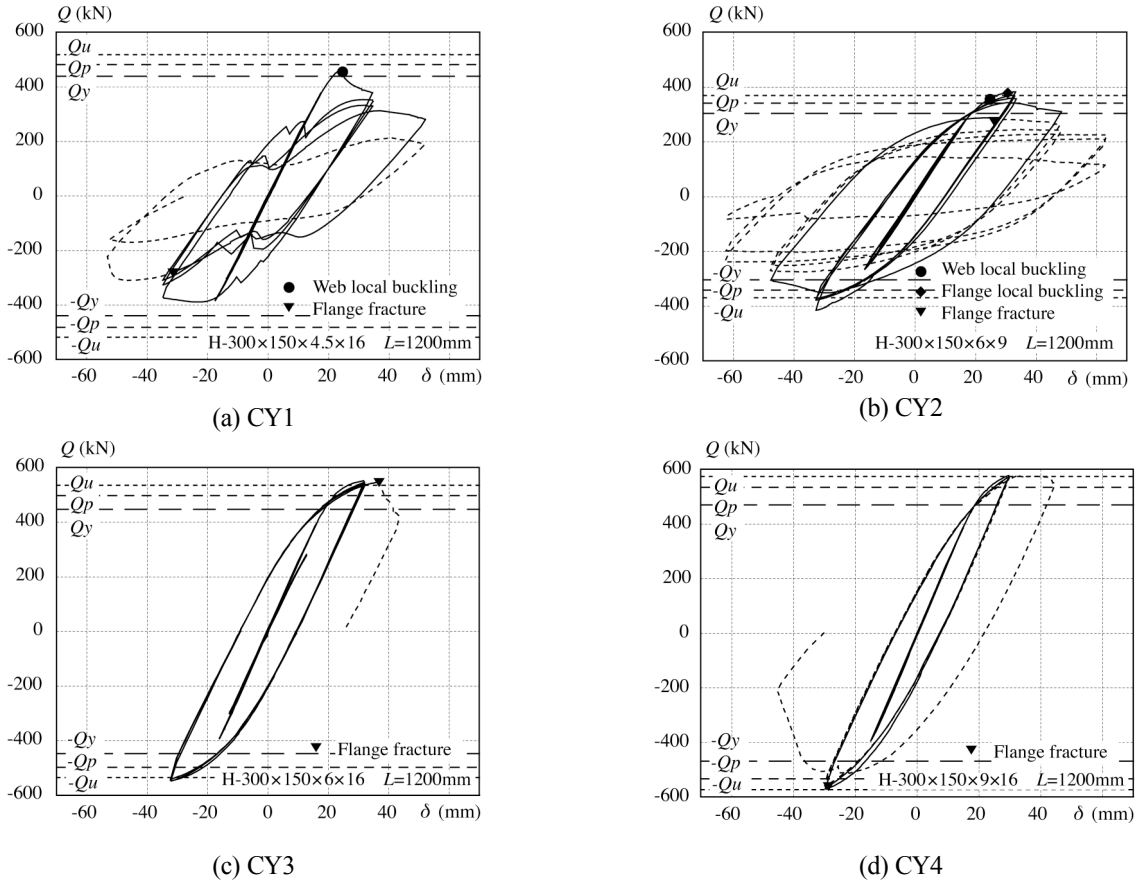

Fig.6: Load-Deformation Curve

are values that consider bend and shear deformation. And lateral buckling is prevented.

3. THE CYCLIC BEHAVIOR AND COLLAPSE MODE OF H-SECTION BEAMS WITH HIGH STRENGTH STEEL

3.1 The Cyclic Behavior and Collapse Mode

Figure 6 shows load-deformation curve of each specimen. The dotted line, broken lone, and long broken line designates Q_F , Q_y , and Q_u . Their actual value is in table 1. ● mark and ◆ mark in the graph designate the point when local buckling of the web or flange occurred. These local buckling points are judged by typical increment of remainder of the value of strain gauges or observation. And ▼ mark designates the fracture point of plate element, and hysteresis curves after the point drawn by dotted line.

CY1, it has the largest web depth-thickness ratio, causes web local buckling when the load gets over Q_y , and reduces the strength suddenly. Then though it causes transient strength deterioration due to buckling wave reversing, it increased the strength by forming tension field. Finally, the web collapsed intensively and flange causes only bending deformation, didn't cause local buckling.

CY2 shows stable hysteresis curve. After the flange fracture, it didn't cause sudden strength deterioration and then the fracture that grew up by steps made it collapse. Finally, although the flange collapse widely and supervened web local buckling, its total displacement until clear strength deterioration is best of all.

Both CY3 and CY4 fractured their welded edges of flange, didn't cause local buckling. Their maximum load get over Q_u , but their weld couldn't deform enough to correspond the flange tensile deformation so that it fracture.

It is not good for H-section beams with high strength steel to make its depth-thickness ratio small. If we use it, the edge can fracture early in plastic range as fig.6 (c) and (d) indicates. This phenomenon is also found in Ref. [5]. In contrast, although H-section beams with relatively large depth-thickness ratio cause local buckling and strength deterioration, their collapse mode is very gentle, as fig.6 (b) indicates, and they are also superior in energy absorption.But it is related to yield ratio or detail either the fracture causes sudden deterioration or local buckling decides the maximum strength. We may leave the details to other opportunity.

3.2 The Influence of the Joint Detail Upon the Deformation Mode of Beams

In cyclic loading, the influence of the weld may affect the mode of beams because cyclic specimens are

endplate type. Thus monotonic specimens are continuous beams like in Fig.7 to eliminate the influence of the weld. The experiment is monotonic loading. Each specimen is distinguished from the cyclic specimen that has same section by changing its initial C to M.

Figure 8 are examples of load-displacement curves. ▼ mark in graph designates the maximum load. Chain line and dotted lines are cyclic hysteresis curves of same section. Their behavior and collapse mode in elastic range are similar to cyclic specimens that have same sections. But collapse mode in plastic range is different from the result of cyclic loading, either they collapse by local buckling or by flange fracture.

CY1, CY2, MY1 and MY2 causes strength deterioration results from local buckling after the maximum strength. The maximum load displacement and deteriorating inclination corresponds to cyclic loading. Hence specimens that their maximum strength are defined by local buckling has no difference between the endplate type and the continuous beam type. And cyclic behavior can be predicted by the result of monotonic loading.

On the other hand, CY3, CY4, MY3 and MY4 differ in their behavior whether they cause the sudden strength deterioration by flange fracture in about $2\delta_y$ or gentle strength deterioration after they deform considerably. This difference comes from whether their edges are welded or not. It seems that the ductile fracture mode of the material appears in load-displacement curve because the continuous beam type doesn't cause strain concentration.

Finally, MY1 and MY2, those collapse by local buckling wave that is similar to the endplate. MY3 and MY4, those collapse by flange facture, decrease their flange width and thickness.

4. THE ELASTIC BEHAVIOR OF H-SECTION BEAMS WITH HIGH STRENGTH STEEL AND PROPOSAL OF THE LIMIT OF PLATE SLENDERNESS

4.1 The Influence of Cyclic Loading on Stiffness, Strength, and Process of Strain distribution

Figure 9 shows 10 cycles from the beginning of the load-displacement curve of each specimen, cyclic behavior in yield moment at the edge. In graphs, value of shear force Q_F and Q_y correspond to allowance moment M_F or yield moment M_y each other. All specimens keep their load-curves linear. Now the gap in CY3 comes from trouble of jigs. Their inclination of line, stiffness of beams, is about 90% of the theory value. Consider decline of the stiffness, it is a safety consideration to limit the moment that is provided by allowable stress.

Figure 10 shows strain distributions of cyclic specimens. The above and bellow graphs are flange strain distributions along the joint line of web and flange, and the left graph are web strain distribution as the average of the value of strain at 30mm from the edge on both sides.

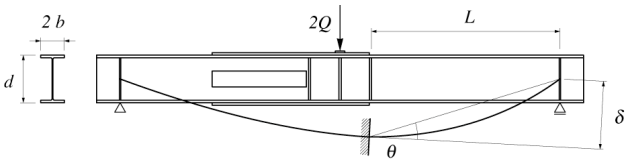

Fig.7: Monotonic Specimen

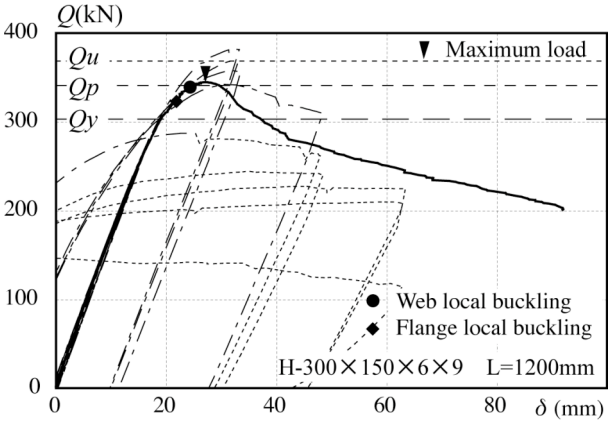

(a) MY2

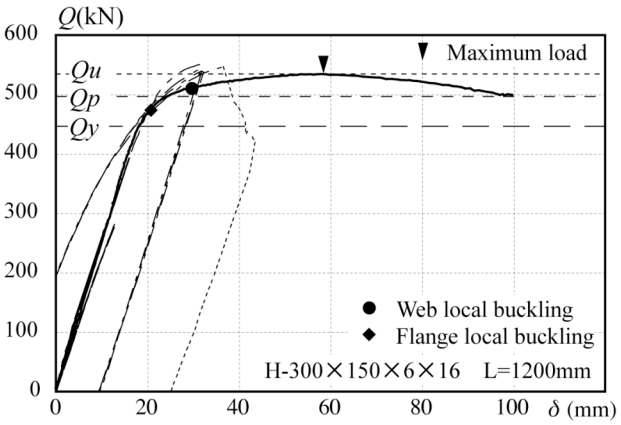

(b) MY3

Fig.8: Load-Deformation Curve

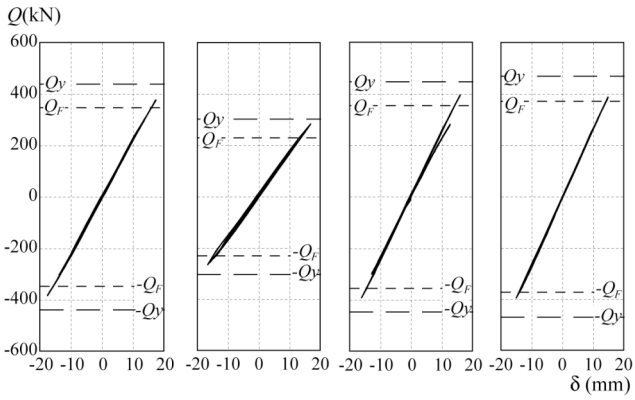

Fig.9: Elastic Behavior

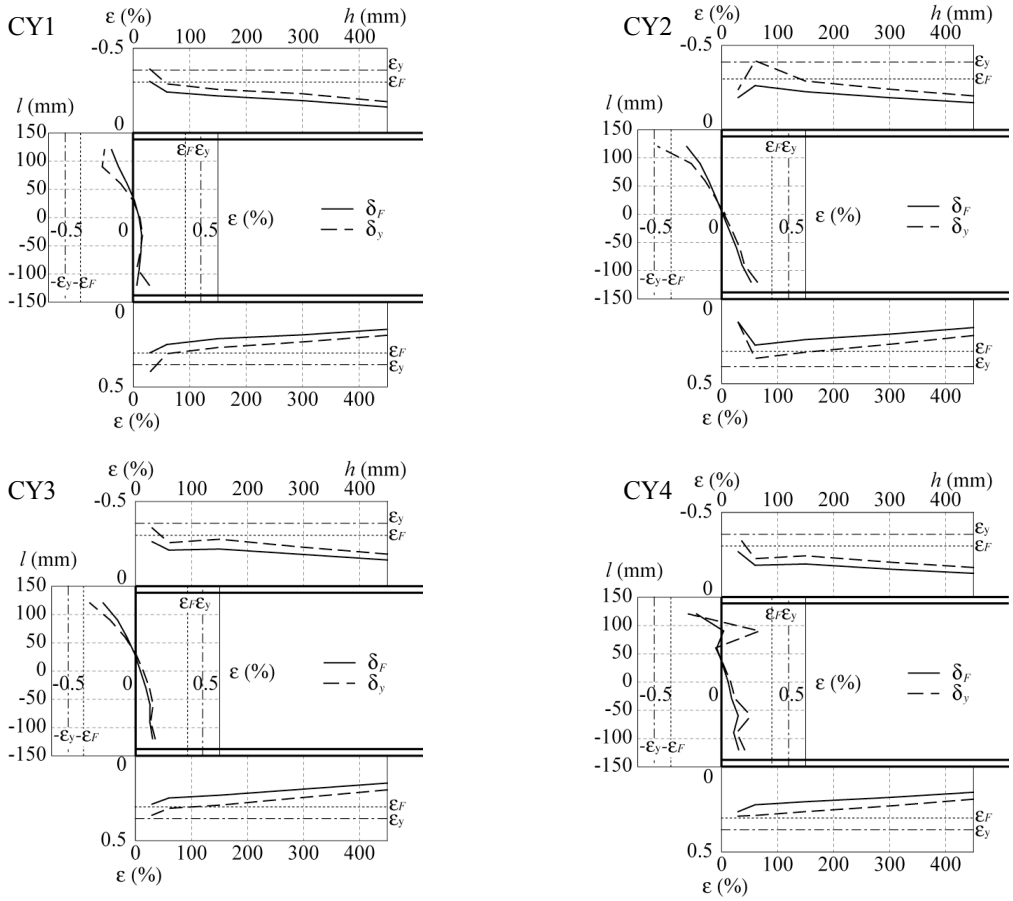

Fig.10: Strain Distributions of Cyclic Specimens

δ_F and δ_y are values in 5th cycle of each displacement, and real line is δ_F , broken line is δ_y . Yield strain ε_F (=σ_y /E) and allowance strain ε_y (=σ_F /E) is also designated. Because of the influence of the endplate, flange strain distributions aren't linear and the more approach the edge, the more their strain increases.

It is possible that the moment at the edge gets over the elastic range locally, although the load level is in elastic range. However, there is not any point that gets over ε_y when the displacement is δ_F . Therefore, local plasticity can be prevented by controlling the load level. Thus, the concept about referenced strength in this study and its value seem to be appropriate.

4.2 The Limit Value of Plate Slenderness in Which the Stress Condition of Beams and Coupled Local Buckling of Plates are Considered

In this study, we chose H-section beams with comparatively large web depth-thickness ratio for specimens. Many of them don't satisfy current standard because we examine the indication that current standards and recommendation are too severe if we consider the stress condition of beams.

Fig.11 is a relationship between the yield strength obtained by the experiment (M_{ye}) and dimensionless depth-thickness ratio. M_{ye} is the strength when the stiffness decrease to 1/6 compare with elastic stiffness. WF, the dimensionless depth-thickness ratio is expressed by following Eq.1~Eq.4 [4]

$$WF = \frac{d/t_w}{BTW} = \frac{b/t_f}{BTF} = \left[\frac{(d/t_w)^3}{BTW0^3} + \frac{4.63(b/t_f)^3}{(E/\sigma_y)^{3/2}} - \frac{(b/t_f)^3}{BTW0^3} \right] \quad (1)$$

$$\left(\frac{BTW}{BTW0}\right)^3 + \left[4.63 - 125\left(\frac{\sqrt{E/\sigma_y}}{BTW0}\right)^3\right]\left(\frac{BTW}{\sqrt{E/\sigma_y}}\right)^3 = 1 \quad (2)$$

$$\frac{BTW0}{\sqrt{E/\sigma_y}} = \begin{cases} 4.9 & \alpha < 1/6 \\ 5.75 - 5.1\alpha & 1/6 < \alpha < 1/2 \\ 3.2 & 1/2 < \alpha \end{cases} \quad (3)$$

$$\alpha = \left(\frac{1}{6} + \frac{A_f}{A_w}\right)\frac{\beta}{\lambda_w} \quad (4)$$

Now BTW : limit value of web plate slenderness, BTF : limit value of flange plate slenderness, A_w : web sectional area, A_f : flange sectional area, b : bending inclination ($0 \leqq b \leqq 2$, 0 : equal bending, 2 : anti-symmetric bending), λ_w : web aspect ratio, E : Young's modulus, σ_y : yield point of each plate.

Beams are grouped into shear buckling type or bending local buckling type, whether α is more than 1/2

or less than 1/6 . This new proposed limit by Eq.2 is the one in which the stress condition of beams and coupled local buckling of plats is considered[4], and it is applicable to beams with practical section. Besides, it follows the fundamental concept of current standard[1], that prevent plates to buckle until it yield, and derived from same concept. Figure 11 indicates that the yield strength of specimens those *WF* is under 1, in other word, those depth-thickness ratio satisfy Eq.2 clear the full plastic strength. Hence, we can say with fair certainty that H-section beams clear yield strength to satisfy the limit value of Eq.2 even if they don't satisfy current limit. Figure 12, it differ the expression to Fig.11, is limit carve that derived from Eq.2 and plot of depth-thickness ratio of each specimen. As we see Fig.12, CY2, CY3, and CY4 satisfy the limit value proposed in this study.

For reasons mentioned above, this study propose Eq.2 in which the stress condition of beams and coupled local buckling of plates is considered as a new limit value of plate slenderness that is based on allowable stress concept. This limit carve is set to pass over the point A for simplicity. Hence, plates of H-section beams in the rectangle area that is determined by A and the origin (inside of the bold line) are safe and don't cause buckling until they yield. Though it is fairly safe, we can simply use $0.6\sqrt{E/F}$ for flange, and $3.0\sqrt{E/F}$ for web as the limit value individually.

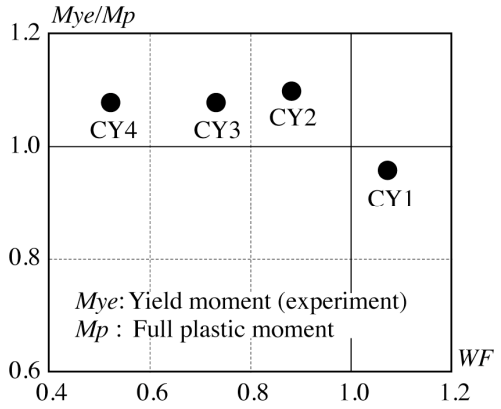

Fig.11: Securing Full Plastic Moment by New Limit Value of Plate Slenderness

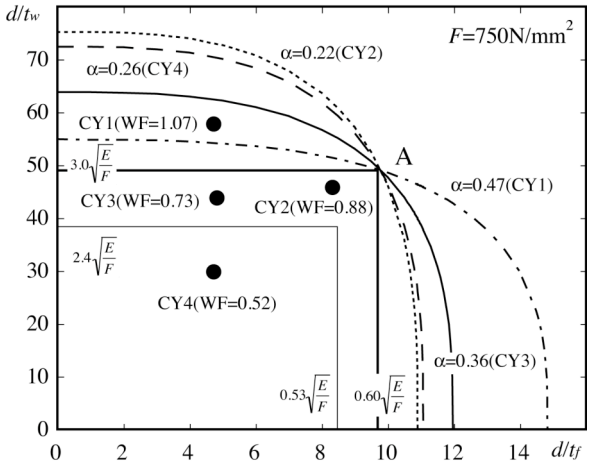

Fig.12: Proposal of Limit Value of Plate Slenderness

7. CONCLUSION

1. Experiments of build-up H-section beams with high strength steel were carried out. It is clear that their performance were not deteriorated in elastic range until yield moment. But the possibility of local plasticity were indicated. So in order to prevent it, the load must be under the strength obtained from allowable stress.
2. Collapse mode of High strength steel H-section beam with thick plate is sometimes fracture of beam end. In order to improve the plastic deformation capacity of beams, it is necessary to avoid a fracture. And it is clear that Beam buckling occurs, the strength degradation is not rapid.
3. In beam with slender web plate, the beam may have sufficient plastic deformation capacity. But the plate slenderness of beams is necessary to satisfy the limit value of plate slenderness proposed in Ref. [4]. Finally, in this study, the single limit value of plate slenderness about web and flange plate each other are proposed as safety consideration.

References:

[1] Architectural Institute of Japan (2005), "Design Standard for Steel Structures -Based on Allowable Stress Concept-"

[2]Architectural Institute of Japan (1990), "Recommendation for Limit State Design of Steel Structures"

[3] Suzuki, T., Ikarashi, K., Azuma, T., and Satsukawa, K. (1998), "A Study on Plastic Deformation Capacity of 590N/mm^2 High Strength Steel Beams with Large Depth-Thickness Ratio", J. Struct. Constr. Eng., AIJ, No.522, 113-119.

[4] Ikarashi, K., and Wang, T. (2008), "Evaluation of Width-Thickness Ratio Limitation of H-Shaped Beam Members Based on Coupled Buckling Analysis", J. Struct. Constr. Eng., AIJ, No.629, 1177-1184.

[5] Suzuki, T., Ogawa, T., Ikarashi, K., Obata, M., Koiwa, K., "Plastic Deformation Capacity of H-Shaped High Strength Steel Beams Depended on Mutual Effect of Plate Local Buckling and Ductile Fracture", J. Struct. Constr. Eng., AIJ, No.481, 127-135.

[6] Architectural Institute of Japan (2009), "Evaluation Procedures for Performance -Based Seismic Design of Buildings – Calculation of Response and Limit Strength, Energy Balance -Based Seismic Resistant Design, Time History Response Analysis-"

JOINT CONFERENCE PROCEEDINGS
7th International Conference on Urban Earthquake Engineering (7CUEE) &
5th International Conference on Earthquake Engineering (5ICEE)
March 3-5, 2010, Tokyo Institute of Technology, Tokyo, Japan

Plastic Deformation Capacity and Post Buckling Behavior of H–Shaped Beam with Large Depth-Thickness Ratio under Cyclic Loading

Tao Wang[1] and Kikuo Ikarashi[2]

1) *Postdoctoral researcher, Center for Urban Earthquake Engineering, Tokyo Institute of Technology, Japan*
2) *Associate Professor, Dept. of Architecture Engineering, Tokyo Institute of Technology, Japan*
wantao2@gmail.com, ikarashi@arch.titech.ac.jp

Abstract: This paper presents an experimental study on H–Shaped Beams subjected to cyclic loading in large range of deformation with large width-thickness ratio of webs which are beyond or near to the limit value those restricted in the current standards. According to the result, it is by no means to declare that the plates with lower Depth-Thickness Ratio have more advantage of the capacity for earthquake resisting because Plastic Deformation Capacity may be significantly affected by the other geometric parameters. The effects of these parameters such as aspect ratio, section area as well as the Plate Slenderness are relevantly identified to evaluate the Plastic Deformation Ratio, and the new division for Plastic Deformation Ratio of H–Shaped beam is proposed.

1. INTRODUCTION

Plate Slenderness (Width-Thickness Ratio or Depth –Thickness Ratio) was generally assumed to be the major parameter to estimate the Plastic Deformation Capacity of thin plates formed steel structure. Up to now, many experimental and analytical researches have been reported aimed to reveal the relationship between Plastic Deformation Capacity and Plate Slenderness. These results have now been incorporated in all sorts of standard and recommendations of steel structures. In regard to the Stability Design of Steel Structure in many countries, Plate Slenderness is strictly restrained in order to retain the stability of steel structures in elastic region[1] especially for Depth –Thickness Ratio. In Japan, the division of Plate Slenderness about H–Shaped beam is provided in compliance with Plastic Deformation Capacity as a general provision which is only applicable in a limited region where the Depth-Thickness ratio is relatively small[2].

It is well known that coupled local buckling may dominate the beam behavior when the Depth-Thickness ratio of web is relatively large. Moreover, resent studies subjected to H–Shaped Beam with large Depth-Thickness Ratio of web had shown the practical use of such thin plate as the earthquake-resisting element even if it is beyond the restricted value in some cases[3].

However, no standardized method is currently available for estimating the Plastic Deformation Capacity of such beams. In such a context, a theoretic study was undertaken to develop an easy evaluation for the coupled local buckling strength of H–Shaped beam in elastic range[4]. Based on the knowledge of this study, an adequate method was proposed to restrict the Slenderness of H–Shaped beam plates[5].

Based on these two studies[4, 5], this paper is intended to develop an easy method to estimate the Plastic Deformation Capacity of H–Shaped beam when the Depth-Thickness ratio is beyond or near to the current restricted value. Moreover, this paper also aims at revealing the post buckling behavior under the cyclic loading situation by contrast with the monotonous loading situation.

2. CYCLIC LOADING TEST

This test aims to investigate the local buckling behavior of H–Shaped beam. Therefore, the lateral direction (z) was restrained in the test arrangement. Figure 1 shows the static testing device for the H–Shaped beam. It can be modeled as shown in Figure 2. Figure 4 shows the cyclic testing program. M_y And M_p denote the bending moment at the end plate on the yielded condition which can be expressed as bellow:

$$M_y = Q_y \cdot l = \frac{1}{6}\sigma_{wy} \cdot t_w (d - t_f)^2 + 2\sigma_{fy} \cdot bdt_f \qquad (1)$$

$$M_p = Q_p \cdot l = \frac{1}{4}\sigma_{wy} \cdot t_w (d - t_f)^2 + 2\sigma_{fy} \cdot bdt_f \qquad (2)$$

The deformations δ_y, δ_p corresponding to M_y, M_p are given by Eq. (3) and (4):

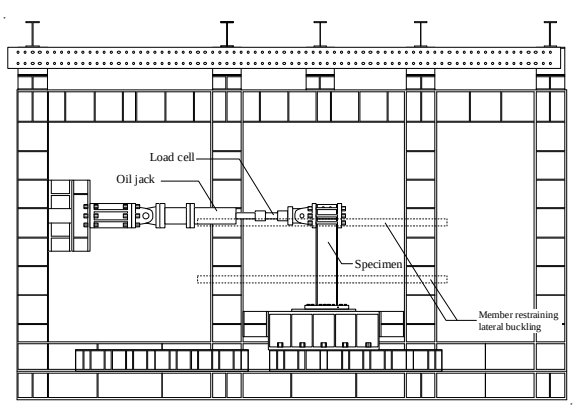

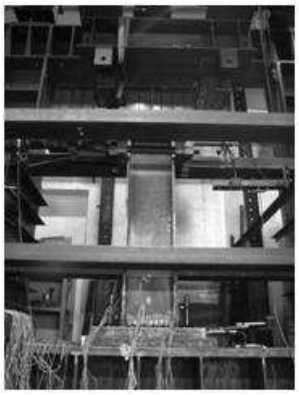

Figure 1 Testing Device, Setting Photo

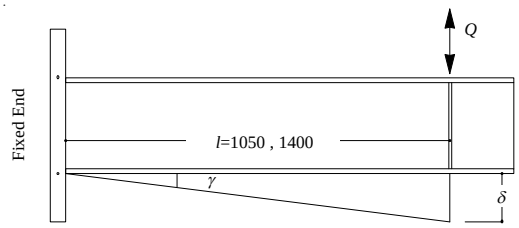

Figure 2 Loading Model

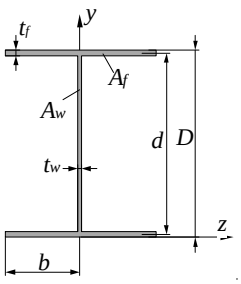

Figure 3 Beam Section

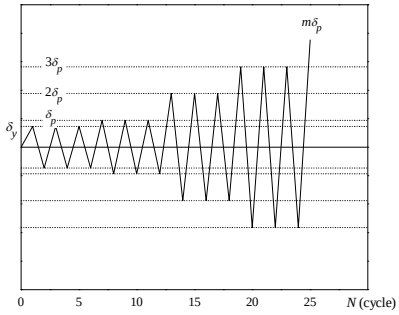

Figure 4 Loading Program

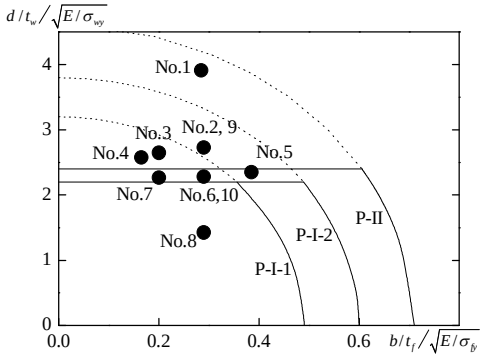

Figure 5 Plate slenderness division

$$\delta_y = \frac{M_y l^2}{3EI} + \frac{M_y}{GA_w} \quad (3)$$

$$\delta_p = \frac{M_p l^2}{3EI} + \frac{M_p}{GA_w} \quad (4)$$

Figure 3 shows the beam section and its geometric marks. These geometric parameters and marks used in this study are defined in Table 1. The dimension of each specimen given a number is shown in Table 2.

In the test, the following 7 types of plates with different Width (Depth)-Thickness Ratio are adopted. They are the same sort of material but a little different from each other in the tension test due to their different thickness. The mechanical property of each plate is show in Table 3.

According to the Standard for Limit State Design of

Table 1 Parameter Definition

marks	meaning
l	length of beam
$\lambda_w = l/d$	aspect ratio of web
$\lambda_f = l/b_f$	aspect ratio of flange
$A_w = b_w t_w$	section area of web
$A_f = 2b_f t_f$	section area of flange
d/t_w	depth-thickness ratio of web
b/t_f	width-thickness ratio of flange
β	bending incline(β=1 tested)
σ_{wy}, σ_{fy}	yield stress of web, flange

Table 2 Specimen List

specimen	section(nominal value)	(surveyed value)		l
	H-D-2b-t_w-t_f	d/t_w	b/t_f	
No.1	H-350-175-3.2-12	105	7.4	1400
No.2	H-350-175-4.5-12	76	7.5	
No.3	H-350-175-4.5-16	73	5.6	
No.4	H-350-175-4.5-19	71	4.7	
No.5	H-350-175-6-9	59	10.2	
No.6	H-350-175-6-12	57	7.5	
No.7	H-350-175-6-16	56	5.6	
No.8	H-350-175-912	38	7.5	
No.9	H-350-175-4.5-12	76	7.5	1050
No.10	H-350-175-6-12	58	7.5	

Table 3 Material Property

test-piece	t (mm) thickness	σ_y (N/mm^2) yield stress	σ_u (N/mm^2) tensile strength	E (kN/mm^2) Yong's modulus	ε_u (%) Max strain	*Elng.* (%) fracture strain	*Y.R.* (%) yield ratio
SS400	3.2	281	424	206	19.8	29.4	66.3
	4.5	267	417	205	20.9	27.8	64.0
	6.0	332	433	205	17.7	29.4	76.7
	9.0	291	439	206	15.0	30.4	66.3
	12	306	479	205	13.0	32.6	63.9
	16	266	412	209	12.3	31.8	64.6
	19	257	410	206	11.8	33.1	62.7

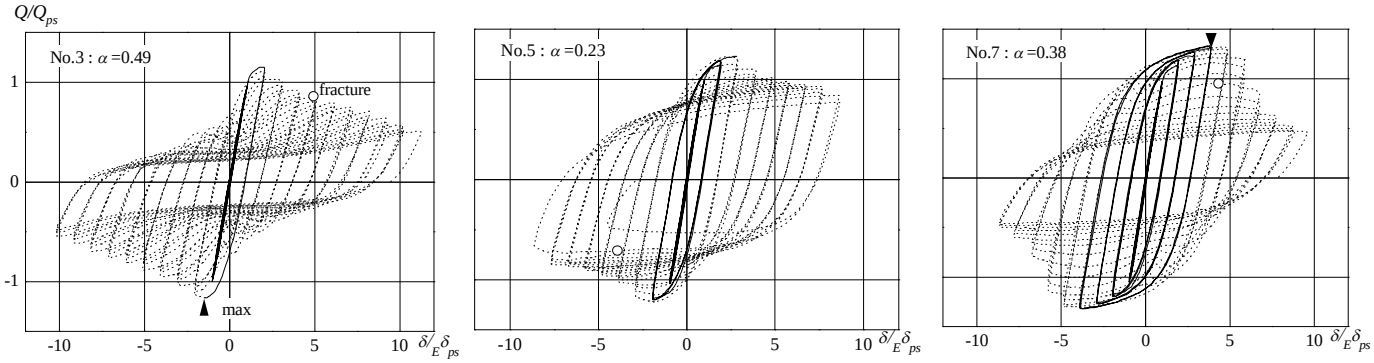

(a) No.3 (b) No.5 (c) No.7

Figure 6 Load-Deformation Curve

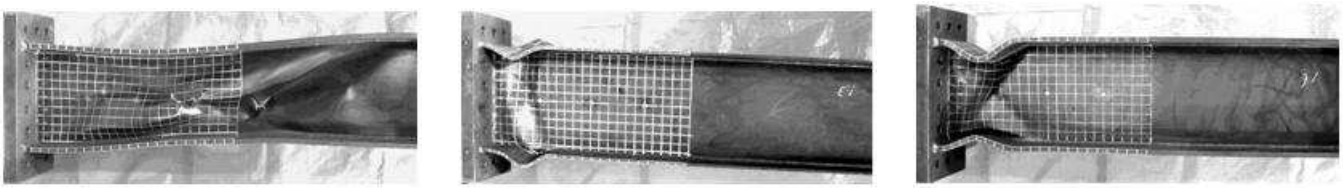

(a) No.3 Web Buckling Type (W.type) (b) No.5 Couple Buckling Type (C.type) (c) No.7 Vertical Buckling Type (V.type)

Figure 7 Buckling Mode

Steel Structures of Japan[2], the division curves with three ranks for Width (Depth)-Thickness Ratio are shown in Figure 5. The relationship between Width-Thickness Ratio of flange and Depth-Thickness Ratio of web about each specimen is also shown by plots in the same Figure.

3. EXPERIMENTAL RESULTS AND DISCUSSION

3.1 Hysteresis Curve and Post Buckling Behavior

Figure 6 shows the historic curve obtained by this test. The horizontal and vertical axes show the dimensionless numbers for the deformation and load. In the elastic region, the relationship between them is defined as Eq. (5) bellow:

$$Q / Q_{ps} = \delta / {}_E\delta_{ps} \tag{5}$$

According to Ref.6), Q_{ps} can be expressed by Eq. (6) bellow:

$$\frac{Q_{ps}}{{}_wQ_p} = \begin{cases} 1 - \left[\dfrac{\sqrt{\dfrac{{}_wM_p^2}{M_p^2} - 4sb\left(1 - sb - \dfrac{{}_wM_p}{M_p}\right)} - \dfrac{{}_wM_p}{M_p}}{2sb} \right]^2 & sb > 1 - \dfrac{{}_wM_p}{M_p} \\ 1 & otherwise \end{cases} \tag{6}$$

Where, Q_{ps} denotes the yield shear load on the condition of taking account of bending effect. ${}_wQ_p$ is the yield load on pure shear condition, ${}_wM_p$ denotes the full plastic moment born on web, sb denotes the ratio of shear to bending on the yield condition. They are given as Eq. (7) –(9):

$$ {}_wQ_p = A_w\sigma_{wy} / \sqrt{3} \tag{7}$$

$$ {}_wM_p = \frac{1}{4}t_w d^2\sigma_{wy} \tag{8}$$

$$ sb = \frac{\lambda_w / \beta}{(0.25 + A_f / A_w)\sqrt{3}} \tag{9}$$

In the Figure 6, each historic curve shows a stable behavior until the local buckling happens. For each specimen, the load drops down soon after the buckling. Then a fracture is caused server cycles later, and the beam collapse in the end. The photos of collapsed beams are shown bellow Figure 6 in Figure 7. As shown in Figure 7, the buckling modes can be divided into three typical types: (a) shows web buckling type (W.type); (b) shows coupled buckling type (C.type); (c) shows vertical buckling type (V.type). The mode of flange buckling type is not discussed due to large Depth-Thickness Ratio of web used in this test.

Compared with the other two types, the degradation incline of V.type shown in Figure 6(c) is extremely sharp. Vertical buckling may be induced by web local buckling when flanges are not strong enough to support the buckled web. As a consequence, the bending rigidity of beam quickly falls down once the buckled web makes a dent in flange. The vertical buckling does not happen even though web bucking dominates in case of Figure 6(a) because the bending burden on flange is relatively small or α (Eq.(10)) is large, hence they can resist the vertical buckling. On the other hand, the vertical buckling does not happen in case of Figure 6(b) because the Depth-Thickness Ratio of web is relatively small or $(d/t_w)/(b/t_f)$ is small. As a discussion result, the degradation incline of non-V.type is about 7% of the elastic incline; the necessary conditions for non-V.type are about α>0.5 or $(d/t_w)/(b/t_f)$<6 by estimation.

Where, α is the ratio of shear stress to bending stress express by Eq. (10)

$$\alpha = \left(\frac{1}{6} + \frac{A_f}{A_w}\right)\beta / \lambda_w \tag{10}$$

3.2 Bone Curve and Restriction for Plate Slenderness

According to Ref.7), the bone curve is defined as Figure 8 on the right side transformed from cyclic curve on the left side by joining the renewal points before reaching the maximum load. After the maximum load, the bone curve is treated as wrapping line.

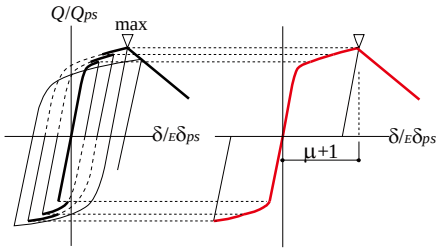

Figure 8 Definition of Bone Curve

Based on the rule defined in Figure 8, the bone curve of each specimen is obtained in Figure 9. The maximum load of No.2 and No.3 shown in Figure 9 are over the Plastic shear load Q_{ps} even though their Depth-Thickness Ratios are beyond the restricted value. This result indicates that the restriction for Depth-Thickness Ratio can possibly be alleviated in some degree.

According to Ref.5), a new method for restriction of Width (Depth)-Thickness Ratio had been proposed. The restriction curve is given as Eq. (11) bellow:

$$\left(\frac{BTW}{BTW0}\right)^3 + \left[4.63 - 125\left(\frac{\sqrt{E/\sigma_{wy}}}{BTW0}\right)^3\right]\left(\frac{BTF}{\sqrt{E/\sigma_{fy}}}\right)^3 = 1 \tag{11}$$

Where, α is given as Eq. (10), $BTW0$ is given as Eq. (12) bellow:

$$\frac{BTW0}{\sqrt{E/\sigma_{wy}}} = \begin{cases} 4.9 & \alpha < 1/6 \\ 5.75 - 5.1\alpha & 1/6 \le \alpha \le 1/2 \\ 3.2 & \alpha > 1/2 \end{cases} \tag{12}$$

BTW and *BTF* are the restriction value of Depth and Width –Thickness Ratio. They are proposed by taking account of the effect of Plate Slenderness and the other geometric parameters comprising plate section area and aspect ratio based on the calculation of buckling strength.

As a sample shown in Figure 10 where the rectangular plots are the value on restriction curves obtained by Eq. (11), circle plots are the real Width (Depth)-Thickness Ratio of each beam, the ratio of the value at circle plots to rectangular plots on each situation can be express as Eq. (13) bellow.

$$WF = \frac{d/t_w}{BTW} = \frac{b/t_f}{BTF} \tag{13}$$

Here, *WF* denotes the normalized Plate Slenderness.

Substituting Eq. (11) into Eq. (13), *WF* is given as Eq. (14) bellow:

$$WF = \left[\frac{(d/t_w)^3}{BTW0^3} + \frac{4.63(b/t_f)^3}{(E/\sigma_y)^{3/2}} - \frac{125(b/t_f)^3}{BTW0^3}\right]^{1/3} \tag{14}$$

Figure 11 shows the relationship between *WF* and ${}_EQ_{ps}$(defined in Figure 11) based on this test and FEM subjected to the same scale specimens under monotonous loading. In the figure, it is shown that ${}_EQ_{ps} > Q_{ps}$ when $WF<1$. Therefore, *WF* can be regarded as a parameter to restrict the beam dimension to prevent elastic local buckling.

4. Plastic Deformation Capacity

In Figure 8, μ denotes the Plastic Deformation Ratio at the point of maximum load, it is a parameter defined to express the Plastic Deformation Capacity in this study. As shown in Figure 5, the division curve of P-I-1 is to ensure $\mu>4$, the curve of P-I-2 is to ensure $\mu>2$, the curve of P-II is to ensure $\mu>0$.

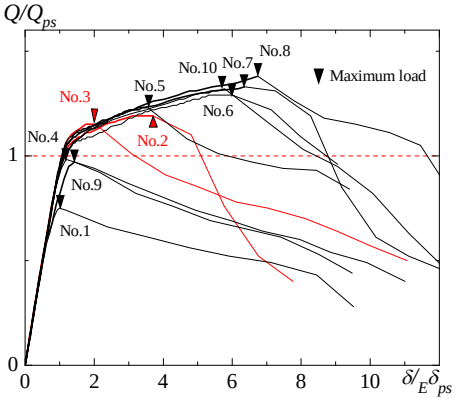

Figure 9 Bone Curves

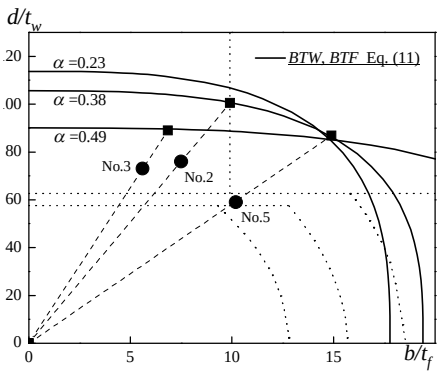

Figure 10 restriction curves (Eq. (11))

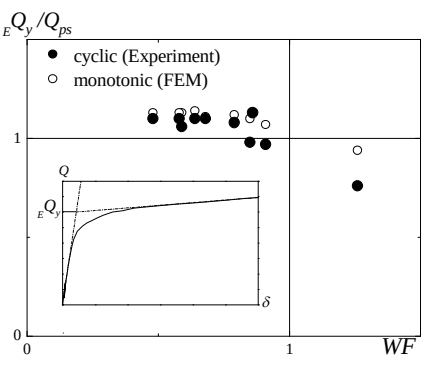

Figure 11 restriction based on *WF*

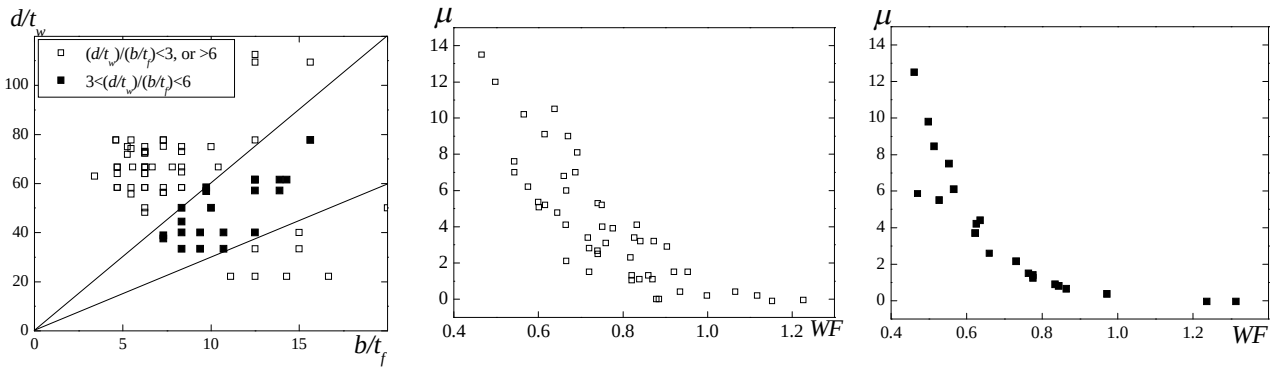

(a) Object of Depth and Width-Thickness Ratio (b) $(d/t_w)/(b/t_f)$ <3, or >6 (c) 3<$(d/t_w)/(b/t_f)$ <6

Figure 12 Plastic Deformation Capacity and *WF*

Figure 12(b) and (c) show the relationship between *WF* and μ obtained by this experiment and a number of FEM analysis subjected to monotonous loading where the same model as Figure 2 was adopted. As to the FEM analysis and experiment, the Width-Thickness and Depth-Thickness Ratio about each beam is shown in Figure 12(a). The aspect ratio of web of each beam is set at $2<\lambda_w=l/d<12$. According to the buckling modes, the results are divided into two parts in Figure 12(a). Figure 12(b) shows the plots in case of $(d/t_w)/(b/t_f)$ <3, or $(d/t_w)/(b/t_f)$>6 where a large part of their buckling modes are single buckling modes or non-coupled buckling modes. Figure 12(c) shows the plots in case of $3<(d/t_w)/(b/t_f)<6$ which are assumed to be the coupled buckling modes. According to the plots showing the relationship between *WF* and μ in both Figure 12(b) and (c), μ tends to become larger as *WF* becomes smaller. Therefore, *WF* can be reasonably regarded as a major parameter to estimate the Plastic Deformation Ratio.

As mentioned in chapter 2, the load falls down soon after the buckling without reference to the buckling modes in case of cyclic loading situation. But the load does not fall down soon after the single buckling in case of monotonous loading situation. Consequently, there is some dispersion in the Figure 12(b). But the dispersion in Figure 12(c) is small due to coupled buckling modes.

Figure 13 shows relationship between Bone Curve and Monotonous Curve as a sample. These curves are well in agreement with each other in case of No.5 specimen which belong to C.type, but they are not in agreement with each other in case of non-C.type as shown in Figure 13(a) where Plastic Deformation Ratio μ at Monotonous Curve is always larger than Bone Curve.

To minimize the dispersion and evaluate the Plastic Deformation Capacity safely, *WF* expressed in Eq. (14) is modified as Eq. (15) bellow:

$$WF=\sqrt{\frac{(d/t_w)^2}{BTW0^2}+\left(\frac{5\sigma_{fy}}{E}-\frac{36}{BTW0^2}\cdot\frac{\sigma_{fy}}{\sigma_{wy}}\right)(b/t_f)^2} \qquad (15)$$

Where, α is given as Eq. (10), *BTW*0 is given as Eq.

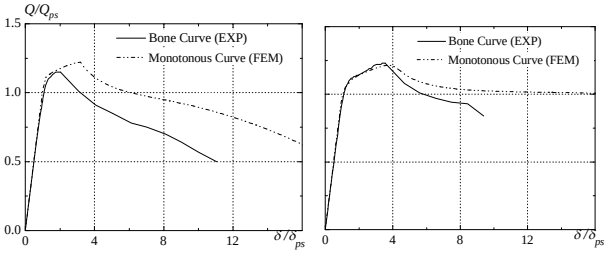

(a) No.3 (W.type) (b) No.5 (C.type)

Figure 13 Bone Curve and Monotonous Curve

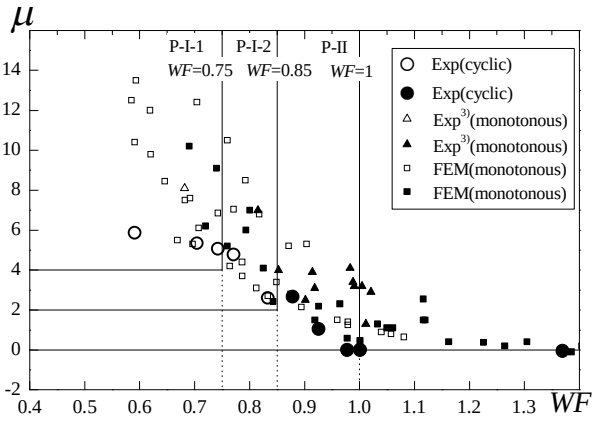

Figure 14 Division for Plastic Deformation Capacity

(16) bellow:

$$\frac{BTW0}{\sqrt{E/\sigma_{wy}}}=\begin{cases}4.4 & \alpha<1/6\\ 5.18-4.6\alpha & 1/6\le\alpha\le1/2\\ 2.9 & \alpha>1/2\end{cases} \qquad (16)$$

Figure 14 shows the relationship between μ and *WF* related to Eq. (15). Each black plot denotes the case when Plate Slenderness is over the restricted value[1]. According to these black plots, the restriction can be alleviated in many case of WF<1. The circle plots denoting the results under cyclic loading in this test are smaller than the other cases. They are distributed in the lower limit. This phenomenon reflects the knowledge mentioned above. To estimate the Plastic Deformation Capacity reasonably, the lower limit of μ must be adopted due to the disadvantageous loading

situation. According to the result shown in Figure 14, the division for Plastic Deformation Capacity is proposed as bellow:

P-I-1(μ>4): WF<0.75,

P-I-2(μ>2): WF<0.85,

P-II(μ>0): WF<1

5. CONCLUSIONS

This study shows the possibility that Depth-Thickness Ratio of H–Shaped beam can be alleviated in some cases through cyclic loading test.

Hysteretic curves and load degradation of post bucking behavior was examined. The vertical buckling induced by web local buckling was found to be the major effect of degradation. The approximation of the necessary conditions for non-V.type was given.

Compared with experiment and a number of numerical analysis under monotonous loading situation, the Plastic Deformation Ratio of the beams under cyclic loading is relatively small especially in case of beam with non-C.type buckling mode. The restriction curve based on calculation of local buckling strength in Ref.5) was relevantly examined. The division for Plastic Deformation Capacity was proposed by using normalized Plate Slenderness WF as a new parameter modified from restriction curve.

Acknowledgements:

The authors acknowledge support from the Japan Ministry of Education, Culture, Sport, Science, and Technology (MEXT) for establishing the Center for Urban Earthquake Engineering (CUEE) in Tokyo Institute of Technology. This support makes possible the forthcoming international conference, as well as international joint research projects and exchange programs with overseas universities.

References:

1) Architectural institute of Japan, "Design Standard for Steel Structure," 2005

2) Architectural institute of Japan "Standard for Limit State Design of Steel Structure," 2002

3) Suzuki, T. Ikarashi, K. and Tsuneki, Y, "A Study on Collapse Mode and Plastic Deformation Capacity of H-Shaped Steel Beams under Shear Bending" *Journal of Structural and Construction Engineering, Arch, inst. of Japan,* No.547, 185-191, 2001 .9

4) Ikarashi, K. and Wang, T, "A Method for Evaluation of Elastic Buckling Strength of H-Shaped Steel Member under Bending-Shear and Axial Force," *Journal of Structural and Construction Engineering, Arch, inst. of Japan,* No.613, 137-146, 2007.3

5) Ikarashi, K. and Wang, T, "Evaluation of Width-Thickness Ratio Limitation of H-Shaped Beam Members Based on Coupled Buckling Analysis," *Journal of Structural and Construction Engineering, Arch, inst. of Japan,* No.629, 1177-1184, 2008.7

6) Japan Society of Civil Engineers, "Guidelines for Stability Design Steel Structures," 2005

7) Architectural institute of Japan, "Evaluation Procedures for Performance –Based Seismic Design of Buildings –Calculation of Response and Limit Strength, Energy Balance –Based Seismic Resistant Design, Time History Response Analysis– ," 2009.2

Appendix:

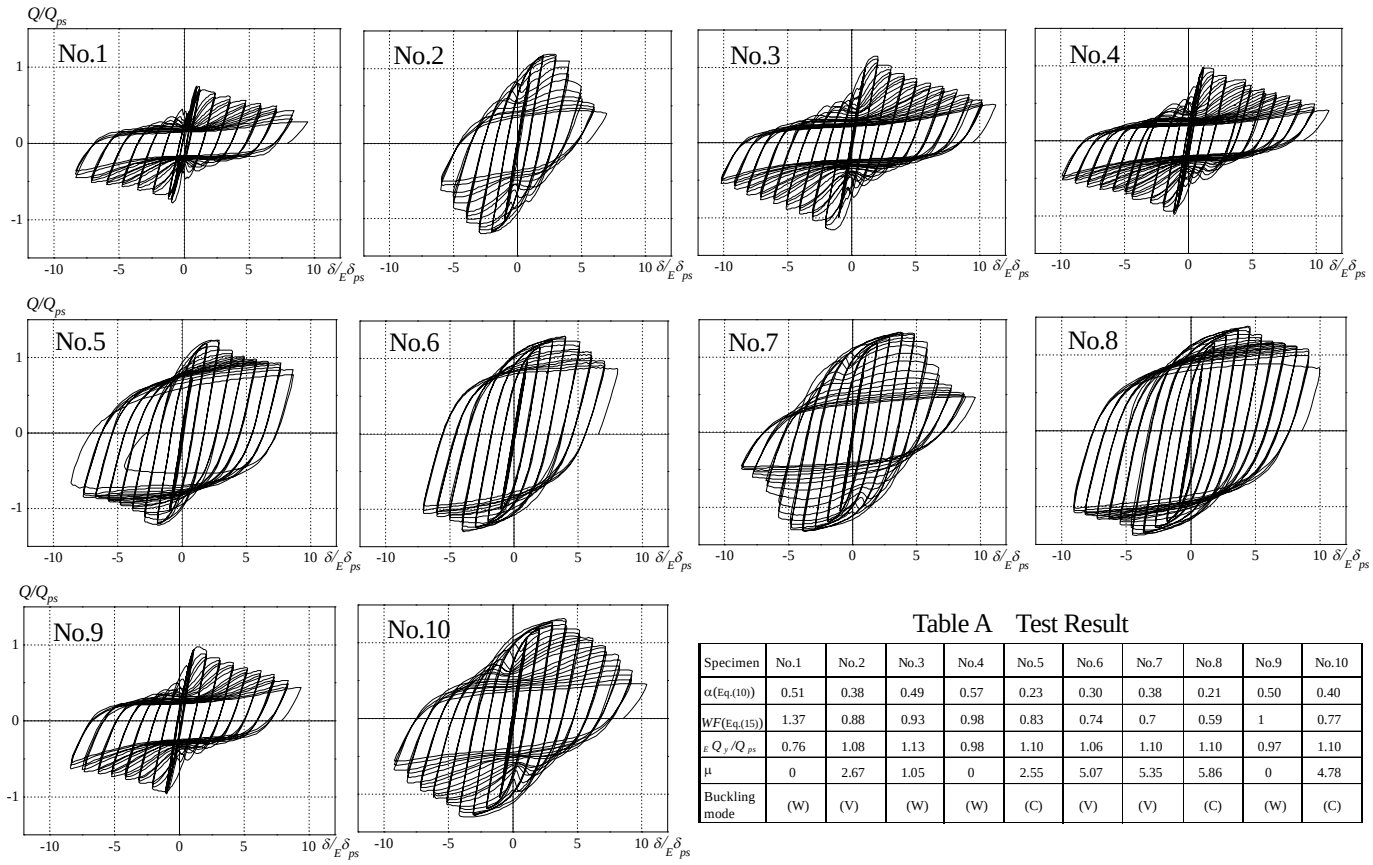

Figure A Loading –Deformation Curve (all specimen)

Table A Test Result

Specimen	No.1	No.2	No.3	No.4	No.5	No.6	No.7	No.8	No.9	No.10
α(Eq.(10))	0.51	0.38	0.49	0.57	0.23	0.30	0.38	0.21	0.50	0.40
WF(Eq.(15))	1.37	0.88	0.93	0.98	0.83	0.74	0.7	0.59	1	0.77
$_E Q_y / Q_{ps}$	0.76	1.08	1.13	0.98	1.10	1.06	1.10	1.10	0.97	1.10
μ	0	2.67	1.05	0	2.55	5.07	5.35	5.86	0	4.78
Buckling mode	(W)	(V)	(W)	(W)	(C)	(V)	(V)	(C)	(W)	(C)

JOINT CONFERENCE PROCEEDINGS
7th International Conference on Urban Earthquake Engineering (7CUEE) &
5th International Conference on Earthquake Engineering (5ICEE)
March 3-5, 2010, Tokyo Institute of Technology, Tokyo, Japan

CRACK FRACTURE OF H-SECTION CANTILEVER BEAM UNDER STRONG CYCLIC LOAD

Katsuhiko Goto[1)], Motoo Saisho[2)]

1) Assistant Professor, Department of Architecture, Miyakonojo National College of Technology, Japan
2) Professor, Department of Architecture and Civil Engineering, Kumamoto University, Japan
goto@cc.miyakonojo-nct.ac.jp

Abstract: Crack fracture of H-section cantilever beam under strong cyclic load was tested. It is shown that there are two types of crack fractures even if the fracture in the weld zone at the fixed-end of beam is prevented. The analysis method to calculate it as the very low-cycle fatigue behavior is proposed since these crack fractures occur in very low cycle loading. Comparing the analyzed values with the test results it is ascertained that the proposed analysis method can predict the type of fracture precisely enough and it is useful to calculate the very low-cycle fatigue of H-section beam.

1. INTRODUCTION

When strong alternating repeated load is applied to the H-section cantilever beam, flange buckles locally and fractures after that even if the crack fracture at the welded-joint is avoided. According to the dynamic loading tests of H-section cantilever beam, there are two types of crack fracture as shown in Fig.1-Fig.2. They are the fracture at the locally buckled flange of beam (B-type) and the fracture at the end of beam flange that is butt-welded and affected by the weld heat (W-type). In any case the fracture occurs at the flange of beam near the fixed-end in brittleness and it becomes extremely disadvantageous behavior to secure earthquake resistance performance for multi-story frame which is composed of H-section beams.

In this study two types of crack fractures are regarded as very low-cycle fatigue fracture behavior. On the basis of this consideration the fatigue fracture equation is proposed. The validity of the proposed equation is investigated by comparing with test results.

2. VERY LOW-CYCLE FATIGUE TEST OF H-SECTION BEAM

2.1 Specimens and Test Conditions

Very low-cycle fatigue tests of H-section cantilever beam under strong cyclic load have been carried out (Saisho et al. 2008). In these tests the cyclic loading of every specimen is continued until specimen is fractured completely. As the test results, the flange of H-section beam have cracked and fractured at the ultimate state as shown in Fig.1-Fig.2.

Test conditions are explained in Fig.3. To test the crack fracture of H-section cantilever beam under strong cyclic load, the dynamic and cyclic vertical load (F) is given by the actuator. There are two kinds of time-histories of the vertical displacement (δ) at the loading point. They are the sinusoidal wave with constant amplitude after gradually increasing amplitude (C-wave) and the random wave (R-wave) as shown in Fig.4. The maximum vertical velocity at the loading point is dδ/dt=100mm/second and the measured data are acquired in every 0.02 second or acquired in every 0.05 second in case of small displacement amplitude.

Specimens are rolled H-section beams (SS400). Their sections and lengths of cantilever beam are explained in

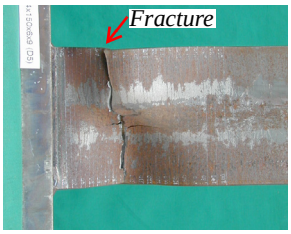

R194x150-2

Figure 1 Crack fracture at locally buckled flange of beam (B-Type)

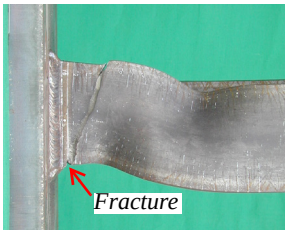

R148x100-1

Figure 2 Crack fracture at the end of beam (W-Type)

Table 1. The material properties of H-section beam flange using the tensile specimen (JIS-5 type) are shown in Table 2. In Table 2, the fracture elongation (ε_f), which is closely related to the very low-cycle fatigue equation, is defined when the stress deteriorates to $0.9\sigma_u$ (σ_u: tensile strength) after the stress reaches σ_u on the tension test since the remarkable stress deterioration occurs after that.

The fixed-end of specimen, which is supposed to be welded to the column flange, is butt-welded to the end-plate that thickness is 28mm. The end-plate is fixed on the frame that stiffness is enough. Welding conditions of the fixed-end of specimen are the non-scallop method and the overmatching welding to prevent the fracture of welded metal and to fracture the flange of specimen. Moreover, the fixed-end of specimen is welded by low heat input and low interpass temperature enough (less than 40kJ/cm and 350 degrees Centigrade). As the test results, the crack of all specimens has not occurred at the welded metal.

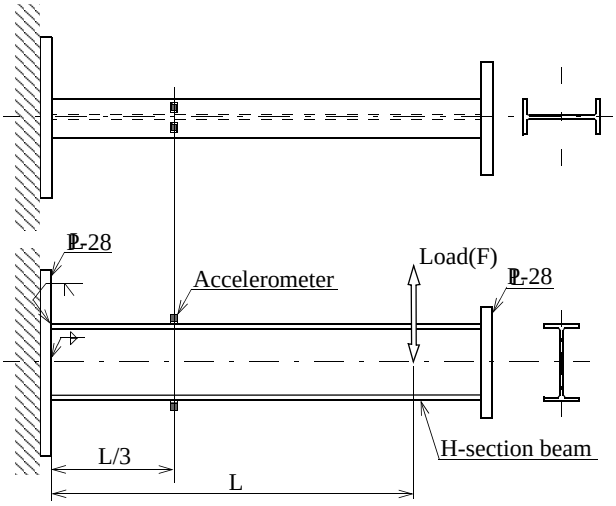

Figure 3 Loading condition of H-section cantilever beam

2.2 Measurement of Crack Fracture

To observe the crack fracture point involves strong shock, the accelerometers which measure the axial acceleration of specimen are attached on the flange of specimen as shown in Fig.3. The measured axial acceleration of flange is shown in Fig.5 as an example. There is remarkable acceleration change around 125

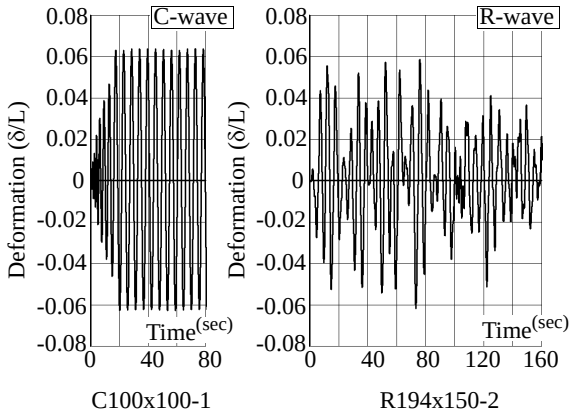

Figure 4 Time-history of vertical deformation

Table 1 Specimens and test conditions

Specimen	Section	L	Load	δ_{max}/L	FT	$(2N_f)_{Test}$	$(2N_f)_{Cal}$
C100x100-1	H-100x100x6x8	672	C	0.064	W	73	48
C100x100-2	"	"	"	0.099	B	52	25(W), 27(B)
C100x100-3	"	"	"	0.128	B	31	20(W), 21(B)
R100x100-1	"	"	R	0.113	B	205	34(W), 47(B)
R100x100-2	"	"	"	0.125	B	50	21(W), 23(B)
C150x75-1	H-150x75x5x7	772	C	0.098	B	30	16
C150x75-2	"	"	"	0.047	W	48	36
R150x75-1	"	"	R	0.086	B	53	17
R150x75-2	"	"	"	0.087	B	18	18
R150x75-3	"	"	"	0.090	B	30	16
C148x100	H-148x100x6x9	772	C	0.097	W	19	17(B), 18(W)
R148x100-1	"	"	R	0.097	W	38	19(B), 20(W)
R148x100-2	"	"	"	0.084	W	28	23(B), 25(W)
C200x100-1	H200x100x5.5x8	972	C	0.064	B	27	27
C200x100-2	"	"	"	0.077	B	21	20
C200x100-3	"	"	"	0.089	B	19	18
R200x100-1	"	"	R	0.069	B	62	65
R200x100-2	"	"	"	0.073	B	79	67
R200x100-3	"	"	"	0.068	B	58	65
C194x150-1	H194x150x6x9	972	C	0.065	B	43	75
C194x150-2	"	"	"	0.078	B	25	59
R194x150-1	"	"	R	0.045	W	350	1040(B), 1084(W)
R194x150-2	"	"	"	0.066	B	160	307
R194x150-3	"	"	"	0.072	B	186	208

L: cantilever beam length (mm), Load: loading hysteresis (C-wave, R-wave)
δ_{max}/L: maximum deformation angle until fracture, FT: Type of fracture (B-type, W-type)
$(2N_f)_{Test}$, $(2N_f)_{Cal}$: number of half-cycles to fracture

Table 2 Material properties

H-section	σ_y	σ_u	ε_u	ε_f
H-100x100x6x8	367	455	27.7	34.1
H-150x75x5x7	307	436	23.4	27.1
H-148x100x6x9	326	473	24.8	29.8
H-200x100x5.5x8	333	468	24.0	29.5
H-194x150x6x9	326	512	26.4	31.8

σ_y : yield stress (N/mm^2), σ_u : tensile strength (N/mm^2)
ε_u : uniform elongation (%), ε_f : fracture elongation (%)

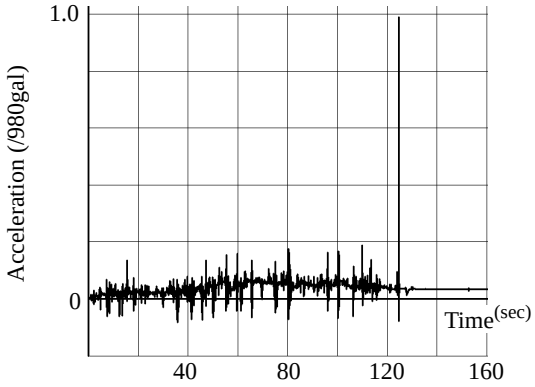

Figure 5 Time-history of axial acceleration (R100x100-2)

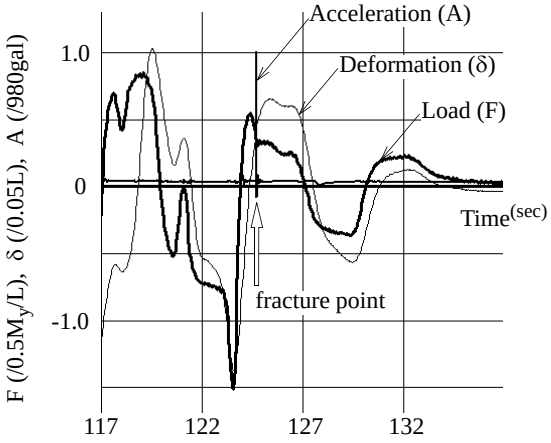

Figure 6 Time-history of axial acceleration, deformation and load (R100x100-2)

seconds. Fig.6 which expands the time axis of Fig.5 shows the time-history of the axial acceleration of flange (A), the dynamic load applied to the free-end of specimen (F) and deformation (δ). The crack fracture behavior and how to decide the crack fracture of specimen are shown in these time-histories. The crack fracture of each specimen is obtained on the basis of the following three conditions.

i) The axial acceleration of flange (A) changes suddenly and remarkably.

ii) The restoring force of H-section beam (F) falls down even if the deformation (δ) increases monotonically.

iii) After that the restoring force (F) becomes to be small and almost constant.

The point indicated by thick allow in Fig.6 is satisfied with the above three conditions and shows the crack fracture point. The number of half-cycles to the crack fracture ($(2N_f)_{Test}$) of each specimen is shown in Table 1.

2.3 Test Results

From test results, there are two types of crack fractures are shown in Fig.1-Fig.2. One is the fracture at the locally buckled flange of beam (B-type) and the other is the fracture at the end of beam flange that is butt-welded and affected by the weld heat (W-type). The distance from the fixed-end to fracture of the former fracture is about 40-70mm, that is corresponding with the inelastic local buckling length (Lay 1965). The fracture type of each specimen is shown in Table 1. 18 specimens were fractured as B-type and 6 specimens were fractured as W-type.

Table 1 also shows the number of half-cycles to the crack fracture of H-section beam ($(2N_f)_{Test}$), that is derived from the above conditions in section 2.2 and the reversal point number of cyclic plastic strains at the fracture point of specimen. Therefore, the cycle that the strain between the reversal points is less than $2\varepsilon_{cr}$ ($\varepsilon_{cr}=(\sigma_u-\sigma_y)/E_p$, σ_y: yield stress, $E_p=E/20$, E: young's modulus) is excluded. In this study, $(2N_f)_{Test}$ represent not the number of cycles until crack is generated but those until all section of flange is fractured.

3. VERY LOW-CYCLE FATIGUE ANALYSIS

3.1 Damage Ratio Equation

From test results, the flange of H-section beam is fractured in very low-cycle loading (N_f=10-50) except for several specimens. Based on this behavior, the fracture of H-section beam is considered as the very low-cycle fatigue, and the fracture condition is derived on the basis of the Coffin-Manson relationship and the Palmgren-Miner rule (Dowling 2007) in this study.

According to the Coffin-Manson relationship, the low cycle fatigue life (N_f) under alternating repeated load is expressed by the plastic strain amplitude (ε_{pa}) as shown in Eq.(1).

$$\varepsilon_{paj} = \varepsilon_f (2N_{fj})^c \tag{1}$$

in which ε_f: fracture elongation, c: material modulus, N_{fj}: number of cycle to fracture under the j-th cycle load.

The very low-cycle fatigue of H-section beam is assumed to be approximated by the Palmgren-Miner rule in this study. From the Palmgren-Miner rule, the damage ratio of H-section beam is given by the accumulation of the each cycle damage. Therefore, the damage ratio (D_{cr}) at each instant under repeated load can be expressed by Eq.(2).

$$D_{cr} = \sum_j \left(\frac{1}{N_{fj}}\right) \tag{2}$$

The damage ratio (D_{cr}) can be expressed by the plastic strain amplitude (ε_{paj}) because the fatigue life (N_{fj}) in Eq.(2) is given by it. The crack fracture condition by calculation is D_{cr}=1.0.

3.2 Plastic Strain Equation of H-Section Beam

In this analysis, the plastic strains of H-section beam under alternating repeated load, which is closely related to

the very low-cycle fatigue of it, are given by the collapse mechanism (Saisho et al. 2008) which is roughly the same with that proposed by Climenhaga and Johnson (1972). This collapse mechanism shows the local buckling deformation of H-section beam as shown in Fig.7 and Fig.8. The plastic compression strain (ε_{c1}) on compression side caused by the local buckling deformation, which is shown at point P and point A in Fig.7, are given by Eq.(3).

$$\varepsilon_{c1} = \frac{t_f}{wL_f}(2L_f \cdot L_o\theta - L_o^2\theta^2)^{1/2} \quad (3)$$

in which t_f: thickness of flange, w: plastic zone of the locally bucked flange, L_f, L_o: parameters to show the collapse mechanism (Saisho et al. 2005), θ: plastic deformation of H-section beam.

The plastic compression strain (ε_{c2}) of the yield surface PQRS on compression side are given by Eq.(4).

$$\varepsilon_{c2} = \frac{L_o}{L_f}\theta \quad (4)$$

The plastic tension strain (ε_t) of flange on tension side are given by Eq.(5).

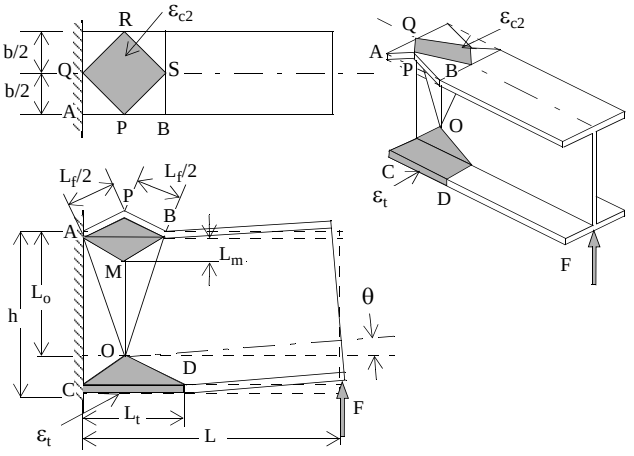

Figure 7 Local buckling collapse mechanism of H-section cantilever beam

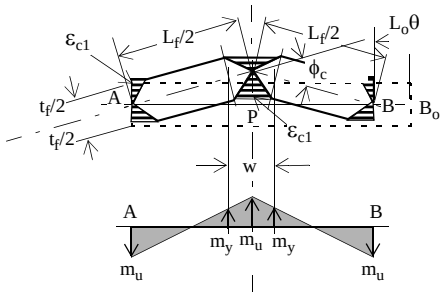

Figure 8 Plastic strain in the locally buckled compression flange (ε_{c1})

$$\varepsilon_t = \frac{1}{L_f}(h - L_o)\theta \quad (5)$$

in which h: depth of beam, L_t: parameter to show the collapse mechanism (Saisho et al. 2005).

The plastic strains (ε_C, ε_T) which are closely related to the low-cycle fatigue are obtained by using Eq.(3)- Eq.(5). The plastic strains of the B-type fracture generated at point P in Fig.7 are (ε_C, ε_T)=(ε_{c1}+ε_{c2}, ε_t) and those of the W-type fracture generated at point A in Fig.7 are (ε_C, ε_T)=(ε_{c1}, ε_t) respectively. By applying the relation between the plastic strain amplitude (ε_T -ε_C)/2 (=ε_{pa}) and the number of cycle to fracture (N_f), Eq.(1) is expressed by Eq.(6).

$$\frac{1}{2}(\varepsilon_T - \varepsilon_c) = \varepsilon_f(2N_f)^c \quad (6)$$

The plastic strains (ε_T, ε_C) of H-section beam can be expressed by the plastic deformation (θ) of H-section beam by using Eq.(3)- Eq.(5). From this reason not only the number of cycle to fracture (N_f) in Eq.(6) but also the damage ratio (D_{cr}) in Eq.(2) can be expressed by the plastic deformation (θ) of H-section beam.

4. MODULUS (c) IN COFFIN-MANSON RELATIONSHIP

On the basis of calculating the crack fracture by the proposed method, the modulus (c) in the Coffin-Manson relationship (Eq.(1), Eq.(6)) is obtained under the condition that the calculated fatigue life coincides with the test results. Fig.9 shows both the moduli of the B-type specimens and those of the W-type specimens. Both moduli are calculated under the condition that the fracture elongation (ε_f) is not changed even if the flange of beam-end is affected by the weld heat. However, it seems that the fracture elongation at the beam-end is deteriorated by the effect of weld heat. Thus, our object is only the B-type specimens except for the W-type specimens. As shown in Fig.9, the calculated moduli (c) of the B-type specimens are nearly constant and the average value of moduli (c) is almost c=-0.30.

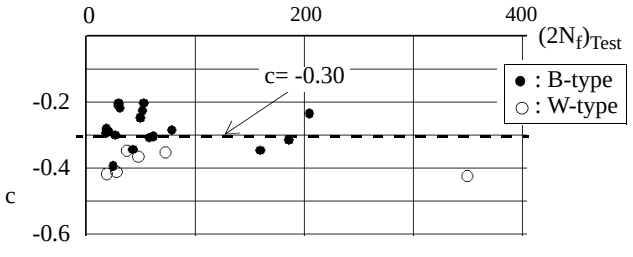

Figure 9 Modulus (c) in Coffin-Manson relationship when calculations are coincides with test results

4. FRACTURE ELONGATION OF WELDED H-SECTION BEAM

4.1 Specimens and Test Conditions

The fracture elongation of the beam-end flange is supposed to be changed from the base material because of the effect of weld heat. For the W-type specimens, the fracture elongation affected by the weld heat must be used in the Coffin-Manson relationship (Eq.(1), Eq.(6)). Therefore, the welded specimens as shown in Fig.10 are cut from the H-section beam specimen and butt-welded to the steel plate and tension tests using the tensile specimens cut from the welded specimens are carried out to obtain the fracture elongation in this study. The welding design and condition of each welded specimen are equal, which are 35 degrees single bevel groove, 5mm root gap and CO_2 gas shielded arc welding with the backing plate as shown in Fig.11. The welding condition is equal to the end of H-section beam specimen and that is overmatching welding. To investigate the effect of weld heat, the gage length of tensile specimen is 20mm from the weld toe and the gage width is 10mm as shown in Fig.11. The surfaces of tensile specimen are cut down thinly.

Tension tests are carried out by using the 250kN universal testing machine. Strain is measured by both the strain gage and the linear variable differential transformer (LVDT). To remove the loading rate effect, the maximum strain rate in the plastic range is less than 3000με/minute.

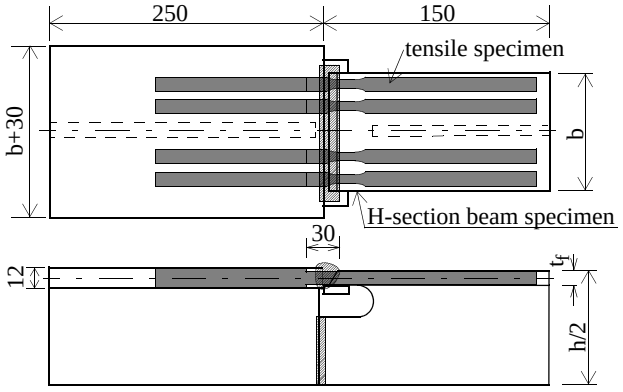

Figure 10 Welded specimen and tensile specimen (unit: mm)
(b: beam width, h: beam depth, t_f: thickness of flange)

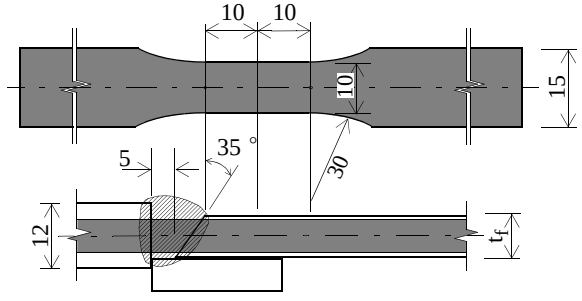

Figure 11 Details of welding and tensile specimen (unit: mm) (t_f: thickness of flange)

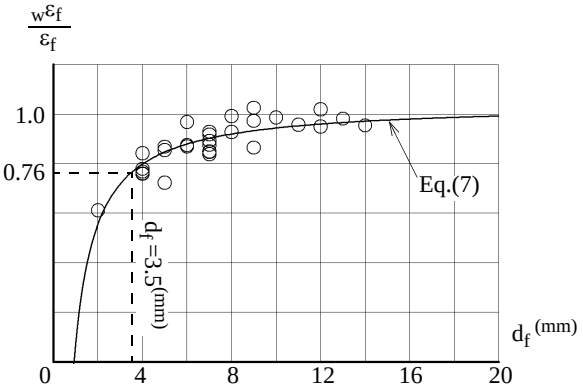

Figure 12 Fracture elongation ratio ($_w\varepsilon_f/\varepsilon_f$) versus distance from weld toe to fracture (d_f)

4.2 Test Result

Fig.12 shows the relation between the ratio of the fracture elongation affected by the weld heat ($_w\varepsilon_f$) to that of base material (ε_f) that the tensile specimen is the same size each other and the distance from the weld toe to fracture (d_f). According to the test results the fracture elongation affected by the weld heat ($_w\varepsilon_f$) deteriorates in inverse proportion when the position of fracture approaches the weld toe. From this relation, it is approximated as the following equation in this study.

$$\frac{{}_w\varepsilon_f}{\varepsilon_f} = 1.04 - \frac{0.970}{d_f} \qquad (7)$$

It is also investigated the distance from the welded flange-end of the H-section beam which shows the W-type to fracture. From this investigation, the average distance is 3.5mm and substituting this value into Eq.(7), the deteriorating ratio of the fracture elongation becomes $_w\varepsilon_f/\varepsilon_f=0.76$.

4.3 Analytical Result

On the basis of calculating the crack fracture of H-section beam by the proposed method, the fracture elongation in the Coffin-Manson relationship (Eq.(1), Eq.(6)) is obtained under the condition that the calculated fatigue life coincides with the test results and the modulus (c) in the Coffin-Manson relationship is c=-0.30. Fig.13 shows the relation between the ratio of the calculated fracture elongation affected by the weld heat ($(_w\varepsilon_f)_{Cal}$) to that of base material (ε_f) and the fatigue life of test result ($(2N_f)_{Test}$) concerning the W-type specimens. According to the calculated results, the fracture elongation ratio ($(_w\varepsilon_f)_{Cal}/\varepsilon_f$) is nearly constant and the average value is $(_w\varepsilon_f)_{Cal}/\varepsilon_f=0.70$ except for the R194x150-1 specimen ($(2N_f)_{Test}=350$) which is different from the very low-

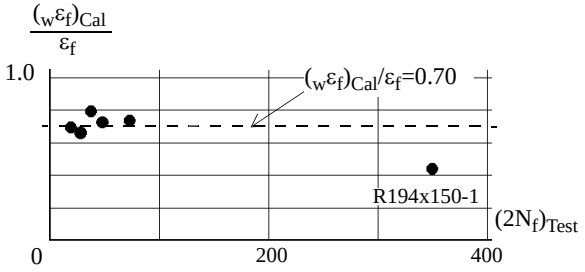

Figure 13 Calculated fracture elongation ratio ($(_w\varepsilon_f)_{Cal}/\varepsilon_f$) when calculations are coincides with test results

cycle fatigue. Moreover, this average value is well corresponding with the tension test result.

From both experimental and analytical results, the fracture elongation affected by the weld heat ($_w\varepsilon_f$) is approximated by $_w\varepsilon_f/\varepsilon_f$=0.70 in this study.

5. VERY LOW-CYCLE FATIGUE TYPE

The fatigue lives of all specimens are calculated by the proposed method and compared with the test results as shown in Fig.14 and Table 1. It is shown that the proposed method is possible for the very low-cycle fatigue specimens (except for R100x100-1 and R194x150-1) to predict the type of fracture and to calculate the very low-cycle fatigue life of H-section beam. However, it is recognized that there are 6 specimens which do not correspond with the calculated results. But their differences of cycles are less than 1 cycle (2 half-cycles), so it is considered that both fatigue fractures almost occur simultaneously.

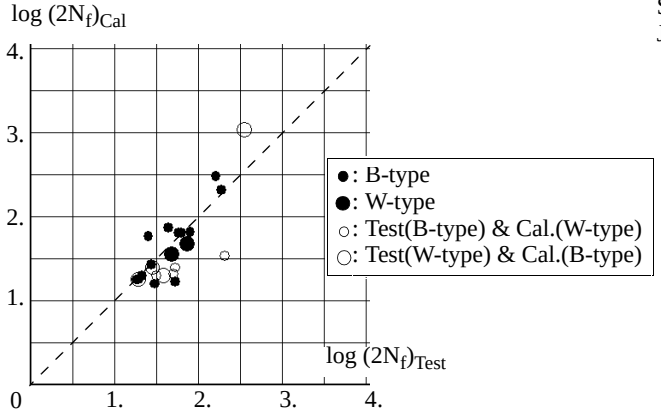

Figure 14 Very low-cycle fatigue predictions compared with test results

6. CONCLUSION

On the basis of the very strong cyclic loading tests of H-section cantilever beam, it is shown that two types of fractures occur at the nearly beam-end flange even if the fracture of welded metal at the beam-end is prevented. One is the fracture at the locally buckled flange of beam and the other is the fracture at the end of beam flange which is affected by the weld heat. Both fractures occur in very low cycle loading. On the basis of this behavior the fracture of H-section beam under strong cyclic load is considered as the very low-cycle fatigue fracture and the fatigue fracture equation is derived on the basis of the Coffin-Manson relationship and the Palmgren-Miner rule. By using this proposed method the fatigue lives of specimens are calculated and are compared with test results. From the calculated results it is shown that the proposed method can predict the type of fracture and calculate the very low-cycle fatigue of H-section beam.

Acknowledgements:

A part of investigation reported herein was supported by the foundation for applied research and technological uniqueness at Nagaoka university of technology.

References:

Saisho, M., Higashi, K., Nakashima, T., and Fujiki, T. (2008), "Very-Low Cycle Fatigue Fracture of H-Section Cantilever Beam under Strong Cyclic Load," *Journal of Constructional Steel*, Japanese Society of Steel Construction, Vol. 16, 13-20. (in Japanese)

Lay, M.G. (1965), "Flange Local Buckling in Wide-Flange Shapes," *Journal of Structural Division*, American Society of Civil Engineers, Vol. 91, No. ST6, 95-116.

Dowling, N.E. (2007), "Mechanical Behavior of Materials," Person Prentice Hall.

Climenhaga, J.J. and Johnson, R.R. (1972), "Moment-Rotation Curves for Locally Buckling Beams," *Journal of Structural Division*, American Society of Civil Engineers, Vol. 98, No. ST6, 1239-1254.

Saisho, M., Goto, K., Hayamichi, D., Takaira, A., and Kanamoto, N. (2005), "Very-Low Cycle Fatigue Fracture of H-Section Beam," *Journal of Constructional Steel*, Japanese Society of Steel Construction, Vol. 13, 283-290. (in Japanese)

JOINT CONFERENCE PROCEEDINGS
7th International Conference on Urban Earthquake Engineering (7CUEE) &
5th International Conference on Earthquake Engineering (5ICEE)
March 3-5, 2010, Tokyo Institute of Technology, Tokyo, Japan

ASSESSMENT OF THE SEISMIC PERFORMANCE OF A SUSPENDED ZIPPER FRAME WITH HYBRID TESTING

Andreas Stavridis[1] and Benson P. Shing[2]

1) Postdoctoral Researcher, Dept. of Structural Engineering, University of California San Diego, United States
2) Professor, Dept. of Structural Engineering, University of California San Diego, United States
andreas@ucsd.edu, pshing@ucsd.edu,

Abstract: This paper presents an analytical and experimental study conducted to evaluate the seismic performance of a three-story suspended zipper steel frame. The frame was concentrically braced and had zipper struts to transfer the unbalanced forces induced on the beams due to the buckling of the lower-story braces. The experimental study was conducted with the hybrid test technique, in which only the bottom-story braces of the three-story frame were physically tested, while the behavior of the rest of the frame was modeled using a general structural analysis software. The analytical model of the entire frame was validated with the hybrid tests and was able to accurately capture the material and geometric nonlinearities that developed when the braces yielded and buckled. This study has demonstrated the usefulness of hybrid testing in improving analytical models and modeling assumptions and providing information that cannot be obtained from an analytical study alone. The results have shown that the suspended zipper frame can distribute the brace nonlinearity over the first two stories as intended in the design and will not have catastrophic failure under the design level earthquakes considered in this study, despite the significant inelastic deformations.

1. INTRODUCTION

Steel frames with inverted-V braces are commonly used as the lateral load-resisting system in buildings. Recent earthquakes, such as the 1994 Northridge earthquake, have demonstrated the undesirable consequences of severe seismic loading on these buildings (EERI 1994). Field evidence and past research have indicated that, under lateral loads, the braces on the first and possibly the second story of such structures may buckle, inducing a soft story mechanism and an unbalanced force on the beam of the story above. This force may cause inelastic bending and lateral torsional buckling of the beam if the latter is not properly designed. However, the proper design of the beam may require large and un-economical cross-sections that are also not desired architecturally.

A possible design solution proposed by Khatib et al. (1988) is to transfer the unbalanced force to the upper stories of the building via vertical struts connected to the top of the beams at the locations of the gusset plates for the lower-story braces. The struts are called zipper struts and the frame is a zipper frame. The zipper struts are placed at the second story and up and are subjected to axial tensile loads once a brace in the story below buckles. Therefore, they can transfer the unbalanced force to the upper stories and significantly reduce the design loads for the beam leading to a more economical design. The advantage of a zipper frame over a conventionally braced frame is that inelastic deformation, namely, the brace yielding and buckling, is distributed over the entire height of a structure through the zipper struts. This leads to a more ductile behavior and a better energy dissipation mechanism as it prevents the development of a soft-story mechanism, which has been a common failure pattern of braced frames. However, a collapse mechanism may still develop if all braces along the height of the structure buckle. To prevent this failure mechanism, a design concept called suspended zipper frame has been proposed by Yang et al. (2008) to ensure that the top story will remain elastic.

A three-story frame designed with the suspended zipper concept was studied in a project with researchers from Georgia Institute of Technology (GT), the University at Buffalo (UB), the University of California, Berkeley (UCB), and the University of California, San Diego (UCSD). In this collaboratory research project, one-third scale models of the frame were tested on a shake table at UB (Schachter and Reinhorn 2006) and quasi-statically at GT by Yang et al. (2010). In the latter tests, the story displacements generated by nonlinear dynamic analyses prior to the tests were imposed quasi-statically on the specimens. The researchers from UCB (Yang et al. 2009) and UCSD conducted hybrid tests where only the bottom-story braces were physically tested with the rest of the frame modeled in a computer. The overall aim of the project was to attain a better

understanding of the seismic performance of zipper frames and assess the usefulness and accuracy of the hybrid test method for evaluating the performance of such complicated systems.

This paper presents an overview of the hybrid test method and the substructure tests of four zipper frame models conducted by the UCSD researchers in the hybrid test facility at the University of Colorado, Boulder (CU). This facility is part of the George E. Brown Jr. Network for Earthquake Engineering Simulation (NEES). The test system is based on the substructure pseudodynamic test concept (Dermitzakis et al. 1985). It combines the realism of physically testing the critical structural subassemblage with the efficiency of modeling the rest of the structure in a computer during a test. The main distinction, however, is that this system can keep the actuators in continuous motion and deliver a rate of loading significantly higher than that in a conventional pseudodynamic test.

For the hybrid tests of the first three specimens, the model of the analytical substructure was extracted from a model of the entire frame that was developed and calibrated with the data from the shake table tests conducted at UB. Based on the additional data obtained from the first three hybrid test specimens and an extensive numerical study, the material parameters and brace model were re-calibrated and a final model was developed and used for the tests of the fourth specimen. The validated final model of the entire frame was used for additional numerical studies to attain a better understanding of the behavior of the suspended zipper frames and assess their seismic performance under strong earthquake events. This paper demonstrates how hybrid testing can be combined with numerical simulation to yield information on structural performance that may not be provided by either method alone.

2. ZIPPER FRAME DESIGN

A three-story suspended zipper frame designed by Yang et al. (2008) was selected as a prototype structure for this study. The structure had the same configuration as a moment-resisting frame studied in the SAC program (FEMA 2000). The seismic demand considered in the design was for a structure located at a site with stiff soil, i.e., site class D per ASCE-7-05 (2006), in the downtown Los Angeles area. The mapped spectral accelerations (S_S and S_1) for the short and 1-sec periods were 2.16 and 0.72g, respectively. The frame was designed with an importance factor of 1.5. Therefore, the resulting design response spectrum, shown in Figure 1, corresponds to a Maximum Considered Earthquake (MCE) for the Los Angeles area.

The prototype structure was scaled down with a length factor of 1/3 to obtain a test model that could be accommodated by the respective laboratory facilities at GT, UB, UCB, and CU. Furthermore, to comply with the capacity of the shake table at UB, the total floor weight of the specimen was 267 KN (60 kips) (Schachter and Reinhorn 2006), which is 1/18 of that of the prototype. As a result, the scale factors for the time and horizontal acceleration were calculated to be 1/2.45 and 2, respectively, to satisfy the similitude requirements (Harris and Sabnis 1999). A partial list of the scale factors is presented in Table 1, and the design of the 1/3-scale specimen is presented in Figure 2 and Table 2. The beams and columns were fabricated from A572 Grade 50 steel, while the braces and zipper struts are fabricated from A500 Gr. C. steel with a minimum yield strength of 318 MPa (46 ksi). The specimens tested in the four laboratories were all fabricated by a single fabricator.

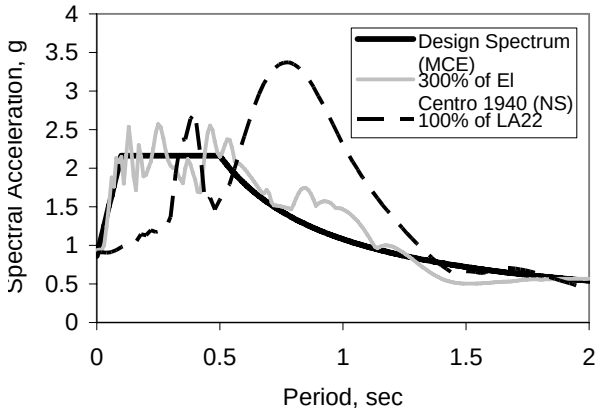

Figure 1: Elastic response spectra for 5% damping.

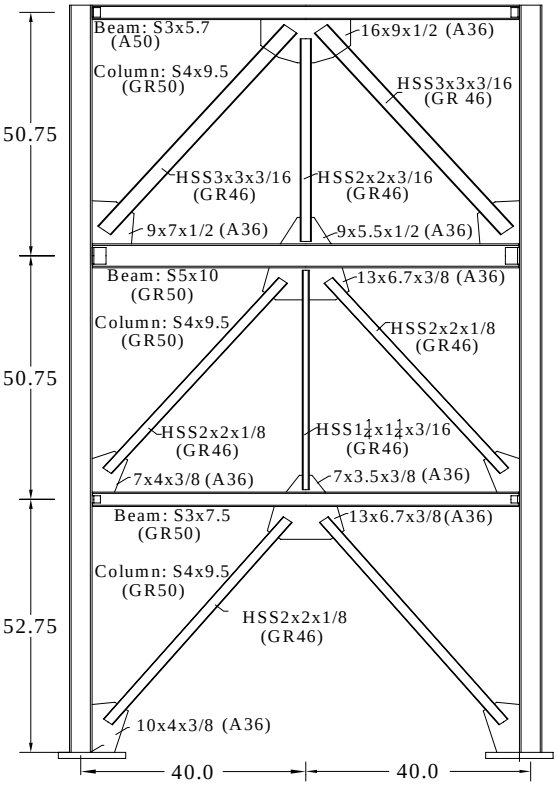

Figure 2: Test structure [4] (measurements in inches, 1 in.=25.4 mm).

Table 1: Scale factors.

Quantity	Scale Factor
Length	**1/3**
Elastic modulus	**1.00**
Mass	**1/18**
Seismic Acceleration	2.00
Force	1/9
Stress	1.00
Strain	1.00
Time	0.41
Gravitational acceleration	1.00

Table 2: Summary of floor masses and member sizes for the test members.

Story	1	2	3
Mass per story	9050	9050	9050
Braces	HSS 2x2x1/8	HSS 2x2x1/8	HSS 3x3x3/16
Columns	S4x9.5	S4x9.5	S4x9.5
Beam	S3x7.5	S5x10	S3x5.7
Zipper Column		HSS 1.25x1.25 x3/16	HSS 2x2x3/16

3. HYBRID TEST SETUP, INSTRUMENTATION, AND TEST SEQUENCE

The tests discussed here were conducted with the Fast Hybrid Test (FHT) system developed and implemented in the NEES facility at CU (Shing et al. 2004 and 2005, and Jung et al. 2007). The system used OpenSEES (McKenna and Fenves, 2000), an open-source object-oriented structural analysis framework which was adapted to serve as the computational platform for the FHT system.

The partition of the zipper frame into an analytical and an experimental part, and the setup for the hybrid tests are illustrated in Figure 3. The experimental part consisted of only the bottom-story braces connected to the base supports and the loading beam with the same type of gusset plates as those shown in Figure 2. During the test, three actuators were used to control the degrees of freedom of the experimental substructure at the node connecting the two braces. This node was at the interface between the analytical and experimental substructures. It was assumed that the experimental substructure had only two translational degrees of freedom at this node. This is a reasonable assumption in view of the fact that the braces were expected to buckle out-of-plane and the bending stiffness of the braces is much lower than that of the beam to which they were connected to in the zipper frame model.

Figure 4 shows that Linear Variable Differential Transformers (LVDT) and a Heidenhain digital linear encoder were used to monitor the displacements at the two controlled degrees of freedom, the out-of-plane displacement at the middle of each brace, the axial deformations of the braces, and the support movements, if any. Eight strain gauges were attached on each brace to measure strains, which can be used to calculate the axial forces in the braces as long as the strains are within the elastic limit. The forces in the braces can be also calculated from the equilibrium conditions between the braces and the actuator forces measured by the load cells. This is especially useful when the strains in the braces exceed the elastic limit.

Four sets of bottom story braces were tested and they are designated as Specimens 1 through 4. Except for the last test conducted on Specimen 4, the hybrid tests used base motions that were recorded from the shake table tests performed at UB on their first zipper frame specimen. The input motions for the shake table tests were scaled versions of the LA22 record derived in the SAC research program by Somerville et al. (1997). The record was obtained by scaling up the fault parallel component of the ground acceleration recorded at the JMA station in the 1995 Kobe earthquake by 15% (Somerville, 2008), and has a 2% probability of exceedance in 50 years for the Los Angeles area. The elastic response spectrum of the LA22 record is compared to the design spectrum in Figure 1. In the shake table tests, the acceleration level in each run was scaled to 15, 30, 45, 60, 80, and 100% of the original record, respectively. Since the scaling factor required for the horizontal acceleration is 2.0, these acceleration levels correspond to 7.5, 15, 22.5, 30, 40, and 50% of the LA22 ground motion intensity with respect to the full-scale prototype. The ground motion levels referred to from this point on are all with respect to the full-scale prototype. Moreover, the acceleration records used in the tests had to be compressed in time by a scale factor of 2.45.

Due to malfunctions of the digital control system caused by defective network connections, Specimens 1 and 2 were accidentally damaged by erroneous displacement commands generated during the initial, low amplitude, tests when elastic behavior of the structure was expected. These specimens were, however, further tested only to identify and correct the hardware problems. Specimens 3 and 4 were tested successfully. The 100% level ground motion used for Specimen 4 was based on the original LA22 record since it was beyond the maximum level used in the shake table test.

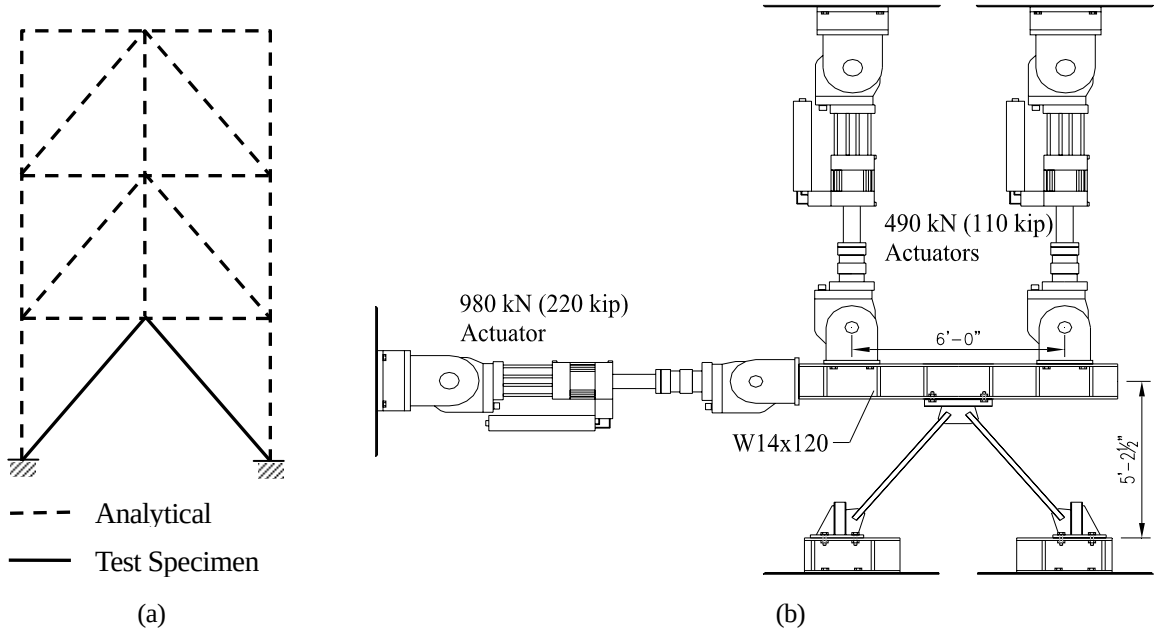

(a) (b)

Figure 3: (a) Structural partitioning and (b) test setup for hybrid tests.

4. DEVELOPMENT AND CALIBRATION OF THE MODEL OF THE ANALYTICAL SUBSTRUCTURE

The zipper frame was designed to spread the inelasticity into the second- and third-story braces, which were part of the analytical substructure in the hybrid tests. This presented a greater challenge for the development of the analytical model than a case in which the analytical substructure would undergo only mild inelastic deformation. Since the accuracy of the analytical model was critical for the success of the hybrid tests, the calibration of the model was carried out progressively in two stages. In both stages, an analytical model for the full zipper frame was considered. Once the full zipper frame model was calibrated, the analytical substructure was then extracted from the full model for the hybrid tests. The full-frame model was initially calibrated with the shake table tests conducted on the first zipper frame at UB [4]. This model was used for the hybrid tests on Specimens 1, 2, and 3. It was improved later on with the data obtained from the hybrid tests conducted on Specimens 2 and 3 at CU to arrive at the final model that was used for the hybrid testing of Specimen 4.

For the calibration of initial model the suite of six horizontal acceleration time histories recorded on the shake table as mentioned previously was used as input excitation. In the analytical model, each brace was modeled with two flexibility-based inelastic beam-column elements (Spacone et al. (1996) connected at the middle of the brace with a slightly offset node. This initial imperfection combined with the corotational formulation allowed for the simulation of the buckling behavior of a brace. All elements had cross-sections divided into fibers to capture progressive plasticization. The uniaxial stress-strain behavior of each fiber was represented by the Menegotto–Pinto (1973) steel model .

The issues considered in the model calibration included the damping properties of the structure, the initial imperfection of the braces and the rigidity of the brace-to-frame connections, which affect the buckling resistance of a brace, and the material properties. Furthermore, both the time integration interval and mass distribution in a brace affect the convergence of the numerical solution once a brace buckles. This was given appropriate attention in the model development. The values of the modeling parameters selected for the final model are shown in Table 3. Stavridis and Shing (2010) discuss issues pertinent to the calibration of the computer model for the analytical substructure as well as for the entire frame, including the selection of an appropriate damping matrix, and the modeling of the buckling behavior of the braces and bracing connections.

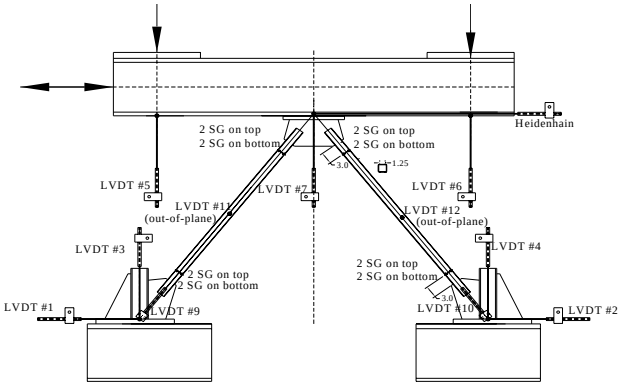

Figure 4: Instrumentation scheme.

In view of the restraints provided by the gusset plates, all beam-to-column connections were assumed to be rigid. However, due to the lack of pertinent information and the weak rotational restraint of the gusset plates against the

out-of-plane buckling of a brace, the brace connections were initially assumed to be hinged. This assumption was revised in the final model as the tests on Specimens 2 and 3 indicated that rotational springs provided more accurate representation of the actual behavior. The initial imperfection in the modeled braces was assumed to be equal to 1/535 of the brace length. This was also revised based on the test data and in the final model it was set equal to 1/313. The steel material model was initially calibrated with results of coupon tests carried out at UB but was later revised based on coupon tests obtained from Specimen 2, as discussed in Stavridis and Shing (2010). The strain-hardening slope was determined to be 1% of the Young's modulus for the braces and zipper struts, and 0.5% for the beams and columns based on the available test data.

Table 3: Modeling assumptions in the final model used for the analytical substructure in the tests on Specimen 4.

Beam-to-Column connections	Fixed	
Brace end condition	Restrained by elastic spring	
Brace initial imperfection ratio	1/313	
Material properties (steel02 in OpenSEES	**Beams, columns and zipper struts**	**Braces**
E (GPa)	200	200
F_y (MPA)	344	365
Strain hardening ratio	0.005	0.001
Mass Distribution	- Story mass equally distributed among the three nodes at each story - The center node of each brace had an additional mass equal to 1/120 of the story mass to assure the positive definiteness of the effective secant stiffness matrix and ensure convergence of modified Newton iteration.	
Damping	Rayleigh damping based on the initial stiffness ($C = \alpha_1 M + \alpha_1 K$) $\alpha_0 = 1.06, \quad \alpha_1 = 0.001043$	

5. TEST RESULTS FROM SPECIMEN 4

Specimen 4 was subjected to a sequence of three ground motions. The first two were again the 15 and 40% level motions from the UB tests, while the last motion was the original LA22 record compressed in time and with its acceleration scaled up to 200% so that it is equivalent to the 100% motion for the prototype frame. Because of the reduced time integration interval of 0.0035 sec and the time required to record the numerical data on a hard-drive in each time step, the test was about 83.7 times slower than a real-time test.

Figure 5 shows that an almost exact match of the test and simulation results was obtained for the 15% level earthquake. It also compares the test results obtained from Specimens 3 and 4. In these tests, both the analytical and experimental substructures remained elastic. Since the experimentally tested braces had similar properties and the same excitation was used, the difference in the responses can be attributed to the differences in the brace models used in the analytical substructure.

The first-story displacement time histories for the 40% test are shown in Figure 6 and indicate a good agreement between the test and the analysis. Figure 7 shows the close match of the hysteresis loops for the two bottom-story braces, which exhibit moderate inelastic deformation and brace buckling. It can be observed that the brace forces in the analytical model are influenced by the inertia effect of the small mass at the middle node and, therefore, the hysteresis loops are not very smooth; however, the influence is not significant. Figure 7 also presents the hysteretic curves for the zipper strut and the second-story braces. As the west brace of the bottom story mildly buckled, the zipper strut transferred an axial tension that forced the west brace of the second-story into the nonlinear regime. Figure 6 shows that the difference between the displacement responses of Specimens 3 and 4 is more distinct for the 40% ground motion level, with Specimen 3 showing a larger displacement. This difference highlights the importance of having an accurate model for the analytical substructure.

The displacement time histories obtained from the 100% level test and simulation are shown in Figure 8. During this last test, the west brace suddenly fractured in tension right outside the gusset plate during the first cycle of strong motion when it reached a drift ratio of 2.9%. The failure of Specimen 4 is shown in Figure 9. The maximum axial strain that was recorded in the brace right before fracture was about 0.008. This brittle failure was probably caused by a problem introduced by the welding of the slotted end of the brace to the gusset plate and could have been prevented if the regions next to the brace-to-gusset plate connections were strengthened according to the current design specification (AISC 2005). Since this failure was not captured in the simulation, the analysis continued beyond the point of fracture resulting in a maximum drift ratio of 5.3%. Until the brace fractured, the experimental and simulation results show close correlation, even for the hysteretic behavior of the braces as shown in Figure 10. Figure 10 also presents the forces in the zipper strut and the second-story braces, which indicate that the zipper mechanism was activated inducing the buckling of the second-story braces after the bottom-story braces buckled.

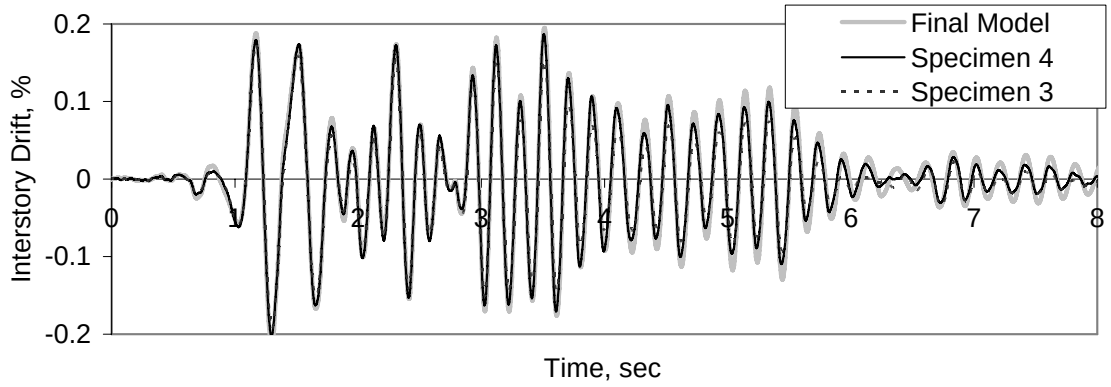

Figure 5: Comparison of bottom-story drifts obtained from the final analytical model and Specimens 3 and 4 under the 15% ground motion.

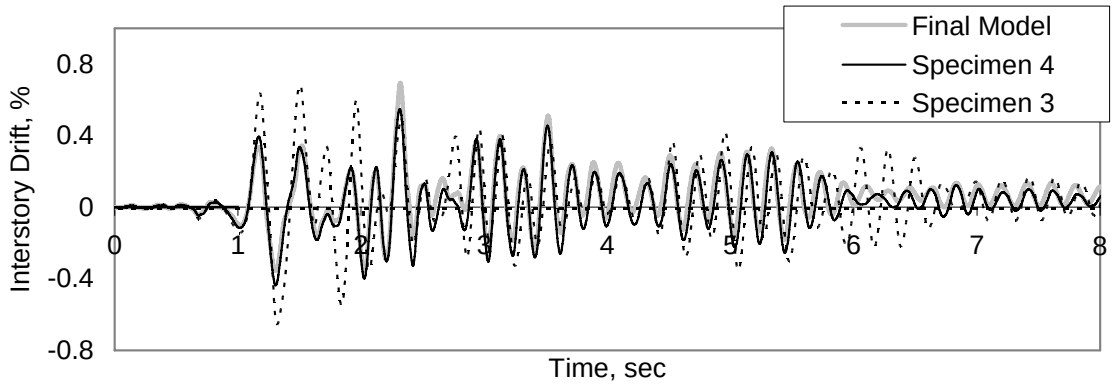

Figure 6: Comparison of bottom-story drifts obtained from the final analytic model and Specimens 3 and 4 under the 40% ground motion.

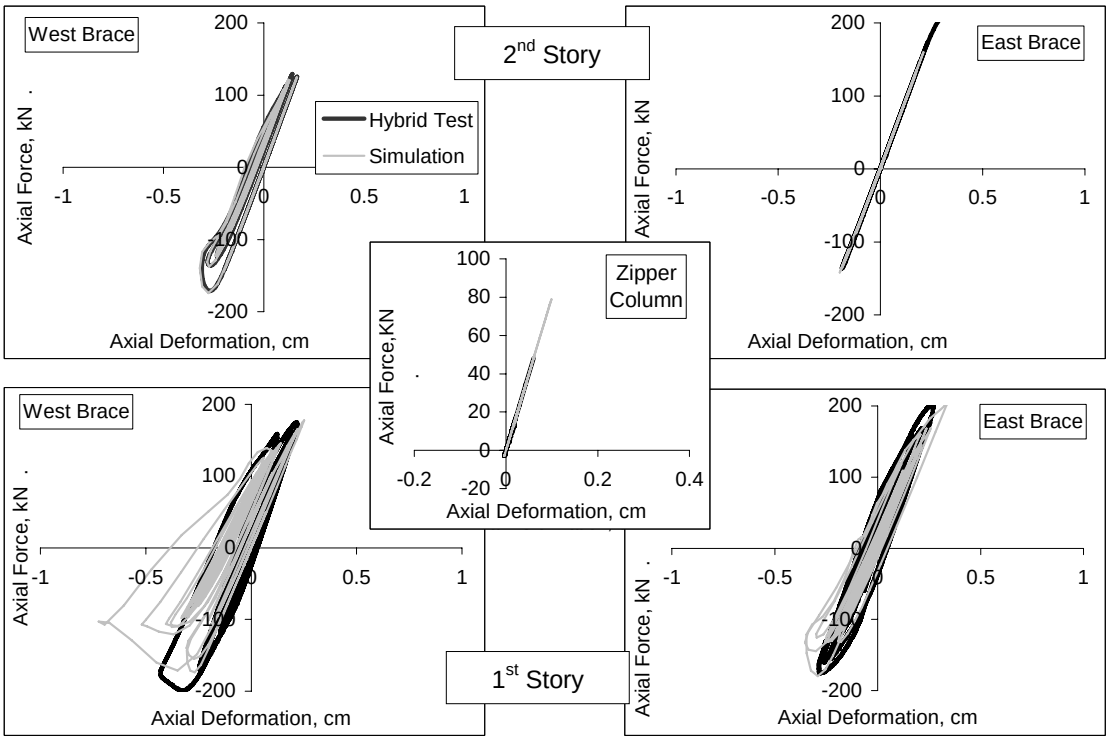

Figure 7: Comparison of analytically and experimentally obtained hysteresis loops of Specimen 4 under the 40% ground motion. (Note: the curves for the 2nd story were obtained from the analytical substructure in both cases.)

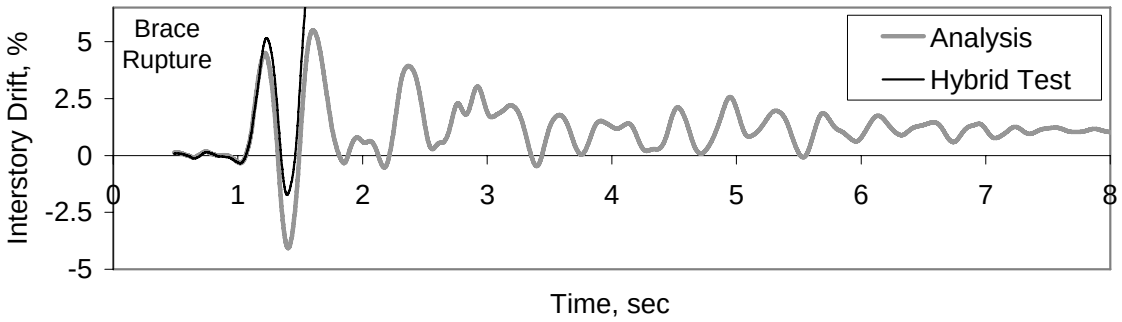

Figure 8: Comparison of analytically and experimentally obtained first story drifts of Specimen 4 under the 100% ground motion.

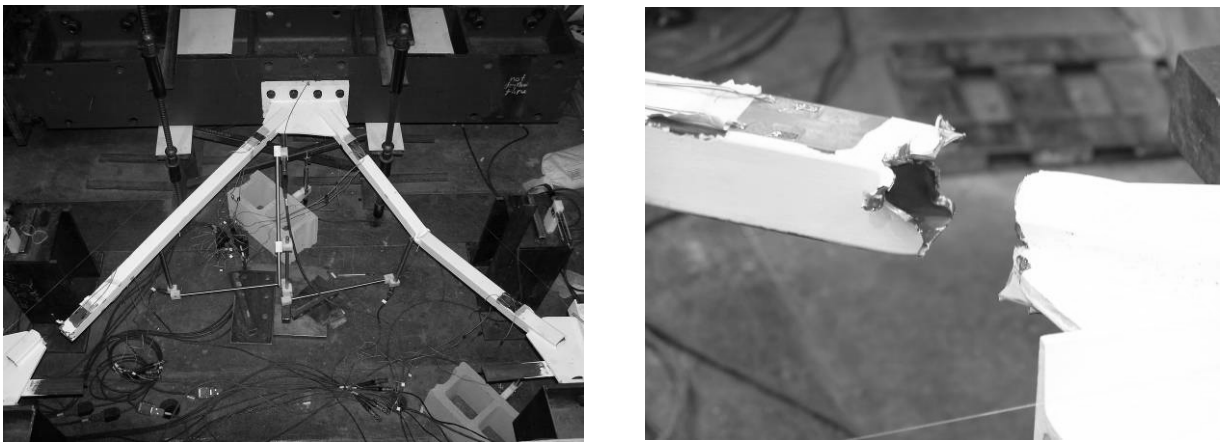

Figure 9: Failure of Specimen 4.

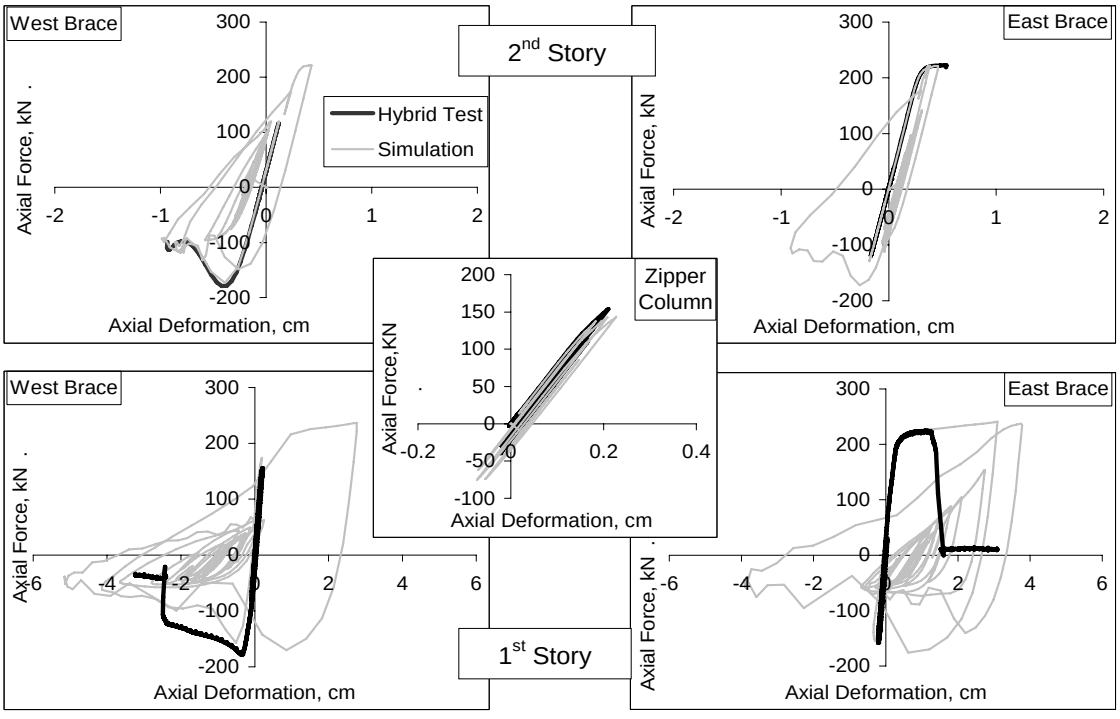

Figure 10: Comparison of analytically and experimentally obtained hysteresis loops of Specimen 4 under the 100% ground motion. (Note: the curves for the 2nd story were obtained from analytical brace models in both cases.)

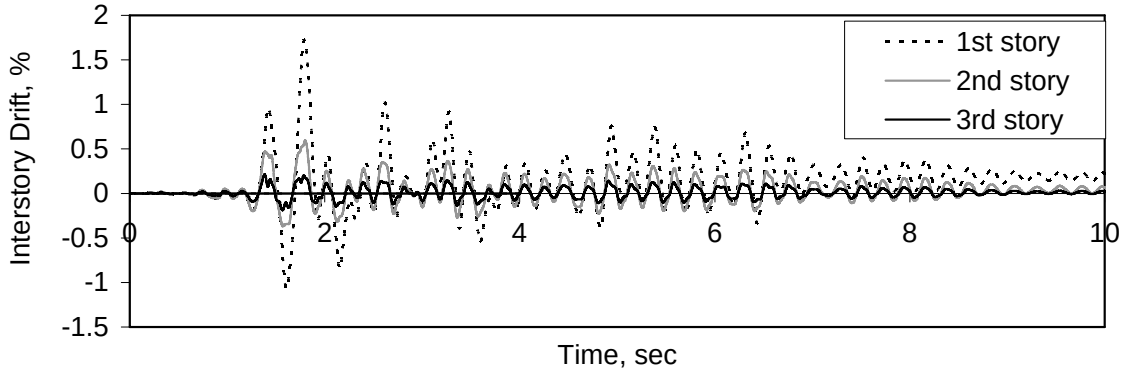

Figure 11: Interstory drifts of the zipper frame subjected to 100% of LA22 record without prior damage.

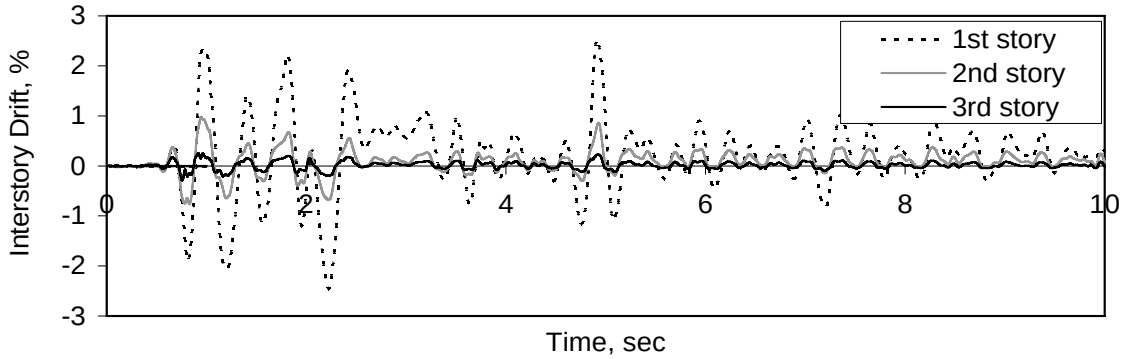

Figure 12: Interstory drifts of the zipper frame subjected to 300% of El Centro 1940 (NS) ground motion without prior damage.

6. SEISMIC PERFORMANCE ASSESSMENT OF ZIPPER DESIGN

In the tests described in this paper, the specimens were subjected to sequences of ground motions scaled to different levels. This was a more demanding loading scenario than what would have been experienced by a structure in a seismic event. In particular, the analytical and experimental substructures were already damaged when the 100% LA22 record was applied. To investigate how the same structure would respond if it had not sustained prior damage, the same record was applied to the final analytical model of the frame. The first-story drift obtained is shown in Figure 11. It can be observed that the maximum story drift developed is 1.7%, while in the case of the same model pre-damaged by the 40% level ground motion, it exceeds 5% as shown in Figure 14. With the maximum drift of 1.7%, the bottom-story braces buckled but are not expected to fracture since brace fracture occurred at a drift of 2.9% in the test.

As shown in Figure 1, the response spectrum of LA22 is quite different from that used for the design of the prototype zipper frame. The fundamental frequency of the undamaged full-scale prototype frame is 0.34 sec., at which the spectral acceleration given by LA22 is close to that given by the spectrum used in the design. However, the response to LA22 can be significantly higher than that given by the design spectrum when the structure softens and its fundamental period elongates. Therefore, it is interesting to investigate the performance of the same frame for a ground motion that has a spectral shape resembling the design spectrum. For this purpose, the NS component of the acceleration time history recorded in El Centro, during the 1940 Imperial Valley earthquake was considered. This time history was scaled by a factor of 3 to match the design spectrum as illustrated in Figure 1. The time and acceleration of the record were then scaled accordingly to satisfy the similitude requirements for the scaled model. The response of the zipper frame is presented in Figure 12. The peak interstory drifts were 2.5, 1.0, and 0.25% for the first, second, and third floor, respectively. The analysis indicated that the bottom-story braces severely buckled but did not reach the deformation at which one brace of Specimen 4 fractured. The second-story braces had moderate buckling, while the top braces remained elastic as intended according to the suspended zipper design. However, according to ASCE 7, the maximum allowed story drift for the frame is 2.25% based on the importance factor of 1.5 and the Occupancy Category IV. The analysis conducted with the scaled El Centro motion has indicated that this requirement was violated by the frame. However, the frame could effectively distribute the inelastic behavior and would not fail in a catastrophic manner.

8. CONCLUSIONS

This study demonstrates the usefulness of the hybrid test technique to evaluate the seismic performance of a zipper frame structure that exhibited severe inelastic behavior not only in the experimental substructure but also in the analytical part. The analytical model has been successfully validated with the tests conducted on the last specimen and it can accurately capture the highly nonlinear buckling behavior of the braces. The validated analytical model of the full frame has been used for further analytical studies to investigate the performance of an undamaged structure of the same design under severe seismic excitations. The results have shown that the suspended zipper frame can distribute the brace nonlinearity over the first two stories as intended in the design and will not have catastrophic failure under the design level earthquakes, despite the fact that the allowable story drift can be slightly violated. The model, however, does not account for the brace fracture. The fracture observed in Specimen 4 could have been prevented if the braces regions next to brace-to-gusset plate connections were strengthened according to the current design specification.

Acknowledgements:

This study was supported by the National Science Foundation under Award No. 0324468. The first author would also like to acknowledge the Graduate Fellowship from UCSD that partially supported his graduate study. The authors would like to thank Prof. Andrei Reinhorn and Dr. Macarena Schachter from the University at Buffalo for sharing their shake table test data and their assistance in specimen design and fabrication and Dr. Walter Yang for the design of the prototype structure. This project would not be possible without Prof. Roberto Leon's dedication in developing and coordinating this collaborative research effort. Finally, the authors would like to express their gratitude to the staff in the NEES facility at the University of Colorado at Boulder. Without their dedicated professional support, the tests could not have been successfully completely. However, opinions expressed in this paper are those of the authors and do not necessarily represent those of the sponsor or the aforementioned collaborators.

References:

Earthquake Engineering Research Institute. (1996). "1994 Northridge Earthquake Reconnaissance Report." *Earthquake Spectra*, Vol 12, Issues S1 and S2.

Khatib IF, Mahin SA, Pister, KS. (1988). "Seismic behavior of concentrically braced steel frames." *UBC/EERC-88/01*, Earthquake Engineering Research Center, University of California, Berkeley, Ca.

Yang CS, Leon RT, DesRoches R. (2008). "Design and behavior of zipper-braced frames." *Journal of Engineering Structures* 2008; Vol 30, 1092-1100.

Schachter,M, Reinhorn AM. (2006). "On the importance of 3D Analysis for zipper frame structures." *Proceedings of 14th National Conference on Earthquake Engineering, San Francisco*, Ca.

Yang CS, Leon RT, DesRoches R. (2010). "Cyclic Behavior of Zipper-Braced Frames." *Earthquake Spectra. (under review).*

Yang TY, Stojadinovic B, and Moehle J. (2009). "Hybrid simulation of zipper-braced steel frame under earthquake excitation." *Journal of Earthquake Engineering and Structural Dynamics*. 38:95-113.

Dermitzakis SN, Mahin, SA. (1985). "Development of substructuring techniques for on-line computer controlled testing." *UBC/EERC-85/04*, Earthquake Engineering Research Center, University of California, Berkeley, Ca.

FEMA-355C. (2000). State of the art report on systems performance of steel moment frames subjected to earthquake ground shaking. FEMA 355C/September 2000. Washington (DC): *Building Seismic Safety Council*.

Minimum design loads for buildings and other structures. American Society of Civil Engineers, *ASCE/SEI 7-05*; 2006.

Harris HG, Sabnis GM. (1999). *Structural modeling and experimental techniques*. CRC Press, Boca Raton, Fl.

Shing PB, Wei Z, Jung RY, Stauffer E. (2004). "NEES fast hybrid test system at the University of Colorado." *Proceedings of the 13th World Conference on Earthquake Engineering*. Vancouver, Canada.

Shing PB, Stavridis A, Wei Z, Stauffer E, Wallen R, Jung RY. (2005). 'Validation of a Fast Hybrid System with Substructure Tests.' *Proc. 17th Analysis and computation specialty conference.* Saint Louis, Mi.

Jung RY, Shing PB, Stauffer E, Thoen B. (2007). 'Performance of a real-time pseudodynamic test system considering nonlinear structural response.' *Earthquake Engineering and Structural Dynamics*; Vol. 36, 1785-1809.

McKenna F, Fenves GL. (2007). "An Object-oriented software design for parallel structural analysis." *Proceedings of the SEI/ASCE Structures Congress*, Philadelphia, Pa.

Somerville PG, Smith N, Punyamurthula S, Sun J. (1997). "Development of ground motion time histories for phase 2 of the FEMA/SAC steel project." *SAC background document*. report no. SAC/BD 97/04; 1997.

Somerville PG. (2008). *Personal communication*.

Spacone E, Filippou FC, Taucer FF. (1996). "Fibre beam-column model for nonlinear analysis of R/C frames: Part I. Formulation." *Journal of Earthquake Engineering and Structural Dynamics*; 25:711-725.

Menegotto M, Pinto PE. (1973). "Method of analysis for cyclically loaded reinforced concrete plane frames including changes in geometry and nonelastic behavior of elements under combined normal force and bending." *IASBE Symposium on Resistance and Ultimate Deformability of structures Acted on by Well-Defined Repeated Loads*, Final Report, Lisbon, Portugal.

Stavridis, A**.** and P.B. Shing. (2010). "Hybrid Testing and Modeling of a Suspended Zipper Steel Frame." *Journal of Earthquake Engineering and Structural Dynamics*. 39:187-207.

American Institute of Steel Construction, AISC Seismic (2005). *Seismic provisions for steel buildings*. Chicago, IL.

JOINT CONFERENCE PROCEEDINGS
7th International Conference on Urban Earthquake Engineering (7CUEE) &
5th International Conference on Earthquake Engineering (5ICEE)
March 3-5, 2010, Tokyo Institute of Technology, Tokyo, Japan

EFFECTS OF EDGE DISTANCES ON SHEAR CAPACITY OF ANCHOR BOLT FASTENING STEEL COLUMN BASE TO CONCRETE FOUNDATION

Hayato Asada[1], Shoichi Kishiki[2], and Satoshi Yamada[3]

1) Graduate Student, Structural Engineering Research Center, Tokyo Institute of Technology, Japan
2) Assistant Professor, Structural Engineering Research Center, Tokyo Institute of Technology, Japan
3) Associate Professor, Structural Engineering Research Center, Tokyo Institute of Technology, Japan
asada@serc.titech.ac.jp, kishiki@serc.titech.ac.jp, naniwa@serc.titech.ac.jp

Abstract: This paper focuses on shear resistance of anchor bolts with deep embedment fastening steel column base to reinforced concrete foundation. The shear loading tests of a single anchor bolt were conducted to discuss effects of edge distances and anchor geometries on shear capacity. From the test results, it is found that the prediction based on 45 degree concrete cone method does not adequately takes into account effects of edge distance in perpendicular to loading direction, on the other hand, CCD method advanced by Hofmann was good agree with experimental results regardless of large or small of its edge distances.

1. INTRODUCTION

Anchor bolts are widely used to anchor the base plate of steel column to reinforced concrete foundation. In current anchorage designs for steel column-base in Japan, large anchor bolts with deep embedment (embedment length exceeding 20 times of its diameters) are generally used. Anchor bolts may be subjected not only to tensile force but also to shear force during severe earthquake excitation. Especially, in case of the column-base with brace, large shear force acts on anchor bolts. If anchor bolts with sufficient embedment to prevent concrete cone failure locate near the edges of reinforced concrete foundation, concrete edge failure may be caused by shear force. Whereas concrete edge failure of small anchors such as headed studs with shallow embedment have been studied extensively (Klingner, (1982), Fuchs, (1995)) anchor bolts with deep embedment have not been adequately addressed (Kawano, (2003), (1996)).

it has been known that capacity of concrete edge failure is affected by tensile strength of concrete, concrete edge distances and anchor geometries.

However, the complete determination of capacity of concrete edge failure has not been formed yet. For this reason, the shear loading tests of a single anchor bolt were conducted to discuss effects of edge distances and anchor geometries on shear capacity, as governed by concrete edge failure. The tests results were also intended to assess the applicability of existing predictions.

2. SHEAR LOADING TESTS

2.1 Test specimens

To evaluate effects of edge distances and anchor geometries on shear capacities of single anchor bolts, 8 specimens with various edge distances and amchor geometries were selected and performed. Test program is summarized in Table 2. Edge distances from free edges that is main parameters in this study were defined as shown in Figure 3. Experimental parameters are given as edge distances and the ratio corner distance c_2 (edge distance in perpendicular to loading direction) to edge distance in loading direction c_1. Specifically, c_1=100 and 160mm c_2/c_1=1.9, 1.5, 1.25, 1.0, 0.5. Thus, the test were mainly planned to discuss effects of edge distances in perpendicular to loading direction.

Configuration of test specimen is shown in Figure 1. All specimens were composed of anchor bolt and concrete block whose bottom parts were placed reinforcements. These reinforcements do not significantly influence the failure. They were not reinforced around anchor bolts using lateral reinforcements. The upper concrete test blocks of all specimens were same size of 600x600x500. Details of anchor bolt are shown in Figure 3. All anchor bolts used in the tests were fabricated of SBPR1080/1230 with nominal yield strength of 1080N/mm^2 to prevent steel failure before concrete edge failure occurs. They have ϕ19 or 23mm diameter, and embedment length of 400mm.

The average concrete strength at the time of testing is shown in Table 2(a). The concrete for the all specimen was placed from one batch. Table 2(b) shows the material

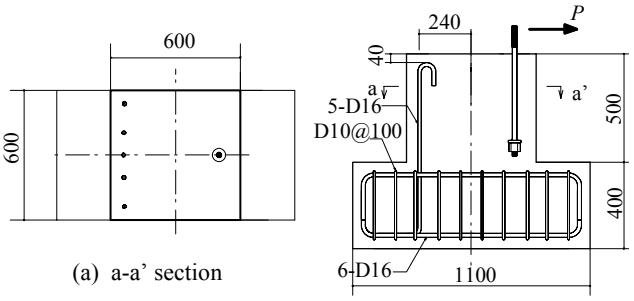

(a) a-a' section

(b) elevation

Figure 1 Configuration of Test specimen

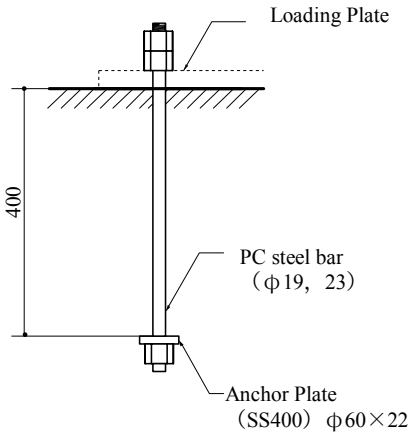

Figure2 Details of Anchor bolt

Table 1 List of Test Specimens

Specimen	diameter of A.bt d [mm]	edge distance c_1[mm]	corner distance c_2[mm]
U-1	ϕ23	100	300
U-2		160	(over1.9c_1)
U-3		100	100(=1.0・c_1)
U-4		160	240(=1.5・c_1)
U-5			200(=1.25・c_1)
U-6			160(=1.0・c_1)
U-7			80(=0.5・c_1)
U-8	ϕ19		300

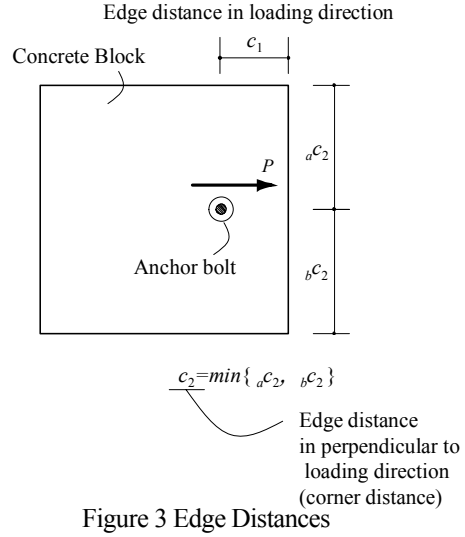

Figure 3 Edge Distances

Table 2 Material Properties

(a) Concrete

Tensile Strength σ_t [N/mm^2]	Compresive strength σ_B [N/mm^2]	Elastic modulus E_c [N/mm^2]
2.03	24.7	2.36×10^4

(b) Anchor bolts

Steel grade	Yield strength $_s\sigma_y$ [N/mm^2]	Ultimate Strength $_s\sigma_u$ [N/mm^2]	E.L. [%]
PC steel bar (φ19) *1	1187*2	1269	12
PC steel bar (φ23) *1	1217*2	1282	12

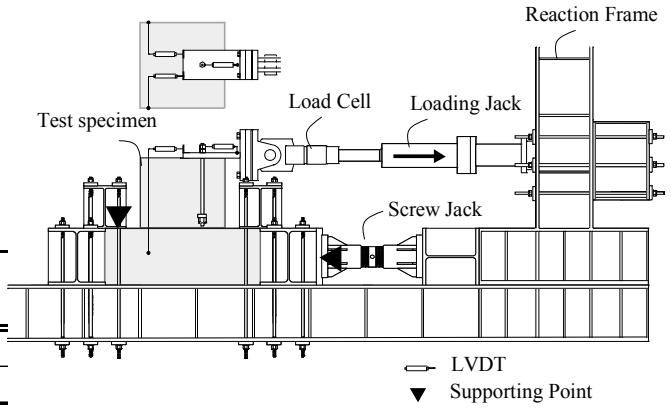

Figure 4 Test Setup

properties of anchor bolts.

2.2 Test setup and measurements

The test setup is shown in figure 7. Top face and side surface of the bottom part of concrete block were fixed to the reaction frame with Steel beam and screw jack. Shear load was applied monotonically to the anchor bolt through the steel plate. A Teflon sheet was inserted between the concrete surface and the steel plate to reduce friction resistance. The applied load was measured by load cell embedded in loading Jack. Additionally, strains of the anchor bolt were measured. Furthermore, the lateral displacement of Anchor bolt was measured by a couple of displacement transducers.

3. TEST RESULTS AND DISCUSSIONS

3.1 Failure mode and load-displacement behavior

Failures of all specimens were caused by forming of concrete breakout. Typical failure surface of specimens are shown in Figure 5. The depths of failure Surface were measured by laser displacement sensor after removal of broken piece of concrete block. Quasi-tensile force obtain from multiplying concrete tensile strength obtain from

cleave test by measured failure surface area, was much larger than measured capacity of concrete edge failure regardless of size of failure surface. As past study on pull out behavior of anchor bolt by Asada et al, (2010) has been shown, quasi-failure surface capacity did not directly correspond to measured failure capacity of concrete edge failure.

Figure 6 shows load-displacement curve of specimens with various edge distances. As show in this figure, stiffness of load-displacement curve did not affected by edge distances, even though edge distances affected lateral displacement at ultimate load.

3.2 Existing predictions of concrete edge failure Load

In this study, predicted capacities were calculated by following two methods to compare with measured capacity and discuss the accuracy of existing predictions for the shear capacity of anchor bolt with large embedment.

One design method is called 45 degree concrete cone method. Japanese anchorage design provision (AIJ, 1985) is subjected to this method. Another is Concrete capacity design (CCD) method improved by Hofmann (Hofmann, (2004)) which is the basis of US and European anchorage design

[45 degree concrete cone method]

45 degree concrete cone method assumes half cone failure surface, whose the angle of inclination is 45° as shown in Figure 7. Then, concrete capacity of a single anchor bolt is calculated assuming a constant strength equal to $0.31\sqrt{\sigma_B}$ (tensile strength) acting on projected area of assumed failure surface:

$$_{AIJ_c}P_u = 0.31\sqrt{\sigma_B}\cdot A_c = 0.31\sqrt{\sigma_B}\cdot\frac{\pi\cdot c_1^{\,2}}{2} \tag{1}$$

where A_c: projected area, c_1: edge distance in loading direction, σ_B: compressive strength of concrete. If the edge distances perpendicular to loading direction is small ($c_2<c_1$), the shear capacity has to be reduced with the projected area on side of the concrete block.

[CCD method improved by Hofmann]

CCD method is based on regression analysis of a large number of test data. The concrete capacity of a single anchor bolt is calculated by equation (2).

In this procedure, failure block as half pyramid with the angle of 35° is assumed as shown in Figure 8. Note that the concrete capacity calculated using CCD method improved by Hofmann is proportional to $c_1^{1.5}$. This is attributable to the size effect. Anchor geometries are also considered in equation.

$$_{CCD_c}P_u = \frac{A_{cc}}{A_{cco}}\cdot\Psi_{s,v}\cdot P_0 \tag{2}$$

$$P_0 = 3.0\cdot d^{\alpha}\cdot l_e^{\,\beta}\sqrt{\sigma_B}\cdot c_1^{\,1.5} \tag{3}$$

where

$$\alpha = 0.1\cdot\left(\frac{l_e}{c_1}\right)^{0.5} \qquad \beta = 0.1\cdot\left(\frac{d}{c_1}\right)^{0.2}$$

$$\Psi_{s,v} = 0.7 + 0.3\cdot c_2/(1.5\cdot c_1) \le 1$$

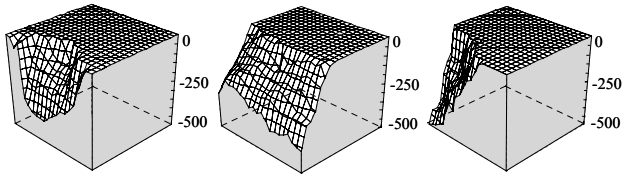

(a) U-1 (b) U-2 (c) U-6

Figure 5 Failure Surface

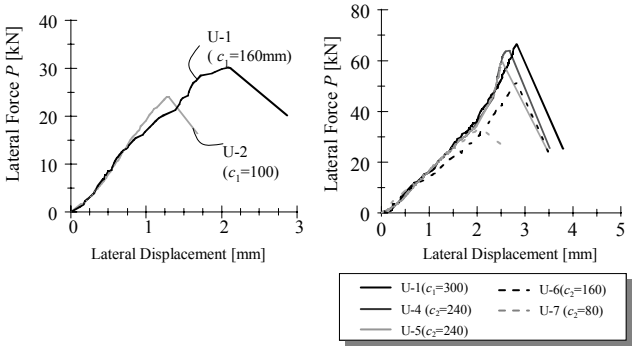

(a) Effect of edge distance c_1 (b) Effect of edge distance c_1

Figure 6 Load-Displacement Curves

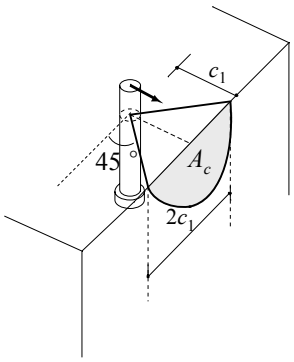

Figure 7 Idealized Concrete Failure Body of Individual Anchors in Shear (45 degree concrete cone method)

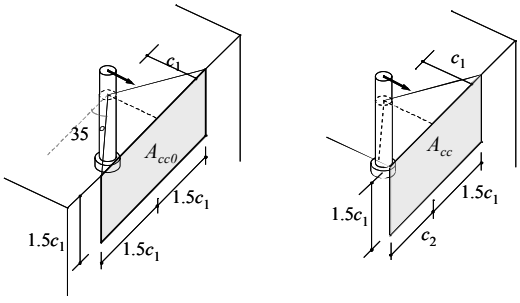

(a) $c_2 \geqq 1.5\,c_1$ (b) $c_2 < 1.5\,c_1$

Figure 8 Idealized Concrete Failure Body of Individual Anchors in Shear (CCD method)

where d: diameter of anchor bolt, l_e: effective embedment length c_1: edge distance in loading direction, c_2: corner distance (edge distance in perpendicular to loading direction). If the edge distances perpendicular to loading direction is smaller than 1.5 times of c_1, the concrete capacity load has to be reduced with the projected area and reduction factor $\Psi_{s,v}$

3.3 Concrete edge failure load

[Effects of edge distances]

Measured capacity in the current test and predicted capacity are summarized in Table 3. To discuss effects of corner distance c_2 on concrete capacity, The ratio of measured failure load of each test to measured failure load of The specimen U-6 with c_2/c_1 =1.0 in the current test are plotted as a function of ratio c_2 to c_1 in Figure 9. this figure shows that the failure load were reduced with c_2 is smaller than 1.5 times of c_1. The results indicate that 45° concrete cone method can not properly evaluate the effects of corner distance c_2 on concrete capacity because the reduction of concrete capacity due to corner distance cannot be appropriately evaluated if c_2 doesn't become small more than c_1.

Measured failure loads are plotted as a function of edge distance c_1 in Figure 10. The results of 31 previous tests conducted by Kawano (1996, 2004) and Ichihashi (1987) are also plotted. Table 4 give the range of varied parameters of previous tests. The previous tests carried out using anchor bolt with large embedment greater than 250mm. and corner distance greater than 1.5 times of edge distance. All specimens were failed by concrete breakout. And also, the tests were performed with different compressive strength of concrete. Therefore, the measured failure loads were normalized by divided by square roots of compressive strength of concrete.

It can be observed that failure loads strongly are influenced by edge distances c_1. In conjunction with test results, approximate curve are plotted. The coefficient of correlation R^2 is also described in Figure 10. Approximate curve was proportional to $c_1^{1.6}$. This result indicates that CCD method with $c_1^{1.5}$ can estimate the effect of edge distance in loading direction c_1 better than 45° concrete cone method with c_1^2.

[Effects of anchor geometries]

Figure 10 shows that the effects of anchor geometries on measured failure load.

Measured failure loads were normalized by divided by edge distance $c_1^{1.6}$ and square roots of compressive strength

Table 3 Test results and Predicted Loads

Specimen	${}_eP_u$ *1 [kN]	${}_{AIJ_c}P_u$ *2 [kN]	${}_{CCD_c}P_u$ *3 [kN]	${}_eP_u/{}_{AIJ_c}P_u$	${}_eP_u/{}_{CCD_c}P_u$
U-1	66.27	61.92	74.39	1.07	0.89
U-2	30.16	24.19	43.63	1.25	0.69
U-3	24.02	24.19	32.72	0.99	0.73
U-4	63.99	61.92	74.39	1.03	0.86
U-5	59.57	61.92	64.78	0.96	0.92
U-6	51.43	61.92	55.79	0.83	0.92
U-7	33.34	49.82	39.67	0.67	0.84
U-8	63.35	61.92	71.08	1.02	0.89

*1 ${}_eP_u$:Measured failure load

*2 ${}_{AIJ}P_u$: Predicted failure load according to 45 degree concrete cone method

*3 ${}_{CCD}P_u$: Predicted failure load according to CCD method

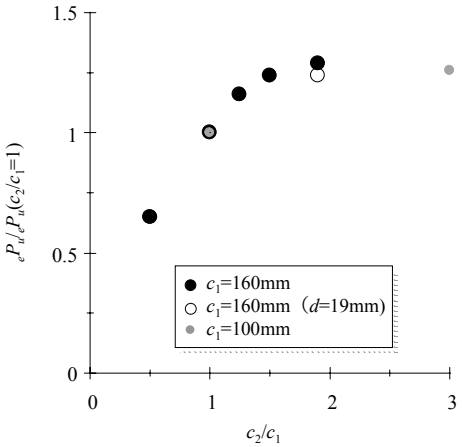

Figure 9 Relation between Ratio ${}_eP_u$ / ${}_eP_u$ with c_2/c_1=1.0 and Ratio c_2/c_1 in the Current Tests

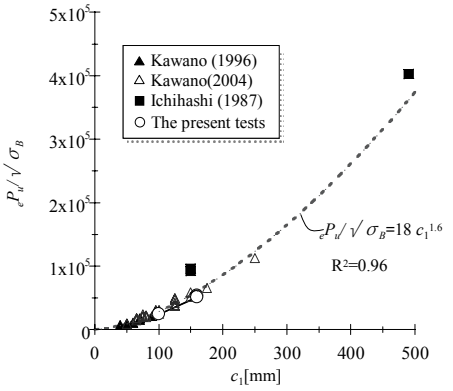

Figure 10 Relation between Measured Failure Load and Edge Distance c_1

Table 4 Range of varied Parameters of the Previous Tests Influence Shear Capacity of Anchor bolt

	σ_B [N/mm2]	c_1 [mm]	c_2 [mm]	l_e [mm]	d [mm]
Kawano(2003) (n=8)	20.4~29.7	40 ~100	200	213~394	11~20
Kawano (1996) (n=26)	29.6	50~250	200~575	200~350	12.4~47.8
Ichihashi (1987)(n=3)	27.6~29.1	150~490	900	399	42

σ_B: compressive strength of concrete; c_1: edge distance; c_2: corner distance,; le: effective embedment depth; d : anchor diameter

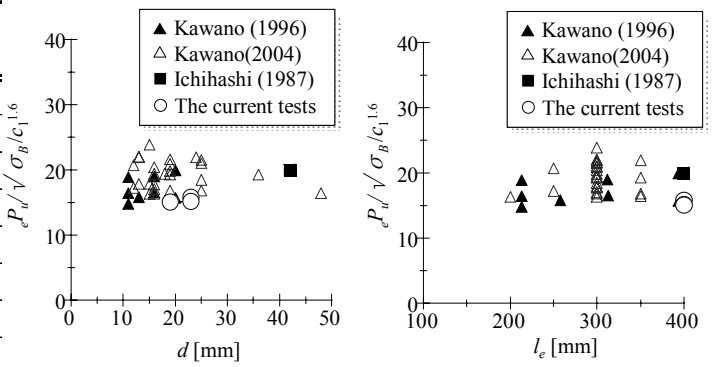

(a) Effect of Anchor Diameter (b) Effect of Effective Embedment Depth

Figure 10 Relation between Measured Failure Load and Anchor geometries

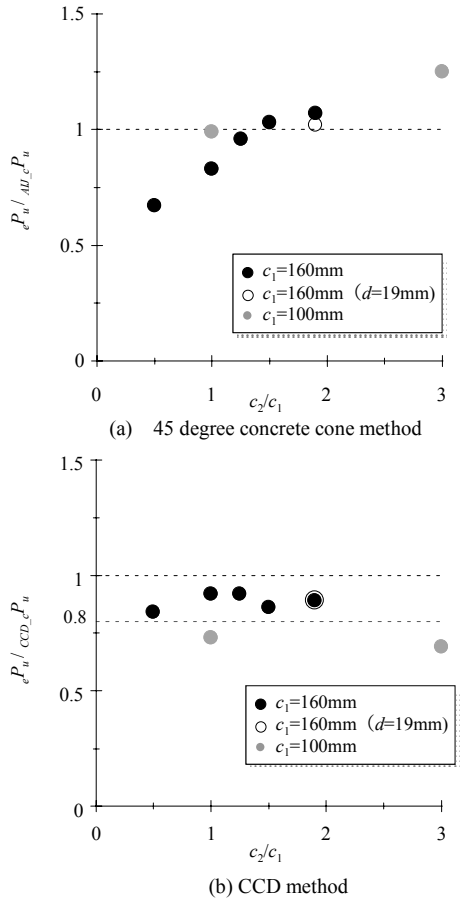

Figure 12 Ratio of Measured to Predicted Failure Load as Function of Ratio c_2/c_1

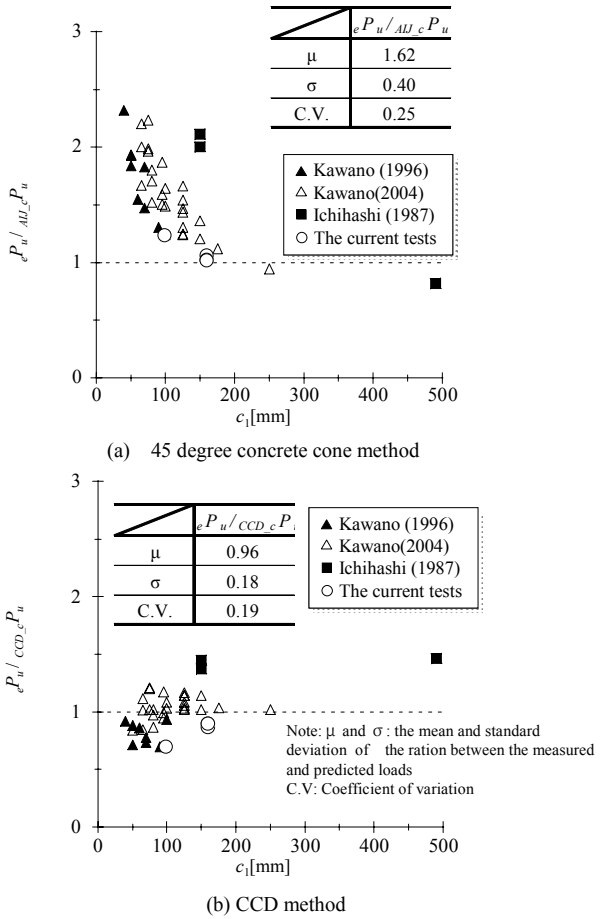

Figure 13 Ratio of Measured to Predicted Failure Load as Function of Edge Distance c_1

of concrete to eliminate their effects. Anchor geometries have little effects on concrete capacity for anchors have diameter of 12mm to 42mm and effective embedment depth of 200mm to 400mm.

3.4 Comparison of predictions with Test data

Figure 12 shows the measured failure loads of each test compared with predicted loads according to 45 degree cone method $_{AIJ}P_u$ and CCD method $_{CCD}P_u$ as function of the ratio c_2/c_1. As previous mentioned, It is confirmed that 45 degree concrete cone method overestimate when corner distance c_2 is smaller than 1.5 times of c_1. On the other hand, CCD method can estimate the effects of reduction of c_2. As a result, CCD method can predict well measured capacity regardless of corner distance c_2. However, CCD method slightly overestimates measured failure loads

In Figure 13, Comparison of measured failure loads of each test with the predicted loads are plotted as function of edge distance c_1. As can be seen, 45 degree concrete cone method was conservative for anchor bolts with small edge distance. However, when c_2 become larger, 45 degree concrete cone method tends to overestimate measured failure loads. These results are due to the size effect of edge distance. In contrast, CCD method has good agreement with the measured loads. in wide range of

4 CONCLUSIONS

From the present and previous results, it is found that prediction according to 45 degree concrete cone method does not adequately takes into account effects of edge distance in perpendicular to loading direction. On the other hand, the prediction proposed by Hofmann based on Concrete capacity method can predict test results well because this prediction can appropriately describes effects of edge distances.

.

References:

Klingner, R. et al. (1982), "Shear Capacity of Short Anchor Bolts and Welded Studs：Literature Review," *ACI Journal*, Vol.79, No.4, 270-279

Fuchs, W. et al. (1995), "Concrete Capacity Design (CCD) Approach for Fastening to Concrete," *ACI Structural Journal*, V.92, No.1, 73-94

Kawano, H., et al. (2003), "Experimental Study on Shear Resistance of anchor bolts in Exposed-type of Steel Column

Bases," *Journal of Structural and Construction Engineering*, AIJ, No.567, 141-148

Kawano, H., et al. (1996), "An Experimental Study on Shear Strength of Anchor Bolts Embedded in Concrete", *Steel Construction Engineering*, JSSC, 12-3, 31-38

Asada, H. et al. (2010), "Pull-out Behavior of Anchor Bolt Fastening Lead Damper to Concrete Foundation," *Journal of Structural and Construction Engineering*, AIJ, No.649

Hofmann, J. (2004), Tragverhalten und Bemessung vonBefestigungen unter beliebiger Querbelastung in ungerissenem Beton, (in German)

Eligehausen, et al. (2006), "Anchorage in Concrete Construction," Ernst & sohn,

Ichihashi, K., (1987), "Strength of the Embedded Plates with anchor bolts in Nuclear Power Plants –Part 2- Shear Strength of Large Size Anchor bolts," *Proceedings of annual meeting*, AIJ, 159-160

JOINT CONFERENCE PROCEEDINGS
7th International Conference on Urban Earthquake Engineering (7CUEE) &
5th International Conference on Earthquake Engineering (5ICEE)
March 3-5, 2010, Tokyo Institute of Technology, Tokyo, Japan

SEISMIC PERFORMANCE EVALUATION OF THE STEEL INTERMEDIATE MOMENT FRAME SYSTEMS WITH RBS WITH BOLTED WEB

Seong-Hoon Hwang[1], Sang Whan Han[2], Ki-Byung Kang[3], and Ki-Hoon Moon[4]

1) Researcher, Construction Research Center at Hanyang University, Seoul, Korea
2) Professor, Hanyang University, Seoul, Korea
3) Graduate student, Hanyang University, Seoul, Korea
4) PhD Candidate, Hanyang University, Seoul, Korea
Hoonic@gmail.com, swhan@hanyang.ac.kr, kkb84@hanyang.ac.kr, acttr@hotmail.com

Abstract: The purpose of this study is to evaluate seismic performance of the Intermediate Moment Frame (IMF) systems with Reduced Beam Section with bolted web connections (RBS-B). Previous studies have demonstrated that the formation of an interior plastic hinge within the reduced beam section improves seismic performance. Some experimental tests showed that some RBS-B specimens fractured at early loading stage. This may be attributed to poor prediction of the accurate moment strength of beam-to-column connection. Accurate equation for predicting connection was proposed by the previous study. In this study, 3- and 6-story IMF systems were designed in accordance with AISC seismic design provisions with the connection design procedure specified in ANSI/AISC 358-05. The seismic performance of IMF systems with RBS-B connections was evaluated according to ATC-63 methodology.

1. INTRODUCTION

FEMA-350 (FEMA 2000) permits the RBS with a bolted web (RBS-B) connection to be used in Special Moment Frames (SMF). In ANSI/AISC 358 (AISC 2005a), which represents an updated version of FEMA-350, the RBS-B moment connection is not prequalified for use in SMF. Only the RBS with Welded web (RBS-W) connection is qualified for SMF. The experimental testing data that some RBS-B specimens failed to achieve 0.04 radian of total rotation required for SMF prequalified connections have been reported (Lee et al. 2005). This may be attributed to insufficient moment strength at face of columns and overestimate of the beam strength at the beam-to-column connection calculated using the current building standards.

Consequently, the objective of this study is to evaluate the seismic performance of the moment frames with RBS-B connection. For this purpose, the three- and six-story buildings having major differences in configuration, design ground motion intensity, and period domain are considered as index archetype models. For this purpose, nonlinear analyses are conducted on the index archetype models. According to ATC-63, Collapse Margin Ratio (*CMR*) of the models is evaluated for performance evaluation.

2. OVERVIEW OF ATC-63 METHODOLOGY

In the ATC-63 Methodology (ATC 2009), collapse level ground motions are defined as the intensity that would result in median collapse of the seismic load resisting system. Median collapse occurs when 50% of the structures under this intensity of ground motion would collapse. Set of ground motions are used in nonlinear dynamic analysis in order to evaluate the collapse capacity of the seismic load resisting system. The collapse capacities of the archetype models are evaluated to determine whether the system provided adequate collapse safety in terms of the Collapse Margin Ratio, *CMR*. The *CMR*, as given in the Eq. (1), which is the ratio of the median spectral response acceleration of the collapse level ground motions, $\hat{S}_{CT}$ to the 5% damped spectral response acceleration of the MCE ground motions, S_{MT} at the fundamental period of the seismic load resisting system:

$$CMR = \frac{\hat{S}_{CT}}{S_{MT}} \tag{1}$$

3. INDEX ARCHETYPE MODELS

3.1 Nonlinear Model for RBS-B moment connections

The M2 model is used for simulating the cyclic behavior of RBS-B moment connections (Gupta and Krawinkler 1999). This model can reflect the exact dimensions of a panel zone. In this model, three different spring elements are used to simulate connection behavior: beam plastic spring; beam end fracture spring; panel zone spring.

(1) Beam Plastic Spring

The beam plastic spring at the center of the reduced beam section used in this study is developed based on bilinear hysteretic model with strength limited (Ibarra 2005). The equation for predicting the plastic rotation capacity of the RBS connection proposed by (Lignos and Krawinkler 2008) was used for simulating the RBS moment connection as follows:

$$\theta_p = 0.22\left(\frac{h}{t_w}\right)^{-0.45}\left(\frac{b_f}{2\cdot t_f}\right)^{-0.14}\left(\frac{d}{21''}\right)^{-0.854} \quad (2)$$

where, h/t_w is the fillet-to-fillet web depth over web thickness ratio, $b_f/2t_f$ is the flange width to thickness ratio, and d beam depth in inches.

(2) Beam End Fracture Spring

In the case of RBS-B moment connections, the moment strength equation of RBS-B connections suggested by Han et al. (2009) was used for considering the possibility of brittle fracture at the beam-to-column connection. This equation explicitly reflects the contributions of the bolted web connection ($M_{n\text{-}bolt}$) and the welded flange connections ($M_{n\text{-}flange}$) to the moment strength of the RBS-B connection as follows:

$$M_n = M_{n-flange} + M_{n-bolt} \quad (3)$$

(4) Panel Zone Spring

The panel zone shear strength and stiffness is modeled by two bilinear springs. The superimposed bilinear springs can simulate the tri-linear behavior of the panel zone (Gupta and Krawinkler 1999). Fig. 1 illustrates that the analytical model for the RBS moment connections accurately predicts actual hysteretic curves.

3.2 Description of Index Archetype Models

As shown in Table 1, 3- and 6-story buildings, which have differences in configuration, design ground motion intensity, and period domain, were considered as index archetype models to evaluate the seismic performance of steel moment frames having RBS-B moment connection. All archetype models were designed in accordance with ASCE/SEI 7-05 (ASCE 2005) and ANSI/AISC 341-05 (AISC 2005b), and soil conditions were assumed to be a stiff soil defined as Site Class D in the ASCE/SEI 7-05.

Two basic configurations are used in steel moment frames with RBS-B moment connections, with 3 and 6 m by widths, respectively. Design ground motion intensities are represented by maximum and minimum Seismic Design Category (SDC) C in accordance with ASCE/SEI 7-05. For example, S_{DS} is 0.499 g and S_{D1} is 0.200 g for SDC C_{max} and S_{DS} is 0.338 g and S_{D1} is 0.133 g for SDC C_{min}. Table 2 shows that the design properties of each of the archetype models used in this study.

4. NONLINEAR ANALYSIS

The models were used to investigate the seismic performance of steel intermediated moment frames system by both nonlinear static pushover analyses and nonlinear dynamic analyses using OpenSees program (Mazzoni et al. 2007). Yield strength of 344.5 MPa was assumed for the design of the steel used in the various structural elements. For the analysis of models, a value of 396.9 MPa was selected to represent the mean value of actual yield strength. For the nonlinear dynamic analyses, 5% Rayleigh damping is assigned to the first mode and the mode at which the cumulative modal mass participation exceeds 90%.

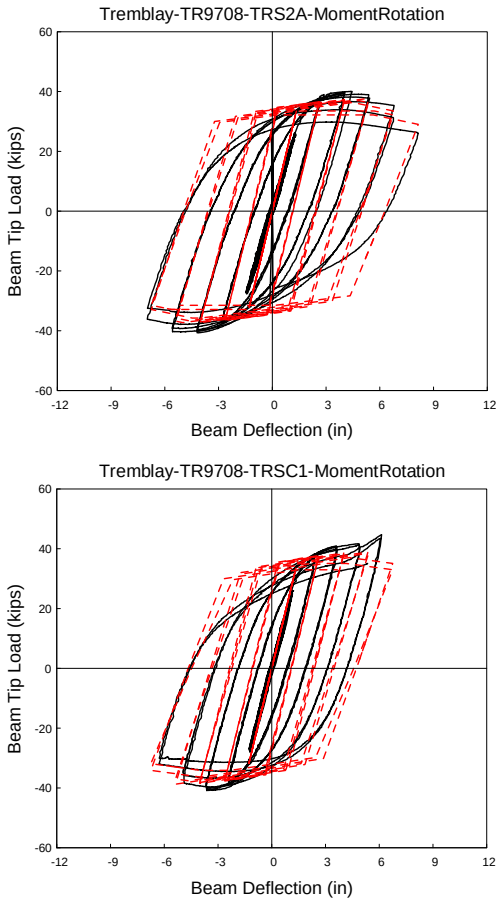

Figure 1. Measured (Tremblay et al. 1997) and Calculated Hysteretic Curves of RBS moment connections

4.1 Nonlinear Static Analysis

In this study, a nonlinear static pushover analysis is conducted for quantifying the maximum base shear capacity, V_{max} and the ultimate displacement, δ_u which are used to estimate archetype overstrength, Ω and period-based ductility, μ_T using the vertical distribution of the lateral force in proportion to the fundamental mode shape of the model.

As shown in Fig. 2, V_{max} is the maximum base shear strength on the pushover curve, and δ_u is taken as the roof displacement at the point of 80 % of maximum base shear strength. The overstrength factor for index archetype, Ω, is the ratio of maximum base shear strength, V_{max} to design base shear, V. The period-based ductility for a given index archetype model, μ_T, is taken as the ratio of ultimate roof drift displacement, δ_u, to the effective yield roof drift displacement , $\delta_{y,eff}$ as follows:

$$\mu_T = \frac{\delta_u}{\delta_{y,eff}} \tag{4}$$

The effective yield roof drift displacement is as given by:

$$\delta_{y,eff} = C_0 \frac{V_{\max}}{W}\left(\frac{g}{4\pi^2}\right)\left(\max\left(T,\ T_1\right)\right)^2 \tag{5}$$

where C_0 relates fundamental-mode (SDOF) displacement to roof displacement, W is building weight, g is gravity acceleration, T is fundamental period The fundamental period of index as defined in Sec 12.8.2 of ASCE/SEI 7-05, and T_1 is fundamental period of index determined from eigenvalue analysis. The coefficient C_0 is given by:

$$C_0 = \phi_{1,r}\frac{\sum_{x=1}^{N} m_x\phi_{1,x}}{\sum_{x=1}^{N} m_x\phi_{1,x}^2} \tag{6}$$

where m_x is the mass at level x, $\phi_{1,x}$ and $\phi_{1,r}$ are the ordinate of the fundamental mode at level x and roof, respectively, and N is the number of levels. Table 2 summarizes important quantities obtained from the nonlinear static pushover curves.

Table 1. Performance Groups for Evaluation of Steel Moment Frames Archetypes

Group No.	Grouping Criteria			
	Basic Configuration	Seismic Design Category	Period Domain	No. of Stories
1	6 m Bay width	SDC C_{min}	Long	3
				6
2		SDC C_{max}	Long	3
				6
3	9 m Bay width	SDC C_{min}	Long	3
				6
4		SDC C_{max}	Long	3
				6

4.2 Nonlinear Dynamic Analysis

Collapse under ground motion is considered here as the limit state in which dynamic sidesway instability is occurred. 44 ground motions of Far-Field record set is used for Incremental Dynamic Analysis (IDA) (Vamvatsikos and Cornell 2005) which are used to estimate the median collapse capacity, $\hat{S}_{CT}$, and collapse margin ratio, *CMR*, for each of the models.

The median collapse capacity, $\hat{S}_{CT}$ is defined as the ground motion spectral intensity when half of the ground motions cause the structure to collapse. Ground motion intensity, S_T, is defined based on the median spectral intensity of the record set, computed at the upper limit on fundamental period, C_uT_a defined in ASCE/SEI 7-05. The results of IDA analyses are shown in Table 3.

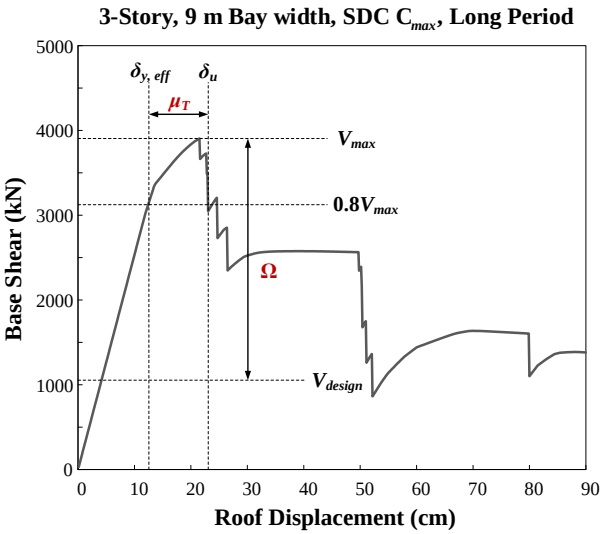

Figure 2. Nonlinear static pushover curves of the three-story archetype model (SDC C_{max}, with 9 m bay width)

Table 2. Pushover results for 8 index archetype models

Group No.	No. of Stories	V_{max} (kN)	Ω	$\delta_{y,eff}$ (cm)	δ_u (cm)	μ_T
1	3	631.69	2.05	10.54	14.50	**1.38**
	6	1095.86	3.11	19.77	27.34	**1.38**
2	3	1653.82	3.53	9.93	14.15	**1.43**
	6	1327.70	2.46	16.50	22.59	**1.37**
3	3	1814.98	2.61	12.38	17.12	**1.38**
	6	2966.70	3.74	25.47	52.07	**2.04**
4	3	3905.38	3.71	12.56	23.77	**1.89**
	6	3808.19	3.14	22.86	36.85	**1.61**

5. PERFORMANCE EVALUATION

The collapse margin ratio is converted into adjusted collapse margin ratio, ACMR, which aims for accounting for the proper spectral shape of rare ground motions through the spectral shape factor, SSF as follows:

$$ACMR_i = SSF_i \times CMR_i \tag{7}$$

In ATC-63 Methodology, individual values of adjusted collapse margin ratio, *ACMR* for each index archetype within a performance group exceeds acceptable values of adjusted collapse margin ratio having collapse probability of 20%, $ACMR_{20\%}$. Table 4 shows the collapse margin ratio, *CMR* obtained from IDA, the SSF, the adjusted collapse margin ratio, *ACMR*, and acceptable values.

6. CONCLUSIONS

The purpose of this study is to evaluate the seismic performance of the moment frames with RBS-B connection. 3- and 6-story buildings, design ground motion intensity, and period domain, were considered as index archetype models to

evaluate the seismic performance of steel moment frames having RBS-B moment connection. The results of seismic performance of RBS-B frames are follows:

1) The overstrength, Ω was calculated from 2.05 to 3.74 according to the results of nonlinear static pushover analysis. overstrengths of some buildings (3-story in group 1: 2.05, 6-story in group 2: 2.46, 3-story in group 3: 2.61) are smaller than 3 proposed by ASCE 7-05. And period-based ductility, μ_T of RBS-B frames was estimated very poor from 1.21 to 1.89. It is known that fracture of the RBS-B connections severely affect to seismic performance of frames as the causes of the low overstrength and poor ductility.

2) The results of dynamic analysis were shown that 3-story RBS-B frames designed for SDC C_{max} with 6 m bay widths is not satisfied by performance of the IMF system. Adjusted collapse margin ratios (ACMR) of this RBS-B frame is estimated to 1.50. This value of ACMR is lower than acceptable values of ACMR. For the safety of RBS-B frames under earthquake load, the RBS-B connections should be re-designed or the response modification of RBS-B frames was re-evaluated.

Table 3. IDA Results for 8 Index Archetype Models

Group No.	No. of Stories	$S_{MT}(g)$	$\hat{S}_{CT}(g)$
1	3	0.23	**1.01**
	6	0.13	**0.24**
2	3	0.38	**0.80**
	6	0.22	**0.30**
3	3	0.23	**0.62**
	6	0.13	**0.39**
4	3	0.38	**1.64**
	6	0.22	**0.49**

Table 4. Results of Adjusted Collapse Margins and Acceptance Criteria for Steel Intermediate Moment Frame Archetype models

Group No.	No. of Stories	*CMR*	*SSF*	*ACMR*	*Accept. ACMR*	*Pass /Fail*
1	3	4.35	1.06	4.61	1.74	Pass
	6	1.78	1.10	1.95	1.74	Pass
2	3	2.11	1.06	2.23	1.74	Pass
	6	1.38	1.09	1.50	1.74	**Fail**
3	3	2.68	1.06	2.83	1.74	Pass
	6	2.91	1.15	3.35	1.78	Pass
4	3	4.29	1.08	4.63	1.77	Pass
	6	2.22	1.11	2.47	1.75	Pass

Acknowledgements:
This work was supported by National Research Foundation of Korea Grant funded by the Korean Government (KRF-2008-313-D01140) and a grant (07-UR-B04) funded by Ministry of Land, Transport and Maritime Affairs. It is greatly appreciated

References:

AISC. (2005a). "Prequalified Connections for Special and Intermediate Steel Moment Frames for Seismic Applications." ANSI/AISC 358, American Institute of Steel Construction Inc (AISC), Chicago, IL.

AISC. (2005b). "Seismic provisions for structural steel buildings including Supplement No. 1." ANSI/AISC 341, American Institute of Steel Construction Inc, Chicago, IL.

ASCE. (2005). "Minimum design loads for buildings and other structures." ASCE/SEI 7-05, American Society of Civil Engineers, Reston, VA.

ATC. (2009). "Quantification of building seismic performance facters." ATC-63, Applied Technology Council, Redwood City, CA.

FEMA. (2000). "Recommended seismic design criteria for new steel moment frame buildings." FEMA 350, Federal Emergency Management Agency, Washington, D.C.

Gupta, A., and Krawinkler, H. (1999). "Seismic demands for performance evaluation of steel moment resisting frame structures." John A. Blume Earthquake Engineering Center Rep. No. 132, Dept. of Civil and Environmental Engrg., Stanford Univ., Palo Alto, CA.

Han, S., Moon, K., and Stojadinovic, B. (2009). "Design equations for moment strength of RBS-B connections." Journal of Constructional Steel Research, 65(5), 1087-1095.

Ibarra, L. F. (2005). "Global collapse of frame structures under seismic excitations." John A. Blume Earthquake Engineering Center Rep. No. 152, Dept. of Civil and Environmental Engrg., Stanford Univ., Palo Alto, CA.

Lee, C.-H., Jeon, S.-W., Kim, J.-H., and Uang, C.-M. (2005). "Effects of Panel Zone Strength and Beam Web Connection Method on Seismic Performance of Reduced Beam Section Steel Moment Connections." Journal of Structural Engineering, 131(12), 1854-1865.

Lignos, D., and Krawinkler, H. (2008). "Sidesway collapse of deteriorating structural systems under seismic excitations," Phd dissertation, Dept. of Civil and Environmental Engrg., Stanford Univ., Palo Alto, CA.

Mazzoni, S., McKenna, F., Scott, M. H., and Fenves, G. L. (2007). OpenSees command language manual, The Univ. of California, Berkeley, Calif., http://opensees.berkeley.edu/index.php.

Tremblay, R., Tchebotarev, N., and Filiatrault, A. (1997), "Seismic performance of RBS connections for steel moment resisting frames: Influence of loading rate and floor slab," Behavior of Steel Structures in Seismic Areas (Proceedings of the Second International Conference, STESSA '97), Kyoto, pp. 664-671.

Vamvatsikos, D., and Cornell, C. A. (2005). "Seismic performance, capacity and reliability of structures as seen through incremental dynamic analysis." John A. Blume Earthquake Engineering Center Rep. No. 151, Dept. of Civil and Environmental Engrg., Stanford Univ., Palo Alto, CA.

JOINT CONFERENCE PROCEEDINGS
7th International Conference on Urban Earthquake Engineering (7CUEE) &
5th International Conference on Earthquake Engineering (5ICEE)
March 3-5, 2010, Tokyo Institute of Technology, Tokyo, Japan

EVALUATION OF PLASTIC ENERGY DISSIPATION CAPACITY OF STEEL BEAMS UNDER VARIOUS LOADING HISTORIES

Yu Jiao[1], Satoshi Yamada[2], Shioichi Kishiki[3], and Yuko Shimada[1]

1) Graduate student, Department of Environmental Science and Technology, Tokyo Institute of Technology, Japan
2) Professor, Structural Engineering Research Center, Tokyo Institute of Technology, Japan
3) Assistant Professor, Structural Engineering Research Center, Tokyo Institute of Technology, Japan
jiao.y.aa@m.titech.ac.jp, yamada.s.ad@m.titech.ac.jp, kishiki.s.aa@m.titech.ac.jp, shimada.y.ab@m.titech.ac.jp

Abstract: In energy based seismic design, the structural performance is determined by the energy dissipation capacity. Due to the wide use of the weak-beam mechanism, it is necessary to evaluate the energy dissipation capacity of steel beams. Seismic effects with significantly different characteristics are applied to the structural components during different types of earthquakes. This paper focuses on the energy dissipation capacity of the steel beams that end in ductile fracture under various loading histories. The material's mechanical characteristics, the beam's geometric characteristics, the beam-to-column connection details and the loading histories are the principal factors that determine the plastic deformation capacity of the steel beams. In this study, first, the effect of the material's mechanical characteristics, the beam's geometric characteristics and the connection details were discussed through the steel beams subjected to monotonic loading. A bi-linear model of the beam's load-deformation relation was introduced. Following that, the cyclic loading tests of the steel beams were carried out to investigate the influence of different loading histories. Together with the experimental data from some other similar experiments, the energy dissipation capacity of the steel beams suffering from ductile fracture under random loading histories was evaluated.

1. INTRODUCTION

In the energy based seismic design, the balance between the seismic input energy and energy dissipation capacity of the structures is the principle concept (Akiyama 1985). The structural performance is determined by the energy dissipation capacity, which depends greatly on the structural components. The steel moment frames with weak-beam mechanism are frequently used to resist earthquakes. Thus, it is very important to study the behavior of the steel beams. This paper focuses on the beams that end in ductile fracture at the flange under various loading histories. The seismic behavior of the beams is discussed in terms of energy concept.

The load-deformation hysteresis loops of the steel beams under cyclic loading can be decomposed into three parts: the skeleton curve, Bauschinger part and elastic unloading part (Akiyama 1985), as illustrated in Fig 1. Two basic empirical rules show that, first, the load-deformation relations of the steel beams under monotonic loading have an approximate correspondence to the skeleton curves, when the steel beams fracture within relatively fewer loading cycles under cyclic loadings; second, the results of the earthquake response analysis show that usually the number of the large deformation amplitude loading cycles that decisively affect the plastic deformation capacity of steel beams is relatively small. Therefore, the energy dissipation capacity of the skeleton curves has been adopted to characterize the behavior of the beams (AIJ 1990).

Nevertheless, the structures are subjected to a large number of loading cycles with relatively small deformation amplitudes under long duration ground motion. With the decreasing of the deformation amplitudes, the energy dissipation of the skeleton curves decreases while that of the Bauschinger parts increases. The relationship between the energy dissipation of the skeleton curves and Bauschinger parts has been quantitatively studied through the cyclic loading tests of the structural steel (Akiyama 1995). Yet no similar work has been done in the field of steel components. Moreover, in most of the cyclic loading tests of the steel beams, the recommended standard loading protocols were applied to the specimens (Sumner 2002, Ricles 2002). However, the structures are subjected to random seismic effects during different earthquakes; the comparison between multiform specimens under various loading

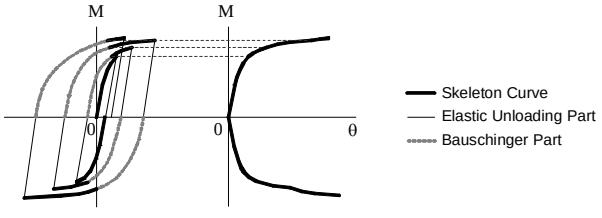

Figure 1 Decomposition of the Beams' Hysteresis Loops

histories is very difficult. Thus, it is extremely important to seek a feasible common method to investigate the seismic performances of diverse steel beams subjected to various loading histories, which is the main purpose of this study.

2. EVALUATION MATHODOLOGY

2.1 Variables That Affect the Energy Dissipation Capacity of Steel Beams

There are many factors that affect the energy dissipation capacity of the steel beams. In this study, several principal factors: The material's mechanical characteristics, the beams' sections and spans; the beam-to-column connection details that include the columns' cross section; and the loading histories were discussed.

For the ideal cantilever steel beam, the material's mechanical characteristics (yielding point, yield ratio and elongation) and the beam's section and span are the determining factors of its load-deformation behavior. The full plastic moment, initial stiffness and the post-yielding stiffness of the beam are strongly affected by these factors.

In the real structures, the beam-to-column connection details (including the column's section) also influence the plastic deformation capacity of the beam. The shop welded flanges and webs connection seems to have good plastic cyclic behavior, which is being widely used in Japan and also raises great attention of the designers and researchers from other countries. The details of this kind of welded-flange-welded-web connections can be found in many literatures (Tremblay 1996, Nakashima 1999). The shape of the weld access holes is one of the decisive parameters that considerably affect the energy dissipation capacity of the beams, because the sudden change in geometry at the toe of the weld access holes causes a stress/strain concentration that consequentially leads to the initial ductile cracks. Furthermore, the loss of the web section due to the weld access holes directly results in the decrease of the moment transmission ability (the joint efficiency). There are different sorts of weld access holes with distinct shapes in Japan (Fig. 2) (AIJ 1996). Before the 1995 Kobe earthquake, the conventional weld access holes were used, while the improved type was introduced since around 1996 in order to avoid stress (and strain) concentration. Besides, the no weld access hole design was also put into used in Japan recently to reduce the strain concentration, which allows the beams to be welded onto the columns without obvious weld access holes. In addition to the weld access holes, the shape of the column sections is also an important factor. Generally speaking, two types of cross sections are commonly used as steel columns: the RHS columns and wide flange columns, of which the former is widely used in Japan while the latter is more frequently used in the United States and some other countries. The RHS columns do not have the weak axis problem but the skin plates at the connections tend to have out-of-plane deformation when the beams are subjected to bending, which is another main reason that causes the inefficiency of

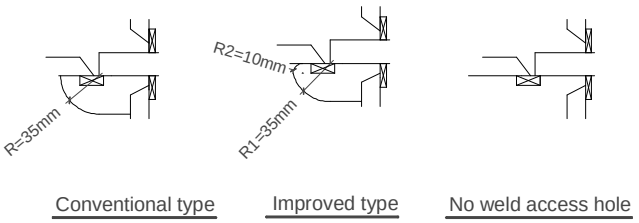

Figure 2 Shapes of the Weld Access Holes

the connection's moment transmission (Okada 2003), i.e., the joint efficiency of the beam web is less than 100%.

In earthquake engineering, the beams' deformation and energy dissipation capacity depend on the cumulative damage, and thus, the loading history is known as the most definitive factor that affect the capability of the beams. Seismic effects of significantly different characteristics are applied to the structures during distinct earthquakes. Furthermore, the number and amplitudes of the loading cycles the beam experiences during earthquakes depend on the configuration, strength, stiffness of the structures and so on. There is no unique best loading history that can represent all kinds of seismic effects input to the beams (Krawinkler 2009). A practical way to assess the consequences of the cumulative damage is to consider various loading histories the beam might undergo. Most of the cyclic loadings employed in the steel beams testing are the recommended standard (usually incremental) loading protocols. It is necessary to introduce more loading histories in addition to these standard loading protocols. Krawinkler (2009) also indicates that a comprehensive testing program for a structural component should include a monotonic test in addition to cyclic tests and the near fault effect should also be taken into consideration.

2.2 Evaluation Methodology

The evaluation of the steel beam's energy dissipation capacity in this study was conducted in two steps. In the first stage, the energy dissipation capacity of the steel beams under monotonic loading was evaluated to investigate the effect of the material's mechanical characteristics, the beam's geometric characteristics and the beam-to-column connection details. According to the current research, a strong correlation between the beam flange's strain concentration and the beam web's joint efficiency was pointed out through experimental research (Matsumoto 1999). The concept of a bi-linear model of the beam's load-deformation relation under monotonic loading was used to illustrate this correlation (Okada 2003). Nevertheless, this bi-linear model is still in the conceptional stage, and there is still a lack of the quantitative study of the energy dissipation capacity. In this study, the conceptional bi-linear model was developed by evaluating the web's joint efficiency at its ultimate state, so that it is possible to obtain the monotonic plastic deformation capacity. Here, the experimental results of 11 specimens from some related beam tests (Okada 2003, Akiyama 1998) were introduced to verify the evaluation.

In the second stage, the energy dissipation capacity of the steel beams under random cyclic loadings was discussed based on that under monotonic loading by considering the effect of cyclic loadings. First, 5 beam-column subassemblies were tested under 5 different loading histories with incremental, decremental as well as constant amplitudes. In addition, 13 specimens from 4 cyclic loading tests (Kishiki 2005, Suita 2003, Kobayashi 2005, Nakagomi 1997) were also investigated. Based on the whole experimental database, the energy dissipation capacity of the steel beams with the failure mode of ductile fracture under various cyclic loading histories was evaluated.

3. ENERGY DISSIPATION CAPACITY OF THE STEEL BEAMS UNDER MONOTONIC LOADING

3.1 The Equivalent Cumulative Plastic Deformation Ratio

The energy dissipation capacity of steel beams under monotonic loading is discussed through a bi-linear load-deformation model, where the effect of the material's characteristics, the beam's section and span as well as the connection details including the column's cross section were studied.

The energy dissipation capacity of steel beams was expressed by means of the Equivalent Cumulative Plastic Deformation Ratio ($\bar{\eta}$), which is one of the indexes used to express the cumulative damage, i.e., the energy dissipation of the steel beams in the energy based seismic design. Equation (1) shows the definition of $\bar{\eta}$:

$$\bar{\eta} = \frac{W_p}{M_p \cdot \theta_p} \tag{1}$$

where W_p is the plastic energy dissipation of the steel beam; M_p is the full plastic moment of the steel beam; and θ_p is the beam rotation when the moment at the beam end reaches M_p. The equivalent cumulative plastic deformation ratio of the steel beams subjected to monotonic loading $\bar{\eta}_0$ can be illustrated in Fig. 3, which is defined by Equation (2),

$$\bar{\eta}_0 = \frac{W_{p0}}{M_p \cdot \theta_p} \tag{2}$$

where W_{p0} is the plastic energy dissipation of the steel beam under monotonic loading.

3.2 Effects of the Material's Characteristics and the Beam's Geometry

As mentioned previously, the material's characteristics and the beam's section and span affect the full plastic moment and the stiffness of the load-deformation relation. It is possible to calculate the full plastic moment and the initial stiffness of the bi-linear load-deformation model from the basic material and structural information. In order to obtain their effect on the second stiffness ratio, a parametric study of the material characteristics and the beam's moment gradient was conducted through the in-plane analysis (Kato 1966, Yamada 1966) of the ideal cantilever W-beams subjected to monotonic shear bending (without out-of-plane deformation).

Two types of steel with different yielding points and elongations that are commonly used in Japan as steel beams, SN400 and SN490, were chosen as the typical material. The tensile coupon test results of these two types of steel were used as the basic stress-strain models (engineering stress and strain). The experimental yield ratio of SN400 was around 60% while that of SN490 was around 70%. It is possible to obtain two relevant stress-strain models with different yet reasonable yield ratios (70% for SN400 and 80% for SN490), by varying the post-yielding stress value of the tensile coupon tests results. Thus, the material database in this parametric study consisted of four stress-strain relation models with various strength, yield ratios and elongations (Fig. 4). Moreover, the stress and strain under compression ε_c, σ_c were derived through Equation (3) from those under tension (Akiyama 1995):

$$\varepsilon_c = \frac{-\varepsilon_t}{1+\varepsilon_t}; \quad \sigma_c = -(1+\varepsilon_t)^2 \cdot \sigma_t \tag{3}$$

where ε_t is the engineering strain under tension; and σ_t is the engineering stress under tension. This equation is valid under the assumption of a constant volume of the steel elements and that the true strain-stress relation under compression and tension is center-symmetric.

The cross section of the cantilever beam was set to wide-flange section 600 mm (depth) × 300 mm (width) × 13 mm (web thickness) × 25 (flange thickness). In order to change the beam's moment gradient, three different beam spans were defined: 3m, 4m and 6m.

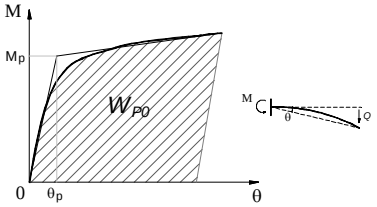

Figure 3 Plastic Energy Dissipation of Steel Beam under Monotonic Loading

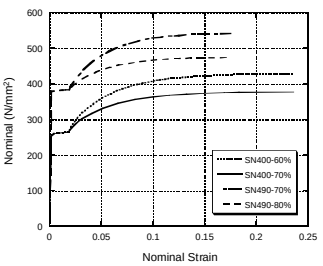

Figure 4 Material Database of the Parametric Study

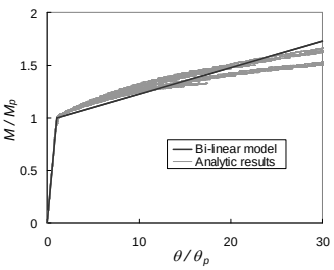

Figure 5 Results of the Parametric Study

The analytic result of each parameter composition is shown in Fig. 5 (thin gray lines). The beam rotation plotted on the X-axis was normalized by θ_P and the moment on the Y-axis was normalized by M_P. There is hardly any significant distinction between the second stiffness ratios of the load-deformation relations obtained with variable parameters. Therefore, it is feasible to assume that the second stiffness ratio of the ideal steel W-beams' load-deformation relations under monotonic loading is a constant, which is considered to be around 2.5%. The bi-linear model of the load-deformation relation with the second stiffness ratio of 2.5% is shown in the graph with the thick line, which agrees well with the analytic results.

In order to study the load-deformation relation of the steel beams, the experimental results of the monotonic loading tests and the shaking table tests were investigated here. In the monotonic loading tests (Okada 2003), four beam-column subassemblies numbered 1~4 were tested under monotonic loading. The details of the tests are listed in Table 1. For the beam section, H is the beam depth; B is the beam width; t_w and t_f is the web and flange thickness. For the column section, D is the column width, and t is the thickness. The shape of the column's cross section (RHS column / wide flange column), the thickness of the column and the shape of the weld access holes (improved type / non-hole type) were the variables of this experiment. The W-beams' cross sections and their spans are exactly the same. Here the definition of the span is the beam length from the loading point to the column's face. The loading points were at the cantilever ends of the beams. The load-deformation relation obtained in this experiment is shown in Fig. 8, which would be discussed later. The ultimate states of all specimens were confirmed as ductile fracture.

In addition to the monotonic loading tests, the data of seven W-beam-to-RHS-column connection specimens numbered 5~11 from a full-scale shaking table test (Akiyama 1998) were also collected (Table 1). The NS component of JMA Kobe Record (According to the Japan Meteorological Agency of Kobe, 1995) which was scaled to a peak velocity of 1.0 m/s, was inputted during the testing. All specimens fractured ductilely during the ultimate excitations. According to the characteristics of the input record (near fault earthquake record), each specimen fractured within few loading cycles, which means the skeleton curves obtained from this experiment are very similar to the load-deformation relations of these beams if they were subjected to monotonic loading. Therefore, it is reasonable to approximately regard the skeleton curves in this shaking table tests as the load-deformation relations of these specimens under monotonic loading.

The experimental results were from these two experiments plotted in Fig. 7 as gray lines together with the bi-linear model. The experimental beam rotation plotted on the X-axis was normalized by the experimental value of θ_P and the moment on the Y-axis was normalized by the experimental value of M_P. There is no considerable difference between the second stiffness of all these specimens. The plastic parts of these experimental results run almost parallel to the 2.5% second stiffness ratio line. Therefore, it is feasible to set the second stiffness ratio of this bi-linear model as 2.5%.

3.3 Effects of the Beam-to-column Connection Details including the Column's Cross Section

In addition to the initial stiffness and second stiffness, it is still essential to study the influence of the different column's section and the weld access holes (beam-to-column connection details). These factors inevitably affect the monotonic load-deformation relation, especially the ultimate plastic deformation capacity. Here, the beam's plastic behavior was first studied based on the experimental results of the monotonic loading tests. Following that, the joint efficiency of the beam web at the ultimate state was evaluated by modifying the Japanese Architectural Institute of Japan (AIJ) design recommendation equations (AIJ 2006). In most cases the joint efficiency is less than 100%, which causes the decrease of the beam's load carrying and deformation capacity.

According to the experimental results of the monotonic loading tests (Fig. 6), there is no considerable difference between the initial stiffness and the second stiffness of all specimens despite the varying parameters. On the other hand, for the specimens with weld access holes (No. 3, 4), the plastification moments are impressively lower than that of the specimens without weld access holes (No. 1, 2).

In order to obtain the ultimate state (load and beam rotation) of the beam, it is necessary to discuss the joint efficiency of the ultimate state. Under bending, the loss of the beam's web section due to the weld access holes and the potential out of plane deformation of the column's skin plates (of RHS-columns) are the main reasons of the beam web being unable to fully transmit the moment. In other

Table 1 Details of the monotonic loading tests and the shaking table tests

Number	Beam						Connection	Column		Loading History
	Cross Section W-H×B×t_w×t_f	Span (mm)	Flange		Web		Weld Access Hole	Cross Section □-D×t	σy (N/mm²)	
			σ_y (N/mm²)	YR (%)	σ_y (N/mm²)	YR (%)				
1	W-300×150×6.5×9	1500	334	70	375	76	None	W-250×250×10×14	348	Mono
2	W-300×150×6.5×9	1500	334	70	375	76	None	□-250×9	364	Mono
3	W-300×150×6.5×9	1500	334	70	375	76	Improved	□-250×9	364	Mono
4	W-300×150×6.5×9	1500	334	70	375	76	Improved	□-250×6	312	Mono
5	W-600×300×12×25	2729	330	64	413	76	Conventional	□-500×16	501	Shaking
6	W-600×300×12×25	2729	330	64	413	76	Conventional	□-500×22	498	Shaking
7	W-600×300×12×25	2729	330	64	413	76	Improved	□-500×22	498	Shaking
8	W-600×300×12×25	2729	330	64	413	76	Improved	□-500×22	498	Shaking
9	W-600×300×12×25	2729	330	64	413	76	None	□-500×22	342	Shaking
10	W-600×300×12×25	2729	330	64	413	76	Conventional	□-500×32	405	Shaking
11	W-600×300×16×32	2729	316	62	378	70	Conventional	□-500×32	405	Shaking

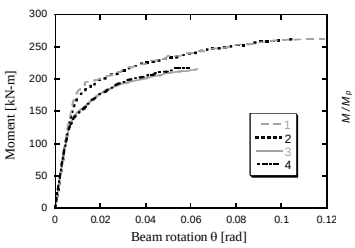

Figure 6 Results of the Monotonic Loading Tests

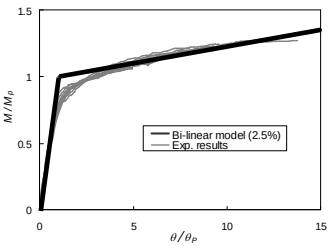

Figure 7 Verification of the Analysis

words, the joint efficiency of the beam web at the beam-to-column connection is less than 100%. Consequently, the plastic strain tends to concentrate on the beam flanges, which causes the decrease of the beam's ultimate deformation capacity as well as the energy dissipation capacity (Fig. 8).

The ultimate joint efficiency of the beam web at the connection γ_w is defined by Equation (4),

$$\gamma_w = \frac{{}_jM_{wu}}{M_{wu}} \tag{4}$$

where ${}_jM_{wu}$ is the maximum moment of the beam web at the connection considering the loss of the beam cross section and out of plane deformation of the skin plate; $M_{wu} = \sigma_{wu} \cdot Z_{wp}$ is the ideal maximum moment of the beam web at the connection; σ_{wu} is the ultimate stress of the beam web; and Z_{wp} is the plastic section modulus of the full section beam web.

In this study, ${}_jM_{wu}$ is calculated by a modified evaluation method based on the Japanese "Recommendation for design of connections in steel structures" (2006) (hereinafter to be referred as "Recommendation"). According to the Recommendation, the actual maximum moment of beam web at the connection ${}_jM_{wu}$ can be calculated through Equation (5) (The symbols mentioned here are illustrated in Fig. 9),

$${}_jM_{wu} = m \cdot Z_{wpe} \cdot \sigma_{wy} \tag{5}$$

where σ_{wy} is the yielding stress of the beam web; $Z_{wpe} = \frac{1}{4}(D_b - 2t_{bf} - 2S_r)^2 \cdot t_{bw}$ is the plastic section modulus of the beam web considering the loss of cross section; and m is the normalized bending strength of the beam web at the beam-to-column connection considering the out-of-plane deformation of the column's skin plate by comparing the yielding stress of both the skin plate and beam web. For the wide flange columns (strong-axis direction), $m = 1$; and for the RHS columns, $m = \min\left\{1, \quad 4\frac{t_{cf}}{d_j}\sqrt{\frac{b_j \cdot \sigma_{cy}}{t_{bw} \cdot \sigma_{wy}}}\right\}$, where σ_{cy} is the yielding stress of the column; D_b is the beam height; t_{bf} is the thickness of the beam flange; S_r is the loss of cross section in the dimension of beam height (usually the length of weld access hole along beam height); t_{bw} is the thickness of the beam web; t_{cf} is the steel plate thickness of the RHS column; d_j is the inner distance of two diaphragms; $b_j = B_c - 2t_{cf}$ is the width of the yielding area on the RHS column obtained from the Yield-line Theory; and B_c is the width of the RHS column.

In Equation (5) the steel's yielding stress σ_{wy} is used. The maximum web moment is a little underestimated to guarantee the safety of the design. Nevertheless, strain hardening occurs to the real structural steel. In case of the W-beams without weld access holes when the joint efficiency of the beam web is higher, the web is more likely to be in its plastic region reaching ultimate stress σ_{wu} when the beam fractures. Therefore, the modified method divides beams into two categories, with and without weld access holes, expressed by Equations (6) and (7) respectively:

$${}_jM_{wu} = m \cdot Z_{wpe} \cdot \sigma_{wy} \tag{6}$$

$${}_jM_{wu} = m \cdot Z_{wpe} \cdot \sigma_{wu} \tag{7}$$

For beams without weld access holes, the ultimate stress σ_{wu} is introduced. The experimental results of the eleven specimens (No. 1~4 from the monotonic loading tests and No. 5~11 from the shaking table tests) from section 3.2 were investigated to verify the proposed evaluation method of the joint efficiency.

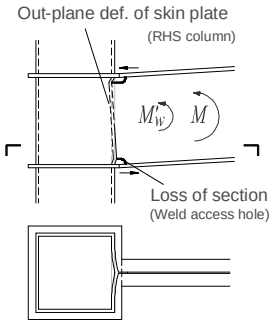

Figure 8 Out-plane Deformation of Skin Plate and the Loss of Web Section

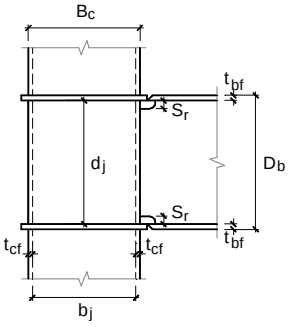

Figure 9 Symbols Mentioned in Equation 5

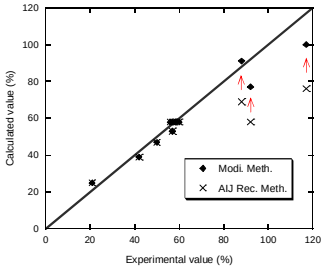

Figure 10 Verification of the Calculation Method

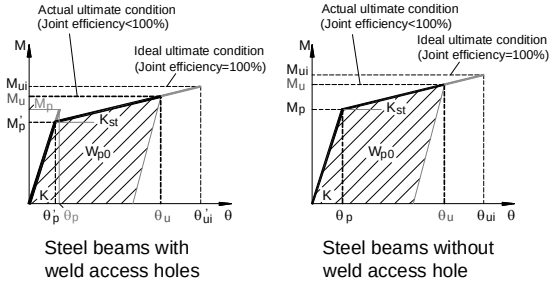

Figure 11 Bi-linear Load-deformation Relation Model of Steel Beams under Monotonic Loading

The calculated joint efficiencies of these 11 specimens were obtained through the original evaluation method from the Recommendation as well as the modified evaluation method. The calculated results were compared with the experimental values (Okada 2003). The verification of the evaluation methods is shown in Fig. 10 with the experimental results plotted on the X-axis and the calculated results plotted on the Y-axis. The modified method shows good accuracy. Particularly for the specimens without weld access holes, the results of the modified method are considerably closer to the experimental results (arrows in Fig. 10), although the Recommendation method is known to be safer in structural design.

A bi-linear load-deformation relation model is proposed here based on the model mentioned by Okada (2003) to evaluate the energy dissipation capacity of steel beams under monotonic loading. Fig. 11 shows the details of the model. According to the previous discussion, it is necessary to divide the beams into two categories: with and without weld access holes. For both categories, K is the initial stiffness and $K_{st} = 2.5\% \cdot K$ is the second stiffness. For beams without weld access holes, the plasticification moment can be represented as M_p and θ_p. M_{ui} and θ_{ui} are the ideal maximum moment and beam rotation when the joint efficiency γ_w is 100%, which can be obtained from the model with some basic structural information. M_u and θ_u are the actual ultimate condition considering the decrease of the joint efficiency. For beams with weld access holes, it is necessary to consider the decrease of the plastification moment, i.e., to calculate the full plastic moment from the net beam section. Therefore, the plasticification moment $M_p^{'}$ and the corresponding beam rotation $\theta_p^{'}$ are smaller than the commonly defined M_p and θ_p. M_{ui} is the same as the ideal ultimate fracture moment of the beams without weld access holes, while $\theta_{ui}^{'}$ is the corresponding beam rotation. M_u and θ_u is the actual ultimate condition considering the decrease of the joint efficiency. M_u can be expressed in Equation (8),

$$M_u = M_{fu} + \gamma_w \cdot M_{wu} \tag{8}$$

where $M_{fu} = \sigma_{fu} \cdot Z_{fp}$ is the maximum moment of the beam flange at the connection; and Z_{fp} is the plastic section modulus of the full section beam flange. With the joint efficiency γ_w known, it is possible to obtain the maximum beam rotation θ_u from the bi-linear model. It is possible to calculate the energy dissipation capacity W_{p0} as well as $\bar{\eta}_0$ of steel beams subjected to monotonic loading through this model.

The experimental results from the monotonic loading tests were investigated to verify the evaluation method. Fig. 12 shows the verification. The equivalent cumulative plastic deformation ratio of steel beams under monotonic loading $\bar{\eta}_0$ is calculated from the model to estimate the energy dissipation capacity. The experimental results of $\bar{\eta}_0$ from the monotonic loading tests are plotted on the X-axis and the calculated results of $\bar{\eta}_0$ are plotted on the Y-axis. This graph shows the good correspondence between the experimental and calculated values of the monotonic energy dissipation capacity.

4. ENERGY DISSIPATION CAPACITY OF STEEL BEAMS UNDER CYCLIC LOADING

4.1 Equivalent Cumulative Plastic Deformation Ratio of the Steel Beams under Cyclic Loading

In this section, the influence of various loading histories is studied by investigating the beams under cyclic loadings. The load-deformation hysteresis of the steel beam subjected to cyclic loading is composed of the skeleton curve, Bauschinger part and elastic unloading part (Akiyama 1985). Here, the skeleton curve is obtained by connecting parts of the load-deformation relation sequentially, when the beam experiences its maximum load (both positive and negative) for the first time.

With the decomposition of the hysteresis loop, the plastic energy dissipation of the steel beam W_p can be expressed as the sum of that from both its skeleton curve and Bauschinger part, as shown in Equation (9) and Fig. 13:

$$W_p = W_S + W_B \tag{9}$$

where W_S is the plastic energy dissipation from the skeleton curve; and W_B is the plastic energy dissipation from the Bauschinger part. Consequently, it is possible to express the equivalent cumulative plastic deformation ratio of steel beams under cyclic loading $\bar{\eta}$ in Equations (10)-(12).

$$\bar{\eta} = {}_S\bar{\eta} + {}_B\bar{\eta} \tag{10}$$

$${}_S\bar{\eta} = W_S / (M_p \cdot \theta_p) \tag{11}$$

$${}_B\bar{\eta} = W_B / (M_p \cdot \theta_p) \tag{12}$$

where ${}_S\bar{\eta}$ is the equivalent cumulative plastic deformation ratio of the skeleton curve; and ${}_B\bar{\eta}$ is the equivalent cumulative plastic deformation ratio of the Bauschinger part. In this study, the equivalent cumulative plastic deformation ratio of each part of the hysteresis loop was studied to discuss the energy dissipation capacity of the steel beam subjected to cyclic loading.

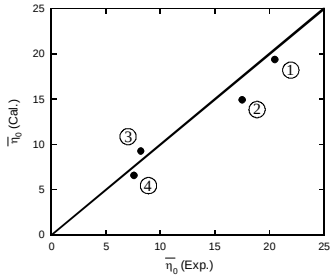

Figure 12 Verification of the Energy Dissipation Capacity of Steel Beams under Monotonic Loading

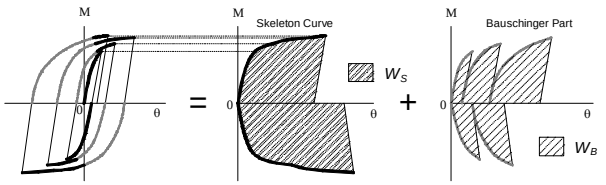

$$W = W_S + W_B$$

Figure 13 Decomposition of the Hysteresis Loop & Plastic Energy Dissipation of Steel Beam under Cyclic Loading

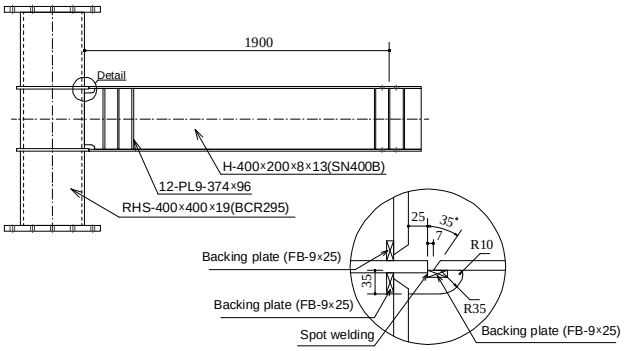

Figure 14 Details of the Specimens

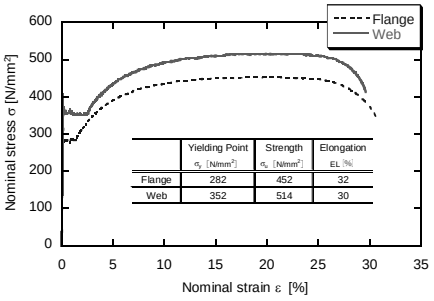

	Yielding Point σ_y [N/mm²]	Strength σ_u [N/mm²]	Elongation EL [%]
Flange	282	452	32
Web	352	514	30

M_P [kN-m]	383
θ_P [rad]	0.0058
M_U [kN-m]	599
K_e [kN-m/rad]	66000

Figure 15 Coupon Tests Results and the Specimen's Mechanical Characteristics

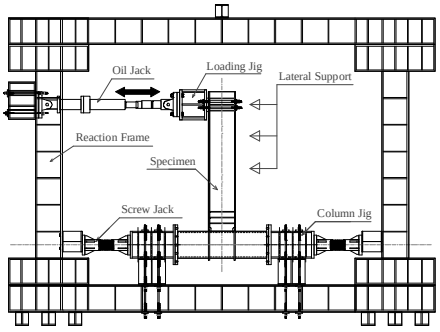

Figure 16 Setup Details of the Cyclic Loading Tests

4.2 Cyclic Loading Tests of the Steel Beams

The cyclic loading tests of five T-type beam-column subassemblies (No. 12~16 in the whole database) with exactly the same structural details were conducted to investigate the effect of the loading history to the energy dissipation capacity of steel beams. The only variable in this experiment is the loading history.

The column of the specimen is the RHS 400 mm × 400 mm × 19 mm (BCR295) while the beam is the wide-flange section 400 mm (depth) × 200 mm (width) × 8 mm (web thickness) × 13 (flange thickness) (SN400B) (Fig. 14). The beam was shop welded onto the column via through-diaphragms, with the improved type of weld access holes and solid end tab in accordance with the Japanese Standard Specification JASS6 (AIJ 1996). Steel plates of the column and panel zone were thick enough so that both did not yield even when the beam reached its maximum strength. Furthermore, in order to prevent local buckling, stiffeners were welded to the beam near the panel zone of the connection as well as the loading point. The results of the tensile coupon tests are shown in Fig. 15. The engineering stress and strain are shown here. Mechanical characteristics of the specimen are also listed.

The specimen, which was rotated 90° with its beam standing vertically and column lying horizontally, was set up through column jigs and screw jacks, with the former fastened onto the reaction frame to offer vertical support and the latter contacting the reaction frame to get horizontal support (Fig. 16). A loading jig connecting the beam free-end of the specimen and the oil jack which was installed horizontally on the reaction frame composed the loading system. Moreover, the lateral supports (stiffening systems) were set at three locations to avoid lateral buckling of the beam.

Five different deformation-controlled cyclic loadings shown in Fig. 17 were applied to the specimens during the test with the unit beam rotation set to θ_P (0.0058 rad by calculation), which is the elastic beam rotation when the moment of the beam's cantilever end equals its full plastic moment M_P (383kN·m by calculation). The five loading histories are as follows: 1) Incremental cyclic loading starting from $\pm 2\theta_P$, with intervals of $2\theta_P$. For each load step, two cycles were applied. 2) Decremental cyclic loading completely converse of 1), i.e. loading starting from the fracture loading amplitude of specimen 1) with intervals of $-2\theta_P$. For each load step, two cycles were applied. 3)-5) Cyclic loading with constant amplitude of $\pm 3\theta_P$, $\pm 4\theta_P$ and $\pm 5\theta_P$. Here, loading 1) is recommended by the Building Research Institute and the Japan Iron and Steel Federation (Building Research Institute 2002); and loadings 3)-5) are employed to simulate the earthquake effect under long duration ground motion.

The load-deformation relations obtained from the cyclic loading tests are shown in Fig. 18. Ductile cracks on the beam flange were first observed near the toe of the weld

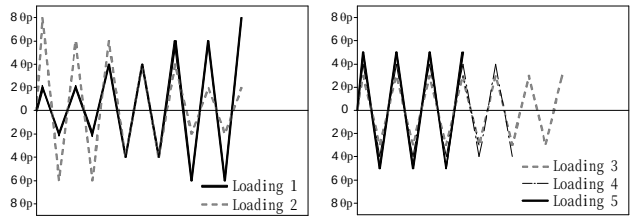

Figure 17 Loading Histories

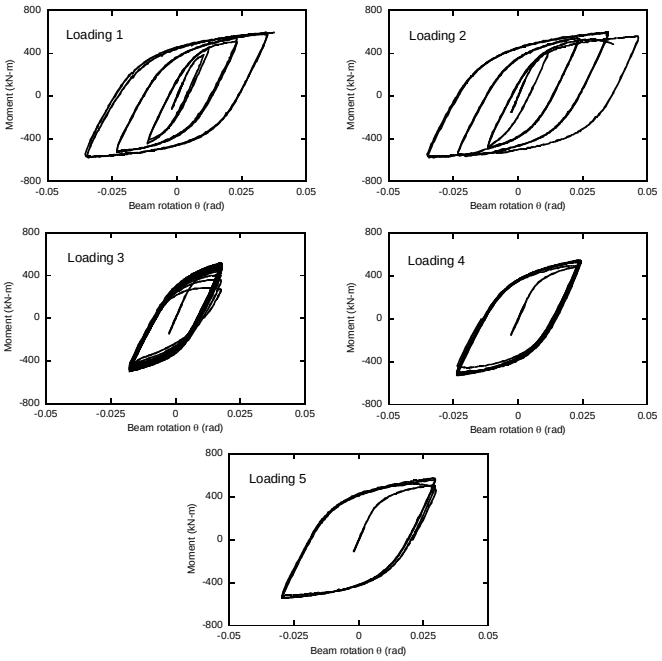

Figure 18 Loading-deformation Relations

Table 2 Details of the related cyclic loading tests

Number	Beam						Connection	Column		Loading History
	Cross Section W-H×B×t_w×t_f	Span (mm)	Flange		Web		Weld Access Hole	Cross Section □-D×t	σy (N/mm²)	
			σ_y (N/mm²)	YR (%)	σ_y (N/mm²)	YR (%)				
17	W-600×200×9×12	2050	291	68	385	74	Improved	□-400×19	388	Incr.
18	W-600×200×11×17	3725	299	62	334	68	None	PL-50		Incr.
19	W-600×200×11×17	3725	299	62	334	68	None	PL-50		Incr.
20	W-600×200×11×17	3725	299	62	334	68	None	PL-50		Con.
21	W-600×200×11×17	3725	299	62	334	68	None	PL-50		Con.
22	W-600×200×11×17	2225	299	62	334	68	None	PL-50		Incr.
23	W-600×200×11×17	2225	299	62	334	68	None	PL-50		Incr.
24	W-600×200×11×17	2225	299	62	334	68	None	PL-50		Con.
25	W-600×200×11×17	2225	299	62	334	68	None	PL-50		Con.
26	W-400×200×8×13	1900	314	71	368	78	Improved	□-400×19	359	Incr.
27	W-400×200×8×13	1900	314	71	368	78	Improved	□-400×19	359	Incr.
28	W-488×300×11×18	2150	386	73	396	71	Conventional	□-400×19	397	Incr.
29	W-488×300×11×18	2150	318	72	318	72	Conventional	□-400×19	267	Incr.

access hole of each specimen, which evolved longer and wider during the test until the specimen reached fracture. Here, fracture is defined as the point when the measured load started to decrease while specimen's deformation was still increasing. Due to the limitation of the specimens, it is still necessary to collect additional experimental data.

4.3 Relevant Cyclic Loading Tests of the Steel Beams

Thirteen specimens (No. 17~29) from 4 cyclic loading tests were collected (Table 2). Eight of them are steel beam specimens with 50 mm thick end-plates (PL in Table 2), and the others are the beam-column subassemblies with W-beams and RHS columns, of which the beam parts were tested. Different types of structural steel were used in each experiment for beams and columns. Both the conventional and the improved type of the weld access holes can be found

Table 3 Detailed results of the whole database

Number	Loading History		Equivalent Cumulative Plastic Deformation Ratio						
	Loading Pattern	Number of Cycles	Cal. Value	Experimental Value					
			$\bar{\eta}_0$	$_S\bar{\eta}$	$_B\bar{\eta}$	$\bar{\eta}$	$_S\bar{\eta}/\bar{\eta}_0$	$_B\bar{\eta}/\bar{\eta}_0$	$\bar{\eta}/\bar{\eta}_0$
1	Monotonic	0.5	19.36	20.30	0.00	20.30	1.05	0.00	1.05
2	Monotonic	0.5	14.94	17.34	0.00	17.34	1.16	0.00	1.16
3	Monotonic	0.5	9.26	8.09	0.00	8.09	0.87	0.00	0.87
4	Monotonic	0.5	6.59	7.58	0.00	7.58	1.15	0.00	1.15
5	JMA Kobe NS Record	2	18.87	41.50	16.75	58.25	2.20	0.89	3.09
6	JMA Kobe NS Record	3	20.69	43.30	37.83	81.13	2.09	1.83	3.92
7	JMA Kobe NS Record	3	20.69	43.71	38.15	81.86	2.11	1.84	3.96
8	JMA Kobe NS Record	3	20.69	43.55	55.96	99.51	2.10	2.70	4.81
9	JMA Kobe NS Record	14	24.64	44.28	122.96	167.24	1.80	4.99	6.79
10	JMA Kobe NS Record	14.5	20.69	45.59	98.37	143.95	2.20	4.75	6.96
11	JMA Kobe NS Record	2.5	23.14	52.16	65.03	117.19	2.25	2.81	5.06
12	2×±2θp, 2×±4θp, 2×±6θp, +8θp	6.5	19	21.56	47.69	69.25	1.13	2.51	3.64
13	8θp, 2×±6θp, 2×±4θp, 2×±2θp, 8θp	7	19	25.82	53.30	79.12	1.36	2.81	4.16
14	±3θp	26.5	19	7.85	137.95	145.80	0.41	7.26	7.67
15	±4θp	10	19	13.28	82.74	96.02	0.70	4.35	5.05
16	±5θp	3.5	19	18.96	29.23	48.19	1.00	1.54	2.54
17	1×±1/100, 1×±1/50, 1×±1/33	3	7.21	9.86	8.56	18.42	1.37	1.19	2.55
18	2×±2θp, 2×±4θp, n×±6θp	8	29.53	27.74	88.26	116.00	0.94	2.99	3.93
19	8×±2θp, 8×±4θp, n×±6θp	17.5	29.53	18.67	141.85	160.52	0.63	4.80	5.44
20	±4θp	11.5	29.53	17.34	120.01	137.35	0.59	4.06	4.65
21	±6θp	4.5	29.53	28.69	67.77	96.46	0.97	2.30	3.27
22	2×±2θp, 2×±4θp, n×±6θp	8.5	29.53	29.02	102.13	131.15	0.98	3.46	4.44
23	8×±2θp, 8×±4θp, n×±6θp	18.5	29.53	21.33	118.66	139.99	0.72	4.02	4.74
24	±4θp	8.5	29.53	16.40	75.68	92.08	0.56	2.56	3.12
25	±6θp	7	29.527178	30.33	129.06	159.39	1.03	4.37	5.40
26	2×±0.01, 2×±0.02, 2×±0.03, 2×±0.04	6.5	12.16	15.09	24.12	39.21	1.24	1.98	3.22
27	5×±0.01, 5×±0.02, 1×±0.05	11	12.16	19.27	27.41	46.68	1.58	2.25	3.84
28	±10p, 2×±20p, 2×±30p, 2×±40p…	10	12	7.88	24.41	32.29	0.66	2.03	2.69
29	±10p, 2×±20p, 2×±30p, 2×±40p…	10.5	11.8	14.44	56.34	70.78	1.22	4.77	6.00

in these specimens. In addition, the steel beam specimens with end-plates were welded onto the thick end-plate without weld access holes. In these experiments, the specimens were tested under various loading histories consisted of the incremental cyclic loadings (Incr.), the constant amplitude cyclic loadings with relatively small or large amplitudes (Con.). The ultimate states of all these specimens were confirmed as ductile fracture at the beam flanges near the connections.

4.4 Evaluation of the Energy Dissipation Capacity

In order to remove the influence of the material characteristics and structural details, the equivalent cumulative plastic deformation ratio of the skeleton curve ($_S\bar{\eta}$) and Bauschinger part ($_B\bar{\eta}$), as well as the overall equivalent cumulative plastic deformation ratio $\bar{\eta}$, were normalized by the equivalent cumulative plastic deformation ratio of steel beams under monotonic loading $\bar{\eta}_0$. The normalized values $_S\bar{\eta}/\bar{\eta}_0$, $_B\bar{\eta}/\bar{\eta}_0$ and $\bar{\eta}/\bar{\eta}_0$ can be regarded as the energy dissipation capacity of the steel beam with the same material and structural characteristics, which is only affected by the loading histories. The detailed results of the whole database are listed in Table 3.

The number of loading cycles till the beam fractures N various from 0.5 to 26.5 in the database. The relations of normalized equivalent cumulative plastic deformation ratios and the number of loading cycles till fracture are plotted in Fig. 19. $_S\bar{\eta}/\bar{\eta}_0$ decreases with the increasing of N, while $_B\bar{\eta}/\bar{\eta}_0$ and $\bar{\eta}/\bar{\eta}_0$ show opposite trends.

The fitted line of each relation is also plotted in these graphs. It is possible to approximate the normalized equivalent plastic deformation ratios as the functions of $\ln(N^n)$ with tolerant errors, illustrated in Equations (13)~(15).

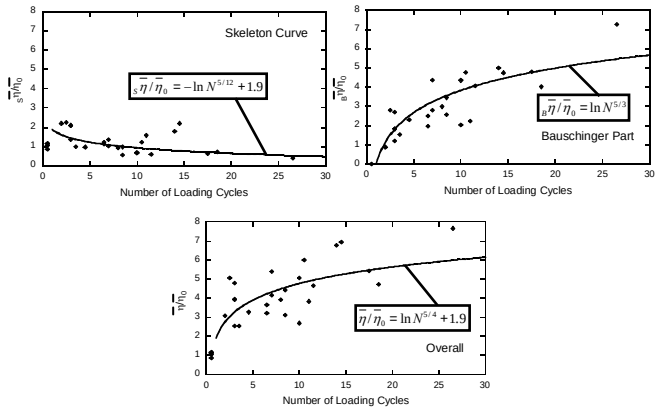

Figure 18 Relation between the normalized equivalent cumulative plastic deformation ratio of skeleton curve and the number of loading cycles till fracture

$$\begin{cases} {}_S\bar{\eta}/\bar{\eta}_0 = \ln N^{5/4} + 1.9 & (0.5 \le N \le 1) \\ {}_S\bar{\eta}/\bar{\eta}_0 = -\ln N^{5/12} + 1.9 & (N > 1) \end{cases} \quad (13)$$

$$\begin{cases} {}_B\bar{\eta}/\bar{\eta}_0 = 0 & (0.5 \le N \le 1) \\ {}_B\bar{\eta}/\bar{\eta}_0 = \ln N^{5/3} & (N > 1) \end{cases} \quad (14)$$

$$\bar{\eta}/\bar{\eta}_0 = \ln N^{5/4} + 1.9 \qquad (N > 0.5) \quad (15)$$

5. Conclusion

This study aims at the evaluation of the energy dissipation capacity of the steel beams fracture ductilely under various loading histories. First, a modified bi-linear model of the beam's load-deformation relation under monotonic loading was suggested for the evaluation of the beams' energy dissipation capacity under monotonic loading, where the effect of the material's mechanical characteristics, the beam's section/span as well as the beam-to-column connection details were discussed. Following that, the cyclic loading tests of steel beams were conducted and some similar experiments were also investigated. The relation between the energy dissipation capacity of steel beams and the number of loading cycles until fracture was obtained. The errors observed are within acceptable range. The conclusions of this study can be summarized as follows:

(1) It is possible to evaluate the energy dissipation capacity of steel beams under monotonic loading through the bi-linear load-deformation model with the second stiffness ratio of 2.5% despite the different material, beam section/span as well as the connection details. The ultimate moment and beam rotation of the model are obtained by considering the webs' joint efficiency.

(2) The normalized equivalent plastic deformation ratio of each part of the beam's load-deformation relation (${}_S\bar{\eta}/\bar{\eta}_0$ and ${}_B\bar{\eta}/\bar{\eta}_0$) and the overall normalized equivalent plastic deformation ratio ($\bar{\eta}/\bar{\eta}_0$) can be approximately fitted as the natural logarithm functions of the number of loading cycles the beam experiences in its plastic region till fracture (N).

Acknowledgements:

Grateful acknowledgement is given to Prof. Keiichiro Suita of Kyoto University for providing his experimental data of steel beams under cyclic loading.

References:

Akiyama H. (1985), Earthquake-resistant limit-state design for buildings, Tokyo: University of Tokyo Press.

Architectural Institute of Japan. (1990), Ultimate strength and deformation capacity of buildings in seismic design (In Japanese). Tokyo: AIJ.

Akiyama H, Takahashi M, Shi Z. (1995), Ultimate energy absorption capacity of round-shape steel rods subjected to bending (In Japanese). Journal of Structural and Construction Engineering, Transactions of AIJ; No 475: 145-54.

Sumner EA, Murray TM. (2002), Behavior of extended end-plate moment connections subject to cyclic loading. Journal of structural engineering; Vol. 128, No. 4: 501-8.

Ricles JM, Mao C, Lu LW, Fisher JW. (2002), Inelastic cyclic testing of welded unreinforced moment connections. Journal of structural engineering; Vol. 128, No. 4: 429-40.

Tremblay R, Bruneau M, Nakashima M, Prion HGL, Filiatrault A, DeVall R. (1996), Seismic design of steel buildings: lessons from the 1995 Hyogo-ken Nanbu earthquake. Canadian Journal of Civil Engineering; Vol. 23: 727-56.

Nakashima M, Roeder CW, Maruoka Y. (1999), Steel moment frames for earthquakes in United States and Japan. Journal of structural engineering; Vol. 126, No. 8: 861-8.

Architectural Institute of Japan. (1996), Japanese architectural standard specification JASS 6 steel work (In Japanese). Tokyo: AIJ.

Okada K, Matsumoto Y, Yamada S. (2003), Evaluation of effect of joint efficiency at beam-to-column connection on ductility capacity of steel beams (In Japanese). Journal of Structural and Construction Engineering, Transactions of AIJ; No 568: 131-8.

Krawinkler H. (2009), Loading histories for cyclic tests in support of performance assessment of structural components. 3rd International Conference on Advances in Experimental Structural Engineering, San Francisco.

Matsumoto Y, Akiyama H, Yamada S. (1999), Relation between deformation capacity of beam at steel beam-to-column connection and joint efficiency (In Japanese). Journal of Structural and Construction Engineering, Transactions of AIJ; No 523: 117-24.

Akiyama H, Yamada S, Matsumoto Y, Matsuoka S, Ogura K, Kitamura H. (1998), Study on fracture of beam-to-column connections by means of full scale shaking table test (In Japanese). Journal of structural and construction engineering, Transactions of AIJ; No 512: 165-72.

Kishiki S, Uehara D, Yamada S, Suzuki K, Saeki E, Wada A. (2005), New ductile steel frames limiting damage to connection elements at the bottom flange of beam-ends: Part 3 Experimental evaluation of composite effects and

damage to concrete slab (In Japanese). Journal of structural and construction engineering, Transactions of AIJ; No 595: 123-30.

Suita K. (2003), Flexural strength demand for beam-to-column connections in earthquake resistant design of steel moment frames (In Japanese). Journal of structural and construction engineering, Transactions of AIJ; No 567:165-71.

Kobayashi A. (2005), Evaluation of ultimate energy dissipation capacity of steel under cyclic loading (In Japanese). Master Thesis submitted to Tokyo Institute of Technology.

Nakagomi T, Fujita T, Minami K, Lee K, Murai M. (1997), Study on beam-end detail for the method of non-scallop on beam-to-column welded joints (In Japanese). Journal of structural and construction engineering, Transactions of AIJ; No 498: 145-51.

Kato B, Akiyama H, Uchida N. (1966), Ultimate strength of structural steel members (I) (In Japanese). Transactions of the AIJ; No 119: 22-30.

Yamada M, Sakae K, Tadokoro T, Shirakawa K. (1966), Elasto-plastic bending deformation of wide flange beam-columns under axial compression, Part I: Bending moment curvature and bending moment deflection relations under static loading (In Japanese). Transactions of the AIJ; No 127: 8-14.

Architectural Institute of Japan. (2006), Recommendation for design of connections in steel structures (In Japanese). Tokyo: AIJ.

Building Research Institute and the Japan Iron and Steel Federation. (2002), Study on testing method for structural performance evaluation of steel structures. Tokyo.

JOINT CONFERENCE PROCEEDINGS
7th International Conference on Urban Earthquake Engineering (7CUEE) &
5th International Conference on Earthquake Engineering (5ICEE)
March 3-5, 2010, Tokyo Institute of Technology, Tokyo, Japan

THE INFLUENCE OF THE LATERAL LOAD PATTERN ON THE MINIMUM COLUMN-TO-BEAM MOMENT STRENGTH

Se Woon Choi[1], Sung Woo Park[1], Bub Ryur Kim[1] and Hyo Seon Park[2]

1) Graduate Student, Dept. of Architectural Engineering, Yonsei University, Korea
2) Professor, Dept. of Architectural Engineering, Yonsei University, Korea
watercloud@yonei.ac.kr, paksungwoo@naver.com, rlaqjqfuf@hanmail.net, hspark@yonsei.ac.kr

Abstract: The 'Strong Column-Weak Beam' condition is generally used to improve the ductility of a building. But many researchers showed that a reinforced condition above the column-to-beam moment strength ratio of the provision was required. The structural design of examples used in these researches was based on the experience of engineers. The examples used in this study are designed by the optimal seismic design method to guarantee more objectivity than the existing researches. The purpose of this study identifies the minimum moment strength ratio of column-to-beam joints required to ensure the beam-hinge mechanism and the influence of the lateral load pattern on the ratio. The lateral load patterns considered in this paper are an inverted triangular pattern and a uniform pattern. The optimal method used in this paper is to minimize the structural weight and the column-to-beam moment strength ratio ratios through the objective functions and to induce the beam-hinge mechanism through the constraint which is to prevent the formation of plastic hinge in the column part consisting of the joints. A 2D steel moment frame is used as an example.

Keywords: strong column-weak beam, plastic hinges, lateral load pattern, optimization

1. INTRODUCTION

Moment resisting frames are a representative seismic resisting system that consists of beams and columns. The beams of them rigidly were connected to the columns to resist the seismic loads. They are widely used in the many regions of high seismicity because of their high ductility and architectural versatility.

Seismic Provisions for Structural Steel Buildings(ANSI/AISC 341-05) presents the concept of 'Strong Column-Weak Beam' for ensuring a high ductility of steel moment resisting frames. This is the design concept that the sum of moment strength of columns is greater than the sum of those of beams at the column-to-beam joint. The purpose of this concept is to prevent the concentration of deformation at the specific story due to the occurrence of the soft-story. If the plastic deformations are concentrated on the columns, which is called 'column-hinge mechanism', the possibility of abrupt failure of the building will increase. So we need to design buildings that plastic deformations are concentrated on the beams, which is called 'beam-hinge mechanism'.

'Strong Column-Weak Beam' condition used in the seismic design code and provision is based on elastic analysis and assumes that the inflection point of a column is located near the center of the column. However, Park and Paulay(1975) showed that the inflection point of a column could move to the end part of it or that the bending moment distribution of it could form a single curvature due to the influence of the inelastic behavior and higher modes. If this case happens, the corresponding column will be subject to a larger load than anticipated and be damaged.

Numerous studies have shown that a design satisfying this condition can still experience the formation of plastic hinge on the columns consisting of joints. So many design methods are proposed to induce the bema-hinge mechanism of moment resisting frames(Lee 1996, Nakashima et al. 2000, Dooley et al. 2001, Kuntz et al. 2003, Medina 2005). However, these studies were based on the examples designed by the engineer's experience. Choi and Park(2009) presented an optimal seismic design model to ensure the beam-hinge mechanism for the steel moment frames. Their study only used an inverted lateral load pattern. However the lateral load pattern of low-rise buildings generally is more similar with the uniform pattern rather than the inverted triangular pattern. If the applied lateral load pattern is different, the minimum moment strength ratio of the column-to-beam joints required to ensure the beam-hinge mechanism will become different. The reason is that the behaviors of a structure become different according to the applied lateral load pattern.

The purpose of this study identifies the minimum moment strength ratio of column-to-beam joints required to ensure the beam-hinge mechanism and the influence of the lateral load pattern on the ratio. The lateral load patterns used in this paper are an inverted triangular pattern and an

uniform pattern. A 2D steel moment frame is used as an example.

2. FORMULATION

This study uses an optimal algorithm to obtain designs which ensure a beam-hinge mechanism. Non-dominated sorting genetic algorithm-II(Deb 2002) is used as an optimal algorithm. The objective function and the constraints of this study are identical with those of Choi and Park(2009).

2.1 Objective Functions

Two objective functions as Eq. (1) and (2) are used in this study. The first objective function is to minimize the structural weights, and the second objective function is to minimize the maximum ratio among moment strength ratios of joints consisting of the structure. It is prevented that the moment strength ratio of a specific joint becomes excessive by the second objective function.

$$\min \sum_{i=1}^{m} \rho_i A_i l_i \quad (1)$$

$$\min \alpha_{\max} \quad (2)$$

where,

ρ_i : the density of the ith element
A_i : the cross-sectional area of ith element
l_i : the length of ith element
m : the number of elements consisting of the structure
$\alpha_{\max}$: the maximum moment strength ratio among joints of the structure

ANSI/AISC 341-05 doesn't consider the joints of the top floor when checking the strong column-weak beam condition. This study also does not consider the column-to-beam joints of the top floor when calculating the moment strength ratios of column-to-beam joints. This study uses Eq. (3) to calculate the column-to-beam strength ratio of each joint consisting of the structure.

$$\alpha = \frac{\sum (F_y Z)_c}{\sum (F_y Z)_b} \quad (3)$$

where,

$\sum (F_y Z)_c$: Sum of plastic bending moment strengths of columns
$\sum (F_y Z)_b$: Sum of plastic bending moment strengths of beams

2.2 Constraints

This study uses the following Eq. (4) to (8) constraints, which are the strength constraints for columns and beams, the inter-story drift constraint, the constraint on the formation of plastic hinges on column parts consisting of joints, and the cross-sectional area constraint on continuous columns.

$$\frac{\sigma_{column}}{\sigma_{a,column}} \le 1.0 \quad (4)$$

$$\frac{\sigma_{beam}}{\sigma_{a,beam}} \le 1.0 \quad (5)$$

$$\frac{\Delta}{\Delta_a} \le 1.0 \quad (6)$$

$$1.0 + \frac{N_{plastic\ hinges}}{2N_{joints}} \le 1.0 \quad (7)$$

$$\frac{A^c_{i+1,j}}{A^c_{i,j}} \le 1.0 \quad (8)$$

where,

σ_{column} : the required stress of column
$\sigma_{a,column}$: the allowable stress of column
σ_{beam} : the required stress of column
$\sigma_{a,beam}$: the allowable stress of column
Δ : the maximum inter-story drift obtained from the elastic analysis
Δ_a : the allowable inter-story drift
$N_{plastic\ hinges}$: the number of plastic hinges developed on the column part of the considering joints
N_{joints} : the total number of the considering joints
$A^c_{i,j}$: the cross-sectional area of the ith floor and jth column

The curvature of a column plastic hinge is calculated by Eq. (9). If the curvature value obtained from the pushover analysis is greater than the value calculated by Eq. (9), we consider that a plastic hinge on the corresponding column part of the joint has been formed.

$$\kappa = \frac{M_p}{EI} \quad (9)$$

where,

κ : the curvature of column
E : the modulus of elasticity of the corresponding column
I : the moment of inertia of the corresponding column
M_p : the plastic moment strength of the corresponding column

3. APPLICATION

This study evaluates the minimum moment strength ratio of column-to-beam joints and the influence of the lateral load pattern on the minimum ratio using a 3-story steel moment structure of figure 1, which was also used in Hasan et. al. (2002) and Xu et. al. (2006). The number of

beams and columns DB used in the algorithm is 16 respectively. The DB lists of beams and columns are tabulated like table 1. The load combinations for the strength design use the following Eq. (10) to (12) chosen among the load combinations of ASCE 7-05.

$$1.4DL \quad (10)$$
$$1.2DL+1.6LL \quad (11)$$
$$1.2D+1.0E+1.0LL \quad (12)$$

where,
DL: Dead load
LL: Live load
E: Earthquake load

AISC/AISC 360-05 is used to check strength constraints. An analysis tool used OpenSees (2006). We considered the rigid offset of beams and columns instead of modeling panel zones. We assume that plastic hinges are formed at end parts of a member. In FEMA 273 the maximum inter-story drift ratio of moment structure is limited to 5.0% for the collapse prevention performance level. For this reason we set the target displacement for the pushover analysis as 5.0% of the height of a building. To evaluate the influence of the lateral load pattern on the minimum moment strength ratio of column-to-beam joints, we use two lateral load patterns, which are the inverted triangular pattern and the uniform pattern.

Figure 2 shows the results obtained from applying the proposed algorithm to the example. The maximum moment strength ratio among joints α_{max} of the feasible solutions shows that the minimum moment strength ratio required to ensure the beam-hinge mechanism is greater than '1.0' recommended in ANSI/AISC 341-05. As the weight of the solution increases, the minimum moment strength ratio required to ensure the beam-hinge mechanism decreases. The distribution of feasible solutions by the inverted lateral load pattern is similar with that by the uniform lateral load pattern. However, the case of the uniform lateral load pattern need more structural weight than the case of the inverted lateral load pattern when comparing their structural weight at the same α_{max} .

4. CONCLUSIONS

In this study, we identified the minimum moment strength ratio of the column-to-beam joints required to ensure the beam-hinge mechanism in steel moment resisting frame using an optimal algorithm. Also we identified the influence of the lateral load pattern on the ratio. An inverted triangular lateral load pattern and a uniform lateral load

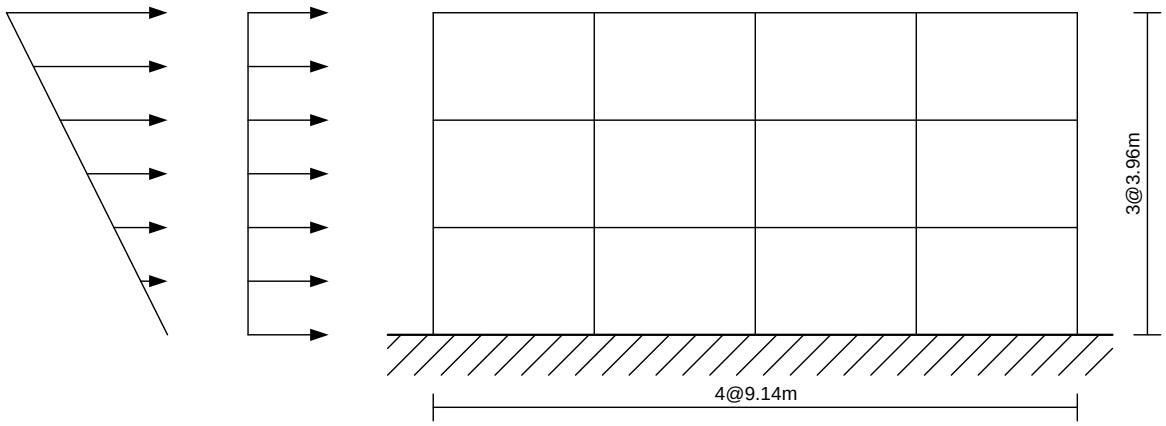

Figure 1. The lateral load patterns and elevation diagram of the example considered in this study.

Table 1. Beam DB and Column DB used in this study

Beam		Column	
W24x229	W24x104	W14x370	W14x176
W24x207	W24x103	W14x342	W14x159
W24x192	W24x94	W14x311	W14x145
W24x176	W24x85	W14x283	W14x132
W24x162	W24x76	W14x257	W14x120
W24x146	W24x68	W14x233	W14x109
W24x131	W24x62	W14x211	W14x99
W24x117	W24x55	W14x193	W14x90

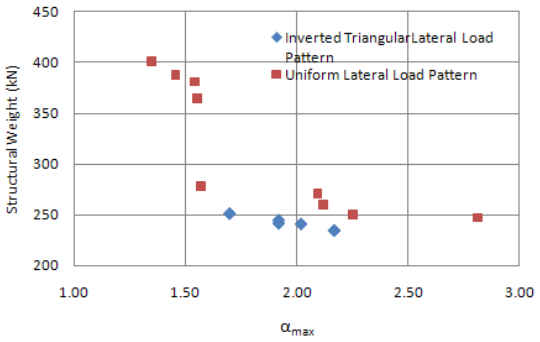

Figure 2. Results obtained from the optimal algorithm used in this study

pattern are used. We used a 2D steel moment frame as an example and obtained the following results through numerical simulation.

1) Feasible solutions obtained from applying the proposed algorithm to the example showed that a higher ratio than '1.0' specified in ANSI/AISC 341-05 is required.
2) Regardless of the shape of lateral load pattern, it is necessary the more structural weight to decrease the minimum moment strength ratio of column-to-beam joint required to ensure the beam-hinge mechanism.
3) The case of the uniform lateral load pattern needs more structural weight than the case of the inverted lateral load pattern when comparing their structural weight at the same α_{max}.

Acknowledgements:

The work presented in this paper was supported by the National Research Laboratory Program(Project No. 2005-01504) of the Ministry of Science and Technology of Korea.

References:

AISC, ANSI/AISC 341-05 Seismic Provisions for Structural Steel Buildings, American Institute of Steel Construction, Inc: Chicago, I.L, 2005.

AISC, ANSI/AISC 360-05 Specification for Structural Steel Buildings, American Institute of Steel Construction, Inc: Chicago, IL., 2005

ASCE, Minimum design loads for buildings and other structures, SEI/ASCE Standard No. 7-05, ASCE

Deb, K., Pratap, A., Agarwal, S., Meyarivan, T., A Fast and Elitist Multiobjective Genetic Algorithm: NSGA-II, IEEE Transactions on Evolutionary Computation, 6(2), pp. 182-197, 2002

Dooley, L. and Bracci, J. M., Seismic evaluation of column-to-beam strength ratios in reinforced concrete frames, ACI Structural Journal, 98(6), pp. 834-851, 2001

Federal Emergency Management Agency, NEHRP guideline for the seismic rehabilitation of buildings (FEMA 273), Building Seismic Safety council, Washington, D.C., 1997

Hasan, R., Xu, L., Grierson, D. E., Push-over analysis for performance-based seismic design, Computers and Structures, pp. 2483-2493, 2002

Kuntz G. L. and Brouning, J., Reduction of Column Yielding During Earthquakes for Reinforced Concrete Frames, ACI Structural Journal, 100(5), pp. 573-580, 2003

Lee, H., Revised Rule for Concepts of Strong-Column Weak-Girder Design, Journal of Structural Engineering, 122(4), pp. 359-364, 1996

Medina, R. A., Krawinkler, H., Strength Demand Issues Relevant for the Seismic Design of Moment-Resisting Frames, Earthquake Spectra, 21(2), pp. 415-439, 2005

Nakashima M. and Sawaizumi S., Column-to-beam strength ratio required for ensuring beam-collapse mechanisms in earthquake responses of steel moment frames, Proceedings of the 12th World Conference on Earthquake Engineering, New Zealand Society for Earthquake Engineering, paper No. 1109, Auckland, New Zealand, 2000

Park, R. and Paulay, T., Reinforced Concrete Structure, John Wiley and Sons, New York, 1975.

Silvia AK, Frank Mckenna, Michael H. Scott, Gregory L, Fenves, Opensees Command Language Manual, Open System for Earthquake Engineering Simulation, 2006

Xu, Lei., Gong, Y., Grierson, D. E., Seismic Design Optimization of Steel Building Frameworks, Journal of Structural Engineering, 132(2), pp. 277-286, 2006

Se Woon Choi and Hyo Seon Park, Eavluation of the Minimum Column-to-Beam Strength Ratios to Prevent the Formation of Plastic Hinges on the Column Parts Consisting of Joints in Special Steel Moment Frames, Proceedings of the 8th International Conference on Civil and Environmental Engineering, 2009

JOINT CONFERENCE PROCEEDINGS
7th International Conference on Urban Earthquake Engineering (7CUEE) &
5th International Conference on Earthquake Engineering (5ICEE)
March 3-5, 2010, Tokyo Institute of Technology, Tokyo, Japan

SEISMIC BEHAVIOR OF A NEW STEEL BEAM-COLUMN CONNECTION USING STEEL FIBER REINFORCED CEMENTITIOUS COMPOSITE (SFRCC)

Yao Cui[1)], Toru Tai[2)], Shuhai Song[2)], Toko Hitaka[3)], and Masayoshi Nakashima[4)]

1) Postdoctoral Researcher, Disaster Prevention Research Institute, Kyoto University, Japan
2) Graduate Student, Dept. of Architecture and Architectural Engineering, Kyoto University, Japan
3) Associate Professor, Disaster Prevention Research Institute, Kyoto University, Japan
4) Professor, Disaster Prevention Research Institute, Kyoto University, Japan
snoopy.cy@steel.mboc.media.kyoto-u.ac.jp, tai-toru@t04.mboc.media.kyoto-u.ac.jp, seasong@t05sxx.mboc.media.kyoto-u.ac.jp, toko.h@ay2.ecs.kyoto-u.ac.jp, nakashima@archi.kyoto-u.ac.jp

Abstract: Steel fiber reinforced cementitous composites (SFRCC) is a promising material with high strength in both compression and tension compared with normal concrete. The ductility is also greatly improved because of 6% volume portion of straight steel fibers (diameter of 0.4 mm, length of 12.0 mm, and tensile strength of 1350 MPa). The new beam-column connection is proposed aimed at solving the brittle fracture caused by the welding. In this connection, the SFRCC slab is applied on both the top and bottom beam flange, which are not welded to columns. Headed studs are densely located close to the beam end, and welded on the beam flange to transfer the beam force to the SFRCC slab. The connection is designed such that hinge is formed close to the end of the SFRCC slab. Behavior of the new beam-column connection is investigated based on a series of cyclic loading test. According to the test results, the new beam-column connection was found to be a promising connection for seismic design of ductile steel moment frames.

1. INTRODUCTION

During the 1994 Northridge earthquake and the 1995 Hyogoken-Nanbu earthquake, a large number of steel building structures sustained severe damage or even collapsed (AIJ 1995, Nakashima et al. 1998). One of the most serious damage appeared to be cracks and brittle fracture at welded beam-to-column connections. Similar to the observation in the 1994 Northridge earthquake (Youssef et al. 1995), the location where premature fractures initiated was typically in the vicinity of the weld between the beam bottom flange and the column. After the earthquakes, numerous efforts were made to address the source of structural damage and to provide structural systems with enhanced safety and functionality. However, most of the practical solutions have been developed within the domain of conventional approaches.

In steel frame buildings, structural steel is typically used together with concrete, for example, steel beam with concrete floor slabs. Composite structures made of structural steel and concrete maximize the advantages of the two components. It is a fact that engineers are increasingly designing composite building systems of steel and concrete to produce more efficient structures when compared to design using either material alone.

In recent decades, material development in response to the call for more durable infrastructures has led to many exciting advancements. Advanced concrete is one example. One of advanced concrete named SFRCC (steel fiber reinforced cementitious composites) is adopted in the proposed beam-column connection as shown in Fig. 1.

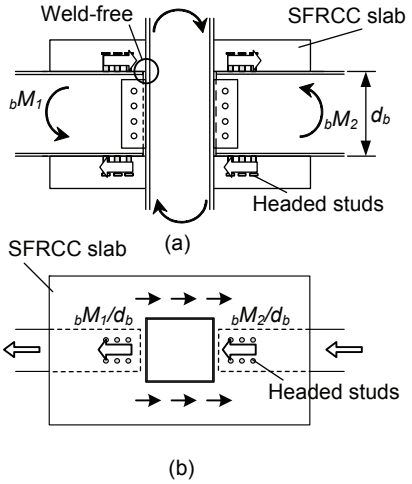

Fig.1 Proposed beam-column connection:
(a) elevation view, and (b) plane-view

The portion of floor slab around the column is cast by SFRCC and designed to transfer the load from the beam to

the column. The SFRCC floor slab is applied on both the top and bottom beam flange. There is no welding between the column and beam flange. The headed studs are welded with small intervals on the beam flange to transfer beam load to the SFRCC floor slab. The beam hinge is expected to form at the end of the slab edge.

The primary objective of this study was to experimentally prove the feasibility of the proposed connection system. Based on the test results, important design parameters, i.e., the elastic stiffness, maximum strength, and energy dissipation of the connection, are examined. The effect of using SFRCC slab instead of the conventional welding was investigated by comparing the behavior with the conventional bare steel beam-column connection in terms of the maximum strength and energy dissipation.

2. SFRCC PROPERTIES

The mix design of SFRCC differs significantly from that of conventional concretes: SFRCC mix compositions are characterized by cement, superplasticizer and silica fume contents. Furthermore, the water-binder ratio is lower than 0.20 (Bache 1987, Kaneko et al. 2001). The size of the coarsest aggregate used in SFRCC generally lies between 0.5 and 4 mm. Compared to conventional concrete, SFRCC has a remarkably large compressive strength and a better tensile behavior in terms of the strength and the ductility, as shown in Fig. 2.

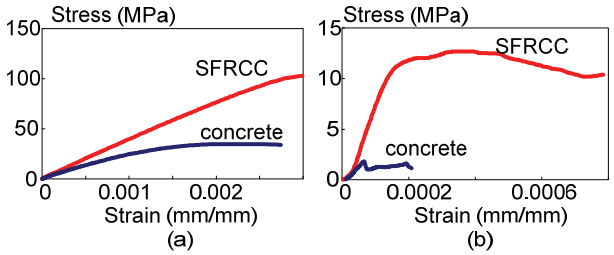

Fig. 2 Stress-strain behavior of concrete and SFRCC: (a) in compression, and (b) in tension

Strain-hardening behavior is achieved by incorporating a high percentage of steel fibers (6 vol.%). Because of the presence of steel fibers, the deformation and energy absorption capacities of SFRCC are significantly improved. Therefore, it is also combined with closely spaced steel bars. Furthermore, the spacing and cover layer of rebars can be as small as 15mm, because relatively small sizes of the fibers and fine aggregate are used. Because of the highly compacted material structures of SFRCC, durability and resistance to corrosion are also to be good, so that such a small cover to reinforcement is still sufficient.

3. TEST PROGRAM

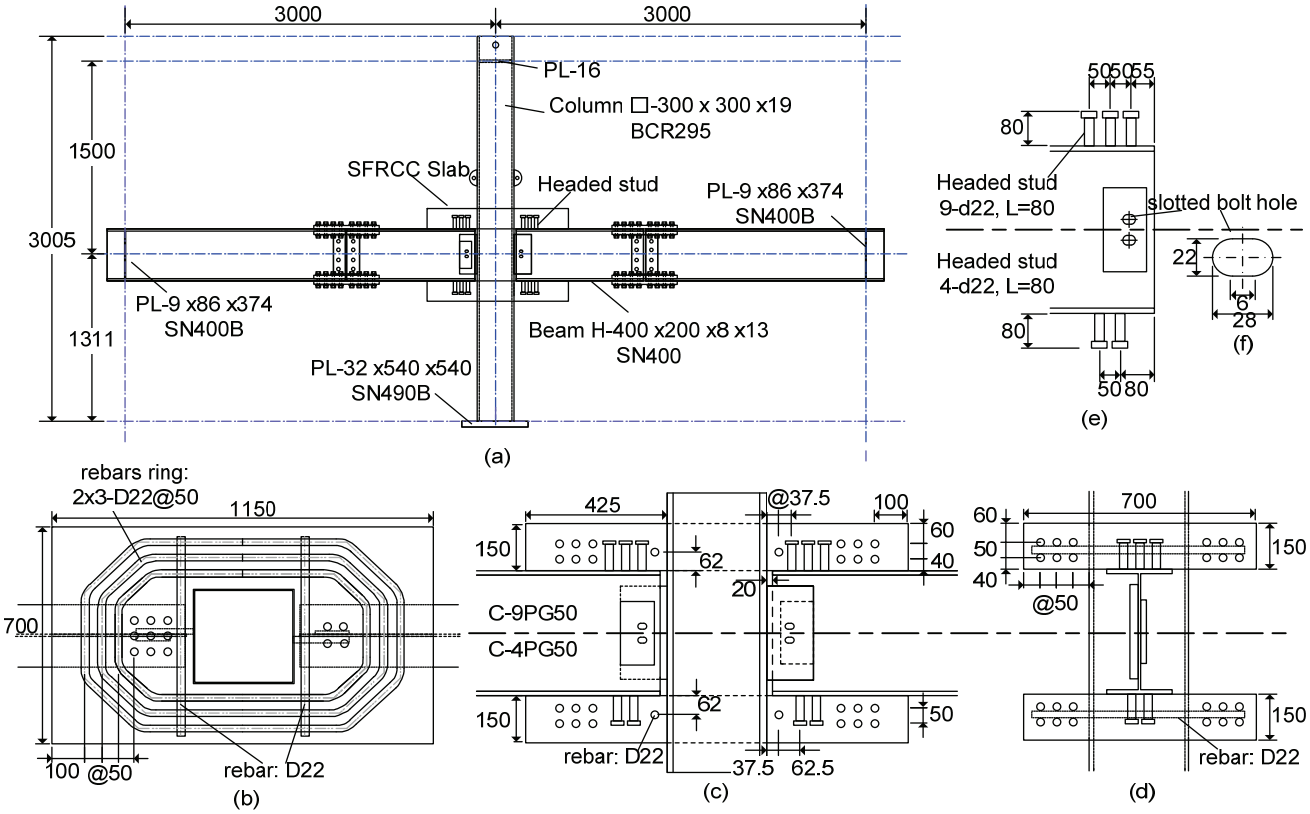

Fig. 3 Test specimen: (a) global view, (b) plane view of slab, (c) front view of slab, (d) side view of slab, (e) arrangement of studs, and (f) slotted bolt hole (unit: mm)

3.1 Test Specimens

The test specimens were designed to simulate interior moment-resisting connections of a four-story steel structure with a story height of 3 m and a span length of 6 m. Two specimens 'C-4PG50' and 'C-9PG50' were fabricated in the full-scale as shown in Fig. 3. The detailing of these two specimens was the same expect the number of the studs. A relatively strong column was used to ensure that the beams can initiate the development of yielding during cyclic loading before significant deformation or damage to the column. All specimen comprised a cold-formed, square-tube cross section column (300 mm in the width, with a thickness of 19 mm), two H-shaped steel beams (400 mm in the height and 200 mm in the width, with a thickness of 8 mm and 13 mm for the web and flange, respectively). Two SFRCC slabs were casted on the top and bottom beam flanges, as shown in Fig. 3 (a). The size of the SFRCC slab is 1150 mm along the beam (the ratio to the span is 0.1) and 700 mm orthogonal to the beam. The thickness of the SFRCC slab is 150 mm, which is the same as the concrete slab thickness in the steel buildings. In this test, the concrete slab on the beam was not considered. The slotted bolt holes (Fig. 3 (f)) were designed for beam web to transfer the shear load only.

In specimen 'C-4PG50', four studs were welded on the beam flange to transfer the load. This specimen was designed to investigate the connection behavior when the studs fracture prior to the beam yielding. Specimen 'C-9PG50', in which nine studs were utilized to transmit the load, was designed to investigate the connection behavior when the beams yield prior to the stud fracture.

The number of studs was determined based on the test results of the push-out test. The shear resistance per stud with the diameter of 22 mm is 190kN when the studs are arranged with 50 mm spacing along the loading direction. Therefore, the bending moment transferred by an individual stud with the diameter of 22 mm is 76kNm. The bending moment governed by the stud fracture was was 0.68 times and 1.54 times of the full-plastic moment M_p of beam (458 kNm) for Specimen 'C-4PG50' and 'C-9PG50', respectively.

The SFRCC slab was provided with rebars. The rebar in the longitudinal direction, i.e., along the beam direction, was designed to resist the tensile load in the SFRCC slab, while the rebar in the transverse direction, i.e., perpendicular to the beam direction, was designed to prevent the split cracks induced by the studs. Twelve D22 rebars for each SFRCC slab were arranged to transfer all the flange force when the full-plastic moment of beam was achieved at the column face. Rebar rings were adopted for the slab by considering the spacing and cover layer limitation, since the rebars in longitudinal and transverse direction overlapped at the corners of the slab. The rebars were bent by 45° at the corner to directly transfer the force from the transverse direction to the longitudinal direction. As illustrated in Fig.3 (b) to (d), two layers of three rebars rings are placed around the studs group and column at a 50 mm space both vertically and horizontally.

The material properties of the steel and SFRCC used for the specimens were obtained from the associated material tests and are summarized in Table 1.

Table 1 Material properties (steel and SFRCC) (unit: MPa)

		Yield strength σ_y	Tensile strength σ_u
Column (BCR295)		430	439
Beam (SN400)	Flange	306	460
	Web	374	484
Rebar (SD295)		396	566

	Compressive strength f_c'	Split strength f_{sp}'
SFRCC	115	18.1

3.2 Test Setup and Loading Program

The test specimen was placed in the loading frame shown in Fig. 4. The top and bottom of the column and free ends of the beams were pinned supported. The beams were supported vertically by pin-ended struts. The lateral load was applied as a cyclic drift displacement at the top of the column. The drift angle was measured as the displacement at the top of the column divided by the height of the column (3000 mm). Drift angles of 0.005, 0.01, 0.02, 0.03, 0.04, and 0.06 rad were adopted, and two cycles were performed for each drift angle. Loading of specimens was terminated till the specimen lost the resisting capacity completely.

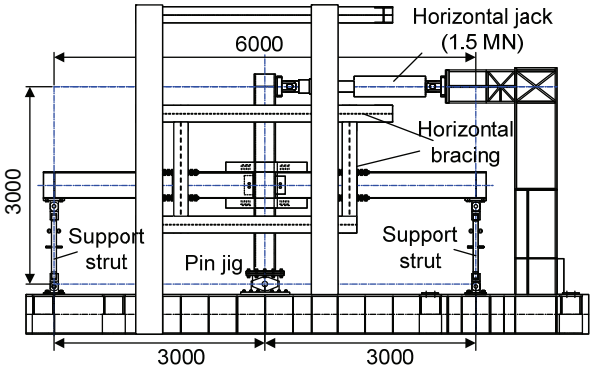

Fig. 4 Test setup (unit: mm)

3.3 Instrumentation

In-plane displacement LVDT measured the deflection at the top of the column. Four LVDTs were fixed on the steel flange at the elevation corresponding to the middle of the stud group, while the head of the LVDT was attached to an acrylic resin plate glued onto the surface of the slab at the same elevation. Measurement of beam rotations was around the connection, tracking the horizontal displacements with respect to the column located above and below the beam.

The strut located at the end of each beam was attached with gauges to measure the reaction force. A grid was drawn on the slab and the cracks were marked at various peak displacements. At each level of the peak displacement, these cracks served as a qualitative measure of the level of damage. Meanwhile, slip between the SFRCC slab and the beam was

also measured by way of strips of paper, resembling tape measures at each end of the SFRCC slab.

4. TEST RESULTS

4.1 Moment-Rotation Relationships

The performance of each side connection (East and West) is studied in Fig. 5 in terms of the normalized beam end moment versus beam-to-column rotation. In the positive loading, the top beam flange in west is in tension. The beam moment is estimated at the face of the column, and the moment is normalized by the full plastic moment of the beam M_p. The applied load was calculated based on the strain measurements of the two support struts attached with strain gauges. The rotation of the beam relative to the column was measured using two LVDTs that were placed near the top flange and bottom flange. Both specimens showed stable behavior till the story drift of 0.02 rad. For Specimen 'C-4PG50', studs fractured during at the first cycle of 0.03 rad story drift. As illustrated in Fig. 5, the connection of Specimen 'C-9G50' exhibits more stable hysteretic behavior up to 0.04 rad of story drift. While the specimen lost its strength during the first cycle of 0.06 rad story drift because of the failure of slab, which will be discussed later. It is notable that Specimen 'C-9PG50' showed fatter hysteretic curves than Specimen 'C-4PG50'.

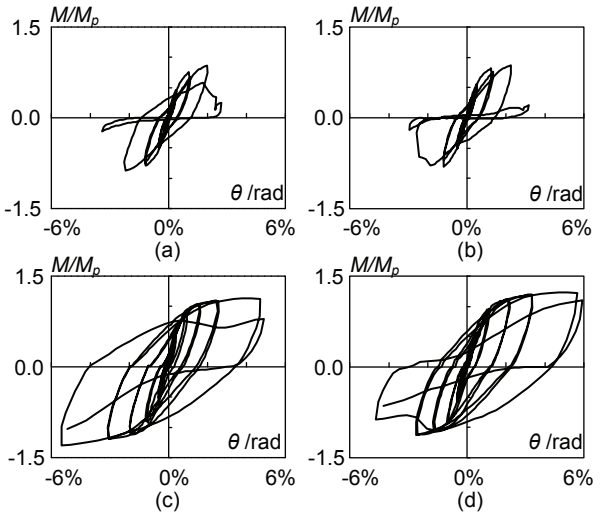

Fig.5 Beam moment versus beam-to-column rotation curves: (a) East connection of Specimen 'C-4PG50', (b) West connection of Specimen 'C-4PG50', (c) East connection of Specimen 'C-9PG50', and (d) West connection of Specimen 'C-9PG50'

Table 2 summarizes the results, including the elastic stiffness (K_0), the maximum moment of each beam (M_{max}), the dissipated energy of each beam (E_p), and the failure mode. The elastic stiffness of the specimen is defined as the secant stiffness between the points at ±0.5% rad of the load (P) versus story drift (Δ) curves. The maximum moment of the East and West beam (M_{max}) are calculated at the column face for both specimens. And the maximum moments in the positive and negative direction were averaged. The dissipated energy (E_p) was estimated from the total area of the hysteretic loops. For both specimens, the calculation was made from the start of loading to the completion of loading with the 3% rad drift angle amplitude.

Table 2 Test results

Spec.		K_0 (kN/m)	M_{max} (kN·m)	E_p (kN·m·rad)
'C-4PG50'	East	6804	390	25.69
	West		376	24.93
'C-9PG50'	East	7143	548	29.00
	West		527	34.87

4.2 Elastic stiffness

As shown in Table 2, the two specimens showed almost the same elastic stiffness with the difference of 5%. The number of studs had a minimal influence of the initial stiffness. It is speculated to be because the studs of Specimens 'C-4PG50' and 'C-9PG50' were able to transfer the same amount of flange force during initial loading. In addition, the theoretical elastic stiffness based on the unit virtual load method using the rigid connected beam-column connection frame mode is 7391 kN/m. The difference between the test and theoretical elastic stiffness is 8% and 3% for Specimens 'C-4PG50' and 'C-9PG50', respectively. However, the contribution of the SFRCC slab is not counted in the frame model. The beam and column are in part rigidly connected using the studs in the new connection system. The slip between beam flange and SFRCC slab reduced the stiffness, but the SFRCC slab still exhibited a large stiffness. The contribution of the SFRCC slab is speculated to cancel the reduction of the stiffness caused by possible slips. Therefore, it is assumed that the new beam-column connection has similar stiffness properties as the rigid connected beam-column connection.

4.3 Maximum strength

The maximum beam moment of Specimen 'C-9PG50', in which the beam yielded before the slab fracture, was 30% larger than the moment of Specimen 'C-4PG50', which failed by stud fracture. A conventional bare steel beam-column connection with through diaphragm details (Suita et al. 2009) was chosen to compare with the new beam-column connection specimens. As shown in Fig. 6, the beam moments are normalized by the full plastic moment of the corresponding beam, M_p. Since Specimen 'C-4PG50' failed by stud fracture, the maximum moment of the East and West beam are about $0.8M_p$. While the maximum beam moment of Specimen 'C-9PG50' were about $1.2M_p$, which is similar to the moment resistance of the bear steel beam-column connection. It is experimentally proved that the new beam-column connection can sustain similar moment resistance as the bare steel beam-column connection.

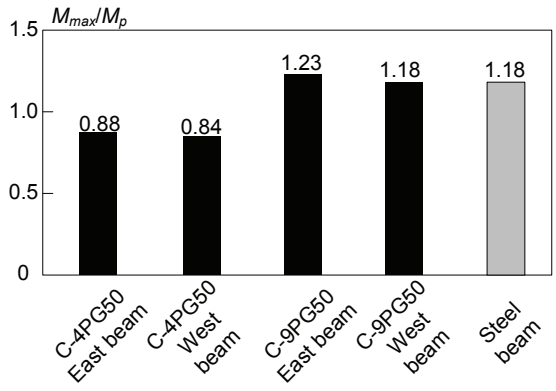

Fig. 6 Normalized maximum moment

4.4 Energy dissipation

Up to 3% rad story drift, the energy dissipation of Specimen 'C-9PG50' is about 1.3 time that of Specimen 'C-4PG50'. The equivalent viscous damping coefficients of both specimens are compared with that of the aforementioned bare steel beam-column connection specimen (Suita et al. 2009) in Fig. 7. The equivalent viscous damping coefficient of Specimen 'C-4PG50' is reduced at 3% rad story drift, because of the stud fracture. The coefficient of Specimen 'C-9PG50' is reduced at 6% rad story drift, because of the slab fracture. In comparison with the bare steel beam-column connection specimen (Suita et al. 2009), the new beam-column connection specimens shows similar energy dissipation up to 1% rad story drift. After that, the new beam-column connection specimens dissipated less energy. It is speculated that the SFRCC around the studs are locally crushed, which promoted the pinching of the hysteretic curves.

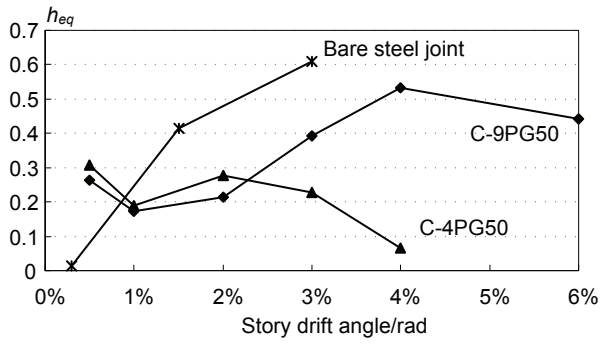

Fig. 7 Equivalent viscous damping coefficient

4.5 Failure Mechanism

Two failure modes occurred in the specimens as shown in Fig.8 (a) and (b). Specimen 'C-4PG50' failed by stud fracture, and there were no significant cracks observed during the loading. And Specimen 'C-9PG50' failed by the slab fracture following the beam yielded. It is notable in Fig. 8 that the SFRCC slab of Specimen 'C-9PG50' deformed seriously than that of Specimen 'C-4PG50'.

The two specimens exhibited similar behavior under the loading cycles up to 3% rad story drift. As shown in Fig. 9 (a) and (b), the horizontal slip and vertical separation between the beam flange and SFRCC slab kept increasing as the load increased. The separation was 11 mm and 8 mm after the competition load of 3% story drift for Specimen 'C-4PG50' and Specimen 'C-9PG50', respectively. Specimen 'C-4PG50' failed by stud fractures in the first cycle of 3% rad story drift. Several cracks formed at the surface of slab and from the root of the stud. However, these cracks did not propagate seriously, with the maximum crack width of 0.85 mm, till the specimen failed.

The beam flange of Specimen 'C-9PG50' yielded (Fig. 9 (c)) in the first cycle of 4% story drift. Meanwhile there are several transverse cracks formed in the SFRCC slab. As shown in Fig. 9 (d), these transverse cracks were originated from the root of the studs, which was the same as the cracks observed in Specimen 'C-4PG50'. At the end of loading, the maximum width of transverse cracks was 15 mm.

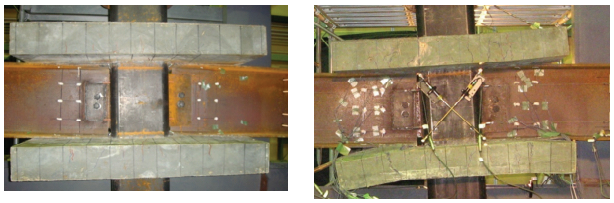

Fig. 8 Failure of specimens: (a) stud fracture (Specimen 'C-4PG50'), and (b) combination of slab fracture and beam yield (Specimen 'C-9PG50')

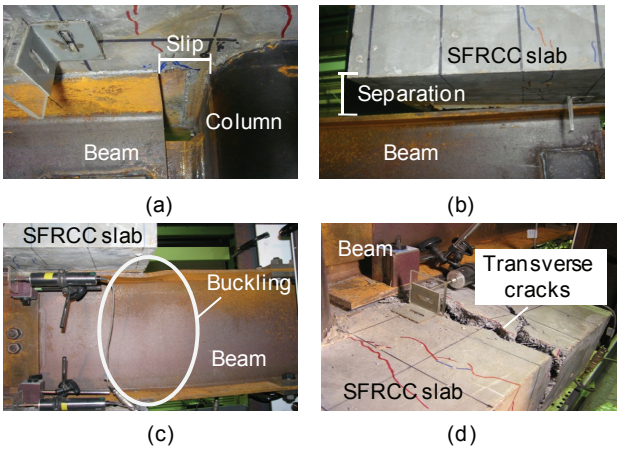

Fig.9 Experimental observation: (a) slip between beam flange and SFRCC slab, (b) separation between slab and beam flange, (c) local buckling of beam, and (d) transverse cracks of SFRCC slab

5. CONCLUSIONS

To examine the constructability, seismic performance and failure mechanism of the new beam-column connections, two full scale cruciform connection specimens were tested under horizontal cyclic loading. According to the test results, the new beam-column connection was found to be a

promising connection for seismic design of ductile steel moment frames. Major findings obtained from the tests are as follows:

(1) The specimen with four studs (Specimen 'C-4PG50') failed by stud fracture, while the specimen with nine studs (Specimen 'C-9PG50') failed by beam yielding followed by slab fracture. The specimen failed by beam yielding exhibited fatter hysteretic curves than the other specimen.
(2) The number of studs showed minimal effect on the elastic stiffness. The two specimens showed nearly the same elastic stiffness with a difference of 5%. In addition, the measured elastic stiffness agreed with the theoretical elastic stiffness well with a difference not greater than 10%.
(3) The experimental results revealed that the new beam-column connection has a potential to assure the formation of plastic hinges in the beam and achieve large energy dissipation and ductile behavior. In terms of the energy dissipation, the new beam-column connection showed the same value as the conventional beam-column connection up to 0.01 rad.

Workability of the new beam-column connection was experimentally proved. The new beam-column connection is designed to fail by beam yielding at the end of the SFRCC slab. A strong SFRCC slab and sufficient number of studs are needed to guarantee the failure mode. To develop a reasonable stiffness and strength evaluation procedure for the new beam-column connection, further work, both experimental and numerical, are needed.

Acknowledgements:

The writers are grateful for invaluable suggestions provided by Prof. Yoshio Kaneko of Kyoto University.

References:

Architectural Institute of Japan (AIJ). (1995). Reconnaissance Rep. on Damage to Steel Building Structures Observed from the 1995 Hyogoken Nanbu Earthquake, Kinki Branch, Osaka (in Japanese).

Architectural Institute of Japan (AIJ). (1996). Japanese architectural standard specification: JASS 6 steel work, Tokyo (in Japanese).

Bache, H. H. (1987). "Compact Reinforced Composite, Basic Principles." CBL Report No.41, Aalborg Portland.

Kaneko Y., Mihashi H., and Kirikoshi K. (2001). "Mechanical Properties and Application of Steel Fiber Reinforced Cementitious Composite." *Cement Science and Concrete Technology*, Vol. 54, 723-730.

Nakashima, M., Inoue, K., and Tada, M., (1998). "Classification of damage to steel buildings observed in the 1995 Hyogoken-Nanbu earthquake." *Eng. Struct.*, 20(4-6), 271-281.

Suita Keiichiro, Kitamura Yukiko, and Hashida Isao. (2009). "Seismic performance and retrofit of beam-to-column connection for early high-rise buildings." *Journal of structural and construction engineering*, *Transactions of AIJ*, 74 (636), 367-374.

Youssef, N.F.G., Bonowitz, D., and Gross, J. L. (1995). "A survey of steel moment resisting frame buildings affected by the 1994 Northridge earthquake." NISTIR 5625, National Institute of Standards and Technology, Gaithersburg, Md.

JOINT CONFERENCE PROCEEDINGS
7th International Conference on Urban Earthquake Engineering (7CUEE) &
5th International Conference on Earthquake Engineering (5ICEE)
March 3-5, 2010, Tokyo Institute of Technology, Tokyo, Japan

SYSTEM-LEVEL SEISMIC EVALUATION OF PARTIAL-STRENGTH SEMI-RIGID STEEL FRAMES USING HYBRID SIMULATION

Hussam Mahmoud[1], Amr Elnashai[2], Billie Spencer[2], and David Bennier[3]

1) Ph.D. candidate, Civil and Environmental Engineering Department, University of Illinois at Urbana-Champaign
2) Professor, Civil and Environmental Engineering Department, University of Illinois at Urbana-Champaign
3) Engineer in training, Kansas City, MO
hmahmoud@illinois.edu, aelnash@illinois.edu, bfs@illinois.edu, dbennier@hntb.com

Abstract: The available information on the behavior of semi-rigid connections has been collected through either experimental component testing or detailed 3D finite element models of beam-column subassemblies. Despite the promising potential of this type of connection, previous experiments were conducted under idealized loads and boundary conditions; hence the results are not directly applicable to real situations. In addition, the developed finite element models are computationally expensive and have primarily been used under monotonic loadings. Accurate assessment of the full potential of the connection requires a system-level investigation whereby the effect of the local behavior of the connection on the global response of the structural system is considered, while the connection is tested under natural and realistic boundary and loading conditions. This paper represents a new system-level hybrid simulation framework aimed at investigating the seismic performance of partial-strength semi-rigid steel frame. The analytical component of the simulation comprises a detailed 2D nonlinear finite element model. The experimental component of the simulation comprises a full-scale beam-column subassembly with loading and boundary conditions that are in full interaction with the rest of the frame. The simulation was conducted successfully using the state-of-the-art instrumentation and control equipments at the MUST-SIM facility at the University of Illinois; part of the NSF Network for Earthquake Engineering Simulation (NEES).

1. BACKGROUND

1.1 Introduction

During the Northridge (1994), and Hyogo-ken Nanbu (1995) earthquakes, numerous cracks were developed in the welded beam-to-column joints of steel frames. The damage was attributed to the low toughness welds and poor connection detailing practices that were typical prior to the earthquakes (SAC 2000). The cracks originated in the heat-affected zone of the weld and propagated in the flange and the web of the columns as shown in Figure 1.



Figure 1 Fractured Connection in a Steel Moment Frame during the Northridge Earthquake

The uncertainly in the performance of welded connections spiked interest in investigating the use of bolted connections in the construction of steel frames in seismic regions. With their lower construction costs and simple fabrication process, bolted partial-strength semi-rigid connections were evaluated as a viable alternative and their fundamental characteristics were assessed both experimentally and analytically. The cyclic behavior of the connection was evaluated through testing of beam-column subassemblies. The experimental results demonstrated the large energy absorption capabilities of these connections under cyclic loading with stable hysteretic behavior (Azizinamini et al. 1989 and Bernuzzi et al. 1994).

In addition, analytical models aimed at capturing the complicated behavior of the connection such as slip, friction between surfaces in contact and prying action were heavily investigated. The previously conducted experimental and analytical studies were aimed at assessing the behavior of the connection on component level bases. The assessment of the seismic performance of steel frames is then conducted using an idealized moment-rotation relationships obtained from the experimental results or the finite element models. The drawback of using such approach, in addition to idealizing the moment-rotation relationships, is that the interaction between the beam and column flanges and the

angles comprising the connection is not captured. Such interaction is essential as it influences the spread of yielding in the beam. This paper presents new system-level approach for the seismic assessment of steel frames with top-and-seat angle with double web angle connections using hybrid simulation.

1.2 Analytical Models

Early work on the development of analytical models for representing the moment-rotation relationship of semi-rigid connections focused on simplified linearized and curve fitting models compared to experimental data (Frye et al. 1975, Richard et al. 1975, Chen et al. 1985, Kishi et al. 1986). Although large effort has been made to calibrate such models, the models fell short of predicting the rotational capacity when the tension capacity of the bolts governs the behavior. Furthermore, none of the above models limit the rotational capacity of the connection since they are based on tests with flexible angles (Leon et al. 2004).

With advances in computational techniques, 2D and 3D finite element representations of the connections were developed with the aim of better quantifying and representing the localized behavior (Krishnamurthy 1979, Kukreti et al. 1987, Gendron et al. 1989, Gebbeken et al. 1994, Bose et al. 1996, Sherbourne et al. 1997, Bursi 1998, Citipitioglu et al. 2002). A comparative study was conducted on extended endplate connections to correlate stresses and displacement obtained using 2D and 3D linear elastic models with bolt pretension alone (Krisnamurthy et al. 1976). A similar procedure was proposed to reproduce moment-rotation relationships of end plate connections (Kukreti et al. 1987). The advancement in computational power shifted the attention to the development of 3D models which have proven to be capable of capturing the true behavior of the connection. An example of such detailed model is shown in Figure 2. Despite their effectiveness in capturing the complex behavior, 3D models are computationally intensive and difficult to construct, thus limiting their ability to be used in large parametric studies.

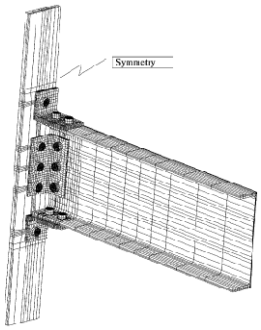

Figure 2 Detailed 3D FEM Aimed at Capturing the Localized Performance of a Top-and-seat Angle with Double Web Angle Connection (Citipitioglu et al. 2002)

2. HYBRID SIMULATION METHODOLOGY

2.1 Description of the Structure

The structure considered is a 2-story, 4-bay (longitudinal) and 2-bay (transverse) steel frame. The height of the first and second story is 4.57 m and 4.11 m, respectively and the bay width is 9.14 m. The outer frames are special moment resisting frames (SMRF) designed according to the Structural Seismic Design Manual, Volume 3 (IBC 2006) while the inner frames are only responsible for carrying their share of gravity load. The strong-column weak-beam design approach was used for the SMRF and resulted in beam and column sizes of W18 x 40 and W14 x 159, respectively. Plan view of the structure and an elevation of a typical SMRF are shown in Figure 3.

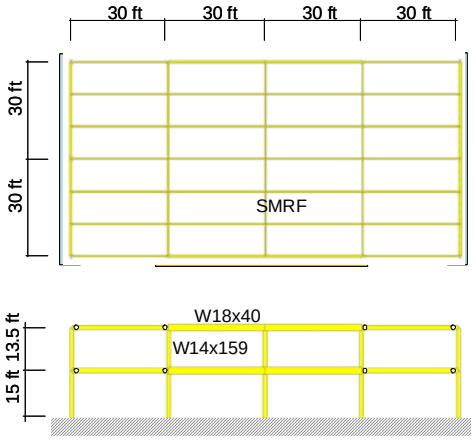

Figure 3 Plan View of the Structure Considered and an elevation of the SMRF with Red-dashed Line Representing the Physical Specimen to be Tested

Following the sizing of the beams and columns, the assumed rigid connections in the frame were redesigned to reflect partial strength. Three different frames are considered with the connections in each frame designed as top-and-seat angles with double web angles according to the Eurocode 3 (prEN 2005). The sizes of the angles and the bolts were optimized such that the resulting connection capacity in frame 1, 2 and 3 is 30%, 50%, and 70%, respectively, of the plastic moment capacity of the beam. Figure 4 shows the 30% Mp connection as an example of the connection geometry used in all three simulations.

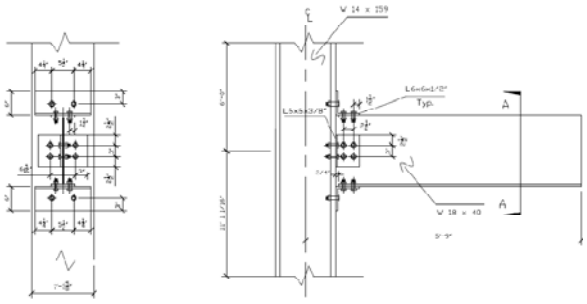

Figure 4 Detailed Geometry of the Connection with 30% Mp Capacity

2.2 Experimental Component

The experimental component of the simulation utilizes the Multi-Axial Full-Scale Sub-Structured Testing and

Simulation Facility (MUST-SIM) which is part of the 15 sites of the Network of Earthquake Engineering Simulations (NEES). The main components of the facility include three Load and Boundary Condition Boxes (LBCBs) and the L-shaped strong wall (Elnashai et al. 2004). The experimental component of the simulation represents a full-scale bolted beam-column subassembly. The beam comprises a portion of first story beam in the first bay while the column includes portion of the first and second story columns in the same bay for a total number of three points to be controlled during the simulation. At each of the three control points, an LBCB should be used to provide the required deformation commands during the simulation. However, the base of the column was fixed to the lab floor and only two LBCBs were used as shown in Figure 5. The fixity of the column base was accounted for during the simulation through the use of relative deformation between all three control points.



Figure 5 Overview of the Experimental Setup

The instrumentation plan was developed and installed to capture the local response of the connection and the global response of the beam-column subassembly. In each test, a total of 175 channels were installed on the specimen and recorded using a National Instrument Data Acquisition (NI-DAQ) system. In addition, each LBCB houses 6 load cells and 6 LVDTs for displacement and load measurements, respectively, for each actuator.

Various types of sensors were used and included strain gauges, linear potentiometers, string pots, still cameras and video cameras. Strain gauges were installed to measure the global and local strain in the beam, column and angles. Linear potentiometers were used to measure the column panel zone deformation and the localized slip of the bolts used for connecting the angles to the beam and column. String pots were installed to measure the global deformation of the column with respect to a fixed reference. Figure 6 shows an example of linear pot arrangements used for measuring the localized slip in the connection. In addition to the conventional instruments used, the advanced non-contact displacement measurement systems (Krypton) was utilized to measure global and local displacement of the beam-column subassembly.

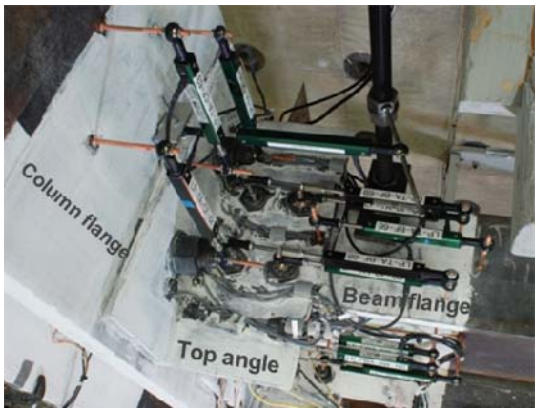

Figure 6 Linear Potentiometer Arrangement For Measuring the Localized Behavior of the Connection

2.3 Analytical Component

Analytical models of frames have utilized line elements connected with springs representing the load deformation characteristics of the connection. Due to its minimal computational demands, this modeling approach has been viewed as the best alternative for hybrid simulation since the number of elements in this case is small and significant time is not required to complete a simulation step. However, the models typically represent idealized behavior and in many cases cannot capture the local response of the various connection components. Furthermore, the deformation and the spread of yielding in the beam are not well represented since the prying action between the beam flanges and the top and seat angles is neither physically modeled nor accounted for.

In light of the above arguments, the use of 2D or 3D finite element models in hybrid simulations can pay significant dividends since the localized connection behavior and its interaction with the beam and column is physically modeled. The decision to employ 2D or 3D models in hybrid simulations has been primarily driven by the notion that 2D models cannot properly capture the complex localized behavior of the connection. However, for planar problems or problems that could be idealized as planar, 2D models may be much more efficient when compared to 3D models. This is due to the fact that 3D models contain large number of nodes and elements rendering them computationally expensive and rather impractical particularly when used in a closed-loop hybrid simulation where hundreds of steps are expected.

An inelastic finite element model is employed in the current investigation. The model comprises 2D plane strain elements for the beam-to-column connections and 1D beam elements between subsequent connections and is developed using ABAQUS which is a general purpose commercial package (Hibbit, Karlsson and Sorenson 2007). The model includes various behavioral features namely; 1) bolt preload, 2) friction between faying surfaces, 3) connection slip, 4) the effect of bolt-hole ovalization, and 5) hot-rolling residual stresses in the angles. In addition, the effect of the inner gravity frames on the stability of the moment resisting frame (i.e. large P-Δ effect) is included in the model through a

leaner column modeled as two truss elements pinned at the base and at the first floor level. Tie multi-point constraints were used to provide rigid links between the SMRF and the leaner column. Figure 7 shows the described model. A zoom-in view of the deformed shape of the middle connection in the first floor is shown in Figure 8.

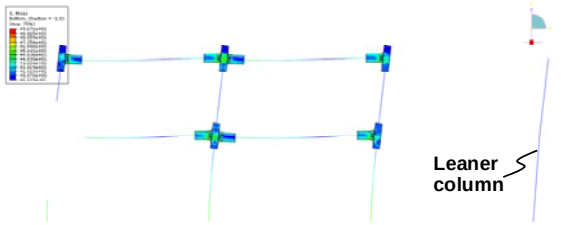

Figure 7 Finite Element Model Used in the Hybrid Simulation

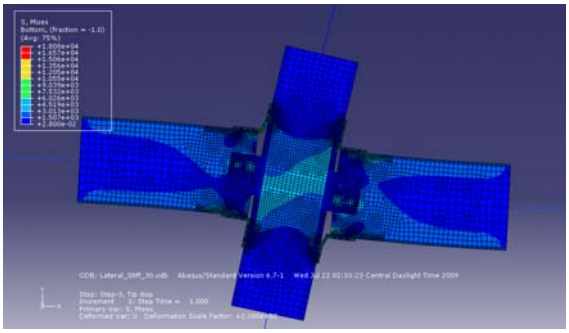

Figure 8 Zoomed View of the Deformed Shape of the Connection

2.4 Integration Scheme for PSD Testing

The integration of the experimental and analytical modules was conducted using UI-SIMCOR which is a hybrid simulation framework developed at the University of Illinois (Elnashai et al. 2004). UI-SIMCOR starts the simulation with a stiffness evaluation step where predefined deformation values are sent to both modules for the evaluation of the system stiffness matrix. In the gravity load application step, following stiffness evaluation, gravity load on the moment resisting frame was applied in the finite element model as distributed load on the beams. As a result of such, target deformation commands were sent to the LBCBs to enforce equilibrium between the experimental and analytical modules which resulted in the deformation of the physical specimen in a way which corresponds to the application of distributed load on the specimen. In the dynamic step, time integration is conducted using the α-Operator Splitting method. A schematic of the hybrid simulation framework is shown in Figure 9. Details on the features of UI-SIMCOR and its applications can be found in (Spencer et al. 2007).

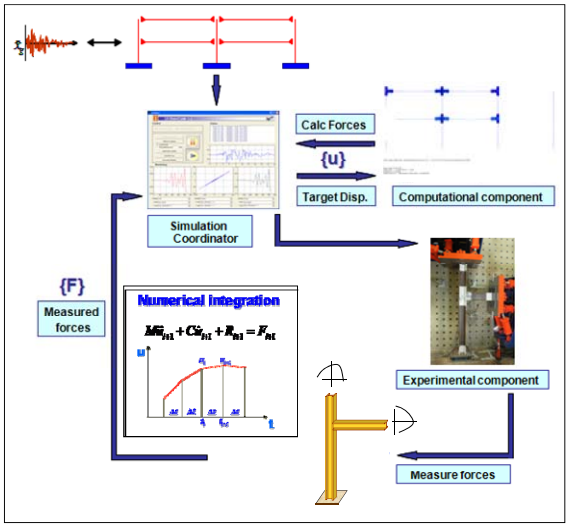

Figure 9 Schematic of the Hybrid Simulation Framework

3. PREMILINARY RESULTS

The Loma Prieta earthquake was selected for the hybrid simulation. The station used was USGS 1662 Emeryville, 77 km from the epicenter of the earthquake, on soft soil (Vs30 = 199 m/s) with peak ground acceleration of 0.26 g. The hybrid simulation was conducted successfully for 321 simulation steps and terminated after passing the large peaks in the record. The deformed shape of the top angle at the end of the simulation and the moment-rotation characteristics of the connection is shown in Figure 10 and Figure 11, respectively.

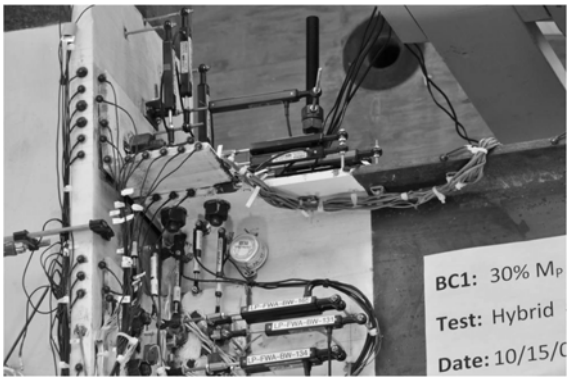

Figure 10 Zoomed View of the Deformed Shape of the 30% Mp Connection

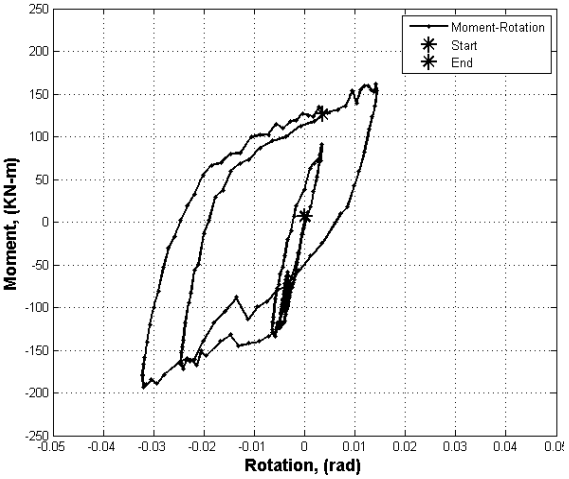

Figure 11 Moment-rotation response of the 30% Mp Connection

3. CONCLUSIONS

An innovative framework was developed for system-level seismic assessment of steel frames with partial-strength semi-rigid connections using hybrid simulation. The simulation includes experimental and analytical modules, and utilizes the large-scale Multi-Axial Full-Scale Sub-Structured Testing and Simulation facility at the University of Illinois. The experimental module comprises a beam-column subassembly with top-and-seat angles with double web angle connection. The analytical modules included an inelastic 2D finite element model which captures the localized behavior of the connection including bolt pretension, friction between surfaces, the effect of bolt hole ovalization and hot-rolling residual stresses in the angles. The sample results presented confirm the accurate and controllable behavior of the hybrid simulation setup.

Acknowledgements:

This research is funded by the Mid-America Earthquake Center project SV-01, the NEES at UIUC and NEES Inc. The Mid-America Earthquake Center is an Engineering Research Center funded by the National Science Foundation under cooperative agreement reference EEC-9701785. NEES at UIUC is funded by the George E. Brown, Jr. Network for Earthquake Engineering Simulation (NEES) program of the National Science Foundation under award reference CMS-0217325 and NEESgird is funded by the same NSF Program, award reference CMS-0117853.

References:

Abaqus/Standard Users' Manual (2007), Version 6.7.1, Hibbitt, Karlsson & Sorensen, Inc.

Azizinamini, A. and Radziminski, J. (1989), "Static and Cyclic Performance of Semirigid Steel Beam-to-Column Connections," *Journal of Structural Engineering*, ASCE, Vol. 115, No. 12

Bernuzzi, C., Zandonini, R., and Zanon, P., (1996) "Experimental Analysis and Modeling of Semi-rigid Steel Joints under Cyclic Reversal Loading," *Journal of Construction Steel Research*, Vol. 38, No. 2.

Bose, B., Sarkar, S. and Bahrami, M. (1996), "Extended Endplate Connections: Comparison between Three-Dimensional nonlinear Finite-Element Analysis and Full-scale Destructive Tests," *Structural Engineering Review*, 8(4):315–28.

Bursi, O.S. & Jaspart, J.P. (1998), "Basic Issues in the Finite Element Simulation of Extended End Plate Connections," Computers & Structures, 69:361–82.

Citipitioglu, A.M.., Haj-Ali, R.M. and White, D.W. (2002), "Refined 3D Finite Element Modeling of Partially Restrained Connections Including Slip," Journal of Construction Steel Research, 58:995–1013.

Elnashai, A., Spencer, B., Kuchma, D., Ghaboussi, J., Hashash, Y. and Can, Q. (2004), "Multi-Axial Full-Scale Sub-Structured Testing and Simulation (MUST-SIM) Facility at the University of Illinois at Urbana-Champaign," *Proceedings of the 13th World Conference on Earthquake Engineering*, Vancouver, B.C., Canada, Paper No. 1756.

Frye, J.M. and Morris, G.A. (1975), "Analysis of Flexibly Connected Steel Frames," *Canadian Journal of Civil Engineering*, 2:280–291.

Gebbeken, N., Rothert, H. and Binder, B. (1994), "On the Numerical Analysis of Endplate Connections," *Journal of Construction Steel Research*, 30:177–196.

Gendron, G., Beaulieu, D. and Dhatt G. (1989), "Finite Element Modeling of Bolted Connections," *Canadian Journal of Civil Engineering*, 16:172-181.

IBC Structural/Seismic Design Manual. (2006), "Volume 3: Building Design Examples for Steel and Concrete,"

Kishi, N. and Chen, W. (1986) "Database of Steel Beam-to-Column Connection," Structural Engineering Report no. CESTR- 86-26, School of Civ. Engrg., Purdue University, West Lafayette, Ind.

Kim, S. J., Holub, C. and Elnashai, A. S. (2008), "Analytical and Experimental Investigations of the Effect of Vertical Ground Motion on RC Bridge Piers," *Proceedings of the 14th World Conference on Earthquake Engineering*, Beijing, China.

Krishnamurthy, N. (1979), "Modeling and Prediction of Steel Bolted Connection Behavior", *Computers and Structures*, 11:75–82.

Kukreti, A.R., Murray, T.M. and Abolmaali, A. (1987), "End Plate Connection Moment-Rotation Relationship," Journal *of Construction Steel Research*, 8:137-57.

Leon, R.T., Hu, J.W. and Corey, S. (2004), "Rotational Capacity and Demand in Top-and-Seat Angle Connections Subjected to Seismic Loading," *Connections in Steel Structures V* – Amsterdam.

prEN 1993-1-8. Eurocode 3. (2003), "Design of Steel Structures, Part 1.8: Design of Joints," European Standard, CEN, Brussels.

Richard, R.M. & Abbott, B.J. (1975), "Versatile Elastic–Plastic Stress–Strain Formula", *Journal of Engineering Mechanics*, ASCE 101(4):511–5.

SAC Joint Venture. (2000), "Recommended Seismic Evaluation and Upgrade Criteria for Existing Welded Steel Moment-Frame Structures" Report no. FEMA-351, Federal Emergency Management Agency, Washington, D.C.

Sherbourne, A.N. & Bahaari M.R. (1997), "3D Simulation of End-Plate Bolted Connections," *Journal of Structural Engineering*, ASCE 120(11):3122–3136.

Spencer, B.F., Elnashai, A.S., Kwon, O-S., Park, K-S. and Nakata, N., (2007), "The UI-SIMCOR: Hybrid Simulation Framework," *2nd World Forum on Collaborative Research in Earthquake Engineering*, EC/JRC, Ispra, Italy.

JOINT CONFERENCE PROCEEDINGS
7th International Conference on Urban Earthquake Engineering (7CUEE) &
5th International Conference on Earthquake Engineering (5ICEE)
March 3-5, 2010, Tokyo Institute of Technology, Tokyo, Japan

NUMERICAL SIMULATION OF LARGE SCALE SEISMIC FRAME STRUCTURES

Yi-Jer Yu[1] and Keh-Chyuan Tsai[2]

1) Assistant Research fellow, National Center for Research on Earthquake Engineering, Taiwan
2) Professor, Dept. of Civil Engineering, National Taiwan University, Taiwan and
Director, National Center for Research on Earthquake Engineering, Taiwan
yjyu@ncree.org, kctsai@ncree.org

Abstract: This paper describes the numerical simulations on earthquake engineering research. The applications of a general-purpose structural analysis computer program PISA3D, developed in Taiwan National Center for Research on Earthquake Engineering (NCREE), for the seismic frame structures are introduced. In this paper, a four-story building is used as a case study to investigate modeling techniques for nonlinear structural responses and collapse analysis. This paper presents several numerical models in detail. The models for the simulation of steel hollow structural column buckling are discussed. A column model incorporating fibered beam-column element using cyclic buckling fibers proposed in this study can satisfactorily simulate the degrading force versus deformation relationships of the ABAQUS column due to the local buckling. A frame model incorporating the same type of fibered column element could predict the collapse time of the test building.

1. INTRODUCTION

In September 2007, the world's largest 3-directional earthquake simulation table, E-Defense shaking table, was utilized for experimental tests of a full-scale four-story steel building shaken to collapse. Before the tests were executed, a blind prediction contest was held (HEERC 2007). Three groups of researchers from the Taiwan National Center for Research on Earthquake Engineering (NCREE) participated in the blind contest (Ohsaki et al. 2008). One team used a general purpose nonlinear structural analysis program PISA3D, and submitted the 3-D and 2-D predictions. This PISA3D/NCREE team was awarded second place in the 2-D analysis research category. In this paper, this four-story building is used as a case study to investigate modeling techniques for nonlinear structural responses and collapse analysis. This paper presents several numerical models in detail. The models for the simulation of steel hollow structural column buckling are discussed. A basic model incorporating non-degrading column elements was constructed first. Then the refinements were carried out by replacing the 1st-story columns in the basic model with the degrading column elements. Two types of degrading column are considered including the fiber and hinge models, with and without the effects of axial-flexural interaction, respectively. Based on these nonlinear response analyses, it is illustrated that the collapse responses of the building can be estimated satisfactorily by incorporating degrading fibered columns.

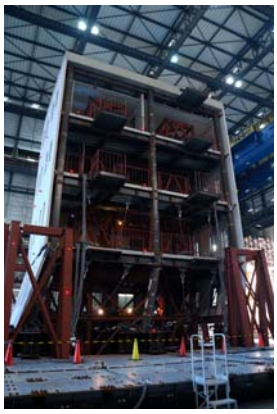

Figure 1 Collapse of the four-story steel building

The photo of the full-scale four-story steel building is shown in Fig. 1. The contestants were required to predict the key maximum experimental responses of the specimen under the three-directional incipient-collapse level shaking as well as the specimen's collapse time under the collapse level earthquake. Before the four-story frame tests, cyclic loading test results of two column specimens and two separate beam-to-column subassemblies were also provided by the organizer to allow the contestants to gain a better insight into the force-deformation characteristics of individual structural members.

The floor framing plan and the elevations are shown in Figures 2a and 2b, respectively. The longitudinal and transverse directions of the building are defined as Y and X directions, respectively. The structural configuration consists of two-bays of 5 m each in the Y direction and one-bay of 6 m in the X direction. Each story height is 3.5 m except the

first story which is 3.875 m. The thickness of the concrete slab is 175 mm for the 1st, 2nd and 3rd floor and 150 mm for the 4th floor. The 75 mm deep metal deck was spanning in the Y direction. Wide flange sections are used for beams, and rectangular hollow structural sections (HSS) for columns. The steel material is SN400B for the frame beams and BCR295 for the columns. The building was designed following the current Japanese specifications and practices (Suita et al. 2008). In particular, the column wall width to thickness ratio of 31.3 is between 37 (λr) and 29.6 (λp) prescribed in the US provisions (AISC 2005).

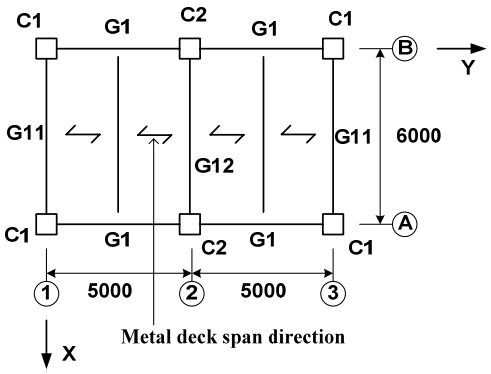

(a) Floor framing plan

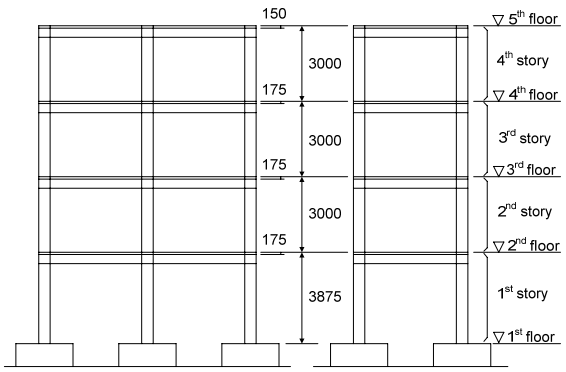

(b) Frame elevations

Figure 2 Floor framing plan and elevations (mm)

The building specimen was subjected to 3-directional ground motions recorded during the 1995 Kobe earthquake at the Takatori train station. The test consisted of repeated applications of the records with progressively increasing scale factors. The Takatori motion scaled by 0.6 was designated as the incipient-collapse level motion, and the full scale Takatori motion was designated as the collapse level motion. For the purposes of discussion, the incipient-collapse level and collapse level excitations are defined as EQ-I and EQ-C, respectively. The required submission of the predicted responses included (Ohsaki et al. 2008):

For the EQ-I: absolute maximum values of relative displacement from base, absolute maximum acceleration and overturning moment at each floor; absolute maximum values of story shear, story drift angle; absolute maximum engineering strain at a specified point in an elastic region; and residual story drift at each story.

For the EQ-C: time, measured from the beginning of the EQ-C, at which the drift angle of any story in X or Y direction reached 0.13 or -0.13 radians.

2. PISA3D

The Platform of Inelastic Structural Analysis for 3-D Systems (PISA3D) (Lin et al. 2009) is developed in the Dept. of Civil Engineering of National Taiwan University and maintained in NCREE. It is an object-oriented general-purpose computational platform for nonlinear structural analyses. The PISA3D incorporates the object-oriented concept and the Design Patterns to construct the software framework, making it easy to maintain and extend. PISA3D provides a rather large variety of nonlinear materials and elements. PISA3D users could build 3-D analytical models and perform nonlinear analyses to investigate the responses of structures under the combined load effects. Users can download the program for free from http://pisa.ncree.org.tw In this paper, PISA3D is adopted to present the response simulations of the frame specimen.

3. BASIC MODEL

In the basic model, the frame mass is considered as a lump mass located at the top of the slab of each floor. However, the location of the mass is eccentric due to the asymmetric configuration of the exterior walls. The Newmark method of constant average acceleration scheme (β=1/4) is used for the time integration. Rayleigh damping is adopted, and the damping ratios are assumed to be 2% for the first and second modes of the 3D model. The modeling techniques of the basic model are described below.

3.1 Fibered Beam Model

The frame beam member is considered as the steel and concrete full-composite beam in the basic model. This beam model adopted fibered beam-column element to represent the composite floor beam. The fibered beam-column element in PISA3D is flexibility-based. The element formulation relies on force interpolation functions that strictly satisfy the equilibrium of the bending moments and the axial force along the element (Spacone et al. 1996; Neuenhofer and Filippou 1997).

As shown in Figure 3, the influence of the metal deck orientation to the composite beam properties has been taken into account. Figure 3a illustrates the fiber section of the composite beam along the Y direction. Figure 3b represents the fiber section of the composite beam along the X direction. For the beams along the Y direction, it is assumed that the concrete between the top and bottom of the metal deck contributes the composite beam action (Figure 3a). However, along the X direction, only the concrete on the top of the metal deck is considered in the fibered beam elements (Figure 3b). Assuming that the composite beam section is mainly subjected to the strong axis bending (z axis in Figure

4a), the fiber distribution was defined only along the local y axis (Figure 4a) to reduce the total number of fibers and the computational effort. Then, the fiber section model for the beams along the Y direction (Figure 3a) was defined as shown in Figure 4a. The beam-to-column subassembly test results were used to define the effective width (b_E) of the concrete slab. It was found that the effective concrete slab width was only 300 mm when the simulation result as shown in Fig.4b was obtained.

The concrete below the top of the metal deck was incorporated using one half of the width of the part above the metal deck. The concrete slabs of the beams along the Y and X direction consist of 7 and 4 compression-only fibers, respectively. The steel beam consists of 13 fibers using the steel yield strength provided by the organizers for the bilinear steel material. The "stress versus strain" relationship of the concrete provided by the organizer was used for concrete fibers. The concrete material follows the recommendations provided by Popovics (1973) and the unloading/reloading responses are according to the work of Karsan and Jirsa (1969). Five integration points along the fibered beam-column element were chosen to integrate the element responses.

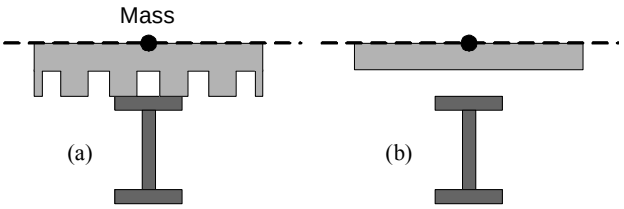

Figure 3 Elevation of floor mass and the cross section of composite beam along (a) Y direction and (b) X direction

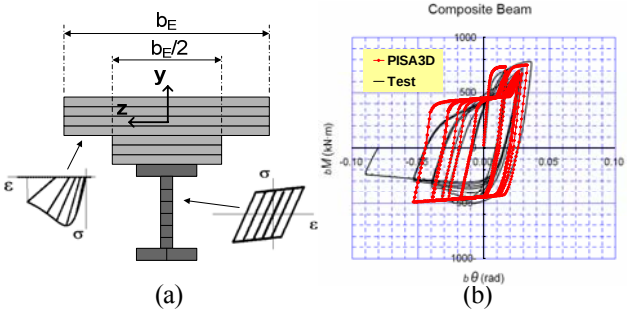

Figure 4 (a) Schematic of the fiber section (b) Comparing the cyclic force versus deformation responses of the fibered beam with test results

3.2 Panel Zone Joint

From the beam-to-column subassembly tests (Shimada et al. 2009), shear deformations were evident in the panel zone. Thus, in the basic model, shear deformations of the panel zones were specifically included by introducing zero-length joint elements while the member rigid end offset feature for the joining beam and column ends were incorporated into the analytical model. In the present study, rotational stiffness, K and yield capacity, M_y for all panel zone joint elements were calculated using the following two equations (Tsai and Popov 1990):

$$K = \frac{G d_b d_c t_j}{\left(1 - \frac{d_b}{H}\right)} \quad (1)$$

$$M_y = \frac{0.55 F_y t_j d_b d_c}{\left(1 - \frac{d_b}{H}\right)} \quad (2)$$

Where d_b is depth of beam, d_c is depth of column, t_j is the thickness of panel zone, and H is the story height. Figure 5 shows the response simulation of the panel zone using the Joint Element and the Bilinear Material in PISA3D. The analytical results suggest that the Joint Element incorporating the stiffness and the yield capacity given in Eqs. 1 and 2 could well simulate the cyclic responses of the panel zone in the beam-to-column subassembly without concrete slab.

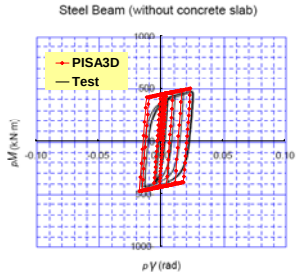

Figure 5 Comparing the cyclic force-deformation responses of the panel zone joint element with the test results

3.3 Hinge Model for Column

In the basic model, hinge-model beam-column element was adopted for all the column members. This beam-column element is a lumped-plasticity model. It has an elastic component that is series-connected by one shear and one flexural plastic hinges at each end. All the nonlinear deformations can only take place in these hinges. The bilinear material property was adopted. The plastic section modulus and the steel yield strength provided by the organizers were used. No axial-flexural interaction is considered in this model. The material strain hardening ratio was assumed to be 0.02.

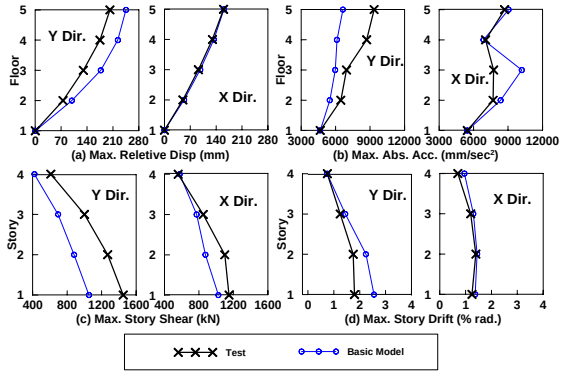

Figure 6 Absolute maximum responses of basic model subjected to the EQ-I

3.4 Comparison Between Basic Model Simulation and Test Results

Figures 6a to 6d show the absolute peak responses of the basic model under the EQ-I. It is evident from Figs. 6a and 6d that the displacement-related responses (maximum floor displacements and story drift) in the X direction are very close to the test results. Figures 6a shows that the maximum floor displacements computed from the basic model were larger than the test results. The basic model underestimated the story shear responses (Figure 6c). For some unknown reasons, this under-prediction on story shear has been found common in most groups participated in the blind contest (Hikino et al. 2009).

From Fig. 6a, it can be found that the analytical Y-direction displacement responses were somewhat greater than those in the X direction. This finding agrees with the observed test responses. Under the EQ-C, the test frame did collapse primarily along the Y direction (Suita et al. 2008). Figure 7 shows the first story drift time history responses in the Y direction of the basic model under the EQ-C. It can be found that the collapse drift ratio of 0.13-radian defined by the contest organizers was never reached in the response history analysis using this basic model. Further studies are necessary.

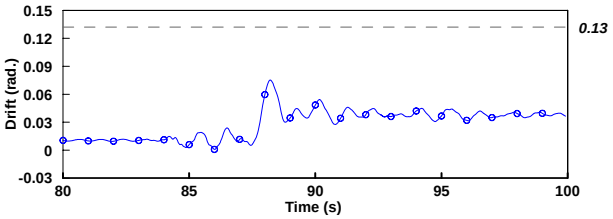

Figure 7 First story drift time histories in the Y direction under the EQ-C for the basic model



Figure 8 Local buckling of the first-story column (at the intersection of frame line A and 2) at the end of the tests

4. REFINE COLUMN USING PARALLEL MATERIAL HINGE MODEL

When the specimen was subjected to the EQ-C, local buckling occurred at both the bottom and top ends of several first story columns (Suita et al. 2008). Figure 8 shows the bottom column end local buckling of the 1st-story column at the intersection of Frame Line A and 2 (Figure 2a). This local buckling led the building into a side-sway collapse mechanism in the first story (Suita et al. 2008). Recall in the basic model that the column strength degradation due to the local buckling was not specifically considered as all the column elements were represented using bilinear material. This should be helpful in explaining why the basic model failed to predict the collapse of the specimen.

In order to refine the column properties in the frame model, an independent ABAQUS (2006) finite element (FE) column model was constructed to study the local buckling response. This column analytical model is 1938 mm high (one half of the 1st-story column of the specimen) and the cross section is HSS300×300×9 mm, identical to the column members in the test frame. The column bottom end is fixed but the top end is free. The FE model was constructed using the 4-node, quadrilateral, stress/displacement shell elements with the reduced integration and a large-strain formulation (S4R). The bilinear steel material model was adopted for a total 936 shell elements. This FE column model was subjected to a constant axial load of 257 kN (observed from the gravity load in the bottom corner column in the five basic models) and cyclic increasing lateral displacements in one direction only.

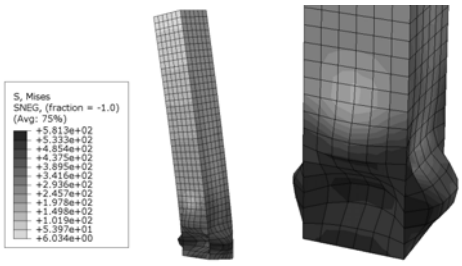

Figure 9 Local buckling of the ABAQUS column model

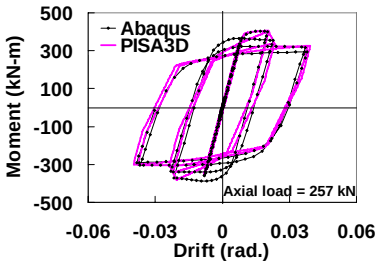

Figure 10 Comparing the HBC cyclic column lateral force versus deformation responses with the ABAQUS FE results

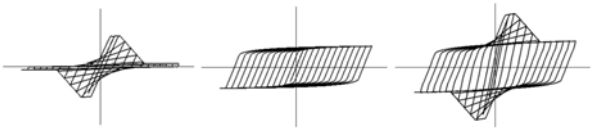

(a) Degrade Material (b) Hardening Material (c) Parallel Material

Figure 11 Parallel material model in PISA3D (a) + (b) = (c)

Figure 9 shows the local buckling response of the ABAQUS column model when the column top end reached 0.04 radians lateral drift. Figure 10 shows the FE column base moment versus top end lateral drift relationships. It is evident that the HSS300×300×9 mm column strength degradation is rather pronounced when the lateral drifts are greater than 0.02 radians. In order to refine the column element properties in the frame model, the "Parallel" material model in PISA3D was adopted in this study. The construction of the hinge-buckling-column "HBC" model utilized two material properties and the feature of parallel

material to simulate the cyclic local buckling response of the column. In the present study, the parallel material property as shown in Fig. 11c is a result of combining the degrade material given in Fig. 11a with the hardening material illustrated in Fig. 11b. The cyclic responses of a PISA3D "HBC" model for the 1938 mm high HSS300×300×9 mm column using the Parallel material are also plotted in Fig. 10. It can be found from comparing the ABAQUS and PISA3D results that the cyclic strength degradation due to local buckling can be better simulated from using the HBC model than the bilinear-HC model. The effects of axial loads on the accuracy of the HBC models will be discussed later.

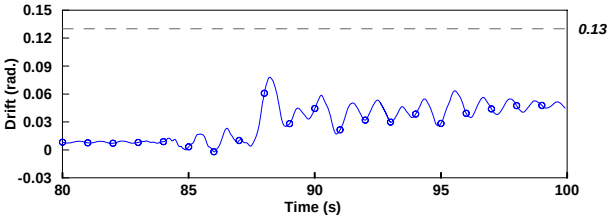

Figure 12 First story drift time histories in the Y direction under the EQ-C for the HBC model

From the findings stated above, the refined HBC model was constructed and studied by replacing the 1st-story columns in the basic model with HBC model columns. The responses of the refined HBC model were very similar to the basic model. Figure 12 shows the first story drift time history response of the refined HBC model under the EQ-C. It can be found that the 0.13-radian drift was still not reached in the refined HBC model. The basic and refined models introduced so far never considered the effects of interactions among the varying axial loads and bi-axial bending moments in columns as hinge models were adopted. Using the fiber model for column, the axial-flexural interactions can be conveniently incorporated into the frame model. In this approach, the compressive stress degradation characteristic has been implemented into the buckle-material fiber model in order to capture the local buckling responses of the column.

5. REFINE COLUMN USING BUCKLE MATERIAL FIBER MODEL

The Buckle material in PISA3D adopted the cyclic response rules proposed by Maison and Popov (1980) as shown in Fig. 13. Users could specify the values of control points and control slopes to adjust the hysteresis responses. The "FBC" column model adopted fibered beam-column element with a cross section consisting of 44 fibers using the Buckle material model given in Fig. 13. Five integration points were used. In this study, the degradation characteristics in the cyclic responses obtained from the afore-mentioned ABAQUS FE column analysis was used to calibrate the parameters of the FBC column model. Two levels of column axial loads (257 and 515 kN for corner column and center column, respectively) were chosen. Figure 14 shows that at both two axial force levels, the FBC column model can satisfactorily simulate the cyclic degrading responses of the ABAQUS FE model. It can be found that under the 515 kN constant axial load, the cyclic degradation of the ABAQUS FE model is severer than in the case of 257 kN axial load. This phenomenon has been well captured by using the same set of degrading parameters in the two FBC models. Based on this finding, a more refined model was constructed.

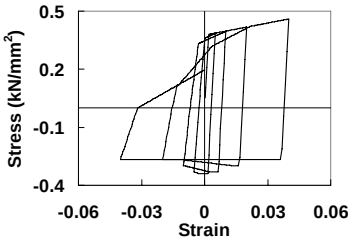

Figure 13 The stress versus strain relationship of each fiber in the FBC model

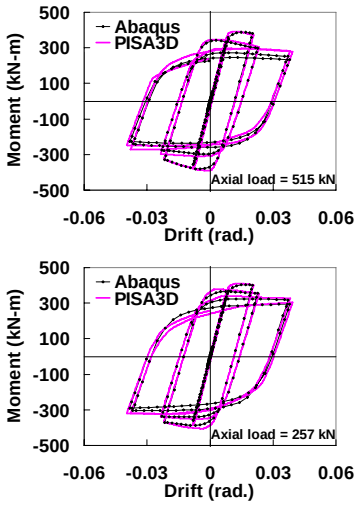

Figure 14 Comparing the FBC cyclic column lateral force versus deformation responses with the ABAQUS FE results for two levels of column axial loads

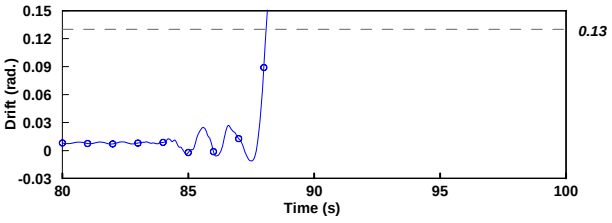

Figure 15 First story drift time histories in the Y direction under the EQ-C for the FBC model

The refined "FBC" frame model was constructed by replacing the 1st-story columns of the basic model with the FBC model columns. Figure 15 shows the 1st-story drift time histories under the EQ-C for the FBC frame model. It can be found in the figure that this model reached the 0.13-radian collapse criterion and very close to the test results (Tada et al. 2008). Figures 16 and 17 show the "HBC" and "FBC" center column base moment (toward the longitudinal direction of the frame collapse) versus 1st story

drift relationships for two levels of excitations, respectively. Under the EQ-I, the strength degradation was not yet developed in Model HBC as shown in Fig. 16a. However, it is evident that the strength deterioration in Fig. 17a (representing the column buckling) has occurred in Model FBC during the EQ-I. As a result, the column base responses of the two models are very different during the EQ-C as evidenced in Figs. 16b and 17b. The reduced strength as observed in the beginning of the FBC model in Fig. 17b was very similar to the response reported in the reference (Suita et al. 2008). The strength deterioration was not reached in Model HBC during EQ-I (Figure 16a) and its initial strength in the beginning of EQ-C (Figure 16b) was higher than that in Model FB_PZ_FBC. These results seem to fail Model HBC to predict the collapse responses. The FBC frame model incorporating the effects of interactions among the varying axial loads and bi-axial bending moments in columns have captured the collapse of the building specimen. This should suggest that the collapse of the test frame is strongly governed by the severe local buckling of the columns in the first story. The cyclic column axial and bi-axial flexural interactions are critical in developing the local buckling of the columns. The proper column analytical model of reasonable degrading rules is important for the collapse simulation.

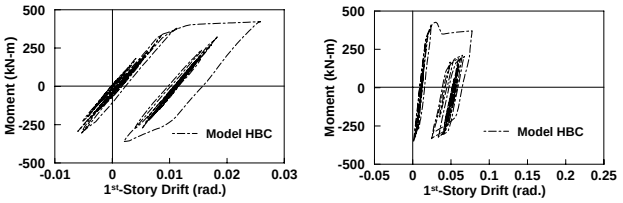

(a) EQ-I (b) EQ-C

Figure 16 Column bottom end moment versus 1st-story drift relationships in Model HBC

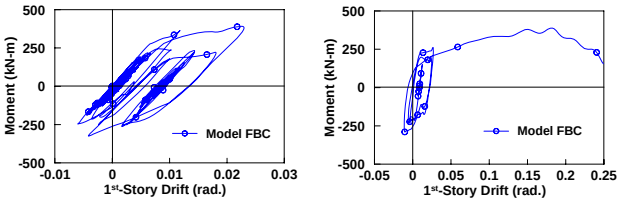

(a) EQ-I (b) EQ-C

Figure 17 Column bottom end moment versus 1st-story drift relationships in Model FBC

Figure 18 compares the X and Y directions' 1st-story drift time histories of Model FBC and test results (Tada et al. 2008) under the EQ-C. In the both directions, the analytical results show good correspondence with the test responses. In addition, the time instant at which the inter-story drift of the analytical model reached 0.13 radians appears very close to that measured from the test (Figure 18b). It is illustrated that the refined FBC analytical model made in this study can satisfactorily simulate the collapse of the specimen.

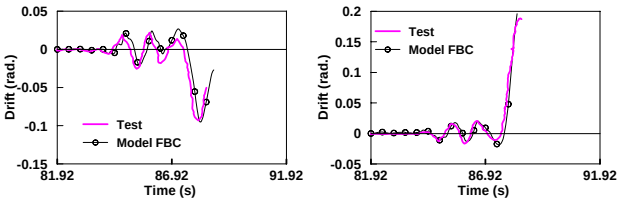

(a) X-direction (b) Y-direction

Figure 18 First-story drift time histories under the EQ-C

6. SUMMARY AND CONCLUSIONS

Based on the analytical and experimental studies, summaries and conclusions can be made as follows:

1. The basic frame model using bilinear hinge-model column elements have failed to predict the frame collapse time. The key reason is that the column strength degradation due to the local buckling has not been considered.
2. Under the EQ-I, the strength degradation was not yet developed in the HBC frame model but was evident in the FBC frame model. The reduced strength as observed in the beginning of the FBC model was very similar to the response of the test specimen. This strength deterioration was not reached in the HBC frame model during EQ-I and its initial strength in the beginning of EQ-C was higher than that in the FBC frame model. These results seem to fail the HBC frame model to predict the collapse responses.
3. The ABAQUS column local buckling responses can be represented using the PISA3D fiber-model column with Buckle Material. The proposed FBC column model can conveniently incorporates the combined cyclic strength degrading effects among the varying axial loads and bi-axial bending moments. The collapse of the test frame is strongly governed by the severe local buckling of the columns in the first story. The collapse time of the test building can be simulated in all the FBC frame model using this column model element. This suggests that the analytical force versus deformation relationships of the first story columns strongly affects the collapse prediction of the frame. The proper column analytical model of reasonable degrading rules is important for the collapse simulation.

Acknowledgements:

The shaking table experiment is a part of "NEES/E-Defense collaborative research program on steel structures." The authors greatly appreciate the organizers conducting the tests, the blind prediction contest, and sharing the test results. This interesting test and the valuable experimental data have stimulated the interests of many researchers and engineers in studying the analytical modeling techniques for steel structures under earthquake ground motions.

References:

ABAQUS. (2006), "ABAQUS analysis user's manual," *ABAQUS Inc.*, Version 6.6.

American Institute of Steel Construction (AISC). (2005),

"Specification for Structural Steel Buildings," Chicago, Illinois.
HEERC, Hyogo Earthquake Engineering Research Center. (2007), *Blind Analysis Contest Application Site*, Web page: http://www.blind-analysis.jp/index_e.html.
Hikino, T., Ohsaki, M., Kasai, K., and Nakashima, M. (2009), "Simulation of E-Defense full-scale shake-table test results of moment-resisting steel frame," *Proceedings of 6th International Conference on Behavior of Steel Structures in Seismic Areas*, Philadelphia, Pennsylvania, USA.
Karsan, I. D., and Jirsa, J. O. (1969), "Behavior of concrete under compressive loading," *Journal of Structural Division ASCE*, 95(ST12).
Lin, B. Z., Chuang, M. C. and Tsai, K. C. (2009), "Object-oriented development and application of a nonlinear structural analysis framework," *Advances in Engineering Software*, 40, pp. 66-82.
Maison, B. F., and Popov, E. P. (1980), "Cyclic response prediction for braced steel frames," *Journal of the Structural Division,* Vol. 106, No. 7, p.1401–p.1416.
Neuenhofer, A., and Filippou, F. C. (1997), "Evaluation of nonlinear frame finite-element models," *Journal of Structural Engineering*.
Ohsaki, M., Kasai, K., Hikino, T., and Matsuoka, Y. (2008), "Overview of 2007 E-Defense blind analysis contest results," *Proceeding of 14th World Conference on Earthquake Engineering*, Beijing, China.
Popovics, S. (1973), "A numerical approach to the complete stress strain curve for concrete," *Cement and concrete research*, 3(5), 583-599.
Shimada, Y., Kishiki, S., Yamada, S., Matsuoka, Y., and Suita, K. (2009), "Panel zone performance in a weak panel-type moment frame consisting of a composite beam and a square hollow section column," *Proceedings of 6th International Conference on Behavior of Steel Structures in Seismic Areas*, Philadelphia, Pennsylvania, USA.
Spacone, E., Ciampi, V., and Filippou, F. C. (1996), "Mixed formulation of nonlinear beam finite element," *Computers and Structures*, Vol. 58.
Spacone, E., Filippou, F. C., and Taucer, F. F. (1996), "Fibre beam-column model for non-linear analysis of R/C frames: part 1. formulation," *Earthquake engineering and structural dynamics*, Vol. 25. 711-725.
Suita, K., Yamada, S., Tada, M., Kasai, K., Matsuoka, Y., and Shimada, Y. (2008), "Collapse experiment on 4-story steel moment frame: Part 2 Detail of collapse behavior," *Proceeding of 14th World Conference on Earthquake Engineering*, Beijing, China.
Tada, M., Tamai, H., Ohgami, K., Kuwahara, S., and Horimoto, A. (2008), "Analytical simulation utilizing collaborative structural analysis system," *Proceeding of 14th World Conference on Earthquake Engineering*, Beijing, China.
Tsai, K. C. and Popov, E. P. (1990), "Seismic panel zone design effect on elastic story drift in steel frames," *Journal of Structural Engineering*, 116(12), pp. 3285-3301.

JOINT CONFERENCE PROCEEDINGS
7th International Conference on Urban Earthquake Engineering (7CUEE) &
5th International Conference on Earthquake Engineering (5ICEE)
March 3-5, 2010, Tokyo Institute of Technology, Tokyo, Japan

TEST ON RETROFIT EFFECTS OF STEEL BEAM-TO-COLUMN CONNECTIONS WITH RC FLOOR SLABS

Yulin Chung[1], Tomohiro Matsumiya[2], Takuya Nagae[3], Kunio Fukuyama[4], Toko Hitaka[5] and Masayoshi Nakashima[6]

1) Graduate Student, Disaster Prevention Research Institute, Kyoto University, Japan
2) Assistant Professor, Facility of Science and Engineering, Kinki University, Japan
3) Senior Researcher, E-Defense, National Institute for Earth Science and Disaster, Japan
4) Visiting Researcher, E-Defense, National Institute for Earth Science and Disaster, Japan
5) Associate Professor, Disaster Prevention Research Institute, Kyoto University, Japan
6) Professor, Disaster Prevention Research Institute, Kyoto University, Japan
yulin.chung@ks7.ecs.kyoto-u.ac.jp, matsumiya@arch.kindai.ac.jp, nagae@bosai.go.jp, fuku-kn@bosai.go.jp, toko.h@ay2.ecs.kyoto-u.ac.jp,nakashima@archi.kyoto-u.ac.jp

Abstract: A series of quasi-static member tests were conducted to characterize the deformation capacity of retrofitted beam-to-column connections of high-rise buildings. In reference to some previous tests on retrofitted connections, three types of retrofit methods were adopted, considering the construction feasibility and the effect of RC slab. Connections were tested by applying multiple plastic cycles of long-period ground motions until the connection fractured. The test results indicate that supplemental welds along the shear tab changes the strain distribution of connection but does not improve the ductility. Retrofit the bottom flange using wing plates and straight haunch significantly improved the cumulative plastic rotation about 4 times of that of the original connection.

1. INTRODUCTION

Occurrences of large earthquakes having a magnitude over eight along subduction zones in the southwestern part of Japan have been predicted. Such subduction zone earthquakes would generate long-period ground motions in land and might cause significantly large cumulative deformation to high-rise buildings (JSCE, AIJ. 2006; AIJ. 2007). A large scale E-Defense shaking table test had been conducted to verify the capacity of high-rise buildings subjected to long-period ground motions (Chung et al. 2008). The ground motions generated fifteen times larger story cumulative ductility to the tested high-rise building specimen than that obtained from the design wave and caused the field-welded connection, which had welded flanges and bolted web, fractured at multiple locations. More then 80% of the existing connection of high-rise buildings adopted the field–welded connection. Thus, retrofitting of the existing connections to make them able to sustain the demands of long-period grounds is very important.

After the 1994 Northridge and 1995 Hyogoken-Nabu earthquakes, connections like reduced beam section (RBS), welded bottom haunch (WBH) among others have been recommended, and all have been qualified as the ductile connections (FEMA 350). For the retrofit of existing connections, however, these recommended connections have difficulties in application because of the presence of RC floor slab. It is also notable that most of the tests based on which the recommendations were stipulated were for bare beams rather than for beams with RC floor slab. According to the past tests (Kim et al. 2004), the slab could significantly effect the performance of connections. The actual data about the seismic performance of retrofitted connections are deemed still very limited.

Therefore, to characterize the deformation capacity of retrofitted beam-to-column connections of high-rise buildings, a series of quasi-static member tests were conducted in this study. In reference to some previous tests on retrofitted connections, three types of retrofit methods were adopted, considering the construction feasibility and the effect of RC slab. Retrofit performance and capacity of these connections are evaluated by applying multiple plastic cycles that considering the effects of long-period ground motions.

2. TEST OUTLINE AND DESIGN OF THE TEST SPECIMEN

2.1 Beam-to-Column Connections

Figure 1(a) to (d) show four types of connections, all arranged with the RC floor slab. Dimensions and connection

details of the specimens were designed by taking the field -welded connection of high-rise buildings built in 1960~70 as the prototype. Due to the capacity of the loading system, dimension of specimens were scaled down to three quarters. The beam was a built-up wide flange section of H 600×150×9×12 and a square tube column of 300×300×19 (BCR295) was adopted. The column beam strength ratio ($_{column}M_p/_bM_p$) was 1.6. $_{column}M_p$ and $_bM_p$ are the full plastic moment of the column and beam section. The column was expected to remain in elastic throughout the loading. The common connection details applied at all connections are shown in Figure 1(e). The top flange weld access hole has a one quarter circle and the toe of the bottom flange weld access hole ends at the boundary of penetration welding. The number and arrangement of the bolts were determined in reference to the following policies. The maximum bending moment obtained from the shear strengths of these bolts should be larger than the estimated full plastic bending moment of the shear plate. Also, the bolts should be able to sustain the beam shear force, while the connection meets the requirement for the combination of maximum strength and long term vertical loadings. Table 1 shows the member sizes and material properties adopted in the test. The SM 490A steel was adopted in all beams.

To evaluate the performance of retrofitted connections, the original connation was tested as the baseline (Figure 1(a)). Base on the connection details, three types of retrofit methods were adopted considering both their retrofit performance and construction feasibility in the filed (Figure 1(b) to (d)). The basic policy of the retrofit is to do the best to enhance the seismic capacity with most practical retrofit techniques rather than to set up the required performance for the retrofit.

In the Figure 1(b), the connection was modified slightly, and the shear tab was welded to the beam web as a possible retrofit. Supplemental welds had been commonly applied between the shear tab and the web of the pre-Northridge connection (WUF-B) when their performance was improved by some tests (Tsai et al. 1988). After the 1994 Northridge earthquake, the ductility demand for beam-to-column connections was raised significantly. Since that time, the supplemental weld connection has been considered unable to satisfy the demand.

Although the supplemental weld is no longer considered as a reliable alternative for the improvement of ductility, the possibility was explored once again in this study to examine how much (or less) the supplemental weld would be effective, this time against cyclic rotations characterized by many cycles, say, more than ten times, but with relatively smaller amplitudes of about 1.0 to 1.5% in the story drift angle (Chung et al. 2008). In this test, the shear tab was all welded to the beam web to increase the web resistance as much as possible.

Attaching wing plates on the top and bottom flanges or

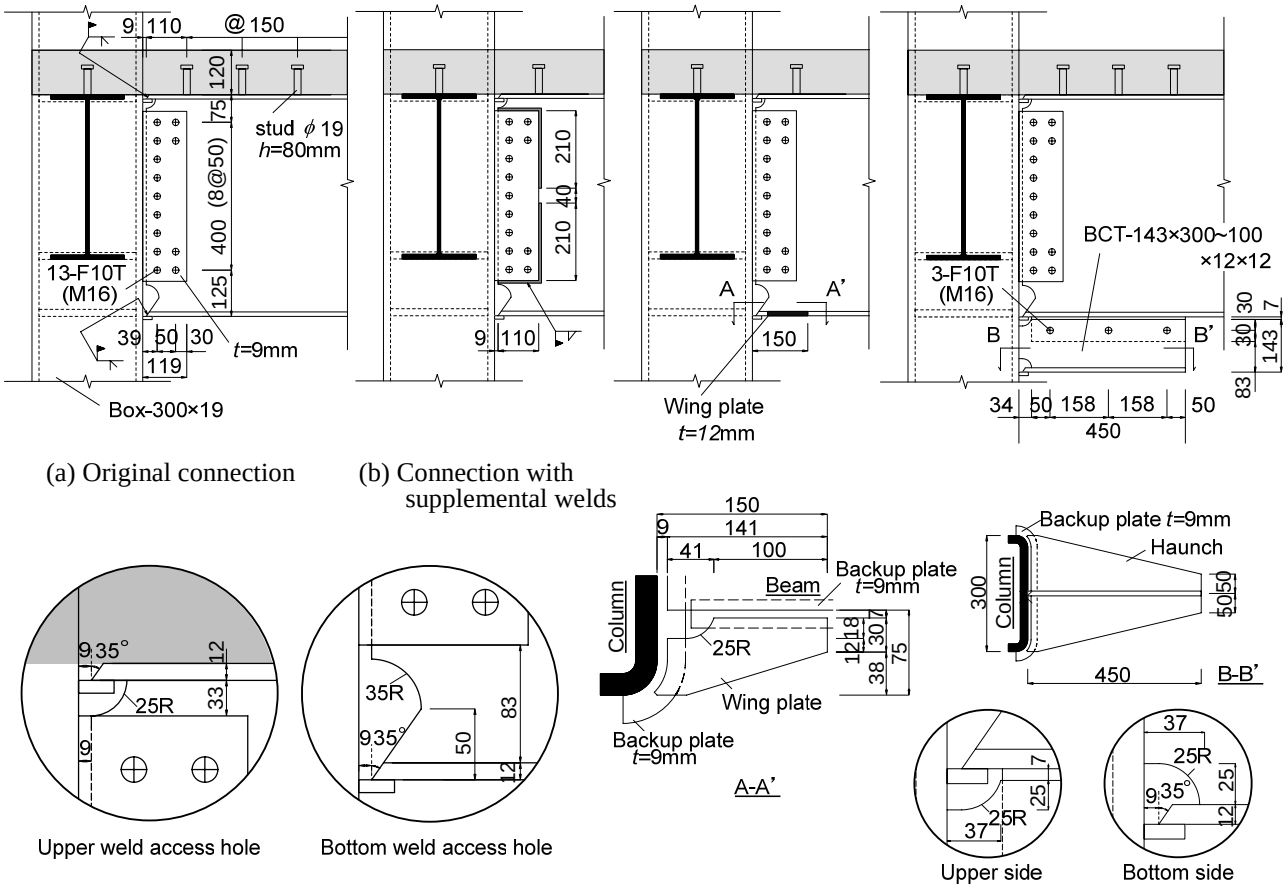

(a) Original connection (b) Connection with supplemental welds

(e) Details of weld access holes (c) Wing plate connection (d) Haunch connection

Figure 1 Test connections Unit: mm

Table 1 Specimen specifications and material properties

Member		σ_y (MPa)	σ_u (MPa)
Box-300×19		435	455
H-600×150×9×12	Flange	350	508
	Web	358	509
Haunch		344	508
Concrete		F_c=21.1 MPa	

attaching a haunch below the bottom flange of field-welded connection were proposed and qualified based on several tests (Tsai et al. 1996, Uang et al. 2000). The concept of the wing plate and haunch connections are to move the weakest spot from the beam end where welds and weld access holes were present to a continuous beam without geometrical discontinuities.

The design of retrofitted connections adopted in this test followed those previous studies. Because of the presence of RC floor slabs, retrofit was mostly limited to the bottom flange or to the web (Figure 1(b)). Besides, the constructability was very critical particularly in high-rise buildings. Along this line, two types of retrofit methods shown in Figure 1(c) and (d) were adopted in this test. In Figure 1(c), the wing plates were only attached at the bottom flange. In Figure 1(d), the haunch was designed to create a reasonable mechanism for the box column.

2.2 Design and Construction

Table 2 summarizes the estimated strengths of connections based on the measured material properties. ${}_bM_p$ is the full plastic moment of the bare beam (638kN・m). ${}_jM_u$ is the maximum strength of connection (AIJ 2006). Effect of RC floor slab was not considered in the calculation.

Table 2 Estimated strength of connections

Connections	${}_jM_u/{}_bM_p$
Original	1.11
Supplemental welds	1.11
Wing plates	1.39
Haunch	1.50

(a) Original connection

The maximum flexural strength of the web connection was controlled by the strength of the shear plate. The connection strength ratio (${}_jM_u$ / ${}_bM_p$) was 1.11. The Japanese code (AIJ 2006) recommends the connection strength ratio of not smaller than 1.2. The ratio in this test was slightly smaller than the recommended value.

(b) Connection with supplemental welds

Basing on the design for the original connection, supplemental welds were applied to the web. To improve the moment transfer of the web as large as possible, the shear plate was all fillet welded to the beam web (Figure 1(b)). The length dimension of horizontal weld at both the top and bottom sides of the shear plate were 110 mm long. The vertical weld was interrupted in the middle by a 40 mm clearance to prevent excessive heat input and residual stresses resulting from a long distance welding.

The maximum flexural strength of the web was controlled by the strength of the shear plate. The connection strength ratio (${}_jM_u$ / ${}_bM_p$) remained 1.11. If the flexural strength of the web was obtained from the combination of the friction force of the bolts and the supplemental welds at shear plate, the connection strength was increased to 1.10 from 0.94 when the supplemental welds were applied.

(c) Wing plate connection

Dimensions of the wing plates were determined using the following policies. The thickness of the plate was identical with the thickness of the beam flange. This ensured the alignment between the flange and wing plate that were welded together. The width of the wing plate was 75 mm to widen the bottom flange to the column width (A-A' in the Figure 1(b)). Because of the presence of the end tab that commonly existed in the field weld connection, one 1/4 circle hole with a radius of 25 mm was adopted in the plates. The length between the wing plate and column (50 mm for each side) could be token as the effect width without considering the out of plane deformation of the square tube column, owing to the presence of the inner-diaphragm in the column. The weld length between the wing plate and beam bottom flange (l_1=100 mm) was determined to ensure the shear force transfer from the wing plate to the beam flange, while the weld between the wing plate and column (l_2=50 mm) arrived at its maximum tensile strength (Figure 2). The connection strength ratio ${}_jM_u$ / ${}_bM_p$ of the wing plate connection was 1.39.

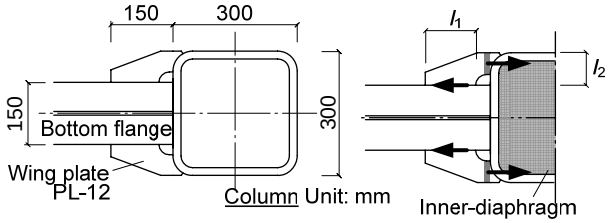

Figure 2 Design concept of wing plate

(d) Haunch connection

Attaching wing plates at the bottom flange sometime meets difficulties. The presence of the end tab and/or a small size column section would leave very limit space for attaching the wing plates and may make the retrofitted connection not able to satisfy the strength ratio of at least 1.2 (AIJ 2006). Attaching a haunch below the bottom flange is another choice for retrofit. The design policies of the haunch retrofit are described below. The thickness of the bottom flange of the haunch was 12 mm that was identical with the thickness of the beam flange. The flange of the haunch was

widened to the column width (300 mm) to transfer the force to the column (Figure 3). Because there is no inner-diaphragm at the location where the haunch flange is connected to the column, an effective width (l_3, showed in Figure 3) of the haunch flange was taken to be 3.5 times of the thickness of the column plate (66.5 mm), measured from each side of the edge (AIJ. 2001). The length of the haunch (l_4=450 mm, showed in Figure 3) was determined to ensure the shear force transfer between the haunch web and the bottom flange of beam when the haunch flange reaches its maximum tensile force. The maximum flexural strength of the haunch connection was determined as the sum of the plastic section modular of the beam and haunch. The strength ratio of the connection ${}_jM_u / {}_bM_p$ reached 1.50.

In the fabrication work, the haunch was first bolted to the shear tab, which was pre-welded to the bottom flange of the beam. The shear tab also worked as a backup plate when the penetration weld was applied between the haunch web and bottom flange of beam. Then, the welder applied the horizontal, vertical and downward welding at the web and flange of the haunch. All welds of all four connections fabricated in this study were ultrasonically tested by qualified inspectors, and no default was inspected.

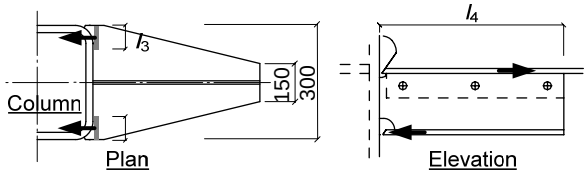

Figure 3 Design concept of haunch

2.3 Loading System and Loading Program

Loading system

The test setup and test specimen are shown in Figure 4. The specimen consists in one column and two beams with respective beam-to-column connections. In one of the specimens, one side of the beam was arranged with the original connection. On the other side of the beam, the connection was modified slightly, and the shear tab was welded to the beam web as a possible retrofit. In the other specimen, the wing plates and haunch connections were arranged on each side of the beams. The top and bottom of the column and the two ends of the beams were pin supported. The horizontal load was applied at the top of the column by the 1,500kN oil jack. A RC floor slab with the thickness of 120 mm was placed on top of the beams. The dimension of the RC slab was limited to 1 m in width and 1.9 m in length on each side. The left and right beams were loaded independently by releasing the pin at the other beam.

Loading program

The loading history was determined in reference to the response obtained from the response of past test (Figure 5(a)). According to the story drift angle history subjected to the long-period ground motion (San wave) in the second story in which the story drift angle was the largest, the specimen experienced cycles between the 0.9 to 1.1% drift

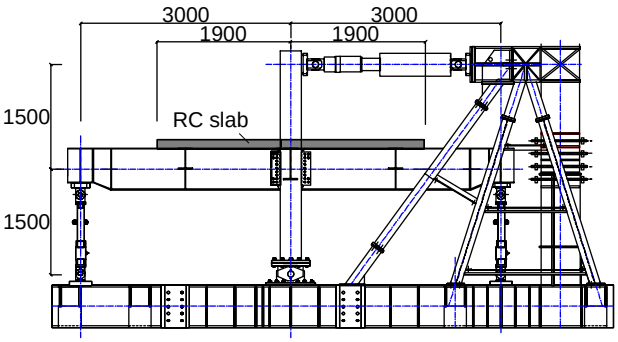

Figure 4 Quasi-static loading test setup (unit: mm)

angle amplitudes for eleven times, and cycles between 1.1% to 2.0% for three times (Chung et al. 2008). To make the experienced amplitudes as close as possible between the past test and this test, the following loading history was adopted for the member test: elastic loading with the 0.2% drift angle for two cycles, followed by the 0.5 % drift angle for two more cycles and inelastic loading, with the 1 % drift angle for eleven cycles, followed by the 2% drift angle for two cycles and 3 % drift angle until the connection fractured (Figure 5 (b)).

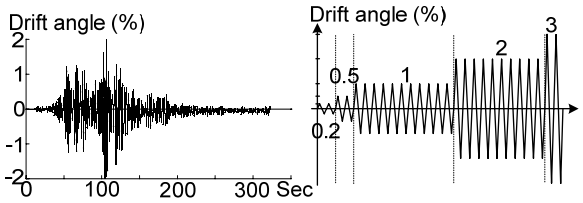

(a) (b)

Figure 5 Loading history: (a) Seismic response; (b) loading history of the test

3. OBSERVATIONS AND HYSTERETIC BEHAVIORS

(a) Original connection

The normalized bending moment versus rotation relationship and a close-up of fractures are shown in Figure 6(a). The rotation represents the rotation angle between the beam end to the pin support. The hysteretic behavior shows stable loops under the 11 cycles of 1% drift angle loadings (beam rotation was about 0.006 rad). A crack extended from the toe of the weld access hole in the first positive cycle of the 2% drift angle, with the beam rotation of 0.018 rad. The crack leaded to fracture of the bottom flange in the next positive bending and made the resistance reduced significantly in the positive bending.

(b) Connection with supplemental welds

In the connection with supplemental welds, a crack was observed at the toe of the bottom flange weld access hole during the first positive bending of the 2% drift angle (Figure 6(b)), with the beam rotation of 0.017 rad. In the negative bending, local buckling was formed in the bottom flange, while fractured in the second cycle of the 2% drift

angle. The connection fractured at nearly the same instant with the original connection. Both the maximum deformation capacity and fracture pattern were very similar between these two connections.

(c) Wing plate connection

The connection was able to sustain more cycles than the previous two connections (Figure 6(c)). Local buckling occurred at the tip of the wing plates under the first negative bending of the 2% drift angle, with the beam rotation of 0.015 rad. A crack initiating from the toe of weld access holes of the top flange was observed in the next 2% drift angle cycle and lead to an eventual fracture after experiencing 10 cycles of the 2% drift angle loading. The fracture at the top flange lead a rapid strength loss in the negative bending.

(d) Haunch connection

Both the strength and deformation capacity were greatly improved by attaching the haunch. A crack at the top flange and buckling at the tip of the haunch (450 mm from the column face) were observed at the first 2% drift angle loading (Figure 6(d)). The strength and stiffness gradually decreased after the buckling. The negative bending moment decreased to 70% of the maximum strength under the 3% drift angle amplitude. After the second cycle of the 3% drift angle, the test was terminated due to severe buckling. The presence of the hunch effectively moved the plastic hinge of the beam outside the haunch region as intended in the design.

4. RETROFIT PERFORMANCE

4.1 Maximum Strength

The maximum strength of the connections are summarized in Table 3. The strength in the positive and negative bending was normalized by the full plastic strength ${}_bM_p$ of the corresponding bare beam.

The haunch connection was able to sustain about two times the full plastic moment of the bare beam. Comparing the maximum negative flexural strength ratio ($M_{max}^-/{}_bM_p$) with the connection strength ratio ${}_jM_u/{}_bM_p$ estimated in the design stage, the test result of each connection shows good correlation (Table 2). In the retrofitted connections, the maximum strength of the haunch connection was the largest, 1.5 times larger than that of the original connection. The $M_{max}^+/{}_bM_p$ of the connection with supplemental welds and the wing plate connection were 1.1 and 1.2 times of that of the original connection.

Table 3 Maximum strength

	$M_{max}^+/{}_bM_p$	$M_{max}^-/{}_bM_p$
Original	1.36	1.16
Supplemental welds	1.55	1.22
Wing plates	1.67	1.34
Haunch	2.04	1.34

4.2 Cumulative Plastic Rotation

Figure 7 shows the cumulative plastic rotation ($\Sigma {}_b\theta_p$) of all connections which were calculated until the fractures of the connections. The connection with supplemental welds fractured at nearly the same instant with the original connection and caused very similar cumulative plastic rotation. Retrofit performance in terms of the cumulative plastic rotation capacity was not notably improved using the supplemental welds at web. For the haunch connection, the rotation was calculated until the strength was reduced to 90% of the maximum strength. The cumulative deformation capacities of the wing plate and haunch connections were both at least four times larger than those of the original connection.

4.3 Strain at The Top and The Bottom Flanges

Figure 8 summarizes the maximum strain at the top and

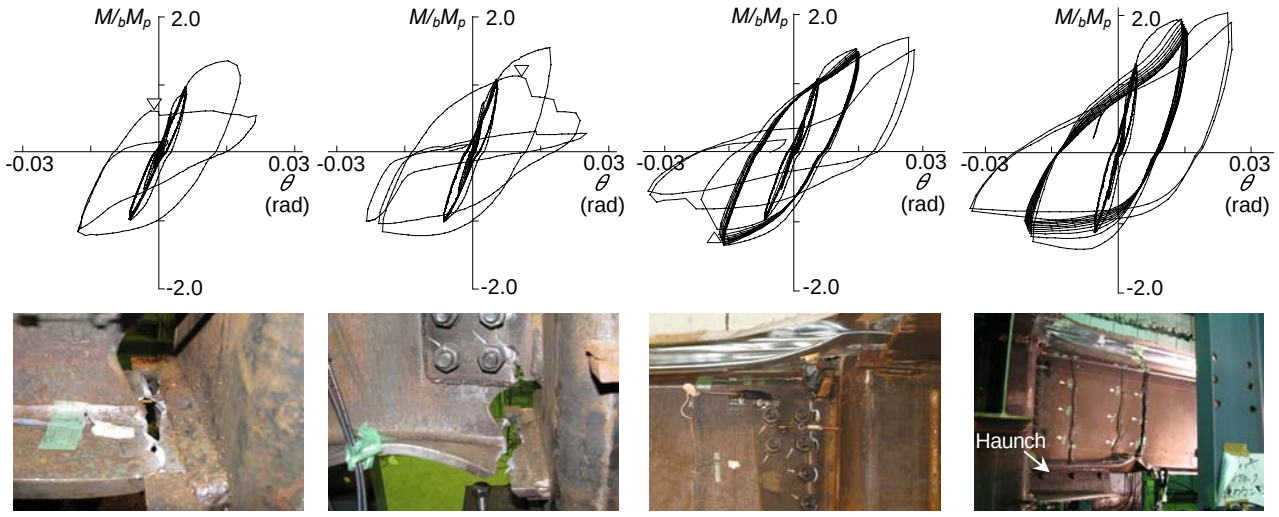

(a) Original connection (b) Connection with supplemental welds (c) Wing plate connection (d) Haunch connection

Figure 6 Test results

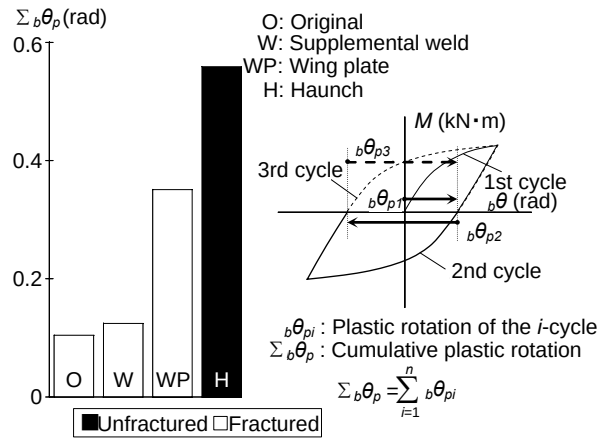

Figure 7 Cumulative plastic rotation

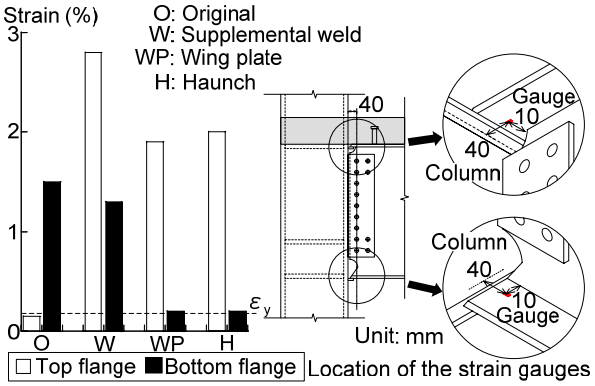

Figure 8 Strain values at flange weld access holes in top and bottom flanges

bottom flange weld access hole under the 1% positive and negative drift loadings. The bottom flange sustained about 10 times larger satin value that the top flange. The supplemental weld at web was not likely to reduce the strain at the bottom flange and made the connection fractured at the same cycle as in the original connection. It is notable that the supplemental weld significantly increased the strain at top flange to about 2.5%, which was about 25 times of that of the original connection. The wing plates and haunch effectively decreased strain concentration at the bottom flange; instead they caused larger strains in the top flange. The wing plate connection finally fractured at the top flange after experiencing ten cycles of this large strain value. As the result, deformation capacity was significantly improved in the two connections.

5. CONCLUSIONS

A quasi-static test on beam-to-column subassemblages that represented the early time field-welded connection of high-rise buildings was conducted. Retrofit was considered, and the original connection was modified by three types of retrofit particularly in consideration of constructability. The connections were tested by multiple plastic cycles that considering the effects of long-period ground motions. The main observations are summarized below:

1. The strain of the original connection highly concentrated at the bottom flange weld access hole at a value of 1.5% under the 1% drift angle loading. The high strain concentration made a crack occur at the toe of weld access hole and fractured along the base metal of beam under the 2% drift angle loading.
2. The supplemental welds at the web changed the strain distribution at the connection. The strain concentration at the bottom flange was not reduced, but it increased at the top flange instead. The connection fractured eventually at the same instant with the original connection. The cumulative plastic rotation remained unchanged.
3. The cumulative plastic rotation of the wing plate and haunch connections were at least four times the value obtained for the original connection. The connections were not fractured at the bottom flange at the end of loading, because the strain concentration at the bottom flange was effectively reduced by the retrofit in the bottom flange. Retrofit on the bottom flange increased the strain concentration on the top flange and lead to fracture of the wing plate connection after experiencing ten cycles of the 2% drift angle loading.

References:

Architectural Institute of Japan. (2006). Recommendation for Design of Connections in Steel Structures. (in Japanese)

Architectural Institute of Japan. (2001). Standard for Structural Calculation of Steel Reinforced Concrete Structures, Allowable Stress Design and Horizontal Load-Carrying Capacity. (in Japanese)

Architectural Institute of Japan. (2007). Long-period ground motions and the seismic resistance of buildings. (in Japanese)

Chung, Y.L., Nagae T., Fukuyama K., Kajiwara K., Inoue T., Hitaka T., and Nakashima M. Seismic Resistance Capacity of High-Rise Buildings subjected to Long-Period Ground Motions - E-Defense Shaking Table Test. *Proc. 14th World Conf. Earthq. Eng*., Beijing, China, 2008, No.95.

Federal Emergency Management Agency (FEMA-350) Recommended Seismic Design Criteria for New Steel Moment-Frame buildings, 2000.7.

Japan Society of Civil Engineering. Architectural Institute of Japan. (2006). Report of seismic performance improvement of civil, architectural structures subjected to long-period ground motions generated by subduction zone. (in Japanese).

Kim, Y. J., Oh, S. H., Moon, T. S. (2004) Seismic behavior and retrofit of steel moment connections considering slab effects. *Eng. Struct.*, 26(13), 1993-2005.

Tsai, K. C., Popov, E. P., (1988) Steel beam-column joints in seismic moment resisting frames, Rep. No. UCB/EERC-88/19, Earthquake Engineering. Research Center, University of California, Berkeley.

Tsai, K. C. and Chen, C. Y. (1996) Performance of Ductile Steel Beam-Column Moment Connections, Paper No. 405 in *Eleventh World Conference on Earthquake Engineering*, Acapulco.

Uang, C. M., Yu, Q. S., Noel, S., Gross, J., (2000) Cyclic testing of steel moment connections rehabilitated with RBS or welded haunch, *J. Struct. Engrg.*, Volume 126, Issue 1, pp.57-68.

JOINT CONFERENCE PROCEEDINGS
7th International Conference on Urban Earthquake Engineering (7CUEE) &
5th International Conference on Earthquake Engineering (5ICEE)
March 3-5, 2010, Tokyo Institute of Technology, Tokyo, Japan

EVALUATION OF ROTATION CAPACITY FOR REDUCED BEAM SECTION WITH BOLTED WEB

Ki-Hoon Moon[1], Sang Whan Han[2], Seong-Hoon Hwang[3], and Sang-Jae Lee[4]

1) PhD Candidate, Hanyang University, Seoul, Korea
2) Professor of Architectural Engineering, Hanyang University, Seoul 133-791, Korea
3) Researcher, Construction Research Center at Hanynag University, Seoul, Korea
4) Graduate student, Department of Architectural Engineering, Hanyang University, Seoul 133-791, Korea
acttr@hanmail.net, swhan82@hotmail.com, Hoonic@gmail.com, tarbang@nate.com

Abstract: RBS connections can be classified into two types according to the web attachment details: reduced beam section with welded web (RBS-W) connections and reduced beam section with bolted web (RBS-B) connections. Some experimental specimens have been demonstrated that RBS-B connection was abnormally failed at the face of column and did not provide the sufficient plastic rotation capacity required for special moment resisting frames that of region of high seismicity. In ANSI/AISC 358-05, the usage of RBS-B is limited to the connections in Intermediate Moment Frames (IMF) instead of SMF. The purpose of this study is to propose new design criteria for RBS-B connections for seismic applications at IMF system. This study conducted a parametric study to determine parameters affected the rotational capacity of RBS-B connections and proposed limiting values of main parameters to satisfy the rotational demand (0.02 radian) specified in ANSI/AISC 358

1. INTRODUCTION

Reduced Beam Section (RBS) moment connection (Fig 1) can be classified into two types, depending on the type of web connection details: a welded (RBS-W) and a bolted web (RBS-B) connection. There is experimental data showing that RBS-B connections were experimented the brittle fracture at the beam flange to column flange welds beyond 0.04 radian of total rotation (Engelhardt et al. 2000). In ANSI/AISC 358-05(AISC 2005), which is updated from FEMA-350, only the RBS-W connection is applicable to SMF system as a prequalified connection. RBS-B connections shall be permitted only for to be used in Intermediate Moment Frames (IMF) system. However, it is necessary to evaluate the possibility of RBS-B connections to be used in IMF system. Lee et al. (2005) reported that some RBS-B specimens did not provide the total rotation of 0.02 which is required for IMF connections.

For this purpose, this study conducted a parametric study to determine major parameters for the rotational capacity of RBS-B connection. Particularly, from the collected data complicity of RBS-B connection experienced fracture, this study proposed an equation for computing the rotational capacity of RBS-B connections.

2. PARAMETERS INFLUENCE OF ROTATION CAPACITY OF RBS-B CONNECTIONS

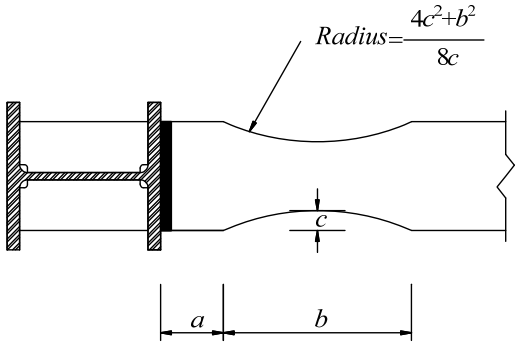

Figure 1 Reduced Beam Section connection

In order to investigate the plastic rotation capacity, θ_p of the connections showing the brittle fracture, it was performed using the response parameters used in previous researches. Uang and Fan (2001) conducted the comprehensive investigation on relationship between the plastic rotation capacity of RBS moment connections and the three slenderness parameters for the flange local buckling (FLB), web local buckling, and lateral torsional buckling (LTB). Plastic rotation capacity, θ_p in this study was defined as the total plastic rotation beyond which the connection strength starts to degrade below 80% of the maximum strength. (Uang and Fan, 2001) shown that based on the result of nonlinear regression analysis for relationship between the plastic rotation capacity and slenderness ratios including FLB, WLB, and LTB, plastic rotation capacity of

RBS moment connection tend to decrease with increasing the values of each response parameter. In addition, equation to predict the plastic rotation capacity of RBS moment connections was proposed as follows:

$$\theta_p = 5.8\left(\frac{b_f}{2t_f}\right)^{-0.12}\left(\frac{h}{t_w}\right)^{-0.5}\left(F_{yf}\right)^{-0.5} \quad (1)$$

where, $b_f/2t_f$ is the flange width to thickness ratio, h/t_w is the fillet-to-fillet web depth over web thickness ratio, and F_{yf} is the expected yield strength of the flange of the beam.

Same trend regarding dependence of θ_p on the slenderness parameters was shown in the research implemented by Lignos (2008). The definition of the plastic rotation, θ_p in research conducted by Lignos (2008) is shown in Fig. 2 and plastic deformation, δ_p is defined as the difference between deformation at the point of maximum strength and at yield strength. Lignos (2008) quantified the dependence of θ_p on beam depth, d, the shear span to depth ratio of the beam, L/d, FLB, and WLB and proposed the equation to predict θ_p of the connections. The proposed equation derived using the major influential parameters on θ_p is given by

$$\theta_p = 0.22\left(\frac{h}{t_w}\right)^{-0.45}\left(\frac{b_f}{2t_f}\right)^{-0.14}\left(\frac{d}{21''}\right)^{-0.854} \quad (2)$$

where, d is beam depth in inches. Both of these studies considering the FLB and WLB shown that rotation capacity of the connections tended to decrease as these slenderness parameters increased.

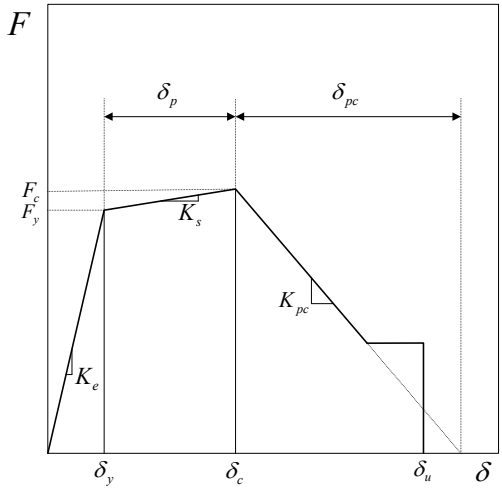

Figure 2Backbone curve of modified Ibarra-Krawinkler model (Lignos, 2008)

In this study, the characteristics of hysteretic behavior of RBS-B moment connection were reviewed prior to assessing the rotation capacity of the RBS-B moment connection. The hysteretic behavior of RBS-B moment connections are characterized by two distinct ways, as shown in Fig.3. Fig. 3(a) illustrates the backbone curves of the RBS-B specimens, which were not occur the fracture at the beam flange of the beam-to-column connection, and Fig. 3(b) shows those of the specimens showing brittle fracture at the beam flange to column flange welds of column face. In Fig. 3(a), gradual strength degradation in RBS-B moment connections after attaining the maximum strength occurs when the connection strength reduced due to local and lateral torsional buckling at the reduced beam section of the beam. In Fig. 3(b), RBS-B moment connection, however, shown that brittle fracture occurred at the beam flange to column flange welds of column face without showing the local buckling, as the strength was increased due to strain hardening effect. This suggests that rotation capacity of RBS-B moment connections and key response parameters on rotation capacity differ, depending on whether or not the occurrence of brittle fracture at the beam flange of column face (Fig. 3). Because the connection fracture already occurred prior to exhibiting the local buckling, moment strength at beam-to-connection is great impact on plastic rotation capacity of the connection.

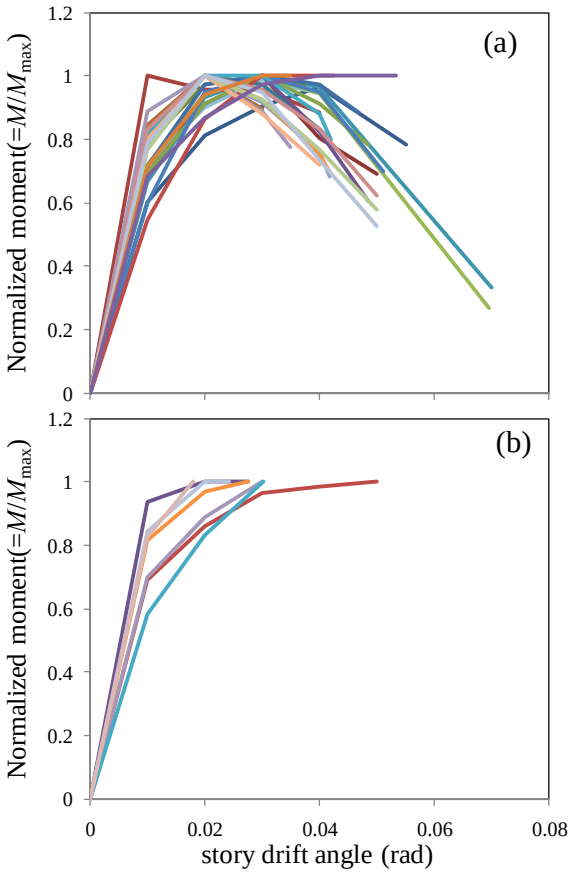

Figure 3 Backbone curves of RBS-B connections: (a) non-fracture specimens, and (b) fracture specimens

3. EQUATION FOR COMPUTING ROTATION CAPACITY

Figure 4 shows rotation capacity of specimen with RBS-B and Welded Unreinforced Flange with Bolted web (WUF-B) moment connections for each response parameter,

which are excluded from the effect of local buckling terms, as mentioned earlier because brittle fracture at the connections occurred without local buckling. (SAC database, 1998) The reason for including the results of WUF-B specimens is that the web connection of WUF-B is similar to that of RBS-B connections. In Fig. 4, solid lines represent the results of regression analysis for specimens with RBS-B and WUF–B moment connections. Overall, the plastic rotation capacity of the connections decrease as the beam depth, d, the shear span to depth ratio of each of the beam, L/d, and the expected yield strength of the flange of the beam, F_{yf} increases (Fig. 4 (a), (b), and (c)). Especially, dependence of plastic rotation capacity on ratio of maximum moment strength, M_{max} to plastic moment, $M_{plastic}$ is significant. M_{max} is measured in previous tests of RBS-B and WUF-B connections and $M_{plastic}$ is estimated from moment at the face of the column, transferred from plastic hinge within the beam and is computed from as follows:

$$M_{plastic} = F_{y,actual} Z_{RBS} \frac{L_b}{L_b - s_h} \quad (3a)$$

$$M_{plastic} = F_{y,actual} Z_b \quad (3b)$$

Where, $F_{y,actual}$ is the actual yield strength measured at a coupon test; Z_{RBS} is the plastic section modulus at the center of the reduced beam section; L_b is clear length of the beam; S_h is distance from the plastic hinge to the column face (see Fig. 1); and Z_b is the plastic section modulus at the unreduced beam section.

Fig. 5 (a) shows plastic rotation capacity, θ_p for moment strength ratio, $M_{max}/M_{plastic}$ of the moment connections showing the brittle fracture and total rotation capacity, θ_{total} for $M_{max}/M_{plastic}$ of the connections is shown in Fig. 5 (b). Because d, L/d, and Fyf terms is less significant effect on plastic rotation capacity of the connections, these terms are exclude from the equation in herein. In this study, simplified equation for predicting the plastic and total rotation capacity for RBS-B moment connections showing brittle fracture is proposed by authors as follows:

$$\theta_{plastic} = 0.0674 \frac{M_{max}}{M_{plstic}} - 0.0631 \quad (4)$$

$$\theta_{total} = 0.0685 \frac{M_{max}}{M_{plastic}} - 0.055 \quad (5)$$

Computation of plastic moment capacity at the center of reduced beam section, as specified in ANS/AISC 358-05, includes strain hardening effect, Cpr as follows:

$$M_{pr} = C_{pr} R_y F_y Z_{RBS} \quad (7a)$$

$$C_{pr} = \frac{F_y + F_u}{2F_y} \leq 1.2 \quad (7b)$$

Where, C_{pr} is a coefficient to accounts for the amplification of the peak connection strength; R_yF_y is the effective yield strength of the beam; and Z_{RBS} is the plastic section modulus at the center of the reduced beam section; and F_y and F_u is nominal yield and tensile strength of steel, respectively.

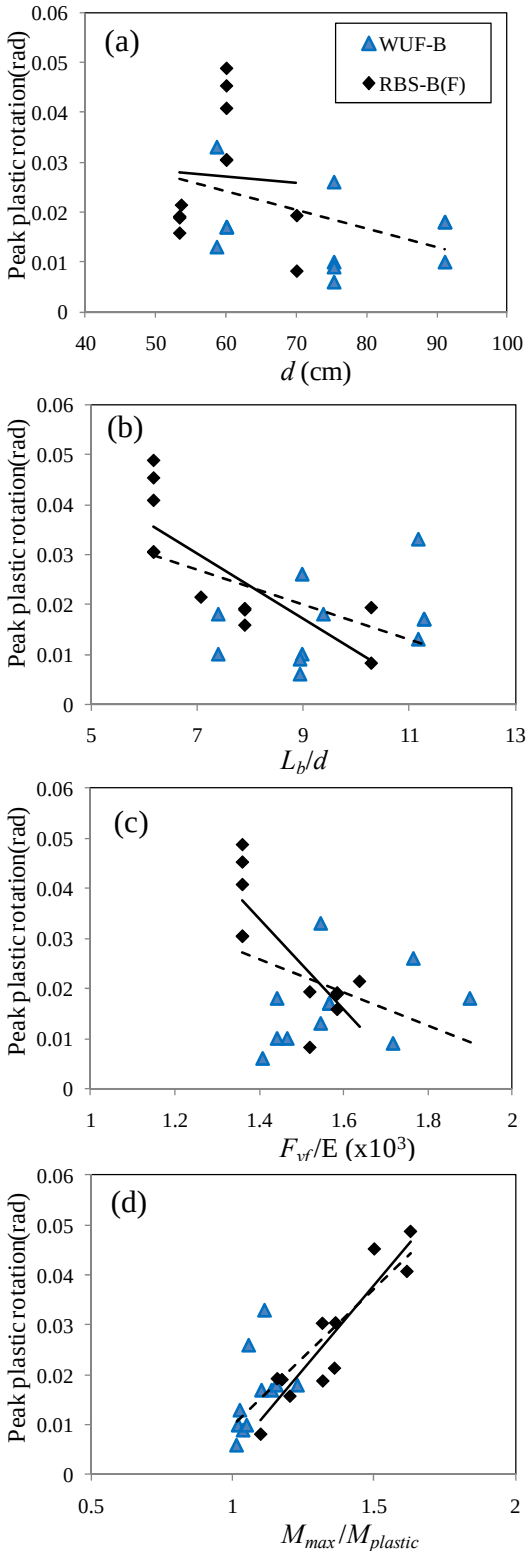

Figure 4 Peak plastic rotation capacity of WUF-B and fracture RBS-B connections: (a) d, (b) L/d, (c) F_{yf}/E, and (d) $M_{max}/M_{plastic}$

It is required that moment demand at the face of column transferred from probable maximum plastic moment at the center of reduced beam section does not exceed the plastic moment at the unreduced beam section using the following equations:

$$M_f = M_{pr} + V_{RBS} s_h \quad (8)$$

$$M_{pe} = R_y F_y Z_b \quad (9)$$

$$M_f \le \phi_d M_{pe} \quad (10)$$

where, V_{RBS} is larger of the two values of shear force at the center of the reduced beam section at each end of the beam: resistance factor, ϕ_d is taken by 1.

Moment diagram for RBS-B moment connections and moment demand for rotation at beam-to-column connection are shown in Fig. 9(a) and (b). Moment strength ratio, of RBS-B moment Connection designed according to above design criteria is equivalent to C_{pr} as follows:

$$\frac{M_f}{M_{plastic}} = \frac{M_{pr}\dfrac{L}{L-S_h}}{M_{p,RBS}\dfrac{L}{L-S_h}} = \frac{M_{pr}}{M_{p,RBS}} = \frac{C_{pr}R_y F_y Z_{RBS}}{R_y F_y Z_{RBS}} \quad (8)$$

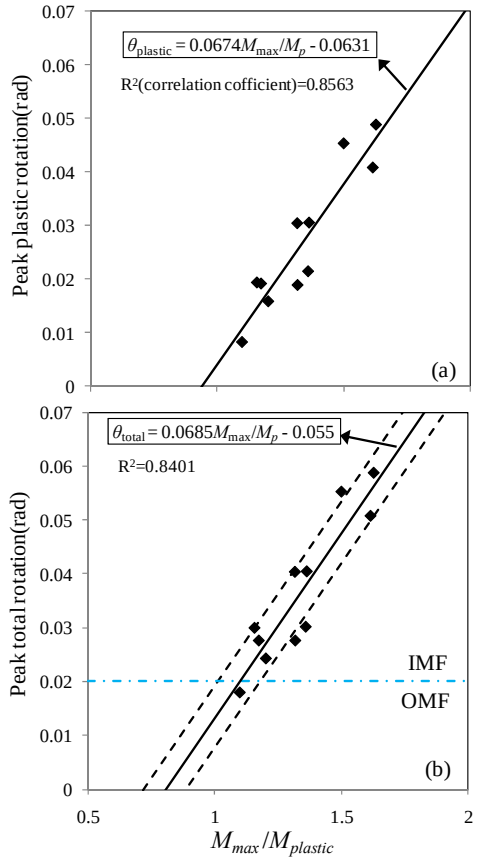

Figure 5 Rotation capacity of fracture RBS-B connections: (a) Plastic rotation , and (b) Total rotation

For ASTM A572 Grade 50 (F_y=345Mpa, F_u= 448 MPa), moment strength ratio, $M_f/M_{plastic}$ is the value of 1.15, and total rotation is 0.023 rad. However, lower moment strength ratio may be shown when fracture was occurred at beam-to-column connection and the total rotation capacity will be lower than 0.02 rad. Therefore, in order to use RBS-B moment connections as prequalified connections of IMF systems, design criteria should be considered moment to cause the brittle fracture at the beam-to-column connection.

4. CONCLUSIONS

From this study, the following conclusion is made:

This study collected test results of 75 RBS-B connections specimens. From the parameters study, moment strength ratio ($M_{max}/M_{plastic}$) is the most influential parameter from contribute rotation capacity of RBS-B connection experiencing fracture. Based on the collected data, This study proposed equations for computing rotation capacity of RBS-B connection experiencing fracture.

Acknowledgements:

Authors acknowledge the financial supports provided by a grant funded by Research Institute of Industrial Science and Technology (RIST) and a grant (07-UR-B04) funded by Ministry of Land, Transport and Maritime Affairs. The views expressed are those of authors, and do not necessarily represent those of the sponsors.

References:

AISC. (2005). "Prequalified connections for special and intermediate steel moment frames for seismic applications." ANSI/AISC 358-05, American Institute of Steel Construction, Chicago, Ill.

Engelhardt, M. D., Fry, G. T., Jones, S. L., Venti, M. J., and Holliday, S. D. (2000). "Behavior and design of radius-cut, reduced beam section connections," *SAC/BD-00/17*, SAC Joint Venture, Sacramento, Calif.

FEMA. (2000). "Recommended seismic design criteria for new steel moment-frame buildings," FEMA-350, Federal Emergency Management Agency, Washington, D.C.

Lee, C.-H., Jeon, S.-W., Kim, J.-H., and Uang, C.-M. (2005). "Effects of panel zone strength and beam web connection method on seismic performance of reduced beam section steel moment connections," *Journal of Structural Engineering*, **131**(12), 1854-1865.

Lignos, D. (2008). "Sidesway collapse of deteriorating structural systems under seismic excitations," PhD thesis, Civil and Environmental Engineering, Stanford University, Stanford, Calif.

SAC. (1998). "SAC Connections databases."

Uang, C. M., and Fan, C. C. (2001). "Cyclic stability criteria for steel moment connections with reduced beam section," *Journal of Structural Engineering*, **127**(9), 1021-1027.

JOINT CONFERENCE PROCEEDINGS
7th International Conference on Urban Earthquake Engineering (7CUEE) &
5th International Conference on Earthquake Engineering (5ICEE)
March 3-5, 2010, Tokyo Institute of Technology, Tokyo, Japan

APPLICABILITY OF SIMULATED GROUND MOTIONS IN DESIGN OF TALL BUILDINGS IN CALIFORNIA

Pierson Jones[1)], Farzin Zareian[2)]

1) Graduate Student Researcher, Dept. of Civil and Environmental Engineering, University of California, Irvine, CA, USA
2) Professor, Dept. of Civil and Environmental Engineering, University of California, Irvine, CA, USA
pjones@uci.edu, zareian@uci.edu

Abstract: This study utilized nonlinear response history analysis to compare the seismic demand for five buildings in the Los Angeles region considering simulated ground motions for the Puente Hills fault and spectrally matched ground motions from the Next Generation Attenuation of Ground Motions (NGA) database, largely composed of recorded motions. The five buildings under consideration were a six-story and a twenty-story moment frame structure (MFS) designed to the 1994 Uniform Building Code (UBC) as well as three variants of a forty-story Buckling Restrained Braced Frame (BRBF). Non-linear models were developed considering all significant contributions to the stiffness and strength of the buildings' lateral load resisting systems. The simulated ground motions are broadband signals, generated from a moment magnitude (M_w) 7.15 scenario rupture of the Puente Hills fault (Somerville and Graves, 2005) for two near fault regions and exhibit long period energy content that significantly exceeds the uniform hazard spectrum. Using spectral matching, NGA ground motions were selected and scaled to five hazard levels. Structural performance was assessed in terms of exceedance of a safe a safe inter-story drift ratio (IDR). It was seen that the simulated ground motions impose higher inter-story drift demands on the structures than the spectrally matched NGA ground motions. Furthermore, the number of instances of exceedance of a safe inter-story drift is substantially higher for the simulated ground motions, pointing to the importance of considering such motions in the collapse prevention of tall buildings on a site-specific basis.

1. INTRODUCTION

Large magnitude, near-fault ground motions tend to be saturated with long period energy to which tall buildings are most vulnerable. As recordings of such ground motions are rare, broadband ground motion simulation procedures are used to generate simulated ground motion records. Recently, SCEC scientists have simulated ground motions for parts of Los Angeles from earthquakes caused by ruptures of the San Andreas and Puente Hills fault systems (Graves and Somerville, 2005). These ground motions have high-amplitude waves generated by rupture directivity especially in the long-period range. Recent studies have shown many structures in the region, including tall special steel moment resisting frames, to be vulnerable to them (Field *et al*, 2005, Olsen 2008, Jones and Zareain 2009).

While nonlinear response spectra have been computed to compare the inelastic demands of simulated motions (Naeim and Graves, 2005) to uniform hazard spectra, to fully portray structural response nonlinear response history analysis is required, such that contributions of higher modes and period lengthening effects are included.

In this paper nonlinear response history analysis was used to assess the seismic demand in terms of maximum IDR for 5 structures located in downtown Los Angeles near the Puente Hills fault. The analysis employed spectrally matched recorded ground motions to five hazard levels as well as near-fault simulated ground motions for a scenario M_w = 7.15 rupture of the Puente Hills fault. Structural performance was assessed in terms of exceedance of a safe inter-story drift ratio.

This paper is part of an ongoing research effort that has two objectives. The first objective is to examine the performance of high-rise buildings with different lateral load resisting systems located in downtown Los Angeles using simulated ground motions from major earthquakes generated from Puente Hills and San Andreas fault systems. The second objective is to assess the difference in performance of these structures when subjected to simulated motions compared to that of recorded ground motions that are selected and scaled to represent the same seismic hazard of the simulated motions. It is envisioned that this research can provide understanding about safety of buildings in a high seismic region such as downtown Los Angeles and the applicability of employing simulated ground motions for design of tall buildings in the future.

2. STRUCTURES USED IN STUDY

Five structures were considered in this study and modeled in PERFORM®3D (version 4.03) structural analysis software by Computers and Structures Inc., 2008. Two of the structures were steel moment frames (SMF) designed to the 1994 UBC and three were 40-story buckling restrained braced frames (BRBF) with varying design criteria.

SMF structures are a common building type in the Los Angeles region and the two SMF under consideration, one six- and one twenty-stories tall, are typical configurations. The buildings were designed to meet the requirements of the 1994 UBC by Hall (1999). Plan and elevations of the buildings are shown in figure 1. The structures are denoted as U6-postNR and U20-postNR respectively as the moment connections in the frames are considered to be Post-Northridge connections characterized by ductile, non-fracturing behavior.

Lumped plasticity models were used in the analysis of the SMF. The models considered all of the structural elements that would be expected to make significant contributions to the lateral strength and stiffness of the structure, including gravity frame members. Non-linear behavior in the beams and columns was modeled with plastic hinges located at the member ends and in the panel zones with a Krawinkler mechanical model. The plastic hinges belonging to the moment frame beams included the effect of the connection behavior and the strengthening effect of the floor slab (Lignos, 2008). Shear tab

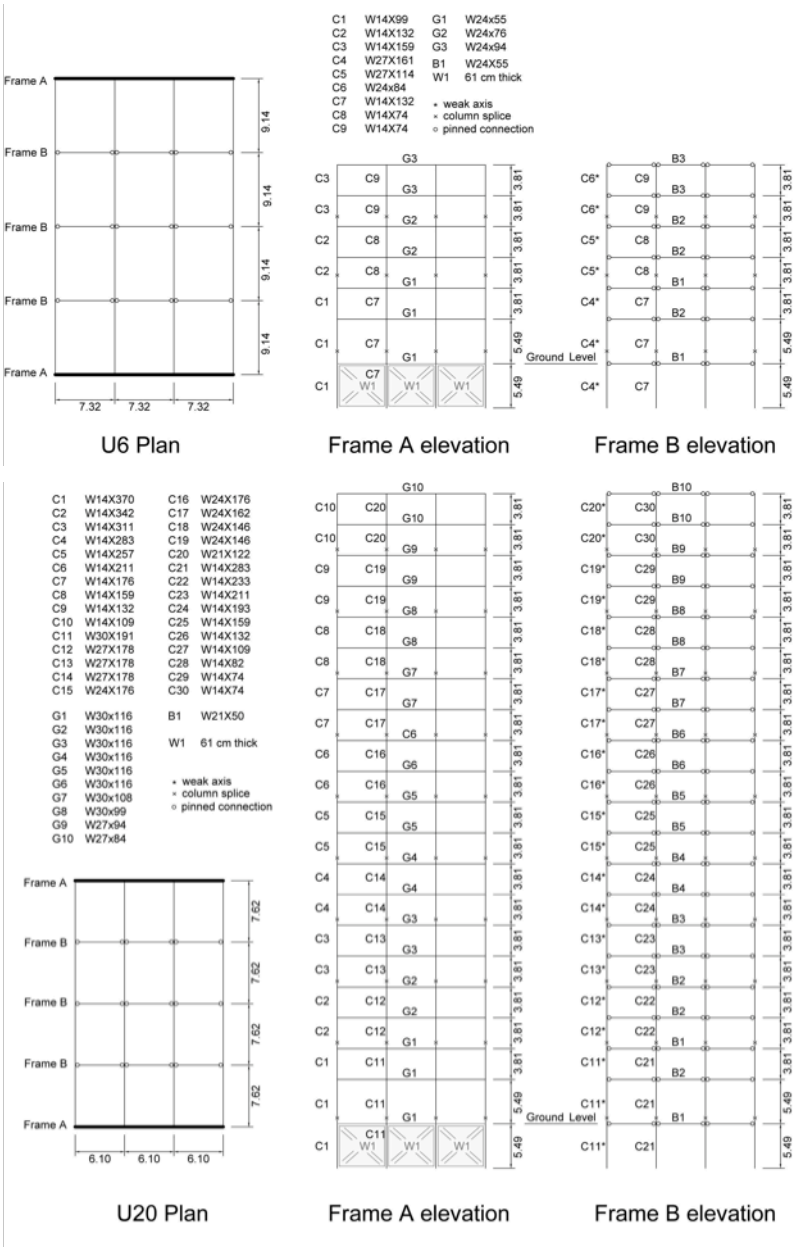

Figure 1. Plan and elevation of the SMF structures, U6-postNR and U20-postNR. Dimensions given in meters. Image source: Jones and Zareian (2009)

connections for the gravity frame members were modeled with semi-rigid moment connections, utilizing backbone curves based on the approximate method developed by Liu and Astahneh-Asl (2004). In addition, the floor slabs were considered to behave as a rigid diaphragm. The basement walls were not explicitly modeled however the perimeter nodes at the ground level were fixed against lateral translation in the plane of the walls. The effects of cladding and other non-structural elements were not considered. A moderate level of cyclic deterioration was assumed. Additional information on the modeling of the structures can be found in Jones and Zareain (2009).

For the SMF structures, the largest inter-story drifts were expected to occur along the short (or transverse) axis of the structure. For this reason the structure was not subjected to bi-axial ground motions. Although the models are 3-dimensional, the analysis of the structures is essentially planar in that ground motions were applied to the short axis of the building only. The top half of table 1 shows the first 3 periods of the SMF structures considering only modal

Table 1 Periods, Mode numbers, and direction of mode shape for the 5 structures. The h1 and h2 designations correspond to the 3-d views of results shown in figures 5-8.

		mode number*		
structure name		1	2	3
U6-postNR	period (s)	1.837	0.6094	0.3179
	direction	→	→	→
U20-postNR	period (s)	3.382	1.152	0.6618
	direction	→	→	→

*considering short axis only for U20 and U6

		mode number			
structure name		1	2	3	4
BRBF40-CBD	period (s)	5.252	3.802	3.74	1.476
	direction	↑ h2	→ h1	↶ tors.	↑ h2
BRBF40-PBD	period (s)	6.47	4.993	4.49	1.774
	direction	↑ h2	↶ tors.	→ h1	↑ h2
BRBF40-PBD+	period (s)	5.736	4.387	4.166	1.639
	direction	↑ h2	↶ tors.	→ h1	↑ h2

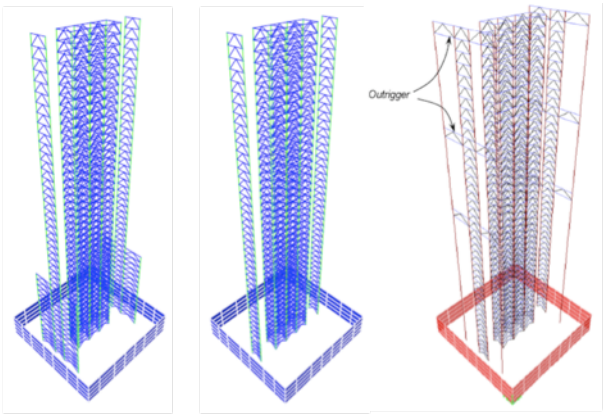

a.) BRBF40-CBD b.) BRBF40-PBD c.) BRBF40-PBD+

Figure 2 3-d view of the three variations on the 40-story BRBF structures: a.) Code-based design b.) Performance-based design c.) Performance-based design plus. The structures have 4 subterranean levels and 40 stories above grade.

shapes that deform in the plane of the short axis of the structure.

The three 40 story BRBF structures share identical footprints but their lateral load resisting frames vary in member sizing and bracing configuration in order to satisfy differing design criteria. Figure 2 shows the three bracing configurations. There is a code based design (denoted as BRBF40-CBD) designed to meet the requirements of the 2006 International Building Code, a performance based design (denoted as BRBF40-PBD) designed to meet the 2008 Seismic Design Criteria for the Los Angeles Tall Buildings Structural Design Council, and finally an performance 'plus' based design (denoted as BRBF40-PBD+) designed to meet newer criteria currently under consideration by the researchers at Pacific Earthquake Engineering Research (PEER) center. Additional information about the CBD PBD, PBD+ structures can be found in Dutta and Hamburger (2009) and Moehle *et al*, 2009.

Buckling-restrained braces were modeled using a built-in component in Perform 3D. 30% of the length of buckling-restrained braces are considered as "End Zone" The backbone curve of buckling restrain-braces are developed assuming Ry = 1.1, ω = 1.25, and β = 1.1. Columns and Beams were modeled with elastic elements. Elastic behavior was verified in these elements by monitoring their demand-capacity ratios and ensuring that they remained in the elastic range. Diaphragms are modeled as rigid and the same mass properties were assigned to each floor down to the foundation. The perimeter shear walls were modeled with elastic wall elements with 50% of the gross stiffness and 40% of elastic shear modulus to account for cracked section properties (Moehle *et al*, 2009, Ch 5).

The first 4 modal periods are shown for the 40 story BRBF structures in the lower half of table 1. As opposed to the SMF structures, the 3-dimensional characteristics of the building are of more importance, and the response history analysis was performed bi-axially. While the BRBF structures have significant torsional periods, they do not have eccentric mass or stiffness so the torsional mode shapes of the structure are not excited. Accidental torsion is not considered in this analysis.

3. GROUND MOTIONS USED IN STUDY

Two batches of ground motions were applied in the study. The first batch was selected and modified from the NGA database using spectral matching criteria for five hazard levels considering a site in the Los Angeles basin near the Puente Hills Fault and was primarily made up of recorded ground motions. The second batch, specifically chosen for long-period energy content, was made up entirely of simulated ground motions for two sites in the LA region for a M_w = 7.15 scenario rupture of the Puente Hills fault.

The spectrally matched ground motions consisted of five sets, with each set considering a target hazard level and made up of fifteen pairs of orthogonal horizontal

components. The hazard levels were specified with return periods of 4975, 2475, 475, 43, and 25 years (denoted as OVE, MCE, DBE, SLE43, and SLE25 respectively). The OVE set, with the longest return period, was largely comprised of recorded ground motions but included several validated simulated motions while the four smaller return period ground motion sets are comprised entirely of recorded ground motions. Additional information on the selection and modification of the ground motions can be obtained from Moehle *et al,* (2009), Ch. 2.

Somerville and Graves (2005) simulated ground motions for the Puente Hills fault by using a hybrid of deterministic and stochastic techniques. The ground motions are broadband signals with frequencies between 0 and 10hz (f=0.0-10.0hz). For low frequency waves (f<1.0hz.) a deterministic method was used, in which a 3-dimensional finite difference model simulates fault rupture, wave propagation to a site, and the site response for 66,000 sites within a 110 km by 150 km expanse of the LA area. The deterministic simulation used a kinematic fault rupture model to incorporate slip and rupture velocity. For high frequency waves (f>1.0hz) stochastic methods were used. Three M_w = 7.15 fault rupture scenarios were simulated with varying rupture models. It should be noted that other scenarios are possible, and that the location of fault rupture and direction of rupture propagation cannot be predicted.

The simulated ground motions used in this study were extracted from the largest of the three Puente Hills simulations. They consisted of two sets, with each set corresponding to a near fault region and made up of nine pairs of orthogonal horizontal components. These motions exhibited strong directivity effects with pulse like characteristics and were chosen for their extreme long period energy content (Naeim and Graves, 2006). The long period energy in these simulated motions is the direct result of the fault rupture model, a buried rupture event with short rise time and large rupture area. The first set, called WHT, was from the high slip region of the rupture where the largest peak ground velocities were observed. The second set, called LAD, was taken from a low slip region of the fault rupture. Due to the long-period energy these ground motions possess, the demands they impose on tall structures reside at the extreme end of demands to which tall structures at the site would be subjected.

In terms of seismic hazard, a direct comparison between the spectrally matched ground motions and the simulated ground motions is difficult to make. Firstly, the spectrally matched ground motions are based on a uniform hazard spectrum and attempt to account for all earthquake sources at all distances for a single site, while the simulated motions are based on a single earthquake scenario and consider 2 near fault sites (Lew, 2009). It is important to note that the most devastating ground motions, those belonging to the WHT set, can be attributed to a very small region of peak ground velocity, while the LAD set are derived from a region of peak ground velocity characteristic of much larger area. In short the likely spatial distribution of these two types of ground motions should be kept in perspective. Secondly, the uncertainty in the location and direction of fault rupture point to the need to consider other rupture scenarios to effectively quantify the seismic hazard at the site using simulated ground motions. And finally, knowledge of the recurrence interval of simulated events may not be particularly precise. For example, a M_w = 7.0 multi-segment rupture of the Puente Hills fault system the return period was estimated to range from 500 to 2000 years (Shaw and Shearer, 1999). More recently, an investigation utilizing paleoseismology revealed at least four large events ($7.2 \leq M_w \leq 7.5$) have occurred on the fault during the past 11,000 years (Dolan, 2003) suggesting a return period of 2,750 years.

4. RESULTS OF RESPONSE HISTORY ANALYSIS

The results of the response history analysis are plotted in figures 3-7 for the five structures studied. Each plot shows the maximum IDR plotted against the story number of the structure for a given direction of the structure (BRBF40 structures) or for a given ground motion component (U6 and U20 structures). In each figure the five sets of spectrally scaled ground motions are plotted above the 2 sets of simulated motions. The spectrally scaled ground motions that are listed in the left column descend from the 4975 year hazard level (OVE) to the 25 year hazard level (SLE25). Individual earthquakes are plotted with light gray lines. The mean response is shown with a heavy black line while the 16th and 84th percentiles are shown with a dashed gray line (appears yellow in color version). For the spectrally matched ground motions, the maximum IDR increases as the return period increase and are highest for the OVE motions as would be expected. In general the simulated maximum IDR exceed that of the spectral matched motions.

Structural performance is judged by the authors to be "safe against collapse" structures that do not exceed an IDR of 0.03 (Moehle *et al*, 2009). Structures that exceed these levels of IDR do not necessarily collapse, however at these levels extreme inelastic demands have been imposed on the structure. For the purpose of safety, this study will consider these IDR levels as collapse prevention performance limits. Figure 9 shows a plot of the percentage of structures exceeding this limit for all five structures and each of the 7 ground motion sets. From the figure it can be observed that the highest percentage of exceedance occur under the simulated motions, especially the WHT set, for all five structures. This result points to the importance of considering large magnitude simulated motions in the collapse prevention of tall structures where important site conditions may not be adequately accounted for when selecting ground motions based on a uniform hazard spectrum.

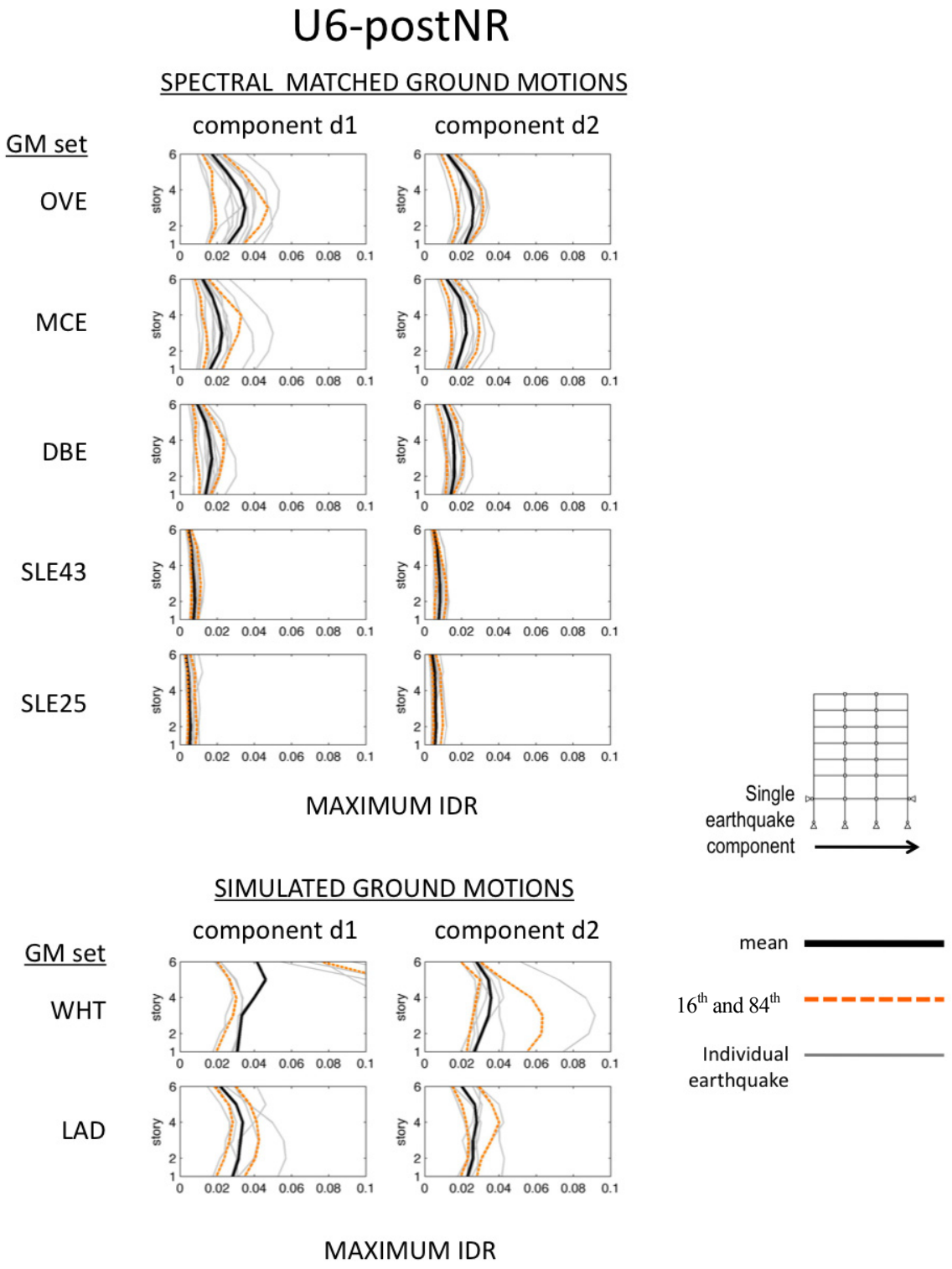

Figure 3. Results for the U6-postNR structure. Maximum IDR is plotted against story number. For the Spectral matched ground motions the ground motions sets in the left column descend from the 4975 year hazard level (OVE) to the 25 year hazard level (SLE25).

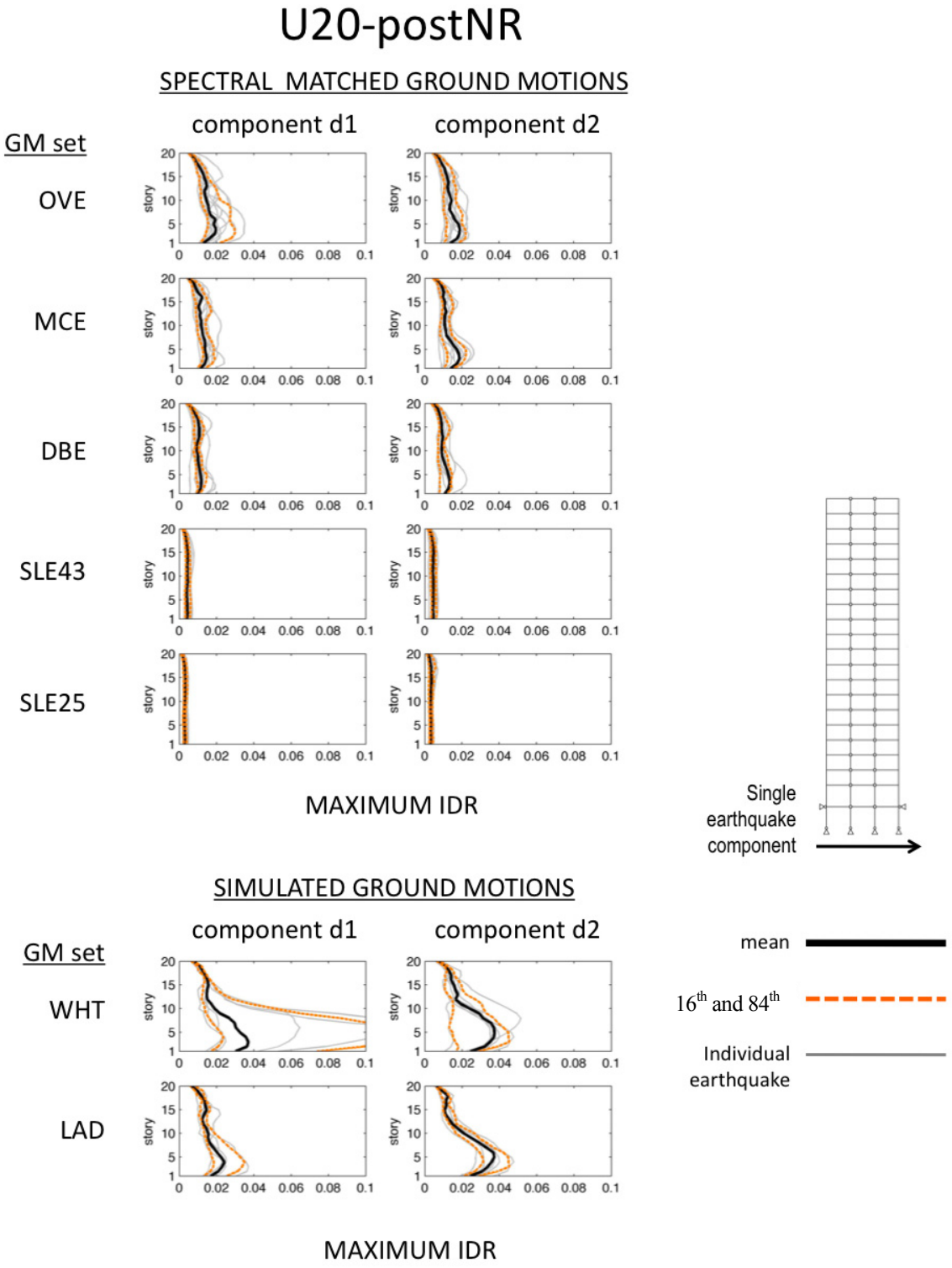

Figure 4. Results for the U6-postNR SMF structure. Maximum IDR is plotted against story number. For the Spectral matched ground motions the ground motions sets in the left column descend from the 4975 year hazard level (OVE) to the 25 year hazard level (SLE25).

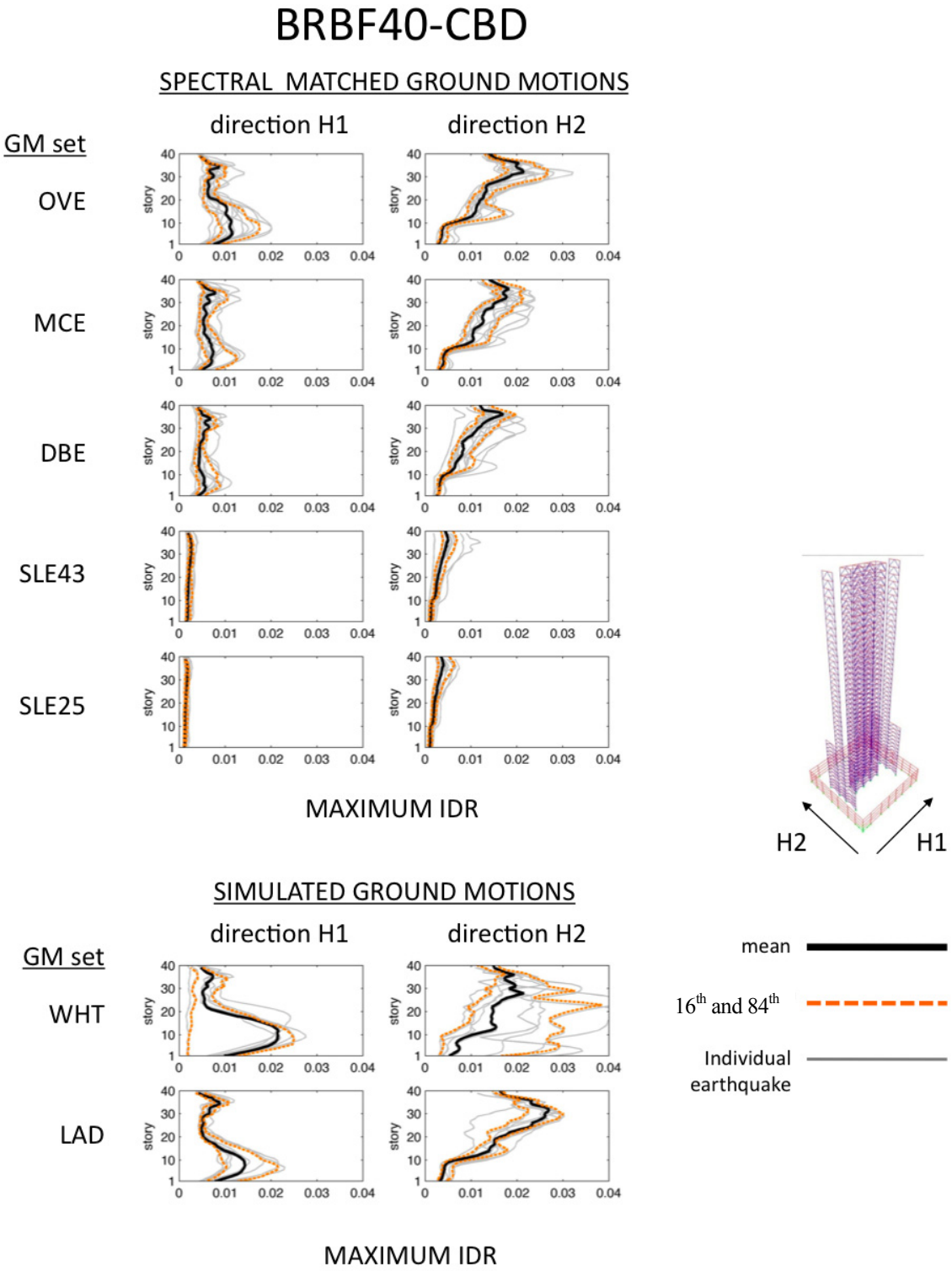

Figure 5. Results for the 40-story BRBF code based design. Maximum IDR is plotted against story number. For the Spectral matched ground motions the ground motions sets in the left column descend from the 4975 year hazard level (OVE) to the 25 year hazard level (SLE25). In the h2 direction, from floors 1-10, there is a stiff region where the IDR are relatively small due the presence of additional bays (compared to the PBD structure).

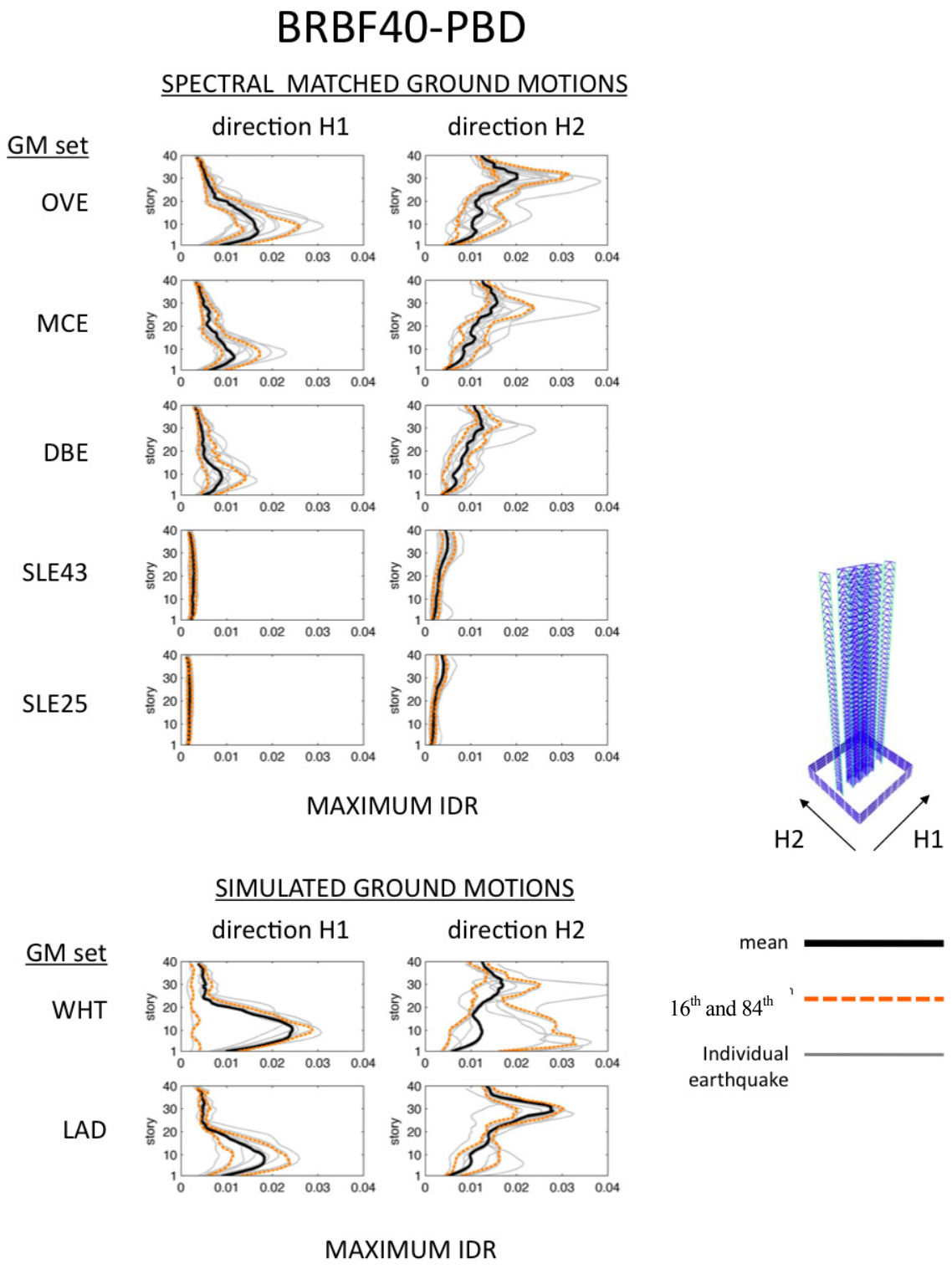

Figure 6. Results for the 40-story BRBF Performance based design. Maximum IDR is plotted against story number. For the Spectral matched ground motions the ground motions sets in the left column descend from the 4975 year hazard level (OVE) to the 25 year hazard level (SLE25). Compared to the CBD and PBD+ structures, which have additional bays in the h2 direction, the IDR is more uniformly distributed throughout the buildings height.

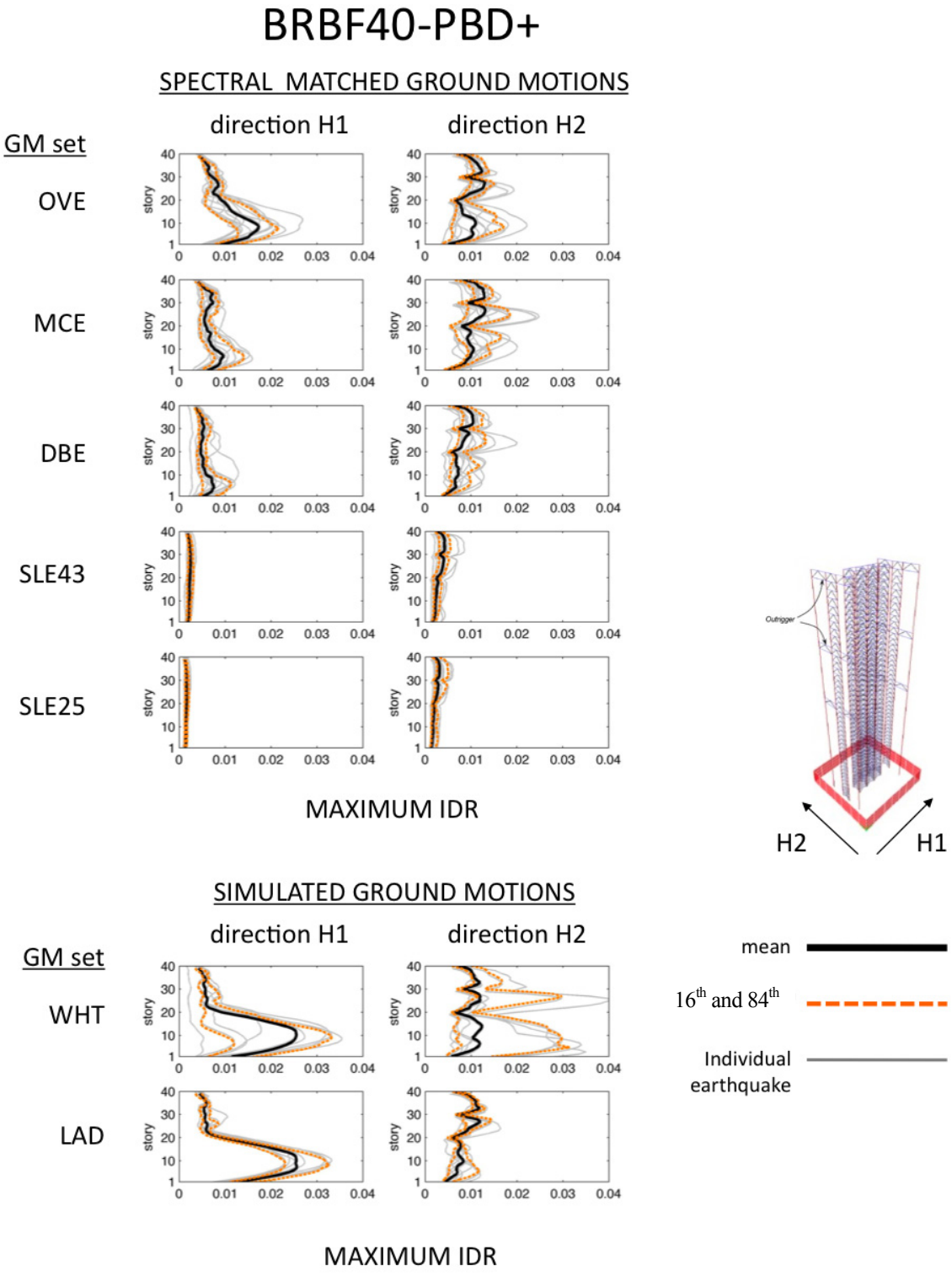

Figure 7. Results for the 40-story BRBF performance 'plus' based design. Maximum IDR is plotted against story number. For the Spectral matched ground motions the ground motions sets in the left column descend from the 4975 year hazard level (OVE) to the 25 year hazard level (SLE25). In the h2 direction 3 bands can be seen where the maximum IDR are pulled back to smaller values due additional stiffness gained from the presence of the hat truss.

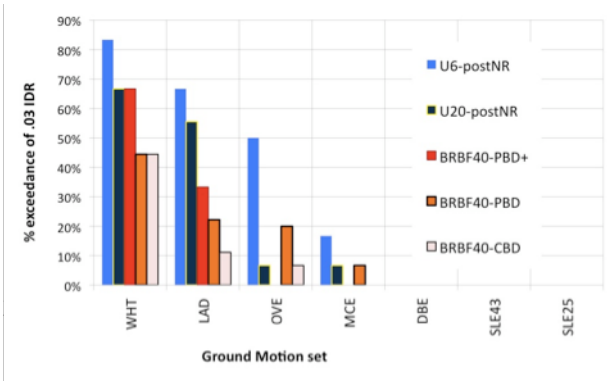

Figure 8 Plot of percent exceedance of .03 IDR during the response history analysis for the five structures and seven ground motions. Structures exhibited significantly worse performance under the simulated ground sets (WHT and LAD) shown on the left than under the spectrally matched ground motions (OVE, MCE, DBE, SLE43, and SLE25).

5. CONCLUSIONS

This research used nonlinear response history analysis to study the affects of simulated ground motions as compared to spectrally matched ground motions in assessing the seismic performance of five structures in the Los Angeles region. Structural performance was assessed in terms of exceedance of a safe inter-story drift ratio (IDR). It was seen that the simulated ground motions impose higher inter-story drift demands on the structures than the spectrally matched NGA ground motions of similar hazard level. Furthermore the number of structures that were considered to collapse is substantially higher for the simulated ground motions than the spectrally matched ground motions. These results point to the importance of considering simulated motions in the collapse prevention of tall buildings on a site-specific basis. Finally, the results also indicate that the consideration of broadband simulated near fault motions may improve estimations of probability distributions for seismic demand parameters in tall buildings, such as IDR, if it can be shown that the demands they impose on a structure reside at the extreme to which a structure will be subjected for a given site.

Acknowledgements:

This study is based on work supported by the PEER Tall Building Initiative through City of Los Angeles under Contract No. C-114158. This financial support is gratefully acknowledged. Any opinions, findings, and conclusions or recommendations expressed in this paper are those of the authors and do not necessarily reflect the views of sponsors. The authors would also like to acknowledge the support from the Japan Ministry of Education, Culture, Sport, Science, and Technology (MEXT) for establishing the Center for Urban Earthquake Engineering (CUEE) in Tokyo Institute of Technology. This support makes possible the forthcoming international conference, as well as international joint research projects and exchange programs with overseas universities.

References:

Computers and Structures, Inc. 2008. PERFORM®3D (version 4.03) [computer software] Berkeley, CA, USA.

Dolan, J. F., Christofferson, S. A. & Shaw, J. H. 2003. Recognition of paleoearthquakes on the Puente Hills blind thrust fault, California. Science, 300, 115-118.

Dutta, A. & Hamburger, R. O. 2009. Case study of a 40-storey buckling-restrained braced frame building located in Los Angeles. The Structural Design of Tall and Special Buildings, 9999, n/a.

Field, E. H., Seligson, H. A., Gupta, N., Gupta, V., Jordan, T. H. & Campbell, K. W. 2005. Loss estimates for a Puente Hills blind-thrust earthquake in Los Angeles, California. Earthquake Spectra, 21, 329-338.

Graves RW, Somerville PG. 2005. "Broadband ground motion simulations for scenario ruptures of the Puente Hills fault." Proceedings of the 8th National Conference on Earthquake Engineering, San Francisco, CA.

Hall, J. F. 1998. Seismic response of steel frame buildings to near-source ground motions. Earthquake Engineering & Structural Dynamics, 27, 1445-1464.

International Code Council (2006). 2006 International BuildingCode. ICC, USA.

LATBSDC (2008). An Alternative Procedure for Seismic Analysis and Design of Tall Buildings Located in the Los Angeles Region, Los Angeles Tall Buildings Structural Design Council.

Lew M, Naeim F, Hudson MB, Koring BO. Challenges in specifying ground motions for design of tall buildings in high seismic regions of the United States, 14th World Conference on Earthquake Engineering, Beijing, October 12–17, 2008.

Lew, M. 2009. The relationship of ground motion hazard to the design of tall buildings. The Structural Design of Tall and Special Buildings, 9999, n/a.

Lignos, D. & Stanford University. Dept. Of Civil And Environmental Engineering. 2008. Sidesway collapse of deteriorating structural systems under seismic excitations. Thesis (Ph D), Stanford University, 2008.

Liu, J. & Astaneh-Asl, A. 2004. Moment-rotation parameters for composite shear tab connections. Journal of Structural Engineering-Asce, 130, 1371-1380.

Moehle, J., Bozorgnia, Y., Hurtado, G., Jones, P., Tuna, Z., Wallace, J., Yang, T. & Zareian, A. F. 2009. Final report to the city of Los Angeles for the Tall Buildings Initiative. Sponsored Projects Office. University of California, Berkeley. Berkeley, CA, USA.

Naeim, F. & Graves, R. W. 2005. The case for seismic superiority of well-engineered tall buildings. Structural Design of Tall and Special Buildings, 14, 401-416.

Olsen AH. 2008. "Steel Moment-Resisting Frame Responses in Simulated Strong Ground Motions: or How I learned to Stop Worrying and Love the Big One." Ph.D. Dissertation, California Institute of Technology, Pasadena, CA.

Shaw, J. H. & Shearer, P. M. 1999. An elusive blind-thrust fault beneath metropolitan Los Angeles. Science, 283, 1516-1518.

Somerville, P. G., Graves, R. W., Day, S. M. & Olsen, K. B. 2006. Ground motion environment of the Los Angeles region. Structural Design of Tall and Special Buildings, 15, 483-494.

JOINT CONFERENCE PROCEEDINGS
7th International Conference on Urban Earthquake Engineering (7CUEE) &
5th International Conference on Earthquake Engineering (5ICEE)
March 3-5, 2010, Tokyo Institute of Technology, Tokyo, Japan

TESTING OF A FULL-SCALE APARTMENT BUILDING AT E-DEFENSE: DESIGN AND PERFORMANCE

John W. van de Lindt[1], Shiling Pei[2], Steven E. Pryor[3], Hidemaru Shimizu[4], Kazuki Tachibana[5], Hiroshi Isoda[6], and Izumi Nakamura[7]

1) Associate Professor, Dept. of Civil Engineering, Colorado State University, Fort Collins, Colorado, USA
2) Post Doctoral Researcher, Dept. of Civil Engineering, Colorado State University, Fort Collins, Colorado, USA
3) International Director of Building Systems, Simpson Strong-Tie, Pleasanton, California, USA
4) Researcher, National Research Institute for Earth Science and Disaster Prevention/E-Defense, Miki, JAPAN
5) Doctoral Student Researcher, Department of Architecture, University of Tokyo, Tokyo, JAPAN
6) Associate Professor, Dept. of Architectural and Civil Engineering, Shinshu University, Nagano, JAPAN
7) Researcher, National Research Institute for Earth Science and Disaster Prevention, Tsubka, JAPAN
jwv@engr.colostate.edu, slpei@lamar.colostate.edu, spryor@strongtie.com, hidemaru@bosai.go.jp, ktachi@iis.u-tokyo.ac.jp, hisoda@gipwc.shinshu-u.ac.jp, izumi@bosai.go.jp

Abstract: In July 2009 a full-scale mid-rise light-frame apartment building was subjected to a series of earthquakes at the world's largest shake table in Miki, Japan. The test program consisted of two major phases: the first phase building consisted of a single story of steel with six stories of wood on top, and the second phase consisted of locking down the steel story and testing the six-story light-frame wood building. This paper presents the building design and test results for phase II. The objectives of the test program were to (1) demonstrate that the performance-based design procedure developed as part of the NEESWood project worked, i.e. validate the approach; and (2) gain a better understanding of how mid-rise light-frame wood buildings respond in a major earthquake while providing a landmark data set to the seismic engineering research community. The building had 1350 square meters of living space and consisted of twenty-three apartment units; approximately half one-bedroom units and half two-bedroom units. In the seven story hybrid (steel + wood) configuration of Phase I the building also had room for two medium size retail stores or restaurants at the first story. The building was constructed over a 14 week period and lifted to the shake table where it was subjected to three earthquakes ranging from seismic intensities corresponding to the 72 year to the 2500 year event for Los Angeles, CA over a two week period. An anchor tiedown system, essentially steel rods running from the bottom of building to roof level at the ends of each shear wall, were used to prevent overturning and allow the shear walls to engage rather than uplift. The building, known as the NEESWood Capstone building, was instrumented with over 300 sensors and 50 LED optical tracking points to measure the component and global responses, respectively. In this paper the construction of the building is explained and the resulting seismic response in terms of base shears, wall drifts, global inter-story drifts, accelerations, and roof drifts are presented. Detailed damage inspection was performed following each test and those results are also presented in detail. The building was found to perform excellently with little damage even following the 2500 year earthquake thus validating the performance expectations outlined during the design phase. The global drift at roof level was approximately 0.25 meters and maximum inter-story drifts were under 3%.

1. INTRODUCTION

Light-frame wood buildings represent the vast majority of the building stock in North America. Most of these types of buildings are single- and multi-family dwellings with a moderate percentage being light commercial construction. Over the last decade progress has been made to better understand the seismic response of light-frame wood buildings. These advances have, in turn, resulted in the evolution of building codes for these types of buildings. Specifically, the move toward performance-based seismic design (PBSD) for light-frame wood buildings necessitates that wood frame buildings be accurately modeled during seismic loading. In turn, accurate modeling requires either a fully mechanistic or constitutive understanding of the components, sub-assemblies, and their interaction to form a complex structural system.

Full-scale seismic tests, i.e. shake table testing has

only been performed a handful of times worldwide for wood frame buildings. During the CUREE Caltech Woodframe project, Filiatrault et al (2001) tested a rectangular two-story house with an integrated one-car garage. The specimen was limited by the size of the available shake table, but provided a state-of-the-art data set nonetheless. The building was subjected to two 1994 Northridge recordings, i.e. the Canoga Park and Rinaldi motions. It was concluded that overall the performance was adequate and that non-structural finishes such as gypsum wall board (GWB) and stucco contributed significantly by increasing both the strength and stiffness of the system (Folz and Filiatrault, 2004). In 2006, as part of the NEESWood project (van de Lindt et al, 2006), Filiatrault et al (2009) conducted full-scale tri-axial tests of a two-story three-bedroom 160m^2 (1800 sq ft) townhouse with an integrated two-car garage utilizing the twin shake tables at the University at Buffalo's SEESL laboratory. This building, termed the Benchmark structure, was designed to the 1988 Uniform Building Code (UBC, 1988) and was intended to benchmark the seismic performance of existing buildings in California and other high seismic regions. The benchmark structure performed relatively well by seemingly protecting life safety of would-be occupants, but suffered substantial and costly damage. Filiatrault et al (2009) was also able to validate the earlier conclusion that non-structural elements such as GWB and exterior stucco significantly increase the strength and stiffness thereby contributing to the improved seismic performance of wood-frame buildings. A three-story apartment building with a tuck-under garage was also tested as part of the CUREE-Caltech Wood Frame Project (Mosalam, 2003). The results of that series of tests confirmed that these types of structures were prone to torsional response and subsequent soft-story collapse mechanisms.

1.1 Overall Objectives

The NEESWood Capstone tests at E-Defense had three (3) major objectives:

Objective 1: To confirm that a representative mid-rise woodframe structure designed using the NEESWood PBSD philosophy satisfies the performance objectives, as pre-defined during the design process. These performance objectives are under development and seek to limit damage and losses while protecting life safety.

Objective 2: Provide a general understanding of the behavior of a mid-rise woodframe structure similar to those currently in place in the Western U.S. and provide a full-scale data set for verification and calibration of nonlinear dynamic models.

Objective 3: Confirm that a representative mixed-use seven-story steel-woodframe mixed-use building designed using the NEESWood design philosophy satisfies the performance objectives, as pre-defined during the design process.

1.2 Performance Objectives

Performance-based seismic design necessitates combining certain prescribed performance expectations with seismic intensity levels. These combinations, while prescribed, are subject to the owners' and overall stakeholders' input; thus any combination, provided it meets current design standards, is acceptable. The NEESWood project team, with input from the project advisory committee, defined the four seismic intensity levels as:

Level 1: Earthquake intensity having a 50% chance of being exceeded in 50 years. This corresponds to a 72 year return period.

Level 2: Earthquake intensity having a 10% chance of being exceeded in 50 years. This corresponds to a 475-year return period. Corresponds *approximately* to the Design-Basis Earthquake (DBE).

Level 3: Earthquake intensity having a 2% chance of being exceeded in 50 years. This corresponds to a 2500-year return period. Corresponds to the Maximum Credible Earthquake (MCE).

Level 4: Optional Near Fault: Un-scaled near-fault ground motions. This is an optional seismic hazard for use depending on the location of a building with respect to the fault and/or the owner's desired performance expectation.

Each of the seismic intensity levels described above can be combined with a particular performance expectation. Based on the Benchmark tests at the University at Buffalo, four performance expectation levels were developed by Christovasillis et al. (2007) as:

Level A: Corresponding to *0.1~1.0%* inter-story drift. Structure may experience minor splitting and cracking of sill plates (some propagation); slight sheathing nail withdraw. slight cracking of GWB; diagonal propagation from door/window openings; partial screw withdraw; and cracking at ceiling-to-wall interface.

Level B: Corresponding to *1.0~2.0%* inter-story drift. Structure may experience Permanent differential movement of adjacent panels; Corner sheathing nail pullout; Cracking/splitting of sill/top plates; Crushing at corners of GWB; and Cracking of GWB taped/mud joints.

Level C: Corresponding to *2.0~4.0%* inter-story drift. Structure may experience Splitting of sill plates equal to anchor bolt diameter; Cracking of studs above anchor bolts; Possible failure of anchor bolts; Separation of GWB corners in ceiling; and Buckling of GWB at openings.

Level D: Corresponding to *4.0~7.0%* inter-story drift. Structure may experience Severe damage across edge nail lines, separation of sheathing; Vertical posts uplifted; Failure of anchor bolts; Large pieces separated from framing; and

Entire joints separated and dislodged.

Each performance level is specified by a probability of non-exceedance (NE) of an inter-story drift limit at a specified level of seismic hazard as shown in Table 1. For example, at seismic intensity level 1 the building should not exceed a median inter-story drift of 1%. At a level 3 seismic intensity the non-exceedance percentile was moved from the 50th percentile, i.e. median, to the 80th percentile because the 4% drift limit was close to what was felt to be the threshold between repairable damage and collapse. Thus it was assumed to be more critical during the design.

Table 1. Capstone Structure Design Expectations

	Seismic hazard (Intensity) Level			
Performance Expectations	Level 1	Level 2	Level 3	Level 4
Level A (1%)	50% NE			
Level B (2%)		50% NE		
Level C (4%)			80% NE	
Level D (7%)				50% NE

2. SPECIMEN CONSTRUCTION

The preparation of the construction began in early 2008 with a joint meeting including the CSU research team, the contractor, and representatives from Simpson Strong-Tie Company. The construction materials were shipped from the U.S. and Canada to Japan in 20 containers at the end of 2008 and beginning of 2009. From the first piece of steel lifting frame being laid on the ground to the move of the specimen onto the shake table, the construction of the test specimen last exactly four months, from February 23rd 2009 to June 22nd 2009. The construction schedule outlined in advance was generally kept with minor adjustment due to some revisions made in the early stages of the construction.

Following the planning of the construction and finalization of the testing schedule, construction materials purchased or donated in the U.S. and Canada were shipped to the Miki shake table site. The first shipment left the U.S. in October, 2008. By the start of construction in February 2009, the majority of the materials had been delivered to the E-defense site and were being stored outside the shake table laboratory.

Shear walls in Capstone building used mostly 2x6 framing. The nail schedule was mostly 2"/12" or 3"/12" in the lower floors. Some of the walls were also sheathed on both sides (double sided) with OSB. Incorporation of a new wall type was also investigated in the project. A double Midply wall system designed to handle high shear demand that exceeds the capacity of traditional shear walls was included. Also because of the high shear capacity of shear walls, high strength shear screws were used at the top and sill plates of the shear walls instead of bolts. These SDS screws had a tested ultimate capacity of approximately 1 kip per-connector in shear.

The wood building was approximately 18m x 12m (60ft x 39ft) in plan view and about 17m (56 ft) tall. The elevation views, presented in Figure 1a, show the significant openings on all sides of the building requiring shear wall stacks in many locations. The floor plan for the first story is shown in Figure 1b and consisted of two small one-bedroom units (Unit A) and two two-bedroom units (Unit B). The floor plan for stories two through five were the same as story one with only a slight change to unit A since no entrance door to the building was needed at those levels. The top story, story 6, was modified from the other stories to combine the space for Unit B into one large two-bedroom unit. This change in floor plan meant some of the shear walls in story 5 did not extend into story 6. For reference, the short direction of the building is designated as the X direction and the long direction as the Y direction.

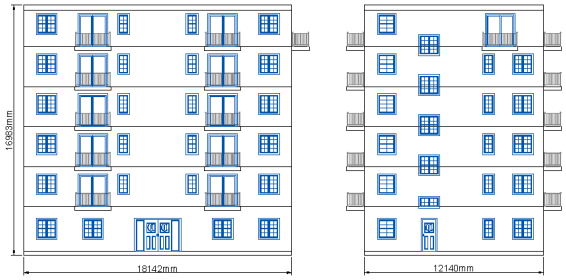

(a)

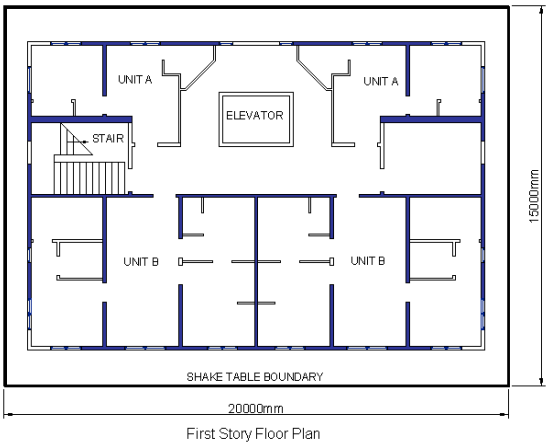

(b)

Figure 1 Elevation and Floor Plan for Capstone Specimen

Wood shear walls were designed as stacked wall systems with a combination of steel rod hold-downs (ATS) with mechanical shrinkage compensating devices at each end to prevent overturning, reduce uplift, and remove slack from the tie-down system that would otherwise develop from in-situ reductions in wood moisture content and natural settling of the structure. Figure 2a shows a schematic of a typical 2x6 wood shear wall in the first story and Figure 2b shows a shear wall in lower story with framing member and compression stud packs exposed. Details for each wall in the

Capstone building can be found in the forthcoming report by Pei et al (2009). The design details of the building were quite extensive and only a basic description of the structural configuration is provided here for brevity. Each shear wall stack included glulam beams as shear collectors in between stories. Floor systems were made up of standard 18mm (23/32 inch) T&G Oriented Strand Board (OSB) with wood I-joists that were hung on the glulam beams with nailed metal hangers. The glulams were fully supported by shear

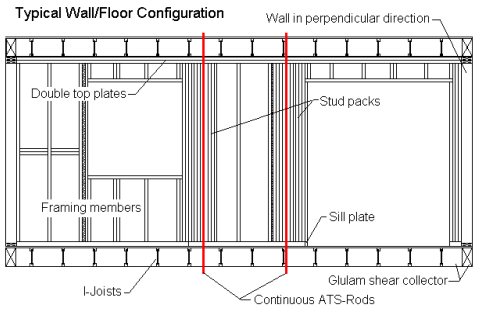

(a)



(b)

Figure 2 Typical Shear Wall Schematic for Capstone Building

walls except in one line between the elevator shaft and stairwell where they acted as beams since no bearing and/or shear wall was present. Wood shear walls had 12mm (15/32 inch) OSB on either one or both sides depending on



Figure 3 Completed Specimen on E-defense Table

the design requirements. Nail spacing ranged from sheathing panel exterior nail spacing of 50 mm (2 in) to as large as 152 mm (6 in), with a constant field nail spacing of 300 mm (12 in) for all walls.

Because there were many shear walls in the Capstone building, it is not possible to shown the details of each shear wall. Shear transfer from the wall to the floor system was achieved using either a nailed channel or two lines of self tapping screw, i.e. SDS screws.

Gypsum wall board (GWB) was installed on all walls and ceilings with tape and putty on all joints except the wall-to-ceiling joints and corners. Finishing as many joints as possible was desirable in order to provide realistic damage inspection results.

In addition to the as-built dead load, seismic mass was added to each story in the form of steel plates in order to bring the total floor seismic mass to a realistic level thereby accounting for all the insulation, gypcrete flooring, exterior finish, plumbing, HVAC, and floor finishes. The weight of the building was carefully calculated based on the construction materials used. Then the added steel plates were placed during the construction of each story and fastened to each floor and the roof. After all the additional masses were added, the total weight of the building was 285 ton (628 kips). The finished test building seating on the E-defense shake table was shown in Figure 3.

The seismic test program consisted of multiple shake table tests during three separate test days. As mentioned, during the first test day a steel special moment frame (SMF) at the base of the building was not braced and therefore participated in the testing. Then the SMF was fully braced for the tests focused on the response of the six-story wood frame building. The Northridge ground motion recorded at the Canoga Park station was used throughout the tests with different scale factors. Figure 4 shows the spectral accelerations in the X, Y, and Z directions of the un-scaled Canoga Park record, with the Y-component (which has a higher PGA value) applied in the long direction of the building. The shear capacity of the building was the same

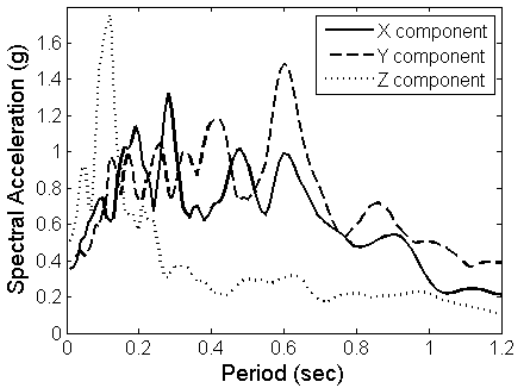

Figure 4 Spectral Acceleration for Unscaled Ground Motion used in Shake Table Test

in both directions by design. The ground motion was scaled to the peak ground acceleration levels listed in Table 2

to represent seismic hazard levels with 50%, 10%, and 2% probability of exceedance in 50 years, which corresponds to return periods of 72, 475, and 2500 years, respectively.

Table 2 Peak Ground Accelerations for the Canoga Park Record

Northridge Canoga Park		Seismic Test		
		Level 1	Level 2	Level 3
Hazard level		50% 50 years	10% 50 years	2% 50 years
Scaling factor		0.53	1.20	1.80
PGA (g)	X	0.19	0.43	0.64
	Y	0.22	0.50	0.76
	Z	0.26	0.59	0.88

3. EXPERIMENTAL RESULTS

Because of the size of the building, it was not possible to find a fixed reference to instrument the absolute displacements of the structure, i.e. a frame beside the shake table. Therefore, an optical tracking measurement system was employed in the test program to capture the building movement with 50 LED light markers attached to the exterior of the building at each diaphragm level. The location of these markers is shown in Figure 5. There were no markers on the back side of the building due to camera limitations.

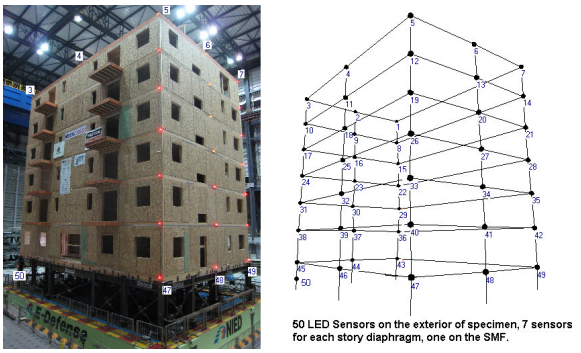

Figure 5 Optical Tracking System for Displacement Measurements

The averaged displacement at the centroid of the floor diaphragm can be estimated based on the measurements from seven optical tracking markers for each floor. The maximum roof displacements relative to the shake table were measured to be 60mm, 140mm, and 211mm for seismic intensities 1, 2, and 3 respectively. The maximum displacement occurred in the long direction of the floor plan, namely the Y direction. The building deformation shapes at the point in time of the maximum roof displacement levels in the X and Y directions are presented in Figure 6. The shape of the deformed grid was generated directly from the optical tracking sensor measurements and is exaggerated for clarity. Although the building was designed to be symmetric and added seismic mass was distributed approximately uniformly over the building floor plan, torsional response was clearly observed during testing. The torsional response was synchronized with the lateral response of the building, which means the point in time at which the torsion reached a maximum value is very close to the occurrence of the maximum value of the lateral response, as one might expect. Due to the presence of torsion, the maximum inter-story drift of some shear walls at the upper levels near the building corners slightly exceeded 3% during the level 3 seismic test.

Inter-story drift is often used in displacement based procedures to evaluate the performance of a wood frame building. The resulting inter-story drift of the Capstone building was calculated by subtracting the absolute displacement measurement between stories and dividing the value by the story height. The maximum values for the average inter-story drift are presented in Table 3.

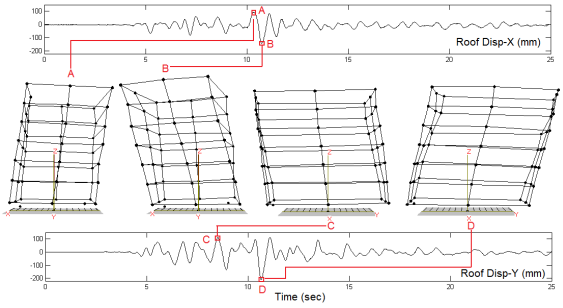

Figure 6 Observed Displacement Response from Optical Tracking System

Table 3. Averaged peak inter-story drift measured during the three tests

Peak Inter-story Drift (%)	Seismic Test 1		Seismic Test 2		Seismic Test 3	
	X	Y	X	Y	X	Y
St1	0.26	0.44	0.49	0.77	0.84	1.12
St2	0.35	0.42	0.63	1.05	0.97	1.46
St3	0.29	0.54	0.64	1.02	0.89	1.64
St4	0.30	0.44	0.77	1.22	1.10	1.48
St5	0.36	0.46	0.64	1.14	1.00	1.88
St6	0.40	0.21	0.88	0.58	1.35	1.11

From Table 3 one can see that the heightwise distribution of inter-story drifts for the building under all three seismic test is close to uniform among the stories, which indicates the absence of a soft story mechanism. Recall this soft story

mechanism was observed in wood frame buildings during large earthquakes (such as the 1994 Northridge and the 1995 Kobe earthquakes). The approach used to design the Capstone test specimen which is outlined in Pang et al (2009) vertically distributes the shears according to the deformed state of the structure essentially eliminating or at least drastically reducing the probability of a soft story being present. Interestingly, the maximum drifts were observed in the upper stories instead of the bottom story, which was, in fact, consistent with numerical model predictions performed prior to testing.

The global hysteresis loops for the building are presented in Figure 7. Similar behavior from one seismic intensity level to the next is observed since the same ground motion (Northridge-Canoga Park) was scaled for each test. As the ultimate base shear capacity of the building, which was used in the performance-based seismic design, is about 2500 kN (562 kips), for the Y direction at intensity level 3 one can see that the test specimen resisted 1824 kN (410 kips) which is approximately 73% of the ultimate value.

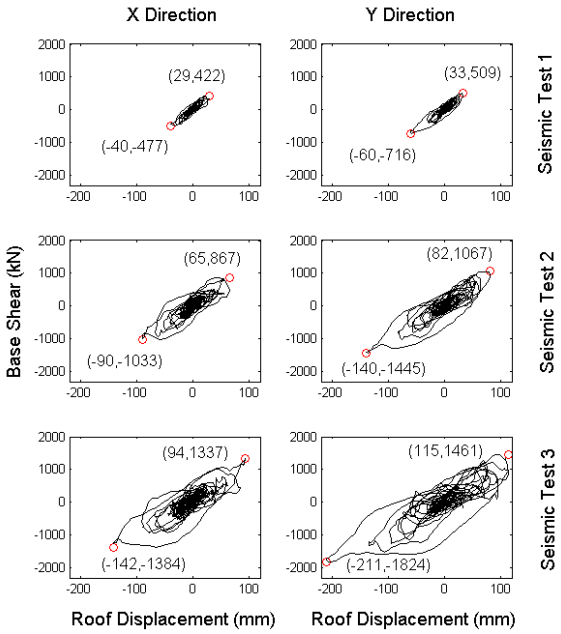

Figure 7 Global Hysteresis Loops for Capstone Building

As mentioned earlier, the damage to the test specimen from the three seismic tests was not felt to be significant even for the 2500 year (MCE level) earthquake. There was no visible damage to any structural components or assemblies of the building, with damage limited to the gypsum wall board (GWB). The GWB damage was observed primarily around the corners of openings as illustrated by the post-shake photographs in Figure 6. The damage and its correlation to inter-story drifts will be presented in its entirety in a forthcoming paper by several of the authors and can be found detailed in the forthcoming report by Pei et al. (2009).

4. SUMMARY AND CONCLUSIONS

A series of three shake table tests on a six-story light-frame wood building was completed in July 2009 in Miki, Japan. Designed with the performance based design procedure developed within the NEESWood project, the building was able to achieve very good performance under both DBE and MCE level earthquakes, with maximum averaged inter-story drifts on the order of 2%. The damage to the structural and non-structural components of the building was very minor, mostly repairable. Peak shear wall drifts at one corner slightly exceeded 3% for the MCE level test. The Capstone building performed very well and did not experience a soft story mechanism at any of the test levels. The averaged floor accelerations were felt to be reasonable at the higher story levels, although objects would still need to be anchored as recommended by FEMA. Even with the approximately symmetric floor plan and evenly distributed seismic mass, considerable torsional response was still observed during the seismic tests. Inclusion of torsion is needed within PBSD for mid-rise light-frame wood buildings. The hold down system employed in the design of the specimen serves the critical role of transferring uplift forces down to the foundation and thereby preventing overturning. Although installed for each shear wall, the hold down rods acted as a system to provide overturning restraint to the entire floor plan, and only at times did they act as a semi-isolated shear wall stack.

Acknowledgements:
The material presented in this paper is based upon work supported by the National Science Foundation under Grant No. CMM-0529903 (NEES Research) and CMMI-0402490 (NEES Operations). Any opinions, findings, and conclusions or recommendations expressed in this material are those of the author(s) and do not necessarily reflect the views of the National Science Foundation. The overall NEESWood project team made up of John W. van de Lindt, David V. Rosowsky, Andre Filiatrault, Rachel A. Davidson, and Michael D. Symans contributed to all facets of the NEESWood project. Thank you also to Weichiang Pang of Clemson University for his participation in the design portion of the Capstone test specimen. Thank you to NSF REU's Doug Allen and Kathryn Pfrefzschner, researchers Chikahiro Minowa of NIED and Mikio Koshihara at the University of Tokyo. Graduate student Tomoya Okazaki, contributed to the construction and instrumentation of the test specimen and a former Ph.D. student Kimberly Cronin helped with the design. Thank you also to Tim Ellis of Simpson Strong Tie Co. and David Clyne of Maui Homes USA. Technical collaborators beyond the authors affiliation included the U.S. Forest Product Laboratory, FP Innovations-Forintek Division, and Maui Homes U.S.A. Financial and in-kind product and personnel donations were provided by Simpson Strong Tie, Maui Homes, B.C. Ministry of Housing and Social Development, Stanley Bostitch, Strocal Inc., Structural Solutions Inc., Louisiana Pacific Corp., Natural Resources Canada, Forestry Innovation Investment, APA-The Engineered Wood Association, American Forest and Paper Association, Howdy, Ainsworth, and Calvert Glulam.

References:

Christovasilis, I.P., Filiatrault, A., and Wanitkorkul, A. (2007). "Seismic testing of a full-scale two-story wood light-frame building: NEESWood benchmark test" Neeswood *Report No. NW-01*, Dept. of Civil, Structural and Environmental Engineering, University at Buffalo, State University of New York, Buffalo, available on-line at http://www.engr.colostate.edu/NEESWood/.

ICBO. (1988). “Uniform Building Code, 1988 ed.” International Conference of Building Officials, Whittier, CA.
Filiatrault, A., Christovasilis, I.P., Assawin Wanitkorkul, and John W. van de Lindt (2009) “Seismic Response of a Full-Scale Light-frame Wood Building: Experimental Study” Journal of Structural Engineering, In Press.
Folz, B. and Filiatrault, A. (2004) “Seismic analysis of woodframe structures. II: Model implementation and verification” Journal of Structural Engineering, v 130, n 9, p 1361-1370.
Mosalam, K.M., C. Mochado, K.U. Gliniorz, C. Naito, E. Kurkel, and S.A. Mahin (2003) “Seismic evaluation of an asymmetric three-story woodframe building” CUREE Report W-19.
Pang, W.C., and Rosowsky, D.V. (2007) “Direct displacement procedure for performance-based seismic design of multistory woodframe structures” Neeswood Report No. NW-02, Zachry Dept. of Civil Engineering, Texas A&M University, College Station, available on-line at http://www.engr.colostate.edu/NEESWood/.
Pei S., and van de Lindt J.W. (2007). User’s manual for SAPWood for Windows, Version 1.0. SAPWood program user’s manual, available on-line at http://www.engr.colostate.edu/NEESWood/.
Pei, S., van de Lindt, J.W. (2008). “Coupled bending-shear seismic analysis of Stacked Wood Shearwall Systems”, Earthquake Engineering and Structural Dynamics, 38: 1631-1647.
Pei, S., J.W. van de Lindt, S.E. Pryor, H. Shimizu, H. Isoda, and D. Rammer. (2010). “The NEESWood Capstone Tests at E-Defense: Testing of a Full-Scale Six-Story Woodframe and Seven-Story Mixed Use Building”, Publication anticipated on-line (NEESWood Report NW-07) and via the U.S. Forest Products Laboratory in 2010.
van de Lindt, J.W., Pei, S., Pryor, S.E., Shimizu, H. and Isoda, H. (2009) “Experimental seismic response of a full-scale six-story light-frame building” Submitted to Journal of Structural Engineering.
van de Lindt, J.W., D.V. Rosowsky, A. Filiatrault, M.D. Symans, R.A. Davidson. (2006). “The NEESWood Project: Progress on the Development of a Performance-Based Seismic Design Philosophy for Mid-Rise Woodframe Construction”. Proc of the 2006 World Conference on Timber Engineering, Portland, OR.

JOINT CONFERENCE PROCEEDINGS
7th International Conference on Urban Earthquake Engineering (7CUEE) &
5th International Conference on Earthquake Engineering (5ICEE)
March 3-5, 2010, Tokyo Institute of Technology, Tokyo, Japan

SEISMIC AASESSMENT FOR RESTORATION OF PRAMBANAN WORLD HERITAGE TEMPLES DAMAGED BY THE CENTRAL JAVA EARTHQUAKE OF 2006, INDONESIA

Toshikazu Hanazato[1)], Satoshi Yamato[2)], Yasufumi Uekita3), Chikahiro Minowa[4)], Suprapt Siswosukarto[5)], Subagyo Pramumijyo[6)], Kunihiko Ono[7)], Noriko Koresawa[8)] and Mai Taneichi[9)]

1) Professor, Division of Architecture, Faculty of Engineering ,Mie University, Japan
2) Director, Architectural and other Structural Division, Department of Cultural Properties, Agency of Cultural Affaire, ,Japan
3) Associate Professor, Graduate School, World Heritage Studies, The University of Thsukuba, Japan
4) Chief Research Engineer, National Research Institute for Earth Science and Disaster Prevention, Japan
5) Associate Professor ,Geotechnical Engineering Department, Faculty of Engineering, Gadjahmada University, Indonesia
7)Associate Professor, Graduate School of Civil Engineering, Gadjahmada University, Indonesia
7) Associate Professor, ,Faculty of World Heritage, Cyber University, Japan
8) Associate Professor, Graduate School of Engineering, Nagoya Institute of Technology, Japan
9) Graduate School Student, Mie University, Japan

hanazato@arch.mie-u.ac.jp, yamato53@bunka.go.jp,,uekita@heritage.tsukuba.ac.jp, Ccmino@aol.com, S2@tsipl.ugem.ac.id,bagyo@ugem.ac.jp , kunihiko_ono@cyber-u.ac.jp, koresawa@,nitech.ac.jp, mai_bow510@yahoo.co.jp

Abstract: A devastating earthquake of magnitude 6.4 that struck Central Java, Indonesia, on May 27, 2006 affected a number of architectural heritages in and around the one of the historic cities in Indonesia, Yogjakarta. The serious damage that attracted world wide concern immediately after the earthquake was to the Prambanan Temple Compounds, World Heritage of stone structures. As the Indonesian government requested in emergency the cooperation of Japanese Government to assess the earthquake damage to the Prambanan Temples for starting the restoration project, an interdisciplinary team of Japanese experts was organized in collaboration of Indonesian experts and has been conducting structural architectural survey for three years in consideration of ISCARSAH guideline. The present international cooperative project is introduced as a successful case study of seismic assessment of the stone monuments damaged by the recent earthquake in Asia. The scope of the present paper is 1) to briefly review the unique history of the Prambanan Temples from a structural point of view, 2) to outline the features of the earthquake damage, 3) and to show the architectural structural survey of the stone temples for the restoration. In particular, it focuses on the structural analysis to clarify the cause of the earthquake damage for designing the structural strengthening. The structural monitoring to assess the present state of the stability is also described.

1. INTRODUCTION

1.1 History of Prambanan

The heritage structures, of the local andesite blocks, composing Prambanan Temples originated in the 9th century. Although they had been ruined during their long histories, the structures were reconstructed in the 20th century (Candi Siva was reconstructed first by Dutch engineers in the middle of 20th century; the other buildings were reconstructed by Indonesian engineers during the end of 1980s and beginning of 1990s.using their technology). In 1991, those architectural heritages were registered as World Heritage by UNESCO. Photo.1 shows an overview of the Prambanan Temples, taken by a radio control helicopter in February, 2007.

The stone monuments were reconstructed by introducing inner concrete structures composed of reinforced concrete frames and infill rubble materials. The reinforced concrete frame was employed to confine infill concrete frames and infill rubble materials(See Fig.1).

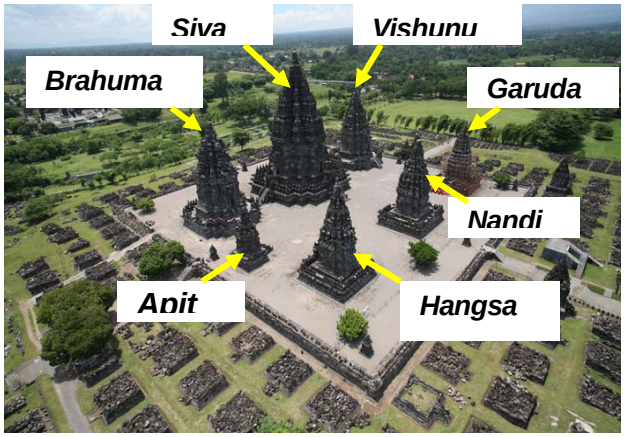

Photo.1 Overview of Prambanan Temples

The reinforced concrete frame was employed to confine infill rubble material structure for ensuring structural stability. The decorative stones of "ratna" and "stupa" were connected to the inner concrete structure by use of metal anchor bolts. Structural issues to assess the seismic safety concerning possibility of structural damage of the inner concrete structure therefore rose, as is discussed in the next section.

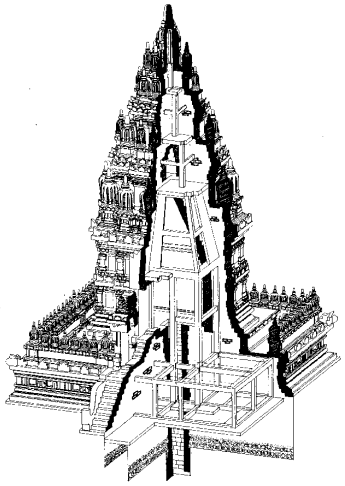

Fig.1 Inner structure (Provided by Archeological Site Office of Yogyakarta Special Province)



Photo.3 Damage of decorative stones



Photo.4 Fall of Ratona



Photo.5 Damaged spire of Candi Garuda

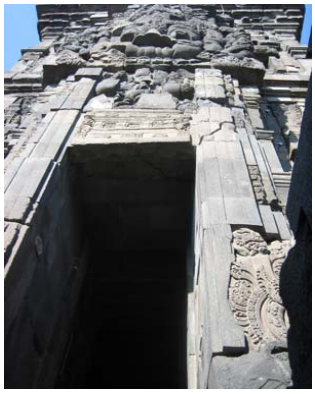



Photo.6 Cracks and gap of stones at the entrance of Candi Siva

1.2 Outlines of Earthquake Damage

A devastating earthquake of magnitude (M_w) 6.4 struck Central Java, Indonesia, having affected various structural types of architectural heritages in and around the historic city of Yogyakarta which locates 25 km from the epicenter. A traditional timber building in Royal Palace of Sultan, Kraton, constructed in the unique Java architectural style, totally collapsed. The historical stone masonry in the former royal palace, Taman Sari, also suffered severe damage. The earthquake affected Koda Gede, a historic area where a number of traditional types of masonry and timber buildings had been maintained and preserved with historic townscape. The damage that attracted worldwide concern immediately after the earthquake was to World Heritage Prambanan Temple compounds. Features of damage to Prambanan Temple Compounds are outlined as follows:

Of the six main temples composing Prambanan Temple, Candi Brahma and Candi Garuda suffered apparently the most severe damage. Many ratna and stupa that decorated the nave roof fell, shown in Photos 3 and 4. The upper part of the roof of Candi Garuda appeared seriously unstable(See Photo.5). Significant relative displacement and horizontal openings between the stone elements were found at the freestanding gate on the platform in front of the entrance. Candi Siva, the largest monument in Prambanan Temples, suffered serious cracks at its base and wall of the nave, shown in Photo 6.

1.3 Establishment of Interdisciplinary Team

As the Indonesian government requested the cooperation of the Japanese government in surveying cultural heritages damaged by the Central Java Earthquake for their restoration and rehabilitation, the Japan Consortium for International Cooperation in Cultural Heritages organized an interdisciplinary team of experts. This interdisciplinary team composed of the experts in conservation of cultural heritages, Indonesian architectural history and structural engineering. Having been sent there in both 2006 and in 2007 to conduct architectural and structural survey for proposing the restoration plan, we focused our efforts on the Prambanan Temple. The structural survey is outlined as an international cooperation project and as a case study of seismic safety evaluation of the cultural heritages damaged by the recent earthquake in Asia.

1.4 Scope of Structural Survey

One of the basic principles for structural restoration of cultural heritages is "minimal intervention". In the case of the Prambanan Temple compound, the fact that the monuments had suffered varying degrees of damage had to

be taken into consideration. In order to minimize intervention, the causes of earthquake damage should be identified by scientific approach in the discussion of structural restoration. Geotechnical investigation at the site, microtremor measurements of the structures and investigation of material properties were performed together with the literature survey of the structural and construction conditions. For both identification of causes of damage and

2. GEOLOGICAL AND STRUCTURAL SURVEY

2.1Geitechnical Survey and Microtremore Measurements

The Prambanan Temples are located to the south foot of the active volcano, Mt. Merapi, which has a number of stream/rivers from near the mountain top. There is a river Opak on the west side of the Prambanan Temples. This

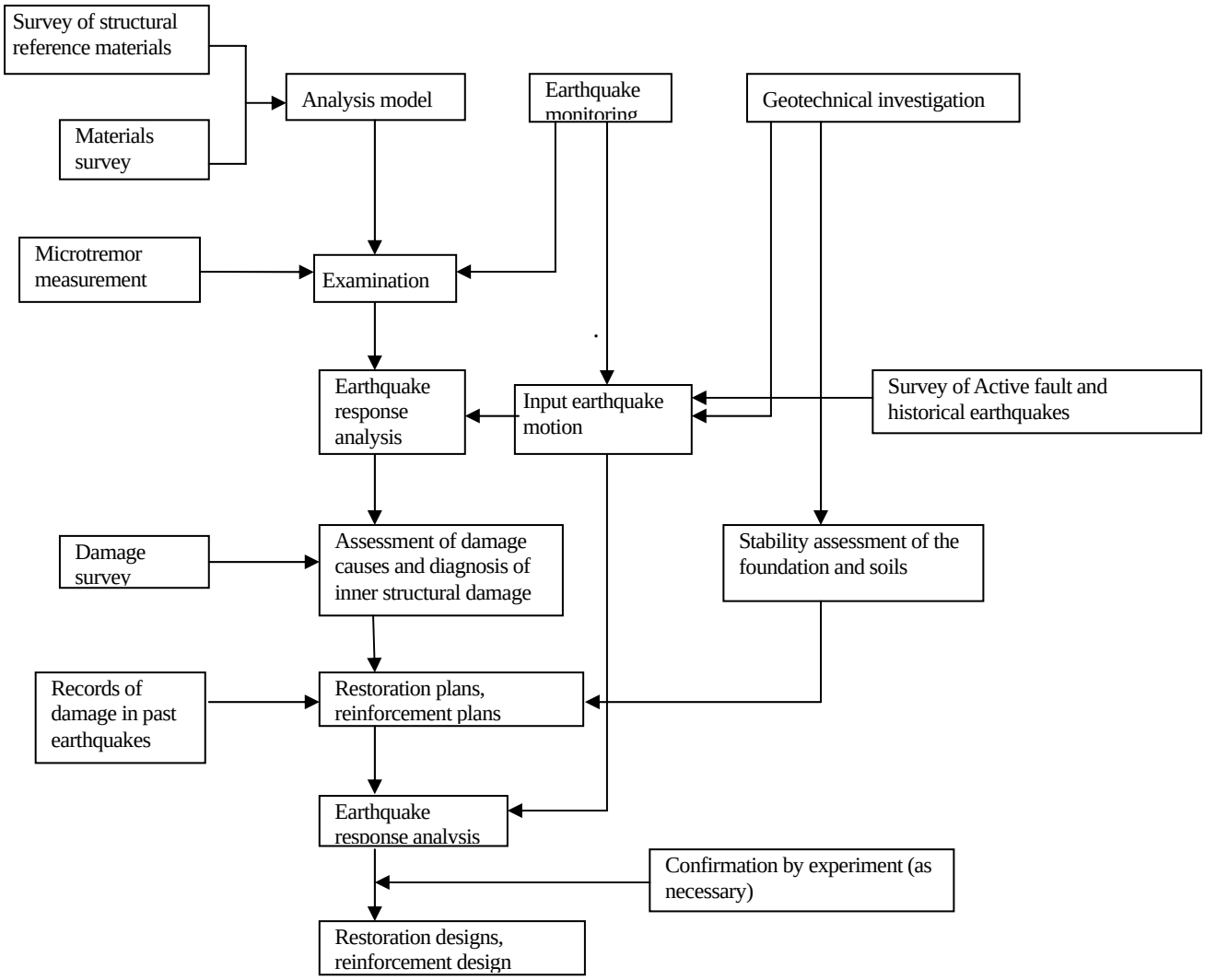

Fig.2 Flow of structural surveys proposed for the formulation of restoration plans

diagnosis for safety evaluation, structural analysis should be performed as quantitative approach. In the present project, therefore, seismic response analysis using 3-deimentional FE model was performed. Structural analysis would furthermore make it possible to assess whether the inner concrete structures of the Prambanan Temple were damaged or intact. Fig.2 shows the structural survey's flowchart proposed at the first phase of the survey in 2006 for the restoration project. In addition to these surveys, the monitoring of crack displacement was initiated in 2008 to investigate the structural stability at the present state.

geological condition indicated that the structures were constructed on the natural sedimentary soils carried by the river.

As a fundamental investigation, standard penetration tests with boring were performed as shown in Photo.7. In order to understand the soil response during the earthquake, PS-logging along the boring holes and the surface wave profiling tests (See Photo.8) were also performed. Fig.3 shows the cross-section ofS-wave velocity of sub-surface soils, evaluated by the surface wave profiling test. It was found that the first surface layer of 5m thickness was embankment, and that the bearing stratum of the structures was the natural sandy layer with Vs=260m/s beneath the

man-made embankment. As results of these surveys, the soil model was successfully provided for the dynamic soil



Photo.7 Boring and standard penetration test



Photo.8 Surface profiling test

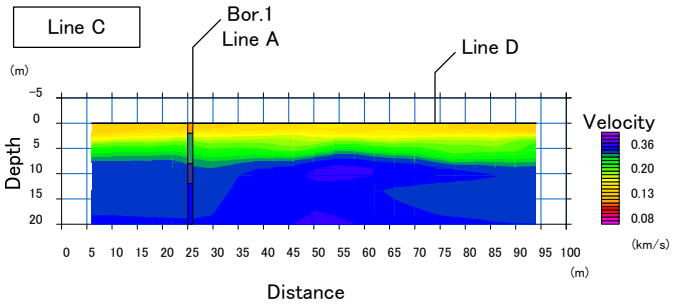

Fig.3 Cross-section of shear wave velocity

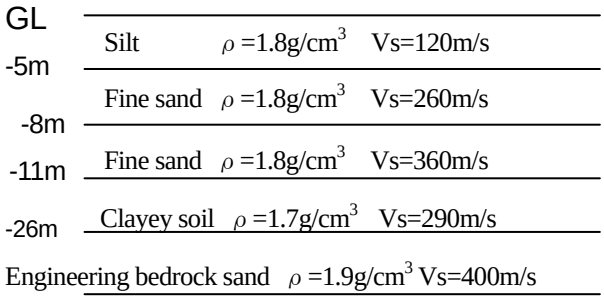

Fig.4 Soil model for dynamic response analysis

response analysis at the site, shown in Fig.4. By employing the one-dimensional shear wave propagation theory (so-called SHAKE), the amplification characteristics as a function of frequency was given, shown in Fig.5. In this soil response analysis, the effect of the dynamic strains on soil stiffness and damping factor was taken into account for the estimated ground motion level. Fig.5 indicates that the predominant frequency of the ground motions would range from 2 to 5Hz at the site (In particular, the amplification at around 5Hz takes high value of 2.2.

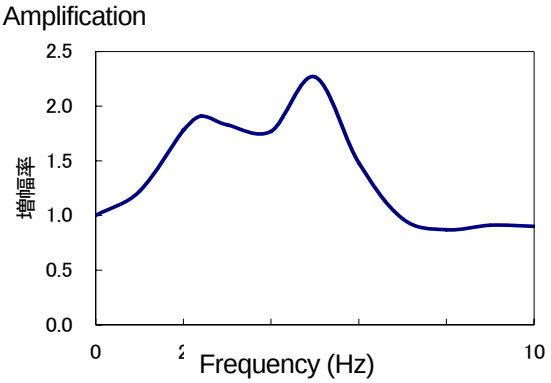

Fig.5 Amplification by soil response

According to the survey conducted by the Indonesian experts, there found a significant differential settlement as high as 50mm at Candi Vishnu and 20mm at Candi Siva. To understand whether such irregular settlement was caused by the earthquake or not, we estimated the earth pressure induced by the seismic response of the structure (The analysis model is described in the following section). Fig.6 shows the simulated earth pressure at the base of the foundation, which was induced by the earthquake motions assumed for the analysis. The peakearth pressure during the earthquake was estimated to be 250kN/m^2. On the other hand, the allowable bearing capacity of the foundation for earthquake loads was evaluated to be 720-760kN/m^2 on the basis of the Recommendation for Design of Building Foundation published by Architectural Institute of Japan.

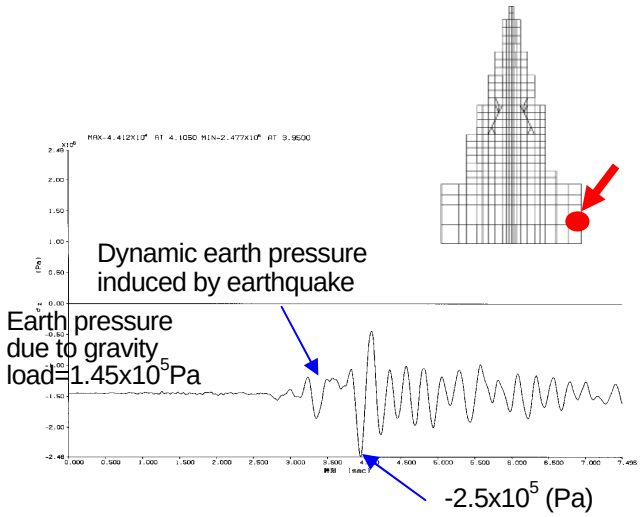

Fig.6 Simulated dynamic earth-pressure induced by earthquake

These analysis results indicated that such apparent irregular settlement was not caused by the earthquake, and that the behaviors of the foundation were stable during that earthquake. Geotechnical investigation and the earthquake response analysis also indicated that the soil conditions at the monuments' bases were the natural deposits enough stable to support the structures even during this and future earthquakes.

As microtremore measurement is a useful technique that can clarify fundamental dynamic characteristics of structures such as natural period, the microtremor for every structure in the courtyard of the Prambanan Temples was recorded in the present project, shown in Photo.9. Fig.7 presents the relationship between the natural period and the height of the historical masonry buildings, including not only the present measurements but also the literature survey. The measured natural frequency of the structures of the Prambanan Temples ranged from 2.2Hz (Candi Siva) to 4.8Hz (Candi Apit), shown in Fig.7. Note that such frequency range is agreement with the predominant frequency of the soil response amplification shown in Fig.5. It indicates that the rise of the structural response due to so-called resonant effect caused serious damage to the historical masonry monuments during the Central Java Earthquake.



Photo.9 Microtremor Measurements

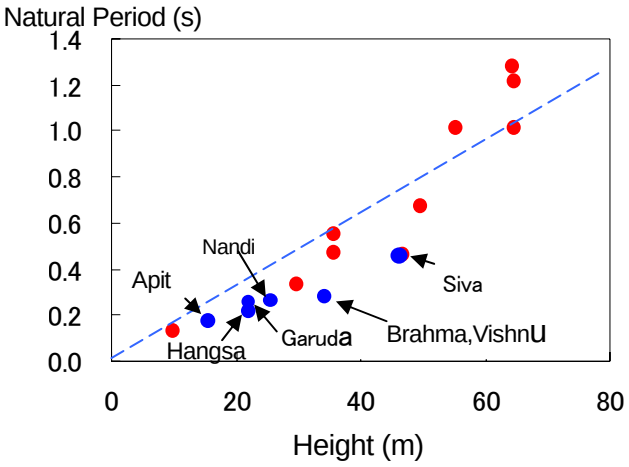

Fig.7 Relationship between natural period and height of historical masonry buildings

2.2 Earthquake Ground Motions

Note that earthquake ground motions should be essential for evaluating seismic safety of heritage structures. Since the earthquake ground motions were not recorded near the Prambanan and in the epicentral area as well, the ground motion level (PGV) was estimated to be approximately 10kine (10cm/s) at the epicentral distance of 20-25km from the attenuation curve based on the earthquake records in the far-field(See Fig.8). The strong motions recorded during the past earthquakes of similar magnitude with severe damage to historical buildings were utilized as the input motions in the earthquake response analysis. In the present study, the earthquake record of Athens Earthquake of September 7, 1999(Mw=5.7), Greece, was selected and utilized. (The acceleration record of T-component at the site of SPLA1 of which PGV and PGA were 12.4kine and 217Gal, respectively, was referred as the input ground motion for the seismic response analysis.) The waveform of the acceleration record of Taft 1952 EW was also utilized in the present project. The soil response characteristics of the sub-surface layers (See Fig.5) were considered to simulate the input ground motions for the seismic response analysis.

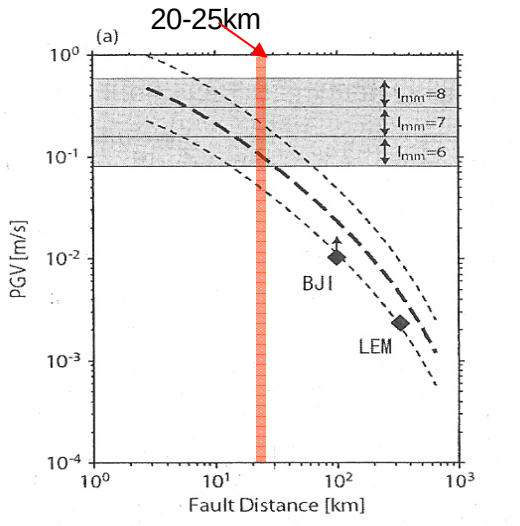

Fig.8 Attenuation curve of PGV proposed in the report of A.I.J.

Fig.8 Attenuation curve of PGV proposed in the report of A.I.J.

3. SRRUCTURAL ANALYSIS

3.1 Analysis Method

Shown in Fig.1, as the buildings of the Prambanan Temples is structurally characterized by the inner reinforced concrete structure, it was needed for the structural restoration to investigate whether the inner structures were damaged or intact. We discussed non-destructive or minor-destructive tests that might be applied to investigate the inner structural conditions in this case, however, it was not possible to find

any non- or minor- destructive tests being appropriate for the present project. In place of the non- or minor- destructive tests, structural analysis was employed to discuss the earthquake damage to the inner structure. At the same time, the seismic response analysis must be useful for understanding the cause of the significant damage of ratona's and stupa's fall, which should be also employed to design the strengthening methods of ratona and stupa against future earthquakes.

Candi Garuda, the most severely damaged building, was focused upon and analyzed in the present study. Figs.9 describe the analysis model using 3-demensional finite solid elements combined with beam elements (Computer Code TDAP III was utilized.). Material mechanical properties used for the analysis model were evaluated as follows (See Table.1) ; i) the stiffness of both the inner rubble concrete and the concrete used for reinforced concrete structure was determined from the laboratory tests of the specimen sampled during the dismantlement of the top part of Candi Garuda(See Fig.5). ii) the stiffness of the andesite blocks was determined from the parametric analysis so that the natural frequency of the structure could agree with the microtremore measurement of Candi Hansa.

By normalizing the peak ground velocity to 13.8kine from an earthquake engineering point of view, the peak acceleration and velocity of the input ground motions were given as 218Gal, 13.8kine at the ground surface, and 138Gal, 10.4kine at the engineering bedrock (GL-26m). Rayleigh damping of 5% at 1st and 2nd modes was assumed in the present dynamic analysis

Table 1 Material Stiffness and Natural Frequency of Analysis Model

Andesite (N/mm^2)	1.8x10^3
Filling Concrete (N/mm^2)	1.6x10^3
RC Frame (N/mm^2)	1.9x10^4
Tuff (N/mm^2)	Equivalent to andesite
Natural frequency (Hz)	4.2

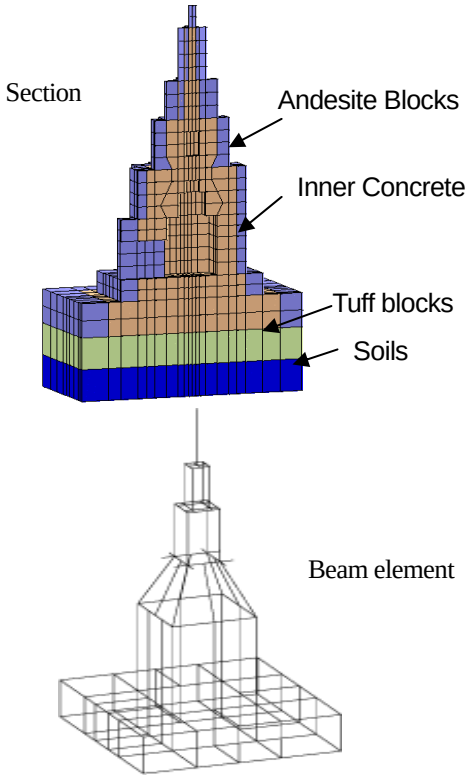

Figs.9 Analysis model (Elevated section of FE-model using solid and beam elements)

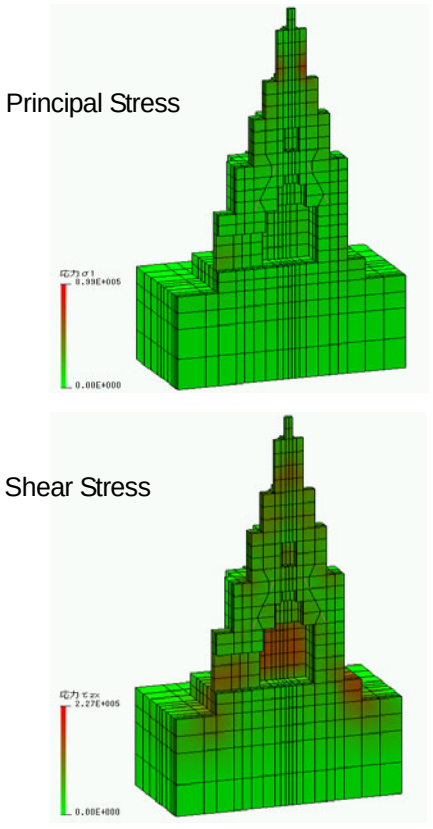

Figs.10 Distribution of principal stress σ_1 and shear stress τ

3.2 Analysis Results

As results, Fig.10 and Fig.11 show the peak tensile and shear stress distributions in the structure, and the peak flexural moment induced in the reinforced concrete members. The analysis results demonstrated that, judging from the induced stress, there was little possibility of serious damage to the inner concrete structure, and that the maximum flexural moment induced in the reinforced concrete frame, 21,700Nm, was less than the short term allowable moment, 38,900Nm. At the same time, it was evaluated that the peak acceleration at the top of the roof reached a level of 2G(G: gravity acceleration), shown in Fig.12. This simulation agreed well with the fact that a number of "ratna" and "stupa" fell from the upper layers. Such numerical results can be used as the design load for proposing strengthening method for the restoration of "ratna" and "stupa".

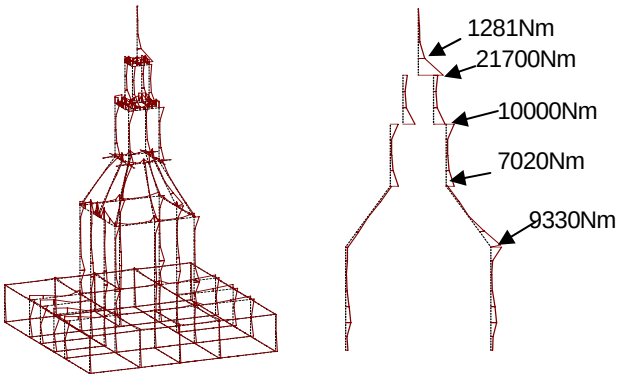

Figs.11 Peak flexural moment induced in RC frame

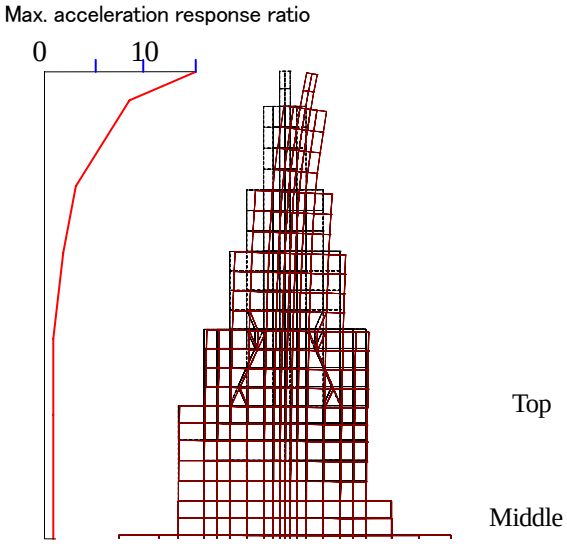

Fig.12 Elevated distribution of acc. Response ratio

4. SRRUCTURAL MONITORING

4.1 Earthquake Monitoring

Earthquake monitoring was initiated in the end of November 2007 to verify the analysis model, and at the same time, to observe the actual dynamic behaviors during strong motions. A total of 4 seismograms were installed at Candi Hangsa, shown in Fig.13.

Since their installation, several small earthquake motions were observed at the site. Fig.14 shows an example of earthquake records, which was recorded on March 25, 2008. The amplitude was so small and affected by noise, therefore, it was difficult to use this data for verification of the analysis model. It would be expected that larger earthquake motions could be recorded.

To investigate the natural frequency of the structure, Fig.15 shows the Fourier spectrum of the earthquake record at the top. It was considered that the spectral peak at 3.3Hz would correspond to the natural frequency. The natural frequency obtained by the microrremore measurement of Candi Angsa was 4.1Hz. The significant difference of the observed natural frequency between the earthquake and microtremor records, although the earthquake record was so small, was caused by strain-dependent characteristics (non-linearity) of the structural response. In general, dynamic behaviors of such rigid and massive structure is affected by soil-structure interaction. Further study should be needed to understand the effect of soil-structure interaction.

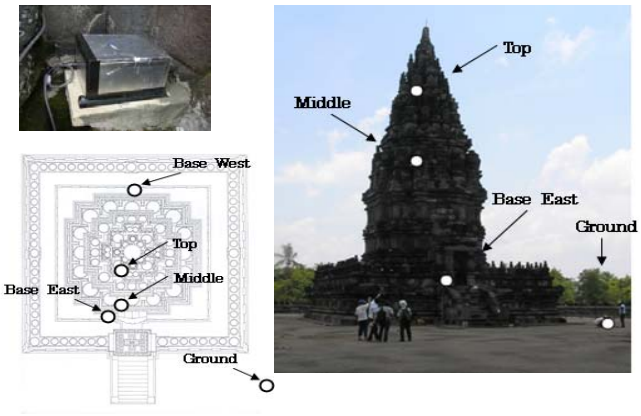

Fig.13 Earthquake monitoring points

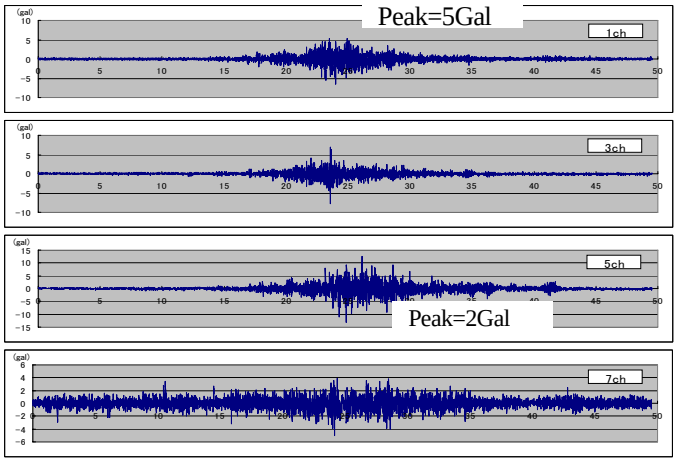

Fig.14 Acceleration records of the small earthquake of March 25, 2008 (NS-component)

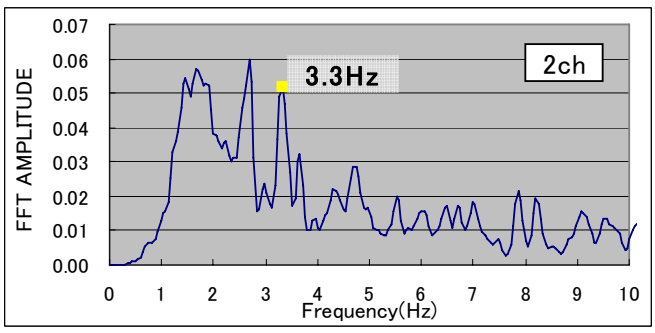

Fig.15 Fourier Spectrum of the earthquake record at the top of Candi Angsa shown in Fig.14

4.2 Monitoring of crack, temperature and humidity

As there found the serious cracks at the walls and the entrances of Candi Siva, the highest monument of the Prambanan Temples, its structural stability should be investigated, the displacement of cracks has been monitored together with temperature and humidity at Candi Siva since October 2008, shown in Fig.16. As structural monitoring has become of importance in the research area of structural engineering for conservation, the records would be expected to provide significant data to conduct the structural conservation.

Fig. 17 describes the monitoring data to understand the variation of the crack displacement with temperature and humidity. It can be noticed that the crack displacement varies in correlation with temperature. At the same time, no progressive variation of the crack displacement can be found.

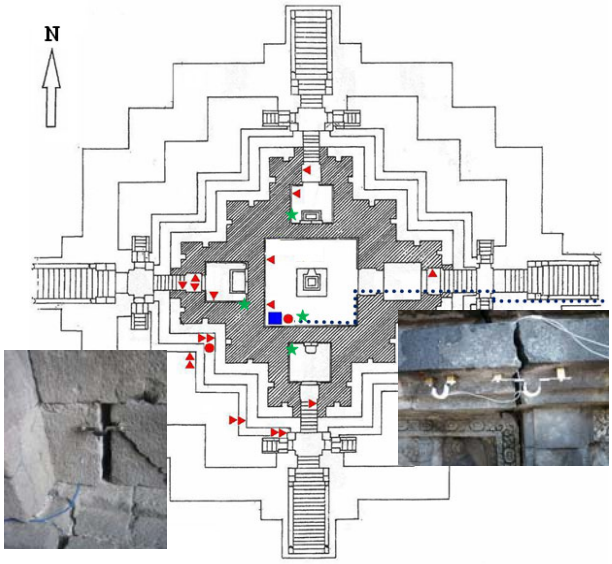

■ Data logger (1) ▲ Crack-gage (18) ● Thermocouple (2)
★ Temperature and Humidity transmitter (4)

Fig.16 Crack monitoring with temperature and humidity

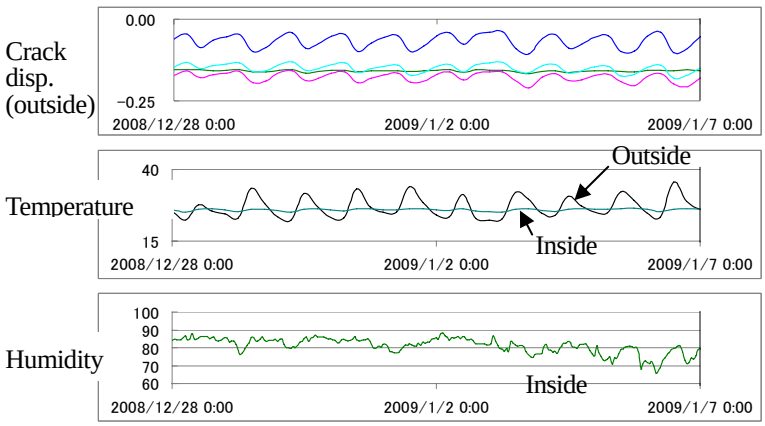

Fig.17 Relationship among crack displacement, temperature and humidity

As well as, no progressive phenomena have been observed for a year since Nov. 2008 even when some earthquakes occurred during the observation period. These records indicate that the structure is stable at the present time.

5. CONCLUDING REMARKS

Safety assessment of the stone heritage structures affected by earthquakes has been studied for structural restoration.

1. The structural analysis indicate that the inner concrete structures were not seriously damaged by the earthquake for the cases of Candi Garuda and Angsa
2. The analysis also indicate that the apparent differential settlement of the foundation was not caused by the earthquake.
3. Whipping phenomena of the structural response caused the serious damage to the decorative stones of stupa and ratona. The simulation provided the seismic loads for designing strengthening of the decorative stones.
4. The predominant period of the surface soil response corresponded to the natural frequency of the structures. Such resonant behaviors might cause the serious damage to the Prambanan Temples.
5. No progressive phenomena can be seen in the crack monitoring records at Candi Sive, the highest and oldest monument. This indicates that it is structurally stable at the present time. Such structural monitoring of crack displacement with temperature & humidity can be used for assessment of structural stability for both and short term.

It is expected that Japan-Indonesia international collaborative study will contribute to the restoration of Prambanan World Heritage Temples.

ACKNOWLEDGEMENT

The present project had been conducted during 2006 and 2007 by the expert team organized in Japan Consortium for International Cooperation in Cultural Heritage being set up at National Research Institute for Cultural Properties, Tokyo. Since 2008, their activities have been financially supported by Grant-Aid-for Scientific Research, provided by Japanese Government. The project have been successfully performed in collaboration with Ministry of Culture and Tourism, Indonesia

[References]

1]Architectural Institute of Japan, 2006 Central Java Earthquake Damage Report, pp8, 2007

2]Japan Center for International Cooperation in Conservation, Survey Report and Restoration Plan on Prambanan World Heritage Temples, 2008.

JOINT CONFERENCE PROCEEDINGS
7th International Conference on Urban Earthquake Engineering (7CUEE) &
5th International Conference on Earthquake Engineering (5ICEE)
March 3-5, 2010, Tokyo Institute of Technology, Tokyo, Japan

EXPERIMENTAL STUDY ON SHEAR BEHAVIOR OF THICK STRUCTURAL PLYWOOD SHEETED FLOOR FRAMING WITH OPENING

Hiroyasu Sakata[1)], Shota Nakano[2)], Hiromichi Ito[3)], Azuma Fujishiro[3)], and Hitoshi Ooguchi[3)]

1) Associate Professor, Structural Engineering Research Center, Tokyo Institute of Technology, Japan
2) Sumitomo Mitsui Construction Co. Ltd, Japan
3) Technological Development Division, NCN Co., Ltd, Japan
hsakata@serc.titech.ac.jp, snakano@smcon.co.jp, ito@ncn-se.co.jp, fujishiro@ncn-se.co.jp, ohguchi@ncn-se.co.jp

Abstract: It is important to retain shear stiffness and strength of floor framing in order to make horizontal bearing members operate more efficiently, such as bearing walls in structures. However, openings in the floor framing reduce the shear stiffness and strength of the floor, and the level of reducing depends on an opening scale, reinforcing members for openings and all that. It is necessary to make consideration of an opening influence in the thick structural plywood sheeted floor framing for working out safety wooden structures. In this study shear experiments of 28 mm structural plywood sheeted floor framings were carried out for non-opening specimen and opening specimen, and grasps the shear property of them. Experiments of 11 specimens were carried out under gradual increase cyclic loading, drift angle is equal to 1/600, 1/450, 1/300, 1/200, 1/150, 1/100, 1/75, 1/50, 1/15rad.. Parameters of specimens are beams arrangement, nail pitch, with/without reinforcing members for openings, position and size of openings, and differentiate of framing wood species. Furthermore, we suggest effectiveness coefficients for shear stiffness and strength of the floor framing with openings individually, and show the validity of the evaluation of them by use of the proposed effectiveness coefficients.
Obtained findings from experiments are summarized as follows:.
1) We grasped the influence for the shear property of beams arrangement, nail pitch, with/without reinforcing members, position and size of openings, and differentiate of wood species.
2) Shear strength and stiffness of the floor framing without opening can be obtained by summing the shear strength and stiffness of constitutive plywood elements.
3) Shear strength and stiffness of the floor framing with opening can be obtained by multiplying the effectiveness coefficients by ones of the floor framing without opening.

1. INTRODUCTION

It is important to verify the tensile stiffness and strength of floor framing members to ensure the practicality of horizontal bearing members such as bearing walls in wooden houses. However, openings in floors change the in-plane stiffness and strength of these members, and the extent of the change depends on opening size, presence of reinforcing members, etc. It is necessary to rationalize construction and take into account the effects of openings in floor framing directly sheeted with thick structural plywood that can ensure high tensile stiffness and strength.

This paper describes experiments conducted to determine the shear behavior of this kind of floor framing. The study focused on floor framing with/without openings sheeted with 28mm-thick structural plywood (hereinafter called plywood). Effectiveness coefficients are proposed for shear stiffness and strength, taking into account opening effects. The study also aimed at demonstrating the adequacy of a method for evaluating the strength of floor framing with openings.

2. IN-PLANE SHEAR TEST ON FLOOR FRAMING WITH OPENINGS

2.1 Test outline

Specimen FL1 is shown as an example in Figure 1, and the experimental set up, is shown in Figure 2. The specimen outline and material properties are shown in Table 1 and Table 2, respectively, The specimen's dimensions were 3P x 3P (P = 910mm). The main beam and sub beam forming the framing members had cross-sections 120mm wide x 150mm high. The reinforcing members employed in FL4 and FL10 were 105mm square. Glued laminated timber used for the main beam, sub beam and reinforcing members was Oshu-akamatsu (European red pine). Main beam – Sub beam and Sub beam – Sub beam were jointed with hardware as shown in Photo 1. The reinforcing members were attached to the main beam and sub beam using hardware as shown in Photo 2. They were used as cradles for nailing. Plywood of 28mm-thick Japanese larch and 30mm-thick Japanese cedar were employed. CN75 nails were used. Rabbet joints were employed to joint the plywood at the edge where nails did not work. The

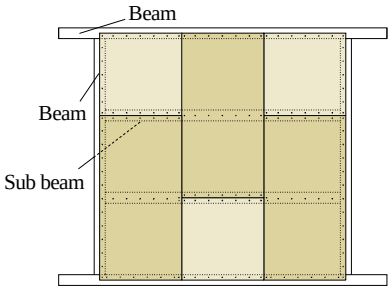

Figure 1 Experimental Specimen (FL1 LSP28-@150-BB.0-Un-Op)

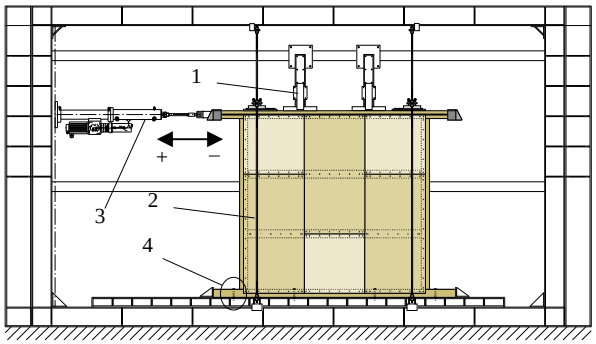

1 : Out-of-plane buckling hamper, 2 : Tie-rod, 3 : Oil jack, 4 : Anchor-bolt

Figure 2 Loading Apparatus



Photo 1 Beam-Sub beam, Sub beam-Sub beam Joint Metal



Photo 2 Beam/Sub beam-Reinforcing Member Joint Metal

Table 1 Specimen

No	Name	Size	Plywood species (thickness)	Number (Nail)	Pitch of a nail	Sub-beam layout	Opening space	Opening position	Rainforceing Metal
FL1	LSP28-@150-BB.0-Un.Op	2730 × 2730	Japanes Larch (28)	CN 75	150	Parallel	—	—	without
FL2	LSP28-@150-BB.90-Un.Op					Orthogonal			
FL3	LSP28-@75-BB.0-Un.Op				75	Parallel			
FL4	LSP28-@150-BB.0-Un.Op-RM				150				with
FL5	LSP28-@75-BB.0-1Px1PCo.Op				75		910×910	Corner	without
FL6	LSP28-@75-BB.0-1Px1PCe.Op							Center	
FL7	LSP28-@75-BB.0-1Px2PCo.Op						910×1820	Corner	
FL8	LSP28-@75-BB.0-2Px1PCo.Op						1820×910		
FL9	LSP28-@75-BB.0-2Px2PCo.Op						1820×1820		
FL10	LSP28-@75-BB.0-2Px2PCo.Op-RM								with
FL11	CSP30-@150-BB.90-Un.Op		Japanese Cedar(30)		150	Orthogonal	—	—	without

LSP28 : Japanese Larch Plywood 28mm thick, CSP30 : Japanese Cedar Plywood 30mm thick, @_ : Pitch of a nail, BB.0 : Align sub beam parallel to loading direction, BB.90 : Align sub beam orthogonal to loading direction, ●P x ▲P : Opening size (1P = 910 mm), Un. Op : Without opening, Co.Op : Corner opening, Ce.Op : Center opening, RM : Reinforcing member

Table 2 Material Properties

Pinus sylvestris (E105F300)				
Laminate thickness	Bending young Coef.		Bending stress	
mm	kN/mm^2		N/mm^2	
	$E_{wx\text{-}x}$	$E_{wy\text{-}y}$	x-x	y-y
31.0	11.0	9.7	51.7	44.4

Water Content	Specific gravity
%	
14.7	0.53

experimental parameters were loading direction, nail pitch, presence or absence of reinforcing members, location and size of openings and kind of plywood material.

The loading method was determined to be the tie-rod method in compliance with "Design of allowable stress for houses with wooden framework construction"[1)] issued by the Japan Housing and Wood Technology Center. Loading was controlled by the true shear deformation angle of the specimen framing (hereinafter called drift angle). After cyclic loadings of 1/600, 1/450, 1/300, 1/200, 1/150, 1/100, 1/75 and 1/50 were executed, the loading finished at about 1/15 rad.

2.2 Test results

The relationship between shear force and drift angle, and conditions of ultimate failure common for all specimens are shown in Figure 3 and Photo 3, respectively. Plywood unsticking took place due to nail detachment in all the specimens. Plywood damage caused by plywood collision was observed in FL6 through FL10 of the floor framing with openings. Breaking failure took place in members after γ = 1/25 rad. at the main-beam/sub-beam jointing in FL9 and FL10 of opening size 2P x 2P. Because FL9 suffered only slight damage by breaking failure of the members, it did not show rapid load decrease. However, FL10 showed rapid load decrease. In FL11, which used Japanese cedar plywood, there were more detached nails with heads buried in the plywood than for the specimens using Japanese larch. The following compares the effects of changing parameters.

[Loading direction] It was found from FL1 and FL2 that there were almost no effects.

[Nail pitch] It was found from FL1 and FL3 that both shear stiffness and strength greatly increased with decreasing nail pitch.

[Presence of reinforcing members] It was found from FL1 and FL4 that shear stiffness and strength increased with the introduction of reinforcing members and application of surrounding nailing for all the plywood. Thus, the effectiveness of the reinforcing members was confirmed.

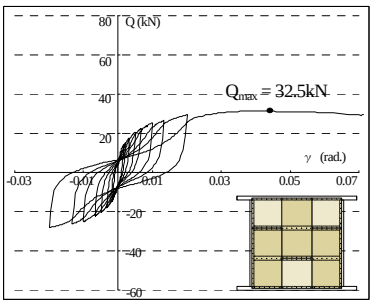

FL1 (LSP28-@150-BB.0-Un.Op)

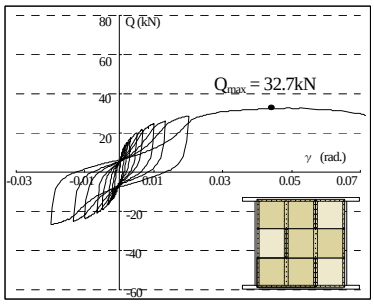

FL2 (LSP28-@150-BB.90-Un.Op)

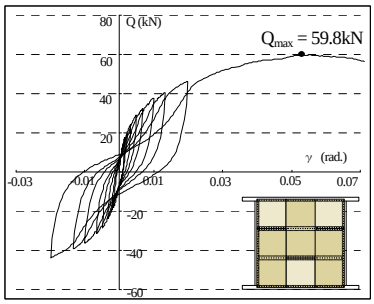

FL3 (LSP28-@75-BB.0-Un.Op)

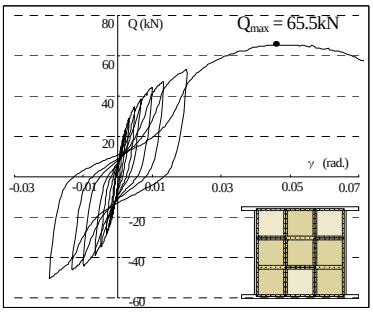

FL4 (LSP28-@150-BB.0-Un.Op-RM)

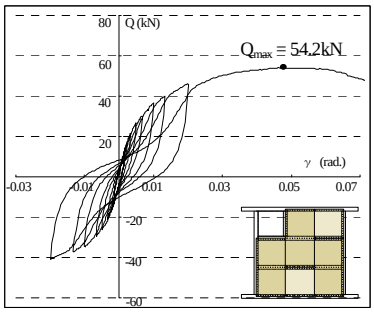

FL5 (LSP28-@75-BB.0-1Px1PCo.Op)

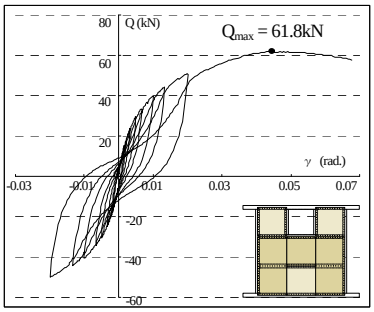

FL6 (LSP28-@75-BB.0-1Px1PCe.Op)

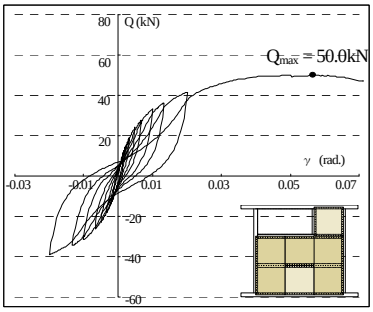

FL7 (LSP28-@75-BB.0-1Px2PCo.Op)

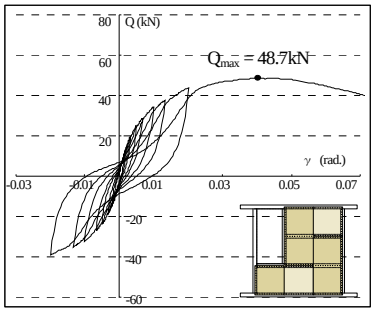

FL8 (LSP28-@75-BB.0-2Px1PCo.Op)

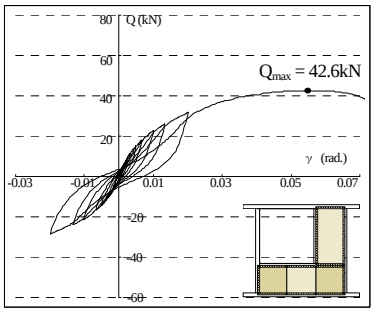

FL9 (LSP28-@75-BB.0-2Px2PCo.Op)

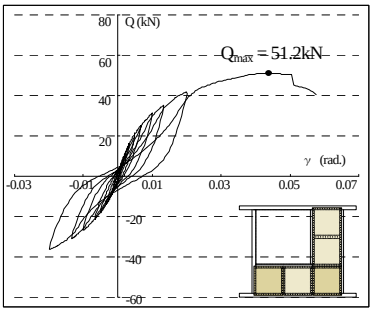

FL10 (LSP28-@75-BB.0-2Px2PCo.Op-RM)

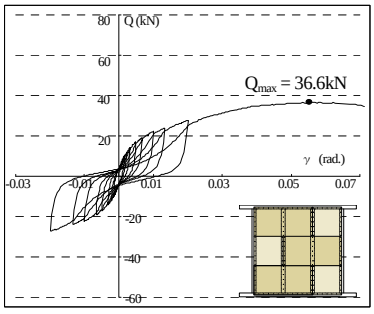

FL11 (CSP30-@150-BB.90-Un.Op)

Figure 3 Shear force Q(kN) – Drift angle γ(rad.) relationship



Photo 3 Ultimate failure mode(FL3)

[Opening location] It was evaluated from FL3, FL5 and FL6 that if the opening was up to 1P x 1P, its effects on strength were small, although a small decrease in strength was observed in FL5.

[Opening size] Comparison of FL3, FL5, and FL7 through FL10 confirmed that shear stiffness and strength decreased with increasing opening size.

[Plywood material] The following were observed from FL1, which used 28mm Japanese larch plywood, and FL11, which used 30mm Japanese cedar plywood. The strength of FL11 slightly increased, although its shear stiffness was lower. It was evaluated that the strength increased because

the nail was buried into the plywood. The burying of nails delayed the unsticking of the plywood due to nail detachment. Many of the nails driven into the specimen were considered to have demonstrated their shear capabilities.

3. SHEAR TEST ON NAILS USING PLYWOOD WITH FRAMING

3.1 Test outline

Specimen outline and specimen set-up are shown in Table 3 and Figure 4, respectively. 8 specimens were prepared with various nail arrangements, plywood material and specimen height. The framing materials, plywood and nails employed for the specimens were made the same as those employed for the floor framing tests. Short tenon and holddown hardware were used for the beam-to-beam jointing. A nail pitch of 150mm was used for all.

Loading was carried out by a method of column-base fixing. The beam was fixed at the mid-point using pins. The lower framing member was fixed to beam supported with rollers. The tests were controlled by the true drift angle of the framing member of the specimen. The cyclic loading was repeated in 3 cycles of 1/600, 1/450, 1/300, 1/200. 1/150, 1/100, 1/75 and 1/50. The tests on specimens of 1P x 1P and 1P x 2P finished with 1/15 and 1/20, respectively. To investigate the resistance force of the framing without panels, loading applied only to the framing was also carried out for each specimen.

3.2 Test results

It was confirmed that the members were unsticked due to nail detachment after the maximum shear force was reached in all specimens. The cause of decreasing shear force after maximum shear force was reached was the detached nails, as shown in the envelope of positive loading on shear force – drift angle, where the resistance force of the framing member was deducted (Figure 5). The shear force was larger for the Japanese cedar plywood than for the Japanese larch plywood for the specimens with the = shaped arrangement, as found in the floor framing tests.

Table 3 Specimens

No.	Name	Size	Plywood		Pitch of a nail (mm) (CN75)
		width x height	Wood species	Thickness (mm)	
U1	LSP28-@150-1P- =	910 x 910	Japanes Larch	28	150
U2	LSP28-@150-1P-U				
U3	LSP28-@150-1P-□				
U4	CSP30-@150-1P- =		Japanes Cedar	30	
U5	LSP28-@150-2P-□	910 x 1820	Japanes Larch	28	
U6	LSP28-@150-2P-3				
U7	LSP28-@150-2P-≡				
U8	LSP28-@150-2P-U& ―				

=, U, □, 3 ≡, ― show the figure of nailing

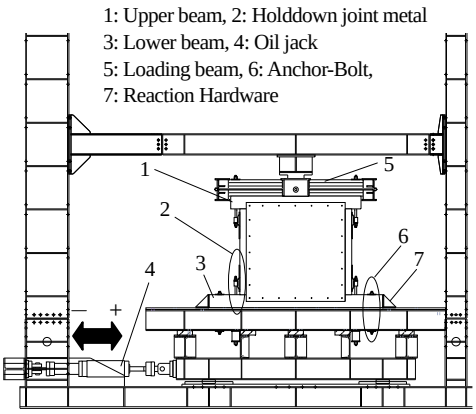

Figure 4 Loading Apparatus

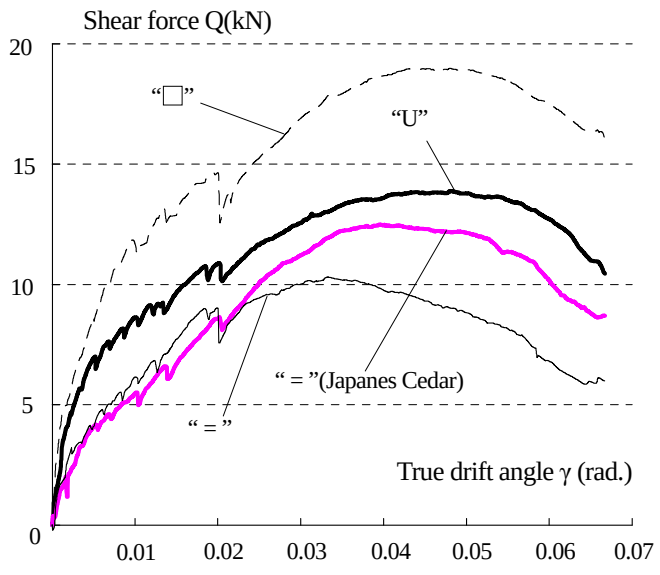

(a) 1P×1P Specimen (U1 - U4)

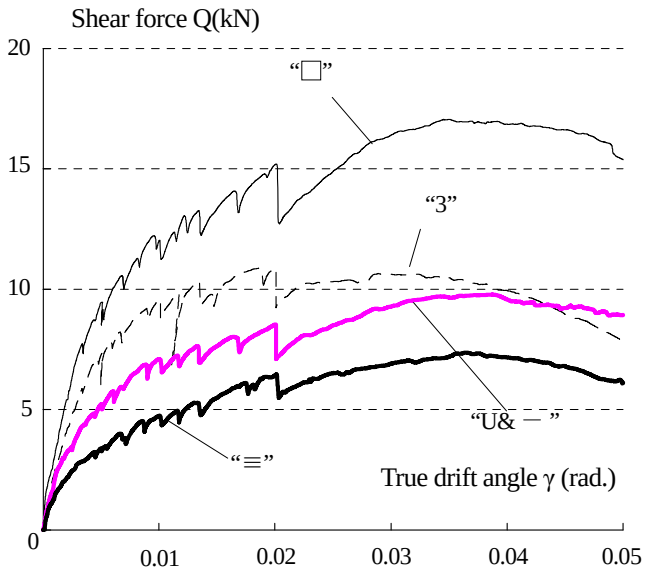

(b) 1P×2P Specimen (U5 - U8)

Figure 5 Envelope of shear force Q(kN)―True drift angle γ

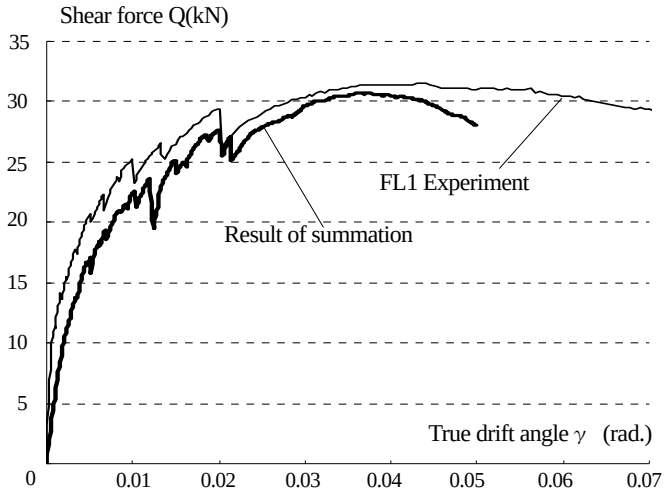

Figure 6 Comparison FL1 with summation of U1, U2, U6 and U7

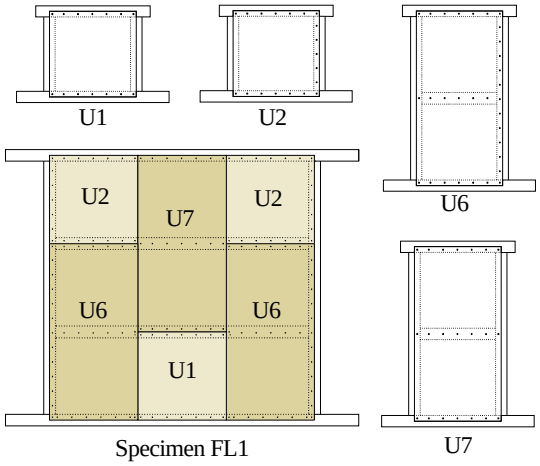

Figure 7 Specimens using summation

3.3 Comparison of Q – γ envelopes for floor framing with openings FL1

The test results for U1, U2, U6 and U7 with graphs comparing the envelopes of shear – drift angle for Specimen FL1 for the tests on the floor framing with openings are shown in Figure 6. The configurations of the specimens used for the above estimation are shown in Figure 7. As a result, it is considered that the effects of friction due to plywood collision, plywood rabbet joint, etc. were small with this construction method. Then, the shear stiffness and strength of a single piece of plywood that formed the floor framing were evaluated. The floor framing without openings was evaluated by summing those values.

4. EVALUATION OF SHEAR STIFFNESS AND STRENGTH OF FLOOR FRAMING WITH OPENING

4.1 Effectiveness coefficient

The Sugiyama method [2] was utilized to evaluate the shear stiffness and strength of the bearing walls with openings in the framing wall construction methods. This method provided the results shown in Figure 8, which led to underestimation of the experimental results described in Section 2.2. Thus, by referring to the method for designing the floor framing in the wooden framework construction method and the concept of the Sugiyama method, coefficients to reduce the shear stiffness and strength of the floor framing without openings (hereinafter called

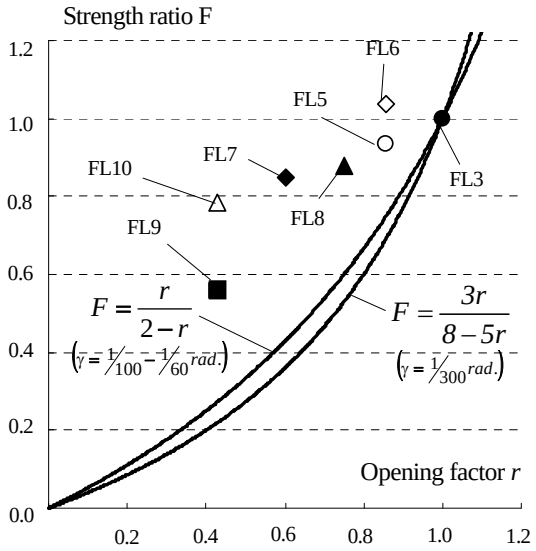

$$F = \frac{3r}{8-5r} \quad (\gamma = 1/300\ rad.)$$

$$F = \frac{r}{2-r} \quad (\gamma = 1/100 - 1/60\ rad.)$$

$$r = \frac{1}{1+\alpha/\beta}, \quad \alpha = \frac{\Sigma A_i}{H \cdot L}, \quad \beta = \frac{\Sigma L_i}{L}$$

F: Strength ratio (=Floor strength with opening / Floor strength without opening, "Strength" is shear force Q when drift angle is 1/300.)

α : Opening area ratio, Ai : Opening area (mm^2), H : Floor height (mm), L : Floor width (mm), β : Wall length ratio, Li : Floor width un-opening side(mm)

Figure 8 Comparison of experimental value (γ=1/150rad.) with Sugiyama equation's evaluation

$$C_k = \frac{K_{op}}{K_{noop}} = \frac{\sum_i^n I_{xy,i}}{\sum_j^m I_{xy,j}} \left\{ 1 - \frac{A_{op}}{A_f} \left(1 - \frac{\sum_k^u l_k}{L} \right) \right\} \quad \cdots (1)$$

$$C_q = \frac{Q_{op}}{Q_{noop}} = \frac{\sum_i^n Z_{xy,i}}{\sum_j^m Z_{xy,j}} \left\{ 1 - \frac{A_{op}}{A_f} \left(1 - \frac{\sum_k^u l_k}{L} \right) \right\} \quad \cdots (2)$$

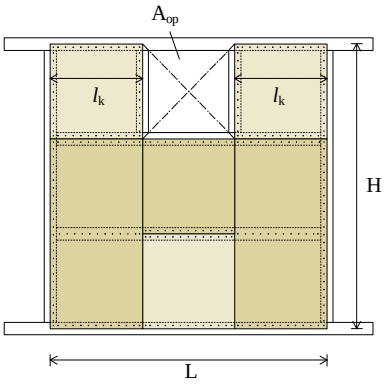

C_k: Effectiveness coefficient of stiffness, K_{op}: Shearing stiffness of floor with opening, K_{noop}: Shearing stiffness of floor without opening, A_{op}: Opening area, A_{noop}: Floor area (H×L), l_k : Floor width of no opening parts of the opening side, u: The number of no opening parts of the opening side, L: Width of Floor, C_q: Effectiveness coefficient of strength, Q_{op}: Strength of floor with opening, Q_{noop}: Strength of floor without opening, $Z_{xy,I}$, $Z_{xy,j}$: Nail arrangement coefficient of each constitution plywood[3)], m: The number of plywood constituting a floor without opening, n: The number of plywood constituting a floor with opening, $I_{xy,i}$, $I_{xy,j}$: Second-moment with nail arrangement of each constitution plywood[3)]

Figure 9 Eq.1 & Eq.2 with symbols

effectiveness coefficients) are proposed. Then, the stiffness and strength of the floor framing with openings were evaluated. The effectiveness coefficients for the shear stiffness and strength are shown in equations (1) and (2), respectively (Figure 9). C_k in equation (1) and C_q in equation (2) denote stiffness effectiveness coefficient and strength effectiveness coefficient, respectively.

The stiffness coefficient is expressed by the product of two terms: the ratio of the sum of the second moments of the nail arrangement in the plywood forming the floor framing with/without openings, and a term expressing the opening ratio and the depth ratio. The latter takes into account the tendency of the shear stiffness of the floor framing with/without openings estimated from the various parameters with the secant stiffness at the drift angle γ = 1/150rad.

The strength effectiveness coefficient is expressed by the product of two terms: the ratio of the sum of the coefficients of the nail arrangement in the plywood forming the floor framing with/without openings, and a term expressing the opening ratio and the depth ratio used for the stiffness effectiveness coefficient.

4.2 Evaluation of shear stiffness and strength of floor framing with opening

The figures evaluated from the experimental results obtained in Section 2.2 and from the effectiveness coefficients are shown in Table 4. The relationship between the stiffness ratio and the stiffness effectiveness coefficient is shown in Figure 10. The relationship between the strength ratio and the strength effectiveness coefficients is shown in Figure 11. The stiffness ratio and strength ratio are the ratio of stiffness and strength of the specimens with/without openings to FL3. It was found that decrease in shear stiffness and strength due to the incorporated openings could be accurately evaluated in the currently employed specimens.

Table 4 Result of experiment and analysis

No.	Name	Strength			Stiffness		
		analysis	experiment	ratio	analysis	experiment	ratio
		Q_{cmax}	Q_{emax}	Q_{emax}/Q_{cmax}	K_{c150}	K_{e150}	K_{e150}/K_{c150}
FL1	LSP28-@150-BB.0-Un.Op	33.8	31.5	0.93	2655	3319	1.25
FL2	LSP28-@150-BB.90-Un.Op	33.8	32.7	0.97	2655	3145	1.18
FL3	LSP28-@75-BB.0-Un.Op	59.8	59.8	1.00	4834	4834	1.00
FL4	LSP28-@150-BB.0-Un.Op-RM	68.7	65.5	0.95	4661	5765	1.24
FL5	LSP28-@75-BB.0-1Px1PCo.Op	51.9	54.2	1.04	4413	4513	1.02
FL6	LSP28-@75-BB.0-1Px1PCe.Op	66.8	61.8	0.93	4829	5021	1.04
FL7	LSP28-@75-BB.0-1Px2PCo.Op	46.5	50.0	1.07	3557	4104	1.15
FL8	LSP28-@75-BB.0-2Px1PCo.Op	46.2	48.7	1.05	3805	4249	1.12
FL9	LSP28-@75-BB.0-2Px2PCo.Op	37.2	42.6	1.15	2634	2701	1.03
FL10	LSP28-@75-BB.0-2Px2PCo.Op-RM	53.1	51.2	0.96	3380	3805	1.13

K_{150}:Secant stiffness when Drift angle γ =1/150rad., Q_{max}: Maximum

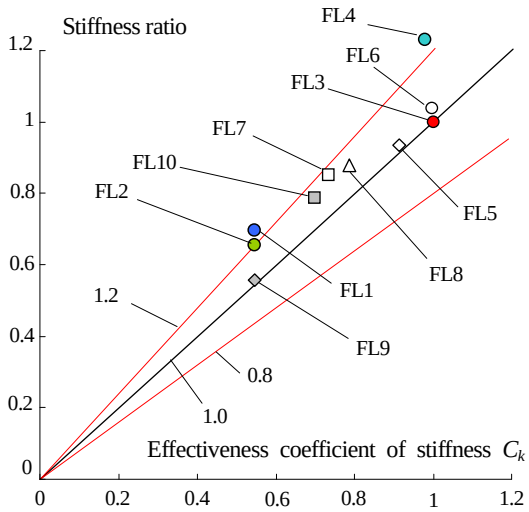

Figure 10 Stiffness ratio - Effectiveness coefficient of stiffness (γ=1/150rad.)

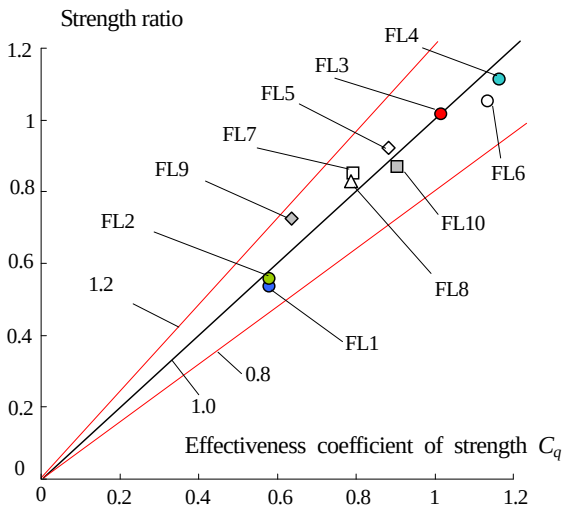

Figure 11 Strength - Effectiveness coefficient of strength

5. CONCLUSIONS

1) Effects of shear properties on floor framing with changing parameters, i.e. arrangement of small beam, nail pitch, presence of reinforcing members, opening location/size, and plywood material were determined from in-plane shear tests on floor framing with openings sheeted with the 28mm-thick structural plywood.
2) It was found that shear stiffness and strength of the floor framing without openings could be evaluated by summing the resistance forces for each kind of plywood.
3) Shear stiffness and strength of floor framing with openings could be generally evaluated by multiplying the proposed effectiveness coefficients by the shear stiffness and strength obtained from in-plane shear tests on floor framing without openings.

References:

1) The Japan Housing and Wood Technology Center: “Design of allowable stress for houses with wooden framework construction”, 2008.12

2) Hideo SUGIYAMA, Tadashi MATSUMOTO: “Empirical Equations for the Estimation of Racking Strength of a Plywood - Sheathed Shear Wall with Openings”, Summaries of Annual Meeting of Architectural Institute of Japan, CII, pp.89 - 90, 1994.9

3) Masahide MURAKAMI and Masahiro INAYAMA: “Formulae to Predict the Elastic and Plastic Behavior of Sheathed Walls with any Nailing Arrangement Pattern”, Journal of Structural and Construction Engineering (Transaction of AIJ), No.519, pp.87 – 93, 1995.5

JOINT CONFERENCE PROCEEDINGS
7th International Conference on Urban Earthquake Engineering (7CUEE) &
5th International Conference on Earthquake Engineering (5ICEE)
March 3-5, 2010, Tokyo Institute of Technology, Tokyo, Japan

RECENT LARGE-SCALE WOOD CONSTRUCTION IN JAPAN
-DEVELOPMENT AND CONSIDERATION OF MID-RISE TIMBER BASED STRUCTURE-

Hiroshi Isoda[1)], Naohito Kawai[2)] and Mikio Koshihara[3)]

1) Associate Professor, Dept. of Architectural and Civil Engineering, Shinshu University, Nagano, JAPAN
2) Chief Research Engineer Building Research Institute, Tsukuba, JAPAN
3) Associate Professor, Institute of Industrial Science, the University of Tokyo, Tokyo, JAPAN
hisoda@shinshu-u.ac.jp, kawai@kenken.go.jp, kos@iis.u-tokyo.ac.jp

Abstract: The Building Standard Law of Japan was revised from specific provision to performance based requirement in June 1998. After the revision, the potential to accept large-scale and high-rise timber buildings was added with provisions of performance-based code. Before the revision, we could not construct the timber based structure which has more than four stories, but after the revision the structure have been able to be built under the law. Main consideration of the mid-rise timber based building in Japan is a fireproof performance in addition to a seismic performance. In this paper, the requirement of fireproof performance in Japanese building standard law is briefly summarized and some members which have a fire resistance performance also are shown. Reinforced concrete structure or steel structure were installed on the base in mid rise timber based structure normally. And the results of numerical analysis on seismic distribution at the each story of the building with reinforced concrete first story are described.
.

1. INTRODUCTION AND CURRENT STATE

The effective utilization of timber is urged from the point of preservation of natural resources and global environment also in Japan. And the effective composite of timber and other materials is expected to extend the possibility of building structures because of the possibility to realize high performance in both structural safety and fire safety. The Building Standard Law (BSL) of Japan was revised in June 1998 and the potential to accept large-scale and high-rise timber buildings was added with provisions of performance-based code. Before the revision, only large scale buildings such as dome and gymnastic hall have been able to be constructed under special approval of ministry. Structurally effective composite systems also have been used in dome and gymnastic hall constructions. After the revision, the composite system began to be used for the purpose of both fireproof measurement and high structural performance.

According to the current BSL of Japan, the main structural members such as columns, beams, floors and walls for buildings with more than four stories are required 1 hour performance in fireproof. Table 1 briefly shows the requirements of fireproof performance for members in accordance with the stories of the building. According to the BSL, five stories building is required 2 hour fire proof performance at the first story and 1 hour performance at from the second to the fifth story. For considering the fireproof performance of timber base members, some fire tests were executed. Based on the testing method under the BSL to confirm the 1 hour fire proof performance of members with combustible materials, members are exposed to the fire for 1 hour and left in the furnace for 3 hours and confirmed that they can support the load even after the test, it means, they can support the load during the test and there is no fear to lose the ability by re-ignition, progress of char, or a rise of temperature after the test. In case of members with 2 hour performance in fireproof, 1 hour is replaced by 2 hours and 3 hours is replaced by 6 hours in the above explanation.

As the results of some tests, floors and walls with covering of gypsum boards or other non-combustible materials with some construction methods were revealed as 1 hour or 2 hour fireproof performance member. The examples are shown in photo1 which has 2 hour fireproof performance in woodframe construction which is so called as “2x4 construction” in Japan and a major construction method in the US. Some walls and floors with 1 hour fireproof performance have been developed and the details between them have been examined and tested. Now a manual for woodframe construction with fireproof performance is published and the buildings can built only with test result certifications. Table 2 shows the number of buildings with fire proof performance

surveyed by the Japan 2x4 home builder association. More than 1000 buildings have completed since the revision.

For columns and beams construction, two member types are found to be solutions of fireproof members with using timber based material. One is the type of members with covering of gypsum boards or other non-combustible material, but this type dose not fascinate designers and owners because the same texture and space are achieved using steel members which are cheaper than timber and easy to use. Another is the type of members with shape steel inserted. This type members have, if made with some special construction specifications, the self-extinguish property. They are burnt when exposed to the fire but the progress of char stops while left in the furnace after the exposure to the fire. Figure 1 shows examples of members whose 1 hour fireproof performance was confirmed in the tests.

For the multi-story timber building, the first and/or second story are used for shops, parking lot normally. Main construction material of their stories is a reinforced concrete and a steel frame. They are also effective to anchor the uplifting load and to support inside steel member of composite column.

In this paper, the timber based multi stories building with reinforced concrete at the bottom are focused on. First, five story post and beam timber based composite system which is unique all over the world will be introduced. And then seismic distribution which is the major consideration in seismic design of the composite structure consisting of reinforce concrete or steel structure base and timber top will be discussed.

Table 2 Number of Woodframe Construction with fire-proof performance (update September 2009)

Number of floors	Number of cases
1	10
2	184
3	859
4	32
5	1

*Fire proof performance is required with all stories building in fire protection area

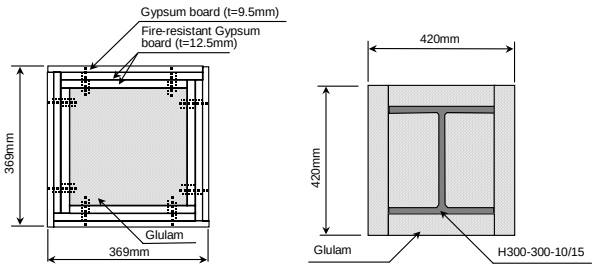

Figure 1 Examples of members whose fireproof performance was confirmed

Table 1 Requirement of property to withstand the heat under BSL

Parts of buildings		Stories of buildings		
		Uppermost story, and second to fourth stories from the uppermost story	Fifth to fourteenth stories from the uppermost story	Fifteenth story or more from the uppermost story
Shear Walls	Partition walls	1 hour	2 hours	2 hours
	External walls	1 hour	2 hours	2 hours
Columns		1 hour	2 hours	3 hours
Floors		1 hour	2 hours	2 hours
Beams		1 hour	2 hours	3 hours
Roofs		30 minutes	30 minutes	30 minutes
Stairs		30 minutes	30 minutes	30 minutes



Before test | After test | No damage of studs (After test)

Covering : 25mm thickness of calcium silicate board+ 35mm thickness of ALC board

Photo 1 Fire tests

2. Five story post and beam timber based composite building

The five-story Kanazawa M Bldg shown in photo 2 (height: 14.237 m, area: 6.195m x 12.100 m) was constructed in Kanazawa City, Ishikawa Prefecture. The first story has a reinforced concrete structure and the second to fifth stories have a timber based composite structure with built-in steel materials as shown in Figure 2. The floor plan and elevation are shown in Figure 3. The building mainly uses the structural members to satisfy the requirements for vertical load performance and seismic performance. So this building is also required fire resistive construction, and structural elements are required 1 hour fire resistive period.

Similar to ordinary timber buildings, a five stories timber based composite structure requires verification of its safety against self weight, live load, vertical load by snow coverage, and horizontal load under a horizontal force, such as an earthquake or wind. Fire resistive buildings are also required to maintain building integrity in the event of a fire. Based on these structural performance requirements, the following structural verification was conducted (Koshihara, Isoda and et.al 2005, Yusa and et al. 2005).

2.1 Vertical Load

The timber and steel frame function together as a structural member in the second to fifth stories of a timber based composite structure. To clarify the function of the timber and the steel frame about each member, the joint was designed as follows:

(1) Beam

Since the vertical deformation is equal between the timber and the steel beam, vertical load should be shared depending on their ratio of flexural rigidity, EI. The flexural rigidity ratio EI / ΣEI is shown in Table 2. The timber and steel frame of the beam are joined at a beam edge using drift pins to transmit the load from the timber to the steel frame, so the steel frame supports all the shear force at the edge. The gusset plate from the steel bar of the column and the steel plate of the beam are joined with high tension bolts. The holes in the side of the timber beam are filled with timber after high tension bolts are clamped. Snow load stress on both the timber and steel frame of the beam are designed not to exceed the short-term allowable limit, even in the very rare case of a snow load with a vertical depth of 1.2 m.

(2) Column

Vertical load is transmitted to the steel bar of a column through a gusset plate, and vertical loading of the timber is avoided through a 2.5 mm clearance, which is essential for combining the timber with the steel frame. The timber of the column functions as a buckling restraint for the steel bar, and the only steel bar of the column buckles at about 20% of the yield stress. According to the bucking tests, the timber based composite column did not buckle when the steel frame yielded to axial force compression because the timber functioned as a buckling restraint.

2.2 Horizontal Load

The structural planning of the building is different from each direction. A timber based composite beam is suspended laterally and supported by columns of identical material, and the longitudinal beam is built in a reinforced concrete slab. Seismic force at the damage limit produces greater horizontal force than the load exerted by very rare wind, as prescribed in the BSL, so horizontal resisting elements are braces the lateral roof face and the longitudinal plywood walls.

(1) Beam

A lateral timber based composite resists axial force and produces a reaction force of braces during an earthquake. The steel frame resists axial force, the timber frame functions as a buckling restraint, and calculations confirmed the absence of buckling within the safety limits of applied axial force.

(2) Column

During an earthquake, a timber based composite column produces a reaction force by braces. This column does not buckle when the steel frame yielded to axial force compression as mentioned above. During a longitudinal earthquake, vertical shear force is transmitted from the plywood shear wall to the timber of the column through the vertical frame. The timber has a bearing plate of the steel frame (PL-19) at both ends of the timber of the column, and when the timber collides against the bearing plates, axial force is transmitted to the steel frame of the column. Therefore, during an earthquake, the timber functions as a buckling restraint.

(3) Brace

A brace bears axial force during a lateral earthquake. Only one steel frame (PL-22x65), at the center, contributes to the structure as the steel frames. Buckling of the brace was not observed under significant plastic deformation of the steel frame by compression axial force.

(4) Plywood shear wall

Plywood shear walls resist horizontal force during a longitudinal earthquake, and consists of structural plywood (thickness: 24 mm), screws (diameter: 8 mm) and both vertical and horizontal frames of laminated timber arranged around the plywood. Shear force is transmitted from the structural plywood to both the horizontal frame and the downstairs plywood shear wall through anchor bolts (M16) embedded in the reinforced concrete slab.

2.3 After Fire

(1) Beam

Only the steel frame supports vertical load on the assumption that the timber had burnt completely. Although timber actually stops burning, the remaining timber cannot be used as a structural member under current BSL. The vertical load is assumed to be the same as before a fire, and for safety reasons, the steel frame stress should not exceed the long-term allowable limit.

(2) Column

The column also supports vertical load only using the steel frame and the stress applied should not exceed the long-term allowable limit for buckling.

(3) Brace

The timber of a brace is also assumed to have completely burned. The wind pressure, at the maximum momentary wind velocity of 15 m/s, is set as the constant wind load, and both brace tension and beam bending resist the lateral horizontal force. In this case, the steel frame stress is prevented from exceeding the short-term allowable limit.

(4) Plywood shear wall

Plywood shear walls are assumed to have completely burned out.

(5) Longitudinal RC beam

An reinforced concrete slab has a built-in reinforced concrete beam in the longitudinal direction of the edge. The rigid frame structure composed by the RC beam and the steel par of the column resists the longitudinal horizontal force produced by the constant wind.



Photo 2 M-Bldg.

Table 2 Flexural rigidity ratio of timber and steel frame

	E(N/mm)	I(mm^4)	EI(Nmm^2)	$EI/\sum EI$
Timber frame	$1.05x10^4$	$5.55x10^8$	$0.583x10^{13}$	0.366
Steel frame	$2.05x10^5$	$4.95x10^7$	$1.01x10^{13}$	0.634

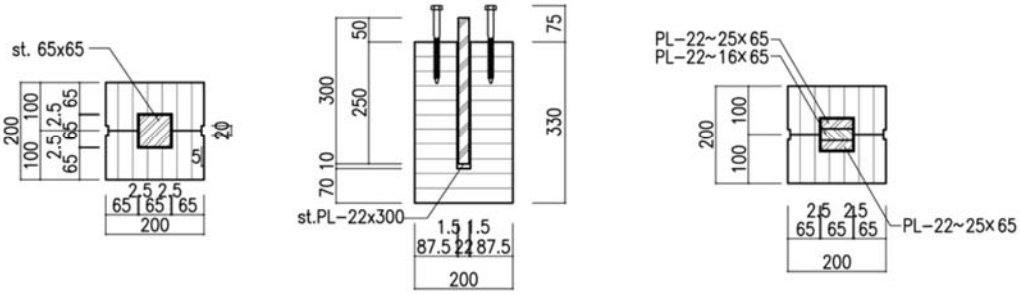

Figure 2 Cross section of column beam and brace

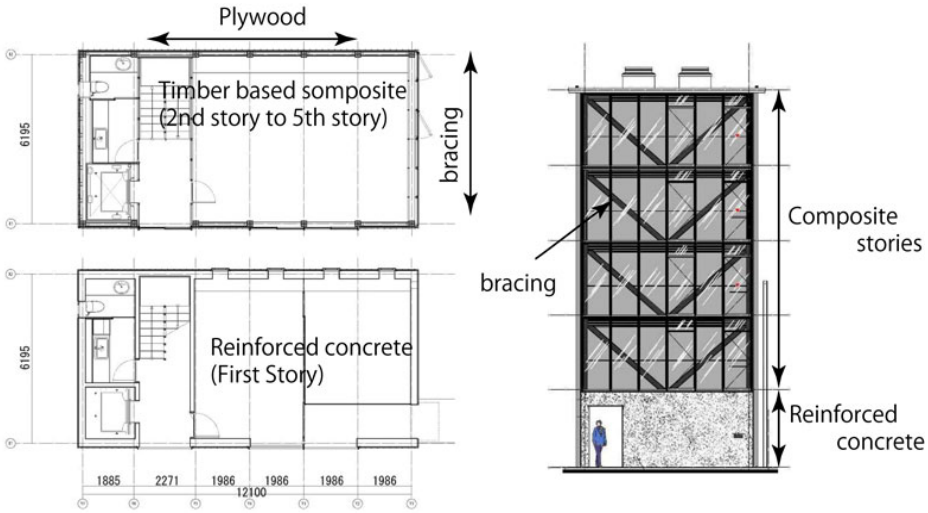

Figure 3 Plan and elevation

3. SEISMIC DISTRIBUTION

3.1 SRSS Analysis

Seismic force distribution of story shear coefficients according to the vibration characteristics of building is calculated using "*Ai* distribution" defined in Japanese Building standard law notification No.1793 as shown in the following equation.

$$Ai = 1 + \left(\frac{1}{\sqrt{\alpha_i}} - \alpha_i \right) \frac{2T}{1+3T} \quad (1)$$

α_i :the value obtained by dividing the sum of the seismic vertical load of the parts supported by the height which is used to calculated for Ai of the building by the sum of the seismic vertical load of the building above ground, T: the fundamental natural period of building in seconds obtained by following equation.

$$T = h(0.02 + 0.01\alpha) \quad (2)$$

h: the height of the building in meters, α :the ratio of the total height of stories of steel construction and wood construction of the building

In case of timber based composite structure composed of stiff and heavy structure at the bottom and soft and light weight timber structure on the top story, Ai distribution based on BSL can be used but following equation, which is called as the SRSS analysis, recommended.

$$A_i = \sqrt{\sum_{j=1}^{k} \left(\sum_{m=i}^{M} \left\{ W_m \cdot \beta_j \cdot u_{mj} \cdot Rt(\tilde{T}_j) \right\} \right)^2 / \sum_{m=1}^{M} W_m} \quad (3)$$

N: the number of stories, $W_{m::}$ the weight of m story, $\beta_j \cdot u_m$: Participation vector in j-th mode, $Rt(\tilde{T})$: the design spectral coefficient in natural period $\tilde{T}$

Numerical result of two cases for timber based composite structure to confirm the applicability of Ai distribution will be described below.

3.2 CASE STUDY1

The SRSS analysis is conducted to evaluate the seismic distribution in composite structure. Table 3 shows the parameter of the seismic weight of the structure. In this case study, five stories building with reinforced concrete first story is assumed because the building can built with 1 hour fireproof members and it is practical. The weights of M1 and M2 are extremely lighter than the reinforced concrete structure, because it is not necessary to consider the fire-proof measurement. M3 is assumed as the structure consisting of members with fire proof performance. The weight of the steel structure is the same as the wooden structure and the stiffness of the steel moment resisting structure is also the same as the wood. Bracing structure is regarding as the stiff structure in the same weight. Table 4 show the combination of the story drift under the Ai seismic distribution defined by the BSL. The stiffness at the each story is calculated from combination of mass and shear force,

Figure 4 shows the result of the SRSS analysis. Ai distribution is also put in the same figure in natural period calculated from both equation (2) (*To*) and modal analysis(*Ty*). In this analysis $R(\tilde{T})$ is assumed as 1.0. Ai distribution from *To* is reasonable for 4 and 5 story building but it underestimates for 3 story building. Natural period calculated from modal analysis is reasonable for 3 story building.

Table 3 Combination of seismic mass (kN/m^2)

	M1	M2	M3
Roof	1.20	2.50	3.50
Normal	2.50	3.50	6.50
R/C Floor	8.0		

Table 4 Combination of story drift

	K1	K2	K3	K4	K5	K6
Timber	1/200	1/400	1/200	1/400	1/200	1/400
R/C	1/2000		1/500		1/200	

3.3 CASE STUDY 2

The SRSS analysis and time history analysis are conducted for the seven stories structure of NEESWood project. Seven ground motions which are 1940 El Centro, 1994 Canoga part, Rinaldi, 1995 JMA Kobe JR Takatori, 2003 k-net Ojiya, and BCJ artificial wave were used in elastic time history analysis for lumped mass model. Figure 5 shows the result of the SRSS analysis in bracing steel first story and six story building without steel story. Ai distribution without steel story expresses from the second story to compare the case of with/without steel. The shear force of second story which is the bottom story of the woodframe is 20% higher than that of the first story without steel bracing story. Figure 6 show the result of time history analysis. The SRSS analysis is reasonable in this case.

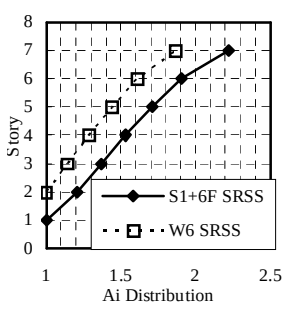

Figure 5 the SRSS analysis

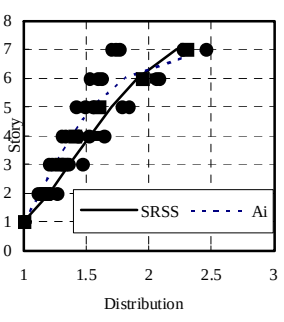

Figure 6 Time-history analysis

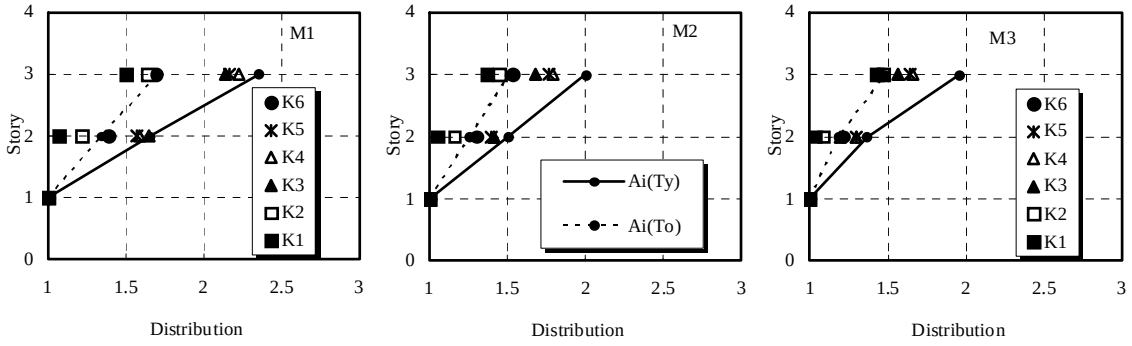

3 stories building

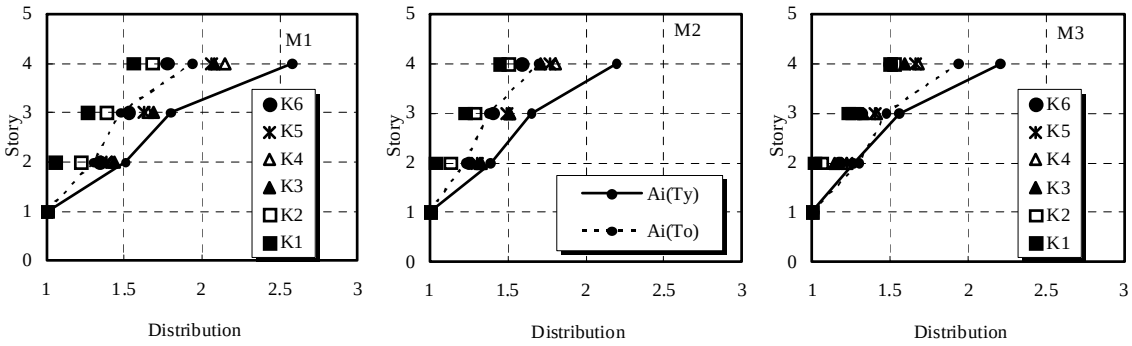

4 stories building

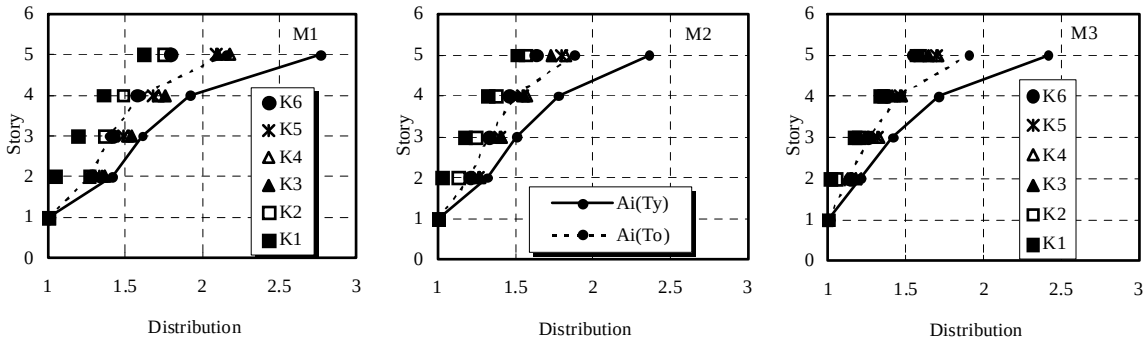

5 stories building

Figure 4 comparison of the SRSS and Ai distribution

4. CONCLUSIONS

The building standard law was revised in 1998 and there have been the potential to build medium and high rise timber based structure with fire and seismic performance in Japan. In this paper, recent mid rise timber based building is shown and consideration of the seismic distribution of the composite structure which have reinforced concrete first story and timber story on the top. The distribution of the shear force calculates using Ai distribution defined in the building standard law in Japan.

References:

Sakamoto, I., Kawai, N., Okada, H., Isoda, H and Yusa, S. “Final report of a Research and Development project on Timber based Composite Building Structures”, Proceedings of 8th WCTE, Aug., 2004

Koshihara, M., Isoda, I. and et al.: “A Study of five storied timber based composite building for practical use (Part 1-3)”, Summary of Technical Papers of Annual Meeting Architectural Institute of Japan, C-1, pp.201-206, 2005

Yusa, S., Yoshikawa, T and et.al “ Research in practice on 5-story fire resistance composite wooden structure building”, Summaries of Technical Papers of Annual Meeting Japan Society for Finishings Technology, pp.7, 2005

JOINT CONFERENCE PROCEEDINGS
7th International Conference on Urban Earthquake Engineering (7CUEE) &
5th International Conference on Earthquake Engineering (5ICEE)
March 3-5, 2010, Tokyo Institute of Technology, Tokyo, Japan

INSTRUMENTAL EARTHQUAKE INTENSITIES VS. DUCTILITY DEMAND: CORRELATION STUDY USING DATA FROM EUROPE & THE MIDDLE EAST

J. Enrique Martinez-Rueda[1] and Tilemachos Vlachos[2]

1) Senior Lecturer, School of Environment & Technology, University of Brighton, UK
2) Postgraduate Student, School of Environment & Technology, University of Brighton, UK
jem11@bton.ac.uk

Abstract: This article is about the degree of association of a number of ground motion parameters with the displacement ductility demands imposed by strong ground motion recorded in Europe and the Middle East. The ground motion parameters used in the study are: peak ground acceleration, spectral acceleration, Housner intensity, Arias intensity and cumulative absolute velocity. For a given combination of strength and initial period of vibration of a structure under analysis, a ground motion parameter with optimum degree of association with displacement ductility demand is identified. The ground motion parameters so identified define the recommended instrumental intensity to be used for the amplitude scaling of natural accelerograms.

1. INTRODUCTION

A rigorous assessment of the ductility demand imposed by strong ground motion on a structure requires of a nonlinear inelastic time-history analysis. On the other hand, the amplitude, the frequency content and the duration are parameters of the seismic input that affect structural response. And a number of ground motion parameters (GMPs) account for one or more of these effects. In fact, it is generally believed that GMPs provide quantitative compact descriptions of important characteristics of strong ground motion (Kramer, 1996). One can even argue that GMPs work as instrumental intensities as they can define in an objective way the severity of an earthquake based on instrumental observations derived from natural accelerograms. Traditionally, ground motion prediction equations (GMPEs) have been implemented primarily for the estimation of peak ground acceleration *PGA* or spectral acceleration *SA*. Because of their relevance in seismic hazard analysis these GMPEs are regularly updated and improved (*e.g.* Ambraseys, *et al.* 2005, Akkar and Bommer, 2010, Bommer *et al*. 2010). More recently however, a number of GMPEs to estimate other GMPs such as Arias Intensity I_A (*e.g.* Travasarou, *et al.* 2003), Housner Spectrum Intensity SI_H (*e.g.* Martinez-Rueda, 2006) and cumulative absolute velocity *CAV* (*e.g*. Danciu & Tselentis, 2007) have been introduced.

Two detailed studies on the ability of Housner Intensity to correlate with displacement ductility demand μ_Δ were conducted by Martinez-Rueda (1998, 2006). These studies demonstrated that SI_H correlates well with μ_Δ particularly for short and intermediate period structures. To a structural engineer this correlation is meaningful as ductility demand is a simple and yet very effective damage index that characterizes damage potential once ductility capacity is established. On the other hand, the above studies also showed that the degree of association between SI_H and μ_Δ is sensitive to the period of the structure and its inelastic strength characterized by its yield seismic coefficient.

There have been also a number of more recent studies to assess the correlation between some GMPs and maximum structural displacement (Riddell, 2007; Yakut and Yilmaz, 2008); however, these two studies have not considered displacement ductility demand as the metric for inelastic response in their analysis of correlation. Other limitations of the above two studies include the use of a narrow range of structural periods and, more importantly, the disregard of the influence of the strength of the structure under analysis, which has been found to have an influence (Martinez-Rueda, 1998) on the degree of association between intensity and ductility demand.

The distinction between elastic and inelastic displacement in the evaluation of the efficiency of GMPs as well as the influence of structural parameters of strength and stiffness on this effciency all have significant implications. Hence, there is still a need of a more elaborate identification of the degree of correlation of a group of practical GMPs with a measure of inelastic response such as μ_Δ.

Accordingly, the main objective of this article is to assess the efficiency of the GMPs: *PGA*, *SA*, SI_H, I_A and *CAV* in terms of their degree of association with μ_Δ. The above GMPs were selected as they are well known and because of their simplicity they are easy to use in practice for the scaling of natural accelerograms.

2. GMPs *vs.* DUCTILITY DEMAND

To assess the performance of the selected GMPs in terms of their degree of association with ductility demand a number of empirical relationships between GMPs and the ductility demand imposed on a family of structures by an ensemble of strong motion earthquake records were first generated and then analyzed as described in detail below.

2.1 Selected strong ground motion

A sample of natural accelerograms recorded on rock were first identified. This sample is the subset of natural accelerograms recorded on rock used by Ambraseys *et al.* (2005) for the derivation of a GMPE for *SA* in Europe and the Middle East. In fact, the accelerograms used in this article are the same as those used by Ambraseys *et al.* (2005). Details on the adopted filtering and base line corrections are described in the above reference.

For the preliminary assessment of the GMPs it was considered appropriate to select from the above subset only accelerograms representative of strong ground motion. In the interest of simplicity for each available record, only the stronger horizontal component with *PGA* greater than 0.10 g was chosen. This lead to an ensemble of 68 accelerograms with a distribution of intensities and seismological parameters (M_w is Moment Magnitude and d is distance to the surface projection of the fault) as summarized in Table 1.

Table 1. Summary of statistical properties of the accelerograms used .

	PGA [m/sec^2]	SI_H [m/sec]	I_A [m/sec]	CAV [m/sec]	M_w	d [km]
Min	0.996	0.011	0.025	0.596	5.000	1.000
Max	8.750	1.236	9.759	26.797	7.600	76.000
Mean	2.556	0.164	0.603	4.112	5.975	15.733
S.D.	1.727	0.199	1.283	4.017	0.671	13.008
C.O.V	0.676	1.217	2.125	0.977	0.112	0.827

2.2 Structures

The family of structures under study was idealised as inelastic single degree of freedom systems characterised by their yield periods T_y (as controlled by their initial stiffness K_y), their yield seismic coefficients C_y , and the postyield stiffness ratio α:

$$C_y = \frac{H_y}{Mg} \quad (1)$$

$$\alpha = \frac{K_h}{K_y} \quad (2)$$

where H_y is the yield strength of the structure and M is the mass of the structure. Four seismic coefficients were considered, *i.e.* C_y = 0.1, 0.2, 0.3 and 0.4 and seventeen periods T_y = 0.1, 0.2, 0.3, ... 1.0, 1.2, 1.4,..2.0, 2.5, 3.0 sec to account for different combinations of strength and stiffness. A single value of α equal to 0.02 was used in all the analyses. This is a realistic typical value that allows the estimation of overstrength due to inelastic response. The hysteretic response of the structures was assumed as bilinear with kinematic hardening. Viscous damping of 5% was assumed in all the analyses. The Runge-Kutta method was adopted to solve for the time-history response of the structures.

3. ANALYSIS OF RESULTS

Figure 1 exemplifies the observed relationships between μ_Δ and the GMPs under study. This example corresponds to structures with T_y = 0.5 sec and C_y = 0.2; each plot in the figure contains 25 points as it was found that for the above combination of stiffness and strength only 25 accelerograms out of the 68 originally selected imposed inelastic response. As expected each GMP has a different degree of association with μ_Δ as evaluated by the coefficient of determination R^2. For the example of Figure 1 the GMP of best performance is SI_H as it has the highest R^2 value equal to 0.7087. In contrast, the worst GMP is I_A as indicated by a very low R^2 = 0.0906 . This very low value of the coefficient of determination indicates that for the above combination of strength and stifness there is a very weak relation between I_A and μ_Δ.

3. 1 Overall trends

As exemplified above the number of points in the relationships GMPs *vs.* μ_Δ varied according to the combination of strength and stiffness under study. No bias against a particular GMP took place as the performance of each GMP in terms of R^2 was assessed using exactly the same number of points. In general, as the strength and stiffness increased the number of points in the relationships decreased, and this lead to a reduction in the number of inelastic structures available to assess the degree of association between the GMPs and μ_Δ. Relationships containing less than 10 points of inelastic response were not considered reliable enough to estimate R^2 and were not used for further analysis. A visualization of the number of inelastic structures as a combination of the structural parameters C_y and T_y is presented in Figure 2. It is observed that as the strength increases the range of periods at which inelastic response occurs becomes narrower.

Figures 3 to 6 present a complete visualization of the performance of the GMPs as a function of the period of the structures for different levels of strength. These figures reveal that there is not a single GMP with best performance over the entire period range under study; however it is rather apparent that the GMPs of the period domain (*i.e. PGA*, *SA* & SI_H) tend to perform much better in comparison with

those of the time domain (*i.e.* I_A & CAV). In fact, for a given combination of strength and stiffness the best performance is always associated with a GMP of the period domain.

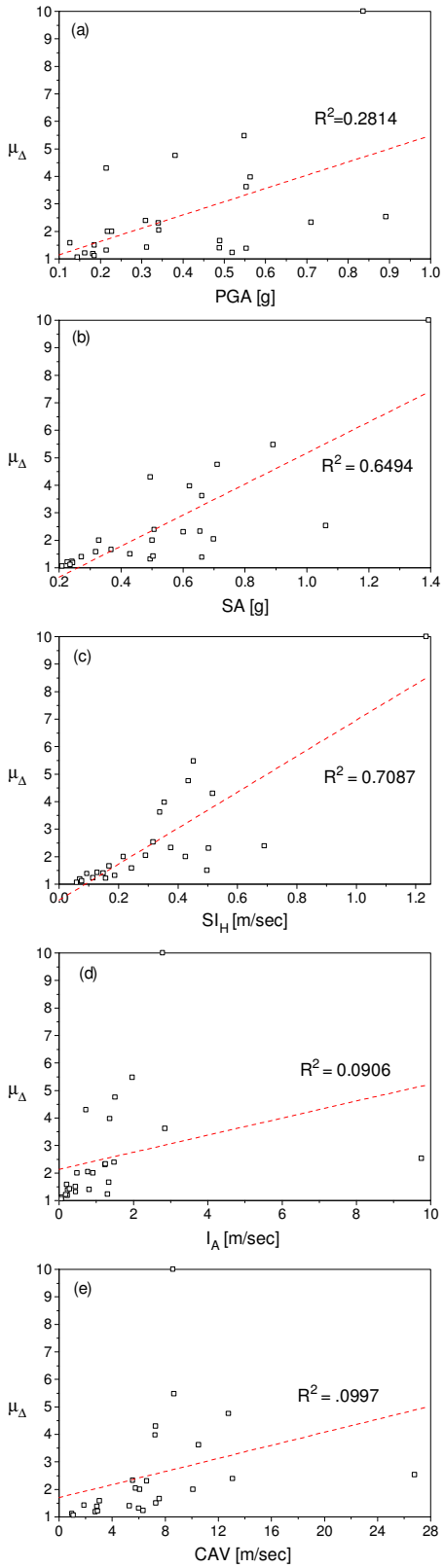

Figure 1. Relationships between GMPs and μ_Δ for structures with T_y = 0.5 sec and C_y = 0.2

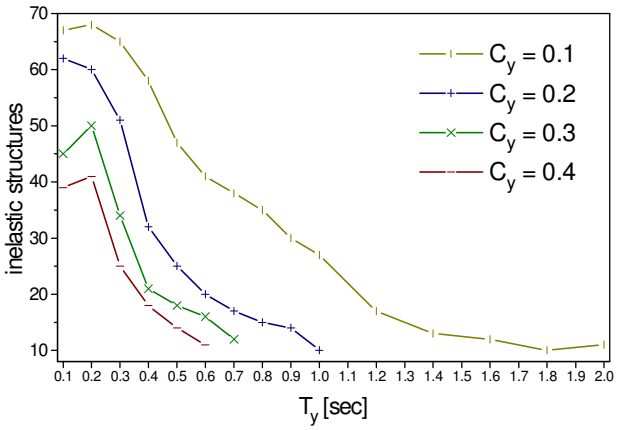

Figure 2. Number of structures behaving inelastically as a function of T_y for different values of C_y

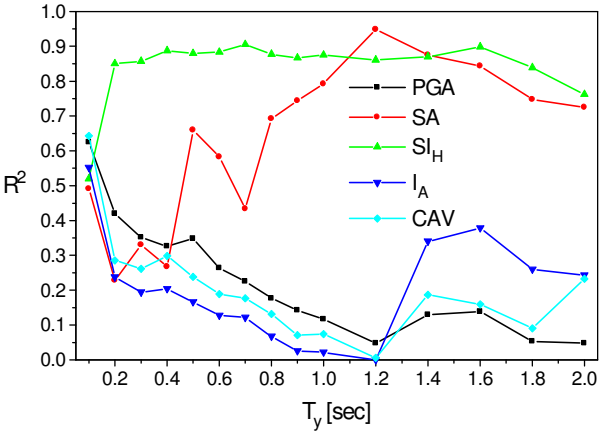

Figure 3. Comparison of GMPs performance for C_y = 0.1

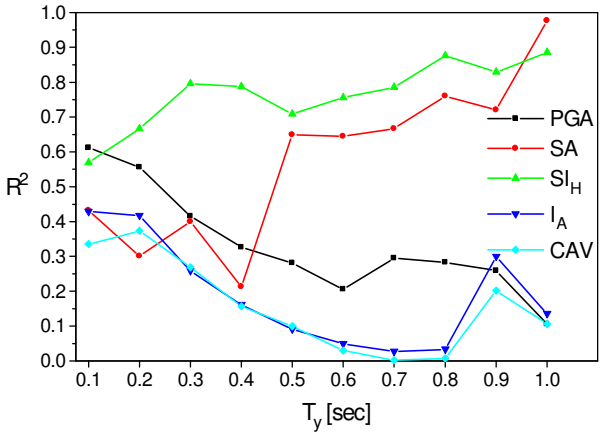

Figure 4. Comparison of GMPs performance for C_y = 0.2

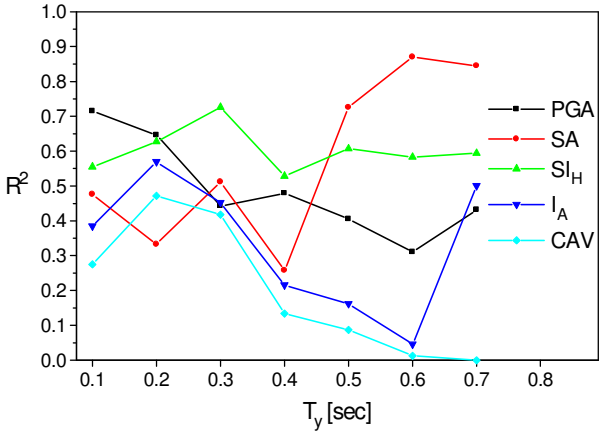

Figure 5. Comparison of GMPs performance for $C_y = 0.3$

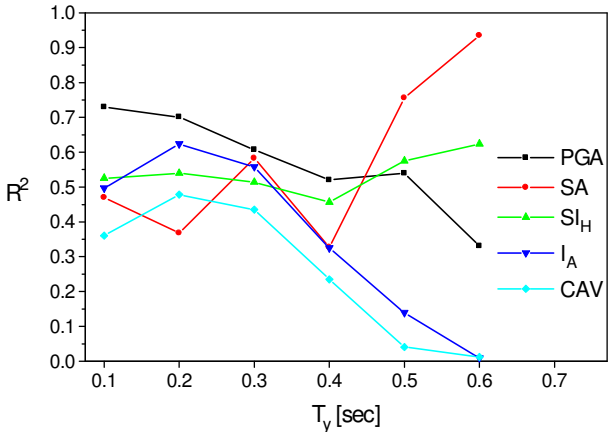

Figure 6. Comparison of GMPs performance for $C_y = 0.4$

Figure 7 shows the overall performance of the GMPs in terms of the average R^2 over the period ranges implied in Figures 3 to 6. It is evident that the GMP of overall best performance is SI_H followed by *SA* and *PGA*. The figure also reveals that SI_H markedly decreases its efficiency as the strength of the structure increases. On the other hand, the efficiency of *PGA* markedly increases with increasing values of strength. In contrast the efficiency of *SA* appears to be virtually unaffected by the strength of the structure.

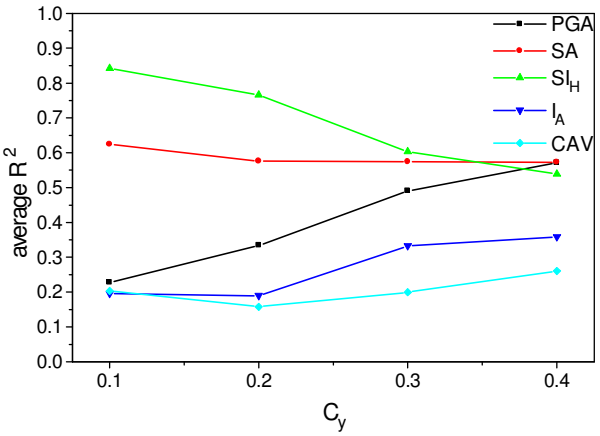

Figure 7. Overall comparisons between GMP in terms of average R^2.

Clearly, I_A and *CAV* cannot compete against the effectiveness of *PGA*, *SA* or SI_H to correlate with μ_Δ. In fact, with the exception of accelerograms of long duration and narrow band frequency content, duration has an effect on hysteretic energy dissipation rather than on peak inelastic response (O'Connor and Ellingwood, 1992). And this might explain why I_A and *CAV* are weakly associated with ductility demand despite the fact they both account explicitly for duration while neglecting the effect of frequency content in the evaluation of ground motion intensity.

4. CONCLUDING REMARKS

This study identified the efficiency of a number of ground motion parameters in terms of their degree of association with ductility demand for different combinations of strength and stiffness of the structure under analysis.

Overall comparisons indicated that the GMPs of the period domain (*i.e. PGA*, *SA* or SI_H) are far better correlated with ductility demand than the GMPs of the time domain (*i.e.* I_A and *CAV*). This finding has important practical implications for time-history analysis. The above GMPs of the period domain can be directly linked to the design spectrum and the target instrumental intensity implied by this spectrum can be achieved, within reason, by the scaling of natural accelerograms to define the seismic input for nonlinear inelastic analysis.

For a given combination of strength and stiffness results obtained in this work indicated that the selection of a GMP of best association with ductility demand depends on the strength and the stiffness of the structure under analysis. A compromise between simplicity and generality lead to the identification of the GMPs judged as of best performance for accelerogram scaling as defined by the following selection criteria:

For $C_y \le 0.2$: *PGA* if $T_y \le 0.1$ sec
SI_H if $T_y > 0.1$ sec

For $0.2 < C_y < 0.4$: *PGA* if $T_y \le 0.2$ sec
SI_H if $0.2 < T_y < 0.5$ sec
SA for $T_y \ge 0.5$ sec

For $C_y \ge 0.4$: *PGA* if $T_y \le 0.4$ sec
SA if $T_y > 0.4$ sec

However, one should be mindful that the above recommendations are supported by the work in progress described in this article which has considered only strong ground motion on rock. Futher studies using a larger number of accelerograms and additional seismic sites such as stiff and soft soil are currently underway to find out if the seismic site has actually a relevant influence on the boundaries that demark the regions of best performance of the GMP.

It is important note that the most well known criterion to define spectrum intensity, *i.e.* that of Housner (1952) was the only one considered here in the interest of simplicity.

Alternative criteria to define spectrum intensity such us the criterion of Matsumura (1992) and that of Martinez-Rueda (1997) have been compared (Martinez-Rueda, 1998) with that of Housener in terms of the degree of association between spectrum intensity and ductility demand. Results indicate that, in some cases, the alternative criteria provide a better option when compared with that of Housner.

Finally, this research has confirmed that, in general, amplitude and frequency content are far more important than duration in regard to the parameters of the seismic input that control the magnitude of ductility demands in inelastic structures. Nevertheless, further studies currently underway considering only the 'strong motion duration' of the accelerograms in the evaluation of I_A and *CAV* might reveal if this refinement can actually improve the performance of the these GMP of the time domain.

Acknowledgements:

The first author gratefully acknowledges the generosity of Dr. John Douglas who provided a copy of the filtered and base line corrected accelerograms used for the derivation of GMPE of Ambraseys *et al.* (2005)

References:

Akkar, S. and Bommer, J.J. (2010), "Empirical Equations for the prediction of PGA, PGV and Spectral Accelerations in Europe, the Mediterranean Region and the Middle East," *Seismological Research Letters*, Manuscript accepted for publication,

Ambraseys, N.N., Douglas, J., Sarma, K., and Smit, P.M. (2005), "Equations for the estimation of strong ground motions from shallow crustal earthquakes using data from European and Middle East: horizontal peak ground acceleration and spectral acceleration," *Bulletin of Earthquake Engineering*, **3**(1), 1-53.

Bommer, J.J., Akkar, S. and Stafford, P.J. (2010) , "Current empirical ground-motion prediction equations for Europe and their application to Eurocode 8," *Bulletin of Earthquake Engineering*, **8**(1), 5-26**.**

Danciu, L., and Tselenis, G. (2007), "Engineering Ground Motion Parameters Attenuation Relationhsips for Greece," *Bulletin of the Seismological Society of America*, **97**(1b), 162-183.

Housner, G.W. (1952), "Spectrum intensities of strong motion earthquakes," *Proceedings of Symposium on Earthquake and Blast Effects on Structures*, EERI.

Kramer, S.L. (1996) "Geotechnical Earthquake Engineering," Prentice-Hall Inc.

Martinez-Rueda, J.E. (1997), "Energy dissipation devices for seismic upgrading of RC structures," *PhD Thesis,* Imperial College, London

Martinez-Rueda, J.E. (1998), "Scaling Procedure for Natural Accelerograms Based on a System of Spectrum Intensity Scales," *Earthquake Spectra*, 14(1), 135-152.

Martinez-Rueda, J.E. (2006), "Proposal of an Attenuation Relationship of Housner Spectrum Intensity in Europe," *Proceedings of 1st European Conference on Earthquake Engineering and Seismology*, Paper No. 1193.

Matsumura, K. (1992), "On the intensity measure of strong motions related to structural failures," Proceedings of the 10th World Conference on Earthquake Engineering, **1**,375-380.

O'Connor, J.M. and Ellingwood, B.R. (1992), "Site dependent models of earthquake ground motion," *Earthquake Engineering and Structural Dynamics*, **21**(7), 573-589.

Ridell, R. (2007), "On ground motion intensity indices," *Earthquake Spectra*, **23**(1), 147-173.

Travasarou, T., Bray. D.J., and Abrahamson, N.A. (2003), "Empirical Relationship for Arias Intensity," *Earthquake Engineering and Structural Dynamics,* **32**(7) , 1133-1155.

JOINT CONFERENCE PROCEEDINGS
7th International Conference on Urban Earthquake Engineering (7CUEE) &
5th International Conference on Earthquake Engineering (5ICEE)
March 3-5, 2010, Tokyo Institute of Technology, Tokyo, Japan

INDIAN BAMBOO AS AN ALTERNATIVE TO TIMBER: A CRITICAL EVALUATION FROM STRENGTH OF MATERIAL PERSPECTIVE

Parthasarathi Mukhopadhyay[1)], and Sekhar Chandra Dutta[2)]

1) Assistant Professor, Dept. of Architecture, Town and Regional Planning, Bengal Engineering and Science University, Shibpur, India
2) Professor and Head, School of Infrastructure, Indian Institute of Technology, Bhubaneswar, India
parthasm@gmail.com, scdind2000@gmail.com

Abstract: Bamboo, as a sustainable building material, is in the process of replacing depleting timber resources in tropical countries like India. However, one of the major hindrances in engineered application of bamboo is dearth of strength of materials data. This paper reports initial observations in this regard. Samples of one bamboo species, *Bambusa balcooa*, having wide traditional application in building construction in India, were subjected to standard mechanical tests in an 'Amsler Wood Testing Machine' to obtain its *compressive strength*, *modulus of rupture*, *energy absorbed in impact-bending* and *cleavage strengths*. The very low *coefficient of variation* of the data, obtained while undertaking the various tests related to the strength properties of bamboo, prove reliability of the same. Primary analyses of the experimental data show that the average permissible compressive strength and modulus of rupture of the bamboo samples exceed the corresponding values of sal, a much appreciated timber by about 14.10% and 131.38% respectively. Further, the very high value of energy absorbed during impact bending proves the material to be well capable in absorbing shocks. Again, the values of cleavage tests prove its handiness during nailing, screwing and other cutting and joining operations needed for constructions. The study may be considered as a small step towards standardization of bamboo as an alternative to wood.

1. INTRODUCTION

1.1 Predominant Building Materials for Indian Households

Next to food, shelter is the prime need of man. The developing countries like India, whose major populations are below poverty line, cannot afford to provide a healthy, safe and long lasting shelter for their people. As per the Census of India 2001, 187 million houses have been reported to be used as residence or residence-cum-other uses by about 192 million 'Households', where a household is defined as a group of persons who normally live together and take their meals from a common kitchen unless the exigencies of work prevent any one of them from doing so. A detailed distribution of the households of India, based on the predominant building material used at the roofs, walls and floors, is given in Table 1. A detailed scrutiny of the Table shows that 47.6% of the roofing materials and 56.3% of the walling materials of the different housing units of India are built of non-engineered materials. In fact, poor people generally use second or third class bricks or timber for their buildings. It is only them who cannot afford the same uses bamboo as a building material. However, Table 1 shows that bamboo and other non-serviceable materials constitute a

Table 1 Distribution of Households of India by Predominant Building Materials as on 2001

Predominant building material	No. of households (in million)	Percentage
Roof:		
Concrete	38	19.8
Tiles	63	32.6
Grass, thatch, bamboo, wood, mud etc.	42	21.9
Others	49	25.7
Wall:		
Burnt brick	84	43.7
Mud, unburnt brick	62	32.2
Grass, thatch, bamboo, wood, mud, etc.	21	10.2
Others	25	13.9
Floor:		
Mosaic, Floor tiles	14	7.3
Cement	51	26.5
Mud	110	57.1
Others	17	9.1

Source: Housing Tables, Census of India, 2001

sizable percentage of the roofing and walling materials. The use of such non-engineered materials in buildings on one hand reduces their longevity, and on the other, increases the chances of them getting devastated during natural catastrophes. Hence, it becomes an urgent task before the architects and structural engineers to attribute adequate 'engineering' or 'technology' to such so called 'non-engineered' structures in order to enable them to resist the lateral forces exerted by earthquakes or cyclones.

1.2 Bamboo: The Sustainable Building Material

Bamboo is an enduring, versatile, and sustainable material that people and communities have utilised for thousands of years. It also has a history of use in buildings, being common to the vernacular architecture of south-east Asia and Latin America. The natural characteristics of bamboo, being tubular, light in weight, fibrous in morphology and its reported tensile strength, make it a highly flexible material (Mukhopadhyay 2008). However, its use as a building material has so far been more traditional than technical. Meanwhile, the globe is witnessing an alarming rate of shrinking of forest-cover. All these have forced developing tropical nations like India, who are bestowed with variety of bamboo species, to rediscover the traditional material as an alternative to rapidly depleting wood resources. However, one of the major hindrances in engineered application of bamboo is dearth of its strength of material data.

2. STRENGTH DATA OF BAMBOO: EARLIER INVESTIGATIONS

Hidalgo (2003) observed that the mechanical properties of bamboo vary from species to species, which depend on the environmental conditions within which they have grown. "For the above reason, one cannot use the strength values, for example, of *Guadua angustifolia*, and apply them to other species of the same genus, even if the other species grows in the same area, for example, *Guadua amplexifolia*". Thus it becomes important to determine the strength data for all the Indian bamboo species which may be considered, from traditional experiences, as good for construction purpose. However, before actually going into the process, it is thought prudent to undertake a literature survey of the experiences of various countries while determining different types of strength properties for diverse species of bamboo.

2.1 Tensile Strength

The first notable study on the mechanical properties of bamboo was carried out by Baumann (1912) in Germany where he investigated on the species *Phyllostachys nigra* popularly known as the 'black bamboo'. He found that tensile strength of the outer layer culm wall was 300.86MPa, which is twice as strong as that of the interior layer which was 156.32MPa. Uno (1932) undertook research at the Utsunomiya Agricultural College, Japan, where he experimentally verified that middle portion of bamboo is stronger than its upper and lower portions in tension. He also observed that tensile strength is maximum at the outermost fibres and decreases gradually as one takes samples from inner layers. During his visit to China, Fugl-Meyer (1937) tested the bamboo cables used in the construction of suspension bridges and found their tensile strength to be around 179.27Mpa. The next notable research work is contributed by Glenn (1950) of Clemson Agricultural College in South Carolina, USA, who embarked in exploiting the tensile strength of bamboo by using it as a reinforcement in cement concrete in lieu of steel. He used the test procedures laid down by the American Standard for Testing Materials (ASTM) for determination of mechanical properties of timber. Another exhaustive investigation on the tensile strength of bamboo for using it as reinforcement in cement concrete was carried out by Sera et al. (1990) at the Asian Institute of Technology, Bangkok, Thailand. Rajeev et al. (1998) reports the work regarding the use of bamboo for manufacturing bamboo mat, a wood veneer composite, under the auspices of Indian Plywood Industries Research & Training Institute (IPRITI), Bangalore, India.

2.2 Compressive Strength

A bamboo piece, when used as column, bears compressive load in a direction parallel to its grains. The compressive load that a bamboo column can bear thus depends upon the capacity of the bamboo fibres to resist longitudinal compression. The relationship between compressive strength parallel to the grain and the moisture content of bamboo is reported by Hidalgo (2003) to be similar to that of wood; this means that there is an increase in maximum crushing stress from the green to the air-dry condition. Uno (1932) experimentally found that the upper portion of a bamboo culm is stronger than its middle and lower portions in compression. He reported the compressive strengths in the upper, middle and lower portions of the culm of *Phyllostachys bambusoides* were found to be respectively 81.89MPa, 33.54MPa and 43.35MPa, and in *Phyllostachys lithophila* the strengths were found to be respectively 125.92MPa, 65.41MPa and 63.15MPa. It was further confirmed by Hidalgo (1978) by testing 76 specimens of the species *Guadua angustifolia* that the compressive strength of bamboo increases with age and the maximum values for compressive strengths occur in specimens which are 3-5 years old. However Syafii (1984) based on his studies on the mechanical properties at the internodes of the lower part of the culms of four bamboo species namely, *Dendrocalamus giganteous*, *Dendrocalamus asper*, *Gigantochloa robusta*, and *Bambusa vulgaris var. striata*, reports that the internodes of the same culm has different mechanical properties, which do not follow a progressive value from the bottom to the top of the culm.

2.3 Bending Strength

Under bending, the inner portion of a bamboo culm compresses and at the same time the upper portion suffers tension. When any one of the compressive or tensile forces acting on the bamboo structural component exceeds the

capacity of the bamboo species, the bamboo culm cracks. According to Takenouchi (1932), if the thickness of the wall of a culm internode is in between $1/8^{th}$ - $1/5^{th}$ of the diameter of the cylinder, then the culm cylinder is, as a rule, much more resistant to bending forces than a solid culm of the same diameter. Baumann (1912) concluded that the bending strength of the bamboo fibres at outer layers is more than that of those at the inner layers. He drew this conclusion from his experiments with the 'black bamboo', where he found the bending strengths of the outer and inner layers to be 248.60MPa and 93.16MPa respectively. As the thickness of the bamboo culm wall decreases with increase in its height, there is an increase in specific gravity and mechanical strength of the inner portions, whereas in the outer portions of the bamboo culm these two properties change only slightly (Hidalgo 2003).

2.4 Shear Strength

Unlike timber, bamboo does not contain radial cells which increase shear strength of timber samples parallel to the axis (Hidalgo 2003). This low shear is advantageous in manufacturing bamboo strips necessary for weaving or for making cables, but is at the same time disadvantageous for building construction purposes. Hidalgo (1978) reports on the basis of his experimentation with 27 specimens of different ages of *Guadua angustifolia* a maximum shear strength of 14.12MPa, and a minimum shear strength of 4.41MPa.

2.5 Impact Tests

Baumann (1912) undertook impact tests of samples of 'black bamboo' with distance between supports at 250mm; the work to failure was reported to be in between the range of 0.22-0.32MPa. Jain et al. (1993) carried out pendulum impact tests with samples of bamboo strips measuring 75mm long with a cross-section 10mm x 10mm. The impact strength of bamboo, derived from these tests, is reported to be $3.02kJm^{-2}$ across the fibre and $63.54kJm^{-2}$ along the fibre. The results again confirm the understanding that bamboo has minimum strength at a direction perpendicular to the fibre direction.

2.6 Strength as a Function of Density: An Universal Approach

Dutch researcher Janssen (1995), while acknowledging the various botanical, environmental and chemical factors affecting the strength properties of bamboo, has attempted to simplify the results by taking an universal approach based on his experiences. He suggests that a ratio exists between the density of a piece of bamboo and the allowable stresses in it, which is shown in Table 2.

He suggests that dry bamboo has a moisture content of 12% when in equilibrium with air of 70% relative humidity, which he considers is a fair mean for many tropical countries. It is further suggested that for very humid climate, the mean values of dry and wet bamboo is to be considered. The National Building Code of India (NBC), 2005 has accepted the above stated approach suggested by Janssen in its totality.

Table 2 Relation between density in kgm^{-3} and allowable stress in MPa

	Compression without buckling	Bending	Shear
Dry bamboo (12% moisture content)	0.013	0.020	0.003
Wet or green bamboo	0.011	0.015	—

Source: Janssen (2005) and NBC 2005.

Janssen comments that the allowable stress for any material is not a constant factor, but a factor of the length of time for which the force is applied, that is, whether loading is of permanent duration, temporary duration or very short duration. The allowable stresses obtainable from Table 2 are for 'dead load' of floors, walls and roofs, that is, for permanent loading. In cases, when 'live load' is a major constituent, the allowable stresses may be increased by 25%, because part of the load is of short duration. Similarly, if wind is likely to be the major load, the allowable stresses given in Table 2 may be increased by 50%, as wind load tends to have an even shorter duration.

2.7 Rediscovering Bamboo in India: Government Initiatives

The consolidated taxonomical account of bamboo in the Indian subcontinent was first brought out by J.S. Gamble in 1896 (Bennet and Gaur 1990), as a part of the *Annals of Royal Botanical Garden, Calcutta*. The account of studies conducted on different species of bamboo thereafter remained somewhat scattered and could not be consolidated. The Forest Research Institute at Dehra Dun, India has also been working with different species of bamboo for decades and in 1990 they came up with the publication 'Thirty Seven Bamboos Growing in India' consisting of information primarily concerning physical and botanical properties of thirty-seven important bamboo species found in India, and the book further mentions uses and applications of these species. However, none of these publications contain any data regarding mechanical property of any Indian bamboo species. The NBC was revised in 2005 to include for the first time a sub-section concerning bamboo. Apart from adopting the density based approach of calculating allowable stresses, the NBC 2005 tabulates 'density', 'modulus of rupture', 'modulus of elasticity' and 'maximum compressive strength' of twenty Indian bamboo species (in round form) in green condition. It further tabulates 'density', 'modulus of rupture' and 'modulus of elasticity' of twelve among the above stated twenty Indian bamboo species (in round form) in air dried condition. Apart from this, the NBC 2005 has further tabulated 'extreme fibre stress in bending' and 'allowable compressive stress' of sixteen Indian bamboo species (in round form) in green condition, considered suitable for the purpose of structural designing. The Code further

acknowledges that the "strength of split bamboo is more than those of round bamboo", but provides basic shear stress values in split form in green condition for only three of the above mentioned sixteen species, suitable for structural applications. No data regarding any other Indian bamboo species in split condition is available. In this context, Dr. P.S. Rana, Chairman and Managing Director, Housing and Urban Development Corporation (HUDCO) noted "in order to exploit the real potential bamboo has, research and development efforts need to be directed at the key areas of concern; such as preservation, jointing, structural design, codification" (HUDCO 2005). The present paper reports initial observations to achieve this end.

3. EXPERIMENTAL SET UP

3.1 Bamboo Species Selected for Experiment

The NBC 2005 has classified the sixteen bamboo species, considered suitable for structural applications, into three groups, namely, Group A, Group B and Group C, based on the range of their 'Modulus of Rupture' and 'Modulus of Elasticity in Bending' (refer Table 3).

Table 3 Classification of Bamboo Species suitable for Structural Application

	Modulus of Rupture (R′) (in MPa)	Modulus of Elasticity (E) in Bending (in Mpa)
Group A	R′ > 70	E > 9
Group B	70 ≥ R′ > 50	9 ≥ E > 6
Group C	50 ≥ R′ > 30	6 ≥ E > 3

Source: NBC 2005.



Figure 1 Felling of *Bambusa balcooa* for the experiment

Bambusa balcooa, the species selected for felling (refer Figure 1) for the purpose of experimentation is one of the above mentioned sixteen species, falling in the Group B. However, no mechanical property related to air dry condition in split form is available regarding this species. Moreover, it is one of the largest available species of the Ganges-Brahmaputra delta of the Indian subcontinent. According to Gamble (1896), "It is probably the best and strongest species for building purposes and is greatly esteemed in Calcutta, and is much used for scaffolding and is very durable if well seasoned by immersion in water".

3.2 Amsler Universal Wood Testing Machines

In spite of the morphological differences between wood and bamboo, it was mentioned in the previous section that Glenn (1950) followed the test procedures laid down by ASTM for determination of mechanical properties of timber for bamboo samples at Clemson Agricultural College in South Carolina, USA. Similarly, Li et al. (1994) followed the testing standards of wood for determining sizes of bamboo specimens to be tested at International Centre for Materials Physics and Institute of Metal Research in Shenyang, China. The methods of testing for round and split bamboo pieces recommended by the Bureau of Indian Standards (BIS) are respectively, IS: 6874-1973 (Reaffirmed 2002) and IS: 8242-1976 (Reaffirmed 2004). These Indian standards, under the Timber Sectional Committee of the BIS, are also following the procedures laid down for testing of timber. Accordingly, the tests were undertaken in the 'Amsler Universal Wood Testing Machine' (refer figure 2), manufactured by the Alfred Amsler Company at the Strength of Materials Laboratory of the Bengal Engineering and Science University (BESU), Shibpur, India. The machine is capable for undertaking the following tests, viz. (i) Compression test, (ii) Cross Bending test, (iii) Impact



Figure 2 Amsler Universal Wood Testing Machine, Strength of Materials Laboratory, BESU, Shibpur

Bending, (iv) Double Cleavage test, and (v) Single Cleavage test. The capacity of the machine is as follows:

(a) 4000kg in compression;
(b) 400kg in static bending; and,
(c) 10kg-m in impact bending.

3.3 Preparation of Bamboo Samples

The bamboo samples, necessary for undertaking the five different types of strength tests, were required to be fabricated as per the dimensions of the specimens recommended for the Amsler Universal Wood Testing Machine (refer Figure 3). However, the diameter of a bamboo culm is much less compared to that of timber; and the bamboo culm is hollow. Thus it is much difficult to prepare the bamboo specimens with an uniform cross-section of 20mm x 20mm. In order to facilitate this, each bamboo culm was split into five equal parts as shown in Figure 4. The curvature of these bamboo splices was much less, and upon planing, they could be flattened in order to produce specimens of uniform rectangular cross-section. The specimens of required dimensions were fabricated from these flattened bamboo splices.

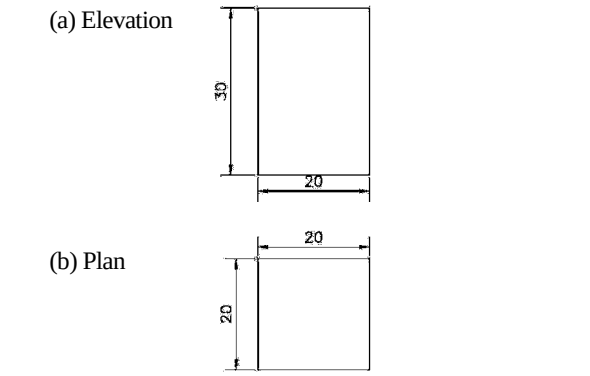

3.1 Compression Specimen

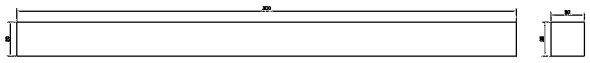

(a) Plan and Elevation (b) Cross-section

3.2 Specimen for Cross-Bending and Impact Bending

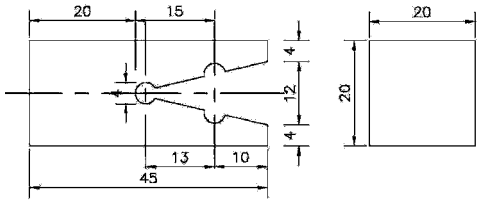

(a) Plan (b) Cross-Section

3.3 Single Cleavage Specimen

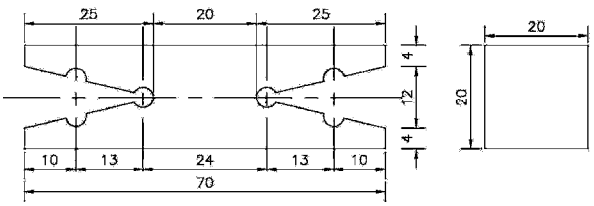

(a) Plan (b) Cross-section

3.4 Double Cleavage Specimen

Figure 3 Drawings for Bamboo Specimens



Figure 4 Fabrication Process of Bamboo Samples

4. RESULTS AND DISCUSSION

4.1 Compression Test

Seventeen samples of *B. balcooa*, each measuring approximately 30mm in length and 20mm x 20mm in cross-section (refer Figure 3.1), were put under compressive load. The direction of grain of all these samples was along the length, that is, parallel to the direction of application of force. The proportional details of each sample were meticulously measured, from which the cross-sectional area (A) was calculated for each sample. The ultimate compressive load (P_{fc}) at which each sample failed was further noted, and the corresponding values of ultimate compressive stress (f_c) were recorded from Eq. (1) below. The values are plotted in Figure 5, in which one finds the mean value of 'f_c' to be 36.54MPa.

$$f_c = P_{fc} / A \quad (1)$$

Again, the NBC 2005 recommends a safety factor of 3.5 for deriving permissible compressive stresses of bamboo. Thus the mean permissible compressive stress for the selected bamboo samples is equal to 10.44MPa. Here it may be stated that the same for sal (*Shorea robusta*), a Group B

category of timber recommended by NBC 2005 for structural purpose is 7.7-10.6 MPa, the mean of which is 9.15MPa. Thus the species *B. balcooa* is found to have average permissible stress in compression along the grain very much comparable to that of sal, if not more.

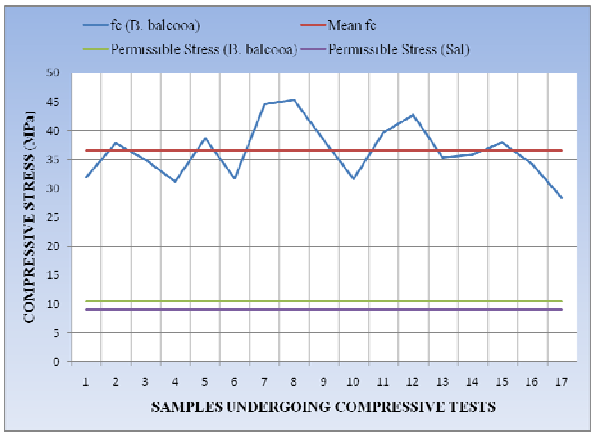

Figure 5 Illustration and analysis of the results of Compressive Tests of samples of *B. balcooa*

Five samples of the species *B. balcooa* were fabricated in a manner so that the direction of grain was across the direction of application of load. In all cases, the ultimate compressive value could not be properly ascertained as the value of P_{fc} went beyond the capacity of the machine in compression, viz. 4,000kg, which implies that compressive stress across the grain is more than many varieties of timbers of Group B category of timbers recommended for structural purposes by the NBC 2005. Here it may be mentioned that the same for sal is 2.9-4.6MPa.

4.2 Bending Tests

Twenty samples of *B. balcooa*, each measuring approximately 300mm in length and 20mm x 20mm in cross-section (refer Figure 3.2) were fabricated for undergoing bending tests. Ten samples were put under impact bending test and the rest ten were put under cross bending test.

(a) Impact Bending Test

The impact bending tests illustrated an interesting property of *B. balcooa*. Barring one example, when the value of the energy absorbed in impact bending was 9.2kgm, in all the other cases the nature of the failure of the samples were observed to be incomplete and the full-capacity value of the machine of 10kgm in impact bending was reached. This preliminary observation indicates that *B. balcooa* can well absorb shocks that cause stress beyond the proportional limit.

(b) Cross Bending Test

The cross-bending test is important because bamboo will be used to fabricate beams, rafters and other important structural members which are subjected to bending. This test exposes weakness caused by defects better than any other test. Like the previous test, the proportional details of each sample were meticulously measured, from which the cross-sectional area (*A*) was calculated for each sample. The maximum load (P) at which each sample failed in bending was noted, and the corresponding values of maximum bending moment at failure load (M_m) and moment of inertia of the cross-section about the neutral axis (*I*), were both recorded respectively from the Eqs. (2) and (3) given below:

$$M_m = Pl/4 \tag{2}$$

where, '*l*' is the unsupported length of the member undergoing cross-bending, which is 240mm in this case.

$$I = (b).(d^3)/12 \tag{3}$$

where, '*b*' is the width of the specimen, and,

'*d*' is the depth of the specimen.

The strength of bamboo in cross-bending is indicated by 'Modulus of Rupture' (*R'*), which is a measure of the ultimate unit stress to the extreme fibre, computed by expression given in Eq. (4) below:

$$R' = \left(\frac{M_m}{I}\right).(C) \tag{4}$$

where, '*C*' is the distance from neutral axis to extreme fibre. The values are plotted in Figure 6, in which one finds the mean value *R'* to be 130.04MPa.

Again, the NBC 2005 recommends a safety factor of 4.0 for deriving permissible extreme fibre stresses in beams of bamboo. Thus the mean permissible extreme fibre stress in bending for the selected bamboo samples is equal to 32.51MPa. Here it may be stated that the same for sal is 11.2-16.9 MPa, the mean of which is 14.05MPa. Thus the species *B. balcooa* is found to have average permissible stress in bending more than that of sal.

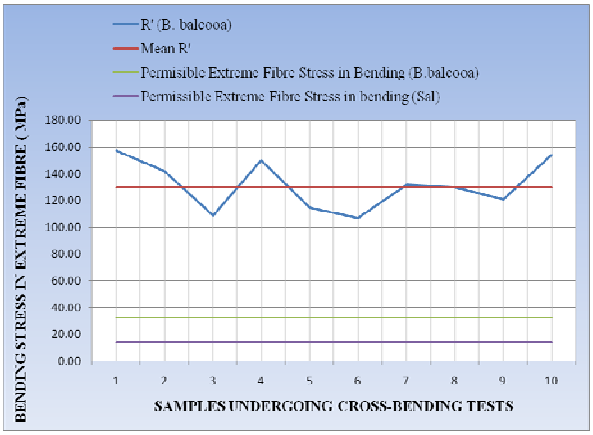

Figure 6 Illustration and analysis of the results of Cross Bending Tests of samples of *B. balcooa*

4.3 Cleavage Test

The cleavage test of a bamboo specimen indicates its resistance to splitting. This is important as far as working of bamboo is considered. Bamboo pieces need to be nailed and/or screwed while fastening, and hence require high cleavage strength. The cleavage tests can be of two types, viz. single cleavage test and double cleavage test.

Thirty nine samples of *B. balcooa*, each measuring

approximately 20mm x 20mm in cross-section, and other shapes and dimensions as per Figure 3.3, were fabricated for undergoing single cleavage tests. Similarly, forty three samples of the species, each measuring approximately same as the single cleavage test in cross-section, and other shapes and dimensions as per Figure 3.4, were fabricated for undertaking double cleavage tests.



Figure 7 Splitting of samples of *B. balcooa* while undertaking single cleavage test at Strength of Materials Laboratory, BESU, Shibpur



(a) Placing a sample for double cleavage test



(b) Double cleavage failure of a sample

Figure 8 Undertaking double cleavage test of a sample of *B. balcooa* in the Amsler Universal Wood Testing Machine at Strength of Materials Laboratory, BESU, Shibpur

Like the compression tests, the cross-sectional area (*A*) of each sample was calculated, and the maximum load (P) at which each sample failed in splitting due to cleavage action was noted. The respective cleavage stress values were obtained and shown in Figures 9 and 10. The average single cleavage stress is found to be 1.11MPa, while the same for double cleavage tests is found to be 2.10MPa. Since splitting during cleavage tests is accomplished by wedging apart the bamboo samples in longitudinal direction, it is closely related to tension across grain.

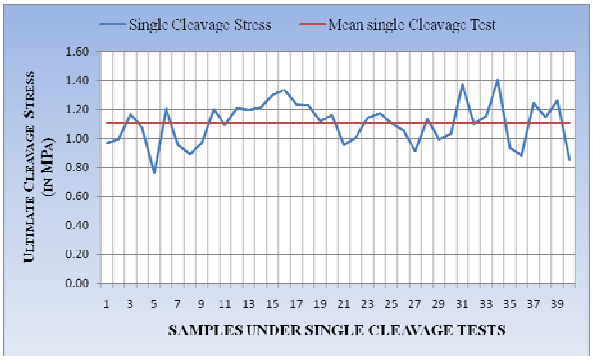

Figure 9 Illustration and analysis of the results of Single Cleavage Tests of samples of *B. Balcooa*

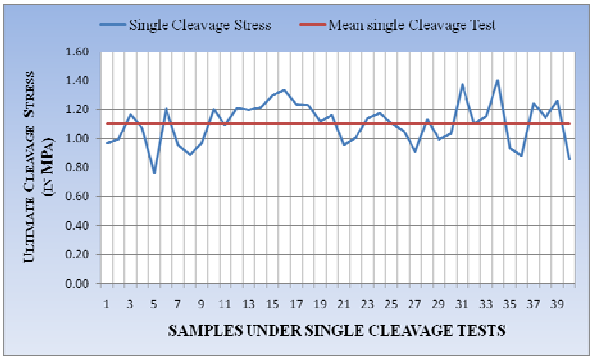

Figure 10 Illustration and analysis of the results of Double Cleavage Tests of samples of *B. balcooa*

4.4 Statistical Reliability of the Data Collected

It is very important to verify statistically the reliability of the strength data collected during the different sets of experiments. The deviation of the highest and the lowest values of the data presented in Figures 5, 6, 9 and 10 from the respective mean values ($\bar{x}$) apparently seem to be within limit. However for statistical purpose, one needs to verify the extent to which the individual data differs from the average or mean value. For this purpose the standard deviation (σ) of each set of data was calculated. However, standard deviations of the data of different mechanical properties are not mutually comparable. This is because the range of data for each set is different. For example, the mean value of the set of data representing single cleavage tests is 1.11MPa, whereas the mean value of the set of data

representing Modulus of Rupture is 130.04MPa. In such cases, unit less ratios are better indicators for comparison of dispersion. This warrants calculation of the coefficient of dispersion (*CV*) for each set of data. Karl Pearson's coefficient of variation is defined by Eq. (5) stated below. The 'mean value', the 'standard deviation', and the 'coefficient of variation' of data collected during each set of experiment are tabulated below in Table 4.

$$CV = \left(\frac{\sigma}{\bar{x}} \right) \times 100 \quad (5)$$

Table 4 Statistical Interpretation of the Data Collected during the Experiments

	Mean value (MPa)	Standard deviation (MPa)	Coefficient of variation (%)
Ultimate compressive Stress	36.54	4.82	13.20
Modulus of Rupture	130.04	18.96	14.58
Single Cleavage Stresses	1.11	0.15	13.18
Double Cleavage Stresses	2.10	0.38	18.08

The low values of the coefficient of variations with very small deviation from each of the different sets of experiments indicate that the data used for taking analytical decisions in this paper are consistent and hence statistically reliable.

5. CONSLUDING REMARKS AND FURTHER SCOPE

The authors would like to put forward a few concluding remarks on certain broad issues related to structural application of *B. balcooa*, which at times also raise questions regarding certain existing provisions of the Indian Code.

(a) The data for extreme fibre stress in bending and for compression, both at failure, are derived from the tests undertaken with the samples of *B. Balcooa* made from present study, tested in air dry condition. These two data are divided by the two different safety factors, recommended by the NBC 2005, to arrive at the corresponding permissible stress values. These permissible values are compared with the corresponding data for samples of *B. balcooa* in green condition, obtained from NBC 2005 in Table 5, which raises a peculiar situation. Whereas the 'Safe Extreme Fibre Stress in Bending' is found to have almost doubled in 'air dry condition' compared to 'green condition', the 'allowable compressive stress' value has decreased by 20%. This situation may be explained by the observations of Uno (1932) that the compressive stress value varies within the same bamboo culm, and it is maximum at the upper portion than at the middle and lower portions. The samples taken by the authors were certainly from lower culm; may be the samples considered by NBC were from upper portions. The difference of strength value at different positions of the same culm may account for this 20% variation. However, this needs further investigation.

Table 5 Comparison of Safe Working Stresses of *B. balcooa* in Green and Air Dry Conditions

Mechanical Property	Green Condition (MPa)	Air Dry Condition (MPa)
Extreme Fibre Stress in Bending	16.4	32.51
Allowable Compressive Stress	13.3	10.44

(b) There is no doubt that these two stress values are well comparable to more than those of sal timber, irrespective of whether the bamboo samples are tested in green or air dry condition. Primary analyses of the experimental data show that the average permissible compressive strength and modulus of rupture of the bamboo samples exceed the corresponding values of sal by about 14.10% and 131.38% respectively. Here 'sal' is especially mentioned because it finds wide use in building construction and interior design purposes in India, and other countries.

(c) The samples used in this experimentation are all prepared from lower portions of bamboo culms. It is worthy to repeat the tests with samples from middle and lower portions. The lowest of the three values may be recommended for inclusion in the Codes.

(d) The very high value of energy absorbed during impact bending proves the material to be well capable in absorbing shocks. This may prove worthy during shocks produced by disasters.

(e) Again, bamboo buildings need different types of fastening systems for creating good junctions, which is especially necessary to withstand cyclonic storms. The high values of cleavage tests prove the species to be effective during nailing, screwing etc.

(f) The general value of density given in NBC 2005 for *B. balcooa* in wet condition is 783kgm^{-3}; the corresponding value in air dry condition is not provided. The authors have experimentally derived the density of the air dry *B. balcooa* samples in laboratory. The value varies between 795kgm^{-3} (found at upper portion) and 830kgm^{-3} (found at lower portion).

(g) Lastly, the authors find a fundamental difference in opinion regarding the method of testing bamboo for obtaining their mechanical properties. Whereas the North American, Asian and European researchers use wood testing machines for the purpose, South American scholars like Hidalgo (2003) raises question regarding this. He considers it to be "a big mistake because bamboo anatomy and morphology are quite different from wood." He observes that because of the natural hollow nature of bamboo, the specimen sizes for wood testing may be erroneously too small for bamboo. This issue needs further investigation.

Acknowledgements:

The authors acknowledge financial support from Bengal Engineering and Science University, Shibpur in the form of seed money for undertaking the investigation as an in-house research project of the University.

References:

Baumann, R. (1912), "Tests on the Elasticity and Strength of Bamboo, Acacia, Ash and Hickory Timbers (Versuche über die Elastizität und Festigkeit von Bambus, Akazien, Eschen und Hickoryholz)," *Zeitschrift des Vereines deutscher Ingenieure*, Düsseldorf, **56**(6), 229-232, [in German].

Bennet, S.S.R. and Gaur, R.C. (1990), "Thirty Seven Bamboos Growing in India," Forest Research Institute, Dehra Dun, India.

Bureau of Indian Standards (2005), "SP7: 2005, National Building Code of India 2005," BIS, New Delhi, India.

Bureau of Indian Standards (1973), "IS: 6874-1973 (Reaffirmed 2002), Method of Tests for Round Bamboos," BIS, New Delhi, India.

Bureau of Indian Standards (1977), "IS: 8242-1976 (Reaffirmed 2004), Methods of Tests for Split Bamboos," BIS, New Delhi, India.

Fugl-Meyer, H. (1937), "Chinese Bridges," Kelly and Walsh, Ltd., Shanghai, [in Danish].

Gamble, J.S. (1896), "The Bambuseæ of British India," in *Annals of Royal Botanical Garden, Calcutta, Vol. VII*, Bengal Secretariat Press.

Glenn, E.H. (1950), "Bamboo reinforcement in Portland Cement Concrete," *Bulletin of the Clemson Agricultural College of South Carolina*, War Production Board (Contact No.78), **4**.

Hidalgo, O. (1978), "Nuevas técnicas de construcción con bambú," Estudios Técnicos Colombianos, Universidad Nacional de Colombia, [in Spanish].

Hidalgo, O. (ed.) (2003), "Bamboo: The Gift of the Gods," Oscar Hidalgo-López, Columbia.

Housing and Urban Development Corporation Ltd. (2005), "Bamboo In Construction," HUDCO, New Delhi, India, iii.

Jain, S., Jindal, U.C., and Kumar, R. (1993), "Development and fracture mechanism of the bamboo/polyester resin composite," *Journal of Materials Science Letters*, Springer Netherlands, **12**(8), 558-560.

Janssen, J.J.A. (1995), "Building with Bamboo: a Handbook (2nd ed.)," Intermediate Technology Publications.

Li, S.H., Fu, S.Y., Zhou, B.L., Zeng, Q.Y., and Bao, X.R. (1994), "Reformed bamboo and reformed bamboo/aluminium composite," *Journal of Materials Science*, Springer Netherlands, **29**(22), 5990-5996.

Ministry of Housing and Urban Poverty Alleviation (2001), "Census of India, Housing Tables," Government of India, New Delhi.

Mukhopadhyay, P. (2008), "Role of bamboo in seismic architecture," *Indian Architect & Builder*, JMPL, **22**(2), 102-106.

Rajeev, B.N., Naidu, M.V., Rangaraju, T.S., Zoolagud, S.S., and Aswathanarayana, B.S. (1998), "Development of Bamboo Mat: Wood Veneer Composites as Wood Substitute," *Indian forester*, Forest Research Institute, Dehra Dun, **124**(9), 705-713.

Sera, E.E., Robles-Austriaco, L., and Pama, R.P. (1990), "Natural Fibres as Reinforcement," *Journal of Ferrocement*, International Ferrocement Information Centre, AIT, Bangkok, **20**(2), 109-124.

Syafii, L.I. (1984), "Pengujian sifat fisik dan mekanis conton kecil bebas cacat beberapa jenis bambu," MSc. Thesis, Faculty of Forestry, Bogor Agricultural University, Indonesia, [in Bahasa Indonesia].

Takenouchi, Y. (1932), "The study on bamboos," Youkendo, Tokyo [in Japanese].

Uno, S. (1932), "Studies on Bamboo: Relations between Chemical Composition and Strength," *Bulletin of the Utsunomiya Agricultural College*, **2**.

JOINT CONFERENCE PROCEEDINGS
7th International Conference on Urban Earthquake Engineering (7CUEE) &
5th International Conference on Earthquake Engineering (5ICEE)
March 3-5, 2010, Tokyo Institute of Technology, Tokyo, Japan

ANALYTICAL STUDY ON SEISMIC RESPONSE CONTROLLED EFFECT OF WOODEN HOUSES USING FRAME MODEL

Kazuhiro Matsuda[1)], Kazuhiko Kasai [2)], and Hiroyasu Sakata[3)]

1) Assistant Professor, Structural Engineering Research Center, Tokyo Institute of Technology, Japan
2) Professor, Structural Engineering Research Center, Tokyo Institute of Technology, Japan
3) Associate Professor, Structural Engineering Research Center, Tokyo Institute of Technology, Japan
matsuda@serc.titech.ac.jp, kasai@serc.titech.ac.jp, hsakata@serc.titech.ac.jp

Abstract: This paper focuses on framed analysis of wooden structure having passively controlled scheme. At first, accurate framed analytical models for the wooden energy dissipation wall with damper and plywood shear wall are proposed. The analytical model was constructed by using many spring elements whose properties derived from the experimental results of the joint tests. The analysis is able to duplicate the many kinds of test results with high accuracy. The seismic response controlled effect due to applying the energy dissipation wall is discussed by parametric analysis using the frame model. By the joint part which consists of axial, rotation and shear spring, an accurate framed analytical model is able to be made. The analytical model is useful for designing and improving the energy dissipation wall, because the effect of each member is regarded to the model. The detailed response of the wooden wall with passive control system could be obtained from the analysis. In the case of applying plywood shear wall, maximum seismic displacement decreases in a linear fashion against the increment of the plywood shear wall. On the other hand, in the case of applying our energy dissipation wall, maximum seismic displacement decreases considerably even if the amount is a little. Therefore the availability of the energy dissipation wall is confirmed.

1. INTRODUCTION

In the Hanshin-Awaji (Kobe) Earthquake that occurred in 1995, the number of collapses or seriously damaged of wooden houses were approximately 250,000. It is said that approximately 10 million wooden houses are insufficient for earthquake resistant in Japan, and those houses need to be reinforced immediately. Moreover, to design new wooden houses to be resistant to earthquakes, it is important to investigate rational methods applying the passive control to wooden houses.

In order to mitigate the damage of wooden houses and seismic response, K-brace passive control wall was developed (Kasai and Sakata et al. 2005, Appendix 1) and a lot of experimental studies using the wall were carried out, such as dynamic cyclic loading tests of the passive control walls (Matsuda et al. 2008), shaking table tests of 1-story or 2-story wooden frames (Sakata et al. 2007 and Matsuda et al. 2007), and so on. However, analytical studies need to be carried out to develop more effective passive control wall and to propose the design method.

Therefore the objective of this study is to propose accurate, framed analytical model for the K-brace passive control wall and plywood shear wall. To make the model, modeling the joint between column and horizontal member is important. In this study, the analytical model is constructed by using spring elements whose properties derived from the experimental results of the joint tests. Also the accuracy of the framed analytical model is confirmed by the comparison between the analytical results and many test results. In addition, parametric study is carried out using the frame model.

2. DEVELOPMENT OF FRAME MODEL

2.1 Outline of Frame Model

Figure 1 illustrates frame model of the energy dissipation wall. Basically linear beam elements which have same condition to the test members, are arranged in the center of the members. Each beam elements are connected by the joint elements which consist of three springs: axial spring, shear spring and rotation spring (Figure 2). The area between the edge of the beam and the surface of the column are assumed rigid and the steel pipe brace is set for truss elements.

Viscoelastic element which was proposed by Kasai et al. (2001, 2002), is arranged at between the intersection of the brace and the steel plate. There are two types of joint element: FC3x2, FC5x1 (Table 1). The L-type metal

includes “FC5” and “FC3” which indicate the number of screws on the column. “x1” and “x2” indicate the number of the metals. Detail of setting the each spring will be described in section 2.3. The two nodes which are framed in by break line at Figure 1, are set so that the two nodes behave together about horizontal displacement and rotation, due to assuming only shear slippage between the column and steel plate. The shear springs between the two nodes are set depending on shear performance of per screw which is set from the test of the joint, because the steel plate is screwed on column by a number of screws. Also the axial springs of bolt are set from the test of joint.

Figure 3 illustrates frame model of the plywood shear wall. Basically constructing method of the exterior frame is same as energy dissipation wall. Therefore linear beam

Table 1 Joint Types

ST (common specification)		SC2	HD
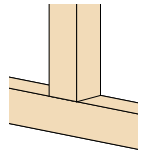		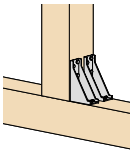	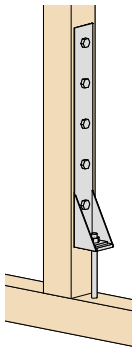
FC5x2	FC5x1	FC3x2	
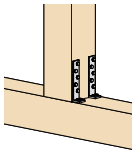	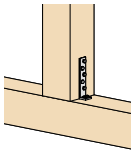	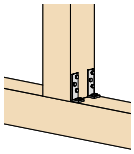	

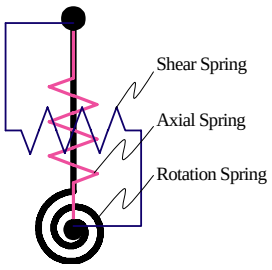

Figure 2 Joint Element

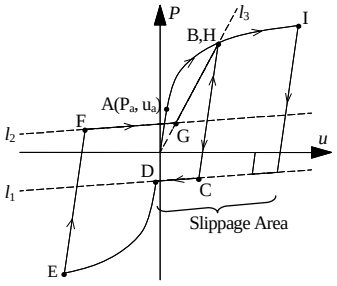

Figure 4 Hysteresis Rule

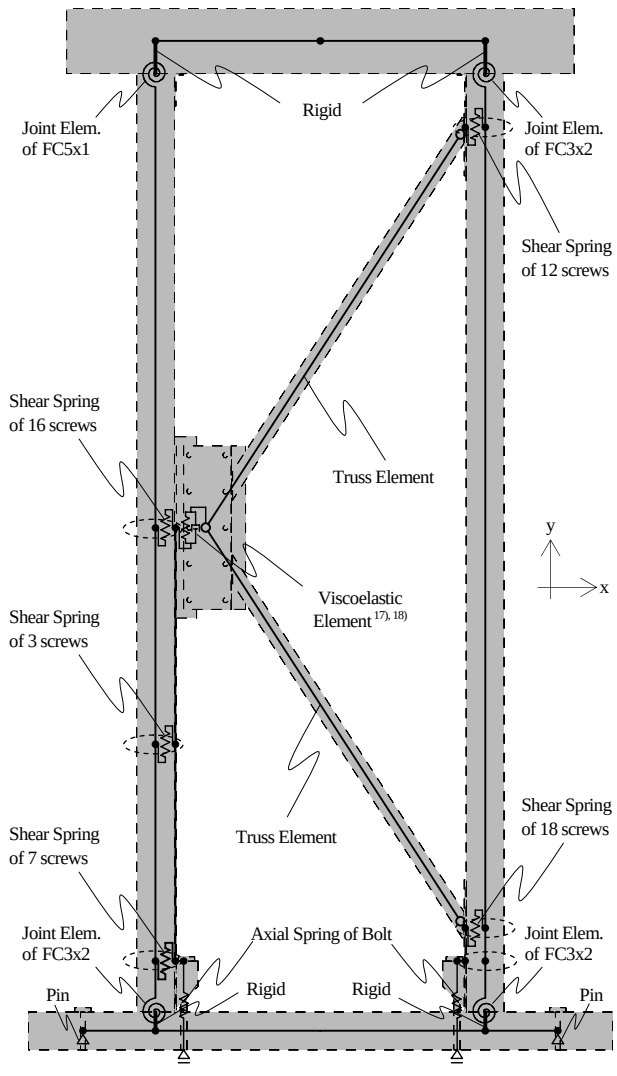

Figure 1 Frame Model of Energy Dissipation Wall

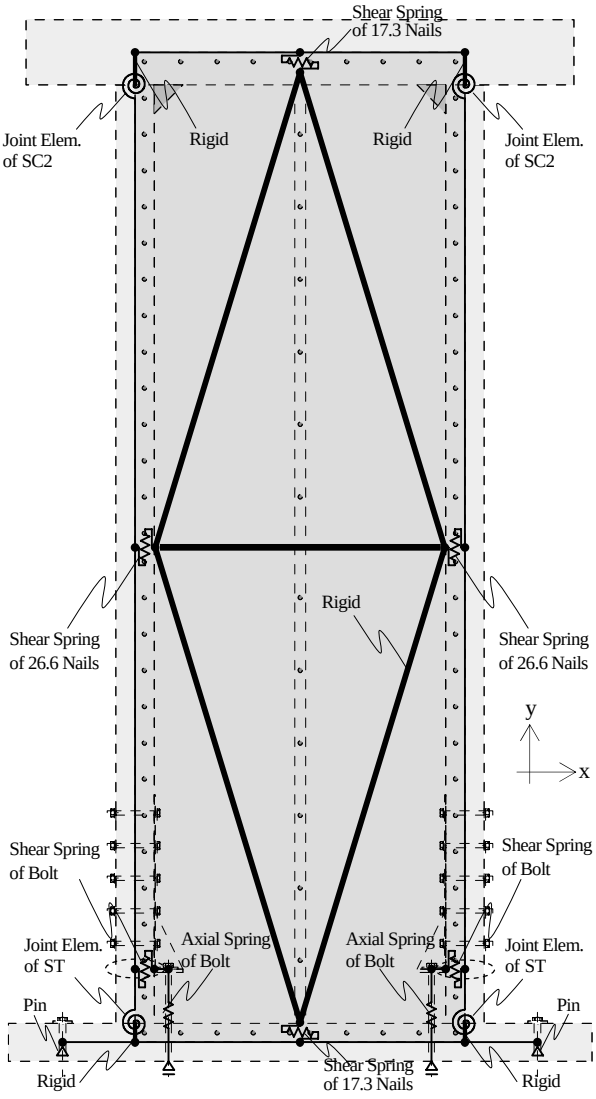

Figure 3 Frame Model of Plywood Shear Wall

elements which have same condition to the test members, are arranged in the center of the members. Each beam elements are connected by the joint elements which consist of three springs. There are two types of joint element: ST and SC2 (Table 1). There are shear springs and axial springs of the bolts. The effect of the nails is contracted to four shear springs using the shear property of a nail and the sheeted wall theory (Murakami et al. 1999). It was confirmed that the contracted method was able to duplicate the real behavior.

2.2 Hysteretic Rules of Springs

Figure 4 illustrates hysteresis rule. After arriving at the elastic limit (Figure 4 A), force increases gradually, and the envelope curve is calculated by Equation (1).

$$\Delta P_x = \frac{(k_i - k_p)\Delta u_x}{\left(1.0 + (k_i \Delta u_x / M_0)^n\right)^{1/n}} + k_p \Delta u_x \qquad (1)$$

Where ΔP_x and $\Delta \upsilon_x$ are increment from P_a and u_a. k_i and k_p are initial and second stiffness. n and M_0 are coefficient to decide the shape of the curve.

This hysteretic rule is applied to the six springs: axial, rotation and shear springs of the joint, and shear springs of the screw, bolt and nail. In the slippage area, the force is set 0 to make the models into simple.

2.3 Envelope Curves of Springs

[Axial springs of the joint]

Figure 5 illustrate the envelope curve of axial spring of the joints. The appraised curve is fitted to the average of four envelope curves which are obtained by the joint tests. ST of the positive direction doesn't bear the pull force. There are two types of depth D = 105mm and 180mm. In the case of negative direction, the effect of metal was ignored, considering the timber bears most of axial compression force. The specimen whose maximum displacement is the smallest of all curves, is regarded when the average curve is obtained.

[Rotation springs of the joint]

Figure 6 illustrates the appraised curve of rotation spring of the joints. As for ST, SC2 and FC5x2, the envelope curves of rotation spring were obtained by using a past data (Kasai et al. 2004). The appraised curves of FC3x2 and FC5x1 are fitted to 0.75 times and 0.5 times of FC5x2. Because FC3x2 and FC5x1 had 0.75 and 0.5 times smaller stiffness than FC5x2 in the axial loading tests of the joints (see Figure 5(b)). SC2 has higher stiffness than FC5x2 in consequence of the haunch.

[Shear springs of the joint]

Figure 7 illustrates the appraised curve of shear spring of the joints. As for ST, SC2 and FC5x2, the envelope curves of shear spring were obtained by using a past data (Kasai et al. 2004). The appraised curve of FC5x1 is fitted to the average curve of FC5x2 and ST. The appraised

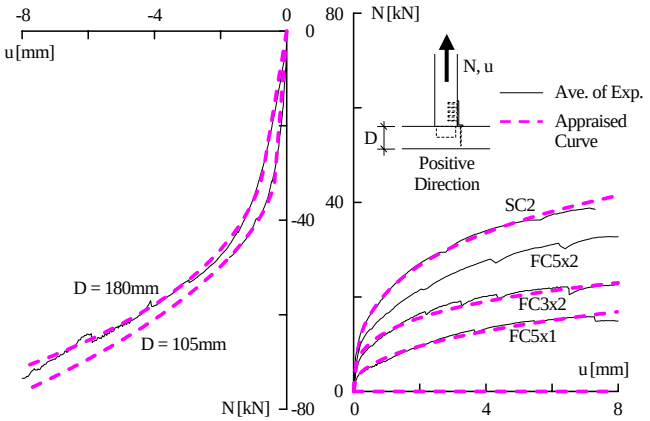

(a) Negative Direction (b) Positive Direction

Figure 5 Appraised Curves of Axial Spring of Joints

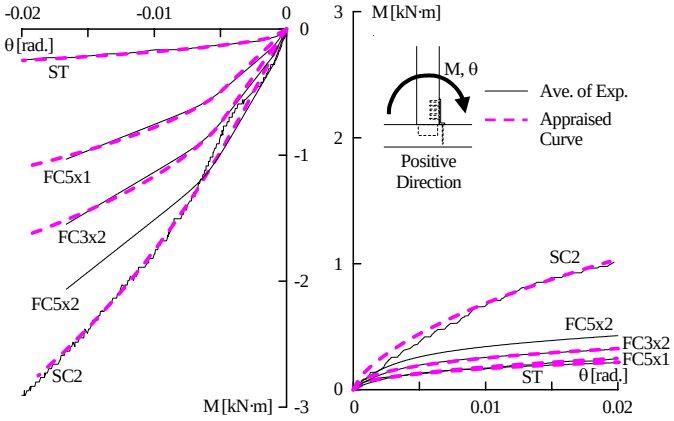

(a) Negative Direction (b) Positive Direction

Figure 6 Appraised Curves of Rotation Spring of Joints

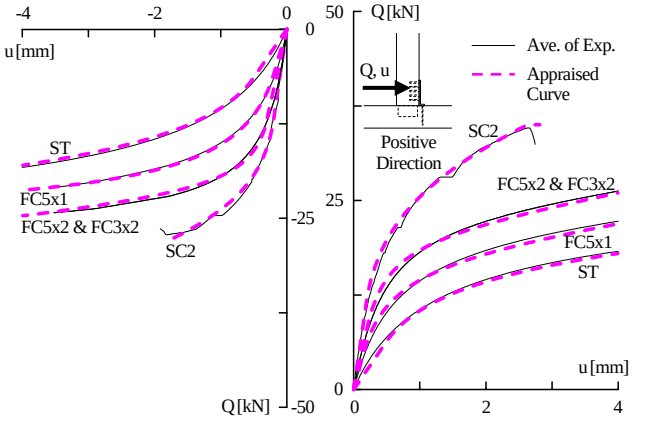

(a) Negative Direction (b) Positive Direction

Figure 7 Appraised Curves of Shear Spring of Joints

curve of FC3x2 is fitted to the curve of FC5x2. Because a few screws which are arranged at the edge part of the joint metal, hardly have the effect of the shear force on the joint.

[Shear springs per screw, bolt and nail]

It is assumed that each screw or bolt behaves in the same way, although the number of the staff varies on each joint. Figure 8 illustrates the appraised curve of a screw and bolt. The shear force per screw or bolt was calculated by dividing axial force of the bolt F_B by the existing number, and the slippage was obtained by u_{slip} (see Appendix 1). The appraised curve is fitted to the average of four envelope curves which were obtained by the past test (Matsuda et al. 2009).

In order to estimate the shear performance of the nail, additionally shear tests of the nails were curried out according to JAS. Figure 9 and 10 illustrate the shear test of the nail and the appraised curve of a nail. The number of specimen is six, and the appraised curve is fitted to the average of six envelope curves as other springs.

[Axial springs of bolt]

Figure 11 illustrates the appraised curve of axial spring of the bolt. The relationships (Figure 11(a)) were obtained by the tests (see Appendix 1). u_B was calculated by Equation (2), regarding the lift of the horizontal member and the slippage of the metal.

$$u_B = u + u_{lift} - u_{slip} \tag{2}$$

In the case of experimental curves, the curves start from N_B = 10kN because of the initial tension 10kN of the bolt. Therefore u_B is moved by 0.8mm or 1.2mm regarding the displacement of initial tension 10kN. The appraised curve is fitted to the enveloped curve which was moved by 0.8mm or 1.2mm like Figure 11 (b). Figure 12 shows hysteresis rule of bolt. In the negative direction the spring hardly bears the strength, in the positive direction the spring behaves with bilinear and slippage hysteresis.

3. COMPARING ANALISIS AND TEST RESULT

3.1 Dynamic Loading Test

As for hysteresis of 1P and 3P, energy dissipation wall and plywood shear wall, Figure 13 illustrates the comparison of experimental results (Matsuda et al. 2008) and analytical results. Where P means 910mm length and 3P framed model has two energy dissipation walls at both ends symmetrically. In the case of 1P energy dissipation wall, also relationships between damper force and damper displacement are indicated. Analytical results are obtained by liberating enforced deformation to the center of the beam and the enforced deformation is same to test (Matsuda et al. 2008). In both 1P and 3P, energy dissipation wall and plywood shear wall, analytical results correspond to experimental results with high accuracy.

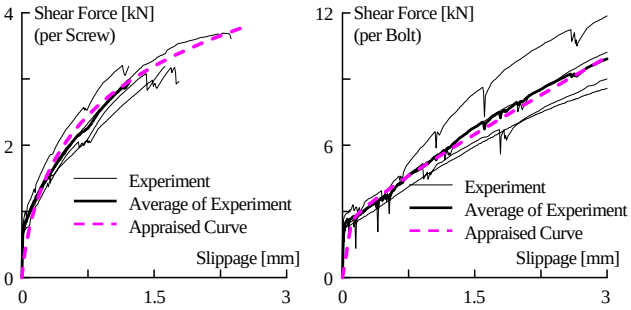

Figure 8 Appraised Curve of Screw and Bolt

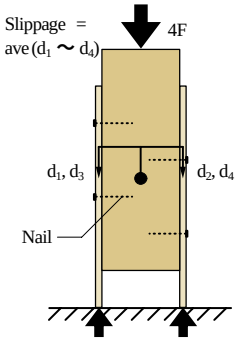

Figure 9 Shear Test of Nail

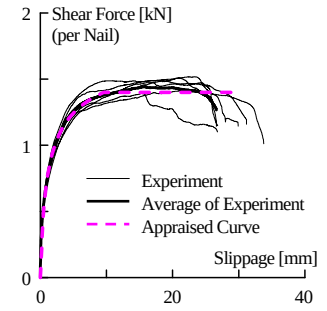

Figure 10 Appraised Curve of Nail

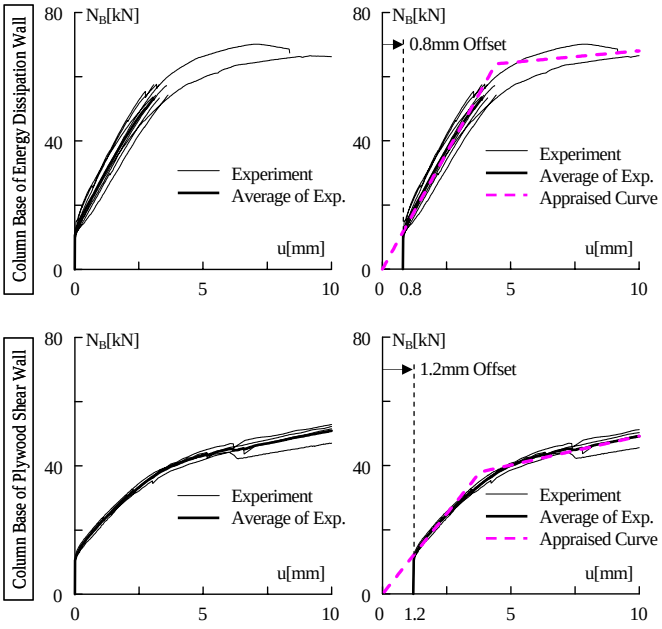

(a) Experimental Results (b) Appraised Curve

Figure 11 Appraised Curves of Axial Spring of Bolt

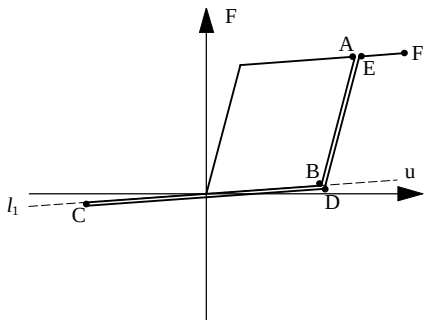

Figure 12 Hysteresis Rule of Bolt

3.2 Shaking Table Tests

As for shaking table test of two story wooden frame (see Picture 1), Figure 14 illustrates the comparison of experimental results (Matsuda et al. 2008) and analytical results. In both the plywood shear wall and the energy dissipation wall, the analytical results fit the test result about the stiffness and maximum displacement. However, in the case of plywood shear wall, after the maximum displacement the analytical result behaves smaller than the test result. The real timber structure behaves with pinched hysteresis having slippage, looks like inverse "S" symbol after the large displacement. The analytical model is not good at this point, hence there is a little error between analysis and test.

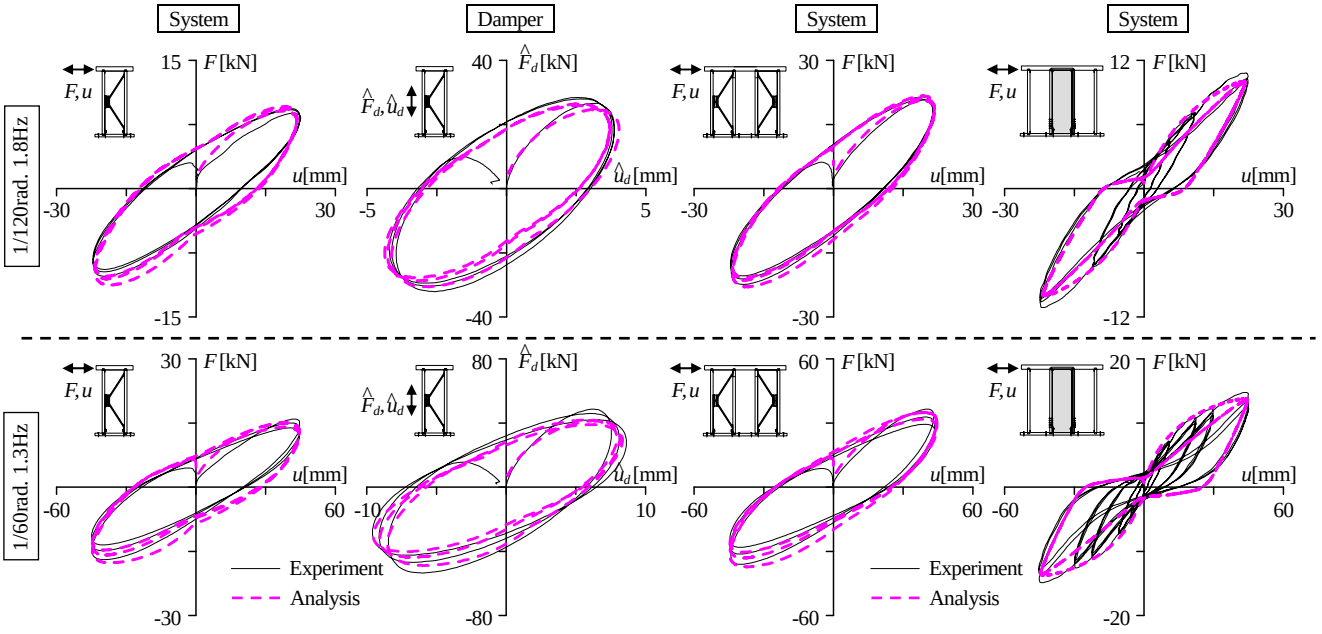

Figure 13 Comparison of Experiment and Analysis by Loading Test

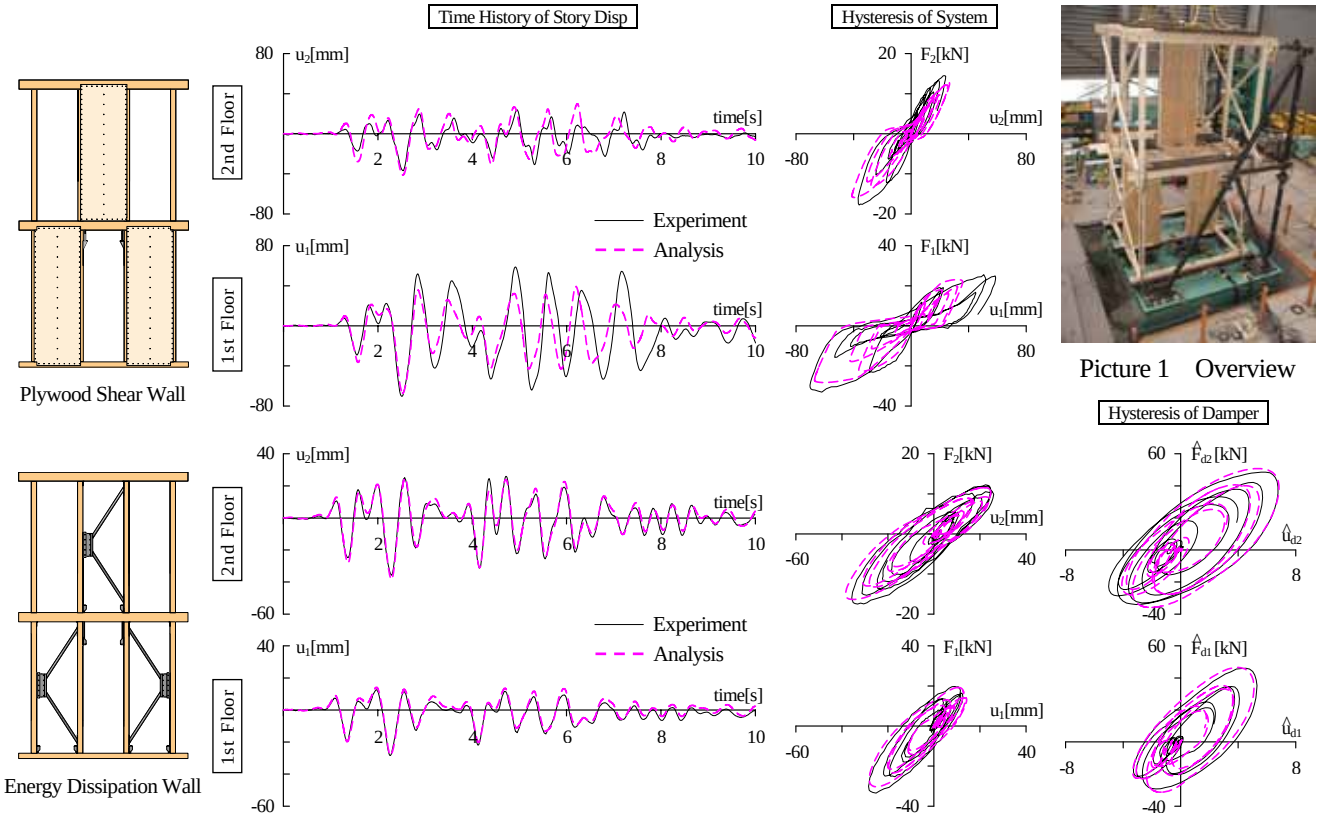

Picture 1 Overview

Figure 14 Comparison of Experiment and Analysis by Shaking Table Test

4. PARAMETRIC ANALYSIS

Parametrically seismic response analyses are carried out by inserting energy dissipation walls or plywood shear walls to the frame model of wooden structure. The frame model is set as below description.

- The floor area is determined as reason that the structure reaches necessary wall-quantity of building standard low when there are two plywood shear walls in the first floor.
- Assuming heavy roof and house where the area of the 1st-floor is equal to that of the 2nd- floor, the condition correspond to 16.6m^2.
- The mass of 2,430kg is allocated to the beam of 2nd floor, and the mass of 2,810kg is allocated to the beam of 1st floor, considering the weight for designing per floor unit.
- In order to consider the effect of nonstructural elements, seven internal walls are allocated in each floor by reference to the amount of internal wall per floor area.

To satisfy above conditions, the frame model is made up like figure 15. The frame model has below condition.

- the energy dissipation wall or the plywood shear wall whose stiffness and strength are changed, are allocated in the three points of "?" symbol in figure 15.
- 2% of stiffness proportional damping is used.

The stiffness and strength of the energy dissipation walls and plywood shear walls are changed, and standard property is defined as 1.00, such as 1.00V and 1.00W. The number indicates coefficient of the stiffness and strength, and 0.33V, 0.67V, 0.33W and 0.67W are prepared.

Reduction effect of seismic displacement by passively controlled scheme is shown in Figure 16. The vertical axis indicates maximum displacement of 1st floor when the frame model is subjected to JMA Kobe earthquake. The horizontal axis indicates the ratio of existing wall-quantity of plywood shear wall to necessary wall-quantity. In the case of applying plywood shear wall, maximum seismic displacement decreases in a linear fashion against the increment of the plywood shear wall. On the other hand, in the case of applying our energy dissipation wall, maximum seismic displacement decreases considerably even if the amount is a little. Therefore the energy dissipation wall is effective obviously.

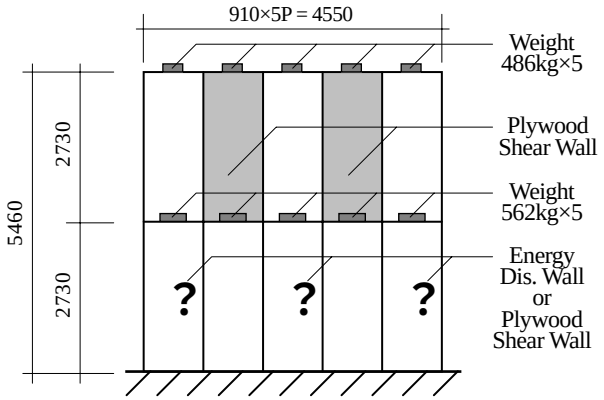

Figure 15 Outline of Analytical Model

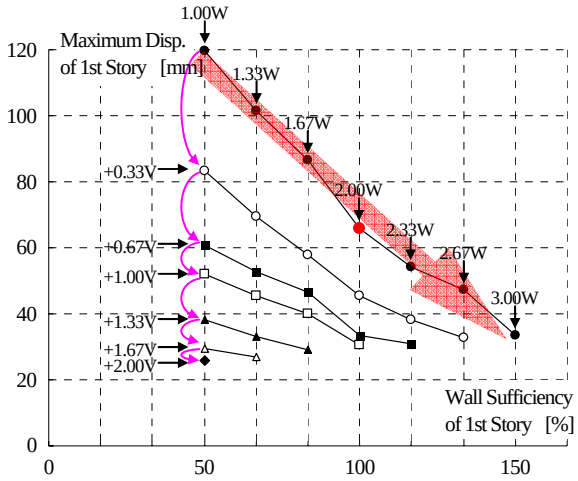

Figure 16 Outline of Analytical Model

6. CONCLUSIONS

Accurate framed analytical models for the wooden energy dissipation wall with damper and plywood shear wall were proposed. In addition, parametric study was carried out using the frame model. Major finding are

- The analytical model was constructed by using many spring elements whose properties derived from the experimental results of the joint tests. The analysis was able to duplicate the many kinds of test results with high accuracy.
- By the joint part which consists of axial, rotation and shear spring, an accurate framed analytical model was able to be made. The analytical model was useful for designing and improving the energy dissipation wall, because the effect of each member was regarded to the model. The detailed response of the wooden wall with passive control system could be obtained from the analysis.
- In the case of applying plywood shear wall, maximum seismic displacement decreased in a linear fashion against the increment of the plywood shear wall. On the other hand, in the case of applying our energy dissipation wall, maximum seismic displacement decreased considerably even if the amount was a little. Therefore the energy dissipation wall was effective obviously.

References:

Kasai, K., Sakata, H., Wada, A. and Miyashita, T. (2005): "Dynamic behavior of a wood frame with shear link passive control mechanism involving k-brace", Journal of Structural and Construction Engineering, No.598, 2005.12, pp.51-60 (In Japanese)

Matsuda, K., Sakata, H., Kasai, K. and Ooki, Y. (2008): "Experimental study on dynamic response of wooden frames with passive control", Journal of Structural Engineering, Vol.54B, 2008.3, pp.149-156 (In Japanese)

Sakata, H., Kasai, K., Wada, A., Midorikawa, M., Ooki, Y., Nakagawa, T. and Matsuda, K. (2007): "Shaking table tests of wood frames with velocity-dependent dampers", Journal of Structural and Construction Engineering, No.615, 2007.5, pp.161-168 (In Japanese)

Matsuda, K. and Kasai, K. and Sakata, H. and Ooki, Y. and Wada, A. (2007): "Shaking table tests of two-story frames with passive control system", Proceedings of 4th International Conference on Urban Earthquake Engineering, Center on Urban Earthquake Engineering, 2007.3, pp.369-374, Yokohama, JAPAN

Kasai, K., Teramoto, M., Okuma, K and Tokoro, K. (2001): "Constitutive rule for viscoelastic materials considering temperature frequency, and strain sensitivities, part 1 Linear model with temperature and frequency sensitivities", Journal of Structural and Construction Engineering, No.543, 2001.5, pp.77-86 (In Japanese)

Kasai, K. and Tokoro, K. (2002): "Constitutive rule for viscoelastic materials considering temperature frequency, and strain sensitivities, part 2 Nonlinear model based on temperature-rise, strain and strain-rate", Journal of Structural and Construction Engineering, No.561, 2002.11, pp.55-63 (In Japanese)

Kasai, K., Wada, A., Sakata, H., Ooki, Y. and Miyashita, T. (2004): "Passive control for mitigating seismic damage to wood houses, part 1 Behavior and design of joints, dampers, and system", Passive control symposium 2004, 2004.11, pp.169-184 (In Japanese)

Murakami, M. and Inayama, M. (1999): "Formulae to predict the elastic and plastic behavior of sheathed walls with any nailing arrangement pattern", Journal of Structural and Construction Engineering, No.519, 1999.5, pp.87-93 (In Japanese)

Appendix 1: Outline of Energy Dissipation Wall

The feature of K-brace passive control wall is shown below (Figure A2). When the wall deforms by horizontal force, there is vertical deformation between the brace and the steel plate and the damper is inserted in the place. The wall is classified in to a series of so-called shear link type. In order to reduce the effect of the column's bending, the edge of the brace is fixed near the joint of the column and horizontal member. There are many advantages because the contents of the wall are able to fit in inside of frames. For example it is possible to fix without an attachment of other walls. K-brace is screwed on wooden frames by a lot of screws because of high factor of safety.

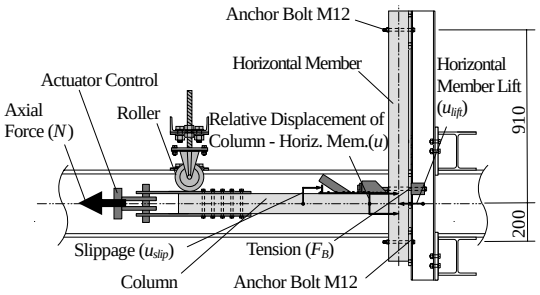

Figure A2 Setup and Measurement Method of Joint Test

A stub tenon, L-type metal and bolt (hold-down metal) are allocated in the joint of the column and horizontal member. The square steel pipe is fillet-welded to steel plate B and C (Figure A1 (e), (f)). Energy absorption capacity is increased as much as possible by allocating the bolt closer to the column, and integrating the steel plate C into the hold-down metal.

Appendix 2: An Example of Joint Test

As shown Figure A2, the horizontal member is fixed on the steel beam by two anchor bolts, and the column is pin-connected with the actuator. The locations of the anchor bolts are considered for the wall tests. The relative displacement between the column and the horizontal member (u), the slippage of the column and metal (u_{slip}) and the lift of horizontal member (u_{lift}) are measured. In the case of having a bolt, the axial force of the bolt (N_B) is measured, and initial axial force is 10 ± 0.5kN. is measured.

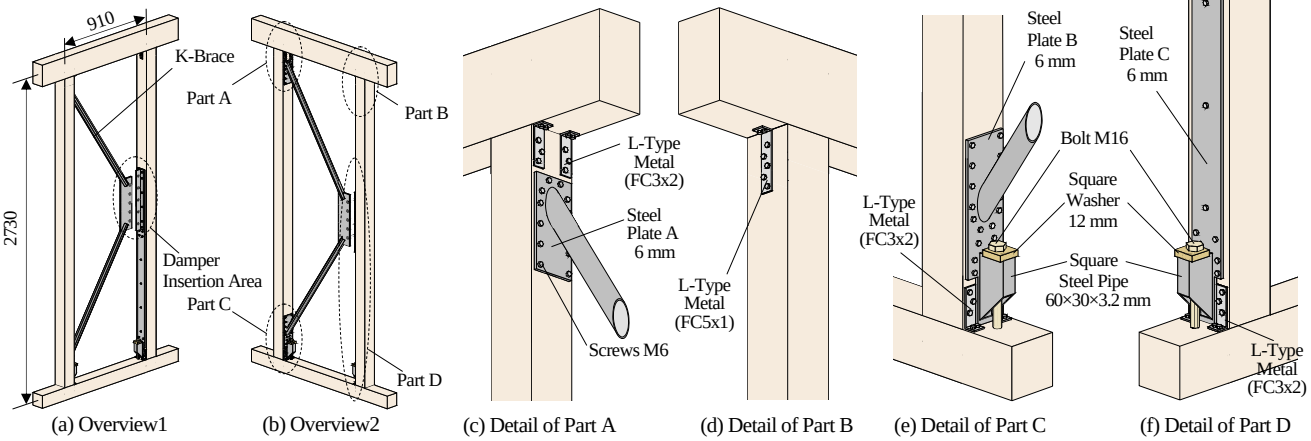

(a) Overview1 (b) Overview2 (c) Detail of Part A (d) Detail of Part B (e) Detail of Part C (f) Detail of Part D

Figure A1 Detail of K-Brace Energy Dissipation Wall

JOINT CONFERENCE PROCEEDINGS
7th International Conference on Urban Earthquake Engineering (7CUEE) &
5th International Conference on Earthquake Engineering (5ICEE)
March 3-5, 2010, Tokyo Institute of Technology, Tokyo, Japan

SEISMIC RESILIENCE OF SELF-CENTERING STEEL BRACED FRAMES WITH REPLACEABLE ENERGY-DISSIPATING FUSES – PART I: LARGE-SCALE CYCLIC TESTING

Jerome F. Hajjar[1], Matthew Eatherton[2], Xiang Ma[3], Gregory G. Deierlein[4], and Helmut Krawinkler[4]

1) Professor, Dept. of Civil and Environmental Engineering, University of Illinois, Urbana, Illinois, USA
2) Graduate Research Assistant, Dept. of Civil and Environmental Engineering, University of Illinois, Urbana, Illinois, USA
3) Graduate Research Assistant, Dept. of Civil & Environmental Engineering, Stanford University, Stanford, California, USA
4) Professor, Dept. of Civil & Environmental Engineering, Stanford University, Stanford, California USA
jfhajjar@illinois.edu, meather2@illinois.edu, maxiang@stanford.edu, ggd@stanford.edu, krawinkler@stanford.edu

Abstract: This paper reports the response of large-scale quasi-static cyclic and hybrid simulation testing of steel braced frames with replaceable energy-dissipating steel fuses. The frames are free to rock at their base and vertical post-tensioning ensures self-centering of the structure at the end of the cyclic excitation. Experimental test results are summarized from one-half scale tests of this system having several different configurations of the replaceable steel fuses. The paper highlights one of the primary framing configurations, consisting of a set of specimens having two independent braced frames, each having a set of replaceable fuses with differing characteristics, located at the central base of the frames. This configuration is comparable to that tested dynamically at the E-Defense shake table in Miki Japan in August, 2009, as summarized in a companion paper. The seismic behavior, energy dissipation, self-centering characteristics, and resilience of this system when subjected to large story drifts are explored.

1. INTRODUCTION

The controlled rocking braced-frame system is a high performance seismic force resisting system for steel-framed buildings. By virtually eliminating residual floor and roof drifts and concentrating structural damage in replaceable fuse elements, the system allows targeted structural repair after an earthquake. In contrast, traditional seismic force resisting systems rely on inelastic actions in structural members throughout the building to dissipate seismic energy and may experience significant residual drifts after large earthquakes making the building uneconomical to repair. It is expected that the controlled rocking system will provide owners and engineers a more repairable high performance alternative to traditional systems.

The controlled rocking system consists of three main components: (1) Steel frames that remain essentially elastic and are allowed to rock about the column bases. As shown in Figure 1, the column base details permit column uplift and restrain horizontal motion by bumpers or an armored foundation trough. The configuration in Figure 1 uses a single frame, although alternative configurations with two side-by-side frames have also been investigated (Eatherton et al. 2008). (2) Vertical post-tensioning strands provide active self-centering forces. The strands are initially stressed to less than half of their ultimate strength, so as to permit additional elastic straining when the frames rock. The configuration in Figure 1 employs post-tensioning down the center of the frame; other configurations with strands oriented on the column lines are also feasible (Roke et al. 2009). (3) Replaceable energy dissipating elements act as structural fuses that yield, effectively limiting the forces imposed on the rest of the structure. In Figure 1, the fuse is configured as yielding shear elements that are anchored down to the foundation with a steel assembly and connected to the rocking frame with a pinned strut. Other configurations that have been tested as part of this project include steel plates configured between two rocking frames, thus engaging these steel plates in shear, and buckling restrained braces oriented vertically at the base of the rocking frame. A number of different types of shear fuses were also tested as part of this work.

This paper briefly summaries the large-scale quasi-static cyclic tests conducted at the University of Illinois at Urbana-Champaign. Other phases of this project, discussed in Hall et al. (2006), Eatherton et al. (2008), and Deierlein et al. (2010), include: tests on a range of fuse topologies to identify steel plates with diamond-shape cutouts as the most effective fuse topology; finite element modeling of the fuses to validate their performance; a parameter study to determine key system variables; additional large-scale cyclic and hybrid simulation tests at the MUST-SIM facility; an SDOF study on self-centering systems including ambient building resistance; and

two-thirds scale shake table tests at the E-Defense facility in Miki, Japan.

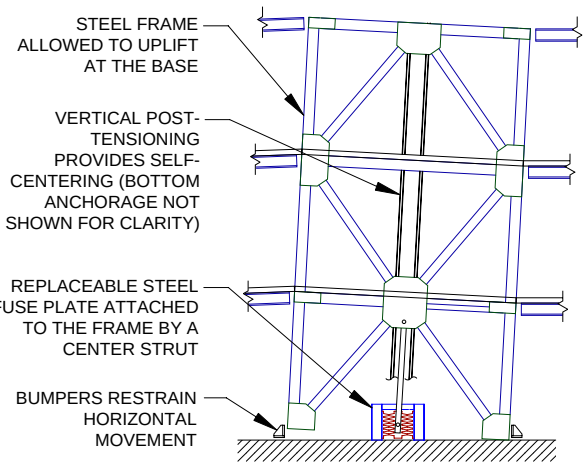

Figure 1 Example of the Controlled Rocking System

2. TEST CONFIGURATION

A series of large-scale cyclic and hybrid simulation tests were conducted at the University of Illinois at Urbana-Champaign MUST-SIM facility which is part of the George E. Brown, Jr. Network for Earthquake Engineering Simulation (NEES). As shown in Figure 2, for the configuration highlighted in this paper, two specimens were tested simultaneously, each representing an independent lateral force resisting frame. The left frame is referred to as Specimen B1 in this paper and the right frame is Specimen B2. The testing series at MUST-SIM consisted of eight specimens, seven of which not shown here made up the "A" series and utilized a double frame configuration with shear acting fuse plates attached between the frames.

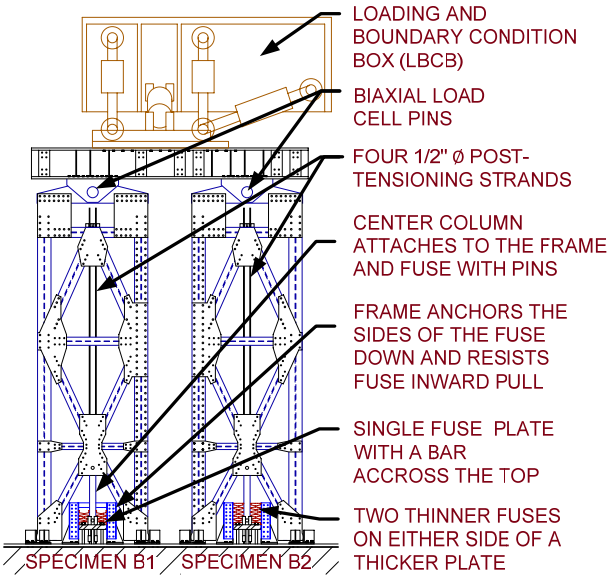

Figure 2 – Quasi-Static Test Setup at MUST-SIM

The system was proportioned based on a three-story prototype building that is 36.6 m x 54.9 m (120' x 180') located in Los Angeles, California. The specimen design strength was calculated using an assumed response modification factor of R = 8.0 (to be used in conjunction with U.S. building codes such as ASCE 7-05 (ASCE 2005), ten frames in each direction, and a scale factor of 0.43 relative to the prototype. The three-story frames were constructed using wide flange sections turned minor axis and connected using gusset plates on the front and back sides of the frames. Base plates were welded to the bottom of the columns and sat unattached on bearing plates surrounded by steel bumpers on all sides. Each frame utilized four 12.7 mm (1/2") diameter post-tensioning strands oriented vertically at the center of the frame and anchored between the roof beam and an anchorage plate at the base that was connected to the strong floor.

The two different fuse assemblies used in Specimen B1 and Specimen B2 are shown in Figure 3. Specimen B1 used a 19 mm (3/4") thick A36 steel plate with specially designed diamond shaped cutouts that create tapered links on either side of a central solid portion of the plate where the center column shown in Figure 2 connects to the fuse through a pin connection. The tapered links of Specimen B1 are designed to promote plastic hinging at the middle of the tapered length away from any discontinuities allowing large inelastic deformations without fracture. A small steel assembly is used to anchor the sides of the fuse plate down to the strong floor and brace the sides of the fuse against the inward pull developed from tension in the fuse at large displacements. The fuse plates for Specimen B2, as shown in Figure 3, use similar link geometry and result in similar capacity, but are thinner and were allowed to experience lateral-torsional buckling. Two 5mm (3/16") thick plates are used on each side of a thicker bracing plate. The bracing plate is not connected to the center column pin and thus does not become engaged in resisting shear forces. Instead, the bracing plate counteracts the inward pull the fuses apply to the side vertical supports and restrains the fuse lateral-torsional buckling to occur in one direction only.

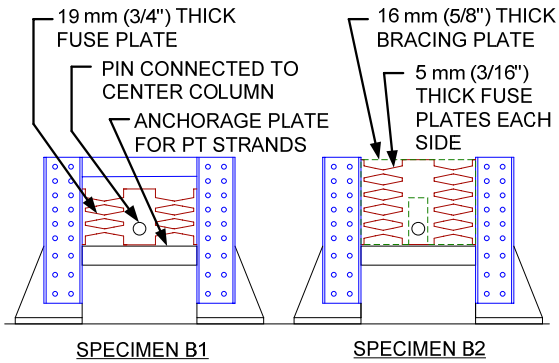

Figure 3 Blow-Up View of the Fuse Assemblies

Biaxial load cell pins shown in Figure 2 measured the forces imparted to each frame as a specified displacement history was applied to both frames simultaneously. The displacement history shown in Figure 4 was calculated to apply a shear strain history to the fuse in accordance with the

requirements of AISC 341-05 (AISC 2005) for eccentrically braced frame links. This loading protocol is designed to apply the cumulative link rotation demand and total number of inelastic cycles similar to what might be experienced in the 90th percentile of earthquake ground motions with a 10% chance of exceedance in 50 years (Richards and Uang 2006). The resulting displacement history shown in Figure 4 consists of many small amplitude cycles that transition into single cycles at each large amplitude level. Three cycles were performed at the final displacement level to assess any cyclic degradation in the system. A photograph of the test setup is shown in Figure 5.

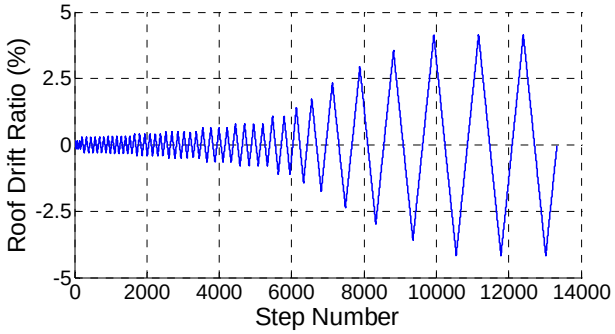

Figure 4 Applied Displacement History

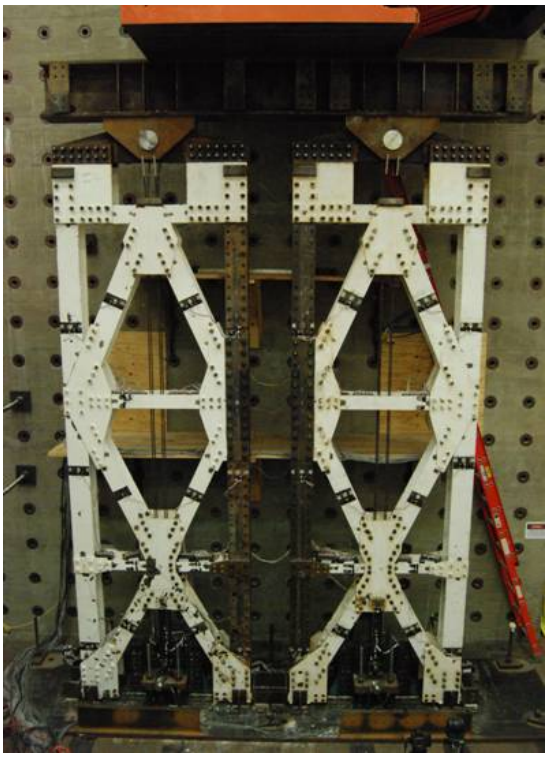

Figure 5 Picture of the Test Setup at MUST-SIM

3. COMPUTATIONAL MODEL

One of the goals of the experimental program was to verify and improve computational models to be used in conducting computational studies to further examine the application, design, and performance of the controlled rocking system in varied configurations. A two-dimensional model was created using the OpenSees software (Mazzoni et al. 2009) including geometric nonlinearities. The model consists of elastic frame elements using nominal cross-section properties with a few important exceptions. The base of the columns have a rigid element extending to the pivot point which is then connected to a restrained node through gap elements that are stiff in compression, but have zero stiffness in tension. The post-tension strands are modeled by a single truss element with bilinear elastic-plastic constitutive relationship connected to a gap element at the base that is stiff in tension but has zero stiffness in compression. The center column that attaches to the fuse uses a gap element to simulate the pin hole tolerance. This gap element generates near zero force up to a specified displacement and then becomes very stiff.

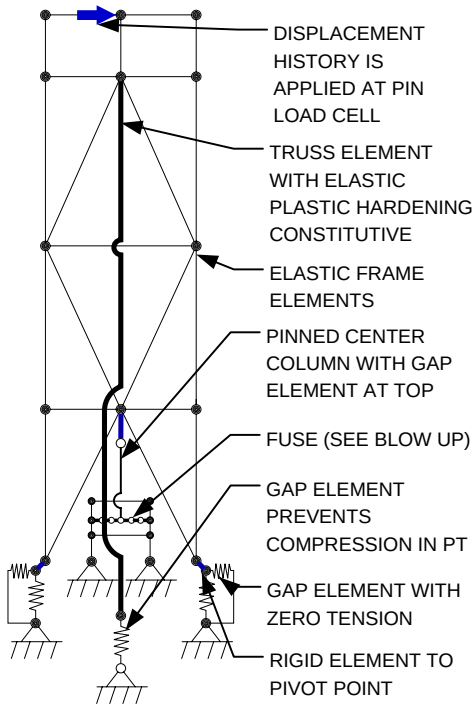

Figure 6 Computational Model Simulating the Test Setup

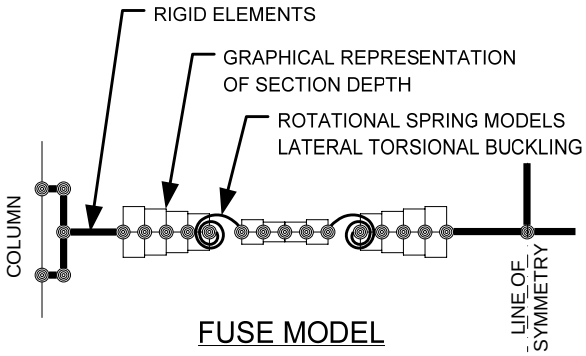

Figure 7 Blow-Up View of the Fuse Model

The fuse model, shown in Figure 7, uses fiber sections

that are segmented to allow definition of the actual varying link depth. The width of the fiber section is equal to the total thickness of all the fuse links combined, and the material is defined to be a standard steel constitutive relationship using measured material yield stress as shown in Figure 8. Rotational springs are included at the third points to simulate lateral-torsional buckling in thinner fuse plates. The moment-rotation relationship for the rotational spring is defined to be stiff and elastic up to a critical buckling moment after which the moment resistance degrades and is modeled using a pinching hysteretic response as shown in Figure 8.

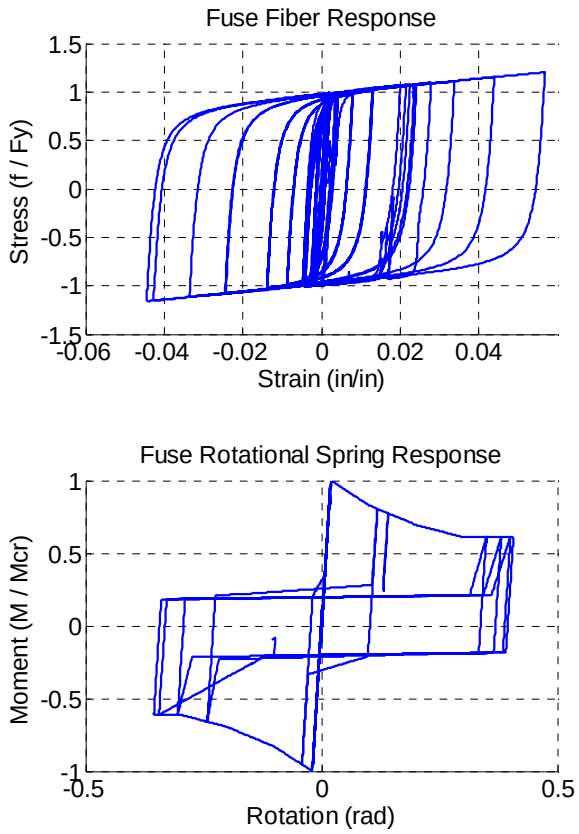

Figure 8 Typical Constitutive Relationships Used in the Fuse Fiber Sections (Top) and the Lateral-Buckling Rotational Spring (Bottom)

4. TEST RESULTS

Approximately 500 channels of data were recorded during the test including five automated digital still cameras that took over 1000 pictures each, four web based video cameras, and two high resolution video cameras. Instrumentation included linear potentiometers, LVDT's, string potentiometers, the Krypton system for measuring 3D coordinates of a set of LED's, inclinometers, strain gages, and load cells. Only a small portion of the data is presented here. Figures 9, 10, and 11 show the behavior of Specimen B1 whereas Figures 12, 13, and 14 show the behavior of Specimen B2.

The force-displacement figures included here (e.g., Figure 9) use overturning moment as the vertical axis which is equal to the lateral force multiplied by the height of application divided by the calculated design overturning moment. The design overturning moment, M_y is given in Equation (1) based on the plastic fuse capacity, V_p, the initial post-tensioning force, F_{pti}, and the frame width, A. Overturning moment is shown instead of base shear because the response is dominated by first mode rocking rather than shear related deformations and overturning moment removes the dependence on the height of load application. The horizontal axis shows the roof drift ratio, equal to roof displacement divided by roof height.

$$M_y = \left(V_p + F_{pti}\right)\frac{A}{2} \qquad (1)$$

The force-displacement response of the controlled rocking system as shown in Figure 9 and Figure 12 produces flag-shaped hysteresis loops that are characteristic of self-centering systems. When the lateral loads are removed, the frame returns to its initial position.

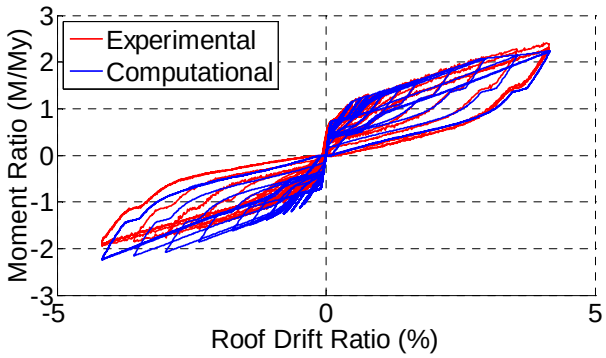

Figure 9 Force-Displacement Response of Specimen B1

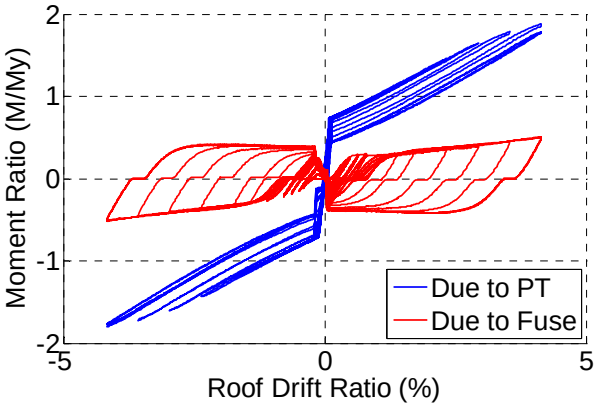

Figure 10 Decoupled System Response for Specimen B1

The flag shape is made of two parts that can be decoupled, as shown in Figure 10. Up until roof drifts of approximately 2.5%, the post-tensioning exhibits a bilinear elastic behavior for which the initial slope is due to frame deformation prior to the base of the frame lifting off its support, and the secondary slope is due to increasing force as

the post-tensioning strands subsequently elongate further. The base of the frames experienced almost 76 mm (3") of uplift, which translates into approximately 38 mm (1.5") of elongation in the post-tensioning strands.

The portion of the response due to the Specimen B1 fuse is mostly elastic-plastic with some added features as shown in Figure 10. As the frame approaches and passes through zero roof drift ratio, the fuse pin is being loaded downward, reaches its lowest vertical location, and begins to be loaded in an upward direction. This creates an unloading and reloading at zero roof drift. The fuse is only loaded in one direction relative to its original position as shown in Figure 11. In this figure, the horizontal axis is shear strain, calculated as the vertical displacement of the center of the fuse divided by the length of the fuse link which is 152 mm (6") and the vertical axis is the shear force divided by the fuse plastic capacity, V_p, which is calculated based on plastic hinges at the quarter points of the fuse links. The plastic fuse capacity as given in Equation (2) for tapered links, with a ratio of middle depth to end depth equal to one-third, is a function of the number of links, n, the link depth at the end, b, the plate thickness, t, the measured material yield stress, F_y, and the link length, L.

$$V_p = \frac{4}{9}\frac{nb^2tF_y}{L} \qquad (2)$$

The hardening shown in Figure 11 is due to material strain hardening and due to axial forces being generated within the fuse links due to the geometric lengthening caused by the large shear deformations. The experimental yield strength was found to be approximately 70% of the plastic capacity and therefore below the fuse response predicted by the computational model.

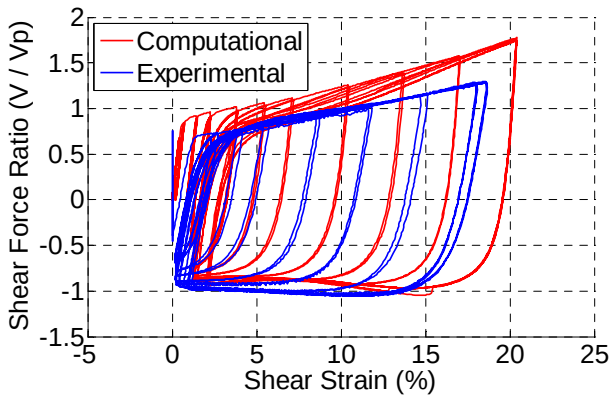

Figure 11 Fuse Hysteretic Response for Specimen B1

Figure 10 also shows flat portions in the fuse response at zero moment ratio due to the pin hole tolerance in both ends of the pinned strut connecting the frame to the fuse. The force in the fuse remains at zero until all the pinned connections again become engaged. This lag due to pin hole tolerance is also noted in the global response shown in Figure 9. The lag in force was found to correspond to 4.7 mm (0.19") and 5.1 mm (0.20") of center column displacement for Specimen B1 and B2, respectively. Since this is the total for engaging two separate plies at both ends of the member and assuming all four holes have approximately the same tolerance, this implies that each hole was 1.25 mm (0.05") larger than the pin, which is within the specified tolerance of 1.59 mm (1/16"). As previously described, the computational model utilizes a gap element at the connection of the center column to the frame representing this pin hole tolerance. The system response of the computational model shown in Figure 12 demonstrates the ability of this gap element to reproduce the same lag as experienced in the experiment.

As shown in Figure 10, the post-tensioning strands in Specimen B1 underwent yielding. The yielding occurred in all of the post-tensioning strands and caused a small loss in restoring force. The yielding was modeled reasonably well by the bilinear elastic-plastic constitutive used in the computational model as demonstrated in Figure 9.

Specimen B2 exhibited many of the same response characteristics as described above for Specimen B1 with a few differences, most notably degradation of the fuse behavior and the occurrence of post-tensioning wire fracture. As shown in Figure 12, there is less energy dissipation for the large displacement cycles than exhibited for Specimen B1. This reduction is reinforced by the fuse behavior shown in Figure 13 and Figure 14. Figure 14 shows that lateral-torsional buckling initiated in the links of the fuse during the second to last displacement level, at which point the fuse experienced significant reduction in strength and stiffness. The computational model response shown in Figure 14 simulates lateral-torsional buckling through pinching, but is a simplification of the experimental behavior, which is a complex interaction of flexure, buckling, and axial forces.

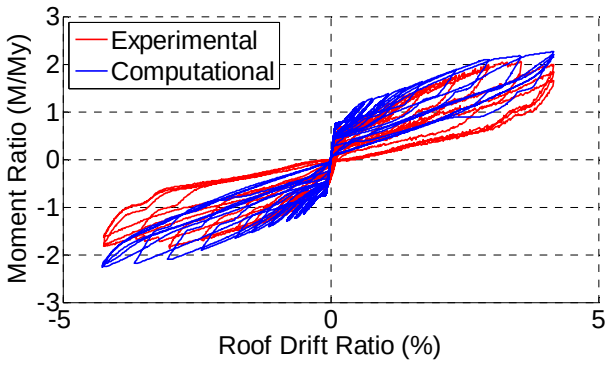

Figure 12 Force-Displacement Response of Specimen B2

Figure 15 shows the post-tensioning strand fracture as the five sharp losses in the post-tension force. Accompanying the loss of force is a loss in stiffness caused by reduced post-tensioning area. Each post-tensioning strand consists of seven individual steel wires wound together. At large elongations (near 1% strain), some of the post-tensioning strands in Specimen B2 started to fracture individual wires. However, as shown in Figure 15, the loss of one wire did not propagate through to the other wires in

this displacement controlled test setup. Five wires of the total 28 wires contained in the 4 post-tensioning strands fractured in Specimen B2, whereas none of the strands fractured in Specimen B1. There were no apparent significant differences between the construction of each frame or the installation of the post-tensioning strands between the two, but since the majority of the fractures were concentrated in the right frame throughout the testing program it is expected that there were minor differences in the anchorage and that post-tensioning strand fracture is sensitive to these differences. Each fracture caused a proportionate loss in the restoring force, but not a significant loss of load-carrying capacity of the system.

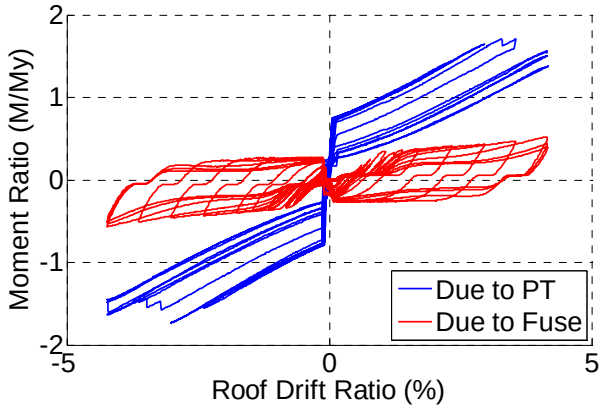

Figure 13 Decoupled System Response for Specimen B2

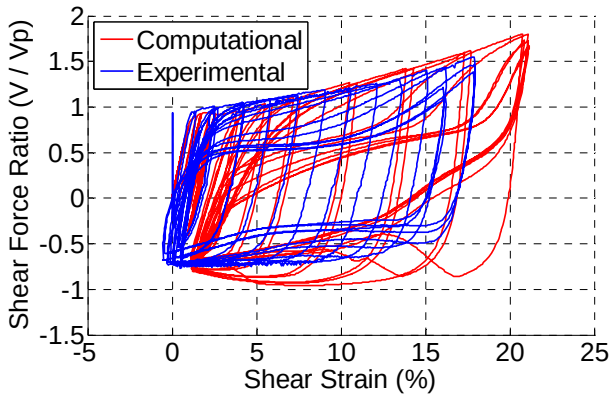

Figure 14 Fuse Hysteretic Response for Specimen B2

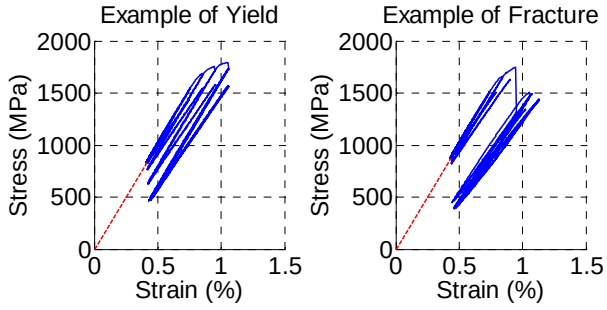

Figure 15 Examples of Stress Strain Responses for Single Post-Tensioning Strands

Since the post-tensioning element in the computational model utilizes a bilinear elastic-plastic constitutive relationship, the computational model does not capture the effect of wire fracture. As a result, the computational model prediction shown in Figure 12 does not exhibit as much loss of strength and stiffness as the experiment.

5. DISCUSSION OF EXPERIMENTAL RESULTS

The controlled rocking system successfully concentrated structural damage in the replaceable fuse elements, which was best demonstrated by the fact that the same steel frames were used in all eight specimens. Through the course of the testing series, fuses and post-tensioning strands were replaced, and different configurations were tested, but the frames did not sustain any significant damage. Furthermore, the controlled rocking system also successfully eliminated residual drifts as demonstrated by the zero displacement when the load is removed as shown in Figure 9 and Figure 12. The system therefore satisfied the specified performance goals related to repairability after large earthquakes.

It was also concluded that the connection details at the base of the columns that allow uplift and pivoting but restrained horizontal movement using bumpers as well as the post-tensioning anchorage details which are also not currently common in steel structures performed well. Since bearing connections were incorporated in a form that allowed slip between adjacent elements, tolerances become an important consideration in designing connections such as the pinned strut connecting the frame to the fuse and the gap left between the base of the frame and the bumpers.

The pin hole tolerances are cumulative in the frame to fuse strut connections creating a lag in the fuse response upon load reversal. This lag, however, did not affect the ability of the fuse to dissipate significant seismic energy throughout the test, nor did it affect the overall performance goals for the system. The effect of the tolerances in these connections was also reduced considerably in the related E-Defense shake table test specimen by fixing the connection at the top of the strut and reducing the pin hole tolerance in the connection to the fuse.

Similarly, consideration should be given to designing the amount of gap to be left between the base of the frames and the bumper. The size of this gap was varied in other tests not reported here and the sliding at the base between the bumpers had an effect on the overall response of the system. In Specimens B1 and B2 reported in this paper, the gap was small such that the effect on system response was negligible. It is expected that in practice, reasonable construction tolerances may be used, and the gap between the bumper and the frame could be eliminated by shimming between the two.

The specially designed steel fuse plates with butterfly shaped links exhibited large deformation capacity and the ability to absorb considerable amounts of energy without fracturing. The results from a thinner fuse that was allowed to experience lateral-torsional buckling, and a thicker fuse that did not buckle, were reported above. The strength and

stiffness of the thinner fuses degrades at large displacements after lateral-torsional buckling occurs whereas the thicker fuse plates do not. The degradation of the fuse resistance can be considered beneficial in that configurations where some restoring force is lost at large displacements due to post-tensioning strand yield or fracture, will experience improved self-center capability because of the reduced fuse resistance. On the other hand, since the thick fuses did not degrade or fracture in any of the tests, even after repeated testing in some cases, the thick fuses may not require replacement after most earthquakes.

At elongations of greater than 0.8%, the post-tensioning strands started to experience yielding. Five wires out of the total 56 wires that made up the eight post-tensioning strands, fractured during the test as the strands were stressed to elongations up to 1.2%. The fractures however, did not propogate through the other wires in the strand or cause fracture in other strands. After testing to a roof drift ratio of 4%, post-tensioning strand yield and strand fracture caused some reduction in the restoring force provided by the post-tensioning, but the system still had considerable load carrying capacity and the ability to eliminate displacements when the force was removed.

6. CONCLUSIONS

A series of large-scale tests were conducted on a self-centering steel braced-frame system with replaceable energy-dissipating fuses. This paper reports the results of cyclic tests on configurations consisting of a single steel braced frame with a fuse assembly at the center base of the frame. Cyclic tests and hybrid simulation tests were also conducted on a configuration with fuses attached between two rocking frames. Large-scale shake table tests conducted at the E-Defense facility in Miki, Japan are reported in a companion paper. The results of all of these tests demonstrate the ability of this system to concentrate structural damage in replaceable steel fuse plate elements and eliminate drifts when the lateral loads are removed.

Ongoing work involves further computational studies to characterize the performance of the system as it is applied to different configurations as well as the development of design recommendations. It is hoped that this work will provide the engineering community with a high performance alternative to traditional seismic force resisting systems that allows targeted structural repair after large earthquakes.

Acknowledgements:

This material is based upon work supported by the National Science Foundation under Grant No. (CMMI-0530756), the American Institute of Steel Construction, Stanford University, and the University of Illinois at Urbana-Champaign. In-kind funding was provided by Tefft Bridge and Iron of Tefft, Indiana, MC Detailers of Merrillville, Indiana, Munster Steel Co. Inc. of Munster, Indiana, Infra-Metals of Marseilles, Indiana, and Textron/Flexalloy Inc. Fastener Systems Division of Indianapolis, Indiana. The authors thank Prof. Sarah Billington, graduate students, Kerry Hall, Alejandro Pena, Eric Borchers, and Paul Cordova, practicing structural engineers, David Mar and Gregory Luth, and our Japanese collaborators for their contributions to this research. The LBCB Operations Manager and LBCB Plugin used in this research were developed by Narutoshi Nakata, Matt Eatherton, Oh Sung Kwon, Sung Jig Kim, and Curtis Holub with support from NEES@UIUC, Grant No. A6000 SBC NEES OMSA-2004, and the Mid-America Earthquake Center, NSF Grant No. EEC-9701785. Any opinions, findings, and conclusions or recommendations expressed in this material are those of the authors and do not necessarily reflect the views of the National Science Foundation or other sponsors.

References:

American Institute of Steel Construction (2005) *ANSI / AISC 341-05 Seismic Provisions for Structural Steel Buildings*, Published by the American Institute of Steel Construction , Chicago, Illinois

American Society of Civil Engineers (2005) *ASCE / SEI 7-05 Miminum Design Loads for Buildings and Other Structures*, Published by the American Society of Civil Engineers

Deierlein, G. G., Ma, X., Hajjar, J. F., Eatherton, M., Krawinkler, H., Takeuchi, T., Midorikawa, M., Hikino, T., and Kasai, K. (2010), "Seismic Resilience of Self-Centering Steel Braced Frames with Replaceable Energy-Dissipating Fuses – Part 2: E-Defense Shake Table Test" *7th International Conference on Urban Earthquake Engineering*, Tokyo, Japan, March 3-5, 2010.

Eatherton, M., Hajjar, J. F., Deierlein, G. G., Krawinkler, H., Billington, S.,and Ma, X. (2008). "Controlled Rocking of Steel-Framed Buildings with Replaceable Energy-Dissipating Fuses," *Proceedings of the 14th World Conference on Earthquake Engineering*, Beijing, China, October 12-17, 2008.

Hall, K. S., Eatherton, M., and Hajjar, J. F. (2006) *Nonlinear Behavior of Controlled Rocking Steel-Framed Building Systems with Replaceable Energy Dissipating Fuses*, UIUC Report No. ST-06-01, Department of Civil and Environmental Engineering, University of Illinois at Urbana-Champaign, Urbana, Illinois, 2006.

Mazzoni, S., McKenna, F., Scott, M. H., and Fenves, G. L. (2009) *Open System for Earthquake Engineering Simulation User Command-Language Manual*, OpenSees version 2.0, Pacific Earthquake Engineering Research Center, University of California, Berkeley, CA, May.

Richards, P. W., and Uang, C.-M. (2006) "Testing Protocol for Short Links in Eccentrically Braced Frames" ASCE *Journal of Structural Engineering*, Vol. 132, No. 8

Roke, D., Sause, R., Ricles, J. M., and Gonner, N. (2009) "Design Concepts for Damage-Free Seismic-Resistant Self-Centering Steel Concentrically Braced Frames" *ASCE Structures Congress*, April 30- May 2, 2009, Austin Texas

JOINT CONFERENCE PROCEEDINGS
7th International Conference on Urban Earthquake Engineering (7CUEE) &
5th International Conference on Earthquake Engineering (5ICEE)
March 3-5, 2010, Tokyo Institute of Technology, Tokyo, Japan

SEISMIC RESILIENCE OF SELF-CENTERING STEEL BRACED FRAMES WITH REPLACEABLE ENERGY-DISSIPATING FUSES – PART II: E-DEFENSE SHAKE TABLE TEST

Gregory G. Deierlein[1], Xiang Ma[2], Jerome F. Hajjar[3], Matthew Eatherton[4], Helmut Krawinkler[1], Toru Takeuchi[5], Mitsumasa Midorikawa[6], Tsuyoshi Hikino[7], and Kazuhiko Kasai[5]

1) Professor, Dept. of Civil and Environmental Engineering, Stanford University, USA
2) Graduate Research Assistant, Dept. of Civil and Environmental Engineering, Stanford University, USA
3) Professor, Civil and Environmental Engineering, University of Illinois, USA
4) Graduate Research Assistant, Civil and Environmental Engineering, University of Illinois, USA
5) Professor, Structural Engineering Research Center, Tokyo Institute of Technology, Japan
6) Professor, Division of Architectural and Structural Design, Hokkaido University, Japan
7) National Research Institute for Earth Science and Disaster Prevention, Japan

ggd@stanford.edu, maxiang@stanford.edu, jfhajjar@illinois.edu, meather2@illinois.edu, krawinkler@stanford.edu, ttoru@arch.titech.ac.jp, midorim@eng.hokudai.ac.jp, hikino@bosai.go.jp, kasai@serc.titech.ac.jp

Abstract: This is the second of two papers that describes research to develop a new type of steel braced frame system that employs controlled rocking and replaceable energy dissipating fuses to resist earthquake ground motions. This paper focuses on the planning, design and results of a large-scale three-story frame that was tested at the E-Defense shake table facility in August 2009. Test results are summarized from shaking table tests of specimens with three different fuse types under varying ground motions. The frames were subjected to the strong ground motion records from the 1994 Northridge and 1995 Kobe earthquakes, scaled to represent various ground motion intensities, up to and beyond Maximum Considered Earthquake (MCE) intensities. Under MCE motions, the peak drift ratios were on the order of about 2% to 2.5% with no residual drifts or damage to the steel frame, except moderate yielding of the replaceable steel fuse. The tests further confirmed the (a) accuracy of nonlinear analyses to simulate the frame response, (b) robustness of the steel post-tensioning and the column rocking behavior, and (c) models to establish design requirements for the frame components. Research is ongoing to generalize the test results and establish performance-based design provisions for the rocking frame systems.

1. INTRODUCTION

A controlled rocking steel braced frame system is developed to provide buildings with self-centering and damage control capability under earthquake attacks. This system allows columns to uplift at their bases, and thus reduce force demand in the frame members which are sized to remain elastic during the motion. Meanwhile, post-tensioning strands and steel shear fuses are employed to provide overturning resistance, energy dissipation and self-centering capability. Intended behavior and desirable seismic performance was confirmed by static pushover and pseudo-dynamic testing of the system conducted at the University of Illinois at Urbana-Champaign. More details about the concept and test results can be found in part 1 of this paper series (Hajjar et. al, 2010). To further corroborate the system's performance under dynamic loading, large scale (2/3 scale) shake table tests were conducted at the E-Defense facility in Miki, Japan.

Multiple configurations of the system were examined as shown in Figure 1. These alternatives primarily differ in the locations of the post-tensioning strands and shear fuses. Option 2 has the fuses located at the center of the first-story bay and the post-tensioning strands running down the two columns. Option 3 reverses the locations of the fuses and post-tensioning strands, and option 1 has both of them at the center. Such different arrangements have several implications which are best exemplified by first comparing options 2 and 3. In the case of option 2, only half of the strands are stretched depending on which side of the frame uplifts, whereas in option 3, all of them are effective regardless of to which direction the frame rocks. Given the same amount of column uplifting, strands at the side experience twice as much elongation as those located in the center, which results in higher deformation and force demand in each strand. In terms of overturning resistance, option 2 and 3 need the same total amount of post-tensioning since the length of lever arm in option 2 is twice as long as

that in option 3. Similar comparisons can be made to understand the influence on fuse behavior. Other implications relate to architectural and construction concerns such as space occupation and convenience of installation. A summary of the issues is provided in Table 1.

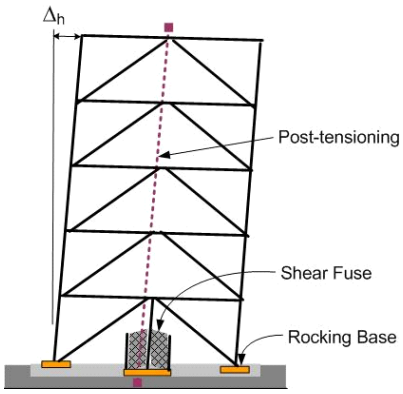

(a)

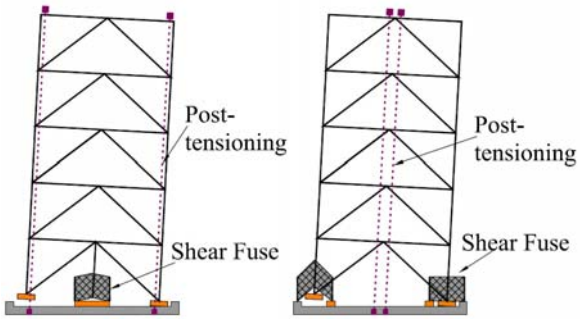

(b) (c)

Figure 1 Rocking Frame Alternative Configurations: (a) Option 1, (b) Option 2 and (c) Option 3

Table 1 Summary of Single Frame Design Alternatives

Factors	Option 1 All at Center	Option 2 Center Fuse	Option 3 Side Fuse
Amount of PT & fuse	Same	Same	Same
PT deformation demand	Lower	Higher	Lower
Fuse deformation demand	Lower	Lower	Higher
Space occupation	Less	Less	More
PT/fuse installation	Crowded at the center	Cumbersome for PT	Cumbersome for fuse

Option 1 was chosen for the E-Defense shake table test. This decision was based on concerns about post-tensioning deformation demand and space usage. Since the specimen was a 2/3 scale three-story frame, the total length of post-tensioning strands is limited to about 8 m which allows only about 70 mm elongation before the strands yield. Having the strands in the center has the advantage of reducing strand deformation demand and increasing safety margin again strands yielding and fracturing. The fuses are placed in the center to avoid intruding into space outside the frame span and make the design look more compact. In practice, since the buildings are generally taller, constraint on post-tensioning deformation demand is more relaxed. Space usage requirement also varies. Therefore a decision in practice may lead to other choices among the options depending on the actual situation.

An example of a shear fuse tested at Stanford University as part of this research is shown in Figure 2. This fuse was fabricated, using standard water-jet cutting, from a thin (6 mm thick) steel plate. For the initial loading region, up to about 7% shear distortion in this example, the fuse links resisted shear force through flexural action with fat hysteresis loops. Beyond deformations of about 7% shear distortion, the links began to buckle in a torsional-flexural mode. At this stage, the flexural resistance of the links decreases and the links begin to resist forces through tension field action. Upon load reversal, the hysteresis loops become pinched as the links buckle in compression and then pick up force again as they stretch in tension. While the pinching decreases the amount of energy dissipated at each cycle, the drop in resistance at large deformations tends to improve the self-centering characteristics of the rocking frame.

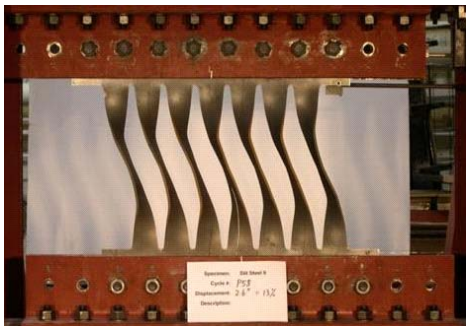

(a)

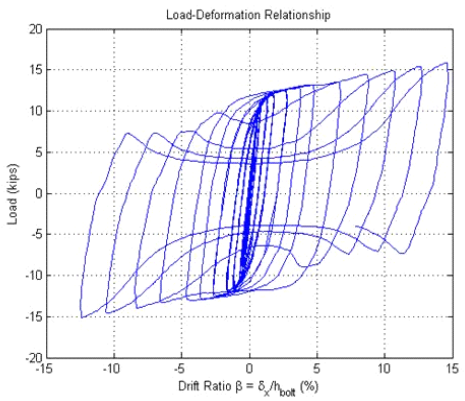

(b)

Figure 2 Butterfly Shear Fuse: (a) Test Specimen and (b) Load-Deformation Hysteresis

2. SHAKE TABLE TEST

2.1 Prototype Building and Similitude Rules

The prototype building for the shake table specimen is based on the SAC building configuration referenced in Gupta et al. (1999). Figure 3 shows the floor plan and the elevation of the building. It's a three-story four bay by six bay structure with typical floor and roof framing, assumed to be located near Los Angeles in California. Lateral resistance is provided solely by the controlled rocking system, while the rest of the structure carries gravity load. Four rocking units are located on the perimeter in each direction, with each unit comprising a single frame rocking system. The total weight of a typical story is 958 ton, and each rocking frame shares 958/4=240 ton.

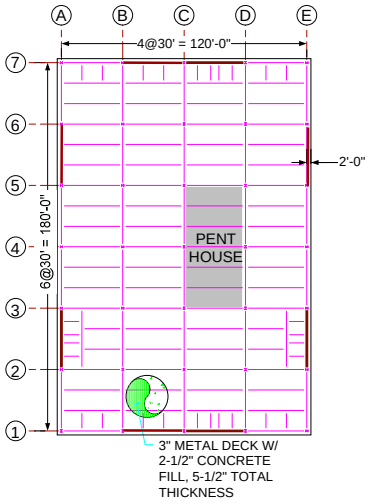

(a)

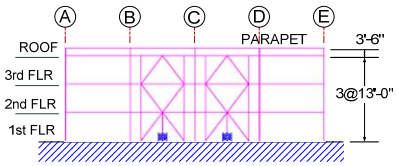

(b)

Figure 3 Prototype Building: (a) Floor Plan and (b) Elevation

Table 2 Similitude Rules

Quantities		Derivation	Ratios
Length	l_r	decided by test design	0.68
Young's modulus	E_r	decided by test design	1.00
Acceleration	a_r	decided by test design	1.00
Mass	m_r	$= E_r l_r^2 / a_r = l_r^2$	0.46
Time	t_r	$= [m_r/(E_r l_r)]^{0.5}$	0.82
Strain	ε_r	dimensionless	1.00
Stress	σ_r	$= E_r$	1.00

Similitude relationship is shown in Table 2. The dimensional scale is determined by the 2.7 m story height of the test specimen and mass testbed. More details about the mass testbed are given later. Story height of a real building is 4 m which results in a dimensional scale of 2.7/4 ≈ 0.68. A number of similitude rules have been examined by Moncarz and Krawinkler (1981). The set of rules adopted here are chosen to avoid altering material property such as Young's modulus, reduce tonnage of required mass, and minimize distorting acceleration and time scales. According to the mass scale m_r, the required weight at each floor for a rocking specimen is 240 ton x 0.46 = 110 ton.

2.2 Test Specimen Design

Details of the specimen frame are shown in Figure 4. The specimen is a relatively stiff three-story braced steel frame. H-shape members in weak axis bending are used for all the members for the convenience of detailing the welded connections. The member sizes are determined by performing dynamic analysis in advance to ensure that the frame remain elastic throughout the motion.

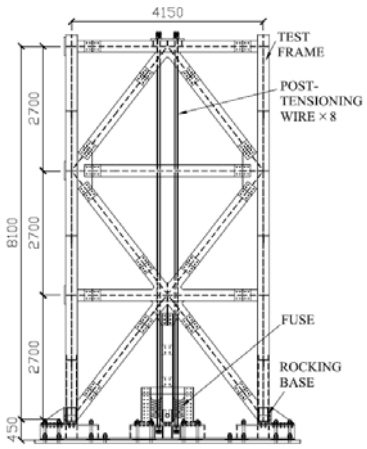

(a)

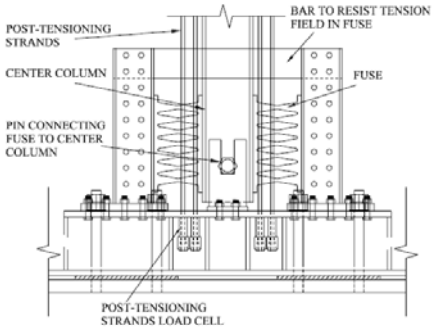

(b)

Figure 4 Specimen Drawing: (a) Specimen Frame (b) Fuse Assembly

2.3 Test Setup

As shown in Figure 5a, the shaking table specimen is located inside a re-usable testbed assembly (shown in grey in Figure 5) that provides the inertial mass and bracing for out-of-plane stability (Takeuchi et al., 2008). The testbed consists of multiple mass units stacked on top of each other

with linear sliders between each story. The mass comprises a concrete block and steel plates, which provides slightly more than 50 ton for each unit. At each story, the added mass is the sum of the weights of two testbed units, or about 101 ton which is close to the estimate of 110 ton based on the prototype mass that is scaled down by similitude rules.

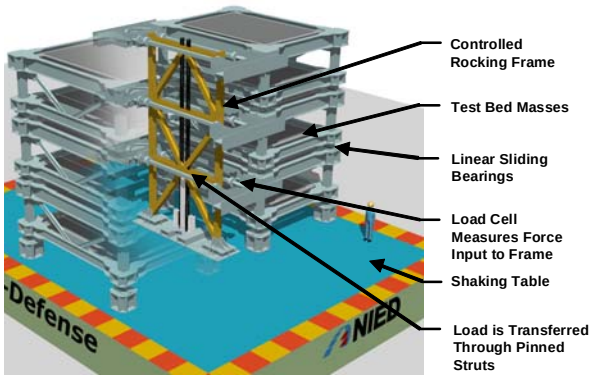

(a)

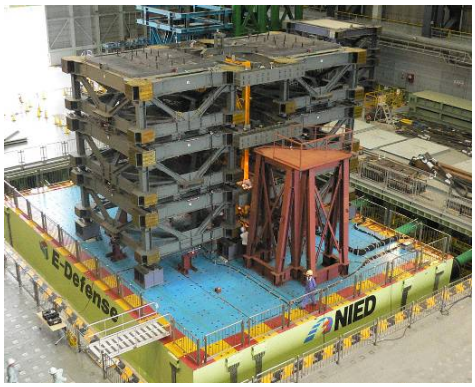

(b)

Figure 5 Test Setup: (a) 3D Schematic (b) Photo

2.4 Ground Motions

Ground motions recorded in the 1994 Northridge and 1995 Kobe earthquakes were selected for the test. Original acceleration spectra are shown in Figure 6 (a). To scale the record to various intensity levels, a pushover analysis of the structure was performed to obtain the load-deflection backbone curve of the structure. Then the initial stiffness and secant stiffness at the expected maximum roof drift were used to find that the period of the structure ranges roughly between 0.3 and 2.0 sec. Finally, as shown in Figure 6 (b), the least square error method was used to match the spectra with design spectrum between the aforementioned range of periods. The resulting scale factors for maximum considered earthquake (MCE) level is 0.69 for the JMA Kobe record and 1.4 for the Northridge record.

2.5 Test Matrix

Four tests of the rocking frame were conducted to investigate alternative fuse designs and effect of different ground motion inputs, as summarized in Table 3. Each specimen was subjected to multiple shakings with varying degrees of intensity. The non-degrading fuse is made of a 22 mm thick steel plate, with it links expected to sustain repeated shear drifts beyond 30% without degradation. The degrading fuse is only 6 mm thick, and typically would buckle under larger drifts as described previously. In test C, the fuse assembly was removed and a buckling-restrained brace (oriented vertically) was used in its place.

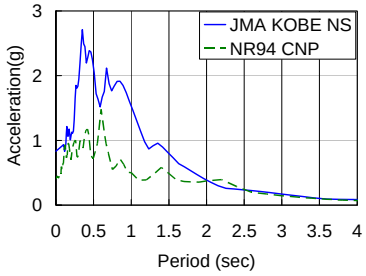

(a)

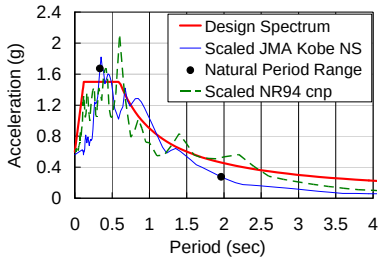

(b)

Figure 6 Response Spectra of Ground Motions: (a) Original Records (b) Scaled Records

Table 3 Test Matrix

Test ID	Fuse	Ground Motions	Motion Intensity
A1	Non-degrading Butterfly Fuse	JMA Kobe NS	30%~65% (MCE)
A2	Non-degrading Butterfly Fuse	Northridge Canoga Park	25%~140% (MCE), 175%
B	Degrading Butterfly Fuse	JMA Kobe NS	10%~60%
C	Buckling Restrained Brace	JMA Kobe NS	10%~65% (MCE)

3. TEST RESULT

3.1 Overall System Behavior

Results from test A1 with 65% of JMA Kobe (MCE) ground motion are shown in Figure 7, together with the numerical prediction performed prior to the test. Numerical modeling is explained in section 4 of this paper. Uplift ratio is defined as the ratio of column uplift to frame bay width, which almost coincides with roof drift ratio since the frame

was primarily undergoing rigid rotation. It can be seen from Figure 7 (a) that the maximum uplift is about 2%. It was confirmed from strain gauge readings that all the frame members and post-tensioning strands remained elastic, as intended in the design. Inelastic deformation only occurred in the shear fuses, which dissipated energy through hysteretic behavior as evidenced in Figure 7 (b). The loops always returned to the origin, thus confirming the self-centering capability of the system. No residual deflection existed after the shake.

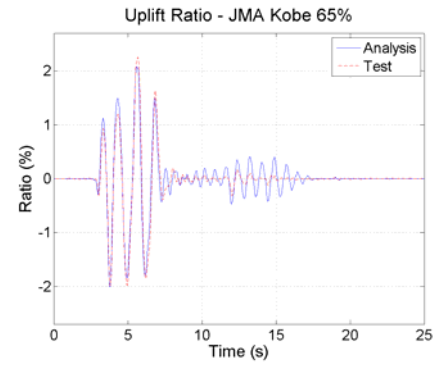

(a)

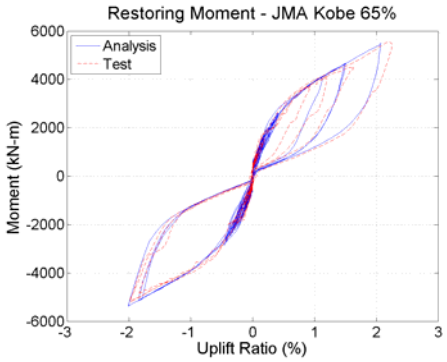

(b)

Figure 7 Test and Analysis Results from Test A1: (a) Uplift Time-History and (b) System Restoring Moment Hysteresis

3.2 Fuse Behavior

The effect of different fuses is examined by comparing the response from test A1, B and C. For the same ground motion input, the shapes of load-deformation hysteresis for the non-degrading shear fuse and BRB are similar. System response such as uplift ratio in the two cases was almost identical. The degrading fuse, on the other hand, led to considerable difference in response as shown in Figure 8. The fuse hysteresis loops of the degrading fuse are significantly pinched, which results in less overturning resistance and energy dissipation. Under the 55% JMA Kobe motion, the specimen with a non-degrading fuse had a maximum uplift ratio of 1.8%, whereas specimen with a degrading fuse had 2.2% uplift. The specimen with a BRB had a maximum response of 1.7%. These differences show how the hysteretic response and energy dissipation of the fuse influence the system's response. Moreover, the non-grading fuse is almost equally effective as BRB in limiting the frame's maximum uplift.

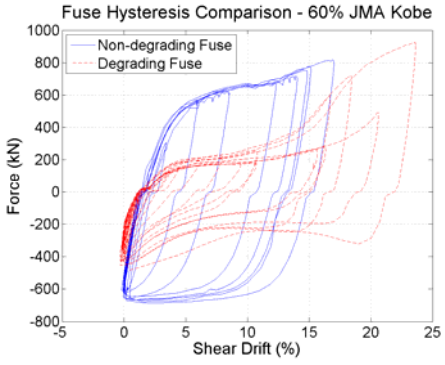

(a)

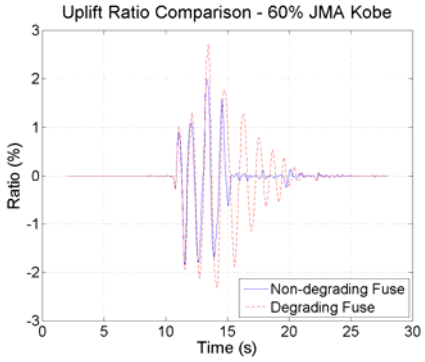

(b)

Figure 8 Influence of Fuses from Comparing Test A1 and Test B: (a) Fuse Hysteresis and (b) Frame Uplift Ratio

3.3 Ground Motions

Comparison between A1 and A2 demonstrates the variability of response resulting from ground motions. Figure 9 shows that the maximum uplift ratios for the MCE level JMA NS and Northridge ground motions are 2.3% and 2.8%, respectively. It can be observed from the uplift time-history that the system has a dominant period of about 1.2 s. At this period, Figure 6 (b) shows the acceleration of JMA Kobe record is significantly lower than that of the Northridge record, which is the likely reason for the large difference in response.

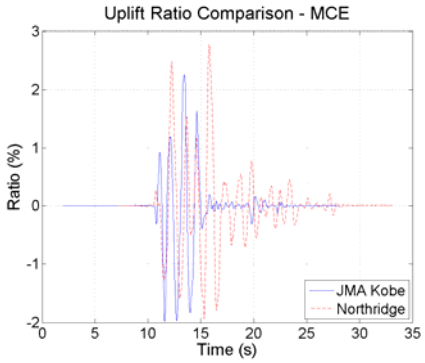

Figure 9 Influence of Ground Motions

4. NUMERICAL MODELING

A 2D numerical model was built using the program OpenSees (Mazzoni et al., 2009) to perform FEM analysis of the system. As shown in Figure 10, co-rotational beam-column elements were used to model the braced frame. Compression only springs are defined at the base to allow free uplifting of the columns. The butterfly shaped fuse links are modeled by truss and rotational spring elements with equivalent axial and bending capacities. The mass testbed is represented by lumped masses on three nodes that are constrained to move horizontally. Springs are placed between the mass nodes to simulate friction in the linear sliders. Rayleigh damping of 0.5% is assumed based on data reported in a comparable test conducted by Midorikawa et al. (2006).

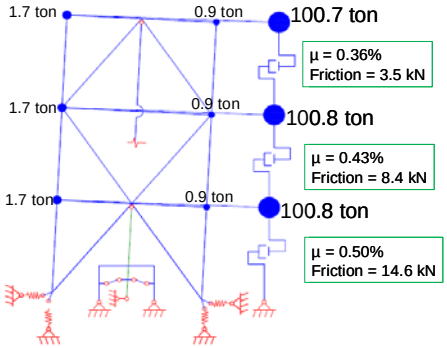

Figure 10 OpenSees Model

As shown in Figure 7, agreement between numerical prediction and test result is reasonably good. Difference in maximum response is less than 10%, with the analysis generally under-predicting the result. Notable differences can be observed in uplift ratio time-history response after 10 sec, where the measured response quickly damps out, whereas the calculated response requires a few more cycles of rocking before the frame completely settles down. The difference may be attributed to damping effects that are not captured in the model such as pounding at the column bases, other collisions in the load path, and friction at the pin connections.

5. CONCLUSIONS

Overall, the large-scale shaking table tests confirmed the behavior and reliability of the controlled rocking frame system. In particular, the tests demonstrated,

(1) the successful self-centering and damage control capabilities of the frame;
(2) validity of criteria and guidelines for capacity design of the braced frame components that are intended to remain elastic, including the effects of pounding impact on the columns and base plate details;
(3) reliability of the steel post-tensioning tendons and the influence of modest levels of tendons on the response;
(4) the influence on fuse degradation and energy dissipation capacity on the rocking response;
(5) that the simplified OpenSees numerical model is effective in predicting the system's seismic response.

Finally, the successful design, fabrication, erection and testing of the large-scale specimen demonstrated the viability of overall controlled rocking frame concept and its practical implementation through the steel braced-frame system.

Acknowledgements:

This research is supported by the National Science Foundation (Grant No. CMMI-0530756), NIED in Japan, the American Institute of Steel Construction, Stanford University, and the University of Illinois). Additional support and materials for the test frame were provided by the Japanese Iron and Steel Federation and the Nippon Steel Corporation. The authors acknowledge contributions of our industry partners from the US (David Mar and Gregory Luth), the excellent NIED staff at E-Defense, the Japanese construction and instrumentation team (Tomoe Corporation, Tomoe Giken, Maekawa Construction Co., Ltd., Kanden Plant Corp., Seitech, Tokyo Sokki Kenkyujo Co., Ltd), and students and collaborators from Tokyo Institute of Technology, Hokkaido University, and Kyoto University.

References:

Gupta, A., and Krawinkler, H. (1999). "Seismic Demands for Performance Evaluation of Steel Moment Resisting Frame Structures." John A. Blume Earthquake Engineering Center Report, No. 132, Stanford University.

Hajjar, J. F., Eatherton, M., Ma, X., Deierlein, G. G. and Krawinkler, H. (2010). "Seismic Resilience of Self-Centering Steel Braced Frames with Replaceable Energy-Dissipating Fuses – Part 1: Large Scale Cyclic Testing" *7th International Conference on Urban Earthquake Engineering*, Tokyo, Japan.

Mazzoni, S., McKenna, F., Scott, M. H., and Fenves, G. L. (2009). "Open System for Earthquake Engineering Simulation User Command-Language Manual", Pacific Earthquake Engineering Research Center, University of California, Berkeley.

Midorikawa, M., Azuhata, T., Ishihara,T., and Wada, A. (2006). "Shaking Table Tests on Seismic Response of Steel Braced Frames with Column Uplift." Earthquake Engng Struct. Dyn., 35, pp. 1767–1785.

Moncarz, P. D., and Krawinkler H. (1981), "Theory and Application of Experimental Model Analysis in Earthquake Engineering", John A. Blume Earthquake Engineering Center Report, No. 50, Stanford University.

Takeuchi, T., Kasai, K., Midorikawa, M., Matsuoka, Y., Asakawa, T., Kubodera, I., Kurokawa, Y., Kishiki, S., and Ando, H. (2008). "Shaking Table Test Using Multipurpose Test Bed", 14th World Conference on Earthquake Engineering, Beijing, China.

JOINT CONFERENCE PROCEEDINGS
7th International Conference on Urban Earthquake Engineering (7CUEE) &
5th International Conference on Earthquake Engineering (5ICEE)
March 3-5, 2010, Tokyo Institute of Technology, Tokyo, Japan

SEISMIC BEHAVIOR OF STEEL ROCKING FRAMES BY THREE-DIMENSIONAL SHAKING TABLE TESTS

Mitsumasa MIDORIKAWA[1], Tadashi ISHIHARA[2], Tatsuya AZUHATA[3], Tetsuhiro ASARI[4], Hirotake HORI[5] and Takayoshi KUSAKARI[6]

1) Professor, Graduate School of Engineering, Hokkaido Univ., Japan
2) Senior Researcher, National Institute for Land and Infrastructure Management, MLIT, Japan
3) Division Head, National Institute for Land and Infrastructure Management, MLIT, Japan
4) Assistant Professor, Graduate School of Engineering, Hokkaido Univ., Japan
5) Kajima Corp., Japan (Former Graduate Student of Hokkaido Univ.)
6) Graduate Student, Graduate School of Engineering, Hokkaido Univ., Japan
midorim@eng.hokudai.ac.jp

Abstract: The seismic response of three-story, one-by-two bay, one-third-scale steel rocking frames with columns allowed to uplift is evaluated and compared with that of fixed-base frames by three-dimensional shaking table tests. The base plates with four wings, yielding due to tension of column, are installed at the bottom of each column of the first story of the rocking frames. The test frames are the moment-resisting frames and the braced frames in the longitudinal and transverse directions, respectively, and are vibrated in three different input-motion conditions; one horizontal component for each direction, two horizontal components and three components of a ground motion record. The earthquake motion used for the tests is the JMA Kobe record of the 1995 Kobe earthquake with its time scale shortened to $1/\sqrt{3}$. The results are summarized as follows: 1) The maximum base shears of the rocking frames are effectively reduced from those of the fixed-base frames; 2) While the maximum uplift displacements of the column bases of the rocking frames increase with the increase of the number of components of the input motion, the horizontal response values such as the roof drifts and base shears are not affected by that.

1. INTRODUCTION

It has been pointed out by past studies (Housner 1963, Rutenberg et al. 1982, Hayashi et al. 1999) that the effects of rocking vibration accompanied with uplift motion might reduce the seismic damage to buildings subjected to strong earthquake ground motions. The influence of uplift motion on the seismic behavior of building structures has been reasonably explained through the simple analysis (Meek 1975, 1978) followed by other studies (Chopra and Yim 1985, Yim and Chopra 1985, Oliveto et al. 2003, Wada et al. 2005, Ishihara et al. 2009).

Based on these studies, structural systems have been studied and developed which allow the rocking and uplift motion under proper control during strong earthquake motions (Clough and Huckelbridge 1977, Huckelbridge 1977, Kasai et al. 2001, Iwashita et al. 2002, Midorikawa et al. 2003, 2006). One of the features of a rocking structural system is that the maximum strain energy associated with the horizontal deformation of a superstructure is reduced, because a portion of the total earthquake input energy exerted to the system is substituted by the potential and kinetic energy associated with the vertical motion of the system as shown in the previous works (Iwashita et al. 2003, Azuhata et al. 2004).

A rocking structural system under research and development by the authors (Midorikawa et al. 2003, 2006) makes use of the uplift yielding mechanism of specially designed flexing base plates. When the base plates yield due to column tension during a strong earthquake motion, the columns uplift and allow the building structure to rock.

Most of the previous studies mentioned above have evaluated the two-dimensional behavior of an uplift structural system. Although the three-dimensional response of an uplift structural system has been evaluated by the analysis (Midorikawa et al. 2009), it has not been examined through an experimental study.

In this paper, the seismic response of three-story, one-by-two bay, one-third-scale steel rocking frames with columns allowed to uplift is evaluated and compared with that of fixed-base frames by three-dimensional shaking table tests. The inelastic three-dimensional behavior of base-plate-yielding (BPY) rocking frames is discussed that were retested under three different input-motion conditions; one horizontal, two horizontal and three components of the 1995 JMA Kobe record. The objectives of the study are to improve the understanding of the seismic response of rocking frames subjected to a three-dimensional strong

earthquake motion and to validate the feasibility of designing steel frames to enable the rocking response through column base-plate deformations.

2. TEST STRUCTURES AND EXPERIMENTAL PROCEDURES

Three-story, one-by-two bay, one-third-scale braced steel frames were tested on the shaking table of the weight capacity of 500 kN. The test frames were retested using two different base conditions: base-plate-yielding uplift-base (BPY model) and fixed-base (FIX model). The test frames are composed of yielding base plates, columns, girders, and bracing members, as shown in Figure 1. There is no significant difference between two frames in the longitudinal direction, and among three frames in the transverse direction. The total height of the test structure is 3 m, 1 m for each story. The floor dimension is 4×2 m and the total weight of the test frame is 182 kN.

In the longitudinal (X) direction, the test frame has two moment-resisting frames with a span of 2 m each. In the transverse (Y) direction, the test frame has three braced frames with a span of 2 m. The bracing member is a high-strength steel bar with a diameter of 9.2 mm and tensile strength of 980MPa. These bracing members are prestressed to a half of the yield strength so that they resist both compression and tension forces.

Yielding base plates are installed at the bottom of each column of the first story of BPY models, as shown in Figure 2. The base plate of BPY model has four wings that are each 110mm long and 60mm wide. The outside end of each wing of yielding base plate is constrained and connected to a steel foundation beam by a steel plate 40mm thick and two high-strength bolts (M24) so that plastic hinge lines are formed at both ends of each wing.

The test frames are vibrated in three different input-motion conditions; one horizontal, two horizontal and three components of the 1995 JMA Kobe record with its time scale shortened to $1/\sqrt{3}$. Each test frame is subjected to earthquake ground motions several times with the maximum input velocity of the vector sum of two horizontal components scaled to a range of levels to simulate various earthquake intensities from 0.05 to 0.5 m/s for BPY model and from 0.05 to 0.2 m/s for FIX model, respectively. Figure 3 shows the acceleration response spectra for the 1995 JMA Kobe ground motion record.

The instrumentation was designed to measure both global structural response and local element response in critical portions of the test frames. The measured data include: horizontal accelerations on the shaking table, horizontal accelerations and relative horizontal displacements at each floor level, axial strains of the first-story columns and bracing members, and uplift displacements of the first-story column bases. The maximum sampling frequency is 1000 Hz. The column shears are calculated from the moment distribution using measured values of strain gauges attached to the first-story columns. The base shear is calculated by summing the shears of the columns and bracing members at the first story. This value corresponds quite well with the base shear obtained from the measured accelerations and masses on each floor.

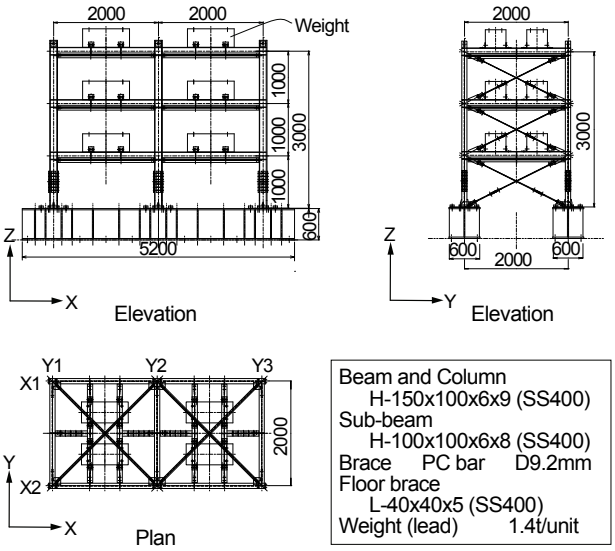

Figure 1 Test frame

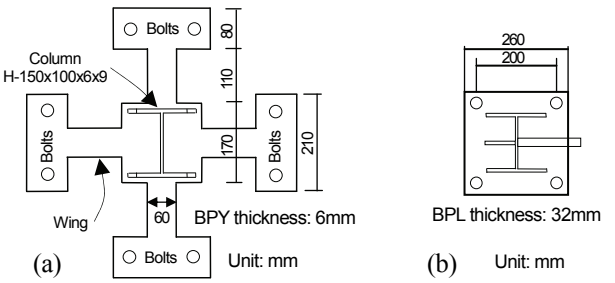

Figure 2 Plan of Base Plates:
(a) Uplift yielding base plate, and (b) Fixed base plate

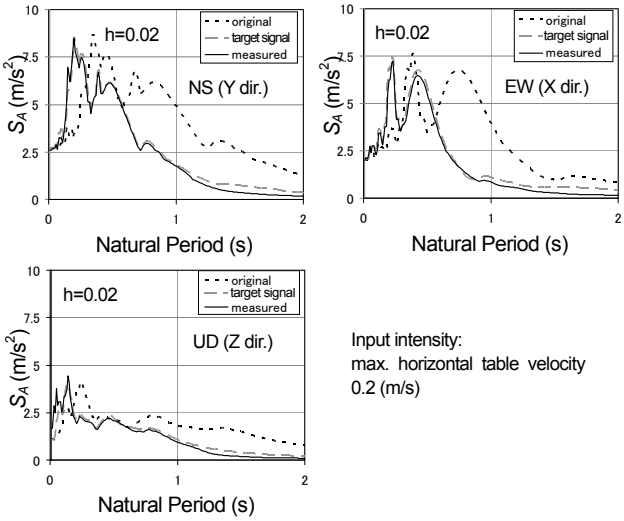

Figure 3 Acceleration Response Spectra of Measured Table Accelerations

3. TEST RESULTS AND DISCUSSION

3.1 Dynamic Characteristics of Test Structures

The fundamental natural periods and the critical damping ratios for the first mode of the test frames estimated from the impact tests using a wooden hammer are listed in Table 1. The critical damping ratios were obtained from the bandwidth method. The fundamental natural period of BPY model is longer than that of FIX model by 28 % and 8 % in the longitudinal and transverse directions, respectively.

Table 1 Natural Periods and Damping Ratios of the First Mode

Model		Period (s)	Damping ratio (%)
BPY	Long.	0.245	2.0
	Trans.	0.181	1.7
FIX	Long.	0.192	1.5
	Trans.	0.168	1.2

3.2 Time Histories of Roof Drift, Uplift Displacement and Base Shear

Figure 4 illustrates the time histories of the roof drift response of the test frames. BPY and FIX models are indicated by bold and thin lines, respectively. The responses of FIX model indicated by dashed lines in Figures 4 and 5 is extrapolated from the test results subjected to the maximum input table velocity of 0.2 m/s, based on the assumption that the response of FIX model is elastic as is observed in the tests. While the maximum roof drifts of BPY model are larger than those of FIX model in the transverse direction, the former are almost equal or smaller than the latter in the longitudinal direction.

Figure 5 shows the time histories of the base shear response of the test frames. The base shears of BPY model are smaller than those of FIX model regardless of the input-motion intensity. Furthermore, along with the increase of the input-motion intensities, the difference between two models also increases.

3.3 Relationships of Base Shear vs. Roof Drift and Uplift Force vs. Displacement

Figure 6 shows the relationships of the base shear and roof drift of the test frames. The response of FIX model was kept in elastic in the test for the maximum input table velocity of 0.2 m/s. In the response of BPY model, the superstructure was kept in elastic but the base plates yielded in the tests for the maximum input table velocity of 0.2 and 0.5 m/s. The higher mode effect is observed in the hysteretic behavior of BPY model.

The relationships of the uplift force and displacement of yielding base plates are illustrated in Figure 7. The uplift force is estimated from the column axial force and the vertical component of brace axial force at the first story. The effect of the dead loads is excluded since the initial values of strain gauges in each shaking test cycle were reset to zero positions in instrumentation. It is pointed out that the characteristics of uplift hysteretic behavior at the column base obtained from the three-dimensional dynamic tests are consistent with the results obtained from the statically cyclic loading tests of yielding base plates subjected an uplift force (Ishihara et al. 2003).

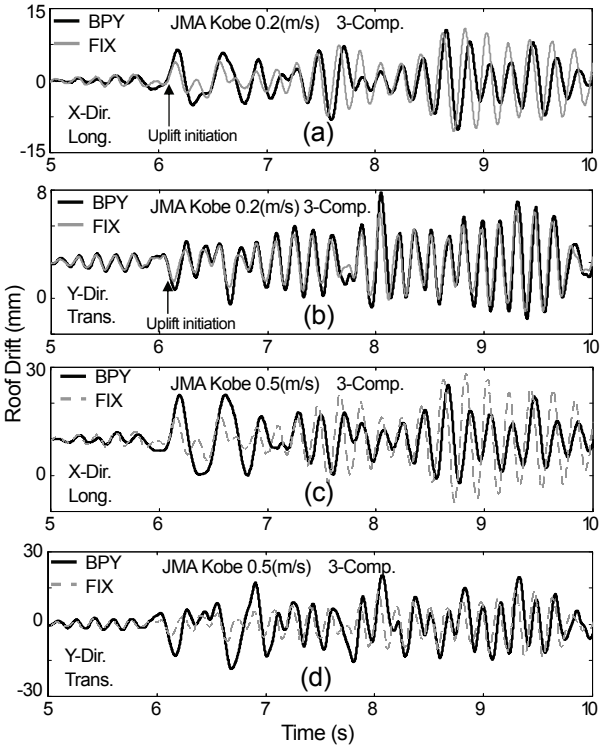

Figure 4 Time Histories of Roof Drift

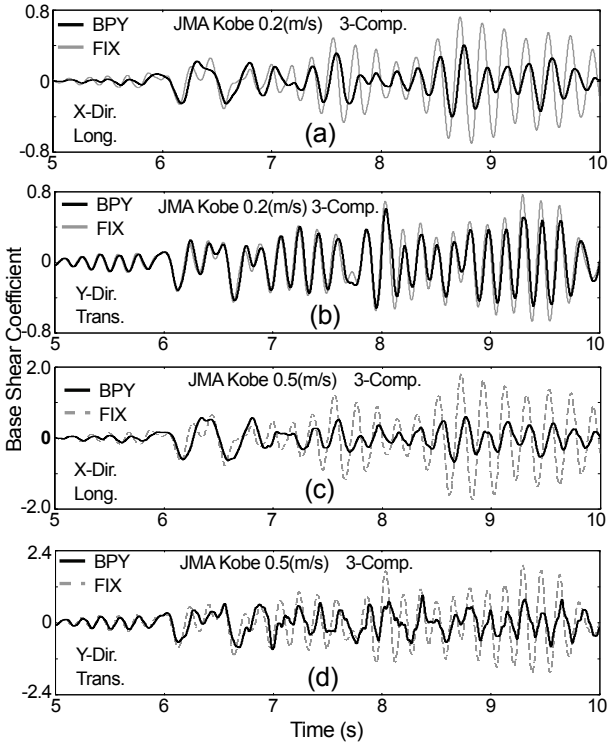

Figure 5 Time Histories of Base Shear

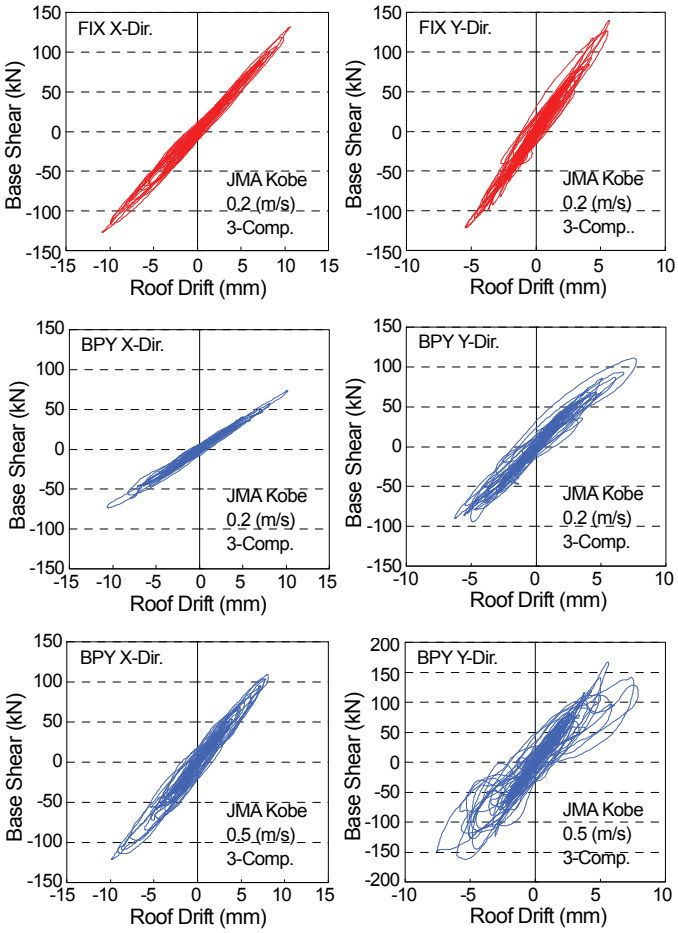

Figure 6 Base Shear vs. Roof Drift

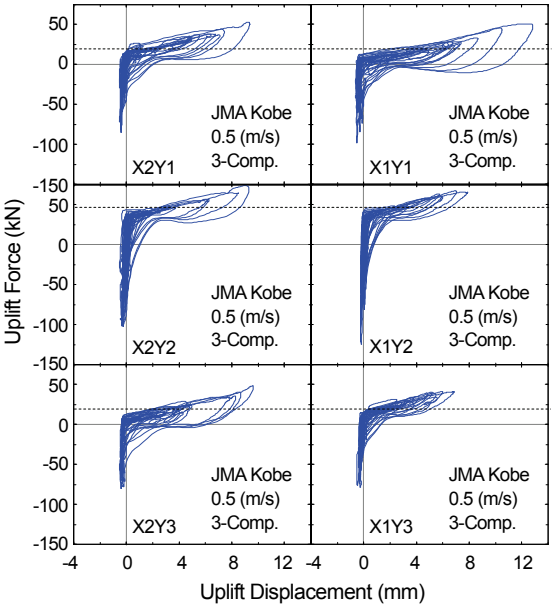

Figure 7 Uplift Force vs. Displacement

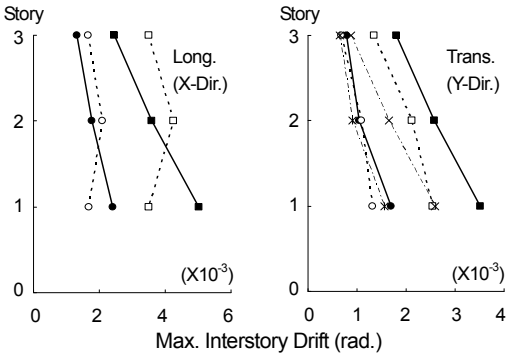

(a) Max. Interstory Drift

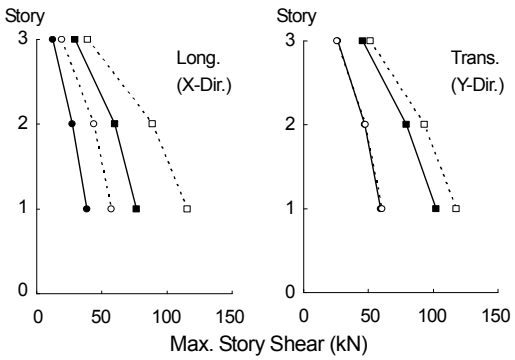

(b) Max. Story Shear

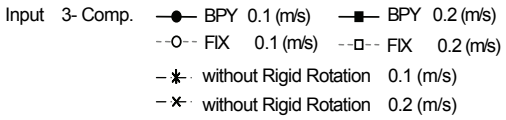

Figure 8 Distribution of Maximum Response Envelopes

3.4 Distribution of Maximum Response Envelopes along the Height

Figure 8 shows the distribution of the maximum response envelopes of interstory drift and story shear along the height of the test frames. The maximum interstory drifts of BPY model are smaller than those of FIX model in the longitudinal direction except for the first story. Although the maximum interstory drifts of BPY model are larger than those of FIX model in the transverse direction, the response values excluding the rocking component of BPY model are almost equal to or smaller than those of FIX model. When the maximum input table velocity becomes 0.2 m/s, the response reduction effect of BPY model is clearly observed and all story shears of BPY model are smaller than those of FIX model in both directions. It is pointed out that the response deformation of the superstructure of BPY model is suppressed because of the rocking component of the response displacement.

3.5 Relationships of Maximum Responses vs. Input-motion Intensity

The relationships of the maximum roof drift of the test frames and input table velocity are illustrated in Figure 9(a). When the maximum input velocity is less than 0.3 m/s, the response values are almost the same between both models in the longitudinal direction. Along with the increase of the maximum input velocity over 0.3 m/s, the response values of BPY model become smaller than those of FIX model, and the difference between two models increases. In the transverse direction, the response values of BPY model are

larger than those of FIX model by about 40 % regardless of the input-motion intensity.

Figure 9(b) shows the relationships of the maximum base shear of the test frames and input table velocity. The response values of BPY model are smaller than those of FIX model in both directions. Furthermore, the difference between both models increases in accord with the increase of the maximum input velocity.

Figure 9(c) shows the relationships of the maximum column axial force of the test frames and input table velocity. The column axial force does not include the effect of dead loads. The variable range of the axial forces is symmetrical in tension and compression before the uplift motion is induced. The tensile axial forces for BPY model are limited to a relatively constant value after the uplift motion occurs. The compressive axial forces for BPY model are less than or about the same as those for FIX model. Consequently, the maximum column axial forces of BPY model never exceed those values of FIX model.

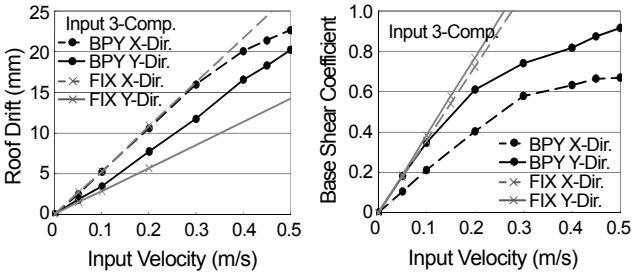

(a) Max. Roof Drift (b) Max. Base Shear Coefficient

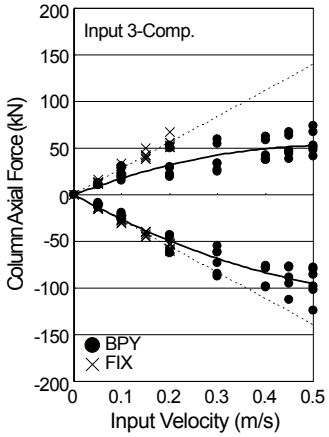

(c) Max. Column Axial Force

Figure 9 Maximum Response Envelopes vs. Input Intensity

3.6 Effect of Components of Input Motion on Maximum Responses

The relationships of the maximum response of BPY models for three different input-motion conditions and input table velocity are illustrated in Figure 10. Plotted are the maximum response values for the input motion of one horizontal, two horizontal and three components, respectively.

Figure 10(a) shows the relationships of the maximum roof drift and input velocity. The maximum roof drifts are not affected by the number of components of the input motion in both directions.

Figure 10(b) shows the maximum uplift displacement of X1Y1 and X2Y3 column-bases and input velocity. The maximum uplift displacements of the both column bases increase with the increase of the number of components of the input motion over the maximum input velocity of 0.2 m/s. Consequently, the uplift displacement of BPY model is somewhat affected by the number of components of the input motion.

Figure 10(c) shows the relationships of the maximum base shear and input velocity. The increase rates of base shears are reduced along with the increase of the maximum input velocity over 0.2 m/s, at which the uplift displacements of column bases are definitely observed, in both directions. While the number of components of the input motion does not affect the base shears in the longitudinal direction, it has a slight effect on those in the transverse direction.

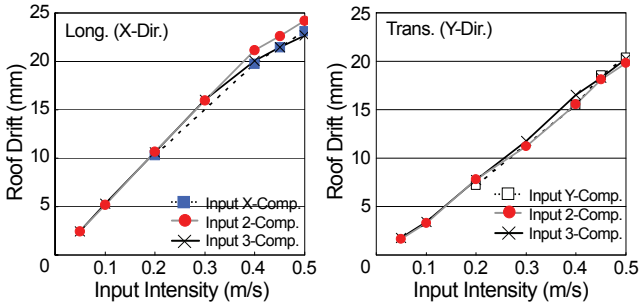

(a) Max. Roof Drift

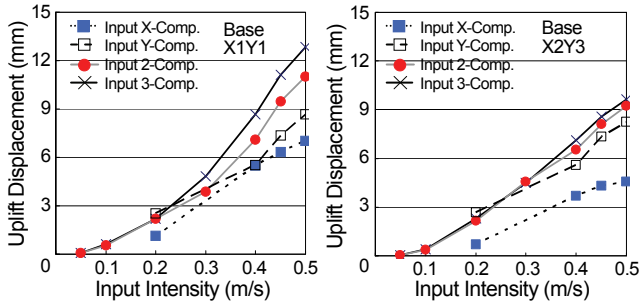

(b) Max. Uplift Displacement

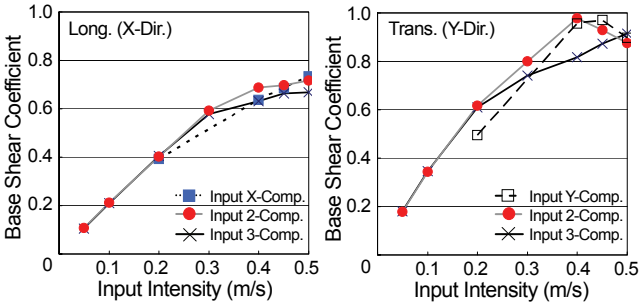

(c) Max. Base Shear Coefficient

Figure 10 Effect of Components of Input Motion on Maximum Responses: BPY model

4. CONCLUSIONS

The results of the study are summarized as follows:

1) The maximum base shears of the rocking frames are effectively reduced from those of the fixed-base frames in the longitudinal and transverse directions.

2) The maximum interstory drifts of the rocking frames are almost equal to or larger than the elastic response values of the fixed-base frames regardless of the input motion intensity, because the rotational rigidity of the column base of the rocking frames is smaller than that of the fixed-base frames. However, the response deformation of the superstructure of the rocking frames excluding the rocking component is nearly equal to or smaller than the elastic response value of the fixed-base frames.

3) The maximum tensile forces at the column bases for the rocking frames are limited to certain values less than those for the fixed-base frames after the rocking motion occurs. This is primarily caused by the self-limiting tensile force in the column base due to base plate yielding. The maximum compressive forces for the rocking frames are almost equal to or less than those for the fixed-base frames. Consequently, it is pointed out that the impact effect is small.

4) While the maximum uplift displacements of the column bases of the rocking frames increase with the increase of the number of components of the input motion, the horizontal response values such as the roof drifts and base shears are not affected by that.

Acknowledgements:

This work has been stipulated by the Comprehensive Research and Development Project on Development of Performance Evaluation Method for Building Structures Using Innovative Structural Materials supported by the Ministry of Land, Infrastructure, Transport and Tourism (MLIT) of Japan. The authors would like to acknowledge all project members for their useful advice and suggestions. The authors express their gratitude to Mr. S. Takai and Mr. M. Kanagawa for their excellent support in the shaking table tests at the Technical Research Institute of Nishimatsu Corp. Part of this work is supported by the Ministry of Education, Culture, Sports, Science and Technology (MEXT) of Japan under Grants-in-Aid for Scientific Research, Projects No. 19360244 and 21560607.

References:

Azuhata, T., Midorikawa, M. and Ishihara, T. (2004), "Energy dissipation mechanism and maximum response displacement prediction of steel frames with yielding base plates in uplift motion for seismic response reduction," *Journal of Structural and Construction Engineering*, AIJ, 583, 61-68. (in Japanese)

Chopra, A. K. and Yim, S. C.-S. (1985), "Simplified analysis of structures with foundation uplift," *Journal of Structural Engineering*, ASCE 111(4), 906-930.

Clough, R. W. and Huckelbridge, A. A. (1977), "Preliminary experimental study of seismic uplift of a steel frame," *Report No. UBC/EERC-77/22*, EERC, University of California, Berkeley, Calif.

Hayashi, Y., Tamura, K., Mori, M. and Takahashi, I. (1999), "Simulation analyses of buildings damaged in the 1995 Kobe, Japan, earthquake considering soil-structure interaction," *Earthquake Engineering and Structural Dynamics*, 28(4), 371-391.

Housner, G. W. (1963), "The behavior of inverted pendulum structures during earthquakes," *Bulletin of the Seismological Society of America*, 53(2), 403-417.

Huckelbridge A. A. (1977), "Earthquake simulation tests of a nine storey steel frame with columns allowed to uplift," *Report No. UBC/EERC-77/23*, EERC, University of California, Berkeley, Calif.

Ishihara, T., Midorikawa, M., Azuhata, T. and Wada, A. (2003), "Hysteresis characteristics of column base for rocking structural systems with base plate yielding," *Journal of Constructional Steel*, JSSC, 11, 51-56. (in Japanese)

Ishihara, T., Midorikawa, M. and Azuhata, T. (2009), "Modal properties and free vibration of uplifting behavior of multistory buildings modeled as uniform shear-beam," *Journal of Structural and Construction Engineering*, AIJ, 74(640), 1055-1061. (in Japanese)

Iwashita, K., Kimura, H., Kasuga, Y. and Suzuki, N. (2002), "Shaking table test of a steel frame allowing uplift," *Journal of Structural and Construction Engineering*, AIJ, 561, 47-54. (in Japanese)

Iwashita, K., Taniguchi, H. and Ishihara, T. (2003), "Energy approach to the earthquake response of building allowing uplift at pile head," *Journal of Structural and Construction Engineering*, AIJ, 564, 23–30. (in Japanese)

Kasai, K., Kanada, M. and Okuma, K. (2001), "Real example for a passively controlled building with stepping column: analysis and full-scale damper experiment," *Proceedings of Passive Control Symposium 2001*, Structural Engineering Research Center, Tokyo Institute of Technology, Yokohama, Japan, 235-249. (in Japanese)

Meek, J. W. (1975), "Effect of foundation tipping on dynamic response," *Journal of the Structural Division*, ASCE, 101(7), 1297-1311.

Meek, J. W. (1978), Dynamic response of tipping core buildings," *Earthquake Engineering and Structural Dynamics*, 6(5), 437-454.

Midorikawa, M., Azuhata, T., Ishihara, T. and Wada, A. (2003), "Dynamic behavior of steel frames with yielding base plates in uplift motion for seismic response reduction," *Journal of Structural and Construction Engineering*, AIJ, 572, 97–104. (in Japanese)

Midorikawa, M., Azuhata, T., Ishihara, T. and Wada, A. (2006), "Shaking table tests on seismic response of steel braced frames with column uplift," *Earthquake Engineering and Structural Dynamics*, 35(14), 1767-1785.

Midorikawa, M., Sudo, T., Asari, T., Azuhata, T. and Ishihara, T. (2009), "Three-dimensional seismic response of ten-story steel frames with yielding base plates allowed to uplift," *Journal of Structural and Construction Engineering*, AIJ, 74(637), 495-502. (in Japanese)

Oliveto, G., Calio, I. and Greco, A. (2003), "Large displacement behavior of a structural model with foundation uplift under impulsive and earthquake excitations," *Earthquake Engineering and Structural Dynamics*, 32(3), 369-393.

Rutenberg, A., Jennings, P. C. and Housner, G. W. (1982), "The response of Veterans Hospital Building 41 in the San Fernando Earthquake," *Earthquake Engineering and Structural Dynamics*, 10(3), 359-379.

Wada, A., Yamada, S., Ono, Y., Kobayashi, K. and Sasaki, Y. (2005), "Shaking table tests of uplift behavior of buildings on elastic foundation during earthquake," *Journal of Structural and Construction Engineering*, AIJ, 595, 57-64. (in Japanese)

Yim, S. C.-S. and Chopra, A. K. (1985), "Simplified earthquake analysis of multistory structures with foundation uplift," *Journal of Structural Engineering*, ASCE, 111(12), 2708-2731.

JOINT CONFERENCE PROCEEDINGS
7th International Conference on Urban Earthquake Engineering (7CUEE) &
5th International Conference on Earthquake Engineering (5ICEE)
March 3-5, 2010, Tokyo Institute of Technology, Tokyo, Japan

SHAKING TABLE TEST ON CONTROLLED ROCKING FRAME OF WOODEN STRUCTURES

Shoichi Kishiki[1] and Akira Wada[2]

1) Assistant Professor, Structural Engineering Research Center, Tokyo Institute of Technology, Japan
2) Professor, Structural Engineering Research Center, Tokyo Institute of Technology, Japan
kishiki@serc.titech.ac.jp, wada@serc.titech.ac.jp

Abstract: Many wooden structures suffered damage in Hyogo-ken Nanbu earthquake 15 years ago. Structural damage caused the termination of social and industrial activities, and severe economic loss. New technology which realizes not only seismic resistances but also protecting their functions will be needed for small residential buildings. In this study, wooden wall with column-base allowed to uplift is proposed. Rocking-controlled walls make conventional walls work following the 1st mode. Carrying out shaking table test of rocking-controlled wooden wall, non-degrading natural frequency of test specimen was achieved by pre-compression of rocking-controlled devices. And column-base uplift led to decrease in damage to wall.

1. INTRODUCTION

In the Northridge and Kobe earthquakes, some buildings lost structural functions, although many buildings avoided collapse as to save human life. The loss caused the termination of social and industrial activities, and severe economic loss. At the stage of seismic design, it is important to consider restoring structures immediately after an earthquake. As stated in the Uniform Building Code, "The purpose of the earthquake provisions herein is primarily to safeguard against major structural failures and loss of life, not to limit damage ore maintain function (ICBO 1997)". Also in Japan, a heavy earthquake country, the differences of a thought concerning actual seismic performances between the people and structural engineers have been pointed out after the Kobe earthquake. New technology which realizes not only seismic resistances (strength, stiffness, and plastic rotation capacity) but also protecting their functions will be immediately needed.

On the other hand, it has been observed that some building structures with uplifting of foundation have been no-damaged in structural functions after the past earthquakes. Analytical study on damage-decrease due to uplifting had been carried out (Hayashi 1996). RC and steel structures with base-column or foundation allowed to uplift (stepping column) have been developed in the US and Japan (Huckelbridge et al. 1977; Midorikawa et al. 2002; Iwashita et al. 2003). And then, some technologies have been applied to actual structures (Kasai et al. 2001; Buckle 2002).

Recently, controlled rocking frame composed of rigid braced frames, vertical post-tensioning strands, and replaceable dampers has been proposed (Deierlein and Hajjar et al. 2005). The controlled rocking system, a large (2/3) scale three-story frame has been tested at the E-Defense facility in August 2009 (Deierlein et al. 2009). In addition to demonstrating the reliability of the system and its components, this test has been an important proof-of-concept of the design criteria, constructability, and performance of the system. The test is jointly planned with collaborators from Stanford University (Gregory G. Deierlein and H. Krawinkler), University of Illinois (J. Hajjar), Tokyo Institute of Technology (T. Takeuchi, K. Kasai and S. Kishiki), Hokkaido University (M. Midorikawa), and E-Defense (M. Nakashima and T. Hikino). And also in Japan, controlled rocking "wooden wall" composed of similar components has been proposed by the authors (Kishiki and Wada 2009). The authors focused on damage distribution of rocking rigid-wall (braced frame). Rocking rigid-wall forces the other earthquake-resisting components to work following the 1st mode-shape which is led to same story drift at every floor. Therefore, brittle shear failures of old wooden and RC walls are avoided by damage-distribution of rocking rigid-wall. Retrofit projects using damage-distribution of rocking controlled wall are in progress (Wada et al. 2009).

In this paper, controlled rocking "wooden wall" composed of rigid braced frames, vertical post-tensioning strands, and replaceable dampers, has been proposed. Shaking table tests of a large scale model of a two-story wooden house were performed to evaluate dynamic response, and to get an important proof-of-concept of the design criteria.

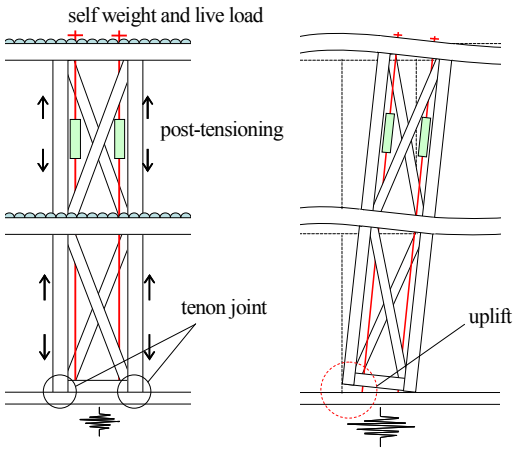

Figure 1 Conceptual illustration of Controlled Rocking Frame

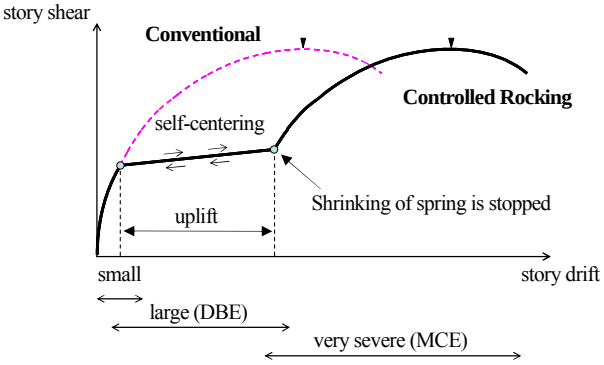

Figure 2 Behavior of Controlled Rocking Frame

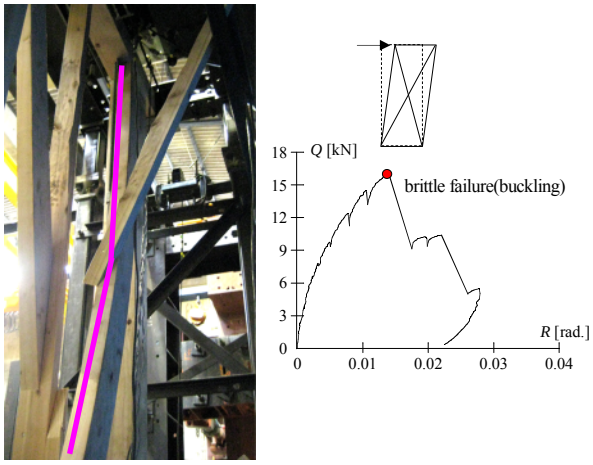

Figure 3 Brittle Shear failure of Conventional Wooden Walls (Braced Frames)

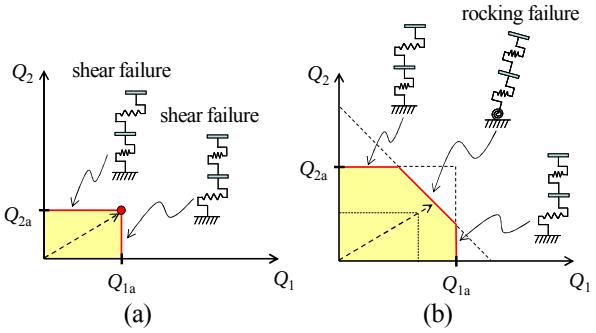

Figure 4 Lateral Strength Interaction between 1st and 2nd story: (a) Conventional Walls and (b) Controlled Rocking Walls

2. CONTROLLED ROCKING WOODEN FRAME

2.1 Detail of System

Conceptual illustration of controlled rocking wooden wall is shown in Figure 1. And structural behavior of the system is illustrated in Figure 2. The system composed of rigid braced frames, vertical post-tensioning strands, and replaceable dampers. Two steel bars with a diameter of 12mm are installed to inside columns of two-story braced-frame. The bars are through from the concrete foundation (anchor) to the roof beam, and fasten. Special devices composed of an elastic spring and a viscoelastic damper are installed among the bars. The elastic spring with a stiffness of 200N/mm control the uplift strength of column-base, and avoid decrease of post-tensioning stress by creep of wooden members. The viscoelastic damper eases the rapid uplifting and the landing impact at the column-base. Two-story wooden house has 5.9kN total weight summing self-weight and live load for corner columns and 8.0kN for the other columns, respectively. In the proposed system, 15kN post-tensioning is given to each 120×120mm squared columns of rocking controlled wall. During a small earthquake, the post-tensioning stress enables the system to behave such as a conventional wooden wall. Column-bases are connected to ground sill by tenon joints, although column-bases of conventional wooden wall are rigidly fastened by hold-down fastener or others. Tenon joints enable column-base to uplift easily. In addition to this, the joints are able to transfer lateral shear force to ground sill. During a severe earthquake such as DBE level or more, the system allows column-base to uplift to decrease damage to structural members. Meanwhile, the elastic springs are shrinking. And then, the post-tensioning stress of the elastic springs leads the structure to self-centering after the earthquake. At the ultimate state under very severe earthquake such as MCE level, uplifting is stopped by the limitation of shrinking of the elastic springs (30mm). Therefore, the system is able to exert enough strength the original wooden wall has.

2.2 Effects on Dynamic Response of the Other Conventional Walls

Conventional wooden walls, especially braced frames, have brittle characteristics, shown in Figure 3. Therefore, using conventional wooden walls, story failure of 1st or 2nd floor would be caused, even if the structure has strength same to standard horizontal seismic coefficient and its distribution, shown in Figure 4(a). In other words, the conventional walls cannot exert their strength capacity at the both floor. On the other hand, the strength of two-story controlled rocking wooden wall is decided by uplifting of column-base. In other words, strength decided by

overturning moment is be able to select innumerable combination of lateral force at the 1st and 2nd floors, shown in Figure 4(b). Therefore, using the controlled rocking wooden walls with conventional walls, the conventional walls are forced to follow deformation shapes of the rocking walls. The rocking walls divide the story shear to the conventional walls which have enough strength, and receive the story shear from the conventional walls which have a lack of strength. Wooden houses with the controlled rocking walls are able to exert the overall strength of the existing walls. Mentioned above, brittle shear failures of old RC walls are avoided by damage-distribution of rocking rigid-walls. Retrofit projects using damage-distribution of the rocking controlled wall are in progress (Wada et al. 2009).

3. SHAKING TABLE TEST PLAN

Shaking table tests of a large scale model of a two-story wooden house were performed in 2008 at the Tokyu Construction Technical Research Institute. The facility has 4×4m shaking table (excitation capacity is ±50cm, ±150 cm/sec, and ±980 cm/sec^2). Test structures have two-story, 2×2 bay braced frame, shown in Figure 5. In the both horizontal direction, the test structure has two braced members at the each floor of exterior frame. The total height of the test structure is 5.91m, 2.955m for each story. The floor dimension is 3×3m and the total weight of the test

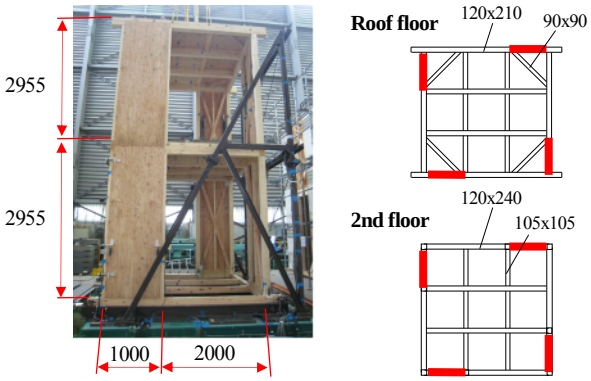

Figure 5 Test Structure (unit:mm)

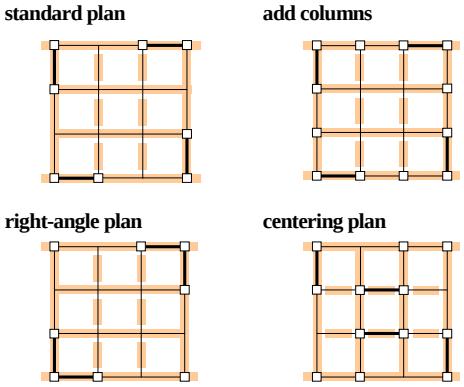

Figure 6 Plans of Shear Walls and Columns

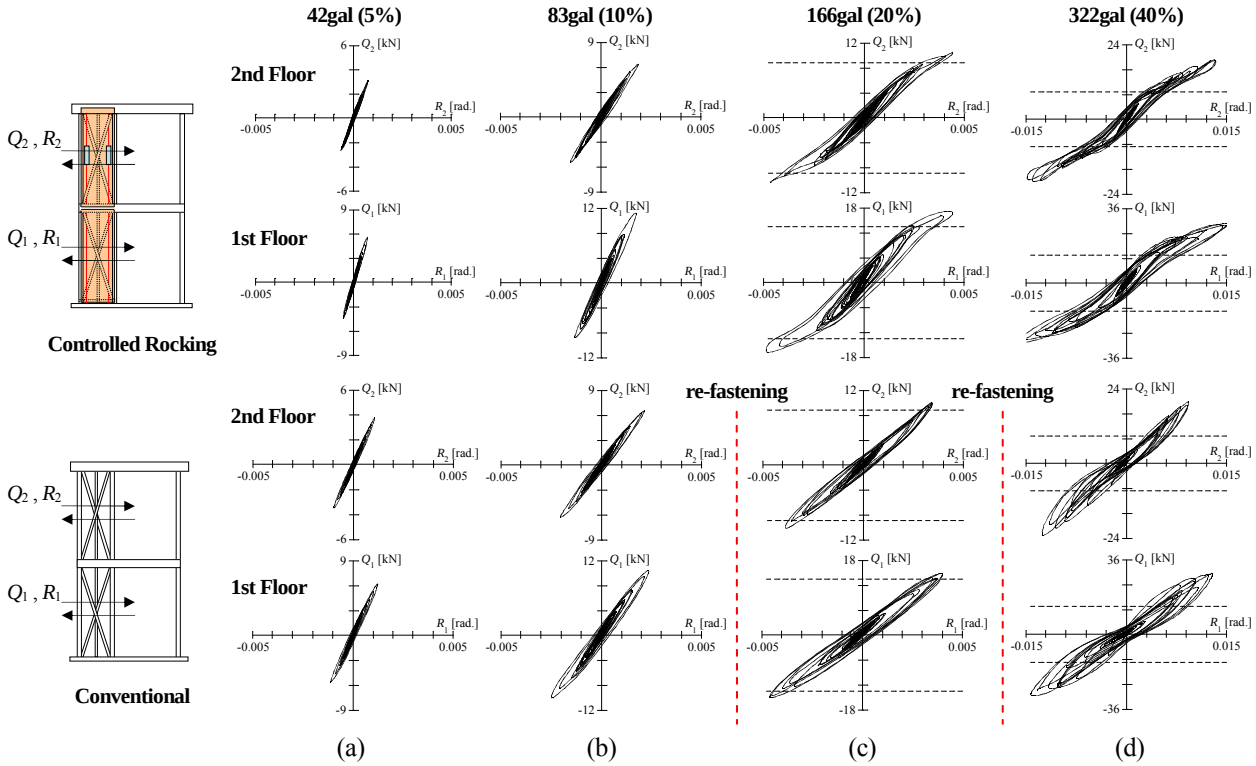

Figure 7 Story Shear and Story Drift Ratio Relation:
scaled to a peak acceleration (a) 5%, (b) 10%, (c) 20%, and (d) 40%

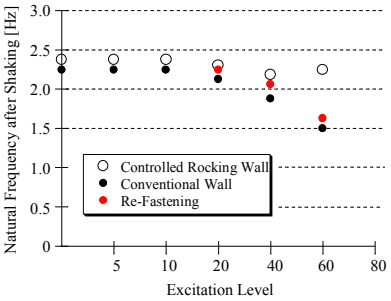

Figure 8 Change of Natural Frequency After Shaking

structure is 12kN. Capacity limitations of the testing facility, heavy steel weights were put on the each floor. The total weight is 67.8kN.

Test structures with two kinds of shear walls, the conventional or the controlled rocking walls, were tested. In addition to this, testing parameter for test structure with the controlled rocking walls is plan of shear walls and columns, illustrated in Figure 6. Four plans were compared to evaluate bending-resistant of the roof and 2nd floor's beam after uplifting of base-columns.

NS component of JMA Kobe Record (according to the Japan Meteorological Agency of Kobe, 1995), which was scaled to a peak acceleration was used in the test. Each test structures was subjected to earthquake ground motions several times with maximum input acceleration scaled to a range of levels to simulate various earthquake intensities from 5% to 100% of actual record.

The instrumentation was designed to measure both global structural response and local elemental response. The measured data include the following: horizontal accelerations on the shaking table, horizontal accelerations and relative lateral displacement at each floor level, vertical displacement (uplift) of the column-base. Inertia forces on the each floor were calculated by using both the measured accelerations and masses. And then, the story shear-story drift ratio relation at the each floor was obtained from these excitations.

4. TEST RESULTS AND CONSIDERATIONS

4.1 Global Behavior of Test Structures

Story shear and story drift ratio relations at the 1st story and the 2nd story are plotted for test structures with the controlled rocking walls and with the conventional walls in Figure 7. As observed in from Figure 7(a) to (b), two test structures exhibited approximately elastic behavior. It indicated that the 15kN post-tensioning stress fastened column-base to groundsill instead of hold-down fastener or others of the conventional wooden wall. At the next scaled excitation to 20% in Figure 7(c), uplift initiations have been observed in the controlled rocking structure. Design story shear forces in allowable stress design, based on standard shear coefficient are illustrated by short dashed line. The controlled rocking structure has uplifting shear strength

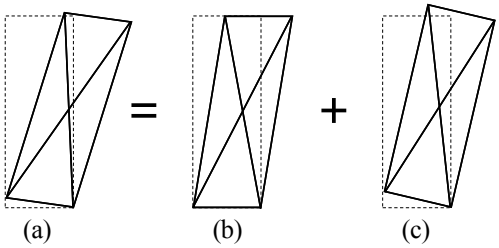

Figure 9 Overall Deformation Decomposed into Shear and Rocking: (a) Overall Deformation, (b) Shear Deformation, and (c) Rocking Behavior

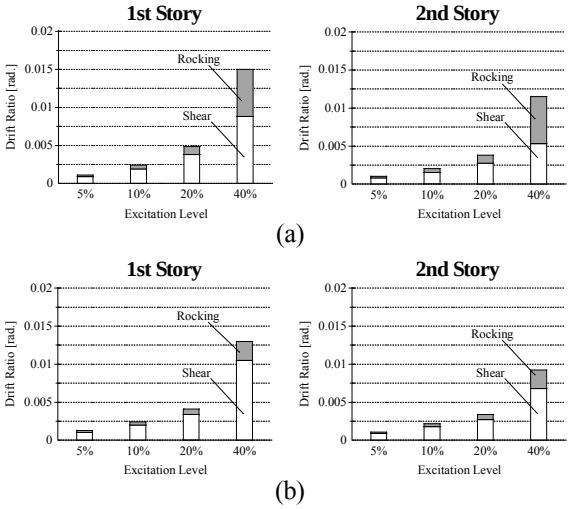

Figure 10 Contribution of Shear Deformation and Rocking Deformation: (a) The Controlled Rocking Wall and (b) Conventional Wall

more than the design force. The viscoelastic dampers cause energy dissipation to uplifting behavior of the structures. The controlled rocking structure has the secondly stiffness obtained by bending-resistant of the roof and 2nd floor's beam after uplifting. And after the shaking, the post-tensioning stress of the elastic springs leads to self-centering. On the other hand, the conventional structure showed slipping hysteresis behavior taken by damage to walls and hold-down fasteners.

4.2 Damage to Walls and Fasteners

Changes of natural frequency obtained white noise wave shaking between the Kobe earthquake shakings, and are shown in Figure 8. After excitation scaled to 20%, natural frequency of the conventional structure is decreased although that of the controlled rocking structure is not changed. In 20% excitation, the conventional structure showed slipping hysteresis behavior, and uplifting initiations were observed in the controlled rocking structure. Therefore, the uplift allowing brings a damage-decreasing of walls and fasteners to the test structure.

Damage to walls is discussed by dividing overall deformation to shear deformation and rocking behavior. Overall story drift ratio is be able to be decomposed of shear deformation of walls and rocking behavior of column base,

shown in Figure 9. And then, Figure 10 shows shear-and-rocking distributions obtained from the maximum story drift between 5% and 40% excitation, respectively. From 5% to 10% excitation, the post-tensioning stress brings same distributions of the conventional structure to the controlled rocking structure. And then, uplifting leads to damage-decreasing to walls, shear deformations of the system in 20% and 40% excitations.

5. CONCLUSIONS

This paper proposed new controlled rocking wooden frame composed of rigid braced frames, vertical post-tensioning strands, and replaceable dampers. In the proposed system, lateral story shear strength decided by overturning moment is be able to select innumerable combination of lateral force at the 1st and 2nd floors. Therefore, using the controlled rocking wooden walls with conventional walls, the conventional walls are forced to follow deformation shapes of the rocking walls. The rocking walls divide the story shear to the conventional walls which have enough strength, and receive the story shear from the conventional walls which have a lack of strength. Wooden houses with the controlled rocking walls are able to exert the overall strength of the existing walls.

Shaking table test of the controlled rocking wooden wall is addressed in this paper. Test results obtained from small excitation is indicated that the 15kN post-tensioning stress fastened column-base to groundsill instead of hold-down fastener or others of the conventional wooden wall. And in DBE level excitation, uplifting initiations were observed, and it leaded to decrease damage to walls and fasteners. In addition to this, the post-tensioning stress of the elastic springs leads to self-centering after shaking.

Acknowledgements:

This system is developed by the following members: Tama Home (Mr. Y.Tamaki, Mr. K.Somei, and Mr. S.Tanaka), Tokyo Institute of Technology (Prof. A.Wada and Dr. S.Kishiki), JUST (Mr. J.Ando, Mr. T.Yanase, and Miss T.Iwaya), KANAI (Mr. T.Namiki and Mr. K.Kanai), Sumitomo 3M (Mr. K.Okuma, Mr. K.Tokoro), NHK Spring (Mr. A.Takahashi and Mr. O.Sasa). The authors acknowledge their support. And the authors express their gratitude to Mr. M.Toyoshima and Mr. S.Takeda for their excellent support in the shaking table tests at the Tokyu Construction Technical Research Institute.

References:

Huckelbridge, A. A. 1977. Earthquake Simulation Tests of a Nine Story Steel Frame with Columns Allowed to Uplift. Report No. UBC/EERC-77/23, EERC, University of California, Berkeley, CA.

Hayashi, Y. 1996. Damage reduction effect due to base-mat uplift of buildings (In Japanese). Journal of Structural and Construction Engineering, Transactions of AIJ No.485, 53–62.

International Conference of Building Officials. 1997. Uniform Building Code, ICBO, Whittier, CA.

Midorikawa, M., Azuhata, T., Ishihara, T., Matsuda, Y., Matsushima, Y., and Wada, A. 2002. Earthquake Response Reduction of Buildings by Rocking Structural Systems. SPIE's 9th Annual International Symposium on Smart Structures and Materials, 4696–33.

Kasai, K., Kaneda, M., and Okuma, K. 2001. Real example for a passively controlled building with stepping column: analysis and full-scale damper experiment (In Japanese). Proceedings of Passive Control Symposium 2001:235–249.

Iwashita, Y., Kimura, H., Kasuga, Y., and Suzuki, N. 2002. Shaking table test of a steel frame allowing uplift (In Japanese). Journal of Structural and Construction Engineering, Transactions of AIJ No.561, 47–54.

Buckle, I. 2002. Protecting Concrete Structures from Earthquake Using Seismic Isolation: From Concept of Reality. Concrete Journal, Japan Concrete Institute, vol.40 No.1:116–122.

Deierlein, G. G., Hajjar, J. F., Billington, S., and Krawinkler, H. 2005. NEESR-SG: Controlled Rocking of Steel-Framed Buildings with Replaceable Energy Dissipating Fuses. Proposal submitted to the National Science Foundation, Arlington, Virginiai.

Deierlein, G. G., Ma, X., Eatherton, M., Krawinkler, H., Billington, S., and Hajjar, J. F. 2009. Collaborative research on development of innovative steel braced frame systems with controlled rocking and replaceable fuses. Proceedings of Sixth International Conference on Urban Earthquake Engineering, Tokyo, Japan.

Kishiki, S., Kubota, H., Yanase, T., Somei, K., and Wada, A. 2009. Shaking table test of rocking-controlled wooden wall with column base allowed uplift behavior (In Japanese). Journal of Structural and Construction Engineering, Transactions of AIJ No.644, 1803–1812.

Wada, A., Qu, Z., Motoyui, S., and Sakata, H. 2009. Integrity, strength and deformability in seismic design of multi-story structures. the 3rd WFEO-JFES-JSCE joint international symposium on disaster risk management

JOINT CONFERENCE PROCEEDINGS
7th International Conference on Urban Earthquake Engineering (7CUEE) &
5th International Conference on Earthquake Engineering (5ICEE)
March 3-5, 2010, Tokyo Institute of Technology, Tokyo, Japan

THREE-DIMENSIONAL ANALYSIS FOR SQUARE SEISMIC ISOLATION BEARINGS UNDER LARGE SHEAR DEFORMATION AND HIGH AXIAL LOADS

Masaru Kikuchi[1)], Ken Ishii[1)], Takahito Nakamura[2)], and Ian D. Aiken[3)]

1) Graduate School of Engineering, Hokkaido University, Japan
2) Research and Development Division, Oiles Corporation, Japan
3) Seismic Isolation Engineering, Inc., U.S.A.
mkiku@eng.hokudai.ac.jp, ishii@eng.hokudai.ac.jp, ta.nakamura@oiles.co.jp, ida@siecorp.com

Abstract: Square elastomeric bearings can provide effective and economical seismic isolation for buildings, with the same performance as circular bearings. With simple connection details they offer the advantage of easy installation during construction. The space required for a square bearing is less than that for a circular bearing for the equivalent vertical load. To facilitate the use of square seismic isolation bearings, a new mechanical model for predicting their large shear deformation behavior is presented in the paper. The model comprises multiple shear springs at its mid-height and two series of axial springs at the top and bottom boundaries. The model has the advantage that the shear hysteresis constitutive relation need not incorporate the influence of axial load, since the influence of axial load on shear behavior is implicitly captured by the material nonlinearity of the axial springs and the geometrical nonlinearities in the model itself. To confirm the validity of the model, analyses of square lead-rubber isolation bearing tests were performed. The analysis results showed very good agreement with the bearing test results. The analyses demonstrated that the model can successfully capture the influence of loading direction, axial load magnitude, and load history on bearing behavior.

1. INTRODUCTION

Square elastomeric bearings were first used for building seismic isolation in New Zealand and the U. S. A. in the 1980s, however, in Japan, square lead-rubber bearings were only used for the first time for building isolation in 2002. Square elastomeric bearings can provide effective and economical seismic isolation for buildings, with the same general properties and performance as circular bearings. There are efficiencies in the quantities of both rubber and steel required to manufacture square bearings compared with circular bearings, and they also offer the advantage of potentially simple connection configurations to the structure. Also, the space required for a square bearing is less than that for a circular bearing for the equivalent vertical load. With these advantages, square bearings have the potential to increase the use of seismic isolation to protect structures from the damaging effects of earthquakes.

Existing design equations for circular lead-rubber bearings have been used for the design of square lead-rubber bearings in Japan. These equations are generally applicable for bearing horizontal deformations up to 250 percent shear strain. The suitability of the design equations is based on the assumed isotropy of the horizontal properties of square lead-rubber bearings. It is generally assumed that any effects of horizontal loading direction on bearing behavior can be neglected for moderate shear strain, design-level horizontal displacements. Less investigation of the ultimate behavior of square bearings, however, has been undertaken and it is expected that at very large shear deformations the bearing behavior will be anisotropic. The more widespread use of square elastomeric isolation bearings has demanded better understanding of some of the more complex aspects of their behavior, such as the influence of large shear deformations and high compressive stresses.

The actual behavior of an elastomeric isolator depends on the interaction between shear and axial forces (Aiken et al. 1989). Two of the authors recently proposed a new analytical model which includes interaction between shear and axial forces as a function of varying vertical load on a bearing during earthquake loading (Yamamoto et al. 2009). The model comprises shear and axial springs at the mid-height and two series of axial springs at the top and bottom boundaries. The model has the advantage that the shear hysteresis model used needs not incorporate the influence of axial load, since the influence of axial load on shear behavior is implicitly captured by the material nonlinearity of the axial springs and the geometrical nonlinearities in the model itself. The analytical results produced by the model show very good agreement with experimental results of bearing shear tests under varying vertical load. The model, however, was developed only for two-dimensional behavior (i.e., shear and axial), and thus its applicability is limited to two-dimensional analyses of

seismic isolation systems. This means that the previously-developed two-dimensional model is not applicable for the prediction of the ultimate behavior of square isolation bearings under multi-directional excitations. In this paper, a three-dimensional analytical model for elastomeric bearings with these capabilities is proposed. The new model has tri-axial interaction among two horizontal components and one vertical component. Because of its generalized characteristics, the new three-dimensional model is expected to be useful for the prediction of the multi-directional horizontal behavior of not only square, but also circular seismic isolation bearings.

2. MECHANICAL MODEL

Figure 1 shows the mechanical model postulated to represent the three-dimensional behavior of square elastomeric isolation bearings. The model comprises multiple shear springs and an axial spring at the mid-height, and two series of axial springs at the top and bottom boundaries. The multiple shear spring (MSS) model was originally proposed by Wada and Hirose to simulate the bi-axial behavior of a building (Wada and Hirose, 1989). The MSS model consists of a series of identical shear springs arranged radially to represent isotropic behavior in the horizontal plane. Each spring in the series of axial springs at the top and bottom ends is a uniaxial, nonlinear spring, and represents an individual fiber of the bearing cross-sectional area. The concept of the series of axial springs to represent coupled axial force and bending moment is the same as that with fiber elements for reinforced concrete members (Kaba and Mahin, 1984). When this collection of springs is combined in the model, the nonlinear, interaction behavior is achieved. The rigid columns, which represent the height of the bearing, are combined between the top and bottom series of axial springs and the mid-height multiple shear springs and the axial spring.

The forces and displacements on the model are shown in Figure 2. There are six displacement degrees of freedom - three translations and three rotations - at the external nodes, *a* and *b*. The internal nodes, *m* and *n*, have three displacement degrees of freedom, translation *A*, and rotations *B* and *C*. The displacements for translations *B* and *C* and rotation *A* of the internal node, *m*, are equal to those of the external node, *a*. The same definition for nodes *a* and *m* is made for nodes *b* and *n*.

By using incremental displacements of nodes *a* and *m* and assuming that plane sections remain plane, the incremental normal deformation of the *i*-th axial spring between nodes *a* and *m*, $\Delta_i\delta_{Na}$, is calculated using Equation (1):

$$\Delta_i\delta_{Na} = \begin{bmatrix} -1 & -{}_il_C & {}_il_B & 1 & {}_il_C & -{}_il_B \end{bmatrix} \Delta\mathbf{u}_{am} \quad (1)$$

where ${}_il_C$ and ${}_il_B$ are the distances between the *i*-th spring and

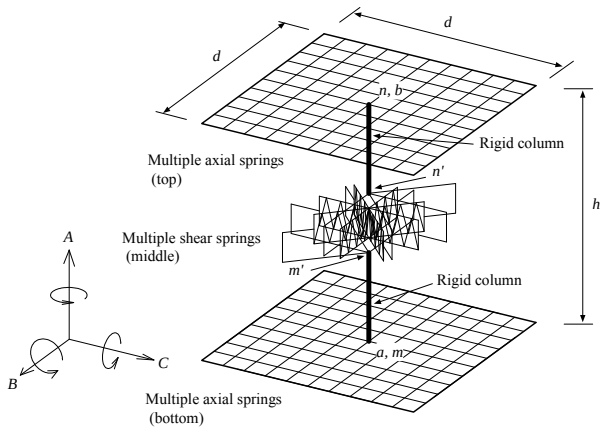

Figure 1 Three-dimensional multi-spring mechanical model.

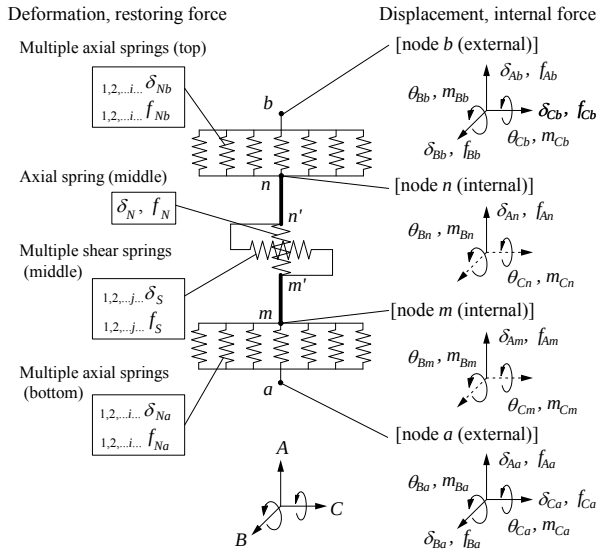

Figure 2 Forces and displacements on the mechanical model.

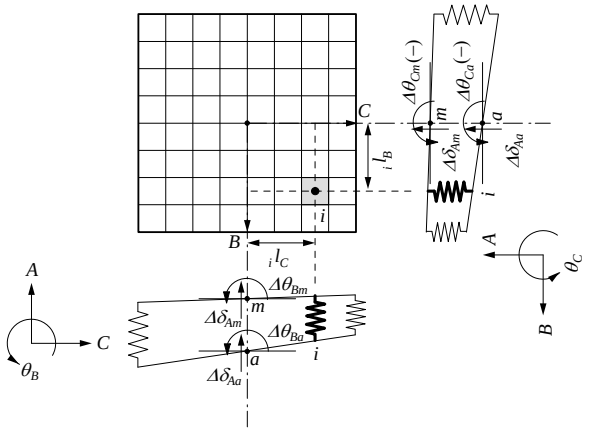

Figure 3 Deformations of the axial springs at the top and bottom boundaries of the model.

the centroid of the cross-sectional area of the bearing along the *B* and *C* axes, respectively (Figure 3), and $\Delta\mathbf{u}_{am}$ is the incremental displacement vector at nodes *a* and *m* expressed as:

$$\Delta\mathbf{u}_{am} = \left\{\Delta\delta_{Aa} \quad \Delta\theta_{Ba} \quad \Delta\theta_{Ca} \quad \Delta\delta_{Am} \quad \Delta\theta_{Bm} \quad \Delta\theta_{Cm}\right\}^{\mathrm{T}} \quad (2)$$

The incremental normal restoring force of the *i*-th axial spring between nodes *a* and *m*, $\Delta_i f_{Na}$, is expressed as:

$$\Delta_i f_{Na} = {}_ik_{Na} \cdot \Delta_i \delta_{Na} \quad (3)$$

where ${}_ik_{Na}$ is the tangential stiffness.

The incremental forces and bending moments on nodes *a* and *m* are expressed as follows:

$$\left.\begin{aligned} \Delta f_{Aa} &= -\Delta f_{Am} = -\sum \Delta_i f_{Na} \\ \Delta m_{Ba} &= -\Delta m_{Bm} = -\sum \Delta_i f_{Na} \cdot {}_il_C \\ \Delta m_{Ca} &= -\Delta m_{Cm} = \sum \Delta_i f_{Na} \cdot {}_il_B \end{aligned}\right\} \quad (4)$$

Equations (1) - (4) may be expressed by the following matrix equation:

$$\Delta\mathbf{f}_{am} = \mathbf{K}_{am} \cdot \Delta\mathbf{u}_{am} \quad (5)$$

where

$$\Delta\mathbf{f}_{am} = \left\{\Delta f_{Aa} \quad \Delta m_{Ba} \quad \Delta m_{Ca} \quad \Delta f_{Am} \quad \Delta m_{Bm} \quad \Delta m_{Cm}\right\}^{\mathrm{T}}$$

$$\mathbf{K}_{am} = \begin{bmatrix} {}_1k_{am} & {}_2k_{am} & -{}_3k_{am} & -{}_1k_{am} & -{}_2k_{am} & {}_3k_{am} \\ & {}_4k_{am} & -{}_5k_{am} & -{}_2k_{am} & -{}_4k_{am} & {}_5k_{am} \\ & & {}_6k_{am} & {}_3k_{am} & {}_5k_{am} & -{}_6k_{am} \\ & & & {}_1k_{am} & {}_2k_{am} & -{}_3k_{am} \\ & \textit{symm.} & & & {}_4k_{am} & -{}_5k_{am} \\ & & & & & {}_6k_{am} \end{bmatrix}$$

$${}_1k_{am} = \sum {}_ik_{Na}, \quad {}_2k_{am} = \sum {}_ik_{Na} \cdot {}_il_C,$$
$${}_3k_{am} = \sum {}_ik_{Na} \cdot {}_il_B, \quad {}_4k_{am} = \sum {}_ik_{Na} \cdot {}_il_C^2,$$
$${}_5k_{am} = \sum {}_ik_{Na} \cdot {}_il_C \cdot {}_il_B, \quad {}_6k_{am} = \sum {}_ik_{Na} \cdot {}_il_B^2$$

The relationship between the incremental forces and displacements on nodes *b* and *n* can be obtained by replacing *a* by *b* and *m* by *n* in Equation (5) as follows:

$$\Delta\mathbf{f}_{bn} = \mathbf{K}_{bn} \cdot \Delta\mathbf{u}_{bn} \quad (6)$$

where $\mathbf{K}_{bn}$ is the stiffness matrix, $\Delta\mathbf{f}_{bn}$ is the incremental force vector and $\Delta\mathbf{u}_{bn}$ is the incremental displacement vector of nodes *b* and *n*.

Now consider the force-displacement relationships for the multiple shear springs and the axial spring at the mid-height of the model. The force-displacement relationship on nodes *n*' and *m*' in Figure 2, which excludes the rigid columns, may be expressed as follows:

$$\Delta\mathbf{f}'_{mn} = \mathbf{K}'_{mn} \cdot \Delta\mathbf{u}'_{mn} \quad (7)$$

where

$$\Delta\mathbf{f}'_{mn} = \left\{\Delta f'_{Am} \quad \Delta f'_{Bm} \quad \Delta f'_{Cm} \quad \Delta f'_{An} \quad \Delta f'_{Bn} \quad \Delta f'_{Cn}\right\}^{\mathrm{T}}$$
$$\Delta\mathbf{u}'_{mn} = \left\{\Delta\delta'_{Am} \quad \Delta\delta'_{Bm} \quad \Delta\delta'_{Cm} \quad \Delta\delta'_{An} \quad \Delta\delta'_{Bn} \quad \Delta\delta'_{Cn}\right\}^{\mathrm{T}}$$

$$\mathbf{K}'_{mn} = \begin{bmatrix} k_N & 0 & 0 & -k_N & 0 & 0 \\ & {}_1k'_{mn} & {}_2k'_{mn} & 0 & -{}_1k'_{mn} & -{}_2k'_{mn} \\ & & {}_3k'_{mn} & 0 & -{}_2k'_{mn} & -{}_3k'_{mn} \\ & & & k_N & 0 & 0 \\ & \textit{symm.} & & & {}_1k'_{mn} & {}_2k'_{mn} \\ & & & & & {}_3k'_{mn} \end{bmatrix}$$

$${}_1k'_{mn} = \sum {}_jk_S \cos^2{}_j\varphi, \quad {}_2k'_{mn} = \sum {}_jk_S \cos{}_j\varphi \sin{}_j\varphi,$$
$${}_3k'_{mn} = \sum {}_jk_S \sin^2{}_j\varphi$$

${}_jk_S$ is the tangential stiffness and ${}_j\varphi$ is the angle to the *B* axis of the *j*-th shear spring (Figure 4), and k_N is the stiffness of the axial spring at the mid-height.

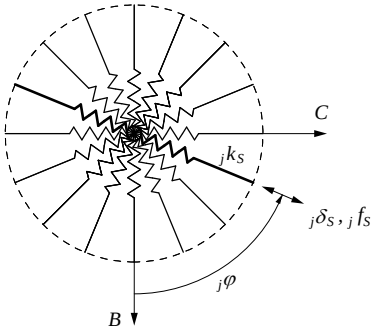

Figure 4 Multiple shear springs at the mid-height of the model.

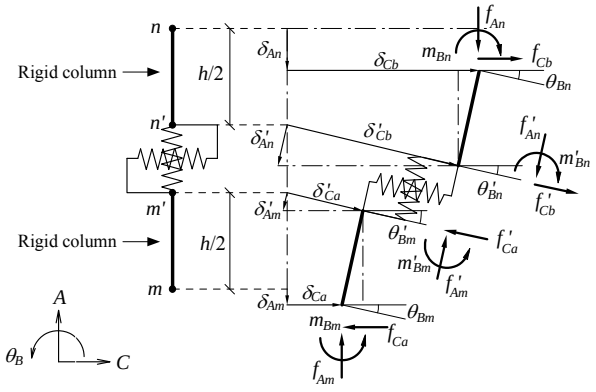

Figure 5 Geometrical relationships of the deformations and forces in the *A*-*C* plane.

In order to convert the force-displacement relationship on nodes *m*' and *n*', expressed by Equation (7), to nodes *m* and *n*, which includes the rigid columns, a transformation matrix is employed. Taking the geometrical relationships of the deformations, the force-equilibrium condition, and the *P*–Δ effect into account gives the transformation matrix. As an example, Figure 5 shows the geometrical relationships of the deformations and the forces in the *A*–*C* plane. Let ${}_{AC}\mathbf{T}$ be the transformation matrix in the *A*–*C* plane, $\Delta_{AC}\mathbf{u}'_{mn}$ and $\Delta_{AC}\mathbf{f}'_{mn}$ be the displacements and the forces on nodes *m*' and *n*', and $\Delta_{AC}\mathbf{u}_{mn}$ and $\Delta_{AC}\mathbf{f}_{mn}$ be those on nodes *m* and *n*. The transformation of the displacements and the forces may be expressed by:

$$\Delta_{AC}\mathbf{u}'_{mn} = {}_{AC}\mathbf{T}\cdot\Delta_{AC}\mathbf{u}_{mn} \tag{8}$$

$$\Delta_{AC}\mathbf{f}_{mn} = {}_{AC}\mathbf{T}^{\mathrm{T}}\cdot\Delta_{AC}\mathbf{f}'_{mn} \tag{9}$$

where

$$\Delta_{AC}\mathbf{u}'_{mn} = \left\{\Delta\delta'_{Am} \quad \Delta\delta'_{Ca} \quad \Delta\theta'_{Bm} \quad \Delta\delta'_{An} \quad \Delta\delta'_{Cb} \quad \Delta\theta'_{Bn}\right\}^{\mathrm{T}}$$

$$\Delta_{AC}\mathbf{u}_{mn} = \left\{\Delta\delta_{Am} \quad \Delta\delta_{Ca} \quad \Delta\theta_{Bm} \quad \Delta\delta_{An} \quad \Delta\delta_{Cb} \quad \Delta\theta_{Bn}\right\}^{\mathrm{T}}$$

$$\Delta_{AC}\mathbf{f}'_{mn} = \left\{\Delta f'_{Am} \quad \Delta f'_{Ca} \quad \Delta m'_{Bm} \quad \Delta f'_{An} \quad \Delta f'_{Cb} \quad \Delta m'_{Bn}\right\}^{\mathrm{T}}$$

$$\Delta_{AC}\mathbf{f}_{mn} = \left\{\Delta f_{Am} \quad \Delta f_{Ca} \quad \Delta m_{Bm} \quad \Delta f_{An} \quad \Delta f_{Cb} \quad \Delta m_{Bn}\right\}^{\mathrm{T}}$$

$${}_{AC}\mathbf{T} = \begin{bmatrix} 1 & -\theta_{Bm} & \dfrac{\delta'_{Cb}-\delta'_{Ca}}{2} & 0 & 0 & 0 \\ 0 & 1 & -\dfrac{h}{2} & 0 & 0 & 0 \\ 0 & 0 & 1 & 0 & 0 & 0 \\ 0 & 0 & 0 & 1 & -\theta_{Bn} & -\dfrac{\delta'_{Cb}-\delta'_{Ca}}{2} \\ 0 & 0 & 0 & 0 & 1 & \dfrac{h}{2} \\ 0 & 0 & 0 & 0 & 0 & 1 \end{bmatrix}$$

and *h* is the total height of the bearing.

The transformation matrix, ${}_{AB}\mathbf{T}$, in the *A*–*B* plane can be constructed using the same procedure as for the *A*–*C* plane, expressed by Equations (8) and (9). The transformation matrix, **T**, is formed by assembling the associated components of ${}_{AB}\mathbf{T}$ and ${}_{AC}\mathbf{T}$. Finally, the force-displacement relationship on nodes *m* and *n* may be expressed as follows:

$$\Delta\mathbf{f}_{mn} = \mathbf{K}_{mn}\cdot\Delta\mathbf{u}_{mn} \tag{10}$$

$$\mathbf{K}_{mn} = \mathbf{T}^{\mathrm{T}}\cdot\mathbf{K}'_{mn}\cdot\mathbf{T} \tag{11}$$

The overall stiffness matrix, $\mathbf{K}_{ab}$, is obtained by arranging the elements of the partial stiffness matrices, $\mathbf{K}_{am}$, $\mathbf{K}_{mn}$ and $\mathbf{K}_{nb}$ into an 18 by 18 matrix, and adding a linear torsional stiffness component. Finally, the relationship of the forces and displacements at the external and internal nodes in the model may be expressed as follows:

$$\begin{Bmatrix}\Delta\mathbf{f}_{ex}\\ \Delta\mathbf{f}_{in}\end{Bmatrix} = \mathbf{K}_{ab}\begin{Bmatrix}\Delta\mathbf{u}_{ex}\\ \Delta\mathbf{u}_{in}\end{Bmatrix} \tag{12}$$

where

$$\Delta\mathbf{f}_{ex} = \left\{\Delta f_{Aa} \quad \Delta f_{Ba} \quad \Delta f_{Ca} \quad \Delta m_{Aa} \quad \Delta m_{Ba} \quad \Delta m_{Ca} \quad \Delta f_{Ab} \quad \Delta f_{Bb} \quad \Delta f_{Cb} \quad \Delta m_{Ab} \quad \Delta m_{Bb} \quad \Delta m_{Cb}\right\}^{T}$$

$$\Delta\mathbf{f}_{in} = \left\{\Delta f_{Am} \quad \Delta m_{Bm} \quad \Delta m_{Cm} \quad \Delta f_{An} \quad \Delta m_{Bn} \quad \Delta m_{Cn}\right\}^{T}$$

$$\Delta\mathbf{u}_{ex} = \left\{\Delta\delta_{Aa} \quad \Delta\delta_{Ba} \quad \Delta\delta_{Ca} \quad \Delta\theta_{Aa} \quad \Delta\theta_{Ba} \quad \Delta\theta_{Ca} \quad \Delta\delta_{Ab} \quad \Delta\delta_{Bb} \quad \Delta\delta_{Cb} \quad \Delta\theta_{Ab} \quad \Delta\theta_{Bb} \quad \Delta\theta_{Cb}\right\}^{T}$$

$$\Delta\mathbf{u}_{in} = \left\{\Delta\delta_{Am} \quad \Delta\theta_{Bm} \quad \Delta\theta_{Cm} \quad \Delta\delta_{An} \quad \Delta\theta_{Bn} \quad \Delta\theta_{Cn}\right\}^{T}$$

and $\Delta\mathbf{f}_{ex}$ and $\Delta\mathbf{u}_{ex}$ are the incremental forces and displacements on the external nodes, *a* and *b*, respectively, and $\Delta\mathbf{f}_{in}$ and $\Delta\mathbf{u}_{in}$ are those on the internal nodes, *m* and *n*, respectively.

3. HYSTERESIS MODEL

3.1 Shear Springs

The hysteresis relationship for the shear springs in the MSS model has been previously developed by the authors, and is capable of predicting the behavior of high-damping rubber bearings under large shear deformations (Kikuchi and Aiken, 1997). A small change is made to the original model to extend its applicability to lead-rubber bearings (Kikuchi et al. 2007). The shear force of *j*-th spring in the MSS model, ${}_jf_S$, is the combination of an elastic component, F_1, and a hysteretic component, F_2, and is given by the following equations (Figure 6):

$${}_jf_S = F_1 + F_2 \tag{13}$$

$$F_1 = \left(1-u\right){}_jf_{peak}\left\{\left(1-p\right)\xi + \mathrm{sgn}\left({}_j\delta_S\right)p\left|\xi\right|^m\right\} \tag{14}$$

$$F_2 = \pm u\,{}_jf_{peak}\left\{1-2e^{-a(1\pm\xi)} + b\left(1\pm\xi\right)e^{-c(1\pm\xi)}\right\} \tag{15}$$

where ξ is the normalized displacement t ($\xi = {}_j\delta_S/{}_j\delta_{peak}$), ${}_jf_{peak}$ is the peak force and ${}_j\delta_{peak}$ is the peak displacement. The parameters, *u*, *m*, *a*, *b*, *c* and *p* in Equations (14) and (15) define the hysteresis loop shape. Bi-linear hysteresis modeling is usually used for lead-rubber bearings (Ikenaga et al. 2001). The values of these parameters are established using bi-linear model design equations. Detailed descriptions of the evaluation of these parameters are available in (Kikuchi et al. 2007, Yamamoto et al. 2009).

The incremental relative displacement of the *j*-th spring, $\Delta_j\delta_S$, is given by:

$$\Delta_j\delta_S = \Delta\delta_{S,B}\cos_j\varphi + \Delta\delta_{S,C}\sin_j\varphi \tag{16}$$

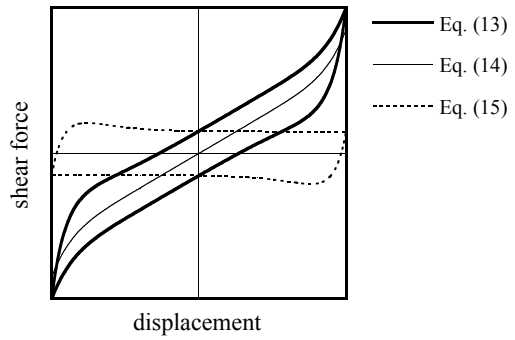

Figure 6 Hysteresis relationship for the shear springs in the MSS model.

where $\Delta\delta_{S,B}$ and $\Delta\delta_{S,C}$ are the incremental relative displacements along the *B* and *C* axes of the MSS model, respectively. These displacements are obtained from the incremental displacements at nodes *a*, *b*, *m* and *n* using Equation (17):

$$\left.\begin{aligned}\Delta\delta_{S,B} &= \left(\Delta\delta_{Bb} - \Delta\delta_{Ba}\right) - \frac{h}{2}\left(\Delta\theta_{Cn} + \Delta\theta_{Cm}\right)\\ \Delta\delta_{S,C} &= \left(\Delta\delta_{Cb} - \Delta\delta_{Ca}\right) + \frac{h}{2}\left(\Delta\theta_{Bn} + \Delta\theta_{Bm}\right)\end{aligned}\right\} \quad (17)$$

The shear hysteresis model defines the restoring force of the component springs in the MSS model using the incremental relative displacement given by Equation (16). The elements of the inner force vector that act on the nodes *m*' and *n*' along the *B* and *C* axes may be expressed by:

$$\left.\begin{aligned}f'_{Bn} &= -f'_{Bm} = \sum\nolimits_j f_S \cos\varphi_j\\ f'_{Cn} &= -f'_{Cm} = \sum\nolimits_j f_S \sin\varphi_j\end{aligned}\right\} \quad (18)$$

The shear stiffness along the *B* or *C* axis of the MSS model may be expressed as follows:

$$K_S = \sum_{j=1}^{n} {}_j k_S \cos^2{}_j\varphi \quad (19)$$

where *n* is the number of radial springs (which is also the same as the number of uniform circumferential divisions, see Figure 4).

The assumption of isotropic shear behavior in the elastic range is made here, that is, ${}_jk_S$ is the same for all radial springs, k_S. Here, we assume that the number of radial springs, or the number of divisions, *n*, is 8 (Wada and Hirose, 1989). Finally, the spring constant, k_S, is given by Equation (20):

$$k_S = \frac{K_S}{\sum_{j=1}^{8}\cos^2{}_j\varphi} = \frac{K_S}{4} \quad (20)$$

Equation (20) indicates that, for the case of n = 8, the mechanical properties for one quarter of the isolator should be applied to each spring of the MSS model.

3.2 Axial Springs

The proposed mechanical model has two kinds of axial springs: a series of axial springs at the top and bottom boundaries and an axial spring at the mid-height of the model. It is assumed that the series of springs at the top and bottom represent the axial properties of the bearings, and the stiffness of the mid-height axial spring is assumed infinite. Figure 7 shows the stress-strain relationship for the series of axial springs at the top and bottom boundaries (Yamamoto et al. 2009).

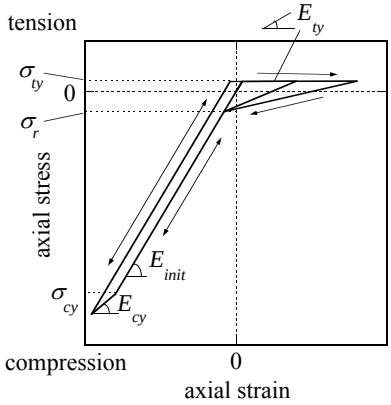

Figure 7 Stress-strain relationship for the axial springs at the top and bottom boundaries of the model.

The incremental strain of the *i*-th axial spring between nodes *a* and *m* is calculated from:

$$\Delta_i\varepsilon_a = \frac{\Delta_i\delta_{Na}}{l} \quad (21)$$

where $\Delta_i\delta_{Na}$ is the incremental relative normal deformation obtained from Equation (1), and *l* is the imaginary length of each spring in the series of axial springs at the top and bottom boundaries. One half of the total height of rubber in the bearing is used for this imaginary length.

The hysteresis relationship shown in Figure 7 defines the tangential compression modulus, ${}_iE_a$, and the incremental axial stress, $\Delta_i\sigma_a$, of the *i*-th spring using the incremental axial strain, $\Delta_i\varepsilon_a$. Then the stiffness and the incremental force are obtained from:

$${}_ik_{Na} = \frac{{}_iE_a \cdot {}_iA_a}{l} \quad (22)$$

$$\Delta_i f_{Na} = \Delta_i\sigma_a \cdot {}_iA_a \quad (23)$$

where ${}_iA_a$ is the incremental area corresponding to the *i*-th

axial spring between nodes *a* and *m*.

The stiffness and the incremental force in the individual axial springs between nodes *b* and *n* are obtained by the same procedure as for the axial springs between nodes *a* and *m*.

4. VERIFICATION OF PROPOSED MODEL

Simulation analyses were conducted for tests of square lead-rubber bearings to demonstrate the validity of the proposed model. The design of the bearing tested is shown in Figure 9. The bearing had 31 2.0 mm thick, 250 mm square rubber layers, with a 50 mm diameter lead plug. The layers shape factor, S_1, was 32.5, and the bearing aspect ratio or second shape factor, S_2, was 4.0.

The tests were conducted with constant compressive stresses of σ= 1, 5, 10 and 20 MPa, and comprised sinusoidal horizontal displacement-controlled loading with four fully-reversed cycles of loading at shear strain amplitudes of 50, 100, 200, 300 and 400 percent. Three square lead-rubber bearings were tested, one bearing for each of the horizontal loading directions, 0, 22.5 and 45 degrees, respectively. The loading directions are shown in Figure 8, and the parameters for the bearing tests are summarized in Table 1.

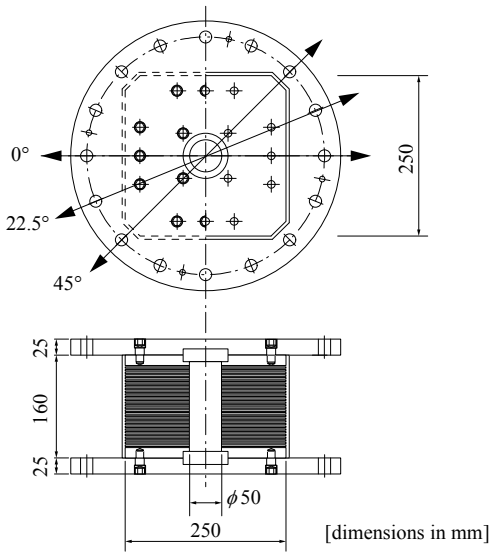

Total rubber thickness: 62 mm (2.0 mm x 31 layers)
Total steel plate thickness: 66 mm (2.2 mm x 30 layers)
Shape factor S_1 : 32.5
Aspect ratio S_2 : 4.0

Figure 8 Square lead-rubber bearing design tested and loading directions.

Table 1 Parameters varied in the bearing tests.

Peak shear strain	50, 100, 200, 300, 400 percent
Compressive stress	1, 5, 10, 20 MPa
Loading direction	0, 22.5, 45 degrees

In the proposed model, the reduction of horizontal stiffness and eventual buckling behavior due to high axial load is represented by the interaction between the shear and axial forces in the tilted MSS model and the axial springs. Therefore, the hysteresis properties to be used for the shear springs in the MSS model should be those under low compressive stress, ideally zero compressive stress. The parameters for the shear hysteresis model were identified by regression analyses of the experimental hysteresis loop under σ=1 MPa compressive stress. Empirical formulae for bearing parameters, as functions of shear strain, were identified from the test results (as Table 2). C_{Kd}, C_{Qd} and C_{heq} are the coefficients for the post-yield stiffness, K_d, characteristic strength, Q_d, and equivalent viscous damping ratio, h_{eq} (Kotsuki et al. 2007, Kikuchi et al. 2007).

Table 2 Empirical formulae for the tested square lead-rubber bearings.

$$C_{Kd}=\begin{cases}0.779\gamma^{-0.43} & (\gamma<0.25)\\ \gamma^{-0.25} & (0.25\le\gamma<1.0)\\ \gamma^{-0.12} & (1.0\le\gamma<2.0)\\ 0.0415(\gamma-2.0)^2+0.920 & (2.0\le\gamma<4.0)\end{cases}$$

$$C_{Qd}=\begin{cases}2.036\gamma^{0.41} & (\gamma<0.1)\\ 1.106\gamma^{0.145} & (0.1\le\gamma<0.5)\\ 1.0 & (0.5\le\gamma<4.0)\end{cases}$$

$$C_{heq}=\begin{cases}1.0 & (\gamma<2.0)\\ 0.0616(\gamma-2.0)^2+1.0 & (2.0\le\gamma<4.0)\end{cases}$$

$$p=\begin{cases}0.0 & (\gamma<2.0)\\ 0.1775\gamma-0.355 & (2.0\le\gamma<4.0)\end{cases}$$

$m=8$ (const.) $(\gamma<4.0)$

$c=6$ (const.) $(\gamma<4.0)$

γ : shear strain

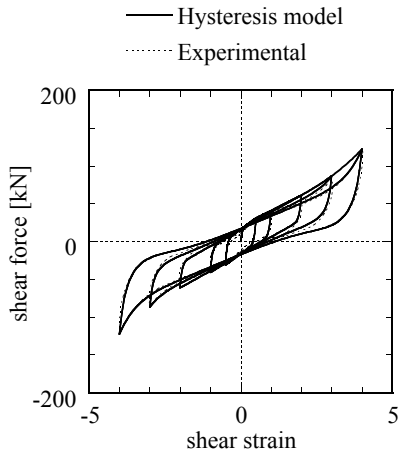

Figure 9 Shear force-shear strain relationship for the multiple shear springs.

The parameters *p*, *m* and *c* are the parameters in Equations (14) and (15). Figure 9 shows the shear force-shear strain relationship up to 400 percent stain used for the MSS model compared with the third cycle hysteresis loop obtained from the test under σ = 1 MPa compressive stress. The shear hysteresis model can capture well the behavior of the tested bearings under low compressive stress. The bearing parameters used for the simulation analyses are summarized in Table 3.

The loading sequence used for the analyses was exactly the same as for the tests. The axial load was applied to the top of the model first, then the horizontal displacement histories were applied. The results show that the proposed model can successfully predict the complex nonlinear

Table 3 Parameters used for the simulation analyses.

Increments in the top and bottom boundaries	30 x 30
Number of springs in MSS model	8
Shear modulus, G	0.392 MPa
Bulk modulus, E_∞	2000 MPa
Tension yielding stress, σ_{ty}	1 MPa
Compression stress for load reversal, σ_r	5 MPa
Tension yielding modulus, E_{ty}	E_{init}/500
Compression yielding stress, σ_{cy}	100 MPa
Compression yielding modulus, E_{cy}	E_{init}/2

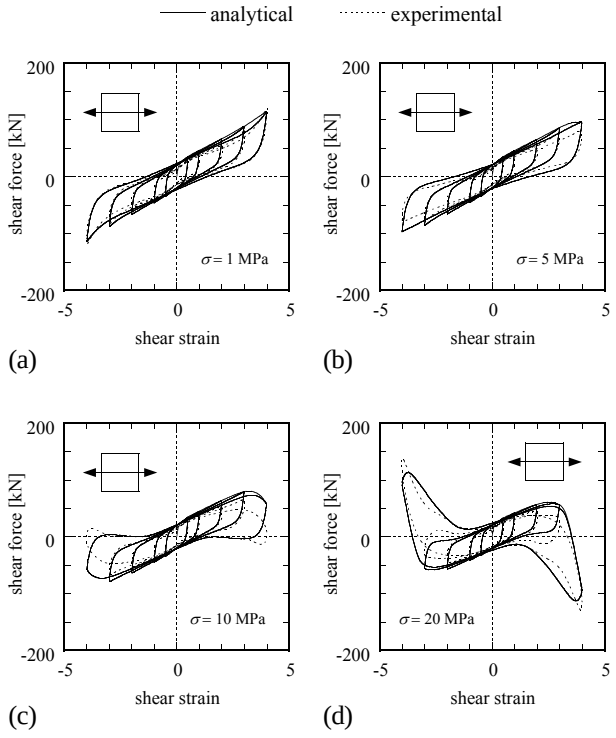

Figure 10 Analysis results for 0 degree horizontal loading: (a) σ=1 MPa; (b) σ=5 MPa; (c) σ=10 MPa; (d) σ=20 MPa.

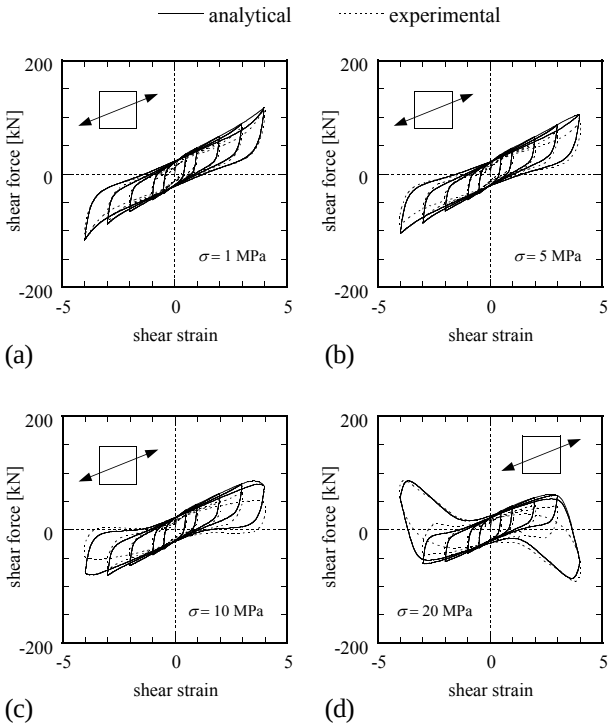

Figure 11 Analysis results for 22.5 degree horizontal loading: (a) σ=1 MPa; (b) σ=5 MPa; (c) σ=10 MPa; (d) σ=20 MPa.

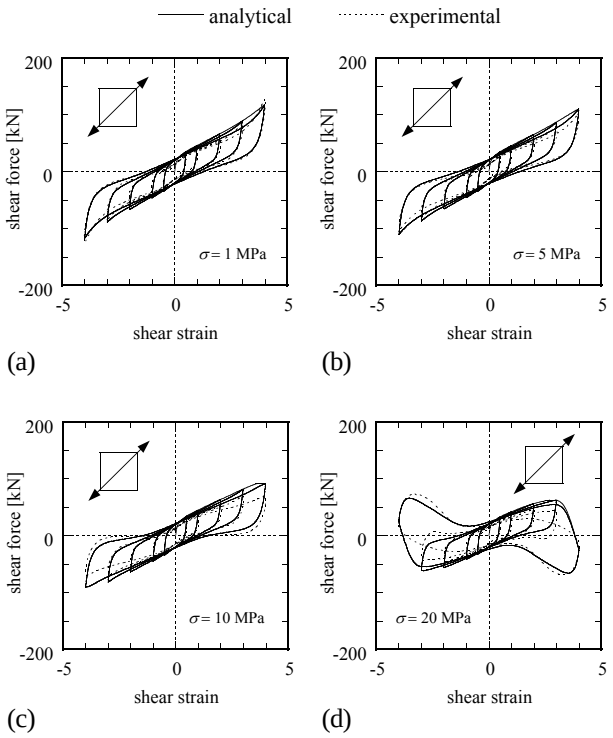

Figure 12 Analysis results for 45 degree horizontal loading: (a) σ=1 MPa; (b) σ=5 MPa; (c) σ=10 MPa; (d) σ=20 MPa.

behavior of square lead-rubber bearings under large deformations, as influenced by the magnitude of the applied vertical load and different horizontal loading directions (Figures 10-12). However, the points of buckling predicted by the analyses (the point on the shear force-displacement plots at which the tangential stiffness is zero) are slightly higher than from the experimental results. This indicates that the proposed model still needs further improvement for the more accurate prediction of limit state behavior.

5. CONCLUSIONS

A three-dimensional mechanical model for square seismic isolation bearings under large shear deformations and high axial loads has been developed by expanding to three dimensions an existing two-dimensional model. The model comprises multiple shear springs at its mid-height, and two series of axial springs at the top and bottom boundaries. The model can capture the interaction between multi-directional shear displacement and axial force, nonlinear hysteresis, and dependence on varying vertical load by considering both material and geometrical nonlinearities in its formulation.

Simulation analyses of bearing tests were performed to validate the proposed model. Analyses of all of the tests were conducted, and the analysis results showed very good agreement with the bearing test results. The model successfully captured the influence of horizontal loading direction, axial load magnitude and axial load history on bearing behavior. The enhanced capabilities of the new model will allow for more accurate three-dimensional dynamic response analyses of seismically-isolated structures, including the effects of varying vertical load and large, multi-directional horizontal displacements.

Acknowledgements:

The authors acknowledge support from the Japan Ministry of Education, Science, Sports and Culture, Grant-in-Aid for Scientific Research (B), 2008, 20360245.

References:

Aiken, ID., Kelly, JM., Tajirian, FF. (1989). "Mechanics of low shape factor elastomeric seismic isolation bearings," Report No. UCB/EERC-89/13, Earthquake Engineering Research Center, University of California, Berkeley.

Yamamoto, S., Kikuchi, M., Ueda, M., Aiken, ID. (2009). "A mechanical model for elastomeric seismic isolation bearings including the influence of axial load," *Earthquake Engineering and Structural Dynamics*, **38**, 157-180.

Wada, A., Hirose, K. (1989). "Building frame subjected to 2D earthquake motion," *Proceedings, Structures Congress '89, ASCE*, San Francisco, 388-397.

Kaba, SA., Mahin, SA. (1984). "Refined modeling of reinforced concrete columns for seismic analysis," *Report No. UCB/EERC-84/03*, Earthquake Engineering Research Center, University of California, Berkeley.

Kikuchi, M., Aiken, ID. (1997). "An analytical hysteresis model for elastomeric seismic isolation bearings," *Earthquake Engineering and Structural Dynamics*, **26**, 215-231.

Kikuchi, M., Yamamoto, S., Aiken, ID. (2007). "An analytical model of lead-rubber bearings under large deformations," *Proceedings of the 8th Pacific Conference on Earthquake Engineering*, Singapore, Paper ID 222.

Ikenaga, M., Suzuki, A., Miyazaki, M. (2001). "Examples which applied anti-seismic devices to existing building and the new approval system for seismic isolator in Japan," *Proceedings of the 7th International Seminar on Seismic Isolation, Passive Energy Dissipation and Active Control of Vibration of Structures*, Assisi, Italy.

Kikuchi, M., Yamamoto, S., Nakamura, T., Nishimura, T., Tamura, K., (2009). "A Three-dimensional multi-spring model for square lead-rubber bearings under large shear deformations," J. Struct. Constr. Eng., AIJ, Vol.74 No.638, 647-655. (in Japanese)

Kotsuki, A., Yamamoto, S., Kikuchi, M., Koshikawa, T., Ueda, M., (2007). "An analytical model for lead-rubber bearing under large shear deformations," *Journal of Structural Engineering*, Vol.53B, 9-16. (in Japanese)

JOINT CONFERENCE PROCEEDINGS
7th International Conference on Urban Earthquake Engineering (7CUEE) &
5th International Conference on Earthquake Engineering (5ICEE)
March 3-5, 2010, Tokyo Institute of Technology, Tokyo, Japan

STRUCTURAL RESPONSE CONTROL BY CONTROLLABLE DAMPERS SETTING AT INTER-STORY OF BUILDINGS

Hideto Kanno[1], Tetsuya Nishida[2], Jun Kobayashi[3] and Norio Inoue[4]

1) *Assistant Professor, Dept. of Architecture & Environment Sytems, Akita Prefectural University, Japan*
2) *Professor, Dept. of Architecture & Environment Sytems, Akita Prefectural University, Japan*
3) *Professor, Dept. of Architecture & Environment Sytems, Akita Prefectural University, Japan*
4) *Professor, Graduate School of Engineering, Tohoku University, Japan*
kanno@akita-pu.ac.jp, tetsuya_nishida@akita-pu.ac.jp, jun.kobayashi@akita-pu.ac.jp, inoue@archi.tohoku.ac.jp

Abstract: This paper discusses the characteristics of the dynamic response of a structure with simple semi-active control system. The control system consists of controllable dampers that are set at each inter-story level. At first, a proposed control method of the damper force was examined. The method, which based on potential energy of inter-story, controls the hysteretic shapes of the damper. The proposed algorithm aims at reducing a displace response without increasing an acceleration response. To examine the performance of the proposed control scheme under seismic excitations, numerical analysis based on equivalent linearization method were conducted. Then extension of this control method to a multi-story building is discussed. As a result, it is confirmed that MDOF model was well controlled by the proposed methods under seismic excitations.

1. INTRODUCITON

In recent years, vibration control systems have been adopted in many buildings in Japan, a lot of which utilize passive supplemental damping schemes. These passive device methods are unable to adapt to structural changes and to varying usage patterns and exciting condition. Active, semiactive structural control systems are evolution of passive control techniques. Especially, semiactive control systems, which need energy in order to alter damping characteristics, are different from active control, which needs more huge energy to suppress seismic response directly. Semiactive control is stable as compared with the active control. Thus, semiactive control schemes are expected to play a much more significant role in future stages of civil engineering and can enhance structural safety during severe earthquakes.

Various types of semiactive control methods have been proposed. A typical approach is to apply a modern control theory such as linear quadratic optimal control. However, the variable damper's highly nonlinear dynamics makes it difficult to determine the optimal control parameter in such an approach. On the other hands, simple control methods have been also proposed. On/off switching control using variable hydraulic damper is to optimize the force-displacement loops (Kurino et al. 1998). Using variable slip-force level damper, Nishitani et al. (2003) proposed a simple control method in such a way that the damper exhibits bilinear hysteresis with a ductility factor equal to two. Shiozaki et al. (2002) proposed EF control that controls damping force depending on vibration energy of a base isolated structure using magnetorheological fluid (MR) damper. MR damper whose damping force can be variable is one of the semiactive control devices.

This paper proposes a simple semiactive control method utilizing controllable dampers which were set up in each inter-story level of building structure. The proposed control method of the damper force based on potential energy of inter-story and controls the hysteretic shape. The basic concept of this semiactive control method is first explained in the following. The control effectiveness of this scheme is then discussed through shaking table tests on a one-story steel structure model. To extend of this control method to a multi-story building, numerical analysis is conducted.

2. OUTLINE OF THE CONTROL METHOD

2.1 Structural Model with Controllable Damper

Structural frame with controllable dampers which were set up in each inter-story of building is showing in Figure 1. A simplified analytical model to represent it is shown in Figure 1b, where m is the mass of the frame, k_f is the stiffness of the original frame. In this paper, a controllable damper consisted of a variable frictional element F_d and dashpot c_d in parallel. This controllable damper model is in series with a spring element which represents the damper support members (k_b indicates the stiffness of the brace). It was assumed that k_f and k_b

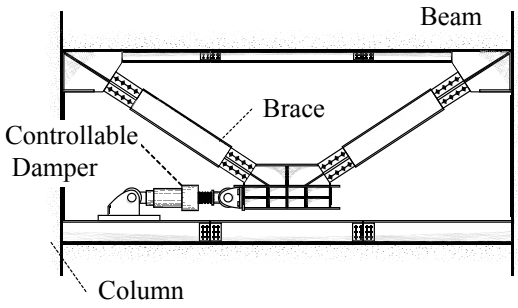

(a) Installation of controllable damper at inter story

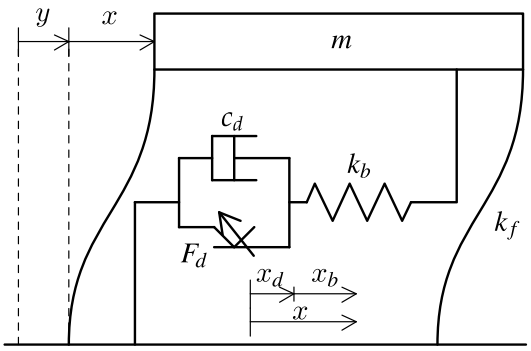

(b) Analytical model

Figure 1 Analytical model of the structure with Controllable Damper

are linear, and only F_d can only be variable while c_d is constant.

Here, a parameter α represents the stiffness ratio of damper support members to the frame stiffness defined as:

$$\alpha = \frac{k_b}{k_f} \tag{1}$$

2.2 Semiactive Control Algorithm

The frictional force of the variable damper was controlled according to the following law.

$$|F_{Ctrl}| = \begin{cases} \lambda\sqrt{\frac{1}{2}k_f x_p^2} = \Lambda|x_p| & \\ & \operatorname{sgn}(x) \neq \operatorname{sgn}(\dot{x}) \\ \Lambda|x_p|\left(1 - \frac{|x|}{|x_{\max}|}\right) & \\ & \operatorname{sgn}(x) = \operatorname{sgn}(\dot{x}) \;\&\; |x| \leq |x_{\max}| \\ 0 & \\ & \operatorname{sgn}(x) = \operatorname{sgn}(\dot{x}) \;\&\; |x| > |x_{\max}| \end{cases} \tag{2}$$

where x is the displacement of the frame and $\dot{x}$ is the velocity of the frame. A parameter x_p indicates peak displacement which occurs at the time of zero velocity. At the time of zero velocity ($\dot{x} = 0$), controlled frictional force of the controllable damper is determined based on a potential energy of the structure. The control force can be calculated as follows: the square root of the potential energy multiplied by a control gain λ. In addition, if equation (2) is rearranged using $\Lambda = \sqrt{\frac{1}{2}k_f}$, the control force at the time of peak displacement is simply evaluated as $F_d = \Lambda|x|$. When the sign of displacement of the frame (x) is not same as the velocity ($\dot{x}$), the control force F_d, which was evaluated just at the peak displacement, was kept fixed. When x and $\dot{x}$ have the same sign, F_d is reduced proportionally in such way that F_d becomes zero when x reaches its maximum value. The hysteresis loop of this semiactive control, when subjected to sinusoidal excitation, is shown in Figure 2.

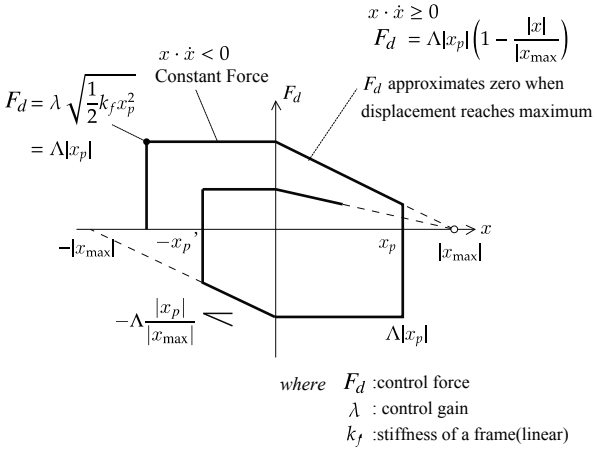

Figure 2 Hysteresis loop with the semiactive control

3. SHAKING TABLE TESTS FOR SDOF MODEL

3.1 Configuration of the testing system

As a controllable damper, MR damper setting into a one-story steel structure was tested. The size of the frame was 1,645 mm high, 2,540 mm long and 1,440 mm wide as illustrated in Figure 3. The mass of the structure was 2,200 kg. The frame without any damper added had a minimal damping (damping ratio was 0.06 %). The natural frequency of the structure without any damper added was 1.8 Hz and the stiffness was 280.6 kN/m. Three kinds of damper support members were used to attach the MR damper to the frame. T3 and T9 were fabricated from two plate sections (T3: 7x75 and T9: 10.5x75) and HH consists of 148x100x6x9 H-section steel. Stiffness ratio α of them follows: T3 and T9 was 0.3 and 0.9 respectively. HH was stiff enough compared to the frame stiffness.

3.2 Properties of the MR damper

Sodeyama et al, (2004) have proposed MR dampers, which have a bypass-flow type magnetizing mechanism. The MR dampers developed by them have a bypass portion in which the electromagnets are installed. The MR fluid passing through the narrow orifice in the bypass portion is applied the magnetic field by electromagnets.

In this paper, the bypass-type MR damper which has a capacity of 2 kN was used. The schematic structure of the MR damper is shown in Figure 4. The piston stroke is 73 mm. MR fluid was enclosed in the cylinder and the bypass portion.

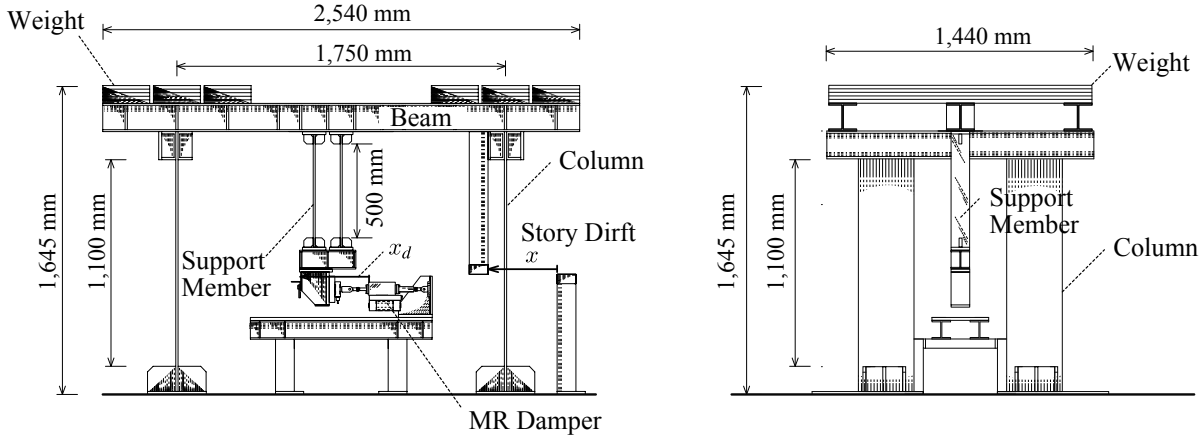

Figure 3 Configuration of tested structural model

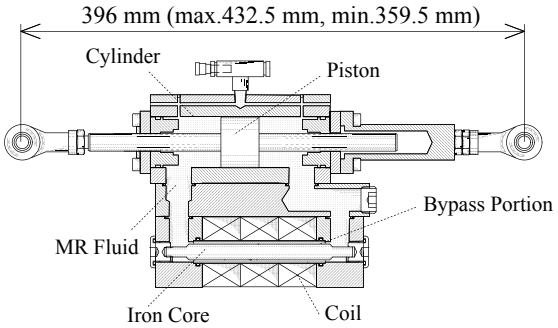

Figure 4 Schematic of 2 kN MR damper

The cyclic loading tests were carried out to clarify the fundamental dynamic characteristics of the MR damper. Figure 5 shows displacement-force hysteresis loops at several exciting current inputted. These are measured under the sinusoidal loading conditions as following: amplitude 15 mm; piston velocity 10 cm/s.

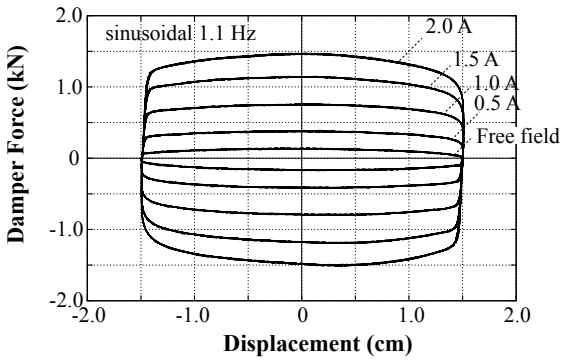

Figure 5 Displacement-force hysteresis loops inputted some exciting currents

3.3 Experimental Method

Shaking table tests also have been carried out using a simulated earthquake ground motion. The simulated ground motion (Figure 6a) was obtained using the phase characteristics of the 1978 Miyagi-ken Oki Earthquake. The peak ground acceleration (PGA) was 0.12G. From the input wave, the spectral characteristics were calculated (Figure 6b) based on the design spectrum stipulated in the Japanese design code.

These tests aim to confirm a seismic response mitigation effectiveness of the semiactive control scheme and to clarify an influence of the support stiffness on the damping properties and control effectiveness. Constant exciting current inputting to the MR damper (i.e. passive control) were also examined during the tests.

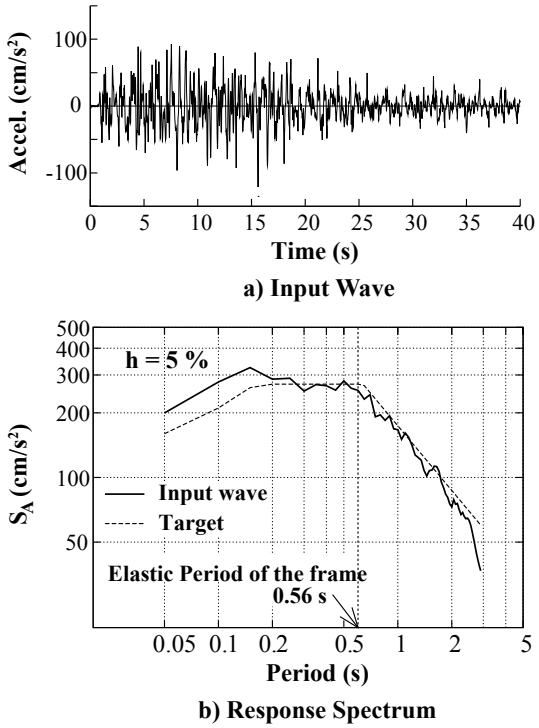

Figure 6 Simulated seismic wave and its response spectrum used in shaking table tests

3.4 Results of Shaking Table Tests

Figure 7 gives damper force - frame displacement hysteresis loops at the maximum damping force for the damper support member HH and T3, in the case of semiactive control and passive control. These loop shapes are well controlled by the proposed algorithm. However, in the case of T3, shapes of loops perform like

a linear spring k_b because damper force is so large that support member is deformable under such large force. Thus, it is clear that α is a major parameter in both the semiactive control and the passive control.

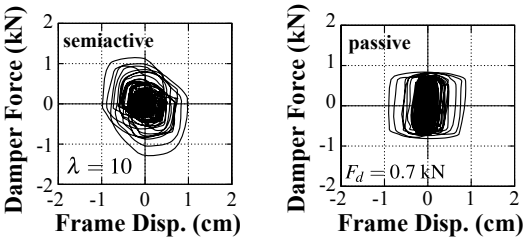

(a) support memeber HH (stiff enough)

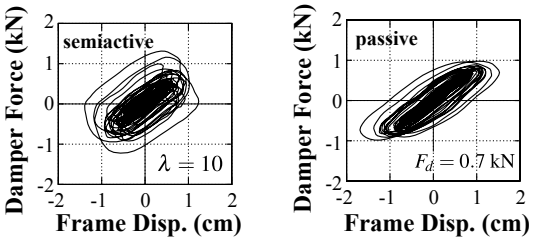

(b) support memeber T3 ($\alpha = 0.3$)

Figure 7 Damper force - frame displacement hysteresis loops of the shaking table tests

4. NUMERICAL ANALYSIS USING EQUIVALENT LINEARIZATION METHOD

4.1 Analytical Method

To examine the performance of the proposed control scheme under seismic excitations, numerical analysis based on equivalent linearization method were conducted. This method, which has been first introduced by Caughey, T.K. (1960) is very useful and practical because of the simplicity of its theory.

For this proposed semiactive method, a parameter η , which represents the ratio of loss stiffness of damping force to the frame stiffness, is defined as

$$\eta = \frac{\lambda\sqrt{\frac{1}{2}k_f}}{kf} = \frac{\Lambda}{k_f} \tag{3}$$

Hysteresis shapes of this scheme are depended on magnitude relation between α and η as shown Figure 8. So equivalent elastic period T_{eq} and equivalent damping ratio h_{eq} are defined by two parameters (i.e. α and η) conditions.

For the semiactive controlled structure vibrating in resonance with steady state sinusoidal excitation, equivalent elastic period T_{eq} and equivalent damping ratio h_{eq} are given by

$$T_{eq} = \frac{1}{\sqrt{1+\alpha C(\alpha,\eta)}} \cdot T_f \tag{4}$$

$$h_{eq} = 0.8\left\{\frac{-\alpha S(\alpha,\eta)}{2(1+\alpha C(\alpha,\eta))} + \frac{h_f}{\sqrt{1+\alpha C(\alpha,\eta)}}\right\} \tag{5}$$

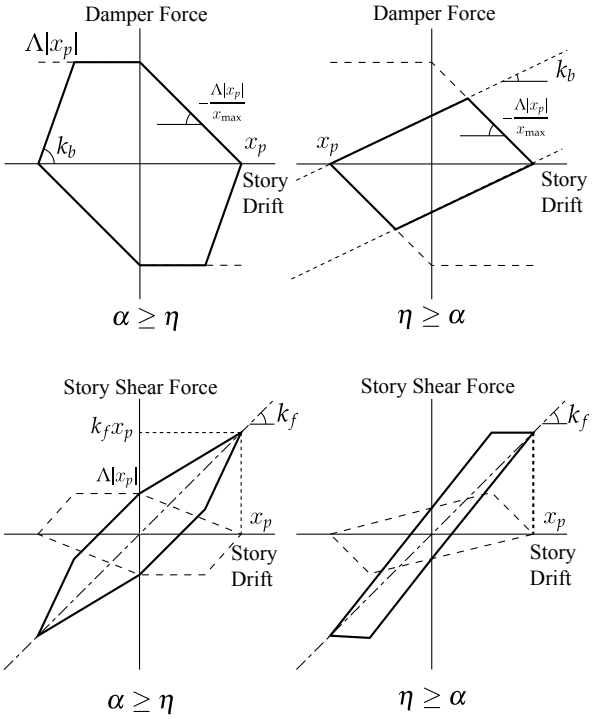

Figure 8 Hysteresis loops with the control depend on the magnitude relation between α and η

where T_f is elastic period and h_f is damping ratio of the frame without the damper added. In the case of this semiactive control algorithm, C and S are functions of α and η as following

$$C(\alpha,\eta) = \begin{cases} \frac{1}{\pi}\left\{\alpha\theta^* - (\alpha-\eta)\sin\theta^* - \frac{\pi}{2}\eta\right\} & \alpha \geq \eta \\ \frac{1}{\pi}\left\{(\alpha+\eta)\theta^* - (\alpha-\eta)\sin\theta^* - \pi\eta\right\} & \alpha < \eta \end{cases} \tag{6}$$

$$S(\alpha,\eta) = \begin{cases} \frac{1}{\pi}\left\{\alpha\sin^2\theta^* + \frac{\alpha}{2}(\alpha-\eta)^2 - 2\alpha - \eta\right\} & \alpha \geq \eta \\ \frac{1}{\pi}\left\{-(\alpha+\eta)\sin^2\theta^*\right\} & \alpha < \eta \end{cases} \tag{7}$$

where θ^* is given by

$$\cos\theta^* = \begin{cases} 1 - \frac{\eta}{\alpha} & \alpha \geq \eta \\ \frac{\alpha-\eta}{\alpha+\eta} & \alpha < \eta \end{cases} \tag{8}$$

Under constant spectral acceleration, response reduction ratio of acceleration R_a and that of displacement R_d are given by

$$R_d = D_h \left(T_{eq} / T_f \right)^2 \qquad R_a = R_d \left(T_f / T_{eq} \right)^2 \qquad (9)$$

where D_h indicates a damping effect factor, which is introduced by Kasai et al. (2003). For simulated seismic excitation, D_h is given by

$$D_h = \sqrt{\frac{1+75h_f}{1+75h_{eq}}} \qquad (10)$$

4.2 Analytical Results using Equivalent Linearization Method

Figure 9 shows predicted maximum displacement and acceleration curves and their comparison with the experimental results. The predicted values using equivalent linearization method agree well with the experimental values. The result suggests that parameter α and η are significantly influential on the seismic control effectiveness. In the case of using rigid support member (HH), this proposed control scheme appears to be more effective in reducing the acceleration than the displacement. Moreover, using soft support member (T9 and T3), in the case of passive control, the seismic response increases as the damper force crosses a certain value. However, the semiactive proposed control method does not show such tendency.

5. EXTENSION TO A MULTI-STORY BUILDING

For the purpose of assessing the simple design method of semiactive control parameters for a semiactive seismic response controlled multi-story building, numerical analysis were conducted using an MDOF model. A 10-story steel building model is set up for the study of an MDOF model and its specifications are shown in Figure 10 and Table 1. The parameters of this model were determined according to the data for the proposed model structure which was designed by Ohbuchi et al. (2002). The stiffness matrix for this model was constructed by the static push-over analysis as an shear structural system. The first three fundamental frequencies without any dampers were 0.54, 1.56 and 2.69 Hz. The structural damping was assumed to be proportional to the stiffness matrix such that a viscous damping ratio of 2% with respect to the first mode.

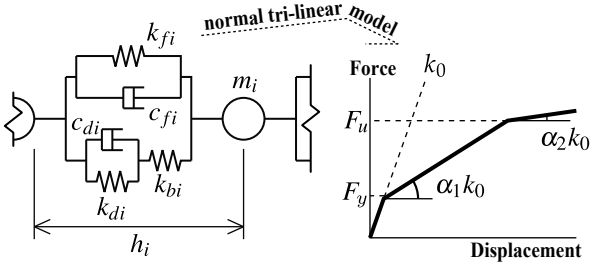

Figure 10 Analytical Model for 10-Degrees-Of-Freedom Model Building

Table 1 Parameters for Analytical Model

Story	h_i (m)	m_i (kN)	k_0 (kN/cm)	F_y (kN)	α_1	F_u (kN)	α_2
10	4.0	7739.4	2152.6	4031.9	0.575	4868.4	0.001
9	4.0	5543.6	2489.0	4903.1	0.716	6926.1	0.001
8	4.0	5617.9	2848.6	5842.1	0.749	8597.7	0.009
7	4.0	5639.5	3050.0	6679.8	0.746	10043.0	0.007
6	4.0	5689.2	3155.8	7323.4	0.740	11213.2	0.010
5	4.0	5707.9	3305.3	7535.2	0.761	12216.3	0.014
4	4.0	5755.5	3457.8	8373.2	0.741	13091.9	0.012
3	4.0	5774.1	3511.5	8843.4	0.724	13686.3	0.016
2	4.0	5774.1	3504.0	8901.0	0.740	14032.1	0.053
1	6.0	5931.2	2650.6	8835.2	0.821	14777.2	0.009

Variable dampers were installed on each inter-story level of the structure. An important issue in the design of this semiactive control scheme is balancing the structural stiffness and loss stiffness of damping force and damper support members stiffness in each story of the building. In this study, these control parameters of each story of the MDOF model were determined by stiffness tuning method, which was proposed by Kasai et. al.(2002), as following:

- Establish the equivalent SDOF system of multi-story structure.
- Determine representative stiffness ratio α and η based on the previous discussion on the SDOF model.
- Damper support member stiffness k_{bi} and control gain η_i on each story are given by

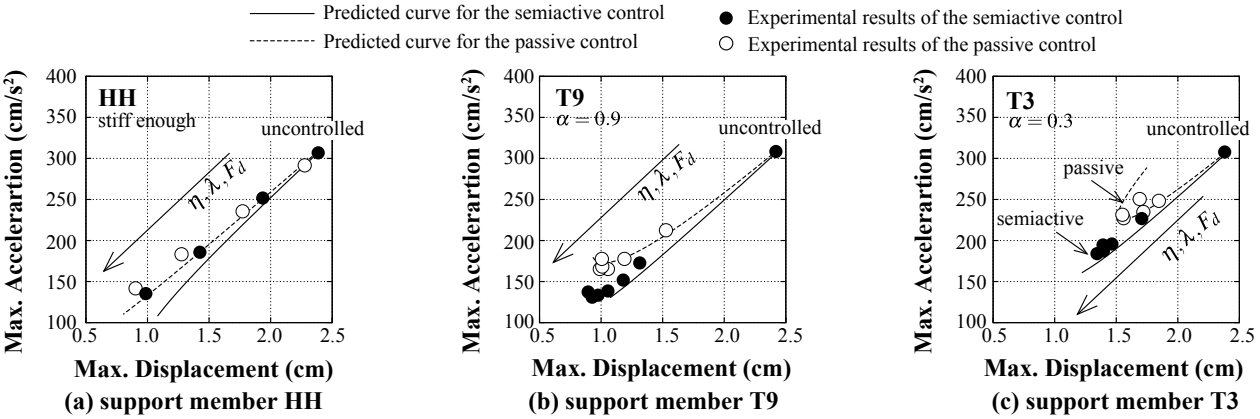

Figure 9 Predictions of Maximum Displacement and Acceleration

$$k_{bi} = \frac{\alpha}{\eta} \cdot \frac{Q_i}{h_i} \cdot \frac{\sum_{i=1}^{n} (k_{fi} h_i^2)}{\sum_{i=1}^{n} (Q_i h_i)} (1+\eta) - \frac{\alpha}{\eta} k_{fi} \qquad (11)$$

$$\eta_i = \frac{k_{bi}}{\sqrt{\frac{1}{2} k_{fi}}} \cdot \frac{\alpha}{\eta} \qquad (12)$$

where Q_i is the lateral earthquake force distribution along the building height, and h_i is story height on each story. In this study, damper support member stiffness k_{bi} and control gain λ_i of each story were designed to the following : target story drift angle every each story were 0.01. The parameters thus determined are provided in Table 2. Using these parameters, numerical analysis subjected to the simulated earthquake ground motion such as previous discussion with PGV 0.5m/s was conducted.

Figure 11 shows the distributions of the maximum values compared with the uncontrolled responses of the building model without any controllable dampers added. Each story drift angle reached approximately 0.01 as the target value and it is confirmed that the simple design method of the proposed control scheme using equivalent linearization method is quite practical. Maximum acceleration of each floor were effectively reduced as compared to the uncontrolled results and it can be said that the proposed scheme can control to the target story drift with acceleration reducing.

Table 2 Control Parameters for MDOF Modle

Story	k_b (kN/cm)	λ_i	
10	NONE		at 10th story, without controllable dampers
9	7321.5	133.0	
8	12666.5	170.8	designed parameter equivalent SDOF as following : $\alpha = 2.0$ $\eta = 0.22$
7	7314.1	131.2	
6	17435.6	199.4	
5	41486.0	258.1	
4	49925.6	272.9	it was assumed that damper stiffness k_d was assumed four times k_f
3	12518.0	173.8	
2	19695.9	214.9	
1	4230.7	91.6	

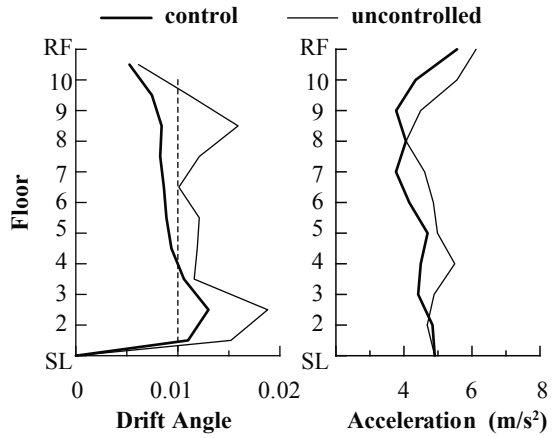

Figure 11 Distributions of Maximum Responses

6. CONCLUSION

A simple semiactive control based on energy response of the structure utilizing controllable dampers has been presented. The response reduction of this scheme was confirmed though the shaking table tests performed on a one-story steel structure model. The control performance could be predicted by equivalent linearization method discussed here. It was found that the proposed scheme can control to the target story drift with acceleration reducing. For a multistory building, the simple design method of the proposed control scheme using equivalent linearization method is practical.

Acknowledgements:

This research was partially supported by the Ministry of Education, Culture, Sports, Science and Technology (MEXT) , Japan, under the Grant-in-Aid for Young Scientists (A), (Grant No. 18686046) and the Grant-in Aid for Young Scientists (B) (Grant No. 21760437) .

References:

Spencer Jr. B. F. (2003). State of the Art of Structural Control. *ASCE Journal of Structural Engineering* **129**(7). 845-856.

Kurino,H. and Kobori,T.(1998). Semi-active Structural Response Control by Optimizing the Force-deformation Loop of Variable Damper. *Proc., 2nd World Conf. on Structural Control*, 407-416.

Kurino,H., Tagami, J., Shimizu,K. and Kobori,T.(2003). Switching Oil Damper with Built-in Controller for Structural Control. *ASCE Journal of Structural Engineering* **129**(7), 895-904.

Shiozaki,Y., Hiwatashi,T., Fujitani,H. and Soda,S.(2003). Simple Semi-active Control for Base-isolated Building by MR Damper. *AIJ Journal of Structural and Construction Engineering* **570**, 37-43

Nishitani,A., Nitta,Y. and Ikeda,Y.(2003). Semiactive Structural-Control Based on Variable Slip-Force Level Dampers. *ASCE Journal of Structural Engineering* **129**(7), 933-940.

Spencer Jr. B. F., Dyke S.J., Sain M.K. and Carlson J.D.(1997). Phenomenological Model of a Magnetorheological Damper. *ASCE Journal of Engineering Mechanics* **123**(3), 230-238.

Sodeyama,H., Suzuki,K. and Sunakoda.K.(2004). Development of Large Capacity Semi-Active Seismic Damper using Magneto-Reheological Fluid. *ASME Journal of Pressure Vessel Technology* **126**, 105-109.

Caughey.T.K.(1960). Sinusoidal Excitation of a System with Bilinear Hysteresis. *ASME Journal of Applied Mechanics* **27**(50), 640-643.

Kasai,K., Ito,H. and Watanabe,A.(2003). Peak Response Prediction Rule for a SDOF Elasto-plastic System Based on Equivalent Linearization Technique. *AIJ Journal of Structural and Construction Engineering* **571**, 53-62.

Ohbuchi,T., Mori,H., Yoshie,K, *et. al.*(2002). Proposed Theme Structure and Analytical Modeling Study for Passive Control System. *Passive Control Symposium 2002 Tokyo Institute of Technology*, 195-219

Kasai,K. and Ito,H. (2005). Passive Control Design Method Based on Tuning of Stiffness, Yield Strength, and Ductility of Easto-plastic Damper. *AIJ Journal of Structural and Construction Engineering* **595**, 45-56.

JOINT CONFERENCE PROCEEDINGS
7th International Conference on Urban Earthquake Engineering (7CUEE) &
5th International Conference on Earthquake Engineering (5ICEE)
March 3-5, 2010, Tokyo Institute of Technology, Tokyo, Japan

EXPERIMENTAL VALIDATION OF MARKET-BASED CONTROL USING WIRELESS SENSOR AND ACTUATOR NETWORKS

R. Andrew Swartz[1)], Yang Wang[2)], Jerome P. Lynch[3)], Kincho H. Law[4)], and Chin-Hsiung Loh[5)]

1) Assistant Professor, Dept. of Civil and Environmental Engineering, Michigan Technological University, Houghton, MI, USA
2) Assistant Professor, Dept. of Civil and Environmental Engineering, Georgia Institute of Tech., Atlanta, GA, USA
3) Associate Professor, Dept. of Civil and Environmental Engineering, University of Michigan, Ann Arbor, MI, USA
4) Professor, Dept. of Civil and Environmental Engineering, Stanford University, Stanford, CA, USA
5) Professor, Dept. of Civil Engineering, National Taiwan University, Taipei, Republic of China
raswartz@mtu.edu, yang.wang@ce.gatech.edu,jerlynch@umich.edu, law@stanford.edu, lohc0220@ccms.ntu.edu.tw

Abstract: Structural control is a powerful tool that can effectively limit the undesired responses of civil structures resulting from base motion occurring during a major seismic event. In particular, low cost semi-active control devices (such as varying dampers) are gaining popularity because they accomplish their control objectives by strategically changing the properties of the structure under low power requirements. However, these devices are limited in the amount of force that they can deliver compared to larger (and more costly) active control devices. As a result, high actuator densities are often required to achieve adequate control of a large structure using semi-active control devices. This dense actuator network, coupled with sensors and the structure itself, represents a complex dynamic system that is best controlled through a decentralized approach. In this study, a decentralized market-based control (MBC) solution is adopted for controlling tall buildings that employ a large number of semi-active varying dampers for response mitigation. Specifically, wireless nodes are used to collect response data from sensors (accelerometers) and to command magnetorheological (MR) dampers. The computational capabilities of the wireless nodes are also utilized to formulate the control solution based on the MBC strategy. Wireless nodes collocated with the MR dampers are modeled as marketplace buyers vying for control energy made available by power sources modeled as market sellers. The buyer demand for control action is formulated as a function of the local response of the structure while the seller counter balances the market demand by having the market supply function correlated to the total reserve energy available in the control system. A market price is arbitrated at each point in time by determining the price at which the demand and supply functions equal one another. The theoretical basis of the MBC algorithm is first presented. Next, the method is experimentally validated using a six-story steel structure controlled by MR dampers and excited by a shake table. The results indicate the MBC solution to be effective in minimizing the displacement of the test structure.

1. INTRODUCTION

Limiting the response of civil structures to large external lateral disturbances (*e.g.*, wind loads, earthquakes) helps to ensure overall stability while limiting damage. Aside from the use of lateral-load resisting systems that are designed to resist seismic forces imposed on large buildings, structural control technology offers an additional avenue to designers to limit vibrations. Early structural control systems tended to be characterized by a small number of large and expensive actuators that were either passive (*e.g.*, tuned mass dampers, viscoelastic dampers, metallic yield dampers) or active (*e.g.*, active mass dampers). In passive control systems undesired response energy is passively drawn out of the system while for active systems, the dynamic behavior of the system is limited through a direct application of energy (Spencer and Nagarajaiah 2003). Passive dampers are effective within the specific bandwidth to which they are tuned but provide less protection outside this bandwidth. In contrast, the electrical energy needed to power active devices is large; this leaves the control system vulnerable because the supply of grid power can be interrupted during a large seismic event. Furthermore, active dampers offer no inherent guarantee of stability for the system.

More recently, semi-active control devices that combine the performance advantages of both passive and active devices have been developed for the control of large civil structures. Semi-active devices consume energy only to modify the configuration of the device; device configurations then minimize the effects of large system disturbances. These devices have a smaller form factor, consume less energy, and are considerably less expensive than active devices (Spencer and Nagarajaiah 2003). Furthermore, unlike passive devices, they can be actively commanded in real time giving them a wide operational bandwidth. Examples of semi-active actuators include variable stiffness devices, variable orifice dampers (*e.g.*,

Kajima's HiDAX device), as well as electro- and magneto-rheological (MR) dampers. The drawback of this class of device is that their control potential is limited, thus necessitating dense installations to effectively control large structures such as high-rise buildings.

The large number of actuators and sensors needed for the control system, coupled with the large spatial dimensions of the structure itself, represents as extremely complex environment for the deployment of a cost-effective control system. Specifically, the wiring required to connect these devices to a central computer (*i.e.*, controller) represents a significant installation cost, potentially thousands of dollars on a per channel basis (Celebi 2002). In light of the high installation cost of a wired control system, one solution is to forego connectivity altogether, operating each semi-active actuator as an independent device, such as is implemented in Kajima Corporation's HiDAX system (Kajima Corporation 2006). However, wireless telemetry also presents an attractive alternative. A feedback control system based on the use of wireless communications allows information to be exchanged between sensors and actuators yet avoids the costs commonly associated with the installation of wires. Wireless sensing and actuation devices can be installed at a significantly reduced cost (as low as a few hundred dollars per device) compared with their cabled counterparts. In addition, the computing capabilities integrated with each wireless node (Straser and Kiremidjian 1998; Lynch, *et al.* 2004) may also be harnessed for the real-time computation of the control solution (Wang, *et al.* 2007; Swartz and Lynch 2009).

A network of low-cost wireless sensing and actuation nodes provides an economical computing platform for the implementation of feedback control solutions. Wireless sensing and actuation nodes with embedded computational abilities can be installed to sense the dynamic response of the structure, to compute control forces, and to command semi-active control devices in a manner that achieves the desired control force. Unlike the traditional centralized control system architecture in which one controller calculates the control solution, the wireless system is characterized by the spatial distribution of its computational resources and measurement data. Furthermore, data transmission over the wireless communication channel imposes a cost in terms of power (a critical issue for battery powered wireless nodes) and communication bandwidth (Wang, *et al.* 2007; Swartz and Lynch 2009). These limitations point to the need for decentralized control methods when implementing on the distributed computational system offered by a wireless sensor and actuator network. In this context, decentralized control methods enjoy two distinct advantages over centralized methods. First, employing a decentralized control solution reduces the communication load on the wireless communication channel, thereby improving communication performance (*e.g.*, channel reliability) while simultaneously reducing the amount of energy expended by each node. Second, distributed controllers avoid dependence on a single computational node; therefore, such systems are less susceptible to systemic failure due to the loss of the centralized controller.

In this study, a decentralized control algorithm based on free market economies is adopted for wireless control of a six-story steel frame structure. This study provides the first experimental validation of the market-based structural control methods proposed and simulated by Lynch and Law (2002; 2004). In the implemented control system, wireless nodes are installed at each structural degree of freedom (DOF) to measure its response using accelerometers. In addition, wireless nodes are integrated with the MR dampers installed on each floor. The wireless sensors and actuators are modeled as market buyers vying to acquire control energy. As the structural response of their associated DOF increases, the demand function of the DOF wireless sensor increases in tandem. Energy sources, modeled as market sellers, have their own associated supply function. The supply and demand functions are aggregated (by wireless communication) in a virtual marketplace so that a Pareto optimal price of control energy can be determined. This competitive equilibrium price is then the basis for the amount of control energy each DOF purchases (and applies in the form of a control force). The subject of this study is a six-story steel laboratory shear building controlled using magnetorheological (MR) dampers located between floors. *Narada* wireless sensing and actuation nodes (Swartz, *et al.* 2005) are installed with each actuator and are responsible for measuring the floor response, computing supply and demand functions, allocating control energy, converting control energy into a control force, and commanding the MR damper to apply that force. In this paper, the theoretical foundation of market-based control is presented followed by a description of the *Narada* wireless sensing and actuation nodes. These sections are followed by a description of the experimental setup and test procedure. Finally, results and conclusions are presented as well as recommendations for future work necessary to advance market based control.

2. MARKET-BASED CONTROL

The installation of large numbers of semi-active actuators (such as MR dampers) in a civil structure renders the disturbance rejection control problem as highly complex due to the sheer size of the actuator network. Commanding this actuator network using a distributed network of low cost wireless nodes introduces additional complexities in the form of distributed data, deterministic computing delays, and stochastic communication delays. These complexities make it difficult to administer control actions in a centralized manner. For complex distributed systems, a decentralized, agent-based approach is often more appropriate (Siljak 1991). While many agent-based control methods have been proposed, this study focuses on market-based control (MBC) because of its effectiveness when applied to structural control problems (Lynch and Law 2002).

In market-based control, decentralized controllers are

designed to exercise autonomous action as economic agents operating within a marketplace. In free market systems, scarce system resources are allocated from seller agents, (according to their supply) to buyer agents (according to their demand) (Clearwater 1996). The aggregated effect of the buy-sell interaction between market agents results in an equilibrium market price, *p*, for the scarce resource. Based on the equilibrium price, the amount of resource allocated to each buyer is determined. When buying power (wealth) is distributed equitably and demand is generated rationally, market systems produce an optimal allocation of resources. In MBC, power sources (*e.g.*, batteries) represent the sellers of control energy while control devices (*e.g.*, actuators) represent buyers. Control devices seek to maximize their utility by purchasing power based on the demand imposed on them by vibration of the structure, P_B. Power sources seek to maximize their profit from the power they have to sell, P_S. In a closed system with *n* sellers and *m* buyers, the aggregated power supplied from all *n* sellers will be equal to the aggregated power demanded by all *m* buyers:

$$\sum_{i=1}^{n} P_{Si} = \sum_{i=1}^{m} P_{Bi} \tag{1}$$

Through aggregation of the supply and demand from all buyers and sellers in the network, the individual buyers' utility functions and sellers' supply functions are maximized within the constraints imposed by the utility and supply functions of all of the other buyers and sellers (respectively) in the system (Lynch and Law 2002). The multiple objectives of these agents are balanced in a Pareto optimal sense through computation of the equilibrium price dictated by the aggregated supply and demand functions. The way in which the supply and demand functions are defined will determine the allocation of control power in the MBC system during extreme loading events.

The objective of the control system is to protect the structure during extreme loading events by minimizing the vibration associated with these unwanted disturbances; thus, the demand for control power is naturally tied to structural response. The demand generated by the ith DOF (and its associated buyer agent), is modeled as a function of displacement, x_i, and velocity, $\dot{x}_i$. A linear demand function is selected for simplicity, with a negative slope to ensure that an increasing price for power will result in a decreasing buyer demand:

$$P_B = -|f(x,\dot{x})|p + |g(x,\dot{x})| \tag{2}$$

where *f* is the slope of the demand function, *g* is the intercept, and p is the price for power, *P*. Both the intercept and magnitude of the slope increase with structural response. Various tuning constants, *Q*, *R*, *S*, and *T* are introduced into the demand function to provide freedom in establishing the relationship between response and demand (Lynch and Law 2004):

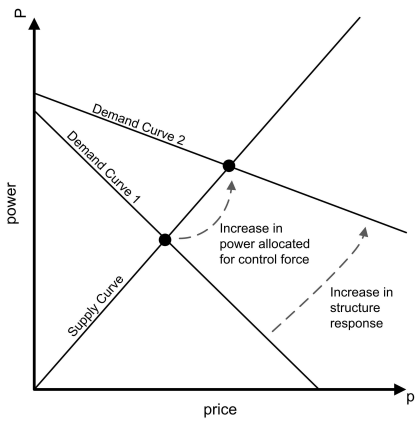

Figure 1 Equilibrium price increase due to increase in demand.

$$f(x,\dot{x}) = \frac{1}{Tx + Q\dot{x}} \tag{3}$$

$$g(x,\dot{x}) = Rx + S\dot{x} \tag{4}$$

As shown in Figure 1, the linear demand function effectively moves on the *p*-*P* plot as the response of the structure varies.

A simple linear supply function is selected with a positive slope such that power sources are encouraged to supply additional control power as the price of power increases. Furthermore, in the absence of demand, the supply function should be zero, necessitating the supply function intercept to be at the origin. With adequate tuning ability built into the demand function, a constant supply function with slope of $1/\alpha$ is selected:

$$P_S = \frac{1}{\alpha}p \tag{5}$$

A graphical depiction of the interaction of the supply and demand functions is presented in Figure 1. As demand increases, the price of power increases thereby stimulating additional supply. In a single DOF system, equating the supply (5) and demand (2) functions yields the control force, *U*:

$$U = K\left(\frac{|Rx + S\dot{x}|}{|Tx + Q\dot{x}| + \alpha}Tx + \frac{|Rx + S\dot{x}|}{|Tx + Q\dot{x}| + \alpha}Q\dot{x}\right) \tag{6}$$

where *K* is a conversion constant that translates equilibrium price to control force (Lynch and Law 2004). Generalizing this formulation to a multiple degree of freedom (MDOF) system introduces a true energy marketplace. To allow the allocation differential control authority in the design of the MBC system, each controller (market buyer) is allocated a fictitious wealth (*e.g.*, W_i for the ith controller). The wealth factor is included as a multiplier to the ith MDOF demand

function (Lynch and Law 2002):

$$P_{Bi} = W_i\left(-\left|\frac{1}{Tx + Q\dot{x}}\right| p + |Rx + S\dot{x}|\right) \quad (7)$$

To maintain balance in the system, selling agents are not allowed to accumulate wealth gained by selling control power to buyers. Rather, the money spent by each buyer is aggregated and redistributed evenly back to the buyers. Heavy consumers of energy will find their wealth gradually diminished, reflecting depletion of their local power supply. The MDOF equilibrium price is (Lynch and Law 2002):

$$p_{eq} = \frac{\sum_{i=1}^{m} W_i|Rx + S\dot{x}|}{\frac{n}{\alpha} + \sum_{i=1}^{m}\frac{W_i}{|Tx + Q\dot{x}|}} \quad (8)$$

If a buyer retains sufficient wealth in excess of the equilibrium price of power, the buyer will purchase control power to generate the control force it desires (Lynch and Law 2002):

$$U_i = K\left(\frac{-p_{eq}W_i}{|Tx + Q\dot{x}|} + W_i|Rx + S\dot{x}|sign(Rx + S\dot{x})\right) \quad (9)$$

The buyer's wealth will be debited by the amount of the control power purchased. The total wealth expended by all buyers is then summed and redistributed equally to all buyers in the network. Finally, the MBC generated control force is translated into a command voltage to be applied to the local semi-active controller.

3. NARADA WIRELESS SENSING AND ACTUATION NODES

Wireless control systems must include the functionality of traditional wired control systems. For example, high-fidelity response data is required for effective feedback control; thus, a wireless sensing node must incorporate sufficient sampling range and resolution to properly characterize the structural response under both relatively large and relatively small excitation levels. Another important functional feature of structural control is the commanding of actuators; hence, a wireless actuation node must be capable of commanding actuators. To exchange information between nodes, a wireless communication interface that introduces minimal communication latency is important to keep the sampling and actuation rate sufficiently high so as to preserve control performance and robustness. Finally, decentralized agent-based structural control (*e.g.*, MBC) over a wireless network requires network nodes capable of embedded, local data processing. These functional requirements strongly influence the design of the wireless nodes used for sensing, actuation and computing. The wireless sensing and actuation device employed in this study has been designed at the University of Michigan for real-time feedback control applications. The *Narada* wireless sensing and actuation node (Figure 2) incorporates a high-resolution, 16-bit sensor interface accommodating up to four sensing channels, an integrated actuation interface, a Zigbee-compatible wireless transceiver capable of communicating data rates up to 250 kbps, and a microcontroller capable of carrying out calculations.

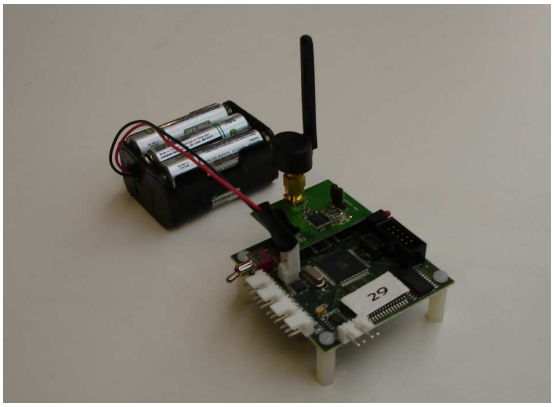

Figure 2 *Narada* wireless sensing and actuation node

The sensing interface of the *Narada* wireless node consists of a Texas Instruments ASD8341, 16-bit, 4-channel, low-power analog-to-digital converter (ADC). Sensor data digitized by the ADC is transmitted to the computational core of the *Narada* node via the serial-peripheral interface (SPI) of the node's microcontroller. The microcontroller is the Atmel Atmega128, a low-power, 8-bit microcontroller with 128 kB of flash memory for program instructions and 4 kB of static random-access memory (SRAM) for data and variable storage. An additional 128 kB of external SRAM is also provided for additional data storage on the sensor node. *Narada*'s link to the world (and other *Narada* nodes) is the Texas Instruments CC2420 IEEE802.15.4-compliant wireless transceiver. The CC2420 has been developed for low-power, ad-hoc wireless network applications, supports 16 independent channels in the 2.4 GHz range, can communicate up to 50 m (line of sight), and consumes approximately 60 mW of power. The *Narada* wireless node also includes an integrated actuation interface consisting of a Texas Instruments DAC7612, 12-bit, 2-channel digital-to-analog converter (DAC). The full capabilities of the wireless node are employed to execute the market-based control tasks outlined herein .

4. EXPERIMENTAL METHODS

The structure that is the subject of this study is a partial-scale, six-story steel structure (Figure 3) employing MR-dampers located between floors to provide control forces that reject seismically induced disturbances. Seismic disturbances are simulated by use of a 5 m x 5 m



Figure 3 Six-story test structure mounted to the 25 m^2 shaking table at the National Center for Research on Earthquake Engineering (NCREE), Taipei, Taiwan

6-degree of freedom (DOF) shaking table. The structure is composed of 2 cm steel plate floors supported at their perimeter by 5 cm x 5 cm x 0.5 cm angles; each floor is vertically spaced by 1.0 m. Floors are supported by 15 cm x 2.5 cm rectangular columns bolted to the corners of the floors and oriented such that lateral loading introduced by the shaking table is applied in their weak direction. Rigid connections are provided for the columns at the base of the structure. Diagonal braces mounted to the bottom of each floor provide the connection points for MR-dampers (Lord Corporation RD-1005-3 MR dampers) that indirectly actuate control forces between floors. By changing the current supplied to the MR-dampers, the level of damping between the floors may be changed in real-time. The interstory force applied by the MR-damper is a function of the input current as well as the differential velocity between those floors.

Narada wireless sensing and actuation nodes are installed on every floor in the structure as well as at the base. Each node is equipped to measure the acceleration response of the floor upon which it is located (using low-cost Crossbow CXL02 capacitive accelerometers). The acceleration measurements are input to a static Kalman state estimator to compute the displacement and velocity of each DOF. The displacement and velocities are input to the MBC demand function embedded in the wireless node measuring acceleration. Local demand functions are calculated at each sensor with the slope and intercept of each DOF's demand function communicated to the network over the wireless channel. Assuming a constant supply function, an equilibrium price for power can be calculated based on the aggregated demand. The equilibrium price is determined based on the aggregated demand and supply functions. The equilibrium price allows each MR damper to determine the power (and amount of control force) to be applied to the structure. However, because the MR-dampers do not generate force directly, computation of a hysteretic bi-linear, bi-viscous model is necessary within the *Narada* node based on the desired control force, damper velocity, and damper state (Lynch, *et al.* 2008). The *Narada* node commands the MR-damper over its actuation interface by issuing an analog command voltage that is converted into a proportional current supply for the damper.

Aggregation of buyer demand and seller supply information implies the existence of a "marketplace" in which market agents interact in a competition. To carry out such a market place, wireless communication would need to take place at each time step so that buyer and seller agents could exchange their information (namely, demand and supply functions). However, heavy use of wireless data transmissions would incur cost in terms of increased latency in the control solution due to deterministic effects (*e.g.*, transmission time and packet overhead) as well as stochastic effects (*e.g.*, lost packets and resend protocols) (Wang, *et al.* 2007). In structural control applications, the latency introduced due to wireless communication has a significant effect on performance (Wang, *et al.* 2007), therefore redundant embedded computation of control parameters can decrease the reliance on the wireless channel, decrease latency, and improve both control performance and reliability of the wireless communications within the network (Swartz and Lynch 2009). In this study's implementation of the market-based control solution, each wireless sensor contains a predetermined supply function that is never transmitted. Rather, the communication channel is reserved only for communication of each buyer agent demand function. In this case, each sensor in the structure takes its displacement and velocity measurement to determine its linear demand function (Equation 7). This information is broadcast by each node with every other node receiving and aggregating all of the demand functions. Once local energy demand is communicated over the network, individual agents will each perform the market aggregation and computation of the equilibrium price in a parallel and redundant fashion, thus trading communication bandwidth for computing. Using the equilibrium price, local control forces can be calculated using the local demand function. In addition, the wireless sensors each determine their wealth, W_i, available for the next time step. This process continues for each time step of the control system.

Design of the MBC controller requires the assignment of values to the tuning parameters in the supply and demand functions in equations (6), (7), and (8), namely, Q, R, S, T, α, and K as well as the initial wealth values, W_i, allocated to each controller. Preliminary studies in the simulation environment found that placing a relatively high weight on the scaling factor applied to the displacement term in the denominator of the demand function (T) yielded the best results in terms of keeping the peak interstory drift experienced by the structure during an earthquake as small as possible. Therefore, the weighting parameters derived

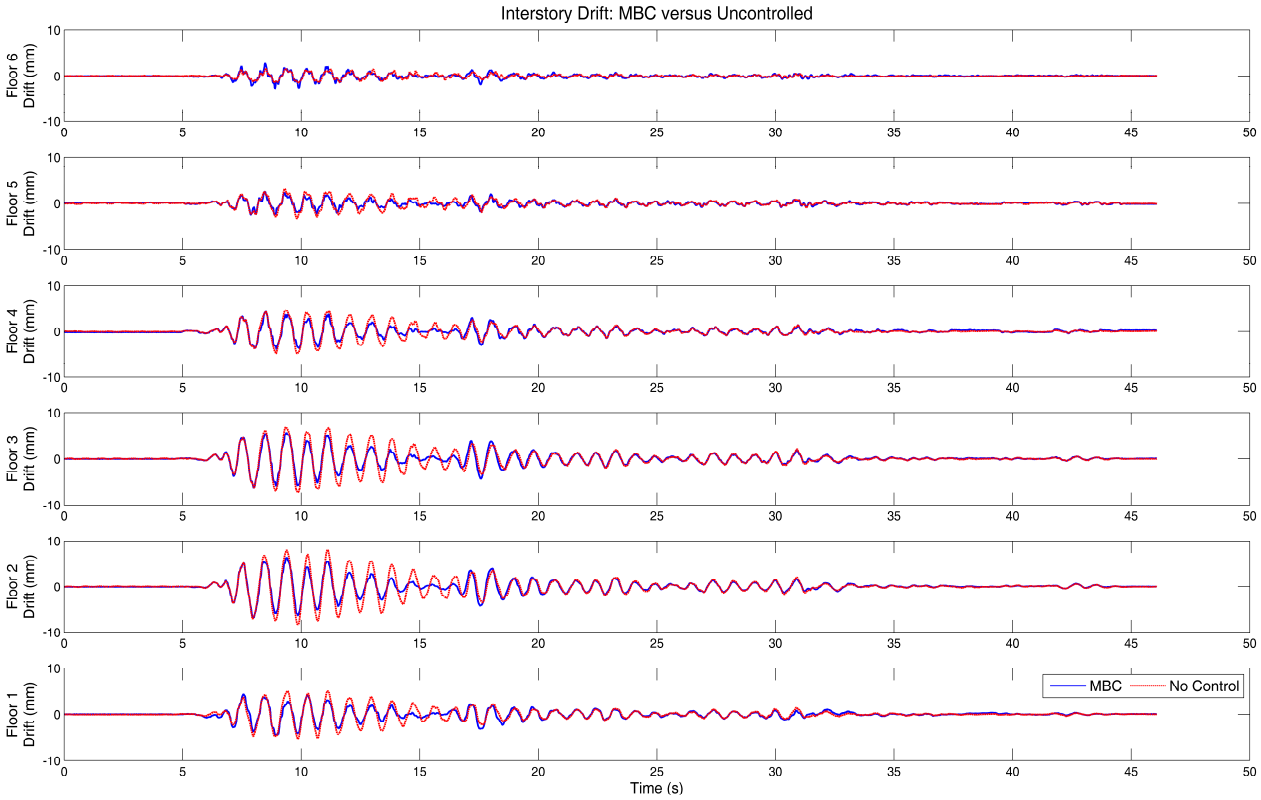

Figure 4 Time-history drift response of the six-story structure to the scaled El Centro ground motion system under MBC ($K = 20$ and initial wealth $W_i = 1000$ for all floors)

from the tuning of the method in a simulation environment (MATLAB) and implemented experimentally are:

$$Q = 1,\ R = 1,\ S = 1,\ T = 1000,\ \alpha = 1 \qquad (10)$$

In the MBC formulation, the magnitude of control force can be calibrated in one of two ways. The first method is to adjust the balance between the price of power and the wealth of the controllers (more wealth or lower price results in more aggressive use of control force). The second method is to simply increase the conversion factor, *K*. In this study, increasing levels of initial controller wealth are allocated to the wireless control agents coupled with varying levels of the conversion factor to explore the effects of these two different computational mechanisms. Tests utilizing uniform (all DOFs) initial wealth values of 400, 700 and 1000 are performed and varying *K* values of 4, 6, 8, 10, 20, and 30 are applied. The resulting control performance is measured in terms of interstory drift performance during repeated table motions with accelerations corresponding to the El Centro (1940 NS USGS Station 117) ground motion record scaled to a peak acceleration level of 1.0 m/s^2 (100 gals). A parallel tethered data acquisition system is installed in parallel to the wireless system to record displacement, velocity and acceleration of all six DOFs; these tethered measurements will aid in validation of the method. Results are presented in the following section

5. RESULTS

The MBC algorithm is run over the wireless network during eight identical El Centro ground motions simulated using the shaking table. A sample time-history response of the interstory drift recorded at each floor, with *K* equal to 20 and initial wealth equal to $W_i = 1000$ is presented in Figure 4. Here, the effectiveness of the MBC algorithm in mitigating the most extreme instances of seismically induced drift is evident. The first six ground motions are carried out with identical MBC parameters with the exception of the *K* factor which varies from 4 to 30. The peak interstory drift and normed interstory drift measured at each floor is presented for each value of *K* in Figure 5. It is demonstrated that control performance generally improves as the *K* value increases, particularly in the normed drift benchmark which is an indirect measurement of the average drift at a floor during the record. This is not true after a certain point however, as the performance suffers when *K* is increased from 20 to 30 suggesting a point at which the controller becomes too aggressive. Interestingly, extremely low values of *K* result in very mild improvements in normed drift (as one would expect) but worse performance than the uncontrolled structure as measured by peak drift.

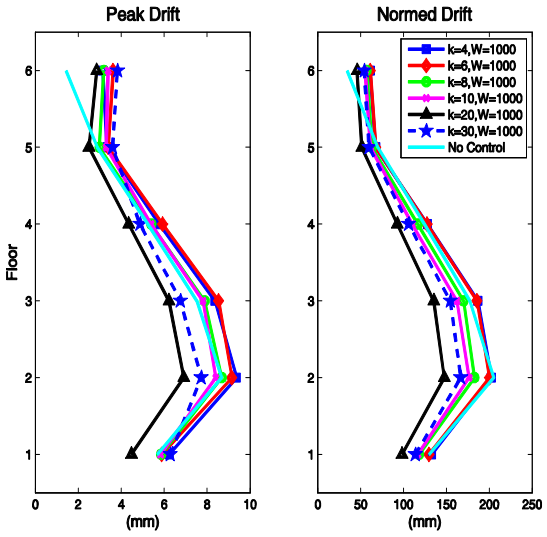

Figure 5 Peak and normed drift by floor due to the El Centro ground motion under MBC as the price to control force conversion factor increases

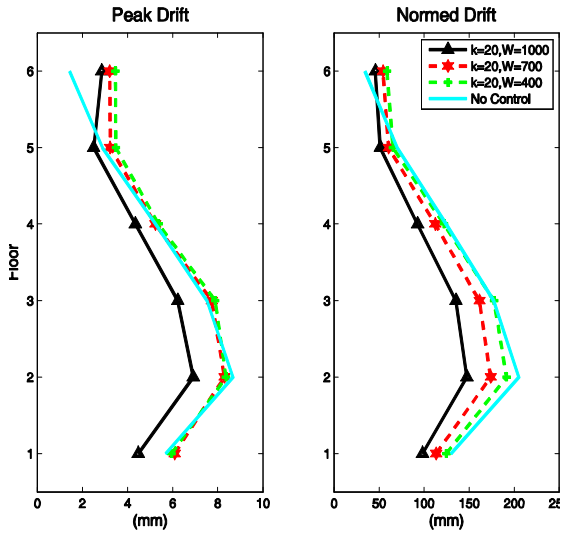

Figure 6 Peak and normed drift by floor due to the El Centro ground motion under MBC as the with diminishing initial wealth allocations

The level of response at which the buyers begin to purchase and exercise control power is affected by the wealth allocated to the agents. Without adequate wealth, the agents do not purchase power even when it would be beneficial to do so. This fact is evident in Figure 6 where peak and normed drift levels are plotted by floor for a constant K (K = 20) and varying values of initial wealth. Here, the lesser values of initial wealth result in very mild control effort (small improvements in interstory drift). With small allocations of wealth, the agents in the system are more successful in reducing the response of the structure as measured in the average sense (normed drift) than in the maximum sense (peak drift) as they are able to purchase power when the price is low. During periods of greater excitation that generate the peak drift values, the price of power increases to the point where it is not affordable to buyers with limited wealth thus demonstrating the need to allocate sufficient wealth to buyers in the system to accomplish the control objective.

6. CONCLUSIONS

This study experimentally assesses the feasibility of the MBC algorithm posed for structural control by Lynch and Law (2002). The algorithm is deployed within a wireless network composed of *Narada* wireless sensing and actuation nodes. *Narada* nodes are responsible for collecting feedback data regarding the response of the structure in the form of acceleration, computing control forces based on the MBC algorithm, and issuing commands to collocated MR-dampers. To find MBC control forces, the nodes must first find displacement and velocity using a Kalman state estimator. This response data is then used to generate demand functions defining the amount of control power desired by the network. A virtual marketplace for power is executed within the wireless network designed to minimize the data transmitted between wireless nodes. Control energy is distributed to controller agents based on the aggregated supply and demand according to their local demand. The power purchased by an agent is subtracted from its individual remaining wealth total. At the end of the control step, wealth collected by the sellers is returned to the buyers, divided equally regardless of how much each buyer purchased.

The MDOF MBC algorithm, as posed, includes several designer defined tuning parameters including demand function response multipliers (Q, R, S, and T), a supply function slope factor (α), a price to control force conversion factor (K) and initial wealth factors for each DOF (W_i). To maximize the effectiveness of the experiments run while the shaking table is available, effective values for the demand function response multipliers and the supply function slope factor are selected based on results found in simulation. For this experimental feasibility study, the effects of the conversion factor and the initial wealth factors on control performance are explored. It is demonstrated that careful tuning of the price-to-control force conversion factor is required to generate control forces large enough to produce meaningful results but not so large as to saturate the controller (similar to a gain factor is more traditional control algorithms). Similarly, adequate wealth allocation is necessary to allow control devices within the MBC network to purchase power when it is necessary. Depending on the price-to-force conversion factor, initial wealth allocation levels will affect the level of control force applied and the effectiveness of the control algorithm.

Future validation work on the MBC algorithm would be beneficial to further explore the effects of the tuning parameters on control performance. In addition, detailed stability analysis of the algorithm should be performed. This study exploits the inherent stability of the semi-active

actuators employed to impart the control algorithm, but guaranteed stability for the generic actuator case would be preferable. Furthermore, this feasibility study uses the simplified case in which initial wealth is allocated in a uniform manner to all buyer agents. A rigorous study of the effects of wealth allocation would provide valuable insight into future design of MBC systems.

Acknowledgements:

The authors acknowledge support from the National Center for Research in Earthquake Engineering (Taipei, Taiwan), Dr. P. Y. Lin (NCREE) and Mr. K. C. Lu (National Taiwan University). Support for this research was provided by the Office of Naval Research (Contracts N00014-05-1-0596 and N00014-09-C0103 awarded to Jerome P. Lynch) and the National Science Foundation (Grant 0824977 awarded to Kincho H. Law)

References:

Celebi, M. (2002), "Seismic Instrumentation of Buildings (with Emphasis on Federal Buildings)," Menlo Park, CA, United States Geologic Survey (USGS).

Clearwater, S. (1996), "Market-Based Control: A Paradigm for Distributed Resource Allocation," World Scientific Publishing, Singapore.

Kajima Corporation (2006), "Advanced Structural Control Technologies, HiDAX: High Damping System in the Next Generation," Technical Pamphlet 06-134E, Tokyo, Japan, Kajima Corporation.

Lynch, J. P. and K. H. Law (2002), "Market-based control of linear structural systems," *Earthquake Engineering and Structural Dynamics* **31**(10), 1855-1877.

Lynch, J. P. and K. H. Law (2004), "Decentralized energy market-based structural control," *Structural Engineering and Mechanics* **17**(3-4), 557-572.

Lynch, J. P., A. Sundararajan, K. H. Law, A. S. Kiremidjian and E. Carryer (2004), "Embedding damage detection algorithms in a wireless sensing unit for attainment of operational power efficiency," *Smart Materials and Structures, IOP* **13**(4), 800-810.

Lynch, J. P., Y. Wang, R. A. Swartz, K.-C. Lu and C.-H. Loh (2008), "Implementation of a closed-loop structural control system using wireless sensor networks," *Journal of Structural Control and Health Monitoring*.

Siljak, D. (1991), "Decentralized Control of Complex Systems," Academic Press, Boston, MA.

Spencer, B. F. and S. Nagarajaiah (2003), "State of the art of structural control," *Journal of Structural Engineering* **129**(7), 845-856.

Straser, E. and A. S. Kiremidjian (1998), "Modular, Wireless Damage Monitoring System for Structures," Stanford, CA, John A. Blume Earthquake Engineering Center.

Swartz, R. A., D. Jung, J. P. Lynch, Y. Wang, D. Shi and M. P. Flynn (2005), "Design of a wireless sensor for scalable distributed in-network computation in a structural health monitoring system", 5th International Workshop on Structural Health Monitoring, Stanford, CA.

Swartz, R. A. and J. P. Lynch (2009), "Strategic utilization of limited bandwidth in a wireless control system for seismically excited civil structures," *Journal of Structural Engineering* **135**(5), 597-608.

Wang, Y., R. A. Swartz, J. P. Lynch, K. H. Law, K.-C. Lu and C.-H. Loh (2007), "Decentralized civil structural control using real-time wireless sensing and embedded computing," *Smart Structures and Systems* **3**(3), 321-340.

JOINT CONFERENCE PROCEEDINGS
7th International Conference on Urban Earthquake Engineering (7CUEE) &
5th International Conference on Earthquake Engineering (5ICEE)
March 3-5, 2010, Tokyo Institute of Technology, Tokyo, Japan

PERFORMANCE-BASED SEISMIC DESIGN OF BUILDING SYSTEMS WITH DAMPERS: EXPERIMENTAL VALIDATION USING REAL-TIME HYBRID SIMULATION

James M. Ricles[1], Richard Sause[2], Theodore L. Karavasilis[3] and Cheng Chen[4]

1) Burce G. Johnston Professor of Structural Engineering, ATLSS Engineering Research Center, Lehigh University, USA
2) Joseph T. Stuart Professor of Structural Engineering Professor, ATLSS Engineering Research Center, Lehigh University, USA
3) Department Reader, Department of Engineering Science, University of Oxford, Oxford OX1-3PJ, UK
4) Assistant Professor, School of Engineering, San Francisco State University, San Francisco, USA
jricles@lehigh.edu, rsause@lehigh.edu, thk207@live.com, chcsfsu@sfsu.edu

Abstract: This paper presents an experimental program using real-time hybrid simulation to verify the performance-based seismic design of a two story, four-bay steel moment resisting frame (MRF) building equipped with compressed elastomer dampers. The laboratory specimens, referred to as experimental substructures, are two individual compressed elastomer dampers, while the remaining part of the building is modeled as an analytical substructure. The proposed experimental technique enables an ensemble of ground motions to be applied to the building, resulting in various levels of damage, without the need to repair the experimental substructures since the damage is within the analytical substructure. Statistical experimental response results incorporating the ground motion variability show that an MRF with compressed elastomer dampers can be designed to perform better than a conventional steel special moment resisting frame (SMRF), even when the MRF with dampers is significantly lighter in weight than the conventional SMRF.

1. INTRODUCTION

Passive damping systems can significantly enhance the seismic performance of buildings by reducing inelastic deformation demands on the primary lateral load resisting system and by reducing drift, velocity, and acceleration demands on non-structural components.

Among the different kinds of passive damping systems, viscoelastic dampers have been extensively studied. Karavasilis et al. (2009a) evaluated the hysteretic behavior of an innovative compressed elastomer damper (Sweeney and Michael 2006) and based on the results of nonlinear dynamic history analyses found that steel moment resisting frames (MRFs) with compressed elastomer dampers can be designed to perform better than conventional special moment resisting frames (SMRFs), even when the MRF with dampers is significantly lighter in weight than the conventional SMRF.

To demonstrate and verify the full potential of new types of dampers, damper designs and performance-based design procedures for structural systems with dampers should be experimentally validated. Full-scale testing is a reliable but, at the same time, a challenging experimental technique. In particular, full-scale testing of structural systems designed to experience inelastic deformations may be cost and time prohibitive since the damaged components of the structural system need to be repaired or rebuilt after each test.

Real-time hybrid simulation combines physical testing and numerical simulation such that the dynamic performance of the entire structural system can be considered during the simulation.

When real-time hybrid simulation is utilized to evaluate the performance of structures with rate-dependent damping devices, the damping devices may be tested as experimental substructures while the remaining part of the structural system is modeled analytically. The added benefit of this experimental technique is that it enables a large number of ground motions to be applied to the structure, resulting in various levels of damage, without the need to repair the test specimens since the damage will be within the analytical substructure.

This paper discusses an experimental program using real-time hybrid simulation to verify the performance-based seismic design of a two story, four-bay steel MRF building equipped with compressed elastomer dampers. The experimental substructures are two individual compressed elastomer dampers with the remaining part of the building modeled as an analytical substructure. The explicit unconditionally stable CR integration algorithm (Chen and Ricles 2008a, Chen et al. 2009a), a robust nonlinear finite element code (Karavasilis et al. 2009b) and an adaptive compensation scheme to minimize actuator delay (Chen and Ricles 2009b) are integrated together and used in the real-time hybrid simulation to compute the structural

response based on feedback restoring forces from the experimental and analytical substructures.

2. STEEL MRFs WITH COMPRESSED ELASTOMERIC DAMPERS

2.1 Prototype Building

Figure 1(a) shows the plan view of the 2-story, 6-bay by 6-bay prototype office building used for the study. The study focuses on one typical perimeter MRF, which is comprised of four bays. This MRF is designed either as a conventional steel SMRF as defined in the 2006 International Building Code (ICC 2006), referred to herein as IBC 2006, or as a steel MRF equipped with compressed elastomer dampers. In the latter case, dampers and supporting diagonal braces are added to the two interior bays, as shown in Figure 1(b).

The members of the MRF are assumed to be A992 steel with a nominal yield stress of 345 MPa. The gravity loads considered in the design are those described in IBC 2006. A smooth design response spectrum with parameters S_{DS}=1.0, S_{D1}=0.6, T_0=0.12 sec and T_s=0.6 sec., defined by IBC 2006, represents the Design Basis Earthquake (DBE) which has a probability of exceedance of approximately 10% in 50 years.

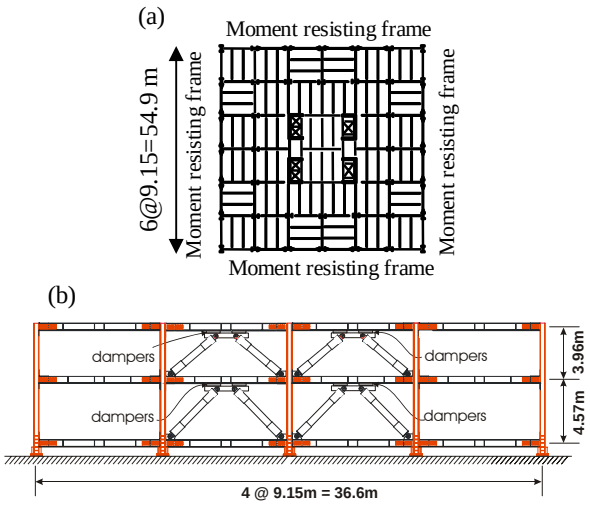

Figure 1 Prototype Building Structure: (a) Plan View, and (b) Perimeter MRF with Dampers and Diagonal Bracing

2.2 Design of Perimeter MRF as a Conventional SMRF

The perimeter MRF in Figure 1(b) is initially designed as a conventional SMRF using the equivalent lateral force procedure in the IBC 2006. This SMRF design without dampers, referred to herein as UD100V, satisfies the member strength criteria of the IBC 2006 with a response modification factor R equal to 8 and also the 2% story drift limit of IBC 2006 with a deflection amplification factor C_d equal to 5.5.

To study whether MRFs with compressed elastomer dampers can be designed to have less strength than a conventional SMRF (without dampers) but achieve similar or better levels of seismic performance, a perimeter MRF was designed without dampers using a design base shear equal to 0.50V, where V is the design base shear for UD100V. The resulting MRF design, referred to herein as UD50V, does not satisfy the drift criteria of the IBC 2006. This MRF design is significantly lighter than UD100V.

Table 1 summarizes the properties of the two MRF designs, where the properties for UD50V are without the dampers. The table lists the column section, beam sections, steel weight, fundamental period of vibration, T_1, and the predicted maximum story drift, θ_{max}, under the DBE earthquake. The maximum story drift, θ_{max}, is determined on the basis of the equal displacement principle.

Table 1 Properties of MRF Designs

MRF	Column Section	Beam Section	Steel Weight (kN)	T_1 (sec)	θ_{max} (%)
UD100V	W14x211	1st story: W24x84 2nd story: W21x50	200	1.08	2.40
UD50V	W14x120	1st story: W24x55 2nd story: W18x40	124	1.48	3.23

2.3 Design of Dampers for MRF

The damper designs are based on the new generation of compressed elastomer dampers presented in Karavasilis et al. (2009a). The thickness and the area of these dampers are 4 times larger than the thickness and the area of the dampers used in the real-time hybrid simulations presented herein. The mechanical properties of these compressed elastomer dampers, namely the equivalent stiffness and loss factor, were derived from the experimental data presented in Karavasilis et al. (2009a) and used to design the compressed elastomer dampers for the UD50V MRF with the aid of the simplified design procedure (SDP) developed by Lee et al. (2005). The SDP idealizes the damper hysteresis loops as linear viscoelastic ellipses and the damper design variables are the equivalent damper stiffness and the loss factor. More details on the SDP and the design of the compressed elastomer dampers for the UD50V MRF can be found in Karavasilis et al. (2009a). Under small deformation (less than 15 mm) the damper hysteretic behavior resembles elastomeric behavior. When the deformation is larger than 15 mm, slip of the elastomer compressed inside a steel tube occurs, and the hysteretic behavior is a combined elastomeric-frictional behavior.

Table 2 provides information for the UD50V MRF with dampers. The story drift and damper deformation demand estimates are for the DBE. It is observed that the UD50V MRF with 8 and 5 compressed elastomer dampers in the first and second stories, respectively, exhibits a significantly better anticipated performance (θ_{max} = 1.60%) than that of

the conventional UD100V SMRF (θ_{max} = 2.40%). Moreover, the UD50V MRF with dampers has a steel weight equal to 124 kN (UD50V) + 17.2 kN (braces) = 141.2 kN, while the steel weight of the conventional UD100V SMRF is 200 kN.

Table 2 Design of UD50V MRF with Dampers

Brace Steel Weight (kN)	T_1 (sec)	θ_{max} (%)	No. Dampers per Story	
			1st	2nd
17.2	1.04	1.60	8	5

3. REAL-TIME HYBRID SIMULATION

3.1 Real-time Integrated Control System and Analytical Substructure Modeling

The performance of the MRF with compressed elastomer dampers is experimentally evaluated by conducting real-time hybrid simulations. The experimental substructures are two individual compressed elastomer dampers with the remaining part of the building modeled as an analytical substructure.

Since the dampers at a story level are placed in parallel in the prototype MRF (Figure 1(b)), they are subjected to the same velocity and displacement. Therefore, each of the dampers setups in the laboratory represents all of the dampers in one story. In a real-time hybrid simulation the measured restoring force from a compressed elastomer damper is multiplied by the number of dampers to obtain the total restoring force of all the dampers at a story level in the MRF.

As discussed previously, the thickness and the area of the elastomer of the dampers that are used in UD50V MRF are considered to be 4 times larger than the thickness and the area of the elastomer of the dampers in the experimental substructure. Consequently, in the real-time hybrid simulation the command displacement of the dampers was scaled down by a factor of 4 and the measured restoring force was amplified by a factor of 4.

A nonlinear finite element code (Karavasilis et al. 2009b) has been implemented into the real-time integrated control system at the NEES Real-Time Multi-Directional (RTMD) Facility at Lehigh University (Lehigh RTMD 2009). The architecture for the RTMD system is shown in Figure 2. A digital servo controller (RTMDctrl) with a 1024 Hz clock speed (sampling time δt=1/1024 sec) controls the motion of the servo-hydraulic actuators and is integrated with the real-time target workstation (RTMDxPC), simulation workstation (RTMDsim), and data acquisition workstation (RTMDdaq) using a shared common RAM network (SCRAMNet). SCRAMNet has a communication rate of about 180ns which enables the transfer of data among the integrated workstations in real-time with minimal communication delay. The nonlinear finite element code has been developed in a manner that enables the analytical substructure modeling, servo-hydraulic control law, and actuator compensation scheme to be integrated into a single SIMULINK model on the simulation workstation and then downloaded onto the target workstation using Mathworks xPC Target Software (MATLAB 2007).

The model of the MRF has a total of 122 degrees of freedom and 71 elements. Inelastic behavior is modeled by means of a bilinear hysteretic lumped plasticity beam-column element with 3% hardening and appropriate axial-moment yield surfaces. Diaphragm action is assumed at every floor level in the building due to the presence of the floor slab. A lean-on column is used to model P-Δ effects on the MRF from gravity loads carried by gravity columns of the building.

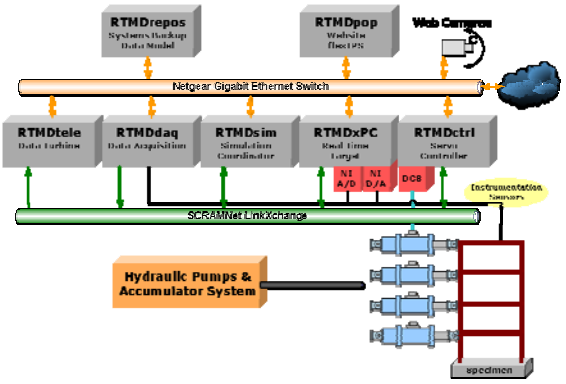

Figure 2 RTMD Integrated Control System Architecture

(a)

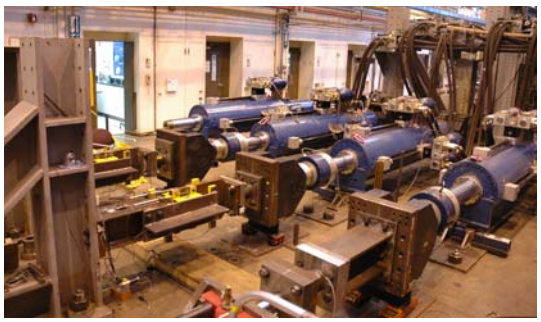

(b)

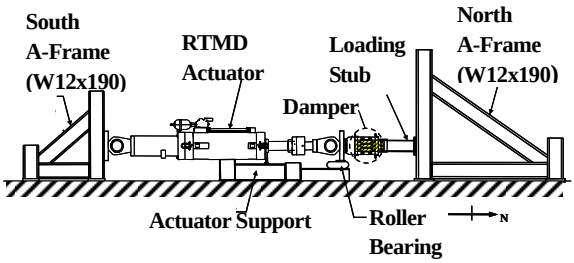

Figure 3 Compressed Elastomer Dampers: (a) Photograph, and (b) Details of Test Setup for each Damper

3.2 Experimental Substructure Test Setup

Figure 3 shows the experimental setup for the real-time hybrid simulation, which consists of the experimental

substructures (two large-scale compressed elastomer dampers), two servo-hydraulic actuators with supports, roller bearings, and reaction frames. The two actuators have a load capacity of 2300 kN and 1700 kN with a maximum velocity of 840 mm/sec. and 1140 mm/sec, respectively, when three servo valves are mounted on each actuator. The servo-controller for the actuator used in the real-time hybrid simulations consists of a digital PID controller with a proportional gain of 20, integral time constant of 5.0 resulting in an integral gain of 4.0, differential gain of zero, and a roll-off frequency of 39.8 Hz.

3.3 Real-time Integration of the Equations of Motion

For the MRF structure with dampers shown in Figure 1(b), the temporal discretized equations of motion at the i+1th time step can be expressed as

$$\boldsymbol{M}\cdot\ddot{\boldsymbol{x}}_{i+1}+\boldsymbol{C}\cdot\dot{\boldsymbol{x}}_{i+1}+\boldsymbol{r}^{a}_{i+1}+\boldsymbol{r}^{e}_{i+1}=\boldsymbol{F}_{i+1} \qquad (1)$$

where $\ddot{\boldsymbol{x}}_{i+1}$ and $\dot{\boldsymbol{x}}_{i+1}$ are the acceleration and velocity vectors of the structure, respectively; $\boldsymbol{r}^{a}_{i+1}$ and $\boldsymbol{r}^{e}_{i+1}$ are the restoring force vectors of the analytical and experimental substructures, respectively; $\boldsymbol{M}$ and $\boldsymbol{C}$ are the mass and damping matrices of the structure, respectively; and $\boldsymbol{F}_{i+1}$ is the excitation force.

The CR unconditionally stable explicit integration algorithm (Chen and Ricles 2008a, Chen et. al. 2009a) is used to solve Equation (1) for the structural displacement vector $\boldsymbol{x}_{i+1}$. According to the CR algorithm, the variations of the displacement and velocity vectors of the structure over the integration time step Δt are defined as

$$\dot{\boldsymbol{x}}_{i+1}=\dot{\boldsymbol{x}}_{i}+\Delta t\cdot\boldsymbol{\alpha}_1\cdot\ddot{\boldsymbol{x}}_{i} \qquad (2.a)$$

$$\boldsymbol{x}_{i+1}=\boldsymbol{x}_{i}+\Delta t\cdot\dot{\boldsymbol{x}}_{i}+\Delta t^{2}\cdot\boldsymbol{\alpha}_2\cdot\ddot{\boldsymbol{x}}_{i} \qquad (2.b)$$

where $\boldsymbol{x}_i$, $\dot{\boldsymbol{x}}_i$ and $\ddot{\boldsymbol{x}}_i$ are the displacement, velocity and acceleration vectors of the structure at the ith time step, respectively; and $\boldsymbol{\alpha}_1$ and $\boldsymbol{\alpha}_2$ are matrices of integration parameters defined as

$$\boldsymbol{\alpha}_1=\boldsymbol{\alpha}_2=4\cdot\left(4\cdot\boldsymbol{M}+2\cdot\Delta t\cdot\boldsymbol{C}+\Delta t^{2}\cdot\boldsymbol{K}\right)^{-1}\cdot\boldsymbol{M} \qquad (3)$$

In Equation (3) $\boldsymbol{K}$ is the initial stiffness matrix of the structure. It should be emphasized that this matrix includes the stiffness and damping contribution of the experimental substructures, i.e., the equivalent stiffness and damping of the two compressed elastomer dampers.

In real-time hybrid simulation, Equations (2.a) and (2.b) are used to obtain the velocity $\dot{\boldsymbol{x}}_{i+1}$ and displacement $\boldsymbol{x}_{i+1}$ vectors at the i+1th time step. The displacement vector $\boldsymbol{x}_{i+1}$ is decomposed into the analytical displacement vector $\boldsymbol{x}^{a}_{i+1}$ and the experimental (or command) displacement vector $\boldsymbol{x}^{e}_{i+1}$, which are imposed onto the analytical and experimental substructures, respectively, to obtain the restoring force vectors $\boldsymbol{r}^{a}_{i+1}$ and $\boldsymbol{r}^{e}_{i+1}$. Strictly speaking, $\boldsymbol{x}^{e}_{i+1}$ contains deformations, i.e., displacement differences of the nodes defining the connectivity of each of the experimental substructures. The analytical restoring force vector $\boldsymbol{r}^{a}_{i+1}$ is obtained with a standard nonlinear beam-column element state-determination procedure, while the experimental restoring force vector $\boldsymbol{r}^{e}_{i+1}$ is obtained from the feedback forces measured using load cells that are placed in each compressed elastomer damper test setup. The equilibrium Equation (1) is then employed to calculate the acceleration response vector $\ddot{\boldsymbol{x}}_{i+1}$ at the i+1th time step, and the velocity $\dot{\boldsymbol{x}}_{i+2}$ and displacement $\boldsymbol{x}_{i+2}$ vectors for the next i+2th time step are readily available from Equations (2.a) and (2.b). This process is repeated to obtain the response over the whole duration of the earthquake ground motion.

Due to inherent servo-hydraulic dynamics, the actuator has an inevitable time delay in response to the displacement command. This time delay is usually referred to as actuator delay and will result in a desynchronization between the measured restoring forces from the experimental substructures and the integration algorithm in a real-time hybrid simulation. Studies on the effect of actuator delay (Wallace et al. 2005, Chen and Ricles 2008b) show that actuator delay is equivalent to creating negative damping and can destabilize a real-time hybrid simulation if not compensated properly.

To minimize the detrimental effect of actuator delay during a real-time hybrid simulation, an adaptive inverse compensation (AIC) method was developed (Chen and Ricles 2009b). The AIC method can be expressed using the following discrete transfer function that relates the compensated command displacement to the original command displacement

$$G_c(z)=\frac{(\alpha_{es}+\Delta\alpha)\cdot z-(\alpha_{es}+\Delta\alpha-1)}{z} \qquad (4)$$

where in Equation (4) z is the complex variable in the discrete z-domain; α_{es} is the estimated actuator delay constant; and $\Delta\alpha$ is an evolutionary variable with an initial value of zero. The AIC method uses an initial estimated α_{es} for actuator delay compensation at the beginning of the hybrid simulation. The evolutionary variable $\Delta\alpha$ is used to adjust the initial estimated value for α_{es} to achieve accurate actuator control during a real-time hybrid simulation. The adaptation of the evolutionary variable $\Delta\alpha$ is based on a tracking indicator (Mercan 2007) which is defined as the enclosed area of the synchronized subspace plot between the actuator command displacement and the actuator measured response. Chen et al. (2009c) used the AIC method for real-time hybrid simulation of passive MR dampers, resulting is good actuator tracking.

4. REAL-TIME HYBRID SIMULATION RESULTS

An ensemble of 5 earthquake ground motions recorded on stiff soil sites (without near-fault effects) was used in the real-time hybrid simulations to evaluate the performance of the MRF with compressed elastomer dampers. The ground

motions were scaled to the DBE and the Maximum Considered Earthquake (MCE) levels using the scaling procedure of Somerville (1997). The MCE has an intensity that is 1.5 times the DBE, and a 2% probability of exceedance in 50 years. Table 3 provides the scale factors and information for the 5 ground motions.

Time history results from the real-time hybrid simulations are presented for the HSP090 record. The hysteresis of the compressed elastomer dampers is presented in Figure 4. The dampers are able to undergo numerous seismic induced deformation cycles without degradation of their behavior. Under the DBE the dampers at both floors exhibit a elastomeric behavior with fairly rounded peaks. Under the MCE the damper at the second floor develops some minor slip, while the damper at the first floor experiences an elastomeric-frictional behavior with slip that results in permanent deformation, but the damper maintains its energy dissipation capacity. Figure 5 shows the floor displacement time history of the MRF with dampers, UD50V MRF. Also presented in Figure 5 is the floor displacement time history of the conventional UD100V SMRF from a numerical analysis. The real-time hybrid simulation results show that the lighter UD50V MRF with dampers experiences significantly lower transient and residual story drifts than the conventional UD100V SMRF. Under the DBE the UD50V MRF with dampers has negligible story drift since the dampers do no slip and the frame remains essentially elastic. Under the MCE the dampers act as sacrificial elements, which develop permanent deformation due to slip, however, the dampers can be replaced after the earthquake. Some modest yielding occurs in the beams and at the ground level of the columns.

Table 3 Ground Motions for Real-time Hybrid Simulations

Earthquake	Station/Component	Scale Factor	
		DBE	MCE
Loma Prieta 1989	Hollister/HSP090	1.99	2.99
Manjil 1990	Abbar/Abbar-T	0.96	1.44
Northridge 1994	N Hollywood/CWC270	1.70	2.56
Chi Chi 1999	TCU049/TCU049-E	1.92	3.67
Chi Chi 1999	TCU105/TCU105-E	2.45	2.89

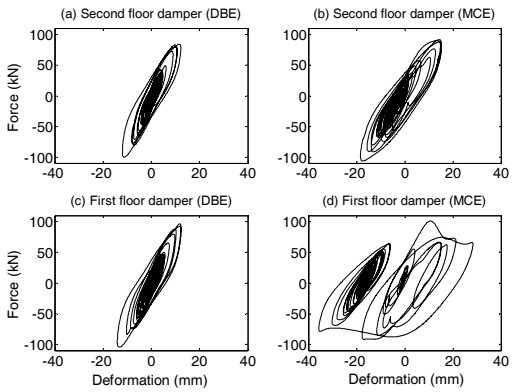

Figure 4. Damper Hysteresis from Real-time Hybrid Simulation

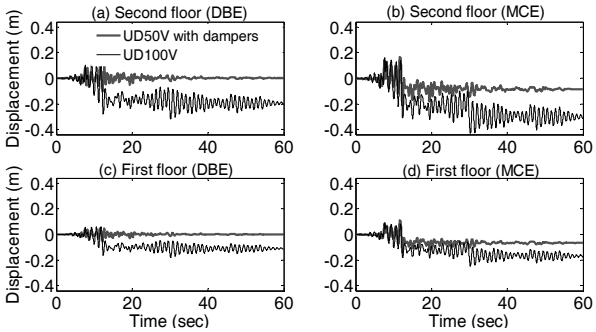

Figure 5. Floor Displacement Time History from Real-time Hybrid Simulation

Table 4 presents the median experimental response values for the maximum story drift, θ_{max}; beam maximum plastic hinge rotation θ_{pl,bm_max}; column maximum plastic rotation θ_{pl,cl_max}; maximum floor absolute velocity v_{max}; and floor absolute acceleration a_{max} of UD50V MRF from the real-time hybrid simulations. Also presented in Table 4 are the median values of the same response quantities for the conventional UD100V SMRF from numerical analysis. Table 4 shows that for the DBE the median θ_{max} value of 1.40% for the MRF with dampers is slightly less than the θ_{max} design demand of 1.60% used in the SDP (Table 2), while the θ_{max} value of 2.60 for the UD100V SMRF is slightly larger than the θ_{max} design demand of 2.40% determined using the equal displacement principle (Table 1). It is also observed that the MRF with dampers has a significantly better performance than the UD100V SMRF in terms of the maximum story drift, plastic hinge rotations, absolute floor velocities and accelerations. Decreases in plastic hinge rotations in UD50V compared to UD100V are approximately 75% and 57% for the DBE and MCE, respectively.

Table 4 Median Values of Response Parameters

Design		θ_{max} (%)	θ_{pl,bm_max} (%)	θ_{pl,cl_max} (%)	v_{max} (m/s)	a_{max} (m/s^2)
		DBE/ MCE	DBE/ MCE	DBE/ MCE	DBE/ MCE	DBE/ MCE
UD50V	Story 1	1.35/2.50	0.0/0.01	0.0/0.01	0.6/0.9	4.2/5.7
	Story 2	1.40/1.80	0.0/0.0	0.0/0.0	0.8/1.1	5.2/6.5
UD100V	Story 1	2.60/2.90	0.01/0.02	0.01/0.02	0.8/1.0	5.3/6.6
	Story 2	2.40/2.60	0.0/0.01	0.0/0.0	1.1/1.3	5.7/6.4

5. SUMMARY AND CONCLUSIONS

An experimental program using real-time hybrid simulation to verify the performance-based seismic design of a steel MRF equipped with compressed elastomer dampers was presented. The experimental substructures consist of two individual large-scale compressed elastomer dampers with the remaining part of the building modeled as an analytical substructure. The real-time hybrid simulations allowed an ensemble of ground motions to be applied to the

structure resulting in various levels of damage, without the need to repair the test specimens since the damage was within the analytical substructure. Statistical experimental response results show that a steel MRF with compressed elastomer dampers can be designed to perform better than a conventional steel SMRF, even when the MRF with dampers is significantly lighter in weight than the conventional SMRF.

Acknowledgements:

This paper is based upon work supported by grants from the Pennsylvania Department of Community and Economic Development through the Pennsylvania Infrastructure Technology Alliance, and by the National Science Foundation under Grant No. CMS-0402490 within the George E. Brown, Jr. Network for Earthquake Engineering Simulation Consortium Operation. The compressed elastomer dampers were manufactured and donated to the research project by Corry Rubber.

References:

Chen, C., Ricles, J.M. (2008a), Development of direct integration algorithms for structural dynamics using discrete control theory. *Journal of Engineering Mechanics*, **134**(8): 676-683.

Chen, C. and Ricles, J.M. (2008b), Stability analysis of SDOF real-time hybrid testing systems with explicit integration algorithms and actuator delay. *Earthquake Engineering and Structural Dynamics* **37**(4):597-613.

Chen, C., Ricles, J.M., Marullo, T.M., Mercan, O. (2009a), Real-time hybrid testing using the unconditionally stable explicit CR integration algorithm. *Earthquake Engineering and Structural Dynamics,* **38**(1):23-44.

Chen, C. and Ricles, J.M. (2009b), Tracking error-based servo-hydraulic actuator adaptive compensation for real-time hybrid simulation. *Journal of Structural Engineering*, **136**(4), in press.

Chen, C., Ricles, J.M., Karavasilis, T., and Sause, R. (2009c), Real-time hybrid simulation system for investigation of structural response under earthquake loading**.** *Journal of Structural Engineering*, submitted, in review.

International Code Council (ICC) (2006), International Building Code, Falls Church, VA.

Karavasilis, T.L., Sause, R., Ricles, J.M. (2009a), Seismic design and evaluation of steel MRFs with compressed elastomer dampers. *Earthquake Engineering and Structural Dynamics*, submitted, in review.

Karavasilis, T.L., Ricles, J.M., Marullo, T., Chen, C. (2009b), HybridFEM. A program for nonlinear dynamic time history analysis and real-time hybrid simulation of structures. ATLSS Engineering Research Center Report.

Lee, K.S., Fan, C.P., Sause, R., Ricles, J. (2005), Simplified design procedure for frame buildings with viscoelastic or elastomeric structural dampers. *Earthquake Engineering and Structural Dynamics*, **34**:1271-1284.

Lehigh RTMD Users Guide. (2009), http://www.nees.lehigh.edu/index.php?page=rtmd-user-s-manual.

MATLAB. (2007), The Math Works, Inc., Natick, MA.

Mercan, O. (2007), *Analytical and experimental studies on large scale, real-time pseudodynamic testing*. PhD. Dissertation, Department of Civil and Environmental Engineering, Lehigh University, Bethlehem, PA.

Somerville P. (1997), Development of Ground Motion Time Histories for Phase 2 of the FEMA/SAC Steel Project, Report No. SAC/DB-97/04, Sacramento, CA.

Sweeney, S.K., Michael, R. (2006), Collaborative product realization of an innovative structural damper and application. Proceedings of IMECE2006, ASME International Engineering Congress and Exposition, Chicago, Illinois, USA.

Wallace, M.I., Sieber, J., Neild, S.A., Wagg, D.J., Krauskopf, B. (2005), Stability analysis of real-time dynamic substructuring using delay differential equation models. *Earthquake Engineering and Structural Dynamics* **34**(15):1817-1832.

JOINT CONFERENCE PROCEEDINGS
7th International Conference on Urban Earthquake Engineering (7CUEE) &
5th International Conference on Earthquake Engineering (5ICEE)
March 3-5, 2010, Tokyo Institute of Technology, Tokyo, Japan

EXPERIMENTAL SEISMIC RESPONSE OF A FULL-SCALE SEVEN-STORY MIXED-USE STEEL/WOOD APARTMENT BUILDING

Steven E. Pryor[1)], John W. van de Lindt[2)], Shiling Pei[3)],

1) International Director of Building Systems, Simpson Strong-Tie, Pleasanton, California, USA
2) Associate Professor, Dept. of Civil Engineering, Colorado State University, Fort Collins, Colorado, USA
3) Post Doctoral Researcher, Dept. of Civil Engineering, Colorado State University, Fort Collins, Colorado, USA
spryor@strongtie.com, jwv@engr.colostate.edu, slpei@lamar.colostate.edu,

Abstract: On June 30, 2009 a seven-story building was subjected to two earthquakes at the world's largest shake table in Miki, Japan. Configured to represent a mixed-use retail and residential structure, the first floor was a new type of innovative steel framing system providing the openness needed for the retail area, which then supported six stories of wood light-frame construction used for the apartment areas above. The objectives of the test program were to (1) demonstrate that the performance-based design procedure developed as part of the NEESWood project worked for this mixed-use structure; (2) validate the new steel moment frame connection system specifically developed to work with wood floor diaphragms while providing high ductility; and (3) obtain better understanding of how to combine wood and steel to provide more building options in areas of high seismicity. The building had 220 square meters of retail space with 1350 square meters of living space above which consisted of twenty-three apartment units; approximately half one-bedroom units and half two-bedroom units. Constructed over a 16 week period, the steel first story was also configured with removable elements to create a three-dimensional lifting truss which was used to lift the entire structure onto the shake table where it was subjected to earthquakes corresponding to the 72 year and the 675 year event for Los Angeles, CA. To prevent overturning in the wood shear walls and allow them to develop their full shear capacity, an anchor tie-down system consisting of steel rods, bearing plates and shrinkage compensating devices, was used at each end of all shear walls and ran from the top of the steel beams to the roof level. The building, known as the NEESWood Capstone building, was instrumented with over 300 sensors and 50 LED optical tracking points to measure the component and global responses, respectively. This paper will focus on the design and construction of the steel frame optimized for use with wood light-frame construction, and the resulting performance of the building during the test. A companion paper will focus on subsequent testing of the upper six story structure that was achieved when the steel moment frame was reconfigured as a highly rigid braced frame, thus functioning as an extension of the table. The building performed very well under the 675 year earthquake. Only minor damage occurred, with global roof drift at approximately 1% and maximum interstory drifts less than 2%.

1. INTRODUCTION

Wood light-frame construction represents the most common method of building single and multi-family residential units in the United States. While it has always seen some use in commercial structures, the push for "green" construction is leading to more use in that market as well. While wood has historically proven to be a good performer in seismic events, the ever increasing use of engineered lumber and the expansion of the use of wood in mid-rise construction has fundamentally changed the nature of these buildings compared to what was built 50 years ago.

These changes have lead to structures with inherently less redundancy and a reduced lateral strength overall. The ability of engineered lumber to span longer distances in both floors and roofs has created an environment in which there are fewer interior walls. The desire for more and more openings in these remaining walls concentrates lateral demand into shorter and shorter wall segments. Consequently, our need to understand the true systems-level behavior of these types of structures has increased substantially.

Over the last 12 years a few projects have incorporated full-scale shake table tests of light-frame wood structures. The CUREE-Caltech Woodframe Project (Filiatrault et al 2001) tested a modest two story structure under uniaxial ground motion and was an important step in understanding

nonlinear modeling issues as well as the influence of nonstructural finish materials. Filiatrault et al (2009) as part of the NEESWood project (van de Lindt et al, 2006) also tested a larger 160m^2 (1800 sq ft) two story townhouse on the shake tables at the University at Buffalo's SEESL laboratory. Utilizing triaxial ground motion input, this "benchmark" structure as it was referred to helped establish the expected seismic performance of California-type building stock designed in accordance with modern seismic codes, in this case the 1988 Uniform Building Code (1988 UBC). While providing another data set to measure the success of predictive modeling it also confirmed and augmented the previous findings with respect to nonstructural finish materials adding strength, stiffness and damping. The CUREE-Caltech Woodframe Project also tested a three story apartment building with "tuck-under" parking (Mosalam, 2003). This type of structure has one open side on the lowest level to facilitate parking. The tests confirmed that these types of structures are likely to experience torsional problems and/or soft story mechanisms making them susceptible to collapse.

This research has helped pave the way toward implantation of performance-based seismic design (PBSD) for these types of structures. Inherent in the assumptions of PBSD is that structural modeling is accurate enough to warrant confidence that a building really will perform in accordance with the predictions. For wood light-frame structures, this is perhaps more difficult because the load path is not as discrete as it is in typical steel or concrete structures. The Capstone project, given the large size of the test structure and triaxial input motions, represents a quantum leap forward in providing a data set to test and refine our abilities to predict structural response as well as validate new and existing construction methods.

1.1 Overall Objectives

The phase I testing of the NEESWood Capstone tests at E-Defense had three (3) major objectives:

Objective 1: Confirm that a representative mixed-use seven-story steel-woodframe mixed-use building designed using the NEESWood design philosophy satisfies the performance objectives, as pre-defined during the design process.

Objective 2: Validate a new type of high-ductility steel special moment frame connection specifically engineered for use with wood-framed structures

Objective 3: Obtain a better understanding of how to combine wood and steel to provide more building options in areas of high seismicity

1.2 Performance Objectives

The goal of performance-based seismic design is to allow design professionals to meet an owner/stakeholder's expectation of how their building will perform under a given level of seismic demand, all within a probabilistic framework. As such, the demand, or more specifically the seismic hazard (intensity) used for design, needs to be defined along with the expected performance, and both of these have to be defined in relevant terms of input/output related to the engineering design process. Provided that current minimum building code requirements are met, any combination of demand and desired performance can be considered. The NEESWood project team, with input from the project advisory committee, considered four seismic hazard levels defined as:

Level 1: Earthquake intensity having a 50% chance of being exceeded in 50 years. This corresponds to a 72 year return period.

Level 2: Earthquake intensity having a 10% chance of being exceeded in 50 years. This corresponds to a 475-year return period. Corresponds *approximately* to the Design-Basis Earthquake (DBE).

Level 3: Earthquake intensity having a 2% chance of being exceeded in 50 years. This corresponds to a 2500-year return period. Corresponds to the Maximum Credible Earthquake (MCE).

Level 4: Optional Near Fault: Un-scaled near-fault ground motions. This is an optional seismic hazard for use depending on the location of a building with respect to the fault and/or the owner's desired performance expectation.

Each of the seismic intensity levels described above can be combined with a particular performance expectation. Based on the Benchmark tests at the University at Buffalo, four performance expectation levels were developed by Christovasillis et al. (2007) as:

Level A: Corresponding to *<1.0%* inter-story drift. Structure may experience minor splitting and cracking of sill plates (some propagation); slight sheathing nail withdraw. slight cracking of GWB; diagonal propagation from door/window openings; partial screw withdraw; and cracking at ceiling-to-wall interface.

Level B: Corresponding to *1.0~2.0%* inter-story drift. Structure may experience Permanent differential movement of adjacent panels; Corner sheathing nail pullout; Cracking/splitting of sill/top plates; Crushing at corners of GWB; and Cracking of GWB taped/mud joints.

Level C: Corresponding to *2.0~4.0%* inter-story drift. Structure may experience Splitting of sill plates equal to anchor bolt diameter; Cracking of studs above anchor bolts; Possible failure of anchor bolts; Separation of GWB corners in ceiling; and Buckling of GWB at openings.

Level D: Corresponding to *4.0~7.0%* inter-story drift. Structure may experience Severe damage across edge nail lines, separation of sheathing; Vertical posts uplifted; Failure

of anchor bolts; Large pieces separated from framing; and Entire joints separated and dislodged.

Each performance level is also associated with given non-exceedance (NE) probability. Table 1 shows how these were associated with a given seismic hazard level to determine the desired performance of the Capstone building. At a level 3 seismic intensity the non-exceedance percentile was moved from the 50th percentile, i.e. median, to the 80th percentile because the 4% drift limit was close to what was felt to be the threshold between repairable damage and collapse. Thus it was assumed to be more critical during the design.

Table 1. Capstone Structure Design Expectations

	Seismic hazard (Intensity) Level			
Performance Expectations	Level 1	Level 2	Level 3	Level 4
Level A (1%)	50% NE			
Level B (2%)		50% NE		
Level C (4%)			80% NE	
Level D (7%)				50% NE

2. SPECIMEN CONSTRUCTION

The preparation of the construction began in early 2008 with a joint meeting including the CSU research team, the contractor, and representatives from Simpson Strong-Tie Company. The construction materials were shipped from the U.S. and Canada to Japan in 20 containers at the end of 2008 and beginning of 2009. From the beginning of steel erection to the move of the specimen onto the shake table, the construction of the test specimen last exactly four months, from February 23rd 2009 to June 22nd 2009.

The first story of the seven story structure was structural steel and served a dual purpose. First, it contained a new type of (proprietary) partial strength moment-resisting beam-to-column connection for structural steel. Operating bi-directionally in the structure, the moment frame was laterally active during the first two tests on the structure (phase I). The purpose of the new connection is to provide high rotational ductility in a manner that creates a plastic hinge outside of the beam itself. This is important because the beam needs to remain elastic and unbraced from column to column due to the adjacent wood floor diaphragm's inability to provide the required brace strength and stiffness necessary to prevent lateral-torsional buckling if the plastic hinge were formed in the beam itself.

The second purpose of the steel frame was to serve as a three dimensional space truss to facilitate lifting the entire structure onto the shake table. While not part of the original intent, this plan emerged during the design process when it became apparent that securing a steel grillage to serve as the lifting base would be difficult. For phase II testing it was intended that a bracing system would be installed into the moment frame thereby increasing lateral stiffness to the point where it would have no impact on the upper six stories of wood, effectively becoming an extension of the shake table. Expanding this to a 3D space truss meant a modest increase in the size of the bracing, the addition of a layer of steel at ground level to serve as the bottom chords of the space truss, and the creation of nodes at the web to bottom chord intersections that could interface with the steel column's bolt pattern above and the shake table's bolt pattern below.

In the short (X) direction of the building the steel frame consisted of seven primary lines, and distributed throughout were 16 moment resisting beam-column joints, with the remainder being simple shear connections. In the long (Y) direction of the building, 16 moment resisting beam-column joints were distributed along its four primary lines, and again the reminder were designed using simple shear connections. Column bases were designed as nominally pinned. The elevation views, presented in Figure 1a, show the large openings provided by the moment frame, while the framing layout is shown in Figure 1b.



(a)

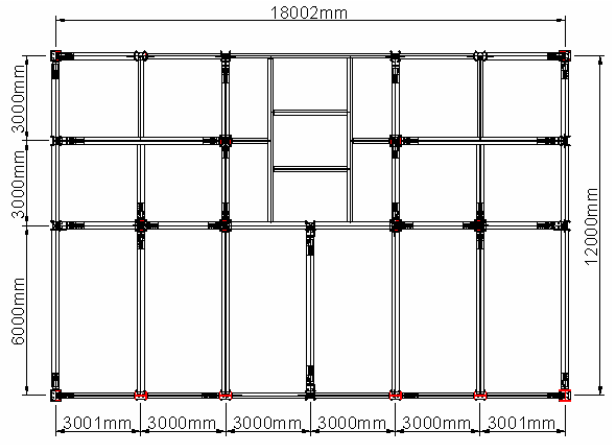

(b)

Figure 1 Elevation and Steel Frame Layout for Capstone Specimen

The partial strength moment-resisting beam-column connection is an all-bolted snug-tight connection consisting

of three separate elements, two that facilitate moment transfer and one for shear transfer. Beam shear is transferred through a simple shear tab connection wherein the center bolt is a standard hole but additional bolts above and below the center bolt are placed in short slots with the slots perpendicular to the direction of shear force. This effectively eliminates any beam moment from being transferred through the shear tab while allowing the center bolt to transfer any net axial force from the beam to the column. To transfer moment from beam to column, a T-shaped element is bolted to both column and beam at both beam flanges, typically with four bolts at the column and four to eight at the beam. In the stem portion of the T that bolts to the beam flange, the central area is reduced to create a zone that will yield under axial load. By controlling the net area and length of the yielding zone, both moment capacity and rotational stiffness of the beam-column joint can be optimized for the end use. In order to prevent buckling of this area when under compression, a restraining plate is placed over the T stem and secured to the beam flange, as shown in Figure 2. Figure 3 shows the completed structure on the shake table at E-Defense.



Figure 2 Partial Strength Moment Resisting Connection



Figure 3 Completed Structure on Shake Table

Using SAPWood (Pei et al 2007), a 2D/3D nonlinear time history analysis program, the target global lateral strength and stiffness demands for the first story were determined by assuming a simple bilinear hysteretic response for the steel, with a more sophisticated multi-parameter hysteretic model for the wood shear walls above. The steel frame was then designed using SAP2000 (CSI 2008) to meet the requirements identified by the SAPWood program, and the SAPWood analysis was then rerun using a full three dimensional model with the as-delivered frame performance at each frame line. Figure 4 shows the final design shear capacity of each story in each direction.

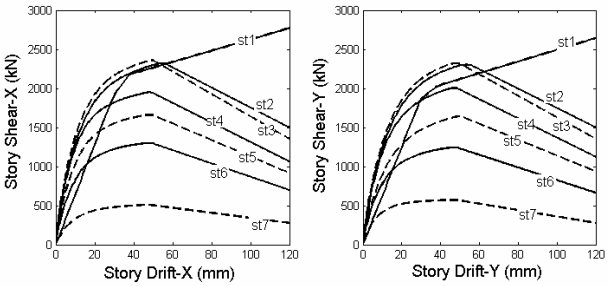

Figure 4 Design Global Pushover Capacity

To secure the upper six stories of wood light-frame construction to the first story of steel, a combination of wood and steel connections were employed. To address shear transfer, wood nailers were bolted to the top flange of the steel beams and shear transfer connections from the floor above were secured to this nailer. Overturning forces in the shear walls above were delivered to the steel frame through a combination of steel rods for tension and wood posts for compression. While the compression side forces were transferred into the steel frame elements through bearing, the rod tension forces where transferred through inverted U-shaped weldments. These weldments contained a hole through which the steel rod could pass and be secured via a nut, and then in turn they were welded to the top flange of the beam. Figure 5 shows the wood nailers being installed. Details on the wood construction of stories two through seven can be found in the upcoming report by Pei et al (2009).



Figure 5 Wood Nailers and Weldments on Beams

Phase I of the test program consisted of two tests on the same day wherein the moment frames were not braced and thus the full seven story structure was active. Ground motions recorded at the Canoga Park station during the 1994 Northridge earthquake were used as input with varying scale factors. Figure 6 shows the spectral accelerations in the X, Y, and Z directions of the un-scaled Canoga Park record, with the Y-component (which has a higher PGA value) applied in the long direction of the building. The ground motion was scaled to the peak ground acceleration levels listed in Table 2 to represent seismic hazard levels with 50%, and 5% probability of exceedance in 50 years, which corresponds to return periods of 72 and 675 years, respectively.

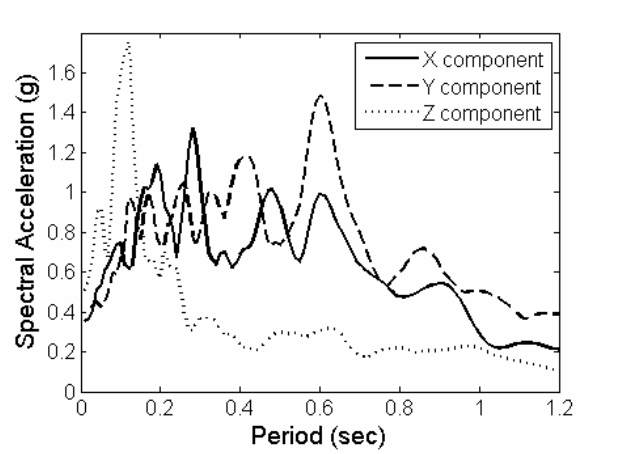

Figure 6 Spectral Acceleration for Unscaled Ground Motion used in Shake Table Test

3. EXPERIMENTAL RESULTS AND DISCUSSION

Because of the size of the building, it was not possible to find a fixed reference to instrument the absolute displacements of the structure, i.e. a frame beside the shake table. Therefore, an optical tracking measurement system was employed in the test program to capture the building movement with 50 LED light markers attached to the exterior of the building at each diaphragm level. The location of these markers is shown in Figure 7. There were no markers on the back side of the building due to camera limitations.

Table 2 Peak Ground Accelerations for the Canoga Park Record

Northridge Canoga Park		Seismic Test	
		Level 1	Level 2b
Hazard level		50% 50 years	5% 50 years
Scaling factor		0.53	1.4
PGA (g)	X	0.19	0.5
	Y	0.22	0.58
	Z	0.26	0.69

The averaged displacement at the centroid of the floor diaphragm can be estimated based on the measurements from seven optical tracking markers for each floor. The maximum roof displacements relative to the shake table were measured to be 65mm and 166mm for seismic intensities 1 and 2, respectively. The maximum displacement occurred in the long direction of the floor plan, namely the Y direction. The building deformation shapes at the point in time of the maximum roof displacement levels in the X and Y directions are presented in Figure 8. The shape of the deformed grid was generated directly from the optical tracking sensor measurements and is exaggerated for clarity. Although the building was designed to be symmetric and added seismic mass was distributed approximately uniformly over the building floor plan, torsional response was clearly observed during testing. The torsional response was synchronized with the lateral response of the building, which means the point in time at which the torsion reached a maximum value is very close to the occurrence of the maximum value of the lateral response. Average peak interstory drift for both tests is shown in Table 3, and global hysteresis loops are shown in Figure 9.

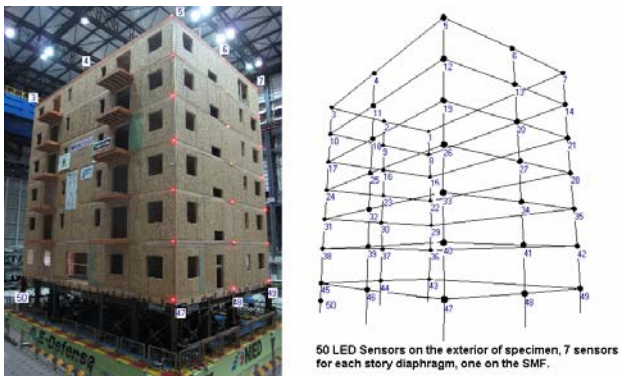

Figure 7 Optical Tracking System for Displacement Measurements

Interstory drifts across all stories are low and fairly uniform with the exception of the steel first story. Interstory drifts there were smaller than anticipated, likely due to two factors: a) stiffer columns utilized when converted to become part of the lifting frame; and b) not explicitly accounting for the rotational stiffness of the nominally "pinned" column base connection. This typical column base connection of a flat steel plate with four central bolts designed only for shear and axial column reactions is often considered by designers as pinned, when in reality it does have moment resistance that will stiffen a frame. More research is needed on this subject.

As would be expected for interstory drifts of this magnitude, damage to the structure was minor and confined to nonstructural gypboard sheathing elements, manifesting itself primarily as diagonal cracking around window and door openings. Figure 10 shows typical damage. This was not unexpected because while severe in its own right, the maximum phase I shaking was still significantly smaller than the maximum phase II earthquake testing in order to prevent too much damage from occurring in phase I.

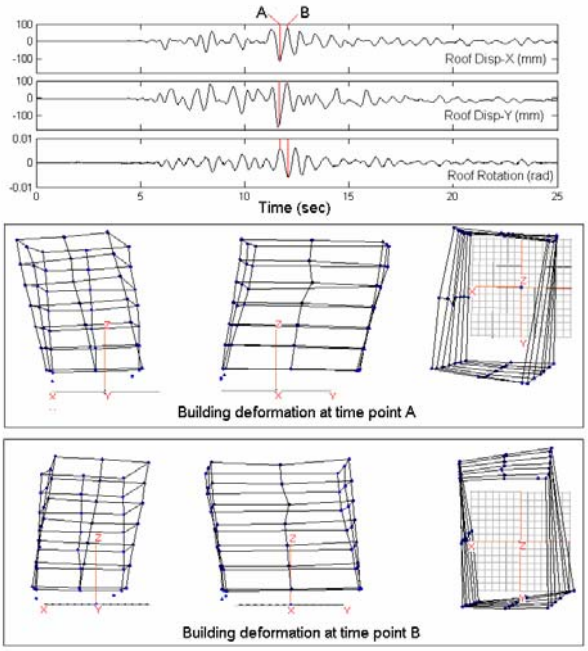

Figure 8 Observed Displacement Response from Optical Tracking System

Table 3 Averaged Peak Interstory Drift Measured During the Two Tests

Peak Inter-story Drift (%)	Seismic Test 1		Seismic Test 2	
Direction	X	Y	X	Y
St1 (SMF)	0.19	0.32	0.34	0.51
St2	0.35	0.38	0.6	0.91
St3	0.41	0.58	0.77	1.14
St4	0.35	0.41	0.75	1.2
St5	0.36	0.45	0.92	1.31
St6	0.33	0.35	0.83	1.15
St7	0.38	0.29	0.96	0.65

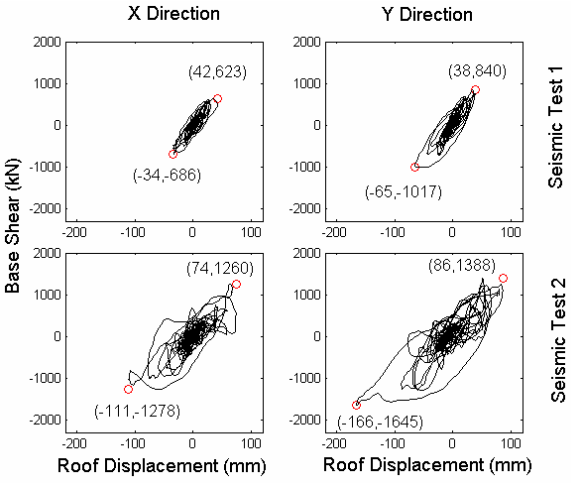

Figure 9 Global Hysteresis Curves



Figure 10 Gypboard Damage at Door (L) and Window (R)

4. SUMMARY AND CONCLUSIONS

A series of two shake table tests on a seven story steel and light-frame wood building was completed on July 30, 2009 in Miki, Japan. With overall design objectives provided by the performance based design procedure developed within the NEESWood project, a new type of partial strength steel moment frame connection was proven to be capable of supplying excellent performance in a mixed-use steel-wood hybrid structure under heavy shaking. The building overall was able to achieve very good performance under excitations exceeding the DBE level earthquake, with maximum averaged inter-story drifts less than 1.5%. Only non-structural damage occurred in the building and was limited to readily repairable minor cracking in the gypsum wall finish material. Typical design approaches for anchoring wood to steel were shown to be easily scalable to secure the upper six story wood superstructure to the steel frame below.

Acknowledgements:
The material presented in this paper is based upon work supported by the National Science Foundation under Grant No. CMM-0529903 (NEES Research) and CMMI-0402490 (NEES Operations). Any opinions, findings, and conclusions or recommendations expressed in this material are those of the author(s) and do not necessarily reflect the views of the National Science Foundation. The overall NEESWood project team made up of John W. van de Lindt, David V. Rosowsky, Andre Filiatrault, Rachel A. Davidson, and Michael D. Symans contributed to all facets of the NEESWood project. Thank you also to Weichiang Pang of Clemson University for his participation in the design portion of the Capstone test specimen. Thank you to NSF REU's Doug Allen and Kathryn Pfrefzschner, researchers Chikahiro Minowa, Izumi Nakamura, and Hidemaru Shimizu of NIED, Hiroshi Isoda of Shinshu University and Mikio Koshihara at the University of Tokyo. Graduate students Kazuki Tachibana and Tomoya Okazaki, contributed to the construction and instrumentation of the test specimen and a former Ph.D. student Kimberly Cronin helped with the design. Thank you also to Tim Ellis of Simpson Strong Tie Co. and David Clyne of Maui Homes USA. Technical collaborators beyond the authors affiliation included the U.S. Forest Product Laboratory, FP Innovations-Forintek Division, and Maui Homes U.S.A. Financial and in-kind product and personnel donations were provided by Simpson Strong Tie, Maui Homes, B.C. Ministry of Housing and Social Development, Stanley Bostitch, Strocal Inc., Structural Solutions Inc., Louisiana Pacific Corp., Natural Resources Canada, Forestry Innovation Investment, APA-The Engineered Wood Association, American Forest and Paper Association, Howdy, Ainsworth, and Calvert Glulam.

References:

Christovasilis, I.P., Filiatrault, A., and Wanitkorkul, A. (2007). "Seismic testing of a full-scale two-story wood light-frame building: NEESWood benchmark test" Neeswood Report No. NW-01, Dept. of Civil, Structural and Environmental Engineering, University at Buffalo, State University of New York, Buffalo, available on-line at http://www.engr.colostate.edu/NEESWood/.

CSI (2008), SAP2000 Version 12.0, http://www.csiberkeley.com

ICBO. (1988). "Uniform Building Code, 1988 ed." International Conference of Building Officials, Whittier, CA.

Filiatrault, A., Christovasilis, I.P., Assawin Wanitkorkul, and John W. van de Lindt (2009) "Seismic Response of a Full-Scale Light-frame Wood Building: Experimental Study" Journal of Structural Engineering, In Press.

Folz, B. and Filiatrault, A. (2004) "Seismic analysis of woodframe structures. II: Model implementation and verification" Journal of Structural Engineering, v 130, n 9, p 1361-1370.

Mosalam, K.M., C. Mochado, K.U. Gliniorz, C. Naito, E. Kurkel, and S.A. Mahin (2003) "Seismic evaluation of an asymmetric three-story woodframe building" CUREE Report W-19.

Pang, W.C., and Rosowsky, D.V. (2007) "Direct displacement procedure for performance-based seismic design of multistory woodframe structures" Neeswood Report No. NW-02, Zachry Dept. of Civil Engineering, Texas A&M University, College Station, available on-line at http://www.engr.colostate.edu/NEESWood/.

Pei S., and van de Lindt J.W. (2007). User's manual for SAPWood for Windows, Version 1.0. SAPWood program user's manual, available on-line at http://www.engr.colostate.edu/NEESWood/.

Pei, S., van de Lindt, J.W. (2008). "Coupled bending-shear seismic analysis of Stacked Wood Shearwall Systems", Earthquake Engineering and Structural Dynamics, 38: 1631-1647.

Pei, S., J.W. van de Lindt, S.E. Pryor, H. Shimizu, H. Isoda, and D. Rammer. (2010). "The NEESWood Capstone Tests at E-Defense: Testing of a Full-Scale Six-Story Woodframe and Seven-Story Mixed Use Building", Publication anticipated on-line (NEESWood Report NW-07) and via the U.S. Forest Products Laboratory in 2010.

van de Lindt, J.W., Pei, S., Pryor, S.E., Shimizu, H. and Isoda, H. (2009) "Experimental seismic response of a full-scale six-story light-frame building" Submitted to Journal of Structural Engineering.

van de Lindt, J.W., D.V. Rosowsky, A. Filiatrault, M.D. Symans, R.A. Davidson. (2006). "The NEESWood Project: Progress on the Development of a Performance-Based Seismic Design Philosophy for Mid-Rise Woodframe Construction". Proc of the 2006 World Conference on Timber Engineering, Portland, OR.

JOINT CONFERENCE PROCEEDINGS
7th International Conference on Urban Earthquake Engineering (7CUEE) &
5th International Conference on Earthquake Engineering (5ICEE)
March 3-5, 2010, Tokyo Institute of Technology, Tokyo, Japan

CYCLIC LOADING TESTS ON BUCKLING-RESTRAINED BRACES USING ROUND STEEL BAR CORES AND DOUBLE STEEL TUBES

Shunji Fujii[1] and Hiroshi Tagawa[2]

1) Okabe Corporation, Japan
2) Associate Professor, Graduate School of Environmental Studies, Nagoya University, Japan
s-fujii@okabe.co.jp, tagawa@genv.nagoya-u.ac.jp

Abstract: This paper presents an experimental study of a buckling-restrained brace (BRB) in which round steel bars and double steel tubes are used, respectively, as core members and buckling restrainers. Cyclic loading tests were conducted using full-scale BRB members. Test results revealed that the proposed BRB has sufficient capability as a hysteretic damper under the control of compressive axial force by the number of contraction allowance parts and the fixing methods of inner tubes.

1. INTRODUCTION

The buckling-restrained brace (BRB) has recently become popular for its ability to mitigate structural damage during seismic events. During large earthquakes, the BRBs absorb seismic energy and reduce the seismic response of structures. In practice, BRB of various types have been developed and used. For core members, steel plate assemblies or steel tubes are often used to resist strong axial forces acting on the brace members. In contrast, round steel bars are rarely used as core members.

This study developed a new type of BRB to resist low axial forces for medium and low-rise building frames. Figure 1 portrays elements of the proposed BRB, which consists of round steel bar cores and double steel tubes. The inner tube directly restrains buckling of the core members. The outer tube restrains buckling of the inner tube through the spacers. The round steel core member is divided into two bars, which are connected with a central coupler. The outer tube is welded to the central coupler to prevent the outer tube from falling under its own weight. This paper presents results of cyclic loading tests on the proposed BRB.

2. TEST OUTLINE

Five test specimens are presented in Table 1 and portrayed in Figure 2. The main test parameters are the fixing methods of the inner tubes and the number of contraction allowance parts allowing compressive deformation of the core members. Each specimen has two round steel bar cores of ϕ22 (SNR490B) in series with M24 thread rolling screws manufactured at each end. End couplers are used to avoid hinge-like mechanisms in the core members after compression yielding. They act as a guide along the outer steel tubes.

Figure 3 presents definitions of clearances c_1–c_4: c_1 represents the clearance between the screw of the core member and the inner tube; c_2 is that between the shaft of the core member and the inner tube; c_3 is that between the spacer and the outer tube; and c_4 is that between the end coupler and the outer tube. The values of c_1–c_4 were determined to prevent problems during the manufacture of test specimens. In specimen I4-O12-A, the central coupler and the outer tube were fixed by a bearing with M16 bolts attached with M16 nuts welded on the outer tube. In the other specimens, the central coupler and the outer tube were fixed by welding. The inner tube and the outer tube are separated with spacers for all specimens except specimen

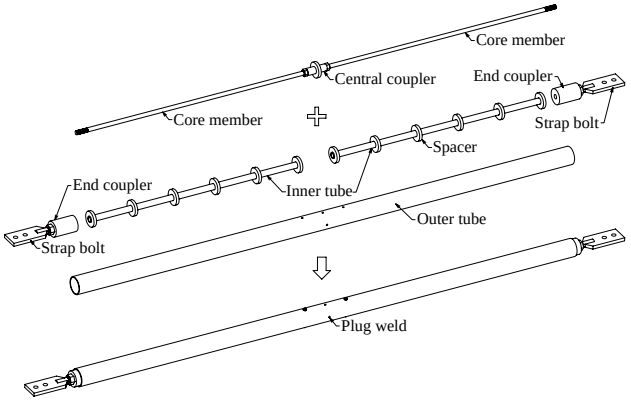

Figure 1 Elements of proposed BRB

Table 1 List of specimens

Specimen	Core member (SNR490B)	Buckling restrainer (STKM13A)		Clearance				Number of contraction allowance
		Inner tube	Outer tube	c_1 (mm)	c_2 (mm)	c_3 (mm)	c_4 (mm)	
I4-O12-A	ϕ22-M24	ϕ42.7×8	ϕ120×13	2.7	4.7	-	2.3	2
I3-O8-A		ϕ34×4.5	ϕ80×6	1.0	3.0	2.0	1.0	
I3-O8-E								
I3-O10-E			ϕ101.6×5					
I3-O10-F								4

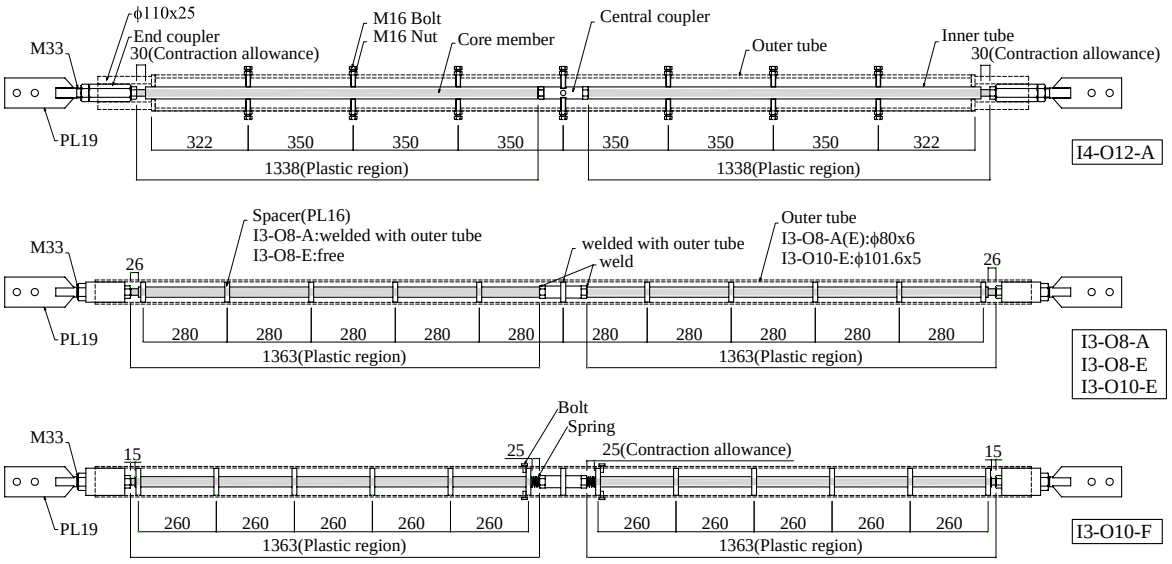

Figure 2 Details of test specimens

I4-O12-A, where M16 bolts were used instead of spacers. For preventing the inner tube from detaching from the central coupler because of self-weight and cyclic loads, the inner tubes were welded to the central coupler for all specimens except specimen I3-O10-F, where the inner tubes were separated from the central coupler with a designated distance using M10 bolts and springs, as shown in Figure 4. Specimens other than I3-O10-F have two contraction allowance parts; specimen I3-O10-F has four contraction allowance parts. Test results revealed that compressive deformation of the core members occurs mainly near the contraction allowance parts. In specimen I3-O8-A, the outer tube and all spacers were fixed by plug-welding.

The specimens were designed so that the inner and outer tubes can restrain buckling of the core member according to the following equations (Fujimoto et al., 1988).

$$ {}_{I}M_y > \frac{N_y c_2}{1 - N_y / {}_{I}N_E} \quad , \quad {}_{I}N_E = \frac{\pi^2 {}_{I}E_{I}I}{{}_{s}d^2} \qquad (1),\ (2) $$

$$ {}_{O}M_y > \frac{N_y (c_2 + c_3)}{1 - N_y / {}_{O}N_E} \quad , \quad {}_{O}N_E = \frac{\pi^2 {}_{O}E_{O}I}{l_k^{\,2}} \qquad (3),\ (4) $$

Therein, ${}_{I}M_y$ and ${}_{O}M_y$ respectively denote the flexural strengths of inner and outer tubes. The axial yield strength, based on material tests of the core member, is N_y . Also, ${}_{I}N_E$ and ${}_{O}N_E$ respectively signify the buckling strengths of inner

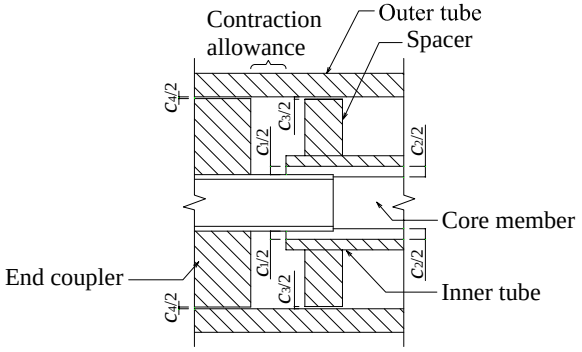

Figure 3 Definition of clearances

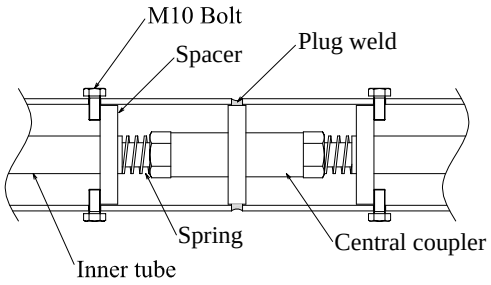

Figure 4 Central part of specimen I3-O10-F

and outer tubes. Furthermore, l_k is the length shown in Figure 5, ${}_sd$ is the distance between spacers, and ${}_IE\ {}_II$ and ${}_OE\ {}_OI$ are the respective flexural stiffnesses of inner and outer tubes.

Figure 5 depicts the test setup. Cyclic loading P was applied at the column top using a 300 kN jack. Rotation R was defined as δ/h, where h denotes the column height and δ denotes the lateral displacement measured at the column top; R corresponds to the story drift angle. The lateral load P was varied to obtain increasing increments of rotation R equal to 1/400, 1/200, 1/100, 1/67, 1/50, and 1/40 radians. For each rotation increment, two full cycles of loading were performed. The loading direction in which a bracing member is subjected to tensile force is defined as positive. The strap bolts attached to both ends of the specimen have about twice the axial strength of the core member. The gusset plates are ensured to be rigid.

3. TEST RESULTS

Test results are shown in Table 2. The N/N_y and R relations are shown in Figure 6, where N and N_y respectively denote the brace axial force and yield strength of the core member. Fairly stable hysteresis loops were observed in the loading cycles up to R = 1/67 in all specimens. For specimens I3-O8-A and I3-O8-E, the brace axial force exceeded the buckling strength of the outer tube. Global buckling of braces took place in the cycle of R = 1/50. The ratio of the axial force in the compressive loading process to that in the tensile loading process increases as R increases. For specimens I3-O10-E and I3-O10-F, stable hysteresis loops were exhibited up to the final cycle. Increased compressive axial force was the smallest for specimen I3-O10-F, which has four contraction allowance parts. Photo 1 shows higher modes of buckling observed in the post-test residual deformations of core members.

4. DISCUSSION

4.1 Increase of compressive axial force

Figure 7 shows variation of the ratio of the axial compressive force to the axial tensile force for each loading cycle. Ratio α increases as R increases for all specimens. The rate of increase of α is lower for specimen I3-O8-E, in which the inner tubes were fixed



Photo 1 Higher mode buckling of the core member

Table 2 Test results

Specimen	N_{max} (kN)	N_{min} (kN)	$\left\|\frac{N_{min}}{{}_ON_E}\right\|$	$\frac{N_{max}}{N_y}$	$\left\|\frac{N_{min}}{N_y}\right\|$	Failure mode
I4-O12-A	185	-342	0.28	1.25	2.31	-
I3-O8-A	166	-205	1.10	1.12	1.39	global buckling
I3-O8-E	162	-203	1.09	1.09	1.37	global buckling
I3-O10-E	182	-259	0.75	1.23	1.75	-
I3-O10-F	180	-230	0.67	1.22	1.55	-

N_{max}: maximum tensile force, N_{min}: maximum compressive force

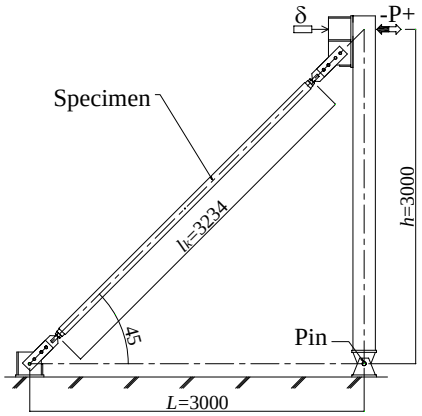

Figure 5 Test setup

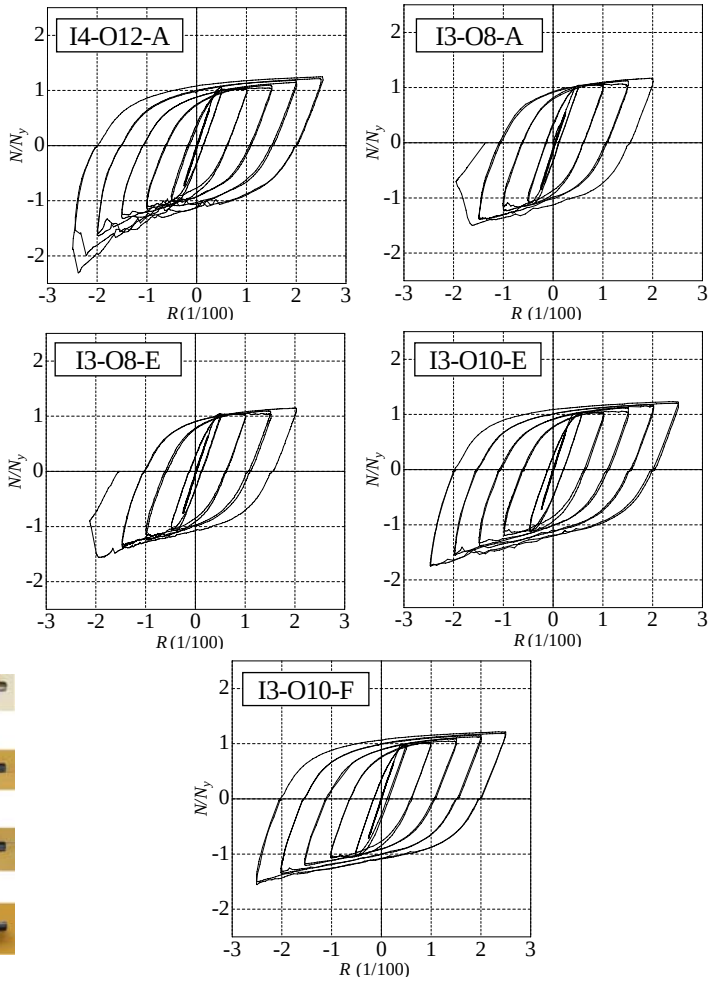

Figure 6 N/N_y and R relationships

with only the central coupler, than that for I3-O8-A, in which the inner and outer tubes were fixed by welding via all spacers. The difference in the rate of increase of α between I3-O10-E and F is discussed using Figure 8 as follows. Observation of the post-test residual deformation of the core members exhibited that the higher mode buckling of the core members was large near the contraction allowance parts. This possibly increases friction between the core member and the inner tube at that part and engenders restriction of compressive deformation. Consequently, the brace axial force increases during the compressive loading process. Figure 8 shows that compressive deformation of the core member in specimen I3-O10-F appears near both ends.

4.2 Strain distribution in steel tube buckling restrainers

Figure 9 shows the strain distribution in the inner and outer tubes at the maximum compressive load. For specimens I3-O8-A and I3-O8-E, only outer tube strains were measured. The outer tube strain in specimen I3-O8-A was much greater than that in specimen I3-O8-E because the friction force between the core member and the inner tube is transmitted to the outer tube via every spacer for specimen I3-O8-A. This increases the brace axial force in the compressive loading process. The strain in the inner and outer tubes in specimen I3-O10-F was less than that in specimen I3-O10-E. Especially, the outer tube strain in specimen I3-O10-F was very slight. In addition, the strain at the central part of inner tube in specimen I3-O10-F was much less than that in specimen I3-O10-E, possibly because the four contraction allowance parts prevented contact between the inner tube and the central coupler. Yielding of the inner tube did not take place for any specimen.

The axial force ratio variation for the outer tube, the inner tube and the core member in the compressive loading is shown in Figure 10 (I3-O10-E, I3-O10-F). The compressive axial forces of the outer and inner tubes are calculated from strain data; that of the core member is obtained by subtracting the inner and outer tube force from the total compressive force of the brace. In specimen I3-O10-E, the axial force ratio of the buckling restrainer tubes reaches 40% at the final loading cycle. In contrast, that ratio in specimen I3-O10-F is rather small. The ratio of the outer tube is extremely small.

5. CONCLUSIONS

A novel buckling restrained brace (BRB) was proposed. The BRB comprises round steel bar cores and double steel tube buckling restrainers. Full-scale cyclic loading tests conducted for the proposed BRB revealed the influences of fixing methods of steel tubes and the number of contraction allowance parts on the cyclic behavior of the proposed BRB.

References:

Fujimoto, M. Wada, A. Saeki, E. Watanabe, A. and Hitomi, Y. (1988), "A study on the unbonded brace encased in buckling-restraining concrete and steel tube" *Journal of Structural and Construction Engineering*, AIJ, Vol.34B, 249-258.

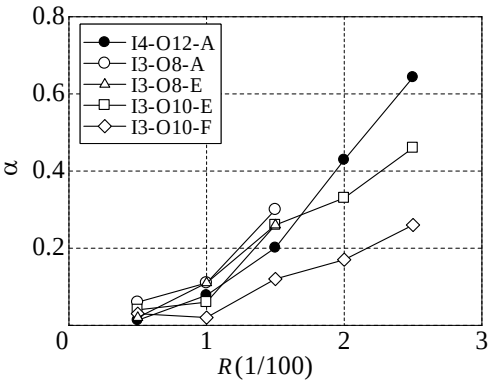

Figure 7 Ratio of compressive axial force to tensile one

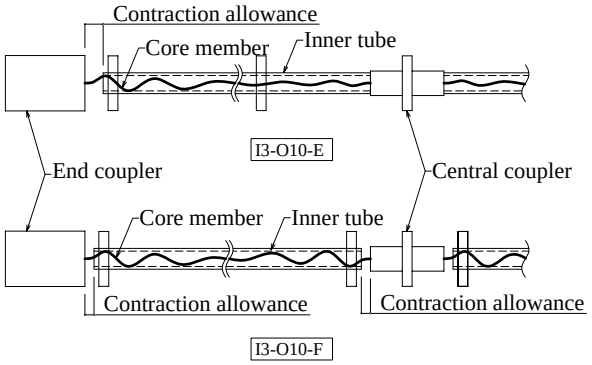

Figure 8 Buckling of the core member

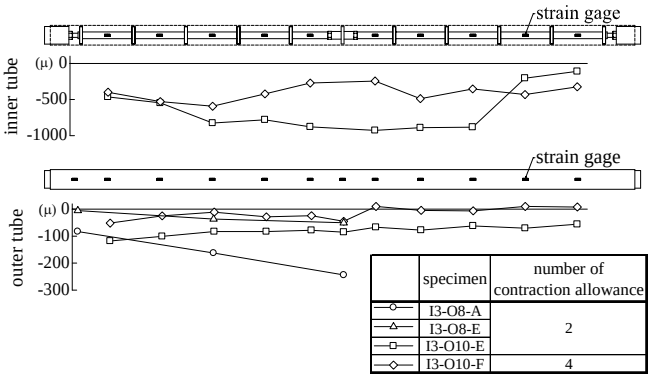

Figure 9 Strain distribution on buckling restrainers

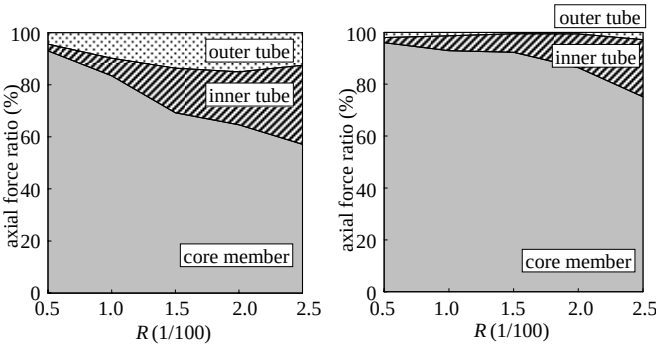

(a) I3-O10-E (b) I3-O10-F

Figure 10 Relationship between story drift angle and axial force ratio

JOINT CONFERENCE PROCEEDINGS
7th International Conference on Urban Earthquake Engineering (7CUEE) &
5th International Conference on Earthquake Engineering (5ICEE)
March 3-5, 2010, Tokyo Institute of Technology, Tokyo, Japan

PARAMETRIC STUDIES OF PARTICLE DAMPERS UNDER MULTI-AXIS EXCITATIONS

Xilin Lu [1], Zheng Lu[1], and Sami F. Masri[2]

1) Professor, State Key Laboratory of Disaster Reduction in Civil Engineering, Tongji University, Shanghai ,China
2) Ph.D student, State Key Laboratory of Disaster Reduction in Civil Engineering, Tongji University, Shanghai ,China
3) Professor, Viterbi School of Engineering, University of Southern California, Los Angeles, California, USA
lxlst@tongji.edu.cn, luzheng111@gmail.com, masri@usc.edu

Abstract: This paper studies the influence of system parameters to the performance of particle damper under multi-axis excitations. The Discrete-Element Method is applied here to capture the behavior of the entire system in detail. With this technique, the positions and contact forces of particles and the primary system can be traced at every tiny time step. Based on high-fidelity simulations, it is shown that: increasing the mass ratio can improve the damper's effectiveness, but only up to a certain level; applying particles with a high value of the coefficient of restitution can result in a broader range of acceptable response levels; friction has a complex influence on particle dampers in a generally detrimental form; a lightly-damped primary system can achieve a considerable reduction in its response with a small weight penalty; and that a cylindrically-shaped container provides a higher level of effectiveness than a rectangularly-shaped one.

1. INTRODUCTION

It is very important to control the dynamic response of structures in engineering. In particular, passive control methods are widely used due to their mechanical simplicity and lack of power requirement. Impact dampers are simple and efficient passive devices (Masri and Caughey 1966). They are used to attenuate the vibrations of lightly damped structures, by momentum exchange and energy dissipation during the impact between solid particle and the primary system, to which they are attached. However, during the impact process, impulsive loads are transmitted between the two coupled systems and will cause a high-level noise; simultaneously, large contact forces will result in material deterioration and local deformation accompanying plastic collisions. Furthermore, the performance of a single-particle impact damper may become sensitive to the coefficient of restitution, level and frequency of the excitation, as well as the container dimension. To reduce these problems, smaller size particles with the same mass ratio are used to replace the single solid particle, thus resulting in a potentially more efficient particle damper.

Many theoretical, numerical, and experimental studies have been carried out for the characterization of particle dampers. Papalou and Masri (1996, 1998) introduced an equivalent single-particle impact damper model to evaluate the performance of multi-particle dampers. Friend and Kinra (2000) developed an analytical approach by treating multi particles as a lumped mass system. Liu et al. (2005) used an equivalent viscous damping model to represent the nonlinearity which was extracted from experimental results. Xu et al. (2004) presented an empirical method for particle damping design. Fang and Tang (2006) developed an improved analytical model by multiphase flow theory based on the previous work of Wu et al. (2004).

Although these equivalent models or empirical-based studies have given many new insights, they are essentially phenomenological, and the results are difficult to extrapolate beyond their respective experimental conditions. Recently, a discrete element method (DEM), which can take interactions between particles into account, has been used to perform limited studies of particle dampers (Saeki 2002, 2005, Mao et al. 2004). Moreover, many parameters influence the behaviors of particle dampers; however, it is not feasible to investigate the numerous particle damper parameters experimentally. Hence, there is a need for a comprehensive study of influence of various system parameters on their performance.

2. SIMULATION METHOD

The simplified model shown in Figure 1 represents a two-degree-of-freedom system equipped with an auxiliary nonlinear particle damper, in which a certain number of particles are placed. The whole system is positioned in the *x*-*y* plane, and is excited by stationary random excitations *fx* and *fy* in the *x* and *y* directions. By letting *x* and *y* be the relative displacements of the primary system in the *x* and *y* directions, respectively, the equation of motion for the primary system is:

$$M\ddot{x} + kx + c\dot{x} = F_x + f_x \quad (1)$$

$$M\ddot{y} + ky + c\dot{y} = F_y + f_y \quad (2)$$

or

$$\ddot{x} = -\omega_n^2 x - 2\zeta\omega_n \dot{x} + (F_x + f_x)/M \quad (3)$$

$$\ddot{y} = -\omega_n^2 y - 2\zeta\omega_n \dot{y} + (F_y + f_y)/M \quad (4)$$

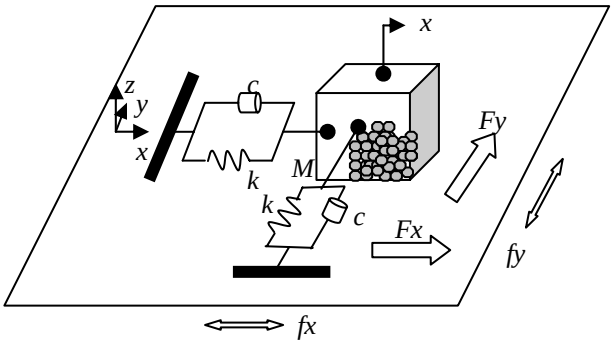

Figure 1 Model of the particle damper

where M, k and c are the mass, equivalent stiffness, and damping constant of the primary system, respectively. Fx and Fy are the decomposed contact forces acting on the primary system in the directions of the x-axis and y-axis, $\omega_n = \sqrt{k/M}$ is the primary system natural frequency, and $\zeta = c/2M\omega_n$ is the primary system fraction of critical damping. The dimensions of the rectangularly-shaped container of the primary system are dx (length), dy (width) and dz (height), which are parallel to the x, y and z direction, respectively. The dots denote a time derivative.

The discrete-element method (Cundall 1979) is a numerical scheme that allows finite rotations and displacements of discrete bodies which are interacted by local contact laws, and are described by Newton's equations of motion. It is based on the idea that the time step chosen may be so small that, during a single time step, disturbances cannot propagate from any particle further than its immediate neighbors. Then, at all times, the forces acting on any particle are determined exclusively by its interaction with the particles with which it is in contact. This method is applied in this study to capture the behavior of the entire system in detail. With this technique, the position and contact force of the individual particle and the primary system can be traced at every single time step. As it is a macroscopic problem, molecular level forces (i.e., the Coulomb force and van der Waals force) are not considered; consequently, the governing equation for a particle i can be written as

$$m_i \ddot{\mathbf{p}}_i = m_i \mathbf{g} + \sum_{j=1}^{k_i} (\mathbf{F}_{ij}^n + \mathbf{F}_{ij}^t) \quad (5)$$

$$\mathbf{I}_i \ddot{\varphi}_i = \sum_{j=1}^{k_i} \mathbf{T}_{ij} \quad (6)$$

where m_i is the mass of particle i, $\mathbf{I}_i$ is the moment of inertia of particle i and $\mathbf{g}$ is the acceleration vector due to gravity; $\mathbf{p}_i$ is the position vector of the center of gravity of particle i, φ_i is the angular displacement vector, $\mathbf{F}_{ij}^n$ is the normal contact force between particle i and particle j (if particle i is in contact with container wall, then j denotes that wall) and $\mathbf{F}_{ij}^t$ is the tangential contact force. The contact forces act at the contact point between particle i and particle j rather than the particle center, and they will generate a torque, $\mathbf{T}_{ij}$, causing particle i to rotate. For a spherical particle of radius r_i, $\mathbf{T}_{ij}$ is given by $\mathbf{T}_{ij} = r_i \mathbf{n}_{ij} \times \mathbf{F}_{ij}^t$, where $\mathbf{n}_{ij}$ is the unit vector from the center of particle i to the center of particle j and $\times$ denotes the cross product. These inter-particle forces are summed over the k_i particles in contact with particle i.

A number of contact models can be used to quantify the normal and tangential contact forces; however, this is still an active research topic, particularly for the tangential forces (Du and Wang 2009, Elperin and Golshtein 1997, Renzo and Maio 2004). The present simulation study uses a linear contact model in the normal direction, and Coulomb's law of friction in the tangential direction.

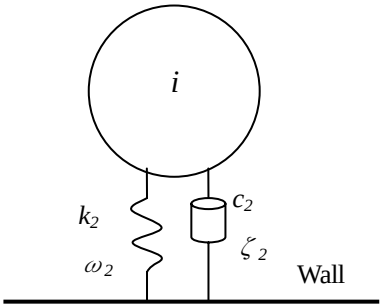

Figure 2 Normal contact force model between a particle and the wall

Figure 2 presents the linear contact model between the particle and the wall in the normal direction, where k_2 is the stiffness of the impact damper "stops", c_2 is the damping constant of the impact damper "stops", and $\omega_2 = \sqrt{k_2/m}$ is the natural frequency, which can be used to simulate a rigid barrier to any degree of accuracy, by a proper choice. Based on previous studies (Masri 1973), the ratio of $\omega_2/\omega_n \geq 20$ is appropriate to represent a "stiff" barrier. The parameter $\zeta_2 = c_2/2m\omega_2$ is the fraction of critical damping, which can be used to simulate inelastic impacts, ranging from the completely plastic up to the elastic one, so that value of any desired coefficient of restitution e can be adjusted by selecting the proper value for ζ_2 Similarly, k_3, ω_3, c_3 and ζ_3 are the stiffness, natural frequency of the spring, and the damping coefficient and fraction of critical damping of the damper, respectively, in the inter-particle contact model along the normal direction. Hence, the normal contact force is expressed by

$$F_{ij}^n = \begin{cases} k_2\delta_n + 2\zeta_2\sqrt{mk_2}\,\dot{\delta}_n & \delta_n = r_i - \Delta_i \\ k_3\delta_n + 2\zeta_3\sqrt{\dfrac{m_i m_j}{m_i + m_j}k_3}\,\dot{\delta}_n & \delta_n = r_i + r_j - |\mathbf{p}_j - \mathbf{p}_i| \end{cases} \quad (7)$$

where δ_n and $\dot{\delta}_n$ are the displacement and velocity of particle i relative to particle j, respectively, and Δ_i is the

distance from the center of particle *i* to the wall.

Considering Coulomb's law of friction, the tangential contact force is expressed by

$$F_{ij}^{t} = -\mu_s F_{ij}^{n} \dot{\delta}_t / |\dot{\delta}_t| \qquad (8)$$

where μ_s is the coefficient of friction between any two particles or between a particle and the wall of the container, and $\dot{\delta}_t$ is the velocity of particle *i* relative to particle *j* or the wall, in the tangential direction.

With the above in mind, the procedure for calculating the response of the particle dampers used in this study can now be illustrated. First, consider the relative position of the particles and walls. If $\delta_n > 0$, the contact force acting on the particle can be determined from equations (7) and (8); while if $\delta_n \le 0$, no contact force is produced. Second, sum all the contact forces acting on this particle, including inter-particle forces and particle-wall forces, if they exist. Third, the particle motion can be analyzed by equation (5) and (6). The same procedure is repeated for all the particles. Finally, the component of the contact force *Fx* and *Fy* acting on the primary system in the *x*-axis and *y*-axis are given by the summation of all the contact forces between the particles and the wall of the container, respectively. By using the components of the contact force *Fx* and *Fy*, the equation of motion for the primary system, equation (1) - (4) is updated.

As a part of the study reported herein, a code was programmed and implemented according to the above mentioned procedure, and the fourth order *Runge-Kutta* method was applied to solve the resulting system of nonlinear ordinary differential equations (Lu et al. 2009).

3. PARAMETRIC STUDY

In this section, different parameters, such as the mass ratio (μ), the coefficient of restitution (*e*), excitation levels, damping ratio of the primary system (ζ), container shape and coefficient of friction (μ_s) are investigated to get a broader view of the performance of particle dampers with a two-degree-of-freedom system. In these simulations, the primary system natural frequency is 11.4 Hz, and the mass is 0.573 kg, the stiffness in the *x* and *y* directions are the same. Two uncorrelated stationary random excitations based on the same probability distribution in both the *x* and *y* directions are exerted. The random excitation is generated based on a normal (Gaussian) distribution with a bandwidth from zero to five times the primary system's natural frequency. The initial positions of the particles are assigned randomly. In order to facilitate the presentation of the results, 2D plots are used hereafter, in which the normalized attenuation level is plotted versus the normalized container size. The width of the container is dy/σ_{r0} =3.8 and 16 particles with the same diameter of d/σ_{r0} =0.8 are placed in the container. The ratio of root-mean-square (r.m.s) value of the displacement of the primary system with a particle damper and that without a particle damper (σ_r/σ_{r0}) is used to quantify the vibration control effectiveness of the particle damper.

3.1 Effect of Mass Ratio

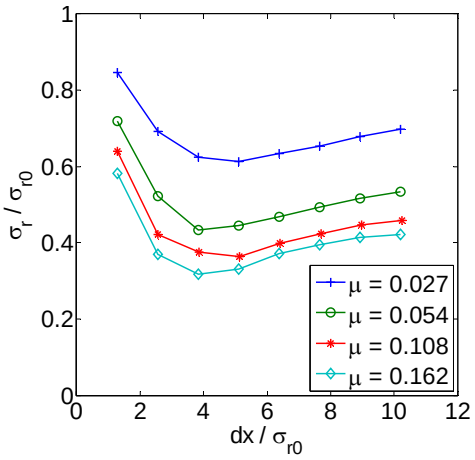

Figure 3 R.M.S displacement magnitude response levels for the primary system with *e* = 0.75, ζ = 0.004, and μ_s = 0.5 (effect of mass ratio)

Figure 3 shows that increasing the mass ratio of particles can reduce the response of the primary system, but the reduction is not linearly proportional to the increase in mass ratio; in fact, the effectiveness per unit mass ratio will decrease in a nonlinear manner as the mass ratio increases.

Another interesting observation is that indefinitely increasing the mass of the particles may not reduce the response any further, especially for large container sizes. This phenomenon can be explained by considering the conservation of momentum between the particles and the system. As a specific particle's mass increases, its absolute velocity immediately after the impact decreases which, in turn, reduces its relative velocity, and it takes a longer time to travel towards the other wall of the container. The force of friction also contributes to the reduction in the velocity while the particle is in motion. As the mass is increased beyond a certain value, its relative velocity immediately after the impact does not allow it to overcome the frictional force while in motion, and it comes to rest relative to the system prior to reaching the other wall. At that point, if the system resumes its motion in the same direction and its acceleration is large enough to overcome the force of friction, the particle starts traveling in the opposite direction relative to the system. If a similar situation arises prior to reaching the other container's boundary, the particle reverses it direction once again. It is possible for the particle to reciprocate between the container's boundaries, while the system goes through several cycles of motion before making the next impact.

3.2 Effect of Coefficient of Restitution

The coefficient of restitution *e* determines the rebound velocity of the particle and is the ratio between the relative velocity immediately following the impact and the relative velocity just prior to impact. It depends on the type, shape, and surface area of the materials coming in contact.

Figure 4 shows that higher *e*'s lead to a less reduction of the primary system's response in small-size containers,

while a more reduction in large-size containers, compared to lower *e*'s. The reason for this behavior is that a higher *e* can get a higher relative velocity immediately following the impact, which results in more collisions under a small clearance. In these collisions, much adverse momentum exchange happens and the Effective Momentum Exchange is reduced. As to dissipated energy, lower *e*'s will cause the loss of more energy during impacts, and this seems to be dominant when the container sizes are small. Another significant observation that can be gleaned from Figure 4 is that the sensitivity of a particle damper to changes in *dx* increases as *e* decreases, which results in the narrower optimum clearance for smaller *e*'s. Consequently, a particle damper designed with a relatively high value of *e* can tolerate a broader range of excitation levels, while still performing around the optimum level.

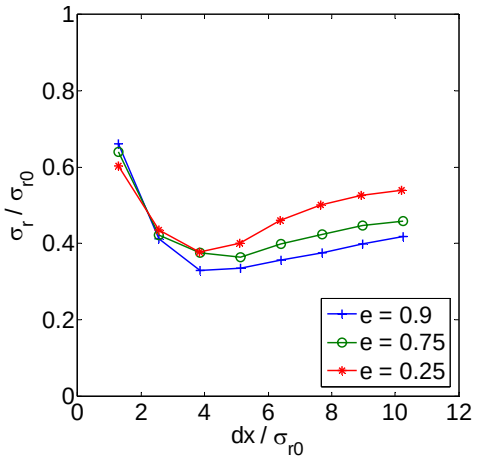

Figure 4 R.M.S displacement magnitude response levels for the primary system with μ = 0.108, ζ = 0.004, and μ_s = 0.5 (effect of coefficient of restitution)

3.3 Effect of Excitation Levels

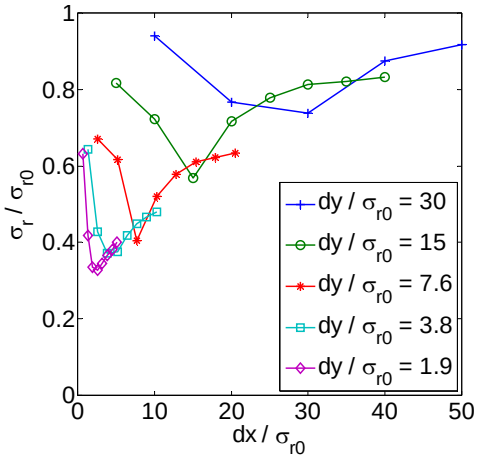

Figure 5 R.M.S displacement magnitude response levels for the primary system with μ = 0.108, *e* = 0.75, ζ = 0.004, and μ_s = 0.5 (effect of excitation level)

In this test, five levels of excitation are used to investigate the influence of the excitation level on the performance of the particle damper. As shown in Figure 5, the level of excitation plays a very important role. As the level of excitation increases, the efficiency of the damper increases due to the fact that the more energetic motion of the particles increase the exchange of momentum and dissipation of energy. On the other hand, when the excitation is high enough to mobilize all the particles, the response amplitude becomes independent of the intensity of the excitation, provided the dimensionless clearance ratio is maintained constant.

3.4 Effect of Primary System Damping

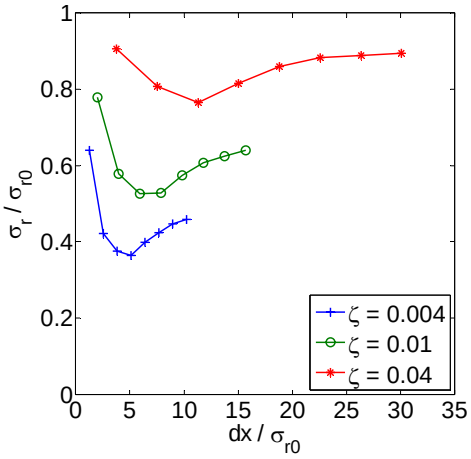

Figure 6 R.M.S displacement magnitude response levels for the primary system with μ = 0.108, *e* = 0.75, and μ_s = 0.5 (effect of primary system damping)

Figure 6 shows that the effectiveness of the particle damper increases as the primary system damping decreases. Consequently, the maximum effect of a particle damper would be achieved for a primary system with a negligible amount of inherent damping.

3.5 Effect of Primary System Damping and Mass Ratio

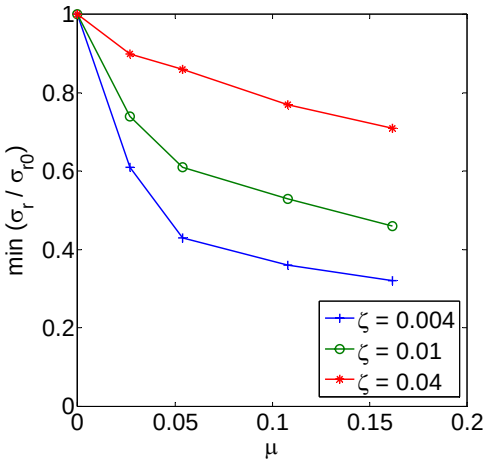

Figure 7 Effect of primary system damping and mass ratio on the performance of particle damper with *e* = 0.75, and μ_s = 0.5

Figure 7 summarizes the effects of mass ratio and primary system damping on the optimum performance of a particle damper. It is clear that, for a given ζ, the optimum response reduction is not a linear function of the mass ratio. Also, one can conclude that even with very small mass ratios, a properly designed particle damper is capable of substantial attenuation of the r.m.s response level.

3.6 Effect of Container Shape

In this test, a cylinder container is used to investigate the effect of container shape. Figure 8 displays the root-mean-square response of the primary system with a cylindrical particle damper, which is filled with 16, 64 and 128 particles, respectively. Optimum clearance ranges can easily be found in all cases, in which the particle damper with 128 particles has a broader range, compared to 16-particle case. Moreover, a particle damper with 16 particles is slightly less effective in reducing the response; however, there is not much difference in the best root-mean-square response level between all cases.

Compared with the behavior of a rectangularly-shaped particle damper with the same parameters (found the μ = 0.108 case in Figure 3), a cylindrical particle damper has better response reduction in the optimum range, that is 64% r.m.s response level reduction for a rectangular particle damper compared with 70% reduction for a cylindrical particle damper. The reason may lie in the symmetric shape, which could cause more beneficial collisions between particles and the container. Additionally, a cylindrically-shaped container is not influenced by the excitation axis.

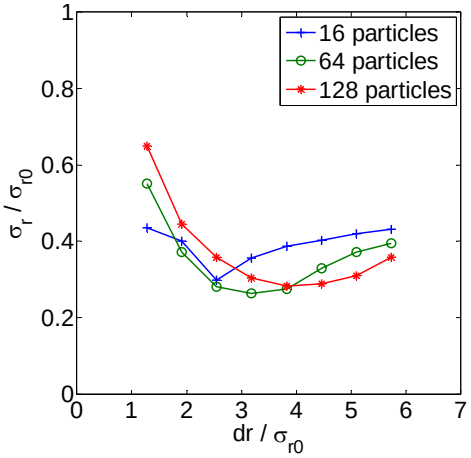

Figure 8 R.M.S displacement magnitude response levels for the primary system with a cylindrical particle damper, with μ = 0.108, e = 0.75, ζ = 0.004, and μ_s = 0.5 (effect of container shape)

3.7 Effect of Coefficient of Friction

Figure 9 shows that a particle damper with a small coefficient of sliding friction can get more r.m.s level reduction compared to that with a large coefficient of friction. The reason is that small friction results in more energetic motions of the particles, and the primary system has increased momentum exchange, in addition to the fact that energy is dissipated more by normal impacts. However, a large friction can dissipate more energy during sliding and oblique collisions. Consequently, friction introduces a complex influence on the behavior of particle dampers.

According to the theoretical and numerical work of Bapat on multi-unit impact damper, the effect of Coulomb friction is generally detrimental (Bapat and Sankar 1985). This phenomenon is also shown in Figure 10, which is performed by a multi-unit impact damper device. Both Figures show that in large-size containers, less friction leads to more response reduction. This indicates that the momentum exchange between particles and the primary system, and the particles' mobility, play very important roles in large-size container cases.

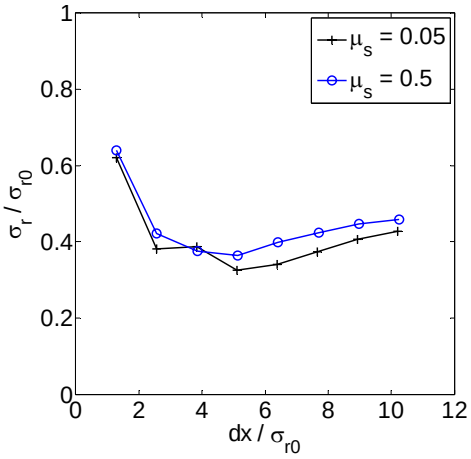

Figure 9 R.M.S displacement magnitude response levels for the primary system with μ = 0.108, e = 0.75, and ζ = 0.004 (effect of coefficient of friction)

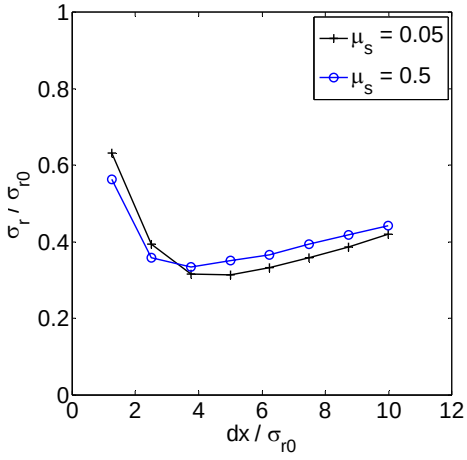

Figure 10 R.M.S displacement magnitude response levels for the primary system with multi-unit impact damper, with μ = 0.108, e = 0.75, and ζ = 0.004 (effect of coefficient of friction)

4. SUMMARY AND CONCLUSION

Although Papalou and Masri (1996, 1998) have presented the results of many experiments with particle

dampers under dynamic loads, the performance of such nonlinear devices is a highly complex nonlinear process involving energy dissipation and momentum exchange, and is not amenable to exact analytical solutions.

This study uses the discrete-element method to simulate the highly nonlinear motion of a primary system that is subjected to multi-component random excitations. Using well-established discrete particle modeling approaches, all significant interaction forces among the particles and with the rigid walls of their container are properly accounted for, including sliding friction, gravitational forces, and oblique impacts.

Extensive parametric studies are presented to evaluate the influence of various system parameters such as: mass ratio, coefficient of restitution, relative strength of excitation, primary system damping, container dimensions, container shape, number of particles, and sliding friction.

It is shown that properly designed particle dampers can significantly attenuate the response of lightly-damped primary systems that are subjected to stationary random excitation. Using a cylindrically-shaped particle container makes this class of dampers quite robust when handling multi-axis excitations, whose relative intensity is not known in advance --- a strong advantage when dealing with applications such as those involving earthquake excitation applied to primary structures, (an advantageous attribute compared to damping augmentation approaches utilizing conventional tuned-mass-dampers that are designed for a specific axis of excitation).

Acknowledgements:

Financial support from the National Natural Science Foundation of China (NSFC) through grant 90815029 and NSFC-JST (Japan Agency of Science and Technology) joint research project are highly appreciated.

References:

Masri, S.F. and Caughey, T.K. (1966), "On the Stability of the Impact Damper," *Journal of Applied Mechanics*, **33**(3), 586-592

Papalou, A. and Masri, S.F. (1996), "Performance of Particle Dampers under Random Excitation," *Journal of the Vibration and Acoustics – Transactions of the ASME*, **118**(4), 614-621

Papalou, A. and Masri, S.F. (1998), "An Experimental Investigation of Particle Dampers under Harmonic Excitation," *Journal of Vibration and Control*, **4**(4), 361-379

Friend, R.D. and Kinra, V.K. (2000), "Particle Impact Damping," *Journal of Sound and Vibration*, **233**(1), 93-118

Liu, W., Tomlinson, G.R., and Rongong, J.A. (2005), "The Dynamic Characterization of Disk Geometry Particle Dampers," *Journal of Sound and Vibration*, **280**(3-5), 849-861

Xu, Z.W., Chan, K.W., and Liao, W.H. (2004), "An Empirical Method for Particle Damping Design," *Shock and Vibration*, **11**(5-6), 647-664

Fang, X. and Tang, J. (2006), "Granular Damping in Forced Vibration: Qualitative and Quantitative Analyses," *Journal of Vibration and Acoustics – Transactions of the ASME*, **128**(4), 489-500

Wu, C.J., Liao, W.H., and Wang, M.Y. (2004), "Modeling of Granular Particle Damping Using Multiphase Flow Theory of Gas-Particle," *Journal of Vibration and Acoustics – Transactions of the ASME*, **126**(2), 196-201

Saeki, M. (2002), "Impact Damping with Granular Materials in a Horizontally Vibrating System," *Journal of Sound and Vibration*, **251**(1), 153-161

Saeki, M. (2005), "Analytical Study of Multi-Particle Damping," *Journal of Sound and Vibration*, **281**(3-5), 1133-1144

Mao, K.M., Wang, M.Y., Xu, Z.W., and Chen, T.N. (2004), "DEM Simulation of Particle Damping," *Powder Technology*, **142**(2-3), 154-165

Cundall, P.A. and Strack, O.D.L. (1979), "A Distinct Element Model for Granular Assemblies," *Geotechnique*, **29**, 47-65

Du, Y.C. and Wang, S.L. (2009), "Energy Dissipation in Normal Elastoplastic Impact Between Two Spheres," *Journal of Applied Mechanics*, **76**

Elperin, T. and Golshtein, E. (1997), "Comparison of Different Models for Tangential Forces Using the Particle Dynamics Method," *Physica A*, **242**(3-4), 332-340

Renzo, A.D. and Maio, F.P.D. (2004), "Comparison of Contact-Force Models for the Simulation of Collisions in DEM-Based Granular Flow Codes," *Chemical Engineering Science*, **59**(3), 525-541

Masri, S.F. (1973), "Steady-State Response of a Multidegree System with an Impact Damper," *Journal of Applied Mechanics – Transaction of the ASME*, **40**(1), 127-132

Lu, Zheng, Masri, S.F., and Lu, Xilin (2009), "Parametric Studies of the Performance of Particle Dampers under Harmonic Excitation," *Structural Control and Health Monitoring*, Doi: 10.1002/stc.359

Bapat, C.N. and Sankar, S. (1985), "Multiunit Impact Damper - Reexamined," *Journal of Sound and Vibration*, **103**(4), 457-469

JOINT CONFERENCE PROCEEDINGS
7th International Conference on Urban Earthquake Engineering (7CUEE) &
5th International Conference on Earthquake Engineering (5ICEE)
March 3-5, 2010, Tokyo Institute of Technology, Tokyo, Japan

A TRACKING SYSTEM TO MAXIMIZE THE EFFICIENCY OF TMD

Ali Bozer[1] and Gülay Altay[2]

1) Phd., Dept. of Civil Engineering, Bogazici University, Istanbul,Turkey
2) Professor., Dept. of Civil Engineering, Bogazici University, Istanbul,Turkey
bozerali@gmail.com, askarg@boun.edu.tr

Abstract: In this study a hybrid system is suggested in which a tracking type controller is used together with a passive undamped TMD unit. When a structure is excited with a single frequency disturbance, it is well known that TMD is most effective when it is tuned to input frequency and no damping is introduced. For earthquake loads the input has a broadband frequency range therefore some damping is introduced to TMD unit to smoothen the sharp peaks of the frequency response function out of the operating range however, in this case the effectiveness of TMD unit in the operating range is adversely affected. The proposed control strategy aims to alter the system response to coincide with the operating frequency of TMD unit. Then the response of the controlled structure matches the desired operating frequency of TMD unit no matter what the frequency content of the input is, hence a passive undamped TMD unit can be utilized in full effectiveness. This is further verified by numerical simulations on a simple 1 +1 DoF system under actual earthquake records and under white noise simplification.

1. INTRODUCTION

The conventional approach for earthquake resistant design is a strength-base one where the load-bearing components are designed to resist earthquake demands with sufficient strength and ability to absorb and dissipate seismic energy through a large number of hysteretic cycles. This has a direct effect of increased energy dissipation through inelastic deformations and it also has an indirect effect of structural softening so that the amount of input energy transmitted to the structure is decreased.

On the other hand, the challenge to find better means of new designs or strengthening existing ones leads to development of some innovative concepts. One of the innovative systems for structural protection is passive energy dissipation where input seismic energy is dissipated not only by the structure itself but also with some type of damping devices. Tuned mass damper (TMD) is one example of passive energy dissipation which is in the essence a mass-spring-dashpot system that is tuned to a particular vibration mode of the structure on which it is installed. The modern concept of tuned-mass dampers emerged from the early studies of Den Hartog (1956). He developed the basic principles and the procedure for proper selection of the absorber parameters when there is no damping in the main structure. McNamara (1977) extended the work of Den Hartog (1956) and investigated the effectiveness of TMD when there is damping in the main structure. Consequently in his extensive paper Warburton (1982) derived absorber parameters for undamped single-degree-of-freedom systems under harmonic and white noise random excitations as force and acceleration inputs. Some of the numerous researchers studied in obtaining optimal parameters of TMD can be cited as Xu and Igusa (1992), Yamaguchi and Harnpornchai (1993), Tsai and Lin (1994), Abe and Fujino (1994), Abe and Igusa (1995), Kareem and Kline (1995), Sadek et. al. (1997), Joshi and Jangid (1997), Li (2000), Park and Reed (2001), Li and Liu (2002), Li and Zhu (2006), Hoang et. al. (2008). It is a common agreement that tuned mass damper (TMD) is most effective when the TMD is tuned to input frequency, however in civil engineering it is not possible to know the input characteristics since building are subjected to environmental excitations which are random in nature such seismic loads. Thus, the best course of action taken is usually to tune the TMD to building's natural frequency since the worst case scenario will be a resonance case in which a dominant input frequency coincides with the building's natural frequency. However, operational range of such a system is band-limited i.e a narrow frequency range around the natural frequency and do not cover a broad band frequency range as in the case of seismic loads. A widely accepted remedy to this situation is to introduce some damping to TMD unit which will broaden the operational range by compromising effectiveness.

Alternatively, the efficiency of TMD can be improved by the addition of an active force to the mass damper as a substitute to inertia forces excerted by TMD unit. This addition of an active force enables achieving the same effectiveness of a large TMD with a small active TMD. Up to date active tuned mass dampers have been extensively

studied by many researchers such as Chang and Soong (1980), Abdel-Rohman and Leipholz (1983), Abdel-Rohman (1984,1987), Suhardjo et. al. (1992), Chang and Yang (1995), Ankireddi and Yang (1996), Mackriell at. al. (1997), Adhikari and Yamaguchi (1997), Nagashima (2001), Li (2004) , Collins et. al. (2006), Bani-Hani (2007), Guclu and Yazici (2008).

In this paper apart from introducing an active controller to TMD unit an alternative approach is proposed to utilize TMD in its full effectiveness. In the proposed approach main structure is equipped with an active controller and the response of the structure is altered to fall into operating range of undamped TMD. The suggested controller is a tracking type controller and forces the system to track a single frequency reference input which coincides with the operating frequency of TMD unit. Then the response of the controlled structure matches the desired operating frequency of TMD unit even if the structure is excited by a broadband input such as earthquake.

2. TUNED MASS DAMPER

By use of the reduced order method the MDOF structure is model as a SDOF structure. To gather with the TMD unit total degrees of freedom of the combined TMD/structure is two and the equation of motion of this system subjected to seismic forces can be written as follows:

$$m_s\ddot{y}_s + [c_s\dot{y}_s + c_1(\dot{y}_s - \dot{y}_1)] + [k_s y_s + k_1(y_s - y_1)] = -m_s\ddot{y}_g(t) \quad (1)$$

$$m_1\ddot{y}_1 + c_1(\dot{y}_1 - \dot{y}_s) + k_1(y_1 - y_s) = -m_1\ddot{y}_g(t) \quad (2)$$

where, subscript s donates for the main structure and subscript 1 donates for the TMD. $\ddot{y}_g(t)$ is the seismic acceleration; m, k, c are respectively the mass, stiffness, and damping coefficients; x_s is the displacement of the main structure with respect to the ground and x_1 represents the displacement of the TMD with respect to the ground. Let's define:

$$\mu = \frac{m_1}{m_s}; \lambda = \frac{\omega_1}{\omega_0}; \zeta_s = \frac{c_s}{2m_s\omega_0}; \zeta_1 = \frac{c_1}{2m_1\omega_1};$$
$$\omega_0 = \sqrt{k_s/m_s}; \omega_1 = \sqrt{k_1/m_1}$$

Transferring Equations (1) and (2) into frequency domain by Laplace transform which is defined as Z(s) = L[z(t)] and introducing the above parameters gives (Li and Zu 2006):

$$X_s s^2 + [2\omega_0\zeta_s X_s + 2\lambda\omega_0\zeta_1\mu(X_s - X_1)]s + [\omega_0^2 X_s + \mu\lambda^2\omega_0^2(X_s - X_1)] = -\ddot{X}_g \quad (3)$$

$$(\mu X_1)s^2 + [2\lambda\omega_0\zeta_1\mu(X_1 - X_s)]s + [\mu\lambda^2\omega_0^2(X_1 - X_s)] = -\mu\ddot{X}_g \quad (4)$$

Equations (3) and (4) can be written in matrix form as:

$$\begin{bmatrix} A(s) & B(s) \\ B(s) & G(s) \end{bmatrix}\begin{bmatrix} X_s \\ X_1 \end{bmatrix} = \begin{bmatrix} -1 \\ -\mu \end{bmatrix}\ddot{X}_g \quad (5)$$

In which:

$$A(s) = s^2 + (2\omega_0\zeta_s + 2\lambda\omega_0\zeta_1\mu)s + \omega_0^2 + \mu\lambda^2\omega_0^2$$
$$B(s) = (-2\lambda\omega_0\zeta_1\mu)s - \mu\lambda^2\omega_0^2$$
$$G(s) = \mu s^2 + (2\lambda\omega_0\zeta_1\mu)s + \mu\lambda^2\omega_0^2$$

Transfer Function of the main structure can be found by solving the Equation (5).

$$TF_s(s) = \frac{X_s}{\ddot{X}_g} = \frac{-G(s) + \mu B(s)}{A(s)G(s) - B(s)B(s)} \quad (6)$$

Once the Transfer Function is obtained Dynamic Amplification Factor can be calculated through setting s=iω in the Transfer Function and computing $\omega_0^2|TF_s(i\omega)|$. Then optimum values are calculated using the minimum-maximum amplitude procedure.

Let's consider a single-degree-of-freedom (SDOF) system with following structural parameters:

ks= 1.10^5 kN/m
cs= $3{,}16.10^3$ kN/s (%5 damping)
ms= 1.10^4 tons

The calculated optimum parameters of a TMD with a mass ratio μ=0.01 would be 0.973 for frequency ratio λ and %6.5 for damping ratio ζ. In Figure 1 bode magnitude plots of the plant, combined non-optimum TMD/plant and finally combined optimum TMD/plant systems are plotted for displacement response. As can be observed, the sharp peak of the plant at resonance frequency is smoothed by the attachment of the optimum TMD. The reduction in peak response is about %40 even though for a small mass ratio μ=0.01. On the other hand when we look at the non-optimized TMD/plant system the great reduction in response can be observed around tuning frequency, however there are now two resonance peaks since the combined system is a two-degree-of-freedom system. These two new resonance peaks are the sole reason why we have to resort to optimal TMD since we can not guarantee to have a disturbance which's driving frequency falls into the operating range, which is defined as the narrow zone between the two resonance peaks where non-optimal TMD is most effective.

It is well known that when a system is excited by a harmonic input, the steady state response is also harmonic with the same frequency of the input. That is to say output frequency of the system matches the input frequency of the system in steady sate, and since the TMD is tuned to the frequency of the structure it is also tuned to the input excitation where TMD is most effective. Consider that we might able to force the structure to mimic a steady state response to a single frequency harmonic excitation. Then what ever the actual frequency content of the excitation, the

shaped structure will response as if it is excited by a single frequency harmonic input. This can be achieved by a tracking type controller. In a tracking system, if a reference signal is chosen to be a harmonic function, than the response of the controlled system will try to track the reference command.

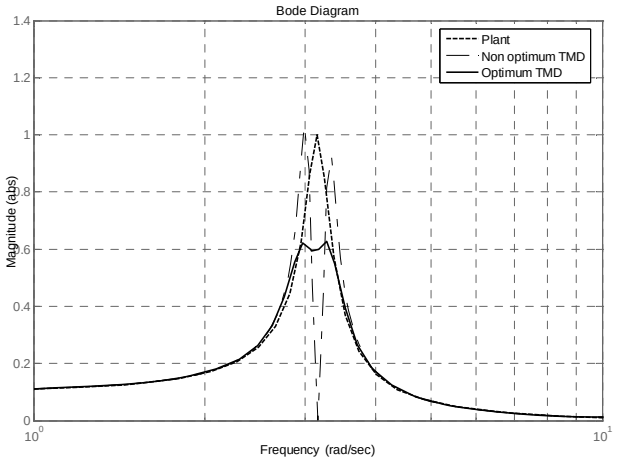

Figure 1. Bode magnitude plots of plant, non-optimal TMD and optimal TMD

3. H_∞ CONTROL AS A TRACKING PROBLEM

3.1 Analytic Formulation

By specifying/grouping signals into sets of external inputs, outputs, input to the controller and output from controller, a general feedback control system can be recast into a standard configuration as in Figure 3 in which all the external inputs such as process and measurement noise vectors are denoted by w(s) and output signals to be minimized/penalized are denoted by z(s), Y(s) is the vector of measurements available to the controller K(s) and U(s) is the vector of control signals. P(s) is called the generalized plant or interconnected system.

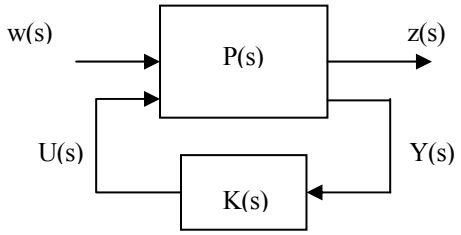

Figure 2. The standard H_∞ configuration

The plant's transfer matrix can be partitioned as:

$$P(s) = \begin{bmatrix} P_{11}(s) & P_{12}(s) \\ P_{21}(s) & P_{22}(s) \end{bmatrix} \quad (7)$$

Such that,

$$z(s) = P_{11}(s)w(s) + P_{12}(s)U(s) \quad (8)$$

$$Y(s) = P_{21}(s)w(s) + P_{22}(s)U(s) \quad (9)$$

Substituting the control law, U(s) = K(s)Y(s), into Equations (8) and (9), we can write the following relationship between the error and the external inputs vector:

$$z(s) = \left[P_{11}(s) + P_{12}(s)K(s)(I - P_{22}(s)K(s))^{-1}P_{21}(s)\right]w(s) \quad (10)$$

The transfer matrix multiplying w(s) on the right hand side of Equation (10) can be denoted as F(s). Then we can re-write Equation (10) as:

$$z(s) = F(s)w(s) \quad (11)$$

The H_∞ optimal control synthesis procedure consists of finding a stabilizing controller, K(s), such that the H_∞-norm of the closed loop transfer matrix, F(s), is minimized. Obtaining the H_∞-norm of a transfer matrix requires calculating the singular values of the transfer matrix with s=iω at a range of frequencies, and then obtaining the maximum of the largest singular value over the given frequency range. It is a well known fact that the requirements of robustness conflict with the requirements of optimal control and tracking performance. While robustness to process noise is obtained by minimizing the largest singular value of weighted sensitivity matrix, *S(s)*, optimal control requires minimizing the largest singular value of *K(s)S(s)*, and good tracking performance to a changing desired output requires maximizing the smallest singular value of the complementary sensitivity matrix, *T(s)=I-S(s)*. However, high-frequency measurement noise rejection requires minimizing the largest singular value of *T(s)* at high frequencies. Such conflicts can be resolved by choosing different frequency ranges for maximizing and minimizing different singular values. The different frequency ranges for the various optimizations can be specified as three frequency weighting matrices, $W_1(i\omega)$, $W_2(i\omega)$,and $W_3(i\omega)$ such that H_∞-norm of the mixed sensitivity matrix, $\|M(i\omega)\|_\infty$ is minimized where [49]

$$M(i\omega) = \begin{bmatrix} W_1(i\omega)S(i\omega) \\ W_2(i\omega)K(i\omega)S(i\omega) \\ W_3(i\omega)T(i\omega) \end{bmatrix} \quad (12)$$

Generally there are no analytic formulae for the solution of the mixed sensitivity optimization problem. In practical design, it is usually sufficient to find a stabilizing controller K(s) such that the H_∞-norm of the mixed sensitivity matrix, $\|M(i\omega)\|_\infty$ is less than a given positive number,

$$\|M(i\omega)\|_\infty < \gamma \quad (13)$$

where $\gamma > \gamma_0 := \min K_{stabilizing} \|M(i\omega)\|_\infty$. This is called the H_∞

suboptimal problem. An optimal solution is reached by iteratively reducing γ.

3.2 Numerical Illustration

Let's consider the single-degree-of-freedom (SDOF) structure in chapter 2. This structure is equipped with an undamped TMD unit which is tuned to the natural frequency of the SDOF system, so the combined SDOF sytem/TMD unit is a 2DOF system. The structural parameters for the SDOF plant and the undamped TMD unit are given as: $k_s=1.10^5$ kN/m,$c_s=3,16.10^3$ kN/s (%5 damping) ,$m_s=1.10^4$ tons; k_{TMD}= 1000 kN/m (λ=1.00),m_{TMD}= 100 tons (μ=0.01),c_{TMD}= 0 N/s (%0 damping)

The frequency of the plant is calculated as 3.16 rad/sec. When the plant is equipped with TMD the frequencies of the combined 2-DOF system are 3.03 rad/sec and 3.30 rad/sec. The TMD is tuned to the frequency of the plant, thus operating frequency is also 3.16 rad/sec. The control goal is to track sinusoidal signal with frequency 3.16 rad/sec and amplitude of 0.1m which is the static deflection of the plant to a unit step disturbance. Then the response of the controlled structure will match the desired operating frequency of TMD unit no matter what the frequency content of the input is.

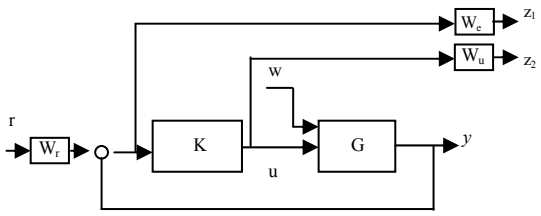

Figure 3. Reference Tracking Configuration in H_∞ setting

As can be followed from Figure 3, in the tracking problem the main difference from a standard regulator problem is that we have a non-zero reference command. Thus the error, *e,* and control force, *u,* are weighted with weighting functions W_e and W_u respectively. The transfer function W_r is used to describe the frequency content of the reference signal and can be described in laplace domain as:

$$W_r(s) = \frac{3.16}{s^2 + 0.2s + 3.16^2} \tag{14}$$

By introducing a weight W_r in to the generalized plant we mathematically say to the optimization algorithm that our reference command is a signal at 3.16 rad/sec frequency. So, the general control configuration shown in Figure 2 can be constructed by setting:

$$P_{11} = \begin{bmatrix} 0 & (W_r - G)W_e \\ 0 & 0 \end{bmatrix} P_{12} = \begin{bmatrix} 0 \\ W_u \end{bmatrix} P_{21} = \begin{bmatrix} 0 & I \\ G & 0 \end{bmatrix} P_{22} = \begin{bmatrix} 0 \\ G \end{bmatrix} \tag{15}$$

In Figure 4 controlled system response to a sinusoidal reference signal is shown. In this case external disturbance is a white noise disturbance with a power of 0 dBW, and main structure is able to track the reference signal successfully. Thus, it can be concluded that with a tracking system we are able to alter the response so that what ever the actual frequency content of the excitation, the shaped structure will response as if it is excited by a single frequency harmonic input.

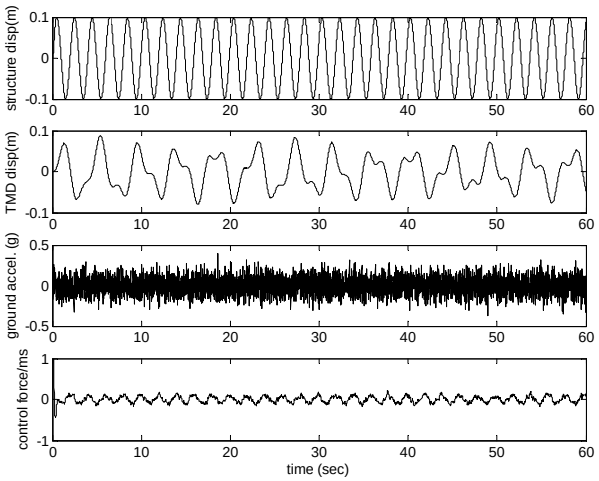

Figure 4. H_∞ tracking performance when the control system is excited with a white noise excitation

Figure 4 reveals that we are able to shape response into desired frequency content; on the other hand it might not be a sound idea to track a constant amplitude reference signal. Because in this case if the response level is lower than the preset constant level than the controller will work against the system to maintain the displacement response at constant. The problem could have been solved if we could be able to track only the frequency of a reference signal but not its amplitude, unfortunately in literature tracking systems are defined to track the trajectory of a reference signal. Thus error functions are defined in time domain and frequency domain error definitions are not present. However, some how if we can manage to render the reference command in harmony with the closed-loop system output in terms of amplitude than it is possible to alleviate the problem. An acceptable solution will be to track a reference model instead of a reference signal. This is called model matching problem and controller tries to match the states of the plant with the states of an idealized mathematical model. If we chose a simple oscillator as a reference model and set the natural frequency of the reference model as the operating frequency of the TMD, under same disturbance the response levels of the actual system and idealized mathematical system will be more or less the same. Thus by tracking the response of an idealized model two aspects are accomplished. First, frequency of the reference signal is the desired frequency which is the operating frequency of the TMD and second, the amplitude of the reference signal is more or less in harmony with the closed-loop response.

4. H_∞ CONTROL AS A MODEL MATCHING PROBLEM

4.1 Analytic Formulation

As can be observed from Figure 5 that model matching problem is very similar to reference signal tracking. The only difference is instead of a reference command signal, we now have reference model output as a reference signal. In this case the reference signal should be in harmony with the plant output since they are both excited with the same external disturbance.

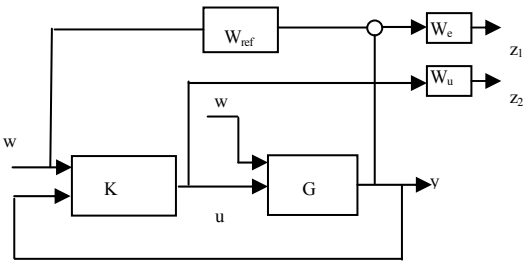

Figure 5. Model Matching Configuration in H_∞ setting

The error, *e,* and control force, *u,* are again weighted with weighting functions W_e and W_u respectively. The selected reference model is an oscillator with natural frequency 3.16 rad/sec which is the operating frequency of TMD. If we introduce %5 damping to reference model, the state equations become:

$$\begin{bmatrix} \dot{r}_1 \\ \dot{r}_2 \end{bmatrix} = \begin{bmatrix} 0 & 1 \\ -9.986 & -0.3 \end{bmatrix} \begin{bmatrix} r_1 \\ r_2 \end{bmatrix} \tag{16}$$

$$\tilde{y} = \begin{bmatrix} 1 & 0 \end{bmatrix} \tag{17}$$

The plant's transfer matrix can be partitioned as follows:

$$\begin{bmatrix} z \\ y \end{bmatrix} = P \begin{bmatrix} w \\ u \end{bmatrix} = \begin{bmatrix} P_{11} & P_{12} \\ P_{21} & P_{22} \end{bmatrix} \begin{bmatrix} w \\ u \end{bmatrix} \tag{18}$$

where we may set

$$P_{11} = \begin{bmatrix} W_{ref} W_e - G W_e \\ 0 \end{bmatrix} P_{12} = \begin{bmatrix} 0 \\ W_u \end{bmatrix} P_{21} = \begin{bmatrix} I \\ G \end{bmatrix} P_{22} = \begin{bmatrix} O \\ G \end{bmatrix} \tag{19}$$

4.2 Numerical Simulations

To verify the effectiveness of the proposed control scheme, a single-degree-of-freedom (SDOF) system is considered as a benchmark case. In the first run, SDOF system namely plant is equipped with standard H_∞ regulator. Then to investigate the effect of TMD unit on control performance a combined plant/optimal TMD structure is equipped with standard H_∞ regulator. In this 2DOF system TMD unit is equipped with a damper and optimal parameters are decided with minimum-maximum amplitude procedure explained in Section 2. In the third run TMD unit is not equipped with a damper, so its operating range is limited and not optimized to cover large bandwidth inputs such as earthquake. This combined plant/non-optimal TMD structure is again equipped with H_∞ regulator. The final run is the proposed hybrid system where combined plant/non-optimal TMD structure controlled with H_∞ tracking controller. In this control strategy system response is altered to coincide with the operating frequency of TMD unit. Then the response of the controlled structure matches the desired operating frequency of TMD unit no matter what the frequency content of the input is, hence a passive undamped TMD unit can be utilized in full effectiveness. The structural parameters for the SDOF plant and the both optimal and non optimal TMD unit are given as:

SDOF Plant: $k_s = 1.10^5$ kN/m, $c_s = 3{,}16.10^3$ kN/s (%5 damping), $m_s = 1.10^4$ tons
Non-optimal TMD unit: $k_{TMD} = 1000$ kN/m (λ=1.00), $m_{TMD} = 100$ tons (μ=0.01), $c_{TMD} = 0$ N/s (%0 damping)
Optimal TMD unit: $k_{TMD} = 960.4$ kN/m (λ=0.98), $m_{TMD} = 100$ tons (μ=0.01), $c_{TMD} = 43386$ N/s (%7 damping)

To effectiveness of the proposed strategy is assessed through statistical analyses in two parts. In the first part the compared systems are excited with 200 artificially generated white noise inputs. Then the mean values and standard deviations corresponding to each control system is noted and compared to each other. In the second part statistical analyses are rerun with actual seismic records to evaluate the effectiveness in real cases.

Table 1 Mean and standard deviation of closed loop response

(Closed Loop Displacement Energy)$^{1/2}$

	SDOF	Optimum TMD	Non-optimum TMD	H_∞ Model Match
μ	0,4467	0,4306	0,4443	0,4312
σ	0,0327	0,0306	0,0326	0,0286

(Normalized Control Energy)$^{1/2}$

	SDOF	Optimum TMD	Non-optimum TMD	H_∞ Model Match
μ	16,1894	16,2464	16,2298	15,4935
σ	0,5136	0,519	0,5177	0,5335

Closed Loop Displacement (m)

	SDOF	Optimum TMD	Non-optimum TMD	H_∞ Model Match
μ	0,0177	0,0171	0,0176	0,0174
σ	0,0022	0,0021	0,0022	0,002

Control Force / m_s

	SDOF	Optimum TMD	Non-optimum TMD	H_∞ Model Match
μ	0,7675	0,7708	0,7701	0,7315
σ	0,0665	0,0664	0,0664	0,0631

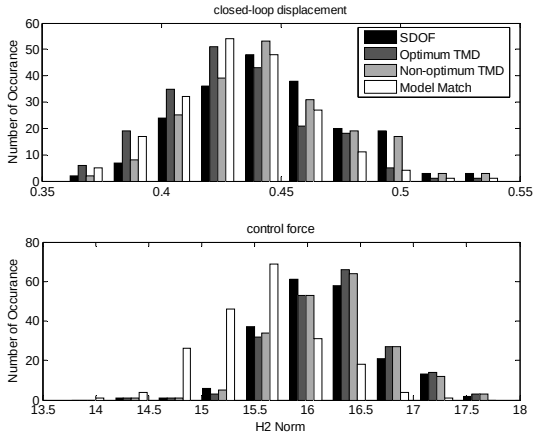

Figure 6. H_2 norm of closed-loop disp. and control forces

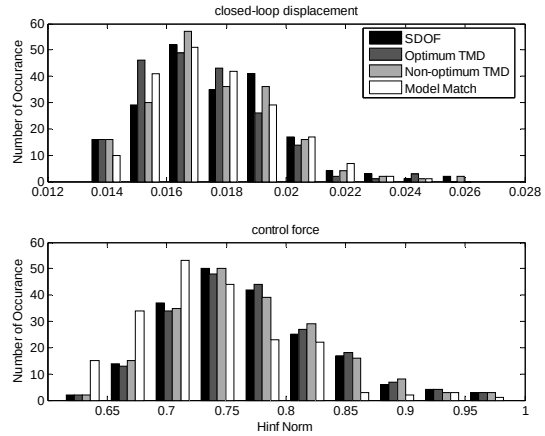

Figure 7. H_∞ norm of closed-loop disp. and control forces

Table 2 Seismic records used in the statistical study

Earthquake	Magnitude	Station Name	Station No	Comp.	Peak Acceleration (g)
Imperial Valley 1979	6.6	Calexico Fire Station	1	H315	0,171
			2	H225	0,275
			3	H315	0,187
		Brawley Airport	4	H225	0,160
San Fernando 1971	6.6	Santa Felicia Dam	5	H172	0,148
			6	H262	0,152
		Whittier Narrows Dam	7	H143	0,081
			8	H233	0,107
San Fransisco 1957	5.3		9	H010	0,093
		Golden Gate	10	H100	0,112
Kocaeli 1999	7.4		11	H000	0,150
		Arçelik	12	H090	0,108
			13	H000	0,076
		Botaş	14	H090	0,076
			15	H000	0,074
		Bursa Tofaş	16	H090	0,095
Whittier Narrows 1987	5.9		17	H270	0,374
		Obregon Park	18	H360	0,234
			19	H000	0,158
		MT Wilson	20	H090	0,142

Table 3 (Closed loop displacement energy)$^{1/2}$ of seismic records

Station No	SDOF H∞	TMDopt H∞	TMD H∞	Model Match H∞
1	0,304	0,305	0,304	0,333
2	0,279	0,278	0,278	0,302
3	0,400	0,392	0,398	0,428
4	0,498	0,459	0,494	0,467
5	0,213	0,204	0,212	0,212
6	0,145	0,137	0,144	0,146
7	0,162	0,154	0,161	0,157
8	0,187	0,176	0,185	0,184
9	0,016	0,016	0,015	0,017
10	0,024	0,025	0,024	0,027
11	0,181	0,173	0,180	0,172
12	0,454	0,432	0,452	0,412
13	0,147	0,144	0,146	0,158
14	0,164	0,159	0,163	0,164
15	0,431	0,414	0,429	0,443
16	0,455	0,455	0,455	0,506
17	0,062	0,063	0,062	0,069
18	0,135	0,139	0,135	0,158
19	0,019	0,019	0,019	0,020
20	0,015	0,015	0,015	0,016
μ	0,215	0,208	0,214	0,220
σ	0,160	0,154	0,160	0,162

Table 4 (Normalized control energy)$^{1/2}$ of seismic records

Station No	SDOF H∞	TMDopt H∞	TMD H∞	Model Match H∞
1	14,92	14,90	14,93	14,20
2	17,74	17,72	17,76	16,71
3	14,75	14,78	14,78	14,42
4	12,17	12,39	12,23	11,97
5	7,86	7,89	7,86	7,66
6	6,11	6,14	6,13	5,92
7	6,01	6,03	6,02	5,70
8	7,13	7,16	7,15	6,82
9	2,04	2,04	2,04	1,85
10	2,62	2,62	2,63	2,39
11	7,66	7,68	7,68	7,26
12	9,10	9,24	9,14	8,92
13	6,52	6,52	6,53	6,33
14	6,48	6,49	6,49	6,28
15	15,61	15,66	15,63	15,34
16	19,40	19,39	19,41	19,20
17	8,11	8,11	8,14	7,35
18	10,45	10,43	10,46	9,87
19	2,69	2,69	2,70	2,42
20	2,55	2,54	2,56	2,27
μ	9,00	9,02	9,01	8,64
σ	5,21	5,22	5,22	5,12

Table 5 Max. closed loop displacement of seismic records

Station No	SDOF H∞	TMDopt H∞	TMD H∞	Model Match H∞
1	0,0121	0,0133	0,0122	0,0156
2	0,0125	0,0123	0,0125	0,0130
3	0,0328	0,0327	0,0327	0,0344
4	0,0263	0,0241	0,0257	0,0258
5	0,0069	0,0069	0,0069	0,0077
6	0,0053	0,0051	0,0052	0,0052
7	0,0075	0,0072	0,0075	0,0074
8	0,0059	0,0065	0,0059	0,0065
9	0,0020	0,0020	0,0020	0,0021
10	0,0028	0,0029	0,0028	0,0031
11	0,0092	0,0087	0,0091	0,0079
12	0,0239	0,0228	0,0238	0,0220
13	0,0076	0,0074	0,0075	0,0083
14	0,0088	0,0081	0,0087	0,0088
15	0,0147	0,0148	0,0150	0,0176
16	0,0187	0,0190	0,0187	0,0215
17	0,0068	0,0068	0,0068	0,0073
18	0,0170	0,0170	0,0169	0,0183
19	0,0021	0,0021	0,0021	0,0021
20	0,0018	0,0018	0,0018	0,0019
μ	0,0112	0,0111	0,0112	0,0118
σ	0,0087	0,0084	0,0086	0,0090

Table 6 Max. normalized control force of seismic records

Station No	SDOF H∞	TMDopt H∞	TMD H∞	Model Match H∞
1	1,174	1,173	1,176	1,100
2	1,319	1,319	1,323	1,195
3	1,141	1,154	1,143	1,163
4	0,822	0,816	0,821	0,798
5	0,413	0,411	0,413	0,381
6	0,451	0,451	0,452	0,416
7	0,386	0,384	0,387	0,336
8	0,438	0,439	0,438	0,419
9	0,273	0,273	0,274	0,246
10	0,328	0,328	0,328	0,306
11	0,662	0,663	0,666	0,578
12	0,607	0,611	0,610	0,581
13	0,468	0,469	0,468	0,451
14	0,472	0,466	0,471	0,448
15	0,663	0,657	0,665	0,639
16	0,728	0,723	0,728	0,699
17	1,242	1,242	1,246	1,123
18	1,278	1,284	1,280	1,228
19	0,492	0,492	0,494	0,440
20	0,370	0,369	0,371	0,331
μ	0,69	0,69	0,69	0,64
σ	0,35	0,35	0,35	0,34

Table 1. suggests that the addition of TMD in both optimal and non-optimal configuration has a marginal effect on control energy and max. control forces when used with standard H∞ regulator. On the other hand best answer is obtained with the proposed strategy both in control energy and max. control forces. The improvement is %4.3 in the former case and %4.7 in the latter case.

Under the excitation of actual seismic records, it is seen that proposed controller give the best answer. Appropriate weights are selected in order to equate the displacement energy and max. displacement among the various controllers, thus closed-loop performance is more or less the same as can be observed from Tables 3 and 5. Then the deciding factor is the control energy. Tables 4 and 6 suggest that the improvement in terms of control energy is %4 and %7.2 respectively with the proposed controller when the mean values are considered.

It is also observed that the effectiveness of the proposed strategy depends on the nature of the input force. The proposed controllers render the closed-loop response to fall into operating frequency of the TMD unit. The operating frequency is the resonance frequency of the TMD unit thus effectiveness is gradually increasing with time and closely linked to the TMD displacement. However, for pulse like inputs as in the case of earthquakes the maximum input acceleration comes so early that TMD unit couldn't find time to operate effectively. On the other hand it is seen that for stations 4,7,11 and 12 the displacement energy and max. displacement is smaller in proposed controllers. Close inspection reveals that the seismic input in station 7 is more uniform in amplitude and the pulses in seismic inputs corresponding to stations 11 and 12 appear later in the record.

5. CONCLUSIONS

The concluding remarks of this paper can be summarized as follows:

1. When a structure is excited with a single frequency disturbance, it is well known that TMD is most effective when it is tuned to input frequency and no damping is introduced. However, for earthquake loads the input has a broadband frequency range and the driving frequency is not known a priori. Therefore some damping is introduced to TMD unit to smoothen the sharp peaks of the frequency response function out of the operating range but in this case the effectiveness of TMD unit in the operating range is adversely affected.
2. In the proposed strategy controller is formulated to track a reference model in order to match the states of the plant with the states of an idealized mathematical model which is selected as a simple oscillator with natural frequency set to the operating frequency of the TMD unit. Thus by tracking the response of an idealized model two aspects are accomplished. Firstly, frequency of the reference signal is the desired

frequency, which is the operating frequency of the TMD unit. Secondly, the amplitude of the reference signal is maintained to be more or less in harmony with the closed-loop response.

3. To verify the effectiveness of the proposed control scheme, the performances of standard regulator controllers are compared with the proposed controllers in terms of closed-loop displacement and required control force. Compared closed-loop systems include a SDOF plant controlled H_∞ regulator, a combined plant/optimal TMD structure controlled with H_∞ regulator, a combined plant/non-optimal TMD structure controlled with H_∞ regulators, and proposed hybrid system of combined plant/non-optimal TMD structure controlled with H_∞ tracking controller. In the first run effectiveness of the proposed strategy is assessed through statistical analyses in which the compared systems are excited with 200 artificially generated white noise inputs. In the second run statistical analyses are repeated with actual seismic records to evaluate the effectiveness in real cases.
4. The time domain response of the compared systems reveal that the proposed closed-loop systems need less control effort for the same closed-loop performance in terms of plant displacement. When compared to standard regulators the improvement is %4.3 in control energy requirement, and %4.7 in maximum control force. With actual seismic records the improvement is %4 in control energy requirement, and %7.2 in maximum control force.
5. It is also observed that the effectiveness of the proposed strategy depends on the nature of the input force. For more uniform inputs or pulses appear later in the record, it is observed that proposed strategy performs better.

References:

J.P. Den Hartog (1956), Mechanical Vibrations, 4th ed., McGraw-Hill, New York.

McNamara, R. J. (1977), "Tuned Mass Damper for Buildings" *Journal of the Structural Division*, ASCE, **103**(9) ,1785-1797.

Warburton G. B. (1982), "Optimum absorber parameters for various combination of response and excitation parameters", *Earthquake Engineering and Structural Dynamics,* **10**, 381-401.

Xu K and Igusa T. (1992), "Dynamic characteristics of multiple substructures with closely spaced frequencies", *Earthquake Engineering and Structural Dynamics*, **21**, 1059-1070.

Yamaguchi H and Harnpornchai N. (1993), "Fundamental characteristics of multiple tuned mass dampers for suppressing harmonically forced oscillations", *Earthquake Engineering and Structural Dynamics*, **22**, 51-62.

Tsai H.C. and Lin G. C. (1994), "Explicit formulae for optimum absorber parameters for force excited and viscously damped systems", *Journal of Sound and Vibration*, **176**(5), 585-596.

Abe M and Fujino Y. (1994), "Dynamic characteristics of multiple tuned mass dampers and some design formulas", *Earthquake Engineering and Structural Dynamics*, **23**,813-835.

Abe M. and Igusa T., (1995) "Tuned mass dampers for structures with closely spaced natural frequencies", *Earthquake Engineering and Structural Dynamics*, **24**, 247-261.

Kareem A and Kline S. (1995), "Performance of multiple mass dampers under random loading", *Journal of Structural Engineering*, **121**(2), 348-361.

Sadek F., Mohraz B., Taylor A.W. and Chung R.M. (1997), "A Method of Estimating the Parameters of Tuned Mass Dampers for Seismic Applications", *Earthquake Engineering and Structural Dynamics*, **26**, 617-635.

Joshi A.S. and Jangid R.S. (1997), "Optimum Parameters of Multiple Tuned Mass Dampers for Base-Excited Damped Systems" *Journal of Sound and Vibration*, **202**(5), 657-667.

Li C (2000), "Performance of multiple tuned mass dampers for attenuating undesirable oscillations of structures under the ground acceleration", *Earthquake Engineering and Structural Dynamics*, **29**, 1405-1421.

Park J. and Reed D. (2001), "Analysis of uniformly and linearly distributed mass dampers under harmonic and earthquake excitation", *Engineering Structures*, **23**, 802-814.

Li C and Liu Y. (2002), "Further Characteristics for Multiple Tuned Mass Dampers", *Journal of Structural Engineering*, **128**(10), 1362-1365

Li C. and Zhu B. (2006), "Estimating double tuned mass dampers for structures under ground acceleration using a novel optimum criterion", *Journal of Sound and Vibration,***298**, 280-297.

Hoang N., Fujino Y. and Warnitchai P. (2008), "Optimal tuned mass damper for seismic applications and practical design formulas", *Engineering Structures*, **30**, 707-715.

Chang J. C. H and Soong T. T. (1980), "Structural Control Using Active Tuned Mass Dampers", *Journal of the Engineering Mechanics Division*, ASCE, **106**(6), 1091-1098.

Abdel-Rohman M. and Leipholz H. H. (1983), "Active Control of Tall Buildings", *Journal of Structural Engineering*, ASCE, **109**(3) ,628-645.

M. Abdel-Rohman (1984), "Optimal Design of Active TMD for Building Control", *Building and Environment*,**19**(3),191-195.

M. Abdel-Rohman (1987), "Feasibility of Active Control of Tall Buildings against Wind", *Journal of Structural Engineering*, ASCE, **113**(2), 349-362.

Suhardjo J., Spencer Jr. B. F. and Kareem A. (1992), "Frequency Domain Optimal Control of Wind-Excited Buildings", *Journal of Engineering Mechanics*, ASCE, **118**(12), 2463-2481.

Chang C. C. and Yang H. T. Y. (1995), "Control of Buildings Using Active Tuned Mass Dampers", *Journal of Engineering Mechanics,* ASCE, **121**(3), 355-366.

Ankireddi S. and Yang H.T.Y. (1996), "Simple ATMD Control Methodology for Tall Buildings Subject to Wind Loads", *Journal of Structural Engineering*, ASCE, **122**(1), 83-91.

Mackriell L. E., Kwok K. C. S. and Samali B. (1997), "Critical Mode Control of a Wind Loaded Tall Building Using an Active Tuned Mass Damper", *Engineering Structures*.**19**(10), 834-842.

Adhikari R. and Yamaguchi H. (1997), "Sliding Mode Control of Buildings with ATMD", *Earthquake Engineering and Structural Dynamics*, **26**, 409-422.

Nagashima I. (2001), "Optimal Displacement Feedback Control Law for Active Tuned Mass Damper", *Earthquake Engineering and Structural Dynamics*, **30**, 1221-1242.

Cao H, and Li Q. S. (2004), "New Control Strategies for Active Tuned Mass Damper Systems", *Computers and Structures*, **82**, 2341-2350.

Collins R., Basu B. and Broderick B. (2006), "Control Strategy Using Bang-Bang and Minimax Principle for FRF with ATMDs", *Engineering Structures*, **28**, 349-356.

Bani-Hani K. A. (2007), "Vibration Control of Wind-Induced Response of Tall Buildings with an Active Tuned Mass Damper Using Neural Networks", *Structural Control and Health Monitoring*, **14**, 83-108,.

Guclu R. and Yazici H. (2008), "Vibration Control of a Structure with ATMD Against Earthquake Using Fuzzy Logic Controllers", *Journal of Sound and Vibration*, **318**, 36-49.

JOINT CONFERENCE PROCEEDINGS
7th International Conference on Urban Earthquake Engineering (7CUEE) &
5th International Conference on Earthquake Engineering (5ICEE)
March 3-5, 2010, Tokyo Institute of Technology, Tokyo, Japan

PRACTICAL NONLINEAR RESPONSE ANALYSIS METHOD OF VISCOELASTIC DAMPER CONSIDERING TEMPERATURE, FREQUENCY, AND STRAIN DEPENDENCIES

Naohiro Nakamura[1], Takuya Suzuki[2], Kazuhiko kasai[3] and Yoji Ooki[4]

1) Chief Researcher, R&D Institute, Takenaka Corporation, Japan
2) Researcher, R&D Institute, Takenaka Corporation, Japan
3) Professor, Structural Engineering Research Center, Tokyo Institute of Technology, Japan
4) Assistant Prof., Structural Engineering Research Center, Tokyo Institute of Technology, Japan
nakamura.naohiro@takenaka.co.jp, suzuki.takuya@takenaka.co.jp, kasai@serc.titech.ac.jp, yoji_ooki@mbe.mhi.co.jp

Abstract: Recently, various kinds of viscoelastic dampers are used for the vibration control of buildings. Some materials have complex properties concerning temperature, frequency, and strain dependency. Although many constitutive models of them have been proposed, most of the models treated these dependencies independently. Models that can consider these dependencies accurately are very limited, because it is very difficult to develop these accurate models since high mathematical knowledge and heavy studies are essential. In this paper, a simple and practical method to calculate the constitutive model considering these dependencies for the nonlinear time history response analysis was proposed, using the interpolation method of experimental data and the transform method of frequency dependent data into the time domain. The efficiency of the method was confirmed by the comparison with both the experiment results and more accurate model results.

1. INTRODUCTION

Various types of viscoelastic dampers are being used as means of vibration control of buildings. Some of them exhibit complex properties in terms of the temperature, frequency and amplitude dependencies. Traditional design evaluations have used simple models in which temperature, frequency and other conditions are limited (e.g. Soda et al.(1998), Asano et al.(2000)). Many of such models treat the frequency and amplitude dependencies separately.

On the other hand, the recent expansion of the range of application of viscoelastic dampers has resulted in the need for more accurate models that can take into account the effects of these complex dependencies. However, previous studies on such models are very few and limited to those conducted by Kasai et al. (2001), (2002), (2003), (2004) and Ooki et al. (2007), which proposed highly accurate constitutive models capable of fractional derivative-based time history analyses for acrylic and isobutylene materials and demonstrated their effectiveness through comparisons with results of experiments.

Such high-accuracy models are clearly useful in that they (1) make it possible to make various detailed evaluations through nonlinear time history response analyses (hereinafter referred to as nonlinear response analyses) instead of experiments and (2) make it possible to perform analyses in the frequency domain and develop various theories by representing various dependencies with a small number of parameters. However, formulating such constitutive models requires substantial knowledge of chemical properties of materials and advanced mathematical knowledge and skills, as well as numerous numerical evaluations and analyses.

Therefore, if a new material with complex temperature, frequency and amplitude dependencies were presented at this moment in time, it would be very difficult to make earthquake response and wind response evaluations through nonlinear response analyses taking into consideration such dependencies. For this reason, a versatile method is being sought that can be used widely for nonlinear response analyses of new materials.

This paper proposes a new method that allows, when experiment data on a new material with such dependencies is provided, nonlinear response analyses to be made through numerical data processing only without requiring material-by-material formulation. Although this method is not superior to traditional methods in terms of analyses in the frequency domain, it can be said that it is a highly practical nonlinear response analysis method because it is versatile, highly accurate and relatively easy to use.

Chapter 2 of this paper provides an overview of the proposed analysis method. Nakamura (2006a), (2006b), (2008a) proposed transfer methods of frequency dependent complex stiffness data into the time domain. Nakamura (2008b) also presented a nonlinear response analysis method for dynamic stiffness data with frequency and strain dependencies, whereby dynamic stiffness data are represented in the frequency domain as strain level-specific

impedance function values. The values are transformed into time domain values and strain level-specific impulse response function values are obtained. By switching among the obtained values based on the current strain level, nonlinear response analyses that reflect both frequency and strain dependencies can be performed. In this paper, the method is expanded and applied to a material with temperature, frequency and amplitude dependencies.

In Chapter 3, the acrylic material adopted for the evaluations in this study, which is identical to the ones evaluated in the studies reported in Kasai et al. (2001), (2002), (2004) is explained. Next, evaluations to select the data interpolation methods and the time domain transform method, which are important elements of the proposed method, are made. Then, simulation analyses that correspond to sinusoidal wave response experiments and random wave response experiments are conducted with the strain amplitude varied.

The adequacy and effectiveness of the proposed method are verified by means of a comparative analysis with the results of analyses performed using a high-accuracy constitutive model that is based on the fractional derivatives presented in Kasai et al. (2001), (2002), (2004).

2. OVERVIEW OF THE PROPOSED ANALYSIS METHOD

Fig.1 shows a flowchart of the proposed analysis method. An overview of the proposed analysis method follows.

2.1 *Arrangement and Interpolation of the Experiment Data*

Assuming that storage stiffness (G') data and loss factor (η) data for the material for different temperature, frequency and maximum strain levels has already been obtained from experiments, the complex stiffness $G(\omega)$ values are calculated from the G' and η data using the equation $G(\omega) = G'(\omega)(1+\eta(\omega)\,i)$ and plotted on the frequency axis, to obtain the frequency-dependent dynamic stiffness values (hereinafter referred to as the "complex stiffness" values) that correspond to specific temperature and maximum strain conditions. At this stage, the complex stiffness values are distributed sparsely and unevenly along the frequency axis. To achieve appropriate time domain transforms, it is desirable for the complex stiffness values to be distributed relatively densely and evenly along the frequency axis. Therefore, an appropriate interpolation method is selected and the data is interpolated along the frequency axis.

Because it is usually the case that the temperature and strain level data too are given as discrete data, the complex stiffness values can be arranged in a matrix fashion with each row associated with a temperature value and each column with a strain level value (Fig.2). This matrix will hereinafter be referred to as the "complex stiffness table."

It is considered that, in a response analysis, the temperature and strain level change continuously. This means that the temperature and strain level data must be interpolated as well.

2.2 Transforms into Time Domain Values

A time domain transform of each of the complex stiffness values in the complex stiffness table arranged in the previous step (See Section 2.1) is made, to obtain the corresponding impulse response value. Because it is considered that the complex stiffness values have significant damping and exhibit strong non-causality (e.g. Makris et al. (2000)), the transform method that is classified as Method C in Nakamura (2006b) is used. Upon completion of the transforms of all complex stiffness values, this time domain transform step will produce an impulse response table of the same format as the complex stiffness table shown in Fig.2.

2.3 Time History Response Analysis

In the nonlinear response analysis step, interpolations between values contained in the impulse response table are made based on the temperature and strain level values for the current time to calculate the corresponding impulse response values, and then the reaction forces are calculated.

The past maximum strain value and the temperature value for the current time rarely coincide with a point in the table (an experiment data value), and in most cases, they fall between points. Therefore, interpolations are made between the values of 4 adjacent points to obtain the exact impulse response value (See Fig.2).

3 PROPERTIES OF THE MATERIAL USED FOR EVALUATIONS IN THIS STUDY (AN ACRYLIC MATERIAL)

In this study, the applicability of the proposed method is evaluated using an actual material, that is, an acrylic material that is identical to the ones evaluated in the studies reported in Kasai et al. (2001), (2002), (2004). This chapter provides a summary of the dynamic properties of the material and explains the high-accuracy constitutive model used in this study (hereinafter referred to as the high -accuracy model), which is a model based on the fractional derivatives presented in these papers.

3.1 Summary of the Dynamic Properties of the Material

Table 1 shows the values of the properties of the acrylic material used for evaluations in this study. These are values obtained from a set of experiments. The stress-strain relationship in an acrylic material follows an elliptical pattern, with the inclination angle and area of the ellipse increasing as the temperature becomes lower or as the frequency increases. In other words, the shape of the ellipse is determined by the temperature and frequency. At lower strain amplitudes, the shape of the ellipse is invariable and the size of the ellipse is proportional to the amplitude (linear behavior). At larger strain amplitudes, the ellipse exhibits nonlinear behavior and the inclination of the ellipse

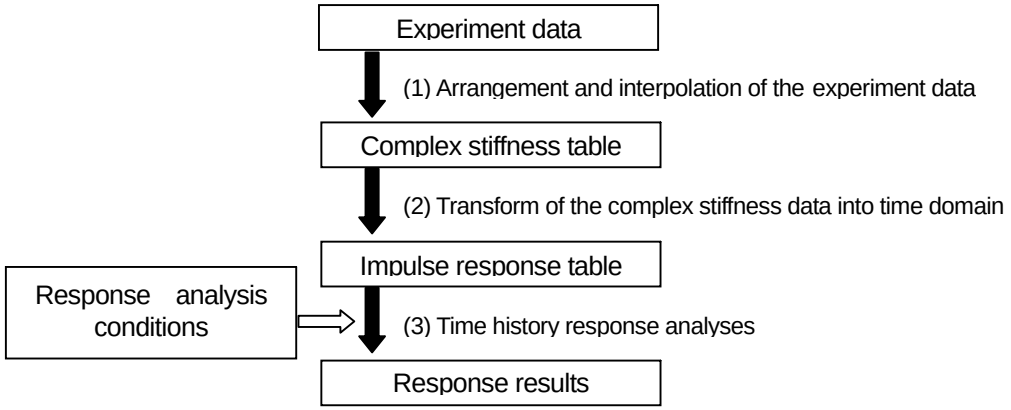

Figure 1 Flowchart of the Proposed Analysis Method

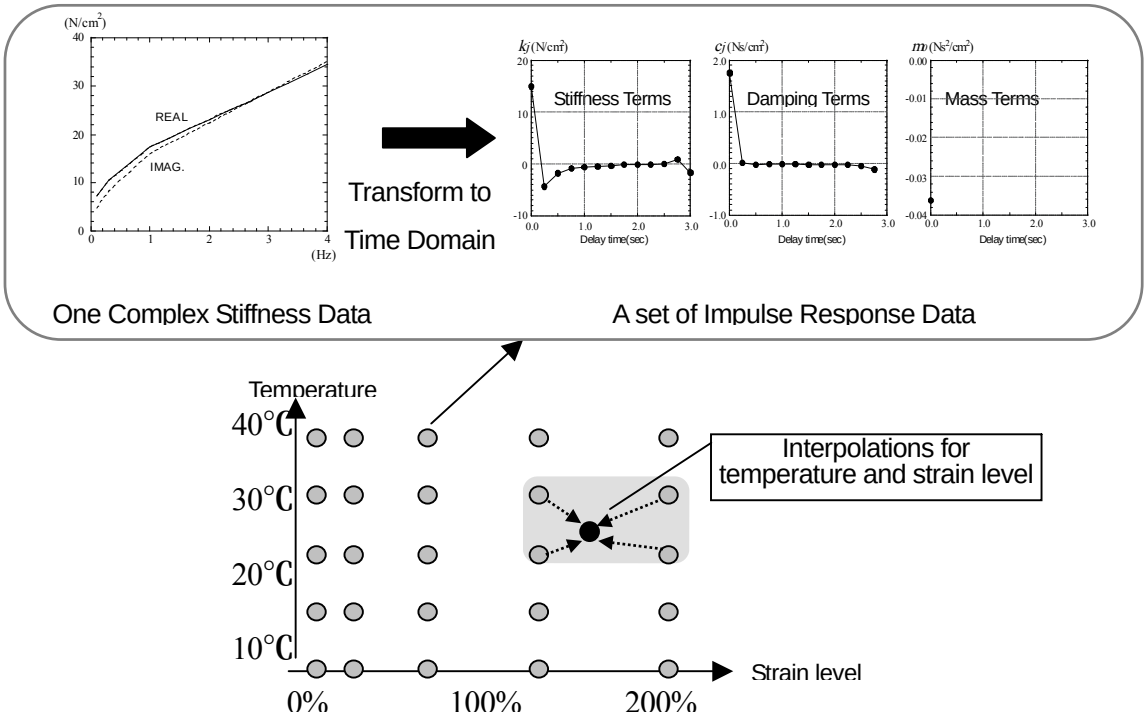

Figure 2 Complex Stiffness and Impulse Response Data Arranged in a Matrix Fashion and a Conception of Interpolations

decreases as the strain increases.

With regard to temperature, the property changes according to the value at the current time. With regard to strain, it is assumed that the property changes according to the past maximum value, because it is known that the property will not change once the maximum value is reached.

In the sinusoidal wave excitation experiment, the stress increases significantly in the first half wave. It is considered that this is due to a hardening phenomenon caused by the sudden application of a high strain rate immediately after the start of the loading.

3.2 Detailed Constitutive Laws that Take into Consideration the Dependencies (High-accuracy Model)

The storage stiffness $G'(\omega)$ and loss factor $\eta(\omega)$ of the material are expressed by Equations (1) and (2). The dependency on the past maximum strain γ_{max} is expressed by Equations (3) and (4). The inequality signs of Equation (4) indicate that the dependency of the material on strain is defined by $\gamma_{max} \geq 100\%$ and is invariable when $100\% \geq \gamma_{max} \geq 0\%$.

With regard to the parameters, the following values were obtained: $a_{ref} = 5.60 \times 10^{-5}$; $b_{ref} = 2.10$; $G_{ref} = 3.92 \mathrm{N/cm^2}$; $\alpha = 0.558$; $C_1 = 0.124$; $C_2 = -0.182$. The temperature dependency of the material is represented by the λ in Equation (5). θ_{ref} represents the reference temperature of the material ($= 20^\circ C$). The p_1 and p_2 values are 14.06 and 97.32, respectively.

$$G'(\omega) = G\frac{1+ab\omega^{2\alpha}+(a+b)\omega^{\alpha}\cos(\alpha\pi/2)}{1+a^2\omega^{2\alpha}+2a\omega^{\alpha}\cos(\alpha\pi/2)} \quad (1)$$

$$\eta(\omega) = \frac{(-a+b)\omega^{\alpha}\sin(\alpha\pi/2)}{1+ab\omega^{2\alpha}+(a+b)\omega^{\alpha}\cos(\alpha\pi/2)} \quad (2)$$

$$a = a_{ref}\lambda^{\alpha}, \quad b = b_{ref}\lambda^{\alpha}\lambda_1, \quad G = G_{ref}\lambda_2 \quad (3)$$

$$\lambda_1 = 1+C_1(\gamma_{\max}-1) \geq 1, \quad \lambda_2 = 1+C_2(\gamma_{\max}-1) \leq 1 \quad (4)$$

$$\lambda = \exp[-p_1(\theta-\theta_{ref})/(p_2+\theta-\theta_{ref})] \quad (5)$$

To represent the stress increase that often observed in initial half cycle of sinusoidal loading, a nonlinear spring model for high strain rates is added in parallel with the above-mentioned spring. Equation (6) expresses the stiffness of the nonlinear spring G_h, and Equation (7) expresses the hardening reduction coefficient β. γ_0 represents the absolute strain that occurs at the start of the half wave of interest (i.e. at the moment of the reversal of the sign of the strain rate). The C_3 and C_4 values are 0.278 (Nsec/mm^2) and -0.549, respectively.

$$G_h = \beta \cdot C_3 \min[\lambda\dot{\gamma}_{\max}, 100] \quad (6)$$

$$\beta = \exp[C_4(\gamma_0 - 0.5)] \leq 1 \quad (7)$$

The increase in the temperature of the material due to the absorption of energy by the material is expressed by Equation (8). θ and θ_0 represent the current temperature and initial temperature, respectively. s_ρ is the product of specific gravity and specific heat, and the value is 187 (N/(cm^2°C)) for this material.

$$\theta = \theta_0 + \int \tau \, d\gamma / s_\rho \quad (8)$$

4. TIME DOMAIN CONVERSION

The transform conditions are as shown in Table 2. Interpolated data points were added between the data point for 0.1Hz and that for 3Hz so that the data points are almost evenly spaced. In addition, the values for 3.333, 3.666 and 4.0Hz are added by means of extrapolation, in order to ensure that the transform results are accurate up to 3Hz.

As an example, this section outlines the transform made for the case for the temperature of 20°C and the strain of 200% after linear interpolations along the frequency axis had been made. Fig.3 shows the complex stiffness data points for the transform, and Fig.4 shows the obtained impulse response values. In the graph for the stiffness terms k_j (Fig.4(a)) and the graph for the damping terms c_j (Fig.4(b)), the value for "Delay time = 0" constitutes the simultaneous component (k_0 and c_0) and the other values constitute the time delay component. The graph for the mass term (Fig.4 (c)) has the simultaneous component (m_0) only. The transform results showed that the time delay component was substantial with regard to the stiffness terms but was negligible with regard to the damping terms.

In both the graph for k_j and the graph for c_j, there are deviations of the last terms and terms close to them (the points in the gray circles) as mentioned above. By excluding the deviated terms and the terms whose values were too small to affect the results, the numbers of time delay component data points to be used in the nonlinear response analyses could be reduced to 5 (n' = 5). The results of past studies show that the use of about 5 data points suffices in ordinary cases, and the use of about 10 data points suffice even in the complicated cases when the complex stiffness values are fluctuated sharply.

To verify the adequacy of the transform, the complex stiffness values are reconstructed from the impulse response

Table 1 Values of the Properties of the Material from Experiment

	Max. Strain	10%				50%				100%				200%				300%			
	Freq.	0.1 Hz	0.3 Hz	1 Hz	3 Hz	0.1 Hz	0.3 Hz	1 Hz	3 Hz	0.1 Hz	0.3 Hz	1 Hz	3 Hz	0.1 Hz	0.3 Hz	1 Hz	3 Hz	0.1 Hz	0.3 Hz	1 Hz	3 Hz
Storage Stiffness G' (N/cm^2)	0°C	35.2	60.3	113	213	34.2	57.8	104	173	32.9	54.1	90.1	116	29.6	43.3	-	-	-	-	-	-
	10°C	15.2	23.6	41.0	71.8	14.8	23.0	39.5	69.5	14.2	22.4	39.8	66.6	13.4	21.4	37.5	60.3	12.8	19.5	-	-
	20°C	8.50	11.9	18.6	30.1	8.33	11.8	18.8	31.0	8.02	11.5	18.4	29.8	7.21	10.5	17.4	28.7	6.82	10.2	17.2	28.7
	30°C	6.06	7.73	11.0	16.3	5.86	7.54	10.8	16.3	5.54	7.21	10.4	15.7	4.83	6.31	9.54	15.4	4.19	5.71	8.94	14.4
	40°C	5.02	6.03	7.86	10.7	4.82	5.82	7.55	10.4	4.45	5.42	7.17	9.97	3.68	4.67	6.41	9.24	3.17	3.95	5.72	8.48
Loss Factor η	0°C	1.07	1.21	1.26	1.23	1.14	1.27	1.36	1.41	1.09	1.20	1.32	1.60	1.04	1.14	-	-	-	-	-	-
	10°C	0.80	0.97	1.12	1.23	0.87	1.02	1.18	1.29	0.88	1.03	1.17	1.28	0.85	0.97	1.05	1.15	0.79	0.91	-	-
	20°C	0.57	0.73	0.91	1.05	0.61	0.79	0.97	1.11	0.62	0.80	0.96	1.11	0.66	0.79	0.92	1.00	0.64	0.77	0.87	0.93
	30°C	0.42	0.55	0.71	0.87	0.43	0.57	0.75	0.91	0.44	0.59	0.76	0.93	0.49	0.63	0.76	0.91	0.47	0.64	0.76	0.86
	40°C	0.32	0.40	0.53	0.68	0.35	0.43	0.56	0.71	0.36	0.44	0.57	0.73	0.39	0.48	0.58	0.75	0.41	0.51	0.62	0.74

Table 2 Transform Conditions

Complex Stiffness		Impulse Response		
Number of data points *N*	Frequencies for which there are data points (Hz)	Δt (sec)	Simultaneous component	Time delay component data points used in time history response analyses
13	0.1, 0.3, 0.65, 1.0, 1.333, 1.666, 2.0, 2.333, · ·3.666, 4.0	0.25	k_0, c_0, m_0	$k_1 \sim k_5$, $c_1 \sim c_5$ (n'= 5)

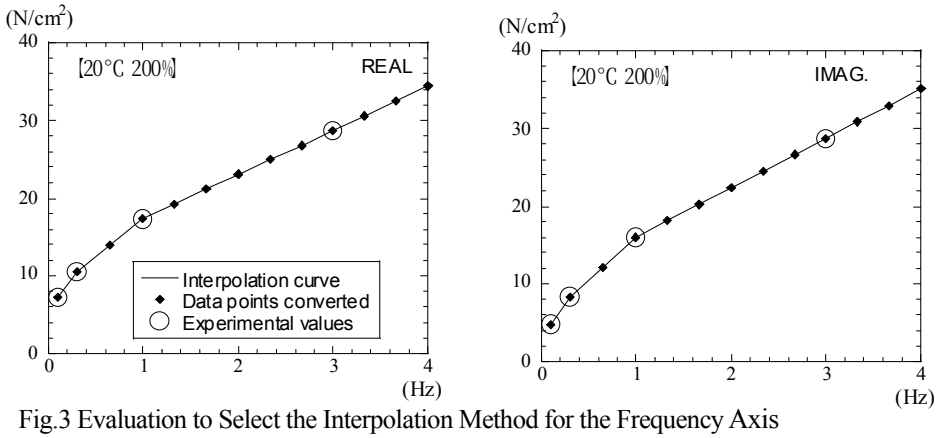

Figure 3 Fig.3 Evaluation to Select the Interpolation Method for the Frequency Axis
(a) Temperature = 0 °C , strain = 100%, and (b) Temperature = 40 °C , strain = 300%

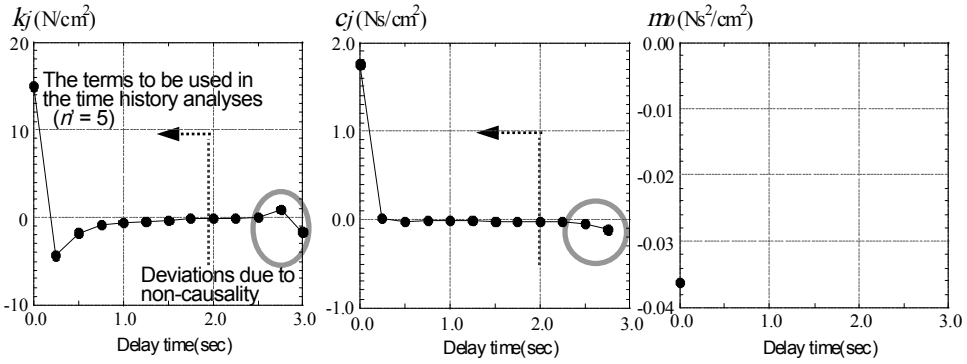

Figure 4 Evaluation to Select the Interpolation Method for the Temperature Axis
(a) Strain = 100%, frequency = 3Hz, and (b) Strain = 200%, frequency = 0.1Hz

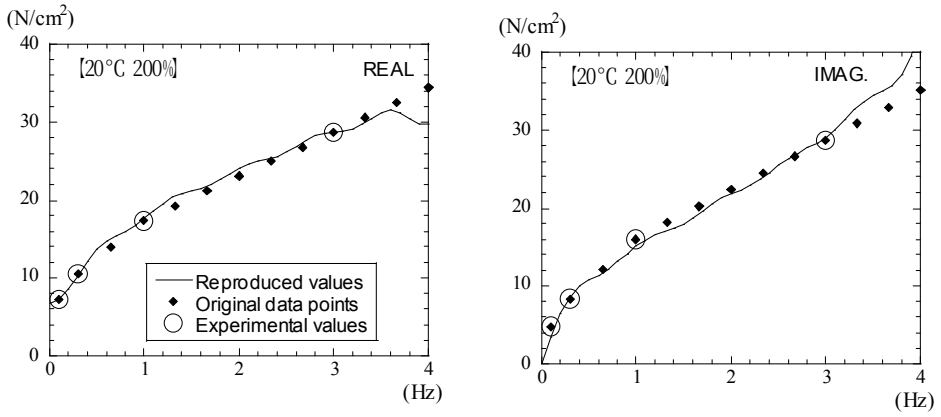

Figure 5 Evaluation to Select the Interpolation Method for the Strain Axis
(a) Temperature = 40 °C , frequency = 3Hz, and (b) Temperature = 10 °C , frequency = 0.1Hz

values obtained. Fig.5 shows the relationship between the reconstructed complex stiffness values and the data points used for the transform. It can be seen from the figure that there is good correspondence between them, which means that the time domain transform results are adequate.

4. VERIFICATIONS OF TIME HISTORY ANALYSIS RESULTS THROUGH COMPARISONS WITH EXPERIMENT RESULTS

4.1 Responses to Sinusoidal Waves

Analyses of sinusoidal wave excitation experiments were made using the proposed model and the high-accuracy model. Fig.6 shows the results of the analyses made using the high-accuracy model and the proposed model of an experiment for the strain amplitude of 200%. The results obtained with the high-accuracy model corresponded well with the experiment results at all frequencies and temperatures as described in Kasai et al. (2002), (2004). The results obtained with the proposed model also corresponded well with the experiment results, with the overall level of correspondence roughly matching that achieved by the high-accuracy model. However, detailed comparison with the experiment results revealed the following differences:

1) The proposed model's history loop for the frequency of 0.1Hz was a little smaller compared with the experiment value. Because a function obtained from a time domain transform must be causal, the imaginary part must be 0 at 0Hz. Therefore, the reconstructed value for the imaginary part shown in Fig.5(b) becomes a little smaller than the experiment value at 0.1Hz. It is considered that this is the reason for the smaller loop area at 0.1Hz.
2) In the 3.0Hz case, there is a little difference in the shape of the first 1/2 loop. This is attributable to deviations that occurred in the proposed model as a result of sudden occurrence of a high speed at the start of the vibrations. This is also attributable to an impulsive input that has many high-frequency components, although the accuracy of the model is only up to 3Hz. This point will be discussed again in Section 4.3.
3) In the low-temperature (0 to 10$^\circ C$) cases, the first 1/2 loop is very bulgy in the experiment results but not so in the results obtained with the proposed model except for the case described in 2). The high-accuracy model increases the accuracy to solve this problem by adding a nonlinear spring defined by Equation (6). However, the proposed model does not do this because it aims to set the properties from Table 1 only. It is considered that this is the reason for the difference. This effect will be discussed again in the section about random wave inputs (Section 4.2) and the section about impulsive wave inputs (Section 4.3).

4.2 Responses to Random Waves

The deformation of the first floor damper of each of a 3-story structure, a 12-story structure and a 24-story structure that would be caused by a strong earthquake motion was calculated by means of time history analysis. The deformations were used as inputs for the experiment and analysis. TAFT (1952, EW) was used as the input earthquake motion. For each of the 3 structures, evaluations for 3 strain levels (the maximum strains of 50%, 150% and 300%) were made. The natural frequencies of the structures were set at 2.86, 0.76 and 0.35Hz, respectively, and the initial temperature was set at 20$^\circ C$.

Fig.7 compares the experiment results with the analysis results. In the 300% case for the 3-story structure, both the results obtained with the high-accuracy model and the results obtained with the proposed model are slightly different from the experiment results with regard to the loop immediately after the start of the loading. However, it can be said that the overall levels of correspondence with the experiment results achieved by the high-accuracy model and the proposed model are very good.

The rightmost columns of Fig.7(a) and Fig.7(b) show the amounts of absorbed energy calculated from the areas of the loops. The results obtained with the proposed model are slightly different from the experiment results in the case with the strain level of 300% for the 3-story structure. However, overall, they correspond well with the experiment results.

On the basis of the above evaluations, it can be said that the proposed model is capable of achieving an overall level of correspondence with experiment results that is roughly equivalent to that achievable with high-accuracy models. In addition, it can be said that the effects of the differences in the first 1/2 loop mentioned in 4.1 2) and 3) are relatively small. Therefore, it can be concluded that the accuracy of the proposed model regarding nonlinear response analyses is sufficiently high for practical purposes.

4.3 Responses to Impulsive Waves

Evaluations were made based on Kasai et al. (2002), (2004) to verify the accuracies of the high-accuracy model and the proposed model regarding inputs containing impulsive waves caused by collisions between buildings. The frequency component of each building before collision is 0.5Hz, but the buildings are subjected to 30Hz impulsive waves upon collision.

Fig.8 shows the shear strain-shear stress relationships obtained with the high-accuracy model and the proposed model together with the relationships obtained from experiments. Evaluations for 2 strain levels (the maximum strain levels of 50% and 300%) were made.

The results obtained with the high-accuracy model correspond well with the experiment results, but the results obtained with the proposed model differ from the experiment results with regard to the shape of the protrusion that appears upon collision. This is attributable to the fact that the accuracy of the proposed model has only been confirmed up to 3Hz.

Therefore, we created new complex stiffness data points up to 10Hz by making extrapolations along the frequency axis, and made time domain transforms of the newly created data points. In making these extrapolations, G and η values for the maximum strain of 10% and the

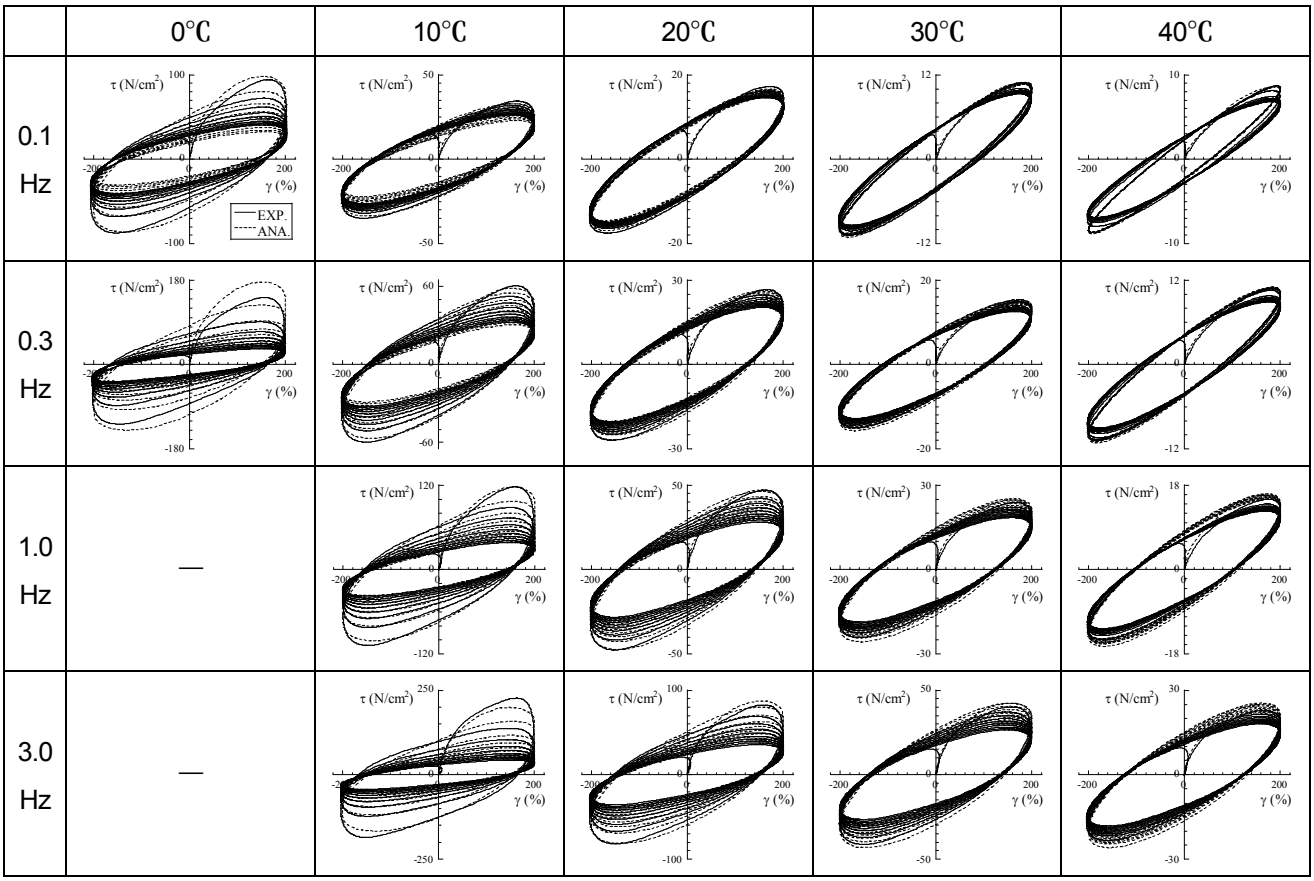

(a)

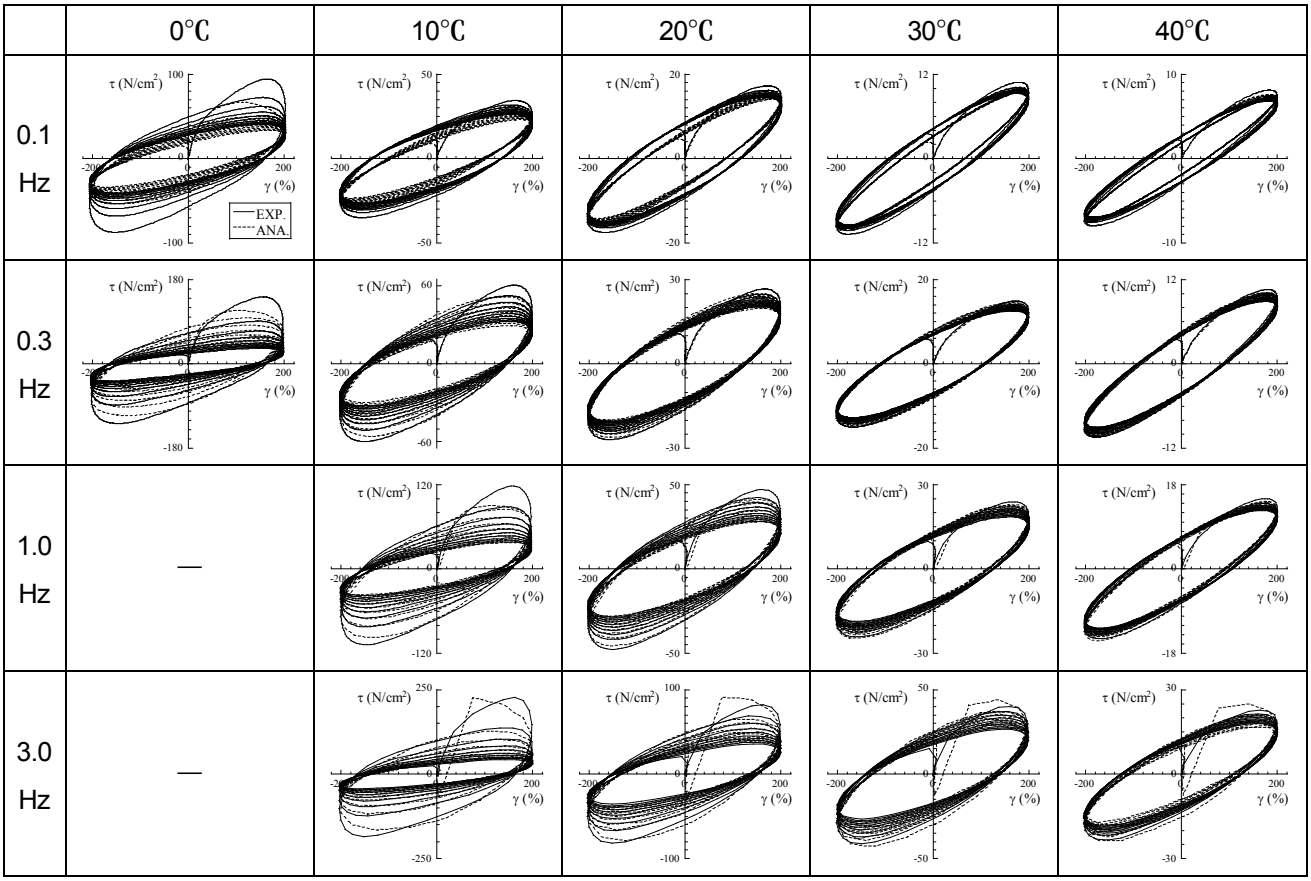

(b)

Figure.6 Evaluations of Responses to Sinusoidal Wave Inputs (maximum shear strain: 200%)
(a) High-accuracy Model, and (b) Proposed Model

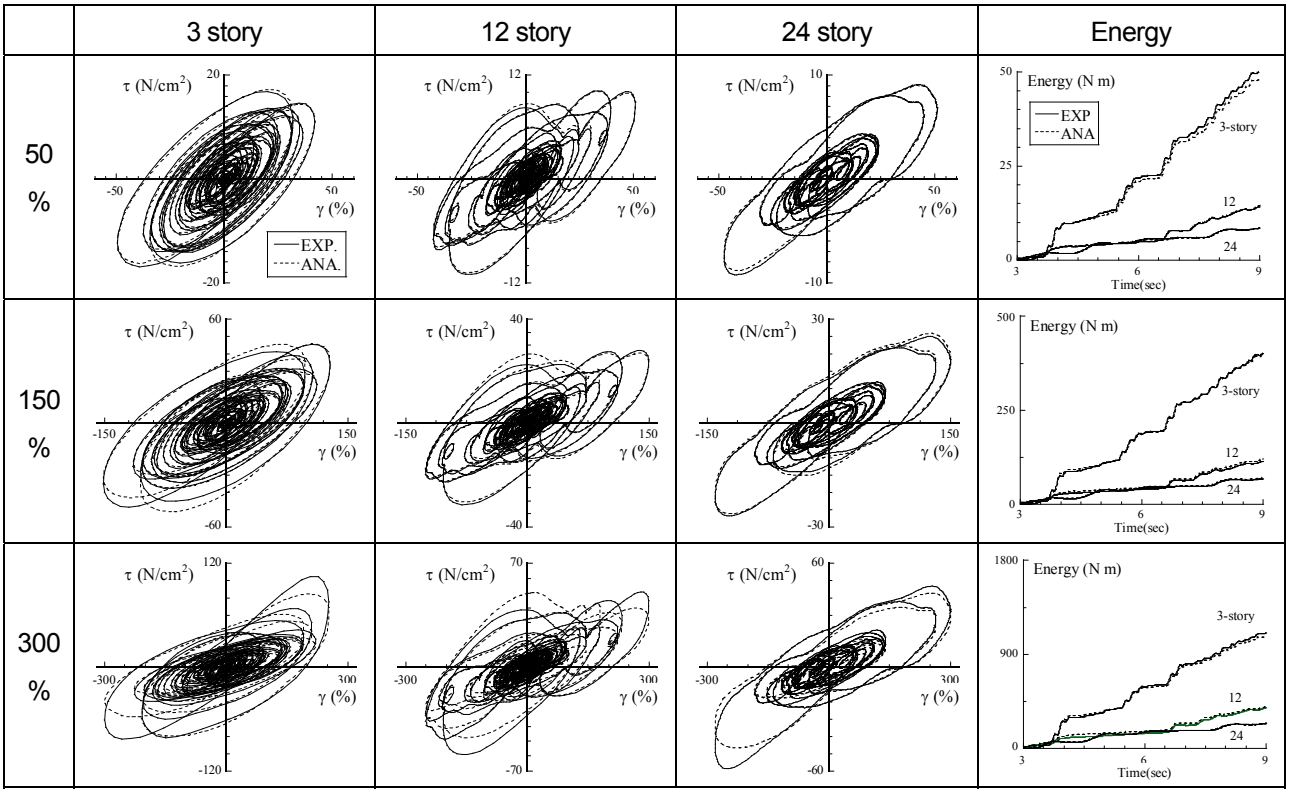

(a)

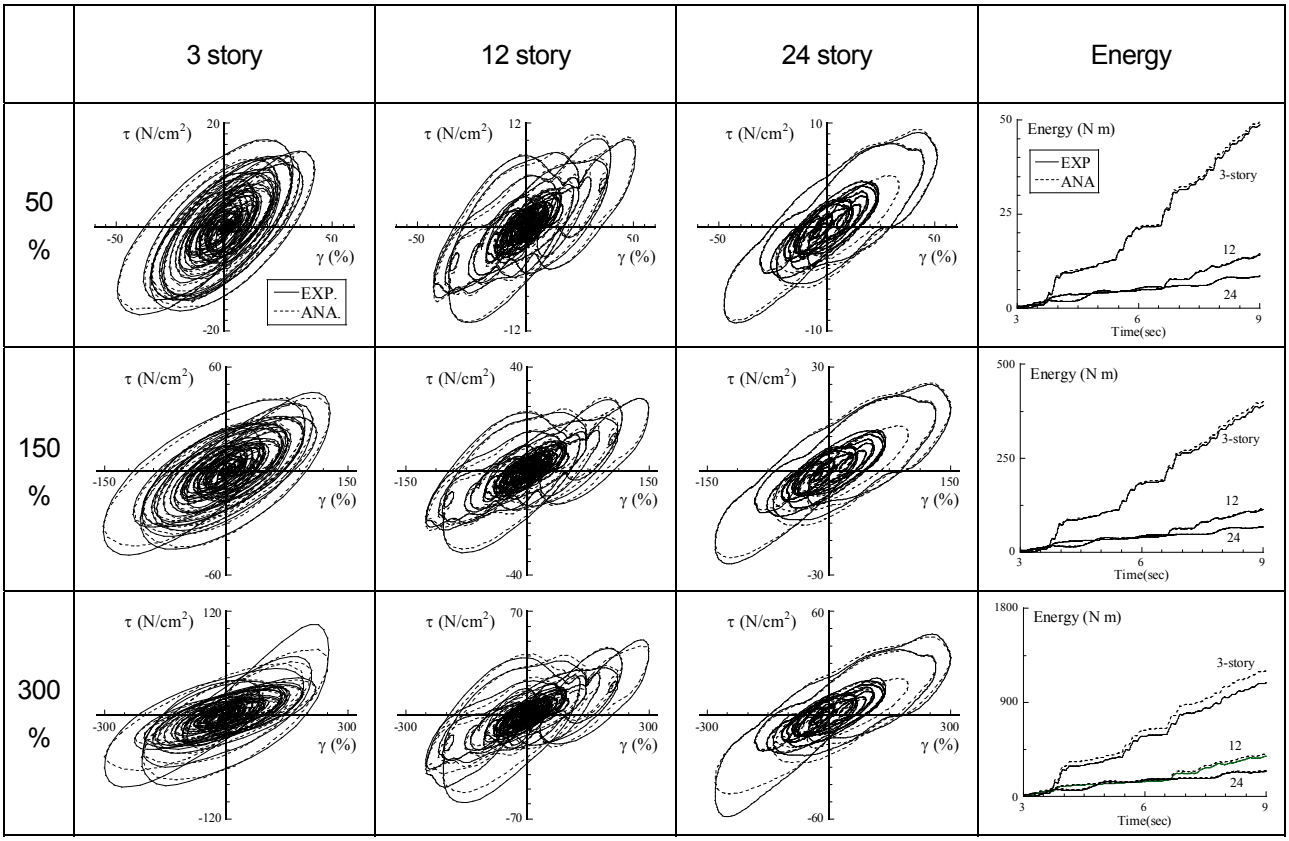

(b)

Figure 7 Evaluations of Responses to Random Wave Inputs (TAFT wave)
(a) High-accuracy Model , and (b) Proposed Model

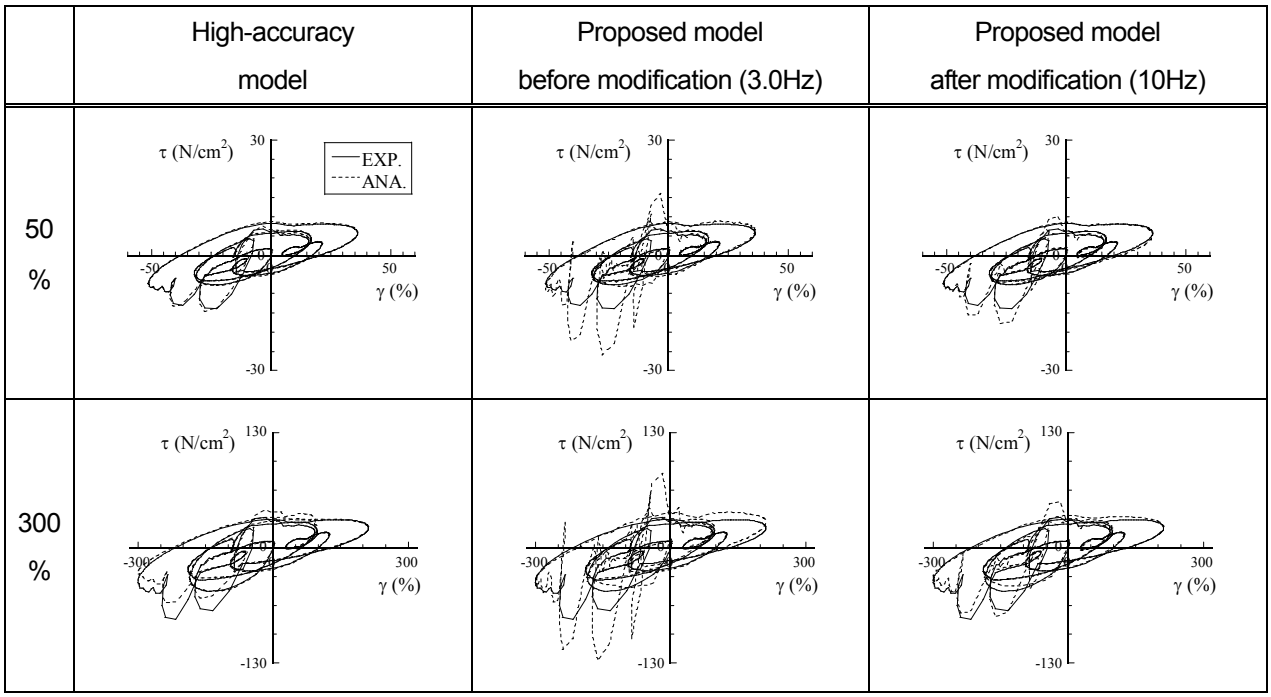

Figure 8 Evaluations of Responses to Impulsive Inputs

Table 3 Transform Conditions

Complex Stiffness		Impulse Response		
Number of data points N	Frequencies for which there are data points (Hz)	Δt (sec)	Simultaneous component	Time delay component data points used in time history response analyses
31	0.1, 0.3, 0.65, 1.0, 1.333, 1.666, 2.0, 2.333, · ·9.666, 10.0	0.10	k_0, c_0, m_0	$k_1 \sim k_5$, $c_1 \sim c_5$ (n'= 5)

frequency of 10Hz presented in Kasai et al. (2001), (2004) were used as reference. The transform conditions are as shown in Table 3. We then performed response analyses using the impulse responses obtained. As a result of these steps, the accuracy was improved and acceptable results were obtained.

5. CONCLUSIONS

This paper proposed a simple and practical nonlinear response analysis method for viscoelastic dampers that takes into consideration the temperature, frequency and amplitude dependencies. Analyses of sinusoidal and random wave response experiments were made, and it was confirmed that the level of accuracy of the proposed model was roughly equivalent to that achievable with high-accuracy models. On the basis of this finding, it can be said that the proposed model is an effective model that provides a sufficient level of accuracy to qualify as a practical nonlinear response analysis method.

In addition, this method has potential for use in a wide range of other applications than evaluations of viscoelastic dampers.

Acknowledgment:

The authors would like to express their gratitude to Mr. Ken Tokoro and Mr. Kiyoshi Ohkuma, Sumitomo 3M Limited., who kindly provided the authors with the experiment data for this study.

References:

Soda, S. and Takahashi, Y. (1998), "Random Loading Method to Quantify Frequency- and Temperature-dependent Properties of Visco-elastic Dampers", Proc. of the 2nd World Conference on Structural Control, Kyoto, Japan, Vol.1, 199-206

Asano, M., Higashino, M. and Yamamoto, M. (2000), "The Experimental Study on Viscoelastic material Dampers and the Formulation of Analytical model", Proc. of 12th World

Conference of Earthquake Engineering, paper Number 1535
Kasai, K., Ooki, Y., Tokoro, K., Amemiya, K. and Kimura, K. (2004), "JSSI Manual for Building Passive Control Technology; Part-11 Time-History Analysis Model for Viscoelastic Dampers", CD-ROM, 13th World Conference on Earthquake Engineering, Vancouver, B.C., Canada
Kasai, K., Teramoto, M., Okuma, K. and Tokoro, K. (2001), "Constitutive Rule for Viscoelastic Materials Considering Temperature, Frequency, and Strain Sensitivities: Part 1 Linear model with temperature and frequency sensitivities", Journal of structural and construction engineering. Transactions of AIJ, 543, 77-86, (In Japanese)
Kasai, K. and Tokoro, K. (2002), "Constitutive Rule for Viscoelastic Materials Considering Temperature, Frequency, and Strain Sensitivities: Part 2 Nonlinear model based on temperature-rise, strain and strain-rate", Journal of structural and construction engineering. Transactions of AIJ, 561, 55-63, (In Japanese)
Kasai, K., Ooki, Y., Amemiya, K. and Kimura K. (2003), "Constitutive Rule for Viscoelastic Materials Combining Iso-butylene and Stylene Polymes: Part 1 Linear model considering temperature and frequency sensitivities", Journal of structural and construction engineering. Transactions of AIJ, 569, 47-54, (In Japanese)
Ooki, Y., Kasai, K., Amemiya, K. and Kimura K. (2007), "Constitutive Rule for Viscoelastic Materials Combining Iso-butylene and Stylene Polymers: Part2 Non-linear model considering temperature, frequency, and strain sensitivities", Journal of structural and construction engineering. Transactions of AIJ, 617, 77-85, (In Japanese)
Nakamura, N. (2006a), "A Practical Method to Transform Frequency Dependent Impedance to Time Domain", Earthquake Engineering and Structural Dynamics, 35, 217-231
Nakamura, N. (2006b), "Improved Methods to Transform Frequency Dependent Complex Stiffness to Time Domain", Earthquake Engineering and Structural Dynamics, 35, 1037-1050
Nakamura, N. (2008a), "Transform Methods for Frequency Dependent Complex Stiffness to Time Domain Using Real or Imaginary Data Only", Earthquake Engineering and Structural Dynamics, 37, 495-515
Nakamura, N. (2008b), "Time history Response Analysis Considering Dynamic Stiffness with Both Frequency and Strain Dependencies", Journal of Engineering Mechanics, ASCE, 134(4), 530-541
Makris, N. and Zhang, J. (2000), "Time Domain Viscoelastic Analysis of Earth Structures", Earthquake Engineering and Structural Dynamics, 29, 745-768

JOINT CONFERENCE PROCEEDINGS
7th International Conference on Urban Earthquake Engineering (7CUEE) &
5th International Conference on Earthquake Engineering (5ICEE)
March 3-5, 2010, Tokyo Institute of Technology, Tokyo, Japan

SEISMIC RISK EVALUATION OF SCHOOL GYMNASIA BASED ON DYNAMIC NONLINEAR RESPONSE ANALYSIS

Shoji Nakazawa[1)], and Shiro Kato[2)]

1) Associate Professor, Dept. of Architecture and Civil Engineering, Toyohashi University of Technology, Japan
2) Professor, Dept. of Architecture and Civil Engineering, Toyohashi University of Technology, Japan
nakazawa@tutrp.tut.ac.jp, kato@tutrp.tut.ac.jp

Abstract: The paper discusses the seismic performance of a relatively small spatial structure such as school gymnasia subjected to earthquake motions. The method is based on a seismic risk analysis. First, an equivalent lumped mass model for evaluating the seismic responses of longitudinal direction simply is proposed, and the validity of the model is investigated. Second, a seismic risk and an expected loss of the structure are calculated based on the results of the elasto-plastic response analysis. Finally, the relation between the expected losses and yield base shear coefficients used for the substructures is examined, and the yield base shear coefficient is discussed in order to suppress the expected loss below to a certain threshold.

1. INTRODUCTION

Spatial structures are required not only to protect peoples they accommodate during an earthquake but also to serve as shelters and to maintain property after earthquakes. In the recent earthquakes in Japan (Kato et al. 1995 and Kawaguchi et al. 2005), the damage such as fall of ceilings, finishing materials and lighting equipments have attracted a greater attention in addition to the structural damage to spatial structures. Consequently, a necessity arises to evaluate a seismic performance in consideration of the damages of not only major structures but also these secondary components.

Seismic risks are evaluated by the basis of a seismic risk analysis (SRA). SRA is a tool to quantify the seismic risk of an individual facility, aiming at providing information for decision making on risk mitigations of facilities. In the present procedures (Mizutani 1997) , risks are quantified as expected losses using an event tree of the seismic damages. In the previous study (Nakazawa et al. 2006, 2007) , an index for evaluation of seismic performance was proposed in terms of maximum deformation of each component. As an index showing economical loss, a seismic loss function F_{SL} used in the research field of SRA were adopted.

Damages to the wall braces in the substructure as anti-seismic elements subjected to longitudinal earthquake motions have been often reported in the damage investigations. Previous preliminary studies (Nakazawa et al. 2006, 2007 and Kato 2008) discussed about a fundamental aspect with an emphasis on economical loss and a functional loss probability based on seismic risk analysis. Although there are several studies (Shima et al. 2003 and) about seismic response characteristics of such structures, the relation between the yield base shear coefficient of wall braces and the expected losses has not been studied enough. In this study, the expected losses subjected to longitudinal earthquake motions are investigated to lead a relationship between the losses and yield base shear coefficient for design use.

2. STRUCTURAL MODEL

2.1 Model for Structural Analysis

Figure 1 shows a model for a typical school gymnasium. The structure is a steel frame with light roof finishing and lightweight concrete panels for side walls. The structure for the present model has been retrofitted for both of the roof and wall braces for the performance in the X direction and the sections of the braces were proportioned as tension braces with slip type characteristics. In the present study, the structural system in the X direction is to be investigated, since wall braces have been often damaged in earthquakes.

Here the part of roof is described as a roof structure, while the part of wall as a substructure. The self weight is 55 kg/m^2 for the roof structure and 65 kg/m^2 for the substructure, including the steel frame and ceilings or wall finishing. The total mass of the structure is 84,400 kg. Both of the roof and wall braces are modeled as truss elements. The Young's modulus of the braces is E = 205,000 N/mm^2, and yield stress σ_y is 235 N/mm^2. The force-deformation relationship of the braces is assumed for investigation of seismic loss in two cases ; one is a slip type hysteresis and the other is a bilinear type hysteresis.

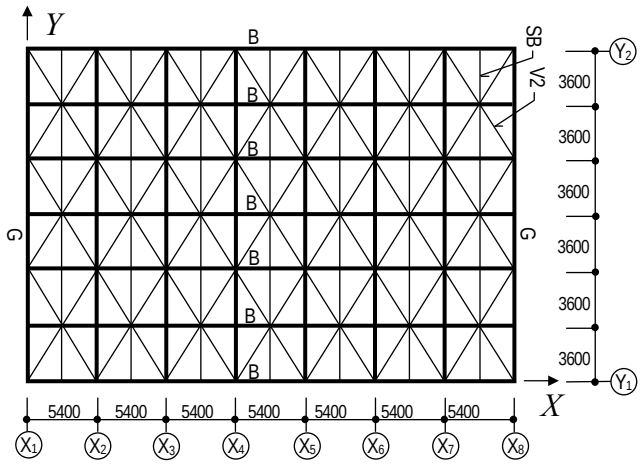

(a) Roof plan

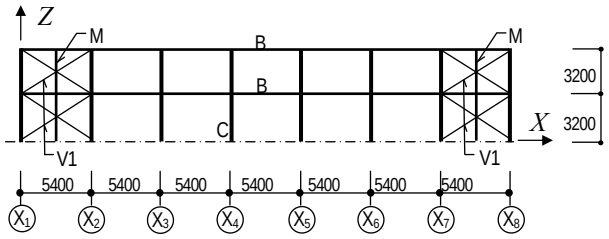

(b) Framework elevation on grid line Y_1 or Y_2

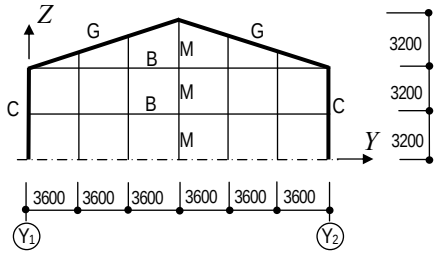

(c) Framework elevation on grid line X_1 or X_2

(d) List of members

C	H-350x175x7x11
G	H-350x175x7x11
B	H-200x100x5.5x8
SB	2C-100x50x20x3.2
M	H-200x100x5.5x8
V1	L-75x75x6
V2	L-65x65x6

Figure 1 Structural Model

2.2 Equivalent Lumped Mass Model

Figure 2 illustrates an equivalent lumped mass model for evaluating the seismic response of longitudinal direction (X direction). An initial shear stiffness, K_{0i} and a yield shear force Q_{yi} of the i-th layer are determined for brace elements as follows,

$$Q_{yi} = A_{BRi}\,\sigma_y \cos\theta_i \tag{1}$$

$$K_{0i} = \frac{E\,A_{BRi}}{\ell_{BRi}}\cos^2\theta_i \tag{2}$$

where A_{BRi} and ℓ_{BRi} are a sectional area and a length of the brace of the i-th layer, respectively. A bending rigidity of the frame is ignored. Parameters of the equivalent lumped mass model are listed in Table 1. C_{yi}, δ_{yi} and Δ_{yi} represent a yield base shear coefficient, a yield displacement and a yield drift angle of the i-th layer, respectively.

Table 1. K_{0i}, Q_{yi} and C_{yi} of the i-th layer

i	M_i [kg]	K_{0i} [kN/m]	Q_{yi} [kN]	C_{yi}	δ_{yi} [cm]	Δ_{yi}
5	5056	79958	723.7	14.61	0.905	1/415
4	10112	79958	723.7	4.87	0.905	1/415
3	10112	79958	723.7	2.92	0.905	1/415
2	9328	42512	353.2	1.04	0.863	1/385
1	7800	42512	353.2	0.85	0.863	1/385

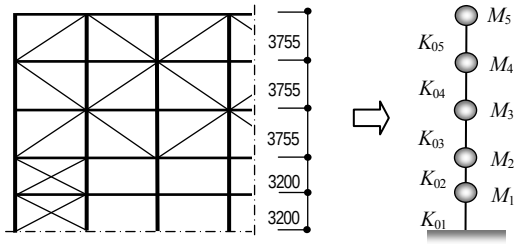

Figure 2 Equivalent lumped mass model

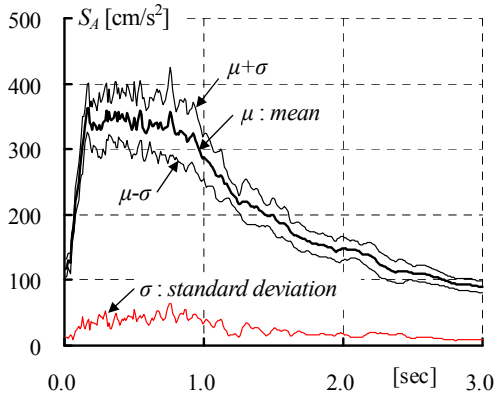

Figure 3 Mean and standard deviation of acceleration response spectra of input seismic motions (h=2 %, λ_E =1.0)

2.3 Input Earthquake Motions

Input earthquake motions are artificial motions simulating the design acceleration response spectrum given in the Building Standard Law of Japan (Midorikawa 2005), corresponding to a soil column of the kind II for ordinary soil condition. Several levels for seismic intensity, λ_E, are assumed. The serviceability limit level is specified as λ_E = 1.0, and the safety limit level is specified as λ_E = 5.0. In this study, twelve phases of the observed ground accelerations, expressed by limited number Fourier series, are used to generate the corresponding time history accelerations. With respect to the serviceability limit level, the mean and standard deviation of acceleration response spectra of the artificial earthquake motions are illustrated in Figure 3.

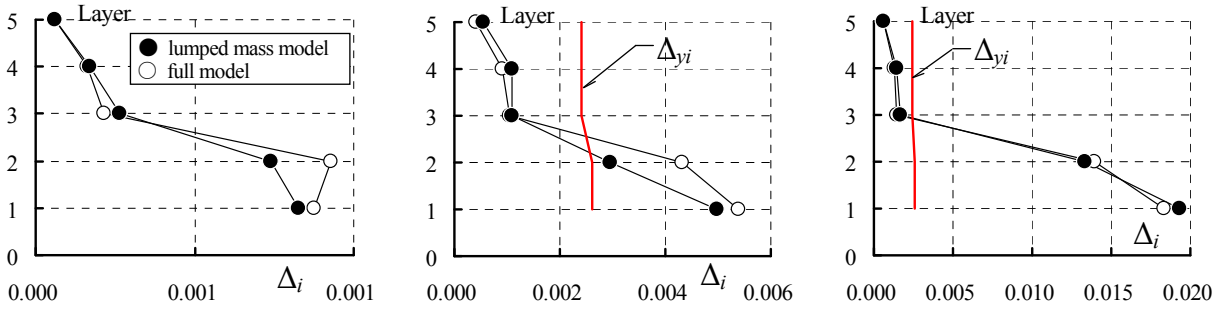

(a) λ_E=1.0 (elastic) (b) λ_E=4.0 (c) λ_E=5.0

Figure 4 Distributions of maximum story drift angle in cases of λ_E=1.0, 4.0, 5.0.

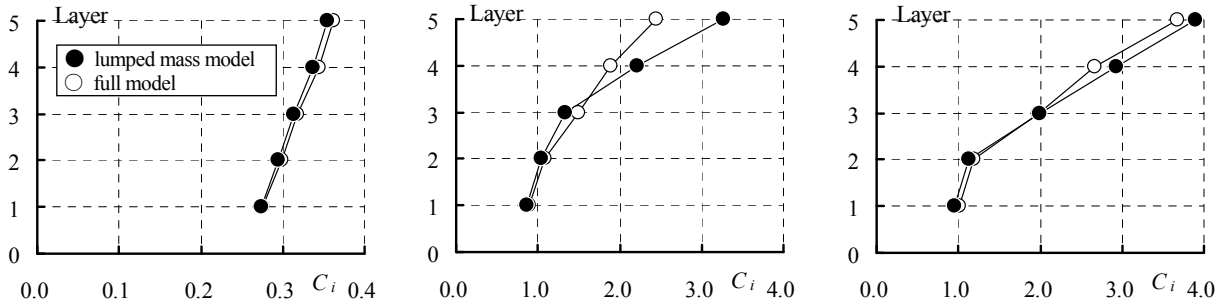

(a) λ_E=1.0 (elastic) (b) λ_E=4.0 (c) λ_E=5.0

Figure 5 Distributions of response shear coefficient in cases of λ_E=1.0, 4.0, 5.0.

Table 2 Numerical Parameters

model	A [cm^2]	K_0 [N/m]	Q_y [kN]	C_y	Hysteresis type
C85S	8.727	43.218	36.040	0.850	Slip Type
C75S	7.703	38.145	31.809	0.750	
C63S	6.419	31.787	26.508	0.625	
C50S	5.135	25.430	21.206	0.500	
C38S	3.851	19.072	15.905	0.375	
C32S	3.267	16.177	13.490	0.318	
C40B	4.108	10.171	8.482	0.400	Bi Linear Type
C35B	3.594	8.900	7.421	0.350	
C30B	3.081	15.256	12.722	0.300	
C25B	2.567	12.714	10.602	0.250	
C20B	2.054	10.171	8.482	0.200	

3. SEISMIC RESPONSE CHARACTERISITICS

3.1 Numerical Method and Eignvalue Analysis

A Newmark-β scheme with β =1/4 is used for numerical integration, and the time interval for response calculation, Δt, is 0.002 s. The damping matrix is assumed as Rayleigh damping with 2 % for the first and second periods of 0.3 s and 0.1 s.

By considering its 3-D arrangement of members, the first natural period of a full model with C_y of 0.85 (C85S model) is 0.285 s, and a corresponding effective mass ratio is 0.915. From the results of equivalent lumped mass model shown in Figure 2, the first natural period is 0.295 s and the corresponding effective mass ratio is 0.932, respectively. From the results of dynamic eigenvalue analysis, the natural periods and the corresponding effective mass ratios of both models are well in agreement with each other.

3.2 Elasto-Plastic Dynamic Response Characteristics

Figures 4 illustrate the distributions of maximum story drift angle Δ_i of the i-th layer in case of λ_E= 1.0, 4.0 and 5.0, respectively. Δ_{yi} represents a yield story drift angle of the i-th layer. The story drift angles of the roof remain in elastic range even in case of λ_E=5.0, relatively smaller compared with the story drift of the substructure. Accordingly, the damage is concentrated on the substructure.

Figures 5 show the distributions of response shear coefficients for comparison between the full model and the lumped mass model. The results of both models are almost in agreement each other, and the validity of the equivalent lumped mass model of Figure 2 is confirmed.

4. EVALUATION OF EXPECTED LOSS

4.1 Parameters for Loss Evaluation

The results described in Chapter 3 reveals that the damage is concentrated on the wall braces, since the roof braces have been retrofitted stronger so that the braces of the walls may yield before the roof braces. Therefore, several types for wall braces as shown in Table 2 are analyzed in

order to investigate the effects of the magnitude of C_y and hysteresis types on the expected loss (seismic risk). C_y is the yield base shear coefficient of wall braces, while A, K_0 and Q_y express the sectional area, initial shear stiffness and yield shear force, respectively. The force-deformation relationship of the braces is assumed, as mentioned before, as two types of the bilinear hysteresis with high ductility and the slip hysteresis.

4.2 Damage Evaluation Index of the Substructure and its Criteria

The damages on the substructure are estimated in terms of the maximum story drift angle of the first layer, Δ_1. A set of five damage states (FEMA 1999) is set up for defining the damage degree as shown in Table 3. A restoration cost ratio corresponding to damage state is also assumed as listed in Table 3. The damage of equipments is not taken into consideration in this research.

4.3 The median and Variation of Maximum Responses

Figs.6 (a) and (b) illustrate the maximum story drift angle of 1st layer Δ_1 depending on the seismic intensity λ_E in the cases of C85S and C32S. The maximum story drift angle increases nonlinearly with increment of λ_E.

In order to calculate SFC (seismic fragility curve), it is necessary to research for the median of maximum responses and its variations. According to the reference (Mizutani 1997, Nakazawa 2006) , the median for relating maximum responses of story drift angle Δ_1 and seismic intensity λ_E are expressed in terms of the following nonlinear formula.

$$\Delta_1 = a \times (\lambda_E)^b \tag{3}$$

A least-squares method is applied to the maximum response Δ_{1k} ($k = 1, \ldots, n$) which are obtained from response analysis for the parameter of λ_E, leading to determination of the coefficients a and b.

4.4. Calculation of Seismic Fragility Curve

Generally, when the probability distributions of load and resistance are given, a failure probability, p_f , can be calculated based on a reliability theory. Seismic Fragility Curve (SFC) means a probability of failure at a certain seismic intensity, λ_E, and is expressed as $F(\lambda_E)$. When probability distributions of response and resistance follow a log normal distribution and the average responses with a variation of ξ_A can be approximated by an expression like Eq.(4), SFC can be expressed as follows (Mizutani 1997, Nakazawa 2006) ,

$$F(\lambda_E) = p_f(\lambda_E) = \Phi\left(\frac{\ln(\lambda_E) - \ln(\lambda_{E0}{}^i)}{\xi_A} \right) \tag{4}$$

in which $\Phi(*)$ is the probability distribution function of standard normal distribution.

SFC is calculable as a probability distribution function in terms of a lognormal distribution with a mean value $\lambda_{E0}{}^i$ and a lognormal standard deviation ξ_A. ξ_A is assumed 0.4 in our research. The values of $\lambda_{E0}{}^i$ are determined as

$$\lambda_{E0}{}^i = (\Delta_{1m}{}^i / a)^{1/b} \tag{5}$$

where a, b are the coefficients in Equation (3). In our research, approximate expressions for relationships between the median of maximum story drift angle Δ_1 and λ_E are estimated as Equation (3). $\Delta_{1m}{}^i$ is a value of the story drift angle in case that a certain damage state i occurs, the values of $\Delta_{1m}{}^i$ corresponding to damage states of "Slight", "Moderate", "Extensive", and "Collapse" are assumed 1/200, 1/100, 1/50 and 1/30 as shown in Table 3. The values of $\lambda_{E0}{}^i$ are determined as the median using the criteria of damage state, and $\lambda_{E0}{}^i$ corresponding to each damage state is shown in Table 4.

Table 3 Damage state and its criteria

	damage state	restoration cost
$\Delta_1 < 1/200$	No damage	0.00
$1/200 \leqq \Delta_1 < 1/100$	Slight	0.05
$1/100 \leqq \Delta_1 < 1/50$	Moderate	0.10
$1/50 \leqq \Delta_1 < 1/30$	Extensive	0.50
$\Delta_1 \geqq 1/30$	collapse	1.00

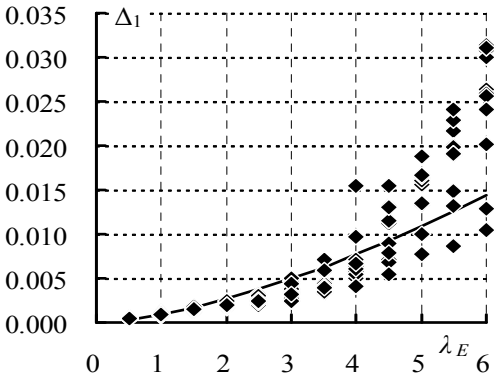

(a) C85S (C_y=0.85)

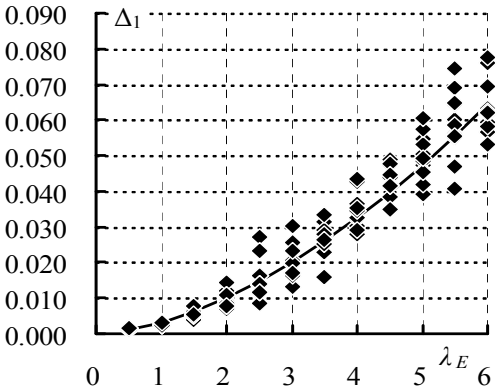

(b) C32S (C_y=0.32)

Figure 6 Relationship between story drift angle of 1st layer Δ_1 and seismic intensity λ_E

Figure 7 illustrates the examples of SFC in case of C85S and C32S. As shown in Figure 7, a occurrence probability p_i of each damage state is calculable. $\lambda_{E0}{}^i$ corresponds to the seismic intensity λ_E from which the occurrence probability of each damage state i becomes 50%.

4.5. Event Tree Modeling and Seismic Loss Function

In Seismic Risk Management, a seismic risk is quantified as an expected loss that is the product of the probability of damage state and its corresponding loss amount associated with the state. A seismic loss function, $F_{SL}(\lambda_E)$, is used for evaluation of economical loss as follows.

$$F_{SL}(\lambda_E) = \sum_{i=1}^{4} [\, C_i \times p_i(\lambda_E) \,] \qquad (6)$$

where $p_i(\lambda_E)$ represents the occurrence probability of damage state-i, and the variable of C_i is the cost corresponding to the damage state-i.

Figure 8 displays the seismic loss function of each model. As shown in Figure 8, the expected loss decreases with an increment in C_y. The seismic loss function of C50S (C_y=0.5, slip type) and C30B (C_y =0.3, bilinear type) is almost same. Since the energy absorption performance of a bilinear type is higher compared with a slip type, the expected loss in case of a bilinear type can be suppressed in comparison with a slip type if the yield base shear coefficient is same.

4.6. Relationship between expected loss and yield base shear coefficient

The relationships between the yield base shear coefficients C_y of substructure and the expected losses in the cases of λ_E = 3.0, 4.0 and 5.0 are shown in Figure 9. The expected loss can be reduced with an increment in C_y. In the case of the same yield base shear coefficient, the expected loss of bilinear type is smaller in comparison with those of slip type.

Generally based on the standard in Japan for seismic evaluation of existing gymnasia and public halls, a seismic performance index of structure, Is, is used, and it is expressed as follows as a product of a yield base shear coefficient, C_y, and a ductility index, F.

$$Is = C_y \times F \qquad (7)$$

The ductility index F of braces of slip type is assumed 2.2 in the reference (Ministry of Education, Culture, Sports, Science and Technology, 2006). Although sufficient arguments have not been made about the ductility index F for hysteresis dampers, for examples, buckling restrained braces, the value of F for a bilinear type structural component is assumed here as 3.8 taking into consideration of a note that the maximum value of the ductility index is 4.0 in reference (Ministry of Education, Culture, Sports, Science and Technology, 2006). The relationships between the value of Is and the expected loss are illustrated in Figure 10 for both of slip type and ductile braces. As shown in Figure 10, the expected losses depend on the design seismic intensity λ_E,

Table 4 λ_{E0} corresponding to each damage state

	Slight	Moderate	Extensive	Collapse
C85S	3.02	4.74	7.43	10.36
C75S	2.59	4.02	6.23	8.61
C63S	2.20	3.36	5.13	7.01
C50S	1.85	2.79	4.21	5.69
C38S	1.46	2.20	3.31	4.48
C32S	1.31	1.98	2.99	4.06
C40B	1.91	3.24	5.52	8.16
C35B	1.68	2.83	4.77	7.01
C30B	1.46	2.44	4.08	5.98
C25B	1.31	2.17	3.59	5.21
C20B	1.11	1.84	3.04	4.41

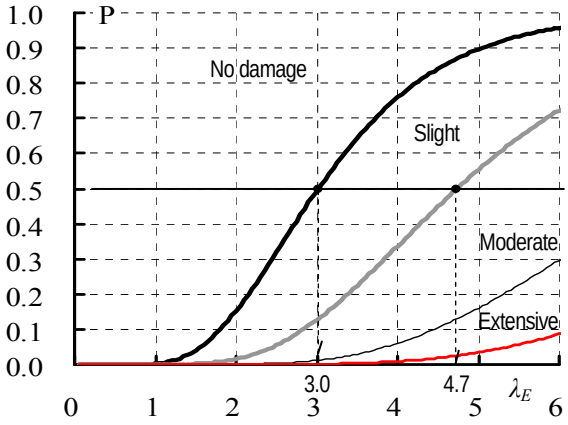

(a) C85S

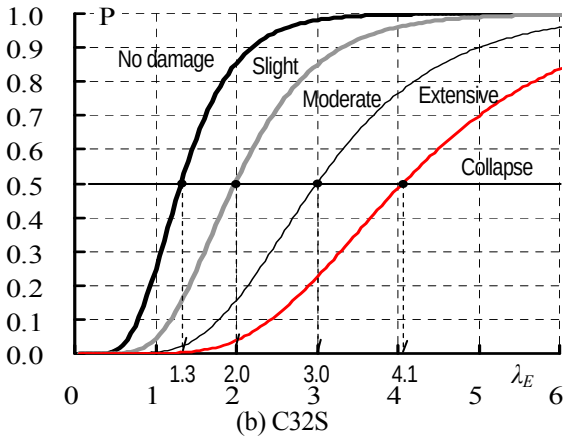

(b) C32S

Figure 7 Seismic fragility curves (SFC)

and the losses are almost same regardless of the hysteresis characteristic of a brace, if a seismic performance index of structure, Is, is same. Accordingly, an important characteristic is found that, if a suitable ductility index F is applied, the expected losses depend only the value of Is and seismic intensity λ_E.

In Japan, seismic retrofit of school gymnasia and public halls has been continued using a criteria that Is value should become beyond 0.7. As observed in Figure 10, the expected losses of, for example, C32S model (Is=0.7) in Table 2 corresponding to the seismic intensity λ_E = 3.0, 4.0, and 5.0 are 0.40, 0.65, and 0.80, respectively. On the other

hand, the expected losses of C85S model (Is=1.87) corresponding to λ_E = 3.0, 4.0, and 5.0 can be greatly reduced to 0.04, 0.08, and 0.15, respectively. We are confronted by a question if the value of Is = 0.7 is proper for retrofitting of school gymnasia because the seismic loss increases almost 0.4 or over 0.4 in the cases of 3.0, 4.0 and 5.0 for seismic intensity λ_E.

5. CONCLUSION

The paper discusses the seismic performance of the small spatial structures due to longitudinal earthquake motions based on a seismic risk analysis. First, an equivalent lumped mass model for evaluating the seismic response of longitudinal direction simply is proposed, and the validity of the model is examined. Second, the expected losses are calculated based on the results of the elasto-plastic response of this model. Finally, the relationship between the expected losses and yield base shear coefficient C_y of the substructure are illustrated, and the required yield base shear coefficient which suppresses the expected loss below to a certain value is discussed, followed by a question that the minimum value of Is=0.7 is enough for retrofitting of school gymnasia because the seismic loss increases almost 0.4 or over 0.4 in the cases of 3.0, 4.0 and 5.0 for seismic intensity of λ_E.

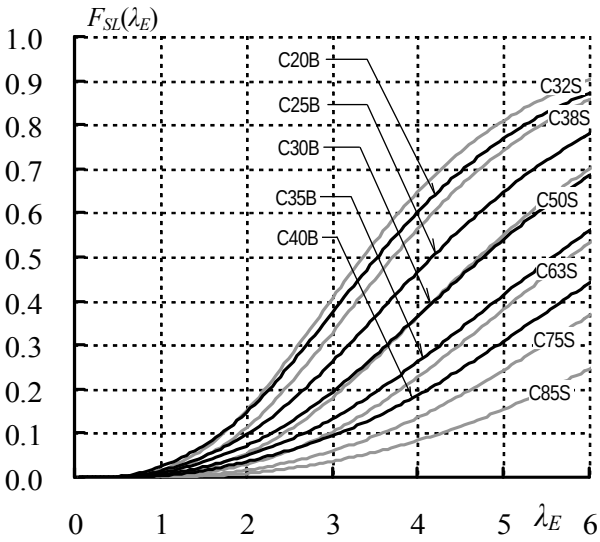

Figure 8 Seismic Loss Functions

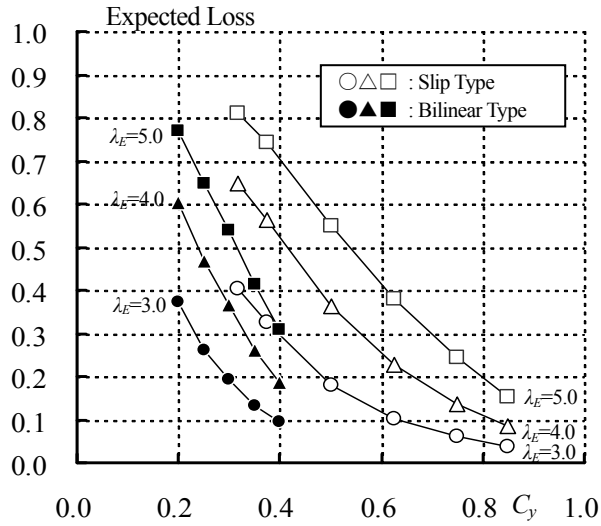

Figure 9 Relationship between Expected Loss and C_y

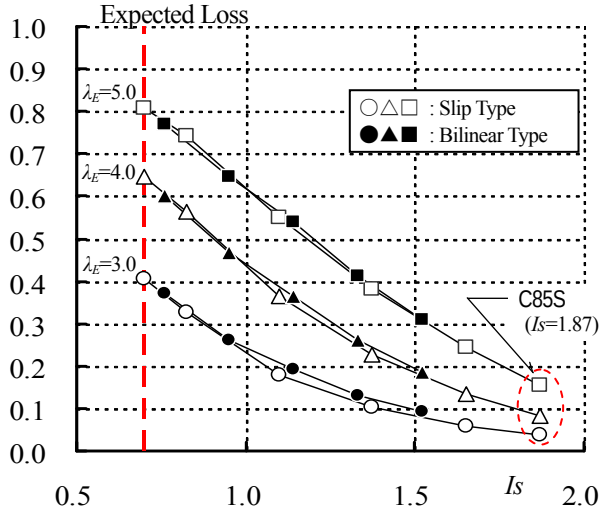

Figure 10 Relationship between the Expected Loss and Is

References:

S. Kato, K. Kawaguchi, T. Saka (1995), "Preliminary report on Hanshin Earthquake", *Proceedings of IASS1995 Symposium*, Vol.2, pp.1059–1066

K.Kawaguchi and Y.Suzuki (2005), "Damage Investigations of Public Halls in Nagaoka City After Nigata-Chuetsu Earthquake 2004 in Japan", *Proceedings of IASS2005*, pp.421-428.

S. Nakazawa, T. Shima, I. Tatemichi, S. Kato and K. Hirano (2006) , "Evaluation for seismic risk based on damage ratio and seismic resistance of spatial Structures", *Proceedings of IASS-APCS 2006 Symposium*, AO16, Beijing

S. Nakazawa, S. Kato and K. Hirano (2007), "Methodology to evaluate the effectiveness of retrofit proposal based on the discounted cash flow method", *Proceedings of IASS 2007* Symposium, PN368, Venice, Italy

M. Mizutani (1997), "Basic Methodology of a Seismic Risk Management Procedures, I*COSSAR'97*, Vol.3, pp.1581-1588

S. Kato and S. Nakazawa (2008), "Seismic risk analysis of large lattice dome supported by buckling restrained braces", *Proceedings of IASS-IACM2008*, pp.98, Cornell University, NY, USA

T. Shima, I. Tatemichi, T. Ueki, S. Kato (2003), "Some Consideration in Structural Planning of Small Gymnasiums Based on Their Dynamic Behavior", *Proc. of IASS APSC 2003*

I. Tatemichi and S. Kato (2005), "A Study on the Seismic Performance of Shell and Spatial Structures", IASS 2005 Symposium, 325-328

Ministry of Education, Culture, Sports, Science and Technology (2006) , "Standard for seismic evaluation of school gymnasia and public halls" (in Japanese)

M. Midorikawa, "Performance-Based Seismic Design Provisions for Buildings in Japan", IASS 2005 Symposium, 2005, pp.307-316, Bucharest, Romania

FEMA, HAZUS99 technical manual, Washington, D.C., NY, 1999

JOINT CONFERENCE PROCEEDINGS
7th International Conference on Urban Earthquake Engineering (7CUEE) &
5th International Conference on Earthquake Engineering (5ICEE)
March 3-5, 2010, Tokyo Institute of Technology, Tokyo, Japan

RESPONSE CONTROL OF LATTICE DOME ROOFS USING SEISMIC ISOLATION

Toru Takeuchi[1)], Kengo Takamatsu[2)], Tomohiko Kumagai[3)] and Toshiyuki Ogawa[1)]

1) Professor, Dep. of Arch. & Build. Eng., Tokyo Institute of Technology, Japan
2) Structural Engineer, Arup Japan, Japan
3) Assistant Professor, Dep. of Arch. & Build. Eng., Tokyo Institute of Technology, Japan
ttoru@arch.titech.ac.jp, kengo.takamatsu@arup.com, kuma@arch.titech.ac.jp, togawa@arch.titech.ac.jp

Abstract: Seismic responses of raised lattice domes with substructures are known to be complicated, and not only horizontal response but also vertical response is excited under horizontal seismic input. Such action causes damage on structures and non-structural elements such as ceiling and suspended lightning equipments. A seismic isolation system is effective to reduce such responses, and will be a solution for safer indoor spaces which are usable for evacuation spaces after large earthquake. In this paper, the effects of seismic isolation bearings on roof response are analytically discussed, and simple response evaluation methods without time-history analyses are proposed using response amplification factors and linearization techniques. Their validities are also discussed against detailed time history analyses.

1. INTRODUCTION

Seismic response of lattice domes includes vertical vibration modes even under horizontal seismic input, and their amplitude against seismic input changes drastically along the relationship between domes and substructures (Figure 1). Such action causes damage to both structures and non-structural elements such as ceiling and suspended lightning equipments. Introducing seismic isolation bearings between the roof and substructure is effective to reduce these seismic responses as indicated by Kato et al. 1998; however, they generally require complicated design process as time-history analyses. For ordinary domes with sub-structures, simple formulas for evaluating the distributions of maximum response accelerations were proposed using amplification factors by Takeuchi et al. 2007 and 2009. In these studies, analytical models of domes supported by seismic isolation bearings with elasto-plastic dampers or viscous dampers are constructed, and simple response evaluation methods of lattice domes with seismic isolation system are proposed. Their validities are discussed against the results of time history analyses including the accuracies for using them as equivalent static loads.

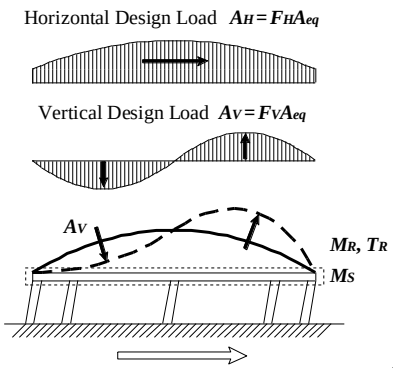

Figure 1 Excited Response of the Dome Roofs under Horizontal Seismic Input

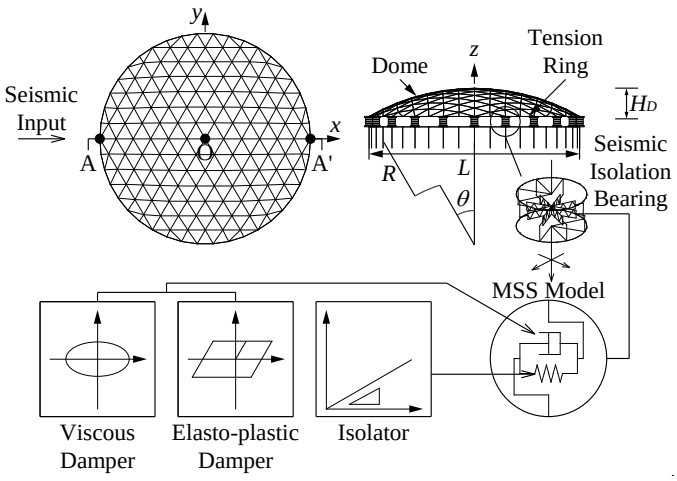

Figure 2 Lattice Dome with Seismic isolation Bearings

2. ANALITICAL MODEL

The analytical models of rigidly jointed medium-span latticed domes with substructures as shown in Figure 2 are constructed for evaluation. The diameter of the dome is 60m, and its half-subtended angle θ is 30°. The out-of-plane bending stiffness are 100 times of the single layer dome roof,

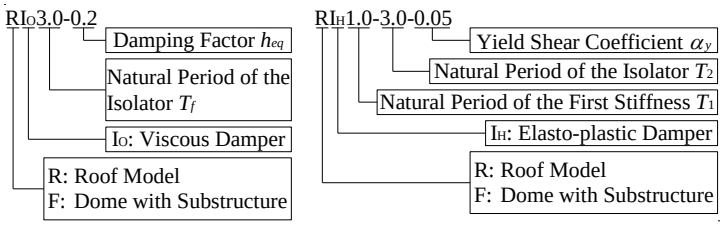

Figure3 Analytical Model Index

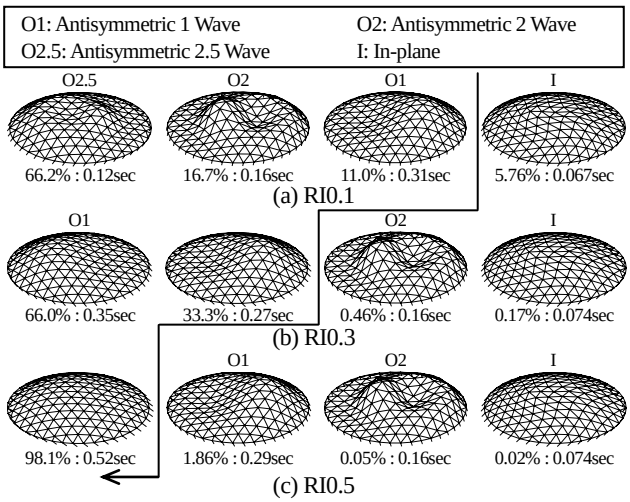

Figure 4 Principal Modes along Seismic Isolation Periods:

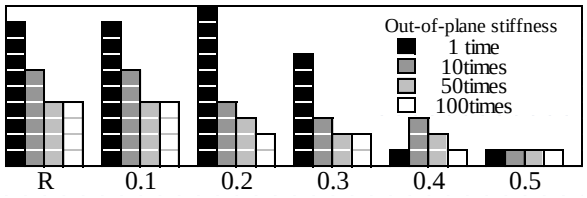

Figure 5 Number of Modes Satisfying Total Effective Mass Ratio as 90% of Total

which are equivalent to double layered domes with depth/span ratio of 1/50. The line connects A-O-A' in Figure 2 is called as the ridge of the dome. The seismic isolation bearings are composed of elastic spring of isolator and viscous or elasto-plastic dampers. Viscous damper has linear viscous, and elasto-plastic damper has bi-linear hysteresis, and they are laid out as Multi Shear Spring (MSS) elements in analyses. Their stiffness and damping ratio are changed, and each model is named as in Figure 3.

The major natural vibration modes for R0.1, R0.3 and R0.5 are shown in Figure 4 together with effective mass ratios and natural periods. The major vibration modes for R0.1 are governed by out-of-plane deformation. On contrary, in R0.5, the major vibration modes become sway in the horizontal direction. Also, the out-of-plane bending stiffness of the dome is increased by 10, 50 and 100 times of single layer dome, which is equivalent to double layered domes of depth/span ratio of about 1/170, 1/70, 1/50, respectively. When the natural period of isolation system exceeds 0.5 sec, the numbers of modes satisfying their total effective mass ratio as 90% of total are unified to sway mode regardless the out-of-plane stiffness as shown in Figure 5. This indicates that the vibration of even single-layer dome is simplified

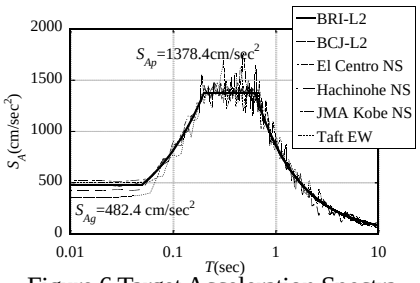

Figure 6 Target Acceleration Spectra (h_0=0.02)

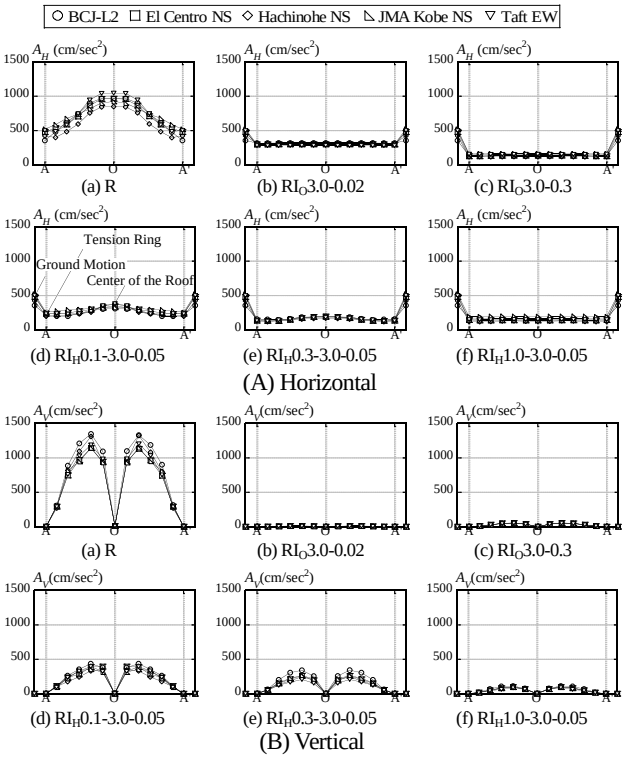

Figure 7 Acceleration Distributions for Roof Models:

with base-isolation bearings.

3. RESPONSE WITHOUT SUBSTRUCTURES

Firstly, time history response analyses considering geometrical nonlinearity are carried out for various seismic isolated domes without substructure, whose natural periods are varied as 0.1 to 3.0 sec., damping ratio of h_{eq}=0.02 to 0.4 for viscous damper, and yield shear force coefficient of 0.01 to 0.5 for elasto-plastic damper. The input earthquake motions are artificial earthquake BCJ-L2, observed earthquake El Centro NS (1940), Taft EW (1952), Hachinohe NS (1968) and JMA Kobe NS (1995), all adjusted to the target spectrum as shown in Figure 6.

Figure 7 shows the maximum response accelerations along the ridge of the dome. In all cases, maximum accelartion in horizontal and vertical directions are reduced with base isolation comparing to ordinary roofs marked as "R". The horizontal response accelerations in RI_O with viscous dampers are reduced as the damping factor is

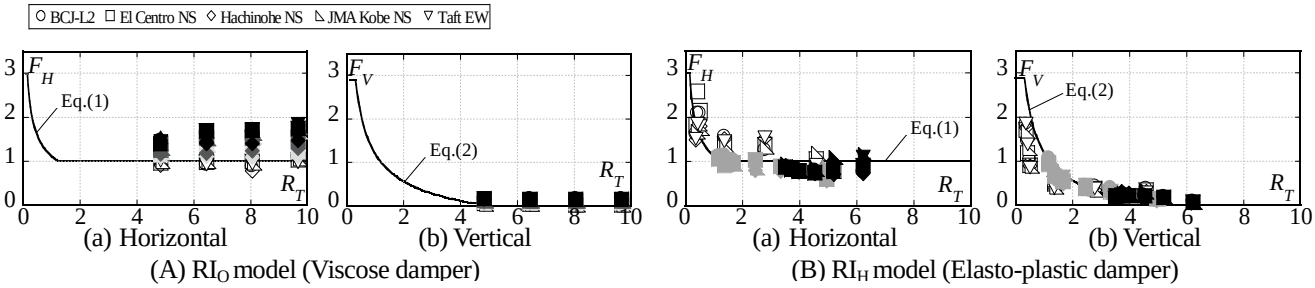

(a) Horizontal (b) Vertical (a) Horizontal (b) Vertical

(A) RI_O model (Viscose damper) (B) RI_H model (Elasto-plastic damper)

Figure 8 Amplification Factors along R_T:

Table 1 Parameters of Substructure

K_S	R_M	T_S(sec)
1.0	1.2	0.18
0.1	1.2	0.58
10	1.2	0.06
1.0	3	0.29
1.0	22	0.78

Table 2 Damper Parameters for Substructure Model Analyses:

(a) Viscous Damper

Model Name	h_{eq}	C_d(kNsec/m)	T_f(sec)
FI_O3.0-0.2	0.2	332.8	3.0

(b) Elasto-plastic Damper

Model Name	α_y	δ_y(mm)	T_1(sec)	K_1(kN/m)	T_2(sec)	K_2(kN/m)
FI_H0.1-3.0-0.05	0.05	0.12	0.1	1.568×10^6	3.0	1.742×10^3
FI_H0.3-3.0-0.05		1.12	0.3	1.742×10^5		
FI_H1.0-3.0-0.05		12.42	1.0	1.568×10^4		

increased. However, the vertical response accelerations are not decreased despite the increasing damping factor. In RI_H with elasto-plastic dampers, the vertical response accelerations are increased as initial stiffness of dampers become larger. This is because of the out-of-plane deformation mode being excited by the elastic natural period of the damper.

These models are applied to the already proposed response evaluation method for ordinary domes as in previous studies by Takeuchi et al. 2007. In these studies, the amplification factors to estimate maximum roof acceleration are expressed in the following equations for relatively shallow (θ<40°) domes.

Horizontal: $$F_H = \begin{cases} 3 & (0 \le R_T \le 5/36) \\ \sqrt{\dfrac{5}{4R_T}} & (5/36 < R_T \le 5/4) \\ 1 & (5/4 < R_T) \end{cases} \quad (1)$$

Vertical: $$F_V = \begin{cases} 3C_V\theta & (0 \le R_T \le 5/1) \\ \left(\sqrt{\dfrac{5}{R_T}} - 1\right)C_V\theta & (5/1 < R_T \le) \\ 0 & (5 < R_T) \end{cases} \quad (2)$$

Where C_V=1.85, and R_I=T_{eq}/T_R is ratio of natural periods between the roof and seismic isolation system. The relationship between the response amplitude factors F_H, F_V calculated from Eq. (3) (4) and the period ratio R_T are plotted in Figure 8,

Horizontal: $$F_H = A_{H\max} / A_{eq}(T_{eq}, h_{eq}) \quad (3)$$

Vertical: $$F_V = A_{V\max} / A_{eq}(T_{eq}, h_0) \quad (4)$$

Where $A_{H\max}$, $A_{V\max}$ are the maximum horizontal and vertical response accelerations in the dome roof respectively, $A_{eq}(T_{eq}/h_{eq})$ and $A_{eq}(T_{eq}/h_0)$ are accelerations estimated by response spectrum in the SDOF model estimating roof as rigid body. The equivalent natural period T_{eq} is calculated from isolator stiffness K_f for viscous dampers. For elasto-plastic damper, we propose to use the average of integration between T_1 and $T_{\max}$ which is expressed in Eq.(5), where T_1 is the natural period derived from the elastic stiffness, and $T_{\max}$ is that from the stiffness lead by maximum shear force including damper forces divided by maximum displacement. This reflects that the equivalent natural period varies depending on the amplitude.

$$A_{eq} = \frac{1}{T_{\max} - T_1}\int_{T_1}^{T_{\max}} S_A(T, h_{eq})dT \quad (5)$$

For this range of present study, Eq. (5) corresponds roughly to A_{eq} calculated by using T_{eq} that is the mean value of T_1 and $T_{\max}$.

$$T_{eq} = (T_1 + T_{\max})/2 \quad (6)$$

The acceleration A_{eq} for the vertical amplitude factors ignores the influence of additional damping in Eq. (4). The proposed methods and time-history analyses on the amplitude factors are compared in Figure 8. They generally agree each other and the proposed response evaluation method is considered to be applicable even for base isolated domes.

4. RESPONSE WITH SUBSTRUCTURES

Next, the response characteristic of those lattice domes supported by substructures with a seismic isolation system is

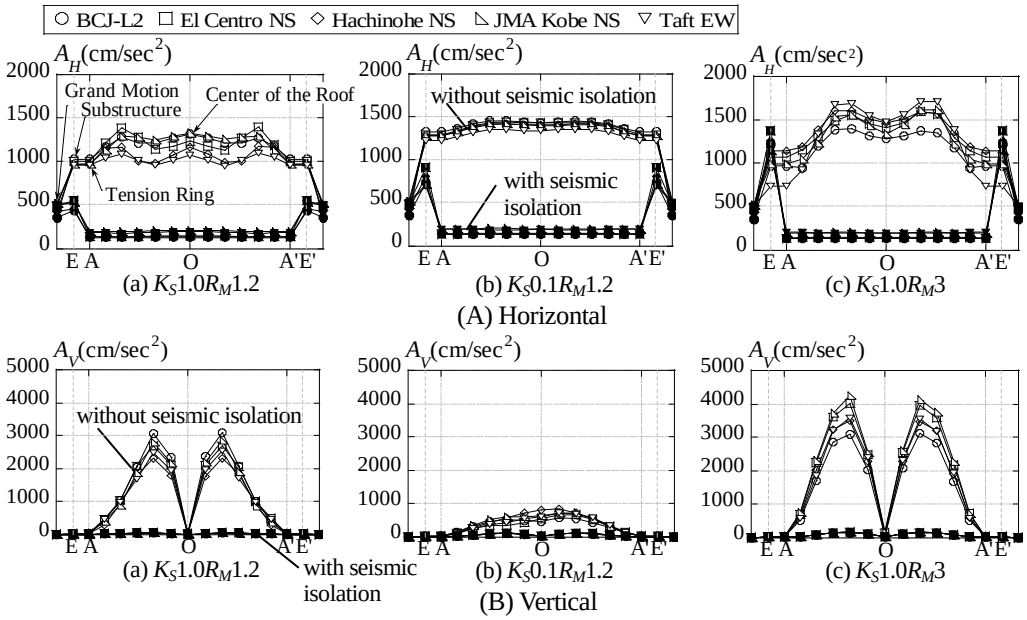

Figure 9 Acceleration Distributions for Substructure Models

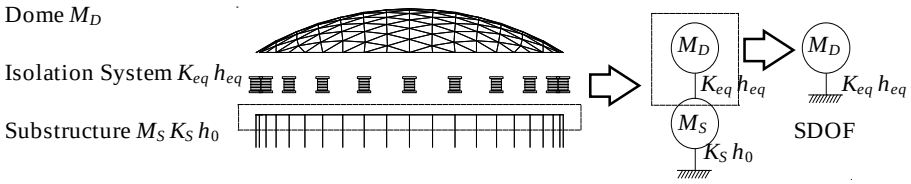

Figure 10 Conversion to Simplified Models

investigated. The beams of the substructures are modeled as rigid, and columns are designed to keep story drift against base-shear coefficient as 0.2 within 1/200. Then the column stiffness K_S and mass ratio R_M are changed as 0.1 to 1.0 and 1.2 to 22 respectively as shown in Table 1. Where, T_S is the natural period of total mass of the roof and bearings estimated as rigid body, being supported by substructures. Here the mass ratio RM is defined as the ratio between the mass of the dome (M_R), and the total mass of dome (M_R) and substructure (M_S).

$$R_M = M_{eq}/M_R = (M_R+M_S)/M_R \quad (7)$$

The parameters of dampers are shown in Table 2, and time history analyses were carried out for these models. Figure 9 shows the maximum response accelerations along the ridge of the dome. The response of models without seismic isolation system is heavily affected by substructure characteristics. On the other hand, the responses of the domes with seismic isolation system are insensitive against substructure, together with the reduction of acceleration. Response evaluation of these models is also investigated in the following.

Firstly, the amplitude factors evaluated in the SDOF model in Figure 10 regarding the substructures as rigid as are shown in Figure 11 by black plots. In RM1.2 models, this method is roughly appliciable. However, in heavy substructures as RM22 models, the error increases because of responses of the roof being amplified by the response of the substructure.

For the model with the mass ratio exceeding $R_M1.2$ and the natural periods ratios between isolation system and substructure $\beta = T_{eq}/T_S < 5.0$, the responses should be calculated in DDOF models as proposed by Matsui et al. 2006, as following process.

1) Estimate the natural period T_{eq} and equivalent stiffness K_{eq} of a seismic isolation system. For the elasto-plastic damper, assume a response displacement δ_S in seismic isolation layer, and obtain the equivalent natural period $T_{\max}$ by the equivalent stiffness at the point of maximum amplitude.

$$T_{eq} = (T_1 + T_{\max})/2 \quad (8)$$

$$K_{eq} = 4\pi^2 M_R / T_{eq}^2 \quad (9)$$

2) Calculate the response of the roof (the upper part mass) of DDOF as shown in Figure 10 by combining two mode responses obtained by response spectrum with SRSS.
3) If the response displacement in the seismic isolation layer calculated by 2) does not correspond to assumed displacement, repeat the steps from 1) to 2).
4) Calculate period ratio R_T(=T_{eq}/T_R) of natural period of 1st modes (T_{eq}) to natural period of asymmetric 1 wave mode for dome roof (T_R)
5) Evaluate the maximum acceleration in the dome, by multiplying the amplification factors calculated by Eq. (1)(2) on $A_{eq}(T_{eq}, h_{eq})$ for horizontal, and $A_{eq}(T_{eq}, h_0)$ for

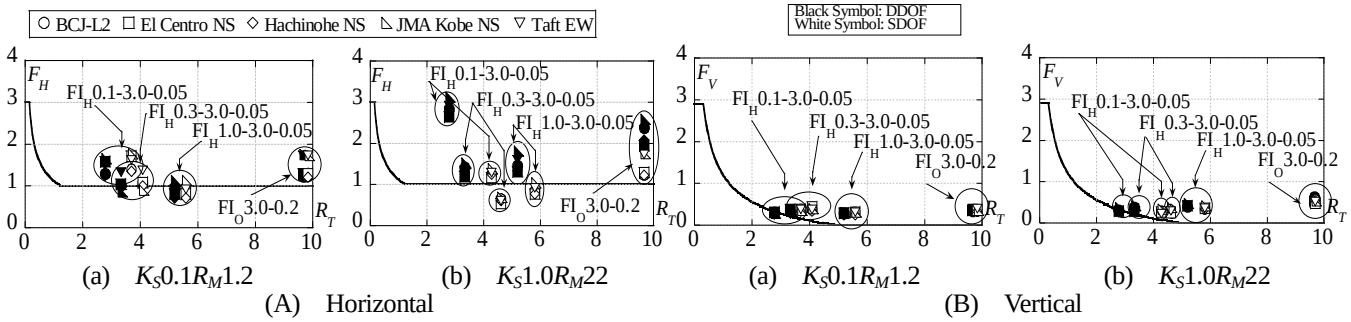

(a) $K_S0.1R_M1.2$ (b) $K_S1.0R_M22$ (a) $K_S0.1R_M1.2$ (b) $K_S1.0R_M22$

(A) Horizontal (B) Vertical

Figure 11 Amplification Factors along R_T:

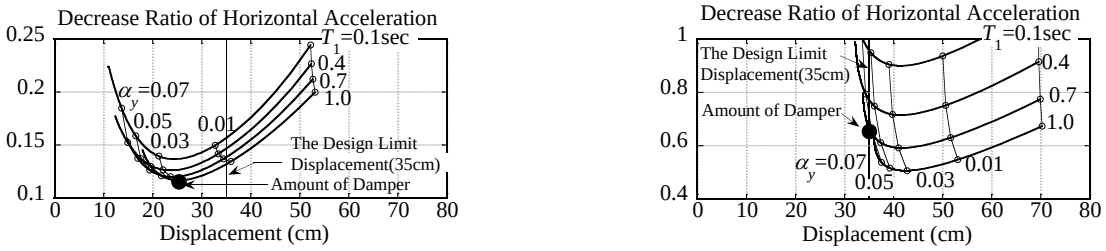

(a) $R_M1.2T_S0.2$ (b) $R_M22T_S1.0$

Figure 12 Response Evaluation in FI_H Model:

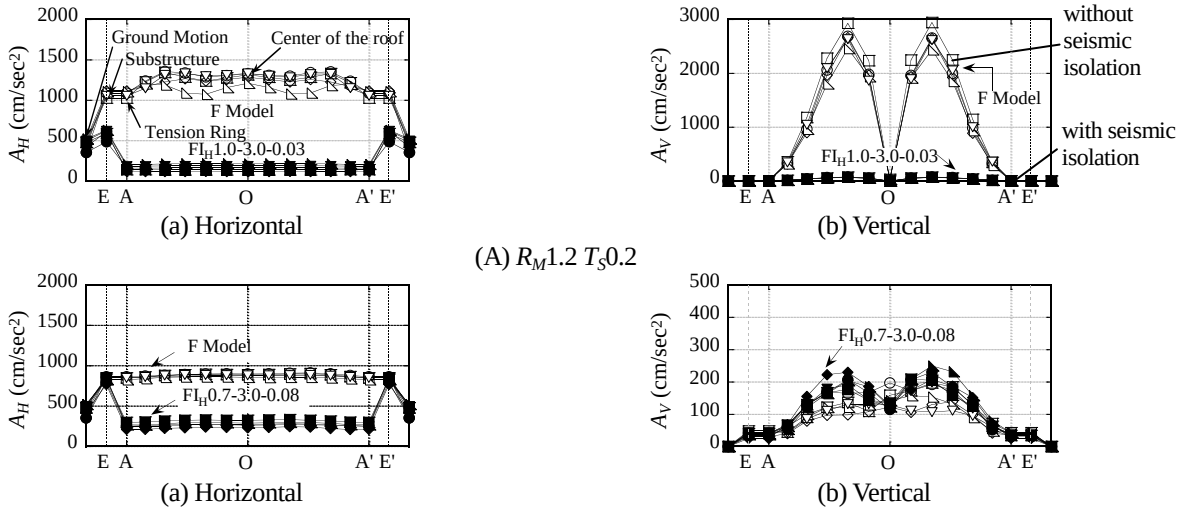

(a) Horizontal (b) Vertical

(A) $R_M1.2\ T_S0.2$

(a) Horizontal (b) Vertical

(B) $R_M22\ T_S1.0$

Figure 13 Acceleration Distributions for Detailed Examples:

vertical response. Comparison of the above method andtime-history analyses in the amplitude factors are compared in Fig 11 by white plots. In $R_M1.2$ models, F_H and F_V calculated in DDOF generally correspond to those calculated in SDOF, however horizontal errors are mitigated in R_M22 models.

5. RESPONSE EVALUATION EXAMPLE

The proposed methods are applied to two detailed design examples; a model with a light, stiff substructure ($R_M1.2T_S0.2$) and the other with a heavy substructure having a low degree of stiffness ($R_M22T_S1.0$), and the response reduction effect of the seismic isolation system is evaluated. The natural period of the isolator (T_I) is set as 3.0 sec and the maximum displacement in seismic isolation system is assumed to be 35cm. In $R_M1.2T_S0.2$ model, the effects of substructures are ignored because the stiffness of the substructure is sufficiently greater than the stiffness of seismic isolation system. In $R_M22T_S1.0$ model, where β <5.0, the response of the roof is calculated in consideration of amplification by the substructure. Figure 12 shows the relation between the horizontal response acceleration reduction rate and the displacement of a seismic isolation layer in the case with elasto-plastic dampers. The response acceleration distributions along the ridge line in each model are shown in Figure 13. The horizontal and vertical response decreased already in $R_M1.2T_S0.2$. In $R_M22T_S1.0$ model, although the horizontal response accelerations are reduced, the vertical accelerations are even slightly increased because of the close natural period between substructure and seismic isolation system. However, the vertical response of the roof has already been reduced enough before the introduction of the seismic isolation devices.

From evaluated maximum acceleration $A_{H\max}$ and $A_{V\max}$ with the modified amplification factors, acceleration

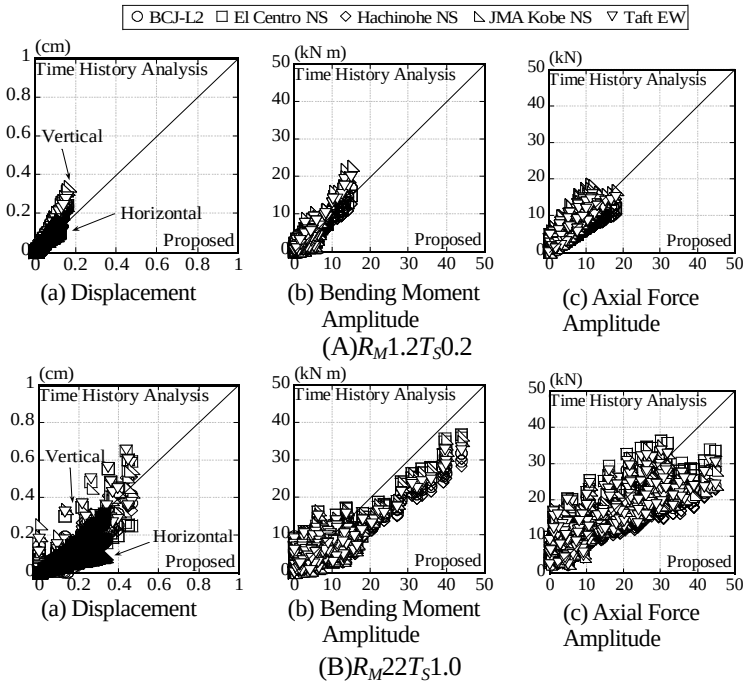

Figure 14 Accuracies of Proposed Evaluation Method:

response distribution can be calculated by the following equations as indicated in the previous paper (Takeuchi et al. 2007 and 2009).

$$\text{Horizontal:}\quad A_H(x,y) = A_{eq}\left\{1+(F_H-1)\cos\frac{\pi\sqrt{x^2+y^2}}{L}\right\} \quad (10)$$

$$\text{Vertical:}\quad A_V(x,y) = A_{eq}F_V\frac{x}{\sqrt{x^2+y^2}}\sin\frac{2\pi\sqrt{x^2+y^2}}{L} \quad (11)$$

By using Eq.(10)(11), the maximum acceleration distribution in each model is estimated, and displacements and each member force is calculated by using the acceleration as the equivalent static load coefficient. The results at all the connections in the roof are shown in Figure 14, compared with those of time history analysis. As observed in Figure 13, although the results in axial forces and bending moments are distributed relatively widely, the proposed method is considered to be valid for rough estimations.

6. CONCLUSIONS

Seismic response of raised domes supported by substructures with a mid-story seismic isolation system was investigated, and the following results were obtained.

1) For the roof model with seismic isolation system, the vertical response accelerations are reduced by extending the natural period, however, little reduction effect by additional damping was observed for vertical response. For the seismic isolation system with elasto-plastic dampers, the vertical response is more reduced when the elastic stiffness of damper is reduced. By considering these effects, the proposed method can evaluate the response more accurately.

2) When the substructure is light and stiff, the effect of the substructure is negligible and the amplitude factor can be estimated by SDOF model regarding the substructures as rigid.

3) When the substructure is much heavier than the roof, natural period of the substructure approaches that of the seismic isolation system, and the maximum response of the roof can be evaluated by combining the equations of amplification factors and a predictive method using DDOF models.

Acknowledgements:

The authors acknowledge a support from the Japan Ministry of Education, Culture, Sport, Science, and Technology (MEXT) for establishing the Center for Urban Earthquake Engineering (CUEE) in Tokyo Institute of Technology.

References

Kato, S., Nakazawa S., Uchikoshi, M., Ueki, T. and Osugi, F. (1998) "Earthquake Response of Domes Implemented by Hysteresis Dampers for Earthquake Isolation", *Proccedings of IASS (Sydney)*, 451-459

Takeuchi, T., Kumagai, T. and Ogawa, T. (2007) "Seismic Response Evaluation of Lattice Shell Roofs with Substructures", *Journal of IASS*, **48**(3), 197-210.

Takeuchi, T., Kumagai, T. and Ogawa, T. (2009), "Seismic Response Evaluation of Lattice Roofs with Substructures", *Proceedings of 6th International Conference for Urban Earthquake Engineering, Tokyo Institute of Technology*

Matsui, T. and Furuike, H. (2006) "Seismic Response Prediction for Base-Isolated Spatial Structures by the Response Spectrum Method", *Summaries of technical papers of Annual Meeting Architectural Institute of Japan. B-1*, 781-784 (in Japanese)

JOINT CONFERENCE PROCEEDINGS
7th International Conference on Urban Earthquake Engineering (7CUEE) &
5th International Conference on Earthquake Engineering (5ICEE)
March 3-5, 2010, Tokyo Institute of Technology, Tokyo, Japan

Shaking Table Tests of Cylindrical Lattice Shell Roofs Supported by Substructure with Viscous Damper Subjected to Horizontal Earthquake Motions

Tomohiko KUMAGAI[1], Toru TAKEUCHI[2], Fumi USHIWATA[3], and Toshiyuki OGAWA[2]

1) Assistant Professor, Dept. of Architecture and Building Engineering, Tokyo Institute of Technology, Japan
2) Professor, Dept. of Architecture and Building Engineering, Tokyo Institute of Technology, Japan
3) Takenaka Research & Development Institute, Takenaka Corporation, Japan
kuma@arch.titech.ac.jp, ttoru@arch.titech.ac.jp, togawa@arch.titech.ac.jp

Abstract: In this paper, the seismic vibration tests are carried out using small scale models of cylindrical lattice shell roofs supported by substructure with viscous damper under horizontal motions.

The cylindrical lattice shell roofs used in the experiments are made of steel plates 0.8mm thick. The arch span is 75 cm. The substructures consist of a linear motion slider, compression or tension springs and weights. The natural periods of substructures are adjusted by varying the spring constants and the weights. The shell roofs are subjected to earthquake motions with gable (arch) direction. The viscous damper is selected as the additive damping is 20%. The coefficient of viscosity of damper is 1100kg/s at velocity with 20cm/s. The shell roofs and substructures are in elastic range under earthquake motions.

From the experimental results, the response reduction effect by adding the viscous damper is examined. At first, the fundamental vibrational characteristics of shell roof and fundamental characteristics of viscous damper are examined. The effects of relationship between mechanical properties of roofs and substructures, existence of damper and shortening of time axis on response behavior of shell roofs are made clear. In addition, it is confirmed that the simple response evaluation methods proposed in previous papers apply to the responses with viscous damper.

1. INTRODUCTION

The cylindrical lattice shell structures are used for the roofs of a gymnasium, an exhibition hall and so on. These structures are also used for evacuation facility and disaster prevention base in a time of disaster such as an earthquake or a typhoon. Therefore, it is hoped that these structures have sufficient earthquake performance for resisting large earthquake motions. It is effective in avoiding the failures of members of roof for large earthquake motion adding the damping devices at substructure. By adding the devices, the seismic input to shell roof decreases.

In this paper, the seismic vibration tests are carried out using small scale models of cylindrical lattice shell roofs supported by substructure with viscous damper under horizontal motions. It is confirmed that the simple response evaluation methods proposed in previous papers apply to the responses with viscous damper (Takeuchi et al. (2004), Takeuchi et al. (2005), Takeuchi et al. (2007)).

2. OUTLINES OF VIBRATION TESTS OF CYLINDRICAL LATTICE SHELL

2.1 Specimens and Experimental Devices

The roof structure for experimental model is the cylindrical lattice shell roof as shown in Photo 1 and Fig.1. The span of gable direction of lattice shell L_x is 75cm. The half subtended angle θ is 30deg.. The shell roof is made of cold rolled steel plates (SPCC) 0.8mm thick. The line through AOA' in gable direction is called "center line". The line through BOB' in longitudinal direction is called "ridge line". The names of models are

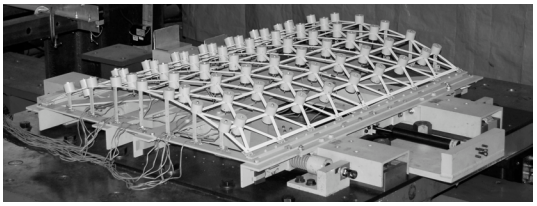

Photo 1 Experimental Device of Cylindrical Lattice Shell Structure with Viscous Damper

shown at the right of Fig. 1. Fig. 2 shows the schematic diagrams for experimental models. The models are the following 3 types. R model is the model of shell roof without substructure, F model is the model of shell roof with substructure and E model is the equivalent single-mass model with mass of shell roof and substructure. In addition, d model is the model with viscous damper and n model is that without damper on F and E models. The parameters for experiments are shown in Table 1. The ratios R_T of the natural period of E model to that of 1st mode of R model are adjusted to 0.8, 1.0 and 1.2. The experimental device is shown in Fig.3. The shell roofs are fixed with hinges, the boundary of roof is a pin support. The substructures consist of a linear motion slider, compression springs and weights. The natural periods of substructures are adjusted by varying the spring constants. The brazen weights is attached to the nodes of shell for the purpose of lengthening the period of shell roof and the stresses occurring uniformly under the dead load. The viscous damper is selected as the additive damping is 20%. The coefficient of viscosity of damper is 1100kg/s at velocity with 20cm/s.

2.2 Measurement and Loading Programs

The responses of structures are measured with the accelerometers, the motion capture systems (MC) and the strain gauges. The positions for measurements are shown in Fig.4. The accelerations of shell structures are obtained by differentiating the measured displacements by MC twice with respect to time t. The accuracies of these accelerations are verified by comparison of the response values by the motion capture systems with those by the accelerometers. The input earthquake motions are BCJ-L1 which is an artificial earthquake motion of the Building Center of Japan, El Centro NS (1940) and JMA Kobe NS (1995). The time axes of earthquake motions are shortened in quarter (T/4). In addition, earthquake motions with half (T/2) and original (T/1) time axes are used at JMA Kobe. The maximum accelerations of input earthquake motions A_g^{max} are standardized to be 150~200 cm/s^2. The shell roofs and substructures are in elastic range under these earthquake motions.

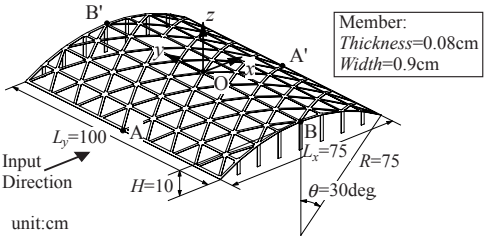

Figure 1 Shape of Cylindrical Lattice Shell Roof

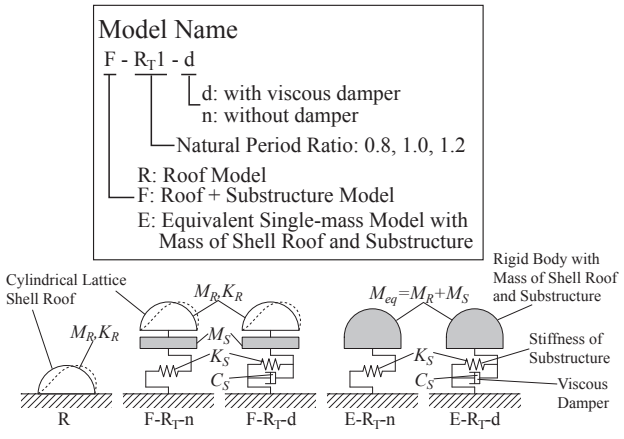

Figure 2 Schematic Diagrams for Experimental Models

Table 1 Parameters for Experiments

Natural Period Ratio $R_T(=T_{eq}/T_R)$	Stiffness of Substructure (N/mm)	Mass of Roof M_R(kg)	Whole Mass M_{eq} (kg)	Mass Ratio $R_M(=M_{eq}/M_R)$
0.8	293.6	18.2	47.1	2.6
1.0	187.9			
1.2	130.5			

3. VIBRATIONAL CHARACTERISTICS OF CYLINDRICAL LATTICE SHELLS

3.1 Vibrational Characteristics of Roof Model

The eigenmodes of R (roof) model are measured by inputting sweep waves and sine waves. The number of measured eigenmodes is 7. Fig.5 shows the natural vibrational characteristics for R model. Phase difference between the measureing points is observed. Therefore, the shapes of eigenmodes with maximum amplitude at all nodes are shown in figures. The natural periods are

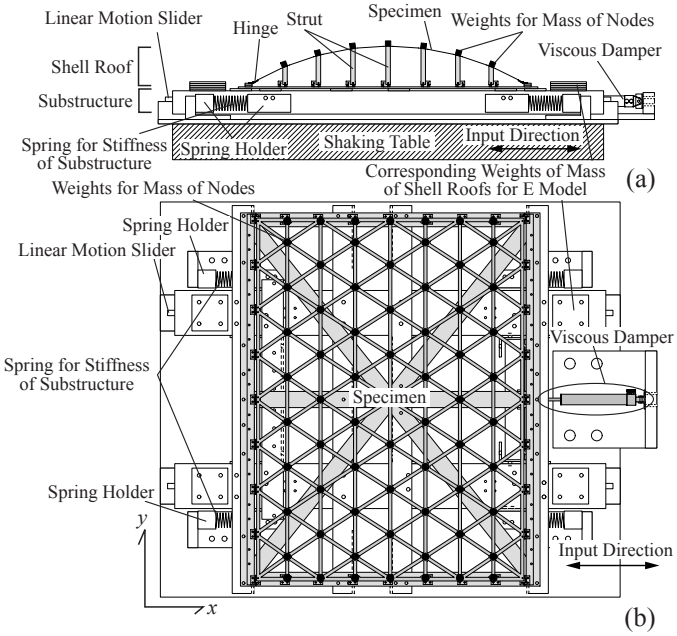

Figure 3 Experimental Device:
(a) Elevation, and (b) Plan

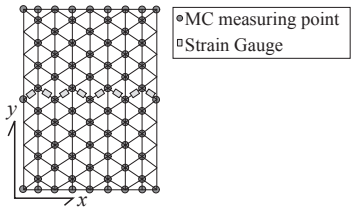

Figure 4 Positions for Measurements

0.098sec for 1st mode and 0.079sec for 5th mode. The shape of 1st mode is antisymmetrical 2 waves mode (O2). That of 5th mode is symmetrical 1.5 waves mode. Fig. 6 shows the vertical response magnification factor at node with maximum response of shell roof subjected to sine wave with natural period of each mode. The magnification factor of 5th mode is larger than those of other modes.

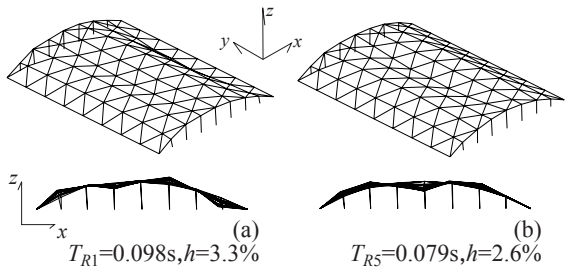

Figure 5 Natural Vibrational Characteristics (R model): (a) 1st Mode, and (b) 5th Mode

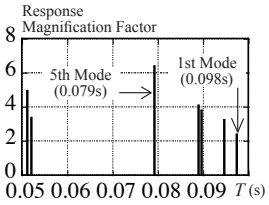

Figure 6 Vertical Response Magnification Factors of Each Mode (Node with Maximum Response, Sine Wave)

3.2 Vibrational Characteristics of Equivalent Single-mass Model

The vibrational characteristics of E (equivalent single-mass) models are shown in Table 2. In the case of E model, the amplitude dependence occurs in the relationships between the damping factors and the amplitude of response. Therefore, the damping factors at the maximum value of responses under each earthquake motion are applied to the damping factor of E model.

Table 2 Natural Vibrational Characteristics (E model)

Addition of Damper	Model Name	Natural Period T_{ei}(sec)	Natural Period Ratio R_T (=T_{ei}/T_{R1})	Damping Factor h(%)
without Damper	E-R_T0.8-n	0.082	0.84	0.6
	E-R_T1-n	0.101	1.03	0.6
	E-R_T1.2-n	0.128	1.31	0.4
with Damper	E-R_T0.8-d	0.081	0.83	11.2
	E-R_T1-d	0.099	1.01	19.1
	E-R_T1.2-d	0.123	1.26	7.9

(Damping Factor: JMA Kobe NS T/4 input)

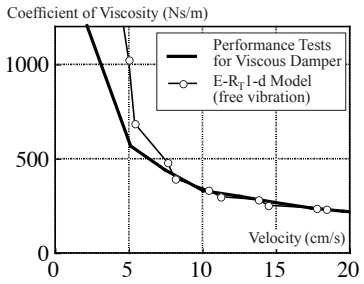

Figure 7 Performance Tests for Viscous Damper (Sine Wave 10Hz input)

The damping factors of E-R_T-d model with damper are about 7~18% larger than those of E-R_T-n model without damper. However, There is little difference of natural period by the existence of damper. Fig.7 shows the relationships between coefficient of viscosity and velocity by the performance tests for viscous damper. The tests are carried out by inputting the sine waves or moving with uniform velocity. The viscous damping coefficients are calculated from the energy consumption per 1 cycle obtained from the load-displacement curve by tests. The test results approximately agree with the curve obtained by free vibration of E-R_T1-d model.

4. SEISMIC RESPONSE BEHAVIOR OF CYLINDRICAL LATTICE SHELLS

4.1 Seismic Response Behavior of Roof Model

Fig.8 shows the distributions of maximum response accelerations of R model on the center line AOA' and entire shell roof. In the case of vertical response, the shape of distribution is an almost symmetrical shape about the ridge line BOB'. However, the node with maximum response is located in left side. The reason for this is that the shell roof is the asymmetrical shape about the ridge line with geometric initial imperfection. On the other hand, in the case of horizontal response, the shape of antisymmetrical 2 waves is observed in Fig.8(A). Fig.9 shows the distributions of maximum response displacements. The larger displacements occur in the vicinity of boundary on the side of Node A in any direction.

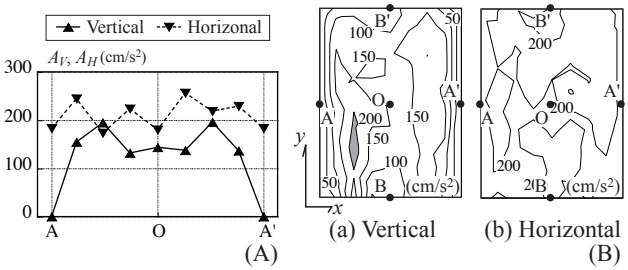

Figure 8 Distributions of Maximum Response Accelerations of R model (JMA Kobe NS T/4, Ag^{max}= 200cm/s^2):
(A) on Center Line, and (B) on Entire Shell Roof

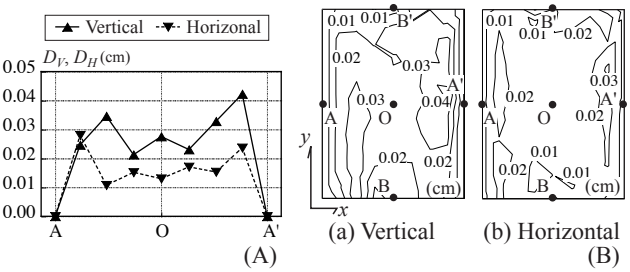

Figure 9 Distributions of Maximum Response Displacements of R model (JMA Kobe NS T/4, Ag^{max}= 200cm/s^2):
(A) on Center Line, and (B) on Entire Shell Roof

4.2 Response Reduction Effect by Vibration Control Device

First, the response reduction effects of E (equivalent single-mass) models by addition of viscous damper are examined. The amplification factors of maximum response acceleration of E model A_{eq} to the maximum acceleration of input earthquake motion A_g^{max}, and response spectra are shown in Fig.10. The amplification factors of E-R_T-n model correspond to the response spectrum with h=0.003~0.01, those of E-R_T-d model correspond to the response spectrum with h=0.1~0.2. These damping factors approximately agree with the damping factors of E models shown in Table 2.

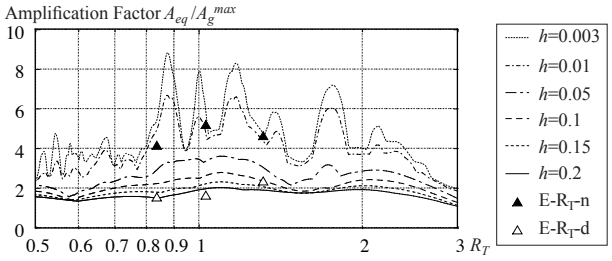

Figure 10 Acceleration Response Amplification Factors of E Model to Input Acceleration of Earthquake Motion, and Response Spectra (JMA Kobe NS T/4)

Next, the response reduction effects of F (shell roof with substructure) models are examined. Fig.11 shows the distributions of maximum response accelerations of F model on the center line AOA'. Regardless of R_T, the response accelerations of F-R_T-d models are reduced to half in comparison with those of F-R_T-n models in any response direction. In the case of vertical response accelerations of F-R_T-n models, the shapes of distribution are shapes with two peaks about the apex O in any R_T. In the case of F-R_T-d models, the shapes of distribution of R_T=1, 1.2 models are shapes with two peaks about the apex. However, in the case of R_T=0.8 model, maximum vertical response acceleration occurs at the apex O. The distribution shape of F-R_T0.8-d model is similar to shape of 5th mode of shell roof. This behavior indicates that the 5th mode appears due to shift of natural period by addition of viscous damper. Fig.12 shows the distributions of maximum response accelerations of F-R_T1 model on entire shell roof. The distribution of horizontal response becomes uniformly by addition of damper. In the case of vertical response, the accelerations increase sharply at the boundary regardless of the addition of damper. The maximum response accelerations occur in the vicinity of center line near boundary (near node A or A').

Fig.13 shows the maximum and minimum values of axial forces and bending moments on the center line AOA' for F-R_T1 model. These member forces are evaluated from the measured value of strain gauges using Eqs. (1) and (2) shown in Fig.13. The member forces are reduced to half by addition of damper as in the case of response accelerations. The absolute values of maximum and minimum values are almost equal.

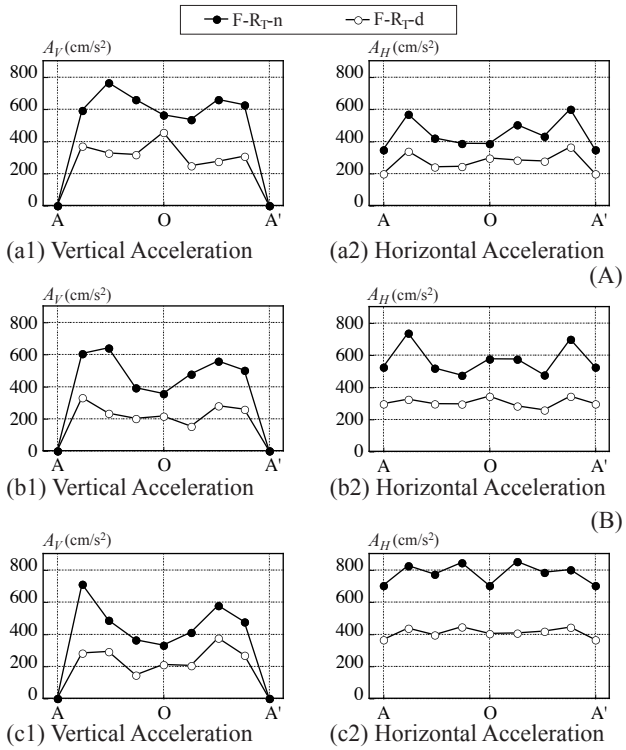

Figure 11 Distributions of Maximum Response Accelerations of F model (Center Line AOA', JMA Kobe NS T/4):
(A) F-R_T0.8 , A_g^{max}= 150cm/s^2, (B) F-R_T1 , A_g^{max}= 150cm/s^2, and (C) F-R_T1.2 , A_g^{max}= 200cm/s^2

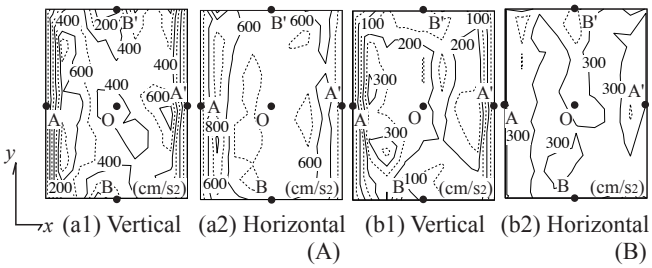

Figure 12 Distributions of Maximum Response Accelerations of F-R_T1 model (Entire Shell Roof, JMA Kobe NS T/4, A_g^{max}= 150cm/s^2):
(A) F-R_T1-n, and (B) F-R_T1-d

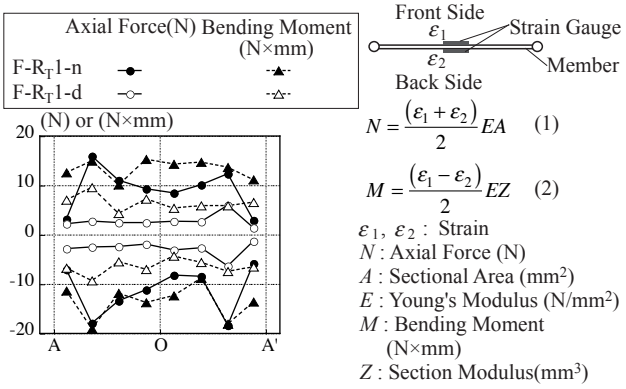

Figure 13 Maximum and Minimum Velues of Axial Forces and Bending Moments on Center Line AOA' (F-R_T1 model, JMA Kobe NS T/4, A_g^{max}= 150cm/s^2)

Next, the acceleration response amplification factors of F model are examined.

Fig.14 shows the acceleration response amplification factors of F-R_T1 model on center line AOA'. The acceleration response amplification factors are obtained by dividing the maximum response accelerations of shell roof A_V, A_H by the response acceleration of E model. The response accelerations reduced by addition of viscous damper as shown in Fig.11. However, the results of F-R_T1-d model are larger than those of F-R_T1-n model on the response amplification factor. This fact indicates that the response reduction by addition of damper for F model is smaller than that for E model.

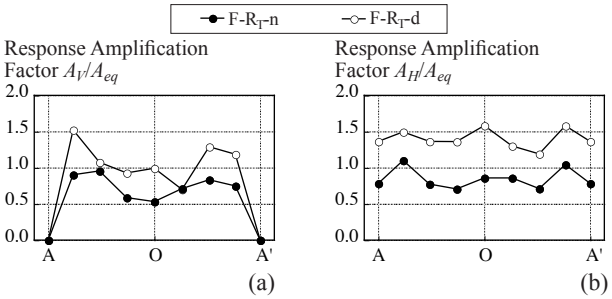

Figure 14 Response Amplification Factors of F-R_T1 model (Center Line AOA', JMA Kobe NS T/4, A_g^{max}= 150cm/s^2):
(a) Vertical Amplification Factor, and (b) Horizontal Amplification Factor

Fig.15 (a) and (b) show the relationships between acceleration response amplification factor under earthquake motion with T/4 and natural period ratio R_T. In these figures, the evaluation formulae for acceleration response amplification factor (Takeuchi et al. (2007)) are indicated together (Eqs.(3)~(6)).

Vertical:

$$F_{RV0} = \begin{cases} 3 & (0 < R_T \le 5/16) \\ \sqrt{5/R_T} - 1 & (5/16 < R_T \le 5) \\ 0 & (5 < R_T) \end{cases} \quad (3)$$

Horizontal:

$$F_{RH0} = \begin{cases} 3/2 & (0 < R_T \le 1/4) \\ (\sqrt{1/R_T} + 1)/2 & (1/4 < R_T \le 1) \\ 1 & (1 < R_T) \end{cases} \quad (4)$$

correction formulae considering the resonance at around R_T=1.0:

Vertical:

$$F'_{RV0} = \sqrt{F_{RV0}^2 + \frac{1}{\left(1 - R_T^2\right)^2 + \left(1/R_M\right)}} \quad (5)$$

Horizontal:

$$F'_{RH0} = \sqrt{F_{RH0}^2 + \frac{1}{\left(1 - R_T^2\right)^2 + \left(1/R_M\right)^\theta}} \quad (6)$$

The results of R (roof) model are dealt with as those of F model with R_T=0 in these figures. In addition, the response amplification factors are defined again as

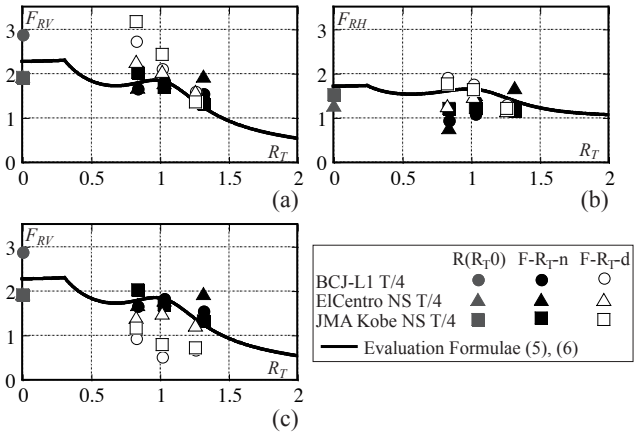

Figure 15 Relationships between Acceleration Response Amplification Factor and Natural Period Ratio, and Evaluation Formulae (Earthquake Motions with T/4): (a) Vertical Direction (with Additive Damping), (b) Horizontal Direction, and (c) Vertical Direction (without Additive Damping)

following equations according to the paper by Takeuchi et al. (2007).

$$F_{RV} = A_{Vmax} / A_{eq} C_V \theta \quad (C_V = 1.33, \theta(\text{rad.})) \quad (7)$$

$$F_{RH} = A_{Hmax} / A_{eq} \quad (8)$$

where A_{Vmax} and A_{Hmax} are maximum vertical and horizontal response accelerations for all nodes of roof, A_{eq} is maximum response acceleration of equivalent single-mass model, C_V is constant for half subtended angle of shell roof θ.

The application range for evaluation formulae of previous paper is the cases of the natural period of shell structure existing in the range of constant acceleration and antisymmetrical 1 wave mode being a predominant mode. Therefore, the condition of shell structure of this study is different from that of previous paper. However, the responses of F-R_T-n model without damper approximately correspond to the evaluation formulae. The vertical responses of F-R_T-d model with damper exceed the evaluation formulae at R_T=0.8, 1. Assuming that the response reduction effect by additive damping for vertical response accelerations of shell structure is smaller than that for response accelerations of equivalent single-mass model, the response amplification factors for F-R_T-d model are evaluated again by using the responses of E-R_T-n model without response reduction effect by additive damping. As a result of reevaluation, the response amplification factors of F-R_T-d model can be estimated on safe side as shown in Fig.15(c).

Next, it is examined why the response amplification factors of F-R_T-d model are larger than those of F-R_T-n model. Fig.16 shows the relationships between response amplification factor A_S/A_{eq} and natural period ratio R_T. Here, A_S is the horizontal response acceleration of substructure of F model. The response amplification factors of F-R_T-n model are less than one time at R_T =0.8, 1. This behavior is elucidated by the following

reason. The shell roof and substructure resonate because the natural periods of shell roof and substructure exist closely. Therefore, the input energy is consumed by the vibration of shell roof, the response of substructure reduces. On the other hand, this vibration behavior does not occur in F-R_T-d model due to the vibration control of shell roof by viscous damper. The amplification factors are about 1.0 at R_T=1.2 regardless of the addition of damper because of non-resonant vibration.

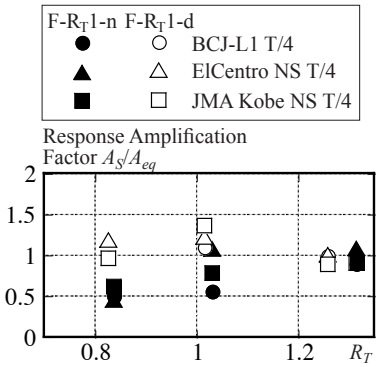

Figure 16 Relationships between Acceleration Response Amplification Factor of Substructure of F Model and Natural Period Ratio

4.3 Effects of Natural Period Ratio and Input Earthquake Motion on Response Reduction Ratio

The relationships between the acceleration response reduction ratio and natural period ratio are shown in Fig.17. The acceleration response reduction ratio is defined as the ratio of response with damper to response without damper. The predicted values are evaluated as the values of response spectrum with damping factor of F-R_T-d model divided by those with damping factor of F-R_T-n model. The relationships between the response reduction ratios and the natural period ratios of predicted and experimental values show similar tendencies on BCJ-L1 and JMA-Kobe NS. In addition, the predicted values correspond better to the experimental values at R_T=1.2 than other R_T. The reduction effect at R_T=1.0 is largest in any direction.

Fig.18 shows the relationships between the acceleration response reduction ratio and the time axis of input earthquake motion. The reduction effect of time axis T/1 of earthquake motion with long period is smaller than the effects of other time axes regardless of R_T. In the case of input earthquake motion with long period, the reduction effect by damper becomes small because the velocity of response is small and the quasi-static response occurs.

Finally, the comparisons between the experimental values and the predicted values of acceleration response reduction ratios for each seismic wave are shown in Fig.19. With a slight dispersion in El Centro NS T/4 and JMA Kobe NS T/1, the predicted values approximately agree with the experimental results. Therefore, it is possible to predict the acceleration response reduction ratios of shell structures by using additive damping and response spectrum.

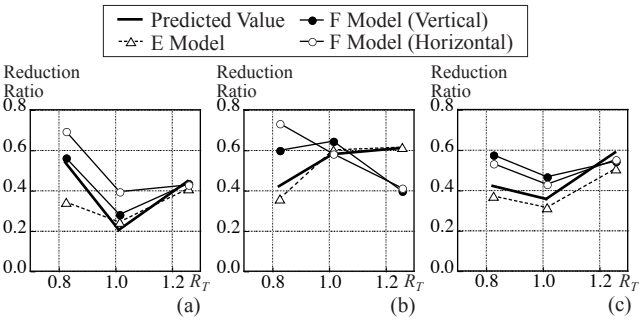

Figure 17 Relationships between Acceleration Response Reduction Ratio of Response of F-R_T-d Model to Response of F-R_T-n Model and Natural Period Ratio: (a) BCJ-L1 T/4, (b) El Centro NS T/4, and (c) JMA Kobe NS T/4

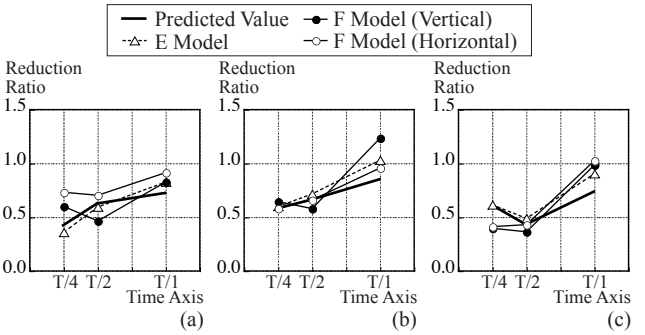

Figure 18 Relationships between Acceleration Response Reduction Ratio of Response of F-R_T-d Model to Response of F-R_T-n Model and Natural Period Ratio (JMA Kobe NS): (a) R_T0.8, (b) R_T1, and (c) R_T1.2

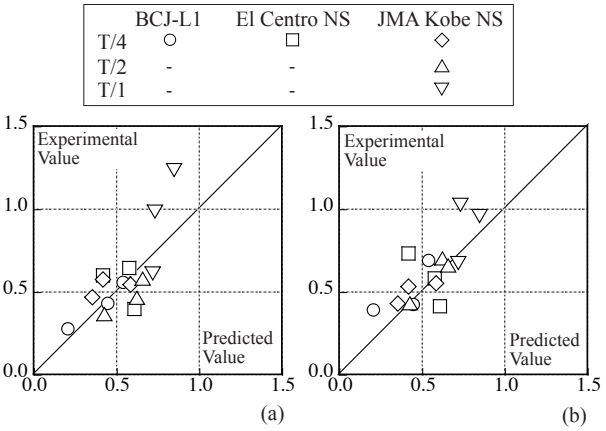

Figure 19 Comparisons between Experimental Values and Predicted Values of Acceleration Response Reduction Ratio of Response of F-R_T-d Model to Response of F-R_T-n Model: (a) Vertical Direction, and (b) Horizontal Direction

5. CONCLUSIONS

It is concluded as follows, from the above results.

1) It is possible to reduce the maximum vertical and horizontal response accelerations, and maximum axial forces and bending moments of shell roof by adding the viscous damper to the substructure and

consequently decreasing the horizontal response acceleration of substructure.

2) It is necessary to note that the reduction effect of shell roof by additive damping is smaller than that of equivalent single-mass model by additive damping in regard to the calculation of acceleration amplification factor to the response of equivalent single-mass model.
3) It is possible to predict the acceleration response reduction ratios of shell structures by using additive damping and response spectrum.

Acknowledgements:
The present paper was supported in part by a grant from Grant-in-Aid for Young Scientists (B) (Research No.18760414) and Grant-in-Aid for Scientific Research (B) (Research No.19360247) by Japan Society for the Promotion of Science (JSPS). The experiments in this paper are carried out using the facility by JSPS the 21st Century COE Program "Evolution of Urban Earthquake Engineering".

References:

Takeuchi, T., Ogawa, T., Nakagawa, M. and Kumagai, T. (2004), "Response Evaluation of Medium-Span Lattice Domes with Substructures Using Response Spectrum Analysis," *Shell and Spatial Structures from Models to Realization, IASS2004 symposium*, Montpellier, TP076 (CD-ROM 1-8)

Takeuchi, T., Ogawa, T., Yamagata, C. and Kumagai, T. (2005), "Seismic Response Evaluation of Cylindrical Lattice Roofs with Substructures Using Amplification Factors," *Proceedings of IASS 2005*, Bucharest, 391-398

Takeuchi, T., Ogawa, T. and Kumagai, T. (2007), "Seismic Response Evaluation of Lattice Shell Roofs using Amplification Factors," *Journal of the International Association for Shell and Spatial Structures*, **Vol. 48** n. 3, n. 160, 197-210.

JOINT CONFERENCE PROCEEDINGS
7th International Conference on Urban Earthquake Engineering (7CUEE) &
5th International Conference on Earthquake Engineering (5ICEE)
March 3-5, 2010, Tokyo Institute of Technology, Tokyo, Japan

STRUCTURAL DESIGN AND RESEARCH OF A LARGE-SPAN SINGLE-LAYER ELLIPSOID LATTICED SHELL WITH COMPLEX BOUNDARY

Zhang Hui[1], Yang Lianping[2], Li Yaming[3], Zhang Lianglan[4],and Zhou Deyuan[5]

1) Dr., Shanghai Institute of Architectural Design & Research Co., Ltd. P.R.C.
2) Dr., Shanghai Institute of Architectural Design & Research Co., Ltd. P.R.C.
3) Professor, Shanghai Institute of Architectural Design & Research Co., Ltd. P.R.C.
4) Master, Shanghai Institute of Architectural Design & Research Co., Ltd. P.R.C.
5) Professor, Department of Civil Engineering, Tongji University, P.R.C.
zhanghui@siadr.com.cn, lianping_yang@xd-ad.com.cn, liym@siadr.com.cn, zhangll@siadr.com.cn, dyzhou@tongji.edu.cn

Abstract: In this paper, a shaking table test of a large-span single-layer ellipsoid latticed shell with its concrete frame support was carried out. The dynamic characteristics (such as the natural frequencies, the natural vibration modes, the damping factors etc.) of the model were measured. The seismic responses of the shell due to small, middle and large seismic excitation were observed. The damage of the concrete support was observed too. An analysis model was established for earthquake response analysis. Comparison between the results calculated by ANSYS and the test results was carried out. The effect of the boundary condition of the latticed shell (such as the joint of the shell and the frame support, the lateral rigidity of RC frame support, etc.) to the dynamic behavior of the shell is also analyzed. Based on the test and research, some advices are provided for the design of the actual shell.

1. INTRODUCTION

The latticed shell is a structure which is often used in the large-span space for its beautiful shape, reasonable bearing capacity and economical efficiency. Through the information we have gathered, static analysis, which tends to be mature, and stability analysis, which is based on many computing/analytical theories, were mainly focused on for the time being. As for the dynamic analysis of the latticed shell, it is limited to some extent and needs further improvement.

Compared with the theoretic research, the experiment research of the earthquake-resistant capacity of the latticed shell is far less than enough. There are only researches about dynamic buckling and vibration control in very few references and literatures, and the model adopted in the experiment is quite different to the one in engineering practice.

Based on the engineering background of Shanghai Oasis Center, this paper represents a shaking table test on the large-span single-layer ellipsoid latticed shell structure with a complex boundary. The natural vibration property of the structure is studied. Also the seismic response of the RC frame support in the low part of the shell system is observed. The three-dimensional global structure model including the RC frame that supports the latticed shell system and the ring beam is established, as well the single latticed shell structure. ANSYS software is adopted to calculate the three-dimensional structure and to analyze the vibration property of the structure and the seismic response.

2. ENGINEERING OVERVIEW

Building No.7 in Shanghai Oasis Center, consists of a main building and a skirt building with a 2 story basement, having a floor area of 36,544 square meters. The main building has 12 stories with a total height of 49.4 meters, and the skirt building has 3 stories with a height of 9.55 meters. Frame-shear wall structure is adopted as a structure system. The large-span single-layer latticed shell structure is adopted to part of the skirt building due to the architectural requirements. The horizontal plane and vertical plane are shown in Figure 1 and Figure 2.

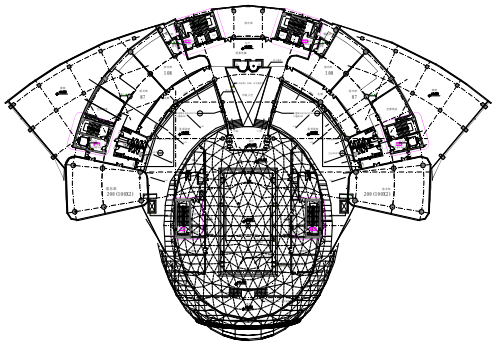

Figure 1 The horizontal plane of the shell

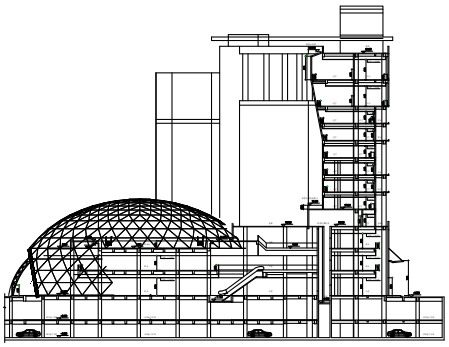

Figure 2 The vertical plane of the shell

The major axis of the shell is 52.6 meters, the minor being 40.0 meters and the height being 20 meters. The shell has a projection area of 1280 square meters and a developed area of 1843 square meters. The latticed shell has a shape of ellipsoid with a complex peripheral bound. Different parts are supported at different elevations: the front two sides are supported by ±0.000 on the roof plate in the basement, with the connection of two-wing support and the RC wall; the middle is supported on the RC ring beam in the skirt building roof with an elevation of 9.55 meters; the door at the back end is supported on the RC wall; the front gate is consisted of a RC arched beam connected with the latticed shell, which is shown in Figure 3.

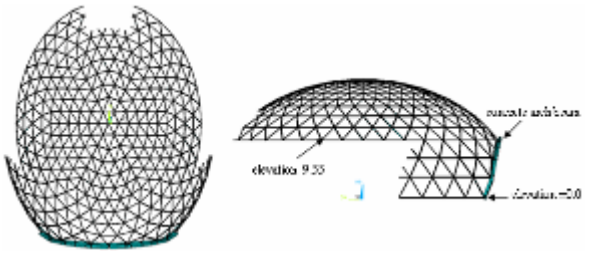

Figure 3 The support boundary of the shell

Both computing analysis and optimization of the different forms and sizes of lattice have been done in this project. The length of a member bar ranges from 2.0 to 4.0 meters, and the main length is about 2.8 meters. Also, the top and the bottom of the latticed shell accept different adoptions of forms and density of lattice so as to enhance the stable capacity. All the joints are welded ball ones.

3. DESING OF THE MODEL

The test was conducted on the MTS six-degree of freedom simulated earthquake shaking table in the State Key Laboratory of Disaster Reduction in Civil Engineering of Tongji University. The size of the shaking table is 4m by 4m, which is available to the input of the three-dimensional earthquake waves.

If the whole structure (including the latticed shell and the RC structure) is made as an test model to experiment on the shaking table, the latticed shell would be very small because of the limited size of the shaking table. The experiment will lose credibility for the huge difference between the latticed shell and the real shell. Thus, in order to do a better research of the seismic behavior of the latticed shell, only the latticed shell and the 3-storiy RC frame which is directly connected with the shell will be taken into the account in this experiment.

The real latticed shell, different from the latticed shell studied in the experiment, has 889 member bars and 345 joints, which is so large a number and is so difficult to make experiment if we make the model conformed to its real amount. So the structure will be simplified in this experiment, which means to increase the size of the latticed shell and the joints, to reduce the number of member bars and joints, and the variety of member bars. The simplification is based on the elaborated computing analysis that both the dynamic and the static properties will be close before and after the simplification of the latticed shell. After the simplification, there are 271 member bars and 131 joints, and only 2 kinds of section of member bars and welded ball joints each.

According to the condition in the lab, we choose the scaling factor of length to be 1/10. The experimental model is shown in Figure 5. The main scaling factors are shown in Table 1.

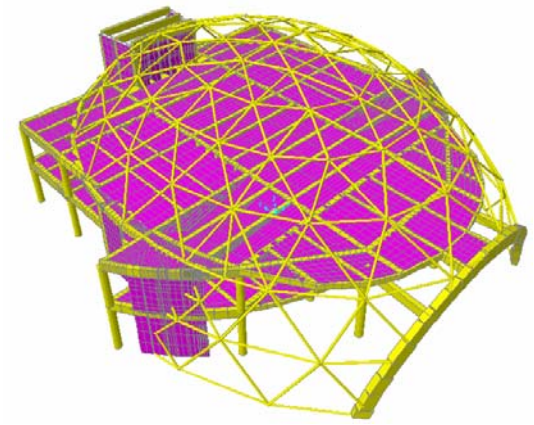

Figure 4 The experimental analytical model



Figure 5 The experimental model

Table 1 The main scaling factors of the experimental model

Physical quantity	L (length)	E (modulus elasticity)	A (accelerate)	T (cycle)	F (frequency)	Σ (stress)
Scaling factor	1/10	1/4	1	0.3162	3.1626	1/4

According to the natural frequencies and the classification of the sites where the constructions are located, the earthquake waves adopted in the experiment are El-Centro wave, Pasadena wave and SHW wave. Referring to the seismic code for building structures in China and the rule of latticed shell structure technique, the peak ground acceleration (PGA) is 0.035g, 0.10g, and 0.22g for minor, moderate, and major earthquake levels of seismic intensity 7, respectively. PGA for the major earthquake of intensity 8 is 0.40g.

4. MODEL TEST

4.1 Description of the Observations in the test

The model structure is basically in elastic stage and meets the requirements that the structure is not damaged by earthquake according to the rules before the effect of the major earthquake. After an effect of major earthquake of intensity 8, there are several cracks in the parts of the RC frame, and the cracks are distributed in the beam joints in the east, west, and north facade. The cracks also appear in the joints area of the beam and the shear wall. The propagation of the cracks is slight and the width is small. The latticed shell hasn't been distorted. There is some damage to the structure after the effect of major earthquake of intensity 8 but quite slight. Thus, the structure meets the requirements that it does not collapse by major earthquake according to the codes.

4.2 Natural vibration property of the model structure

We make a scanning test to the structure model by white noise both before and after the effect of different levels of the earthquakes. We can find out the natural vibration property of the model structure through the spectral characteristics of each measuring point of acceleration, the transfer function and the analysis of the reaction of the time interval.

In the test, we've measured that before the effect of the earthquake, the first vibration frequency of the model structure is 10.35Hz (lateral translation mainly in the bottom frame), and the second vibration frequency is 12.671Hz (vertical translation mainly in the bottom frame). After the effect of major earthquake of intensity 8, the first vibration frequency of the model structure has reduced to 6.644Hz, with a reduction of 35.83%, and the second vibration frequency has reduced to 9.426Hz, with a reduction of 25.61%.

The natural vibration frequencies of the model are very dense except first frequency, which are corresponding to the results of other kinds of latticed shells. The lower mode of vibration of the model structure represents a lateral translation of the whole structure, and the higher mode of vibration represents an oscillation of the latticed shell structure. As the value of the input earthquake amplitude increases, the frequency of the model structure becomes lower. This is mainly due to the crack of the concrete frame. However, there's no great change in the rigidity of the latticed shell.

4.3 The joints of the model structure and the response of member bars

4.3.1 The displacement response of the joint of the model structure

The value of the displacement response of the joint of the model structure can be obtained by the displacement pickup. Several maximum and minimum values of the joint displacements are shown in Figure 6 to Figure 8.

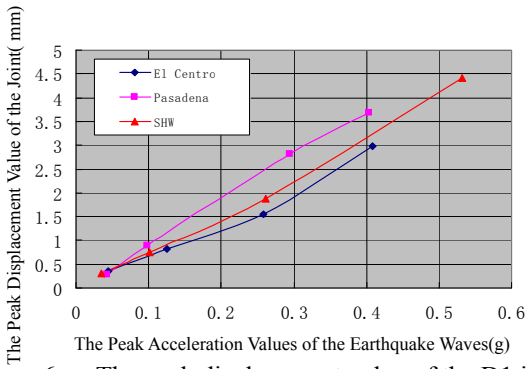

Figure 6 The peak displacement value of the D1 joint in the effect of the earthquake waves in X direction

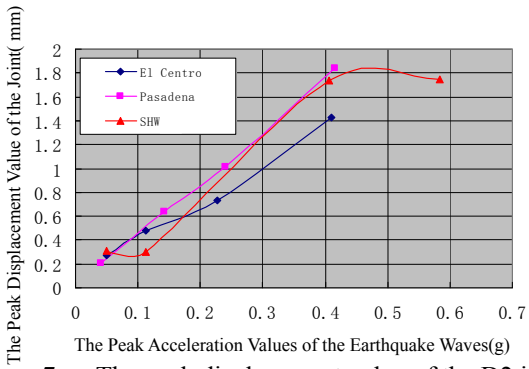

Figure 7 The peak displacement value of the D2 joint in the effect of the earthquake waves in Y direction

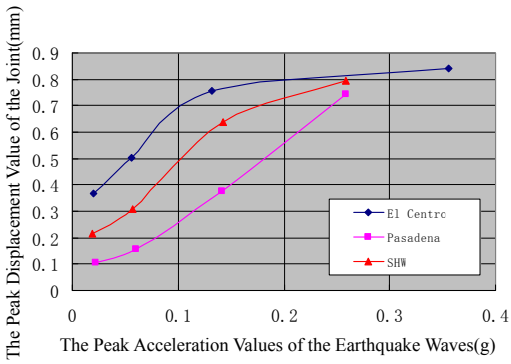

Figure 8 The peak displacement value of the D3 joint in the effect of the earthquake waves in Z direction

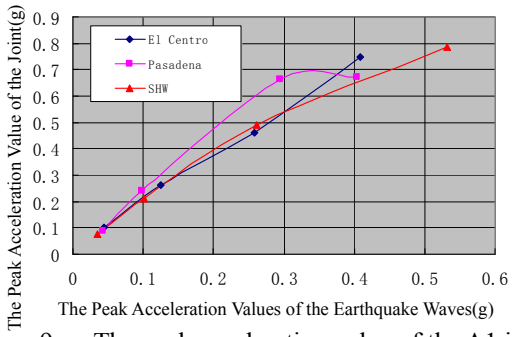

Figure 9 The peak acceleration value of the A1 joint in the effect of the earthquake waves in X direction

It can be shown from the Figure 6 to Figure 8 that there isn't mutation in the displacement response of the joint of the latticed shell when experiencing the effect of the earthquake in each stage, which means that there's no obvious plastic deformation of the structure after the effect of major earthquake of intensity 8.

In the course of being affected by frequent earthquake of intensity 7 to the rare earthquake of intensity 8, all the joint displacements of the model structure are 10mm smaller than the limitation of the code (1/400 short-span). In the effect of z-direction earthquake, the joints of latticed shell caused by El-Centro wave receive the strongest response of the z-direction displacement, the SHW wave being the second and the Pasadena wave being the least. In the effect of the main X, Y- direction earthquake, the joints caused by the three waves receive a quite close response of x-direction displacement. In the effect of the vertical earthquake, the joints receive less response to the vertical displacement than the response to the displacement caused by a lateral earthquake, but the displacement responses in the three directions of the latticed shell are in the same magnitude. This is corresponding to the result of the response to the acceleration. Therefore, the effect of the earthquake in three directions should be taken into consideration when designing the latticed shell.

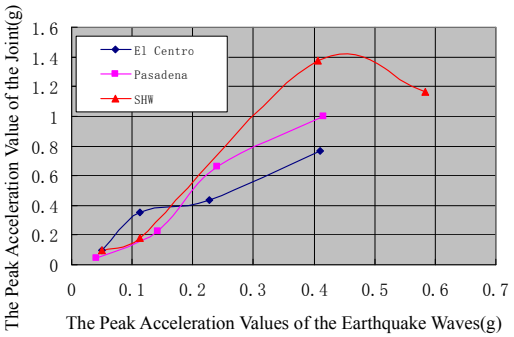

Figure 10 The peak acceleration value of the A2 joint in the effect of the earthquake waves in Y direction

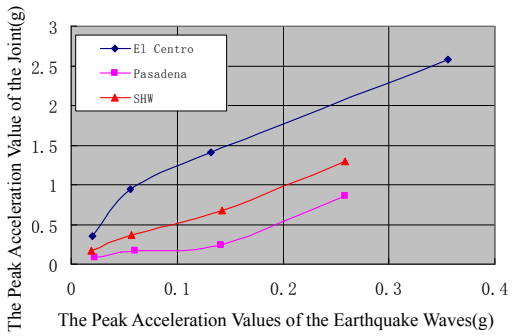

Figure 11 The peak acceleration value of the A3 joint in the effect of the earthquake waves in Z direction

4.3.2 The acceleration response of the joints of the model structure

The values of the acceleration response of the joints of the model structure are measured by the piezoelectric acceleration transducer. The maximum and minimum values of some joints are shown in the Figure 9 to Figure 11.

It can be shown from the Figure 9 to Figure 11 that after experiencing the effect of the frequent earthquake of intensity 7 and the rare earthquake of intensity 8, there's no abnormal phenomenon in the acceleration response of the joints of the model structure. The acceleration response of the joints changed its curve into line with the change of the value of the earthquake amplitude, which means that there's no mutation of the structure stiffness and no obvious plastic deformation of the structure.

In the effect of z-direction earthquake, the z-direction acceleration receives the strongest response of the structure caused by El-Centro, the SHW wave being the second and the Pasadena wave being the least. In the effect of the main x-direction earthquake, the structure caused by the three waves receives a quite close response of the x-direction acceleration. In the effect of the main y-direction earthquake, the structure caused by the three waves also receives a quite close response of the y-direction acceleration. While in the effect of a major earthquake, the response caused by SHW wave was much stronger than other two waves.

In the earthquake effect, acceleration responses of the different direction of the joints are in the same magnitude. Therefore, the earthquake effect in z-direction should be taken into consideration when designing the latticed shell structure. The acceleration

response of the latticed shell structure does not increase as the elevation of the joints increases. The joints in the middle elevation receive stronger response.

4.3.3 The response of member bars of the model structure

The strain response of the member bars can be measured by the strain gauges on the member bars. The S3 member bars response are shown in the Figure 12; the maximum and the minimum values of the member bars response in the effect of the earthquake waves are shown in Figure 13 to Figure 15.

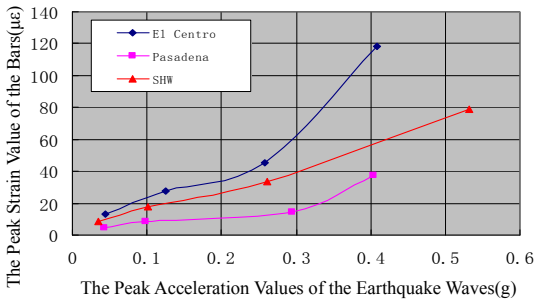

Figure 12 The strain response of the S3 member bar in the effect of the earthquake waves

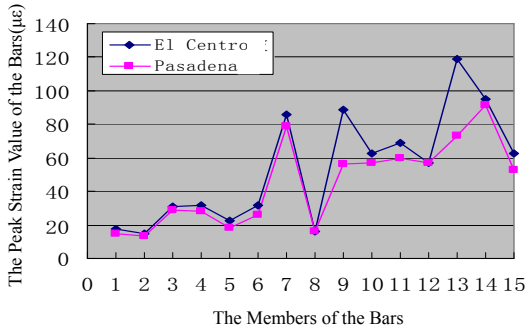

Figure 13 The peak values of the member bars response in the effect of the earthquake waves in X direction

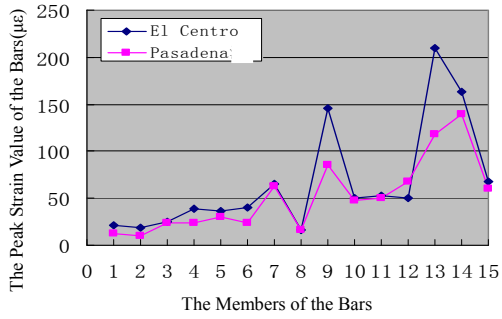

Figure 14 The peak values of the member bars response in the effect of the earthquake waves in Y direction

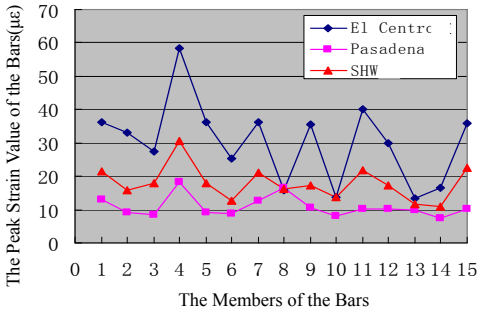

Figure 15 The peak values of the member bars response in the effect of the earthquake waves in Z direction

It can be shown from the figures that there isn't mutation in the strain response of the member bars when experiencing the effect of the earthquake in each stage, which is corresponding to the criteria of the acceleration and replacement response. In the effect of z-direction earthquake, the member bars stress caused by El-Centro is the maximum, the SHW wave being the second, and the Pasadena wave being the least. This is corresponding to the conclusion drawn above.

In the effect of the lateral earthquake, the stress response of the member bars between the first floor and the ring beam is the stronger. As the increase of the elevation, the stress of the member bars tends to reduce. While in the effect of the vertical earthquake, the stress response of member bars in each elevation is quite close. The stress response caused by El-Centro is the strongest, the SHW being the second, and the Pasadena wave being the least.

5. THEORETICAL ANALYSIS

In this paper, two analytical models are established (shown in Figure 16 to 17). One is the single latticed shell structure, the other is the three-dimensional global structure model including the single latticed shell structure, the infrastructure that supports the latticed shell system and the ring beam. ANSYS is adopted to calculate and analyze the three-dimensional structure. In the analytical model, the beam element is adopted for space bar system and main structure beam while the shell element is adopted for the concrete shear wall and the floor plate.

When choosing the seismic design parameters, steel structure response spectrum is chosen for analytical model of the single latticed shell. Considering that the concrete structure plays a leading role in the structure property, we choose concrete structure response spectrum for the global model. The effect of the X,Y , Z direction earthquake should be taken into consideration respectively to analyze the structure.

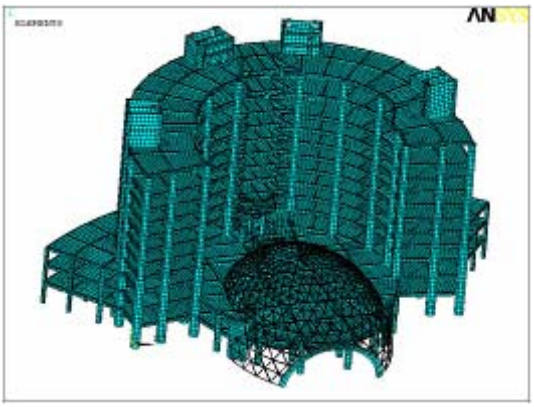

Figure 16 The global structure analysis model

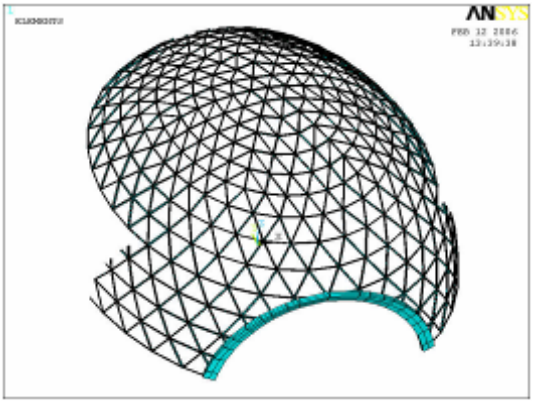

Figure 17 The single latticed shell structure analysis model

5.1 Analysis of the single latticed shell model

The natural frequencies of the first 20 orders of the structure are shown in Table 2. The first 4 orders of the vibration mode are shown in Figure 18 to 21.

It can be shown from the figure of the latticed shell structure that the stiffness in the short-span is relatively weak. The first vibration mode is mainly lateral vibration; the second one is mainly vertical vibration; the third one is mainly vertical vibration with some torsional vibration; and the fourth to the tenth one are the combination of lateral and vertical vibration, mainly with vertical vibration. The torsional effect is occurred along with high order vibration mode. The vertical vibration type accounts for 50% in the first 30 vibration mode. In the effect of the vertical component of the ground motion, the earthquake effect which is corresponding to the vertical vibration type of the structure will increase. Thus, we should pay special attention to the vertical vibration.

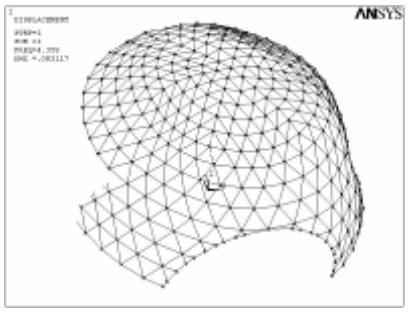

Figure 18 The first order of the vibration mode

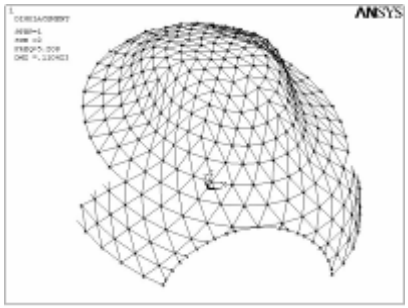

Figure 19 The second order of the vibration mode

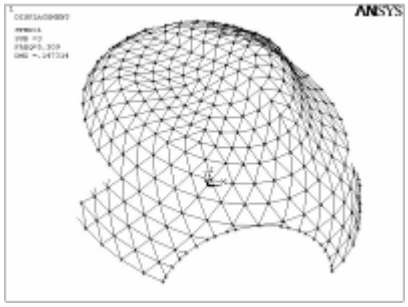

Figure 20 The third order of the vibration mode

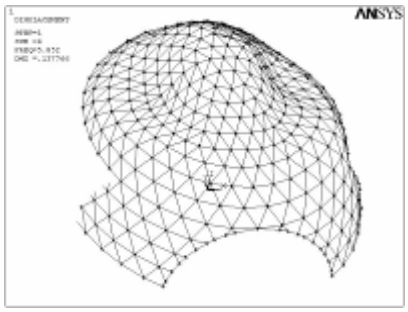

Figure 20 The fourth order of the vibration mode

Table 2 The natural frequencies of the first 20 orders of the structure of The single latticed shell structure

number	1	2	3	4	5	6	7	8	9	10
frequency	**4.3578**	**5.2076**	**5.3092**	**5.8517**	**5.8832**	**5.9686**	**6.0769**	**6.1505**	**6.4864**	**6.5375**
number	11	12	13	14	15	16	17	18	19	20
frequency	**6.5981**	**6.903**	**6.9342**	**7.0264**	**7.1119**	**7.2019**	**7.2771**	**7.4011**	**7.6309**	**7.6733**

The calculating result of the member bars' internal force shows that the internal force caused by the lateral earthquake has reached about 20% to 60% of the static internal force, and the stronger internal force caused by the earthquake is located in a position where the member bars' static internal force is stronger. The internal force caused by the vertical earthquake has reached about 2% to 8% of the static internal force, and the strongest dynamic and static internal force share a quite similar distributing rule. The dynamic internal force of the hoop and the slanting member bar is stronger in the place near the support in the short-span and near the front arched beam. Therefore, though the structure is located in the seismic fortification area of intensity 7, the internal force of the member bars caused by the effect of the lateral and the vertical earthquake is relatively high. The earthquake effect should be taken into consideration during designing process.

5.2 The calculation and analysis of the global structure model.

The natural frequencies of the first 20 orders of the structure are shown in Table 3. The vibration modes of the first 4 orders are shown in Figure 22 to 25.

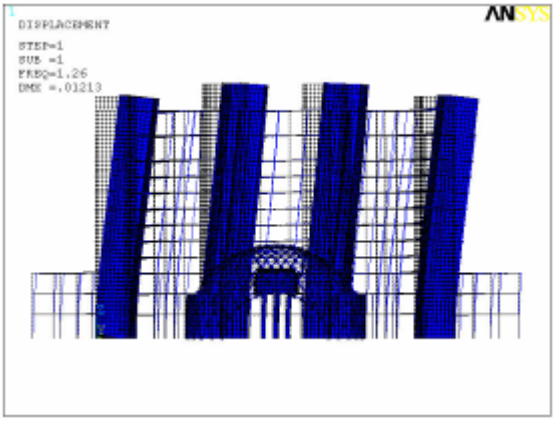

Figure 22 The first order of the vibration mode

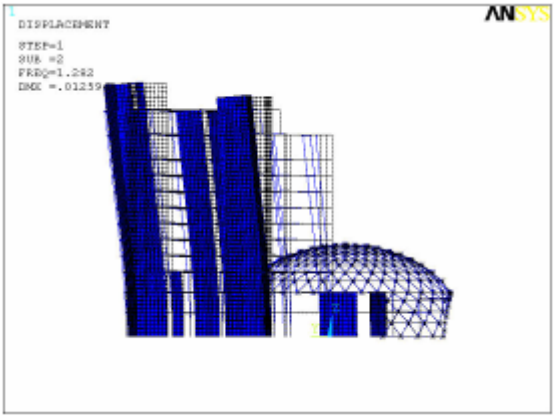

Figure 23 The second order of the vibration mode

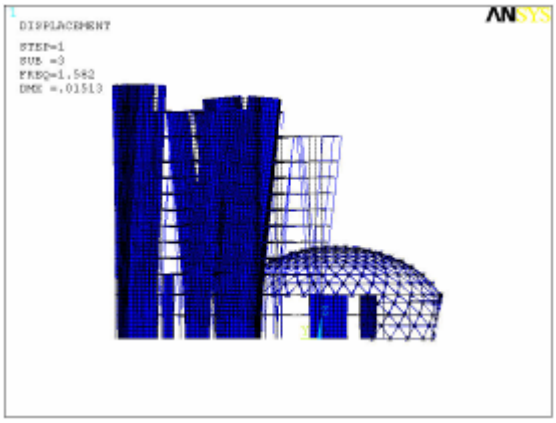

Figure 24 The third order of the vibration mode

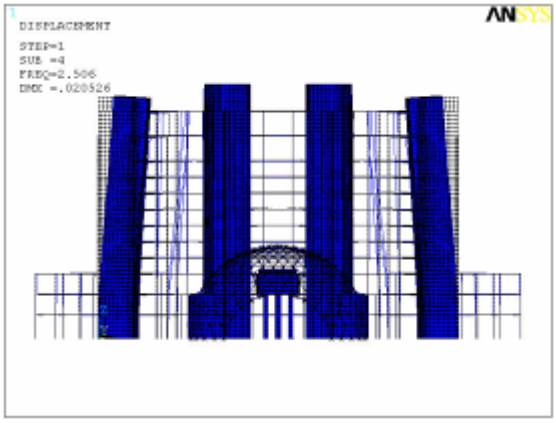

Figure 25 The fourth order of the vibration mode

It can be learnt from the calculating results that in the effect of the lateral earthquake, the maximum axial force of the member bar appears in the front arched beam and in the diagonal web members which is near the two sides of the gate hole. In the effect of the x-direction earthquake, the greatest dynamic internal force of the member bar of the global model is 18% more than that of the single model; in the effect of the y-direction earthquake, the greatest dynamic internal force of the member bar of the global model is 3.76 times more than that of the single model. In the effect of the vertical earthquake, the greatest dynamic internal force appears in the ring bar near the support in the span center and there's not much difference between the results of the global model and the single model, and the value is relatively small compared with that in the effect of the lateral earthquake.

Through the analysis, we can learn that in the effect of the lateral earthquake, the value of the internal force of the global model is obviously bigger than that of the single model. However, in the effect of the vertical earthquake, the two values are quite close. This result is corresponding to the one of the analysis of the vibration mode. There are more translations in the global model, and they occurred in the low-frequency modes of the first orders. The first order vibration mode is mainly in x-direction translation, while other vibration modes are mainly in vertical direction. Since the major part of the

latticed shell is connected with the frame structure below, the bottom supporting structure will bring to inertial effect. If we do calculation and analysis only by using single model, the design of the member bars and the support may not be safe. Therefore, global model should be adopted in the seismic design analysis of the space structure, and the reality of the simulated bottom structure will directly affect the accuracy of the calculating results.

6. CONCLUSIONS

Through the shaking table test research and theoretical analysis on the large-span single-layer ellipsoid latticed shell structure with a complex boundary, several conclusions can be drawn as followed:

1. The model structure studied in this paper has a high stiffness, a small distortion, and a good seismic behavior, which meet the needs of seismic design code in China.
2. Being the same as the other major kinds of latticed shell structure, the large-span single-layer ellipsoid latticed shell structure has a dense frequency distribution and a complex structure vibration mode.
3. In the effect of the lateral earthquake, the responses are quite close caused by 3 kinds of earthquakes adopted in the experiment. While in the effect of the vertical earthquake, the response caused by El-Centro is the strongest, the SHW wave are the second, and the Pasadena wave are the least. In the effect of the earthquake, the latticed shell joint which receives a stronger response of displacement and acceleration is not at the top point but in the 3 to 5 circles below the top point. In the effect of the lateral earthquake, the stress response of the member bars between the first floor and the ring beam is the strongest. As the increase of the elevation, the stress of the member bars tends to reduce. While in the effect of the vertical earthquake, the stress responses of member bars in each elevation are quite close.
4. *Latticed shell structure technique rules* in China stipulates that the latticed shell structure needs no calculation of the vertical earthquake-resistance in the area where the seismic fortification intensity is 7. But the experiment and the calculation result show that though the response in the z-direction is weaker than that in the x and y direction in the effect of the earthquake, the response of the three directions should be in the same magnitude. Hence, the earthquake effect of the three directions should be taken into consideration, which is corresponding to the single-layer cylinder latticed shell, wide-span single-layer saddle latticed shell, single-layer hyperbolic paraboloid latticed shell and double-layer ellipsoid latticed shell.

Reference:

Feng Fan, Shizhao Shen: The Simulated Earthquake Shaking Table test on Single-Layer Sphere Shell and research on structure shock absorption, …*Journal of Harbin University of Civil Engineering and Architecture*, the 33rd Volume, the 3rd issue, 2000.6.

Ming Zhang: the static and dynamic property analysis of K-shape single-layer sphere latticed shell structure, *Building Science*, the 18th volume, the 6th issue, 2002.12.

Dasheng Li, Zhaoquan Zhu: the analysis of the natural property and the earthquake response of the single-layer cylinder latticed shell, *Journal of Xuzhou Institute of architectural Technology*, the 2nd volume, the 1st issue, 2002.3.

Yigang Zhang: the seismic behavior of single-layer hyperbolic paraboloid latticed shell, Journal of Beijing University of Technology, the 27th volume, the 1st issue, 2001.3.

The Occupation Standard in China: Technical specification for latticed shells(JGJ 61-2003), Beijing, 2003.

JOINT CONFERENCE PROCEEDINGS
7th International Conference on Urban Earthquake Engineering (7CUEE) &
5th International Conference on Earthquake Engineering (5ICEE)
March 3-5, 2010, Tokyo Institute of Technology, Tokyo, Japan

IMPLEMENTATION OF BIO-INFORMATICS ON STRUCTURAL HEALTH MONITORING

Tzu-Kang Lin[1)], Chang-Hung Ku[2)], Li-Chen Yu[2)], Chih-Shiuan Lin[3)], Kuo-Chun Chang[4)]

1) Associate Research Fellow, National Center for Research on Earthquake Engineering, Taipei, Taiwan
2) Bachelor Student, Department of Civil Engineering, National Taiwan University, Taipei, Taiwan
3) Research Assistant, National Center for Research on Earthquake Engineering, Taipei, Taiwan
4) Professor, Department of Civil Engineering, National Taiwan University, Taipei, Taiwan
tklin@ncree.org, b95501031@ntu.edu.tw, b95501011@ntu.edu.tw, jasonlin_1130@yahoo.com.tw, ciekuo@ccms.ntu.edu.tw

Abstract: A structural health monitoring system based on Bayesian damage classification and DNA expression data is studied in this paper. Transplanted from the DNA array concept in molecular biology, the proposed structural health monitoring system is constructed by utilizing a double-tier AR-ARX regression process to extract the expression array from the structural time history recorded during external excitations. The AR-ARX array is symbolized as the various genes of the structure in the viewpoint of molecular biology to reflect the possible damage condition existing in the structure. A scale-down six-story steel building located at the shaking table of the National Center for Research on Earthquake Engineering was used as the benchmark structure, and the structural response with different damage levels and locations under ambient vibration was collected to support the database for structural health monitoring. To improve the feasibility of the proposed structural health monitoring system in practical application, a SHM prototype detection system is developed. Three hot-pluggable type modules including the sensing input module, the GPS module, and the data storage module are integrated to form the prototype system. As designed, the micro vibration data will first be measured by the sensor deployed and then transmit through the input module to the built-in micro processor. Both acceleration and velocity of the structure can be measured simultaneously to evaluate the health condition of the structure. Test results from ambient data have shown that the damage condition and location of the specimen can be successfully detected by the structural health monitoring prototype system. The feasibility of transplanting the DNA array concept from molecular biology into the field of structural health monitoring has been demonstrated by the proposed SHM prototype.

1. INTRODUCTION

Structural health monitoring (SHM), a brand new multidisciplinary filed, gradually emerges in various branches of engineering over the last fifteen years. Generally, SHM is defined as the implementing of damage detection and characterization strategy for engineering structures. For the regularity and mass production characteristics of the monitoring objectives, some developed SHM technologies have been successfully applied to aircrafts, vessels, and vehicles in both aeronautics and mechanical engineering. For civil engineering, the goal of SHM is to provide rapid condition screening and reliable information regarding the integrity of the structure in near real time after extreme events, such as earthquakes or blast loading. To reach this target, researchers have been focusing on developing some specific techniques and customized systems.

Recently, how to apply the concept of pattern recognition technique to the field of SHM has been widely discussed. By using pattern recognition technique, the SHM system should be able to classify the measured data based on a priori knowledge or statistical information extracted from the collected patterns. As this concept is increasingly accepted by worldwide researchers, SHM systems based on pattern recognition technique are established and verified. For example, a novel time series analysis integrating pattern recognition is first proposed by Sohn et al. [Sohn and Farrar 2001]. The statistical process control (SPC) technique is then combined to improve the performance of the system [Sohn et al. 2000]. To prove the practical feasibility of pattern recognition based system, experimental data measured from full-scale civil structures are used. It is found that although damage can be consistently detected, however, problems still exist when localizing or quantifying are required [Cheung et al. 2008].

Bioinformatics, the application of information technology to the field of molecular biology, rapidly attracts the vision from researchers of all fields after it was coined in 1979. The research conducted by Dominggos and Pazzani demonstrates that attributes can be dependent in a simple Bayesian classifier (SBC) and makes the application of SBC in bioinformatics possible [Domingos and Pazzani 1996]. Later, the concept of gene expression monitoring was proposed and implemented by T. R. Golub in 1999 [Golub et al. 1999]. The new method offers a new vision for classifying cancer cells from normal ones and ignited a

series of researches on detecting diseases from gene expression array. Following the study, a new research using Naïve Bayes (NB) algorithm to identify the DNA array of cells was proposed [Keller et al. 2000]. Different cancer cases were classified by comparing the DNA patterns of cells with the NB algorithm. According to the research result, the possible disease can be reliably diagnosed by the new proposed system. The subsequent research from Slonim et al. once again demonstrated the feasibility of combining the NB algorithm and the DNA array data for multi-class cancer diagnosis [Slonim et al. 2000].

Inspired by the above-mentioned researches, a new SHM system is proposed in this paper. The structural damage characteristic was first extracted by an AR-ARX model which is composed of a double-tier auto-regressive (AR) and auto-regressive with exogenous inputs (ARX) prediction model. By evaluating the AR-ARX array calculated from the measured structural response with the database created from different structural damage conditions under the support of NB algorithm, the possible damage location and level can be rapidly detected. The developed SHM system is then implemented on a SHM prototype composed of a sensing input module, a GPS module, and a data storage module. Finally, a brief description of the experimental verification is carried out.

2. PRELIMINARY VERIFICATION

The proposed SHM system is composed of three parts: the AR-ARX expression array database which is converted from the time history of structural response under specific damage conditions, the Naïve Bayes method which has been demonstrated to have superior performance in array classification, and the likelihood selection process to optimize the SHM system. To verify the feasibility of the proposed SHM system in practical structure, a series of experiment was conducted on the scale-down six-story specimen at National Center for Research on Earthquake Engineering (NCREE).

Different from monitoring the structural response during strong earthquakes, which is commonly seen in some existing SHM systems, the proposed system tries to use signals measured from ambient vibration in the daily life to enhance its practicability. The structure damages were classified into four major groups with 13 different cases and were simulated by loosening four of the 16 bolts in each floor (1/4 of the beam-column connection). By collecting the experiment database at night, the unwanted noise due to the machine operation or human activity from the laboratory can be carefully avoided and suppressed to improve the reliability of the structural feature arrays. A list of the thirteen damage conditions is listed in Table 1.

As shown in Figure 1, six high-sensitivity velocity meters were deployed on the specimen to measure the micro vibration of each floor. The sampling rate was set to 200 Hz, and 90 cases with each of 20 seconds under every damage condition were recorded while the 13 damage cases were achieved by switching the location of the loosened fasteners. The SHM database was then established by transforming the time histories into the above mentioned AR-ARX models as the DNA array of the structure. The three fundamental parameters (p, a, and b) of the basic ARA-

RX model described is designed to be 12-8-4 after an optimization process. Meanwhile, the advantage of utilizing array expression data for SHM is evaluated by using five different array orders of 60-40-20, 72-48-34, 84-56-28, and 96-64-32 under the basis of the 12-8-4 form. As indicated itself, the 60-40-20 AR-ARX array uses 120 coefficients to monitor the health condition of the structure, and the 96-64-32 AR-ARX array uses 192 coefficients accordingly. To execute the independent testing of the SHM system, 80 patterns in each damage case were used to create the SHM array database, and the rest 10 patterns were used to verify the performance of the system. The results of all 13 cases by sensor V6 is shown in Figure 2. The 13 damage cases are indicated in the longitudinal axis as UN, S1, S2, S3, S4, S5, S6, M12, M34, M56, S123, S234, and S456, and the detected damage condition is reflected in the latitudinal bar. The AR-ARX order is increased from 60-40-20 from the top subplot to the final 96-64-32 in the bottom subplot. All the 10 testing patterns are expressed by the individual bar among every damage case.

According to the results shown in the figures, the performance of the SHM system can be enhanced by increasing the order of the AR-ARX array data. For the cases of 60-40-20 and 72-48-24, serious fluctuation is observed among all testing cases. It is estimated that structural damage characteristics may not be reflected by using only few coefficients. With considering high-order array expression data, the minute damage existing in the structure can successfully detected. For the 96-64-32 AR-ARX system, the accuracy can be expected to approximately 85 to 90 %. Although the feasibility of the proposed SHM system with high-order AR-ARX has been demonstrated by the previous examination, however, any SHM system without 100 % precision could still be classified as a failed system. For that reason, the developed SHM system is upgraded again by using the likelihood selection method in the next section.

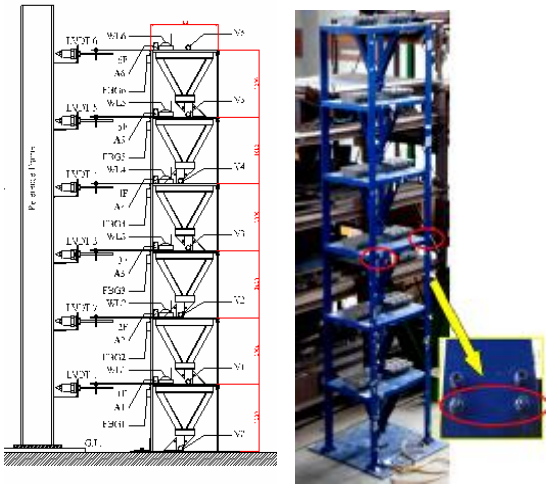

Figure 1 The Six-Story Specimen at NCREE

Table 1. List of the 13 damage cases

1	Undamaged	None
2	Slight damage	1F
3		2F
4		3F
5		4F
6		5F
7		6F
8	Moderate damage	1F&2F
9		3F&4F
10		5F&6F
11	Severe damage	1F&2F&3F
12		2F&3F&4F
13		3F&4F&5F

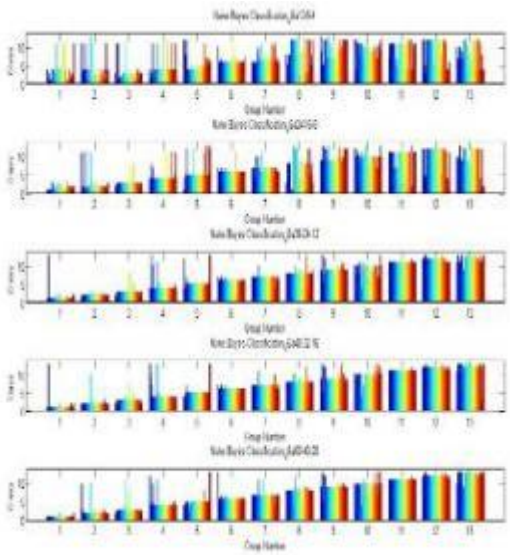

Figure 2 Independent Testing Result from Ambient Vibration of V6

3. MOBILE SHM PROTOTYPE

In order to implement the SHM concept in practice, a SHM prototype detection system is developed. As shown in Figure 3, three hot-pluggable type modules including the sensing input module, GPS module, and the data storage module are integrated to form the prototype system. Meanwhile, by using the customized rectangular tin on the prototype system, power for the sensing unit can be easily provided, and the sensor may operate normally to become a relay station in collecting the data required. As designed, the micro vibration data will first be measured by the sensor deployed and then transmit through the input module to the built-in micro processor. Both acceleration and velocity of the structure can be measured simultaneously to evaluate the health condition of the structure. In addition, different SHM prototype systems can be extend to SHM network by connecting network wires between each prototype system.

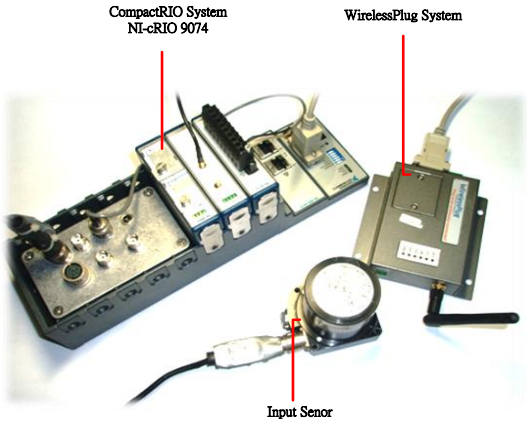

Figure 3 The SHM Prototype System

In order to execute the developed SHM algorithm on the prototype system properly, the driving software is transplanted into the firmware of the mobile module. The software can be divided into two parts: the onsite program in the local machine and the demonstration program in the remote server where all the damage information of structures is collected and released. As shown in Figure4, the on-site program is composed of four parts: Data Pre-Processing, Coefficient Extracting, Health Condition Diagnosis, and GPRS & Wireless.

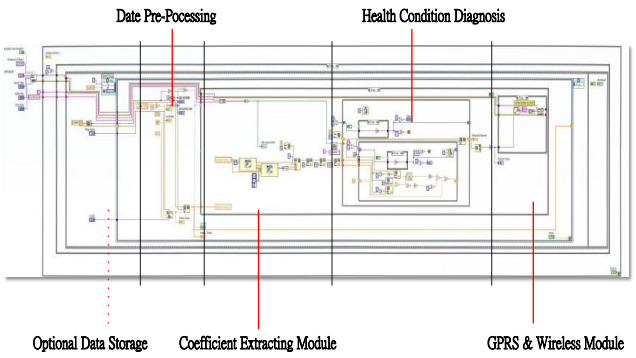

Figure 4 The On-Site Program

3.1 Data Pre-Processing

The Pre-Processing program is composed of three parts including the collection of the input data, the design of the digital filter, and the settings of the data size for SHM processing. By using the Pre-Processing program, the unnecessary noise from the ambient environment can be successfully avoided to ensure the accuracy of the input data. In this study, the sample rate of the data is selected as 200Hz, and the filter is chosen as band-passed filter to filter out the unwanted high and low frequency set as 90Hz and 0.1Hz. The errors caused by the voltage conversion between the analog and digital signals can also be eliminated to collect the proper data required while the accuracy of the data is also guaranteed. The setting and selecting of filter

parameters is indicated in Figure 5.

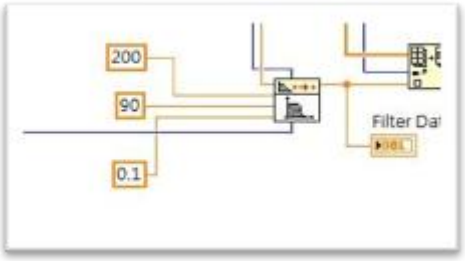

Figure 5 Data Pre-Processing

3.2 Coefficient Extracting Module

The Coefficient Extracting module is designed based on the specific SHM algorithm developed for the monitoring objective, which is the 8-story down-scale steel structure. In this study, the AR-ARX model is first established and then implemented by codes written with the LabView program, and the settings of the order required is shown in figure 6. By using the Coefficient Extracting module, the time history of the structure response can be quickly transformed into the AR-ARX array form and the damage condition of the structure can be evaluated by comparing with the deposited database in the next stage.

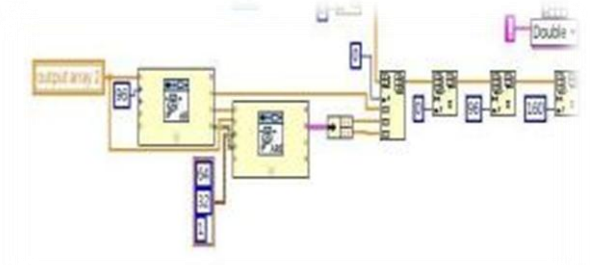

Figure 6 The Coefficient Extracting Module

3.3 Health Condition Diagnosis

The Naïve Bayes-based SHM algorithm is applied in this part. By comparing the AR-ARX array calculated from the previous block with the stored database, the occurrence probability of all 19 damage cases is estimated by a designated loop, and the structural damage condition and location can be easily determined. The detail of the Health Condition Diagnosis module is shown in Figure7

We can further determine the conditions of structural damages and the damage location, the case result will be shown in number from 1 to 19.

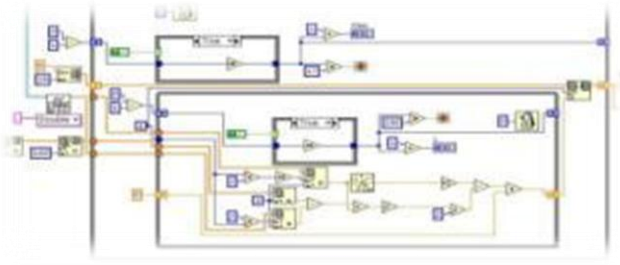

Figure 7 Coefficient Extracting Module

3.4 GPRS & Wireless Module

In order to achieve the goal of real-time monitoring after the analysis of damage classification, the utilization of GPRS Module to transfer the data back to the monitor is necessarily. In this study, we can see the images presented in LabView out of GPRS and select the set value we need, and send the data back to the real-time monitor to carry the structural health monitoring out with the combination of hardware as the LabView program is functioning. For the purpose of the safe-transmission of data and the accuracy of reception, data transmission will be transmitted with encryption. In this study, the skill to encrypt and decrypt is to add AA in the front end, and to give instructions to the receiving end. To determine whether an instruction is received, it depends on the AA in the front-end of information. As shown in Figure 8 & Figure 9.

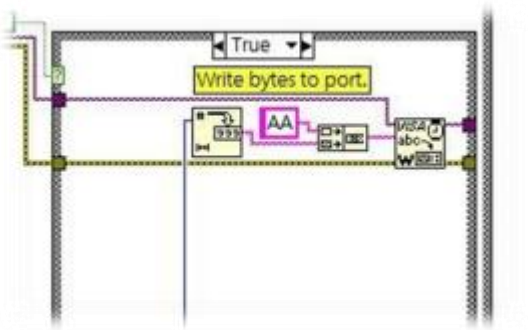

Figure 8 The Program Design of Transmission

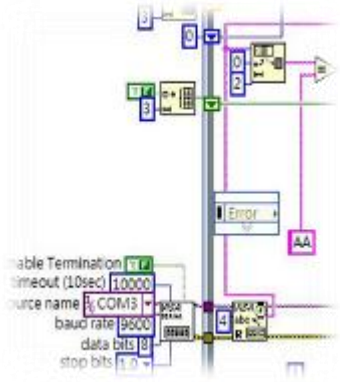

Figure 9 The Program Design of Receiver

When the steps mentioned above (Data Pre-Processing、Coefficient Extracting Module、 Health Condition Diagnosis、 GPRS Module) have been completed, the program will automatically input a classification through GPRS Module and send a message back to the monitor. Therefore, we created a monitoring interface in order to dissect which category the received information belongs to on the real-time monitor. (Figure 10) As mentioned above, the prototype of mobile type SHM detecting system can be applied practically on real structures, after combining the software and hardware parts.

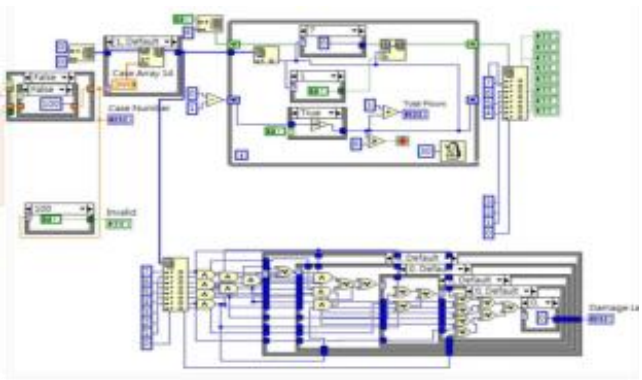

Figure 10 The Monitoring Interface

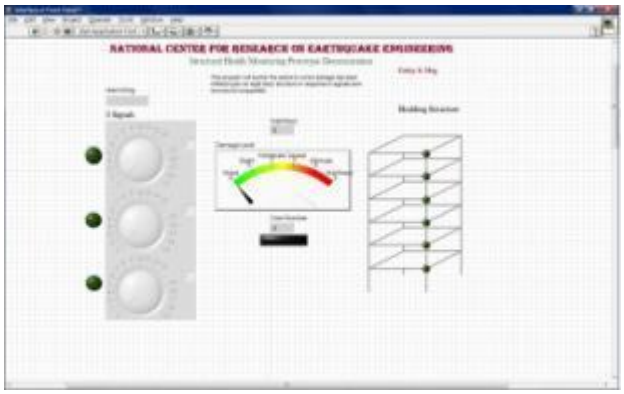

Figure 11 The Real-Time Monitoring Interface

4. PRACTICAL VERIFICATION

In order to test the performance and the consistence between the software and hardware of the SHM prototype, an experimental verification was arranged. The scaled-down six-story steel building mounted on the shaking table at NCREE was again used as the practical testing structure. The testing structural damage was simulated by loosening four bolts on the third floor, which is damage case 4, and then the ambient vibration response measured by the sensor of the roof was analyzed by the on-site SHM prototype for testing. By comparing the AR-ARX array obtained from the micro vibration data with the database deposited in the SHM system, the results of the structural health condition can be evaluated immediately.

The real-time monitoring result is shown in Figure 11 where the SHM results can be determined every 20 seconds on the left side of the figure. The numbers shown in the panel represent the classification result. To avoid false alarm in practical application, the SHM algorithm is designed to operate three times per 60 seconds to determine the damage condition and location of the structure which is shown on the right side of Figure 11. The damage level of the structure, which is either none, slight, moderate, severe, ultimate, or nonlinear is shown in the middle of the figure. Furthermore, not only the real-time structural damage can be monitored by the mobile type SHM system, but the software parameters can also be remotely controlled. This flexible monitoring design can make the SHM system optimal to fit all kinds of conditions and evaluate the structural damage immediately. The high mobility and prompt execution concepts of the proposed mobile SHM prototype are finally implemented.

5. SUMMARY AND CONCLUSIONS

An ambient vibration based SHM system using the concept of AR-ARX array, and Naïve Bayesian damage classification is proposed in this research. By using the ambient vibration data measured from three different floors of a scale-down six-story building located at NCREE, which can be easily achieved in our daily life, a specific data array was extracted and treated as the DNA array of the structure to form the SHM database. Based on the Naïve Bayesian damage classification, the coefficients obtained from any unknown damage case was compared with the individual mean values and standard deviations of the array in the pre-collected database of multiple damage conditions to detect the possible damage location and level of the structure. To improve the feasibility of the proposed structural health monitoring system in practical application, a SHM prototype detection system is developed. Test results from ambient data have shown that the damage condition and location of the specimen can be successfully detected by the structural health monitoring prototype system. The feasibility of transplanting the DNA array concept from molecular biology into the field of structural health monitoring has been demonstrated by the structural health monitoring prototype system.

References:

[1] Sohn, H. ;Farrar, C.R., 2001. Damage diagnosis using time series analysis of vibration signals, Smart Materials and Structures 10 (3), 446-451.

[2] Sohn, Hoon ; Czarnecki, Jerry A.; Farrar, Charles R., 2000. Structural health monitoring using statistical process control, Structural Engineering New York 126 (11), 1356-1363.

[3] Cheung, A. ; Cabrera, C.; Sarabandi, P.; Nair, K.K.; Kiremidjian, A.; Wenzel, H., 2008. The application of statistical pattern recognition methods for damage detection to field data, Smart Materials and Structures 17 (6).

[4] Domingos, P. and Pazzani, M., 1996. Beyond independence: Conditions for the optimality of the

simple Bayesian classifier. Proceedings of the Thirteenth International Conference on Machine Learning, 105-112, Bari, Italy. Morgan Kaufmann.

[5] T.R. Golub, D.K. Slonim, P. Tamayo, C. Huard, M. Gaasenbeek, J.P. Mesirov, H. Coller, M.L. Loh, J.R. Downing, M.A. Caligiuri, C.D. Bloomfield and E.S. Lander, 1999. "Molecular Classification of Cancer: Class Discovery and Class Prediction by Gene Expression Monitoring", Science 15 286 (5439), 531-537, 10.1126/science.286.5439.531.

[6] Andrew D. Keller, Michel Schummer, Lee Hood and Walter L. Ruzzo, 2000. "Bayesian Classifiction of DNA array Expression Data", Technical Report UW-CSE-2000-08-01.

[7] Donna K. Slonim, Pablo Tamayo, Jill P. Mesirov, Todd R. Golub and Eric S. Lander, 2000. "Class Prediction and Discovery Using Gene Expression Data", Annual Conference on Research in Computational Molecular Biology, Proceedings of the 4th annual international conference on Computational molecular biology, 263-272, 1-58113-186-0, Tokyo, Japan,.

[8] L. Ljung, 1986. "System Identification: Theory for the User", Prent-Hall, NJ, USA.

[9] Hoon Sohn, Charles R. Farrar, Norman F. Hunter and Keith Worden, 2001. "Structural Health Monitoring Using Statistical Pattern Recognition Techniques", J. Dyn Sys., Meas., Control 123, 10.1115/1.1410933.

[10] Asadollah Bassam, Seyed ; Ansari, Farhad, 2008. Post-seismic structural health monitoring of a column subjected to near source ground motions, Material Systems and Structures 19 (10), 1163-1172.

[11] Fraraccio, G.; Brügger, Adrian; Betti, R., 2008. Identification and damage detection in structures subjected to base excitation, Experimental Mechanics 48 (4), 521-528, Inverse Problems in Experimental Mechanics.

[12] Yi, Jin-Hak; Kim, Dookie; Feng, Maria Q., 2009. Periodic seismic performance evaluation of highway bridges using structural health monitoring system, Structural Engineering and Mechanics 31 (5), 527-544.

JOINT CONFERENCE PROCEEDINGS
7th International Conference on Urban Earthquake Engineering (7CUEE) &
5th International Conference on Earthquake Engineering (5ICEE)
March 3-5, 2010, Tokyo Institute of Technology, Tokyo, Japan

STRUCTURAL CONTROL USING GLOBAL VIBRATION SENSING AND MODEL UPDATING BASED ON LOCAL INFRARED IMAGING

Chun-Hung Lin[1], Nebojsa Sebastijanovic [2], Henry T.Y. Yang [3], and Xiaoyan Han [4]

1) Research Assistant, Department of Mechanical Engineering, University of California, Santa Barbara, CA 93106, USA
2) Research Assistant, Department of Mechanical Engineering, University of California, Santa Barbara, CA 93106, USA
3) Professor, Department of Mechanical Engineering, University of California, Santa Barbara, CA 93106, USA
4) Professor, Department of Electrical and Computer Engineering, Wayne State University, Detroit, MI 48202, USA
lin@engineering.ucsb.edu

Abstract: This paper presents the basic idea of combining a hybrid structural health monitoring system with an adaptive structural control system. The proposed global damage detection method is combined with a local damage identification method using sonic infrared imaging to update the computational structural model for continuous structural monitoring and control. The previously developed damage diagnosis technique is enhanced by including an equivalent simplified lumped-mass model deduced from a complex frame structure. Changes in global dynamic response characteristics due to damaged members or joints are first observed, and the damage can be detected and located during the earthquake event. After the earthquake event, local damages are inspected in detail by sonic infrared imaging. The example of a three-story steel frame model with a damaged column and a damaged joint is presented to demonstrate and evaluate the usefulness and effectiveness of the proposed concept. Results from the numerical simulations show that the adaptive control strategy based on model updating can improve the control performance.

1. INTRODUCTION

A global method for identifying and locating structural damages has been presented in previous studies (Ma et al. 2005; Sebastijanovic et al. 2006). The measured structural responses were assumed to be displacements, velocities, or accelerations. In the examples considered, the authors have shown that the developed algorithm was capable of detecting assumed damages based on the changes in dynamic responses and characteristics.

In the study of the present global damage detection algorithm, the previously developed global damage detection algorithm is enhanced by including an equivalently simplified lumped-mass model deduced from the complex high rise frame structure. This enhanced technique can identify specific values for the floor masses and bending spring constants, whereas only parameters for state space representation of a simplified lumped mass model were identified using the previous method (Wrobleski and Yang 2003).

In this study, the concept of combining the proposed global damage detection algorithm with the available local damage identification methods is considered and discussed. Once the proposed global damage detection algorithm has determined the condition of a structure based on the changes in dynamic responses and characteristics, local damage identification techniques can be used to provide more detailed and accurate assessment about the severity and extent of the damage. This can be performed after the earthquake is over since all local damage detection methods currently are based on the concept of active sensing. However, real time inspection and feedback would be preferred and advantageous but it would require a series of embedded interconnected sensors to collect data in real time. One of the main advantages of monitoring for damages in real time is that the structural model can be continuously updated so that an accurate model is readily available and may be used for control. In order to design an effective control system it is important to have an accurate model that can be used to provide current information about the dynamic system in response to a particular earthquake input, especially when the system dynamics is changing due to damages.

Among all the available damage identification techniques, sonic infrared imaging technique has been developed and used for this study due to its ability to detect poor welds, cracks or other defects that are invisible or only partially visible (Favro et al. 2001; Han et al. 2001; Han et al. 2003; Han et al. 2006). It is a novel non-destructive evaluation technology that overcomes many drawbacks of traditional non-destructive evaluation techniques. It is an effective, fast, and wide-area non-destructive evaluation method. Sonic infrared imaging combines acoustic excitation and infrared sensing technologies for local

damage and defect detection. This technique employs a pulse of ultrasound/sound excitation to cause self heating in damaged/defect areas, which results in the rise of infrared (thermal) radiation from the damaged/defect areas and their surroundings. Infrared sensors are used to image the thermal radiation from the target. The damaged/defect areas can be identified from the changes in thermal radiation in the infrared images. The location of the damage/defects can be accurately identified and the severity of the damage can be evaluated at the same time as well.

The progress on combining a hybrid structural health monitoring system with an adaptive control system is illustrated through a three story model with local defect of a column with channel cross section. Once the existence of damage is indicated through the global damage detection algorithm, sonic infrared imaging can be used immediately and quickly for detecting and evaluating local damages. Based on the results of the hybrid structural health monitoring system, local members can be updated with new bending stiffness of a beam or column or rotational stiffness of a joint to instantly update the global structural model. Thus, new local or perhaps smaller damages can be located by this continuously updating method in real time. The control strategy can be modified as well. The concept of combing the global sensing and local infrared imaging, where the global sensing is used to predict the existence of damage in a structure, and infrared imaging is used for local damage identification and evaluation, is shown in Figure 1. In addition to its ability to detect invisible or partially visible defects, sonic infrared imaging technique has the potential of being used remotely, i.e. without the need for local active sensing, and remote sensing could potentially be used to identify damaged components and joints. The use of such remote sensing system in real time may become reality in the near future. With such expectations and assumptions, the development of a hybrid structural health monitoring and control system that can be implemented for real time structural health monitoring is illustrated in this paper conceptually, although for the most part realistically.

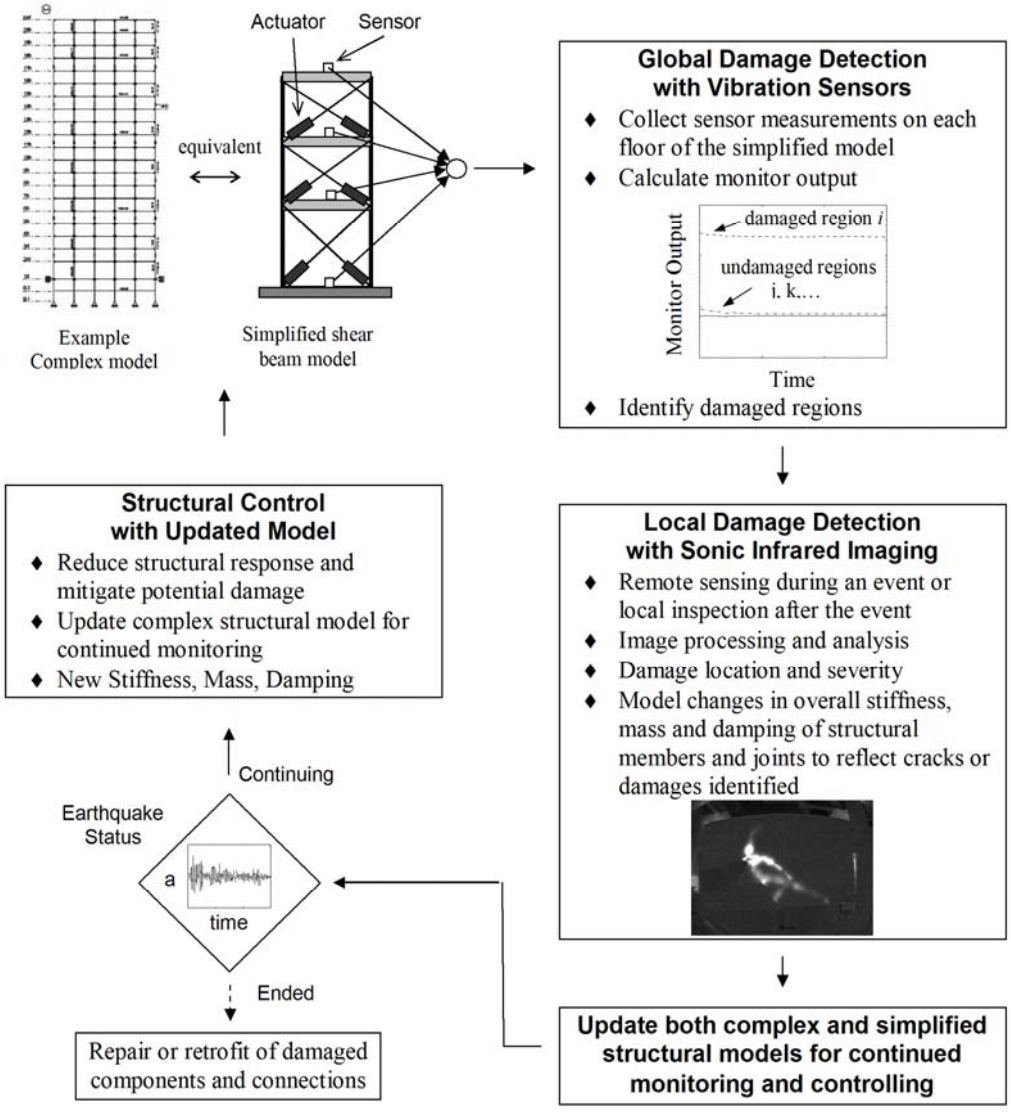

Figure 1 Schematic diagram of the hybrid structural health monitoring and control system combining global sensing and local sonic infrared imaging

2. GLOBAL DETECTION OF DAMAGES

The global damage diagnosis algorithms presented in the previous studies (Ma et al. 2005; Sebastijanovic et al. 2006; Sebastijanovic et al. revised version submitted in November 2009 with tentative acceptance) have been using one of three kinds of measurements, displacements, velocities, or accelerations, as inputs. Displacement feedback is used in this study for the purpose of simplicity.

For a simple shear beam model, monitors are designed to measure damages of each floor separately, which is achieved by decoupling of the damages. This makes it possible to identify the damaged floor, but not detailed damages such as cracks in structural members, welding, and joints, etc. A system identification method is presented here to enhance the previous damage detection method and enable the detection of damages in a complex frame structure.

2.1 System identification technique

In this study, the previously developed damage detection method has been improved by including a system identification technique. This technique can identify an equivalently simplified lumped-mass model deduced from a complex high rise frame structure, and can be used in the damage diagnosis algorithm. The concept of coordinate transformation with mode shapes and modal matrix (Craig Jr 1981) is utilized here.

First, natural frequencies and mode shapes can be obtained by implementing the finite element frame-based model. The jth mode shape which corresponds to the desired degree of freedom is selected and defined as Φj. The orthonomal modal matrix Φ for the n-degree-of-freedom system then can be written as

$$\mathbf{\Phi} = \begin{bmatrix} \phi_1 & \phi_2 & \dots & \phi_j & \dots & \phi_n \end{bmatrix} \tag{1}$$

Second, the mass of ith floor of the simplified lumped-mass model mi can be obtained by summing mass of every member of the finite element frame-based model to each floor, i.e. the mass of each story is divided in half and lumped at the column-beam joint. The modal stiffness kjj and modal damping cjj can be calculated as

$$k_{jj} = \omega_j^2 \tag{2}$$

$$c_{jj} = 2\xi_j\omega_j \tag{3}$$

where ωj is the natural frequency and ζ j represents the damping ratio of the jth mode.

Then, the mass, damping, and stiffness matrices of the simplified model can be determined by coordinate transformation and denoted as M, C and K, respectively.

$$\mathbf{M} = diag\left[m_i\right] \tag{4}$$

$$\mathbf{C} = \mathbf{\Phi}^{-T} diag\left[c_{jj}\right] \mathbf{\Phi}^{-1} \tag{5}$$

$$\mathbf{K} = \mathbf{\Phi}^{-T} diag\left[k_{jj}\right] \mathbf{\Phi}^{-1} \tag{6}$$

The governing equation of the simplified lumped-mass model under external excitations can now be constructed as

$$\mathbf{M}\ddot{z} + \mathbf{C}\dot{z} + \mathbf{K}z = \mathbf{F}(t) \tag{7}$$

where z is the displacement vector and F(t) is the external forces depending on time, t.

It is shown that in addition to matching frequencies and structural responses, the present technique can also identifies specific values for the masses and stiffness, whereas only parameters of the transfer function and state space representation of a lumped-mass model are identified using the previous method (Wrobleski and Yang 2003). This enhanced system identification technique thus may be used to identify a simplified lumped-mass model for a complex frame model.

3. LOCAL SONIC INFRARED IMAGING

Sonic infrared imaging is a novel non-destructive evaluation technology that combines acoustic excitation and infrared sensing methods to overcome many drawbacks of traditional non-destructive evaluation techniques. The main advantage is in its versatility and ability to detect defects in different materials and structures, including poor bonding in welded or brazed joints, open or fatigue cracks, or other defects that are invisible or only partially visible (Favro et al. 2001; Han et al. 2001; Han et al. 2003; Han et al. 2006). It is important to note that the accuracy of the semi-rigid frame design is determined by the accuracy of the joint parameters, as shown by Wald (1990). The prediction of the joints' parameters is affected by joint imperfections, e.g., lack of fit, bolt holes' sizes, position variation, tightening differences and even cracks. For simplicity, the practically important and complex problem of determining the percentage reductions of rotational stiffness in a joint due to various scenarios of joint damages has not been investigated in this preliminary study; only the effect of assumed reduction in rotational stiffness of the joint has been considered in order to determine the effectiveness of the proposed global damage detection algorithm. It should be noted that a similar approach can be used to determine changes in joint stiffness for semi-rigid connections. It would be of interest to further investigate the limitations of the proposed algorithm in terms of its sensitivity to rotational stiffness reduction of joints as well as its ability to distinguish between beam or column member and joint damages with examples of multi-story frames in further studies, along with practical assessments of percentage reduction of rotational stiffness due to joint damage and reduction of bending stiffness due to beam or column damage under various practical damage scenarios.

3.1 Determine stiffness reduction in columns and beams

The assumed damage due to an open crack is modeled

as an 18% reduction of the moment of inertia in a column. The formulation for modeling variation in beam stiffness due to damages follows the study by Sinha et al. (2002) which is based on the concept presented by Christides and Barr (1984).

Schematic drawing of using the sonic infrared imaging technique for local damage detection of a steel C channel (AISC C5x6.7) of the 1st floor column is shown in Figure 2. Ultrasonic or acoustic waves are injected by the transducer to cause heating in damaged area/defects, and an infrared camera is used to image the structure to locate the damage for evaluation. The structural elements can be scanned in sections whose size would depend on the infrared camera resolution until the exact location and severity is determined. It is assumed that all selected sections along the beam have been scanned and cracks were discovered in the top beam. Therefore, only the damaged segment of the C channel is presented and analyzed. For the segment considered, the excitation source is 15 kHz, the focal plane array of the infrared camera has 640x512 infrared detectors which can come up with 85 frames per second, and the infrared sensors are sensitive to mid-wavelength infrared, in the range of 2-5 microns. It is obvious that a structure of this size can be imaged as a whole and the infrared image will still have sufficient spatial resolution to identify the damages in the structure. Interior cracks in the C channel are created through thermal fatigue with external impact to simulate the damage. The crack and its dimensions that are discovered during local infrared inspection are shown in Figure 3(a). It can be seen that there are quite a few interconnected cracks along the beam segment considered. For simplicity, a rough approximation of the damaged area is described by an opening, as shown in Figure 3(b). For lack of a more detailed modeling of these cracks with accurate theory and approximations for the distribution of the moment of inertia (I) through the length of the column, a rough approximation method is proposed for simplicity. The moment of inertia has been approximated at ten cross sections along the column length as indicated by I_i in Figure 3(b). Based on this approximation, an estimate of the variation in moment of inertia is shown in Figure 3(c) so as to roughly illustrate the proposed concept although rigorous theory and approximation method have yet to be developed. In order to use the global damage detection algorithm, the damaged column on the first floor is represented by an equivalent column with its "effective" moment of inertia determined using the approach presented by Chehil and Jategaonkar (1987). In that study, the authors used the concept of effective moment of inertia to develop a method for estimating natural frequencies of beams with linear inertia variation in a non-continuous manner. It is shown that the effective moment of inertia can be calculated using the expression (Chehil and Jategaonkar 1987)

$$I_{eff} = I_0 \pm i\left[\frac{1}{4} + \frac{1}{2n^2\pi^2}(1-\cos n\pi)\right] \tag{8}$$

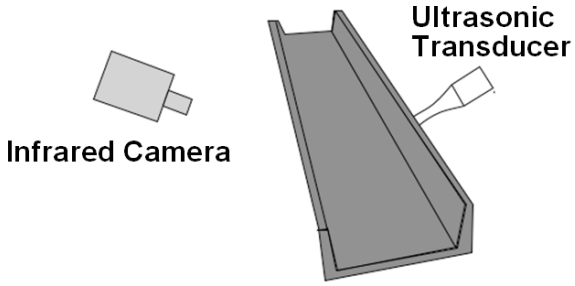

Figure 2 Schematic drawing of sonic infrared imaging for local damage detection

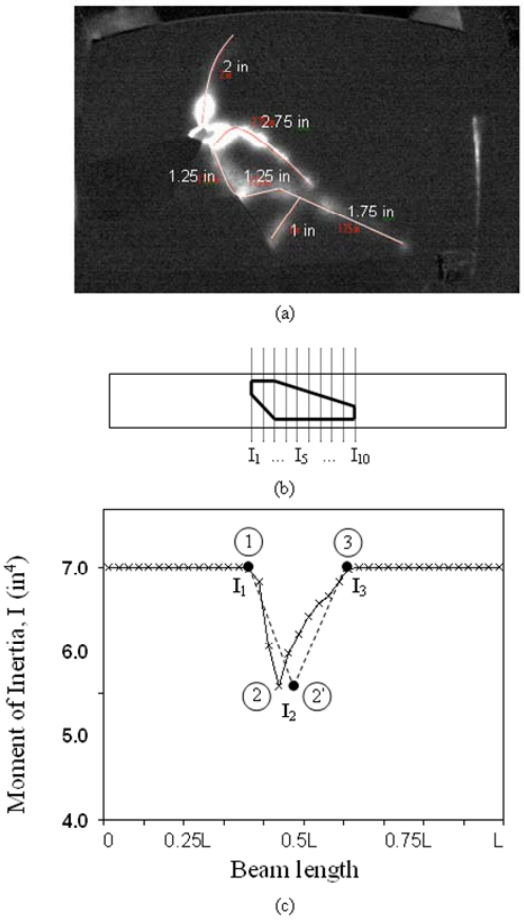

Figure 3 (a) Dimensions of cracks found in the steel C channel, (b) Rough approximation of the damaged segment due to cracks, (c) Variation in moment of inertia along the column due to approximated damage

which simplifies to $I_{eff} = I_0 + i/4$ as $n \to \infty$, where n is the number of modes, I_0 is the moment of inertia of the undamaged column, and i represents the variation in moment of inertia along the column, i.e. rate of change in the moment of inertia multiplied by I_0.

Consider the column shown in Figure 3, $i = (I_2 - I_1)/\Delta L = (5.58 - 7.03)/(2) = -0.725 \times I_0$ from point 1 to point 2 and $i = (I_3 - I_2)/\Delta L = (7.03 - 5.58)/(2) = 0.725 \times I_0$ from point 2 to point 3. For simplicity, it is assumed that the moment of inertia linearly reduces from point 1 to point 2 and linearly increases from point 2 to point 3. It should be also noted that because the approximation suggested by Chehil and Jategaonkar (1987) is based on the assumption that the moment of inertia curve is symmetrical, the valley of the actual curve 1-2-3 representing the reduction of moment of inertia is slightly shifted to the right to become a symmetrical V-shaped curve 1-2'-3. Therefore, the reduction in the moment of inertia of the C channel based on the estimated dimensions of the cracked zone over the damaged channel segment would result in the effective moment of inertia of $I_{eff} = 0.82 \times I_0$. This indicates an 18% stiffness reduction in the first floor column 2-4 of the frame model shown in Figure 4(a), which can be identified by the global damage detection algorithm. This damage is equivalent to a 9% stiffness reduction in the first floor, k_1, of the simplified lumped mass model (Figure 4(b)). Damaged and undamaged outputs are clearly distinguished by a jump in the value of the normalized monitor output. Detected changes in certain structural parameters of damaged members or joints can be used to update the existing structural model for continued monitoring during the earthquake event. Only those critical members and joints that are potentially vulnerable to occurrence of damages will need to be identified and monitored in real time. Based on the concept presented, it seems that a hybrid structural health monitoring system could be developed by combining the method for global damage detection and a method for local damage identification so that both the exact location of the damage and its degree of severity can be determined in real time.

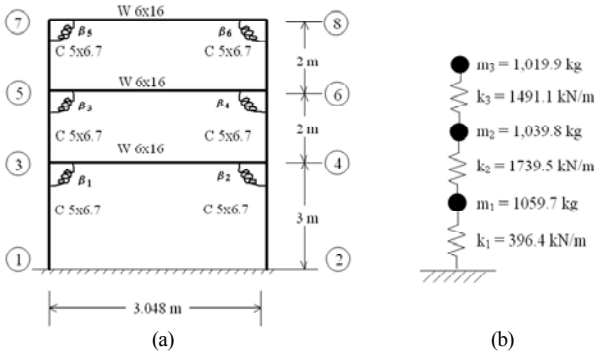

Figure 4 (a) Three-story frame model, (b) Equivalent simplified 3 degree-of-freedom lumped-mass model

3.2 Determine stiffness reduction in connections and joints

For the example considered, once the changes in joint flexibility have been determined using the proposed global damage detection algorithm, local damage identification methods can be used to find damaged/failed joints. Figure 5 shows the experiment of applying sonic infrared imaging technique on a damaged joint with cracks along the welded joint. The crack can be easily detected by the local damage identification method.

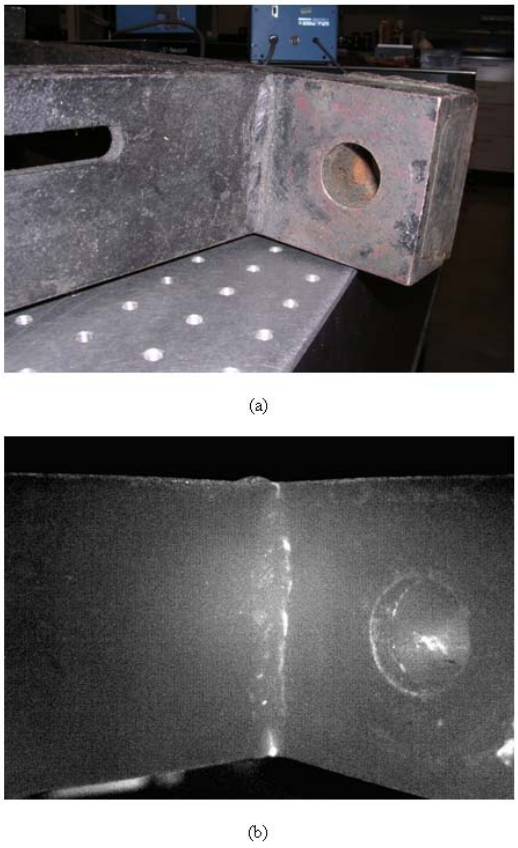

Figure 5 (a) Optical image of the welded joint, where the beam is 7.5cm (3") thick, (b) Sonic infrared image of the joint showing subsurface cracks along the joint

4. EXAMPLE

The example of the single bay, three-story frame model considered in the previous study (Wrobleski and Yang 2003) is modified by changing all the columns to C5x6.7 and all the beams to W6x16 as shown in Figure 4(a). The reason for this change to a channel beam is due to the availability of such a beam and the practical simplicity for experimental creation and detection of embedded cracks of such a specimen in the present laboratory.

The frame is modeled using beam and column elements with two degrees of freedom at each joint, i.e. horizontal displacement and rotation. System identification technique described in the previous section is used to identify an equivalent simplified lumped mass model shown in Figure 4(b) that can be used in the global damage detection and structural control algorithm. The frequencies for the first three modes are identified to be $\omega_1 = 10.89$ rad/s, $\omega_2 = 38.94$ rad/s, $\omega_3 = 70.30$ rad/s, respectively.

The frame model is excited by the N-S component of acceleration of the 1940 El Centro earthquake and structural responses measured are assumed to be displacements at each floor. The concept of applying adaptive structural control using global vibration sensing and model updating based on local sonic infrared imaging has been explored on this frame model as well.

Global damage detection is assumed to be performed in real time in this study. The monitors directly analyze structural response measurements in the time domain. Once the existence of damage has been determined using the proposed global damage detection algorithm, in this case in the first floor column and then the third floor joint, sonic infrared imaging is proposed to investigate the damage locally. The model updating is based on the detailed information provided by both the global and local damage detection methods. The new model which includes information about the damage is then used to improve the control performance. Even though global damage detection can only identify a general location of the damage, i.e. a damaged floor, it is still useful since sonic infrared imaging can focus on a smaller region and reduce the delay in feedback real time required to locate damaged members. Currently, sonic infrared imaging can only be used after the earthquake has ended to detect local damages so that they can be inspected in detail for the purpose of repair and retrofit. However, sonic infrared imaging technique has the potential of being used remotely and the current study is based on the premise and expectation that the use of such remote sensing in real time will become reality in the near future.

4.1 Detecting damages in a three-story structure with damaged column and damaged joint

The following example is presented here to test the ability of the proposed damage detection method.

First, a crack is assumed to occur in the column between joint 1 and joint 3 as shown in Figure 4(a), and the equivalent moment of inertia of this column is reduced by 18%. The global damage detection method is used and damage is detected on the first floor. Monitor 1 indicates that the first floor stiffness, k_1, is decreased by 9% (Figure 6). After the damage is located, the sonic infrared imaging local damage detection method is used to discover the crack. The equivalent moment of inertia of the damaged column is calculated and shown to be decreased by 18% using the method described in Section 3.1. Based on the information, the frame model is updated and the parameters in the global damage diagnosis algorithms are recalculated using the system identification technique. Then, a new crack is assumed to occur in joint 8 as shown in Figure 4(a). The joint, assumed to be damaged, becomes semi-rigid. The rotational stiffness β_8 in Figure 4(a) is then reduced to 10^7 N m/rad (for rigid joint, it is assumed as 10^{11} N m/rad). The global damage detection method is used and the new damage is detected on the third floor (Figure 7). Finally, the crack in joint 8 can be found by implementing the local damage detection method (Figure 5). The process can be continued to monitor new damages.

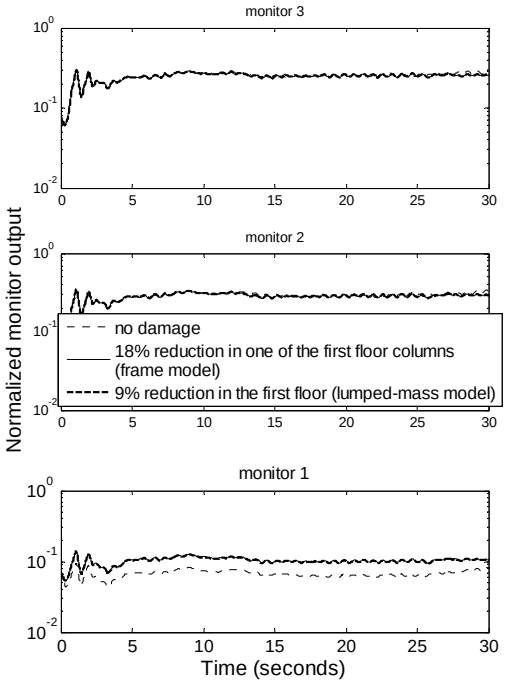

Figure 6 Damage detection for the three-story steel frame model using displacement feedback and assuming 18% stiffness reduction in the top beam of the first floor

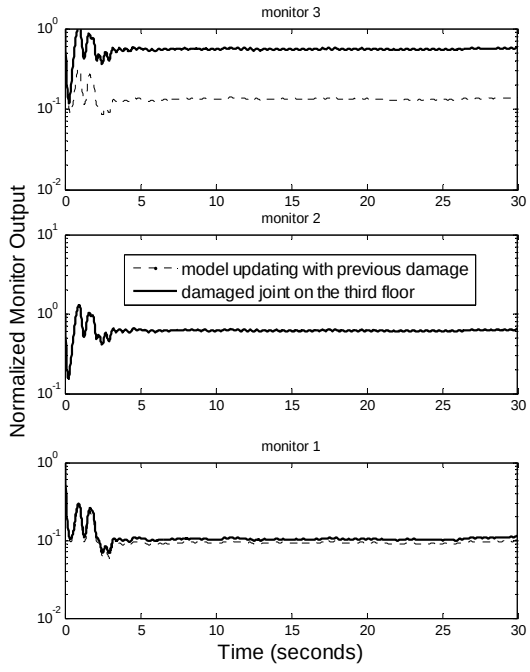

Figure 7 Damage detection for the three-story steel frame model using displacement feedback and assuming stiffness reduction in one of the joints of the third floor

4.2 Adaptive structural control with model updating

In the previous example, the stiffness reduction of the damaged C channel on the first floor was determined to be 18%, which is equivalent to 9% stiffness reduction for the first floor stiffness (k_1) of the simplified lumped-mass model. This information can be fed back to the computational model (model updating) for continues structural health monitoring and adaptive control. In our simulation, the structure is controlled by an actuator on the first floor using LQR active control algorithm, which minimizes the cost function:

$$J = \lim_{t\to\infty} \int_{-\infty}^{t} \left(2.07\times10^{4}\,\ddot{x}_3^2 + 6.2\times10^{10}\,x_1^2 + f_1^2\right)dt \qquad (9)$$

where $\ddot{x}_3$ is the acceleration measured on the third floor of the structure model, x_1 and f_1 are the displacement and control force on the first floor, respectively.

The comparison of peak responses of the three-story frame model over N-S acceleration component of the 1940 El Centro earthquake with and without model updating are shown in Table 1. Although the effect of 18% reduction of stiffness in the first floor column might not be significant, it does show advantages of using control with model updating.

5. CONCLUSIONS

In this study, the previously presented global damage detection algorithm has been improved by including a system identification capability. This enables monitoring of complex structures by identifying an equivalent simplified lumped-mass model with specific values for floor mass and bending spring stiffness. An example of identifying the simplified lumped mass model of the three-story frame model was presented to illustrate the effectiveness of the improved system identification technique.

The improved global damage detection algorithm is then evaluated using a three-story steel frame model with a damaged column and a damaged joint. For the example presented, it is shown that the proposed global damage detection algorithm can detect stiffness changes due to the assumed (or actual) damages, as well as changes in joint stiffness.

The concept of combining the improved global damage detection algorithm and local infrared imaging technique in order to develop a hybrid structural health monitoring and adaptive control system has been presented and discussed as well. This concept is illustrated using a three-story steel frame building with a local damage of a column with channel cross section and a semi-rigid joint. The damage in the column is approximated based on the experimental results. Once the changes in stiffness due to damages are indicated by the global damage detection algorithm, sonic infrared imaging technique is used to detect and evaluate local damages more accurately. Sonic infrared imaging technique has been developed and used for this study due to its ability to detect poor welds, cracks or other defects that are invisible or only partially visible. It also seems that its potential of remote monitoring can be used for real time structural health monitoring once the necessary technology for real time passive sensing is developed. Currently, the proposed concept may be quite useful after the earthquake has ended. Once the global damage detection identifies a general location of the damage, sonic infrared imaging can focus on a smaller region and reduce the delay in feedback real time required to locate damaged members so that they can be inspected in detail for the purpose of repair and retrofit.

For the adaptive control using model updating, it is noted that the effect of 18% reduction of stiffness in the first floor column might not be significant, but it does show advantages of using control with model updating. Further studies on more severe damage in beams, columns, and joints are in progress.

Table 1 Comparisons of peak responses with and without updated model for frame model

		Uncontrolled	LQR optimal control *without* model updating	LQR optimal control *with* model updating	Percentage of reductions due to model updating
Displacement (cm)	x_1	8.023	3.227	3.124	3.20
	x_2	9.205	3.857	3.752	2.74
	x_3	9.917	4.243	4.131	2.63
Drift (cm)	d_1	8.023	3.227	3.124	3.20
	d_2	1.182	0.668	0.660	1.15
	d_3	0.712	0.403	0.398	1.14
Acceleration (cm/s^2)	a_1	982	596	585	1.95
	a_2	1141	772	763	1.17
	a_3	1229	800	791	1.15
Max force (N)	f	0	6927	7046	-1.72

Acknowledgements:

This study is sponsored by the National Science Foundation grant CMS 0511046. The guidance of program director, Dr. S. C. Liu, is gratefully acknowledged. Valuable discussions with Tian-Wei Ma are acknowledged.

References:

Chehil, D. S., and Jategaonkar, R. (1987). "Determination of natural frequencies of a beam with varying section properties." *Journal of sound and vibration*, 115(3), 423-436.

Christides, S., and Barr, A. D. S. (1984). "One-dimensional theory of cracked Bernoulli-Euler beams." *International Journal of Mechanical Sciences*, 26(11-12), 639-648.

Craig Jr, R. R. (1981). "Structural Dynamics," John Wiley & Sons, Inc.

Favro, L. D., Thomas, R. L., Han, X., Ouyang, Z., Newaz, G., and Gentile, D. (2001). "Sonic infrared imaging of fatigue cracks." *International Journal of Fatigue*, 23, 471-476.

Han, X., Favro, L. D., Ouyang, Z., and Thomas, R. L. (2001). "Thermosonics: Detecting cracks and adhesion defects using ultrasonic excitation and infrared imaging." *The Journal of Adhesion*, 76(2), 151-162.

Han, X., Favro, L. D., and Thomas, R. L. (2003). "Recent developments in sonic IR imaging." *AIP Conference Proceedings*, 657, 500.

Han, X., Islam, M. S., Newaz, G., Favro, L. D., and Thomas, R. L. (2006). "Finite element modeling of the heating of cracks during sonic infrared imaging." *Journal of Applied Physics*, 99, 074905.

Ma, T.-W., Yang, H. T., and Chang, C.-C. (2005). "Structural Damage Diagnosis and Assessment under Seismic Excitations." *Journal of Engineering Mechanics*, ASCE, 131(10), 1036-1045.

Sebastijanovic, N., Ma, T., and Yang, H. T. Y. (2006). "Structural damage detection and assessment using acceleration feedback." T. Masayoshi, Y. Chung-Bang, and G. Victor, eds., *SPIE*, 61742L.

Sebastijanovic, N., Yang, H. T. Y., and Ma, T. W. (revised version submitted in November 2009 with tentative acceptance). "Structural Damage Detection and Assessment Using Acceleration Feedback." *Journal of Engineering Mechanics*, ASCE.

Sinha, J. K., Friswell, M. I., and Edwards, S. (2002). "Simplified models for the location of cracks in beam structures using measured vibration data." *Journal of sound and vibration*, 251(1), 13-38.

Wald, F. (1990). "Sensitivity of semi-rigid frames to initial imperfections." *3rd Stability Colloquium*, Budapest, Hungary, 2, 305-311.

Wrobleski, M. S., and Yang, H. T. Y. (2003). "Identification of Simplified Models Using Adaptive Control Techniques." *Journal of Structural Engineering*, ASCE, 129(7), 989-997.

JOINT CONFERENCE PROCEEDINGS
7th International Conference on Urban Earthquake Engineering (7CUEE) &
5th International Conference on Earthquake Engineering (5ICEE)
March 3-5, 2010, Tokyo Institute of Technology, Tokyo, Japan

STATISTICAL-BASED STRUCTURAL DAMAGE DETECTION USING STRAIN POWER MODE SHAPE

Eun Hyung Cho[1], and Jae Kwan Kim[2]

1) Engineer, POSCO Engineering & Construction, Korea

2) Professor, Dept. of Civil and Environmental Engineering, Seoul National University, Korea

ehcho@ poscoenc.com, jkwankim @ snu.ac.kr

Abstract: As structures have become larger and more complicated, possibility of collapse of structures and the extent of damage have increased. This paper presents the new damage detection method based on strain power mode shape. One characteristic of this algorithm is that it is based on the usage of statistical properties of strain signals. Further, it is unnecessary to perform the modal analysis. Strain power mode shape is calculated from the statistical features of response strain signals, specifically, the Root Mean Square (RMS) properties of strain data measured by FBG sensors. Strain Power Mode Shape (SPMS) index and Strain Power Flexibility (SPF) index are proposed based on strain power mode shape to detect the location of damage. Numerical and experimental analysis are performed to investigate the effectiveness and possibility of field application of proposed algorithm using the experimental model, a 3-story building. Comparisons between previous damage detection method and newly proposed damage detection method are carried out. The experimental results indicate that the proposed algorithm functions well to detect the location of damage. Also, the stability of proposed algorithm to random noise is investigated by considering random noise, and the results show that this algorithm is robust to Gaussian random noise.

1. INTRODUCTION

As structures such as bridges and buildings have become larger and more complicated, the possibility of the collapse of structures and the extent of damage have increased. As a result, integrity monitoring has become more important than ever to prevent the collapse of large-sized structures and minimize the extent of damage. Recently, a number of studies have been done on the real-time integrity monitoring using FOS(Fiber Optic Sensor) to complement existing non-destructive testing methods used on large-sized structures.

A. K. Pandey et al. developed the damage detection method based on evaluation of changes in the flexibility matrices of the structure. D. Zonta proposed the damage detection method using a strain-flexibility matrix based on strain mode shapes, which are estimated by the analytic differentiation of displacement mode shapes. Park et al. presented modal flexibility-based damage detection technique of steel beam by dynamic strain measurement using FBG sensors. S.-E. Fang et al. established non-modal-based damage indices using statistical properties of displacement signals.

In this study, the new damage detection method is

proposed. The new concept of this algorithm is the strain power mode shape, and this is calculated from the statistical features of response strain signals. The Strain Power Mode Shape (SPMS) index and Strain Power Flexibility (SPF) index, which are the damage indices proposed in this study, are solved based on the strain power mode shape. The dynamic strain data are measured by FBG strain sensors at various nodes of the structure. The numerical and experimental verification of damage detection method are done on a 3-story building model.

2. THEORETICAL BACKGROUNDS

2.1 Fiber Optic Sensors

The principle of light propagation in fiber is the principle of total reflection. This phenomenon can only be observed when light travels from a medium with a higher refractive index to one with a lower refractive index. The core has a higher refractive index than the cladding and light entering in the fiber core is totally reflected at the boundary of core and cladding.

When the light from a broadband source interacts with the grating of the FBG sensor, a single wavelength called Bragg wavelength is reflected. The Bragg wavelength is the function of the effective refractive index, n_{eff}, and grating period, Λ, as expressed in Eq. (1).

$$\lambda_B = 2n_{eff}\Lambda \tag{1}$$

Strain and temperature can be calculated measuring the shift of the Bragg wavelength. The equation between the shift of the Bragg wavelength and physical quantities is expressed in Eq. (2) where p_e is Photo-elastic constant.

$$\Delta\lambda_B = \lambda_B[(1-p_e)\varepsilon + (\alpha_f + \xi_f)\Delta T] \tag{2}$$

If there are no abrupt temperature changes as in the laboratory circumstance and no temperature differences between each FBG sensor, the terms related to temperature change can be ignored and the strain can be calculated by Eq. (3).

$$\varepsilon = \frac{\Delta\lambda_B}{(1-p_e)\lambda_B} \tag{3}$$

2.2 Strain-Flexibility index

In this part, one method of damage detection methods based on modal analysis, strain-flexibility index, is introduced. This index is based on the strain-flexibility matrix, which is determined using modal frequencies and strain mode shapes.

The modal properties can be extracted using Frequency Domain Decomposition (FDD) which was suggested by Brincker et al.. FDD method is that modal frequencies and mode shapes are calculated by singular value decomposition of Power Spectral Density (PSD) and Cross Spectral Density (CSD) matrices of responses.

D. Zonta suggested the strain-flexibility matrix $\mathbf{F}^{\varepsilon}$ expressed in Eq. (4).

$$\mathbf{F}^{\varepsilon} = \Phi^{\varepsilon}\Lambda^{-1}(\Phi^{\varepsilon})^{T} \tag{4}$$

where Φ^{ε} is the strain mode shape, Λ^{-1} is the matrix whose diagonal term is $1/\omega_p^2$, and ω_p is the p th modal frequency. Strain-flexibility index is proposed by the absolute difference between diagonal elements of strain-flexibility matrix before and after damage.

2.3 Damage detection procedure

The new damage detection processing from measured strain data is as follows. First of all, PSD functions of each measured point are estimated from strain data and Root Mean Square (RMS) values of each measured node are calculated by integrating PSD functions. Provided that the stationary and ergodic random excitation function of a linear

structure excited at point r is $x_r(t)$, the strain response function of a structure at point i is $y_i^{\varepsilon}(t)$. When the time lag $\tau = 0$, Root Mean Square (RMS) of $y_i^{\varepsilon}(t)$, $\psi_{y_i}^{\varepsilon}$, can be directly computed by integrating the PSD function, $S_{y_i}^{\varepsilon}(\omega)$.

$$(\psi_{y_i}^{\varepsilon}) = \{\int_{-\infty}^{\infty} S_{y_i}^{\varepsilon}(\omega) d\omega\}^{\frac{1}{2}} \quad (5)$$

When the excitation point is r and response point is i, Strain Frequency Response Function(SFRF) is defined as Eq. (6).

$$H_{i,r}^{\varepsilon}(\omega) = \sum_{p=1}^{n} \frac{\phi_{ip}^{\varepsilon}\phi_{rp}}{k_p - \omega^2 m_p + j\omega c_p} \quad (6)$$

where ϕ_{rp} represents the p th displacement mode shape at r th node and ϕ_{ip}^{ε} represents the p th strain mode shape at i th node; ω_p and ω are the frequency of p th mode and the external excitation, respectively; n is the number of modes considered.

The relationship between the input PSD function, $S_{x_r}(\omega)$, and the output PSD function, $S_{y_i}^{\varepsilon}(\omega)$, can be expressed by SFRF, $H_{i,r}^{\varepsilon}(\omega)$, in Eq. (7).

$$S_{y_i}^{\varepsilon}(\omega) = (H_{i,r}^{\varepsilon}(\omega))^* H_{i,r}^{\varepsilon}(\omega) S_{x_r}(\omega)$$
$$= \left|H_{i,r}^{\varepsilon}(\omega)\right|^2 S_{x_r}(\omega) \quad (7)$$

Substituting Eq. (7) into Eq. (5) and considering each p mode respectively in specific integrated frequency bandwidth, $[\omega_{p1}, \omega_{p2}]$, Eq. (8) can be derived as a bandwidth-localized RMS:

$$\psi_{y_i,p}^{\varepsilon} = \sqrt{\left\{(\phi_{ip}^{\varepsilon})^2 \int_{\omega_{p1}}^{\omega_{p2}} \left|\frac{\phi_{rp}/m_p}{\omega_p^2 - \omega^2 + j\omega c_p/m_p}\right|^2 S_{x_r}(\omega)\, d\omega\right\}}$$
$$= D' \phi_{ip}^{\varepsilon} \quad (8)$$

Where D' is the coefficient of the relationship between $\psi_{y_i,p}^{\varepsilon}$ and ϕ_{ip}^{ε}. If damages occur on the structure, the changes in structural properties affect conventional strain mode shapes as well as RMS based on Eq. (8). As a result, RMS can be used in determining whether or not damages occur, similar to conventional strain mode shapes.

Same principle that limits the integrated frequency bandwidth as $[\omega_{p1}, \omega_{p2}]$ is applied to Eq. (5), and $[\omega_{p1}, \omega_{p2}]$ is defined as $\left[\frac{f_{j(i-1)} + f_{ji}}{2}, \frac{f_{ji} + f_{j(i+1)}}{2}\right]$ (f_{ji} : the i th peak frequency at j th node) by analyzing PSD function of each point. The RMS of p th mode can be calculated by the following expression.

$$(\psi_{y_i,p}^{\varepsilon}) = \{\int_{\omega_{p1}}^{\omega_{p2}} S_{y_i}^{\varepsilon}(\omega) d\omega\}^{1/2} \quad (9)$$

By assembling all the RMSs of p th mode of every measured node, a p th strain power mode shape of the structure is generated.

Since the effect of damage is also reflected on strain power mode shapes themselves based on Eq. (8), the new damage index, Strain Power Mode Shape (SPMS) index, is

proposed as Eq. (10).

$$\Delta\psi^{\varepsilon}_{y_i,p} = \left|(\psi^{\varepsilon}_{y_i,p})_{damage} - (\psi^{\varepsilon}_{y_i,p})_{undamage}\right| \quad (10)$$

Then, the detection of damage locations can be found by the largest absolute differences between RMS values.

Strain power flexibility matrix is function of strain power mode shapes and the natural frequency, which is determined by averaging the p th peak frequencies of each node. The strain power flexibility matrix is defined in Eq. (11).

$$\mathbf{PF}^{\varepsilon} = (\Psi^{\varepsilon})\Lambda^{-1}(\Psi^{\varepsilon})^{T} \quad (11)$$

Strain Power Flexibility (SPF) index is defined as the absolute difference between diagonal terms of undamaged and damaged strain power flexibility matrix.

$$(\Delta\mathbf{PF}^{\varepsilon})_{diag} = \left|((\mathbf{PF}^{\varepsilon})_{damaged})_{diag} - ((\mathbf{PF}^{\varepsilon})_{undamaged})_{diag}\right| \quad (12)$$

The diagonal terms are only considered in the damage index because the contribution of each natural frequency and strain power mode shapes of each node is only regarded in the diagonal terms.

3. NUMERICAL AND EXPERIMENTAL ANALYSIS

A 3-story building is the experimental model for verification of damage detection algorithm using strain power mode shapes. The detailed descriptions of the experimental model and the natural frequencies of undamaged modeling are summarized in Table 1 and Table 2, respectively.

The locations which strain data are collected for numerical and experimental analysis are the 1/4 and 3/4 location of each column and beam element, and are indicated in Figure 1. The upper one shows the location of sensors of column and the lower one shows that of beam.

Table 1 Description of the experimental model

Material	Aluminum
Elastic constant E	69.69 GPa
Beam element	$40\times4\times246$ mm^3
Column element	$40\times3\times446$ mm^3
Lumped mass	666.58 g
	$40\times40\times55$ mm^3
T-shaped element	15.6 g

Table 2 Natural Frequencies of Undamage Modeling

1st natural freq.	2nd natural freq.	3rd natural freq.
1.9484 Hz	5.7474 Hz	8.8727 Hz

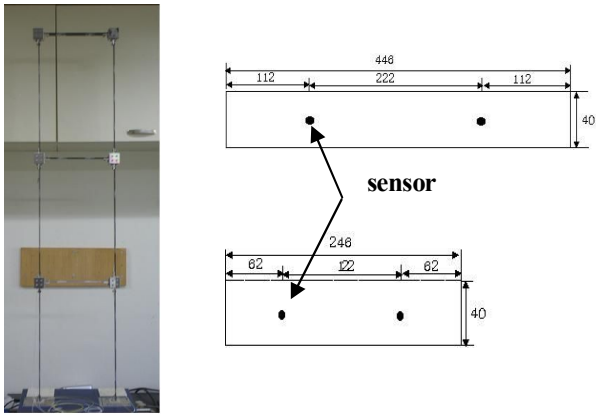

Figure 1 Location of Sensors (unit: mm)

To calculate Strain Power Flexibility (SPF) index, 1st, 2nd, and 3rd strain power mode shapes are used, because the strain power flexibility matrix can detect the location of damage just using the information of first few fundamental strain power mode shapes. Also, the same information is used to compute Strain Power Mode Shape(SPMS) index.

In field application, structures are exposed to the environment which experimenters cannot control. Thus many unknown parameters can affect the results of the experiments. Hence, the robustness of the proposed method to random noise should be investigated before the field application of the proposed algorithm. In this study,

Gaussian random noises are generated using MATLAB and the sizes of the Gaussian random noise are dependent on the sizes of undamaged and damaged dynamic strain data. The standard deviation of the random noise is set from 5% to 20% of the RMS level of the maximum reference signal, with increments of 5%.



Figure 2 The damage of vicinity of fixation

Damage scenarios are simulated considering the real situation. One of them is the damage of vicinity of fixation. There is a lot of potential that damages are processed at the vicinity of fixation when an earthquake occurs, because large moment and shear force are generated at the vicinity of fixation. Figure 2 shows the damage scenario regarded in this study. The numbers indicated in Figure 2 are the numbering of total sensors in the experimental model.

The damage of vicinity of fixation is simulated by damaging the vicinity of fixation of left first story column, and the impact hammer is used to impact the locations of lumped masses randomly. The three results using the same noise free dynamic strain data are shown according to the applied algorithms. Figure 3 is generated using the modal analysis results. However, Figure 4 and Figure 5 are calculated without the modal analysis.

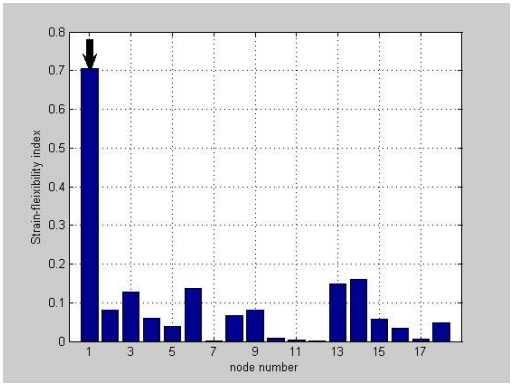

Figure 3 Strain-Flexibility Index

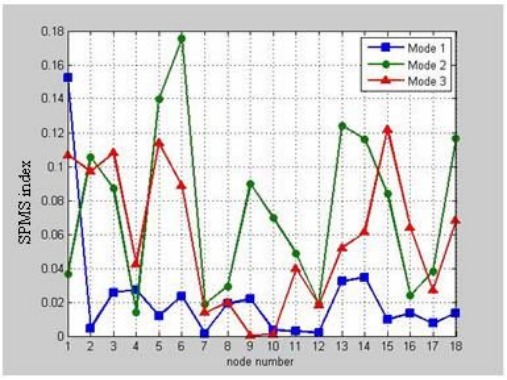

Figure 4 Strain Power Mode Shape (SPMS) Index

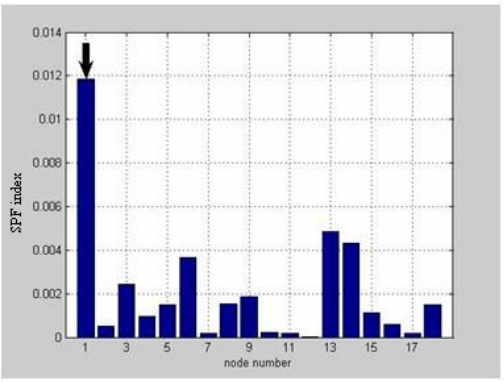

Figure 5 Strain Power Flexibility (SPF) Index

Comparing Figure 3 and Figure 5, the distributions of these two damage indices are similar and these two methods detect the same location as the location of the damage. This indicates that Strain Power Flexibility (SPF) index infers the location of damage without the modal analysis.

The biggest Strain Power Mode Shape (SPMS) index occurs at the node 6 related to 2nd mode in Figure 4. The indices related to the 1st mode are smaller compared to those

related to 2nd and 3rd mode. There are no clear peaks at the location of damage and Strain Power Mode Shape (SPMS) index performs moderately in this case.

Figure 5 shows that Strain Power Flexibility (SPF) index is the highest at node 1 compared to those of other nodes. The values of damage index at node 13 and node 14 are also bigger than those of other nodes except that of node 1. But the value of the damage index of node 2 is lower. Since the data related to the 1st mode contribute most to Strain Power Flexibility (SPF) index, the value is peaked at node 1 in Figure 5. Considering all the facts mentioned above, the damage occurs between the fixation of left column and node 1. This means that strain Power Flexibility (SPF) index detects the location of damage.

In this case, Strain Power Flexibility (SPF) index detects the location of the damage better than Strain Power Mode Shape (SPMS) index does.

Figure 6 shows the results of Strain Power Flexibility index with noise. The values of Strain Power Flexibility (SPF) index are changed only a little in quantity and the distributions of the index are similar. Namely, there is no distinct difference between the results of different noise level. Therefore, it is found that the proposed method is robust to the Gaussian random noise.

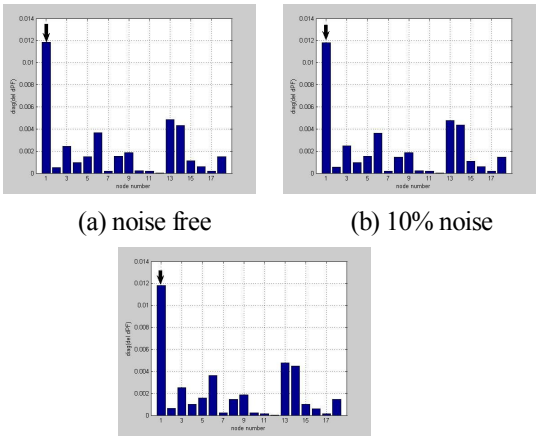

(a) noise free (b) 10% noise

(c) 20% noise

Figure 6 Strain Power Flexibility (SPF) index with noise

4. CONCLUSIONS

The new damage detection procedure using measured strain data is proposed. First of all, PSD functions of each measured points are estimated and Root Mean Square (RMS) values of each measured node are calculated by integrating PSD functions. Then, Strain power mode shapes are computed by assembling RMS values of each node. Finally, Strain Power Mode Shape (SPMS) index and Strain Power Flexibility (SPF) index is used to detect the location of damage.

By comparing Strain-flexibility index and SPF index, the location of peak value and distribution of two indices are similar. Unlike Strain-flexibility index, SPF index is based on statistical parameters without the modal analysis. From facts mentioned above, SPF index is effective to detect the location of damage. Also, SPF index works out better than SPMS index comparing the experimental results. There is only one value for each node using SPF index. On the other hand, engineers should examine all values of every mode of each node thoroughly using SPMS index. Considering the facts mentioned above, SPF index is a more effective and convenient method than SPMS index.

The robustness of the proposed method to random noise is investigated. The results show that the values of SPF index changed only a little in quantity and the distributions of the index are similar. Therefore, it is found that the proposed method is robust to the Gaussian random noise.

Acknowledgements:

This work is supported partly by Korea Ministry of Land, Transport and Maritime Affairs (MLTM) through Korea Construction Engineering Development Collaboratory Program Management Center (KOCED PMC) at Seoul National University, and partly by the fund of Korea Science and Engineering Foundation(KOSEF) through Korea Earthquake Engineering Research Center (KEERC) at Seoul National University. The authors wish to

express their gratitude for the financial supports.

References:

A. K. Pandey and M. Biswas (1994) "Damage Detection In Structures Using Changes In Flexibility", *Journal of Sound and Vibration*, **169**(1), 3-17.

D. Zonta, A. Lanaro and P. Zanon (2003) "A Strain-Flexibilty-Based Approach to Damage Location", *Key Engineering Materials*, **245-246**, 87-94.

Park, H.J., Koo, K.Y., Yun, C.B. (2007) "Modal Flexibility-based Damage Detection Technique of Steel Beam by Dynamic Strain Measurements using FBG sensors", *Steel Structures*, **7,** 11-18.

S.-E. Fang and R. Perera (2009) "Power mode shapes for early damage detection in linear structures", *Journal of Sound and Vibration*, **324**, 40-56.

Brincker, R., Zhang, L. and Andersen, P. (2001) "Modal Identification of Output-only systems using Frequency Domain Decomposition", *Smart Materials and Structures*, 1(10), 441-445.

JOINT CONFERENCE PROCEEDINGS
7th International Conference on Urban Earthquake Engineering (7CUEE) &
5th International Conference on Earthquake Engineering (5ICEE)
March 3-5, 2010, Tokyo Institute of Technology, Tokyo, Japan

A HIGH RESOLUTION DISTRIBUTED MOISTURE SENSING SYSTEM TO QUANTIFY EARTHQUAKE INDUCED VOID REDISTRIBUTION

Jonathon Fagert[1], Bin Zhang[2] and Xiong (Bill) Yu[3],

1) BS/MS student, Department of Civil Engineering, Case Western Reserve University, USA
2) Ph.D. Candidate, Department of Civil Engineering, Case Western Reserve University, USA
3) Assistant Professor, Department of Civil Engineering, Case Western Reserve University, USA

Abstract: This paper describes the preliminary study targeting at developing a high resolution distributed moisture sensing system. The goal is for this sensor to be able to measure the moisture distribution with sufficient spatial and temporal resolution so that it can detect the earthquake induced void redistribution and the consequent on-set of ground liquefaction. Such sensor is currently unavailable. Therefore, an important application of this sensor is to establish the liquefaction criteria due to void redistribution, which occurs under stratified ground conditions. The sensing principles for moisture distribution are described. A feasibility analysis is conducted on improving the sensor design to achieve the desired resolution. A few prototype sensor designs are described. The results indicate a spiral shaped design further increased the spatial resolution. The sensor is under further refinement and testing to be suitable for applications.

1. INTRODUCTION

Ground liquefaction during earthquake can lead to catastrophic consequences. Because of this, study the triggering mechanism of liquefaction has been carried out for decades. According to Seed (1987), "The major emphasis in a soil liquefaction potential investigation should be placed on the triggering problem and on exploring the conditions that cause sufficient pore pressure development to trigger liquefaction in a soil". Most existing study focuses on determining the liquefaction criteria for uniform soils. For slopes and embankments constructed of layered soils, it was found that a unique phenomenon called void redistribution occurs, which accelerate liquefaction at the interface between layers. Due to the discontinuity of hydraulic conductivity, a portion of the liquefied soil locally loosens (or dilates) whereas another portion densifies (or contracts) (Kulasingam et al. 2004, Malvick et al. 2006, e.g. Fig. 1). Void redistribution has been observed in a number of laboratory experiments and field studies (Seed 1987, DeAlba 1987, Boulanger and Truman 1996, Malvick et al. 2006, Malvick et al. 2008).

The redistribution of water content, especially the accumulation of water at the interface area between liquefied soil and soil layer of low permeability can cause significant loss of shear strength in slopes and embankments during and after earthquake (Malvick et al. 2006). This is one of the most likely failure mechanisms of slopes made of stratified soil layers (NRC 1985). Over the years, investigators had implemented a variety of experimental studies, trying to verify this mechanism. In an award winning paper, Kulasingam et al (2004) conducted a group of centrifuge tests on seismic stability of a sand slope with or without a layer of low permeability silt. Based on the recorded excess pore pressure and deformation, they concluded that this mechanism is probably the right one. It illustrated clearly how important this topic is in geotechnical earthquake engineering under stratified ground conditions.

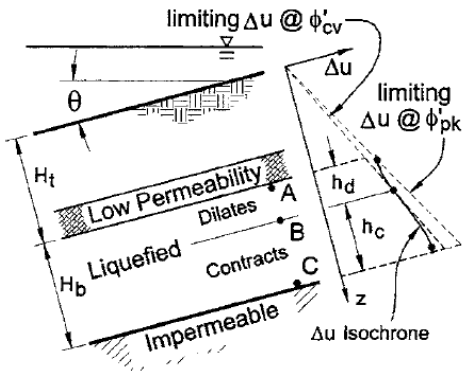

Fig. 1 Void redistribution mechanism (liquefied soil layer embedded between low permeability layers causing formation of dilation and contraction zones) (Malvick et al. 2006)

However, as Kulasingam et al (2004) rightfully pointed out "it remains a challenging task to develop reliable methods for quantifying the degree of void redistribution in the field…, such methods are necessary for judging the extent to which a site may be more or less prone to strength loss or localizations due to void redistribution." Therefore, it is very important and beneficial to develop a reliable method that can quantify the void redistribution during and immediately after an earthquake.

2. BACKGROUND

2.1 Liquefaction Induced Void Redistribution

The void redistribution and the consequent shear band localization in liquefied soils have been studied by recent research efforts (e.g., Kulasingam et al (2004), Malvick et al. (2006) and Malvick et al. (2008)). A few assumptions are typically made, for example, the thickness of shear band is generally assumed to be in tens of D_{50}. Studies by Boulanger and Truman (1996) and Malvick et al. (2003) have shown that the dilating shear zone is much larger than this assumption. In addition, in most existing study, the void redistribution is indirectly estimated by inferring from pore pressure measurement using pore pressure transducers placed at different depths within the layered soil slope. This does not provide direct measurement on the onset and development of void redistribution. Moreover, the size of pore pressure transducers limit the spatial resolution such sensors could provide. Considering the thickness of shear band, which is in minimeter range for common types of sand, a higher resolution will be needed to directly measure the thickness of shear band and the extent of void redistribution (the contraction and dilation zones along the depth, Fig. 1). Direct measurement of these quantities will help clarify a number of fundamental questions on earthquake triggering mechanism in stratified soil layers.

For saturated soils, sensors to real time monitoring the distribution of moisture along strategically-set directions in earth slopes would provide data to directly measure the onsite and development of void redistribution. While measurement of moisture content is a basic activity by many disciplines using different scientific principles, technology suitable for measuring the moisture distribution with required high spatial and time resolution are currently lacking. Developing a technology to overcome the limitations of the existing method is the focus of this paper.

2.2 Time Domain Reflectometry

TDR is a guided electromagnetic wave technology, which measure the material properties based on the speed and attenuation of electromagnetic wave. It works by generating a small-magnitude electromagnetic field excitation and measures the material response. The schematic of a TDR measurement system is shown in Fig. 2a. Dipoles (originated from the molecular geometry or charges of the particles) oscillate under the excitation. The overall responses of the material are dependent on the excitation frequencies and is described by the dielectric spectra. Certain ions drift freely under the electrical field and the macroscopic phenomena correspond to electrical conductivity (Yu and Drnevich (2004)). Typical information obtained from a TDR signal includes the apparent dielectric constant , Ka, and the electrical conductivity, ECb.

TDR was originally used by electrical engineers for locating discontinuities in electrical cable. It is being increasingly used for Civil and Environmental applications (O'Connor and Dowding (1999)). Examples include characterization of soils and concretes (Topp and Davis (1985), Benson and Bosscher (1999), O'Connor and Dowding (1999), Noborio (2001), Yu and Drnevich (2004), Hager and Domszy (2004)), monitoring of infrastructure conditions (Yankielun and Zabilansky (1998), Dowding (2001), Su and Chen (2003), Chen, et al. (2004), Lin et al. (2005)), and study of contaminants transport (Elrick et al. (1992), Haridy et al. (2005)).

Measurement of soil water content is an important application area for TDR technology (O'Connor and Dowding (1998)). The ability of TDR to measure soil water content lies in the much larger dielectric constant of water (around 81) than those of air (around 1) and soil solids (around 3 to 5). TDR signals and the related information (dielectric constant, Ka, and electrical conductivity, ECb) are very sensitive to the variations of soil water content (Fig. 2b). It is used to measure the soil water content in most major pavement instrumentation programs (Gary et al. (2003)). Compared with widely used nuclear method, TDR-based instrument has the advantages such as fast, non-radioactive, cost-effective, and easily automated.

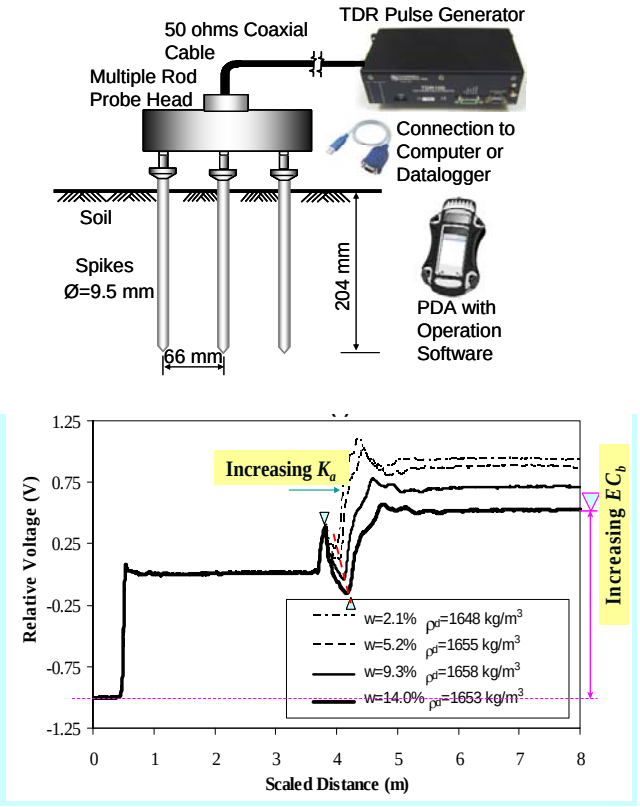

Fig. 2 a) Example TDR system for point measurement; b) Effects of water content, *w*, on TDR signals

3. TECHNICAL FEASIBILITY ANALYSIS

Sensitivity: A sensitivity analysis is conducted using theoretical dielectric mixing models.

$$K_{a,b}^{1/m} = (1-n)\cdot K_{a,s}^{1/m} + n\cdot K_{a.w}^{1/m}$$

where n is the porosity, m is a factor related to the particle orientation, a typical value set for m is 2, $K_{a,b}$ is the bulk dielectric constant, $K_{a,s}$ is the dielectric constant of soil solids,

$K_{a,w}$ is the dielectric constant of water.

For saturated sand, the results of model prediction are plotted in Figure 3, which shows the relationships between the void ratio, soil dry density and soil bulk dielectric constant. The bulk dielectric constant of saturated sand is described using classic dielectric mixing model (Topp et al. 1980). Figure 3 shows that as the dry density of sand reduces (i.e., soil dilates), the dielectric constant increases significantly, i.e., the dielectric constant increases from around 20 at void ratio of 0.5 (or volumetric water content of 33%) to 55 at the void ratio of around 3 (or volumetric water content of 75%). It has been independently verified that sensors based on TDR principles can achieve an accuracy of within 1-2% of volumetric water content upon proper calibration (Roth et al. 1990). This corresponds to a resolution of around 0.2 (via (3-0.33)/((75%-33%)/2%))) in detecting the change of void ratio. Such accuracy should be sufficient to detect the void redistribution in the shear band.

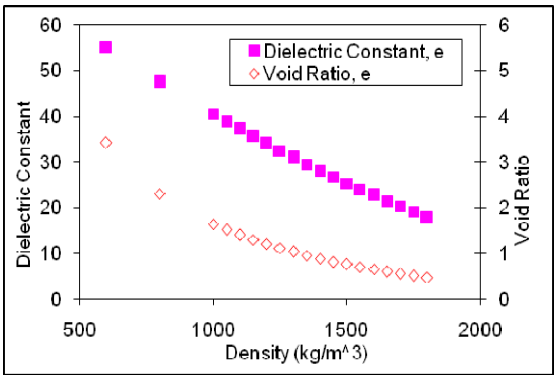

Fig. 3 The effects of the void ratio variation on the dielectric constant of saturated sand

Spatial and Temporal Resolution: To detect void redistribution and shear band during liquefaction, the system needs to have a spatial resolution in the millimeter range. For the purpose of real time detection, the sampling rate for signal acquisition needs to be sufficiently high to achieve the desired temporal resolution. The advancement in the electric pulse technology and high speed samplers have made it possible to achieve the required high spatial and temporal resolution. The spatial and temporal resolution can be achieved by the integration of advance pulser technology and data storage and retrieval strategy.

Advanced Pulser Technology to Achieve Required Spatial Resolution: The spatial resolution in sub-millimeter range can be achieved by incorporating a state of the art pulse generator recently produced by Picoseconds Pulse Labs Inc.. This advanced pulse generator can produce electrical pulse with a rise time of 10 picoseconds (1 picosecond equals to 10^{-12} second). This corresponds to 3 mm spatial resolution in vacuum (rise time x speed of electromagnetic wave) or around 0.3 mm spatial resolution in water (the travel speed of EM wave in water is only around 1/9 that in vacuum). It is anticipated that a spatial resolution of less than 1 mm can be achieved for saturated sand by use of this state of the art pulser technology.

Data Storage and Retrieval Strategy to Achieve Required Temporal Resolution: The length of TDR pulse is typical in milliseconds (e.g., 14 ms for commonly used TDR100 pulse generator[@]). This is also the time required for accomplishing a complete TDR measurement. More than 50 TDR readings can be taken within one second. This should provide be sufficient to detect the onsite and dynamic development of void redistribution. To achieve the maximum signal rate, a strategy for TDR data storage and transfer will be needed. Due to the limitation in the data transferring rate by serial or Ethernet communication protocol, it might need to temporally store TDR signals in an on-board memory card and transfer the data to host computer for further analyses after the experiment. These alternative strategies need to be designed and evaluated.

4. PILOT STUDY OF DISTRIBUTED SENSING AND INCREASING THE SPATIAL RESOLUTION

4.1 Distributed Moisture Sensing

A pilot study was conducted to validate the ability of TDR for distributed moisture sensing. Figure 4a shows the prototype from this preliminary effort (Zhang et al. 2007). The sensing component is composed of a special designed flat sensing cable of 40mm in the width, 1mm in the thickness and 1.0 m long. The sensor cable is fabricated with inexpensive stainless steel strips, with the total materials costing less than $100. Evaluation shows that the TDR sensor signals are very sensitive to moisture variations (Fig. 4b). As shown in Fig. 4, the three artificial wet spots (by wet sponges and moisture tin with water) clearly demonstrate the EM signal response. This is indication that the distributed moisture sensing capability can be achieved.

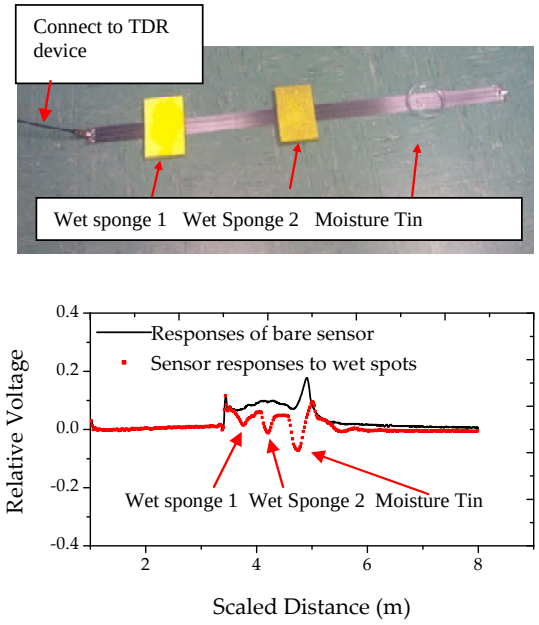

Fig. 4 View of TDR strip and example signal responses (Zhang et al. 2007)

4.2 Increasing Resolution for Interface Detection

Efforts have been attempted to further increase the spatial resolution of the sensor. The cross section of the sensor was scaled down to in millimeter range in an effort to further improve the spatial sensitivity (Fig. 5a). The sensor prototype includes two metal wires of approximate 1 mm in diameter. The sensing wires are aligned to achieve the required electrical impedance.

To further increase the spatial resolution in the length direction, a spiral shaped sensing rod was also fabricated, where the sensing wires are circled around a plastic tube with 5mm diameter in spiral shape (Fig. 5b). This increased the travel length of the electromagnetic wave per unit depth. Assuming the spiral wire is mounted on the rod at density of N circles per unit length, the length ratio of spiral shaped sensing wire to the straight sensing wire is

$$\frac{L_{spiral}}{L_{straight}} = \frac{\pi D N \Delta h}{\Delta h} = \pi D N$$

where D is the diameter of the rod.

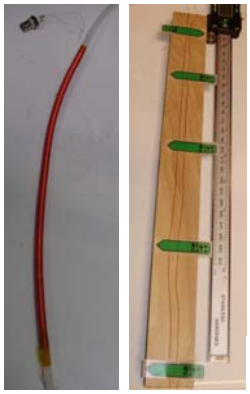

Fig. 5 a) spiral sensor; b) straight wire sensor

For the fabricated spiral sensor, the N number is around 20 cyle/cm. This gives a length ratio of around 31.4.

Both sensors were evaluated for the spatial resolution in detecting the interfaces. The following procedures were applied during the process:

- Fill a transparent tube with water
- Take a reading of the straight/spiral wire exposed in air
- Dip portion of the straight/spiral wire into water, take TDR reading and save the signal
- Gradually increase the length of the portion of the straight/spiral wire dipped into water, take TDR readings and save signals

(a)

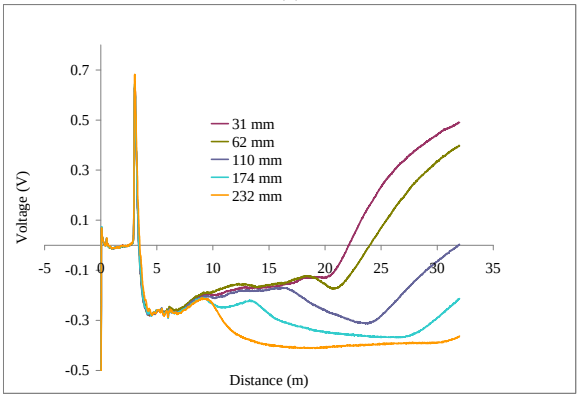

(b)

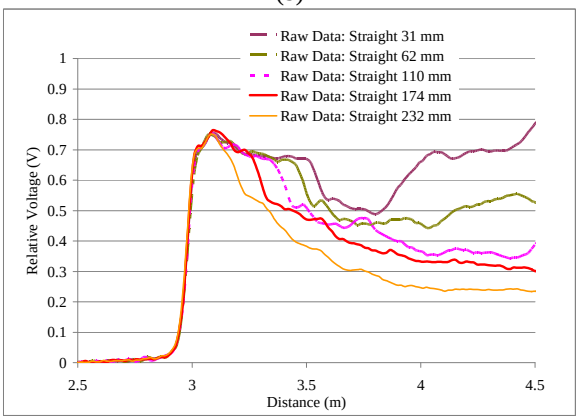

Fig. 6 Example of measured signals when different length of the sensor is submerged into water.

Examples of the measured signals by two different sensors are shown in Figure 6. The locations of the characteristic points, i.e., the peaks or steepest slopes, were determined from the measured signals. Figure 7 plots the water level versus the location of these characteristic points. Two observation can be made from Fig. 7. Firstly, there is very good linear relationships between the water level (or water/air interface) and the location of the characteristic points in TDR signals for both the straight and spiral wire sensors. Secondly, the spiral coil has much larger sensitivity to the variations of the interface location. The ratio of the slopes of the calibration curves by these two

different sensors is around 29 (0.0576/0.002). This means the spiral sensing wire is around 29 times more sensitive to detect the interfaces compared with a straight wire. The results is similar to what is predicted from Eq. (2). The resolution can be further increased by increasing the diameter of the spiral coil or by increasing the N numbers.

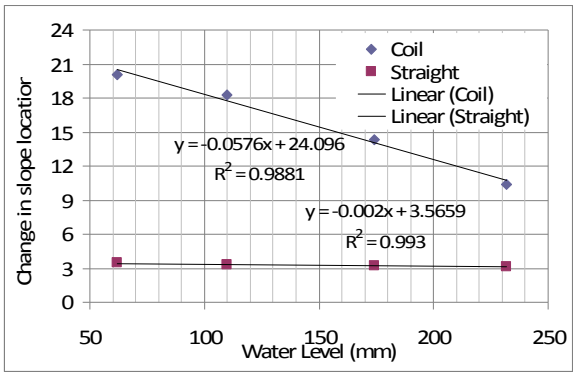

Fig. 7 Relationship between water level and the location of characteristic points for two different sensors

5. CONCLUSIONS

Earthquake induced void redistribution is a major triggering mechanism of liquefaction under stratified ground conditions. This paper describes the preliminary study targeting at developing a high resolution distributed moisture sensing system to help establish the liquefaction criteria due to void redistribution. A distributed moisture sensor based on TDR was fabricated. The sensor was found to have distributed sensing capability. The size of sensor was reduced for detecting the spatial event with high resolution. A special spiral wire sensor design was also fabricated. The comparison indicates that the spatial resolution are significantly improved with the spiral shape design. The sensor is under further refinement and testing for field applications.

Acknowledgements:

The authors acknowledge the partial support from the National Science Foundation (0700524, 0846475, 0900401) for this study. The help from Dr. S.C. Liu, NSF program director is highly appreciated.

References:

Benson, C. H., and Bosscher, P. J. (1999). "Time-domain reflectometry (TDR) in Geotechnics: A review, nondestructive and automated testing for soil and rock properties." *ASTM SPT 1350*, W. A. Marr, and C. E. Fairhurst, eds., American Society for Testing and Materials, West Conshohocken, Pa.

Boulanger R.W. and Truman S.P. (1996). Void Redistribution in Sand under Post-earthquake Loading, *Can. Geotech. J.* 33:829-834.

Chen, G.D., Mu, H.M., Pommerenke, D., and Drewniak, J.L., (2004), "Damage detection of reinforced concrete beams with novel distributed crack/strain sensors", *Structural Health Monitoring*, Vol 3(3): 225-243.

Gary E. Elkins, Peter Schmalzer, Travis Thompson, and Amy Simpson, (2003), "Long-term pavement performance information management system pavement performance database user guide", U.S. Department of Transportation, Federal Highway Administration, Research, Development, and Technology Turner-Fairbank Highway Research Center, Report No. FHWA-RD-03-088

Hager, N.E. and Domszy R.C. (2004). "Monitoring of cement hydration by broadband time-domain-reflectometry dielectric spectroscopy", *Journal of Applied Physics*, Vol. 96, No.9, pp.5117-5128.

Haridy, A.S., Persson, M., and Berndtsson, R., (2004), "Estimation of LNAPL saturation in fine sand using time-domain reflectometry", *Hydrological Sciences Journal*, Vol. 49, No. 6, pp987-1000

Kulasinggam, R. Malvick, E.J., Boulanger, R.W., and Kutter, B.L. (2004). "Strength loss and localization at silt interlayers in slopes of liquefied sand," *ASCE Journal of Geotechnical and Geoenvironmental Engineering*, Vol.130, No.11, 1192-1202.

Kulasinggam, R. Malvick, E.J., Boulanger, R.W., and Kutter, B.L. (2004). "Strength loss and localization at silt interlayers in slopes of liquefied sand," *ASCE Journal of Geotechnical and Geoenvironmental Engineering*, Vol.130, No.11, 1192-1202.

Lin, M.W., Thaduri, J. and Abatan, A.O., (2005), "Development of an electrical time domain reflectometry (ETDR) distributed strain sensor", *Meas. Sci. Technol*. Vol 16: 1495-1505.

Malvick E.J., Kutter, B.L. and Boulanger R.W. (2006). Postshaking Shear Strain Localization in a Centrifuge Model of a Saturated Sand Slope. *Journal of Geotechnical an Geoenvironmental Engineering*, Vol. 134, No. 2, 164-174.

Malvick E.J., Kutter, B.L., Boulanger R.W. and Kulasingam R. (2008). Shear Localization Due to Liquefaction-Induced Void Redistribution in a Layered Infinite Slope. *Journal of Geotechnical an Geoenvironmental Engineering*, Vol. 132, No. 10, 1293-1303.

National Research Council (1997). Nonconventional Concrete Technologies: Renewal of the Highway Infrastructure. 1997, NMAB-484, National Academy Press: Washington, DC.

Noborio, K. (2001). "Measurement of soil water content and electric conductivity by time domain reflectometry: a review." C*omput. Electron. Agric*., 31(3), 213–237.

O'Connor K. and Dowding, C. (1999). "Geo Measurements by Pulsing TDR Cables and Probes", CRC Press, Boca Raton, FL, 1999, 340 pps.

Seed, H.B. (1987). Design Problems in Soil Liquefaction. *Journal of Geotechnical Engineering*, Vol. 113, No. 8, August.

Su, M.B. and Chen Y. J., (1998), "Multiple reflection of metallic time domain reflectometry", Exp. Tech., No. 22, pp26–35.

Topp, G. C. and Davis, J. L., 1985, "Measurement of Soil Water Content Using Time Domain Reflectometry (TDR): A Field Evaluation," *Soil Science Society of America Journal*, Vol. 49, pp. 19–21.

Yu, X. and Drnevich, V.P. (2004). "Soil water content and dry density by time domain reflectometry", *Journal of Geotechnical and Geoenvironmental Engineering*, Vol. 130, No. 9, pp.922-934.

JOINT CONFERENCE PROCEEDINGS
7th International Conference on Urban Earthquake Engineering (7CUEE) &
5th International Conference on Earthquake Engineering (5ICEE)
March 3-5, 2010, Tokyo Institute of Technology, Tokyo, Japan

APPLICATION OF DIFFERENT CONTINUOUS WAVELET FUNCTIONS ON CYLINDRICAL GUIDED WAVE SIGNALS FOR UNDERGROUND PIPE INSPECTION

Rais Ahmad[1] and Tribikram Kundu[2]

1) Assistant Professor in Residence, Dept. Civil & Environmental Engineering, University of Connecticut, USA
2) Professor, Dept. of Civil Engineering & Engineering Mechanics, University of Arizona, USA
rahmad@engr.uconn.edu, tkundu@email.arizona.edu

Abstract: Over the past decade, wavelets provided a powerful and flexible set of tools for handling fundamental problems in science and engineering. Wavelet analyses are being used for solving problems in different engineering areas like audio de-noising, signal compression, object detection, image decomposition, speech recognition etc. Wavelet analysis employs orthonormal as well as non-orthonornal functions. This research investigates the effectiveness of wavelet analysis in detecting defects in underground steel pipe networks. Continuous Wavelet Transforms (CWT) has been performed on the received signals of cylindrical guided waves. Cylindrical Guided waves are generated and propagated through the pipe wall boundaries in a pitch-catch system. Piezo-electric transducers are used to generate as well as receive guided waves. Several mother wavelet functions such as Daubechies, Symlet, Coiflet and Meyer have been used for the Continuous Wavelet Transform to investigate the most suitable function for defect detection. This research also investigates the effect of surrounding soil on wavelet transforms for different mother wavelet functions.

1. INTRODUCTION

Early forecasting of the degradation process caused by adverse environmental effects or mechanical damages in pipe network systems can save many catastrophic accidents. Now a days, the detection of the existing defects in pipes is one of the major challenges for the structural health monitoring of pipes. Propagation of cylindrical guided waves through pipes for damage detection is becoming an increasingly popular technique for pipe inspection.

Gazis [1959a and 1959b] first analytically solved the propagation of harmonic waves in an infinitely long elastic hollow cylinder. Many investigators [Silk *et al.* (1979) and Brook *et al.* (1990)] used guided wave modes for detecting wall thinning defects in cylindrical pipes. Rose and coworkers (1994a and 1994b) designed a special probe which can be used both as a transmitter and a receiver during the pipe inspection. Guo and Kundu (2000 and 2001) designed a new transducer holder mechanism for pipe inspection using cylindrical guided waves. Using those transducer holders Na *et al*. (2002 and 2003) generated cylindrical guided waves for detecting delaminations between steel bars and concrete interface.

Successful damage detection requires proper use of signal processing techniques or tools. In recent years wavelet analysis has become a popular technique for processing received signals with time-varying spectra. Many investigators have used the wavelet analysis to characterize damages in materials. Cho *et al.* (1996) discussed the detection of subsurface lateral defects using wavelet transform on propagating Lamb waves. Rioul and Vitterli (1991) and Abbate *et al.* (1995) used wavelet transform for processing signals with non-stationary spectral contents. Kaya *et al.* (1994) used wavelet decomposition to detect flaws in stainless steel samples. Ahmad *et al* (2006 and 2005) used daubechies wavelet transforms for detecting defects in free and embedded pipes.

Gabor transform can be used as another form of wavelet analysis. Gabor (1947) adapted the Fourier transform to analyze only a small section of the signal at a time – a technique called windowing of the signal. Gabor Transform (also known as 'Short Time Fourier Transform', STFT), maps a signal into a two-dimensional space of time and frequency. Gabor's work was not widely known until 1980 when Bastiaans *et al.* (1980, 1981 and 1985) related the Gabor expansion and the short time Fourier transform. Bastiaans introduced the sampled short time Fourier transform to compute the Gabor coefficients and successfully derived a closed form Gaussian function.

Murase and Kawashima (2002) tried out different wavelet transforms and showed that when Gabor functions are used as mother wavelets then one can plot group velocity curves for a thin aluminum plate. Ahmad and Kundu (2004) also used the Gabor wavelet transform to plot group velocities for defective and defect-free cylindrical pipes from experimental data. Ahmad *et al.* (2009) used daubechies

mother wavelet functions to identify defects in transmission pipes.

2. THEORY

A wavelet is described by the function $\psi_{a,b}(t)$, which is obtained by dilation and translation of a function $\psi(t)$ as defined by

$$\psi_{a,b}(t) = \frac{1}{\sqrt{|a|}} \psi\left(\frac{t-b}{a}\right); \text{ with } a > 0, \text{ and } b \in \Re \quad (1)$$

Where, $\Re$ is the set of real numbers. The function $\psi_{(a, b)}$ is traditionally called mother wavelet. The parameter a represents the scale index and b indicates the time shifting or translation. The approximation of a function $f(t)$ by wavelets is carried out using the coefficients C given by

$$C(a,b) = \langle f ; \psi_{a,b} \rangle \quad (2)$$

Where, <* ; *> defines the scalar product

The continuous wavelet transform or CWT, is given by

$$CWT \quad f(a,b) = \frac{1}{\sqrt{|a|}} \int_{-\infty}^{+\infty} f(t) \psi^* \left(\frac{t-b}{a}\right) dt \quad (3)$$

Where, * denotes the complex conjugate of the function.

In simple words, the continuous wavelet transform is defined as the sum over all time of the signal multiplied by scaled, shifted version of the wavelet function, ψ;

$$C(scale, position) = \int_{-\infty}^{\infty} f(t) \psi(scale, position, t) dt \quad (4)$$

The results of the CWT are many wavelet coefficients C, which are a function of scale and position.

A wavelet is a waveform of effectively limited duration that has an average value of zero. Wavelet analysis is the breaking up of a signal into shifted and scaled version of the original mother wavelet. Wavelets have scale aspects and time aspects and consequently a wavelet analysis produces a time-scale view of a signal. Scaling a wavelet means stretching it. The smaller the scale factor, the more compressed the wavelet. Higher scales correspond to the more stretched wavelets. When the wavelets are stretched more then longer is the portion of the signal with which the wavelets are compared, then the coarser signal features are measured by the wavelet coefficients. Thus, there is a correspondence between wavelet scales and frequency:

Low scale $a \Rightarrow$ Compressed wavelet $\Rightarrow$ Rapidly changing details $\Rightarrow$ High frequency, ω.

High scale $a \Rightarrow$ Stretched wavelet $\Rightarrow$ Slowly changing, coarser features $\Rightarrow$ Low frequency, ω

3. EXPERIMENTS

The primary objective of this research is to investigate how cylindrical guided waves can be used effectively to detect defects in embedded pipes. Another issue of this research is to find out how the guided waves behave when pipes are embedded in soil. Continuous wavelet analyses were performed using daubechies, symlet, coiflet and meyer mother wavelet functions on the signals received for both defect free and defective pipes. The pipes were kept in two different boundary conditions - 1) traction free boundary condition for free pipes open in the air and 2) for soil embedded pipes the outer surface of the pipe is not traction-free.

3.1 Specimens

A specimen set, consisting of three steel pipes were fabricated. All three pipes were 1200 mm (~4ft) long and had 21.4 mm (13.5/16 inch) outer and 15.6 mm (10/16 inch) inner diameters. One pipe was defect-free and the other two had mechanical defects - a gouge and a dent that were artificially fabricated on the pipe. The gouge anomaly was fabricated by pressing the outer wall of the pipe while keeping the inner diameter unchanged by placing a rigid rod inside. The dent type anomaly was formed by pressing the outer wall, keeping the inner wall free to deform. In both types of defect the outer walls were cold pressed. The defect covered a complete (360°) revolution. Table 1 gives all dimensions of the pipes and the defects. Table 2 shows the acoustic properties of steel – the pipe material. Properties of the surrounding soil used in this experiment are given in Table 3.

Table 1. Different types of pipe defects and their dimensions

Type	Pipe Length (mm)	Diameter		Thickness (mm)	Damage Dimension	
		Outer (mm)	Inner (mm)		Depth (mm)(% of thickness)	Width/ Diameter (mm)
Defect Free (Pipe A)	1200	21.4	15.6	2.9	-	-
Gouge (Pipe B)	1200	21.4	15.6	2.9	1.26 (43.4%)	5.92
Dent (Pipe C)	1200	21.4	15.6	2.9	1.41 (48.6%)	5.21

Table 2. Acoustic properties of steel

P-wave speed (km/s)	S-wave speed (km/s)	Density (gm/cc)
5.96	3.26	7.932

Table 3. Soil Properties

1. Coefficient of Uniformity, $C_U = 5.0$
2. Coefficient of Concavity, $C_C = 0.8$
3. Moisture Content = 0.58 %
4. Compressional wave velocity, C_p ~ 220 m/s. [23] (Ref. Velea, D. *et al*. (2000))
5. Shear Wave Velocity, C_s ~ 140 m/s. [24] (Ref. Velea, D. *et al.* (2000))

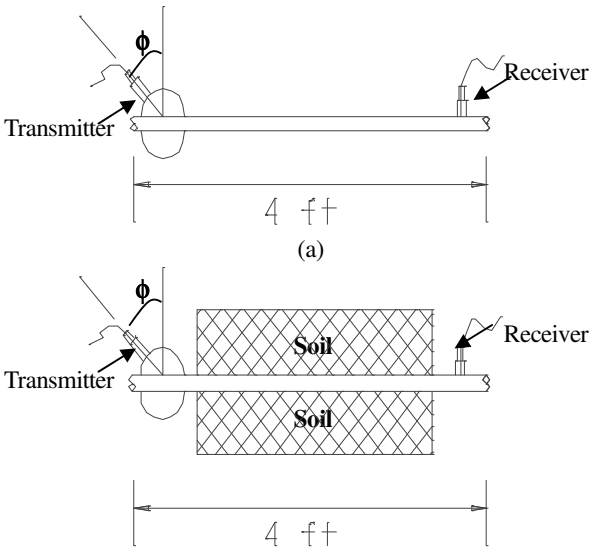

Figure1. Experimental setup, (a) traction free boundary condition, (b) soil embedded condition.

4. RESULT

4.1 Traction Free Boundary Condition

The experiments were carried out for two different boundary conditions. First the pipes, both the defect free and the defective pipes were tested for the free boundary conditions. Cylindrical guided waves are generated by piezo-electric transducers. The guided waves are propagated through the pipe wall and received at the other end by another transducer. The time series (amplitude versus time) signals which are obtained from the receiving transducers are used for the continuous wavelet transforms. From the time series of the signals, it was observed that the signals were associated with significant amount of noise. Using wavelets, noise from the signals are removed by identifying which component or components contain the noise. The signals are then reconstructed omitting those noisy components. Figures 2 (a), (b) and (c) show the de-noised signals for the defect-free (pipe A) and defective pipes (pipes B and C – pipe B has gouge and pipe C has dent) under traction-free boundary conditions.

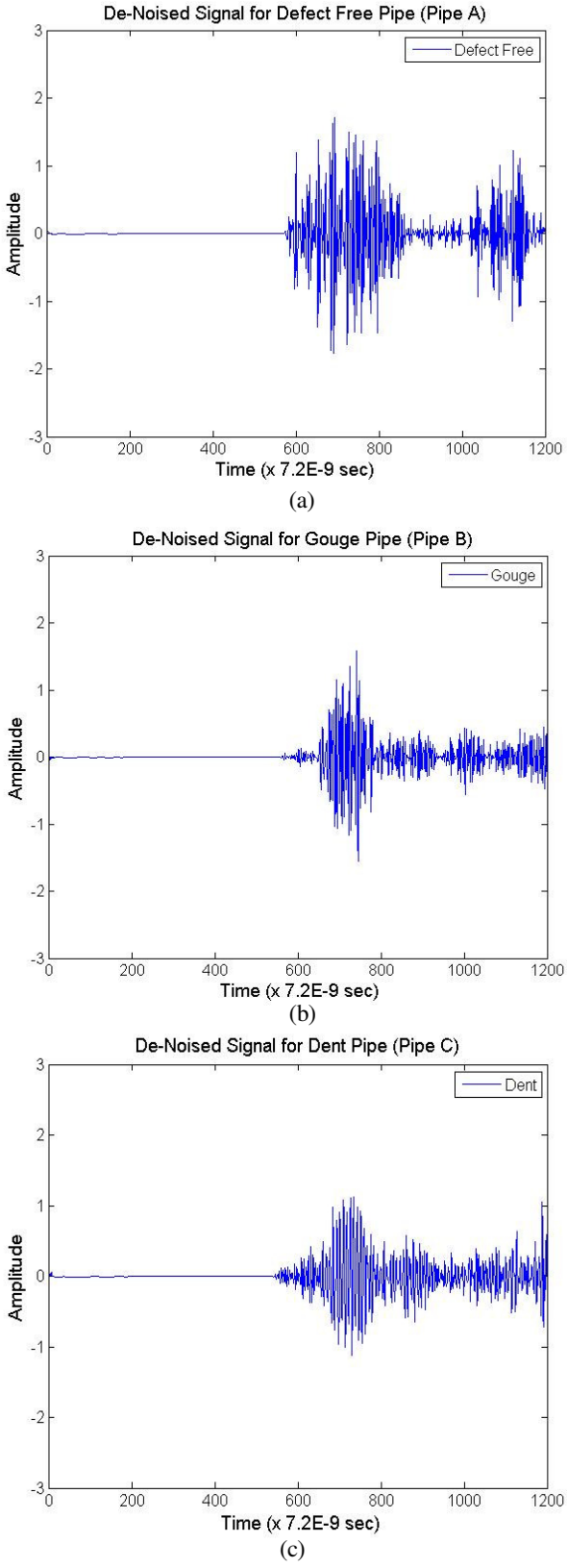

Figure 2. De-noised signals under traction-free boundary conditions, (a) defect free pipe, (b) gouged pipe, (c) dented pipe.

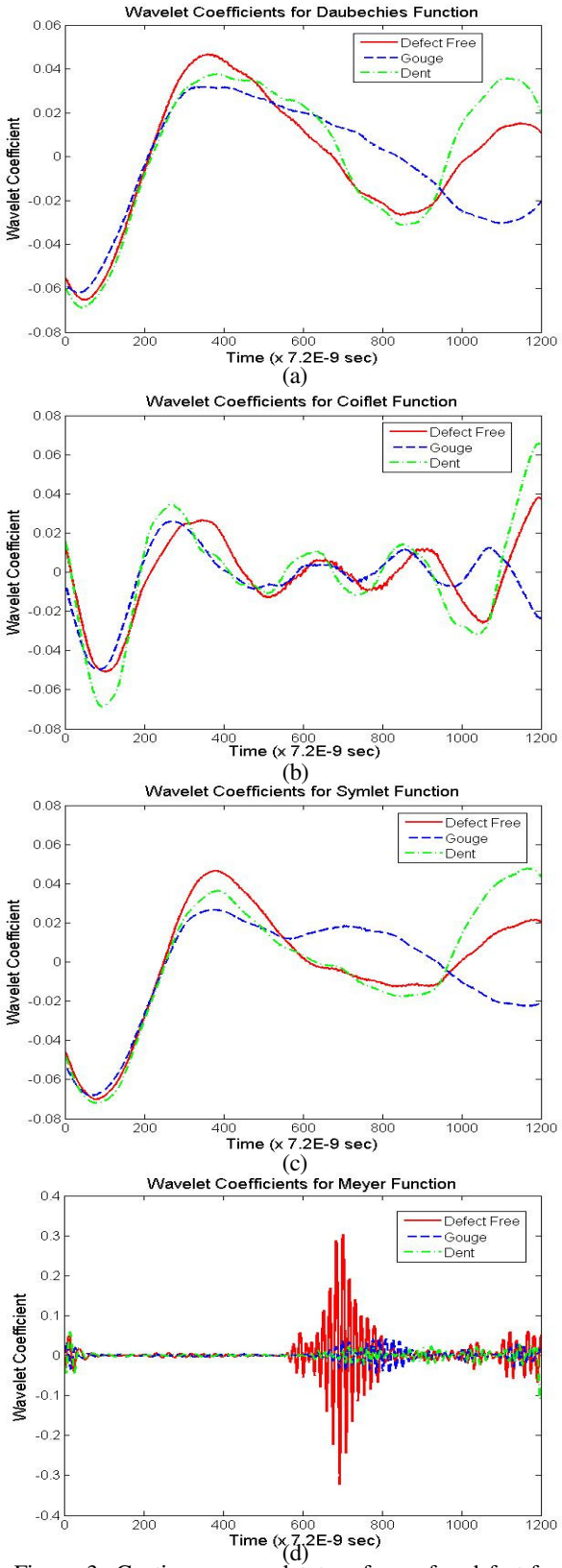

Figure 3. Continuous wavelet transforms for defect-free, gouged and dented pipes under traction-free boundary conditions, (a) for daubechies function, (b) for coiflet function, (c) for symlet function and (d) for meyer function.

Continuous wavelet transforms (CWT) have been performed on the received signals for both defect-free and defective pipes. Daubechies (db4), coiflet (coif2), symlet (sym4) and meyer mother wavelet functions are used for the CWT. The scaling for the daubechies, coiflet, symlet and meyer wavelet transforms are taken as 512, 256, 512 and 16 respectively. The appropriate functions db4, coif2, sym4 and meyer and their respective scaling are chosen in such a way that they produce significant results. Figures 3 (a), (b), (c) and (d) show the calculated wavelet coefficients for the above mentioned functions with respect to time. The time scale is shown in 1200 equal divisions where each division accounts for 7.2 ns (nano seconds). From Figures 2 (a) and (c) it can be observed that between time divisions 600 and 800, where the first patch of modes in the time series (Figures 2 (a), (b) and (c)) appears, the wavelet coefficients for the defect free and dente pipes match well but there is a significant difference in wavelet coefficients for the gouged pipe. In Figure 3(c), some difference in the wavelet coefficients can be observed, but it is not so pronounced. In Figure 3(d), where meyer function is used for the CWT, significant difference in wavelet coefficients can be seen. The calculated coefficients for the defect-free pipe are much stronger than those for gouged and dented pipe. It shows a clear difference between defect-free and defective pipes.

4.2 Pipe Embedded in Soil

Figures 4 (a), (b) and (c) show the de-noised signals for the defect-free (pipe A), gouged (pipe B) and dented pipes (pipe C) when the pipes are kept embedded in soil. The arrangement for the soil embedment is shown in Figure 1 and the acoustic properties for the surrounding soil are provided in Table 3. As for the traction-free boundary condition, the time length of the signal is taken upto 1200 division where each division is 7.2 nano seconds.

The continuous wavelet transforms for the defect-free and defective pipes embedded in soil are shown in Figures 5 (a), (b), (c) and (d) using daubechies, coiflet, symlet and meyer functions, respectively. For this condition, the scaling for the wavelet analyses were kept same as before for the traction-free boundary condition. In Figures 5 (a) and (c), where daubechies (db4) and symlet (sym4) functions are used, the wavelet coefficients for the defect-free pipe differs considerably from the defective pipes (gouge and dent) occurring between the time divisions 600 and 800 where the first patch modes propagate. It can also be noted that the pattern for the defective pipes (gouged and dented) are similar and they differ from the pattern shown by the defect-free pipe. It differs significantly from the traction-free boundary conditions. The presence of surrounding soil makes the defective pipes, gouge and dent, behave similarly when wavelet analyses are performed using daubechies and symlet functions. The CWT using coiflet functions provides some dissimilarities in wavelet coefficients for the defective and the defect-free pipes.

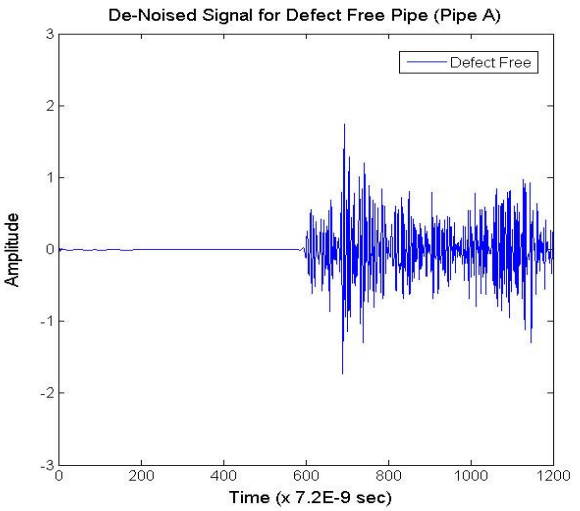

(a)

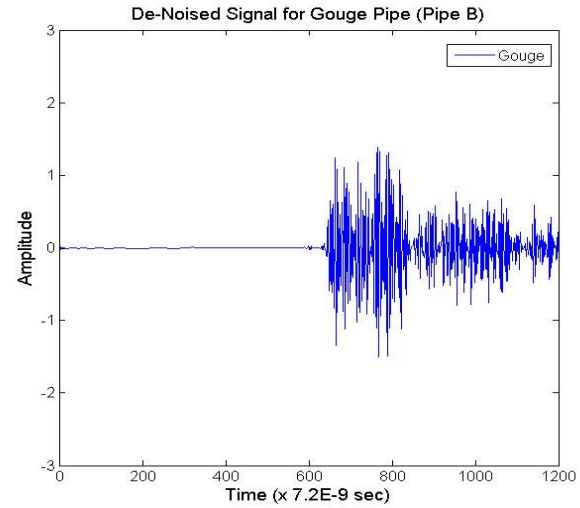

(b)

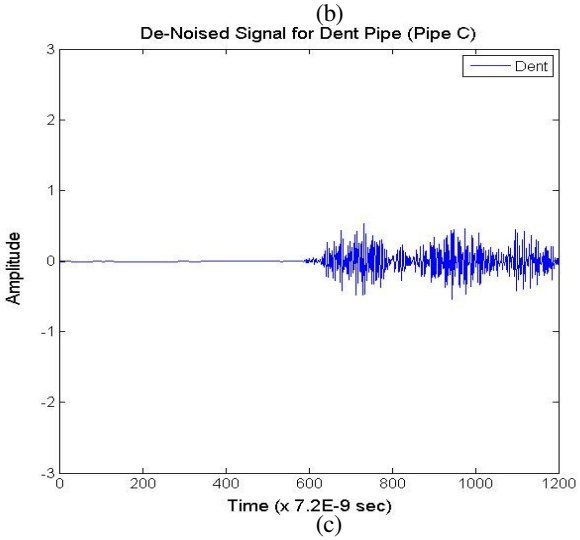

(c)

Figure 4. De-noised signals in embedded pipes, (a) defect-free pipe, (b) gouged pipe, (c) dented pipe.

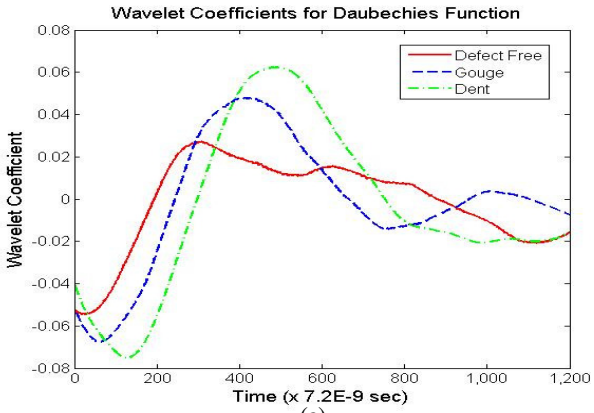

(a)

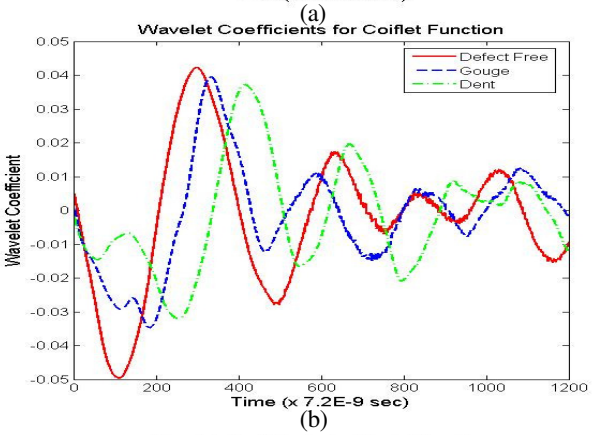

(b)

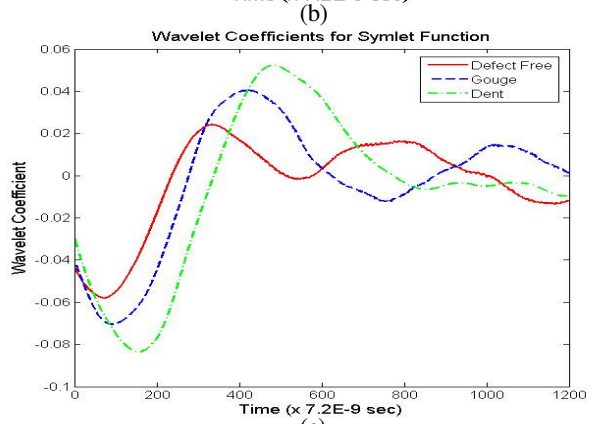

(c)

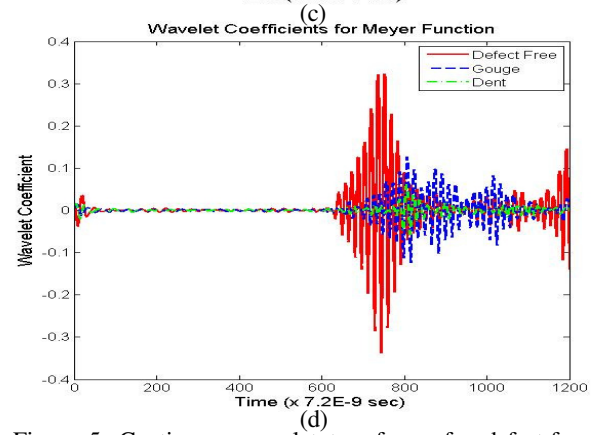

(d)

Figure 5. Continuous wavelet transforms for defect-free, gouged and dented pipes embedded in soil, (a) for daubechies function, (b) for coiflet function, (c) for symlet function and (d) using meyer function.

In Figure 5(d) significant difference in wavelet coefficients can be observed between the defect-free pipe and the defective pipes where meyer function is used. This phenomenon is also observed for the traction-free boundary. Even for the soil embedded condition, where the acoustic signal is expected to loose significant amount of energy, CWT using meyer's function provide considerable evidence for identifying possible defects in embedded pipes and can easily be distinguished from the defect-free pipe.

5. CONCLUSION

This research investigates the application of continuous wavelet analysis for identifying defects in pipe networks when pipes are free in the air (or vacuum) and embedded in the soil. From these investigations it can be concluded that the proper selection of wavelet functions and scaling aspects are important in detecting anomalies. Daubechies, symlet and meyer wavelet functions can be used efficiently to investigate the integrity of underground pipes.

Acknowledgement

This research was financially supported from the National Science Foundation, Grant No. CMS-9901221 and CMMI-0530991, Program Manager – S. C. Liu.

Reference:

Gazis D. Z. (1959a), "Three Dimensional Investigation of Propagation of Waves in Hollow Circular Cylinders. I. Analytical Foundation", Journal of Acoustical Society of America, Vol. 31, No. 5, pp.568-573.

Gazis D.Z. (1959b), "Three Dimensional Investigation of Propagation of Waves in Hollow Circular Cylinders. II. Numerical Results", Journal of Acoustical Society of America, Vol.31, No.5, pp. 573-578.

Silk, M. G. and Bainton, K.F. (1979), "The Propagation in Metal Tubing of Ultrasonic Wave Modes Equivalent to Lamb Waves", Ultrasonics, pp.11-19.

Brook, M., Ngoc, T.D.K. and Eder, J. (1990), "Ultrasonic Inspection of Stem generator Tubing by Chemical Guided Waves", Review of Progress in QNDE, Vol 9, eds. D.O. Thomson and D.E. Chimenti, Plenum Press, New York, pp. 243-249.

Rose, J. L., Ditri, J. J., Pilarski, A., Rajana K. and Carr, F. (1994a), "A Guided Wave Inspection Technique for Nuclear Steam Generator Tubing", NDT & E International, Vol. 27, No. 6, pp. 307-310.

Rose, J. L, Rajana K.M. and Carr, F. T. (1994b), "Ultrasonic Guided Wave Inspection Concepts for Steam Generator Tubing", Materials Evaluation, Vol. 52, No. 2, pp. 134-139.

Guo, D. and Kundu, T. (2000), "A New Sensor for Pipe Inspection by Lamb Waves", Materials Evaluation, Vol. 58, No. 8, pp. 991-994.

Guo, D. and Kundu, T. (2001), " A New Transducer Holder Mechanism for Pipe Inspection", Journal of the Acoustical Society of America, Vol. 110(1), pp 305-309.

Na, W.B., Kundu, T. and Ehsani, M.R. (2002), "Ultrasonic Guided Waves for Steel Bar-Concrete Interface Inspection", Materials Evaluation, Vol. 60(3), pp. 437-444.

Na, W.B., Kundu, T. and Ehsani, M.R. (2003), "Lamb Waves for Detecting Delamination Between Steel Bars and Concrete", Journal of Computer Aided Civil and Infrastructure Engineering, Vol. 18, pp. 57-62.

Cho, H., Ogawa, S. and Takemoto, M. (1996), NDT & E International, Vol. 29(5), pp. 301-306.

Rioul, O. and Vetterli, M. (1991), "Wavelets and Signal Processing", IEEE Trans. Signal Processing, pp. 14-38.

Abbate, A., Frankel, J. and Das, P. (1995), "Wavelet Transform Signal Processing for Dispersion Analysis of Ultrasonic Signals", Proc. of IEEE Ultrasonic Symposium.

Kaya, K., Bilgutay, N.M. and Murthy, R. (1994), "Flaw Detection in Stainless Steel Samples, using Wavelet Decomposition", Proc. Ultrasonic Symposium, Vol. 94CH3468-6, pp. 1271-1274.

Ahmad, R., S. Banerjee and T. Kundu (2006), "Cylindrical guided waves for damage detection in underground pipes using wavelet transforms", *Health Monitoring and Smart Nondestructive Evaluation of Structural and Biological Systems*, Ed. T. Kundu, SPIE's 11th Annual International Symposium on NDE for Health Monitoring and Diagnostics, March, 2006, San Diego, California.

Ahmad, R., S. Banerjee and T. Kundu (2005), "Underground Pipe Inspection by Guided Waves Using Wavelet Analysis", *Health Monitoring and Smart Nondestructive Evaluation of Structural and Biological Systems*, Ed. T. Kundu, SPIE's 10th Annual International Symposium on NDE for Health Monitoring and Diagnostics, March 6-10, 2005, San Diego, California.

Gabor, D. (1947), "Theory of Communication", *IEEE*, vol. 93, no. III, pp. 429-457, London.

Bastiaans, M.J. (1980), "Gabor's Expansion of a Signal into Gaussian Elementary Signals", *Proceedings of the IEEE*, vol. 68. pp 538-539.

Bastiaans M.J. (1981), "A Sampling Theorem for the Complex Spectrogram and Gabor's Expansion of a Signal in Gaussian Elementary Signals", *Optical Engineering*, vol. 20. no. 4, pp 594-598.

Bastiaans, M.J. (1985), "On the Sliding- Window Representation in Digital Signal Processing", *IEEE Trans. Acoustics, Speech, Signal Processing*, vol. ASSP-33, no. 4, pp 868-873.

Murase, M. and Kawashima, K. (2002), "Non-contact Evaluation of Defects in Thin Plate With Multimode Lamb's Wave and Wavelet Transform", Proc. IMECE 2002, ASME, Int. Mechanical Engineering Congress & Exposition, New Orleans, Louisiana, USA.

Ahmad, R. and Kundu, T. (2004), "Guided Wave Technique to Detect Defects in Pipes using Wavelet Transform", Proceedings of the 2nd European Workshop on Structural

Health Monitoring, Munich, Germany, July 7 - 9, 2004, Eds. C. Boller and W.J. Staszewski, Pub. DEStech, Lancaster, PA, USA, pp. 645-652.

Ahmad, R., S. Banerjee and T. Kundu (2009) "Pipe Wall Damage Detection in Buried Pipes Using Guided Waves", ASME Journal of Pressure Vessel Technology, Vol. 131(1), pp. 011501-1 to 8.

Velea, D., Shields, F.D. and Sabatier, J.M. (2000), "Elastic wave Velocities in Partially saturated Ottowa Sand: Experimental Results and Modeling", Soil Sci. Soc. Am. J. 64, pp. 1226-1234.

JOINT CONFERENCE PROCEEDINGS
7th International Conference on Urban Earthquake Engineering (7CUEE) &
5th International Conference on Earthquake Engineering (5ICEE)
March 3-5, 2010, Tokyo Institute of Technology, Tokyo, Japan

EXPERIMENTAL AND THEORETICAL STUDY ON SELF-CENTERING ISOLATORS MADE OF SHAPE MEMORY ALLOY METALLIC RUBBER

Suchao LI[1)], Chenxi MAO[2)], Hui LI[3)], Yagebai ZHAO[4)], and Wentao WANG[5)]

1) PhD student, School of Civil Engineering, Harbin Institute of Technology, China
2) Associate professor, Institute of Engineering Mechanics, China Earthquake Administration, China
3) Professor, School of Civil Engineering, Harbin Institute of Technology, China
4) PhD student, College of Construction Engineering, Jilin University, China
5) Undergraduate Student, School of Civil Engineering, Harbin Institute of Technology, China
lisuchao@hit.edu.cn, maochenxi@iem.ac.cn, lihui@hit.edu.cn, yagebai@sina.com, wangwentao8797@163.com

Abstract: In order to improve the behavior of isolators used for structures or equipments, a novel metallic rubber material made by Shape Memory Alloys (SMAs) was investigated in this paper. The Shape Memory Alloy Metallic Rubber (SMAMR) has self-centering ability to eliminate plastic deformation after earthquake or other dynamic loads due to the shape memory effect of SMA. In this paper, three types of SMAMR with various processing technologies were made to study the restoring ability of these specimens.

Firstly, both static and dynamic experiments for the SMAMR specimens under compression and shear loading were carried out to investigate the mechanical behavior. The results indicate that SMAMR was an ideal candidate material for three-dimensional isolator due to the low elastic modulus on both compression and shear directions. Secondly, the self-centering tests of these three types of SMAMR were carried out through temperature rising approaches, and some suggestions on selecting the manufacturing technologies were given according to the restoring ability of the specimens. Finally, based on the theory of porous materials and the least-squares method, the constitutive model of metallic rubber under compression loading was proposed and compared with the experimental results.

1. INTRODUCTION

Earthquakes or other dynamic excitations often cause damages to structures and instruments, and isolation is proved to be one of the most effective strategy to eliminate the loss (Zhou, F.L 2001; Melkumyan 2002). Nowadays, most of the isolators used in engineering are made of rubber or its composite materials, and there will exist some potential disadvantages such as the aging of the material. As we know, many isolators will remain some residual deformation after earthquakes because of its small stiffness in horizontal direction, and this residual deformation will decrease the performance of the isolators in the frequent aftershocks. However, it is impossible to replace or repair the isolators duly after each aftershock. Then it is very important to make the isolators has self-centering ability after earthquakes.

Metallic rubber (MR) is a kind of porous material with high elasticity and large restorable deformation, and Shape Memory Alloy Metallic Rubber (SMAMR) is an improved material from ordinary metallic rubber. The manufacturing technology of MR is as follows: first, the thin metal wires whose diameters vary from 0.03 to 0.30mm are made into elastic spirals; second, the spirals are stretched and woven according to certain technics; then the spirals are put into a cubic mould and loaded in the axial direction, and finally become the product. In the micro element of metallic rubber, numerous micro springs contact each other through point-to-point, and make up the porous and elastic entity. When SMAMR is under the action of quasi-static or dynamic cyclic loading, relatively sliding will occur between the contact pairs of the micro spirals and the friction will dissipate energy during the loading and unloading process. Consequently, SMAMR has damping (energy dissipation ability). Except for the advantages aforementioned, another advantage of SMAMR is the excellent self-centering ability after the plastic deformation occurred. By using the shape memory effect (Dolce 2001; Humbeeck 2003), the residual deformation of the SMAMR which is made of the martensite SMA can restore easily. SMAMR is a good candidate for developing novel isolator with deformation self-centering ability for civil infrastructures.

As a novel material, the mechanical properties of SMAMR including both quasi-static and dynamic behavior are very important for research and engineering

applications. In this study, three types of SMAMR with different processing technologies were made aiming at improving their deformation restoring ability. Thereafter, the mechanical properties of these SMAMR specimens under static and dynamic compression/shear loading were test. After the plastic deformation occurs, the deformation restoring ability of the three types of SMAMR was addressed through temperature rising tests. At last, the constitutive model of SMAMR along the compression direction is obtained according to the experiment results and least-squares method, and the performance in other cases is predicted according to the above constitutive equation.

2. SPECIMENT FABRICATION AND TEST METHOD

2.1 Fabrication of SMAMR Specimens

The SMAMR specimens used in this study were all fabricated by the Metal Rubber Technique Research Centre in Harbin Institute of Technology. The SMAMR specimens were made of SMA wires with 0.2mm diameter. The martensite SMA ($A_s \approx 50℃$) wires were adopted to build up the cubic-like model. The general fabrication process of three different types of specimens can be divided into three steps: (1) tension and wrap each wires on a thin bar to make them become micro springs with diameter of 1.7mm; (2) knit and roll the micro springs form a spongy entity; and (3) put the entity into a mould and stamping it to fix the shape. The modelling pressure was 5t/cm^2.

The first type of SMAMR (called type A SMAMR) was fabricated just following above general three steps. For the second type (called type B SMAMR), a heat treatment was carried out between the aforesaid first and second fabrication steps. The heat treatment technology was heating the SMA micro springs at 500℃ for 30 minutes and then cooling it to 300℃ before the second step. In the third processing technology (called type C SMAMR), the aforesaid heat treatments were carried out two times, one was between the first and second aforesaid fabrication steps, and the other one was after the third fabrication step. All the types A, B and C SMAMR have deformation self recovery ability but their ability are different. For type A, its residual deformation recovers because the SMA wires in it remember their original shape (the straight line shape). Type A SMAMR has the strongest deformation recovery ability but its recovery can not be controlled easily. The deformation of specimens maybe over recover and the dimension of specimens maybe become bigger than their original size. For type B, the SMA wires in the specimens remember the shape of micro springs. So this type of SMAMR has weaker deformation recovery ability but its recovery process can be controlled easier. The type C SMAMR has the weakest recovery ability but it will not over recover. In order to address the mechanical behavior of SMAMR under static and dynamic compression/shear loading, 6 specimens with various materials and various nominal densities were fabricated for compression loading and 1 specimen for shear test. The parameters of these specimens are list in Table 1. The photographs of SMAMR specimens used in this study are shown in Figure 1.



Figure 1 The SMAMR Specimen.

Table 1 Parameters of the SMAMR Specimens

SMAMR Specimens	Diameter of wires (mm)	Nominal density	Mass (g)	Dimension (mm)
Type A	0.2	0.23/0.25	28/30	≈25×25×25
Type B	0.2	0.23	28	≈25×25×25
Type C	0.2	0.23	28	≈25×25×25

2.2 Test Apparatus and Method

For the static compression tests, an Instron 4504 test machine was used. For the dynamic compression test, the Instron 8801 test machine was adopted. The force and deformation of the specimens were recorded by the load cell and displacement sensor in the test machines. Then the stress and strain of the specimens were calculated according to their cross section area and dimension. The compression load was applied along the stamping and forming direction of the specimens, and the shear load was applied along its orthogonal direction with the compression one. For the static compression tests, 4 strain amplitudes (5%, 10%, 15% and 20%) were applied for all the specimens. The loading speed was 5mm/min. Five cycles were repeated for each working condition. While for the dynamic compression test, dynamic compression load with 5 different loading frequencies (0.1Hz, 0.5Hz, 1Hz, 3Hz and 5Hz) were applied. Also 4 strain amplitudes (5%, 10%, 15% and 20%) were adopted for each loading frequency. 10 cycles were repeated for each working condition. The static and dynamic shear test was only focused on three shear angle amplitudes (15°,20° and 30°) due to the restricted number of the specimens.

3. MECHNICAL PROPERTIES OF SMAMR UNDER STATIC AND DYNAMIC COMPRESSION LOADING

3.1 Mechanical Properties under Static Compression Loading

The nominal densities of these specimens are 0.23 and 0.25 respectively as shown in Table 1. Fig. 2 (a) and (b) shows the stress-strain curves of type A SMAMR specimens under various strain amplitudes. It is noted that the loading part of the hysteretic stress-strain curves has strain hardening phenomenon. And this phenomenon becomes evident when

the strain is larger than 15%. That means the isolator made by SMAMR will provide larger restoring force if its deformation exceed a certain value. This is beneficial to preventing the isolator from overturning that result from its large deformation. However, the cyclic number has a little influence on the hysteretic property of SMAMR. The stress-strain curves become stable and coincide well with other curves after the third loading cycle. It also can be noted from Figure 2 that the SSMR with larger nominal density has larger elastic modulus and larger restoring force.

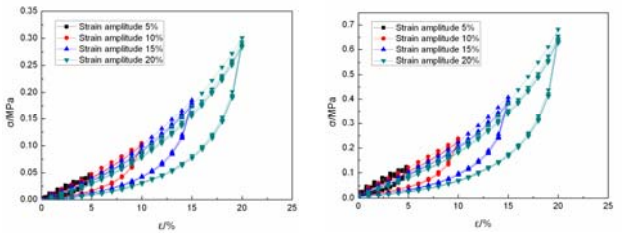

(a) (b)

Figure 2 The Stress-strain Curves of Type A SMAMR under Various Strain Amplitudes: (a) Curves of 0.23 Nominal Density; (b) Curves of 0.25 Nominal Density

In order to address the effect of processing technology of SMAMR on its mechanical properties, the stress-strain curves of type B and C SMAMR specimens (both have 0.23 nominal density) under static compression load at 20% and 11.3% stain amplitude are shown in Figure 3(a) and (b). It is observed that type B specimen has larger elastic modulus and restoring force than that of the type A specimen and the type C specimen has the largest elastic modulus. However, the elasticity of type A specimens are best. Type B specimen has worse elasticity than the type A one because 2% residual strain is observed from the stress-strain curves of this type of specimen when its strain amplitude only reach to 20%. Type C specimen has the worst elasticity because it has about 4.5% residual strain at 11.3% strain amplitude. Then it can be concluded that the heat treatment can increase elastic modulus and restoring force of SMAMR but decrease its restorable deformation limit. The three types of SMAMR specimens with residual deformation were put into a temperature controlling stove in the subsequent experiments. Their residual deformation was then recovered through heating them above the austenitic phase transition temperature. Also, the influence of processing technology on the deformation recovery ability was addressed.

The tests were carried out to address the mechanical properties of the SSMR and SMAMR under static and dynamic compression loading. All the tests were carried out in the Mechanics Test Centre in Harbin Engineering University. For the static compression tests, an Instron 4504 test machine was used. For the dynamic compression test, another Instron 8801 test machine was adopted. The force and deformation of the specimens were recorded by the load cell and displacement sensor in the test machines. Then the stress and strain of the specimens were calculated according to their cross section area and dimension. The compression load was applied along the stamping and forming direction of the specimens. For the static compression tests, 4 strain amplitudes (5%, 10%, 15% and 20%) were applied for all the specimens. The loading speed was 5mm/min. Five cycles were repeated for each working condition. While for the dynamic compression test, dynamic compression load with 5 different loading frequencies (0.1Hz, 0.5Hz, 1Hz, 3Hz and 5Hz) were applied. Also 4 strain amplitudes (5%, 10%, 15% and 20%) were adopted for each loading frequency. 10 cycles were repeated for each working condition.

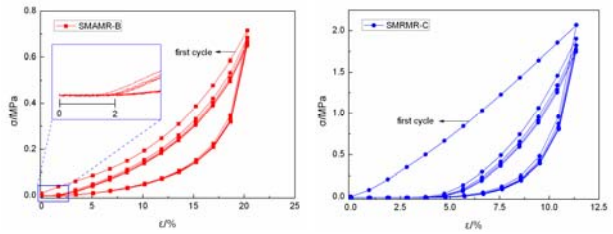

(a) (b)

Figure 3 Stress-strain Curves of Type B and C SMAMR under Static Compression Loading at 20% Strain Amplitude: (a) Curves of Type B Specimen; and (b) Curves of Type C Specimen

3.2 Mechanical Properties under Dynamic Compression Loading

Dynamic tests were also carried out for the SMAMR specimens. The loading frequencies adopted were from 0.1Hz to 5Hz, which is the same as that used in the dynamic tests of SSMR. Figure 4(a) shows the stress-strain curves of SMAMR (0.25 nominal density, type A) under various frequencies of compression loading at 20% strain amplitude. It is noted that the dynamic loading frequency (within the frequency range of 0.1Hz to 5Hz) has no influence on the hysteretic property of SMAMR. Figure 4(b) gives the stress-strain curves of SMAMR (0.25 nominal density, type B) under dynamic compression loading (1Hz). Similar to the results under static load, type B and type C SMAMRs have larger elastic modulus and restoring force than type A. The type C specimen has largest elastic modulus but smallest restorable deformation.

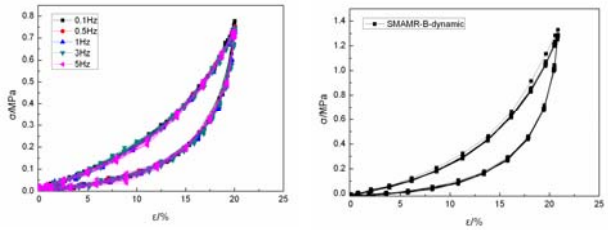

(a) (b)

Figure 4 Stress-strain Curves of SMAMR under Dynamic Compression Loading at 20% Strain Amplitude: (a) Curves of Type A SMAMR under Various Frequencies of Dynamic loading; (b) Stress-strain Curves of Type B SMAMR under 1Hz Cyclic Loading

4. MECHNICAL PROPERTIES OF SMAMR UNDER STATIC AND DYNAMIC COMPRESSION LOADING

Like the properties of compression, SMAMR has similar behavior under static and dynamic shear loading, and the stress-shear angle curves of the dynamic case is shown in Figure 5.

As shown in Figure 5, the shear modulus is even smaller than the compression modulus, and nonlinear relationship between stress and shear strain occurs with the increase of the shear angle. It is beneficial to preventing the isolator from occurring overlarge displacement. Consequently, the SMAMR based isolator is a good choice in structural protection.

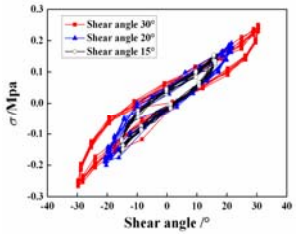

Figure 5 Stress-shear Angle Curves of SMAMR under Dynamic Shear Loading

5. DEFORMATION RESTORABLE ABILITY OF THREE TYPES OF SMAMR

In order to study the deformation restorable ability of the three types of SMAMR specimens, they were compressed by the Instron machine to the 48% strain amplitude and then unload. Different residual deformation was observed on the three types of specimens.

The experiments results show that type A SMAMR had the smallest residual deformation, while type C one had largest residual deformation. Thereafter, the specimens were put into a temperature controlling stove and were heated. The recovery strain versus temperature relationship was recorded during heating. Figure 6 gives the strain-temperature curves of the three types of SMAMR specimens (the residual strain of specimens is represented as minus strain). It could be noted that the residual deformation all of threes three types of SMAMR can recovery fully. For type A and type B specimen, the recovery process is difficult to be controlled. Once the temperature exceeds A_f the deformation of this type of specimen will restore but the size of specimen will continue to increase very quickly (as shown in Figure 6). Although type C SMAMR has the largest residual deformation during compression, but its residual deformation can restore totally and its deformation recovery process is also easy to be controlled. The original shape that the specimens remember and the number of the heat treatment are main factor for the restore ability of SMAMR.

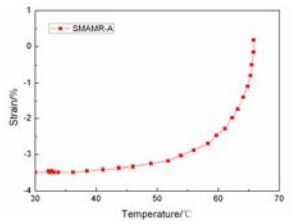

(a)

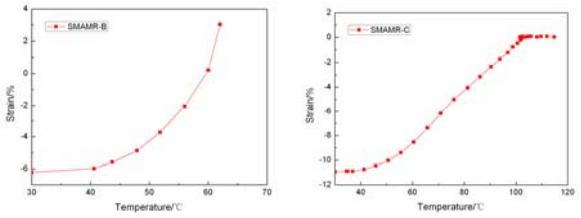

(b) (c)

Figure 6 Strain-temperature Curves of Three Types of SMAMR Specimens

6. THE CONSTITUIVE MODEL OF METALLIC RUBBER

6.1 Theory of Micro-beam Model with Rectangular Section

Metallic rubber is a kind of porous material in which elements are distributed randomly. In order to illustrate the factors which affect the mechanical behavior of the rubber, a micro-beam model with rectangular section is presented. The schematic illustration of this model is shown in Figure 7. The results of the above experiments show that we can assume that it is isotropic continuous along the compression direction and the Poisson ratio is smaller than that of metal. Therefore, in this micro-beam model, the axial and shear deformation of beam are neglected under static loading, whereas the bending displacement is taken into account. Besides, the friction between the contacted beams is also neglected.

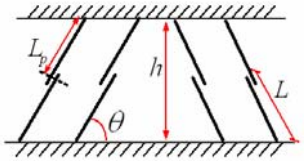

Figure 7 Schematic Illustrations of Micro-beam Model with Rectangular Section

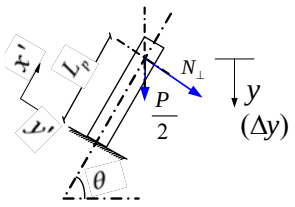

Figure 8 Mechanical Calculation Diagram of Micro-beam

For a beam of one contact pairs, under a compressive load *P/2*, the mechanical calculation diagram of micro-beam is shown in Figure 8. The area of the micro-beam is equal to the area of the wire, and the large quantity of the beams is estimated in the following analysis.

The interaction force between the inclined beams, both of whose one end is fixed, can be written as

$$N_{\perp} = \frac{P}{2} \cdot \frac{1}{\cos\theta} \tag{1}$$

Where θ is the angle between the axis of the micro-beam and the horizontal line.

And the moment of the end of the beam is given by

$$M(x) = N_{\perp} \cdot x' \tag{2}$$

And,

$$EIy'' = -M(x') \tag{3}$$

we get

$$y' = \frac{PL_p^3}{6EI} \tag{4}$$

Where L_p is the length from the contact center to the fixed end.

Then, transform the variables from local coordinate system to global coordinate system, we obtain

$$y' = \Delta_{\perp} = \frac{\Delta y}{2} \cdot \cos\theta \tag{5}$$

Substituting Eq. (4) into Eq.(5) and according to Hooke Law, we obtain

$$C = \frac{P}{\Delta y} = 3EI\cos^2\theta \frac{1}{L_p^3} \tag{6}$$

Where θ and L_p are parameters related to the metallic rubber materials, and they can be obtained as follows (Li, Z. Y. 2000):

$$\theta = 0.3(0.5 - \bar{\rho})(18 - \bar{d}) \tag{7}$$

$$\bar{d} = \frac{D}{d}$$

Where $\bar{d}$ is the ratio of the diameter of the spiral to the diameter of the metal wire.

$$L_p = 14.5/\sqrt{\bar{d}}\,(0.6 - \bar{\rho})(0.47 - \bar{\rho}_s) \tag{8}$$

Where $\bar{\rho}_s$ is the nominal density before pressed in the cubic mould, and usually in the range of 0.3~0.8g/cm^3.

6.2 Numerical Constitutive Model of Metallic Rubber

A large number of experimental data were used for parameter identification. It was found that the restoring force was nonlinear and that mainly the cubic-nonlinearity of displacements was responsible for the stress-strain characteristics of the dry friction system (Li, Y. Y 2004). However, during the initial stage of unloading, the restoring force is a little different from the loading, and this phenomenon results from the interaction of mutual connection between the SMA wires. When unloading happens, the spirals and wires can not release themselves immediately because the specimen is denser than the initial stage of loading. It is found that quintic-nonlinearity of displacements is more reasonable for a short stage after the beginning of unloading. Therefore, the unloading process includes two parts, one of which is in the range of 0~0.8ε and the other is 0.8ε~1.0ε, where ε is the target strain we need.

According to the above assumptions, the constitutive model can be expressed as follows,

The nonlinear stress-strain relation of metallic rubber in loading process is given by

$$\sigma = \sum_{k=1}^{n} NZ_k C\varepsilon^k = NZ_1 C\varepsilon + NZ_2 C\varepsilon^2 + NZ_3 C\varepsilon^3 \tag{9}$$

Where *N* is the number of micro-beam in the specimen.

Besides, the nonlinear stress-strain relation of metallic rubber in unloading process is given by

$$\begin{aligned}\sigma &= \sum_{k=1}^{n_A} NA_k C\varepsilon_A{}^k + \sum_{k=1}^{n_B} NB_k C\varepsilon_B{}^k \\ &= N\left(A_1 C\varepsilon_A + A_2 C\varepsilon_A{}^2 + A_3 C\varepsilon_A{}^3 + A_4 C\varepsilon_A{}^4 + A_5 C\varepsilon_A{}^5\right) \\ &\quad + N\left(B_1 C\varepsilon_B + B_2 C\varepsilon_B{}^2 + B_3 C\varepsilon_B{}^3\right)\end{aligned} \tag{10}$$

The section area of the metal wire is given by

$$A_0 = \frac{\pi}{4} d^2 \tag{11}$$

The total length of the metal wire is given by

$$L_{wire} = \pi DN \tag{12}$$

So, the total mass of the metallic rubber can be expressed as follows:

$$M_0 = \rho_0 A_0 L_z = \rho_0 \frac{\pi}{4} d^2 \pi DN \tag{13}$$

And the total mass of the finished product is given by

$$M_0' = \rho_s V \tag{14}$$

By using law of Mass Conservation, the number of micro-beam can be obtained as follows

$$M_0' = M_0 = \rho_s V = \rho_0 \frac{\pi}{4} d^2 \pi DN \tag{15}$$

Finally, the number of the micro-beam can be obtained

$$N = \frac{\rho_s}{\rho_0} \cdot \frac{4V}{\pi^2 d^2 D} = \bar{\rho}_0 \frac{4V}{\pi^2 d^2 D} \tag{16}$$

The least-squares method was used for data processing,

Table 2 Average Values of Coefficients of Constitutive Model

Strain	Loading process			Unloading process A					Unloading process B		
	Z3	Z2	Z1	A5	A4	A3	A2	A1	B3	B2	B1
10%	4.6751	-1.065	0.2118	1.170E+07	-5.127E+05	8638.2	-56.35	0.4343	3.419	-0.121	0.027
15%	9.2649	-1.119	0.2102	6.432E+06	-3.830E+05	8381.2	-70.23	0.5478	5.5635	-0.204	0.0543
20%	14.844	-2.41	0.2815	3.731E+06	-2.994E+05	8871.6	-101.5	0.9443	5.7361	-0.479	0.067

and every coefficient of Eqs. (9) and (10) can be obtained from the experimental data (including the specimens with different nominal densities). Consequently, the average values of coefficients of the nonlinear constitutive equation for metallic rubber are taken in this study. The coefficients of the above equation are presented in Table 2. Based on the constitutive model, the stress-strain curves with different nominal densities could also be predicted. The numerical and predicted results are shown in Figure 9.

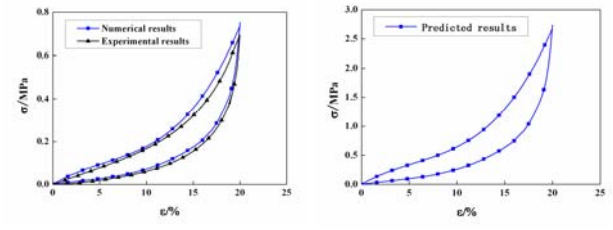

(a) (b)

Figure 9 Numerical Stress-strain Curves of SMAMR specimen: (a) Numerical and Experimental Results; (b) Predicted Results of static compression of SMAMR with nominal densities equal 0.4

7. CONCLUSIONS

Three kinds of SMAMR with different processing technology were investigated to develop deformation self-centering isolators for civil infrastructures in this study. The mechanical behaviors and deformation restorable ability of the SMAMR specimens were also tested and analyzed. Besides, based on the least-squares method, a simplified micro-beam constitutive model was presented. Main conclusions in this study are summarized below:

(1) SMAMR has stable static and dynamic nonlinear mechanical properties and low compression and shear modulus. Strain hardening phenomenon exists in both compression and shear experiments and the frequency of exciting has no influence on the mechanical properties. It is an ideal 3D-isolator for structural roof or precision instruments.

(2) All of these three types of SMAMR have good residual deformation recovery ability. The residual deformation can all be recovered through the temperature rising approach. Although the type A and B specimens have the strongest recoverable ability, they are not easy to be controlled.

(3) The contacted micro-beams with rectangular section were proper to build up the constitutive model of SMAMR. The least-squares method was used for data processing, and the loading process and unloading process should be considered independently. Generally, cubic-nonlinearity in loading stage and both of cubic-nonlinearity (0~0.8ε)and quintic-nonlinearity (0.8ε~1.0ε)in unloading stage were recommended. A new micro-beam contacted modal is under analyzing in which the fiction between the surfaces of the couple of beams is considered, and the results will be presented in the near future.

Acknowledgements:

This study is financially supported by NSFC with grant no. 50808165 and the special project of Institute of Engineering Mechanics, China Earthquake Administration with grant no. 2007B15. In addition, the authors would like to thank Prof. H. Y. Jiang for his help in fabricating all the MR specimens.

References:

Melkumyan, M.G. (2002), "Seismic Isolation of Civil Buildings in Armenia," *Progress in Structural Engineering and Materials*, Volume 4, 344-352.

Zhou, F. (2001), "Seismic Isolation of Civil Buildings in the People's Republic of China", *Progress in Structural Engineering and Materials*, 3(3).

Dolce, M. et.al (2001), "Mechanical Behaviour of Shape Memory Alloys for Seismic Applications 1. Martensite and Austenite NiTi Bars Subjected to Torsion", *International Journal of Mechanical Sciences*, Volume 43, 2631-2656.

Humbeeck, J.V. et.al (2003), "Damping Capacity of Thermoelastic Martensite in Shape Memory Alloys", Journal of Alloys and Compounds, Volume 355, 58-64.

Li, Y, Huang, X., and Mao, W. (2004), "Investigation on the computational method of vibration response of a dry friction system with cubic non-linearity for metal rubber," *Journal of Aeronaut. Materials*, Volume 24, 56-60.

Li, Z. (2000), "Design of Metal Rubber Components," *National Efence Industry Press*, Beijing.

Douglas, T.Q., and Haydn N.G. (2005), "Cellular Metal Lattices with Hollow Trusses," *Journal of Acta Materialia*, Volume 53, 301-313.

JOINT CONFERENCE PROCEEDINGS
7th International Conference on Urban Earthquake Engineering (7CUEE) &
5th International Conference on Earthquake Engineering (5ICEE)
March 3-5, 2010, Tokyo Institute of Technology, Tokyo, Japan

PASSIVE ENERGY DISSIPATION DEVICE USING U-SHAPED STEEL DAMPERS BASED ON QUASI-LINEAR MOTION MECHANISM

Jinhe Gao[1] and Hiroshi Tagawa[2]

1) Graduate Student, Nagoya University, Japan
2) Assoc. Professor, Nagoya University, Japan
jinhegao@urban.env.nagoya-u.ac.jp, tagawa@genv.nagoya-u.ac.jp

Abstract: This paper presents a new steel energy dissipation device for protection of structures from earthquakes. The proposed device achieves dissipation of seismic energy into the structure through yielding of U-shaped steel dampers. The system uses a quasi-linear motion mechanism. Consequently, bracing members are subjected only to tensile force. This feature can eliminate the brace-buckling problem. Cyclic loading tests of the portal moment frames are conducted using the proposed device. Results and discussion are presented with emphasis on key features that affect the energy dissipation capabilities. Furthermore, nonlinear finite element analysis is conducted for the steel moment frames considering the proposed device.

1. INTRODUCTION

Recent studies have examined passive energy dissipation for earthquake risk mitigation of structures extensively. During a severe earthquake, a large amount of energy is imparted to a structure, possibly causing structural damage. Passive energy dissipation is intended to reduce such structural damage. With designated energy dissipation devices installed within a structure, a portion of the input seismic energy can be diverted to these devices. Various dampers have been investigated as energy dissipation devices. For velocity-dependent dampers, whose damping effects are dependent on velocity (Ibrahim et al. 2007), numerous mechanical models and damper devices have been developed. On the other hand, steel dampers, also known as non-velocity dependent dampers, have been developed. They dissipate seismic energy into a structure through the yield deformation of steel dampers, which are inexpensive, require minimal maintenance, and which have been widely adopted to reduce the seismic response of structures. Steel dampers are classifiable into three types by their yield deformation: axial-yield type such as buckling-restrained braces (Sabelli et al. 2003); shear-yield type such as shear panels (Chan et al. 2009); and bending-yield type. As dampers of the bending-yield type, U-shaped dampers were applied to base isolation systems with rubber bearings (Yoshikawa et al. 1999) and to beam-column connections (Iwasaki et al. 2002). In comparison with the axial-yield type and shear-yield type, the applications of bending-yield type are few, but they can eliminate the buckling problem and provide stable and reasonably large energy dissipation capabilities according to the boundary conditions.

This study investigated passive energy dissipation devices using U-shaped steel dampers (U-dampers) based on a quasi-linear motion mechanism. In the proposed device, the U-dampers exhibit only bending deformation. Only tension force is generated in bracing members. Therefore, the brace buckling consideration is unnecessary. In this paper, cyclic loading tests of portal frames are conducted to reveal fundamental characteristics of the proposed device. Nonlinear finite element analysis is also conducted for three-story moment-resisting frames to demonstrate the effectiveness of the proposed device.

2. OUTLINE OF ENERGY DISSIPATION DEVICE

Figure 1 portrays the Chebyshev linkage, which realizes a quasi-linear motion mechanism. While hinges J and K move rightward and leftward, the middle point M moves on the approximate straight line g. Figure 2 presents the proposed energy dissipation system. As shown in Figure 2(a), a connection member is pin-supported and U-dampers are installed between the connection member and the beam. Two rods are intersected from the edge of the connection member. As shown in Figure 2(b), when the frame deforms under a lateral load, the U-dampers exhibit plastic deformation in tension and compression. Tensile axial force is generated in the rods, but compression axial force is not generated. When the direction of lateral load reverses, tensile axial force is generated immediately in an opposite rod. This behavior is based on the characteristics of the quasi-linear motion mechanism. Thereby, the load-displacement loop exhibits a spindle type without slipping.

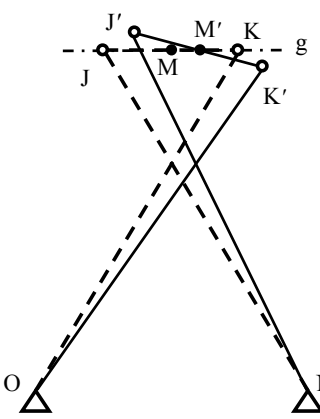

Figure 1 Quasi-Linear Motion Mechanism

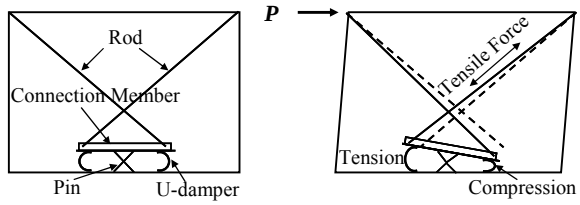

(a) Before Deformation (b) After deformation

Figure 2 Proposed Energy Dissipation System

3. CYCLIC LOADING TESTS

3.1 Test Specimens

Table 1 and Figure 3 show the four test specimens. The column and beam members of H-150x150x7x10 (steel grade: SN400B) were connected with pin-joints. The columns were also supported by pin supports at the bottom. Therefore, the lateral stiffness of the test specimens is dependent only on the damper system. Out-of-plane movement of the frame was prevented at the column tops. The bracing members were 25 mm diameter tension rods (SS400). A cross-turnbuckle component was used for the intersection part of the bracing members. Three rib plates were placed to eliminate connection member deformation. Filler plates of 60 mm width were placed outside of the U-dampers, and plates of 12 mm thickness and 60 mm width were placed inside of the U-dampers, as shown in Photo 3.

Figure 4 depicts the U-damper of 9 mm thickness steel plate (SN400B), which is formed with the annealing process and has yield stress of 308 N/mm^2, ultimate stress of 438 N/mm^2 and an elongation rate of 32.2% based on the tensile coupon test results.

3.2 Loading Program

Figure 3 shows that lateral load P was applied at the right beam-to-column connection under control of the lateral displacement δ measured at the left beam-to-column connection. Figure 5 presents the applied loading history considering the story drift R (=δ/1568). The lateral load P was varied to obtain increasing increments of rotation R equal to 0.005, 0.01, 0.02, 0.03, 0.04, and 0.05 radians. For each rotation increment, two full cycles of loading were performed. For specimens BN and BP, loading was terminated after the 0.04 radian cycle because the U-damper reached its limit deformation (Photo 3).

Table 1 Test Specimens

Specimen	Damper Placement	Rod Pre-tension
AN	⊃ · ⊂	No pre-tension
AP	⊃ · ⊂	Pre-tension (450 $\mu\varepsilon$)
BN	⊂ · ⊃	No pre-tension
BP	⊂ · ⊃	Pre-tension (450 $\mu\varepsilon$)

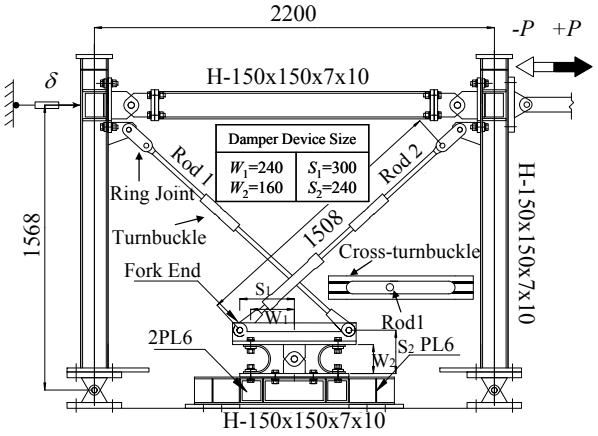

(a) Specimen AN and AP

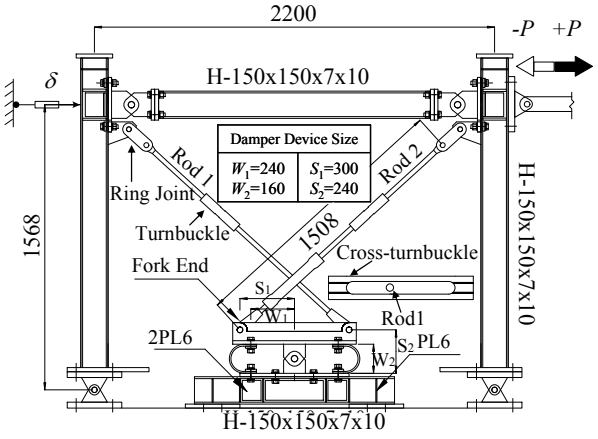

(b) Specimen BN and BP

Figure 3 Test Specimens

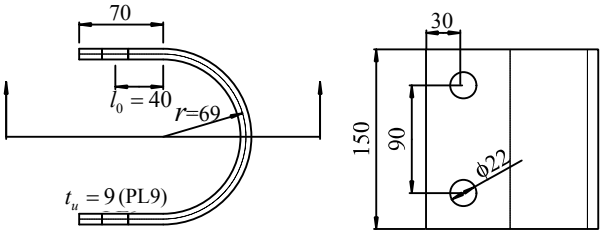

Figure 4 U-Shaped Damper

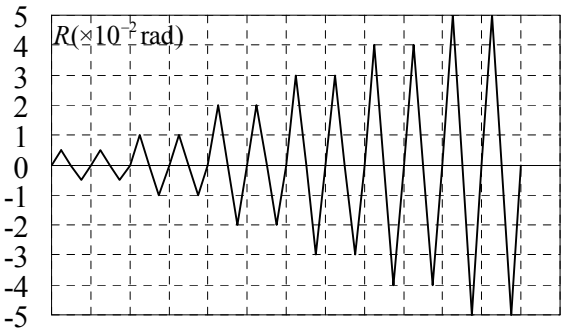

Figure 5 Loading History

3.3 Test Results

3.3.1 Load and Story Drift Relation

Figure 6 shows the load and story drift relations obtained in the cyclic loading tests. All four specimens exhibits stable and spindle-type hysteretic loops. For specimens AN and BN, when the story drift reaches a high level, slipping becomes apparent around P=0 in the load and story drift relation curves. In contrast, for specimens AP and BP, in which pre-tension was introduced into rods, the slipping disappears.

Skeleton curves of all specimens are shown in Figure 7. The skeletons of specimens AN and AP and those of BN and BP are, respectively, almost identical. The specimens in which pre-tension was introduced into the rods—AP and BP—are slightly stiffer than those in which pre-tension was not introduced: AN and BN.

Photo 1 shows the deformation of specimen AP at R = -0.04 rad. Photo 2 shows that of specimen BP at R=0.04 rad. Photo 3 shows the deformation of the compression damper of specimen BP at R = 0.04 rad.

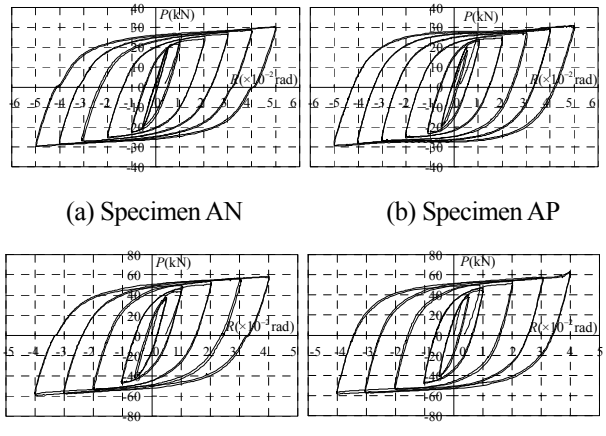

(a) Specimen AN (b) Specimen AP

(c) Specimen BN (d) Specimen BP

Figure 6 Load and Story Drift Relation

3.3.2 Influence of Pretension in Rods

Figure 8 shows relations between the lateral load and rod strain for specimens AN and AP. The rod strain was obtained as a mean value of two strain gauges mounted on both sides near the upper edge. For non-pre-tension specimen AN, when the load acted in positive way, the strain of the rod 2 increased, although the strain of rod 1 was almost zero because the ring joint with two hinges was used for a rod connection. Consequently, compression force was not generated in rods. When the load acted in a negative way, rods 1 and 2 behaved in an opposite manner. In contrast, for specimen AP, it was observed that the rod strain remained positive, which means that the pre-tension introduced into the rods did not disappear during the test.

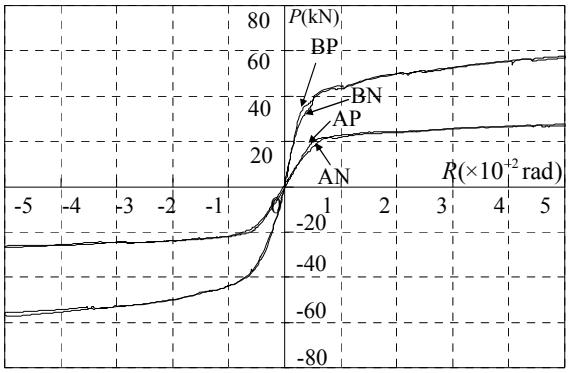

Figure 7 Skeleton Curves



Photo 1 Specimen AP (R=-0.04 rad)



Photo 2 Specimen BP (R=0.04 rad)



Photo 3 Compressive Deformation of Damper in Specimen BP (R=0.04 rad)

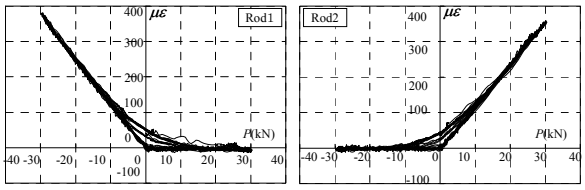

(a) Specimen AN

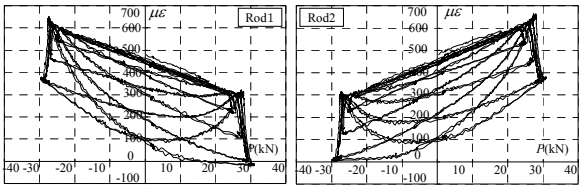

(b) Specimen AP

Figure 8 Load and Rod Strain Relation

4. FINITE ELEMENT ANALYSIS

This section presents results of nonlinear finite element analysis for moment frames with and without proposed devices. The characteristics and advantages of the proposed device are examined through comparison of analysis results.

4.1 Model Description

Finite element analyses were performed for the three-story, three-bay frames as shown in Figure 9. The analysis models comprise Model A (bare frame), Model B (with proposed devices), and Model C (with proposed devices). Models B and C were used to examine the influence of the damper placement method on frame behavior. Sections of H-250x250x9x14 for columns and H-350x175x7x11 for beams were used in the model. The damper system dimensions are presented in Table 2. The beam-to-column joint panels were reinforced with doubler plates. Vertical stiffeners and web-doubler plates were placed in the part of the beam where the damper system is attached.

Table 2 Damper System Dimensions

Damper Device				U-shaped Damper			Rod
S_1	S_2	W_1	W_2	r	l_0	t_u	Φ_B
900	620	800	560	200	100	36	40

r, l_0, t_u: defined in Figure 4. Φ_B: rod diameter.

S_1, S_2, W_1, W_2: defined in Figure 3.

4.2 Finite Element Modeling and Material Properties

The nonlinear finite element analysis program ANSYS ver. 11.0 was adopted for this study. For the elements of the columns and beams near the connections, the U-shaped dampers and the connection member, four-node three-dimensional quadrilateral shell element "SHELL 163" with six degrees of freedom at each node was adopted. For the elements of the columns and beams apart from the connections and the components between the U-shaped dampers and the connection members, two-node three-dimensional beam element "BEAM188" with six degrees of freedom at each node was adopted. The elements of CONTA175 and TARGE170 were adopted at the boundaries between the shell163 and beam188 elements. The pin components of the connection member were molded using two-node three-dimensional spar element "LINK 8" with three degrees of freedom at each node. The rods were molded using the tension-only spar element "LINK 10". Figure 10 shows the stress–strain relation of the material. The yield stress of the frame and connection member is 300 MPa; that of the U-shaped dampers is 225 MPa. The rods were assumed to be elastic considering high strength steel. Young's modulus is 205000 MPa; Poisson's ratio is 0.3. The components between the U-shaped dampers and the connection members (BEAM 188) and the pin components of the connection member (LINK 8) were assumed to be rigid.

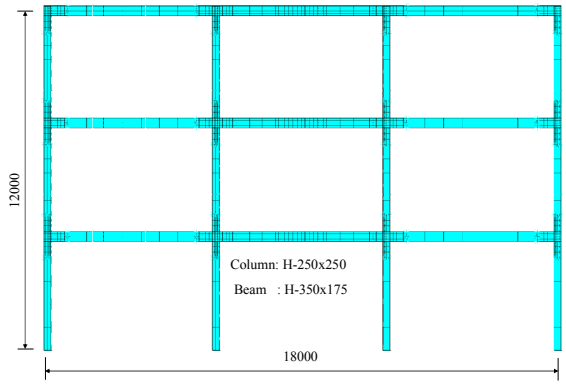

(a) Model A

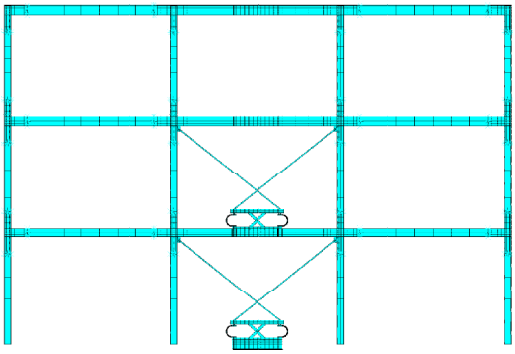

(b) Model B

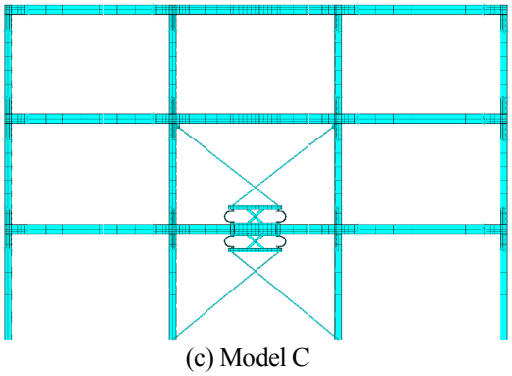

(c) Model C

Figure 9 Finite Element Modeling

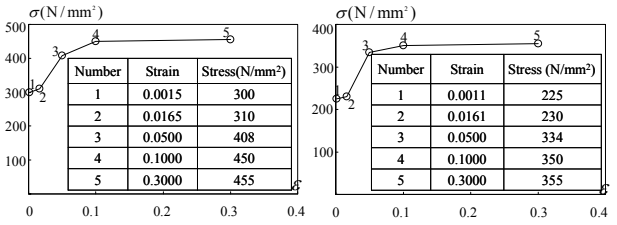

(a) Frame and Connection Member (b) U-Shaped Damper

Figure 10 Stress and Strain Relation

4.3 Load Application and Boundary Condition

The nonlinear static pushover analysis was conducted. The lateral load ratio acting on the first, second and third story was assumed to be 1:1.47:2.42 considering the design earthquake force profile based on the Ai distribution in the Japanese seismic code. The lateral loads acted on each center of beam-to-column panel. The geometrical nonlinearity was considered in the analysis. Out-of-plane movement of the frames was prevented at each center of beam-to-column panel. The column bases were fixed.

4.4 Nonlinear Analysis Results

4.4.1 Story Shear and Story Drift Relation

Figure 11 presents the story shear and drift relations (Q and R curves). Figure 11(a) shows that the Q and R curves of Model C are almost identical with those of Model B. Figure 11(b) portrays the damper device contribution as the difference between the Model A of the bare frame and the Model C with the proposed device.

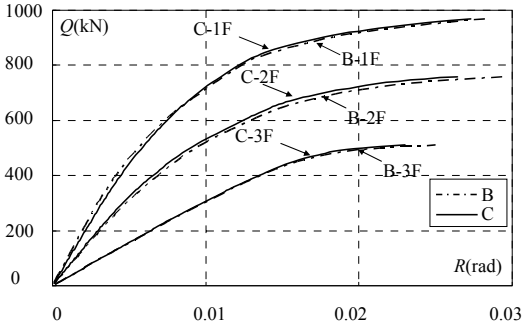

(a) Model B and C

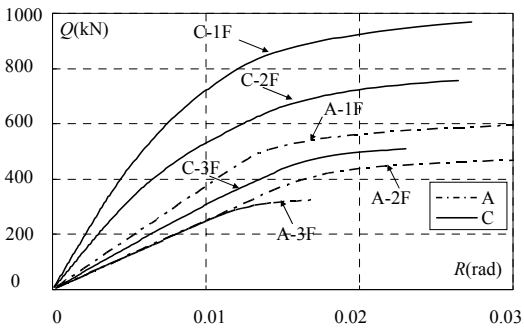

(b) Model A and C

Figure 11 Story Shear and Story Drift Relations

4.4.2 Stress Distribution

Figure 12 shows the stress distribution of Model B and Model C at the respective points where the first-story drift angle reaches 0.0027 rad and 0.015 rad. When the first-story drift angle reaches 0.0027 rad, the U-damper in tension has yielded, although that in compression has not yielded because of the elastic deformation of the connection member.

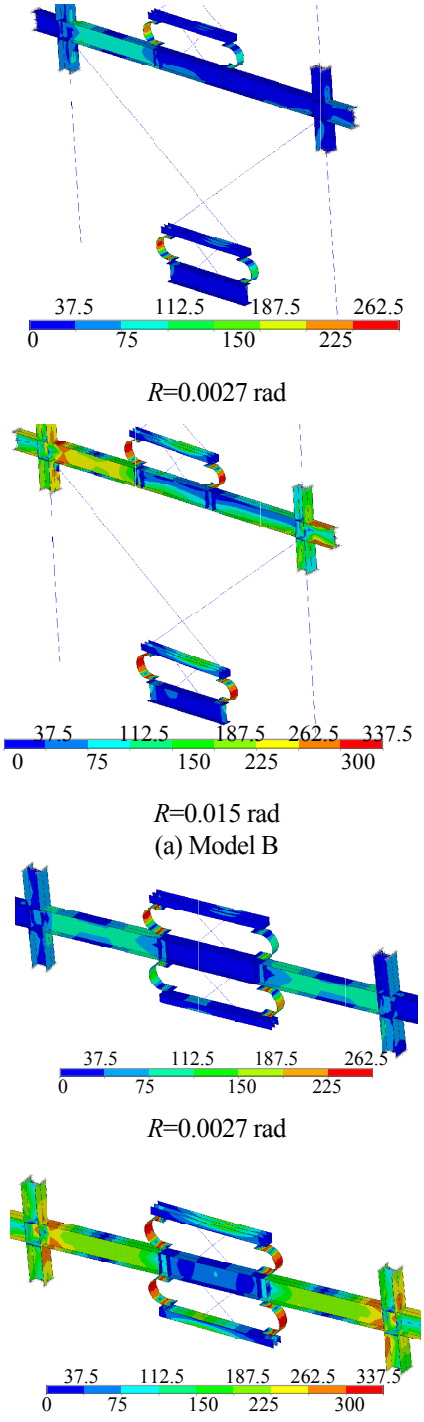

(a) Model B

(b) Model C

Figure 12 Stress Distribution

When the first-story drift angle reaches 0.015 rad, both U-dampers have yielded. In Model B, the stress of the left-side beam-web is much greater than that of the right-side beam-web because of the tensile force from the rod in the upper story. In contrast, in Model C, the stress of the left-side beam-web is almost identical to that of the right-side beam-web. This is because the tensile forces acting from the rods in the upper and lower story reduce the unbalanced stress distribution.

5. CONCLUSION

A passive energy-dissipation device using U-shaped steel dampers based on a quasi-linear motion mechanism was proposed. The device can eliminate brace buckling problems. Four cyclic loading tests conducted for the portal frame with proposed devices revealed that the load and story drift relation curve exhibits stable and spindle type, which indicates that the proposed device can offer good energy dissipation capability. The influences of the U-damper placement and pre-tension in bracing members were revealed.

To confirm the applicability of the proposed device, nonlinear finite element analyses were also conducted for three-story, three-bay frames with and without the proposed device. The analysis results demonstrated that the proposed device increases the frame stiffness and that the U-shaped damper yields in the lower range of story drift angle. It is noteworthy that only tension force is generated in the bracing members; this force possibly engenders large stress in the beam. One method to resolve this problem is mounting of damper devices in opposite ways in upper and lower stories.

References:

Chan, R.W.K., Albermani, F. and Williams, M.S. (2009), "Evaluation of Yielding Shear Panel Device for Passive Energy Dissipation," Journal of Construction Steel Research，65，260-268.

Iwasaki, A., Inoue, K., Suita, K., Koetaka, Y. and Uno, N. (2002), "Study on Dampering Mechanism for H-section Beam-to-Column Connections," Summaries of Technical Papers of Annual Meeting Architectural Institute of Japan C-1, Structure III, 639-640.

Ibrahim, Y.E., Marshall, J. and Charney, F.A. (2007), "A visco-plastic device for seismic protection of structures," Journal of Construction Steel Research, 63, 1515-1528.

Sabelli, R., Mahin, S. and Chang, C. (2003), "Seismic Demands on Steel Braced Frame Buildings with Buckling-Restrained Braces," Engineering Structures, 25, 655-666.

Yoshikawa, H., Saeki, E., Watanabe, A. and Suzuki, K. (1999), "Experimental Study of U-shaped Steel Damper (Part 2: Test of U-shaped Dampers with Rubber Bearings)," Summaries of Technical Papers of Annual Meeting Architectural Institute of Japan B-2, Structure II, 667-668.

JOINT CONFERENCE PROCEEDINGS
7th International Conference on Urban Earthquake Engineering (7CUEE) &
5th International Conference on Earthquake Engineering (5ICEE)
March 3-5, 2010, Tokyo Institute of Technology, Tokyo, Japan

ADAPTIVE NOISE VARIANCE IDENTIFICATION FOR FUSION OF ACCELERATION AND DISPLACEMENT USING SUBSPACE-BASED TECHNIQUE

Zhen Li[1)] and Chih-Chen Chang[2)]

1)Ph.D student, Dept. of Civil and Environmental Engineering, The Hong Kong University of Science and Technology, China
2)Professor, Dept. of Civil and Environmental Engineering, The Hong Kong University of Science and Technology, China
lizhen@ust.hk, cechang@ust.hk

Abstract: The Kalman filter is commonly employed to fuse the information from both displacement and acceleration responses. The fusion technique can produce more accurate displacement responses. The fusion performance however significantly depends on the estimation accuracy of noise variances. The noise variances are generally estimated empirically *a priori* and fixed throughout the whole fusion procedure, which may induce a large estimation error especially when the noise characteristics are time-varying. In this study, a subspace-based technique is developed to identify the noise variances adaptively. The approach is based on the principal component analysis technique which could decompose noisy signals into the signal subspace and the noise subspace. The noise variances are then estimated from the noise subspace. The proposed method estimates the variances of acceleration and displacement responses independently and the positive definite of the variances could be ensured. The projection approximation subspace tracking technique is employed to track the signal subspace and the noise variances could then be obtained in an on-line fashion, hence, the technique can be incorporated into an adaptive Kalman filter. A numerical example is used to validate the proposed approach.

1. INTRODUCTION

Displacement/deformation measurements are of paramount importance for the structural health monitoring and safety assessment. It is however a fairly difficult and challenging task. A commonly used approach is to perform a double integration on acceleration data that can be readily acquired from accelerometers. This integration process, however, is not easy to be achieved as it requires the selection of filters and baseline correction (Hudson 1979). Some direct techniques have been developed and widely adopted for displacement measurements over the past few decades. The current most popular technique is the global positioning system (GPS), which could provide subcentimeter tracking on two orthogonal axes at sampling rates up to 20 Hz in a real time fashion (Chan et al. 2006; Kijewski-Correa et al. 2006). Although the GPS can provide rather accurate real-time displacement measurements, its performance depends greatly on many factors such as vibration frequency, satellite coverage, atmospheric effect (Roberts et al. 2004). Another commonly used approach is the videogrammetric technique, which use digital cameras to capture displacement responses of civil structures (Chang and Ji 2007; Ji and Chang 2008a, b). This video-based technique can be performed remotely at a distance from the structure to be measured. Although this technique is much more flexible and cost-effective than the GPS, it also suffers from a relatively low sampling frequency. It is also found that the measured results are susceptible to measurement noises especially when the distance between the camera and the structure is long.

One remedy is to compensate displacements using accelerations that contain more accurate information of high-frequency responses. It is argued the most effective scheme is to fuse accelerations and displacements with the Kalman filter, which provides the optimal estimation for displacements and velocities based on the noise characteristics of accelerations and displacements (Roberts et al. 2004). Noting that the rate of displacement measurements is commonly slower than that of acceleration measurements, Smyth and Wu (2007) proposed using a multi-rate Kalman filter for the data fusion. Various kinds of simulations have validated the proposed technique.

It is noted the performance of the Kalman filter relies on the correct determination of process and measurement noise statistics, which are generally obtained *a priori* and remained fixed throughout the whole fusion process. This scheme leads to two possible problems. On the one hand, inaccurate estimations of the noise statistics will reduce the precision of results. On the other hand, it can not deal with the case when the noise characteristics are time-varying. To circumvent these difficulties, the adaptive Kalman filters have been proposed for data fusion (Mohamed and Schwarz 1998; Hide et al. 2003). These techniques use the innovation sequences as the basis for adapting the noise variances. An appropriate window function has to be determined to compromise the adaptivity and the stability. The

positive definite of the noise variances can not be ensured either. The identification process also implies the noise of accelerations and displacements are correlated, which may not be the truth.

This paper proposes a new paradigm of the adaptive Kalman filter (Fig. 1). The subspace-based technique is developed to estimate the noise variances of acceleration and displacement responses adaptively and independently. The noisy signal is first decomposed into the signal subspace and the noise subspace through the principal component analysis technique. The noise variances could then be estimated from the noise subspace. To estimate the noise variances adaptively, the projection approximation subspace tracking technique (PAST) is adopted to track the signal subspace and the noise subspace. A numerical example is used to illustrate the performance the proposed approach.

2. KALMAN FILTER WITH SMOOTHING

Assume that in addition to the displacement responses, the collocated acceleration responses are also available. The Kalman filter technique is commonly adopted to fuse the two types of responses. Denote the acceleration, velocity and displacement at time instant k as $\ddot{x}_k$, $\dot{x}_k$ and x_k respectively, the following formulations could be obtained from the basic physical law

$$x_{k+1} = x_k + T\dot{x}_k + T^2\ddot{x}_k/2 \quad (1a)$$

$$\dot{x}_{k+1} = \dot{x}_k + T\ddot{x}_k \quad (1b)$$

where T denotes the sampling interval of the accelerations and the subscript indicates the time step. To complete the modeling work, assume outputs are the displacements and it is further assumed the accelerations and displacements are both corrupted by noises, the following state-space model could then be formulated

$$\mathbf{X}_{k+1} = \mathbf{A}\mathbf{X}_k + \mathbf{B}\ddot{x}_k^m + \mathbf{B}w_k \quad (2a)$$

$$x_k^m = \mathbf{O}\mathbf{X}_k + v_k \quad (2b)$$

Where

$$\mathbf{X}_k = \begin{bmatrix} x_k \\ \dot{x}_k \end{bmatrix} \mathbf{A} = \begin{bmatrix} 1 & T \\ 0 & 1 \end{bmatrix} \mathbf{B} = \begin{bmatrix} T^2/2 \\ T \end{bmatrix} \mathbf{O} = \begin{bmatrix} 1 & 0 \end{bmatrix} \quad (3a\text{-}d)$$

Note that $\ddot{x}_k^m$ and x_k^m represent the measured accelerations and displacements respectively. The measured noises for the accelerations and the displacements, denoted as w and v, are assumed to be independent zero mean Gaussian white noise with variance q_k and r_k respectively. The Kalman filter estimates a process using a form of feedback control: the filter estimates the process state at some time and obtains feedback in the form of measurements, as such, the equations for the Kalman filter are separated into two groups: time update and measurement update. The time update equations project forward the state and error covariance to obtain a *priori* estimates for the next time step,

$$\hat{\mathbf{X}}_{k+1}^- = \mathbf{A}\hat{\mathbf{X}}_k + \mathbf{B}\ddot{x}_k^m \quad (4a)$$

$$\mathbf{P}_{k+1}^- = \mathbf{A}\mathbf{P}_k\mathbf{A}^T + \mathbf{Q}_k \quad (4b)$$

where $\hat{\mathbf{X}}_{k+1}^-$ and $\hat{\mathbf{X}}_k$ are the *a priori* and *a posteriori* state estimates, respectively; $\mathbf{P}_{k+1}^-$ and $\mathbf{P}_k$ are the *a priori* and *a posteriori* error covariance estimates respectively. The covariance matrix $\mathbf{Q}$ is

$$\mathbf{Q}_k = \mathbf{B}\mathbf{B}^T q_k \quad (5)$$

The superscript T indicates the matrix transpose. The projected state and error covariance estimates are then updated by measurements as,

$$\hat{\mathbf{X}}_{k+1} = \hat{\mathbf{X}}_{k+1}^- + \mathbf{G}_{k+1}\left(x_{k+1}^m - \mathbf{O}\hat{\mathbf{X}}_{k+1}^-\right) \quad (6a)$$

$$\mathbf{P}_{k+1} = \left(\mathbf{1} - \mathbf{G}_{k+1}\mathbf{O}\right)\mathbf{P}_{k+1}^- \quad (6b)$$

where the Kalman gain $\mathbf{G}$ is

$$\mathbf{G}_{k+1} = \mathbf{P}_{k+1}^-\mathbf{O}^T\left(\mathbf{O}\mathbf{P}_{k+1}^-\mathbf{O}^T + r_k\right)^{-1} \quad (7)$$

Where $(*)^{-1}$ indicates the inverse of a matrix. As the displacements are commonly measured at a slower rate than the accelerations, a muti-rate Kalman filter could be applied for the estimation of the displacement and velocity. In that case, only time updating in Eq. (4) is performed between any two consecutive displacement measurements. When both the accelerations and displacements are available at the same time instant k, measurement updates in Eq. (6) is also performed to obtain the optimal results.

The smooth technique could be further employed to improve the accuracy of the estimation. It is a non-real-time operation where all the available data are processed to obtain a state estimate. There are three types of smoothing: fixed-point, fixed-interval and fixed-lag smoothing. In this paper, the celebrated RTS fixed-interval smoother which combines the backward filter and smoother into one single backward recursion is adopted. The smoothed estimates $\hat{\mathbf{X}}_{k|N}$ for the whole time interval can be obtained by

$$\hat{\mathbf{X}}_{k|N} = \hat{\mathbf{X}}_k + \mathbf{F}_k\left(\hat{\mathbf{X}}_{k+1|N} - \hat{\mathbf{X}}_{k+1}^-\right) \quad (8a)$$

$$\mathbf{F}_k = \mathbf{P}_k\mathbf{A}^T\left(\mathbf{P}_{k+1}^-\right)^{-1} \quad (8b)$$

With $k=N-1, N-2, \ldots, 1, 0$. N is the total number of data points in the time interval.

3. NOISE VARIANCE IDENTIFICATION THROUGH SUBSPACE TECHNIQUE

The preceding discussion indicates that the fusion performance can be divided into two parts: The modeling problem and the estimation problem. The modeling problem concerns with the development of a model to describe the relationship between accelerations and displacements accurately.

Although the model in Eq. (2) is an approximation of the true integral, it is argued the modeling error could be ignored when the sampling frequency is sufficiently high. The optimality of the estimation is closely connected with the quality of the *a priori* information of the process noise and the measurement noise, whose identification will be discussed in the following contents.

3.1 Estimation of Noise Variance Using Principal Component Analysis

The equation of motion of an *m*-degree-of-freedom structure can be expressed as

$$\mathbf{M}\ddot{\mathbf{y}}(t)+\mathbf{C}\dot{\mathbf{y}}(t)+\mathbf{K}\mathbf{y}(t)=\mathbf{f}(t) \tag{9}$$

in which **M**, **C** and **K** are the mass matrix, damping matrix and stiffness matrix respectively with a dimension $m\times m$. **y**(t) is an $m\times 1$ displacement vector and **f**(t) is the input force vector. The system response could be readily calculated by the modal superposition if the structure is lightly damped or with classical damping. That is, the response of the structure collected from *M* different points can be expressed as a linear sum of normal modes

$$\mathbf{Y}(t)=\sum_{i=1}^{m}h_i(t)\boldsymbol{\varphi}_i \tag{10}$$

where **Y**(t) is an *M*-dimensional vector representing the measurements. $h_i(t)$ denotes the *i*th normal coordinates and $\boldsymbol{\varphi}_i$ is the *i*th mode shape at the measurement points. Given that all the sensors (the same type) are corrupted by noises with the same variance, the measured response could then be expressed in a concise way as

$$\mathbf{Y}(t)=\boldsymbol{\Phi}\mathbf{H}(\mathbf{t})+\mathbf{V}(t)=\mathbf{S}(\mathbf{t})+\mathbf{V}(t) \tag{11}$$

where **Φ** is the ensemble of the *N* mode shapes with a dimension of $M\times N$. *N* denotes the modes whose contribution is distinguishable from measurement noise. **H**(t) is a vector referring to the *N* normal coordinates with distinct frequencies. **V**(t) denotes the *M*-dimensional zero mean noise process, which is assumed to be zero mean white noise process and uncorrelated with the clean signal. An important assumption in Eq. (11) is the number of measurement points are more than the modes that could be identified. In other words, it is assumed *M* is larger than *N*. This model in Eq. (11) is commonly used in the principal component analysis (PCA). It turns out the exact type of the signal model is of no importance. It is the relationship *M*>*N* that plays a crucial role for noise filtering, since it implies that the signal only occupies the first *N* subspaces. Without loss of generality, it is assumed **Y**(t) is zero mean random vector process. Consider the covariance matrix of **Y**(t), $\mathbf{R}_{YY}=\mathbf{E}(\mathbf{Y}(t)\mathbf{Y}^T(t))$. Eq. (12) can be obtained from Eq. (11) as the noise is uncorrelated with the signal

$$\mathbf{R}_{YY}=\mathbf{R}_{SS}+\sigma^2\mathbf{I} \tag{12}$$

where $\mathbf{R}_{SS}=\mathbf{E}(\mathbf{S}(t)\mathbf{S}^T(t))$ and $\sigma^2=\mathbf{E}(\mathbf{V}(t)\mathbf{V}^T(t))$. **E**(*) denotes the mathematical expectation. Consider the following eigen-decompsition

$$\mathbf{R}_{SS}=\mathbf{U}\boldsymbol{\Sigma}\mathbf{U}^T \tag{13}$$

where **U** is an othonormal matrix with a dimension $M\times M$. $\boldsymbol{\Sigma}=diag(\lambda_1,\lambda_2,...,\lambda_M)$ denotes a diagonal matrix consisting of all the eigenvalues. Without loss of generality, it is assumed the eigenvalues are given in a descending order. Since the rank of the covariance matrix $\mathbf{R}_{SS}$ is *N*, it is obtained that

$$\lambda_1\geq\lambda_2\geq....\lambda_N>\lambda_{N+1}=0=.....\lambda_M \tag{14}$$

Then the eigendecomposition of $\mathbf{R}_{YY}$ is given by (Katayama 2005)

$$\mathbf{R}_{YY}=\mathbf{U}\boldsymbol{\Lambda}U^T \tag{15}$$

where $\boldsymbol{\Lambda}=diag(\lambda_{Y1},\lambda_{Y2}...\lambda_{YM})$ with

$$\lambda_{Yi}=\begin{cases}\lambda_i+\sigma^2 & i=1,.....,N\\ \sigma^2 & i=N+1,.....,M\end{cases} \tag{16}$$

Hence, the noise variance could be estimated from the average of the last *M*-*N* eigenvalues. The procedure to estimate the noise variance is summarized as follows:

1. Select the measurements from *M* sensors and estimate the covariance matrix of $\mathbf{R}_{YY}$

$$\overline{\mathbf{R}}_{\mathbf{YY}}=\frac{1}{L}\sum_{k=1}^{L}\mathbf{Y}_k\mathbf{Y}_k^T \tag{17}$$

where $\mathbf{Y}_k$ is the measurement at time instant *k*

2. Perform the eigen-decomposition to the estimated covariance matrix and arrange the eigenvalues in a descending order. Another alternative is to perform the singular value decomposition (SVD), which arranges the singular values in a descending order automatically.

3. Determine the true system order *N* or the number of principal components (PCs) to be retained. A popular ad hoc rule is to use the plot which plots the eigenvalues in a decreasing order and search for an elbow where the signal eigenvalues are on the left side and the noise eigenvalues on the right. Another approach is to compute the cumulative percentage of the total variation explained by the PCs and retain the number of PCs that represent the predefined threshold of the total variation. Various other methods have also been proposed, interested people are referred to Ulfarsson and Solo (2008).

4. Estimate the noise variance from the smallest *M*-*N* eigenvalues

$$\overline{\sigma}^2=\frac{1}{M-N}\sum_{i=M-N+1}^{M}\lambda_{Yi} \tag{18}$$

3.2 Adaptive Estimation of Noise Variance

To the end of the adaptive estimation, it is necessary to consider another form of Eq. (18). Let $\mathbf{U}=[\mathbf{U}_S, \mathbf{U}_N]$ where $\mathbf{U}_S$ denotes the $M \times N$ matrix which represents the principal components or the signal subspace of the random process $\mathbf{Y}(t)$. On the other hand, $\mathbf{U}_N$ represents the noise subspace. Eq. (15) could then be reformulated as follows

$$\mathbf{R}_{YY} = \mathbf{U}_S \mathbf{\Lambda}_S \mathbf{U}_S^T + \mathbf{U}_N \mathbf{\Lambda}_N \mathbf{U}_N^T \quad (19)$$

$$\mathbf{\Lambda}_S = diag(\lambda_{Y1} ..... \lambda_{YN}), \mathbf{\Lambda}_N = diag(\lambda_{YN+1} ..... \lambda_{YM}) \quad (20)$$

It is required to project the measurements into the noise subspace to estimate the noise variance. Since $\mathbf{U}_N$ is an orthogonal matrix, the following projection matrix could be defined

$$\mathbf{P} = \mathbf{U}_N \mathbf{U}_N^T \quad (21)$$

The matrix $\mathbf{P}$ is idempotent and Hermitian, which is the orthogonal projector onto the noise subspace. Consider the following linear transformation

$$\boldsymbol{\chi}(t) = \mathbf{P}\mathbf{Y}(t) \quad (22)$$

Then the covariance of $\boldsymbol{\chi}(t)$ is

$$\mathbf{R}_{\chi\chi} = \mathbf{U}_N \mathbf{\Lambda}_N \mathbf{U}_N^T \quad (23)$$

Comparing Eq. (19) and (23), it is seen only the noise component is retained after projection. The noise variance could then be estimated as

$$\overline{\sigma}^2 = \frac{trace(\mathbf{R}_{\chi\chi})}{M - N} \quad (24)$$

in which *trace*(*) denote the trace of a matrix. Since $\mathbf{U}$ is othonormal

$$\mathbf{P} = \mathbf{I} - \mathbf{U}_S \mathbf{U}_S^T \quad (25)$$

Hence, the adaptive estimation of noise variance could be achieved through the adaptive estimation of the signal subspace. The PAST technique proposed by Yang (1995) is adopted to track the signal subspace. Differing from the SVD, the PAST considers subspace tracking as seeking the solution of an unconstrained optimization problem. Consider an M-dimension random process $\mathbf{Y}$ with the autocorrelation matrix $\mathbf{R}_{YY}=\mathbf{E}(\mathbf{Y}\mathbf{Y}^T)$ and the following optimization problem

$$J(\mathbf{W}) = \arg\min_{\mathbf{W}} E \| \mathbf{Y} - \mathbf{W}\mathbf{W}^T\mathbf{Y} \|^2 \quad (26)$$

where $\mathbf{W}$ is an $M \times N$ matrix ($N<M$). Without loss of generality, It is assumed $\mathbf{W}$ has a full rank N. Yang (1995) proved the global minimum of $\mathbf{J(W)}$ is attained if and only if $\mathbf{W}= \mathbf{U}_S\boldsymbol{\psi}$ where $\mathbf{U}_S$contains the N dominating eigenvectors of $\mathbf{R}_{YY}$ and $\boldsymbol{\psi}$ is an arbitrary unitary matrix. In order to extract signal subspace recursively, the expectation operator in Eq. (26) is replaced with the exponentially weighted sum and the following approximation is also adopted

$$\mathbf{z}(k) = \mathbf{W}^T(k-1)\mathbf{Y}(k) \quad (27)$$

Then Eq. (26) will be modified as

$$J(\mathbf{W}(k)) = \sum_{i=1}^{k} \lambda^{k-i} \| \mathbf{Y}(i) - \mathbf{W}(k)\mathbf{z}(i) \|^2 \quad (28)$$

where λ ($0 < \lambda \leq 1$) is the forgetting factor. The solution of this optimization problem in Eq. (28) is

$$\mathbf{W}(k) = \mathbf{C}_{Yz}(k)\mathbf{C}_{zz}(k)^{-1} \quad (29)$$

where the sample covariance matrix $\mathbf{C}_{Yz}(k)$ and $\mathbf{C}_{zz}(k)$ are defined as follows

$$\mathbf{C}_{Yz}(k) = \sum_{i=1}^{k} \lambda^{k-i} \mathbf{Y}(k)\mathbf{z}(k)^T \quad (30a)$$

$$\mathbf{C}_{zz}(k) = \sum_{i=1}^{k} \lambda^{k-i} \mathbf{z}(k)\mathbf{z}(k)^T \quad (30b)$$

Based on the celebrated matrix inversion lemma, an RLS-like algorithm could be derived to extract $\mathbf{W}$ recursively. The projection matrix in Eq. (25) could then be constructed using $\mathbf{W}$ instead of $\mathbf{U}_S$ and the noise variance could be estimated adaptively following the previous discussions. It is noted the modified cost function in Eq. (28) has been minimized instead of the original one in Eq. (26), Hence, the columns of $\mathbf{W}$ is not exactly orthonormal. However, the deviation is small especially when the forgetting factor is close to one.

4. NUMERICAL EXAMPLE

A four degree-of-freedom shear-beam structure subject to an earthquake excitation (Fig. 2) is used to demonstrate the proposed approach. The mass of each floor is m_1=3452.4 kg, m_2=m_3=2652.4 kg, m_4=1809.9 kg. The stiffness of each story is k_1=k_2=k_3=k_4=67.9 MN/m. The model is actually a simplified version of the ASCE benchmark structure (Johnson et al. 2004). The damping matrix is assumed to be proportional to the mass matrices and the damping ratio of the first mode is assumed to be 5%. Damping matrix could then be obtained. The frequencies of the four modes are 9.41, 25.54, 38.66 and 48.01 Hz respectively. The damping ratios are 5%, 1.8%, 1.2% and 1.0% respectively. The excitation earthquake is modeled as filtered Gaussian white noise (Gaussian white noise passed through a six order low-pass Butterworth with a 20Hz cutoff). The sampling frequencies of

both the acceleration and displacement responses are 512Hz. It is assumed the acceleration and displacement responses of all the four degrees are obtained. All the acceleration responses are superimposed with uncorrelated white noises with the same variance such that the noise-to-signal ratio of the roof floor is 5%. Likewise, uncorrelated white noises with the same variance are added to all the displacement quantities such that the noise-to-signal ratio of the roof floor is 10%. Fig. 3 presents the measurements of the roof floor and their power spectrum density (PSD) function. Since the input force is concentrated within 0-20 Hz, the highest two modes has small contribution to the responses, which is especially true for the displacements as observed from Fig. 3. The covariance matrices are estimated using the first 5s data and it is found the cumulative percentage of the total variation explained by the first three PCs are 99.9% and 99.6% for the acceleration and displacement respectively. Thus, the first three PCs are retained. Fig. 4 shows the estimated noise variances using the batch method. It is seen the estimations approaches to the true values when more data are employed. Another observation is that limited data (e.g. 1s data) could provide fairly accurate results. As to the adaptive estimation of the noise variances, the first 1s data are used to obtain an initial value for the signal subspace. The forgetting factor is set to be 0.999. Fig. 5 indicates that the estimated results could converge to the true values in a quite quick and stable way. It is also observed all the estimations for the noise variances are positive, which is critical for incorporating this estimator to the Kalman filter and smoother. Making use of the estimated noise variances, the Kalman filter and smoother is exploited to fuse the measured accelerations and displacements. The time interval for the smoother is one second. The fused displacements of the roof floor using both the true noise variance and from the adaptive estimator are shown in Fig. 6(a). The clean signal is also presented for comparison. A zoomed part of this figure is taken out to show clearly the fusion results of these two schemes in Fig. 6(b). The difference of the fused displacements with theoretical one is displayed in Fig. 6(c). It is seen the proposed approach could reach almost the same accuracy as the optimal solution.

The time-varying case is next studied. It is assumed the noise level of the accelerations is changed abruptly at t=5s such that the noise-to-signal ratio of the roof floor is increased from 5% to 10%. On the other hand, the noise level of the displacements is also changed such that the noise-to-signal ratio of the roof floor is reduced linearly from 20% to 10% from 4s-6s. The first 1s data are used to initialize the algorithm as the first case and the forgetting factor is set to be 0.995. Fig. 7 presents the trajectory of the noise variances. It is seen the proposed approach is capable of tracking the noise variances accurately in the time-varying case. Some tracking delays are also observed, which could be decreased by adopting a smaller forgetting factor. However, it is noted a smaller forgetting factor will induce larger variations to results and even instability simultaneously. The fusion displacements of the roof floor based on the adaptive noise estimator are plotted in Figs. 8. The results using constant noise variances are also given for comparison. It indicates that the two schemes could provide almost the same results in the beginning stage where the noise variances are constant while the constant scheme could only provide suboptimal results when the noise variances become time-varying. The adaptive scheme is then desired in the case, since the noise variances could be adapted instantaneously.

5. CONCLUSIONS

A new adaptive tracking method based on the subspace concept has been proposed to identify noise variances in the time-varying case. The noisy signal is first decomposed into the signal subspace and the noise subspace through the principal component analysis technique. The projection approximation subspace tracking technique is adopted to track the signal subspace and the noise subspace such that the noise variance could be estimated adaptively. This estimator is then combined with the Kalman filter to fuse the information from measured accelerations and displacements. A numerical example has been given to demonstrate the performance of the proposed technique. Simulation shows that the proposed technique could ensure the estimate of noise variances be positive and outperforms the conventional Kalman filter in the time-varying case.

The approach is based on the two assumptions. Firstly, both the accelerometers and the displacement sensors in the structural health monitoring system are more than the modes that could be identified. Secondly, the noise variances are the same for all the same type sensors. These two assumptions are great limitations in practice. The research is untaken to release the limitations.

References

Chang, C. C., and Ji, Y. F. (2007). "Flexible videogrammetric technique for three-dimensional structural vibration measurement." *J. Eng. Mech*., 133(6), 656-664.

Chan, W. S., Xu, Y. L., Ding, X. L., Xiong, Y. L. and Dai, W. J. (2006). "Assessment of dynamic measurement accuracy of GPS in three directions." *J. Surv. Eng*., 132(3), 108-117.

Roberts, G., Meng, X. and Dodson, A. (2004). "Integrating a global positioning system and accelerometers to monitor the deflection of bridges." *J. Surv. Eng*., 130(2), 65-72.

Hudson, D. E. (1979). "Reading and interpreting strong motion accelerograms." EERI Engineering monographs on earthquake criteria, structural design, and strong motion records, Vol. 1, Earthquake Engineering Research Institute, Berkeley, Calif.

Hide, C., Moore, T. and Smith, M. (2003). "Adaptive kalman filtering for low-cost INS/GPS." *J. Navigation*, 56, 143-152.

Ji, Y. F. and Chang, C. C. (2008a). "Nontarget image-based technique for small cable vibration measurement." *J. Bridge Eng*., 13(1), 34-42.

Ji, Y. F. and Chang, C. C. (2008b) "Nontarget stereo vision technique for spatiotemporal response measurement of line-like structures." *J. Eng. Mech*., 134(6), 466-474.

Johnson, E. A., Lam, H. F., Katafygiotis, L. S., and Beck, J. L. (2004). "Phase I IASC-ASCE structural health monitoring benchmark problem using simulated data." *J. Eng. Mech*., 130(1), 3–15.

Katayama, T. (2005). "Subspace Methods for System Identification.",Springer-Verlag, London

Kijewski-Correa, T., Kareem, A. and Kochly, M. (2006). "Experimental verification and full-scale deployment of global positioning systems to monitor the dynamic response of tall buildings." *J. Struct. Eng.*, 132(8), 1242-1253.

Mohamed, A. H. and Schwarz, K. P. (1999). "Adaptive kalman filtering for INS/GPS." *J. Geodesy*, 73, 193-203.

Smyth, A., and Wu, M. (2007). "Multi-rate kalman filtering for the

data fusion of displacement and acceleration response measurements in dynamic system monitoring." *Mech. Syst. Signal Process*., 21(2), 706-723.
Ulfarsson, M. O. and Solo, V. (2008). "Dimension estimation in noisy PCA with sure and random matrix theory." *IEEE Trans. Signal Process*., 56(12), 5804-5816.
Yang, B. (1995). "Projection approximation subspace tracking." *IEEE Trans. Signal Process*., 43 (1995), 95-107.

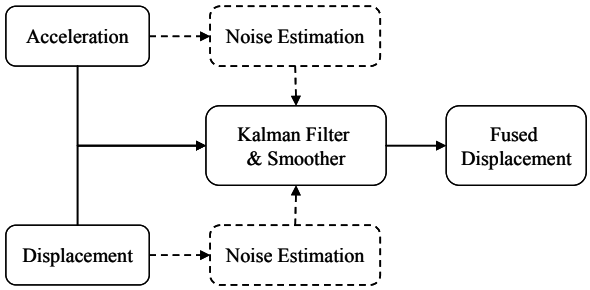

Fig. 1 Diagram of the proposed method

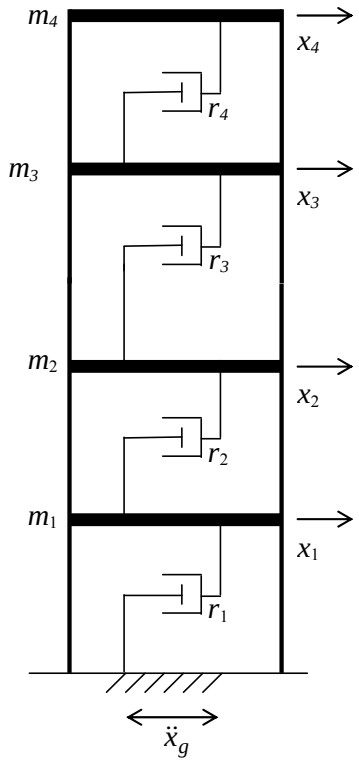

Fig. 2 A 4-DOF shear-beam building with earthquake excitation

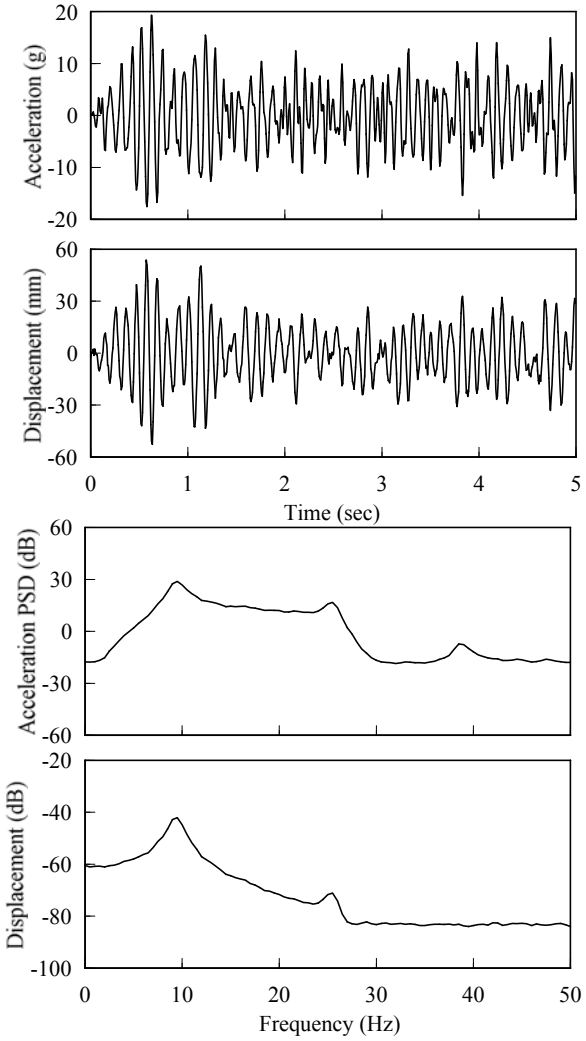

Fig. 3 Measured displacement and acceleration of the roof floor and their power spectral densities (PSD's)

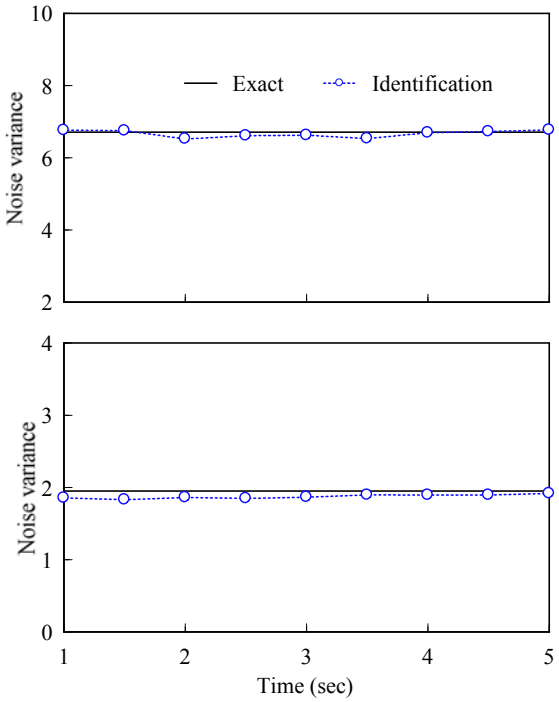

Fig. 4 Noise variance estimation (a) for acceleration and (b) for displacement

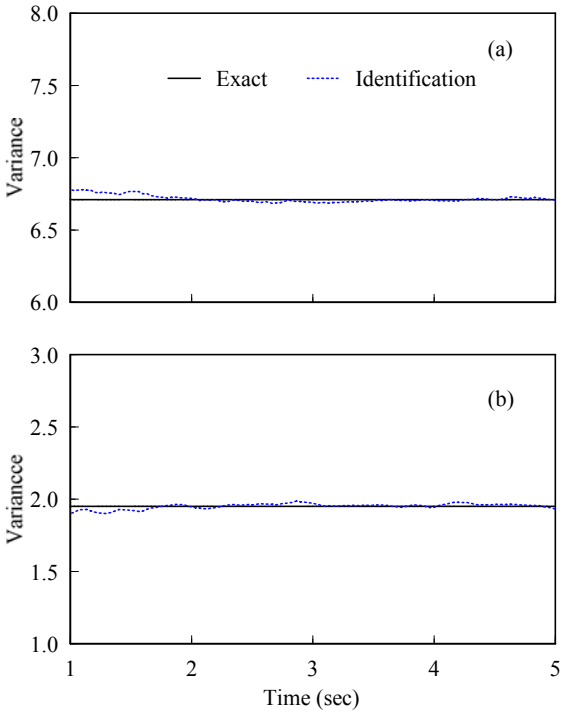

Fig. 5 Adaptive noise variance estimation (a) for acceleration and (b) for displacement

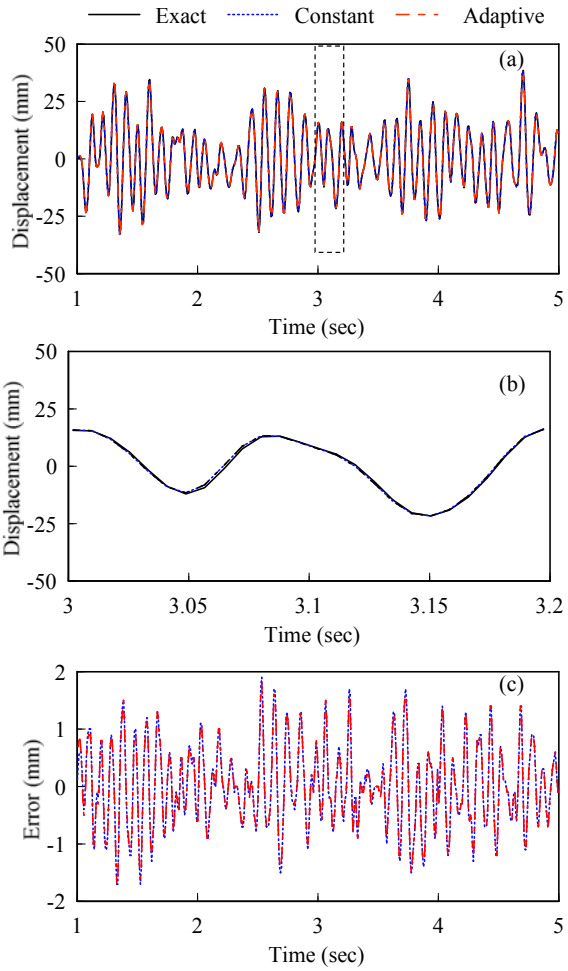

Fig. 6 Fused results of the roof floor for the first case

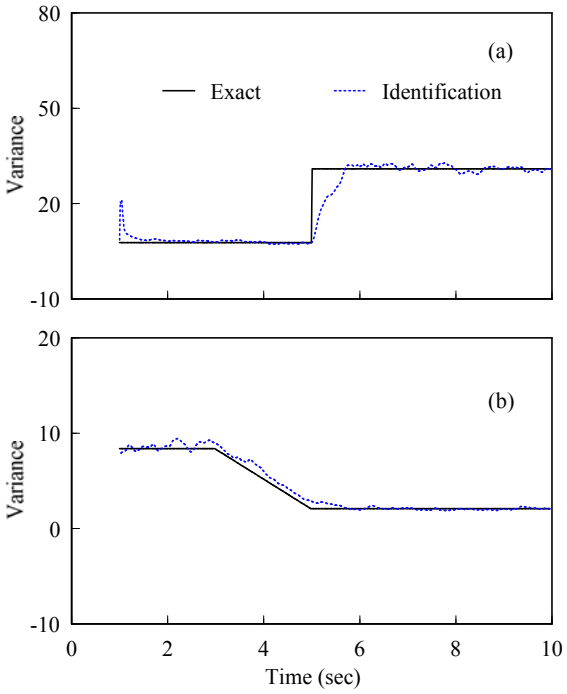

Fig. 7 Adaptive noise variance estimation for the time-varying case (a) for acceleration and (b) for displacement

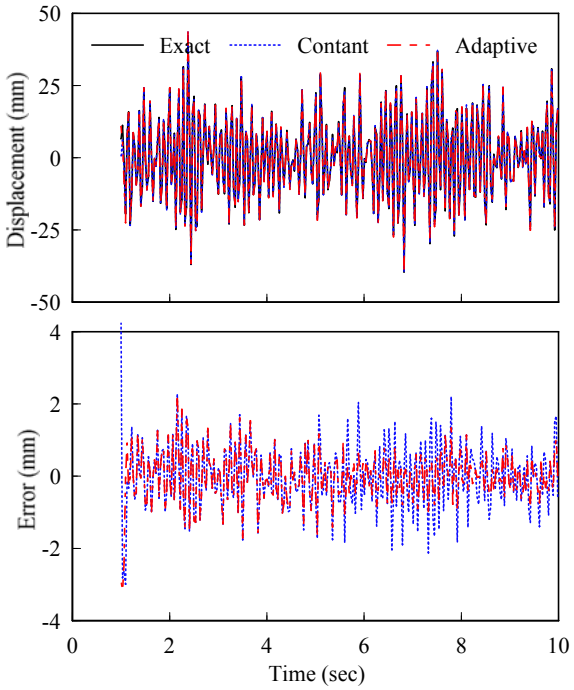

Fig. 8 Fused results of the roof floor for the time-varying case

JOINT CONFERENCE PROCEEDINGS
7th International Conference on Urban Earthquake Engineering (7CUEE) &
5th International Conference on Earthquake Engineering (5ICEE)
March 3-5, 2010, Tokyo Institute of Technology, Tokyo, Japan

EFFECTIVE BUCKLING LENGTH OF BUCKLING RESTRAINED BRACES CONSIDERING ROTATIONAL STIFFNESS AT RESTRAINER ENDS

Ryota Matsui[1], Toru Takeuchi[2], Kohji Nishimoto[3] Satoshi Takahashi[4] and Tatsuya Ohyama[5]

1) Doctoral Student, Dept. of Architecture and Building Engineering, Tokyo Institute of Technology, Japan
2) Professor, Dept. of Architecture and Building Engineering, Tokyo Institute of Technology, Japan
3) Manager, Nippon Steel Engineering, Japan
4) Structural Engineering Department, Division of Architectural Design and Engineering, Kajima Corporation, Japan
5) Master Student, Dept. of Architecture and Building Engineering, Tokyo Institute of Technology, Japan
matsui.r.aa@m.titech.ac.jp, ttoru@arch.titech.ac.jp, nishimoto.kohji1@nsc-eng.co.jp
takahsat@kajima.com, ohyama.t.aa@m.titech.ac.jp

Abstract: Buckling Restrained Braces (BRBs) are commonly used as ductile bracing elements in seismic design. A key requirement in BRB design is the prevention of flexural buckling. At present, when both ends of a BRB are assumed as pin connections, the effective buckling length of the BRB is evaluated as the distance between the two ends without any initial imperfection by applying an eccentric force. However, the effective buckling length is affected by the stiffness and strength of the connection zones. In order to precisely evaluate the effective buckling length, it is essential to assess the connection stiffness of the braces. In this study, each connection zone is modeled using two rotational elastic springs attached to a gusset plate and two rotational elasto-plastic springs attached to the end zone of the restrainer. The stiffness and strength are evaluated by performing mock-up experiments and analyses, and their evaluation methods are proposed.

1. INTRODUCTION

Buckling restrained braces (BRBs) comprise a steel core plate restrained by a concrete-filled tube. Developed in the 1980s for use by Watanabe and Wada et al. (1988) in Japan, BRBs have been employed in more than three hundred buildings as ductile bracing members or hysteretic dampers. BRBs are designed using a design code such as Eq. (1) so that the axial force is not transferred to the restrainers and the BRBs exhibit no elastic buckling and bending yielding (e.g., Xie 2005 and Koetaka et al. 2009).

$$\begin{cases} M_c^B = \dfrac{P_{cu}\left(a+e+s\right)}{1-P_{cu}/P_{cr}} \le M_y^B \\ P_{cr} = \dfrac{\pi^2 E I_r}{L_k^2} \end{cases} \quad (1)$$

Here, P_{cu} denotes the maximum axial force of the core plate; P_{cr}, the Euler buckling force of the restrainer; a, the initial imperfection of the restrainer; e, the eccentricity of the core plate; s, the clearance between the core plate and the restrainer; M_y^B, the yield bending moment of the restrainer; E, the elastic modulus of steel; I_r, the geometrical moment of inertia of the restrainer; and L_k, the effective buckling length of the BRB. The buckling conditions for a BRB are normally determined by applying an out-of-plane buckling force; some researchers have shown that the buckling force is affected by the rotational stiffness at connections. For instance, Koetaka et al. (2009) and Inoue et al. (2004 and 2007) carried out a thorough evaluation of the buckling force of a BRB by considering the beam sway and torsional displacement that occurs when a plastic hinge is attached at the restrainer end. Takeuchi and Yamada et al. (2004) evaluated the buckling force by considering a BRB as a linear model with four rotational spring stiffnesses. In this case, effective buckling length L_k is essential to calculate the buckling force, and some design codes consider L_k as the distance between the centers of a beam L and a column or between the surfaces of a beam L_0 as shown in Figure 1. However, the relationship between the strength and stiffness at the end of the restrainer and an overlap length of the core plate stiffener, the condition under which the bending moment is transmitted from the core plate to the restrainer of the BRB against an assumed story drift, and the effective buckling length of the BRB have not been clarified by considering the rotational stiffness at the connections and restrainer ends. In this study, the strength and rotational stiffness of a BRB are investigated as the bending moment is transmitted between the core plate and the restrainer. The BRB specimens

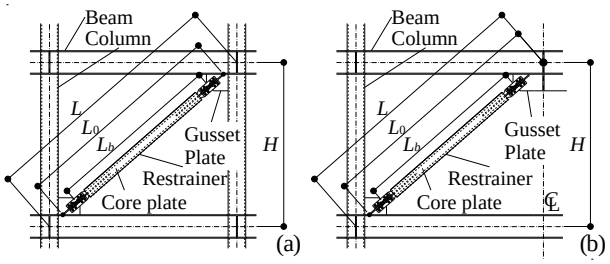

Figure 1 BRB Layouts:
(a) N-type Layout, and (b) K-type Layout

employed in this study comprise cruciform stiffeners fixed to a flat steel core plate at the restrainer ends; the stiffener and core plate are restrained by a mortar-filled steel tube. The rotational strength and stiffness at the restrainer ends are evaluated by considering the shape of the restrainer at the ends to be parametric. Subsequently, the out-of-plane rotational stiffness of three types of connections is calculated by a finite element method. Finally, the condition under which bending moment is transmitted and the effective buckling length of the BRB are estimated by considering the rotational stiffness at each connection and restrainer end.

2. EFFECTIVE BUCKLING LENGTH OF BRB

The buckling force for a BRB is calculated by taking account of the rotational stiffness at the restrainer ends and connections. Here, the rotational stiffness at a restrainer end is located at the edge of the core plate stiffener as shown in Figure 2(a). Two BRB layouts are assumed in order to calculate the buckling force. In the N-type layout, both edges of a BRB are arranged at the beam-column connections, as shown in Figure 1(a). On the other hand, in the K-type layout, one edge of a BRB is arranged at the beam-column connection, and the other edge is arranged at the center of a beam, as shown in Figure 1(b). Further, the buckling force for a BRB in the K-type layout is studied using the connection rotational stiffness at the center of a beam by Inoue and Koetaka et al. However, in this study, the connection rotational stiffness at the center of a beam is assumed to be located at the pin end and restrained in the horizontal direction. In addition, the buckling modes of a BRB are considered to be as depicted in Figures 2(a) and (b) against each BRB layout shown in Figure 1. In the N-type layout, the boundary condition is symmetric; therefore, the buckling force is calculated by treating each of the two modes as a half model in Figures 3(a) and (b). In the K-type layout, the buckling force is calculated by treating the single mode as the complete model in Figure 3(c). The lateral deflection of a BRB in each range is calculated using Eqs. (2) and (3) in the N-type layout, and in the K-type layout, Eq. (4) is added to calculate the lateral deflection.

$$y_1 = {}_1C_1 \sin\frac{\alpha}{\sqrt{\gamma}}x + {}_1C_2 \cos\frac{\alpha}{\sqrt{\gamma}}x + {}_1C_3 x + {}_1C_4 \tag{2}$$

$$y_2 = {}_2C_1 \sin\alpha x + {}_2C_2 \cos\alpha x + {}_2C_3 x + {}_2C_4 \tag{3}$$

$$y_3 = {}_3C_1 \sin\frac{\alpha}{\sqrt{\gamma}}x + {}_3C_2 \cos\frac{\alpha}{\sqrt{\gamma}}x + {}_3C_3 x + {}_3C_4 \tag{4}$$

Here, ${}_iC_j$ (i = 1, 2, 3; j = 1, 2, 3, 4) is a constant defined by the boundary conditions, $\alpha^2 = P/EI$, γ denotes the bending stiffness ratio between the restrainer tube and the cruciform core plate at the BRB end, and ξL_0 represents the distance from the edge of the core plate stiffener to the beam-column surface (in the K-type layout, the center of a beam). From these boundary conditions, Eqs. (5)–(12) are obtained for the N-type layout. Subsequently, from Eqs. (5)–(12), the buckling force is obtained using the condition of ${}_iC_j$ indefiniteness, as expressed in Eq. (13).

$$x = 0;\ y_1 = 0 \tag{5}$$

$$x = 0;\ \gamma EI\left(\frac{d^2 y_1}{dx^2}\right) = K_{Rc}\left(\frac{dy_1}{dx}\right) \tag{6}$$

$$x = \xi L_0;\ y_1 = y_2 \tag{7}$$

$$x = \xi L_0;\ P\left(\frac{dy_1}{dx}\right) + \gamma EI\left(\frac{d^3 y_1}{dx^3}\right) = P\left(\frac{dy_2}{dx}\right) + EI\left(\frac{d^3 y_2}{dx^3}\right) \tag{8}$$

$$x = \xi L_0;\ -\gamma EI\left(\frac{d^2 y_1}{dx^2}\right) = K_{Rr}\left(\frac{dy_1}{dx} - \frac{dy_2}{dx}\right) \tag{9}$$

$$x = \xi L_0;\ -EI\left(\frac{d^2 y_2}{dx^2}\right) = K_{Rr}\left(\frac{dy_1}{dx} - \frac{dy_2}{dx}\right) \tag{10}$$

$$x = \frac{L_0}{2};\ \frac{dy_2}{dx} = 0 \tag{11}$$

$$x = \frac{L_0}{2};\ EI\left(\frac{d^3 y_2}{dx^3}\right) = 0 \tag{12}$$

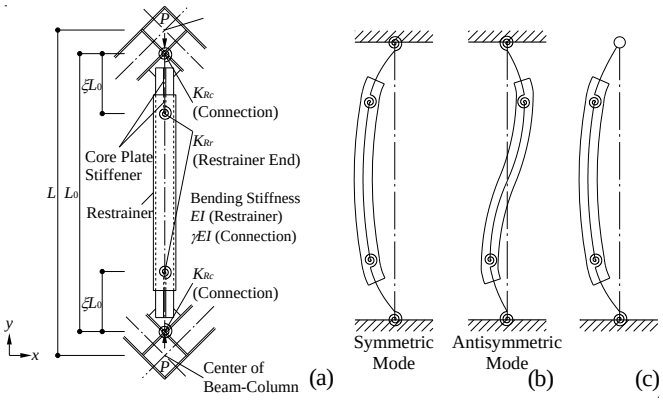

Figure 2 Out-of-plane Buckling Modes of BRB:
(a) Scale and Stiffness,
(b) Both Spring Ends (N-type Layout),
and (c) One Spring End and One Pinned End (K-type Layout)

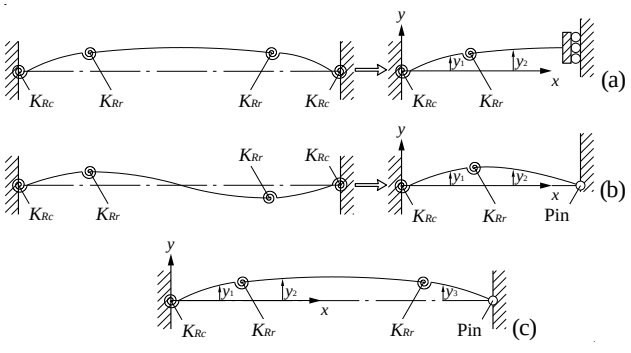

Figure 3 Boundary Conditions for BRB:
(a) Symmetric Mode in N-type Layout,
(b) Antisymmetric Mode in N-type Layout,
and (c) K-type Layout

Table 1 Specimen Parameters

Specimen	Restraint Tube			Core Plate		L_{in}/B_c
	Shape	Practical	Specimen	Practical	Specimen	
RB65	Rectangular	□-300 × 300 × 5.0 (Tall) □-200 × 200 × 3.0 (Small)	□-150 × 150 × 2.3	PL-250 × 36 (Tall) PL175 × 25 (Small)	PL-125 × 19	0.5, 1, 2
RB125		□-300 × 300 × 2.4 (Tall) □-200 × 200 × 1.7 (Small)	□-150 × 150 × 1.2			1, 2
CB83	Circular	ϕ-355.6 × 4.0 (Tall) ϕ-216.3 × 2.6 (Small)	ϕ-165.2 × 2.0			0.5, 1, 2, 3

Table 2 Material Properties

Specimen	Material	Yield Stress (N/mm^2)	Ultimate Stress (N/mm^2)	Yield Strain (%)
Core Plate	SS400	259	413	0.11
Restraint Tube (2.3mm)	SPHC-P	347	457	0.36
Restraint Tube (1.2mm)	SPCC-SD	184	316	0.49
Restraint Tube (2.0mm)	SPHC-P	235	330	0.18

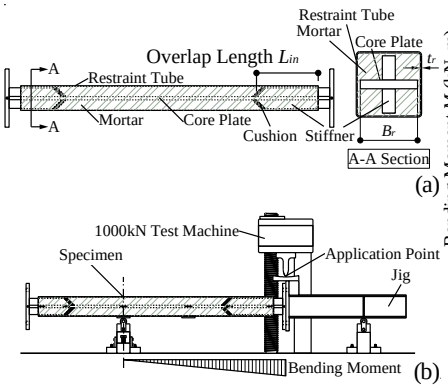

Figure 4 Specimen and Setup for Measuring Stiffness at Restrainer End: (a) Specimen, and (b) Setup

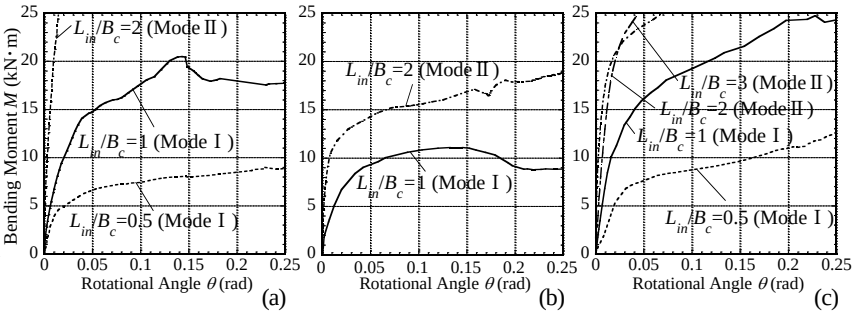

Figure 5 Bending Moments vs. Rotational Angle Curve at Restrainer End: (a) Rectangular, t_r = 2.3 mm, (b) Rectangular, t_r = 1.2 mm, and (c) Circular, t_r = 2.0 mm



(a) (b)

Photo 1 Failure Modes of Restrainer End: (a) Failure Mode I, and (b) Failure Mode II

$$\alpha^2(EI)^2 S_1C_2 + \alpha EI\left(-\frac{K_{Rc}+K_{Rr}}{\sqrt{\gamma}}C_1C_2 + K_{Rr}S_1S_2\right) + K_{Rc}K_{Rr}\left(-\frac{S_1C_2}{\gamma} - \frac{C_1S_2}{\sqrt{\gamma}}\right) = 0 \quad (13)$$

$$\alpha^3(EI)^2 L_0S_1S_2 - \alpha^2 EIL_0\left(K_{Rr}S_1C_2 + \frac{K_{Rc}+K_{Rr}}{\sqrt{\gamma}}C_1S_2\right) + \alpha EIK_{Rc}S_1S_2 - \alpha K_{Rc}K_{Rr}L_0\left(\frac{1}{\sqrt{\gamma}}C_1C_2 + \frac{1}{\gamma}S_1S_2\right) - 2K_{Rc}K_{Rr}\left(S_1C_2 + \frac{1}{\sqrt{\gamma}}C_1S_2\right) = 0 \quad (14)$$

$$\begin{aligned}
&-\frac{K_{Rr}L_0\alpha^2EI}{\gamma}S_3(S_1^2 - C_1^2) + \frac{K_{Rr}^2L_0\alpha}{\gamma}C_3(S_1^2 - C_1^2) \\
&-\frac{K_{Rr}^2L_0\alpha^2EI}{K_{Rc}}S_3(S_1^2 - \frac{C_1^2}{\gamma}) - K_{Rr}^2S_3(S_1^2 - \frac{C_1^2}{\gamma}) - 2K_{Rr}\alpha EIS_1^2C_3 \\
&-2\frac{K_{Rr}L_0\alpha^3(EI)^2}{K_{Rc}}S_1^2C_3 + \alpha^2(EI)^2S_1^2S_3 + \frac{L_0\alpha^4(EI)^3}{K_{Rc}}S_1^2S_3 \\
&+2\frac{K_{Rr}^2L_0\alpha^2EI}{\sqrt{\gamma}K_{Rc}}S_1C_1C_3 - 2\frac{K_{Rr}L_0\alpha^3(EI)^2}{\sqrt{\gamma}K_{Rc}}S_1C_1S_3 + \frac{K_{Rr}^2L_0\alpha}{\gamma\sqrt{\gamma}}S_1C_1S_3 \\
&+2\frac{K_{Rr}L_0\alpha^2EI}{\sqrt{\gamma}}S_1C_1C_3 + 2\frac{K_{Rr}^2}{\sqrt{\gamma}}S_1C_1C_3 - 2\frac{K_{Rr}\alpha EI}{\sqrt{\gamma}}S_1C_1S_3 \\
&+\frac{K_{Rr}^2L_0\alpha}{\sqrt{\gamma}}S_1C_1S_3 - \frac{L_0\alpha^3(EI)^2}{\sqrt{\gamma}}S_1C_1S_3 = 0
\end{aligned} \quad (15)$$

$$\left(\begin{aligned}
&S_1 = \sin\frac{\alpha}{\sqrt{\gamma}}\xi L_0, C_1 = \cos\frac{\alpha}{\sqrt{\gamma}}\xi L_0 \\
&S_2 = \sin\alpha L_0\left(\frac{1}{2} - \xi\right),\ C_2 = \cos\alpha L_0\left(\frac{1}{2} - \xi\right) \\
&S_3 = \sin L_0(1-2\xi),\ C_3 = \cos L_0(1-2\xi)
\end{aligned}\right) \quad (16)$$

The effective buckling length of the symmetric buckling mode in the N-type layout is obtained by regarding the minimum buckling force that satisfies Eqs. (13) and (16) as Euler buckling force. Similarly, the buckling force of the antisymmetric buckling mode in the N-type layout is obtained by Eqs. (14) and (16), and the buckling force in the K-type layout is calculated using Eqs. (15) and (16).

3. ROTATIONAL STIFFNESS AT RESTRAINER END

3.1 Experiment

The rotational stiffness at a restrainer end was experimentally investigated. Here, an overlap length L_{in} is defined as the length of the core plate overlapping the restrainer as shown in Figure 4(a). The ratio between the overlap length L_{in} and the core plate width B_c is defined as the overlap length ratio L_{in} / B_c, and this ratio is used as a parameter for the specimens, as listed in Table 1. In previous study by Takeuchi et al. (2004), it was found that the rotational stiffness at a restrainer end develops after the core plate stiffener rotates for restoring the clearance between the core plate and the restrainer; however, in this study, the clearance is considered to be zero and any change in it is ignored. The size of the specimens is assumed to be 1/2–1/1.4 that of the size used in practical design. Restraint tubes having rectangular and circular cross-sections are used. The width-to-thickness ratio of the rectangular restraint tubes ranges from 65 to 125, and that of the circular restraint tube is 83. The

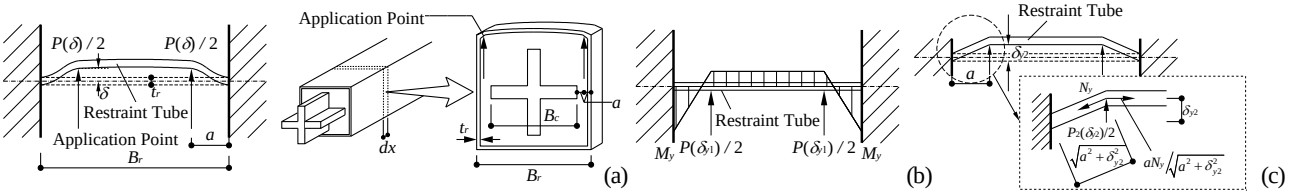

Figure 6 Failure Models of Rectangular Restraint Tube:
(a) Shear Force Transmit Points of Core Plate, (b) Bending Yielding, and (c) In-plane Stress Yielding

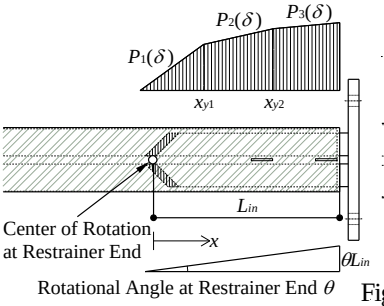

Figure 7 Shear Force Distributions in Core Plate

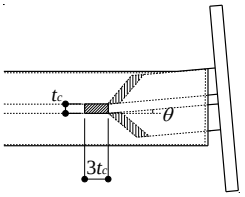

Figure 8 Plastic Deformation at Restrainer End

core plate is PL-125 × 19, as listed in Table 1. Table 2 shows material properties. The bending moment distribution of a BRB possesses a point of contraflexure when out-of-plane displacement occurs, and the setup is made assuming that one side of the BRB and specimen were arranged in the form of a pin-roller support, as shown in Figure 4(b). In Figure 5, the bending moments vs. rotational angle curve at a restrainer end. The restrainer end exhibited two failure modes, as presented in Photo 1. When the overlap length ratio is small, the failure of the restrainer end occurs locally and this failure mode is called mode I as shown in Photo 1(a). On the other hand, when the overlap length ratio is large a complete failure occurs, and this failure mode is referred to as mode II as shown in Photo 1(b). In addition, the rotational stiffness and the strength at the restrainer end increase as the overlap length ratio increases and the width-to-thickness ratio of the restraint tube decreases.

3.2 Modeling of Failure Modes

In this section, the failure mechanism at the restrainer end is hypothetically modeled and compared with the experimental results. In the range of the overlap length, the restraint tube is subjected to a force concentrically and in the longitudinal direction from the core plate stiffener. When the lateral deflection attains a value of δ at the application point of shear force $P_1(\delta)$ as Figure 6(a), $P_1(\delta)$ is calculated as Eq. (17) in the elastic range.

$$P_1(\delta) = \frac{EB_r t_r^3}{2B_r a^3 - 3a^4}\delta dx \tag{17}$$

Here, a represents the distance between the shear force application point and the outer surface of the restraint tube. When the bending stress at the corner of the restraint tube attains the yield stress σ_{ry} as shown in Figure 6(b), the lateral deflection at the shear force application point δ_{y1} is calculated as Eq. (18).

$$\delta_{y1} = \frac{\sigma_{ry}}{3}\frac{2B_r a^2 - 3a^3}{Et_r(B_r - a)} \tag{18}$$

The restraint tube is postulated to resist the shear force of the core plate stiffener by adding the in-plane stress prior to in-plane stress yielding, and the transmitted shear force $P_2(\delta)$ is estimated as Eq. (19) that linearly interpolates the in-plane stress yielding with the bending yielding.

$$\begin{aligned} P_2(\delta) &= \frac{EB_r t_r^3}{2B_r a^3 - 3a^4}\delta_{y1}dx \\ &+ \left\{\frac{2\delta_{y2}\sigma_{ry}t_r}{\sqrt{a^2+\delta_{y2}^2}} - \left(\frac{EB_r t_r^3}{2B_r a^3 - 3a^4}\delta_{y1}\right)\right\}\frac{\delta - \delta_{y1}}{\delta_{y2} - \delta_{y1}}dx \end{aligned} \tag{19}$$

δ_{y2} is defined as the lateral deflection at the shear force application point when in-plane stress yielding occurs per unit length in the cross-section, as shown in Eq. (20). The in-plane stress distributed in the restraint tube become constant after the in-plane stress yielding as shown in Figure 6(c), and the transmitted shear force $P_3(\delta)$ is calculated using Eq. (21).

$$\delta_{y2} = B_r\sqrt{\left(\frac{\sigma_{ry}}{2E}\right)^2 + \frac{a\sigma_{ry}}{B_r E}} \tag{20}$$

$$P_3(\delta) = 2\frac{\delta}{\sqrt{a^2+\delta^2}}\sigma_{ry}t_r dx \tag{21}$$

At the shear force application point, the lateral deflection attains the values δ_{y1} and δ_{y2} as the distance between the force application point and the rotational center of the core plate stiffener assumes the values x_{y1} and x_{y2}, respectively, as shown in Figure 7. The lateral deflection at the shear force application point is $\delta = \theta x$, and the bending moment at the restrainer end M_r is evaluated as a function of the rotational angle at the restrainer end θ by integrating the transmitted shear force to the longitudinal as Eq. (22).

$$\begin{aligned} M_r &= \int_0^{x_{y1}} P_1(\theta x)x dx + \int_{x_{y1}}^{x_{y2}} P_2(\theta x)x\,dx + \int_{x_{y2}}^{L_e} P_3(\theta x)x dx \\ &= M_1 + M_2 + M_3 \end{aligned} \tag{22}$$

Each term of M_r (M_1, M_2, and M_3) is calculated using Eqs. (23)–(25). In this regard, x_{y1} and x_{y2} are not larger than the overlap length, and these values are defined as the minimum values in Eq. (26).

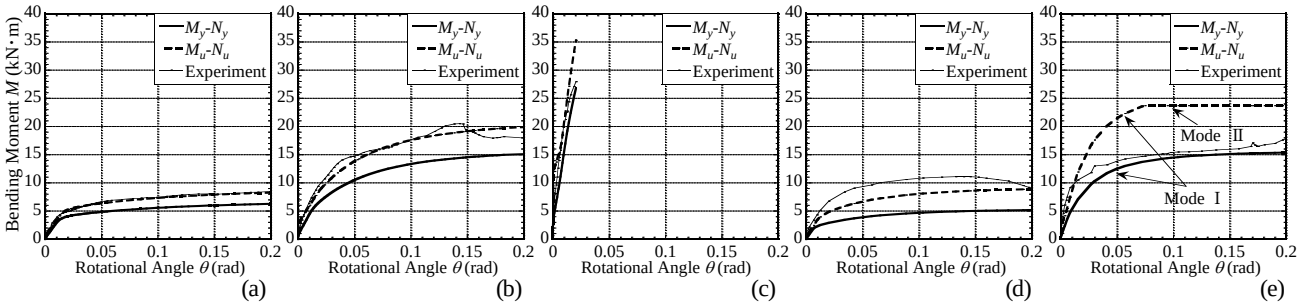

Figure 9 Bending Moments vs. Rotational Angle Curve at Restrainer End for Rectangular Restraint Tube:
(a) L_{in} / B_c = 0.5, RB65, (b) L_{in} / B_c = 1.0, RB65, (c) L_{in} / B_c = 2.0, RB65
(d) L_{in} / B_c = 1.0, RB125, and (e) L_{in} / B_c = 2.0, RB125

$$M_1 = \frac{EB_r t_r^{\,3} x_{y1}^{\,3}}{3(2B_r a^3 - 3a^4)}\theta \tag{23}$$

$$M_2 = \left(\frac{EB_r t_r^3}{2B_r a^3 - 3a^4}\delta_{y1}\right)\frac{x_{y2}^2 - x_{y1}^2}{2} + \left\{\frac{2\delta_{y2}\sigma_{ry}t_r}{\sqrt{a^2+\delta_{y2}^2}} - \left(\frac{EB_r t_r^3}{2B_r a^3 - 3a^4}\delta_{y1}\right)\right\}\left\{\frac{\theta\left(x_{y2}^3 - x_{y1}^3\right)}{3\left(\delta_{y2} - \delta_{y1}\right)} - \frac{\delta_{y1}\left(x_{y2}^2 - x_{y1}^2\right)}{2\left(\delta_{y2} - \delta_{y1}\right)}\right) \tag{24}$$

$$M_3 = \sigma_{ry} t_r \left\{\left(L_{in}\sqrt{L_{in}^2 + \left(\frac{a}{\theta}\right)^2} - x_{y2}\sqrt{x_{y2}^2 + \left(\frac{a}{\theta}\right)^2}\right) - \left(\frac{a}{\theta}\right)^2 \log_e\left(\frac{\theta L_{in} + \sqrt{a^2 + \left(\theta L_{in}\right)^2}}{\theta x_{y2} + \sqrt{a^2 + \left(\theta x_{y2}\right)^2}}\right)\right\} \tag{25}$$

$$x_{y1} = \min\left\{\frac{\delta_{y1}}{\theta}, L_{in}\right\},\ x_{y2} = \min\left\{\frac{\delta_{y2}}{\theta}, L_{in}\right\} \tag{26}$$

Subsequently, the bending moment of the core plate is evaluated. When the core plate yields on the compression side, it is not expected to have bending moment; however, this evaluation is modeled to simulate the experimental result. The bending moment of the core plate distributes in the range of $3t_c$ at the restrainer end as shown in Figure 8, and is calculated as Eq. (27).

$$M_c = \frac{E}{3t_c}\frac{B_c t_c^{\,3}}{12}\theta = \frac{EB_c t_c^{\,2}}{36}\theta \tag{27}$$

When the core plate exhibits bending yielding, the rotational angle at the restrainer end θ_{cy} is calculated as Eq. (28). Here, σ_{cy} denotes the core plate yield stress; Z_c, the section modulus of the core plate.

$$\theta_{cy} = \frac{6\sigma_{cy}}{E} \tag{28}$$

The bending moments of the core plate prior to and after the yielding are defined as Eq. (29).

$$\begin{cases} M_c = \dfrac{EB_c t_c^{\,2}}{36}\theta & \left(\theta \le \dfrac{6\sigma_{cy}}{E}\right) \\ M_c = \dfrac{B_c\sigma_{cy}}{4}t_c^{\,2} - \dfrac{3B_c\sigma_{cy}^{\,3}}{E^2\theta^2}t_c^{\,2} & \left(\theta \ge \dfrac{6\sigma_{cy}}{E}\right) \end{cases} \tag{29}$$

Because the mortar was crushed in the experiments, the mortar is assumed to make no contribution to the bending moment at the restrainer end in failure mode I, and the bending moment at the restrainer end is calculated as Eq. (30).

$$M = M_r + M_c \tag{30}$$

The bending moment at the restrainer end increases as the overlap length ratio is large in failure mode I, as seen from Eqs. (23)–(25); however, it does not exceed the value at the point where the entire core plate and restraint tube yield. Under these experimental conditions, the mortar on the tensile side is not effective because it is crushed, and on the compression side, the stress is considered to be distributed in the form of a triangle as the core plate surface is neutral. The bending moment in the failure mode II is estimated as Eq. (31).

$$M = Z_{rp}\sigma_{ry} + Z_{cp}\sigma_{cy} + (1/4)Z_{mp}\sigma_{my} \tag{31}$$

Here, Z_{rp}, Z_{cp}, and Z_{mp} denote the plastic section modulus of the restraint tube, core plate, and mortar, respectively, and σ_{my} (= 43.1 N/mm^2) represents the compressive strength of the mortar. In the ultimate stage, the restraint tube stress attains the ultimate stress σ_{ru} because of hardening. In Figure 9, M_y–N_y is calculated from the yield stress σ_{ry}; M_u–N_u, from the ultimate stress σ_{ru} by using Eqs. (17)–(31). Figure 9 shows that the experimental values approximately distribute between the yield stress value M_y–N_y and the ultimate stress value M_u–N_u.

On the other hand, for the circular restraint tube, the in-plane stress yielding is considered to precede the bending yielding caused by the transmitted shear force. The in-plane stress ranges to the half of the cross-section, and the lateral deflection of the restraint tube at the in-plane stress yielding δ_y is calculated using Eq. (32) and is shown in Figure 10.

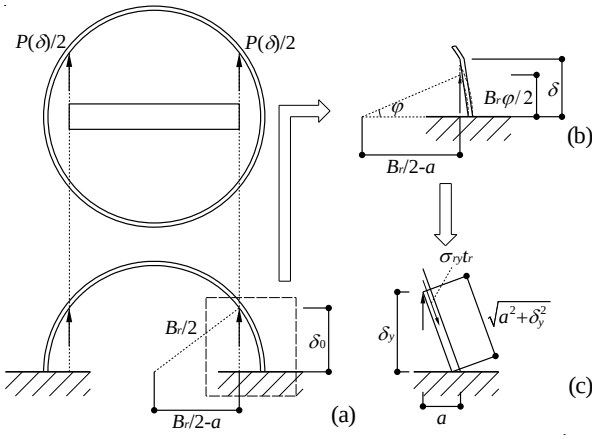

Figure 10 Failure Models of Circular Restraint Tube: (a) Initial Situation, (b) Restraint Tube Elongation, and (c) In-plane Yielding

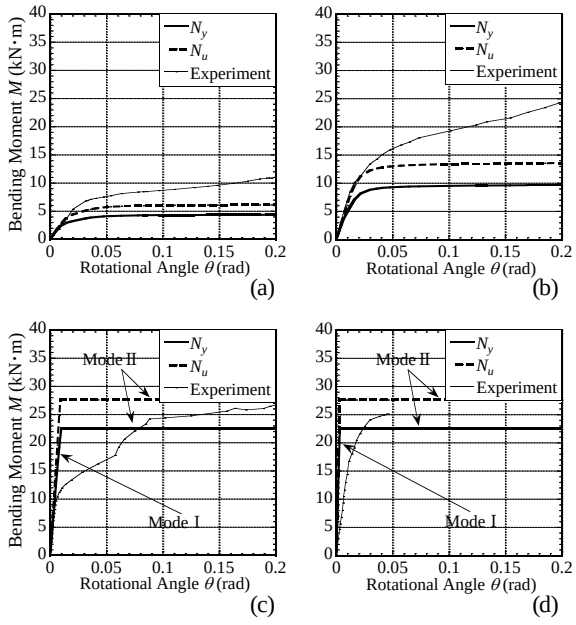

Figure 11 Bending Moments vs. Rotational Angle Curve at Restrainer End for Circular Restraint Tube: (a) L_{in} / B_c = 0.5, CB83, (b) L_{in} / B_c = 1.0, CB83, (c) L_{in} / B_c = 2.0, CB83, and (d) L_{in} / B_c = 3.0, CB83

$$\delta_y = \sqrt{\left(\frac{\pi B_r \sigma_{ry}}{4E} + \frac{B_r}{2}\cos^{-1}\left(\frac{B_r - 2a}{B_r - 2t_r}\right)\right)^2 - a^2} \tag{32}$$

The transmitted shear force before the in-plane stress yielding $P_1(\delta)$ is calculated by performing linear interpolation between the bending yielding and the in-plane stress yielding as Eq. (33).

$$P_1(\delta) = 2\sigma_{ry} t_r \frac{\delta_y}{\sqrt{a^2 + \delta_y^2}} \frac{(\delta - \delta_0)}{\delta_y - \delta_0} \tag{33}$$

Here, δ_0 represents the distance between the core plate surface and the shear force application point when the shear force is not applied, and $\delta = \theta x + \delta_0$. After the in-plane stress yielding, the in-plane stress is not assumed to increase, and the transmitted shear force $P_2(\delta)$ is calculated using Eq. (34).

$$P_2(\delta) = 2\sigma_{ry} t_r \frac{\delta}{\sqrt{a^2 + \delta^2}} \tag{34}$$

The restraint tube yields at the distance x_y from the rotational center of the core plate stiffener, and the bending moment at the restrainer end is calculated as Eqs. (35)–(37).

$$\begin{aligned} M_r &= \int_0^{x_y} P_1(\theta x)\, x dx + \int_{x_y}^{L_{in}} P_2(\theta x)\, x\, dx \\ &= M_1 + M_2 \end{aligned} \tag{35}$$

$$M_1 = \frac{P_1(\delta_y)}{3(\delta_y - \delta_0)} \theta x_y^3 \tag{36}$$

$$\begin{aligned} M_2 &= \int_{x_y}^{L_{in}} \frac{2\sigma_{ry} t_r (\theta x + \delta_0)}{\sqrt{a^2 + (\theta x + \delta_0)^2}} x dx \\ &= \frac{2\sigma_{ry} t_r}{\theta^2}\left\{\left(\frac{\delta'}{2} - \delta_0\right)\sqrt{a^2 + \delta'^2} - \left(\frac{\delta_y}{2} - \delta_0\right)\sqrt{a^2 + \delta_y^2} - \frac{a^2}{2}\log\left(\frac{\delta' + \sqrt{a^2 + \delta'^2}}{\delta_y + \sqrt{a^2 + \delta_y^2}}\right)\right\} \end{aligned} \tag{37}$$

Here, δ' represents the lateral deflection at the distance L_{in} from the rotation center of the core plate stiffener. From Eq. (36), the elastic rotational stiffness K_{Rr1} at the restrainer end is defined as Eq. (38).

$$K_{Rr1} = \frac{2\sigma_{ry} t_r L_{in}^3}{3\sqrt{a^2 + \delta_y^2}} \frac{\delta_y}{\delta_y - \delta_0} \tag{38}$$

The yield rotational angle at the restrainer end is defined as Eq. (39).

$$\theta_y = (\delta_y - \delta_0) / L_{in} \tag{39}$$

Similarly, the bending moment in failure mode II of circular restraint tube is defined as Eq. (31), as in the case of the rectangular restraint tube. In Figure 11 N_y is calculated from the yield stress σ_{ry}; N_u from the ultimate stress σ_{ru}. It is observed that the experimental values approximately distribute between N_y and N_u. From these deliberations, the M_y–N_y evaluation is used for the rectangular restraint tube and N_y evaluation is for the circular restraint tube when the effective buckling length is calculated.

3.3 Evaluation of Rotational Stiffness

In this section, the rotational stiffness at the restrainer end is evaluated considering the deliberations presented in the previous section. In this evaluation, the core plate is postulated to be plastic and having no bending moment. The rotational stiffness at the restrainer end is modeled as bilinear or trilinear, consisting of the bending yielding and in-plane stress yielding. In the bending moment vs. rotational angle relationship, the stiffness prior to pseudo yielding is defined as elastic; plastic, after the pseudo yielding; and zero, after the in-plane stress yielding, as shown in Figure 12. When the restraint tube is rectangular, the elastic rotational stiffness K_{Rr1} is calculated as Eq. (40).

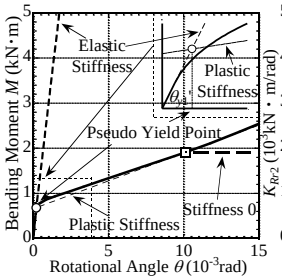

Figure 12 Rotational Stiffness at Restrainer End

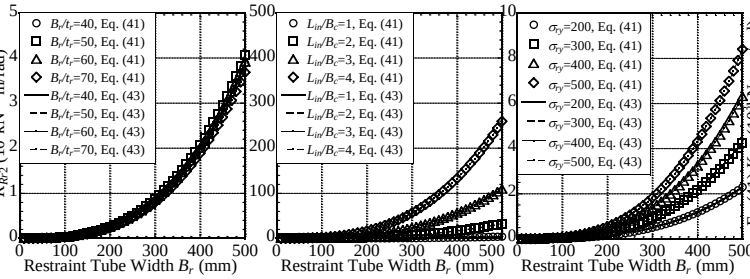

Figure 13 Variations in Plastic Stiffness K_{Rr2} at Restrainer End: (a) Width-to-thickness Ratio, (b) Overlap Length, and (c) Yield Stress

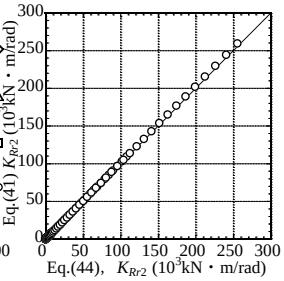

Figure 14 Proposed Values of Plastic Stiffness K_{Rr2}

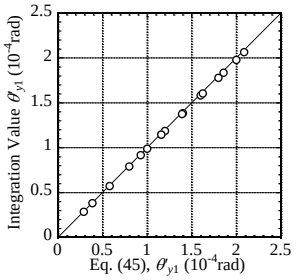

Figure 15 Proposed Values Of Pseudo Yield

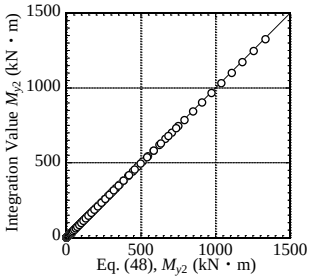

Figure 16 Proposed Values Of In-plane Stress Yield

$$K_{Rr1} = \frac{dM}{d\theta} = \frac{EB_r t_r^3 L_{in}^3}{3\left(2B_r a^3 - 3a^4\right)} \tag{40}$$

In failure mode I, the plastic rotational stiffness K_{Rr2} is calculated from Eq. (24) as a tangent modulus of the bending moment vs. rotational angle curve and is expressed as Eq. (41).

$$K_{Rr2} = \left.\frac{dM}{d\theta}\right|_{\theta=\theta_{y2}} = \frac{P_1\left(\delta_{y1}\right)}{3}\frac{\delta_{y1}^2}{\theta_{y2}^3} + \frac{P_2\left(\delta_{y2}\right) - P_1\left(\delta_{y1}\right)}{3\left(\delta_{y2} - \delta_{y1}\right)}\left(L_{in}^3 - \left(\frac{\delta_{y1}}{\theta_{y2}}\right)^3\right) \tag{41}$$

θ_{y2} represents the rotational angle when the restraint tube exhibits the in-plane stress yielding and is given as Eq. (42).

$$\theta_{y2} = \frac{B_r}{L_{in}}\sqrt{\left(\frac{\sigma_{ry}}{2E}\right)^2 + \left(\frac{a\sigma_{ry}}{B_r E}\right)} \tag{42}$$

Here, pseudo yielding is defined as the intersection of the elastic stiffness and the tangent drawn to the bending moment vs .rotational angle curve at the in-plane stress yielding, as shown in Figure 12. The plastic rotational stiffness K_{Rr2} is calculated by these equations as shown in Figure 13, and basically the restraint tube thickness is t_r = 5.0 mm; the overlap length ratio, L_{in} / B_c = 1.0; the core plate width, B_c = 0.85B_r; the core plate thickness, t_c = 0.12B_r; the yield stress, $\sigma_y = \sigma_{ry} = \sigma_{cy}$ = 290 N/mm^2; and the elastic modulus E = 205000 N/mm^2. The width-to-thickness ratio B_r / t_r = 40–70, the yield stress σ_y = 200–500 N/mm^2, and the overlap length ratio L_{in} / B_c= 1.0–4.0 are treated as parametric. Except for the width-to-thickness ratio, the plastic rotational stiffness K_{Rr2} increases with the overlap length ratio and the yield stress in Figure 13, and K_{Rr2} is defined by a function of the restraint tube width as Eq. (43).

$$K_{Rr2} = f(L_{in} / B_c, \sigma_{ry})\, B_r^3 \tag{43}$$

K_{Rr2} is estimated as a function by an approximation using the restraint tube width, the overlap length ratio, and the yield stress as Eq. (44).

$$K_{Rr2} = 0.11\sigma_{ry} B_r^3 (L_{in} / B_c)^3 \tag{44}$$

Figure 14 shows that Eq. (44) is consistent with the integral values in Eq. (41). Similarly, the pseudo yield point is approximated as Eq. (45), and the approximation values of Eq. (45) agree with the integration values, as shown in Figure 15.

$$\theta'_{y1} = 1.64 \times 10^{-3} (\sigma_{ry} / E)(B_r / t_r)(B_c / L_{in}) \tag{45}$$

From these equations, the elastic rotational stiffness K_{Rr1} is defined by Eq. (40); the plastic rotational stiffness K_{Rr2}, by Eq. (44); the pseudo yield point θ'_{y1}, by Eq. (45); and the in-plane stress yielding point θ_{y2}; by Eq. (42). The rotational stiffness at the restrainer end K_{Rr} is defined by Eq. (46); the yield bending moment M'_{y1} and M_{y2}, by Eqs. (47) and (48), respectively. These bending moments do not exceed the bending moment strength in failure mode II as Eq. (49).

$$K_{Rr} = \begin{cases} K_{Rr1} & (0 \le \theta \le \theta'_{y1}) \\ K_{Rr2} & (\theta'_{y1} \le \theta \le \theta_{y2}) \\ 0 & (\theta_{y2} \le \theta) \end{cases} \tag{46}$$

$$M'_{y1} = K_{Rr1}\theta'_{y1} \tag{47}$$

$$M_{y2} = K_{Rr1}\theta'_{y1} + K_{Rr2}\left(\theta_{y2} - \theta'_{y1}\right) \tag{48}$$

$$M'_{y1}, M_{y2} \le Z_{cp}\sigma_{cy} + (1/4)Z_{mp}\sigma_{my} \tag{49}$$

Here, Eqs. (46)–(49) represent rotational stiffness and yield point value. The bending moment at the in-plane stress

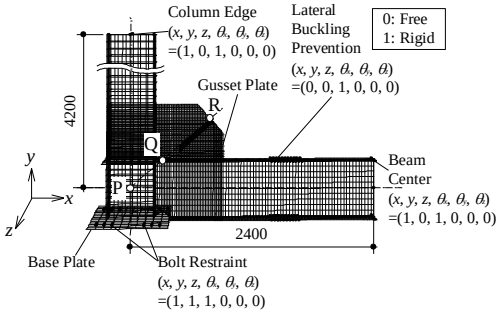

Figure 17 FEM Analysis Model for Connection Rotational Stiffness

Table 3 FEM Displacement Calculation

	x (10^{-3}mm)	y (10^{-3}mm)	z (10^{-3}mm)
P	-3.3	-5.7	2.8
Q	-9.4	-7.4	11.2
R	-12.1	-6.2	-1233.9

Table 5 Assumed Models for Effective Buckling Length

Specimen	Restraint Tube	Core Plate
RB55	□-300 × 300 × 5.5 (Tall) □-200 × 200 × 3.6 (Small)	PL-250 × 36 (Tall) PL-175 × 25 (Small)
CB67	ϕ-355.6 × 5.3 (Tall) ϕ-216.3 × 3.2 (Small)	

Table 4 Assumed Models for Connection Rotational Stiffness in FEM Analysis Calculation

Building Connection Model	BRB Axial Force (kN)	Core Plate	Restraint Tube	Connection Stiffness (kN・m/rad)
Tall A	2511	PL-36 × 310	ϕ-355.5 × 6.4	7.00×10^3
Tall B				9.80×10^3
Tall C				1.81×10^4
Small A	1249	PL-25 × 222	ϕ-267.4 × 5.0	1.73×10^3
Small B				2.64×10^3
Small C				4.85×10^3

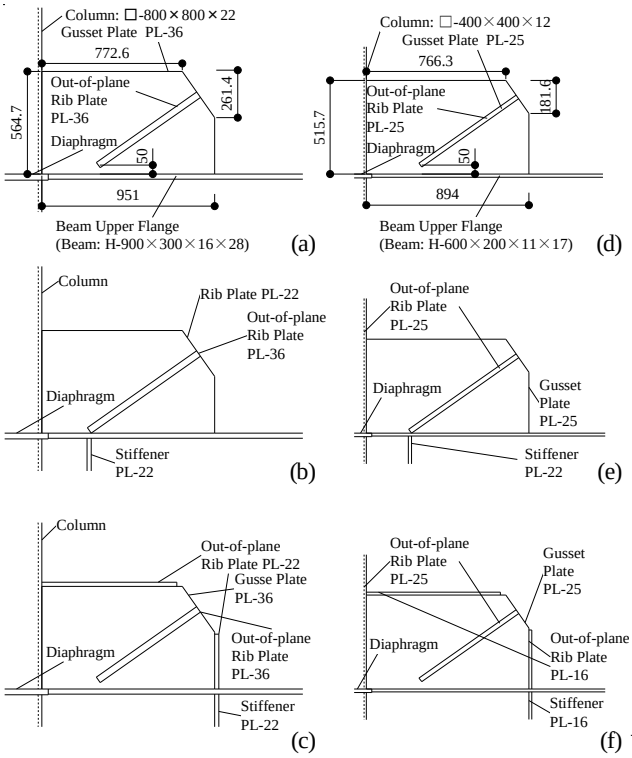

Figure 18 Connection Shapes:
(a) Tall A, (b) Tall B, (c) Tall C,
(d) Small A, (e) Small B, and (f) Small C

yielding M_{y2} calculated from Eqs. (46)–(48) are consistent with those calculated using Eqs. (23)–(25) in Figure 16, and this evaluation of the in-plane stress yielding is considered to be effective in modifying the failure mode I. When the restraint tube is circular, the bending moment vs. rotational angle relationship is modeled as a bilinear function by Eqs. (38) and (39), and Eqs. (50) and (51) represent rotational stiffness and yield point value respectively. The in-plane stress yielding calculated from Eq. (51) does not exceed that calculated for failure mode II by using Eq. (49).

$$K_{Rr} = \begin{cases} K_{Rr1} \ (0 \le \theta \le \theta_y) \\ 0 \ (\theta_y \le \theta) \end{cases} \tag{50}$$

$$M_y = K_{Rr1}\theta_y \tag{51}$$

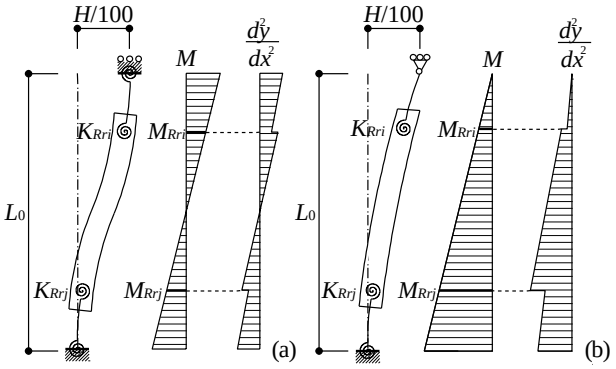

Figure 19 Bending Moment Distributions in BRB:
(a) N-type Layout, and (b) K-type Layout

4. CONNECTION ROTATIONAL STIFFNESS

In order to investigate the rotational stiffness at connections, FEM analysis was carried out using the software ABAQUS (ver.6.4-1). Figure 17 shows the FEM analysis model and boundary conditions. Further, Table 3 lists the displacements of the points P, Q, and R when the bending moment is applied to the point R, and it is observed that the displacement mainly occurs between the points Q and R. The stiffener rib rotates as a rigid body, and this spring stiffness of the connection simulates the mechanical model shown in Figure 2. The rotational stiffness between the points P and R is 9.23×10^2 kN·m/rad. The error between an experimental value and the analytical value is smaller than 10%, and this analysis model is effective in modifying the rotational stiffness at the connection. Thus, the rotational stiffness of three common-type connections shown in Figure 18 is calculated by this FEM model. Here, the rotational angle at the connection is standardized by the distance between the points Q and R. Table 4 shows the analytical rotational stiffness for the three types of connections. From these calculations, the rotational stiffness at the connection is found to distribute in the range of about 1.0×10^3–2.0×10^4 kN·m/rad, and the rotational stiffness at the connection of type C shown in Figure 18(c) and (f) has the highest value.

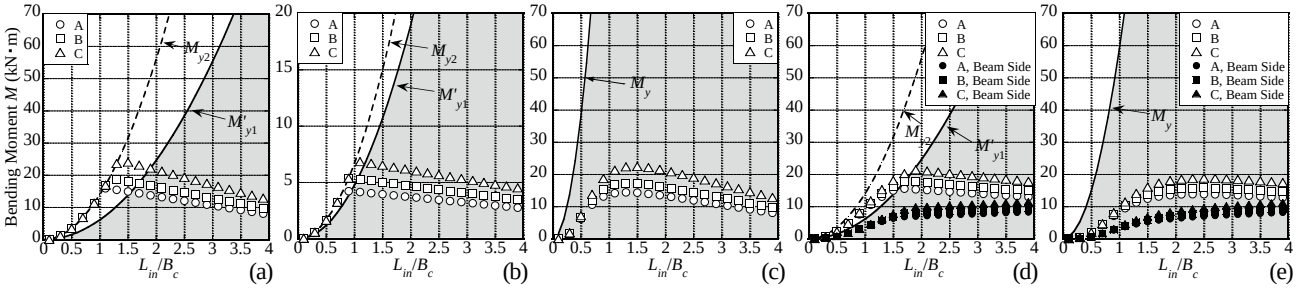

Figure 20 Bending Moments at Restrainer End when Story Drift Angle is 1/100 (Overlap Length Ratio Comparison): (a) Tall N-type RB55, (b) Small N-type RB55, (c) Tall N-type CB67, (d) Tall K-type RB55, and (e) Small K-type RB55

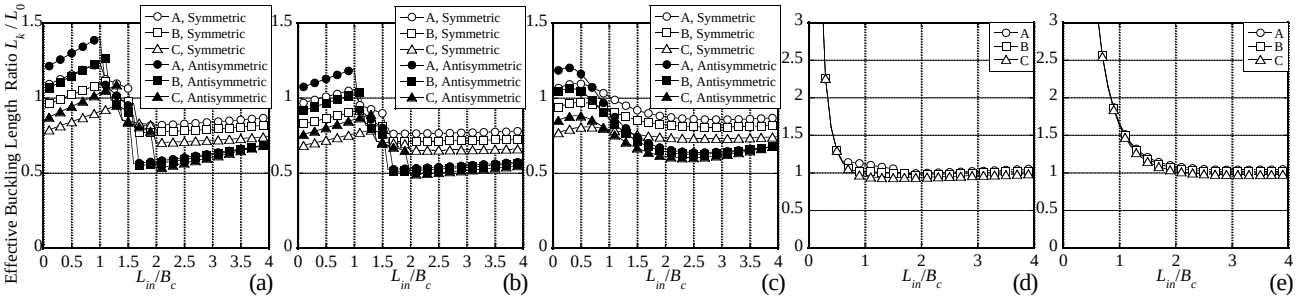

Figure 21 Effective Buckling Length Ratios of BRB when Story Drift Angle is 1/100 (Overlap Length Ratio Comparison): (a) Tall N-type RB55, (b) Small N-type RB55, (c) Tall N-type CB67, (d) Tall K-type RB55, and (e) Small K-type RB55

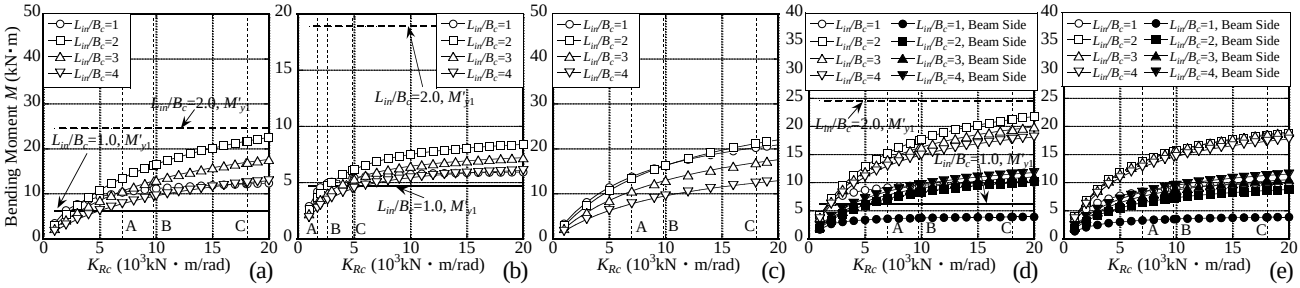

Figure 22 Bending Moments at Restrainer End when Story Drift Angle is 1/100 (Connection Rotational Stiffness Comparison): (a) Tall N-type RB55, (b) Small N-type RB55, (c) Tall N-type CB67, (d) Tall K-type RB55, and (e) Small K-type RB55

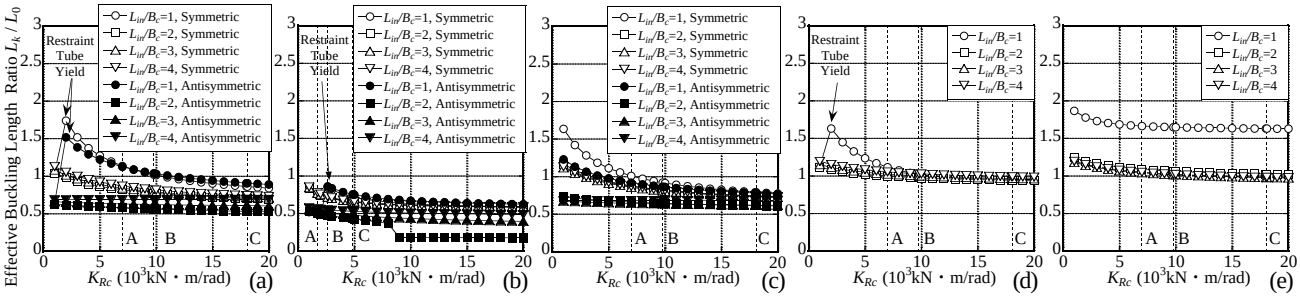

Figure 23 Effective Buckling Length Ratios of BRB when Story Drift Angle is 1/100 (Connection Rotational Stiffness Comparison): (a) Tall N-type RB55, (b) Small N-type RB55, (c) Tall N-type CB67, (d) Tall K-type RB55, and (e) Small K-type RB55

5. EVALUATION OF EFFECTIVE BUCKLING LENGTH

In the previous sections, the rotational stiffness at both the restrainer end and the connections was evaluated through experiment and analysis. In this section, the effective buckling length of a BRB and the conditions for transmitting the bending moment are evaluated from the rotational stiffness. Table 5 shows the scales for the restraint tube and the core plate. When the restraint tube is rectangular, the bending moment vs. rotational angle curve for the restrainer end exhibits the trilinear relationship, as expressed by Eqs. (46)–(49); when the restraint tube is circular, the curve exhibits the bilinear relationship, as shown in Eqs. (50)–(51). The rotational stiffness at the restrainer end depends on the bending moment at the restrainer end. Here, the rotational stiffness at the restrainer end is defined by the bending moments at a story drift angle of 1/100 for the out-of-plane displacement in

order to evaluate the effective buckling length of the BRB as Figure 19. The frame of a tall building is similar to that of a small building. The BRB layout of N-type is, ξL_0-L_{in} is 1000 mm (K-type, 1600mm on beam side), L_0 is 5400 mm, and H is 3800 mm, as shown in Figures 1, 2, and 4. Figure 20 shows the bending moments at the restrainer end and the yield points against the story drift angle of 1/100. Here, A, B, and C represent the connection types listed in Table 4. For rectangular and circular restraint tubes, the bending moment at the restrainer end increases with the overlap length ratio. Figure 21 shows the effective buckling length ratios calculated from Eqs. (13)–(15) by considering the rotational stiffness at the restrainer end and the connection. From these figures, it is found that in order to prevent the restrainer end from yielding, the overlap length ratio should be larger than $1.5L_0$–$2.0L_0$. For a rectangular restraint tube, the effective buckling length of a BRB ranges between $0.6L_0$ and L_0 when the restrainer end does not yield. The effective buckling length ranges between $0.7L_0$ and $1.4L_0$ in the case of an N-type layout, and it considerably exceeds L_0 in the case of a K-type layout when the restrainer end yields. On the other hand, for the circular restraint tube, the restrainer end does not yield; however, the effective buckling length ranges in almost the same range as that of the rectangular restraint tube. For rectangular and circular restraint tubes, the bending moment at the restrainer end increases with the rotational stiffness at the connection in Figure 22. When the restrainer end yields, the effective buckling length increases considerably in Figure 23. Thus, when the rotational stiffness at the restrainer end is expected to possess stiffness, it might be appropriate that the rotational stiffness at the connection is designed to be less than that at the restrainer end. In this study, it is appropriate for ensuring safety that the distance between the surfaces of beam L_0 (in the case of the K-type layout, distance between the surface of the beam and the center of the beam and column) is considered to be the effective buckling length under the condition that the restrainer end does not yield.

6. CONCLUSION

In this study, the rotational stiffness and the strength at the restrainer end and the connection are evaluated through experiment and numerical analysis. The following conclusions are derived:

(1) The buckling modes of a BRB with N-type and K-type layouts are postulated to calculate its effective buckling length from the rotational stiffness at the restrainer end and the connection.

(2) The failure mechanism of the restraint tube is modeled to evaluate the rotational stiffness as a multilinear function. The rotational stiffness at the restrainer end increases as the ratio between the overlap length of the core plate stiffener and the restraint tube width-to-thickness ratio increase. The hypothetical values are consistent with those obtained from experiment.

(3) An FEM analysis is carried out for the calculation of the rotational stiffness at the connection, and the rotational stiffness of three common-types of connections is calculated.

(4) From (1), (2), and (3), the condition for transmitting the bending moment from the core plate to the restrainer end and the effective buckling lengths are evaluated. In order to avoid restrainer end yielding, the overlap length should be more than 1.5–2.0 times as large as the core plate width. When the restrainer end does not yield, the effective buckling length ranges between $0.6L_0$ and L_0. On the other hand, when the restrainer end yields, the effective buckling length ranges between $0.7L_0$ and $1.4L_0$ for the N-type layout, and it is considerably larger than L_0 for the K-type layout. It is possible that the restrainer end yields when the rotational stiffness at the connection is larger than that at the restrainer end.

References:

Watanabe, A., Hitomi, Y. Saeki, E., Wada, A., and Fujimoto, M. (1988), "Properties of Brace Encased in Buckling-restraining Concrete and Steel Tube," *Proceedings of 9th World Conference on Earthquake Engineering*, **Vol. IV(8)**, 719-724.

Xie, Q. (2005), "State of the Art of Buckling-restrained Braces in Asia," *J. Constr. Steel Research*, Elsevier, **61(5)**, 727-748.

Koetaka, Y. and Kinoshita, T. (2009), "Design Criteria of Buckling-restrained Brace to Prevent Out-of-plane Buckling," *J. Struct. Constr. Eng.*, AIJ, **641(7)**, 1371-1378. (in Japanese)

Tembata, H., Koetaka, Y., and Inoue, K. (2004), "Out-of-plane Buckling Load of Buckling-restrained Braces Including Brace Joints," *J. Struct. Constr. Eng.*, AIJ, **581(7)**, 127-134. (in Japanese)

Kinoshita, T., Koetaka, Y., Inoue, K., and Iitani K. (2007), "Criteria of Buckling-restrained Braces to Prevent Out-of-plane Buckling," *J. Struct. Constr. Eng.*, AIJ, **621(11)**, 141-148. (in Japanese)

Takeuchi, T., Yamada, S., Kitagawa, M., Suzuki, K. and Wada, A. (2004), "Stability of Buckling-restrained Braces Affected by the Out-of-plane Stiffness of the Joint Element," *J. Struct. Constr. Eng.*, AIJ, **575(1)**, 121-128. (in Japanese)

JOINT CONFERENCE PROCEEDINGS
7th International Conference on Urban Earthquake Engineering (7CUEE) &
5th International Conference on Earthquake Engineering (5ICEE)
March 3-5, 2010, Tokyo Institute of Technology, Tokyo, Japan

AN EXPERIMENTAL STUDY ON ASNLSE METHOD FOR HEALTH MONITORING OF BASE-ISOLATED STRUCTURES

Qiang Yin[1], Li Zhou[2], and Jann N. Yang[3]

1) Ph. D. Candidate, MOE Key Lab of Structure Mechanics and Control for Aircraft, Institute of Structures & Strength, Nanjing University of Aeronautics and Astronautics, Nanjing, 210016, China
2) Professor, MOE Key Lab of Structure Mechanics and Control for Aircraft, Institute of Structures & Strength, Nanjing University of Aeronautics and Astronautics, Nanjing, 210016, China
3) Professor, Department of Civil & Environmental Engineering, University of California, Irvine, CA92697, USA
yinqiang@nuaa.edu.cn, lzhou@nuaa.edu.cn, jnyang@uci.edu

Abstract: Recently, a new data analysis method, referred to as the sequential non-linear least-square estimation (SNLSE) approach, has been proposed in the literature for the identification of structural parameters. And an adaptive tracking technique has been implemented in the proposed SNLSE to identify the time-varying system parameters of the structure. Simulation and experimental studies for linear structures have demonstrated that the adaptive SNLSE (ASNLSE) approach is capable of tracking the variations of structural parameters, such as the degradation of stiffness, due to damages. In this paper, experimental studies are performed and presented to verify the capability of the adaptive sequential non-linear least-square estimation ASNLSE approach for identifying and tracking damages in nonlinear structures. A base-isolated building model, consisting of a scaled shear-beam type building model mounted on a rubber-bearing isolation system, has been tested experimentally in the laboratory. To simulate structural damages during the test, an innovative device, referred to as the stiffness element device (SED), is proposed herein to reduce the stiffness of the model abruptly. Different types of excitations have been applied at different locations of the test model, including the white noise and earthquake excitations. Various damage scenarios have been simulated and tested. Measured acceleration response data and the ASNLSE approach are used to track the variation of stiffness during the test. The tracking results for the stiffness variations correlate well with that estimated by the finite-element method. It is concluded that the ASNLSE approach is capable of tracking the variation of hysteretic structural parameters leading to the detection of structural damages.

1. INTRODUCTION

An objective of structural health monitoring systems is to identify the state of the structure and to detect the damage when it occurs. In this regard, analysis techniques for damage identification of structures, based on vibration data measured from sensors, have received considerable attention. Various approaches for system identification and damage detection have been proposed in the literature. When a structural element is damaged, such as cracking, the stiffness of the damaged element is reduced. Hence, the structural damage may be reflected by the changes of parametric values of the damaged element. During a severe dynamic event, such as a strong earthquake, a structure may be damaged, and the damage events or the reductions of the stiffness of damaged elements will be contained in measured vibration data. To identify the structural damages using vibration data that contain damage events, system identification techniques in time domain have been developed for nonlinear and/or multi-degree-of freedom (MDOF) structural systems, such as the least-square estimation (LSE) (Loh et al. 2000, Smyth et al. 2002, Yang & Lin 2005, Yang et al. 2007), the extended Kalman filter (EKF) [Hoshiya & Saito 1984, Sato & Takei 1998, Yang et al 2006a, Yang et al. 2007a, Zhou et al. 2008], and others (e.g., Yun et al. 1997, Yang et al. 2009, Huang et al. 2009). Recently, a new data analysis method, referred to as the sequential non-linear least-square estimation (SNLSE) approach (Yang et al. 2006b) has been proposed in the literature for the identification of structural parameters. And an adaptive tracking technique has been implemented in the proposed SNLSE to identify the time-varying system parameters of the structure. Simulation and experimental studies for linear structures have demonstrated that the adaptive SNLSE (ASNLSE) approach is capable of tracking the variations of structural parameters, such as the

degradation of stiffness, due to structural damages.

In this paper, experimental studies are performed and presented to verify the capability of the ASNLSE approach for identifying and tracking damages in nonlinear structures. A base-isolated building model, consisting of a scaled shear-beam type building model mounted on a rubber-bearing isolation system using a particular type of rubber-bearing (GAN110), has been tested experimentally in the laboratory. To simulate structural damages during the test, an innovative device, referred to as the stiffness element device (SED), is used herein to reduce the stiffness of the model abruptly. Different earthquake excitations have been used to drive the shake table, including the El Centro earthquake and Kobe earthquake. Various damage scenarios have been simulated and tested. Measured acceleration response data and the ASNLSE approach are used to track the stiffness variation of the upper structure during the test. The tracking results for the stiffness variations correlate well with that estimated by the finite-element method. It is concluded that the ASNLSE approach is capable of tracking the variation of structural parameters leading to the detection of structural damages.

2. ADAPTIVE SEQUENTIAL NON-LINEAR LEAST SQUARE ESTIMATION

In this section, a brief summary of adaptive sequential nonlinear least-square estimation (SNLSE) approach is given, and the details are referred to (Yang et al. 2006b). The equation of motion of an mDOF nonlinear structure can be expresses as

$$\mathbf{M}\ddot{\mathbf{x}}(t)+\mathbf{F}_c[\dot{\mathbf{x}}(t)]+\mathbf{F}_s[\mathbf{x}(t)]=\boldsymbol{\eta}\mathbf{f}(t) \tag{1}$$

in which $\mathbf{M}$=(m×m) mass matrix; $\mathbf{x}(t)=[x_1,x_2,\cdots,x_m]^{\mathrm{T}}$ = m-displacement vector; $\mathbf{F}_c[\dot{\mathbf{x}}(t)]$ = m- damping force vector; $\mathbf{F}_s[\mathbf{x}(t)]$ =m-stiffness force vector; $\mathbf{f}(t)$ =excitation vector, and $\boldsymbol{\eta}$ =excitation influence matrix. The acceleration responses $\ddot{\mathbf{x}}(t)$ and the excitation forces $\mathbf{f}(t)$ are measured, and the unknowns to be identified are the state vector $\mathbf{X}=[\mathbf{x}^{\mathrm{T}},\dot{\mathbf{x}}^{\mathrm{T}}]^{\mathrm{T}}$, including displacement and velocity vectors, and the parametric vector $\boldsymbol{\theta}=[\theta_1,\theta_2,\cdots,\theta_n]^{\mathrm{T}}$, involving n unknown parameters, such as stiffness, damping, and nonlinear parameters.

The observation associated with the equation of motion, Eq. (8), can be written as

$$\boldsymbol{\varphi}[\mathbf{X};t]\boldsymbol{\theta}+\mathbf{e}(t)=\mathbf{y}(t) \tag{2}$$

in which $\mathbf{y}(t)=\boldsymbol{\eta}\mathbf{f}(t)-\mathbf{M}\ddot{\mathbf{x}}(t)$ is known and $\mathbf{e}(t)$ is the model noises. Eq. (9) can be discredited at $t=t_k=k\Delta t$ as

$$\boldsymbol{\varphi}_k(\mathbf{X}_k)\boldsymbol{\theta}_k+\mathbf{e}_k=\mathbf{y}_k \tag{3}$$

Instead of solving $\mathbf{X}_k$ and $\boldsymbol{\theta}_k$ simultaneously by forming an extended state vector as in the EKF approach, the SNLSE approach will solve $\mathbf{X}_k$ and $\boldsymbol{\theta}_k$ in two steps. The first step is to determine $\boldsymbol{\theta}_k$ by assuming that $\mathbf{X}_k$ is given using the LSE solution. The second step is to determine $\mathbf{X}_k$ through a nonlinear LSE approach, referred to as the SNLSE, as follows:

Step I: Suppose the state vector $\mathbf{X}_k$ is known and the parametric vector $\boldsymbol{\theta}_k$ is constant, the classical LSE recursive solution $\hat{\boldsymbol{\theta}}_{k+1}$ that is the estimate of $\boldsymbol{\theta}_{k+1}$ can be obtained as

$$\hat{\boldsymbol{\theta}}_{k+1}=\hat{\boldsymbol{\theta}}_k+\mathbf{K}_{k+1}(\mathbf{X}_{k+1})[\mathbf{y}_{k+1}-\boldsymbol{\varphi}_{k+1}(\mathbf{X}_{k+1})\hat{\boldsymbol{\theta}}_k] \tag{4}$$

$$\begin{aligned}\mathbf{K}_{k+1}(\mathbf{X}_{k+1})=&(\boldsymbol{\Lambda}_{k+1}\mathbf{P}_k\boldsymbol{\Lambda}_{k+1}^{\mathrm{T}})\boldsymbol{\varphi}_{k+1}^{\mathrm{T}}(\mathbf{X}_{k+1})\times\\&[\mathbf{I}-\boldsymbol{\varphi}_{k+1}(\mathbf{X}_{k+1})(\boldsymbol{\Lambda}_{k+1}\mathbf{P}_k\boldsymbol{\Lambda}_{k+1}^{\mathrm{T}})\boldsymbol{\varphi}_{k+1}^{\mathrm{T}}(\mathbf{X}_{k+1})]^{-1}\end{aligned} \tag{5}$$

$$\mathbf{P}_k=[\mathbf{I}-\mathbf{K}_k(\mathbf{X}_k)\boldsymbol{\varphi}_k(\mathbf{X}_k)](\boldsymbol{\Lambda}_k\mathbf{P}_{k-1}\boldsymbol{\Lambda}_k^{\mathrm{T}}) \tag{6}$$

in which $\mathbf{K}_{k+1}(\mathbf{X}_{k+1})$ is the LSE gain matrix. And in equations above, $\boldsymbol{\Lambda}_{k+1}$ is a diagonal matrix, referred to as the adaptive factor matrix, with diagonal elements $\lambda_1(k+1)$, $\lambda_2(k+1)$, …, $\lambda_n(k+1)$, where $\lambda_j(k+1)$ is referred to as the adaptive factor associated with the jth unknown parameter of θ_{k+1} at $t_{k+1}=(k+1)\Delta t$. The determination of the adaptive factor matrix $\boldsymbol{\Lambda}_{k+1}$ has been described in (Yang & Lin 2005, Yang et al. 2007).

Step II: The recursive solution for $\hat{\mathbf{X}}_{k+1|k+1}$, that is, the estimation of $\mathbf{X}_{k+1}$ can be obtained as

$$\hat{\mathbf{X}}_{k+1|k+1}=\hat{\mathbf{X}}_{k+1|k}+\bar{\mathbf{K}}_{k+1}[\mathbf{y}_{k+1}-\hat{\mathbf{y}}_{k+1}(\hat{\mathbf{X}}_{k+1|k})] \tag{7}$$

$$\hat{\mathbf{X}}_{k+1|k}=\boldsymbol{\Phi}_{k+1,k}\hat{\mathbf{X}}_{k|k}+\mathbf{B}_1\ddot{\mathbf{x}}_k+\mathbf{B}_2\ddot{\mathbf{x}}_{k+1} \tag{8}$$

$$\bar{\mathbf{K}}_{k+1}=\bar{\mathbf{P}}_{k+1|k}\boldsymbol{\Psi}_{k+1,k}^{\mathrm{T}}[\mathbf{I}+\boldsymbol{\Psi}_{k+1,k+1}\bar{\mathbf{P}}_{k+1|k}\boldsymbol{\Psi}_{k+1,k+1}^{\mathrm{T}}]^{-1} \tag{9}$$

$$\bar{\mathbf{P}}_{k+1|k}=\boldsymbol{\Phi}_{k+1,k}\bar{\mathbf{P}}_{k|k}\boldsymbol{\Phi}_{k+1,k}^{\mathrm{T}} \tag{10}$$

$$\bar{\mathbf{P}}_{k|k}=\bar{\mathbf{P}}_{k|k-1}-\bar{\mathbf{K}}_k\boldsymbol{\Psi}_{k,k}\bar{\mathbf{P}}_{k|k-1} \tag{11}$$

where

$$\hat{\mathbf{y}}_{k+1}[\hat{\mathbf{X}}_{k+1|k}]=\boldsymbol{\varphi}_{k+1}(\hat{\mathbf{X}}_{k+1|k})\hat{\boldsymbol{\theta}}_{k+1}(\hat{\mathbf{X}}_{k+1|k}) \tag{12}$$

$$\boldsymbol{\Phi}_{k+1,k}=\begin{bmatrix}\mathbf{I} & (\Delta t)\mathbf{I}\\ \mathbf{0} & \mathbf{I}\end{bmatrix},$$

$$\boldsymbol{\Psi}_{k+1,k+1}=\left.\frac{\partial\hat{\mathbf{y}}_{k+1}(\mathbf{X}_{k+1})}{\partial\mathbf{X}_{k+1}}\right|_{\mathbf{X}_{k+1}=\mathbf{X}_{k+1}(\hat{\mathbf{X}}_{k+1|k})} \tag{13}$$

$$\mathbf{B}_1=\begin{bmatrix}(0.5-\tilde{\beta})(\Delta t)^2\mathbf{I}\\ (1-\tilde{\gamma})(\Delta t)\mathbf{I}\end{bmatrix},\qquad \mathbf{B}_2=\begin{bmatrix}\tilde{\beta}(\Delta t)^2\mathbf{I}\\ \tilde{\gamma}(\Delta t)\mathbf{I}\end{bmatrix} \tag{14}$$

in which $\tilde{\beta},\tilde{\gamma}$ are parameters used in Newmark-β method (usually $\tilde{\beta}=0.25$, $\tilde{\gamma}=0.5$ are used). The details of SNLSE approach are referred to the literature by Yang and Huang, et al.

3. ANALYTICAL HYSTERETIC MODEL

Several hysteretic models for describing the dynamic behavior of rubber-bearings have been proposed in the literature, including bi-linear model (Tan & Huang 2000), tri-linear model (Furukawa et al. 2005), Bouc-Wen (Nagarajaish et al. 1991, Wen & Ang 1987, Wen 1976, 1989), etc. However, the determination of an appropriate model for the base isolation system using actual response data is important in civil engineering applications. To date, no single model has proven entirely satisfactory for all

hysteretic systems for one reason or another. For rubber-bearing isolators, the Bouc-Wen model seems to be quite reasonable.

Consider a single-degree-of freedom hysteretic system (SDOF). The equation of motion can be expressed as

$$m\ddot{x}(t) + r(x, \dot{x}) = f(t) \tag{15}$$

where m is the mass, x is the relative displacement, and $f(t)$ is the excitation. $r(x, \dot{x}) = F_c(\dot{x}) + F_s(x)$ is the total restoring force with $F_c(\dot{x}) = c\dot{x}$. The Bouc-Wen model will be used for $r(x, \dot{x})$ as follows:

$$\dot{r} = c\ddot{x} + k\dot{x} - \beta|\dot{x}||r|^{n-1} z - \gamma\dot{x}|r|^n \tag{16}$$

in which $\dot{r} = \dot{r}(x, \dot{x})$, c and k are, respectively, the damping and stiffness coefficients, and β, γ and n are hysteretic parameters. Some literatures (Chen 2006, Huang & Zhao 2000) have suggested that $\beta = 0.5$, $\gamma = 0.5$, $n = 2$ are available for rubber bearings. Thus, in this paper, these parametric values are adopted.

4. EXPERIMENTAL STUDIES

4.1 Experimental Set-Up

A base-isolated building model, consisting of a 400 mm by 300 mm small-scale shear-beam type building model mounted on a 600 mm by 500 mm rubber-bearing isolation system, as shown in Fig. 1, is used for the experiments. The total height of this building model is 660 mm, where the height of upper story is 345mm and the height of the isolation storey is 315mm. The total weight of the model is 350 kg, in which the mass of upper floor is 50 kg and the mass of the base is 300 kg. The first two natural frequencies of the test specimen are: 1.955 Hz and 5.376 Hz, respectively. Based on the discretized 2-DOF shear-beam model, the stiffness of each story are obtained as 52 kN/m and 46 kN/m using the finite-element approach. The building model is placed on the shake table that simulates different kinds of earthquakes.

Two earthquake excitations will be used, including the El Centro and Kobe earthquakes. During the tests, each floor is installed with one acceleration sensor and one displacement sensor to measure the floor responses.

The damage in a story unit is assumed to be reflected by the reduction of its stiffness. To simulate the reduction of stiffness in the upper story, a stiffness element device (SED) (Wu et al. 2006, Zhou et al. 2008), consisting of a hydraulic cylinder-piston (HCP) and a bracing system, with an effective stiffness of K_{hi} is installed in the upper storey, so that stiffness of the upper storey is increased by K_{hi}. During the experimental test, the effective stiffness of the SED is reduced to zero to simulate the reduction of the stiffness in the upper storey.



Figure 1 The tested based-isolated model using shake table with tracks

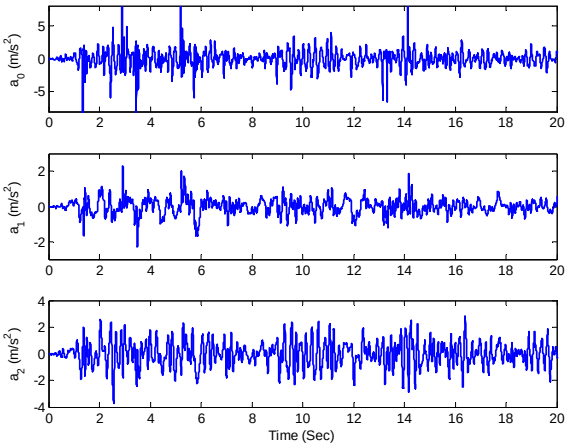

(a) El Centro earthquake for Case 1

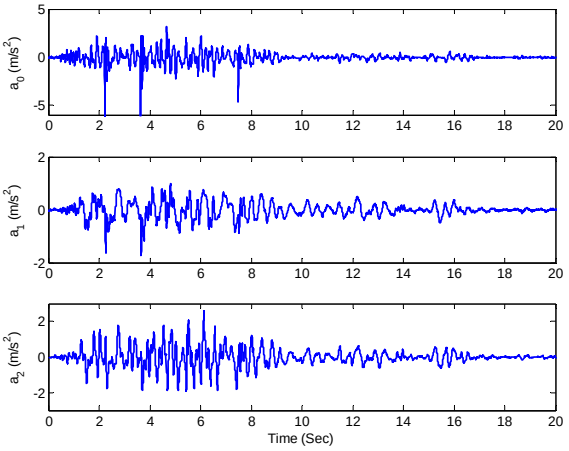

(b) Kobe earthquake for Case 2

Figure 2 Measured acceleration responses and shake table acceleration

4.2 Experimental Results

To demonstrate the capability and accuracy of the ASNLSE approach [Yang et al (2006a)] for tracking the damage of base-isolated structures, experimental tests are conducted herein for different damage scenarios. For shake table tests, two earthquakes will be used, including the El Centro and Kobe earthquakes. For each earthquake, the acceleration responses (a_1, a_2) of both floors and the shake table acceleration a_0 were measured and presented in Fig.2. The sampling frequency of all measurements is 500 Hz.

4.2.1 Case 1: El Cento Earthquake

In this test, a stiffness element device (SED) is installed in the upper storey unit as shown in Fig. 1. The cylinder of the SED is filled by air with an air pressure of 0.75 MPa. From the experimental test, an air pressure at P_0 = 0.75 MPa results in an effective stiffness of 7.5 kN/m for the SED, i.e., K_{hi} = 7.5 kN/m. Thus, the stiffness of the upper storey is k_2 = 46 kN/m + 7.5 kN/m = 53.5 kN/m, whereas the stiffness of base-isolated storey is k_1 = 52 kN/m. During the test with the El Centro earthquake excitation, both valves of the SED unit were open simultaneously at t = 14 seconds, so that the stiffness of the upper storey reduces abruptly from 53 kN/m to 46 kN/m at t = 14 seconds. The acceleration responses of both floors, a_1 and a_2 in m/s^2, were measured and presented in Fig. 2(a). Further, the displacement responses of both floors and the base were also measured for correlation studies later.

For the ASNLSE approach, the test specimen is considered as a 2-DOF shear-beam building model, and the equations of motion can be written, in which the stiffness and damping of each storey of the base-isolator, are unknown parameters. Consequently, the equation of motion, Eq. (3), can be established analytically. With the measured shake table acceleration a_0 and acceleration responses (a_1, a_2) shown in Fig. 2(a), the unknown structural parameters, i.e., k_i, c_i (i = 1, 2), can be identified on-line using the recursive solution, Eqs. (4)-(11), of the ASNLSE approach.

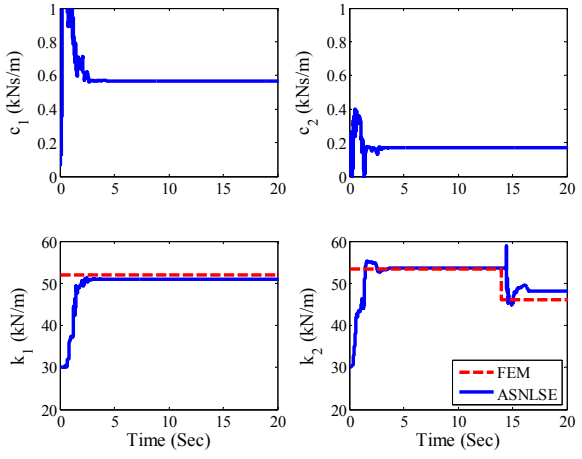

(a) Identified structural parameters

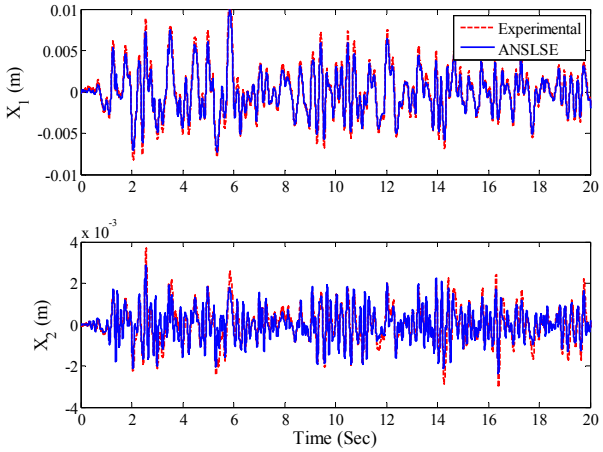

(b) Identified inter-storey drifts

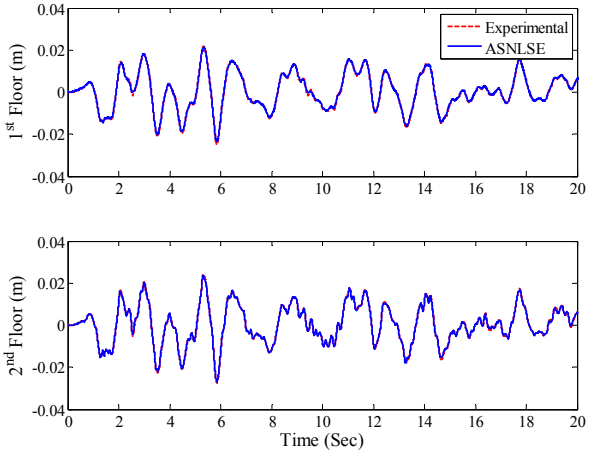

(c) Identified displacements

Figure 3 Identified results for damage at 14 sec. due to El Centro earthquake (Case 1)

For the ASNLSE approach described previously, the following initial values were assumed: (i) the initial values for k_i and c_i are: $k_{i,0}$ = 30 kN/m and $c_{i,0}$ = 0.1 kN.s/m (i = 1, 2), (ii) the initial values for the displacements and velocities are zero, i.e., $\mathbf{x} = 0$, $\dot{\mathbf{x}} = 0$, (iii) the initial gain matrix $\mathbf{P}_0$ for the estimation of the parametric vector and the initial gain matrix $\bar{\mathbf{P}}_{0|0}$ for the estimation of the state vector, are set to be $\mathbf{P}_0 = 100\mathbf{I}_4$ and $\bar{\mathbf{P}}_{0|0} = \mathbf{I}_4$, respectively, where $\mathbf{I}_j$ is a (j×j) identity matrix. In all the experimental studies to be presented later, these same initial values will be used.

Based on the ASNLSE approach and the measured data, the identified unknown parameters for both stories are presented in Figure 3(a) as solid curves (blue color). Also shown in Fig. 3(a) as dashed curves (red color) for comparison are the results based on the finite-element method. Further, the identified inter-storey drifts and

displacements of each floor using the ASNLSE approach are presented in Fig. 3(b) and (c) as solid curves (blue color). Also shown in Fig. 3(b) and (c) as dashed curves (red color) are the measured experimental results. The numerical results of the ASNLSE estimation are as follows: (i) prior to damage, k_1 = 50.95 kN/m and k_2 = 53.55 kN/m, and (ii) after damage, k_1 = 50.95 kN/m and k_2 = 48.08 kN/m. It is observed from Fig. 3(a) (solid curves) and the numerical results above that the identified structural parameters based on the ASNLSE approach are reasonable in comparison with that predicted by the finite element method (dashed curves). The difference between the solid and dashed curves has been expected due to the structural uncertainty of the test model, including the shear-beam assumption. Fig. 3 clearly demonstrates that the ASNLSE approach is capable of tracking the variation of stiffness parameters, leading to the detection of structural damages.

4.2.2 Case 2. Kobe Earthquake

Instead of the El Centro earthquake, the Kobe earthquake was used to drive the shake table. The test configuration is identical to that of Case 1 presented previously, the air pressure of the SED installed in the first storey is P_0 = 0.7 MPa. This results in a stiffness of 7.0kN/m for the SED. Hence, the stiffness of the upper storey prior to a damage is k_1 = 52 kN/m and k_2 = 53 kN/m. During the test, valves of the SED were open at about t = 6 seconds, following the most intensive portion of the earthquake, at that time k_2 is reduced to 46 kN/m. Acceleration responses (a_1, a_2) of both floors and the shake table acceleration a_0 were measured and presented in Fig. 2(b). Based on the measured data in Fig. 2(b) and the ASNLSE approach, the identified unknown parameters for both stories are presented in Fig. 4(a) as solid curves (blue color), whereas the dashed curves (red color) are the finite-element results. The predicted inter-storey drifts and displacements of each floor are presented in Fig. 4(b) and (c) as solid curves (blue color), whereas the dashed curves (red color) are the measured data for comparison. The numerical results of the ASNLSE are as follows: (i) prior to damage, k_1 = 51.26 kN/m and k_2 = 52.83 kN/m, and (ii) after damage, k_1 = 51.26 kN/m and k_2 = 46.96 kN/m. As observed from Fig. 4, the ASNLSE predictions are quite reasonable, and that the trend of predictions is consistent with that of the previous case.

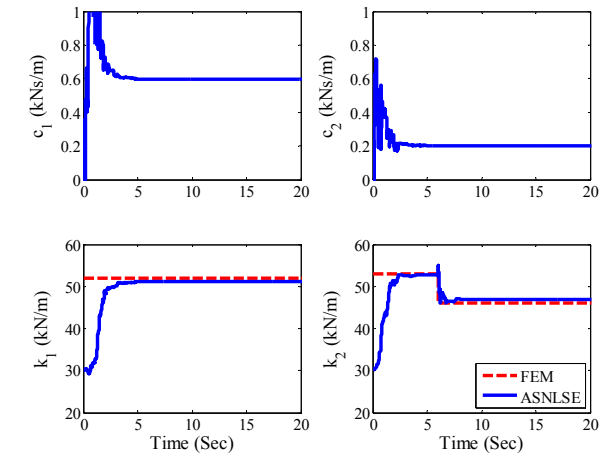

(a) Identified structural parameters

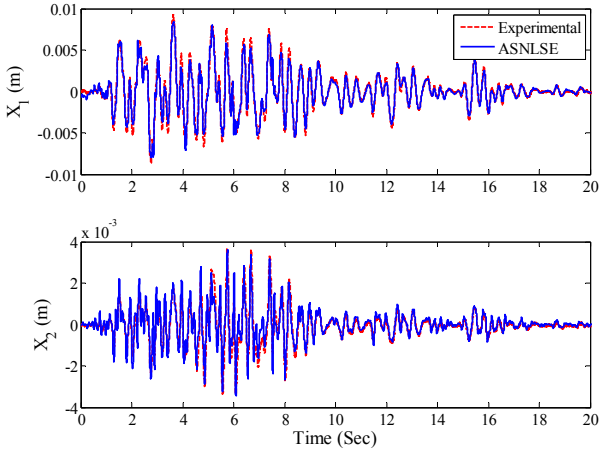

(b) Identified inter-storey drifts

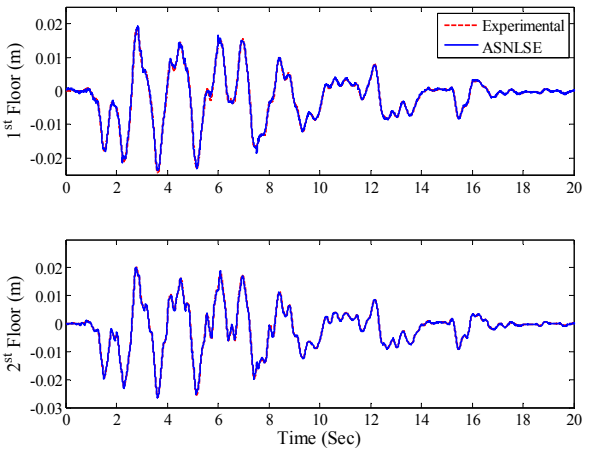

(c) Identified displacements

Figure 4 Identified results for damage at 6 sec. due to Kobe earthquake (Case 2)

5. CONCLUSION

Recently, a new adaptive sequential nonlinear estimation (ASNLSE) approach [Yang et al (2006b)] has been proposed for the on-line damage identification of structures based on simulation results. In this paper, we have performed experimental studies to verify the capability of this ASNLSE in identifying the damage of base-isolated structures by conducting a series of experimental tests on a scaled rubber-bearing isolated building model. To simulate the structural damage during the test, an innovative stiffness element device (SED) has been used to reduce the stiffness of the upper storey. Different damage scenarios under different earthquakes have been simulated and tested. Measured acceleration response data and the ASNLSE approach have been used to identify the unknown structural parameters, and to track the stiffness variation of the structure during the test. The identified stiffness parameters based on the ASNLSE approach correlate reasonably well with that predicted by the finite-element method. Experimental studies conducted herein demonstrate that the ASNLSE approach is capable of tracking the variation of stiffness parameters leading to the detection of structural damages.

Acknowledgments:

This research is partially supported the Science Foundation of Aeronautics of China grant No.2008ZA52012, the National Natural Science Foundation of China grant No. 10572058, and the US National Science Foundation grant No. CMMI-0853395.

References

Chen, B.J., Tsai, C.S. and Chung, L.L., Chiang, T.C., (2006), "Seismic behavior of structures isolation with a hybrid system of rubber bearings," *Structural Engineering and Mechanics*, **22**(6):761~783.

Furukawa T., Ito M. and Noori M.N. (2005), "System Identification of Base-Isolated Building Using Seismic Response Data," *Journal of Engineering Mechanics*, ASCE, **131**(3), 268-273.

Hoshiya, M. and Saito, E. (1984), "Structural Identification By Extended Kalman Filter," *Journal of Engrg. Mechanics,* ASCE*,* **110**(12), 1757-1771.

Huang, H., and Yang, J.N. (2008), "Damage Identification of Substructure for Local Health Monitoring," *Journal of Smart Structures and Systems*, **4**(6), 795-807.

Huang, H., Yang, J.N., and Zhou, L. (2009), "Adaptive quadratic sum-squares error with unknown inputs for damage identification of structures," *journal structural Control and Health Monitoring*, Published online in Wiley InterScience, DOI: 10.1002/stc.318.

Huang, J.W. and Zhao, B. (2000), "The nonlinear dynamic response of multistory base isolated building with laminated rubber bearings," *Journal of Xi'an University of Science & Technology*, **20**(4), 317-321.

Lin, J.W., Betti, R., Smyth, W.A. and Longman, R.W. (2001), "On-line Identification of Nonlinear Hysteretic Structural System Using A Variable Trace Approach," *Earthquake Engineering and Structural Dynamics*, **30**, 279-1303.

Loh, C.H., Lin, C.Y. and Huang, C.C. (2000), "Time Domain Identification of Frames Under Earthquake Loadings," *J. Engrg. Mechanics*, ASCE, **126**(7), 693-703.

Ma, F., Zhang, H., Bockstedte, A., Foliente, G.C. and Paevere, P. (2004), "Parameter Analysis of the Differential Model of Hysteresis," *Journal of Applied Mechanics*, ASCE, **71**, 342-349.

Nagarajaiah, S., Reinhorn, A.M. and Constantinou, M.C. (1991), "Nonlinear dynamic analysis of 3D-base isolated structures," *Journal of Structural Engineering*, ASCE, **117**(7), 2035-2054.

Sato, T. and Takei, K. (1998), "Development of A Kalman Filter with Fading Memory," *Proc. Structural Safety and Reliability*, ICOSSA, Balkma, Rotterdam, 387-349.

Smyth, A.W., Masri, S.F., Kosmatopoulos, E.B., Chassiakos, A.G and Caughey, T.K. (2002), "Development of Adaptive Modeling Techniques for Non-linear Hysteretic Systems," *International Journal of Non-linear Mechanics*, **37**(8), 1435-1451.

Tan, R.Y. and Huang, M.C. (2000), "System identification of a bridge with lead-rubber bearings," *Computers and Structures*, **74**, 267-280.

Wen, Y.K. (1976), "Method for random vibration of hysteretic systems," *J. Eng. Mech. Div.*, **102**(2), 249-263.

Wen Y. K. and Ang A. H. (1987), "Inelastic Modeling and System Identification," *Proceedings. Structural Safety Evaluation Based on System Identification Approaches*, International Workshop, Lambrecht, Germany, pp. 142-160.

Wen Y. K. (1989), "Methods of Random Vibration For Inelastic Structures," *Applied Mechanical Reviews*, **42**(2): 39–52.

Wu, S.Y., Zhou, L. and Yang J.N. (2006), "Experimental study of an adaptive extended Kalman filter for structural damage identification," *Proceedings of 4th International Conference on Earthquake Engineering*, Taipei, Taiwan, October 2006.

Yang, J.N., Kim, J.H. and Agrawal, A.K. (2000), "A Resetting Semi-Active Stiffness Damper for Seismic Response Control," *Journal of Structural Engineering*, ASCE, **126**(12), 1427-1433.

Yang, J.N. and Lin, S. (2005), "Identification of Parametric Variations of Structures Based on Least Square Estimation and Adaptive Tracking Technique," *Journal of Engineering Mechanics*, ASCE, **131**(3), 290-298.

Yang, J.N., Lin, S., Huang, H.W. and Zhou, L. (2006a), "An Adaptive Extended Kalman Filter for Structural Damage Identification," *Journal of Structural Control and Health Monitoring*, **13**, 849-867.

Yang, J.N., Huang, H. and Lin, S. (2006b), "Sequential non-linear least-square estimation for damage identification of structures," *International Journal of Non-linear Mechanics*, **41**, 124-140.

Yang, J.N., Pan, S., and Huang, H. (2007a), "An Adaptive Extended Kalman Filter for Structural Damage Identification II: Unknown Inputs," *Journal of Structural Control and Health Monitoring*, **14**(3), 497-521.

Yang, J.N., and Huang, H. (2007b), "Sequential Non-Linear Least Square Estimation for Damage Identification of Structures with Unknown Inputs and Unknown Outputs," *International Journal of Non-Linear Mechanics*, **42**, 789-801.

Yang, J.N., Pan, S., and Lin, S. (2007c), "Least Square Estimation with Unknown Excitations for Damage Identification of Structures," *Journal of Engineering Mechanics*, ASCE, **133**(1), 12-21.

Yang, J. N., Huang, H. and Pan, S. (2009), "Adaptive Quadratic Sum Squares Error for Structural Damage Identification," *Journal of Engineering Mechanics*, ASCE, **135**(2), 67-77.

Yun, C.B., Lee, H.J. and Lee, C.G. (1997), "Sequential Prediction Error Method for Structural Identification," *Journal of Engineering Mechanics*, ASCE, **123**(2), 115-123.

Zhou L., Wu, S.Y. and Yang, J.N. (2008), "Experimental study of an adaptive extended kalman filter for structural damage identification," *Journal of Infrastructure Systems*, ASCE, **14**(1), 42-51.

JOINT CONFERENCE PROCEEDINGS
7th International Conference on Urban Earthquake Engineering (7CUEE) &
5th International Conference on Earthquake Engineering (5ICEE)
March 3-5, 2010, Tokyo Institute of Technology, Tokyo, Japan

A STUDY ON THE STABILITY OF STEP-OVER ISOLATED STRUCTURE

Yosuke Yamamoto[1], Toru Takeuchi[2], Yasuhiro Nakata[3], Eiichirou Saeki[4]

1) Graduate Student, Tokyo Institute of Technology, Japan
2) Professor, Tokyo Institute of Technology, Japan
3) Manager, Nippon Steel Engineering
4) General Manager, Nippon Steel Engineering

Abstract: The authors have proposed Step-Over Isolated Structure which is one of the extension methods for multistory housing occupied by residents. In structural design, the extension floors are being supported by slender columns with long natural period similar as ordinary base-isolation, and connected to existing structure by energy dissipation devices for displacement control. In this method, stability conditions for the supporting columns are essential, including *P-δ* effects and plastic deformation of these members. In this paper, these effects of complex non-linearity of components on the stability and response characteristics are analyzed, and the conditions to ensure the robustness are discussed. Next, shaking table tests for de-scaled mockup models are carried out. Their results are compared with analytical results, and the validity of proposed criteria is discussed.

1. INTRODUCTION

From the aspect of the reduction of environmental impact, it is not suitable to keep 'scrap and build' concept for urban metabolism, so what is recommended in urban areas is the development method to retrofit the urban infrastructures utilizing existing buildings. In Japan, there are many low or middle rise housings. Especially, large amount of housings are in difficulty to redevelop because occupants have no place to move out and lack of scrap-and-build construction costs. For solving this problem, adding floors on the existing housing is becoming popular in Europe. Besides, base isolated structure is wide-spread in Japan.

For the practical application in seismic areas, extending floors with Step-Over Isolated Structure is proposed. This structure consists of elements as follows. Extension floors are supported by additional steel columns arranged in two rows. Existing and extension floors are structurally independent each other in this stage. Then energy dissipation devices are distributed between the two for reducing response displacement and velocity. The natural period of the extension floors are longer because of slender steel columns, and the effect of decreasing seismic response is almost as same as the ordinary base isolation. For the supporting columns work as part of isolators in the ordinary base isolation, the seismic force transferred from extension floors to existing floors becomes few in comparison with an ordinary extension, so reinforcements to existing floors are minimized.



Figure 1 Perspective

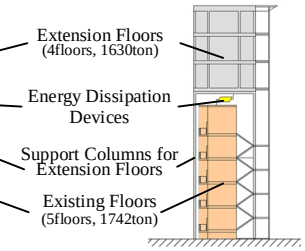

Figure 2 Section

2. NUMERICAL ANALYSIS OF SLENDER COLUMNS

The supporting columns are modeled by the element as in Figure 3. The column base has a rotational stiffness k_θ, modeling the rotation of foundations. Column's weight is ignored in analysis. Firstly, *i*-th element from lower end is shown in Figure 4. The sums of horizontal and vertical component of axial force and shear force at lower and upper end are equal to horizontal and vertical loads respectively. Assuming the length of element *ds* as constant, the deformations of the element are evaluated

by iteration process as shown in Figure 5. Besides, deformation states of columns are calculated by summing up deformations of all elements. Figure 6 shows the flow chart of the analysis until the column's end reaches full plastic bending moment M_p. It is assumed that the axial force ratio is not large as influential to M_p, and a material characteristic is estimated as perfect linear elastoplasticity. When the load applied to the element increases, the moment at the end of a column increases, the moment of the upper end M_B firstly reaches yield moment M_y, subsequently full plastic moment M_p. Assuming that the upper end coordinate (u, x) and the lower end moment M_A, then operate iteration until the sum of ds fits to column's length l. When the horizontal load increases furthermore, M_A of the lower end reaches M_y and M_p, both displacement and load are fixed to satisfy equation (1) condition.

$$2M_p = Pu + Hx \quad \cdots (1)$$

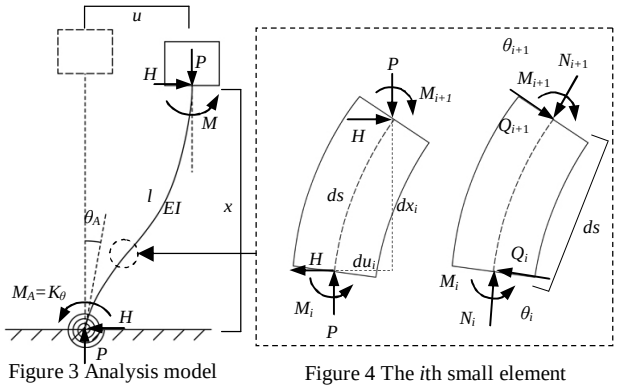

Figure 3 Analysis model

Figure 4 The ith small element

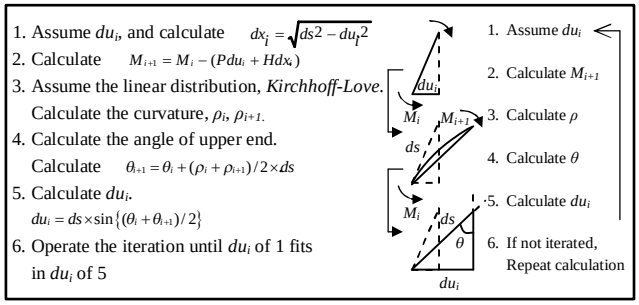

Figure 5 The deformation of the small element

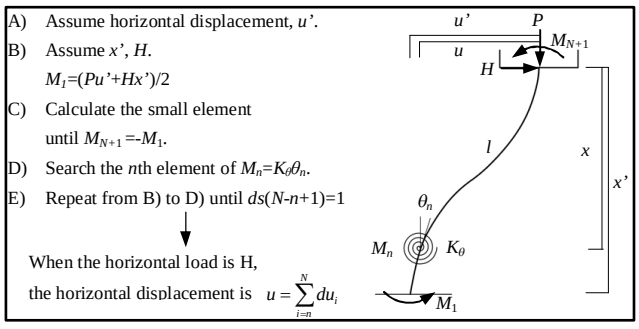

Figure 6 The numerical analysis process for load-deformation relationship

3. RESTORING FORCE CHARACTERISTIC WITH ELASTIC COLUMNS

3.1 Effect of Vertical Load

The theoretical load deformation relationships in elastic conditions can be evaluated by using equation (2)-(4) in Figure 7 with buckling slope-deflection method. Equation (5) and (6) show nondimensional vertical load p and rotational stiffness k_θ, and equation (7) shows the relationship between load and deformation using these parameters. Figure 8 shows the nondimensional load deformation relationships. Each plot in this figure is the numerical analysis value from section 2, and each line is the elastic theoretical value derived from equation (2)-(7). At the range of large horizontal displacement, numerical analysis results become larger than linear theoretical value. This is because of the ignorance of the non-linear vertical displacement. However, at the range of u/l<0.2, errors between analysis value and theoretical one is negligible. Load deformation relationships can be estimated by linear equations. Nondimensional stiffness k has a constant value with each k_θ or P, and load is proportionally related to deformation. Figure 9 shows the effect of k_θ to k. When k_θ is less than 10, the effect increases rapidly. Figure 10 shows the effect of p to k. k_0 means the nondimensional stiffness at p=0. (k- k_0)/p plots spread in range 11-12, and k is estimated approximately as equation (8) in the following studies.

3.2 Effect of Overturning Moment

Next, the effect of the overturning moment is discussed for the extension with high aspect-ratios. When the center of the extension part is subjected to both of horizontal load 2H and vertical load 2V, the axial force of the columns changes by the effect of the overturning moment. Axial forces in supporting columns

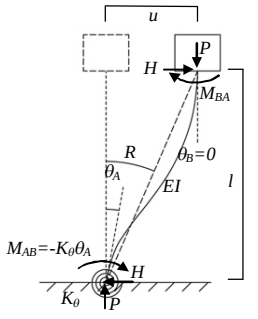

Figure 7 The analysis model concerned about P-δ effect

$$\left.\begin{aligned} M_{AB} &= \frac{EI}{l}(\alpha\theta_A + \beta\theta_B - \gamma R) \\ M_{BA} &= \frac{EI}{l}(\alpha\theta_B + \beta\theta_A - \gamma R) \end{aligned}\right\} \quad (2)$$

$$\left.\begin{aligned} \alpha &= \frac{Z\sin Z - Z^3\cos Z}{2(1-\cos Z) - Z\sin Z} \\ \beta &= \frac{Z^2 - Z\sin Z}{2(1-\cos Z) - Z\sin Z} \\ \gamma &= \alpha + \beta = \frac{Z^2(1-\cos Z)}{2(1-\cos Z) - Z\sin Z} \end{aligned}\right\} \quad (3)$$

$$Z = l\sqrt{\frac{P}{EI}} \quad (4)$$

$$p = \frac{P}{P_{cr}} \qquad P_{cr} = \frac{\pi^2 EI}{l^3} \quad \cdots (5) \qquad k_\theta = \frac{K_\theta l}{EI} \quad \cdots (6)$$

$$H = k\frac{EI}{l^3}u \qquad k = \left\{\gamma\left(\frac{2k_\theta + \alpha - \beta}{k_\theta + \alpha}\right) - \pi^2 p\right\} \quad \cdots (7)$$

$$k = k_0 - 12P/P_{cr} \quad \cdots (8) \qquad k_0 = 6\left(\frac{2k_\theta + 2}{k_\theta + 4}\right) \quad \cdots (9)$$

P_{cr}: Euler buckling load p: nondimensional P_{cr}
K_θ: Rotational stiffness k_θ: nondimensional K_θ

in compression and tension side of the axial force are expressed by equation (10).

$$P^{+} = P_0 + \frac{2Hh}{a} + \frac{2P_0 u}{a} \qquad P^{-} = P_0 - \frac{2Hh}{a} - \frac{2P_0 u}{a} \quad \cdots (10)$$

The sum of both columns' load deformation relationships are expressed as eq. (11).

$$2H = H^{+} + H^{-} = (k^{+} + k^{-})\frac{EI}{l^3}u \quad \cdots (11)$$

k^{+} and k^{-} are evaluated by exchanging P at (3)-(7) to (10), however, these are the functions of H and u, and it needs iteration until the results fit to the assumption. Figure 12 shows the comparison of the theoretical value by iteration of load deformation relationships, with the results by equation (8). All of them indicate similar values, however, the approximate equation (8) is slightly smaller. Figure 13 shows the comparison of the theoretical value including large overturning moment effect with not including one. Although the gap of the theoretical values is large in large horizontal displacement area, the gap is relatively small in the range of $H^{+}>0$ ($u/l<0.2$). Therefore, the effect of the overturning moment to the system can be neglected in this range.

4. RESTORING FORCE CHARACTERISTIC OF ELASTO-PLASTIC COLUMNS

Figure 14-a) and b) are the numerical analysis results including the columns in the condition of the material characteristic is elasto-plastic. Figure 14-a) shows the case of base rotational stiffness is rigid, and Figure 14-b) shows the case of that is soft. In each figure, the result neglects the effect of overturning moment because the effects of these additional axial forces are negligible as same as in elastic range. From these, the simple method for estimating the load deformation relationships can be proposed as follows. Firstly, the initial gradient is required from equation (8). Secondly, the third gradient is required from equation (1) and $u^2+x^2=l^2$. M_B is calculated by equation (12), and the displacement ${}_{u}u_p$ where the moment of the upper end of the column reaches to M_p is calculated by equation (13). When the connection at the lower end is rigid, the displacement ${}_{g}u_p$ where the both end form the plastic mechanism is calculated from equation (14). And, when the connection at the lower end is semi-rigid, the displacement at the mechanism ${}_{l}u_p$ is approximately calculated by equation (15) assuming the mechanism as Figure 15. ${}_{u}u_p$ and ${}_{l}u_p$ are plotted on the load deformation relationships, and the line between two plots can be drawn as the second gradient. The process indicated above, the restoring force characteristic under the elasto-plastic condition can be estimated.

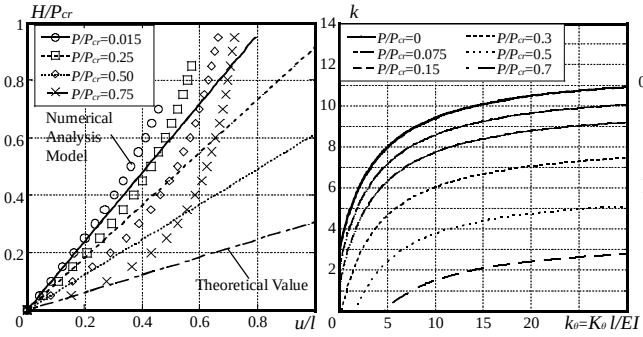

Figure 8 Load-deformation relationship

Figure 9 The effect of rotational stiffness

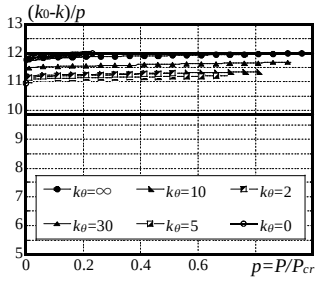

Figure 10 The effect of the vertical load to the column's stiffness

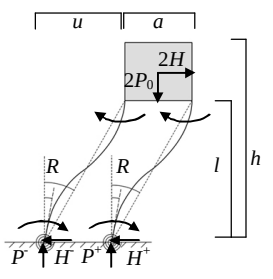

Figure 11 The analysis model concerned about overturning

5.1 Analysis model

Extension floors and existing floors can be replaced as multi degrees of freedom analysis model shown in figure 16. The extension and existing floors are connected by elasto-plastic dampers. The stability of step-over isolated structure is verified by the time-history

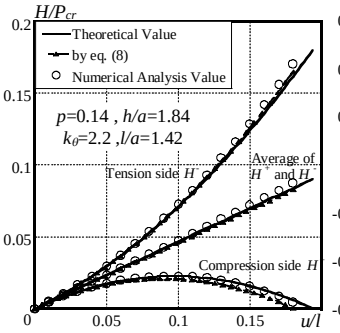

Figure 12 Load-deformation relationship concerned about overturning

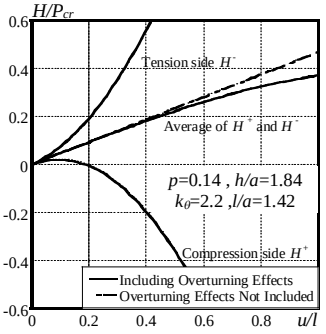

Figure 13 Nonlinearity by overturning

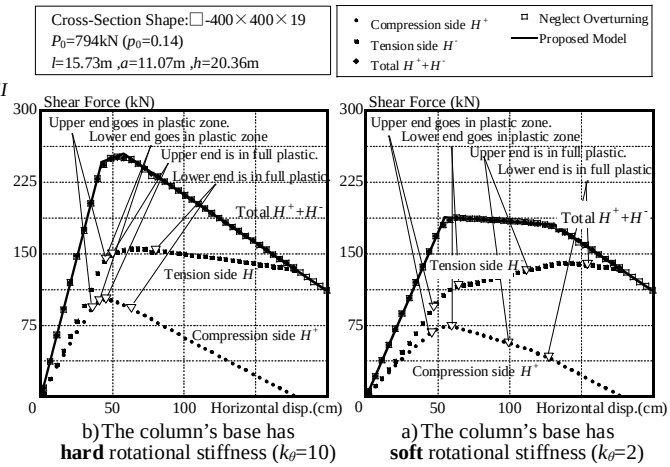

b) The column's base has **hard** rotational stiffness (k_θ=10)

a) The column's base has **soft** rotational stiffness (k_θ=2)

Figure 14 Load-deformation relationship

5. DETAILED ANALYSES WITH MULTISTORY MODEL

analyses using Wilson-θ method (θ=1.4). The characteristics set up in the previous section are used for the restoring force characteristics of the columns, and modeled with Masing's rule as in Figure 17. Table 1 shows the structural parameters. Seismic input are artificial earthquake (BCJ-L2 (V_{max}=57.4cm/sec)) and recorded ones (El-Centro-NS, Taft-EW, JMA-Kobe-NS, Hachinohe-EW (V_{max}=50 cm/sec)).

5.2 Effect of Geometrical and Material Nonlinearity

Figure 18 shows the comparison of the result of time -history analysis between columns with elasto-plastic characteristics of both rigid end and the simple model in which columns have the simple shear stiffness of $12EI/l^3$. When yield shear coefficient distribution of damper α_s is larger than 0.02, the gap of the maximum response displacement of the column is very small; however there is some gap in the maximum shear force when α_s<0.02.

5.3 Effect of Rotational Stiffness of Column End

The effect of rotational stiffness of the column base is shown in Figure 19 with the comparison of k_θ=10 and k_θ=2. In k_θ=2 as soft stiffness model, the natural period becomes longer than those of k_θ=10, then the maximum response shear force is smaller in k_θ=2, however, the effect of the rotational stiffness to the response displacement is not remarkable.

5.4 Effect of Plasticity of the Existing Part

Next, the effect of plasticity of the existing part is discussed. It is assumed that the existing part goes into plastic range at base shear 0.3, and the restoring force characteristic is bi-linear model. Figure 20 shows the comparison of the analysis result with the result in elastic range. In elastic range, the story drift of the existing part decreases along α_s, in contrast, in plastic range, the story drift increase in case of larger damping. Even then, the response of the extension part in plastic range is not so different from the response in elastic range.

5.5 Stability at Excessive Input

Finally, the collapse behavior with larger input is examined. Figure 21 shows the time-history of response displacement for BCJ-L2 (V_{max}=75.0cm/sec) input to the extension part without dampers. When the maximum displacement of columns goes to the negative gradient,

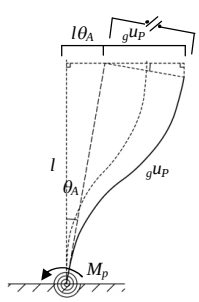

Figure 15 The displacement in Mechanism

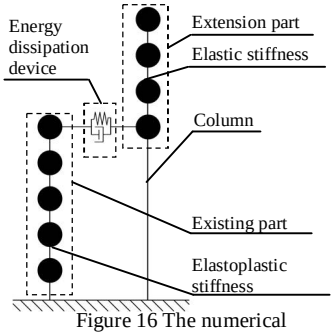

Figure 16 The numerical response analysis model

$$M_B = \frac{Pu}{1-\cos(k_0/12\pi)} + Hl\sqrt{3/k_0} \quad \cdots (12)$$

$$_uu_p = M_p \Big/ \left\{ \frac{Pu}{1-\cos(k_0/12\pi)} + k\sqrt{3/k_0}\,\frac{EI}{l^2} \right\} \quad \cdots (13)$$

$$_gu_p = 2M_p \Big/ \left\{ P + \frac{(12-12P/P_{cr})EI}{l^2} \right\} \quad \cdots (14)$$

$$_lu_p = {}_gu_p + l\frac{M_p}{K_\theta} \quad \cdots (15)$$

Table 1 Structural Diagram

Additional part

story	mass(ton)	damping factor	stiffness (kN/mm)
9	444.9	0.01	460.1
8	400.2	0.01	480.3
7	399.9	0.01	420.4
6	384.5	0.01	-

Existing part

story	mass(ton)	damping factor	initial stiffness (kN/mm)	yield disp. (mm)	2nd stiffness (kN/mm)
5	282.5	0.03	220.11	7.41	1.82
4	359.2	0.03	279.61	8.24	3.33
3	357.8	0.03	378.52	8.52	5.47
2	368.2	0.03	425.64	9.32	6.56
1	374.7	0.03	878.93	5.79	9.71

Elstoplastic damper

yield disp. (mm)
7.5

Support Column

rotational stiffness	initial stiffness (kN/mm)	yield disp. (mm)	2nd stiffness (kN/mm)	2nd yield disp. (mm)	3rd stiffness (kN/mm)	3rd yield disp. (mm)	4th stiffness (kN/mm)
k_θ=10	5.83	377.5	2.73	487.6	-0.56	786.5	-1.02
k_θ=2.0	3.46	503.3	1.258	613.4	-1.04	1289.8	-1.02
k_θ=∞	7.64	330.3	3.02	377.7	0.266	440.4	-1.02
simple model	8.8	-	-	-	-	-	-

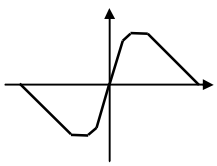

Figure 17 Load -deformation relationship

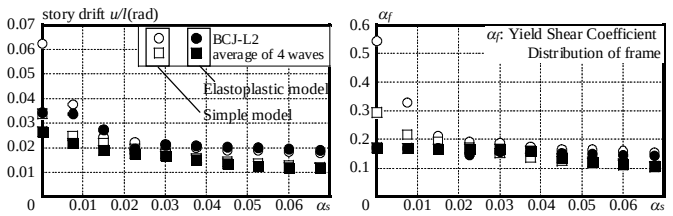

a) Max disp. of column b) Max shear force of column

Figure 18 The effect of nonlinearity

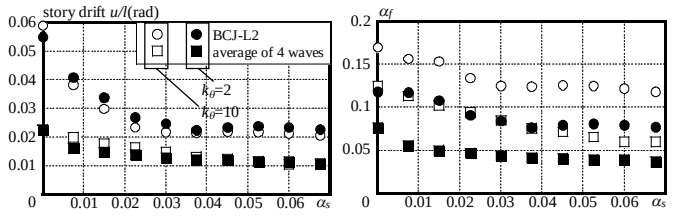

a) Max disp. of column b) Max shear force of column

Figure 19 The effect of the rotational stiffness at the end of the column

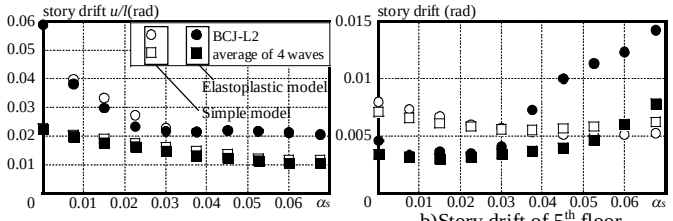

a)Time-historical response disp. b)Story drift of 5th floor of existing part

Figure 20 The effect of plasticity of the existing part

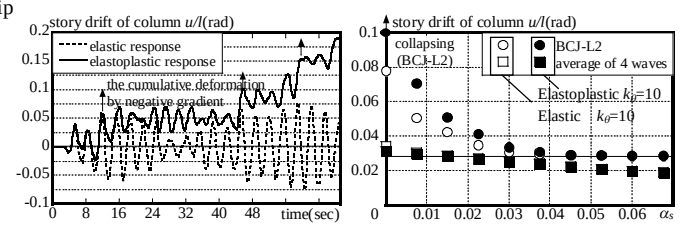

Figure 21 The process of collapsing

Figure 22 Relationship between damper and story drift

horizontal deformations increases drastically, and reaches to the collapse. Figure 22 shows the plots of response displacement with alternation of α_s to V_{max}=75.0cm/sec input. If α_s is larger than 0.045, the unstable domain can be avoided. This condition is satisfied when the maximum response displacement is less than ${}_u u_p$ at equation (13).

6. SHAKING TABLE TEST USING MOCK-UP MODELS

To confirm the validity of the analytical results, the shaking table tests using mock-up model are carried out. Figure 23 shows the set-up configuration and the measurement arrangement, and Figure 24 shows the layouts of strain gages. The scale factor of the test is set as λ=1/20 (Table 2). The mock-up model consists of three extension floors and five existing floors. Flat roller bearings are placed in the space between the floors, and steel plates modeling shear stiffness are placed in each floor. The extension part is supported by four steel columns of φ21.7×4.0. The weight of each floor is 144kg in an existing floor (57.6ton in full scale size), 349kg in an extension floor (139.6ton in full scale size). The natural period of an extension part alone is almost 0.525sec (2.35sec in full scale size). The plates of the existing part can be changed, modeling the RC-building, Steel-building, et al. 2 types of dampers are modeled with an elasto-plastic damper and a viscous damper as shown in photo 1 and 2. The scheme of shaking test is three types, as sweep vibration tests, sine waves tests, and seismic shaking tests of V_{max}=25cm/sec and 50cm/sec.

6.1 Results with Elasto-plastic Dampers

The shaking test is performed using the model with elasto-plastic dampers. First, the sweep vibration tests containing the frequency range of 0.1to 15Hz by 0.1Hz are performed to confirm the natural frequency in each model, and the natural frequencies are showed at Figure 26. Those of extension parts come closer to those of extension parts only as the damper decreases. In addition, the difference of the stiffness of an existing part causes the change of natural frequency of an extension part at the same α_s. Secondly, the test of the sine wave of the same frequency as each model is performed to confirm damping values. Equivalent damping constant h is derived from each amplitude ratio d and the equation (16). Figure 27 shows the relationship between h and d. The result shows that the damping constant is affected by the stiffness of an existing part and the amount of the damper, however, not by amplitude. If the stiffness of an existing part is small and the amount of dampers is large, the damping performance goes down. Thirdly, the seismic shaking test is performed. Figure 28 and 29 show the reduction ratio of displacement and acceleration of an extension part compared with the time history response analysis results. In the response analysis, the restoring force characteristics are determined by the simple

$$h = \frac{\ln d}{2\pi} \Big/ \sqrt{1+\left(\frac{\ln d}{2\pi}\right)^2} \quad \cdots (16)$$

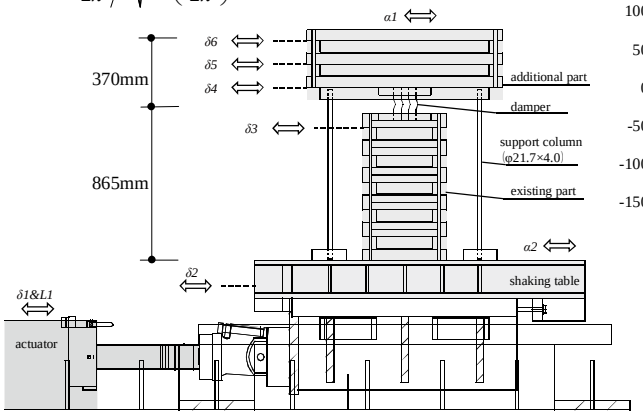

Figure 23 The set-up diagram and the measurement

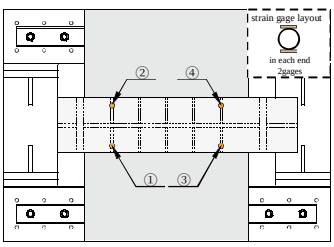

Figure 24 The points of strain gages

Table 2 Similarity rule

		full scale	descale mockup
scale factor	l	$l\lambda$	
mass	m	$m\lambda^2$	
acceleration	a	a	
time	t	$t\lambda^{0.5}$	
natural period	T	$T\lambda^{0.5}$	
stiffness	k	$k\lambda$	
displacement	δ	$\delta\lambda$	
damping constant	C	$C\lambda^{1.5}$	
velocity	v	$v\lambda^{0.5}$	

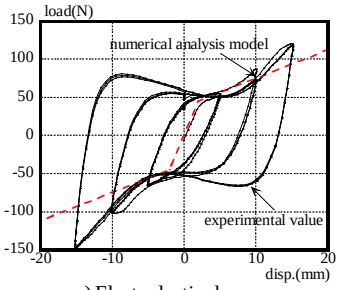

a) Elastoplastic damper
load-displacement relationship

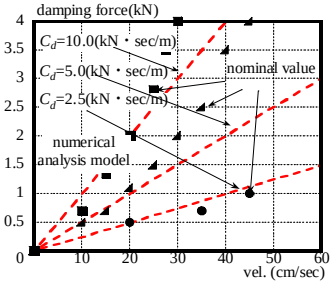

b) Viscous damper
damping force-velocity relationship

Figure 25 Damping characteristics

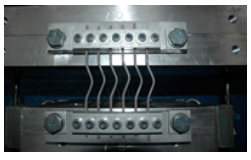

Photo 1 Elastoplastic damper



Photo2 Viscous damper

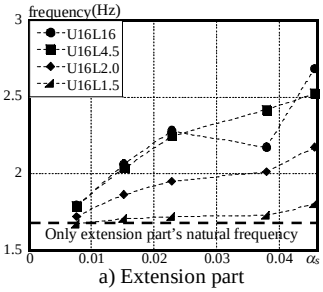

a) Extension part

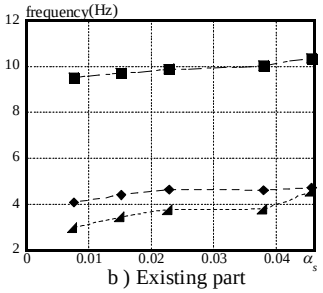

b) Existing part

Figure 26 Relationship between frequency and damping

method of section 5. U16L16-model is equivalent to RC-existing building, U16L4.5 is equivalent to Steel-existing building. In both case, the shaking test results are almost same as the analysis results. It is observed that the reduction effect becomes larger for larger response displacement and α_s becomes larger, and the acceleration response becomes larger when α_s becomes too large. In the case of impulsive wave like JMA-Kobe-NS input, acceleration response does not reduces as the other waves.

6.2 In the Case of Viscous Dampers Attached

The shaking table test is performed with viscous dampers. First, the sweep vibration tests containing the frequency range of 0.1to 15Hz by 0.1Hz is performed to confirm the natural frequency in each model, and the natural frequencies are showed at Figure 30. Despite the amount of the damper is larger or smaller, each model has the constant value about natural frequency. This result means that the viscous damper has the certain stiffness regardless the amounts of dampers. Secondly, the test of the sine wave with the same frequency as each model is performed to confirm damping values. Figure 31 shows the comparison of nominal value with experimental value. Even when the nominal damping becomes larger than 0.4, the actual performance increases. In comparison with the damping of the extension part and the damping of the viscous damper, if the viscous damper's performance become larger, the damping of the extension part does not become larger because the existing part absorbs the seismic energy as shown in Figure 32. Finally, the seismic shaking table tests are performed. Figure 33 and 34 show the reduction ratio of displacement and acceleration of an extension part compared with the time-history response analysis results. In both case, the shaking table test results are in almost same ranges as the analysis results as same as elasto-plastic damper models. It is indicated that the reduction ratio of response displacement becomes larger when constant value h_{eq} becomes larger. In addition, in the case of impulsive wave as JMA-Kobe-NS, acceleration response does not decrease drastically.

6.3 Collapse Mechanism with Excessive Inputs

In this section, the collapse conditions of the extension part are confirmed. The scheme of the shaking table test includes 2 cycles of BCJ-L2 (50cm/sec), 3cycles of El-Centro-NS (50cm/sec), and multi-cycles of sine waves by increasing the level until the collapse of the extension part. Figure 35-a) to c) show the typical load deformation relationships. These results mean that the yield of the column has progressed gradually, the plastic hinge is firstly formed at the upper end of the column, and secondly the hinge is formed at the lower end of the column subsequently. *P-δ* effect causes the negative gradient about the load deformation relationships, and the system collapses as photo 3 finally. The restoring force characteristics are made by overlaying these hysteresis curves. Figure 35-d) shows the comparison of the test's result with the analysis result. The numerical analysis model includes the complex nonlinearity indicated in section 5. Both are almost same, and it is confirmed that the analysis model and proposed equation has some amount of validity. The stability ratio which is proposed by Yamazaki and Endo is calculated and estimated as 0.13, 0.19 to BCJ-L2 and El-Centro-NS. Although 1.0 ratio means the system being all collapse, it means that estimated structure is stable enough for the earthquake of V_{max}=50cm/sec.

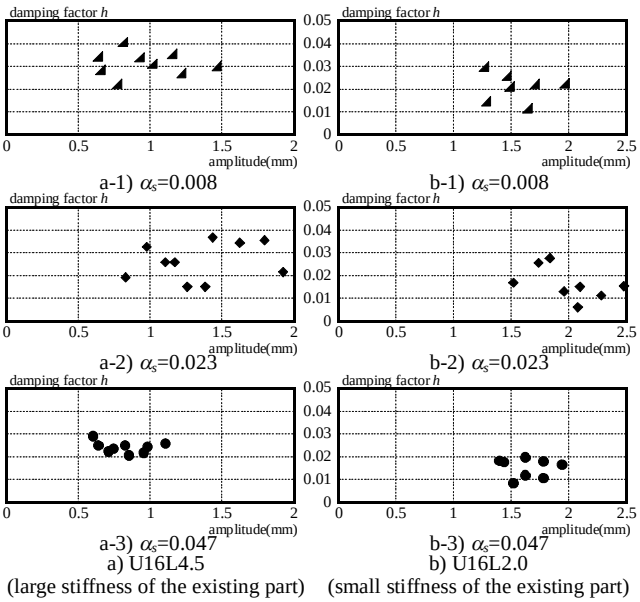

a) U16L4.5 (large stiffness of the existing part)
b) U16L2.0 (small stiffness of the existing part)

Figure 27 Relationship between amplitude and damping factor

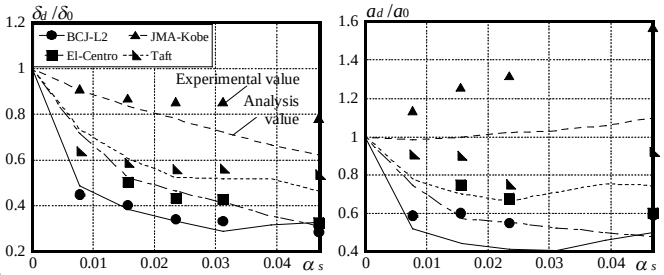

a) Reduction ratio of disp. response
b) Reduction ratio of acc. response

Figure 28 Relationship between reduction ratio and the amount of damper (case: U16L16)

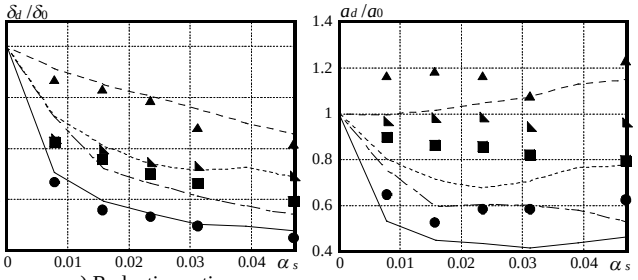

a) Reduction ratio of disp. response
b) Reduction ratio of acc. response

Figure 29 Relationship between reduction ratio and the amount of damper (case: U16L4.5)

7. CONCLUSIONS

The following conclusions are derived in this study.

1) The effect of the geometrical stiffness accompanied by the horizontal deformation to the restoring force relationships is very small when the story drift is less than 1/5 (rad). The nonlinearity effect of the rotational stiffness to the restoring force relationships can be neglected when the shear force of the column in the compression side is in the positive range. As a whole, in the range of that the story drift is less than 1/5 (rad), it is enable to evaluate the restoring force relationships by the theoretical linear value. On the other hand, the effect of rotational stiffness at the column base is larger in the range of the nondimensional rotational stiffness k_θ is less than 10.
2) In the above range, the simple method of calculating the restoring force relationships is proposed.

Subsequently, the following conclusions are derived from results of the shaking table test with the mockup model.

3) When the elasto-plastic dampers are attached to the step-over isolated structure, the natural period decreases and both of response displacement and acceleration decrease as the amount of the dampers becomes larger. In the case that the viscous dampers are attached to this structure, despite the damping constant h_{eq} increases, the damping constant of the total structure does not increase than 10%. For the seismic response, the results with viscous dampers are as same as that of elasto-plastic dampers attached. The seismic test's results are almost same to the numerical analysis results.
4) As the results of excessive inputs to the extension part without dampers, the load deformation relationships until collapse fits well to the proposed hysteresis and validity of the analysis model and proposed equation has been confirmed.

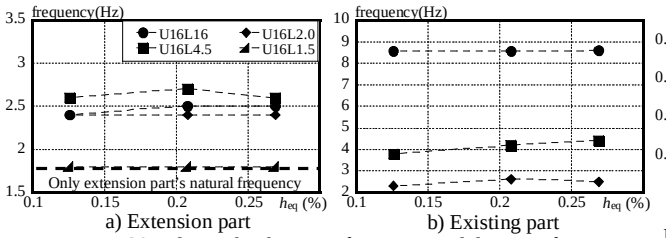

a) Extension part b) Existing part

Figure 30 Relationship between frequency and damping factor

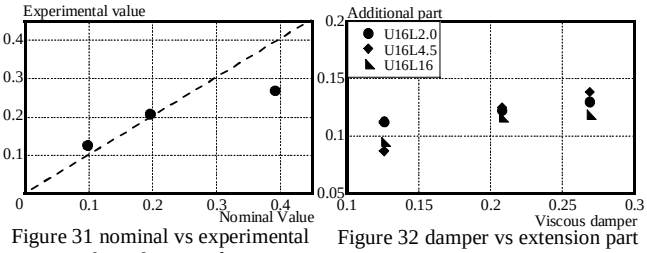

Figure 31 nominal vs experimental about damping factor

Figure 32 damper vs extension part about damping factor

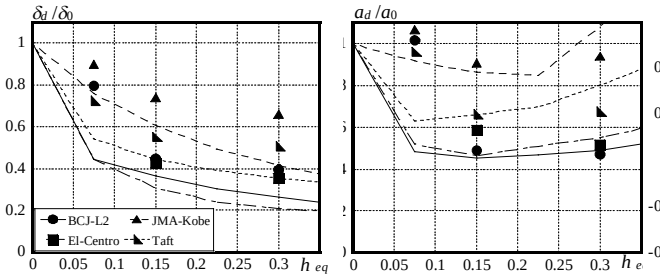

a)Reduction ratio of disp. response b)Reduction ratio of acc. response

Figure 33 Relationship between reduction ratio and the amount of damper (case: U16L16)

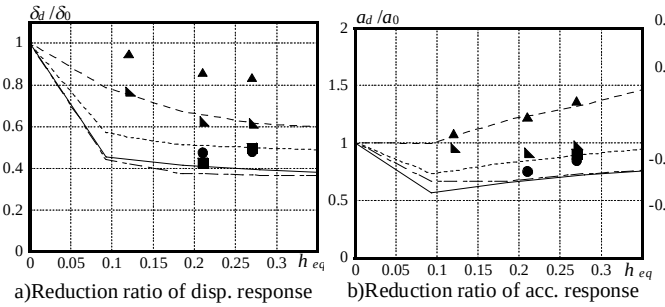

a)Reduction ratio of disp. response b)Reduction ratio of acc. response

Figure 34 Relationship between reduction ratio and the amount of damper (case: U16L4.5)

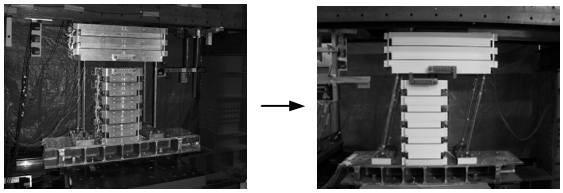

Photo 3 Backward and forward state of the mock-up model

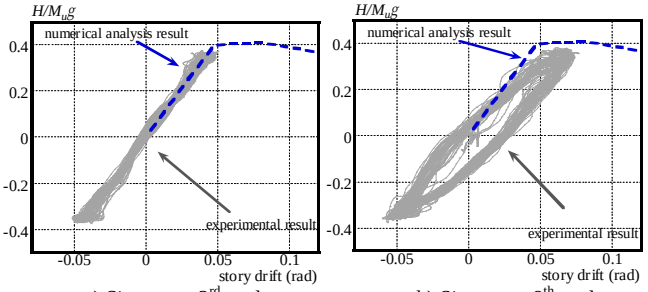

a) Sine wave 3rd cycle b) Sine wave 8th cycle

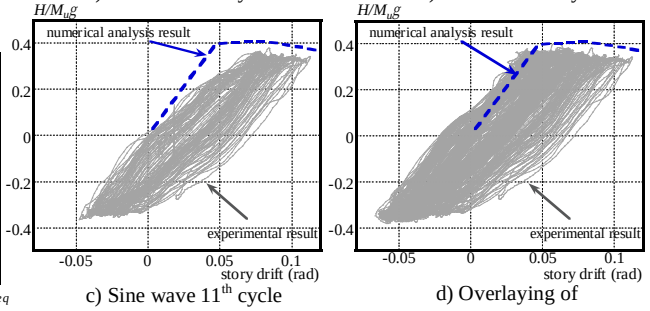

c) Sine wave 11th cycle d) Overlaying of the hysteresis curves

Figure 35 The load deformation relationship of the column

References:

Takeuchi, T., Ohshima, Y., Nakata, Y. and Saeki, E. (2007), "Response Characteristics of Step-Over Isolated Structure," AIJ Journal of Technology and Design, **13**(25), 153-155.

Yamazaki, S,. Endo, K,. (2000), "Stability Ratio and Dynamic P-Δ Effect in Inelastic Earthquake Response," Journal of Structural and Construction Engineering, **527**, 71-78.

JOINT CONFERENCE PROCEEDINGS
7th International Conference on Urban Earthquake Engineering (7CUEE) &
5th International Conference on Earthquake Engineering (5ICEE)
March 3-5, 2010, Tokyo Institute of Technology, Tokyo, Japan

OPTIMUM DESIGN OF PARTICLE DAMPERS UNDER RANDOM EXCITATION

Zheng Lu[1], Xilin Lu[1], and Sami F. Masri[2]

1) Ph.D student, State Key Laboratory of Disaster Reduction in Civil Engineering, Tongji University, Shanghai ,China
2) Professor, State Key Laboratory of Disaster Reduction in Civil Engineering, Tongji University, Shanghai ,China
3) Professor, Viterbi School of Engineering, University of Southern California, Los Angeles, California, USA
luzheng111@gmail.com, lxlst@tongji.edu.cn, masri@usc.edu

Abstract: This paper presents an investigation of the performance of particle dampers under random excitation, focusing on their optimum strategies. Correlation functions, the amount of dissipated energy due to impact and friction, and the concept of Effective Momentum Exchange are shown to be suitable means to interpret the physics involved in the behavior of particle dampers. Using three different types of random excitation, the optimum operating regions are all determined, within which particles move in a plug flow pattern and correlation functions decay fast, while the dissipated energy and the Effective Momentum Exchange are large compared with inefficient operating conditions.

1. INTRODUCTION

Particle dampers, which evolved from the single-particle impact damper (Masri and Caughey, 1966), are containers or structural voids partially filled with particles (e.g., ball bearings, tungsten powders, etc.). With the advantages of ruggedness, reliability, and insensitivity to extreme temperatures, these simple and efficient passive devices are used to attenuate the vibrations of lightly damped structures, especially in harsh environments where traditional approaches fail. The main damping mechanics are momentum exchange and energy dissipation during the impact between the particles and the primary system.

There is a long history of research in the modeling, analysis, simulation, design and deployment of this class of vibration control devices. Masri (1967, 1969, 1970) gave a closed solution for the steady-state motion of a multi-unit impact damper attached to a periodically excited primary system. Bapat and Sankar (1985) studied the effect of Coulomb friction on the performance of identical multi-unit impact damper. Popplewell and Semercigil (1989) compared the performance of a resilient bean bag (a plastic bag filled with lead shots) and a conventional rigid impact damper under sinusoidal excitation. Bryce et al. (2000) discussed the effectiveness and predictability of particle dampers, and also developed a complete design methodology which had been validated in laboratory studies. Michael et al. (2004) developed a pair of two-dimensional master design curves with unitless axes which are comprised of combinations of design parameters. Bai et al. (2009) proposed and investigated the behavior of a piston-based particle damper.

Despite all these efforts, due to the system's high nonlinearity and the complexity involving a large number of parameters, the understanding of the particle damping mechanism has still not been well developed. The studies listed above have all focused on one-degree-of-freedom system with a particle damper. The performance of particle dampers with a two-degree-of-freedom system, which involves correlations in two directions, is seldom investigated. Moreover, the behavior of particle dampers in their optimum operating regions is not thoroughly studied, either. Consequently, there is a need for a comprehensive study of the performance of particle dampers when operating with a multi-degree-of-freedom system that is subjected to multi-axis dynamic loads.

2. PERFORMANCE ANALYSIS

In this section, the performance of a particle damper attached to a two-degree-of-freedom system under different stationary random excitation is studied. In these simulations, the primary system natural frequency is 11.4 Hz, and the mass is 0.573 kg, the stiffness in the x and y directions are the same. The random excitation is generated based on a normal (Gaussian) distribution with a bandwidth from zero to five times the primary system's natural frequency. The initial positions of the particles are assigned randomly so as to account for realistic situations where there is always a certain level of uncertainty in even nominally identical physical parameters.

The collisions within particle dampers can be separated into three types according to the relative velocity of the particle and the primary system at the instant of impact: (1) Type 1: The absolute velocities of both particle and the primary system are opposite to each other at the instant immediately before contact, which is the face-to-face impact; (2) Type 2: Although the particle and the primary system's

absolute velocities have the same direction, the relative velocity of the particle is opposite prior to contact, which is the case for the primary system catching up with the particle; and (3) Type 3: The particle and system's absolute velocities and the particle's relative velocity have the same direction just before contact, which is the case for the particle catching up with the primary system.

Collisions of Type 1 and Type 2 can reduce the response of the primary system, because a collision force which is in the direction opposite to the velocity of the primary system tends to prevent its moving. This kind of momentum exchange can be defined as "beneficial momentum exchange" and this kind of impact can be called "beneficial impact". On the other hand, a collision of Type 3 is inclined to accelerate the primary system, thus such type of momentum exchange is harmful to the response reduction of the primary system. Consequently, it is defined as "adverse momentum exchange" and the impact is defined as "adverse impact". A concept of Effective Momentum Exchange (EME) is proposed herein to conveniently describe the combined effect of a beneficial momentum exchange minus an adverse momentum exchange.

2.1 Stationary Random Excitation in the *x* Direction Only

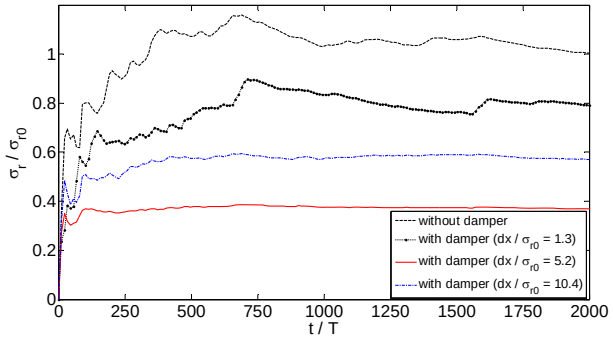

Figure 1 R.M.S response time history of the displacement magnitude $\sqrt{x^2 + y^2}$ for the primary system with μ = 0.108, e = 0.75, ζ = 0.004, μ_s = 0.5, dy/σ_{r0} = 3.9, d/σ_{r0} = 0.8 and 16 particles, under a stationary random excitation in the *x* direction

This test uses a stationary random excitation in the *x* direction. Figure 1 shows a typical root-mean-square response time history for different container sizes. After an operating time span of 1000 times the primary system's natural period, the system reaches a stationary response, thus this time duration is used for the following simulations. Choosing a suitable container size, the particle damper can achieve optimum response reductions. As expected, the main response is observed along the direction of the excitation, and negligible movement exists along the orthogonal direction. The reason for this behavior is that particles are excited mainly in the *x* direction, although the oblique collisions may cause particles to move in the *y* direction, they move randomly along the *y* direction and counteract the effects of each other. The effective contacts of particles and walls in the *y* direction are at a very low level, consequently; so is the Effective Momentum Exchange.

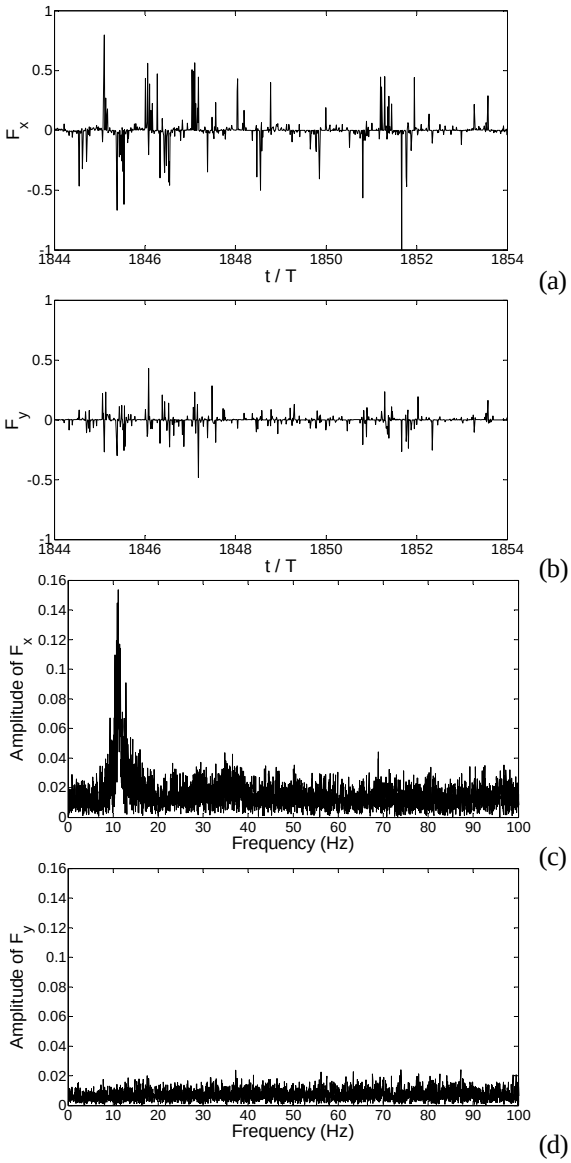

Figure 2 Time history (a-b) and Fast Fourier Transforms (c-d) of the contact force between the primary system and particle container: (a, c) Force *Fx* in the *x* direction; (b, d) Force *Fy* in the *y* direction. System parameters are: μ = 0.108, e = 0.75, ζ = 0.004, μ_s = 0.5, dy/σ_{r0} = 3.9, dx/σ_{r0} =5.2, d/σ_{r0} = 0.8 and 16 particles, under a stationary random excitation in the *x* direction

As to the contact forces *Fx* and *Fy*, they exhibit different behaviors. Figure 2(a-b) shows a sample time history for both contact forces, which is made dimensionless by dividing the maximum force during this sample duration. In Figure 2(a), the negative forces are on the left hand side (LHS) edge of the container, while the positive forces are on the right hand side (RHS) edge; similarly, in Figure 2(b), the negative ones are on the front edge and the positive ones are on the back. One can see that in Figure 2(a), *Fx* is larger than *Fy* in Figure 2(b), and it occurs at a dominant frequency. Figure 2(c) shows that this *Fx* frequency is the same as that

of the primary system. While *Fy* is smaller and randomly excited, as shown more clearly in Figure 2(d) that the energy of *Fy* is generally low in all bandwidth of frequencies. Figure 2(c-d) shows the Fast Fourier Transforms of *Fx* and *Fy*.

2.2 Correlated Stationary Random Excitations in the *x* and *y* Directions

This test uses the same stationary random excitation in both the *x* and *y* directions, which is equivalent to the case situation in which the excitation is applied to the primary system in a diagonal direction. Figure 3(a) shows that the primary system without a particle damper, moves back and forth along the diagonal direction. Due to the disturbances induced by the collisions (both between particles and the container), the trajectory of the primary system with a particle damper departs from the diagonal direction a slight amount, but still remains mainly along the diagonal line. This is mostly because of the correlated excitation. However, the displacement is reduced a lot in this case, which indicates that particle dampers can be operated in a more robust and efficient way compared to a tuned mass damper (TMD), which can only reduce the response along the installation axis of the TMD.

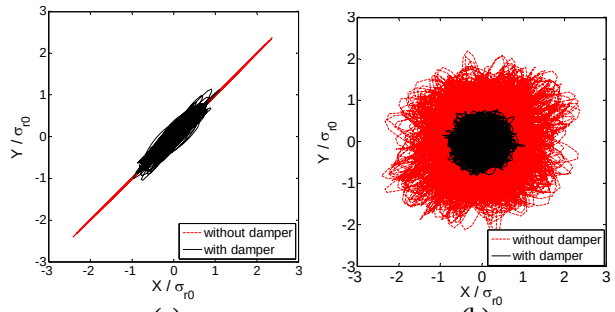

Figure 3 Trajectory of the primary system with μ = 0.108, e = 0.75, ζ = 0.004, μ_s = 0.5, dy/σ_{r0} = 3.8, dx/σ_{r0} =5.1, d/σ_{r0} = 0.8 and 16 particles, under two simultaneous (a) *correlated* and (b) *uncorrelated* random excitations in the *x* and *y* directions

2.3 Uncorrelated Stationary Random Excitations in the *x* and *y* Directions

This test uses two uncorrelated stationary random excitations based on the same probability distribution in both the *x* and *y* directions. Compared with Section 2.2, Figure 3(b) shows that the trajectories of the primary system are different due to the different excitation manner. Both trajectories are centered at the equilibrium position and move in a circular form. The orbit radius in the particle damper case is much smaller than the corresponding case without a particle damper.

Figure 4 shows a sample root-mean-square response of the primary system in different container sizes, which also displays a certain optimum operation. It can be seen that an operating time of about 1000 the primary system's natural periods is sufficient for the primary system to reach a stationary vibration.

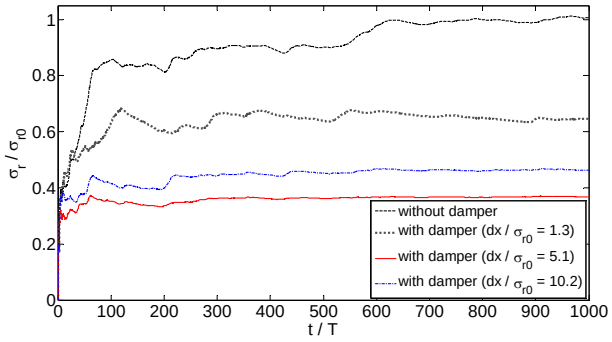

Figure 4 R.M.S response time history of the displacement magnitude $\sqrt{x^2 + y^2}$ for the primary system with μ = 0.108, e = 0.75, ζ = 0.004, μ_s = 0.5, dy/σ_{r0} = 3.8, d/σ_{r0} = 0.8 and 16 particles, under two simultaneous uncorrelated random excitations in the *x* and *y* directions

3. DISCUSSION

The nature of the movements of particles is different in the region of the optimum operating conditions compared with other inefficient operating conditions. Basically, plug flow motions of the particles, rather than random movements, can be observed in the optimum cases in all of the above mentioned three types of excitations. This is similar qualitative behavior to what occurs in a single-particle impact damper when operating with two-impacts-per-cycle (Masri, 1973). In plug flow mode, the particles tend to move together, hence cross correlation functions are used here to indicate the different behavior of the particle dampers.

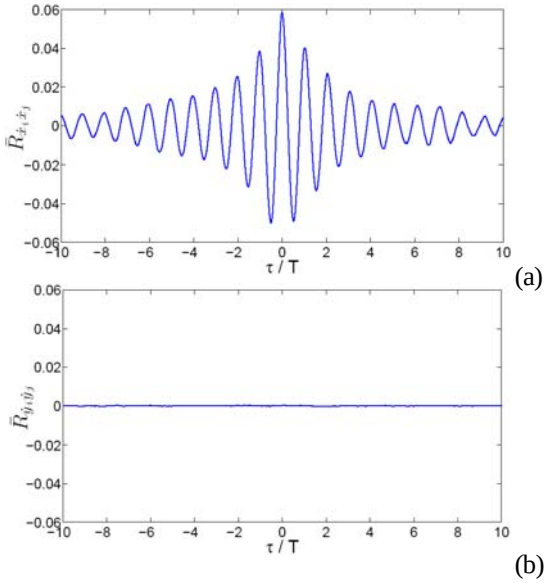

Figure 5 Normalized cross-correlations of velocities of two randomly picked particles in the optimum operating range: (a) in the *x* direction and (b) in the *y* direction. System parameters are: μ = 0.108, e = 0.75, ζ = 0.004, μ_s = 0.5, dy/σ_{r0} = 3.9, dx/σ_{r0} =5.2, d/σ_{r0} = 0.8 and 16 particles, under a stationary random excitation in the *x* direction

Figure 5 shows the normalized velocity cross

correlation in the x direction of two randomly picked particles under a stationary random excitation in the optimum operating range, which is discussed in Section 2.1. The normalized cross correlation ($\bar{R}_{\dot{x}_i\dot{x}_j}$) used here is defined as

$$\bar{R}_{\dot{x}_i\dot{x}_j}(\tau)=\frac{E[\dot{x}_i(t)\dot{x}_j(t-\tau)]}{E[\dot{x}_{np}(t)\dot{x}_{np}(t)]}=\frac{\frac{1}{T}\int_0^T \dot{x}_i(t)\dot{x}_j(t-\tau)dt}{\frac{1}{T}\int_0^T \dot{x}_{np}(t)\dot{x}_{np}(t)dt} \quad (1)$$

where τ is the time lag, T is the operating time, $\dot{x}_{np}$ is the velocity in the x direction of the primary system without a particle damper, $\dot{x}_i$ is the velocity in the x direction of a randomly picked particle i, and E is the mean-value operator. Figure 5 shows that $\bar{R}_{\dot{y}_i\dot{y}_j}$ is much smaller than $\bar{R}_{\dot{x}_i\dot{x}_j}$. This is so because particles are moving in a plug flow mode in the x direction, while moving randomly in the y direction.

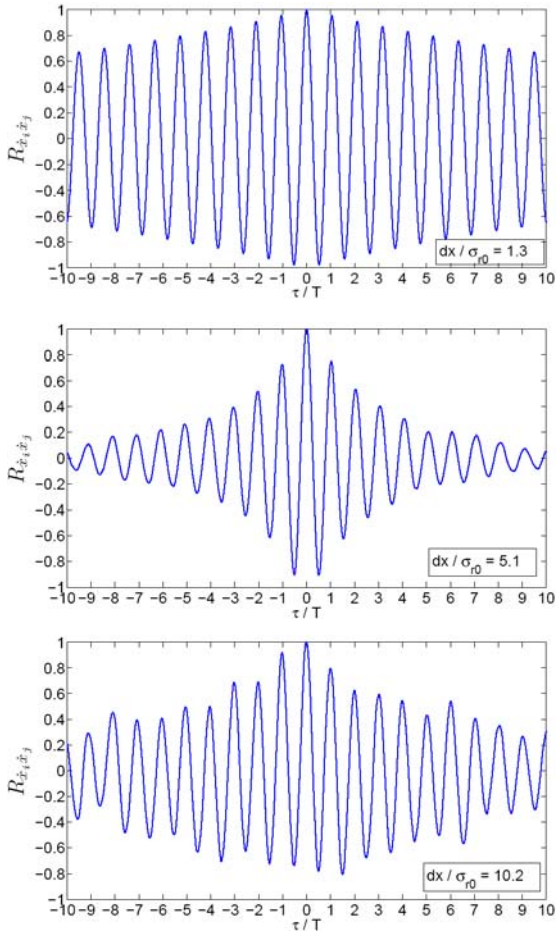

(a) (b) (c)

Figure 6 Normalized cross-correlations of velocities in the x direction of two randomly picked particles. (a) small container size, in the inefficient operating range; (b) medium container size, in the optimum operating range; and (c) large container size, in the inefficient operating range. System parameters are: μ = 0.108, e = 0.75, ζ = 0.004, μ_s = 0.5, dy/σ_{r0} = 3.8, d/σ_{r0} = 0.8 and 16 particles, under two simultaneous uncorrelated random excitations in the x and y directions

Corresponding to Figure 4, Figure 6 gives a general impression of how the normalized velocity cross correlations of two randomly picked particles behave under different operating conditions. The normalized cross correlation ($R_{\dot{x}_i\dot{x}_j}$) here is defined as

$$R_{\dot{x}_i\dot{x}_j}(\tau)=\frac{E[\dot{x}_i(t)\dot{x}_j(t-\tau)]}{E[\dot{x}_i(t)\dot{x}_j(t)]}=\frac{\frac{1}{T}\int_0^T \dot{x}_i(t)\dot{x}_j(t-\tau)dt}{\frac{1}{T}\int_0^T \dot{x}_i(t)\dot{x}_j(t)dt} \quad (2)$$

An interesting observation is that the velocity correlation function decays much faster in the optimum operating range than that in the inefficient operating range, which is shown more clearly in Figure 7. It can be seen that the exponential decay ratio is ~ 4.5% for a medium container size in the optimum range, compared to ~ 2.2% for a relatively large container size and ~ 0.7% for a small container size in the inefficient operating range.

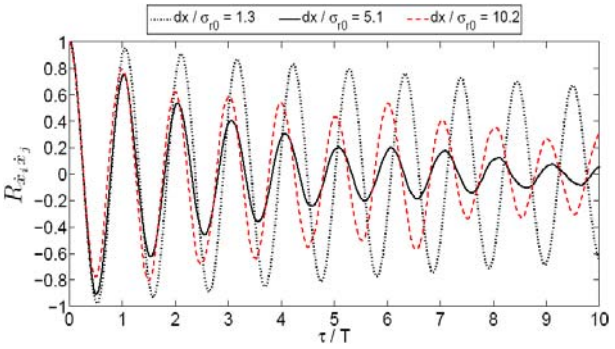

Figure 7 Normalized cross-correlations of velocities in the x direction of two randomly picked particles. dx/σ_{r0} = 1.3 corresponds to a small container size, in the inefficient operating range; dx/σ_{r0} = 5.1 corresponds to a medium container size, in the optimum operating range; and dx/σ_{r0} = 10.2 corresponds to a large container size, in the inefficient operating range. System parameters are: μ = 0.108, e = 0.75, ζ = 0.004, μ_s = 0.5, dy/σ_{r0} = 3.8, d/σ_{r0} = 0.8 and 16 particles, under two simultaneous uncorrelated random excitations in the x and y directions

Consequently, it is found that the cross correlation of velocity of random particles is a good "global" tool to indicate the performance of the particle damper.

Besides the cross correlation functions, the auto correlations of the primary system displacement with or without a particle damper, are also informative. As shown in Figure 8, the former decays quickly in an exponential form, which indicates that the particle damper increases the system damping a lot; while the latter decays in a slower exponential manner, only due to the inherent system damping.

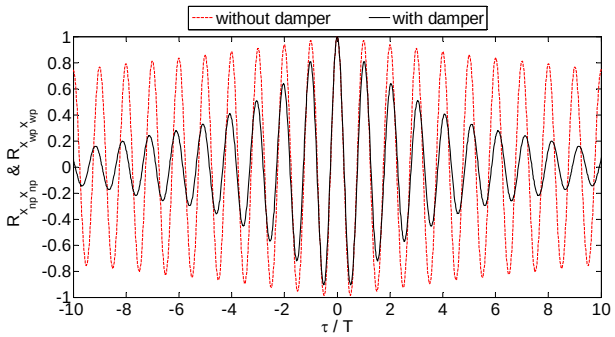

Figure 8 Normalized auto-correlations of the primary system displacement in the x direction, with μ = 0.108, e = 0.75, ζ = 0.004, μ_s = 0.5, dy/σ_{r0} = 3.8, dx/σ_{r0} =5.1, d/σ_{r0} = 0.8 and 16 particles, under two simultaneous uncorrelated random excitations in the x and y directions

The correlation functions are not the only useful interpreters for optimum behavior of particle dampers; other measures such as the amount of energy dissipation due to impact and friction, and the Effective Momentum Exchange are also useful tools.

Figure 9(a) gives a general impression of how a particle damper is working within a range of container sizes, including lengths and widths (as the height does not influence the behavior very much, it is not included in this study). An optimum region, within which the primary system can get more than 60% reduction of the r.m.s response, is clearly shown in the contour plot Figure 9(b). In Figure 9(c), the dissipated energy is plotted in dimensionless form by dividing by the energy of the excitation force (*Ee*). One can find a high ratio of dissipation in the optimum region. Similarly, a normalized version of the Effective Momentum Exchange, which is divided by the momentum exchange of the excitation force *(Me*), is plotted in Figure 9(d), and results a relatively high value in the optimum range, too. The reasons for this behavior is that in small container sizes, the particles are piled together in many layers, which minimizes the motion of the lower layers, and only created a vigorous motion in the top-most layers. In large container sizes, the particles need to spend a long time transiting from one wall to the opposite wall, which leads to fewer impacts with the primary system; hence a trade-off exists, which is the reason why an optimum performance of the particle damper can be obtained.

The above results clearly indicate that particle dampers can yield a good performance under different types of stationary random excitations, and this robustness is a significant advantage, which can be used in practical applications. Thus, the correlation functions, the dissipated energy and the Effective Momentum Exchange are suitable means to characterize the physics involved in particle damper operations.

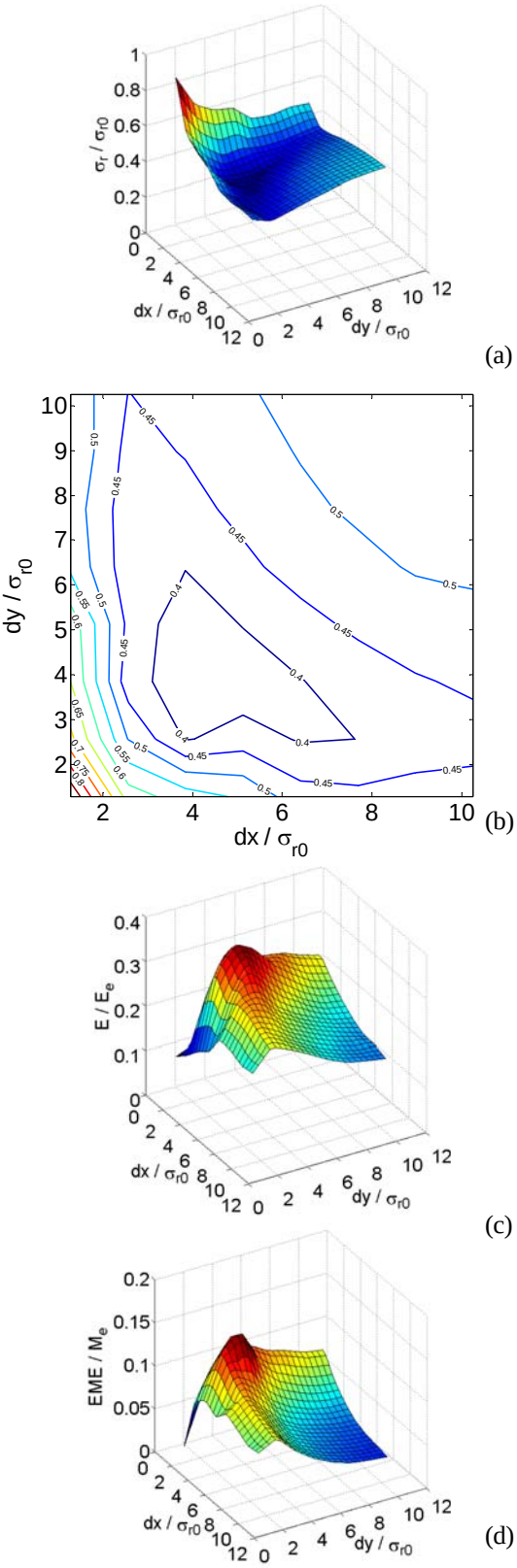

Figure 9 (a) R.M.S displacement magnitude response levels; (b) Contour plot of σ_r/σ_{r0} ; (c) Dissipated energy; (d) Effective Momentum Exchange for the primary system with μ = 0.108, e = 0.75, ζ = 0.004, μ_s = 0.5, d/σ_{r0} = 0.8 and 16 particles, under two simultaneous uncorrelated random excitations in the x and y directions

4. SUMMARY AND CONCLUSION

Even though several previous studies of particle dampers have been reported in the literature, currently there are no satisfactory guidelines for determining the optimum design strategy for maximizing the performance (i.e., response attenuation capability) of this class of highly nonlinear dampers when attached to a primary system subjected to broad-band random excitations.

This study simulates the highly nonlinear motion of a primary system that is subjected to multi-component random excitations of arbitrary degree of correlation. The primary system can be thought of as a reduced order single-degree-of-freedom system that is capable of motion in two orthogonal directions (x, y) aligned with the directions of assumed excitations (e.g., a single-story building under multi-axis earthquake base motion). The particle damper may have an arbitrary number of particles ranging from a single one to virtually any number of interacting particles that move in a three-dimensional trajectory within the confines of their container. Even though the primary system is assumed linear and its two components of motion are independent of each other if there is no particle damper attached, due to the multi-component motion of the colliding particles, the combined 2DOF plus damper system's motion in the x and y directions do interact and introduce qualitatively complex response.

In order to analyze and interpret the very complicated behavior of inter-particle as well as particle-container interactions, several "global" measures are presented to obtain some useful indices that can provide an overall indication of the performance of the damper, particularly as these measures relate to the optimum primary system response attenuation. It is found that the following quantities provide good "illumination" of the underlying complex physical phenomena occurring among the system components: (1) the Effective Momentum Exchange, (2) the amount of internal energy dissipation due to impact and friction, and (3) the cross-correlation of the velocity of random particles.

Acknowledgements:

Financial support from the National Natural Science Foundation of China (NSFC) through grant 90815029 and NSFC-JST (Japan Agency of Science and Technology) joint research project are highly appreciated. Financial support from the China Scholarship Council for the first author's work at the University of Southern California as a visiting scholar is gratefully acknowledged.

References:

Masri, S.F. and Caughey, T.K. (1966), "On the Stability of the Impact Damper," *Journal of Applied Mechanics*, **33**(3), 586-592

Masri, S.F. (1967), "Effectiveness of Two-Particle Impact Dampers," *Journal of the Acoustical Society of America*, **41**(6),1553-1554

Masri, S.F. (1969), "Analytical and Experimental Studies of Multiple-Unit Impact Dampers," *Journal of the Acoustical Society of America*, **45**(5), 1111-1117

Masri, S.F. (1970), "General Motion of Impact Dampers," *Journal of the Acoustical Society of America*, **47**(1P2), 229-237

Bapat, C.N. and Sankar, S. (1985), "Multiunit Impact Damper - Reexamined," *Journal of Sound and Vibration*, **103**(4), 457-469

Popplewell N. and Semercigil, S.E. (1989), "Performance of the Bean Bag Impact Damper for a Sinusoidal External Force," *Journal of Sound and Vibration*, **133**(2), 193-223

Bryce, L.F., Eric, M.F., and Steven, E.O. (2000), "Effectiveness and Predictability of Particle Damping," *Smart Structures and Materials 2000: Damping and Isolation*, **3989**(1), 356-367

Michael, Y.Y., George, A.L., Stephen, A.H., and Gary, H.K. (2004), "Development of a Design Curve for Particle Impact Dampers," *Smart Structures and Materials 2004: Damping and Isolation*, **5386**, 450-465

Bai, X.M., Shah, B., Keer, L.M., Wang, Q.J., and Snurr, R.Q. (2009), "Particle Dynamics Simulations of a Piston-Based Particle Damper," *Powder Technology*, **189**(1), 115-125

Masri, S.F. (1973), "Steady-State Response of a Multidegree System with an Impact Damper," *Journal of Applied Mechanics – Transaction of the ASME*, **40**(1), 127-132

JOINT CONFERENCE PROCEEDINGS
7th International Conference on Urban Earthquake Engineering (7CUEE) &
5th International Conference on Earthquake Engineering (5ICEE)
March 3-5, 2010, Tokyo Institute of Technology, Tokyo, Japan

MEASUREMENT OF PERFORMANCE AND ESTIMATION OF SCALABILITY FOR ENHANCED IES WITH HIGH PERFORMANCE COMPUTING TECHNIQUES

Gholamreza Sobhaninejad[1], Muneo Hori[2], Ichimura Tsuyoshi[3], Maddegedara L.L. Wijerathne[4]

1) Ph.D. Student, Dept. of Civil Eng., University of Tokyo, Japan
2) Professor, Earthquake Research Institute, University of Tokyo, Japan
3) Ph.D., Earthquake Research Institute, University of Tokyo, Japan
4) Ph.D., cSUR. The Global Center of Excellence, Dept. of Civil Eng., University of Tokyo, Japan
sobhani@eri.utokyo.ac.jp, hori@eri.utokyo.ac.jp,ichimura@eri.utokyo.ac.jp,lalith@eri.utokyo.ac.jp

Abstract: Integrated earthquake simulation (IES) is a seamless simulation of the three earthquake processes, namely, the earthquake hazard process, the earthquake disaster process, and the anti-disaster action process. High performance computing is essential if IES or particularly, the simulation of the earthquake disaster process is applied to an urban area in which 10^6 structures are located. IES is enhanced with parallel computation, and its performance is examined, so that virtual earthquake disaster simulation will be made for a model of an actual city by inputting observed strong ground motion. It is shown that parallel IES has good scalability even when advanced nonlinear seismic structure analysis is used.

1. INTRODUCTION

While basic physical characteristics of the earthquake hazard have not changed, earthquake disaster it evolves itself as society changes. In Japan, for instance, the earthquake disaster impacts on domestic and global economy activities will be tremendous if an inter-plate earthquake hits large cities. The shortage of the work force in the construction industry might cause difficulties in repairing damaged assets. To improve preparation, the first step will be to develop a hazard map of next generation that is able to show such consequences of the earthquake.

The authors have been developing Integrated Earthquake Simulation (IES) as a candidate of a simulation based prediction system for earthquake hazard and disaster Hori (2006), Nallathamby et al. (2007), Ichimura et al. (2004). This simulation is a seamless simulation of the following three processes: 1) the earthquake hazard process in which earthquake waves propagate in the crust; 2) the earthquake disaster process in which structures are shaken by strong ground motion; and 3) the anti-disaster action process, which includes urgent evacuation or recovery of social functions. Simulation of the third process is essential in predicting secondary or indirect disasters that includes impacts on economic activities. Suitable models are constructed from GIS (Geographic Information System) and other data resources, and the prediction is made by analyzing these models with numerical analysis methods.

High Performance Computation (HPC) is required for IES, when it is used for a larger urban area. In particular, HPC is essential for the earthquake disaster process that makes use of linear or nonlinear numerical analysis methods to compute responses of structures located in the area; strong ground motion is generated by earthquake waves which are synthesized in the simulation of the earthquake hazard process, and the seismic responses are computed for all structures by inputting the strong ground motion at a site of each structure.

In order to enhance IES with HPC, the authors are making the following two improvements: 1) layer-based design of IES architecture and the Common Modeling Data (CMD) class for interlayer communication; and 2) the Generic Distributable (GD) class and the MPI_Process_Manager class for sending data of complicated structure and massive amount through Message Passing Interface (MPI) library. The basic concepts of these improvements are not original; the authors regard making such improvements as a standard practice to enhance an existing system with HPC. However, since IES uses data of various kinds, complex structure, and huge amount, efforts have to make to materialize the concepts.

The contents of this paper are as follows. In Section 2, the first improvement that is related to the IES architecture is explained, and advantages of the current IES architecture are discussed. In Section 3, the second improvement for parallel computing is explained. Emphasized is the treatment of data of complex structure and huge amount through the MPI library. By using IES, which is enhanced with HPC, a simulation of the earthquake disaster process is made for a part of Tokyo in which around 10,000 structures are located. The simulation results are presented in Section 4, and scalability of this IES computation is discussed. Concluding remarks are made in Section 5. It should be noted that IES employs C++, and a class is used to designate an object which is used

in IES.

2. IMPROVEMENT OF IES DESIGN

2.1 Drawbacks of wrapper-based design

Originally, IES employs wrapper-based design to facilitate data conversion among the three processes of the IES simulation as well as the visualization of the simulation results, Nallathamby et al. (2007). A wrapper is constructed for each simulation program of seismic structure analysis, so that it is responsible for interpreting input and output data for the analysis method. More specifically, the wrapper reads data from GIS and other data resources, and converts and combines the data to an appropriate form so that they can be used as input data of the analysis method. A model to which the program is applied is thus constructed for each structure. The wrapper visualizes analysis results, reads and interprets the output of the program, and then makes suitable data for a visualization tool. A schematic view of the wrapper-based design is illustrated in Figure 1.

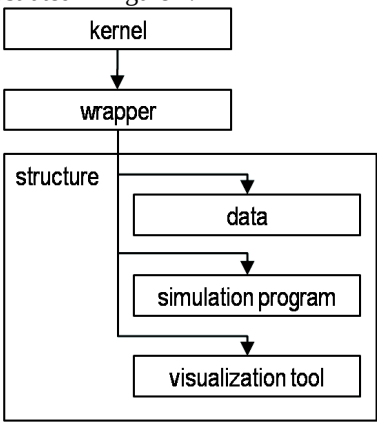

Figure 1 Schematic view of wrapper-based design of IES

As an interpreter, a wrapper has to convert data of one type to data of a different type. As the variation of GIS and data resources, simulation programs, and visualization tools increases, the wrappers must include new functions, and as a result, their program structure becomes complicated. This complication is essentially in contradiction with the KISS (Keep It Simple, Straightforward) software development principal, see Tanaka et al. (2008). Also the wrappers increase cohesion between computation processes; for instance, cohesion happens if several wrappers simultaneously use the same set of data resources.

2.2 Layer-based design of IES

To overcome the disadvantages of the wrapper-based design, current IES employs a layer-based design. The layer-based design is described in terms of one control room, which is called the kernel, and three layers, namely, data, simulation, and visualization layers. A schematic view of the layer-based design is shown in Figure 2. As the control room, the kernel manages initialization, connection, and execution of each layer. The data layer reads data from several GIS's or other data resources. The simulation layer encapsulates the three processes of the IES simulation. For the sake of simplicity, these three processes are regarded as an item in the simulation layer since after. The visualization layer visualizes results of the simulation layer.

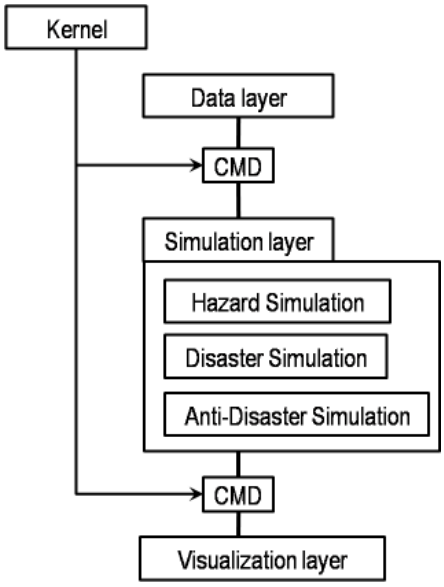

Figure 2 Schematic view of layer-based design of IES

The key feature of the layer-based design is the data conversion between the two neighboring layers. As it will be explained later in detail, the CMD class is introduced for this interlayer data conversion. That is, when a certain entity in one layer makes data and tries to send them to another entity in the neighboring layer, the data are first converted to the form of CMD, from which data of a specific form are made for the receiving entity. Although two data conversions are made in the receiving and sending CMD, the complexity of the data conversion is drastically reduced compared with the wrapper-based design; for instance, if the numbers of GIS, analysis methods and visualization tools are N, M, L, respectively, the number of the data conversion required for the layer-based design is N + M + L while that is required for the wrapper-based design is N*M *L.

It is certainly true that quantifying the improvement in the simulation coherency is difficult by employing the layer-based design instead of the wrapper-based design. However, naturally, less conjunction of the simulation coherency could happen for the layer-based design that limits the data conversion between the neighboring layers.

The interlayer data conversion of the IES is demonstrated in Figure 3. As for IES, the simulation cohesion between different layers is limited to the data conversion and data communication. Each layer changes CMD to appropriate data, which can be used as intra-layer data. For instance, after the simulation layer receives CMD from the data layer, it converts receiving data to a simulation layer entity, structural model, which is used by simulation program. After executing a simulation program, results are converted to CMD, and can be used by visualization layer as an input data.

It might be worth mentioning that the authors are aimed at developing Integrated Natural Disaster Simulation (INDS) as an extension of IES, see Sobhaninejad (2008). The

layer-based design is foundation to achieve flexible and expandable software architecture for INDS, which must integrate a larger number of data resources and numerical analysis methods than IES. As schematically shown in Figure 2, analysis methods for natural disasters such as flooding or volcano eruption can be interpreted as three phase of hazard, disaster, and anti-disaster simulations to be integrated in INDS.

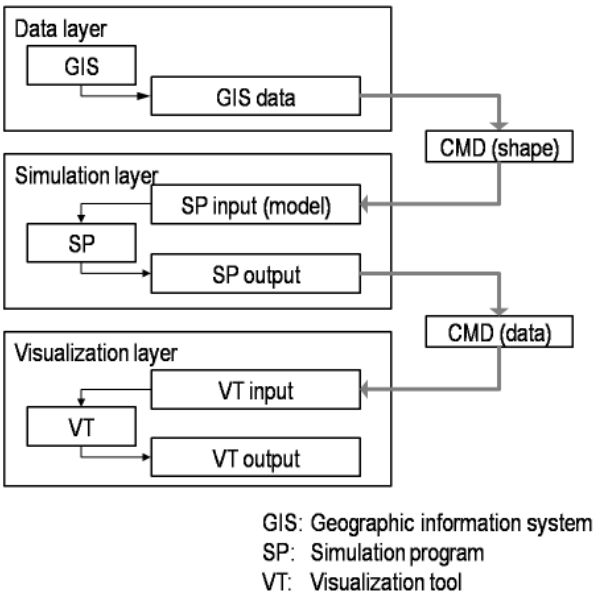

Figure 3 Diagram of inter-layer data conversion

2.3 Realization of data conversion by means of CMD

To achieve robust and efficient interlayer data communication, CMD class is developed; see Figure 3. Introducing CMD to IES would be a solution to solve the basic problem of describing resources that are stored in the data layer in such a general form as is to be understood by other layers. In the other layers, a suitable model or files for input/output data can be generated by using CMD.

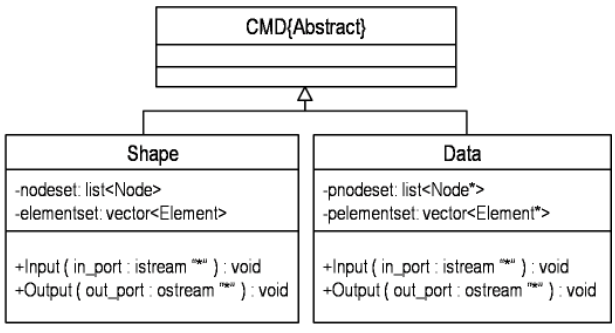

Figure 4 Component of CMD

The authors regard CMD class as a tool which is used for the inter-layer communication; this tool is more transparent than the data conversion made by a wrapper which must interpret data of other resources in the format or form that can be understood only by the corresponding analysis method.

At this moment, CMD class has two derived classes, i.e., Shape and Data classes; see Figure 4. The data structure of these classes is inspired from the input data of finite element analysis. Shape class carries geometric description of a structure, and hence it is aggregated with Node and Element classes; nodes and elements are commonly used by the finite element method. Data class is a container for the information that is generated before, during or after executing simulation of different layers. For instance, the information about the strong ground motion is generated after executing a simulation of the hazard simulation layer. This information is saved in an instantiated object from Data class, so that it is used as input data for a simulation of the disaster simulation layer. Data class associates with Shape class.

Shape and Data classes have a method of Input() or Output() which writes or reads their attributes with a coherent format in or from a standard C++ stream. The Input() or Output() methods establishes interlayer communication among different layers. Recall that IES carries out a simulation for numerous buildings located in an urban area and cannot keep all the information in the memory; once the object information is written to a file or a stream, the object is deleted from the memory.

3. GD class and MPI_Process_Manager class

Among HPC architectures, clusters have the most popularity since they are more economical and accessible. In parallel computation, data have to be transferred among cluster nodes by using the MPI library. For IES, however, the use of the standard MPI library is not feasible; see McCandless et al. (1996). This is because CMD class has complicated data structure. Data stored in CMD cannot be transferred by using the MPI library as well as its extensions in Grama et al. (2003). To overcome the inability for IES to use the MPI library, the authors develop GD (Generic Distributable) class and MPI_Process_Manager class. They are specially tuned so that the MPI library is indirectly used and the data transmission between cluster nodes has sufficient robustness.

3.1 GD class

GD class is an abstract class which offers two pure virtual methods, Serialization() and De_serialization() which; see Figure 5 for the class diagram of GD class. Serialization() interprets a class data structure as a primitive one, and De_serialization() regenerates the object from the interpreted data. These two methods actually overload Pack() and Unpack() functions of the MPI library, respectively.

As shown in Figure 5, CMD class is a subclass of GD class; specific consideration must be made to the complex structure of each concrete class of CMD. As shown in Figure 4, Shape and Data classes have two methods, Input() and Output(), which inputs and outputs their data for an input and output stream, respectively. Overridden methods from GD class in Shape and Data classes, Serialization() and

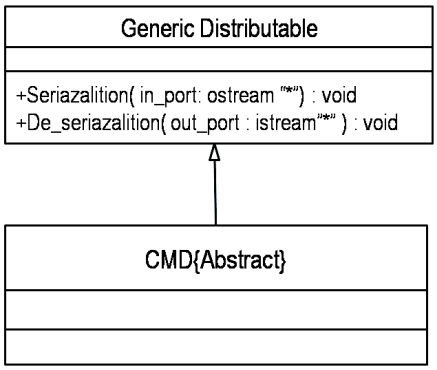

Figure 5 Schematic view of GD class

De_serialization(), use Input() and Output() respectively, and read and write complementary information, like length of a stream, from and to the stream. Serialization() and De_serialization() are achieved with GD class.

As shown in Figure 5, CMD class is a subclass of GD class; specific consideration must be made to the complex structure of each concrete class of CMD. As shown in Figure 4, Shape and Data classes have two methods, Input() and Output() , which inputs and outputs their data for an input and output stream, respectively. Overridden methods from GD class in Shape and Data classes, Serialization() and De_serialization(), use Input() and Output() respectively, and read and write complementary information, like length of a stream, from and to the stream. Serialization() and De_serialization() are achieved with GD class.

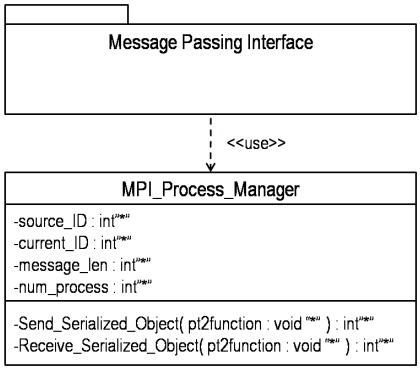

Figure 6 Schematic view of MPI_Process_Manager class

3.2 MPI_Process_Manager class

MPI_Process_Manager class is introduced to make easy use of the MPI library. As shown in Figure 6, attributes of this class are ID's for source and current cluster nodes, message length and process number. These attributes are used to initialize a cluster node and transfer data between cluster nodes.

MPI_Process_Manager class has two methods of Send_Serializable_Object() and Rceive_Serializable_Object(). These methods are made so that they play a role of a wrapper for Serialization() and De_serialization() of GD class. Access to Serialization() and De_serialization() is prepared through a function pointer, so that implementation of these two methods are encapsulated.

3.3 IES process hierarchy

The IES process hierarchy in the parallel environment is explained by using Figure 7. The data layer makes CMD (Shape) to send its data to the simulation layer, and this layer makes another CMD (Data) to deliver the analysis results to the visualization layer. Parallel computing enhancement is achieved by assigning a separate computational node to conduct simulation and visualization for each Shape. The data conversion via CMD corresponds to inter-node communication which is realized by inheriting GD class to CMD class and applying MPI_Process_Manager class for cluster nodes.

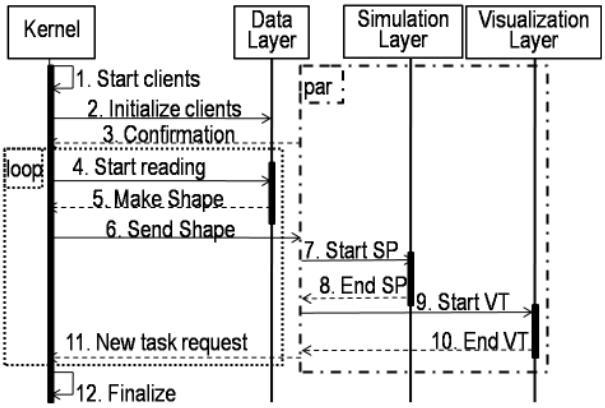

Figure 7 Sequence of IES parallel computation process

Regarding the nature of IES simulation, this system can be categorized as an it embarrassingly parallel system; see Sommervill (2006). This is because only data conversion needs an inter-node process; actual analysis or computation of the layers is an intra-node process. Therefore, the client-server model is selected for the parallel computing load balancing model, and first-come-first-served is used as load balancing strategy. The kernel in association with the data layer works as server, while an aggregation of simulation and visualization layers makes client part.

Figure 7 is the sequence diagram for the parallel communication process in IES. The Kernel and Data remain on the server node as the control room and the source of data respectively. The Kernel initializes client nodes for the Simulation and Visualization. Each client node sends a confirmation message, starts a process of modeling, starts a simulation program (which is running a plug-in structural seismic analysis program), makes the visualization, and sends a finalizing message to the server node. These series of communications are repeated until the server node finishes all the required simulations.

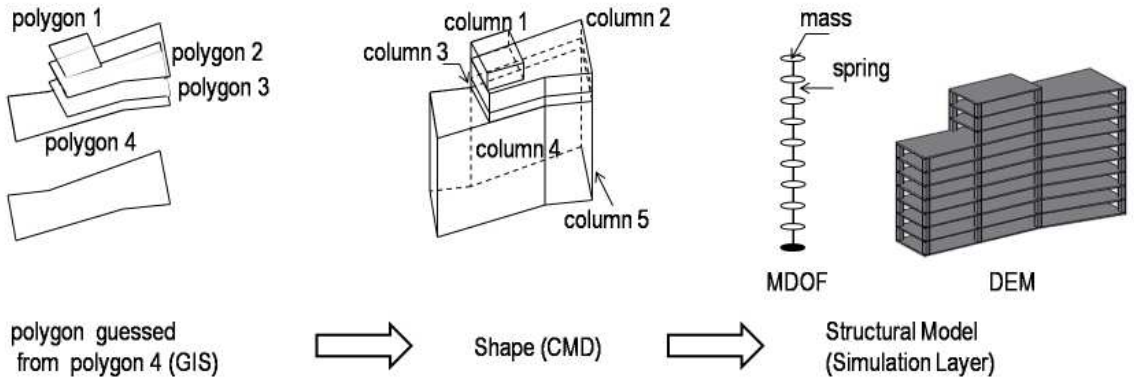

Figure 8 Schematic view of data conversion from GIS data to structural model

4. Results of IES Simulation

4.1 Model construction

Two analysis methods for the seismic response analysis are used to measure the performance of IES that is enhanced with HPC. They are linear Multi-Degree-Of-Freedom (MDOF) analysis and nonlinear Distinct Element Method (DEM) analysis; complexity of the analysis methods is examined by using these methods which require utterly different computational resources. For one building, two models are constructed from the data layer of GIS, one for linear MDOF and another for nonlinear DEM. The data conversion from the data layer to the simulation layer takes on a constant amount of time for an urban area of a specific size. Entities of Shape class are generated before executing the parallel computation, in order to omit the constant amount of time of the data conversion. The performance is measured in terms of speedup and efficiency, and scalability is studied using iso-efficiency function as an index.

The data conversion from the data layer to the simulation layer is schematically shown in Figure 8. While the data conversion produces two analysis models from one set of GIS data, one entity of Shape class, which is generated for the GIS data, is used for the data conversion. Analysis models of different type are constructed from this Shape class entity.

Table 1 Structure categorization based on the floor area and building height

Height(m)	10 < Floor Area (m^2) <=100	Floor Area (m^2) >100
3 ~ 12	Timber	Steel
12 ~ 50	RC	RC
> 50	Steel RC	Steel

The data conversion from a Shape class entity to an MDOF model is not new to the authors, who have developed a wrapper for the MDOF analysis. The procedures of the data conversion are summarized as follows: 1) the number of floors is calculated from the structure height using a typical value of floor height; 2) for each floor, the weight is calculated from the floor area, assuming a typical value for the floor thickness and density; and 3) spring constants between the floors are determined so that the natural frequency and damping constant of the first and second modes coincide with the empirical formulas. Since GIS does not contain any information about structure type, floor area and building height are used to guess type of structure. Table 1 shows an assumed relation between these values and the structural type.

DEM is a nonlinear numerical analysis method, which models a structure as an assembly of rigid body elements; these elements mimics' structure members such as columns, foundation, or floor slab, and they are connected by virtual joints which are expressed in terms of nonlinear springs and dashpots. The equation of motion of these elements is solved for a given input strong ground motion; see Kiyono et al. (2004); it can simulate the collapse of a structure by fully breaking the joints. The present DEM analysis uses two sets of spring and dashpot; see Figure 9.

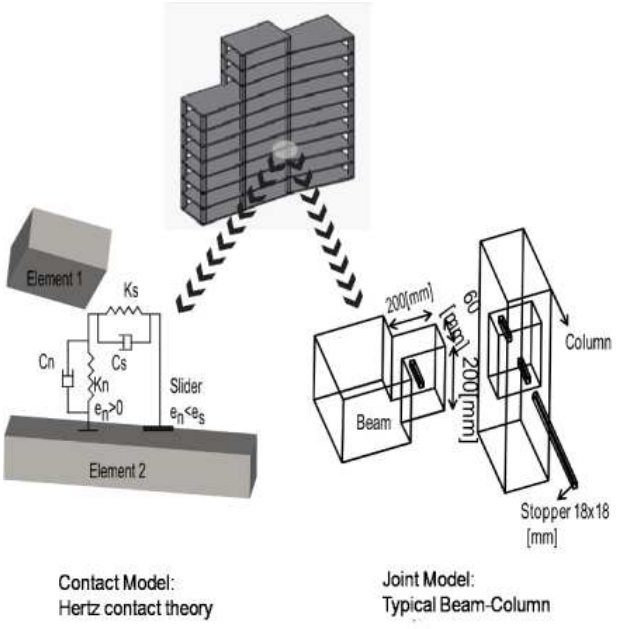

Figure 9 DEM joint model

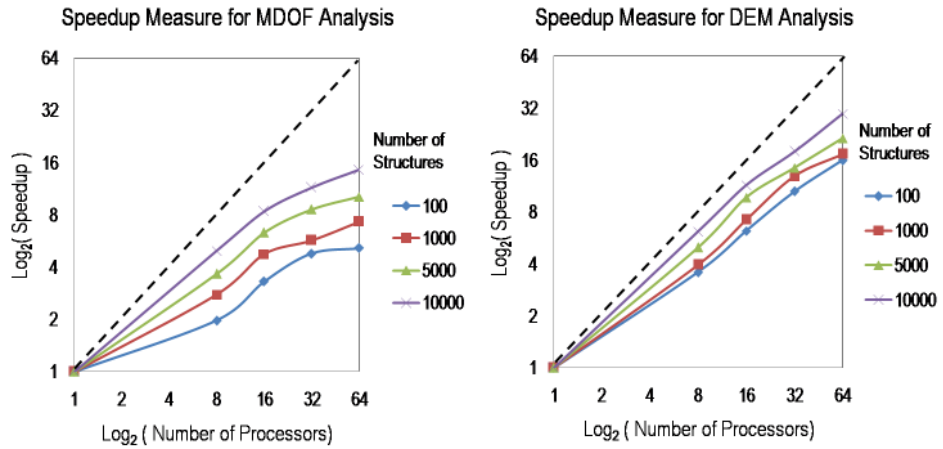

Figure 10 Speedup: left for MDOF and right for DEM

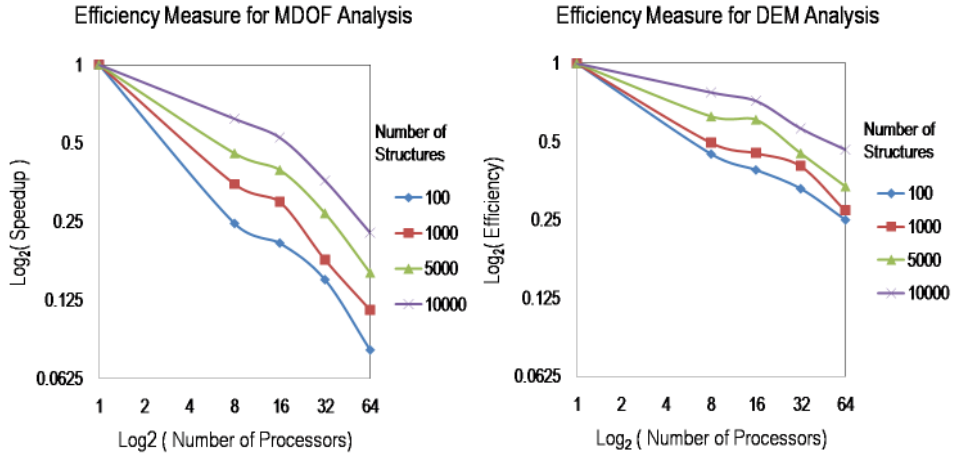

Figure 11 Efficiency: left for MDOF and right for DEM

The first set represents contact between elements, and the mechanical properties are estimated based on Hertz contact theory Kiyono et al. (2004). The second set represents joint of wooden house whose mechanical properties have been experimentally measured. Note that all the structures in a target area are assumed as a wooden house when the nonlinear DEM analysis is made.

DEM is a nonlinear numerical analysis method which models a structure as an assembly of rigid body elements; these elements mimics structure members such as columns, foundation or floor slab, and they are connected by virtual joints which are expressed in terms of nonlinear springs and dashpots. The equation of motion of these elements is solved for a given input strong ground motion; see Kiyono (2004); it can simulate the collapse of a structure by fully breaking the joints. The present DEM analysis uses two sets of spring and dashpot; see Figure 9. The first set represents contact between elements, and the mechanical properties are estimated based on Hertz contact theory. The second set represents joint of wooden house whose mechanical properties have been experimentally measured. Note that all the structures in a target area are assumed as a wooden house when the nonlinear DEM analysis is made.

4.2 Performance measurement

Speedup, efficiency, and iso-efficiency function are used as an index which measures the performance of IES parallel computation; see Pacheco (1996). These indexes are obtained by executing the IES simulation for 100, 1,000, 5,000, and 10,000 structures on 8, 16, 32, and 64 computational nodes. A cluster with 8 AMD Opteron 2356 QuadCore processors (2.3 GHz) which has 4GB memory for each processor is used for the performance measurement.

4.2.1 Speedup

The execution time of the IES simulation that uses p computational nodes is denoted by T(p). Speedup is then defined in terms of this execution time as follows:

$$S(p) = \frac{T(1)}{T(p)} \tag{1}$$

in the ideal case of parallel computation, the relation between p and S(p) becomes linear.

Figure 10 shows speedup for the MDOF and DEM analyses. As is seen, the speedup curve tends to be close to

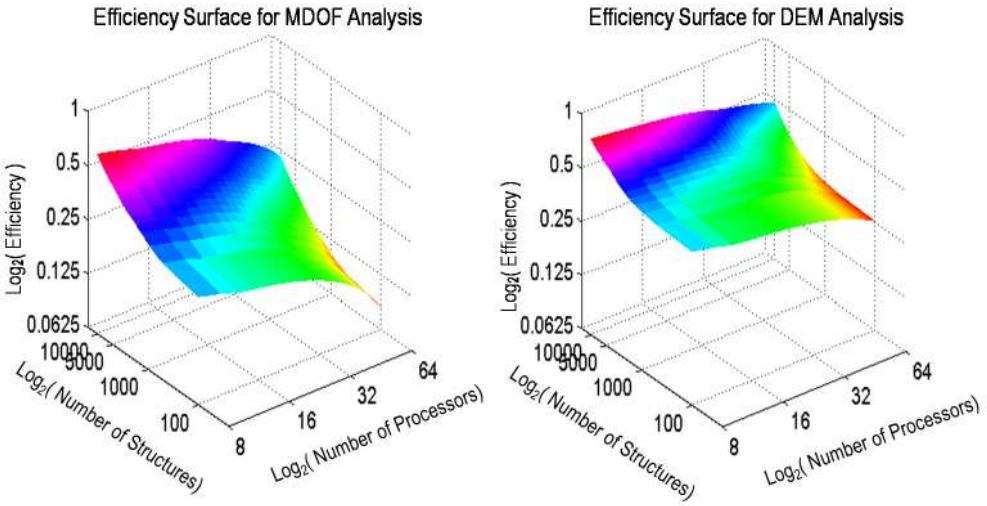

Figure 12 Efficiency surface: left for MDOF and right for DEM

the ideal one, which is designated by a dashed line. The speedup moves toward the ideal line as the number of simulated structures increases. The tendency toward to the ideal case is more obvious for the DEM analysis than for the MDOF analysis. The difference between these analyses

4.2.2 Efficiency

Efficiency is defined by normalizing speedup by the number of computational nodes, i.e.,

$$E(p) = \frac{S(p)}{p} \tag{2}$$

As is easily, the ideal number of efficiency is 1 and E(p) cannot exceed this value.

Figure 11 illustrates an efficiency curve for the MDOF and DEM analyses. As is seen, for the MDOF analysis, the efficiency is small; this is another evidence that message passing overhead is dominant in saved time for the MDOF analysis. As the number of analyzed structures increases, the efficiency increases for a fixed number of computational

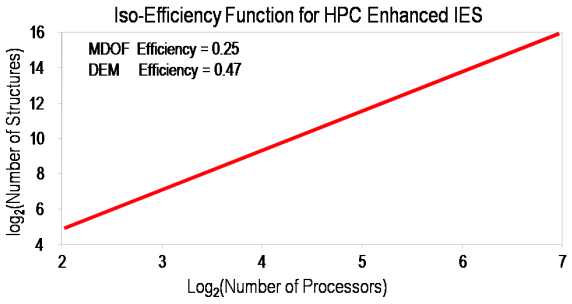

Figure 13 Iso-efficiency function for IES

nodes. However, the efficiency decreases as the number of computational nodes increases.

4.2.3 Efficiency surfaces and iso-efficiency function

IES simulation can provide a more realistic prospective stems from the fact that message passing overhead is dominant for time saved by parallel computing for the MDOF analysis. Since IES is eventually aimed at megacities like Tokyo, the increase in speedup for larger number of structures is a good sign of the performance.
regarding to the consequences of an earthquake hazard on an urban area. This information can be used by residents and government officials to keep up the level of readiness against of such a natural hazard. Therefore, having the ability of predicting the performance of IES simulation is essential.

Figure 12 shows efficiency surfaces for MDOF and DEM simulations. Efficiency surfaces can be used to predict the parallel execution efficiency of IES for a determined configuration of number of structures and number of processors. As it can been seem, regardless of type of structural seismic analysis method the both curves shows the same trend, which is a good indication of appropriate design of IES.

A system, a program or an algorithm is called scalable if there is a function of the number of processors, which gives the problem size that is solved with constant efficiency. Therefore, efficiency surfaces can be used to estimate iso-efficiency functions for the different level of efficiency. As an example, the following equation gives the relation between number of processors and the number of structures for the both MDOF and DEM analyses when efficiency is 25% and 47% in order for both cases,

$$n = 1.44 * p^{2.23} \tag{3}$$

Figure 13 shows an estimated iso-efficiency function; the thick line is the iso-efficiency function given as Eq. 3. The iso-efficiency function is of the power low, and hence it is shown that the present IES has the scalability from degree two. Several factors influence the scalability degree, such as message passing latency, external storage access. For IES, non-homogeneity of analysis models could be a significant

factor of the scalability; non-homogeneity is caused by different type of structures, which needs specific model construction from Shape entity and an analysis method inherent to it so that execution and data processing times are changed.

5. CONCLUSIONS

This paper presents the two improvements of IES to enhance it with HPC by means of parallel computing. Major techniques developed are CMD and GD classes; although the authors do not think that the basic concept of GD class is original, well-structured CMD and GD classes are developed so that complicated and huge data for structures are easily handled through several layers of IES. In particular, CMD class improves task distinction between layers by proposing a standard data type for interlayer communication. Urban area model for 10,000 is constructed by interpreting GIS data to CMD form, which indicates the robustness of such a data conversion. Moreover, the concept of serialization/de-serialization is used to distribute CMD components through distributed memory architecture by leveraging the power of MPI_Process_Manager class.

The scalability of IES simulation is studied, by employing the linear MDOF and nonlinear DEM analyses so that effects of the numerical analysis method complexity on the scalability is examined. The resemblance of two efficiency surfaces shows that IES design provides a suitable foundation to achieve a scalable system independent from the analysis methods. The iso-efficiency function is estimated for both the numerical analysis methods. Even though the efficiency level is 25% and 47% for the MDOF and DEM analyses, respectively, a unique iso-efficiency function can be used to predict the IES performance. It can be expected that IES has similar good efficiency for other analysis methods with different levels of efficiency. Efficiency can be improved by using shared memory parallelization in client side, which should be studied in the future.

Acknowledgements:

We are grateful for Associate Prof. Aiko Furukawa (Kyushu University) for providing the source code of the DEM analysis method, and Pasco Co. for providing GIS data. We are grateful for the support provided by the Japanese Government (MEXT).

References:

Hori M. (2006), "Introduction to Computational Earthquake Engineering," Imperial College Press.

Nallathamby S., Hori M., Ariga Y. (2007), "Improvement of IES Wrapper for Plug-in of Advanced Simulation Programs," Journal of Applied Mechanics, **10**, 573-579.

Ichimura T., Hori M. (2004), "Development of prototype of Integrated Earthquake Disaster Simulator using digital city and strong ground motion simulator with high resolution,"
13th Conference on Earthquake Engineering, No.1418.

Tanaka K., Sobhaninejad Gh., Hori M. (2008), "Data Conversion of GIS to Urban Area Model for Natural Disaster Simulation," Journal of Applied Mechanics, **11**, 647-654.

Sobhaninejad Gh., Hori M., (2008), "Common Modeling Data: New Approach in Designing Integrated Natural Disaster Simulation Software," Annual conference of JSCE.

McCandless B.C., Squyres J.M., Lumsdaine A. (1996), "Object Oriented MPI (OOMPI), a class library for the Message Passing Interface," MPI Developer's Conference, Proceedings, 87-94.

Grama A., Karypis G., Kumar V., Gupta A. (2003), "Introduction to Parallel Computing, 2/E," Addison-Wesley.

Sommervill I. (2006), "Software Engineering, 8/E," Addison-Wesley.

Kiyono J., Furukawa A. (2004), "Casualty occurrence mechanism in the collapse of timber-frame houses during an earthquake," Earthquake Engineering and Structural Dynamics, **33**(12), 1233-1248.

Pacheco P.S. (1996), "Parallel programming with MPI," Morgan Kaufmann Publishers Inc.

JOINT CONFERENCE PROCEEDINGS
7th International Conference on Urban Earthquake Engineering (7CUEE) &
5th International Conference on Earthquake Engineering (5ICEE)
March 3-5, 2010, Tokyo Institute of Technology, Tokyo, Japan

A NEW MODEL PARAMETER IDENTIFICATION TECHNIQUE FOR MAGNETORHEOLOGICAL DAMPERS

Aditya Venkatesan

Senior Undergraduate Student, Department of Civil Engineering, National Institute of Technology-Allahabad, Allahabad, U.P., India.
venkatesan.aditya@gmail.com

Abstract— Magnetorheological (MR) Dampers offer rapid variation in damping properties, making them ideal in semi-active control of structures. They potentially offer highly reliable operation and can be viewed as fail safe, in that in the worst case, they become passive dampers. Perfect understanding of the response is necessary when implementing these in operation in conjunction with a control mechanism. There are many models used to predict the behavior of MR dampers. One of these is the Bouc-Wen model. It is extremely popular as it is numerically tractable, very versatile and can exhibit a wide range of hysteretic behavior. It is necessary to first identify the characteristic parameters of the model before response prediction is possible. However, characteristic parameters identification of the Bouc-Wen model needs an experimental base, which has its own limitations. The extraction of these characteristic parameters by trial and error and optimization techniques leaves significant difference between observed and simulated results. This paper deals with a new approach to extract characteristic parameters for the Bouc-Wen model.

I. INTRODUCTION

Magnetorheological (MR) dampers have emerged as one of the most promising devices to control and protect structural systems from dynamic environmental hazards. A magnetorheological damper or magnetorheological shock absorber is a damper filled with magnetorheological fluid, which is controlled by a magnetic field, usually using an electromagnet. This allows the damping characteristics of the shock absorber to be continuously controlled by varying the power of the electromagnet. The mechanical simplicity, high dynamic range, low power requirements, large force capacity and robustness have made MR dampers the ideal devices for vibration suppression.

II. MR FLUIDS

MR Fluids are a special type of smart fluids containing a suspension of micro sized particles in a carrier liquid, usually oil. When subjected to a magnetic field, the fluid greatly increases its apparent viscosity, to the point of becoming a viscoelastic solid. This effect is due to the formation of chain-type structures within a fluid in response to a magnetic field. These are aggregations of solid particles, and dominate the flow of the liquid and can prevent flow entirely at lower stresses. The particles are suspensions in inert carrier liquids. These are typically of the order of 1 to 10 μm in size are added to fluid such as mineral oils or silicone oils, in weight fractions as large as around 30% or so. Most fluids contain a small amount of additives that affect the polarization of particles or stabilize the structure of suspension against settling.

In the absence of external magnetic fields, the fluid behavior may be characterized as Newtonian i.e. resisting shear strain (γ) with a shear stress (ζ) proportional to the product of the strain rate (dγ/dt) and viscosity (η).

$$\zeta = \eta \left[\frac{d\gamma}{dt}\right] \quad (1)$$

This however, is widely regarded as an approximation as even under no field conditions, there exists a certain amount of non-Newtonian response. The presence of a magnetic field on an MR fluid causes the particles to form chain, or fibrils, in the direction of the field. This process of fibration occurs in a few milliseconds after application of the field. When there is no motion of the fluid or the walls of the container, the fibrils are static structures and span the gap of the walls if the particle concentration is large enough.

MR fluids differ from conventional magnetic fluids which contain particles of much smaller size, mostly in the region of 10 nm or so, where the effects of Brownian motion are more predominant. These particles as a result are unable to form fibrils. The magnetic fluid experiences a body force proportional to the magnetic field gradient.

III. MODELING OF AN MR DAMPER

Modeling of an MR damper refers to the definition of MR damper behavior, by means of a given set of equations. It is essential to the prediction of damper response. There are many different models that have been used to define MR damper behavior. One of the very important factors to achieve successful control performance is to have an

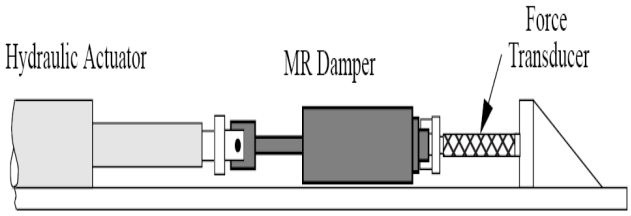

Figure 1. Test setup for MR damper identification.

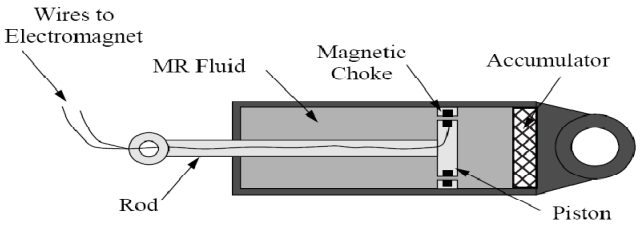

Figure 2. Schematic of an MR

accurate damping force model which can capture the inherent hysteresis phenomenon of MR dampers. Damper models have been classified into two categories, quasi-static or dynamic in nature. For quasi-static models, there are several works reported in literature. The most elementary of these is the Bingham Model, where a set of non-dimensional variables defined the corresponding quintic equation for pressure gradient in a parallel duct. Further development around this model led to the observation that a quasi-static model, while quite easily describing the force-displacement behavior, did not perform as well when it came to describing the force-velocity behavior. The need for development of a different line of approach was clear. This led to the development of the dynamic models to predict the behavior of MR fluids.

The most fundamental of models around which all parametric models are built is the Bingham viscoelastic-plastic model. One of the most popular models to have evolved around this framework is known as the Bouc-Wen model. The Bouc-Wen model was initially formulated (Bouc 1971) as an analytical description of a smooth hysteresis model and later generalized (Wen 1976). This model is very popular due to its numerically tractable nature. It is extremely versatile and can represent a wide range of hysteretic behavior. This model has the ability to capture in a continuous function a range of shapes of hysteresis loops which represent the properties of a wide range of real non linear hysteresis loops [1, 2]. However one of the inherent problems of this model is the evaluation of the constant parameters. Many attempts have been made to overcome this particular shortcoming. Optimization techniques such as Sequential Quadratic Programming (SQP) and other attempts based on Trial and error methods have been used to determine the parameters in such a manner that the error between the experimental and simulation results reduce to as insignificant a value as possible [1,3]. Combining of such parameters however, could be significantly large and often there exists no unique exact solution. In other words the final solution usually does not match the actual observed hysteresis phenomenon. Considerable differences have been reported between the generated simulation and the experimental data [1, 3]. The Bouc-Wen model has thus hence been criticized due to its inherent difficulties in predicting the characteristic parameters [4].

The aim of this paper is to demonstrate a parameter identification procedure (extraction of the characteristic parameters) for the Bouc-Wen model. The data used to simulate a model for illustration purposes of the parameter identification procedure is first generated. A force-displacement curve is plotted for the Bouc-Wen equation using the values of the characteristic parameters as obtained from the experiment performed by Spencer et al. [1]. This is then used as a reference and the extraction procedure is illustrated. It is important to note a characterization procedure for the Bouc-Wen model proposed by Dominguez *et al* [5, 6], using the force velocity plots along similar lines. It is the objective of this study to develop a force-displacement based extraction procedure along parallel lines for sinusoidal inputs. It makes use of the force-displacement plot to obtain the characteristic parameters that govern the response of the damper. This method has the advantage of direct incorporation with a displacement based sensor. Also as the Bouc-Wen model shows closer similarity between experimental and simulated plots for force-displacement as opposed to force-velocity, it is likely to produce a more true representation of the characteristic parameters.

IV. THE BOUC-WEN MODEL

The Bouc-Wen damper model consists of a spring, a viscous dashpot, and a hysteretic curve generator, all in parallel. Referring to Figure 3, the total damping force can be represented as shown in Equation (2). [2]

$$F(x(\tau), \dot{x}(\tau), 0 \le \tau \le t; t) = c_0\dot{x} + k_0 x + \alpha z \qquad (2)$$

The first term describes the force associated with the viscous damper. The second portion represents the force due to the linear part of the damper, cause by the compressed gas in the accumulator. The third term represents the response of the evolutionary force due to the hysteretic portion. The sum of the three components represents the force response of the damper. z is the

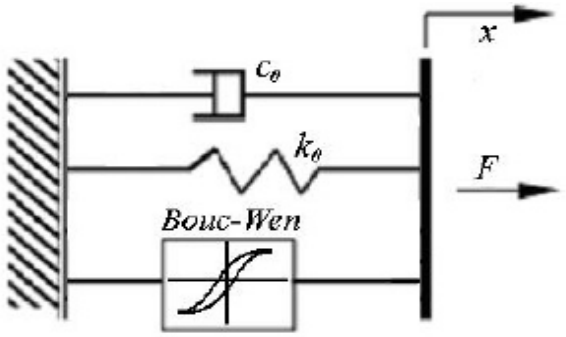

Figure. 3 Schematic representation of the Bouc-Wen model

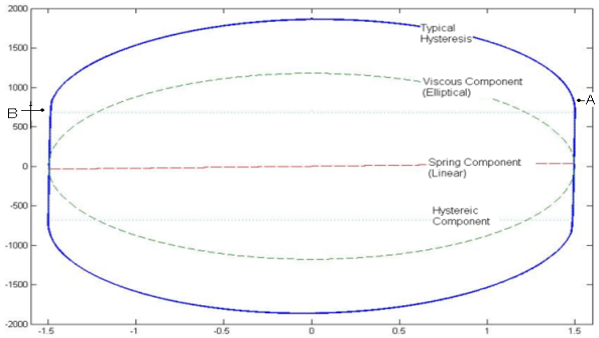

Figure. 4. Force-Displacement plots, representing the Hysteretic Forces, along with the individual Bouc-Wen components

evolutionary shape variable described by the first order differential equation as,

$$\dot{z} = -\gamma|\dot{x}||z|^{(n-1)}z + A\dot{x} - \beta\dot{x}|z|^n \qquad (3)$$

The parameters $c_0, k_0, \alpha, \beta, \gamma$ and A are called the characteristic parameters of the Bouc-Wen model. They are not functions of current, amplitude and frequency [6]. It should be noted that the values of the characteristic parameters are constant for a constant value of current, amplitude and frequency. These will of necessity have to be recalculated for differing excitation conditions. For the characterized MR damper which was used by Spencer et al [1] the values of the constant parameters are

$\alpha = 880N/cm$
$k_0 = 25N/cm$
$\beta = 100\ cm^{-2}$
$c_0 = 50\ N\ sec/cm$
$\gamma = 100\ cm^{-2}$
$A = 120$
The other parameter defining the curve is n = 2 .

V. PARAMETER IDENTIFICATION

A major difficulty in using the Bouc-Wen model is the evaluation of the characteristic parameters. The most common approach is the use of optimization techniques, or trial and error methods [1]. The problem however remains that the solution space is infinite and these techniques require high computational costs. The generated parameters generally fall short, and the description of MR damper behavior remains inaccurate.

An efficient methodology to determine the constant parameters of the Bouc–Wen model in order to better characterize the hysteresis behavior of the MR damper has been presented by Dominguez et al. [5]. In this methodology, the required parameters have been determined by considering the individual effect of each term of Equation (2) over the hysteresis curve. It has been demonstrated that it is possible to extract some information from the experimental data in order to obtain directly the values of the characteristic parameters without using any method to match the experimental data with simulation results.

This paper deals with a similar approach, employing the Force-Displacement relationship as opposed to the Force-Velocity analysis as employed by Dominguez et al [5, 6]. The advantage is that this approach eliminates the need for optimization or trial and error to generate the values of the parameters, similar to what has been done by Dominguez et al. [5, 6]. In that view the proposed methodology is in parallel to the one proposed in [5, 6]. This method has the advantage that it can be directly integrated with a displacement based sensor and the raw data can be analyzed directly.

The sign of $\dot{x}$ and z will decide the nature of the differential equations. They can be broken down into the four that are shown below in the Equations 4 (i, ii, iii, iv)

$$\frac{dz}{dx} = A - (\gamma + \beta)z^n \qquad for\ z \geq 0, \dot{x} \geq 0$$
$$\frac{dz}{dx} = A + (\gamma - \beta)z^n \qquad for\ z \geq 0, \dot{x} < 0$$
$$\frac{dz}{dx} = A + (-1)^{n-1}(\gamma + \beta)z^n \qquad for\ z < 0, \dot{x} < 0$$
$$\frac{dz}{dx} = A + (-1)^{n-1}(-\gamma + \beta)z^n \qquad for\ z \geq 0, \dot{x} \geq 0$$

The individual effects of parameters n and β were discussed by Spencer et al. [2]. It was concluded that as n increases, the radius of curvature in the vicinity of transition points decreases (points known as transition velocity points). The value of n = 2 is used in solving the equation [1, 7, 8]. The effect of β on the hysteresis curve has been well documented. It is seen that as β increases the smoothness of the curve in the vicinity of the transition

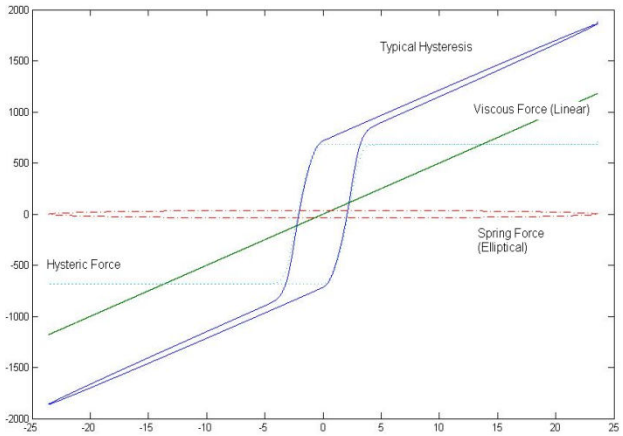

Figure 5. Force-Velocity plots, representing the Hysteretic Forces, along with the individual Bouc-Wen components.

points decreases. For simplicity of calculation the value of β=0, but it is quite obvious that the methodology remains the same for any other value of β [9]. Upon substitution of the values into the Equations 4(i, ii, iii, iv), the four equations simplify into the two cases shown in Equation (5)and (6).

$$\frac{dz}{dx} = A - \gamma z^2 \; ; \; for \;\; z \geq 0, \dot{x} \geq 0 \; or \; z < 0, \dot{x} < 0 \qquad (5)$$

$$\frac{dz}{dx} = A + \gamma z^2 \; ; \; for \;\; z \geq 0, \dot{x} < 0 \; or \; z \geq 0, \dot{x} \geq 0 \qquad (6)$$

On integrating the Equations (5) and (6) the solutions are obtained in Equations (7) and (8) which define the hysteretic curves.

$$z = \frac{\sqrt{A\gamma}}{\gamma} \, tanh\left[\sqrt{A\gamma}(x + c_1)\right] ; \; for \; z \geq 0, \dot{x} \geq 0 \; or \; z < 0, \dot{x} < 0 \qquad (7)$$

$$z = \frac{\sqrt{A\gamma}}{\gamma} \, tan\left[\sqrt{A\gamma}(x + c_2)\right] \;\; ; \; for \;\; z \geq 0, \dot{x} < 0 \; or \; z \geq 0, \dot{x} \geq 0 \qquad (8)$$

Assuming A = 1, the integration constant is determined by making use of the coordinate point($F_{z0}, x = 0$); where F_{z0}represents the force at the point of zero displacement. The constant in Equations (7) and (8) are first extracted. Equations (7) and (8) represent the upper and lower bounds of the hysteretic curves. [5, 6]

$$c_1 = \frac{1}{\sqrt{\gamma}} \text{atanh}\left(\frac{F_{z0}}{F_{z,max}}\right)$$

$$F_{z,max} = F_{max} - k_0 x_{max} \qquad (9)$$

$F_{z,max}$ is the evolutionary force at maximum displacement or simply put, the maximum evolutionary force. It is also written as

$$F_{z,max} = \frac{\alpha}{\sqrt{\gamma}} \qquad (10)$$

F_{max} is the maximum total hysteresis force. The parameter k_0 can be determined from the graph. It is seen that the parameter k_0 is the slope of the line connecting the points A and B in Figure 4. The points can be identified as the points where the linearity of the vertical boundaries end and the curvilinear nature of the horizontal bounds begin. It can easily be isolated by visual inspection. Thus, the value of k_0 equals,

$$k_0 = \frac{F_A - F_B}{x_A - x_B} \qquad (11)$$

where $F_A, F_B$are the values of the total force at points A and B; x_A, x_B are the values of displacement at points A and B.

The value of F_z can now be ascertained, by using the value of F and F_k , at the point $x = x_{max}$. Since $F_c = 0$ at the point of maximum displacement, the total force can be expressed as (F) as, $F = F_k + F_z$. The value of F and $F_k$being known, the value of F_z can be obtained. The value of F_z remains constant, except at the points of maximum displacement where it changes sign.

Considering the force plot at the point represented by x=0, it is clear that the value of F_k , representing the force due to the accumulator equals zero at the origin. The sum of forces can be written as $F = F_c + F_z$. As the value of F and F_z are known, value of F_c at the centre is obtained.

It is obvious that, the variation of force due to the viscous component varies elliptically with respect to displacement. The parameter c_0 , can be determined using Equation (12).

$$c_0 = \frac{x_{max} F_c}{\sqrt{(x_{max}\dot{x}_{\max})^2 - (\dot{x}_{max} x_i)^2}} \qquad (12)$$

where F_c is the value of the viscous component, established in the preceding lines, $\dot{x}_{max} = \omega \, x_{max}$, x_{max} is the maximum displacement and x_i = point on the curve, corresponding to the established value of F_c .
Using the coordinate point ($F_z = 0$, x_{z0}), the value of γ can be obtained using Equation (13).

$$0 = F_{z,max} \, tanh\left[\sqrt{\gamma}(x_{z0} + \frac{1}{\sqrt{\gamma}} \text{atanh}\left(\frac{F_{z0}}{F_{z,max}}\right)\right] \qquad (13)$$

Subsequently the value of α is obtained by the use of Equation (10), in which the values of γ and $F_{z,max}$ are substituted.

Upon substitution of the integration constant c_1 into Equation (7) the value of z is determined.

VI. Conclusion

As demonstrated, it is rather easy to extract the parameters that define the response of a MR damper as predicted by the Bouc-Wen model. This model is likely to predict characteristic parameters more representative of the dampers true nature as the simulated and experimental force-displacement plots are a closer match than simulated and experimental force-velocity plots, for the Bouc-Wen model. Since this method employs the force displacement plots, it can be directly integrated with a displacement based sensor. Validation of the work is ongoing.

VII. Acknowledgment

The author would like to acknowledge the guidance of Mr. Sharad K. Purohit in the research without whom none of this would have been possible. The author is also grateful to the guidance of Dr. N.K. Chandiramani of IIT-Bombay, who took a great deal of time to aid me in this work.

VIII. References

[1] B.F. Spencer, S.J. Dyke, M.K.Sain, J.D.Carlson 1996 – "*Phenomenological Modelling of an MR damper"* – ASCE Journal of Engineering Mechanics

[2] Spencer B F 1986 Jr. *"Reliability of Randomly excited hysteretic structures"* (Berlin : Springer)

[3] Yang G 2001 – "*Large Scale Magnetorheological fluid damper for vibration mitigation: modeling testing and control"* PhD dissertation University of Notre Dame, Indiana.

[4] Wang E R, Ma X Q, Rakheja S and Su C Y 2003 Modeling the hysteric characteristics of a Magnetorheological fluid damper *Proc. Inst. Mech. Eng.* D 217 537–50

[5] A Dominguez, R. Sedaghati, R.Stiharu 2004 -*"Modelling the hysteresis phenomenon of MR damper"*- Institute of Physics Publishing Smart Materials and Structures : 13 1351-1361.

[6] A. Dominguez, R. Sedaghati, R. Stiharu 2006 – *"A new dynamic hysteresis model for MR dampers*" – Institute of Physics Publushing Smart Material and Structures :15 1179-1189

[7] S.B. Choi, S.K. Lee 2001-*"A hysteresis model for field dependant damping force of a MR damper"*- Journal of Sound and Vibration 245(2), 375-383.

[8] G.Z. Yao, F.F. Yap, G. Chen, W.H. Li, S.H. Yeo 2002 -*"MR damper and its application for semi-active control of vehicle suspension system"* –Mechatronics : 963-973

[9] C.W. Wong, Y.Q. Ni, S.L. Lau 1994 –"*Steady State oscillation of Hysteretic Differential Model Response Analysis*"- Journal of Engineering Mechanics. 120 No. 11 November 1994

[10] C.W. Wong, Y.Q. Ni, J.M. Ko 1994 – "*Steady State oscillation of Hysteretic Differential Model Performance Analysis"*- Journal of Engineering Mechanics : 120 No. 11 November 1994

[11] Smart Structures- Analysis and Design by A.V Srinivasan and Michael McFarland.

JOINT CONFERENCE PROCEEDINGS
7th International Conference on Urban Earthquake Engineering (7CUEE) &
5th International Conference on Earthquake Engineering (5ICEE)
March 3-5, 2010, Tokyo Institute of Technology, Tokyo, Japan

TORSIONAL SEISMIC RESPONSE REDUCTION BY PASSIVE CONTROL DEVISE FOR CONVENTIONAL POST-AND-BEAM ONE-STORY WOODEN HOUSE WITH STIFFNESS ECCENTRICITY

Yoshihiro Yamazaki[1)], Kazuhiko Kasai[2)], and Hiroyasu Sakata[3)]

1) JSPS Research Follow, Department of Built Environment, Tokyo Institute of Technology, Japan
2) Professor, Structural Engineering Research Center, Tokyo Institute of Technology, Japan
3) Associate Professor, Structural Engineering Research Center, Tokyo Institute of Technology, Japan
yamazaki.y.ai@m.titech.ac.jp, kasai@serc.titech.ac.jp, hsakata@serc.titech.ac.jp

Abstract: Shaking table tests for full-scale wood frame specimens with large stiffness eccentricity are conducted. Specimen is single story, and its plan dimension is 1.82m in X-direction and 2.73m in Y-direction. Stiffness of specimens are unbalanced in X direction, along which input motions are provided by the shaking table. The eccentricity ratio R_e, defined by Japan Building Standard Law is about 0.6 for the standard specimen. Six specimens are tested : one does not have any dampers and the others are provided with viscoelastic dampers in various arrangements. The performance of specimens is discussed by referring to story drift, damper deformation and dynamic properties. Finally, we propose a methodology of effective torsional response reduction by passive control devises on the basis of this test.

1. INTRODUCTION

1.1 BACKGROUND

Extremely much amount of wooden houses were collapsed or got terrible damage in 1995 Hyogoken Nanbu earthquake. Damage investigation reported that eccentric arrangement of shear walls presumably led many houses to crucial torsional response. Seismic resistant structure which decipate energy by damage of structural members are not likely to protect weaker members or frames like a large opening. Certainly, more effective solution is required to reduce seismic damage caused by torsional response.

We have demonstrated effectiveness of passively controlled walls applied to wooden structure and conducted a lot of dynamic loading tests and shaking table tests. We found that passive control system is very effective solution to reduce torsional response even if the devices are arranged in proper layout and appropriately attached to structural members.

1.2 PREVIOUS RESEARCH

Noguchi(2006) has applied viscoelastic damper to wooden houses and verified effectiveness by conducting shaking table test for scaled models and time history analyses. However, the states of timber shear walls which reacted well-known complicated non-linear behavior were assumed elastic in this research, and the tested models seemed not to be actual passive controlled timber houses. Soda(2004) has proposed compressive knee brace oil dampers for wooden houses. Although the proposed dampers were compact and easily attached to wooden houses, they were not likely to be effect on reducing torsional response because of their relatively small damper force. Koshihara and Agawa(2002) have tested full-scale timber shear wall structure with stiffness eccentricity. In this research, a theory on stiffness eccentricity and strength eccentricity for wooden houses was established

On the other hand, there is no design method considering damping eccentricity except for individual time history analysis by designers. In the case of 1-story linear model considering not only stiffness eccentricity but also damping eccentricity, Kasai et al.(2009) have proved by time history analyses that arranging center of damping in opposite side of center of stiffness leads to reduction of seismic torsional response. In addition, they proposed simplified maximum response prediction rule.

1.3 OBJECTIVE

In this paper, shaking table tests for full-scale 1-story specimens which are provided with passively controlled walls in various arrangements are performed. By assuming stiff horizontal diaphragms, effectiveness of response reduction by passively controlled walls is made clear. We demonstrate the effects of damping eccentricity and damping force of transverse frames in particular. Although passively controlled walls which the authors designed can include several types of damper, viscoelastic dampers are selected in this shaking table test. Therefore the advanced characteristics of passively controlled walls against timber shear walls are high energy dissipation capacity and linearity. The important objective is to present some significant points of applying passively controlled walls to 3D wooden frame

structure. Our study is likely to be contributed to a basic study and solid development for a methodology of effective torsional response reduction by passive control devises.

2. OUTLINE OF SHAKING TABLE TESTS

2.1 SPECIFICATION OF SPECIMENS

As shown in Figure 1, all the specimens are single story, and its plan dimension is 1.82m in X-direction and 2.73m in Y-direction, which are modeled on conventional post-and-beam wooden houses. The groundsills of specimen are fixed to steel foundation beams which are set to shaking table. In this test, each groundsill and foundation beam is separated in order to measure shear force bore by each frame.

Timber shear walls and passively controlled walls are installed in outer frames of the plan. Stiffness of one frame in X-direction to which input motions are applied is decreased with large opening. This frame is described as '*flexible side frame*'. Similarly, the opposite side frame is '*stiff side frame*', and the two frames in Y-direction are '*transverse frames*'.

As shown above, center of stiffness (c.s.) is located away in Y-direction from the center of mass (c.m.), and input motions are applied to specimen in X-direction by shaking table. Five additional loaded weights are distributed to the roof in order that rotatory inertia of these weights equals to one of uniformly distributed weight.

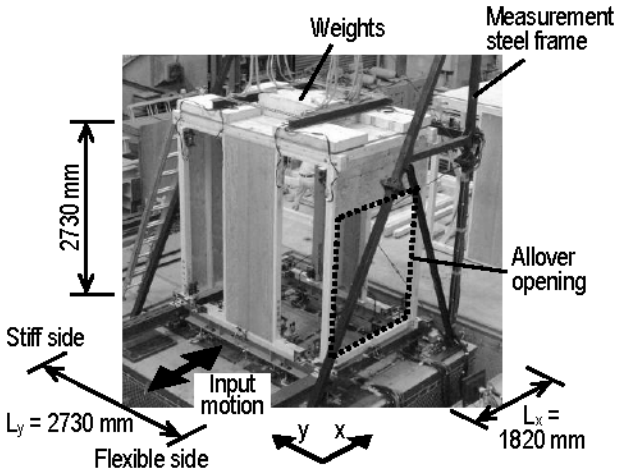

Figure 1 Setup of specimen

2.2 PROPERTIES OF TIMBER SHEAR WALLS AND PASSIVELY CONTROLLED WALLS

Timber shear walls and passively controlled walls which are added to specimen are shown in Figure 2. Two types of timber shear walls are tested ; one is '*plywood sheathing hanging wall*' installed in flexible side frame, and another is '*plywood sheathing allover wall*' installed in stiff side frame and transverse frames. They are described as 'HW (*hanging wall*) ' and 'AW (*allover wall*) ' respectively. Similarly, two types of passively controlled walls are tested.

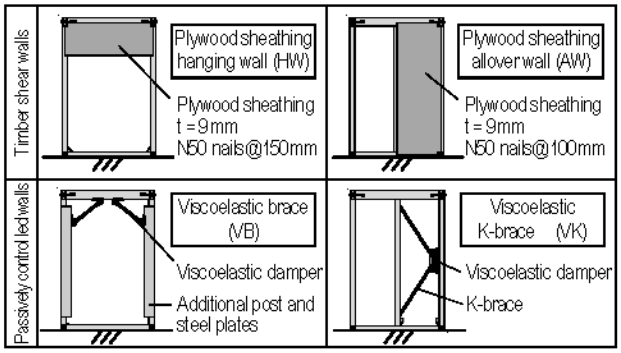

Figure 2 Teted timber shear walls and passively controlled walls

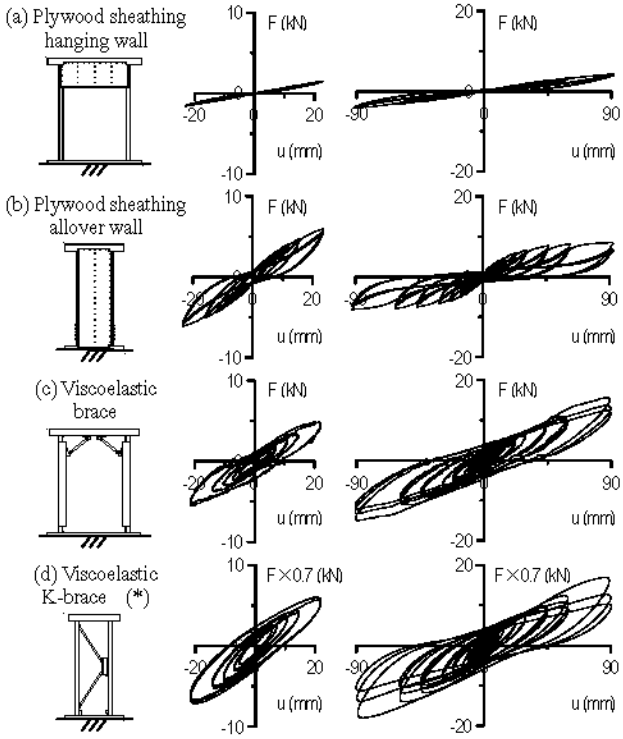

Figure 3 The shear force-deformation relationships of timber shear walls and passively controlled walls
(*) Note : Shear force of VK is multiplied by 0.7.

One is '*viscoelastic brace*' described as 'VB'. Although VB has a large opening so that it can be installed in flexible side frame as well as HW, it can give supplemental stiffness and damping to flexible side frame. Another is '*viscoelastic K-brace*' described as 'VK'. It is installed in stiff side frame and transverse frames.

In our previous research, static lateral loading tests for HW and AW, and dynamic lateral loading tests for VB and VK were conducted. The shear force-deformation relationships obtained are shown in Figure 3. Stiffness and strength of HW are clearly much less than those of AW. Compared to the hysteresis of AW, those of HW seem to be nearly elastic. This is because the shear resistant mechanism of HW consists of two types of components ; one is shear resistance of nails fastening plywood sheathings, and another is bending of column which reacts nearly

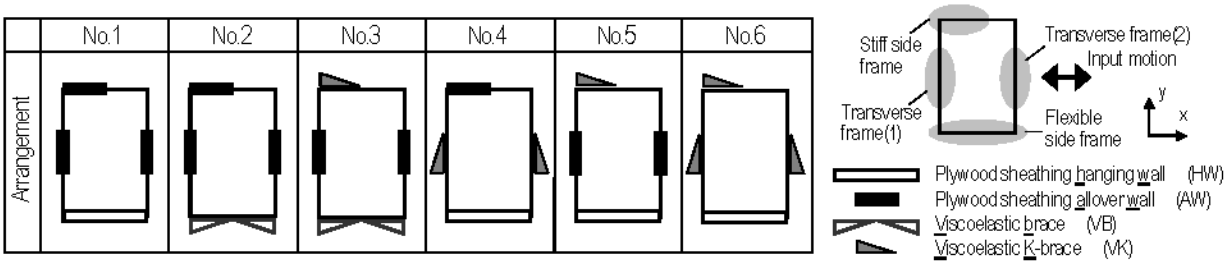

Figure 4 The list of specimens

elastically. On the other hand, the hysteresis of VB and VK are constantly ellipse from small deformation to large deformation by adding viscoelastic damper. They do not show slip-type hysteresis, which is unique to timber structure. The obtained multiplier of bracing unit of these walls are HW = 0.4, AW = 3.3, VB = 1.6 and VK = 5. In this paper, it should be noted that multipliers of bracing unit are the index of shear strength when drift angle of the walls are 1/120 rad. divided by standard strength (= 1.96 kN) and the wall length. It turns out that stiffness and strength of VK are much more than those of AW. For this reason, the amount of viscoelastic material of VK is reduced to 0.7 times that in the following shaking table tests. It means that strength of VK becomes the same as that of AW when drift angle of the walls are 1/240 rad. by referring to our previous dynamic characteristics prediction rule for passive control system. Since stiffness of VK almost depends on damper stiffness, 0.7 times tested shear force are shown in Figure 3(d), which is likely to give a good agreement with hysteresis obtained in the following shaking table tests.

2.3 PARAMETER OF SPECIMENS

The list of tested specimens and predicted behavior in dynamic state are shown in Figure 4 and 5, and design aims of each specimen are described as follows.

No.1 : all the four frames consists of timber shear walls. In other words, it has no passive control devises. Referring to stiffness of each frame obtained from Figure 3, we can find that the eccentricity ratio R_e, defined by Japan Building Standard Law is 0.56 for this specimen. Since R_e must not exceed 0.3 in Japanese design code of wooden house, severe torsional vibration probably occurs. The disarrangement between c.m. and c.s. causes torque corresponding to rotatory inertia multiplied by angular acceleration around c.m..

No.2 : Flexible side frame is reinforced with VB. In other words, supplemental stiffness and damping are added to opening. As a result, c.s. is approached to c.m., and the above torque is reduced. In addition, damping force applied by VB located in flexible side can effectively damp torsional response.

No.3 : VB and VK are installed in flexible and stiffness side frames respectively. Both frames in X-direction of this specimen are passively controlled in order to reduce translation as well as rotation.

No.4 : VKs are installed in transverse frames, which aims to reduce rotation by viscous force perpendicular to input motion. This specimen is expected to control torsional response without reinforcement in X-direction.

No.5 : VK is installed in stiff side frame. Although unexpected large torque can be caused by viscous force in stiff side frame, main aim for this specimen is to reduce translation.

No.6 : VKs are installed in stiff side frame and transverse frames. All the frames except for flexible side frame are passively controlled, and its effectiveness is examined.

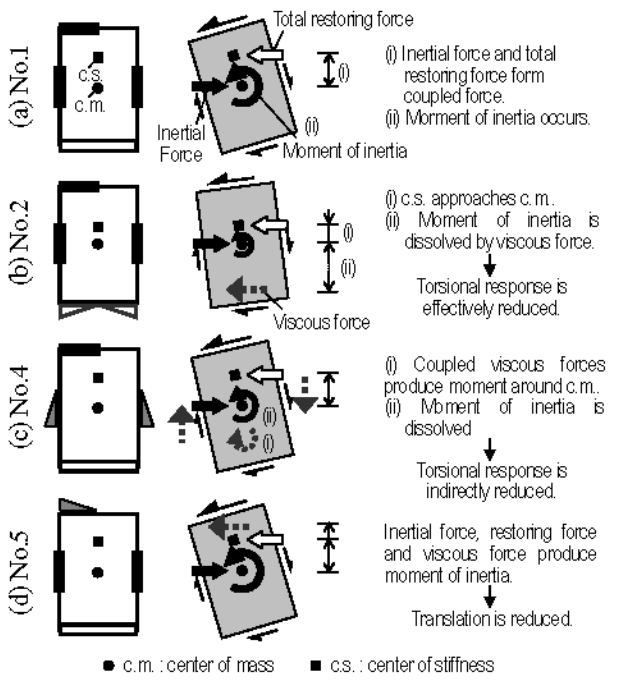

Figure 5 Predicted behavior in dynamic state

2.4 MEASUREMENT METHOD

As shown in Figure 6, relative displacement of each frame are measured from measurement steel frame, and geometrically calculated by assuming stiff horizontal diaphragm. By way of parenthesis, the adequacy of above assumption is confirmed. Shear force bore by each frame are also measured. It is calculated by subtracting inertial force applied in lower side of specimen out of base shear force measured by shear-type load cell set under each steel foundation beam. Besides, damper deformation, temperature of viscoelastic material, post-and-beam joints deformation and tensile force of bolts for metal joints are measured.

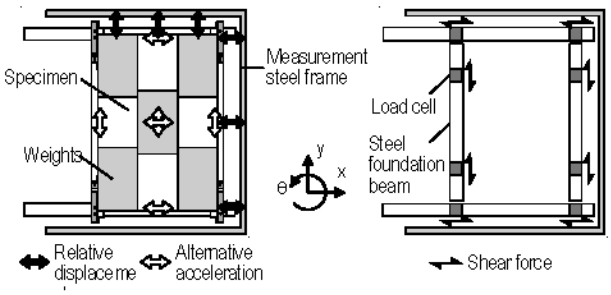

(a) Relative displacement and absolute acceleration (b) Shear force

Figure 6 The measurement method of displacement and shear force

2.5 SCHEDULE OF INPUT MOTIONS

The schedule of input motions is shown in Table 1. 1995 JMA Kobe record NS component (described as Kobe wave in this paper) and 1952 Taft record EW component (described as Taft wave) are selected, which are different in dominant frequency and duration time of main wave. White Noise motions whose maximum acceleration is scaled to 0.05g are applied to specimen between input earthquakes in order to observe change of dynamic properties. At first, Kobe wave whose maximum acceleration scaled to 0.1g is applied. In the following statement, this input motion is described as '*0.1g Kobe wave*', and the others input motions are described similarly. After that, 0.2g Kobe wave, 0.2g Taft wave, 0.6g Kobe wave and 0.2g Kobe wave(2) are applied in order to observe behavior against small earthquake after experiencing severe earthquake. Tensile force is applied to the bolts for metal joints again, and 0.83g Kobe wave which is full-scale motion is applied. In the case of No.2, No.3 and No.6, 1g Kobe wave is applied after that.

Table 1 Schedule of input motions

Input No.	Input motion	Max acc.
1	JMA Kobe NS	0.1g
2	JMA Kobe NS	0.2g
3	Taft EW	0.2g
4	JMA Kobe NS	0.6g
5	JMA Kobe NS	0.2g
Reinforcement of the metal joints bolts		
6	JMA Kobe NS	0.83g (Full scale)
Reinforcement of the metal joints bolts		
7	JMA Kobe NS	1g

Note : Input No.7 is conducted for Specimen No.2, No.3 and No.6. White Noise motions are applied between each input motion.

3. RESULTS OF SHAKING TABLE TESTS

3.1 SHEAR FORCE-DEFORMATION RELATIONSHIPS AND MAXIMUM DEFORMATIONS OF EACH FRAME

Shear force and deformation relationships for (a) flexible side frame and stiff side frame, and (b) transverse frames subjected to 0.2g Kobe wave, 0.6g Kobe wave, 0.2g Kobe wave(2) and 0.83g Kobe wave are shown in Figure 7. Since there are little differences in two pairs of hysteresis of transverse frames, the result of transverse frame(2) are shown in Figure 7(b). Let F_{x1}, F_{x2} and u_{x1}, u_{x2} be shear force and deformation of flexible and stiff side frame respectively. Similarly, let F_{y1}, F_{y2} and u_{y1}, u_{y2} be those of transverse frame(1) and (2). The results of all the specimens are summarized as follows.

As for No.1, behavior of all the frames is almost liner in the case of 0.2g Kobe wave. However, stiffness of both flexible and stiff side frame are decreasing, and especially hysteresis of stiff side frame becomes slip-type one in the case of 0.6g Kobe wave. In comparison between the results of 0.2g Kobe wave and 0.2g Kobe wave(2), stiffness of all the frames are decreasing after strong earthquake. At last, all the frames get severe damage, and deformation angle of transverse frames exceed 1/120rad. in the case of 0.83g Kobe wave. It is noted that plasticity of transverse frame due to uni-directional input motion is unique phenomenon to asymmetric structure.

As for No.2 and No.3, installing VB in flexible side frame can significantly increase their stiffness, and their hysteresis become thick ellipses compared to those of No.1. As a result, both translation and rotation decrease, and these torsional response reduction effects also contribute to decreasing deformation of transverse frames. In other words, the behavior of No.2 and No.3 become nearly translation not including rotational component. Stiffness of stiff side frame of No.2, however, decreases a little in the case of 0.83g Kobe wave. No.3 has VK in stiff side frame, which keeps its behavior linear through all input motions.

As for No.4, since the specification of flexible and stiff side frame is the same as that of No.1, hysteresis of these frames is similar. The maximum deformation of transverse frame are much less than those of either flexible side frame or stiff side frame, which means dissipation energy of VKs is relatively less than those of HW or AW despite their high damping capacity. The reason for it seems to be as follows. Deformation of transverse frames is attributed to the roof's rotation only, and the contribution is affected by the ratio of plan dimension in X-direction to Y-direction. The length from c.m. to transverse frame is shorter than that from c.m. to flexible or stiff side frame as to tested specimens. Therefore bearing forces of transverse frames do not greatly contribute to resistant moment. In other words, installing passively controlled walls in transverse frames is more likely to be effective for the structure with long plan in X-direction.

As for No.5, the hysteresis of stiff side frame becomes very thick ellipse, and most of input earthquake energy is dissipated by VK in stiff side frame. As described in 2.2., VK is modified so that its strength in 1/240 rad. becomes the same as that of AW based on their result of static and dynamic loading test. Stiffness and strength of AW in this shaking table test, however, are higher than it has been assumed especially in small deformation. As a result, the stiffness eccentricity of No.5 is small compared to that of No.1.

Maximum deformations of flexible and stiff side frame through all input motions are summarized in Figure 8.

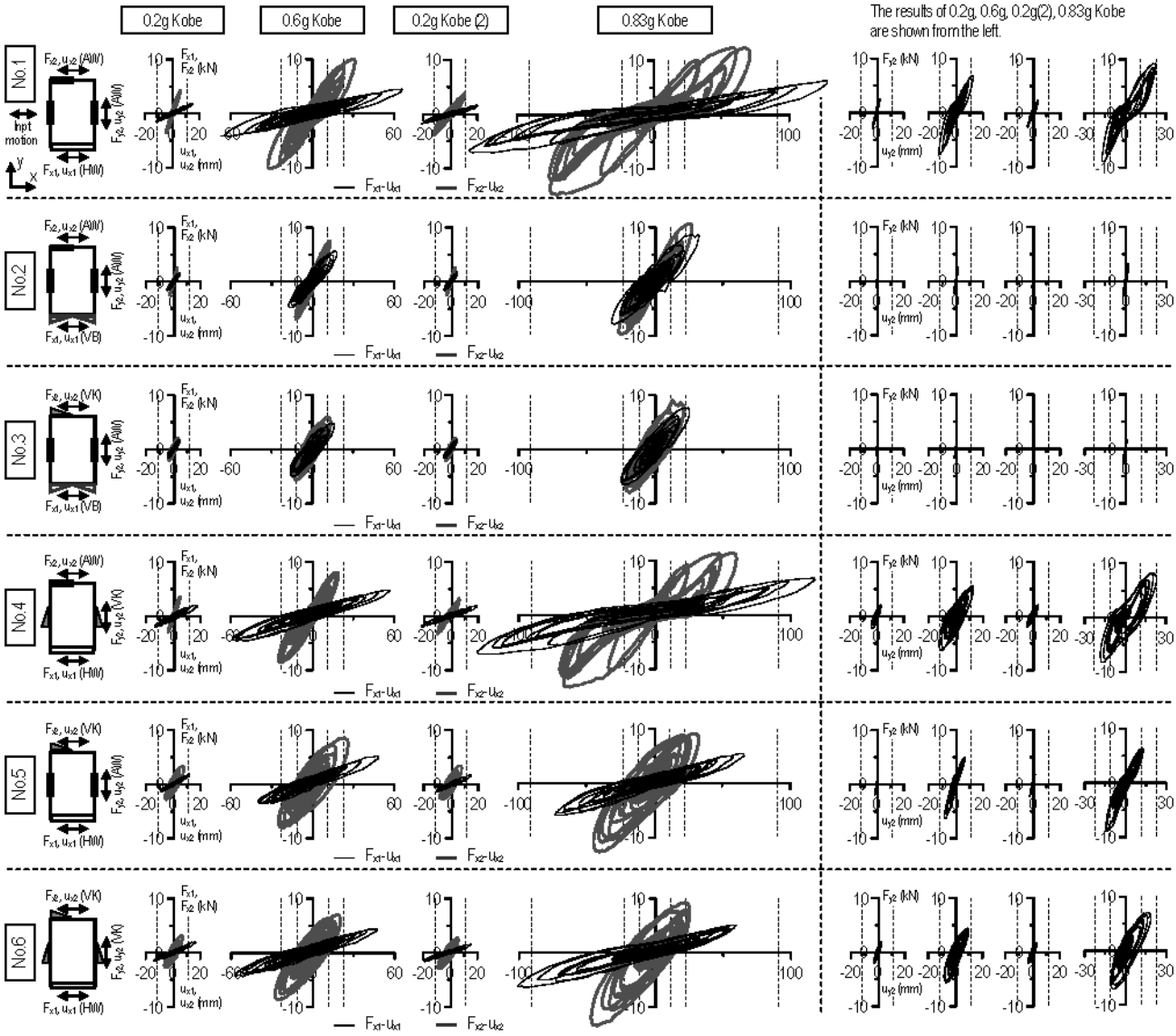

(a) Flexible side frame and stiff side frame (b) Transverse frame

Figure 7 Shear force-deformation relationships of each frame

Those of both flexible and stiff side frame of No.2 and No.3 are remarkably small compared to those of the other specimens. Moreover the differences of maximum deformations between flexible and stiff side frame become small, which means rotation are so decreased as not to affect translation. In addition, their response reduction effects are clearly confirmed in strong input motions rather than small input motions. This is because the states of their frames are relatively linear through all input motions although those of the other specimens become strong non-linear. In comparison between the results of 0.2g Kobe wave and 0.2g Kobe wave(2), maximum deformations in the case of 0.2g Kobe wave(2) become larger, as is especially definite as to No.1 and No.4. Since stiffness of VK is lower than that of AW as described above, maximum deformations of No.4 and No.6 are nearly the same as those of No.1. Maximum deformation of No.2 and No.3 subjected to 0.2g Taft wave become a little larger than those subjected to 0.2g Kobe wave, and opposite results are observed as for the other specimens. However, these differences are trivial.

Length of stiffness eccentricity, e_y of each specimen subjected to 0.2g Kobe wave is summarized in Table 2. The index e_y means distance from c.m. to c.s., and it is calculated using secant stiffness of each frame when its deformation becomes maximum value. We would like to emphasize that e_y is not so small as for No.2 in spite of its torsional reduction.

3.2 MAXIMUM ACCELERATION

As shown in Figure 9, inertial force and torque caused by excited acceleration are applied to c.m., which are caused by absolute acceleration of c.m. ($\ddot{u}_x + \ddot{u}_g$) and angular acceleration around c.m. ($\ddot{\theta}$) respectively. When angular acceleration increases, a distribution of acceleration becomes triangle or trapezoid. Therefore it is important to examine a distribution of acceleration. Those when 0.2g

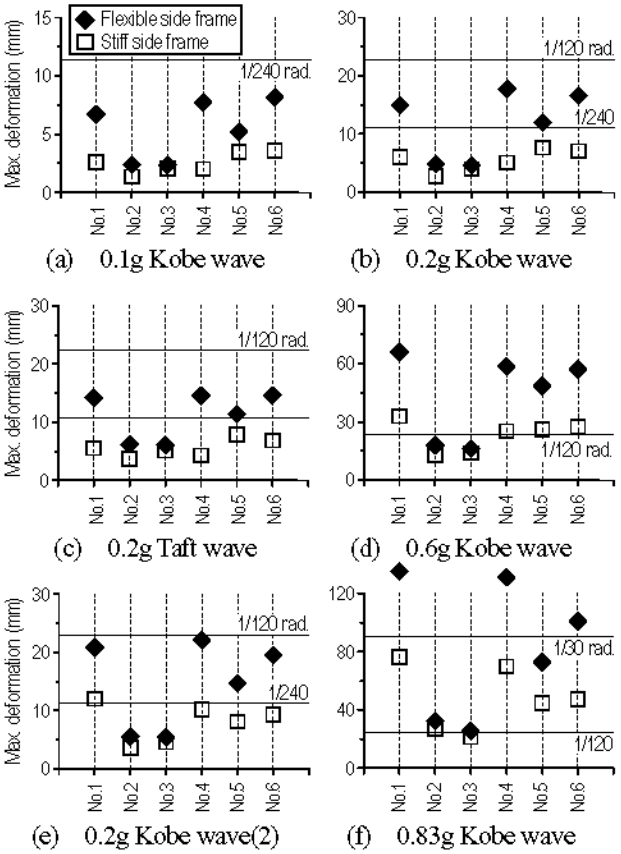

Figure 8 Maximum deformations of flexible side frame and stiff side frame

Table 2 Length of stiffness eccentricity e_y

Specimen	e_y (mm)	e_y/L_y (-)
No.1	976	0.36
No.2	664	0.24
No.3	231	0.08
No.4	1006	0.37
No.5	608	0.22
No.6	774	0.28

Kobe wave and 0.83g Kobe wave are applied are shown in Figure 10. It is note that they are affected by nonlinearity and higher mode response, which is differs to displacement response. For above reason, each distribution shape when acceleration of c.m., flexible and stiff side frame becomes largest is shown with bold lines, dot lines and thin lines respectively. And maximum acceleration and angular acceleration of c.m. are summarized in Table 3.

In the case of 0.2g Kobe wave, acceleration of c.m., flexible and stiff side frame become largest in the same distribution shape. The longer length of stiffness eccentricity e_y is, the larger the eccentricity of acceleration distribution become as to No.1, No.4 and No.6. As a result, about 0.2 times acceleration of c.m. occurs in transverse frames. Although No.2 has larger e_y than No.3 and No.5, angular acceleration of No.2 is the smallest in all the specimens. Angular acceleration especially decreases in the case of No.2 and No.3. In addition to it, translational acceleration also decreases, which means story shear force are also decreased.

In the case of 0.83g Kobe wave, three kinds of the acceleration distribution shapes differ as to No.1, No.2, No.4 and No.5, which means maximum acceleration of each frame become largest in different distribution shapes. The eccentricity of acceleration distribution of No.1, No.4, No.5 and No.6 when acceleration of c.m. becomes largest are a little loose slope compared to those in the case of 0.2g Kobe wave. The effect of angular acceleration, however, is large for No.1 and No.4, and maximum acceleration of transverse frames reaches 840 cm/s^2 for No.1 and 700 cm/s^2 for No.4. These values are about 0.5 times those of c.m.. Angular acceleration of reverse rotation occurs in the case of No.2.

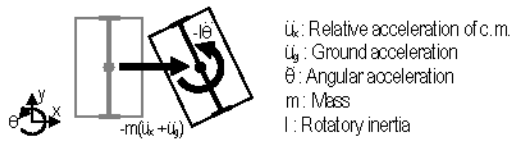

Figure 9 External forces

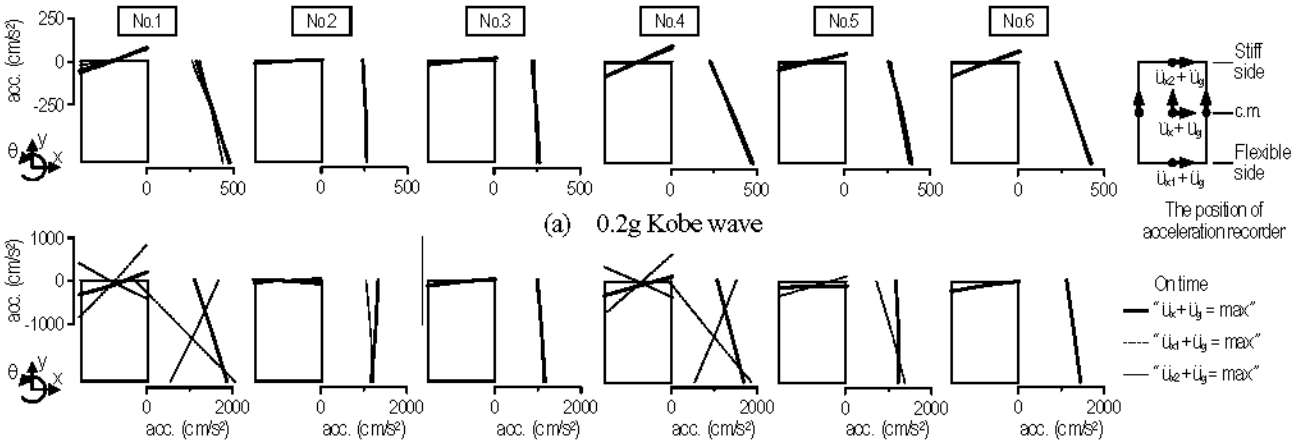

(a) 0.2g Kobe wave

(b) 0.83g Kobe wave

Figure 10 The distribution of maximum acceleration

Table 3 Maximum acceleration

	0.2g Kobe wave		0.83g Kobe wave	
	$(\ddot{u}_x+\ddot{u}_g)_{max}$	$\ddot{\theta}_{max}$	$(\ddot{u}_x+\ddot{u}_g)_{max}$	$\ddot{\theta}_{max}$
No.1	384	0.070	1509	0.276
No.2	258	0.009	1271	-0.058
No.3	246	0.017	1083	0.064
No.4	358	0.092	1385	0.226
No.5	336	0.050	1235	0.021
No.6	326	0.073	1290	0.119

$(\ddot{u}_x+\ddot{u}_g)_{max}$: Maximum acceleration of center of mass (cm/s²)
$\ddot{\theta}_{max}$: Maximum angular acceleration around center of mass on time "$\ddot{u}_x+\ddot{u}_g$ = max" (rad./s²)

3.3 THE EFFECT OF TORSION ON RESPONSE IN OUTER FRAMES

As shown in Figure 11(a), let u_x and Δu_x be translational displacement of c.m. and relative displacement in edge to c.m. respectively. The ratio of u_x to Δu_x is assumed a rotation effect index, and torsional responses of each specimen are compared quantitatively. In this part, torsional behavior of specimens subjected to 0.2g Kobe wave and 0.83g Kobe wave are discussed in order to examine the differences between small and large levels of deformation. The values of $\Delta u_x / u_x$ when deformation of c.m. becomes largest are shown in Figure 11(b).

In the case of No.1, the value of $\Delta u_x / u_x$ decreases from 0.43 to 0.28 as input motion increases. It also decreases as for No.4. However, there is important difference in the behavior between No.1 and No.4. In the case of No.4, the states of transverse frames which are passively controlled subjected to 0.83g Kobe wave. This behavior prevents keep their states nearly linear even though specimen is rotational stiffness from decreasing and leads to larger reduction degree of $\Delta u_x / u_x$ than that of No.1 as input motion increases. In the case of No.2, stiffness eccentricity is dissolved because flexible side frame keeps its state linear, and the state of stiff side frame becomes plastic when 0.83g Kobe wave is applied. Therefore the value of $\Delta u_x / u_x$ decreases as input motion increases. In the case of No.3 and No.5, the values of $\Delta u_x / u_x$ increase a little as input motion increases, as are different tendency from the other specimens. This is because stiff side frames keep their states linear, and stiffness eccentricity becomes larger in large deformation rather than in small deformation. In the case of No.6, the value of $\Delta u_x / u_x$ decreases a little because No.6 has intermediate character of No.4 and No.5.

We obtained the fact that when severe earthquake like 0.83g Kobe wave is applied, torsional response behavior changes as long as not all the frames are passively controlled. In this shaking table tests, the only passively controlled frames can keep their states linear. As a result, the following design methodology on the basis of plasticity in severe earthquake can be proposed. In order to reduce torsional response, installing passive control devises in flexible side frame or transverse frames is presumably effective. Oppositely, installing passive control devices in stiff side frame is likely to cause larger torsional response in sever earthquake rather than in small earthquake.

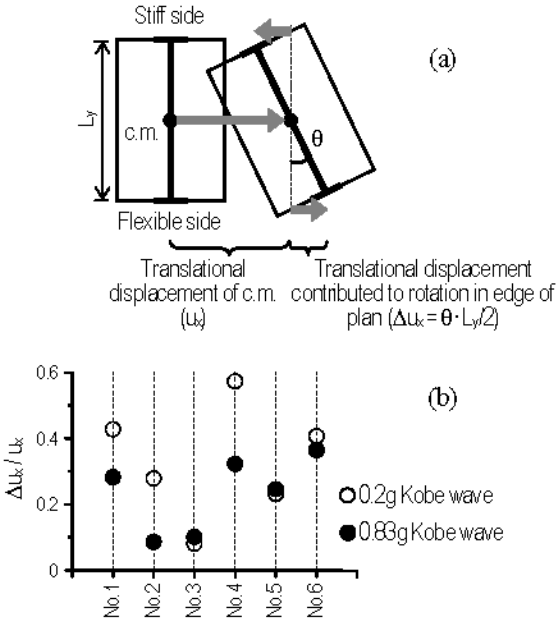

Figure 11 The effect of translational displacement contributed to rotation

3.4 DAMPER DEFORMATION

We describe the ratios of damper deformation to story drift as '*damper deformation ratio*' in the following statement. These values are defined as those when story drift becomes largest and compared in the cases of 0.2g Kobe wave, 0.6g Kobe wave, 0.2g Kobe wave(2) and 0.83g Kobe wave. The results are shown in Table 4.

Although VBs are used in flexible side frame where larger deformation is applied rather than that in c.m., damper deformation ratios of VBs are lower than those of VKs used in stiff side frame. This is the critical defect in VB or knee bracing system. In order to dissipate much energy with such small deformation, dampers are required to put out large force with high stiffness. Damper deformation ratios in transverse frames are approximately half of those in stiff side frames in these tests, which is likely to depend on the degree of torsinal response. Therefore high stiffness is also needed for dampers installed in transverse frames.

In the former subsection (3.3), we presented the change of torsional response behavior in small and large input motions and its dependency on the arrangement of passively controlled walls. However, all the damper deformation ratios decrease as input motion increases except for those of No.3 wherever passively controlled walls are installed. These reductions of damper deformation ratio are attributed to stiffness decreasing of the other timber shear walls. It prevents deformation from concentrating on damper. Therefore if not linear viscoelastic dampers but elasto-plastic dampers are used, damper deformation ratios can be increased in severe earthquake.

3.5 EVALUATION OF DYNAMIC PROPERTIES CONSDERING NON-PROPORTIONAL DAMPING

Dynamic properties for each specimen subjected to White Noise motions are evaluated. The tested models are

Table 4 The ratios of damper deformation to story drift

	No.2	No.3		No.4	No.5	No.6	
(Plan) θ, y, x Story drift Damper deformation	VB	(ii) VK (i) VB	(i) (ii)	VK	VK	(i) VK (ii) VK	(i) (ii)
0.2g Kobe	0.097	0.084	0.192	0.088	0.167	0.125	0.064
0.6g Kobe	0.089	0.102	0.204	0.058	0.152	0.132	0.056
0.2g Kobe (2)	0.077	0.079	0.171	0.061	0.162	0.122	0.055
0.83g Kobe	0.082	0.094	0.199	0.046	0.146	0.118	0.054

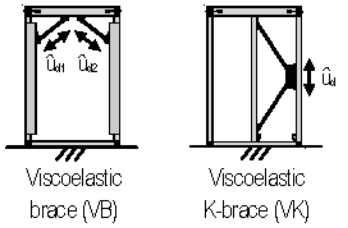

In the case of VB, $\hat{u}_d$ is defined as average of $\hat{u}_{d1}$ and minus $\hat{u}_{d2}$.
Note : $\hat{u}_{d1}$ and $\hat{u}_{d2}$ have opposite sign.

Table 5 Dynamic properties based on the results of White Noise input

	Before input motions				After 0.6g Kobe wave				After 0.83g Kobe wave			
	T_1 (sec.)	T_2 (sec.)	h_1 (%)	h_2 (%)	T_1 (sec.)	T_2 (sec.)	h_1 (%)	h_2 (%)	T_1 (sec.)	T_2 (sec.)	h_1 (%)	h_2 (%)
No.1	0.27	0.10	2.2	2.1	0.31	0.11	4.1	3.1	0.43	0.14	14.4	6.1
No.2	0.23	0.10	5.8	2.3	0.24	0.10	5.9	2.0	0.24	0.10	6.4	2.3
No.3	0.26	0.11	14.6	9.7	0.27	0.11	14.5	10.0	0.27	0.11	14.6	10.0
No.4	0.30	0.11	8.7	8.7	0.33	0.12	9.6	11.3	0.44	0.15	17.5	20.3
No.5	0.29	0.11	12.7	9.0	0.30	0.11	12.8	9.3	0.32	0.12	13.0	8.5
No.6	0.32	0.12	13.0	22.0	0.35	0.13	15.2	23.4	0.37	0.14	15.5	24.7

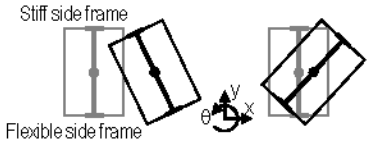

(a) 1st. mode (b) 2nd. mode

Figure 12 Typical mode shapes for 1-story structure with uni-axial eccentricity

non-proportional damping system, because viscous elements like passively controlled walls are arranged in non-proportion to stiff elements. The following study takes this effect into account.

Fourier spectra are calculated from acceleration records on the roof and the groundsills, and transfer functions for two degrees of freedom (2DOF) are obtained. These transfer functions can be determined in three positions (c.m., flexible and stiff side frame). Each of them is fitted to theoretical transfer function for 2DOF non-proportional damping system, and natural period and damping ratio of 1st. and 2nd. mode T_1, T_2 and h_1, h_2 are obtained respectively.

The dynamic properties in three states (before input motions, after 0.6g Kobe wave and 0.83g Kobe wave) are shown in Table 5, and typical mode shapes for 1-story structure with uni-axial eccentricity are shown in Figure 12. 1st. mode is dominant to translation, and 2nd. mode is dominant to rotation for regular structure. At first, the comparison of the dynamic properties of 1st. mode is summarized as follows.

In the case of before input motions, T_1 equals to 0.27 sec. and h_1 equals to 2.2 % as for No.1. Comparing these values of No.2 and No.3 to those of No.1, we can find that T_1 become short, and h_1 increase to 5.8 % and 14.6 % respectively because of their supplemental stiffness and damping in flexible side frame. As for No.4, No.5 and No.6, T_1 become long, and h_1 increase to 8.7 %, 12.7 % and 13.0 % respectively. Such increasing of h_1 for No.4 is notable although dampers are attached only to the transverse frames. This is a unique phenomenon for asymmetric structure in which translation and rotation are coupled. Maximum response of No.4, however, is almost the same as that of No.1 as shown in Figure 8. Therefore it is required that the enough amounts of supplemental stiffness and damping are added in proper arrangement, and natural period and damping ratio are controlled in order to reduce torsional response effectively.

In the case of after 0.6g Kobe wave, test results show that T_1 become long and h_1 increase through all specimens compared to those of before input motions. Especially, h_1 increase to 4.4 % as for No.1, and T_1 become about 1.1times long as for No.1, No.4 and No.6.

In the case of after 0.83g Kobe wave, T_1 of No.1 becomes 0.43 sec. which is 1.43 times longer than that before input motions, and h_1 increases to 14.4 % which is 6.5 times larger. Clearly No.1 gets severe damage. Compared to the above dynamic properties of No.1, those of No.2 and No.3 are kept almost the same as those before input motions. In other words, damage of No.2 and No.3 are remarkably reduced even though they are subjected to full-scale Kobe wave. T_1 of No.4 becomes 1.5 times longer than that before input motions. The comparison of No.5 and No.6 shows that No.5 can reduce more damage.

The change of 2nd. mode dynamic properties is summarized as follows. T_2 become long as frames get damage, which is similar to the tendency of T_1. No.1 and No.2 have almost the same value of h_2 before input motions. This is because a component of 2nd. mode shape in flexible

side frame is smaller than those in stiff side frame or transverse frames as shown in Figure 12. Oppositely saying, installing passively controlled walls either in stiff side frame or transverse frames is effective to increase h_2, and No.6 has the highest h_2 in all specimens.

Although it is omitted in this paper, above presented results are compared to the case that the tested model are assumed conventional proportional damping system. The results show that by assuming proportional damping, T_1 are overestimated from 1.01 times to 1.03 times and h_1 are evaluated from 0.77 times to 1.19 times, which has some dispersion. The dynamic properties evaluation method for proportional damping system as a whole gives a good agreement with that for non-proportional damping system.

3.6 DISTRIBUTION OF ENERGY DISSIPATION

In this part, we present distribution of energy dissipation when 0.2g Kobe wave and 0.83g Kobe wave are applied. The ratios of energy dissipated by each frame to energy provided by earthquake are shown in Figure 13. The amount of energy dissipated by each frame is calculated as a summation of area of shear force-deformation relationship, and the amount of earthquake input energy is a summation of them. By the way, it can be assumed that energy dissipated by timber shear walls consists of damage like nails' plastic deformation or local compression of timber materials in connection. On the other hand, it is confirmed that the amount of energy dissipated by VB mostly consists of damper dissipation energy, and their ratios are from 60% to 80 %. In the case of VK, they are from 80 % to 90 %. Therefore passively controlled walls can convert most earthquake energy to thermal energy by attached viscoelastic damper, and they can reduce damage of other members.

In the case of 0.2g Kobe wave, 40 % of input energy to No.1 is concentrated to flexible side frame. The other specimens can dissipate more energy in passively controlled frame. As for No.2, No.4 and No.5, the dissipation energy ratios in passively controlled frames are about 60 %, 50 % and 70 % respectively. No.3 dissipates almost all energy in two passively controlled frames.

In the case of 0.83g Kobe wave, the dissipation energy ratios in passively controlled frames decrease through all specimens. This is because hysteretic energy of timber shear walls increase as input motions increase. As for No.2 and No.4, those ratios decrease to 40 % and 20 % respectively, as is affected by plasticity of stiff side frame. Those ratios for No.3 and No.6, however, are not so decreased.

In addition, the relationship between T_1 before input motions and equivalent velocity with earthquake input energy, V_e are shown in Figure 14. As we know, V_e is nearly proportion to T_1 in short period. Since T_1 of No.4, No.5 and No.6 become longer than those of the other specimens due to lower stiffness of VK than that of AW, earthquake input energy to these specimens are relatively large. However, increasing stiffness of supplemental passive control devises is likely to lead to decrease of earthquake input energy.

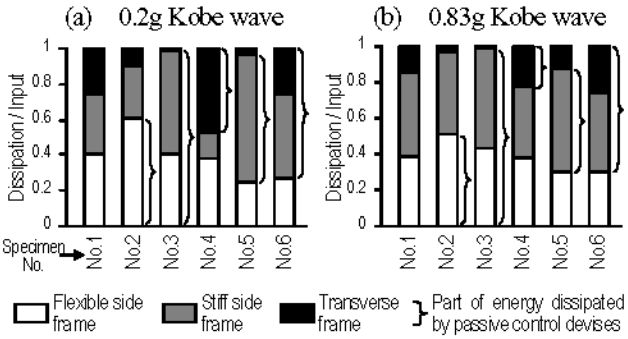

Figure 13 The distribution of energy dissipation

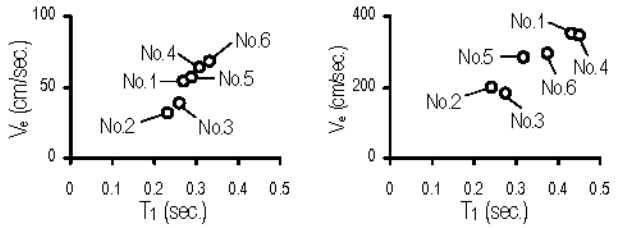

(a) 0.2g Kobe wave (b) 0.83g Kobe wave

Figure 14 The relationships between T_1 and V_e

4. CONCLUSION

In this paper, torsional seismic response reduction method by passive control devise is proposed, and its effectiveness is demonstrated. The following are findings obtained in this research.

(a) The most effective method for torsional response reduction is installing viscoelastic braces in flexible side frame.

(b) We propose the following design methodology on the basis of nonlinearity in severe earthquake. In order to reduce torsional response, installing passive control devises in flexible side frame or transverse frames is effective. Oppositely, installing passive control devices in stiff side frame can cause larger torsional response in sever earthquake rather than in small earthquake.

(e) In order to control torsional response, designers should use dampers with high stiffness for knee bracing system and transverse frames because of their small damper deformation.

(f) Installing passive control devises in flexible side frame contributes to increasing of damping ratio of 1st. mode. Moreover, installing passive control devises in transverse frames can increase damping ratio of 1st. mode and 2nd. mode when the structure has large stiffness eccentricity. It is notable that mode natural period and damping ratio are not changed whether the structure is assumed proportional damping system or non-proportional damping system.

Finally, it is necessary to pay attention to some assumption that considering model is 1-story structure with uni-axial eccentricity and stiff horizontal diaphragm, which is subjected to uni-directional input motion. Moreover attached passive control devises are only viscoelastic

dampers. Therefore restricted models are researched in this paper. Further research must be conducted in the future.

Acknowledgements:

This shaking table test is supported by Mr. Toyoshima, Mr. Miwa and their co-worker at Institute of Technology, Tokyu Construction Co., Ltd.. The specimens and dampers are provided by Mr. Kanai and Mr. Kajisa at Housing Structure Research Institute, Co., Ltd. and Mr. Tokoro at Sumitomo 3M Limiteds. We would like to express our gratitude to them.

References:

Murakami, M., Tahara, M., Fujita, Y. and Misawa, F. (1996). "Damage of Urban Wooden Houses by Hanshin-Awaji Earthquake," *Journal of structural and construction engineering. Transactions of AIJ*, Architectural Institute of Japan, (481), 71-80

Kasai, K., Sakata, H., Wada, A. and Miyashita, T. (2005). "Dynamic Behavior of A Wood Frame with Shear Link Passive Control Mechanism Involving K-Brace," *Journal of structural and construction engineering. Transactions of AIJ*, Architectural Institute of Japan, (598), 51-59

Sakata, H., Kasai, K., Wada, A. and Miyashita, T. (2005). "Experimental Study on Dynamic Behavior of A Wood Frame with Shear Link Passive Control Mechanism Involving Plywood Panel," *Journal of structural and construction engineering. Transactions of AIJ*, Architectural Institute of Japan, (594), 65-73

Sakata, H., Kasai, K., Wada, A. et al. (2007). "Shaking Table Tests of Wood Frames with Velocity-Dependent Dampers," *Journal of structural and construction engineering. Transactions of AIJ*, Architectural Institute of Japan, (615), 161-168

Kasai, K., Sakata, H., Wada, A. et al. (2005). "Shaking Table Tests of Wood Frames with Deformation-Dependent Dampers," *Journal of structural and construction engineering. Transactions of AIJ*, Architectural Institute of Japan, (594), 101-110

Sakata, H., Kasai, K., Ooki, Y., and Matsuda, K., (2008). "Experimental Study on Dynamic Behavior of Passive Control System Applied for Conventional Post-and-Beam Two-Story Wooden House Using Shaking Table," *Journal of structural and construction engineering. Transactions of AIJ*, Architectural Institute of Japan, (631), 1607-1615

Noguchi, H. et al. (2006). "Earthquake Response Control of Timber Structure with Unbalanced Distribution of Shear Walls Utilizing Viscoelastic Damper : Shaking Table Test with Three-Dimensional Model and Analysis of Response Mechanism," *Journal of structural and construction engineering. Transactions of AIJ*, Architectural Institute of Japan, (600), 123-130

Soda, S. et al. (2004). "Seismic Strengthening of Existing House with Compressive Oil Dampers," *Summaries of technical papers of Annual Meeting Architectural Institute of Japan*, Architectural Institute of Japan, B-2, 105-106

Koshihara, M. et al. (2002). "Experimental Study on Seismic Performance of Wooden Shear Wall Structure with Eccentricity Subjected to Static Loading," *Journal of structural and construction engineering. Transactions of AIJ*, Architectural Institute of Japan, (558), 165-171

Agawa, M. et al. (2002). "Experimental Study on Dynamic Properties of Timber Shear Wall Structures with Eccentricity," *Journal of structural and construction engineering. Transactions of AIJ*, Architectural Institute of Japan, (558), 157-164

Kasai, K., Yamashita, T., Yamazaki, Y. and Igusa, T. (2009). "Spectrum-Based Response Prediction of Asymmetric Structure with Supplemental Viscous Dsmping," *Journal of structural and construction engineering. Transactions of AIJ*, Architectural Institute of Japan, 74(636), 225-234

JOINT CONFERENCE PROCEEDINGS
7th International Conference on Urban Earthquake Engineering (7CUEE) &
5th International Conference on Earthquake Engineering (5ICEE)
March 3-5, 2010, Tokyo Institute of Technology, Tokyo, Japan

ANALYSIS AND EXPERIMENTAL APPROACHES ON SEISMIC PERFORMANCE OF ARCHITECTURAL CURTAIN WALLS

Wensheng Lu[1)], Baofeng Huang[2)], Shiming Chen[1)]

1) State key laboratory of disaster reduction in civil engineering, Tongji University, P.R. China
2) College of Civil Engineering, Tongji University, P.R. China

wenshenglu@vip.163.com, ceowolf@163.com, chensm@tongji.edu.cn

Abstract: Seismic performance of the curtain wall system being treated as nonstructural components is analyzed. The seismic mechanism including acceleration initiation, deformation behavior as well as the interactive action between the curtain wall and the main structure is discussed. Curtain walls are types of hybrid sensitive components, so that different seismic mechanisms would occur for the curtain walls in different buildings. Two seismic indices, AAFs and ISDRs are presented. The advisable specific indices are proposed based on the scaled structural modeling for the shaking table test of highrise buildings, which are slightly greater than those proposed in the current specification. Seismic test approaches are discussed and commented. The methodology in further verified both the static and the shaking table tests is suggested, and problems arising in both the static and the dynamic tests are also analyzed.

1. INTRODUCTION

For years, few researchers have been care for the seismic performance of architectural curtain walls since they are very light in mass, and also known as the secondary members attached to the main structures of buildings. Being formed as an envelope system, architectural curtain walls do not share the action of the main structure. Conventionally, unit curtain wall system is suspended to the structural members at each floor. The history of curtain walls is less than 60 years since they have been utilized as a member of the building. During that period there were not so much serious earthquakes occurred and the seismic performance of curtain wall have not been tested actually. Until the end of last century, the novel theory-performance based seismic design was advocated, researchers and designers started to pay more attention to the seismic performance of the nonstructural components considering economic and functional issues. Improving the seismic performance of nonstructural components including architectural curtain walls is one of the aims of performance based seismic design. Seismic study of curtain wall consists of seismic mechanism analysis and experimental investigation approaches.

2. SEISMIC MECHANISM

There are various seismic mechanisms depending on the different materials used and different structural types of curtain walls. Curtain wall components are possibly displacement sensitive, acceleration sensitive and hybrid sensitive since their structural characteristics respectively. FEMA74 (USA, 1994, 2005) suggests that use of tempered glass and laminated glass can reduce seismic hazard greatly because the falling of the relative large glass panels from the buildings can be avoided efficiently. Earthquake action adaption is the prominent property of the curtain wall instead of bearing and transferring it. Deformation and acceleration action would occur at each floor level where the curtain wall is installed on the main structure during earthquake are the real action which the curtain wall members have to endure (Huang and Lu, 2009). Some researchers (Pantelides, 1994, Behr et al. 1995, 1996) paid more attention to the deformation ability of the glass panels as the inertial force is below their bearing capacity, while the in-plane stiffness may not allow the possibly large deformation passing from the main structure. Since deformation and acceleration at each floor are varying, the curtain wall systems are usually large in scale, so that it is very difficult to scale down the curtain wall specimen in a laboratory to investigate their seismic performance. Current test methodologies would only be applicable to individual members while the interaction between them is still unclear. It should be essential to improve the seismic test methodologies in base of fully understanding the seismic mechanisms of different curtain wall systems.

2.1 Acceleration Initiated Mechanism

2.1.1 Acceleration Distribution

Curtain wall system receive the earthquake acceleration

action at each floor passes by the main structure. The peak ground acceleration (PGA) was amplified on every floor level. The floor responses in time history are different from each other on different levels. Therefore, the peak floor acceleration (PFA) is various along the height of the buildings. Obviously, the PFA value is increasing from the foundation to the top of the structure for first mode controlled building. As for highrise buildings, their higher modes can also prominent comparing to the lower modes, thus their acceleration distribution are complicated.

The acceleration distribution may diversify on certain floor levels if the cross section of the main structure irregular. As for large span structures such as gymnasiums, auditoriums and airport terminals, the acceleration may various in three dimensions especially on the irregular roofs and the elevations.

2.1.2 Acceleration Transfer

Generally, curtain wall system consists of anchoring members, supporting frames, clue and panels. First, the ground acceleration response was passed to the main structure through the foundation. Then the main structure starts to vibrate under the action of the ground motion. The acceleration response was transferred to the anchoring members, if the anchoring members are rigid enough, the acceleration was then transferred to the supporting frames without reduction connected with them. However, if the anchoring members are flexible or the anchoring details allow a certain displacement, the acceleration will be reduced comparing to the original one.

Types of curtain wall's supporting systems are various. If the frames are absolutely rigid, they will not amplify the acceleration they acquire from the anchoring members. But they are flexible actually because their flexible structural types, small cross sections, and flexible materials. Therefore, the acceleration is frequently amplified by them and then is transferred to the glass frames or the glass panels.

As for framed curtain wall, the glass frames are frequently made up of aluminum alloy, their sections are usually thin and the modulus is smaller than steel. The acceleration value can be amplified in the middle span of the unit type curtain wall. As for point supported curtain wall, however, the rigidness of the metal claw determined its acceleration transferring ability.

Silicone was buried between the aluminum alloy frame and the glass panel. Its mechanical performance is relative tender than the frame and the panel. This way, the deformation deference between the frame and the panel is allowed because the existence of the silicone. Consequently, the acceleration value in the direction parallel and perpendicular to the panel surface is thus reduced.

Nowadays, the curtain wall glass panels are large in scale, this lead to the inertial force action different from the sides to the middle of the panel. The acceleration response is amplified by the curtain wall panel. But the amplification value is determined by the panel shape, material and so on.

Besides the horizontal acceleration transfer action, vertical transfer action occurred in the large span curtain wall systems. The transfer procedure is equivalent except for the different transfer ability and then the amplification factors.

In summary, acceleration transfer action running through the overall curtain wall system, it starts from the anchoring members and ceases at the panels. The process is clear but the specific transfer factors are not so easy to determine as it comprising structural, material, and constructional issues. Once the acceleration transfer mechanism are clear, the seismic performance analysis come to be efficient since it provides an analytical approach.

2.2 Deformation Initiated Mechanism

2.2.1 Deformation Distribution

As for low-rise buildings, the first mode controlled its overall deformation shape. The inter storey drift ratio achieves maximum value at first storey, while it reduces to minimum at the highest storey. As for highrise building, however, the inter storey drift ratio distribution is complicated because the higher modes have unignorable effect to the overall deformation shape. As a kind if secondary system, the curtain wall has to endure the deformation acted by each storey. Therefore, the deformation demands are different along every storey. The specific deformation demands of the curtain wall will be discussed in the following section of this paper. As for large span structures, the deformation demands are even more complicated because the deformation distribution of the main structure almost has no united rules. Special seismic analysis and dedicate test should be done to prove its security under earthquake action.

2.2.2 Deformation Transfer

The curtain wall system has to adapt to the deformation acted by the storey drift. Flexible anchoring details reduce the deformation action to the supporting system. Then, the supporting system can also reduce the deformation, finally, the last deformation which was reduced for two times was acted to the panels. The reason of the deformation reduction action is the curtain wall components (anchoring members, supporting systems, clue and panels) have the deformation ability on the base of their structural types and materials.

Just because the deformation reduction ability is prominent, curtain wall system thus has the excellent seismic performance to endure the earthquake action. According to this, many people consider the seismic performance of the curtain wall is outstanding, and some other people think the deformation ability is more important than the acceleration resistance ability during earthquake. However, it is not so clear that how the deformation occurred and how to acquire a uniform equation to calculate it in a very accurate way. Furthermore, it is very hard to say which kind of ability of the curtain wall controls the overall earthquake response because the dynamic characteristics is various on different curtain wall systems, panels and materials. And even the structural types, site conditions, the height and the span of the building pose importance to the curtain wall. Cautious and comprehensive analysis is very necessary to understand this mechanism.

2.3 Curtain Wall-Structure Interaction

It is difficult to calculate the natural frequency of the curtain wall system. But it is believe that the fundamental period is longer than the one of the main structure. Therefore, as for the low-rise building, whose natural period is shorter than the curtain wall's. The dynamic interaction is not so obvious. As for the highrise buildings, their natural period are identical, thus the interaction may be prominent in certain stories. As for the large span structures, the curtain wall is the important part of the whole. Curtain wall- structure interaction upgrades into a structural problems for seismic calculation and analysis.

The direct action to the curtain wall unit is the floor response. According to the floor spectra, it is easy to identify whether the interaction is important or not. As the spectra acceleration achieves peak value at the natural period of the curtain wall unit, the interaction will be serious because of the resonance. Consequently, the floor response analysis is necessary to determine the interaction level. It is believe that the interaction accounts for small part of the overall earthquake action of the whole building. But it will be serious to the curtain wall systems in economic and structural issue.

3. DISCUSSION ON THE SEISMIC INDICES

Normally, curtain wall is a kind of hybrid sensitive nonstructural component. It is flexible in the direction perpendicular to the surface of the façade, while it is rigid in the direction parallel to the surface. Therefore, curtain wall is acceleration sensitive in the direction of out-of-plane and displacement sensitive in direction of in-plane. Acceleration index and deformation index should be determined before the seismic test and relative seismic performance study.

3.1 Acceleration Index

3.1.1 Current Research Results

Chinese codes (JGJ102-2003 and JGJ133-2001) mention that the peak acceleration value of the curtain wall members should be the 5.0 times of the designed peak ground acceleration. It is only an experienced specification without serious research works. According to shaking table tests and relative seismic analysis, Huang and Lu (2009) prove that the acceleration amplification factor (AAF) above could not promise the security of curtain wall members especially for the curtain walls installed on the high-rise buildings. Uniform Building Code (UBC1994, UBC1997, USA) provides a equation to calculate the inertial force of the nonstructural components, the maximum AAF is 5.0. According to the records observed by the accelerographs installing in the 405 buildings, FEMA303 (1997) obtained the AAF distribution along the height of the buildings. The maximum value is less than 4.0. In order to get the AAF of each floor of a certain building, comprehensive analysis is necessary. This is usually time consuming and uneconomical especially for complicated structures in real project. M.P. Singh (2006) presented simplified methods for calculating the seismic force coefficient for flexible nonstructural components in buildings. His research work showed that the maximum AAF value of multistory building is near to 6.0. Miranda (2005) and Taghavi (2005) also analyzed the floor acceleration demands in multistory building, as for high-rise buildings, the method itself might be uneasy to execute efficiently. The specifications and research results above are mainly aim at equipments or facilities anchored on the buildings and they may not efficient to curtain walls. Shaking table test on scaled model of high-rise buildings is convenient to acquire the AAF.

3.1.2 Shaking Table Test Study of Model Structure on AAF

According to the shaking table test research reports on the super highrise buildings, complicated highrise buildings, and buildings with various structural types, AAF distribution curves (Figure 1) along the height of the model structures (Lu and Huang, 2008).

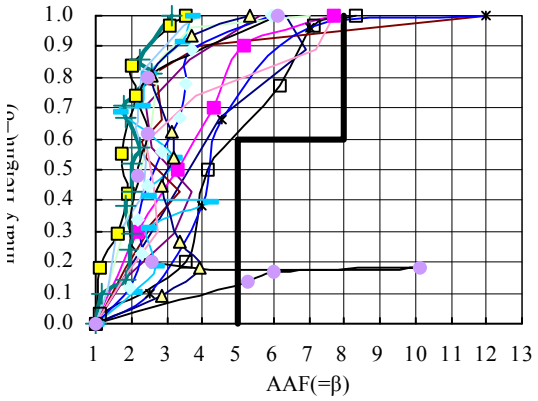

Figure 1 AAF Distribution along the Unitary Height

According to Figure1, it is advised to regulate the curve of β along the height of the main structure, β=5.0 as δ<0.6, β=8.0 as δ>0.6 (refer to the black bold line in Figure 1). At the same time, near the top of the building β could be increased according to the site conditions, height, intensity, structural type and the importance classification of the main structure, the amplitude should be less than 2.0. As for the floors near the ground, β can be reduced, but the amplitude should be less than 3.0.

3.1.3 Acceleration Index Selection

Current research results do not provide the designers an efficient AFF value in curtain wall design and test. Thus the acceleration index selection seems to be very subjective and it lies on the designer's experience and understanding of the aseismic performance of curtain wall.

The author introduces the AAF value as 5.0 for design and test for normal curtain wall of midrise buildings. For highrise buildings, large span buildings, however, 8.0 is a advisable choice if there is no enough research material to reference to. Group discussion and review is necessary when determining the AAF of super highrise buildings and complicated structures, seismic tests are surely to be efficient in AAF determination.

Considering the acceleration distribution along the height of the building, the AAF value should be diversified along the building height as mentioned by Lu and Huang (2008).

3.2 Deformation Index

3.2.1 Current Research Results

It is specified that the deformation ability of the curtain wall system should be no less than three times of the elastic inter storey drift limit ratio (JGJ102-2003, 2003 and JGJ133-2001, 2001). But the Elastic inter storey drift ratios (ISDR) are far more smaller than the elasto-plastic ones (see table 1 and table 2, GB 50011-2001, 2001). It is obvious that the curtain wall deformation ability is not efficient as the ISDR value in the elasto-plastic area of the main structure in far more bigger than the three times specification. Under the issue of performance based seismic design, this specification seems more improper. FEMA 302 also recommends allowable storey drift for various buildings (1997, See Table 3). The ISDR values are different according to the seismic group. It does not mentions the bearing state of the main structure. Moreover, the maximum value specified by FEMA 302 is bigger than the one of the GB 50011-2001. However, neither of them mentions the deformation distribution along the height of the building.

Table 1 Elastic Inter Storey Drift Ratio Limitation

Structural Types	ISDR
RC frame	1/550
RC frame-shear wall, Plate column-shear wall and Frame-tube	1/800
RC shear wall, Tube system	1/1000
RC frame support storey	1/1000
Steel structure	1/300

Table 2 Plastoelastic Inter Storey Drift Ratio Limitation

Structural Types	ISDR
Single storey RC frame	1/30
RC frame	1/50
Frame-shear wall of bottom frame masonry structure	1/100
RC frame-shear wall, Plate coloum-shear wall and Frame-tube	1/100
RC shear wall, Tube system	1/100
Steel structure	1/50

Table 3 Allowable Storey Drift

Structure	Seismic Group		
	I	II	III
Structures, other than masonry shear wall or masonry wall frame structures, four stories or less in height with interior walls, partitions, ceilings, and exterior wall systems that have been designed to accommodate the story drifts	0.025	0.020	0.015
Masonry cantilever shear wall structures	0.010	0.010	0.010
Other masonry shear wall structures	0.007	0.007	0.007
Masonry wall frame structures	0.013	0.013	0.010
All other structures	0.020	0.015	0.010

3.2.2 Shaking Table Test Study of Model Structure on ISDR

According to the shaking table test research reports on the super highrise buildings, complicated highrise buildings, and buildings with various structural types, ISDR distribution curves (Figure 2) along the height of the model structures.

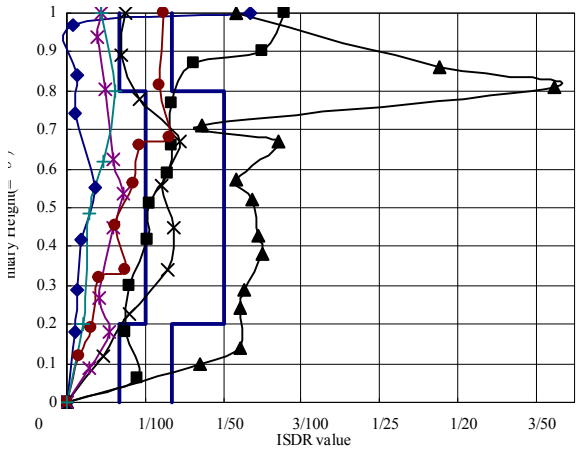

Figure 2 ISDR Distribution along the Unitary Height

According to Figure 2, it is concluded that:

1) The ISDR values were almost below 1/50, and many θ values were about 1/100.

2) Generally, ISDR distributions along the height of the main structure were various as various main structural types. As for the shearing deformation leading structures, ISDR values were near the lower stories, as for the moment deformation leading structures, the peak ISDR values might move to the mid-height of structures. As for the moment-shearing deformation leading structures, however, the peak ISDR values might occur along lower stories and the mid-height of structures. As for the structures with slender higher stories, the θ values could increase abruptly.

The moment-shearing deformation is the primary deformation style as for many high-rise buildings. According to Figure2, it could be found that:

1) Near the first floor of the structure, where δ is between 1.00 and 0.20, θ is increasing along the height of the structure.

2) As δ is between 0.20 and 0.80, θ is relatively bigger and 3) as δ exceeds 0.80, θ decrease.

As for the same the building structure, the deformation of the mid-height of the structure is bigger, thereby, the curtain wall installing in this area should have enough deformation capacity to adopt the plastic deformation requirement. According to Code for Seismic Design of Buildings (GB 50011-2001), parameters of the drift angles of the curtain wall could be referenced. Near the base and the top of the structure, where $\delta>0.80$ and $\delta<0.20$, ISDR is the 2/3 of the plastic deformation capacity of the main structure, as shown in table 4.

Table 4 Advised Storey Drift

Structure Type	0.20<δ<0.80	δ<0.20 or δ>0.80
R.C frame	1/50	1/50
R.C frame-shear wall or Slab column–shear wall or Frame-tube	1/100	1/150
R.C. shear wall or tube system	1/100	1/150
Steel structure	1/50	1/75

Note: 1. The content of the table is applicable to bending-shearing leading building structure, as for other structures, this table could be referenced according to experience and experiment.

2. As for R.C frame supported story, ISDR shall be selected according to its location, ISDR =1/120 is advisable.

3.2.3 Deformation Index Selection

There are no universal deformation indices applicable to various kinds of curtain walls and main structural types. Anyway, it is a guideline that the deformation ability (ISDR value) of the curtain wall should be no less the deformation ability of the main structure. The designer can use the ISDR which is not discussed in this paper once he has reasonable technical basis.

4. EXPERIMENTAL APPROACHES

Seismic mechanism and seismic indices are premises of seismic test of curtain wall. There are two kinds of test approaches, one is static test, the other is shaking table test. Experimental methodology design and practice are important to the seismic performance investigation.

4.1 Static Test

Many studies reported in-plane seismic test of curtain wall panels (Behr, 1995, 1996, 2006; Brueggeman, 2000; Memari, 2003, 2004; Pantelides, 1994, 1996). AAMA (2001) also provides a recommended test methodology to guild the experiment seismic performance evaluation. But they all focus on the deformation capacity of the curtain wall panels without considering the acceleration action bearing by the panels during earthquake action, and the test results are proved the to be efficient only to the framed curtain wall. However, it is not yet to be applicable to the point supported panels or the bear supported ones. The test loading plan and test setup should be improved according to the curtain wall types and capacity of the loading equipments.

4.1.1 Test Setup

Frequently, test setup of curtain wall consists of actuator, steel test frame and curtain wall specimens (Figure 3, AAMA, 2001). As for unit curtain wall, it is installed on each storey, and the framed panels are arranged in a vertical plane as the façade of the building, so the specimen should includes no less than three framed panels. The middle panel is the experimental target as the interaction between the neighboring curtain wall panels is easy to investigate. The steel test frame should be rigid enough to endure the load acted by the actuator. Furthermore, the natural frequency of the frame should be far from the loading frequency, otherwise, resonance is to be occurred and this experiment will be failed. The upper beam, lower beam and the adjust brace should have enough rigidness and bending resistant strength. Protection measures are necessary to prove the out-of-plane stability and the security of the actuator during the test. Finally, the connection between the actuator and the upper beam should be absolutely rigidity to reduce the displacement loss. Vertical displacement is another problem that should not be ignored once the obvious horizontal deformation occurred.

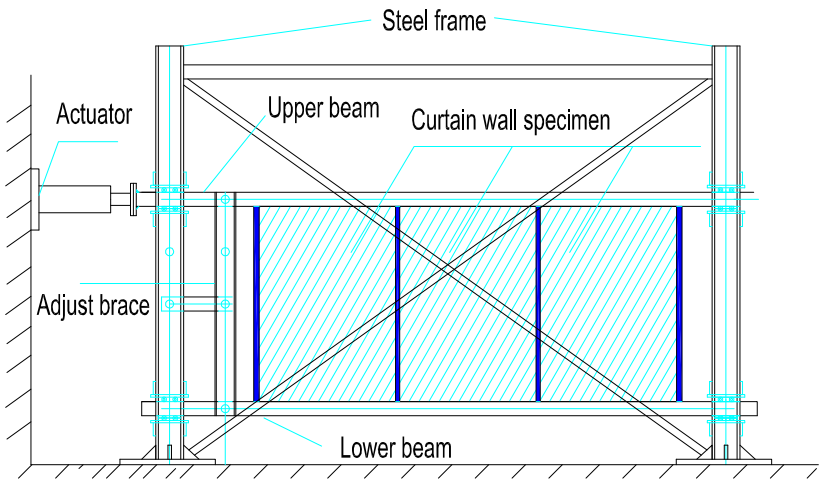

Figure 3 Static test setup

4.1.2 Loading Plan

Loading plan relates to the working performance of

actuator and loading demand of the curtain wall specimen. Behr (1995, 1996, 1998, 2006) and AAMA (2001) use two-stage loading curve, the loading frequency is about 0.8Hz in the first two minutes, and 0.4Hz until the specimen failed. Actually, as has been discussed in this paper, the earthquake action to the panel has a certain frequency, peak acceleration and time duration. The loading plan should realize the earthquake action in great effort.

Usually, the hydraulic power supply, flow rate, stroke and diameter of the rod are the fundamental parameters of a certain actuator. The dynamic relationship between the acceleration, velocity and displacement are describes by the following equation bellow.

$$d = A \bullet \sin \omega t \quad (1)$$

$$v = A \bullet \omega \sin \omega t \quad (2)$$

$$a = A \bullet \omega^2 \sin \omega t \quad (3)$$

Where, d=displacement, A=peak displacement, v=loading velocity, a=loading acceleration, ω=circular frequency.

1Hz 0.8Hz

Figure 4 Loading Curve

From equation (1) to (3), it is easy to find that once the peak displacement increase, the peak acceleration and loading frequency will certainly reduce because of actuator's performance limitation. As the building's design peak inter storey ratio is relatively big (1/50 for example), and the average distance between every neighboring floor is 3.0m, so the peak relative displacement is 3000×1/50=60mm. Once the loading amplitude is less than ±60mm, the loading frequency and acceleration should not be less than the peak floor acceleration. This demand the loading equipment have powerful capacity, of course, it needs plenty of financial investigation. Actually, this requirement is not so easy to be satisfied as the performance of the actuator is limited. The researchers have to prove at least one parameter in the experiment to realize the test purpose possibly. Furthermore, carefully designed test frame can reduce the difficulty through displacement amplification (Figure 3). The advisable loading curve see Figure 4 below, it is proved to be efficient in curtain wall seismic test.

4.1.3 Seismic Performance Evaluation

Seismic performance of the specimen is determined by the inter storey ratio of the main structure. Even under the same ground motion, the seismic demand can be different for different buildings or floor levels. As for the specimen itself, the seismic behavior comprise the excellent integrity and fallout resistance ability under peak floor acceleration and relative deformation. The researchers can get the aseismic ability of the specimens according to their damage levels under series of tests.

4.2 Shaking Table Test

Static test could not reproduce the earthquake action in time history. So the validity of the test result is doubtful. Shaking table can simulate the earthquake action very precisely once the test frame, floor responses, and test procedures are provide reasonably. Few researchers outside China execute shaking table test on curtain wall. In main land of China, however, as curtain wall is widely used in various buildings, people start to think much of its seismic performance. And thus many shaking table test on curtain wall were done each year. Due to the seismic mechanism and seismic indices are not so clear, the evaluation results distinguish with each other very much. Therefore, the methodology is necessary to develop. Lu and Huang (2008) put forward an improved shaking table test method for curtain wall, but it need further improvement to fit all the curtain wall types.

4.2.1 Steel Frame Design

Due its excellent flexibility, the steel frame is the first choice to be selected as the test frame for curtain wall shaking table test. The steel should have the deformation ability to satisfy the inter storey drift ratio demand of the curtain wall specimen. Besides this, it should also have the acceleration resistance ability to satisfy the bearing capacity during the earthquake action. It means that during the whole process of the test, the frame should be elastic and no damage appears. The most important thing is that the steel frame can provide peak acceleration and drift ratio at the same time under the floor response action (Figure 5).



Figure 5 Steel Frame

4.2.2 Earthquake Wave Selection

It is not correct to input the ground motion as the earthquake action to investigate the seismic performance of curtain wall specimen. Many curtain walls are installed on the tall buildings. The action they endured directly is

the floor response. So, the input wave should be relative floor response (RFR) between the upper and lower end of the curtain wall unit. In order to acquire the RFR of a certain building, comprehensive seismic analysis is necessary. The characteristic of the RFR in time history and floor spectra is very useful in the whole research. The exemplified floor response in time history and floor spectrum are shown in figure 6 and figure 7.

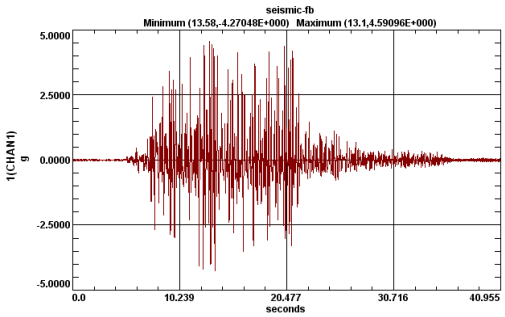

Figure 6 Floor Acceleration Time History

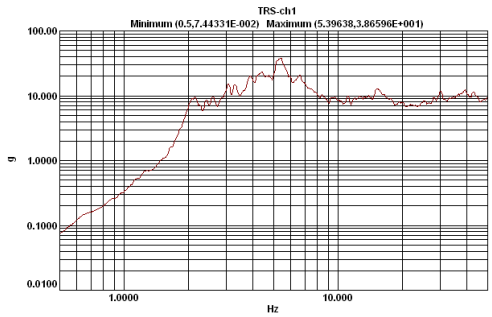

Figure 7 Floor Spectrum



Figure 8 Test Setup

As a result of the floor response is difficult to acquire, it is advisable to reference to the test wave used in shaking table test of equipment. Of course, it need long time test practice to summarize the experimental experience and methodology.

4.2.3 Sensor Disposition

Accelerometers, displacement sensors and strain gauges should be placed in the key locations of the specimen and frame according to the researcher's experience and estimation.

4.2.4 Test Procedure

Floor response should be input in an increasing order to detect the response of the specimen in elastic and post elastic area. Before and after each test, white nose wave should be input to get the dynamic characteristic of the specimen. The test setup example of a shaking table experiment on curtain wall exhibited in figure 8.

4.2.5 Seismic Performance Evaluation

According to the observation of the sensors and the experimental phenomenon during the test, the research can provide a objective evaluation of the seismic performance of the specimen.

5. CONCLUSIONS

As a kind of nonstructural components, the seismic performance of curtain wall system is analyzed. The seismic mechanism including acceleration initiated mechanism, deformation initiated mechanism and interaction between the curtain wall and the main structure are discussed. Curtain wall is hybrid sensitive component, and its seismic mechanism differs in different types of building. The seismic indices including AAFs and ISDRs are proposed, and the specific advisable indices are listed according to scaled model structure shaking table test of high-rising buildings. They are slight greater than those adopted in the current specification. Seismic test approaches are discussed, and the methodology for further improved static and dynamic tests are mentioned. Problems of the two test types are analyzed. It also mention that the seismic mechanism is the basis of the seismic research and test, and then to enhance the seismic performance of curtain wall.

Acknowledgements:

The financial and technical supports from Shanghai Science & Technology Committee (08ZR1420200) and State Key Laboratory for Disaster Reduction in Civil Engineering are gratefully acknowledged.

References:

Federal Emergency Management Agency (1994), "Reducing the Risks of Nonstructural Earthquake Damage: A Practical Guide," Wiss, Janney, Elstner Associates, Inc.

Federal Emergency Management Agency (2005), "Earthquake Hazard Mitigation for Nonstructural Members," Wiss, Janney, Elstner Associates, Inc.

National Standard of the People's Republic of China (2003), "Technical Code for Glass Curtain Wall Engineering (JGJ102-2003)," Beijing: China Architecture & Building Press. (in Chinese)

National Standards of the People's Republic of China (2001), "Technical Code for Metal and Stone Curtain Walls Engineering (JGJ133-2001)," Beijing: China Architecture & Building Press. (in Chinese)

Baofeng Huang, Wensheng Lu and Wenqing Cao (2009), "Discussion on Seismic Performance Indexes of Architectural Curtain Walls," *China Civil Engineering Journal*, China Civil Engineering Society, **42**(9), 7-12. (in Chinese)

International Conference of Building Officials (1994), "Uniform Building Code," Whittier, California.

International Conference of Building Officials (1997), "Uniform

Building Code," Whittier, California.
Behr, R.A., and Brown, A.T. (1995a), "Seismic Performance of Architectural Glass in a Storefront Wall System," *Earthquake Spectra*, Earthquake Engineering Research Institute, **11**(3), 367-391.
Behr, R.A., and Belarbi, A. and Culp, J. H.(1995b), "Dynamic Racking Tests of Curtain Wall Glass Elements with In-plane and Out-of-plane Motions," *Earthquake Engineering and Structural Dynamics*, International Association for Earthquake Engineering, **24**(1), 1-14.
Behr, R. A., and Belarbi, A.(1996), "Seismic Test Methods for Architectural Glazing Systems," *Earthquake Spectra*, Earthquake Engineering Research Institute, **12**(1), 129–143.
Behr, R. A.(1998), "Seismic Performance of Architectural Glass in Mid-rise Curtain Wall," *Journal of Architectural Engineering*, American Society of Civil Engineers, **4**(3), 94–98.
M.P. Singh, L.M. Moreschi, L.E. Suárez, and E.E. Matheu (2006), "Seismic Design Forces II: Flexible Nonstructural Components," *Journal of Structural Engineering*, American Society of Civil Engineers, **132**(10), 1533-1542.
Wensheng Lu, Baofeng Huang (2008), "Discussion on Seismic Performance Indices of Architectural Curtain Walls," 14WCEE, paper ID: 12-01-0193
National Standards of the People's Republic of China (2001), "Code for seismic design of buildings (GB 50011-2001)," Beijing: China Architecture & Building Press. (in Chinese)
Building Seismic Safety Council for the Federal Emergency Management Agency (1997), "NEHRP Recommended Provisions for Seismic Regulations for New Buildings and Other Structures," Building Seismic Safety Council, Washington, D.C.
Brueggeman, J. L., Behr, R. A., Wulfert, H., Memari, A. M., and Kremer, P. A.(2000), "Dynamic Racking Performance of an Earthquake-isolated Curtain Wall System," *Earthquake Spectra*, Earthquake Engineering Research Institute, **16**(4), 735–756.
Memari, A., Behr, R. A., and Kremer, P. A.(2003), "Seismic Behavior of Curtain Walls Containing Insulating Glass Units, *Journal of Architectural Engineering*, American Society of Civil Engineers, **9**(2), 70–85.
Memari, A., Behr, R. A., and Kremer, P. A.(2004), "Dynamic Racking Crescendo Tests on Architectural Glass Fitted with Anchored Pet Film, *Journal of Architectural Engineering*, American Society of Civil Engineers, **10**(1), 5–14.
Pantelides, C.P., and Behr, R.A.(1994), Dynamic In-plane Racking Tests of Curtain Wall Glass Elements," *Earthquake Engineering and Structural Dynamics*, International Association for Earthquake Engineering, **23**(2), 211-228.
Pantelides, C. P., Truman, K. Z., Behr, R. A., and Belarbi, A.(1996), "Development of a Loading History for Testing of Architectural Glass in a Shop-front Wall System," *Engineering Structures*, **18** (12), 917–935.
AAMA 501.6-01 (2001), "Recommended Dynamic Test Method for Determining the Seismic Drift Causing Glass Fallout from a Wall System," American Architectural Manufactures Association, Schaumburg, IL.
Behr, R. A.(2006), "Design of Architectural Glazing to Resist Earthquakes," *Journal of Architectural Engineering*, American Society of Civil Engineers, **12**(3), 122–128.
Wensheng Lu, Baofeng Huang (2008), "Study on the Shaking Table Test Methods of Architectural Curtain Walls," *Journal of Disaster Prevention and Mitigation Engineering*, China Association for Disaster Prevention, **28**(4):447-453. (in Chinese)

JOINT CONFERENCE PROCEEDINGS
7th International Conference on Urban Earthquake Engineering (7CUEE) &
5th International Conference on Earthquake Engineering(5ICEE)
March 3-5, 2010, Tokyo Institute of Technology, Tokyo, Japan

DYNAMIC CHARACTERISTICS OF JAPANESE STYLE OF CEILING

Shojiro Motoyui[1)], Yasuaki Satoh[2)], and Takuto Kawanishi[2)]

1) Associate Professor, Dept. of Built Environment, Tokyo Institute of Technology, Japan
2) Graduate Student, Dept. of Built Environment, Tokyo Institute of Technology, Japan
motoyui@enveng.titech.ac.jp, yasuaki.s.aa@m.titech.ac.jp, kawanishi.t.ab@m.titech.ac.jp

Abstract: The damage of non-structural components has occurred during the recent earthquakes. Especially, the damage of hanging ceiling was severe while the measured acceleration was not so great. The falling down of ceiling may injure persons or cut off an evacuation route. The damage of ceiling probably causes the loss of business continuity even if there are not any injured persons. Then, it is important to prevent ceiling from any damage against earthquakes. To clarify the process of damage in ceiling, the shaking table test with the E-defense for the whole of full-sized steel building including ceiling was executed. In this paper, the experimental results are reported. Particularly, we focus on the degradation phenomenon under the input acceleration corresponding to the middle class of earthquakes. Finally, the numerical result is shown to identify the damage situation of the ceiling.

1. INTRODUCTION

In the recent earthquakes in Japan, some serious damage and falling down of ceilings occurred while the measured acceleration was not so great. Actually no damage of building structures was observed. The falling down of ceiling may injure persons or cut off an evacuation route. The damage of ceiling probably causes the loss of business continuity even if there are not any injured persons. Then, it is important to prevent ceiling from any damage against earthquakes. The hanging ceiling in Japan which is composed of steel members and plaster boards as shown in Fig.1. They are built up on site and each steel member, called "Channel" or "M-bar" is connected with unique metal connection parts called "Hanger" and "Clip". See Figure 1. It is obvious that the detachment behavior of "Clips" caused the falling of ceiling since plaster boards with "M-bars" fell down through the observation of the actual damage after earthquakes. However, the reason why "Clips" detached during earthquakes has not been clarified.

To clarify the process of damage in ceiling, the shaking table test with the E-defense for the whole of full-sized steel building including ceiling was executed as shown in Figure 2. In this experiment, the acceleration recorded at Takatori in Kobe(1995) is applied as the input acceleration to the shaking table. Totally the five cases of tests were executed. The maximum value of the input acceleration in each case was set to 5%, 20%, 30%, 40% and 70%. The ceiling fell down in the fourth test, Takatori-40%. In this paper, The dynamic characteristics, especially initial dynamic properties and the degradation process of properties for the Japanese style of ceiling will be described via experimental results.

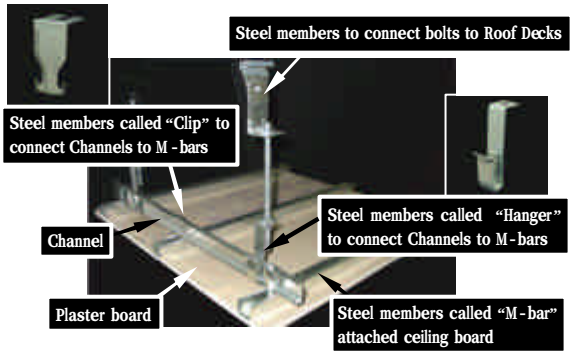

Figure 1 Japanese style of hanging ceiling

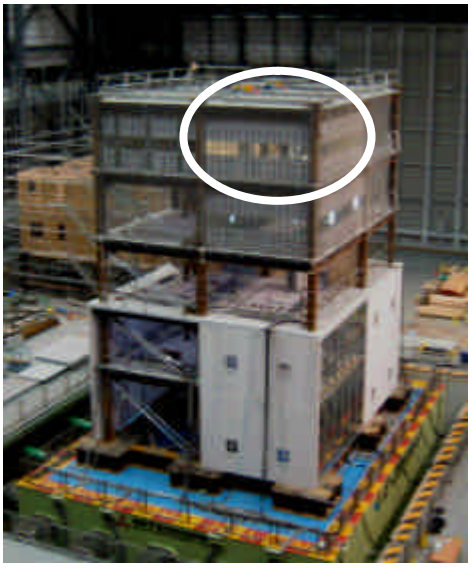

Figure 2 Test specimen of full-sized building

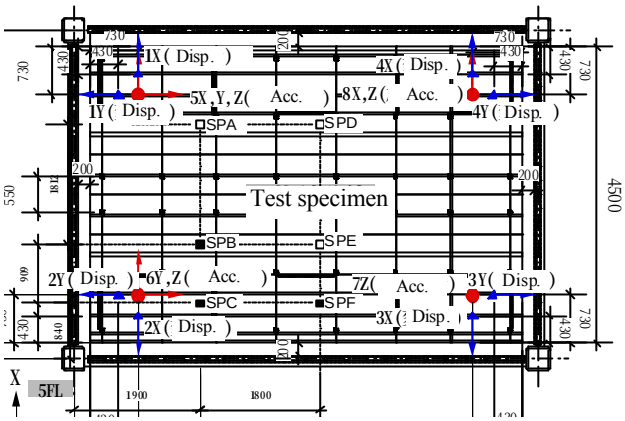

Figure 3 Test specimen of ceiling

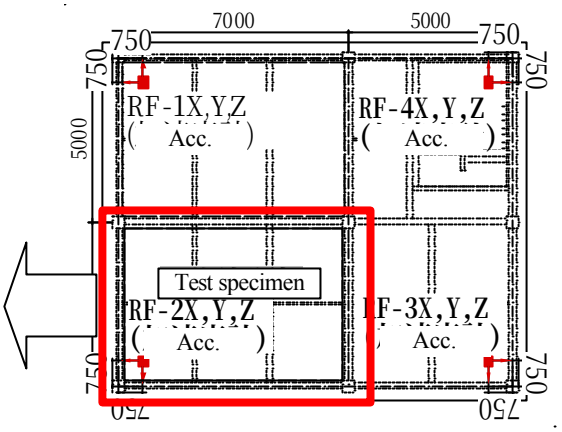

Figure 4 Plan at 5th floor

2. Outline of Shaking Table Test

2.1 Test specimen

The ceiling test specimen is set at the fifth floor and is hung from a slab at the roof as shown in Figure 4. Figure 5 shows the ceiling test specimen. The size is 4,500mm by 6,500mm and the depth which means the distance between the plaster board level and the bottom of the slab at the roof is 590mm. The mass of the ceiling is 585kg and the average mass per unit area is 20kg/m^2 and the value was determined taking account of the size (scale) effect. Because, our true target of ceiling has wider area like a ceiling at gymnasium. Then, the value is heavier than that of the usual ceiling (14kgm^2). The spacing (clearance) between the plaster board and the surrounding walls is 200mm for the ceiling not to pound the surrounding wall. The six diagonal members and eight ones are arranged for Y and X direction respectively not to swing during testing.

2.2 Experiment Results

Figure 5 shows the power spectrum is calculated by using relative acceleration which is relative to the motion at the roof, under the white noise before testing. The eigen frequency and period at the virgin condition, are 3.25Hz and 0.308sec. The values agree with the predicted one with the evaluation method proposed by us. Figures 6 and 7 are the response acceleration and relative response displacement of the ceiling for the Takatori-5%. Each maximum value is close to the predicted one through the response spectra at the roof with the damping ratio of the ceiling set to be 3.0%. The matter means that the ceiling behaves as a linear system.

Figure 8 compares the response acceleration of the ceiling for the Takatori-20% with 4 times of the one for the Takatori-5%. The result for the Takatori-20% is quite different from the one for the Takatori-5%x4 though the both results are close until 5.5sec. Namely, the eigen period becomes longer and the time of the maximum acceleration changes from 5.8sec to 7.6sec. The matter means that the behavior of ceiling is not linear but nonlinear. As I mentioned before, the present test specimen fell down during the Takatori-40% but any damage of the ceiling had already occurred during the Takatori-20%.

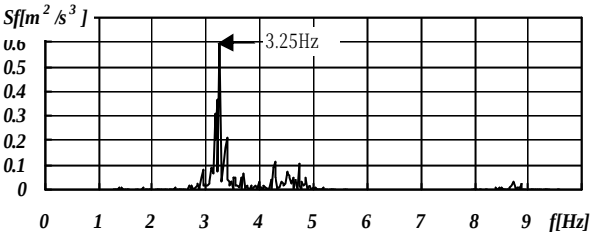

Figure 5 power spectrum of ceiling at virgin

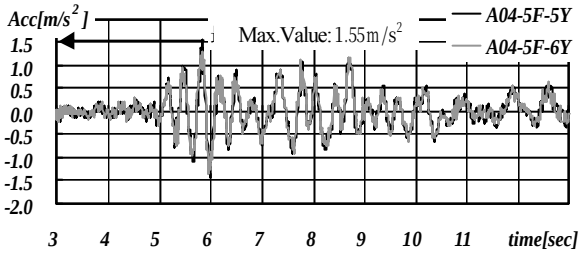

Figure 6 Absolute response acceleration for 5%

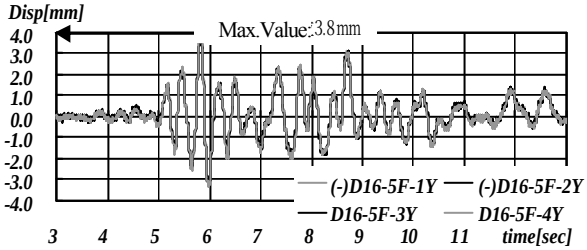

Figure 7 Relative response displacement for 5%

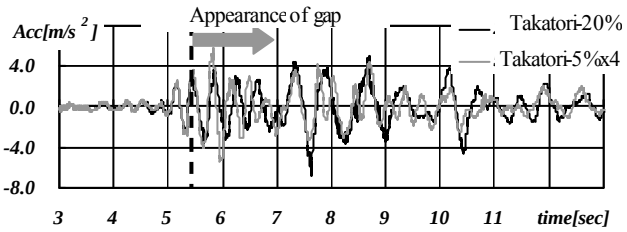

Figure 8 Comparison between results for 5% and 20%

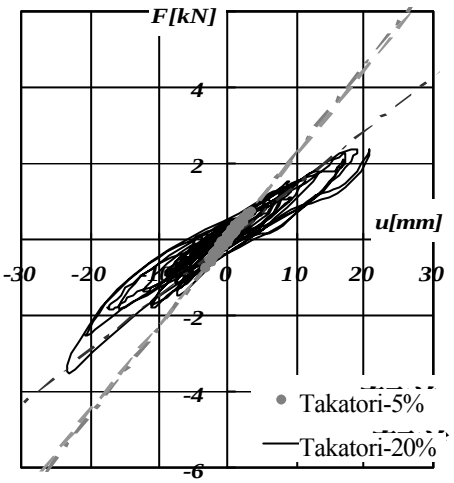

Figure 9 Relationship between Inertia force and displacement for 5% and 20%

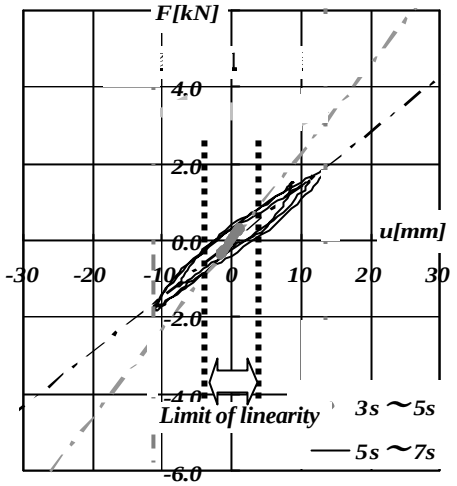

Figure 10 Change of Relationship between Inertia force and displacement for 20%

Figure 9 shows the relationship between the inertia force and the relative displacement for the Takatori-5% (Light gray) and 20% (Black). These can be considered to be the relationship between the internal force of the ceiling and the displacement if the damping force can be neglected. The result for the Takatori-20% shows the ceiling system behaves as a nonlinear system while the result for the Takatori-5% remains the linearity as I mentioned above. Figure 10 shows the extracted relationship only for two periods; 3second to 5second and 5second to 7second easily to understand the change of the relationship in testing for the Takatori-20%. In the former period, the relationship can be judged to keep the linearity as well as the one for the Takatori-5%. In the latter one, the behavior of the ceiling becomes nonlinear. The limit displacement to remain the linearity for the present ceiling specimen can be considered to be approximately $\pm$4mm, which corresponds to the maximum displacement measured in the Takatori-5%. The change to the nonlinear relationship means that any damage occurs in the ceiling system. However, any remarkable damage was not observed through the image by surveillance cameras. Then, in the next section, we will examine the behavior of the specimen via numerical results

3. Numerical Analysis for ceiling system

3.1 Numerical Method

Next, we executed the numerical simulation of the ceiling system to judge what damage makes a progress. The slipping and detachment behaviors of a clip are important and should be considered in a numerical simulation of the ceiling damage. We introduced so-called Master-Slave model by Crisfield in order to express slipping and detachment. See Figure 11. In this model, the relative position vector $\boldsymbol{x}_R$ between a master node and a slave node is introduced. The position vector $\boldsymbol{x}_S$ and the local unit basis $\boldsymbol{Q}_S$ at the slave node can be expressed as;

$$\boldsymbol{x}_S = \boldsymbol{x}_M + \boldsymbol{x}_R = \boldsymbol{x}_M + \boldsymbol{Q}_A \bar{\boldsymbol{x}}_R \quad (1)$$

$$\boldsymbol{Q}_S = \boldsymbol{Q}_M \boldsymbol{Q}_R(\bar{\boldsymbol{\beta}}_R) \quad (2)$$

where $\boldsymbol{x}_M$ is the position vector of the master node, $\bar{\boldsymbol{x}}_R$ is the relative position vector consists of components to the local unit basis $[\boldsymbol{m}_x, \boldsymbol{m}_h, \boldsymbol{m}_z](=\boldsymbol{Q}_A)$ at the master node. The infinitesimal variation of position vector (=displacement vector) can be calculated as

$$\begin{aligned} d\boldsymbol{u}_S &= d\boldsymbol{u}_M - \boldsymbol{W}(\boldsymbol{Q}_M \bar{\boldsymbol{x}}_R) d\beta_M + \boldsymbol{Q}_M d\bar{\boldsymbol{x}}_R \\ d\boldsymbol{\beta}_S &= d\beta_M + \boldsymbol{Q}_M d\bar{\beta}_R \end{aligned} \quad (3)$$

Or $$d\boldsymbol{U}_S = \boldsymbol{H}_M d\boldsymbol{U}_M + \boldsymbol{H}_R d\boldsymbol{U}_R \quad (3')$$

Inserting Eq.(3') into the virtual work equation for slave node gives

$$\begin{bmatrix} \boldsymbol{K}_{MM} & \boldsymbol{K}_{MR} \\ \boldsymbol{K}_{RM} & \boldsymbol{K}_{RR} \end{bmatrix} \begin{Bmatrix} d\boldsymbol{U}_M \\ d\boldsymbol{U}_R \end{Bmatrix} = \begin{Bmatrix} -\boldsymbol{q}_M \\ -\boldsymbol{q}_R \end{Bmatrix} \quad (4)$$

where

for example, $\boldsymbol{K}_{MM} \cong \boldsymbol{H}_M{}^T \boldsymbol{K}_S \boldsymbol{H}_M$ and $\boldsymbol{q}_M = {}^t\boldsymbol{H}_M{}^T \boldsymbol{q}_S$

Here, relative components depend on only the variables for the present elements. It is not necessary to consider the relative variables when the global equation is solved and the relative ones can be eliminated through the condensation at each element level.

$$\left[\boldsymbol{K}_{MM} - \boldsymbol{K}_{MR}\boldsymbol{K}_{RR}{}^{-1}\boldsymbol{K}_{RM}\right] d\boldsymbol{U}_M = -\boldsymbol{q}_M + \boldsymbol{K}_{MR}\boldsymbol{K}_{RR}{}^{-1}\boldsymbol{q}_R \quad (5)$$

If the internal force is released, the slave node slides in the direction of the released inner force. If all of internal forces are released, the slave node is detached.

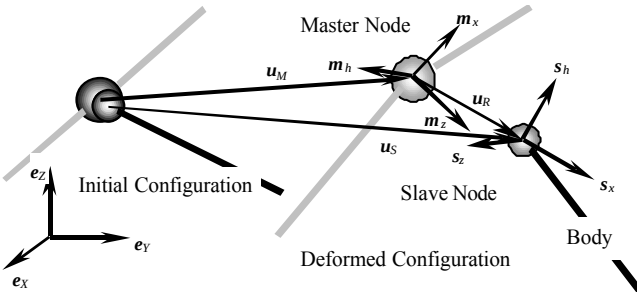

Figure 11 Master-slave model

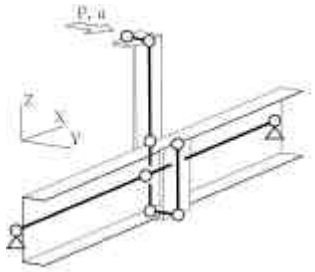

Figure 12 Analytical model for Joint with "Hanger"

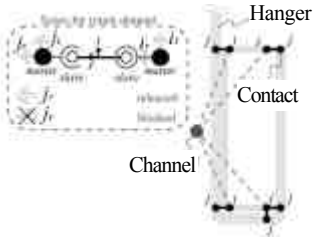

Figure 13 Modeling for Joint with "Hanger"

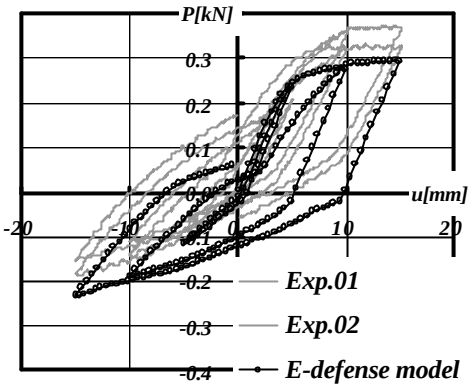

Figure 14 Validation of modeling for Joint with "Hanger"

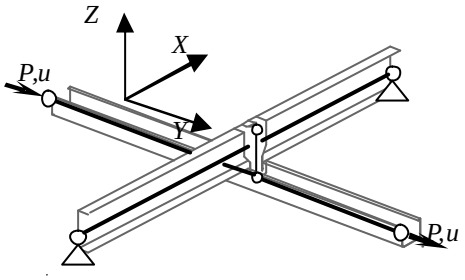

Figure 15 Analytical model for Joint with "Clip"

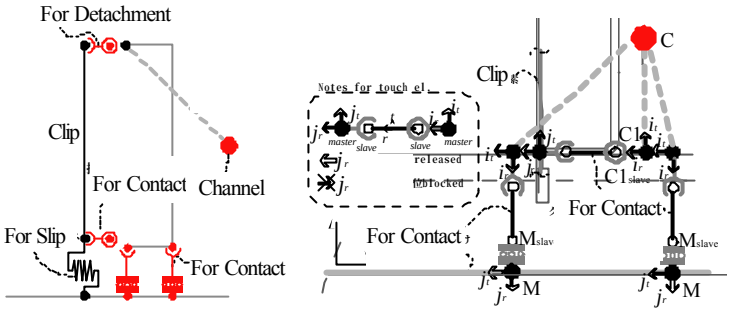

Figure 16 Modeling for Joint with "Clip"

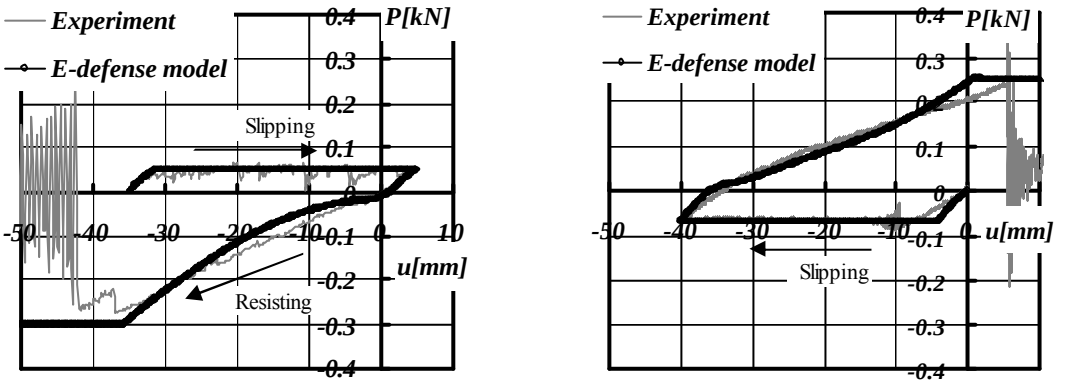

Figure 17 Validation of modeling for Joint with "Clip"

3.2 Validation of modeling for Joints

Figures 12 and 13 show the analytical model for a test of the joint with a "Hanger". The model includes a few dummy elements to represent the contact behavior, slipping and detachment behavior. The round-house type of stress-strain curve is applied for the material property of a "Hanger" to consider the cold metal form process of a "Hanger". The numerical result is shown in Figure 14. The light gray is the experimental result and the black is the present solution. The present result agrees with the experimental one.

Figures 15 and 16 show the analytical model for the connection with a "Clip" and the arrangement of dummy elements between "Channel" and "Clip", "M-bar" and "Clip" or "Channel" and "M-bar". The numerical result is compared with the experiment ones in Figure 17. The present solution agrees with the experimental results in the situation of slipping and resisting. Then, we can simulate the non-linear behavior of a ceiling including the slipping of a "Clip" numerically.

It is noted that the detachment behavior of a "Clip" is not taken account of in this paper, because we focus on the process that the ceiling system change from the linear system to nonlinear system. Therefore, the post detachment behavior is neglected. So, the strength of a "Clip" after yielding the limit of detachment remain the detachment strength without vanishing the strength.

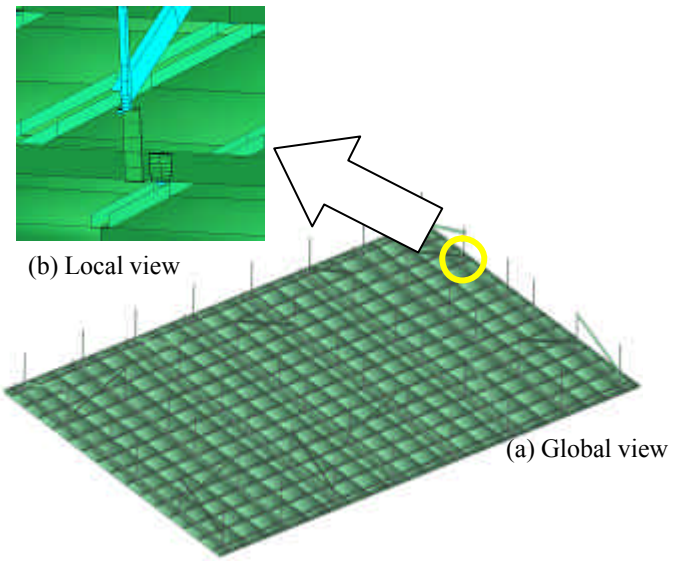

Figure 18 Analytical model for the ceiling specimen

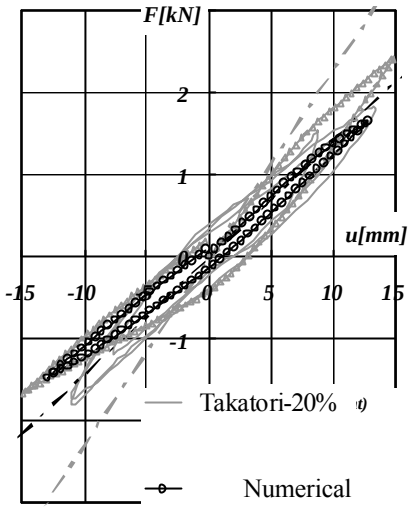

Figure 19 Numerical result for ceiling

3.2 Numerical analysis of the ceiling

The modeling for the joint with the "Hanger" and "Clip" shown in the previous section is applied to the analytical model for the whole of ceiling. Figure 18 shows the analytical model. Beam elements are applied to all of steel members including dummy elements while shell elements are applied to the plaster board. The applied load is only the statically cyclic horizontal load as the object of the present numerical analysis is to identify the damage situation in the Takatori-20%.

Figure 19 shows the numerical result only for the final loop. The result is close to the experimental one. In the state of final loop, we found the damage of the six "Clips" near the six diagonal members in the direction of Y while most of "Clips" remained the virgin (no damage) condition. The matter means that "Clips" near diagonal members may be damaged under the slight horizontal load though the detachment behavior of "Clips" can not be observed at a glance.

4. Conclusion

We reported the results by the shaking table test for the ceiling which is set at the full-sized building. Particularly, we focus on the degradation phenomenon in the middle class of earthquakes; Takatori-5%～Takatori-20%. We made sure that the degradation in the Takatori-20% is caused with the damage of some "Clips" near diagonal members.

Acknowledgment

This study is a part of "NEES/E-Defense collaborative research program on steel structures". The Japan team leader for the overall program is Kazuhiko Kasai at Tokyo Institute of Technology. The writers acknowledge the support of members of Damper Isolation System WG (leader: Kazuhiko Kasai) and financial support provided by the National Research Institute for Earth Science and Disaster Prevention.

References:

Crisfield, M.A. (2000), "Non-linear Finite Element Analysis of Solids and Structures Volume 2 Advanced Topics", John Wiley & Sons Inc.

JOINT CONFERENCE PROCEEDINGS
7th International Conference on Urban Earthquake Engineering (7CUEE) &
5th International Conference on Earthquake Engineering (5ICEE)
March 3-5, 2010, Tokyo Institute of Technology, Tokyo, Japan

ESTIMATION OF FLOOR ACCELERATION DESIGN SPECTRA

Hossein Akhlaghi[1)] , Abdolreza S. Moghadam[2)]

1) Research Associate, Iranian Earthquake Engineering Association (IEEA), Tehran, IRAN
2) Assistant Professor, International Institute of Earthquake Engineering and Seismology (IIEES), Tehran, IRAN
akhlaghi_civilengineer@yahoo.com, moghadam@iiees.ac.ir

ABSTRACT : The excitations felt by nonstructural component within a building is due to effects such as the location within the building and the relationship between the building frequency of motion and those of the nonstructural component. Several methods have been used to estimate the effect of earthquake excitations on nonstructural components. Building codes and recommended provisions have included approximate formulas for calculating an effective seismic force for both rigid and flexible acceleration sensitive nonstructural components. The design force for the acceleration sensitive nonstructural components on floor are based on acceleration design spectra calculated for each floor of the building, however the calculation of the normalized Floor Acceleration Design Spectra (FADS) is a cumbersome task to be used for most buildings. Since the value of FADS at a particular level of building depends on its dynamic properties; the level of nonlinearity induced; and the ground excitation intensity, the FADS cannot be formulated as a function of height without considering these aspects. In this study, FADS are calculated by Nonlinear Time History Dynamic Analyses (NTHDA) for a total of five 2D steel moment-resisting frame models. An ensemble of 28 different ground motions recorded on four soil types are used as earthquake excitation input for NTHDA. The results of these analyses are compared to the International Building Code (IBC 2006) procedure for calculating the design force of nonstructural components on floor.

KEYWORDS : Floor Acceleration Design Spectra, Nonstructural Components.

1. INTRODUCTION

The design forces for acceleration sensitive nonstructural components are a function of the seismic demand and the expected ductility and overstrength. The seismic demand depends on the ground motion, the amplification of the ground motion at the location within the building to which the component is attached, and the amplification of the nonstructural motion due to resonance with the building at a certain model period (Kehoe and Hachem 2003). The components that can be considered rigid are identified by their fundamental period that should be lower than 0.06 seconds. In the paper of Akhlaghi and Moghadam (2008) presented a simplified method for the height-wise distribution of Peak Horizontal Floor Acceleration (PHFA) to estimate the input acceleration for rigid acceleration sensitive nonstructural components.

If the weight of the nonstructural component is small compared to the weight of the structure, and also if the fundamental period of nonstructural component is more than 0.06 seconds, it is considered as a flexible nonstructural component. However, the dynamic interaction between the flexible acceleration sensitive nonstructural components and the input acceleration in this type of nonstructural components will be different and often higher from PHFA so acceleration demands can be estimated using Floor Acceleration Design Spectra (FADS). FADS provide information of the inensity of the floor motion at different frequencies, and hence provide far more information than only the PHFA (Reinoso and Miranda 2004). Since the response of a flexible nonstructural component varies with its fundamental period, this variation in the response characteristics is best represented by the FADS curves of the floor on which the flexible nonstructural component is supported (Singh et al. 2005).

This paper investigate the acceleration demands for the flexible acceleration sensitive nonstructural components. Since flexible nonstructural components could amplify the motion applied at their base, the 2003 NEHRP Provisions (BSSC 2003), the 2006 International Building Code (ICC 2006), and the SEI/ASCE 7-05 Standard (ASCE 2005) prescribe the use of an amplification factor (a_p) that related to rigidity of nonstructural components to estimate the seismic coefficient.

It reality, this amplification factor depends in a rather complex manner upon several parameters such as the ratio of the component period to the building period, component and building damping ratios, also the location of the component in the building (Singh et al. 2005). However, these complications are simplified and fixed numerical values for the a_p, either 1.0 or 2.5, have been provided in tables in the 2003 NEHRP Provisions (BSSC 2003), the

2006 International Building Code (ICC 2006), and in SEI/ASCE 7-05 Standard (ASCE 2005) for various components. The value of $a_p = 1$ is for rigid components and rigidly attached components and the value of $a_p = 2.5$ is for flexible components and flexibly attached components or the components that are of some safety concerns or higher importance. The values of the amplification factors were based on the simplified amplification curve proposed by Soons et al. (1993). There are several investigations about floor response spectrum, e.g., Reinoso and Miranda (2004), Singh (2005), and others. To estimate FADS, information about the fundamental period, damping ratio and also the dominants modes of the building is needed.

In this investigation, the structural models and recorded ground motions introduced by the paper of Akhlaghi and Moghadam (2008) are used. The FADS are calculated by the time history acceleration of floor obtained from NTHDA of structural models. The results of these analyses are compared to the the 2006 International Building Code (ICC 2006) procedure for calculating building floor accelerations.

2. THE BUILDING MODELS

For this study, five steel moment-resisting frame (SMRF) buildings with four, eight, twelve, sixteen and twenty stories each with three 5 m span are considered. The five structural models, have the same story height of 3 m, and have a uniform mass distribution over their height and a non-uniform lateral stiffness distribution. They were designed using the lateral load distribution specified in the Iranian Building Codes and Standards (2005). Results of eigenvalue analyses of the different models, are provided in Table 1. The fundamental periods of these structures is ranging from 0.5-1.8 second. Numerical models were developed for analyses, using a representative 2D frame of the buildings along the transverse direction. It is assumed that the beam members can develope flexural plastic hinges. The flexural plastic hinges in column are considering the axial load-flexural moment interaction. The nonlinear direct integration time history analyses is used with a 5% damping coefficient for the first and the second modes of structural models.

Table 1 Dynamic Parameters of Structures

Model	Period (sec)		Modal Participating Mass Ratio Mode 1	Modal Participating Mass Ratio Mode 2
	Mode 1	Mode 2		
4 Story	0.50	0.16	81.4%	12.5%
8 Story	0.91	0.32	76.5%	13.0%
12 Story	1.19	0.42	75.4%	12.7%
16 Story	1.48	0.51	74.1%	13.7%
20 Story	1.83	0.62	71.9%	14.7%

3. GROUND MOTIONS CONSIDERED

For this study, 28 ground motions recorded on four soil types (classified by shear wave velocity in soil layers) are used. These ground motions were generated for the UC Science building as a part of PEER (Pacific Earthquake Engineering Research Center) test bed project (2007). The ground motions are derived from actual ground motion records considering their magnitude and distance from the fault to site. The list of the ground motions used along with some of their parameters is provided in Table 2. The peak ground acceleration (PGA) for these motions varies from 0.26g to 0.821g. The range of peak ground velocity (PGV) is 12.2 – 120.7 cm/sec, and the range of peak ground displacements (PGD) is 1.9 – 41.3 cm.

Table 2 Earthquake Motions Records

Type of Soils	Earthquake	Station	PGA (g)
Type 1	Kobe 1995/01/16	0 KJMA	0.821
	Landers 1992/06/28	Luceme	0.785
	Loma Prieta 1989/10/18	Corralitos	0.644
	Northridge 1994/01/17	LA - Univ. Hospital	0.493
	Parkfield 1966/06/28	Temblor pre-1969	0.357
	San Fernando 1971/02/09	Lake Hughes #12	0.366
	Victoria, Mexico 1980/06/09	Cerro Prieto	0.621
Type 2	Cape Mendocino 1992/04/25	Rio Dell Overpass - FF	0.549
	Landers 1992/06/28	Coolwater	0.417
	Whittier Narrows 1987/10/01	LA - Obregon Park	0.45
	Loma Prieta 1989/10/18	Saratoga - Aloha Ave	0.512
	Morgan Hill 1984/04/24	Anderson Dam	0.423
	Northridge 1994/01/17	Beverly Hills - Mulhol	0.617
	N. Palm Springs 1986/07/08	North Palm Springs	0.694
Type 3	Imperial Valley 1979/10/15	SAHOP Casa Flores	0.506
	Loma Prieta 1989/10/18	Capitola	0.529
	Northridge 1994/01/17	Glendale - Las Palmas	0.357
	Parkfield 1966/06/28	Cholame #5	0.442
	Coyote Lake 1979/08/06	Gilroy Array #2	0.339
	Morgan Hill 1984/04/24	Gilroy Array #4	0.348
	Chi-Chi, Taiwan 1999/09/20	TCU072	0.4
Type 4	Imperial Valley 1979/10/15	El Centro Array #3	0.266
	Chi-Chi, Taiwan 1999/09/20	CHY041	0.639
	Loma Prieta 1989/10/18	APEEL 2 - Redwood City	0.274
	Kobe 1995/01/16	Takatori	0.616
	Kobe 1995/01/16	Takarazuka	0.694
	Kobe 1995/01/16	Nishi-Akashi	0.509
	Kobe 1995/01/16	Kakogawa	0.345

The Seismosignal computer program (2007) is used to estimate the Ground Motion Parameters. For example, the effective duration is based on the significant duration concept but both the start and end of the strong shaking phase are identified by absolute criteria. Also, the predominant period (Tp) is the period at which the maximum spectral acceleration occurs in a 5% damped acceleration response spectrum.

4. COMPARISON OF FLOOR ACCELERATION DESIGN SPECTRA (FADS)

To investigate the Floor Acceleration Design Spectra (FADS) in this study, for each structural model and each earthquake time history, acceleration response spectra at four floors were generated. The four floors considered were taken as the roof level, the level at three-quarter of the height, the mid-height level, and the one-quarter height level of the structural model. Figure 1 show a comparison of ratio of 5% damped acceleration response spectra of floor to acceleration response spectra of ground obtained from NTHDA

(normalized spectrum) for each one of the four soil types at the level of 0.25 of 4 story model. In this figure, the acceleration design spectra is obtained from the average of acceleration response spectra of four soil types.

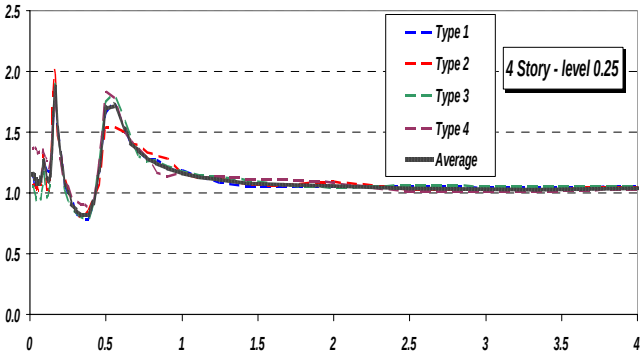

Figure 1 Comparison of Normalized Aacceleration Response Spectra of Floor Versus Period for each one of the four Soil Types at the Level of 0.25 of 4 Story Model with Average of Acceleration Response Spectra

And also for all structural models at the level of 0.25 to 1, the Floor Acceleration Design Spectra (FADS) show in the figures 2 to 5. In these figures, the FADS obtained from the each level for all structural models have approximately the same magnitude and same shape. Also, these figures show how the frequency content of the FADS are varied as height increases. For example the FADS at all levels of structural models, have two peaks that occur at fundamental periods of first and second modes of structural models. At level of 0.25, these two peaks have the same magnitude and the peak on the fundamental period of first mode is amplified as level increases. It means that at level of 0.25, the contribution of both the first and the second modes are equal, and at higher levels the contribution of the first mode increases.

5. COMPARISON OF FADS and INTERNATIONAL BUILDING CODE (IBC 2OO6)

According to the International Building Code (IBC 2006), the amplification factor (a_p) for flexible nonstructural component is equal to 2.5. Also according to it's proposed distribution of acceleration, the values of amplification coefficients of flexible nonstructural component at different levels are between 2.5 to 7.5.

Figure 6 show a comparison of ratio of 5% damped normalized Floor Acceleration Design Spectra (FADS) obtained from NTHDA using the 28 earthquake excitations for each one of the structural models to the International Building Code (IBC 2006) procedure at the levels of 0.25, 0.5, 0.75 and 1.

In this figure, the intensity of amplification factor for flexible nonstructural component proposed from the International Building Code (IBC 2006), at the levels of 0.25 and 0.5 is conservative, and for other levels is approximatly equal to the peak ratio of FADS.

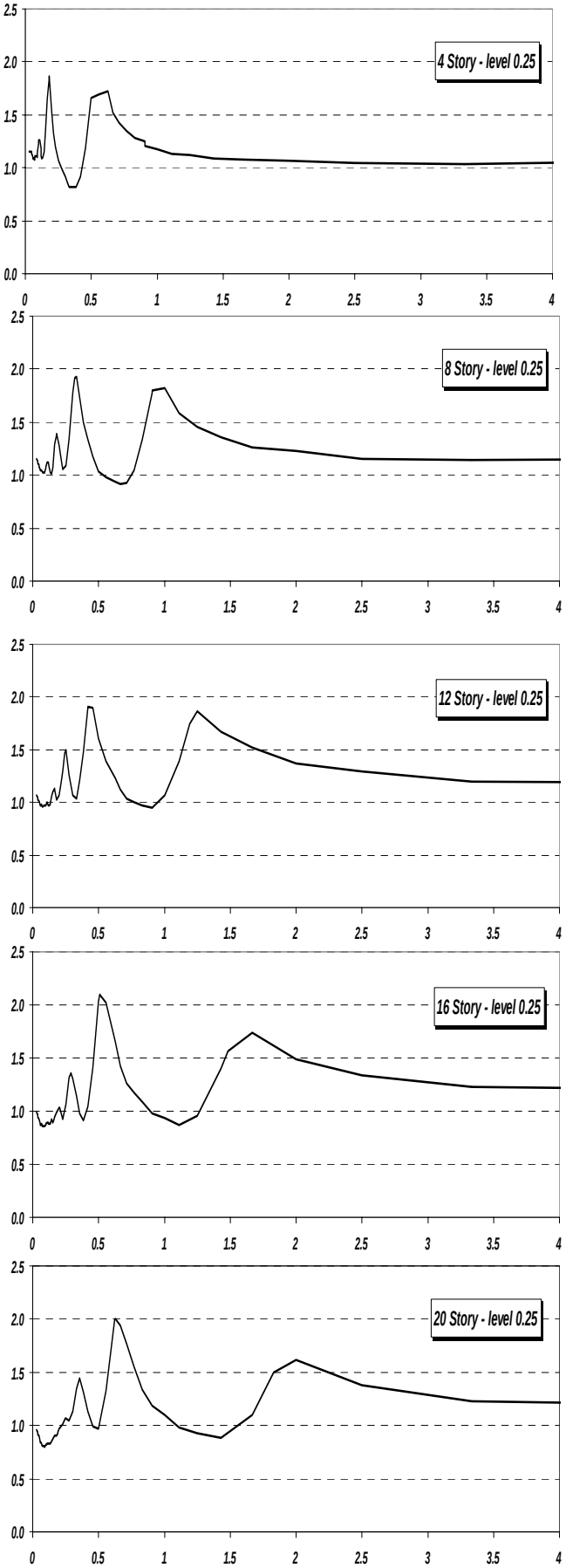

Figure 2 Relative FADS Versus Period at the Level of 0.25 for 4, 8, 12, 16 and 20 Story Models

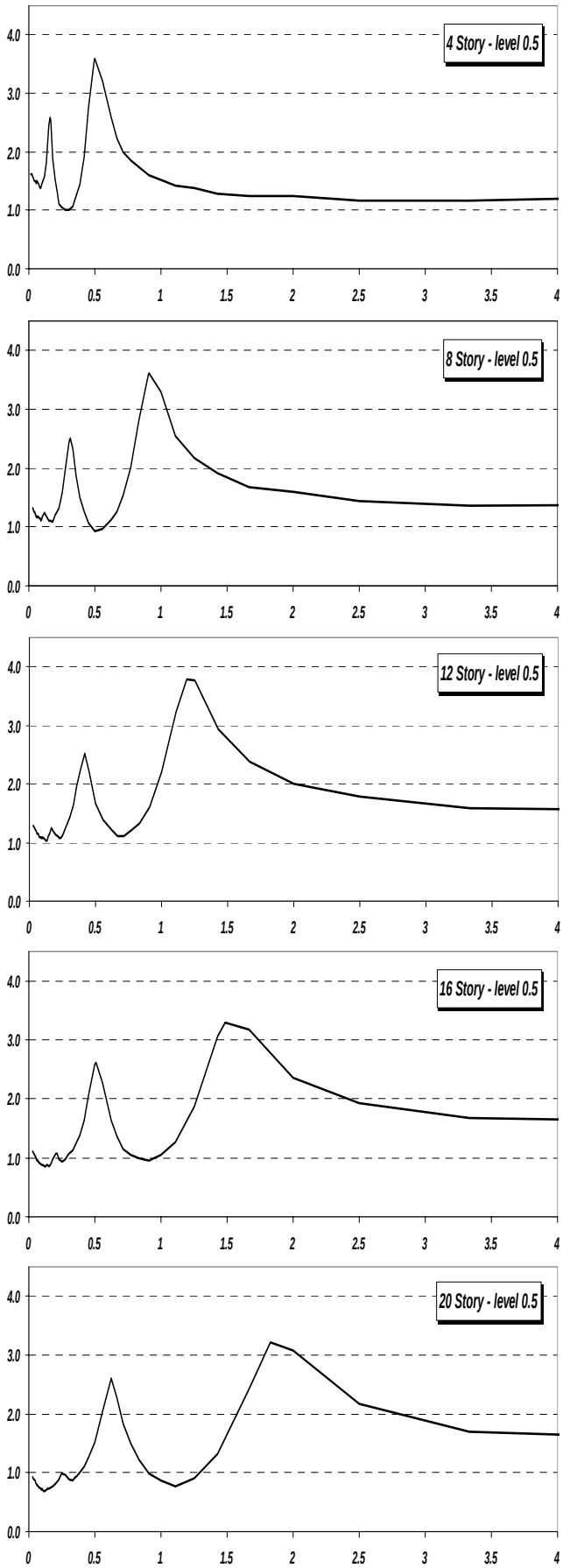

Figure 3 Relative FADS Versus Period at the Level of 0.5 for 4, 8, 12, 16 and 20 Story Models

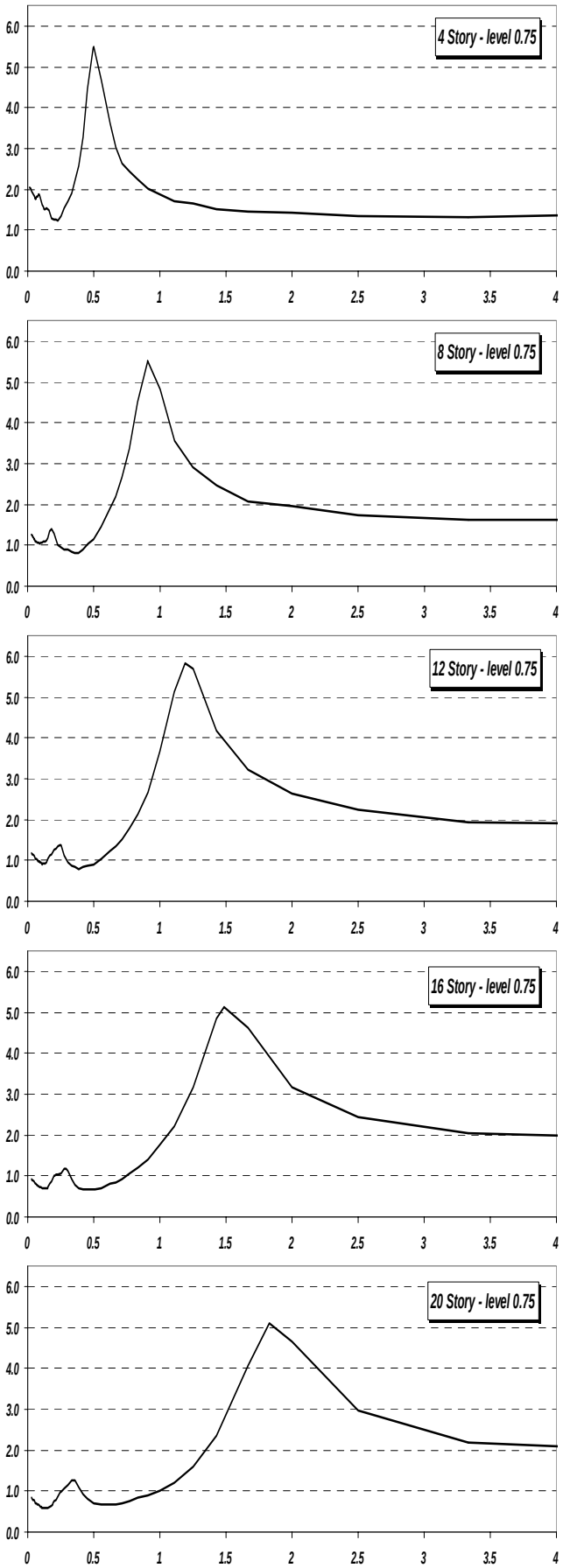

Figure 4 Relative FADS Versus Period at the Level of 0.75 for 4, 8, 12, 16 and 20 Story Models

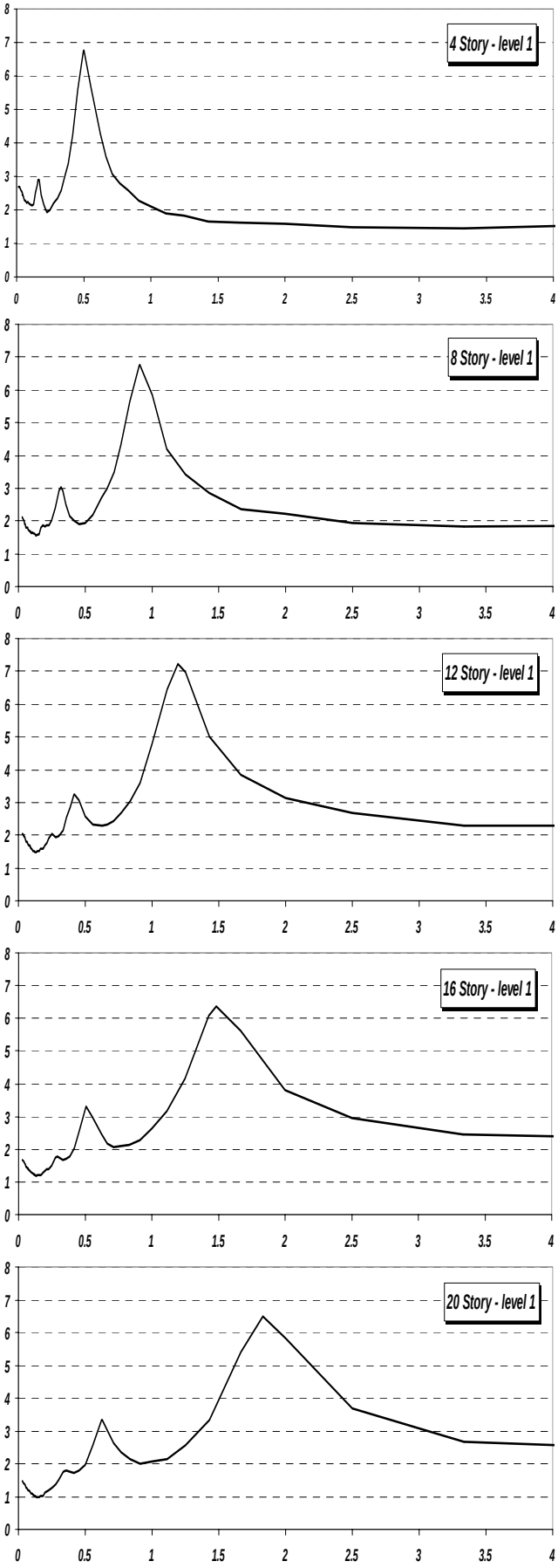

Figure 5 Relative FADS Versus Period at the Level of 1 for 4, 8, 12, 16 and 20 Story Models

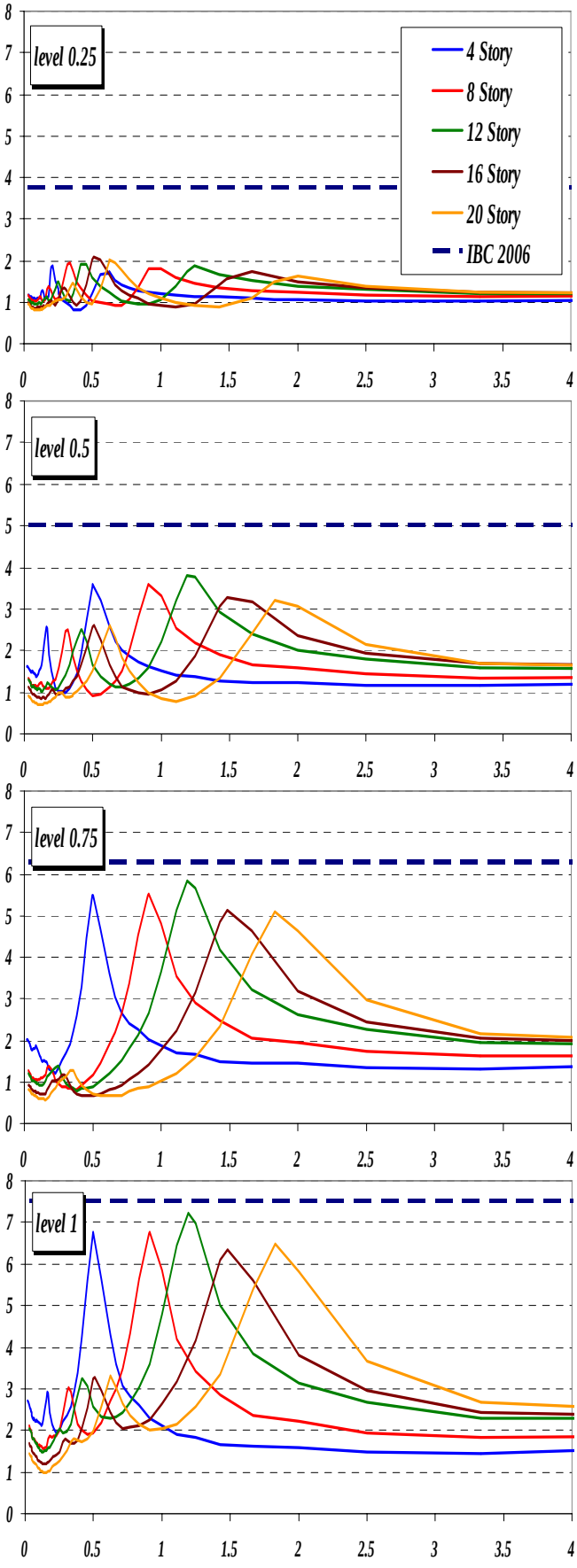

Figure 6 Comparison of Normalized FADS for each one of the Structural Models and the IBC 2006 Versus Period at the Levels of 0.25, 0.5, 0.75 and 1.

6. SUMMARY AND CONCLUSIONS

The paper presents an investigation about the Floor Acceleration Design Spectra (FADS) for calculating the input acceleration for flexible acceleration sensitive nonstructural components.

The ratio of 5% damped normalized Floor Acceleration Design Spectra (FADS) obtained from the structural models at the levels of 0.25, 0.5, 0.75 and 1 of the height.

Finally, the results of these analyses are compared to the International Building Code (IBC 2006) procedure for calculating building floor accelerations. The results show that the intensity of amplification factor for flexible nonstructural component proposed from the 2006 IBC provisions, at the levels of 0.25 and 0.5 is conservative, and for other levels is approximatly equal to the peak normalized FADS.

References:

Akhlaghi, H. and Moghadam, A. S. (2008), "Height-Wise Distribution of Peak Horizontal Floor Acceleration (PHFA)." *14TH World Conference on Earthquake Engineering (14WCEE), Beijing, China.*

International Code Council (ICC). (2006), International Building Code (IBC), Whittier, Calif.

Iranian Building Codes and Standards. (2005), Iranian code of practice for seismic resistant design of buildings. Standard No. 2800-05, 3th Ed., BHRC Publication No. S-253, Building and Housing Research Center, Tehran, Iran

Kehoe, B. E., and Hachem, M. M. (2003), "Procedures for Estimating Floor Accelerations." *Proceedings of the ATC-29-2 Seminar on Seismic Design, Performance, and Retrofit of Nonstructural Components in Critical Facilities, Applied Technology Council, Redwood City, Calif.*

Reinoso, E., and Miranda, E. (2005), "Estimation of Floor Acceleration Demands in High-Rise Buildings During Earthquakes." *Struct. Design Tall Spec. Build.*, **14**, 107-130.

SeismoSignal, ver 3.2.0. (2007), On-line documentation at: http://www.seismosoft.com

Singh, M. P., Moreschi, L. M., Suarez, L. E., and Matheu, E. E. (2005), "Seismic Design Forces. II: Flexible Nonstructural Components." *J. Struct. Eng.*, **132**(10), 1524-1532.

Singh, M. P., Suarez, L. E., Matheu, E. E., and Maldonado, G. O. (1993), "Simplified Procedure for Seismic Design of Nonstructural Components and Assessment of Current Code Provisions." *Technical Rep. No. NCEER-93-0013, National Center for Earthquake Engineering Research, State Univ. of New York, Buffalo, N.Y.*

JOINT CONFERENCE PROCEEDINGS
7th International Conference on Urban Earthquake Engineering (7CUEE) &
5th International Conference on Earthquake Engineering (5ICEE)
March 3-5, 2010, Tokyo Institute of Technology, Tokyo, Japan

THE DEVELOPMENT AND USE OF THE CONTINUOUS COLUMN CONCEPT

Gregory MacRae

Civil and Natural Resources Engineering, University of Canterbury, Christchurch, New Zealand
gregory.macrae@canterbury.ac.nz

Abstract: The "continuous column concept" recognizes that all continuous columns and walls in a multistory building provide stiffness which discourages the formation of a soft-storey mechanism. The concept is more powerful, and it is more general, than the "capacity design" approaches that have been advocated in the past. This paper describes the background to the development of this methodology, quantification of the amount of drift concentration for specified column stiffness, and the importance of the continuous column concept in reducing the tendency of the structure to develop significant drifts in one direction due to P-delta effects. Finally, some applications of the concept are described.

1. INTRODUCTION

For good behaviour, structures subjected to strong earthquake shaking are required to have element deformation demands that are less than their capacities. The deformation demands are often related to the structural drifts. For a long period structure the displacement at the centre of mass can be estimated for a specified earthquake record or response spectrum. If the structure moves over with a linear shape distribution, then we can say that there is no drift concentration and the drift is related to the structural displacement. However, most structures do not move over uniformly, and a drift concentration factor, *DCF*, may be defined in Equation 1 and Figure 1 where the roof drift, δ_r, is simply the roof displacement, Δ_r, divided by the height of the roof from the ground, H, and the storey drift, δ_s, is the maximum value of interstorey displacement, Δ_{si}, divided by storey height, h_i, for all stories, i, as shown in Equation 2. If the *DCF* is unity, then the structure is moving over linearly. Otherwise, *DCF* is greater than unity.

$$DCF = \frac{\delta_s}{\delta_r} \quad (1)$$

$$\delta_s = \max_i\{\delta_{si}/h_i\} \quad (2)$$

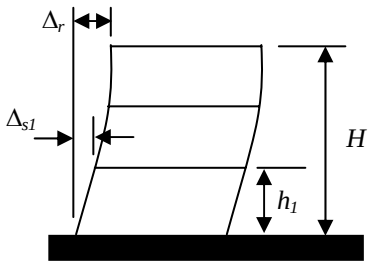

Figure 1. DCF Definition

In some structures, such as base-isolated structures, high drift concentrations may be expected or desired. In other short structures they may be permitted in certain cases. MacRae et al. (2004) have shown that that for a frame in which all of the yielding occurs in the bottom storey of a frame designed for a ductility, μ_t, then a good approximation to the *DCF* is Equation 3.

$$DCF \doteq \frac{(\mu_t - 1)\frac{H}{h_1}}{\mu_t} \quad (3)$$

For a 10 story structure with constant interstorey height designed to for a ductility, μ_t, of 5, the *DCF* is 8. This implies that the drift demands are 8 times what they would be if the structure were designed to move over linearly. Such an increase in demand may mean that the member capacities are exceeded, energy is all dissipated in a few locations (so redundancy of energy dissipation is lost), and the structure is more likely to be susceptible to deformations in one direction as a result of P-delta and other dynamic effects. For this reason it is generally considered to be more desirable if tall structures are designed with a *DCF* close to unity.

This paper describes some ways that this soft storey, or drift concentration, effect has been considered in the past. Then the development of a relatively new concept, the Continuous Column Concept (CCC) is described, along with its implications for design. In particular, the following questions are addressed:

1) What methods are currently used to limit the concentration of storey drift in frames?
2) Can an improved method be developed considering continuous columns?
3) What is the relationship between continuous column stiffness and storey drift?
4) How does the continuous column influence the

frame stability?

5) How can the continuous column be considered for frame design?
6) Are there some innovative applications of the continuous column concept?

2. LIMITING DRIFT CONCENTRATIONS

In moment frame design, the most common way of discouraging a soft-storey mechanism is by using a "capacity design" approach. In capacity design, a desired inelastic mechanism is specified. Locations of expected inelastic deformation are provided with sufficient ductility capacity that the structure can sustain the desired mechanism. Then, locations not expected to yield and which may be brittle are provided with sufficient strength to ensure that they do not yield. Their strength is related to the "capacity" of the ductile regions. In tall moment frames, the mechanism selected generally involves columns above the base remaining elastic, with plastic hinging occurring at the ends of the beams and at the base of the columns. This is generally referred to as the strong column weak beam (SCWB) mechanism shown in Figure 2. Here, the column flexural strength is specified to be significantly stronger than the demands likely to be imposed by the yielding beams.

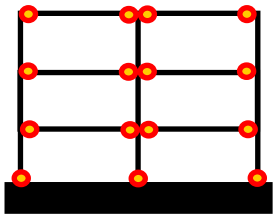

Figure 2. SCWB Mechanism

Code provisions for concrete moment frames differ around the world. Under the influence of Professor Tomas Paulay, the New Zealand (NZ) concrete code (NZS3101:1982, 2008) was one of the first to attempt to rigorously implement a capacity design approach. This approach had the dual aims of (i) discouraging column yielding due to the lower ductility of concrete columns detailed according to the code, and (ii) discouraging a soft storey mechanism. The column flexural strength is made greater than the demands imposed by the beams yielding in flexure considering strain hardening and dynamic inelastic effects. This capacity design methodology, because of its conceptual simplicity, became part of NZ earthquake engineering for reinforced concrete moment frame structures. When these techniques were being developed for RC structures, there was initially no similar development for steel framed structures.

The methods propounded by Paulay received ready acceptance but there were a number of issues in their general application. Some of these relating to reinforced concrete frames include:

(i) The moment frame capacity design approach is applied on a level-by-level basis. Therefore, according to the approaches considered, the frame in Figure 3 (in which there are perfect pins at the column points of inflection) would be expected to behave in a similar way to the frame in Figure 2. However, in reality, the Figure 3 frame response may be significantly different, with significantly more drift concentration and drift demand especially if stories have a negative post-elastic stiffness.

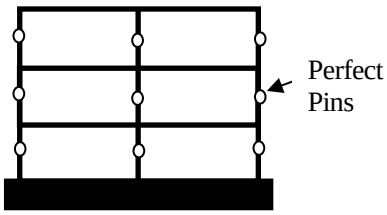

Figure 3. Modelling Steel Frame as Series of Subassemblies

(ii) The capacity design recommendations do not normally prevent a mechanism involving column hinging above the base in tall frames. This has been shown by Pekcan et al. (1997) using a simple plastic analysis of a moment frame subject to lateral forces. In general, as the column flexural strength increased, the location of the column hinge moved higher up the frame. The type of frame mechanism which often occurs is given in Figure 4.

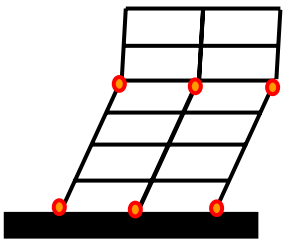

Figure 4. Plastic mechanism
due to Pushover of Capacity Designed Frame

(iii) Modifications to the capacity design methods described above were required for some structures to ensure that the final design is not unreasonable or uneconomical. This includes some low-rise frames as well as frames with large gravity loads along the beams.

One of the mandates of my PhD work, which was started in 1986, was to develop a capacity design methodology for steel framed structures. Steel moment-frames have a number of different characteristics than RC frames which can make capacity design even more difficult. In particular, a rolled steel beam section has the same flexural capacity in both positive (sagging) and negative (hogging) flexure. Often the size of a beam is determined based on the required hogging moment at the beam ends. The application of the concrete capacity design procedures to these steel frames can lead to very big column sizes. Also, the member strength-to-stiffness ratio of steel members is greater than that considered for concrete structures. Therefore, frame flexibility and drift considerations, rather than strength considerations, often

governed the member sizes. How was I, as a new postgraduate student, going to develop a design approach for steel structures that was simple, rational for NZ designers? A discussion with Prof. Paulay was the first step.

Prof. Paulay told me that since steel columns possessed some ductility capacity, there was not the same need to try to prevent any column yielding as there was for reinforced concrete structures. The most important thing was to make sure that columns demands did not become too significant, and this could generally be achieved for design level shaking by preventing a soft storey mechanism. Paulay advocated ensuring that there was at least one column in the structure that did not yield. An exterior column was the natural choice as it only had one beams from one direction framing into it. Thus, an acceptable mechanism became that in Figure 5. Following the advice of Paulay, I wrote my first conference paper on this topic (MacRae and Carr, 1987).

While I followed Paulay's advice, I had some questions/concerns about the procedure. These were:

i) Since the external columns provide all the restraint for a soft storey mechanism, there should be an effect of the number of bays in the frame, as shown in Figure 6. Here, each external column has to provide restraint for half of the frame width. It seemed to me that as the frame width increased, the exterior column stiffness should also increase. However, this effect was not considered in the capacity design approach where the capacity of the column was only based on the flexural capacities of the beams framing into it.

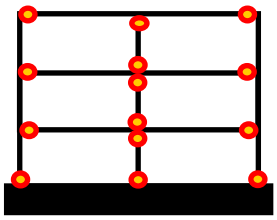

Figure 5. Plastic Mechanism Proposed by Paulay for Steel Frames

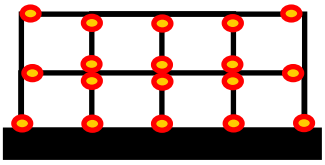

Figure 6. Plastic Mechanism for Frame with Many Bays

ii) If the beams framing into the exterior columns were perfectly pinned, as shown in Figure 7, then the moment applied to the external columns is zero. It is difficult then to perform capacity design using the traditional method. It was not clear to me whether or not this type of frame would perform badly.

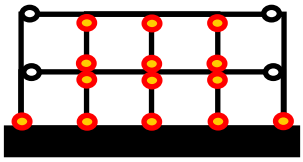

Figure 7. Frame with Pinned Beams beside Strong Column

iii) Even if we performed capacity design according to the method by Paulay for the frame shown in Figure 5, and the exterior column were made of a material that were very strong but very flexible in flexure, then it would only sustain large moments at very large interstorey drifts. While a soft-storey mechanism would be discouraged, a soft storey could still occur with the majority of the demands occurring over one storey.

iv) Realistic effects of the slab passing outside the column width were not always included (and are still often not included) explicitly in analysis of the frames in current design codes, and or in procedures for frame assessment (e.g. AISC, 2005). These effects are additional to that of the beam and slab acting directly on the column face. They cause additional forces imposed on the column as shown in Figure 8. These forces are similar to those imposed on a coconut tree by a monkey climbing it! Here, the lateral strength of the subassembly is increased because the longitudinal reinforcing steel in the slab extending outside the column width is subjected to tension due to the moment on the left hand beam. This tension force is resisted by a compressive force on the right hand side of the column slab as shown. To resist the moment applied by the left-hand beam, there is also a compressive force at the bottom of the left hand beam on the column face. The magnitude of the compression forces acting on the column depends on the amount of steel outside the column width in the participating slab. This width of participating slab, and the amount of steel, increases as the beam deformation increases. Note that there is no force shown at the end of the right hand beam. This is because the tension steel yielding at the bottom of the right hand beam limits the moment that can be imposed there and the slab effect is not large.

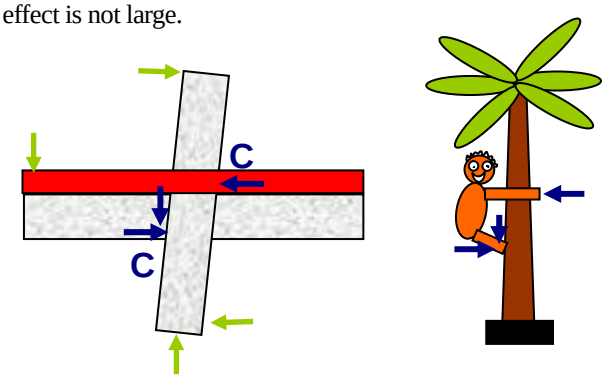

(a) Subassembly (b) Monkey Idealization

Figure 8. Additional Forces on Column (tree) due to Slab (monkey) Extending around Column

Studies have shown (e.g. Wolfgram (1984), French and Boorojerdi (1989)) a strength increase of more than 70% due to the presence of the slab for a RC frame. A simple method to consider these effects in all types of frame has been proposed by Umarani and MacRae (2007). For steel frames, the increase in moment can be significantly less than that for RC frames (where a slab tributary width approach may be used) because yielding of the steel section occurs at the bottom of the left hand beam. Using the concept above, methods are now considered in the NZ Steel Structures code (NZS3404, 2007) to compute the maximum demands that can be imposed on the column.

In addition to these concerns for moment-frames, my doctoral work looked at the performance of braced frame structures. In particular, appropriate design of eccentrically braced frames (EBFs) was studied. In these frames, whether or not the connections of the beams and columns to the column were modelled as fixed does not have a major effect on the column sizes because the forces are predominantly governed by truss action. The is an issue for a frame designed and detailed as a truss away (except for beside the yielding link) with the perfect pinned connections shown in Figure 9a. Here, after the first link yields, there is a soft-storey mechanism which results in large demands. (The storey drift demands were doubled to 5.3% in the analysis of a 10 storey EBF without continuous columns in analyses by MacRae et al. (1990)). A method to limit this type of deformation by using vertical tension ties at each end of the link was proposed, as shown in Figure 9b. While this concept to reduce a soft-storey mechanism was effective, no general prescription was provided as to the total strength and stiffness of these elements. Professor Egor Popov was the reviewer of my doctoral thesis. I spoke to him as part of a cruise on the San Francisco bay as part of a bridge workshop at Berkeley in 1993. He said that in all the analyses of EBFs he had been involved with he had not seen a problem with the type of soft-storey we were concerned about.

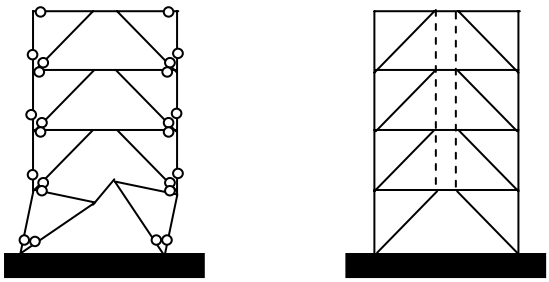

(a) Possible Frame Mechanism (b) Proposed Solution

Figure 9. EBF Considerations (MacRae et al. 1990)

Concentrically braced frames (CBFs) also have the same issues as EBF frames. Analyses have shown that if the structure is analysed as designed, with pinned connections everywhere, significant member demands can occur in the storey with the drift concentration.

It may be seen from the discussion above that capacity design methods have been used to limit large storey deformations and to discourage column yielding in moment frame structures. While these methods work for some cases, they do not always work. In addition, these methods cannot be applied in a reasonable and economic way to steel moment frames, and there is no clear way of limiting drift concentrations in braced frames.

The concept for a better, simpler and more rational means of limiting drift concentrations came many years after the doctoral work. I had the privilege of being involved in frame analyses for the SAC Steel Project while I was working at the University of Washington, Seattle. As part of this project there were some discussions on modelling. I was not involved in these directly, but they probably reignited my thinking in this issue. It was in 2000 at a conference that I had a simple idea. I do not recall exactly which conference it was, but it could have been the ASCE Structures Congress in Philadelphia. I do remember thinking that it was a powerful concept. Because it was a concept, I would not be able to get funding to develop it in the US system, but it was something that I should develop it and publish before talking about it too much. It is one of those things that is so simple, that once explained, people say it is common sense and there is nothing new about it. While other people may have realized the significance of it, no-one had discussed it, or written specifically about it, before. I was able to work on it initially with Dr. Yoshihiro Kimura. Dr. Kimura was doing post-doctoral studies at Tokyo Institute of Technology, and who had obtained funding to study at the University of Washington for several months where he worked on the behavior of CFT framed structures with Professor Charles Roeder and myself. Our work on limiting drift concentration occurred while he was back at Tokyo Institute of Technology and while I was on sabbatical leave at the University of Canterbury.

3. THE CONTINUOUS COLUMN CONCEPT (CCC)

The continuous column concept simply acknowledges that:

> *If columns are continuous over several stories of a structure, then the stiffness of the columns will limit the amount of drift concentration that can occur.*

The major difference between this simple concept and previous concepts is that:

1) It emphasizes the importance of *stiffness* rather than *strength*, as was considered in the capacity design approaches. In fact, strength may be regarded simply as a means of maintaining stiffness.

2) It considers the frame behaviour over the height rather than on a level-by-level basis.

3) It considers the effects of all of the continuous columns in the building, as they provide stiffness that resists the drift concentration. These include all in-plane and out-of-plane

seismic columns, and all gravity columns in the structure.

4) The concept can be applied to shear-type frames of all types and materials in a consistent way. It is the same for RC, timber and steel structures designed as moment frames or braced frames.

In the words of Paulay, this concept "allows the designer to tell the structure what to do". The paper describing the basic concept is described by MacRae, Kimura and Roeder (2004).

4. COLUMN STIFFNESS – DCF RELATIONSHIP

While the concept is simple, designers need to know what level of *DCF* is associated with what level of drift. This is characterized by MacRae, Kimura and Roeder (2004) for frames with pinned continuous columns at the ground floor level. (Other papers describing both the developments are also listed in the references section at the end of this paper).

The first part of the paper quantifies the performance of the 2 storey shear type structure with continuous columns as shown in Figure 10. The stiffnesses of all continuous columns in the building were lumped together and modelled as one single continuous column with section flexural stiffness, *EI*. Closed form expressions were developed for the deflections of the frame due to an inverted triangular force distribution considering continuous column effects. Separate expressions were developed for the 3 stages of inelasticity (i) the elastic structure; (ii) after the base storey had yielded; and (iii) after both stories of the frame had yielded.

The expressions developed indicated that the *DCF* was dependent on a non-dimensional column stiffness, α, given by Equation 4, where k is the storey stiffness. When α tends to infinity then DCF tends to unity as would be expected. Also, when α is zero, the response is that for a frame without a continuous column. Computer generated pushover analysis was conducted to ensure that the derivation was accurate. Time history analyses performed were also in agreement with the pushover analysis results.

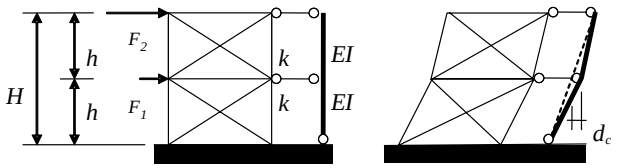

(a) Parameters (b) Deformed Shape

Figure 10. System with Gravity Column

$$\alpha = \frac{EI}{kh^3} \qquad (4)$$

For multistory shear-type structures, it is not possible to determine a simple closed form solution for the response. The non-dimensional column stiffness ratio, α, developed from the 2 storey structure analyses was again used and empirical expressions were used to develop expressions for the *DCF* and maximum moment in the column due to pushover analyses. These expressions developed were based on analyses of frames with a strength distribution up the height ranging from uniform to one which matched the shear demand distribution from the imposed forces. Inelastic dynamic analyses were also undertaken. Empirical techniques were used to allow the dynamic response to be estimated from the pushover response.

An interesting finding from these analyses is that the peak moment in the continuous columns can occur high up in the frame. Often it is above the mid-height. If gravity columns are required to resist these moments, then a partial strength splice may not be sufficient to ensure satisfactory behaviour.

The study summarized in the 2004 paper concentrated on continuous columns with pinned bases. An attempt was also made to develop simple expressions for continuous columns with fixed bases (like shear walls on a rigid foundation). While some expressions could be obtained, they are more complex than those considering the pinned base (Kimura and MacRae, 2006).

5. STABILITY EFFECTS

There was another mystery relating to the behaviour of steel frames which has been solved with the CCC. This involves the dynamic stability of frames subjected to dynamic loading. The concept of dynamic stability had been developed at the Public Works Research Institute, Tsukuba, Japan with Dr. Kazuhiko Kawashima in 1990-1991 (MacRae and Kawashima, 1993). This concept related both to *P*-delta effects and to the likelihood of permanent (or residual) displacements after a major earthquake (Kawashima et al. 1994, 1998 and MacRae, 1994). The concept was inspired by at chat with Prof. Uetani from Kyoto University who kindly spend some time with me when I dropped into his office on a visit there.

In simple terms, the dynamic stability concept states that a bilinear oscillator with a negative post-elastic stiffness has a tendency to yield in the direction away from the initial displacement position and to have large peak and permanent displacements which are a function of the duration of the strong motion shaking. Conversely, structures with a positive post-elastic stiffness, which have already yielded in one direction, tend to yield toward the zero displacement location. Their permanent displacements tend to be lower as the post-elastic stiffness ratio increases.

Some considerations relating to this effect are included in seismic code P-delta provisions. Generally, these are the same for all types of structure, even though different types of structure have different types of hysteresis loop and are affected differently by P-delta effects. The parameter used to

describe the P-delta effect, θ, is given in Equation 5. It is dependent on the axial force on the level considered, *P*, the lateral stiffness of the level, *k*, and the height of the level, *h*. It has been developed based on elastic frame considerations (MacRae, 1994) and codes usually specify that it is used on a level-by-level basis.

$$\theta = \frac{P}{kh} \tag{5}$$

Hiroyuki Tagawa, a postgraduate student who had completed his undergraduate study as part of Prof. Fumio Watanabe's group from Kyoto University, was working with me at the University of Washington on the seismic response of steel frames. He found that the post-elastic stiffness of the lower stories of steel frames often had a significant negative post-elastic stiffness. (The storey/level post-elastic stiffness was computed for subassemblies of the frame at each level by inserting pins at the column mid-storey heights as shown in Figure 3). However, when dynamic inelastic was conducted, the large permanent displacements that had been seen in single-degree-of-freedom analyses were not observed.

Tagawa carefully studied the frame response and determined the effective post-elastic stiffness factor for a multi-storey frame. He did this by comparing the instantaneous eigenvalue of the first mode with that of the elastic frame. He also isolated the P-delta term in a consistent way to that for a single degree of freedom structure. While post-elastic stiffnesses of the bottom storey/levels were significantly negative (using the Figure 3 approach), he found from the time history analyses that the effective post-elastic stiffness factor of a frame (and the lowest instantaneous eigenvalue) was almost always positive during the analysis. This was due to the continuous columns providing significant stiffness between stories. When the continuous columns were not provided, large drift concentrations and demands resulted.

6. APPLICATION OF CCC

(a) Estimation of frame likely drift concentrations

The continuous column stiffness for a number of steel frames has been evaluated by Tagawa (2005). Some of these are shown as vertical lines in Figure 11 for the seismic columns alone (w/o Gravity Column) and with the seismic and gravity columns together (w/ gravity column) for frames of different heights. Here the C.C. Ratio on the *x*-axis is α. It can be seen that the continuous column ratio, α, for the seismic frame columns alone is close to, or greater than, 0.20 for all the SAC Steel Project Los Angeles frames. When the gravity columns in the building are also considered, α is greater than, 0.30.

The *DCF* is also given as a function of α on these graphs for various scale factors of the NF05 record from the SAC suite. The maximum scale factor for the severe NF05 record is 0.50 for the LA 20 frame because more severe records cause collapse. The *DCF* change over the range of a seen in the structures, α = 0.2 to 0.3, is not very large. The gravity column stiffness range is plotted on a log scale indicating that it takes a large increase in stiffness α to significantly reduce the *DCF*.

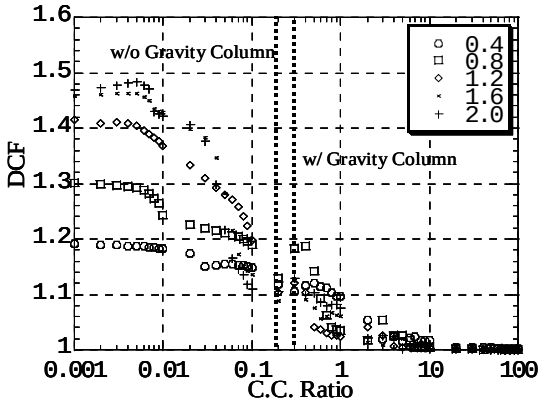

(a) LA 3 storey frame

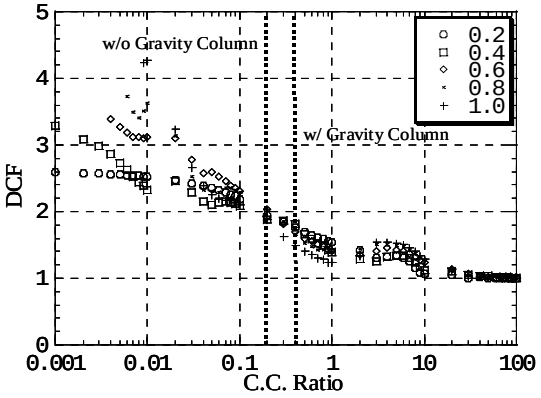

(b) LA 9 storey frame

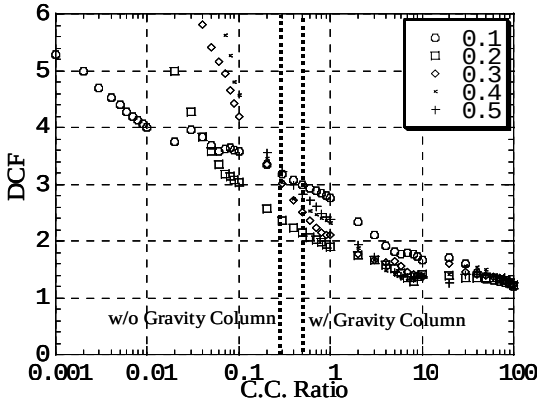

(c) LA 20 storey frame

Figure 11. DCF – α plots (from Tagawa 2005)

If buildings are provided with an α value of 0.2 then the *DCF* may be estimated from the response of the frame for various records. It can be seen that the response does not differ a lot for the different levels of the earthquake record used in the plots in Figure 11. From the records shown, an

approximate estimate of *DCF* as a function of the number of stories in the frame, *N*, is given by Equation 5. For example, for a 9 storey frame the DCF estimated is 2.06. Further analyses would be needed to increase the robustness of this type of equation which could be used in building codes.

$$DCF = 0.132\,(N - 1) + 1 \qquad (5)$$

The fact that realistic frames tend to have significant seismic and gravity column continuous stiffness is a reason that significant problems with a soft-storey mechanism, such as that shown in Figure 9a, have not been seen in analyses of many frames, as had been described by Popov.

(b) CC-Slab Connection Strength

The required strength of connections between continuous columns and floor slabs at the building perimeter is not only related to the inertial force resulting from accelerations, but also to the continuous column stiffness as shown by Tagawa, MacRae, Lowes and Wada (2008).

7. INNOVATIVE USES OF THE CCC

The CCC has also been used in an innovative way by Prof. Akira Wada of Tokyo Institute of Technology. Here, an older multistory SRC structure has been retrofitted by placing a number of 600mm x 4,400mm post-tensioned walls on top of a pinned base steel structure and connecting it to the structure through a steel base with a pin at the ground level as shown in the schematic of Figure 12. This pin is featured so people using the structure can appreciate the engineering solution. This form of retrofit has little effect on the structural first-mode period and on the maximum likely base shear. This means that very little foundation work is required. Some dampers are also provided at the top of the wall to further reduce the response. In such a frame there is almost no drift concentration (i.e. the DCF = 1.0) as the structure moves over in a linear first mode fashion. This reduces the overall demands on the structure and increases earthquake resistance.

7. CONCLUSIONS

The paper describes a new paradigm in the prevention of large deformations due drift concentrations in multistory frames. This involves explicit consideration of the stiffness of the continuous columns over the height of the structures. The background to the development of this new method is described. In particular, it is shown that:

1) Capacity design methods have previously been developed to limit large storey deformations and to discourage column yielding in moment frame structures. However, these methods are inadequate for general moment frames and cannot be applied easily to other types of frame.

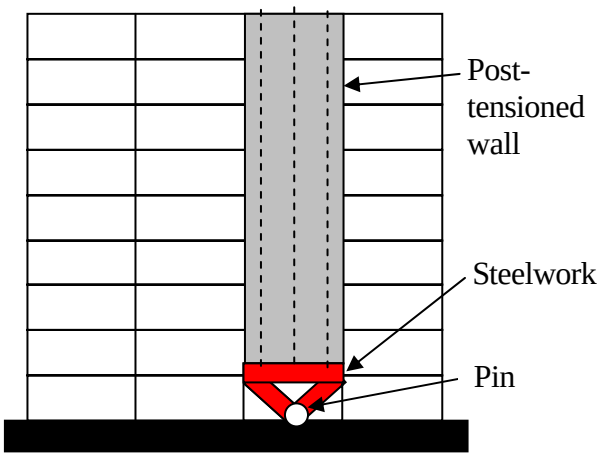

Figure 12. Schematic of Retrofit of SRC Structure in Tokyo

2) The Continuous Column Concept (CCC) is proposed which emphasizes the importance of the *stiffness* of all continuous columns in the building structure for controlling drift concentrations. Strength is necessary, but only as a means of maintaining stiffness.
3) Relationships between CC stiffness and drift concentration are developed and described in a non-dimensional form. By specifying appropriate CC stiffness it is possible to control the structural behaviour.
4) It is shown that the CC stiffness is critical in ensuring that multistory structures behave in a dynamically stable way during an earthquake, so that large permanent displacements are discouraged.
5) Relationships developed between drift concentration factor and continuous column stiffness may be used for design.
6) An interesting application of the CCC has already been implemented by Prof. Wada's group in Japan.

Acknowledgements:

It is through the diligent efforts of Prof. Yoshihiro Kimura and Dr Hiroyuki Tagawa that the continuous column concept was developed. The author also wishes to thank Prof. Wada for informing him about the innovative application, as well as the organizing committee of CUEE for providing the invitation, support and opportunity to present this work.

References:

AISC 341 – 05, (2005), "AISC 341 – 05, Seismic Provision for Structural Steel Buildings", *American Institute of Steel Construction* (AISC), November.

French, C. W., and Boroojerdi, A., (1989), "Contribution of R/C Floor Slabs in Resisting Lateral Loads," *Journal of Structural Engineering, ASCE*, 115(1), January, pp. 1-18.

Iwan, W D. (1997), "Drift spectrum: Measure of demand for earthquake ground motions", Journal of Structural Engineering, ASCE, 123(4), April, p.397-404.

Kawashima K., MacRae G. A., Hoshikuma J. and Nagaya K., (1994), "Residual Displacement Response Spectrum and Its Application", *Journal of the Japan Society of Civil Engineers*, No. 501/I-29, October, pp. 183-192. (In Japanese).

Kawashima K., MacRae G. A., Hoshikuma J. and Nagaya K., (1998),

"Residual Displacement Response Spectrum", *ASCE Journal of Structural Engineering*, ASCE, May, pp. 523-530.

Kimura, Y., MacRae, G. A and Roeder, C. W., (2002), "Effect of Column Flexural Stiffness on Braced Frame Performance", *7th National Conference on Earthquake Engineering*, Boston, July 21-25.

Kimura, Y. and MacRae, G. A., (2002), "The Effect of the Column Flexural Stiffness on Story Drift Concentration Mechanism of Two Story Braced Frames", *Architectural Institute of Japan, Journal of Constr. Eng.*, No. 560, pp 189-195, October.

Kimura, Y. and MacRae, G., (2003), "Effect of the Column Flexural Stiffness and Strength to Limit Story Drift Concentration Braced Multi Story Frames", *9th East Asia Pacific Conference on Structural Engineering and Construction*, December, pp.40-45.

Kimura, Y. and MacRae, G.. (2004), "Effect of Cantilever Column Flexural Characteristic on Braced Frame Displacements", *13WCEE*, Vancouver, August.

Kimura, Y. and MacRae, G., (2004), "Effect of Column Flexural Stiffness and Strength on Story Drift Concentration for Two Story Braced Frames", *1st International Conference on Urban Earthquake Engineering*, Vol. 1, March, pp.71-70.

Kimura, Y. and MacRae, G. A., (2005), "Effect of the Column Flexural Stiffness and Strength on Story Drift Concentration Mechanism of Two Story Braced Frames with Fixed Column Base", *Architectural Institute of Japan, Journal of Struct. Constr. Eng.*, No. 593, pp 153-160, July.

Kimura, Y. and MacRae, G., (2006), "Application of Elastic Cantilever Column to Limit Story Drift Concentration of Braced Two Story Frames", *10th East Asia Pacific Conference on Structural Engineering and Construction*, August, pp.771-776.

Kimura, Y. and MacRae, G., (2006), "Effect of Column Flexural Characteristic on Seismic Behavior of Braced Frame with Fixed Column Base", *STESSA*, Yokohama, Japan, 14-17 August.

MacRae, G. A. and Carr, A. J., (1987). "Capacity Design of Steel Moment-Resisting Frames", Proceedings, *Pacific Conference on Earthquake Engineering*, Wairakei, New Zealand, Vol. 2, pp. 47-58, 1987.

MacRae, G. A., Carr, A. J. and Walpole, W. R., (1990). "The Seismic Response of Steel Frames", *Research Report 90-6, Department of Civil Engineering, University of Canterbury*, New Zealand, March.

MacRae, G. A. and Kawashima, K., (1993). "The Seismic Response of Bilinear Oscillators Using Japanese Earthquake Records", *Journal of Research of the Public Works Research Institute*, Vol. 30, Ministry of Construction, Japan.

MacRae, G. A., Kimura, Y., and Roeder, C. W., (2004), "Effect of Column Stiffness on Braced Frame Seismic Behavior", *Journal of Structural Engineering, ASCE*. March, **130**(3), pp. 381-391.

Pekcan G., Mander J. B. and Chen S. C. (1997), "Design and Retrofit Methodology for Building Structures with Supplemental Energy Dissipating Systems", *Report MCEER-99-0021, State University of New York, Buffalo*, NY14261.

Peng, B. H. H., (2009), "Seismic Performance Assessment of Reinforced Concrete Buildings with Precast Concrete Floor Systems", *Doctoral Thesis, University of Canterbury*, July.

Standards Association of New Zealand, (1982), "NZS 3101:1982, Code of Practice for Design of Concrete Structures", *Standards Association of New Zealand*, Wellington.

Standards New Zealand, (2006), "NZS 3101:2006, Code of Practice for Design of Concrete Structures". Standards Association of New Zealand, (1982), "NZS 3101:1982, Code of Practice for Design of Concrete Structures", *Standards New Zealand*, Wellington.

Standards New Zealand, (2007), "NZS 3101:2006, Code of Practice for Design of Concrete Structures". Standards Association of New Zealand, (1982), "NZS 3101:1982, Code of Practice for Design of Concrete Structures", *Standards New Zealand*, Wellington.

SNZ 2007, "NZS 3404.1 and 2:1997 Steel Structures Standard": *Standards New Zealand*, with 2001 and 2007 Amendments, Wellington.

Tagawa, H., MacRae, G., and Lowes L. (2004), "Evaluations of 1D Simple Structural Models for 2D Steel Frame Structures", *13th World Conference on Earthquake Engineering*, Vancouver, August 2004.

Tagawa, H., (2005), "Towards an Understanding of Seismic Response of 3D Structures – Stability & Reliability", *Doctoral Thesis*, University of Washington, Seattle.

Tagawa, H., MacRae, G., and Lowes, L., (2006), "Probabilistic Evaluation of Seismic Performance of 3D One-way and Two-way Steel Moment Frame Structures", *STESSA*, Yokohama, Japan, 14-17 August.

Tagawa, H., MacRae, G. A. and Lowes, L., (2007), "Seismic Behavior and Dynamic Stability of 2D Steel Moment Frame Structures", *Pacific Structural Steel Conference*, Wairakei, NZ.

Tagawa, H., MacRae, G. A., and Lowes, L., (2007), "Evaluation of Seismic Response of Multi-Story Structures Using Dynamic Stability Coefficients - Continuous Column Effects in Steel Moment Frames in Perspective of Dynamic Stability (Part 1)", *Journal of Structural and Constructional Engineering, Transactions of the Architectural Institute of Japan, AIJ*. No. 618 (20070830), pp. 57-64. ISSN:13404202.

Tagawa, H., MacRae, G., Lowes, L. and Wada, A., (2008), "Analytical Simulation of Progressive Collapse of Perimeter Frames Due to Out-of-Plane Behavior", *14th World Conference on Earthquake Engineering*, Beijing, China, 12-17 October, Paper ID: 05-05-0087.

Tagawa, H., MacRae, G. A., and Lowes, L., (2010), "Continuous Column Effects of Gravity Columns in U.S. Steel Moment-resisting Frame Structures- Continuous Column Effects in Steel Moment Frames in Perspective of Dynamic Stability (Part 2)", *Journal of Structural and Constructional Engineering, Transactions of the Architectural Institute of Japan, AIJ*. Vol. 75, No. 650.

Tremblay, R. (1993), "Seismic Behaviour and Design of Friction Concentrically Braced Frames for Steel Buildings", *Doctoral Thesis, University of British Colombia*.

Umarani, C. and MacRae, G. A., (2007), "A New Concept For Consideration Of Slab Effects On Building Seismic Performance", *Journal of Structural Engineering*, Structural Engineering Research Centre, Chennai, India, No. 34-3, April-May, pp. 25–32.

Wolfgram, C. E., (1984). "Experimental modelling and analysis of three one-tenth scale reinforced concrete frame-wall structures," *Doctoral thesis, University of Illinois at Urbana.*

JOINT CONFERENCE PROCEEDINGS
7th International Conference on Urban Earthquake Engineering (7CUEE) &
5th International Conference on Earthquake Engineering (5ICEE)
March 3-5, 2010, Tokyo Institute of Technology, Tokyo, Japan

A NOVEL APPROACH TO PERFORMANCE-BASED SEISMIC DESIGN OF BRIDGE USING FUZZY GENETIC OPTIMIZATION

Yu-Chi Sung [1], Chin-Kuo Su [2], and Dyi-Wei Chang [3]

1) Professor, Department of Civil Engineering, National Taipei University of Technology ,Taipei 106, Taiwan
2) Senior Engineer-3, CECI Engineering Consultants, Inc., Taipei 106, Taiwan
3) General Manager, CECI Engineering Consultants, Inc., Taipei 106, Taiwan
sungyc@ntut.edu.tw, CKSu@ceci.com.tw, dwchang@ceci.com.tw

Abstract: This paper presents a fuzzy genetic optimization for performance-based seismic design (PBSD) of reinforced concrete (RC) bridge piers with single-column type. The design is modeled as a constrained optimization problem with the objective of minimizing construction cost subject to the constraints of qualified structural capacity and suitable reinforcement arrangements for the designed RC pier. A violation of the constraints is combined with construction cost to serve as the objective function. The fuzzy logic control (FLC), which adapts the penalty coefficients in the genetic algorithm (GA) optimization solver, was employed to avoid a penalty that is too strong or too weak through the entire calculation so that a feasible solution can be obtained efficiently.

The reported results of cyclic loading tests for three piers with squared section, rectangular section and circular section, respectively, were employed as the data-base of investigation. Furthermore, a case study on the PBSD of a squared RC bridge pier with four required performance objectives (fully operational, operational, life safety and near collapse) corresponding to different peak ground accelerations (PGAs) of earthquakes was analyzed. Two feasible designs of the pier were determined successfully and the optimal one with minimum construction cost was obtained accordingly. The result obtained shows that the proposed algorithm gives an acceptable design for the PBSD of the RC bridge piers.

The superiorities of GA and FLC were incorporated and the availability of the proposed procedure was investigated. Moreover, through the proposed systematic design procedure, the discrepancy in the PBSD from different design engineers will be lessened effectively and the design efficiency as well as the design precision will also be enhanced significantly.

1. INTRODUCTION

The performance-based seismic design (PBSD) of a reinforced concrete (RC) bridge pier with single-column type intends to find a feasible design consistent with multiple-level structural performances with respect to different levels of earthquake. Its primary goal is to determine the nonlinear performance of structures under different scales of severe earthquakes for safety or retrofitting considerations, or the linear performance of structures under moderate earthquakes for detecting their serviceability or operational functions (SEAOC 1995; ATC-40 1996). In other words, the complete structural performance excited from moderate earthquakes up to the maximum loading, which may lead to ultimate states, is required for design. Making a qualified design that satisfies the rigorous limitations is difficult even for the senior engineers, and an indirect investigation procedure is widely adopted as an alternative. A set of design parameters for an RC pier including the material strengths, the arrangement of reinforcements and the size of pier section is able to be tried initially, based on the designer's experience. Certain important characteristics such as plastic hinge property (PHP) and sensitivity to structural nonlinearity of the pier can be determined accordingly (Sung et al. 2005). Sequentially, the seismic response of the single-column pier is able to be evaluated rapidly via a pushover analysis if a simple model of the cantilever structure is considered. If the response obtained does not meet the target of structural performance, the design parameters need to be revised and the process needs to be repeated until the targeted structural performance is satisfied. A highly iterative trial-and-error design procedure is often used and the accuracy as well as the efficiency of the design is strongly sensitive to the designer's experience. Therefore, the goal of this work is to create a systematic design procedure to avoid the man-made discrepancy and enhance the design precision.

In this paper, the PBSD of an RC bridge pier was modeled as a constrained optimization problem with the objective of minimizing construction cost subject to the constraints of qualified structural capacity and suitable reinforcement arrangements for the designed RC pier. The structural capacity, represented by the structural force-displacement relation, obtained from the pushover

analysis is required to satisfy the extreme case of multiple-level structural performances with respect to various earthquakes; the reinforcement arrangements is limited to the specification of the seismic design code of RC structure (ACI Committee 318 2005). A violation of the constraints is combined with construction cost to serve as the objective function. Since the objective function is not able to be formulated in an explicit mathematical function, conventional optimization solvers (such as the sequential quadratic method or the dual method) are not suitable for this problem (Bazaraa and Shetty 1979).

Based on the Darwin's survival-of-the-fittest, the GA does the optimization with a group of chromosomes known as a population. Since a population provides a list of solutions at the same time, it gives a stronger search than traditional optimizers by skipping the local optimal points. For the constrained optimization problem, the penalty function is employed by penalizing the infeasible solutions by reducing their fitness values in proportion to their degrees of constraint violation. Although the GA can give potential solutions, the efficiency as well as the precision of the solutions is sensitive to the penalty coefficients. The infeasible solutions with high original fitness values may remain in subsequent generations in the case where the penalty coefficient is too small, which results in the search moving toward false peaks in the infeasible region. On the contrary, the feasible solutions with low original fitness values will have no chance to retain their good characteristics in subsequent generations in the case where the penalty coefficient is too large, which yields premature convergence resulting in poor solutions. If a constant coefficient is adopted through the entire calculation, an improper penalty during different generations may be inevitable and, accordingly, give imprecise results (Sarma and Adeli 2000).

Nanakorn and Messomklin (2001) proposed an adaptive penalty function in the GA for structural design optimization. The main idea of their scheme is to fix the chance to be selected to the matting pool of the best infeasible members throughout all generations. The parameter was set as the ratio between the fitness value of the best infeasible members and the fitness value of the feasible average members. Accordingly, a modified bilinear scaling technique was employed for fitness scaling. In this way the penalty is always adjusted so that the desired degree of penalty is achieved in all generations.

Fuzzy logic control (FLC) can deal with vagueness and impreciseness in knowledge representation by the theory of fuzzy set and it is suited modeling real-world design problems that are difficult to represent in precise mathematical forms (Zadeh 1965). The FLC can handle the decision-making problem with imprecise data and provides valuable information in deciding the predominant parameters in the model. As a result, the use of FLC to adapt the penalty coefficients in the GA is appropriate.

Soh and Yang (1996) proposed a fuzzy-controlled genetic-based search for structural shape optimization. In their model, each constraint of the shape optimization problem was represented by fuzzy set theory. By introducing a fuzzy knowledge-based system (FKBS), the applicability of coupling a fuzzy rule-based system to a GA to enhance the GA search efficiency and improve its decision-making performance was illustrated.

The present paper aims at using the FLC to control the penalty of the constraints in the GA used as the optimizer for the PBSD of the RC bridge piers with single-column type. The envelopes of the reported experimental hysteresis loops of three piers were simplified to a bilinear form of the structural force-displacement relation and served as the design target. Based on the proposed procedure, several feasible solutions of pier design were determined and their structural capacities were compared with the envelopes of the experimental loops to validate the accuracy of the proposed fuzzy genetic optimization. Furthermore, a case study on the PBSD of a square RC bridge pier with four required performance objectives (fully operational, operational, life safety and near collapse) corresponding to earthquakes with peak ground accelerations (PGAs) of 0.12g, 0.18g, 0.30g and 0.40g was analyzed. Two feasible designs of the pier were determined successfully and the optimal one with minimum construction cost was obtained accordingly.

2. OPTIMAL MODEL FOR PDSD OF THE RC BRIDGE PIERS WITH SINGLE-COLUMN TYPE TWO GROUPS OF CROSS-SECTION

Section commonly used for the RC bridge piers were taken into account in the present paper. For the rectangular (or square) section, ten design parameters are used as the design variables. They include: (1) the length of the long side; (2) the length of the short side; (3) the number of longitudinal reinforcements along the long side; (4) the number of longitudinal reinforcements along the short side; (5) the diameter of the longitudinal reinforcement; (6) the diameter of the transverse reinforcement; (7) the spacing of the transverse reinforcement; (8) the strength of the concrete; (9) the strength of the longitudinal reinforcement and (10) the strength of the transverse reinforcement. The ten parameters are represented by a design variable vector $\mathbf{x}$ for the optimization design of RC columns with rectangular (or square) section.

For the circular section, eight design parameters are used as the design variables. They include: (1) the dimension of diameter; (2) the number of the longitudinal reinforcements; (3) the diameter of the longitudinal reinforcement; (4) the diameter of the transverse reinforcement; (5) the spacing of the transverse reinforcement; (6) the strength of the concrete; (7) the strength of the longitudinal reinforcement and (8) the strength of the transverse reinforcement. The eight parameters are represented by a design variable vector $\mathbf{x}$ for the optimization design of RC columns with circular section.

The construction cost of a designed RC bridge pier can be expressed as:

$$\psi = V_C C_C + C_S (W_{SL} + W_{ST}) \tag{1}$$

where, V_C is the volume of concrete in the designed pier, C_C is the construction cost per volume of concrete, W_{SL} and W_{ST} are the weights of the designed longitudinal reinforcements and transverse reinforcements, respectively, and C_S is the construction cost per weight of reinforcement.

The design target (DT) of structural performance for a bridge pier is ideally modeled with a structural bi-linear system characterized by the four physical quantities which include the yielding displacement δ_Y (i.e. DT_1), the yielding force P_Y (i.e. DT_2), the ultimate displacement δ_U (i.e. DT_3), and the ultimate force P_U (i.e. DT_4). In other words, the design objectives for the target pier can be represented by (DT_i, i=1~4).

On the other hand, the four design quantities (DQ): δ_Y^* (i.e. DQ_1), P_Y^* (i.e. DQ_2), δ_U^* (i.e. DQ_3) and P_U^* (i.e. DQ_4), have similar physical meanings to the design targets, and can be obtained through the pushover analysis, based on a set of design variables. Therefore, the penalties ω_i can be expressed as

$$\omega_i = \frac{|DQ_i - DT_i|}{DT_i} \tag{2}$$

The optimization problem which seeks to minimize the function F_0 can be expressed as

$$Minimize \quad F_0(\mathbf{x}) = \psi(1 + \sum_{i=1}^{4} \omega_i)^2 \tag{3}$$

where, the square of the bracket was used to enhance the penalty for violation of the constraints (Zou and Chan 2005).

Based on the seismic design code for a RC structure (ACI Committee 318 2005), the ratio of the cross-sectional area of the longitudinal reinforcement to the gross cross-sectional area of the RC section is defined as ρ and ρ must be between 0.01 and 0.06. The violation of the design code can be quantified by a coefficient η defined as follows:

$$\eta = \begin{cases} 0 & if \quad 0.01 \le \rho \le 0.06 \\ (\rho - 0.06)/0.06 & if \quad \rho > 0.06 \\ (0.01 - \rho)/0.01 & if \quad \rho < 0.01 \end{cases} \tag{4}$$

Moreover, based on ACI 318-05, the cross-sectional area A_{sh} (rectangular section) or the volumetric ratio ρ_s (circular section) of transverse reinforcement should satisfy the following equations

$$A_{sh} \ge \begin{cases} 0.09\left(sh_c \dfrac{f_c'}{f_{yh}}\right) \\ 0.3\left(sh_c \dfrac{f_c'}{f_{yh}}\right)\left(\dfrac{A_g}{A_c} - 1\right) \end{cases} \quad \text{for rectangular section} \tag{5a}$$

$$\rho_s \ge \begin{cases} 0.12 \dfrac{f_c'}{f_{yh}} \\ 0.45\left(\dfrac{A_g}{A_c} - 1\right)\dfrac{f_c'}{f_{yh}} \quad ; \quad f_{yh} \le 420\ MPa \end{cases}$$

for circular section (5b)

where h_c is the cross-sectional dimension of the column core measured center to center of confining reinforcement; A_g is the gross cross-sectional area of the column; A_c is the cross-sectional area of the column core measured out to out of transverse reinforcement; s is the spacing of transverse reinforcement that must be smaller than 10 cm and a quarter of the effective depth ($d/4$) of the column.

The violation of the design code with respect to A_{sh} (rectangular section) or ρ_s (circular section) can be quantified by a coefficient ξ as follows

$$\xi = \max \begin{cases} 0 \quad if \quad A_{sh} \ge 0.09\left(sh_c \dfrac{f_c'}{f_{yh}}\right) \\ 0 \quad if \quad A_{sh} \ge 0.3\left(sh_c \dfrac{f_c'}{f_{yh}}\right)\left(\dfrac{A_g}{A_{ch}} - 1\right) \\ \left(0.09\left(sh_c \dfrac{f_c'}{f_{yh}}\right) - A_{sh}\right) \Big/ 0.09\left(sh_c \dfrac{f_c'}{f_{yh}}\right) \quad if \quad A_{sh} < 0.09\left(sh_c \dfrac{f_c'}{f_{yh}}\right) \\ \left(0.3\left(sh_c \dfrac{f_c'}{f_{yh}}\right)\left(\dfrac{A_g}{A_{ch}} - 1\right) - A_{sh}\right) \Big/ 0.3\left(sh_c \dfrac{f_c'}{f_{yh}}\right)\left(\dfrac{A_g}{A_{ch}} - 1\right) \quad if \quad A_{sh} < 0.3\left(sh_c \dfrac{f_c'}{f_{yh}}\right)\left(\dfrac{A_g}{A_{ch}} - 1\right) \end{cases} \tag{6a}$$

$$\xi = \max \begin{cases} 0 \quad if \quad \rho_s \ge 0.12 \dfrac{f_c'}{f_{yh}} \\ 0 \quad if \quad \rho_s \ge 0.45\left(\dfrac{A_g}{A_c} - 1\right)\dfrac{f_c'}{f_y} \\ \left(0.12 \dfrac{f_c'}{f_{yh}} - \rho_s\right) \Big/ 0.12 \dfrac{f_c'}{f_{yh}} \quad if \quad \rho_s < 0.12 \dfrac{f_c'}{f_{yh}} \\ \left(0.45\left(\dfrac{A_g}{A_c} - 1\right)\dfrac{f_c'}{f_y} - \rho_s\right) \Big/ 0.45\left(\dfrac{A_g}{A_c} - 1\right)\dfrac{f_c'}{f_y} \quad if \quad \rho_s < 0.45\left(\dfrac{A_g}{A_c} - 1\right)\dfrac{f_c'}{f_y} \end{cases} \tag{6b}$$

The normalized coefficients η and ξ defined in eqs. (4) and (6) quantify the degree of violation of the longitudinal and transverse reinforcement, respectively, and are adopted as the input variables to the FLC which finds a scale factor $FLC(\eta,\xi)$ of the penalty coefficient λ in the GA. The details of $FLC(\eta,\xi)$ are discussed in the next section.

The constrained optimization model can be regarded as an extension of Equations (3) and expressed as

$$minimize \quad F(\mathbf{x}) = \psi\left[1 + \sum_{i=1}^{4} \omega_i + \lambda \cdot FLC(\eta, \varsigma)\right]^2 \tag{7}$$

3. FUZZY LOGIC CONTROL (FLC) FOR ADAPTION OF PENALTY COEFFICIENT

The membership functions (MFs) used for the input and output variables to the FLC are shown in Fig. 2 and Fig. 3, respectively. In which, according to the interpretation of the fuzzy linguistic terms [8], the following five fuzzy variables were used in this study: very small (VS), small (S), medium (M), large (L) and very large (VL).

The rule-based fuzzy inference system shown in Table 1 is determined based on the Mamdani Model, the structure of which is the popular system of multi-input single output (MISO).

Table 1. The rule-based fuzzy inference system.

η \ ξ	VS	S	M	L	VL
VS	VS	VS	VS	S	M
S	VS	VS	S	M	L
M	VS	S	M	L	VL
L	S	M	L	VL	VL
VL	M	L	VL	VL	VL

Following lists the procedure in determining the $FLC(\eta,\xi)$.

1. Determine the membership values corresponding to the input η and ξ

$$Poss(A_{i1} \mid \eta) = \max_{x_1 \in U_1} (A_{i1}(x_1) \wedge \eta) \quad i = 1 \sim 5 \tag{8}$$

$$Poss(A_{i2} \mid \xi) = \max_{x_2 \in U_2} (A_{i2}(x_2) \wedge \xi) \quad i = 1 \sim 5 \tag{9}$$

where $i=1\sim5$ orresponds to five fuzzy variables of VS, S, M, L and VL, respectively, η and ξ are fuzzy singletons, x_1 and x_2 are the underlying domains between 0 to 1 corresponding to normalized coefficients η and ξ, respectively, and $A_{i1}(x_1)$ and $A_{i2}(x_2)$ are input MFs.

2. Find the maximum τ_i of the two values above

$$\tau_i = Poss(A_{i1} \mid \eta) \cap Poss(A_{i2} \mid \xi) \quad i = 1 \sim 5 \tag{10}$$

3. Find the output fuzzy function corresponding to each τ_i

$$R_i(y) = \tau_i \wedge B_i(y) \quad i = 1 \sim 5 \quad \forall y \in Y \tag{11}$$

where $B_i(y)$ is the output MFs and Y is the universe of discourse between 0 to 1 representing the normalized output domain space.

4. Aggregate the output fuzzy functions

$$R(y) = \bigcup_{i=1}^{5} R_i(y) = R_1(y) \cup R_2(y) \cup \ldots \cup R_5(y), \quad \forall y \in Y \tag{12}$$

5. Defuzzify the aggregated output fuzzy function to find the scale factor $FLC(\eta,\xi)$ of the penalty coefficient based on center of gravity method (COG). (Zadeh 1965)

$$FLC(\eta, \xi) = \frac{\sum_{i=1}^{5} b_i^* \sum_{j=1}^{N} R_i(y_j)}{\sum_{i=1}^{5} \sum_{j=1}^{N} R_i(y_j)} \tag{13}$$

where N is the number of intervals in calculating the summation of aggregated output fuzzy functions and b^* is the centroid of the output fuzzy functions.

4. GENETIC ALGORITHM (GA) AS OPTIMIZATION SOLVER

Equations (7) is used as the fitness function of the GA, the chromosomes with higher fitness values have a greater chance to be selected into the mating pool. The probability of the i-th chromosome $\mathbf{x}_i$, the vector indicating the design variables illustrated previously, being selected is

$$P(\mathbf{x}_i) = \frac{F(\mathbf{x}_i)}{\sum_{j=1}^{N} F(\mathbf{x}_j)} \tag{14}$$

where N is the population size. The real values, rather than the binary encoding, of the continuous variables were employed directly. The cross-over method of generating the children chromosome X_{new}, the vector indicating the design variables of the new generation, is based on a combination of the parents, i.e.,

$$\mathbf{x}_{new} = \gamma \mathbf{x}_{ma} + (1 - \gamma)\mathbf{x}_{da} \tag{15}$$

where γ is a random number on the interval [0, 1], and X_{ma} and X_{da} are the vectors of design variable vectors of the mother chromosome and father chromosome, respectively.

The mutation is performed by adding a normally distributed random number to the variable selected as follows

$$x_i' = x_i + \sigma N(0,1) \tag{16}$$

where σ is the standard deviation of the normal distribution, $N(0,1)$ is the standard normal distribution with zero mean and variance equal to 1 (Haupt and Haupt 2004), and x_i is the i-th gene indicating the i-th design parameter of the design vector $\mathbf{x}$.

In this paper, six significant factors sensitive to the analytical results of the GA, which include the chromosome number, the size of the population, the maximum number of

the iterative generation, the fraction rate of the kept population, the crossover rate and the mutation rate, were set to be adapted flexibly to enhance the efficiency of the calculations.

5. INVESTIGATIONS OF THE PROPOSED ALGORITHM

In order to investigate the algorithm, the reported results of cyclic loading tests on three RC columns (Nagaya and Kawashima 2001; Chang and Chang 1999; Chung 2000) were employed as case studies, in which a square section, a rectangular section, and a circular section of the columns were involved. Table 2 contains the details of the experiments. All of the real capacity curves enveloping the experimental hysterestic loops were taken into account as the targets of these designs. Four important parameters, which include the yielding displacement δ_Y, the yielding force P_Y, the ultimate displacement δ_U, and the ultimate force P_U, were taken into account as the design objectives for our optimal model. All the specimens were modeled structurally as a cantilever column for the pushover analysis.

Table 2. Details of specimens for cyclic loading tests of RC column (Nagaya and Kawashima, 2001; Chang and Chang, 1999; Chung, 2000)

	Unit	Specimen 1 Square section	Specimen 2 Rectangular section	Specimen 3 Circular section
Concrete compression stress	MPa	29.4	22.05	26
Yielding stress of longitudinal reinforcement	MPa	372	436.8	490.5
Yielding stress of transverse reinforcement	MPa	363	450.8	490.5
Yielding stress of tie reinforcement	MPa	-	450.8	490.5
Cross section	mm	400×400	600×750	Diameter 760
Height	mm	1350	3250	3250
Cover	mm	27.5	25	25
Arrangement of longitudinal reinforcement	-	20-D13	32-D19	34-D19
Spacing of transverse reinforcement	mm	D6@50	D10@100	D10@70
Axial load (kN)	kN	157	1400	1400

The design parameters, such as the size of the column section, the number of longitudinal reinforcements, the diameter of the longitudinal reinforcement, the spacing of the transverse reinforcement and the diameter of the transverse reinforcement, were set as discrete design variables, whereas others the continuous design variables.

5.1 Square section of RC pier

Based on the experimental result, the design objectives selected were the yielding displacement $\delta_{Y,\,squared}$=10 mm, the yielding force $P_{Y,\,squared}$=130 kN, the ultimate displacement $\delta_{U,\,squared}$=50 mm, and the ultimate force $P_{U,\,squared}$=135 kN.

5.2 Rectangular section of RC pier

Based on the experimental result, the design objectives selected were the yielding displacement $\delta_{Y,\,rectangular}$=40 mm, the yielding force $P_{Y,\,rectangular}$=430 kN, the ultimate displacement $\delta_{U,\,rectangular}$=180 mm and the ultimate force $P_{U,\,rectangular}$ =410 kN.

5.3 Circular section of RC pier

Based on the experimental result, the design objectives selected were the yielding displacement $\delta_{Y,\,circular}$=45 mm, the yielding force $P_{Y,\,circular}$=480 kN, the ultimate displacement $\delta_{U,\,circular}$=165 mm, and the ultimate force $P_{U,\,circular}$=470 kN.

5.4 Analytical results

Fig. 1 (a)~(c) shows the corresponding capacity curves via the pushover analyses of two analytical results of the designs for all kinds of section. These curves are found to be in good agreement with the envelope of the experimental hysteretic loop.

Since these designs are inverse problems, the solution of every problem will not be unique. It can be seen that the design parameters obtained from the algorithm are not exactly the same as those of the experiments, however, they are all feasible solutions because the corresponding capacity curves from the pushover analyses of these designs are consistent with the envelopes of the experimental hysteretic loops. As a result, the utility of the proposed algorithm has been demonstrated.

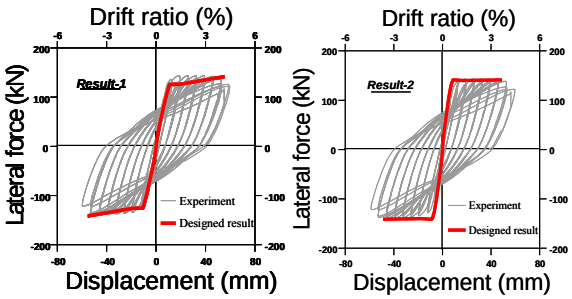

Figure 1 (a). square section

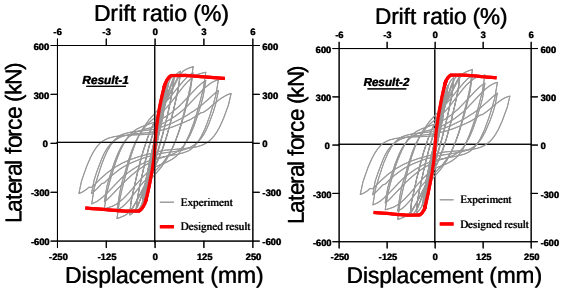

Figure 1 (b). rectangular section

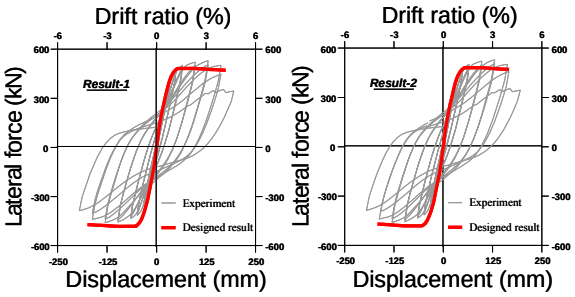

Figure 1 (c). circular section

6. CASE STUDY ON PBSD OF A SQUARE RC BRIDGE PIER

A square RC bridge pier with a height of 6m was modeled structurally as show in Fig. 2. Because the pier and superstructure are separate, it was modeled as a cantilever column with a lumped mass at the top. The pier was subjected to four performance objectives (fully operational, operational, life safety and near collapse) with respect to different levels of earthquake shown in Table 3. The peak ground accelerations (PGAs): 0.12g, 0.18g, 0.30g and 0.40g corresponding to the return periods of the earthquake: T_r =30 *yr*, T_r =75 *yr*, T_r =475 *yr*, and T_r =2500 *yr*, respectively, were determined based on the seismic hazard analysis at the bridge site. On the basis of the displacement-based design method, the corresponding spectral displacements S_{ds} can be specified and listed. Suppose that the S_d of the second performance objective PO_2 was regarded as the yield spectral displacement, i.e. $S_{d2} = S_{dy}$, the ductility ratio of the spectral displacement for each performance objective can be calculated accordingly and represented by $\mu = (S_{di}/S_{dy})$, i = 1~4.

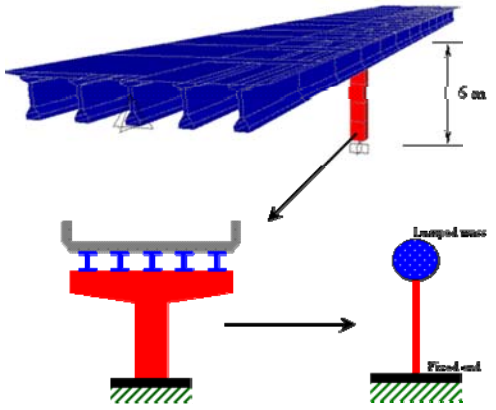

Figure 2. Square RC bridge pier.

Table 3. Performance objectives of the RC bridge column.

	Fully Operational PO_1	Operational PO_2	Life Safety PO_3	Near Collapse PO_4
PGA	0.12 g (T_r=30yr)	0.18 g (T_r=75yr)	0.30 g (T_r=475yr)	0.40 g (T_r=2500yr)
S_d	2.80 cm	3.70 cm	12.00 cm	17.50 cm
μ^*	0.75	1.00	3.25	4.73

Sung et al. selected more than two hundred ground motions recorded in the Chi–Chi earthquake (Chang 1999) as the seismic inputs for the time history analyses of two SDOF systems where one is a bi-linear system and the other is a linear one with identical mass, viscous damping and elastic stiffness. The responses of these two systems are shown in Fig. 3. According to the analyses, the following formulations have been regressed (Sung et al. 2007):

$$\Omega = \left[\mu - (\mu - 1) \exp\left(\frac{-a}{\mu^b} \right) \right] \tag{17}$$

where $\Omega = S_{ae}/S_{ay}$ is the ratio of the elastic pseudo spectral acceleration S_{ae} of the linear system to the pseudo spectral yield acceleration S_{ay} of the bi-linear system when the two systems are subjected to the same seismic excitation. On the other hand, $\mu = (S_{di}/S_{dy})$ is the ratio of the inelastic spectral displacement S_{di} to the spectral yield displacement S_{dy} of the bi-linear system. The coefficients a and b are the parameters dependent upon the fundamental period of the structure T, the soil condition, and the post-yield stiffness ratio α.

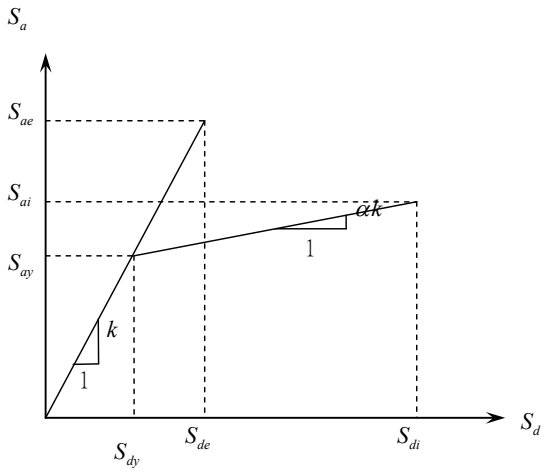

Figure 3. Relationship between Linear and Bi-linear SDOF Systems.

Based on the performance objectives PO_1 and PO_2, the fundamental period of the pier can be determined by the following equation

$$T = \min_j \left(2\pi \sqrt{\frac{S_{dj}}{(S_{ae})_j}} \right), j = 1,2 \tag{18}$$

In this case, the calculated fundamental period is $T = 0.64\,\text{sec}$, and the pseudo spectral yield acceleration is given as

$$S_{ay}^{*} = \left(\frac{2\pi}{T} \right)^2 S_{dy} \tag{19}$$

Assuming that the post-yield stiffness ratio, and the pseudo spectral acceleration reduction factor $SAR = S_{ai}/S_{ae}$ relates to Ω as

$$SAR = \frac{1}{\Omega}\left[1 + \alpha\left(\mu - 1\right)\right] \tag{20}$$

The inelastic pseudo spectral acceleration($(S_{ai})_3$, $(S_{ai})_4$) and the pseudo spectral yield acceleration ($(S_{ay})_3$, $(S_{ay})_4$) with respect to PO_3 and PO_4 can be given as

$$(S_{ai})_3 = SAR_3 \times (S_{ae})_3 = SAR_3 \times PGA_3 \times C \tag{22}$$

$$(S_{ai})_4 = SAR_4 \times (S_{ae})_4 = SAR_4 \times PGA_4 \times C \tag{23}$$

$$(S_{ay})_3 = \frac{(S_{ai})_3}{1 + \alpha(\mu_3 - 1)} \tag{24}$$

$$(S_{ay})_4 = \frac{(S_{ai})_4}{1 + \alpha(\mu_4 - 1)} \tag{25}$$

Finally, the pseudo spectral yield acceleration of the bridge pier can be chosen as the maximum of S_{ay}^{*}, $(S_{ay})_3$ and $(S_{ay})_4$, i.e.

$$S_{ay} = \max\left[S_{ay}^{*},\ (S_{ay})_3,\ (S_{ay})_4 \right] \tag{26}$$

The pseudo spectral ultimate acceleration of the pier is

$$S_{au} = S_{ay}\left[1 + \alpha\left(\mu - 1\right)\right] \tag{27}$$

The properties of a bilinear system that relate S_a and S_d (capacity spectrum) as shown in Fig. 4, characterized by the calculated S_{ay} = 356 cm/sec^2, S_{dy} = 3.69 cm, S_{au} =369 cm/sec^2 and S_{du} = 17.45 cm, cannot simultaneously satisfy all the specified performance objectives, however, it is in agreement with the extreme requirements among the objectives and therefore can be adopted for practical design. Based on the theory of structural dynamics, the capacity spectrum can then be transferred into the capacity curve (ACI Committee 318x 2005) represented by P_Y= 5,059 kN, δ_Y=48 mm, P_U= 5,244 kN and δ_U= 192 mm, which is able to be taken into account as the design target of the pier.

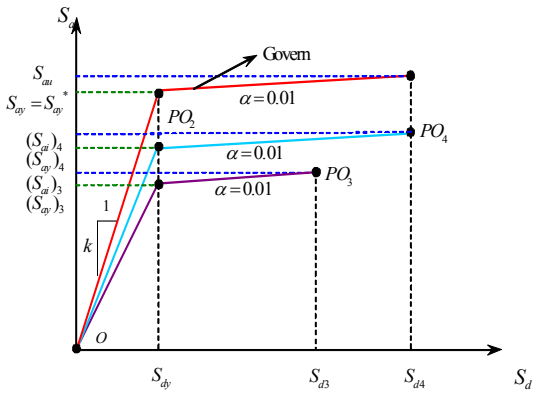

Figure 4. The capacity spectrum of the target column.

To simplify the design, the strength of concrete was fixed to be fc'=34.3 *MPa*, the strength of longitudinal reinforcement together with transverse reinforcement was set to be the same $f_y = f_{yh}$ = 411. 8 MPa, and the spacing of the transverse reinforcement $s = 100\ mm$, which are all usually employed by engineers for RC structural design. The number of the longitudinal reinforcements, the diameter of the longitudinal reinforcement, and the diameter of the transverse reinforcement were set to be discrete design variables. Based on the proposed algorithm, two design results shown in Table 4 were obtained and their corresponding pushover analyses associated with the specified design target are shown in Fig. 5. It is clear that the discrepancy between each analysis result and the target seem to be insignificant and the designs fulfill the specified requirements.

Table 4 shows the construction cost as well as the design parameters of the two pier sections obtained. All the design results satisfy the specifications of the design code. It can be seen that the result of Design-2 with the minimum construction cost of NT$1,651,810 is the optimal one.

Table 4 Details of two design results of the RC column.

Designed results	Design - 1	Design - 2
Section (mm)	1500×1500	1550×1550
Arrangement of Longitudinal Reinforcement (Section Ratio)	104-36φ (4.70 %)	96-36φ (4.07 %)
Arrangement of Transversal reinforcement	19φ@ 100 mm	19φ@ 100 mm
Strength of Concrete (MPa)	34.3	
Strength of Longitudinal Reinforcement (MPa)	411.8	
Strength of Transversal reinforcement (MPa)		
Total Cost (NT dollars)	1,717,770	1,651,810

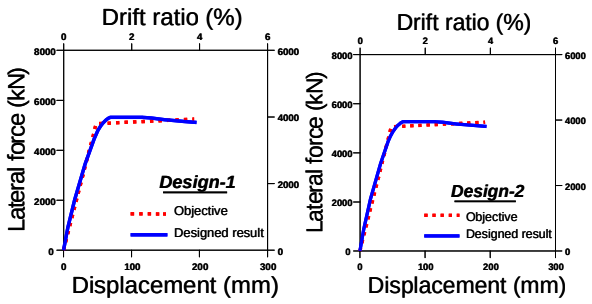

Figure 5. Comparison between the pushover analyses of the two designs obtained and the designed capacity curve.

7. CONCLUSIONS

Based on the analyses presented in this paper, the following conclusions may be made:

1. The performance-based seismic design (PBSD) of the RC bridge pier with single-column type can be modeled as a constrained optimization problem with the objective of minimizing construction cost and constraints of multiple-level structural performance with respect to different levels of earthquake together with the limitations on the arrangement of reinforcements specified in the seismic design code for RC structures. The penalty for violating the constraints were combined with construction cost to serve as the objective function of the optimization algorithm. Since the model cannot be formulated in an explicit mathematical function, a genetic algorithm (GA) with a penalty function was chosen to be the optimization solver.
2. Fuzzy logic control (FLC), based on the fuzzy inference system with the structure of multi-input single output (MISO), was implemented to adapt the penalty coefficient to prevent the penalty from being too weak or too strong through the entire calculation of the GA. The individual superiority of the GA and the FLC were developed significantly through the proposed approach.
3. The reported results of cyclic loading tests of three RC columns served as the data base for the necessary investigations to show the utility of the proposed algorithm.
4. This paper is focused on the PBSD of an RC bridge pier with single-column type. The pushover analysis is applied on a modeled cantilever structure with either a vertical centric or eccentric dead load. This study is essential for the PBSD of the entire bridge structure. Because all the bearings and the piers can be modeled as substructures of the whole bridge system in cases where the structural nonlinearities are given, an equivalent bilinear system of spring elements can be modeled to represent the structural nonlinearities of the piers or the bearings, and linked to the beam elements representing the girders of the bridge. Accordingly, the whole bridge system can be simplified and the pushover analysis performed easily. The fuzzy genetic algorithm can also be used to solve this PBSD problem and give a good solution search to determine the optimal structural nonlinearities of the equivalent spring elements to satisfy various performance requirements of the bridge system. As a result, the required structural nonlinearities of the piers can be obtained and their detailed designs can be completed through the proposed processes.

Acknowledgements:

The financial supports received from the National Science Council, Taiwan, through Grants No. NSC-94-2625-Z-027-004 and No. NSC-95-2625-Z-027-003 are gratefully acknowledged.

References:

SEAOC (1995), "Performance-Based Seismic Engineering of Buildings," Structural Association of California, Sacramento, CA, USA.

ATC-40 (1996), "Seismic Evaluation and Retrofit of Concrete Building," Applied Technology Council, Redwood City, California.

Sung, Y. C., Liu, K. Y., Su, C. K., Tsai, I. C. and Chang, K. C. (2005), "A Study on Pushover Analyses of Reinforced Concrete Columns," *Journal of Structural Engineering and Mechanics*, vol. 21.-1, pp. 35-52.

ACI Committee 318(2005). "Building code requirements for reinforced concrete and commentary (ACI 318-05)," American Concrete Institute, Farmington Hill, USA.

Bazaraa, M. S. and Shetty, C. M. (1979), "Nonlinear Programming: Theory and Algorithms," Published by John Wiley and Sons, New York.

Sarma, K. C. and Adeli, H. (2000), "Fuzzy Genetic Algorithm for Optimization of Steel Structures," *Journal of Structural Engineering*, ASCE, vol. 126(5), pp. 596-604.

Nanakorn, P. and Messomklin, K. (2001), "An adaptive penalty function in genetic algorithms for structural design optimization, " *Journal of Computers and Structures*, vol. 79, pp. 2527-2539.

Zadeh, L. A. (1965), "Fuzzy Sets," *Journal of Information and Control*, vol. 8. pp. 338~353.

Soh, C. K. and Yang, J. (1996), "Fuzzy Controlled Genetic Algorithm Search for Shape Optimization," *Journal of Computing in Civl Engineering*, ASCE, vol. 10(2), pp. 143-150.

Zou, X. K and Chan, C. M. (2005), "Optimal seismic performance-based design of reinforced concrete buildings using nonlinear pushover analysis," *Journal of Engineering Structures*, vol. 27, pp. 1289–1302.

Haupt, R. L., and Haupt, S. E. (2004), "Practical Genetic Algorithms," Second Edition, Published by John Wiley and Sons, Inc. New Jersey.

Nagaya, K. and Kawashima, K. (2001), "Effect of Aspect Ratio and Longitudinal Reinforcement Diameter on Seismic Performance of Reinforced Concrete Bridge Columns," Report No. TIT/EERG 01, Institute of Technology, Tokyo, Japan.

Chang, K. C. and Chang, H. F. (1999), "Seismic retrofit study of rectangular bridge column with CFRP jackets," Report No. NCREE-00-030, National Center for Research on Earthquake Engineering, Taipei, Taiwan.

Chung, L. L. (2000), "Seismic retrofit study of RC bridge columns," Report No. NCREE-00-035, National Center for Research on Earthquake Engineering Taipei, Taiwan.

Chang, K. C. (1999), "Seismic investigation of bridge damage in Chi-Chi Earthquake," Report No. NCREE-90-055, National Center for Research on Earthquake Engineering, Taipei, Taiwan.

Sung, Y. C., Lin, T. W., Tsai, I. C., Chang, S. Y. and Lai, M. C. (2007), "Application of Normalized Spectral Acceleration-Displacement (NSAD) Format on Performance-Based Seismic Design of Bridge Structures," *Journal of Mechanics*, vol. 23(2), pp. 86-93.

JOINT CONFERENCE PROCEEDINGS
7th International Conference on Urban Earthquake Engineering (7CUEE) &
5th International Conference on Earthquake Engineering (5ICEE)
March 3-5, 2010, Tokyo Institute of Technology, Tokyo, Japan

STUDY ON SEISMIC RETROFITTING USING ROCKING WALLS AND STEEL DAMPERS

Hiroshi Ito[1], Yuta Uchiyama[2], Hiroyasu Sakata[3], Shojiro Motoyui[4] , and Akira Wada[5]

1) Researcher, Structural Engineering Research Center, Tokyo Institute of Technology, Japan
2) Graduate Student, Interdisciplinary Graduate School of Science and Engineering, Tokyo Institute of Technology, Japan
3) Associate Professor, Structural Engineering Research Center, Tokyo Institute of Technology, Japan
4) Associate Professor, Interdisciplinary Graduate School of Science and Engineering, Tokyo Institute of Technology, Japan
5) Professor, Structural Engineering Research Center, Tokyo Institute of Technology, Japan
ito.h.ac@m.titech.ac.jp, uchiyama.y.ab@serc.titech.ac.jp, hsakata@serc.titech.ac.jp, motoyui.s.aa@m.titech.ac.jp, wada@serc.titech.ac.jp

Abstract: In this paper, new and advanced approach of seismic retrofit for the existing 11- and 9-story SRC buildings constructed in 1970's are introduced. From the results of seismic inspection, it was found that strength and ductility of these buildings are very low due to lack of steel members and reinforcing bars, in addition Is value, which is seismic index of structure, of them didn't meet 0.7 of the required value. In order to reduce the seismic responses and damage of these two buildings, mainly PC rocking walls and steel dampers have been utilized as reinforcing members in these projects. The PC rocking walls give the existing frame structural stability to prevent story collapse of the building, and the steel dampers dissipate the input energy of earthquake ground motion. Extensive nonlinear time history analysis is carried out to assess the seismic performance of both the existing and retrofitted buildings.

1. INTRODUCTION

From the damage and the collapse of the buildings subjected to the major earthquakes such as Kobe Earthquake (1995) as shown in Photo 1, in recent years, it has strongly been insisted on necessity of seismic retrofit of the old ramshackle existing building, especially designed before the major revision of the seismic design provisions in the Building Standard Law of Japan in 1981. As seismic retrofit scheme for the old existing building, installation of steel bracing frame increasing the strength capacity of each story of the building has been most general and practical.

On the other hand, as suggested by many researchers, rocking systems are effective in preventing the damage to concentrate at some specified locations regardless of the variety of earthquakes ground motions. By inserting damping devices in these locations, the energy dissipating capacity of the structure can be significantly increased.

Seismic retrofit projects to employ a rocking wall system for the existing 11-story (G3 Bldg.) and 9-story (R1 Bldg.) buildings were carried out and to be completed in March, 2010. They are educational buildings located in Suzukake-dai Campus of Tokyo Institute of Technology in Japan.

In this paper, a rocking wall system is proposed and to concept of these retrofit designs is explained. The details of the retrofit project are then introduced. Extensive nonlinear time history analysis is carried out to assess the seismic performance of both the existing and retrofitted buildings.

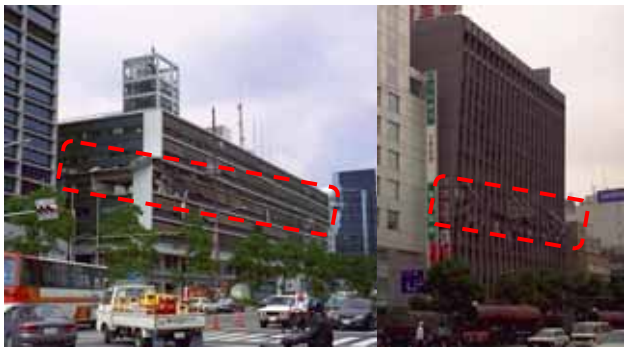

Photo 1. Examples of the Intermediate Stories Collapse of Buildings Subjected to Kobe Earthquake (1995)

2. SEISMIC RETROFIT DESIGN FOR EXISTING BUILDINGS

2.1 Existing Buildings

Photo 2 shows front view and side view of G3 Bldg. and R1 Bldg. before seismic retrofit. G3 Bldg. has 11 stories above the ground and the roof elevation is 39.7m and its total weight and is about 186,000kN (Table 1). It consists of mainly SRC frames. R1 Bldg. has 9 stories above the ground and the roof elevation is 31.7m and its total weight and is about 133,000kN (Table 1). It consists of SRC frames below 5-story and RC frame above 5-story. They were built in 1979 and 1977, respectively, before the major revision of the seismic design provisions in the Building Standard Law of Japan in 1981.

According to seismic inspections carried out for G3 Bldg. and R1 Bldg. in 2006, the both existing structures can not fulfill the current requirements of the Japanese Building Standard Law and related specifications, especially in their longitudinal direction i.e. *x* direction in Figure 1.

The seismic capacity index *Is* of the existing structures of both G3 and R1 Bldg. along both their *x* (longitudinal) and *y* (transverse) direction given by the seismic inspection are shown in Figure 1. According to the Japanese codes (Japan Building Disaster Prevention Association, 1997-2001), the building has to be demolished if *Is* value is below 0.3. Otherwise, retrofit is required if *Is* value is below 0.7. It can be seen in Figure 1 that *Is* in the *x*-direction of the G3 Bldg. below the 9-story and in that of the R1 Bldg. at the 5- and 6-story are only around 0.4, which leads to an urgent effort to strengthen the structure.



Photo 2. Front View and Side View of (a)11-story (G3 Bldg.), and (b)9-story (R1 Bldg.) Existing Buildings (Before Retrofit)

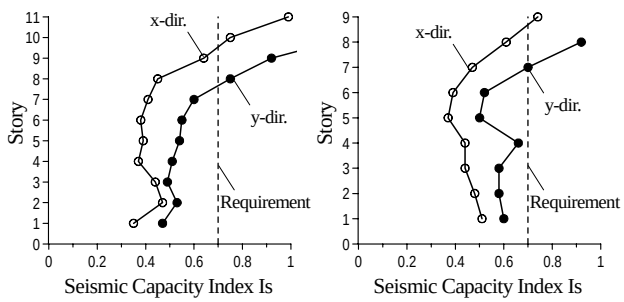

(a) G3 Bldg. (b) R1 Bldg.

Figure 1. Is Value of Existing Buildings

Table 1. Story Height and Seismic Weight of Existing Buildings

(a) G3 Bldg.

Story	Story Height (mm)	Seismic Weight (KN)
11	3,500	23,517
10	3,500	16,024
9	3,500	15,883
8	3,500	15,841
7	3,500	15,695
6	3,500	15,904
5	3,500	16,355
4	3,500	16,157
3	3,600	16,537
2	3,600	16,495
1	4,500	17,888
Total	39,700	186,296

(b) R1 Bldg.

Story	Story Height (mm)	Seismic Weight (KN)
9	3,443	17,943
8	3,412	13,057
7	3,400	13,103
6	3,400	13,223
5	3,400	13,391
4	3,400	14,199
3	3,463	14,215
2	3,650	15,200
1	4,125	16,002
Total	31,693	130,331

2.2 Design Concept

Instead of strengthening each member of the existing SRC and SRC/RC frames, a different retrofit concept is employed, which emphasizes the control of the global behavior rather than increasing the strength and deformation capacity of each story of the building. Since same design concept is employed in both G3 Bldg. and R1 Bldg., retrofit scheme only for G3 Bldg. is described below. Figure 2 shows floor plan of G3 Bldg. after retrofitting.



Figure 2. Floor Plan of G3 Bldg. (After Retrofit)

6 pieces of very strong prestressed concrete (PC) walls with pin connections at the bottoms are attached to the building in the existing slots (Figure 2). These walls are connected at their centers to the floor slabs by horizontal steel braces frame as can been seen in Figure 2. When the structure is subjected to severe earthquakes along its *x*-direction, these PC walls are expected to rotate around their bases without being damaged or even cracking. The deformation pattern of the whole building is expected to be well controlled by these rocking walls.

In the gaps between the rocking walls and the existing SRC frame, dozens of steel dampers and stiffener plate are inserted (Figure 2, 3). When the rocking walls rotate, these dampers are supposed to yield extensively due to the vertical displacement between the rocking walls and their adjacent SRC columns. These dampers will provide considerable additional moment-resisting capacity as well as energy dissipation. Photo 3 shows front view and side view of G3 Bldg. after seismic retrofitting. More details of the rocking walls, steel dampers, and so on are given in Photo 4 to 5 and Figure 4 to 5.

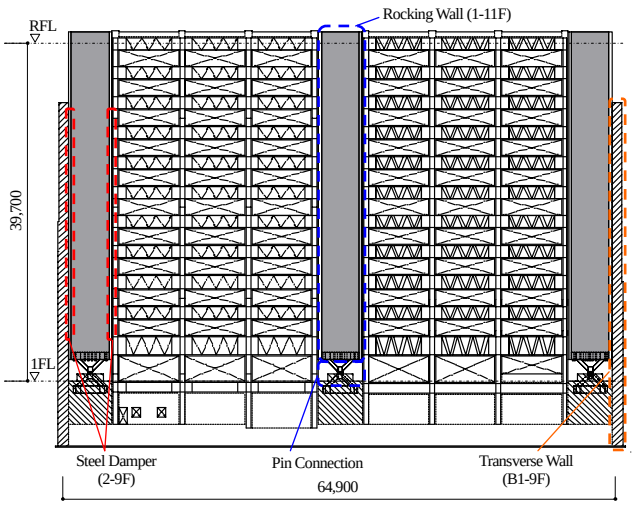

Figure 3. Elevation of G3 Bldg. (After Retrofit)



Photo 3. Front View and Side View of G3 Bldg. after Retrofitting

2.3 Rocking Wall

All the 6 rocking walls have identical cross-sections of 4400mm in width and 600mm in depth. The total cross section area of the rocking walls in each story is about 51% to 62% of that of the existing SRC frame from the bottom to the top. To increase the cracking strength of the rocking walls, concrete with specified design compressive strength of 36 MPa and post-tension prestressed strands with yield strength of 1580MPa are applied (Figure 4). The control pretension for each rocking wall is determined to be 18,000kN, and control prestress for each strand is 1,266MPa, which is 80% of the strand's yield strength. To prevent severe damage at the bottom of the walls when rocking, pin connection as shown in Figure 4 and Photo 4 is proposed. The rocking wall is resting on a steel beam on which the steel strands are anchored. The steel beam is supported by two opposite pairs of steel braces connected in the center by a tooth-shaped pin connection, which allows for no lateral translation but rotation. The lower pair of steel braces is encased in a reinforced concrete footing.

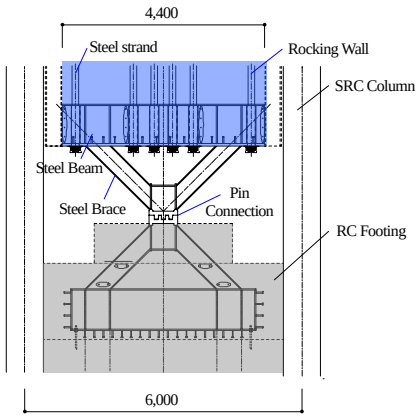

Figure 4. Detail of Pin Connection at the Bottom of Rocking Wall



Photo 4. (a)Rocking Wall and (b)Pin Connection at the Bottom

2.4 Steel Damper and Stiffener Plate

For all the rocking walls, steel dampers and stiffener plates are installed from the 2- to 9-story at the middle of each story, from the 1st to roof story at the level of wall girder of each story, respectively (Photo 4, 5). This is why it is to prevent damage of adjacent SRC column by seismic lateral force between existing building and rocking wall transmitted by stiffener plates. Low yield strength steel with yield strength of 225MPa is utilized as steel damper. All the steel dampers and stiffener plates have identical depths of 350mm. The thickness of the web plates of all the dampers and stiffener plates are 6mm. The widths of the dampers are 1500mm for the walls at the center, and from 1000mm at lower stories to 750mm at upper stories for the walls at both ends. All the dampers are designed to be replaceable against their damage by sever earthquake.

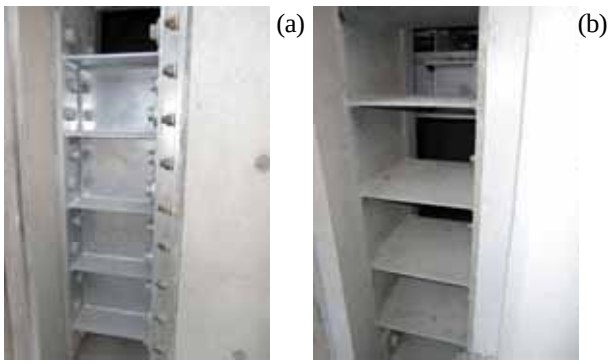

Photo 5. (a)Steel Damper and (b)Stiffener Plate Installed between Existing Building and Rocking Wall

2.5 Horizontal Brace Frame

Horizontal steel braces frames (Figure 5) are expected to transmit seismic lateral force between existing building and rocking wall as well as stiffener plates, and prevent torsional behavior of rocking walls as stabilizer.

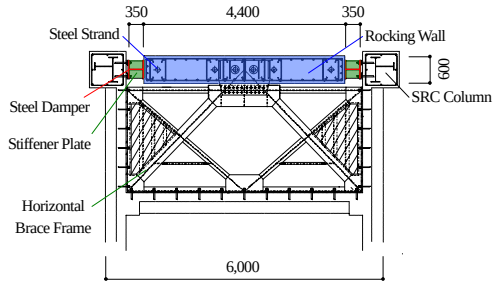

Figure 5. Detail of Horizontal Brace Frame

3. SEISMIC PERFORMANCE EVALUATION

3.1 Modeling Assumption

In this section, analysis model for dynamic analysis of G3 Bldg. in *x*-direction shown in Figure 6 is explained, omitting it of R1 Bldg.. Existing building is modeled as

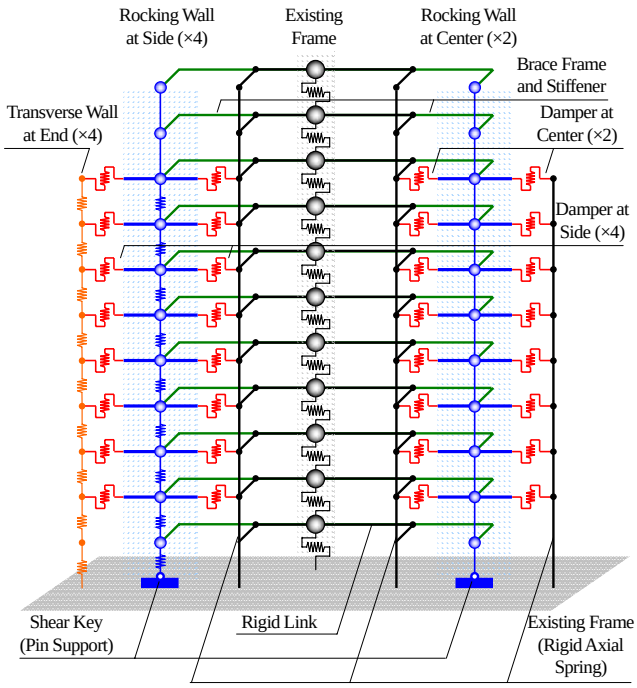

Figure 6. Analysis Model of G3 Bldg. for Dynamic Analysis

Table 2. Structural Parameter of Existing Structure

(a) G3 Bldg.

Story	Q_c [kN]	Q_u [kN]	K_1 [kN/mm]	K_2 [kN/mm]	K_3 [kN/mm]
11	5243	10107	4680	2588	234
10	8093	15571	6372	3210	319
9	9530	19120	7176	3729	359
8	12957	27360	8496	3717	425
7	14550	31288	8760	4249	438
6	16197	35117	9444	4315	472
5	17784	38692	9600	6246	472
4	19039	42259	10452	5072	472
3	20161	44598	12756	6235	472
2	21306	46031	18876	7797	472
1	22715	48359	16404	9109	472

(b) R1 Bldg.

Story	Q_c [kN]	Q_u [kN]	K_1 [kN/mm]	K_2 [kN/mm]	K_3 [kN/mm]
9	6876	12667	6369	770	6
8	7639	16061	5305	695	7
7	8331	18995	5295	713	9
6	8827	21589	5555	846	10
5	9484	24929	5197	1060	18
4	13423	38100	5779	1308	84
3	14094	40839	6176	1430	89
2	16015	44433	6740	1530	49
1	17201	45279	9135	1796	60

※Q_c, Q_u: Cracking Strength, Ultimate Strength
K_1, K_2, K_3: Story Stiffness Parameter

11-DOF shear-bar model and hysteretic rule of each shear spring is tri-linear Takeda model based on plain frame model of its moment-resisting frame with shear walls. Since the rocking walls are designed to keep elastic during severe earthquakes, they're modeled by elastic beam elements with rigid horizontal beams connected with the dampers. Steel dampers are model as shear spring, and behave bi-linearly. RC transverse walls added at both ends of building for *y*-direction are modeled as truss spring in vertical direction, and they are assumed elastic. Since seismic lateral force between existing building and rocking wall is transmitted by stiffener plates and horizontal brace frames, and they are modeled as link element.

3.2 Ground Motion Records

The seismic responses of both the existing and retrofitted structure to a suite of 5 artificial earthquake motion records, which are considered as extremely severe earthquake level in Japan, are evaluated by nonlinear time history analysis. Design response spectrum and response spectra of them for 5% damping are shown in Figure 7. Peak ground acceleration (PGA) of artificial earthquake motions are shown in Table 3. Note that natural period of both the existing and retrofitted structures of G3 Bldg. are 0.59s and 0.50s, and those of R1 Bldg. are 0.58s and 0.50s, respectively.

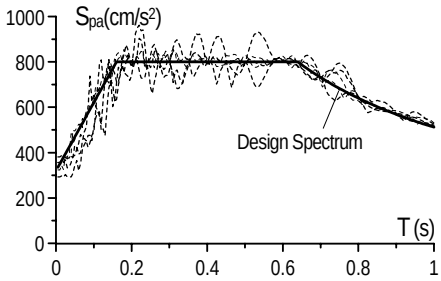

Figure 7. Response Spectra of Artificial Earthquake Ground Motions ($h_0 = 0.05$)

Table 3. List of Input Artificial Earthquake Ground Motions

	PGA (cm/s^2)
Hachinohe EW (1968) Phase	356.3
Tohoku Univ. NS (1978) Phase	293.0
JMA Kobe NS (1995) Phase	381.2
NGT NS (on site)	356.7
NGT EW (on site)	324.3

3.3 Analysis Results

Peak lateral displacement and story drift angle of both existing and retrofitted structures of G3 Bldg. and R1 Bldg. subjected to the 5 ground motions are shown in Figure 8, 9. To better comprehend the seismic contribution of the rocking walls and the steel dampers, the mean values and each case of the peak lateral displacement and story drift angle of the existing structure, the structure with only the rocking walls, and the structure with both the rocking walls and steel dampers obtained by numerical analysis are compared in Figure 8, 9.

For the existing structure of G3 Bldg., the 2nd story is vulnerable to some of the ground motion records while some upper stories, such as the 9- to 11-story becomes weak story when the structure is subjected to other ground motions. For the existing structure of R1 Bldg., some middle stories, such as the 5- and 6-story becomes weak story, this is why it consists of SRC frames below 5-story and RC frame above 5-story, and distribution of ultimate strength of the existing structure changes significantly at 5-story. The distribution of deformation as well as the location of deformation concentration is quite different and unpredictable (Figure 8, 9). By adding only the rocking walls for both buildings, the maximum peak story drift angle is reduced but peak lateral displacement increases, the deformation pattern becomes much more uniform for various ground motions, since the rocking walls are effective in suppressing higher mode vibrations and preventing weak story mechanism. Moreover by adding the rocking walls and steel dampers for both building, peak lateral displacement and story drift angle decrease significantly.

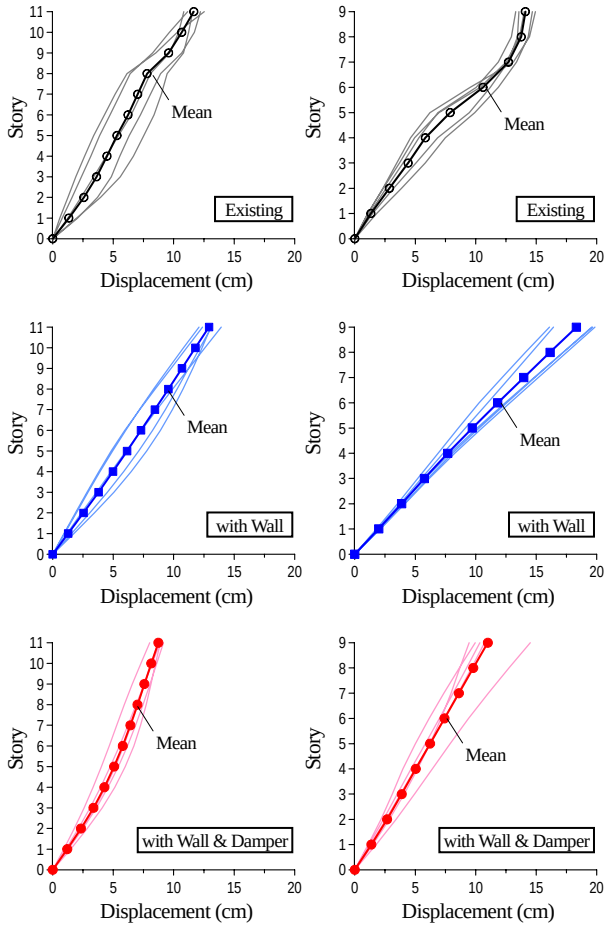

(a) G3 Bldg. (b) R1 Bldg.

Figure 8. Peak Lateral Displacement (Before and After Retrofit)

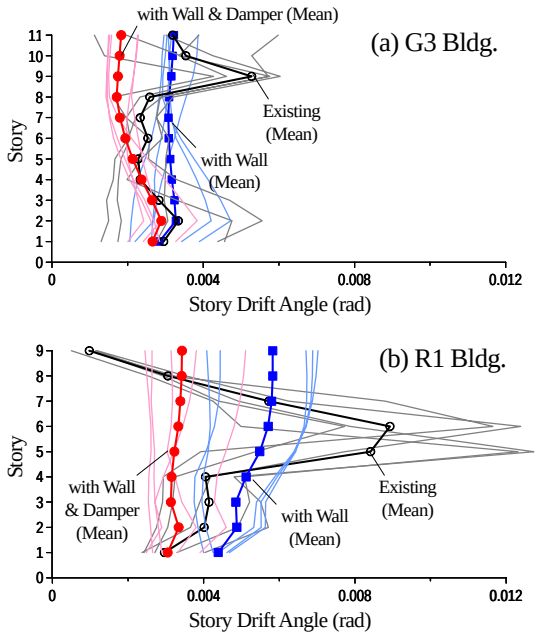

Figure 9. Peak Story Drift Angle (Before and After Retrofit)

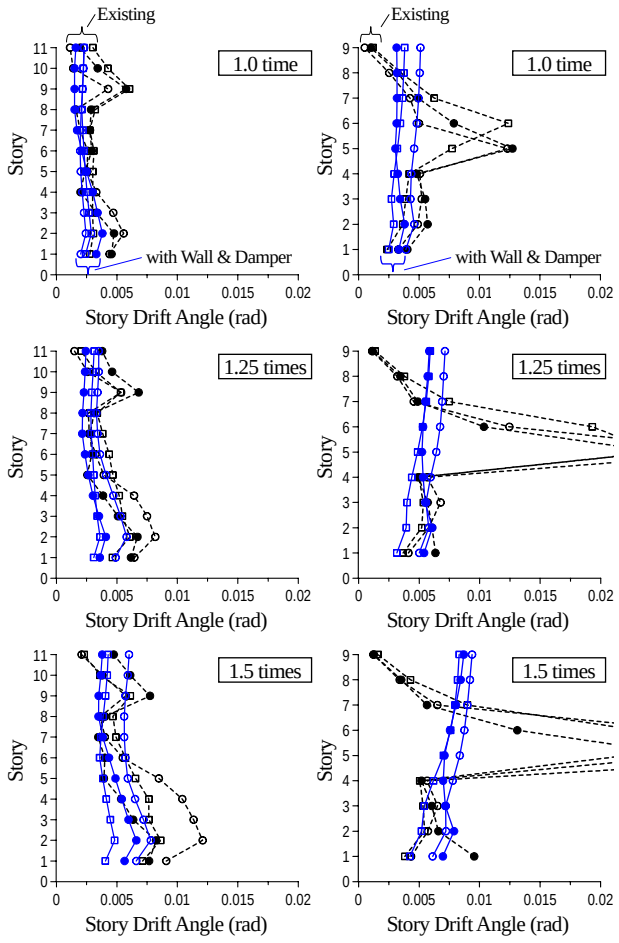

(a) G3 Bldg. (b) R1 Bldg.

Figure 10. Peak Story Drift Angle by Incremental Dynamic Analysis

To better demonstrate the seismic effect by the rocking walls and the steel dampers, incremental dynamic analysis shown in Figure 10, was carried out. Ground motion records used in this study are 1.0, 1.25, and 1.5 times of original records. It is expected that rocking walls crack when subjected to large earthquake, they are also modeled as elastic element in this study. From Figure 10, by adding the rocking walls and the steel dampers, both buildings keep almost uniform deformation patter preventing weak story mechanism for 1.5 times large original ground motions.

The story drifts are further reduced by setting up the steel dampers, which, together with the rocking walls, provide additional lateral force resisting capacity and energy dissipating capacity. It is seen that the rocking walls play an essential role in this retrofit scheme, which effectively controls the deformation pattern and the damage of the structure.

4. CONCLUSIONS

In this paper, new and advanced seismic retrofit scheme for the old 11- and 9-story SRC buildings are introduced. Extensive nonlinear time history analysis was carried out to assess the seismic performance of both the existing and retrofitted buildings. It is demonstrated that the PC rocking walls give the existing frame structural stability to prevent story collapse of the building, and the steel dampers dissipate the input energy of earthquake ground motion.

References:

Midorikawa M., Azuhata T., Ishihara T., Wada A., (2007), "Shaking table tests on seismic response of steel braced frames with column uplifts", Earthquake Engineering and Structural Dynamics 35: 1767-85.

Japan Building Disaster Prevention Association, "Seismic Evaluation Standards, Guidelines for Seismic Retrofit and Their Application Examples: Reinforced Concrete Buildings (2001), SRC Composite Buildings (1997) and Steel Buildings (1998)"

Building Center of Japan. (2004), "The Building Standard Law of Japan"

JOINT CONFERENCE PROCEEDINGS
7th International Conference on Urban Earthquake Engineering (7CUEE) &
5th International Conference on Earthquake Engineering (5ICEE)
March 3-5, 2010, Tokyo Institute of Technology, Tokyo, Japan

A STUDY ON EARTHQUAKE RESPONSE ANALYSES OF BUILDINGS USING ENERGY TRANSMITTING BOUNDARY IN THE TIME DOMAIN

Naohiro Nakamura[1)]

1) Chief Researcher, R&D Institute, Takenaka Corporation, Japan

nakamura.naohiro@takenaka.co.jp

Abstract: The energy-transmitting boundary, using in the models of the finite element method (FEM), is a quite efficient technique for the earthquake response analysis of buildings considering soil-structure interaction. However, it is applicable only in the frequency domain. The author has proposed methods for transforming frequency dependent impedance into the time domain. In this paper, an earthquake response analysis method for a soil-structure interaction system, using the energy-transmitting boundary in the time domain, was proposed. First, the transform of the transmitting boundary matrices to the time domain using the proposed transform method was studied. Then, time history earthquake response analyses using the boundary were performed. Through these studies, the validity and efficiency of the proposed methods were confirmed.

1. INTRODUCTION

It is important to consider the effects of soil-structure interaction to accurately estimate the behavior and the damage of buildings during. In the FEM analyses, wave boundary models are necessary at the side or bottom of the soil model to express a semi-infinite extent of the soil. In this paper, the side boundary is studied, since it is more important generally.

As side boundary models, the viscous boundary (Lysmer et al. 1969), and the non-reflecting boundary (e.g. Smith 1973, Kunar et al. 1980) are well known to be applicable to analyses in the time domain.

In the viscous boundary (hereafter referred to as VB), a viscous damper is installed between the ends of the inner field model and a 1-dimensional model indicating the infinite far field (hereafter referred to as the free field model). It is well known that a wave motion propagated at right angles to the boundary is completely absorbed, but the wave motion in an oblique direction is not absorbed completely. Therefore, the region of the inner field model must be expanded to improve the analysis accuracy.

The non-reflective boundary is applied to the analyses in the time domain as a method of eliminating the reflected wave. However, this method is rarely used due to many problems in actually applying it to the analyses.

As mentioned above, currently the cyclic and viscous boundaries are generally used as side boundary models. However, since the accuracy of these models is not particularly high, the boundary cannot be placed in the vicinity of the structure that is the main subject of analysis. Therefore, the modeling region for the inner field is enlarged, and the computational burden for the analyses is increased.

On the other hand, the energy-transmitting boundary (hereafter referred to as TB) is generally known as a highly accurate wave boundary (Lysmer et al. 1972, Waas 1972, Lysmer et al. 1975a, Kausel 1974, Lysmer et al. 1975b). The use of TB can sharply reduce the modeling region.

TB is composed of an impedance matrix with strong frequency dependency and an additional force vector. It has been difficult, so far, to transform the former to the time domain. Therefore, the application of TB is limited to an equivalent linear analysis in the frequency domain.

The author has been carrying out investigations related to the transform of the frequency dependent dynamic stiffness to the time domain (Nakamura 2006a, 2006b, 2008). Furthermore, using the transform methods, a practical causal hysteretic damping model, in which the damping ratio is nearly independent of the frequency, was proposed (Nakamura 2007).

In this paper, application of TB to the 2-D in-plane problem is described as the first stage of development. Then, an earthquake response analysis method, using this TB in the time domain, is proposed. This proposed method corresponds to the time history analysis version of the FLUSH program (Lysmer et al. 1975a).

First, outline of TB is introduced and the summary of the proposed transform methods is shown. Next, the validity of the transform of the TB impedance matrix to the time domain is investigated. Then, a time history response

analysis method using TB is proposed.

By conducting time history response analyses for a soil-structure interaction model, the validity of the proposed method is demonstrated. The analysis results are compared with the results using TB in the frequency domains and the results using VB.

2. OUTLINE OF TRANSMITTING BOUNDARY

TB, which is called "the energy transmitting boundary" or "the consistent transmitting boundary," is applied at the ends of the inner field model. The main assumption of TB is that the free field consists of horizontally layered soil on rigid bedrock. TB is a highly accurate boundary, rigorous in a horizontal direction, and obeys the displacement interpolation function of elements in a vertical direction. (In the case of first-order linear elements, the displacement varies linearly.) As a result, this boundary can almost completely absorb wave motions propagating from any direction.

TB was first proposed by Lysmer & Waas (1972) for the 2-D anti-plane problem. Waas (1972) expanded TB to the in-plane problem. Based on these studies, Lysmer et al. developed the soil-structure interaction system analysis program, FLUSH (Lysmer et al. 1975a). In this program, pseudo-3D analyses can be carried out using the anti-plane VB. Kausel (1974) expanded this program for 3-D problems using a cylindrical coordinate system, and Lysmer et al. developed an axi-symmetric analysis program, ALUSH (Lysmer et al. 1975b).

As mentioned above, it is well known that TB is accurate, but can be analyzed only in the frequency domain. Therefore, it has been thought that TB cannot easily be applied in the time domain while maintaining its accuracy. In this study, investigations on the 2-D in-plane (Rayleigh wave) problem, corresponding to the FLUSH, are carried out. The outline of the TB used in this problem is introduced below.

As shown in Figures 1 and 3, half-scale models, each with TB only on its right side (a skew-symmetric condition at the central axis) are considered in this study. To the left of the TB is the inner field, and to its right is the free field. The wave equation of the free field in the 2-D in-plane problem is shown by Eq.(1).

$$([A]k^2 + i[B]k + [G] - \omega^2[M])\{u^*(\omega)\} = \{0\} \quad (1)$$

Here k: wave number, $\{u^*(\omega)\}$: displacement vector of the free field, and $[A]$,$[B]$,$[G]$,$[M]$: matrices of $2n \times 2n$ (n: node number), which can be given as the superposition of the sub-matrices $[A]_j$,$[B]_j$,$[G]_j$,$[M]_j$ for each of the following elements.

$$[A]_j = \frac{h_j}{6}\begin{bmatrix} 2(2G_j+\lambda_j) & 0 & (2G_j+\lambda_j) & 0 \\ 0 & 2G_j & 0 & G_j \\ (2G_j+\lambda_j) & 0 & 2(2G_j+\lambda_j) & 0 \\ 0 & G_j & 0 & 2G_j \end{bmatrix} \quad (2)$$

$$[B]_j = \frac{1}{2}\begin{bmatrix} 0 & (G_j-\lambda_j) & 0 & (G_j+\lambda_j) \\ -(G_j-\lambda_j) & 0 & (G_j+\lambda_j) & 0 \\ 0 & -(G_j+\lambda_j) & 0 & -(G_j-\lambda_j) \\ -(G_j+\lambda_j) & 0 & (G_j-\lambda_j) & 0 \end{bmatrix} \quad (3)$$

$$[G]_j = \frac{1}{h_j}\begin{bmatrix} G_j & 0 & -G_j & 0 \\ 0 & (2G_j+\lambda_j) & 0 & -(2G_j+\lambda_j) \\ -G_j & 0 & G_j & 0 \\ 0 & -(2G_j+\lambda_j) & 0 & (2G_j+\lambda_j) \end{bmatrix} \quad (4)$$

$$[M]_j = \frac{\rho_j h_j}{6}\begin{bmatrix} 2 & 0 & 1 & 0 \\ 0 & 2 & 0 & 1 \\ 1 & 0 & 2 & 0 \\ 0 & 1 & 0 & 2 \end{bmatrix} \quad (5)$$

Where, under the condition of Eq. (6), the eigenvalue problem related to the wave number in Eq. (7) is solved.

$$[C] = [G] - \omega^2[M] \quad (6)$$

$$\left| [A]k^2 + i[B]k + [C] \right| = \{0\} \quad (7)$$

From the obtained $4n$ eigenmodes, $2n$ modes corresponding to the waves propagating toward the right are extracted, and the mode matrix $[V]$ is set using these modes. $[K]$ is the diagonal matrix consisting of the eigenvalues. With this, the TB matrix on the right side of the model can be indicated with $[R]$ in Eq. (8). $[D]$ is set with the superposition of the sub-matrix $[D]_j$ in Eq. (9). Although $[R]$ is not symmetric originally, in the following discussion, the matrix is made symmetric by averaging terms at symmetric positions.

$$[R] = i \cdot [A][V][K][V]^{-1} + [D] \quad (8)$$

$$[D]_j = \frac{1}{2}\begin{bmatrix} 0 & \lambda_j & 0 & -\lambda_j \\ G_j & 0 & -G_j & 0 \\ 0 & \lambda_j & 0 & -\lambda_j \\ G_j & 0 & -G_j & 0 \end{bmatrix} \quad (9)$$

Accordingly, the equation of motion for the entire model is given by Eq. (10), where $[M_I]$: mass matrix of the inner field, $[K_I]$: stiffness matrix of the inner field, and $\{u(\omega)\}$: displacement vector of the inner field

$\{F(\omega)\}$ of Eq. (11) indicates the boundary force vector and $-[D]$ $\{u^*(\omega)\}$ shows the additional force vector, in the case of seismic motion being input from a vertical lower direction. $[R]$, $\{u^*(\omega)\}$, and $\{F(\omega)\}$ are defined with $2n$ degrees of freedom in the boundary part up to Eq. (8). However, hereafter they are extended to the number of degrees of freedom of the inner field to superimpose them on the values of the inner field.

$$(-\omega^2[M_I]+[K_I]+[R])\{u(\omega)\} = -\ddot{y}(\omega)[M_I]\{1\}+\{F(\omega)\} \quad (10)$$

$$\{F(\omega)\} = ([R]-[D])\{u^*(\omega)\} \quad (11)$$

3. TRANSFORM TB MATRIX TO TIME DOMAIN

Next, the transform of Eq. (10) to the time domain is considered. The vectors $F(\omega)$, $u(\omega)$, and $\dot{u}(\omega)$ can be transformed to the time domain using the usual inverse Fourier transform. Since the mass [M] and stiffness matrices [K] are not frequency dependent, there is no problem in the transform to the time domain. On the other hand, it is not easy to transform the frequency dependent TB matrix [R] to the time domain. Therefore, the problem in the transforming Eq.(10) to the time domain reduces to transforming [R] to the time domain. This chapter investigates this problem. First, the proposed transform methods are explained; then, the equation of motion in the time domain is described.

Although many methods to transform frequency dependent complex stiffness to the time domain have been proposed, most of them employed either the past displacement or the past velocity in the formulation of the impulse response. The author [9] proposed some transform methods using both the past displacement and velocity.

In this paper, following Method B' and Method C were used for the transform. The complex stiffness and the reaction of method B' are expressed as shown in Eqs. (12) and (13) respectively.

$$S'_B(\omega) = -\omega^2 \cdot m_0 + i\omega \cdot c_0 + k_0 + \left\{ i\omega \cdot \sum_{j=1}^{n'} c_j \cdot e^{-i\omega t_j} + \sum_{j=1}^{n'} k_j \cdot e^{-i\omega t_j} \right\} \quad (12)$$

$$F'_B(t) = m_0 \cdot \ddot{u}(t) + c_0 \cdot \dot{u}(t) + k_0 \cdot u(t) + \left\{ \sum_{j=1}^{n'} c_j \cdot \dot{u}(t-t_j) + \sum_{j=1}^{n'} k_j \cdot u(t-t_j) \right\} \quad (13)$$

Where $u(t)$ is the displacement. $t_j = j\Delta t$ where Δt is discrete time interval for the transform. It should be noted that Δt is usually different from ΔT (the time interval of the time history response analysis) as shown in Nakamura (2006a). c_j (= $c(t_j)$) and k_j (= $k(t_j)$) are the damping term and the stiffness term of the obtained impulse response function at t_j respectively. c_0 and k_0 are those of simultaneous components and c_1~$c_{n'}$ and k_1~$k_{n'}$ are those of the time-delay components. m_0 is the simultaneous component of mass term. All the unknown impulse response components are solved by simultaneous equations with given complex stiffness data $D(\omega_i)$ (i=0,1,2…N).

In the case of the hysteretic damping being large, the accuracy of the recovered value of the complex stiffness tends to deteriorate. In order to improve this problem, the simultaneous components (m_0, c_0, k_0) are corrected. This method is called method C'. The simultaneous components for the modified impulse response are set to be $m'_0=m_0+\Delta m$, $c'_0=c_0+\Delta c$ and $k'_0=k_0+\Delta k$. Where, Δm, Δc and Δk indicate the modification terms determined by the least square method (Nakamura 2008). The recovered value of the complex stiffness can be expressed using Eq. (14).

$$S'_C(\omega) = S'_B(\omega) - \omega^2 \cdot \Delta m + i\omega \cdot \Delta c + \Delta k \quad (14)$$

Using Eq.(13), the equation of motion in the frequency domain shown in Eq. (10) can be indicated in the time domain by Eq. (15), where $\{u(t)\}$ and $\{F(t)\}$ are values obtained by inverse Fourier transform, corresponding to $\{u(\omega)\}$ and $\{F(\omega)\}$, respectively. The force $[R]\{u(\omega)\}$ in the frequency domain is separated into the simultaneous component $\{R_0(t)\}$ and the time delay component $\{R_I(t)\}$ in the time domain, as shown in Eqs.(15) and (16).

$$[M_I]\{\ddot{u}(t)\}+[K_I]\{u(t)\}+\{R_0(t)\} = -\ddot{y}(t)[M_I]\{1\}+\{F(t)\}+\{R_I(t)\} \quad (15)$$

Where

$$\left.\begin{aligned} \{R_0(t)\} &= [m_0]\{\ddot{u}(t)\}+[c_0]\{\dot{u}(t)\}+[k_0]\{u(t)\} \\ \{R_I(t)\} &= -\sum_{j=1}^{n'}[c_j]\{\dot{u}(t-t_j)\} - \sum_{j=1}^{n'}[k_j]\{u(t-t_j)\} \end{aligned}\right\} \quad (16)$$

4. CAUSAL HYSTERETIC DAMPING MODEL

In this study, a causal hysteretic damping model [12] is used for the inner field, to express the frequency independent material damping in the time history response analysis. This model is used for the quad element indicating the soil and for the shear spring element indicating the building. A summary of the model is shown below (details in Nakamura 2007). Eq. (17) shows the element displacement–element force relation in the frequency domain including hysteretic damping. This was obtained using the causal unit imaginary function $Z'(\omega)$ in place of the function sgn(ω) i of the complex damping model $[K_e](1+2h\,\mathrm{sgn}(\omega)\,i)$.

$$\{F_e(\omega)\} = [K_e](1+2h\cdot Z'(\omega))\cdot\{u_e(\omega)\} \quad (17)$$

Where $[K_e]$: element stiffness matrix, h: damping factor, $\{F_e\}$: element force vector, and $\{u_e\}$: element displacement vector. The imaginary part of $Z'(\omega)$ is set as a function, which has an almost constant value (=1) in a certain frequency range. The real part is set as a causal function, calculated using Hilbert transform of the imaginary part. $Z'(\omega)$ is transformed into the impulse response in the time domain. The obtained impulse response consists of both the damping term simultaneous component (c_0) and the stiffness term time delay components (k_1, k_2, …, k_n, where k_j = $k(\Delta t\cdot j)$, Δt is the time step). From this, Eq. (17) can be expressed as Eq.(18) in the time domain.

$$\{F_e(t)\} = [K_e]\left[\{u_e(t)\}+2h\left(c_0\{\dot{u}_e(t)\}+\sum_{j=1}^{n}k_j\{u_e(t-t_j)\}\right)\right] \quad (18)$$

This study focused on the frequency range of 0–20Hz and Δt= 0.05 s for this damping model. Nine data points were used for the transform (2, 4, 6, … 18Hz). This model is equivalent to "the 8 term model" in Nakamura (2007).

5. EXAMPLE ANALYSES

The validity of the transform of TB to the time domain and the efficiency of the proposed time history response analysis method are investigated through example analyses. First, after making a TB matrix in the frequency domain for the soil model, the behavior of the transform in the time domain is investigated. Furthermore, considering a building embedded in this soil, time history seismic responses to the soil–structure interaction system are analyzed.

5.1 Transform of the TB Matrix to the Time Domain

The soil model used for the investigation is shown in Figure 1. Table 1 lists the properties of the soil. The model has a unit thickness in the anti-plane direction. The anti-plane VB is not taken into consideration in this study.

First, the TB matrix [R] in Eq. (8) and the boundary force vector $\{F(\omega)\}$ in Eq. (11) are calculated in the frequency domain. The 6 × 6 TB matrix composed of horizontal and vertical degrees of freedom. The frequency range under consideration is 0–20 Hz for both [R] and $\{F(\omega)\}$. Next, the transform of TB matrix to the time domain is carried out using method C. Table 2 shows the conditions for the transform.

Figure 2 compares the matrices recovered from the obtained impulse response and the original data points. For recovery from the impulse response, the simultaneous components k_0, c_0, and m_0 and the time delay components k_1–k_{10}, and c_1–c_{10} are used. The recovered values correspond quite well with almost all the data points. Therefore, the results of the transform of the TB matrix by method C are valid.

5.2 Seismic Response Analysis

Next, to carry out response analyses, seismic ground motions were input into the soil–structure interaction system. The analysis model is shown in Figure 3, and the physical properties of the model are shown in Table 1. The building is a reinforced concrete structure. It has three stories above ground and a rigid basement. The plan of the building is 20m × 20m. Table 3 shows the data of the building model. The TB matrix is the same as that in Figure 2, however, the thickness in the anti-plane direction of Figure 3 is 20 m, while that in Figure 1 is 1 m. El Centro 1940 NS wave (Δt = 0.005 s, continuous time = 10s, maximum acceleration =323.4 Gal) was used for the input ground motion.

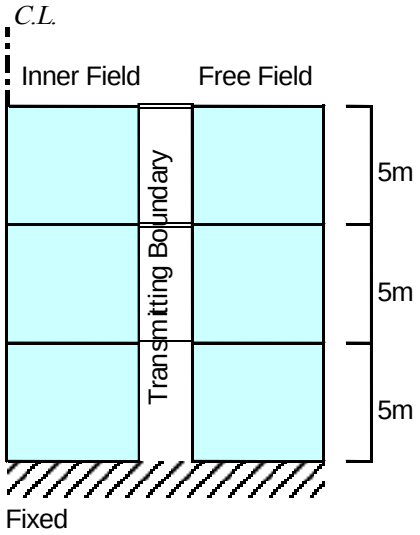

Figure 1: Soil model (skew-symmetric model)

Table 1: Properties of Soil

Shear Velocity Vs (m/s)	400
Poisson's Ratio ν	0.4
Density ρ (t/m^3)	2.0
Damping ratio h	0.02

Table 2: Conditions for Transform into the Time Domain

Impedance	
No. of data	Frequencies of data (Hz)
21	0.1, 1.0, 2.0, 3.0, … 19.0, 20.0

Impulse response		
Δt (s)	Simultaneous components	Time delay components
0.05	k_0, c_0, m_0	$k_1 \sim k_{20}$, $c_1 \sim c_{19}$

Table 3: Data for the building model

No.	Mass (t)	Rotational inertia (tm^2)	Shear stiffness (×10^6 kN/m)	Damping ratio h
1	480	-	1.755	0.03
2	480	-	2.924	
3	480	-	3.509	
4	480	-	∞	
5	720	88000	-	-

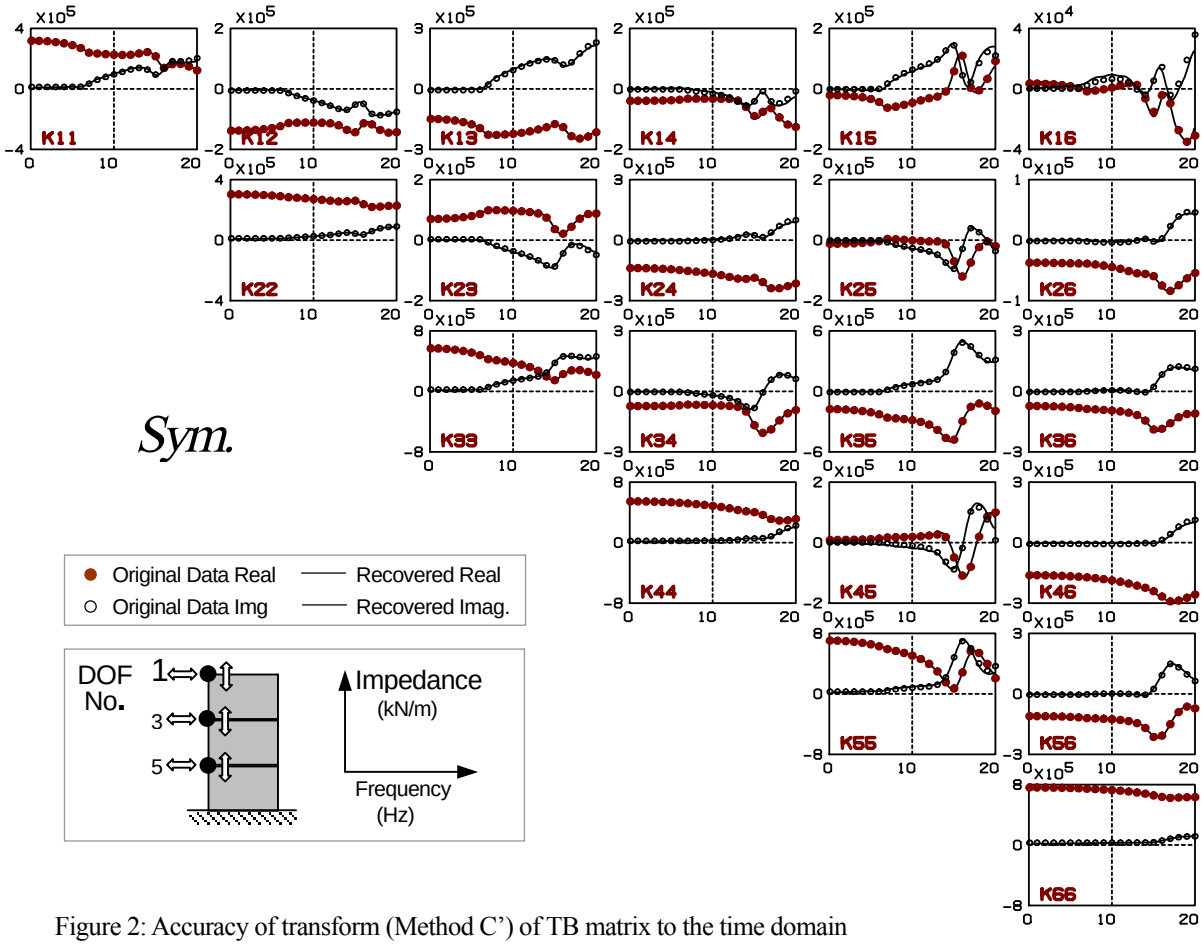

Figure 2: Accuracy of transform (Method C') of TB matrix to the time domain
(Comparison between values recovered from obtained impulse response and original data point)

Table 4 Comparison of maximum response horizontal acceleration (Gal) (Inner field problem)

Node No.	Results of frequency response	Results of time history response					
		Stiffness proportional damping model		Strain energy proportional damping model		Causal hysteretic damping model	
1	2837	2762	0.97	2772	0.98	2908	1.03
2	2099	2015	0.96	2031	0.97	2101	1.00
3	1270	1253	0.99	1243	0.98	1273	1.00
4	749	700	0.93	736	0.98	720	0.96
5	723	667	0.92	703	0.97	694	0.96
6	515	477	0.93	516	1.00	510	0.99
7	321	323	1.01	323	1.01	323	1.01
34	811	755	0.93	805	0.99	780	0.96
35	722	667	0.92	702	0.97	693	0.96
36	518	494	0.95	521	1.01	506	0.98
37	321	323	1.01	323	1.01	323	1.01

Note: Gray parts show the ratio to the results of frequency response

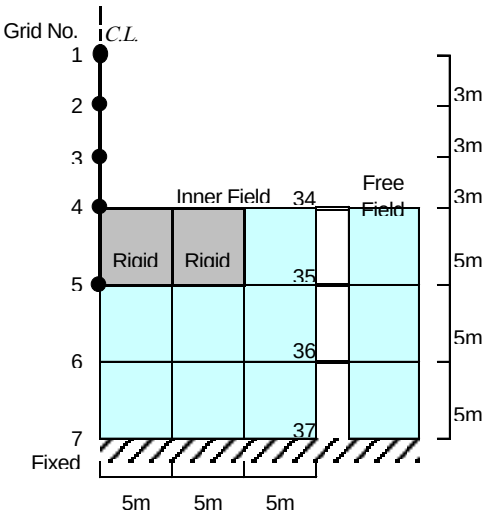

Figure 3: Soil-structure interaction analysis model

5.2.1 Investigations of the Material Damping Model

Damping models were investigated using the inner field model with a free boundary, as shown in Figure 3. The stiffness proportional damping model, the strain energy proportional damping model, and the causal hysteretic damping model are studied.

The results of the time history response analyses using these damping models are compared to those of the frequency response analysis using the complex damping. With the stiffness proportional model, the damping ratios for the soil (2%) and the building (3%) are set at the primary eigenfrequency of the total model (4.92 Hz).

Table 4 indicates the maximum horizontal acceleration of the soil and building nodes. Using each damping model, the time history response analyses were carried out. The numbers 1–7 show the nodes on the central axis, and the numbers 34–37 show the nodes on the outer ends. The numbers in the colored parts in each column show the ratio of the time history response analysis results to the results of the frequency response analysis, which is considered the accurate value in this study.

For the stiffness proportional model, the maximum differences are about 8% at the nodes on both the central axis and at the outer ends. Thus, the accuracy of this model is not high. The strain energy proportional model and the causal hysteretic damping model showed a maximum difference of 3% and 4% at the nodes, on both the central axis and the outer ends, respectively. Both values are fairly favorable. Thus, the causal hysteretic damping model, for which the quad elements are used, has relatively good accuracy — almost the same degree as the strain energy proportional model.

5.2.2 Response Analyses using the TB Matrix Transformed to Time Domain

The results of the proposed time history response analyses, carried out using the TB matrix transformed to the time domain, are compared with the response analysis results in the frequency domain (Super FLUSH/2D by Kozo Keikaku Engineering (1999) is used here to investigate the validity of the proposed method.

For a damping model, both the strain energy proportional model and the causal hysteretic damping model were used, because of their high accuracy.

The simultaneous components (k_0, c_0, and m_0) and the time delay components (k_1–k_{10} and c_1–c_{10}) were used for the TB matrix from among the impulse response components obtained from the transform to the time domain. These are identical to the components used for the recovery calculation in Figure 2.

Table 5 compares the maximum response horizontal acceleration from the proposed method with that obtained from frequency analysis. The nodes subjected to comparison were positioned on the central axis and the outer ends. These are the same nodes shown in the previous section. The outer edge was set as TB in this section, whereas it was a free boundary in the previous section.

As shown in Table 5, in comparing the time history response results using the causal hysteretic damping model with the frequency analysis results, the difference is ≤ 2% at almost all nodes, except for a node on the outer edge where the difference is 8%. This comparison indicates that, on the whole, the results obtained from both analyses correspond well, and confirms the validity of the proposed method.

On the other hand, when the results from the strain energy proportional model, which was nearly equivalent in accuracy to the causal hysteretic damping model in the previous section, are compared with the frequency analysis results. The difference is ≥ 5% at half of the nodes, and the maximum difference is 14% at the node on the outer edge. This is a decrease in accuracy from the previous section. The reason for this decrease is thought to be as follows.

In this study, the damping matrix was computed using all eigenmodes, by carrying out eigenvalue analyses of the inner field with the outer edge considered as the free boundary (the same conditions as in the previous section). It is thought that the connection of the TB matrix to the inner field causes a variation in the eigenvalue of the model, and this variation causes the decrease in accuracy. If this is true, the obtained damping matrix might be modified based on component mode synthesis methods (e.g. Craig et al. 1968).

However, the efficiency of the strain energy proportional damping model appears low. This is because the model uses full matrix damping and requires eigenvalue analyses to obtain the total eigenmodes. Therefore, the computational burden of using the model is heavy for large-scale problems.

It is necessary to memorize the past displacement and velocity when using the causal hysteretic damping model, however, eigenvalue analyses and full matrix damping are not necessary. This lightens the computational burden is to a high degree. Thus, the causal hysteretic damping model can be effective as the damping model in this proposed method.

Table 5 Comparison of maximum response horizontal acceleration (Gal)

Node No.	Results using TB (Freq. domain)	Results using TB (Time domain)			
		Strain energy proportional damping model		Causal hysteretic damping model	
1	4092	3836	0.94	4152	1.01
2	2692	2551	0.95	2736	1.02
3	1380	1318	0.96	1365	0.99
4	669	608	0.91	703	1.05
5	674	588	0.87	682	1.01
6	519	483	0.93	514	0.99
7	321	323	1.01	323	1.01
34	744	639	0.86	758	1.02
35	684	604	0.88	700	1.02
36	515	497	0.97	556	1.08
37	321	323	1.01	323	1.01

Note: Gray parts show the ratio to the results of frequency response

Table 6 Comparison of maximum response horizontal acceleration (Gal)

Node No.	Results using TB			Results using VB					
	Freq. Domain	Time Domain (Proposed)		(a) Base width × 1.5		(b) Base width × 5		(c) Base width × 10	
1	4092	4152	1.01	4756	1.16	4013	0.98	3962	0.97
2	2692	2736	1.02	2940	1.09	2677	0.99	2668	0.99
3	1380	1365	0.99	1305	0.95	1378	1.00	1379	1.00
4	669	703	1.05	978	1.46	803	1.20	771	1.15
5	674	682	1.01	976	1.45	831	1.23	791	1.17
6	519	514	0.99	648	1.25	645	1.24	591	1.14
7	321	323	1.01	323	1.01	323	1.01	323	1.01

Note: Gray parts show the ratio to the results using TB

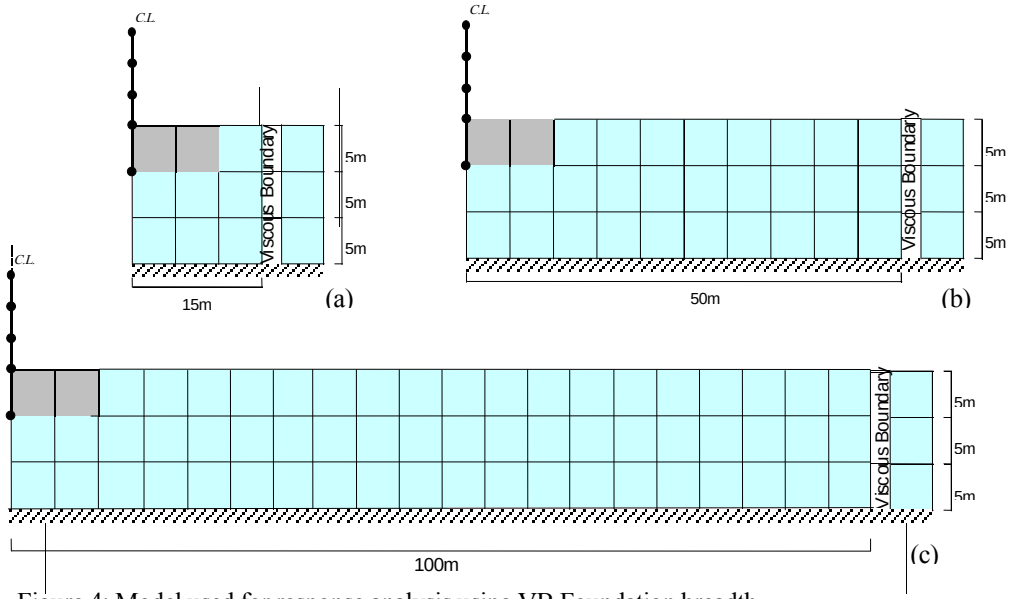

Figure 4: Model used for response analysis using VB Foundation breadth
(a) Base width × 1.5, (b) Base width × 5, (c) Base width × 10

5.2.3 Comparison with Response Analysis using VB

The validity of the proposed method was investigated by comparison with the viscous boundary (VB), which is a representative boundary model in the time domain. Figure 4 shows the analysis models used in this investigation. The causal hysteretic damping model served as the inner damping model.

The width of the inner field of the analysis model was varied to (a) 1.5 times, (b) 5 times and (c) 10 times the base width (20m). Since a 1/2 scale skew-symmetric model is used, the width of the inner field in the figure is set to 1/2 of the width mentioned. Model (a) has the same shape as the analysis model used for TB, as shown in Figure 3.

Table 6 compares the maximum horizontal acceleration at the central axis position of each model with the results of frequency response analysis using TB. Model (a), showed a difference of 16% at the building's top (node # 1) and ≥45% at the foundation (nodes # 4 and 5) — its accuracy is low. For models (b) and (c), however, which had a wider inner field, the difference is improved. Compared with these results, the accuracy of the model using TB in the time domain (proposed model) is higher than model (c).

6 CONCLUSIONS

In this study, the transmitting boundary for the 2-D in-plane problem (corresponding to the boundary in the FLUSH program) was transformed to the time domain, and a method for carrying out time history seismic response analyses for a soil–structure interaction system using this boundary was proposed.

It was confirmed that the frequency dependent impedance matrix of the transmitting boundary can be transformed to the time domain with excellent accuracy. Then, through earthquake response analyses, the validity of the proposed method was confirmed. Furthermore, by comparison with the viscous boundary, which is a representative boundary model in the time domain, the efficiency of the proposed method was shown.

Acknowledgement:

This work was supported by the Grand-in-Aid for Scientific Research C (No. 20560543) from Japan Society for the Promotion of Science.

References

Lysmer, J. Kuhlelameyer, R.L. (1969), "Finite Dynamic Model for Infinite Area", J. Eng. Mech. Div., ASCE, 95(EM3), 859-877.

Smith, W. (1973), "A Non-reflecting Plane Boundary for Wave Propagation Problems", Journal of Computational Physics, 15, 492-503.

Kunar, R.R. Rodriguez-Ovejero, L. (1980), "A Model with Non-reflecting Boundaries for Use in Explicit Soil-Structure Interaction Analysis", Earthquake Engineering and Structural Dynamics, 8, 361-374.

Lysmer, J. Waas, G. (1972), "Shear Wave in Plane Infinite Structures", J. Eng. Mech. Div., ASCE; 98(EM1), 85-105.

Waas, G. (1972), "Earth Vibration Effects and Abatement for Military Facilities Analysis Method for Footing Vibrations Through Layered Media", Technical Report S-71-14, U.S. Army Engineer Waterways Experiment Station.

Lysmer, J. Udaka, T. Seed, H.B. Hwang, R.N. (1975a), "FLUSH, a Computer Program for Approximate 3-D Analysis of Soil-structure Interaction Problems", Report No.EERC75-30, University of California, Berkeley.

Kausel, E. (1974), "Forced Vibration of Circular Foundations on Layered Media", Research Report R74-11 Soils Publication No. 336, Dept. of Civil Eng., M.I.T.

Lysmer, J. Udaka, T. Tsai C.F. Seed, H.B. (1975b), "ALUSH a Computer Program for Seismic Response Analysis of Axisymmetric Soil-structure Systems", Report No. EERC75-31, University of California, Berkeley.

Nakamura, N. (2006a), "A Practical Method to Transform Frequency Dependent Impedance to Time Domain", Earthquake Engineering and Structural Dynamics, 35, 217-234.

Nakamura, N. (2006b), "Improved Methods to Transform Frequency Dependent Complex Stiffness to Time Domain", Earthquake Engineering and Structural Dynamics, 35, 1037-1050.

Nakamura, N. (2008), "Transform Methods for Frequency Dependent Complex Stiffness to Time Domain Using Real or Imaginary Data Only", Earthquake Engineering and Structural Dynamics, 38, 495-516.

Nakamura, N. (2007), "Practical Causal Hysteretic Damping", Earthquake Engineering and Structural Dynamics, 36, 597-617.

Kozo Keikaku Engineering Inc., (1999), Jishin kougaku kenkyusho Inc, "Super FLUSH/2D Theoretical Manual"

Craig, R.R. Bampton, M.C.C. (1968), "Coupling of Substructures for Dynamic Analysis", AAIA Journal, 6(7), 1313-1319.

Nakamura, N. (2009), "Nonlinear Response Analysis of Soil-Structure Interaction System Using Transformed Energy Transmitting Boundary in the Time Domain", Soil Dynamics and Earthquake Engineering, 29, 799-808.

JOINT CONFERENCE PROCEEDINGS
7th International Conference on Urban Earthquake Engineering (7CUEE) &
5th International Conference on Earthquake Engineering (5ICEE)
March 3-5, 2010, Tokyo Institute of Technology, Tokyo, Japan

PERFORMANCE BASED SEISMIC DESIGN FOR THE SHANGHAI TOWER

Jiemin Ding[1], Xin Zhao[2] and Si Chao[3]

1) Professor, Architectural Design & Research Institute of Tongji University
2) Senior Engineer, Architectural Design & Research Institute of Tongji University
3) Professor, Architectural Design & Research Institute of Tongji University
djm@tjadri.com, kenkicn@gmail, 22cs@tjadri.com

Abstract: The performance based seismic design methodology was applied in the structural design of the Shanghai Tower project. This paper firstly addresses the performance design objectives and the related design criteria for the overall structure and structural members of the Shanghai Tower. According to the seismic importance and the design overall structural plasticity development mechanism, the earthquake performance levels of the overall structure and structural members were determined for different earthquake design levels. The design criteria for the overall structure and structural members were then set based on the earthquake performance levels. Secondly, the determinations of the design earthquake levels, ground earthquake parameters and the input ground motions are discussed. The specifications in Chinese seismic code and the recommendations of the site seismic safety report were considered during the determination of the design spectrum parameters. During the selection of the input ground motions, the site specific characteristic and the structural dynamic properties were considered. Finally, the seismic performance assessment method and process of the Shanghai Tower project were addressed. The seismic performance of the overall structural and critical connections were precisely analyzed and assessed and the seismic performance assessment results were smoothly integrated in the seismic design of the Shanghai Tower project. The performance based seismic design methodology applied in the Shanghai Tower project could be a typical case study for the super tall buildings in earthquake-prone areas.

1. INTRODUCTION

Beside the Jinmao Tower and the World Financial Center, the Shanghai tower project is located in the Lujiazui central financial district in Shanghai. The Shanghai tower has a height to architectural top of 632m and a height to structural roof of about 580m. It has 124 stories and a gross area of 380,000m^2 above grade, and 5 stories and 160,000m^2 below grade. Due to its super height and the mega structural system applied, the in-depth understanding of the seismic performance and optimized structural design can hardly be achieved using the current code-based design method. The performance based seismic design (PBSD) methodology was then applied for the seismic design of the Shanghai tower. By using PBSD methodology, quantified and detailed performance objectives were applied for assessing the seismic performance of the structure (Bertero and Bertero 2002, Xu et al 2005). The seismic performance of the structural system was thoroughly analyzed and optimized structural design was obtained.

This paper addresses the analysis and design issues with the PBSD of the Shanghai tower, including the design seismic action analysis, the selection of the performance objectives and the design criteria and the assessment of the seismic performance.

2. STRUCTURAL SYSTEM DESCRIPTION

Mega frame core wall structural system is applied for the Shanghai tower (Figure 1). Totally 6 levels of outriggers are set along the height of the building at zone 2, 4, 5, 6, 7 and 8 respectively. A two story high belt truss is set for each zone of the building. The maximum section size of the super column is 5300mm by 3700mm and the maximum thickness of the core wall is 1200mm at the bottom of the building. For supporting the twisting curtain wall on the building façade, radial trusses are installed at the refugee floor for each zone. The mega frame is composed of the super columns, two story high outriggers and belt trusses at all zones.

The eight perimeter supper columns are extended to zone 8, while the four corner supper columns stop at zone 5. The four corner supper columns are arranged mainly for reducing the spans of the belt trusses below zone 6. The belt trusses are not only parts of the mega frame, but also the transferring trusses for the secondary structure of each zone. The core wall plan changes according to the architectural plans along the height of the building. The core is 29m by 29m at the bottom of the building. The core corners are partially removed in the middle height of the building. The core corners are further removed and a cross arrangement is left at the top of the building. At the bottom of the building, steel plates are imbedded in the fin walls and web walls of the core to form composite shear walls. By using steel plate imbedded composite core, the wall thickness can be reduced and the ductility can be significantly improved.

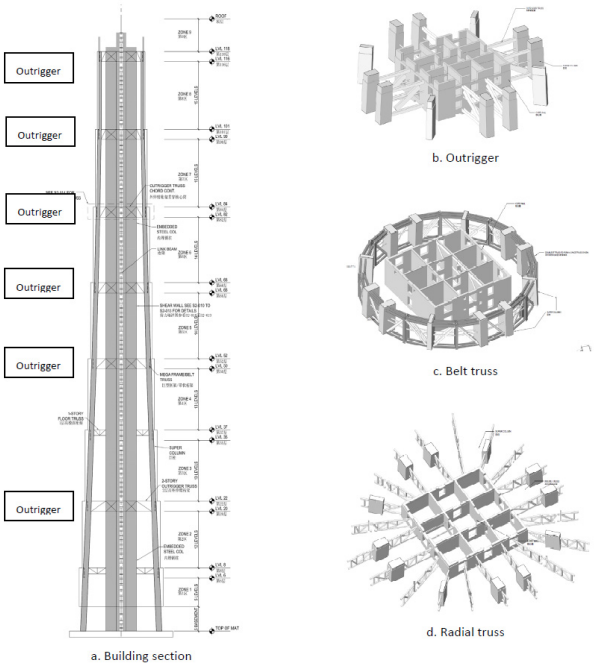

Figure 1 Structural system

3. DEFINING SEISMIC PERFORMANCE OBJECTIVES

3.1 Design earthquake level

The design reference period is commonly taken as 50 years for the structural design in Chinese code. Three design earthquake levels are defined for each design reference period, namely the minor earthquake, moderate earthquake and major earthquake. Under the specific design reference period set by the Chinese code, the probability of exceedance is 63.2% for the minor earthquake, 10% for the moderate earthquake and 2~3% for the major earthquake. The return periods for the minor earthquake, moderate earthquake and major earthquake under different design reference periods are listed in Table 1.

Table 1 Return periods for the design earthquake levels for different design reference periods

Design reference period (years)	Design earthquake level		
	Minor earthquake (63.2%)	Moderate earthquake (10%)	Major earthquake (2.5%)
50	50	475	1975
100	100	950	3950

The seismic action of a site is related to the seismic fortification intensity of this site. According to the "Seismic ground motion parameter zonation map of China (GB18306-2001)", the seismic fortification intensity of Shanghai is 7°.

The envelop spectrum of code-based design spectrum and site-specific spectrum is applied for the minor earthquake of the Shanghai tower project, and the code-based design spectra are applied for the moderate and major earthquake. The damping ratios for the minor, moderate and major earthquakes are chosen as 4.0%, 4.0% and 5.0%. The corresponding period reduction factors are 0.90, 0.95 and 1.00 respectively. The Shanghai tower design spectra for the minor and moderate earthquakes are shown in Figures 2~3.

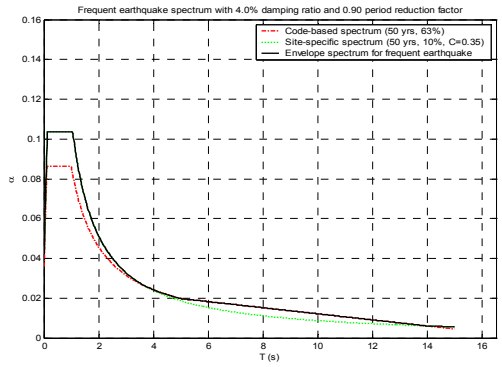

Figure 2 Design spectrum for the minor earthquake of the Shanghai tower project

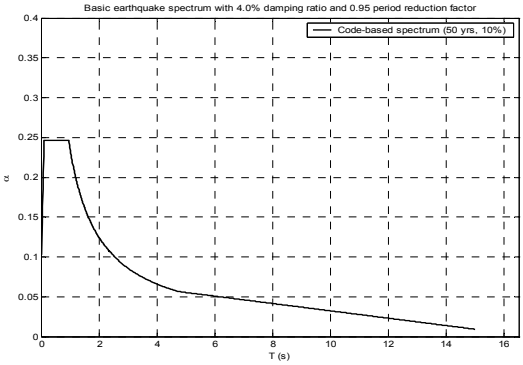

Figure 3 Design spectrum for the moderate earthquake of the Shanghai tower project

As a supplementary counterpart of the response spectrum analysis, the time history analysis method allows structural analysts to select the ground motions regarding different site spectrum characteristics and thus obtain the dynamic responses of the structure under specific ground motions. By considering both the responses spectrum analysis results and the time history analysis results, the seismic structural performance can be revealed generally and specifically. To make the responses spectrum analysis results and the time history analysis results comparable, the ground motions for the time history analysis should be chosen according to the requirements of the site characteristic, stochastic properties, effective peak value, lasting time and source mechanism specified in Chinese code. 7 sets of ground motions were selected for the elastoplastic analysis of the Shanghai tower projects. The time histories and response spectra of the two of the 7 sets of ground motions are shown in Figures 4~7.

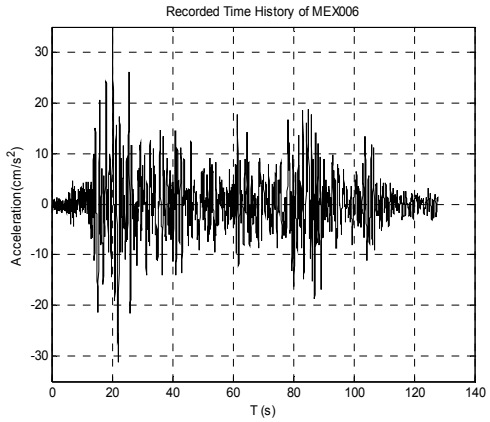

Figure 4 Recorded Time History of Mexico City Earthquake (1985)

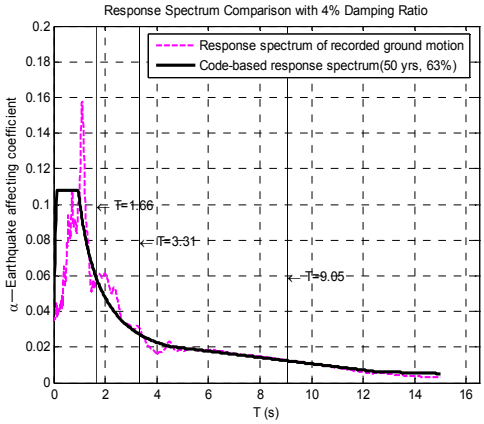

Figure 5 Response Spectrum of Mexico City Earthquake (1985)

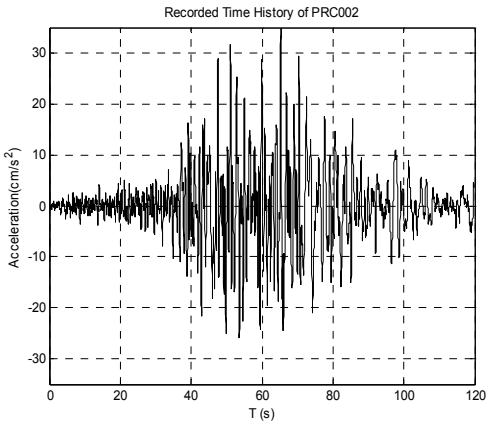

Figure 6 Recorded Time History of Tangshan earthquake, China (1976)

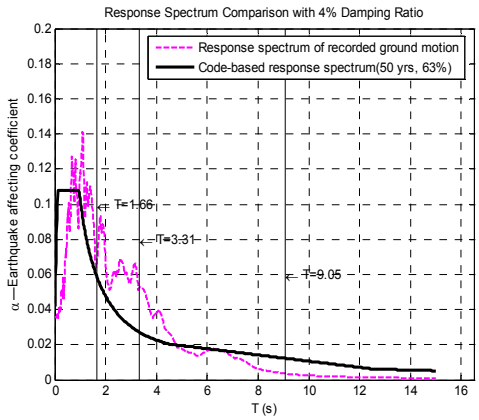

Figure 7 Response Spectrum of Tangshan Earthquake, China (1976)

3.2 Seismic performance levels

The seismic performance level describes the seismic performance under specific design earthquake level (Chen and Liu 2006). Four seismic performance levels are commonly applied in Chinese seismic design practice, say operational, immediate occupancy, damage control and life safety (Li and Cheng 2004). The general descriptions of the four performance levels are listed in table 2.

Table 2 General description of the seismic performance levels

Seismic performance level	Description
Operational	No damage with the structure, fully operational and can be occupied without repair.
Immediate occupancy	Small damage with the structure. The bearing capacity and properties remain unaffected for the main structural members. The building functions are affected but the building can be occupied with few repairs.
Damage control	The structure is damaged and the building functions are affected and can hardly be promptly repaired. The building can be repaired under acceptable cost.
Life safety	The structure is seriously damaged but the structural bearing capacity is not affected. The building functions are highly affected. The lives in the building are safe.

3.3 Seismic performance objectives

According to the importance of the building, the seismic protection level of the tall buildings can be categorized as special seismic protection level (SPL A), important seismic protection level (SPL B) and standard seismic protection level (SPL C). Due to its high importance, the Shanghai tower can be classified as important seismic protection level. Lv (2009) gives suggestions on the seismic performance levels for the beyond-code tall buildings of SPL A, B and C respectively. The seismic performance

objectives are listed in Figure 8. The seismic performance objectives for the important protection level (SPL B) are applied for the Shanghai tower. The seismic performance levels for the minor, moderate and major earthquake are respectively operational, immediate occupancy and life safety respectively. Under minor earthquake, the structure remains intact and elastic. Under moderate earthquake, the structure is basically intact and almost elastic, and the dynamic properties after the earthquake are almost the same as those before the earthquake. The super columns, core walls, outriggers and main connections remain elastic. Secondary members such as frame beams and link beamshave small cracks. The energy dissipation members become yield. Under major earthquakes, the structure is seriously damaged but the main connections are not broken. The structure will not partially and totally collapse. The shear failure of the main lateral resisting structural members, such as super columns, corner columns and core walls will not happen.

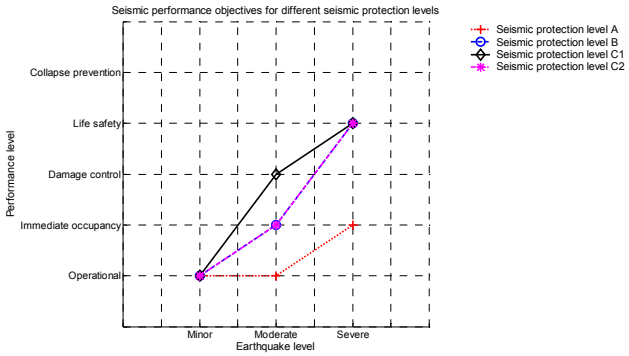

Figure 8 Seismic performance objectives for different seismic protection levels

The structural design criteria for different design earthquake levels are determined according to the seismic performance objectives. Under minor earthquake, the maximum story drift will be less than 1/500, and the ground floor story drift will be less than 1/2000. Under the moderate earthquake, the maximum story drift will be less than 1/250. The design seismic capacity of the super columns, corner column, corewalls and outriggers are to be checked using the design values of the combined internal forces under moderate earthquake, without considering internal force amplification and wind load. The steel and reinforcement stresses for the frame beams, link beamsare below the 85% of the yielding stress.

Under the major earthquake, the maximum story drift is to be less than 1/100. The plastic hinges appear for the secondary members such as the frame beams and spandrels, but the rotational angle of the plastic hinges are below 1/50. The rebar or steel stresses can beyond the yielding stress, but below the ultimate strength. The controlling shear capacity limit should be checked using the characteristic values of the material strength and the elastic seismic internal forces under major earthquake. The ultimate shear capacity of the super columns and corewalls should also be checked. The seismic performances for different structural members are listed in table 3.

Table 3 Seismic performance of structural members for different design earthquake levels

Structural member	Earthquake level	Seismic performance
Core	Minor	Remain elastic
	Moderate	Remain elastic for the core walls at the bottom strengthening zone, outrigger floors and the one story just above and below the outrigger floors. Non-yielding for the other floors. The rebar or steel stresses are below 85% of the yielding strength.
	Major	Satisfy the controlling shear capacity limit for the core walls at the bottom strengthening zone, outrigger floors and the one story just above and below the outrigger floors. Check the ultimate shear capacity. The characteristic value of the tension stress at the bottom of the corewall is less than 1.5 f_{tk}
Spandrel	Minor	Remain elastic
	Moderate	Remain Non-yielding. The rebar or steel stresses are below 85% of the yielding strength.
	Major	Formation of plastic hinge, and the hinge rotation is below 1/50. Rebar stress is beyond the yielding stress, but below the ultimate strength.
Super column	Minor	Remain elastic
	Moderate	Remain elastic.
	Major	Satisfy the controlling shear capacity limit. Satisfy the ultimate shear capacity. Rebar stress is beyond the yielding stress, but below the ultimate strength.
Belt truss	Minor	Remain elastic
	Moderate	Remain elastic.
	Major	Remain Non-yielding. The rebar or steel stresses are below 85% of the yielding strength.
Outrigger	Minor	Remain elastic
	Moderate	Remain Non-yielding. The rebar or steel stresses are below 85% of the yielding strength.
	Major	Steel stress is beyond the yielding stress, but below the ultimate strength.
Crown	Minor	Remain elastic
	Moderate	Remain elastic
	Major	Steel stress is beyond the yielding stress, but below the ultimate strength.
Key Connections	Minor	Remain elastic
	Moderate	Remain elastic
	Major	Remain Non-yielding. The rebar or steel stresses are below 85% of the yielding strength.

4. Seismic Design and Analysis

By the definition of the Chinese seismic design code, the super building height of Shanghai tower is beyond the scope of the code and the main irregularity of the Shanghai tower is the abrupt stiffness and capacity changes due to the setting of outriggers and belt trusses. Several measures were taken during the seismic design procedure to improve the seismic safety of the structure and structural members.

The gravity loads of the Shanghai tower are mostly sustained by the eight super columns and four corner columns. To ensure the ductility of the super columns, the compression ratio of the super columns under seismic combination is set below the code specified limit of 0.65. The steel ratio of the super columns at outrigger levels is also increased to 5%. The seismic grade of the super columns is set as the ultra A grade, which will lead to highest member ductility. To improve the seismic performance of the mega frame, the base shear of the mega frame is taken as no less than 25% of the overall base shear of the tower, and the super columns will remain elastic under moderate earthquake.

The core is the most important earthquake resisting members. The safety of the bottom strengthening zone is critical for the safety of the whole structure. The compression ratio of the core wall strengthening zone is strictly controlled to be below 0.5, and the steel embedded composite shear wall is applied. The seismic grade of the core is set as the ultra A grade. Steel columns are embedded at the corners of the core to improve the ductility and ensure the integrity of the core corners. Multi layer rebars are set for relatively thick core walls, thus to make the shear stress evenly distributed across the shear wall thickness and reduce the shrinkage cracks of the concrete. The shear stresses and axial stresses at the bottom of the core are strictly controlled.

To ensure the continuous force transferring between the outriggers and the core walls, the outriggers are continuous across the core section. The axial compression ratios for the adjacent upper and lower floor for the outrigger levels are strictly controlled. The reinforcement and embedded steel columns for the outrigger strengthening floors are increased. The contribution of the floor slabs are not considered for the design of the outriggers and the connections between outriggers and core walls. The construction sequence is analyzed based on assumed construction procedure and the outriggers will be locked at the top-out of the tower to reduce the secondary forces induced by the gravity loads.

The eight belt trusses of the Shanghai tower will support the loads of the dozen floors for each zone. The stress ratio of the structural members of the belt trusses are controlled to be below 0.85 in the design. The seismic performance of the belt trusses are set as remaining elastic for moderate earthquake and Non-yielding for major earthquake. The upper and lower chords and the posts of the double trusses are connected using steel plates to improve the global torsional resisting capacity of the belt trusses.

To ensure the accuracy and completeness of the calculation results, three software were employed for the global analysis of the tower structure. The elastic and elastoplastic time history analysis were conducted according to the code requirements and the weak positions of the tower were identified and strengthened accordingly. The P-Δ effect, vertical ground motion and the construction sequence were considered during the structural analysis.

6. SEISMIC PERFORMANCE ANALYSIS AND ASSESSMENT

Elastic and elastoplastic analysis methods were utilized to analyze and assess the seismic performance of the critical connections, structural members and the overall structure. The analysis results are partially shown in Figure 10~14. According to the analysis results, the seismic performance that the outriggers remaining Non-yielding during moderate earthquake and the belt trusses remaining Non-yielding during major earthquake can be satisfied. The base shear can also satisfy the preset requirements. The story drift ratio under major earthquake is below 1/100. During the major earthquake, the super columns mostly remain elastic, and the structural members of the belt trusses, outriggers, and radial trusses mostly remain elastic. Only few members along the earthquake directions become partially plastic.

The strengthening zone of the core wall will be locally plastic under major earthquake. The most seriously damaged positions are at the bottom of zone 6 and 7. The corner core walls at the top of zone 4 are also seriously damaged. Those places with large story drift ratio are also plastically damaged to some extent. The link beams for all zones become obviously plastic under major earthquake and the most seriously damaged locations are the top floors of zone 7 and 8. The link beams are seriously damaged under major earthquake. The link beams are also the major energy dissipation members. The main structural parts of the tower can satisfy the performance objectives that the structure is seriously damaged under major earthquake, but the critical connections will not be broken and the structure will not locally or globally collapse. The shear failure of the super columns, core walls will not happen.

During construction design phase, further tests on critical connections, super column members and global structure are to be conducted. Structural performance monitoring will also be considered to capture the real seismic performance and assess the structural safety during potential earthquake.

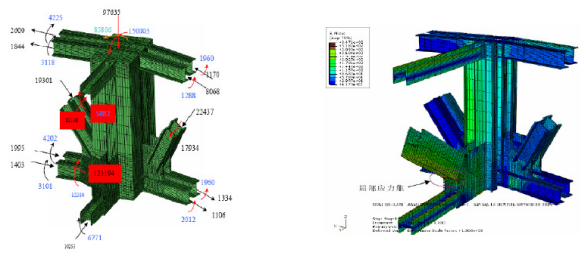

Figure 10 Super column outrigger connection and Mises stress results under the moderate earthquake

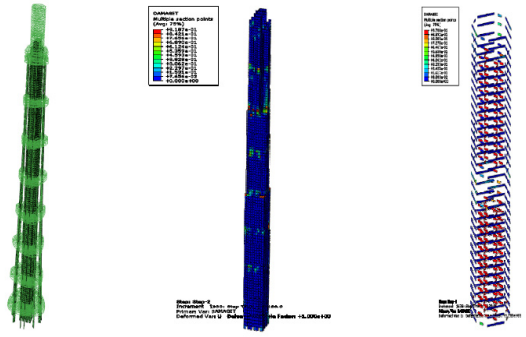

Figure 11 ABAQUS model and the compression damage development of the core walls and spandrels

7. CONCLUSIONS

The performance based seismic design of the Shanghai tower project is addressed in this paper. A design reference period of 50 years was applied in the determination of the design earthquake levels. The envelop of the site-specific spectrum and code-based spectrum was employed for the minor earthquake level, and the code-based spectra were applied for the moderate and major earthquake level. The ground motions for the time history analysis were chosen according to the requirements of the site characteristic, stochastic properties, effective peak value, lasting time and source mechanism specified in Chinese code. The seismic performance objectives for the important protection level are applied for the Shanghai tower. The seismic performance levels for the minor, moderate and major earthquake are respectively operational, immediate occupancy and life safety respectively. Several measures were taken regarding the super height problem and abrupt stiffness and capacity changes due to the setting of outriggers and belt trusses to improve the seismic safety of the structure and structural members. Elastic and elastoplastic analysis methods were utilized to analyze and assess the seismic performance of the critical connections, structural members and the overall structure. The performance assessment results show that the preset performance objectives can be mostly satisfied. To investigate the real seismic performance of the structure, further structural tests and performance monitoring will be conducted in the construction drawing design phase.

Project team:

Owner:	Shanghai Tower Construction & Development Co.
Architect	Gensler/Architectural Design and Research Institute of Tongji University (Group) Co. Ltd.
Structural	Thornton Tomasetti/Architectural Design and Research Institute of Tongji University (Group) Co. Ltd.
MEP	Cosentini/Architectural Design and Research Institute of Tongji University (Group) Co. Ltd.

Acknowledgements:

The authors acknowledge the support of Dennis Poon, Ling-En Hsiao, Yi Zhu, Steve Zuo and Paul Fu from Thornton Tomasetti in providing valuable comments and suggestions.

References:

Bertero, R.D. and Bertero, V.V. (2002), "Performance-based Seismic Engineering: the Need for a Reliable Conceptual Comprehensive Approach," E*arthquake Engineering and Structural Dynamics*, **31**:627-652

Xu, P.F., Fu, X.Y., Wang, C.K. and Xiao, C.Z. (2005), "Structural Design of Complicated Tall Buildings", China Architecture and Building Press

Lv, X.L (2009), "Seismic Design Guidelines for Tall Buildings beyond the Scope of Design Codes (2nd version)," Tongji University Press

Li, G. and Cheng, G.D.(2004), "Performance based Seismic Design – Theory, Method and Application," Science Press

Chen, W.F. and Liu, E.M. (2006), "Earthquake Engineering for Structural Design," CRC press

JOINT CONFERENCE PROCEEDINGS
7th International Conference on Urban Earthquake Engineering (7CUEE) &
5th International Conference on Earthquake Engineering (5ICEE)
March 3-5, 2010, Tokyo Institute of Technology, Tokyo, Japan

PRESCRIPTIVE SEISMIC CODES: SOCIETAL INCONVENIENCES

F. Casciati[1], A. Marcellini[2], A. Tento[2], D. Gerosa[3]

1) Professor, Dept. of Structural Mechanics, University of Pavia, Italy
2) Institute of Environmental Dynamic Processes, National Research Center (CNR), Milan, Italy
3) Consulting Geologist., Milan, Italy
fabio@dipmec.unipv.it,

Abstract: There are countries, all around the world, where the structural codes have the juridical nature of a law. When something is written in them, situations in conflict with it are illegal. These structural codes, however, does not apply to existing buildings until one is not obliged to retrofit them for some reason. Nevertheless, the managers of strategic buildings, as hospital, are quite sensitive to maintain them consistently with the update codes. Under these premises, it is common in these countries that a hospital is found to be at seismic risk, thus requiring immediate retrofitting at costs that sometimes are unaffordable by the hospital authority. This contribution explain how a process of micro-zonation could suitably avoid such inconveniences.

1. INTRODUCTION

The Italian structural code evolved during the past century at discrete times (Casciati-Marcellini, 2009). The basic jump occurred with the law 64 of 1974 (Law February 2, 1974) which represents the frame inside which updates are written. This law introduced the seismic macro-zonation. It sought at the beginning a partial coverage of the national territory by two different classes. It became a full coverage in four classes (Civil Protection, 2006) and it is presently provided in NTC 2008 (Ministry Decree, 2008) by a matrix which associates site coordinates with the spectral parameters. All the documents are national laws. But a part from the temporary document (Ministry Decree, 2005) which was of the performance-based type, all the other steps enforce Italy to adopt a prescriptive scheme.

Months before the Southern Italy strong seismic event of 1980, the team elaborating the seismic hazard, working with the name Group of Geodynamics within the National Research Council, had evidence that the municipality of Rome (the largest across Italy due to historical reasons) should have been assigned to a seismic class (Hazard Working Group, 1979). But the costs associated with such a decision would result economically unbearable and a cost-benefit analysis delayed such an update.

A fully opposite policy dominated the current scheme: the values of the parameters resulting from the hazard analysis were written as part of the law and the designer must respect them. The team in charge of its elaboration forgot that there is a micro-zonation ring in the chain which could deeply change the forces exciting a structures.

Two main problems arise:

1) how does such an evolution of the code prescriptions at a given site influence the management of existing buildings?
2) where is the local authority supposed to collect the money for the upgrades such a decision obliges to introduce?

In this paper the first item is not further considered, despite the two documents (Ministry Decree, 2005) and (Ministry Decree, 2008) introduced from scratch a chapter on Existing Buildings.

Attention is focused on the fact that a manager of a strategic construction, as a school or a hospital, is put under pressure when the text of a law says that at the site, where his/her facility was built, there is a hazard more aggressive than the one assumed in the design process.

The aim of this contribution is to explain how a process of micro-zonation could suitably avoid such inconveniences.

2. THE CASE STUDY

San Gerardo (Figure 1) is the most important hospital in the town of Monza, which counts 120000 inhabitants. It is located at some 20 km on the Nord-East of the metropolitan town of Milan. Nevertheless, Monza was recently given the

rank of Province, with a local council in charge of the territorial needs.

The major Italian newspaper *Corriere della Sera*, published on October 23, 2009, a first article on this hospital, followed by a second article on October 24, 2009, signed by different authors. In synthesis: the hospital construction started in the Sixties, but the building became fully operative in 1980. With a design 50 years old and a operational life of 30 years, the building requires a retrofit. But its design must now be consistent with the document (Ministry Decree, 2008), with more stringent seismic constraint than those adopted in the design, ruled by the old law of 1939!

Two solutions are discussed to accomplish the task:

1) reinforcement of 5000 pilasters with an extra cost of 35 millions euro to be added to the global cost of the retrofit (140 millions euro);
2) removal of the upper three floors (with their reconstruction at ground level) for a budget of 80 millions.

The province of Monza did not belong to any official Italian seismic zone till 2003. Actually the seismicity of the area is not significant: in the past thousand years Monza was hit by one earthquake only, the earthquake of 1396 with an estimated MCS Intensity of 7-8, with an estimated magnitude of 5.3 and probably with epicenter located very close to the town.

Presently Monza has been included into the seismic zones and classified in the 4th seismic category. According to the recently issued Italian seismic code NTC 2008 (Ministry Decree, 2008) the design response spectrum has a site dependent shape and the PGA (peak ground acceleration) value a_g is determined by the probabilistic seismic hazard. It coincides with the spectral acceleration S_a computed at the abscissa T=0, where T denotes the period.

With reference to a hospital, it is conveniently assumed a nominal life of 100 years, in addition the hospital belongs to the 4th destination category. That is: considering the design at the ultimate limit state SLV (safe life limit state) the seismic input a_g would be the seismic hazard PGA for 945 years return period. But a nominal life multiplication factor of 2 must be introduced for the destination 4th category, which brings to a reference return period of 1950 years.

The Monza area, situated in the Po valley, is characterized by fluvial and glacio-fluvial quaternary deposits of relevant thickness. From a lithological point of view the soil is mainly composed by loose sediments mainly coarse grained, of gravelly-sand and/or pebbly, sometimes cemented, and in silty-clay matrix. The oldest Pleistocene deposits are sometimes covered by silty deposits of eolinian origin (loess). The soil of San Gerardo site is characterized (from surface to depth) by few meters (approximately 2 m) of clayley silt and landfill, sand and gravel silty clayed weakly pebbly for some 20 meters, 2 meters of a cemented layer like 'Ceppo' that overlays a thick layer of gravels and sandy pebbly weakly silty clay. According to the lithological description the soil belongs to the B category of the NTC 2008 (Ministry Decree, 2008) soil type.



Figure 1 Monza: the San Gerardo Hospital.

The elastic response design spectrum prescribed by the code for SLV design at the site of the San Gerardo Hospital is presented in Figure 2.

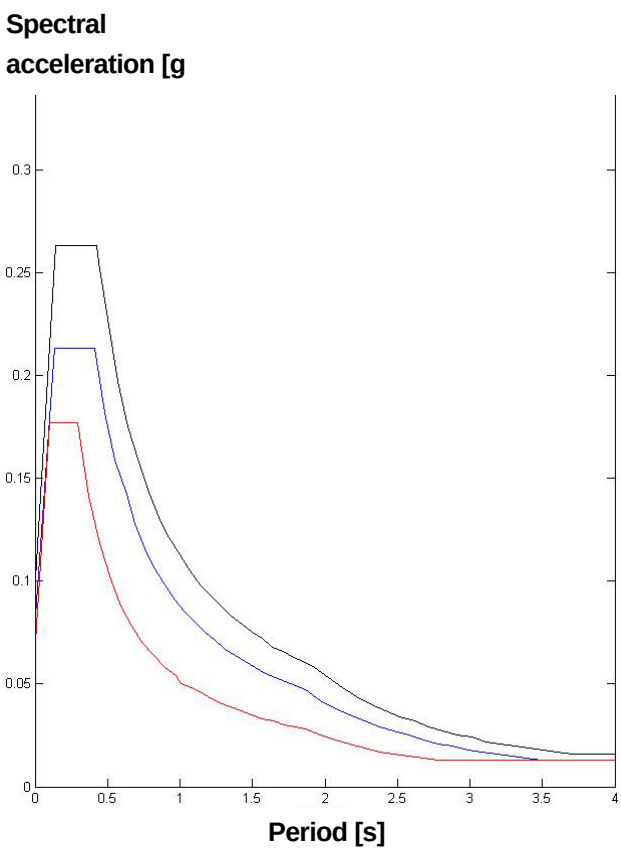

Figure 2 The Italian seismic code NTC2008 (Ministry Decree, 2008) prescribes both horizontal and vertical design spectra. The parameters T_B, T_C, T_D (which define the discontinuity abscissae), and Sa can be modified by coefficients dependent on site conditions. The bottom line denotes the elastic horizontal response spectrum, in a rock-site and for a return period of 945 years, in the town of Monza. The 945 hazard PGA of Monza is 0.067 g. The other horizontal elastic design spectrum lines refer to the San Gerardo hospital site ,soil type B, assuming either 50 years (middle) and 100 years (top) nominal life and a destination factor of 2 (as required for the SLV design).

3. SITE EFFECT ANALYSIS

To check the actual influence of the soil conditions at the San Gerardo site, a site effects analysis was conducted by using a uni-dimensional (1D) approach. The following steps are envisaged:

1) Definition of the input motion: this is achieved by fitting (Casciati et al., 2003) the 5%-damping elastic response spectrua of the accelerograms of the European data base (Ambraseys et al., 2004) with the target response spectra (that is the 945 years return period response spectra reported in App: A-B of NTC08 (Ministry Decree, 2008)). The resulted accelerograms are reported in Figure.3. The quality of fit with target spectrum is shown in Figure 4.

2) Soil shear wave velocity (V_s) profile: it is obtained by MASW (Multichannel Analysis of Surface Waves) geophysical investigation. Figure 5 reports the soil profile with the associated standard deviation. To account for the uncertainties several models compatible with the profile were adopted as input data in the 1-D computer code.

3) 1D viscoelastic analysis: a standard 1D viscoelastic program was used to calculate the site effects. The input data described at point 1 and 2 were adopted , together with the shear modulus decay and the damping curves reported in the microzonation regulations of the Lombardia region, where the Monza province is located

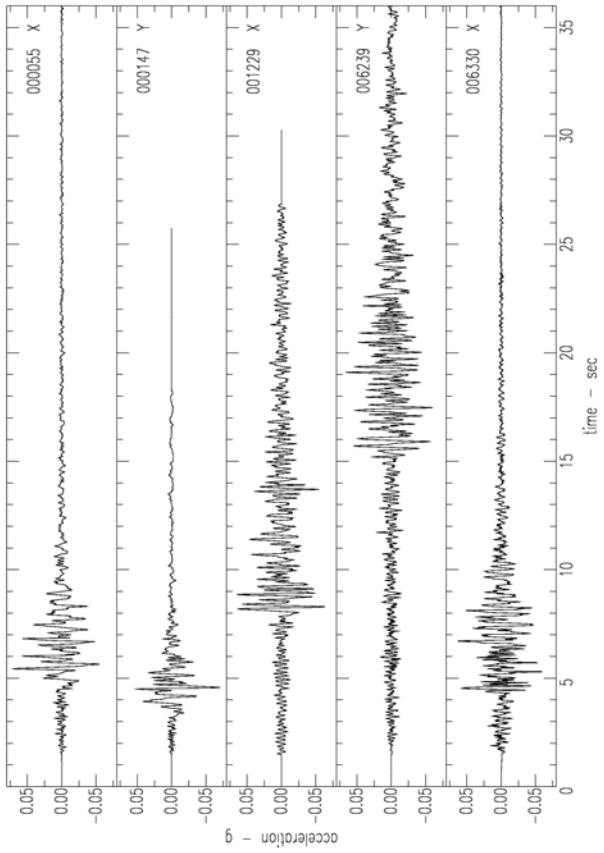

Figure 3. Selected accelerograms adopted as input motion on rock soil type

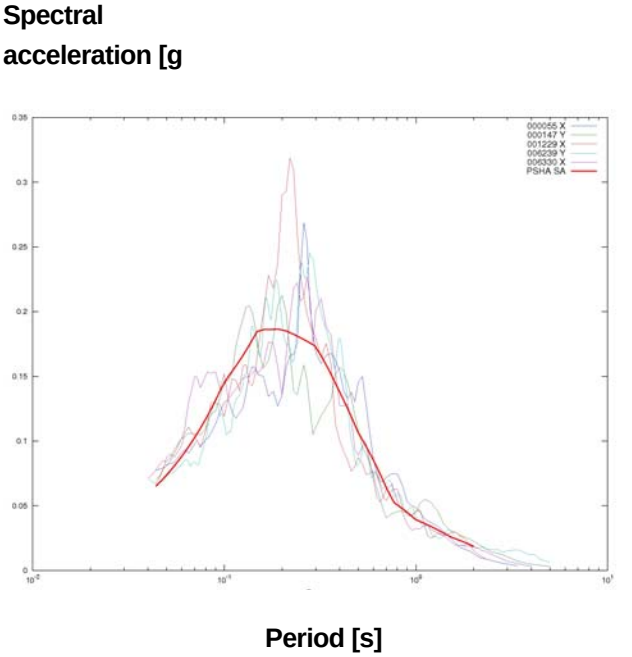

Figure 4. 5%-damping elastic response spectra of the accelerograms reported in Figure.3 compared with target response spectrum (tick-line)

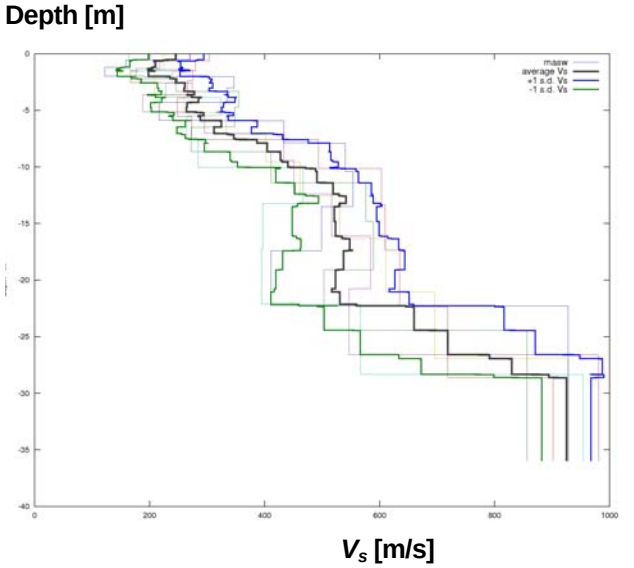

Figure 5. V_s profile of San Gerardo site: average value plus/minus 1 standard deviation

The results are summarized in Figure 6. It is possible to observe that the site conditions double the rock site figure Finally the above mentioned results (the expected response spectrum) were compared with the response spectrum prescribed by the code. Figure 7 summarizes the results by comparing the 5%-damping response spectra computed at the site of the San Gerardo hospital with the elastic design spectrum drawn according to NTC 08 (Ministry Decree, 2008) assuming a soil of type B, a nominal life of 100 years nominal life and an SLV ultimate limit state design.

Spectral acceleration [g

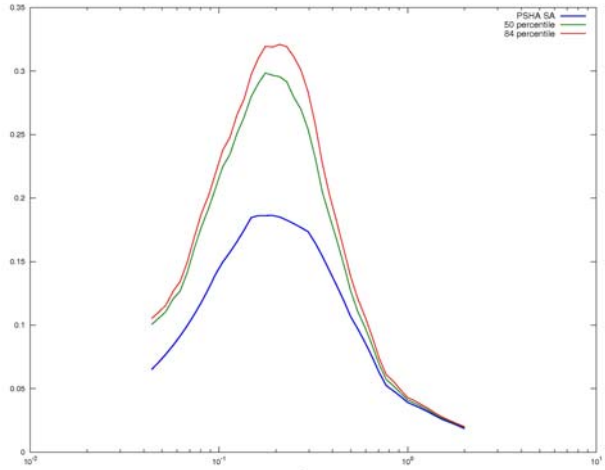

Figure 6. 5% damping response spectra computed at San Gerardo, compared with the rock soil type spectrum at the same site (lowest ordinates). The intermediate response spectrum is the 50percentile; the top spectrum is the 84 percentile

Spectral acceleration [g]

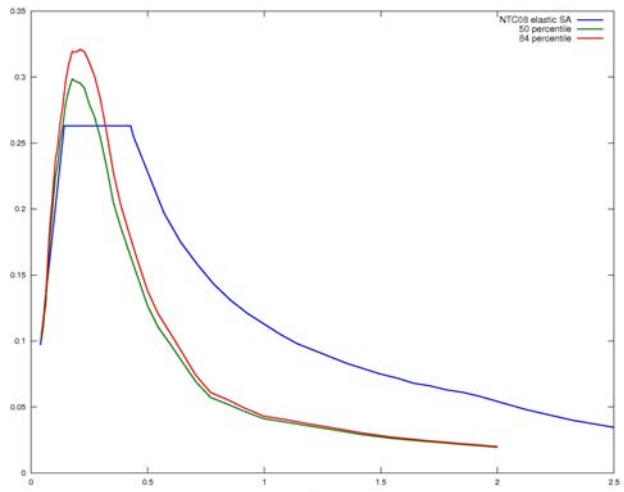

Figure 7. 5% damping response spectra computed at the site of the San Gerardo hospital (see also Figure 6), compared with the horizontal elastic design spectrum (curve with the flat plateau) drawn according to NTC 08 (Ministry Decree, 2008). It is assumed a soil of type B, assuming, 100 years of nominal life and a design at the ultimate limit state SLV (safe life limit state). The response spectrum of lowest ordinates is the 50percentile; the other is the 84 percentile.

In the whole procedure the investigation was limited to consider the horizontal component only.

From figure 7 it is possible to observe that there is a strong amplifiaction in short periods range .

Viceversa the spectrum prescribed by the NTC08 (Ministry Decree, 2008) largely overestimates the expected motion at intermediate and large periods, which are likely to be the most significant for the massive structure of the hospital.

4. CONCLUSIONS

With reference to a significant case study, this paper emphasizes the societal inconveniences of a prescriptive approach in the elaboration of the seismic structural code.

This approach, 30 years ago suggested, to be silent on the seismic hazard in a metropolitan area as the one of Rome, due to the high costs involved by preventing it. The same approach, with the seismic hazard parameters written in a text which is a national law, obliges the managing administrations of strategic facilities to invest a lot of money in retrofit, independently of a suitable cost-benefit analysis.

Indeed this paper outlines the following remarks to be deeply considered in view of a general amelioration of the seismic codes matter:

1) it is quite dangerous to remove any responsibility from the professional operators as geologists, seismologists and structural engineers; such professions are replaced by texts with the vigor of a national law, independently of the scientific bases of their elaboration;
2) the retrofit of existing building should be the subject of appropriate instructions demanding a global cost-benefit analysis and not simply the consistency with always more stringent prescriptions;
3) even ignoring the two remarks above, a fully prescription nature of the seismic code is obliged to neglect the local aspects of the seismic micro-zonation. It offers the chance to significant cost reductions in the case study discussed along this paper, but it can also result in a quite un-conservative design.

Acknowledgements

The first author acknowledge support of the Athenaeum Research Funds from the University of Pavia (FAR 2009). The cooperation between the authors is framed within the Graduate School of Civil Engineering at the University of Pavia.

References:

N. N. Ambraseys, P. Smit, J. Douglas, B. Margaris, R. Sigbjörnsson, S. Ólafsson, P. Suhadolc and G. Costa , 2004, CD-ROM European Strong-Motion Database, vol. 2,.

F. Casciati and A. Marcellini , 2009, “L’Aquila, Central Italy, April 6, 2009: a Further Lesson to Civil Engineers”, ***The Open Construction and Building Technology Journal,*** **3**, Bentham Open.

F. Casciati, S. Casciati, A. Marcellini, 2003, “PGA and Structural Dynamics at a Given Site”, *Journal of Earthquake Engineering and Engineering Vibration*, **2** (1), pp. 25-34.

Civil Protection Department, 2006, Seismic classification 2006 (in Italian),. http://www.protezionecivile.it/cms/attach/editor/

Hazard Working Group, 1979, Preliminary hazard maps of the national territory (in Italian), C.N.R. P.F. Geodinamica. Publ 227, ESA, Roma, 25 pp..

Law February 2, 1974, N. 64

Ministry Decree 14-09-2005 (in Italian), Gazzetta Ufficiale, 222, 23-09-2005.

Ministry Decree 14-01-2008 (in Italian), Gazzetta Ufficiale 29, 04-02-2008.

JOINT CONFERENCE PROCEEDINGS
7th International Conference on Urban Earthquake Engineering (7CUEE) &
5th International Conference on Earthquake Engineering (5ICEE)
March 3-5, 2010, Tokyo Institute of Technology, Tokyo, Japan

A METHODOLOGY FOR THE SEISMIC DESIGN OF TALL BUILDINGS INCORPORATING BASE ISOLATION DEVICES

Troy A. Morgan[1] and Kazuhiko Kasai[2]

1) Assistant Professor, Center for Urban Earthquake Engineering, Tokyo Institute of Technology, Japan
2) Professor, Structural Engineering Research Center, Tokyo Institute of Technology, Japan
morgan@cuee.titech.ac.jp, kasai@serc.titech.ac.jp

Abstract: The design of tall buildings in Japan have recently incorporated seismic isolation systems as a means of providing enhances seismic protection. Whereas seismic isolation has traditionally been applied to short, stiff structures, several successful projects have demonstrated the viability of seismic isolation for tall buildings. However, a general methodology describing an approach for selecting appropriate isolation system parameters given a range of superstructural characteristics has yet to be developed. In this paper, a procedure for generating an equivalent viscoelastic system to describe a tall isolated building is described. In this procedure, the problem of a significant non-proportionally damped multi-DOF structure is overcome by introducing an assumption of steady-state vibration combined with a correction to account for the difference in peak velocity compared to peak pseudo-velocity. Analysis of a wide range of isolated building models indicates excellent agreement between response prediction from response history analysis of the non-proportionally damped model and the proposed spectrum-based equivalent viscoelastic analysis.

1. INTRODUCTION

Recent trends in urban planning have led to the development of high-density residential and commercial areas. Due to limitations in available space, tall buildings must be constructed to accommodate such high-density areas. Given the large number of occupants in these tall buildings, combined with the financial significance of organizations which inhabit them, the consequences of damage due to a seismic event must be carefully assessed. In the past 25 years, seismic isolation has been applied worldwide to achieve enhanced seismic performance in structures subjected to earthquakes. There have been recent applications of seismic isolation technology to tall, flexible building in Japan [Ariga, et al. 2006, Kani 2009, Miyazaki 2009]. Given this trend, there has been recent research dedicated to examining the behavior of tall buildings with seismic isolation systems [Takewaki 2007, Takewaki and Fujita 2009.]

Traditionally, base isolation has been seen as applicable only to short, stiff structures. For tall, flexible structures, the period is already longer than the predominant period of most ground motions. Therefore, it is assumed that the addition of an isolation system is ineffective for the enhancement of seismic performance. However, the addition of an isolation layer can alter the mode shape such that a significant portion of the deformation response is concentrated in the isolations system rather than the supported structure. Since there is very little information about the behavior of tall or flexible structures on isolation systems, it is necessary to develop robust design methodologies to target desired levels of performance.

2. DEFINITION OF PARAMETERS

To develop equations of motion for generic 2-DOF isolated structures, a coordinate system must be chosen. Since relative deformations of the superstructure and isolation system are of primary interest, equations of motion are expressed using relative deformations. Relative to some fixed reference frame, let the ground displacement, isolation level displacement, and structural displacement be u_g, x_b, and x_s, respectively. Here we define the isolator displacement as $u_b = x_b - u_g$ and the structural displacement as $u_s = x_s - x_b$. We also define the mass at the isolator and structure level as m_b and m_s, respectively. Between the ground and base mass, the isolation system is represented as a Kelvin element having spring stiffness k_b and linear viscous damping coefficient c_b. Between the base mass and superstructure mass, a second Kelvin element with spring stiffness k_s and linear viscous damping coefficient c_s is defined to represent the superstructure. The 2-DOF structure with the above parameters is depicted in Figure 1.

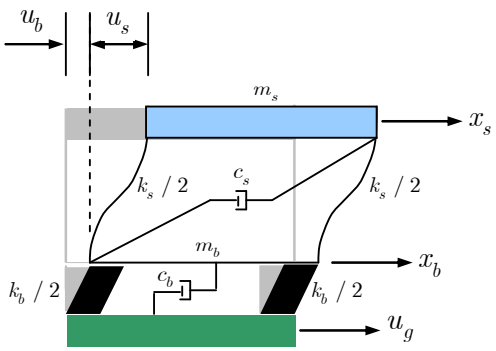

Figure 1: Definition of parameters for 2-DOF isolated structure

With these definitions, it is possible to develop the equations of motion for this system subjected to some ground acceleration $\ddot{u}_g$. First, it is convenient to define a mass ratio $\gamma = m_s / (m_s + m_b)$, which tends to unity at the superstructure mass becomes very large compared to the base mass. Additionally, it is useful to define the natural frequencies of the isolation system and the superstructure. The squares of the natural frequencies of the isolation system and superstructure, ω_b^2 and ω_s^2 are defined as

$$\omega_b^2 = \frac{k_b}{m_s + m_b}, \quad \omega_s^2 = \frac{k_s}{m_s} \tag{1}$$

Notice that ω_b is the natural frequency of the isolated structure assuming the superstructure is infinitely rigid. This definition follows that of modern building codes (e.g. ASCE-7, 2005.) Similarly, we can define critical viscous damping ratios for the isolation system and superstructure as

$$\zeta_b = \frac{c_b}{2(m_s + m_b)\omega_b}, \quad \zeta_s = \frac{c_s}{2m_s\omega_s} \tag{2}$$

3. VISCOELASTIC REPRESENTATION

In order to develop an equivalent SDOF system which may be used to estimate the response of the previously-described 2DOF structure, a steady-state response approach is taken. For tall isolated buildings, the superstructure mass will be much larger than the base mass, which implies that γ approaches unity. If the superstructure mass m_s is assumed to be much larger than the base mass m_b (i.e. $\gamma \to 1$), the isolated structure may be represented by a viscoelastic (VE) system subjected to some forcing function *f*, as shown in Figure 2. All other definitions remain as defined above, except the damping ratio of the superstructure, ζ_s, is assumed negligible compared to that of the isolation system, and is therefore assumed to be zero.

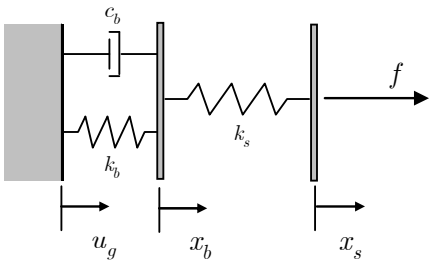

Figure 2: Viscoelastic representation of isolated 2DOF structure

We define the displacement of the equivalent system as $u = x_s - u_g$, which could be expressed equivalently as $u = u_b + u_s$. Suppose that the response of the equivalent system is described by

$$u = u_0 \sin \omega_{eq} t \tag{3}$$

Where u_0 is the maximum displacement response and ω_{eq} is some frequency of excitation of the equivalent VE system. With no loss of generality, we assume the mass of the equivalent VE system is equal to unity. As a result, the total mass-normalized force *f* acting on the system can be described by either the isolation system force f_b as

$$f = f_b = \omega_b^2 u_b + 2\zeta_b \omega_b \dot{u}_b \tag{4}$$

or the superstructure force f_s as

$$f = f_s = \omega_s^2 u_s \tag{5}$$

The individual component deformations may be expressed as

$$u_b = \frac{f - 2\zeta_b \omega_b \dot{u}_b}{\omega_b^2}, \quad u_s = \frac{f}{\omega_s^2} \tag{6}$$

Applying the relations $u = u_b + u_s$ and $\dot{u} = \dot{u}_b + \dot{u}_s$, the deformation *u* is given by

$$u = \frac{f - 2\zeta_b \omega_b (\dot{u} - \dot{u}_s)}{\omega_b^2} + \frac{f}{\omega_s^2} \tag{7}$$

Substituting $u = u_0 \sin \varpi t$, $\dot{f} = \omega_s^2 \dot{u}_s$, and applying algebraic manipulation leads to the following first-order differential equation

$$f\left(\frac{\omega_b^2 + \omega_s^2}{\omega_b^2 \omega_s^2}\right) + \dot{f}\left(\frac{2\zeta_b}{\omega_b \omega_s^2}\right) = u_0 \sin \omega_{eq} t + u_0 \omega_{eq} \left(\frac{2\zeta_b}{\omega_b}\right) \cos \omega_{eq} t \tag{8}$$

It can be shown that the solution to this differential equation is given by

$$f = \left(\frac{\omega_s^2 \omega_b^2}{\omega_b^2 + \frac{\omega_s^2}{\Gamma}} \right) u_0 \sin \omega_{eq} t + \left\{ \frac{\omega_s^2 \omega_b^2 \eta_b}{\left(\omega_b^2 + \frac{\omega_s^2}{\Gamma} \right) \left[1 + \frac{\omega_b^2}{\omega_s^2} \left(1 + \eta_b \right)^2 \right]} \right\} u_0 \cos \omega_{eq} t \tag{9}$$

Where the loss factor $\eta_b = 2\zeta_b$ and the non-dimensional parameter Γ is defined as

$$\Gamma = 1 + \frac{\omega_s^2 \eta_b^2}{\omega_s^2 + \omega_b^2} \tag{10}$$

In general, the total force in the equivalent VE system undergoing stead-state vibration can be described as

$$f = k'_{eq} u_0 \left(\sin \omega_{eq} t + \eta_{eq} \cos \omega_{eq} t \right) \tag{11}$$

where k'_{eq} is the storage stiffness and η_{eq} is the loss factor. Here, we introduce a term to account for the inexact assumption of steady state response for a system subjected to earthquake excitation. Under steady-state response, the peak velocity of the system can be computed through differentiation as

$$\dot{u}_0 = \max \left[\dot{u}(t) \right] = \omega_{eq} u_0 \tag{12}$$

This definition follows that of the peak pseudo-velocity (Chopra, 2007) where u_0 is the peak earthquake displacement response of an SDOF oscillator having natural frequency ω_{eq}. However, the damping force is related to the actual velocity, whose peak is generally not equal to the peak pseudo-velocity. For some ground motion excitation, we define a correction term

$$\alpha_v = \frac{\dot{u}_0}{\omega_{eq} u_0} \tag{13}$$

where u_0 and $\dot{u}_0$ are the peak displacement and velocity at frequency ω_{eq}, respectively. The correction term α_v is generally a function of frequency and damping, and varies depending on the ground motion under consideration. Using the relationship $\dot{u}_0 = \alpha_v \omega_{eq} u_0$, the corrected force in the VE system is described by

$$f = k'_{eq} u_0 \left(\sin \omega_{eq} t + \eta_{eq} \alpha_v \cos \omega_{eq} t \right) \tag{14}$$

An important observation is that the maximum force in the VE system can be expressed as

$$f_{\max} = k'_{eq} u_0 \sqrt{1 + \eta_{eq}^2 \alpha_v^2} \tag{15}$$

The derived force from Eq. (9) can be expressed in the same form as Eq. (15) where

$$k'_{eq} = \frac{\omega_s^2 \omega_b^2}{\omega_b^2 + \frac{\omega_s^2}{\Gamma}}, \quad \eta_{eq} = \frac{\eta_b}{\left[1 + \frac{\omega_b^2}{\omega_s^2} \left(1 + \eta_b \right)^2 \right]} \tag{16}$$

Therefore, the equivalent VE representation of the 2DOF isolated structure undergoing steady-state vibration is described by the parameters k'_{eq} and η_{eq}. From this we can conclude that the natural frequency of the equivalent system is given by $\omega_{eq} = \sqrt{k'_{eq}}$, or

$$\omega_{eq} = \sqrt{\frac{\omega_b^2 \omega_s^2}{\omega_b^2 + \frac{\omega_s^2}{\Gamma}}} \tag{17}$$

Similarly, the viscous damping ratio of the equivalent system can be computed by recognizing that the critical damping $\zeta_{eq} = \eta_{eq} / 2$, or

$$\zeta_{eq} = \frac{\zeta_b}{1 + \left[\frac{\omega_b}{\omega_s} \left(1 + 2\zeta_b \right) \right]^2} \tag{18}$$

The relationship of the equivalent period $T_{eq} = 2\pi / \omega_{eq}$ and the equivalent damping ζ_{eq} to the isolation period T_b for various fixed-base periods T_s and isolation damping ζ_b is shown below in Figure 3.

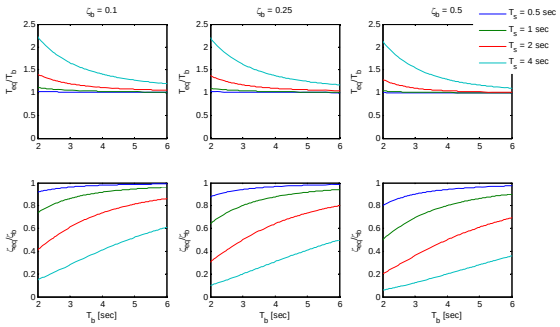

Figure 3: Equivalent period T_{eq} and equivalent damping ζ_{eq} as a function of isolation period T_b

With these definitions, it is possible to analyze an equivalent SDOF system subject to earthquake ground motion, and obtain an estimate for the maximum displacement response u_0. However, it is important that the individual displacements of the isolation system and superstructure are captured from this equivalent analysis. Therefore, a procedure is needed to extract u_{b0} and u_{s0} from the computed u_0. Suppose the steady-state isolator displacement is described by $u_b = u_{b0} \sin \omega_{eq} t$. Substituting u_b and its derivative into Eq. (4), the maximum force developed in the isolation system is

$$f_{b\max} = u_{b0} \sqrt{\omega_b^4 + 4\alpha_v^2 \zeta_b^2 \omega_b^2 \omega_{eq}^2} \tag{19}$$

Noting $f_{b\max} = f_{\max}$ and solving for u_{b0} gives

$$u_{b0} = u_0 \frac{\omega_{eq}^2}{\omega_b^2} \sqrt{\frac{1+4\alpha_v^2\zeta_{eq}^2}{1+4\alpha_v^2\zeta_b^2\left(\frac{\omega_{eq}^2}{\omega_b^2}\right)}} \tag{20}$$

Similarly, we let $u_s = u_{s0} \sin \omega_{eq} t$ and substitute $f_{s\max} = f_{\max}$ from Eq. (15) into Eq. (19) to obtain

$$u_{s0} = u_0 \frac{\omega_{eq}^2}{\omega_s^2} \sqrt{1+4\alpha_v^2\zeta_{eq}^2} \tag{21}$$

With these definitions, it is straight-forward to estimate the peak deformation in both the isolator and superstructure based on a ground motion displacement spectrum developed for a damping level of ζ_{eq}.

4. TRANSFORMATION OF NDOF TO 2DOF

To conduct realistic analytical simulations, a procedure is needed to convert a generic *N*-story building to an idealized 2DOF structure. The necessary properties for the 2DOF system are: number of stories *N*, superstructure period T_s, superstructure damping ratio ζ_s, isolation period T_b, isolation damping ratio ζ_b, and mass ratio γ. It is necessary to make some assumption regarding T_s based on *N*, so the well-known approximation $T_s = 0.1N$ is made here. Therefore, assuming equal floor weights, the mass ratio γ can be expressed as $\gamma = (N-1)/N$. This idealization is described below in Figure 4.

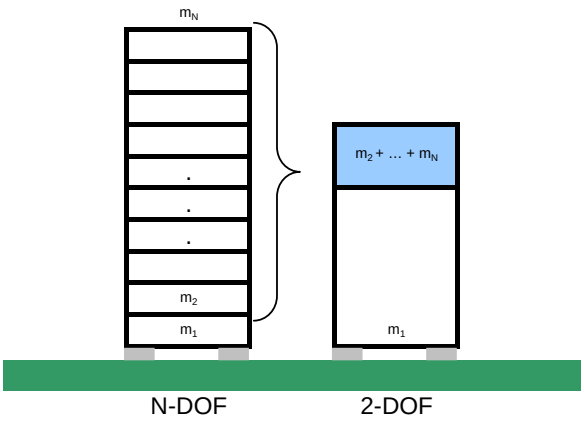

Figure 4: Description of the idealization of N-story building to a 2DOF structure

Given the assumptions of T_s, ζ_s, T_b, and ζ_b, we can define the properties of the 2DOF system, shown in detail in Figure 1, as follows. For the superstructure, the spring stiffness k_s and damping coefficient c_s are computed as

$$k_s = \left(\frac{2\pi}{T_s}\right)^2 \sum_{i=2}^{N} m_i, \quad c_s = 2\zeta_s \left(\frac{2\pi}{T_s}\right) \sum_{i=2}^{N} m_i \tag{22}$$

Similarly, for the isolation level, the spring stiffness k_b and damping coefficient c_b are computed as

$$k_b = \left(\frac{2\pi}{T_b}\right)^2 \sum_{i=1}^{N} m_i, \quad c_b = 2\zeta_b \left(\frac{2\pi}{T_b}\right) \sum_{i=1}^{N} m_i \tag{23}$$

These parameters are sufficient to characterize the 2DOF system for response history analysis.

5. GROUND MOTIONS

To both facilitate the development of statistical descriptions of demand and to consider a variety of seismic characteristics, an ensemble of ground motions is selected to represent possible realizations of ground motion at a site. As part of the SAC Steel Project, several ensembles of ground motions were developed for the Los Angeles basin. Since the objectives of these studies is to identify demand parameter sensitivities to inputs having multiple frequencies of occurrence, three ground motions ensembles were selected. Each of the three ensembles contains 20 acceleration records, and were developed for return periods of 72-years, 475-years, and 2475-years. For further details of the development of the SAC ground motions, see Somerville et al. [1997.]

Figure 5 through Figure 7: Elastic response spectra for 2475-yr records (median shown bold) show the elastic response spectra for each ground motion for the 72-yr, 475-yr, and 2475-yr ensembles, respectively. Figure 8 shows a comparison of the median spectra for all three return periods, including an overlay of the USGS prescriptive spectra with best fit parameters. Best-fit parameters are determined by selecting S_{DS} and S_{D1} such that the error between the median spectrum and the USGS spectrum is minimized for both constant acceleration and constant velocity regions, for all three return periods.

A key ingredient of the VE analysis procedure described previously is a relationship that describes the ratio between peak velocity and peak pseudo-velocity, defines as α_v. While estimates of this ratio are available in the literature for the period range $0.1\,\text{sec} \le T \le 3\,\text{sec}$ (Kasai et al., 2009,) there is little information regarding its characteristics at long-periods of vibration, which are important for isolated tall buildings. For the purpose of estimating this parameter, linear least-squares regression analysis was performed using the SAC suite of ground motions and the following 6-parameter linear model for α_v:

$$\begin{aligned} \alpha_v(T,\zeta) &= \frac{\dot{u}_0}{\omega_{eq} u_0} \\ &= \beta_0 + \beta_1 T + \beta_2 T^2 + \beta_3 \zeta + \beta_4 \zeta^2 + \beta_5 T\zeta \end{aligned} \tag{24}$$

Where the input factors T and ζ are the period and damping of an SDOF oscillator. From this analysis, the following least-squares estimates were determined for each regression coefficient:

$$\begin{aligned} &\hat{\beta}_0 = 0.7062,\ \hat{\beta}_1 = 0.1186,\ \hat{\beta}_2 = 0.0265, \\ &\hat{\beta}_3 = 1.5101,\ \hat{\beta}_4 = -1.1248,\ \hat{\beta}_5 = 0.0334 \end{aligned} \tag{25}$$

This equation defines the assumed relationship for $\alpha_v(T,\zeta)$ used in subsequent analyses, and is valid for the period range $2\,\text{sec} \le T \le 10\,\text{sec}$ and a damping range $0.02 \le \zeta \le 0.40$.

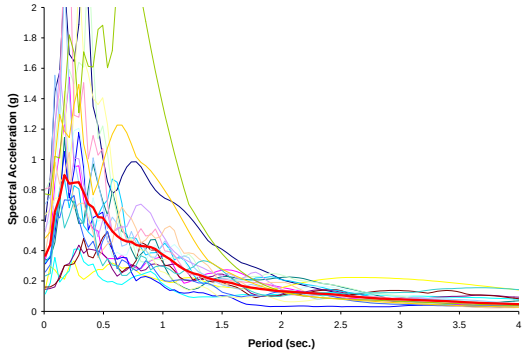

Figure 5: Elastic response spectra for 72-yr records (median shown bold)

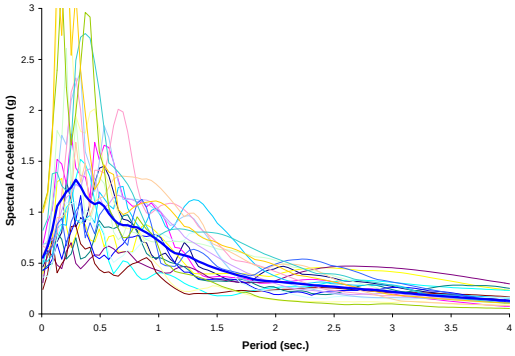

Figure 6: Elastic response spectra for 475-yr records (median shown bold)

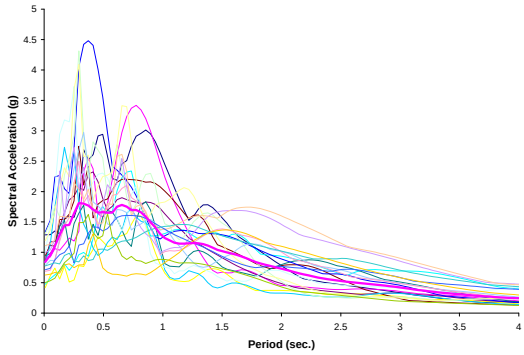

Figure 7: Elastic response spectra for 2475-yr records (median shown bold)

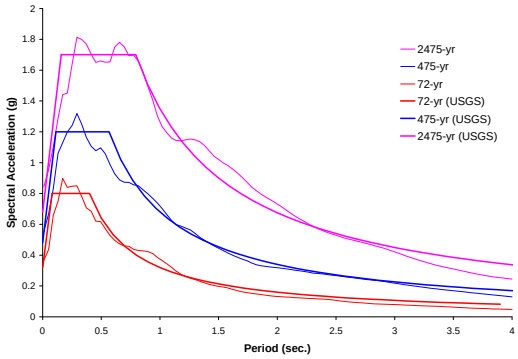

Figure 8: Median elastic response spectra for all three ground motion ensembles, including overlay of best-fit USGS prescriptive spectra

6. LINEAR 2DOF STUDIES

To study the accuracy of the equivalent VE analysis method presented previously, a comparison of displacement demands based on response spectrum and explicit response history analysis (RHA) is made. In the case of response history analysis, the 2DOF system with non-classical damping behavior is analyzed exactly through numerical integration using input earthquake acceleration records. The peak isolator displacement $\max[u_b(t)]$ and peak structural displacement $\max[u_s(t)]$ is computed for each of the 60 ground motions described. These peak deformations of the isolation system and superstructure are compared to those estimated by Eq. (20) and (21) based on the VE approximation and individual ground motion response spectra.

Figure 9 describes the response of a 2DOF structure having T_b = 4 sec, T_s = 1 sec (i.e. N = 10 stories.) It appears that, for both levels of isolation system damping ζ_b considered (10% and 25%) there is very close agreement between the 2DOF RHA and the equivalent SDOF analysis, with very little observable bias and dispersion.

Figure 10 through Figure 12 present similar response comparison data for 2DOF and SDOF analyses, but for superstructure periods T_s = 2, 3, and 4 sec (N = 20, 30, and 40 stories) respectively. It is clear that, as the superstructure period becomes longer, there is similar variation in the estimate of isolator displacement u_b and structural displacement u_s, with negligible bias and dispersion. The results presented here demonstrate that an accurate, response spectrum-based method of estimating isolator displacements and superstructural drift is feasible for tall, isolated buildings with a range of period and damping characteristics.

To investigate the accuracy of the proposed method for *all* SDOF systems studied, the statistical relationship between the exact and the estimated displacement response is described. Here we assume some linear relationship $u_{RHA} = \lambda u_{VE}$ where u_{RHA} is the exact displacement response computed from response history analysis and u_{VE}

is the same displacement response estimated from the proposed equivalent viscoelastic method. The slope parameter λ may be estimated using least-squares regression from the computed data for all 60 ground motion records. If we define $\hat{\lambda}$ as the least-squares estimate of the true slope $\lambda = u_{RHA} / u_{VE}$, then $\hat{\lambda} > 1$ indicates unconservative bias, $\hat{\lambda} < 1$ indicates conservative bias, and $\hat{\lambda} = 1$ indicates a lack of bias. The estimated slope parameters for both isolator and structural displacement are summarized for ζ_b = 10% and 25% in Table 1 and Table 2, respectively. This data demonstrates that the proposed method gives reliable estimates of both isolator displacement and superstructure drift for buildings having natural periods between 1 and 4 seconds (number of stories between 10 and 40) and isolation systems between 2 and 4 seconds for both levels of isolation system damping considered (ζ_b = 10% and 25%.) The estimates for isolator displacement show negligible unconservative bias ($\hat{\lambda} < 1.014$) and those for structural drift show low unconservative bias ($\hat{\lambda} < 1.070$.)

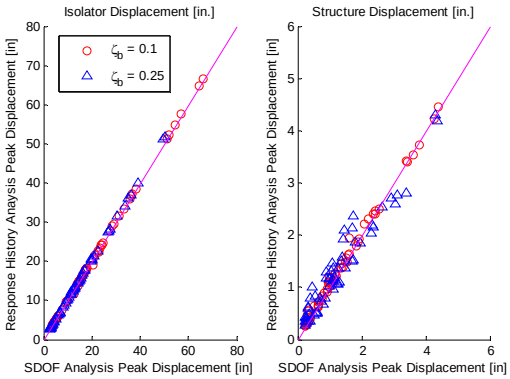

Figure 9: Response of moderately-damped 2DOF structures having T_b = 4 sec, T_s = 1

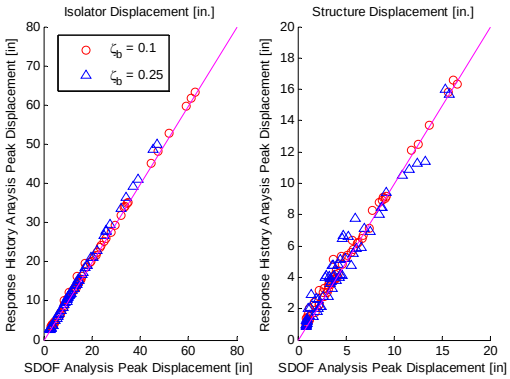

Figure 10: Response of moderately-damped 2DOF structures having T_b = 4 sec, T_s = 2

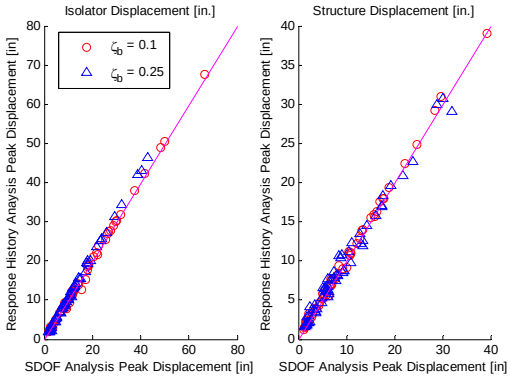

Figure 11: Response of moderately-damped 2DOF structures having T_b = 4 sec, T_s = 3

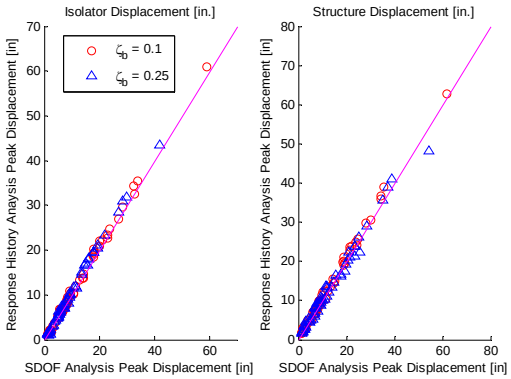

Figure 12: Response of moderately-damped 2DOF structures having T_b = 4 sec, T_s = 4

Table 1: Estimated slope parameter $\hat{\lambda}$ of isolator displacement and structural displacement regression lines between response history result and equivalent viscoelastic result for ζ_b = 10% (slope = 1.0 indicates lack of bias)

	Isolator Displacement			Structural Drift		
	T_b = 2 s	T_b = 3 s	T_b = 4 s	T_b = 2 s	T_b = 3 s	T_b = 4 s
T_s = 1 s	1.0043	1.0059	1.002	1.0329	1.0429	1.031
T_s = 2 s	0.9983	1.004	1.0037	1.0258	1.0346	1.0357
T_s = 3 s	0.9887	1.0009	0.9937	1.0227	1.0318	1.0314
T_s = 4 s	0.9456	0.9908	1.0129	0.9771	1.0211	1.0519

Table 2: Estimated slope parameter $\hat{\lambda}$ of isolator displacement and structural displacement regression lines between response history result and equivalent viscoelastic result for $\zeta_b = 25\%$ (slope = 1.0 indicates lack of bias)

	Isolator Displacement			Structural Drift		
	$T_b = 2$ s	$T_b = 3$ s	$T_b = 4$ s	$T_b = 2$ s	$T_b = 3$ s	$T_b = 4$ s
$T_s = 1$ s	0.9889	1.002	1.0127	1.0314	1.0568	1.0696
$T_s = 2$ s	0.9459	0.9927	1.0135	0.9819	1.0294	1.0665
$T_s = 3$ s	0.9297	0.9636	0.9858	0.9621	0.9875	1.0443
$T_s = 4$ s	0.9942	0.9558	0.9655	1.026	0.9948	1.0165

3. CONCLUSIONS AND FUTURE STUDIES

This study focuses on the response of isolated tall buildings subjected to seismic excitation. A methodology is described to convert a generic *N*-story isolated structure to an idealized 2DOF system using basic natural parameters such as isolation system period and damping, and superstructure period and damping. An equivalent viscoelastic SDOF system is derived in such a away to allow closed-form expressions for isolator and structure displacements given some earthquake response spectrum. This development is made tractable by letting the superstructure mass become large relative to the base bass, which is reasonable for tall isolated buildings. The described approach leads to accurate estimates of peak isolator displacement and peak structural drift through the simple use of a response spectrum. The proposed method gives accurate results even in cases of long isolation period and high isolation system damping, both of which give are characterized by highly non-proportional damping.

Future work includes:

1. Development of spectrum-based design procedures that give estimates of displacement *and* acceleration demand
2. Investigation of the relationship between linear and nonlinear response for isolated tall buildings considering MDOF representations
3. Quantification of the relative reliability of isolated tall buildings compared to conventional tall buildings in terms of probabilistic hazard analysis.

ACKNOWLEDGEMENTS:

The first author is grateful for research funding provided under the Global Center of Excellence (GCOE) Program at the Tokyo Institute of Technology.

REFERENCES:

Ariga T, Kanno Y, Takewaki I. [2006] "Resonant behavior of base-isolated high-rise buildings under long-period ground motions," *Struct. Design Tall and Special Bldgs*; **15**(3): 325–338.

Fu, Y. and Kasai, K. [1998] "Comparative Study of Frames Using Viscoelastic and Viscous Dampers," *J. Struct. Eng.*, ASCE, **124**(5): 513–522

Kani N. [2009] "Current State of Seismic Isolation Design," *J. Disaster Res.*; **4**(3): 175-181

Kasai, K., Yamashita, T., Yamazaki, Y., and Igusa, T. [2009] "Spectrum-Based Response Prediction of Asymmetric Structure with Supplemental Viscous Damper," *J. Struct. Constr. Eng.*, AIJ, **74**(636): pp. 225-234 (in Japanese)

Miyazaki M. [2009] "The Next Generation of Seismic Isolation: Going Beyond Seismic Design Dominated by Earthquakes," *J. Disaster Res.*; **3**(6): 479-502

Somerville, P., Anderson, D., Sun, J., Punyamurthula, S., and Smith, N. [1998] "Generation of Ground Motion Time histories for Performance-Based Seismic Engineering," *Proceedings*, 6th National Earthquake Engineering Conference, Seattle, WA

Takewaki I, Fujita K [2009] "Earthquake input energy to tall and base-isolated buildings in time and frequency dual domains," *Struct. Design Tall and Special Bldgs*; Online: 589-606

Takewaki I. [2007] "Robustness of base-isolated high-rise buildings under code-specified ground motions," The Structural Design of Tall and Special Buildings; **17**(2): 257–271

JOINT CONFERENCE PROCEEDINGS
7th International Conference on Urban Earthquake Engineering (7CUEE) &
5th International Conference on Earthquake Engineering (5ICEE)
March 3-5, 2010, Tokyo Institute of Technology, Tokyo, Japan

SCALING THE GROUND MOTION RECORDS IN ORDER TO ESTIMATE THE PROBABILISTIC SEISMIC DEMAND USING BAYESIAN STATISTICS

Mehdi Banazadeh[1] and Mehdi Mahdavi Adeli[2]

1) Assistant Professor, Dep. of Civil Engineering, Amirkabir University of Technology, Tehran, Iran
2) PhD Candidate, Dept. of Civil Engineering, Amirkabir University of Technology, Tehran, Iran
mbanazadeh@aut.ac.ir, mehmahad@yahoo.com

Abstract: A reliable estimation of seismic demand is an essential part of recently developed performance based earthquake engineering. In this estimation a probabilistic seismic demand model must be implemented to predict the mean value of the demand at the specific value of earthquake intensity measure parameter. To do so, however the full Incremental Dynamic Analysis (IDA) has been widely used by researchers, due to cumbersome and time consuming nature of IDA, it is not easily applicable to complicated structures. An unbiased model calibration and estimation of the unknown parameter through incorporating the results of nonlinear dynamic structural simulation subjected to minimum possible number of scaled ground motion records selected based on a bin strategy are a matter of concern in this paper. An attempt to replace full IDA-based estimation with an efficient, unbiased and fast probabilistic seismic demand analysis incorporating appropriate scale factors to a suit of ground motion records selected based on a bin strategy is carried out. It is shown that model estimation using only a single scale factor is achievable in the case of 3 and 6-sorey frames. For 9, 12 and 15-storey frames, the combination of scaled and un-scaled records can lead to reliable estimation of parameters.

1. INTRODUCTION

A reliable estimation of seismic demand is an essential part of recently developed performance based earthquake engineering. In this estimation the randomness and uncertainty in the ground motion and nonlinear structural response need to be considered. Because of these inherent uncertainties, a probabilistic methodology, which is usually called Probabilistic Seismic Demand Analysis (PSDA), is necessary to estimate the seismic demand of a structure at a designed site. PSDA is an approach to calculate the mean annual frequency (or annual probability) of exceeding a specified seismic demand for a given structure at a designed site (Cornell 1996). Although some different methods have been proposed to PSDA so far (Han and Wen 1997), today the suggested method by Cornell and co-workers (e.g., Bazzurro et al. 1998 and shome 1999) is the most applicable method to estimate seismic demand.

In short, this new method combines a ground motion Intensity Measure (IM) parameter (e.g., first mod spectral acceleration) hazard curve for the designed site, typically computed trough probabilistic seismic hazard analysis, with the demand (e.g., maximum inter-storey drift) resulted from Nonlinear Dynamic Analysis (NDA) of the given structure under a suite of earthquake ground motion records (Luco 2002). The approach is an application of the total probability theorem. In order to estimate the maximum inter-storey drift ratio of a specific structure, denoting by *DR* based on first mode spectral acceleration as IM parameter, denoted by *Sa*, the PSDA can be expressed mathematically as follows:

$$P[DR > x] = P[DR > x \mid Sa = y].\mid dH_{Sa}(y)\mid \qquad (1)$$

In this equation $P[DR > x]$ means annual frequency of *DR* exceeding the value *x*, $H_{Sa}(y)$ spectral acceleration hazard function at $Sa = y$, means annual frequency that *Sa* at a given site will equal or exceed value *y* and notation $|d\ldots|$ means its differential with respect to *Sa*, also evaluated at *y*.

The term $P[DR > x \mid Sa = y]$ means the probability of *DR* exceeding the value *x* given (i.e., conditioned on knowing) that *Sa* equals *y*. By assuming a normal distribution (Φ), for dispersion of naperian logarithm of drift along its mean, this probability can be calculated as:

$$P[DR > x \mid Sa = y] = 1 - \Phi\left(\frac{\mu(Sa = y) - \ln(x)}{\sigma}\right) \qquad (2)$$

In this equation μ and σ are the mean and standard deviation of selected probabilistic seismic demand model. A demand model is a mathematical expression relating the ground motion IM (here *Sa*) to the structure specific demand measure (here *DR*). The main purpose of using such a model is to predict the mean value of the demand, means μ, at the specific value of IM. Although selecting an applicable,

sufficient, efficient and effective demand model is a matter of concern until now (Mackie and Stojadinovic 2001), in this article, the following model, proposed by Cornell et al. (2002) based on extensive regression analysis of response of steel structures, is selected.

$$\ln(DR) = a.\ln(Sa) + w + \sigma.\varepsilon \quad (3)$$

Where epsilon is a normal random variable with median equal to zero and standard deviation equal to unity, σ is the unknown standard deviation of model and, a and w are the unknown model parameters.

All of these unknown parameters must be estimated based on the results of NDA of structure subjected to the selected ground motion records. In the other word, estimating the unknown standard deviation and model parameters required a database which consists of the results of NDA of designed structures subjected to the selected ground motion records. Incremental Dynamic Analysis (IDA) is a common approach to create such a database (Mackie and Stojadinovic 2001). To do so, however the full Incremental Dynamic Analysis (IDA) has been widely used by researcher, due to cumbersome and time consuming nature of IDA, it is not easily applicable to complicated structures. An unbiased model calibration and estimation of the unknown parameter through incorporating the results of nonlinear dynamic structural simulation subjected to minimum possible selected scaled ground motion records are a matter of concern in this paper. An attempt to replace full IDA-based model estimation with an efficient, unbiased and fast probabilistic seismic demand analysis incorporating appropriate scale factors to a suit of ground motion records selected based on a bin strategy is carried out in this research. The NDA results of scaled records are used to create the required database. Later through a state-of-the-art Bayesian regression analysis the model parameters are estimation and compared to those extracted from full IDA. Furthermore the ability of combination of scaled and un-scaled records to estimate the model parameter in a similar manner to the IDA results is investigated.

In order to consider both inherent randomness and uncertainty, associated with seismic events and response of structures, Bayesian regression analysis, which is a powerful tool to simultaneous modeling of randomness and uncertainty, is used to estimate all unknown parameters. Also the target structures are generic Steel Moment-Resisting Frames (SMRFs).

2. GENERIC SMRF

In this article, NDA is carried out using a family of two-dimensional single-bay generic SMRFs with number of stories equal to 3, 6, 9, 12 and 15, and first mode periods equal to 0.3, 0.6, 0.9, 1.2 and 1.5 second respectively. Some main characteristics of this family of frames are as follows, more details can be found in (Medina and Krawinkler 2005):

- The same mass is used at all floor level
- Relative stiffness are turned so that the first mode is straight line
- Plasticization just occurs at the end of the beams and the bottom of the first storey columns
- Frames are designed so that simultaneous yielding at all plastic hinge locations is attained under a parabolic (NEHRP, k=2) load pattern.
- Moment-rotation hysteretic behavior is modeled by using rotational springs with peak-oriented hysteretic rules and cyclic deterioration parameter equal to 30 and 3% strain hardening.

These frames are modeled using the opens system for earthquake engineering simulation (OpenSees 2009).

3. SELECION OF GROUND MOTION RECORDS

An appropriate estimation of seismic demand through NDA requires a suitable selection of ground motion records which must represent the seismic hazard condition of target territory at different return periods. In this article, using a bin strategy, 80 records are selected from the PEER Center Ground Motion Database (http://peer.berkeley.edu/smcat/) and are classified into four magnitude-distance bins for the purpose of time history analysis of SMRFs (Medina and Krawinkler 2003). The record bins are designated as follows:

- Large Magnitude-Short Distance Bin, LMSR, (6.5 < Mw < 7.0, 13 km < R < 30 km),
- Large Magnitude-Long Distance Bin, LMLR, (6.5 < Mw <7.0, 30 km < R < 60 km),
- Small Magnitude-Short Distance Bin, SMSR, (5.8 < Mw < 6.5, 13 km < R < 30 km), and
- Small Magnitude-Long Distance Bin, SMLR, (5.8 < Mw < 6.5, 30 km < R < 60 km).

4. ESTIMATION OF THE STANDARD DEVIATION AND MODEL PARAMETERS USING IDA RESULTS

In this section in order to create a widespread database, the 80 selected records are used in an IDA, the dynamic equivalent to familiar static pushover analysis. Given a structure and a ground motion, IDA is done by conducting a series of NDA. In this process the *IM* of ground motion (here *Sa*) is incrementally increase and the selected seismic demand parameter (here *DR*) is monitored during each analysis (Vamvatsikos and Cornell 2002). The extreme values of demand parameter are plotted against the corresponding value of the *IM* for each level to produce a database and then the unknown model parameters are estimated based on this database. In this section, using a scale factor which can be less, equal or more than one, the *Sa* of the records have been increased with 0.05g steps starting from 0.05g incrementally to reach a high level limit which leads to overall collapse of the modeled structure. Overall collapse is considered here as the ultimate limit state in which dynamic sideways instability in one or several stories of the structural system is attained or the drift of structure exceeds a value

which is defined as collapse in design codes (Ibarra and Krawinkler 2005, FEMA 350).

By following this process and removing the collapse cases, a database consists of 80 or less pairs of (*Sa* and *DR)* at each level is produced. This database, shown in figure 1 for 3 and 15-sroey frames for example, is applied to a Bayesian regression analysis to estimate the unknown standard deviation (σ) and model parameters (a and w) of defined demand model. These estimated results, listed in table 1, are the target values for estimation in later sections.

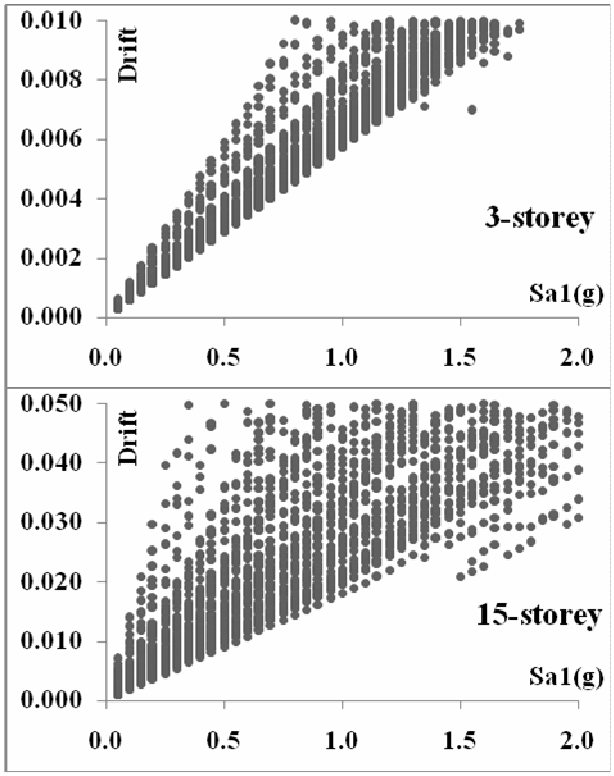

FIGURE 1 Examples of IDA results to estimate the unknown model parameters in 3 and 15-storey frames.

Table 1 Estimated model parameters (a and **w**) and standard deviation (SD) from IDA results, using Bayesian regression

		Number of Stories				
		3	6	9	12	15
Estimated Parameter	*w*	-5.91	-4.99	-4.36	-3.88	-3.52
	a	0.98	0.96	0.94	0.89	0.87
	SD	0.19	0.19	0.25	0.32	0.39

5. ESTIMATION OF THE STANDARD DEVIATION AND MODEL PARAMETERS USING SCALED GROUND MOTIONS RECORDS

In this section in order to scale the records and create 30 databases, 80 selected ground motion records have been multiplied by a scale factor, which is defined as an integer number between 1 and 30. Then each scaled bin including 80 records are incorporated into a NDA. Then a data base is assembled collecting pairs of the drift and corresponding *Sa*. Most of the time the original ground motion are not strong enough to impose collapse in structures, however when multiplied with a large scale factor, it would be possible that some ground motion records lead to overall collapse of structure. These points are removed from the corresponding database, so in some databases the number of points remained to estimate the model parameters is less than 80. In figure 2 the number of remained points at each database for different frames and scale factor are shown.

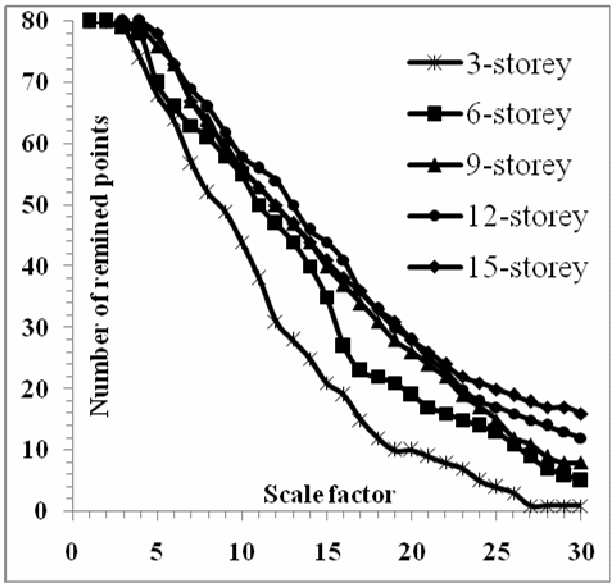

FIGURE 2 Number of remained points at each database for different frames and scale factor.

Applying Bayesian regression analysis for each scaled bin consisting the output of NDA through scaled ground motion records, is used to estimate the model parameters (a and w) and standard deviation for each frame. Figures 3, 4, 5, 6 and 7 show these parameters by discrete points and their comparison to the parameters that estimated from IDA results, which are represented by a solid line. Generally the following hints can be concluded form this figure:

- In 3-storey frame, applying a scale factor less than 7 to a suit of 80 ground motions selected based on a bin strategy, and implementation of the Bayesian regression estimation of the drift probabilistic model in the format of equation 3 would result in an adequately similar estimation to the ones out of a full IDA, specially for the parameter (a) which is the slope of the *Sa-DR* equation in a logarithmic space. Using a larger scale factor, however, will reduce the value of (a) and increase the value of (w) with an indistinct trend which is due to the fact that more ground motion would impose

severe nonlinear behavior and in some cases collapse to the structure. Evaluation of model dispersion in term of Standard Deviation (SD) through applying different scale factors would result in very close SD to the one extracted from IDA in the range of 4 to 6.

- In 6-storey frame, increasing the scale factor, results in a raise to (a) and a decrease to (w) in the same way observed in 3-storey structure. The scale factor of 3 and 4 will produce the same value for (a) and (w). However, regarding SD, the scale factor of 6 and 7 results in the same SD out of IDA.
- In 9-storey frame, although scale factor of 3,4 and 5 cause a very satisfactory value for (w) in comparison to IDA, there is no distinct scale factor resulting a similar value for (a). Roughly concluding, the scale factor 4 can be suggested for estimation the parameter (a) and (w) while there is no single scale factor can be regarded for estimation the value of SD. It can be attributed to more complicated nonlinear behavior resulted from upper vibration model in 9-storey frame before reaching the overall collapse.

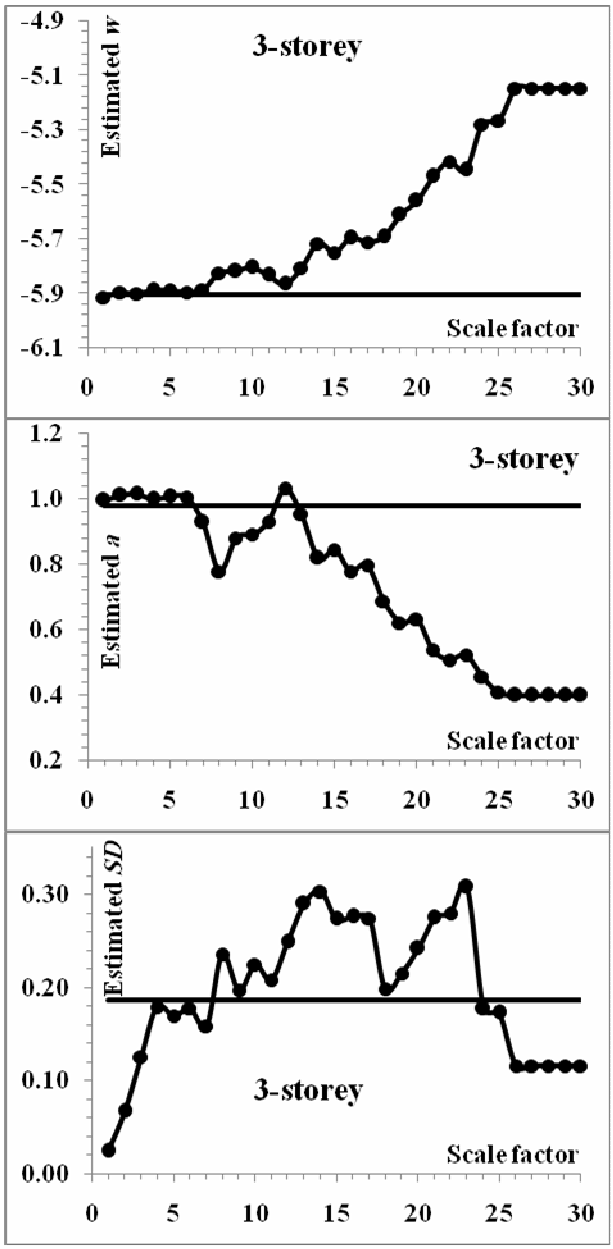

FIGURE 3 Estimated model parameters (a and w) and standard deviation (SD) from NDA results of scaled record, using Bayesian regression and comparison to IDA estimated parameters (solid line) in 3-stoery frame.

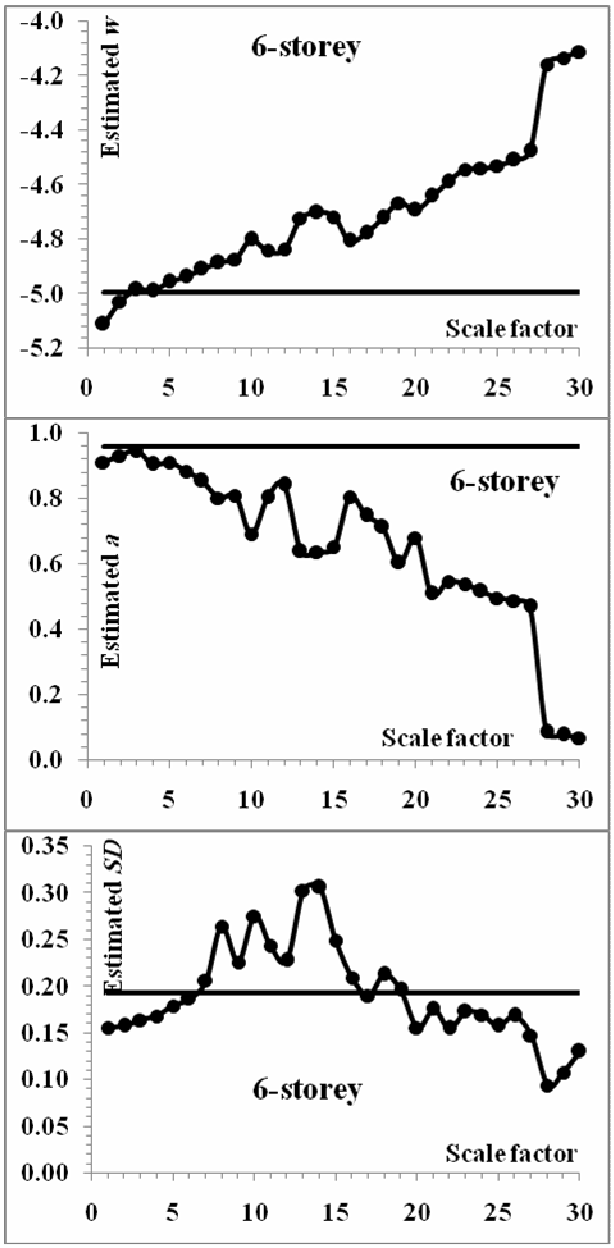

FIGURE 4 Estimated model parameters (a and w) and standard deviation (SD) from NDA results of scaled record, using Bayesian regression and comparison to IDA estimated parameters (solid line) in 6-stoery frame.

- In 12-storey frame applying a scale factor of 5 to 8 would result in a similar (w) while there is no single factor for estimation of (a). SD can be produced with scale factors less than 4 with adequate accuracy. It can again be attributed to more complicated nonlinear behavior resulted from upper vibration model in 12-storey frame before reaching the overall collapse. Since the drift model for taller frames has two near to linear part, the data base must be included the un-scaled records along with the scaled ones (Gardoni et al. 2002).

- In 15-storey frame, using a scale factor of 6 will result in the same estimation for (w). The value of (a) has been estimated less than the one form IDA for all factors in the range of 1 to 30. The trend of SD is however more or less irregular and no single factor can be introduced for producing SD within acceptable accuracy. The observed difference between the estimated parameters in this case and estimated parameters from IDA results is higher in comparison with other cases.

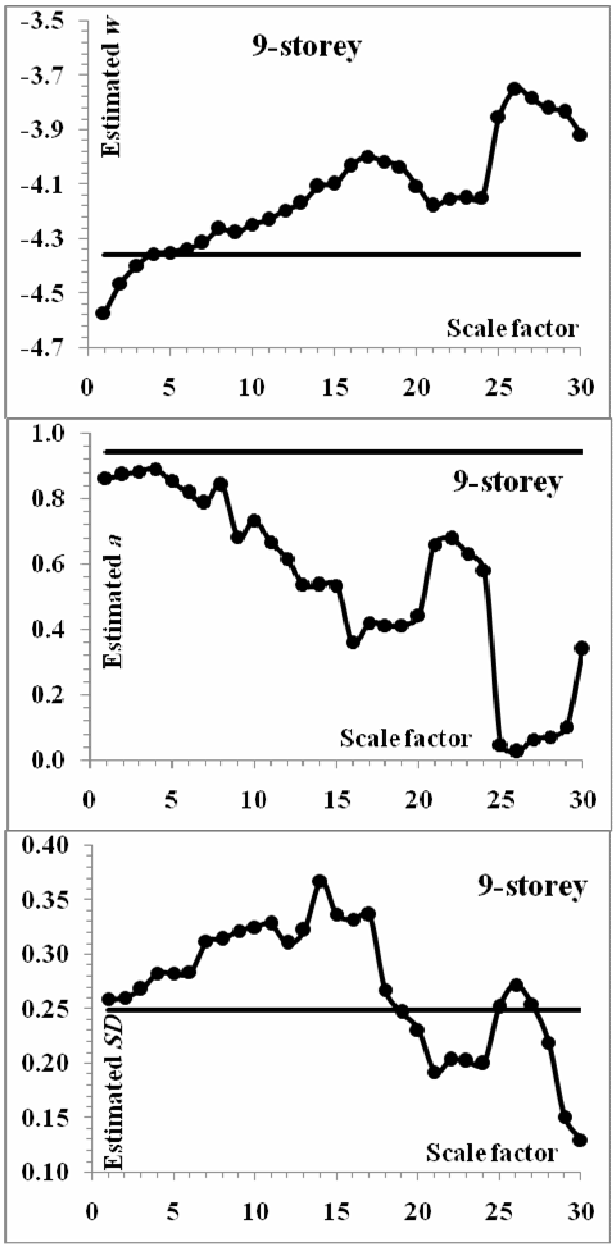

FIGURE 5 Estimated model parameters (a and w) and standard deviation (SD) from NDA results of scaled record, using Bayesian regression and comparison to IDA estimated parameters (solid line) in 9-stoery frame.

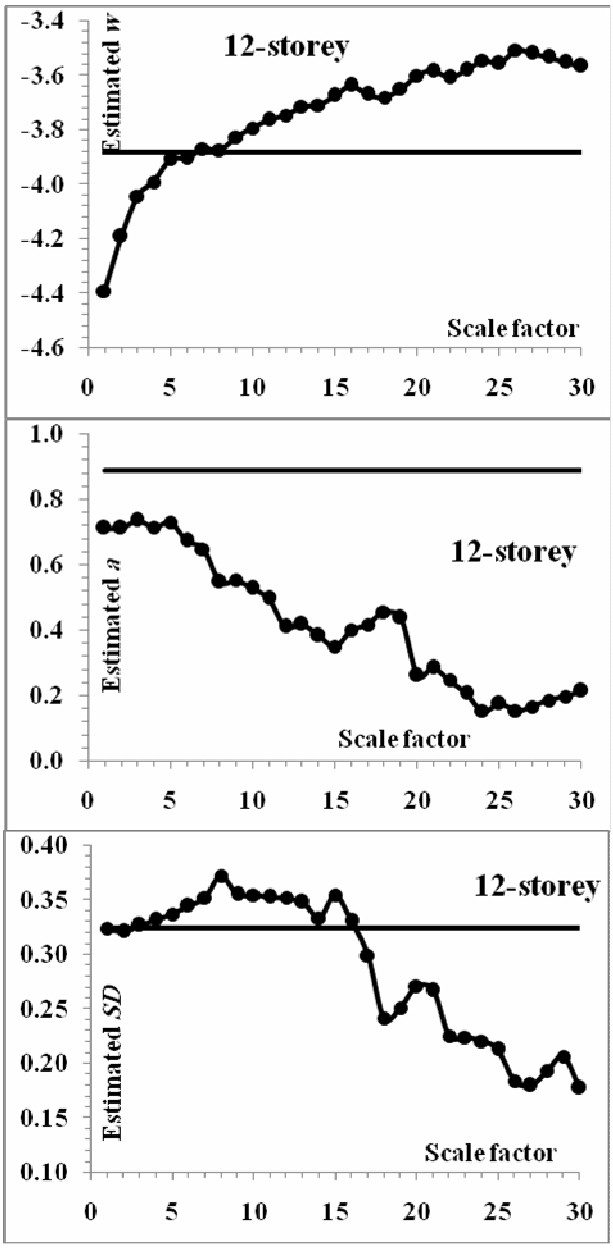

FIGURE 6 Estimated model parameters (a and w) and standard deviation (SD) from NDA results of scaled record, using Bayesian regression and comparison to IDA estimated parameters (solid line) in 12-stoery frame.

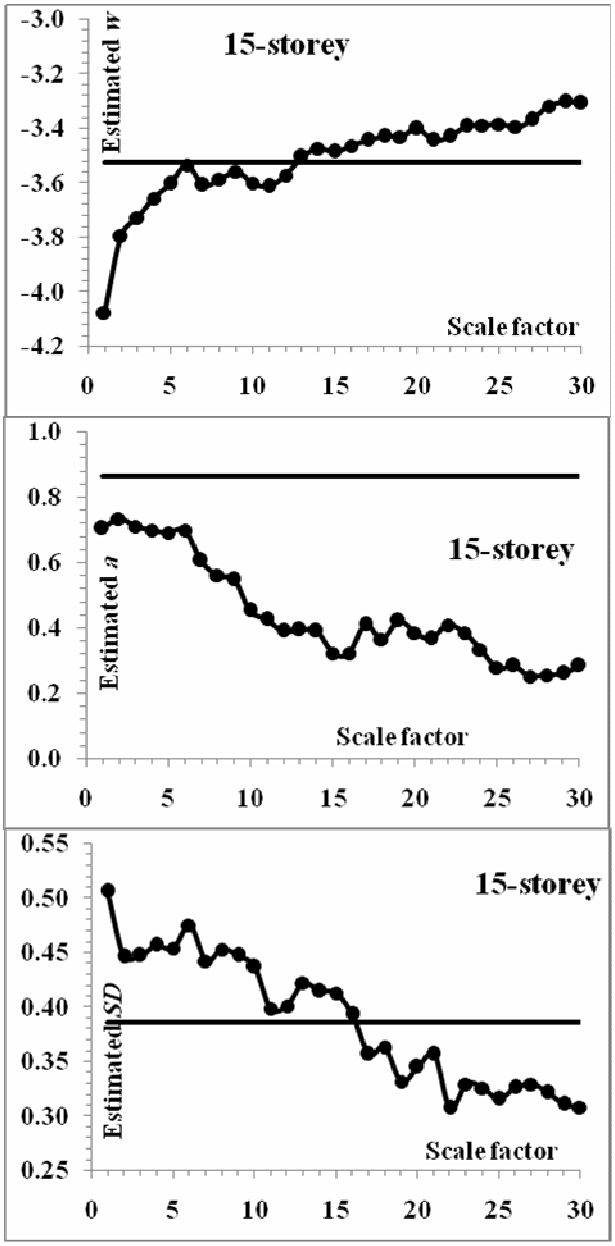

FIGURE 7 Estimated model parameters (a and w) and standard deviation (SD) from NDA results of scaled record, using Bayesian regression and comparison to IDA estimated parameters (solid line) in 15-stoery frame.

6. ESTIMATION OF THE STANDARD DEVIATION AND MODEL PARAMETERS USING COMBINATION OF SCALED AND UN-SCALED GROUND MOTIONS RECORDS

As seen in the previous section, although it is possible to find the scale factors those using to scale the records can lead to estimate model parameters similar to IDA estimated parameters in the case of 3 and 6-storey frames, in the case of 9, 12 and 15-storey frames there is no such a scale factor. In this section instead of using a group of scaled records, a combination of scaled and un-scaled ground motion (or the records scaled with scale factor equal to 1) is used to create the databases to estimate the parameters. Because of removed overall collapse cases from data points, each database consists of 160 or less data points. Using these databases in a Bayesian regression analysis to estimate the standard deviation and model parameters lead to remarkable results, which are shown in figures 8, 9, 10, 11 and 12. In order to compare the results by previous section the charts were drawn in same scale. Generally the following hints can be concluded form these figures:

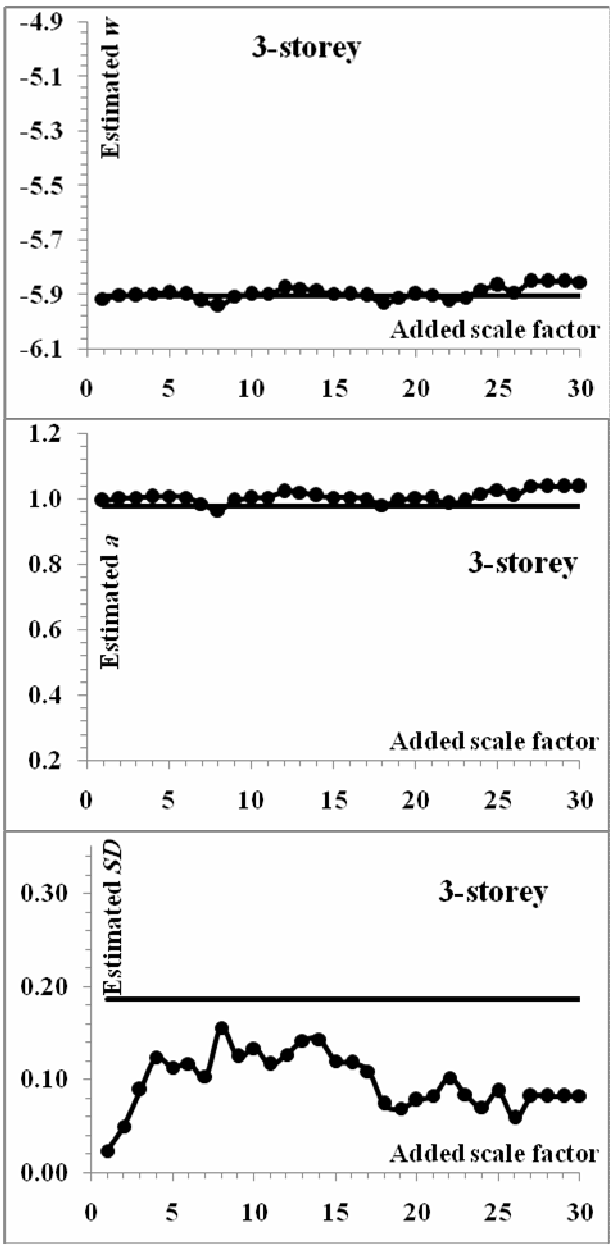

FIGURE 8 Estimated model parameters (a and w) and standard deviation (SD) from NDA results of combination of scaled and un-scaled record, using Bayesian regression and comparison to IDA estimated parameters (solid line) in 3-stoery frame.

- In 3-storey frame combination of the un-scaled records selected with the ones scaled with any value less than 25 would result in unbiased and accurate (a) and (w) comparing to the ones calculated through IDA. However SD calculated through IDA is slightly larger than the one calculated by above methodology.
- In 6-storey surprisingly scaling the ground motions with any factor less than 25 and mixing it with the un-scaled records would result in a unbiased and completely accurate estimation for (a), (w) and SD comparing those from IDA.
- In 9 & 12-storey frame, scaling the ground motions with any factor between 4 and 18 and combining it with the un-scaled records would result in an unbiased estimation for (a) and (w) comparing those from IDA. The estimated SD is always biased to a larger value comparing to that of calculated form IDA.
- In 15-storey frame the same trend for estimation of (a) and (w) has been observed with reservation that the SD is tangibly larger than the one calculated form IDA.

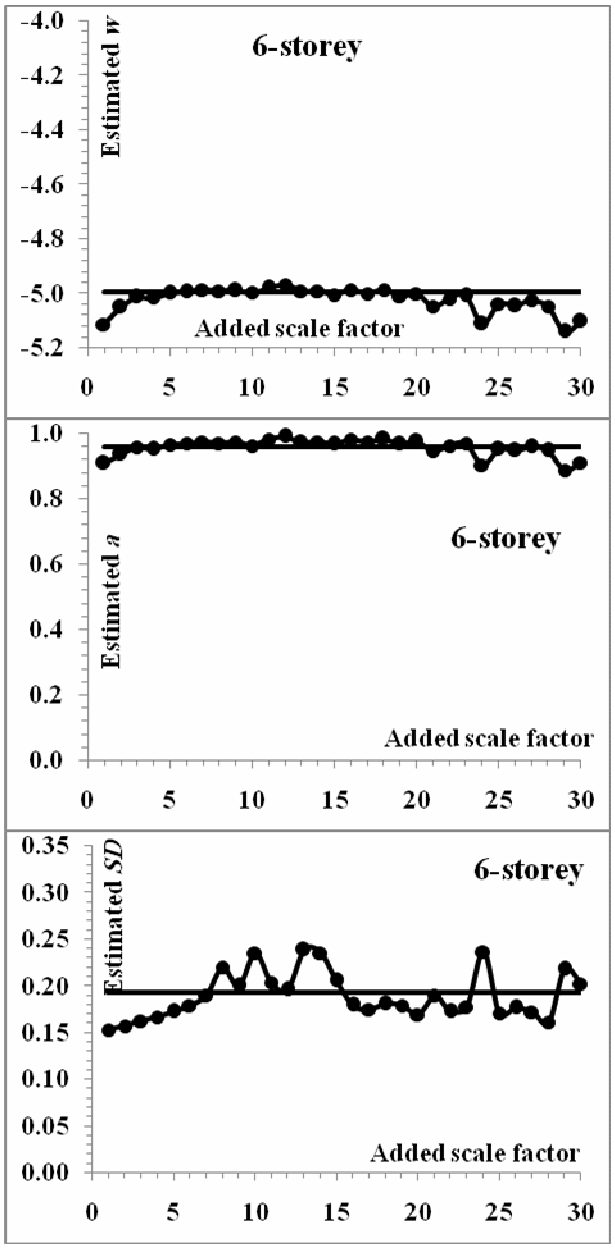

FIGURE 9 Estimated model parameters (a and w) and standard deviation (SD) from NDA results of combination of scaled and un-scaled record, using Bayesian regression and comparison to IDA estimated parameters (solid line) in 6-stoery frame.

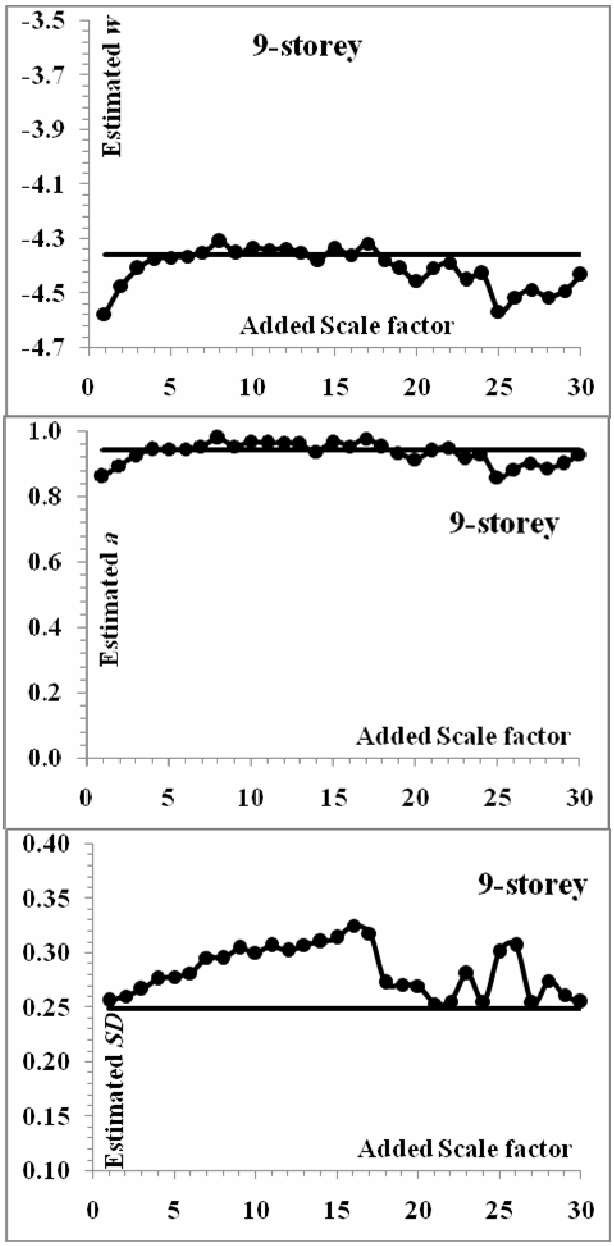

FIGURE 10 Estimated model parameters (a and w) and standard deviation (SD) from NDA results of combination of scaled and un-scaled record, using Bayesian regression and comparison to IDA estimated parameters (solid line) in 9-stoery frame.

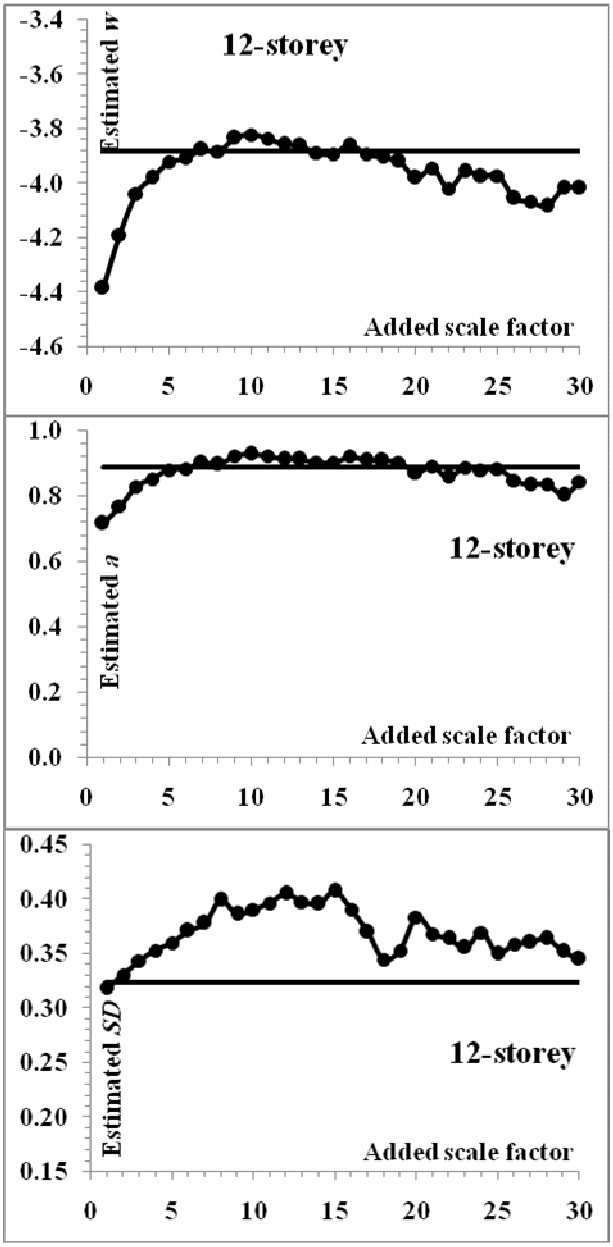

FIGURE 11 Estimated model parameters (*a* and *w*) and standard deviation (SD) from NDA results of combination of scaled and un-scaled record, using Bayesian regression and comparison to IDA estimated parameters (solid line) in 12-stoery frame.

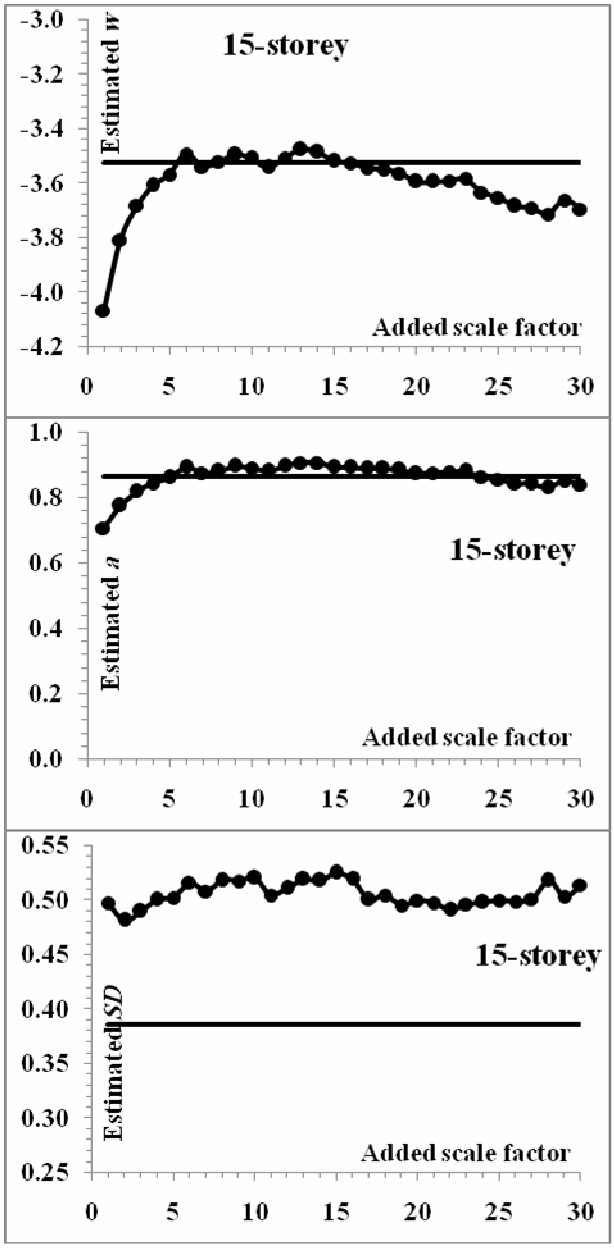

FIGURE 12 Estimated model parameters (*a* and *w*) and standard deviation (SD) from NDA results of combination of scaled and un-scaled record, using Bayesian regression and comparison to IDA estimated parameters (solid line) in 15-stoery frame.

7. CONCLUSIONS

In this article a Fast, reliable and efficient methodology for probabilistic seismic drift demand estimation through implementing a single scale factor into a suit of seismic ground motions selected based on bin strategy has been proposed. This method in some way can be a substitute for a full cumbersome Incremental dynamic Analysis (IDA) especially for complicated structures. Here the basis for efficiency assessment of the proposed scale factor is the similarity of model parameter estimated using a single or combined scaled bins with those extracted through full IDA-based model estimation.

The model selected as the seismic drift demand model in this study is the model that estimates the drift based on first mode spectral acceleration and can be defined in the format of the Eq. (3) and its unknown model parameters and standard deviation can be estimated based on the results of nonlinear dynamic analysis of the selected ground motion records. The full Incremental Dynamic Analysis (IDA) has

been widely used by researcher; however, due to cumbersome and time consuming nature of IDA, it is not easily applicable to complicated structures. It has been concluded that in low rise generic steel moment-resisting models (3 and 6-storey), a scale factor around 5 can adequately estimate the model parameters (*a* and *w*) and its standard deviation (σ). This can be attributed to brittle and stiff behavior of low rise frame and exhibition of near to linear behavior before the overall collapse point. The ductile behavior of mid to high rise models (9, 12 and 15-storey), on the other hand, causes somehow more complicated trend to find a single scale factor. Overcoming this problem, in this paper, it has been shown that a combination of the un-scaled bin with the one scaled with an adequate factor can lead to a surprisingly similar results comparing to the ones extracted from IDA. The adequate scale factor for these models can be suggested to be an integer between 5 and 15. As a general conclusion, the results of this study show that using the appropriate combination of scaled and un-scaled ground motion records in nonlinear dynamic analysis leads to results which can be used as replacement of results of laborious IDA method to estimate the seismic demand. This new method can be a beneficial progress in performance based design engineering. Further investigation on different drift models as well as ground motion suits, however, is needed to endorse the result of this paper in more extent.

References:

Bazzurro P., Cornell C. A., Shome, N. and Carballo J. E. (1998), "Three proposals for characterizing MDOF nonlinear seismic response," *Journal of Structural Engineering*, **124**(11), 1281-1289.

Cornell, C.A. (1996), "Calculating building seismic performance reliability: a basis for multi-level design norms," *Proceedings of the 11th World Conference on Earthquake Engineering*, Paper No. 2122, Acapulco, Mexico

Cornell, C. A., Jalayer, F., Hamburger, R. O. and Foutch, D. A. (2002), "Probabilistic basis for the 2000 SAC Federal Emergency Management Agency steel moment frame," *Journal of Structural Engineering*, **128**(4), 526-533.

FEMA 350, (2000), "Recommended seismic design criteria for new steel moment-frame buildings," *Report No. FEMA-350*, SAC Joint Venture, Federal Emergency Management Agency, Washington, DC.

Gardoni, P., Der Kiureghian, A. and Mosalam K. M. (2002), "Probabilistic models and fragility estimates for bridge components and systems," *Report No. PEER 2003-13*, University of California at Berkeley, Berkeley, California.

Han, S. W., and Wen Y. K., (1997), "Method of reliability-based seismic design. I: Equivalent nonlinear systems," *Journal of Structural Engineering* **123**(3), 256-263.

Ibarra, L. F. and Krawinkler, H. (2005), "Global Collapse of Frame Structures under Seismic Excitations," *Report No. PEER 2005-05*, University of California at Berkeley, Berkeley, California.

Luco, N. (2002), "Probabilistic seismic demand analysis, SMRF connection fractures, and near source effects," *Ph.D. Thesis*, Department of Civil and Environmental Engineering, Stanford University, Stanford.

Mackie, K. and Stojadinovic, B. (2001), "Probabilistic seismic demand model for California highway bridges," *Journal of Bridge Engineering,* **6**(6), 468-481.

Medina, R. A. and Krawinkler, H. (2003), "Seismic demands for non-deteriorating frame structures and their dependence on ground motions," *Report No. 144*, Stanford University, Stanford.

Medina, R. A. and Krawinkler, H. (2005), "Evaluation of drift demands for the seismic performance assessment of frames," *Journal of Structural Engineering*, **131** (7), 1003-1013.

OpenSees (2009), "Open System for Earthquake Engineering Simulation," *Pacific Earthquake Engineering Research Center*, http://peer.berkeley.edu/

Shome, N. (1999), "Probabilistic seismic demand analysis of nonlinear structures," *Ph.D. Thesis*, Department of Civil and Environmental Engineering, Stanford University, Stanford.

Vamvatsikos, D. and Cornell C. A. (2002), "Incremental dynamic analysis," *Earthquake Engineering & Structural Dynamics*, **31**(3), 491-514.

JOINT CONFERENCE PROCEEDINGS
7th International Conference on Urban Earthquake Engineering (7CUEE) &
5th International Conference on Earthquake Engineering (5ICEE)
March 3-5, 2010, Tokyo Institute of Technology, Tokyo, Japan

EVALUATION OF THE DYNAMIC PRESSURE ENVELOPES IN EMBEDDED STORAGE TANKS UNDER NEAR FIELD EARTHQUAKES

Fayaz R. Rofooei[1)], Nader K. A. Attari[2)], and Navid K. A. Attari[3)]

1)Professor, Department of Civil Engineering, Sharif University of Technology, Tehran, Iran
2) Assistant Professor, Building and Housing Research Center (BHRC), Tehran, Iran
3) Graduate student, Department of Civil Engineering, Rensselaer Polytechnic Institute, *N.Y., USA*
rofooei@sharif.edu, n.attari@bhrc.ac.ir, khajen@rpi.edu

Abstract: The dynamic behavior of embedded rectangular storage tanks under near and far field earthquakes is investigated taking into account both soil-structure and fluid-structure interactions. Considering a bounded soil domain, transmitting boundaries are used in proper distance to prevent the wave reflection at the boundaries. Contact elements are used in the soil-structure interface to include the surface separation and the friction between the tank's sides and the surrounding soil. The fluid behavior is considered Eulerian, while the soil's nonlinear characteristics is modeled using the elasto-plastic Dracker-Prager criteria. Nonlinear dynamic analyses carried out using near and far field earthquake records. The resulting dynamic soil and fluid pressure envelopes are compared with those obtained from pseudo-static methods. The near field effects on the dynamic soil and fluid pressure envelopes have been investigated.

1. INTRODUCTION

The hydrodynamic interaction between fluid and structure, the surrounding soil medium, the soil boundaries as a state of semi infinite medium, and possible sliding and separation at the interfaces of the buried structure and the soil are among the major issues to be considered in modeling and analyzing the dynamic behavior of buried fluid-storage tanks. Due to large number of parameters involved, the dynamic time history analysis of the whole system could become extremely difficult and time consuming. Therefore, various attempts have been made to simplify the modeling process, while preserving the required level of accuracy. The added mass method is one of these approaches, which widely is employed in various engineering applications. Housner formulated a simplified model for fluid's behavior in rigid cylindrical and rectangular tanks under seismic excitation. He presented an equivalent added mass model that could properly estimate the forces and the moments exerted by fluid on the tank's side walls [Housner 1957]. Housner and Haroum [Haroun1982] and Cho et al. [Cho 2001] have extended that model to include flexible tanks. They divided the fluid hydrodynamic pressure in rigid containers to the impulsive fluid that moves rigidly with tank's body and the convective fluid that experiences sloshing at the fluid's free surface. The latter can be modeled using a number of mass-spring and/or dashpots.

On the other hand, the Lagrangian and Eulerian finite elements are commonly used for modeling the behavior of the fluid continuum. In Eulerian approach [Morand 1995, Ohayon2001, Pal 1999, Chen 1999], the system is divided in two separate domains. The velocity or pressure potential function describes the fluid behavior, while the displacement domain describes the structural movement. This method leads to a coupled system of equations of motion with unsymmetrical matrices that could numerically be solved using a number of available techniques developed for these types of equations.

Lagrangian approach [Hamdan 1999, Bermudez 2001, Virella 2008], describes both the fluid and structural movements in the same displacement domain. The static and dynamic compatibility and equilibrium conditions are then automatically satisfied at the boundaries. The Lagrangian formulation is usually employed to predict the transient response of systems with fluid–structure interaction and complex boundary conditions under small fluid motions, while the Eulerian method is appropriate for modeling the systems with large fluid motions. Mixed Eulerian –Lagrangian method is also used in some studies [Silva Santos 2007].

For the surrounding soil, considering unbounded soil domain is not practical, thus making it necessary to prevent the wave reflection at the boundaries of the finite soil medium [Livaoglu 2008]. For this purpose, local boundaries such as transmitting, absorbing or non-reflective boundaries can be used. The simplest type of local absorbing boundaries was presented by Lysmer and Kuhlimer in 1969. This model is independent from the external excitation frequencies and applicable in time domain. After the introduction of transmitting boundaries by Lindman in 1975, different types of boundaries have been proposed by researchers. Kellezi presented transmitting boundaries using first order operators that clearly have a better performance in comparison to the simple absorbing boundaries [Kellezi 2001].

The long-period directivity pulse (rupture directivity) and the fling step are probably the most important characteristics of the near-source strong ground motions in earthquake engineering [Hisada 2004, Somerville 1997]. Earthquake rupture towards a site tends to produce a short-duration, large amplitude "pulse" of motion that is called forward directivity. Fling step is associated with the permanent displacement that occurs across a ruptured fault, and involves a large, unidirectional velocity pulse to accommodate this displacement in the slip-parallel direction. The rupture directivity affects intensity measures related to the duration or long-period energy content of ground motions, while the fling step affects their peak velocity and displacement. Nonlinear structural analyses have shown the velocity pulse of the forward directivity as the most damaging to structures [Abrahamson 2001].

In mathematical modeling of the problem, both the soil-structure and fluid-structure interactions are considered. Using contact element for modeling the soil-structure interface, the Lagrange multiplier method in normal direction and penalty function method in tangent direction are implemented in soil-structure interfaces to allow the surface separation and formation of the friction forces between the tank walls and the soil. Having placed the transmitting boundaries with the proper distance from the tank, the Drucker-Prager criterion which is an elastic-perfectly plastic model is considered for modeling the soil's nonlinear behavior.

The objective of this study is to determine the dynamic soil and fluid pressure envelopes caused by the near and far field earthquakes along the buried and semi-buried tank walls. The results are compared with those obtained using the pseudo-static methods. Also, the effects of the near field earthquakes on the envelope of the lateral dynamic soil and fluid pressures have been investigated. Numerical simulation were carried out using seven near source and far source earthquake excitations. ANSYS program is used for numerical analyses.

2. Modeling

2.1 The Fluid-Structure Interaction

The governing differential equation for non-viscous and irrotational fluid domain is the following Helmholtz equation:

$$\frac{1}{c^2}\frac{\partial^2 P}{\partial t^2} - \nabla^2 P = 0 \qquad (1)$$

In the above equation, P and c represent the pressure and the sound propagation speed in fluid respectively. The governing differential equation of the structural domain is:

$$\sigma_{i,jj}(u) + \rho_s \ddot{u}_i = 0 \qquad (2)$$

in which $\sigma_{i,jj}$, $\ddot{u}_i$ and ρ_s are structure's stress, acceleration and density respectively. According to Eulerian theory, the interaction between the fluid pressure and the structural displacement can be defined with the following equation,

$$\{n\}.\{\nabla P\} = -\rho\{n\}\frac{\partial^2\{u\}}{\partial t^2} \qquad (3)$$

where {n} is the normal unit vector to the fluid – structure interface. Using Eqs. (1) and (2), and considering the fluid – structure interaction from Eq. (3), yields to the following equations:

$$\begin{bmatrix}[M^s] & [0]\\ [M^i] & [M^f]\end{bmatrix}\begin{Bmatrix}\{\ddot{u}\}\\ \{\ddot{p}\}\end{Bmatrix} + \begin{bmatrix}[K^s] & [K^i]\\ [0] & [K^f]\end{bmatrix}\begin{Bmatrix}\{u\}\\ \{p\}\end{Bmatrix} = \begin{Bmatrix}\{F\}\\ \{0\}\end{Bmatrix} \qquad (4)$$

$$[M^i] = \rho.[R]^T \quad [K^i] = -\rho.[R] \qquad (5)$$

where $[M^s]$, $[K^s]$, $[M^f]$, $[K^f]$ are the structural mass, structural stiffness, fluid mass and fluid stiffness matrices respectively. Also, $[M^i]$ and $[K^i]$ are the coupling terms in the mass and stiffness matrices of the system, $\{N\}$ is fluid elements shape function and $[R]$ is the so-called fluid–structure interaction matrix, which is derived from the following equation [*Zienkiewicz* 1991]:

$$\rho.[R] = \rho\int_S \{V\}\{n\}^T\{N\}^T.dS \qquad (6)$$

2.2 Structural modeling in soil medium, Direct Solution

In the direct solution of a structural model located in a soil medium, the structure and the surrounding soil medium are modeled and analyzed together in each step. The most important advantage of this method is its ability in considering the nonlinear behavior of soil. In this method, different types of boundary conditions are employed for considering a finite domain instead of unbounded soil media. Boundary conditions, like roller support, reflect the incoming waves from the structure back into the domain, leading to considerable error in results. In order to prevent the wave reflection, viscous energy absorbent boundaries are used in this study. Using one-dimensional wave propagation theory in a 3-D domain and adopting the Lysmer approach, one can assume that the P and the S waves are propagated in a cone shape at Z direction:

$$u(z,t) = \frac{1}{\sqrt{z}} f(z - C_S t)$$
$$w(z,t) = \frac{1}{\sqrt{z}} f(z - C_P t) \qquad (7)$$

In which C_p and C_s are calculated from the following equation:

$$C_P = a.\rho.V_p.A \quad , \quad C_S = b.\rho.V_s.A \tag{8}$$

In the above equation, V_s and V_p are shear and pressure wave velocities respectively, by (a) and (b) being non-dimensional parameters. Using these equations, the stress-strain relationships at the boundaries can easily be obtained. For example the strain-stress relation for the S waves is:

$$\tau(z,t) = \mu\gamma = \rho {C_S}^2 u_{,Z} = \rho {C_S}^2 \left(\frac{-1}{2\sqrt{Z}} f + \frac{1}{\sqrt{Z}} f' \right) \tag{9}$$

where, τ, μ and γ are the shear stress, shear modulus and shear strain respectively. The velocity of the domain's particles caused by the wave propagation is:

$$u_{,t}(z,t) = -\frac{C_S}{z} f'(z - C_S t) \tag{10}$$

and the shear stress at the boundaries are obtained from the following equation:

$$\tau(z,t) = -[\frac{\rho {C_S}^2}{2z} u(z,t) + \rho C_S u_{,t}(z,t)] \tag{11}$$

The governing differential equations for the P wave can be obtained in a similar manner. Using Eqs. (9-11), the stress-strain relationship at the boundaries can be derived as follow:

$$\left[\frac{\partial}{\partial t} + \frac{C_S}{2z} + C_S \frac{\partial}{\partial z} \right] u = 0$$
$$\left[\frac{\partial}{\partial t} + \frac{C_P}{2z} + C_P \frac{\partial}{\partial z} \right] w = 0 \tag{12}$$

In which, u and w are the lateral and normal components of velocity amplitude. Using the above equations, one could arrive at:

$$\{\sigma\} = [D_K]\{u\} + [D_C]\{u_{,t}\} \tag{13}$$

where the damping and stiffness matrices are defined as:

$$[D_C] = \rho C_P(n.r)[N] + \rho C_S(n.r)\{[I] - [N]\} \tag{14}$$

$$[D_K] = \frac{\rho {C_p}^2}{2r}(n.r)[N] + \frac{\rho {C_S}^2}{2r}(n.r)\{[I] - [N]\} \tag{15}$$

In the above equations, "r" represents the distance between the boundaries and the source of vibration. This type of boundaries is called Transmitting boundaries [*Kellezi* 2001]. As it was mentioned before, a comprehensive pressure dependent model such as Drucker-Prager is suitable for certain soil type such as aggregates. Finally, as it was mentioned before, the contact element is used between the tank walls and the surrounding soil to model the existing friction between them.

3. Numerical Examples

In this study, a 2-D, $10m \times 5.4m$ partially filled rectangular water tank is considered. The dynamic behavior of the embedded tank is investigated in two different cases: fully embedded with 5 meters of overlaying soil and the semi-embedded without any overlaying soil. The dimensions of the soil medium is $40m \times 100m$ and the level of water inside tank is assumed to be 5.0m.

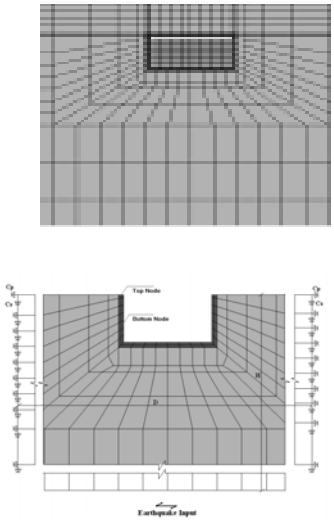

Figure 1. Embedded and Semi- Embedded tank models

Two layers of elements are considered within the wall thickness to model their flexural behavior. The roof-wall connections are assumed to be clamped for the fully embedded case. The plain strain elements were used for modeling the tank body, while Eulerian elements were considered for the fluid medium (Figure 1). Also, the soil nonlinear behavior is considered to follow the Dracker-Prager criteria. The transmitting boundaries are placed in a proper distance from the tanks to prevent wave reflection.

The friction between the tank's walls and soil is assumed to be $\mu = tg(2/3\varphi)$. The displacement time histories of the horizontal earthquake excitations are applied to the nodes underneath the soil domain which is assumed to be the seismic bedrock. Tables (1) and (2) shows the 7 near source and 7 far source earthquake excitations used for the parametric studies. The records are scaled in a way that the ground level PGA be equal to 0.4g. Also, the fluid surface pressure is assumed to be zero. The density, the Poisson ratio and the yield strength of concrete is assumed to be 2400 kg/m^3, 0.15 and 350 kg/m^2 respectively. Material damping in soil media is considered to be 5% for the first and third vibration modes of the system using the Rayleigh damping. Parametric studies carried out to evaluate the effect of the near field earthquakes and the overlaying soil on the dynamic soil and fluid pressure envelopes along the tank walls.

Table 1 Near field earthquake excitations

N	Station, Earthquake	Mag. (M)	PGA	PGV	PGD	Closest fault rupture(km)
1	Gilroy Array #1 Loma Prieta. 1989	6.9	0.473	33.9	8.03	11.2
2	Whitewater Trout FarmN. Palm Springs 1986	6.0	0.612	31.5	4.58	7.3
3	LucerneLanders 1992	7.3	0.785	31.9	16.42	1.1
4	Cape Mendocino Cape Mendocino 1992	7.1	1.497	127.4	41.01	8.5
5	Pacoima Dam (upper left)Northridge 1994	6.7	1.585	55.7	6.06	8.0
6	Pacoima DamSan Fernando 1971	6.6	1.226	112.5	35.5	2.8
7	TCU084Chi-Chi, Taiwan 1999	7.6	1.157	114.7	31.43	10.39

Table 2 Far field earthquake excitations

N	Station,Earthquake	Mag. (M)	PGA	PGV	PGD	Closest fault rupture(km)
1	TCU047 Chi-Chi, Taiwan 1999	7.6	0.413	40.2	22.22	33.01
2	Hayward - BART Sta Loma Prieta 1989	7.1	0.159	15.1	3.72	58.9
3	Coolwater Landers 1992	7.3	0.417	42.3	13.76	21.2
4	Lake Hughes #12 San Fernando 1971	6.6	0.366	17.0	1.65	20.3
5	Silent Valley - Poppet F N. Palm Springs	6.0	0.139	3.9	0.55	25.8
6	N Hollywood - Coldwater Can Whittier Narrows 1987	6.7	0.25	14.3	1.11	30.8
7	San Gabriel - E. Grand Ave Northridge 1994	6.7	0.256	9.8	2.79	41.7

4. Results

Figures 2-3, compare the dynamic fluid pressure envelope along the fully and semi-embedded tank walls for the near and far field earthquakes, as well as their mean and mean± standard deviation. Figure 4 shows the dynamic soil pressure envelope for the semi-embedded tank, while Figure 5 illustrates the results for the embedded tank under near and far field earthquakes. As the results indicate, the near field responses have smaller standard deviations in comparison to that of far field earthquakes.

Figure 6 compares the average dynamic fluid pressure for near and far fields earthquakes. As it is shown, the fluid pressure envelope is larger for the near source earthquakes. The difference is more clear for the semi-embedded tanks. Comparison of Figures 7a and 7b shows that the fluid pressure in semi-embedded tanks especially under the near field earthquakes has larger amplitudes.

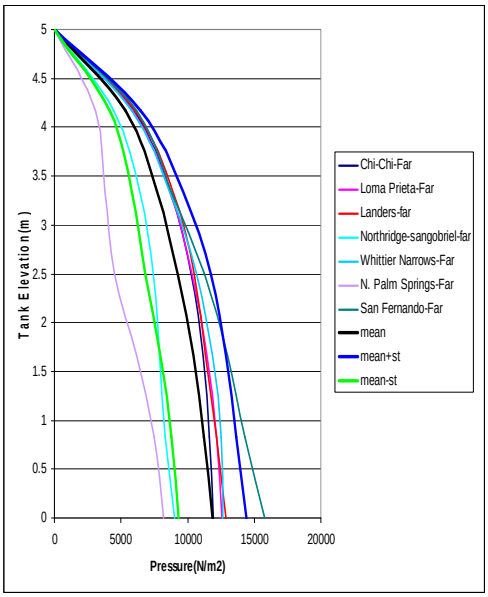

(a)

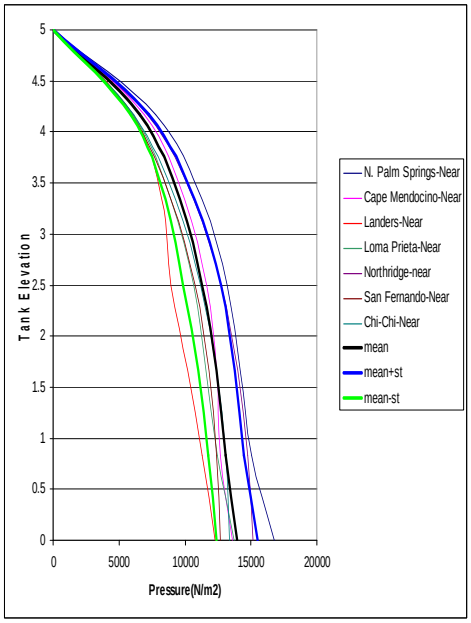

(b)

Figure 2: The dynamic fluid pressure envelope along the semi-embedded tank walls; (a) far field; (b) near field

The dynamic soil pressure for near and far source earthquakes are shown in Figure 8. Results indicate that near field earthquakes cause larger dynamic soil pressure on the tank's wall in both semi- embedded and embedded tanks. As Figure 9 show, the dynamic soil pressure in embedded tanks is specifically larger than semi- embedded tanks.

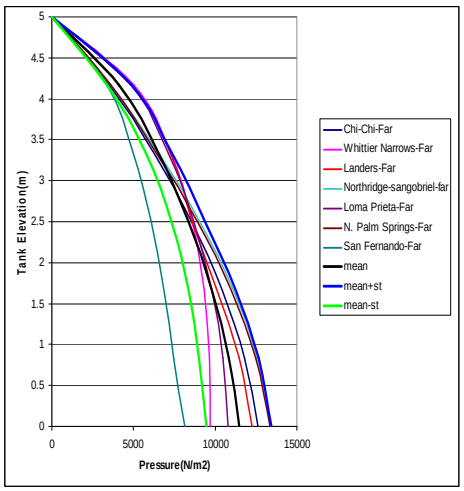

(a)

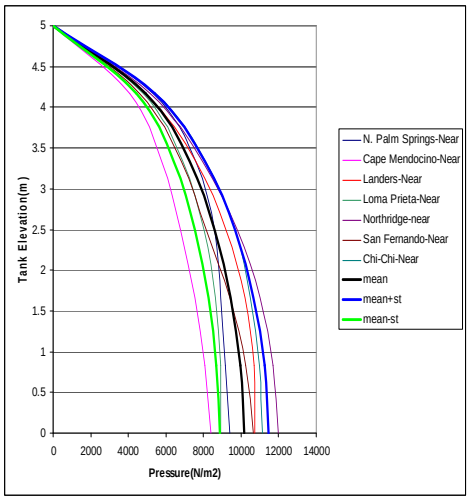

(b)

Figure 3: The dynamic fluid pressure envelope along the embedded tank walls; (a) far field; (b) near field

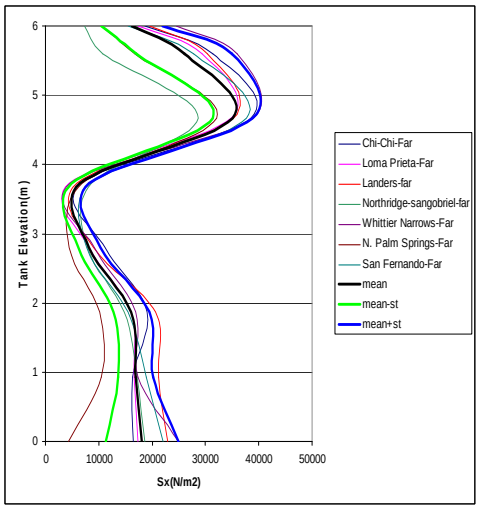

(a)

Figure 4-a: The dynamic soil pressure envelope along the semi- embedded tank walls; (a) far field

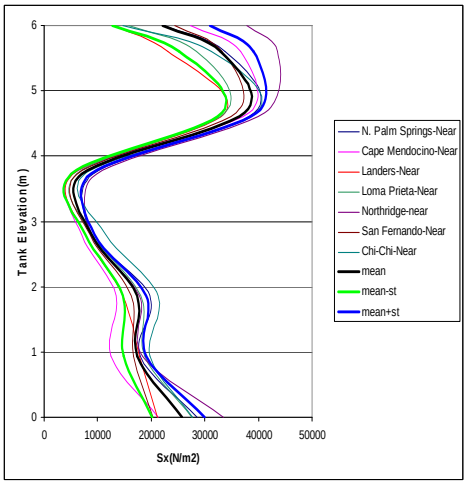

(b)

Figure 4-b: The dynamic soil pressure envelope along the Semi- embedded tank walls; (b) near field

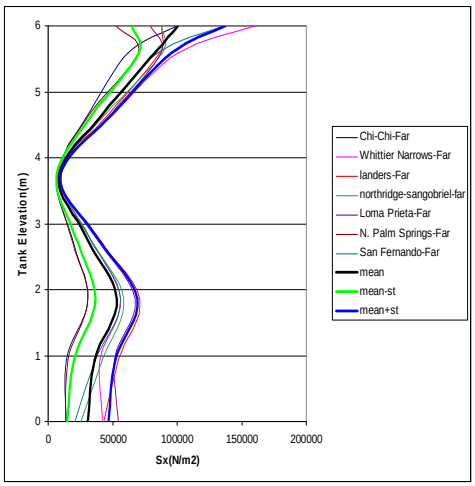

(a)

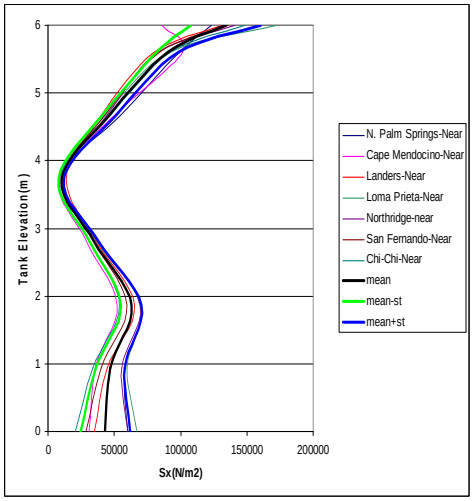

(b)

Figure 5: The dynamic soil pressure envelope along the embedded tank walls (a) far field (b) near field

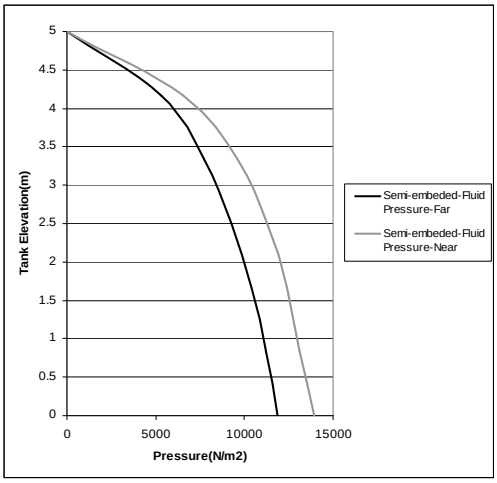

(a)

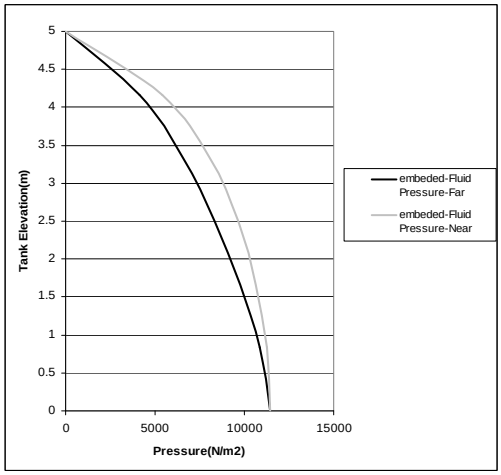

(b)

Figure 6: Comparison of the dynamic fluid pressure envelope under far and near field earthquakes; (a) semi- embedded; (b) embedded

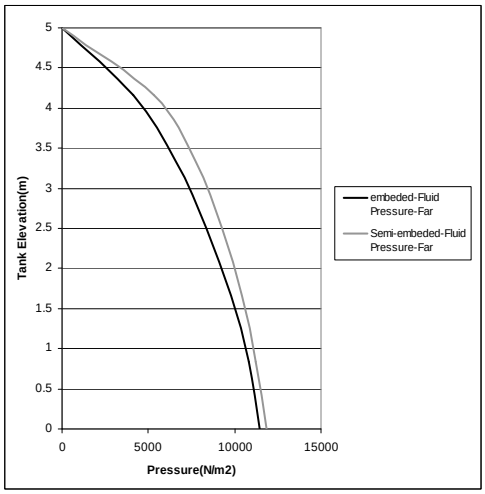

(a)

Figure 7-a: Comparison of the dynamic fluid pressure envelope for the embedded and semi- embedded tanks; (a) Far field

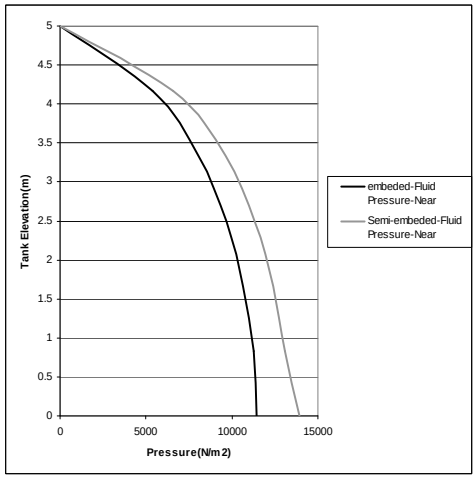

(b)

Figure 7-b: Comparison of the dynamic fluid pressure envelope for the embedded and semi- embedded tanks; (b) near field

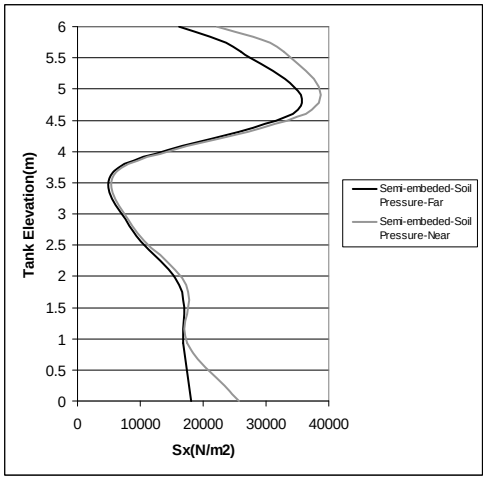

(a)

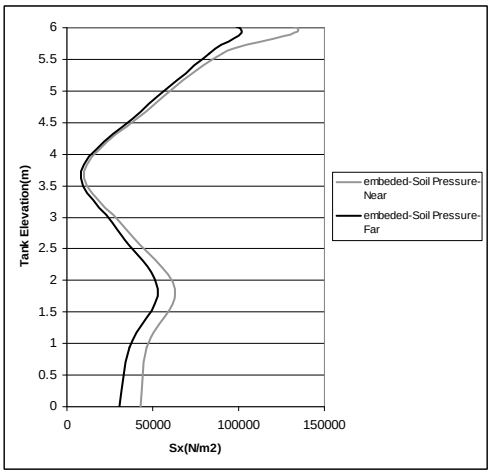

(b)

Figure 8: The dynamic soil pressure envelope along tank walls under near and far field earthquakes; (a) semi- embedded (b) embedded

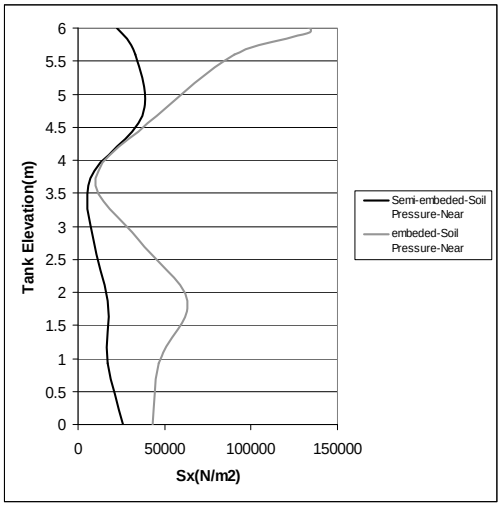

(a)

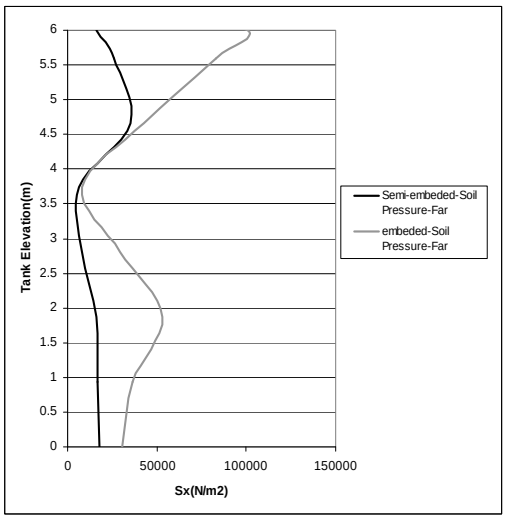

(b)

Figure 9: The dynamic soil pressure envelope for embedded and semi- embedded tank walls; (a) far field; (b) near field

Table 3 shows the resultant of the dynamic soil pressure applied on the tank walls for the embedded and semi-embedded tanks in near and far field earthquakes. These results are compared with those obtained from the Mononobe-Okabe relation in a number of pseudo-static methods. The results show that in near field earthquakes, the total dynamic forces, for the same level of ground motion intensity are 13% and 18.5% higher than those for the far field earthquakes for both semi-embedded and embedded tanks respectively. As it is shown in Table 3, the total forces suggested by the pseudo-static methods are not a good estimate of the actual dynamic forces, as they are larger than actual forces for semi- embedded tanks, and smaller of those in embedded tanks. However, the Seed and Whitman's suggestion for the line of action of the dynamic resultant force is safe.

Table 3: Dynamic Soil Pressure

N	Model Type	Total Force	Total Moment	Point of Application of The Dynamic Force
1	semi-embedded tank far field earthquakes	106384.1	354888.3	3.336
2	semi-embedded tank near field earthquakes	120427.4	403439.6	3.350
3	embedded tank far field earthquakes	248347.6	830910.1	3.346
4	embedded tank near field arthquakes	294291	958441.6	3.257
5	Mononobe-Okabe Method	188234	376458	2
6	Seed and Whitman	188234	677625	3.6

Table (4) shows the resultant dynamic fluid pressure on the tank walls. As it clearly shows, the determined force is larger for the near field earthquakes in comparison to the far field ones. However, the results are close for all four cases. Furthermore, as it is shown, the Westergaard's pseudo-static pressure distribution given by $p_d = 0.875Wk\sqrt{Hh}$ in which p_d is hydrodynamic pressure, W is the unit weight of the fluid, k is the design seismic coefficient, H is the maximum level of the fluid inside the tank, and h is the distance between the fluid surface to the point of action of the hydrodynamic pressure resultant, provides a good estimate for the dynamic fluid pressure and its point of application.

Table 4: Dynamic Fluid Pressure

N	Model Type	Total Force	Total Moment	Point of Application of The Dynamic Force
1	Semi-Buried tank far field earthquakes	41602.7	84349.9	2.028
2	Semi-Buried tank near field earthquakes	49948.3	102609.8	2.054
3	Buried tank far field earthquakes	37850.9	73782.0	1.949
4	Buried tank near field earthquakes	37716.2	77507.5	2.055
5	Westergaard	57225	114450	2.0

5. CONCLUSIONS

The dynamic response of the semi-embedded and embedded tanks under near and far field earthquake records are studied and the envelope of the dynamic soil and fluid pressure along the tank walls are determined. The results for different cases are compared with each other and with those obtained from the pseudo static method. The total dynamic soil force under near field earthquakes are about 15% to 20% lager than those for far field earthquakes with the same ground motion intensity. However, the point of application

of the dynamic force is almost the same in all cases. According to the results of this limited study, the resultant of the hydrodynamic pressure is at $0.404h_f$, where the h_f is the fluid level in storage tank. For soil pressure, the application point of the resultant is at 0.55h where h is height of tank's wall. Pseudo-static methods all lead to inaccurate estimates for the dynamic soil pressure especially in embedded tanks. But Westergaard method provides a very good estimate for the dynamic fluid pressure and its point of application. Obviously the results obtained in this limited study is very much dependent on the eigen-structure of the structural model, the directivity pulse period of the near field earthquakes, the soil type, modeling assumptions, etc., and a more comprehensive study is needed to separately investigate the effect of all those parameters.

References:

Housner G.W., (1957), "Dynamic pressures on accelerated fluid containers", *Bull. Seismolog. SOC*, 47(1).

Haroun M.A., Housner G.W., (1982), "Dynamic characteristics of liquid storage tanks", *Journal of Engineering Mechanic Division Proc ASCE,* 108(EM5).

Cho J.R., Song J.M., Lee J.K., (2001), "Finite element techniques for the free-vibration and seismic analysis of liquid-storage tanks", *Finite Elements in Analysis and Design*, 37, 467-483.

Morand H.J., Ohayon R, (1995), "Fluid-Structure Interaction", New York, John Wiley & Sons.

Ohayon R, (2001), "Reduced symmetric models for modal analysis of internal structural-acoustic and hydro elastic-sloshing systems", *Computer Methods Applied Mechanics Engineering,* 190, 3009-3019.

Pal N.C., Bhattacharyya S.K., Sinha P.K., (1999), "Coupled sloshing dynamics of liquid-filled, composite cylindrical tank", *Journal of Engineering Mechanics,* 25, 491-495.

Chen B.F. Chiang H.W., (1999), "Complete 2D and fully nonlinear analysis of ideal fluid in tanks", *Journal of Engineering Mechanic,* 25, 70-78.

Hamdan F.H., (1999), "Near field fluid-structure interaction using lagrangian fluid finite element", *Computers and Structures,* 71, 123-141.

Bermudez A., Neeto L.N., Rodrigues R., (2001), "Finite element computation of the vibrations of a plate-fluid system with interface damping", *Computer methods in applied mechanics and engineering,* 190, 3021-3038.

Virella J., Prato C., Godoy l., (2008), "Linear and nonlinear 2D finite element analysis of sloshing modes and pressures in rectangular tanks subject to horizontal harmonic motions", *Journal of Sound and Vibration,* 312, 442–460.

Silva Santos C., Greaves D., (2007), "A mixed Lagrangian –Eulerian method for non-linear free surface flows using multi grid on hierarchical Cartesian grids", *Computers & Fluids,* 36, 914–923.

Livaoglu R., (2008), "Investigation of seismic behavior of fluid–rectangular tank–soil/foundation systems in frequency domain", *Soil Dynamics and Earthquake Engineering*, 28,132–146.

Kellezi L., (2000), "Local transmitting boundaries for transient elastic analysis", *Journal of Soil Dynamics and Earthquake Engineering,* 19, 533-547.

Hisada Y., Bielak J., (2004), "Effects of Sedimentary Layers on Directivity Pulse and Fling Step", *13th World Conference on Earthquake Engineering, Vancouver, B.C., Canada,* August 1-6, 1736-1751.

Somerville P.G., Smith N.F., Graves R.W., Abrahamson N.A., (1997), "Modification of empirical strong ground motion attenuation relations to include the amplitude and duration effects of rupture directivity", *Seismological Res. Letter,* 68, 199-222.

Abrahamson, N., (2001), "Incorporating effects of near fault tectonic deformation into design ground motions", *a presentation sponsored by EERI Visiting Professional Program, hosted by the University at Buffalo*, October 26,

Zienkiewicz OC, Taylor RL. (1991), "The Finite Element Methods", Fourth Edition, New York: Mc-Grow Hill, Vol.2.

JOINT CONFERENCE PROCEEDINGS
7th International Conference on Urban Earthquake Engineering (7CUEE) &
5th International Conference on Earthquake Engineering (5ICEE)
March 3-5, 2010, Tokyo Institute of Technology, Tokyo, Japan

A NEW DESIGN IDEA FOR MITIGATING SEISMIC DAMAGE OF FRAME COLUMNS BY USING SMA RELATED DEVICE

Yun Chen [1)] and Xilin Lu [2)]

1) Doctoral students, State Key Laboratory of Disaster Reduction in Civil Engineering, Tongji University, Shanghai, China
2) Professor, State Key Laboratory of Disaster Reduction in Civil Engineering, Tongji University, Shanghai, China
chenyunhappy@163.com, lxlst@tongji.edu.cn

Abstract: The authors of this article first proposed a new design idea for mitigating the seismic damage of the first storey columns. By setting anchorage device below and near the inflection point of the first storey columns, a set of force cable and energy dissipation cable using shape memory alloys （SMA） are installed symmetrically in the anchorage device and the bottom of them fixed in the ground. Under an earthquake, columns generate deformation, but one-way bending occurs below the inflection point. In this case, anti-torque is applied to the column by the tension force cables, which can reduce the moment of the first storey columns while the compression force cables do not work. At the same time, the earthquake energy is dissipated through repeated non-linear deformation by the energy dissipation cables.

Analytical study was carried out, the push-over and time-history analysis was completed by ANSYS finite element program to a new CFST frame and an ordinary CFST frame. Analysis shows that the device can effectively mitigate the response of first storey columns under an earthquake, so the design idea may be used in the future engineering practices, while more research work is still going to be done.

Key words: inflection point; force cables; energy dissipation cables; P-delta effects; push-over analysis

1. INTRODUCTION

In order to avoid the collapse of frame structures under strong earthquakes, it is required the key structural components can not be seriously damaged. Consequently, anti-seismic requirements are “strong column-weak beam”, “strong shear-weak bending” and “strong node- weak elements”. For frame structures, the design idea is to make the beam appear plastic hinges firstly, which can avoid the loss of stability of the structure, leading to collapse. However, practice has shown that plastic hinges, due to the uncertainty of earthquake action and some factors not fully taken into account in structural design, frequently occurred at the column end in frame structures. This phenomenon is caused by the fact that the overall shear force applied to the building by an earthquake is higher at the base (A. Plumier et al. 2005), in addition, as a result of the largest P-delta effects at the bottom storey of structures, the bottom storey columns is more prone to damage and their repair after an earthquake is very difficulty. Figure 1 and Figure 2 shows two examples of plastic hinges at the level of bottom storey in Dujiangyan in Sichuan Province in China on May 12, 2008（Figure 1 and Figure 2 pictured by Alireza Mohyeddin-Kermani et al. 2008）.

As an attempt to provide an idea to solve this problem, the article firstly presents a new design idea for mitigating seismic damage of frame columns by using SMA related device. Later, Static push-over analysis and time-history analysis were calculated to study the seismic performance of the device. Calculation shows that it is effective to mitigate the damage of frame columns by the device, which also has the advantage of some degree of energy-consuming and easiness to repair after the earthquake.



Figure 1 Examples of Plastic Hinges at the Level Of Bottom-storey in Dujiangyan in 5.12 Wenchuan Earthquake, China



Figure 2 Examples of Plastic Hinges at the Level Of Bottom-storey in Dujiangyan in 5.12 Wenchuan Earthquake, China

2. WORKING PRINCIPLE DESCRIPTION

For frame structures, under the seismic action, the structural column generally has an inflection point, and usually one-way bending deformation occurred below the inflection point. According to the deformation of frame columns under earthquake, the article proposed a new design idea, as was shown in Figure 3, by setting anchorage device below and near the inflection point of the first storey columns, a set of force cable and energy dissipation cable are installed symmetrically in the anchorage device and the bottom of them fixed in the ground.

Under an earthquake, columns generate deformation, but mainly one-way bending occurs below the inflection point. In this case, anti-torque is applied to the column by the tension force cables, which can reduce the moment of the first storey columns while the compression force cables do not work. At the same time, the earthquake energy is dissipated through repeated non-linear deformation by the energy dissipation cables.

Energy dissipation cables consisted of wire ropes and SMA（shape memory alloy）ropes and force cables consisted of wire ropes and steel bars or springs.

SMA is a kind of super-elastic material and has found applications in many areas due to their high power density, solid state actuation, high damping capacity, durability and fatigue resistance. When integrated with civil structures, SMA can be passive, semi-active, or active components to reduce damage caused by environmental impacts or earthquakes（G. Song et al. 2006, Jin-Ho Roh et al. 2008, Qiang Pan et al.2007）.

In engineering applications, SMA generally has to go through repeated tensile cycle test until their performance stabilizes. The super-elastic strain of SMA is generally 8% ～10%, and its hysteresis loop is relatively full. By a device installed in the structure, SMA can dissipate lots of seismic energy under the earthquake with little residual deformation.

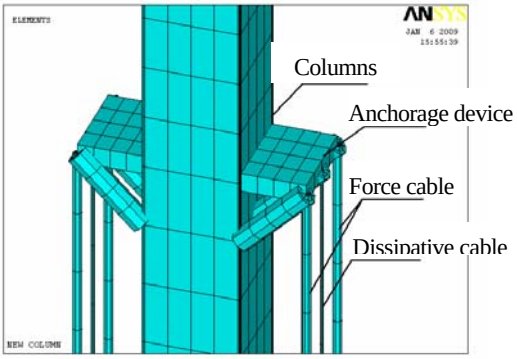

Figure 3 Design Details of New Seismic Column and its FE Model

3. COMPUTER MODEL

In this section, two one-span, one-storey CFST （concrete-filled steel tube）frames are investigated to validate the workability of the proposed design idea. The first one is an ordinary CFST frame, while the second one is a CFST frame with a set of force cable and energy dissipation cable symmetrically installed. According to the working principle discussed above, ANSYS finite element program is used to carry out the push-over and time-history analysis of the two frames. The design parameters of the CFST frame are shown in Table.1. The steel tube and steel beam used in the model is Q235 with yield strength of 235MPa, and the diameter of force cable is 28mm, with yield strength of 335MPa. The diameter of SMA bar is 10mm. H shaped steel beam is equivalent to rectangle cross-section to simplify modeling.

Solid 65 element is used to simulate concrete, and solid 45 element is utilized in the modeling of steel tube and steel beam. The used steel was assumed to behave as an elastic plastic material. Link10 element was used to simulate wire ropes while Solid 185 element is adopted to simulate SMA. This kind of element is a special element of ANSYS to represent the material property of SMA. Figure 4 is the FE model of the new CFST frame. The detail of joint is shown in Figure 3.

Table 1 Design Parameters of CFST Frame Structure

Span of frame (mm)	Storey height (mm)	Steel tube section(mm)
6000	6000	300×300×8
Steel beam section(mm)	Concrete strength (N/mm^2)	Axial-load ratio
300×300	40	0.4

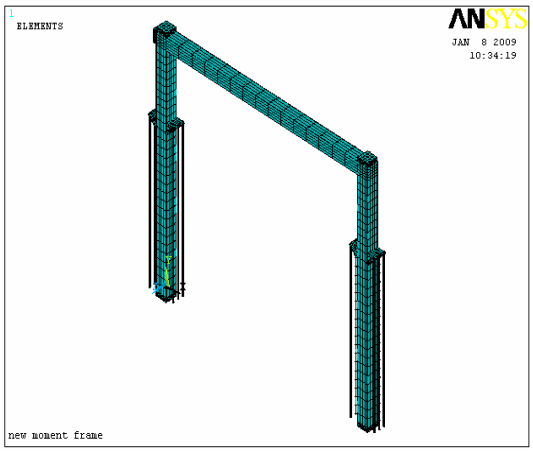

Figure 4 Finite element model of new CFST frames

4. STATIC PUSH-OVER ANALYSIS

For a detailed comparison of the performance of two frames, a static push-over analysis was studied. In FE analysis, the force cable and energy dissipation cable in compression side would unload, thus, the compression side elements were not considered. In addition, the anti-torque imposed by energy dissipation cable is ignored because of its less contribution. Later, the role of energy dissipation cable will be considered in the dynamic time-history analysis.

An axial load of 3480kN was first applied until the axial-load ratio of the CFST column reached 0.4. Then, displacement controlled load was applied with the level maximum displacement of 80mm until storey drift angles of both frame reached 1/73. In this case, both of frames have been yielding. The base shear-top displacement of common frames and new frames obtained from the analysis are shown in Figure 5.

From the base shear-top displacement curves, we can find the deformation of both frames is stable. Due to the action of force cable, maximum bearing capacity of the new frame is higher than the common one by 13%. In addition, more cross section of column is used to resist the pressure. To compare the yield shear force of both frames, the method proposed by FEMA-273 is used to calculate the base yield shear force of the two frames.

The equivalent lines in Figure 5 show that the yield shear force of the ordinary frame is 170.246kN, and the yield displacement is 44mm, while the yield shear force of the new frame is 195.672kN, with yield displacement of 45mm. In other words, the yield shear force of the new frame is 1.15 times higher than ordinary frame. And its yield displacement is also larger than ordinary frame. The Initial stiffness of new frame is 4.352kN/mm with the post-yield stiffness of 0.362kN/mm, and the stiffness degrading ratio is 8.3%; the initial stiffness of ordinary frame is 3.857kN/mm with the post-yield stiffness of 0.369kN /mm. the stiffness degrading ratio is 9.6%. With the similar stiffness degrading ratio, the new frame has a higher bearing capacity. Figure 6 shows the deformation of the new frame.

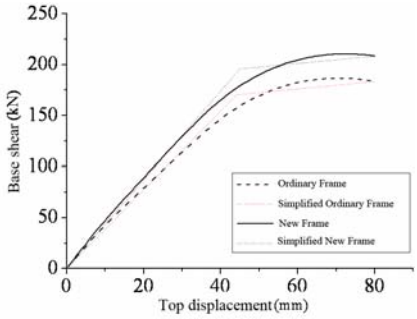

Figure 5 Base shear-top displacement of common frames and new frames

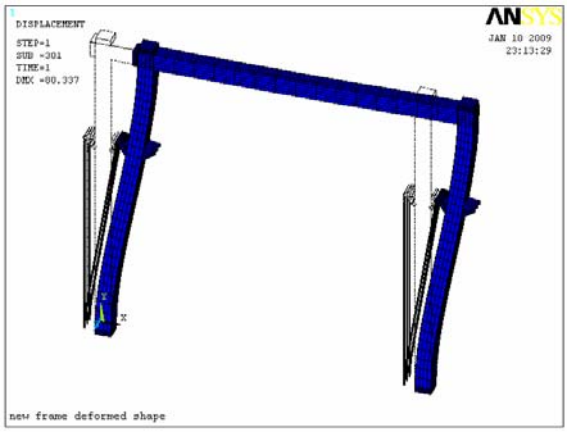

Figure 6 Deformation diagram of new frame

5. DYNAMIC TIME-HISTORY ANALYSIS

In order to further study the effects of force cable and energy dissipation cable, and especially investigate the effects of energy dissipation cable, a dynamic time-history analysis was researched in this section. The analysis model is the same as Figure 4 shown and the El Centro waves were input as seismic waves. Seismic wave peak was 200cm/s^2, and its waveform was shown as Figure 7.

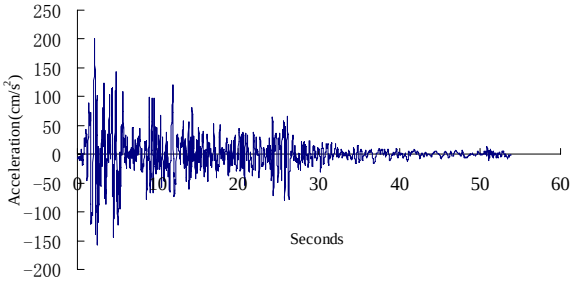

Figure 7 The input El Centro waves

In the section, a total of three kinds of structure were compared, the first for ordinary CFST frame, named frame1 ; the second CFST frame only setting force cable,

named frame 2; the third CFST frame setting both force cable and energy dissipation cable, named frame 3. A parameter was defined to compare the structural vibration control effects. As was shown in Eq. (1) below:

$$\beta_x = \frac{\max\{abs[x_o(t)]\} - \max\{abs[x_n(t)]\}}{\max\{abs[x_o(t)]\}} \times 100\% \quad (1)$$

where β_x is the structural vibration control effects, it includes displacement control effects and acceleration control effects; $x_o(t)$ is the response peak of ordinary structure, it includes displacement response peak and acceleration response peak; $x_n(t)$ is the response peak of new structure, it also includes the above mentioned.

5.1 Displacement Control Effect

As was show in the Figure 8 and table 2, the displacement-time curve of three kinds of frame was compared. During the whole course of time history, the frame 1 has maximum displacement, and its maximum displacement reached 55mm, at the same time, its maximum inter-story drift angle reached 1/109; frame 2 has maximum displacement of 42mm while frame 3 has maximum displacement of 37mm, and their maximum inter-story drift angles reached 1/143 and 1/162 respectively. Frame 2 has control effects of 23.6%, while frame 3 has control effects of 32.7%. So, comparing with frame 2,frame 3 has the better control effects.

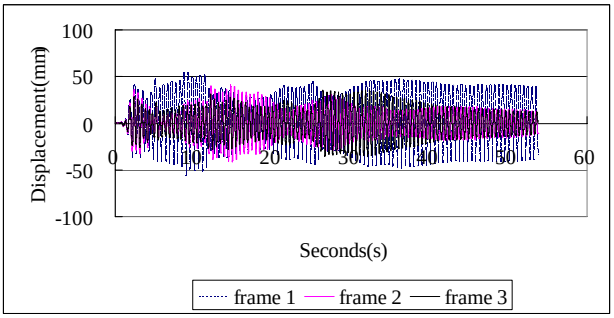

Figure 8 Comparison of displacement-time curve

Table 2 Comparison of Displacement Control Effects

Ordinary frame	Force cable frame	Force+energy cable frame
55mm	42mm	37mm
Control effects	Control effects	Control effects
	23.6%	32.7%

5.2 Acceleration Control Effect

As was shown in the Figure 9 and table 3, the acceleration-time curve of three kinds of frame was compared. During the whole course of time history, the frame 1 has maximum acceleration of 8410 mm/s^2; frame 2 has a maximum acceleration of 7245 mm/s^2, while frame 3 has a maximum acceleration of 6497 mm/s^2. Frame 2 has control effects of 13.9%, while frame 3 has control effects of 22.7%, so, comparing with frame 2, frame 3 has the better control effects

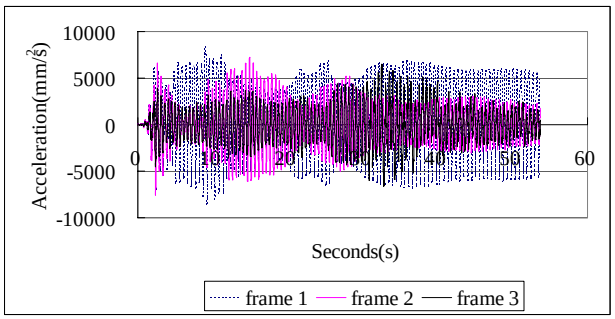

Figure 9 Comparison of acceleration-time curve

Table 3 Comparison of Acceleration Control Effects

Ordinary frame	Force cable frame	Force+energy cable frame
8410 mm/s^2	7245 mm/s^2	6497 mm/s^2
Control effects	Control effects	Control effects
	13.9%	22.7%

6. FORCE COMPARISON OF CABLE

In order to understand deeply change process of internal forces of cable in vibration, Figure 10 compared the internal forces of force cable of frame 2 and frame 3. From the Figure 10, we can find that the maximum tension of force cable of frame 2 was 91.6 kN; for frame 3, due to both force cable and energy dissipation cable being set and some energy being to dissipated by energy dissipation cable, the maximum tension of force cable was 82.2 kN, less than the frame 2.

As was shown in Figure 11, the maximum internal forces of energy dissipation cable were 16.1 kN, much less than internal force of the force cable. So, the anti-torque afforded by the energy dissipation cable could be ignored and only its energy-consuming effects should be considered in design.

To attain the better energy-consuming effects, the strain of SMA should be bigger. Therefore, energy dissipation cable consists of two segments of steel wires and a segment of SMA and Energy dissipation effects depends on the length of SMA. So, it is important to calculate the length of

SMA. If the length of SMA is too long, the effects is much worse, in contrast, if the length of SMA is too short, it may be pulled off in vibration. In design, the length of SMA should be decided according to the maximum displacement that may occur as well as the nature of the material.

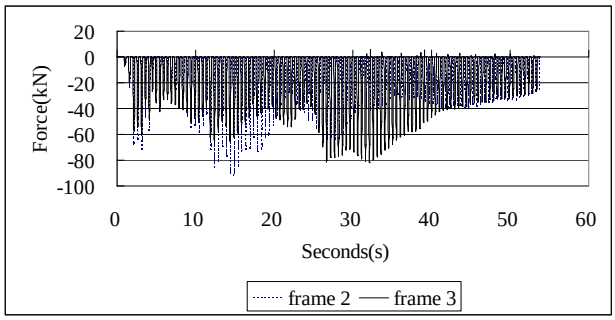

Figure 10 Internal force comparison of force cable

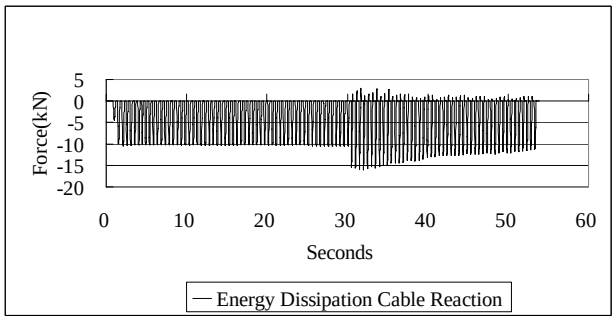

Figure 11 Internal force of energy dissipation cable

7. CONCLUSIONS

The authors firstly proposed a new idea to mitigate the damage of frame bottom columns, by setting a set of force cable and energy dissipation cable symmetrically near and below the inflection point, the structural anti-shear capacity can be improved effectively. It should be noted that force cable has better control effects to the response of displacement and acceleration, but the control effects of energy dissipation cable was not remarkable, because it did not reached enough plastic strain. So, lots of work was still to be done to study the energy dissipation capacity of SMA. Another advantage of the new idea was that when the cable was damaged under the earthquake, it can be easily replaced. In order to have a deeper understanding of the role of both cables, the following work is necessary to further expand:

（1）Optimal design should be further studied, such as the performance parameters of force cable and energy dissipation cable , the accurate location of anchorage device, and the width of anchorage device, etc.

（2）How to better simulate SMA, that is, to develop a better SMA unit, which can undergo super large strain and well reflect the nature of the material.

（3）Experimental method can also be used to further study the structure deeply.

Acknowledgements:

The authors acknowledge the support from National Natural Science Foundation Major Research Projects (90815029), 973 projects(2007CB714202), and State Key Laboratory of Disaster Reduction in Civil Engineering, Tongji University.

Reference:

A. Plumier, C. Doneux, L. Stoychev, T. Demarcot.(2005), “Mitigation of Soft Storey Failures of R.C. Structures Under Earthquake by Encased Steel Profiles,” *Fourth International Conference on Advances in Steel Structures*,Pages 1193-1198

G. Songa, N. Maa, H.-N. Lib. (2006), “Applications of shape memory alloys in civil structures,” *Engineering Structures*, 28,1266–1274

Jin-Ho Roh, In Lee and Jae-Hung Han. (2008), “Damping characteristics of SMA films and their application for passive vibration isolation,” *International Journal of Applied Electromagnetics and Mechanics*, 27,225–241

Qiang Pan and Chongdu Cho. (2007), “The Investigation of a Shape Memory Alloy Micro-Damper for MEMS Applications,” *Sensor*s, 7, 1887-1900

JOINT CONFERENCE PROCEEDINGS
7th International Conference on Urban Earthquake Engineering (7CUEE) &
5th International Conference on Earthquake Engineering (5ICEE)
March 3-5, 2010, Tokyo Institute of Technology, Tokyo, Japan

FIBER REINFORCED POLYMER (FRP) STRENGTHENING OF UNREINFORCED MASONRY BEARING WALL BUILDINGS - A NEW APPROACH

Geoff Sharp,BE, PE[1], Bill Tremayne,BE, PE[2], Paul Littler, Meng[3] and Zander Sivyer, BE, SE[4]

1) Senior Engineer, Holmes Culley Structural Engineers, San Francisco, USA
2) Project Manager, Holmes Culley Structural Engineers, San Francisco, USA
3) Project Engineer, Holmes Culley Structural Engineers, San Francisco, USA
4) Principal & CEO, Holmes Culley Structural Engineers, San Francisco, USA
GeoffS@Holmesculley.com, BillT@Holmesculley.com, PLittler@Holmesculley.com, ZanderS@Holmesculley.com

Abstract: The traditional approach to strengthening unreinforced masonry bearing wall buildings (UMBs) has been to add supplementary lateral load resisting elements assuming little to no contribution from the masonry. It is common to see the addition of new reinforced concrete shear walls or steel moment or braced frames. The obvious drawbacks of these systems include the additional seismic weight, the difficulties in achieving deformation compatibility with the base building and the aesthetic impact of adding large structural elements. The introduction of new structural elements in UMBs often requires significant removal of existing historic fabric and can impact the building functionality.

This paper describes the implementation of a new approach to strengthening unreinforced masonry bearing wall buildings utilizing surface applied fiber reinforced polymer for both shear and flexural enhancement. The use of FRP to locally enhance the shear capacity of masonry has been well studied. However, the use of FRP as a complete building strengthening system to address both shear and flexure in UMBs has not been well documented. Furthermore, little to no guidance is currently provided in building codes with regard to this application.

In the absence of codified guidelines this paper presents the approach which has been developed to improve component and global building performance. Similar in mechanics to traditional hold down techniques, externally bonded vertical strips of FRP are used to increase the flexural capacity of unreinforced masonry wall piers. This allows the full shear capacity of the section to be developed where it would otherwise be limited by rocking. By implementing this throughout a UMB, less additional structure is required and hence the impact on the existing architecture is minimized. In the development of this approach a number of technical issues were addressed including consideration of single sided FRP application, anchorage of the hold downs and global building response.

Two case studies involving the seismic retrofit of historic buildings in the San Francisco Bay Area are presented where the benefits of this methodology are described. These benefits included minimizing the aesthetic impact of strengthening, enhancement of the building's existing lateral load paths and the sustainable re-use of the existing structure. The verification methodology used for these case studies, limitations of this approach and opportunities for further research and testing are also discussed.

1. INTRODUCTION

As advances are made in the understanding of earthquakes and their impact on the built environment the awareness of building owners and the general public to the risks associated with seismically unsafe buildings is increased. Of particular interest in California is the large stock of unreinforced masonry bearing wall buildings (UMBs), which are particularly susceptible to damage during a seismic event. Finding cost effective, historically sensitive, and structurally robust retrofit solutions for UMBs is a significant challenge for structural engineers in California. This paper discusses the implementation of a new approach to the use of fiber reinforced polymers (FRP) in strengthening UMBs.

1.1. Unreinforced Masonry Bearing Wall Buildings

Unreinforced masonry bearing wall buildings became common in San Francisco during the early 1900s. UMBs were very popular due to their inherent fire resistance despite the fact that a large number of brick structures collapsed during the 1906 San Francisco earthquake.

Of the 25,945 UMBs estimated to be in California (Holmes 2009), 18,144 buildings have received some level of mitigation. While this means an impressive 70 % have received some level of seismic rehabilitation there is still a significant number of UMBs that have not.

A typical UMB consists of unreinforced masonry bearing walls with flexible wood floor diaphragms. UMB façades often include a large number of door and window

openings. Particularly relevant to this paper are buildings between 3 and 5 stories tall. UMBs by virtue of their base material are both heavy and brittle. Typical clay brick has low tensile strength and performs poorly under cyclic loading. For this reason conventional seismic retrofits of UMBs involve adding new lateral load resisting structure to supplement or entirely replace the masonry itself.

1.2. Fiber Reinforced Polymers as retrofit materials

Glass and carbon fiber reinforced polymers (FRP) have been used in the building industry for several decades. Applications have primarily focused on the retrofit of existing concrete structures, to enhance axial, flexural or shear strength of elements.

Research in the last 10 years has also focused on the benefits of strengthening unreinforced masonry for flexure and shear at a component level. However, there are few documented cases of FRP being used as a strengthening system for the complete rehabilitation of existing unreinforced masonry buildings.

1.3. Previous Research by others

Grillo (2003) and Holberg and Hamilton (2002) investigated the use of FRP to provide flexural strengthening to unreinforced clay masonry walls. Significant increases in strength (over 150%) and drift capacity (up to 1.6% drift) compared with unreinforced specimens were reported for single-sided FRP applications. However, their results also indicated that further refinement of the retrofit detailing was required to ensure robust performance. In particular, it appeared that closer attention to the FRP anchorage details and proportions (area provided) would be beneficial to inhibit premature and undesirable failure mechanisms such as laminate rupture.

Foster et al (2005) also investigated the benefits of retrofitting unreinforced masonry walls with FRP. Strains in the FRP were successfully limited to between 0.5 and 0.8%, thus avoiding rupture in the laminates prior to the onset of more ductile mechanisms such as horizontal joint-bed sliding (shear yielding). This study also highlighted the importance of considering and inhibiting other, less desirable and ductile, failure modes including diagonal tension (shear) cracking in the plane of the wall.

Testing undertaken at University of California, Irvine (UCI) and California State University, Fullerton (CSUF) by Haroun and Masallam (2002) was focused on the shear strengthening of unreinforced masonry wall panels using a single-sided application of glass FRP (GFRP). This test demonstrated that a single-sided application of GFRP could be used to enhance the shear capacity of an unreinforced masonry wall by 20%.

Research performed by Billington et al (2009) also indicated beneficial contribution of single-sided FRP to the flexural capacity of unreinforced masonry infill panels in concrete frames. However, the testing also indicated that out-of-plane deformations and forces developed at drifts greater than 1% and limited the effectiveness of this application. This behavior was likely attributable to the singled sided (eccentric) FRP application.

The design approach presented for the case studies in this paper draws primarily upon the UCI/CSUF testing but also addresses the issues identified by the other aforementioned researchers. In particular, the out-of-plane effects associated with the use of a single-sided FRP tension "hold-downs" is investigated in detail.

2.0 CODE REQUIREMENTS

The poor performance of unreinforced masonry buildings during seismic events has been well documented. Following the damaging 1989 Loma Prieta earthquake in Northern California the City and County of San Francisco looked at ways to improve the seismic safety of its large stock of unreinforced masonry bearing wall buildings. As a result of this effort the 1992 Unreinforced Masonry Building Ordinance has been made part of the local building code. This ordinance mandates that all UMBs be evaluated to determine their risk level. Where strengthening is required the ordinance does not prescribe or limit the techniques used to address the seismic deficiency. This provides the opportunity to pursue alternate strengthening systems subject to the review and approval of the local permitting authority.

The extent to which UMBs are strengthened often depends on the use of the building, its particular configuration, the intensity of seismic forces expected and whether strengthening is financially viable. It is often impractical to design retrofit solutions which are equivalent to current code loads for new buildings. As such, a number of design codes and standards prescribe varying levels of strengthening for existing buildings. This ranges from mitigating against specific collapse hazards, often termed "bolts plus", through to full code seismic strengthening. The approach presented in this paper applies to the latter.

2.1. Current Code provisions

Prescriptive building codes such as the San Francisco Building Code (2007), International Building Code (2006) and the referenced loading standard ASCE 7 (2005) define unreinforced masonry as a seismic force-resisting system with limited ductility capacity. Consequently, seismic force demands are high compared with those of seismic force-resisting systems typically used in new construction. No guidance is given in either of these reference standards as to how to categorize or design unreinforced masonry buildings which incorporate FRP.

The strengthening methodology utilizing FRP is intended to be "low-tech" and can be applied in conjunction with either a simple static analysis or modal/dynamic analyses. Thus far we have utilized this approach for strengthening buildings in accordance with the previous edition of the San Francisco Building Code (SFBC 2001) and more recently with the requirements of the International

Existing Building Code (IEBC 2006). Both codes have a prescribed methodology for considering the in-plane shear capacity of unreinforced masonry walls. This procedure considers rocking or shear governed behavior at each masonry pier that contributes to lateral load resistance. As described graphically in Figure 1 below.

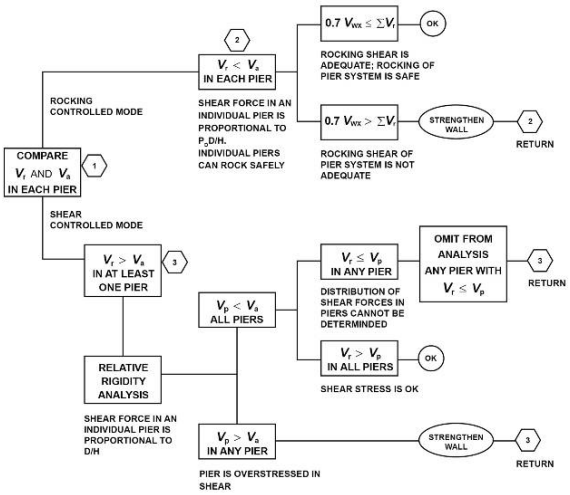

V_a = Allowable shear strength of a pier.
V_p = Shear force assigned to a pier on the basis of a relative shear rigidity analysis.
V_r = Rocking shear capacity of pier.
V_{wx} = Total shear force resisted by the wall.
ΣV_r = Rocking shear capacity of all piers in the wall.

Figure 1 Analysis of URM Wall In-Plane Shear Forces - Appendix A IEBC (2006)

Limited design guidance for FRP strengthening applied to unreinforced masonry is provided by Acceptance Criteria for Concrete and Reinforced and Unreinforced Masonry Strengthening Using Fiber-Reinforced Polymer Composite Systems (AC 125, 1997) and the Guide for the Design and Construction of Externally Bonded FRP Systems for Strengthening of Unreinforced Masonry Structures (ACI 440M, draft). Neither publication addresses the single-sided application of FRP as a tension hold-down strengthening system.

3 STRENGTHENING APPROACH AND ANALYSIS

3.1. The Mechanics

In the absence of comprehensive codified guidelines, the retrofit system presented herein has been developed to envelope the prescriptive, code-based requirements for unreinforced masonry buildings and a "capacity design" approach to the design of the composite FRP strengthening.

The approach involves using vertical, surface applied FRP strips to improve global building response by providing flexural tension capacity to the walls (hold downs). The use of FRP hold down strips has been specifically developed for three to five-story UMBs with short aspect ratio wall piers which respond to lateral loads by rocking or overturning. This mechanism occurs when the lateral force applied at the top of the pier causes a moment in the pier which exceeds the overturning resistance provided by the weight of the pier and its tributary dead load, assuming negligible tension contribution from the mortar. This is represented in the simplified rocking mechanism diagram below, Figure 2.

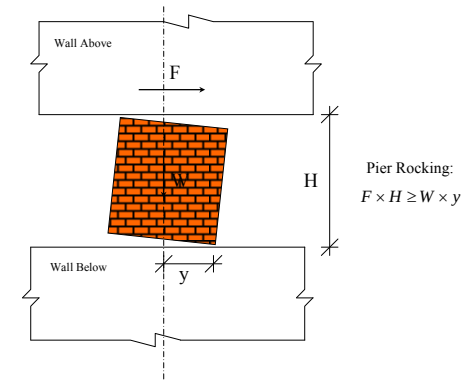

F = Force applied at the top of the pier
W = Weight of the pier including tributary dead load of building above
H = Pier height
y = Lever-arm between center of mass of pier and center of masonry compression block

Figure 2 Pier Rocking Mechanism

It is common for the shear capacity of a multi-wythe unreinforced masonry pier to be higher than the equivalent horizontal force required to cause rocking. The full shear capacity of the section can be developed by adding vertical strips of FRP at each end of the masonry pier. For this to be achieved the vertical strips of FRP must be developed above and below the pier to wall interface. The modified mechanics of the strengthened case are represented below in Figure 3.

Strains in the vertical FRP strips are limited to 0.4%, to ensure a sufficient margin of safety against fiber rupture and to limit bond stress with the masonry substrate as well as at anchorages. This strain limit is based on the recommendations of AC 125 (1997) for shear strengthening and appears to be slightly conservative based on the testing undertaken by Foster et al (2005).

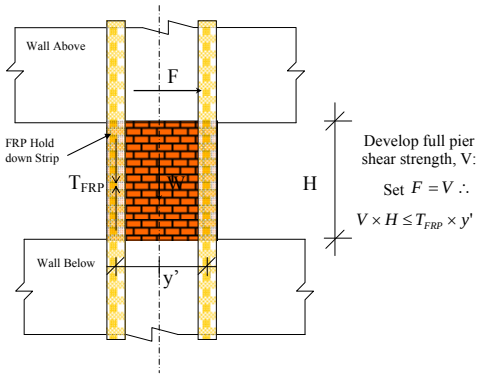

F = Force applied at the top of the pier
W = Weight of the pier including tributary dead load of building above
H = Pier height
T_{FRP} = Tension in FRP Hold Down Strip
y' = Lever-arm between center of FRP Hold Down Strip and center of masonry compression block

Figure 3 Restrained Wall Pier with FRP "hold downs"

The flexural capacity of the strengthened wall pier is evaluated using conventional limit-state bending theory for a reinforced masonry section. An equivalent rectangular compression stress block is assumed at the ultimate limit state, based on the lesser of the mortar or brick compressive strength. The FRP is assumed to behave linear-elastically and proportioned such that tensile strains do not exceed the limit described above. Compressive strains in the masonry/mortar are limited to ensure that crushing failure does not occur at the toe of the wall pier; this typically imposes a limit on the amount of FRP strengthening that can be applied.

Resisting rocking at individual wall piers increases the overall shear capacity and stiffness of the wall line being considered. By implementing this system throughout an existing building it is possible to limit the need for additional lateral load resisting elements.

When necessary, horizontally oriented FRP overlays can also be applied to enhance the shear strength of wall piers and in particular, inhibit the formation of non-ductile failure mechanisms including diagonal tension (shear) cracking.

Given the inherently non-ductile behavior of the FRP material, a capacity design approach needs to be adopted whereby the strengthening is proportioned to resist either an elastic level of seismic load, or the maximum force that can be delivered via a yielding element. For a wall strengthened for flexure only, this maximum force may be limited by the wall's shear capacity. This acknowledges that joint-bed sliding shear failure of a masonry wall pier is a relatively ductile mechanism.

The single sided application of FRP is not intended to directly improve the performance of unreinforced masonry walls for out-of-plane loads. Typically, building codes address the need to strengthen masonry walls for out of plane forces based on the wall's height to thickness ratio. In the two case studies for which this strengthening approach has been applied the height to thickness ratio of the walls proved limited additional structure was needed to satisfy the out-of-plane requirements.

3.2. Validation and Analysis

Whilst the global mechanics described above are relatively simple, careful attention must be given to response at the component level. When FRP is applied to both faces of a masonry pier to act as a hold down, the resulting net section is symmetric. In-plane loads are resolved by a force couple consisting of compression of the brick masonry, and equal tension via the FRP strips on both faces. There are no theoretical out-of-plane force components as the section is symmetric.

Most practical applications of strengthening overlays to masonry façades are single-sided due to access or architectural constraints. In this case the net section becomes asymmetric. The resulting force couple of the masonry compression block and the tension force via the FRP strip is not parallel with the major axis of the masonry pier. The eccentricity between the centroid of the compression block in the masonry and the line of tension force in the FRP causes a rotation of the neutral axis. An out-of-plane deformation is induced if loads are applied parallel to the major axis of the pier, as observed in testing by Billington et al (2009).

3.3. Finite Element Analysis

In order to study the effect of the rotated neutral axis, a three-dimensional volumetric finite element (VFE) analysis was performed. A representative volume element was modeled with the relevant material properties of typical masonry.

Boundary conditions at the base of the VFE solid were assigned accordingly to represent the non-linear force-displacement characteristics of brick masonry. At the locations of FRP strips, the boundary conditions also represent the tensile force-displacement characteristics of FRP. Figure 4 shows the Force-Displacement relationship for the non-linear supports at the locations of FRP overlay, compression only springs were used elsewhere.

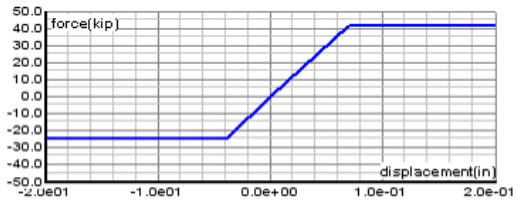

Figure 4 Non-linear support modeling characteristics for FRP

External actions were uniformly distributed across the top surface of the VFE solid, as would be expected for a robust floor diaphragm to wall connection. The self weight of the pier was also included in conjunction with the applied external actions. A series of static non-linear analyses were performed.

Analyses were performed on a number of masonry pier models with varying aspect ratios. Each masonry pier model had the same thickness (t), height (H) and load (V) applied, with the length (L) being the variable. Each masonry pier was modeled with the same area of FRP, typically a 300 mm (12") long by 2.5 mm (0.1") thick equivalent strip at each end. Figure 5 shows the physical condition of a masonry wall pier which the computational model is based on.

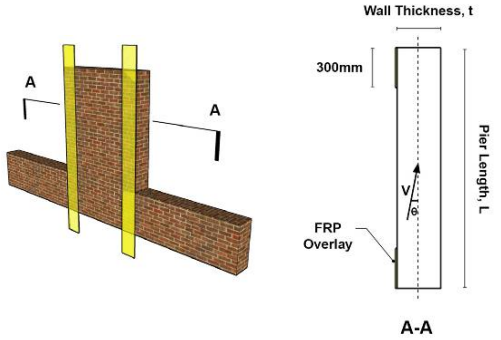

Figure 5 Masonry wall pier showing FRP "hold downs" and model parameters

VFE models of varying aspect ratios were analyzed for different angles, θ, of the load, V. The angles of loading applied range from zero degrees, pure in-plane loading, to 7 degrees, positive to the side of FRP.

Figure 7 shows the plot of the (average) out of plane displacement against angle of rotated load for each of the aspect ratios of masonry piers analyzed.

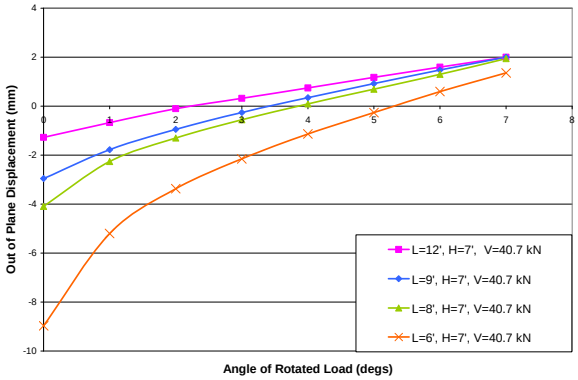

Figure 6 Plot of pier displacement out-of-plane versus angle of loading for four different pier sizes

Figures 7 and 8 show a comparison of the amplified deflected shapes for one of the masonry pier models, when subjected to pure in-plane loading (parallel to the major axis) and subjected to rotated loading which results in no out of plane displacement at the top.

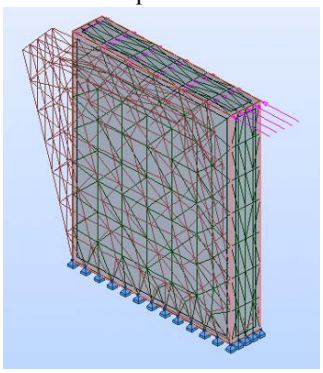

Figure 7 Amplified deflected shape for loading along major axis

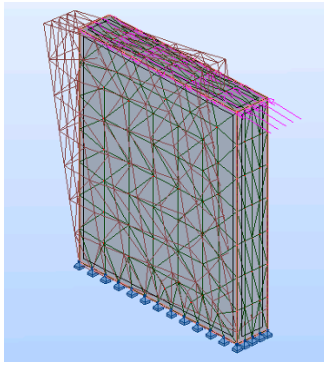

Figure 8 Amplified deflected shape for loading along rotated principal axis

As seen from Figure 6, each wall pier configuration has an optimal angle at which the load can be applied. At this angle, no out-of-plane displacement occurs. This is analogous to loading a steel angle about its principal axes.

The practical implication of this result is that in order to avoid significant out-of-plane deformation in the wall pier, the floor diaphragm must be capable of applying the story shear force at an angle parallel to the rotated principal axis. This can be achieved by designing and detailing the diaphragm and anchor bolts for the resultant combined shear and tension.

The net effect is that the overall shear capacity of the reinforced section is reduced as a trigonometric function of the rotated principal axis and the major axis of the wall pier. For small angles of rotation these effects are negligible.

4 CASE STUDIES

4.1. 235 O'Farrell Street, San Francisco, California

The owner of this building was required to undertake a full seismic upgrade of a 1920's-era, five-story building as part of the City and County of San Francisco's Unreinforced Masonry Building Ordinance. This mandatory upgrade was complicated by a historically significant façade, due in part to the building's location within the vicinity of San Francisco's Union Square district.



Figure 9 North-west perspective view of 235 O'Farrell Street

The existing structure consisted of riveted steel frames with masonry infill from the foundation to second floor, and unreinforced masonry bearing walls from the second floor to the roof. In particular the façade walls in the north-south direction, lacked sufficient shear and flexural (rocking) strength to adequately resist in-plane seismic loads, due in part to a large number of windows and poor wall pier aspect ratios.

Conventional retrofit solutions were infeasible, due to their significant intrusion into the usable floor area. A retrofit scheme was developed that utilized glass FRP in conjunction with the existing masonry façade to upgrade the building to fully comply with the requirements of the San Francisco Building Code (2001 edition). As this was not a codified

retrofit technique, the design required review and approval from the San Francisco UMB Appeals Board. The design approach and criteria described in this paper was presented to the Board, who unanimously accepted the proposal for this and all future UMB projects under their jurisdiction.

The final retrofit methodology consisted of internally applied GFRP to the masonry walls, with reinforced concrete shear walls at the lower levels to complete the vertical load path. GFRP tension hold-down strips forced the masonry wall piers with existing flexural "rocking" failure modes into shear governed modes, with higher strength and stiffness. In addition, overlays of GFRP sheets with horizontally oriented primary fibers were applied to specific wall piers where required to enhance their shear strength and inhibit diagonal tension (shear) cracking, prior to the onset of horizontal joint-bed sliding.



Figure 10 Vertical FRP strips used as tension "hold downs"



Figure 11 Horizontal FRP sheets applied to wall pier to enhance shear strength and inhibit diagonal tension (shear) cracking

This approach added substantial value to the project; as the retrofit had no impact upon the exterior façade and there was minimal impact upon the interior space due to the thin profile of the composite fibers. Furthermore, the costs of the retrofit were significantly less than a conventional UMB retrofit solution, which would have neglected the contribution of the existing masonry façade to the building's lateral load resisting capacity.

4.2. Presidio Building 103, Presidio of San Francisco, California

Located in the Presidio National Park, adjacent to the world famous Golden Gate Bridge, Presidio Building 103 is an historic three story UMB. Originally constructed in 1895 as an army barracks the 40,000 square foot building is going to be seismically strengthened as part of a full building rehabilitation project.

The project was completed on behalf of The Presidio Trust, a federal agency responsible for managing the interior 80% of the Presidio of San Francisco. The major goals for the structural rehabilitation of Building 103 were to improve the seismic safety of the building while preserving its historic fabric. The seismic strengthening needs be in accordance with the 2003 International Existing Building Code.



Figure 12 Presidio Building 103

In order to establish the best method of strengthening for this project three separate schemes were developed simultaneously. The three schemes were:

1. Center-coring to install new vertical reinforcing into the brick piers
2. Internally applied reinforced concrete wall overlay
3. A combination of new internal concrete shear walls and perimeter wall strengthening using FRP

Despite being an emerging retrofit technology for UMBs, FRP strengthening was selected as the optimal scheme as it presented the lowest construction cost with the least impact on the existing building.

The full scheme involved single-sided FRP hold down strips at the perimeter unreinforced masonry walls to fully develop their inherent shear strength. The FRP strips extended the full height of the building providing overturning restraint for piers on two levels. The cumulative hold down forces were then resolved into a new reinforced concrete basement wall overlay. The new basement wall was required to bridge the structural discontinuity associated with the existing stone rubble wall. Adding the new overlay also allowed the waterproofing of the basement space to be significantly improved. In addition to the FRP strips, the scheme included two new reinforced concrete shear walls at the building interior where there was insufficient existing wall. Figure 13 highlights the main strengthening features.

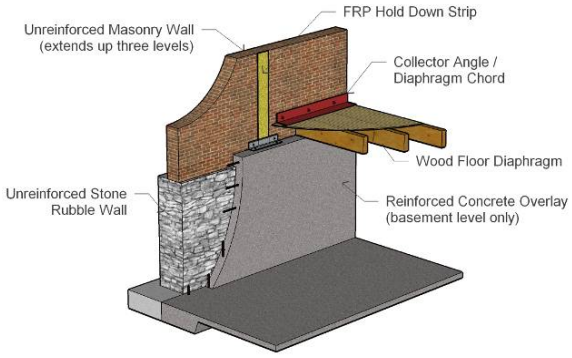

Figure 13 Building cut-away model showing the key strengthening features adopted for Presidio Building 103

A benefit of this approach is that once the FRP is installed and covered over there is little visible evidence that the building has been modified. In general, FRP overlays are in the order of 2 to 5 mm thick and thus, allowing existing finishes to be locally removed then reapplied with no discernable change in appearance.

The structural engineering design for this project was kept simple with a static analysis completed in accordance with the General Procedure for strengthening a UMB. To provide a greater level of validation of the scheme and to accurately represent the global response of the building a non-linear time history (NLTH) analysis was performed. The analysis was performed using in-house NLTH software and the results were compared with the requirements of ASCE 41-06: Seismic Rehabilitation of Existing Buildings. This analysis yielded positive results and concluded that the global response of the building achieved the requirements for life safety at the code mandated level of load. More specifically, maximum strains in the FRP strips were well below ultimate rupture and story drifts below 1 %.

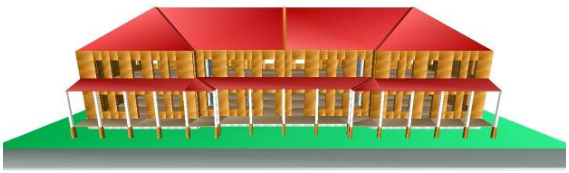

Figure 14 3-D rendering of the NLTH model prepared for Building 103

In recent years, applying sustainable and environmentally friendly practices to the building and construction industry has become very important. In particular, looking at the sustainable reuse of existing buildings has gained traction as organizations including the US Green Building Council (USGBC), who promote the LEED building certification system, recognize the positive environmental impact of rehabilitating existing buildings instead of new construction. In their recent paper, Hays and Cocke (2009), described the embodied energy tied up in existing buildings and compare that with demolition and new build energy consumption as an argument for the reuse of existing buildings. Developing new techniques for the rehabilitation of buildings prone to seismic damage is a sustainable and environmentally friendly practice. Additionally, the approach described in this paper has the potential to limit the use of traditional building materials like steel and concrete. The Presidio Building 103 project has been documented with a focus on sustainability with the aim of achieving LEED Gold status. The innovation in design credit has been sought in addition to requesting the sustainability credits associated with using recycled materials and cement replacement.

Construction on this rehabilitation project is expected to begin in early 2010.

5 CONCLUSIONS

Fiber Reinforced Polymers can be used to enhance overall performance in unreinforced masonry bearing wall buildings. In particular, UMBs which have inherent shear strength benefit significantly from additional local hold down resistance provided at individual wall piers by FRP strips.

Significant research has been carried out by others to evaluate FRP as a retrofit material. This research, combined with the analysis carried out in the preparation of this paper, indicates that there are a number of technical issues to be aware of when implementing this approach. While not prohibitive, these issues include eccentricity effects of single sided FRP application and anchorage of hold downs.

The approach has been implemented in the design of UMB seismic strengthening projects and has proven to be a cost effective method with limited aesthetic impact on the existing structures.

While a number of testing programs have investigated this type of application of FRP, future research should include a full pier and spandrel wall assemblage. This would capture the effects of double curvature, spandrel interaction and the out-of-plane effects on the wood floor diaphragm caused by single sided application of the FRP

References:

American Concrete Institute (2004), "Guide for the Design and Construction of Externally Bonded FRP Systems for Strengthening Unreinforced Masonry Structures (ACI 440M)".

American Society of Civil Engineers (2005), "Minimum Design Loads for Buildings and Other Structures (ASCE 7-05)".

Billington, Kyriakides, Blackard, William, Stavridis and Shing, "Evaluation of a Sprayable, Ductile, Cement-based Composite for the Seismic Retrofit of Unreinforced Masonry Infills", *ATC & SEI Conference on Improving the Seismic Performance of Existing Buildings and Other Structures, 2009.*

California Building Standards Commission (2007), "California Building Standards Code".

City and County of San Francisco (2007), "San Francisco Building Code".

Foster, P.B., Gergley, J., Young, D.T., McGinley, W.M., Corzo, A. (2005), "FRP Repair Methods for Unreinforced Masonry Buildings Subject to Cyclic Loading," *SP-230: 7th International Symposium on Fiber-Reinforced (FRP) Polymer Reinforcement*

for Concrete Structures.
Grillo, V.E. (2003), "FRP/Steel Strengthening of Unreinforced Concrete Masonry Piers", University of Florida.
Haroun and Mosallam, UCI/CSUF Test Report #Fyfe-MW Cyclic Shear Test of Multi-Wythe Existing Brick Wall, University of California, Irvine/California State University, Fullerton, February 2002.
Hays, B. and Cocke, D. (2009), "The Sustainable Practice of Reusing Buildings", *Structural Engineer's Association of California (SEAOC) conference proceedings*, 295-301.
Holberg, A.M. and Hamilton, H.R. (February 2002), "Strengthening URM with GFRP Composites and Ductile Connections", Earthquake Spectra, Earthquake Engineering Research Institute.
Holmes, W.T. (2009), "Progress of Seismic Rehabilitation of Buildings in the U.S", *ATC & SEI Conference on Improving the Seismic Performance of Existing Buildings and Other Structures*.
International Code Council (2006), "International Building Code"
International Code Council (2006), "International Existing Building Code"
International Conference of Building Officials, "Acceptance Criteria for Concrete and Reinforced and Unreinforced Masonry Strengthening Using Fiber-Reinforced Polymer, Composite Systems (AC 125)", 1997.
Naguib, Talaat, Citipitioglu, "FRP Retrofit for Collapse Mitigation of RC Frames with URM Infills: 3-D Computational Modeling of an As-Built and Retrofitted One Story Building", *ATC & SEI Conference on Improving the Seismic Performance of Existing Buildings and Other Structures, 2009.*
National Research Council (2004), "Guide for the Design and Construction of Externally Bonded FRP Systems for Strengthening Existing Structures" (CNR-DT200

JOINT CONFERENCE PROCEEDINGS
7th International Conference on Urban Earthquake Engineering (7CUEE) &
5th International Conference on Earthquake Engineering (5ICEE)
March 3-5, 2010, Tokyo Institute of Technology, Tokyo, Japan

A DESIGN APPROACH USING VISCOUS-TYPE DAMPER TO CONTROL SEISMIC VIBRATION OF SLIP-HYSTERETIC STRUCTURE

Wuchuan Pu[1)], Kazuhiko Kasai [2)]

1) GCOE Researcher, Center for Urban Earthquake Engineering, Tokyo Institute of Technology, Japan
2) Professor, Structural Engineering Research Center, Tokyo Institute of Technology, Japan
pu.w.aa@m.titech.ac.jp, kasai@serc.titech.ac.jp

Abstract: This paper proposed a passive control design method for structures with slip hysteresis added with viscous-type dampers. The dynamic properties of the passive system are described, and the variation of equivalent parameters of system is discussed. The performance curves for slip-hysteretic structures, which show the interaction between dampers, structural component, and seismic input intuitively, are developed, and the passive control design method for slip-hysteretic structure is proposed based on the performance curve. The time history analysis over a wide range of system parameters and input earthquakes shows good accuracy of the proposed method.

1. INTRODUCTION

Timber-framed buildings subjected to earthquake excitation generally show slip hysteresis due to localized deformation in connections, and the energy dissipation capability of structures is accordingly limited because of stiffness degradation. Such characteristics need to be taken into account during aseismic analysis and design. In order to reduce the structural vibration and damage produced by earthquake or wind, vibration control devices are being more and more widely used in timber house structure in recent years. As an effective way to improve the structural energy dissipating capacity, the small-sized viscous (VS) dampers and visco-elastic (VE) dampers are popularly used due to their economy and constructional efficiency. Viscous damper and visco-elastic damper can be classified as the same group, namely, the viscous-type damper, because both of them dissipate energy in terms of the viscosity of viscous materials. Compared to other types of dampers, the viscous-type dampers have the advantage of dissipating energy from very small to large vibration amplitude.

To achieve an effective vibration control design, it is important to understand the seismic behavior of damping devices as well as that of main frame, and then to provide a design with good balance between the stiffness and strength of structural components. In the so-called trial and error method, time history analysis with adjusted quantity of dampers needs to be performed for several times until the target performance of main structure is satisfied. Even though the target of design can be reached in this way, the mechanism of vibration control is difficult to understand, and repeated computation to determine an appropriate quantity of damper is inefficient in practice. In view of this, a general principle is necessary to clarify the complex interaction among the damper, frame, seismic input, and the structural performance. One representative study of such a design criteria can be found in Kasai et al. (2003; 2006 etc.). Kasai et al. has carried on a series of researches on the passive control design method of structures added with various types of dampers, based on the performance curve which describes the relationship between the responses of structure and the damper properties in plot intuitively.

Some experimental studies on the passively controlled timber structure have been carried out (Kasai et al. 2005; Sakata el al. 2005), and the effectiveness of damping devices on reducing the response of timber structures has been verified. However, the general design approach as aforementioned is still lack, and the study on the effect of slip hysteresis on response of passive control system is deficient. In this study, the performance curve will be applied into the slip-hysteretic structures controlled by viscous-type dampers, and a passive control design method particularly for slip-hysteretic structures will be developed. When installing dampers into a frame, supporting braces are generally needed. The damper and the brace constitute the so-called “added component”. Because the force of brace is in-phase with deformation, no matter VS damper or VE damper is used, the added component will produce both in-phase and out-of-phase forces. Namely, the mathematical descriptions of systems with either VS damper or VE damper used can be unified (Fu and Kasai 1998). As example, the VE damper will be considered in this paper.

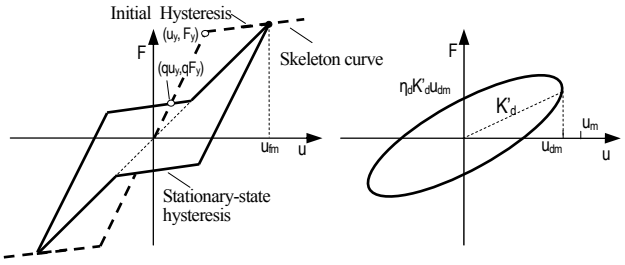

(a) Hysteresis of Slip Element (b) Hysteresis of VE Damper

Figure 1 Hysteresis of Slip Element and VE Damper

2. DYNAMIC PROPERTIES OF SYSTEM

2.1 Constitution Element of SDOF System

Within the hysteresis models previously proposed for timber shearwalls, the combination model of bilinear model and slip model has relatively simple mechanism, and is capable of reproducing exactly the dynamic behavior of shearwall (Araki et al. 2004; Isoda and Kawai 2007). In the present study, this hysteresis model is adopted for simulating the slip-hysteretic structure. Figure 1(a) shows the stationary-state hysteresis of slip element subjected to sinusoidal excitation $u(t) = u_{fm}\sin(\omega t)$. The elastic stiffness, post-yield stiffness ratio, yield deformation, and yield force of slip element are denoted by K_f, p_f, u_y, and F_y, respectively. The skeleton curve of slip element is bilinear, the force corresponding to the deformation at which the elastic hysteresis and the slip hysteresis curves intersect is defined as qF_y, with $q(\leq 1)$ referred to as slip strength ratio. The q describes the degree of slip occurring in hysteresis of structure, and q=1 gives bilinear hysteresis.

Figure 1(b) shows the typical stationary-state hysteresis for visco-elastic damper subjected to sinusoidal excitation $u(t) = u_{dm}\sin(\omega t)$. The stiffness and viscosity possessed by VE damper produce the elastic force and viscous force proportional to the damper's deformation and its velocity, respectively, so the VE damper develops hysteresis loop of an inclined ellipse. We define the secant stiffness at maximum deformation as "storage stiffness" K'_d, the force at deformation u=0 divided by maximum deformation u_{dm} as "loss stiffness" K''_d, and the ratio of loss stiffness to storage stiffness as "loss factor" $\eta_d (= K''_d / K'_d)$.

Figure 2 shows the constitution of passive control system. The damper is connected in series to elastic brace, and the damper-brace assembly is called as "added component". The added component is connected to main structure in parallel to form the VE system. Obviously, the forces of damper and brace are equal, and the added component and frame experience the same deformation.

2.2 Dynamic Properties of VE System

Given the stiffness of brace K_b, storage stiffness of damper K'_d, and loss factor of damper η_d, the storage stiffness K'_a and loss factor η_a for added component are obtained as following.

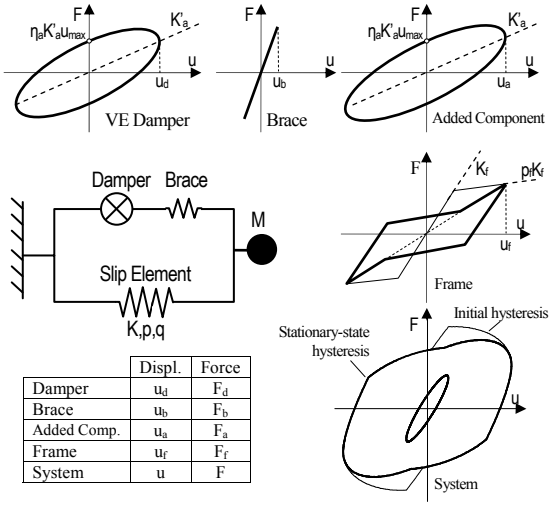

	Displ.	Force
Damper	u_d	F_d
Brace	u_b	F_b
Added Comp.	u_a	F_a
Frame	u_f	F_f
System	u	F

Figure 2 Constitution of System

$$K'_a = \frac{K'_d}{1/\Gamma_d + K'_d / K_b}, \quad \Gamma_d = 1 + \frac{{\eta_d}^2}{1 + K_b / K'_d}, \qquad (1a\text{-}c)$$

$$\eta_a = \frac{\eta_d}{1 + (1 + {\eta_d}^2) K'_d / K_b}$$

Similar to Eq. (1), the system's storage stiffness K' and loss factor η are obtained as

$$K' = K_f + K'_a, \quad \eta = \eta_a \frac{K'_a}{K_f + K'_a} \qquad (2a,b)$$

Let T_f, h_f denote the initial period and damping ratio of frame, the natural period T_0, damping ratio h_0, post-yield stiffness ratio p of the elastic system with added component can be easily obtained.

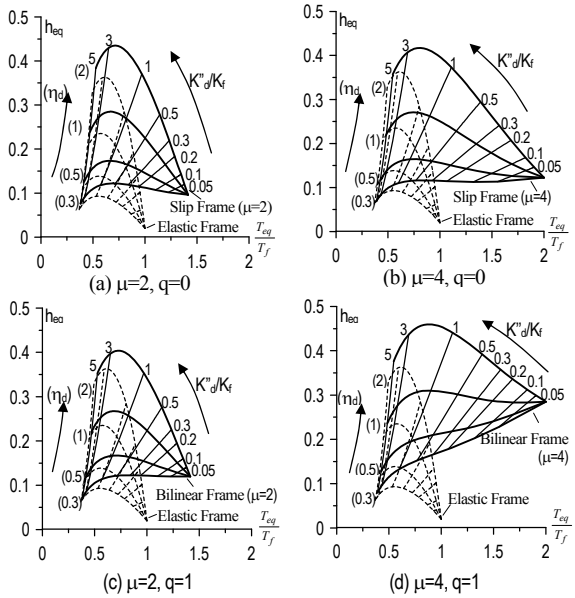

Figure 3 Variation of Equivalent Period and Damping (K_b/K_f=10, p_f=0)

$$T_0 = T_f\sqrt{K_f/(K_f + K'_a)} \qquad (3a\text{-}c)$$

$$h_0 = h_f + 0.9\frac{\eta}{2}, \qquad p = \frac{p_f K_f + K'_a}{K'}$$

where the factor 0.9 in Eq. (3b) reflects the decrease in damping effect of system in random response compared to that in stationary-state response (Kasai & Okuma 2004).

For elasto-plastic system, the secant stiffness at the maximum deformation is defined as the equivalent stiffness, as given by Eq. (4).

$$T_{eq} = T_f\sqrt{\frac{\mu}{1 - p_f + (p_f + K'_a/K_f)\mu}} \qquad (4)$$

where μ ($=u_m/u_y$) is the maximum ductility ratio.

In random response, the slip element develops slightly different hysteresis loops because the stiffness after slipping depends on the maximum deformation experienced by structure. The writers have studied the energy dissipation of slip-hysteretic structure in random response detailedly, and found that the energy dissipation calculated by stationary-state formulas can be used to approximate the total energy dissipation of slip-hysteresis with undervaluation by less than 10% generally (Kasai et al. 2009). Meanwhile, in view of the convenience in application, the stationary-state hysteresis is recommended for use in design. In random response, the ductility ratio of frame varies from 0 to maximum randomly. The average damping method proposed by Newmark & Rosenbluth (1971), which gives the average damping ratio of hysteresis loops with amplitude between 0 and maximum ductility ratio, is adopted. Based on these criteria, the average damping ratio of system was derived as shown in Eq. (5).

$$h_{eq} = \frac{(1+q)^2}{2\pi p\mu}\ln\left(\frac{f(\mu)}{\mu^p}\right) + \frac{h_0}{\mu}\left\{\frac{\sqrt{\mu\cdot f(\mu)}+p-1}{p} + \ln\left(\frac{\sqrt{p\mu}+\sqrt{f(\mu)}}{\sqrt{p}+1}\right)^{\frac{p-1}{p\sqrt{p}}}\right\},$$

$$f(\mu) = 1 + p\mu - p \qquad (5a,b)$$

Based on the above equations, one can obtain the plots for T_{eq}/T_f and h_{eq}, with respect to storage stiffness ratio of K''_d/K_f and loss factor of damper η_d. As examples, brace stiffness ratio K_b/K_f = 10, post-yield stiffness ratio of main frame p_f=0 are fixed, and storage stiffness ratio K''_d/K_f =0.05~5, loss factor η_d= 0.3~2, ductility ratio μ=2 or 4, slip strength ratio q=0 or 1 are assumed. The T_{eq}/T_f and h_{eq} corresponding to these parameters are plotted in Fig. 3 in solid line. For comparison, the T_{eq}/T_f and h_{eq} for elastic system with μ=1 and the same other parameters are plotted in broken line.

Figure 3 shows that a larger storage stiffness ratio K''_d/K_f leads to a smaller equivalent period T_{eq}, and moreover, increase in loss factor η_d leads to significant increase in h_{eq}. On the other hand, in case of a small loss factor η_d, a larger K''_d/K_f leads to more significant decrease in T_{eq} than the increase in h_{eq}. These results indicate that

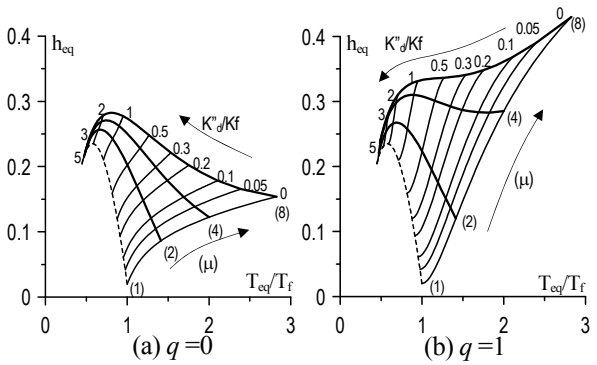

Figure 4 Variation of Equivalent Period and Damping with Respect to Ductility Ratio (K_b/K_f=10, p_f=0, q=0 and 1, η_d=1)

vibration control effect of adding damper into structure is due to the increase of h_{eq} in case of a large loss factor η_d, and to the combination effect of both T_{eq} and h_{eq} in case of a small η_d. In addition, the energy dissipation capability of structure with smaller slip strength ratio q is relatively smaller, so the increase in the equivalent damping h_{eq} accompanying with the increase of yielding of structure is accordingly small for a structure with small q, and vise versa.

Figure 4 shows the variation of T_{eq}/T_f and h_{eq} with respect to ductility ratio μ and storage stiffness ratio K''_d/K_f. Loss factor η_d =1 is assumed. As the slip strength ratio q becomes small, the effect of q on the equivalent damping h_{eq} becomes weak. There is no significant increase in h_{eq} even though the yielding of structure increases, and consequently the responses tend to be large. In contrast, the h_{eq} is influenced greatly by yielding degree of structure with large slip strength ratio q. Figure 4 also shows that when large damper is used, the influence of q becomes small, and the same values will be obtained for equivalent parameters.

3 PASSIVE CONTROL DESIGN BASED ON PERFORMANCE CURVE

3.1 Response Reduction of VE System

Kasai et al. (2003) have developed the response reduction of vibration-controlled structure based on the common linear response spectrum. In this paper, the method will be applied into the slip-hysteretic structure considered. We define the displacement spectrum, pseudo-velocity spectrum, pseudo-acceleration spectrum as S_d, S_{pv}, and S_{pa}, respectively. From any one of the three spectra, the other two spectra can be calculated in terms of Eq. (6) for a structure with period T_f and damping ratio h_f.

$$S_d(T_f, h_f) = \frac{T_f}{2\pi}S_{pv}(T_f, h_f) = \left(\frac{T_f}{2\pi}\right)^2 S_{pa}(T_f, h_f) \qquad (6)$$

The response reduction is the combination effect of vibration period decrease and viscous damping increase after the installation of damper into structure. We define the ratios of the displacement u, force F of passive system to the

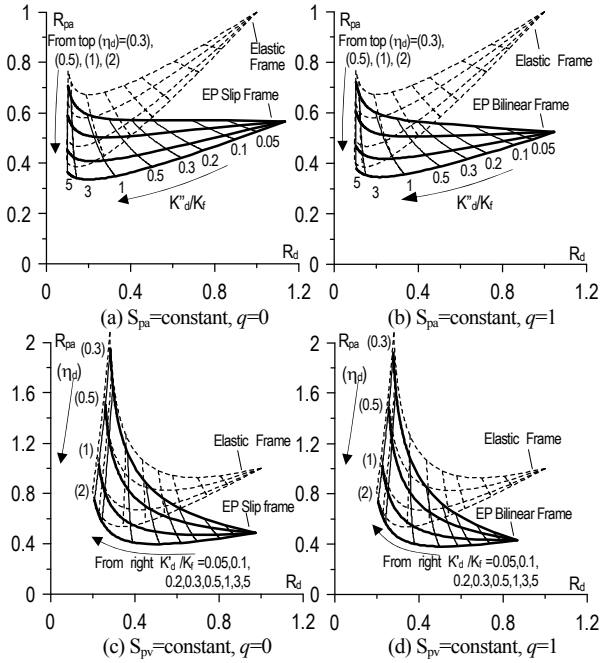

Figure 5 Performance curves

displacement and force of original elastic structure u_{el}, F_{el} as displacement reduction ratio R_d, pseudo-acceleration reduction ratio R_{pa}, respectively.

$$R_d = \frac{S_d(T_{eq}, h_{eq})}{S_d(T_f, h_f)} = D_h \frac{T_{eq}}{T_f} \frac{\bar{S}_{pv}(T_{eq}, h_f)}{S_{pv}(T_f, h_f)} \tag{7a}$$

$$R_{pa} = \frac{S_{pa}(T_{eq}, h_{eq})}{S_{pa}(T_f, h_f)} = D_h \frac{T_f}{T_{eq}} \frac{\bar{S}_{pv}(T_{eq}, h_f)}{S_{pv}(T_f, h_f)} \tag{7b}$$

where $\bar{S}_{pv}(T_{eq}, h_f)$ is the average pseudo-velocity spectrum over period range from T_0 to T_{eq}. The reason to use averaged pseudo-velocity spectrum is in that by such a way the spectrum is smoothed and the possible difference between the spectrum value at T_f and T_{eq} can be reduced.

Assume the pseudo-acceleration spectrum in short-period and pseudo-velocity spectrum in medium- to long-period are identical, respectively, the response reductions of structure can be rewritten readily as

$$R_d = D_h \frac{T_{eq}}{T_f} \frac{T_{eq}/T_f + T_0/T_f}{2}, \quad R_{pa} = R_d \left(\frac{T_f}{T_{eq}} \right)^2 \quad (S_{pa}\text{=const.}) \tag{8a,b}$$

$$R_d = D_h \frac{T_{eq}}{T_f}, \qquad R_{pa} = R_d \left(\frac{T_f}{T_{eq}} \right)^2 \qquad (S_{pv}\text{=const.}) \tag{9a,b}$$

In the above equations, the items except D_h at the right-hand sides of Eqs. (8) and (9) reflect the effect of vibration period decrease, and D_h is the "damping effect factor" reflecting the damping increase effect of adding damper into structure. The following equation is used.

$$D_h = \sqrt{\frac{1+\alpha h_0}{1+\alpha h_{eq}}} \tag{10}$$

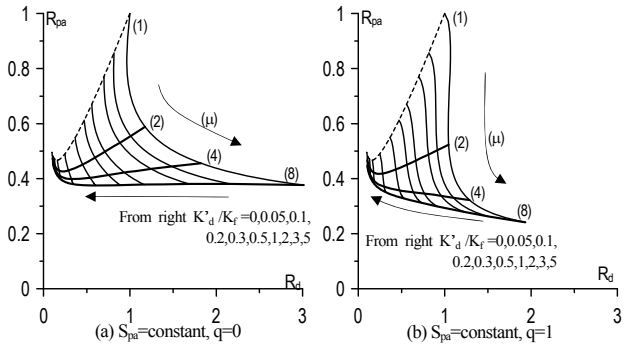

Figure 6 Performance curves with respect to ductility ratio μ (S_{pa}=constant, K_b/K_f=10, p_f=0, q=0 and 1, η_d=1)

where 25 will be used for α in case of a real earthquake, and other different value will be used for artificial earthquake depending on the earthquake's characteristics (Kasai et al. 2003).

Due to the phase difference existing between the damping force and deformation, the maximum pseudo-acceleration occurs before the maximum deformation is reached. To calculate the peak pseudo-acceleration reduction, the following equation is used (Kasai and Kawanabe 2005).

$$R_a = R_{pa}\,\mu\sqrt{1+\eta^2}\,/(1+p\mu-p) \qquad (1 \le \mu \le \mu_A)$$

$$R_a = R_{pa}\,\mu(\sqrt{p^2+\eta^2}+1-p)/(1+p\mu-p) \quad (\mu_A \le \mu) \tag{11a-c}$$

$$\mu_A = (\sqrt{1+\eta^2}+\sqrt{p^2+\eta^2})/(1+p)$$

Given the loss factor η_d and storage stiffness ratio $K"_d/K_f$, calculate the T_0/T_f, T_{eq}/T_f, and h_{eq}, and then obtain R_d and R_{pa} based on Eqs. (8) and (9). Repeating the calculation with different values of parameters produces the R_d-R_{pa} curves, and we call the curves as "performance curve".

Assume initial damping ratio h_f=0.02, ductility ratio μ=2, the performance curves with η_d=0.3~2.0, $K"_d/K_f$=0~5.0 are plotted in solid line in Fig. 5(a) and Fig. 5(b) for S_{pa}=constant and S_{pv}=constant, respectively. For comparison, the performance curves for elastic system with μ=1 and the same other parameters are plotted in broken line.

The performance curves like plotted in Fig. 5 shows the ratios of the responses of elasto-plastic VE system to those of initial elastic system. Using the performance curves, the responses of elasto-plastic VE system can be obtained as long as the elastic response of initial system is given.

3.3 Parametric Effect on Structural Response

From the performance curves shown in Fig. 5, in case of S_{pa} = constant, a larger storage stiffness ratio leads to a smaller displacement response, and this tendency is more significant than that observed in case of S_{pv} = constant. As described in the previous section, the period decrease due to supplementation of damper's stiffness lead to significant decrease in displacement (Eq.(9)). However, in case of S_{pa} = constant, even though the displacement response can be

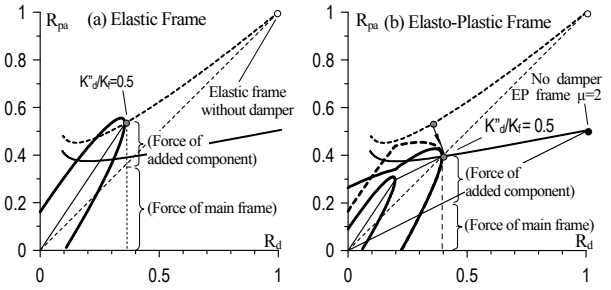

Figure 7 Response properties obtained from performance curves (q=0.5)

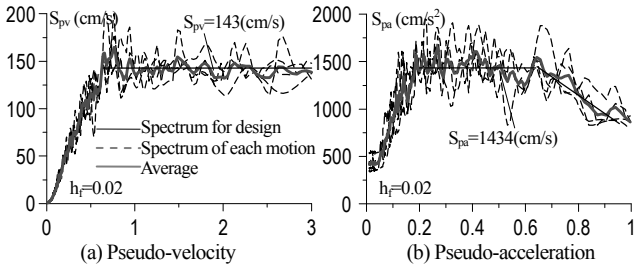

Figure 8 Response spectra of input earthquake motions

reduced greatly, the pseudo-acceleration response keeps on the same level or reduces slightly only.

In case of S_{pv} = constant, as the K''_d/K_f increases, both the displacement and pseudo-acceleration decrease till some degree, and after that the reduction effect becomes weak, and peak pseudo-acceleration becomes larger but not smaller.

As discussed previously, as the degree of structural yielding increases, the equivalent period and damping will be changed accordingly. Figure 6 shows the performance curves with ductility ratio μ ranging from 1 to 8, where S_{pa} = constant is assumed. It is observed that the peak pseudo-acceleration decreases as the ductility ratio increases for a fixed K''_d/K_f, that is because the necessary yield force becomes small. On the other hand, for a fixed ductility ratio, a larger K''_d/K_f leads to a smaller displacement response, and the pseudo-acceleration is controlled under a low level. It is also noted that significant increase in displacement response occurs when the ductility ratio of a system with large q increases.

Figure 7 shows the distribution of force between the frame and added component. Assume S_{pa} is constant and the displacement and force responses of system are already known. In Fig. 7(a), the elastic stiffness of main structure is represented by the straight line connecting the origin and the point of K''_d/K_f =0.5, μ=1 (white circle), the distribution of force between the main frame and damper is obtained readily as shown in Eq. (12). Similarly, Fig. 7(b) shows the information for elaso-plastic structure with ductility ratio μ=2. In R_d-R_{pa} coordinate, the second stiffness of VE system is represented by the line with slope of $(p_fK_f+K'_a)/K_f$. From the point of K''_d/K_f=0.5, μ=2 to draw the line with slope of $(p_fK_f+K'_a)/K_f$, it will cross the elastic stiffness line at the yield point (u_y/u_{el}, F_y/F_{el}). Accordingly, the ductility ratio μ=2 can also be verified. Moreover, the straight line connecting the origin with the point of K''_d/K_f=0, μ=2 shows the equivalent stiffness of main structure with given ductility ratio, and its slope is $(1+p_f\mu-p_f)/\mu$. In consequence, the distribution of force between main structure and damper is obtained as shown in Eq. (13).

$$\frac{F_f}{F'}=\frac{R_d}{R_{pa}},\quad \frac{F'_a}{F'}=1-\frac{R_d}{R_{pa}} \qquad (12a,\ b)$$

$$\frac{F_f}{F'}=\frac{1+p_f\mu-p_f}{\mu}\cdot\frac{R_d}{R_{pa}},\quad \frac{F'_a}{F'}=1-\frac{1+p_f\mu-p_f}{\mu}\cdot\frac{R_d}{R_{pa}} \qquad (13a,\ b)$$

3.3 Passive Control Design Based on Performance Curve

Based on the performance curve, the passive control design to determine the quantity of damper can be performed as following. The already-known include the initial period T_f, initial damping h_f, elastic stiffness K_f, post-yield stiffness ratio p_f, slip strength ratio q, yield displament u_y, brace stiffness ratio K_b/K_f, target ductility ratio μ, and target shear force (or acceleration).

(1). Make the performance curves.
(2). Calculate the elastic responses u_{el}, F_{el}.
(3). Calculate the response reductions R_d, R_{pa}.
(4). Determine the storage stiffness ratio K''_d/K_f, with an assumed loss factor η_d.
(5). Get the pseudo-acceleration reduction R_{pa}, and calculate the reduction of the maximum shear force by Eq. (11).

If both the target maximum force and maximum displacement are satisfied, the design is finished.

4. ACCURACY VERIFICATION

This chapter will carry on the time history analysis to verify the accuracy of the proposed design method. Four artificial earthquake motions are used. They include the BCJ-L2 wave which is used widely in Japanese seismic design, and other 3 motions which possess the phase characteristic of Hachinohe EW wave (HAC), JMA Kobe NS wave (JMA), Tohoku University NS wave (THK) recorded in Japan. The four motions produce almost constant S_{pa} in the period range of 0.16~0.64s, and produce almost constant S_{pv} in the period range larger than 0.64s. As shown in Fig. 8, S_{pa}=1434cm/s^2 for period range of constant S_{pa} and S_{pv}=143cm/s for period range of constant S_{pv} are used for design.

Generally, the properties of visco-elastic materials are frequency-dependent and temperature-dependent. In this paper, the temperature is fixed at 20°, and the increase of temperature due to the energy absorbing is ignored, and the strain-independent material is assumed.

The period of the initial main structure T_f=0.3s, 2s, slip strength ratio q=0, 0.2, 0.5, 1, storage stiffness ratio K''_d/K_f=0.1, 0.3, 0.5, loss factor η_d=0.3, 0.5, 1.0, and ductility ratio μ=2, 4 are assumed. The response reduction obtained from the performance curves are compared with that obtained from time history analysis. A total of 576 cases are considered.

For each of the cases mentioned above, the ratio of prediction result to analysis result is calculated, and they are averaged over 3 kinds of storage stiffness ratio, 3 kinds of loss factor. Figure 9 compares the response reductions

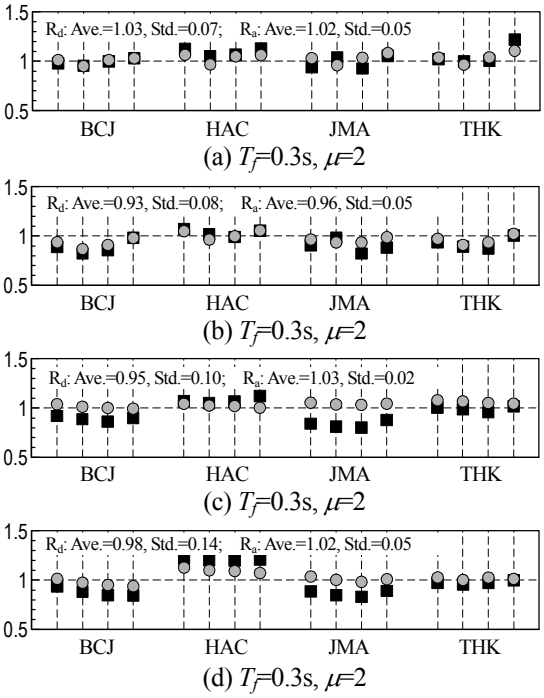

Figure 9 Accuracy of the proposed design method (Legend: ■=R_d,●=R_a)

obtained from the proposed approach and time history analysis per initial period and per ductility ratio. For each of the four motions, the result of slip strength ratio q = 0, 0.2, 0.5, 1, respectively, are shown from left to right.

Table 1 shows the ratios of the response reduction R_d, R_a obtained form time history analysis to those obtained from performance curves, and each value is the average of that obtained from 4 earthquake motions, 3 storage stiffness ratios, and 3 kinds of loss factor. The comparison shows that the time history analysis agrees well with the results of performance curve proposed.

5. CONCLUSIONS

This paper proposed a passive control design method for slip-hysteretic structure added with elasto-plastic damper based on the equivalent linearization and response spectrum. The dynamic properties of the system constituted by the main frame and the added component in parallel are discussed, the variation of equivalent period and damping with respect to system's parameters were described.

The simplified theory which clarify the complex connection between the stiffness of system element, dynamic properties of system and the response properties were described, and the performance curve which illustrate these relations intuitively was proposed. The passive control design based on performance curves can be performed effectively and efficiently, and the mechanism of the passive control can be understood by designer. The time history analysis on structures with a wide range of parameters was performed, and the good accuracy of the proposed method was verified.

Table 1 Accuracy of the proposed design method

		T_f=0.3s				T_f=2s			
		q=0	q=0.2	q=0.5	q=1.0	q=0	q=0.2	q=0.5	q=1.0
R_d	μ=2	0.89 (0.08)	0.87 (0.09)	0.88 (0.09)	0.91 (0.09)	0.95 (0.10)	0.95 (0.11)	0.96 (0.12)	1.03 (0.13)
	μ=4	0.99 (0.09)	0.98 (0.10)	1.02 (0.10)	1.02 (0.11)	0.94 (0.13)	0.95 (0.14)	0.96 (0.15)	1.03 (0.15)
R_a	μ=2	0.87 (0.05)	0.91 (0.04)	0.85 (0.06)	0.93 (0.05)	0.86 (0.05)	0.85 (0.05)	0.86 (0.05)	0.99 (0.04)
	μ=4	0.95 (0.06)	0.98 (0.05)	0.95 (0.05)	0.99 (0.05)	0.90 (0.06)	0.90 (0.07)	0.90 (0.08)	1.00 (0.07)

REFERENCE

Kasai K., Sakata H., and Wada A. et al., "Dynamic Behavior of a Wood Frame with Shear Link Passive Control Mechanism Involving K-Brace," *Journal of Structure and Construction Engineering*, No.598, pp. 51-59, 2005.12

Sakata H., Kasai K., and Wada A. et al., "Experimental Strudy on Dynamic Behavior of Wood Frame with Shera Link Passive Control Mechanism Involving Plywood Panel," *Journal of Structure and Construction Engineering*, No.594, pp. 65-73, 2005.8

Kasai K., Ito H., and Watanabe A., "Peak Response Prediction Rule for a SDOF Elasto-Plastic System Based on Equivalent Linearization Technique," *Journal of Structure and Construction Engineering*, No.571, pp.53~62, 2003.9.

Kasai K., Minato N., and Kawanabe Y., "Passive Control Design Method Based on Tuning of Equivalent Stiffness of Visco-Elastic Damper," *Journal of Structure and Construction*, No. 610, pp. 75-83, 2006.12.

Fu Yaomin and Kasai Kazuhiko, "Comparative Study of Frames Using Viscoelastic and Viscous Dampers," *Journal of Structural Engineering*, Vol. 124, No. 5, pp. 513-522, 1998.5.

Araki Y., Koshihara M., Ohashi Y. et al., "A Study on Hysteresis Model for Earthquake Response Analysis of Timber Structures," *Journal of Structure and Construction Engineering*, No.579, pp. 79-85, 2004.5

Isoda H. and Kawai N., "Hysteresis Model of Walls on Japansese Conventional Construction: Study on seismic behavior of wooden construction," *Journal of Structure and Construction Engineering*, No.616, pp. 157-163, 2007.6

Kasai Kazuhiko and Okuma Kiyoshi, "Evaluation Rule and Its Accuracy for Equivalent Period and Damping of Frequency-Dependent Passive Control Systems: Global damping model of one-mass system having elastic frame and either viscoelastic or oil damper," *Journal of Structure and Construction Engineering*, No. 580, pp. 51~59, 2004.6.

Kasai K., Nishihara K., Pu W. et al." Peak Response Evaluation Method for Slip-Hysteretic Structure Added with Visco-elastic Damper," *Journal of Structure and Construction Engineering*, No.646, pp.2227~2236, 2009.12.

Newmark, N.M. and Rosenblueth, E. "Fundamentals of Earthquake Engineering." Prentice-Hall Inc., 1971.

Kasai K., Kawanabe Y., "Equivalent Linearization to Predict Dynamic Properties and Seismic Peak Responses of a Structural System with High Viscous Damping and Hysteretic Damping," *Journal of Structure and Construction Engineering*, No. 591, pp.43~51, 2005.5.

JOINT CONFERENCE PROCEEDINGS
7th International Conference on Urban Earthquake Engineering (7CUEE) &
5th International Conference on Earthquake Engineering (5ICEE)
March 3-5, 2010, Tokyo Institute of Technology, Tokyo, Japan

STRUCTURAL DAMAGE ASSESSMENT BASED ON 3D NONLINEAR DYNAMIC RESPONSE AND ITS SEISMIC DESIGN

Yongle Zhang[1)], Jianqun Jiang[2)], Jiajin Liu[3)]

1) Graduate, College of Civil Engineering and Architecture, Zhejiang University, China
2) Professor, College of Civil Engineering and Architecture, Zhejiang University, China
3) HydroChina HuaDong Engineering Corporation, Hangzhou, China
3031243006@zju.edu.cn, jianqun@zju.edu.cn, liu_jj@ecidi.com

Abstract : The obvious double-epicenter made the Wenchuan earthquake ground motion distinctive, that hasn't been considered in the present Chinese seismic design code. An appropriate damage model used for evaluation of the progress of structural damage should take both the damage correspond to dissipated energy and displacement overpass into consideration. Four damage models were described, and one of which has been improved. Comparisons of the damage models were made in 3D nonlinear dynamic analysis of a 9-storey RC structure subjected to a real Wenchuan earthquake excitation. The results show that damage in the structural members increased mainly in the first shock. A damage-based approach based on target damage index has been proposed and verified in conjunction with present seismic design method for high intensity earthquake.

1. INTRODUCTION

The Wenchuan earthquake measured 8.0 on the Richter scale struck China on 12 May 2008 caused 69185 deaths, 18458 missing persons and 370,000 injuries according to the statistics of Ministry of Civil Affairs (ended on 25 June 2008), 7,780,000 houses collapsed and 24,590,000 were damaged (Information Department of National Disaster 2008). Data of previous events show that most of the dead were crushed or suffocated in collapsed dwellings after strong earthquakes (Tanaka et al. 1999). RC structures show well seismic performance in Wenchuan earthquake (Civil And Structural Groups Of Tsinghua University 2008), while the strong-columns and weak-beams concept required in Chinese seismic code of buildings is not well achieved (Li Ying-min et al. 2008).

High peak ground acceleration (PGA), long duration and obvious double-epicenter made the Wenchuan earthquake distinctive from the others, thus the impact should be evaluated. A reinforced concrete structure is weakened or damaged by a combination of stress reversals and high stress excursion (Park and Ang 1985). By using a seismic damage index taking in to account the maximum deformation and the effect of repeated cyclic loadings, the cumulative process of damage and the ultimate damage of members can be obtained, which are significant to damage based seismic design.

2. DAMAGE MODELS

2.1 Park-Ang Model

Park and Ang (1985) proposed a damage model based on extensive test data which was widely applied:

$$D = \frac{\delta_m}{\delta_u} + \frac{\beta}{Q_y \delta_u} \int dE \tag{1}$$

$$\beta = \left(-0.447 + 0.073 l/d + 0.24 n_0 + 0.314 p_t\right) \times 0.7^{\rho_w} \tag{2}$$

where δ_m = maximum deformation under earthquake; δ_u = ultimate deformation under monotonic loading; Q_y = calculated yield strength; dE = incremental absorbed hysteretic energy; β = coefficient for cyclic loading effect. l/d = the shear span ratio; n_0 = normalized axial stress; p_t = longitudinal steel ratio; ρ_w = confinement ratio.

$D \geq 1.0$ represents total collapse.

2.2 Kunnath Model

A modified version of the Park and Ang damage model is proposed by Kunnath et al. (1992):

$$D = \frac{\delta_m - \delta_y}{\delta_u - \delta_y} + \frac{\beta}{F_y \delta_u} \int dE \tag{3}$$

The threshold of damage caused by displacement excursion is δ_y.

2.3 Bracci Model

Bracci et al. (1989) suggested a damage model as follows:

$$D = D_M + D_\phi - D_M D_\phi \tag{4}$$

where $D_M = \frac{\Delta M}{M_y} = \frac{c \int dE}{M_y \phi_y}$ represents the deterioration of strength (c = constant) and $D_\phi = \frac{\phi_m - \phi_y}{\phi_u - \phi_y}$ represents the plastic deformation.

2.4 Kumar Model

Kumar and Usami proposed a comprehensive damage model in 1994 and then modified it in 1996 as follows:

$$D = (1-\beta) \sum_{j=1}^{N_j} \left(\frac{\delta_{m,j} - \delta_y}{\delta_u - \delta_y} \right)^c + \beta \sum_{j=1}^{N} \left(\frac{E_i}{Q_y (\delta_u - \delta_y)} \right)^c \tag{5}$$

where N_1 = the number of half cycles producing $\delta_{m,j}$ for the first time. E_i = hysteretic energy dissipated in the ith half-cycle.

2.5 Modified Kumar Model

A member has damaged after the cracking of concrete before yielding, hence a parameter k was introduced in Kumar model to adjust the damage caused by displacement excursion.

$$D = (1-\beta) \sum_{j=1}^{N_j} \left(\frac{\delta_{m,j} - k\delta_y}{\delta_u - k\delta_y} \right)^c + \beta \sum_{j=1}^{N} \left(\frac{E_i}{Q_y (\delta_u - k\delta_y)} \right)^c \tag{6}$$

where $0 \leq k \leq 1$.

3. 3D DYNAMIC DAMAGE ANALYSIS of RC STRUCTURE

3.1 Analytical Models of RC Members

Several models for the nonlinear response analysis of RC structures have been developed, including global models, discrete finite element models and microscopic finite element models, among which discrete finite element models are the best compromise between simplicity and accuracy in nonlinear seismic response studies, thus it is widely used.

Lumped plasticity models and distributed nonlinearity models can be used to model and analyze RC structures in the inelastic range of response. (Taucer et al. 1991)

3.2 Damage Assessment of RC Members

A 9-storey RC structure (Fig. 1) was selected to evaluate damage of members subjected to a real Wenchuan earthquake excitation. The strength of concrete used for column with a cross-section of $0.6 \times 0.6 m^2$ is C30 and that for beams (1st-3rd storey with a cross-section of $0.4 \times 65 m^2$ and 4th-9th storey with a cross-section of $0.3 \times 0.65 m^2$) is C25. The longitudinal steel ratio of columns = 2% and that of beams = 1.5%.

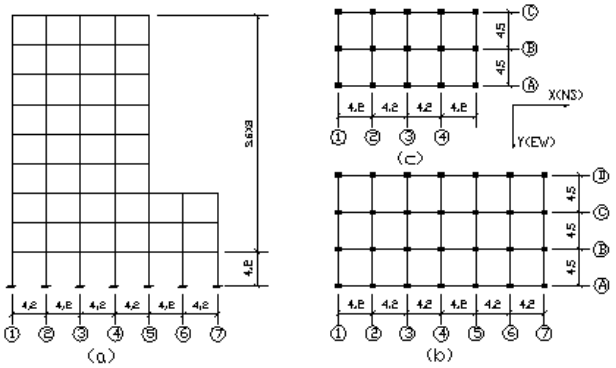

Figure 1 Details of 9-Storey RC Structure
(a) Elevation of Structure, (b) Plans of Structure (1st-3rd) and (c) Plans of Structure (4th-9th)

Table 1 Eigenvalues of Structure

Mode	Eigenvalue (Hz)
1 (EW)	1.370
2 (NS)	1.538
3 (EW)	3.704
4 (NS)	4.167

The computer program CANNY is developed for structural analysis using the multi-spring model to include the three-dimensional nonlinear behavior of structures, thus was used in this paper. The beam was idealized by elastoplastic uniaxial spring, two rotational

springs at element-end, and shear and axial springs located in mid span. The column element was modeled by multi-spring model including multi-axial spring model and multi-shear spring model (Li 2003). The first four eigenvalues of the structure are listed in Table 1, and the corresponding eigenmodes are shown in Fig. 2.

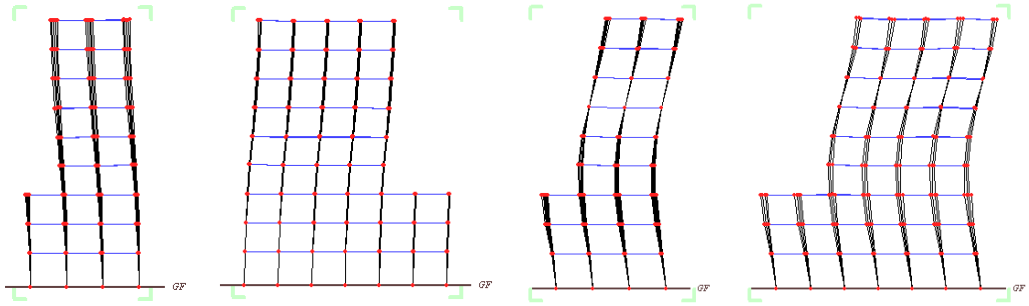

Model 1 Model 2 Model 3 Model 4

Figure 2 Vibration Modes of the Structure

A real Wenchuan earthquake ground motion scaled to PGA of 0.95g (EW), 0.65g (NS) and 0.95g (UD) respectively obtained in Wolong has been selected for analyzing (Fig. 3). The Newmark-β method has been utilized as a numerical integration scheme and the time increment 0.01s has been adopted taking into account the P-Δ effect. 5% damping proportional to instantaneous stiffness was assumed.

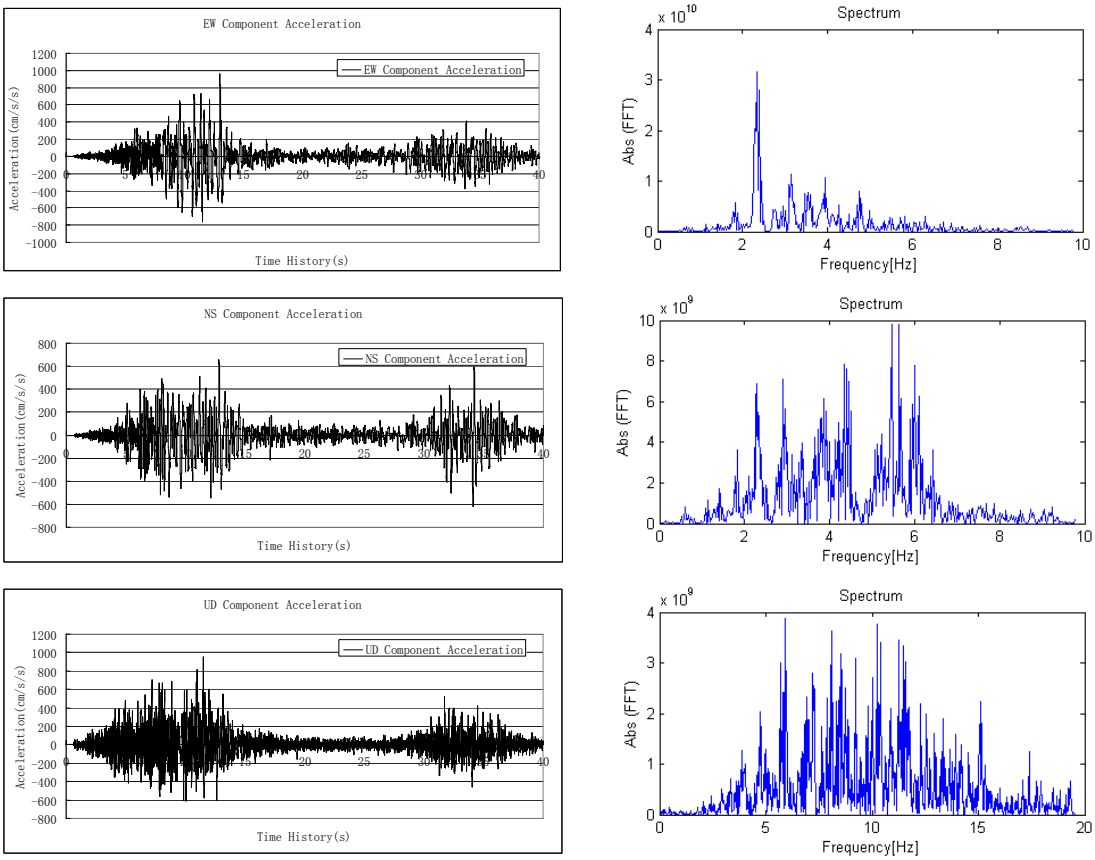

Figure 3 Ground Accelerations and Spectra of Wenchuan Earthquake

3.2.1 Damage Assessment of Beams

For comparison, B240 (X=5, A-B) which located on the 7th storey was selected, β=0.11 for all models, c=1 for Kumar model and modified Kumar model (Kumar and Usami 1996), experiments should be taken out to determine the value of k, a rough estimate value of k= 0.5 was used in this paper only to illustrate the modification of Kumar model. The ultimate damage indices were listed in Table 2, and the cumulative process of damage can be seen in Fig. 4 and 5.

The ultimate damage indices vary from 0.54 to0.79 in the initial end and from 0.45 to 0.69 in the terminal end among the above five models, damage index of Park-Ang model is the largest, and that of Bracci model is the smallest, for the threshold of displacement

excursion caused damage = 0 according to Park-Ang, and the product of D_M and D_ϕ was subtracted in Bracci model.

The value of damage index climbed up rapidly in 8-13s corresponding to the first shock, while increased slightly during the second shock (30-37s). The probably reason may be that the first shock is far larger than the second one, the structure has been damaged severely after the first shock, and the vibration characteristic of the structure has changed.

Table 2 Final Damage of B240

Location	Park-Ang	Kunnath	Bracci	Kumar	Modified Kumar
Initial End	0.7901	0.6392	0.5429	0.7162	0.7554
Terminal End	0.6929	0.5198	0.4545	0.5875	0.6450

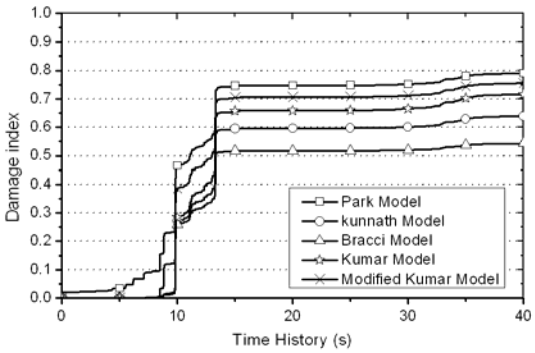

Figure 4 Damage in the Initial End of B240

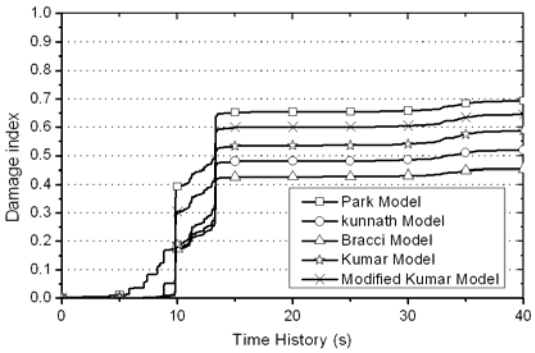

Figure 5 Damage in the Terminal End of B240

3.2.2 Damage Assessment of Columns

C14 (ground storey, X=4, Y=B) was chosen for damage assessment, damage index of the column should take multi-axial load interactions in to consideration, thus Eq. (7) was used to represent damage caused by biaxial bending according to Li and Zhao (Li and Zhao 2000).

$$D = D_x + D_y - A\sqrt{D_x D_y} \tag{7}$$

where D_x and D_y represent damage caused in x and y directions respectively, A=0.58.

The ultimate damage indices were listed in Table 3, and the cumulative process of damage can be seen in Fig. 6 and 7.

Table 3 Final Damage of C10

Location	Park-Ang	Kunnath	Bracci	Kumar	Modified Kumar
Initial End	0.5772	0.4016	0.3862	0.4120	0.4603
Terminal End	0.1123	0.0112	0.0112	0.0131	0.0212

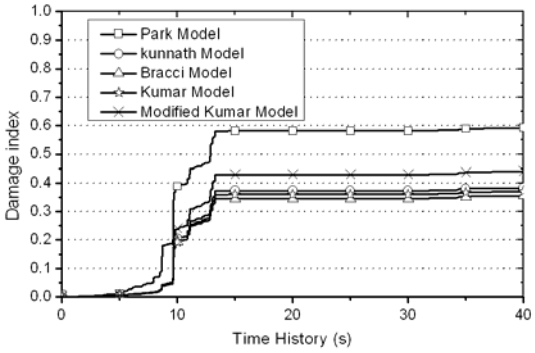

Figure 6 Development of Damage in the Bottom of C10

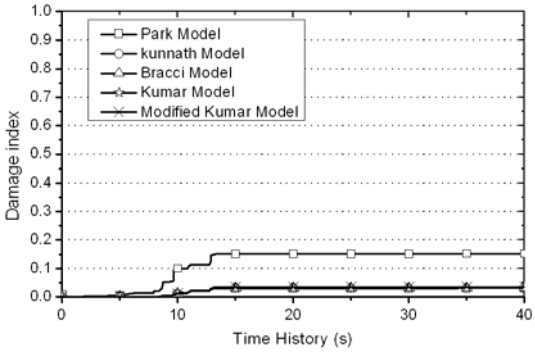

Figure 7 Development of Damage in the Top of C10

As can be seen from Fig. 6 and 7, damage in the bottom of C10 soared dramatically in 8-13s corresponding to the first shock, and remained nearly constant during the second shock. Steels in the capital of the C14 didn't yield in the earthquake. Park-Ang gave a ultimate damage index of 0.11 because of the 0-threshold of displacement excursion caused damage, while others gave nonzero but negligibly small values of damage indices.

4. DAMAGE-BASED SEISMIC DESIGN

4.1 Damage-Based Seismic Design Method of RC Buildings

Early damage-based seismic design was only applied in checking process (Ou et al. 1999). Wang (2007) proposed a direct damage-based seismic design method based on Park-Ang model, at first a value of displacement ductility factor was assumed and then verified. A concise method was proposed in this paper based on the Park-Ang model as well, the demanded value of ductility factor could be derived from calculation rather than assumption.

The damage index of Park-Ang model is the largest among the above five models, thus this model is conservative for seismic design. A parameter γ was introduced by Fajar for Single-Degree-Of-Freedom (SDOF) system (Fajfar et al. 1992) :

$$\gamma = \sqrt{\frac{E_H / m}{\omega \delta_m}} \tag{8}$$

where E_H = the dissipated hysteretic energy, δ_m = the maximum displacement, m = the mass of the system and ω = its natural frequency. For $m\omega^2\delta_y = Q_y$, $\delta_m = \mu\delta_y$, γ can be expressed as follows:

$$\gamma = \frac{1}{\mu}\sqrt{\frac{E_H}{Q_y\delta_y}} \tag{9}$$

where γ is function of period of structure, hysteretic model and ground motion (Fajfar and Vidic 1994).

Substituting Eq. (9) into Eq. (1) yields

$$\mu = \frac{\sqrt{1+4D\beta\gamma^2\mu_u}-1}{2\beta\gamma^2} \tag{10}$$

where $\mu_u = \delta_u / \delta_y$. μ_u = ultimate monotonic ductility.

Wang feng (Wang 2007) deduced the $\mu - D$ relationship of Multi-Degree-Of-Freedom (MDOF) system, yielded

$$\mu_i = \frac{\sqrt{1+4D_i\beta\gamma^2\mu_u}-1}{2\beta\gamma^2} \tag{11}$$

where μ_i = the ductility factor of i th storey, D_i = damage index of i th storey. It is as the same form as that of SDOF. By assuming damage indices of columns on the same storey are of the same value, Eq. (11) represents $\mu - D$ relationship of columns on i th storey as well.

Comparison between damage-based seismic design method proposed in this paper and traditional damage checking procedure was shown in Fig. 8. A target damage index can be specified by users or designers. The basic steps of the method are summarized as follows:

(1) Assume cross-sections of beam and column members, transform Multi-Degree-Of-Freedom (MDOF) system to Equivalent Single-Degree-Of-Freedom (ESDOF) system, calculate the fundamental period of the structure T_1;

(2) Determine parameter γ, β and μ_u; specify target D, thus displacement ductility demand can be obtained from Eq. (10);

(3) Determine ductility dependent reduction factor R_μ (Zhuo and Fan 2001);

$$R_\mu = 1+(\mu-1)(1-e^{-4.84T})+\frac{\mu-1}{0.8+0.89\mu}T\bullet e^{-0.4T}$$

site of class 1 (12a)

$$R_\mu = 1+(\mu-1)(1-e^{-3.95T})+\frac{\mu-1}{0.76+0.09\mu-0.003\mu^2}T\bullet e^{-0.65T}$$

site of class 2 (12a)

$$R_\mu = 1+(\mu-1)(1-e^{-1.38T})+\frac{\mu-1}{0.41+0.06\mu-0.03\mu^2}T\bullet e^{-0.87T}$$

site of class 3 (12a)

(4) Determine elastic earthquake force F_E using elastic response spectrum according to the Code for Seismic Design of Buildings (2003), then earthquake force of ESDOF F_y can be obtained as follows:

$$F_E = \alpha_1 G_{eq} \tag{13}$$

where α_1 = horizontal seismic coefficient, G_{eq} = total equivalent seismic weight of the building. When the structure is modeled as multi-mass system, 85% of the representative of the total gravity load may be used.

$$F_y = F_E / R \tag{14}$$

(5) Transform earthquake force of ESDOF to base shear of MDOF

$$V_b = \Gamma_1^2 \bullet F_y \tag{15}$$

(6) The lateral force, F_i at each storey can be expressed in terms of the base shear

$$F_i = \frac{G_i H_i}{\sum G_i H_i} V_b \tag{16}$$

where G_i = representative value of gravity load concentrated at the mass of i, taken as the combination of dead load and live load, H_i calculated height of mass i from the base of building.

Target damage index can be used as a design parameter at the beginning of the designing process.

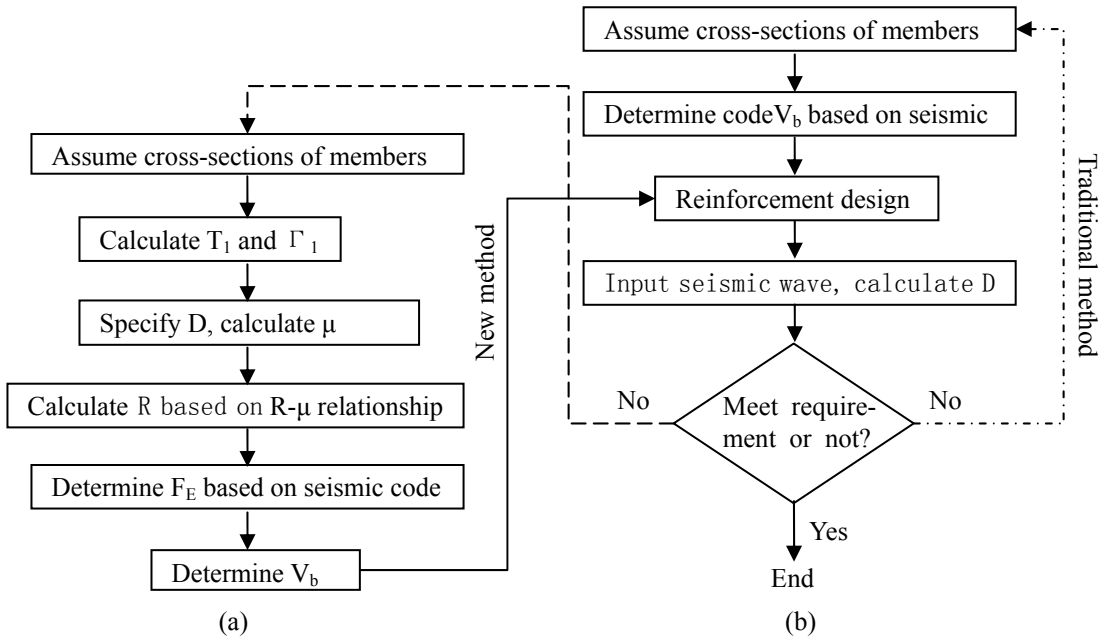

Figure 8 Comparison Between Damage-Based Seismic Design Method Proposed in This Paper and Traditional Damage Checking Procedure: (a) New Method (b) Traditional Method

4.2 Example of Damage-Based Seismic Design

For demonstration an assumed 6-storey RC building structure was chosen for designing with a storey height of 3.6m, plans of the structure can be seen in Fig. 9. Roof dead load= 6.6kN/m^2, roof live load= 1.0 kN/m^2, storey dead load=4.7 kN/m^2, storey live load=2.0 kN/m^2, the building sited in seismic intensity areas of degree 8.

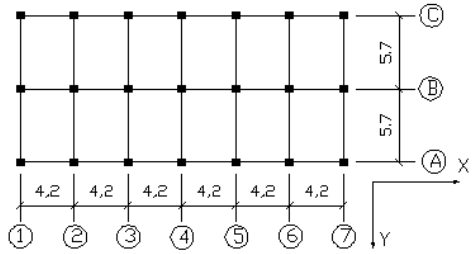

Figure 9 Plans of the Structure

A cross-section of 0.6×0.6m^2 and that of 0.55×0.55m^2 were selected for columns of the 1st-3rd floor and 4th-6th floor respectively, and a cross-section of 0.25×0.65m^2 was selected for all beams. The fundamental period of the structure was 0.54 s, the first mode participation coefficient was 1.316. It was assumed that γ =1.2 (Wang 2007), β =0.15, μ_u =6 (Fajfar 1992). Assuming target damage index = 0.9, hence μ =3.20 was obtained from Eq.(10), and R =4.66 from Eq. (12a), F_E =13371kN, F_y =2868.7kN, V_b =4700.1kN, which was used for reinforcement design. Fig. 10 shows the sketch of the building and the longitudinal steel demand.

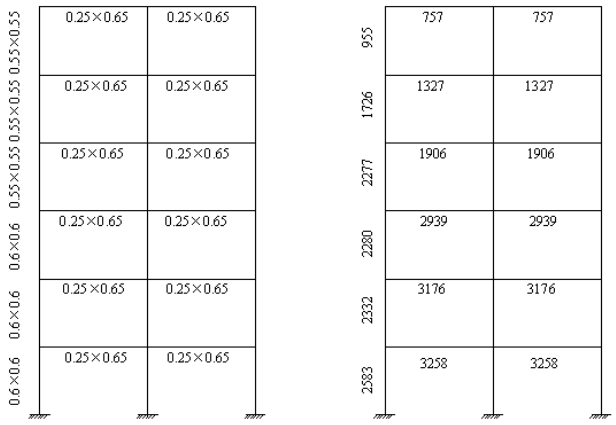

Figure 10 Details of the Building:

(a) Sketch of the Building (b) Longitudinal Steel Demand

An actual seismic record (EI Centro earthquake, 1940) was selected for checking, PGAs of the ground motion were adjusted to 0.4 m/s^{2}and 0.34 m/s^2 in Y-direction and X-direction respectively, according to Chinese seismic code. The column C1 (ground floor, X=A, Y=1) was the most severely damaged member, thus was chosen for checking. The cumulative process of damage in the bottom of C1 was shown in Fig. 11.

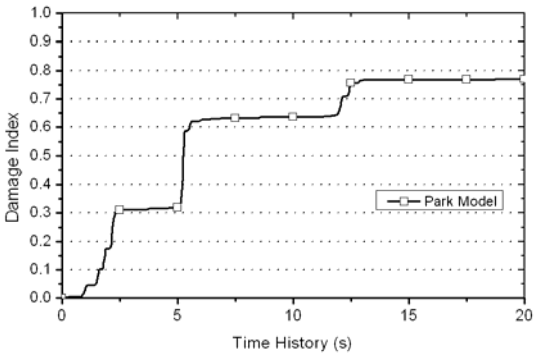

Figure 11 Development of Damage in the Bottom of C1

The ultimate damage index = 0.77, lesser than the target damage index =0.9, thus satisfied the requirement.

5. CONCLUSION

By introducing a damage index in seismic analysis, the development of damage in members of structures during earthquakes can be obtained, which may better reflect the damage process of the members.

Analysis in this paper shows that damage indices of B240 and C10 of the structure turned out to be fairly large after the first main shock, while only increased slightly during the second main shock, the probably reason may be that the ground motion is extremely large in Wenchuan earthquake, hence the structure has damaged seriously after the first main shock, and the vibration characteristic of the structure has changed. However, more researches are needed taking into consideration the variations of different ground motions.

A direct damage-based seismic design method was proposed based on the Park-Ang model, owners or designers may designate different target damage indices according to different performance demand. The simple steps of the method proposed in this paper make it easy for application.

References:

Information Department of National Disaster. (2008). "Comparison of Wenchuan earthquake and Tangshan earthquake." *Natural Disaster Reduction in China*, (7) , 46-47.

Tanaka, H., Oda, J., and Iwai, A., et al. (1999). "Morbidity and mortality of hospitalized patients after the 1995 Hanshin-Awaji earthquake," *The American journal of emergency medicine*, **17**(2), 186-191.

Civil and Structural Groups of Tsinghua University, Xinan Jiaotong University and Beijing Jiaotong University. (2008). "Analysis on seismic damage of buildings in the Wenchuan earthquake." *Journal of Building Structures*, **29**(4) , 1-9.

Li Yingmin, Han Jun, Liu Liping, Xia Hongliu. (2008). "Surveying and Discussing on Wenchuan earthquake between Chinese and Janpanese structure experts." *8th Conference on Constructional and Structural Technologies of China and Japan*, Beijing, China, 51-56.

Park, Y. J., and Ang, A. H. S. (1985). "Mechanical seismic damage model for reinforced concrete," *Journal of Structural Engineering*, **111**, 722-739.

Kunnath, S. K., Reinhorn, A. M., and Lobo, R. E. (1992). "IDARC 3.0: A program for the inelastic damage analysis of RC structures." *Technical Report NCEER-92-0022*, National Center for Earthquake Engineering Research, Buffalo.NY.

Bracci, J. M., Reinhorn, A. M., and Mander, J. B., et al. (1989). "Deterministic model for seismic damage evaluation of RC structures." , State University of New York at Buffalo.

Kumar, S., and Usami, T. (1994). "A note on the evaluation of damage in steel structures under cyclic loading," *Journal of Structural Engineering*, **40**, 177–188.

Kumar, S., and Usami, T. (1996). "Damage evaluation in steel box columns by cyclic loading tests," *Journal of Structural Engineering*, **122**(6), 626-634.

Taucer, F. F., Spacone, E., and Filippou, F. C. (1991). "A fiber beam-column element for seismic response analysis of reinforced concrete structures." *UCB/EERC-91/17*, Earthquake Engineering Research Center, College of Engineering, University of California, Berkeley.

Li Kangning. (2003). "CANNY Technical Manual.".

Li Junqi, Zhao Shichun. (2000). "Damage model of reinforced concrete member." *Journal of Lanzhou Railway University(Natural Sciences)*, **19**(3) , 25-27.

Ou Jinping, He Zheng, Wu Bin, Qiu Fawei. (1999). "Seismic damage performance-based design of reinforced concrete structures." *Earthquake Engineering and Engineering Vibration*, **19**(1) , 21-30.

Wang Feng. (2007). "Studies on Performance-based seismic

design methods of structures subjected to multi-dimensional earthquake excitations." *Dalian: Dissertation of Dalian University of Technology*.

Fajfar, P., Vidic, T., and Fischinger, M. (1992). "On energy demand and supply in SDOF systems." in *Nonlinear Seismic Analysis and Design of Reinforced Concrete Buildings*, Elsevier, Amsterdam, 41-62.

Fajfar, P., and Vidic, T. (1994). "Consistent inelastic design spectra: hysteretic and input energy," *Earthquake Engineering & Structural Dynamics*, **23**(5), 523-537.

Zhuo Weidong, Fan Lichu. (2001). "On strength reduction factors used for seismic design of structures." *Earthquake Engineering and Engineering Vibration*, **21**(1) , 84-88.

China Ministry of Construction. (2003). "Code for seismic design of buildings (GB50011-2001)." , China Architecture & Building PressBeijing.

Fajfar, P. (1992). "Equivalent ductility factors, taking into account low-cycle fatigue," *Earthquake Engineering & Structural Dynamics*, **21**(10), 837-848.

JOINT CONFERENCE PROCEEDINGS
7th International Conference on Urban Earthquake Engineering (7CUEE) &
5th International Conference on Earthquake Engineering (5ICEE)
March 3-5, 2010, Tokyo Institute of Technology, Tokyo, Japan

SEISMIC RESPONSE OF ROCKING BRIDGES SELF-CENTERING DUE TO GRAVITY

Mostafa Masoudi[1)]

1) PhD Student of Earthquake Engineering, ROSE School, IUSS Pavia, Italy
mmasoudi@roseschool.it

Abstract: This paper aims to introduce a seismic resistant scheme of ordinary bridges that can be allowed to rock during strong ground shaking without losing stability due to excessive rocking. Rocking instability is avoided by means of stop abutments and self centering is provided only based on gravity acceleration. In this paper evaluation of earthquake response is presented. It has been shown that this innovative system can survive severe strong motions and reduce inertial forces like an isolated bridge while satisfies desired drift limit. Also two simplified procedures have been proposed to calculate peak response for design purposes. The first one considers peak ground velocity of the design ground motion as the key value to calculate peak structural response. The second proposed method estimates maximum response by introducing new spectral values calculated according to the gap value between deck and abutments. Since in this new system no special devices or technologies have been used, it has economical privilege compared with isolated bridges and post-tensioned self-centering piers.

1. INTRODUCTION

Self-centering is one the most important characteristics of a modern earthquake resistant structural system. Several attempts have been done to design such systems which meet the desired performance objective. Up to now, modern proposed structural systems contain isolation devices or unbounded post-tensioned tendons or combination of them to dissipate energy. Post-tensioning technology is used to design self centering bridge piers while preventing excessive rocking that cause instability. Necessary items in the technical literature of these kinds of structures have been addressed in this study.

In this study instead of using special devices or technology, it has been focused on the inherent self centering due to gravity acceleration to introduce a simple earthquake resistant scheme. This bridge structural system can rock during earthquakes. Excessive rocking is prohibited by using stop abutments. Abutments exist in most of bridge structures. The bridge deck hits stop abutments if a large rocking response occurs. They need to be designed for deck impacts.

This paper considers only the dynamic behavior of the proposed scheme and does not provide information relating to detail design. For example if this system is used in transverse direction then an appropriate earthquake resistant system should be considered for longitudinal direction which avoids any conflict with the transverse one.

2. DYNAMICS OF THE SYSTEM

Transverse motion of a typical bridge bent in Figure 1 is considered in this study. Only rocking response in allowed. Thus an appropriate detail should be designed for connection between piers and deck and foundation. As an example of such a connection is two steel rings circumvent each pier at the top and bottom. They are connected to the deck and foundations. However, they have enough tolerance with piers to make rocking possible. The duty of this connection is to avoid the sliding response of the deck on piers and also to transfer the inertial forces of the deck into the piers when small sliding compensates for the tolerance between piers and ring connections. The other alternative for this purpose is steel bars coming out from piers and going into deck and foundation. However, these bars should be unbounded in the deck and foundation to avoid any moment transfer.

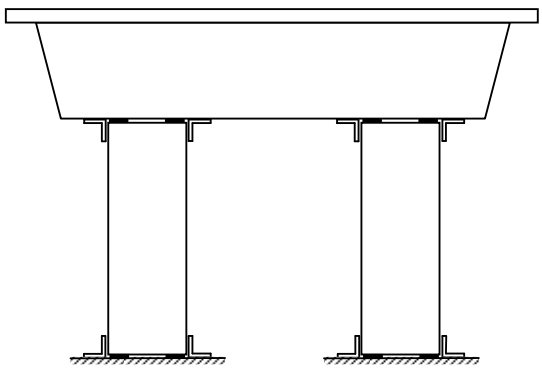

Figure 1 A typical bridge bent with appropriate foundation-pier-deck connections to ensure a rocking motion

After rocking by increases in displacement the stiffness of the rocking system reduces. Rocking response is nonlinear and it is hardly acceptable to represent it by a single degree of freedom system (Zhang and Makris 2001). Housner (1963) analyzed the free oscillations of a free-standing rocking block and addressed the rocking period and energy loss accordingly. Shenton (1996) showed it is incorrect to assume that the rocking mode will govern if static friction is simply greater than the aspect ratio of the block, D/H.

To obtain dynamic characteristics of such a system the following assumptions have been considered:

- All elastic deformations prior to and during the rocking response are negligible.
- Translational and rotational masses of the piers are negligible compared with the deck mass.
- The bridge deck is considered as a rigid body in the transverse bending plane.
- The system can show only a rocking response without sliding.
- When the direction of the deck displacement changes then a certain amount of energy loss is considered to calculate the restitution factor.

It does not matter how many piers a bent has. The following figure shows the free body diagram of a bent during the rocking response. In Figure 2 the free body diagram of a two pier bent is shown.

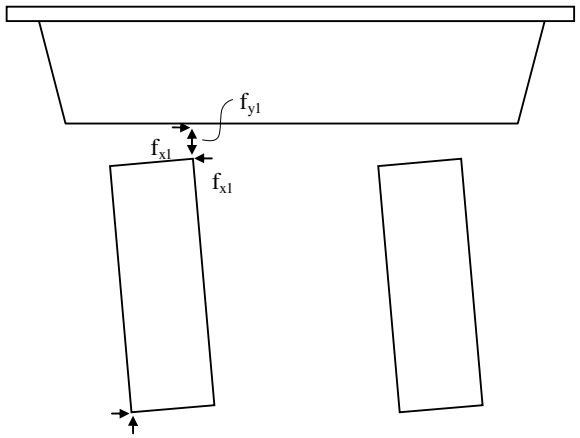

Figure 2 Free body diagram of a rocking bent

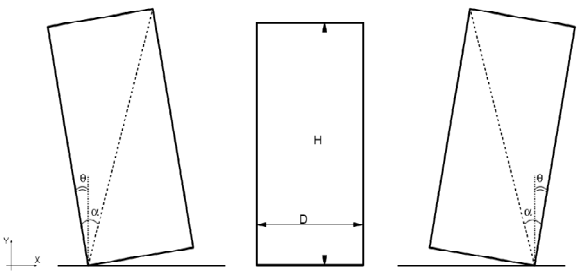

Figure 3 Rocking motion of a bent pier

Figure 3 shows possible rocking motion for a pier with required parameters for analytical model.

The following kinematic relationships are applicable to a bridge deck and obtained by considering the motion of pier corners which is in contact with the deck. For clockwise motions, $\theta > 0$ and for counter-clockwise motions, $\theta < 0$ we can write:

$$x = R\cos(\alpha \mp \theta)\,\theta \quad , \quad y = \pm R\sin(\alpha \mp \theta)\,\theta \qquad (1)$$

where, the negative sign is for clockwise and positive sign is for counter-clockwise motions. Aforementioned relationships are also valid for first and second derivatives of the motion i.e. velocity and acceleration.

$$\frac{y}{x} = \frac{\dot{y}}{\dot{x}} = \frac{\ddot{y}}{\ddot{x}} = \tan(\alpha \mp \theta)\,\dot{\theta} \qquad (2)$$

Considering instantaneous rotational equilibrium for each pier while neglecting their mass, we can write:

$$f_y = \mp \frac{f_x}{\tan(\alpha \mp \theta)} \qquad (3)$$

where, fx and fy are shown in Figure 2.

Equations of motion of the deck in x and y direction can be written as the following.

$$\sum f_x = m_d(\ddot{x} + \ddot{x}_g) \qquad (4)$$

$$\sum f_y - W_d = m_d\ddot{y} \qquad (5)$$

where, md and Wd are the deck mass and weight, respectively.

By substituting Eq. (4) into Eq. (5) we can write:

$$\sum f_x = m_d(\ddot{x} + \ddot{x}_g) \qquad (6)$$

Considering the following definition we can write 5 6 simpler.

$$A = \ddot{x}/g \quad ; \quad A_g = \ddot{x}_g/g \qquad (7)$$

where, g is gravity acceleration. So, the rotational acceleration of piers is:

$$\ddot{\theta} = -\frac{g}{R}\left(\sin(\alpha\,\mathrm{sgn}(\theta) - \theta) + A_g\cos(\alpha\,\mathrm{sgn}(\theta) - \theta)\right) \qquad (8)$$

It is very important to consider the impact problem when piers recover to their initial configuration and energy is dissipated through impacts between piers and foundation and deck. Free vibration response of a rigid block indicates

that the restitution factor i.e. the ratio of velocity immediately after and before impact is equal to the square root of kinetic energy of the system immediately after and immediately before impact for the linear limit of response (Housner 1963). Here, it is considered all impacts to be Inelastic.

To solve the equation of motion which it is a second order differential equation the Runge-Kutta-Nyström method (Kreyszig 1993) has been applied. This is done by a MATLAB codes.

The level of acceleration that causes rocking initiation is calculated by the following relationship. It depends on the geometrical dimensions of piers.

$$W_d D = m_d \ddot{x}_g H \Rightarrow A_g = \frac{D}{H} \quad (9)$$

To prevent excessive rocking that cause instability, it is necessary to consider something like stop walls. For ordinary bridges it is possible to build abutments as stop walls. A certain gap should be provided between the bridge deck and stops in the transverse direction. The rough estimation of this gap is calculated based on the desired drift limit. Since, stop walls have a finite stiffness the drift response will exceed the first considered drift which is equal to the ratio of the gap over the deck height. To solve the deck-abutment impact problem in this preliminary stage, we simply represent each stop wall as a spring and dashpot.

$$\sum f_x - K(x \mp \delta) - C\dot{x} = m_d(\ddot{x} + \ddot{x}_g) \quad (10)$$

$$\sum f_y - W_d = m_d \ddot{y} \quad (11)$$

Considering Eq. (3) which is also valid in this case and substituting ∑fx from Eq. (10) into Eq. (11) result in:

$$\mp \frac{m_d(\ddot{x} + \ddot{x}_g) + K(x \mp \delta) + C\dot{x}}{\tan(\alpha \mp \theta)} - W_d = m_d \ddot{y} \quad (12)$$

If we transfer x and y to the polar coordinate then:

$$\ddot{\theta} = -\frac{g}{R}(\sin(\alpha \mathrm{sgn}(\theta) - \theta) + A_g \cos(\alpha \mathrm{sgn}(\theta) - \theta)) + \frac{\cos^2(\alpha \mathrm{sgn}(\theta) - \theta)}{m_d}(K(\theta \mathrm{sgn}(\theta) - \beta) + C\dot{\theta}\mathrm{sgn}(\theta)) \quad (13)$$

Relationship for the rotational equilibrium of the deck results is:

$$\left(\sum f_x - K(x \mp \delta) - C\dot{x}\right) H' + \sum (f_y d_i) = I_d \ddot{\theta}_d \quad (14)$$

where, H' is the distance between the top of the pier to the deck center of gravity and $\ddot{\theta}_d$ is equal to zero. From Eq. (10) we have:

$$\left(m_d(\ddot{x} + \ddot{x}_g)\right) H' + \sum (f_y d_i) = 0 \quad (15)$$

We know $\ddot{x}$ because we have calculated $\ddot{\theta}$. Now, if we consider the vertical equilibrium and the rigid deck assumption we can calculate forces in each pier.

3. EXAMPLE BRIDGE

A simple bridge is considered as an example. This bridge has three identical bents and each bent has two piers. It is designed in a way that the abutments do not carry any gravity load from the deck. Pile abutments are designed as stops to prevent excessive rocking response. Only pile stiffnesses are considered for transverse stiffness of stops and the contribution of soil pressure is not considered. Here, only the translational response is considered.

8 sever ground motion which are listed in Table 1 has been selected for these analyses. Selected response spectra have been shown in the appendix.

Table 1 Sever seismic excitations used in analyses

Earthquake	PGA (g) PGV (cm/s) PGD (cm)	Duration of strong motion (sec)	Component	Station details	Site category	Closest distance to fault (km)	Database
San Fern. 1971	1.226 112.5 35.5	33.60	SFERN/ PUL164	CDMG #279	Rock	1.81	PEER
Gazli 1976	0.852 71.6 23.71	10.61	GAZ090	9201 Karakyr	Rock	5.46	PEER
Tabas 1978	0.852 121.4 94.58	27.88	TR	9101 Tabas	Rock	2.05	PEER
Nahanni 1985	1.096 46.1 14.58	13.12	S1280	6097 Site 1	Rock	9.60	PEER
Landers 1992	0.721 97.6 70.31	33.27	LCN275	24 Lucerne	Rock	2.19	PEER
Northridge 1994	1.779 113.6 33.22	27.32	TAR090	CDMG 24436 Tarzana	Shallow (stiff) soil	15.60	PEER
Chi Chi 1999	0.814 126.2 92.57	44.88	TCU 065-W	TCU065	Deep broad soil	0.59	PEER
Bam 2003	0.815 124 34	39.23	N278E	3168/02	Deep hard soil	< 1	BHRC

Required details to conduct analyses are given in the following:

- Height of piers, H = 7 m
- pier diameter, d = 1 m
- Provided transverse gaps between deck and stop abutments are associated to 1%, 3%, 5% and 10% drifts.
- Stiffness of each abutment = 4×7 = 28 kN/mm
- Damping ratio of abutments = 5%
- Restitution factor = √0.8

Considering results of analyses, displacement and velocity responses are very sensitive to the duration of major acceleration pulses.

Even for a very high level of PGA if PGD is small then the bridge can survive ground motion without hitting stop abutments while stability is not violated.

4. SIMPLIFIED METHODS TO EVALUATE RESPONSE

For design purposes it is necessary to develop a simplified approach to estimate reasonable values for peak responses. Here tow methods have been proposed to obtain design values.

4.1 Velocity Based Method

Consider Eq. (13) while θ > 0. If we multiply both sides of this equation by Rcos(α–θ) and add the ground acceleration then the total horizontal acceleration is obtained.

$$A_T = -\frac{1}{2}\sin\big(2(\alpha-\theta)\big) + A_g(1-\cos^2(\alpha-\theta)) + \frac{R\cos^3(\alpha-\theta)}{W_d}\big(K(\theta-\beta)+C\dot{\theta}\big) \quad (16)$$

The first term can be replaced by –(α–θ). The second term can be neglected because cos(α–θ) is very close to one. In the third term we can neglect the effect of damping in this stage. Also from the results of analyses it is possible to obtain a rational value for θ–β for each considered drift associated to the gap i.e. β. Therefore, Eq. (16) is reduced to:

$$\mathrm{A_{T,max}} = -(\alpha-\theta_{\max}) + \frac{\mathrm{RK}}{\mathrm{W_d}}(\theta_{\max}-\beta) \quad (17)$$

When the deck hits stops we can assume the deck and the stop as a single degree of freedom system during the impact time. Just before each impact, this SDOF system has an initial velocity which is equal to the velocity when θ is equal to β. So, the displacement response of such a system is:

$$\mathrm{u(t)} = \frac{\dot{u}_0}{\omega_n}\sin(\omega t) = \dot{u}_0\sqrt{\frac{m_d}{K}}\sin(\omega t) \quad (18)$$

Therefore the maximum displacement response is:

$$u_{\max} = \dot{u}_0\sqrt{\frac{m_d}{K}} \quad (19)$$

Also we know that:

$$\theta_{\max} - \beta = \frac{u_{\max}}{H} \quad (20)$$

Without conducting a time history analysis for the rocking system for each specific earthquake it is impossible to find the maximum of ů0 in all impacts. Therefore, it is necessary to estimate a rational value for the maximum of initial velocity for the largest impact that leads to the maximum horizontal acceleration. For a system without stopping block or abutment if it can rock without instability due to excessive rocking, the maximum velocity of such a system cannot exceed the peak ground velocity i.e. PGV because when rocking initiates there is always a restoring acceleration due to the gravity in the opposite direction of the relative system displacement. Although in a real case when there are stops this assumption maybe violated due to several impacts and complexity of the response, it can be a good assumption for preliminary design. So, we can obtain a design value for θ.

$$\theta_{\mathrm{des}} = \frac{\mathrm{PGV}}{H}\sqrt{\frac{m_d}{K}} + \beta \quad (21)$$

For the conventional range of bridge pier's aspect ratios, R and H are very close. Considering Eq. (21) we can reduce Eq. (17) to:

$$\mathrm{A_{T,des}} = \beta - \alpha + \mathrm{PGV}\left(\frac{1}{g}\sqrt{\frac{K}{m_d}} + \frac{1}{H}\sqrt{\frac{m_d}{K}}\right) \quad (22)$$

For a near fault motion PGV maybe assumed equal to 1 m/sec. As an example PGV for Tabas 1978 earthquake is equal to 1.21 m/sec which results in AT,des = 0.921 for β = 0.03. Exact solution results in 0.89g as the maximum value of total horizontal acceleration in deck.

This method is shorting to consider the effect of provided gap between deck and stop abutments. It gives same value for all gap limits. However, in the next proposed method one may develop a design spectrum associated to different gap limits and obtain a better estimation of design values. This is described in the next section.

4.2 Displacement Based Method

At onset of rocking, this acceleration is equal to the product of the aspect ratio of piers and gravity acceleration i.e. rocking initiation acceleration. Restoring acceleration reduces when horizontal displacement of the deck increases. Thus, we may neglect the restoring acceleration due to gravity. In this case, it is possible to assume deck and abutments like a SDOF system while between the system mass and spring-dashpot there is a certain gap. This SDOF

system is shown in Figure 4. Before oscillation starts, provided gaps in both sides of the mass are equal.

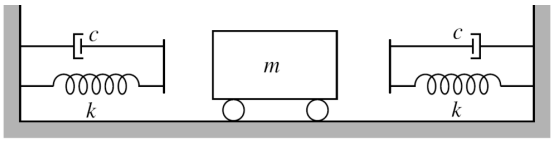

Figure 4 Idealized deck-abutments system to calculate Gap Spectra

Response spectra for the shown system are calculated using a Matlab code. Different gaps associated to 1%, 3%, 5% and 10% drift of the example bridge considered to obtain response spectra which are referred as Gap Spectra. Displacement gap spectra for several earthquakes show that it is reasonable to consider all gap spectra intersect at corner period of the idealized displacement spectrum. Therefore, we may develop gap spectrum from design displacement spectra. At zero period, the ordinate of the gap spectrum should be equal to the provided gap because the spring stiffness is infinite thus displacement cannot exceed the gap value. According to Figure 7 and 8, it is reasonable to assume an identical corner period and spectral ordinate for gap spectrum and standard spectrum. The proposed displacement design spectrum for SDOFs with gap i.e. the gap spectrum is shown in Figure 5. Selected spectra have been shown in the appendix.

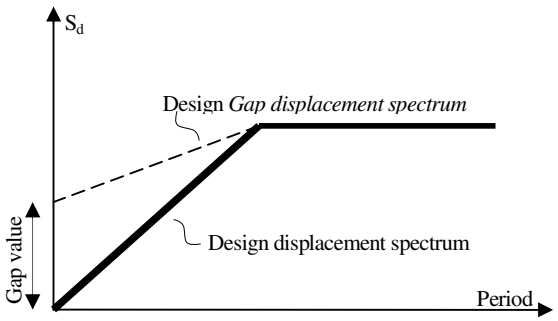

Figure 5 Idealized design displacement spectrum

Once we have design displacement then we can subtract gap values from design displacement to find displacement demand for abutment spring. Therefore, the design value of inertial force is the product of the abutment stiffness and displacement.

Same idea can be develop as design Gap Velocity Spectrum. It means that instead of PGV we may put the design spectral value for velocity or impact velocity into Eq. (22).

5. CONCLUSIONS

Results show that this scheme can be very promising earthquake resistant model if it is adopted into practice. The proposed structure has advantage of an isolated structural system without imposing extra price.

Simple design methods can be developed for this scheme like what have been proposed. However, to obtain better result these methods should be more studied.

A new spectrum namely Gap Spectrum introduced here for SDOF systems which have a predetermined gap between the system mass and spring-dashpot assemblage.

This scheme opens a broad insight into future researches to implement this idea into practice. Several researches should be done to account for different parameters that can affect earthquake response and components behavior. Some of them can be addressed like effects of elastic deformation of piers, investigation of restitution factor for piers, plastic deformation of the corners of piers during rocking response and behavior of abutments under deck impact.

References:

Housner, G. W. (1963), "The behavior of inverted pendulum structures during earthquakes," *Bulletin of the Seismological Society of America,* **53**(2), 403 -417.

Kreyszig, E. (1993), " Advanced Engineering Mathematics," 7th edition, JohnWiley, New York.

MATLAB Version 7.5., (2007), "The Language of Technical Computing," The Mathworks Inc., Natick, MA.

Shenton, H.W., III, (1996), "Criteria for initiation of slide, rock, and slide-rock rigid-body modes," *Journal of Engineering Mechanics (ASCE)* **122**(7), 690 -693.

Zhang, J., and Makris, N. (2001), "Rocking response of free-standing blocks under cycloidal pulses," *Journal of Engineering Mechanics (ASCE),* **127**(5), 473 -483.

Appendix:

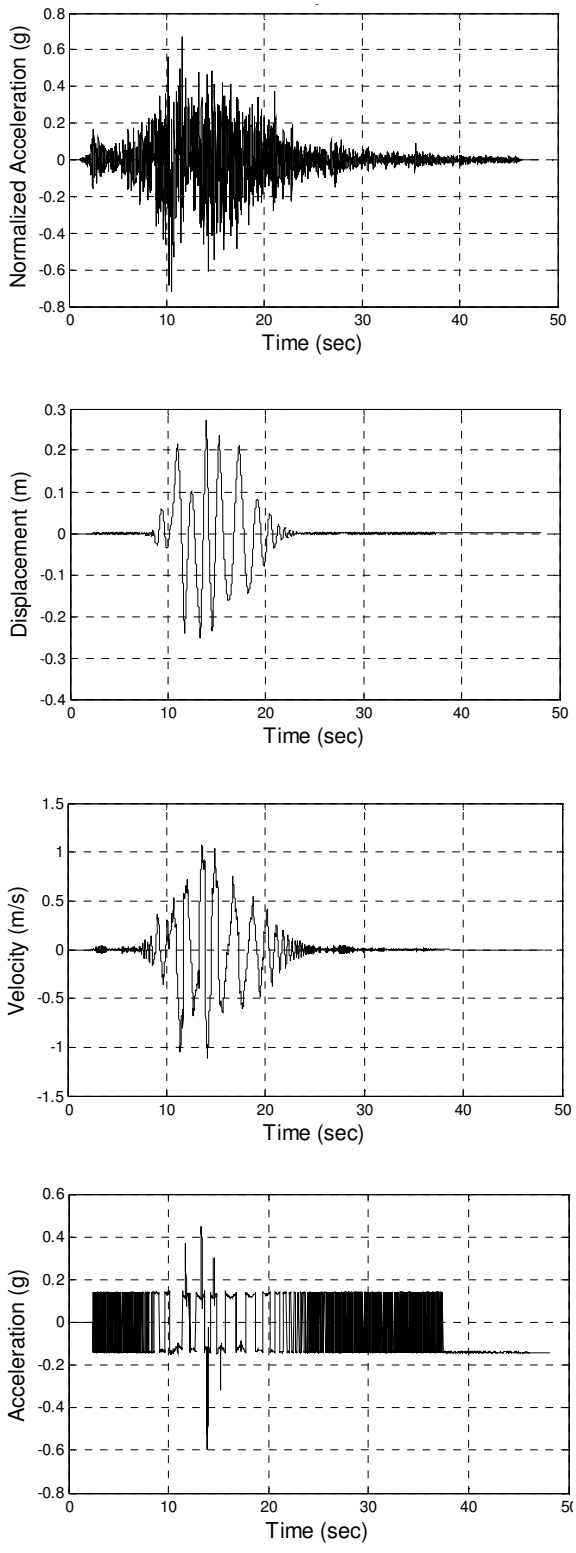

Figure 6 Ground acceleration, deck displacement, velocity and total horizontal acceleration response for Landers 1992 while the gap value is associated to 10% drift

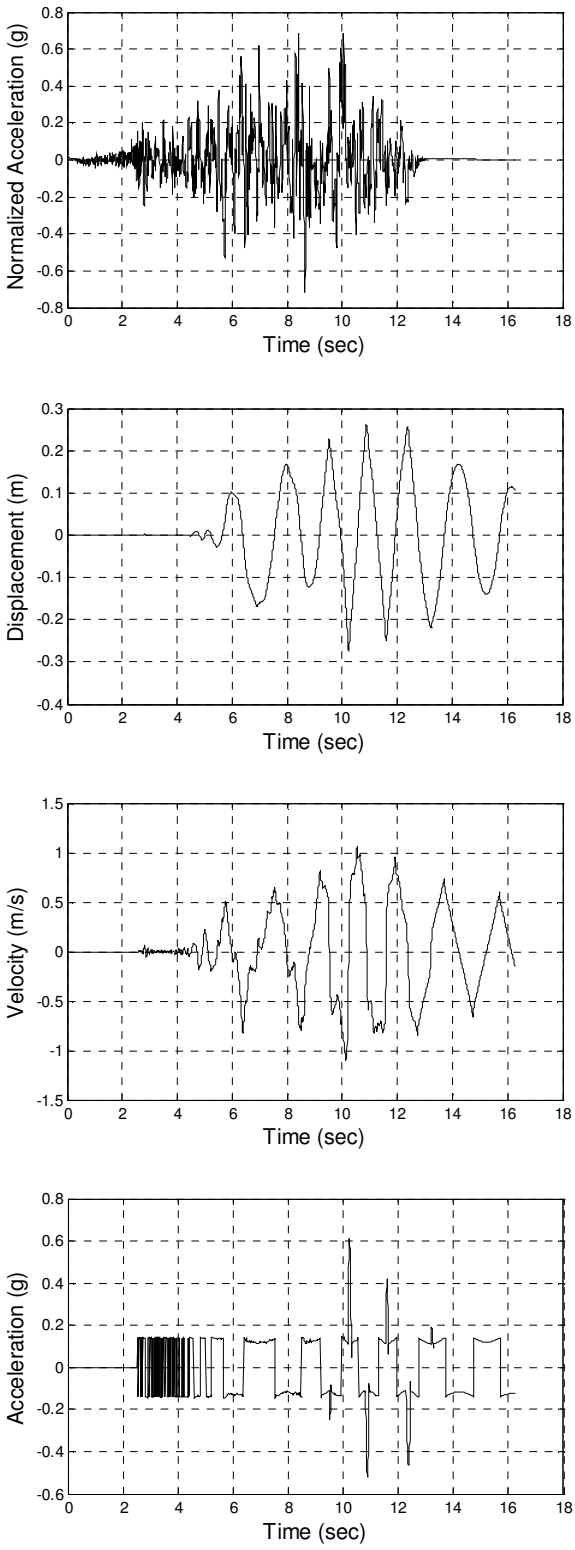

Figure 7 Ground acceleration, deck displacement, velocity and total horizontal acceleration response for Gazli 1976 while the gap value is associated to 3% drift.

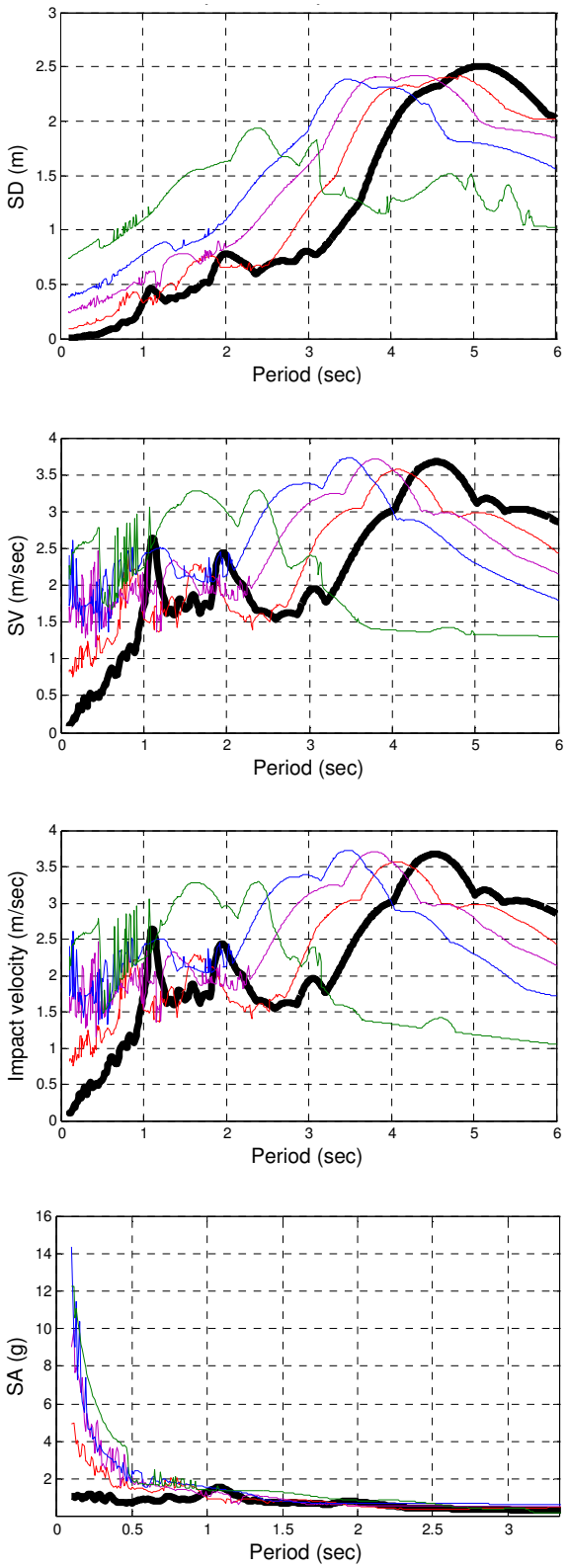

Figure 8 Response spectra for Chi Chi 1999 for the gap values associated to 0, 1%, 3%, 5% and 10% drift are shown with thick black, red, pink, blue and green, respectively.

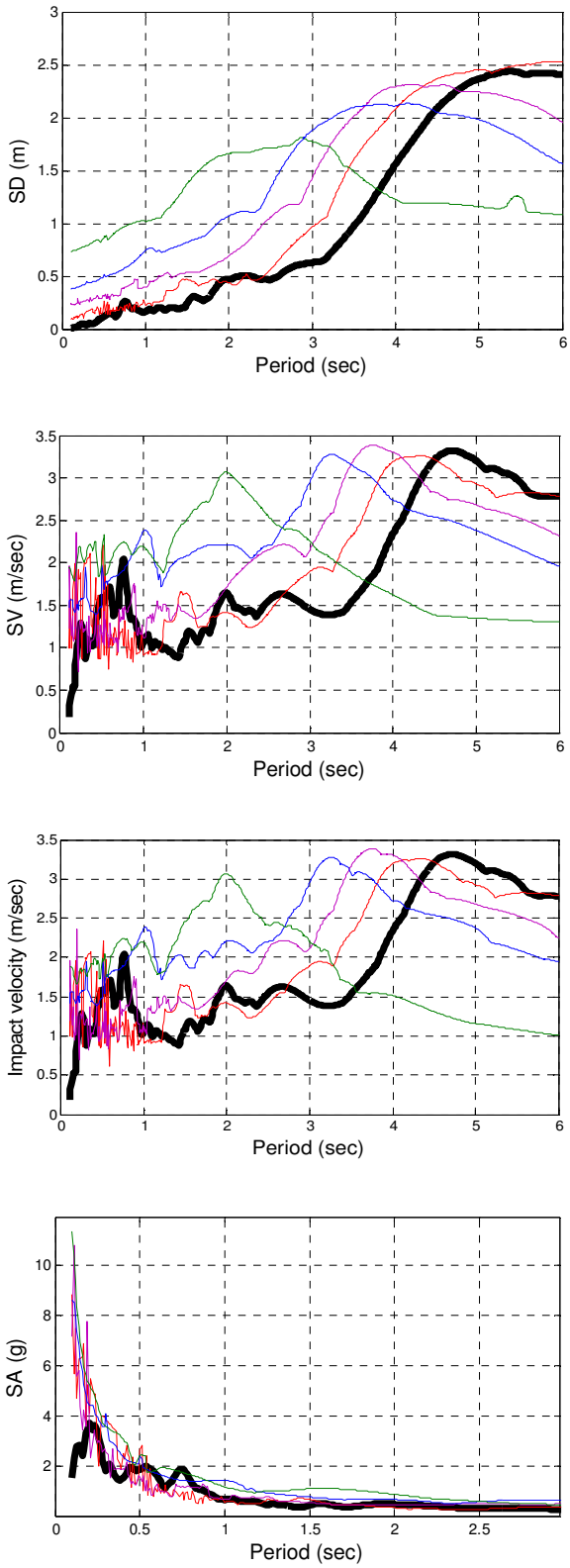

Figure 9 Response spectra for Tabas 1978 for the gap values associated to 0, 1%, 3%, 5% and 10% drift are shown with thick black, red, pink, blue and green, respectively.

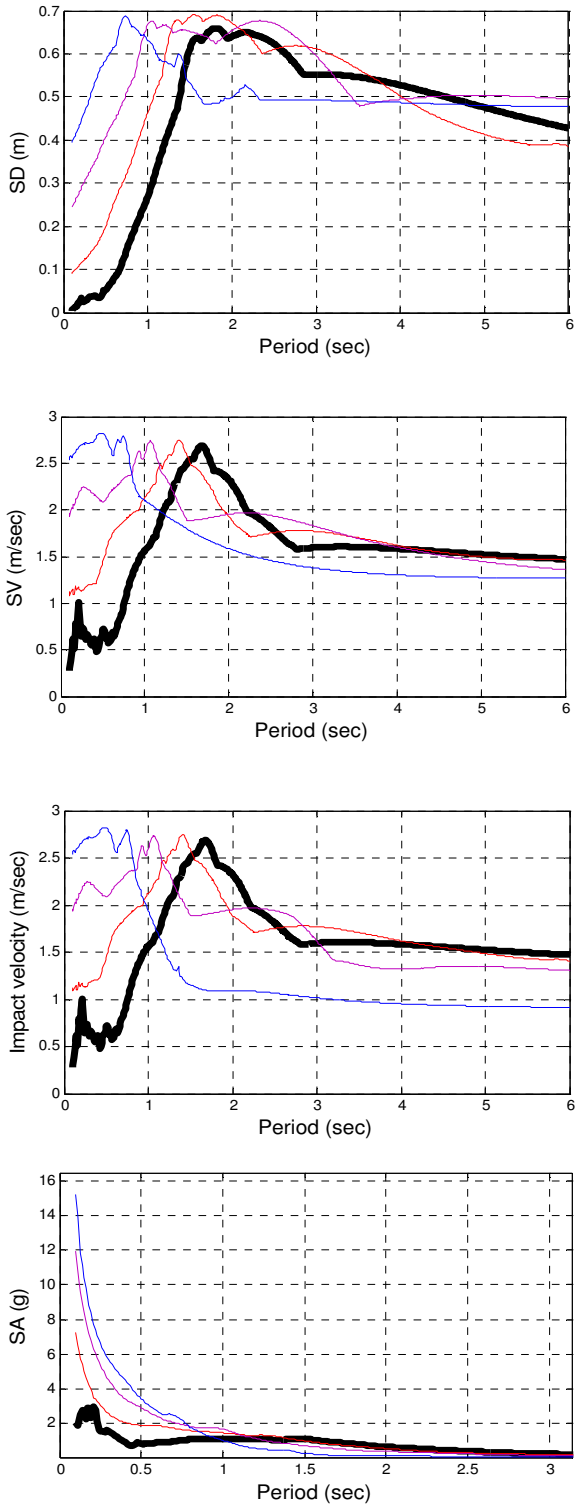

Figure 10 Response spectra for Bam 2003 for the gap values associated to 0, 1%, 3% and 5% drift are shown with thick black, red, pink and blue, respectively. Note that drift cannot reach to 10%.

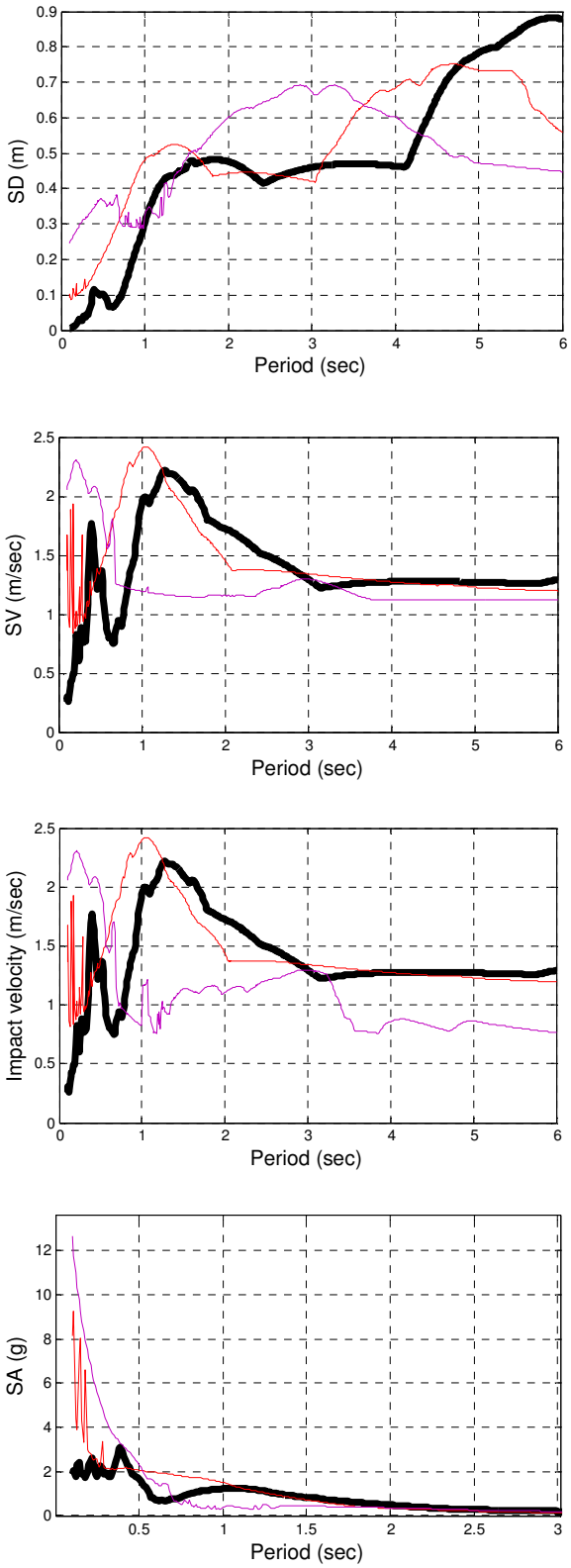

Figure 11 Response spectra for San Fernando 1971 for the gap values associated to 0, 1% and 3% drift are shown with thick black, red and pink, respectively. Note that drift cannot reach to 5%.

JOINT CONFERENCE PROCEEDINGS
7th International Conference on Urban Earthquake Engineering (7CUEE) &
5th International Conference on Earthquake Engineering (5ICEE)
March 3-5, 2010, Tokyo Institute of Technology, Tokyo, Japan

ANALYSIS OF EARTHQUAKE DAMAGE FOR VARIOUS TYPES OF BUILDING STRUCTURES IN WENCHUAN EARTHQUAKE

SUN Bai-tao[1)], and ZHANG Gui-xin[2)]

1) Professor, Institute of Engineering Mechanics, China Earthquake Administration, China
2) Graduate student, Institute of Engineering Mechanics, China Earthquake Administration, China
sunbt@iem.net.cn, zhangguixin1010@163.com

Abstract: This paper focuses on the description and analysis of the damage phenomena of typical structures based on the on-site investigation of the earthquake damage in Wenchuan earthquake. Some valuable lessons learned from this extreme earthquake are presented including three kinds of structural damage characteristics, namely masonry structures, reinforced concrete frame structures and masonry buildings with bottom frame. The vulnerability of these three kinds of buildings in different intensities has been analyzed and compared. The content in this paper may be as a reference to seismic design of buildings, reconstruction of disaster area and revision of corresponding codes and regulations.

1. INTRODUCTION

At 14:28:04 on May 12, 2008(Beijing Time), a great earthquake (Ms=8.0) occurred in Wenchuan, Sichuan province, China. A large number of buildings have been affected to a various degree because of the fault movement and strong ground motion. Especially in the intensities of Ⅶ or higher, buildings and the infrastructure were severely damaged or destroyed.

After the earthquake, an investigation group (led by IEM) was set up quickly. They walked for million kilometers covering disaster areas and took more than three months for investigating engineering structures from Ⅵ to Ⅺ scientifically. Finally, about 5000 single samples of the buildings were obtained, which has great significance to grasp the overall vulnerability of the structure, with which we received persuasive statistical analysis of seismic vulnerability, and results play an irreplaceable role in guiding the seismic fortification of the building structures and Earthquake Disaster Mitigation Planning in the future in the disaster region or even the entire country.

2. EARTHQUAKE DAMAGE OF TYPICAL BUILDINGS IN THE EARTHQUAKE-AFFECTED AREA

Due to the large magnitude of the earthquake, the range of ground motion field was very wide. There were 324080 square kilometers areas in the region above the intensity of Ⅵ. The region above the intensity of Ⅶ contained prefecture-level cities, counties with more developed economics, towns and villages. So many types of engineering structures were damaged in the earthquake and damage characteristics were plentiful. Such as steel structures, reinforced concrete structures, masonry structures (brick structures), masonry buildings with bottom frame, timber structures, adobe structure and stone structures and so on, among which three typical types of structures were discussed and analyzed.

2.1 Masonry structure (Brick structure)

Masonry structure accounts for 70%~80% in our country according to statistics by experts, especially in the underdeveloped regions or townships the proportion is much larger. Three typical earthquake damage of masonry structures appeared in the affected areas: (1) Buildings with formal seismic design and construction in accordance with the local fortification intensity of Ⅶ, most of which were built after 1992, had a considerable seismic potential in Wenchuan earthquake. Many buildings were basically undamaged or only slightly damaged (Fig.1). (2) Unfortified brick structures with imperfect or completely no seismic measures most were built before1992. In late of 1980 s, public or residential buildings built by a number of underfunded factories or units have a relatively poor seismic capacity. These buildings were severely damaged or collapsed (Fig.2), especially schools and hospitals, which was the main reason for the victims and injuries. (3) Self-built brick building without formal design mostly were built less than 3 storeys in the township and villages, which were severely damaged in the different intensities in the seismic zone [1].

Because of low cost, broken sandstones were often used instead of river sand in this area to form mixed cement mortar during the construction. High mud content in broken sandstone induces low shear strength of connections

between cement mortar and brick masonry, and lateral resisting capacity of the wall reduced, which is another important reason for the serious earthquake damage of masonry structure. This phenomenon usually appeared in self-built buildings in the townships and rural areas.



Figure 1 The first floor of the fortified masonry building destroyed in Beichuan County (XI)



Figure 2 Unfortified masonry building fully collapsed in Dujiangyan (IX)

2.2 Reinforced concrete frame structure

In this earthquake, reinforced concrete frame structure showed a good seismic performance. In addition to varying degrees of damage on decoration and subsidiary structures, other characteristics behaved mainly in the following forms: (1) The destruction of filled wall. Obvious inclined and cross cracks of filled walls would appear in low-intensities, and the filled walls with poor mortar quality would collapse above intensity Ⅷ. (2) The destruction of the column cap. The main characteristics were uncoupled in the junctions between enclosure walls or infill walls and beams or columns, and walls and part of the column cap showed inclined and cross cracks. (3) Collapsed wholly. A small number of structures collapsed in meizoseismic area [2].

2.3 Masonry building with bottom frame

Since earthquake damage examples of this structure type were few before and seismic test study on them has not been given the same attentions as reinforced concrete structure. The seismic research results are also few. Fortification requirement for the masonry building with the bottom frame in <code for seismic design of buildings>GB50011-2001[3] is reflected in terms of masonry structure. However, masonry building with bottom frame was one of the more common types in this earthquake.

This type of structure was mostly ones with reinforced concrete structure in the first or two floors but masonry structure in the upper. Its failure phenomena were similar to masonry structure in the regions with intensities of Ⅷ or lower. But in high-intensity zone, they showed following damage characteristics: (1) In meizoseismic area, the structure mostly was damaged or collapsed in stiffness conversion layer, which commonly known as the middle layer "sitting layer". We can see that two bottom floors of Yingxiu hotel collapsed in Fig.3. (2) The column on the first floor of the frame structure was skewed (Fig.4).



Figure 3 Two collapsed bottom floors of the Yingxiu hotel



Figure 4 The collapsed column cap

3. SURVEY METHODS FOR BUILDING EARTHQUAKE DAMAGE AND THE DISTRIBUTION OF SURVEY SPOTS

Aimed at various building structures in the affected areas, a detailed outline of scientific investigation and investigation table were compiled. The survey contents aiming at the monomers of different architectural structures in the stricken region of intensities from VI to XI were as followings:

1. Structural form, for example, with or without collar beam, constructional column, roof type, ect.
2. Material properties, such as strength of brick materials, mortar grade and so on.

3. Construction methods, such as reinforced concrete slabs are cast-in-place or precast etc.
4. Sizes of the structures and components, such as section size of beam and column in each floor, the overall size of building etc.
5. Fortification intensity and site conditions etc.

Then the group took a lot of photographs in multi-angle and made a detailed description of the phenomenon of the earthquake damage degree.

202 survey spots (Fig.5) were mainly distributed in about twenty states and cities such as Aba Tibetan and Qiang Autonomous Prefecture, Chengdu, Deyang, Mianyang and Guangyuan and so on, according to distribution of seismic intensity of Wenchuan earthquake (Fig.6).

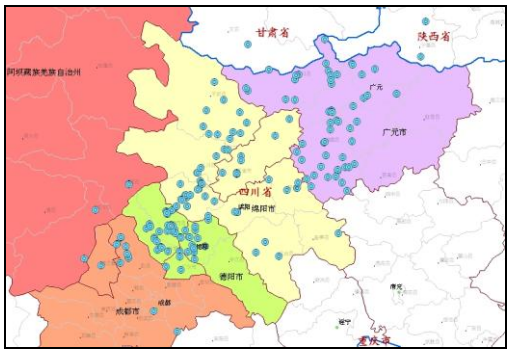

Figure 5 Distribution of survey points in administrative regional map

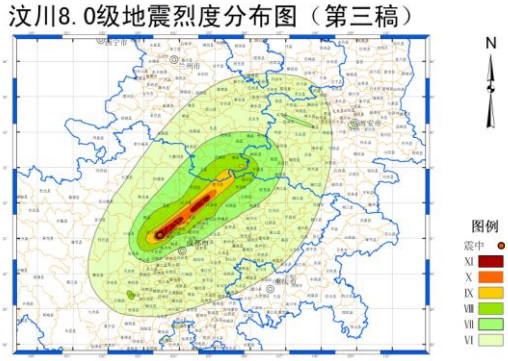

Figure 6 Distribution of earthquake intensity

It is shown from the map that the survey spots are distributed uniformly in the stricken region with intensities from VI to XI, which could better reflect integral vulnerability and distribution features of different structures throughout the disaster area. Survey spots in the Northwest region where were on the hanging side of the fracture zone were very few because it was mountain area and Tibetan and Qiang residential area where distributed Sparse settlements (Fig.5).

Survey method of each sampling spot was that different types of structures were investigated one by one on a street or a district selected randomly. Relevant drawings were collected and structure or component sizes were measured using laser geodimeter on site. Strength of mortar or concrete was judged based on experience or instrument testing. Then all results of the investigation were filled on a survey table and a detailed description of the characteristics and extent of earthquake damage was recorded, and multi-angle photographs of structural damage were taken.

4. ANALYSIS OF SEISMIC VULNERABILITY OF TYPICAL STRUCTURES

The engineering seismic damage investigation group contained nearly 200 experts in earthquake engineering coming from more than ten research institutions and universities of our country. The group was divided into more than 20 professional teams and walked for hundreds of kilometers covering disaster areas and took more than three months for a detailed investigation on 202 sampling spots and obtained about 5000 single samples of the buildings in the regions with intensities from VI to XI. By statistics, the more perfect building data of 4539 single samples whose areas are about 5737 thousand square meters have been analyzed. The amounts of the different structures are in the following table.

Table 1 Surveyed Buildings

Structure Types	Number of buildings	Area ($\times 10^4$ m^2)	Inventory Distribution(%)
Masonry structures	2782	281.218	61.29
Reinforced concrete structures	505	106.329	11.13
Masonry structures with bottom frame	665	112.526	14.65
High-rise buildings	60	53.778	1.32
Industrial plants, spacious buildings	122	9.573	2.69
Others	405	10.245	8.92
Total	4539	573.669	100

Then, vulnerability of each type has been analyzed. Vulnerability matrices for the above six types of structures are calculated. Finally, twenty-four vulnerability matrices have been obtained. And comparison of each type has been analyzed. Then we only made a comparison on vulnerability matrix between fortified and unfortified masonry structures. From table 2 we can see that unfortified structure accounts for a higher proportion than fortified one, which is reflected obviously in the column of “Destroy”. The situation was same also under the same intensity. All of above fully showed that fortified and unfortified structure behaved very different in the earthquake. Fortified structure showed much better seismic performance than the unfortified one, and increasing as the intensities, there was an upward trend in seismic damage indices, which meant the higher of the intensity the larger of the damage index. Therefore, seismic performance of buildings in the areas with high intensity needs to be enhanced.

Table 2 The vulnerability matrix comparison between fortified and unfortified masonry structure (%)

Intensity	Intact	Slight damage	Medium damage	Serious damage	Destroy
Ⅵ	/20	33.33/	/60	66.67/20	0
Ⅶ	28.68/43.47	32.45/35.26	25.28/16.26	11.70/4.56	1.89/0.46
Ⅷ	9.52/22.13	25./25.78	20.83/27.87	34.52/22.82	10.12/1.39
Ⅸ	6.28/9.8	7.11/16.25	19.25/29.97	56.49/35.29	10.88/8.68
Ⅹ	9.8/32.18	19.61/25.29	13.73/25.29	31.37/13.79	25.49/3.45
Ⅺ	7.25/22.37	10.14/22.37	8.7/9.21	31.88/34.21	42.03/1.3

The black number is vulnerability matrix of unfortified masonry structures while the red one is the fortified one.

Masonry building with bottom frame was one of the more serious forms in this earthquake, which showed varying degrees of damage in the regions with the intensities from Ⅶ to Ⅺ. Especially in the regions with the intensity of Ⅺ, nearly thirty percent buildings of this type were serious damaged, and about fifteen percent was collapsed. Figure 7 was percentage of the five destructive states of masonry building with bottom frame according numbers.

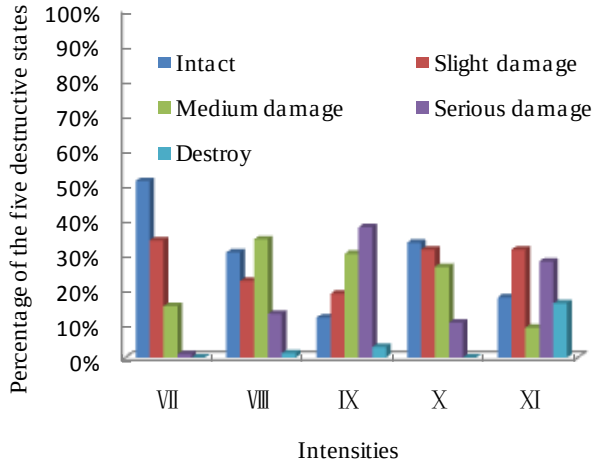

Figure 7 Percentage of the five destructive states of masonry building with bottom frame according numbers

Through investigating, it was obvious that the earthquake resistant capabilities successively decreased: reinforced concrete structure, masonry building with bottom frame, masonry building. The number of these three types accounts for 87 percent of all buildings, and they were damaged severely in the regions with the intensities of Ⅸ and Ⅺ. Average damage index of masonry structure was up to 0.6, which meant that buildings in these regions reached the extent of serious damage on average.

5. SOME UNDERSTANDINGS

1. The differences of the seismic capacity of buildings with different types of structures were understood-analyzed, which were built following codes for seismic design of buildings in different ages.
2. Masonry structures fortified in code behaved much better than ones unfortified. For example, the structure with collar beams and constructional columns basically showed the ability of seismic resistance that should have, but the spandrel walls of fortified masonry structures damaged obviously. By survey and analysis, if we put more than two constructional steel bars in the spandrel walls, their shear capacity would be enhanced greatly.
3. In low-intensity area, masonry structure with bottom frame built in standard behaved well and was not seriously damaged, and its anti-seismic performance is similar to the fortified masonry structure. But in high-intensity areas, this type of structure was all damaged severely whether its seismic fortification was considered. It is suggested that masonry structure with bottom frame should be strictly limited in high-intensity areas in the future.
4. Fortified reinforced concrete frame behaved well in Wenchuan earthquake. But the phenomenon of earthquake damage caused by weak column/strong beam was still obvious. So we'd better to enhance the strength of column reasonably in the construction in the future.
5. Vulnerability matrixes of different structures obtained from this scientific investigation have important reference value and guide significance to the reconstruction of Wenchuan and our country's urban and rural disaster prevention planning in the future.
6. Every large earthquake is a test to the relevant codes issued. After Wenchuan earthquake, scientific survey and research analysis have an important significance to the revise of our country's code for seismic design of buildings.

Acknowledgements:

This Work was supported by the National natural science foundation (50938006), National 973 planning topics (2007CB714205) and Special research in Chinese seismological industry (200708041).

References:

[1] Yuan Yifan, Sun Baitao. General Introduction to Engineering Damage during Wenchuan Earthquake [J]. Science Press, 2008:37-44.
[2] Sun Baitao, Yan Peilei, Hu Chunfeng, Zhang Mingyu. Overview on seismic damage to different structures in Yingxiu Town during Wenchuan Earthquake [J]. Earthquake engineering and engineering vibration, 2008, 28(5):1-9.
[3] The national standard in the People's Republic of China, Code for seismic design of buildings (GB50011-2001) [s]. Beijing: China Architecture & Building Press,2001.

JOINT CONFERENCE PROCEEDINGS
7th International Conference on Urban Earthquake Engineering (7CUEE) &
5th International Conference on Earthquake Engineering (5ICEE)
March 3-5, 2010, Tokyo Institute of Technology, Tokyo, Japan

BI-SPECTRA FOR TWO-WAY ASYMMETRIC-PLAN STRUCTURES UNDER BI-DIRECTIONAL GROUND EXCITATIONS

Jui-Liang Lin[1], Wen-Chia Yang[2], and Keh-Chyuan Tsai[3]

1) Associate Research Fellow, National Center for Research on Earthquake Engineering Research Center, Taipei, Taiwan
2) Assistant Research Fellow, National Center for Research on Earthquake Engineering Research Center, Taipei, Taiwan
3) Director, National Center for Research on Earthquake Engineering. and Professor, Department of Civil Engineering, National Taiwan University, Taiwan
jllin@ncree.org.tw, wcyang@ncree.org.tw, kctsai@ncree.org.tw

Abstract: The conventional inelastic response spectra are constructed from the peak responses of single-degree-of-freedom (SDOF) vibrators. Nevertheless, the force-deformation relationships of the SDOF vibrators merely represent the relationships of the roof translation versus the base shear force. Therefore, the translation-rotation interaction effect of asymmetric-plan structures is not considered by using the conventional inelastic response spectra. Furthermore, the rotational responses of asymmetric-plan structures are not available from the conventional inelastic response spectra. The authors have developed the three-degree-of-freedom (3DOF) modal system based on the relationships of roof translations versus base shears and roof rotation versus base torque for two-way asymmetric-plan buildings. The 3DOF modal system represents the coupled vibration mode of two-way asymmetric-plan structures. In this study, the 3DOF modal systems are used to construct the bi-directional inelastic response spectra, referred to as bi-spectra, representing the modal responses of two-way asymmetric-plan structures subjected to bi-directional seismic excitations. In order to construct bi-spectra, the independent elastic parameters of the 3DOF modal systems were identified and the inelastic 3DOF modal parameters versus the strength ratio relationships were established. The parametric study of the key 3DOF modal parameters was conducted for getting the variation trend of these key parameters.

1. INTRODUCTION

Although the responses of one-way asymmetric systems have been studied widely under uni-directional seismic motions, two-way asymmetric systems subjected to bi-directional seismic motions have received less investigation. De-La-Colina (1999) concluded that additional study should be carried out to assess the equivalence between uni-directional and bi-directional analyses in studying torsion-related problems. Hernandez and Lopez (2000) pointed out that the simultaneous action of two horizontal seismic components should be considered in the analysis of one-way and two-way asymmetric plans in order to avoid incursions in the inelastic range, hence, to reach an adequate design for serviceability conditions. Cruz and Cominetti (2000) concluded that if the purpose of the analysis is to know the level of damage to which the columns of a structure are exposed, or the elastic or inelastic torsional behavior of building excited by seismic ground movements, the evaluation should be carried out considering the bi-directional earthquake. From the study results mentioned above, it is evident that the consideration of bi-directional ground excitations is in deed necessary for a satisfactory assessment of the seismic performance of a two-way asymmetric-plan structure under actual earthquake events. In the past decades, systematical investigation of response spectra with a wide variety of SDOF systems and earthquake characteristics is well considered as an effective approach for understanding and assessing the seismic demand of structures (Newmark and Hall 1973; Nasar and Krawinkler 1991; Vidic, Fajfar and Fischinger 1992; Miranda and Bertero 1994). Nevertheless, the conventional response spectra, constructed from the peak responses of SDOF vibrators subjected to one component of earthquakes, are obviously incapable of representing the seismic behaviors of two-way asymmetric-plan structures under bi-directional earthquakes.

In this study, the 3DOF modal system (Lin and Tsai 2008) representing the translation-rotation coupled vibration mode of two-way asymmetric-plan buildings are used to construct the bi-directional response spectra, referred to as bi-spectra. The key tasks enabling the construction of bi-spectra are introduced in this paper. Some of bi-spectra are also presented herein.

2. THEORETICAL BACKGROUNDS

2.1 3DOF Modal System

The two plan axes are the X- and Z-axis. The Y-axis is upward (opposite to the direction of gravity). The

proportionally damped two-way asymmetric-plan buildings with each floor simulated as a rigid diaphragm are considered in this research. The equation of motion for an *N*-storey two-way asymmetric-plan building subjected to bi-directional ground excitations is

$$\begin{aligned}
&\mathbf{M}\ddot{\mathbf{u}}+\mathbf{C}\dot{\mathbf{u}}+\mathbf{K}\mathbf{u}=-\mathbf{M}\boldsymbol{\iota}_x\ddot{u}_{gx}(t)-\mathbf{M}\boldsymbol{\iota}_z\ddot{u}_{gz}(t)\\
&=-\sum_{n=1}^{3N}\mathbf{s}_{xn}\ddot{u}_{gx}(t)-\sum_{n=1}^{3N}\mathbf{s}_{zn}\ddot{u}_{gz}(t)\\
&=-\sum_{n=1}^{3N}\Gamma_{xn}\mathbf{M}\boldsymbol{\varphi}_n\ddot{u}_{gx}(t)-\sum_{n=1}^{3N}\Gamma_{zn}\mathbf{M}\boldsymbol{\varphi}_n\ddot{u}_{gz}(t)\\
&=-\sum_{n=1}^{3N}\left(\Gamma_{xn}\ddot{u}_{gx}+\Gamma_{zn}\ddot{u}_{gz}\right)\mathbf{M}\boldsymbol{\varphi}_n
\end{aligned}\tag{1}$$

, in which the displacement vector, **u,** mode shape, $\boldsymbol{\varphi}_n$, mass matrix, **M,** stiffness matrix, **K**, influence vectors, $\boldsymbol{\iota}_x$, $\boldsymbol{\iota}_z$, modal inertia force distributions, $\mathbf{s}_{xn}$, $\mathbf{s}_{zn}$, and modal participation factors, Γ_{xn}, Γ_{zn}, are

$$\mathbf{M}=\begin{bmatrix}\mathbf{m}_x & \mathbf{0} & \mathbf{0}\\ \mathbf{0} & \mathbf{m}_z & \mathbf{0}\\ \mathbf{0} & \mathbf{0} & \mathbf{I}_0\end{bmatrix}_{3N\times 3N},\quad \mathbf{K}=\begin{bmatrix}\mathbf{k}_{xx} & \mathbf{k}_{xz} & \mathbf{k}_{x\theta}\\ \mathbf{k}_{zx} & \mathbf{k}_{zz} & \mathbf{k}_{z\theta}\\ \mathbf{k}_{\theta x} & \mathbf{k}_{\theta z} & \mathbf{k}_{\theta\theta}\end{bmatrix}_{3N\times 3N}$$

$$\mathbf{u}=\begin{bmatrix}\mathbf{u}_x\\ \mathbf{u}_z\\ \mathbf{u}_\theta\end{bmatrix}_{3N\times 1},\quad \boldsymbol{\varphi}_n=\begin{bmatrix}\boldsymbol{\varphi}_{xn}\\ \boldsymbol{\varphi}_{zn}\\ \boldsymbol{\varphi}_{\theta n}\end{bmatrix}_{3N\times 1},\quad \boldsymbol{\iota}_x=\begin{bmatrix}\mathbf{1}\\ \mathbf{0}\\ \mathbf{0}\end{bmatrix},\quad \boldsymbol{\iota}_z=\begin{bmatrix}\mathbf{0}\\ \mathbf{1}\\ \mathbf{0}\end{bmatrix}$$

$$\mathbf{s}_{xn}=\Gamma_{xn}\mathbf{M}\boldsymbol{\varphi}_n,\quad \mathbf{s}_{zn}=\Gamma_{zn}\mathbf{M}\boldsymbol{\varphi}_n$$

$$\Gamma_{xn}=\frac{\boldsymbol{\varphi}_n^T\mathbf{M}\boldsymbol{\iota}_x}{\boldsymbol{\varphi}_n^T\mathbf{M}\boldsymbol{\varphi}_n},\quad \Gamma_{zn}=\frac{\boldsymbol{\varphi}_n^T\mathbf{M}\boldsymbol{\iota}_z}{\boldsymbol{\varphi}_n^T\mathbf{M}\boldsymbol{\varphi}_n}\tag{2}$$

When only the force $-\left(\Gamma_{xn}\ddot{u}_{gx}+\Gamma_{zn}\ddot{u}_{gz}\right)\mathbf{M}\boldsymbol{\varphi}_n$ is applied to the building, the equation of motion (Eq. 1) becomes

$$\mathbf{M}\ddot{\mathbf{u}}_n+\mathbf{C}\dot{\mathbf{u}}_n+\mathbf{K}\mathbf{u}_n=-\left(\Gamma_{xn}\ddot{u}_{gx}+\Gamma_{zn}\ddot{u}_{gz}\right)\mathbf{M}\boldsymbol{\varphi}_n,\quad n=1\sim 3N\tag{3}$$

, in which $\mathbf{u}_n$ is the *n*-th modal displacement response and $\mathbf{u}=\sum_{n=1}^{3N}\mathbf{u}_n=\sum_{n=1}^{3N}\boldsymbol{\varphi}_n D_n$. D_n is the generalized modal coordinate. The 3DOF modal equation of motion for the *n*-th vibration mode is

$$\mathbf{M}_n\ddot{\mathbf{D}}_n+\mathbf{C}_n\dot{\mathbf{D}}_n+\mathbf{K}_n\mathbf{D}_n=-\left(\Gamma_{xn}\ddot{u}_{gx}+\Gamma_{zn}\ddot{u}_{gz}\right)\mathbf{M}_n\mathbf{1}\tag{4}$$

where

$$\mathbf{M}_n=\begin{bmatrix}\boldsymbol{\varphi}_{xn}^T\mathbf{m}_x\boldsymbol{\varphi}_{xn} & 0 & 0\\ 0 & \boldsymbol{\varphi}_{zn}^T\mathbf{m}_z\boldsymbol{\varphi}_{zn} & 0\\ 0 & 0 & \boldsymbol{\varphi}_{\theta n}^T\mathbf{I}_0\boldsymbol{\varphi}_{\theta n}\end{bmatrix}_{3\times 3}\tag{5}$$

$$\mathbf{C}_n=\begin{bmatrix}\boldsymbol{\varphi}_{xn}^T\mathbf{c}_{xx}\boldsymbol{\varphi}_{xn} & \boldsymbol{\varphi}_{xn}^T\mathbf{c}_{xz}\boldsymbol{\varphi}_{zn} & \boldsymbol{\varphi}_{xn}^T\mathbf{c}_{x\theta}\boldsymbol{\varphi}_{\theta n}\\ \boldsymbol{\varphi}_{zn}^T\mathbf{c}_{zx}\boldsymbol{\varphi}_{xn} & \boldsymbol{\varphi}_{zn}^T\mathbf{c}_{zz}\boldsymbol{\varphi}_{zn} & \boldsymbol{\varphi}_{zn}^T\mathbf{c}_{z\theta}\boldsymbol{\varphi}_{\theta n}\\ \boldsymbol{\varphi}_{\theta n}^T\mathbf{c}_{\theta x}\boldsymbol{\varphi}_{xn} & \boldsymbol{\varphi}_{\theta n}^T\mathbf{c}_{\theta z}\boldsymbol{\varphi}_{zn} & \boldsymbol{\varphi}_{\theta n}^T\mathbf{c}_{\theta\theta}\boldsymbol{\varphi}_{\theta n}\end{bmatrix}_{3\times 3}$$

$$\mathbf{K}_n=\begin{bmatrix}\boldsymbol{\varphi}_{xn}^T\mathbf{k}_{xx}\boldsymbol{\varphi}_{xn} & \boldsymbol{\varphi}_{xn}^T\mathbf{k}_{xz}\boldsymbol{\varphi}_{zn} & \boldsymbol{\varphi}_{xn}^T\mathbf{k}_{x\theta}\boldsymbol{\varphi}_{\theta n}\\ \boldsymbol{\varphi}_{zn}^T\mathbf{k}_{zx}\boldsymbol{\varphi}_{xn} & \boldsymbol{\varphi}_{zn}^T\mathbf{k}_{zz}\boldsymbol{\varphi}_{zn} & \boldsymbol{\varphi}_{zn}^T\mathbf{k}_{z\theta}\boldsymbol{\varphi}_{\theta n}\\ \boldsymbol{\varphi}_{\theta n}^T\mathbf{k}_{\theta x}\boldsymbol{\varphi}_{xn} & \boldsymbol{\varphi}_{\theta n}^T\mathbf{k}_{\theta z}\boldsymbol{\varphi}_{zn} & \boldsymbol{\varphi}_{\theta n}^T\mathbf{k}_{\theta\theta}\boldsymbol{\varphi}_{\theta n}\end{bmatrix}_{3\times 3}$$

$$\mathbf{D}_n=\begin{bmatrix}D_{xn}\\ D_{zn}\\ D_{\theta n}\end{bmatrix}_{3\times 1},\quad \mathbf{1}=\begin{bmatrix}1\\ 1\\ 1\end{bmatrix}_{3\times 1}\tag{5}$$

D_{xn}, D_{zn}, and $D_{\theta n}$, are referred to as the X- and Z-directional modal translations and modal rotation respectively. The corresponding *n*-th 3DOF modal system is shown in Fig. 1. The elastic properties of the *n*-th 3DOF modal system are as follows:

$$\begin{aligned}
&m_{xn}=\boldsymbol{\varphi}_{xn}^T\mathbf{m}_x\boldsymbol{\varphi}_{xn},\quad m_{zn}=\boldsymbol{\varphi}_{zn}^T\mathbf{m}_z\boldsymbol{\varphi}_{zn},\quad I_n=\boldsymbol{\varphi}_{\theta n}^T\mathbf{I}_0\boldsymbol{\varphi}_{\theta n}\\
&k_{xn}=\frac{\boldsymbol{\varphi}_{xn}^T\mathbf{k}_{xx}\boldsymbol{\varphi}_{xn}}{C^2},\quad k_{zn}=\boldsymbol{\varphi}_{zn}^T\mathbf{k}_{zz}\boldsymbol{\varphi}_{zn}-k_{xn}S^2\\
&k_{\theta n}=\boldsymbol{\varphi}_{\theta n}^T\mathbf{k}_{\theta\theta}\boldsymbol{\varphi}_{\theta n}-e_{xn}^2k_{zn}-\left(e_{xn}S-e_{zn}C\right)^2k_{xn}\\
&\begin{bmatrix}e_{xn}\\ e_{zn}\end{bmatrix}=\begin{bmatrix}k_{xn}SC & -k_{xn}C^2\\ k_{zn}+k_{xn}S^2 & -k_{xn}SC\end{bmatrix}^{-1}\begin{bmatrix}\boldsymbol{\varphi}_{xn}^T\mathbf{k}_{x\theta}\boldsymbol{\varphi}_{\theta n}\\ \boldsymbol{\varphi}_{zn}^T\mathbf{k}_{z\theta}\boldsymbol{\varphi}_{\theta n}\end{bmatrix}\\
&\beta_n=\tan^{-1}\left(\frac{\boldsymbol{\varphi}_{zn}^T\mathbf{k}_{zx}\boldsymbol{\varphi}_{xn}}{\boldsymbol{\varphi}_{xn}^T\mathbf{k}_{xx}\boldsymbol{\varphi}_{xn}}\right)
\end{aligned}\tag{6}$$

where $C=cos\beta_n$ and $S=sin\beta_n$. In this study, β_n is assumed approximately equal to zero, i.e. $\mathbf{k}_{zx}$ is neglected. This assumption is justified for most of common buildings with all the lateral force resisting elements (LFREs) placed along either the X-axis or the Z-axis. The buildings with LFREs obliquely placed in the X-Z plan are not considered in this study. The inelastic parameters of the *n*-th 3DOF modal system, including the yielding moments M_{yxn}, M_{yzn}, $M_{y\theta n}$ and the post-yielding stiffness k'_{xn}, k'_{zn}, $k'_{\theta n}$ of the three rotational springs of the 3DOF modal system (Fig. 1), are

$$M_{yxn}=A_{xny}m_{xn},\quad M_{yzn}=A_{zny}m_{zn}\tag{7a}$$

$$M_{y\theta n}=A_{\theta ny}I_n+A_{xny}m_{xn}e_{zn}-A_{zny}m_{zn}e_{xn}\tag{7b}$$

$$k'_{xn}=\frac{m_{xn}}{\dfrac{m_{xn}}{k_{xn}}+\dfrac{\left(I_n+m_{xn}e_{zn}-m_{zn}e_{xn}\right)e_{zn}}{k_{\theta n}}-\dfrac{\left(I_n+m_{xn}e_{zn}-m_{zn}e_{xn}\right)e_{zn}}{k'_{\theta n}}}\tag{7c}$$

$$k'_{zn}=\frac{m_{zn}}{\dfrac{m_{zn}}{k_{zn}}-\dfrac{\left(I_n+m_{xn}e_{zn}-m_{zn}e_{xn}\right)e_{xn}}{k_{\theta n}}+\dfrac{\left(I_n+m_{xn}e_{zn}-m_{zn}e_{xn}\right)e_{xn}}{k'_{\theta n}}}\tag{7d}$$

$$k'_{\theta n}=k_{\theta n}\cdot\alpha_{\theta n}\tag{7e}$$

where A_{xny}, A_{zny} and $A_{\theta ny}$ are the yielding accelerations and α_{xn}, α_{zn} and $\alpha_{\theta n}$ are the post-yielding stiffness ratios obtained from the three pushover curves of the original asymmetric-plan building pushed by its n-th modal inertia force. The stated three pushover curves, representing the two roof translations versus the two base shears and the roof rotation versus the base torque relationships, are idealized as three bilinear curves in the acceleration-displacement response spectra (ADRS) format. By using the step-by-step integration for solving the 3DOF modal equation of motion (Eq. 4), the n-th modal response history $\mathbf{D}_n$ can be obtained. Then, the total displacement response $\mathbf{u}$ of the original building is calculated as

$$\mathbf{u}=\sum_{n=1}^{3N}\mathbf{u}_n=\sum_{n=1}^{3N}\mathbf{\Phi}_n\mathbf{D}_n$$
$$=\sum_{n=1}^{3N}\begin{bmatrix}\boldsymbol{\varphi}_{xn} & \mathbf{0} & \mathbf{0}\\ \mathbf{0} & \boldsymbol{\varphi}_{zn} & \mathbf{0}\\ \mathbf{0} & \mathbf{0} & \boldsymbol{\varphi}_{\theta n}\end{bmatrix}_{3N\times 3}\begin{bmatrix}D_{xn}\\ D_{zn}\\ D_{\theta n}\end{bmatrix}_{3\times 1} \tag{8}$$

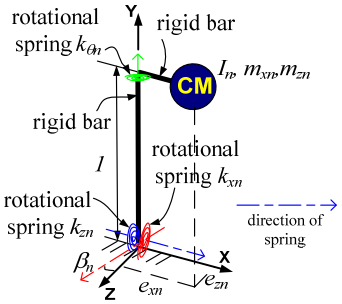

Figure 1 The 3DOF Modal System

2.2 Key Parameters of 3DOF Modal Systems

Similar to the study of the 2DOF modal systems for one-way asymmetric-plan structures (Lin and Tsai 2009), the identification of the independent elastic 3DOF modal parameters and the establishment of the relationships between the strength ratio and the inelastic 3DOF modal parameters were conducted. The results of these two tasks are briefly stated as follows:

The independent elastic 3DOF modal parameters are vibration period T_n, frequency ratios $\Omega_{\theta xn}$, $\Omega_{\theta zn}$, modal eccentricity e_{xn} and normalized modal eccentricity ratio $|e_{xn}|/r_{xn}$. All the elastic 3DOF modal parameters can be determined from these five independent 3DOF modal parameters using Eqs. 9 to 11 with the assumption $\beta \approx 0$.

$$\Omega_{\theta xn}=\sqrt{\left(1+\frac{m_{xn}}{I_n}e_{zn}-\frac{m_{zn}}{I_n}e_{xn}\right)\left(1-e_{zn}\right)} \tag{9a}$$

$$\Omega_{\theta zn}=\sqrt{\left(1+\frac{m_{xn}}{I_n}e_{zn}-\frac{m_{zn}}{I_n}e_{xn}\right)\left(1+e_{xn}\right)} \tag{9b}$$

$$T_n=\frac{T_{xn}}{\sqrt{1-e_{zn}}}=\frac{T_{zn}}{\sqrt{1+e_{xn}}} \tag{10}$$

$$m_{xn}+m_{zn}+I_n=1 \tag{11}$$

The frequency ratios $\Omega_{\theta xn}$, $\Omega_{\theta zn}$, are defined as $\Omega_{\theta xn}=\omega_{\theta n}/\omega_{xn}$ and $\Omega_{\theta zn}=\omega_{\theta n}/\omega_{zn}$, respectively, where ω_{xn}, ω_{zn} and $\omega_{\theta n}$ are the X- and Z-translational and rotational frequencies of the corresponding uncoupled 3DOF modal system. In addition, $T_{xn}=2\pi/\omega_{xn}$ and $T_{zn}=2\pi/\omega_{zn}$. The relationships between the strength ratio and the inelastic 3DOF modal parameters are shown as follows:

$$M_{yxn}=\frac{S_{dn}^{elastic}}{R}\left(-1+e_{zn}\right)k_{xn} \tag{12a}$$

$$M_{yzn}=\frac{S_{dn}^{elastic}}{R}\left(1+e_{xn}\right)k_{zn} \tag{12b}$$

$$M_{y\theta n}=\frac{S_{dn}^{elastic}}{R}k_{\theta n} \tag{12c}$$

Therefore, given the strength ratio, all the yielding moments of the three rotational springs in a 3DOF modal system (Fig. 1) can be determined by using Eq. 12.

2.3 Specification of Bi-Directional Ground Excitations

Since the ground excitation shown at the right hand side of the 3DOF modal equation of motion (Eq. 4) is synthetic, i.e. $\Gamma_{xn}\ddot{u}_{gx}+\Gamma_{zn}\ddot{u}_{gz}$, the way to specify the bi-direction ground excitation is different from that for the uni-axial ground excitation. The synthetic ground motion can be further expressed as $\lambda\left(\gamma_{xn}\ddot{u}_{gx}+\gamma_{zn}\ddot{u}_{gz}\right)$, where

$$\lambda=\sqrt{\Gamma_{xn}^2+\Gamma_{zn}^2} \tag{9a}$$

$$\gamma_{xn}=\frac{\Gamma_{xn}}{\sqrt{\Gamma_{xn}^2+\Gamma_{zn}^2}} \tag{9b}$$

$$\gamma_{zn}=\frac{\Gamma_{zn}}{\sqrt{\Gamma_{xn}^2+\Gamma_{zn}^2}} \tag{9c}$$

The γ_{xn} and γ_{zn} are named as the n-th modal excitation ratios in the X- and Z-directions, respectively, herein.

3. PARAMETRIC STUDY

From the results shown in the previous section, the inelastic response spectra for two-way asymmetric-plan buildings could be constructed by using the 3DOF modal systems if the values of e_{xn}, $|e_{xn}|/r_{xn}$, $\Omega_{\theta xn}$, $\Omega_{\theta zn}$, α_{xn}, α_{zn}, $\alpha_{\theta n}$, R, γ_{xn}, γ_{zn} and damping ratio ξ_n are given. The ranges of values of the strength ratio, R, and damping ratio, ξ_n, have been widely studied. However, the ranges of values of e_{xn}, $|e_{xn}|/r_{xn}$, $\Omega_{\theta xn}$, $\Omega_{\theta zn}$, α_{xn}, α_{zn}, $\alpha_{\theta n}$, γ_{xn}, γ_{zn} are not comprehensive. The study of the conventional SDOF response spectra became meaningful only after the ranges of the associated parameter values have been well understood. Therefore, the goal of this section is to study the ranges of values of e_{xn}, $|e_{xn}|/r_{xn}$, $\Omega_{\theta xn}$, $\Omega_{\theta zn}$, α_{xn}, α_{zn}, $\alpha_{\theta n}$, γ_{xn}, γ_{zn}. Since parametric studies on elastic one-storey asymmetric-plan buildings have been extensively conducted by other

researchers, the ranges of the whole-structure parameter values of the one-storey system are already available. In order to understand the common values of the elastic and the inelastic 3DOF modal parameters, their variations with respect to the changes of the whole-structure parameters of one-storey asymmetric-plan buildings were investigated. Figure 2 illustrates the variation of the values of the first modal eccentricities, i.e. e_{x1}, e_{z1}, of the one-storey systems with an aspect ratio β=0.5. In general, the surface constructed from the values of e_{x1} and e_{z1} is looked like downward domes. Figures 2a and 2b show the values of e_{x1} and e_{z1} are always larger than -1 and less than 1, respectively. It is observed that the values of e_{x1} and e_{z1} are increased as the one-storey frequency ratio $\Psi_{\theta z}$ is increased. On the contrary, the values of e_{x1} and e_{z1} are decreased as the one-storey frequency ratio $\Psi_{\theta x}$ is increased.

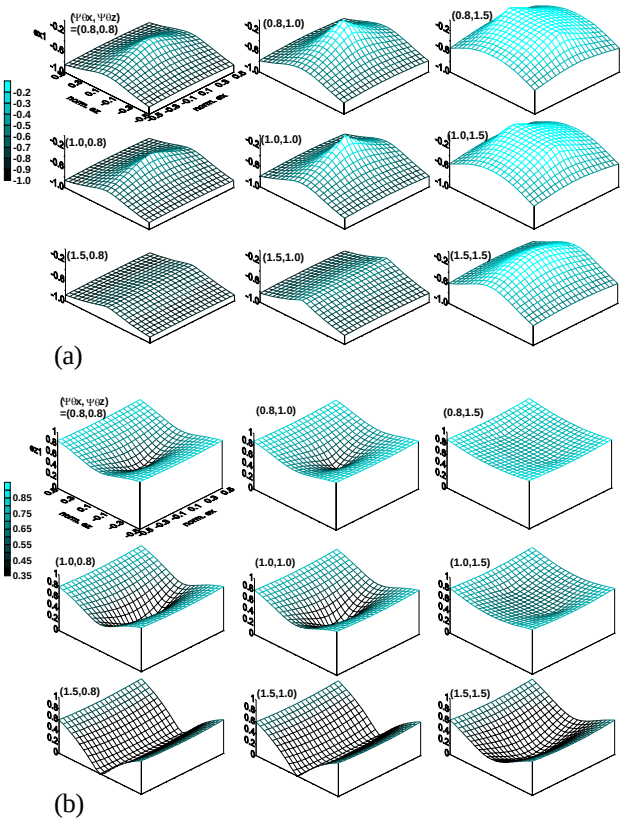

Figure 2 The first modal eccentricities, (a) e_{x1} and (b) e_{z1}, of the one-storey two-way asymmetric-plan buildings with aspect ratio β=0.5.

The ranges of values of post-yielding stiffness ratios α_{xn}, α_{zn} and $\alpha_{\theta n}$ (Fig. 1d) are discussed herein by using two simple one-storey systems (Fig. 3) as the extreme cases. System I (Fig. 3a) represents the rotational stiffness of this system almost contributed from the LFREs placed along the Z-axis. However, System II (Fig. 3b) represents the rotational stiffness of this system almost resulted from the LFREs placed along the X-axis. If only the X-directional LFREs of System I yield, the rotational stiffness of the system would be only lightly affected. Thus, the value of $\alpha_{\theta n}$ would be much larger than the value of α_{xn}. It is noted that the translational deformation at the CM is contributed from two parts: one is the translation at the CR and the other one is the rotation-induced translation. Thus, if the Z-translational stiffness is little influenced by the light softening of the rotational stiffness, the value of α_{zn} would be also much larger than the value of α_{xn}. Figure 4a schematically shows this situation, denoted as Case A. In case of the modal eccentricity is great, the light softening of the rotational stiffness maybe still cause large rotational-induced Z-translation, which is denoted as Case B and shown in Fig. 4b. However, if the direction of the mentioned large rotational-induced Z-translation is opposite to that occurred at the CR, the total Z-translation may be reduced as the modal inertia force increases. That is, a negative post-yielding stiffness ratio for the Z-translational force-deformation curve maybe takes place, which is schematically shown in Fig. 4c and denoted as Case C. Similarly, if the X-directional LFREs of System II yield, the rotational stiffness of the system would be significantly affected. Thus, the value of $\alpha_{\theta n}$ would be close to the value of α_{xn}. Moreover, if the softened rotational stiffness has little influence on the Z-translation, the value of α_{zn} would be much larger than the value of α_{xn}. This discussed situation, denoted as Case D, is sketched in Fig. 4d. However, Fig. 4e shows the Case E, which in case of the softened rotational stiffness considerably enhances the Z-translation, the value of α_{zn} would also be close to the values of α_{xn}. On the contrary, if the softened rotational stiffness makes the Z-translation increase in the opposite direction of the lateral force induced Z-translation, the value of α_{zn} might become negative. Figure 4f shows this situation and denoted as Case F. If only the Z-directional LFREs of Systems I and II yield, the similar discussions can be carried out. The associated possible cases, denoted as Case G to Case L, are illustrated in Fig. 4g to Fig. 4l.

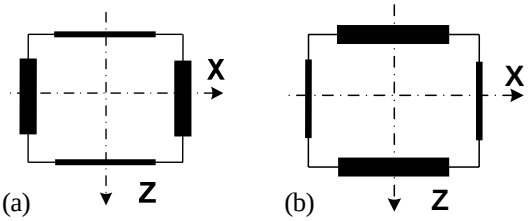

Figure 3 (a) System I (b) System II.

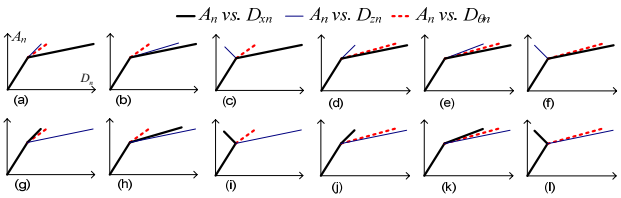

Figure 4 Different cases for the combination of α_{xn}, α_{zn} and $\alpha_{\theta n}$: (a) Case A (b) Case B (c) Case C (d) Case D (e) Case E (f) Case F (g) Case G (h) Case H (i) Case I (j) Case J (k) Case K (l) Case L

4. NUMERICAL VALIDATION

The first three vibration modes of two example buildings (Fig. 5) are investigated for verifying the above established relationships of modal parameters and the ranges of modal parameter values. The one-storey and the three-storey example buildings are denoted as Building I and Building II, respectively. All the columns, beams and braces of these two example buildings are H200×200×12×12, H200×150×6×9 and L90×90×10, respectively. The strong axes of column cross sections are along the X-axis. The floors are simulated as rigid diaphragms. The mass and mass moment of inertia of each floor are lumped at CM and equal to 9450 kg and 23030 kg-m^2, respectively. The location of CM is shown in Fig. 5c. The steel material is A36 and simulated as elastic-hardening material.

The elastic modal parameters of the first three vibration modes of the example buildings are shown in Tables 1a and 1b. Equations 9, 10 and 11 are all satisfied by substituting the elastic modal parameter values shown in Tables 1a and 1b into those equations. The modal pushover curves of the first three vibration modes of the example buildings are shown in Fig. 6. The values of associated properties, A_{xny}, A_{zny}, $A_{\theta ny}$, α_{xn}, α_{zn}, and $\alpha_{\theta n}$, obtained from these pushover curves are shown in Table 2. The corresponding inelastic 3DOF modal parameters computed from Eq. 7 are also listed in Table 2. The correctness of Eq. 7 has been verified in the previous work (Lin and Tsai 2008). Looking at the values of α_{xn}, α_{zn}, and $\alpha_{\theta n}$ shown in Table 2 and comparing Fig. 6 with Fig. 4, the combinations of post-yielding stiffness ratios for the first three vibration mode of Building I can be categorized as Case G, Case F and Case F, respectively. In the same way, the combinations of post-yielding stiffness ratios for the first three vibration mode of Building II can be all categorized as Case E or Case K. Figure 6a confirms the possibility of negative post-yielding stiffness ratios discussed in the previous section.

Table 1 The elastic modal parameters of Building I and Building II.

(a) Building I

Mode	m_{xn}	m_{zn}	I_n	k_{xn}	k_{zn}	$k_{\theta n}$
1	0.001	0.992	0.005	13.46	1015	54.26
2	0.709	0.005	0.284	6569.	5.08	3052.
3	0.289	0.002	0.713	2679.	1.61	7673.

Mode	e_{xn}	e_{zn}	β_n	γ_{xn}	γ_{zn}
1	-0.050	0.889	-5.68E-03	0.038	-0.999
2	5.286	0.302	1.82E-05	0.997	0.083
3	14.877	-0.749	-1.60E-05	0.997	-0.074

(b) Building II

Mode	m_{xn}	m_{zn}	I_n	k_{xn}	k_{zn}	$k_{\theta n}$
1	0.304	0.570	0.129	256.6	61.53	42.71
2	0.424	0.434	0.145	356.7	46.93	48.24
3	0.330	0.532	0.137	2330.1	694.39	515.78

Mode	e_{xn}	e_{zn}	β_n	γ_{xn}	γ_{zn}
1	-0.343	0.913	-0.004	0.591	-0.806
2	0.416	0.822	0.003	0.706	0.708
3	-0.365	0.884	0.002	0.604	-0.797

Table 2 The inelastic properties of Building I and Building II

(a) Building I

Mode	A_{xny}	A_{zny}	$A_{\theta ny}$	α_{xn}	α_{zn}	$\alpha_{\theta n}$
1	73	73	73	0.595	0.132	0.543
2	163	163	163	0.194	-0.049	0.204
3	261	261	261	0.169	-0.015	0.187

Mode	k'_{xn}	k'_{zn}	$k'_{\theta n}$	M_{yxn}	M_{yzn}	$M_{y\theta n}$
1	43.13	128.95	29.46	0.11	72.4	4.08
2	1248.1	6.70	622.63	115.57	0.81	76.92
3	472.38	1.43	1434.9	75.43	0.41	123.5

(b) Building II

Mode	A_{xny}	A_{zny}	$A_{\theta ny}$	α_{xn}	α_{zn}	$\alpha_{\theta n}$
1	25	25	25	0.148	0.126	0.138
2	40	40	40	0.080	0.127	0.068
3	90	90	90	0.049	0.040	0.046

Mode	k'_{xn}	k'_{zn}	$k'_{\theta n}$	M_{yxn}	M_{yzn}	$M_{y\theta n}$
1	178.30	7.42	5.89	7.60	14.25	15.05
2	137.00	4.76	3.28	16.96	17.36	12.52
3	224.59	25.84	23.73	29.70	47.88	56.06

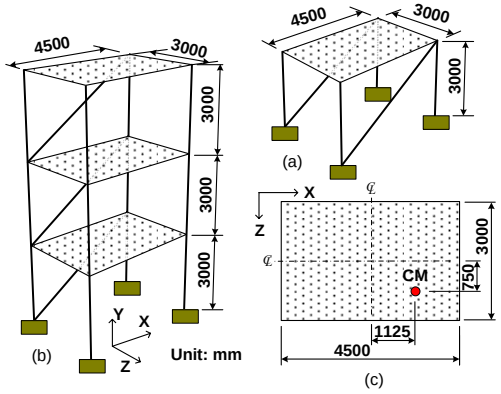

Figure 5 (a) Building I (b) Building II (b) the floor plan.

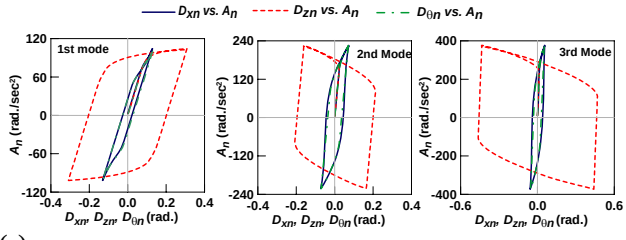

(a)

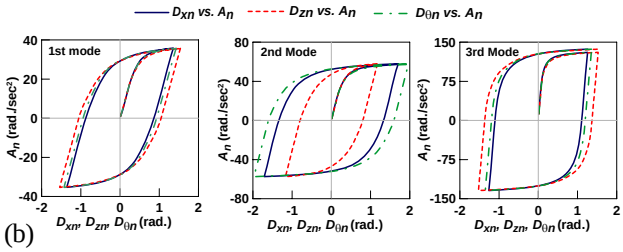

(b)

Figure 6 The modal pushover curves of the first three vibration modes for (a) Building I and (b) Building II.

5. BI-SPECTRA

Figures 7a and 7b show the constant strength response bi-spectra constructed from the proposed 3DOF modal systems with parameter values γ_{xn}=0.25, e_{xn}=-0.75, $|e_{xn}|/r_{xn}$=0.3 and R=3 and 6. There are nine (3×3) plots in each figure. The values of the combinations of $\Omega_{\theta xn}$ and $\Omega_{\theta zn}$ are varied in the nine plots as shown in the corresponding 3×3 table in the right-hand side of each figure. The only different parameter values between Fig. 7a and Fig. 7b are the values of α_{xn}, α_{zn} and $\alpha_{\theta n}$. In Fig. 7a, the values of α_{xn}, α_{zn} and $\alpha_{\theta n}$ are respectively equal to 0.05, 0.35 and 0.30, which represents Case A (Fig. 4a). However, in Fig. 7b, the values of α_{xn}, α_{zn} and $\alpha_{\theta n}$ are respectively equal to 0.05, 0.08 and 0.30, which represents Case B (Fig. 4b). It is evident that the curves of μ_{xn}, μ_{zn} and $\mu_{\theta n}$ are totally different shown in each plot. That is to say, the conventional inelastic response spectra constructed from the peak responses of SDOF modal systems are incapable of simultaneously estimating the three types of seismic demands for two-way asymmetric-plan buildings subjected to bi-directional seismic excitations. Figure 7a shows that μ_{zn} and $\mu_{\theta n}$ are almost equal for all combinations of $\Omega_{\theta xn}$ and $\Omega_{\theta zn}$ except the combinations with $\Omega_{\theta zn}$=1.5. It indicates that the Z-translational ductility demand and the rotational ductility demand are similar while the values of α_{zn} and $\alpha_{\theta n}$ are close. Nevertheless, the stated ductility demands, μ_{zn} and $\mu_{\theta n}$, become obviously different while the vibration mode is torsionally stiff in Z-direction, i.e. $\Omega_{\theta zn}$=1.5, and the vibration period is about larger than 1.0 sec. In Fig. 7a, the ductility curves for vibration periods larger than 1.0 sec. can be obviously categorized as two groups indexed by using the strength ratio R equal to 3 and 6. However, while the vibration mode is torsionally stiff in Z-direction, the rotational ductility demand for R=6 is almost equal to the X-translational ductility demand for R=3. In other words, the rotational ductility demand for Case A being torsionally stiff in Z-direction could be double overestimated by using the conventional inelastic response spectra. Comparing Fig. 7b with Fig. 7a, it is reasonably shown that the Z-translational ductility becomes close to the X-translational ductility because α_{zn} and α_{xn} are close in Fig. 7b.

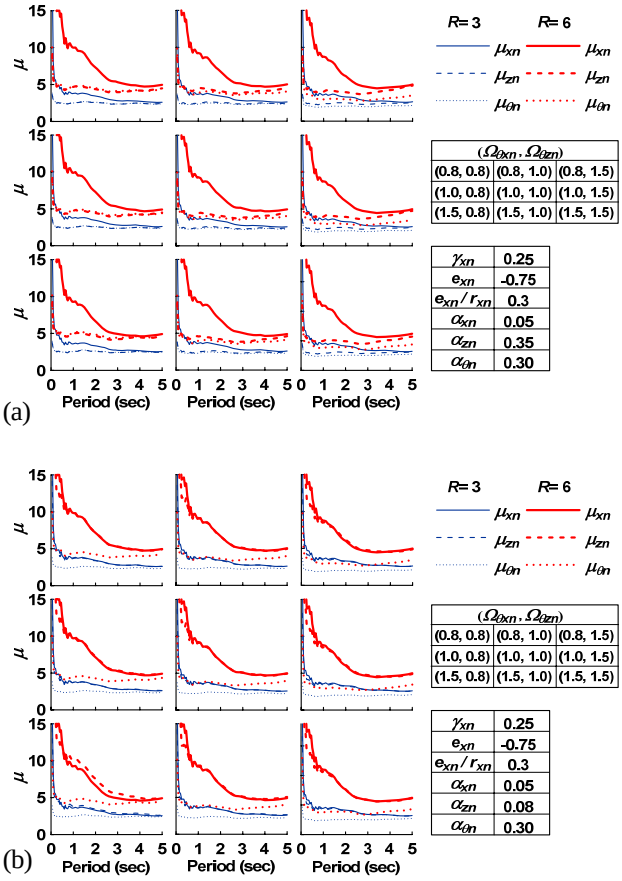

(a)

(b)

Figure 7 The constant strength response bi-spectra (a) Case A and (b) Case B.

6. CONCLUSIONS

In order to construct the bi-spectra for investigating the inelastic modal responses of two-way asymmetric-plan structures subjected to bi-directional ground excitations, some key tasks have been completed in this study. The first completed task is the identification of the independent elastic 3DOF modal parameters as T_n, $\Omega_{\theta xn}$, $\Omega_{\theta zn}$, e_{xn} and $|e_{xn}|/r_{xn}$. All the other elastic 3DOF modal parameters can be determined from these independent elastic parameters. For considering the bi-directional ground excitations in the modal level, the modal excitation ratios are naturally introduced. The second completed task is the establishment of the relationships between the inelastic modal parameters and the strength ratio. These relationships are essential for constructing constant-strength or constant-ductility response spectra. The various possible combinations of modal post-yielding stiffness ratios have been investigated. The third completed task is the investigation of the variation trends of 3DOF modal parameter values by using one-storey buildings with wide ranges of varied structural parameter values. It is found that the values of e_{x1} and e_{z1} are always negative and positive, respectively. Finally, the completed three key tasks have been verified by investigating the modal parameters of two example buildings. Some of the constant strength response bi-spectra are presented and discussed in this paper.

Acknowledgements:

This research was financially supported by the National Science Council of Taiwan, R.O.C. under grant no. NSC 98-2221-E-002-107-MY2, and is hereby gratefully acknowledged.

References:

Cruz, E.F. and Cominetti, S. (2000), "Three-dimensional buildings subjected to bi-directional earthquakes. Validity of analysis considering uni-directional earthquakes," *Proceedings of 12th World Conference on Earthquake Engineering*, Auckland, New Zealand, 2000.

De-La-Colina, J. (1999), "Effects of torsion factors on simple non-linear systems using fully-bidirectional analysis," *Earthquake Engineering and Structural Dynamics*, **28**, 691-706.

Hernádez, J.J. and López, O.A. (2000), "Influence of bidirectional seismic motion on the response of asymmetric buildings," *Proceedings of 12th World Conference on Earthquake Engineering*, Auckland, New Zealand, 2000.

Lin, J.L. and Tsai, K.C. (2008), "Seismic analysis of two-way asymmetric building systems under bi-directional seismic ground motions," *Earthquake Engineering and Structural Dynamics*, **37**, 305-328.

Lin, J.L. and Tsai, K.C. (2009), "Modal parameters for the analysis of inelastic asymmetric-plan structures," *Earthquake Spectra*, **25**(4), 821- 849.

Miranda, E. and Bertero, V.V. (1994), "Evaluation of strength reduction factors for earthquake-resistant design," *Earthquake Spectra*, **10**, 357-379.

Nassar, A.A. and Krawinkler, H. (1991), "Seismic demands for SDOF and MDOF systems," *Report No. 95*, The John A. Blume Earthquake Engineering Center, Stanford University, Stanford, California.

Newmark, N.M. and Hall, W.J (1973), "Seismic design criteria for nuclear reactor facilities," *Report No. 46*, Building Practices for Disaster Mitigation, National Bureau of Standards, U.S. Department of Commerce, 209-236.

Vidic, T., Fajfar, P. and Fischinger, M. (1992), "A procedure for determining consistent inelastic design spectra," *Proc. Workshop on Nonlinear Seismic Analysis of RC Structures*, Bled, Slovenia.

JOINT CONFERENCE PROCEEDINGS
7th International Conference on Urban Earthquake Engineering (7CUEE) &
5th International Conference on Earthquake Engineering (5ICEE)
March 3-5, 2010, Tokyo Institute of Technology, Tokyo, Japan

SELECTION OF EARTHQUAKE RECORDS FOR TIME-HISTORY ANALYSIS OF STRUCTURES

Abbas Moustafa[1], Izuru Takewaki[2] and Anil Wijeyewickrema[3]

1) Visiting Assistant Professor, Department of Urban and Environmental Engineering, Kyoto University, Japan
2) Professor, Department of Urban and Environmental Engineering, Kyoto University, Japan
3) Associate Professor, Department of Civil and Environmental Engineering, Tokyo Institute of Technology, Japan
abbas@archi.kyoto-u.ac.jp, takewaki@archi.kyoto-u.ac.jp, wijeyewickrema.a.aa@m.titech.ac.jp

Abstract: Modern seismic codes require the use of time-history analysis for dynamic assessment of important structures, structures having irregularities in plan or elevation and special structures, such as, base-isolated structures. In that case, a set of appropriate earthquake records and a suitable nonlinear model for the structure are required. The selection of appropriate acceleration records for a given structure from available records represents a crucial task in earthquake engineering. The selection of records for the site is generally based on the magnitude, the site-source distance and the local soil condition. In seismically active regions, a large number of records may be available for the site making the selection of records for the given structure a difficult task. In this paper, we propose a post-selection procedure for identifying a suitable small set of records. The paper covers also recent developments on the identification of critical acceleration records and the uncertainty involved in the selection parameters. Issues related to special classes of ground motions, such as, near-field ground motion with directivity focusing or fling effects, long duration earthquakes, earthquakes with concentrated energy, and accelerations with repeated sequences are also addressed. Examples on the selection of earthquake records for two sites in Japan and USA using the KiK-Net and the PEER Center are provided.

1. INTRODUCTION

Modern seismic codes require time-history analysis for important structures, structures having irregularities in plan or elevation and special structures (IBC 2009, AIJ 2005, Eurocode-8 2003, JRA 2002). Figure 1 shows the level II design response spectrum for seismic zone A and 0.05 damping ratio according to the Japanese Road Association seismic code (JRA 2002). Three simulated time histories compatible with this spectrum and their average response spectrum are also shown in the figure. Unlike response spectra, earthquake records provide full description of the ground motion, since they contain important information, such as, duration and amplitude. Bommer and Ruggeri (2002) identified 8 seismic codes from 33 countries where the time-history analysis is compulsory. In such case, a set of appropriate records and a suitable nonlinear model for the structure are required. Actual, simulated and artificial accelerations can be used as input for the time-history analysis. The use of artificial or simulated accelerations requires the existence of a response spectrum for the site which may not be always available. In addition, artificial accelerations have unrealistic higher frequencies.

Earthquake records are available in CD ROM or can be freely downloaded from the Internet. Table 1 lists some of the popular websites in the world. In Japan, records can be downloaded from the K-Net and the KiK-Net. Two sets of three digitized accelerograms each can be downloaded. The first set is recorded at the earth surface and the second set represents accelerations from underground seismographs.

The selection of earthquake records for dynamic analysis of structures is currently an active research field. Extensive review of records selection and scaling can be found in Housner and Jennings (1977), Anderson and Bertero (1987), Naeim (1993), Uang (1993), Shome et al (1998), Bommer and Ruggeri (2002), Bommer and Acevedo (2004), Naeim et al (2004), Iervolino and Cornell (2005), Baker and Cornell (2006), Watson-Lamprey and Abrahamson (2006), Beyer and Bommer (2007), Zhai and Xie (2007), Elnashai and Sarno (2008), Hancock et al (2008), Iervolino et al (2008), Lew et al (2008), Moustafa (2009a), Moustafa and Takewaki (2009a), Katsanos et al (2009) and Catalan et al (2010). The choice of records for a site is generally based on magnitude, site-source distance and local soil condition (Bommer and Acevedo 2004). This may lead either to (a) large or (b) limited number of records, depending on the site seismicity and availability of records. In seismically active regions, a large number of records may be available making the selection of a few records for the given structure a difficult task. Conversely, for sites with

low-moderate seismicity, a small number of records could be available. For such sites, records from other sites could be used but with similar seismicity level and soil condition. Alternatively, optimization techniques can be used to obtain the critical input that leads to the largest structural response. As well known, engineers are often interested in examining the worst case scenario that can happen to the structure. For that reason, a few studies have dealt with the identification of resonant or critical earthquake records for the structure (Housner and Jennings 1977, Anderson and Bertero 1987, Takewaki 2005, Amiri and Dana 2005, Zhai and Xie 2007, Moustafa 2009a, Moustafa and Takewaki 2009a).

An important aspect that should be taken into account is special classes of ground motion observed at the site, such as, long-duration earthquakes, repeated acceleration sequences and near-fault ground motion with impulsive characteristics. A series of moderate earthquakes can produce more damage in the structure than a single strong event due to accumulation of inelastic deformations (Elnashai et al 1998, Hatzigeorgiou and Beskos 2009, Moustafa and Takewaki 2009b). Near-fault earthquakes with directivity focusing or fling effects are capable of producing large structural deformations due to concentration of energy in narrow frequency band (Moustafa 2009a, b, 2010, Moustafa and Takewaki 2010a, b).

In this paper, we propose a post-selection procedure for identifying a suitable small set of records. The paper covers recent developments on the identification of critical acceleration records. Issues related to special classes of ground motions are addressed. Examples on the selection of earthquake records for two sites in Japan and USA using the KiK-Net and the PEER Center databases are also provided.

2. SELECTION OF EARTHQUAKE RECORDS

2.1 Selection based on magnitude, site-source distance and local soil type

The selection criteria for records at a site are usually based on earthquake magnitude, site-source distance and local soil type. This process may result in several hundred records for certain sites, but a few records for other sites. In case a large number of earthquake records are available for the given site, more refinement for the records can be carried out. Practically, 3-10 records should be selected. This selection could be based on properties of the structure to be designed, such as, its fundamental frequency. In some of the previous works, the above selection parameters, have been treated as being constants (Bommer and Acevedo 2004). However, the magnitude and site-source distance of possible future earthquakes are uncertain quantities. It is, therefore, reasonable to include uncertainties in these parameters. Specific guidelines on the variation in these parameters are currently not available. Elnashai and Sarno (2008) suggested that the range of the earthquake magnitude could be ($M \pm 0.30\ M$) and the range of the site-source distance could be (D $\pm$ 20~40) km. They also reported that the earthquake magnitude is more important than matching the site-source distance. Note that, the range of variation in the site-source distance should be based on the expected site-source distance of future earthquakes. For instance, when the site is close to the source, a small variation should be considered and when the site is far from the source, a large variation should be considered. We propose that the variation in the site-source distance could be ($D \pm \alpha D$), where α is a small positive quantity (e.g. $0.20 \leq \alpha \leq 0.40$). The K-Net and KiK-Net facilitate searching records for a region using the latitude and the longitude of the site. This is a useful option since it provides records for a region. Illustrative examples on this aspect are provided in Section 3.

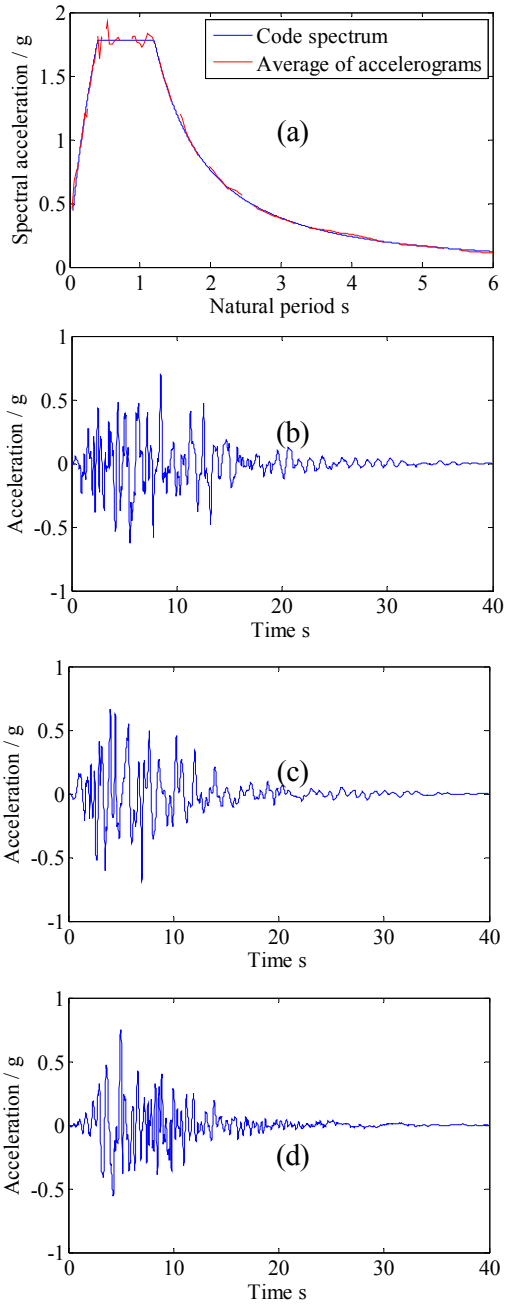

Figure 1: (a) Level II elastic response spectra for seismic zone A ($\xi = 0.05$) and (b-d) Compatible acceleration time histories (JRA 2002)

Table 1: Some popular sources for strong ground motion records (Bozorgnia and Campbell 2004)

Ground motion data source	Internet website
(1) California Strong Motion Instrumentation Program (SCMIP)	http://www.consrv.ca.gov/cgs/smip
(2) California Integrated Seismic Network (CISN)	http://docinet3.consrv.ca.gov/csmip/cisn-edc/default.htm
(3) U.S. Geological Survey (USGS)	http://nsmp.wr.usgs.gov
(4) U.S. Geological Survey (USGS)*	http://nsmp.wr.usgs.gov/cdrom.html
(5) Consortium of Organizations for Strong-Motion Observation System (COSMOS)	http://db.cosmos-eq.org
(6) TriNet and ShakeMap	http://www.trinet.org/ and http://earthquake.usgs.gov/shakemap
(7) University of Southern California (USC)	http://www.usc.edu/dept/civil_eng/Earthquake_eng
(8) US National Geophysical Data Center (NGDC/NOAA)	http://www.ngdc.noaa.gov/seg/hazard/strong.html
(9) Pacific Earthquake Engineering Research (PEER) Center	http://peer.berkeley.edu/smcat/search.html
(10) SAC steel project, strong-motion database	http://nisee.berkeley.edu/data/strong_motion/sacsteel/ground_motions.html
(11) Caltech strong motion database (SMARTS)**	http://www.eerl.caltech.edu/smarts/smarts.html
(12) Pacific Northwest Seismograph Network (PNSN)	http://www.geophys.washington.edu/SEIS/PNSN/SMO
(13) European Strong- Motion Database (ESD)	http://www.isesd.hi.is/ESD_Local/frameset.htm
(14) Kyoshin Net (K-Net) (NIED, Japan)	http://www.k-net.bosai.go.jp
(15) KiK-Net (NIED, Japan)	http://www.kik.bosai.go.jp/kik/index_en.shtml
(16) Mexico, Guerrero Accelerograph Network	http://www.seismo.unr.edu/ftp/zeng/GUERRERO/guerrero.html
(17) Switzerland, National Strong Motion Network	http://seispc2.ethz.ch/strong_motion/home.jsp
(18) Taiwan, Central Weather Bureau (CWB)***	http://www.cwb.gov.tw/V4e/index.htm
(19) Turkey, General Directorate of Disaster Affairs	http://angora.deprem.gov.tr/indexen.htm

*CD ROM of digitized strong-motion accelerograms of North and Central American Earthquakes, 1933–1986 (Seekins et al 1992).
** Diskettes of selected records (http://www.eerl.caltech.edu/smarts/smarts.html)
*** For 1999 Chi-Chi earthquake, a CD of strong motion records was also produced by Lee et al (2001).

When the search yields a large number of records, a refinement could be carried out by performing simple analysis of the available records. For example, the Fourier spectra of the ground acceleration can be used to select those records that have concentrated energy and dominant frequencies close to the structure fundamental frequency (Takewaki 2004, Moustafa 2009b). Moustafa and Takewaki (2009a) have recently proposed deterministic and probabilistic measures to identify resonant or critical earthquake records.

2.2 Selection based on other criteria

Based on the experience of practicing engineers, simple guidelines have been specified in selecting earthquake records as inputs to time-history analysis of structures. These guidelines may not be technically robust, but they serve as suitable criteria for non-specialists with limited knowledge of earthquake engineering (Zhu et al 1988, Broderick and Elnashai 1996, Elnashai and Sarno 2008). The selection is based on the ratio of the peak ground acceleration to the peak ground velocity r = PGA/PGV. For instance, near-fault shallow earthquakes (e.g. 2010 Haiti earthquake) or earthquakes measured on rocks will have high acceleration peaks of short duration (high r), leading to low-velocity cycles. Deep or distant earthquakes or records on soft soil will have lower accelerations and long-duration cycles (low r), leading to high-velocity waves. Intermediate scenarios will lead to intermediate values of r. Note that other criteria, such as, the ratio of PGA/PGD can be also used. For instance, near-fault ground motion with directivity focusing or fling effects, known as pulse-like ground motion, possesses low PGA/PGV and PGA/PGD (Moustafa and Takewaki 2010a, b). Elnashai and Sarno (2008) reported three different ranges for strong ground motion, namely, low ($r < 0.8$), medium ($0.8 \leq r \leq 1.2$), and high ($r > 1.2$), where PGA is represented in g and PGV in m/s.

2.3 Number and duration of earthquake records

Most seismic codes specify the use of 3-10 records as inputs to nonlinear time-history analysis of structures. Bommer and Acevedo (2004) suggested 10-20 records. We believe that the number of earthquake records should be selected such that it adequately represents those records that could be critical to the structure under consideration. In seismically active regions, such as, Japan, more records should be used. In areas with moderate seismicity lower number of records could be adopted. The importance and size of the structure to be designed should be also taken into account.

In case of availability of small number of records, simulated accelerations or records from other sites with similar geological soil condition and seismicity level could be used. In the first case, the duration, magnitude, and other characteristics of the simulated accelerations should be based on the seismicity study of the site. In other words, simulated accelerations should reflect observed properties of earthquake records. Similarly, record selection from other sites should also reflect the major characteristics observed in recorded ground motions at the site.

2.4 Special classes of ground motion

The ground acceleration measured at a certain point in the earth depends on the source mechanism, the travel path and the local soil condition at the site. In other words, the attenuation of the ground acceleration measured by the seismograph from the seismic waves released at the source depends primarily on the site-source distance, the travel path and the local soil type (Moustafa et al 2009). Flexible soils can amplify the amplitudes and filter the frequencies of the seismic waves several times compared to stiff soils. The selection process should be based on the nature of the expected earthquakes at the site, i.e. ground motion resulting from inter-plate and/or from intra-plate.

Attention should be given to special classes of ground motion, such as, near-field ground accelerations with impulsive characteristics, repeated earthquake sequences, long-duration earthquakes, earthquakes with concentrated energy and earthquakes with large amplitudes. Additional discussions on these special classes of ground motions are provided below.

2.4.1 Inter-plate and intra-plate earthquakes

The structural engineer should be careful in selecting records from inter-plate regions and use them for intra-plate regions. This can be handled by studying the seismo-tectonic of the region. Classification of inter- and intra-plate records has been based on remoteness from active tectonic boundaries (Dahle et al 1990). Intra-plate regions have been described also as not being actively deformed and referred as stable continental regions (Johnson et al 1994). The differences between the characteristics of inter-plate and intra-plate strong-ground motions result due to source and path effects (JRA 2002).

2.4.2 Near-field ground motion

Near-field ground motions with directivity focusing or fling effects can produce larger responses and can cause severe damage to the structure compared to ordinary earthquakes. This is attributed to the impulsive nature of the ground motion. This class of ground motion has its energy concentrated in one or very few pulses (Moustafa 2010, Moustafa and Takewaki 2010a, b). These ground motions are generally influenced by the source mechanism and observed within about (0-20) km from the source. The 1994 Northridge, 1995 Kobe and the 2010 Haiti earthquakes are examples of near-field earthquakes causing widespread damage and large life loss.

2.4.3 Multi-sequences ground motion

This class of ground motion is characterized by a

long duration and existence of repeated strong shaking and is known as ground motions with multiple sequences. Such ground motion can cause extensive damage to the structures due to accumulation of inelastic deformations from repeated sequences. The characterization of strong ground motion of repeated sequences has been studied recently by Moustafa and Takewaki (2009b). A set of low-moderate earthquake events can cause more damage to the structure than a single strong earthquake. Care should be given to the existence of such ground motion for the given site. For instance, the 2004 Niigata earthquake consisted of repeated acceleration sequences of 10 minutes total duration followed by 16 after-shocks (Moustafa and Takewaki 2009b). Thus, several structures got severely damaged since they were subjected to repeated strong ground motions before being repaired.

It may be emphasized that, current seismic codes specify design earthquakes as a single strong ground motion event. In reality, however, the structure may get subjected to a series of strong ground motions from the same earthquake or from different earthquakes. In the first scenario, such as, the 2004 Niigata earthquake and the 2010 Haiti earthquake, secondary sequences or aftershocks may cause further damage to the already damaged structure from the main shock or from the first acceleration sequence.

2.4.4 Long-duration earthquakes

Earthquake records of total duration more than 60 s are knows as long-duration earthquakes. This type of ground motion can drive the structure to the inelastic range producing extensive damage.

2.4.5 Large amplitude earthquakes

Ground accelerations with peak ground acceleration greater than 1.0 g and peak ground velocity larger than 1.0 m/s are knows as large amplitude ground motion. Strasser and Bommer (2009, 2010) have studied this class of ground motion. Ground motion with large amplitude has been generally observed in the near-fault region. This class of ground motion can cause severe damage to the structures (e.g. the 1994 Northridge, the 1995 Kobe, the 1999 Chi-Chi and the 2004 Niigata earthquakes). Large amplitude earthquakes could be also observed in far-field strong ground motion due to amplification of seismic waves by soft soils. An example is the ground accelerations recorded during the 2001 Bhuj earthquake at Ahmad Abad about 240 km from the source.

2.5 Nature of recorded accelerograms

2.5.1 Corrected and uncorrected records

Earthquake records available in the Internet or in CDs contain base-corrected ground motions as well as uncorrected ground motions. The use of uncorrected records may lead to unrealistic responses. Therefore, uncorrected records should be corrected before being used with corrected records in dynamic analysis of structures. The correction criterion varies from linear, quadratic to higher orders correction methods. Long-duration records require special correction methods. Earthquake records include higher frequencies, noise and errors due to the response of the recording instruments. Some of these errors can be reduced while others are difficult to be eliminated.

2.5.2 Analog and digital records

Historical and old records have been recorded using analog seismic instruments. This data has been digitized and made available in the form of numerical values of the ground acceleration at discrete time instants. The accuracy of the digitization process does not provide accurate acceleration time-histories compared to those from new digital recording instruments. Old historical records have been digitized at equal time-intervals of 0.02 or 0.01 s. Modern seismographs, on the other hand, provide ground accelerations measured at time-intervals of 0.005 or 0.004 s. Note that the recording time-interval and its relation with the lowest period of the structure are important in the time-history analysis of structures.

2.6. Nature of the structure

For certain structures, such as, hospitals the floor acceleration should be kept as small as possible so that it does not cause falling or movement of medical instruments and equipments. Long-span bridges and extended pipelines are special structures that require the specification of the ground motion at multiple support points. The ground motion at each support is different from those at other support points. In certain cases, the distance between the support points could be several hundred meters. Similarly, the specification of multi-component ground acceleration for seismic design of certain structures (e.g. high-rise buildings) requires special care (Beyer and Bommer 2007).

Base-isolated and tall structures are required to be designed not only for the usual design earthquakes but also for long-period ground motions. This is because long-period earthquakes with large PGV/PGA and PGD/PGA ratios are regarded to be critical for base-isolated and tall buildings (Ariga et al 2006, Takewaki 2008). Important structures, such as, nuclear power plants are usually designed using the response spectrum method. However, some of the individual components, such as, the pipes transmitting chemical materials and the cooling pipes are required to be designed separately using time history analysis. In these cases, ground accelerations of high magnitudes should be selected. This aspect is of essential importance for such structures at seismically active regions.

2.7 Post-selection of records for a given structure

In seismically active regions, a large number of records are usually available. This number could be several hundreds making the time-history analysis of the

structure under this large number of records a time consuming process. In such case, it is appropriate to limit the number of earthquake records to be used as inputs to the dynamic analysis of the given structure to a small number (typically 3-10 records) to reduce the computations. As a general rule, one should not select many records from the same earthquake to avoid biasing towards a single event.

In the context of the potential of the ground motion to damage structures, several authors have attempted to identify the earthquake record that causes the largest damage to the structure. One of the early studies on this subject has been carried out by Housner and Jennings (1977). These authors have attempted to identify the maximum credible ground motion that can be used in seismic design of the structure by developing a simple intensity measure similar to the Arias measure (Arias 1970). The peak ground acceleration (PGA), the effective PGA, the peak ground velocity (PGV), the effective PGV, the energy, the intensity, the duration and the number of cycles of the ground accelerations have been used for this purpose (see e.g. Naeim and Anderson 1993, Amiri and Dana 2005). However, damage of structures is contributed by several parameters of the ground motion. Naeim and Anderson (1993) used the magnitude and PGA ($M \geq 5.0$ and $\text{PGA} \geq 0.05\,\text{g}$) to select 1157 horizontal accelerations from a set of about 5000 accelerograms recorded during 1933-1992. Subsequently, 30 records that have the highest PGA, EPGA, PVA, EPGV, PGD, IV and ID have been selected from the 1157 records. A set of 84 records was further selected based on the bracketed duration and a subset of 36 records with long durations was identified. This led to a database of 120 records. This study provided simple procedures for identifying the most severe real seismic design ground motions. More recently, the critical excitation concept has been used in identifying resonant or unfavorable earthquake records (Zhai and Xie 2007, Moustafa 2009a, Moustafa and Takewaki 2009a). Thus, Zhai and Xie (2007) considered a database of 852 records from 34 earthquakes measured during 1940-2001 and classified it into four groups based on the site soil type. This database was further divided into three groups based on the region (mainland China, Taiwan of China and regions outside China). The most unfavorable records were then determined for each of these three groups by considering their damage potential in terms of the parameters of the ground motion and the associated structural damage criteria, such as, deformation, hysteretic energy and damage indices.

In this paper, we propose the use of the methods suggested by Moustafa (2009a) and Moustafa and Takewaki (2009a) to identify the resonant records and to quantify the associated dominant frequency of each record. This is followed by a ranking of the records based on their resonance or criticality. Subsequently, the first 3-10 records that have narrow frequency content and have their dominant frequency close to the structure fundamental natural frequency are selected.

The methods proposed by Moustafa (2009a) and Moustafa and Takewaki (2009a) for quantifying the frequency content of the ground acceleration, include deterministic and probabilistic measures. The probabilistic measures contain the entropy rate and the dispersion index and are based on the geometric properties of the power spectral density function of the ground acceleration. The deterministic measures include the effective and the dominant frequencies of the ground acceleration.

2.8 The critical ground motion input

Figure 2 shows the Fourier amplitude spectra for four accelerations, namely, the EW component of the 1995 Kobe earthquake (Japan) recorded at Kobe University, the NS component of the 1999 Duze earthquake (Turkey) recorded at DZC, the NS component of the 1940 Imperial Valley earthquake (California) recorded at El Centro array #9, and the critical acceleration for a structure of fundamental natural frequency = 1.0 Hz (Abbas and Manohar 2002, 2007). As can be seen, some of the actual records have concentrated energy in a narrow frequency band. When this frequency band is centered around the structure fundamental frequency, large deformation can be expected (Takewaki 2005, 2007, Cao and Friswell 2009, Moustafa 2009b). The widespread damage caused to structures in the near-field region during the 1994 Northridge, 1995 Kobe, 1999 Chi-Chi, 1999 Duze and Izmit, earthquakes sheds lights on the worst ground motions that can cause severe damage to the structures (Moustafa and Takewaki 2010a, b, Strasser and Bommer 2009, 2010).

The critical excitation method can be employed to generate mathematical earthquake accelerations that can be used as inputs to the time history analysis of important structures. These accelerations can be used in situations where a limited number of records are only available for the given site. The critical or the worst acceleration provides an upper bound on the worst case scenario that can happen to the structure. In such case, the critical acceleration can be expressed as a linear combination of the available accelerograms and these parameters are optimized to produce the maximum response in the structure. Meanwhile, the critical acceleration is constrained to predefined constraints (Wang et al 1978, Pirasteh et al 1988). Since this representation contains mathematical and convergence problems, Abbas and Manohar (2002) used the Fourier series in representing the critical acceleration and employed the available records in evaluating the constraints. Pirasteh et al (1988) imposed constraints on the selection of the of the set of basis records, such as, the use of strong ground motions, the similarity of soil condition and site-source distance and selecting records from different earthquakes to avoid biasing towards any particular earthquake. They further placed bounds on the candidate records, such as, peak

values, Fourier spectra and growth rate for the ground acceleration, velocity and displacement.

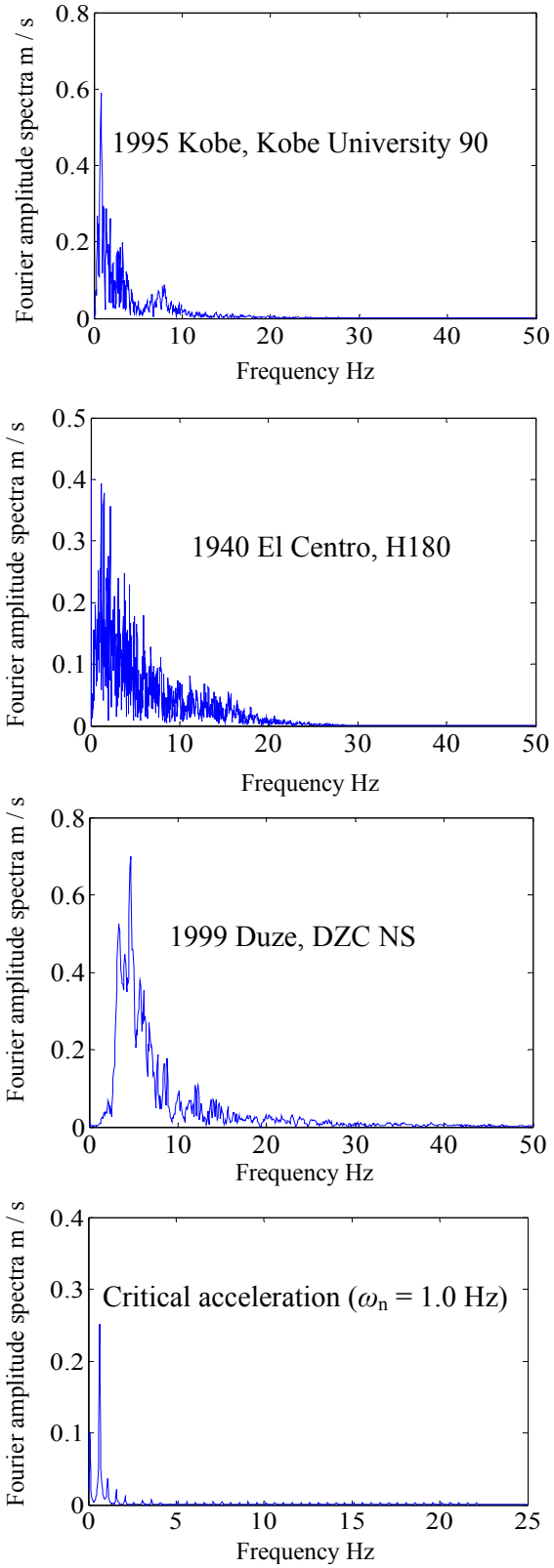

Figure 2: Fourier amplitude spectra for recorded and critical accelerations

3. ILLUSTRATIVE EXAMPLES

3.1 Records search using the KiK-Net

Japan is one of the most seismically active regions in the world. Seismic active areas in Japan, such as Tokyo and Kobe, can experience strong ground motions quite frequently. The Kyoshin Net and the Kiban-Kyoshin Net contain earthquake records from January 1996 onwards (see Table 1) and facilitate: (a) searching earthquakes with the origin time (b) searching earthquakes with the origin time, magnitude, epicenter location, and (c) searching acceleration data independent of earthquakes, based on date and time, site location, site characteristics, maximum acceleration and epicentral distance. The time period of records can be also specified (e.g. from July 1996 to November 2005). One of the attractive and efficient features of the K-Net and the KiK-Net is that they facilitate searching earthquake records for a region by specifying the longitude and the latitude. This feature is not available in other ground motion database sites. These two sites provide detailed information on the recording stations, such as, location, depth, body (P and S) wave velocities, and details of soil layers up to 1000 m below the earth's surface.

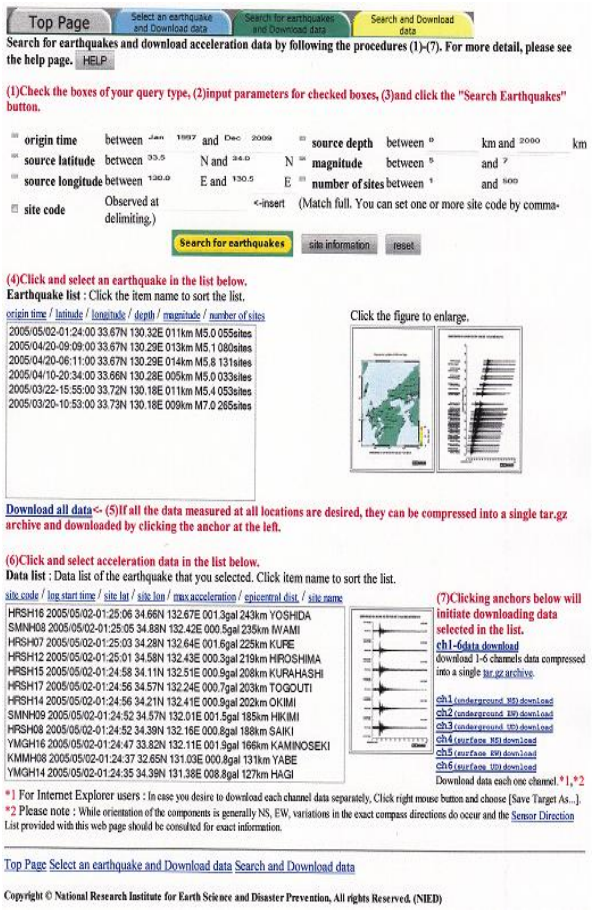

Figure 3: Records search results for a region in Japan using the KiK-Net ($5.0 \leq M \leq 7.0$, 33.5 N ≤ latitude ≤ 34.0 N, 130.0 E ≤ longitude ≤ 130.5 E)

An illustrative example for searching earthquake records for a region of about 55×55 km ($1^{o} \approx 111$ km) and magnitude of $5.0 \leq M \leq 7.0$ is shown in Figure 3. This search led to a total number of 617 records from 6 earthquakes. Specifically, these earthquakes contain 55, 80, 131, 33, 53, and 265 records, respectively. The time period of records considered is taken from January 1996 to December 2009. Note that a post-selection process is necessary in this case (see Section 2.7).

3.2 Records search using the PEER Center

The PEER Center provides a convenient way of searching earthquake records. The search is based on the earthquake magnitude, site-source distance and local soil type. Earthquake records can be searched with upper and lower bounds on the earthquake magnitude and the site-source distance. The local soil type is classified based on the shear velocity as: type A ($v > 750$ m/s), B ($360 \leq v \leq 750$ m/s), C ($180 \leq v < 360$ m/s) and D ($v < 180$ m/s) according to the USGS classification (where v is the shear velocity of the soil). The classification also includes soil type A (Rock), B (Shallow or stiff soil), C (Deep narrow soil), D (Deep broad soil) and E (Soft deep soil). The third soil classification includes soil type 1 (Hard soil), 2 (Medium soil) and 3 (Soft soil) according to the Taiwan CWB. These different classifications of soil types arise due to the difference in defining the soil type for ground motion recorded in Taiwan from those recorded in USA and other parts of the world. An illustrative example for searching earthquake records using the PEER Center for earthquake magnitude $6.0 \leq M \leq 6.5$, site-source distance of 30 km $\leq D \leq$ 35 km and soft soil is shown in Figure 4. This search led to a total of 9 records (6 horizontal and 3 vertical) from two earthquakes (1994 Northridge and 1999 Chi-Chi). Herein, a limited number of records is available. These 9 records can be used in deriving the critical acceleration input for the given structure (see Section 2.8). Note that the search page provides information on the records ID, station code, data source, and peak values of ground acceleration, velocity and displacement.

4. CONCLUSIONS

The widespread damage and the massive loss of life caused by strong motion earthquakes, such as, the 1985 Mexico, 1994 Northridge (USA), 1995 Kobe (Japan), 1999 Chi-Chi (Taiwan), 2001 Bhuj (India) and the more recent 2010 Haiti earthquakes pose a real challenge to structural and earthquake engineers for the mitigation of extensive damage of structures and the prevention of massive loss of life due to earthquake hazards. This requires developing new design concepts and the use of modern methods for seismic design of structures. The identification of the appropriate strong ground motion that best describes the most expected future earthquakes to occur at the site, during the structure's life-time, is an important task.

PEER Strong Motion Database

Introduction | Browse | Search | Documentation | Providers | Credits

Query Results

Record ID	Earthquake	Station	Data Source	Record/Component	HP (Hz)	LP (Hz)	PGA (g)	PGV (cm/s)	PGD (cm)
P1476	Chi-Chi, Taiwan 1999/09/20	TCU113	CWB	CHICHI/TCU113-N	0.03	50.0	0.074	23.4	27.12
P1476	Chi-Chi, Taiwan 1999/09/20	TCU113	CWB	CHICHI/TCU113-V	0.03	50.0	0.077	16.0	17.03
P1476	Chi-Chi, Taiwan 1999/09/20	TCU113	CWB	CHICHI/TCU113-W	0.04	50.0	0.07	27.8	22.21
P1488	Chi-Chi, Taiwan 1999/09/20	TCU140	CWB	CHICHI/TCU140-N	0.03	50.0	0.057	20.5	17.53
P1488	Chi-Chi, Taiwan 1999/09/20	TCU140	CWB	CHICHI/TCU140-V	0.04	50.0	0.071	19.7	17.1
P1488	Chi-Chi, Taiwan 1999/09/20	TCU140	CWB	CHICHI/TCU140-E	0.05	50.0	0.07	24.0	21.44
P0984	Northridge 1994/01/17 12:31	90011 Montebello - Bluff Rd.	USC	NORTHR/BLF296	0.1	30.0	0.128	5.9	2.25
P0984	Northridge 1994/01/17 12:31	90011 Montebello - Bluff Rd.	USC	NORTHR/BLF-UP	0.2	30.0	0.076	2.8	0.48
P0984	Northridge 1994/01/17 12:31	90011 Montebello - Bluff Rd.	USC	NORTHR/BLF206	0.2	30.0	0.179	9.4	1.48

© Copyright 2000, Regents of the University of California

Figure 4: Records search results for soft soil site using the PEER Center ($6.0 \leq M \leq 6.5$, $30 \leq$ Site-source distance ≤ 35 km)

This paper deals with the selection of strong ground motion records for seismic analysis of engineering structures. Alternative methods based on the magnitude, site-source distance and local soil type and those based on empirical assumptions, such as, PGV/PGA and PGD/PGA have been discussed. The paper proposed a simple methodology for generating mathematical ground motion time histories. This approach is based on the critical excitation concept. The ground motion modeled using this approach contains the energy concentrated at the structure fundamental frequency and thus provides an upper bound on the worst case scenario that can happen to the structure. Historical strong ground motion earthquakes which caused widespread structural damage and massive loss of life, such as, the 1985 Mexico, 1994 Northridge, 1995 Kobe, 1999 Chi-Chi, 2001 Bhuj and the more recent 2010 Haiti earthquake provide clear examples on the high level of uncertainty involved in earthquake accelerations. The estimation of the critical earthquake load can be carried out for important structures and critical facilities when a limited number of earthquake records are only available. Numerical illustrations on searching earthquake records for sites in Japan and USA are provided using the KiK-Net and the PEER Center, respectively. In this context, it may be emphasized that the PEER Center and the KiK-Net provide different options in searching earthquake records. For instance, the PEER Center provides records based on the expected magnitude, site-source distance and local

soil type. On the other hand, the KiK-Net provides accelerograms based on the magnitude, source depth, and site location and area (in terms of latitude and longitude).

Acknowledgements:

This research is supported by the Japanese Society for the Promotion of Science (Grant No. JSPS-P-08073) and by the Center for Urban Earthquake Engineering at Tokyo Institute of Technology. These supports are gratefully acknowledged. The authors are also thankful to the NIED (Japan) and to the PEER Center (USA) for providing the ground motion records.

References:

Abbas, A.M. and Manohar, C.S. (2002), "Investigations into critical earthquake load models within deterministic and probabilistic frameworks." *Earthquake Engineering & Structural Dynamics*, **31**, 813-832.

Abbas, A.M. and Manohar, C.S. (2007), "Reliability-based vector nonstationary random critical earthquake excitations for parametrically excited systems," *Structural Safety*, **29**, 32-48.

AIJ (2004), "Recommendations for loads on buildings," Architectural Institute of Japan, Tokyo.

Amiri, G.G. and Dana, F.M. (2005), "Introduction to the most suitable parameter for selection of critical earthquakes,", *Computers & Structures*, **83**, 613-626.

Anderson, J.C. and Bertero, V.V. (1987), "Uncertainties in establishing design earthquakes," *Journal of Structural Engineering*, ASCE **113**(8), 1709-1724.

Arias, A. (1970). "A measure of earthquake intensity: Seismic design of nuclear power plants", Cambridge, MA: MIT press, pp. 438:468.

Ariga, T., Kanno, Y. and Takewaki, I. (2006). "Resonant behavior of base-isolated high-rise buildings under long-period ground motions," *The Structural Design of Tall and Special Buildings*, **15**(3), 325-338.

Baker, J. and Cornell, C.A. (2006), "Spectral shape, epsilon and record selection," *Earthquake Engineering & Structural Engineering*, **35**, 1077-1095.

Beyer, K. and Bommer, J.J. (2007), "Selection and scaling of real accelerograms for bi-directional loading: a review of current practice and code provisions," *Journal of Earthquake Engineering* **11**, 13-45.

Bommer, J.J. and Acevedo, A.B. (2004), "The use of real earthquake accelerograms as design input to dynamic analysis," *Journal of Earthquake Engineering*, **8**(1):43-91.

Bommer, J.J. and Ruggeri, C. (2002), "The specification of acceleration time-histories in seismic design codes," *European Earthquake Engineering*, **1**, 3-17.

Bozorgnia, Y. and Campbell, K.W. (2004), "Engineering characterization of ground motion," Bozorgnia and Bertero (editors), CRC Press, Florida.

Broderick, B.M. and Elnashai, A.S. (1996), "Seismic response of composite frames, I: response criteria and input motion," *Engineering Structures*, **18**(9), 696-706.

Catalan, A., Benavent-Climent, A. and Cahis, X. (2010), "Selection and scaling of earthquake records in assessment of structures in low-to-moderate seismicity zones," *Soil Dynamics and Earthquake Engineering*, **30**(1-2), 40-49.

Cao, H., and Friswell M.I. (2009), "The effect of energy concentration of earthquake ground motions on the nonlinear response of RC structures," *Soil Dynamics and Earthquake Engineering*, **29**, 292-299.

Dahle, A., Bungum, H. and Kvamme, L. (1990), "Attenuation models inferred from intraplate earthquake recordings," *Earthquake Engineering & Structural Dynamics*, **19**, 1125-1141.

Elnashai, A.S., Bommer, J. J., and Martinez-Pereira A (1998), "Engineering implications of strong-motion records from recent earthquakes," *Proceedings of Eleventh European Conference on Earthquake Engineering*, Paris, CD-ROM.

Elnashai, A.S. and Sarno, L.D. (2008), "Fundamentals of earthquake engineering," John Wiley & Sons, England.

European Committee for Standardization (2003), "Eurocode 8: Design of structures for earthquake resistance," Brussels.

Hancock, J, Bommer, J.J. and Stafford, P.J. (2008), "Numbers of scaled and matched accelerograms required for inelastic dynamic analyses," *Earthquake Engineering & Structural Dynamics*, **37**, 1585-1607.

Housner, G.W. and Jennings, P.C. (1977), "The capacity of extreme earthquake motions to damage structures," Structural and Geotechnical Mechanics, A volume honoring Nathan M. Newmark (Ed. W. J. Hall), Prentice-Hall, Englewood Cliffs, NJ, 102-116.

International Building Code (IBC) (2009), International Code Council Inc, USA.

Iervolino, I. and Cornell, C.A. (2005), "Record selection for nonlinear seismic analysis of structures," *Earthquake Spectra*, **21**(3), 685-713.

Iervolino, I., Maddaloni, G. and Cosenza, E. (2008), "Eurocode 8 compliant real record sets for seismic analysis of structures," *Journal of Earthquake Engineering*, **12**, 54-90.

Johnson, A.C., Coppersmith, K.J., Kanter, L.R. and Cornell, C.A. (1994), The earthquakes of stable continental regions: Volume 1-assessment of large earthquake potential. *EPRI Report* TR-10 2261-VI, Electric Power Research Institute, Palo Alto, CA.

JRA (2002), "Specifications for highway bridges, Part V: Seismic design," Japan Road Association, Tokyo.

Katsanos, E.I., Sextos, A.G. and Manolis, G.D. (2009), "Selection of earthquake ground motion records: A state-of-the-art review from a structural engineering perspective," *Soil Dynamics and Earthquake Engineering* (in press, doi:10.1016).

Kiban-Kyoshin Network (2009), "National Research Institute for Earth Science and Disaster Prevention," (http://www.kik.bosai.go.jp).

Kyoshin-Network (2009), "National Research Institute for Earth Science and Disaster Prevention," (http://www.k-net.bosai.go.jp).

Lee, W.H.K., Shin, T.C, Kuo, K.W., Chen, K.C. and Wu, C.F. (2001), "Data files from CWB free field strong-motion data from the 21 September Chi-Chi, Taiwan, earthquake," *Bulletin of the Seismological Society of America*, **91**(5), 1390.

Lew, M., Naeim, F. Hudson, M.B. and Korin, B. (2008), "Challenges in specifying ground motions for design of tall buildings in high seismic regions of the United States," *Fourteenth World Conference in Earthquake Engineering*, 12-17 October 2008, Beijing.

Moustafa, A., (2009a), "Discussion of a new approach of selecting real input ground motions for seismic design: The most unfavourable real seismic design ground motions," *Earthquake Engineering & Structural Dynamics*, **38**, 1143-1149.

Moustafa, A. (2009b), "Discussion of the effect of energy concentration of earthquake ground motions on the nonlinear response of RC structures," *Soil Dynamics and Earthquake Engineering*, **29**, 1181-1183.

Moustafa, A. (2010), "Discussion of analytical model of ground motion pulses for the design and assessment of seismic protective structures," *Journal of Structural Engineering,* ASCE **136**(2), 229-230.

Moustafa, A. and Takewaki, I. (2009a), "Use of probabilistic and deterministic measures to identify unfavorable earthquake records," *Journal of Zhejiang University, Science A*, **10**(5), 619-634.

Moustafa, A. and Takewaki, I. (2009b), "Characterization of earthquake ground motion of multiple sequences,"

Earthquake Spectra, under review.
Moustafa, A. Ueno, K. and Takewaki, I. (2009), "Critical earthquake loads for inelastic structures considering evolution of seismic waves" *Earthquakes and Structures*, under review.
Moustafa, A. and Takewaki, I. (2010a), "Characterization and modeling of near-fault pulse-like strong ground motion via damage-based critical excitation method" *Structural Engineering and Mechanics*, in press.
Moustafa, A. and Takewaki, I. (2010b), "Deterministic and probabilistic representation of near-field ground motion," *Soil Dynamics and Earthquake Engineering*, in press.
Naeim, F. (1993), "Selection of earthquake records for seismic design of tall buildings," *The Structural Design of Tall Buildings* **2**, 255-293.
Naeim, F., Alimoradi, A. and Pezeshk, S. (2004), "Selection and scaling of ground motion time histories for structural design using genetic algorithms," *Earthquake Spectra*, **20**(2), 413-426.
Naeim, F. and Anderson, J.C. (1993), "Classification and evaluation of earthquake records for design," The NEHRP Professional Fellowship Report to EERI and FEMA.
PEER (2005), "Pacific Earthquake Engineering Research Center," (http://peer.berkeley.edu).
Pirasteh, A.A., Cherry, J.L. and Balling, J.A. (1988). The use of optimization to construct critical accelerograms for given structures and sites," *Earthquake Engineering & Structural Dynamics*, **16**, 597-613.
Seekins, L.C., Brady, A.G., Carpenter, C. and Brown, N. (1992), "Digitized strong-motion accelerograms of North and Central American Earthquakes 1933–1986," CD-ROM, U.S. Geological Survey Digital Data Series (DDS) #7.
Shome, N., Cornell, C., Bazzurro, P. and Carballo, J.E. (1998), "Earthquakes, records, and nonlinear responses," Earthquake Spectra, 14(3), 469-500.
Strasser, F.O. and Bommer, J.J. (2009), "Large-amplitude ground-motion recording and their interpretations," *Soil Dynamics and Earthquake Engineering*, **29**, 1305-1329.
Strasser, F.O. and Bommer, J.J. (2010), "Review: Strong ground motions-Have we seen the worst?," *Bulletin of the Seismological Society of America*, **99**(5), 2613-2637.
Takewaki, I. (2004), "Bound of earthquake input energy," *Journal of Structural Engineering*, ASCE **130**(9), 1289-1297.
Takewaki, I. (2005), "Resonance and criticality measure of ground motions via probabilistic critical excitation method," *Soil Dynamics and Earthquake Engineering*, **21**, 645-659.
Takewaki, I. (2007). "Critical excitation methods in earthquake engineering", Elsevier science, Amsterdam.
Takewaki, I. (2008), "Robustness of base-isolated high-rise buildings under code-specified ground motions," The Structural *Design of Tall and Special Buildings*, **17**(2), 257-271.
Uang, C-M. (1993), "An evaluation of two-level seismic design procedure," *Earthquake Spectra*, **9**(1), 121-135.
Wang, P.C., Drenick, R.F. and Wang, W.Y.L. (1978), "Seismic assessment of high-rise buildings," *Journal of the Engineering Mechanics Division*, ASCE, **104**, 441-456.
Watson-Lamprey J., Abrahamson, N. (2006), "Selection of ground motion time series and limits on scaling," *Soil Dynamics and Earthquake Engineering*, **26**, 477-482.
Zhai, C-H., and Xie, L-L., (2007), "A new approach of selecting real input ground motions for seismic design: The most unfavourable real seismic design ground motions," *Earthquake Engineering & Structural Dynamics*, **36**, 1009-1027.
Zhu, T.J., Heidebrecht, A.C. and Tso, W.K. (1988), "Effect of peak ground acceleration to velocity ratio on the ductility demand of inelastic systems," *Earthquake Engineering & Structural Dynamics*, **16**(1), 63-79.

JOINT CONFERENCE PROCEEDINGS
7th International Conference on Urban Earthquake Engineering (7CUEE) &
5th International Conference on Earthquake Engineering (5ICEE)
March 3-5, 2010, Tokyo Institute of Technology, Tokyo, Japan

AN EVALUATION OF COST EFFECTIVENESS OF NEW TECHNOLOGY FOR SEISMIC MITIGATION IN GANSU DURING WENCHUAN EARTHQUAKE

Yongfeng Du[1), 2)] Hui Li[1)]

1) Professor, Western Center for Disa. Mitig. in Civil Engnrg of Ministry of Educ., Lanzhou Univ. of Techn., Lanzhou, 730050, PR China
2) Professor, Institute of Earthquake Protection and Disaster Mitigation, Lanzhou University of Technology, Lanzhou, 730050, PR China
kasai@serc.titech.ac.jp, ecruz@ing.puc.cl, kawasima@cv.titech.ac.jp

Abstract: This paper presents an evaluation on the cost effectiveness of different type of buildings using traditional earthquake resistant design techniques, and compared with the case of application of base isolation technique in the same region. The buildings are divided into 9 categories, i.e., school, dwelling house, office, hospital, life line system, and so on. The correlation of damage ratio, economical loss between the initial economic input and technical input is examined, and the dynamic reliability is used as an index representing the earthquake resistant ability of buildings using traditional earthquake resistant technique and those using base isolation technique. It is found that the economic input of buildings using base isolation technique is much more reasonable than the buildings using traditional earthquake resistant technique, and the dynamic reliability of the former is much higher than the latter.

1. INTRODUCTION

The strong earthquake which hit Wenchuan County, Sichuan Province, Southwest China, on May 12, 2008, caused relatively heavy losses to urban infrastructure and civil engineering structure apart from the serious losses of human lives. As a neighboring province of Sichuan, Gansu Province suffered greatly during the big earthquake in terms of economic losses, and ranked the second place among the provinces in the impact region of this earthquake. Since May 13, Gansu provincial government has dispatched 6 teams of senior researchers of earthquake engineering acted as the emergency evaluation expert to help the local government try to avoid possible secondary disaster during aftershocks. The provincial Construction Department later organized nearly 10 other teams of designers with a total number of 225 people to diagnose the degree of damage of various types of buildings. The author of this paper worked 14 days as emergency evaluation expert in the earthquake disaster region, and made investigation to some public buildings, such as schools, hospitals, and son on. The performance of a group of isolated buildings located 200 km to the epicenter of the May 12 earthquake was also under the examining of the evaluation team head by the author. During the summer of 2008, the author's research team worked more than one month in the disaster region to collect data of the damage extent and evaluate the performance of various types of buildings and other civil engineering structures. This paper presents comparison of damage ratio among different types of buildings and infrastructures, and discusses the cost effectiveness of traditional aseismatic design method versus new technology.

2. EARTHQUAKE INTENSITY DISTRIBUTION AND TYPES OF STRUCTURES EXAMINED

The places with a relatively high intensity induced by the May 12 earthquake in Gansu Province were found to be Longnan City, Tianshui City, and Ganna prefecture. The evaluation in this paper is performed based on the data from Longnan City, mainly located in a seismic intensity from VIII to VI$^+$. which is the highest intensity among the 3 prefectures.

The total number of buildings under evaluation is 3323 with a total area of 4,854,851 m2, and structures under investigation can be classified into the following 9 types: schools, hospitals, communication, power supply, government offices, lifeline, dwelling, urban infrastructures, and others.

3. EVALUATION INDEX

3.1 Damage index

The degree of damage of buildings are classified into the following 5 levels:

Level 1, basically good (BG): no damage occurred in the load bearing members, slight damage in very few non-structural elements and auxiliary structure, the structure can be used without repairing

Level 2, slight damage (SD): slight crack occurred in very few load bearing members, apparent damage in non-structural elements and auxiliary structure, the structure

can be used with little repairing

Level 3, medium damage (MD): slight crack occurred in most load bearing members, partly with apparent crack, severe damage in very few non-structural elements, the structure can be limitedly used after ordinary repairing

Level 4, grave damage (GD): severe damage occurred in most load bearing members, partly collapsed, the structure need heavy repairing and partly demolishing.

Level 5, collapsed or dangerous (CD): most load bearing members collapsed, the structure need to be demolished.

3.2 Performance index

For different typical structures, the reliability are chosen as one of the indices to judge its performance. The local building are made of the cheap materials, such as brick masonry, even partly made of clay soil or combination of soil with timber, quite a few public buildings are made of concrete. Though most part of these materials are less ductile, the structure is modeled as linear elastic form simplicity because most buildings are under action of minor or medium earthquake.

The ground acceleration is assumed to be a stationary, Gaussian, filtered white noise process with zero mean, and dynamic reliability is approximately calculated by setting different limit displacement values for different materials in the following limit state function

$$L_j - Y_j = 0 \tag{1}$$

A representative failure probability is defined as a measure for dynamic reliability by regarding the structure as SDOF system.

3.3 Cost index and loss index

A statistical investigation is made on the initial cost of different types of structures, and a loss index is proposed in this paper for different levels of damage. Considering that the structures of damage Level 1 (BG) require very little repair work on the finishing, thus very little loss in terms of the financial value, while for the structures of damage Level 5 (CD), on the other hand, most of the structures need to be demolished, very little part of their financial value is remained, because only small part of materials might be re-used. By curve fitting based on this ideology, one obtains

$$\begin{aligned} L_r = {} & (L_{r\max} - L_{r\min})/(D_{i\max} - D_{i\min}) \\ & \times (D_i - D_{i\min}) \\ & + \alpha (D_i - D_{i\min})(D_{i\max} - D_i) \end{aligned} \tag{2}$$

Where $D_{i\max}$ and $D_{i\min}$ are the maximum and minimum value of damage index, and L_r is the calculated loss ratio index indicating the of various types of structures, as shown in Fig. 1, in which the straight line stands for its simplified form. With this loss ratio, the total value of the loss can be expressed

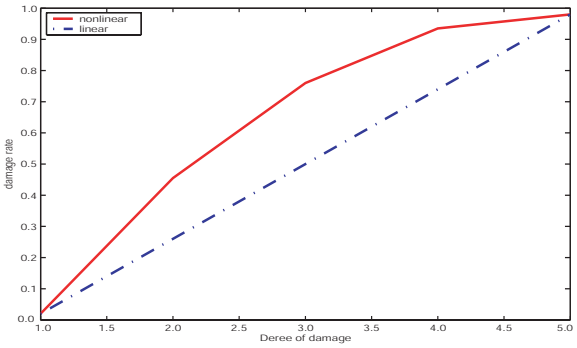

Figure 1 Loss ratio for different damage level

$$V_L = \sum_{i=1}^{L_T} L_{ri} \cdot r_i \cdot A_c \cdot c_u \tag{3}$$

Where, V_L is the total lost value, r_i is area percentage of the ith damage level, which is obtained by the evaluation through field trip investigation. A_c and c_u are the total number of area and the price per unit, respectively, of each type of buildings. Dividing the total lost value by total number of area and the price per unit, one obtains the lost value per unit area with per unit price

$$u_L = \frac{V_L}{A_c \cdot c_u} = \sum_{i=1}^{L_T} L_{ri} \cdot r_i \tag{4}$$

The index defined in Eq. (4) can be used for partly reflecting the effect of financial input on seismic resistant ability. The percentage of buildings of Longnan prefecture at different damage level is listed in Table 1.

Table 1 Percentage of different damage level

Damage level	Nr item	Percenta.	Area m^2	Percenta.
Nr evaluated	3323	100%	4854851	100%
Level 1: BG	641	19.3%	1150937	23.7%
Level 2: SD	1105	33.3%	1629160	33.6%
Level 3: MD	659	19.8%	977302	20.1%
Level 4: GD	498	15.0%	650303	13.4%
Level 5: CD	419	12.6%	447178	9.2%

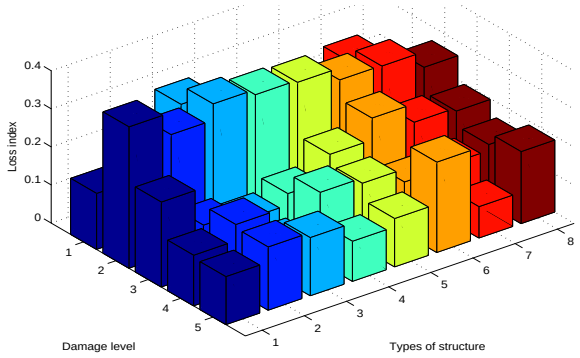

Figure 2 Item damage ratio for different buildings

From Table 1, one can observe that the average damage level of major part of the buildings belong to Damage Level 2 in the above mentioned prefecture, and the data illustrated by distinguishing different types of buildings, the percentage of damage level for different types of buildings might be slightly different, but major part of the buildings belong to Damage Level 2 still hold, as listed in Fig 2, and 3.

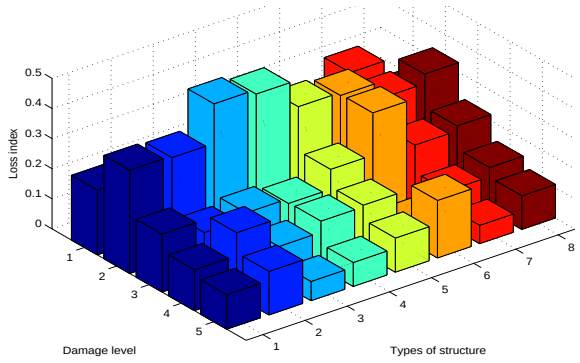

Figure 3 Area damage ratio for different buildings

The percentage of damage for different types of civil buildings in terms of area and item are shown in Figs 4 and 5, respectively. One can observe that communication buildings behave fairly well, this might be explained by the reason of the highest financial input among all the types of buildings under investigation.

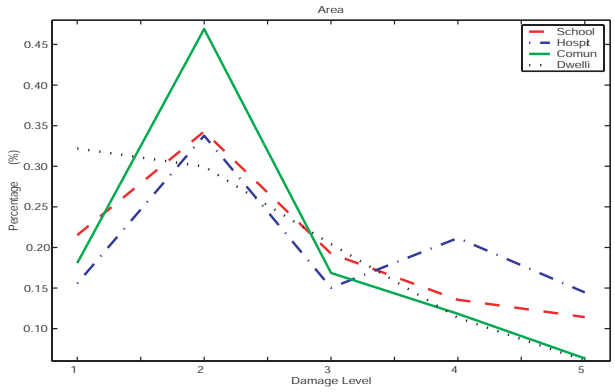

Figure 4 Area damage percentage of civil buildings

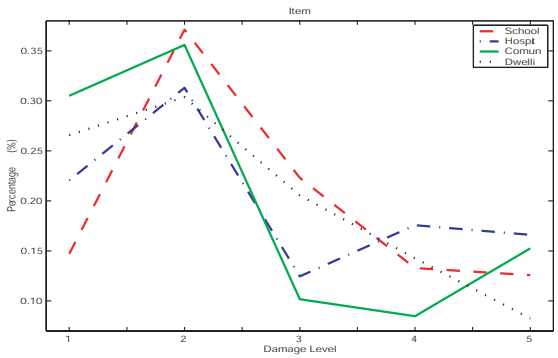

Figure 5 Item damage percentage of civil buildings

The percentage of damage for different types of public structure in terms of item is shown in Figs 6. This figure shows that the life line structures behave not as good as desired, this was considered to be due to the lack of experience for the construction of this type of structures by the local people as compared with dwelling houses.

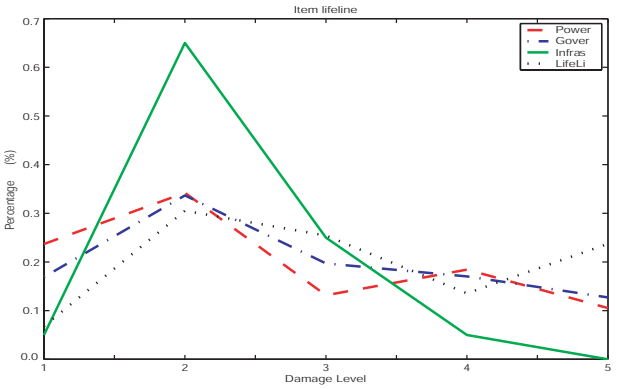

Figure 6 Damage ratio of public buildings, item

Fig 7 shows the variation of lost value with cost per unit area. One may observe from this figure that the lost value is usually smaller for higher financial input.

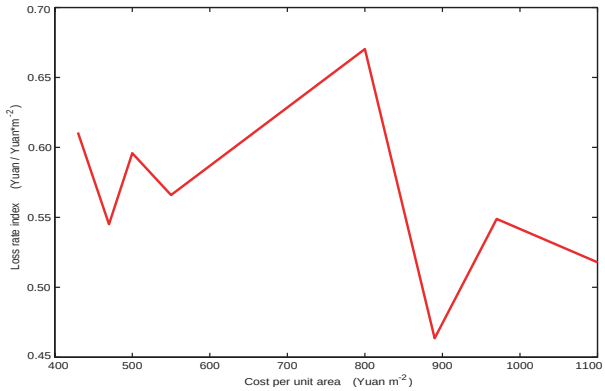

Figure 7 variation of loss index with cost per unit area

Fig 8 shows that the variation of percentage of dangerous structures with PGA of the building site, and it is no doubt that a higher value of PGA corresponding to a higher value of damage ratio, and that the hospital and commander buildings are as weak as school buildings

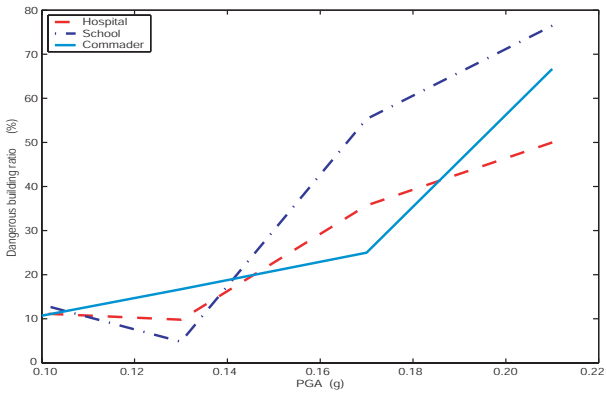

Figure 7 Area damage ratio for different buildings

Damage percentage of some buildings in the highest intensity region is listed in Table 2, where S-T stand for combination of soil-timber structure, B-T stand for combination of brick-timber structure, BM stand for brick masonry structure, FR stand for frame structure, and BI stand for base isolated structure. One may observe from this table that the damage percentage is usually higher for structures with lower reliability. The dynamic reliability of base isolated buildings is apparently much higher than the fixed base ones, and account for the reason of buildings with the best earthquake resistant behavior.

Table 2 Damage percentage of building in the highest intensity region

Str type / Smp Nr	Failure probab $\times 10^{-4}$	Percentage of damage level %				
		BG	SD	MD	GD	CG
S-T/147	563.8	0	2.7	7.5	42.9	46.9
B-T/45	464.5	0	11.1	24.4	35.6	28.9
BM/514	372.7	1.5	38.3	28.0	18.3	13.9
FR/11	124.8	0	91	9	0	0
BI / 1	4.622	100	0	0	0	0

3. CONCLUSIONS

The investigation shows that a higher the initial economic input of buildings usually corresponds to a better earthquake resistant ability of the buildings. Besides the financial input, proper selection of types of structures might be another important factor, choosing such new technique as the base isolation is clearly shown to be much more cost effective.

Acknowledgements:

This research is supported by Natural Science Foundation of China under Project No. 50778087 (Project director: Ming Lei and Jiping Ru). This support is gratefully acknowledged.

References:

Du, YF., Li, H., Han, JP, et al. (2005). Experimental study on behavior of laminated rubber bearing under low temperature, *Proc. 1st Int. Conf. Adv. in Experimental Structural Engineering*, Nagoya, Japan, 213-218.

Du, Y.F., Li, H., and Spencer, Jr., B.F. (2002). Effect of non-proportional damping on seismic isolation. *Journal of Structural Control*, 9(3), 205-236

Du, YF, Zhang, EH, and Li, H, , et al (2004b). Dynamic reliability of isolated structure for "undamaged under minor earthquake". *Earthquake Engineering and Engineering Vibration*, 24(5), 84-91 (in Chinese)

Du, Y.F., Li, H., and J.M. Jin. (2006). Behavior of laminated rubber bearing under low and its effect on the dynamic reliability. *Proc. 4th Int. Conf. on Earthquake Engineering*. Taiwan, October 12-13, Paper No. 167

Zhao, GF, Jin WL, and Gong JX. (2000). *Theory of Structural Reliability*. Beijing: Building Industry Press (in Chinese)

Du, YF, Li, H., and Yan, L., et al (2008). A probe into enhancing ductility of brick masonry structures using fibre mortar with static cyclic test. New building materials in China,10(S):213-216

Du, YF, Li, H., and Mo, Y., et al (2008). Field trip report on emergency evaluation of public buildings in Longnan after May 12 Earthquake. In: (ed) Western Center for Disaster Mitigation in Civil Engineering of Ministry of Education. *A Collection of Field trip report after May 12 Earthquake*. Lanzhou: Lanzhou University of Technology. June, 2008

Provincial Committee of Scientific and Technical Expert of construction of Gansu Province. *A Field trip report on investigation of May 12 Earthquake and emergency evaluation of damaged buildings after May 12 Earthquake*. Lanzhou: Western Center for Disaster Mitigation in Civil Engineering of Ministry of Education, Lanzhou: Gansu Provincial Aseismatic Administration Office, June, 2008

JOINT CONFERENCE PROCEEDINGS
7th International Conference on Urban Earthquake Engineering (7CUEE) &
5th International Conference on Earthquake Engineering (5ICEE)
March 3-5, 2010, Tokyo Institute of Technology, Tokyo, Japan

APPROXIMATE INCREMENTAL DYNAMIC ANALYSIS USING MODAL PUSHOVER

SW Han[1] and TS Lee[2]

1) Professor, Department of Architectural Engineering, Hanyang University, Seoul, Korea
2) Graduated student, Department of Architectural Engineering, Hanyang University, Seoul, Korea
swhan82@hotmail.com , arch_struct@naver.com

Abstract: The purpose of this study is to develop approximate procedure for incremental dynamic analysis (IDA) using modal pushover analysis (MPA) with inelastic displacement and collapse strength ratios. Since this procedure does not require nonlinear response history analysis of multi- or single- degree of freedom systems, IDA curves can be effortlessly obtained. For verifying the accuracy of the proposed procedure, the 20 story steel moment frame was used as a model frame and an ensemble of 20 ground motions was selected as input motions. The result showed that the MPA-based IDA with C_R and R_c produced a fairly accurate IDA curves. The computing time is almost negligible compared to the exact IDA using repeated nonlinear response history analysis (RHA) of a structure and original MPA-based IDA requiring repeated nonlinear RHA of modal SDF systems.

1. INTRODUCTION

Incremental dynamic analysis (IDA) was developed to estimate the seismic demand and capacity of structures (Vamvatisikos and Cornell, 2002). Since the IDA requires repeated nonlinear response history analyses (RHA) of a structure for an ensemble of ground motions, the IDA of practical structures demands extreme computation. Modal Pushover Analysis (MPA) based IDA was also developed (Han and Chopra, 2006) to construct approximate IDA curves with a computationally efficient and accurate procedure. The MPA is an approximate analysis procedure (Chopra and Goel, 2002), estimating seismic demands using nonlinear RHA of modal SDF systems instead of conducting nonlinear RHA of the MDF structure.

The objective of this study is to make more efficient procedure for MPA-based IDA. For this purpose, empirical equations of inelastic displacement (C_R) and collapse strength ratios (R_c) were incorporated into the MPA-based IDA by which the seismic demands and capacities are estimated without conducting nonlinear RHA of modal SDF systems. The accuracy of the proposed procedure (MPA-based IDA with C_R and R_c) was verified by comparing the IDA curves obtained from the proposed procedure with those obtained from exact IDA and original MPA-based IDA, respectively. For this purpose, 20 story steel moment frame was considered as a model frame and an ensemble of 20 ground motions were selected as input ground motions for IDA.

2. MPA-BASED IDA WITH C_R AND R_c

Incremental Dynamic Analysis (IDA)—a procedure developed for the accurate estimation of seismic demand and capacity of structures—requires nonlinear response history analysis of the structure for an ensemble of ground motions, each scaled to many intensity levels, selected to cover the entire range of structural response—all the way from elastic behavior to global dynamic instability. Recognizing that IDA of practical structures is computationally extremely demanding, an approximate procedure based on the modal pushover analysis procedure was developed (Han and Chopra, 2006). The MPA (Chopra and Goel, 2002) is an approximate method to estimate seismic demands subjected to ground motions without conducting nonlinear RHA of the MDF system.

In the MPA procedure, the peak response of the building to the nth-mode component of effective earthquake forces $\mathbf{p}_{\text{eff},n}(t)$ —or the peak "modal" demand r_n — is determined by a nonlinear static or pushover analysis using the modal force distribution $\mathbf{s}_n^* = \mathbf{m}\boldsymbol{\phi}_n$ at the peak roof displacement u_{rn} associated with the nth-mode inelastic SDF system. The peak modal demands r_n are then combined by an appropriate modal combination rule to estimate the total demand. This procedure is directly applicable to the estimation of deformation demands (e.g., floor displacements and story drifts). The MPA procedure has been described in a convenient step-by-step form (Chopra and Goel, 2002).

As motioned earlier, using inelastic displacement ratio (C_R) and collapse strength ratio (R_c), the MPA-based IDA becomes a more efficient procedure to construct IDA curves

since it avoids repeated nonlinear RHA of the MDF or SDF system under an ensemble of ground motions. This study incorporated the empirical equations of C_R and R_c into MPA-based IDA. This study used C_R and R_c equations proposed by the companion researches (Han et al, 2010), which were obtained by nonlinear regression analysis using 3,456,000 values of each of C_R and R_c computed using linear and nonlinear RHA.

2.1 Inelasitc Displacement Ratio, C_R

The inelastic displacement ratio, C_R is defined as the ratio of peak displacement of the inelastic SDF system (D_m) to that of the corresponding elastic SDF system (D_o) [Eq. (1)], which has the same mass, elastic stiffness and damping ratio.

$$C_R = \frac{D_m}{D_o} \tag{1}$$

Note that subscript *R* is defined as the ratio of elastic strength demand f_o of the SDF system to yield strength f_y as shown in Eq. (2).

$$R = \frac{f_o}{f_y} = \frac{mA}{mA_y} = \frac{A}{A_y} = \frac{D_o}{D_y} \tag{2}$$

Where $A_y (= f_o / m)$ and $D_y (= A_y / \omega_n^2)$ are pseudo spectral acceleration (A) and displacement (D) corresponding to yield strength (f_y), and m and ω_n are the mass and natural circular frequency, respectively.

Previous study (Han et al, 2010) proposed empirical equations of C_R and its dispersion for strength limited bilinear SDF systems using nonlinear regression analysis with 3,456,00 computed C_R. Han and Chopra (Han and Chopra, 2006) showed that the strength limited bilinear model accurately simulates the cyclic curves of steel moment frames. The median(50%) C_R for 5% damped strength limited bilinear SDF system [$(C_{R,50\%})_{\zeta=5\%}$] is:

$$(C_{R,50\%})_{\zeta=5\%} = 0.97^R + \frac{10^{a_1} \cdot (R-1)^{a_2}}{(T_n)^{a_3} \cdot R^{a_4} \cdot \mu_c^{\ a_5} \cdot \alpha_s^{\ a_6}} \tag{3}$$

Wherein the coefficients in Eq. (3) are presented in Table 1.

Table 1. Numerical values for coefficients in Eq. (3)

	a_1	a_2	a_3	a_4	a_5	a_6
$T_n \le 0.8$	-1.63	4.26	1.52	2.91	1.29	0.67
$T_n > 0.8$	-5.29	-2.76	0.11	-6.00	2.57	1.77

The dispersion of C_R is represented by standard deviation of $\ln(C_R)$ [$\sigma_{\ln(C_R)}$]. The empirical equation of $\sigma_{\ln(C_R)}$ is:

$$\sigma_{\ln C_R} = -\ln\left(1 + \frac{8 \cdot (12.3 \cdot \zeta + \ln(\zeta \cdot T_n) - 19)}{10^3 \cdot \mu_c^{\ 0.06} (\alpha_s)^{0.08}} \cdot \left|R - 1.6\right|^{0.21}\right) \tag{4}$$

Using median C_R and $\sigma_{\ln(C_R)}$, 16% and 84% fractile C_R can be computed using the following equation:

$$\begin{aligned} (C_{R,16\%})_\zeta &= (C_{R,50\%})_\zeta \times \exp(-\sigma_{\ln C_R}) \\ (C_{R,84\%})_\zeta &= (C_{R,50\%})_\zeta \times \exp(+\sigma_{\ln C_R}) \end{aligned} \tag{5}$$

2.2 Collapse Strength Ratio, R_c

When a system reaches global dynamic instability (GI) state, displacement demand increases without bound. Near GI state, displacement varies significantly with a slight increase of ground motion intensity. Thus, it is difficult to predict (GI) state using displacement computed using C_R and elastic displacement. Instead, GI state can be measured more stably using ground motion intensity, the ordinate of IDA curve, which is often expressed in terms of by the 1st mode pseudo spectral acceleration (A).

In the previous study (Han et al, 2010), the empirical equations of collapse strength ratio R_c were proposed for strength limited bilinear SDF systems. The empirical equation for R_c is summarized as follows.

For systems with 5% damping,

$$\left[(R_c)_{\zeta=5\%}\right]_{50\%} = 1 + \mu_c \left(1 - e^{-2.5T_n}\right)\left(-0.38\mu_c^{a}\alpha_c^{-1}\right)^{\mu_c^{-b}} + 0.03T_n - 0.03\ln T_n \tag{6}$$

Wherein coefficients a and b are presented in Table 2 for selected values of α_S; these parameter values may be determined by interpolation for other values of α_S.

Table 2. Numerical values for coefficients a and b in Eq. (6) for different values of α_S

Coefficients	Strain-hardening stiffness ratio, α_S				
	0.00	0.03	0.05	0.1	0.2
a	0.00	0.30	0.38	0.65	1.57
b	1.09	0.85	0.61	0.51	1.07

The dispersion measure of R_c can be computed using $\sigma_{\ln R_c}$ using the following equation:

$$\sigma_{\ln R_c} = \frac{0.22}{\zeta^{0.05}}\left[(-\alpha_c)^{0.03\mu_c - 0.29} + \frac{0.04\mu_c^{1.12} - 0.14}{\zeta^{0.28} \cdot T_n^{0.36}}\right] \tag{7}$$

Because A_y is assumed to be a deterministic quantity, not a random variable, $\sigma_{\ln A_C} = \sigma_{\ln R_C}$. The collapse intensity A_c is determined from $A_c = R_c A_y$. Using this median value of A_C and $\sigma_{\ln R_C}$, approximate values of the 16, 50, and 84% fractile A_c ($A_{c-16\%}, A_{c-50\%}, A_{c-84\%}$) are computed using a similar equation as Eq.(5). Pervious study (Han et al, 2010) shows that collapse intensity of a MDF system is satisfactorily predicted considering only one mode of the system, which makes simpler to determine collapse intensity of MDF systems. Fractile collapse intensities are intensity measure (IM) given by damage measure (DM). In IDA curves, 16%, 50% and 84% fractile IM given DM almost perfectly matches 84%, 50%, and 16% fractile DM given IM (Vamvatisikos and Cornell, 2002). Thus, 16%, 50% and 84% A_c given DM can be used as ground motion intensity for 84%, 50%, and 16% IDA curves given IM.

3. ACCURACY OF MPA-BASED IDA WITH C_R and R_c

For verifying the accuracy of the proposed method, this study considered the 20 story building having steel moment resisting steel frames (SMRSF) as lateral force resisting systems (Gupta and Krawinkler, 1999). IDA curves were constructed using exact IDA with repeated nonlinear RHA of the structure, original MPA-based IDA with repeated nonlinear RHA of modal SDF systems, and MPA-based IDA with C_R and R_c. For conducting exact IDA and MPA-based IDA, an ensemble of 20 ground motions was selected. Listed in previous work by Ruiz-Garcia and Miranda (2005), these motions were recorded on firm soil, during three earthquakes of M 6.5-6.9 (Loma Prieta, 1989; Superstition Hills, 1987; and Imperial Valley, 1979) at distances ranging from 15 to 32 km. Thus, no near-fault motions with directivity effects are included. The seismic demand parameters (DM) monitored were $\theta_{\max}$ and θ_{roof}.

In MPA, computing each modal demand r_n requires two analyses: (1) nonlinear static analysis of the building subjected to lateral force distribution $\mathbf{s}_n^* = \mathbf{m}\boldsymbol{\phi}_n$, leading to the base shear-roof displacement, $V_{bn} - u_{rn}$, pushover curve; and (2) nonlinear RHA of the *n*th-mode inelastic SDF system. Figure 1 shows the pushover curves for the first three modes of the 20 story building and the 1st mode idealized pushover curve. Observe that the post-yield slope of the first-mode pushover curves is negative because of *P*-Δ effects. The force-deformation relation for initial loading of the modal SDF system is determined by appropriately scaling both axes of the idealized modal pushover curve and plotting V_{bn}/M_n^* versus $u_{rn}/\Gamma_n\phi_{rn}$, where M_n^* is the effective modal mass and ϕ_{rn} is the value of ϕ_n at the roof (Chopra and Goel, 2002). From the idealized hysteretic curve, characteristic parameters for the strength limited bilinear were determined, which are the variables for C_R and R_c equations.

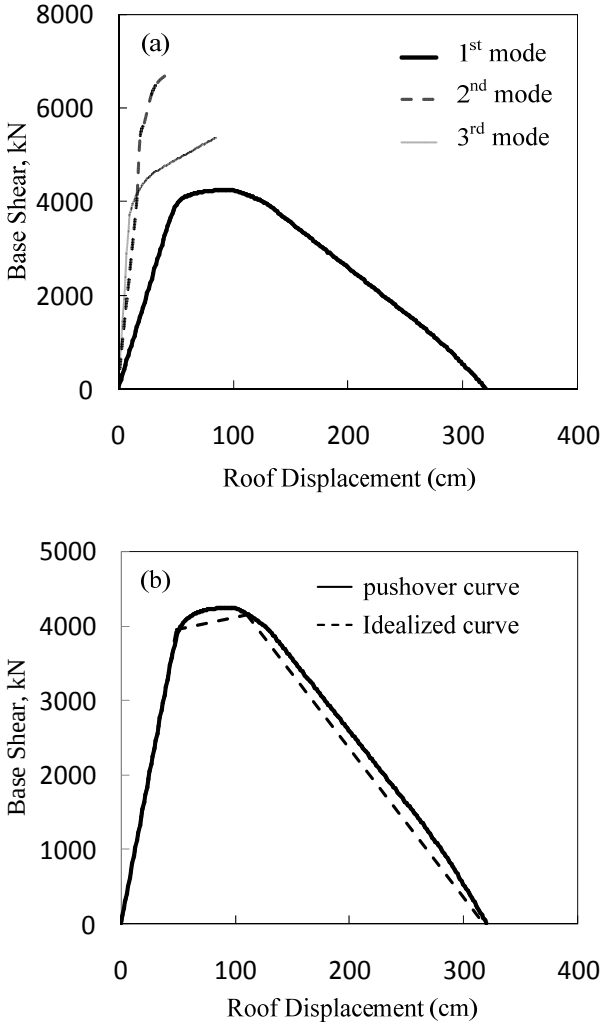

Figure 1 Modal pushover curves for 20-story building (a) first three mode pushover curves, (b) fist mode idealized pushover curves

Since, in the MPA-based IDA using C_R and R_c, the fractile drifts of the higher modes are computed using C_R against the nth mode pseudo spectral acceleration, $A(T_n, 5\%)$, it is necessary to convert $A(T_n, 5\%)$ into $A(T_1, 5\%)$ that is the ordinate of the IDA curve. The ratio (β_n) of $A(T_1, 5\%)$ to $A(T_n, 5\%)$ was computed using the median pseudo acceleration response spectrum for the ensemble of 20 ground motions. Once β_n is found from the spectrum, $A(T_n, 5\%)$ can be converted into $A(T_1, 5\%)$ by multiplying $A(T_n, 5\%)$ by β_n. Then, for $A(T_1, 5\%)$, the modal drifts were combined using the conventional modal combinational procedure.

Figure 2 presents IDA curves corresponding to 16, 50, and 84% fractiles for the 20-story building. The approximate IDA curves estimated by the MPA-based IDA using C_R and R_c including three modes is presented together with the IDA curves obtained from exact IDA and original MPA-based IDA.

Comparison of the curves demonstrates that the IDA curves from the MPA-based IDA using C_R and R_c is fairly

accurate over the entire range of drift ratios, even close to collapse. Like the original MPA-based IDA, there seems to be no systematic bias in the approximate procedure; i.e., it does not always underestimate or overestimate capacities (or demands).

Using the MPA-based IDA using C_R and R_c, which provides good estimates of IDA curves, IDA curves are effortlessly compared with exact IDA and original MPA-based IDA that use nonlinear RHA of MDF systems and modal SDF systems, respectively, to compute demands. If a Pentium 4 processor with 3.0 GHz CPU and DDR 512 MB RAM is used the computer time for analysis of one frame of the SAC Los Angeles 20-story building is reduced from 6 hours for the exact result to 5 minutes for the original MPA-based IDA procedure including 3 modes, whereas computing time for MPA-based IDA using C_R and R_c is only a few seconds. Thus, a fast estimate of the IDA curves for multistory buildings is achieved at only a small loss in accuracy.

4. CONCLUSIONS

This study developed an approximate IDA using MPA with empirical equations of C_R and R_c. Using the proposed procedure, the IDA curves can be effortlessly obtained since this procedure does not require conducting nonlinear RHA of MDF or SDF systems. The MPA-based IDA with empirical equations of C_R and R_c is fairly accurate over the entire range of drift ratio, even close to collapse; there seems to be no systematic bias in the procedure. The IDA curve obtained from the MPA-based IDA with C_R and R_c is as accurate as that obtained from the original MPA-based IDA.

Acknowledgements:

Authors acknowledge the financial supports provided by National Research Foundation of Korea (2009-0086384) and SRC/ERC (R11-2005-056-04002-0). The views expressed are those of authors, and do not necessarily represent those of the sponsor.

References:

Vamvatisikos, D., and Cornell, C. A, (2002), Incremental dynamic analysis, *Earthq. Engrg. Struc.* Dyn., **31**:491-514.

Han, S.W., Chopra A.K. Approximate incremental dynamic analysis using the modal pushover analysis procedure. Earthquake *Engineering and Structural Dynamics* 2006; **l35**:1853-1873.

Chopra, A. K., and Goel, R. K. (2002). A modal pushover analysis procedure for estimating seismic demands for buildings, *Earthq. Engrg. Struct.* Dyn., **31**:561-582.

Han, S.W., Moon, K.H., Chopra A.K.(2010). Application of MPA to estimate probability of collapse of structures, accepted for publication, *Earthq. Engrg. Struct. Dyn.*

Han, S.W., Chopra, A.K., Lee, TS. (2010). Approximate incremental dynamic analysis using MPA-based IDA using C_R and R_c, in preparation for submission, *Earthq. Engrg. Struct. Dyn.*

Gupta, A., and Krawinkler, H. (1999). Seismic demands for performance evaluation of steel moment resisting frame structures (SAC Task 5.4.3*). Report No. 132,* John A. Blume Earthquake Engineering Center, Stanford University, Stanford, CA.

Ruiz-García J, Miranda E. Performance-based assessment of existing structures accounting for residual displacement. *Report No-153*, John A. Blume Earthquake Engineering Center, Stanford University, Stanford, CA, 2005.

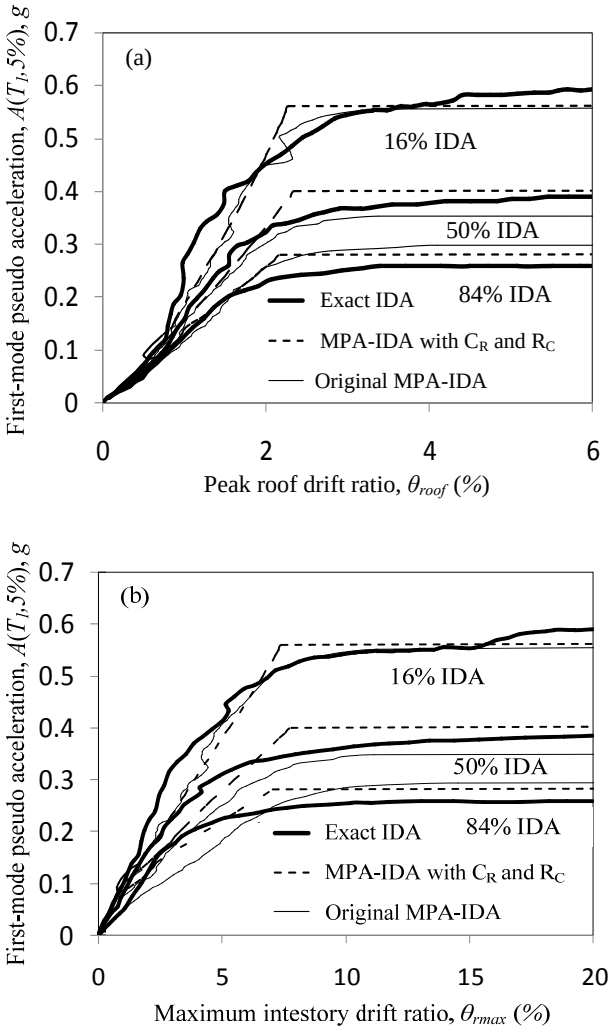

Figure 2 Sixteen, 50, and 84% fractile IDA curves for 20-story building from nonlinear RHA (exact) versus MPA-based approximate procedure, (a) Peak roof drift ratio, (b) Maximum interstory drift ratio

JOINT CONFERENCE PROCEEDINGS
7th International Conference on Urban Earthquake Engineering (7CUEE) &
5th International Conference on Earthquake Engineering (5ICEE)
March 3-5, 2010, Tokyo Institute of Technology, Tokyo, Japan

ANALYSIS AND COMPARISON OF AN INNOVATIVE PARTIAL ISOLATION METHOD AND TRADITIONAL ISOLATION METHOD FOR A SHAKING TABLE LABORATORY

Yifei Ma[1], Xilin Lu[2], Yonghui Ruan[3], and Xueping Li[3]

1) Master, State Key Laboratory of Disaster Reduction in Civil Engineering, Tongji University, Shanghai, China
2) Professor, State Key Laboratory of Disaster Reduction in Civil Engineering, Tongji University, Shanghai, China
3) Structure Engineer, Architectural Design and Research Institute of Tongji University, Shanghai, China
yifei85.ma@gmail.com, lxlst@mail.tongji.edu.cn, 22ryh@tjadri.com

Abstract: In recent years, isolated structures are mainly designed by two most common isolation methods which are base isolation and roof isolation. The newly built Shaking Table Laboratory of Tongji University is a comprehensive laboratory that includes shaking table test division, fatigue test division and office. In order to meet its special requirements for isolation, an innovative partial isolation method is proposed by the designers of the laboratory building. In this method, a lead-rubber bearing is installed at the top of the column that located in the vibration zone. Besides, the bearing joint is consisted of an orthogonal pair of dampers to control the responses in both directions. The feasibility and efficiency of this innovated method will be discussed in this paper. Firstly, the finite element analysis software, named MSC.MARC, was applied in this paper to simulate the local vibration of the new laboratory and the nonlinear time-history analysis was carried out to get the vibration responses of the structure. Secondly, the isolation efficiencies of the structures that designed by two different kinds of isolation methods respectively were compared to verify the feasibility and applicability of the new isolation method designed for the special requirements. In addition, the design procedure of the new isolation method and the possible problems during the engineering practice will be presented in this paper. Finally, the use of the new isolation method to meet the special requirements of the isolated structure during the design was recommended by the author.

1. INTRODUCTION

A newly-build Shaking Table Laboratory in Tongji University, shown in Figure 1, is a comprehensive laboratory that consists of shaking table test division, fatigue test division and office division. The building has an "L" plane shape, as it is shown in Figure 2, and a height of 24m. The shaking table test division is 98m in x direction and 51m in y direction, as well as the fatigue test division is 46mx26m, which is very close to the office division.

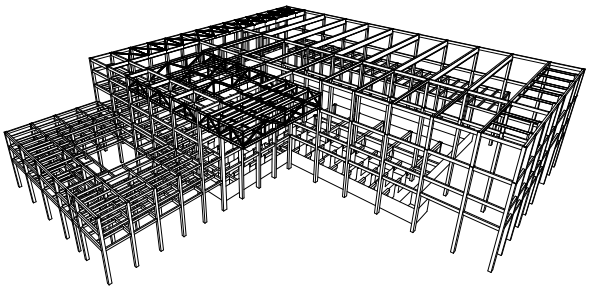

Figure 1 Perspective View of the Structure

As we all know, the shaking table and the fatigue machine will cause a lot vibrations which can be transmitted to the whole structure through the foundation and the superstructure, of course the office division is included. So the occupants' comfort will be reduced due to the vibration. The plan view of the structure appears in Figure 2, the vibration divisions are defined as section A, which is surrounded by a seismic channel. By using this method, the transmission path of the vibration through the foundation can be cut off; however, 12 columns are still located in section A. In order to keep the integrity of the structure architecturally, all these divisions share a same roof. So the vibrations may be transmitted through the columns to the roof and other divisions. In an effort to solve this problem, the author suggests applying an innovative isolation method, named partial isolation. The details will be discussed in the next section.

Recently, isolated structures are developed all over the world and isolation is proofed to be an effective method of reducing effects of seismic events on building structures (Satish Nagarajaiah, et al. 2009). The most widely used isolation methods are base isolation and roof isolation. Instead of these conventional methods, the author suggests another one named partial isolation method. In this paper, the feasibility of the innovative partial isolation method will be verified and also the dynamic response characteristics of

this building designed in different isolation methods will be compared.

In an early study of this partial isolation method, the influence of factors to the isolation efficiency has been determined by the author, which is different to the base isolation system (Beom-Soo Kang, et al. 2009). What's more, it is made clear that the damping of the bearing is a key factor. So the relationships of these factors will not be discussed in this paper.

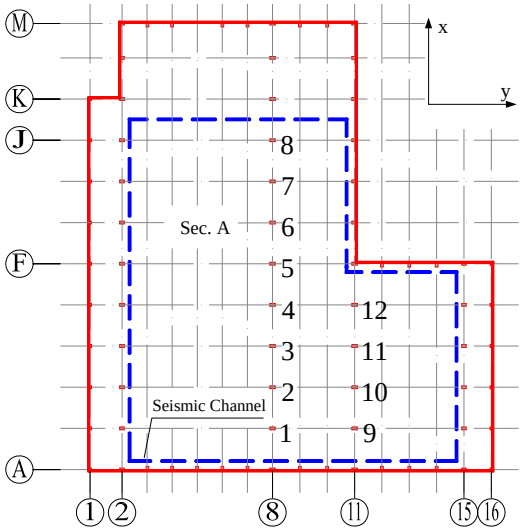

Figure 2 Plan View of the Structure

2. ISOLATION METHODS

In this paper, three isolation methods are taken into consideration including the innovative partial isolation method. Two of them are analyzed and compared to show the feasibility and probability of the new method.

2.1 Base Isolation

Base isolation of building structures is a passive control technique used to protect the building from seismic effects (Daniel Ordonez, et al. 2002). The seismic isolator is installed in the structure's foundation to absorb the seismic energy. But for this specific structure with a hinged bent system, base isolation should not be used mainly because the joints of the reinforced concrete columns and steel beams are approximately considered as hinge joints. So if the base isolation approach is adopted, a column with two ends hinged connections will be a very unfavorable influence of the seismic behavior of the structure which should be avoided during the design phase.

2.2 Roof Isolation

Roof isolation is another well developed method used to absorb the vibrations. In this system, the frictional materials are inserted between the roof slab and the beams that support the roof slab (Roberto, et al. 2002). The roof slab and the supporting beams are connected by springs which deliver lateral stiffness to the system. The roof isolation system is similar to TMD (Tuned Mass Damper) system to a certain degree. During an earthquake, the substructure of a roof isolation system is imposed by the roof with inertial force in an opposite direction of its motion. Thus the seismic response of the structure will be reduced significantly. In this paper, roof isolation method is taken into consideration and the efficiency is assessed in a simple way.

2.3 Partial Isolation

Considering that only 12 columns are located in the vibration zone, using roof isolation may not as efficient as it is supposed to be. As a result of that, a partial isolation design method is proposed that lead-rubber bearings are only applied on top of the columns in vibration zone.

The key element of the partial isolation method is the construction joint of the beam-column connection as it is shown in Figure 3. From this diagram, we can see the joint is consisted of a lead-rubber bearing and an orthogonal pair of viscous dampers, which are connected to the column and beams by connection plates. These devices are embedded between the steel beams and top of columns that are located in the vibration zone. The bottom plate of the lead-rubber bearing is connected with the embedded parts on top of the columns with bolts. Simultaneously, the top plate of the bearing is connected to the bottom flange of the steel beams with bolts, too. These junctions are shown in Figure 4. The construction of the viscous damper joint is a little more complex than that of the lead-rubber bearing. Two ends of the damper are connected with the steel beams and the RC columns, respectively. The construction of the lower end of the damper is similar to that of the bearing's bottom plate, which is also connected to the pre-embedded parts on the side of the column with bolts. The other end of the damper is connected to a connection plate which is welded to the bottom flange of the beam. The joint of the damper and the connection plate can be considered as a hinge, and the angle of the damper and the roof beam is approximately 45 degrees, so the damper will be functional both horizontal and vertical.

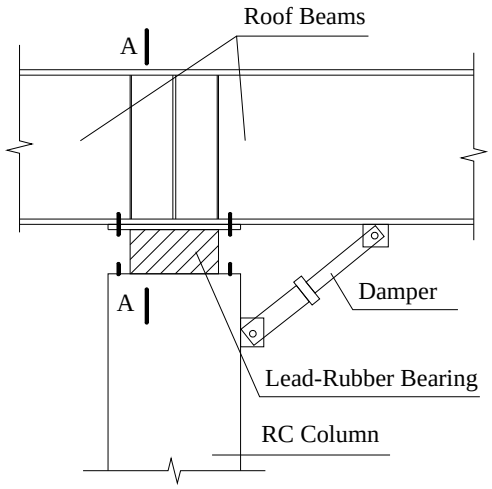

Figure 3 Construction of the Joint

The lateral stiffness of the structure will not be decreased obviously due to there is no isolation layer formed. Moreover, the local vibration of columns can be efficiently

prevented from transmitting to the roof. Thus, this method is valid for this project, as long as the stiffness and damping are adjusted to proper values.

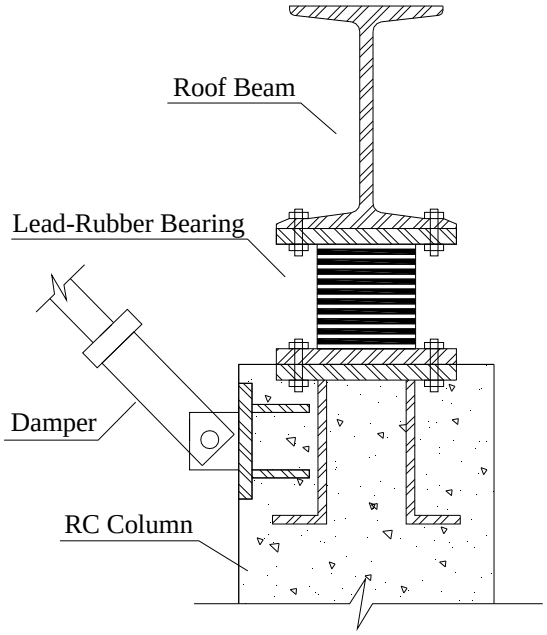

Figure 4 A-A Profile

3. Isolation Scheme Design and Analysis

In this section, No. 3 column shown in Figure 2 is taken as an example to demonstrate the process of the isolation scheme.

3.1 Calculation Diagram and Model

Since the rubber bearing plays a very important role in the isolation system, the construction of the column top joint is designed carefully. As it is shown in Figure 3, the steel beams that support the roof slab are supported on the rubber bearing, which is installed on top of the columns that located in the vibration zone.

Based on the construction of the critical joint, it can be simplified into a finite element modal as shown in Figure 5. The rubber bearing can be considered as a spring, which connects the roof node and the column top node. In the analysis, the nodes mentioned above are taken as the key nodes that the seismic response characteristics are recorded and compared in the paper. Furthermore, the beam-column connection is considered as a hinge joint because the I-section beams are linked together with the upper steel plate of the rubber bearing with bolts, which means the moments in the beam cannot be transferred to the column efficiently. Additionally, for the partial isolation approach, 12 rubber bearings are installed at the top of the columns that located in the vibration zone. Besides, each bearing joint is consisted of an orthogonal pair of dampers to control the responses in both directions.

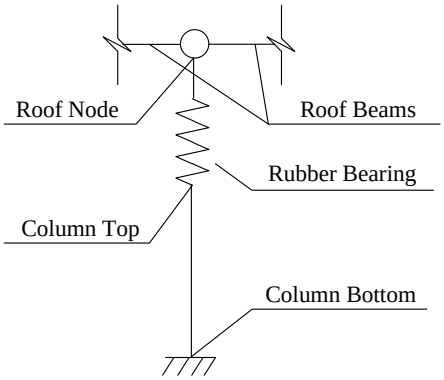

Figure 5 Finite Element Model

3.2 Analysis Method

First of all, the structure can be considered as a single degree of freedom system. Based on the type of isolation methods applied, the models can be divided into 3 groups. The seismic structure that without isolation is modeled as it is shown in Figure 6 (a), where M_a means the total mass of the structure; and k_c means the stiffness of the columns. Figure 6 (b) shows the structure with roof isolation and Figure 6 (c) shows the structure with partial isolation, where k_u is the total stiffness of the rubber bearings. In the partial isolation method, the stiffness of the columns are taken into consideration respectively, where k_{c1} means the stiffness of the columns that without rubber bearings; and k_{c2} means the stiffness of the columns that with rubber bearings. k_c can be expressed as: $k_c=k_{c1}+k_{c2}$.

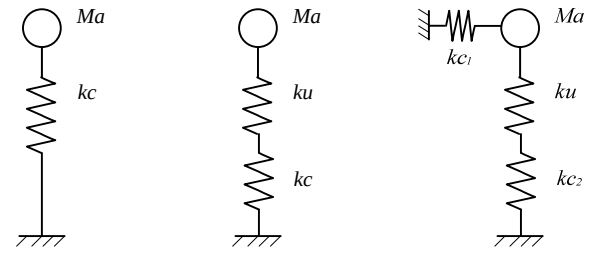

*(a) Se*ismic *(b)* Roof Isolation *(c)* Partial Isolation

Figure 6 Calculating Diagram

3.3 Lead-Rubber Bearing

These bearings are similar to the rubber bearing but a central lead-core is used to provide an additional means of energy dissipation and initial rigidity against minor earthquakes and winds. The energy absorbing capacity by the lead-core reduces the bearing displacement; also the bearings provide an additional hysteretic damping through the yielding of lead core (LU Xilin et al. 2003). The force-deformation behavior of the lead-rubber bearing is generally represented by non-linear characteristics; however, in order to simplify the analysis procedure, a bilinear model is proposed as shown schematically in Figure 7.

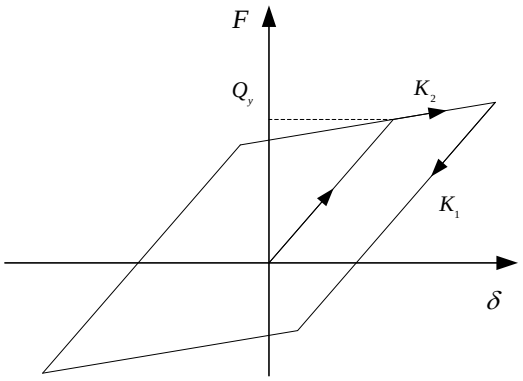

Figure 7 Bilinear Hysteretic Behavior

The mechanical behavior of the rubber bearing under a certain cyclic load could be assumed as linear, as well as the mechanical behavior of the lead core could be assumed as perfect elastoplastic material (Alfonso Vulcano, et al. 1998). These properties could be seen in Figure 8. Based on these assumptions, the key parameters of the bilinear model are as follows:

-K_1: initial stiffness of the lead-rubber bearing, which is equal to the sum of the stiffness of the rubber and lead core before yield, and

-K_2: yield stiffness of the lead-rubber bearing, which is equal to the sum of the stiffness of the rubber and lead core after yield.

-Q_y: yield strength of the bearing.

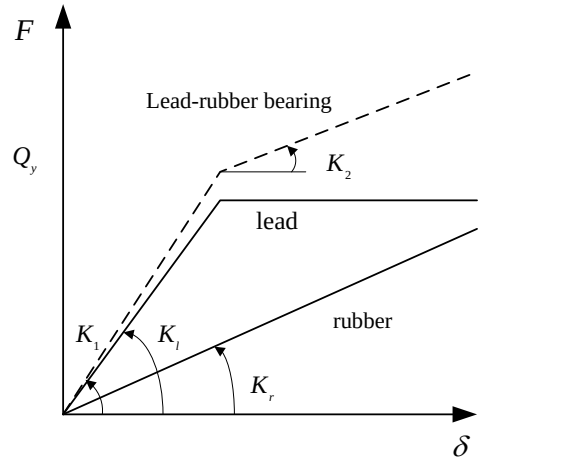

Figure 8 Equivalent Linearization Method

Once these parameters are determined, so do the properties of the isolation bearing. The restoring force developed in the bearing, F_b is given by

$$F_b = K_{eq}\delta + c\dot{\delta} \tag{1}$$

where δ is the relative displacement of the lead-rubber bearing, K_{eq} and c are secant stiffness and damping of the bearing, respectively.

3.4 Calculation Procedures

First of all, the horizontal stiffness of the seismic structure should be determined. The equation of the frequency should be expressed as

$$f = 1/2\pi\sqrt{k_c / M_a} \tag{2}$$

thus, the k_c could be calculated as

$$k_c = (2\pi f)^2 M_a \tag{3}$$

Secondly, assumes the total number of columns is $N=n_1+n_2$, where n_1 means the number of columns that with isolation bearings and n_2 is the other columns total number. Here we define $\gamma=n_1/N$, which means the isolation percentage of the structure ($\gamma=1$ means roof isolation system, $\gamma=0$ means seismic structure). Because of using the isolation bearings, the structural frequency will be shortened. Define α as the frequency reduction factor of the structure, which is given by

$$\alpha = f_{eu} / f \tag{4}$$

where f_{eu} is the frequency of the isolation structure, and $\sqrt{\gamma}<\alpha<1$. According to the series-parallel connection spring theory,

$$\begin{cases} k_c = k_{c1} + k_{c2} \\ k_{eu} = k_{c1} + k_u k_{c2} / (k_u + k_{c2}) \\ k_{eu} = (2\pi\alpha f)^2 M_a \end{cases} \tag{5}$$

where k_{eu} is the equivalent lateral stiffness of the isolation structure and k_u is the lateral stiffness of the lead-rubber bearings, which could be calculated from these equations. For this structure, k_u is the sum value of the isolation layer. Considering each single lead-rubber bearing, the stiffness will be

$$k_{ui} = k_u / n_1 \tag{6}$$

where k_{ui} means a single bearing's stiffness. According to the Japanese design experience, the post-yield stiffness of the bearing is given by

$$k_{di} = k_{ui} / 6.5 \tag{7}$$

where k_{di} is the post-yield stiffness of a single bearing.

Finally, the yield strength of the isolation layer, also according to the Japanese design experience, could be calculated by

$$\sum Q_v = \beta W_e \tag{8}$$

where β is the ratio of the yield strength, and 0.02< β <0.1 (β =0.05 is suggested); and W_e is the equivalent total weight of the superstructure that supported by the isolation bearings.

Moreover, the damping ratio of the structure should be 0.10< ξ<0.30, and the damping could be given by

$$C = 2\xi\sqrt{M_e k_c (1-\gamma)} \tag{9}$$

where C is the damping of the bearing; and M_e is the equivalent total mass of the superstructure that supported by the isolation bearings.

So far, the key parameters of the lead-rubber bearing could be determined. Then the elastoplastic time-history analysis is carried out to assess the efficiencies of the roof isolation and partial isolation.

4. Finite Element Analysis

The feasibility and efficiency of the proposed isolation systems are based on the result of a series of three dimensional finite element analyses. With the secondary development user subroutines, convenient pre and post process functions and extinct nonlinear capacity of general purpose FEA software of MSC. MARC, the spatial partial seismic responds of structure can be simulated in detail.

4.1 Numerical Models

As it is shown in Figure 9, the RC columns and beams are simulated by fiber elements, in which the sections of the elements are divided into a number of fibers and each fiber is under uniaxial force (Asad Ullah Qazi, et al. 2006), therefore the uniaxial stress-strain relations are given for concrete and steel fibers as shown from Figure 10 to Figure 11. Shell elements are used for the floor slabs.

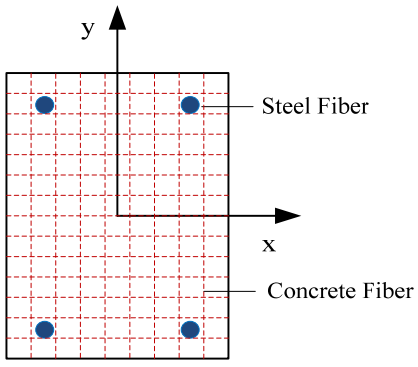

Figure 9 Fiber Column/Beam Model

For the case where the building is analyzed with the isolation system, the isolation bearings are modeled with a spring element that behaves nonlinear as it is shown in Figure 8. The lead-rubber bearing is attached with an orthogonal pair of dampers, which could be simulated in the FEA software Marc by link elements, as shown in Figure 12 (Vasant A.Matsagar, et al. 2006).

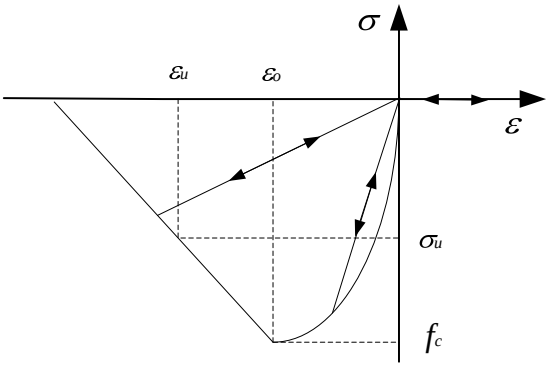

Figure 10 Stress-Strain Relation for Concrete Fibers

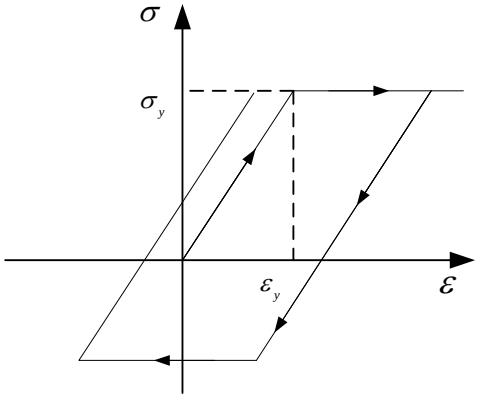

Figure 11 Stress-Strain Relation for Steel Fibers

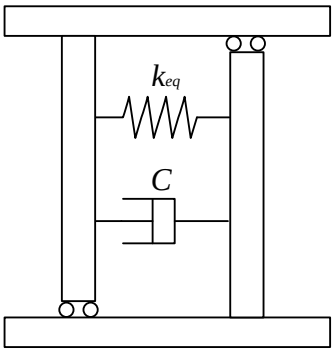

Figure 12 Numerical Model of the Bearing

4.2 Load Case

The ground motion used in the finite element analysis is El Centro record, shown in Figure 13, and the peak value is scaled to 400gal and the dominant frequency is tuned to be close to the fundamental natural frequency. The reasons to select this record are based on the following aspects: (1) It is a record that can induce, when tuned close to the fundamental natural frequency of the structure, a strong structural response. Thus the use of the record is an effective way to test the model and the isolation system components under extreme conditions. (2) The effectiveness of a vibration absorber is more evident when a building is

subjected to a damaging ground motion than when it is subjected to a ground motion that only induces an insignificant building response. Along the same lines, no other ground motions are considered in the finite element analysis because it is known from the previous studies just referred to that vibration absorbers are effective to reduce the response of a structure under different ground excitations, particularly when the excitation is in resonance with the fundamental frequency of the structure. (3) The objective of the investigation is to test whether or not the suggested partial isolation scheme can work effectively as vibration absorber and not in demonstrating that vibration absorbers are effective under different earthquake excitations.

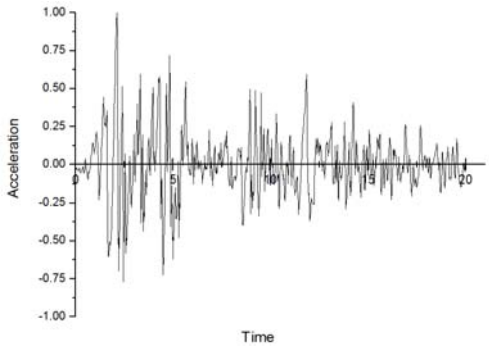

Figure 13 Ground Motion

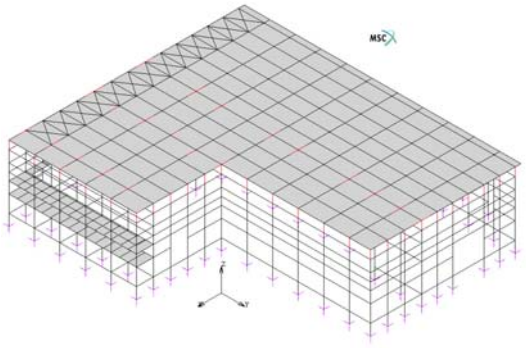

Figure 14 Three-Dimensional Model of the Structure

Different from the conventional dynamic time-history analysis for structures, in this specific analysis, the ground motion is only applied in x direction to the 12 columns that located in the vibration zone. No. 3 column is chosen as the observation object, whose key parameters are recorded and analyzed, including the displacement, velocity, acceleration of the top nodes and the shear force of the bottom nodes. In order to demonstrate the feasibility of each isolation approach, nonlinear time-history analysis were performed on 3 finite element models, respectively. Model-1 is referred to the seismic structure without any isolations and the same structure with roof isolation system is called Model-2, as well as the proposed partial isolation system is modeled as Model-3. Generally speaking, all these three models are the same except for the isolation method. The finite element model is shown in Figure 14 - Figure 17.

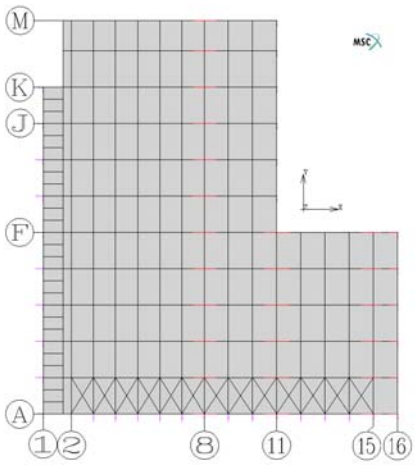

Figure 15 Plan View (z Direction)

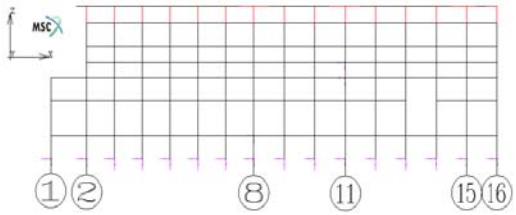

Figure 16 Front View (y Direction)

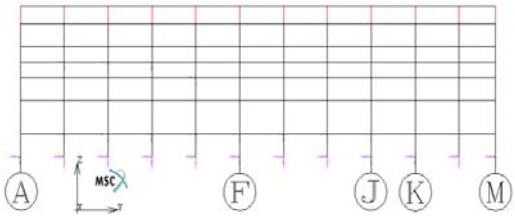

Figure 17 Right View (x Direction)

5. Results

As it is mentioned before, displacement, velocity, acceleration and shear force at different key nodes are recorded, and the maximal values are compared for the 3 numerical models, respectively. The first three are the main parameters to assess the comfort of the occupants and the fourth one is to evaluate the influences of the isolation system to the prototype structure.

5.1 Displacement

The results of the comparative study show that the peak lateral displacement of the isolated structure will be larger than the seismic structure, especially when the building is subjected to a strong ground motion; however, these large displacements seem to be not a serious problem as far as the lead-rubber bearings are concerned and the vibrations caused by the testing machines are not significant due to the short period of time of resonance.

Table 1 Comparison of Displacement

Displacement *(mm)*	Model-1	Model-2	Model-3
Roof	1.26	5.002	1.909
Column	1.26	29.87	17.46

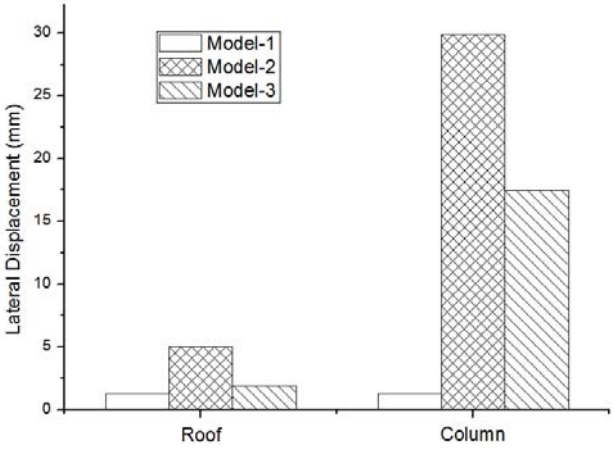

Figure 18 Displacement of the Roof and Column

It demonstrates in Figure 18 that though both isolation methods will enlarge the displacement of the roof and column, still it is within the yield displacement of the bearings, which is 30mm. For the roof isolation system, the isolation efficiency is largely depended on the characteristic of the selected ground motion, such as the dominant frequency and duration. What's more, several former studies show that roof isolation may not work as efficient as expected due to the susceptible. On the contrary, the partial isolation is much better because the lateral stiffness of the structure is not greatly changed due to the small percentage of the isolated columns. Thus the displacement will be decrease compared to the roof isolation system; however, it is still larger than the seismic structure.

5.2 Velocity

The isolation layer will decrease the restrain of the substructure from the roof. As a result of that, the response of the columns will be much greater than that of the seismic structure. But the vibration induced by the testing machines is not so significant that the members will not develop plastic deformation or even be damaged. So the response of the substructure is not taken into consideration for the next two parameters.

From Figure 19, we can see that the velocity of the roof will be decreased due to the use of the roof isolation approach. It is about 8% that is decreased compared to the seismic structure. For the partial isolation structure, the percentage is increased to about 35%, so that the partial isolation method is much more efficient than roof isolation.

Table 2 Comparison of Velocity

Velocity *(mm/s)*	Model-1	Model-2	Model-3
Roof	20.15	18.62	13.2
Efficiency	-	7.6%	34.5%

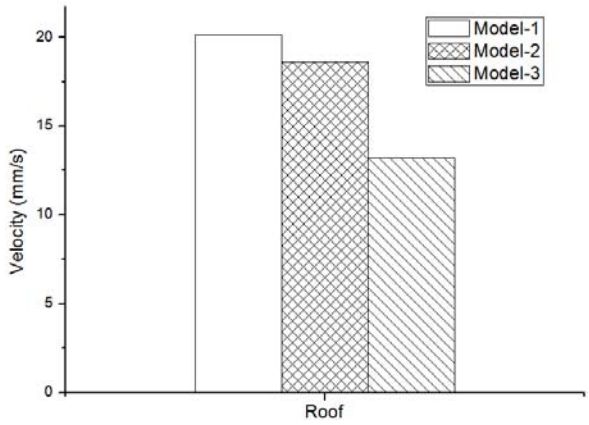

Figure 19 Velocity of the Roof

5.3 Acceleration

The acceleration should be controlled strictly, because the occupants are very sensitive of that, and it is also one of the important issues in the structure influenced by vibrations. From Figure 20, we can see that both isolation methods are effective to reduce the acceleration. What's more, for this specific structure, the number of bearings of the roof isolation structure is 5.6 times that of the partial isolation method. As a result of that, the economic benefit of the proposed isolation method is much higher. Besides, it is clearly observed that the partial isolation will reduce the acceleration to 18% of the seismic structure.

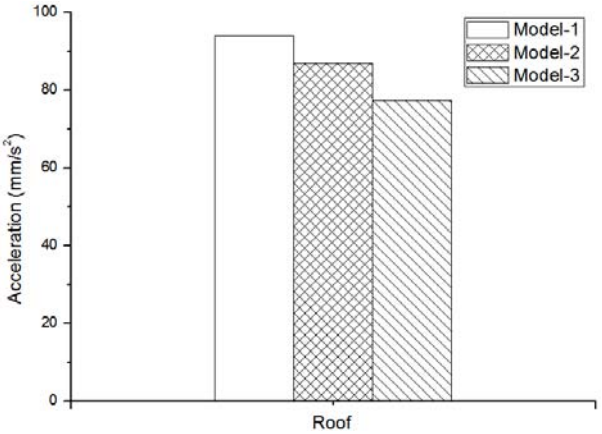

Figure 20 Acceleration of the Roof

Table 3 Comparison of Acceleration

Acceleration *(mm/s²)*	Model-1	Model-2	Model-3
Roof	93.98	86.87	77.27
Efficiency	-	7.6%	17.8%

5.4 Base Shear

Due to the usage of the bearings, the base shear of the column is consisted of the inertial force and the reaction force of the roof. As shown in Table 4, the maximal base shear is recorded for three models, respectively, and for this parameter, both isolation methods acquired nearly the same effectiveness.

Table 4 Comparison of Base Shear

Shear force *(kN)*	Model-1	Model-2	Model-3
Column Bottom	49.89	48.54	50.94

6. Conclusions

Isolation systems are proposed to reduce the vibration of buildings. The results of the comparative nonlinear time-history analysis of three numerical models show that:

(1) The proposed partial isolation system significantly reduces the vibrations induced by the testing machines even if the dominant frequency of the ground motion is close to the fundamental frequency of the building.

(2) Roof isolation system studied in this paper is a reference object to the partial isolation system. Though the roof isolation could reduce the vibration of the roof, it is not proposed because of the susceptibility. According to a former study and early publications, if the dominant frequency of the ground motion that subjected to the structure changed, the effectiveness of the roof isolation will change, too.

(3) The displacement of the roof will increase due to the use of isolation methods; however, it is within the elastic range. In addition, the main purpose of this paper is to assess the efficiency of the partial isolation method under foundation vibration, and the seismic response of the whole structure under earthquakes will be taken into consideration in the next phase study.

Though the proposed partial isolation system has been proofed to be a practical and effective way to reduce vibrations induced by testing machines, further studies are needed to find solutions to overcome some of the practical problems associated with it and some of the assumptions are not precise:

(a) The energy dissipation of the proposed partial isolation is assumed according to a bilinear model. It is found that a nonlinear model will be more precise than that.

(b) The parameters of the lead-rubber bearings are determined by experiences, and some of them, such as the damping, have to be determined by numerical analysis, etc.

Acknowledgements:

The authors acknowledge the financial support partially from the National Natural Science Foundation of China (NSFC) through NSFC-JST joint research program.

References:

JIN Zhangcai, ZHU Yuhua and LU Xilin, "Research on Shaking Table Tests of Model Building with Lead Rubber Bearing under Multi-Intensity ground Motion Inputs," *Structural Engineers*, **2003**, (1), 43-48.

ZHU Yuhua, LU Xilin, SHI Weixing, IKENAGA Masayoshi, Feng Demin, MIYAMA Takafumi, "Study on Shaking Table Tests of Model Building with Lead Rubber Bearing under Multi-Direction Component Input," *Structural Engineers*, **2001**, (1), 34-38.

Pranesh Murnal and Ravi Sinha, "Aseismic Design of Structure-equipment Systems Using Variable Frequency Pendulum Isolator," *Nuclear Engineering and Design*, **2004**, (231), 129-139.

Roberto Villaverde, "Aseismic Roof Isolation System: Feasibility Study with 13-Story Building," *Journal of Structural Engineering*, **2002**, 128(2), 188-196.

Beom-Soo Kang, Le Li and Tae-Wan Ku, "Dynamic Response Characteristics of Seismic Isolation Systems for Building Structures," *Journal of Mechanical Science and Technology*, **2009**, 23, 2179-2192.

Satish Nagarajaiah, Sriram Narasimhan, Anil Agrawal and Ping Tan, "Benchmark structural control problem for a seismically excited highway bridge: Part III, Phase II Sample controller for the fully base-isolated case," *Structural Control and Health Monitoring*, **2009**, 16, 549-563.

Alfonso Vulcano, "Comparative Study of the Earthquake and Wind Dynamic Responses of Base-isolated Buildings," *Journal of Wind Engineering and Industrial Aerodynamics*, **1998**, 74-76, 751-764.

Daniel Ordonez, Dora Foti and Luis Bozzo, "Comparative Study of the inelastic response of base isolated buildings," *Earthquake Engineering and Structural Dynamics*, **2003**, 32, 151-164.

Asad Ullah Qazi, YE Lieping and LU Xinzheng, "Passive Control Reinforced Concrete Frame Mechanism with High Strength Reinforcements and Its Potential Benefits Against Earthquakes," *Tsinghua Science and Technology*, **2006**, 3-15, 640-647.

Vasant A.Matsagar and R.S.Jangid, "Seismic Response of Base-isolated Structures During Impact with Adjacent Structures," *Engineering Structure*, **2003**, 25, 1311-1323.

JOINT CONFERENCE PROCEEDINGS
7th International Conference on Urban Earthquake Engineering (7CUEE) &
5th International Conference on Earthquake Engineering (5ICEE)
March 3-5, 2010, Tokyo Institute of Technology, Tokyo, Japan

STATIC-DYNAMIC ANALYSIS METHOD FOR ENERGY-DISSIPATED DESIGN OF FRAME-SHEAR-WALL STRUCTURES WITH DAMPERS

Gengwen Zhao[1], Aiqun Li[2], and Ruixin Huang[3]

1) Graduate Student, School of Civil Engineering, Southeast University, China
2) Professor, School of Civil Engineering, Southeast University, China
3) Graduate Student, School of Civil Engineering, Southeast University, China
eileenzhao0409@yahoo.com.cn

Abstract: The static-dynamic analysis method is the combination of the static pushover analysis method based on the three-dimensional model and the nonlinear time history analysis method based on the bending-shearing layer model. Taking a 25-floor residential building located in Jiangsu Suqian as the engineering background, the energy-dissipated design of the structure installed with viscous fluid dampers was conducted by the static-dynamic analysis method. Firstly, the three-dimensional static pushover analysis of the structure was conducted in order to get the restoring forces curves of stories. On this basis, the bending-shearing layer model of the structure was established, and the nonlinear time history analysis was conducted. Meanwhile, the vibration control of frame-shear-wall structures seismic responses influenced by the nonlinear viscous fluid dampers was studied. The results show that the static-dynamic analysis could evaluate elastic-plastic seismic behaviors of frame-shear-wall structures, and provide reference for the design of other engineering structures.

1. INTRODUCTION

Dynamic nonlinear time history analysis and static pushover analysis are the main methods for high-rise structure non-linear seismic analysis.

Dynamic nonlinear time history analysis is a dynamic analysis method which gradually integrates the motion differential equations of structures. This method can directly calculate the displacement, velocity, acceleration time-history response of structures, and describe the internal forces of structures during elastic and plastic stages under strong earthquakes, as well as gradual cracking, yield, destruction of structural members and collapses of the entire structures. Although the method can truthfully simulate the behavior of structures under earthquakes, it still remains in the research stage and is far away from broad application. The main reasons are as follows:

1 A huge amount of calculations;

2 The earthquake responses of the same structure under different seismic waves vary significantly. And there is no criterion to decide which one is suitable for the structure design.

With the recent proposal of the concept of performance-based design, static pushover analysis method has got more and more attention. Adding assumed lateral loads on structures, static pushover analysis gradually adds the value of loads and modifies the stiffness matrixes of structures until they reach the performance level points of structures, and then assesses the seismic performance of structures. Avoiding the complexity of nonlinear time-history analysis method, this method is much easier and time-saving.

Both methods have advantages and disadvantages. The static-dynamic analysis method is the combination of the static pushover analysis method based on the three-dimensional model and the nonlinear time history analysis method based on the bending-shearing layer model. Not only can it reduce the amount of calculations, but also it can get the earthquake seismic responses of structures during the whole processes. It is a practical approach for high-rise structures non-linear seismic analysis.

In this paper, using the static-dynamic analysis method, the energy-dissipated design of a 25-floor residential building installed with viscous fluid dampers was conducted. Firstly, the three-dimensional static pushover analysis of the structure was conducted in order to get the restoring forces curves of stories. On this basis, the bending-shearing layer model of the structure was established, and the nonlinear time history analysis was conducted. Meanwhile, the vibration control of frame-shear-wall structures seismic responses influenced by the nonlinear viscous fluid dampers was studied.

2. PROJECT BACKGROUND

The project discussed in this paper is a 25-floor residential building located in Jiangsu Suqian. The total building area is 8473.00m^2, and the full height of this

building is 75.00m. There 25 floors above the ground and one floor underground. Frame-shear-wall is employed as the main structure.

The city of Suqian in Jiangsu Province, located in the middle of the Tan-Lu fault zone, is one of the major seismic fortified cities in our country. The seismic fortification intensity is 8 degree, and the basic design acceleration is 0.3g. Considering the structure characteristic and the condition, it is impossible to improve the seismic capacity of this structure using traditional design methods. In contrast, it is more effective to protect the structure under strong earthquakes by setting damping devices to control the seismic responses of the structure. They can effectively increase the damping ratio of this structure and significantly reduce the seismic response. Therefore, some viscous fluid dampers are installed in appropriate places in this project.

3 BENDING-SHEARING LAYER MODEL

There are two components in the deformation of high-rise frame-shear-wall structures: bending deformation and shear deformation. Their vibration characteristics can be described more precisely using bending-shearing layer model, as shown in Figure 1.

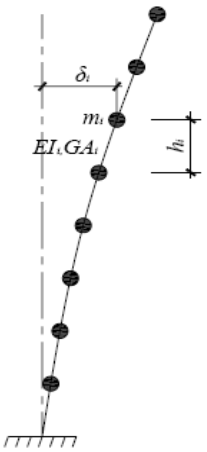

Figure 1 Bending-shearing Layer Model

3.1 Equivalent Bending Rigidity

As shown in Figure 2, according to the axial deformation energy *Wi* of columns and walls of the ith story on the elastic stage (the total strain energy of bending deformation), the equivalent angle increment $\Delta\theta_i$ can be obtained under the assumption that each column and wall remains plane during axial deformation, and then the corresponding equivalent bending stiffness *EIi* can be calculated by the following expression:

$$EI_i = \frac{h}{2\Delta\theta_{i1}}(M_{i+1} + M_i) \qquad (1)$$

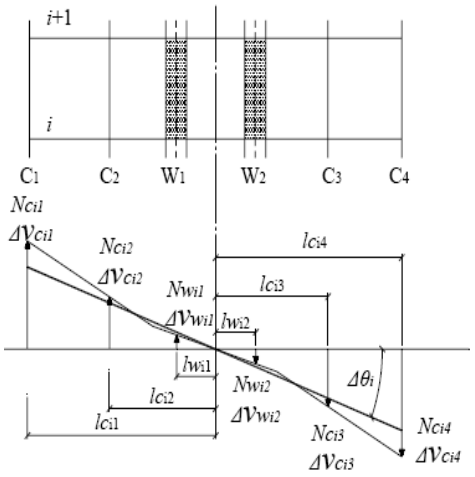

Figure 2 Equivalent Bending Deformation

3.2 Equivalent Shear Stiffness

The bending deformation component δ_{Bi} of the ith story can be calculated by the following expression:

$$\delta_{Bi} = h_i \sum_{k=i}^{i-1} \Delta\theta_k + \frac{h_i^2}{6EI_i}(M_{i+1} + 2M_i) \qquad (2)$$

The shear deformation component δ_{Si} of the ith story can be calculated by the following expression:

$$\delta_{Si} = \delta_{Ai} - \delta_{Bi} \qquad (3)$$

Where, δ_{Ai} is the total deformation of the ith story.

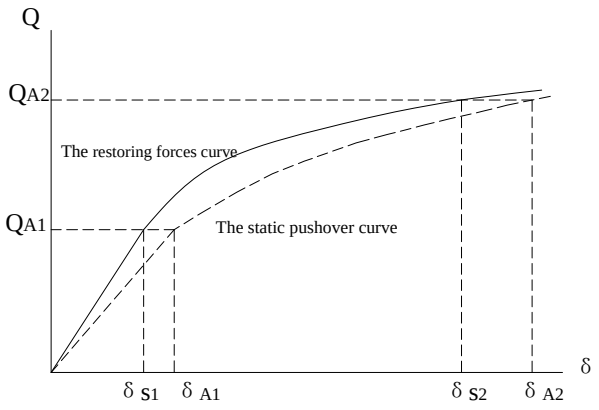

Figure 3 Restoring Forces Curve

As shown in Figure 3, the relationship between the shear forces of each story and the deformation of each story can be obtained by the static pushover analysis. Then the restoring forces curve of bending-shear layer model can be got by subtracting the shear deformation component from the total deformation of the ith story.

3.3 Three Polygon Stiffness

The restoring forces curve can be replace by the three polygon stiffness in this way:

1 The first point (δ_1, Q_1) corresponds to the stage

that the damping members of each story start to yield;

2 The slope of No.2 Line and the second point (δ_2, Q_2)is determined based on the following principles: From the first point to the third point (δ_{75}, Q_{75})which is corresponding to the inter-story drift angle of 1/100, the area between the restoring forces curve and x-axial is the same as that between the three polygon stiffness curve and x-axial;

3 The slope of No.3 Line is the tangent of restoring forces curve at (δ_{75}, Q_{75}).

There exit the following relationships:

$$Q_2 = k_2(\delta_2 - \delta_1) + Q_1 \quad (4)$$

$$Q_2 = Q_3 - k_3(\delta_3 - \delta_2) \quad (5)$$

So the slope of No.2 Line k_2 can be expressed in this equation:

$$k_2 = \frac{Q_3 - Q_1 - k_3(\delta_3 - \delta_2)}{\delta_2 - \delta_1} \quad (6)$$

The δ_{S2} can be calculated in the following expression:

$$\delta_2 = \frac{2A - 2Q_3\delta_3 + (Q_1 + Q_3)\delta_1 + k_3(\delta_3^{\,2} - \delta_1\delta_3)}{(Q_1 - Q_3) - k_3(\delta_1 - \delta_3)} \quad (7)$$

In this way, the second point (Q_2, δ_2) can be determined using the equations motioned above. So the three polygon stiffness curve is established.

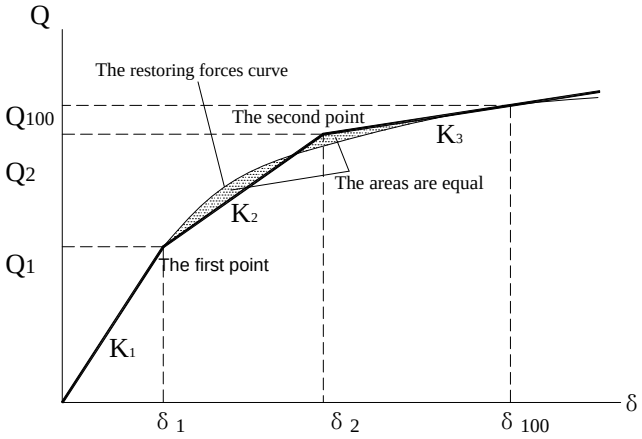

Figure 4 Three Polygon Stiffness

4 ENERGY-DISSIPATED DESIGN BASED ON BENDING-SHEARING LAYER MODEL

4.1 Modeling

A bending-shearing layer model for the 25-floor residential building was established with program SAP2000 using the method mentioned above. The natural vibration period of the three dimensional model and that of the bending-shearing layer model were analyzed, the results shown in Table 1.

Table 1 Natural Vibration Period of the Structure

	X-direction		
Period	3-d Model	Bending-shearing Layer Model	Difference
1st	1.37	1.42	3.6%
2nd	0.41	0.43	4.9%
3rd	0.37	0.40	8.1%
	Y-direction		
Period	3-d Model	Bending-shearing Layer Model	Difference
1st	1.87	1.90	1.6%
2nd	0.50	0.53	6.0%
3rd	0.23	0.25	8.7%

As can be seen from Table 1, the maximum difference between these two models is 8.7%, which meets the project accuracy requirements. So the bending-shearing layer model can be employed in the nonlinear time history analysis of this structure.

4.2 The Layout of Viscous Fluid Dampers

The viscous fluid dampers were installed along two principle axes respectively. Their numbers, models and locations were optimized through many rounds of static-dynamic analysis, as shown in Table 2. Based on "Code for Seismic Design of Buildings"(GB50011-2001) and the architectural design, the structural layout as well as the related analysis models and results, 148 sets of non-linear viscous fluid dampers were installed from the first floor to the 25th floor, which can significantly reduce the seismic response of the structure. The damper force - deformation relationship of non-linear viscous fluid dampers is

$$f = C\dot{u}^{\alpha} \quad (8)$$

Where: C is the damping coefficient, $\dot{u}$ is the deformation rate of the damper, and α is the damping index.

Table 2 Layout of Viscous Fluid Dampers

Story Number	The Damping Index	The Damping Coefficient (Nm/s)	The Number of Dampers
1-4 21-25	0.25	$2.0\text{x}10^6$	x:2 y:2

5-15	0.25	$2.0x10^6$	x:4 y:4
16-20	0.25	$2.0x10^6$	x:3 y:3

4.2 Seismic Waves

Two natural waves and one artificial wave were used in the static-dynamic analysis. They are USER232 wave, AMO wave and Suqian wave respectively, as shown in Figure 5 (peak acceleration is 1cm/s^2). According to "Code for Seismic Design of Buildings"(GB50011-2001) (2008 edition), the peak values of each seismic wave are adjusted to 110 cm/s^2 under frequent earthquake and 510cm/s^2 under rare earthquake.

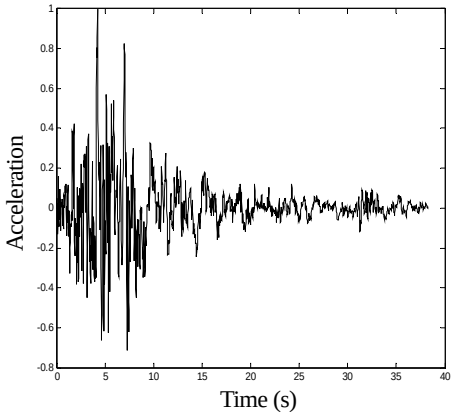

(a)

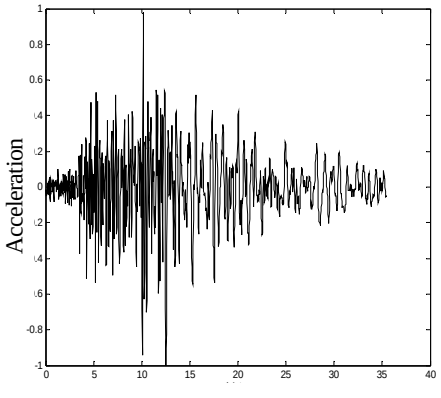

(b)

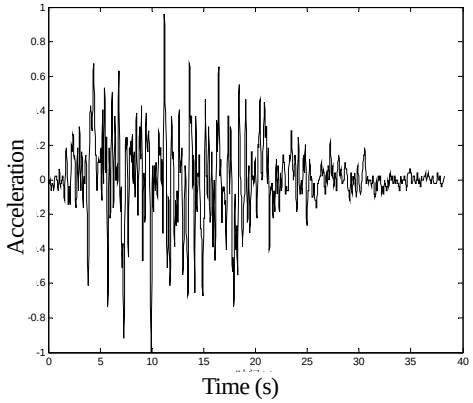

(c)

Figure 5 Seismic Waves:
(a) USER 232, (b) AMO, and (c) Suqian

The base shear forces under frequent earthquake are shown in Table 3. The selection of seismic waves meets the requirement of "Code for Seismic Design of Buildings" (GB50011-2001) (2008 edition). The base shear forces of each seismic wave should not less than 65% those of response spectrum; the averages should not less than 80% the base shear forces of response spectrum.

Table 3 Base Shear Forces under Frequent Earthquake (kN)

Base Shear Forces	Response Spectrum	U232
X direction	17828.28	24356.77
Y direction	14760.17	11336.37
Base Shear Forces	Suqian Wave	AMO
X direction	27569.57	21209.84
Y direction	22381.91	12856.81
Base Shear Forces		Average
X direction		24378.72
Y direction		15525.03

4.4 Damping effect

The inter-story drift angles of the structure are shown in Figure 6 and Figure 7.

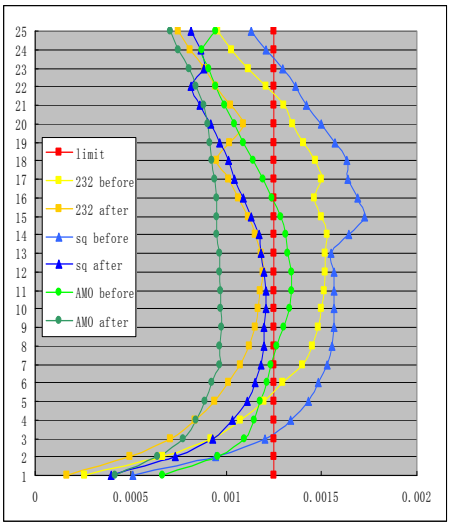

(a)

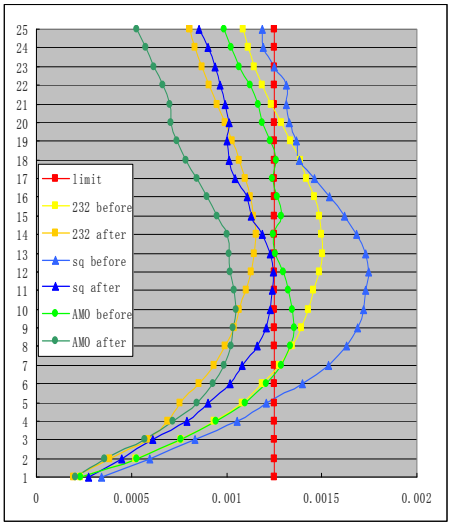

(b)

Figure 6 The Inter-story Drift Angles of the Structure under Frequent Earthquake:
(a) x direction, and (b) y direction

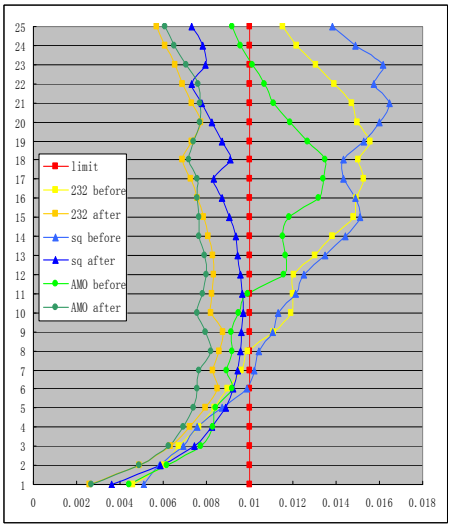

(a)

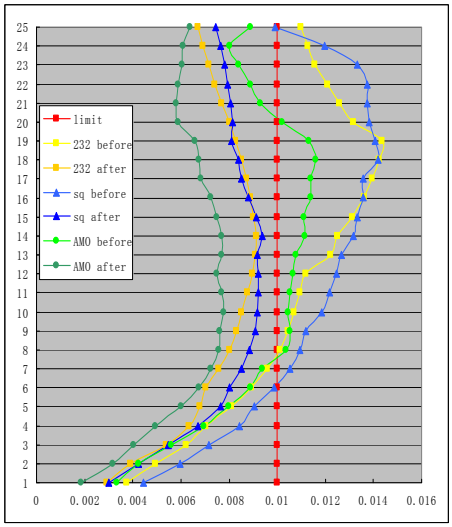

(b)

Figure 7 The Inter-story Drift Angles of the Structure under Rare Earthquake:
(a) x direction, and (b) y direction

5 CONCLUSIONS

The restoring forces curves of stories are simplified as the three polygon stiffness model through the static pushover analysis. On this basis, the bending-shearing layer model of the structure was established, and the nonlinear time history analysis was conducted. The static-dynamic analysis method gets the best of both methods, reducing the amount of calculation and saving time. And it can assess the overall seismic behaviors of structures under earthquakes.

Viscous fluid dampers can effectively increase the structural damping ratio and significantly reduce the seismic response of structures. In the existing condition of damping devices setting, the response of structure are reduced and meet the meet the limits of "Code For Seismic Design of Buildings"

Acknowledgements:

The authors acknowledge the financial support provided by Key Projects in the National Science & Technology Pillar Program in the Eleventh Five-year Plan (Grant No. 2006BAJ03A04).

References:

Yang,Z.Y. and He, R.Q.(2003), "Inelastic Static Dynamic Analysis Method of High Rise Steel Structures under Earthquake Action," *Journal of Building Structures*, 24(3), 25-32.

Yang, J., and Zou, H.D.(2007), "The Progress in Push-over Analysis Method for Earthquake-resistance Structure," *Industrial Construction*, 37, 189-195.

Ministry of construction of the People's Republic of China,(2008). "Code For Seismic Design Of Buildings" (GB50011-2001) China Architecture and Building Press.

Artho, C., Biere, A.(2005), "Combined static and dynamic analysis", *Electronic Notes in Theoretical Computer Science*, 131, 3-14, 20.

The Japan Society of Seismic Isolation (2008), "Passive Seismic Structures Design & Construction Manual (The 2nd edition),"China Architecture and Building Press.

JOINT CONFERENCE PROCEEDINGS
7th International Conference on Urban Earthquake Engineering (7CUEE) &
5th International Conference on Earthquake Engineering (5ICEE)
March 3-5, 2010, Tokyo Institute of Technology, Tokyo, Japan

RESPONSE OF RC BUILDINGS UNDER MULTIPLE EARTHQUAKES

Adel E. Abdelnabi[1)] and Amr S. Elnashai[2)],

1) Research Assistant, Department of Civil and Environmental Engineering, University of Illinois at Urbana-Champaign, USA
2) Bill and Elaine Hall Endowed Professor, Department of Civil and Environmental Engineering, University of Illinois at Urbana-Champaign, USA

abdelna1@illinois.edu, *aelnash@illinois.edu*

Abstract: There are many locations around the world where earthquakes occur as a cluster. It is often not possible to distinguish the individual earthquakes as fore- and after-shocks, or sequences of earthquakes from proximate fault segments. Previous research had been focusing mainly on the response of structures due to one earthquake assuming that damage will occur only during the main shock. Therefore, previous researchers and practitioners usually perform earthquake assessment on the basis of a single event. This approach neglects the accumulated damage induced due to earlier ground shaking which significantly affects the structural dynamic characteristics and hence predicted response under subsequent earthquake ground motion. This paper describes an approach for earthquake assessment of reinforced concrete (RC) structures that considers multiple earthquake effects. In this method: (1) ground motions were developed based on possible earthquake scenarios the fault systems being studied can generate; (2) numerical models that incorporate structural deterioration effects due to earlier shaking were established; and finally (3) the response was predicted and compared with that obtained based on a single earthquake. In addition, the paper presents a system-level hybrid simulation framework test that is required for numerical model verification.

1. INTRODUCTION

Some seismic regions have fault lengths sufficient to generate multiple earthquakes at different epicentral locations. Since the fault rupture does not usually relieve all accumulated strain energy at once therefore high stresses along the fault length are created. Consequently, the energy is first released from zones of weak rock as foreshocks and aftershocks are generated from strong rock zones.

In this paper, examples of multiple earthquakes that occurred at different places around the world are illustrated. Moreover data were obtained from field surveys following these earthquakes. The data indicated that structural damage substantially increases due to successive shaking. Indeed the accumulation of damage in some cases lead to buildings collapse during aftershocks.

Most research work done before did not study the response of structures under repeated shaking. This approach assumes that structures are initially undamaged and hence it neglects: (1) the effects of accumulated damage on system degradation and (2) changes in structural dynamic characteristics due to previous shaking.

This study introduces a new approach that considers repeated shaking in earthquake assessment of reinforced concrete structures. First the region seismicity is studied and then all possible earthquake scenarios generated from the fault systems are predicted, earthquake records along the fault lines based on the estimated magnitude and source-to-site distances for each individual shock are developed. Numerical models are established using available commercial tools that can perform non-linear inelastic dynamic analysis. Ground motions are then applied as fore-, main and after-shocks as ground acceleration successively.

New models were required to be implemented in order to account for the accumulated damage in terms of cracking, stiffness and strength deterioration in concrete as well as fracture and buckling of steel re-bars.

Finally, the expected behavior of structures was discussed and challenges were remaining in order to verify and support the expected results.

2. MULTIPLE EARTHQUAKES EXAMPLES

2.1 Turkey

Kocaeli and Duzce earthquakes (1999): in 1999 two earthquake events hit Turkey. Both earthquakes were generated from the same fault line, the so-called North Anatolian Fault system which was estimated to be 1300 km long. The first earthquake (Kocaeli) of magnitude 7.4 was

associated with 120 km rupture along the western extension of the North Anatolian fault. The earthquake struck Kocaeli and Sakarya provinces on August 17 causing severe damage to buildings, infrastructure and lifelines. In November 12, a second earthquake (Duzce) of magnitude 7.2 was produced due to another rupture in the North Anatolian fault system; however this rupture was at the eastern end, severe damage was revealed especially in the following four districts: Kocaeli, Sakarya, Bolu and Yalova. Many structures survived from the first earthquake and kept intact; however they collapsed due to the second earthquake.

Gediz Earthquake (1970): On March 28, 1970, Turkey was shaken by a severe earthquake of magnitude 7.1. The earthquake occurred in the upper reaches of the Gediz River and affected the region between the towns of Kutahya, Emet, Simav and Usak. Severe shaking was felt in the after-shocks. Figure 1 (left) shows the effect of the main shock of the earthquake on a three story house of mixed, reinforced concrete and brick construction, while Figure 1 (*right*) shows the effect of strong aftershocks a few days after the earthquake of 28 March 1970 in Gediz on the damaged building shown in Figure 1 (*left*)**.**



Figure 1: Damaged building after main-shock (*left*), collapsed building due to an after-shock (*right*).

2.2 Taiwan

Chichi Earthquake: on September 21, 1999, an earthquake of magnitude 7.6 hit Chichi town in Taiwan. A total of 12,911 after-shocks were recorded by the Central Weather Bureau, one strong aftershock struck on September 26 and caused the collapse of some already damaged structures due to the main shock on the 21st. 2,416 people were killed and 44,338 houses were destroyed due to the main and after-shocks.

2.3 New Madrid Zone, USA

1811-1812 earthquakes: it was reported that more than two hundred moderate to large earthquakes occurred on the New Madrid fault between December 16, 1811 and March 15, 1812. Amongst these earthquakes were five major shocks with magnitude (M_S) above 7.7 which struck the region causing soil liquefaction and landslides and also changing the region topology, for example by forming new lakes. It was indicated that at least one of these shocks had a magnitude above 8.0. Furthermore, ten earthquakes of M_S about 6.7 were also reported in addition to thirty five of M_S about 5.9, sixty five of M_S about 5.3, and eighty nine of M_S about 4.3.

The 1811-1812 repeated earthquakes caused low fatalities and damage to buildings since the affected area at that time was sparely settled. However, if the same scenario is repeated it will be a disaster since many cities are highly populated and most of the buildings are not well seismically designed for repeated earthquakes.

It is well known that the New Madrid Fault generates intra-plate earthquakes which usually have longer recurrence periods than their interpolate companions. However, a similar scenario of the 1811-1812 earthquakes within the coming 50 years is very much probable.

2.4 Haiti Earthquake (2010):

Dozens of aftershocks up to 6.1 in magnitude hit Haiti after the major earthquake of magnitude 7 that occurred on January 12, 2010.

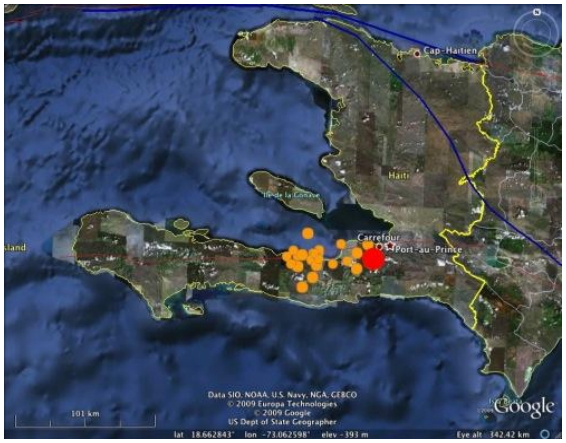

Figure 2: Source locations of main shock (in red) and aftershocks (in orange).

The map shown in Figure 2 represents the source locations of the main shock and aftershocks. Different source locations are revealed along the fault system.

2.5 Other Earthquakes

Many other earthquakes around the world followed similar earthquake scenario to New Madrid Zone 1811-1812 earthquakes, where earthquakes struck as more than one principal shocks and each principal shock generates its own aftershocks. Examples of such earthquakes are the: 1990 Sudan (M 7.3, 6.7, 7.2 in 5 days); 1976-84 Gazli, Uzbekistan (M 6.8, 6.9, 6.9 in 8 years); 1985-88 Nahani, Canada (M 6.6, 6.8, 6.2 in 3 years); 1988 Tennant Creek, Australia (M 6.2, 6.3, 6.6 in 12 hours); and 1982 Miramichi, New Brunswick (M 5.6, 4.9, 5.0 in 3 days). It is worth mentioning that all these earthquakes are intra-plate earthquakes like the 1811-1812 earthquakes that were generated from the New Madrid Fault, however the 1811-1812 earthquakes were reported as the largest known among these earthquakes. In the aforementioned earthquakes, damage was reported to

structures and facilities due to main shocks as well as aftershocks.

3. LITERATURE

Most researchers focused mainly on the response of structures based on a single earthquake record rather than multiple earthquakes. However, few research studies were conducted to propose cumulative damage models for circular bridge piers (El-Bahy et al. 1996) and steel components of steel structures subjected to earthquake ground motions (Krawinkler and Zohrei 1983). These two studies were so specific to certain structural systems and components. For example the study conducted by El-Bahy was limited to circular bridge columns with predominantly flexural response, and moreover the failure was defined only in the bridge pier while other potential damage sources such as foundation failure and deck-abutment connection failures were beyond the scope.

Many other studies were carried out using energy-based damage models for deteriorating systems to account for accumulated damage in structures. However these studies were mainly focused on evaluating the amount of induced damage to structures after an earthquake by defining new damage indices. These models were used to depict the stiffness and strength degradation of steel and reinforced concrete members subjected to cyclic loading (Chung et al. 1989) and (Park et al. 1985) but were not modeled to investigate the response of structures under further earthquake loading.

In 1999, a study was conducted by M. Aschheim and E. Black to determine the "effects of prior earthquake damage on response of simple stiffness-degrading structures". The study involved over 20,000 single degree-of-freedom analyses to assess the effects of prior earthquake damage on the peak displacement response. The analyses used the modified Takeda load-deformation relation that incorporates pinched hysteresis and strength degradation. Eighteen earthquake motions representing different frequency content, duration and directivity effects were selected and applied in different sequences. The final results, as per the study, indicated that the initial stiffness has little influence on peak displacement response. Also it was concluded that the prior damage due to the previous earthquakes did not significantly affect the response since initially undamaged oscillators used to crack in early portions of their loading history and then quickly catch up to the response of their corresponding previously damaged companions (Figure 3). This study done by Aschheim was not supported by any experimental tests; moreover, it was conducted on single degree of freedom oscillators applied to only three series of eighteen random earthquake ground motions. Therefore, these results were assumed to be unrealistic since they do not match with what was presented earlier, from earthquake site visits, about collapse of building due to aftershocks.

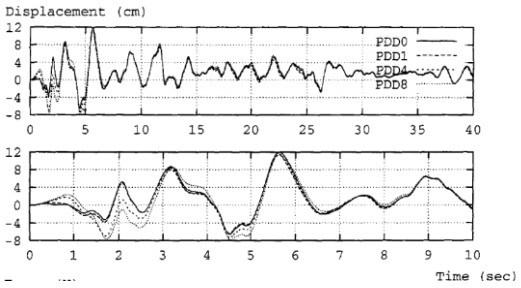

Figure 3: Comparison between initially damaged and undamaged response of SDOF oscillator for different ductility demands (Aschheim 1999).

In some previous research physical structures on shaking tables were subjected to repeated shaking. Although it was incidental and was not the primary focus of the research but it was revealed that the displacements were affected by damage induced due to prior earthquake loadings when compared to the undamaged structures (Cecen 1979) and (Wolschlag 1993).

Therefore, this study is essential to focus on the behavior of different types of structures under properly selected repeated earthquake ground motions. Also this research incorporates all required tools to model structural damage in terms of stiffness and strength deterioration, and applies reasonable earthquake motions based on the region seismicity of the structure of interest.

4. RESEARCH OBJECTIVES

The aim of this research is to provide state-of-art guidelines to researchers in earthquake engineering field and designers of critical structures and facilities under multiple earthquakes hazard. These guidelines are illustrated as follows:

1- Study the region seismicity of the studied structure in terms of active faults and fault lengths.
2- Based on seismological facts and historical earthquake records of the region under scope determine the ability of multiple earthquakes generation.
3- Determine all possible earthquake scenarios using all earthquakes combinations generated at different locations along the fault length or from different fault segments.
4- Develop input ground motions that simulate the actual earthquakes that could be generated from the seismic region, using the information provided about the source-to-site distance, site conditions and estimated magnitude.
5- Establish numerical models that use advanced tools to model the accumulated damage induced to structures as a result of multiple earthquakes.

6- Derive fragility curves for some selected structures subjected to multiple earthquakes and compare their vulnerability with that derived for one earthquake record.

Finally, a case study which summarized all previously mentioned guidelines was done for a typical strucuture in the New Madrid Seismic Zone.

5. RESEARCH METHODOLOGY

In order to achieve the mentioned objectives the research methodology was divided into two major tasks: (1) developing input ground motions; (2) Implementing advanced tools to numerical models to consider accumulated damage induced due earlier shaking; and finally (3) performing hybrid simulation tests to verify the numerical models.

5.1 Input Ground Motions

Input ground motions are developed by first studying the fault systems. And based on fault lengths and number of faults all possible multiple earthquake combinations are recognized. Attenuation relationships are used to consider the effects on ground motions due to wave propagation through rock from source to site. These attenuation relationships, so-called New Generation Attenuation Relationships models (NGA models), are recently developed and are based on motions response spectra and hence they increase the motion predominant period as long as the wave propagates from source-to-site distance. In addition they scale down the peak ground accelerations.

Since the developed motions are predicted on bedrock, site response analyses are required to depict the effects of soil type on motion characteristics due to wave propagation from bedrock to soil surface.

Natural records are used from available records databanks, the records selection criteria are based on similar: fault mechanism, magnitude, distance and site conditions. Attenuation relationships are used and site response analyses are performed for natural records that did not match the distance criterion and records that were measured on bedrock respectively. For some regions, where natural records were not available like the New Madrid Seismic Zone, synthetic records, developed from previous research work done, were used instead.

5.2 Numerical Models

In order to carry out non-linear inelastic time history analyses for multiple earthquakes scenario, new tools needed to be implemented to current numerical models. These tools should be capable of depicting the accumulated damage that has been induced due to previous earthquakes. Since current available commercial packages that perform non-linear inelastic dynamic analyses by applying earthquake motions do not capture the damage deterioration of materials due to earthquake loading as shown in Figure which represents two similar successive strong ground motions applied to a reinforced concrete frame using the non-linear fiber analysis software tool Zeus-NL. Similar responses were revealed from the first and second records as shown from the FFT response for the top acceleration of the frame shown in Figure (*right*).

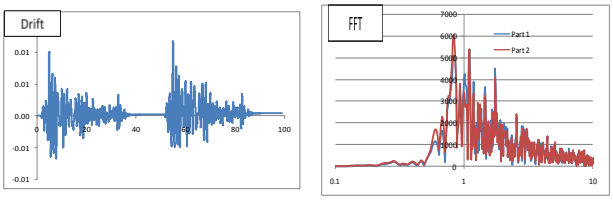

Figure 4: Drift time history response at the top of the frame (left); Fast Fourier Transform of top accelerations at the top of the frame (*right*).

Similar responses were not expected from this analysis since strong ground motion's peak ground acceleration was 0.5g. Material deterioration in terms of stiffness and strength degradation was expected though. Therefore, new material models were implemented for both concrete and reinforcing steel.

A Plastic-Damage Model for cyclic loading of concrete structures developed by Lee and Fenves in 1998 was used. This model uses concepts of fracture-energy-based damage to account for stiffness and strength degradation of concrete under cyclic loading in both tension and compression. Two damage parameters were introduced to this model, one for tensile damage and the other for compressive.

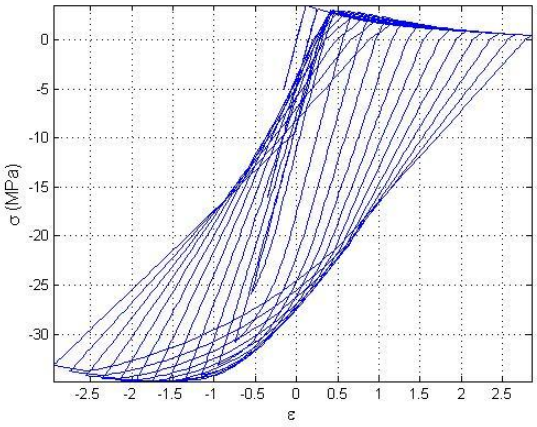

Figure 5: Uniaxial Stress-Strain response of concrete model under cyclic loading.

Figure 5 shows the uniaxial cyclic response of the implemented concrete model. As shown, the compressive behavior depicts the stiffness and strength degradation of concrete while the tensile behavior considers stiffness degradation and also accounts for tension stiffening of concrete after cracking. The model also accounts for stiffness recovery for load reversal from compression to tension and vice versa.

For steel rebars, a modified Menegotto-Pinto cyclic

stress-strain steel relationship was used (Augusto and Appleton 1997). The modification to the commonly used Menegotto-Pinto relationship was developed to account for inelastic buckling of longitudinal rebars under compression in concrete and after concrete spalling.

The actual response of structures under multiple earthquakes could be then predicted after material models implementation.

6. CASE STUDY (NMSZ)

A typical reinforced concrete moment resisting frame structure in the New Madrid Seismic Zone (NMSZ) was selected as a case study. The frame was two bay three storey frame which was not well seismically detailed as typical structures in the region.

6.1 Region Seismicity and Earthquake Records

Aforementioned, the New Madrid Zone is a region of low seismic activity; however the New Madrid fault is capable of generating multiple earthquakes each of which can exceed a magnitude of 8.0.

The New Madrid fault could be divided into three segments, namely, the northeast, southwest and central (reelfoot) segments (Elnashai 2008). The northeast and southwest segments are strike-slip faults while the central segment is a thrust fault. Each segment could generate an earthquake of magnitude 8.0 or more. Seismologists expect that an initial shock will be generated from the either one of the strike-slip segments followed by a third shock from the central segment in order to balance the energy released from the entire fault.

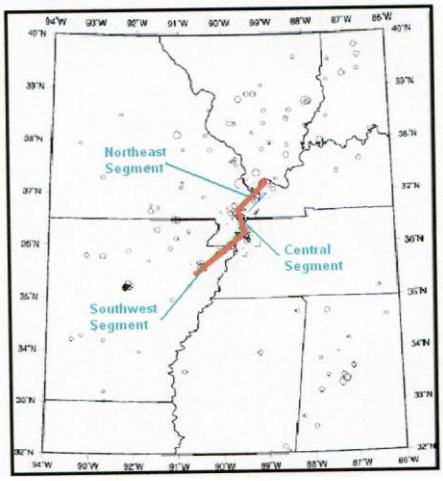

Figure 6: New Madrid Fault segments.

The earthquake records developed by Fernandez and Rix in 2007 were used. However, these records were developed for a specified source-to-site distance and rock site conditions, therefore attenuation relationships were applied to these records to account for different distances of different earthquakes generated from each fault segment, in addition site response analyses were performed to account for site effects.

6.2 Numerical Model

The numerical model of the concrete frame was established. Pushover analysis was performed to study the global response of the structure due to incrementally increasing lateral forces. The analysis revealed a soft story formation at the three lower columns of the frame (Figure 7).

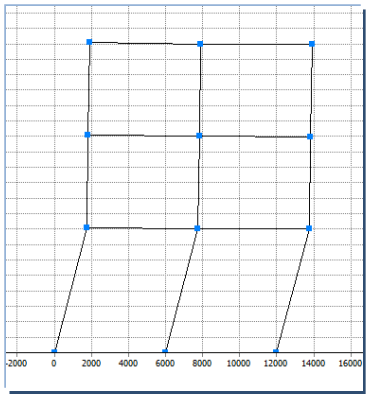

Figure 7: Soft-story in concrete frame (pushover analysis).

A system-level hybrid simulation framework will be conducted. The experimental component of the hybrid model will comprise the three columns at the first story where a soft story is estimated to take place. The analytical component will comprise the rest of the frame were inelastic behavior is unlikely to occur. The experimental component will be tested using three small scale load and boundary condition boxes at University of Illinois at Urbana Champaign (Figure 8). These tests will be required to validate the newly introduced approach of damage accumulation due to earthquake loadings in reinforced concrete structures.

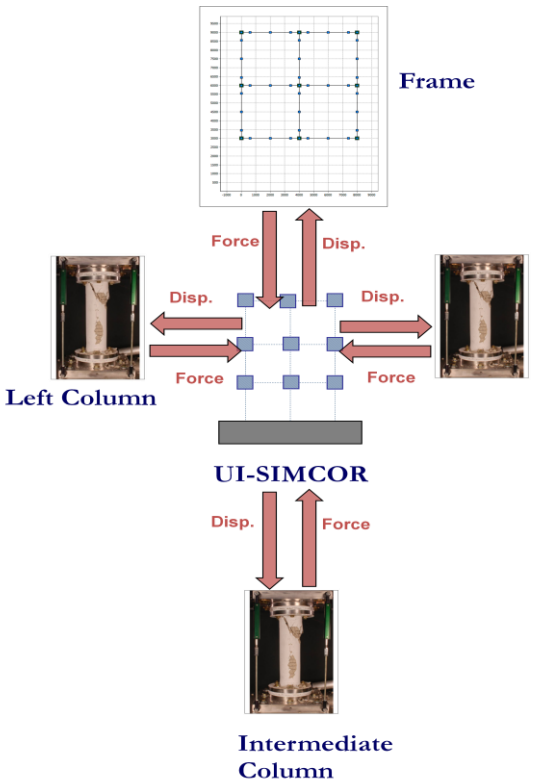

Figure 8: Hybrid simulation framework for the reinforced concrete frame.

7. SUMMARY AND CONCLUSIONS

This paper focused on the potential of including multiple earthquake effects on a structure as opposed to a single event approach especially in regions where series of earthquakes are likely to occur. This approach was not considered in previous research and codes of practice in assessing existing structures or designing new ones. Therefore, previous research and codes of practice may lead to unquantifiable errors, as highlighted in the paper.

Multiple earthquakes significantly affect the structural response of a building since the first earthquake may cause damage that entirely changes the dynamic characteristics of the structure. Therefore, subsequent earthquakes could cause unexpected response that is distinct from that obtained by assuming initially undamaged structures. Accordingly, studies are needed to ascertain the effect of multiple earthquakes on the response of inelastic structures.

Acknowledgements:

The authors acknowledge support from the Japan Ministry of Education, Culture, Sport, Science, and Technology (MEXT) for establishing the Center for Urban Earthquake Engineering (CUEE) in Tokyo Institute of Technology. The first author acknowledges the support of the Mid-America Earthquake Center at the University of Illinois.

References:

"The Chi-Chi, Taiwan Earthquake of September 21, 1999", *EERI Special Report*, December 1999.

Aschheim, M. and Black, E. (1999), "Effects of Prior Earthquake Damage on Response of Simple Stiffness-Degrading Structures", Journal of Earthquake Spectra, **15**(1), 1-24.

Cecen, H. (1979), " Response of Ten-Story, Reinforced Concrete Model Frames to Simulated Earthquakes", *Doctoral Thesis, Department of Civil Engineering, University of Illinois at Urbana Champaign.*

Chung, Y., Meyer, C. and Shinozuka, M. (1989), "Modeling of Concrete Damage", *ACI Structural journal*, **86**(3), 259-271.

El-Bahy, A., Kunnath S., Stone W. and Taylor A. (1999), "Cumulative Seismic Damage of Circular Bridge Columns: Benchmark and Low-Cycle Fatigue Tests", *ACI Structural Journal*, **96**(4), 633-642.

El-Bahy, A., Kunnath S., Stone W. and Taylor A. (1999), "Cumulative Seismic Damage of Circular Bridge Columns: Variable Amplitude Tests", *ACI Structural Journal*, **96**(5), 711-719.

Fernandez, J.A. and Rix, G.J. (2008), "Seismic Hazard Analysis and Probabilistic Ground Motions in the Upper Mississippi Embayment", *Geotechnical Special Publication*, **181**.

Gomes, A. and Appleton, J. (1997), "Nonlinear Cyclic Stress-Strain Relationship of Reinforcing Bars Including Buckling", *Journal of Engineering Structures*, **19**(10), 822-826.

Johnston, A.C. and Schweig, E.S. (1996), "The Enigma of the New Madrid Earthquakes 1811-1812", *Journal of Annual Review of Earthquake and Planetary Sciences*, **24**, 339-384.

Krawinkler, H. and Zohrei, M. (1983), "Cumulative Damage in Steel Structures Subjected to Earthquake Ground Motions", *Journal of Computers and Structures*, **16**(1-4), 531-541.

Lee, J. and Fenves, G.L. (1998), "Plastic Damage Model for Cyclic Loading of Concrete Structures", *ASCE Journal of Engineering Mechanics*, **124**(8), 892-900.

Mahin, S.A. (1980), "Effects of Duration and Aftershocks on Inelastic Design Earthquakes", *Proceedings of the Seventh World Conference on Earthquake Engineering*, Istanbul, **5**.

Menegotto, M. and Pinto, P. (1973), "Method of Analysis for Cyclically Loaded RC Plane Frames Including Changes in Geometry and Non-elastic Behavior of Elements Under Combined Normal Force and Bending", *Resistance and ultimate deformability of structures acted on by well defined repeated loads*, IABSE Reports, **13**.

Saiidi, M. and Sozen, M.A. (1984), "Simple and Complex Models for Nonlinear Seismic Response of Reinforced Concrete Structures", *Structural Research Series*, **465**, Civil Engineering Studies, University of Illinois at Urbana Champaign.

Sucuoğlu, H., and Yılmaz, T., (2001). "Düzce, Turkey: A City Hit by Two Major Earthquakes", *Seismological Research Letters*, **72**(6), 679-689.

Wolschlag, C. (1993), "Experimental Investigation of the Response of R/C Structural Walls Subjected to Static and Dynamic Loading", *Doctoral Thesis*, Department of Civil Engineering, University of Illinois at Urbana.

JOINT CONFERENCE PROCEEDINGS
7th International Conference on Urban Earthquake Engineering (7CUEE) &
5th International Conference on Earthquake Engineering (5ICEE)
March 3-5, 2010, Tokyo Institute of Technology, Tokyo, Japan

EXPERIMENTAL STUDY ON IN-PLANE AND OUT-OF-PLANE BEHAVIOR OF PP-BAND RETROFITTED MASONRY WALLETTE MADE OF SHAPELESS STONES

Kotaro Sakurai[1)], Navaratnarajah Sathiparan[2)], and Kimiro Meguro[3)]

1) Graduate Student, Department of Civil Engineering, The University of Tokyo, Japan
2) JSPS Post Doctoral Fellow, Institute of Industrial Science, The University of Tokyo, Japan
3) Director/Professor, International Center for Urban Safety Engineering, Institute of Industrial Science, The University of Tokyo, Japan
sakurai@risk-mg.iis.u-tokyo.ac.jp, sakthi@risk-mg.iis.u-tokyo.ac.jp, meguro@iis.u-tokyo.ac.jp

Abstract: Unreinforced masonry structure is one of the most popularly used constructions in the world, especially in developing countries. It is also unfortunately, the most vulnerable to the earthquake and its damage has caused many human casualties. Therefore, from global viewpoint, retrofitting of low earthquake-resistant masonry structures is essential to reduce the casualties by earthquake disaster. In developing countries, retrofitting method should be technically feasible and economically affordable, the retrofitting material, accessible, and the workmanship, locally available. Considering these points, PP-band (polypropylene bands, worldwide available and cheap material, commonly used for packing) retrofitting technique has been developed by Meguro Laboratory, The University of Tokyo. In this research, we conducted a series of experiments to verify the suitability of PP-band retrofitting for masonry structures made of shapeless stones. Material tests were conducted to understand the basic parameters of stone masonry, i.e. shear, tension and compression strength. After the material tests, diagonal compression test and out-of-plane test were carried out using masonry wallette made of shapeless stones with and without retrofitting. From both test results, it was clear that PP-band retrofitting improved drastically the overall stability and ductility of stone masonry structures made of shapeless stones.

1. INTRODUCTION

Masonry structure, constructed by piling burned bricks or unburned, just sun-dried, bricks called adobes, stones or concrete blocks, is one of the most popularly used constructions in the world, but also the most vulnerable to earthquakes. Because distribution of the masonry structures overlap with high seismicity area in the world, it has caused many human casualties during earthquake. Therefore in global viewpoint, retrofitting of low earthquake-resistant masonry structures is very important to save people from earthquake disaster. Considering these points, a new retrofitting technique for masonry has been developed based on the use of polypropylene band (PP-band) meshes by Meguro laboratory, The University of Tokyo[1)]. This PP-band retrofitting technique prevents masonry structures from collapsing by giving the stabilization.

Up to now PP-band retrofitting study mainly focus on houses build by regularly shaped bricks and adobes. But the masonry has many different kinds of construction and the effect of PP-band is not confirmed for all kinds of masonry. Especially in the mountainous region in developing countries, stone masonry is constructed using shapeless or shaped stones as constructing material[3)]. But stone masonry house, particularly shapeless stone masonry house is the most vulnerable during earthquake as shown in Table 1. Therefore further test of stone masonry wallettes should be carried out.

Table 1 Vulnerability Table[2)]

	Type of structure	Vulnerability Class					
		A	B	C	D	E	F
MASONRY	Rubble stone, field stone	O					
	Adobe (earth brick)	O——					
	Simple stone	——O					
	Massive stone		——O——				
	Unreinforced, with manufactured stone units	——O——					
	Unreinforced, with RC floors		——O——				
	Reinforced or confined			——O——			
REINFORCED CONCRETE	Frame without earthquake-resistant design (ERD)	——O——					
	Frame with moderate level of ERD		——O——				
	Frame with high level of ERD			——O——			
	Walls without ERD		——O——				
	Walls with moderate level of ERD			——O——			
	Walls with high level of ERD				——O——		
STEEL	Steel structures			——O——			
WOOD	Timber structures		——O——				
O	: Most likely vulnerability class						
——	: Probable range						
·····	: Less probable range, exceptional cases						

2. MATERIAL TEST

2.1 Test Setup

Figure 1 shows the specimens used for shear, tension and compression tests to obtain the mechanical properties of the stone masonry. Shapeless stones whose size range from 60mm to 80mm were used for preparation of specimens. A

mortar with the mixture ratio of cement : lime : sand = 1 : 5 : 14 and cement/water ratio = 0.20 in weight was used. To make the specimens close to real stone masonry structures made of shapeless stones in developing countries, gravel were put between the shapeless stones. The number of shapeless stones used for specimen was 3, 2 and 5 for shear, tension and compression test specimens, respectively as shown in Figure 1. Five identical specimens were constructed for each test. Specimens were tested 28 days after construction under displacement control condition and the loading rate was 0.1mm/min.

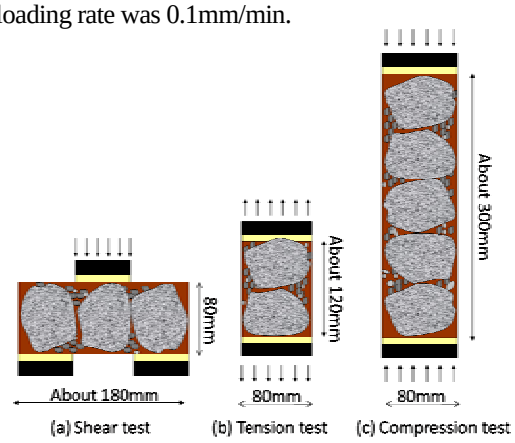

Figure 1 The Structure of The Specimens for Material Test

2.2 Results of Material Tests

Based on the difference of failure mechanism, major failure patterns of masonry can be divided into 3 types[4].

a) Failure occurred within the mortar.
b) Failure occurred along the interface between mortar and stone surface.
c) Failure occurred within the brick or stone.

Type c) failure can be observed only in case of special combination of very strong mortar and very weak brick or stone.

From the shear test's results, it is found that the failure pattern of masonry made of shapeless stones is type b) that is the separation along interface between stone surface and mortar because interface strength is less than that of mortar. Figure 2 shows the average strength of each test, i.e. shear, tension and compression tests. Figure 3 shows the failure pattern of stone masonry made of shapeless stones.

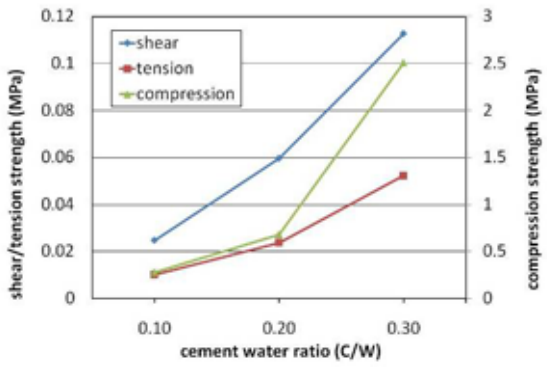

Figure 2 Mechanical Properties Obtained from Material Tests

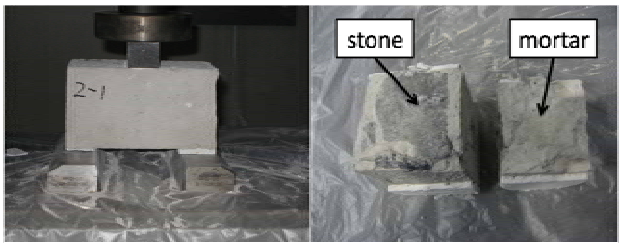

Figure 3 Separation along Stone-Mortar Interface

3. DAIAGONAL SHEAR TEST

3.1 Outline of The Diagonal Compression Test

To verify the suitability of PP-band retrofitting technique for stone masonry, diagonal shear test using 1/4 scaled model was conducted. The wallette dimension was 300×300×150mm^3 and it was composed of 5 × 3 stones, and 2 stones in the direction of depth as seen in Figure 4. Because the size and shape of stones were variable, there is approximately 10mm variation in the height of the specimens. Considering the results of material tests, we used a mortar with the mixture ratio of cement : lime : sand = 1 : 7.3 : 18.7 and cement/water ratio = 0.15 in weight for diagonal shear test to make the specimens close to real masonry structures made of shapeless stones in developing countries.

In this experimental program, masonry wallettes made of shapeless stones with and without retrofitting were prepared. In addition, specimens with 10mm surface finishing were prepared. Three identical wallettes were constructed for each test. Specimens were tested 28 days after construction under displacement control loading condition. The loading rate was 0.5mm/min up to the first 10mm of diagonal deformation, and then it was increased to 2mm/min up to 50mm and 5mm/min up to 100mm of diagonal deformation.

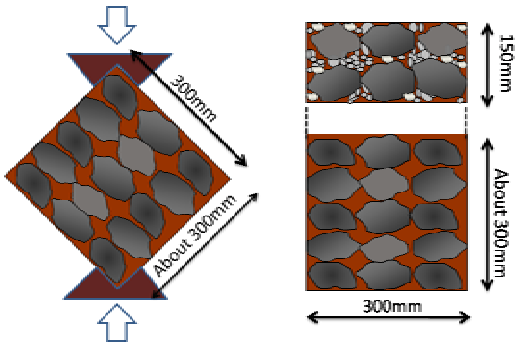

Figure 4 Specimen for Diagonal Shear Test

3.2 The Result of Experiment

Figure 5 shows the diagonal shear stress variation with strain for the non-retrofitted and retrofitted specimens. In the non-retrofitted case, there was no residual strength after the first crack occurred and the specimens split into two pieces at strain equal to 1.1%. If we consider average behavior of

retrofitted specimens, although the initial crack was followed by a sharp drop, at least 64% of the peak stress remained. As the matter of fact, 3 specimens were used for each non-retrofitted and retrofitted case. Subsequent drops were associated with new cracks such as the ones observed in the retrofitted specimen that shown in figure 5, at the strain of 2.5%. After this, the stress was regained by readjusting and packing by PP-band mesh. The stress equal to 72% and 81% of the initial peak stress was remained at the strain equal to 10% and 20%, respectively. The residual peak stress of the specimen was 99% of initial peak stress. If we consider the overall behavior of retrofitted specimens, specimen didn't break at the strain equal to 24%, which indicates that retrofitted specimen was at least 21 times more ductile than non-retrofitted one.

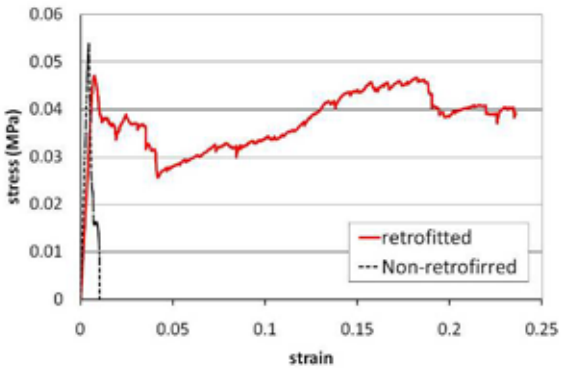

Figure 5 Stress vs. Strain for Stone Masonry Wallette with and without Retrofitting by PP-band Mesh

Figure 6 shows the non-retrofitted and retrofitted specimens at the end of test, which corresponded to the strain equal to 1.1% and 24%, respectively. As strain became larger, due to very low mortar strength, PP-band penetrated to the specimens. Therefore, increase of strength was not observed with strain. However, for specimens used for 1/4 scaled experiment, scaled PP-band whose width was approximately 6mm was used and it increased penetration-rate. But in case of full-scale structure, because 15mm PP-bands are used, penetration of PP-band meshes to the masonry houses are reduced relatively. Therefore additional increase of strength is expected, when the real masonry structures are retrofitted by PP-band meshes.



Figure 6 Failure Pattern of Stone Masonry Wallette (Left: without Retrofitting, Right: with Retrofitting)

Figure 7 shows the diagonal shear stress variation with strain for retrofitted specimens with and without surface finishing. As a surface finishing, mortar with the thickness of 10mm was pasted on specimens. In case of retrofitted specimen without surface finishing, 64% of the peak stress remained after the first crack. On the other hand, if we consider average behavior of retrofitted specimens with surface finishing, 77% of the peak stress was remained after the first crack. By overlaying mortar onto PP-band mesh, surface finishing fill the gap between PP-band mesh and masonry wallette and the residual strength became higher than that of the specimens without surface finishing. It was found that surface finishing makes beneficial effect in residual strength for masonry made of shapeless stones as well as for adobe and brick.

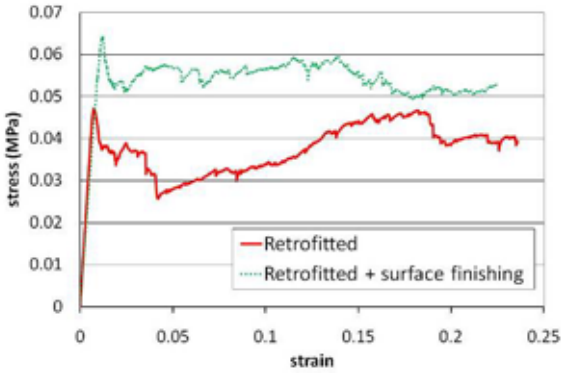

Figure 7 Stress vs. Strain for Retrofitted Stone Masonry Wallette with and without Surface Finishing

4. OUT-OF-PLANE TEST

4.1 Outline of The Out-of-plane Test

Out-of-plane test was carried out to investigate the effectiveness of PP-band mesh in walls exhibiting arching action. Wallette used was 1/4 scaled model and its dimension was 480×240×150mm^3 and it was composed of 4×5 stones, and 2 stones in the direction of depth as seen in Figure 8. Because the size and shape of stones were variable, there is the approximately 10mm variation in the height of the specimens. Considering the result of material tests, we used a mortar with mixture ratio of cement : lime : sand =1 : 4 : 11.2 in weight for out-of-plane test to make the specimens close to real masonry structures made of shapeless stones in developing countries. And also, not to give damage to the specimen before test, the cement/water ratio used was 0.25.

Masonry wallettes made of shapeless stones with and without retrofitting were prepared and three identical wallettes were constructed for each test. Specimens were tested 28 days after construction under displacement control loading condition. The wallettes were simply supported with a 440mm span and steel rods were used to support the wallette at the two ends. The masonry wallettes were tested under a line load which was applied by a 20mm diameter steel rod at the wallette mid span. The loading rate was 0.5mm/min for the first 6mm of vertical deformation, and then it was increased to 2mm/min up to 65mm vertical deformation.

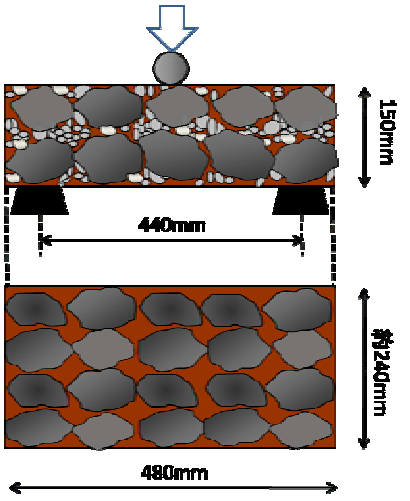

Figure 8 Specimen for Out-of-plane Test

4.2 The Result of Experiment

Figure 9 shows the out-of-plane load variation with net vertical deformation for the non-retrofitted and retrofitted specimens at the mid span. If we consider average behavior of non-retrofitted specimens, the initial strength was 1.34 KN and the specimens split into two pieces at the mid span deformation equal to 1.4mm. In the retrofitted case, although the initial crack was followed by a sharp drop, at least 33% of the peak strength remained. After this, the strength was regained progressively due to the PP-band mesh effects. In the retrofitted specimen shown in figure 9, the strength equal to 225% and 433% of the initial peak strength was observed at the mid span deformation equal to 20mm and 40mm, respectively. The residual peak strength of the specimen was 439% of initial peak strength. Specimen didn't break at the mid span deformation equal to 62mm, which indicates that; retrofitted specimen was at least 45 times more ductile than non-retrofitted one.

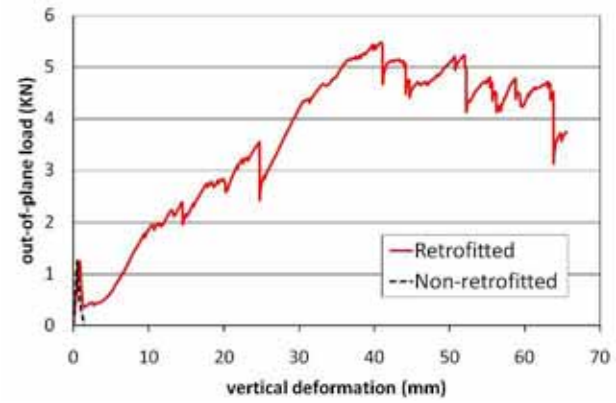

Figure 9 Out-of-plane Load Variation vs. Vertical Deformation

Figure 10 shows the non-retrofitted and retrofitted specimens at the end of test, which corresponded to deformation equal to 1.4mm and 62mm, respectively. In out-of-plane test, the improvement of final strength became much bigger than that of diagonal compression test. The cement/water ratio of the specimens used for the diagonal shear test was 0.15, but in case of out-of-plane test, the cement/water ratio equal to 0.25 was used. Because strength of mortar is high enough, PP-band didn't penetrate to the specimens and the drastic improvement of residual strength was observed.

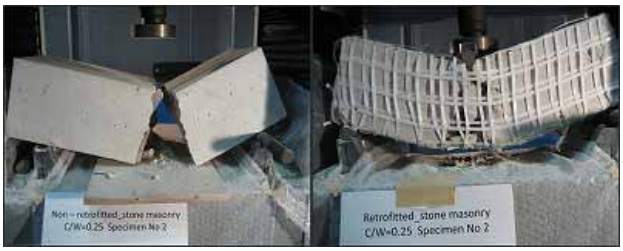

Figure 10 Failure Pattern of Stone Masonry Wallette (Left: without Retrofitting, Right: with Retrofitting)

5. CONCLUSION

This paper mainly discusses the results of a series of diagonal compression and out-of-plane tests that were carried out using both non-retrofitted and retrofitted wallettes by PP-band meshes.

5.1 Summary of Diagonal Compression Test

If we consider average behavior of the specimens

1) Masonry wallette without PP-band mesh lost the entire load bearing capacity after crack appeared.
2) Masonry wallette with PP-band mesh retrofitting lost some of load bearing capacity immediately after the crack-initiation, but 64% of the peak stress was remained. With the effects of the PP-band meshes, it could regain the load bearing capacity, and its strength and deformability improved. According to the experimental result, 1.3 times higher peak stress and at least 21 times larger ductility were observed.
3) By overlaying mortar onto PP-band mesh retrofitted masonry wallette, 77% of the peak stress was remained after the first crack. It was higher than that of the specimens without surface finishing.

5.2 Summary of Out-of-plane Test

If we consider average behavior of the specimens

1) In case of out-of-plane tests, the mesh effect was not observed before the wall cracking. After cracking, the mesh presence positively influenced the wallette behavior. Also in case of retrofitted wallette, 33% of the peak strength was remained after the first crack occurred, and then strength was regained and improved.
2) The retrofitted wallettes could have 2.9 times higher strength and 45 times larger deformation than those of the non-retrofitted ones.

Considering the overall performance of the specimens, we can conclude that PP-band mesh retrofit method can

effectively increase the seismic capacity of masonry wall made of shapeless stones, too. Based on the fact, we can expect that with PP-band mesh retrofit method, seismic capacity of weak stone masonry houses made of shapeless stones can also be improved very much and reduce drastically human casualties due to future earthquakes.

References:

1) Mayorca, P. and Meguro, K. (2004), "Proposal of An Efficient Technique for Retrofitting Unreinforced Masonry Dwellings," Proceedings of The 13th World Conference on Earthquake Engineering, Vancouver B.C., Canada, Paper No.2431.
2) Grunthal, G. (1998), "European Macroseismic Scale" Chaiers du Centre Europèèn de Géodynamique et de Sismologie, 15, Luxembourg.
3) Marjana, L. "STONE MASONRY CONSTRUCTION" (www.world-housing.net), as retrieved on April 1st , 2009.
4) Sathiparan, N. (2005), "Experimental Study of Retrofit of Masonry Buildings by PP-band Mesh", M.Eng. Dissertation, The University of Tokyo, Japan.

JOINT CONFERENCE PROCEEDINGS
7th International Conference on Urban Earthquake Engineering (7CUEE) &
5th International Conference on Earthquake Engineering (5ICEE)
March 3-5, 2010, Tokyo Institute of Technology, Tokyo, Japan

RAPID VISUAL SEISMIC VULNERABILITY ASSESSMENT TOOL AND ITS APPLICATION FOR LOCAL LEVEL DISASTER RISK MANAGEMENT

Youb Raj Paudyal[1], Ryuichi Yatabe[2], Netra Prakash Bhandary[3], Jishnu Subedi[4], Rekha Shrestha[5]

1) Graduate Student, Graduate School of Science and Engineering, Ehime University, Bunkyo-3, Matsuyama, Japan
2) Professor, Graduate School of Science and Engineering, Ehime University, Bunkyo-3, Matsuyama, Japan
3) Assistant Professor, Graduate School of Science and Engineering, Ehime University, Bunkyo-3, Matsuyama, Japan
4) Assistant Professor, Institute of Engineering, Tribhuvan University, Nepal
5) Assistant Professor, Nepal Engineering College, Pokhara University, Nepal
yrpaudyal@gmail.com, yatabe@cee.ehime-u.ac.jp, netra@cee.ehime-u.ac.jp, jishnusubedi@gmail.com, rekha_shrestha@hotmail.com

Abstract: The rapid visual seismic vulnerability assessment method is one of the most economical, reliable, simple and efficient methods to determine the vulnerability level of the buildings. In this paper it is argued that methods used for vulnerability assessment can be different from place to place. In preparing Rapid Visual Seismic Vulnerability Assessment Tool (RVSVAT) special features of buildings in Kathmandu valley of Nepal have been given due considerations and buildings have been evaluated against adherence to code and guidelines, number of stories and column size, plan and vertical irregularity, opening size, condition of building and falling hazards. Vulnerability of the buildings is decided by the final score. Validation of the tool was done by comparing results with the prevailing National Building Code (NBC), 1994 of Nepal. A pilot study in a locality of Kathmandu Valley shows that 84 percent are vulnerable and 16 percent are non-vulnerable buildings and almost all Adobe buildings would severely collapse if the area experienced an earthquake of intensity IX MMI. This tool is useful for identification of the vulnerable and non-vulnerable buildings very quickly and can help to make a plan for implementation of disaster risk reduction program.
Keywords: Vulnerability, Vulnerable, Non-vulnerable, NBC, MMI

1. INTRODUCTION

Nepal has experienced several devastating earthquakes in the past resulting in huge amount of property damage and large number of human deaths. There are incidents of earthquakes in Nepal reported since 1255 A.D. Historical records indicate many instances of earthquake in this region prior to 1934 A.D. Major earthquakes of 1408, 1681, 1810 1833 and 1866 have been reported to have claimed a large numbers of lives and huge amount of property (Gupta, 1988).

The recent major earthquake that severely hit Kathmandu valley the capital area of Nepal was Bihar-Nepal Earthquake of 1934 A.D, which produced an intensity of 9-10 on the Modified Mercalli Intensity (MMI) scale in the Kathmandu Valley. About 8,519 people were killed and around 200,000 houses, temples and historic buildings were destroyed. Kathmandu itself lost a quarter of all its houses and Bhaktapur suffered enormous devastation to its property (Dixit et al., 1999, JICA, 2002). Although the record of historical earthquake is not complete, which poses a problem in assessing the recurrence period of great earthquakes, the available record shows that a major earthquake occurs in an interval of 100 years. As the last one occurred in 1934, there is a real threat that another major earthquake may occur anytime in the next 10-20 years.

Kathmandu Valley falls under active seismic zone. Rapid population growth, poor land use planning, precarious settlement patterns, and inadequate enforcement of building code make Kathmandu vulnerable to earthquakes. Most of the structures are constructed by traditional construction materials with traditional technology (indigenous technology, which applies least of the engineering techniques). Traditional earthquake resistant measures have lost their relevance

as more people use modern construction techniques and building materials. Even the most recent buildings in the urban areas are found to be poorly designed and constructed.

Hence, there is an urgent need to asses the seismic vulnerability of the buildings in Kathmandu Valley. There exist many approaches for vulnerability assessment from very detailed and complicated ones, e.g. detailed Finite Element Method to very simple ones such as Rapid Visual Screening of buildings developed by Federal Emergency Management Agency (FEMA). Finite Element Method is very good approach to find the vulnerability of individual buildings for the area where the detailed design and drawings are available (Roca et al., 2006). In the case of Kathmandu Valley, this method is not feasible because of its time consuming nature and unavailability of detailed design and drawings of buildings.

HAZUS is used for earthquake-hazard mitigation, emergency preparedness, response and recovery planning, and disaster response operations (HAZUS-MH MR1, 2003). This method has a wider application to find out the vulnerability of buildings but this method requires high level skilled manpower and equipments. This method is expensive, time consuming and difficult to understand too. RADIUS method is applicable for the estimation of the vulnerability of the buildings and population of a particular area (RADIUS, 1999). This method seems more appropriate for the study of preliminary earthquake hazard and vulnerability. This method is more appropriate to prepare fast earthquake scenarios that better fit the needs of earthquake-threatened cities in developing countries. This method is not suitable for individual buildings. This method requires generating the mesh. In one mesh there should be only one building types but in reality there may be more than one type of buildings. This method is developed based on the common building types in Latin American cities. Since the building types are different in the case of Kathmandu Valley Nepal, it will not give accurate result. Most of the methods (Ravi Singha and Alok Goyal, Hazus) that are available do not cover the major building topology of the Kathmandu Valley Nepal.

It is therefore very important to use simpler procedures that can help to rapidly evaluate the vulnerability of different types of buildings. Although the simple method such as the one developed by FEMA is very useful tool, it cannot be used in context of Kathmandu because of difference in building types and social acceptance level. Hence it is necessary to develop a method that can be used for specific condition of Kathamndu Valley, Nepal. The general objectives of the study are to develop a Rapid Visual Seismic Vulnerability Assessment Tool suitable for the buildings in Kathmandu Valley and apply the tool for seismic risk assessment of an area in Kathmandu Valley. This method is designed to be implemented without performing any structural calculations. Emphasis is given to make the tool simple, easy to understand and use by any people after simple orientation.

2. STUDY AREA

The main objective of this research is to develop a rapid visual seismic vulnerability assessment tool for the buildings of Kathmandu Valley. For that purpose, Kathmandu Valley is taken as a research area. For application of developed tool, Duwakot Village Development Committee (VDC) – 4 and Jhaukhel Village Development Committee (VDC) – 5, Bhaktapur in Kathmandu Valley as shown below in Figure 1 is taken. Survey of the houses in those areas is performed to find their vulnerability condition. Both VDC are consisted with varieties of buildings in terms of use of building materials and age of buildings. The seismic vulnerability of the different building types depends on the choice of building materials. Building inventory data base plays a vital role to identify the vulnerability of the buildings.

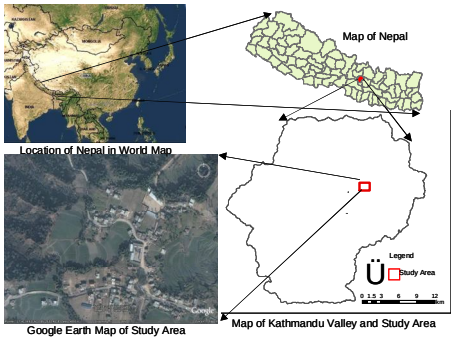

Figure 1 Study Area

Building inventory data collected by JICA (2002) shows that there are basically following five types of buildings in Kathmandu Valley.

1. Adobe and Stone Masonry Buildings (AD & ST)
2. Brick Masonry in Mud Mortar (BM)
3. Brick Masonry in Cement Mortar (BC)
4. Reinforced Concrete Buildings with/without Masonry Wall more than Three Stories (RC5)
5. Reinforced Concrete Buildings with/without Masonry Wall less than or equal to Three Stories (RC3)



AD



BM



BC

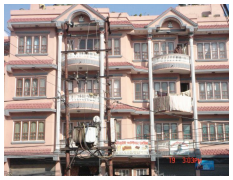

RC5



RC3

Figure 2 Building Type in Kathmandu Valley

3. METHODOLOGY

The general objectives of the study are to develop a Rapid Visual Seismic Vulnerability Assessment Tool suitable for the buildings in Kathmandu Valley and apply the tool for seismic risk assessment of an area in Kathmandu Valley. This method is designed to be implemented without performing any structural calculations. Emphasis is given to make the tool simple, easy to understand and use by any people after simple orientation.

The vulnerability assessment methods are developed according to the nature of the buildings, scope of the job and particular requirement of the projects (Roca et al, 2006). According to the building types, location, method of construction, purpose and need of the survey and other factors such as economic, assessment methods can be different. Moreover, the vulnerability rating may be different according to the social acceptability or economic condition as some countries may consider well built mud mortar house meeting the requirements and some countries may consider that not acceptable at any conditions.

Based on the review of the different literature, the following two methodologies were adopted for the development of the Rapid Visual Seismic Vulnerability Assessment Tool (RVSVAT) for Kathmandu Valley.

3.1 Federal Emergency Management Agency (FEMA) methodology based on Applied Technical Council (ATC) – 13.

Federal Emergency Management Agency (EEMA) has developed a Rapid Visual Screening of Seismically Hazards Buildings (RVSSHB) (FEMA 154, FEMA 155). This method is worldwide accepted method and used for rapid visual vulnerability assessment in different regions. In this method structural score was generated which is related to the probability of the building sustaining life threatening damage. This method is based on expert opinion for which a questionnaire sheet was prepared and distributed to the experts who are familiar with earthquake engineering. The response from the experts was collected for different type of buildings for different scenario of earthquake intensity. According to their response, the basic score and score for performance modification factors were calculated.

FEMA methodology was adopted to develop a scoring technique according to the building types prevalent in Kathmandu valley, so that these scores represent the actual performance of building during earthquake. To obtain the view of different experts about damage percentage of different building types at different Modified Mercalli Intensity (MMI) level, a questionnaire sheet was developed based on Applied Technical Council (ATC-13) and distributed to experts.

Table 1 Questionnaire form

Type of Structure	Year (s) of Experience	Intensity Vs Damage Factor (%) & Confidence Level																	
		VII						VIII						IX					
		L		B		H		L		B		H		L		B		H	
		DF	CL	DF	CL	DF	CL	DF	CL	DF	CL	DF	CL	DF	CL	DF	CL	DF	CL
ST & AD																			
BM																			
BC																			
5RC																			
3RC																			

Where, Damage Factor (DF) is defined as the ratio of amount of loss in a particular type of structure by the earthquake having particular intensity and the amount of replacement value. Confidence Level (CL) or Degree of certainty of each estimated value is rated on a scale from 0 to 3.

3.1.1 Experts' Opinion

After distributing the questionnaire form, a series of discussion was done formally and informally (telephone, email and personal meeting) with different experts. Out of twenty five experts, only five experts responded partially and other experts responded verbally which are summarized below.

1. This methodology is very good and widely accepted but not suitable in our local condition.
2. This methodology is not suitable because we have no such experience of frequent earthquakes.
3. This methodology is only suitable where people experienced frequent earthquake like Japan or to the countries with good record of damage after earthquake.
4. This methodology is complex and not comprehensible as research in earthquake engineering has just started in Nepal.

Based on the experts' response and discussion, the following conclusions were made:

1. The responses from the experts are highly valuable but that much is not sufficient for the research.
2. As Nepal does not experience frequent earthquakes and details of earthquake damages in previous earthquakes are sketchy, it might be difficult to answer the entire question.
3. This methodology cannot be adopted to develop the form and hence an alternate approach which uses experience of researchers in other regions needs to be adopted.

3.2 Method based on review of the existing methods and analysis of building data

The methodology adopted in this research works mainly consists of analysis of past earthquake damage data similar with Kathmandu Valley, analysis of fragility curve developed by JICA (2002) for buildings of Kathmandu Valley. For analysis purposes Structural Analysis Program (SAP) and Geographic Information System (GIS) is used as tool. This assessment tool is prepared after reviewing FEMA-154 and FEMA-155 and other different analysis tools given by experts with some modification in Nepal's context. Tool mainly contains the basic structural score and modifiers score. The final score of a building will be calculated by adding or subtracting the modifiers score from basic score depending upon the types of modifiers. The basic scores represent comparative vulnerability of buildings without consideration of different elements of buildings such as plan irregularity or vertical irregularity. In order to incorporate the elements which affect structural performance of buildings during earthquakes, it is necessary to modify the basic scores according to the additional building features. These modifying scores are termed as performance modification factors.

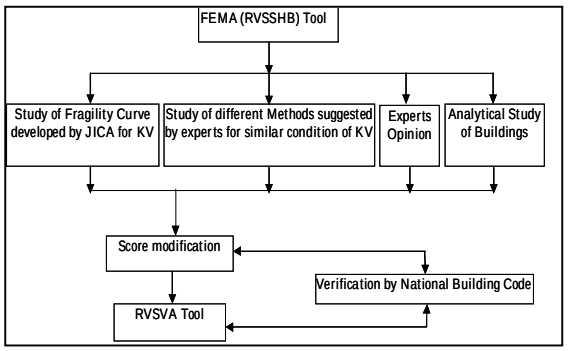

Flow chart of methodology

The performance of buildings during earthquakes depend upon various factors, the most common of which are the code or guidelines followed, plan irregularities, vertical irregularities, number of stories, column size, condition of buildings, opening in buildings etc for the buildings in Kathmandu Valley. These factors are taken for evaluating the vulnerability of buildings and development of assessment tool. Score of performance modification factors can be positive or negative depending upon their influence in buildings vulnerability.

According to the different guidelines, codes and damages from previous earthquakes in different developing countries, it can be underscored that Brick masonry building with cement sand mortar having following parameters can resist scenario earthquake, that is taken for this research, without complete collapse (sustaining life threatening damage).

- Simple rectangular plan and symmetrical both with respect to mass and rigidity.
- Not any vertical irregularity.
- No such falling hazards.
- Storey not more than two.
- Wall thickness should be 230 mm minimum.

This type of building is also recommended in the Nepal National Building Code (NBC 202, 1994). For such building a basic structural score 2 is assumed which is also taken as cut-off score for the evaluation of building vulnerability. Vulnerability of building is evaluated based on the total score of the building. Generally, score less than 2 indicates vulnerable buildings requiring detailed evaluation and score greater than 2 indicates non-vulnerable buildings and hence safe and can sustain life threatening damage.

The probable damage can be estimated based on European Micro-Seismic Scale 1998 (EMS-98) on the score of developed tool as follows (Vaseva et al., 2003).

Score ≥ 2 – High probability of 2 or less Grade damage.
Score < 2 – High probability of 3 or more Grade damage.

In calculation of Basic Structural Score for different types of buildings, the fragility curve prepared by JICA (2002) was studied and damage ratio of different types of building was taken and basic score was calculated on the basis of the assumed score 2 for above type building. The results obtained after analyzing the data were also verified by the damage data of similar type of buildings proposed by AS Arya.

The score for performance modification factors were analyzed based on the existing scoring given in FEMA 154 and score given by experts in different methods for similar type of buildings of Kathmandu Valley. During finalization of the score of the tool, a series of meeting and discussion with the experts who are familiar with vulnerability assessment of buildings, design and construction of buildings were done. For verification purposes, some sample of buildings were taken and final score of the buildings were calculated and verified with Nepal Building Code (NBC 105 1994, NBC 109 1994, NBC 202 1994, NBC 203 1994).

Table 2 Rapid Visual Seismic Vulnerability Assessment Tool for Kathmandu Valley

Building Sketch	Surveyor: _____ Building Use_____ Date of Survey_____ Address: _____ House No:_____ Year built:_____ No of Stories:_____ Photograph No._____
	Occupancy Commercial ☐ Historic ☐ Office ☐ Residential ☐ School ☐ Others ☐
	Max. Number of Persons: 0-10 ☐ 11-20 ☐ 21-50 ☐ 51-100 ☐ 101-1000 ☐ >1000 ☐ Falling Hazards: Large Cantilever Slab ☐ Chimneys ☐ Gamala ☐ Parapets ☐ Others ☐

Basic Score, Modifiers and Final Score

Building Type	ST & AD	BM	BC	RC3	RC5
Basic Score	1	1.5		3	2
Code or Guidelines Followed	+1 Yes 0 No	+1 Yes 0 No	+1 Yes 0 No	+1.5 Yes 0 No	+2 Yes 0 No
Building Stories (BS)	-0.5 BS>2 0 BS≤2	-0.5 BS>2 0 BS≤2	-0.5 BS>2 0 BS≤2	NA	NA
Column Size (CS)	NA	NA	NA	-1 CS≤9" 0 CS>9"	-1 CS≤9" 0 CS>9"
Verticularity Irregularity	-1 Yes 0 No	-1 Yes 0 No	-1 Yes 0 No	-1 Yes 0 No	-1 Yes 0 No
Plan Irrgeularity	-0.5 Yes 0 No	-0.5 Yes 0 No	-0.5 Yes 0 No	-0.5 Yes 0 No	-0.5 Yes 0 No
Poor Condition	-0.5 Yes 0 No	-0.5 Yes 0 No	-0.5 Yes 0 No	-0.5 Yes 0 No	-0.5 Yes 0 No
Opening > 40% for BC & >30% for Others	-0.5 Yes 0 No	-0.5 Yes 0 No	-0.5 Yes 0 No	NA	NA
Final Score					
Comments:				Is Building Vulnerable Yes ☐ No ☐	

Note: If buildings have more than 5 stories and roof having Tile, RBC and Slate please notify in the comments

3.2.1 Structural analysis of building as recommended by Nepal Building Code

Modeling and analysis of structure and also the study of stress variation in buildings were done for the different type of buildings by using structural analysis software SAP 2000. The stress variation due to the presence of modifiers (opening variation) that are taken in development of seismic vulnerability assessment tool was minutely analyzed.

3.2.1.1 Structural Analysis Results

Table 3 Stress in the various levels of two stories masonry with cement sand mortar buildings having rectangular plan without any irregularities

SN	Description	Max. Tensile Stress (kN/m^2)	Max. Comp Stress(kN/m2)	Max. Shear Stress(kN/m^2)	Remarks
1	Bottom West South Corner	95.37	486.35	18.30	
2	Bottom East South Corner	47.60	477.80	17.63	
3	Top Left Corner of Door Opening	78.71	404.46	53.68	
4	Top Right Corner of Door Opening	52.92	431.15	50.46	
5	Top Left Corner of Window Opening	50.89	464.93	61.26	
6	Top Right Corner of Window Opening	34.08	483.88	74.02	

The structural analysis results of two stories brick masonry building with cement sand mortar without any irregularities is found within the acceptable limit. From this type of buildings a minimum acceptable structural safety can be achieved. Near the openings of masonry building, stresses are much higher. Stresses increase as per the increase of opening. When the opening is more than acceptable (40%) the stresses were also found to be more than acceptable.

4. SEISMIC VULNERABILITY ASSESSMENT

Spatial locations of the houses are plotted over the region of the suitable areas identified and further details of these houses like physical features (building type, occupancy, number of storey, score of building, vulnerability), performance characteristics of building during earthquakes were integrated with a database of house features. This type of data base is often known as building inventory data. For vulnerability assessment purposes, some part of the Duwakot Village Development Committee (VDC) - 5 and some part of Jhaukhel Village Development Committee (VDC) - 4 were selected. The creation of the building database in this study was based on the interpretation of Google Earth Image together with field survey. Total 104 buildings were surveyed and analysis of the data was done to find their vulnerability.

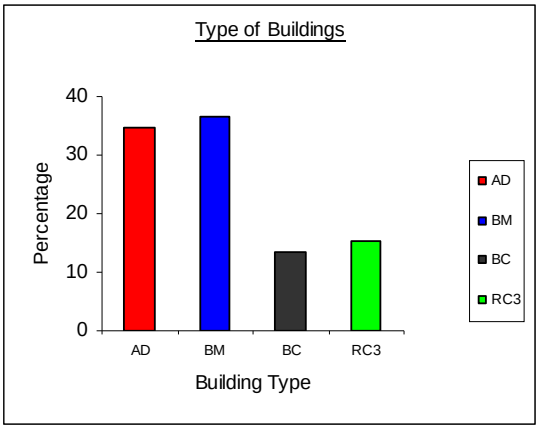

Figure 3 Type of Building in Study Area

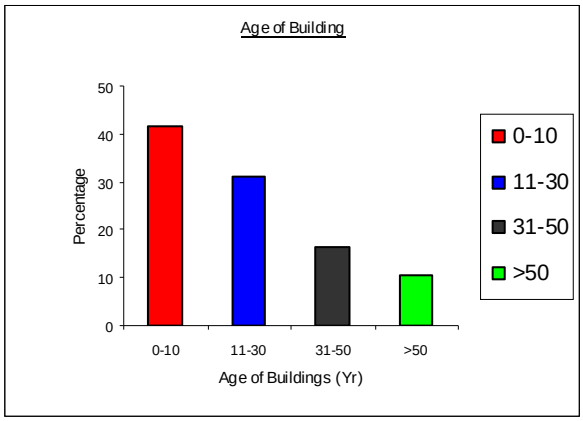

Figure 4 Age of Building in Study Area

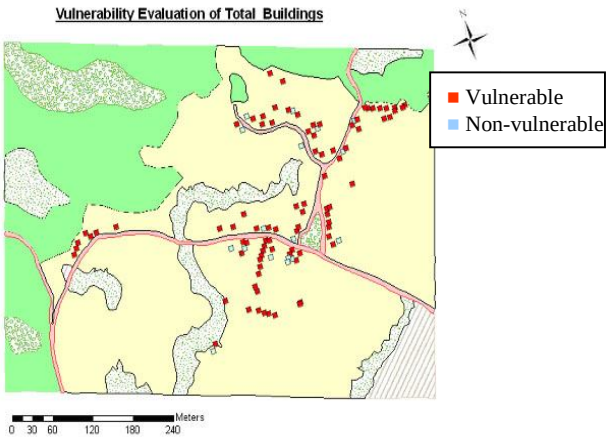

Figure 5 Vulnerability of Building in Study Area

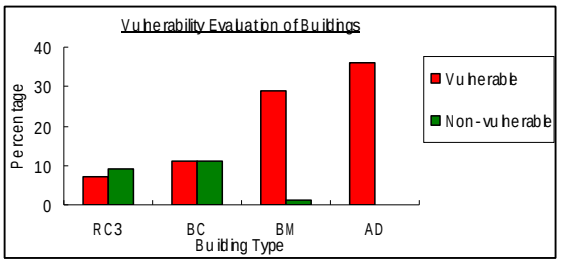

Figure 6 Vulnerability of different type of buildings in study area

5. DISCUSSIONS AND CONCLUSIONS

The development of Rapid Visual Seismic Vulnerability Assessment Tool for Kathmandu Valley was done considering three objectives: to review existing methods of seismic vulnerability assessment to find out their appropriateness for vulnerability assessment of buildings of Kathmandu Nepal, to develop Rapid Visual Seismic Vulnerability Assessment Tool that should be simple and easy to understand, and to apply the tool for vulnerability assessment in one of selected areas in Kathmandu Valley. After processing and analyzing the data, the following important conclusions are drawn.

1. There exist many approaches for vulnerability assessment from very detailed and complicated ones e.g. detailed Finite Element Method to very simple ones such as Rapid Visual Screening of buildings developed by FEMA. Detailed analysis of individual buildings is not a feasible option because of its time consuming feature and unavailability of detailed design and drawing of buildings. Although the simple method such as the one developed by FEMA is very useful tool, it cannot be used for the context of Kathmandu because of difference in building types and social acceptance level.
2. The basic score basically depends upon the type of buildings. The simple two stories rectangular Brick Masonry Buildings constructed with cement sand mortar without any irregularities can sustain the maximum scenario earthquake without collapse (life sustaining damage). From these types of buildings a minimum structural safety can be achieved. For such buildings a basic structural score 2 is assumed which is also taken as cut-off score for the evaluation of building vulnerability. The basic score for AD, BM, BC, RC3 and RC5 buildings are calculated as1, 1.5, 2, 3 and 2 respectively.
3. Vulnerability of building is evaluated based on the total score of the building. If the building score is less than 2, the building is considered as vulnerable building and if building score is more than or equal to 2, the building is considered as non-vulnerable building. The probable damage can be estimated based on EMS- 98 on the score of developed tool as follows:
   a. Score ≥ 2 – High probability of 2 or less Grade damage;
   b. Score < 2 – High probability of 3 or more Grade damage.
4. By using developed tool, the Rapid Visual Seismic Vulnerability Assessment of one of the selected area in Duwakot-5 and Jhaukhel-4 shows that about 16% of buildings are non-vulnerable and 84% buildings are vulnerable. This is because the most dominant types of buildings in that area are AD and BM and the current construction practices still use mud mortar in Brick Masonry buildings without earthquake resistant features.

References:

Arya, A. S., 2006, "Masonry and timber structures including earthquake resistant design" Nem Chada and Bros., Roorkee (UP), 424p.

ATC – 13, 1982, "Earthquake damage evaluation data for California", Applied Technology Council (ATC), Redwood city, California, 492p.

Bothara, J.K., Parajuli, Y.K, Arya, A.S., and D Sharpe, R., 2000, "Seismic safety in owner-built buildings" *Proceedings of the 12th World Conference on Earthquake Engineering*, Auckland Newzeland.

Dixit, A.M., Dwelly-Samant, L., Nakarmi, M., Tucker, B. and Pradhanang, S.B., 1999, "The Kathmandu Valley earthquake risk management action plan," Implemented by National Society for Earthquake Technology (NSET), Nepal and GeoHazards International (GHI), 37p.

FEMA 154, 1988, "Rapid visual screening of buildings for potential seismic hazards: a handbook," Applied Technology Council, Redwood City, California, 185p.

FEMA 155, 1988, "Rapid visual screening of buildings for potential seismic hazards: supporting documentation," Applied Technology Council, Redwood City, California, 137p.

Gupta, S. P., 1988, "Eastern Nepal earthquake 21 August 1988, damage & recommendations for repairs and reconstruction," Asian Disaster Preparedness Center, Asian Institute of Technology, Bangkok, Thailand, 135p.

HAZUS-MH MR1, 2003, "Multi-hazard loss estimation methodology, earthquake model, advanced engineering building module, a technical and user's manual," Department of Homeland Security, Emergency Preparedness and Response Directorate, FEMA Mitigation Division, Washington D.C.

IS 1893 (Part I):2002, "Criteria for Earthquake Design of Structures Part I General Provisions & Buildings (Fifth Revision)," Bureau of Indian Standards, Manak Bhavan, New Delhi, 39p.

ISDR, 2002, "Living with risk: a global review of disaster reduction initiatives," International Strategy for Disaster Reduction, Geneva.

JICA, 2002, "The Study on earthquake disaster mitigation in the Kathmandu Valley Kingdom of Nepal," Japan

International Cooperation Agency (JICA) and Ministry of Home Affairs, His Majesty's Government of Nepal, volume I, Summary, 110+p, volume III, Main Report 2/2, Earthquake Disaster Assessment and Data Base System, 76+p.

NSET, 2000, "Seismic vulnerability of the public school buildings of Kathmandu Valley and methods for reducing it," National Society for Earthquake Technology- Nepal (NSET), 64+p.

NBC 105, 1994, "Seismic design of buildings in Nepal," His Majesty's Government of Nepal, Ministry of Housing and Physical Planning, Department of Buildings, Nepal, 105p.

NBC 109, 1994, "Masonry: unreinforced," His Majesty's Government of Nepal, Ministry of Housing and Physical Planning, Department of Buildings, Nepal, 37p.

NBC 202, 1994, "Mandatory rules of thumb load bearing masonry," His Majesty's Government of Nepal, Ministry of Housing and Physical Planning, Department of Buildings, Nepal, 49p.

NBC 203, 1994, "Guidelines for earthquake resistant building construction: low strength masonry," His Majesty's Government of Nepal, Ministry of Housing and Physical Planning, Department of Buildings, Nepal, 54+p.

RADIUS, 1999, "Risk assessment tools for diagnosis of urban areas against seismic disasters," *IDNDR, United Nations* (http://geohaz.org/radius/)

Roca, A., Goula, X., Susagna, T., Chavez, J., Gonzalez, M. and Reinoso, E., 2006, "A simplified method for vulnerability assessment of dwelling buildings and estimation of damage scenarios in Catalonia Spain," *Bulletin of Earthquake Engineering*, 4, 141-158.

UNDP, 1994, "Seismic hazard mapping and risk assessment for Nepal," His Majesty's Government of Nepal, Ministry of Housing and Physical Planning, UNDP/UNCHS(Habitat) Subproject NEP/88/054/21.03.

Vaseva, E., Marinkostov, Kolera, N., Stefanov, D., Kaneva, A., 2003, "Seismic vulnerability assessment of building stock in a given region according to EMS 98" *Fifth National Conference on Earthquake Engineering*, 26-30 May 2003, Istabbyk, Turkey, Paper No: AE-005, 9p.

JOINT CONFERENCE PROCEEDINGS
7th International Conference on Urban Earthquake Engineering (7CUEE) &
5th International Conference on Earthquake Engineering (5ICEE)
March 3-5, 2010, Tokyo Institute of Technology, Tokyo, Japan

DAMAGE ESTIMATION OF WATER DISTRIBUTION PIPES FOLLOWING RECENT EARTHQUAKES IN JAPAN

Yoshihisa Maruyama[1] and Fumio Yamazaki[2]

1) Associate Professor, Dept. of Urban Environment Systems, Chiba University, Japan
2) Professor, Dept. of Urban Environment Systems, Chiba University, Japan
ymaruyam@tu.chiba-u.ac.jp, yamazaki@tu.chiba-u.ac.jp

Abstract: In this study, fragility curves for water distribution pipes are constructed and used to simulate the distribution of water pipe damage from the Tokyo Metropolitan scenario earthquake in Chiba Prefecture. The damage ratio of water distribution pipes is assumed to follow the scaled log-normal distribution, which is evaluated using the weighted least squares method. The results of this study suggest that the relationship, obtained only from the dataset after the Kobe earthquake, between the peak ground velocity and the damage ratio of water distribution pipes can overestimate the damage ratio.

1. INTRODUCTION

To enhance earthquake security, various governmental organizations in Japan make predictions regarding earthquake-induced damages. For some earthquake source faults, the ground motion intensity and the occurrence of liquefaction are estimated for several events, taking into consideration the geological and topographical conditions. The number of collapsed buildings, burned-out houses, casualties, etc. are derived from the estimated ground motions. Also predicted are the loss of lifeline systems (Hoshiya et al. 2004), e.g., disrupted water and gas supplies, electricity failure, etc. On the basis of various kinds of impacts due to scenario earthquakes, disaster prevention planning and countermeasures are designed by local governments.

Regarding the water supply infrastructure, we assume that only incidents of damage to buried pipes will disrupt water supply. Isoyama et al. (2000) developed the fragility curve of water distribution pipes based on the damage dataset from the 1995 Kobe earthquake in Japan, and this fragility curve was widely used to estimate the number of damage incidents (pipe breaks) after scenario earthquakes. Recently, modifications have been made to estimate damage incidents of water distribution pipes (Kuwata and Takada 2003). Because several events that caused damage to water distribution pipes in Japan have occurred, the fragility curve, which is constructed primarily from the damage dataset of a single event (the Kobe earthquake), can be empirically revised.

In this study, damage datasets from the 1995 Kobe, 2004 Niigata Chuetsu, 2007 Noto-Peninsula, and 2007 Niigata Chuetsu-oki earthquakes are compiled to construct a fragility curve for water distribution pipes. A scaled log-normal distribution is employed for the fragility function. In addition, the damage ratios of water distribution pipes in Chiba Prefecture, Japan, after the scenario Tokyo Metropolitan earthquake are illustrated.

2. METHOD OF ESTIMATING THE DAMAGE RATIO OF WATER DISTRIBUTION PIPES

To estimate the damage ratio of water distribution pipes (i.e., the number of damage incidents per kilometer of water pipe), Isoyama et al. (2000) proposed the following formula:

$$R_m(v) = C_p C_d C_g C_l R(v) \tag{1}$$

where R_m is the damage ratio, C_p, C_d, C_g, and C_l are correction coefficients for the pipe material, diameter, geological condition, and liquefaction occurrence, respectively, and v is the peak ground velocity (PGV).

$R(v)$ estimates the damage ratio for cast iron pipe (CIP) with a diameter of 100–150 mm and is given as

$$R(v) = c(v - A)^b \tag{2}$$

where b, c, and A are regression coefficients. On the basis of the damage dataset for the 1995 Kobe earthquake, Isoyama et al. (2000) obtained the following result for $R(v)$:

$$R(v) = 3.11 \times 10^{-3}(v - 15)^{1.30} \tag{3}$$

In that study, A was assumed to be between 0 and 30 cm/s, and regression analyses were performed by changing A in an interval of 5 cm/s. A was determined to be 15 cm/s because it was for this value that the correlation coefficient between the PGV and damage ratio attained its maximum value.

The constant A gives the minimum PGV that causes damages to water distribution pipes. Thus, the results of Isoyama et al. (2000) given in Eq. (3) indicate that water distribution pipes fail for PGVs greater than 15 cm/s. The constant A obtained from analyzing damage datasets of other earthquake events is sometimes different. For example, the following formula is used to simulate the number of damage incidents for water pipes in the Metropolis of Tokyo (2006):

$$R(v) = 2.24 \times 10^{-3} (v - 20)^{1.51} \qquad (4)$$

3. FRAGILITY CURVE FOR WATER DISTRIBUTION PIPES CONSIDERING RECENT DAMAGE DATASETS

3.1 Damage Dataset from Recent Earthquakes

The damage datasets from the 2004 Niigata Chuetsu, 2007 Noto-Peninsula, and 2007 Niigata Chuetsu-oki earthquakes are also considered in the current study. The damage dataset from the Kobe earthquake gives the damage ratio of water distribution pipe in a 2 x 2 km square area centered on a seismic observation station. Although there are 27 seismic observation stations in the dataset, the 8 damage ratios associated with seismic motion affected by liquefaction and structural responses were excluded from the dataset.

Regarding the three recent earthquakes, detailed damage datasets such as that of the Kobe earthquake are not available. The Health, Labor, and Welfare Ministry of Japan (2004) and the Japan Water Works Association (JWWA 2007) reported the number of damage incidents to the water pipes in every municipality. Because the intensity of ground motion depends on the local topography and the subsurface geological conditions, it is desirable to use a detailed damage dataset such as that of the Kobe earthquake. On the other hand, more damage datasets are expected to be used as long as the fragility curve is empirically obtained. This study includes the damage datasets from three recent earthquakes to investigate differences in ground motion characteristics among earthquake events. In this study, we also compiled the damage ratios from 2 municipalities (Ojiya and Nagaoka) in the 2004 Niigata Chuetsu earthquake, from 5 municipalities (Monzen, Shika, Anamizu, Wajima, and Nanao) in the 2007 Noto-Peninsula earthquake, and from 5 municipalities (Kashiwazaki, Izumozaki, Nagaoka, Joetsu, and Kariwa) in the 2007 Niigata Chuetsu-oki earthquake to construct the fragility curve.

We determine the reference PGV from the ground motion recorded in every municipality. If multiple accelerometers were installed in a municipality, the PGV observed in an area from where more damage incidents were reported is defined as the reference PGV. Figure 1 shows an example of choosing the reference PGV from multiple ground motion records in a municipality. In the 2004 Niigata Chuetsu earthquake, 4 seismic motion records were available in Nagaoka city. Considering the distribution of damaged water pipe reported by the Health, Labor, and Welfare Ministry of Japan, we selected the PGV at K-NET Nagaoka-shisho (NIED 2009) as the reference value (70.57 cm/s). Table 1 shows the damage dataset for water distribution pipe after the three recent earthquakes. The reference PGVs were mainly selected from the seismometers deployed by the National Research Institute for Earth Science and Disaster Prevention (NIED) and the Japan Meteorological Agency (JMA). The damage ratios of water distribution pipes were correlated with the PVG values for different pipe materials, which include cast iron pipe (CIP), ductile cast iron pipe (DIP), and vinyl pipe (VP).

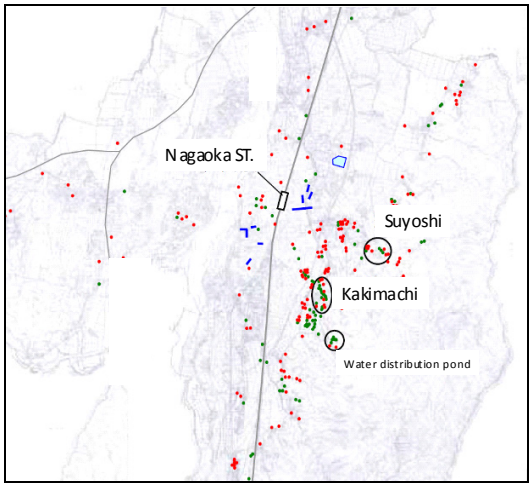

(a)

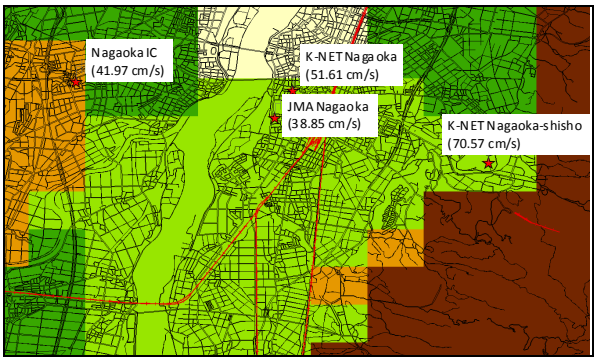

(b)

Figure 1 (a) Location of damaged water distribution pipe in Nagaoka city after the 2004 Niigata Chuetsu earthquake and (b) for seismic observation stations

3.2 Nonlinear Regression Analysis

As shown in Eq. (2), we use a power-law function to estimate the damage ratio of water distribution pipe. If the damage ratio is assumed to follow a power-law function, the

Table 1 Damage dataset for water distribution pipes after the recent earthquakes

Municipality (Seismic observation st.)	PGV (cm/s)	Upper: No. of damage incidents Lower: Length (km) DIP	CIP	VP
2004 Niigata Chuetsu EQ.				
Nagaoka (K-NET Nagaoka-shisho)	70.57	84 777.6	-	154 227.5
Ojiya (JMA Ojiya)	93.5	39 234.4	-	20 29.9
2007 Noto-hanto EQ.				
Monzen (Monzen town office)	110.4*1	15 70.5	-	25 94.2
Wajima (K-NET Wajima)	43.9	1 52.9	3 4.9	8 132.9
Shika (JMA Shika)	55.18	6 198.2	-	13 191.9
Anamizu (K-NET Anamizu)	103.4	7 57.7	0 4	0 26.2
Nanao (K-NET Nanao)	34.79	12 280.8	2 11.5	26 172.4
2007 Niigata Chuetsu-oki EQ.				
Kashiwazaki (Kagami-machi gas holder)	113.7	218 539	13 3.4	249 299.1
Kariwa (Kariwa village office)	156.2	72 52.484	-	17 16.01
Teradomari and Yoita (Nakanoshima city office)	35.5	3 105.2	3 5.7	12 210.1
Kakizaki (Kakizaki ward office)	93.9	7 21.39	-	12 63.3
Izumozaki (JMA Izumozaki)	55.4	0 3.8	-	6 82.2

*1 Estimated value from the peak ground acceleration and JMA seismic intensity

number of damage incidents becomes extremely large under severe ground motion. Hence, the upper limit for the damage ratio of buried pipe is sometimes assigned (Toprak and Taskin 2007). In addition, the lower limit of the PGV [i.e., the constant A in Eq. (2)], which affects the damage ratio, is set according to a series of parameter studies, and is not obtained directly from a regression analysis.

To use the fewest parameters in determining the lowest PGV that cause damage to water distribution pipe and the largest damage ratio, we choose the scaled log-normal distribution (Maruyama et al. 2008). Explicitly,

$$R(v) = C\Phi\left(\left(\ln v - \lambda\right)/\zeta\right) \tag{5}$$

where Φ(x) is the cumulative distribution function of the standard normal distribution, and λ, ζ, and C are constants determined by a regression analysis. With this formula, only three parameters need to be determined to resolve the lowest PGV that causes damage and the largest damage ratio.

We thus performed a nonlinear regression analysis to determine the three parameters in Eq. (5). The error term ε, shown in Eq. (6), was minimized using the quasi-Newton method.

Table 2 Fragility curve parameters determined by nonlinear regression analysis

Material of pipe	ζ	λ	C
CIP and VP	0.860	5.00	2.06
DIP	0.864	6.04	4.99

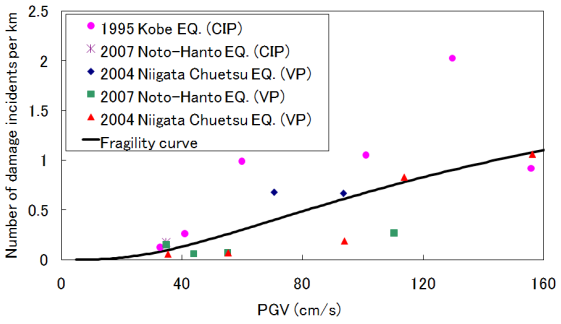

(a)

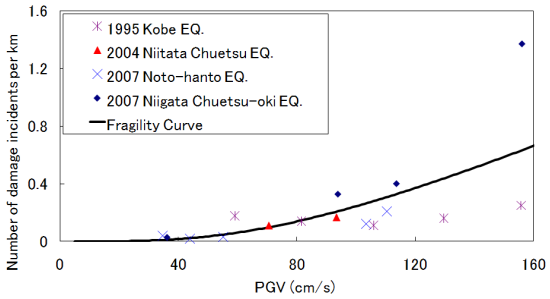

(b)

Figure 2 Fragility curves for water distribution pipe for (a) CIP and VP and (b) DIP

$$\varepsilon = \sum (P_R - R(v))^2 w \tag{6}$$

In this equation, P_R and w represent the actual damage ratio and the length of the water distribution pipe, respectively.

3.3 Fragility Curve for Water Distribution Pipe

The fragility curve for water distribution pipe is constructed on the basis of the damage ratio of CIP in the 1995 Kobe earthquake. Regarding the damage datasets for the three recent earthquakes, CIPs were not widely used as water distribution pipe in the affected areas. Therefore, it is difficult to perform a regression analysis using the damage datasets including the recent earthquakes for CIPs. Conversely, DIPs and VPs were the primary types of pipes used in the areas concerned by the three recent earthquakes. The correction coefficient C_p for the pipe material in Eq. (1) is defined to be 1.0 for VPs on the basis of the damage dataset obtained after the 1995 Kobe earthquake.

On the basis of the correction coefficient C_p and the damage datasets for the recent earthquakes, the fragility curves for water distribution pipe were constructed to estimate the damage ratio of CIPs, VPs, and DIPs.

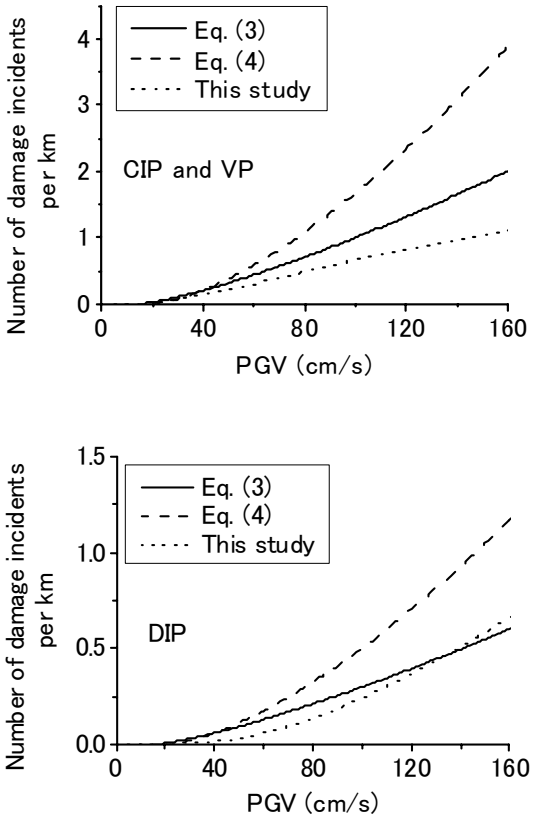

Figure 3 Comparison of the fragility curves for the water distribution pipes

According to statistical data compiled by the JWWA (Nojima 2008), over 50% of water distribution pipes are DIPs. Based on the fact, we also construct the fragility curve for DIPs, which we expect to use in a future research as a standard function for damage estimation.

Table 2 lists the parameters of the obtained fragility curves, which are shown in Fig. 2. Figure 3 compares the fragility curves constructed in the current study with those from Eqs. (3) and (4). The damage ratios for DIP are estimated from Eqs. (3) and (4) by multiplying by C_p, which is set to be 0.3 in the previous study. According to the fragility curves obtained in the current study, the lowest PGV that causes damage to CIPs and VPs is about 20 cm/s, whereas the lowest PGV that causes damage to DIPs is approximately 30 cm/s. Overall, the result of the current study allows one to estimate the minimum number of damage incidents to water distribution pipe.

4. ESTIMATION OF DAMAGE DISTRIBUTION IN CHIBA PREFECTURE DURING THE SCENARIO TOKYO METROPOLIS EARTHQUAKE

To promote earthquake security, local governments in Japan make public predictions of the damages and impacts expected from future earthquakes. Chiba Prefecture estimates the damages of future earthquakes almost every decade, and in the latest damage estimation (Chiba Prefecture 2008), they constructed an earthquake scenario assuming that the epicenter was in the Tokyo Metropolis (M_{JMA} = 7.3). Figure 4 shows the expected PGV and the probability of liquefaction occurrence in different zones of Chiba Prefecture.

For local-government estimates of the damage to water distribution pipe, either Eq. (3) or Eq. (4) is used for the fragility curve. The water-disrupted area, which can be estimated from the spatial density of damage incidents to water distribution pipe, often becomes much larger than the gas-disrupted area. According to the latest estimation by the Tokyo Metropolitan Government (2006), more than 40% of the houses in some eastern districts are assumed to be unable to use water even though the gas supply continues as normal. To close the gap between the water and gas cutoff rates, we first revise the fragility curve of water distribution pipe.

Figure 5 compares the estimated damage ratios of water distribution pipe calculated using Eqs. (3) and (4), and the fragility curve constructed in this study. Both Eqs. (3) and (4) predicted higher damage ratios than the curve from this study did in the Tokyo-Bay areas. Especially, Eq (4) predicts higher damage ratios for the entire area.The results obtained from Eq. (3) and from this study show similar tendencies, although some grid cells have damage ratios higher than 2.0 /km when calculated using Eq. (3).

The predicted damage ratios for Chiba Prefecture were derived from numerical simulations and are therefore not definitive. As long as the fragility curves are constructed empirically, the damage datasets after multiple earthquake events are expected to be considered. In addition, the fragility curves constructed in this study give lower estimations than the previous fragility curves. The gap between the disrupted rates of water and gas can be closed to some extent by using the fragility curves for water pipe proposed herein.

5. CONCLUSIONS

We constructed fragility curves for water distribution pipe considering the damage datasets from three recent earthquakes: the 2004 Niigata Chuetsu, 2007 Noto-Peninsula, and 2007 Niigata Chuetsu-oki earthquakes, and from the 1995 Kobe earthquake. We adopted a scaled log-normal distribution to construct the fragility curves. The lowest PGV for which damage occurs and the largest damage ratio (the number of pipe breaks per kilometer) can be estimated using this fragility.

Compared with previous studies, the fragility curves constructed in the current study lead to lower estimates for the damage ratios of water distribution pipe. Provided the fragility curves are obtained empirically, the curves obtained in this study are preferable because the damage datasets from multiple earthquake events were considered. In some scenario earthquakes, the area where the gas supply is expected to be cut off is much smaller than the area where the water supply is expected to be disrupted. The fragility

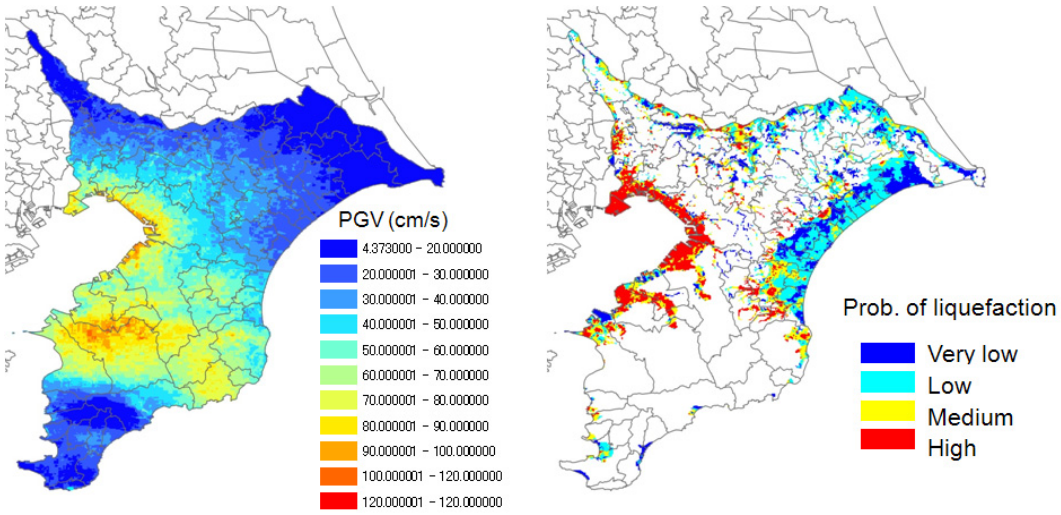

Figure 4 Simulated distribution of the PGV and the probability of liquefaction during the scenario Tokyo Metropolis earthquake

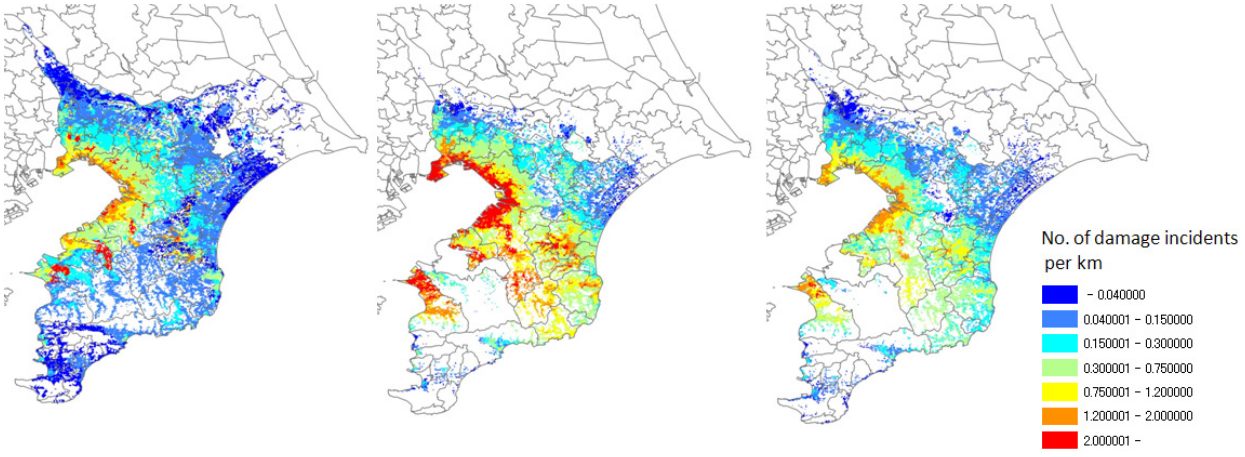

(a) (b) (c)

Figure 5 Comparison of the estimated damage ratios of water distribution pipe in Chiba Prefecture calculated using (a) Eq. 3, (b) Eq. 4, and (c) the fragility curve proposed in this study

curves obtained in this study can close the gap between these predictions.

In a future study, the correction coefficients heretofore determined only from the Kobe earthquake dataset will be revised to include the effects of recent earthquakes.

References:

Chiba Prefecture, Japan. (2008), http://www.pref.chiba.lg.jp/english/index.html

Health, Labor and Welfare Ministry of Japan. (2004), http://www.mhlw.go.jp/topics/bukyoku/kenkou/suido/topics/niigata/index.html (in Japanese)

Hoshiya, M., Yamamoto, K., and Ohno, H. (2004), "Redundancy index of lifelines for mitigation measures against seismic risk," *Probabilistic Engineering Mechanics*, **19** (3), 205-210.

Isoyama, R., Ishida, E., Yune, K., and Shirozu, T. (2000), "Seismic damage estimation procedure for water supply pipelines," *Water Supply*, **18** (3), 63-68.

Japan Water Works Association. (2007), http://www.jwwa.or.jp/houkokusyo/houkokusyo_08.html (in Japanese)

Kuwata, Y., and Takada, S. (2003), "Seismic risk assessment and upgrade strategy of hospital-lifeline performance," *Proceedings of the Sixth U.S. Conference on Lifeline Earthquake Engineering*, 82-91.

Maruyama, Y., Yamazaki, F., Mizuno, K., Yogai, H., and Tsuchiya, Y. (2008), "Development of Fragility Curves for Highway Embankment Based on Damage Data from Recent Earthquakes in Japan," *Proceedings of the 14th World Conference on Earthquake Engineering*, CD-ROM, 8p.

National Research Institute for Earth Science and Disaster Prevention (NIED). (2009), http://www.k-net.bosai.go.jp/

Nojima, N. (2008), "Seismic vulnerability assessment of lifeline networks using vulnerability factor –In application to water distribution pipe–," *Journal of Social Safety Science*, **10**, 137-146 (in Japanese).

Tokyo Metropolitan Government. (2006), http://www.bousai.metro.tokyo.jp/english/index.html

Toprak, S., and Taskin, F. (2007), "Estimation of earthquake damage to buried pipelines caused by ground shaking," *Natural Hazards*, **40**, 1-24.

JOINT CONFERENCE PROCEEDINGS
7th International Conference on Urban Earthquake Engineering (7CUEE) &
5th International Conference on Earthquake Engineering (5ICEE)
March 3-5, 2010, Tokyo Institute of Technology, Tokyo, Japan

POST QUAKE MICROZONING STUDY ON PISCO AND TAMBO DE MORA DUE TO AUGUST 15TH 2007 PISCO QUAKE

Carlos Zavala[1], Zenón Aguilar[2], and Miguel Estrada[3]

1) Professor, CISMID, Structural Lab, Faculty of Civil Engineering Universidad Nacional de Ingeniería, Lima, Perú
2) Professor, CISMID, Geotechnical Lab Faculty of Civil Engineering Universidad Nacional de Ingeniería, Lima, Perú
3) Professor, CISMID, Geomantic Lab Faculty of Civil Engineering Universidad Nacional de Ingeniería, Lima, Perú
czavala@amauta.rcp.net.pe, zaguilar@zergeosystemperu.com, estrada@uni.edu.pe

Abstract: On August 15th 2007 a severe quake occurs on Pisco (200 km from Lima Peru), with heavy damage on non structural buildings and also damage on infrastructure. As a consequence of the quake a Tsunami attacks the coastal area on Pisco and Tambo de Mora. Specially in this last location strong damage was found due to the nature of the soil, where massive liquefaction occurs in front of the shore. This report presents the results of the study of post quake microzoning in the area of Pisco City and Tambo de Mora city. Classification of damage on housing and also on infrastructure is presented. Survey results of the damage are link with the results of a field study developed on the area, to produce seismic microzoning maps using GIS systems. Results shows that in Pisco area soil profile in downtown areas produce amplification of the response on housing and some areas should not be used in future. In Tambo de Mora, field campaign and soil profiles shows that most of the city need to be relocated because the liquefaction problem. Maps of the zones area produced for both locations and recommendation for the decision makers are presented.

1. INTRODUCTION

On August 15th 2007 at 18 hrs., 40 minutes local time, an earthquake of magnitude 8.0 Mw, stroke the south coast of Peru with epicenter at Latitude -13.49° and Longitude: -76.85° with depth of 26 Km. located 74 Km. west of Pisco city. According with INDECI (Peruvian Civil Defense) report, the quake kill 593 persons, with 1,291 injured, and 48,208 collapse houses, and near 90,000 affected houses. Also 14 health services were destroy and 112 health services were affected.

2. DAMAGE ON HOUSING AND TYPES

2.1 Seismic Demand

The damage on a building is related with the seismic demand and the site where the structure is located. According with the Peruvian National Quake Standards (NTE-030), the standard of adobe design (NTE-080) and the standard to build masonry buildings (NTE-070), the structures must resist a severe quake without collapse and moderate quake with acceptable damage among limits of resistance and displacements. A severe quake will demand accelerations in the order of 0.40g, 0.48g and 0.56g on rigid, middle and soft soils respectively. In other words the seismic demand is associated with the soil type and the acceleration of the ground. Better soil gets less demand and bad soil gets more demand. Therefore, a building with more demand has a high probability to be damaged instead of the same structure under low demand.

2.2 Damage Levels

During the Pisco quake the most likely affected buildings were the adobe buildings and the non reinforced masonry structures. Three damage levels were used for classification: Light damage was presented by small cracks (less than 0.5 mm.) on the plaster of the walls, and also small pieces of mortar that fall down from the wall . Moderate damage is presented when small cracks (between 1 mm. to 2 mm.) on walls big pieces of plaster fall down from the walls, cracks on lintels and windows vicinities with diagonal cracks. Severe damage, appears as big cracks on the wall, partial destruction of walls, cracking on part or sections of the structure; collapse of walls and roof in parts or total.

2.3 Damage on Adobe Housing

The adobe houses built on soft soils experience collapse due to the large displacements on soil, the increment of the seismic demand due to site conditions, and due to non reinforce on walls was used on non engineering constructions. Non engineering house don't use any cane, wood, confine element on the ends of walls, therefore, opening of the corners, lost of alignment of walls and overturning on walls (See Photo1 to 4), classifies the damage as severe. As a product of the big displacement, after the damage of walls and the opening of corners appears,

the roof collapse and structural system became unstable and collapse occurs.



Photo 1: Overturning of walls



Photo 2: Collapse of non engineering house



Photo 3: Collapse of roof and walls



Photo 4: Collapse of heavy wood roof

A characteristic of the collapse of walls starts with diagonal cracks on the surrounding area of windows then the area of the wall between the opening and the door is small and very weak, therefore the collapse of the walls occurs. Other characteristic of the adobe walls is lintel beam without enough penetration in the wall, just because these beams don't have enough support on the walls, then horizontal cracks appears and collapse of surrounding adobe blocks broke. If there are not collar beam, strong vertical cracks appears on the corners of walls between walls, the collapse and overturning of walls and collapse of roof.

2.4 Damage on Masonry Housing

On soft soils areas, the houses build with brick masonry walls, but following engineering procedures, experience moderate damage represented by collapse of balconies and non structural walls (see Photos 5, 6 and 7)

Also the collapse of non structural walls due to irregularity is presented on Photo 8. In the process of self construction, many owners used non regulated brick units generating failure on non structural walls or producing collapse on buildings when these walls were used as structural.



Photo 5: Overturning of wall



Photo 6: Damage on non structural wall



Photo 7: Collapse of façade

The masonry structures build by self construction or with irregular configuration or built with non regulated bricks (not permitted by the standards) suffered severe damage and in some cases are impossible to be repaired (see Photo 9, Photo 10 and Photo 11).

Many buildings in the city with severe damage or

collapse were mix structures with first floor of adobe and second floor of masonry (see Photo 12), this type of building is not regulated and is considered a non engineering structure.



Photo 8: Damage due to irregularity


Photo 9: Collapse due to cut on belt beam


Photo 10: Collapse due to irregularity


Photo 11: Collapse due to soft story


Photo 12: Failure on mix building

3. DAMAGE ON TAMBO DE MORA

3.1 Damage due to Tsunami

For the city of Tambo de Mora city the damage had two sources: the tsunami and also the nature of the soft soil with high water level with strongly high potential of liquefaction.

As a consequence of Pisco quake, 23 minutes after the event a tsunami affected the coast of Pisco and Tambo de Mora cities, where the last city was severely affected by the tsunami. Over the coastal line, the tsunami flooded the houses until 1.0 m. where DHN reports that the water reached the level 2.91 m. over the sea.

Flooding on agriculture zones at the south of Tambo de Mora, and also on the Jail of the city and the industrial area where also reported, but the most affected area was the coastal residential area.

A simulation of the tsunami wave propagation (run up, Figure 1) was developed. Then, considering the Yamaguchi theory were determined the of arrival time of the wave to the shore and theoretically floods surface presented in Figure 2, were the extreme run up for the study area was considered.

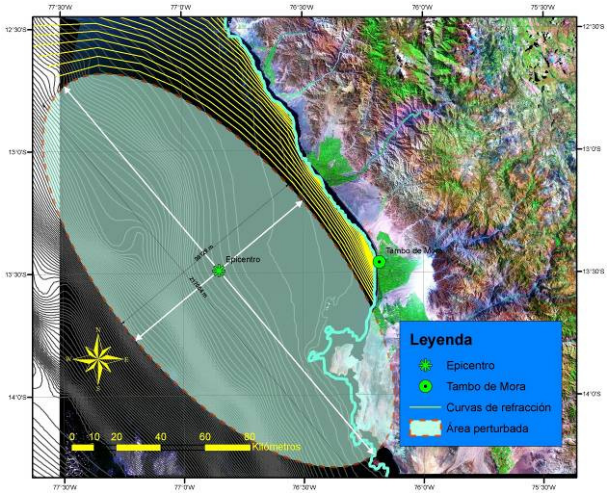

Figure 1: Refractions curves of Tsunami of Pisco Quake at Tambo de Mora

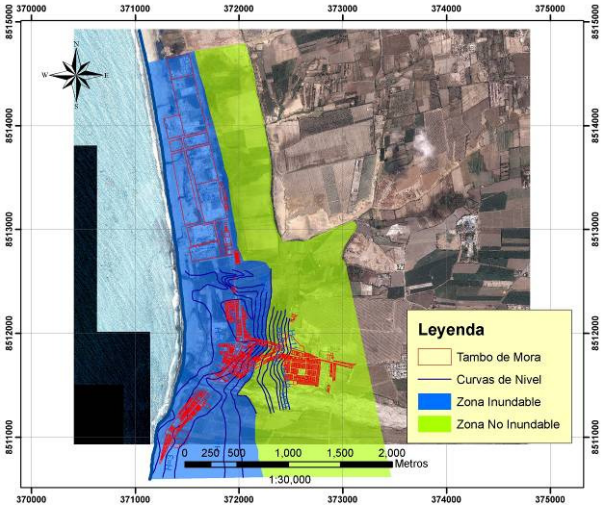

Figure 2: Run up for Extreme Tsunami on Tambo de Mora

3.2 Damage due to Liquefaction

In the case of Tambo de Mora which is located about 100 Km. of the quake epicenter, the nature of the soil with high liquefaction potential produce severe damage and collapse on the structures. On Photos 13 and 14, the engineering structures of the fence of a tower were severe affected by the liquefaction.



Photo 13: Outside view of tower



Photo 14: Inside view of tower with liquefaction

Photo 15 and 16 are examples of how the houses sunk into the liquefied sand, due to the loss of capacity because the nature of the soil. A general view of the streets on Tambo de Mora city and its damage due to the quake and then the tsunami is presented on Photo 17, where it is easy to observe how the water reaches the houses.



Photo 15: Sunk of a house by liquefaction



Photo 16: Collapse of a house by settlement



Photo 17: View of the streets due to tsunami and liquefaction

The flood generated by the tsunami were recorded on three zones on Photo 18, where adobe houses were affected by the floods and also the agriculture areas were inundated by tsunami.



Photo 18: Records of the floods due to tsunami

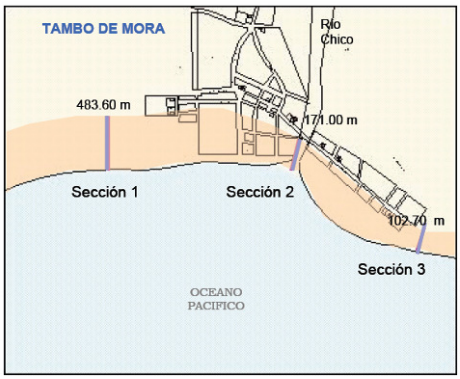

Figure 3: Inundation levels by DHN 15/8/2007

Based on the information of DHN, the tsunami affect not only Tambo the Mora location, also damage was reported on Paracas peninsula, where the water reached almost the level of 7 m over the sea in a large area of 5 km. Tsunami risk analysis reported by DHN found a maximum inundation level of 6 m. for the extreme tsunami for areas like Pisco, Paracas and Tambo de Mora. However during Pisco quake the water reached the level of 3.0 m in the areas on the agriculture areas, located on section 3 of Figure 3 (Photo 18 right photo), a level of 2.6 m. on urban areas, located on section 2 of Figure 3 (Photo 18, left photo), and level 1.73 m. on section 1 of Figure 3.

4. FIELD SURVEY

The authors with the support of professors and students of the Faculty of Civil Engineering of the National University of Engineering carried out a field survey on the two cities involved in the present report with the financial aid of Inter-American Development Bank (IDB) and World Bank (WB). Both cities are located on the coast. However the damage characterization depends of the demand and also the site conditions where different kinds of soil profiles were found. Pisco has areas of soft soil represented by a mix of sand with gravel with high level of humidity and also a middle soil with gravel and compact sand. Tambo de Mora has two types of soils: soft soil represented by high potential liquefied sand and more compact soil as we are near the cliff. Two campaigns were developed to study the cities of Pisco and Tambo the Mora, to implement the damage characterization presented at the beginning of this report, and record the data on a GIS system.

4.1 Field Survey on Pisco City

Figure 4 shows the results of field survey on Pisco City, by damage for each type of material used in the city. From the total of adobe buildings, 82% collapsed, following by quincha buildings with 65% of collapse. Masonry buildings suffer less from the strike of the quake (slight damage and non damage) with 70% of them without high demand.

If we consider the total of buildings of Pisco city, Figure 3 presents the percentage considering the total number of the buildings. The adobe buildings that collapsed in the city represents 15% of the total and the masonry buildings that collapsed represents 10.7% of the total of housing.

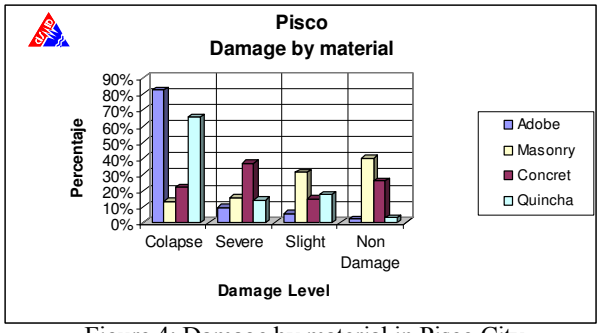

Figure 4: Damage by material in Pisco City

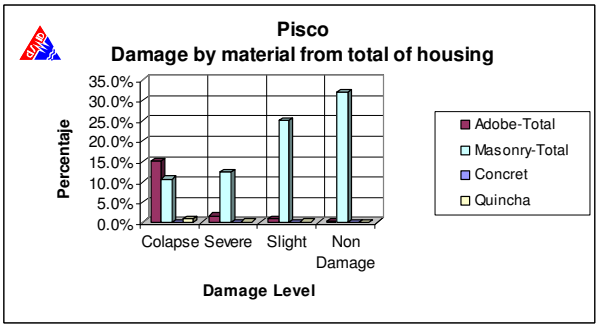

Figure 5: Damage related with total

Figure 6 presents the addition of the collapse plus severe damage in comparison with the addition of slight damage buildings and non damage buildings. It is possible to read that 41.1% of the housing was more affected and collapsed and 58.9% were less affected by the quake. From the severe affected buildings most of them were non engineering structures.

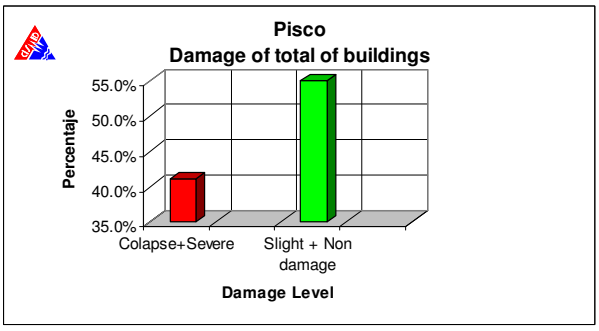

Figure 6: Damage of buildings in Pisco

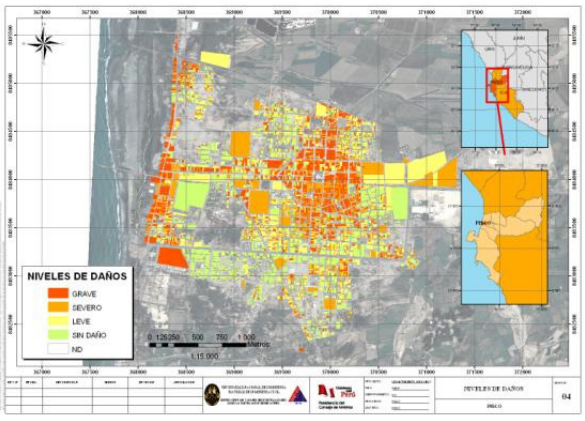

Figure 7: Results of Damage Survey in Pisco

On Figure 7, the red color represents the collapsed structures, in orange the severe damage buildings, in yellow slight damage and light green non damage structures.

4.2 Field Survey on Tambo de Mora

Tambo de Mora city has mainly two kinds of materials on housing: adobe and masonry, so the survey was related with these two kinds of materials. The observed damage was recorded on survey sheets the ones that were implemented on the GIS system.

On Figure 8 presents damage level on adobe housing. It is possible to read that 66% of the houses collapse and 12% had been severely damaged. From the severe affected buildings most of them were non engineering structures.

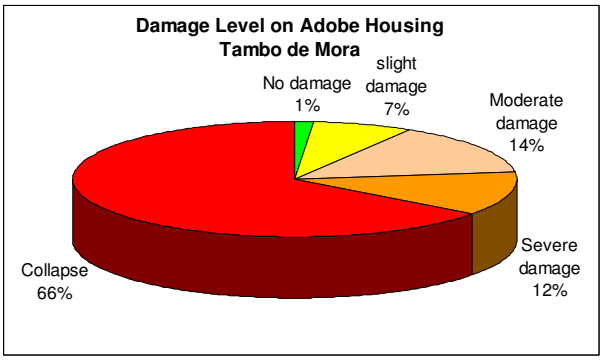

Figure 8: Damage on adobe housing on Tambo de Mora

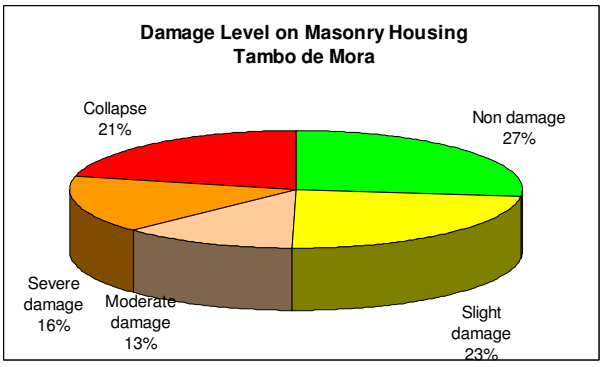

Figure 9: Damage on masonry housing on Tambo de Mora

In the case of masonry houses, Figure 9 presents the damage level for this material. In this case 21% collapsed, and 16% had severe damage. On the other side, the addition of slight damage and non damage houses gave almost 50% . This indicator shows that collapse damage level for masonry structures is lower than adobe buildings.

Figure 10 presents the damage distribution on the city. Red color indicate collapse of the structure, orange indicate severe damage, pink color indicate moderate damage, yellow indicate slight damage and green color shows non damage buildings.

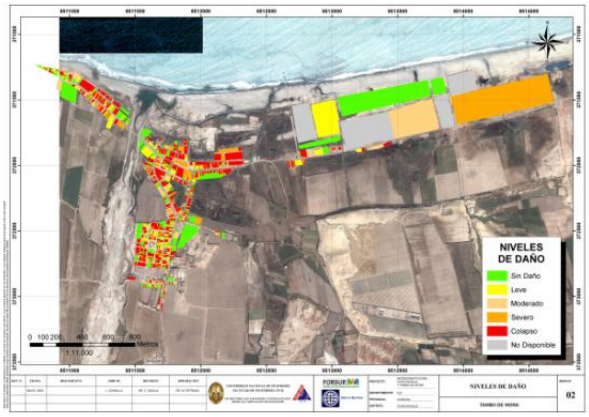

Figure 10: Results of damage survey in Tambo de Mora

5. SEISMIC MICROZONING OF PISCO

A Geotechnical study has been developed by the staff of the CISMID considering the soil profiles and a campaign of boring to determine the capacity and characterization of the soils inside Pisco city. Also dynamic characterization of the soils was performed using Microtremor measurements on soils generating a mesh of soil periods values to produce make the dynamic characterization of the soils.

The soil profiles shows that Pisco city has layers of loose sand and debris with a depth between 0.5 m. to 4 m. This kind of material is not adequate to support buildings specially in the case where the layer is more thick. Under this layer a compacted gravel was found which is adequate for support building foundations. In the north part of the city the underground water level reach depth between 0.5 m. to 2.0 m. Therefore there are four micro zones presented in Figure 11:

- Zone I: with load capacity between 2.0 kg/cm2 to 3.5 kg/cm2 and natural periods less than 0.1 sec.
- Zone II: with load capacity between 1.5 kg/cm2 to 2.0 kg/cm2 and natural periods less than 0.1 sec.
- Zone III: with load capacity between 0.8 kg/cm2 to 1.0 kg/cm2 and natural periods between 0.1 sec to 0.16 sec.
- Zone IV: conformed of soils of debris and wet mud, and also loose sand with high liquefaction potential

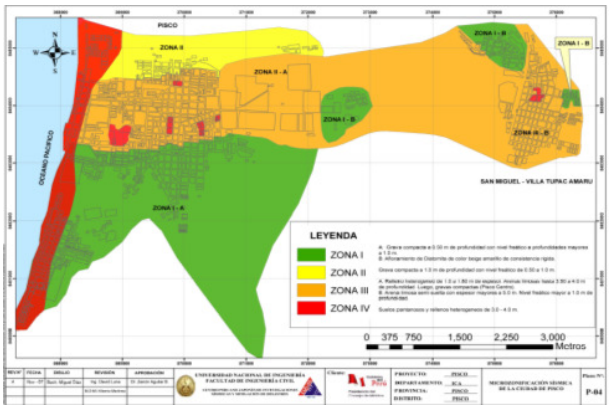

Figure 11: Seismic Microzoning map of Pisco

6. SEISMIC MICROZONING OF TAMBO DE MORA

Using the overlapping of the mechanical behavior, dynamic characterization of soils, potential of liquefaction and inundation surface of tsunami, a microzoning map has been developed for Tambo de Mora city. Three seismic micro zones have been found and presented in Figure 12:

- Zone I: with silt and sand soils of high plasticity and load capacity at 1.2 m. between 2.0 kg/cm2 to 2.5 kg/cm2. The predominant period of this kind of soils is around 0.2 sec.
- Zone II: this soil is an slimy hard clay with a depth between 1.8 to 3.0 m. with load capacity of 1.50 kg/cm2 at 1.0 m. depth. The natural predominant periods of this kind of soils are between 0.15 sec. to 0.2 sec.
- Zone IV: This zone has two geotechnical zones IV-A and IV-B were the phenomena of liquefaction occurs and also tsunami inundation happens. This is the more dangerous zone in the city and must not be considered for house construction.

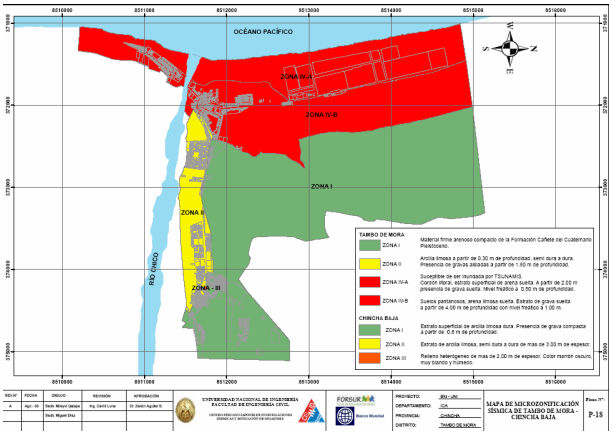

Figure 12: Seismic Microzoning map of Tambo de Mora

7. CONCLUSIONS

- Investigation about the causes and type of damage has been conducted to understand the effects of the 2007 Pisco Earthquake in the affected area.
- Mainly the damage due to the earthquake in Pisco City has been caused by the soil conditions that may amplify the seismic waves, on building materials, like adobe, that have a bad behavior against seismic forces and construction quality that do not comply with the standards.
- As a consequence of 15/8/2007 Pisco quake, damage on housing occurs at Pisco and Tambo de Mora locations, were the most damage construction system was the adobe walls house with 82% of collapse in Pisco and 66% of collapse on Tambo de Mora.
- Masonry housing experiment less damage than adobe due to the confinement of the walls, with only 10% of collapse in Pisco and 21% of collapse in Tambo de Mora. We know the last value is not only related with the material, because in this location liquefaction happens and damage was linked with soil conditions and tsunami inundation.
- It is evident the correspondence between the damage levels and the soil conditions; therefore, the microzoning studies of urban areas constitutes a very important tool for city planning and reconstruction plans.
- Damage levels for both cities were presented. Soft soils and non structural housing were experiment extreme damage on Pisco. In the case of Tambo de Mora city the damage on soft soils is also associated with tsunami inundation.
- Considering the geotechnical campaign and the dynamic characterization of soils, microzoning maps were developed for Pisco and Tambo de Mora cities. In the case of Pisco the center of the city was severe damage due to some of the areas has soft soils and also there are some red spots with debris soils. Here constructions must not be allowable. In the case of Tambo de Mora, due to the high potential of liquefaction of the shore areas and also the tsunami risk, relocation of the population was consider to the zone II by the Local Government.
- It is demonstrated that even in a case of a strong ground motion if the masonry buildings are built following the national standards they do not collapse, given as result the safety of their occupants.
- Liquefaction cause severe damage on buildings that are built on liquefaction prone soils whatever it is its construction type. It is strongly advised to conduct investigation on soils of this type, especially if they are urbanized.
- Also tsunami prone areas should be avoided, the consolidation of urban areas must find a suitable land high enough to avoid the effects of the tsunami. While it is true that a tsunami cannot be avoided, damage to people can be mitigated if people are prepared to act correctly.

Acknowledgements:

The authors acknowledge support from Inter American Development Bank (IDB) and World Bank (WB) for the support this research. Also, our gratitude to the Secretary of First Ministry Board, to trust on our Institution in the development of this microzoning studies. Finally we would like to express our gratitude to all our staff members, specially our young researchers who collaborated in the field survey and implementation of GIS data.

References:

CISMID-FIC-UNI. (2007). Microzoning of Pisco, San Luis de Cañete and Huaytara. Report for Inter American Development Bank (IDB) and Secretary of the Presidency of First Minister (PCM), Lima, PERU.

CISMID-FIC-UNI. (2008). Microzoning of Tambo de Mora and Chincha Baja. Report for World Bank (WB) and FORSUR Ministry of Housing, Lima, PERU.

Dirección de Hidrografía y Navegación Marina de Guerra del Perú (DHN), Reporte del Tsunami del 15/8/2007, Lima PERU.

JOINT CONFERENCE PROCEEDINGS
7th International Conference on Urban Earthquake Engineering (7CUEE) &
5th International Conference on Earthquake Engineering (5ICEE)
March 3-5, 2010, Tokyo Institute of Technology, Tokyo, Japan

ENHANCEMENT OF EARTHQUAKE AND TSUNAMI DISASTER MITIGATION TECHNOLOGY IN PERU: A SATREPS PROJECT

Fumio Yamazaki[1], Carlos Zavala[2], Shoichi Nakai[3], Shun'ichi Koshimura[4], Taiki Saito[5] and Saburoh Midorikawa[6]

1) Professor, Graduate School of Engineering, Chiba University, Japan. yamazaki@tu.chiba-u.ac.jp
2) Professor, CISMID, National University of Engineering, Peru. czavala@uni.edu.pe
3) Professor, Graduate School of Engineering, Chiba University, Japan. nakai@faculty.chiba-u.jp
4) Associate Professor, Graduate School of Engineering, Tohoku University, Japan. koshimura@tsunami2.civil.tohoku.ac.jp
5) Senior Researcher, Building Research Institute, Japan. tsaito@kenken.go.jp
6) Professor, Center for Urban Earthquake Engineering, Tokyo Institute of Technology, Japan. smidorik@enveng.titech.ac.jp

Abstract: This project aims to conduct a comprehensive research towards earthquake and tsunami disaster mitigation in Peru considering regional characteristics, under strong collaboration among researchers of Peru and Japan. Five main research activities are the followings: 1) Strong motion prediction and development of seismic microzonation; 2) Development of tsunami countermeasures based on numerical simulations; 3) Enhancement of seismic resistance of buildings based on structural experiments and field investigation; 4) Development of spatial information database using remote sensing technology and earthquake damage assessment for scenario earthquakes; 5) Development of earthquake and tsunami disaster mitigation plan and its implementation to the society. After signing of the Record of Discussion (R/D) in January 2010 by the responsible organizations of the two nations, the project has just started and will continue for the five year period. This paper introduces the Japan-Peru earthquake and tsunami disaster mitigation research project.

1. INTRODUCTION

A new international research program named "Science and Technology Research Partnership for Sustainable Development (SATREPS)" has started since 2008 under the joint sponsorship of Japan Science and Technology Agency (JST) and Japan International Cooperation Agency (JICA). The scheme of SATREPS is shown in **Figure 1**. Research proposals in the following three fields were invited to apply for the grant: 1) Environment and Energy, 2) Natural Disaster Prevention, and 3) Infectious Diseases Control. A proposal submitted by the present authors, "Enhancement of Earthquake and Tsunami Disaster Mitigation Technology in Peru," was selected as one of the projects in the field of natural disaster prevention in April 2009.

The project aims to conduct a comprehensive research towards earthquake and tsunami disaster mitigation in Peru considering regional characteristics, under strong collaboration among researchers of Peru and Japan. The first author (F. Yamazaki) is the principal investigator (PI) of the Japanese team and the second author (C. Zavala) is the PI of the Peruvian team. After the nomination of our project, the preparatory phase has started to plan the detail of the joint research, considering the needs of the developing country (Peru) and the promotion of science and technology on the global issue (disaster mitigation).

The Record of Discussion (R/D) was signed on 15 January 2010 by the responsible authorities of the two nations (JICA and National University of Engineering, Peru) in Lima, Peru. Then the project has formally started and will continue for the five year period (until March 2014). This paper describes the overall objectives and joint research plan of the project.

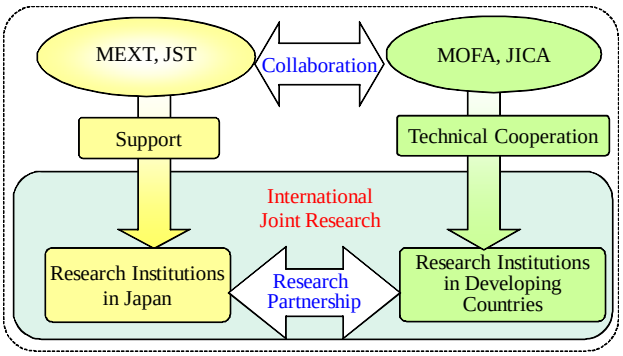

Figure 1 Scheme of Science and Technology Research Partnership for Sustainable Development (SATREPS) (http://www.jst.go.jp/global/english/about.html)

2. BACKGROUND AND OBJECTIVES OF THE PERU PROJECT

Natural disasters are one of the major threads for people in the world. Especially for the countries in the Asia-Pacific region, earthquakes and tsunamis are the major obstacles towards sustainable developments. In order to reduce disaster risks, understanding of natural hazards and upgrading of societal resilience are necessary. Since earthquakes and tsunamis are rare but devastating events, the data collection in a global scale is necessary and international collaboration is inevitable to reduce the losses due these events, as highlighted in Hyogo Framework of Action (International Strategy of Disaster Reduction (ISDR), 2005). In this sense, Japan is expected to serve a leading role in the promotion of international disaster mitigation because of its long history to cope with natural disasters.

Peru locates in the circum-Pacific seismic belt with high seismic and tsunami risks. **Figure 2** shows the tectonic settings and the epicenters of earthquakes in Peru and the surrounding region. It is seen that both Peru and Japan are located in a similar seismic environment, frequently hit by damaging earthquakes and tsunamis In this region, large plate-boundary earthquakes occurred recently in the offshore of Atico (M_w=8.4, 23 June 2001) and in the offshore of Pisco (M_w=8.0, 15 August 2007). A large number of buildings and infrastructures were destructed, hundreds of people were killed, and tsunamis were also generated by these events. Thus, earthquake and tsunami disaster mitigation draws considerable attentions in Peru.

Not just physical similarities of the two countries, Peru and Japan have a long term relationship since 1873, when the official relation has started. A large number of immigrants from Japan settled down in Peru in the early 20 century.

The relationship in the field of disaster mitigation technology also has some history. Japan-Peru Center for Earthquake Engineering and Disaster Mitigation (CISMID) was established within National University of Engineering (UNI) in 1987 by the support of Government of Japan. CISMID became the leading center of earthquake engineering research in South America. CISMID has been in collaboration with many Japanese research institutions, notably, Building Research Institute in Tsukuba, Japan.

Significance of this joint research between Peru and Japan can be summarized as the four points: 1) contribution of Japanese science and technology to disaster mitigation in Peru, 2) providing research fields to Japanese geoscience and earthquake engineering, 3) contribution to international tele-tsunami research for subduction-zone earthquakes, e.g. 1960 Chile earthquake, and 4) promotion of disaster mitigation and capacity building through sharing the knowledge from the international joint research.

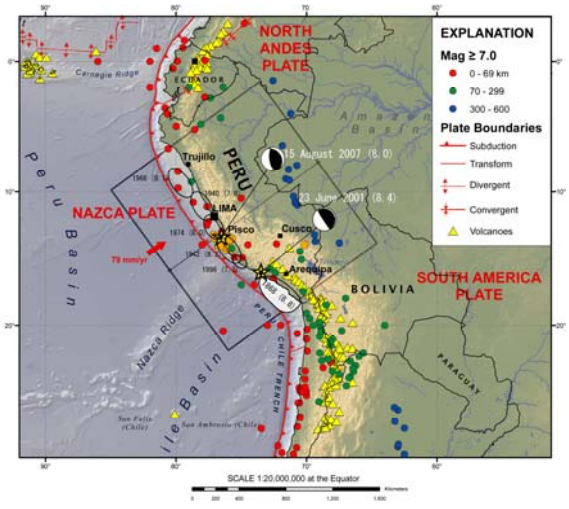

Figure 2 Tectonic setting and the epicenters of earthquakes in Peru and the surrounding region (modified from USGS (2007) and Chlieh et al. (2004))

3. OVERALL RESEARCH PLAN AND ORGANIZATIONAL STRUCTURE

In this research project, a comprehensive research towards earthquake and tsunami disaster mitigation in Peru will be carried out under strong collaboration among researchers of Peru and Japan. **Figure 3** shows the organizational structure of this five year projects. The joint research will be carried out in five main research topics: 1) Strong motion prediction and development of seismic microzonation; 2) Development of tsunami countermeasures based on numerical simulations; 3) Enhancement of seismic resistance of buildings based on structural experiments and field investigation; 4) Development of spatial information database using remote sensing technology and earthquake damage assessment for scenario earthquakes; 5) Development of earthquake and tsunami disaster mitigation plan and its implementation to the society.

Japanese reaserch team consists of five groups (G1 to G5 in Figure 3; the group leaders are the authors of this paper) corresponding to the five topics.

Peruvian research team consists of CISMID/UNI, National Institute of Civil Defense (INDECI), Geophysical Institute of Peru (IGP), Direction of Hydrology and Navigation (DHN), National Committee for Aerospace

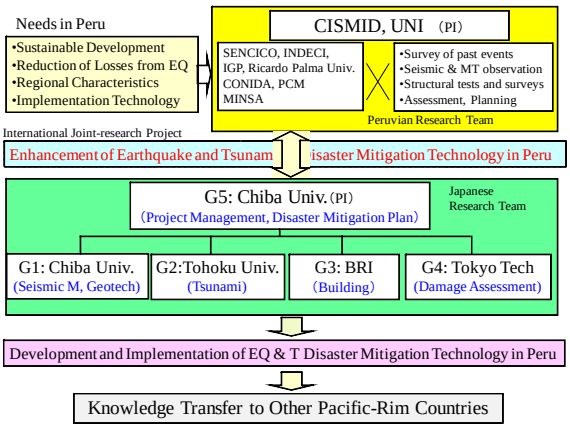

Figure 3 Organizational structure of the project

Research and Development (CONIDA), Disasters Prevention and Study Center (PREDES), National Institute of Culture (INC), Ministry of Housing, Construction, and Sanitation (MVCS), National Service of Training for the Construction Industry (SENCICO), Ricardo Palma University (URP), National Office of Electronic Government and Information (ONGEI-PCM), and Municipalities of the project study areas.

Figure 4 shows the research topics and items of the project and the groups in charge the items. Based on the research outputs from the four groups (G1-G4), the disaster mitigation plan group (G5) will propose and implement earthquake and tsunami disaster mitigation plans to case study areas in Peru. Three case study areas will be decided soon after preliminary surveys. A part of Metropolitan Lima including Callao has already selected as one of the study areas. The other two areas are still in discussion; currently, Chimbote in the north and Moquegua or Tacna in the south are possible candidates. Other than these areas, the affected areas due to the recent earthquakes, Pisco (the 2007 event) and Camana, Arequipa etc. (the 2001 event), will also be considered in developing hazard and damage assessment models.

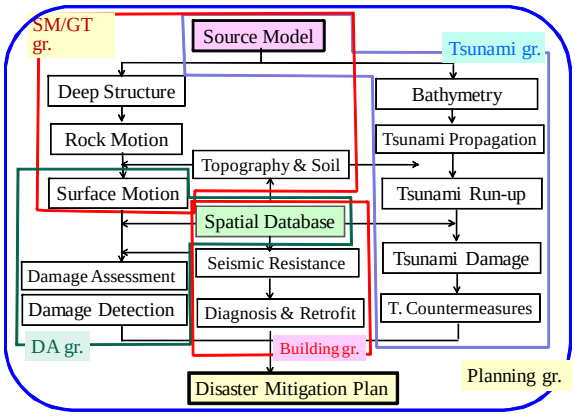

Figure 4 Research topics and items of the project and the groups in charge the items

4. IMPLEMENTATION AND PROSPECTED OUTPUTS OF THE PROJECT

The Japanese Detailed Planning Survey Team organized by JICA visited Peru from August 5 to 13, 2009, for the purpose of working out the details of the technical cooperation program concerning the project. During its stay in Peru, the team exchanged views and had a series of discussions with the Peruvian organizations concerned, led by CISMID/UNI. As a result, the team and the Peruvian organizations concerned agreed on the matters referred to in the document (JICA, 2009).

The objective of this project has agreed as "To develop technologies and measures for assessment and mitigation of earthquake/tsunami disasters caused by large-magnitude inter-plate earthquakes occurring off the coast of Peru." It is further envisaged that such technologies should be widely used in Peru, and also disseminated and applied to pacific-rim countries, especially to neighboring countries, facing the risks of large-magnitude inter-plate earthquakes and tsunamis. In addition, the project is expected to contribute to the enhancement of capacity as well as the advance of research for both Peruvian and Japanese research institutes involved in this project.

The following seven outputs are listed in the master plan agreed.

1. Scenarios of large-magnitude inter-plate earthquakes are identified which will cause the most significant losses in Peru (G1, G2).
2. Geographical information of the study areas is prepared (G4).
3. Tsunami disaster losses in study areas by scenario earthquakes are estimated, and mitigation technologies are developed (G2).
4. Strong motion and ground failure in study areas by scenario earthquakes are simulated (G1).
5. Earthquake disaster losses in study areas by scenario earthquakes are estimated, and mitigation technologies are developed (G4).
6. Technologies for evaluation of seismic-resistance and structural retrofit are developed, adapting to building characteristics of Peru (G3).
7. Earthquake/tsunami disaster mitigation is promoted in the study areas (G5).

Table 1 Schedule of the project

Research Items	Period (2009-2014)				
	1 st	2 nd	3 rd	4 th	5 th
Project Management 【Chiba U and CISMID/UNI】	WS▼	WS▼	WS▼	WS▼	WS▼
G1: Seismic motion & Geotechnical 【Chiba U and CISMID, IGP】 1-1 Source modeling and seismic motion 1-2 Site response & Microzonation 1-3 Slope failure assessment	Source modeling EQ and MT observation, Geological survey Field survey, measurement	Simulation of SM	Seismic Response Analysis	Microzonation Hazard map	
G2: Tsunami 【Tohoku U and DHN, CISMID】 2-1 Tsunami propagation and impacts 2-2 Tsunami hazard mapping 2-3 Tsunami DM technology	Tsunami simulation Data collection Historical tsunami data	Inundation and impact Damage assessment method	Tsunami DM technology	Tsunami damage analysis	
G3: Buildings 【BRI and CISMID】 3-1 Seismic tests database 3-2 Diagnosis and Retrofit 3-3 Retrofit of historical buildings	Literature Survey, Tests Develop diagnosis method Survey, Risk assessment	Retrofit technology, Validation tests Retrofit Technology	Database development	Guideline Guideline	
G4; Damage Assessment 【Tokyo Tech and CISMID, CONIDA】 4-1 Geo-spatial database 4-2 Damage detection using RS 4-3 Damage assessment for Scenario EQ	Data collection Data collection Damage assessment method	Geospatial data Methodology	Database development Damage detection Assessment, risk map		
G5; Disaster Mitigation Plan 【Chiba U and INDECI, CISMID】	Literature Survey		Planning	Dissemination, Education	

The schedule of the five-year project is shown in **Table 1**. To implement the project, JICA will provide the services of the JICA experts (Japanese research members), machinery, equipment and other materials necessary for the implementation of the project, and will receive the Peruvian personnel connected with the project for technical training in Japan. The actual joint research will be carried out by the five joint research groups in Table 1.

Other than group-based technical collaborations, the leading members of the project will meet annually either in Peru or Japan in the occasion of project workshops. The first project workshop will be held soon in Lima on March 15

and 16, 2010. About 25 researchers from Japan and scores of researchers/engineers/stakeholders from Peru will attend this workshop. Earthquake engineering researchers from the surrounding Latin American countries will also participated in the workshop.

The Joint Coordinating Committee (JCC) will be organized soon to oversight the project and meet at least once a year and whenever necessity arises, in order to fulfill the following functions (JICA, 2009):

(1) To approve the annual work plan of the project
(2) To review the progress of the annual work plan
(3) To review and exchange opinions on major issues that may arise during the implementation of the project
(4) To discuss any other issue(s) pertinent to the smooth implementation of the project

5. DETAILED RESEARCH PLANS AND ACTIVITIES

To obtain the expected outputs, the following research activities are planned for the five research groups.

5.1 Source, Seismic Motion and Geotechnical Issues

1-1 Surveying historical records of earthquakes, and grasping the characteristics of inter-plate earthquakes occurring off the coast of Peru
1-2 Developing earthquake source models that are suitable to the characteristics of inter-plate earthquakes occurring off the coast of Peru
1-3 Having preliminary estimation of earthquake/tsunami disaster losses using the source scenarios, and identifying the most devastating scenarios of inter-plate earthquakes
1-4 Observing microtremor in the study areas
1-5 Developing seismic observation networks in the study areas, and observing strong seismic motions
1-6 Collecting existing geological data of the study areas, and undertaking supplementary borehole surveys
1-7 Modeling deep and subsurface ground structures of the study areas
1-8 Simulating strong motions and ground failures in accordance with the inter-plate earthquake scenarios

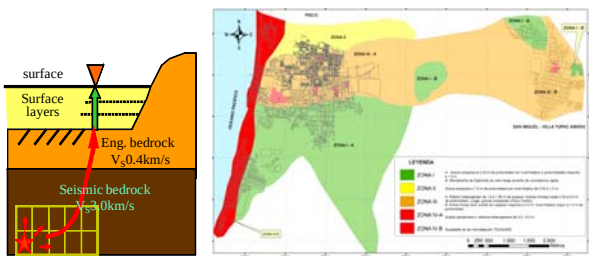

Figure 6 Scheme of simulation of seismic motion (left) and an example of seismic microzonation (right)

5.2 Tsunami Simulation and Damage Mitigation

2-1 Surveying historical records of tsunamis, and grasping the characteristics of tsunami propagation along the Pacific coast of Peru
2-2 Preparing merged bathymetry and topography data of the coastal zones of the study areas
2-3 Evaluating vulnerability of buildings and infrastructures in the study areas
2-4 Simulating tsunami propagation and run-up in accordance with the earthquake scenarios, and estimating tsunami disaster losses
2-5 Making tsunami hazard maps for the study areas
2-6 Making guidelines of designing emergency evacuation facilities

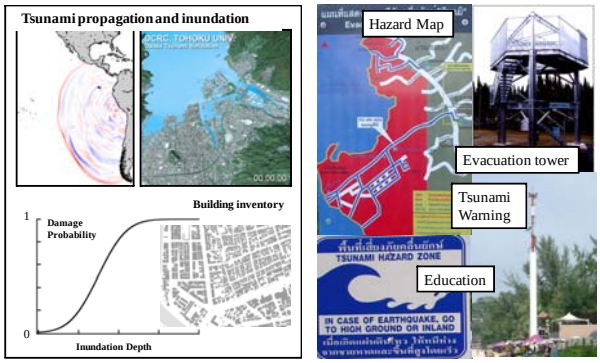

Figure 7 Scheme of tsunami simulation and damage assessment (left) and tsunami countermeasures (right)

5.3 Enhancement of Seismic Resistance of Buildings

3-1 Developing a database of structural test results and material test results for buildings
3-2 Developing technologies of seismic-diagnosis and retrofit for different types of buildings prevalent in Peru
3-3 Identifying historical buildings in the study areas that face significant earthquake disaster risks
3-4 Verifying the effects of structural retrofit technologies through structural tests and numerical analyses

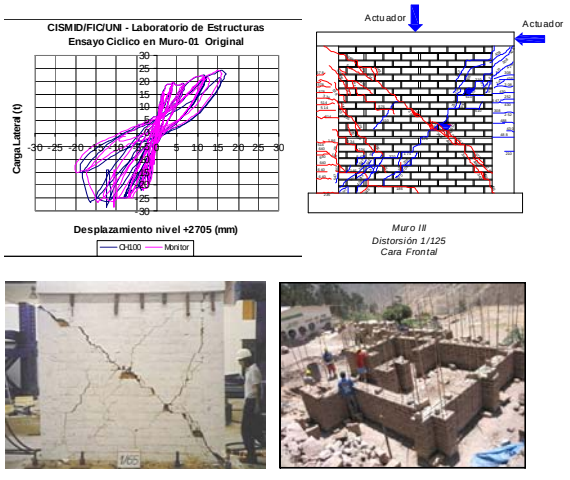

Figure 8 Scheme of structural testing (top) and photos of experiment and construction site (bottom)

5.4 Geo-spatial Database and Damage Assessment

4-1 Making digital surface models (DSMs) of the study areas using satellite images

4-2 Making land-use maps and building maps of the study areas using satellite images

4-3 Estimating earthquake disaster losses of the study areas in accordance with the inter-plate earthquake scenarios

4-4 Developing technology for rapid detection of earthquake/tsunami disaster losses using satellite images

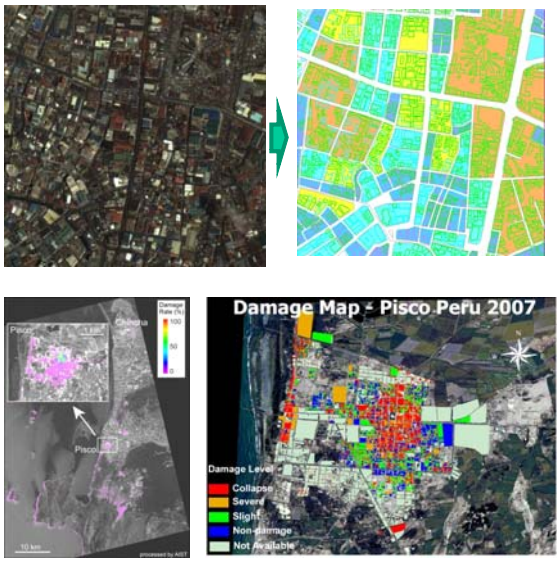

Figure 9 Scheme of developing building inventory (top) and damage assessment of the Pisco earthquake (bottom)

5.5 Development of Disaster Mitigation Plan

5-1 Developing land-use proposals for mitigation of earthquake/tsunami disasters

5-2 Developing local disaster mitigation plans for the study areas

5-3 Undertaking awareness raising and dissemination activities of earthquake/tsunami disaster mitigation for disaster management organizations and local communities

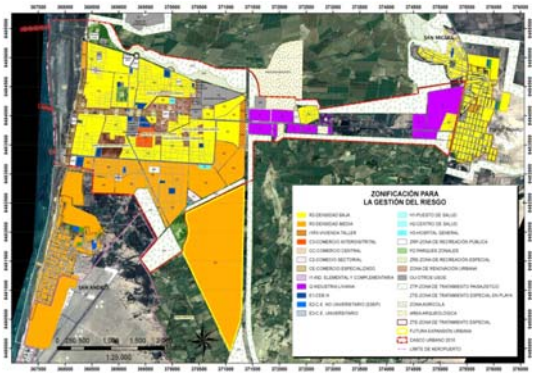

Figure 10 Land-use plan of Pisco city proposed by CISMID after the Pisco earthquake

6. CONCLUSIONS

Under the joint sponsorship of JST and JICA, a new international research program named "Science and Technology Research Partnership for Sustainable Development (SATREPS)" has started, and the proposal submitted by the present authors, "Enhancement of Earthquake and Tsunami Disaster Mitigation Technology in Peru," was accepted in the category of natural disaster prevention. In this paper, the background, objectives and research plan of the project were introduced. The project aims to conduct a comprehensive research towards earthquake and tsunami disaster mitigation in Peru considering regional characteristics, under strong collaboration among researchers of Peru and Japan. The progress of the project will be presented in the near future.

References:

Chlieh, M., de Chabalier, J. B., Ruegg, J. C., Armijo, R.; Dmowska, R., Campos, J., Feigl, K. L. (2004), "Crustal deformation and fault slip during the seismic cycle in the North Chile subduction zone, from GPS and InSAR observations," Geophys. J. Int., 158, 695-711.

ISDR (2005), "Hyogo Framework of Action for 2005-2015: Building the resilience of nations and communities to disasters," http://www.unisdr.org/eng/hfa/hfa.htm

Japan International Cooperation Agency (2009), "Minutes of meeting between JICA detailed planning survey team and the National University of Engineering."

USGS (2007), "Poster of the Ica, Peru Earthquake of 15 August 2007 -Magnitude 8.0, Earthquakes Hazard Program USGS," http://earthquake.usgs.gov/earthquakes/eqarchives/poster/2007/20070815.php

JOINT CONFERENCE PROCEEDINGS
7th International Conference on Urban Earthquake Engineering (7CUEE) &
5th International Conference on Earthquake Engineering (5ICEE)
March 3-5, 2010, Tokyo Institute of Technology, Tokyo, Japan

SEISMIC LOSS ESTIMATION FOR THREE MAJOR CITIES IN BANGLADESH

Pennung Warnitchai[1], Matrin Suthasit[2], Chaiyapat Suesutajit[3], and Kawin Worakanchana[4]

1) Associate Professor, School of Engineering and Technology, Asian Institute of Technology
2) Doctoral Student, School of Engineering and Technology, Asian Institute of Technology
3) Former Research Associate, School of Engineering and Technology, Asian Institute of Technology
4) Former Visiting Researcher, Regional Network Office for Urban Safety, Asian Institute of Technology
pennung@ait.ac.th, suthasit@hotmail.com, heng4004@yahoo.com, kawin@iis.u-tokyo.ac.jp

Abstract: To mitigate earthquake disasters in Bangladesh, the Comprehensive Disaster Management Programme of the Government of Bangladesh engaged an international consulting team consisting of Asian Disaster Preparedness Center (ADPC), Asian Institute of Technology (AIT), National Society for Earthquake Technology of Nepal (NSET), and OYO International Corporation (OIC) to carry out a research project entitled "Seismic Hazard and Vulnerability Mapping of Dhaka, Chittagong, and Sylhet City Corporation Areas". The scope of this project is divided into two main parts: (1) seismic hazard assessment, and (2) seismic loss assessment. This paper focuses on the later part. To conduct a city-scale seismic loss assessment, an integration of multidisciplinary engineering knowledge into a systematic framework is necessary. HAZUS, a multi-hazard loss estimation methodology developed by the Federal Emergency Management Agency of the US (FEMA), provides such a framework and was therefore adopted in this project. The implementation of HAZUS is explained with an emphasis on building related losses. The project works include the development of GIS base maps, building surveys, preparation of input data for HAZUS, development of fragility functions, selection of representative earthquake scenarios, etc. Modifications have been made to several analysis models of HAZUS to make them fit to the specific conditions of Bangladesh. Examples of seismic loss assessment results are presented and discussed. The results are being used for developing a national contingency plan for earthquake disaster management of Bangladesh.

1. INTRODUCTION

Over the past decades the urbanization in Bangladesh has been rapidly taking place without proper guidance. As a result, many urban centers in Bangladesh have been developed haphazardly, and buildings as well as infrastructures were not properly designed and constructed for earthquake resistance. Since there are several seismic sources in the country, there is a possibility of a city being struck by a major earthquake, which would result in disastrous consequences of the entire nation.

To mitigate earthquake disasters, the Comprehensive Disaster Management Programme (CDMP) of the Government of Bangladesh engaged an international consulting team consisting of Asian Disaster Preparedness Center (ADPC), Asian Institute of Technology (AIT), National Society for Earthquake Technology of Nepal (NSET), and OYO International Corporation (OIC) to carry out a comprehensive research project entitled "Seismic Hazard and Vulnerability Mapping of Dhaka, Chittagong, and Sylhet City Corporation Areas".

The main objective of the project is to perform a seismic hazard assessment and a seismic loss assessment for 3 major cities of Bangladesh—Dhaka, Chittagong, and Sylhet City corporation areas. These cities are, respectively, the capital city, the main port city, and one of the most seismically active cities of Bangladesh. The execution of the project started in August 2007 and ended in July 2009. At the time of writing this paper, the project results are being used for developing a national contingency plan for earthquake disaster management of Bangladesh.

The scope of project work was divided into two main parts: (1) seismic hazard assessment, and (2) seismic loss assessment. The former part was carried by the cooperation between ADPC and OIC, and the later part by the cooperation among ADPC, AIT and NSET. This paper focuses on the later part of the project.

In order to carry out a seismic loss assessment in a city scale, an integration of multidisciplinary engineering knowledge into a systematic framework is necessary. There are several well recognized methodologies for such purpose, e.g., KVERMP methodology, GIS GRID-SEDM (JICA), RADIUS, GIS Different Level-SLARIM (ITC), and HAZUS. In this project HAZUS was chosen as it was a comprehensive open-source methodology with sufficiently clear and complete technical support documents.

HAZUS (FEMA 1999) is a multi-hazard loss estimation methodology developed by the Federal

Emergency Management Agency (FEMA) of United States. It is capable of assessing various types of seismic impacts on a wide range of identities at risk. These identities are broadly classified into: (1) general building stock, (2) essential and high potential loss facilities, (3) transportation systems, and (4) utility systems. In this project, all these identities were assessed. However, only the seismic loss assessment of general building stock is explained in this paper due to the page limitation. Detailed descriptions on the seismic loss assessment of the others can be found in the project's final reports (CDMP 2009).

A brief overview of HAZUS methodology is given in the next section. Then, an implementation of HAZUS for the study areas with an emphasis on general building stock is given in subsequence sections. These include the development of GIS base maps for the study areas, building surveys to collect required data, preparation of input data for HAZUS, and an assessment of losses in the study areas for many possible earthquake scenarios. The loss assessment results of the study areas and discussions are given at the end of this paper.

2. AN OVERVIEW OF HAZUS

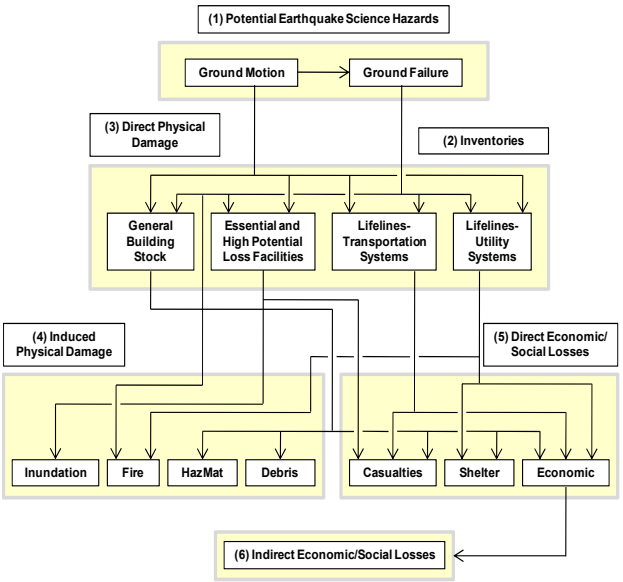

Figure 1 HAZUS seismic loss assessment framework

In HAZUS, several loss estimation models are available for several types of natural hazards. In this project, only the 'Earthquake Model' was utilized. HAZUS is designed to produce loss estimates to assist federal, state, regional, and local authorities in planning earthquake risk mitigation, emergency preparedness, response and recovery. The methodology was implemented in a computer software package named 'HAZUS-MH MR2', which was adopted in this project (the current version is 'HAZUS-MH MR3'). The software operates through any compatible Geographic Information System (GIS) applications such as ArcGIS. The HAZUS framework for seismic loss assessment consists of 6 major modules as depicted in **Fig.1**, detailed descriptions of which are given as follows.

2.1 Potential Earth Science Hazards (PESH)

The PESH module is utilized in describing all possible earthquake related hazards of the study area. These include ground motion, ground failure (i.e., liquefaction, landslide, and surface fault rupture), and tsunami/seiche. Note that the surface fault rupture and tsunami/seiche hazards were not taken into account in this project.

To define the seismic hazard, HAZUS provides two alternatives. In the first alternative, seismic demands are defined by directly providing seismic hazard maps to HAZUS. These maps include, for example, peak ground acceleration (PGA) map, 0.3s period spectral acceleration (S_{as}) map, etc. In the second alternative, the earthquake parameters listed in **Table 1** and the following GIS information—soil classification map, topology map, and ground water level map—are provided to HAZUS. After that, all necessary seismic hazard maps are automatically generated. Since the later method allows the users to conveniently simulate many possible earthquake scenarios, it was adopted in this project. The use of seismic hazard analysis results in preparing the required data for PESH is explained later in section 4.

The calculated ground motion and ground failure parameters are taken as input to 'Direct Physical Damage Module' for estimating the seismic damage of the physical features (see **Fig.1**).

Table 1 HAZUS earthquake parameters

No.	*Parameter*
1	Ground motion attenuation function
2	Epicenter location (latitude and longitude)
3	Earthquake magnitude (M_w)
4	Focal depth (km)
5	Fault width (km)
6	Fault orientation angle (degree)
7	Fault dip angle (degree)

2.2 Inventory

The inventory module is utilized in describing the seismic vulnerability of the study area. It contains tools for describing physical features and demographics inside the study area. As stated previously, the physical features accounted in the seismic loss assessment include (1) general building stock, (2) essential and high potential loss facilities, (3) transportation systems, and (4) utility systems. Here, only detailed descriptions for general building stock (GBS) and demographics are given.

HAZUS evaluates building related seismic losses on cluster-by-cluster basis. Therefore, a study area has to be divided into many sub-areas called clusters. Each cluster is assigned with a specific set of GBS inventory parameters

(**Table 2**) to define its seismic vulnerability. The definition of GBS parameters given in **Table 2** is quite straight forward except for two parameters. They are 'occupancy class' and 'model building type', detailed descriptions of which are given below.

Table 2 Parameters used by HAZUS for describing the general building stock in each cluster

No.	*Parameters*
1	**Square footage by occupancy**–the summation of floor area inside all buildings within each occupancy class.
2	**Full replacement value by occupancy**–the total cost for replacing all buildings within each occupancy class.
3	**Building count by occupancy**–the total number of buildings in each occupancy class.
4	**Occupancy class to model building type correlation matrix**–a matrix used for converting square footage by occupancy class into square footage by model building type.
5	**Demographics**–a table containing housing and population statistics.

The occupancy class indicates the primary function of the building (e.g., residential, commercial, or industrial building). As implied by HAZUS, buildings within the same occupancy class should exhibit the same damage/loss characteristics. For example, when subjected to seismic damage, the repair cost of a hospital building can be approximated by the product of its square footage floor area (a specific property of this building) and an average repair cost per unit area of hospital buildings (a common property or loss characteristic for buildings in this occupancy class).

In HAZUS, there are 7 general occupancy classes: residential (RES), commercial (COM), industrial (IND), agriculture (AGR), religion/nonprofit (REL), government (GOV), and education (EDU). These general classes are further divided into 33 specific classes, descriptions of which are given by HAZUS. These specific classes were intentionally developed for describing buildings in the US. As a result, for this project, the HAZUS descriptions were modified to better suit the Bangladesh local classification (BNBC 1993). The modified classes are given in **Table 3**.

The model building type indicates the primary lateral force resisting system and, thus, the seismic performance of buildings. When subjected to the same ground motion demand, buildings within the same model building type are expected to exhibit a similar level of seismic damage. HAZUS utilizes the following parameters to classify the model building type: structural material (e.g., concrete, steel, masonry), lateral force resisting system (e.g., moment frame, braced frame, shear wall), and building height (e.g., low rise, mid rise, high rise). Based on these parameters, there are 36 model building types in HAZUS. Besides the foregoing parameters, HAZUS further classifies model building type based on 'code level' (the level of seismic code/provision adopted in the design of buildings).

Similar to the case of occupancy classification, several HAZUS model building types are not appropriate for Bangladesh, i.e. some buildings in the study area belong to no class in HAZUS. Therefore, a reclassification was made in this project. The HAZUS model building type classification was replaced by the classification in **Table 4**.

Table 3 Modified occupancy class descriptions for Bangladesh (compatible with BNBC 1993)

Class	*Description*
RES1*	Any building, detached from neighborings by distances required by code (BNBC), having independent access for private dwelling by members of a single family
RES2*	Any building in which one or more families are housed, specifically built for minimum standard accommodation of lower income families, in which the minimum requirements for hygiene and safety are maintained, e.g. multi-storied complexes, cluster houses and rehabilitation housing or housing undertaken by private low income groups approved by the authority.
RES3*	Any building or portion thereof or group of buildings in which living quarters are provided for more than one family, living independently of each other, with independent cooking facility for each family. Flats or apartments may be located in walk up buildings, high rise buildings or in housing complexes
RES4*	Any building or group of buildings under single management in which sleeping and living accommodation, with or without dining facilities but without cooking facilities for individuals are provided for hire on transient or permanent basis. Example, hotels, motels, rest house, lodging house, inns and clubs.
RES5*	Any building in which sleeping and living accommodations are provided for groups of unrelated persons with or without common dining facilities and with common cooking facilities under management control or with individual or group cooking facilities. Examples, mess houses, dormitories, boarding houses, hostels and students' halls of residence.
RES6*	Include sub-standard housings
COM1	Any building or portion thereof used for purpose of display and sale of merchandise, either wholesale or retail or without incidental storage and service facilities with an area not exceeding 300 sq m. Example; large shops, markets, departmental stores, super markets and hyper markets
COM2	Any building or portion thereof used for purpose of display and sale of merchandise, either wholesale or retail or without incidental storage and service facilities with an area more than 300 sq m. Example; large shops, markets, departmental stores, and super markets.

*indicates occupancy classes with modified descriptions

Table 3 (Continue) Modified occupancy class descriptions for Bangladesh (compatible with BNBC 1993)

Class	*Description*
COM3	These are personal and repair services shop. Examples; photocopy shop, automobile workshop etc.
COM4	These are professional or technical services offices
COM5	These are financial institutions or organizations. Examples; banks, money exchange etc.
COM6	Any building or portion thereof used for purpose of providing essential medical facilities having surgery, emergency and casualty treatment areas which is equipped and designated to handle post disaster emergency and is required to remain operational after disaster.
COM7	Any building or portion thereof used single management in which general and specialized medical, surgical and other treatment is provided to persons sufferings from physical limitations because of health. Example; medical office or clinic.
COM8	Include entertainment and recreation facilities. Example: restaurants, bars, snooker club etc.
COM9	Theaters, Cineplex's
COM10*	Any combination of occupancy class (mixed occupancy buildings) such as residential with commercial uses.
IND1	Buildings are heavy industrial factories. Example: large rubber industry, and plastic factory.
IND2	Buildings include light industry. Example; small textile & garments factory, jewelry industry.
IND3	Buildings include food, drugs or chemicals industries. Example; soft drink, pharmaceuticals etc.
IND4	Buildings metals or minerals processing factories. Example: iron & steel industry, brick or cement factories.

*indicates occupancy classes with modified descriptions

Table 4 Modified model building type classification for Bangladesh

Class	*Story*	*Description*
C1L	1-3	Concrete Moment Frame: buildings consisting of reinforced concrete (RC) columns and beams to form the main lateral force resisting system, containing insignificant volume of infill walls.
C1M	4-7	
C1H	8+	
C2L	1-3	Concrete Shear Wall: buildings primarily consisting of shear walls to form the main lateral force resisting system. Examples for shear walls are lift cores and structural walls.
C2M	4-7	
C2H	8+	
C3L*	1-3	Concrete Frame With Masonry Infill Walls: buildings consisting of RC columns and beams to form the main lateral force resisting system, containing significant volume of infill walls.
C3M*	4-7	
C3H*	8+	

*indicates the introduced model building types

Table 4 (Continue) Modified model building type classification for Bangladesh

Class	*Story*	*Description*
C4L*	1-3	Concrete Slab Column Frame: buildings consisting of reinforced concrete columns and slabs to form the main lateral force resisting system with and without infill walls.
C4M*	4-7	
C4H*	8+	
S1L	1-3	Steel Moment Frame: buildings consisting of structural steel columns and beams to form the main lateral force resisting system, containing insignificant volume of infill walls.
S1M	4-7	
S1H	8+	
S3L*	1	Steel Truss-Column Frame: single storied buildings consisting of structural steel roof trusses and columns to form the main lateral load resisting system.
LCL*	1-3	Lightly Reinforced Concrete Frame: buildings similar to concrete moment frames but with substandard designed beams and columns. They were not subjected to engineering design.
LCM*	4-7	
LCH*	8+	
BCL*	1-3	Brick in Cement Mortar Masonry with Concrete Diaphragm: masonry buildings with concrete slabs, concrete roofs, and structural masonry walls.
BCM*	4-7	
BFL*	1-3	Brick in Cement Mortar Masonry with Flexible Diaphragm: masonry buildings with flexible slabs, flexible roofs, and structural masonry walls without confinement from RC columns.
STC*	1	Steel Truss-Concrete Column Frame: single storied buildings consisting of steel roof trusses and RC columns to form the main lateral force resisting system.
STM*	1	Steel Truss-Masonry Wall Frame: single storied buildings consisting of steel roof trusses and masonry walls to form the main lateral force resisting system.
TSL*	1-3	Tin Shed: minimum standard structures consisting of tin shed walls and roofs.
BAL*	1-3	Bamboo: buildings consisting of bamboo as structural components to form both the lateral and gravity load resisting system.

*indicates the introduced model building types

Note that, according to the building surveys (see section 3), most buildings in Bangladesh were designed and constructed without any seismic design provision, even though there has been a legal enforcement since 1993 (BNBC 1993). Therefore, the code level was not utilized in the classification of model building type in this project.

2.3 Direct Physical Damage

Based on information provided from PESH and Inventory Modules, 'Direct Physical Damage Module' estimates the seismic damage of the physical features at risk.

The estimated seismic damage is then taken as input to other modules to obtain induced physical damages, direct and indirect social/economic losses (see **Fig.1**).

For buildings in GBS, the direct physical damage is classified into 5 states: none, minor, moderate, extensive, and complete. The descriptive explanations of these damage states can be found in the HAZUS technical manual (FEMA 1999). The seismic vulnerability of buildings is quantified in terms of *probabilities of reaching or exceeding different damage states for a given ground motion demand*. To calculate such probabilities, HAZUS utilizes (1) building capacity (push-over) curves which are used in conjunction with seismic demand spectra to determine the peak building response in terms of S_{di} (spectral displacement at the performance point) and (2) fragility curves which are functions describing the probability of reaching or exceeding different damage states for a given peak building response.

Although HAZUS provides standard capacity and fragility curves for each and every model building type, they were intentionally developed for buildings in the US and, thus, may not be applicable to buildings in Bangladesh where design and construction practices are significantly different from those in the US. In this project, a new set of capacity curves and fragility functions for buildings in Bangladesh were therefore developed from a series of 3D pushover analyses of typical building models identified from extensive field survey data. Full details on this development are provided in the project's supplementary reports on fragility study of reinforced concrete buildings and masonry buildings (CDMP-c 2009 and CDMP-d 2009).

2.4 Induced Physical Damage

An induced physical damage is defined as consequences of hazards other than the primary hazard (earthquake) that led to losses. These include fire following earthquake, debris generation, inundation, and hazardous materials release. Two former hazards were taken into account in this project. Note, however, that in HAZUS the effects of induced physical damages are not taken into account in the calculation of direct and indirect economic/social losses (see **Fig.1**).

2.5 Direct Economic/Social Losses

Direct physical damages lead to several types of direct losses. HAZUS divides direct losses into two main categories: economic loss and social loss.

The direct 'economic loss' is quantified by the cost of repair or replacement of seismically damaged physical features. The cost calculation takes into account of structural damage, nonstructural damage, and damages to contents inside buildings. The repair/replacement costs due to the different sources of damage are calculated as a fraction of the *full replacement cost*, the value of which is modified in this project to suit the local conditions (further details are given in section 3). Besides the repair/replacement cost, HAZUS is also capable of estimating business inventory loss, building recovery time/loss of function, relocation expenses, loss of proprietors' income, and loss of rental income. These losses, however, were not assessed in this project due to the lack of associated data.

The direct social loss is quantified in terms of casualties. In HAZUS, the casualties are classified into four severity levels: (1) injuries requiring basic medical aid that could be administered by paraprofessionals, (2) injuries requiring greater degree of medical care and technology such as x-ray or surgery but not expected to progress to a life threatening status, (3) injuries that pose an immediate life threatening condition if not adequately and expeditiously treated, and (4) instantaneously killed or mortally injured. Estimation can be carried out by the casualty calculation module for three times of day: 2:00PM (day time), 2:00AM (night time), and 5:00PM (commute time).

The HAZUS methodology for the estimation of casualties is based on the assumption that there is a strong correlation between building damage (both structural and nonstructural) and the number and severity of casualties. The correlation is defined by casualty rates for different model building types and different damage states. In this study, the HAZUS default casualty rates were reviewed by comparing them with the casualty rates derived from available earthquake casualty statistics in the literature. The casualty rates were found to be reasonable except those associated with 'building collapse' state. Though these default collapse related casualty rates might be appropriate for the US, they were adjusted to conform to global earthquake casualty statistics (Coburn et al. 1992) in this project.

2.6 Indirect Economic/Social Losses

This module assesses the broad and long-term implications of the direct damages and losses. Examples of indirect economic losses are changes in employment and personal income. This module was excluded from this project because of the secondary importance of indirect losses and the lack of associated data.

3. DEVELOPMENT OF GENERAL BUILDING STOCK (GBS) INVENTORY

The development of GBS inventory for the three cities is described in the following sub-sections (3.1-3.3). This GIS inventory in the primary input data for HAZUS.

3.1 Development of GIS Base Maps

For Dhaka and Chittagong, several existing GIS maps of the cities were acquired from the city development agencies and some other government departments and were compiled for each city into a single map called 'GIS base map'. The base map shows the occupancy class, footprint, and geographical location of each and every building, and the total number of buildings in the study area. It was, however, found that several data were missing, and some existing data were not properly updated.

To correct these problems, QuickBird images of Dhaka

and Chittagong were acquired. Several ground control points at suitable locations were selected and utilized for georeferencing. After that, the QuickBird images were digitized and compared with the GIS base maps to develop complete maps. Field surveys were also carried out to identify some missing data, such as the occupancy class of some buildings and certain key parameters of lifelines and transportation systems (see **Fig.2**).

For Sylhet, unfortunately there were no any GIS maps available at the beginning of the project. The GIS base map of Sylhet had to be developed from scratch. The development was made by acquiring a QuickBird image of the city, georeferencing the image, making a preliminary GIS base map showing the footprint and geographical location of each and every building, and finally identifying the remaining building attributes (occupancy class, number of stories, etc.) from field (street-walk) surveys.

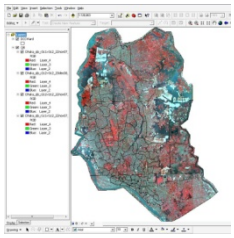

QuickBird Image (Dhaka)



Geo-Referencing by RTK-GPS

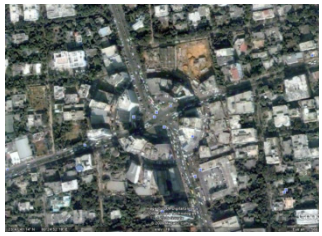

Geo-Referenced Image



Image Digitization

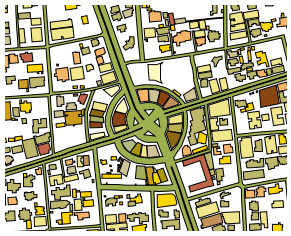

Digitized Physical Features



Field Survey (Base Map Survey) to Collect Parameters

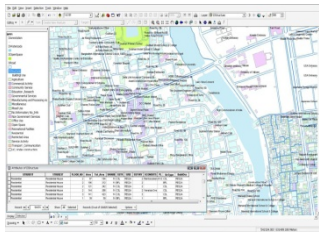

Adding Parameters

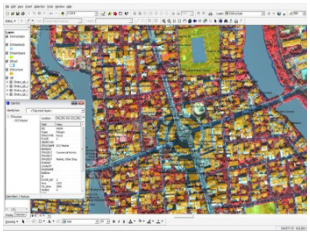

Complete GIS Base Map

Figure 2 Illustration of overall procedure for the development of GIS base maps.

3.2 Cluster Delineation

As explained earlier, HAZUS evaluates building related seismic losses on cluster-by-cluster basis. Therefore, each city has to be divided into many clusters. The size of clusters must be sufficiently small to illustrate the geographical variation of seismic losses, but too small clusters may result in the difficulty in data interpretation.

In this project, the administrative ward boundary in the city was used as the first step in the cluster delineation. Then, some physical features such as roads, lakes, canals, and rivers were taken as boundaries to further divide the administrative wards into smaller clusters. The cluster delineation was made such that the homogeneity of land use with each cluster was reasonably attained. The restricted areas, where the building information must not be exposed to the public (as required by local regulations/laws), were taken as separated clusters. Such areas include military bases, sea ports, and airports. The outcome of the cluster delineation are summarized in **Table 5**.

Table 5 The outcome of cluster delineation

City Corporation	*Admin. Wards*	*Total Clusters*	*Restricted Clusters*
Dhaka	90	552	12
Chittagong	41	285	0
Sylhet	27	82	0

3.3 Building Surveys

For each cluster, the GBS parameters No. 1 and 3 in **Table 2** can be readily extracted from the GIS base map. The remaining parameters, however, are not available and have to be estimated by statistical inference from available data. This process requires the knowledge of statistical correlations between available and missing building attributes. Specially designed building surveys were therefore carried out in this project to determine such correlations. The surveys were a side-walk type, i.e. surveyors were sent to the field with survey forms (see **Fig.3**) to acquire the required data by visual building inspections from the street sides and by interviewing building occupiers.

In this project, to conduct the surveys in each city, several survey teams were set up. Each team consists of a survey supervisor, which is a local civil engineer, and one or two surveyors, which are local civil engineering students. Prior to the actual survey work, to assure a proper understanding of the teams regarding the data required in survey sheets and the data collection procedure, a comprehensive training course was given to the teams. Then, a few trial rounds of survey were conducted, during which the survey teams were closely monitored by experts from AIT and NSET who experienced in such a survey in Thailand and Nepal, respectively. After the trial round survey, a discussion between the survey teams and the experts was arranged to solve practical and technical problems found in the trial round survey.

After the teams were ready, the actual survey work was launched. However, to further guarantee the quality of data, there were periodical reviews and cross checks of survey results by the survey supervisors and the experts. Note that in the initial survey phase a large amount of data were rejected through the quality assurance process. The total numbers of buildings surveyed are summarized in **Table 6**.

3.4 Creating GBS Inventory Input Data for HAZUS

The process to determine the GBS parameters as listed in **Table 2** for each cluster is explained in the following.

(a) *Building count by occupancy*, n_i, is the total number of buildings of the ith occupancy class within the cluster under consideration (the occupancy classification is defined in **Table 3**). This parameter can be determined by direct counting from the GIS base map.

Earthquake and Tsunami Preparedness in Bangladesh
Comprehensive Disaster Management Program

Phase I Survey: Building Inventory Survey Format

General	Date:		
ID: Location:		Road No:	
Name of the Owner:		Grid No:	
Surveyor Name:		Sign:	
Supervisor Name:		Sign:	
Building Details			
Structural Type Code:		No of Storey:	
Occupancy Class:			
Number of Occupants:	a) Day:	b) Night:	
Construction Year: or Age years	(<10 years	10-30 Years	>30 years)
Existence of Shear Wall[1)]	a) Yes	b) No	
Vulnerability Factors			
First Soft/Weak Storey:	a) Yes	b) No	
Heavy Overhangs and Cantilever:	a) Yes	b) No	
Shape of Building in Plan:	a) Rectangular	b) Narrow Rect.	c) Irregular
Shape in Elevation:	a) Regular	b) Setback	c) Narrow tall
Poundings Possibility	a) Yes	b) No	
Building in Slope Land	a) Yes	b) No	
There is visible ground settlement	a) Yes	b) No	
Short Columns:	a) Identified	b) Not Identified	
Visible Physical Condition			
a) Poor b) Average	c) Good		
Photograph Number:			

Figure 3 Building attributes survey form

Table 6 Total numbers of buildings surveyed in three cities

City Corporation	*Buildings in the City Corp. area*	*Surveyed buildings*	*% Survey*
Dhaka	326,825	8741	2.67
Chittagong	182,277	6175	3.39
Sylhet	52,176	3536	6.78

(b) *Square footage by occupancy*, Ao_i, defines the total floor area of buildings of the ith occupancy class within the cluster under consideration. Similar to the previous case, this parameter can be determined by direct counting from the GIS base map.

(c) *Occupancy class to model building type correlation matrix*: In HAZUS, to determine the direct physical damage of buildings, the total floor area of buildings for each model building type (as defined in **Table 4**) must be known. Such information is normally absent in existing GIS base maps because its use is quite specific to engineering purposes. This was also the case for this project. As a result, an occupancy class to model building type correlation matrix is required. It is a two dimensional array showing the model-building-type wise distribution of building floor area for different occupancy classes. An example correlation matrix is given in **Table 7**. Note that the sum of values in each row of the matrix yields 100%. A correlation matrix is used for converting the square footage by occupancy class (Ao_i) into the square footage by model building type (Am_j).

To derive the correlation matrix for the study area, the value in each cell of the matrix can be directly obtained from a statistical analysis of building survey results. From the survey, the following properties of a sample building are known: (1) occupancy class, (2) model building type, and (3) square footage floor area. Ideally, the correlation matrix for a cluster should be derived from the survey results within the cluster. However, in this project, the correlation matrices of all clusters in a city were assumed to be identical. This assumption was carefully examined by using the survey results and was found to be reasonable. Hence, a single correlation matrix was derived from the properties of all sample buildings in each city and was used as the correlation matrix for every cluster in the city.

Table 7 Occupancy class to model building type correlation matrix (values are expressed in percentage).

		Model Building Type				***Sum***
		C1L	C2L	…	BAL	
Occ. Class	RES1	3	27	…	11	100
	…	…	…	…	…	100
	EDU2	51	37	…	0	100

The values shown in this matrix are for demonstration purpose only

d) *Demographics*: Demographics for a cluster under consideration are defined by a set of parameters describing housing and population statistics. Ideally, the exact number of building occupants should be used to define the demographics parameters. However, such information for Bangladesh was not available. As a result, an approximation method described in the ATC-13 report to estimate demographics parameters was adopted in this project (ATC 1982).

According to ATC-13, the number of building occupants can be approximated by the product of the building square footage and the average number of occupants per square footage. Therefore, in this project the average number of occupants per square footage for every occupancy class was identified from the building survey results and was utilized in estimating the total number of building occupants in every cluster.

The method was found to yield reasonable estimates for every occupancy class except the single family dwelling

(RES1). No clear statistical relationship was found between the number of building occupants and the RES1 building square footage. The number of building occupants seemed to be associated to the family size. Therefore, instead of using the ATC-13 method, the total number of RES1 building occupants was taken equal to the building count multiplied by the average number of occupants per building of RES1.

(e) *Full replacement value by occupancy*: The full replacement value of an occupancy class (R_i) defines the cost required to replace all existing buildings in this occupancy class with the new constructions. In this project, the full replacement value was taken equal to the product of the total floor area and the unit construction cost of the occupancy class under consideration. The unit construction cost is expressed in terms of US dollars per sq-ft.

Even though HAZUS provides a set of default values for unit construction costs, it is definitely not applicable to buildings in Bangladesh. Therefore, the unit construction costs for several occupancy classes were collected from three local organizations: Apartment design & Development Ltd., Trimline Consultants Co.Ltd., and Dalan Kotha Ltd. The collected unit construction costs were averaged and tabulated against the default values provided by HAZUS. It was found that the unit construction costs in Bangladesh are approximately equal to 20% of those in the US.

4. EARTHQUAKE SCENARIOS

In order to conduct a seismic loss assessment of the study areas, a set of realistic earthquake scenarios have to be defined. With respect to seismic hazard, these scenarios should cover all possible earthquake events so that the results of seismic loss estimation can be utilized in developing an effective and versatile earthquake disaster contingency plan.

As stated earlier, HAZUS provides two methods for defining the seismic hazard of the study area and the second method, in which the earthquake parameters listed in **Table 1** are provided to HAZUS, was chosen. This section describes the use of seismic hazard analysis results to select earthquake scenarios.

In this project, both deterministic and probabilistic approaches were adopted in the seismic hazard assessment of the study areas. According to the deterministic analysis made by OIC, the maximum possible earthquakes produced by five major faults in and around Bangladesh were suggested for use in the seismic loss assessment. These faults are: Madhupur fault (MF), Dauki Fault (DF), Plate boundary fault 1 (PBF1), Plate boundary fault 2 (PBF2), Plate boundary fault 3 (PBF3). Besides the fault source earthquakes, in order to take into account the effects of background earthquakes, an additional scenario where a $6.0M_w$ earthquake occurring beneath the city was suggested.

According to the probabilistic seismic hazard analysis, two earthquake scenarios were recommended. They are earthquake scenarios which produce ground motion demands equivalent to those with 2% and 10% probability of exeedance in a 50-year exposure period.

Based on both assessment approaches, there were 8 earthquake scenarios suggested for each city. Considering that the interpretation of seismic loss assessment results from all suggested scenarios could be complicated, it was decided to reduce the total number of scenarios. This was accomplished by grouping earthquake scenarios which yield approximately the same level of seismic hazard into a single representative scenario. After grouping, the selected earthquake scenarios can be summarized in **Table 8**.

5. SEISMIC LOSS ESTIMATION RESULTS

In this project, the seismic loss assessment for the study areas was carried out for all selected earthquake scenarios. However, to demonstrate the assessment results, only the scenario where an $M_w = 6.0$ earthquake occurs beneath the city (scenario 3), which yields the highest seismic loss in terms of dollar values, is presented.

Table 8 Earthquake scenarios for seismic loss estimation of Dhaka, Chittagong, and Sylhet.

Scenario number	***Description***
1	The fault-source earthquake which produces the highest seismic demand on the study area. In particular, these are $7.5M_w$ at MF, $8.0M_w$ at PBF1, and $8.0M_w$ at DF earthquakes for, respectively, Dhaka, Chittagong, and Sylhet.
2	The fault-source earthquake which represents the remainings. In particular, these are $8.0M_w$ at PBF2, $8.0M_w$ at PBF2, and $8.3M_w$ at PBF3 earthquakes for, respectively, Dhaka, Chittagong, and Sylhet.
3	This scenario represents the effect of background earthquakes. It is assumed that a $6.0M_w$ earthquake occurs beneath each city.
4[1]	An assumed earthquake which generates the ground motion demands approximately equal to those indicated by the probabilistic seismic hazard map for 10% probability of exceedance in 50 year.
5[2]	An assumed earthquake which generates the ground motion demands approximately equal to those indicated by the probabilistic seismic hazard map for 2% probability of exceedance in 50 year.

[1]For Dhaka, scenario 4 was not assessed because it yields similar ground motion demands as those of scenario 3

[2]For Chittagong, scenario 5 was not assessed because it yields similar ground motion demands as those of scenario 3.

Maps showing spectral acceleration at 0.3s period in Dhaka and Chittagong for scenario 3 are given as examples in **Fig.4**. The short period spectral acceleration is chosen for illustration because it is closely associated with the seismic damage of low- to mid-rise buildings which constitute the major population of buildings in the study areas. In each city

the causative fault is shown by a thick solid line. For Dhaka, the ground motion demand is highest around the fault and attenuates by distance. Nevertheless, for some clusters away, the demand is significantly amplified (see the left-most part of the city) due to the presence of soft soils in such areas. A more pronounced soft soil amplification effect can be found in Chittagong, where the demand at some distance away from the seismic source is higher than that around the source itself.

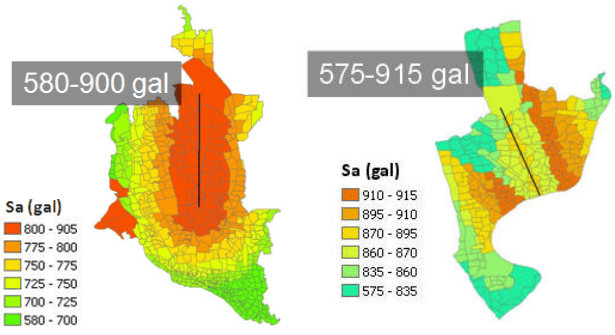

(a) Dhaka (b) Chittagong

Figure 4 Spectral acceleration at 0.3s caused by a 6.0M_w earthquake occurring underneath the city.
Thick solid lines show the assumed causative faults.

The spatial distribution of building damages in Dhaka in earthquake scenario 3 is illustrated in **Fig.5.** In this Figure, the total number of buildings in moderate, extensive, and complete damage states (or in 'at least moderate' damage state) in each cluster is represented by color codes. One can see that the clusters close to the seismic source generally have higher number of damaged buildings than those farther away because of the higher seismic demand. It was estimated that more than 180,000 buildings, which is about 56 % of all buildings in the city, will be at least moderately damaged. Among these damaged buildings, more than 78,000 buildings will be damaged beyond repair. The direct economic losses due to these building damages in Dhaka are shown in **Table 9** along with those in Chittagong and Sylhet.

Table 9 Estimated direct economic losses due to building damages (in millions of US dollars).

Source of Damage	*Dhaka*	*Chittagong*	*Sylhet*
Structural	1076	367	80
Nonstructural	3854	966	211
Content	1494	156	73
Sum	6424	1490	364

The direct social losses in terms of the number of casualties in the three cities are summarized in **Table 10**. It can be observed that the total number of casualties of day time scenario is somewhat close to that of night time scenario. However, the casualties are concentrated in residential buildings for night time scenario, but are distributed to commercial buildings and others for day time scenario. This information is very useful for the development of effective response/recovery plans for day and night time scenarios.

The above results are a few examples of those developed under this project. Further details are given in the project's main report on 'Risk Assessment of Dhaka, Chittagong, and Sylhet City Corporation Area' (CDMP-b 2009).

Table 10 Estimated casualties (outside and inside parentheses are for day and night time scenarios, respectively).

City[1]	*Occ*[2]	*Injury Severity Level*			
		1	**2**	**3**	**4**
DH	RES	*42452* *(125726)*	*8465* *(21808)*	*2039* *(5309)*	*28422* *(94710)*
	COM	*60531* *(837)*	*11782* *(158)*	*3449* *(47)*	*3660* *(333)*
	Others	*19286* *(479)*	*3840* *(89)*	*1103* *(27)*	*6780* *(225)*
CI	RES	*20272* *(58689)*	*4093* *(10383)*	*1049* *(2758)*	*12119* *(39634)*
	COM	*17821* *(254)*	*3213* *(44)*	*899* *(12)*	*12376* *(183)*
	Others	*6657* *(741)*	*1166* *(123)*	*276* *(2799)*	*5276* *(637)*
SY	RES	*2711* *(7451)*	*527* *(1319)*	*156* *(415)*	*1533* *(4677)*
	COM	*1853* *(23)*	*332* *(4)*	*97* *(1)*	*1237* *(17)*
	Others	*610* *(34)*	*107* *(5)*	*28* *(1)*	*473* *(30)*

[1]DH, CI, and SY are Dhaka, Chittagong, and Sylhet, respectively
[2]Occ. stands for occupancy class.

5. CONCLUSIONS

An application of HAZUS in the seismic loss assessment of three major cities in Bangladesh is described in this paper. Even though HAZUS was intentionally developed for use in the US, with proper modifications it can be successfully applied to other countries. Such modifications are demonstrated using the case of Bangladesh as an example. The obtained seismic loss assessment results will certainly be useful as they are currently being used for developing a national contingency plan for earthquake disaster management of Bangladesh.

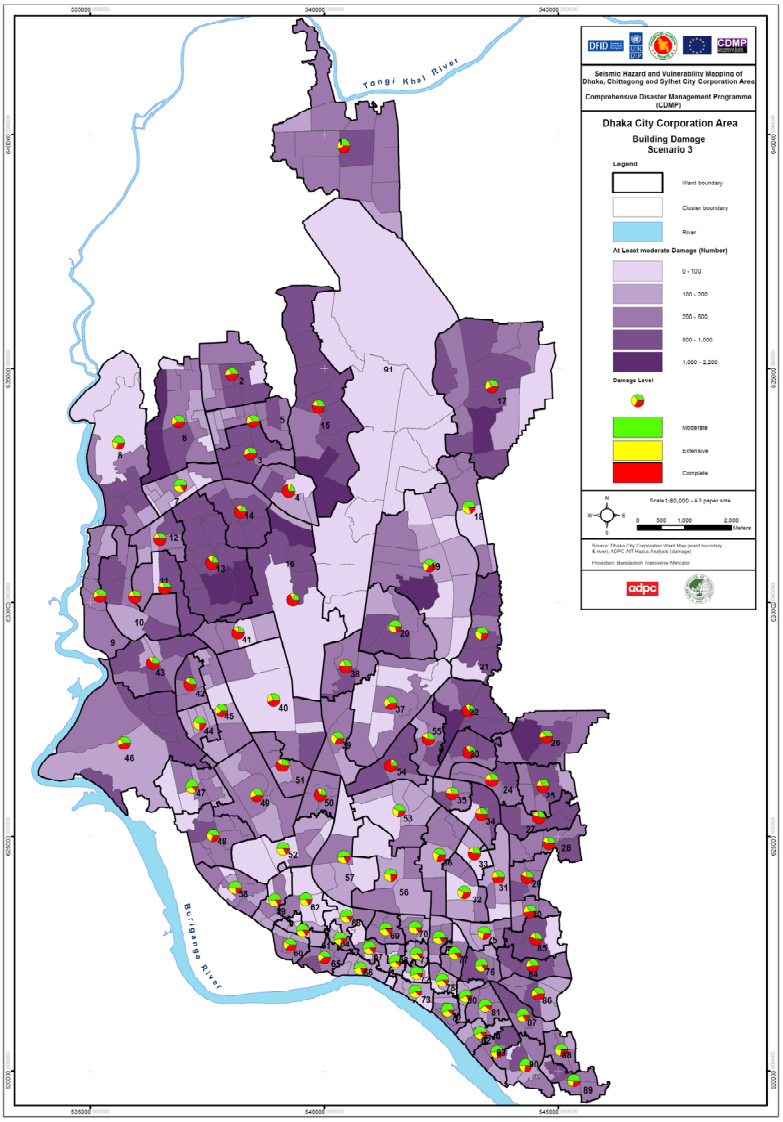

Figure 5 Distribution of building damages in Dhaka in earthquake scenario 3.

ACKNOWLEDGMENT:

The fund for implementing this project is provided by the Comprehensive Disaster Management Programme (CDMP), Government of Bangladesh. Any opinions, findings, and conclusions expressed in this paper are those of the authors and do not necessarily reflect those of CDMP.

REFERENCES:

ATC (1982), *ATC13 Earthquake Damage Evaluation Data for California*, Applied Technology Council, Redwood City, CA, USA.

BNBC (1993), *Bangladesh National Building Code*, Ministry of Construction, Government of Bangladesh.

CDMP-a (2009), *Main Report on Vulnerability Assessment of Dhaka, Chittagong, and Sylhet City Corporation Area*, Comprehensive Disaster Management Programme, Government of Bangladesh.

CDMP-b (2009), *Main Report on Risk Assessment of Dhaka, Chittagong, and Sylhet City Corporation Area*, Comprehensive Disaster Management Programme, Government of Bangladesh.

CDMP-c (2009), *Supplementary Report on Fragility Study of Reinforced Concrete Buildings in Dhaka, Chittagong, and Sylhey City Corporation Area*, Comprehensive Disaster Management Programme, Government of Bangladesh.

CDMP-d (2009), *Supplementary Report on Fragility Study of Masonry Buildings in Dhaka, Chittagong, and Sylhey City Corporation Area*, Comprehensive Disaster Management Programme, Government of Bangladesh.

Coburn, A.W., Spence, R.J.S., and Pomonis, A. (1992), "Factors Determining Human Casualty Levels in Earthquakes: Mortality Prediction in Building Collapse," *Proceedings of the 10 WCEE*, Madrid, Spain, 5989-5994.

FEMA 1999, *HAZUS MH-MR2 Technical Manual*, Department of Homeland Security, Federal Emergency Management Agency, Mitigation Division, Washington, D.C., USA.

JOINT CONFERENCE PROCEEDINGS
7th International Conference on Urban Earthquake Engineering (7CUEE) &
5th International Conference on Earthquake Engineering (5ICEE)
March 3-5, 2010, Tokyo Institute of Technology, Tokyo, Japan

URBAN STRUCTURAL DAMAGE CHARACTERIZATION USING OPTICAL IMAGERY

Tara C. Hutchinson[1] and ZhiQiang Chen[2]

1) Associate Professor, Department of Structural Engineering, University of California, San Diego, USA
2) Postdoctoral Scholar, Department of Structural Engineering, University of California, San Diego, USA
tara@ucsd.edu, zqchen@ucsd.edu

Abstract: Recent research endeavors in civil engineering have attempted to apply remote sensing technology to urban damage assessment to aid in post-disaster reconnaissance and recovery. Typically, urban structural damage is identified based on pre- and post-disaster satellite images with the use of a pattern classification approach. Analysts then present damage maps with categorical levels, such as 'fully collapsed', or 'intact', assigned to urban sub-regions or individual structures within the image(s). A major limitation in past attempts is the use of deterministic approaches to classify damage levels. To address this, a probabilistic classification framework by means of a multi-class classifier is proposed. Notably, by applying this probabilistic approach, classification of urban damage provides posterior probabilities, which can be used to quantify decision uncertainties and to obtain regional urban damage classification. Methods of feature extraction, a key ingredient in interpreting the underlying damage, are also discussed. A numerical experiment is presented using satellites images acquired from the 2003 Bam, Iran Earthquake.

1. INTRODUCTION

Remotely sensed data, in particular satellite imagery, can be a powerful utility for urban damage assessment following large-scale urban disasters, such as earthquakes, tsunamis, or hurricanes. Recently, the civil engineering community has endeavored to apply such data at a variety of urban disaster scales (e.g., Rejaie and Shinozuka, 2004; Rathje and Crawford, 2004; Hutchinson and Chen, 2005; Mansouri et al., 2005; Gusella et al., 2005; Chiroiu, 2005). In these attempts, urban structural damage is identified based on pre- and post-disaster satellite images with the use of a pattern classification approach. The identification result is usually presented in a damage map wherein categorical damage levels, such as 'fully collapsed', 'partially collapsed', or 'intact', are assigned to urban sub-regions or individual structures in images. To generate these categorical descriptions for urban objects in satellite images, structural details that characterize structural conditions, e.g. boundaries or roof details of urban structures, must be distinguishable from image background. This requires that satellite images have sufficiently high resolution. Due to the launching of modern space-borne sensors, such as WorldView-1/2, Quickbird (DigitalGlobe Inc., 2009) or IKONOS (GeoEye Inc., 2009), satellite images at sub-meter accuracy are available, thus the aforementioned structural features in these images are well detectable. These technical advances enable the possibility of performing computational urban damage classification for assessing specific structures or sub-regions within images.

1.1 Damage Characterization Work Flow

Original satellite images acquired from satellite companies usually capture a very large area of the earth's surface. Portions of these images may not cover urban areas, but rather vegetation or water surface. To conduct damage identification at a meaningful object scale, hierarchical processing steps are usually adopted. In Figure 1, a four-step workflow is proposed, which proceeds with sequentially decreasing geospatial scales.

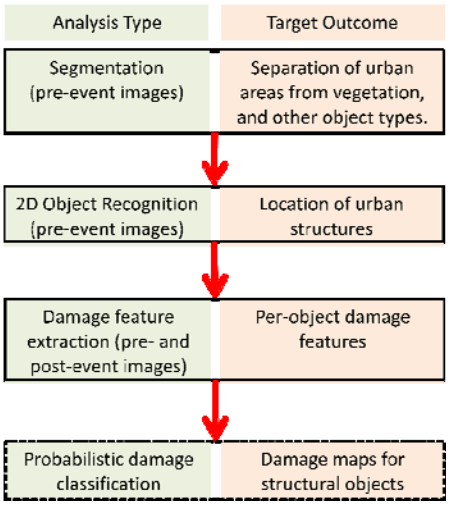

Figure 1. Hierarchical workflow for performing object-based urban structural damage identification using bi-temporal satellite images (Chen and Hutchinson, 2010).

A critical ingredient to the successful characterization of damage and its associated distribution is the classification undertaken in the final step of the workflow. Damage classification has the ultimate objective of outputting

multiple damage levels for structural objects and rendering these damage levels onto a damage map. If a single damage index (namely, a damage feature defined with the hypotheses that it varies monotonically with structural damage) is obtained, simple threshold-based methods may be used to associate structures with different damage levels. However, multivariate features are usually produced; in this case, a more sophisticate pattern classification algorithm is required.

A major limitation in past attempts has been the use of deterministic classification methods to estimate structural damage levels. There are several limitations to such an approach. First, there is no evaluation of the underlying decision uncertainties. Second, due to the categorical nature of classification results, there is no scalable solution that can bridge the damage levels of individual urban buildings to the damage level of an urban sub-region of varying size. Finally, the traditional approaches to classifying damage in arbitrary urban sub-regions do not exclude non-structural coverage (e.g vegetation areas) in the sub-regions. In this paper, these limitations motivate us to investigate a multi-class, object-based probabilistic classification approach. Interested readers may find an extended discussion of the methodology and results in Chen and Hutchinson (2010).

2. PROBABILISTIC DAMAGE CLASSIFICATION

Let us first assume that image-based damage feature extraction has been conducted, which results in a training data set, denoted as:

$$\mathrm{D} = \left\{ (s_n, \mathbf{f}_n) \mid s_n \in \{s1, s2, s3\}, \mathbf{f}_n \in \mathbf{R}^L, n = 1, 2, ..., N \right\} \quad (1)$$

where s_n represents the structural damage levels for the nth structure with three possible states denoted by $s1$, $s2$ and $s3$, and $\mathbf{f}_n$ is the corresponding feature vector. It is noted that for the purpose of image-based urban damage assessment, three states of structural damage usually suffice in distinguishing the different damage levels in images.

Probabilistic classification approaches generally have two types: (i) generative methods and (ii) discriminative methods (Duda et al. 2000). In Methods (i), the classification is modeled via Bayes' theorem as a *posterior probability*: $P(s \mid \mathbf{f}) \propto p(\mathbf{f} \mid s) P(s)$, where the conditional distribution of $\mathbf{f}$ or the likelihood function $p(\mathbf{f} \mid s)$, usually takes an assumed distribution type with unknown parameters. For discriminative methods, the posterior probability $P(s \mid \mathbf{f})$ is directly fitted by a parameterized discriminant function $\sigma(\mathbf{f})$. The training process for these classification methods involves estimating the model parameters in $p(\mathbf{f} \mid s)$ or $\sigma(\mathbf{f})$ based on the training data D using the maximum likelihood estimation method or a Bayesian inference method.

After the classifiers are trained, posterior probabilities can be predicted for a testing feature vector $\mathbf{f}_m$ for the mth structure, denoted by:

$$\{P(s1 \mid \mathbf{f}_m, \mathrm{D}), P(s2 \mid \mathbf{f}_m, \mathrm{D}), P(s3 \mid \mathbf{f}_m, \mathrm{D})\} \quad (2)$$

The most probable damage state for this structure is therefore a state that has the maximum posterior probability:

$$\hat{s}_m = \arg\max_s P(s \mid \mathbf{f}_m, \mathrm{D}), \quad \forall \mathrm{s} \in \{s1, s2, s3\} \quad (3)$$

Hence, one obtains a predicted damage state for the target structure and the associated probability as a decision confidence measure. For decision makers, the prediction can be rejected if the associated confidence measure is lower than a rejection threshold. In contrast, if a deterministic classification approach is used, one only obtains hard-valued estimates of damage levels without knowledge of the underlying decision uncertainties.

An important property of probabilistic classification is that it offers a simple way to perform damage classification for built urban sub-regions of varying sizes. Assume a sub-region containing M urban structures is selected; one can determine the damage state for this sub-region as follows. First, for the mth urban structure with an area of A_m in this sub-region, the posterior probability distribution of damage levels is estimated, denoted by $P(s \mid \mathbf{f}_m, \mathrm{D})$. Subsequently, the distribution of damage levels for this sub-region is obtained by area-weighted averaging of the posterior probability distributions of all the confined structures:

$$Q(s) = \frac{\sum_{m=1}^{M} A_m \, P(s \mid \mathbf{f}_m, \mathrm{D})}{\sum_{m=1}^{M} A_m} \quad (4)$$

The weighting is based on the areas of the confined structures in Eq. (4), which is regarded as an appropriate way to consider the participating importance of the individual structures in this selected sub-region. The regional damage state for this sub-region can be similarly determined by using Eq. (1). Notably, non-structural coverage, e.g. vegetation, ground etc., is excluded in producing this sub-region damage classification.

3. MULTI-CLASS PROBABILISTIC CLASSIFICATION

In this paper, a recent classification development in the machine learning fields termed Relevance Vector Machines (RVM) (Tipping, 2001) is adopted. RVM is a discriminative method, and is capable of producing probabilistic multi-class classification. The popular Support Vector Machines (SVM) (Vapnik, 1998) is not used due to its lack of multi-class probabilistic classification. An RVM classifier places its training process in a Bayesian inference framework, and possesses a sparser kernel-based prediction model than the more popular Support Vector Machines (SVM) approach, yet it has similar classification accuracy as SVM. Due to these appealing merits, RVM has been used in many applications (e.g. Williams et al., 2003; Wei et al., 2005).

3.1 Framework of Multi-class RVM (mRVM)

An original RVM model is in essence a marginalization operation that directly integrates out all model parameters in its discriminant function to obtain posterior probability predictions given training data:

$$P(s|\mathbf{f},\mathrm{D}) = \iint P(s|\mathbf{f},\mathbf{w})p(\mathbf{w}|\mathbf{a},\mathrm{D})p(\mathbf{a}|\mathrm{D})\,d\mathbf{w}\,d\mathbf{a} \quad (5)$$

where $P(s|\mathbf{f},\mathbf{w})$ is the posterior probability to be modeled by a discriminant function with unknown model parameters $\mathbf{w} = \{w_1, w_2, ...\}$; the parameter set $\mathbf{w}$ is further modeled by a prior probability model $p(\mathbf{w}|\mathbf{a})$ in terms of a set of hyper-parameters $\mathbf{a} = \{\alpha_1, \alpha_2, ...\}$. The two posterior probability functions $p(\mathbf{w}|\mathbf{a},\mathrm{D})$ and $p(\mathbf{a}|\mathrm{D})$ characterize the distributions of $\mathbf{w}$ and $\mathbf{a}$, respectively, given the training data D. In the literature, the derivation of RVM is found only for binary classification wherein the logistic function is used for $P(s|\mathbf{f},\mathbf{w})$. In the work of Chen and Hutchinson (2010), the formulation of the multi-class RVM (mRVM) is presented. Herein we present the resulting approximation adopted in the numerical solution, which may be summarized as follows:

$$\boldsymbol{P(s=k|\mathbf{f},D) = \int P(s=k|\mathbf{f},\mathbf{w})p(\mathbf{w}|\mathbf{a}_{MP},\mathbf{D})\,d\mathbf{w}}$$

(6a)

$$= \int \frac{\sigma^{(k)}(\mathbf{f},\mathbf{w})}{(2\pi)^{K/2}\,|\Sigma_{\mathbf{w}_{MP}}|^{1/2}} \exp\left(-\frac{1}{2}(\mathbf{w}-\mathbf{w}_{MP})^T \Sigma^{-1}_{\mathbf{w}_{MP}} (\mathbf{w}-\mathbf{w}_{MP})\right) d\mathbf{w}$$

(6b)

$$\approx \sigma^{(k)}(\mathbf{f},\mathbf{w}_{MP})$$

(6c)

In Eq. (6a) an approximation is adopted whereby $p(\mathbf{a}|\mathrm{D})$ is replaced with a Dirac Delta function $\delta_{\mathbf{a}\mathrm{MP}}$. In Eq. (6b), $p(\mathbf{w}|\mathbf{a},\mathrm{D})$ is approximated by the multivariate Gaussian defined via the Laplace's method. Note that Eq. (6b) does not result in a closed-form solution, therefore Eq. 6c presents an approximation whereby $P(s=k|\mathbf{f},\mathrm{D})$ is directly computed at $\mathbf{w} = \mathbf{w}_{MP}$ using the discriminant function for the kth class. In our study, it is found through simulations that the differences between the resulting estimates from Eq. (6c) and the sampling-based estimates of Eq. (6b) are usually less than 5%.

4. STRUCTURAL DAMAGE FEATURE EXTRACTION

As presented in the urban damage identification workflow in Figure 1, a damage feature extraction step is performed to obtain damage measurements prior to mapping these measurements to categorical damage levels. In our study, it is observed that there are two general types of structural damage in satellite images: i) texture-type damage, and ii) edge-type damage. To evaluate these, two different damage detection methods are considered.

Texture-type damage is characterized by random or non-structured changes in gray-level variations between bi-temporal images of urban areas. This type of structural damage can be easily contaminated by other non-damage variations due to atmospheric, seasonal or other environmental changes in urban areas. However, in case of inundation damage due to tsunami or flood etc, this type of damage may be significant since irradiance from the roof of urban structures can change significantly due to water sediments. To detect this damage, the conventional linear correlation analysis is suitable. Given the pre- and post-event images, denoted by $u_0(x,y)$ and $u_1(x,y)$, respectively, we introduce a neighborhood notation:

$$\mathrm{N}(x,y) = \{(x',y') \mid x-\omega \le x' \le x+\omega,\ y-\omega \le y' \le y+\omega\} \quad (7)$$

to define an image block centered at (x,y). The area of this neighborhood block is $A = (2\omega+1)^2$. The squared linear correlation coefficient $c^{lcc}(x,y)$ is then computed at (x,y):

$$c^{lcc}(x,y) = \frac{\left(\sum_{\mathrm{N}} u_0 u_1 - \sum_{\mathrm{N}} u_0 \sum_{\mathrm{N}} u_1 / A\right)^2}{\left(\sum_{\mathrm{N}} u_0^2 - \left(\sum_{\mathrm{N}} u_0 / A\right)^2\right)\left(\sum_{\mathrm{N}} u_1^2 - \left(\sum_{\mathrm{N}} u_1 / A\right)^2\right)} \quad (8)$$

where the notation $\sum_{\mathrm{N}} u$ is:

$$\sum_{(x',y')\in \mathrm{N}(x,y)} u(x',y') \quad (9)$$

It is noted that in the current study, only gray-level intensities are exploited to detect potential structural damage, while multi-spectral imagery information (e.g. the R, G and B bands in a true color image) is not used.

In earthquake-inflicted areas, structural damage may be more readily characterized by more structured, edge-type changes in gray-level variations; for example, visible collapse of structural boundaries can result in discontinuous edges in the satellite image. Herein, we apply a dissimilarity-based damage detection method to consider this issue (Chen and Hutchinson, 2007). First, the features of interest, edge-like boundaries of urban structures, are extracted by computing image gradient magnitudes on both the pre- and post-disaster images:

$$v(x,y) = u_x^2 + u_y^2 \quad (10a)$$

$$u_x \approx \frac{\partial g(x,y,\tau)}{\partial x} * u(x,y), \quad u_y \approx \frac{\partial g(x,y,\tau)}{\partial y} * u(x,y) \quad (10b)$$

where the first-order image derivatives u_x and u_y are optimally approximated by convolving the image with the first-order derivatives of a Gaussian filter $g(x,y,\tau)$ with a scale parameter τ (Gonzalez and Woods, 2008). Secondly, the structural features within a neighborhood $\mathrm{N}(x,y)$ are normalized, making the summed features equal to unity; therefore, the normalized features confined by $\mathrm{N}(x,y)$ can be viewed as an empirical probability distribution. With the use of some non-parametric dissimilarity measures for probability distributions, such as

Jeffery divergence (Cover and Thomas, 2001), the dissimilarity-based damage measurement at (x, y) is:

$$c^{div}(x,y) = 2\ \mathrm{sigmod}\left(\sum_{N} v_0 \log \frac{v_0}{v_1} \Big/ \sum_{N} v_0 + \sum_{N} v_1 \log \frac{v_1}{v_0} \Big/ \sum_{N} v_1 \right) - 1 \quad (11)$$

where a sigmoid function is applied resulting in a measurement bounded by 0 and 1.

If block-based structural damage identification is sought, the pixel-wise damage measurements given by $c^{lcc}(x, y)$ in Eq. (8) or $c^{div}(x, y)$ in Eq. (11) within user-defined blocks of the same sizes can be directly used as damage features. This block-based approach is easily affected by non-structural coverage in an urban image (e.g., water, grounds and vegetations, etc.). Therefore, it is more desirable to perform an urban structure-based damage identification, which requires a separate vector image containing the spatial locations of urban structures. One may then identify the structure locations within the image domain and confine the damage measurements within individual structures. However, the size of these damage measurements will be different due to the different sizes of the structures in the images. In this work, to form equal-length damage feature vectors, statistical histograms for the damage measurements pertaining to different urban structures are computed by using the same number of histogram bins, which equally divide the numerical range of the extracted damage measurements. For an urban structure, the resulting histogram frequencies (i.e. the number of pixels at which the damage measurements fall into the histogram bins) are used as a damage feature vector, and the dimension of the vector is the number of the histogram bins.

5. NUMERICAL EXPERIMENTS

In this section, we present a numerical experiment using satellite images containing seismic damage. Three general damage levels are adopted, namely, *minor damage* (e.g., nearly or fully intact), *moderate damage* (e.g., partial collapse), and *major damage* (e.g. full collapse). The objective is to illustrate the potential to use the proposed damage classification procedure to perform regional damage classification, which is not possible if a non-probabilistic damage classification is used. Note that a realistic situation is mimicked where only a small number of structures are visually identified with designated damage levels, whereas the damage levels of the remaining structures are unknown.

5.1 Input Images and Training Data

The historical city of Bam, Iran was struck by a major earthquake (M_w = 6.6) on December 24, 2003, which devastated a large number of residential buildings. These structures were mostly constructed of mud-bricks, with little to no seismic resistance. Largely due to the collapse of these structures, approximately 30,000 lives were lost (Eshghi and Zare, 2003). In this study, we use the images captured by the Quickbird satellite (DigitalGlobe Inc., 2009) before and after the earthquake. In Figure 2, two panchromatic images are shown, which both have 1100x1800 pixels and a resolution of 60 *cm/pixel*.

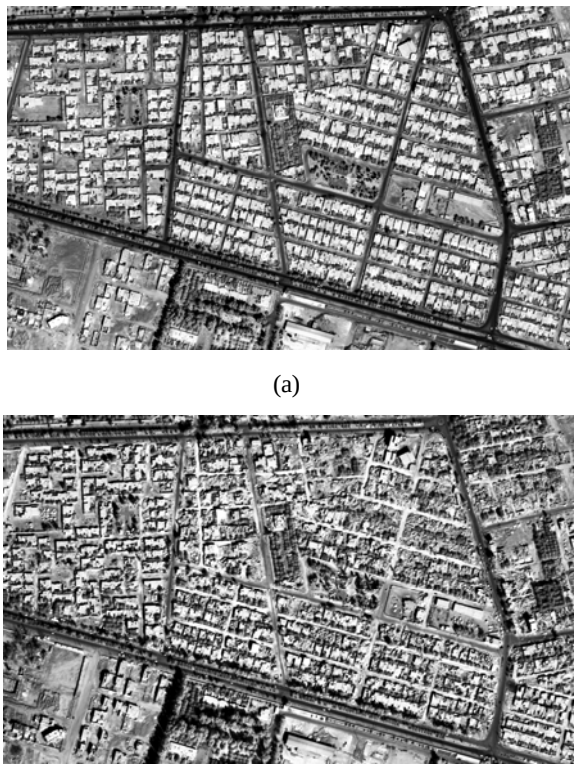

(a)

(b)

Figure 2. Geo-referenced images showing part of an urban area in Bam, Iran (manual histogram equalization was conducted on both images to enhance visibility): (a) pre-event image captured on Sep. 30, 2003; (b) post-event image captured on Jan. 3, 2004 (Images courtesy of DigitalGlobe Inc.).

Damage levels for individual urban buildings were determined manually by an independent analyst. This *visually identified truth* (VIT) is used as the reference data in this work. Note that agreement between the two analyst as to the damage state of individual buildings had to be obtained based on careful inspection of the bi-temporal change of building boundaries and the appearance of the roof structure.

In Figure 3(a), the 121 structures confined in the upper-left **blue** bounding box were selected to prepare training data, among which 37 (30%) structures were determined major-damage, 59 (49%) were moderate-damage, and 25 (21%) were minor-damage. Since structural damage is primarily edge-type, the dissimilarity-based feature extraction method is applied (Eq. 11). With the same parameters used in the first experiment, the resulting damage feature vectors are computed for all 468 structures in the images.



(a)



(b)

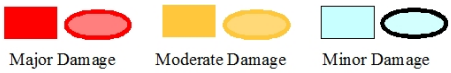

Figure 3: (a) Manually identified and predicted structural damage for individual urban structures. In this map, damage levels for structures in the **blue** bounding box were visually identified and used in preparing the training data, while damage levels for the remaining structures outside of this box were predicted using the proposed damage classification procedure; (b) structural damage classification for the select sub-regions, with the color-rendered damage levels overlaid with the original image of Figure 2(b).

5.2 Generation of Damage Maps for Individual Buildings and Sub-regions

By conducting a five-fold cross validation on the training data, the kernel parameters for mRVM can be defined. The resulting mRVM model has a total of 15 relevance vectors. Probabilistic damage classification is then conducted for the remaining 345 structures, and predicted damage is rendered in Figure 3(a). It is observed that predicted damage is visually consistent. For example, if one observes the structures in the upper right corner, these are generally subject to complete collapse; structures in the center area are mostly partially collapsed, while some structures in the lower left of the image remained almost intact.

In addition to an individual structure-based damage map in Figure 3(a), regional damage classification may be still useful in conducting a practical urban damage assessment. Due to the scalability of the proposed framework, one can compute the average distribution of posterior probabilities for any selected sub-regions in the image domain, which contain multiple urban structures (even part of a structure). In Figure 3(b), we mimic a practical situation by selecting a number of ellipse sub-regions of an analysts' interest. The resulting structural damage classification for the selected sub-regions is illustrated with different color-rendered ellipses. This regional urban structural damage map in conjunction with the individual structure-based damage map can provide a level-of-detail urban damage assessment at user-selected scales.

6. Conclusions

In this paper, we present a probabilistic classification framework for image-based urban structural damage identification using bi-temporal satellite images. With the use of a probabilistic multi-class classifier, the damage levels for individual urban structures may be obtained. As a result, the associated posterior probabilities can be used to quantify decision uncertainties and to analyze damage for user-defined urban objects with different spatial scales. Numerical experiments are conducted using two pairs of real bi-temporal satellite images. The damage classification results, either at the level of individual urban structures or via select sub-regions can quickly be evaluated using color-rendered damage maps. Notably for decision makers, these rendered maps can provide effective damage assessment information and thus guide post-disaster reconnaissance and recovery.

To fully realize an automated urban damage classification process using bi-temporal satellite images, we recognize the following needed future efforts. First, it is necessary to establish large-scale, image-based urban damage database for individual buildings through expert-level visual identification procedure. The used images should incorporate those captured for different natural hazards and different urbanized regions. Only with this availability, can a computational damage feature extraction and object-based damage classification be achieved. Second, currently the processing of image registration between and urban building extraction within large-scale satellite images dominates the processing time in the proposed workflow. Therefore, computationally efficient and accurate image registration methods and urban building extraction methods, where human intervention is minimized, are worthy of further investigation.

Acknowledgements:

The Holmes Fellowship Foundation, a graduate fellowship from the California Institute of Information and Telecommunication Technology and an NSF grant (CMMI-0729357) provided partial support for this work. Digital satellite images were obtained from DigitalGlobe Inc. This support is gratefully acknowledged. Special thanks to Miss Robyn Chung for performing the manual damage identification. Opinions in this paper are those of the authors and in no way reflect those of the supporting agencies.

References:

Chen, Z. and Hutchinson, T. (2007). "Empirical evaluation of dissimilarity measures for use in urban structural damage detection." *In the Proceedings of the IS&T/SPIE Symposium on Electronic Imaging Science and Technology*, San Jose, CA.

Chen, Z. and Hutchinson, T.C. (2010). Probabilistic urban structural damage classification using bitemporal images. *Earthquake Spectra*. 26(1): To Appear (Feb 2010).

Chiroiu, L. (2005). "Damage assessment of the 2003 Bam, Iran, earthquake using Ikonos imagery." *Earthquake Spectra*, 21(S1), S219–S224.

Cover, M. and Thomas, J. (2001). Elements of Information Theory. Wiley-Interscience.

DigitalGlobe Inc. (2009). www.digitalglobe.com

Duda, R. O., Hart, P., and Stork, D. (2000). Pattern Classification. Wiley-Interscience.

Eshghi, S. and Zare M. (2003). "Bam (Iran) earthquake of 26 December 2003, M_w 6.5: a preliminary reconnaissance report. http://www.iiees.ac.ir/English/bam_report_english_recc.html.

GeoEye Inc. (2009). www.geoeye.com.

Gonzalez, R.C. and Woods, R.E. (2008). Digital Image Processing (3rd Edition). Prentice Hall.

Gusella, L., Adams, B., Bitelli, G., Huyck, C., and Mognol, A. (2005). "Object-oriented image understanding and post-earthquake damage assessment for the 2003 Bam, Iran, earthquake." *Earthquake Spectra*, 21(S1), S225–S238.

Hutchinson, T. and Chen, Z. (2005). "Optimized estimated ground truth for object-based urban damage estimation using satellite images from the 2003 Bam, Iran, earthquake." *Earthquake Spectra*, 21(S1), S239–S254.

Mansouri, B., Shinozuka, M., Huyck, C., and Houshmand, B. (2005). "Earthquake induced change detection in the 2003 Bam, Iran, earthquake by complex analysis using Envisat ASAR data." *Earthquake Spectra*, 21(S1), S275–S284.

Rathje, E. and Crawford, M. (2004). "Using high resolution satellite imagery to detect damage from the 2003 northern Algeria earthquake." *In the Proceedings of the 13th World Conference on Earthquake Engineering*, Vancouver, B.C., Canada

Rejaie, A. and Shinozuka, M. (2004). "Reconnaissance of Golcuk 1999 earthquake damage using satellite images." *Journal of Aerospace Engineering, ASCE*, 17(1), 20–25.

Tipping, M. (2001). "Sparse Bayesian learning and the relevance vector machine." *Journal of Machine Learning Research*. 1:211–244.

Vapnik, V. (1998). Statistical Learning Theory. Wiley, New York.

Wei, L., Yang, Y., Nishikawa, R., Wernick, M., and Edwards, A. (2005). "Relevance vector machine for automatic detection of clustered micro-calcifications." *IEEE Transactions on Medical Imaging*, 4(10), 1278–1285.

Williams, O., Blake, A., and Cipolla, R. (2003). "A sparse probabilistic learning algorithm for real-time tracking." *In the Proceedings of the 9th IEEE International Conference on Computer Vision*, Nice, France.

JOINT CONFERENCE PROCEEDINGS
7th International Conference on Urban Earthquake Engineering (7CUEE) &
5th International Conference on Earthquake Engineering (5ICEE)
March 3-5, 2010, Tokyo Institute of Technology, Tokyo, Japan

PREDICTION AND UTILIZATION OF SPATIAL GEOTECHNICAL INFORMATION FOR ADMINISTRATIVE DECISION SUPPORT ON EARTHQUAKE DISASTER IN URBAN AREA

Chang-Guk Sun[1)]

1) Senior Researcher, Earthquake Research Center, Korea Institute of Geoscience and Mineral Resources, Korea
pungsun@kigam.re.kr

Abstract: A number of earthquake disasters have been caused by the site effects relating to the amplification of ground motion. The site effects are strongly influenced by the local geologic conditions such as soil thickness and stiffness. Most of major cities in the world are located across wide plane area where there are various surface topographies and corresponding subsurface geotechnical conditions. To prepare seismic hazards in an urban area, hence, the spatial prediction of geotechnical information in the entire region is not only important but fundamental. In this study, to predict reliably spatial geotechnical information based on restricted number of boring data, a procedural methodology is introduced and applied into GIS tool. Particularly, an urban area, Daejeon, located in the central region of South Korea, was selected for implementing an integrated GIS-based geotechnical information system because the area is represented as a hub of research and development as well as one of the largest metropolises in Korea. To build the geotechnical information system for Daejeon, existing geotechnical data collections were performed over the administrative entire region and a walk-over site survey was additionally carried out to acquire surface geo-knowledge data. Based on the data combined over the area of interest, geotechnical layers information was reliably predicted in the entire region of Daejeon with three-dimensional feature. For practical application of geotechnical information to assessing the site effects in the target urban area, seismic zoning maps of bedrock depth and site period were created and presented as regional basic information on earthquake-induced geotechnical hazards. According to the distribution of site period, seismic zonation of site classification was also carried out to determine the site amplification factors for seismic design at any site in the area of interest. Furthermore, the spatial information of representative site class with administrative unit was presented in the border of target area for the rapid decision support on earthquake disaster.

1. INTRODUCTION

Recent destructive earthquakes demonstrated that earthquake-induced geotechnical hazard and corresponding structural disasters are generally more severe over soft soils than over firm soils or rocks in urban areas (Tsai and Huang 2000, Sun et al. 2005, 2008). This implies that local geologic and soil conditions of a site have a profound influence on the amplification of earthquake ground motions (Sugito et al. 2000, Sun et al. 2005, Sun and Chung 2008). The difference of seismic amplification potential between different sites in a region can be estimated by predicting spatial variations in the subsurface soil thickness and the corresponding seismic responses (Sun et al. 2009). For such predictions, existing geotechnical borehole data across the area of interest can be effectively utilized. Expert geotechnical knowledge can also be utilized for enhancing the reliability of prediction.

Geographic information system (GIS) in recent years has emerged to be a powerful computer-based technique, with the integrated capabilities of spatial analysis, database management and graphic visualization (Codermatz et al. 2003). For geotechnical purposes, the GIS-based information systems have been developed and utilized to forecast and reduce natural hazards such as landslides or earthquakes (Sun et al. 2008). Particularly, in geotechnical earthquake engineering, there have been many researches on GIS technology (Anastasiadis et al. 2001, Sun et al. 2008). And the technical applications of GIS in geotechnical earthquake engineering are increasingly used in seismic zonations for the prediction and mitigation of earthquake-induced hazards (Marinos et al. 2001, Kolat et al. 2006). In this study, for the presentation and reliable estimation of the geotechnical subsurface layers over the selected urban area, Daejeon, which is represented as a hub of research and development and an inland metropolis in Korea, a GIS-based geotechnical information system was built in spatial domain. The implemented geotechnical information system was applied to geotechnical earthquake engineering related problems, particularly, to those dealing with site-specific amplification potentials that depend on the local site effects over the whole administrative region of the model inland urban area.

2. SITE EFFECTS INDUCING SEISMIC HAZARDS

Since a number of sites on recent alluvial deposits are prime locations for the development of urban areas, local

seismic amplification is a major concern not only in earthquake-prone regions but also in weak or moderate seismic regions. The site effects that cause seismic amplification and correspondent disasters are mainly associated with geological and geotechnical site conditions.

2.1 Site Period

Site effects are basically associated with the phenomenon of seismic waves traveling through soil layers. The phenomenon can be explained first by differences in the shear wave velocity (V_S) between the soil layers and the underlying rock, which represent an impedance contrast, and second by the thickness of soil layers or the depth to bedrock. The largest amplification of earthquake ground motion at a nearly level site occurs at approximately the fundamental lowest natural frequency (Rodriguez-Marek et al. 2000, Sun et al. 2005).

The period of vibration corresponding to the fundamental frequency is called the characteristic (or predominant) site period (T_G) and for multi-layered soil can be computed as Eq. (1) below:

$$T_G = 4\sum_{i=1}^{n}\frac{D_i}{V_{Si}} \tag{1}$$

where D_i is the thickness of each soil layer above the bedrock (i.e., the bedrock depth, $H = \Sigma D_i$), V_{Si} is the shear wave velocity of each soil layer, and n is the number of soil layers. The site period is a useful indication of the period of vibration, at which the most significant amplification is expected. Thus, if the spatial variations in the thickness and V_S values of soil layers are known for an entire study area, the spatial variation of the T_G can be readily established and used for regional earthquake hazard estimations.

2.2 Existing Site Classification System in Korea

For seismic design, the local site effects are quantified, in the Korean seismic design guide based on the seismic codes of western United States (Sun 2004, Sun et al. 2005), by the site coefficients for short-period and mid-period, F_a and F_v, for the mean V_S to a depth of 30 m (V_S30) and the corresponding site classes (Dobry et al. 2000, Sun et al. 2005). Accordingly, in the Korean seismic codes, the site characterization is based on the top 30 m of the ground. The site class is determined solely and unambiguously by one parameter, V_S30.

To quantify the site effects, correlations between V_S30 and the site coefficients were established on the basis of empirical and numerical studies without defining the depth to bedrock (Borcherdt 1994, Sun 2004). F_a and F_v were calculated by the average ratio of response spectra or ratio of Fourier spectra between soil and nearby firm to hard rock site, computed in period bands from 0.1 to 0.5 s and from 0.4 to 2.0 s, respectively. The conditions of the site with an exceptional category F can be classified into five categories, namely A to E, according to the V_S30 values of the current seismic codes, including the Korean seismic design guides, the Uniform Building Code (UBC), and the National Earthquake Hazard Reduction Program (NEHRP) provisions (Dobry et al. 2000, Sun 2004, Sun et al. 2005), despite different site classification schemes in other seismic codes. In the above current seismic design guides, the site coefficients quantifying the seismic amplification are used to estimate the design response spectra dependent on both the site categories and the intensity of rock motions. Both F_a and F_v are unity for rock (site class B), but increase as the soil becomes softer with decreasing V_S30 or as the site class evolves through C and D to E.

2.3 Site Classification System with Site Period in Korea

In spite of the common use of V_S30 as the sole criterion considering the geotechnical dynamic property in the current seismic design codes including the Korean guide, the depth to bedrock is not regarded in the current site classification system (Sun 2004). Recently, to use T_G for reasonable seismic design in Korea, considering both the bedrock depth and the geotechnical dynamic property with respect only to the inland sites categorized into classes B, C and D, Sun (2004) proposed a new site classification scheme based on T_G together with V_S30. In the proposed scheme for seismic design, the local site effects are quantified by F_a and F_v according to the site classes, but the site classes C and D are subdivided into four sub-classes. Table 1 illustrates the site classification scheme developed by Sun (2004) according to T_G, especially for the inland region in Korea. This scheme can be used by engineers for preparing the seismic design and evaluating the seismic performance of a site.

Table 1 Site Classes and Site Coefficients Based on Site Period for the Inland Region of Korea (Sun 2004)

Generic Description	Site Class		Criteria		Site Coefficients	
			V_S30 (m/s)	T_G (s)	F_a	F_v
Rock	B		> 760	< 0.06	1.00	1.00
Weathered Rock and Very Stiff Soil	C	C1	> 620	< 0.10	1.20	1.03
		C2	> 520	< 0.14	1.40	1.07
Intermediate Stiff Soil		C3	> 440	< 0.19	1.60	1.12
		C4	> 360	< 0.27	1.80	1.17
Deep Stiff Soil	D	D1	> 320	< 0.34	2.00	1.22
		D2	> 280	< 0.43	2.20	1.27
		D3	> 240	< 0.55	2.40	1.32
		D4	> 180	< 0.68	2.60	1.37

3. FRAMEWORK OF GIS-BASED GEOTECHNICAL INFORMATION SYSTEM

To efficiently manage and use spatial geotechnical information for the ground surface and subsurface, geotechnical information systems have been developed based on GIS technology. The GIS-based geotechnical information system described here incorporates a geostatistical kriging interpolation technique, adopted for reliable spatial prediction of geotechnical data (Sun 2004, Sun et al. 2008, Sun and Chung 2008). Geostatistical kriging

can be regarded as the best linear unbiased estimate and optimal interpolation method for geological and geotechnical predictions in space, because it is a linear combination of weighted sample values having minimum variance (Oliver and Webster 1990). The basic premise of kriging interpolation is that every unknown point can be estimated by the weighted sum of the known points. The estimated value, $Z^*(x_i, y_j)$, at coordinates (x_i, y_j), can be calculated by Eq. (2) below:

$$Z^*(x_i, y_j) = \sum_{\alpha=1}^{n} w_{ij\alpha} \times Z_\alpha \qquad (2)$$

where n is the number of the known values, Z_α. A set of weights, $w_{ij\alpha}$, is calculated for every point. These weights are computed to place greater emphasis on the known points close to the unknown points and less emphasis on known points far from unknown points. This process is performed by calculating a variogram that characterizes the spatial continuity or roughness of a point data set with the distance between each pair of points (Olea 1999).

The GIS-based geotechnical information system was applied here for a densely urbanized inland area, Daejeon, in Korea. As presented in Figure 1, the GIS-based system has four functional components: geo-knowledge database, spatial analysis, geotechnical analysis, and visualization. Arrows in the figure indicate the direction of data flow, which occurs between the database component and mutually geotechnical analysis component (Tsang et al. 2007, Sun et al. 2008). For predicting the spatial geotechnical information more reliably in the area of interest within the GIS framework (Gangopadhyay et al. 1999, Sun et al. 2008), new concepts were applied, such as the use of an extended area encompassing the study area and geo-knowledge to acquire additional surface geotechnical data (Sun et al. 2008). Extended area can provide more reliable geotechnical information for the marginal parts of the area of interest, because interpolations contribute to more reliable spatial estimation than extrapolations.

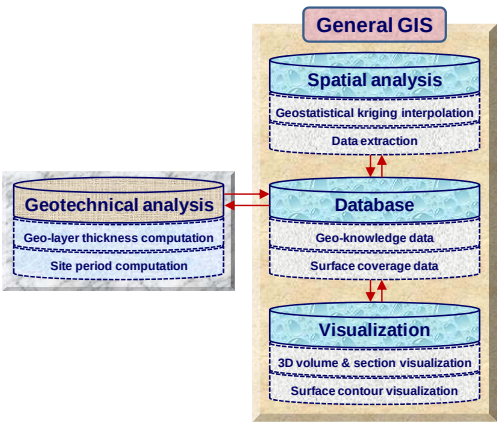

Figure 1 Architecture of Geotechnical Information System

To build a database for the geotechnical information system, surface-to-bedrock borehole data for the area of interest across the extended area was first collected. In addition, for a more reliable prediction of the spatial geotechnical information, geo-knowledge database was built up by undertaking ground survey to acquire surface geotechnical data, particularly in areas where borehole data were lacking (Sun 2004). For the purpose of this study, surface and subsurface geotechnical layers were classified into five categories: fill, alluvial soil, weathered residual soil, weathered rock, and bedrock (Sun 2004). To manage and update the geotechnical data, database (DB) management system was developed for the geo-knowledge data of this study. The system is composed of DB server supported by the FTP server and the DB management program for clients. Basically, the system allows for input and renewal of data through communications between server and client's program by TCP/IP network and for the conversion of general-purpose application into text or spread sheet formats.

4. IMPLEMENTATION OF GIS-BASED GEOTECHNICAL INFORMATION SYSTEM

For estimating the seismic site effects at Daejeon in Korea, GIS-based geotechnical information system was built by predicting the information on spatial geotechnical layers across the area of interest. Daejeon is one of the largest metropolitan areas in Korea and particularly a hub of technical research and development in Korea. Thus, Daejeon is vulnerable for extensive damage during an earthquake.

4.1 Building of Geotechnical Database

As part of building geotechnical information system at Daejeon, the geo-knowledge DB containing the borehole drilling data and the surface geotechnical data referenced with the topographic maps was first created for two areas within the frame of DB management system. On the basis of the DB of the areas, the GIS-based system was implemented for spatial geotechnical characterization using several advanced GIS software tools. Accessing the DB server via the DB management program, a client can open the interface to examine and retrieve data, as shown in Figure 2.

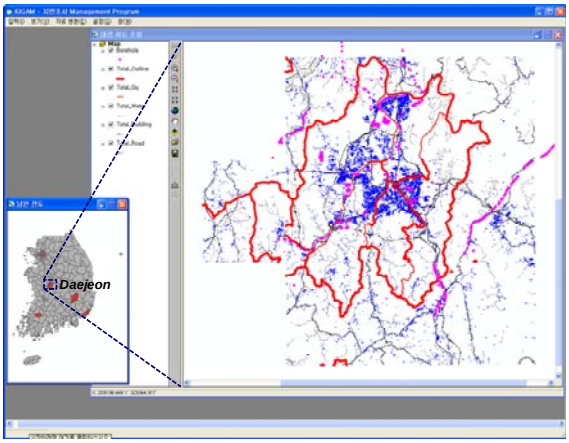

Figure 2 Interface of DB Management Program

The left and right windows indicate the administrative units of South Korea for selecting the study area and the locations of data (indicated with points in the right window) across the study area, which are referenced by topographic features and administrative borders, respectively. In the DB management program, the client can input new data according to the standardized format by opening other interface option. More than 2,500 datasets including about 1,300 borehole data and 1,200 surface geotechnical data were archived into the geo-knowledge database for Daejeon metropolis. The database in the program was exported for analysis and display within the GIS tools.

Figure 3 shows the spatial distribution of existing borehole data and surface geo-knowledge data in the extended area of Daejeon created within the spatial GIS-based system. In Figure 3, it can be examined that most of surface geo-knowledge data acquired from the site visit are located the areas lacking the existing borehole data. In this paper, the vertical scales in three-dimensional figures were exaggerated five times and surface coverage data such as waterways, buildings and/or roads were overlain on ground surface for better visual depiction of surface and subsurface features. The spatial information was built with the unit of meter on the local TM (Transverse Mercator) coordinate system of local origin, on which X and Y represent the directions from west (W) to east (E) and south (S) to north (N), respectively, and Z represents the elevation.

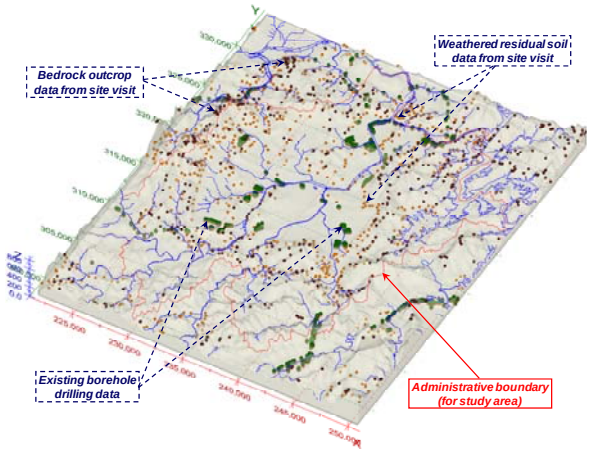

Figure 3 Distribution of Existing Borehole Data and Surface Geo-knowledge Data in the Extended Area of Daejeon

4.2 Implementation of Geotechnical Information System

In geotechnical and earthquake engineering, the GIS can be used either alone or in conjunction with specified model-analysis techniques (Gangopadhyay et al. 1999). In this study, the geotechnical information system with geo-knowledge DB was used with several GIS software tools, ESRI ArcGIS Desktop, EVS-Pro, and AutoCAD LDDT, in combination with various advanced techniques (Sun et al. 2009). Moreover, for better spatial estimation of geotechnical information, a sophisticated kriging interpolation program based on Visual BASIC code was developed and adopted for the spatial analysis component.

To demonstrate the building of GIS-based system, the study and extended areas were selected for target urban area, Daejeon. The rectangular dimension of the extended area measures 29.0 km on WE and 36.0 km on NS. The study area consists of the whole administrative region for Daejeon metropolis. For reliably estimating the spatial geotechnical layers in areas of interest, the kriging prediction method was applied to the extended area. From these estimated values, the geotechnical information for the study area was extracted using a specified GIS cut function. The conceptual steps involved in this extraction are depicted in Figure 4.

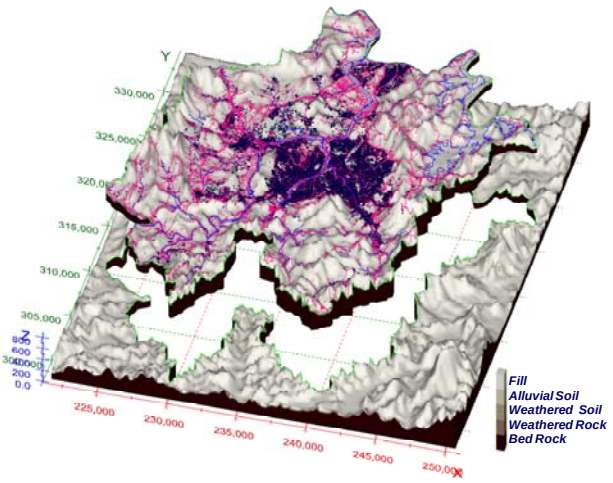

Figure 4 Spatial Geotechnical Layers Predicted Within Geotechnical Information System for Daejeon

The variation of geotechnical information at any section in the area of interest can be examined by using the expert GIS tools, which were adopted in this study. Figure 5 shows a couple of sections of predicted spatial geotechnical layers for several slices of the study area together with the topographic variation illustrated by superposing the satellite image. Particularly, the area along the rivers or creeks has thick soil deposits while thin soil deposits were observed at hilly and mountainous areas, as shown in Figure 5. Thus, the deep soil deposits in Daejeon have been mainly developed the fluvial actions during frequent floods along the rivers and creeks.

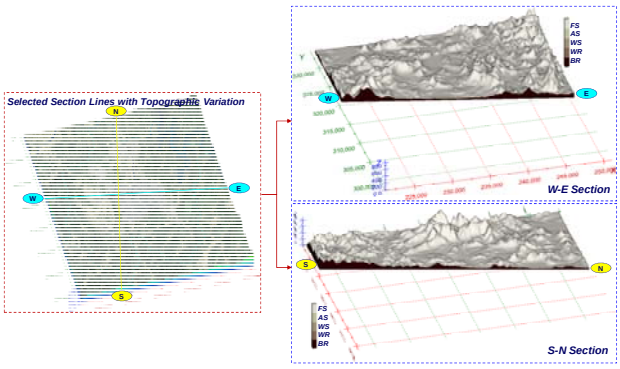

Figure 5 Sections Examined for Subsurface Geological Structures with Topographic Feature in Daejeon

Three-dimensional visualization of geotechnical layers in space is generally quite informative. However, a solid spatial ground volume model cannot be directly applied to engineering projects because from this model subsurface geological structures will not be clear to most users. Therefore, visualizations within GIS tools usually present two-dimensional contour maps (Kolat et al. 2006). The thickness of geotechnical layers and the depth to bedrock are depicted as zoning contour maps on spatial topographic features of the study area (Sun and Chung 2008). Figure 6 presents representative spatial zoning maps showing the distribution of the depth to bedrock at Daejeon, which were computed in the geotechnical analysis component of the GIS-based geotechnical information system.

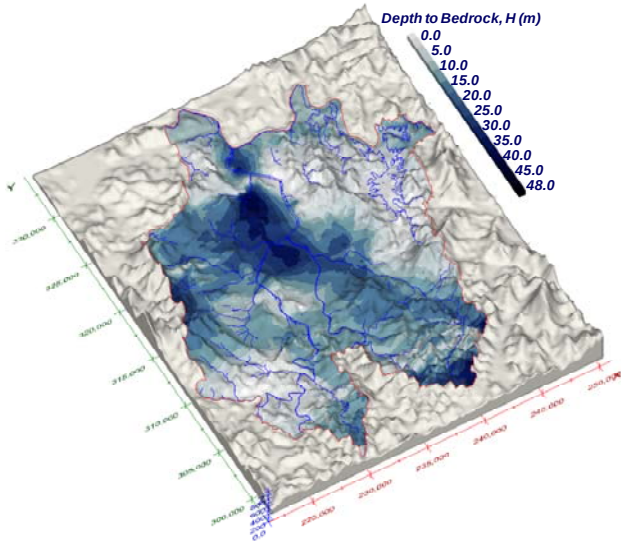

Figure 6 Spatial Distribution of Depth to Bedrock in the Study Area of Daejeon

From Figure 6, it is observed that the 20 to 48 m thick soil deposits are distributed in the plains adjacent to waterways. These characteristics in soil formation generally represent an inland topographical basin, and they could have resulted from fluvial action along the rivers and creeks surrounding mountains during the floods of the geological past. The depth to bedrock is one of the most important geotechnical parameters for addressing various geotechnical problems (Sun 2004), particularly for evaluating seismic site amplification and corresponding hazards (Sun et al. 2008). As shown in Figure 6, the depth to bedrock in the plains, including rivers and creeks, is more than that in surrounding mountain areas. Such zones of deep bedrock are susceptible to ground motion amplification owing to the site effects.

5. SPATIAL GEOTECHNICAL ZONATION ON EARTHQUAKE DISASTER POTENTIAL

Site-specific seismic response characteristics, represented as the site effects, play an important role in evaluating earthquake disasters. Empirical relationships or simple site classification schemes have also been used to evaluate site-specific seismic responses on a regional scale because of their convenience and effectiveness (Wills et al. 2000, Sun et al. 2008). In this study, only the geotechnical parameter of the site period (T_G) was used to evaluate the site effects for the Daejeon area. The results obtained by using the GIS technique are presented on zoning maps showing the locations or zones of earthquake disaster potential.

The T_G was computed using both the thickness and V_S of soil layers over the bedrock. The thicknesses of soil layers were already estimated across the study area using the GIS-based geotechnical information system, but the representative V_S values of geotechnical layers for Daejeon could not be determined. Therefore, these were compiled from the results of the previous in-situ seismic tests conducted for obtaining V_S profiles in the Korean land areas (Sun 2004, Sun et al. 2005). From these results, the V_S was determined representatively to be 350 m/s for fill, 330 m/s for alluvial soil, 450 m/s for weathered residual soil, 550 m/s for weathered rock, and 1,000 m/s for bedrock. For efficient geotechnical zonation based on the T_G values over the study area, the geotechnical thickness data interpolated in the spatial analysis of the GIS-based system and the representative V_S values were imported into the geotechnical analysis component. Then, the T_G was calculated at 100 m intervals based on Eq. (1). The T_G values calculated for the target metropolitan area were spatially modeled, and the results are presented as spatial zoning maps in Figure 7.

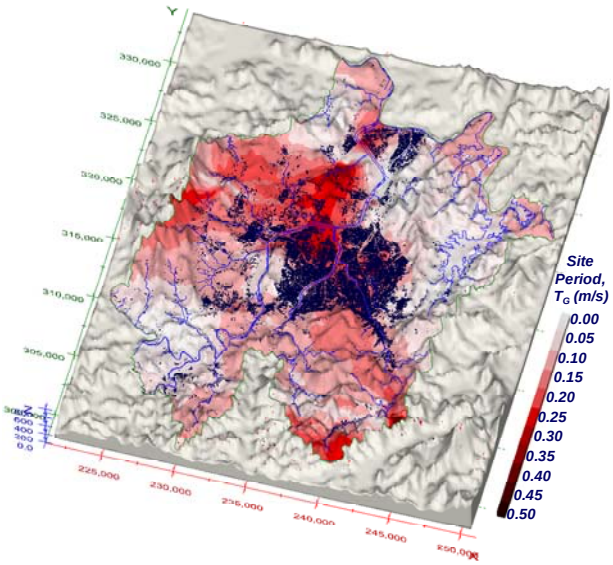

Figure 7 Spatial Zonation of T_G for Earthquake Disaster Potential at Daejeon

Although several parts of mountainous zones show the T_G values higher than other parts, the T_G values for plains are generally higher than those for mountainous and hilly locations, and range mainly between about 0.10 and 0.50 s in the Daejeon area. The distribution of T_G values in space is particularly consistent with the distribution of bedrock depth depicted in Figure 6. In Figure 7, the spatial main building

coverage data are shown as an overlay on the T_G distribution data to examine the seismic vulnerability of buildings. These rigorous zonations, including building coverage, can serve as a fundamental resource for predicting seismically induced structural damage. The natural period of a building is generally accepted to be 0.1 times the number of its stories (Kramer 1996, Sun et al. 2008). Buildings of lower than five stories would therefore be vulnerable to seismic damage caused by earthquake resonance. Zoning information based on the T_G values can contribute to formulating earthquake-related strategies, rational land-use plans, and developmental plans for inland metropolitan areas.

Seismic design and seismic performance evaluation can also be carried out by adopting the site classification system based on the T_G values available from the seismic zoning maps. In this study, the site classification scheme developed by Sun (2004) (see Table 1) for the inland region in Korea was adopted. Figure 8 shows the spatial zoning map with the main road coverage data in respect of seismic site classification in the study area, built within the GIS-based geotechnical information system. The site coefficients, F_a and F_v, according to T_G values for the seismic design of structures are presented as legend to the figure.

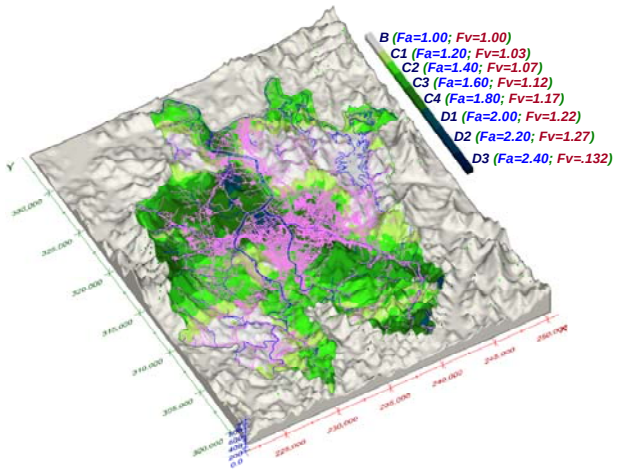

Figure 8 Spatial Zonation on Site Classes for Preliminary Seismic Design at Daejeon

The plains in the area of interest fall within the site classes C (C1 to C4) and D (D1 to D3), which represent the amplifying earthquake ground motions of the sites, and match with the seismically vulnerable areas inferred from T_G values indicated in Figure 7. On the other hand, most of the hilly zones with the exception of western and southeastern zones fall into site class B whose site coefficients (F_a and F_v) are 1.0. These spatial zonation maps of site class provide the information needed for preliminary seismic design of the structure or building. Further, the site classification maps indicate whether the buildings or structures located on the plains need evaluation of their seismic performances. As depicted in Figure 8, the site class can be determined solely and unambiguously by one parameter, T_G. Therefore, if the spatial variations of T_G are known for the entire study area, the site classes and from them the site coefficients can be readily determined for any location in the study area by spatial seismic zonation.

The spatial seismic zonation maps on T_G produced by the geotechnical information system can be used to predict earthquake disasters. Also, the spatial site classification map based on the T_G can be applied in both preliminary seismic design and seismic performance evaluation of structure at any site in the entire study area. Differing from the continuous distribution of site classes illustrated in Figure 8, the information on site class would be uniquely assigned to administrative sub-unit (called 'dong' in Korea) particularly for quickly making a decision against earthquake. The site classes with the administrative sub-units were determined based on the average of T_G values in each district and are shown in Figure 9. Especially, the information of site classes for districts can be usefully applied to the decision-support program against earthquake by the executive or official agency.

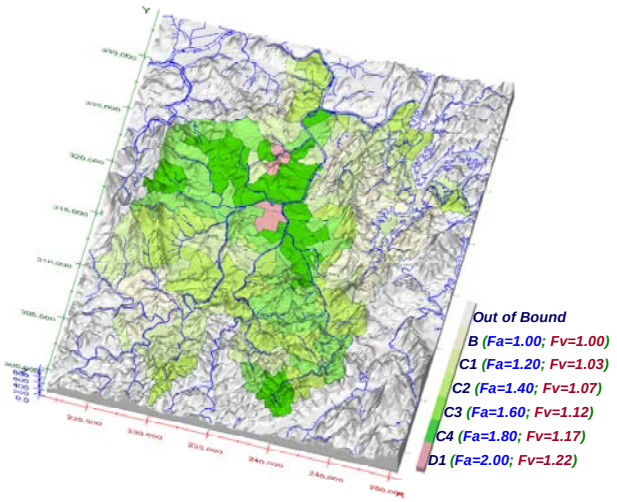

Figure 8 Site Class with Administrative Sub-unit by Computing the Average T_G in Each Unit of Daejeon

The GIS-based geotechnical information system implemented in this case study successfully revealed the spatial geotechnical zonation for estimating systematically the local seismic site effects in an inland urban area of Korea. The fundamental seismic information provided should prove useful to earthquake engineers, regional agencies, and insurance companies. The zoning map and administrative sub-unit map on site classes, which provide short- and mid-period site coefficients across the entire study area, can also be used to develop earthquake preparedness plans and strategies for the target metropolitan area.

6. CONCLUSIONS

This study presented information on earthquake disaster potential in terms of site effects for a densely urbanized area, Daejeon, in Korea. To enhance the reliability of information, the concept of geo-knowledge was applied to acquiring data

in the extended area encompassing the study area. For this study, existing borehole data and surface geotechnical data were utilized, by archiving them into a database. For managing the database, the DB management system was developed and used. With the help of DB, the information on spatial geotechnical layers was reliably predicted by building the GIS-based geotechnical information system for the target metropolis.

Based on the spatially interpolated geotechnical layers for the extended area, the map showing the distribution of the depth to bedrock was prepared for the study area composed of the whole administrative region for Daejeon metropolis. To assess the seismic site effects on a regional scale, the distribution of the T_G was created in the form of spatial zonation map based on the geotechnical layers estimated within the GIS-based system and V_S determined representatively from the prior researches. The T_G map suggests that the buildings with lower than five stories are vulnerable to seismic activity. Based on the distribution of T_G values in the area of interest, seismic zoning map for site classification was also created to determine the short- and mid-period site coefficients for preliminary seismic design. These site classification maps show that the plains in the study areas fall within the site classes C and D in terms of amplifying earthquake ground motion, implying thereby that the structures or buildings on the plains may need seismic performance evaluation. Furthermore, the site class with each administrative sub-unit in the area of interest was informed in order to assist the seismic decision-making in Daejeon. This case study of spatial geotechnical seismic zonation using GIS technology verifies the usefulness of the geotechnical information system as a regional systematic tool for use in earthquake disasters-related planning.

Acknowledgements:

The author would like to acknowledge the support from the Basic Research Project of the Korea Institute of Geoscience and Mineral Resources (KIGAM) funded by the Ministry of Knowledge Economy of Korea.

References:

Anastasiadis, A., Raptakis, D., and Pitilakis K. (2001), "Thessaloniki's Detailed Microzoning: Subsurface Structure as Basis for Site Response Analysis," *Pure and Applied Geophysics*, **158**(12), 2597-2633.

Borcherdt, R.D. (1994), "Estimates of Site-dependent Response Spectra for Design (Methodology and Justification)," *Earthquake Spectra*, **10**(4),617-653.

Codermatz, R., Nicolich, R., and Slejko, D. (2003), "Seismic Risk Assessment and GIS Technology: Applications to Infrastructures in the Friuli-Venezia Giulia Region (NE Italy)," *Earthquake Engineering and Structural Dynamics*, **32**(11), 1677-1690.

Dobry, R., Borcherdt, R.D., Crouse, C.B., Idriss, I.M., Joyner, W.B., Martin, G.R., Power, M.S., Rinne, E.E., and Seed, R.B. (2000), "New Site Coefficients and Site Classification System Used in Recent Building Seismic Code Provisions," *Earthquake Spectra*, **16**(1), 41-67.

Gangopadhyay, S., Gautam, T.R., and Gupta, A.D. (1999), "Subsurface Characterization Using Artificial Neural Network and GIS," *Journal of Computing in Civil Engineering*, American Society of Civil Engineers, **13**(3), 153-161.

Marinos, P., Bouckovalas, G., Tsiambaos, G., Sabatakakis, N., and Antoniou, A. (2001), "Ground Zoning against Seismic Hazard in Athens, Greece," *Engineering Geology*, **62**(4), 343-356.

Kolat, C., Doyuran, V., Ayday, C., and Süzen, M.L. (2006), "Preparation of a Geotechnical Microzonation Model Using Geographical Information Systems Based on Multicriteria Decision Analysis," *Engineering Geology*, **87**(3-4), 241-255.

Kramer, S.L. (1996), "Geotechnical Earthquake Engineering," Prentice-Hall Inc.

Oliver, M.A. and Webster, R. (1990), "Kriging: A Method of Interpolation for Geographical Information Systems," *International Journal of Geographical Information Systems*, **4**(3), 313-332.

Olea, R.A. (1999), "Geostatistics for Engineers and Earth Scientists," Kulwer Adcademic Publishers, Boston.

Rodriguez-Marek, A., Bray, J.D., and Abrahamson, N. (2000), "A Geotechnical Seismic Site Response Evaluation Procedure," *Proceedings of the 12th World Conference on Earthquake Engineering*, CD-ROM, Paper No. 1590.

Sugito, M., Oka, F., Yashima, A., Furumoto, Y., and Yamada, K. (2000), "Time-dependent Ground Motion Amplification Characteristics at Reclaimed Land after the 1995 Hyogoken Nambu Earthquake," *Engineering Geology*, **56**(1-2), 137-150.

Sun, C.G. (2004), "Geotechnical Information System and Site Amplification Characteristics for Earthquake Ground Motions at Inland of the Korean Peninsula," Ph.D. Dissertation, Seoul National University.

Sun, C.G., Chun, S.H., Ha, T.G., Chung, C.K., and Kim, D.S. (2008), "Development and Application of GIS-based Tool for Earthquake-induced Hazard Prediction," *Computers and Geotechnics*, **35**(3), 436-449.

Sun, C.G. and Chung, C.K. (2008), "Assessment of Site Effects of a Shallow and Wide Basin Using Geotechnical Information-based Spatial Characterization," *Soil Dynamics and Earthquake Engineering*, **28**(12), 1028-1044.

Sun, C.G., Kim D.S., and Chung, C.K. (2005), "Geologic Site Conditions and Site Coefficients for Estimating Earthquake Ground Motions in the Inland Areas of Korea," *Engineering Geology*, **81**(4), 446-469.

Sun, C.G., Kim, H.S., Chung, C.K., and Kim, M.M. (2009), "Spatial Assessment of Seismic Site Effects Based on GIS for Inland Urban Areas in Korea," *Proceedings of the International Symposium on Geo-informatics and Zoning for Hazard Mapping*, CD-ROM, 279-284.

Tsai, Y.B. and Huang, M.W. (2000), "Strong Ground Motion Characteristics of the Chi-Chi, Taiwan Earthquake of September 21, 1999," *Earthquake Engineering and Engineering Seismology*, **2**(1), 1-21.

Tsang, H.H., Lam, N.T.K., and Lo, S.H. (2007), "Probabilistic Seismic Hazard Assessment without Source Characterization," *WSEAS Transactions on Environment and Development*, **3**(1), 8-13.

Wills, C.J., Petersen, M., Bryant, W.A., Reichle, M., Saucedo, G.J., Tan, S., Taylor, G., and Treiman, J. (2000), A Site-Condition Map for California Based on Geology and Shear-Wave Velocity, Bulletin of the Seismological Society of America, **90**(6B), 187-208.

JOINT CONFERENCE PROCEEDINGS
7th International Conference on Urban Earthquake Engineering (7CUEE) &
5th International Conference on Earthquake Engineering (5ICEE)
March 3-5, 2010, Tokyo Institute of Technology, Tokyo, Japan

A NEW DISASTER MANAGEMENT MANUAL FOR DISASTER REDUCTION

Shinya Kondo[1] and Kimiro Meguro[2]

1) Research Scientist, Disaster Reduction and Human Renovation Institution, Kobe, Japan
2) Professor, Institute of Industrial Science, the University of Tokyo, Japan
kondos@dri.ne.jp, meguro@iis.u-tokyo.ac.jp

Abstract: In this study, the authors proposed the system "a new style disaster management manual for disaster reduction". The aims of this system, organization and regions can sort out potential problems, with using the functions, "Analysis and Assessment of existing manuals" and "Independent of existing manuals". And they can plan efficient disaster countermeasures, with using the function "Drafting and updating of manual". With repeat this process, they can create a good environment for the disaster management improvement. For application of this system to some organization, scenario based on damage estimation, and Lesson or record of past disaster case should be defined. So time flow and characteristic or scales of damage are considered. And this manual has indexes for explaining each situation and responsibilities. With these indexes, we construct relational database as web application. Then users can use this manual by Internet / Intranet. In this instance, the authors tried to apply this system to some organization that will respond to earthquake in The Islam Public of Iran.

1. INTRODUCTION

The ideal disaster management countermeasures are to be conducted by properly balancing the following three measures: Disaster Mitigation, Preparedness/Disaster Response and Optimum Recovery/Reconstruction Plan (Figure 1). "Disaster Mitigation" means efforts to prevent hazard from becoming a disaster. "Preparedness/Disaster Response" means measures to prevent the disaster from affecting/spreading widely. "Optimum Recovery/ Reconstruction Plan" means to recover and reconstruct from disaster as soon as possible to reduce its effects to a minimum. Moreover, disaster management cannot be improved without user's imagination of real disaster situation or the implementation of these three measures.

For realizing these measures, people should prepare an environment as shown in Figure 2 not only during disaster periods but also during disaster free periods. This environment consists of 5 elements: time and spatial imagination of what will happen after a disaster, sorting out potential problems by analyzing current disaster prevention policies, design and development of countermeasures, implementation or disaster drill, and "assessment of each element". If all the people involved in implementing disaster countermeasures (hereinafter called users) participate in their design, they have the chance to plan them based on the regional characteristics because they have to study the background of each countermeasure. For realization of this scheme, it is important to prepare an environment which consists of ordered past or ongoing disaster responses and provide information to people so that they can imagine the situation after a disaster occurs. Therefore it is necessary to satisfy the following conditions: building up and sharing disaster response information obtained from the current system, analysis/assessment of the information in real-time, and imagination of disaster response and related information.

It is needless to say that a disaster management manual should contribute to the improvement of each of these approaches. Unfortunately, most of the existing manuals are mainly aimed at the "Preparedness/Disaster Response". They are "Government prepared," with inconveniences such as ambiguity over where the responsibility lies and the characteristics of the region and organization. They are "thick printed material," difficult to edit and evaluate. Such manuals do not improve the overall disaster management.

Based on these points, the authors propose the "New Style Disaster Management Manual". Organizations and regions, that actually use this proposed manual, can sort out potential problems, review, conduct and assess countermeasures so that they can create a good environment for the disaster management improvement (see Figure 3). The authors concluded that there are three functions necessary in order to achieve the realization of this manual: "Analysis and Assessment of existing manuals", "Independent edition by each purpose/user", and "Drafting and Updating of manual". In this instance, the authors tried to apply this system to some organization that will respond to earthquake in The Islam Public of Iran (Iran).

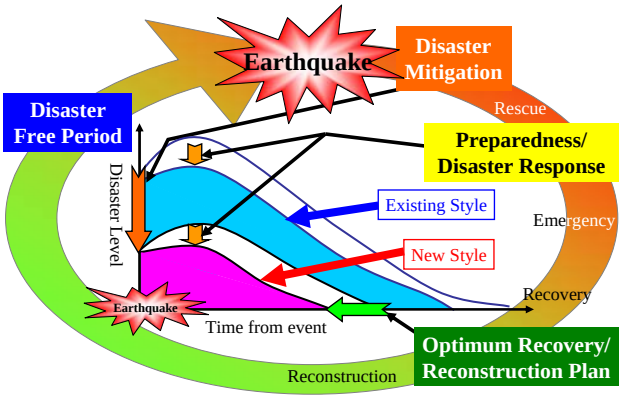

Figure 1 Ideal disaster management countermeasures

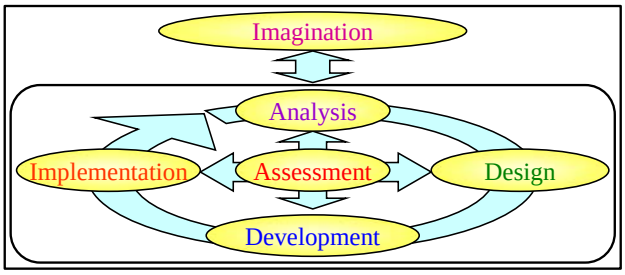

Figure 2 Environment for implementation of ideal disaster management countermeasures

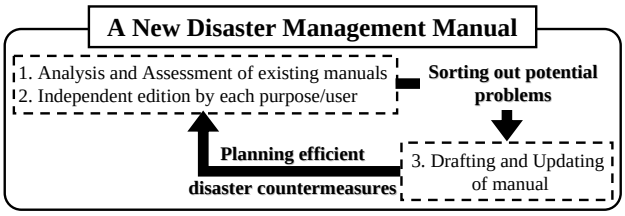

Figure 3 Flowchart of A New Disaster Management Manual



Figure 4 An instance of New Style Disaster Management Manual

2. ORGANIZATION OF THE MANUAL

In a New Disaster Management Manual, the scenario of damage estimation is incorporated. So time flow and characteristic or scales of damage are considered into this manual. This manual has six indexes which are important for analyzing and evaluating disaster management based on the scenario of damage estimation. These contents are "Responsible organization", "Service contents", "Term of measures (Relatively)", "Time to start and finish measures of an event (Absolutely)", "Workloads (man x day)". A relational database is constructed from those indexes. This database is used in web application as disaster management manual (see Figure 4). So, users can use this manual if only they can use Internet / intranet.

3. MAIN FEATURES

3.1 Analysis and Assessment of existing manuals

For the realization of comprehensive disaster management, it is necessary to sort out problems of existing manual. Manual should be analyzed and assessed rationally / objectively. However, most of the existing manuals are "Thick books", it is difficult to judge the quality of manual like relations between each items and the whole balance of contents.

In this study, the authors prepare the function, "Analysis and Assessment of existing manuals". It is easy to know the relation between each works from indexes set at previous section "Organization of the Manual" excluding "Work loads", therefore it is easy to analyze contents of present manual rationally / objectively from various points of view. Figure 5 presents an example of analysis and assessment of the disaster management manual of a big city in the Tokyo metropolitan region. The x-axis is "Time to start from an event". The y-axis represents different "Responsible organization". The z-axis is "Amount of the work" to be done. From the x-axis, we can see actions are not well pointed out after 6-24 hours and four days. Also from the y-axis, it can be seen that amount of work is not balanced among organizations.

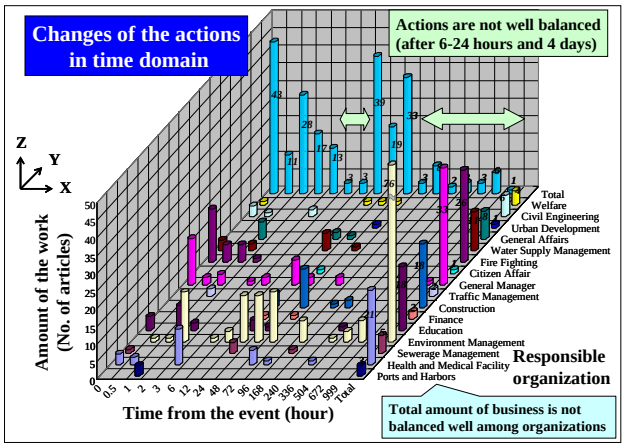

Figure 5 Sample of analytical result of existing manual (after MEGURO, 2001)

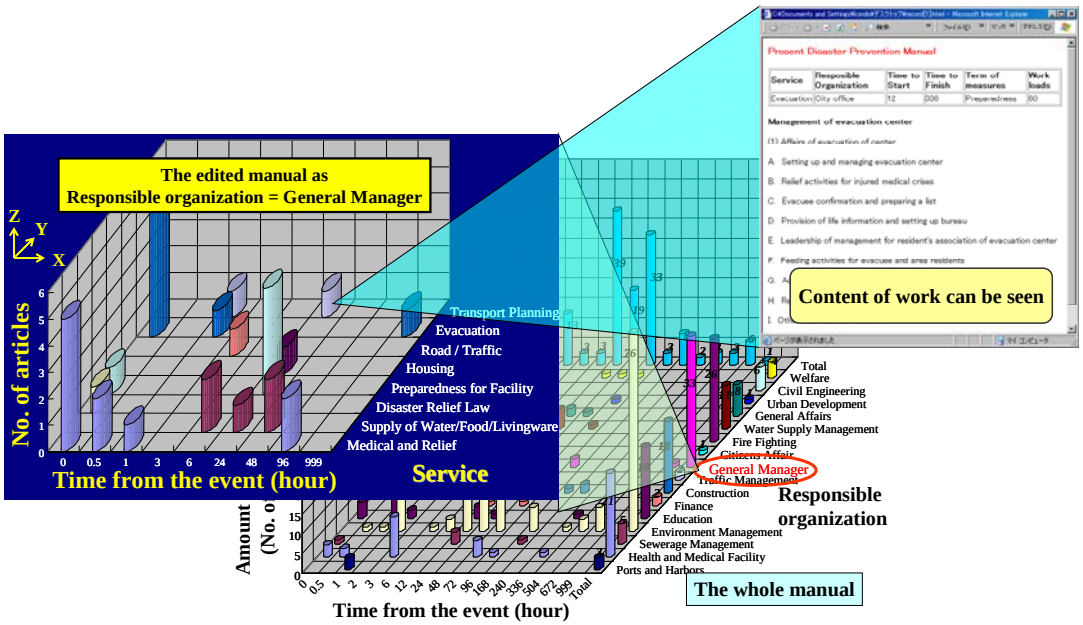

Figure 6 Independent edition by each purpose /user

3.2 Independent edition by each purpose /user

It is essential to analyze / assess disaster management manual from a whole organizational view, but it is not enough. Contents of the total manual become better, if users know how they should act personally and who / when to do some services. To pick information of a latest disaster and to know user's need, directly by accessing the manual is important to assess the real situation of a disaster.

In this study, the authors prepare the function, "Independent edition by each purpose / user". Users choose necessary conditions from indexes set at previous section "Organization of the Manual" excluding "Work loads", picking up necessary items from whole manual, so they can get idea about their own role, during a disaster. Figure 6 shows the application of this feature in the existing government disaster management manual as presented in Figure 5. This figure shows that how a General Manager, (normally mayor or governor) of an organization can select his own responsibility just by clicking a button on his position.

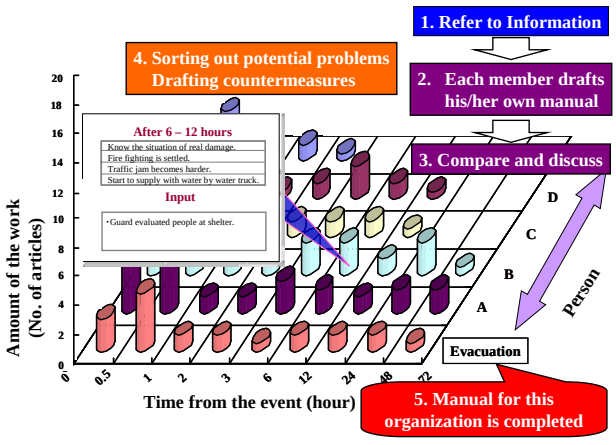

Figure 7 Flowchart of drafting a manual of an organization

3.3 Drafting and Updating of manuals

Drafting and Updating process of the disaster management manual by real users is very important and useful occasion to study and understand contents of the manual, that is, sorting out potential problems and reviewing / assessing measures so users contribute in the improvement of comprehensive disaster management measures. However, most existing manuals are "the Government prepared", which cannot be improved through the process of reviewing the manual by the real users.

In this study, the authors prepare the function, "Drafting / Updating the resulting manuals". With this function, users can review their disaster management manual by themselves. For instance (see flowchart of Figure 7), in case of considering the manual of some organizations of the disaster countermeasures office, each member of this organization drafts his/her own manual by him/herself with information people should consider at each condition set by indexes. And members compare and discuss their own manuals, so they can sort out potential problems and consider and assess disaster prevention measures. It follows that when the manual of this organization is completed, members can understand not only problems of their organization / area but background of each item through this process, so they will be able to do measures without manual smoothly after a disaster occurs.

The features of "Drafting and Updating of manuals" are two. Firstly, users easily know which and how many actions should be added, if potential problems can be found, through analysis of present manual. Secondly, users easily know how many actions can be decreased, if they do proper measures before the event. Figure 8 gives an example of these changes.

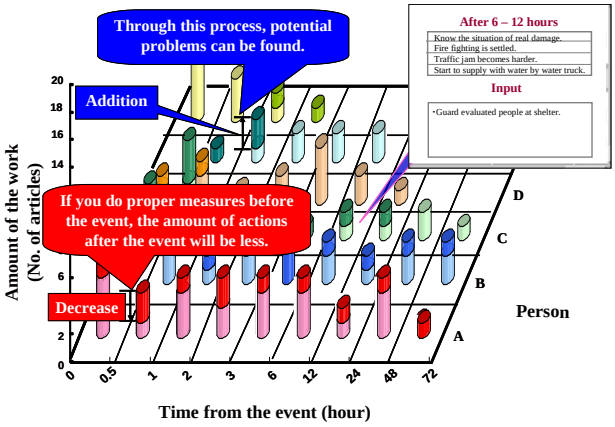

Figure 8 The features of the function, "Drafting / Updating the resulting manuals" (after KONDO et al., 2001)

4. OUTLINE OF FLOWCHART TO INTRODUCE

In this study, the authors introduced Disaster Management System to the organization at Iran followed the flowchart. Figure 9 is the flowchart for introduction of system to the organization. Content of each work is included below.

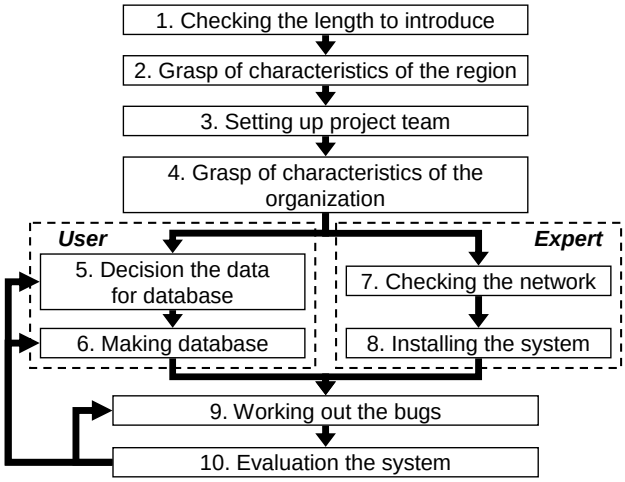

Figure 9 Flowchart for introduction of system

4.1 Checking the length to introduce

For introducing proposed system to the organization, people should check the length that expert can work on-site. So, the schedule and function to install can be decided. At GTGC and IRCS, each length that the authors could work to install is shown in Table 1.

Table 1 The length to install proposed system

Organization	Date	Length
GTGC	27th , June – 6th , July, 2004	9days
IRCS	7th , August – 14th , August, 2004	8days

4.2 Grasp of characteristics of the region

People should grasp characteristics of the region, for installing system adapting to the organization. At this stage, people studied damage estimation (JICA, CEST 2000) at Tehran city.

4.3 Setting up project team

People should set up project team with members of the organization for installing and managing proposed system by themselves. Members of project team consist of expert, facilitator, database creator, and interpreter (Iranian to English).

4.4 Grasp of characteristics of the organization

At this stage, people should know structure of the unit of the organization. So members of the organization were recruited to the project team. The authors could grasp characteristics of the organization from them.

4.5 Decision the data for database

Project team selected data for making database by database creator. At GTGC, existent disaster management manual was used. Based on Disaster Information Database at IRCS, facilitator could ask people who are responded for Bam earthquake to make database.

4.6 Making database

The authors asked database creator to put 7 indexes in Farsi to each measure, "Responsible organization", "Service contents", "Term of measures (relatively)", "Time to start and finish measures from an event (absolutely)", and "Work loads (man x day)". So it is easy for people to imagine situation after disaster happened. Figure 10 shows the people during making database at IRCS.



Figure 10 People making database

4.7 Checking the network

Checking the network is very important because proposed system uses Web application. But network at Iran was poorer than at Japan. Then project team decided to install proposed system to each PC.

4.8 Installing the system

Expert installed proposed system with a policy decided at pre-step. Expert installed proposed system as shown Table 2.

Table 2 Environment of proposed system

Function	Software
OS	Windows XP
Server	Apache
DBMS	MySQL
Server-side Script	PHP

4.9 Working out the bugs

After installing the system, project team should find out the bugs of system. They should fix bugs if found. During this time, one bug was found. Farsi was displayed from left to right (Usually right to left) on screen.

4.10 Evaluation the system

After pre-step, project team asks members of the organization to evaluate installed system. If some problem is pointed out, they feed back to the system. During this time, they asked boss and several directors at GTGC, and some researcher to study about disaster response at IRCS. In each situation, installed system got high evaluation.

5. RESULT OF INTRODUTION

Figure 11 shows a result of analysis GTGC Disaster Management Manual. The x-axis is "Responsible Organization". The y-axis is "Time from the event". The z-axis is "Work loads". The right side of window shows name of responsible organization corresponding to the number on the x-axis. From this figure, we can see that all sections will start all works after 1 hour to 2 months from the event. This result shows database creator has a shortage of imagination for disaster situation. So, the environment members can imagine real situation should be prepared.

Figure 12 shows the example at using Disaster Information Database of disaster response of IRCS in Bam earthquake. The x-axis is "Responsible Organization". The y-axis is "Time from the event". The z-axis is "Work loads". With this system, people can imagine real situation in disaster easier. Therefore this system prepares environment for members to pick out lessons.

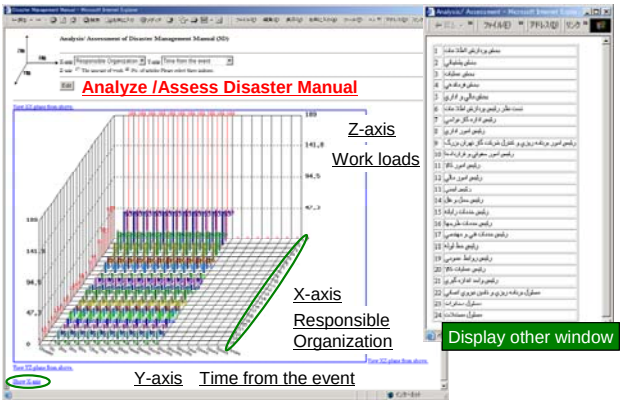

Figure 12 Result of analysis GTGC Disaster Management Manual

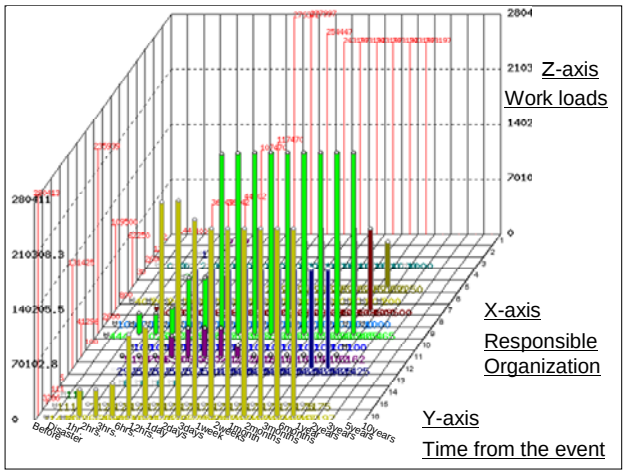

Figure 13 The example to use Disaster Information Database of disaster response of IRCS in Bam earthquake

6. CONCLUSION

In this study, the authors propose "New Disaster Management Manual". As the result of incorporating the scenario of damage estimation, setting indexes, and construction of relational database, three functions as below are achieved: "Analysis and Assessment of existing manuals", "Independent edition by each purpose/ user", and "Drafting and Updating of manual". Organizations and regions can create a good environment to sort out potential problems, review, conduct and evaluate countermeasures like the flowchart in Figure 14. And these can improve comprehensive disaster prevention.

Moreover, the authors tried to introduce some features of this system to the organization which plan disaster reduction at Islamic Republic of Iran. At first, the system "New Style Management Manual" was applied to Greater Tehran Gas Company (GTGC). "New Style Disaster Information Database" about disaster response in Bam earthquake 2003 was constructed at Iranian Red Crescent Society (IRCS). With this system, these organizations can create the environment that people can make disaster management manual by themselves. And they can improve earthquake disaster reduction.

References:

Kondo, S., Hamada, S. and Meguro, K. (2001). Proposal of New Style Disaster Manual for Implementation of Efficient Disaster Countermeasures. Proceedings of the JSCE Earthquake Engineering Symposium 26:2, 1481-1484.

Meguro, K. (2001). Dynamic Evaluation Model for Large Earthquake Disaster. Journal of Geography 110:6, 900-914.

Japan international cooperation Agency (JICA), Center for earthquake and environmental studies of Tehran (CEST), and Tehran Municipality (2000), THE STUDY ON SEISMIC MICROZONING OF THE GREATER TEHRAN AREA IN THE ISLAMIC REPUBLIC OF IRAN

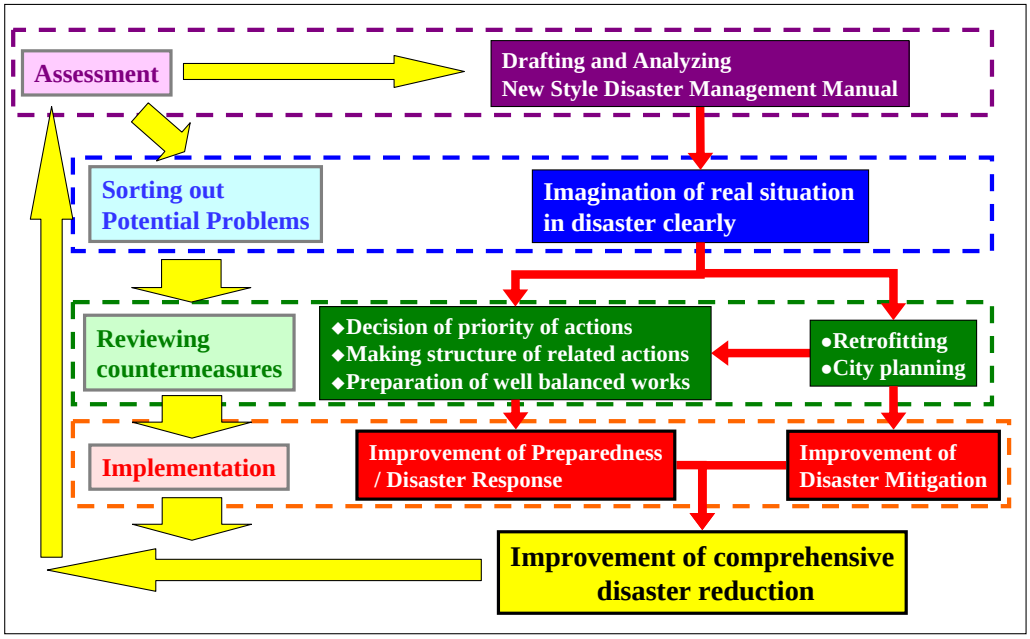

Figure 14 Flowchart of using of proposed manual

JOINT CONFERENCE PROCEEDINGS
7th International Conference on Urban Earthquake Engineering (7CUEE) &
5th International Conference on Earthquake Engineering (5ICEE)
March 3-5, 2010, Tokyo Institute of Technology, Tokyo, Japan

Parallelized fast multipole BEM for seismic analysis in time-domain

Sohichi Hirose[1)] and Takahiro Saitoh[2)]

1) Professor, Department of mechanical and environmental informatics,
Tokyo Institute of Technology, Japan
2) Assistant Professor, Department of mechanical and environmental informatics,
Tokyo Institute of Technology, Japan
shirose@cv.titech.ac.jp, tsaitoh@qnde.mei.titech.ac.jp

Abstract: This paper presents a new parallelized fast multipole boundary element method (FMBEM) based on a convolution quadrature method (CQM) for seismic analysis in time-domain. In this formulation, the convolution integrals of the time-domain boundary integral equations are numerically approximated by the CQM. To achieve the acceleration of the time-domain boundary element method (BEM) based on the CQM, OpenMP and MPI for parallel computing techniques are utilized. Moreover, a fast multipole method (FMM) is adapted to improve the computational efficiency of the resulting matrix-vector products from the boundary integral equations. First, time-domain BEM formulation based on the CQM is described for 3-D elastic wave propagation. Next, a brief description on how to apply the FMM to the time-domain BEM based on the CQM is presented. Finally, some numerical examples are demonstrated for the validation of the proposed method.

1. INTRODUCTION

Seismic motions produced at an earthquake fault propagate in ground as elastic waves and sometimes cause tremendous destruction of buildings and infrastructures. Therefore, the understanding of elastic waves can help not only predict ground motions by earthquake but also reduce seismic damages.

Normally, a seismic problem can be solved by modeling the ground as an infinite or half-space. Since the boundary element method (BEM) is a suitable numerical approach for wave analysis in an infinite or half space domain, the BEM has been used for many years for seismic analysis in frequency domain (Kataoka 1996). However, there are not so many numerical examples using time-domain BEM for seismic analysis (Abe et al. 1993), even though time-domain BEM is a powerful technique in some engineering analyses such as non-linear and transient analysis.

In general, transient problems can usually be solved for unknown time-dependent quantities by a direct time-domain BEM with a time stepping scheme. However, the use of direct time-domain BEM sometimes causes the instability of time stepping solutions. Moreover, the time-domain BEM needs much computational time and memory for large size problems.

To overcome these difficulties, a new time-domain boundary element method is developed for seismic analyses in this research. In the formulation of the new time-domain BEM, the convolution quadrature method (CQM), first proposed by Lubich (1988) is applied to achieve the stability behavior in a time stepping scheme. The convolution integrals of the time-domain boundary integral equations are numerically approximated by the quadrature formulas, whose weights are computed using the Laplace transform of the fundamental solution and a linear multistep method. OpenMP and MPI for parallel computing techniques are applied to direct computations of influence functions for near field and calculations of the CQM in each time-step, respectively. In addition, the fast multipole method (FMM) developed by Greengard and Rokhlin (1987) is utilized to improve the computational efficiency of the time-domain BEM.

As a first step for the development of a seismic wave simulator, in this paper, the new time-domain BEM formulation is presented with the focus on 3-D elastic wave propagation. As numerical examples, elastic wave scattering is demonstrated using the present method.

2. TIME-DOMAIN BEM FOR 3-D ELASTIC WAVE PROPAGATION

We consider a 3-D elastic wave scattering problem in an exterior domain D as shown in Figure 1. When the incident wave u_i^{in} hits the boundary surface S^c of the scat-

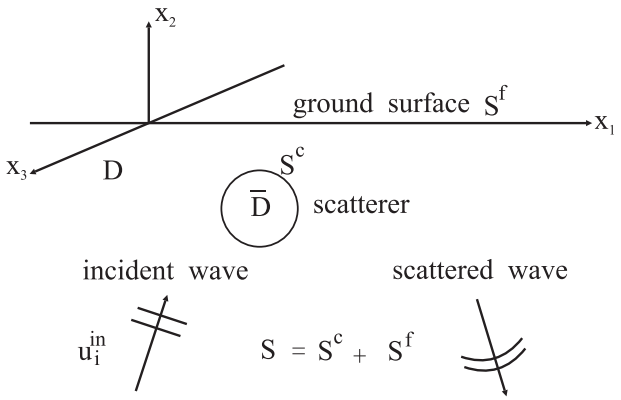

Figure 1 A 3-D seismic analysis model.

terer $\bar{D}$ and the ground surface S^f, scattered and reflected waves are generated by the interaction with the scatterer and the ground surface, respectively. Assuming the zero initial conditions, the elastic wave displacement field u_i at time t satisfies the governing equation and boundary conditions as follows:

$$\mu u_{i,jj}(\boldsymbol{x},t) + (\lambda+\mu)u_{j,ij}(\boldsymbol{x},t) = \rho\ddot{u}(\boldsymbol{x},t) \quad \text{in } D \tag{1}$$

$$\begin{aligned} &u_i(\boldsymbol{x},t) = \hat{u}_i(\boldsymbol{x},t) \ \text{ on } \ S_1, \\ &t_i(\boldsymbol{x},t) = \hat{t}_i(\boldsymbol{x},t) \text{ on } \ S_2 \quad S_2 = S\backslash S_1 \end{aligned} \tag{2}$$

where ρ is the density of an elastic medium, $\dot{(\ )}$ show the time derivative, and λ and μ are Lamé constants. In addition, t_i show traction components corresponding to the displacement components u_i, and $\hat{u}_i(\boldsymbol{x},t)$ and $\hat{t}_i(\boldsymbol{x},t)$ are given boundary conditions.

The time-domain boundary integral equations for 3-D elastic wave propagation can be expressed by

$$\begin{aligned} \frac{1}{2}u_i(\boldsymbol{x},t) =& u_i^{\text{in}}(\boldsymbol{x},t) + \int_S U_{ij}(\boldsymbol{x},\boldsymbol{y},t) * t_j(\boldsymbol{y},t)dS_y \\ &- \int_S T_{ij}(\boldsymbol{x},\boldsymbol{y},t) * u_j(\boldsymbol{y},t)dS_y \ \text{ for } \quad \boldsymbol{x} \in S \end{aligned} \tag{3}$$

where $U_{ij}(\boldsymbol{x},\boldsymbol{y},t)$ and $T_{ij}(\boldsymbol{x},\boldsymbol{y},t)$ denote the time-domain fundamental solution and its double layer kernel (Kobayashi 2000) in 3-D elastodynamics, respectively. In addition, $*$ is the symbol of time convolution. In general, the boundary integral equations shown in Equation 3 are discrized using the appropriate interpolation functions for time and space, and then solved using a time-step algorithm. The time-domain boundary integral equations, however, sometimes cause unstable solutions when time increment is small. Therefore, the CQM is applied to Equation 3 to overcome the difficulty in this research.

3. TIME-DOMAIN BEM BASED ON THE CQM FOR 3-D ELASTIC WAVE PROPAGATION

Since the application of the CQM to the time-domain BEM has been described in detail in other published papers (for example, see the paper of Fukui and Saitoh 2009, Saitoh et al. 2009), the principal formulas will be introduced here.

According to the CQM, Equation 3 is arranged into the following discretized boundary integral equations for n-th time step, e.g.,

$$\begin{aligned} \frac{1}{2}u_i(\boldsymbol{x},n\Delta t) =& u_i^{\text{in}}(\boldsymbol{x},n\Delta t) \\ &+ \sum_{\alpha=1}^{M}\sum_{k=1}^{n}\Big[A_{ij}^{n-k}(\boldsymbol{x},\boldsymbol{y}^\alpha)t_j(\boldsymbol{y}^\alpha,k\Delta t) \\ &- B_{ij}^{n-k}(\boldsymbol{x},\boldsymbol{y}^\alpha)u_j(\boldsymbol{y}^\alpha,k\Delta t)\Big] \end{aligned} \tag{4}$$

where Δt denotes the time increment and M is the number of elements. Moreover, A_{ij}^m and B_{ij}^m are influence functions, which are defined as follows:

$$A_{ij}^m(\boldsymbol{x},\boldsymbol{y}) = \frac{\mathcal{R}^{-m}}{L}\sum_{l=0}^{L-1}\int_S [\tilde{U}_{ij}(\boldsymbol{x},\boldsymbol{y},s^l)dS_y]e^{\frac{-2\pi iml}{L}} \tag{5}$$

$$B_{ij}^m(\boldsymbol{x},\boldsymbol{y}) = \frac{\mathcal{R}^{-m}}{L}\sum_{l=0}^{L-1}\int_S [\tilde{T}_{ij}(\boldsymbol{x},\boldsymbol{y},s^l)dS_y]e^{\frac{-2\pi iml}{L}} \tag{6}$$

where i is the imaginary unit, and $\mathcal{R}$ and L are the parameters of the CQM (Lubich 1988) . Moreover, $\tilde{U}_{ij}(\boldsymbol{x},\boldsymbol{y},s^l)$ and $\tilde{T}_{ij}(\boldsymbol{x},\boldsymbol{y},s^l)$ are the Laplace domain fundamental solutions, which are defined with the Laplace parameter s^l as follows:

$$\begin{aligned} &\tilde{U}_{ik}(\boldsymbol{x},\boldsymbol{y},s_\beta) = \frac{1}{4\pi\mu} \\ &\times\left\{\frac{e^{-s_T r_{xy}}}{r_{xy}}\delta_{ik} - \frac{1}{s_T^2}\frac{\partial^2}{\partial y_i \partial y_k}\left(\frac{e^{-s_T r_{xy}}}{r_{xy}} - \frac{e^{-s_L r_{xy}}}{r_{xy}}\right)\right\} \end{aligned} \tag{7}$$

$$\tilde{T}_{ik}(\boldsymbol{x},\boldsymbol{y},s_\beta) = n_j(\boldsymbol{y})C_{kjpq}\frac{\partial}{\partial y_q}\tilde{U}_{ip}(\boldsymbol{x},\boldsymbol{y},s_\beta) \tag{8}$$

where r_{xy} is given by $r_{xy} = |\boldsymbol{x}-\boldsymbol{y}|$ and $n_j(\boldsymbol{y})$ shows the components of a unit outer normal vector at a source point $\boldsymbol{y}$. C_{kjpq} is the elastic constant, which is related with Lamé constants by $C_{ijkl} = \lambda\delta_{ij}\delta_{kl} + \mu(\delta_{ik}\delta_{jl} + \delta_{il}\delta_{jk})$. Note that s_β is defined by $s_\beta = s^l/c_\beta(\beta = L \text{ or } T)$ due to the simple expression in Equations 7 and 8 where c_L and c_T are velocities of P and S waves. The calculations of Equations 5 and 6 are identical to the discrete Fourier

transform. Therefore, Equations 5 and 6 can be evaluated rapidly by means of the fast Fourier transform (FFT). Arranging Equation 4 and considering the boundary conditions, we obtain

$$\begin{aligned}&\frac{1}{2}u_i(\boldsymbol{x},n\Delta t)+\sum_{\alpha=1}^{M}[B_{ij}^0(\boldsymbol{x},\boldsymbol{y}^\alpha)u_j(\boldsymbol{y}^\alpha,n\Delta t)\\&-A_{ij}^0(\boldsymbol{x},\boldsymbol{y}^\alpha)t_j(\boldsymbol{y}^\alpha,n\Delta t)]=u_i^{\mathrm{in}}(\boldsymbol{x},n\Delta t)\\&+\sum_{\alpha=1}^{M}\sum_{k=1}^{n-1}[A_{ij}^{n-k}(\boldsymbol{x},\boldsymbol{y}^\alpha)t_j(\boldsymbol{y}^\alpha,k\Delta t)\\&-B_{ij}^{n-k}(\boldsymbol{x},\boldsymbol{y}^\alpha)u_j(\boldsymbol{y}^\alpha,k\Delta t)].\end{aligned}\tag{9}$$

For the n-th time step, all the quantities on the right-hand side of Equation 9 are known. Therefore, the unknown values $u_i(\boldsymbol{y}^\alpha,n\Delta t)$ or $t_i(\boldsymbol{y}^\alpha,n\Delta t)$ in the n-th time step can be obtained by solving Equation 9.

Unfortunately, we cannot solve large scale problems with a large number of boundary elements M because the computational time and required memory are proportional to the number of elements. Therefore, the time-domain BEM based on the CQM is accelerated by the fast multipole method (FMM) (Greengard and Rokhlin 1987) in this research.

4. TIME-DOMAIN FAST MULTIPOLE BEM BASED ON THE CQM IN 3-D ELASTODYNAMICS

The FMM, developed by Greengard and Rokhlin (198-7), is a technique for reducing computational time and memory requirements for a large-scale problem. In this section, the essential formulas to implement the fast multipole method is derived in 3-D elastodynamics. Hereafter, the unit vector of $\boldsymbol{x}-\boldsymbol{y}$ is defined as $\hat{\boldsymbol{r}}_{xy}$.

4.1 Multipole expansion

We first consider a point $\boldsymbol{y_0}$ near the source point $\boldsymbol{y}$ on the surface S as shown in Figure 2. The multipole expansion of the fundamental solutions for 3-D elastodynamics is based on the following series expansion :

$$\begin{aligned}&\frac{e^{-s_\beta r_{xy}}}{r_{xy}}\\&=\frac{2s_\beta}{\pi}\sum_{n=0}^{\infty}\sum_{m=-n}^{n}(2n+1)O_n^m(s_\beta r_{xy_0})\bar{F}_n^m(s_\beta r_{yy_0})\end{aligned}\tag{10}$$

where the functions $F_n^m(s_\beta r_{y_0y})$ and $O_n^m(s_\beta r_{xy_0})$ have the following relations;

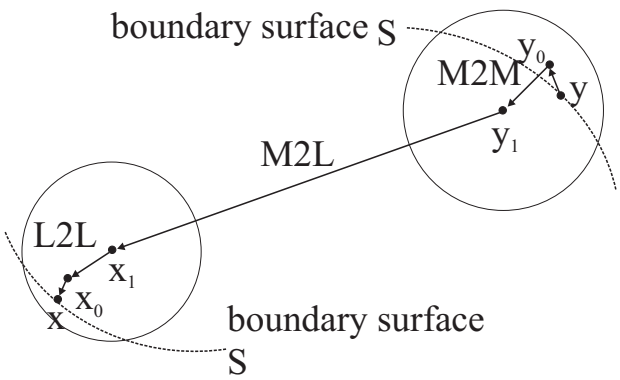

Figure 2 M2M, M2L and L2L.

$$F_n^m(s_\beta r_{yy_0})=I_n(s_\beta r_{yy_0})Y_n^m(\hat{r}_{yy_0})\tag{11}$$
$$\bar{F}_n^m(s_\beta r_{yy_0})=I_n(s_\beta r_{yy_0})\bar{Y}_n^m(\hat{r}_{yy_0})\tag{12}$$
$$O_n^m(s_\beta r_{xy_0})=K_n(s_\beta r_{xy_0})Y_n^m(\hat{r}_{xy_0})\tag{13}$$
$$\bar{O}_n^m(s_\beta r_{xy_0})=K_n(s_\beta r_{xy_0})\bar{Y}_n^m(\hat{r}_{xy_0})\tag{14}$$

where I_n^m and K_n^m are the modified spherical Bessel functions of the first and second kind, respectively. Moreover, Y_n^m is the spherical harmonics defined by

$$Y_n^m(\hat{r}_{y_0y})=\sqrt{\frac{(n-m)!}{(n+m)!}}P_n^m(\cos\theta)e^{im\phi}\tag{15}$$

where θ and ϕ are zenith and azimuthal angles in the spherical coordinate system, respectively, and P_n^m is the associated Legendre function. The functions $\bar{F}_n^m(s_\beta r_{yy_1})$ and $O_n^m(s_\beta r_{xy_0})$ have series expansion forms as follows:

$$\begin{aligned}&\bar{F}_n^m(s_\beta r_{yy_1})=\sum_{n'=0}^{\infty}\sum_{m'=-n'}^{n'}\sum_{l=|n-n'|}^{n+n'}(-1)^{m'+n'+n+l}\\&\times(2n'+1)(2l+1)W_{0,0,0}^{n,n',l}W_{m,m',-m-m'}^{n,n',l}\\&\times\bar{F}_{n'}^{-m'}(s_\beta r_{yy_0})F_l^{-m-m'}(s_\beta r_{y_0y_1})\end{aligned}\tag{16}$$

$$\begin{aligned}&O_n^m(s_\beta r_{xy_0})=\sum_{n'=0}^{\infty}\sum_{m'=-n'}^{n'}\sum_{l=|n-n'|}^{n+n'}(-1)^m(2n'+1)\\&\times(2l+1)W_{0,0,0}^{n,n',l}W_{m,m',-m-m'}^{n,n',l}\\&\times F_{n'}^{-m'}(s_\beta r_{x_0x})O_l^{m+m'}(s_\beta r_{x_0y_0}).\end{aligned}\tag{17}$$

In Equations 16 and 17, $W_{n_1,n_2,n_3}^{j_1,j_2,j_3}$ denotes the Wigner 3j symbol (Messiah 1967) .

In order to obtain the integrated multipole moments for the fundamental solution defined in Equation 7, V_i is defined as

$$V_i=\int_S\tilde{U}_{ik}(\boldsymbol{x},\boldsymbol{y},s)t_k(\boldsymbol{y},k\Delta t)dS_y.\tag{18}$$

Substituting Equations 7 and 10 into Equation 18, and after some manipulation, we have the multipole expansion of influence functions for the fundamental solution as follows:

$$V_i = \sum_{n=0}^{\infty}\sum_{m=-n}^{n} A_n \frac{\partial}{\partial x_i}[O_n^m(s_L r_{xy_0})] M_{n,m}^{U_L}(\boldsymbol{y_0}) + \sum_{n=0}^{\infty}\sum_{m=-n}^{n} B_n e_{rji} \frac{\partial}{\partial x_j}[O_n^m(s_T r_{xy_0})] M_{r,n,m}^{U_T}(\boldsymbol{y_0}) \tag{19}$$

where $A_n = -s_L(2n+1)/(2\pi^2 \mu s_T^2)$ and $B_n = -(2n+1)/(2\pi^2 \mu s_T)$. In addition, e_{rji} is the permutation symbol. The functions $M_{n,m}^{U_L}(\boldsymbol{y_0})$ and $M_{r,n,m}^{U_T}(\boldsymbol{y_0})$ are called the multipole moments on point $\boldsymbol{y_0}$ for P-wave (longitudinal wave) and S-wave (transversal wave), respectively, which are defined as follows:

$$M_{n,m}^{U_L}(\boldsymbol{y_0}) = \int_S \frac{\partial}{\partial y_k}[\bar{F}_n^m(s_L r_{yy_0})] t_k(\boldsymbol{y}, k\Delta t) dS_y \tag{20}$$

$$M_{r,n,m}^{U_T}(\boldsymbol{y_0}) = \int_S e_{rlk} \frac{\partial}{\partial y_l}[\bar{F}_n^m(s_T r_{yy_0})] t_k(\boldsymbol{y}, k\Delta t) dS_y \tag{21}$$

Similarly, W_i is defined as

$$W_i = \int_S \tilde{T}_{ik}(\boldsymbol{x}, \boldsymbol{y}, s) u_k(\boldsymbol{y}, k\Delta t) dS_y \tag{22}$$

to derive the integrated multipole moments for the double layer kernel defined in Equation 8. Substituting Equation 8 into Equation 22, and arranging the resulting equation with Equation 10, we obtain the multipole moments $M_{n,m}^{T_L}(\boldsymbol{y_0})$ and $M_{r,n,m}^{T_T}(\boldsymbol{y_0})$ on point $\boldsymbol{y_0}$ for P and S wave components of double layer kernel respectively as follows:

$$M_{n,m}^{T_L}(\boldsymbol{y_0}) = \int_S C_{kjpq} n_j(\boldsymbol{y}) \frac{\partial}{\partial y_q}\frac{\partial}{\partial y_p}[\bar{F}_n^m(s_L r_{yy_0})] \tag{23}$$

$$M_{r,n,m}^{T_T}(\boldsymbol{y_0}) = \int_S e_{rsp} C_{kjpq} n_j(\boldsymbol{y}) \times \frac{\partial}{\partial y_q}\frac{\partial}{\partial y_s}[\bar{F}_n^m(s_L r_{yy_0})] u_k(\boldsymbol{y}, k\Delta t) dS_y \tag{24}$$

Note that all multipole moments for all source points $\boldsymbol{y}$ can be evaluated independently from a field point $\boldsymbol{x}$.

Once these multipole moments are obtained for each source point $\boldsymbol{y}$, the matrix vector products of Equation 9 can be quickly evaluated using the fast multipole algorithm with an oct-tree structure prepared in advance.

4.2 Local expansion and translation theorems

A local expansion corresponding to the multipole expansion is derived. Substituting Equation 17 into Equation 18, the local expansion of Equation 18 can be obtaned as follows:

$$V_i = \sum_{n=0}^{\infty}\sum_{m=-n}^{n} A_n \frac{\partial}{\partial x_i}[F_n^{-m}(s_L r_{x_0 x})] L_{n,m}^{L}(\boldsymbol{x_0}) + \sum_{n=0}^{\infty}\sum_{m=-n}^{n} B_n e_{rji} \frac{\partial}{\partial x_j}[F_n^{-m}(s_T r_{x_0 x})] L_{r,n,m}^{T}(\boldsymbol{x_0}) \tag{25}$$

where $L_{n,m}^{L}(\boldsymbol{x_0})$ and $L_{r,n,m}^{T}(\boldsymbol{x_0})$ are the local expansion coefficients on the point $\boldsymbol{x_0}$ near the field point $\boldsymbol{x}$ as shown in Figure 2.

The local expansion coefficients $L_{n,m}^{L}(\boldsymbol{x_1})$ and $L_{r,n,m}^{T}(\boldsymbol{x_1})$ on the local point $\boldsymbol{x_1}$ are related with the multipole expansion coefficients $M_{n,m}^{L}(\boldsymbol{y_1})$ and $M_{r,n,m}^{T}(\boldsymbol{y_1})$ on the point $\boldsymbol{y_1}$ by M2L formulas for P and S waves as follows:

$$L_{n,m}^{L}(\boldsymbol{x_0}) = \sum_{n'=0}^{\infty}\sum_{m'=-n'}^{n'}\sum_{l=|n-n'|}^{n+n'} (-1)^{m'} \times (2n'+1)(2l+1) W_{0,0,0}^{n',n,l} W_{m',m,-m-m'}^{n',n,l} \times O_l^{m+m'}(s_L r_{x_0 y_0}) M_{n',m'}(\boldsymbol{y_0}) \tag{26}$$

$$L_{r,n,m}^{L}(\boldsymbol{x_0}) = \sum_{n'=0}^{\infty}\sum_{m'=-n'}^{n'}\sum_{l=|n-n'|}^{n+n'} (-1)^{m'} \times (2n'+1)(2l+1) W_{0,0,0}^{n',n,l} W_{m',m,-m-m'}^{n',n,l} \times O_l^{m+m'}(s_T r_{x_0 y_0}) M_{r,n',m'}(\boldsymbol{y_0}) \tag{27}$$

M2M and L2L formulas are also necessary to achieve the fast multipole method. Substituting Equation 16 into Equation 20 and 21, we obtain M2M formulas for P and S waves to shift the center point $\boldsymbol{y_0}$ of the multipole expansion to the other center point $\boldsymbol{y_1}$ as follows:

$$M_{n,m}^{L}(\boldsymbol{y_1}) = \sum_{n'=0}^{\infty}\sum_{m'=-n'}^{n'}\sum_{l=|n-n'|}^{n+n'} (-1)^{m'+n'+n+l} \times (2n'+1)(2l+1) W_{0,0,0}^{n,n',l} W_{m,m',-m-m'}^{n,n',l} \times F_l^{-m-m'}(s r_{y_0 y_1}) M_{n',-m'}(\boldsymbol{y_0}) \tag{28}$$

$$M_{r,n,m}^{T}(\boldsymbol{y_1}) = \sum_{n'=0}^{\infty}\sum_{m'=-n'}^{n'}\sum_{l=|n-n'|}^{n+n'} (-1)^{m'+n'+n+l} \times (2n'+1)(2l+1) W_{0,0,0}^{n,n',l} W_{m,m',-m-m'}^{n,n',l} \times F_l^{-m-m'}(s r_{y_0 y_1}) M_{r,n',-m'}(\boldsymbol{y_0}). \tag{29}$$

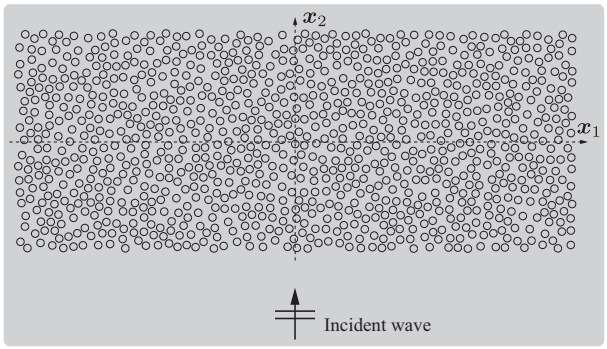

Figure 3 Multiple scattering of SH-waves in a nonhomogeneous media.

Finally, L2L formulas, to shift the center point $\boldsymbol{x_1}$ of the local expansion to the other center point $\boldsymbol{x_0}$ for P and S waves are derived from substituging Equation 16 into 25, which are expressed by

$$L^L_{n,m}(\boldsymbol{x_0}) = \sum_{n'=0}^{\infty}\sum_{m'=-n'}^{n'}\sum_{l=|n-n'|}^{n+n'}(-1)^l \times(2n'+1)(2l+1)W^{n',n,l}_{0,0,0}W^{n',n,l}_{m',-m,-m'+m} \times F_l^{-m'+m}(sr_{x_1x_0})L_{n',m}(\boldsymbol{x_1}) \quad (30)$$

$$L^T_{r,n,m}(\boldsymbol{x_0}) = \sum_{n'=0}^{\infty}\sum_{m'=-n'}^{n'}\sum_{l=|n-n'|}^{n+n'}(-1)^l \times(2n'+1)(2l+1)W^{n',n,l}_{0,0,0}W^{n',n,l}_{m',-m,-m'+m} \times F_l^{-m'+m}(sr_{x_1x_0})L_{r,n',m'}(\boldsymbol{x_1}). \quad (31)$$

Note that infinite summations appeared in the formulations such as M2M, M2L, and L2L are evaluated by truncating them with p terms.

5. NUMERICAL EXAMPLES

Numerical examples using the proposed method are discussed in this section. In this research, boundary elements are discritized with the piecewise constant approximation.

5.1 SH-wave scattering in nonhomogeneous media

To reveal elastic wave behavior in nonhomogeneous media is one of the important problems in the research area of seismic analysis. As a first example of the present method, multiple scattering of SH-waves in a nonhogeneous media as shown in Figure 3 is demonstrated. In this analysis, a nonhomogeneous media is modeled by 1000 cavities with radius a as shown in Figure 3. The boundary conditions are supposed to be antiplane traction component $t_3 = \partial u_3/\partial n = 0$ on the surfaces of each cavity. The

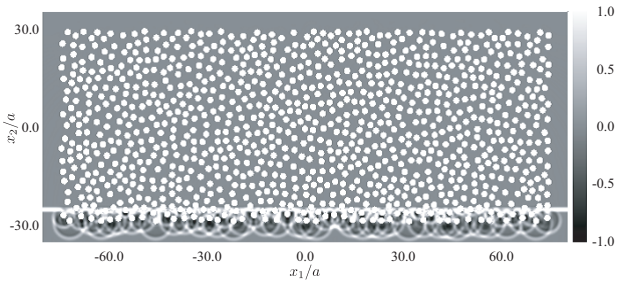

(a)

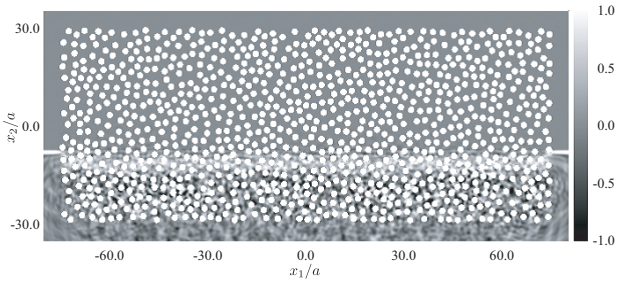

(b)

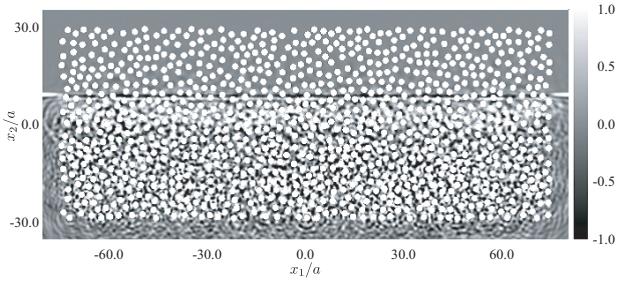

(c)

Figure 4 Time variations of the total SH-wave field around many cavities at (a) $c_Tt/a = 6.0$ (b) $c_Tt/a = 23.0$ and $(c)c_Tt/a = 40.0$.

boundary surface is divided into 128 boundary elements per cavity and the number of the total boundary elements is 128000. In addition, the parameters L and $\mathcal{R}$ are taken as $L = 1024$ and $\mathcal{R} \simeq 0.9139817$, respectively. The displacement of the incident SH-wave with wavelength λ_T is given by

$$u_3^{\rm in}(\boldsymbol{x},t) = u_0(1-\cos 2\pi\alpha),$$
$$\alpha = \begin{cases} \frac{c_T}{\lambda_T}(t-\frac{x_2+30.0a}{c_T}) & \text{for} \quad 0 \le \alpha \le 1 \\ 0 & \text{for} \quad \text{otherwise} \end{cases} \quad (32)$$

In this analysis, the time increment is $c_T\Delta t/a = 0.05$, the wavelength is $\lambda_T/a = 2.0$, and the total time steps $N = 1024$. The summations of infinite series of multipole and local expansions are truncated with $p = 10$ terms. Figures 4-(a),(b) and (c) show the time variations of the total SH-wave field around many cavities at (a) $c_Tt/a = 6.0$ (b) $c_Tt/a = 23.0$ and $(c)c_Tt/a = 40.0$. The multiple scattering can be confirmed by the interaction between 1000 cavities and the incident wave.

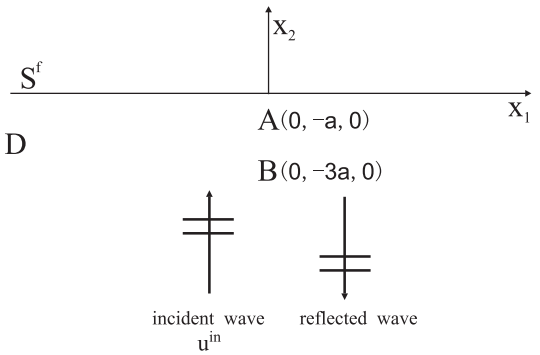

Figure 5 Reflection analysis model.

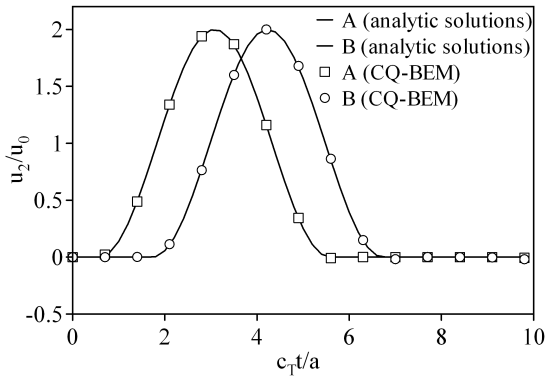

Figure 6 Total displacements u_2/u_0 at points A and B in Figure 5.

In the proposed method, not only the parallelization techniques such as MPI and OpenMP are used but also FMM for more acceleration. MPI is applied to parallelize the summation about l appeared in the calculation of influence functions such as Equation 5 and 6. On the other hand, OpenMP is utilized for the direct computaion part, which is not carried out using FMM.

Needless to say, this problem could not be solved by the conventional time-domain BEM because of the restriction of required memory. In addition, if enough memory is available for this analysis, this problem could not be solved within the range of realistic time. Therefore, the proposed method is very useful for large size problems.

5.2 Reflection by the ground surface

Normally, seismic analysis requires a model which contains a ground surface as shown in Figure 1. In this subsection, therefore, the elastic wave reflection by the ground surface was considered as shown in Figure 5. As an incident wave, an incident plane P wave wavelength λ_L propagating the perpendicular direction for the ground surface was assumed as follows:

$$u_i^{\rm in}(\boldsymbol{x},t) = u_0\delta_{i2}(1-\cos 2\pi\beta)$$
$$\beta = \begin{cases} \frac{c_L}{\lambda_L}(t-\frac{x_2}{c_L}) & \text{for} \quad 0\le\beta\le 1 \\ 0 & \text{for} \quad \text{otherwise} \end{cases} \qquad (33)$$

where u_0 is the displacement amplitude. The time increment is $c_L\Delta t/a = 0.1$, the wavelength $\lambda_L/a = 5.0$, the total time step is $N(=L) = 128$, and Poisson's ratio is $\nu = 0.25$. In this analysis, the number of total boundary elements is 900. Figure 6 shows the displacements of the reflected wave at points A and B in Figure 5. In this analysis, the analytical reflected wave can be easily obtained. Therefore, analytical solutions are also shown by the solid lines in Figure 6 to compare numerical solutions with them. It can be seen that numerical results by the present method are in good agreement with the analytical solutions.

6. CONCLUSIONS

In this paper, parallelized fast multipole BEM in time-domain was developed for 3-D elastodynamics. The proposed method is very effective for large scale problems. Further refinement of the formulations and our Fortran code are desirable for seismic analyses and engineering applications. In addition, large size seismic problems in 3-D elastodynamics will be solved by the proposed method in near future.

Acknowledgement:

The authors gratefully acknowledge the support of this work by N. Segawa, master's student of Univ. of Fukui, Japan.

References:

Kataoka, S. (1996), "Simulation of the 1995 Hyogo-ken Nanbu Earthquake by a 3-D BEM", *Technical Report, Department of Civil Engineering, Tokyo Institute of Technology*, No.54, 11-20 (in Japanese).

Abe, K., Yoshida, Y. and Nakamura, T. (1993), "Near field seismic analysis by three-dimensional time domain boundary element method, *Journals of the Japan Society of Civil Engineers*, No.471/I-24, 125-133 (in Japanese).

Lubich, C. (1988)," Convolution quadrature and discretized operational calculus I", *Numer. Math.*,**52**, 413-425.

Greengard, L. and Rokhlin, V. (1987)," A fast algorithm for particle simulations", *Journal of Computational Physics*, **73**, 325-348.

Kobayashi, S. et al. (2000), "Wave analysis and boundary element methods", Kyoto University Press (in Japanese).

Fukui, T. and Saitoh, T. (2009), " Fast multipole acceleration time-domain boundary element method by Lubich's operational quadrature method", *Journal of the Japan society for simulation technology*, **28**, No.3, pp.119-124 (in Japanese).

Saitoh, T., Hirose, S. and Fukui, T. (2009), "Convolution quadrature boundary element method and acceleration by fast multipole method in 2-D viscoelastic wave propagation, *Theoretical and applied mechanics Japan* (in press).

Messiah, A. (1967), "Quantum Mechanics", John Wiley & Sons (North Holland), New York.

JOINT CONFERENCE PROCEEDINGS
7th International Conference on Urban Earthquake Engineering (7CUEE) &
5th International Conference on Earthquake Engineering (5ICEE)
March 3-5, 2010, Tokyo Institute of Technology, Tokyo, Japan

ANALYTICAL EVALUATION FOR LOCAL BUCKLING BEHAVIOR OF STEEL FRAMED STRUCTURES

Takahiro Ohtsuka[1] and Shojiro Motoyui[2]

1) Associate Professor, Dept. of Architecture, Meijo University, Japan
2) Associate Professor, Dept. of Built Environment, Tokyo Institute of Technology, Japan
ohtsuka@ccmfs.meijo-u.ac.jp, motoyui.s.aa@m.titech.ac.jp

Abstract: In considering local buckling of steel member for the designed structures, analytical models have much more freedom degree number and are very costly. Therefore, in this paper, we will propose a consistent beam element for H shaped and square tube steel member involving local buckling behavior. In this element, we evaluate the influence of local buckling as softening. First, we formulate present beam element based on thermodynamics. Secondly, we show the yield function with local buckling and the softening property by local buckling for H-shaped and square tube steel member. Lastly we will examine the validity and usefulness of our element through some numerical examples.

1. INTRODUCTION

It is significant to analyze the collapse behavior of designed structures. For the strength degradation behavior of the structures composed of steel member, it is necessary to evaluate local buckling. In order to evaluate the influence of local buckling, we usually use the finite element method with discrete model, but it is very costly to evaluate the local buckling by using discrete model because the model requre many elements to acheve accurate results. Then, to analyze a huge structural model economically, special simplified method like the simple plastic hinge model and multi spring model were proposed and the strength degradation by the local buckling was taken into account on their element. These elements indeed involve characteristics of local buckling, but the theoritical background and validity of mechanics in its treatment are not clear.

Then in this paper, we propose a useful beam element based on the thermodynamics for H-section and sqrure tube steel member involving local buckling. In this method, we regard the effect of local buckling as the softening, that is, multi yield surfaces in the space of (M_i,M_j,N) are moving according to the local buckling degree. And the consistent softening property of local buckling is given by investigation into the elastoplastic buckling behavior of flange plate model. Finally we examine the validity and the useful of our method through some numerical examples.

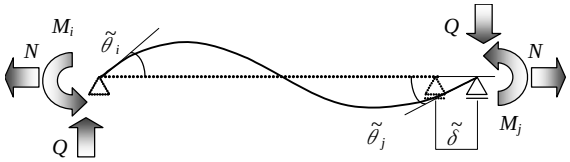

Fig.1 Nodal force and displacement of beam element

2. FORMULATION OF BEAM ELEMENT WITH LOCAL BUCKLING

2.1 Basic Equations

In this paper, we consider for relative displacement in Figure 1. And we assume that total component $\tilde{\boldsymbol{u}}$ can be written by the form of additive decomposition.

$$\tilde{\boldsymbol{u}} = \tilde{\boldsymbol{u}}^{ef} + \tilde{\boldsymbol{u}}^{pb}, \quad \tilde{\boldsymbol{u}}^{pb} = \tilde{\boldsymbol{u}}^{p} + \tilde{\boldsymbol{u}}^{b}, \quad \tilde{\boldsymbol{u}}^{T} = \left\langle \tilde{\delta} \quad \tilde{\theta}_i \quad \tilde{\theta}_j \right\rangle \quad (1)$$

where $(\,)^{\mathrm{T}}$ signifies transpose, $\tilde{\boldsymbol{u}}^{p}$ and $\tilde{\boldsymbol{u}}^{b}$ are the plastic and buckling components of the nodal relative displacement, and we introduce an effective plastic-buckling component $\tilde{\boldsymbol{u}}^{pb}$ and an effective elastic component $\tilde{\boldsymbol{u}}^{ef}$. In this paper, we extend the approximately method for truss beam to H-section beam. The free energy Ψ for H-section beam can be written by

$$\Psi = \frac{1}{2}\tilde{\boldsymbol{u}}^{ef\,T}\boldsymbol{k}^{e}\tilde{\boldsymbol{u}}^{ef} \quad (2)$$

where $\boldsymbol{k}^{e}$ is an elastic stiffness matrix considering shear deformation. In this case, the Clausius-Duhem inequality can be written by

$$-\dot{\Psi} + \boldsymbol{f}^{T}\dot{\tilde{\boldsymbol{u}}} = \left\{\boldsymbol{f} - \boldsymbol{k}^{e}\tilde{\boldsymbol{u}}^{ef}\right\}^{T}\dot{\tilde{\boldsymbol{u}}} + \boldsymbol{f}^{T}\dot{\tilde{\boldsymbol{u}}}^{pb} \geq 0 \quad (3)$$

where $\boldsymbol{f}$ is the nodal forces; $\boldsymbol{f}^{T} = \left\langle N \quad M_i \quad M_j \right\rangle$ as shown in Figure 2. For inequality equation to be true for all values of $\tilde{\boldsymbol{u}}$, their coefficients must be zero, giving

$$\boldsymbol{f} - \boldsymbol{k}^{e}\tilde{\boldsymbol{u}}^{ef} = \boldsymbol{0}, \quad \Gamma = \boldsymbol{f}^{T}\dot{\tilde{\boldsymbol{u}}}^{pb} \geq 0 \quad (4)$$

The first equation corresponds to the elastic constitutive equation and the second inequality represents the plastic dissipation. Here, the principle of maximum plastic dissipation is introduced to specify the post-buckling

behavior. This problem can be solved using Lagrange minimization method subject to yielding condition: $\Phi_\alpha \le 0$. The sub-suffix α means the value according to α -th reference point. So consider the Lagrangian;

$$L = -\Gamma + \sum_{\alpha\in active} \dot\lambda_\alpha^p \Phi_\alpha = -\boldsymbol{f}^T \dot{\tilde{\boldsymbol{u}}}^{pb} + \sum_{\alpha\in active} \dot\lambda_\alpha^p \Phi_\alpha \qquad (5)$$

where $\dot\lambda_\alpha^p$ is a Lagrange multiplier that is called a plastic consistency parameter physically. In generally, Equation (5) becomes simultaneous equations with respect to each active condition according to the reference buckling flange. Differentiation of the Lagrangian with respect to $\boldsymbol{f}$ gives the evolution equations;

$$\frac{\partial L}{\partial \boldsymbol{f}} = -\dot{\tilde{\boldsymbol{u}}}^{pb} + \sum_{\alpha\in active} \dot\lambda_\alpha^p \frac{\partial \Phi_\alpha}{\partial \boldsymbol{f}} = 0 \qquad (6)$$

$$\dot{\tilde{\boldsymbol{u}}}^{pb} = \sum_{\alpha\in active} \boldsymbol{\phi}_\alpha \dot\lambda_\alpha^p, \quad \boldsymbol{\phi}_\alpha = \frac{\partial \Phi_\alpha}{\partial \boldsymbol{f}} = \left\langle \phi_\alpha^N \quad \phi_\alpha^{M_i} \quad \phi_\alpha^{M_j} \right\rangle^T \qquad (7)$$

Namely the associate flow rule is satisfied. It is noted that Equation (7) is similar to the extended Koiter's form. If the yielding condition is active then the following Kuhn-Tucker complementary conditions must be satisfied.

$$\Phi_\alpha = 0, \quad \dot\Phi_\alpha = 0, \quad \dot\lambda_\alpha^p \ge 0 \qquad (8)$$

2.2 Tangent stiffness matrix

Since $\dot\Phi_\alpha = 0$ for $\alpha \in active$,

$$\dot\Phi_\alpha = \left(\frac{\partial \Phi_\alpha}{\partial \boldsymbol{f}}\right)^T \dot{\boldsymbol{f}} + \frac{\partial \Phi_\alpha}{\partial \bar\tau_\alpha}\dot{\bar\tau}_\alpha = \boldsymbol{\phi}_\alpha^T \boldsymbol{k}^e \left(\dot{\tilde{\boldsymbol{u}}} - \dot{\tilde{\boldsymbol{u}}}^{pb}\right) + \frac{\partial \Phi_\alpha}{\partial \bar\tau_\alpha}\dot{\bar\tau}_\alpha$$
$$= \boldsymbol{\phi}_\alpha^T \boldsymbol{k}^e \left(\dot{\tilde{\boldsymbol{u}}} - \sum_{\beta\in active} \boldsymbol{\phi}_\beta \dot\lambda_\beta^p\right) + \frac{\partial \Phi_\alpha}{\partial \bar\tau_\alpha}\dot{\bar\tau}_\alpha = 0 \qquad (9)$$

Then we have the simultaneous equations with respect to $\dot\lambda_\alpha^p$ as follows;

$$\sum_{\beta\in active} G_{\alpha\beta}\dot\lambda_\beta^p = \boldsymbol{\phi}_\alpha^T \boldsymbol{k}^e \dot{\tilde{\boldsymbol{u}}} \qquad (10)$$

Where $G_{\alpha\beta} = \boldsymbol{\phi}_\alpha^T \boldsymbol{k}^e \boldsymbol{\phi}_\beta - \chi_\alpha E_\alpha^{pb} \delta_{\alpha\beta}$ (11)

$\chi_\alpha \equiv \partial\Phi_\alpha/\partial\bar\tau_\alpha$, $E_\alpha^{pb} \equiv \partial\bar\tau_\alpha/\partial\lambda_\alpha^p$, $\delta_{\alpha\beta}$: kronecker delta

By solving this simultaneous equation, we can find $\dot\lambda_\alpha^p$.

$$\dot\lambda_\beta^p = \sum_{\alpha\in active} G^{\beta\alpha} \boldsymbol{\phi}_\alpha^T \boldsymbol{k}^e \dot{\tilde{\boldsymbol{u}}} \qquad (12)$$

where $G^{\beta\alpha}$ is the inverse of $G_{\alpha\beta}$. And from the nodal force rate, the consistent tangent stiffness matrix $\boldsymbol{k}^{epb}$ is given

$$\dot{\boldsymbol{f}} = \left[\boldsymbol{k}^e - \sum_{\beta\in active}\sum_{\alpha\in active} G^{\beta\alpha}\left(\boldsymbol{k}^e\boldsymbol{\phi}_\beta\right)\otimes\left(\boldsymbol{k}^e\boldsymbol{\phi}_\alpha\right)\right]\dot{\tilde{\boldsymbol{u}}} \equiv \boldsymbol{k}^{EPB}\dot{\tilde{\boldsymbol{u}}} \qquad (13)$$

where $\otimes$ signifies tensor product.

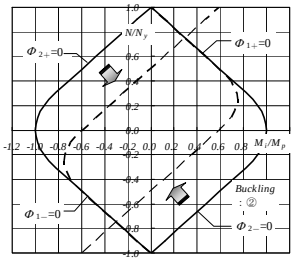

Fig.2 Illustrate yield surface

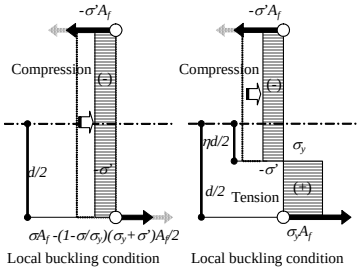

Fig.3 Stress distribution

Table 1 Sign of yield function at each reference point

α	①+, ③+	①−, ③−	②+, ④+	②−, ④−
C_N	+	−	+	−
C_M	+	−	−	+

2.3 Yield function with local buckling

Considering the truss beam involving member's elastoplastic buckling behavior, we guess that the yield surfaces of H-section member move like arrow as shown in Figure 2 according to flange local buckling. In this case, by using the hypothesis of stress block, we assume the condition of stress distribution as follows.

<The neutral axis is in flange>

$$\left|\frac{N}{N_y} + C_N\frac{1}{2}\left(1-\bar\tau_\alpha\right)\right| \ge \frac{1}{2}\left(1+\bar\tau_\alpha\right)\frac{A_w}{A}$$

$$\Phi_\alpha = C_N\frac{N}{N_y} + \frac{1}{2}\left(1-\bar\tau_\alpha\right) + C_M\bar A_1\frac{M_{i,j}}{M_p} - \frac{1}{2}\left(1+\bar\tau_\alpha\right) = 0 \qquad (14\text{-a})$$

<The neutral axis is in web>

$$\left|\frac{N}{N_y} + C_N\frac{1}{2}\left(1-\bar\tau_\alpha\right)\right| < \frac{1}{2}\left(1+\bar\tau_\alpha\right)\frac{A_w}{A}$$

$$\Phi_\alpha = \bar A_2\left\{\frac{N}{N_y} + C_N\frac{1}{2}\left(1-\bar\tau_\alpha\right)\right\}^2 + C_M\frac{1}{2}\left(1+\bar\tau_\alpha\right)\frac{M_{i,j}}{M_p} - \frac{1}{4}\left(1+\bar\tau_\alpha\right)^2 = 0 \qquad (14\text{-b})$$

$$\bar A_1 = \frac{4A_f + A_w}{2A}, \quad \bar A_2 = \frac{A^2}{\left(4A_f + A_w\right)A_w},$$

C_N and C_M are given in Table 1

2.4 Softening properties cased by local buckling

Similarly for H-section beam element, we lead the sofetning properties caused by the local buckling from plate buckling behavior. In this paper, we assume that the effective yield stress (τ_α) and the plastic dissipation (Γ_α) of plate model are satisfied Equation (15) and (16) respectively.

$$\bar\tau_\alpha = C_1 + \left(1-C_1\right)\left\{1-C_2\left(\Theta_\alpha - 1\right)\right\}\exp\left\{C_3\left(\Theta_\alpha - 1\right)\right\} \quad \left(\Theta_\alpha > 1\right)$$
$$= 1 \quad \left(\Theta_\alpha \le 1\right)$$

$$\Gamma_\alpha = n_\alpha \dot u_\alpha \qquad (15),(16)$$

buckling parameter: $\Theta_\alpha = -\frac{u_\alpha}{u_{\alpha cr}}, \quad u_{\alpha cr} = \frac{\sigma_{\alpha cr}}{E} l_\alpha$

where C_1,C_2,C_3 are constant value of each member, and n_α, u_α, l_α are mean axial force, axial stretch and axial

length of plate model. Here we regard l_α as local buckling length and we use the buckling coefficient k for elastic buckling stress of plate model.

By regarding above plastic dissipation as plastic dissipation of α-th reference point Γ_α, plastic dissipation of beam element can be rewritten by

$$\Gamma = \sum_{\alpha \in active} \Gamma_\alpha = \sum_{\alpha \in active} n_\alpha \dot{u}_\alpha = \boldsymbol{f}^T \dot{\tilde{\boldsymbol{u}}}^{pb} = \boldsymbol{f}^T \sum_{\alpha \in active} \boldsymbol{\phi}_\alpha \dot{\lambda}_\alpha^p \qquad (17)$$

Here if we assume that the reference flange axial force n_α according to the α-th reference point is satisfied Equation (18), we can obtain Equation (19).

$$n_\alpha = \boldsymbol{f}^T \boldsymbol{h}_\alpha \qquad (18)$$

$$\boldsymbol{h}_\alpha{}^T = A^{ef} \left\langle \frac{1}{A} \quad \pm(1-\xi_\alpha)\frac{1}{Z} \quad \mp \xi_\alpha \frac{1}{Z} \right\rangle$$

$$\dot{\Theta}_\alpha = -\frac{\dot{u}_\alpha}{u_{cr}} = -\frac{\boldsymbol{f}^T \boldsymbol{\phi}_\alpha}{\boldsymbol{f}^T \boldsymbol{h}_\alpha u_{cr}} \dot{\lambda}_\alpha^p \equiv R_\alpha \dot{\lambda}_\alpha^p \qquad (19)$$

Furthermore, effective yield stress $\bar{\tau}_\alpha$ is a function with respect to Θ_α, therefore the softening property caused by local buckling is given by

$$\dot{\bar{\tau}}_\alpha = \frac{\partial \bar{\tau}_\alpha}{\partial \Theta_\alpha} \dot{\Theta}_\alpha = -\frac{\partial \bar{\tau}_\alpha}{\partial \Theta_\alpha} \frac{\boldsymbol{f}^T \boldsymbol{\phi}_\alpha}{\boldsymbol{f}^T \boldsymbol{h}_\alpha u_{cr}} \dot{\lambda}_\alpha^p \equiv E_\alpha^{pb} \dot{\lambda}_\alpha^p \qquad (20)$$

$$\frac{\partial \bar{\tau}_\alpha}{\partial \Theta_\alpha} = (1-C_1)\{C_3 - C_2 - C_2 C_3(\Theta_\alpha - 1)\}\exp\{C_3(\Theta_\alpha - 1)\}$$

3. NUMERICAL EXAMPLES

We compare some numerical results calculated by the present beam element model with by the discrete model composed of many shell elements in order to examine the validity of our method.

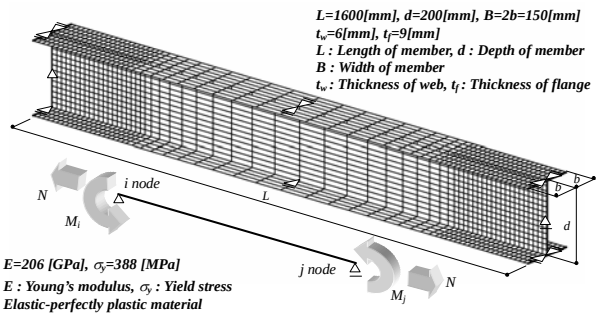

Fig.4 Discrete model and beam element model of H-section member

3.1 H-section member

Analytical model is a simple beam composed of H-200 × 150 × 6 × 9, L=1600[mm], Young's modulus E=206[GPa], Yield stress σ_y=388[MPa], Elastic-perfectly plastic material. The present results are calculated with only one element, and another is done with the discrete model composed of many shell elements as shown in Figure 4. The constant value of present model; local buckling length l_α=B and C_1=0.4, C_2=-0.3, C_3=-0.4. We examine to loading pattern Case I-III.

Monotonic loading:

Case I $\{ M_j = 0 ,(M_i / N = 5,10,20,50 , \ N = 0)\}$

Case II $\{ N/N_y = 0.2 , \tilde{\theta}_i / \tilde{\theta}_j = 2 \}$

Cyclic loading:

Case III $\{ M_j = 0 , \tilde{\delta} = -\tilde{\theta}_i d/2 \}$

In Figure 5-7, plots indicate the results of present model and lines indicate that of discrete model. As shown all figures, for each loading pattern, the equilibrium path of present and discrete model are close and this means the present method is valid.

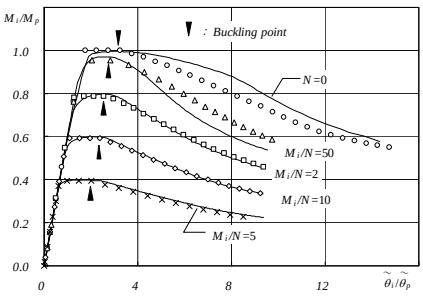

Fig.5(a) Load-displacement curve (CaseI)

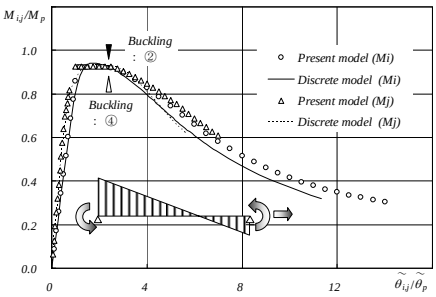

Fig.6(a) Load-displacement curve (Case Ⅱ)

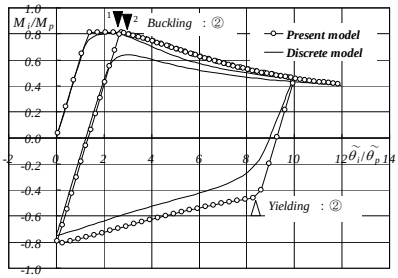

Fig.7(a) Load-displacement curve (CaseⅢ)

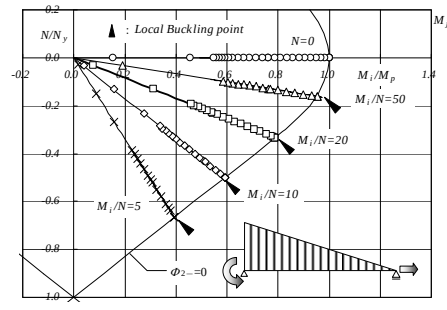

Fig.5(b) N-M_i correlation (Case I)

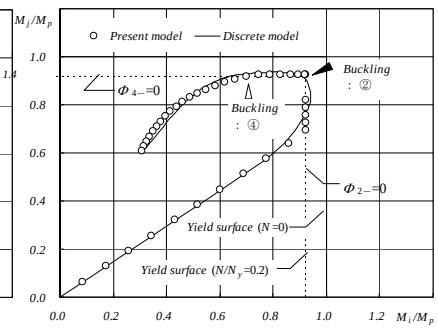

Fig.6(b) M_j-M_i correlation (Case Ⅱ)

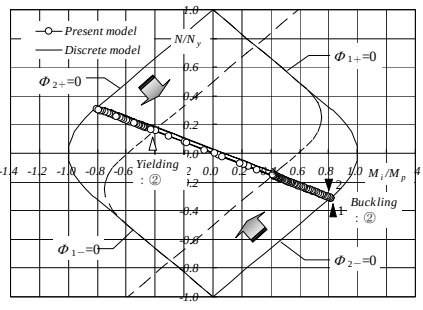

Fig.7(b) N-M_i correlation (CaseⅢ)

3.2 Square tube member

We analyze for a simple beam composed of □-300 ×300×9, L=3500[mm], Young's modulus E=206[GPa], Yield stress σ_y=323[MPa], Elastic-perfectly plastic material. The discrete model composed of shell elements is shown in Figure 8. The constant value of present model; local buckling length $l_\alpha=B$ and C_1=0.3, C_2=-0.3, C_3=-0.6. We examine to loading pattern Case IV,V.

Case IV $\{ M_j = 0 , (M_i / N = 10,30,50 , \ N = 0) \}$

Case V $\{ N/N_y = 0.2 , \theta_i / \tilde{\theta}_j = 2 \}$

In Figure 9,10, for each loading pattern, the equilibrium path of present and discrete model are close and this means that the present element for square steel tube member is valid. But the present element evaluate late for local buckling occur.

3.3 Frame structure

We analyze for a frame structure shown as Figure 11, beam: H-400×200×8×13, column:□-300×300×9.Both material properties: Young's modulus E=206[GPa], Yield stress σ_y=235[MPa], Elastic-perfectly plastic. The constant value of present model; beam : local buckling length $l_\alpha=B$ and C_1=0.4, C_2=-0.3, C_3=-0.4, column : local buckling length $l_\alpha=B$ and C_1=0.3, C_2=-0.3, C_3=-0.6. We loading vertical load P_V =0.3N_y (constant) and horizontal load P_H, P_H is controlled by horizontal displacement u_H. The deformation of discrete model at last condition is shown in Figure 12. And we can see the local buckling occurred at top and bottom of column. Figure 13 show the load displacement of frame structure. Figure 14 show the effective yield stress at bottom of right column and top of left column. This effective yield stress indicates the evolution of local buckling. Then we can evaluate the evolution of local buckling very easy.

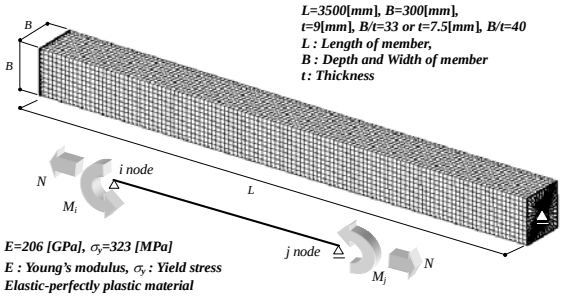

Fig.8 Discrete model and beam element model of squre tube member

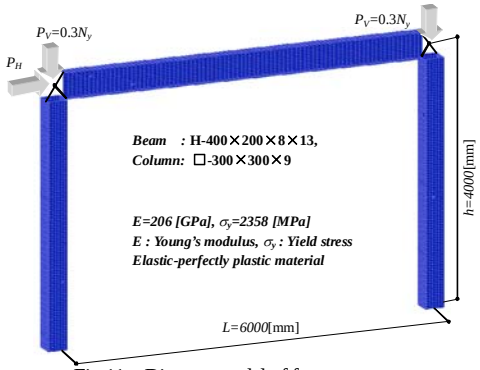

Fig.11 Discrete model of frame structure

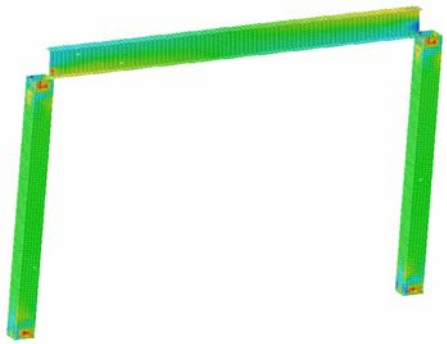

Fig.12 Deformation of discrete model at last step

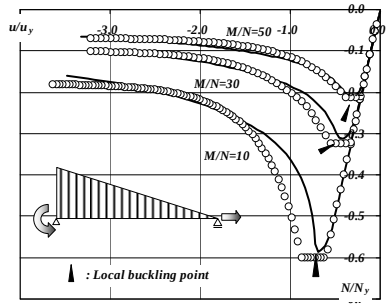

Fig.9(a) Load-displacement curve (CaseIV)

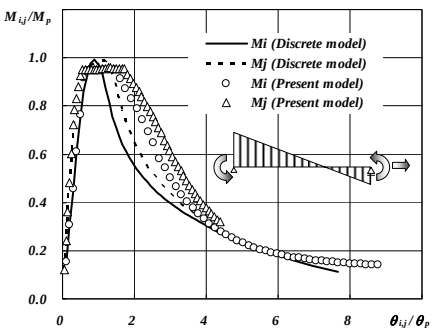

Fig.10(a) Load-displacement curve (CaseIV)

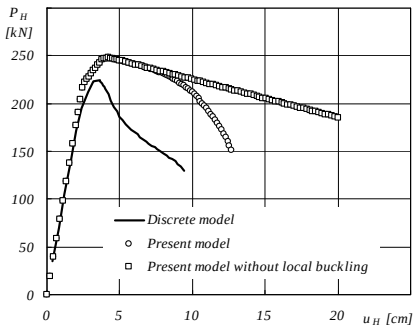

Fig.13 Load-displacement curve of frame model

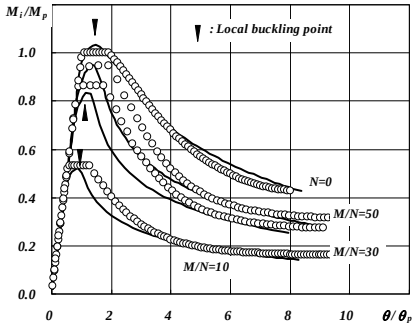

Fig.9(b) Load-displacement curve (Case IV)

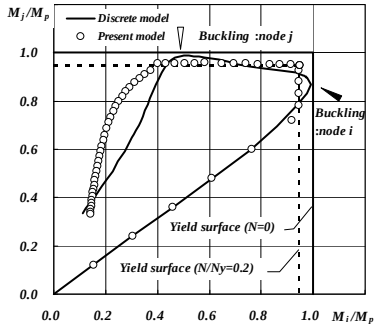

Fig.10(b) M_j-M_i correlation (CaseIV)

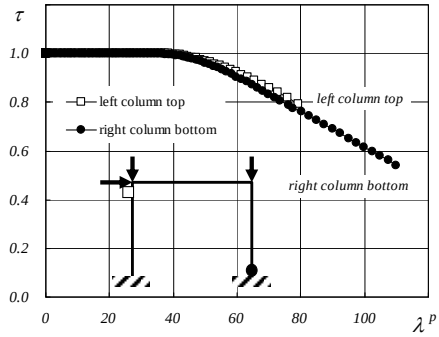

Fig.14 Local buckling evolution in present element

4. CONCLUSIONS

In this paper, we described a consistent and convenient beam element for H-section and square tube beam column including elastoplastic local buckling behavior based on the thermodynamics. The formulation of this element is almost same for H-section and square tube member. In this element, multi-surfaces for yielding and buckling behavior are considered in the space of (M_i,M_j,N). Each couple of surfaces corresponds to the yielding and buckling strength of each flange. And from investigation into the elastoplastic buckling behaviour of plate model, we proposed a consistent softening property caused by local buckling. Furthermore the validity of the present method was examined through some numerical examples.

Acknowledgements:

This study is part of the research program at Meijo University, funded by 'ARCSEC' and The Naito Science & Engineering Foundation.

References:

Ohtsuka, T., Motoyui, S., (2004), “Analytical Evaluation of Local Buckling Behavior of H-Section Steel Member”, Proceedings of The Seventh International Conference on Computational Structures Technology (CST2004), Lisbon, Portugal, 7-9 September 2004, pp.1-10(CD-ROM)

Ohtsuka, T., Motoyui, S., (2008), “Analytical Evaluation for Local Buckling Behavior in Square Steel Tube Members”, Proceedings of The Ninth International Conference on Computational Structures Technology (CST2008), September, 2008, Athens, Greece, pp.1-10(CD-ROM)

JOINT CONFERENCE PROCEEDINGS
7th International Conference on Urban Earthquake Engineering (7CUEE) &
5th International Conference on Earthquake Engineering (5ICEE)
March 3-5, 2010, Tokyo Institute of Technology, Tokyo, Japan

DEVELOPMENT OF INTEGRATED DISASTER INFORMATION SYSTEM AND INFORMATION MANAGEMENT

Kimiro Meguro[1] and Shinya Kondo[2]

1) Director/Professor, International Center for Urban Safety Engineering, Institute of Industrial Science, The University of Tokyo, Japan
2) Researcher, The Great Hanshin-Awaji Earthquake Memorial Disaster Reduction and Human Renovation Institute, Kobe, Japan
meguro@iis.u-tokyo.ac.jp, kondos@dri.ne.jp

Abstract: Quality and quantity of disaster can be discussed by the relations between characteristics of hazard as an input, such as magnitude, location of hypocenter, fault mechanism, etc. in case of earthquake and characteristics of the affected region as a system, such as soil condition, infrastructure and housing condition, politics, economy, religions, education, history, culture, etc. The regional characteristics can be divided into two groups, one is on natural environment and the other is on social environment. Also, since activities of people and society are strongly reflected by time, time related factors, such as season, day of the week, and event occurrence time, etc. should be considered as a part of the system. Disaster can be considered as an output of the above mentioned input-system mechanism. While there are seven countermeasures for disaster reduction, namely, "mitigation", "preparedness", "prediction and early warning", "damage assessment", "emergency disaster response", "recovery", and "reconstruction". For implementation of all seven measures, "information and communication" is a key and information management plays essential role for it. The ideal disaster management measures are to be conducted by properly balancing these seven measures considering hazard characteristics and regional characteristics of the target area. In this paper, the authors sort out important issues on information management and propose their solutions for total disaster management.

1. INTRODUCTION

For total disaster management, there are seven countermeasures as shown in Figure 1. These are "mitigation", "preparedness", "prediction and early warning", "damage assessment", "emergency disaster response", "recovery", and "reconstruction". For implementation of all seven measures, "information and communication" is a key and information management plays essential role for it. The ideal disaster management measures can be conducted by properly balancing these seven measures considering both the hazard characteristics and regional characteristics of the target area.

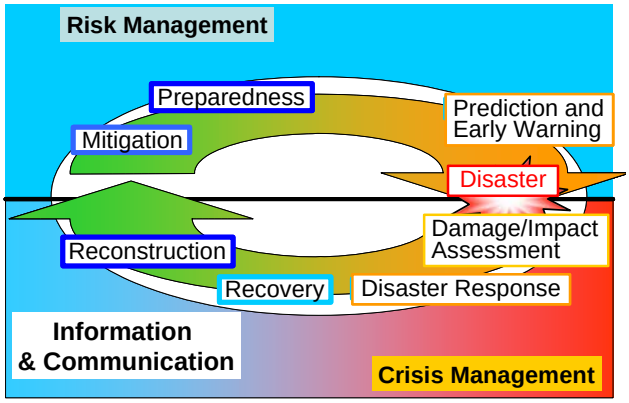

Figure 1 Elements of Disaster Countermeasures and Total Disaster Management System

In this paper, the authors point out important issues on information management and propose their solutions for total disaster management to minimize negative impact due to hazards.

2. CONSTRUCTION OF DATABASE

After a hazard attack, survey on information required by the affected people and/or people who should take care of affected ones is often carried out through questionnaire survey and/or interview survey. Figures 2 and 3 show some examples of these survey results, however, they are not enough for proper actions. As Figure 4 shows, it is important that from before a hazard attack to just after, and to recovery and reconstruction stages, and from national level to prefecture, city and town, and to citizens' levels, all activities by all divisions and information needed for those activities are analyzed. In this chapter, the method for analysis and

database prepared based on the result of analysis will be introduced.

2.1 Information on Disaster Response Activities for Analysis

In Japan, we had an earthquake with the magnitude of 6.8 called the 2004 Mid Niigata Prefecture Earthquake in the central part of Niigata Prefecture on October 23, 2004. The death toll and injured due to this earthquake was 68 and 4,805, respectively. The total number of heavily and partially damaged houses and buildings was approximately 16,000. The records of disaster response activities by the Niigata Prefectural Government during this earthquake disaster were used for analysis. The records summarized by the Niigata Prefectural Government employees contain time series actions of each section with actors and their start and finish times.

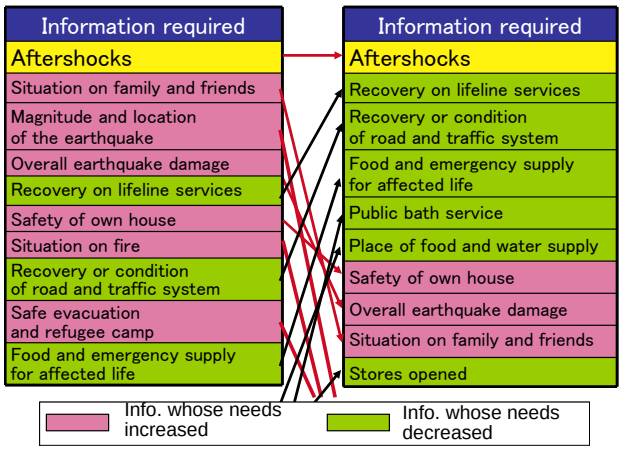

Figure 1 Changes of Needs of Information After the 1995 Kobe Earthquake

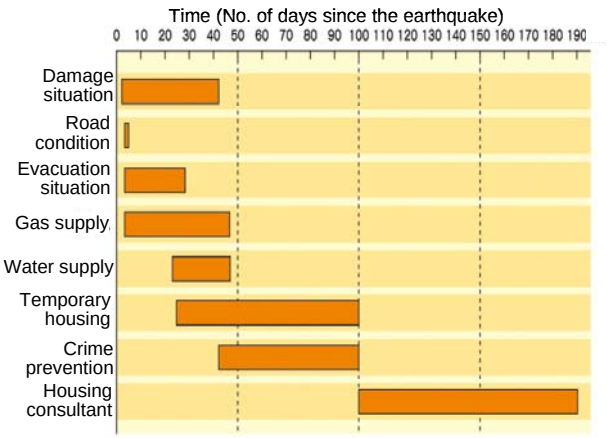

Figure 3 Changes of Information that Niigata Prefecture Government Has Been Disseminating through Web After the 2004 Mid Niigata Prefecture Earthquake

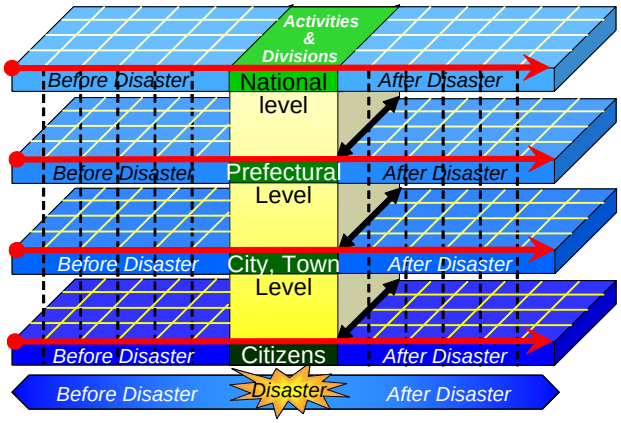

Figure 4 Disaster Information Image of Disaster Information Database

2.2 Activities and Required Information

In order to provide appropriate responses to the various tasks at appropriate times, organizations do not respond to any single situation, but instead they take an overview of the entire situation. Kondo and Meguro [1] have proposed an environment for provision of appropriate responses (see Figure 5). People should improve their temporal and spatial grasp of the environment and what will happen after the disaster (imagination), as well as sort out potential problems (analysis), design and develop countermeasures (design & development), implement disaster drills (implementation), and assess each element (assessment).

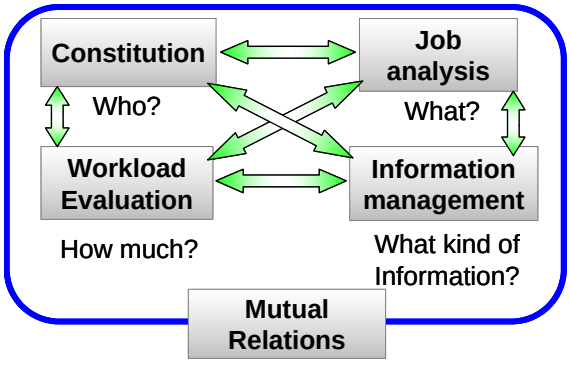

Figure 5 Environment for Provision of Appropriate Responses

Figure 6 shows a series of activities as time goes that need information (A) and (B). Also, actor organization/division and required accuracy on the information are shown in the figure. In order to prepare this figure using real data, we should make clear the relations between information and activity. However, there is no person who can trace activities from the viewpoint of information required for each activity. Therefore in the study, we picked up all works from large scale and broke down these works up to concrete actions by interview survey from all divisions related disaster response as shown in Figure 7 (a). After getting all concrete actions, we asked the people at each division and could get information and accuracy required for each action, and its provider division. About

required accuracy of the information, there are three factors; quantity, location, and time. Accuracy on these three factors becomes quite different with actor division/organization, time, and action. When we can prepare all relations among action, required information, and its accuracy and provider, we finally can trace all activities from the viewpoint of each required information as shown in Figure 7 (b).

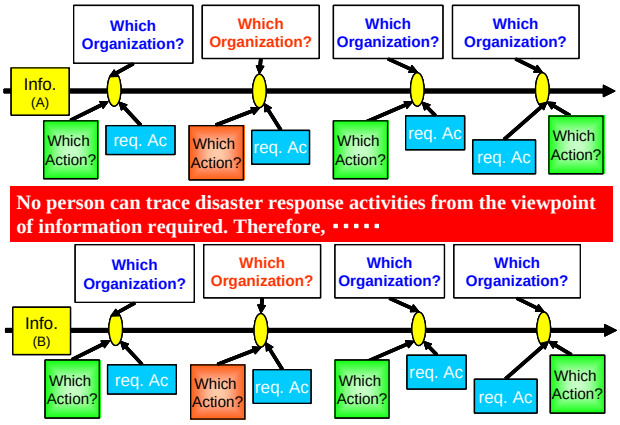

(req. AC: Required Accuracy)

Figure 6 Activities Are Traced from the Viewpoint of Each Information Required for the Activity

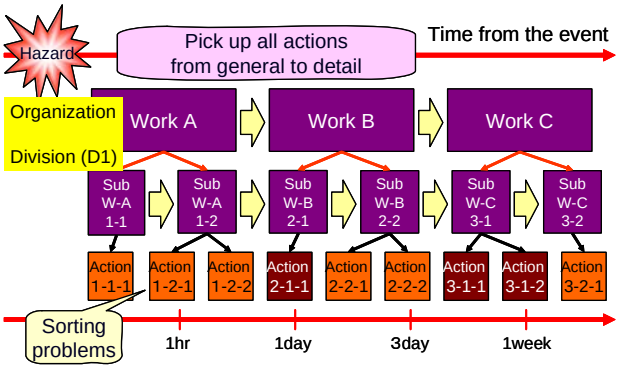

(a) Break Down of Works

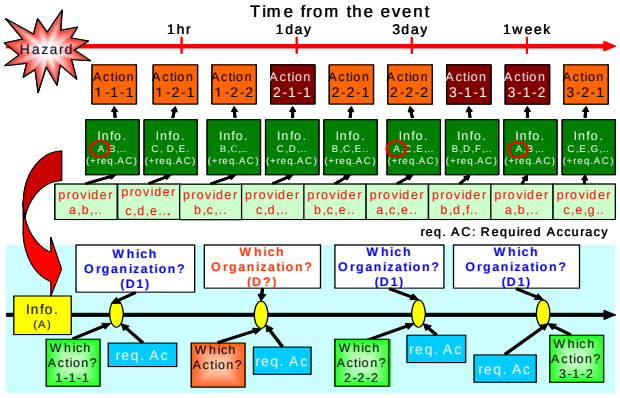

(b) Activity Traceability by Required Information

Figure 7 Method for Trace of Activities from the Viewpoint of Each Information Required for the Activity

Adopting this approach, we can make disaster information matrix and when we make disaster information platform using this concept, each division of all levels from national to city and town levels can get necessary information in favorite time with required resolution. Therefore, with this platform system, people belonging to local governments don't have to report damage situation to the higher level governments. With the following chapters, we will explain this approach using real data.

2.3 Database Specifications

It is necessary to organize the input items for disaster response analysis from the five viewpoints. There were 12 attributes in this study as shown in Figure 8: responsible organizations, services provided, actions taken, terms of measurement, start and finish times of events, workloads, necessary information, division(s) to access information, output information, division(s) of information destinations, and related actions. If some records lacked certain attributes, details from the 2004 Mid-Niigata Prefecture Earthquake were supplied through interviews with Niigata Prefectural Government employees and reference materials [3 – 6] of this earthquake.

For sorting out potential problems, people should analyze the current disaster from five viewpoints, i.e. "Constitution", "Job analysis", "Workload evaluation", "Information management", and "Mutual relations." "Constitution" means defining each group's role, depending on how the situation unfolds after the hazard attack. "Job analysis" means comparing needs in the disaster area with what the organization should do. "Workload evaluation" means estimating the quantity of work to be done for effective use of limited resources (i.e., people, goods, capital, and information). "Information management" means not only obtaining, controlling, communicating, sharing, and using information to do work, but managing cooperation with outside organizations. "Mutual relations" means analyzing disaster response activities from the multiple viewpoints described previously.

If the organization considers countermeasures based on these analyses, each person's actions will be linked so that things will be organized in a timely fashion with spatial efficiency. However, most existing reports lack analysis from these five viewpoints. In a previous paper, the authors proposed "A New Style Disaster Information Database," which was a system for multilateral analysis and assessment of a database consisting of newspaper articles, reconnaissance reports, compilations of lessons [2], and a new method for disaster response assessment using a disaster information database constructed based on current available systems, such as fax machines [1]. This system and method together form an environment that provides information to all people for the development of their mental images of the situation after disaster struck. However, they do not have the five viewpoints to analyze the organization's disaster response. In this study, the authors propose an environment to improve disaster management of the organization in a disaster-free period. Specifically, the

records of disaster response activities in past disasters were analyzed from five viewpoints (constitution, job analysis, workload evaluation, information management, and mutual relations), issues for improvement in disaster management of the organization were sorted out, and the contents and structure of improvements were identified.

In this research, the records of the Niigata Prefectural Government's disaster response activities during the 2004 Mid-Niigata Prefecture Earthquake were collected and used for analysis from five viewpoints. The validity of the analysis from the five viewpoints was verified, and lessons of the organization's disaster response were summarized.

ID	Responsible organization(s)	Service
1	Civil Engineering, Building and Housing	Construction of temporary housing

ID	Action
1	Research construction site for temporary housing

ID	Term(s) of measures	Time to start	Time to finish	Workloads
1	Emergency	100 (hours)	180 (hours)	10 (division x day)

ID	Input information	Division(s) to access information	Output information	Division(s) for information destination
1	No. of households with refugee	Life and environment division	Candidate site for temporary housing	General affairs division, Administrative promotion office

ID	Related action
1	Budget for temporary house construction

Figure 8 Specifics of the Database

3. ANALYSIS OF THE ORGANIZATION'S DISASTER RESPONSE BASED ON THE DATABASE

In this section, the organization's disaster response is analyzed using the database. In this study, "Analysis" is defined as "breaking combined operations down into their constituent parts and sorting those constituents and their characteristics." The current state of disaster response can be understood from an analysis of all operations, but problems are not sorted out quickly. Analysts (the authors and staff who responded to the disaster in this study) determine the constituents and characteristics of the disaster response and discuss its validity from the results of analysis. In addition, problems emerged as gaps between an ideal situation and the actual situation.

3.1 Constitution

After the 2004 Mid-Niigata Prefecture Earthquake struck, 17 departments were established under the Niigata Prefectural Emergency Operation Center (EOC). EOC meetings were held as needed. Some groups, which consisted of several departments, reported on the situation at the time.

Table 1 shows the evolution of the structure. Many groups were established in the EOC meetings: five groups in the first step (October 27, 2004), two groups in the second step (October 31, 2004), and one group in the third step (November 13, 2004). The reason for this was the need to provide careful service. In the fourth step (December 24, 2004), all groups except five were disbanded.

Table 1 Evolution of the Niigata Prefectural EOC Structure

	Local plan for disaster prevention	First	Second	Third	Numbers (Max)	4th
Date		2004/10/27	2004/10/31	2004/11/5		2004/12/24
Structure	Headquaters commission	Headquaters commission	Headquaters commission	Headquaters commission	8	Headquaters commission
	General affairs	General affairs	General affairs	General affairs	5	General affairs
	Countermeasure	Countermeasure	Countermeasure	Countermeasure	15	Countermeasure
	Bulletin	Bulletin	Bulletin	Bulletin	5	Bulletin
		Ministry on-site support team	Ministry on-site support team	Ministry on-site support team	40	Dissolution
	Liaison to ministry	Liaison to ministry	Liaison to ministry	Liaison to ministry		Dissolution
		Control of SDF	Control of SDF	Control of SDF	60	Dissolution
	Liaison to SDF	Liaison to SDF	Liaison to SDF	Liaison to SDF	15	Dissolution
	Liaison to disaster prevension agency	Liaison to disaster prevension agency	Liaison to disaster prevension agency	Liaison to disaster prevension agency	10	Dissolution
	Lifeline	Lifeline	Lifeline	Lifeline	8	Dissolution
		Rescue	Rescue	Rescue	16	Dissolution
		Information on evacuation center	Information on evacuation center	Information on evacuation center	5	Dissolution
		Supply of food	Supply of food	Supply of food	18	Dissolution
			Livingware	Relief goods and logistics	50	Relief goods and logistics
			Liaison to Governers	Liaison to Governers	10	Dissolution
					265	

SDF: Self Defense Force

In other words, the Niigata Prefecture EOC meetings decided on countermeasures that could be implemented from soon after disaster struck to two months after the Mid-Niigata Prefecture Earthquake. Thus, changes in the organization's structure proportional to changes in the disaster-affected community were made.

3.2 Job Analysis

Job analysis means the breaking down and refining of work to lead planning operations to action. The first level was the EOC's work as listed in regional disaster prevention plan. The second level was the division's work listed in the regional disaster prevention plan. The third level was intermediate tasks between the second and fourth levels. The fourth level was concrete action.

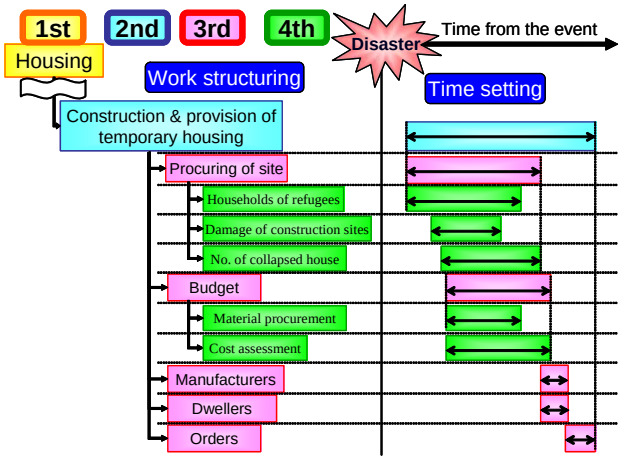

Figure 9 Job Analysis
(Civil Engineering Bureau, Housing Construction)

For the Civil Engineering Bureau Building and Housing division, the first level was “Housing” and the second level, “Construction and provision of temporary housing” consists of the third level: “Procuring of site,” “Budget,” “Manufacturers,” “Dwellers,” and “Orders,” as shown in Figure 9. In addition, the fourth level, “Procuring,” consisted of “Households of refugees,” “Damage to construction sites,” and “Number of collapsed houses.”

3.3 Workload Evaluation

In this section, each type of work to be done was quantified. This was done by compiling the duration of first level works, with eight hours equaling one unit per day. Figure 10 shows the prefectural staff’s workload at each first level. “Setting and management EOC” was the largest category of work in terms of quantity. “Public establishment” and “Agriculture, Forestry and Fisheries” are the second and third-largest categories of work in terms of quantity, respectively. The features of the 2004 Mid Niigata Prefecture Earthquake were collapsed houses, blocked roads, isolated settlements, and floods due to landslides. Local structures – rice terraces and carp ponds – were damaged in Yamakoshi village. Rice terraces fell under the category of “Public Establishments,” carp ponds under the category of “Agriculture, Forestry and Fisheries.” The amount of work to be done by each division was analyzed for clarification of the division’s workload.

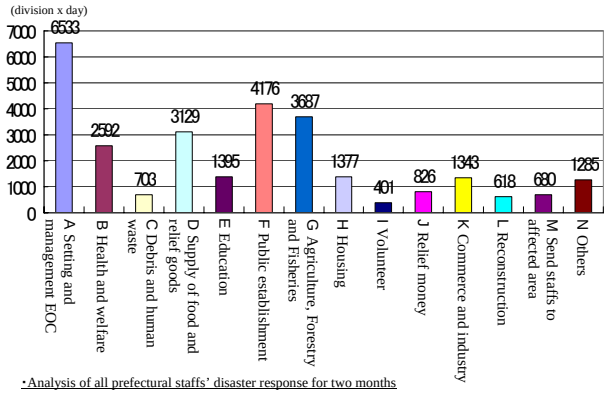

Figure 10 Prefectural Staff’s Workload For Each First-level Task

Table 2 Analysis of the Responsibility for Each Division of the Life and Environment Bureau

	A	B	C	D	E	F	G	H	I	J	K	L	M	N
Crisis management	52	0	0	47	0	0	0	0	0	0	0	0	0	0
Environmental plan	125	1	64	1	0	0	7	0	13	1	0	0	5	20
Environmental measures	124	5	75	2	0	0	0	0	9	0	0	0	0	0
Life	81	0	0	5	0	0	0	0	265	0	8	0	0	0
Nuclear safety measures	142	0	0	0	0	0	0	0	0	0	0	0	0	139
Fire difense	676	0	25	4	0	0	0	0	0	0	0	0	4	133
Promotion of gender equality	4	0	0	2	0	0	0	0	11	0	0	0	0	53
Debris measures	0	0	523	0	0	0	0	0	0	0	0	0	0	0
Cultural administration	18	2	0	0	0	4	0	0	29	0	0	0	0	0
Total	1222	8	687	61	0	4	7	0	327	1	8	0	9	345

・Analysis of all prefectural staffs’ disaster response for two months (division * day)

Table 2 is an analysis of the responsibility of the Living Environment Bureau. The main work of this bureau was the following: A) Setting and management EOC, C) Debris and human waste, and I) Volunteers. These work categories were listed on the local disaster prevention plan. This bureau also worked with other bureaus’ main work categories, such as J) Relief money and K) Commerce and industry. This analysis included each bureau’s work, both its main work and complementary work. The work categories listed in the local disaster prevention plan and carried out in real situations were compared and analyzed.

Figure 11 is an analysis of the Civil Engineering Bureau’s work, where the x-axis is the organization responsible, the y-axis is time from the event, and the z axis is the number of work categories, with the local disaster prevention plan on the left and the real situation on the right. The plan did not have a concept of a timeline; therefore, related records were used in setting the times. This analysis showed concrete actions taken in the implementation of the plan, as well as unplanned work.

Table 3 is an analysis of unplanned work. Local government staff should not only know the tasks listed on the plan, but also recognize “Routine work,” “Conclusion of agreements,” “Assistance to other divisions,” “Publication and notices,” and “Demands and requests.”

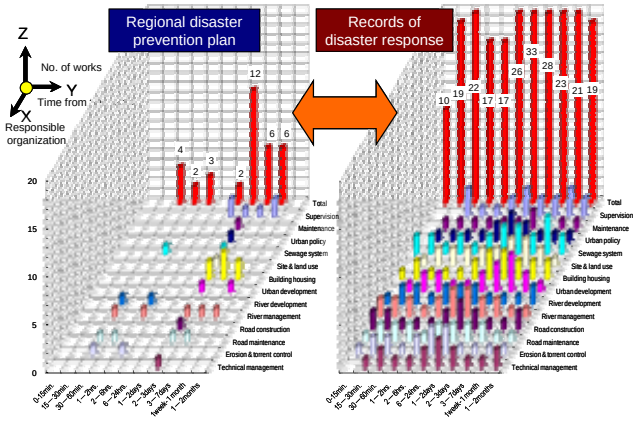

Figure 11 Analysis of Civil Engineering Bureau’s Work

Table 3: Unplanned Work Categories

2nd level
Carrying in and out relief supplies

Classification	Action
Disaster response	Carry in relief supplies at Niigata Airport
	Prepare rice ball at parking
Routine work	Provide house map to related divisions
Conclusion of agreements	Conclude collaboration agreement with prefectural land development corporation
Assistance to other divisions	Assistance to Nagaoka branch office
	Assistance to empty room information center
Publication and notices	Notify regional agency of case example of site acquisition in the 1995 Kobe earthquake disaster through written statements
	Notify regional agency of site acquisition at disaster area through a written statement
Demand and requests	Go off to MLIT to demand special national taxation measures for site acquisition
	Request site office outside disaster area to assistance site acquisition
	Support to respond to the media (Prime Minister inspection)

3.4 Information Management

Disaster response, from information managed at the time, has been analyzed as follows. The work analyzed in Section 3.2 was "set-related" information. Information and work did not always have a one-to-one relationship. Figure 12 shows the result of associating related information with structured second-level work, such as "the Construction and provision of temporary housing." Related information was separated into input and output as seen in Figure 13. Based on these processes, information-related disaster response was arranged on a timeline.

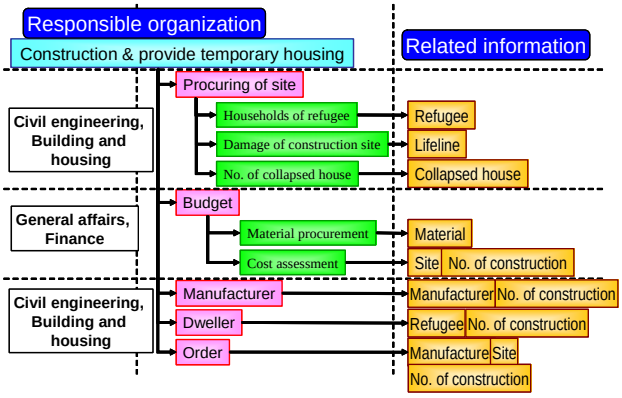

Figure 12 Result of Associating Related Information with Structured Second-level Work

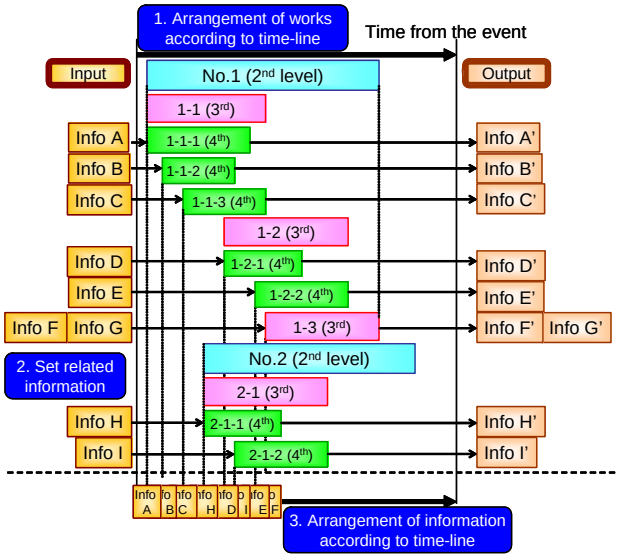

Figure 13 Arrangement of Information by Division

With the introduction of this process into the entire organization, information regarding each division's needs was arranged on the timeline (see the upper part of Figure 14). Which section needs information and which section provides information were focused on and arranged on a timeline. The lower part of Figure 14 shows an example of focus on "Refuge information."

In this study, the above method of analysis was called "information traceability." "Information traceability job analysis" focuses on "Refuge information" and "Road damage information." "Information traceability job analysis" was an analysis of providers, users, and times for information use, arranged in a table. Work related to taking refuge was not routine work and was work related to various bureaus. Road damage information was used by various work categories.

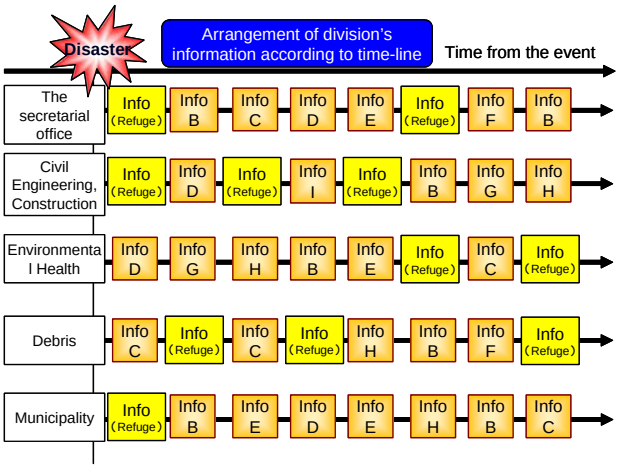

Figure 14 Information Traceability

Figure 15 shows example of "job analysis from information management." The upper table is "Refuge information." and he lower one is "Road damage information." We have focused on 12 hours after the earthquake struck; refuge information is only used for damage surveys on shelters. Road damage information was used for early works, such as damage surveying and traffic regulating, setting up detours for transporting relief supplies, and surveying isolated settlements when making surveys on earthquake victims. Such work was needed for the working out of prefectural policy. Therefore, it was necessary to improve the sharing of road damage information. Figure 16 shows the arrangement of work and the division responsible using refuge information from the timeline. Various divisions provide service to refugees. Based on this figure, the relationships among divisions, which were not listed in the local disaster prevention plan, were shown.

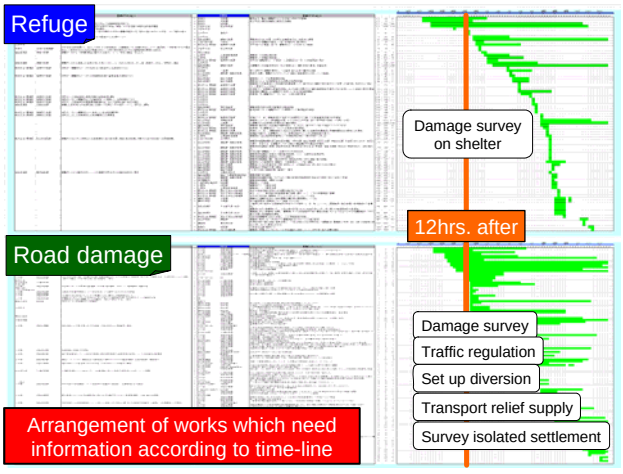

Figure 15 Job Analysis from Information Management

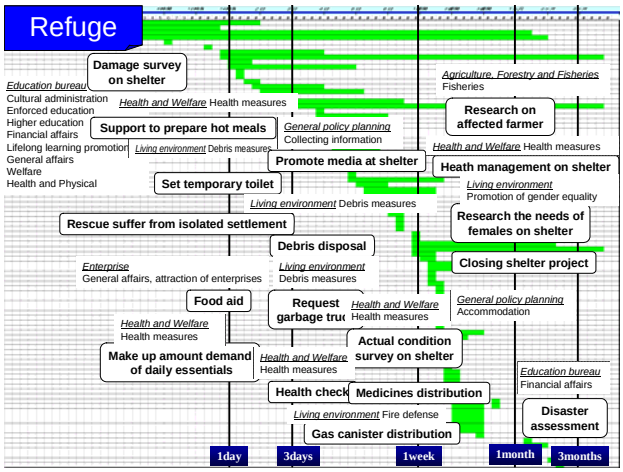

Figure 16 Information Traceability Job Analysis

Figure 17 is an analysis of the effect of information sharing. It was apparent from the "information traceability job analysis" that different divisions collected the same information at different times. It was assumed that the information system would have shared refugee information with the Niigata Prefectural Emergency Operation Center. The effort of collecting information had therefore been decreased. By collecting information early, logistic support, such as the provision of heaters and medicine and the promotion of same via the media, could be done earlier. In other words, information sharing was not for the good of disaster response organizations, but for the good of the victims.

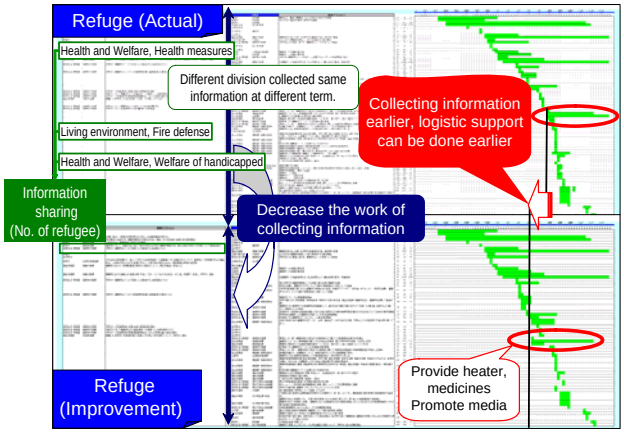

Figure 17 Effect of Information Sharing

3.5 Mutual Relations

In this section, the relationship between information providers and receivers was arranged with focus on types of information. Figure 18 shows an example focus on refuge area information. The left side references the division providing and reporting information. The upper portion references the divisions needing and receiving information. In this study, this figure was defined as an input-output information matrix. From Figure 18, divisions of the Education Bureau provided information to General Affairs. This division edited information and provided it to the national government. Figure 19 shows input-output information matrix- related road damage information. The Civil Engineering Bureau's Road Management Division received this information not only from the Road Construction Division but also from related outside organizations, such as municipalities and the MLIT Regional Development Bureau. This division edited and controlled information and provided it to the prefectural EOC, the city and national governments.

In light of the above results, it was possible to improve the environment-related outside organizations and central division for information management with arrangement of divisions providing or receiving types of information. It was necessary to construct relationships with related organizations and to learn information management.

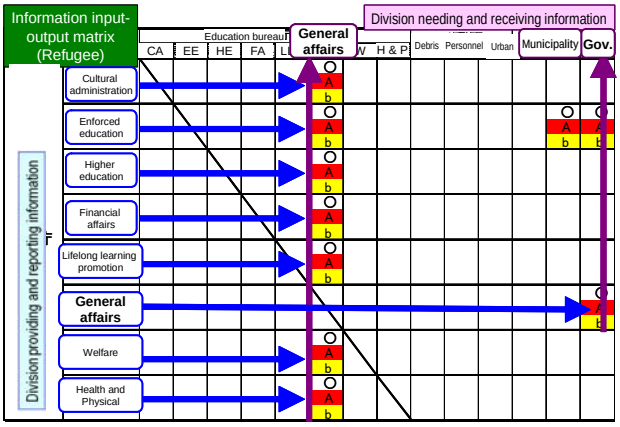

Figure 18 Input-output Information Matrix (Refugees)

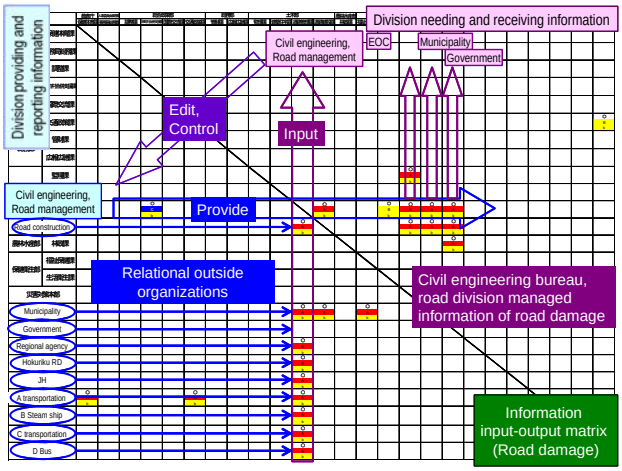

Figure 19 Input-output Information Matrix (Road Damage)

4. CONCLUSIONS

In this study, for implementation of proper disaster management, we have mainly done two issues related disaster information management. One is a proposal of a new approach to make clear the relationship among activities for disaster reduction in different time phases, actor organizations/divisions, required information, its accuracy

and providers in order to make efficient disaster information matrix. Adopting this concept, we have proposed disaster information platform. With this system, damage data collection and report systems become efficient and quite different from conventional one as shown in Figure 20. As Figure 21 shows, when disaster related organizations had this system, efficient information sharing could be done and disaster response activities might be smoother and more efficient.

The other is that we have proposed an environment to improve disaster management of organizations in a disaster-free period. To do so, the records of the Niigata Prefectural Government disaster response activities during the 2004 Mid-Niigata Prefecture Earthquake disaster were analyzed from five points of view (constitution, job analysis, workload evaluation, information management, and mutual relations). Results are shown below.

- From the viewpoint of constitution, changes in the Niigata Prefectural Emergency Operation Center's structure proportional to changes in the disaster-affected community were cleared.
- From the viewpoint of job analysis, the work divisions listed in the regional disaster prevention plan were broken down and refined for putting planning operations into action. This analysis enabled inexperienced people to get a grasp of the time required to carry out the works.
- The workload of each type of work was quantified. The amounts are calculated by compiling the duration of first level work, with eight hours equaling one workday. This analysis included both the main work and complementary work of each bureau.
- The works categorized in the local disaster prevention plan and carried out in real situations were compared and analyzed. This analysis showed concrete actions to be taken to in the implementation of the plan, and also shows unplanned work.
- From the viewpoint of information management, which section needs information and which section provides information were focused on and arranged on a timeline.
- This analysis showed that the relationships between divisions, which are not listed in the local disaster prevention plan, was shown, and the effect of information sharing was not for the good of disaster response organizations but for the good of the victims.
- From viewpoint of mutual relations, the relationships between information providers and receivers were arranged in a matrix with the focus on information input-output.
- From this matrix, it could be understood that it is possible to improve the environment-related outside organizations and central division of information management with arrangement of divisions providing or receiving types of information. It was necessary to construct relationships between related organizations and to learn information management.

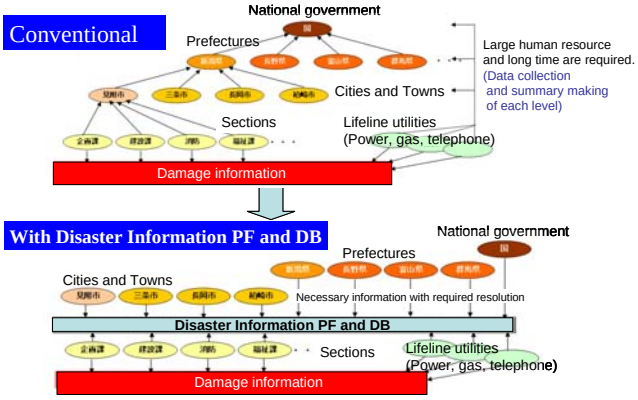

Figure 20 Changes of Damage Data Collection and Report among Disaster Related Organizations with and without Disaster Information Platform

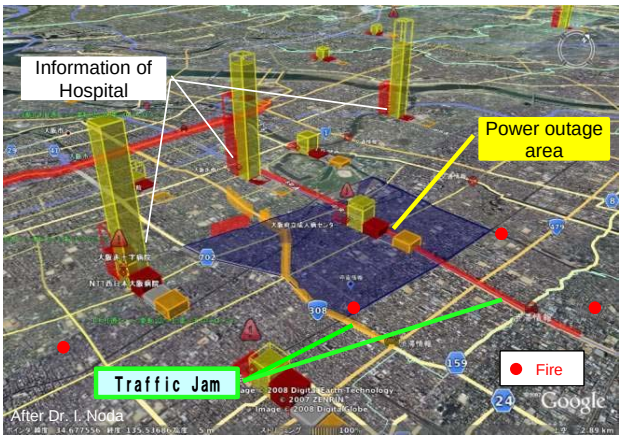

(after Dr. I. Noda)

Figure 21 Disaster Information Sharing using Disaster Information Platform

References:

[1]S. Kondo and K. Meguro, Development of a New Method for Disaster Response Assessment Using Disaster Information Obtained by Current System, *JSCE Journal of Earthquake Engineering*, Vol.28, 2005.

[2]S. Kondo and K. Meguro, Development of New Style Disaster Information Database for Implementation of Efficient Disaster Countermeasures, Journal of Social Safety Science, No.4, pp. 261-266, 2002.

[3]Niigata Prefecture: The local disaster prevention plan –Earthquake measures–, 2004. (in Japanese)

[4]Niigata Prefecture: Information about the Mid-Niigata Prefecture Earthquake in 2004, http://www.pref.niigata.jp/content/jishin/jishin1.html (in Japanese)

[5]Fire and Disaster Management Agency: The Mid-Niigata Prefecture Earthquake in 2004, http://www.fdma.go.jp/concern/index.html (in Japanese)

[6]Disaster Reduction and Human Renovation Institution: Studies on the Niigata Chuetsu Earthquake Disasters of 2004, 2005. (in Japanese)

JOINT CONFERENCE PROCEEDINGS
7th International Conference on Urban Earthquake Engineering (7CUEE) &
5th International Conference on Earthquake Engineering (5ICEE)
March 3-5, 2010, Tokyo Institute of Technology, Tokyo, Japan

THE MEANINGS OF THE APPROVAL SYSTEM FOR BUSINESS CONTINUITY ABILITY OF CONSTRUCTION COMPANIES

Hiroaki Maruya [1)]

1) Professor, Center for Urban Earthquake Engineering, Tokyo Institute of Technology,
Executive Fellow, Research Institute of Construction and Economy
h-maruya@tiara.ocn.ne.jp

Abstract: Kanto Regional Development Bureau of Ministry of Land, Infrastructure, Transport and Tourism started the approval system for the business continuity ability of construction companies in June 2009. In 2007, the bureau formulated their Business Continuity Plan (BCP) mainly for the Tokyo Inland Earthquakes, and they noticed that construction companies were strongly requested to have an ability to correspond quickly and set up their workers and machinery for checking and mending the damages of the roads, ports, river banks and so on at the time of disaster. Therefore, to promote their business continuity ability, the bureau published a simple BCP guidebook for small and middle-sized constructors in 2007. In addition, the bureau introduced above-mentioned approval system considering large-scaled earthquakes. They also published the plans to give merit in the bidding and contracting condition for certain construction works that the bureau orders in future. This is the first systematic incentive of the government related to BCP promotion in Japan. The similar systems have been introduced, and we will expect to spread them more in the future.

1. INTRODUCTION

1.1 Concept of Business Continuity

Business Continuity Management (BCM) is a management strategy by which organizations (including companies, governmental organizations) secure their critical operations even if they have serious damage by disasters and accidents. Recently, the importance of BCM has been widely recognized in Japan.

The Cabinet Office (in charge of natural disaster prevention) of Japanese government has promoted Business Continuity Plan (BCP) by issuing guidelines.[i]

Figure 1 shows the concept of business continuity. If an organization has no countermeasures of business continuity, the degree of the 'critical operations' turns to be zero % by a disaster or an accident, and then gradually recovers. However, such a late recovery would cause serious problems. Those are :

1) Losing customers (seized by other companies),
2) Decline in market share,
3) Serious social inconvenience,
4) Negative impact on a company's reputation.

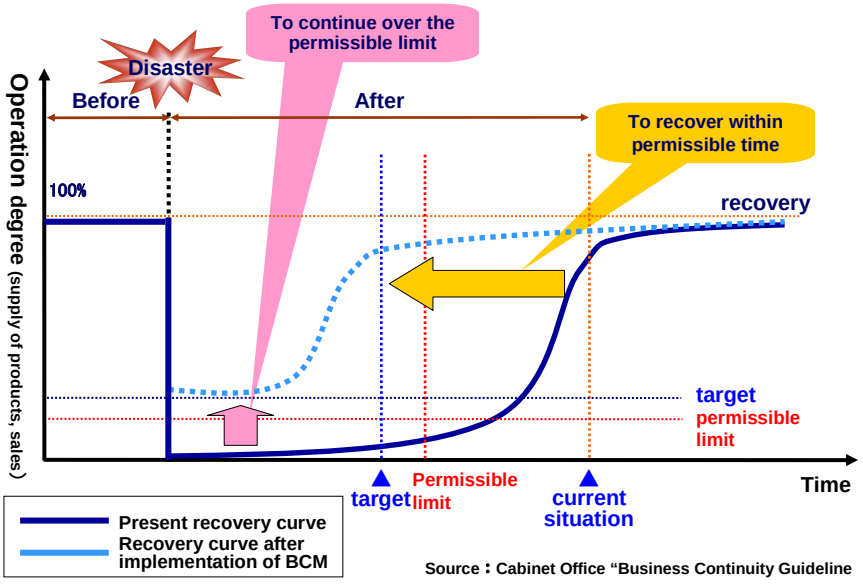

Figure 1 Concept of Business Continuity

Therefore, the organization should recognize 'the permissible limit of recovery time', and should recover the operation degree before the limit. The targeted time is called "recovery time objective (RTO)."

Additionally, even shortly after a disaster or an accident, the company should keep the operational degree above the level of permissive limit. This targeted level is called "recovery level objective (RLO)."

1.2 BCP Diffusion Degree of the Private & Public Organizations

According to a research [ii] by the Nihon Keizai Shimbun Inc. and Disaster Reduction and Human Renovation Institution in December 2008, the diffusion of BCP among Japanese companies was as follows;

Among major companies, for example, listed on the first section of the Tokyo Stock Exchange;

-Already formulated BCP: 41.7%

-Planning to formulate BCP: 50.6 %.

However, BCP has not spread to the small and medium-sized enterprises and this has been a serious problem.

To government organizations, BCP is gradually prevailing. "Business Continuity Guidelines for Ministries of Central Government" was published in June 2007. Based on this, all ministries had completed their BCP assuming the Tokyo Inland Earthquakes before the end of FY2008. Ministry of Land, Infrastructure, Transport and Tourism (MLIT) played the leading role in formulating governmental BCP, and its local branch "Kanto Regional Development Bureau" also formulated its BCP in 2007.

As for prefectural governments, Tokushima, Tokyo, Osaka, Saitama, Aichi and Kanagawa prefecture have drew up their BCP before the end of 2009, and other several prefectures are formulating.

2. NECESITY OF BUSINESS CONTINUITY ABILITY OF CONSTRUCTION COMPANIES

2.1 Recognition of Kanto Regional Development Bureau

When Kanto Regional Development Bureau (KRDB) formulated their BCP in 2007, they strongly recognized the necessity of business continuity ability of construction companies, to which the bureau ordered or requested to secure emergency transport roads and recover dikes, ports and other facilities at the time of disaster. These constructors have to establish their formation quickly and prepare the necessary workers and machinery for the works to execute inspections, clear off obstacles and repair public facilities.

Therefore, the bureau embarked on promotion of the constructors' ability in business continuity and published "Simple Guide for Business Continuity of Constructors at the Time of Disaster"[iii] in December 2007 (Figure 2). The author was asked to assist in drawing up the guide, and proposed to utilize the first half of the "BCP Step-up Guide for Small and Medium-sized Enterprises"[iv] published by the Business Continuity Advancement Organization (BCAO). The Simple Gide of KRDB has 10 steps through the formulating procedure. These steps are shown in Table 1.

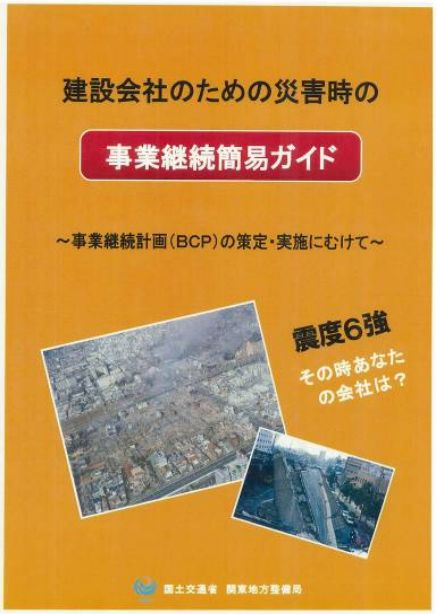

Figure 2 "Simple Guide for Business Continuity of Constructors at the Time of Disaster"

Table 1 10 Steps of the Simple Gide

Steps	Title
1	What are the disaster risks your companies faces?
2	Organizational formation and system of command at the time of disasters
3	Securing the headquarter at the time of disaster
4	Sending & sharing information
5	Confirmation of the safety of company members, etc. (Securing communication method)
6	Ensuring the safety of staff, preventing secondary disaster and Keeping stockpiles
7	Backup of critical information (Data, important documents & drawings, etc.)
8	Procurement of necessary workers, materials and machinery
9	Rough assessment of risks on building and countermeasures without expensive investment
10	Choosing critical operations and deciding time objectives by simple methods

The characteristics of the methods of the Simple Gide are that it utilizes the disaster prevention countermeasures that the company has executed for earthquakes or wind/flood damage. It reinforces them to promote its business continuity ability. Additionally, the effort will not be wasted even if the company stops their procession in mid-course of steps, as some concrete advancement is steadily realized in each step.

KDRB has promoted BCP of construction companies inside its jurisdiction, by using the Simple Gide in lecture

meetings and so on.

2.2 Significance on Existence of Constructors and its Disaster Response Ability

In Japan, construction investment has been rapidly decreasing since Fy1996. These days, the business environment for construction companies has been severer. Bankrupts of major regional constructors have occurred one after another. Continued existence of necessary construction companies is endangered in many regions. Even if the construction works decreased, it is apparent that regional construction companies are requested to fulfill a role to maintain and amend existing infrastructure and buildings and execute disaster recovery works.

To retain constructors that conduct disaster response actions, there are systems that some governments give small merit in tendering and contracting of public works to the companies attending to a "disaster response agreement" with the governments. However, there is no clear method to confirm whether individual construction company is surely able to conduct disaster recovery works quickly. Therefore, the governments cannot distinguish a company with high ability of disaster response from others and give it much priority. In this context, MLIT focused on BCP of construction companies. If governments are able to evaluate companies retaining enough business continuity ability, the companies are expected objectively to execute recovery works smoothly even at the time of serious disaster.

2.3 BCP Promotion Activity of Associated General Constructors of Japan, Inc.

In Japan, large and medium-sized regional construction companies often formulate a constructors association in each prefecture, and their nationwide body is Associated General Constructors of Japan, Inc (AGCJ). In promoting CSR of the member companies, AGCJ has been emphasizing constructor's social contribution activities in a time of disaster.

Since FY2007, AGCJ had conducted to make original BCP promotion materials for member contraction companies. Its achievement is "Manual of Business Continuity at the Time of Disasters for Regional Constructors" published in April 2009 (Figure 3). [v] This manual highly conforms to above-mentioned Simple Gide of KRDB, contains the same 10 steps of the Gide, and supplements its explanations.

Additionally separate volume "An Example of BCP of Regional Construction Company (Simple version)" is also prepared. It is consist of 39 pages and contains simple document forms with commentary. AGCJ members companies can get the electric files of this example from the members-only website of AGCJ, and directly fill in the format.

AGCJ and subordinate constructors associations of each prefecture have promoted BCP by way of organizing lecture meetings of this manual, and the author has also supported these activities. [vi]



Figure 3 The Manual of AGCJ

3. KRDB's RECOGNITION SYSTEM OF BUSINESS CONTINUITY ABILITY

3.1 Background of Introduction of the Approve System

Encouraging construction companies to formulate their BCP, KRDB concerned that they could not diffuse it easily if the concrete merits of holding BCP were not clear. Actually, drawing up BCP generally needs considerable time and efforts. Then in fact, BCP did not be spread to regional constructors easily.

Responding to this situation, KRDB started the system to evaluate basic business continuity ability of construction companies and approve those that fulfill the requirement in June 2009.

KRDB is operating this "Approval System of Constructors' Business Continuity Ability at the Time of Disaster" in coordination with constructors associations. For example, KRDB asked AGCJ to hold a consultation counter of the system. Additionally, constructors that want to apply the approval system are able to utilize the AGCJ's manual for business continuity as a very useful textbook.

3.2 Outline of the Approval System

KRDB conducts the procedure of the approval system in every quarter of the year (June, September, December and March). The examination includes both of document review and an interview. Required documents are the applicant's BCP documents (full documents are not necessarily required). Applicants should clearly present all the points that KRDB will confirm in their documents.

The final decision of approval was made by the Approval Committee of Business Continuity Ability that consists of executive officers of KRDB. Subcommittee for evaluation executes the concrete examination process,

including the interview with applicant companies. The Subcommittee includes BCP specialists, and the author is the one of the specialists at this moment. The requirements of the approval system are shown in Table 2.

Table 2 Requirements of Approval System of KRDB

Check Points		Contents of Confirmation
A	Choice of critical operations and recognition of time objectives	-Damage expectation -Choice of critical operations -Recognition of time objectives
B	Organizational formation at the time of disaster	-Safety confirmation of staff and family -Organizational formation - Substitute members to the chief of the disaster headquarter and their order of substitution
C	Secure the headquarter,	-To secure a headquarter and a substitute headquarter for communication -Criteria of the start
D	Information sending & sharing	-Mutual recognition of contact with national, prefectural and municipal governments -Communication tools usable in a time of disaster
E	To secure workers, material and machinery	-Resources which a company secures in itself -Subcontractors' emergency contact points and mutual recognition of communication methods
F	Training	-Training plans and past result -Improve plans of BCP and past result

It should be aware that the approval system does not confirm whole contents of BCP or BCM. KRDB explains that it evaluates "basic business continuity ability." It is apparently different from the third party certification system on BCM, which the International Standard Organization (ISO) has discussed, or British Standard's BCM system certification has operated. KRDB's system is the confirmation procedure by an ordering party, in other word a transaction counterpart, of the disaster recovery works. Therefore, they focus on whether an applicant constructor can play a role that the government expects in a time of disaster.

Based on this character, "time objective of when the applicant is able to secure its organization formation" and other time objectives are carefully certified. On the other hand, KRDB does not request to explain critical operations such as checkout of the disaster damage on the objects of valued clients in the examination process.

The submission of the first approval procedure started in June 2009 and 33 companies applied, and 31 companies were qualified in September. As for the second examination, 27 companies applied and were 26 companies were qualified in December 2009. The qualified companies are listed on the website of KRDB.[vii]

The reason of the high pass rates was that KRDB made effort to advise applicants to fulfill the criteria and suggest how to amend the problems before final judgment. This kind of certification process that helps applicants' success seems to be necessary at the beginning of the approval system to make settled in construction industry.

3.3 Approval System of Shikoku Regional Development Bureau

Almost the same approval system started in the Shikoku district, south and western part of Japan. Shikoku Regional Development Bureau started the system in December 2009. The applicants are restricted to "C rank" companies of "civil works general" in the bureau's contractor registration system criteria. They are mainly large and medium-sized constructors in each prefecture that are generally in charge of disaster response works. The total number of companies belonging to the C rank is 119. To the first approval examination 49 companies have applied, and it means one fourth of the total. It seems to be a good start in the respect of diffusion

In January 2009, prior to the approval system started, Shikoku Regional Development Bureau, prefectural government of Tokushima, Kagawa, Ehime and Kochi, four national universities in these prefectures, constructers associations of these prefectures and construction consultants association of Shikoku aria formulated the BCP Conference on Construction Industry. By the members of this conference BCP promotion activity had started. Until now, for example, study meetings are continued at the member universities.

Additionally, other Regional Development Bureaus of MLIT are also considering the introduction of similar approval system for construction companies

3.4 Effective Diffusion Method of BCP to Regional Construction Companies

The author has supported small and medium-sized enterprises (SME) to formulate BCP in many prefectures with other members of BCAO. Based on these experiences, it is not easy for SME to formulate BCP without outer support even if they use the Guidelines or manuals of BCP. They often face the process that they cannot easily understand, and frequently they misunderstand the details of the manual. One idea is to get support by an experienced consultant on BCP, but it normally costs some million yen (some ten-thousand dollars) for fulfilling consultation.

Therefore, the author believes that it is effective for the constructors to have a study meeting with other construction companies that want to draw up BCP. IF technical supports by local universities, research institutes, NPOs, governments, industrial associations or SME support

organizations are available, it would be more useful. The study meeting method is low cost, and it should be a good occasion to ask questions each other, and will be a motivation to continue the BCP formulation.

This kind of study meeting have been realized, for example, at Tokushima University, Ehime University in Shikoku area, and BCAO recommends as one type of BCP promotion method for SME.

4. CONCLUSIONS

"Approval System of Constructors' Business Continuity Ability at the Time of Disaster" of KRDB is the first example that the government approves companies' business continuity ability, and it may be the first case that the government objectively evaluates companies' ability of disaster response.

The selection and favorable treatment system for construction companies that have high probability to execute disaster response at the time of serious disaster will be useful to secure the available constructors in each region. If local governments also utilize this approval system, it will be more effective.

However, at present, the approval system is still in the trial stage and we should carefully examine how many regional construction companies will apply to it. If the share of the certified companies remains low, it will be difficult to introduce the merit in the comprehensive evaluation system of public works. Therefore, effective promotion activities in Kanto and Shikoku districts are seriously important. The BCP diffusion rate in these districts in the near future would decide whether the approve system works successful or not.

References:

Maruya, H (2009), "Present Situation and Future Tasks for Diffusion of Business Continuity Plan (BCP) to Small and Medium Enterprises," Proceedings of the Annual Conference, Institute of Social Safety Science, No.24, 17-20

Maruya, H (2008), "Meaning and Economic Effect of Business Continuity Plans," Gyousei Inc

Maruya, H and Sashida, T. (2006), "Commentary and Q&A of Business Continuity Guideline of Central Disaster Prevention Council," Nikkagiren Inc

Maruya, H. (2007), "Study of the Step-up Introduction Measures of BCP for Small and Medium Enterprises," Proceedings of the Annual Conference, Institute of Social Safety Science, No.20, 41-16

Maruya, H. (2007), "The Present State and Regional Difference in the Assistance Measures Provided by the Prefectural Government, etc. for SMEs to Introduce a BCP," Journal of Social Safety Science, Institute of Social Safety Science, No.9, 37-46

Maruya, H. (2006), "Study on the Situation and Difficulty of Introducing Important Elements of Business Continuity Management, Considering Dissemination of BCM to SMEs in Japan," Journal of Social Safety Science, Institute of Social Science, No.8, 269-278

Additional notes:

[i] "Business Continuity Guidelines 1st ed." published in August, 2005. In March 2007, a commentary of the guidelines was published.
http://www.bousai.go.jp/kigyo-machi/jigyou-keizoku/guideline01_und.pdf
Additionally, the second edition of the guidelines was published in November 2009.
http://www.bousai.go.jp/MinkanToShijyou/guideline02.pdf

[ii] "Inquire Survey on Disaster Prevention, BCP and Pandemic Influenza Countermeasures of Companies." Respondent of the survey: 587 companies selected according to the share of the type of business from major companies, mainly those listed on the first section of the Tokyo Stock Exchange. Response rate: 26.6%.

[iii] KRDB website
http://www.ktr.mlit.go.jp/kyoku/saigai/bcp/kanigaido.pdf

[iv] The guide is available from BCAO website
http://www.bcao.org/data/01.html

[v] The manual is available by download from the website of AGCJ.
http://www.zenken-net.or.jp/zenken-jktebiki/index.html
Document creation of the manual was entrusted to Research Institute of Construction & Economy that the author belongs to.

[vi] The first effort to promote BCP by construction industry was the "Construction BCP Guidelines" published in July 2006 by Japan Federation of Construction Contractors, Inc. Main target of this guidelines are large-sized nationwide construction companies.
http://www.nikkenren.com/publication/index2006.html

[vii] Website of KRDB
http://www.ktr.mlit.go.jp/kyoku/saigai/ninteikigyou.htm

JOINT CONFERENCE PROCEEDINGS
7th International Conference on Urban Earthquake Engineering (7CUEE) &
5th International Conference on Earthquake Engineering (5ICEE)
March 3-5, 2010, Tokyo Institute of Technology, Tokyo, Japan

MINING CRITICAL INFRASTRUCTURE INTERDEPENDENCY RELATIONSHIPS TO MITIGATE DISASTERS USING GSP

Ssu-Min Tseng[1)], Te-Che Chen[2)], and Chien-Cheng Chou[3)]

1) Graduate Research Assistant, Department of Civil Engineering, National Central University, Taiwan
2) Senior Engineer, Taiwan High Speed Rail Corporation, Taiwan
3) Assistant Professor, Department of Civil Engineering, National Central University, Taiwan
983402006@cc.ncu.edu.tw, teche_chen@thsrc.com.tw, ccchou@ncu.edu.tw

Abstract: Critical infrastructures are important national assets for producing or distributing continuous flows of essential goods or services. When one critical infrastructure shuts down due to an external disruption, it can be expected that other critical infrastructures that need goods or services provided by the discontinued one will stop shortly, exacerbating the damage caused by the external disruption. Past research has categorized critical infrastructure interdependency (CII) into four relationship types and has proposed several methods to model CII and its effects. This paper presents a knowledge discovery process for CII that can be used to extract frequent patterns of critical infrastructure failure records directly or indirectly triggered by external disruptions. The knowledge discovery process, including integration of critical infrastructure failure records and transformation into the data format needed by the data mining algorithm, is described. Discussion of a disaster mitigation approach to stopping CII-related possible future failure events is addressed, followed by the analysis results of sample critical infrastructure failure records. Disaster mitigation officials can employ the proposed approach to explore CII and to design countermeasures when a disaster hits certain areas.

1. INTRODUCTION

Critical infrastructures are important national assets for producing or distributing continuous flows of essential goods or services (Fisher and Peerenboom 2000). These assets include, but are not limited to, facilities for transportation, communication systems, electric power systems, gas and oil storages and pipelines, water supply systems, wastewater treatment systems, and government services. A critical infrastructure interdependency (CII) relationship between two critical infrastructures can be defined as a bi-directional relationship that one critical infrastructure's output is the other critical infrastructure's input, and vice versa (Rinaldi et al. 2001). For instance, a gas pipeline leaks and an explosion occurs, which in turn engenders shutdown of a nearby telecommunication facility. Since the telecommunication facility does not function well, the emergency information cannot be relayed, and the explosion may cause other severe damage to both the gas pipeline and the telecommunication facility. Obviously, these critical infrastructure interactions often create complex interdependency relationships that cross system boundaries (Haimes 2005). As the complexity and interconnectedness of a country's critical infrastructures evolve, threats and vulnerabilities for the country increase. Investigating how a set of critical infrastructures interact thus becomes an important research topic.

Researchers have classified myriad interdependency relationships of critical infrastructures into four types: physical, cyber, logical and geographic (Rinaldi et al. 2001). Several methods have been proposed for identifying these relationships. Some of them can designate the geographic type of interdependency relationships, based on the complete and accurate baseline data of the critical infrastructures (Laefer et al. 2006; Duenas-Osorio et al. 2007). The others can detect some physical, cyber, or logical types of interdependency relationships, based on the information gathered after the failures of the critical infrastructures (McDaniels et al. 2007). However, it should be noted that not only the baseline data but the failure records of the critical infrastructures need to be well integrated so that their interdependency relationships can be rendered (Pradhan et al. 2007). Further, most infrastructure owners focus on their own facilities and do not pay much attention to such interactions that cross system boundaries (Chou et al. 2007). Hence, comprehensive identification of all four types of interdependency relationships remains to be a challenge.

In addition, a critical infrastructure system usually consists of many sections that are geographically distributed over certain areas (Bagheri and Ghorbani 2006). A critical infrastructure section may consist of numerous components. An interdependency relationship may exist at the component, at the section level, or at the system level. For instance, a pump station of a water supply system may interact with a

facility of a power distribution network. Failures of the two components may not cause the shutdown of the two entire systems, but they may affect certain sections of the systems. Past research has investigated the system-level interdependency relationships (Mendonca and Wallace 2006); however, it may be more economic and feasible to define a disaster mitigation plan only for the affected sections of the critical infrastructures.

In fact, when an external disruption occurs, there will be a series of failure events among the interdependent critical infrastructures. Uddin and Engi (2002) proposed pre-, mid-, and recovery-from-events modes to describe them. Disaster mitigation officials may want to know possible future failure events in order to stop them. For instance, assume that event A occurred and experts said that event B, event C and event D will probably occur. Therefore, the officials might want to investigate the possibility of preventing the occurrence of event B so that events C and D will not occur. Overall, if relevant failure records of critical infrastructures can be collected completely and analyzed, their CII relationships may be unveiled by extracting frequent patterns of the failure records. Past CII-related research does not accommodate this need. Elaboration of such sequence-based CII knowledge may deserve further research and could lead to deeper knowledge of CII.

This paper presents a knowledge discovery process for CII. Specifically, the generalized sequential patterns (GSP) discovery algorithm was employed to find out frequent patterns of critical infrastructure failure records directly or indirectly triggered by external disruptions. The proposed approach aims at investigating section-level interactions among a given set of critical infrastructures and at exploring the possibility of stopping the failure chain. Theoretically, if infrastructure owners will repair damaged facilities to the extent prior to the breakdowns, CII relationships will be repeatedly formulated and frequent patterns of critical infrastructure failure records may help researchers better understand these relationships. Furthermore, comprehensive identification of the CII relationships could be possible if sufficient external disruptions exist and can trigger failures due to each CII relationship.

2. LITERATURE REVIEW

The disaster management process consists of six disaster-related phases (USFDA 2003): (1) identification; (2) prediction; (3) mitigation; (4) preparation; (5) response; and (6) recovery. The identification phase involves ascertaining any opportunity pertaining to community assets, i.e., critical infrastructure systems, fire trucks, hospital beds, etc., that may be affected by a disaster. The prediction phase consists of scientific analysis tasks, including meteorological, geologic, hydrologic, agricultural, environmental, epidemiologic calculations and simulations. The mitigation phase concerns active reductions of a disaster's impact, whereas the preparation phase includes needed actions to contend with the portion of a disaster's impact that cannot be mitigated. The response phase focuses on real-time actions as a disaster evolves, whereas the recovery phase deals with how to restore community assets affected by a disaster (Pradhan et al. 2007).

Researchers have also analyzed requirements of a DMS covering all six phases of the disaster management process (Pradhan et al. 2007). Briefly, a DMS is designed to significantly lessen the loss of human life and the economic costs of a disaster, and should have three components (Uddin and Engi 2002): (1) a baseline database: which contains the basic information of the community assets affected by a disaster; (2) spatial querying: which can provide disaster management officials with a graphical interface showing designated geographical information of the disaster and community assets, e.g., locating the shortest evacuation path and optimizing the resource distribution; and (3) ubiquitous computing: which means redundant computing resources should be allocated to execute the DMS simultaneously (Pradhan et al. 2007).

Although most of the current DMSs have stored critical infrastructure baseline data for disaster management purposes, CII data have not been rigorously documented and analyzed. The rescue operations after September 11, 2001 were recognized as lack of an integrated data repository that can be used to predict possible subsequent infrastructure failures. CII data can play a major role in establishing the knowledge base for the rescue operations during and after a disaster. Disaster management officials or decision makers need to know not only direct impact on community assets of a disaster but indirect impact on other critical infrastructure systems that may be shut down due to CII. However, since managing the interdependencies of critical infrastructure systems is not their owners' top priority, the only way to collect CII data is for transportation agencies to ask infrastructure owners to upload interdependency data as a part of the rights-of-way permitting process. Some infrastructure owners build very detailed computerized models describing their own facilities, but this kind of information may involve a company's confidential data and cannot be completely shared with the others. Security concerns regarding CII data must be addressed in advance of data collection from different infrastructure owners. A formal model that can describe CIIs and predict a disaster's impact on critical infrastructure systems is highly desired.

3. THE CII MODEL

The proposed CII model is shown in Figure 1. Elaboration of each class in the model is described in the following sections. Basically, the model consists of three main parts: (1) infrastructure and management classes; (2) interdependency classes; and (3) infrastructure type classes. The infrastructure and management classes contain information regarding an infrastructure system itself and the owners' organization. The interdependency classes are

designed to capture requirements of the three CII types. The infrastructure type classes are the reflection of the need that each type of critical infrastructure systems has its own attributes. The mechanisms of the model are described as follows.

3.1 Infrastructure and Management Classes

Three classes pertain to this part:

- Organization: this class represents the owner of a critical infrastructure system. It includes a person's contact information so that disaster management officials can get in touch with him or her when potential damage of the infrastructure occurs.

- Enterprise: this class represents the concept of the organization's business entity. For example, a city government may be responsible for the water supply system, the wastewater treatment system, and the power distribution system. There must be three engineering divisions in the city government, so "Enterprise" represents the city government whereas "Organization" represents each engineering division. The "Enterprise-Organization" structure can be easily extended to model any infrastructure owners' organizations.

- Infrastructure: this class represents the most important concept in the CII model, i.e., infrastructure. It consists of six fundamental attributes:

1. Name: the name of the infrastructure.
2. Description: notes or other information regarding this infrastructure.
3. Location PolygonZ: the location and shape of the infrastructure, including the vertical dimension. It should be noted that since an infrastructure object may contain a set of other infrastructure objects via composition, the shape and base reference point of the object should be changed accordingly.
4. ServicePeriod T: the expected service period of the infrastructure. Sometimes an infrastructure service may be stopped due to maintenance. The discontinued service may cause a serious problem if a disaster strikes an area where the regular backup infrastructure is working. In the theory of temporal database or MOD, there are two time dimensions associated with each time-sensitive attribute: valid time and transaction time (Tansel et al. 1993, Guting and Schneider 2005). The valid time refers to the time in the real world when an event occurs or a fact is valid. The transaction time refers to the time when a change is recorded in the database. For example, the service period of an infrastructure is defined by a manager as from 2009/1/1 to 2009/5/1. The manager knows the plan on 2008/11/1, but the plan is changed by another manager on 2009/3/1. Hence, the infrastructure will not provide service after 2009/3/2, although the original plan does not say so. Same rules can be applied to the transaction time dimension. Traditional database techniques do not consider such requirements because only the newest status of an object is recorded.
5. Status T: the working status of the infrastructure. This attribute is also time-sensitive. For example, disaster management officials might want to know when the status of an infrastructure is "Working" or "Stopped." They might want to know when the status data is updated. Persisting historical data of the infrastructure status in a database can help decision makers understand past experience.
6. EstimateStatus T: the estimated status of the infrastructure. Because the CII model is designed to predict the interdependencies between critical infrastructure systems, this attribute will be used to record the predicted status of an infrastructure.
7. RecoveryStatus T: the recovery progress of the infrastructure. If an infrastructure is out of order, its recovery plan will be executed. If RecoveryStatus is equal to "Complete," the Status of the infrastructure should be "Working."

3.2 Interdependency Classes

Four classes pertain to this part:

- Relationship: this class represents the concept of a relationship in the CII model. In the one end of the relationship, it is the dependent infrastructure that needs services or resources provided by the supporting infrastructure. For example, the operation of a power plant depends on the entrance road, whereas the traffic control system on the road needs electricity provided by the plant. Two relationship objects should be created for this interdependency. Additionally, the class consists of six attributes:

1. Name: the name of the relationship.
2. Description: notes or other information regarding this relationship.
3. TimeLag: the time span of the relationship that will cause the dependent infrastructure to stop or reduce the service level.
4. MinStatus: the minimum status of the supporting infrastructure that will activate the relationship, i.e., to shut down the dependent infrastructure.
5. ActiveTime T: the time when the relationship is activated. This attribute is time-sensitive and can provide detailed records of how a disaster propagates.
6. ImportantR: the weight or ratio of the relationship with respect to the dependent infrastructure. For example, two infrastructure systems support the operation of the third infrastructure. The two infrastructure systems may play different roles in supporting the third one. Hence, the weight for each supporting infrastructure is different.

- Physical: this class represents the physical relationship

type in the CII model. Relationship attributes can be easily modeled in the class. In the proposed model, the resource that bridges the two infrastructures is recorded here.

- Geographic: this class represents the geographic relationship type in the CII model. In the proposed model, the radius defining the boundary of two infrastructures that may work or stop at the same time is recorded here.

- Cyber: this class represents the cyber relationship type in the CII model. In the proposed model, the information that is consumed by the dependent infrastructure is recorded here.

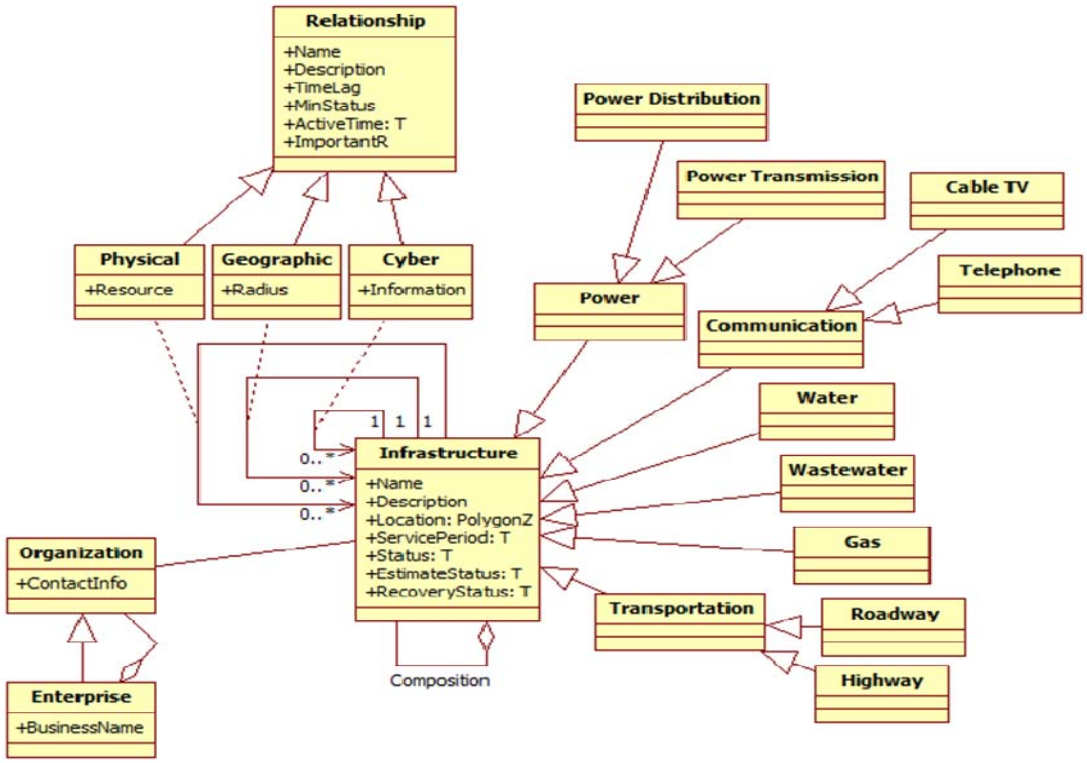

Figure 1 UML Class Diagram of the CII Model

3.3 Infrastructure Type Classes

This part defines various infrastructure types. Specific attributes pertaining to a certain type of critical infrastructure systems are recorded in respective classes. Additionally, because the structures and functions of a power distribution network is quite different that a power transmission network, two classes are designed to accommodate this requirement.

4. DISINTEGRATING SEQUENTIAL PATTERNS FOR CII-RELATED DISASTER MITIGATION

The sequential patterns identified could be utilized to analyze the possibility of breaking up the failure chain for CII-related disaster mitigation. Because CII-related failure events occur sequentially, a mechanism similar to the firewall concept could be employed to limit the spread of critical infrastructure failures. Suppose a frequent sequential pattern with three failure events "<{p1}{p2}{p3}>" was identified. If the component of the power system at Cell 1 location just failed, and if the power component at Cell 3 location is a very important asset that cannot be damaged, protection of the power component at Cell 2 location might be a good prevention strategy against the important asset failure at Cell 3 location, based on the sequential pattern identified. Such firewall strategy can be generalized as the following steps:

(1) Assume that a series of failure events have occurred. We use s0 to represent this sequence and there are k0 events. The support value of s0 is sp0.

(2) Assume that an important asset ij, where i is the type of the critical infrastructure and j is the cell location number, has not be damaged. Disaster mitigation officials would like to protect it against any CII-related impact.

(3) Let sp1 to be the support value of the sequence combining s0 and the failure of the important asset ij. We use s1 to represent this new sequence, and there are k1 events. Note that k1 is equal to the sum of k0 plus one and ij must be the last event of s1.

(4) For all the sequential patterns generated by GSP, filter out the sequential patterns that do not satisfy any of the following requirements:
The pattern should begin with s0, i.e., the failure events of s0 should occur first among all the other events of the pattern.

The pattern should end with ij, i.e., ij should be the last event of the pattern.

Note that the sequential patterns with more than (k1+1) events do not need to be analyzed either because all of their support values are less than or equal to the support values of the patterns that pass Step 4.

(5) After completion of Step 4, there may be a set of sequential patterns. Let s2 to be the sequential pattern with the maximal support value. Let sp2 to be the support value of s2.

(6) The firewall component (s2-s1) would be the one which disaster mitigation officials should strive to protect in order to prevent the failure of ij. For instance, assume that s0 consists of <{p1}>, s1 consists of <{p1}{p3}>, and s2 consists of <{p1}{p2}{p3}>, where p1 is the current failure event, p3 is the important asset, and p2 is the firewall component that disaster mitigation officials can utilize to prevent the failure of p3 from CII-related impact.

(7) Initially, the probability of the failure of the important asset is (sp1/sp0). If adequate measures have been applied in protecting the firewall component, the new probability of the failure of the important asset becomes [(sp1-sp2)/sp0]. The probability of successful protection of ij by preventing the failure of (s2-s1) would be (sp2/sp1).

It should be noted that an important asset may have many CII relationships with other components of critical infrastructures. Because disaster mitigation officials already knew the current failure events (s0), they would like to break the CII chain that can damage the important asset. Once the firewall component (s2-s1) is identified, they can create alternative sources of input for the important asset to continuously operate. For instance, if a water pump station is very important for nearby communities, an alternative power source should be established for it as long as its original power supply component is identified as the firewall component.

5. CONCLUSIONS

With the ever-increasing demand for a streamlined analysis of CII, disaster management officials and decision makers are making substantial efforts to improve the disaster mitigation technology. Because CII data are fundamental to develop a full-fledged DMS and because the management of the time dimension is the most difficult task in modeling CIIs, a rigorous model with time processing capabilities such as the one in this paper can help disaster management officials retrieve relevant information on demand. This research has designed a UML-based model that can describe CIIs with the time-sensitive attributes. Further implementation and evaluation of the CII model proposed is needed in order to demonstrate how such information technology can mitigate a disaster's impact.

References:

Chen, L.C., Wu, J.Y., and Lai, M.J. (2006) "The Evolution of the Natural Disaster Management System in Taiwan." *Journal of the Chinese Institute of Engineers*, 29(4), 633-638.

Chou, C.C., Caldas, C.H., and O'Connor, J.T. (2007) "Decision Support System for Combined Transportation and Utility Construction Strategy." *Transportation Research Record: Journal of the Transportation Research Board*, TRB, 1994, 9-16.

Fisher, R., and Peerenboom, J. (2000) "Interdependencies: A DOE Perspective." *16th Annual Security Technology Symposium & Exhibition*, Office of Critical Infrastructure Protection, June 28, 2000, Williamsburg, Virginia.

Guting R.H., and Schneider, M. (2005) *Moving Objects Databases*, Morgan Kaufmann, San Francisco, CA.

Haimes, Y. (2005) "Infrastructure Interdependencies and Homeland Security." *Journal of Infrastructure Systems*, ASCE, 11(2), 65-66.

Kranc, S.C., Yalcin, A., Tsalatsanis, A., and Collier, N.O. (2007) "The Efficacy of Utility Data Management." *FDOT Research Project BD544-27 Report*, University of South Florida, Tampa, FL.

Kraus, E., Quiroga, C., Brown, R., Stevens, C., and Koncz, N. (2007) "Development of a Utility Conflict Management Tool." *TxDOT Research Project 0-5475 Report*, Texas Transportation Institute, College Station, TX.

Laefer, D., Koss, A., and Pradhan, A. (2006) "The Need for Baseline Data Characteristics for GIS-Based Disaster Management Systems." *Journal of Urban Planning and Development*, ASCE, 132(3), 115-119.

MRA. (2005) *Joint Infrastructure Interdependencies Research Program (JIIRP) Symposium*, the Department of Public Safety and Emergency Preparedness Canada (PSEPC), November 10, 2005, Ottawa, Ontario, Canada.

Peachavanish, R., Karimi, H., Akinci, B., and Boukamp, F. (2006) "An ontological engineering approach for integrating CAD and GIS in support of infrastructure management." *Advanced Engineering Informatics*, Elsevier, 20, 71-88.

Pederson, P., Dudenhoeffer, D., Hartley, S., and Permann, M. (2006) "Critical Infrastructure Interdependency Modeling: A Survey of U.S. and International Research." *INL/EXT-06-11464*, Idaho National Laboratory: Critical Infrastructure Protection Division, Idaho Falls, Idaho.

Pradhan, A., Laefer, D., and Rasdorf, W. (2007) "Infrastructure Management Information System Framework Requirements for Disasters." *Journal of Computing in Civil Engineering*, ASCE, 21(2), 90-101.

Rinaldi, S., Peerenboom, J., and Kelly, T. (2001) "Identifying, Understanding, and Analyzing Critical Infrastructure Independencies." *IEEE Control Systems Magazine*, 21, 11-25.

Tansel, A., Clifford, J., and Gadia, S. (1993) *Temporal Databases: Theory, Design, and Implementation*, Benjamin-Cummings, San Francisco, CA.

Uddin, N., and Engi, D. (2002) "Disaster Management System for Southwestern Indiana." *Natural Hazards Review*, ASCE, 3(1), 19-30.

USFDA. (2003) *Disaster preparedness phases*, U.S. Federal Drug Administration, Rockville MD.

Wolfson, O., Xu, B., Chamberlain, S., and Jiang, L. (1998) "Moving Objects Databases: Issues and Solutions." *Proceedings of the Tenth International Conference on Scientific and Statistical Database Management*, IEEE, Capri, Italy, 111-122.

Wolfson, O. (2002) "Moving Objects Information Management: The Database Challenge." *Lecture Notes in Computer Science*, Springer Berlin / Heidelberg, 2382, 15-26.

JOINT CONFERENCE PROCEEDINGS
7th International Conference on Urban Earthquake Engineering (7CUEE) &
5th International Conference on Earthquake Engineering (5ICEE)
March 3-5, 2010, Tokyo Institute of Technology, Tokyo, Japan

ECONOMIC IMPACTS CAUSED BY BUILDING AND TRANSPORTATION INFRASTRUCTURE DAMAGES: APPLICATION OF INTERREGIONAL COMMODITY FLOW MODEL TO THE 1995 HANSHIN AWAJI EARTHQUAKE DISASTER

Yoshio Kajitani[1)]

1) Research Scientist, Civil Engineering Research Laboratory, Central Research Institute of Electric Power Industry, Japan

Abstract: This paper discusses the economic impact on industrial sectors during natural disasters. Simultaneous damages on utility system (e.g. water, gas, electricity) as well as transportation network are focused on as the major impact sources of industrial activity levels. For this purpose, survey based resilience factors and interregional commodity flow model (ICFM) are adopted. Resilience factor is simply defined as the service level (output base) of each industrial sector under utility damages or any production input reductions, and these factors are available based on empirical surveys to Japanese industries. On the other hand, ICFM is a combined model of interregional input-output model and transportation network (user equilibrium model), which can estimate the traffic flows on each road considering the transportation time and input output structures. In this study, these survey data sets and ICFM are applied to estimate the impact on domestic commodity flow under the damages of utility and transportation infrastructures in the case of 1995 Great Hanshin-Awaji Earthquake. Through the comparison of the estimated result to the actual rerouting situation of several surveyed industries, tasks and future development of the model are discussed in the last part of presentation.

1. INTRODUCTION

When a large-scale disaster occurs, a road network system can be severely damaged. This damage causes economic losses due to the failure of trading goods inside and outside the physically damaged areas. In order to reduce this type of economic loss, it is important t to analyze the relationship between each road link and economic activities and determine which route should be reinforced in advance or quickly recovered after the disaster.

One of promising approaches is utilizing regional economic models, which combine the input-output type of econometric model and transportation network model (user equilibrium model). The input-output type of model can estimate the interregional trades, while transportation network model can assign the traffic flows (cars) on the actual road networks. Therefore, amount of cargo traffics of each sector at the link level can be estimated and utilized for the impact analysis of the damaged link. For example, Kim et al. (2002) utilized the integrated input-output and transportation network model, so called Interregional Commodity Flow Model (ICFM) and applied the model to the economic impact analysis of trunk road network damages.

However, the model is applied to a limited situation only in the United States and its applicability and extensions are not fully investigated on in the more general disaster situations such that other infrastructures and production facilities are damaged and final demands are decreased.

Therefore, this research reviews the performance of ICFM and investigates on the model characteristics and extensionality through the case study of the 1995 Great Hanshin-Awaji Earthquake. Especially, the model performance is demonstrated related to the fitting accuracy to observed data, convergence time, and influences of supply and demand decreases during disasters.

2. PREVIOUS RESEARCHES ON ECONOMIC IMPACTS INDUCED BY TRANSPORTATUON DAMAGE

There are several related researches on estimating economic impacts due to natural disasters. Wide ranges of reviews on past related researches are comprehensively summarized in Okuyama (2007). The following reviews are rather limited to the main focus of this paper; the extension of the economic loss assessment model with transportation networks.

For, example, Cho and Gordon et al. (2001) developed the econometrics model called SCPM (Southern California Planning Model). This model can target at the local traffics in the urbanized area (or populated area), including both personal and material flows. In the SCPM, a gravity type model is applied to estimate the origin-destination flows based on the input-output data and regional population databases. The developed model is applied to the City of Los Angels to estimate the economic impact of the damaged bridges.

Sohn et al. (2003) applied the ICFM, reviewed in the previous section, to the economic impacts of earthquake disaster in New Madrid, the United Sates. As a result, important implication is derived such that the order of economic importance of the roads (links) is different from the order of physical importance (i.e. damage probabilities of the links.).

In Japan, SCGE approach becomes popular to analyze the economic impacts of natural disasters, such as Muto and Ueda (2006), Koike et al. (2004), Tatano and Tsuchiya (2008). Different from regional economic models, Nagae et al. (2007) developed user equilibrium model considering the change of traffic demands during earthquake disasters and applied it to the traffic congestion analysis in the local damaged area. However, the combination of SCGE and transportation model is thought to be still under construction.

On the other hand, ICFM is the succeeded model, which had been intentionally developed in 1980s, focusing on the combination of user equilibrium model and entropy model with the restriction of input-output structure (Boyce, D. 2002). That is, this model can find the equilibrium point of two models; The model to determine the interregional material flows based on the fixed traffic time, and the model to determine the traffic time based on the fixed material flows. Therefore, ICFM can be applied to the decision making problems such as the upgrades of local road network performances, considering the macro economic impacts of natural disasters.

However, as described in the previous sector, model applicability considering the influence of model parameters and data sets, such as the required fineness of road network, should be fully investigated because the damaged area is relatively local and supply-demand conditions are complicated during natural disasters. The examples in Kim et al. (2002) and Sohn et al. (2003) focuses on the relatively large-scale road network and are not applied to the actual natural disasters. From these perspectives, the analysis in this paper is expected to demonstrate the important example of ICFM application to the actual earthquake disaster in 1995, Kobe, Japan and shows the possibilities of future model extensions.

There are several applications of ICFM in Japan. For example, Okuda and Hayashi (1991) adopt ICFM to investigate on the impacts of environmental tax to transportation sector. However, this paper is oriented to only theoretical investigation and not testified in the context of natural disaster.

3. APPLICATION OF ICFM TO THE ECONOMIC IMPACTS ASSESSMENT OF NATURAL DISASTERS

3.1 Outline of ICFM

In the following, basic idea of ICFM is introduced based on the formula shown in Kim et al. and Sohn et al. Essentially, the formula is expressed by the user equilibrium model with entropy function, with the restriction of input-output trading structure. Input-output structure is thought as competitive imports and trading amount is exchanged by the rate of monetary term (yen) to traffic terms(tons).

Consider traffic volumes on each link are defined as:

$$\sum_m \sum_{ijr} h_{ijr}^m \Phi_{ijr}^a = f_a \ , \tag{1}$$

where, f_a : traffic volume on link $a \in A$, h_{ijr}^m : traffic volume of sector m from region $i \in \Omega$ to $j \in \Omega$ by route $r \in R_{ij}$. Φ_{ijr}^a takes the value 0 or 1 ; $\Phi_{ijr}^a = 1$ if link a is used and $\Phi_{ijr}^a = 0$ in the other case.

Then the objective function and restriction conditions in ICFM are expressed as:

$$\min_{h,x} Z(h,x) = \sum_a \int_0^{fa} d_a(\omega) d\omega + \sum_{mj} d_{jj} \frac{x_{jj}^m}{g^m} + \sum_m \frac{1}{\beta^m g^m} \left\{ \sum_{ij} \left(x_{ij}^m \right) \ln \left(x_{ij}^m \right) \right\} \tag{2}$$

s.t.

$$\sum_r h_{ijr}^m = \frac{x_{ij}^m}{g^m}, \tag{3}$$

$$\sum_i \left(x_{ij}^m \right) = \sum_n a^{mn} \left(\sum_k x_{jk}^n \right) + y_j^m + E_j^m - M_j^m, \tag{4}$$

$$h_{ijr}^m \geq 0. \tag{5}$$

Here, x_{ij}^m : outbound domestic exports of sector m from area i to j (Yen), g : exchange coefficient between traffic volumes (PCU: Passenger Car Unit) and trade values (Yen), $d_a(\omega)$: link performance function, β^m : cost sensitivity parameter for sector m, d_{jj}: intraregional travel time. Entropy function performs to avoid so called "aggregation effects" and to produce "hawling effects". These effects produce mutual trading among the same sector and disperse trading routes and regions, which can be observed in the real data sets.

Equations (3) to (5) are used as restriction conditions. Equation (3) is an exchange rate between traffic amount (PCU) and monetary amount (Yen). Equation (4) is a regional input-output structure. The remained parameters are set as follows. a^{mn} : input-output coefficient, y_j^m : regional final output, E_j^m : exports (yen) from region j . M_j^m : imports (yen) to region j . The last constraint in equation (5) indicates the non-negative conditions on the route traffic flow.

Characteristic of the model is that the monetary flow is exchanged to the traffic flows and allocated to the physical road network. For example, in case that the transportation cost increases, the model can express the change of interregional trading with the restriction of regional input-output structure. Impacts on traffic flows are also analyzed in case that final demand decreased during disasters. In this way, economic activities and traffic flows are explicitly analyzed based on the ICFM. The prerequisites to apply the ICFM are raised as follows:

-Exogenous variables: a^{mn}, y, E, M
-Only material flows are considered. (Personal traffic flows are exogenously determined)
-All the interregional flows are assigned on road networks (Transport share of road network exogenously determined.)
-Same cost sensitivity parameter β is used both for the normal and disaster cases.

The last requirements correspond to the assumption that the sizes of impacts of transportation cost to the input-output structure are same both for the normal and disaster cases. In the actual case, alternative production during the disaster requires adjustment cost. Here, alternative production indicates that company in the non-damaged area can tentatively increase production for the companies in the damaged area. Therefore, the prompt change of alternative production might not occur during disaster. However, because the data sets related to the alternative production are limited and influences of this assumption are testified in the case study section in terms of the change of traffic flows.

3.2 Production Capacity During Disasters and Parameter Estimations

As mentioned in the previous sector, not only the transportation network, but also the restriction of supply capacity and decrease of demand are emerged during disasters. These restriction and decrease are caused by several factors such as the stop of lifeline supply and building damages except transportation damages. In the ICFM, demand is exogenously given, and supply in the each region is determined without any upper limitation of production to satisfy the demand.

However, because the production capacity can be reduced in the great manner, the following restrictions are required.

$$\sum_j x_{ij}^m \le \hat{x}_{i\max}^m \quad . \tag{6}$$

Here, $\hat{x}_{i\max}^m$: maximum production capacity (yen) for sector m in region *i*. Equation (6) presumes that the goods of the same sector are identical and substitutable and that the sum of production capacity in the same sector is thought as the production capacity in the entire region. In addition, restoration and upgrade of production facilities, movement of facilities between regions do not occur during the short period after disasters.

Considering equations (2)-(6), Traffic flows are derived based on the first-order conditions of Lagrange multiplier.

$$x_{ij}^m = \delta_i^m \varepsilon_j^m \eta_i^m \exp(-\beta^m \mu_{ij}^m) , \tag{7}$$

$$\delta_i^m = \exp(-\beta^m g^m \sum_l \gamma_i^l a_i^{lm} - 1.0) , \tag{8}$$

$$\varepsilon_j^m = \exp(\beta^m g^m \gamma_j^m) , \tag{9}$$

$$\eta_i^m = \exp(-\beta^m g^m \theta_i^m) . \tag{10}$$

γ, μ, θ are Lagrangian variables regarding with constraint equation (3), (4), (6), respectively. Equation (10) is an inequality condition, which has to satisfy the following condition.

$$\theta = 0, \quad if \quad \sum_j x_{ij}^m \le \hat{x}_{i\max}^m , \tag{11}$$

$$\theta > 0, \quad if \quad \sum_j x_{ij}^m = \hat{x}_{i\max}^m . \tag{12}$$

In addition, the following condition regarding with μ_{ij}^m is obtained.

$$\mu_{ij}^m = \sum_a d_a(f_a) \Phi_{ijr}^a, \quad if \quad h_{ijr}^m > 0 , \tag{13}$$

$$\mu_{ij}^m \le \sum_a d_a(f_a) \Phi_{ijr}^a, \quad if \quad h_{ijr}^m = 0 . \tag{14}$$

Wilson's iterative balancing method (iterative update of δ and ε) is applied to equation (7) and obtain the amount of interregional trading and OD (origin-destination) traffics for each sector. In our research, update of Lagrangian η, which satisfies equations (11) and (12), is additionally estimated in the process of Wilson's method. Based on the result of Wilson's iterative method, solve the minimization problem of objective function and update μ in the equation (13). The simultaneous update of interregional trade and link traffics can be solved by Evans' algorithm (Evans 1986). In total, Wilson's method is a sub-problem of Evans' algorithm.

Parameter estimation is necessary for the cost-sensitive parameter β ($=\beta^m \times g^m$). Several calibration methods are proposed to fit the observed traffics (average moving time). This research adopts Hyman's method (Hyman 1969), which is also adopted in the previous research (Kim et al. 2002).

4. CASE STUDY OF THE 1995 GREAT HANSHIN-AWAJI EARTHQUAKE, JAPAN

4.1 Data Sets for the Case Study

The 1995 Great Hanshin-Awaji Earthquake severely damaged the regional traffic system in the Kobe metropolitan region. Highways and national roads along the coastal area were paralyzed and it takes a long period to recover them. Number of the roads from north to south through Mt. Rokko was limited, which also restricted accessibility to the damaged area from outside areas. As alternative routes, Chugoku Expressway and Maizuru Expressway, which recovered relatively in a short period, were assumed to be utilized (Editorial Committee for the Report on the Hanshin-Awaji Earthquake Disaster, 1998a).

In the following, damage conditions are determined for the period from several weeks to 1 month after the disaster. During this period, Trunk road networks such as Kobe and Wangan lines of the Hanshin Expressway, National Roads 2 and 43 had not yet been recovered. Regions are divided into 9 regions (Hokkaido, Tohoku, Kanto, Chubu, Kansai, Chugoku, Shikoku, Kyusyu, and Okinawa) as in Figure 1.

As a road network data set, the entire expressway in Japan and national roads are added for the Kinki region, surrounding area of the severely damaged area, in order to

conduct the precise commodity flow study. In total, network data consists of 7771 nodes and 8313 links. Figure 2 is the magnified road network around the damaged area; some of the representative trunk roads for the interregional trading are given with their names.



Figure 1 9 regions in Japan and road networks for case study

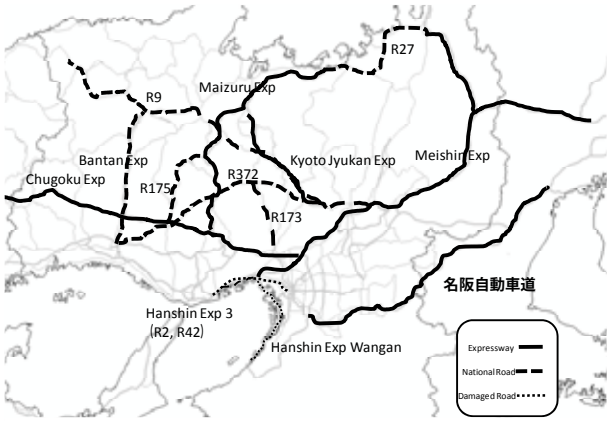

Figure 2 Traffic Network in the Kobe Surrounding Areas

OD nodes for the traffics in each region are arbitrarily set at only one of the nodes of traffic network in each region. Therefore, the congestions near the OD node can be severe due to the restriction of link capacity. Based on the precise distribution of each sector, more detailed and realistic study can be conducted. In addition, OD node for the Okinawa region is set at the most south node of Kyusyu area for a convenience. Traffic time inside the region is set as the half of the shortest traffic time to the adjacent regions as in Kim et al.

Other exogenous variables, their sources and assumptions are summarized in Table 1. Production capacity at non-damage region is set by the largest yearly production amount between 1990 and 1995, based on the assumption in Ashiya and Jinushi (2001). In this case, production capacities in each sector are distributed from 1 to 1.1 (except Mining (=1.5)). On the other hand, production capacity in the damaged area is determined by Kajitani et al. (2004), which utilized the distribution of building damages and utility damages (See Figure 3).

Table 1 Sources and assumptions of exogenous variables

Variables	Sources and assumptions
a^{mn} E_j^m M_j^m	1995 interregional input-output table (12 sectors in Research Institute of Economy (2000)).
y_j^m	1995 interregional input-output table Final demand in the Hyogo Prefecture (Hyogo Prefecture 1996) is modified by the household consumption survey (decrease of household consumption = 0.3).
g^m	Commodity flow census in Table 2 (MLIT 2002)
$\hat{x}_{i\max}^m$	Ashiya and Jinushi (2001) (Stock damage (production level) is based on Figure 2 estimated by Kajitani et al. (2004) .
$d_a(\omega)$	$(d_a(\omega) = a_0\{1+\alpha(\omega/C_a)^{\upsilon}\})$: α=0.48, υ =2.82 21). Link capacity Ca and Traffic speed a0 are set for Express way:72000 (pcu/day) and 100km/h, National Road:12000 (pcu/day) and 60km/h (JSCE 2006).
Others	Ratio of commodity flow in total traffic flows: 0.55, share of road networks: Estimated from commodity flow census in Table 3 (MLIT 2002).

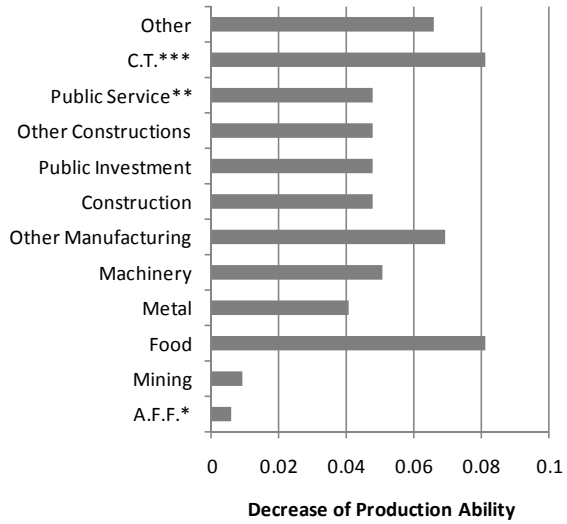

Figure 3 Estimated production capacity in each sector

*Agriculture, Forestry, and Fisheries

**e.g. Utilities ***Commercial and Transportation

g^m (Ton-Yen exchange rate) in the equation (3) is set by the commodity flow census as is given in Table 2. Industries, which are not given in the table, are thought to be the industries of imports only. Personal traffic flows are assumed to be the same proportion to commodity flows. Moreover, commodity flows which use road networks are thought to be the share rate for some categorized travel lengths in Table 3.

Table 2 Basic unit data of commodity flows (MLIT 2002)

	Weight/ Value (Ton/ 10^6 Yen)	Weight/Lot (Ton/PCU)	Lot/Value (PCU/ 10^6 Yen)
F.A.F.*	0.13	1.8	0.07
Mining	5.13	96.02	0.05
Manufacturing	7.30	3.04	2.40
C.T.**	0.80	0.66	1.89

*F.A.F.: Forestry, Agriculture and Fisheries

** Commercial and Transportation (Represented by whole sale sector)

Table 3 Share of road networks for all the commodity flows (MLIT 2002)

Distance	Share
1-100km	89.9%
101-300km	79.9%
301-500km	59.8%
501-1000km	50.4%
1001km 以上	31.2%

4.2 Estimation of Parameters

Estimated results of cost sensitive parameter β based on the setting up conditions in **4.1** are shown in the following. Figure 4 describes the value of β corresponding to the convergence situation of the average travel time (Hour/PCU). Calibration is conducted to fit the estimated average travel time to the average travel time estimated by the simple user equilibrium assignment of the OD data obtained from the interregional input-output table and basic unit data of commodity flows. In this study, β, satisfying the target average travel time (2.78 hours), is obtained after 7 calibrations.

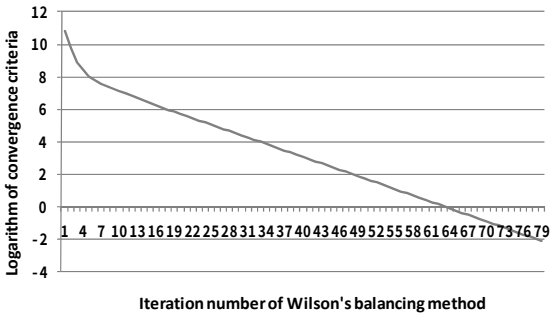

Figure 4 Convergence situation of average travel time

Figure 5 is the convergence situation of Wilson's balancing method at the end of calibration for β. A convergence criterion is a relative gap (maximum value of differences of estimated and observed final demands divided by the observed final demands), which becomes below 0.001, a criterion value of convergence, at 80 times iteration. Because it takes only a few seconds for reaching to convergence for Wilson's method, the total calibration time is equivalent to the computation time of Evans' algorithm.

Figure 6 compares the interregional trades (PCUs) estimated by ICFM to the PCUs estimated only by interregional input-output table. A correlation coefficient between two estimated interregional trades is 0.71 for logarithm data (0.99 for raw data). Underestimation by ICFM occurs at a few traffics area, but, in general, the estimated results by ICFM represent the interregional input-output table.

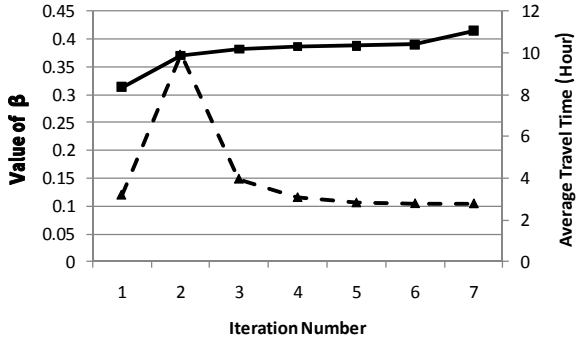

Figure 5 Convergence of Wilson's balancing method at the last calibration

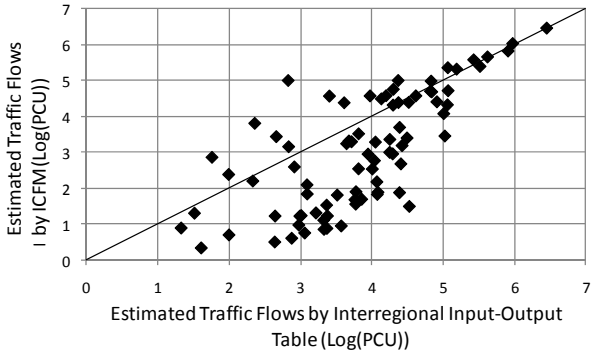

Figure 6 Comparison of the estimated interregional trades (PCU) by ICFM and the estimated pcus only by interregional input-output table

Figure 7 draws the estimated traffic on each link at the normal period (without disaster). Based on the magnified maps around Kobe City, Hanshin Expressway Line 3, National Roads, 2, 43, 372, and Chugoku Expressway are shown to be used for the traffics of the east-west direction. There is no traffic assignment for Maizuru Expressway, which was expected to be used for an alternative route

during the disaster. Travel times from Kinki to Hokkaido, Tohoku, Kanto, Chubu, Chugoku, Shikoku, Kyushu are estimated to be 6, 17, 12, 7, 4, 4, 8 (hours), respectively.

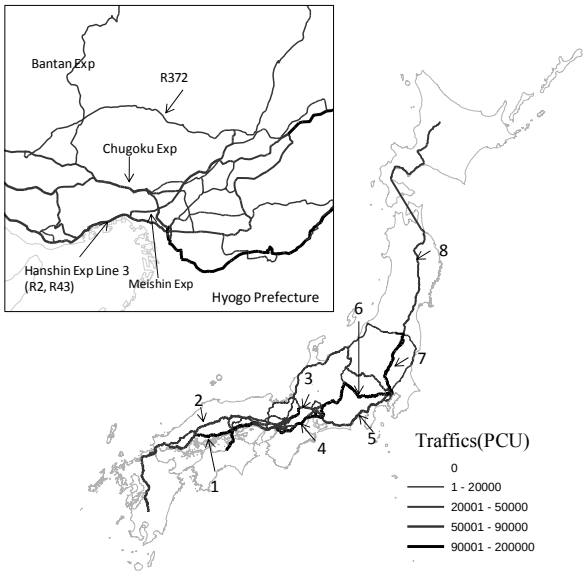

Figure 7 Estimated average traffic flows at the normal time (average of both directions)

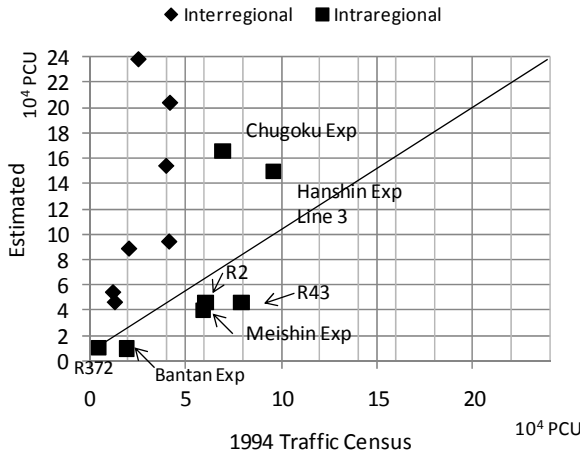

Figure 8 Comparison of the estimated traffic flows by ICFM and traffic census data in 1994 at the major observation points (average of both directions)

Figure 8 compares the estimated traffic flows by ICFM with traffic census data in 1994 at the major observation points. As observation points, 8 points are selected for comparing 24 hour traffic flows on interregional trades in Japan shown in Figure 6 and 24 hour traffic flows on the major roads in the damaged area. Most of the interregional traffic flows are overestimated. On the other hand, traffic flows in the damaged area are relatively better fit by ICFM. As a whole, fitting accuracy is not so excellent, but it could be improved by adding more local road network which can share the interregional traffic flows.

4.3 Impacts of Road Network Damages, Supply Constraint and Demand Decrease

Based on the parameter value of β obtained at (2), simulation is conducted under the actual road network damages. For this simulation, two scenarios regarding with supply constraint and demand decrease are considered (i.e. with supply constraint and demand decrease (more actual case), and without these constraint and decrease). Major trunk roads, national roads 2 and 43 and Hanshin express way are completely damaged and capacity of Chugoku Expressway is set as one third of its original capacity considering the traffic restriction for the emergent vehicles during the disaster.

Figure 9 shows a convergence situation of the objective function in the scenario with supply constraint and demand decrease. Relative gap, a convergence criterion, becomes below a target value 0.001 at 19 times iteration. Convergence is not rapid as the iteration reaches to the final solution.

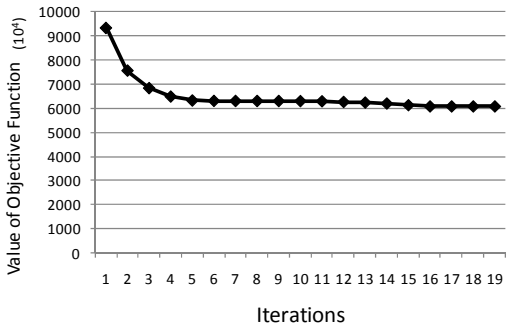

Figure 9 Convergence situation of objective function

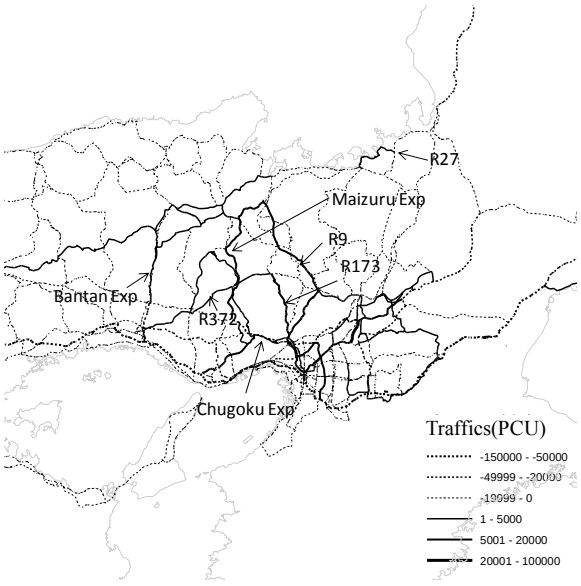

Figure 10 Estimated traffics under the road network damages (traffics with disaster minus traffics without disaster)

Figure 10 expresses the difference between traffic flows at the daily case and at the disaster case (disaster case-daily case). Traffics are increased in detouring routes such as the routes thorough Bantan Expressway-Maizuru Expressway-Route 9 and Route 372-Route 9.

Based on the report by the Hanshin-Awaji Earthquake committee (consists of major related academic society such as Japanese Society of Civil Engineering), 22 samples out of 24 samples changed the routes, among them 11 samples used Maizuru Expressway, then 9 samples used Route 9. Also, it is reported that major access routes to Osaka area were Routes 372 and 173 after taking the Maizuru Expressway, which is consistent with the estimated results. However, any traffic in the large detouring route in the report, Maizuru-Route 27-Hokuriku Expressway are not estimate in this study.

Figures 11 and 12 show the comparison of interregional traffic flows between daily case(without disaster) and with disaster cases. Origin (Figure 11) and destination (Figure 12) of interregional traffic flows in Kinki region are focused. Both figures show the estimated results with and without the assumptions of no restriction on supply capacity and no demand decrease. During disasters, the traffic flows in Kinki region decrease, while the traffic flows between Kinki and Chubu decrease. This is mainly because the travel time in the damaged area increases. Because the maps of traffic flows with and without supply and demand constraints are similar, the map of without case is omitted in this paper.

In the case with supply constraint and demand decrease, the traffic in Kinki region is heavier than the traffics in the without case. One reason is that the decreased demand reduces the intra and interregional trades and finally reduces the travel time in Kinki region by 0.15 hour. The other reason is that the other regions take place of productions in Kinki region, and reduce the traffics from Kinki region to other regions. In order to testify these reasons, it is necessary to collect the empirical data regarding with alternative productions.

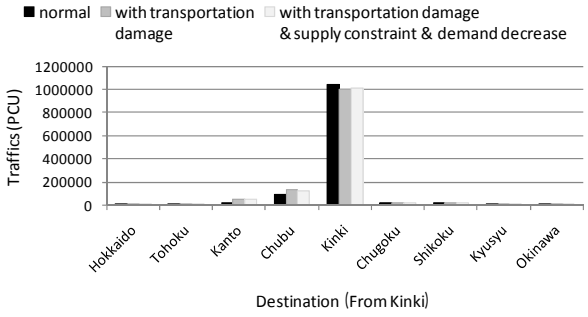

Figure 11 Comparison of interregional traffics (Kinki origin)

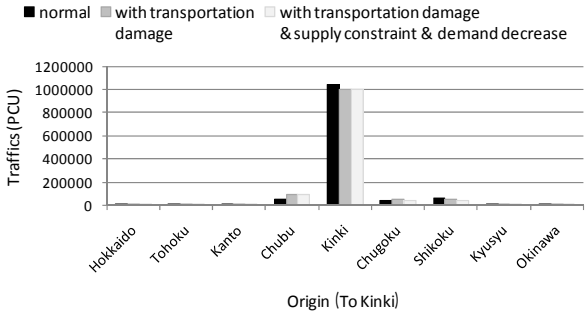

Figure 12 Comparison of interregional traffics (Kinki destination)

5. CONCLUSIONS

This study investigated on the interregional commodity flow model (ICFM) for estimating the economic impact of natural disasters. ICFM has characteristics of integrating both the transportation network model (user equilibrium model) and input-output model, and hence, the model is utilized for identifying the critical link for the intra- and interregional trading.

Considering the complexity of supply and demand situation during the disaster, this study focused on investing on the applicability and extensionality of the model through the case study of the actual earthquake disaster occurred in Kobe city, Japan in 1995. Because the disaster hit the very local area in the Region, it was also necessary to develop the detailed road network in the damaged area.

At first, the ICFM is slightly modified for considering the upper limitation of production, which is also useful for the case of including the impacts of utility damages to firms' production level. Then, based on the data sets, such as road networks and final demands, before and after the 1995 earthquake disaster, model calibration was conducted. The values of parameter were stably estimated in our data sets. It is a future task to demonstrate the model performance under a large-scale network and small-area based interregional input-output table such as the prefecture level. The results of traffic assignments are not so consistent with the observed traffics data mainly due to the rough network data sets for the interregional trading. Not only the network data but also the basic traffic data per a unit production in each sector should be carefully developed.

The case study under the transportation damages, supply constraints and demand decrease, the result of traffic assignments is relatively consistent with the actually reported traffic situation. Supply and demand changes induce the decrease of intra-regional traffics in Kinki region and reduce the travel time in the damaged area compared to the case without supply and demand constraints. In actuality, the emergency vehicles could increase the traffics in the damaged area, which could overwhelm the decrease of traffics from industries. The alternative production outside the damaged area is one of the reasons of decreased traffics

in the damaged area, but this should be testified and model extension is necessary based on the actual data sets of firm's production.

In this way, several findings are obtained in this study. These are the calculations under the relatively simplified conditions. Based on the continuous surveys on the actual disasters, it is necessary to extend the model such as considering the personal trips and cost sensitive parameters under the disaster, and comparison among different models, etc.

Acknowledgements:

Special thanks to Professor Geoffery Hewings for introducing a basic idea of the model in this paper.

References:

Newmark, N.M. and Rosenblueth, E. (1971), "Fundamentals of Earthquake Engineering," Prentice-Hall Inc.

Kim, T.J. (1983), "A combined land use-transportation model when zonal travel demand is endogenously determined," *Transportation Research,* **17**(B), 449-462.

Okuyama, Y. (2007), "Economic Modeling for Disaster Impact Analysis: Past, Present, and Future," Economic Systems Research, **19**(2), 115-124.

Cho, S., Gordon, P., Moore II, J. E., Richardson. H. W., Shinozuka, M. and Chang, S. (2001), "Integrating transportation network and regional economic models to estimate the cost of a large urban earthquake", *Journal of Regional Science*, **41**(1), 39-65.

Kim, T.J., Ham, H., and Boyce, D.E. (2002), "Economic impacts of transportation network changes, Implementation of a combined transportation network and input-output model," *Papers in Regional Science*, **81**, 223-246.

Sohn, J., Kim, T. J., Hewings, G. J. D., Lee, J. S. and Jang, S. G. (2003), "Retrofit priority of transport network links under an earthquake," *Journal of Urban Planning and Development,* **129**(4), 195-210.

Muto, S. and Ueda, T. (2006), "Construction of Small City CGE Model to Evaluate Alternatives of Disaster Countermeasure for Large Social Infrastructure," *Proceedings of Infrastructure Planning,* **34** (CD-R) (In Japanese).

Koike, A., Ueda, T., Akiyoshi, S. (2004) "Economic Damage Assessment of Catastrophe-A Welfare Metrics with the Spatial Computable Equilibrium Model," *Infrastructure Planning Review*, **21**, 367-374, (In Japanese).

Tatano, H. and Tsuchiya, S. (2008), "A framework for economic loss estimation due to seismic transportation network disruption: a spatial computable general equilibrium approach," *Natural Hazards*, **44**, 253–265.

Nagae, T., Fujiwatra, T., Asakura, Y. (2007): Cost-Benefit Analysis of Road Network Reinforcement Using Geographical Information Systems and User Equilibrium with Variable Demand, *Infrastructure Planning Review*, **24**(2), 233-242 (In Japanese).

Boyce, D. (2002), "Combined Model of Interregional Commodity Flows on a Transportation Network," In Hewings, Sonis and Boyce (eds) Trade, Networks and Hierarchies, 29-40, Springer.

Wilson, A.G. (1970), "Entropy in urban and regional modeling. London", Pion, 1970.

Okuda, T., Hayashi, R. (1991), "An Interregional Input/Output Model for Impact Studies of Environmental Tax," *Infrastructure Planning Review*, **11**, 271-278 (In Japanese).

Evans, S.P. (1976), "Derivation and analysis of some models for combining trip distribution and assignment," *Transportation Research*, **10**, 37–57.

Hyman, G.M. (1969): Calibration of trip distribution models. Environment and Planning Vol.1, 105–112.

Editorial Committee for the Report on the Hanshin-Awaji Earthquake Disaster (1998a), "Report on the Hanshin-Awaji Earthquake Disaster (Japan Society of Civil Engineers): Damage and Recovery of Transportation and Agricultural Facilities," Maruzen LTd (In Japanese).

Editorial Committee for the Report on the Hanshin-Awaji Earthquake Disaster (1998b), "Report on the Hanshin-Awaji Earthquake Disaster (Japan Society of Civil Engineers): Effects and Damages on Regional Economics and on Environment," Maruzen LTd. (In Japanese).

Research Institute of Economy. (2000), Trade and Industry:1995 interregional input-output table (In Japanese).

Hyogo Prefecture. (1996), 1995 Statistics in Hyogo Prefecture.

Ministry of Land, Infrastructure, Transport and Tourism (2002): 7th Commodity Flow Census (In Japanese).

Ashiya, T. and Jinushi, T. (2001), "The Great-Hanshin Earthquake and the Industrial Structure ; Estimations and an Application of the Demaged-Area Inout-Output Table," *Journal of political economy and commercial science*, **183**(1), 79-97.

Kajitani, Y., Yamano, N., and Shumuta, Y. (2004), "Estimation of Economic Recovery Function after a Large Scale Disaster," *Proceedings of Infrastructure Planning*, **30**(CD-ROM) (In Japanese).

Japan Society of Civil Engineers (2006): Theory and Application of Traffic Demands Forecasting: Extension of User Equilibrium Model.

Ministry of Construction. (1995), 1994 Traffic Census.

JOINT CONFERENCE PROCEEDINGS
7th International Conference on Urban Earthquake Engineering (7CUEE) &
5th International Conference on Earthquake Engineering (5ICEE)
March 3-5, 2010, Tokyo Institute of Technology, Tokyo, Japan

RELATIVE ANALYSIS BETWEEN A COMMUNITY'S DISASTER RECOVERY POTENTIAL AND SOCIAL CAPITAL

Emi Ishibashi[1)], Eiichi Itoigawa[2)], Michitaka Umemoto[2)] and Yoshio Kumagai[3)]

1) Graduate School of System and Information Engineering, University of Tsukuba, Japan (present ; PASCO Corporation)
2) Graduate School of System and Information Engineering, University of Tsukuba, Japan
3) Japan Science and Technology Agency
eimhis3983@pasco.co.jp

Abstract: This paper aims to construct a quantifying method to measure a community's disaster recovery potential. In constructing a quantifying method, the indexes were selected from literature surveys, and the weight of each index was determined by an expert questionnaire survey using AHP. Also, in order to reinforce a communities disaster recovery potential before an occuring of a disaster, a relative analysis between a community's potential and social capital is executed.

1. INTRODUCTION

1.1 Recent Disasters and Disaster Prevention Power

After a massive natural disaster, there is a limitation to the rescue and recovery activities that can be taken by the government. Therefore it is important that the victims of the disaster themselves are capable to play one of the key roles in mitigating further damage and recovering the community. Such ability is referred to as a community's "disaster prevention power."

In order to empower a community's disaster prevention power, it is essential to quantify and evaluate between communities. In recent studies, quantification methods of community's disaster prevention power have been practiced in several surveys and researches. Presently, as an internet web service for civilians provided by the Japanese government, there is a quantifying method for disaster prevention potentials focused on landslides and floods.[1)] Also, the Shiga prefecture introduced a comprehensive disaster prevention potential number on the community level.[2)] In addition to such approaches taken by the federal and local governments, quantifying methods are proposed by many proceeding studies.[3), 4), 5)].

In these proceeding studies and investigations, most approaches focus mainly on the initial rescue phase where rescue and firefighting activities become composing factors of "disaster prevention power". However, it is also essential to focus on the reconstruction and recovery phase, as the community's power, is also necessary. Especially, in the recovery phase, in order to rebuild the city, the citizens must reach many agreements, and such recovering power (Disaster Recovery Power) lays an important role.

1.2 Disaster Recovery Potential and Social Capital

The power used in the recovery phase potentially lies in the community in normal times, and this potential is said to have relation with the bondage between the citizens of the community.

In the case of the Great Hanshin-Awaji Earthquake, it is said that in many communities, it was difficult to reach agreement on the recovery plans, however in communities like that Mano area in Kobe City, where there was strong bondage between the citizens, the agreement process was pointed out to have been more simple.[6)] From such points, bondage between the citizens of a community is anticipated to be important for post disaster recovery.

However, proceeding studies lack to focus on the relationship between a community's disaster recovery potential and community bondage mainly when considering comparison with a quantified value. Therefore, in order to reinforce disaster recovery ability, it is essential to quantify the relationship between daily community bondage and disaster recovery potential.

From the points given above, this research aims to construct a quantifying method for "Disaster Recovery Potential" which focuses on the potential which can be observed and measured in normal times. Also in order to empower disaster recovery potential in normal times, a relative analysis with social capital which represents community bondage, is executed in order to find what kinds of social capital works positively towards disaster recovery potential.

2. DEFINITION OF KEYWORDS

2.1 Disaster Recovery Potential

2.1.1Outline

In this research, according to the time scale in the post disaster period, "Disaster Prevention Potential" is divided into three types of potential according to each phases; Rescue Potential, Reconstruction Potential, and Recovery Potential, and each potential will be executed as power accordingly as shown in Figure 1,2. Each of the factors of disaster prevention power are not executed after a respective amount of time after the disaster, as it becomes unnecessary,

On the other hand, the potential of this power always exists within the community. The potential of disaster prevention power is divided into each post disaster phase as, rescue potential, reconstruction potential, and recovery potential. Empowering the potential of a community leads the empowering of the power which is executed after the occurring of a disaster.

2.1.2 Definition

Disaster Recovery Potential is the estimated potential of a power that is executed by the citizens after a disaster in the recovery phase. On the other hand, Disaster Recovery Potential is the power that is actually executed, and the strength of this power depends on the strength of the potential in normal times. (Figure 3). In other words, disaster recovery potential can be measured in normal times, where the ability which is actually executed, and can only be measured and evaluated through disaster recovery activities after an actual disaster. Figure 4 shows how the strength of Disaster Recovery Potential leads to the strength of the power actually executed.

Disaster Recovery Potential consists of the factors given below.

・Past experience of disaster
・Possibility of remaining in a community and recovering after a disaster
・Daily disaster preventive activities
・Strength of the will to recover onsite

The Consisting factors were selected from literature reviews and proceeding researches. Also, the lessons learnt from past disasters in Japan, mainly the Great Hanshin Awaji earthquake, referred to in the selection process.

2.1.3 Observation Target

The target type of community for observing disaster recovery potential, is established city areas where there is a danger of massive earthquake damage.

2.2 Social Capital

The idea of social capital emphasizes that network among citizens are a source of capital just as material capital or human capital. According to the research executed by the cabinet of Japan, Social Capital consists of 3 factors; Network, Norms of Reciprocity, and Trustworthiness.

In recent years, the idea of social capital has been referred to in various countries, and quantifying methods have been practiced in proceeding researches.

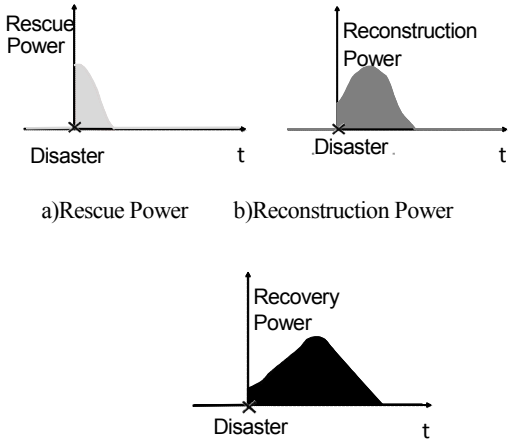

a)Rescue Power b)Reconstruction Power

c) Recovery Power

Figure 1 Image of Disaster Prevention Power

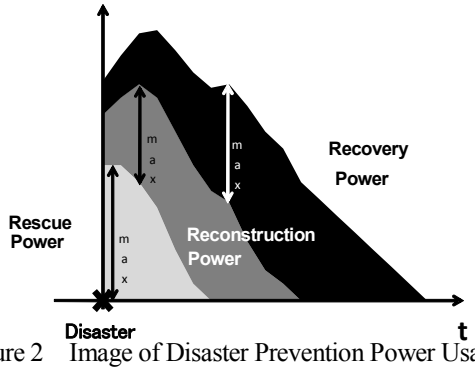

Figure 2 Image of Disaster Prevention Power Usage

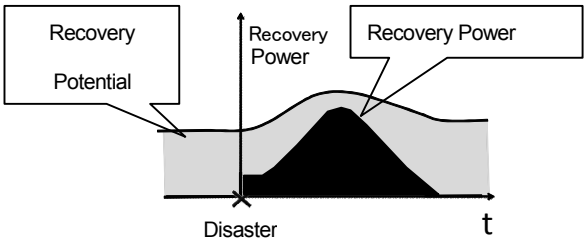

Figure 3 Image of Disaster Recovery Potential

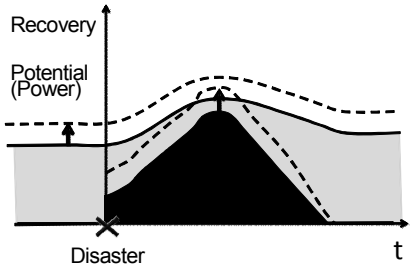

Figure 4 Relation between Recovery Potential and Recovery Power

3. RESEARCH METHOD

3.1 Disaster Recovery Potential

3.1.1 Plan of Analysis

The hypothesis of this research is that disaster recovery potential is strong in areas where social capital is strong. Also, as introduced in the previous chapter, when social capital is broken down into 3 factors (Network, Trustworthiness, Norms of Reciprocity), the effectiveness of each factor is anticipated to differ, Therefore, it is essential to not only recognize social capital as a single value, but to break it down into 3 factors and observe the relationship of each factor towards disaster recovery potential. By clarifying the most effective factor, it becomes clearer what type of policy of social capital would work positively towards the empowering of disaster recovery potential.

3.2 Flow of Research

This research aims to construct a quantifying method to capture a community's disaster recovery potential from survey results of both experts and ordinary citizens. Also, execute further analysis on the relationship between disaster recovery potential and social capital.

3.2.2 Citizen's Survey on Disaster Recovery Potential and Social Capital

Conduct a citizen survey to measure disaster recovery potential and social capital at the community level and the personal level.

3.2.3 Relative Analysis on the Community Level

Conduct a relative analysis between a community's disaster recovery potential and social capital value which is calculated from the average of the personal values. Also, extract the type of social capital which acts positively towards disaster recovery potential.

3.2.4Relative Analysis on the Personal Level

Conduct a relative analysis as above, on the personal level, to capture the characteristics of the relationship between the two factors on the personal level.

4. CALCULATION OF DISASTER RECOVERY POTENTIAL

4.1 Calculation of Disaster Recovery Potential

4.1.2 Determining the Composing Factors

In determining the factors of disaster recovery potential, this research focused on the principal of "On-Site recovery". On-site recovery is important in means of maintaining the community from population loss, leading to a weakening in the power to recover. The factors were chosen from literature review of proceeding research3),4),5)h on disaster prevention power, and literature on lessons learned from past disasters8)~12). The factors are shown in layered structure in Figure 5.

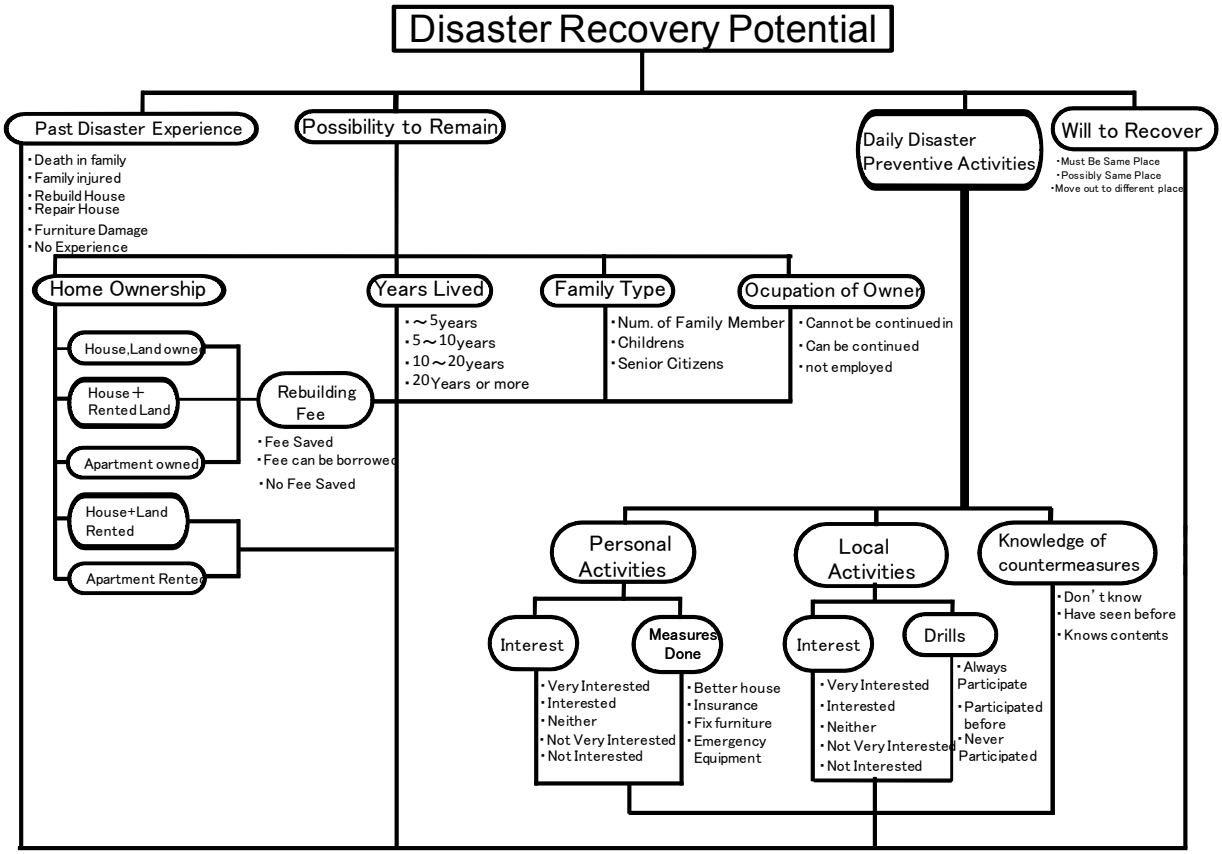

Figure 5 Factors of Disaster Recovery Potential

4.1.3 Calculation Formula

The formulas for calculating disaster recovery potential are shown below.

$$R_j = S_j + a_E \cdot E_j + A_j + a_W \cdot W_j \quad \cdots[1]$$

$$S_j = \sum_{i=1}^{5} a_{Si} \cdot S_{ij} \quad \cdots[2]$$

$$A_j = P_j + D_j + a_G \cdot G_j \quad \cdots[3]$$

$$P_j = \sum_{i=1}^{2} a_{Pi} \cdot P_{ij} \quad \cdots[4]$$

$$D_j = \sum_{i=1}^{2} a_{Di} \cdot D_{ij} \quad \cdots[5]$$

The formulas above are arranged as below

$$R = \sum_{i=1}^{5} a_{Si} \cdot S_{ij} + a_E \cdot E_j + \left(\sum_{i=1}^{2} a_{Pi} \cdot P_{ij} + \sum_{i=1}^{2} a_{Di} \cdot D_{ij} + a_G \cdot G_j \right) + a_W \cdot W_j \quad \cdots[6]$$

R_j: Recovery Potential of area j
S_j: Possibility to remain in district j
S_{1j}: Type of home ownership
S_{2j}: Years inhabited
S_{3j}: Family members
S_{4j}: Savings for home reconstructtion
S_{5j}: Occupation of home owner
E_j: Past disaster experience of district j
A_j: Local disaster prevention activities of district j
P_j: Personal disaster preventive activities
P_{1j}: Interest in personal disaster countermeasures
P_{2j}: Variety of personal disaster countermeasure taken
D_j: Local disaster prevention activities
D_{1j}: Interest in local disaster countermeasures
D_{2j}: Participation in disaster drills
D_{3j}: Knowledge of local community recovery measures
G_j: Knowledge of local governmental disaster recovery measures
W_j: Will to Recover in district j
a_*: Weight of each factor

4.2 Calculation of Social Capital

The calculation method for Social Capital is constructed as below, in reference to the method executed by the investigation by the cabinet 6) Also, in applying the quantifying method to a more smaller size community, factors on charity were excluded. On the other hand, in order to compare the personal relationships with others inside and outside of the community, relationships with co-workers were added to the social capital factors.

4.2.1 Integrated Indicator

$$C_j = (T_j + N_j + NR_j)/3 \quad \cdots[7]$$

C_j: Social Capital of district j
T_j: Trust of district j
N_j: Network of district j
NR_j: Norms of Reciprocity of district j

4.2.2 Trustworthiness

$$T_j = \left(\sum_{i=1}^{6} T_{ij} \right) \Big/ 6 \quad \cdots[8]$$

$$T_{ij} = \sum_{k=1}^{n} x_{Tijk} \Big/ n \quad \cdots[9]$$

T_j : Trustworthiness of district j
T_{ij} : Variables of Trustworthiness （i=1～6）
T_{1j} : Trust of People in General(District average)
T_{2j} : Trust of People in Foreign Places (District average)
T_{3j} : Trust of Neighbors (District average)
T_{4j} : Trust of Friends, aquaintences (District average)
T_{5j} : Trust of Co-workers (District average)
T_{6j} : Trust of Relatives (District average)
n : Citizens in District j (Polls collected in survey)
x_{Tijk} : The T_{ij} value of the num. k citizen of district j

4.2.3 Network

$$N_j = \left(\sum_{i=1}^{6} N_{ij} \right) \Big/ 6 \quad \cdots[10]$$

$$N_{ij} = \sum_{k=1}^{n} x_{Nijk} \Big/ n \quad \cdots[11]$$

N_j : Network in district j
N_{ij} : Variables of Network （i=1～6）
N_{1j} : Degree of interaction with neighbors (District average)
N_{2j} : Number of interacting neighbors (District average)
N_{3j} : Frequency of interaction with friends (District average)
N_{4j} : Frequency of interaction with relatives (District average)
N_{5j} : Frequency of interaction with co-workers (District average)
N_{6j} : Participation in sports and leisure activities (District average)
n : Citizens in District j (Polls collected in survey)
x_{Nijk} : The N_{ij} value of the num. k citizen of district j

4.2.4 Norms of Reciprocity

$$NR_j = \left(\sum_{i=1}^{2} NR_{ij} \right) \Big/ 2 \quad \cdots[12]$$

$$NR_{ij} = \sum_{k=1}^{n} x_{NRijk} \Big/ n \quad \cdots[13]$$

NR_j: Norms of Reciprocity in District j
NR_{ij}: Variables of Norms of Reciprocity （i=1～2）
NR_{1j}: Participation in local activities (district average)
NR_{2j}: Participation in volunteer, NPO, citizen activities (district average)
n : Citizens in District j (Polls collected in survey)
x_{NRijk}: The NR_{ij} value of the num. k citizen of district j

5. CONSTRUCTION FOR THE EVALUATION METHOD OF DISASTER RECOVERY POTENTIAL

5.1 Outline of Expert Survey

The targets of the expert survey were university professors, researchers, and experts in the disaster management field.

The survey was executed at the 23rd Autumn Conference of Social Safety Science in 2008. The outline of the survey are shown in Table 1.

5.2 Questions

In this survey, the importance of the factors shown in figure 5 are measured by the AHP method. In order to evaluate the factors with the AHP method, each of the factors were asked in paired comparison on a scale of 1 to 9.

Table 1 Outline of Survey

Date	Nov. 13th to 15th 2008
Numbers handed out	63
Numbers Collected	19
Valid Polls	17
Validity Rate	27.0%

5.3 Results of Survey

The results of the expert survey are shown in Figure 6. The geometrical mean of each of the evaluation matrix of the examinees were calculated. From this figure, factors of the left block which contains the "Will of on-site Recovery" and "Possibility of remaining" are judged to be most important. This can be assumed from the fact that the definition of Disaster Recovery Potential is based on the principal of "On-site Recovery." However, since "On-site Recovery" is pointed out as an important principal for reasons such as preventing the population to outflow into other areas, these factors are considered to be important for better recovery. On the other hand, "Daily disaster preventive activities" were evaluated low, and this was assumed to be for the reason that most daily disaster preventive activities lacked to focus directly on the recovery phase. So, even though "daily disaster preventive activities" had the positive effect to bond people together, no other direct effects were assumed to exist. From this result, in the promotion of disaster prevention activities, it is important to promote activities focused on the recovery phase, such as the disaster recovery drill introduced by Ichiko[8] and for the importance of such drills to be recognize which would lead to a more important evaluation of such factors in the disaster recovery field. However, participation rates to daily disaster prevention activities are yet low, so results cannot be expected if only drills are conducted. Therefore, in order to empower the potentials of each phase, it is essential that activities and methods outside of the disaster prevention theme that work should be empowered in the community, and one method is to empower a community's social capital .

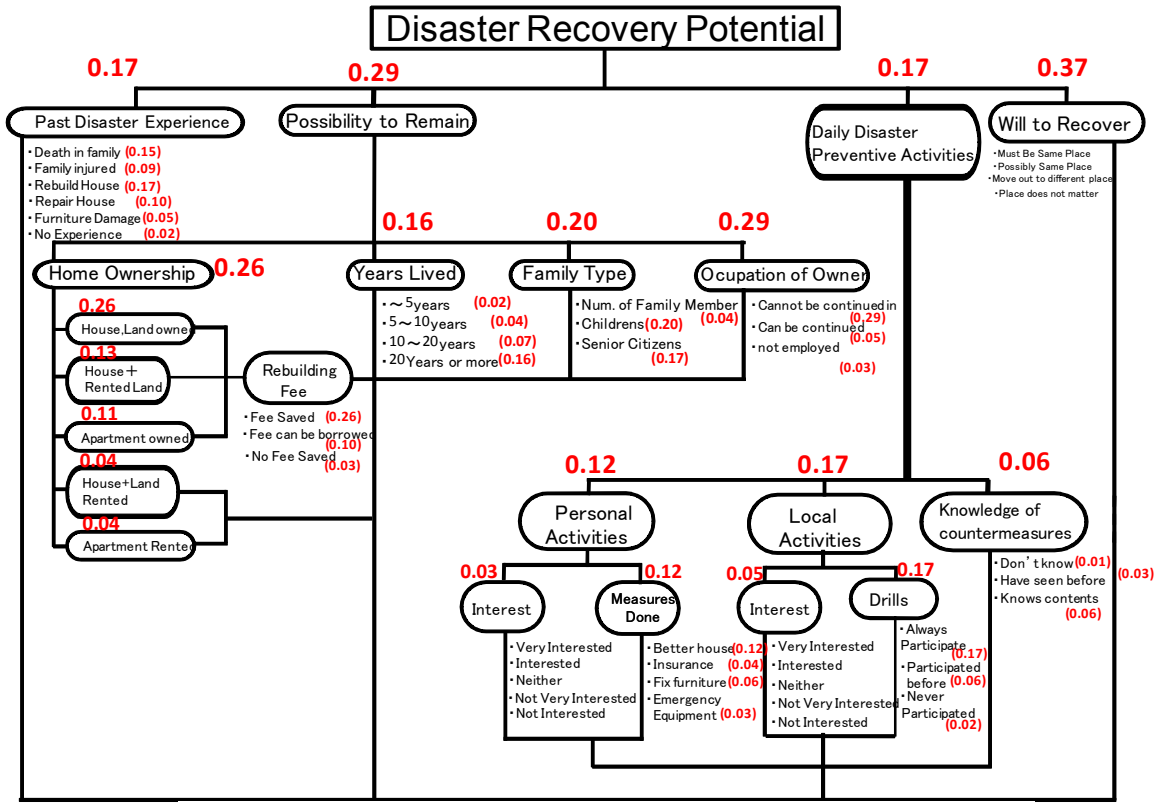

Figure 6 Evaluation Result of the Factors of Disaster Recovery Potential

of the disaster prevention theme that work should be empowered in the community, and one method is to empower a community's social capital .

6. OUTLINE OF CITIZEN'S SURVEY

In order to capture the relationship between disaster recovery potential and social capital, a survey was conducted to ordinary citizens on the both factors.

The area of survey was chosen from 1) established city areas, were 2) massive earthquake disasters are assumed to occur, in the Tokyo special ward area. Also for clearer comparison, areas where disaster recovery potential and social capital were both assumed to be high or low were selected. The rules in selecting the surveying areas are shown in Table 2, where 8 different types of areas were chosen. As a result, the Suginami ward was chosen due to reason that it had all 8 types of areas. The outline of the survey is shown in Table 3.

Table 2 Determination of Area of Interest

		Community Bondage (NPO/Volunteer organizations)			
		Strong (existence)		Weak (no existence)	
		Recovery Ability (Bosai Machizukuri Award)			
		High (Awarded)	Low (Unawarded)	High (Awarded)	Low (Unawarded)
Danger Rate	High	A Asagaya-Minami-3	B Asagaya –Kita-3	C Honamanuma-3	D Amanuma-1
	Low	E Shimoigusa-1	F Narita-Higashi-5	G Minami-Ogikubo-4	H Ogikubo-3

Table 3 Outline of Citizen's Survey

District	Handed out	Valid Polls(Rate)
Asagaya- Minami-3	700	117(16.7%)
Asagaya-Kita-3	700	117(16.7%)
Honamanuma-3	700	120(17.1%)
Amanuma-1	700	124(17.7%)
Shimoigusa-1	700	115(16.4%)
Narita-Higashi-5	700	117(16.7%)
Minami-Ogikubo-4	700	114(16.3%)
Ogikubo-3	700	116(16.6%)

7. RELATIVE ANALYSIS ON THE COMMUNITY LEVEL

7.1 Correlative Analysis of Disaster Recovery Potential and Social Capital

The value of the disaster recovery potential and social capital was calculated by the methods shown previously, and the average of each area is shown in a scatter plot in Figure 7. The correlation coefficient is shown in Table 4. As seen in Figure 7, although in the primary selection of the districts were to select different types of districts, the calculated values were concentrated in a small range. But from Figure 7 and Table 4 , it can be dictated that there is a weak positive correlation between disaster recovery potential and social capital. The observed significance level of test is only of reference, but the correlation coefficient value shows that network has the strongest correlation with disaster recovery potential.

7.2 Social Capital which Empowers Disaster Recovery Potential

To extract the social capital factor which empowers disaster recovery potential, a multiple regression analysis was conducted with the 3 factors of social capital as explanatory variables, and disaster recovery potential value as the explained variable. The results are shown in Table 5.

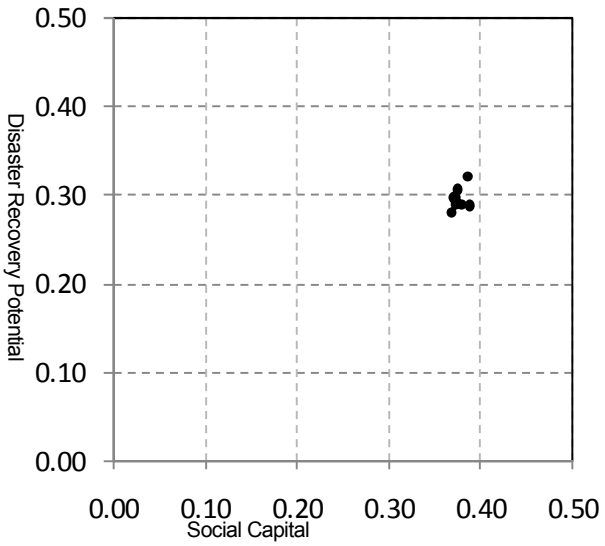

Figure 7 Disaster Recovery Potential and Social Capital (District Level)

The multicollinearity value, VIF was below 5, so it is judged that there is no multicollinearity among the variables. R_2 was 0.454. Observing the standardization coefficient, the weight of network and norms of reciprocity are nearly the same, with network with a heavier weight.

Also from statistical test, trustworthiness was anticipated to have no relation with disaster recovery potential. So further multiple regression analysis was executed using only network and norms of reciprocity as explanatory variables. The results are shown in Table 6. R_2 was 0.560, so it can be weakly explained that network and norms of reciprocity work positively towards disaster recovery potential/

From these results, it can be said from the standardization coefficient that network and norms of reciprocity work positively towards disaster recovery potential, and that network is relatively the strongest positive actor. This is the same conclusion given from the multiple regression analysis using all 3 factors of social capital.

8. RELATIVE ANALYSIS ON THE PERSONAL LEVEL

8.1 Correlative Analysis of Disaster Recovery Potential and Social Capital

This section focuses on if there is relation between disaster recovery potential and social capital on the personal level. The values of disaster recovery potential and social capital are shown in the scatter plot in Figure 8. The correlation coefficient is shown in Table 7.

The results show that the correlation coefficient of disaster recovery potential and social capital is 0.327, and there is a weak positive correlation. When the 3 factors of social capital are divided the correlation coefficient are 0.117 for trustworthiness, 0.340 for network, and 0.290 for norms of reciprocity. Also all factors showed a weak positive correlation. Out of the 3 factors, network showed a relatively stronger correlation, and was assumed to have the strongest relationship with disaster recovery potential. On the other hand, trustworthiness showed the weakest correlation among the 3 factors as seen in the analysis done in the district level.

8.2 Social Capital which Empowers Disaster Recovery Potential

As the same as the analysis done on the district level, multiple regression analysis was conducted on the personal level. The explanatory variables were the 3 factors of social capital, and the explained variable was value of disaster recovery potential. The results are shown in Table 8. Also her, the results show that trustworthiness does not have relation with disaster recovery potential.

So further multiple regression analysis was conducted using only the remaining 2 factors (network and norms of reciprocity, the results are shown in Table 9. The standardization coefficients do not differ for the 2 factors from the analysis done with the original 3 factors, and network shows a relatively larger weight which show the same results as the analysis done on the district level

.

8.3 Weighting the factors of Social Capital

In the previous section, the factors of social capital were divided into 3 factors for multiple regression analysis, However as seen in formulas 8 to 13, these factors are the average values of a lower level of variables and these variables have the possibility to have different importance towards disaster recovery potential. Therefore, further analysis was executed in order to consider the weight of the variables. Since Social capital consists of a massive number of variables, a principal component analysis was conducted in order to combine the variables.

8.3.1 Trustworthiness

The variables of trustworthiness and the result of the principal component analysis are shown in Tables 10 and 11. From the eigenvalue, 2 principal components were extracted and the cumulative proportion was 64.8%.

Table 4 Correlation Coefficient (District Level)

	Correlation Coefficient	Significance Probability (Both Sides)
Social Capital	0.407	0.317
Trustworthiness	−0.091	0.830
Network	0.489	0.219
Norms of Reciprocity	0.267	0.523

Table 5 Result of Multiple Regression Analysis (using 3 explanatory variables)

重相関係数 0.829 決定係数 0.454 （自由度調整済み）	標準化係数 β	T value	VIF	Significance Probability
(定数)		−1.152		0.314
Trustworthiness	−0.052	−0.184	1.026	0.863
Network	0.887	2.730	1.354	0.052
Norms of Reciprocity	0.769	2.348	1.376	0.079

Table 6 Result of Multiple Regression Analysis (using 2 explanatory variables)

R=0.828 R^2= 0.560 （DF Adjusted）	Standardiza--tion coefficient β	T value	VIF	Significance Probability
(Constant)		−1.587		0.173
Network	0.886	3.037	1.353	0.029
Norms of Reciprocity	0.777	2.663	1.353	0.045

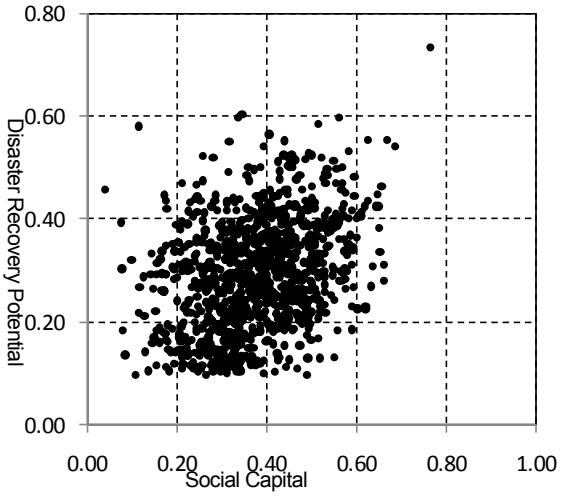

Figure 8 Disaster Recovery Potential and Social Capital (Personal Level)

Table 7 Correlation Coefficient (Personal Level)

	Correlation Coefficient	Significance Probability (Both sides)
Social Capital	0.327	0.000
Trustworthiness	0.117	0.000
Network	0.340	0.000
Norms of Reciprocity	0.290	0.000

Table 8 Result of Multiple Regression Analysis (Using 3 factors)

R=0.379 R^2 =0.141 (DF adjusted)	Standardiza--tion coefficient β	T value	VIF	Significance Probability
(Constant)		15.510		0.000
Trustworthiness	−0.043	−1.284	1.200	0.200
Network	0.281	8.026	1.342	0.000
Norms of Reciprocity	0.183	5.458	1.227	0.000

Observing each principal component score, the scores in the 1st principal component show a plus value, Therefore the 1st principal component is anticipated to represent overall trustworthiness. Compared to the 2nd principal component the scores for "friends, acquaintences", "Relatives", "Neighbors", "Co-workers" showed higher values. This anticipates that within the overall trustworthiness, the 1st principal score shows trust towards people that are known. The 2nd principal component shows minus values towards people that are known, and shows plus values towards people met in foreign places and general trust. Therefore, the 2nd principal component represents trust towards people which are unknown.

8.3.2 Network

In order to extract more interpretable principal components, the variables "expected future leisure, sports activities" and "opportunity to begin leisure and sport activities" were excluded from the analysis. The reason these two variables were excluded, was due to the reason that the objective of this research was to in the empowerment of social capital which reinforced disaster recovery potential. So, the expectance of future activities are anticipated to depend heavily on the present situation of activities done, and it is difficult to change the hopes one has for future activities through policy. Also, for the opportunity of starting activities, personal interest or the consciousness as participation as a custom or ritual, are difficult to develop policies.The results are shown in Table 12 and 13.

As results of the principal component analysis, 3 principal components were extracted according to the cumulative proportion value 62.7%.

From the analysis results, the 1st principal component is anticipated to represent association with people that are known, (association with local people, and friends, acquaintances,)

The 2nd principal component had plus values for association with co-workers outside of work, whereas showed minus values for the variety of people associated through leisure and sports activities. It was assumed that the 2nd principal component represented whether a person spends the weekend with their co-workers, or with friends and acquaintances from a different group of people.

The 3rd principal component represents the frequency of leisure and sports activities and captures the amount of time spent on leisure and sports.

8.3.3 Norms of Reciprocity

The variables of Norms of Reciprocity were selected in the same order as network in order to simplify the understanding the principal components. The results are shown in Table14, and 15.

2 principal components were extracted. The cumulative proportion of the 2 principal components were 55.9%.

The 1st principal component represents the variety of people one participates with in local activities, and the frequency of participation in local activities, and the variety of people one participates with in citizen activities.

Table 9 Result of Multiple Regression Analysis (Using 2 factors)

R=0.377 R^2 =0.140 (DF adjusted)	Standardiza--tion coefficient β	T value	VIF	Significance Probability
(Constant)		17.349		0.000
Network	0.267	8.031	1.206	0.000
Norms of Reciprocity	0.177	5.335	1.206	0.000

Table 10 Principal Component of Trustworthiness (Eigenvalue,Proportion)

	Eigenvalue	Proportion	Cumulative Proportion %
1	2.400	39.996	39.996
2	1.490	24.840	64.836
3	0.724	12.070	76.906
4	0.672	11.204	88.110
5	0.491	8.192	96.301
6	0.222	3.699	100

Table 11 Principal Component Score of Trustworthiness

	1	2
Friends, Acquaintances	0.680	−0.403
Relatives	0.629	−0.357
Neighbors	0.624	−0.179
Co-workers	0.605	−0.438
Trust in foreign places	0.608	0.714
General trust	0.646	0.684

Table 12 Principal Component of Network (Eigenvalue,Proportion)

	Eigenvalue	Proportion	Cumulative Proportion %
1	2.194	31.337	31.337
2	1.129	16.135	47.472
3	1.065	15.216	62.688
4	0.858	12.263	74.951
5	0.717	10.245	85.196
6	0.637	9.098	94.294
7	0.399	5.706	100.000

Table 13 Principal Component Score of Network Variables

	1	2	3
Degree of Interaction	0.768	0.010	−0.336
Num, of Interacting People	0.729	−0.042	−0.482
Interaction with friends, acquaintances	0.633	−0.150	0.344
Interaction with Relative	0.566	0.504	0.008
Interaction with co-workers outside of work	0.243	0.672	0.440
People joined in leisure, sports activities	0.409	−0.562	0.152
Frequency of leisure, sports activities	0.352	−0.289	0.620

Table 14 Principal Component of Norms of Reciprocity (Eigenvalue, Proportion)

	Eigenvalue	Proportion	Cumulative Proportion %
1	1.772	35.430	35.430
2	1.021	20.424	55.854
3	0.959	19.176	75.030
4	0.759	15.188	90.218
5	0.489	9.782	100.000

This describes the amount of participation towards relatively mandatory activities. Concerning local activities, participation is at times mandatory and passed on among the citizens, and also for citizen activities, most of the participants are anticipated to be the same as those who participate in local activities, therefore is grouped as the same principal component,

The 2nd principal component shows a plus value towards the frequency of citizen activities, and on the other hand, show a minus value towards charity. This shows the type of energy one dedicates to citizen activities, time or money, So, this principal component shows the rate of dedication to citizen activities through time. Also, the reason why frequency of citizen activities was not grouped together with the frequency of local activities can be anticipated that citizen activities differ from local activities as participation is more free and one's will to participate is respected.

From the analysis above, the extracted principal components are shown in Table 16.

(4)Social Capital which Empowers Disaster Recovery Potential

From the previous principal component analysis, the principal components with eigenvalue over 1 are chosen too execute a multiple regression analysis with the personal principal components scores as explanatory variables, and personal disaster recovery potential values as the explained variable. The results of the multiple regression analysis are shown in Table 17. The multicollinearity values, VIF were under 5, so it is judged that there is no multicollinearity.

From this analysis, other than the variable of "interaction with private acquaintances", the significance probability is under 5%, therefore the following results of the analysis can only be used as reference. From the results, the principal component which works positively towards disaster recovery potential is, according to the standardization coefficient, is "interaction with private acquaintances, and this is the 1st principal component of the network factor.

From this result, it can be said that daily interaction with friends, acquaintances and relatives within the community generates a strong network, and works positively towards disaster recovery potential. Also, other factors which worked positively, were "Trust towards strangers," and "Interaction based on occupation." The degree which "interaction based on occupation" worked towards disaster recovery potential was relatively smaller, but was anticipated that broader networks constructed in workplaces worked to build networks.

9. CONCLUSION

9.1 Proposal of a Quantifying Method for Disaster Recovery Potential

In constructing a quantifying method for disaster recovery potential, the consisting factors were set based on the principal " on-site recovery", and an expert survey was conducted in order to decide the weight of each factor. From the survey, activities which constructed attachment towards the area, was evaluated to be important.

Also, as the reason why "daily disaster preventive activities" was weighted low, it was anticipated that contemporary activities executed in the communities lacked to be focused on the recovery phase, therefore could not be expected to work positively. This can be explained that citizen disaster prevention organizations are contemporarily expected to do activities based on daily disaster education, maintenance of equipment, detection of dangerous points in the area, and establishment of organizations and active response in the rescue phase. Another reason why daily disaster preventive activities were evaluated to be unimportant was anticipated that in most communities, these activities are not active and have little effect towards the community.

In conclusion, the most important factor of disaster recovery potential was evaluated to be the "will of on-site recovery". This meant that the power of the will to stay within the community was evaluated to act most positively to the recovery of the community.

9.2 Relative Analysis of Disaster Recovery Potential and Social Capital

Relative Analysis of a community's disaster recovery potential and social capital was conducted primarily through a correlative analysis of the average value of its consisting factors. Also, in order to extract the factor of social capital which has a more positive effect, a multiple regression analysis was conducted with the 3 factors of social capital as explanatory variables and disaster recovery potential as the explained variable. The results of the analysis showed that the most positively effective factor of social capital towards disaster recovery potential was network.

This anticipated that the network between the people of the community worked as one of the main reasons for remaining

in the same community and also motivated the citizens to participate to daily disaster preventive activities..

Table 15 Principal Component Score for Norms of Reciprocity

	1	2
Sharing of local activities	0.786	−0.240
Frequency of local activities	0.761	0.126
Participation in citizen activities	0.654	−0.027
Frequency of Citizen Activity	0.266	0.869
Charity Activity	0.276	−0.437

Table 16 Extracted Principal Components

Factor	Principal Component	Principal Component
Trustworthiness	1st principal component	Trust towards acquaintance
	2nd principal component	Trust towards strangers
Network	1st principal component	Private interactions
	2nd principal component	Interaction based on Co-workers
	3rd principal component	Frequency of leisure and sports activities
Norms of Reciprocity	1st principal component	Rate of Mandatory Activities
	2nd principal component	Rate of dedication through time

Table 17 Result of Multiple Regression Analysis

(Using Principal Component Score)

R=0.556 R_2=0.142 (DF Adjusted)	Standariza--tion coefficientβ	T Value	VIF	Significance Probability
(Constant)		16.078		0.000
Trust to Acquaintance	−0.040	−0.252	1.033	0.803
Trust to Others	0.264	1.392	1.510	0.174
Private Interactions with acquaintances	0.563	2.870	1.618	0.008
Interaction based on Co-workers	0.125	0.606	1.795	0.550
Frequency of Leisure and Sports activities	0.070	0.370	1.508	0.714
Rate of mandatory activities	−0.163	−0.816	1.674	0.421
Rate of dedication through time	−0.297	−1.668	1.335	0.106

In the analysis done in the personal level, the 3 factors of social capital was broken down into smaller factors, and an analysis of which variables worked positively towards disaster recovery potential was conducted. However, due to the limitation of the questions of the survey concerning social capital, extracting a specific factor of social capital was not possible.

In conclusion, the most positively effective factor of social capital towards disaster recovery potential was network. This anticipated that a rich and strong network amongst the people of the community work positively to the power to remain within the area after a disaster and reconstruct the city.

References

1) HP of Quantifying Method by Japanese Government <http://www.bousai.go.jp/bousairyoku/index.html>

2) Survey by Shiga Prefecture,2008.7.28 < http://www.pref.shiga.jp/h/ryuiki/tiikibousairyokuankeito/080728bousairyokukekka.pdf >.

3) Gohnai Y., Ohgai A., Kato T.,, Hitaka K.,Murakami M., Watanabe K. (2008),"A development of quantitative evaluation method for capability of community-based disaster mitigation focused on neighborhood community association," Journal of the City Planning Institute of Japan (43), pp.34－40.

4) Okanishi Y. and Sadohara S. (2006) ," A Study on Community and Local Disaster management in Neighborhood Associations for Improving Local Ability of Disaster Prevention: Analysis of questionnaire survey to neighborhood associations in Yokohama city," Journal of architecture and planning (609), pp.77-84.

5) Takita M. and Kumagai Y. (2002), "Assessment of the community response capacity for the shelter management during a large-scale disaster" Journal of social safety science (4), pp.15-24.

6) Konno H. (1995), "Inner Area Community under the Hanshin Great Earthquake: A Case of Mano, Kobe," Hakuoh Daigaku ronshu : the Hakuoh University journal 10(1), pp.225-255

7) Cabinet Office of Japan , Report on Social Capital,2002 年 <http://www.npo-homepage.go.jp/data/report9_1.html>.

8) Ichiko T., OnodaT., Murakami H., Aiba S., Yoshikawa J., Nakabayashi I. (2004), " A Community Training Method for Community-based Urban Reconstruction : Grounded on Preparedness Discussion for Urban Reconstruction," Journal of social safety science (6), pp.357-366.

JOINT CONFERENCE PROCEEDINGS
7th International Conference on Urban Earthquake Engineering (7CUEE) &
5th International Conference on Earthquake Engineering (5ICEE)
March 3-5, 2010, Tokyo Institute of Technology, Tokyo, Japan

EFFECTIVENESS OF A SPORTS FESTIVAL STYLE OF DISASTER DRILL BY PICKED COMMUNITY GROUPS IN THEIR CAPACITY BUILDING FOR RESPONDING TO EARTHQUAKE DISASTERS

Masaki Fujioka[1], Hideki Kaji[2], Jun Mihira[3] and Yoshinari Takanashi[4]

1) Researcher, Center for Urban Earthquake Engineering (CUEE), Tokyo Institute of Technology, Japan
2) Professor, Center for Urban Earthquake Engineering (CUEE), Tokyo Institute of Technology, Japan
3) Doctoral Student of the Graduate Program, Tokyo Institute of Technology, Japan
4) Chief Researcher, Iota Co. Ltd.
fujioka.m.aa@m.titech.ac.jp, kaji@cuee.titech.ac.jp, mihira.j.aa@m.titech.ac.jp, takanasi@iota-lab.com

Abstract: On 8 March, 2009, a sports festival style of disaster drill was held at Himeji City, with the participation of the citizens of 10 community groups which were represented on 72 communities in allover city. This festival was the first attempt to encourage people's interest in the disaster drill that had been depressed in general by most Japanese peoples. This paper examines how effective the festival has been in promoting people's interest and enthusiasm and in fostering social capital among community people, thus resulted in building their capacity of responding to earthquake disasters. Just after the festival, a questionnaire survey was conducted to ask the attitude of all participants towards preparedness for an event, commitment of community people, evaluation of the festival, future expectation, and so on. More than 70 per cent of peoples showed their positive replies to all aspects of this sports festival.

1. INTRODUCTION

The survey on people's attitude toward earthquake disaster being conducted by a private research company (Central Research Services Inc, 2008) indicates that 72.8 per cent of Japanese nations feel fear of occurrence of coming earthquakes in near future. This ratio, which varies slightly depending on the occurrence of practical earthquake in the year, is relatively stable in recent years (see figure 1).

Never-the-less, the proportion of those peoples who have an experience of participating in a disaster training drill during past 5 years being organized by local governments is only 33 per cent (National Census, 2002).

The figure 2 shows the reasons why 67 % of peoples do not participate in the drill. The most frequent response is that they have no time to spare for it due to busy daily work.

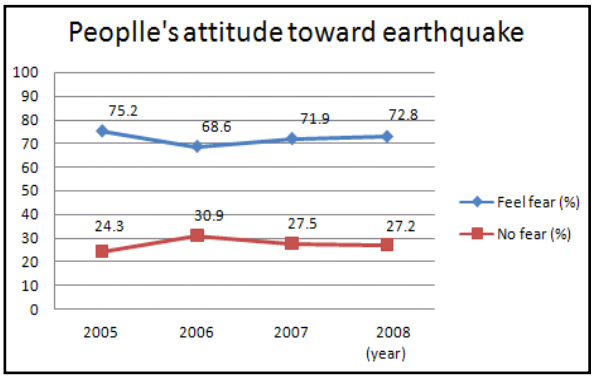

Figure 1 People's Attitude toward Earthquake

2. CHALLENGES OF HIMEJI CITY

2.1 Problems of current disaster training drill

The current disaster training drill targeted to community organizations which is conducted by local government faces on the following problems.

First, it cannot give incentives for the participants to continue the exercise unlike any other training. In fact, there is no training exercise which implies somehow preparatory efforts for trainees to seek immediate award given through a game, competition, presentation and so on. The disaster drill, however, is simple exercise for unforeseen and uncertain future event. Secondly, the current training drill focuses on promoting just individual capacity of responding to disasters. In a practical disaster scene, however, mutual helps of neighbors are more important and thus training practice on group cooperation should be encouraged. Thirdly, most of training participants are regular members who are mostly aged. It is strongly expected for young people to join. Fourthly, community's enthusiasm for disaster training varies from one to another. Some organize the training frequently, while others do never. It is common problems for the local government to popularize the training in their entire jurisdiction.

2.2 Experiment of sports festival style of disaster training drill

The mayor of Himeji City, Dr. Toshikatsu Iwami, decided to introduce the sports festival style of disaster

training drill, in order to attract more citizens. The first experimental festival was held in the fall of 2006. The six active community organizations were requested to participate on the voluntary bases. The festival was highly appreciated and encouraged by the participants in terms of fun. They, however, raised some critics that the each training game event should be reasonably devised to meet the practical response skill to actual disasters as well as to be played by diversified generations from the yang to the aged. It was also recommended that the way to contain as many citizens as possible should be explored.

The City authority thus decided to consult the authors on the idea of responding to these critics. After intensive studies of the past events that had been conducted by some other organizations, six events of disaster training drill on the form of competitive sports game were created. They are;

- A game of making a stretcher by blanket or clothes and carrying the injured on it,
- A game of correcting signboards of emergency kit which are hanged by children,
- A quiz game of an earthquake disaster,
- A game of rescuing those buried alive by cutting wooden beams and columns,
- A game of putting off fires by bucket water, and
- Relay race on clearing disaster obstacles.

The second problem to be solved is on how the sport festival can attract as many citizens as possible and become popular among them. In Himeji city, there were 72 community organizations and it is of course impossible to invite all of them to one place. Himeji Fire Department divides the city area into five jurisdictions. Each of the branch fire station are in charge of guiding respective community group to improve its capacity of responding to disasters and organizes disaster training drill for it at least once ever year. Thus, in order to attract all community groups and also to popularize this sports festival, elimination round on the bases of respective jurisdiction of fire department branch were proposed. Thus two teams from the jurisdiction of one fire department branch would be picked out to the final round.

It was also proposed that a team had to be organized by about 20 to 30 persons with the combination of children, ladies, men, and volunteer firemen, so that mutual-help attitude could be fostered.

The elimination events were organized during the period from October to December 2008 at the five places. And the ten teams were picked out. Thus the final round was held on 8 March, 2009 at the Himeji Sport Ground with the participation of these ten picked teams.

3. AIM AND METHODOLOGY OF THE PAPER

3.1 Objective of the paper

The sports festival of Himeji City was named as "Mamolympic Himeji", which was given by public opinions, and was a coined word of "Mamoru (to prevent) "and Olympic Game. As mentioned, it was originally planed with the strong expectation of making the disaster drill enjoyable, thus attracting many citizens in particular young generations, giving communities a short term goal which helped the participant's incentives to continue the daily exercise, and fostering attitudes of mutual help among neighbors of community. This paper thus aims to examine through a questionnaire survey whether these expectations has been satisfied.

3.2 Questionnaire survey

The six items of questions including their personal attributes were asked to the participants of the final round as follows.

(1) Sex, age, and experiences of disaster training drill,
(2) Impressions of the Sport Festival:
encouragement, enjoyment, and appreciation,
(3) Effectiveness in establishment of solidarity and promotion of mutual-help attitude among neighbors of a community,
(4) Effectiveness in promoting people's incentive to continue disaster drills, and in attracting the young generations,
(5) Aspiration for the following festival and hopes of participating in the final round with reasons, and
(6) Improvement of the festival management.

3.3 Samples collected

Just after the festival, the questionnaire was distributed to 240 persons who were participated athletes, and were collected by a week later. As a result, 186 samples were collected.



Figure 2 A stretcher game



Figure 3 Fire putting off game by bucket water

4. RESULTS OF ANALYSIS

4.1 Face data

The face data of this research are displayed in Table 1 and Table 2. As Table 2 shows that most survey participants are over age 30.

Table 1 sex and affiliation

sex and belong	Number
Male	76(41%)
Female	65(35%)
volunteer firefighter	44(24%)
Sum	185(100%)

Table 2 age

age	Number
10-19	1(1%)
20-29	6(3%)
30-39	51(27%)
40-49	50(27%)
50-59	29(16%)
Over 60	49(26%)
Sum	186(100%)

4.2 Result

The preference comparisons between common disaster drill and sports festival style drill is presented as Figure 4. The result said that 67% participations prefer sports festival style of disaster drill better than common disaster drill.

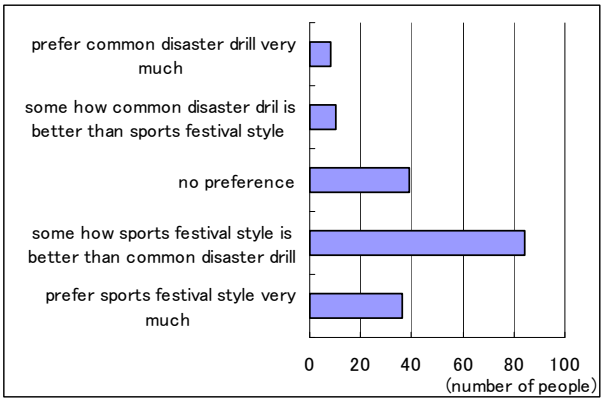

Figure 4 preference comparisons between common disaster drill and sports festival style of disaster drill

Figure 5 presents the survey result of the degree of contribution to network neighbors of a community by sports festival style of disaster drill. Around 78% participations believe that festival style of disaster drill is a good way to network neighbors of community because through sports festival they share the same goal, prepare for the drill, and discuss with each other.

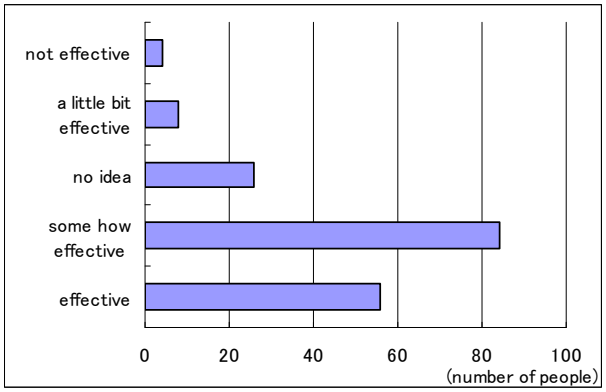

Figure 5 degree of contribution to network neighbors of a community by sports festival style of disaster drill

The festival includes two stages which are elimination round and final game. The team which passes elimination round can go forward to final game. We assume that this game design could lead regional disaster prevention training in a more active way. The survey result from Figure 6 support our assumption that participants think this game system is helpful in region disaster prevention.

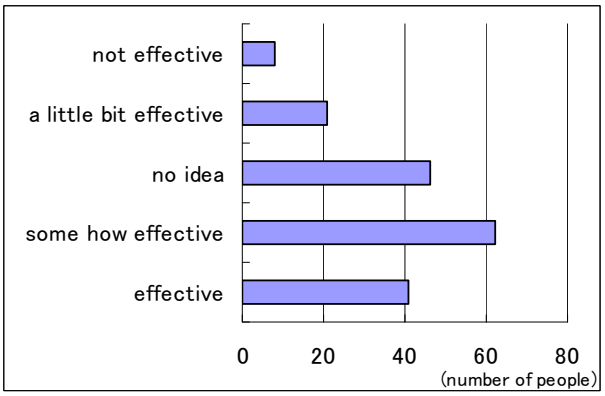

Figure 6 participants believe if the game system leads region disaster drill more active

Figure 7 shows participation experience on disaster drill by ages. We can see the young generations, for example under 40 years old, do not attend disaster drill actively.

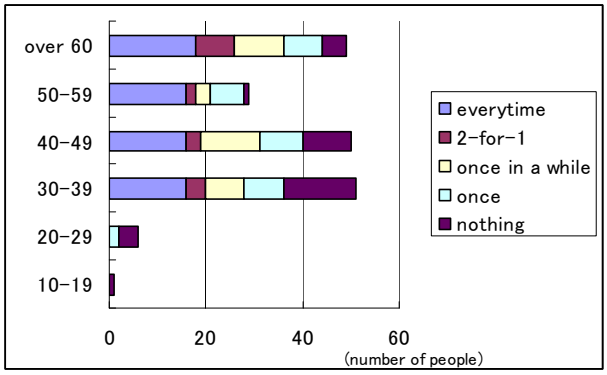

Figure 7 disaster drill experience

Figure 8 shows the participants' willingness to the next festival by ages. We can see people over age 60 show strong interest to the next festival. Moreover, from 30s to 40s more than half participants are willing to attend festival again.

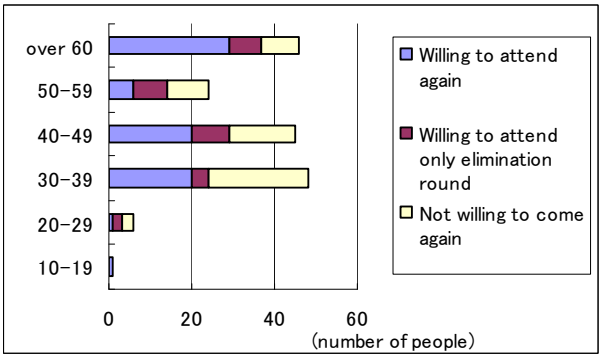

Figure 8 Participants' willingness to the next festival

Given the two stage design of the game system, we expect all the participants to experience solid training programs. We are interested in if this game system could motivate people to join the training festival and how often do people want to have such kind of training festival. Figure 8 shows most participants think this game system helps them to set up target in the training festival and expect such kind of festival to be held frequently.

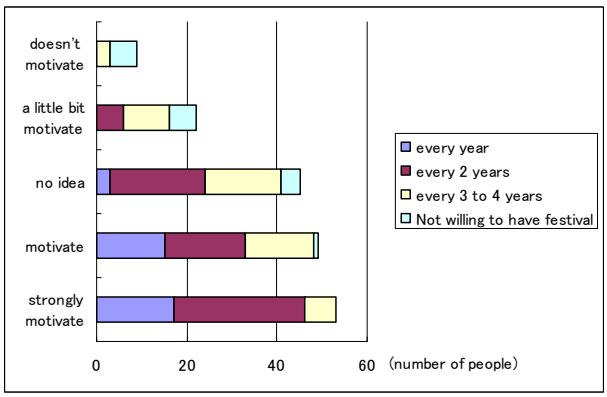

Figure 9 Survey about frequency of holding festival and motivation by the design of game system

Figure 10 shows the relation between participations' target for the next festival and the possibility of young people's participation due to the design of game system.

We can see most people who set the target to the main stage think that the game system makes young people participate the festival training. From this result we can expect young people to play the leader role in region disaster prevention.

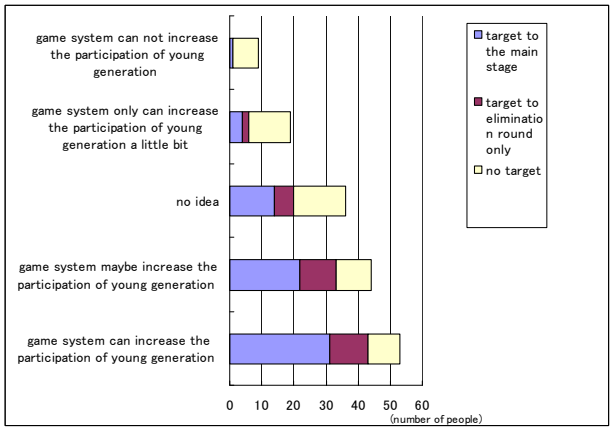

Figure 10 participations' target for the next festival and the possibility of young people's participation due to the design of game system

5. CONCLUSIONS

From this research, we can see this sports type of disaster drill could increase young people participation in regional disaster prevention. More than 50% participants who attend the disaster drill first time consider this sports festival style of disaster drill should continue every year or every two years. In addition, this disaster drill has effectiveness in establishment of solidarity and promotion of mutual-help attitude among neighbors of a community. On the other hand, maintenance of festival as an annual event costs a lot. Not smooth management may bother participants too much and lower their willingness to attend disaster drills. In the future we would like to create more ideas to increase the participation of young generation.

Acknowledgements:

The authors acknowledge support from the Himeji City Government for its cooperation in distributing and collecting the questionnaire.

References:

Central Research Services Inc., (2008), http://www.crs.or.jp/backno.htm

Kaji H. (2008), "Report of Effective Fire Services and Disaster Managements", submitted to the Himeji City Government.

JOINT CONFERENCE PROCEEDINGS
7th International Conference on Urban Earthquake Engineering (7CUEE) &
5th International Conference on Earthquake Engineering (5ICEE)
March 3-5, 2010, Tokyo Institute of Technology, Tokyo, Japan

GLOBALIZATION AND LOCALIZATION OF DISASTER IMPACT: EXAMINATION FOR GLOBAL PROPAGATION

Yasuhide Okuyama

Associate Professor, Center for Urban Earthquake Engineering, Tokyo Institute of Technology, and International University of Japan, Japan
okuyama@cuee.titech.ac.jp

Abstract: Albala-Bertrand (2007) claimed that economic impact of a disaster, which causes localized damages and losses on capital and activities, may not affect negatively the macro-economy in both short-term and longer-term. This appears to contradict with some empirical observations, such as the 1999 Chi-Chi Earthquake in Taiwan and other recent disasters. The propagation process of disaster impact in a global sense is examined in this paper using the empirical case of the 2004 Indian Ocean Earthquake and Tsunami. The results reveal that the potential propagation of economic impact in a global scale; however, the impact to the surrounding countries are relatively limited. Meanwhile, from the risk management perspective, the lack of localized countermeasures against disasters may lead to the spread of local risk over the global economy through international aids and donations.

1. INTRODUCTION

The damages and losses brought by disasters, such as earthquakes, floods, hurricanes and cyclones, and so on, can have significant and intense impacts on a nation's economy. However, despite the importance of assessing the economic impacts of damages and losses in the aftermath of such events, estimating impacts is challenging. The consequences associated with the event will have many other aspects including damages on demand and supply sides, for example, since the event may affect a wide range of economic activities in different ways. The difficulties with impact analysis of disasters are, therefore, 1) disentangling the consequences stemming directly and indirectly from the event, 2) deriving possibly different assessments at each spatial level—cities, region, or nation—(Hewings and Mahidhara, 1996), and 3) evaluating the reaction of households which are poorly understood (West and Lenze, 1994). Data availability for the impact assessment is another issue. West and Lenze (1994) claim that sophisticated economic impact models requiring precise numerical input have to be reconciled with imperfect measurements of the damages. They proposed a systematic way to estimate the impacts from the available data; however, "impact assessment of unscheduled events is an inexact science" (Hewings and Mahidhara, 1996; p. 216).

Albala-Bertrand (2007) claimed that economic impact of a disaster, which causes localized damages and losses on capital and activities, may not affect negatively the macro-economy in both short-term and longer-term. This appears to contradict with some empirical observations, such as the 1999 Chi-Chi Earthquake in Taiwan, which caused a hike in price of computer memory chips in the US and other countries, and the 2005 Hurricane Katrina, which somewhat influenced the crude oil price domestically and internationally. These observations indicate that while the degree of damages and losses is much severer in the areas hit by such natural hazard, the indirect impacts of the event appear to spread over to many other areas and nations. In this regard, the propagation process of disaster impact in a global sense is examined in this paper using the empirical case of the 2004 Indian Ocean Earthquake and Tsunami.

In the following section, Albala-Bertrand's *Globalization and Localization: an Economic Approach* (2007) is reviewed and critiqued. Section 3 defines and describes terminology associated with economic impact assessment of natural disaster. Analysis of empirical case study based on the 2004 Indian Ocean Earthquake and Tsunami is carried out and discussed. The final section concludes the paper with some remarks on future directions for this line of research.

2. REVIEW OF GLOBALIZATION AND LOCALIZATION

Albala-Bertrand has been studying about the economic consequences of natural disasters, especially in the developing country's context. In his studies, he often claimed that economic impacts of natural disasters are rather minor in a macroeconomic sense, even with a catastrophic one. For example, he claimed that the indirect effects of disaster are "more a possibility than a reality"

(Albala-Bertrand, 1993, p. 104). He also argued that in a long run negative impacts from damages made by a disaster and positive impacts from recovery and reconstruction may potentially cancel out and then the estimation of the total impacts often ends up deriving insignificant values (Albala-Bertrand, 1993). While his arguments were based on some empirical evidence of the past disasters (in 1960s and 70s for his 1993 publication), and whereas his conclusions have been agreed with many empirical studies of natural disaster, with the recent progress on globalization and increased interdependency between economies, economic impact of disasters should be re-examined with the augmented complexity of society.

In his recent publication (Albala-Bertrand, 2007), Albala-Bertrand analyzed the effect of globalization on disaster impacts from an economic perspective. His main conclusions are:

1. disaster impacts, such as casualties and economic losses, will be economically localized, and thus are unlikely to influence negatively the macro economy, such as national economy, even in a long run;
2. positive features of globalization, like access to larger markets and suppliers, etc., may lead to even more localization of disaster impacts, while negative features of globalization, which are fast efficiency and productivity improvements through privatization and deregulations and lead to thinner and weaker social fabric against emergency situations, make localized disaster impact much more condensed into the local community than before; and
3. the synchronization of business cycle caused by globalization, especially with the US economy, may regulate the financial capability for disaster response of the world, especially when the leading economies are under recession.

These conclusions reflect his argument on disaster impacts above, while he acknowledges the uncertainty of disaster consequences, shown in 2 and 3, may increase due to globalization.

In a macroeconomic or an aggregated sense, his arguments appear plausible for having not so significant total impacts. However, the total impacts are the sum of negative and positive impacts. The positive impacts are based on the expenditure for recovery and reconstruction, and it can be much smaller if an economy has well equipped and prepared against natural hazard, let alone the opportunity cost of the expenditure for other use. In addition, economic structure can affect the extent and significance of disaster impacts, since the interdependency may act as a path for propagation of negative and positive impacts from disaster and the distribution and volume of negative and positive impacts may differ over space and time. In this line, Albala-Bertrand's claim, which urges for future studies to start classifying disaster impacts over localities, is imperative. This may contradict his claim of negligible total impact of disasters in an aggregate sense, but the disaggregation of disaster impacts, showing disequilibrium between negative and positive impacts over space and time, is necessary and essential on the way to display the nominal macroeconomic impacts. Thus, in this paper, one of his conclusions, the above 1, is re-examined with the case study of the 2004 Indian Ocean Earthquake and Tsunami. His other conclusions, the above 2 and 3 for the effects of globalization, will be analyzed in the future studies.

3. ECONOMIC IMPACTS OF DISASTERS: CONCEPT AND DEFINITION

In order to discuss the economic impacts of disasters, we need to clarify the terminology first, since the use of similar words has created some confusion in many disaster literatures. According to Okuyama and Chang (2004), "hazard is the occurrence of the physical event *per se*, and disaster is its consequence" (p. 2). In this context, while the occurrence of hazards cannot be prevented, the extent and intensity of a disaster can be managed. Hence, the measuring the extent and intensity of economic consequences (disaster) caused by a hazard is necessary to evaluate and determine the countermeasures against hazards and is central to understand how the consequences of a hazard become a disaster.

In terms of disaster economic impacts, many comparable terms, such as damages, losses, impacts, direct losses and indirect losses, have been employed interchangeably without making any distinction or definition of them, and have led to further perplexity. Oftentimes, direct loss refers to the damages on stock, such as buildings, roads, houses, etc. and indirect loss implies the loss of flow due to business disruptions caused by stock damages. And then, in many disaster literatures, the total loss is calculated by adding these direct and indirect losses. However, in economics term, stock and flow are two different things and summing these up leads to potential double counting (Rose, 2004). Also, in the above way, the distinction between flow losses caused directly by the stock loss and flow losses caused via interindustry linkage (often referred as ripple effect) cannot be made, and this distinction is vital to illustrate the extent of disaster impact.

Consequently, the clear definition of disaster impact should be made. Okuyama and Sahin (2009) proposed the following terminology for disaster economic impacts: damages are by economics definition the damages on stocks, which include physical and human capitals; losses are business interruptions, such as production and/or consumption, caused by damages and can be considered as first-order losses; higher-order effects, which take into account the system-wide impact based on first-order losses through interindustry relationships; and total impacts are the total of flow impacts, adding losses (first-order losses) and higher-order effects. Rose (2004) further suggested that listing both damages and losses, but not adding them together, is appropriate for showing the different aspects of economic impact. In the following sections, these terms

are used for the analysis.

What we are going to estimate in this paper is the economic intensity of a natural hazard on flow, while a comprehensive assessment of a natural disaster requires to include both negative impact of a natural hazard and positive effects of recovery and reconstruction activities. More concretely, the results shown in the following section are only the negative impact of a natural hazard over a year, without any restoration, recovery, or reconstruction. This looks a very unlikely scenario, but this serves as the worst-case scenario [1] (do-nothing-scenario) and also provides the extent to which recovery and reconstruction need to be done. In addition, those restoration, recovery, and reconstruction strategies will be decided based on the total impacts of a disaster and the distribution of them; thus, the estimation of negative impact only becomes a basis of decision making and is well worth doing.

4. EMPIRICAL EXAMINATION: 2004 INDIAN OCEAN EARTHQUAKE AND TSUNAMI

In this section, how economic impacts of a local disaster can (or cannot) spread over internationally is examined, employing the 2004 Indian Ocean Earthquake and Tsunami as the case study. While this event was a multi-country incident, involving at least five countries (India, Indonesia, Maldives, Sri Lanka, and Thailand), the damaged areas in each country were relatively limited geographically. Thus, using the Albala-Bertrand's term, this was a localized event for each country. The economic impacts of this event are evaluated using the 2000 Asian International Input-Output table for analyzing whether or not any sizable economic impacts were propagated over other countries, *i.e.* internationally.

4.1 2004 Indian Ocean Earthquake and Tsunami

The December 2004 Indian Ocean disaster was caused by an earthquake, and the earthquake generated a tsunami, carrying many million tons of water in a series of very large waves that traversed the Indian Ocean in a matter of hours. These waves hit beaches, flooding low-lying lands coastal areas. The destruction was widespread: the most seriously affected areas were Banda Aceh, Indonesia, as well as in tourism resorts in Thailand, Sri Lanka, and the Maldives. Many small and medium sized rural villages located along the beachside in the five countries were also wiped out (ADPC, 2005).

According to the preliminary assessment of damages and losses (*ibid.*), total of 281,900 persons died as a result of the earthquake and tsunami; 189,500 persons were injured, physically and psychologically, and required immediate or medium term treatment; and, 1.2 million persons became homeless and even a year after the tsunami many were still housed in temporary camps, a sizable fraction of which still requires shelter, food and health services. The total economic effects of this event were estimated as US$ 5.6 billion of damages and 4.3 billion of losses over five countries—Indonesia, India, Sri Lanka, Maldives, and Thailand. In this paper, the total impacts of this event are estimated and analyzed for Indonesia and Thailand using the 2000 Asian International IO table, since other three countries (India, Maldives, and Sri Lanka) was not included in the IO table.

Indonesia

The total damage and loss in Indonesia were estimated as US$ 2,664 million and 1,136 million, respectively (*ibid.*). The housing sector had the largest damage with 1,398 million (52% of total damage). The transport sector had the second largest damage, 409 million. The productive sector, especially agriculture and industry (manufacturing) sectors, also had some sizable damages. On the other hand, the losses were concentrated on these productive sectors, 550 million for agriculture and 280 million for industry, and together, they had about 73% of total loss.

Thailand

The total damages and losses in Thailand were estimated to US$ 509 million and 1,690 million, respectively. The damages were concentrated on tourism with 376 million (74% of the total damage), resulted from the washed out resorts and hotels on the beaches. Other noticeable damages were on agriculture. The losses were also mostly on tourism with 1,470 million (87% of the total loss), and agriculture and industry had some losses around 100 million each.

4.2 Methodology

There is a wide range of methodologies used to estimate the higher-order effects thus the total impacts of disasters (further detailed discussion of methodologies for impact estimation can be found at Rose (2004), Okuyama (2007), and Greenberg *et al.* (2007)). Input-Output (IO) model has been the most widely used methodology for disaster impact estimate for the recent decades (for example, Cochrane, 1997; Gordon and Richardson, 1996; Rose *et al.* 1997; Okuyama *et al.*, 1999; and, Hallegatte, 2008). The popularity of IO models for disaster related research is based mainly on the ability to reflect the economic interdependencies within an economy in detail for deriving higher-order effects, and partly on its simplicity. On the other hand, this simplicity of the IO model creates a set of weaknesses, including its linearity, its rigid structure with respect to input and import substitutions, a lack of explicit resource constraints, and a lack of responses to price changes (Rose, 2004).

Input-output (IO) framework was developed by Wassily Leontief in the late 1920s and early 1930s. The structure of IO mimics the double-entry style of bookkeeping scheme. For the production side, the output is determined as the sum of intermediate demand and final demand as follows:

[1] There would be potentially some worse scenarios than this, if the recovery and reconstruction activities were misguided to create further negative effects.

$$x_i = \sum_j x_{ij} + f_i \quad (1)$$

where x_i is the output of sector *i*, x_{ij} is intermediate demand from sectors *j* to *i*, and f_i is the final demand for sector *i*. Direct input coefficient, a_{ij}, is calculated by $a_{ij} = x_{ij} / x_j$, and equation (1) can be transformed as follows:

$$x_i = \sum_j a_{ij} x_j + f_i \quad (2)$$

In the matrix notation, (2) becomes:

$$\mathbf{x} = \mathbf{Ax} + \mathbf{f} \quad (3)$$

Solving this relationship for **x** yields:

$$\mathbf{x} = (\mathbf{I} - \mathbf{A})^{-1} \mathbf{f} \quad (4)$$

$(\mathbf{I} - \mathbf{A})^{-1}$ is the Leontief inverse matrix. For the impact analysis, the impact of changes in final demand can produce the changes in output in the following manner:

$$\Delta\mathbf{x} = (\mathbf{I} - \mathbf{A})^{-1} \Delta\mathbf{f} \quad (5)$$

Miyazawa's (1976) extended input-output analysis intends to analyze the structure of income distribution by endogenizing consumption demands in the standard Leontief model. In some sense, Miyazawa's system is considered the most parsimonious in terms of the way it extends the familiar input-output formulation. Miyazawa considered the following system:

$$\begin{pmatrix} \mathbf{x} \\ \hline \mathbf{y} \end{pmatrix} = \left(\begin{array}{c|c} \mathbf{A} & \mathbf{C} \\ \hline \mathbf{V} & \mathbf{0} \end{array}\right) \begin{pmatrix} \mathbf{x} \\ \hline \mathbf{y} \end{pmatrix} + \begin{pmatrix} \mathbf{f} \\ \hline \mathbf{g} \end{pmatrix} \quad (6)$$

where **x** is a vector of output, **y** is a vector of total income for some *r*-fold division of income groups, **A** is a block matrix of direct input coefficients, **V** is a matrix of value-added ratios for *r*-fold income groups, **C** is a corresponding matrix of consumption coefficients, **f** is a vector of final demands except households consumption, and **g** is a vector of exogenous income for *r*-fold income groups. Solving this system yields:

$$\begin{pmatrix} \mathbf{x} \\ \hline \mathbf{y} \end{pmatrix} = \left(\begin{array}{c|c} \mathbf{B}(\mathbf{I} + \mathbf{CKVB}) & \mathbf{BCK} \\ \hline \mathbf{KVB} & \mathbf{K} \end{array}\right) \begin{pmatrix} \mathbf{f} \\ \hline \mathbf{g} \end{pmatrix} \quad (7)$$

where:

B=(I-A)$^{-1}$ is the Leontief inverse matrix;

BC is a matrix of production induced by endogenous consumption;

VB is a matrix of endogenous income earned from production;

L=VBC is a matrix of expenditures from endogenous income; and

K=(I-L)$^{-1}$ is a matrix of the Miyazawa interrelational income multipliers.

In this paper, the IO model used is transformed to the Miyazawa's extended IO framework for the analysis of impact on income generation.

Model used in this paper is the 2000 Asian International Input-Output Table, published by the Institute of Developing Economies (IDE), the Japan External Trade Organization (JETRO). This table includes nine countries and one region (Indonesia, Malaysia, Philippines, Singapore, Thailand, China, Taiwan, Korea, Japan, and the United States) with seven industrial sectors (agriculture, mining, manufacturing, utility, construction, trade and transport, and services). This is the only officially available data source for this type of international input-output table, while the data year, 2000, is a bit earlier than the year when the event occurred, the end of 2004, implying some of the trade relationships may have changed between these years, especially with China.

The sectors in the original model are aggregated as much as possible to fit with the data of damages and losses in order to maintain the feature of the input data. The IO model is a demand driven model so that the input to model should be the form of changes in final demand, and then changes in output will be derived. Therefore, losses (decreased output level) is converted to final demand change in each sector, using Miller and Blair's (1985) method—dividing the changes in output (output loss) by the diagonal term of the Leontief inverse matrix for IO model. Then, the derived changes in final demand model are multiplied with Leontief inverse matrix to calculate impact by sector. Because of extension to the Miyazawa framework, the model can yield both the output impact (higher-order effects) and the impact on income generation (income impact) as the results.

At the end of the estimation, the impact multiplier is calculated by dividing the total output impact (not including income impact) by total converted losses (sum of total output decease and total income decrease). While this is different from the standard output multiplier in IO literature, where the changes in output are divided by the changes in final demand and usually income losses are converted to the changes in final demand, this impact multiplier aims to connect the calculated impact with the original loss data in the respective assessment report, and not to double-count between the impacts on output, which already take into account the income decrease and on income.

4.3 Analysis

The economic impacts of the 2004 Indian Ocean Earthquake and Tsunami for Indonesia and Thailand, and other Asian countries are calculated and evaluated in this subsection. Table 1 shows the input data, damages and losses, and the results, output impact and income impact in Indonesia. The derived total impacts are US$ 2,386 million (0.93% of 2004 GDP) for output and 1,219 million for income. The most significant output impact falls on manufacturing with 814 million (with 280 million of output decrease as loss), followed by agriculture with 672 million. The sectors with large impact tend to be accompanied with large losses, while the other sectors with small or no losses,

such as mining, utilities, and construction, have limited higher-order effects. This may lead to the relatively small impact multiplier of 2.10.

Table 1 Economic Impacts of 2004 Indian Ocean Earthquake and Tsunami: within Indonesia (2007 US million dollars)

Indonesia		Data		Converted			Calculated	
Sector		Damages	Losses	Sectors in model	Output decrease	Demand decrease	Output impact	Income impact
Infrastructure	Housing	1,398	39	Agriculture	550	410	672	
	Transport	409	148	Mining	0	0	69	
	Electricity	68	0	Manufacturing	280	158	814	
	Water and Sanitation	27	3	Utilities	3	3	30	
	Urban and Municipal	132	89	Construction	0	0	20	
	Water Resource			Trade and Transport	148	113	370	
Social	Health and Nutrition	111	9	Services	116	80	412	
	Education	166	18					
Production	Agriculture	186	550					
	Industry	167	280					
	Service			HH Income decrease	39			1,219
	Tourism							
Total		2,664	1,136		1,136		2,386	1,219

The derived impact for Thailand on output and income are US$ 3,205 million (1.99% of 2004 GDP) and 1,240 million, respectively, as seen in Table 2. The total impacts fall mostly on services (including tourism industry) with 1,535 million (48% of the total output impact). Meanwhile, manufacturing has a sizable impact of 872 million (27% of the total output impact), indicating that the Thailand's domestic industries are highly interwoven and interdependent so that the total impacts spread across the sectors. However, the calculated impact multiplier is 1.90, a relatively low value. This implies that while the tourism industry is one of the major industries in Thailand, the losses are concentrated on one industry (tourism) and thus the total impacts are somehow limited and not widely spread to the entire economy.

Table 2 Economic Impacts of 2004 Indian Ocean Earthquake and Tsunami: within Thailand (2007 US million dollars)

Thailand		Data		Converted			Calculated	
Sector		Damages	Losses	Sectors in model	Output decrease	Demand decrease	Output impact	Income impact
Infrastructure	Housing	22	0	Agriculture	102	89	228	
	Transport	7	9	Mining	0	0	33	
	Electricity	4	10	Manufacturing	93	58	872	
	Water and Sanitation	1	3	Utilities	13	10	132	
	Urban and Municipal	15		Construction	0	0	3	
	Water Resource			Trade and Transport	9	7	401	
Social	Health and Nutrition	9	3	Services	1,473	946	1,535	
	Education							
Production	Agriculture	75	102					
	Industry		93					
	Service			HH Income decrease	0			1,240
	Tourism	376	1,470					
Total		509	1,690		1,690		3,205	1,240

As seen above, the impacts of the event appear not so large within the two countries (0.93% of GDP in Indonesia and 1.99% of GDP in Thailand). With increased economic interdependency between countries through international trades, this simultaneous damages and losses in multiple neighboring countries may bring the higher-order effects to other surrounding countries, or globally. As described in the previous section, the model used for this particular event (2000 Asian International IO table) includes the above two countries and six other Asian countries and one region, and the United States so that the impacts to those countries can be estimated.

Table 3 Spatial Distribution of Total Impact in 2004 Indian Ocean Earthquake and Tsunami (2007 US million dollars)

	Sectors in model	*Indonesia*	*Thailand*	Malaysia	Philippines	Singapore	China	Taiwan	Korea	Japan	USA	Total
Output Impact	Agriculture	*672*	*228*	2	1	0	19	2	3	8	13	948
	Mining	*69*	*33*	5	0	0	7	0	0	1	4	118
	Manufacturing	*814*	*872*	36	7	33	96	42	59	230	120	2,307
	Utilities	*30*	*132*	1	1	1	6	1	2	11	7	192
	Construction	*20*	*3*	0	0	0	1	1	0	4	2	30
	Trade and Transport	*370*	*401*	5	2	7	14	9	7	64	47	926
	Services	*412*	*1,535*	9	2	9	14	15	19	110	114	2,239
	Total	*2,386*	*3,205*	58	14	50	156	69	90	428	306	6,761
Income Impact		*1,219*	*1,240*	22	5	12	39	24	26	154	143	2,885

Table 3 indicates the impacts for these countries. Except those directly affected countries, Indonesia and Thailand, Japan receives the largest total impacts (thus the largest higher-order effects, since there are no first-order losses in Japan) in this system, with US$ 428 million. The United States has the second largest total impacts of 306 million. China follows these two countries and has 156 million of the total impacts. Among the sectors, manufacturing has the most significant impact in total (2,307 million) and for each country in this system. This also is an evidence of increasing interdependence among manufacturing firms through international trades. Comparing to the total impacts in Indonesia and Thailand and to their own GDPs, these impacts in the other countries can be considered as negligible. At the same time, for the system as a whole, the aggregated total impacts become 6,761 million with the impact multiplier of 2.39, and these numbers are noticeably larger than the above two countries'. For the multi-country disaster case such as this Indian Ocean Earthquake and Tsunami, this type of international analysis is useful to capture the comprehensive picture of the impacts.

So, does this mean that this type of localized but multi-country disaster can have any global economic impact? The answer would be probably 'NO', since the higher-order effects to other surrounding countries are very small in value. As described in the previous section, the derived economic impacts do not include the positive impacts from recovery and reconstruction activities in the respective countries. If included, the economic impacts to other surrounding countries may become much smaller than the values in Table 3. In the meantime, some parts of recovery and reconstruction activities were done with the cooperation of international organizations and international aids from those surrounding and other countries. If these aids cancel out the higher-order effects in Table 3 by preventing the spread-out of higher-order effects and those countries had no impact from such additional expenditure, the positive feature of globalization worked as Albala-Bertrand argued. But it may not be so simple under the current difficult situation for the global economy caused

by the global financial crisis. In addition, how the negative feature of globalization, which may weaken the local economies, needs to be investigated through how the damaged localities have been recovered and reconstructed.

5. SUMMARY AND CONCLUSIONS

In this paper, the total impacts of 2004 Indian Ocean Earthquake and Tsunami were estimated using the 2000 Asian International Input-Output table. The results show that the higher-order effects and total impacts of disasters are significant and complex domestically. The spread of higher-order effects to other surrounding countries do exist, while the value *per se* is relatively small comparing to the localized higher-order effects and to their respective size of the economy. However, this does not mean there is no global or international ripple effect of the disaster impact; rather, if proper development and domestic policy and appropriate recovery and reconstruction strategies were not practiced, these higher-order effects would spread over globally.

Some researchers claim that the short-term impact of disasters are negligible since the positive impact of relief, recovery, and reconstruction activities starts immediately after the occurrence of hazards and the counteraction measures that a society inherently has against such a calamity would respond to reduce the higher-order effects (Albala-Bertrand, 1993 and 2007). This may be true, if the negative impact of higher-order effects and the positive impact of relief and reconstruction are added up to show the total impact; in many empirical disaster studies, the total impacts are indeed sometimes negligible, offsetting negative and positive impacts, or even positive in some cases. However, these results do not lead to the conclusion that disasters have no impact on the economy. A thorough investigation of disaster impacts requires a detailed and disaggregated analysis, which separates negative and positive impacts, and not merely adding them up, in order to assess how negative and positive impacts interact each other and affect various segments of society differently. Negative impacts of higher-order effects surely exist as seen in this paper, and their proper recognition and estimation can enable policy makers to contemplate how ex-ante loss reduction measures can be formed effectively and efficiently.

The data for damages and losses used as input for estimation in this paper are based mostly on the ECLAC methodology (UN ECLAC, 2003). While the accuracy of these data is the key for the precision of the estimated results and in this regard the data collection methodology needs to be streamlined further (Greenberg, *et al*., 2007), this ECLAC methodology can standardize the assessment of damages and losses of a disaster, and this standardization not only enables inter-disaster comparison but also encourages the discussion of mitigation, preparedness against disasters, and vulnerability analysis of economies based on the common framework. An important next step would be to make the estimation methodology of higher-order effects a part of a standardized methodology – such as the ECLAC methodology – evaluating a more accurate measure of disaster impacts.

Acknowledgements:

This research was supported by the JSPS Grant-in-Aid for Scientific Research (C) [21510199] and partly by the Global Facility for Disaster Reduction and Recovery (GFDRR) and the World Bank. The author would like to express gratitude to Apurva Sanghi and Sebnem Sahin for their support, encouragement, and patience. The author would also like to thank Hirokazu Tatano for his helpful comments at the 2009 ARSC meetings in Yamagata, Japan.

References:

Albala-Bertrand, J.M. (1993) *The Political Economy of Large Natural Disasters: With Special Reference to Developing Countries*, Oxford, UK: Clarendon Press.

Albala-Bertrand, J.M. (2007) "Globalization and Localization: An Economic Approach," in H. Rodriguez, E.L. Quarantelli, and R.R. Dynes ed. *Handbook of Disaster Research*, New York: Springer, 147-167.

Asian Disaster Preparedness Center (ADPC) (2005) *Regional Analysis of Socio-Economic Impacts of the December 2004 Earthquake and Indian Ocean Tsunami*, Bangkok, Thailand.

Cochrane, H.C. (1997) Forecasting the economic impact of a Midwest earthquake, in: B.G. Jones (Ed.) *Economic Consequences of Earthquakes: Preparing for the Unexpected*, Buffalo, NY: National Center for Earthquake Engineering Research: pp. 223-247.

Gordon, P. and Richardson, H.W. (1996) The business interruption effects of the Northridge earthquake, Lusk Center Research Institute, University of Southern California, Los Angeles, CA.

Greenberg, M.R., Lahr, M., and Mantell, N. (2007) Understanding the economic costs and benefits of catastrophes and their aftermath: A review and suggestions for the U.S. federal government, *Risk Analysis*, 27 (1): pp. 83-96.

Hallegatte, S. (2008) An adaptive regional input-output model and its application to the assessment of the economic cost of Katrina, *Risk Analysis*, 28 (3): pp. 779-799.

Hewings, G.J.D. and Mahidhara, R. (1996) Economic impacts: Lost income, ripple effects, and recovery, in S.A. Changnon ed. *The Great Flood of 1993: Causes, Impacts, and Responses*, Boulder, Colorado: Westview Press.

Miller, R.E. and Blair, P.D. (1985) *Input-Output Analysis: Foundations and Extensions*, Englewood Cliffs, N.J: Prentice-Hall.

Miyazawa, K. (1976) *Input-output Analysis and the Structure of Income Distribution*, New York, NY; Springer-Verlag.

Okuyama, Y. (2007) Economic modeling for disaster impact analysis: past, present, and future, *Economic Systems Research*, 19 (2): pp. 115-124..

Okuyama, Y. and Sahin, S. (2009) "Impact Estimation of Disasters: A Global Aggregate for 1960 to 2007," *Policy Research Working Paper 4963*, the World Bank.

Okuyama, Y., Hewings, G.J.D. and Sonis, M. (1999) Economic impacts of an unscheduled, disruptive event: a Miyazawa multiplier analysis, in G.J.D. Hewings, M. Sonis, M. Madden and Y. Kimura (Eds) *Understanding and Interpreting Economic Structure*, Berlin: Springer: pp. 113-144.

Rose, A. (2004) Economic principles, issues, and research priorities in hazard loss estimation, in: Y. Okuyama and S.E. Chang (Eds) *Modeling Spatial and Economic Impacts of Disasters*, New York: Springer: pp. 13-36.

Rose, A., Benavides, J., Chang, S.E., Szczesniak, P. and Lim, D. (1997) The regional economic impact of an earthquake: direct

and indirect effects of electricity lifeline disruptions, *Journal of Regional Science*, 37, pp. 437-458.

United Nations Economic Commission for Latin America and the Caribbean (UN ECLAC) (2003) *Handbook for Estimating the Socio-Economic and Environmental Effects of Disasters*, Santiago, Chile.

West, C.T. and Lenze, D.G. (1994) Modeling the regional impact of natural disaster and recovery: a general framework and an application to hurricane Andrew, *International Regional Science Review*, 17, pp. 121-150.

JOINT CONFERENCE PROCEEDINGS
7th International Conference on Urban Earthquake Engineering (7CUEE) &
5th International Conference on Earthquake Engineering (5ICEE)
March 3-5, 2010, Tokyo Institute of Technology, Tokyo, Japan

EMERGENCY AND TRANSITIONAL SHELTER POST EARTHQUAKE: THE ROLE OF SOCIAL CAPITAL IN JAVANESE COMMUNITY

Ikaputra[1)]

1) Associate Professor, Department of Architecture and Planning, Gadjah Mada University, Indonesia
ikaputra_2001@yahoo.com

Abstract: Disasters are the ultimate test of emergency response capability. The ability to have self reliance is very important to response at emergency. One of the needs for surviving at basic is community capacity to provide a basic emergency shelter after disaster. When emergency shelter is not suitable enough for the normal family life need, people continues to struggle or strive for normality by constructing a transitional shelter to fill the gap between emergency shelter and the high demand on proper housing. This paper focuses on the discussion of how the community provided shelter post Java earthquake 2006 both as one of the human basic needs at emergency stage and as transitional living before survivors able to return to normal and secure permanent house. The discussion contains three issues: (a) The Role of *POSKO*—Community Help Center—to cope with surviving at basic needs at the earlier stage of emergency, (b) The Community Self Reliance to provide shelters for emergency living; and (c) The participatory T-Shelter as useful component for Transitional Living. Those above local initiative and practices of the community in providing shelters post earthquake proved to us that the existing system of mutual self-help so called *gotong royong* within the community is believed to be a valuable social capital to make the emergency response and living in transitional stage in Yogyakarta post earthquake done very rapid and effective.

1. INTRODUCTION: DISASTER RESPONSE

Emergency can be described simply as "a sudden occurrence and need immediate response". The sudden occurrence is usually, unexpected occurrence or an abnormal situation. The unexpected occurrence might be caused by natural disaster (such as earthquake, tsunami, tornado, hurricane, mount eruption, etc.), by man-made disaster, (such as fire, war, terrorist attack, airplane crash, etc.) or by both natural and man-made disaster (such flood, landslide, or other environmental degradation). It is also happened from serious incidents cause by riot, civil conflicts, or employee mistake actions, which make a significant disruption of normal facility or agency procedure, policy, or activity.

To generalize the emergency situation, it can be started from a disaster which produces a sudden change in the physical components of a community. Combined with physical destruction are deaths and injuries. It causes the community can no longer function as before. During the emergency period underlying values and the community norms usually produces a high level of frantic activity, most of which is altruistic. Efforts are made to save persons and property from further damage. Consensus is usually high and the immediate needs and responses are obvious in most instances. (Haas et.al., 1977: xx-xxi)

Why in the emergency situation, it requires immediate response, prompt action and urgent assistance? The sudden occurrence usually creates a crisis situation, where there are serious and immediate danger and threats to human life, property, or environment. The emergency phase is typically a period of high consensus in the community, with much altruistic behavior aimed at preventing or reducing human suffering. (Pelling, 2003:14) The main goal to set up the immediate response and action is to prevent a worsening of the situation, to lessen or avert the threat of disaster.

In the vulnerable disaster, the immediate response is needed formally, by the government to declare a state of emergency. The immediate actions may be from internal or external resources in the short time scale. External resources can be mentioned such emergency medical expert teams, humanitarian NGOs, or technical experts related to the cause of disaster. However the most important resources to cope with the emergency situation come from within the community or survivors. Kate and Pijawka (1977: 3) illustrated clearly to describe the relation between the character of emergency period and the coping capacity as immediate response embedded in the community:

> *Emergency period is characterized by those coping actions stemming from the high portion of the capital stock that has been damaged or destroyed, and by the number of dead, injured, homeless or missing. During this period, normal social and economic activities cease or are drastically changed. The emergency period may be very short in societies with a great capacity to cope with disaster, lasting only*

days or a few weeks, or it may drag on for much longer periods of time in societies with a limited coping capacity. (Kate & Pijawka, 1977: 3)

The coping capacity of society, or known as community self-reliance becomes significant aspect to survive in the emergency period. Disasters are the ultimate test of emergency response capability. The ability to effectively deal with disasters is becoming more relevant because of factors that tend to increase risk. (Auf Der Heide, 1989: 4) The ability to have self reliance is very important to response at emergency. Self reliance has meanings personal independence, or the capacity to rely on one's own capability. It is the ability or capacity to response from within individual to recover quickly from depression, to recover after disturbance, or to bounce back after a perturbation. A self-reliant community exploits to the fullest its own local resources, assets, and capacities to satisfy its own needs. UNHCR (2005: 1-2) "Self reliance" is also defined as social and economic ability of an individual, a household or a community to meet essential needs (including protection, food, water, shelter, personal safety, health and education) in a sustainable manner and with dignity.

Generally, the resilience can be seen as a capability of a system to maintain its basic functions and structures in a time of sudden pressure or shocks. This definition of resilience also implies that a system or unit (such as social system, ecosystem, neighborhood unit, a group of people, etc.) is able to mobilize sufficient self-organization to maintain essential structures and processes within a coping or adaptation process. Self survive at basic is the idea of the resilience. Emergency response by the community is efforts at basis level to recover critical conditions headed for normal functioning and development after being hit by a disaster. One of the needs for surviving at basic is community capacity to provide a basic emergency shelter after disaster. After the emergency stage, when emergency shelter is not suitable enough for the normal family life need, people do struggling or striving for normality. Lack of funding, shortage of materials, and limited supplies of manpower make survivors unable to quickly return to their pre-disaster secure permanent house. There is a clear gap between the high demand on proper housing and the shortage of resources to reconstruct the house after disaster and get back to normal life. If efforts to have permanent living are longer than the expectation, survivors should bridge the gap between emergency shelter and permanent house by considering a transitional shelter. (Ikaputra, 2009: 38)

Community self reliant ability, external supports, and government supports play a role to strive for normality—efforts to restore livelihoods as same as possible to pre-disaster situation. Although government supports usually cover people needs at all stages of post disaster activities, Community self reliance mostly contributes significantly to emergency stage to survive at basic needs, while external supports play a role dominantly at transitional stage when people unable quickly to have normal live.

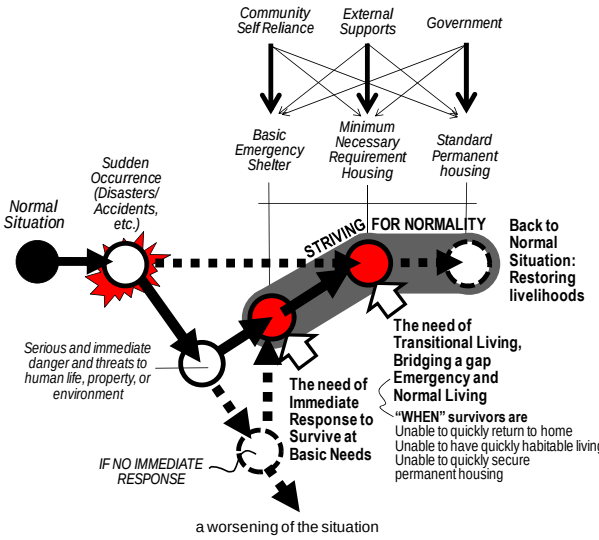

Figure 1. Emergency & Transitional Stage Post Disaster

The case of the vulnerable Java Earthquake 2006 provides a lesson to us how survivors as well as community, local/international NGOs, government, universities, donors and other social components hands in hands to response immediately emergency situation post earthquake by supporting survival at basic needs. This paper focuses on the discussion of how the community provided shelter post earthquake both as one of the human basic needs at emergency stage and as transitional living before survivors able to return to normal and secure permanent house.

2. SURVIVE AT BASIC NEEDS IN EMERGENCY

2.1 The Role of *POSKO:* Community Help Center

1. What is *POSKO* and Who initiated?

What is POSKO? Posko is Indonesian abbreviation for two words: *"Pos* and *Komando."* Those words mean simply "Command Post" or "Command Unit. (Steven & Schmidgall-Tellings, 2004: 769) The original use of the term is for military operation in Indonesia. The *Posko* is set up where military orders are instructed by commander. It is usually located in strategic place and plays a role very important to support the operation. Nowadays the *Posko* term is widely used not only for military purpose, but it has similar meaning and functioned as "command headquarters" or "center of coordinating place". (Uni Apro, 2006) The *Posko* is made for temporary function and often activated in post disaster relief or at emergency time, such as *Posko Bencana Alam*—Earthquake Command Center, (KBRI Canberra, 2006) and Emergency Command Units. (Sukrismanto, 1998: 7) *Posko* is also used by International humanitarian organization to familiarize or fit their existence

within the community as "Emergency center" (IFRC, 2008: 2), or as "Emergency Control Post". (IOM, 2006: 1) The most important *Posko* is the unit that spontaneously developed by the community at the Emergency time. For the community, the *Posko* can be functioned or used as a *First-aid Post* (Lordet, 2006) for survivors. The *Posko* created by the community is aimed basically to be a Help-center or Aid-center.

At the Java Earthquake 2006, most of the Posko was created by the community on the day of the earthquake especially at the area which suffered high vulnerability level. *Who initiated to create a POSKO in the time of emergency*? An interview involving 100 families was aimed to recall their memory on "who was the initiator" for setting up a *Posko* in their neighborhood after the Earthquake event in 2006. There were "6 actors" mentioned by respondents. *Warga* (=citizen) and *masyarakat* (=society, community) were mentioned as initiator by most of respondents. It means the *poskos* were mostly set up spontaneously by the community on the village. The people also mentioned *tokoh masyarakat* (community's figures), *dukuh* (hamlet leader); *RT* leader (neighborhood unit leader) and *aparat* (government staffs or apparatus) as initiators. It is understandable that those people play an important role for *Posko*, because they are the very persons who have the responsibility and good network and accessibility with external connections/supports. The community also told us that NGO/Donors help them to make a *Posko* for survivors within their humanitarian relief's mission. Some of political party and figures were also brought into their mind as the organization or person who helped them for emergency *Posko*. It is clear that the *Posko* in the community mostly was set up by themselves as a part of their capability to cope with the emergency situation. The capability which is believed to be one of the important components of Community self-reliance needed for help themselves in the emergency. (See Figure 2)

.

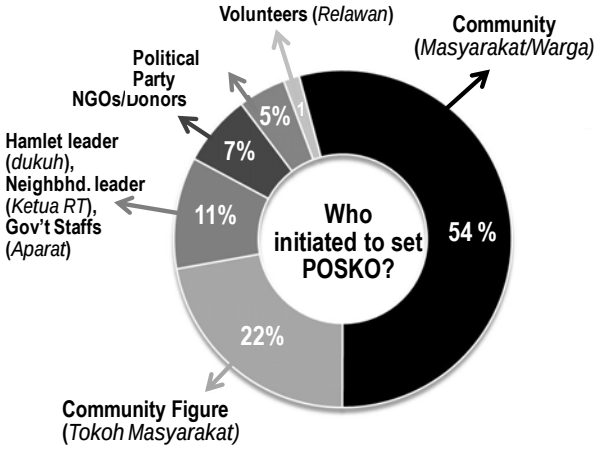

Figure 2. POSKO Initiators

2. What is *Posko* Function and Who involved?

A foreigner who came to Yogyakarta to observe the post disaster emergency activities has reported to IFRC on June 14, 2006—around two weeks after the earthquake. A part of the report that described "*posko*" activities and the *"gotong royong"* among the community can be read as follows:

> *First-aid posts called* "posko*" were set up to centralize the distribution of food and water, ensure fair rationing, count the number of injured people and casualties and also assess the damage. The* "gotong royong*", which means "solidarity" in Javanese and is a sort of community melting pot shows clearly how an emergency response is always most effective when the people themselves get involved in first aid*. (Lordet, 2006)

The report at least gives an illustration of what is the function of the *Posko* from the point of view of foreigner. The *Posko* was viewed as "first-aid community center" and supported by people with "solidarity spirit"—*gotong royong*. *Posko* activities described by the community—as a result of interview of survivors—can be understood from the following figure:

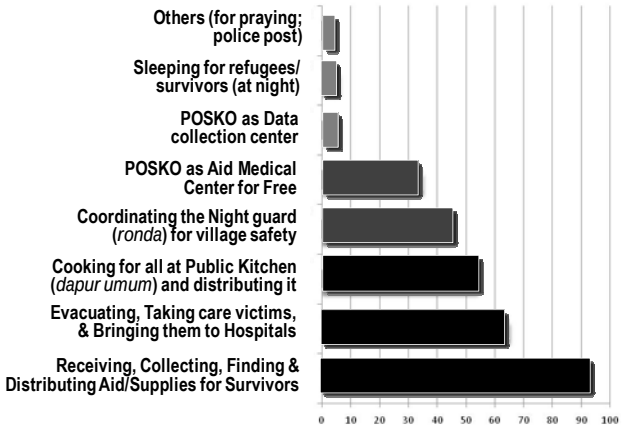

Figure 3. POSKO's Function

The *Posko* has mostly or dominantly by three main activities: helping victims, managing supplies/aid, and providing/distributing foods. The *Posko* was describes as a help center for victim's evacuation, taking care them, and bringing them to Hospitals. Some of the *Poskos* even had a function as an Emergency Hospital (*Rumah Sakit Darurat*) or Emergency Medical Care unit (*Pengobatan Sementara, tenda berobat, tempat Pengobatan*). They were supported by individual's doctor volunteer, or PMI (Indonesian Red Cross), or country donors such as Qatar or Uni-Emirates. People can have medical helps for free. The *Posko* also became a center to receive, collect, find as well as distribute aid/supply for survivors such as clothes, blanket, mats, tents, plastic sheets, cooking tools, soaps, towels, and foods. Some *Poskos* collected aids first then distributed later on so it

needed a storage-like tent. Most of *Poskos* did receiving the aid and soon distributed them to families. The source of aids *(bantuan*) can be from Individuals donors, relatives of the survivors, government, institutions/companies, mass media agencies, religion organizations, political parties, or as a result of proposal submission by the *Posko.* The feeling of same boat (*senasib*) and solidarity made families bring supports/aid directly came to them (usually from relatives, their company, or as private gifts) to the *Posko*. They gave the support with sincerity (*keihklasan*) to the *Posko* for the sake of people needs. This made people solid and bonded better than before. Concerning foods for survivors, they can come and have a meal or food which was cooked at a public kitchen known as *dapur umum* as a part of a *Posko.* At night the *Posko* can be a place for sleeping especially for survivors who were homeless caused by their totally damage houses. After earthquake, there was an issue on pillage/plundering (=*penjarahan*) by outsiders spread over villages. The fears/threats of *stealing survivor's goods*, made the community improving their intensity to do night guard. As a result, the *Posko* added his service as a coordinating center for the night guard activities. Some of *Posko* was run to be a center for data collection (on victims or house damages). One to another *Posko* can vary their services to help survivors at the emergency time.

Who involved in POSKO activities? There were 8 components of community which mentioned as actors who played a role in *Posko* activities. Those are *warga* or can be translated into "community" in common, *tokoh masyarakat* (community figure), *Dukuh/RT* (hamlet/neighborhood unit leader), *Karang Taruna* (the Youth organization in the community), *bapak-bapak* (Household Head, male), *ibu-ibu* (House wives) or PKK (house wife's club); *ronda* club (night guard), and NGO.

Almost all components (except *ibu-ibu* and *ronda* group) were mentioned as actors who manage the *Posko.* Tasks of each component can be described specifically by figure 2.5. The task to collect aids (*bantuan*) and to find financial supports were done by the youth, community figures, and *dukuh/RT* leader. The most dominant activity which involved significantly the people was to distribute the aids/supplies (*bantuan*) for the emergency supports. The village security was handle mostly by existing night guard group supported by the youth and led by the *dukuh/RT*leaders. *Ibu-ibu* and their Village women club—*PKK*—were in charge in operating the *dapur umum* (public kitchen) so that the survivors were able to have enough food in the emergency phase. *Dukuh/RT* leader had an additional obligation to find or provide for families who really needed support on emergency shelter. The *Posko* can be an example of collective management—people hands in hands—to cope with the immediate needs in emergency time. It proved that the community has self-help capability—the community self-reliance.

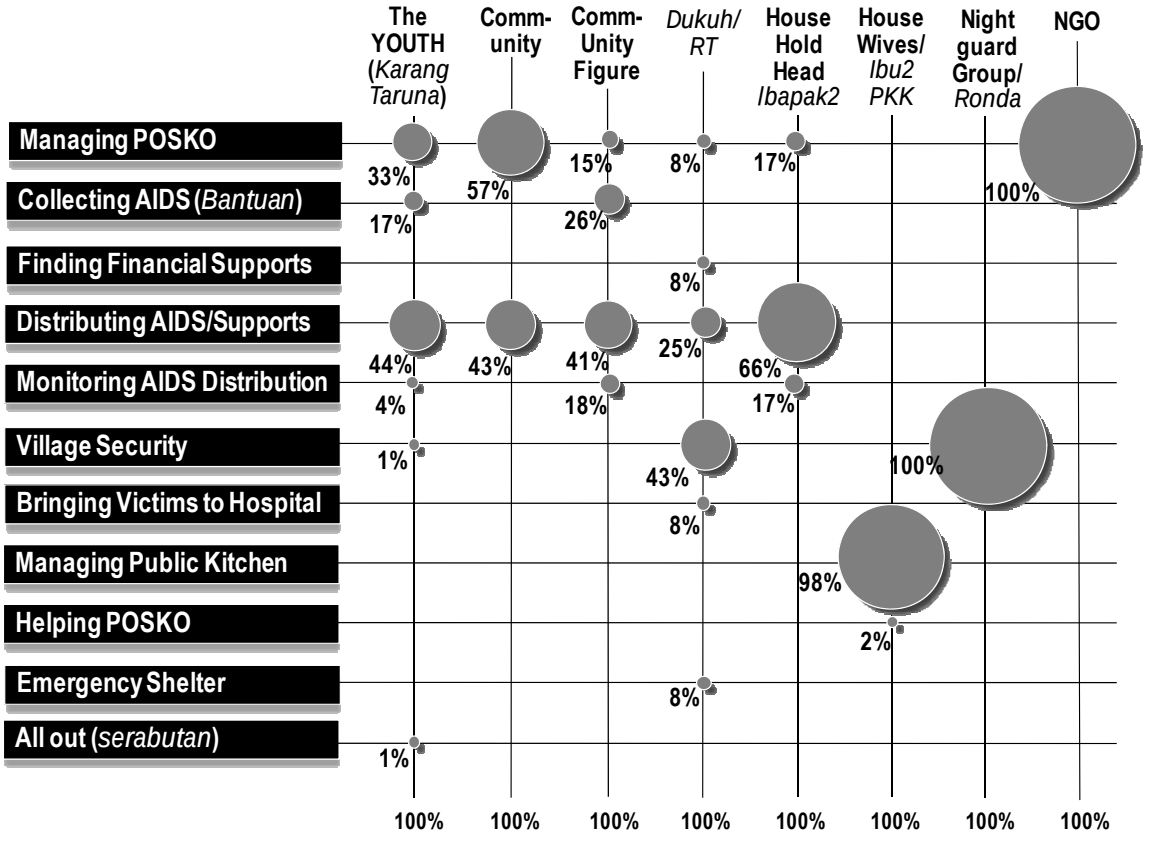

Figure 4. Community Involvement in *Posko* activities

3. *POSKO's* Architecture

"Reconstructive sketches" done by community from 14 sub-districts (*kecamatans*) shows most of *poskos* have a generic type as "simple rectangular architecture." It was usually tents which can be set up within 1-2 hours. They described the *posko* as a big tent with column at the middle. The size was about 12 x 12 m2. This emergency tent was given by or received from army, government, or NGO. Why most of them were tents? When an immediate response should be ready within hours after earthquake or disasters, people are not ready with local materials or are either not available at all. (UNHCR Canada, 2008: 4-5) However, the life span of an erected tend depends on the climate and the care given by its occupants; it may be as long as 2-3 years. Within the better immediate response by the community at emergency, the tent can be used no more than three months. It means the tent will be useful enough for the *posko*.



Figure 5 POSKO's Architecture

The emergency tent as *posko* at the most devastated district—*kabupaten* Bantul had an open-layout with plastic sheets, mats or carpet as flooring and some tables on it. Sometimes the tent was divided into two a room "guest room" and another room for logistic or aid (*bantuan*) storage. This multifunction tent served as community gathering place, storage for the aid goods, and for communal sleeping tents especially for children, infants, ageing, and women. Sometimes *posko* was also utilized as public kitchen and emergency medical care from Indonesia Red Cross (PMI). The *posko* was usually erected on vacant land or open space away and safe from house ruins. It can be at someone house yard, village leader's (*RT* or *Dukuh*) house yard, or at within the complex of *village hall* (*balai desa*, or *pendopo kelurahan*). The location of the *posko* usually accessible from the main road or just at the main road occupied some part of the road.

2.2 Community Self Reliance for Emergency Shelters

One of "survive at basic needs" of the Emergency Response is the need of shelter. People could not wait for having the place for sheltering and protecting them from weather to maintain their physical health and safety immediately after disaster. This part will explain how people in Yogyakarta and middle Java tried to survive with emergency shelter from the first day after the earthquake. Survivors started to create the shelter with very-very limited sources. It can be described the situation for having shelter with no land ready to be the site for building. All land was almost fully filled by the house ruins. Land readiness was almost none. This problem was worsened by the lack of material, financial, and other supports coming from external. It was also technically difficult to have good construction in the time of people should save lives of many injured victims. The only modality of the people was the spirits of *gotong royong*—to work together to cope and solve problem they faced immediately.

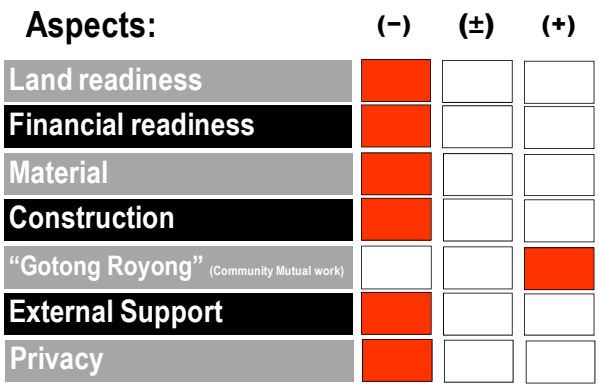

Figure 6 Important Aspect of Emergency Shelter

A qualitative observation to what people afforded and did effort to fulfill the need of shelter during the emergency have been done within first four weeks after earthquake.

(Ikaputra, 2006)[1] The aim of the observation in line with UNHCR-Canada recommendation (2008: 2) that:

> *Refugee should build or assist in building their own housing. This ensures that the housing will meet their particular needs, reduce their sense of dependence, and can costs considerably.*

The observation has resulted various typology of emergency shelter done by community themselves. The typology of "shelter for gathering", "shelter for belonging", "shelter for privacy", "recycled material shelter", and "shelter with material and technical supports" are among the finding which can be shared for other emergency relief on shelter. Those typologies of emergency shelters were developed with different situation and context.

1. Shelter for Gathering

The first 3 days after earthquake, the sudden change of environmental landscape caused by earthquake—the ruins of collapsed houses—were added to people feeling on traumatic, suffer from injured, or have in deep-felt condolences of victims among families. The community hands in hands worked to evacuate victims from ruins, seek for medical helps, got foods for survivors. The community as mentioned by Ursano et.al. (2007: 8) serves as important physical and emotional support system at the emergency situation. The community cohesion was shown by the high feeling of "*senasib*" (same fate or "same boat") and the strong spirit to work together known as "*gotong royong*" (community mutual helps) to cope with the emergency post earthquake.

An emergency shelter was built and functioned as a place for community gathering. This shelter for gathering strengthened the feeling of same fate (*senasib*). The spirit of *gotong royong*, became the social capital in constructing the emergency shelter for gathering within the lack of other resources. The land was still not ready for the individual shelter setting. It was still fully filled by debris and ruins. The lack of financial and material supports for constructing the shelter was the main problem since most of the survivors are villagers without high income. The construction knowledge especially earthquake resistant house was absent or had not yet introduced. The external support was still focused on food, medical aid, and other life line supports. There was no time to think on individual shelter for family privacy.

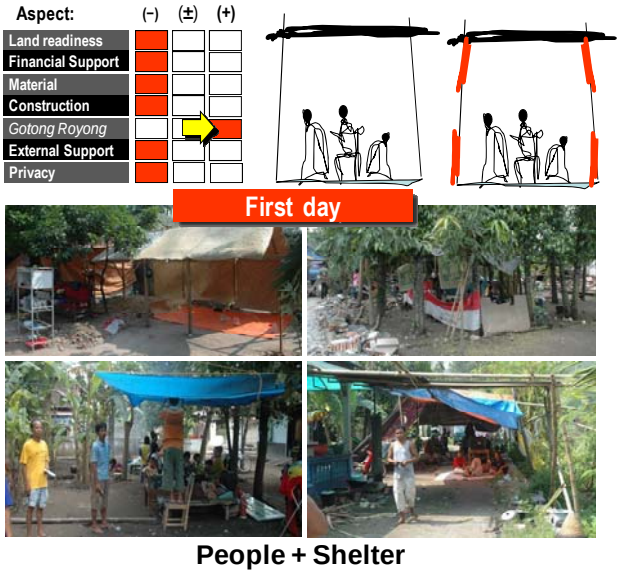

Figure 7 Shelter for Gathering

2. Shelter for Belonging

After the survivors finished working for victim's evacuation and making the shelter for community gathering, they started to think about their owned belongings—the property owned by family. They tried to collect their valuable property as much as possible. They collected house hold properties from ruins carefully with feeling of scare of next coming earthquake shaking. They gathered from small goods such as kitchen ware (dishes, glasses, spoons, etc.), clothes, blankets, electronic ware (Radio, TV, refrigerator, etc.), to big stuffs such as furniture (mats, carpets, chairs, tables, cabinets, beds, etc.).

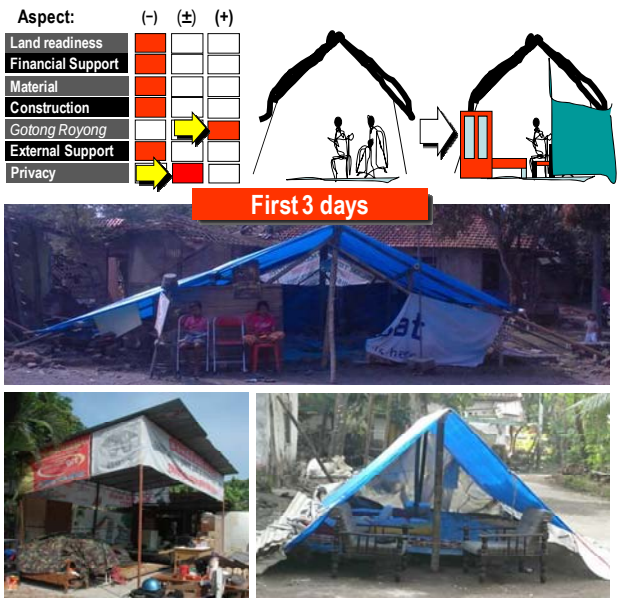

Figure 8 Shelter for Belonging

[1] I prepared the qualitative observation while I was working with Gadjah Mada University team for helping the community after earthquake. The observation was actually requested by UNDP as a part of their workshop on the proposal for *Transitional Shelter* program. The very short qualitative observation was titled "*Current T-Shelter Development in the Community*". It was presented at the workshop on June 26, 2006.

Survivors worked hard to find all useful properties, repaired them if possible, and cleaned them at nearby streams or river. Even it can be illustrated a mother tried hard to bring together scattered valuable books and school block notes for her kids who would had school examination some weeks to go. All family belongings were pull together under emergency roofed shelter or plastic sheet's tent. Each family tried to save their property from rain and for keeping an eye easy.

Personal belongings, beside its functional use, they also became objects of family life history and identity for the family next generation. (Lovell, 1998: 16) This anthropological perspective shows the importance of belongings as a part of identity of people to immediate social world. (Jeanette, 1998: 157)

3. Shelter for Privacy: A concealed-Shelter

Entering the first week aftermath of the earthquake, the survivors felt tired and needed to devote time to restoring their own emotional equilibrium. Beyond securing the physical belongings such as property and things, survivors wanted to comfort themselves to whom they are most closely attached emotionally. This family emotional feeling is called also (intangible) belongings. (Hays, 1977: 291) Each survivor tried to find privacy within their own family. The word "privacy" can be meant by the quality of being secluded from the presence or view of others, or the condition of not being seen by others. The most basic action to find family privacy is to create a territory for emotional security which can be controlled its access from outsider. Territoriality is an important element of how human is organized in space, such as rooms, buildings, local communities, states or regions, nation-states. (Delaney, 2005: 10-13) What territory for? Territoriality is simply for–a means to satisfying–some more basic family private needs, (Delaney, 2005: 18-19) such as gathering, cooking, sleeping, storing, and others. For survivors, the function of shelter after disaster, according to Sphere (2004: 221) is to provide protection from the climate, security and privacy for individual households, including an establishment of territorial claims or rights.

The most basic type of the shelter for privacy is how to make concealed territory or shelter. The boundary of a territory may be expressed by physical things which easily to be found in the emergency times such as used banner, textiles, plastic sheets, furniture, etc. Supports from external community made them easier and possible to create a basic private-concealed shelter. A week after the earthquake event, many donors/agencies usually came to the vulnerable area and distributed aid including plastic sheets and emergency tents. Some families were able to get a good tent for their privacy. When the need of family privacy was higher, the *gotong royong* became slightly decrease due to the need of working for their owned private family shelter. Technically, it had no external assistant for better shelter construction yet, so that people made the very basic of shelter form for privacy—a concealed shelter. It can be tent, half tent and half plastic sheets, or completely concealed plastic sheets' shelter.

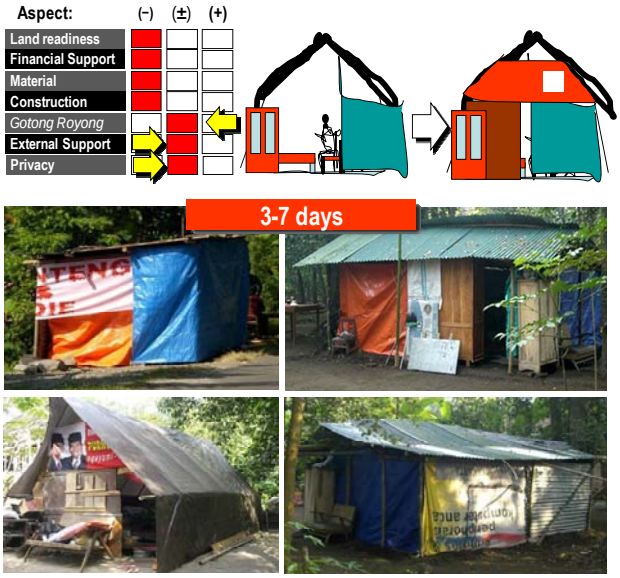

Figure 9 Shelter for Privacy: Concealed Shelter

4. "Recycled Material Emergency Shelter"

Within 2-3 weeks after the disaster, survivors tried to improve the very-very basic "concealed emergency shelter" for privacy, by creating an emergency shelter using recycled materials from ruins or debris of their own damage house. The shelter made from recycled materials, is only possible if there is available materials ready to be reused. When the recycled materials are ready? Two weeks after Yogyakarta's Earthquake, most of survivors did a huge task of clearing debris of their owned damage house. They did not only select components/materials which can be used for the emergency shelter, but also prepared for cleared land for space of the shelter using recycled materials. However, the survivors were still not getting a better shelter construction technique nor receiving financial support from external. Some materials such as plastic sheets may be received by the family as aid supports. As a result there were various forms of "recycled materials emergency shelter". We found a family re-used bamboos, woven bamboo, and thatch roof from their ruined house; other family combined used woods and used zinc roof with new plastic sheets, even often a family utilized a stand-still-walls as vertical enclosures as well as supports for plastic sheet roofs to make private concealed shelter. They did *gotong royong* with really closed neighbors (4-5 families around), with their relatives, or with volunteers who came to them. Survivors did think hard to reuse the house material debris to save money, energy, and time to have improved emergency shelter for their family before better external house support available.



Figure 10 Shelter built with Recycled Materials

5. Emergency Shelter with material from External Supports

Two-three weeks after the earthquake, when a land or part of it ready for shelter, disaster relief donors have also already provided an immediate scheme to support survivors to have emergency shelter. Donors help people to set up their owned shelter by providing material supports to build a temporary shelter. Material supports can be in forms of "a temporary shelter kit" or "a package of materials"—containing plywood, zinc roof, or tin plastic sheets, tarpaulin, wood frame, nails, rope, etc. Sometimes the kit or package was set with a manual to make a temporary shelter. Survivor's families got the kit or package, and then they constructed the emergency shelter by themselves. They could ask their neighbors or relatives to help to build the shelter.

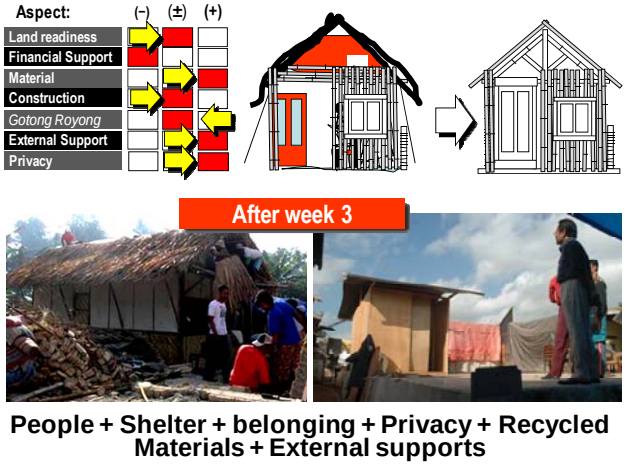

Figure 11 Shelter built with External Supports

They added their owned recycled materials to the "material kits" they got. As a result, there were various types of shelter built using combination of materials from donors and from family own recycled materials. Yet these efforts to have temporary shelters with material supports from donors were still lack of technical assistance to make better shelter secure for aftershock earthquake.

3. COMMUNITY BASED TRANSITIONAL SHELTER

3.1 Government Policy and the Need of T-Shelter

The government of Indonesia adopts two stages of post-disaster recovery: the emergency response phase and the rehabilitation and reconstruction phase. This "one step policy" gives an impact to survivors or community affected by disaster to seek supports to provide transitional living shelter to bridge the gap between emergency shelter and permanent housing. Transitional shelter known as "T-Shelter" has been played an important role to be a useful component in support survivor's living in Transitional period of Java Post Earthquake 2006.

In the case of Java Post Earthquake Reconstruction, by understanding that the government policy moved from emergency directly to the reconstruction of permanent house, and made little allowance for temporary shelter solutions, it raised a question: "*how survivors who lived in around 300,000 houses destroyed by the earthquake did efforts to provide transitional shelter to sustain their living activities after disaster*?" During their waiting for the distribution of government financial support to reconstruct their destroyed houses, it is assumed that around 30 % of more than 300,000 destroyed houses was substitute by T-shelters funded by (most) of International NGOs for all central Java and Yogyakarta Special Province, 10 % by local government, 37 % T-Shelter Construction by Community Owned Sources, and the Rest 23 % combined T-Shelter constructed by Local NGOs, or substitute by Core house, or other permanent houses. (MacRae, 2008: 1995 and Ikaputra, 2009: 39)

3.2 Community based T-Shelter Construction

The improvement of emergency shelter design into better construction led to the ideas of utilizing the shelter as "transitional" living place towards a normal live. There are three aspects in developing and implementing T-shelter in Java Post Earthquake 2006. The three aspects related to design, technical, and implementation aspects. Aspects related to design of T-shelter should consider the minimum necessary requirements, such as minimum floor area for living (18 m2), should accommodate and support the essential house hold activities such as sleeping, eating, and having privacy. To achieve and maintain a healthy internal environment, the T-shelter should have adequate ventilation especially good cross ventilation for tropical climate.

Aspects related to technical issue required its strength and safety to anticipate aftershocks of the 2006 earthquake. Meanwhile considering the life span and shelter cost, most of T-shelter design has been developed by using construction material from local suitable sources especially bamboo and some with palm trees.

Discussing the implementation aspects, almost all of the T-shelter construction was done by the community participation through *gotong royong*. This tradition, which has rural base one, is actually a practice of mutual self-help embedded in the Javanese culture dealt with how people hand-in hand to cope with basic problems of housing, jobs, and social security. (Aldrich, 1980: 272) In the transitional period post earthquake, survivors do automatically *gotong royong* to provide the need of transitional living, with or without external supports. The tradition made easier to donors/agencies or other external supports requesting community based T-shelter construction.

3.3 Commonality of Interest for T-Shelter

A social capital is defined as bonding, bridging and linking relationships that build trust and common interests and the networks that support people within, between and beyond their owned community. (Moore, 2005: 2) The community in the disaster time, according to Handmer and Dover (2007; 60-62) in "*The Handbook of Disaster and Emergency Policies and Institutions*," define a 'community' as a commonality of interest, which holds together, at least at particular times, a group of people and provides the impetus for shared attitudes or actions.

The success in providing living facilities in transitional period post Yogyakarta earthquake is not apart from the fact that there was a commonality of interest among various group of people—not only local community or survivors—who hand in hand working for T-shelter availability. It can be mentioned various actors who played important role in providing the T-shelters such as International and domestic agencies/donors; universities, architects, engineers, professional association and volunteers; Daily newspaper and media; Relatives, neighbors, individual donators, volunteers or companies employee's program on its Corporate Social Responsibility; and of course the local community. The following scheme (See figure 12) can become a reference how some of efforts done by various actors to share their commonality of interest in providing T-shelter whether on behalf of "planned program" or "sporadic non-planned T-shelter" construction.

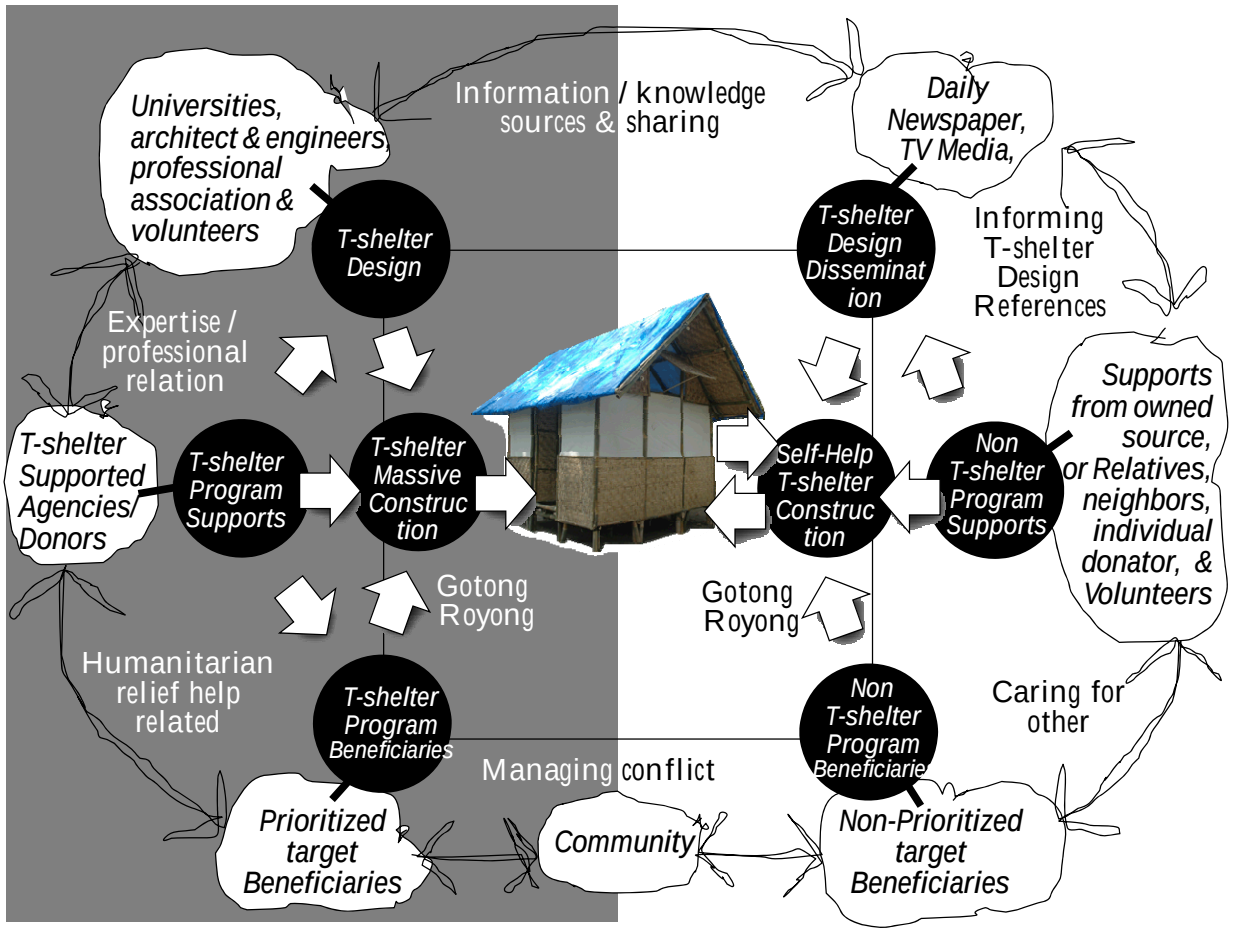

Figure 12 Commonality of Interests among various groups for T-Shelter

4. CONCLUSIONS

The key successes to survive at basic and to strive for normality or to restore livelihood as soon as possible to pre-disaster situation are community self reliant ability, external supports, and government supports.

The existence of the social capital—especially *gotong royong* (mutual work) within the community also helps us to understand the process of survivors to manage various external government or non-government supports, to know how people provide themselves with *poskos*—the community first-aid center, and to share how individuals family make various typology of basic shelters at emergency times, and also to install "Transitional Shelter" before they proceed to better shelter or permanent house reconstruction. The *gotong royong* has been able to build social awareness, sense of togetherness, a sense of feeling of the same boat and tolerance. These local initiatives and practice of *gotong royong* as well as the commonality of interests belong to various groups are believed to be a valuable social capital to make the emergency response and living in transitional period in Yogyakarta post earthquake done very rapid and effective.

Acknowledgements:

I owe a sincere debt of thank to Prof. Ryuzo Ohno (Tokyo Institute of Technology), who makes possible this study to be presented in the conference managed by the Center for Urban Earthquake Engineering (CUEE), thanks to Prof. Erich Lehner and Dr. Ully Herbig (TU-Vienna) for their valuable opinion and input on the study result's report, also to CUEE's secretariat and Rachma San for dealing with invitation, visa, etc. Last but not least, thanks to all people of Yogyakarta who helped me to do field survey and interviewed while we were struggling for Post Earthquake Recovery.

References:

Aldrich, Brian C. (1980), "Formal Neighborhood Social Organization in Five Southeast Asian Cities," In *International Journal of Comparative Sociology* 1980; 21; 268, Published by: SAGE Journals Online at http://www.sagepublications.com.

Auf Der Heide, Erick (1989) "Disaster Response: Principle Preparation and Coordination," In *The Disaster Response Online Book*, ©1989: Erik Auf der Heide Atlanta.

Delaney, David (2005) "Territory: A Short Introduction," Malden-Oxford-Victoria: Blackwell Publishing Ltd

Haas, J. Eugene, et.al. (1977) "Reconstruction Following Disaster," Massachusetts: The MIT Press.

Hays, R. Allen (1977) "Housing," In Vogel, Ronald K (1977) *Handbook of Research on Urban Politics and Policy in the United States*, Published by Greenwood Publishing Group.

IFRC (2008) "Program Update IFRC: Indonesia," *Report Appeal* No. MAAID002, dated 13 August 2008. Source: http://www.ifrc.org/docs/appeals/annual08/MAAID00208pu1n.pdf, accessed on January 10, 2009.

Ikaputra (2006), "T-Shelter Development in the Community," UNDP One-day workshop: *A bridge to Permanent housing*. June 26, 2006, Department of Architecture and Planning Gadjah Mada University.

Ikaputra (2009), "T-Shelter Post Yogyakarta Earthquake 2006: Design Typology and its Implementation," *Journal of Architecture & Planning Studies* (Jurnal Arsitektur & Perencanaan), Vol.3, No.1, April 2009. ISBN 1829-6610, pp. 38-46

IOM (2006), "Emergency and Post Conflict Activities," International Organization for Migration, source: http://www.iom.ch/jahia/webdav/site/myjahiasite/shared/shared/mainsite/published_docs/brochures_and_info_sheets/Infosheet_INO_NIAS_072006.pdf, accessed on January 10, 2009.

Jeanette, Edwards (1998), "The Need for a 'Bit of History': Place and Past in English Identity," In *Locality and Belonging*, Edited by Nadia Lovell. London: Routledge

Kates, Robert W. and Pijawka, David (1977), "From Rubble to Monument: The Pace of Reconstruction," In Book *Reconstruction Following Disaster*. Edited by Haas, J. Eugene, et.al. Massachusetts: The MIT Press.

Lordet, Gilles (2006), "Community Mobilization and Volunteerism prove effective in Yogyakarta Quake Relief," Reported to IFRC on June 14, 2006. Source: http://www.ifrc.org/docs/news/06/06061402/, accessed on January 10, 2009.

Lovell, Nadia (1998), "Belonging in Need of Emplacement," In *Locality and Belonging*, London: Routledge

MacRae, Graeme (2008), "Could the system work better? Scale and Local Knowledge in Humanitarian Relief," *Development in Practice*, Volume 18, Number 2, April 2008. Routledge: Taylor and Francis Group

Moore, Keith M (2005), "Conflict, Social Capital and Managing Natural Resources: A West African Case Study". Edited by Keith M. Moore. Trowbridge: Cromwell Press.

Pelling, Mark (2003), "The Vulnerability of Cities: Natural Disasters and Social Resilience," London: Earthscan Publications Ltd.

SPHERE (2004), "Humanitarian Charter and Minimum Standards," In *Disaster Response*, Published by: The Sphere Project, Switzerland.

Steven, Alan. M., and Schmidgall-Tellings, A. Ed. (2004), "A Comprehensive Indonesian-English Dictionary," Ohio: Ohio University Press.

Sukrismanto, Edi, et.al. (1998), "Framework For An Asean Regional Fire Suppression Mobilization Plan, For Strengthening the Capacity of the Association of Southeast Asian Nations to Prevent and Mitigate Transboundary Atmospheric Pollution**,"** Source: http://pdf.usaid.gov/pdf_docs/PNACW365.pdf, accessed on January 10, 2009.

UNHCR (2005), "Handbook for Self-reliance," Prepared by Reintegration and Local Settlement Section Division of Operational Support UNHCR, Geneva. Geneva: UNHCR.

UNHCR Canada (2008), "Emergency Handbook Notes on Shelter," The UN Refugee Agency. http://www.unhcr.ca/documents/emergency_handbook_shelter_notes.pdf., Retrieved December 20, 2008.

Uni Apro (2006), "UNI Apro and UNI LCJ Mission to Yogyakarta to donate Earthquake victims in Yogyakarta, Indonesia" Report on 26 June 2006.

Ursano, Robert J., Fullerton, Carol S., Weisaeth, Lars, & Raphael, Beverley (2007), "Individual and Community Responses to Disasters," In *Textbook of Disaster Psychiatry*, Edited by Ursano, Robert J., Fullerton, Carol S., Weisaeth, Lars, & Raphael, Beverley. New York: Cambridge University Press.

JOINT CONFERENCE PROCEEDINGS
7th International Conference on Urban Earthquake Engineering (7CUEE) &
5th International Conference on Earthquake Engineering (5ICEE)
March 3-5, 2010, Tokyo Institute of Technology, Tokyo, Japan

HOUSING RECONSTRUCTION AND COMMUNITY

Yoshimitsu Shiozaki

Professor, Department of Architecture, Kobe University, Japan
shiozaki@kobe-u.ac.jp

Abstract: The aim of this paper is to study about the experience of the housing reconstruction process after the Great Hanshin Earthquake and to make clear the way of doing housing reconstruction without losing community.

Housing provision by a public entity usually would be the construction of temporary housing and public rental housing. In the Great Hanshin Earthquake case the strategy of housing reconstruction is called single line housing reconstruction that consisted of evacuation, temporary housing and public rental housing. Although the quality of public rental housing is fairly good and rent is low, some residents complained about the environment of the housing estate and most of them could not accept the location, because they were built in suburban areas far from the residents' home town. Also victims who could enter the new public housing must be selected by a lottery system. This means that they had to live in a new housing situation in a strange place with unfamiliar neighbors. In the end they lost their connection to community and they had a lonely life in their housing units. Many people did not even go for a walk or leave their apartment regularly. Some people died all alone, with no one even realizing that they had passed away.

After the Great Hanshin Earthquake there are some good projects of housing reconstruction, which preserved the former community connections and where people did not suffer from loneliness.

During these 15 years peoples' action created a new system in which government provides some money to victims to build houses. Of course it is not enough for victims. So we have to prepare a better system to deal with a great disaster in the near future.

1. DISASTER MITIGATION STRATEGY

During these 15 years since the Great Hanshin-Awaji Earthquake so many major disasters have occurred in Japan and the world, and it is feared that more disasters will happen in the near future. Particularly Japan is one dangerous area because 10% of major earthquakes over M6 in the world happen in Japan.

The Central Disaster Prevention Committee of the Japanese Government announces that a lot of major earthquakes will happen within the next 30 years with 60% probability. As a counter measure to these earthquakes, the Japanese central government has a target to decrease up to almost half of human and economic damage.

One of the problems of this program is that we can decrease only half of the damage during the next 10 years. The other one is that these counter measures do not have tools to prevent damage after the earthquakes. Major earthquakes bring not only direct damages but also many kind of indirect damages in the process of the reconstruction process after the earthquake itself.

Table 1 Disaster mitigation strategy for the next major earthquakes

	Tokai earthquake		Tonankai / Nankai earthquake		Tokyo eathquake	
	Death (person)	Economic damage (trillion yen)	Death (person)	Economic damage (trillion yen)	Death (person)	Economic damage (trillion yen)
Estimate	9,200	37	17,800	57	11,000	112
Turget	4,500	19	9,100	31	5,600	70

(Source; Central Disaster Prevention Committee,Japan)

2. RECONSTRUCTION DISASTER

Although the number of direct deaths caused by the Hanshin –Awaji Earthquake is 5,502, the number of indirect deaths after the quake is 932, and additionally 804 people have died alone in temporary housing or public housing by 2008. It means that 1700 people and more died after the quake. Housing reconstruction programs and urban reconstruction programs after earthquake have the strong relation to those facts caused by community destruction. Moreover aftereffects of injury, mental damage and economic damage should not be ignored. In the Hanshin-Awaji earthquake more than 10,000 people received heavy injury and not a few people are considered to be a disabled. Nevertheless there has been no survey about these problems during 15 years. In the clean up work of collapsed building a lot of workers were inhaled asbestos particles. Only two persons have been acknowledged as patients of emphysema so far. This disease is considered to appear 40 years later. Also in the U.S. the victims of Hurricane Katrina who moved into trailer house have

suffered from sick houses by formaldehyde. It is said that a similar thing happened in the temporary housing after Sichuan earthquake in China.

We can call these damages after disaster "Reconstruction Disaster", which is avoidable damage for the people who survive disaster itself . It is very important to avoid it for the disaster mitigation which aims to decrease the damage by disaster overall. Housing reconstruction is the most important factor to decrease the reconstruction disaster because housing is a fundamental condition for daily life for everybody.

3. HOUSING RECONSRTRUCTION AFTER THE HANSHIN-AWAJI EARTHQUAKE

In the Hanshin-Awaji Earthquake 104,906 buildings collapsed completely and 144,234 buildings were partly damaged. Housing reconstruction has three steps consisting of evacuation, temporary dwelling and getting permanent housing. After the Hanshin-Awaji Earthquake three programs had been taken, as evacuation shelter, temporary housing and public housing. As it lacked any other wide range support of housing reconstruction we call it a single line program.

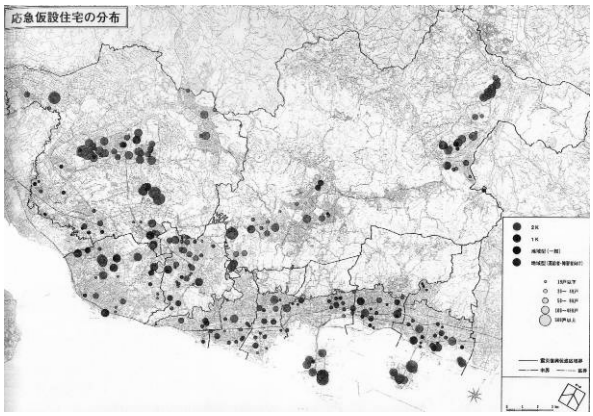

Figure 1 Geographical distribution of public temporary housing

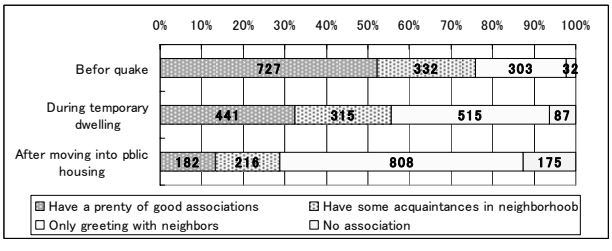

Figure 2 Community change of public housing inhabitants

38,600 units of public housing for victims as permanent housing were built, most of which were located in the area far from affected victims' home town. As the housing unit itself is new, stable and well equipped, almost all inhabitants were satisfied with this situation. Also they were satisfied with the rent of public housing which is fairly cheap. Some people complained about the location of their housing that stands by express highway or in the area far from their home town.

The biggest problem of public housing is that residents can not preserve their local community in which they live before the earthquake. There are many inhabitants of public housing who lost the relationship with their neighbors and friends, and who do not go out of their housing units and do not talk to anybody in one week or more. The worst case of this situation in public housing will be "solitary death". The number of solitary deaths in the temporary housing is 236 and that is 568 in public housing, the total number is 866 by the end of 2009.

Apparently the solitary death is caused by losing community in the reconstruction process not by the natural disaster itself, which can be avoided by a successful reconstruction system. So we can call it "reconstruction disaster".

For the situation of community lost in the public housing the local government has created a observation program by Life Support Advisor (LSA). However it seems effective partially, and could not solve the problem completely.

4. SELF HELP TEMPORARY HOUSING IN KOBE

We can say that community loss was caused by the single line program of housing reconstruction. So in this sense it is important to find out other ways. One of them is self help temporary housing in Japan and the other one is the core house system in Indonesia.

After the Hanshin–Awaji Earthquake not a small number of victims constructed self help temporary housing which can be counted up to 5000 buildings. The self help housing on average were constructed with a cost of 9 million yen and has 65 m2 floor space right after the quake and exists for over 10 years. They are very useful for the victims who wanted to restart their life and small business. As they were built on the former lots of course, victims did not lose their communities. They have been used through maintenance and reform.

This self help housing was constructed by individual power without any public support. Public temporary housing under the law was constructed by the local government with the cost of 4 million yen for one unit, which can be counted

	Public temporary housing	Self-build temporary housing
Institution	Disaster aid act	None
Construction Cost	$40,000(inc. demolition cost)	$90,000 (average)
Floor space	19㎡～26㎡	65㎡ (average.)
Living level	Lower than minimum standard	Good
Location	Far from home town	Home town
Selection of unit	Lottery	Self-decision
Using term	2-5 years	10 years and more
After using	Demolition	Repair or remodel
Community	Collapse	Safe and contingence

Table 2 Comparison of public temporary housing and self-build temporary housing

as 48,300 units totally. As they should have been abolished after the period of use, there is no housing stock. In the end, our government spent a large amount of resources.

In the comparison of public temporary housing and self help temporary housing the latter is better for reconstruction after quake. If there were some support for self help temporary housing, more people would try to take this path. Actually almost 25% of residents of public rental housing lived in their own occupied housing before the quake.

5. CORE HOUSE IN JAVA ISLAND

There is a unique self help housing system on Java island of Indonesia, called the core house system. The mid-Java earthquake happened of May 2006, and hit Yogyakarta city and the surrounding rural area. It caused 5,716 deaths and 190 thousands of buildings were damaged.



Figure 3 Construction of core house by local people supported by university

The core house system is a way to get temporary and permanent housing through building small houses with reinforced concrete structure at first after evacuation, which has only 18 m2 floor space and expands to twice and three times as big a house according to getting more money step by step. The initial cost of building material was supplied by domestic and international NGOs, and construction work was covered for each other by neighbors in the village. The cooperative system in which people support each other in agricultural work and house construction etc. is traditional in Indonesian society, called “Gotong Royong”.

On the other hand construction technology to build reinforced concrete buildings was taught by university professors or engineers and students supervised the construction process. In many universities in Indonesia introduce the KKN program, in which every student must take experience in a local area for two months before graduation. So we can see many students who work voluntarily in affected areas. Some students were involved in core house building as a supervisor.

Core house is a small house but it needs some space for the lot. Many affected houses are located in rural areas where each household has pretty large lots. So they could make core houses on the vacant land in their lots.

The core house system is a very logical method to support temporary and permanent dwelling for victims to fit local conditions in Indonesia. We can lean this lesson and should prepare a similar system under the Japanese condition.

6. SUPPORT PROGRAM FOR SELF RECONSTRUCTION

From the lesson of the Hanshin –Awaji Earthquake reconstruction, it is best to reconstruct housing on their lots for victims. So we have to prepare a supporting system for every victim to get new housing this way.

The supporting act for disaster victim life of 1998 after the Hanshin-Awaji Earthquake was amended in 2007 completely to allow victims to use subsidized money from the central government to reconstruct new housing. The amendment of the act provides up to 3 million yen for the victims who lost their house completely. The new program is very effective to support housing reconstruction.

Noto Peninsular Earthquake in Ishikawa prefecture in 2007 brought complete damage of 684 buildings and partial damage of 1,732 buildings. In Wajima city 250 units of temporary housing were constructed and 539 people lived there. To transition to permanent housing, at first 72 households in the temporary housing wanted to move to public housing, however after introducing the new supporting system 26 households chose instead to construct their own house using the subsidy without moving to public housing.

In Ishikawa prefecture victims can receive not only 3 million yen from the central government but also 1 million yen from the local government, 1.7 million yen from donations and 2 million yen from a special subsidy program of local government. In all they can get up to 7.7 million yen, which covers almost half of the total cost (approximately 15 million yen) for a new standard house in this area. So if they can borrow the rest from relatives or a bank, they can build their own house and not live in public housing.

Another tool to help the self reconstruction of disaster victims is the provision of low cost housing of 100,000 yen per m2 by an NPO. This system can provide a new house with 50 m2 floor space for 5.5 million yen or 90 m2 floor space for 10 million yen. This is still a new pilot project. If it will be popular, the cost will be so much cheaper that it presents a broad way for victims to reconstruct by themselves on their former lots.

There is one more good experience in Kashiwazaki city that Chuetsuoki earthquake hit in 2007. While generally public temporary housing is built with light steel construction, here there is some temporary housing built with a wooden structure. The temporary housing was very comfortable even in summer and winter because of wooden material. One victim liked this housing and got this one as permanent house through negotiation with the city government. The reuse of temporary housing to permanent house is a very wise way to conserve resources. We should



Figure 4 Reuse project of wooden temporary housing in Kashiwazaki city

prepare such a program as a temporary housing reuse system from the first stage of the reconstruction process.

7. DESIGN FOR PUBLIC HOUSING

Although in my opinion self reconstruction is the best way for victims, there are more than a few victims who depend on public housing because of lack of money and of land. As public housing is constructed by public money, the planning and design of housing and allocation system tends to take a bureaucratic approach which contributes to the loss of former community by making a different environment from the former house and neighborhood of victims.

To avoid losing community, the following two points are important;

1) New housing should be located in the area not far from the former neighborhood,

2) Former relationship between neighbors should be secured in the new housing estate.

The second point suggests the principle of planning and design for public housing to preserve the community. In the case of the Chuetsu earthquake in Niigata prefecture semi-detached wooden house is provided as reconstruction public housing in the area near the former village. Following the experience of Tsukiji area and Wakamiya area in Hanshin-Awaji earthquake, we can say that apartment houses should be under 30 units in one building and in less than 5 stories.

8. CONCLUSION

We should understand the reconstruction disaster which occurs after the disaster itself. The reconstruction process can cause great damage in addition to that which occurred directly due to the disaster. To decrease the disaster damage we should avoid reconstruction disaster and prepare good programs for housing reconstruction that can secure the former community. It should consist of supporting systems for the victim to recover their houses on their own lots and good planning and design for public reconstruction housing which avoids the loss of community.

Of course we can not discuss every issue about avoiding reconstruction disaster. The other issues are for instance urban reconstruction programs that do not cause community disruption in high density areas of major cities and revitalization programs for rural areas after disaster. Also it is important how to make good community in the village in the case that affected areas can not be recovered due to geographical destruction. There are many different issues involved in avoiding the reconstruction disaster.

References:

Shiozaki,Y (2009) “Housing Reconstruction and Community”, Nihonkeizaihyoron sha Inc.

Shiozaki,Y, Nishikawa, E and Deguchi, T (2005) “Lessons from the Great Hanshin Earthquake”, Creates Kamogawa, Inc.

JOINT CONFERENCE PROCEEDINGS
7th International Conference on Urban Earthquake Engineering (7CUEE) &
5th International Conference on Earthquake Engineering (5ICEE)
March 3-5, 2010, Tokyo Institute of Technology, Tokyo, Japan

HUMAN FACTORS IN PREPARATION OF EARTHQUAKE DAMAGE MITIGATION

Haruyuki Fujii

Associate Professor, Department of Architecture, Tokyo Institute of Technology, Japan
hfujii@arch.titech.ac.jp

Abstract: This paper reviews, with respect to the constructive methodology, the human factors that have influence on the preparation in the earthquake damage mitigation. The notion of the human factors, in this paper, refers to actions and the attitudes that encourage or discourage one to perform the actions. It is investigated how the preparation by ordinary people, who are not specialists of earthquake engineering, can be facilitated.

1. INTRODUCTION

The objective of this paper is to review the human factors in the earthquake damage mitigation. It depends on the people who have influence on an earthquake damage mitigation system that the system works well or not. Not only the specified people who work for the system but also an unspecified large number of people have such influence. For effective mitigation, the influence of the general public could not be ignored. The final goal of this study is to design an preferable way of effectuating the management of the earthquake damage mitigation. This paper describes a constructive methodology of designing and explains how the human factors are considered with respect to the model.

2. CONSTURCTIVE METHODOLOGY

The constructive methodology is a general framework abstracting methods of creating artifacts, such as a building, an appliance, a social system, and so on. We are going to apply the methodology to an activity of designing effective courses of actions towards the preparation in the earthquake damage mitigation.

2.1 A Model of Designing

The notion of design refers to an activity of forming a new schema coupling things and its assigned significances as well as of embodying the schema in a certain artifact, concurrently. A schema describes the constitution of an artifact, the mechanism how the artifact brings about certain situations, and the course of events where the artifact is embodied. Beliefs about the causalities related to the things or the patterns emerged from the things are employed to determine the features of the schema and those of the artifact. The immediate products of design are a new schema and an artifact as an instance of the schema. The indirect products of design are the expected phenomena as instances of the given significance and the unpredicted phenomena as secondary effects. The secondary effects could be either favorable or not. If the effects are favorable then they may be expected explicitly in the succeeding design. If not, the schema and the artifact are improved so as not to bring about such phenomena.

A scheme of the preparation in the earthquake damage mitigation is (1) to predict the damages without any preparation, (2) to abstract the causalities between the features in non-prepared situations and the earthquake damage from the result of the prediction, (3) to find, on the basis of the causalities, the features to be improved so as to mitigate the predicted damage, (4) to conceive actually the way to improve the features, (5) to predict the damage of the improved situation, and (6) to repeat step-2 to 5 until a promising plan to prepare for earthquake damage. It should be noticed that the cycle described above would not end since the situation is always changing.

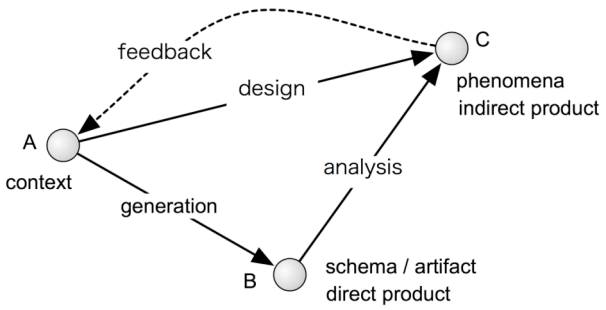

Figure 1 F-Triangle Model of Designing

An image of design is depicted in figure 1. Design is the combination of generation and analysis. The two processes are performed sequentially or synchronized with each other. In generation, a scheme of the artifact that is

expected to have the potentiality to change the current situation into preferred one is formed. Generation produces a course of actions to embody the artifact, too. In analysis, it is predicted what if the artifact is embodied and implemented in a particular environment to let the artifact interact with the environment. The beliefs about the nature of law are used as grounds for the prediction. If it is convinced that the artifact has the expected potentiality based on the consequence of prediction then design finishes. A course of action to change the current situation into preferred one is determined. If not, the schema of the artifact and some beliefs are modified to fill the gap between the preferred situation and the predicted situation. The figure emphasizes that the products of design are not only an artifact but also some phenomena brought about by using the artifact.

Design is constructive. The crucial nature of design is that a new schema has to be formed on the basis of the current beliefs and hypotheses about the nature of law. The beliefs and hypotheses are constructed without the new schema. They will probably be modified when the interactions between an artifact with the schema and its environment are analyzed. If the schema is not consistent with the modified beliefs, the schema loses some of the grounds. It is hard to consider all of important aspects prior to generation. Some aspects that have not been noticed are found to be important through the interaction. Therefore, the concurrent cycle of generation and analysis is repeated until design is almost completed. This means that design is constructive and has dialectic nature.

2.2 Constructive Methodology of Designing

The constructive methodology is the repetition of a constructive cycle whose constituents are the following three sub-processes, i.e., *generation*, *analysis*, and, *focusing*. Figure 2 shows the constructive cycle.

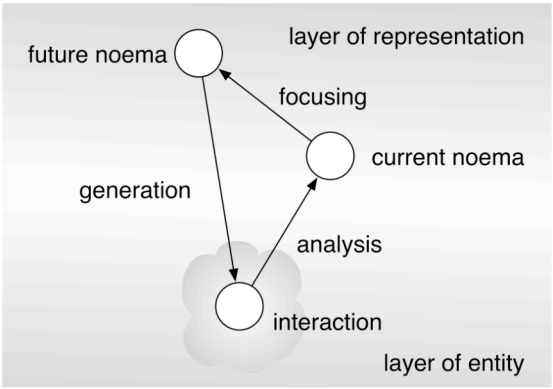

Figure 2 Constructive Cycle (FNS-Diagram)

The generation process is the process of externalizing the designer's internal representation of the artifact to be made and the situation that emerges as the consequence of the interaction between the artifact and the environment. We call such representation as *future noema*. The designer operates on the substances in an empirical world and the world changes as responding to the designer's operations. The internal image of the artifact is embodied in the world and interacts with its environment, which is made of the other constituents in the world. Deductive inference is employed to predict or expect the consequence of making the artifact on the basis of the causality between particular features characterizing the artifact and the changes in a part of the world. The causality doesn't necessarily have to be correct and objective as scientific knowledge. It can be a subjective assumption by the designer. Of course, it is preferable that the causality is correct, though. The ability to express one's internal image and the ability to act so as to actualize the image play important roles in the generation.

The process of analysis is the process of observing the interaction between the embodied artifact and its environment and of analyzing the things in common and differences between what is going on as the consequence of the generation process and what is expected before the process. We call the representation of the things currently observed as *current noema*. If the recent future noema and the current noema are similar, the generation is considered to be successful. If the differences between the recent future noema and the current noema are significant, the rationale for the differences will be searched. The aspect that the designer has in advance affects the observation and analysis. The aspect may be changed for the rationale of the unexpected consequence. In other words, the situation is re-interpreted. The rationale and the new aspect facilitate the succeeding process of focusing. The ability to observe the phenomena existing before one's eyes and the ability to abstract an underlying pattern from the observed phenomena are required in analysis.

The process of focusing is the process of selecting the design features to operate in order to resolve the differences between the expectation and the current consequence. The designer's belief on the causality that implicates the operation on the variables as the resolution of the differences is employed for the selection. It doesn't matter if the causality is subjective assumptions or objective laws. The direction of improving the current artifact is determined. The internal representations of revised artifacts and the situations provided by the artifacts are made. A promising one is selected as the artifact to be embodied in the succeeding generation process. Then, the next cycle of generation, analysis, and focusing starts. The ability to conceive flexibly alternative options in the ways towards a goal and the ability to judge what to do are essentials for focusing.

The cycles are continued as long as the designer seeks for the ways to change the existing situations into preferred ones.

3. HUMAN FACTORS IN PREPARATION

The situations where an issue concerning human factors comes up are as follows. We characterizes the human factors in terms of the actions to prepare against disaster, the attitudes affecting the actions, and the abilities related to the actions and attitudes.

3.1 Actions of Preparation in Mitigation

A lot of manuals to prevent or mitigate damages by earthquake and post earthquake disaster are issued. Some of them are for the specified people, while the others are for the other unspecified people. In these manuals, the actions for preparation in earthquake damage mitigation are classified into three groups, i.e., self-help, mutual-help, and public-help. The balance in the gravity of each of the groups differs with respect to the target of the manual. However, none of them can be out of consideration since the actions in the different groups interact with one another. For example, if a person is prepared enough to prevent fire damage and the preparation works well in the case of fire – self-help -, the salient load upon the fire fighting system – public-help - could be decreased. On the other hand, since there is a good fire fighting system, people can concentrate, through self-help and mutual-help, on complimenting the system and increasing its effectiveness. Otherwise, they have to prepare everything by themselves.

The followings are well-known examples of the self or mutual-help actions contributing the earthquake damage mitigation.

1) To Live in a Safe Place

It is desirable, from a point of view of the earthquake damage mitigation, to live in a safe area and in a safe building if no inevitable circumstances exist. Statistics of the past earthquakes shows that if a strong earthquake occurs, many people are crushed to death by collapsed buildings. Even though a building is strong enough not to be destroyed by an earthquake, it might collapses by a tsunami or a landslide if it is built near the seashore or near a cliff, respectively. In the similar sense, a densely built-up area with buildings made of inflammable materials. However, it is reality that some people choose to live such a place or building because of their occupations, financial situations, and so on. In a certain area, the fishermen and their family wish to live near the seashore since the access to the sea is better than the other places.

2) To Secure Furniture so that it won't Fall Over

It is encouraged to secure furniture so as not to fall over easily. This action decreases the possibility of being hit or caught by Statistics says that a lot of people were killed by collapsed furniture. In a super high-rise building, it is predicted that the shaking can be stronger than that on the ground because of the building's flexible structure. To encourage this action, some local governments or public bodies support the residents to get devices to fasten furniture. The aesthetic design of the fixing devices might encourage or discourage people to use them. If the device fits the furniture or the room where the device is to be used, the possibility that the device is adopted may increase. For the people living in rented houses, the conditions about restoration of the houses in the contract may have an influence of the action to secure furniture. The tenants would tend to secure furniture is the obligation of the restoration is not too much.

3) To Store Foods and Water for Emergency

It is important to store foods and water for emergency. An earthquake would destroy the lifelines such as domestic water supply, energy supply, food supply, communication, and so on. People are obliged to live in an isolated place since they are cut off from the supply systems. It is estimated that a few days are required to restore electric power supply system and that a couples of weeks are required to restore domestic water supply system. For the first few days after an earthquake attack, the foods that can be eaten without cooking, such as canned or retort pouch foods, are recommended to be stored. For the next few days, the easy-to-cook-and-eat foods are recommended. In addition, the situation that tableware cannot be washed up because water supply is not completely restored. In these days, most of all houses and public facilities may store foods and water for emergency. In the latter, it is important to make a plan to distribute the foods and water in the circumstance just after an earthquake.

3.2 Burdens Discouraging the Preparation

1) Lack of the Sense of Crisis

Needless to say, the sense of crisis affects the actions to prepare for the earthquake damage mitigation. If one has an adequate sense of crisis, the one would be motivated to prepare for the crisis. If one has a week sense of impending crisis, the one is likely to lack motivation for the preparation. In this case, the sense of crisis would be amplified if the people become to be able to image what really happens after a big earthquake. It is a promising way to learn a lesson from examples of the past earthquake damage mitigations.

If the lack of the sense of crisis arises from the normalcy bias, the things are not so straightforward. One with the normalcy bias tends to avoid facing an undesirable disaster and to underestimate the possibility of the disaster and the consequences of it. In this case, it might be better to encourage the one with normalcy bias to prepare for earthquake damage without threatening the one with the past earthquake disasters. Since it is said that an undesirable situation may cause the normalcy bias so as not to face the reality.

2) Lack of the Responsibility of Ownership

In addition to the sense of crisis, the responsibility of ownership affects the actions to prepare for the earthquake damage mitigation. Even though one as the sense of crisis, if the one lacks the responsibility of ownership, the one tends to be dependent on someone and to consider that someone would prepare instead of the one. This tendency may discourage self-help, may produce so called a free rider on the mutual-help system, and decrease the effectiveness of the system.

If the lack of the responsibility of ownership comes from the same origin to the lack of the sense of crisis, it may increase the responsibility of ownership to learn a lesson from the past cases that the one with the responsibility of ownership is likely not to be embroiled in unexpected situations and that the one without it would face severe situations.

2) The Sense of Helplessness

The sense of helplessness may override self-help and

mutual-help motivated by the sense of crisis and the responsibility of ownership. If one thinks that it is a useless attempt to prepare for a strong earthquake, the one might give up trying to decrease earthquake damage. It is important in order to avoid the sense of helplessness to have a real feeling that an earthquake damage mitigation plan does work. Again, one can learn a lesson from the past successful examples. In addition, learning a lesson from the current situation is helpful. If one experience personally the situation that let the one image the effectiveness of the actions for earthquake damage mitigation, the one would be encouraged to perform the actions actually.

4. CONSTURCTIVE METHODOLOGY - REPRISE

As described above, the constructive methodology can be applied to the preparation for earthquake damage. One of the most important things in this methodology is to do something actually – generation –, to observe the result and the consequence of the generation – analysis, and to focus on the promising features to improve the succeeding course of actions – focusing -. If the constructive cycle creates the spiral in which the sense of crisis and the responsibility of ownership are enhanced and the sense of helplessness is reduced, the actions to decrease earthquake damage would be promoted.

4. CONCLUSION

This paper reviewed the human factors in earthquake damage mitigation and discussed a way to eliminate the mental burdens and to encourage the actions for the damage mitigation with respect to the constructive methodology

References:

Fujii, H. (2009), "Nature of Design from an Architectural Point of View," *Special Issue of Japanese Society for the Science of Design*, **16-2**(62), 27-30.

Nakashima, H. (2009), "Design of Constructive Design Process," *Special Issue of Japanese Society for the Science of Design*, **16-2**(62), 7-12.

JOINT CONFERENCE PROCEEDINGS
7th International Conference on Urban Earthquake Engineering (7CUEE) &
5th International Conference on Earthquake Engineering (5ICEE)
March 3-5, 2010, Tokyo Institute of Technology, Tokyo, Japan

SPATIOTEMPORAL DISTRIBUTION OF RAILROAD USERS FACING DIFFICULTY IN RETURNING HOME AFTER A DEVASTATING EARTHQUAKE

Toshihiro Osaragi[1] and Ikuko Otani[2]

1) Associate Professor, Graduate School of Information Science and Engineering, Tokyo Institute of Technology, Japan
2) Graduate Student, Graduate School of Information Science and Engineering, Tokyo Institute of Technology, Japan

Abstract: To develop measures for minimizing human damage from a devastating earthquake, it is important to understand the characteristics of the population and its spatiotemporal distribution in an urban area. In the present paper, a model is constructed that simulates the route selection behavior and the transfer choices of railroad users using a geographic information system. The spatiotemporal distribution of users is estimated by applying the model to the Tokyo metropolitan area, using data collected in a person-trip survey. Some numerical examples using the proposed model are shown for detailed disaster prevention planning. In particular, the number and the spatiotemporal distribution of people with difficulty returning home are discussed.

1. INTRODUCTION

In recent years, interest in disaster prevention planning for a devastating earthquake directly below Tokyo has grown, and numerous investigations and studies have been completed that estimate fatalities from such an event. Most previous estimates of human casualties have been estimated based on static population distributions, such as the daytime population distribution or nighttime population distribution obtained from the national census or other sources. However, the actual population distribution varies hourly, and the degree and spatial distribution of human damage are closely linked to the time when the disaster occurs. In particular, the temporal variation in the number of railroad users is extremely large in Tokyo metropolitan area, and cannot be ignored. Consequently, the purpose of the current research is to build a model for estimating the spatiotemporal distribution of railroad users using data extracted from the Tokyo Metropolitan Area Person Trip Survey of 1998 (hereafter referred to as "PT data"), and thereby develop a detailed understanding of the temporal and spatial variations in the number of railroad users.

The advanced model developed in the current study examines the spatiotemporal distribution of people that would encounter difficulty in returning home after a disaster. In addition to the number of individuals with difficulty returning home, the people that remain within the city are also considered in the model. To demonstrate the ability of the constructed model to estimate detailed attributes and anticipated information, the current study includes individuals with a high possibility of remaining in the city in need of support, and discusses the spatiotemporal distribution of these residents in case of disaster.

2. METHODS OF ESTIMATION

2.1 Previous Research

As part of transportation planning, civil engineers have previously conducted research about railroad users (Morichi et al. 2001, Iwakura et al. 2000, Harada et al. 2002). These studies are focused on alleviating rush hour congestion in urban transport regions, and provide the elemental research that supports policy options for leveling out the volume of railroad users at peak times in high traffic time zones (Iwakura et al. 2000). The analyses include the effects of a flex-time system, peak-pricing, and charges per used time zone. However, the users' detailed attributes have not been previously evaluated because the research has focused on the number of railroad users during morning rush hour. Furthermore, although methods of forecasting spatiotemporal user demand have been developed, the forecasting of time-specific user demand has not been sufficiently ad-dressed (Harada et al. 2002).

In contrast, Toriumi et al. (2008) examine impacts on railroad users in the event of an earthquake with an epicenter directly below the Tokyo metropolitan area, using the model developed by Taguchi (2005). Although Toriumi et al. (2008) examine each railroad's temporal movements, their methods differ from the method employed in the current study. That is, their examination is limited to railroad users with commuting passes, using the Metropolitan Transport

Census (2000), and detailed user attributes such as gender, age and occupation and purpose of movement cannot be obtained through their method.

2.2 Features of Proposed Model

A large number of route choice models have been developed over the last few years for route choice in public transit systems and path choice within transit stations. Most of these approaches are based on discrete choice models (Bovy and Stern 1990, Caspar et al. 2007). In the present paper, a model was constructed to estimate the dynamically varying spatiotemporal distribution of railroad users based on their detailed attributes provided in the PT data — i.e. to answer the questions "what types of people (attributes such as age and sex) use the railroad, at what time, in which sectors (position coordinates), and for what reasons (purpose)?" More specifically, position and time information for the departure/arrival railroad stations are extracted from PT data. Based on that information, time specific position information is estimated for railroad users by recreating spatial movements on railroad lines using Geographic Information System (GIS) network analyses. Figure 1 provides the details of estimating the spatiotemporal distribution of railroad users using the present model.

A part of the information provided in the PT data is listed in Table 1. Using PT data, the railroad user position and time information for the departure/arrival stations can be determined. However, the accuracy of time information is not so high and time necessary for transit is unknown. Therefore, the route and transfer stations taken by the user between the departure and arrival stations cannot be directly determined. Thus, the model selects the route that "minimizes the cost of movement (time-cost)" as the spatial movement of railroad users. Route selection by railroad users may be affected by factors such as waiting time before train arrival, physical fatigue, the psychological burden of changing trains, and the base fare payments that arise from transferring among lines under different management (operators). Although changing trains is generally accomplished at one station or between stations with the same name, there are users that change trains by walking to a station located within close proximity of another (walking transfer). The various resistances that arise from needing to transfer between trains are converted to time-cost values and incorporated into the model. The following discussion outlines the specific method for describing time-cost.

For movement along a single train line, movement time is estimated based on the distance between stations and the railroad velocity, and considered to be the "railroad movement cost." However, train velocity will vary among train lines. Thus, a model describing the railroad velocity is developed using the average distance between stations for each line, as shown in Figure 2.

To accommodate transferring between lines, the movement time on the station premises, the waiting time for train arrival, and user resistance to changing trains (i.e., the psychological burden of changing trains) are converted to time-cost values, and the total values are taken to be the "in-station transfer cost." However, movement time at a station depends upon the size of the station, which is indicated by the number of connected lines. The in-station transfer cost is set for links connecting the representative boarding/disembarking points for lines under the same operator with the same station name (corresponding to different platforms). The representative points are assigned as the center of gravity for a group of boarding/disembarking points, which correspond to the station representative points for each operator.

Furthermore, the movement time between stations of the same name with different operators, and resistance to changing trains between operators (base fare resistance) are converted to time-cost values, which are then totaled as the "inter-station transfer cost." The inter-station transfer cost is set for links that connect between representative station points for lines with the same station names under different operators.

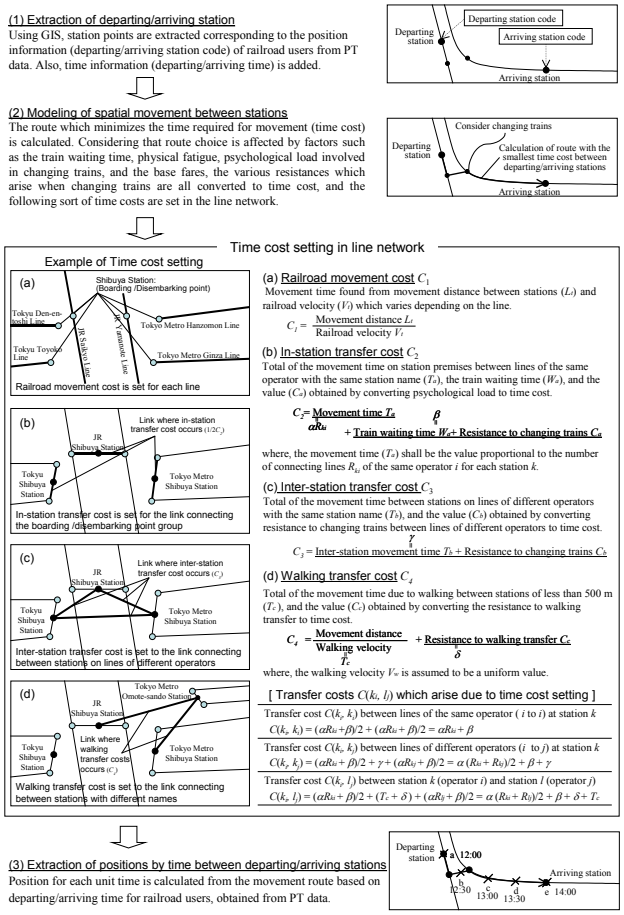

Figure 1 Model for Estimating Spatiotemporal Distribution of Railroad Users

Table 1 Outline of Person Trip Survey (PT data)

Regions subject to survey:	Tokyo, Kanagawa, Saitama, Chiba and Southern Ibaraki Prefectures
Survey time and date:	One weekday, excluding Monday/Friday in October–December of 1998
Object of survey:	Persons living within the region, extracted/selected from persons at least 5 years old
Sampling:	Random sampling based on census data (1,235,883 persons from 32,896,705 persons)
Valid data:	883,044 samples (mean weighting coefficient is around 37.3 (= 32,896,705/ 883,044))
Content of data:	Personal attributes, departure/arrival time and location, purpose of trip, means of trip, etc.
Purpose of trip:	One of the 18 purposes for each trip
Means of trip:	One of the 15 means for each unlinked-trip, one or more means for each trip

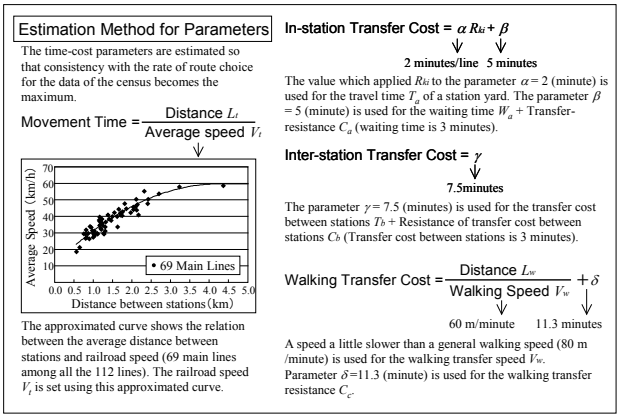

Figure 2 Time-cost Parameter for Railroad Networks

In addition, walking time between stations with different names and resistance to walking transfers (resistance that results from the necessity of walking a long distance) are also converted to time-cost values, and those values are totaled to represent the "walking transfer cost." A walking transfer cost value is set for links connecting representative station points where the distance between stations with different names is 500 meters or less.

The waiting time cost might vary for passengers, depending on their departure times and their egress time from transit lines. Also the walking-transfer resistance might be higher for elderly people. Although all the parameters used in the model might vary between different trip characteristics and age-groups, they are assumed to be constant for the model's simplicity.

2.3 Estimation of Model Parameters

The Metropolitan Transport Census data provides information concerning the use of transfer stations. The information is derived from commuters' monthly-passes, by which they can travel on the specific lines and transfer on the specific stations. Based on these data, transit choices are identified and are constructed as measured values (referred to as the "real value") using the following method. After applying the method, all transfer routes between Station A and Station B are extracted, and represented as R_i (i = 1, 2,⋯, n). Furthermore, the probability of choosing any one of these routes is represented as C_i (i = 1, 2,⋯, n) ($\Sigma_i C_i$ = 1.0). In sum, for multiple routes available as user choices for movement between Station A and Station B, and for which the collective time-costs are approximately equivalent, the ratios of choosing these routes are equivalent. In contrast, when a particular route has a minimum collective time-cost, the ratio of choosing the particular route is close to 1.0.

The route estimation model is calibrated using the following method. Railroad user movement routes are estimated based on the above model, and the model parameter is estimated using the steepest descent method to enhance coincidence with the movement route choice ratio. The data for movement among stations on the same line are not included in the calibration of the model, because they do not include the information about transfer stations and do not contribute to the calibration.The estimated values of the time-cost parameters after model calibration are shown in Figure 2. Given that resistance to changing trains at one station is low, whereas resistance to changing trains between different stations and walking transfers is high, users are tolerant of transfers among trains under the same operator, and tend to select routes that do not require additional initial fares or walking transfers.

2.4 Validation of The Estimated Model

The estimates generated by the calibrated model show that more than eighty-two percent (82.9%) of transfer movement routes were correctly extracted from the Metropolitan Transport Census data; when the data were weighted and converted to reflect user numbers, ninety-four percent (94.0%) of the routes were correctly estimated. To confirm compatibility with other statistical data, the following validations were completed.

Movement routes are calculated using data for all railroad users (number of trips: 497,835). Based on this, a comparison of the estimated value of the number of users per day for stations with multiple connected lines (155 stations) and stations with one connected line (918 stations) with the statistical values reported in the Urban Transport Yearbook (Institution for Transport Policy Studies 2003). The results are shown in Figure 3. There is a strong correspondence between the estimates derived from the model and the statistical values, indicating that the model can reproduce the actual spatial movement with comparatively good precision.

Validation of elapsed time for trips was conducted by comparing the time estimated by the model and based on the PT data. The average margin of error for the actual time minus estimated time is – 3.6 minutes, and the standard deviation is 11.3 minutes. Although standard deviation is somewhat large, the actual time and the estimated time are compatible and reflect accurate results.

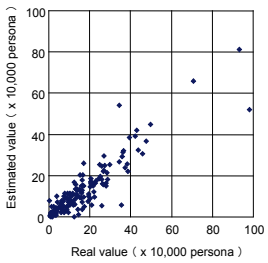

Figure 3 Fitting of The Estimated Model

3. RAILROAD USERS WITH DIFFICULTY RETURNING HOME

3.1 Method for Estimation

Previous research on the difficulty of residents returning home in the event of a disaster evaluated the city's measures for damage prevention, and considered the history and experiences of residents during previous catastrophic

disasters (Nakabayashi 1985, 1995). The Tokyo Metropolis published a report regarding damage forecasts for earthquakes occurring directly below the city (Tokyo Metropolis, 1997). In the Tokyo metropolitan area, a large number of people are traveling for variety of purposes within a one and half hour's distance from home using rapid transit railways. In the event of a major earthquake, public transportation including buses is expected to be paralyzed and unavailable for transport, leaving an extremely large number of people in the city and with difficulty returning home. In the event of a major earthquake, automobiles including buses must stop on roadsides for preventing collateral disasters. Many roads are expected to be damaged and blocked by collapsed buildings and traffic signals will be turned off. The government assumes therefore that there is no alternative way, excepting walking, to get home. This is the same in areas where a dense network of bus route is available.

The spatiotemporal distribution of persons with difficulties returning home was estimated by anticipating which users remain without transportation home in the event of an earthquake based on the data contained in Tokyo Metropolis (1997), as shown in Figure 4. More specifically, the ability or difficulty in returning home was determined in accordance with the distance required to return home, which was set as the distance to the center coordinates of his/her residential zone (a spatial unit of PT data) based on the time-specific position coordinates of the railroad users calculated in the previous chapter. The time-specific position coordinates for low-use time periods are represented as the center coordinates of the residential zone. In actuality, the distance that a person can traverse by walking home differs depending on the time of earthquake occurrence and the degree of damage. However, at present an individual's evaluation of whether the return home is feasible cannot be anticipated. Therefore, a simple historical method is used. In addition, the figures in the current study focus only on railroad users, and address markedly fewer individuals than studies focusing on all persons who are outside their homes during a disaster. However, many of the individuals outside their homes that are traveling a farther distance are railroad users, and this estimate is important to include in disaster planning.

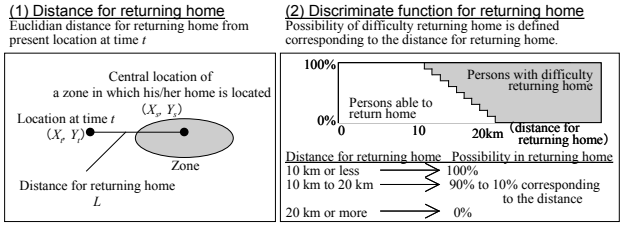

Figure 4 Definition of Persons with Difficulties Returning Home

3.2 Railroad Users with Difficulty Returning Home

The number of persons with difficulty returning home abruptly increases between 7:00 and 9:00, and gradually decreases from 18:00 to 24:00 (Figure 5, left panel), with a maximum (approximately 4.2 million users) reached at approximately 14:00. Riders at the peak account for approximately 45% of all railroad users who would have difficulty returning home in the event that an earthquake interrupts transportation. Figure 5 (right panel) shows that many people are in the process of traveling to a destination in the morning and evening. Particularly the evening, accommodations would need to be provided for travelers experiencing difficulty returning home. The spatial distribution (Figures 6 and 7) confirms that users that would experience difficulty returning home are distributed along railroad lines in the morning, and spread out from the city center to the west side during the day. At night, many remain in the city center.

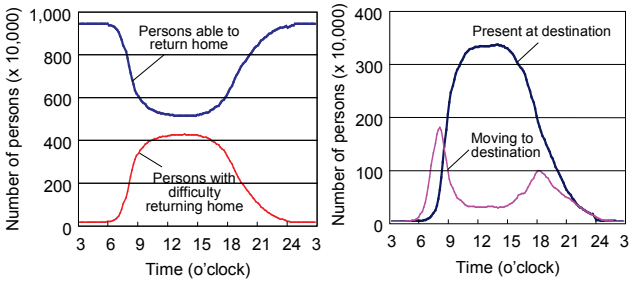

Figure 5 Persons able to Return Home and Persons with Difficulty Returning Home, by Movement Segment

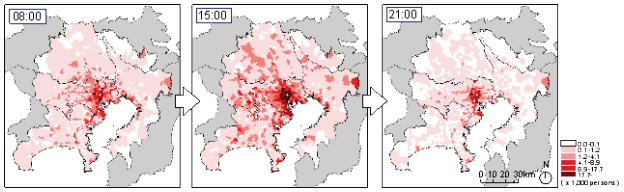

Figure 6 Spatiotemporal Distribution of Persons with Difficulty Returning to Homes, by Present Location

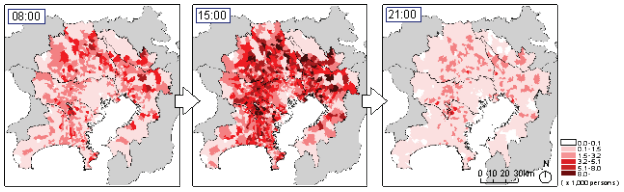

Figure 7 Spatiotemporal Distribution of Persons with Difficulty Returning to Homes, by Location of Residence

3.3 Spatial Distribution by Personal Attributes

The percentage of persons with difficulty returning home in the age group 5–18, which includes pupils, children, and kindergartners, temporarily increases at approximately 8:00. During the day, the percentage of persons over age 80, housewives and househusbands, and the unemployed increases (Figures 8 and 9). In the event of an earthquake during the time period of commuting to school in the morning, emergency response to students, children, kindergartners, and other underage persons in the age group 5–18 will be crucial.

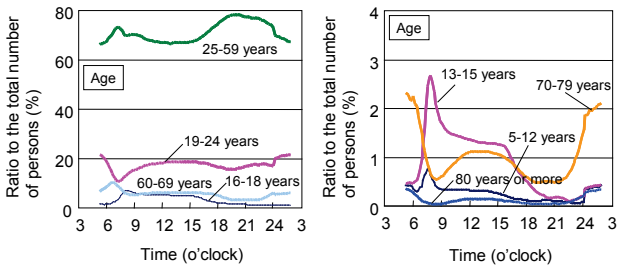

Figure 8 Ratio of Persons with Difficulty Returning Home, by Age

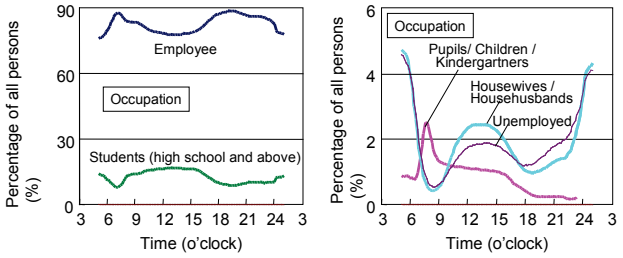

Figure 9 Number of Persons with Difficulty Returning Home, by Occupation

3.4 Spatial Distribution by Purpose for Travel

During the day, a high percentage of persons with difficulties returning home are traveling for purposes such as shopping (Figure 10). A high percentage of persons with difficulties returning home during the day are at their place of work or school. In contrast, at night a high percentage of persons with difficulty returning home are found at locations outside their home for purposes such as shopping. The spatial distribution (Figure 11) shows that persons with difficulty returning home and the purpose of commuting to work tend to concentrate in the city center, while persons with the purpose of commuting to school are distributed over a broad geographic range throughout the day. Persons who travel with a purpose, such as shopping, tend have a wide geographic distribution in the morning, and be concentrated in the city center in the evening. Although individuals that experiences difficulty in returning home are concentrated in the city center (Figure 6), when evaluated by purpose, distinguishing characteristics are evident.

These distinguishing characteristics, such as the distribution over a wide geographic area vary with time. For example, persons with the purpose of commuting to kindergarten or school involve additional users because the young must be met by their parents or guardians, who may not be at the particular location at other times of the day. Similarly, persons with purposes such as shopping who do not belong to any organization may be traveling to different locations in particular time periods. Consequently, the need for emergency measures to assist individuals with difficulties returning home is not limited to the city core, but is spread throughout the metropolitan area depending on the time of day.

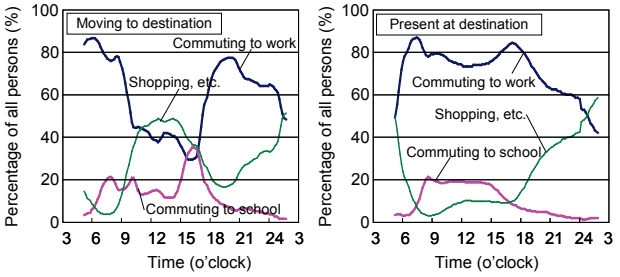

Figure 10 Ratio of Persons with Difficulty Returning Home, by Purpose

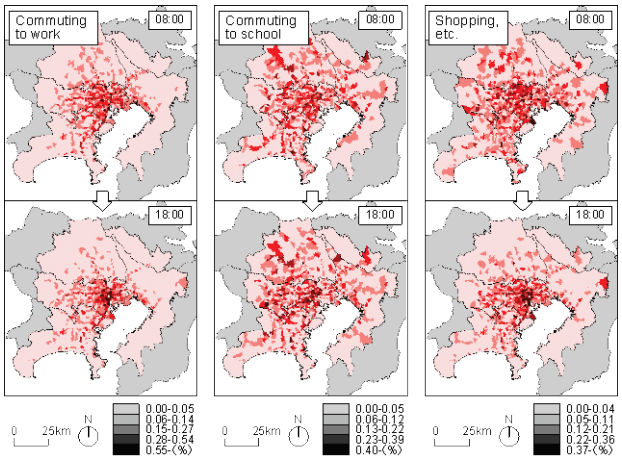

Figure 11 Spatiotemporal Distribution of Persons with Difficulty Returning Home, by Zone and by Purpose

4. SUMMARY AND CONCLUSIONS

We constructed a model for estimating the spatiotemporal distribution of railroad users using PT data, and developed an understanding of the time variation and the variation in location of railroad users by personal attributes and movement purposes. Using this model, it became possible to understand factors that previously could not be understood such as the potential for human damage, and the specific profile of persons affected by an earthquake, which vary greatly with time and location. By combining the profiles of affected persons and their spatiotemporal distribution, it is possible to plan for disaster assistance and to allow for more detailed disaster prevention planning suited to particular time periods and locations. As an application of the spatiotemporal distribution of railroad users estimated by the proposed model, the spatiotemporal distribution of persons with difficulty returning home was examined.

Acknowledgements:

The authors would like to give their special thanks to Mr. Hideki Oshima for his valuable comments at the 14th annual conference of the Geographic Information Systems Association in 2005. This work was sponsored by a Grant-in-Aid for Scientific Research (17310093).

References:

Morichi, S., Iwakura, S., Morishige, T,, Itoh, M. and Hayasaki, S. (2001), "Tokyo metropolitan rail network long-range plan for the 21st century", Transportation Research Board 80th Annual Meeting, Washington, D.C.

Iwakura, S., Watanabe, S. and Doi, A. (2000), "Development of peak-hour train speed model for dynamic commuter travel forecasting", The Infrastructure Planning Committee, JSCE 17, 709-714.

Harada, C., Iwakura, S. and Morichi, S. (2002), "Analysis and modeling of commuters' departure time in urban railway network", The Infrastructure Planning Committee, JSCE, 26, CD-ROM.

Toriumi, S., Kawaguchi, Y. and Taguchi, A. (2008), "Estimation of the damage of railway commuter traffic caused by forthcoming earthquake in Tokyo metropolitan area", Operations research as a management science research 53(2), 111-118.

Taguchi, A. (2005), "Time dependent traffic assignment model for commuter traffic in Tokyo metropolitan railway network", Transactions of the Operations Re-search Society of Japan 48, 85-108.

Bovy, P. and Stern, E. (1990), "Route choice: Wayfinding in transport networks", Kluwer Academic Publishers.

Caspar, C., Molin, E., Arentze, T., Hoogendoorn, S., Timmermans H. and Van Wee, B (2007), "Validation of a multimodal travel simulator with travel information provision", Transportation Research Part C 15, 191-207.

Institution for Transport Policy Studies (2003), "Urban transport Yearbook", Institution for Transport Policy Studies.

Nakabayashi, I. (1992), "Development of estimation method on obstructed home-ward commuters after earthquake disaster", Comprehensive Urban Studies, 35-75.

Nakabayashi, I. (1985), "Study for figuration of damage in a metropolis during an earthquake disaster (4) estimation of difficulty to arrive home from each office", Summaries of Technical Papers of Annual Meeting, Architectural Institute of Japan F, 361-362.

Tokyo Metropolis (1997), "Report on the damage assessment of earthquake directly under Tokyo", Tokyo Metropolis.

JOINT CONFERENCE PROCEEDINGS
7th International Conference on Urban Earthquake Engineering (7CUEE) &
5th International Conference on Earthquake Engineering (5ICEE)
March 3-5, 2010, Tokyo Institute of Technology, Tokyo, Japan

A HUMAN BEHAVIOR MODEL IN REPLACEMENT OF WOODEN HOUSING FOR EARTHQUAKE DAMAGE MITIGATION

Yusuke Meshitsuka[1)]

1) Assistant Professor, Department of Architecture and Building Engineering, Tokyo Institute of Technology, Japan
meshi@arch.titech.ac.jp

Abstract: Building in a densely built-up area has high probability of burning down, because there is an external effect from nearby burning buildings. This study aims to understand quantitatively the external effect especially paying attention to the relation between the ratio of fireproof buildings and the probability of catching fire. To this end, fire probability which is a probability that building is burned out are analytic described. As a result, some characteristics of external effect are explained.

1. INTRODUCTION

There are large densely built-up area in the city in Japan (figure 1 and figure 2). Building in a densely built-up area has high probability of burning down, because there is an external effect from nearby burning buildings.

In this paper, we will try to understand quantitatively the external effect especially paying attention to the relation between the ratio of fireproof buildings and the probability of catching fire.



Figure 1 Scenery of a old residential area in Tokyo



Figure 2 An aerial photograph of a old residential area in Tokyo (Google Earth)

2. FIRE PROBABILITY IN A UNIFORM SITUATION

2.1 Model and Symbols

Once a fire breaks out, other buildings of all the of the area may be involved in a fire by the spread of a fire.

Building Types :

All buildings were classified into 2 building types by means of fire-resistant performance. The former is "fire-resistant building" such as reinforced concrete building, and the latter is "non fire-resistant building" such as wooden building.

Damage Levels :

Once a building start burning, the damage is going to increase with progression of the fire. However in this study, every building are classified into “burned building” or “non

burned building", because we do not consider the progression stage.

When a huge earthquake has occurred, buildings will suffer damage by not only fire but also quaking. However, in order to concentrate on an analysis of the damage suffered by fire, damage from causes except fire are ignored. And all "non burned building" is considered to be "non damaged building". In other words, each building after the earthquake can be classified into 2 types such as "burned and damaged building" and "non burned and non damaged building".

The following signs are used for a further examination.

$\boldsymbol{n}$: a number of buildings in a model city

$\boldsymbol{p}_i$: "fire start probability" which is a probability that fire start from this building.

$\boldsymbol{q}_i$: "fire probability" which is a probability that building is burned out.

$\boldsymbol{p}_{ij}$: "fire spread probability" which is a probability of fire spread from building $\boldsymbol{i}$ to buillding $\boldsymbol{j}$.

2.2 Description of situation

When building i is "non damaged building", fire doesn't start from building i and any fire doesn't spread to building i from buildings which belong to neighborhood set. Then the following equation is represented.

$$1 - q_i = (1 - p_i) \prod_{j \neq i} (1 - p_{ji}\, q_j) \tag{1}$$

Please note that fire start probability pi and fire spread probability pij does not change when the ratio of fire-resistant building change. On the other hand, it is considered that fire probability qi decreases when the ratio of fire-resistant building increases because the probability of fire spread seems to decrease.

First of all, we try to describe fire probabirity when all buildings are non fire-resistant building or when all buildings are fire-resistant buildings.

When all buildings are "non fire-resistant building", equation (1) is represented by following equation.

$$1 - q_W = (1 - p_W)(1 - p_{WW}\, q_W)^k \tag{2}$$

Where

$$p_i = p_W,\ p_{ij} = p_{WW} \tag{3}$$

Equation (2) can be approximated by the following equation.

$$1 - q_W \cong 1 - p_W - k p_{WW}\, q_W \tag{4}$$

Then q_W can be calculated by the following equation.

$$q_W = \frac{p_W}{1 - k p_{WW}} \tag{5}$$

When all buildings are "fire-resistant building", q_W can be calculated by the following equation.

$$q_R = \frac{p_R}{1 - k p_{RR}} \tag{6}$$

Where

$$p_i = p_W,\ p_{ij} = p_{WW} \tag{7}$$

A non fire-resistant building is considered that fire breaks out more frequently than a fire-resistant building. And a couple of non fire-resistant buildings are considered that fire spread more easily than a couple of fire-resistant buildings. Then following inequalities are represented.

$$p_R \leq p_W, \quad p_{RR} \leq p_{WW} \tag{8}$$

According to the comparison of equation (5) and (6), the following equation is obtained.

$$q_R \leq q_w \tag{9}$$

Fire probability $\boldsymbol{q}_i$ is small when there are many fire-resistant buildings. In other words, fire probability $\boldsymbol{q}_i$ depends on the ratio of fire-resistant buildings. Then, we consider that fire probability is a function of the ratio of fire-resistant building.

2.3 The Uniform Solution of Fire Probability

Although it is necessary to explain fire probability of fire-resistant building and fire probability of non fire-resistant building in the case a rate of fire-resistant buildings is $\boldsymbol{x}$. But it is difficult to explain analytic the probability because even when the rate of fire-resistant building is the same, fire probability will change if the layout of fire-resistant and non fire-resistant change. Since the purpose of this study is to understand an external effect metrically, we consider approximating with the evaluation value of average fire probability.

Thus, it is assumed that the number of buildings is large enough and all buildings are arranged layout uniformly. Then, fire probability can be thought that is not based on the spatial relationship of buildings but is decided only by the difference between fire-resistant building or non fire-resistant building.

There are n buildings in model area, n_W of them are non fire-resistant buildings and n_R of them are fire-resistant buildings.

$$n_W + n_R = n \tag{9}$$

Then the ratio of fire-resistant building x is represented by following equation.

$$x = \frac{n_R}{n} \tag{10}$$

When building i is non fire-resistant building, the ratio of fire-resistant building of the other buildings x_W is described by following equation.

$$x_W = \frac{n_R}{n-1} \tag{11}$$

Then

$$1 - q_W(x) = (1 - p_W)\left(1 - p_{WW} q_W(x)\right)^{n_W - 1} \times \left(1 - p_{RW} q_R(x)\right)^{n_R} \tag{13}$$

This equation can be approximated by the following equation.

$$1 - q_W(x) \cong 1 - p_W - (n_W - 1) p_{WW} q_W(x) - n_R p_{RW} q_R(x) \tag{14}$$

When building i is fire-resistant building, the ratio of fire-resistant building of the other buildings x_R is described by following equation.

$$x_R = \frac{n_R - 1}{n - 1} \tag{15}$$

Then

$$1 - q_R(x) = (1 - p_R)\left(1 - p_{WR} q_W(x)\right)^{n_W} \times \left(1 - p_{RR} q_R(x)\right)^{n_R - 1} \tag{16}$$

This equation can be approximated by the following equation.

$$1 - q_R(x) \cong 1 - p_R - n_W p_{WR} q_W(x) - (n_R - 1) p_{RR} q_R(x) \tag{17}$$

A solution can be obtained by solving simultaneous equations (14) and (17) because these equations express the same phenomenon.

Then

$$q_W(x) = \frac{p_W}{1 - (n_w - 1) p_{WW} - (n_R - 1) p_{RR}} \tag{18}$$

$$q_R(x) = \frac{p_R}{1 - (n_w - 1) p_{WW} - (n_R - 1) p_{RR}} \tag{19}$$

When p_{WW} and p_{RR} are small enough, equation (18) and (19) can be approximated by following equations.

$$q_W(x) = p_W\{1 + (n_w - 1) p_{WW} + (n_R - 1) p_{RR}\} \tag{20}$$

$$q_R(x) = p_R\{1 + (n_w - 1) p_{WW} + (n_R - 1) p_{RR}\} \tag{21}$$

$$f(x) = (n_w - 1) p_{WW} + (n_R - 1) p_{RR} \tag{21}$$

$$f(x) = (1 + n) p_{WW} + p_{RR} + nx(-p_{WW} + p_{RR}) \tag{22}$$

Then,

$$q_W(x) = p_W\{1 + f(x)\} \tag{23}$$

$$q_R(x) = p_R\{1 + f(x)\} \tag{24}$$

$f(x)$ expresses an increased part of the fire probability. When $f(x)$ is negligible, fire probability are equal to fire start probability. This means that $f(x)$ is the external effect.

$f(x)$ is the weight sum of fire spread probability which makes weight the number of buildings of fire-resistant buildings and non fire-resistant building.

Reference

Yoshitsugu Aoki (2009) :

http://www.aokilab.arch.titech.ac.jp/lab/y_notes/notes/85_ynote.pdf

JOINT CONFERENCE PROCEEDINGS
7th International Conference on Urban Earthquake Engineering (7CUEE) &
5th International Conference on Earthquake Engineering (5ICEE)
March 3-5, 2010, Tokyo Institute of Technology, Tokyo, Japan

EDUCATIONAL ACTIVITIES TO PROMOTE EARTHQUAKE PREPAREDNESS USING A PORTABLE VIRTUAL REALITY SYSTEM

Shinsuke Tsubota[1], and Ryuzo Ohno[2]

1) Postdoctoral Research Fellow, Center of Urban Earthquake Engineering, Tokyo Institute of Technology, Japan
2) Professor, Dept. of Built Environment, Tokyo Institute of Technology, Japan
tsubota@enveng.titech.ac.jp, rohno@n.cc.titech.ac.jp

Abstract: We develop a portable virtual reality (VR) system to impart earthquake disaster prevention education in the place that participants familiar with. Further, we report information regarding educational activities for disaster prevention using a program that employs photographs and moving images. We conducted demonstrations of this program using portable virtual reality (PVR) at a university and public events aimed at disaster prevention. During one of these events at a survival camp in Tsuzuki, we conducted a questionnaire survey thrice: before the screening, immediately after it, and three months later. The survey results showed that some participants exhibited an increased fear of earthquakes. In addition, the results indicated that the program using the portable VR system is effective in raising awareness about earthquakes and disaster prevention.

1. INTRODUCTION

It is believed that a virtual experience through images of an earthquake will enable an individual to make sound decisions with regard to disaster prevention during the occurrence of an actual earthquake. Moreover, a virtual experience is effective in promoting disaster preparedness among individuals. Today, comprehensive education for disaster prevention is imparted at various related institutions through visuals on a large screen or apparatus to simulate an earthquake. However, the public can receive this education only by visiting such institutions.

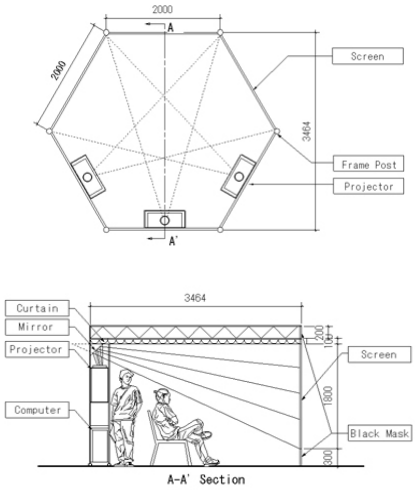

Figure 1 Plan and Section Views of Portable VR System

In this paper, we develop a portable virtual reality (VR) system, using which education on earthquakes can be imparted at any location, for example, a school or a community center. We prepare two programs for portable virtual reality (PVR). The first involves the simulation of an earthquake using computer graphics. The other is a program that employs photographs and moving images. Further, we report information on educational activities aimed at disaster prevention by using the latter program.

2. Imparting education on earthquakes using the portable VR system

By projecting images on a wide screen that in turn comprises three large screens, the portable VR system enables individuals to view images with wide resolutions. Since a wide screen is used, the viewers can have a highly engrossing and realistic experience.

The portable VR system has two main functions aimed at providing a virtual experience to promote earthquake preparedness. One function is to present real-time CG images that are generated through a render computer by synchronizing three computers to create one complete image at a viewing angle of 120° for the combination of three screens. We chose the PhysX engine for this purpose, owing to its stability in simulation and the availability of various supporting documents that facilitated the creation of a new code for our system. Using real-time physics simulation, we could use a suitable physics-based VR room space that could

provide the viewers with an enhanced sense of virtual reality.

The other function is to present high-quality moving images on a wide screen that is created using three projectors. The total resolution of the three screens is up to 3000 ×1000 pixels because the screen comprises three projectors with SXGA resolution.

We created three videos for this function in order to impart education on earthquake preparedness. The first vide is called “Damages caused by earthquake.” The video mainly consists of a high-definition movie on the Great Hanshin Earthquake. This video has three versions with lengths of five minutes, eight minutes, and fifteen minutes.

The second video is called “Promotion on reinforcing a timbered house.” This video includes subject matter on damage caused to houses and housing reinforcement.

The third video is called “Preparedness for an earthquake disaster.” This video comprises seven measures for earthquake preparedness that can be implemented at home.

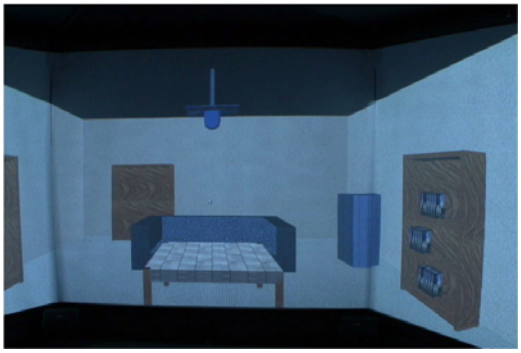

Figure 2 Real Time Physics Simulation

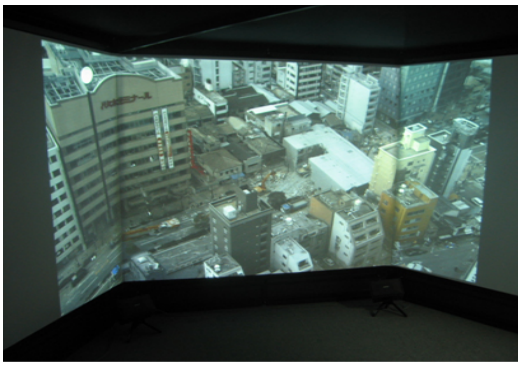

Figure3 High-quality Moving Image on the Wide Screen

3. Implementation of educational programs using the portable VR system

Table 2 presents information on the educational screenings conducted using the portable VR system since April 2008. In addition, we conducted screenings for many visitors to the Suzukakedai campus of the Tokyo Institute of Technology. In 2009, we conducted screenings not only at the university festival in the Suzukakedai campus but also at various public events on earthquake preparedness. In these events, apart from the screenings that employed the portable VR system, we demonstrated educational methods to provide first-aid training to the public and created hazard maps.

Table2 Implementation of Educational Programs from 2008

Event	Date	Promoter	Site	Contens watched	Participant
Excurision for institution	18-Apr-2008	Tokyo Tech	Suzukakedai Campus	Damages Caused by Earthquake	concerned Earthquake About 10
Festival in Suzukakedai	10-May-2008	Tokyo Tech	Suzukakedai Campus	Damages Caused by Earthquake Promotion on Reinforcing Timbered House	Citizen About 30
Class for disaster prevention	23-May-2008	Daruma	Suzukakedai Campus	Damages Caused by Earthquake Promotion on Reinforcing Timbered House	Citizen About 25
NCU Suzukakedai	17-Jul-2008	Tokyo Tech	Suzukakedai Campus	Damages Caused by Earthquake Promotion on Reinforcing Timbered House	concerned Earthquake About 25
Exhibition for crisis management	8-Oct-2008	Yokohama City	Tokyo Big Site	Damages Caused by Earthquake	Citizen About 60
Fair for disaster prevention of house	18-Oct-2008	House Squre Yokohama	House Squre Yokohama	Damages Caused by Earthquake Promotion on Reinforcing Timbered House	Citizen About 30
the Survival Camp	22-Nov-2008	I LOVE Tsuduki	Tokyo City Univ	Damages Caused by Earthquake	Citizen About 30
Festival on safety and security	10-Jan-2009	Yokohama City	Yokohama Red Blick Warehouse	Damages Caused by Earthquake	Citizen About 30
Gathering on Disaster Prevaention 2009	17-Jan-2009	Gathering on Disaster Prevaention	Kanagawa Civilian Center	Damages Caused by Earthquake	Citizen About 25
Research Meeting of Fire and Disaster	30-Jan-2009	Research Institute of Fire and Disaster	Research Institute of Fire and Disaster	Damages Caused by Earthquake Promotion on Reinforcing Timbered House	concerned Earthquake About 25
Festival in Suzukakedai	9-May-2009	Tokyo Tech	Suzukakedai Campus	Damages Caused by Earthquake Promotion on Reinforcing Timbered House	Citizen About 30
Lecture meeting for disaster prevention in Midoriku	27-Jun-2009	Midori-ku	Nakayama area care plaza	Damages Caused by Earthquake	Citizen About80
Fair for disaster prevention in Kanagawa	18-Oct-2009	Center of disaster prevention in Kanagawa	Center of disaster prevention in Kanagawa	Damages Caused by Earthquake	Citizen About 70

Table1 Videos for Portable VR system

title	Damages Caused by Earthquake	Promotion on Reinforcing Timbered House	Preparedness for earthquake disaster
time	7min25sec	7min35sec	5min30sec
table of contents	1 the great Hanshin-Awaji Earthquake 2 the Earthquake at home and abroad the Mid Niigata Prefecture Earthquake the Sumatra Earthquake in late 2004 3 Earthqauke in the Tokyo area	1 Damage from Earthqauke 2 Structure on reinforcement 3 Shaking Experiment by E-defence 4 vibration Control Wall of K style Brace 5 Subsidy System on Reinforcement	1 the Sichuan Earthquake in China 2 Earhquake in Yokohama 3 Preparedness for Earthqauke Disaster seven ways for preparedness

4. Opinions on the screenings using the portable VR system

After the screenings, we compiled the opinions of some visitors on the portable VR system and the videos. It turned out that many visitors had considerable information about an earthquake from the opinions, for example “I understand the fear of earthquake” and “I brought back the past on earthquake”. Some visitors commented on their preparedness for an earthquake disaster, for example “I image it would happen for real. I will prepare”. Moreover, some visitors provided comments for the improvement of the instrumentation and the videos, for example “It is better take in voices of victims” and “I think you'd better take in image of first aid because of education of activities in emergency.”. And some visitors pointed out problems of instrumentation and video, for example “The scene line is too early”. Overall, we verified that the portable VR system is effective at raising awareness among the public about disaster prevention.

5. Questionnaire about the screening in the survival camp

We conducted questionnaire surveys to evaluate the portable VR system at a survival camp in Tsuzuki in November 2008. The survey participants comprised children aged eight to twelve years and their parents. The main theme of the survival camp, which was organized by an NPO called “I LOVE Tsuzuki,” was to provide the public with the experience of spending a night at an evacuation center. Some programs for creating hazard maps and imparting first-aid training in case of an emergency were also conducted at the camp.

We screened the first video “Damage caused by earthquake” for the participants. As mentioned earlier, we conducted a questionnaire survey thrice: before the screening, after it, and three months later. The questionnaire for the first and third instances was related to awareness about earthquakes and disaster prevention. The second questionnaire asked the participants for their opinions on the video and the system. This survey was answered by 18 participants.

Table4 Out-Line of the Survival Camp

promoter	I LOVE Tsuduki
partcipants	primary school chidren and their parents
purpose	experience of evacuation life
first day	gathering **first time questionnaire**
	orientation
	class about first aid in emergency, gas facilitiies and fire figting **performance using portable VR system**
	lunch **second time questionnaire**
	class about earthquake
	walking town and publishing hazard maps
	cooking using tabletop stoves
second day	workshop about evacuation life
	presentation about workshop
three month after	**third time questionnaire (by mail)**

Table3 Comments of participants on Portable VR System

classification	coments	event	sex/age
impression	I thik this is good.	Fair for disaster	M/58
	I feel nature is terrible.	Fair for disaster prevention of house	F/65
	I am impressed. Can I get this program as DVD.	Fair for disaster prevention of house	M/45
	great	Gathering on Disaster Prevaention	M/31
	A tremendous impact	Gathering on Disaster Prevaention	M/50
	This movie is realistic and fulfilling.	Research Meeting of Fire and Disaster	M/60
	This movie is grea,t because of real live-action film.	Fair for disaster prevention in Kanagawa	M/38
	This movie served as useful reference.	Fair for disaster prevention in Kanagawa	M/50
	I thik this is very good.	Fair for disaster prevention in Kanagawa	M/70
	This movie is vigorous because of wide screen.	Fair for disaster prevention in Kanagawa	M/8
awareness of earthquake	I understood fear of earthquak.	Gathering on Disaster Prevaention	M/65
	I bringed back the past about earthquake.	Gathering on Disaster Prevaention	M/69
	I know well, but this movie was thought-provoking about earhquake one more time.	Fair for disaster prevention in Kanagawa	F/48
	Please continue to provide information about earthquake to remind with age,	Gathering on Disaster Prevaention 2009	F/-
	I feeled threatened again.	Gathering on Disaster Prevaention	M/57
	Image and coment are good. I think this system is useful for disaster prevention.	Fair for disaster prevention in Kanagawa	M/58
	I feell myself forgeting that time. This movie remind of earthquake.	Fair for disaster prevention in Kanagawa	M/30
	I feel fear earthquake one more time.	Fair for disaster prevention in Kanagawa	F/10
	I feel fear earthquake.	Fair for disaster prevention in Kanagawa	M/8
promotion of disaster prevention	I understand the damage from earthquake. I find preparedness is imporatant. I think this movie is meanigful.	Fair for disaster prevention of house	M/40
	I want to give serious thougt to earthquake.	Gathering on	M/73
	I want to lool at earthquake and aging of society.	Gathering on Disaster Prevaention	M/55
	I image it would happen for real. I will prepare.	Fair for disaster prevention in Kanagawa	F/53
	I feel to need prepareation for emergency.	Fair for disaster prevention in Kanagawa	F/
	I will prepare myself for earhqukae disaster.	Fair for disaster prevention in Kanagawa	M/10
	Image of Kobe and Sumatra is memorable. I will prepare for earthquake.	Fair for disaster prevention in Kanagawa	F/-
	I see fear of earthquake and daily preparedness for earthquake one more time. It is important to consult on this problem by society.	Fair for disaster prevention in Kanagawa	F/-
	I live in the area where many old houses are, so I will check way to escape in emergency.	Fair for disaster prevention in Kanagawa	M/43
	I will have a think preparedness for my family. I had a positve experienece today.	Fair for disaster prevention in Kanagawa	M/32
suggestion about system	I think you'd better take in image of first aid because of education of activety in emergency.	Research Meeting of Fire and Disaster	M/61
	If you use this system with an earthquake simulation vehicle,It is more effective.	Research Meeting of Fire and Disaster	M/25
	It is better to take in voices on earthquake.	Fair for disaster prevention in Kanagawa	M/36
	It is better to take in way of preparedness for earthquake.	Fair for disaster prevention in Kanagawa	F/65
point out problems	The scene line is too early.	Fair for disaster prevention in Kanagawa	M/38
	It is better to exercise your ingenuity.	Fair for disaster prevention in Kanagawa	M/73
	You'd better make the movie to understand more easily.	Fair for disaster prevention in Kanagawa	F/48
	There are too much information in the movie. I think it is better to narrow down.	Fair for disaster prevention in Kanagawa	M/38
	I thinke we are too close to the screens.	Fair for disaster prevention in Kanagawa	M/56
technology	I think image on 3 screen and narration is in motion with effective.	Gathering on Disaster Prevaention	M/44

Comparing the first and third questionnaires on awareness about earthquakes, we noted that some participants, for example, 2 and 18, were increasingly concerned about the disaster (Fig 4). Further, some participants, for example, 36 and 47, mentioned that the screenings increased their awareness about earthquakes.

As for the questionnaire on earthquake preparedness, we observed an increase in the awareness of some participants in this regard (Fig 5). However, we confirmed that a few participants implemented measures for earthquake preparedness, for example, storing water for daily usage and securing big pieces of furniture.

6. CONCLUSIONS

In this paper, we reported information on screenings aimed at educating the public about earthquakes using a portable VR system and questionnaire surveys.

We screened the related video using a program that involved moving images by means of a portable VR system at various locations. The results deduced from the participants' feedback and the questionnaire survey confirmed that the system was effective at increasing public awareness about earthquakes and disaster preparedness. However, the promotion of disaster preparedness still remains an issue for future research. Furthermore, additional education should be imparted in order to facilitate a more detailed evaluation of the effectiveness of the portable VR system.

Acknowledgements:

The authors acknowledge support from the Center for Urban Earthquake Engineering (CUEE) in Tokyo Institute of Technology. These activities were successfully completed with the help of NPO I LOVE Tsuzuki, staffs of the survival camp and participants.

References:

Ryu, J., Soeda, M., and Ohno, R.,(2006), "Development of an effective tool for virtual experience of environmental hazard -A survey of disaster education facilities in Japan," Third International Conference on Urban Earthquake Engineering, March 6-7, Tokyo, Japan, pp197-203

Ryu, J., Hashimoto, N., Sato, M,. and Ohno, R.,(2007), "Development of Portable Virtual Reality System for Earthquake Disaster Preparedness" Summaries of technical papers of Annual Meeting Architectural Institute of Japan A-2, pp469-470(Japanese)

Ryu, J., and Ohno, R.(2007), "Developing of novel room relayout tool using real-time physics simulation and portable VR system for preparedness of earthquake disaster" Fourth International Conference on Urban Earthquake Engineering, March 5-6, Tokyo, Japan, pp583-589

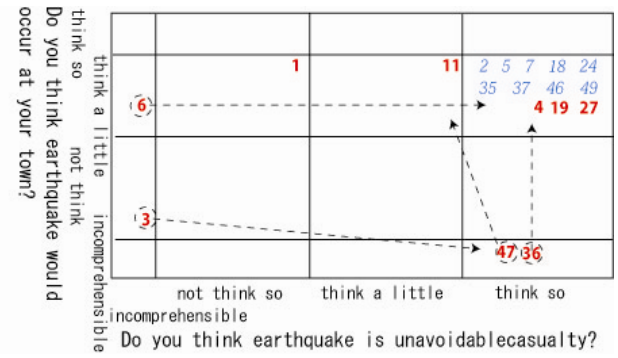

Bold Font : Children Thin Font : Parents

○→ : Change After Three Months

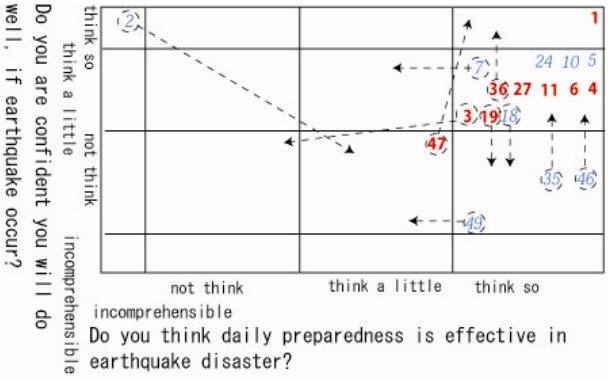

Figure 4 Results of Questionnaire on awareness for Earthquake Disaster

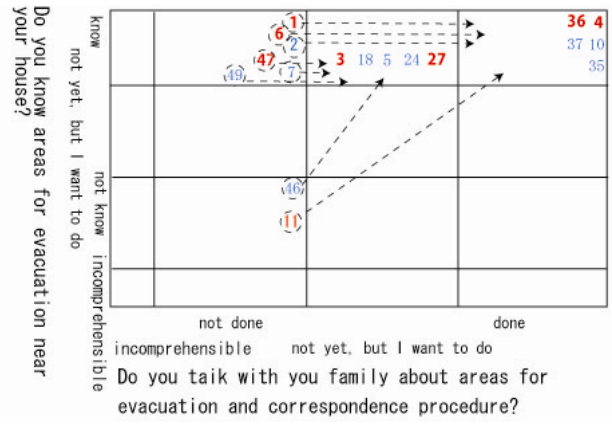

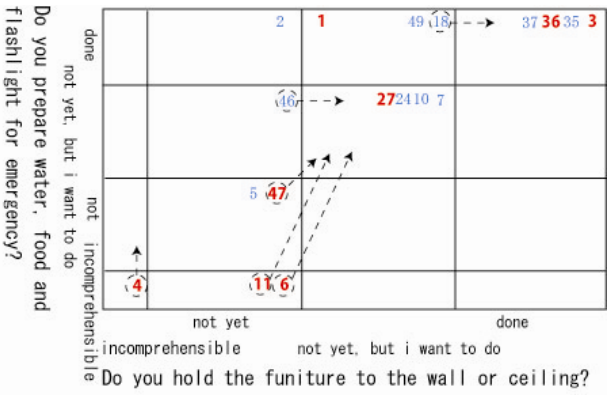

Figure 5 Results of Questionnaire on Disaster Prevention

JOINT CONFERENCE PROCEEDINGS
7th International Conference on Urban Earthquake Engineering (7CUEE) &
5th International Conference on Earthquake Engineering (5ICEE)
March 3-5, 2010, Tokyo Institute of Technology, Tokyo, Japan

RESIDENTS' EVALUATION IN JAVA 2006 EARTHQUAKE POST DISASTER SETTLEMENT
-Case Study of New Ngelepen, Sleman, Yogyakarta-

Syam Rachma Marcillia[1)]

1) Graduate Student, Department of Built Environment, Tokyo Institute of Technology, Japan
syam.r.aa@m.titech.ac.jp

Abstract: Prefabricated materials and modern construction method sometimes are necessary in post disaster housing restoration to accelerate the reconstruction and for better disaster prevention performance. However, sometimes the donated post disaster housing come from other countries that culturally different from local dwellings of the residents. In this paper, the housing and living environment of planned post disaster settlement is evaluated from the residents' perception point of view to understand its relationship to residents' lifestyles. A comprehensive onsite fieldwork survey was conducted using household survey questionnaires and in-depth interviews to collect the data as well as observation of residents' activities. Questionnaires and in-depth interviews contained items related to residents' dwellings condition before and after disaster, their evaluation on post disaster housing and outdoor space design and residents' participation in community activities. The results of the analysis show that housing and living environment conditions were different before and after disaster but their previous lifestyle were still being maintained despite some constraints. Residents' evaluation shows that some constraints such as unchangeable misfit design had result in residents' dissatisfaction.

1. INTRODUCTION

The huge number of damaged and collapsed buildings after the earthquakes creates a housing problem needing urgent attention. In some post disaster housing restoration, survivors of natural disasters did not have many choices than to accept the condition of the given donated housing. For these people, they are not only facing physical and economical impacts caused by the disasters but also psychological and social impact, especially if they are forced to be relocated to different environment. However, when the donated housing is culturally different from their original housing, in a long term it could restrict and change residents' original lifestyle. This condition had been a concern and controversy for post disaster housing settlement in *New Ngelepen*, Yogyakarta. In *New Ngelepen*, the survivors of Java earthquake May 27th 2006 were relocated to a new type of settlement and given dome house post disaster housing that completely different from their Javanese vernacular dwelling.

Various studies on how residents' condition at *New Ngelepen* after the earthquake had been done such as; study on response and adaptation to the dome house (Ikaputra,2008), residents' perception about the new environment (Saraswati,2007), etc. However, a study on how residents' dwellings condition before and after the earthquake and how it influence their evaluation and lifestyles from residents' perception point of view received considerably less attention.

Through questionnaires and in-depth interviews regarding residents' housing condition, their evaluation on the living environment and observation of residents' activities, this study objective is to determine the relationship between the living environment and how it affects residents' lifestyle from residents' perspective. The findings shows that in the daily life and community activities the residents pursued in *New Ngelepen*, although before and after disaster houses and living environment condition were different, their previous lifestyle both in personal daily life or social activities were still maintain despite some constraints. Residents' evaluation findings show that some constraints such as unchangeable mis-fit design results in residents' dissatisfaction.

2. RESEARCH METHOD

In this study, an intensive and comprehensive onsite fieldwork research was conducted not only by encompassing questionnaires and in-depth interviews, but also observation of residents' activities as well as physical changes they made to the original donated houses and site plan. Questionnaires and in-depth interviews contained items related to residents' dwellings condition before and after disaster, their evaluation on the living environment both for house and outdoor space design and also participation in community activities were investigated. To represent and analyze the data, open ended and multiple choices questionnaires with in-depth interview were used. Particularly for asking residents' evaluation and attitude, five points scale questionnaires were asked. However, instead of using

straightforward personal satisfaction questions toward the given donated housing, residents were asked about their capability to overcome house design problems and their agreement related to outdoor space problems. The questioned items for residents' evaluation questions were made based on intensive field observation found at *New Ngelepen* post disaster settlement. Data and onsite observation was conducted and gathered for approximately one month on August 2009 with the help of volunteers from Gadjah Mada Architecture students.

3. OVERVIEW OF SURVEY AREA

The study case area for this research is located at *New Ngelepen*, Sleman Regency, Yogyakarta Special Province, Indonesia. After Java earthquake May 27th 2006, in the original *Ngelepen* village, almost 50 houses were demolished by catastrophic landslide and the area declared as a geographically unbuildable land. As a result, the residents were relocated to *New Ngelepen* post disaster settlement, situated about 1,5km from the original village.
The *New Ngelepen* introduced house clusters site plan design where every 12 houses form a block that shared sanitation, electricity, public toilet/washing area and approach pathways. Dome monolithic with a hemispherical roof and a circular plan were introduced with concrete cast as a single and integral structure as the donated post disaster houses. The diameter of the house is 7 meters, two stories, with the total area about 38 square meters. The development of the houses began in October 10, 2006, and started to be occupied at the end of April 2007. They were built by World Association of Non-Governmental Organization (WANGO) and the Domes for the World Foundation (DFTW), and developed by Emaar Properties. Although the post disaster houses itself are free donated houses, but the land where they were built owned by the local Government, *Sleman's* Regency and were lend to the survivors for free in 3 years. The site plan, cluster typology and dome house type are shown in figure 1.

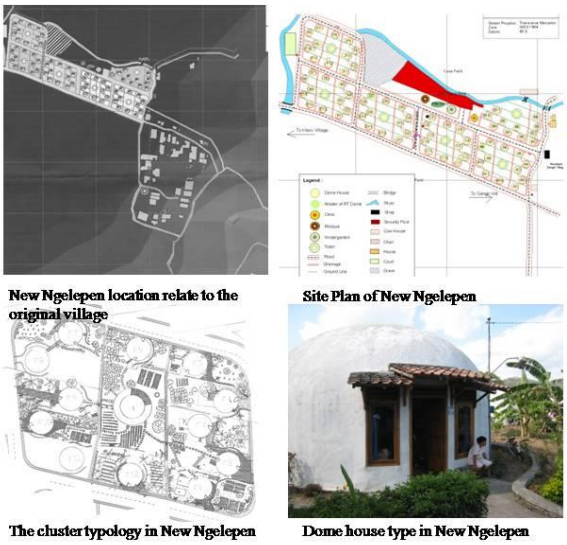

Figure 1 Site plan, cluster typology and dome house type.

Based on observation and confirmation from the village official on August 2009, from the total of 71 dome houses that were built and given to the survivors, only 50 houses were lived in by the residents. The residents in *New Ngelepen* mostly come from the same destructed original *Ngelepen* village and the neighboring villages. The distribution of donated dome houses was made based on lottery. From the residents that lived in the area, only 34 (68%) of the lived in dome houses residents were managed to be questioned and interviewed both the head of the household and the spouses.

4. RESIDENTS' HOUSING CONDITION BEFORE AND AFTER DISASTER

Analyses of residents' before and after disaster housing condition were made based on multiple choice and open ended questions concerning the house condition, comparison of rooms/spaces availability, their future preference to add or fix the condition of donated post disaster housing and the changes residents had made to the original donated house.
Description on residents' before and after disaster housing condition is shown in Table 1.
Table 1 Before and after disaster housing condition.

Remarksc	Residents and House Condition	
	Original House (before disaster)	Dome House (after disaster)
House Type	Rectangular or square plan house with gable, hip or *joglo* roof type	Circular plan house with a hemispherical roof type
House Structure	50% brick with concrete column 25% brick without concrete column 14% ½ brick ½ wood/bamboo with concrete column 11% ½ brick ½ wood/bamboo with wood column	100% concrete cast dome monolithic
House space average	88 m2	38 m2 (7 m in diameter)
Land status	Personally owned 93%	Personally owned 0% (100% owned by Sleman regency goverment)
Occupancy	Lived by more than 1 household 35 %	Lived by more than 1 household 6%

Comparison of rooms/spaces type availability before and after disaster housing shows that the most drastic difference are on the availability of front terrace, dining room (usually integrated with kitchen), family room, praying room, chicken/cow house and water tanks (Figure 2). Interestingly, the residents' acknowledgments to the availability of the room/spaces implicitly show some design mis-fit where the intended available room or spaces in master plan for both site plan and house plan were actually not aligning with residents' usage or perception. For example, the master plan of *New Ngelepen* landscaping were only allowed distinctive fruits and flower plants for each clusters, but in reality most of the land were used for planting harvest crops. Moreover, some of the available spaces such as chicken houses, fish pond, etc were actually prohibited but they were built by the residents to fulfill their needs. In contrary, some of the available room in master plan of the house, such as the room on the 2nd floor of the dome house that were intended for family room, is rarely recognized and use as family

room, instead they use it as storages. These design misfits could happen because designers' interpretation of 'good' design was not aligning with residents' way of life.

Response to an open question of residents' future preference to add or fix the condition of donated post disaster housing shows the importance of adding either kitchen and private/individual bathroom for similar rooms available at *New Ngelepen* (Figure 3). The highest demand of adding kitchen beside the existing kitchen inside the dome had been an important issue since early studies on *New Ngelepen* settlement (such as by Ikaputra, 2008). From the interview and observation in original *Ngelepen*, kitchen is one of the largest rooms in original dwellings that usually act as a multi function area. In conventional Javanese cooking, most of the people are still using cordwood to cook and since Java food use various fresh spices and sometimes fresh from the yard crops, large preparation space and washing area are necessary. A socialization space such as dining room or just benches with preparation table are usually available as neighboring housewives or other family members usually chats together while preparing for cooking. Sometimes a kitchen also acts as storage area for the harvesting crops, equipments for farming and even as garage for bicycle or motorcycle. Most kitchens in original *Ngelepen* located in the back part and often separated but still have a direct access to the main house. Because of the peculiar Javanese cooking habit and other above mentioned functions in the kitchen, that is why most Javanese people usually percept kitchen as *dirty* place. The high demand for another kitchen besides the one in the dome houses is understandable because the available kitchen in the dome houses could not facilitate Javanese cooking customs functionally and differ to the residents' perception.

Some of the largest demands of new additional rooms can be mentioned are garage for vehicle, shops and terrace (Figure 3). The importance of garage is due to the fact that motorcycle and bicycle are considered valuable items for the residents that 85% of their income only 100US$/month or less. However, the need for specific garage was not significance in original house because availability and spaciousness of other rooms to keep the vehicles contrasted to the room space inside dome house that is too limited to use as garage while also use for its functional purpose. The importance to add terrace is to accommodate the residents' way of life which is not facilitated in dome house. As shown in Figure 2, in original house the existence of terrace was more than 80% but it decreases to only 7% in dome houses. For Javanese people, terrace has an essential value especially for social interaction. It functions as 'first' acceptance area for formal guest, family relaxation area and active-passive contacts interaction area with the neighbors. The need for adding shops is new to the residents' lifestyle. It happened because dome houses have attracted many people to come and it becomes an opportunity to do home business.

Although the above results shows the importance and needs of certain rooms/spaces in the house but the residents rarely add permanent rooms beside temporary kitchen, storage and shops (Figure 4). The changes had been made to the original

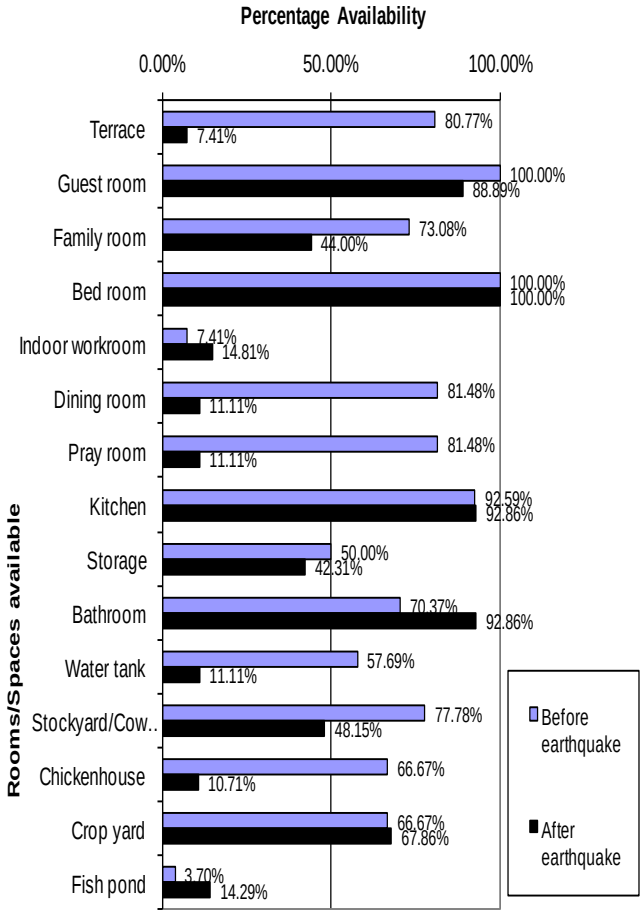

Figure 2 Rooms/spaces availability in residents' before and after disaster housing.

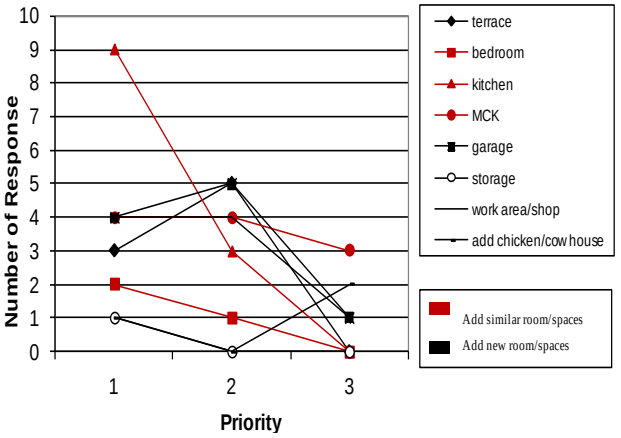

Figure 3 Residents' future preference to add or fix the condition of donated post disaster housing.

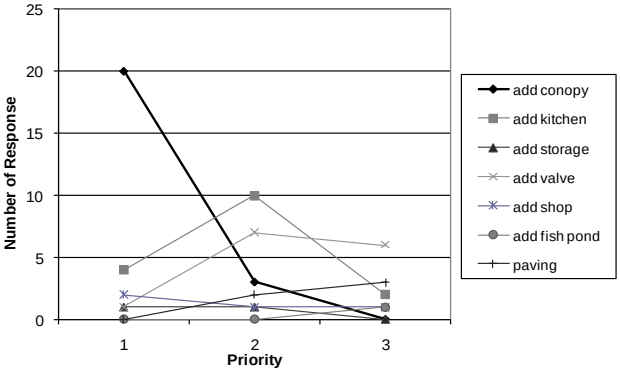

Figure 4 Changes had been made to the donated house.

donated house within 3 years of occupancy were only adding canopy for protection in rainfall season, paving part of yard for social interaction spaces and installation of personal water valve (Figure 4). This condition could be caused by land status conflict; the fact that the land was only lent to them made them reluctant or postponed their needs to add permanent rooms.

An important note to mention is the incapability of the dome houses to accommodate the extended family in one house. In their original houses more than 34% were lived in by more than one household, but in dome houses it decreases to only 6%. Other finding shows that from the original house which had been repaired and still used, 56% of them were used by other family members. These implicit the situation in dome houses where nuclear families were encouraged to each owns a separate house although whether it affect the closeness of family relations or not will need further study.

5. RESIDENTS' POST DISASTER HOUSING EVALUATION

5.1 House Design Evaluation

Three aspects of residents' evaluation about their post disaster house design were investigated; flexibility, personalization and maintenance. Residents were asked in five points response score to evaluate their capability to overcome the house design problems related to those aspects in their post disaster houses.

Evaluation for flexibility shows "very hard" capability of residents to *"to change the order/function of the rooms"* (64%), *"to expand the room"*(57%), and *"to change the location of the doors or windows"* (76%). Only 61% for capability *"to give rooms addition"* shows *"regular"* capability (Figure 5).

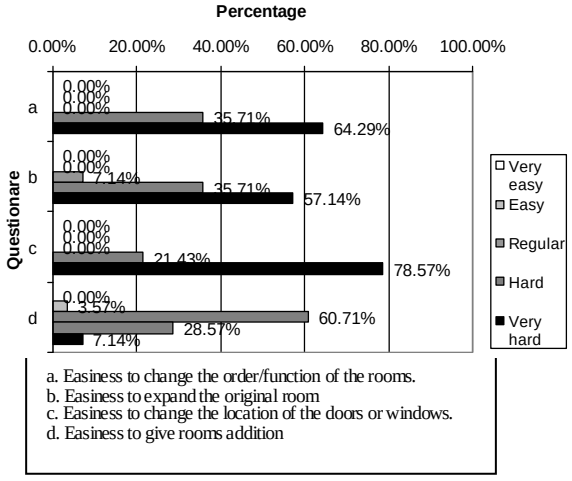

Figure 5 Residents' evaluation for house design flexibility

Evaluation for personalization shows 63% *"hard"* capability for the residents to both *"to reuse or recycle previous doors and windows frames"* and *"to make additional room that compatible with original donated house"* and only 58% shows a *"regular"* capability for *"to decorate own house to look different from the others"* (Figure 6).

Evaluation for maintenance related to *"to fix any damage to wall"*, *"to fix any damage to roof" and "to fix any damage structure joints"* shows *"hard"* capability for 50% and less. Only 45% shows an *"easy"* capability *"to fix/add installation for electricity, water, etc."* (Figure 6).

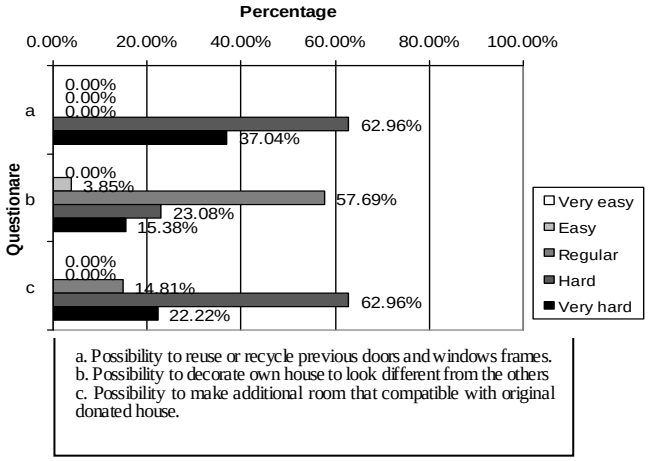

Figure 6 Residents' evaluation for house personalization

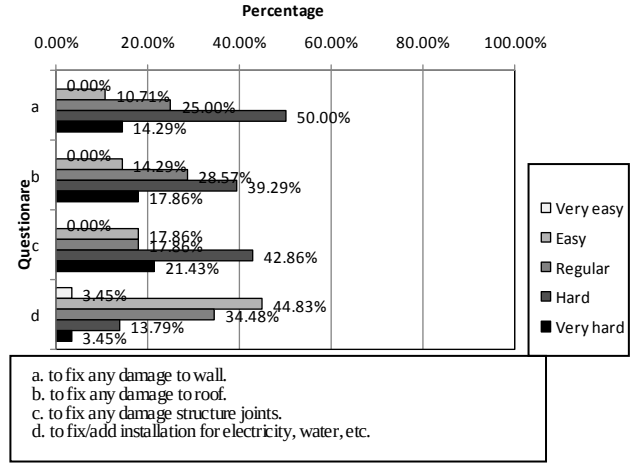

Figure 7 Residents' evaluation for house maintenance

From the residents' evaluation, we can make a conclusion that flexibility in dome houses is one of the most complicated problems for the residents except for capability *"to give rooms addition"*. However, in reality it is also hard for the residents *"to make additional room that compatible with original donated house"*. Maintenance related to elements fixed to dome house structure such as wall, roof and joints also become a point of issues as the residents did not have the knowledge how to repair or maintain dome house structure.

5.2 Outdoor Space Evaluation

Three aspects of residents' evaluation about their post disaster outdoor space conditions were studied; house outdoor space, neighborhood streets and cluster's facilities. Residents were asked in five points response score to evaluate their agreement to some of the problems related to those aspects of outdoor spaces.

Evaluation for house outdoor space shows *"very agree"* attitude toward statement *"it is better for each house to have private approach pathway"* (57%), *"there is not enough yard/room in the house to have social gathering"* (61%) and *"it is important to have a front terrace but the space available is not possible to made one"* (50%), while only 64% shows *"agree"* attitude toward statement *"each house should have own pathway from house to public toilet/washing area"* (Figure 8).

Evaluation for neighborhood streets shows that more than 96% of the residents are *"very agree"* to the statement *"the house front yard space should be larger instead of larger street for better social gathering space"*. However evaluation for statement *"streets inside the neighborhood should not be too large so that cars and motors not easily pass by" were "disagree"* by more than 53% (Figure 9).

Evaluation for common facilities shows that more than 53% *"very agree"* that *"every house should have their own water installation and sanitation"* and only 32% to the statement *"every house should have their own toilet area"*(Figure 10).

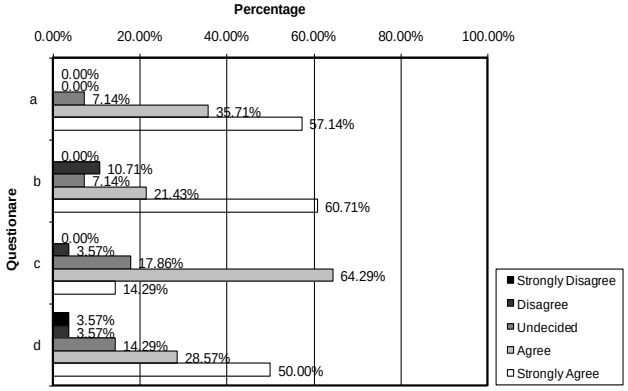

a. It is better for each house to have private approach pathway.
b. There is not enough yard/room in the house to have social gathering.
c. Each house should have own pathway from house to public toilet/washing area
d. It is important to have a front terrace but the space available is not possible to made one.

Figure 8 Residents' evaluation for house outdoor space.

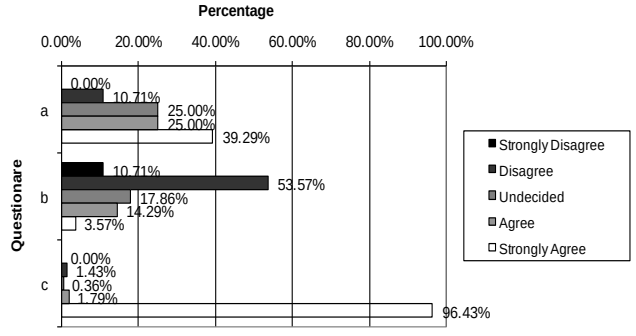

a. neighborhood streets are too dangerous to leave children play by themselves.
b. streets inside the neighborhood should not be too large so that cars and motors not easily pass by
c. The house front yard space should be larger instead of larger street for better social gathering space.

Figure 9 Residents' Evaluation for neighborhood streets.

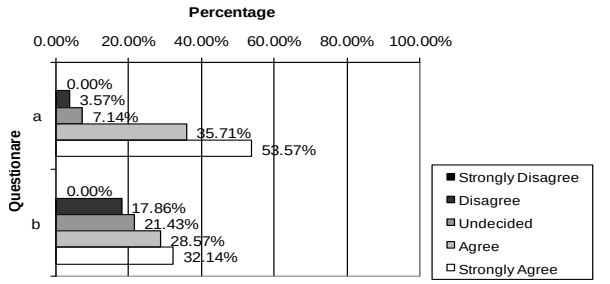

a. every house should have their own water installation
b. sanitation and every house should have their own toilet/washing area

Figure 10 Residents' evaluation for common facilities

From the residents' evaluation we can presume that house outdoor space hold an important role in their activities. Most typical Javanese rural dwellings had large yard that function not only for planting and drying laundry but as drying harvest crops, burning garbage, drying the corkwood, etc. It also hold important role as a socialization space. In daily life, housewives like to chats with the neighbors while looking after their little children playing in the house yard. Occasionally large social gathering are also done in house yard area such as wedding, 'trah' gathering, etc. In *New Ngelepen*, the limitation of house outdoor space made the residents use neighborhood's streets for their activities. From the interview and observation, during the day little children were playing freely on the streets, while housewives chat on side of the streets. The streets were also used as social gathering spaces. Near neighborhood entrance, main street was painted as badminton field where youths and man gather in the evening to play badminton or just to hang around. Social gathering that used to be facilitated in original dwellings but not possible in dome houses, now performed on the streets such as 'ruwahan", etc. Even once the streets were closed for one of the resident's wedding ceremony.

Interestingly, although they responses show a high dissatisfaction toward the outdoor space condition, but when the residents were asked whether they planned to change it, most of their answers are not (Figure 11). These responses become questionable as to whether the residents were indeed does not want to change or they can not change the situation.

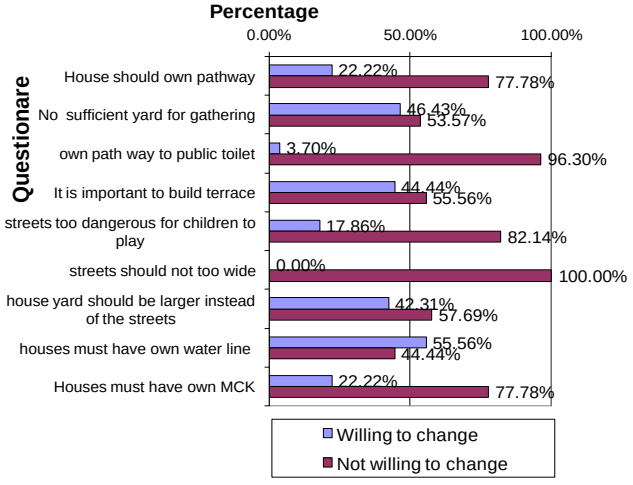

Figure 11 Intention to change outdoor space condition.

6. PARTICIPATION IN COMMUNITY ACTIVITIES

6.1 Overall Status of Participation and Perception

Regarding the residents' willingness of participation in overall community activities, the most frequent response by both heads of household and spouses is A *"I am actively participate"*. If responses A, B, C are taken as *"do participate with their own willingness",* responses D and E are taken as *"do not participate"* and response F is taken as *"do participate as obligation",* then approximately more than 95% for both heads of household and spouses said that they participate with their own willingness, while only less than 5% feel obligated to participate and null for no participation (Figure. 12).

High participation to community activities is supported by their perception on the importance of the value and existence of community activities in their neighborhood. Approximately 65% head of household and 57% of spouses response is A "I feel that community activities are very important" and approximately only about 34% for both heads of household and spouses said that "they are neutral, don't really have certain feeling (Figure.13)

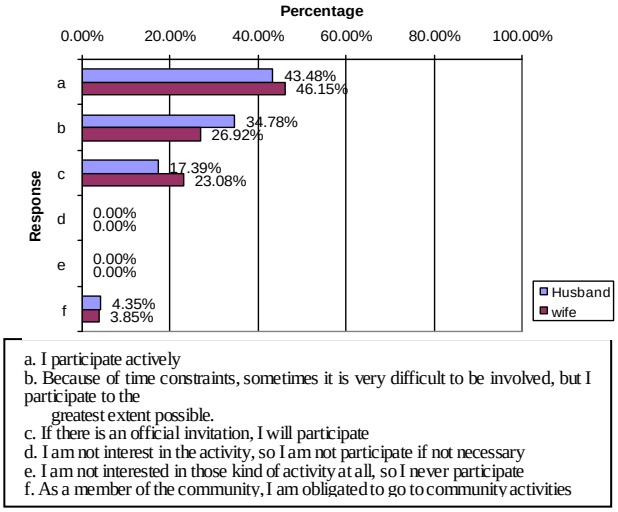

Figure 12 Residents' participation to community activities.

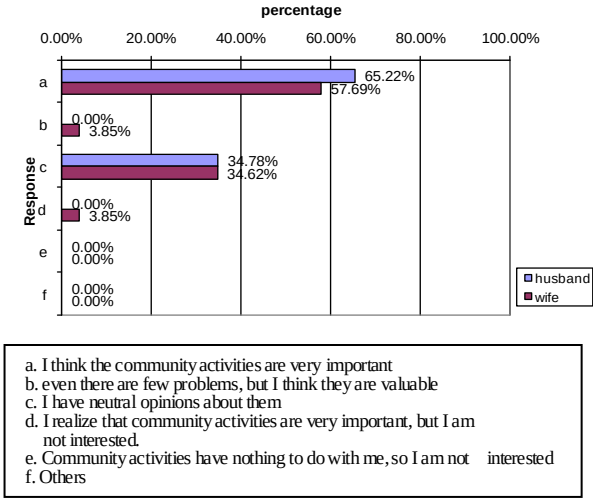

Figure 13 Resident perceptions to community activities.

6.2 Status of Participation Correlated to Certain Community Activities and Location.

Participation in community activities at residents' house such as neighborhood meetings (*RT*'s meeting, *Block* meeting,etc), housewives' meetings (*PKK meetings, Dasa Wisma, Posyandu, etc),* religious gathering (*Wiridan ,Tahlilan,etc.* shows 100% of head households and 96% of spouses participation. Community activities at Community Meeting Hall (*Pendopo/Balai Pertemuan*) such as General meeting, *Karang Taruna* meeting, etc. shows approximately 96% head households and 89% of spouses participation. Community religious activities at neighborhood's mosque such as *Jum'at* prayer, *Tarawih*, preaching, etc. shows 100% of head households and 96% of spouses participation. Neighborhood aesthetics and maintenance activities surround the neighborhood such as cleaning up the cemetery, *Sunday* neighborhood clean-up, etc. shows 68% of head households and 62% of spouses participation. Health and sport activities at neighborhood's field such as badminton, soccer, etc. show 32% of head households and 7% of spouses participation (Figure 14)..

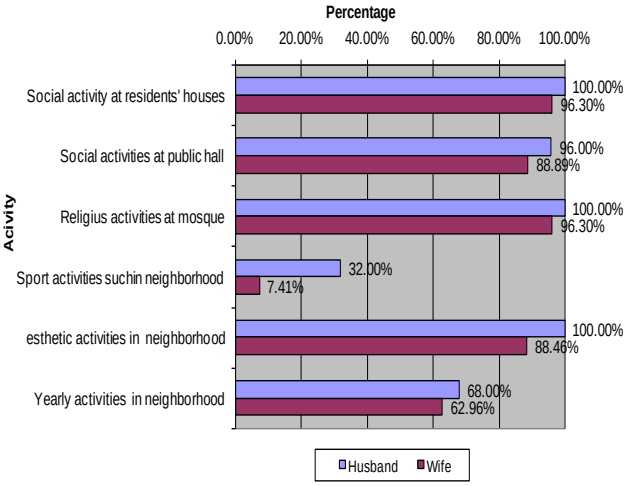

Figure 14 Residents' community activities participation at various locations.

7. CONCLUSION

7.1 Summarization

The results of the above surveys and analyses can be summarized as follows:

(1) The results highlighted that even though physical features condition of the original dwellings before the disaster and post disaster housing environment are different, but in personal daily life or social activities the residents still maintain their previous lifestyle. The facts that the usage of some rooms in the house and planned areas of outdoor space contrary to the master plan shows that there are some misfit design where the "intended" usage are not use as its supposed to. These conditions occur because the built environment could

not facilitate the residents' way of life to fulfill their needs.

(2) Residents' evaluation findings show that there is high level of incapability for the residents to change the condition in their post disaster house design. The need for flexibility, personalization and easiness for maintenance are inevitable as most of the residents used to fix or change their house condition on their own. The condition where misfit in house design and outdoor spaces are unchangeable had resulted in residents' dissatisfaction. Similar evaluations were made to the outdoor space where dissatisfaction is also high. However, the controversy toward their responses to the possibly to change the condition need a further study whether the residents were indeed does not want to change or they can not change the situation.

(3) The results also show that residents still have a high participation and value to their community activities. Various types of community activities located at different neighborhood facilities imply the needs for these facilities to be provided in their settlement. However, there are also community activities that need to be done inside residents' houses and usually the frequency is more intensive.

7.2 Closure

The relationship between people and environment is a result among cultural, environmental (physical planning) and perceptual aspects. Physical features of the environment influenced its capability to facilitate the activities of its users by enhancing and encouraging certain behavior to the extent that it's provided. As a home is the most fundamental base for one's personal life, outdoor spaces around the home and neighborhood are also essential for the residents' daily live. Since misfit in housing could result in residents' dissatisfaction and restrict their original lifestyle, it is important for housing design to facilitate its inhabitants' activities and lifestyle. Especially for post disaster housing, it is necessary that post disaster housing to be built not only for an emergency situation but also to accommodate the survivors' way of life and needs in a long term and help their post disaster recovery process.

.

Acknowledgements:

The author acknowledged support from G-COE Center for Urban Earthquake Engineering (CUEE) in Tokyo Institute of Technology for funding this research. A sincere thanks to Prof. Ryuzo Ohno for his support and guidance for this study. Last but not least, thanks to all Gadjah Mada Architecture students who helped me to do field survey and interviewed and to the people in New Ngelepen who are willing to help in this research.

References:

Bayulke, Nejat (1983). *Lessons to be Learned from Relocation of Villages and Use of Prefabricated Houses in Post-disaster Housing in Turkey*. Proceedings of the Seminar on Socio-Architectural Aspects of Housing in Earthquake-Prone Areas of Turkey, Ankara, the Scientific & Technical Research Council of Turkey Building Research Institute.

Birkman, J. et.al. (2007) *Rapid Vulnerability Assessment in Sri Lanka Post-Tsunami Study of Two Cities:Galle and Batticaloa.* SOURCE **(**Studies of the University: Research, Councel, Education). Paffenholz, Bornheim,Germany: Publication Series of UNU-EHS Vol.7/August 2007.

Dikmen, Nese (2006) Relocation or Rebuilding in the Same Area: An Important Factor for Decision making For Post Disaster Housing Project. Department of Architecture, Suleyman Demirel University

Feinstein, David (2008) *Energy Psychology in Disaster Relief.* The journal *Traumatology* (Vol 14, Issue 1, March 2008). IF Research Group, University of Montreal .

Ikaputra(2008). *Response to Localize the Imported Culture.* Proceeding of the 14 World Conference on Earthquake Engineering October 12-17, 2008, Beijing, China

Saraswati Titien. "The Development of Architecture in Yogyakarta: Are the Reconstruction Buildings of Post-Earthquake Responsive?". Paper presented in the *National Seminar of the Development of Architecture in Indonesia*, Diponegoro University, Semarang, Indonesia, May 05, 2007.

JOINT CONFERENCE PROCEEDINGS
7th International Conference on Urban Earthquake Engineering (7CUEE) &
5th International Conference on Earthquake Engineering (5ICEE)
March 3-5, 2010, Tokyo Institute of Technology, Tokyo, Japan

SURVEY ON CAUSES OF FATALITIES IN RECENT JAPANESE EARTHQUAKES

Masahiro YOSHIMURA[1] and Saburoh MIDORIKAWA[2]

1) Graduate student, Department of Built Environment, Tokyo Institute of Technology, Japan
2) Professor, Department of Built Environment, Tokyo Institute of Technology, Japan
yoshimura.m.ac@m.titech.ac.jp, smidorik@enveng.titech.ac.jp

Abstract: Fatalities in recent Japanese earthquakes are surveyed and discussed. In nine earthquakes after the 1995 Hyogo-Ken Nanbu Earthquake, 114 fatalities have been reported. We surveyed the circumstances where 114 earthquake fatalities occurred. Publications by the nation and local governments, and newspaper articles are collected. Information on fatalities such as age, sex, place, and cause are examined. As a result of the survey, we confirmed chiefly the following points. For fatalities due to building collapse and shock or stress, vulnerability of aged people was observed. Fatalities from those causes would increase in the future earthquake disasters because of aging population and low birthrate in Japan. Fatalities due to shock or stress are occurred in the municipality with comparatively small intensity, such as the 4 or 5 lower.

1. INTRODUCTION

The 1995 Hyogo-ken Nanbu earthquake caused huge damage to the Hanshin region, and 6,437 fatalities due to this event was reported (Fire and Disaster Management Agency, 2006). Approximately 80% of cause of directly earthquake-related deaths was asphyxia and body compression (The Ministry of Health and Welfare, 1995). Circumstances of those were mostly due to building collapse.

Ikuta et al. (2001) analyzed the data of death and seriously injured person during the 1995 Hyogo-ken Nanbu earthquake, and pointed out that both death rate and serious injury rate rose with increasing age. Moreover, Lu and Miyano (1998) analyzed the fatalities of 11 earthquakes from the 1923 Great Kanto earthquake to the 1995 Hyogo-ken Nanbu earthquake. They pointed out that the age and sex distribution of earthquake fatalities have been affected by changes of population characteristics (e.g., aging population, low birthrate and increase of nuclear family), and those changes should be considered in earthquake casualty estimation.

In recent Japanese earthquakes, fatalities caused by the building collapse are fewer than past earthquakes. On the other hand, in the 2004 Niigata-ken Chuetsu earthquake, indirectly earthquake-related deaths (non-trauma deaths) which correspond to psychological shock, stress, tiredness or disease worsening accounted for 70% or more of the entire fatalities. This suggests that the cause of fatalities during earthquakes have been affected by the change of living condition and social environment in recent years. If the causes of fatalities are to be changed, we must understand them. However, there is little research that surveyed and analyzed the causes of earthquake fatalities after the 1995 Hyogo-ken Nanbu earthquake.

In this study, we survey the circumstances where earthquake fatalities occurred after the 1995 Hyogo-ken Nanbu earthquake and analyze its causes. The general trend for causes of earthquake fatalities is presented, and the characteristic of fatalities of earthquakes surveyed is discussed by a comparison of fatalities during the 1995 Hyogo-ken Nanbu earthquake.

2. SURVEY OF EARTHQUAKE FATALITIES AFTER THE 1995 HYOGO-KEN NANBU EARTHQUAKE

2.1 Outline of Survey

We surveyed earthquake fatalities after the 1995 Hyogo-ken Nanbu earthquake. The data are based on publications by the nation and local governments, and newspaper articles. As a result, 114 fatalities resulting from 9 earthquakes were surveyed (Fire and Disaster Management Agency, 2000, 2002, 2004, 2005, 2009a-e). These are summarized in Table l.

The earthquake caused the largest number of fatalities is the 2004 Niigata-ken Chuetsu earthquakes, 68 people. The second is the 2008 Iwate Miyagi Nairiku earthquake, 23 people. The third is the 2007 Niigata-ken Chuetsu-oki earthquake, 15 people. In the other six earthquakes, one or two fatalities have been reported. Age distribution of fatalities for each age-group is shown in Figure 1. Fatalities aged 60-year-old or more account for about 60%.

Table 1 Summary of Earthquake Fatalities after The 1995 Hyogo-ken Nanbu Earthquake.

Name of earthquake	Occurrence date	Maximum seismic intensity	Dead	Missing	Total
2000 Niijima and Kozushima earthquake	July 01, 2000 16:01	6 Lower	1		1
2001 Geiyo earthquake	March 24, 2001 15:27	6 Lower	2		2
2003 Tokachi-oki earthquake	September 26, 2003 4:50	6 Lower		2	2
2004 Niigata-ken Chuetsu earthquake	October 23, 2004 17:56	7	68		68
2005 Fukuoka-ken Seiho-oki earthquake	March 20, 2005 10:53	6 Lower	1		1
2007 Noto Hanto earthquake	March 25, 2007 09:41	6 Upper	1		1
2007 Niigata-ken Chuetsu-oki earthquake	July 16, 2007 10:13	6 Upper	15		15
2008 Iwate-Miyagi Nairiku earthquake	June 14, 2008 08:43	6 Upper	13	10	23
2008 Iwate-ken Engan Hokubu earthquake	July 24, 2008 0:26	6 Lower	1		1
Total			102	12	114

(note) Making from Fire and Disaster Management Agency homepage material (As of May 7, 2009)

Table 2 Cause of Earthquake Fatalities after The 1995 Hyogo-ken Nanbu Earthquake.

Cause / Name of earthquake	Number of fatalities								
	Building collapse	Landslides	Fire	Fence collapse	Furniture overturning	Fall-related injuries	Tsunami	Shock or stress	Other causes
2000 Niijima and Kozushima earthquake		1							
2001 Geiyo earthquake	1			1					
2003 Tokachi-oki earthquake							2		
2004 Niigata-ken Chuetsu earthquake	12	4						50	2
2005 Fukuoka-ken Seiho-oki earthquake				1					
2007 Noto Hanto earthquake				1					
2007 Niigata-ken Chuetsu-oki earthquake	9		1			1		4	
2008 Iwate-Miyagi Nairiku earthquake		19			1				3
2008 Iwate-ken Engan Hokubu earthquake						1			
Total	22	24	1	3	1	2	2	54	5

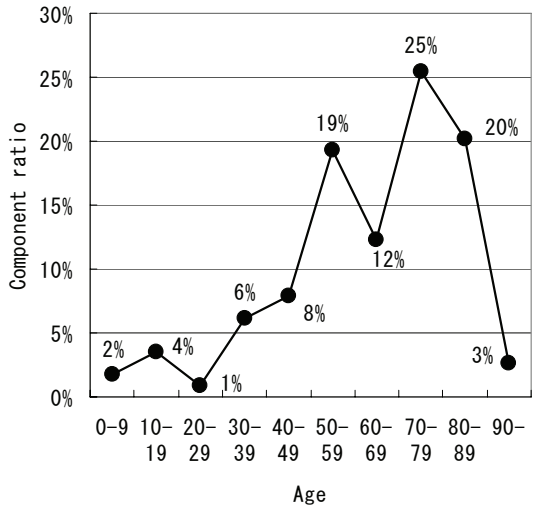

Figure 1 Age Distribution of Earthquake Fatalities after The 1995 Hyogo-ken Nanbu Earthquake

2.2 Causes of Earthquake Fatalities

We classified the causes of earthquake fatalities into nine categories. The categories are shown in Table 2.

The cause with the largest number of fatalities is shock or stress, with 54 fatalities. Shock or stress corresponds to psychological shock, stress, tiredness or disease worsening. The deaths due to those cause is called indirectly earthquake-related deaths or non-trauma deaths. The second major cause (24 fatalities) is landslides. Fatalities due to landslides include those caused by earthquake-induced slope failure and debris flow. The third cause (22 fatalities) is building collapse. Fatalities due to building collapse include those caused by structure collapse and partial building collapse, such as falling walls and debris, etc. The fourth cause is fence collapse, with 3 fatalities. Fence collapse corresponds to collapse of concrete-block walls and stone walls. Fall-related injuries and tsunami (seismic sea waves) rank fifth with two fatalities. Fall-related injuries correspond to slipping or stumbling, falling from bed, and falling from

stairs. Fire following earthquake and furniture overturning caused only one fatality. Other causes account for 5 fatalities. As expected, it accounts for 88% by three major causes (shock or stress, landslides, building collapse) for the entire fatalities.

In three earthquakes with ten or more fatalities, the primary cause of deaths is different respectively. That for the 2004 Niigata-ken Chuetsu earthquake is shock or stress, 50/68 or 74%. That for the 2008 Iwate Miyagi Nairiku earthquake is landslides, 19/23 or 83%. That for the 2007 Niigata-ken Chuetsu-oki earthquake is building collapse, 9/15 or 60%. As this reason, it is probably that the seismic intensity 6 upper or 7 were observed in these earthquakes. Additionally, in the 2004 Niigata-ken Chuetsu earthquake many aftershocks occurred, and in the 2008 Iwate Miyagi Nairiku earthquake epicentral area was mountainous region with many earthquake-induced landslides.

2.3 Profile of Each Cause of Fatalities

In this section, we outline the profile about building collapse and shock or stress among nine categories of causes of earthquake fatalities.

a) Fatalities due to Building Collapse

22 Fatalities due to building collapse have been reported. Of 22 fatalities, one occurred in the 2000 Geiyo earthquake, 12 in the 2004 Niigata-ken Chuetsu earthquake 12, and 9 in the 2007 Niigata-ken Chuetsu-oki earthquake. The breakdown of circumstances of 22 fatalities is that 20 fatalities (91%) are due to structure collapse, one is due to falling walls, and one is due to falling balcony. As a result, it is reconfirmed that one of the important measures to reduce fatalities is to prevent structure collapse.

b) Fatalities due to Shock or Stress

54 Fatalities due to shock or stress have been reported. Of 54 fatalities, 50 occurred in the 2004 Niigata-ken Chuetsu earthquake, and 4 in the 2007 Niigata-ken Chuetsu-oki earthquake. Because this cause had many fatalities, we examined subdivision cause; shock, stress, tiredness, or disease worsening. The results of subdivision are summarized in Table 3.

The breakdown of fatalities in those two earthquakes is shock 28%, stress 30%, tiredness 26%, and disease worsening 17%. Many cases of fatalities due to stress are from strong stress suffered from the earthquake and the living in evacuation shelters. Many cases of fatalities due to tiredness are from overwork because of cleaning up a mess due to earthquake damage and the living in evacuation shelters.

Next, number of municipalities and occurrence time of each subdivision fatalities during the 2004 Niigata-ken Chuetsu earthquake are summarized in Table 4. In either subdivision cause, fatalities have been observed in the large area. The occurrence time of fatalities due to shock corresponds to time when large aftershocks occurred. The occurrence time of fatalities due to stress, tiredness and disease worsening is in two or three months after the main earthquake.

Table 3 Subdivision cause of earthquake fatalities due to Shock and stress etc

subdivision cause	2004 Niigata-ken Chuetsu	2007 Niigata-ken Chuetsu-oki	Total
Shock	15		15
Stress	12	4	16
Tiredness	14		14
Disease worsening	9		9
Total	50	4	54

Table 4 Number of Municipalities and Occurrence time of Each Subdivision Fatalities during The 2004 Niigata-ken Chuetsu Earthquake

subdivision cause	Number of municipalities of fatalities	Occurrence time of fatalities
Shock	10	From October 23, 2004 (occurrence date of main shock) to October 31, 2004
Stress	5	From October 28, 2004 to the middle of December, 2004
Tiredness	9	From October 25, 2004 to the end of January, 2005
Disease worsening	5	From October 25, 2004 to the beginning of January, 2005

3. ANALYSIS OF CAUSE OF FATALITIES IN RECENT JAPANESE EARTHQUAKES

3.1 Age Distribution of Fatalities

In this section, we examine age distribution of fatalities in main municipalities of earthquake damaged area which had five or more fatalities.

Age distribution of fatalities of 9 earthquakes surveyed is shown in Figure 2. In the municipalities of the 2004 Niigata-ken Chuetsu earthquake and the 2007 Niigata-ken Chuetsu-oki earthquake, fatalities aged 60-year-old or more account for high ratio, because these two earthquakes had many fatalities due to building collapse and shock or stress. In Kurihara-city of the 2008 Iwate Miyagi Nairiku earthquake, over 60-year-old persons account for low ratio, because fatalities of landslides occupy the majority. This suggests that age distribution of earthquake fatalities have been affected by the cause of fatalities.

3.2 Analysis of Fatalities due to Three Major Causes

In this section, we analyze the causes of three major damages; shock or stress, building collapse, and landslides. The analysis does from the viewpoint of the age, and brings the feature together. Age distribution of fatalities due to three major causes is shown in Figure 3.

a) Fatalities due to Shock or Stress

The ratio of over 80-year-old persons of fatalities due to shock or stress is 37% and it is twice or more higher than the other two causes. That of 60-79-year-old persons is also high with 41%. Therefore, over 60-year-old persons account for about 80%. As this reason, it is thought that senior citizen is easy to receive the influence of stress and tiredness which are the causes with many fatalities in this classification

The age distribution in 9 earthquakes surveyed is compared with that of indirectly earthquake-related deaths in the 1995 Hyogo-ken Nanbu earthquake. These are shown in Figure 4. When the ratio of over 60-year-old persons is compared, that of the 1995 Hyogo-ken Nanbu earthquake is a little higher than 9 earthquakes. However, there is no large difference between them. This suggests that aged people have the vulnerability to shock or stress induced by earthquake disaster.

Because Japan has faced a rapidly aging population and low birthrate, fatalities of this category would become a large problem more and more in the future earthquake disasters.

b) Fatalities due to Building Collapse

The ratio of 19-year-old or less persons of fatalities due to building collapse is 18% and it is four times or more as high as the other two causes. Over 60-year-old persons account for about 60%. As this reason, it is thought that the children being at home were sacrificed by house collapse because main shock of the 2004 Niigata-ken Chuetsu earthquake occurred on Saturday evening (17:56).

The age distribution in 9 earthquakes surveyed is compared with that of directly earthquake-related deaths in the 1995 Hyogo-ken Nanbu earthquake. These are shown in Figure 5. In the 1995 Hyogo-ken Nanbu earthquake, about 80% of the cause of directly earthquake-related deaths was a crushing death by building collapse etc (The Ministry of Health and Welfare, 1995).

The ratio of over 60-year-old persons in the 1995 Hyogo-ken Nanbu earthquake is 53%, and that of 9 earthquakes surveyed are 63%. This suggests that the senior citizen become a victim easily due to earthquake-induced building collapse. Fatalities of this category would become a large problem more and more in the future earthquake disasters because of aging population and low birthrate in Japan.

c) Fatalities due to Landslides

The ratio of 40-59-year-old persons of fatalities due to landslides is 63% and it is 40% or more higher than the other two causes. Therefore, senior citizen and young people are few in fatalities due to landslides, because the majority of fatalities have been damaged while being out, working outdoor and getting in the car.

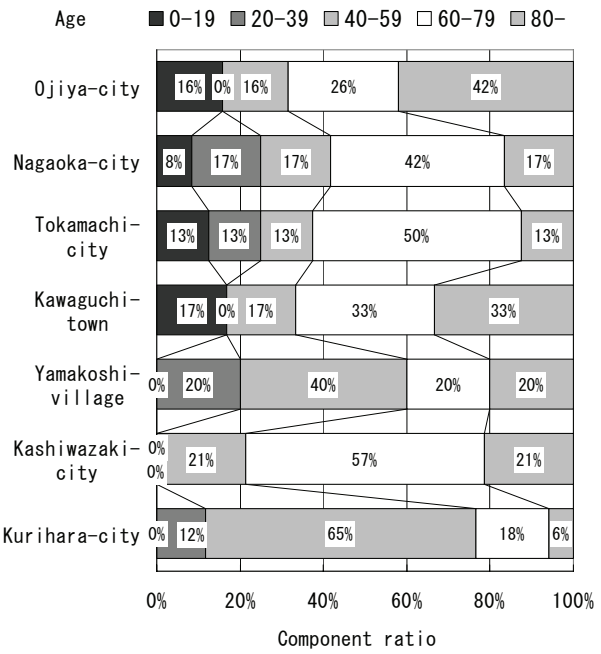

Figure 2 Age Distribution of Fatalities in 9 Earthquakes Surveyed

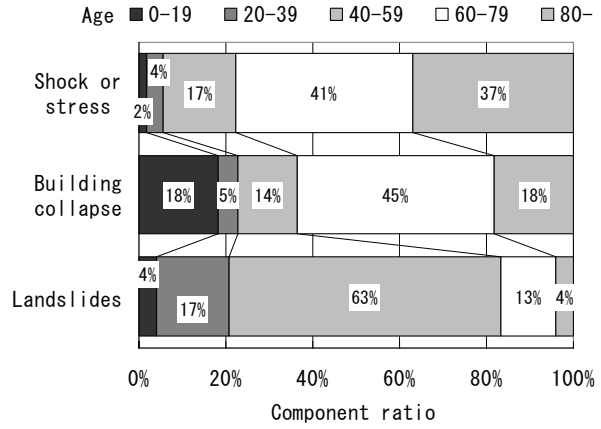

Figure 3 Age Distribution of Fatalities due to Three Major Causes

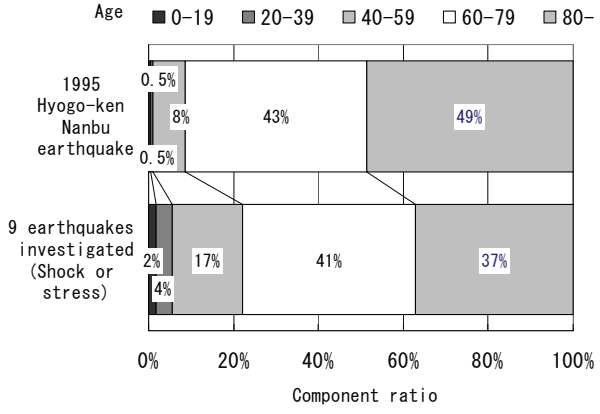

Figure 4 Age Distribution of Fatalities due to Indirectly Earthquake-related Deaths

3.3 Examination of Area of Earthquake Fatalities

In this section, we examine the relationship between the maximum seismic intensity (JMA scale) and the occurrence of earthquake fatalities according to the municipality for the 2004 Niigata-ken Chuetsu earthquake with many fatalities of building collapse and shock or stress. These are summarized in Table 5.

Fatalities due to building collapse have been occurred only in the municipality with the intensity 6 upper or 7. Among fatalities due to shock or stress, many of them have been occurred in the municipality with strong intensity. On the other hand, a few fatalities have been occurred in the municipality with comparatively small intensity, such as the intensity 4 or 5 lower.

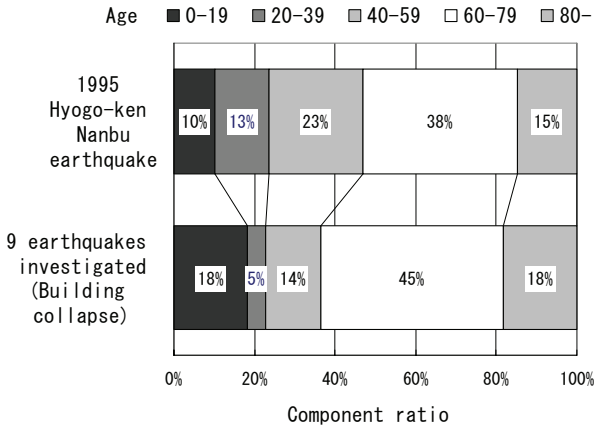

Figure 5 Age Distribution of Fatalities due to Directly Earthquake-related Deaths

4. CONCLUDING REMARKS

In this research, fatalities in recent Japanese earthquakes are surveyed and discussed. In nine earthquakes after the 1995 Hyogo-Ken Nanbu Earthquake, 114 fatalities have been reported. We surveyed the circumstances where 114 earthquake fatalities occurred and analyzed its causes. As a result of the survey, we confirmed the following points:

(1) The causes of 114 earthquake fatalities after the 1995 Hyogo-ken Nanbu earthquake is classified into nine categories that include shock or stress (54 fatalities), landslides (24), building collapse (22), fence collapse (3), fall-related injuries (2), tsunami (2), fire (1), furniture overturning (1), and other causes (5).
(2) The age distribution of earthquake fatalities have been affected by the cause of fatalities.
(3) For fatalities due to building collapse and shock or stress, vulnerability of aged people was observed. Fatalities from those causes would increase in the future earthquake disasters, because Japan has faced a rapidly aging population and low birthrate.
(4) Fatalities due to shock or stress are occurred in the municipality with comparatively small intensity, such as the intensity 4 or 5 lower (JMA scale).

Table 5 Seismic Intensity at Municipalities where Earthquake Fatalities are Observed in The 2004 Niigata-ken Chuetsu Earthquake

Maximum Seismic intensity	Name of municipality	Building collapse	Shock or stress
7	Kawaguchi-town	4	1
6 Upper	Ojiya-city Tokamachi-city Yamakoshi-village Oguni-town	5 1 2	13 7 3 1
6 Lower	Nagaoka-city Koshiji-town Tochio-city Kawanishi-town Yamato-town Horinouchi-town Hirokami-village		8 3 1 1 1 1 1
5 Upper	Mitsuke-city Yunotani-village Koide-town		3 2 1
5 Lower	Tsubame-city		1
4	Yuzawa-town		1

(note) Making from the data only of the municipality where the seismograph station of Japan Meteorological Agency or the municipality existed

References:

Fire and Disaster Management Agency (2000), "The Damage Caused by 2000 Niijima and Kozushima earthquake," 15th report, July 7, 2000, http://www.fdma.go.jp/data/010409211512175018.pdf, (in Japanese)

Fire and Disaster Management Agency (2002), "The Damage Caused by 2001 Geiyo earthquake," Final report, September 24, 2002, http://www.fdma.go.jp/data/010409282212087846.pdf, (in Japanese)

Fire and Disaster Management Agency (2004), "The Damage Caused by 2003 Tokachi-oki earthquake," Final report, March 31, 2004, http://www.fdma.go.jp/data/H160331TokachiJishin.pdf, (in Japanese)

Fire and Disaster Management Agency (2005), "The Damage Caused by 2005 Fukuoka-ken Seiho-oki earthquake," 34th report, May 12, 2005, http://www.fdma.go.jp/data/010600271816273701.pdf, (in Japanese)

Fire and Disaster Management Agency (2006), "The Damage Caused by 1995 Hyogo-ken Nanbu earthquake," Final report, May 19, 2006, http://www.fdma.go.jp/data/010604191452374961.pdf, (in Japanese)

Fire and Disaster Management Agency (2009a), "The Damage Caused by 2004 Niigata-ken Chuetsu earthquake," 75th report, January 13, 2009, http://www.fdma.go.jp/data/010900132148314457.pdf, (in Japanese)

Fire and Disaster Management Agency (2009b), "The Damage Caused by 2007 Noto Hanto earthquake," 49th report, January 13, 2009, http://www.fdma.go.jp/data/010900132150547022.pdf, (in Japanese)

Fire and Disaster Management Agency (2009c), "The Damage Caused by 2007 Niigata-ken Chuetsu-oki earthquake," 50th

report, January 13, 2009, http://www.fdma.go.jp/data/01090013 2154011100.pdf, (in Japanese)
Fire and Disaster Management Agency (2009d), "The Damage Caused by 2008 Iwate-Miyagi Nairiku earthquake," 75th report, January 13, 2009, http://www.fdma.go.jp/data/0109001321571 55289.pdf, (in Japanese)
Fire and Disaster Management Agency (2009e), "The Damage Caused by 2008 Iwate-ken Engan Hokubu earthquake," 25th report, January 13, 2009, http://www.fdma.go.jp/data/01090013 2158172400.pdf, (in Japanese)
Hyogo Prefectural Government. (2005),"Investigation of death during The Great Hanshin-Awaji Earthquake seen", Disaster Management Division, Disaster Management Bureau, press release on December 22, 2005, http://web.pref.hyogo.lg.jp/pa20/ pa20_000000016.html, (in Japanese)
IKUTA, E., MIYANO, M., ITOIGAWA, E. and KUMAGAI, Y. (2001), "Comparison between the death and serious injury due to the Hyogo-ken Nanbu Earthquake on the aspect of those mechanism," *Summaries of Technical Papers of Annual Meeting Architectural Institute of Japan., F-1*, 417-418. (in Japanese)
Kindai-Shoubou editorial office (2000), "Damage situation during The Great Hanshin-Awaji Earthquake (From the material of Fire and Disaster Management Agency as of January 12, 2000.)," Kindai-Shoubou, 38(3), Kindai-Shoubousha, February, 2000., (in Japanese)
LU, H. and MIYANO, M. (1998), "Study on the Age Group and Sex Distinction of Death due to Earthquakes," *Summaries of Technical Papers of Annual Meeting Architectural Institute of Japan. B-2*, 93-94. (in Japanese)
Ministry of Health and Welfare (1995), "Situation of death during The Great Hanshin-Awaji Earthquake seen from Vital Statistics," Statistics and Information Department, Minister's Secretariat, December, 1995. (in Japanese)
Niigata Prefectural government (2008), "The Damage Caused by 2004 Niigata-ken Chuetsu earthquake," 173rd report, September 24, 2008, http://www.pref.niigata.lg.jp/HTML_Article/173,2.pdf, (in Japanese)
Niigata Prefectural government (2009), "The Damage Caused by 2007 Niigata-ken Chuetsu-oki earthquake," 270th report, March 13, 2009, http://www.pref.niigata.lg.jp/HTML_Simple/higai210 3131500.pdf, (in Japanese)

JOINT CONFERENCE PROCEEDINGS
7th International Conference on Urban Earthquake Engineering (7CUEE) &
5th International Conference on Earthquake Engineering (5ICEE)
March 3-5, 2010, Tokyo Institute of Technology, Tokyo, Japan

WORKSHOP FOR DISASTER IMAGINATION IMPROVEMENT OF NURSERY SCHOOL LEADERS

Mariko Abe[1], Kimiro Meguro[2], and Mari Yokoya[3]

1) PhD Candidate, Department of Civil Engineering, The University of Tokyo, Japan
2) Director/Professor, International Center for Urban Safety Engineering, Institute of Industrial Science, The University of Tokyo, Japan
3) Researcher, Institute of Industrial Science, The University of Tokyo, Japan
abe@risk-mg.iis.u-tokyo.ac.jp, meguro@iis.u-tokyo.ac.jp

Abstract: To protect small children from big accidents and disasters, nursery school members and related people should imagine their possible disaster situation and share their images, questions and problems. Based on the situation mentioned, we have designed and conducted a Disaster Imagination Workshops (DI-WS) at nursery schools (Abe and Meguro, 2005). Although this DI-WS had been only possible so far in individual nursery school unit due to the limitation of human resources, it became possible with the support of Ms.Yokoya's NPO to conduct a bigger scale DI-WS, making use of their experiences and resources. So, to let DI-WS more popular and to expand its field of application, we designed a new training program for directors and chiefs of nursery schools using DI-WS, and applied it to the competitive bidding of general risk management training program sponsored by Tokyo Municipality Training Institute. Fortunately, as our proposal was received high evaluation and was selected, we carried out our program and examined the possibility of expanding DI-WS approach. Finally, based on the result, we listed up problems for expanding this approach.

1. INTRODUCTION

Today in Japan, a nursery school is one of the typical places where many small children gather, and the load on adults is very heavy when a big accident or disaster, such as earthquake disaster occurs. There are two important points for nursery school people to protect small children from such disasters. First, each member of nursery school should improve the disaster imagination. Second, members should share their images and experiences with each other.

Therefore, we have designed and conducted a Disaster Imagination Workshop (DI-WS) at a nursery school (Abe and Meguro, 2005). In this WS, the participants first decide the conditions such as season, day of the week, occurrence time, and weather, etc. Then, they start imaging the situation around them as time goes since the hazard attack, and make a story in which they themselves are central figures (Figure 1). In addition, they write down the questions and problems on the memo pads. After writing, they line up their story seats on the table and read each story, comparing along time passage. Sometimes the image of each member is quite different each other. Through this practice, WS members can imagine their possible disaster situation and share their images, questions and problems.

With the definition of nursery school leaders as directors of nursery schools and chiefs who help them, we attempted to design a new training program on general risk management for nursery school leaders using DI-WS to expand the field of DI-WS application and let it popular. However, since Japan is an earthquake disaster prone country and leaders are strongly interested in earthquake disaster, as the first step of the approach, we picked up earthquake disaster as an example from all risks that we should consider. We designed a training program composed of two Workshops. The first half is Problem Sharing Workshop (PS-WS) concerning all risk issues, and the latter half is DI-WS based on PS-WS. Then, we carried out this program and examined the possibility of expanding DI-WS approach. Finally, based on the result, we listed up problems for expanding this approach and proposed a DI-WS support system.

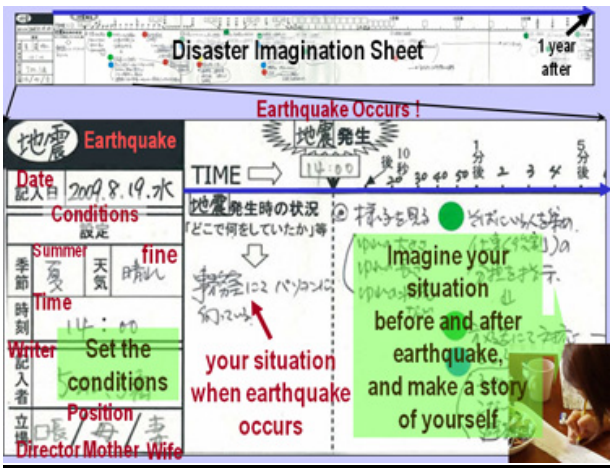

Figure 1 Disaster Imagination Tool

2. DESIGN OF RISK MANAGEMENT TRAINING FOR NURSERY SCHOOL LEADERS

In this chapter, we will introduce today's situation of the risk-management of nursery schools in Japan and the risk management training for nursery school leaders, and explain about the flow of design of the training program.

2.1 Risk Management Training for Nursery School Leaders

National guideline for nursery school, which was revised in 2008, clearly describes that a nursery school director should take responsibility in matters of safety of children at his/her nursery school. Recently, risk management trainings for nursery school leaders are being held and are executed by the social welfare corporation or the municipality. Medical Doctors, lawyers, risk consultants, NPOs and others related to children's safety give lectures in the training. The lecturer is decided by direct nomination or competition, etc. and training takes several hours to several days. However, support system for feedback for participants after going back to their nursery schools, or the succession of the previous year's training data for next year is not enough yet.

2.2 Design of the Training Program

In order to introduce DI-WS into the training for leaders of nursery schools, we designed training program that includes DI-WS, and applied it for the competition of the 2009 risk-management training sponsored by the Tokyo Municipality Training Institute. The competition was nominated tender, and Ms. Yokoya, one of the authors, her NPO was also nominated. The number of participants expected was about 60, and the time of the training planned was 6 hours.

In this study, in order to let DI-WS more popular, we tried to introduce DI-WS into general risk-management training for nursery school leaders. However, since Japan is an earthquake disaster prone country and leaders are strongly interested in earthquake disaster, as the first step of the approach, we picked up earthquake disaster as an example from all risks that we should consider. We designed a training program composed of two Workshops. The first half is Problem Sharing Workshop (PS-WS) concerning all risk issues, and the latter half is DI-WS based on PS-WS.

We divided approximately 60 participants into 9 groups composed of 6-7 members. Emcee, facilitation and recording were done by 6 staffs (2 NPO members and 4 postgraduate students). To share information smoothly among participants, basic information of all nursery schools must be understood first. Therefore, we prepared some basic information seats to fill in the number of staffs and children, construction year of school buildings, indoor map, outdoor map, playground map, and map around the nursery school (route to the park, feature around and so on).

In PS-WS, each participant writes past accidents, shivering events, uneasiness, questions and problems freely on the cards. Then, they arrange the cards on a large paper, discussing in each group. Finally, presenter of each group explains about their discussion result to share information as a whole. We designed the cards in order to arrange the data easily after the training.

In DI-WS, we set 5 conditions - weather, seismic intensity, season, earthquake occurrence time and a day of the week, which may change the situation and the correspondence after the earthquake. The disaster imagination can be widely shared in a limited time by imaging different conditions in each group and sharing them with all participants. However, extreme different conditions may cause confusion when they compare their situations. So, in this program, we set a common condition for weather and seismic intensity as "fine and JMA intensity of 6+" among all groups, and different conditions for season, earthquake occurrence time and a day of the week.

3. RESULTS OF THE PROGRAM

The program we designed received high valuation and was adopted by the Tokyo Municipality Training Institute, and we carried out the program in August, 2009 (Figures 2, 3, 4, and 5). This chapter describes the result of this training program.



Figure 2: Participants



Figure 3: Staffs (2 NPO Members and 4 Postgraduate Students)



Figure 4 PS-WS



Figure 5 DI-WS

PS-WS (Problem Sharing Workshop)

When a big earthquake occurs, can nursery school teachers really move and protect the children?

DI-WS (Disaster Imagination Workshop)

30sec later	Is my house OK? Do fires occur? How about the neighborhood of my house?
5min later	I should go to nursery school, but are families all right?
20min later	Can I bring my mobile phone out of my house? Can I contact with my husband?
1hour later	Usually it takes 7 minutes by walk to the nursery school, but I'm worried about the road condition.
2hours later	Is the building of the nursery school all right? Isn't there any child who has been injured?
others	I should think about the toilet and the meal.

Figure 6 Example of Problems

In PS-WS, participants wrote 304 cards (accident: 102, shivering event: 119, uneasiness/questions/problems: 83). The risk described in the cards varied in topics such as earthquake, accident, suspicious person invasion, allergies, and bees. etc. The number of cards collected concerning earthquake was 21 in PS-WS and 77 in DI-WS. When we compared PS-WS and DI-WS, problems written in DI-WS were more concrete and specific than those of PS-WS (Figure 6). During presentation time in DI-WS, presenters explained peculiar contents due to the conditions of his/her group to understand the difference of the situation by different condition (Table 1). We arranged the cards and the stories, and analyzed the contents according to the type of danger or various characteristics of parties and so on, and applied to design of the support system (proposed in chapter 4).

Table 1 Setting Condition and Content of the Presentation of Each Group

	Season Day of the week Occurring time	Situation when the earthquake occurs	Contents (Extracts)
1	summer weekday 8:00	going to work	・How to contact with the parents?
2	summer weekday 10:00	Taking care of children	・The tasks changes according to the standpoint. The nursery school leaders should think about the whole matters, and the other teachers should take care of children's mental aspect.
3	winter weekday 10:00	Taking care of children	・Can we serve warm meals? ・Because it is cold, small children cannot refuge in clothes alone .
4	summer weekday 12:00	Eating lunch /brushing teeth /children taking a nap	・Tableware may be scattered ・I'm worried about the heat under hot weather.
5	summer weekday 14:00	Children taking a nap, adults taking a break	・Can I understand the whole situation at once? Some of the staffs are taking a rest.
6	summer weekday 16:00	Taking care of children (inside and outside)	・Check the injured children.
7	winter weekday 16:00	Taking care of children	・There is fear of a fire because we use the stoves.
8	summer weekday 18:00	Shifts to the overtime childcare	・Correspondence is difficult because of the time zone shifting to night. ・How can we respond by few people?
9	summer holiday 16:00	Few people are taking care of children /at home	・How can we respond by few people? ・If parents' offices are far, pick-up might be next day.

The 38 questionnaires of participants' impressions were broken down into 3 categories – 22 were positive such as "I felt that the training under the various conditions are necessary", 11 were negative such as "Time was limited", and 5 were both. Most of negative answers concerned about the time scheduling. In the training, the discussion time exceeded 25min-40min than that of what we had expected. Therefore, we had to shorten the time of lecture and presentation (Figure 7). We will redesign the time schedule of the training based on this result.

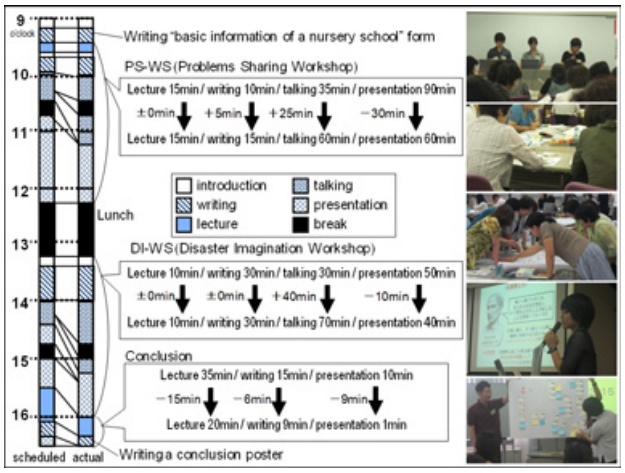

Figure 7 Program (Scheduled/Actual)

From the questionnaire survey, we found some motivation, such as, "I want to download the writing form of DI-WS". Moreover, after the training, we got mails from some participants that “we want to do DI-WS in our nursery school”, and three nursery schools did DI-WS (Figure 8). It shows possibility that DI-WS in the training for the leaders of nursery schools may lead to the DI-WS in nursery schools.



Figure 8 DI-WS in a Nursery School

Based on the situation explained above, we could conclude that there is the high possibility of expanding the field of DI-WS approach by introducing DI-WS into risk management training for nursery school leaders.

4. PROPOSAL OF THE DI-WS SUPPORT SYSTEM BASED ON THE RESULT OF THE TRAINING

For establishing a new DI-WS system in risk management training for nursery school leaders, it is necessary to build the Workshop support system. First of all, it is necessary to improve contents and time schedule of current DI-WS and prepare the DI-WS training set by which nursery school members can carry out Workshop based on their characteristics by themselves smoothly. Moreover, to answer the participant's question in Workshop, the lecturer should know the knowledge on the life patterns of the nursery school members, as well as on disaster mitigation. Therefore, a support system to get information and hints listed below is necessary.

・Various information which helps carrying out DI-WS
・Hints for solving questions and problems arisen from DI-WS

The system will be designed based on the data obtained from the DI-WS. For updating the system, we will add the lessons learned from past disaster and accidents, and knowledge and comments by specialists, and data from the future Workshops. In the future, we will deal with the other risks besides earthquake disaster risk, and make the support system for nursery schools by which they can manage their total risks by improving their risk imagination.

5. CONCLUSIONS

In this paper, we attempted to introduce a Disaster Imagination Workshop (DI-WS) into risk management training for nursery school leaders. As the first step of the research, we picked up earthquake disaster as an example from all risks that we should consider. We have designed a training program composed of two Workshops. The first half is Problem Sharing Workshop (PS-WS) concerning all risk issues, and the latter half is DI-WS based on PS-WS. Then, we carried out this program and examined the possibility of expanding DI-WS approach. Finally, based on this result, we listed up problems for expanding this approach and proposed a DI-WS support system. In the future, we will collect more data for the support system by conducting WSs and hearing surveys.

References:

Abe, M., and Meguro, K.. (2005), “A proposal of disaster imagination Workshop (Meguro-maki WS) for improving total disaster reduction ability of nursery schools and others”, SEISAN-KENKYU –Bimonthly report of the Institute of Industrial Science, the University of Tokyo - 57, pp.538-542 (in Japanese)

Abe, M., and Meguro, K.. (2007), “A study for improving total disaster reduction ability of nursery schools and kinder gartens”, Proceedings of International Symposium on New Technologies for Urban Safety of Mega Cities in Asia, pp.521-528.

JOINT CONFERENCE PROCEEDINGS
7th International Conference on Urban Earthquake Engineering (7CUEE) &
5th International Conference on Earthquake Engineering (5ICEE)
March 3-5, 2010, Tokyo Institute of Technology, Tokyo, Japan

INTRODUCTION OF JAPANESE COASTAL WAVE MONITORING NETWORK

Toshihiko Nagai[1)]

1) Executive Director, Port and Airport Research Institute, Japan
nagai@pari.go.jp

Abstract: History and present situation of Japanese coastal wave monitoring system named as NOWPHAS (Nationwide Ocean Wave information network for Ports and HArbourS) is introduced in this paper. NOWPHAS has been established and operated since 1970 by the Ports and Harbours Bureau of the Ministry of Land, Infrastructure, Transport and Tourism (MLIT) and its associated agencies including the Port and Airport Research Institute (PARI). In the year of 2009, observed data of waves have been recorded at 61 seabed installed acoustic wave gauge stations and 8 deep-sea GPS buoy stations. The data is being collected and analyzed at PARI. Examples of the observed results by the first two sets of the deep-sea GPS buoys are also introduced in this paper.

1. INTRODUCTION

Coastal wave information is very important in various occasions for port and harbor engineers, in the stages such as port and harbor planning, maritime structure design, maritime construction management, and coastal disaster study. This paper introduces history and present situation of Japanese coastal wave-tide observation and information system named as NOWPHAS (Nationwide Ocean Wave information network for Ports and HArbourS). NOWPHAS has been established and operated since 1970 by the Ports and Harbours Bureau of the Ministry of Land, Infrastructure, Transport and Tourism (MLIT) and its associated agencies including the Port and Airport Research Institute (PARI). In the year of 2009, observed data of waves have been recorded at 61 seabed installed acoustic wave gauge stations and 8 deep-sea GPS buoy stations.

2. NOWPHAS

NOWPHAS, the Japanese coastal wave observation and analysis system, has been operated since 1970 by the Ports and Harbors Bureau of the Ministry of Land, Infrastructure, and Transport and its associated agencies including the Port and Airport Research Institute (PARI) (Nagai,et.al, 1994). Development and improvement of the NOWPHAS has been achieved mainly during a recent decade (Nagai, 2002, Nagai, et. al., 2003 and Nagai, et. al., 2008), including the real-time data acquisition, analysis and distribution system using the internet telecommunication system (http://www.mlit.go.jp/kowan/nowphas), and offshore deep-sea GPS buoy system development and application.

The Doppler-type Wave Directional Meter (DWDM) , NOWPHAS principal seabed installed wave gauge now, was put into practical use in 1995 after long years' cooperation research among PARI (Port and Airport Research Institute), JAMSA (JApan Marine Surveyors Association), and Kaijo Co. DWDM enabled us to obtain directional spectrum information with one single sea-bed installed sensor by application of the Doppler Principle of the acoustic signal in the sea. DWDM also realized infra-gravity wave observation with one single seabed installed sensor.



Photo 1. DWDM Seabed Installed Sensor

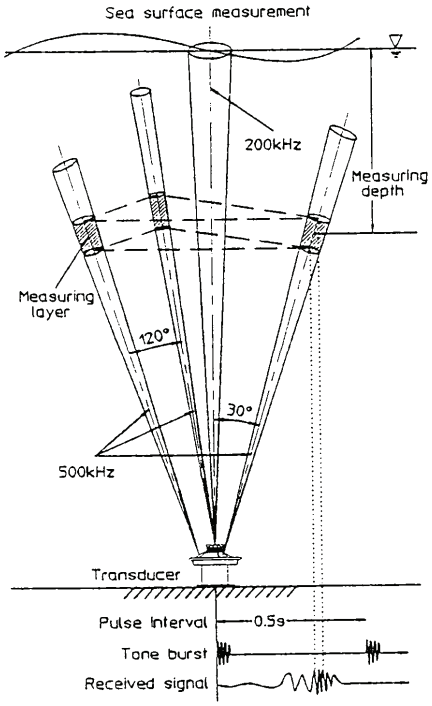

Figure 1. Observation Principle of DWDM

Photo 1 shows the seabed installed DWDM sensor, and Figure 1 shows the observation principle of DWDM (Takayama, et. al. 1994, Hashimoto, et. al., 1996). Ultrasonic signal output to vertical direction takes the same rule to the existing USW. In addition, three components of oblique directional ultrasonic signal output are for the directional wave measurement. By applying the Doppler effect each oblique directional water particle velocity in arbitrary layer can be obtained. Numerical method to obtain directional spectrum from the obtained data has also been developed by PARI (Hashimoto, et. al., 1996). DWDMs have been installed at water depth 20 to 50 m.

3. DEVELOPMENT OF GPS BUOY SYSTEM

3.1 GPS Buoy System

Newly developed GPS buoy system, which applies RTK-GPS techniques to exact measurement of offshore floating buoys, is to be the future of offshore wave and tsunami monitoring system for Japanese coastal line (Nagai, et. al., 2006 and Nagai, et. al., 2007). The GPS buoys can be installed in deeper and more offshore area than the existing seabed-installed wave gauges, making earlier tsunami detection possible with appropriate filtering techniques of observed data. In addition, they can observe deep-sea conditional waves and swells.

Figure 2 shows a concept diagram of the GPS Buoy system (Kato, et. al., 2001). In setting an on-land reference GPS base station within 20km from the buoy, Real-Time Kinematical method is applied. Field pre-experiments conducted at 100m deep and 13km off the Muroto-Misaki cape in 2004, have proved its applicability to offshore wave, tide and tsunami observation (Nagai, et. al., 2004: Nagai, et. al., 2005).

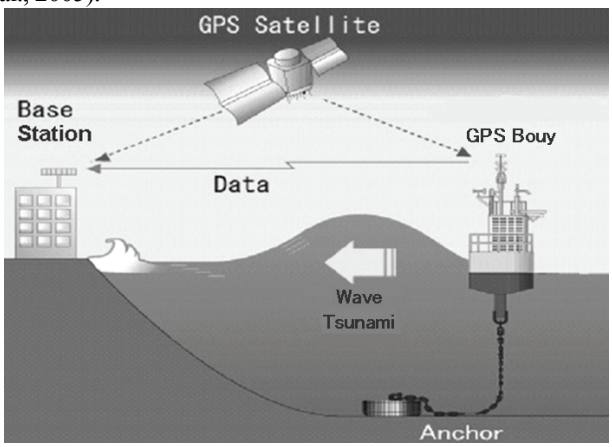

Figure 2 Concept of the GPS Buoy System

3.2 Location of the First GPS Buoys of NOWPHAS

Figure 3 shows locations of the GPS buoys. One is located offshore 144m deep in Miyagi Prefecture (Site M-G) and the other is 204m deep in Iwate Prefecture (Site I-G). In Figure 3 are also shown existing seabed-installed type wave gauges, DWDM off the Ishinomaki-Port 21m deep (Site M-S), and USW (Ultra-Sonic Wave Gauge) off the Kamaishi-Port 50m deep (Site I-S) of NOWPHAS network for comparison (Nagai, et. al., 2008).

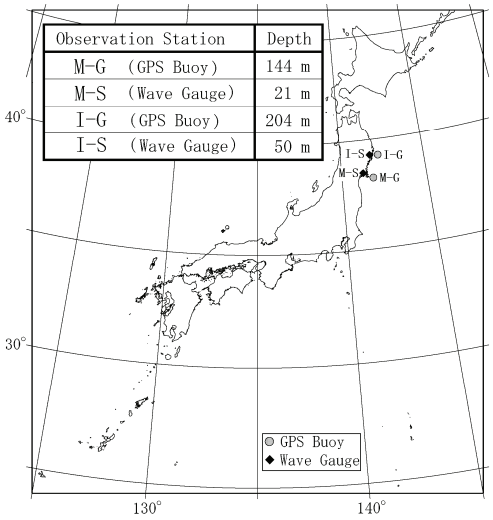

Figure 3 Locations of GPS Buoys and Wave Gauges

3.3 Statistic Wave Climate Analysis

Statistic wave climate analysis was conducted for 6 months Apr-Sept2007. At each wave station, continuous wave data sampling was conducted with intervals of 1.0s for GPS buoys and 0.5s for seabed installed wave gauges.

Zero-up-cross and spectral wave analysis was conducted with every 20 minutes data set. Effective data ratios were 97.7% and 97.6% for M-G and I-G GPS buoys respectively, meaning that only about 2% of the total observation data were missed due to various reasons including GPS positioning errors. While the same were 98.3% and 99.6% for M-S and I-S seabed installed type wave gauges. Statistic wave climate analysis was conducted for 6 months between April and September in 2007. At each wave station, continuous wave data sampling was conducted with the interval of 1.0s for GPS buoys and 0.5s for seabed installed wave gauges. Results of the analysis shows monthly averaged significant wave heights and the lower shows significant wave periods. Obvious difference can be seen in significant wave heights between the deep-sea GPS buoys and the shallower seabed wave gauges, while very little difference can be seen in significant wave periods.

3.4 Frequency Banded Wave Spectrum Analysis

Results of frequency banded wave analysis based on spectral analysis are also introduced in this paper. Table 2 shows defined 6 frequency bands from the lowest band f1, with corresponding periods longer than 30s, to the highest band f6, with corresponding periods shorter than 6s (Nagai, et.al., 2002). The frequency-banded analysis shows wave transformation characteristics for the cases from deep-sea GPS buoy to the shallow seabed wave gauge. little difference can be seen in significant wave periods.

Table.2 Frequency Bands Division

Band	Period	Frequency
f1	30s <	0.003Hz >
f2	15-30s	0.039～0.063Hz
f3	10-15s	0.070～0.094Hz
f4	8-10s	0.102～0.125Hz
f5	6-8s	0.133～0.164Hz
f6	< 6s	0.172Hz <

Figure 4 shows one example of the frequency banded wave statistics. Monthly average frequency banded wave heights are demonstrated in each frequency band. Although wave heights observed by deep sea GPS buoys are bigger than those by shallower seabed sensors in each frequency band, such difference is bigger in the higher frequency bands than in the lower ones. Both GPS buoys show very similar frequency banded wave statistics, meaning that offshore wave statistics do not obviously vary at the two observation sites more than 100km away from each other.

Figure 5 shows distribution of frequency banded wave directions at M-G, M-S and I-G. At Site I-S directional wave observation has not been conducted. GPS buoy observed wave directional analysis needs frequency banded in order to eliminate resonance response of the buoy motion. In the infra-gravity frequency band f1 of the corresponding period longer than 30s, horizontal motion of the GPS buoy was very complicated due to slow drift oscillation. In the highest frequency band f6 of the corresponding period shorter than 6s, horizontal motion of the GPS buoy was also very complicated due to resonance effects of rolling, pitching and heaving motions. Nevertheless, in the other frequency bands of f2, f3, f4 and f5 of corresponding period in between 6s and 30s, wave directions of each frequency band were clearly seen in each band (Shimizu, et. al., 2006a). In the Figure 5, wave directional distributions of f4 and f3 bands with corresponding periods 8-10s and 10-15s respectively are demonstrated. M-G and I-G GPS buoys observed wider range of NE, ENE, E, ESE and SE directions, while shallower M-S DWDM observed narrower range of SE and SSE ones, due to the differences of the topographical sheltering and wave shoaling effects.

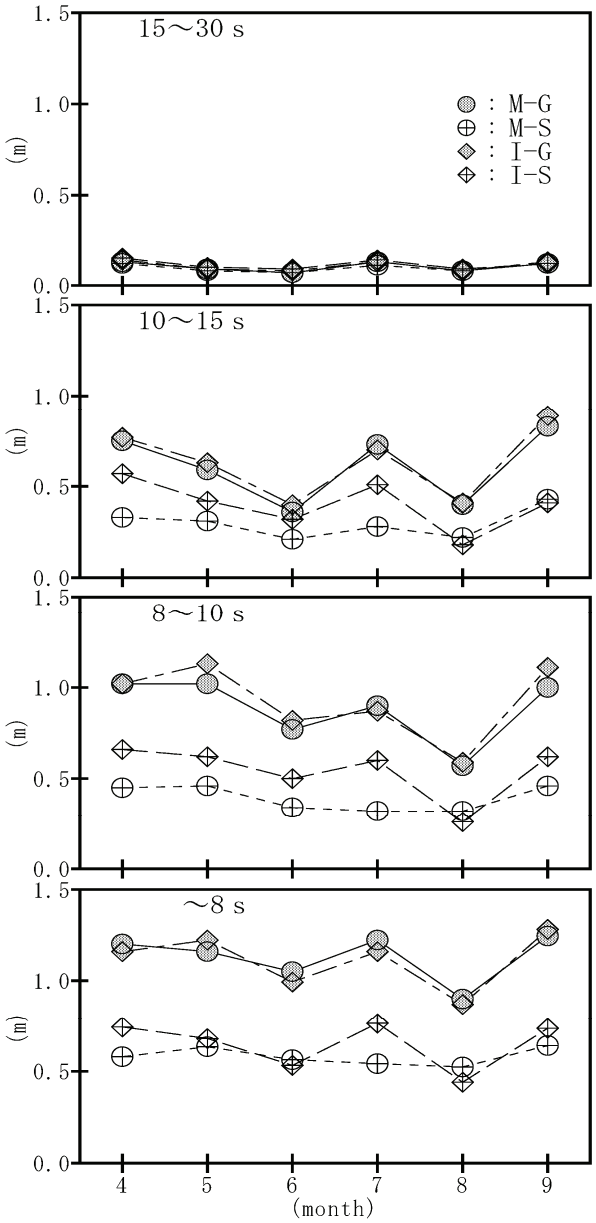

Figure 4 Monthly Averaged Wave Heights

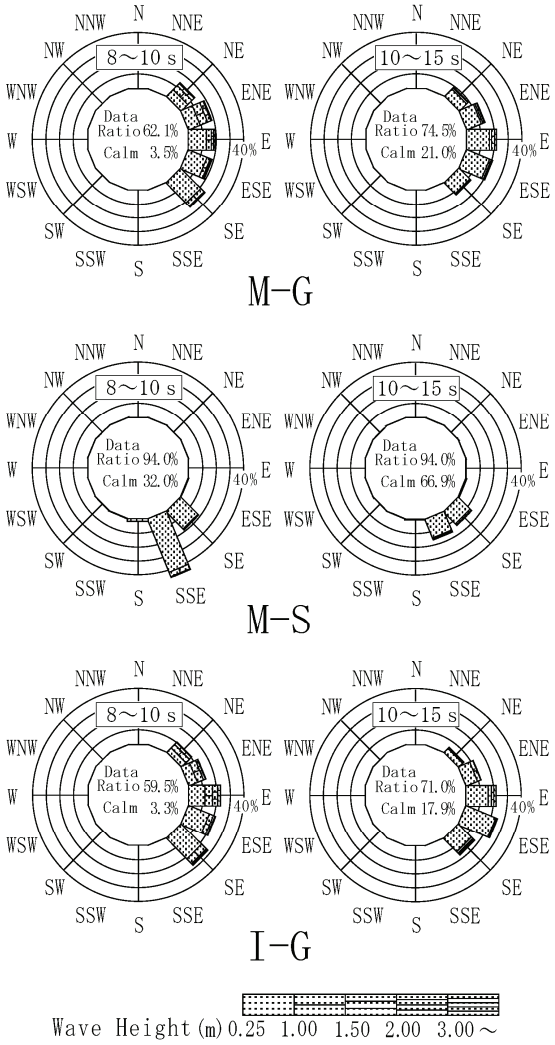

Figure 5 Distribution of the Frequency Banded Wave Directions

3.5 Observation of Abnormal Sea States

Wave climate analysis was conducted for high wave condition due to typhoon attack. Figure 6 is an example, showing time history of significant wave heights and periods for one day on September 7th 2007, when the typhoon No.0709 passed through. The maximum significant wave height of 9.16m with the significant wave period of 11.8s was observed at the M-G GPS buoy, and the maximum significant wave height of 8.11m with the significant wave period of 11.6s was observed at the I-G GPS buoy 3 hours later, as the typhoon was moving from south to north. The GPS buoys observed much bigger significant wave heights in both normal and abnormal sea states than the shallower seabed wave gauges, free from the topographical sheltering effects by peninsulas. It seems that deep-sea wave observation is necessary to evaluate offshore wave conditions.

3.6 2007 Peru Earthquake Tsunami

The 2007 Peru Earthquake Tsunami propagated in the Pacific Ocean and arrived at the Pacific coasts of Japan about one day after the earthquake event. Simulated tsunami arrival time was around JST 4:00 a.m. on August 17, 2007. Figure 7 shows the observed low-pass-filtered low frequency sea level fluctuation data ((Shimizu, et.al.,2006b) near Kamaishi area with 3 sensors: (1) I-G GPS Buoy 204m deep, (2) I-S near-shore seabed acoustic wave gauge at 50m deep, and (3) I-T coastal tide station of the Japanese Coastal Guard.

As the tsunami heights were not so large compared to then existing normal sea's low frequency fluctuation level, the first tsunami wave arrival was not clear in any data at these 3 stations. Nevertheless, after JST 6:00 a.m., low frequency sea surface fluctuation due to the tsunami can be seen in seabed wave gauge and tide station data for several hours, while the GPS buoy was not able to identify the tsunami profile, because tsunami heights are smaller in

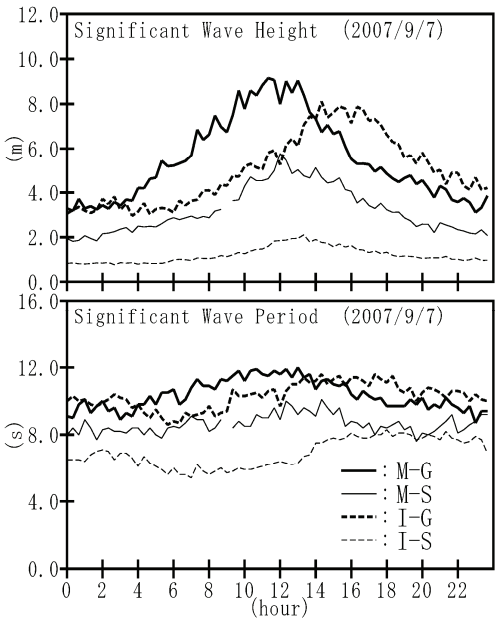

Figure 6 Significant Wave Time History during T0709

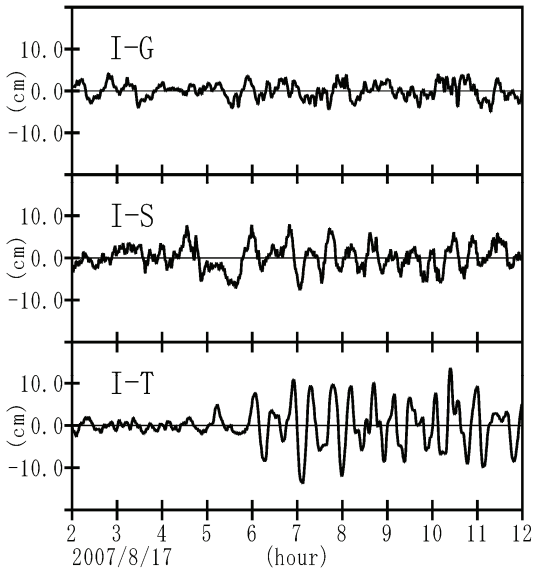

Figure 7 Low Frequency Sea Surface Elevation Data

deeper sea and there existed some noise in the order of several cm (error) due to the RTK-GPS positioning. Such noise level well coincides with the results of GPS vertical error test conducted by the Tohoku District Infrastructure Bureau in March 2006, just before the deployment of M-G GPS buoy.

4. CONCLUSIONS

History and present situation of Japanese coastal wave monitoring system named as NOWPHAS (Nationwide Ocean Wave information network for Ports and HArbourS) is introduced in this paper. NOWPHAS has been established and operated since 1970 by the Ports and Harbours Bureau of the Ministry of Land, Infrastructure, Transport and Tourism (MLIT) and its associated agencies including the Port and Airport Research Institute (PARI). In the year of 2009, observed data of waves have been recorded at 61 seabed installed acoustic wave gauge stations and 8 deep-sea GPS buoy stations.

Examples of the observed results by the first two sets of the deep-sea GPS buoys are also introduced in this paper and following results are obtained.

(1) Obvious wave climate difference can be seen between the deep GPS buoy stations and the shallower sea-bed installed gauge stations. Probability of calm wave condition defined as significant wave height (H1/3) less than 1m is 24.1% (M-G) and 21.7% (I-G) at the deep GPS buoys, while is 82.5% (M-S) and 69.7% (I-S) at the shallower sea-bed installed gauge stations.

(2) Frequency banded wave statistics showed that offshore wave statistics do not obviously change at the two different offshore sites in more than 100km distance. Deep sea GPS buoys observed wider range of NE, ENE, E, ESE and SE directions, while shallower M-S DWDM observed narrower range of SE and SSE ones, due to differences of the topographical sheltering effects.

(3) Offshore GPS buoys observed much bigger significant wave heights in both normal and abnormal sea states than the shallower seabed wave gauges, suggesting that deep-sea wave observation is necessary to obtain offshore wave conditions.

(4) Observed 2007 Peru Earthquake Tsunami profiles were discussed. Low frequency sea surface fluctuation due to the tsunami can be seen in seabed wave gauge and tide station data for several hours, while the GPS buoy were not able to identify the tsunami profile, because tsunami heights are smaller than the existing cm order noise level.

Acknowledgements:

Observed data used in this paper are successful results of the development, improvement and maintenance of the NOWPHAS has been operated by associated agencies of the Ports and Harbours Bureau of the MLIT. Authors have to express sincere gratitude to those concerned persons. Wave gauges and data collecting and processing system adopted in the NOWPHAS were born from more than 40 years' research in the PARI and its cooperative organizations and their associating private companies. Author would like to express sincere gratitude to those concerned persons.

References:

Kato, T., Terada, Y., Kinoshita, M., Kakimoto, H., Isshiki, H., Moriguchi, T., Takada, M., Tanno, T., Kanzaki, M. and James Johnson (2001). "A New Tsunami Monitoring System using RTK-GPS", *ITS 2001 Proceedings*, **5**(12), 645-651.

Hashimoto, N., Mitsui, M., Goda, Y., Nagai, T. and Takahashi, T. (1996). "Improvement of Submerged Doppler-Type Directional Wave Meter and its Application to Field Observation", *Proc. of 25th International Conference on Coastal Engineering (ICCE'96)*, 629-642.

Nagai, T. (2002). "Development and Improvement of the Nationwide Coastal Wave Observation Network", *Techno-Ocean'2002, Paper-TI-1-2*, 1-4.

Nagai, T., Sugahara, K., Hashimoto, N., Asai, T., Higashiyama, S. and Toda, K. (1994). "Introduction of Japanese NOWPHAS System and its Recent Topics", *Proc. of the International Conference on Hydro-Technical Engineering for Port and Harbor Construction (HYDRO-PORT'94),* PHRI, 67-82.

Nagai, T. , Hashimoto, N., Kawaguchi, K., Kudaka, M., and Mitsui, M. (2002). "A New Analysis Method of Observed Directional and Infra-gravity Waves based on Frequency Banded Spectrum Power", *Proc. of the 12th International Offshore and Polar Engineering Conference (ISOPE'2002)*, Vol.4, 49-54.

Nagai, T., Yamamoto, C., Mitsui, M., Shimizu, Y., Ahn, H. D. and Shin S. K., (2003). "Recent Improvement of Coastal Wave-Tide Observation and Textbooks Publication", *Proc. of Annual Meeting of Korean Society of Coastal and Ocean Engineers*, Korean Society of Coastal and Ocean Engineers, 233-239.

Nagai, T., Ogawa, H., Terada, Y., Kato, T. and Kudaka, M. (2004). "GPS Buoy Application to Offshore Wave Tsunami and Tide Observation", *Proc. of the 29th International Conference on Coastal Engineering (ICCE'04)* , ASCE, Vol.1, 1093-1105.

Nagai, T., Satomi, S., Terada, Y., Kato, T., Nukada, K. and Kudaka, M. (2005), "GPS Buoy and Seabed Installed Wave Gauge Application to Offshore Tsunami Observation", *Proc. of the 15th International Offshore and Polar Engineering Conference (ISOPE'2005),* Vol.3, 292-299.

Nagai, T., Kato, T., Moritani, N., Izumi, H., Terada, Y. and Mitsui, M. (2006). "Offshore Tsunami Monitoring Network Design using GPS Buoys and Coastal on-site Sensors" *Proc. of the 30th International Conference on Coastal Engineering (ICCE'06),* ASCE, Vol.2, 1529-1540.

Nagai T., Kato T., Moritani N., Izumi H., Terada Y. and Mitsui M. (2007). "Proposal of Hybrid Tsunami Monitoring Network System consisted of Offshore, Coastal and On-Site Wave Sensors", *Coastal Engineering Journal*, Japan Society of Civil Engineers, **49**(1), 63-76.

Nagai, T., Shimizu, K., Sasaki, M. and Murakami, A. (2008). "Improvement of the Japanese NOWPHAS Network by Introducing Advanced GPS Buoys", *Proc. of the 18th International Offshore and Polar Engineering Conference (ISOPE'2008)*, Vol.3, 558-564.

Shimizu, K. Nagai, T., Satomi, S., Lee, J. H., Kudaka, M. and Fujita, T. (2006a). "Development of the Deep-Sea GPS Buoy Wave Data Processing System", *Proc. of the TECHNO-OCEAN 2006,* JASNAOE, Paper No.27. (CD-ROM)

Shimizu, K., Nagai T., Lee, J.H., Izumi, H., Iwasaki, M. and Fujita, T. (2006b). "Development of Real-Time Tsunami Detection System Using Offshore Water Surface Elevation Data", *Proc. of the TECHNO-OCEAN 2006,* JASNAOE, Paper No.24. (CD-ROM)

Takayama, T., Hashimoto, N., Nagai, T., Takahashi, T., Sasaki, H. and Ito, Y. (1994). "Development of Submerged Doppler-type Directional Wave Meter", *Proc. of the 24th International Conference on Coastal Engineering (ICCE'94),* ICCE, Vol.1, 624-634.

JOINT CONFERENCE PROCEEDINGS
7th International Conference on Urban Earthquake Engineering (7CUEE) &
5th International Conference on Earthquake Engineering (5ICEE)
March 3-5, 2010, Tokyo Institute of Technology, Tokyo, Japan

FIELD SURVEY OF THE 2009 SAMOA EARTHQUAKE TSUNAMI

Shunichi Koshimura[1)], Yuichi Namegaya[2)], Yuichi Nishimura[3)], Yugo Nakamura[4)]
Gerard J.Flyer[5)], Akapo Akapo[6)], and Laura S. L. Kong[7)]

1) Associate Professor, Graduate School of Engineering, Tohoku University, Japan
2) Researcher, Geological Survey of Japan, AIST, Japan
3) Assistant Professor, Institute of Seismology and Volcanology, Hokkaido University, Japan
4) Researcher, Institute of Seismology and Volcanology, Hokkaido University, Japan
5) Geophysicist, Pacific Tsunami Warning Center, NOAA, USA
6) Director, National Weather Service, NOAA, American Samoa
7) Director, International Tsunami Information Center, UNESCO/IOC-NOAA, USA
koshimura@tsunami2.civil.tohoku.ac.jp, yuichi.namegaya@aist.go.jp, yns@mail.sci.hokudai.ac.jp, nyugo@mail.sci.hokudai.ac.jp, Gerard.Fryer@noaa.gov, Akapo.Akapo@noaa.gov, Laura.Kong@noaa.gov

Abstract: A post-tsunami field survey was conducted in Tutuila island of American Samoa after the event of M8.1 earthquake in 2009, focusing on the measurements of the tsunami run-up height, flow depth, extent of inundation zone, coastal erosion/sedimentation, structural damage inspection, and collecting eyewitness accounts.

1. INTRODUCTION

On 29 September, at 17:48 UTC (06:48 Local time), a major earthquake of magnitude 8.1 occurred off the coast of Samoa islands (Figure 1). A tsunami warning was issued by Pacific Tsunami Warning Center at 07:04 (Local time), 16 minutes after the earthquake. The tsunami generated by this earthquake struck the Samoa islands and killed at least 149 people in Samoa, 34 people in American Samoa, and nine people in Tonga (USGS, 2009). And this event resulted the most devastated tsunami disaster in the history of Samoa region.

This paper reports the results of our initial survey in American Samoa to inspect the impact of tsunami such as the tsunami run-up heights, flow depths, spatial extent of tsunami inundation, and the structural damage.

2. POST-TSUNAMI FIELD SURVEY

In order to search the potential impacted area, we first performed an initial analysis by taking an integrated approach of tsunami numerical modeling and GIS analysis with world population data, LandScan™(Dobson et al., 2000). The result suggested that the population along the south-western and central coasts of Tutuila island would be highly exposed against the tsunami (Figure 2).

The post-tsunami field survey was conducted in Tutuila island, American Samoa, from 5 to 8 Oct., 2009, focusing on the measurements of tsunami run-up height, flow depth, extent of inundation zone, structural damage inspection, and collecting eyewitness accounts.

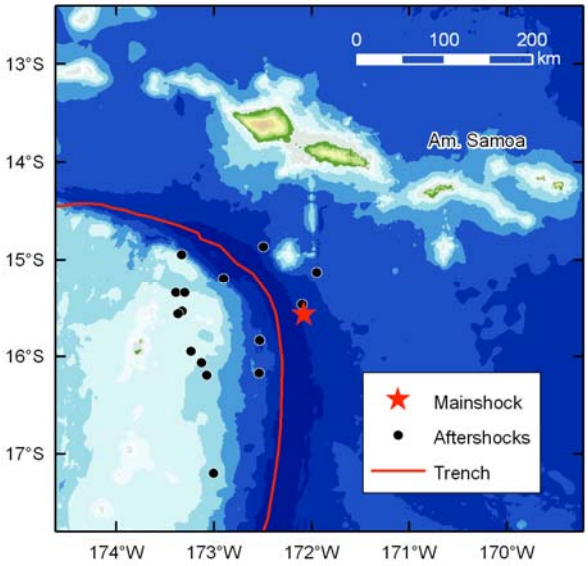

Figure 1 Samoa islands and its vicinity

In total, we measured tsunami heights at 50 points in Tutuila island using the total station, hand-held GPS and survey rods. By using the tide record in Pago Pago harbor, the measured inundation heights were corrected to the height above the background sea level before the tsunami attacked the coast.

3. SURVEY RESULTS

Our measurements in terms of the inundation heights and

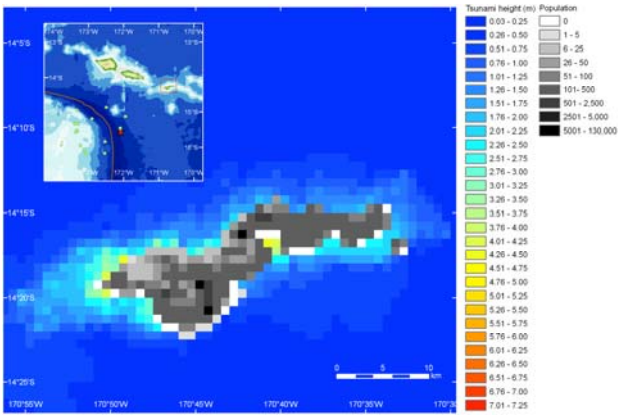

Figure 2 Modeled tsunami height and exposed population in Tutuila island, American Samoa.

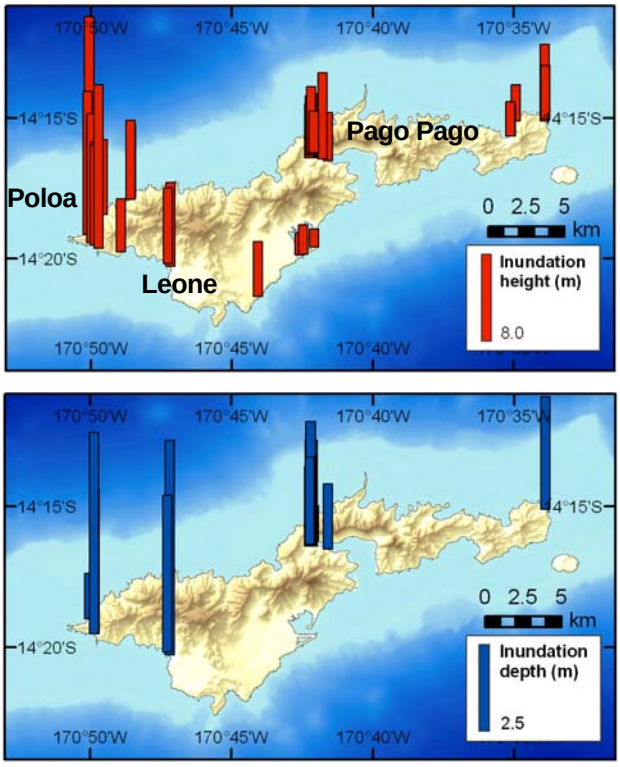

Figure 3 Summary of the measurements.

depths are summarized in Figure 3. The tsunami hit more severely along the western coast of Tutuila island. The highest run-up 16.3m was measured at the village of Poloa which locates on the western coast of the island. The village of Poloa (Figure 4 and Photo 1) was totally devastated or washed-away by the massive tsunami and caused two casualties of village people, 12.4 m inundation height was measured at Amanave (Figure 4, southern coast of the island) where the tsunami penetrated approximately 200 m inland. Severe damage was also found at the village of Leone (Figure 4 and Photo 1), where 6m tsunami attacked. The tsunami penetrated more than 200 m inland and left extensive amount of debris in the lagoon (Photo 1).

Not only along the coast facing outer sea, the tsunami attacked the bottom of the bay. Pago Pago harbor locates in the bottom of the inverse L-shape bay (Figure 2 or 3) and was hit by 5m tsunami that caused more than 500m of inland penetration. We surveyed the structural damage in Pago Pago harbor, by the interpretation of high-resolution satellite images (Figure 6) and on-site inspection with GPS measurement, which leads to the understanding of relations between the tsunami hazard and structural vulnerability. As a preliminary result, we found that 35 houses of 115 houses within the inundation zone were washed-away.

4. SURVIVING FACTORS

During the survey, we interviewed the survivors to collect the eyewitness accounts especially on the tsunami arrival time, the initial sea surface movement, numbers of tsunami attack. Along the southern coast of Tutuila island, the tsunami was likely to have started by depression (Leone, Poloa, and Pago Pago) and the second wave was the highest (Leone), which is consistent with the observed tide record at Pago Pago harbor. The most important part of the interview was that the residents were aware of tsunami and knew that they should move to higher ground as they feel strong ground shaking. In this event, Pacific tsunami warning center issued the warning at 07:04 (16 minutes after the earthquake) and the National weather service office of Pago Pago disseminated the guidance of evacuation through the radio at 07:02 (14 minutes after the earthquake). Probably this awareness would contribute to reducing the number of fatalities in Tutuila island (34 casualties reported). Especially, the school bus driver, who has just left the kids in the school of Poloa, was aware of tsunami after the earthquake and took the children back to the higher ground. This sort of awareness that strong ground shaking is a sign of tsunami, is the most important factor to survive from tsunami disaster.

Acknowledgements:
This study was partially supported by Science and Technology Research Partnership for Sustainable Development (SATREPS) of JST and JICA, and Industrial Technology Research Grant Program in 2008 (Project ID : 08E52010a) from New Energy and Industrial Technology Development Organization (NEDO).

References:

USGS, Earthquake Hazards Program (2009), <http://earthquake.usgs.gov/earthquakes/eqinthenews/2009/us2009mdbi/>

Koshimura, S. (2009), "Inspection of the tsunami impacted area in American Samoa by the Integration of Tsunami Model and High-resolution satellite images," <http://www.tsunami.civil.tohoku.ac.jp/hokusai3/J/events/samoa_090930/inspection_samoa/inspection_samoa.html>

Koshimura, S., M. Matsuoka and S. Kayaba (2009), "Integrated approach to assess the impact of tsunami disaster," Safety, Reliability and Risk of Structures, Infrastructures and Engineering Systems, Furuta, Frangopol & Shinozuka (eds), Taylor & Francis, London, pp.2302-2307.

Dobson, J. E., E. A. Bright, P. R. Coleman, R.C. Durfee & B. A. Worley (2000) "LandScan: A Global Population Data-base for Estimating Populations at Risk," Photogrammetric Engineering & Remote Sensing Vol. 66, No. 7, 849-857.

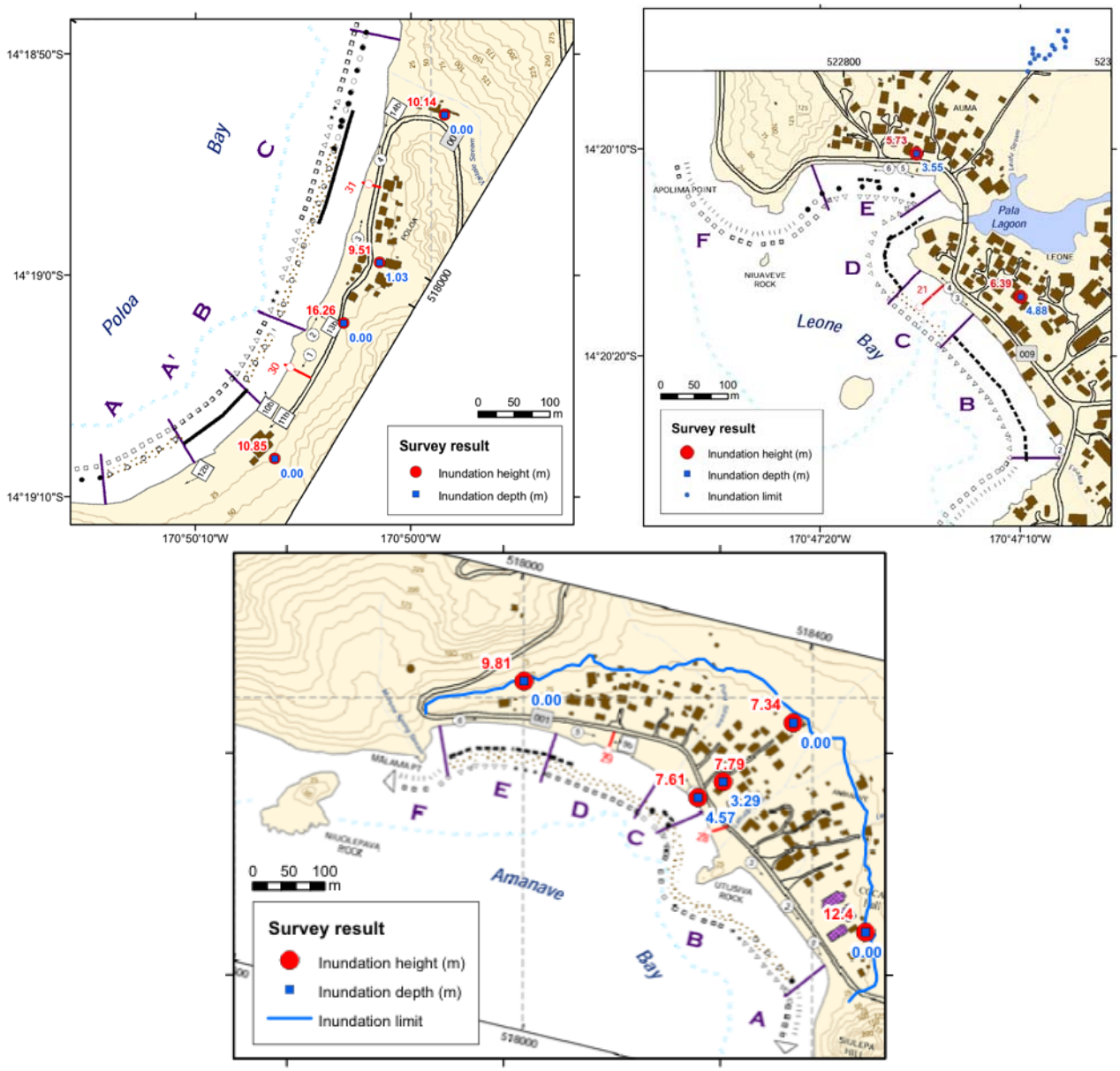

Figure 4 Survey sites of Poloa (upper left), Leone (upper right) and Amanave (bottom)


Photo 1 Devastated villages of Poloa (left) and Leone (right)

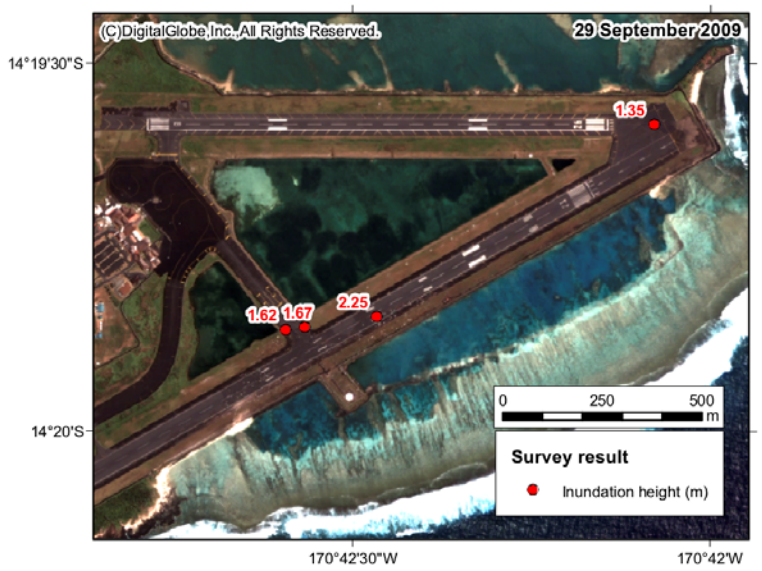

Figure 5 Tsunami run-up on the runway of Pago Pago international airport.

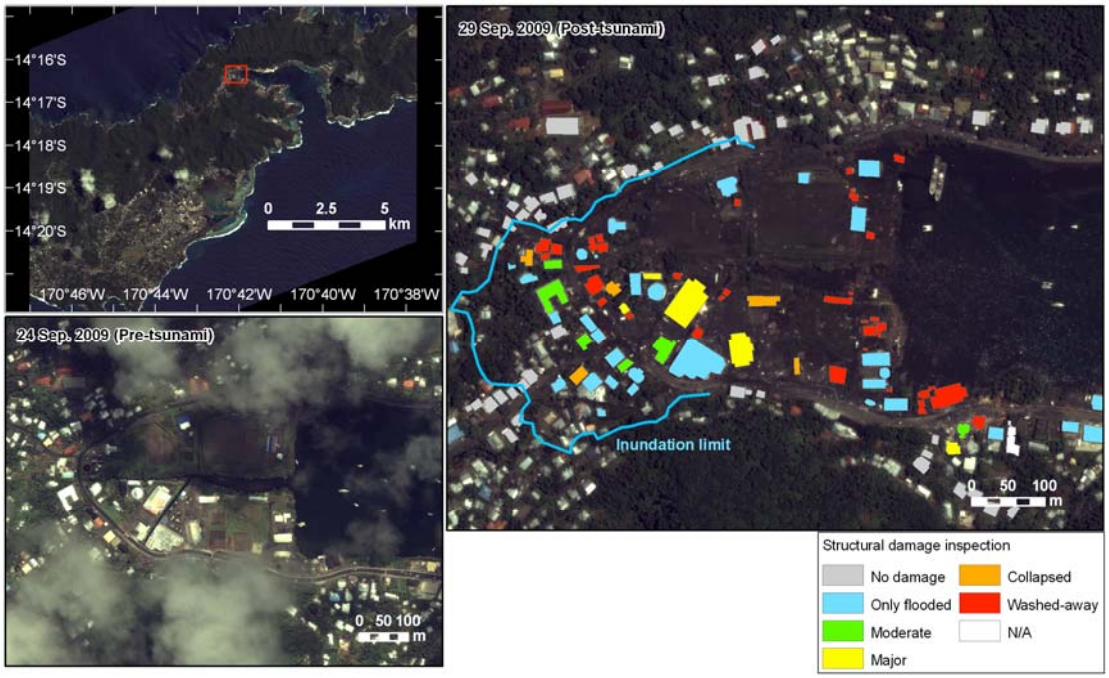

Figure 6 Preliminary result of structural damage inspection in Pago Pago harbor.

JOINT CONFERENCE PROCEEDINGS
7th International Conference on Urban Earthquake Engineering (7CUEE) &
5th International Conference on Earthquake Engineering (5ICEE)
March 3-5, 2010, Tokyo Institute of Technology, Tokyo, Japan

DIFFERENCES OF TSUNAMI WAVES INDUCED BY EARTHQUAKES, SUBMARINE LANDSLIDES AND SEA FLOOR COLLAPSE

K.T. Chau[1)]

1) Chair Professor, Dept of Civil and Structural Engineering, the Hong Kong Polytechnic University, Hong Kong
cektchau@polyu.edu.hk

Abstract: This paper considers the differences of tsunami generation by earthquake, submarine landslides and sea floor collapses. A systematic framework is derived to examine the difference of the water surface undulation induced by three different mechanisms. Sea floor collapse is considered by both moving sea bottom or by rapid water discharge into a sea floor collapsing hole. The mathematical formation is done through the use of linear potential theory for fluid. The problem is specified in terms of velocity potential with appropriate boundary condition imposed on water surface as well as at the sea bottom. Sudden movement of sea bottom is modeled as Heaviside function in terms of a source duration term whereas impulsive sea bottom movement is modeled as Dirac delta function. Hankel transform or Fourier transform is applied to the spatial coordinates while Laplace transform is applied to time variable. Exact solutions were derived for some special cases. In general, the solution will be expressed in terms of infinite integral. For the case of far field and long time solution, the integral can be evaluated by using Kelvin's stationary phase method. The asymptotic forms provide the leading wave structures of the tsunami waves generated by difference sources, including earthquake, landslides and sea floor collapses. The solution of the present problems can provide the initial phase of sea surface condition that can be used as input for traditional tsunami simulations, including TSUNAMI-N2, COST and COMCOT.

1. INTRODUCTION

The economic and infrastructural development in China in recent years has progressed at an unprecedented pace since the "open China" policy about 30 years ago. Formerly sparsely populated coastlines have been developed into big coastal mega cities, with much denser population and important infrastructures, such as cross-harbor tunnels. These recent developments make potential tsunami a big threat to the modern development. A repeat of 2004 Indian Ocean Tsunami along the coastline of China would be much more devastating than any historical tsunami occurred in China. As reported by Chau (2008), according to the historical records compiled by Lu (1984) there are over 200 tsunami of unknown causes occurred along China's coastline since 48 BC. At least six of these tsunami events killed more than 10,000 people (in the years of 1045, 1329, 1458, 1536, 1776 and 1782). Figure 1 shows the locations of some tsunami events of unknown origins in South China.

However, the studies of Mak and Chan (2007) and the number of historical tsunami events announced by State Oceanic Administration of China (Zhou and Adams 1988) are overly underestimated the actual number. The main reason seems that they ignored tsunami events (even with devastation and high fatality) that cannot be linked directly to a felt earthquake. This is a big misconception that tsunami must be linked to earthquake. In fact, according to the well-accepted definition, a tsunami is "a great sea produced by submarine earth movement or volcanic eruption" (e.g. Webster's Ninth New Collegiate Dictionary). In fact, tsunami can be caused by earthquakes, submarine landslides, volcanic eruption, or meteor impact (e.g. Bryant 2001). Therefore, current conception of tsunami hazard level in China is highly underrated.

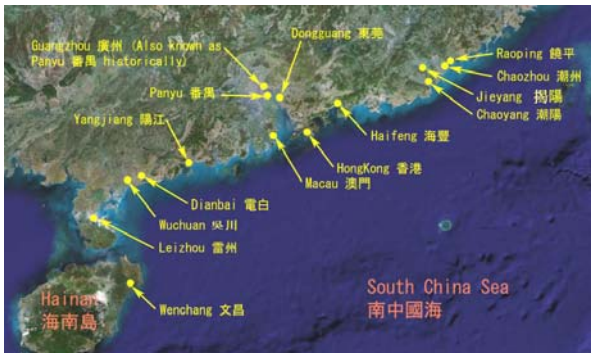

Figure 1 Location of historical tsunami in South China

Before the 2004 Boxing Day Tsunami, not many residents in South Asian countries, such as Thailand, India, and Sri Lanka, would believe that tsunami is a real threat to their lives and properties. Therefore, a more thorough study on tsunami hazard (not restricted to earthquake-induced ones)

in China is of utmost importance and of science merit (Chau et al. 2006).

Submarine landslides have been identified as one of the sources for several destructive tsunamis, such as the devastating Papua New Guinea tsunami in 1998, which killed over 2,000 people (Lynett et al. 2003). It is postulated that some of the historical tsunami events in China are caused by submarine landslides. For example, there are 5 sea floor debris fans have been found at the continental self in the South China Sea (Liu 1992), ranging from 38-98 km in length and 11-39 km in width. Figure 2 shows that near the Pearl River Delta areas, there are 4 debris fans ranging 54-66km in length and 14-50 km in width (Liu 1992). Based on 3.5 Hz-echograms conducted by the Lamont-Doherty Geological Survey ships from 1965-1980 in South China Sea, the largest single slump/debris flow complex near the edge of the continental self is up to 4,500 km^2 (Damuth 1980). These are potential evidences of submarine landslides and their occurrences might link to some historical tsunami of unknown sources (Chau 2009a, 2009b).



Figure 2 Hugh debris fans at sea bottom in South China Sea

In addition, Panyu 30-1 gas field, which is within 100 km of Hong Kong, was developed by the China National Offshore Oil Corporation (CNOOC). Gas extraction from sea bottom may also lead to sea floor collapse or movement, which in turn may lead to local tsunami events. As remarked by Guo (1991), submarine cave-in is not uncommon at where marine deposits are found in abundant. Bursting of submarine shallow-seated gas can also led to catastrophe. To the best knowledge of the author, there is no systematic studies on the tsunami waves or surges generated by sea floor collapse or related events.

The Chinese term "tiankeng" is for "huge collapse doline". In China, tiankengs that were first widely known are in Sichuan Province. In 1994, a number of tiankengs were found unexpectedly in China in caving expeditions in Guangxi and Sichuan Provinces. There are 50 known tiankengs in China accounting for 64% of 78 found in the world (Zhu and Chen 2006). Three of these are giant tiankengs of more than 500 m deep and 500 m in entrance diameter. They are the Xiaozhai Tiankeng in Fengjie of Sichuan, Dashiwei Tiankeng in Leye of Guangxi and Haolong Tiankeng in Bama of Guangxi. Figure 3 shows the Dashiwa Tiankeng. If such huge doline collapse occurs at sea floor, tsunami of considerable size may be generated.



Figure 3 Dashiwei tiankeng in Guangxi

In this paper, we will examine the leading wave characteristics of tsunami induced by submarine landslides, sea floor collapse and earthquakes these different sources. Related studies examining the difference between submarine landslides-induced tsunami and earthquake-induced tsunami include the works by Okal (2003) and Okal Synolakis (2003).

2. TSUNAMI INDUCED BY SEA FLOOR MOVEMENTS

Euler equation for inviscid and incompressible fluid, initially at rest, can be solved in terms of velocity potential Φ (Lamb 1975, Milne-Thomson 1996, Batchelor 2000, DeDontney and Rice 2008):

$$\vec{u} = \nabla\Phi \tag{1}$$

$$p = -\rho g z - \rho\frac{\partial\Phi}{\partial t} - \frac{1}{2}\rho|\nabla\Phi|^2 \tag{2}$$

where p is the pressure, $\vec{u}$ is the velocity field, ρ is the water density, g is the gravitational constant, and z is the vertical coordinate. As it is well-known that substitution of (1-2) into continuity leads to the Laplace equation for potential flow in polar form:

$$\frac{1}{r}\frac{\partial}{\partial r}\left(r\frac{\partial\Phi}{\partial r}\right) + \frac{\partial^2\Phi}{\partial z^2} = 0 \tag{3}$$

where the water domain is defined as $-h < z < 0$ and $0 \le r < \infty$. The kinematic boundary condition at sea

surface (i.e. water particle does not leave the sea surface) and the zero pressure condition at sea surface ($z = 0$) are

$$\frac{\partial \Phi}{\partial z} = \frac{\partial \eta}{\partial t}, \quad \frac{\partial \Phi}{\partial t} = -g\eta \tag{4}$$

Or equivalently, (4) can be combined to eliminate the sea water undulation η to give the boundary condition on $z = 0$

$$\frac{\partial^2 \Phi}{\partial t^2} + g\frac{\partial \Phi}{\partial z} = 0 \tag{5}$$

The sea floor disturbance on $z = -h$ can be prescribed as either vertical fluid flow or vertical velocity

$$\frac{\partial \Phi}{\partial z} = \frac{\partial \eta}{\partial t} = W(r,t) \tag{6}$$

where η is the vertical movement at the sea bottom. In principle, either η or W can be prescribed. Note that (6) provides the source for tsunami generations. In addition, for boundedness requirement, the velocity potential and its derivative must remain finite for large distance r for finite time (i.e. $\Phi, \nabla\Phi \to 0$ as $r \to \infty$).

2. HANKEL-LAPLACE TRANSFORM

To solve the Laplace equation (3) with boundary conditions (5) and (6), we can apply Hankel-Laplce transform to reduce the partial differential equation to lower order. In particular, Hankel transform of an arbitrary function *f(r)* is:

$$\hat{f}(k) = \int_0^\infty rJ_0(kr) f(r) dr\,, \tag{7}$$

where J_0 is the Bessel function of the first kind (Watson 1944, Abramowitz and Stegun 1965), and the corresponding inverse Hankel transform is

$$f(r) = \int_0^\infty kJ_0(kr)\hat{f}(k) dk \tag{8}$$

Laplace transform of an arbitrary function *F(t)* is defined as (Wong 1991):

$$\overline{F}(s) = L\{F(t)\} = \int_0^\infty e^{-st} F(t) dt\,; \tag{9}$$

and the corresponding inverse Laplace transform is

$$F(t) = L^{-1}\{\overline{F}(s)\} = \frac{1}{2\pi i}\int_{\sigma-i\infty}^{\sigma+i\infty} \overline{F}(s) e^{st} ds \tag{10}$$

Apply Hankel-Lapalce transform to the velocity potential Φ, the governing equation becomes

$$\frac{d^2\hat{\overline{\Phi}}}{dz^2} - k^2\hat{\overline{\Phi}} = 0 \tag{11}$$

and the boundary condition on $z = 0$ becomes

$$\frac{d\hat{\overline{\Phi}}}{dz} + \frac{s^2}{g}\hat{\overline{\Phi}} = 0 \tag{12}$$

and that on $z = -h$ becomes

$$\frac{d\hat{\overline{\Phi}}}{dz} = \hat{\overline{W}}(k,s) \tag{13}$$

where

$$\hat{\overline{\Phi}}(k,z,s) = \int_0^\infty \int_0^\infty rJ_0(kr)\Phi(r,z,t)e^{-st} dr\, dt \tag{14}$$

For axisymmetric case (i.e. the velocity potential is independent of θ). General solution form of $\hat{\overline{\Phi}}$ is

$$\hat{\overline{\Phi}} = A\sinh kz + B\cosh kz \tag{15}$$

Substitution of (15) into the left hand side of (12) leads to

$$\begin{aligned}\frac{d\hat{\overline{\Phi}}}{dz} + \frac{s^2}{g}\hat{\overline{\Phi}} &= kA\cosh kz + kB\sinh kz \\ &+ \frac{s^2}{g}(A\sinh kz + B\cosh kz)\end{aligned} \tag{16}$$

Specifying (16) $z = 0$ yields

$$\left[\frac{d\hat{\overline{\Phi}}}{dz} + \frac{s^2}{g}\hat{\overline{\Phi}}\right]_{z=0} = kA + \frac{s^2}{g}B = 0 \tag{17}$$

Substitution of (15) into (13) gives

$$\left[\frac{d\hat{\overline{\Phi}}}{dz}\right]_{z=-h} = Ak\cosh kh - Bk\sinh kh = \hat{\overline{W}}(k,s) \tag{18}$$

Equations (17-18) provides two equations for the two unknown constants A and B and the results can be back substituted into (15) to give

$$\hat{\overline{\Phi}} = \hat{\overline{W}}(k,s)\left(\frac{1}{s^2+\omega^2}\right)\frac{s^2\sinh kz - gk\cosh kz}{k\cosh kh} \tag{19}$$

where

$$\omega^2 = gk\tanh kh \tag{20}$$

Following Mei (1989), the water undulation can be expressed in terms of the velocity potential as:

$$\overline{\eta}(r,s) = -\frac{s}{g}\overline{\Phi}\bigg|_{z=0} = \int_0^\infty \hat{\overline{W}}(k,s)\left(\frac{J_0(kr)}{s^2+\omega^2}\right)\frac{ks}{\cosh kh} dk \tag{21}$$

where

$$\overline{\Phi}(r,z,s)=\int_0^\infty kJ_0(kr)\hat{\overline{\Phi}}(k,z,s)dk \tag{22}$$

Once *W* is given, the surface undulation induced by sea floor movement can be found by (21). The particular case of suddenly applied velocity pulse will be considered next.

3. MODEL FOR SEA BOTTOM COLLAPSE

3.1 Exact Solution for sea floor collapse

In this section, we will prescribe a sea floor condition that resembles the case of sea floor collapse. When a sea bottom collapses, the bottom suddenly moves downward. Mathematically, we can approximate this collapse by a Heaviside step function of time. When a velocity pulse is suddenly applied at $t = 0$ on a circular sea bottom of radius *a* and stopped at $t = \tau$, the sea bottom function *W* can be written mathematically as:

$$W(r,t)=-w_0H(a-r)[H(t)-H(t-\tau)] \tag{23}$$

where *r* is the radial coordinate measured from the center of the circular region, and w_0 is the magnitude of the velocity pulse. Physically, (23) can also be interpreted as a pulse of sea water inflow into a collapsed circular region (see Levin and Nosov 2008). Either way, this function can approximate the situation of sea floor collapse. The corresponding Hankel-Laplace transform of the function *W* is

$$\hat{\overline{W}}(k,s)=-\frac{w_0a}{ks}J_1(ak)(1-e^{-\pi s}) \tag{24}$$

Substitution of (24) into (21) yields the following formula for the sea undulation due to sea floor collapse.

$$\overline{\eta}(r,s)=-\int_0^\infty w_0a\left(\frac{J_0(kr)J_1(ka)}{\cosh kh}\right)\frac{(1-e^{-\pi s})}{s^2+\omega^2}dk \tag{25}$$

Our next task is to take the inverse Laplace transform to yield the solution in time. To do that the following formulas are found useful:

$$L^{-1}\left\{\frac{1}{s^2+\omega^2}\right\}=\sqrt{\frac{\pi t}{2\omega}}J_{1/2}(\omega t)=\frac{\sin(\omega t)}{\omega} \tag{26}$$

$$L^{-1}\{\bar{f}(s)e^{-\pi s}\}=f(t-\tau)H(t-\tau) \tag{27}$$

Applying (26-27) to (25), the sea surface undulation can be found analytically as:

$$\eta(r,t)=\varsigma(r,t)H(t)-\varsigma(r,t-\tau)H(t-\tau) \tag{28}$$

$$\varsigma(r,t)=-w_0a\int_0^\infty\left(\frac{J_0(kr)J_1(ka)}{(gk\tanh kh)^{1/2}\cosh kh}\right)\times\sin[t(gk\tanh kh)^{1/2}]dk \tag{29}$$

This new solution provides the first analytical solution for sea bottom collapse, and this solution can be considered as the 3-D counterpart of the two-dimensional solution given by Levin and Nosov (2008).

3.2 The behavior of leading waves induced by sea floor collapse

If a tide gauge station is located at a position that does not suffer from bay oscillations (or seiches), the tsunami recorded at such a station can be used to study the source mechanism of a tsunami. Kajiura (1963) examined the leading wave of an earthquake-induced tsunami when it is at a far distance from the source. Other similar studies include that by Ben-Menahem and Rosenman (1972).

In this section, we will apply Kelvin's stationary phase method (e.g. Mei 1989, Erdelyi 1956) to examine the asymptotic behavior of the leading wave induced by sea bottom collapse. In particular, we consider the case that the velocity pulse is short (i.e. $\tau << 1$) and the sea depth *h* is big comparing to the collapse size *a* (i.e. $k_{\max}a << 1$). In this case, (28-29) can be simplified to:

$$\eta(r,t)=-\frac{w_0a^2\tau}{2}\int_0^\infty\left(\frac{kJ_0(kr)}{\cosh kh}\right)\cos[t(gk\tanh kh)^{1/2}]dk \tag{30}$$

At far distance from the source, we also set time being long (i.e. $t\to\infty$). It is obvious that (30) becomes an integral that can be simplified using Kelvin's stationary phase method (Mei 1989, Erdelyi 1956):

$$f(x)=\int_\alpha^\beta F(k)\exp\{ixh(k)\}dk \tag{31}$$

$$f(x)\approx\left[\frac{2\pi}{xh''(k_0)}\right]^{1/2}F(k_0)\exp\{ixh(k_0)+\frac{i\pi}{4}\} \tag{32}$$

Note that Kelvin's stationary phase method states that the main contribution of the integration comes from the vicinity of points where the function *h(k)* is stationary (i.e. $h'(k_0) = 0$), and the contributions from the end points α and β are negligible. The function *F(k)* must be continuous whereas *h(k)* must be twice differentiable. Applying this method, (30) can be approximated by:

$$\eta(r,t)=-\left(\frac{w_0a^2\pi k_0}{2\cosh k_0h}\right)\left[\frac{1}{k_0rt|\omega''(k_0)|}\right]^{1/2}\cos[k_0r-\omega(k_0)t] \tag{33}$$

where ω is defined in (20) and k_0 is given by

$$\omega'(k_0)=0 \tag{34}$$

This asymptotic solution shows the leading wave decaying as $t^{-1/2}$ and $r^{-1/2}$.

4. COMPARISON OF LEADING WAVES

4.1 The behavior of leading waves induced by earthquake

Without going into the details, Kajiura (1963) showed that the leading wave of an earthquake-induced tsunami is in the following asymptotic form:

$$\eta(r,t) \sim F(t) r^{-\alpha} \tag{35}$$

where α equals 2/3 for $p_a > 3$ or equals 1 for $p_a < 1$ and p_a is defined as:

$$p_a = (\frac{6}{t}\sqrt{H/g})^{1/3}(a/H) \tag{36}$$

and a is the half the size of the longer side of a rectangular fault surface. The difference of (33) and (35) provides a simple analytical check on the origin of tsunami waves.

4.2 The behavior of leading waves induced by submarine landslides

The analysis of tsunami induced by submarine landslide have been considered by Ward (2001), Okal (2003), and Okal and Synolakis (2003). The case of a simple submarine landslide on a circular region can be approximated by sea bottom uplift of θ-dependence of cosθ and an impulsive time function:

$$W(r,\theta,t) = \frac{A}{a}(a^2 - r^2)^{1/2}\cos\theta\,\delta(t) \tag{37}$$

Physically this model predicts that the upper half of the submarine landslide is modeled by vertical downward movement whereas the lower half of the submarine landslide is modeled by vertical upward movement. Without going into the details, we simple quote the asymptotic formula derived by Mei (1989) for such case:

$$\eta(r,\theta,t) = \cos\theta(\frac{\pi}{2})^{1/2}\frac{Aa}{\cosh k_0 h} J_1^2(\frac{k_0 a}{2})\left[\frac{1}{k_0 rt|\omega''(k_0)|}\right]^{1/2} \times \sin[k_0 r - \omega(k_0)t] \tag{38}$$

Comparison of (38) and (33) shows that the asymptotic form of r and t of sea floor collapse and submarine landslides are the same. But there is no directivity effect from the axisymmetric sea floor collapse whereas there is a strong directivity effect from submarine landslide. In addition, the leading wave from submarine landslides can either be positive or negative, depending on the relative orientation of the tide gauge station comparing to the slide direction whereas sea floor collapse always accompanies with receding water level before the arrival of the first surge. These information will be very useful for studying the source mechanism of tsunami.

5. IMPULSIVE SEA BOTTOM COLLAPSE

Without going into the details, we will report here that the analysis given in Section 3 can easily be applied to the situation of impulsive floor collapse similar to that considered by (37):

$$W(r,t) = -\frac{W_0}{a}(a^2 - r^2)^{1/2}\delta(t) \quad r < a \qquad = 0 \quad r > a \tag{39}$$

The analytical results for this case are similar to the previous solution:

$$\eta(r,t) = -\frac{W_0 a^2}{3}\int_0^\infty (\frac{kJ_0(kr)}{\cosh kh})\cos[t(gk\tanh kh)^{1/2}]dk \tag{40}$$

By applying Kelvin's stationary phase method, we obtain the following asymptotic solution for the leading waves:

$$\eta(r,t) = -W_0 a^2(\frac{\pi}{2a})^{1/2}(\frac{J_{3/2}(k_0 a)}{k_0\cosh k_0 h})\left[\frac{1}{rt|\omega''(k_0)|}\right]^{1/2} \times \cos[k_0 r - \omega(k_0)t] \tag{41}$$

$$\omega'(k_0) = 0 \tag{42}$$

As expected, the asymptotic form of both r and t of (41) are similar to that of (33).

6. CONCLUSION

In this paper, we have formulated a framework to consider sea floor collapse in the form of circular region. Velocity potential was used to formulate the initial boundary problem of tsunami induced by sea floor movements. Both Heaviside step function of time and Dirac delta function of time have been considered. Exact analytical solutions were obtained for the surface undulation induced by sea floor collapse. When the wave is far from the source zone, the leading wave characteristics are examined by using Kelvin's stationary phase method. This result is then compared to the leading wave of earthquake-induced and submarine landslide-induced tsunami. By comparison of these leading waves, we conclude that it is possible to identify the source mechanism of tsunami from their leading waves. For example, the directivity of leading waves observed from different orientations can be used to distinguish sea-floor-collapse -induced tsunami from earthquake-induced tsunami and submarine landslide-induced tsunami.

In addition, computer simulation programs such as TSUNAMI-N2, COST and COMCOT use Okada's (1985) solution for sea bottom movement induced by faulting to directly estimate the sea surface undulation (i.e. assuming the same initial sea bottom and sea surface movements). The

solution of the present problems can thus provide the initial phase of sea surface condition that can be used as input for these tsunami simulations.

Acknowledgements:

The work described in this paper was fully supported by a grant from the Research Grants Council of the Hong Kong Special Administrative region, China (Project No. PolyU 5002/08P). The travel to Phi-Phi Island was supported by Prof. J.M. Ko using Dean's Reserve of FCLU. The project was partially supported by Project No. 1-BBZF of PolyU. The author is grateful to Prof. J.R. Rice of Harvard University by sharing his preliminary report on tsunami analysis when the author visited Harvard University from February to May 2009.

References:

Abramowitz, M., and Stegun, I. A., (1965), "Handbook of Mathematical Functions," Dover, New York.

Batchelor, G., (2000), "An Introduction to Fluid Dynamics," Cambridge University Press.

Ben-Menahem, A., and Rosenman, M., (1972), "Amplitude patterns of tsunami waves from submarine earthquakes," *Journal of Geophysical Research*, 77, 3097–3128.

Bryant, E., (2001), "Tsunami: The Underrated Hazard," Cambridge University Press.

Chau, K.T., (2008), "Tsunami hazard along coastlines of China: a re-examination of historical data," *The 14th World Conference on Earthquake Engineering*, 14 WCEE, October 12-17, 2008 (full paper 015-0041 in CD-ROM).

Chau, K.T., (2009a), "Numerical Simulations of Submarine -Landslide-Induced and Sea-Floor-Collapse-Induced Tsunami Along Coastline of South China," *International Symposium on Prediction and Simulation Methods for Geohazard Mitigation*, May 25-27, 2009, Kyoto, Japan, pp. 247-252.

Chau, K.T., (2009b), "Tsunami formation as a result of sea floor collapse," *South China Sea Tsunami Workshop* 3, 3-5 November 2009, Penang, Malaysia.

Chau, K.T., Wong, R.H.C., Wai, O.W.H., Lin, H.Y., Jhan, J.M., and Dong, Z., (2006), "Tsunami hazard estimation for South China Sea," *The second Guangdong-Hong Kong-Macau conference on Earthquake Technology*, March 1-2, 2006, Macau, China (full paper in CD-ROM).

Damuth, J.E., (1980), "Quaternary sedimentation processes in the South China Basin as Revealed by echo-character mapping and piston-core studies," In *The Tectonic and Geologic Evolution of Southeast Asian Sea and Islands.* Ed. D.E. Hayes, Geophysical Monograph 23, 105-125, American Geophysical Union, Washington DC.

DeDontney, N., and Rice, J.R. (2008), "Role of splay faulting and hydrodynamic dispersion in tsunami waveforms," draft report submitted to NSF.

Erdelyi, A., (1956), "Asymptotic Expansions," Dover, New York.

Guo, X., ed., (1991), "Geological Hazards of China and Their Prevention and Control," Ministry of Geology & Mineral Resources, State Science & Technology Commission, State Planning Commission, Beijing, Geological Publishing House.

Kajiura, K., (1963), "The leading wave of a tsunami," *Bulletin of the Earthquake Research Institute*, 41, 535-571.

Lamb, S. H., (1975), "Hydrodynamics," Cambridge University Press.

Levin, B.W., and Nosov, M.A., (2008), "On the possibility of tsunami formation as a result of water discharge into seismic bottom fractures," *Izvestiya, Atmospheric and Oceanic Physics*, 44(1), 117-120.

Liu, G., (1992), "Geologic-Geophysic Features of China Seas and Adjacent Regions," Beijing, Science Press (in Chinese).

Lu, R. ed., (1984), "Historical tsunamis and related events in China," Beijing, Oceanic Press (in Chinese).

Lynett, P.J., Borrero, J.C., Liu, P.L.-F., and Synolakis, C.E., (2003), "Field survey and numerical simulations: A review of the 1998 Papua New Guinea tsunami," *Pure and Applied Geophysics*, 160, 2119-2146.

Mak, S., and Chan, L.S., (2007), "Historical tsunamis in South China," *Natural Hazards*, 43, 147-164.

Mei, C. C., (1989), "The Applied Dynamics of Ocean Surface Waves," World Scientific.

Milne-Thomson, L. M., (1996), "Theoretical Hydrodynamics," Courier Dover Publications.

Okada, Y., (1985), "Surface deformation due to shear and tensile faults in a half-space," *Bulletin of the Seismological Society of America*, 75, 1135-1154.

Okal, E.A., (2003), "Normal modes energetics for far-field tsunamis generated by dislocations and landslides," *Pure and Applied Geophysics*, 160, 2189–2221.

Okal, E. A., and Synolakis, C. E., (2003), "Theoretical Comparison of Tsunamis from Dislocations and Landslides," *Pure and Applied Geophysics*, 160, 2177–2188.

Ward, S. N., (2001), "Landslide Tsunami," *Journal of Geophysical Research*, 106, 11,201–11,215.

Watson, G.N., (1944), "A Treatise on the Theory of Bessel Functions," Cambridge University Press, Cambridge.

Wong, C.W., (1991), "Introduction to Mathematical Physics," Oxford University Press, New York.

Zhou, Q., and Adams, W.M., (1988), "Tsunamigenic earthquakes in China: 1831 BC to 1980 AD," *Science of Tsunami Hazards* 4(3), 131-148.

Zhu, X., and Chen, W., (2006), "Tiankengs in the karst of China.," *Speleogenesis and Evolution of Karst Aquifers*, 4 (1), 1-18.

JOINT CONFERENCE PROCEEDINGS
7th International Conference on Urban Earthquake Engineering (7CUEE) &
5th International Conference on Earthquake Engineering (5ICEE)
March 3-5, 2010, Tokyo Institute of Technology, Tokyo, Japan

VERIFICATION OF A DYNAMIC TSUNAMI SIMULATION TECHNIQUE BASED ON OBSERVATION RECORDS IN NEAR-FIELD

Shusaku Inoue[1], Tatsuo Ohmachi[2], and Tetsuji Imai[3]

1) Research Associate, Department of Built Environment, Tokyo Institute of Technology, Japan
2) Professor, Department of Built Environment, Tokyo Institute of Technology, Japan
3) Former Graduate Student, Department of Built Environment, Tokyo Institute of Technology, Japan
shusaku@enveng.titech.ac.jp, ohmachi@enveng.titech.ac.jp, t-imai@tokyo-gas.co.jp

Abstract: The 2003 Tokachi-oki earthquake (M_J 8.0) occurred off the southeastern coast of Tokachi, Japan, and excited a large tsunami which arrived at Tokachi Harbor at 04:56 with a wave height of 4.3 m. Japan Marine Science and Technology Center (JAMSTEC) recorded water pressures and sea-bed accelerations at the bottom of the tsunami source region. The records provide valuable information about characteristics of a near field tsunami and its source. We first introduce these records and results derived from Fourier analysis and band-pass filter analysis of them. Water pressure disturbances last for over 30 minutes and the durations are longer than those of accelerations. Next, we conduct tsunami simulation with three types fault models to investigate whether our dynamic tsunami simulation technique can represent water pressure on the seabed during tsunami generation process. The result shows that computed water pressure become smaller than observed data, however the predominant period of those calculated pressure relatively corresponds with those of observed data.

1. INTRODUCTION

A dynamic tsunami simulation technique was developed by Ohmachi et al. (2001a) to simulate generation of tsunamis followed by their propagation, where not only the dynamic displacement of the seabed induced by seismic faulting but also the acoustic effects of the seawater are taken into account. As the dynamic technique assumes weak coupling between the seabed and the seawater, the simulation consists of a two-step analysis. The first step is the dynamic seabed displacement resulting from a seismic faulting, and the second is the seawater disturbance induced by the dynamic seabed displacement. For the first step, the boundary element method (BEM) is used and, for the second step, the finite difference method (FDM) is used to solve the Navier-Stokes equation. A series of dynamic tsunami simulations have demonstrated that in the near-fault area there are some significant features that are water compressibility and short period sea surface disturbances which are mainly excited by Rayleigh waves.

Although most of these findings look quite reasonable, they need to be verified by observed data (Ohmachi et al. 2001b). Hence, in this paper the data obtained by JAMSTEC (Japan Marine Science and Technology Center) for the 2003 Tokachi-oki earthquake and the dynamic tsunami simulation are used in the verification of the findings mentioned above.

2. THE 2003 TOKACHI-OKI EARTHQUAKE AND OFFSHORE MONITORING SYSTEM

The interplate 2003 Tokachi-oki earthquake of JMA magnitude (M_J) 8.0 occurred off the southeastern coast of Tokachi at 04:50 on September 26, 2003. It was reported

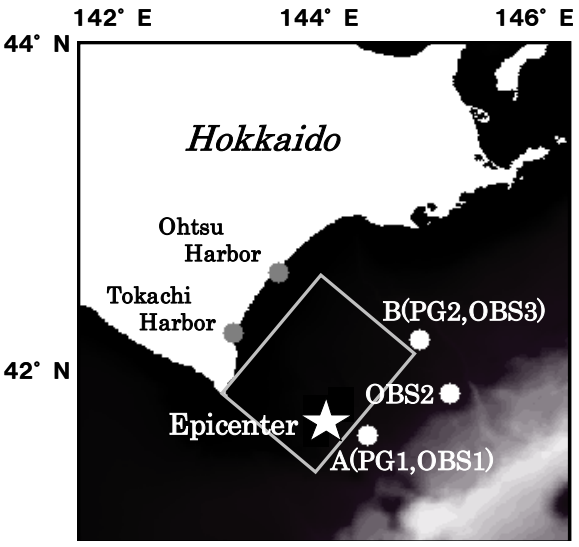

Figure 1 Locations of the JAMSTEC monitoring system equipment and epicenter of the 2003 Tokachi-oki earthquake.

that the tsunami arrived at Tokachi Harbor at 04:56 with a wave height of 4.3 m, while the Japanese nation-wide coastal wave observation network (NOWPHAS) located on the 23m-deep seabed off Ohtsu Harbor recorded the first tsunami arrival at 04:51 (Nagai and Ogawa 2004). The locations of these harbors and the epicenter of the earthquake are shown in Figure 1, where the location of an offshore monitoring system deployed by JAMSTEC is also shown. The system is equipped with three broadband tri-component seismometers (OBS1-3) and two high-precision pressure gauges (PG1-2). The distances between OBS1 and PG1 and between OBS3 and PG2 are rather short; that is, 4.0 km and 3.4 km, respectively. Thus, as shown in Figure 1, the locations where these pairs of instruments are installed are respectively referred to as St. A and St. B, and the distance between these two stations is about 72 km. In Figure 1, the hypocenter of the main shock and a fault model dipping northwest are shown by a star and a rectangle (Koketsu et al. 2004). Sampling rates of the pressure gauges and seismometers are 1 Hz and 100 Hz, respectively. Table 1 shows details of the offshore monitoring system and seawater depth of each sensor (JAMSTEC 2009).

3. TSUNAMI GENERATION PROCESS INFERRED FROM OBSERVED DATA

Time histories of water pressure and ground motion acceleration (vertical component) at St. A and St. B are shown in Figure 2. At both stations, the water pressure change lasted longer than the ground motion acceleration.

Fourier spectra of the time histories are shown in Figure 3. Peak periods of 7.0 s at St. A and 6.5 s at St. B are observed for both water pressure and ground motion acceleration, and each period T can be approximated by T=4H/c, where H is the seawater depth (2.2 - 2.3 km) and c is the acoustic wave velocity of water (1.5 km/s). Hence, these periods are thought to correspond to the acoustic waves traveling between the sea bottom and sea surface (Nosov et al.2005).

Table 1 The JAMSTEC offshore monitoring system and water depth of equipment.

Equipment of the system		Depth（m）	Recorded data
Cable-end Station (DSO)		2,540	Flow velocity
			Velocity according to layer
			Hydrophone
A	Seismometer (OBS1)	2,329	Ground motion acceleration
			Hydrophone
	Tsunami Sensor (PG1)	2,218	Water-Pressure
Seismometer (OBS2)		3,428	Ground motion acceleration
			Hydrophone
B	Seismometer (OBS3)	2,124	Ground motion acceleration
			Hydrophone
	Tsunami Sensor (PG2)	2,210	Water-Pressure

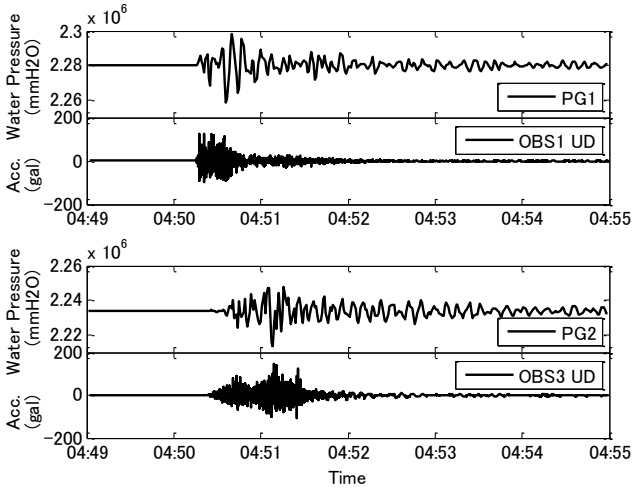

Figure 2 Time histories of water pressure and vertical ground motion acceleration.

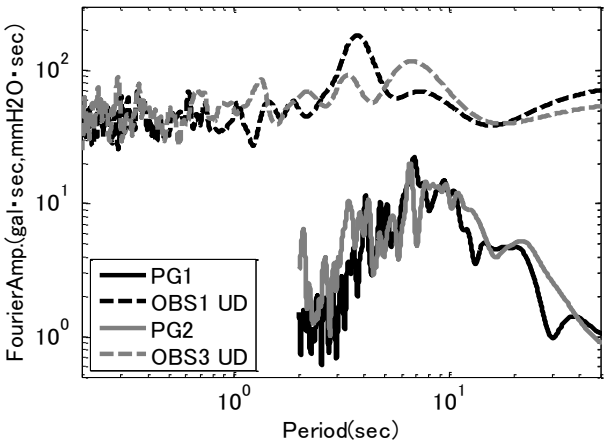

Figure 3 Fourier spectra of time histories shown in Figure 2.

Time histories of the water pressure change shown in Figure 2 consist of many short period components with amplitudes several times larger than the tsunami-induced water pressure. When the components with period less than 50 s are filtered out, the water pressure time histories are indicated by the gray curves in Figure 4. It is evident from the gray curves that, after the main shock, the base-line of the water pressure shifted by about 40 cm at PG1 and about 10 cm at PG2 in terms of the water depth. These base-line shifts were supposedly caused by the uplift of the seabed resulting from the seismic faulting (Watanabe et al. 2004).

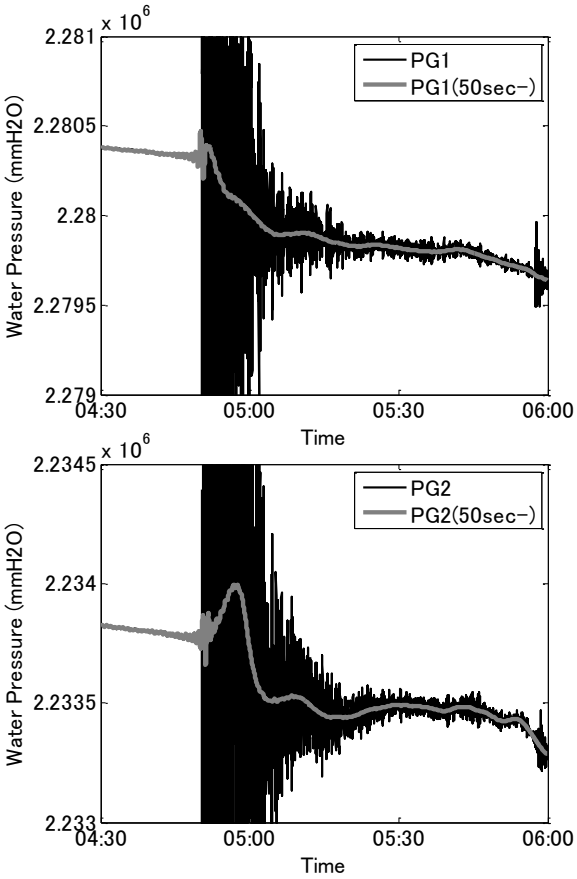

Figure 4 Time histories of water pressure after long-pass filtering of 50 s.

In addition, the gray curves in Figure 4 indicate two important features. First, a generated tsunami was detected with different shapes. At PG2, the tsunami is clearly observed as a solitary wave with a height of about 20 cm and a period of 15 min. At PG1, the wave height and the period of the recently generated tsunami are not as clear as that of PG2, but only a gentle slope can be observed. The difference in the shape of the tsunami is probably due to the difference in the relative location between the observation stations and the tsunami source. As shown in Figure 1, PG1 is located very close to or just above the seismic fault, while PG2 is located a little apart from the fault and about 72 km away

Table 2 Fault parameters

	length(km)	width(km)	depth(km)	Dmax(m)
Koketsu et al (2004)	120	100	25	7.1
Yamanaka and Kikuchi (2004)	90	70	25	5.8
Yagi (2003)	120	130	17	6.1

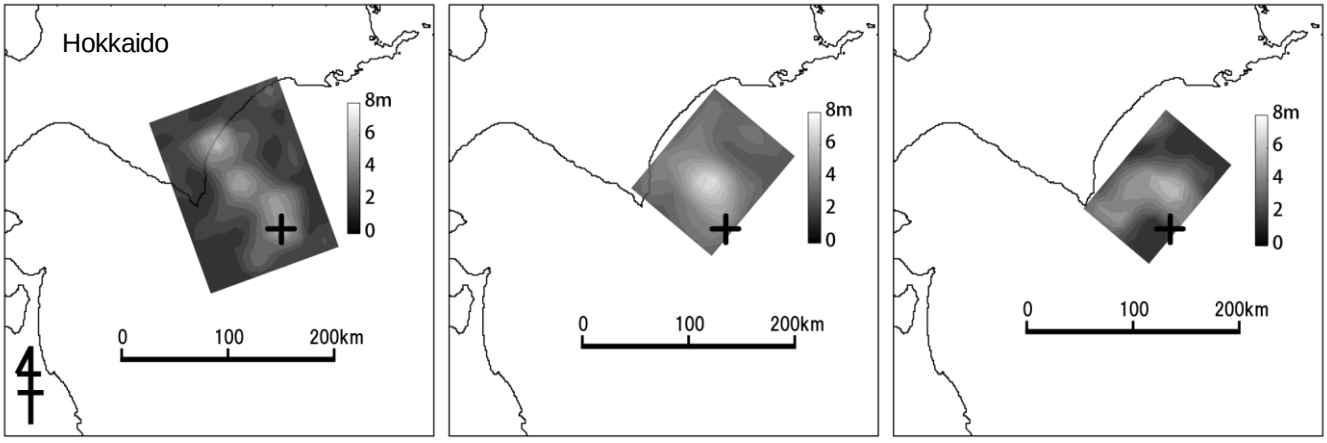

Figure 5 Fault dislocation of each models. (From the left, Yagi2003, Koketsu2004, and Yamanaka2004 model)

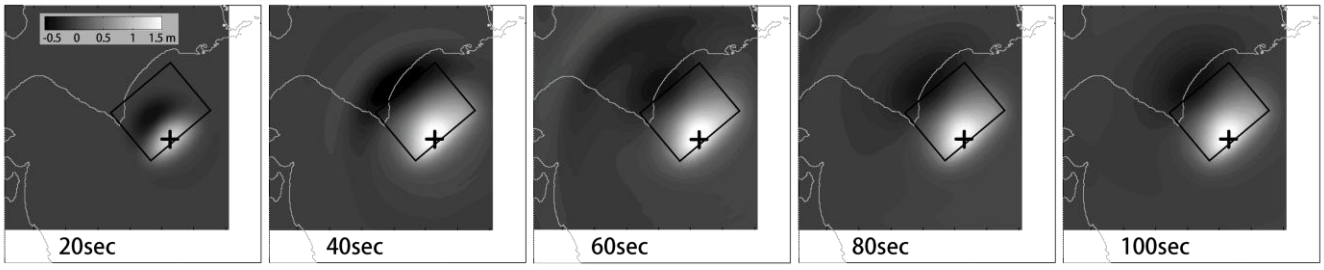

Figure 6 Calculated vertical displacement of the sea-bed by Koketsu 2004 model.

from PG1. Second, another group of water waves preceding the tsunami are seen at the beginning of the short-period water pressure change, and are referred to as preceding waves.

4. DYNAMIC TSUNAMI SIMULATION BY THREE FAULT MODELS

Three fault models proposed by each researchers (Koketsu et el., 2004, Yamanaka and Kikuchi, 2004, and Yagi, 2003) were used to calculate tsunami generation. Differences of these faults models are base on their inversion methods. The parameters of them are shown in Table 2, and the fault projections are shown in Figure 5. Calculation area is 350 km long in the NS direction and 350 km wide in the EW directions.

Snapshots in Figure 6 and 7 show the simulation results of the ground motion at 20, 30, 40, 60, 80 and 100s and water wave height distribution at 20, 60, 80, 100 and 600s after the fault rupturing by Koketsu 2004 model. At 20s the fault rupturing progresses up to middle of the fault plane. From 60s to 80s, the water wave induced by the Rayleigh wave propagates to the Northwest. At 80s when the fault rupture finishes, static uplift and subsidence remain in the near-fault area, and the tsunami profile is almost the same as that of the static displacement of the seabed. Maximum uplift and subsidence are estimated at about 1.3m and 0.6m. These results are correspond to the displacement observed by the GPS.

Figure 8 shows comparison between observed and computed water pressures at PG1 and PG2. From this figure, it is found that the simulated results are smaller than the observed ones. However, Fourier spectral amplitude shown in Fig. 9 indicates that the dominant periods of about 4, 6 to 8, and 20 s correspond with obserbed ones.

5. CONCLUSIONS

Analysis of the JAMSTEC monitoring data have shown that three kinds of water waves were involved in the dynamic tsunami generation process following the 2003 Tokachi-oki earthquake; that is, water pressure waves of short period, a tsunami of long period, and preceding waves of intermediate period.

We performed dynamic tsunami simulation with three kinds of fault model, and compared the simulation results with the observed records. The results showed that computed water pressures became smaller than observed data, however the dominant periods of simulated water pressure relatively correspond with the observed data.

Acknowledgements:
The authors are grateful to JAMSTEC for providing the monitoring system data used in this study.

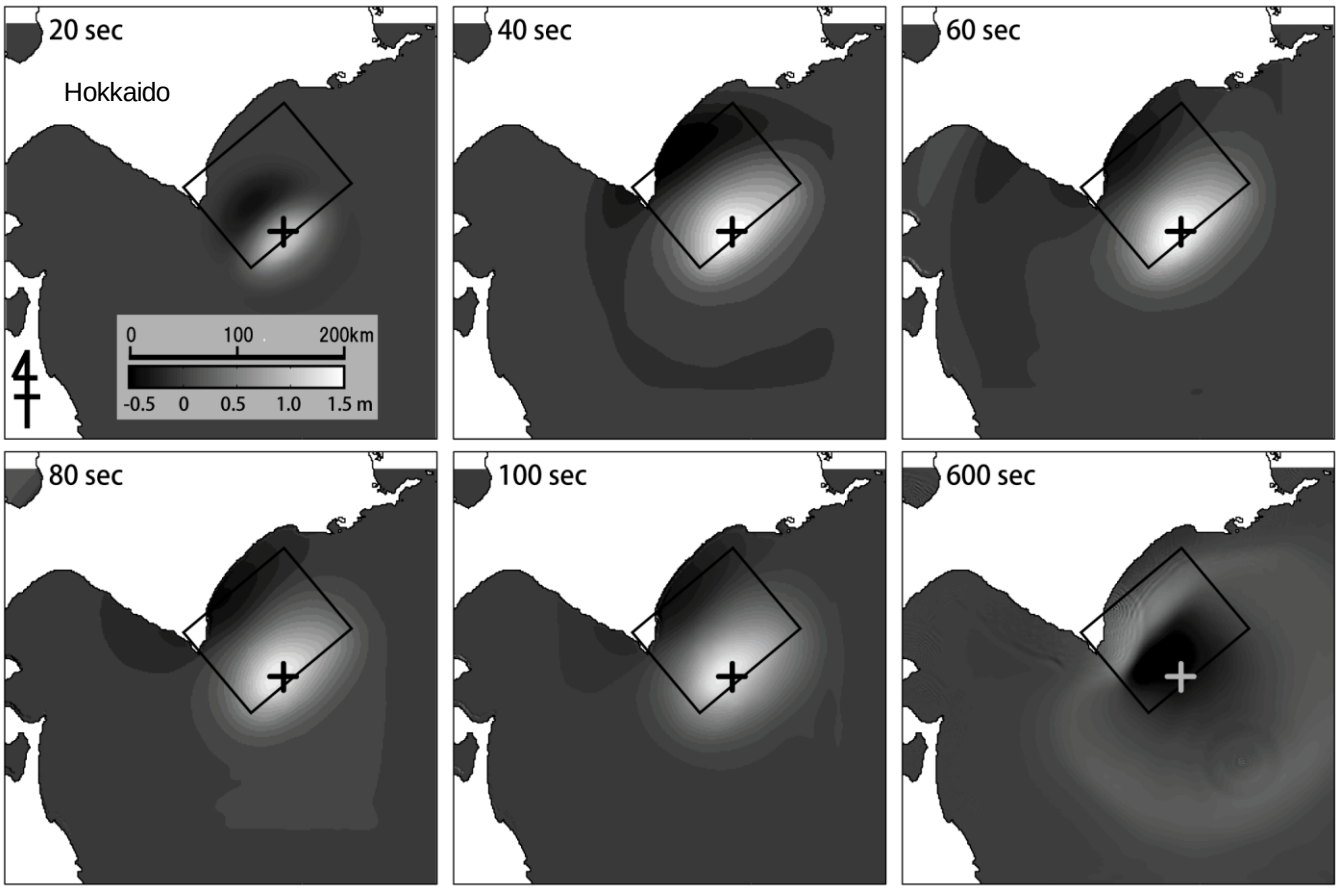

Figure 7 Snapshots of wave height distribution calculated by the dynamic tsunami simulation technique.

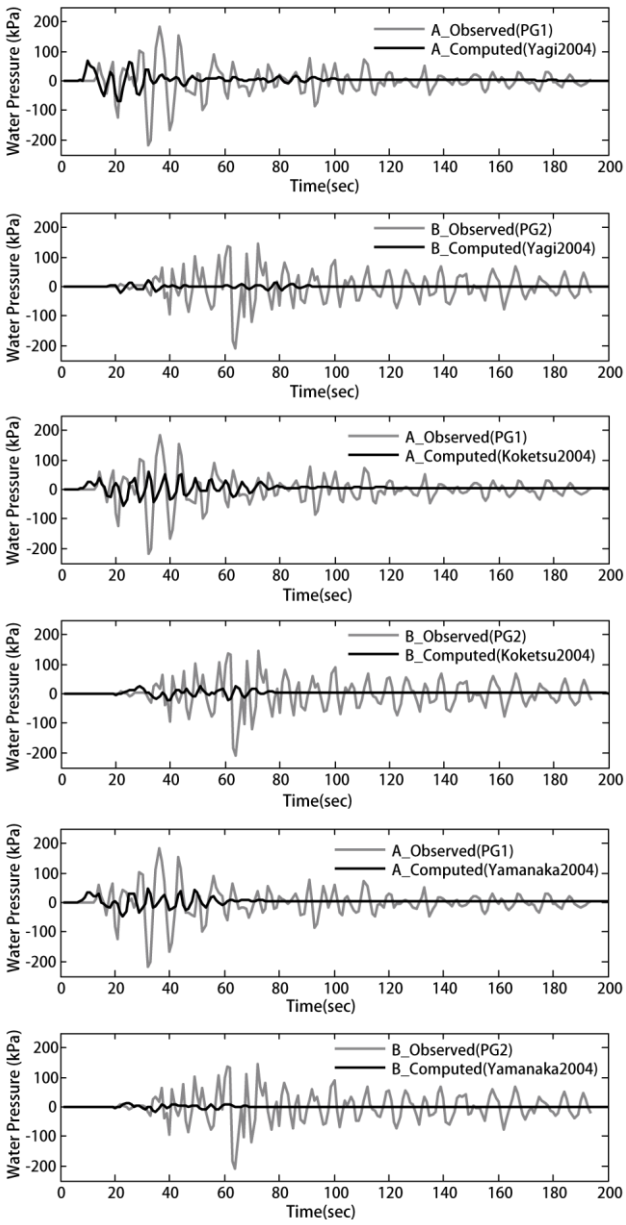

Figure 8 Comparison between observed and computed water pressures at PG1 and PG2.

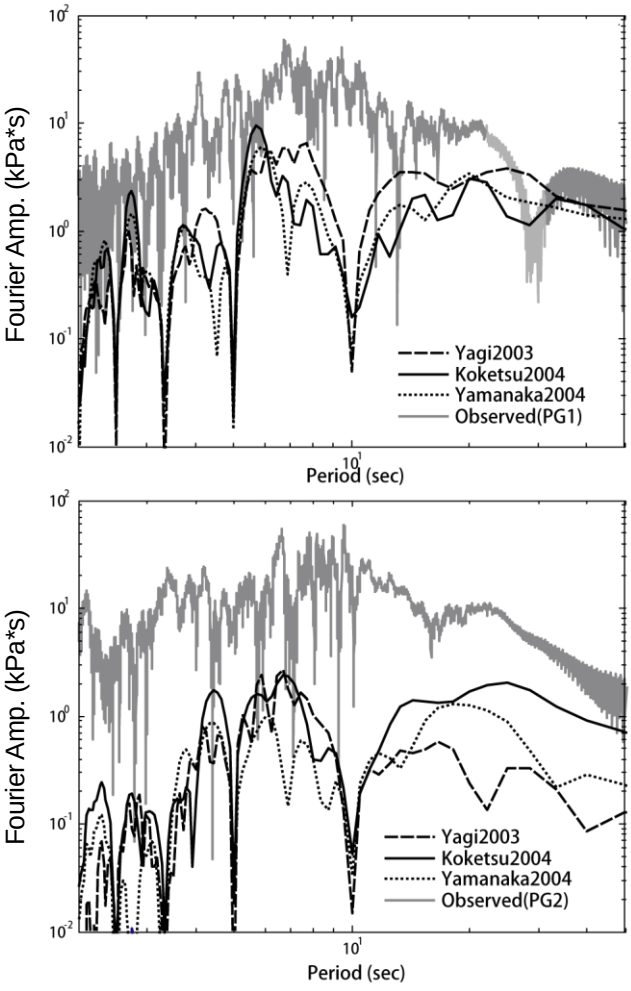

Figure 9 Fourier spectra of oberved and computed water pressures at PG1 and PG2

References:

JAMSTEC (2009), "Submarine Cable Data Center," http://www.jamstec.go.jp/scdc/

K. Koketsu, K. Hikima, S. Miyazaki and S. Ide (2004), "Joint inversion of strong motion and geodetic data for the source process of the 2003 Tokachi-oki, Hokkaido, earthquake," *Earth Planets Space*, **56(**3), 329-334.

T. Nagai and H. Ogawa (2004), "Characteristic of the 2003 Tokachi-off Earthquake Tsunami Profile," *Technical Note on the Port and Airport Research Institute, No. 1070*.

M. Nosov, S. V. Kolesov, A. V. Ostroukhova, A. B. Alekseev and B. M. Levin (2005), "Elastic oscillations of the water layer in a tsunami source," *Doklady Earth Sciences*, **404**(7), 1097-1100.

T. Ohmachi, H. Tsukiyama and H. Matsumoto (2001a), " Simulation of Tsunami Induced by Dynamic Displacement of Seabed due to Seismic Faulting," *Bull. Seis. Soc. Am.*, **91**(6), 1898-1909.

T. Ohmachi, H. Tsukiyama and H. Matsumoto (2001b), " Sea Water Pressure Induced by Seismic Ground Motions and Tsunamis," *ITS2001*, 595-609 (2001b).

T. Watanabe, H. Matsumoto, H. Sugioka, H. Mikada and K. Suyehiro (2004), " Offshore Monitoring System Records Recent Earthquake Off Japan's Northernmost Island," *Eos Trans. AGU*, **85**(2), doi:10.1029/2004EO020003.

Y. Yamanaka and M. Kikuchi (2003), "Source process of the recurrent Tokachi-Oki earthquake on September 26, 2003, inferred from teleseismic body waves," *Earth Planets Space*, **55**, pp. e21-e24.

Y. Yagi, (2004), "Souece rupture process of the 2003 Tokachi-oki earthquake determined by joint inversion of teleseismic body wave and strong motion data," *Earth Planets Space*, **56**, pp. e311-e316

JOINT CONFERENCE PROCEEDINGS
7th International Conference on Urban Earthquake Engineering (7CUEE) &
5th International Conference on Earthquake Engineering (5ICEE)
March 3-5, 2010, Tokyo Institute of Technology, Tokyo, Japan

RECENT PROGRESS ON OFFSHORE TSUNAMI OBSERVATION

Hiroyuki Matsumoto[1)] and Yoshiyuki Kaneda[2)]

1) Research Scientist, Japan Agency for Marine-Earth Science and Technology, Japan
2) Project Leader, Japan Agency for Marine-Earth Science and Technology, Japan
hmatsumoto@jamstec.go.jp, kaneday@jamstec.go.jp

Abstract: Offshore tsunami observation technologies have been developed and their related facilities have been deployed in the recent years, which consist of bottom pressure gauges, kinematic GPS buoys, etc. This paper reports the recent tsunami observation by the offshore cabled observatory off Hokkaido, Japan, both from the far- and the near-field earthquakes. As a far-field event, we introduce the 2006 Kuril Is. earthquake (Mw8.3), and about one hour later from the earthquake, a series of the tsunami signals were detected by two pressure gauges. Tsunami amplitudes observed offshore were about 3 cm, while those observed at the coast were a few tens of centimeters. On the other hand, during the near-field event, i.e., the 2008 off Tokachi earthquake (Mw6.8), a tsunami signal could be detected simultaneously with the earthquake origin with its amplitude of about 4 cm in the source. Offshore pressure gauges possibly become one of the key facilities for early tsunami warning, if an appropriate dataset's processing would be established.

1. INTRODUCTION

After the Indian Ocean tsunami from the Sumatra earthquake on 26 December 2004 (Mw > 9.0), we have realized the importance of the early tsunami warning system and its necessity for mitigating the tsunami disaster. This catastrophic event has been a cue for development of the Indian Ocean early tsunami warning system, and a global tsunami forecast would be established together with the Pacific Ocean tsunami warning system operated by U.S. and Japan. National Center of Geosciences in Germany would challenge to detect relative initial tsunami height distribution by GPS arrays and the seismic stations on land, and deploy GPS buoys along the Sumatra Trench (e.g., Sovolev et al., 2006).

One of the facilities composing the early tsunami warning system is the offshore observatory. NOAA operates a lot of DART buoys receiving water pressure from the ocean bottom in the Pacific and Atlantic Oceans (Titov et al., 2005). On the other hand, other sensors such as in-lined cabled bottom pressure gauges and kinematic GPS buoys are developed and deployed in the seismogenic zone in Japan. We have prepared a few tens of real-time offshore observatories in addition to a lot of traditional tide gauge stations along the coast against for future tsunamis. Figure 1 shows the present tsunami observatories operated in Japan in which black and white points represent offshores and near-shores at the coast, respectively. The first offshore observatory in Japan has been deployed off Omaezaki, central Japan, and followed by seven cabled observatories. Approximately ten kinematic GPS buoys have also been deployed a few kilometers offshore for the last three years after the period of trial and error. They could successfully detect tsunami prior to its arrival at the coast nearby for some tsunamigenic earthquakes (e.g., Matsumoto and Mikada, 2005, Kato et al., 2005). Thus, the offshore observatory has already experienced early tsunami detection and demonstrated an advantage for its early warning.

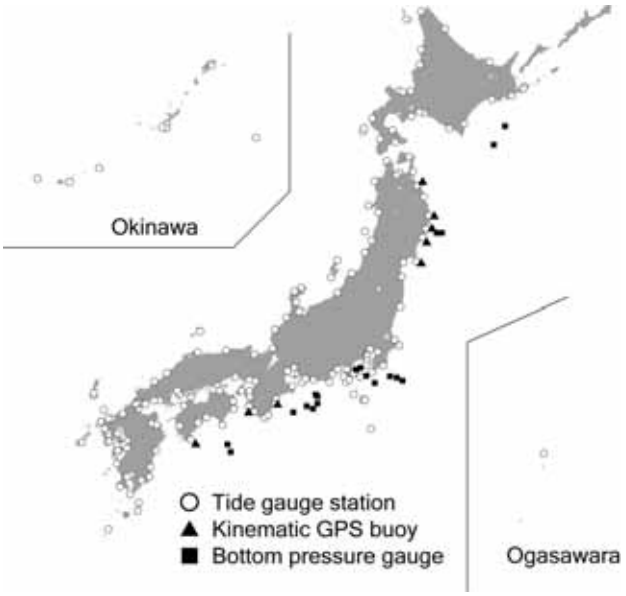

Figure 1 Locations of tide gauge stations (open circles) and offshore tsunami observatories (GPS tsunami meters: triangles; bottom pressure gauges: squares) in Japan.

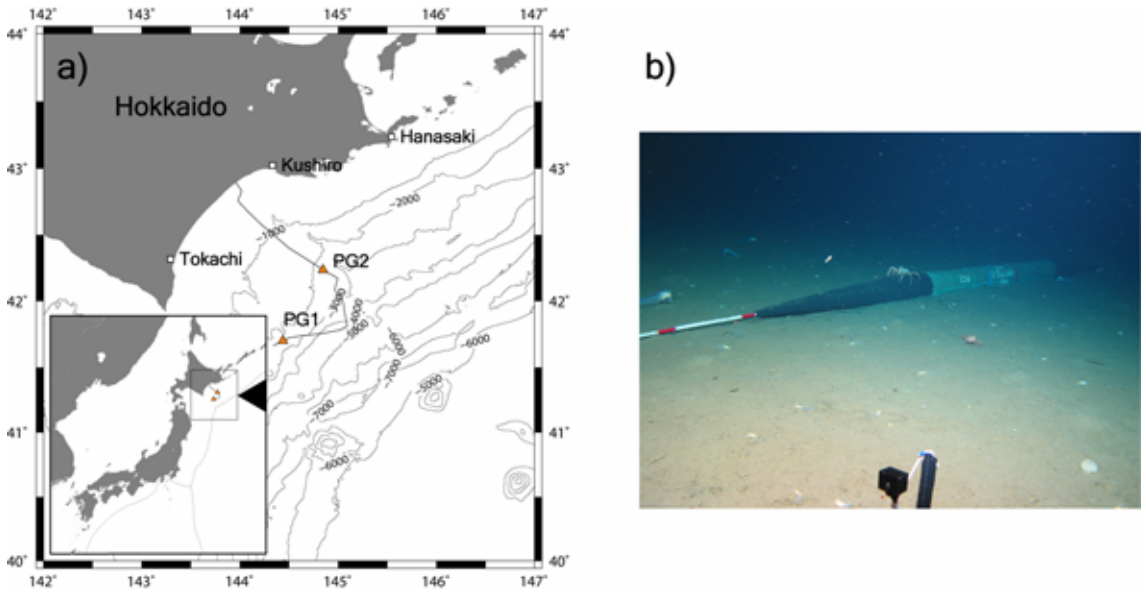

Figure 2 a) Map of bottom pressure gauges PG1 and PG2 locations at the JAMSTEC offshore cabled observatory, Hokkaido, Japan, and b) pressure gauge on the ocean-bottom.

Table 1. Position list of the pressure gauges of the offshore cabled observatory, off Hokkaido, Japan.

	Latitude (deg. N)	Longitude (deg. E)	Water depth (m)
PG1	41.7040	144.4375	2218
PG2	42.2365	144.8454	2210

Japan Agency for Marine-Earth Science and Technology (JAMSTEC) is operating three offshore real-time observatories in the seismogenic zone in Japan, of which the latest system has been deployed off Hokkaido in 1999 (Hirata et al., 2002). The offshore cabled observatory off Hokkaido consists of two permanent bottom pressure gauges (PG1 and PG2), and their dataset are sent to the JAMSTEC office in real-time (Fig. 2). Two pressure gauges, PG1 and PG2 are deployed at the water depth of 2218 m and 2210m, respectively, and their locations are listed in Table 1.

This paper discusses the offshore tsunami observation done by the JAMSTEC offshore cabled observatory off Hokkaido, Japan, for both the far-field and the near-field tsunamis. The tsunami from the 2006 Kuril Is. earthquake (Mw8.3) is reviewed as a far-field tsunami, while the moderate-to-large earthquake off Tokachi (Mw6.8) is introduced as a near-field tsunami.

2. 2006 KURIL ISLANDS EARTHQUAKE TSUNAMI

2.1. Overview

A megathrust earthquake (Mw 8.3) caused off the central Kuril Islands at 11:14:16 UTC on November 15, 2006, was triggered by the Pacific Plate subducting beneath the Okhotsk Plate at 90 mm/year at the quake's epicenter, causing a tsunamigenic earthquake once every century or so.

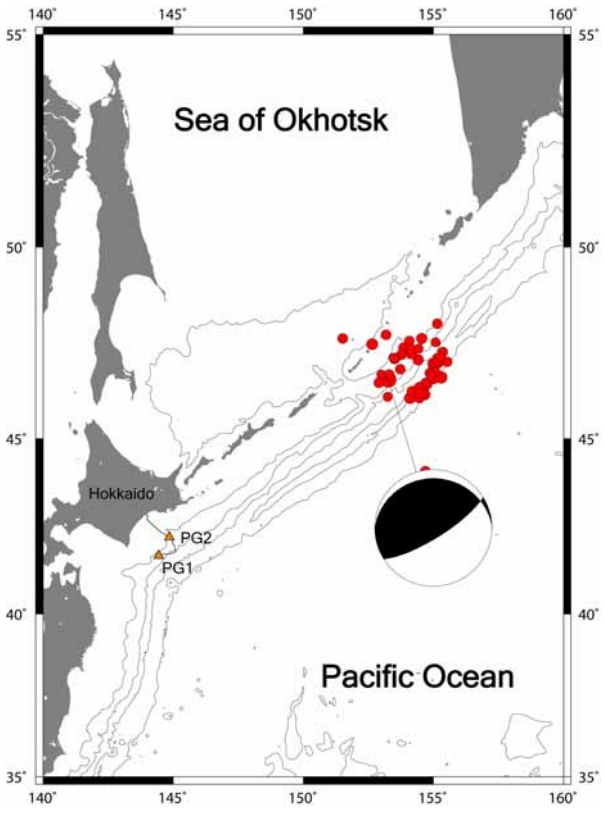

Figure 3 Map of 2006 Kuril Islands earthquake source area. The earthquake's focal mechanism is based on the US Geological Survey (USGS) fast moment tensor solution. Dots are aftershock distribution for 1 day after the earthquake.

Based on the historical earthquake catalog, the most recent large earthquake occurred in 1915 with a magnitude of 7.9 in the central Kuril Islands region. Southwest of the

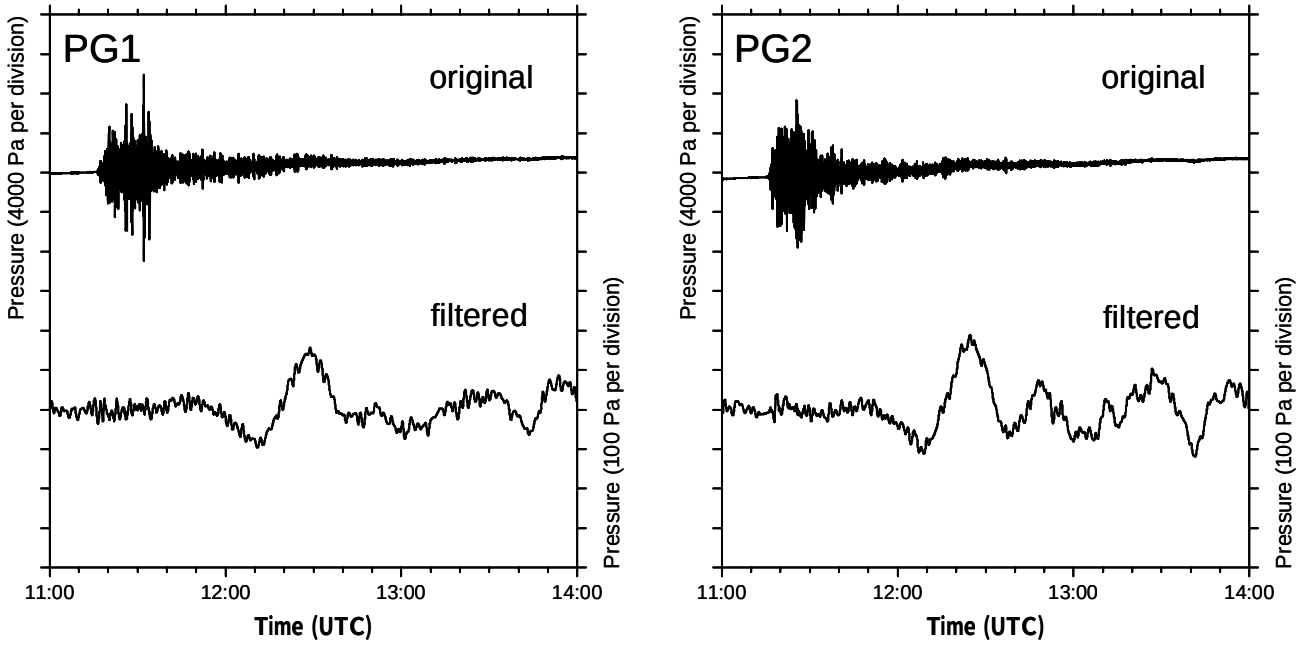

Figure 4 Pressure waveforms observed by 2 bottom pressure gauges during the 2006 Kuril Islands earthquake - above waveform: original; lower waveform: filtered. Note that ordinate (Y axis) values for filtered waveforms are magnified 40 times that of originals.

November 15 earthquake, the largest earthquake occurred in 1963 and, northeast of it, the larges occurred in 1952, as detailed in USGS (2006).

The focal mechanism determined by the USGS fast moment tensor solution resulted in thrust faulting with shallow dipping, indicating a plate boundary earthquake. Aftershock distribution for 1 day suggests that the fracture area extended northeast of the epicenter about 200 km along the Kuril-Kamchatka Trench, as shown in Fig. 3.

Thrust faulting potentially produces relatively large tsunamis. Following the earthquake, the first tsunami warning was issued by the Pacific Tsunami Warning Center (PTWC) at 11:30 UTC to the Pacific region, particular Russia and Japan. The earthquake's magnitude was estimated to be 7.7, 0.6 lower than the revised magnitude found in further analysis. One hour after the earthquake, a second warning was issued, with magnitude modified to 8.1. In Japan, the Japan Meteorological Agency (JMA) issued "tsunami" warnings for Hokkaido and "tsunami attention" warnings for the Pacific coast of NE Japan --the second and the third highest caution categories among Japanese tsunami warnings. Tsunamis from the earthquake were observed at the eastern coast of Hokkaido 1 hour later and at the northeast coast of Japan 2 hours later. The tsunami moving toward the Pacific Ocean hit Hawaii, then arrived at the US west coast 6 to 8 hours later. The JMA withdrew these warnings for the coast in Japan at 16:30 UTC the same day. Three hours after the tsunami warning was canceled, the largest tsunami was to be observed at Miyake Island in southern Japan.

2.2. Tsunami observed by the offshore observatory

Two bottom pressure gauges are located 800 to 900 km from the Kuril Islands earthquake epicenter, as shown in Fig. 3. Figure 4 shows pressure waveforms observed during the earthquake, in which originals contain the astronomical tide, seismic wave, tsunami, etc. To extract tsunami signals conventionally from bottom pressure gauge datasets during an earthquake, a moving average was often applied (e.g., Hino et al., 2001, Matsumoto and Mikada, 2005). We processed time-series datasets of bottom pressure gauges with mathematical filters to remove noise and extract tsunami signals as done by Takayama (2008). Here, we first apply a moving average at 30 min to remove the astronomical tide component, then we apply Chebyshev's low-pass filter at 100 s both forward and backward to remove high-frequency seismic noise, after which we recognize tsunami signals in pressure waveforms, as shown in Fig. 4.

The first tsunami signal rises are seen at 12:09 at PG2 and 12:12 atPG1. The initial PG2 amplitude rise is 3 hPa, while that of PG1 is slightly smaller. Since 1 hPa in a water pressure change corresponds to 1 cm in static water, the first tsunami is estimated at 3 cm at the pressure sensor location. Based on a tsunami observation report released by the JMA, the first tsunamis arrived at 12:29 to 12:46 at tide gauge stations along the Hokkaido coast and had amplitudes of 40 to 80 cm. Offshore pressure sensors detected the first tsunami to arrive at least 20 min in advance, for example, compared to that at Hanasaki, the tide gauge station nearest to the epicenter. The tsunami was amplified 10 times by shoaling effect.

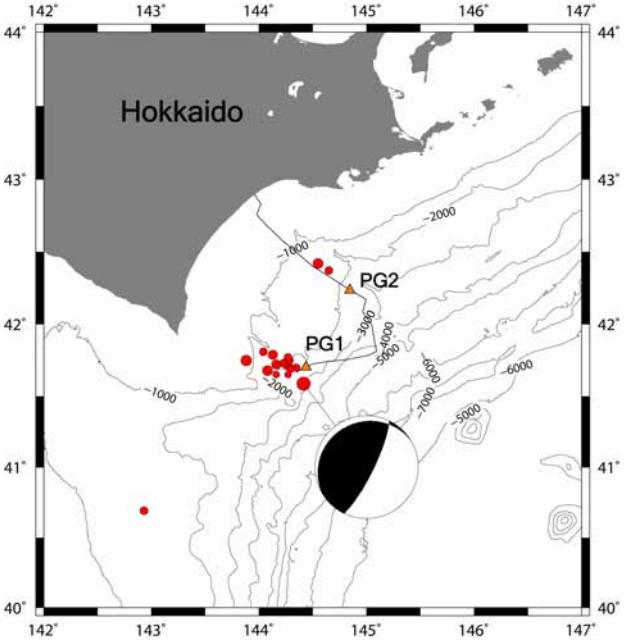

Figure 5 Map of the 2008 off-Tokachi earthquake source area. The earthquake's focal mechanism is based on the USGS fast moment tensor solution. Dots are aftershock distribution for 1 day after the earthquake.

3. 2008 OFF-TOKACHI EARTHQUAKE TSUNAMI

3.1. Overview

Bottom pressure gauges observed another offshore tsunami in the near-field range. An earthquake occurred off Hokkaido, Japan, on September 11, 2008, with a magnitude of 6.8, as shown in Fig. 5, i.e., the 2008 off-Tokachi earthquake. The last prior megathrust earthquake with a magnitude of 8.3 had occurred in 2003 in the same area, and the offshore observatory had observed some geophysical phenomena in the near-field range at that time (Mikada et al., 2006). Based on the USGS catalog (2008), the earthquake originated at 00:20:52 UTC and its hypocenter was located at 41.976N, 143.630E at a depth of 35 km near the JAMSTEC offshore cabled observatory, beneath PG1. Plotting aftershock distribution for 1 day after the earthquake, the segment extends NW-SE near PG1, as shown in Fig. 5. The earthquake involved thrust faulting between the Pacific and Okhotsk Plates, so the JMA issued a tsunami attention warning along the nearby coast 3 minutes after the earthquake. Tsunamis observed along the near coast were 10 to 20 cm high 30 min later. The maximum earthquake seismic intensity for Hokkaido was 5- on the JMA scale.

3.2. Tsunami observed by the offshore observatory

The 2 bottom pressure gauges observed full pressure fluctuations during the earthquake. The nearest bottom pressure gauge, PG1, was 13 km away from the epicenter and PG2 was located 80 km away. PG1 can be regarded as being inside the source region with respect to the earthquake scale. Figure 6 shows the pressure waveforms observed by PG1 and PG2, which were very large amplitude fluctuations in the near-field range. We could not find an offset, i.e., the static pressure change in PG datasets related to crustal deformation, unlike obvious dataset offset following the 2003 megathrust event (Watanabe et al., 2004). Two aftershocks with magnitude of 5.3 and 5.0 occurred at 00:33 and 01:03. Associated pressure fluctuations were recorded in pressure waveforms. Observed pressure waveforms had a large amplitude due to near-field seismic waves and a very low-frequency astronomical tidal component in addition to the tsunami itself. We applied mathematical filtering as same as the previous section to original pressure waveforms and obtained a visible tsunami signal in pressure waveforms after filtering.

Peak-to-peak tsunami amplitudes were 4 hPa and 3 hPa, i.e., 4 cm and 3 cm high for PG1 and PG2. Because PG1 is near the tsunami source, static pressure change related to the tsunami was produced simultaneously with earthquake occurrence. The initial peak of the first wave recorded by PG1 appeared 3 minutes after the earthquake, suggesting that the maximum uplift was beside the bottom pressure gauge. The first tsunami arrived at the coast at 00:56 with flood movement at Tokachi, which is the tide gauge nearest to the source.

4. CONCLUSIONS

Seismic data alone remains insufficient for accurately predicting tsunamis, despite advances in state-of-the-art technology. Offshore observatory tools such as DART and kinematic GPS buoys used in addition to cabled observatories on the open seas are expected to predict and detect tsunamis within a few tens of minutes before such tsunamis reach the nearest coastlines.

We have reported offshore tsunami waveforms observed by bottom pressure gauges during the far-field megathrust earthquake off the Kuril Islands on November 15, 2006, and the near-field off-Tokachi earthquake on September 11, 2008. The Kuril case is, to our knowledge, the earliest detection in Japan of a tsunami - 20 minutes before it arrived at the eastern tip of Hokkaido - and the initial tsunami rising at a height of 3 cm 60 min after the earthquake. In the off-Tokachi case, the tsunami signal at the tsunami source was detected just after the earthquake. Although 2-step mathematical filtering was used for original datasets in our study, appropriate real-time dataset processing is required to extract tsunami signals for both near- and far-field events.

It should be noted that we conducted tsunami calculation for both events based on seismic fault models, reproducing first tsunami wave pressure waveforms and pressure waveforms related to the near-field tsunami at its occurrence. We found, however, that discrepancies still exist for arrival time and the later tsunami phase between observed and calculated waveforms as published in

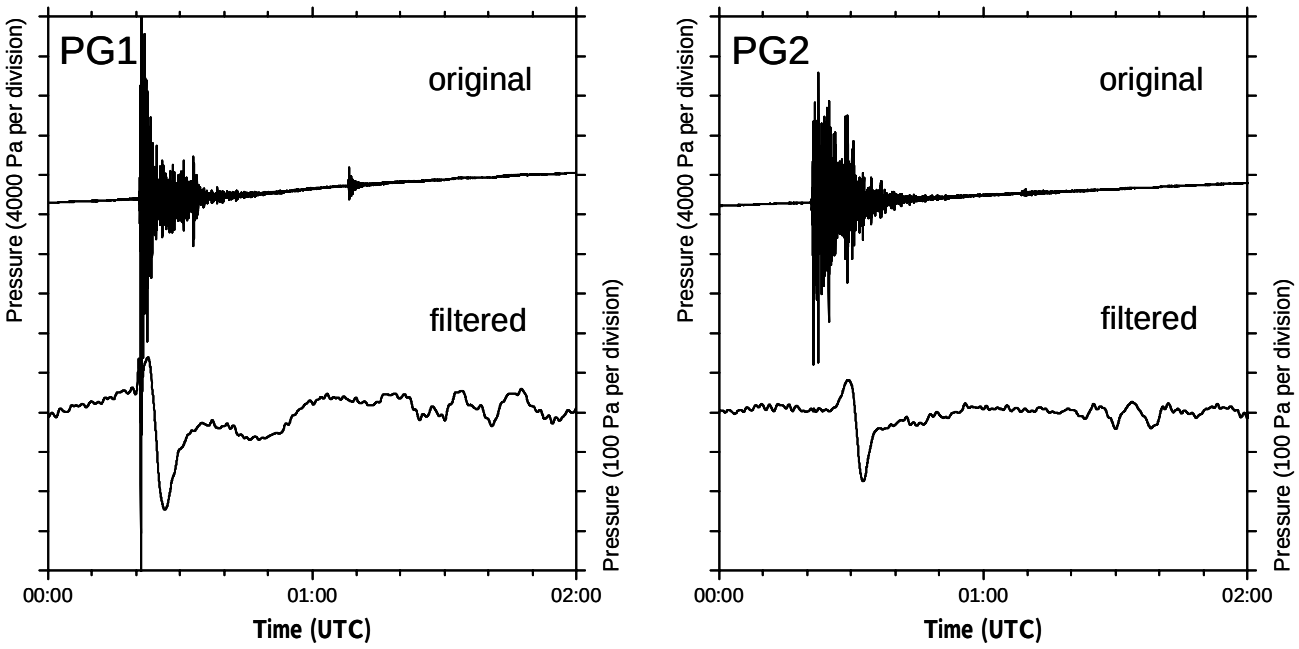

Figure 6 Pressure waveforms observed by 2 bottom pressure gauges during the 2008 off-Tokachi earthquake - above waveforms are original; lower waveforms: filtered. Note that ordinate (Y axis) values for filtered waveforms are magnified 40 times that of originals.

elsewhere (Matsumoto and Kaneda, 2009).

We expect that bottom pressure gauges PG1 and PG2 at the offshore cabled observatory off Hokkaido to be keys in the early warning system detecting tsunamis from the Kuril-Kamchatka trench and from near-field earthquakes, if an appropriate dataset's processing would be applied.

Acknowledgements:

We thank JAMSTEC Submarine Cable Data Center for providing bottom pressure gauges' dataset. Discussions with Ryoichi Iwase and Tomoki Watanabe were useful for this article. Some figures were prepared using GMT software (Wessel and Smith, 1995). This research was supported by Japan Ministry of Education, Culture, Sports, Science, and Technology (MEXT) Grant-in-Aid for Young Scientists Research (B), No. 19710152.

References:

British Oceanographic Data Centre, "The centerary edition of the GEBCO digital atlas (CD-ROM)," 1997.

Hino, R., Y. Tanioka, T. Kanazawa, S. Sakai, M. Nishino, and K. Suyehiro, "Micro-tsunami from a local interplate earthquake detected by cabled offshore tsunami observation in northeastern Japan," *Geophys. Res. Lett.*, **28**, 3533-3536, 2001.

Hirata, K., M. Aoyagi, H. Mikada, K. Kawaguchi, Y. Kaiho, R. Iwase, S. Morita, I. Fujisawa, H. Sugioka, K. Mitsuzawa, K. Suyehiro, H. Kinoshita, and N. Fujiwara, "Real-time geophysical measurements on the deep seafloor using submarine cable in the southern Kurile subduction zone, " *IEEE J. Ocean. Eng.*, **27**, 170-181, 2002

Kato, T., Y. Terada, K. Ito, R. Hattori, T. Abe, T. Miyake, S. Koshimura, and T. Nagai, "Tsunami due to the 2004 September 5th off the Kii Peninsula Earthquake, Japan Recorded by a New GPS Buoy, " *Earth Plants Space*, **57**, 279-301, 2005.

Matsumoto, H. and H. Mikada, "Fault geometry of the 2004 off the Kii peninsula earthquake inferred from offshore pressure waveforms, " *Earth Planets Space*, **57**, 161-166, 2005.

Matsumoto, H., and Y. Kaneda, "Review of recent tsunami observation by offshore cabled observatory", *J. Dis. Res.*, **4**, 489-497, 2009.

Mikada, H., K. Mitsuzawa, H. Matsumoto, T. Watanabe, S. Morita, R. Otsuka, H. Sugioka, T. Baba, E. Araki, and K. Suyehiro, "New discoveries in dynamics of an M8 earthquake -Phenomena and their implications from the 2003 Tokachi-oki Earthquake using a long term monitoring cabled observatory-," *Tectonophysics*, **426**, 95-105, 2006.

Ohmachi, T., H. Tsukiyama, and H. Matsumoto, "Simulation of tsunami induced by dynamic displacement of seabed due to seismic faulting," *Bull. Seism. Soc. Am.*, **91**, 1898-1909, 2001.

Okada Y., "Surface deformation due to shear and tensile faults in a half-space," *Bull. Seism. Soc. Am.*, **75**, 1135-1154, 1985.

Sobolev, S., A. Babeyko, R. Wang, R. Galas, M. Rothacher, J. Lauterjung, D. Sein, J. Schroter, and C. Subarya, "Towards Real-time Tsunami Amplitude Predition, " *EOS Trans. AGU*, **87**, 374-378, 2006.

Takayama, H., "Statiostical relation ship between tsunami maximum amplitudes of offshore and coastal stations," *Pap. Meteor. Geophys.*, **59**, 83-95, 2008 (in Japanese).

Titov, V., F.I. González, E.N. Bernard, M.C. Eble, H.O. Mofjeld, J.C. Newman, and A.J. Venturato, "Real-time tsunami forecasting: Challenges and solutions, " *Natural Hazards*, **35**, 41-58, 2005.

U.S. Geological Survey, "Rupture process of the 2006 NOV 15 Magnitude 8.3 - Kuril Islands Earthquake (Revised)," http://earthquake.usgs.gov/eqcenter/eqinthenews/2006/usvcam/, 2006.

U.S. Geological Survey, http://earthquake.usgs.gov/eqcenter/eqinthenews/2008/us2008wvag/, 2008.

Watanabe, T., Matsumoto, H., Sugioka, H., Mikada, H., Suyehiro, K., and Otsuka, R., "Offshore monitoring system records recent earthquake off Japan's northernmost island," *EOS Trans. AGU*, **85**, 14, 2004.

Wessel, P. and W. H. F. Smith, "New version of the Generic Mapping Tools released," *EOS Trans. AGU*, **76**, 329, 1995.

JOINT CONFERENCE PROCEEDINGS
7th International Conference on Urban Earthquake Engineering (7CUEE) &
5th International Conference on Earthquake Engineering (5ICEE)
March 3-5, 2010, Tokyo Institute of Technology, Tokyo, Japan

TSUNAMI LOADING - FROM EXPERIMENTS TO FIELD LOAD TEST

Panitan Lukkunaprasit [1], and Nuttawut Thanasisathit [2], Anat Ruangrassamee [3]

1) Professor, Department of Civil Engineering, Chulalongkorn University, Thailand
2) Ph.D. Candidate, Department of Civil Engineering, Chulalongkorn University, Thailand
3) Assistant Professor, Department of Civil Engineering, Chulalongkorn University, Thailand
lpanitan@chula.ac.th, nutwut@gmail.com, fcearr@eng.chula.ac.th

Abstract: Federal Emergency Management Agency (FEMA) has recently published the design guidelines for vertical evacuation structures from tsunamis: FEMA P646 (2008). The specification has been verified with limited experimental results, but not with actual field data. The Meteorological Department weather monitoring building in Phang-Nga which survived the 2004 Indian Ocean tsunami attack in southern Thailand served as the case study building. A one-to-fifty scale model of the building was tested in a wave flume under simulated solitary-like waves. The tsunami loading computed in accordance with FEMA P646 was compared with the test results as well as the field tested load on the actual building.

1. INTRODUCTION

The Indian Ocean tsunami on December 26, 2004 caused by an Mw 9.1 mega-earthquake in northern Sumatra, Indonesia (USGS 2008) left severe devastation in many countries in the region. Tsunamis of about 5-12 m heights struck the western coast of southern Thailand with heavy damage to buildings in the affected areas. However, a large number of engineered reinforced concrete (RC) buildings, especially those with openings in the masonry infill panels, survived with minor structural damage even though they were not designed for tsunamis or earthquakes (Lukkunaprasit and Ruangrassamee 2008, Ruangrassamee et al. 2006). Existing guidelines such as FEMA 55 (2000) predict a very large tsunami load; buildings would have collapsed had this load actually acted on the structures, in contradiction to the actual observed performances. Recently, Federal Emergency Management Agency (FEMA) has published FEMA P646 (2008), the design guidelines for vertical evacuation structures from tsunamis. The specification has been verified with limited experimental results, but not with actual field data. To this end, the field load test results of a building that survived the 2004 Indian Ocean Tsunami was utilized to verify the lateral tsunami loading stipulated by FEMA P646 guidelines. Wave flume tests on the building model were also conducted.

2. THE CASE STUDY BUILDING

A weather monitoring building of the Meteorological Department station at Takua Pa, Phang-Nga, which survived the 4.4 m wave height (above the ground) with minor structural damage (Fig. 1) was taken as the case study (Lukkunaprasit et al., 2010). The building is 220 m from the shoreline, and it's elevation is 5 m above the mean sea level.

The single story RC structure, whose plan and elevation are shown in figure 2, has small columns (200 mm x 200 mm in cross section) reinforced with 4 - 12 mm diameter longitudinal reinforcing bars. The main girders are 200 mm x 500 mm with 3-16 mm diameter top and bottom longitudinal bars. The building had essentially nonstructural panels all around the perimeter consisting of large window panes and 900 mm high masonry panels with 120 mm thickness.



Figure 1 Photograph of case study building (front view normal to flow).

The primary members have suffered minor damage, with hairline flexural cracks observed in the columns. The girders are practically intact. The masonry walls essentially perpendicular to the flow were completely destroyed. However, the panels which are essentially parallel to the flow survived, in general, including one major brick wall which is 2.6 m wide and spans the full height as shown in figure 3. This panel, designated as BW, sustained diagonal cracks of about 0.5 mm crack width after the tsunami attack.

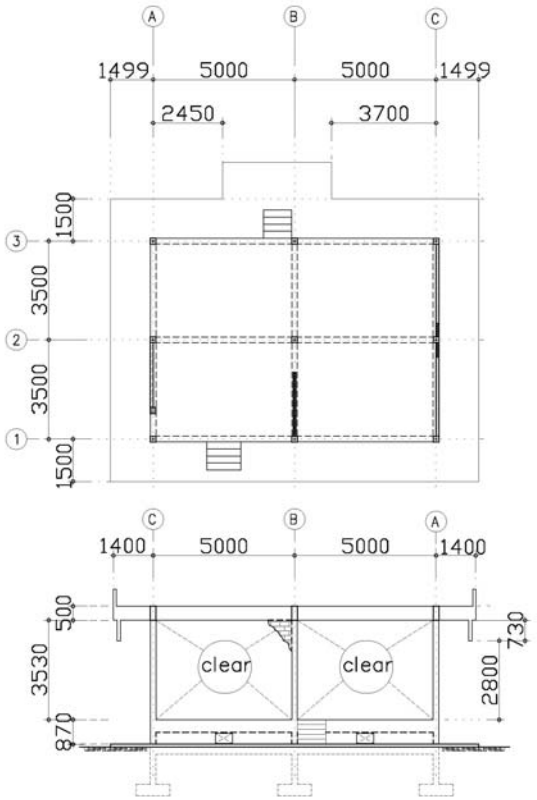

Figure 2 Building plan and elevation.



Figure 3 The interior view of the building showing the remaining structure and brick wall (BW).

3. EXPERIMENTS

3.1 Test Setup

A one-to-fifty scale model of the Meteorological building that remained after the tsunami attack was tested in a 40 m long hydraulic flume with 1 m x 1 m cross section (Fig. 4). A mild slope of 0.5 degree representing the beach condition at Kamala, Phuket, Thailand was modeled in the laboratory. The model dimensions at the ground floor level were 200 mm in width, 140 mm in depth and 103 mm in height (Fig. 5). A high frequency load cell was mounted at the base of the model to record the tsunami forces. The tsunami wave was generated by a sudden release of water through a controlled gate at the bottom of an elevated water tank located at the upstream end of the flume. The nominal wave height investigated was 60 mm. Here the wave height h is defined as the maximum flow depth that would occur in a flow without the presence of the model measured at the location of the model. This wave height was selected (by trial runs) such that the flow approximately reached the level of the fin (4.4 m in prototype) where the water mark was observed in the survived building. The frontal areas of the building submerged in the flow are shown in figure 6.

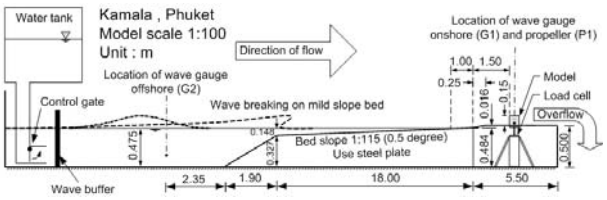

Figure 4 Schematic diagram of test setup.

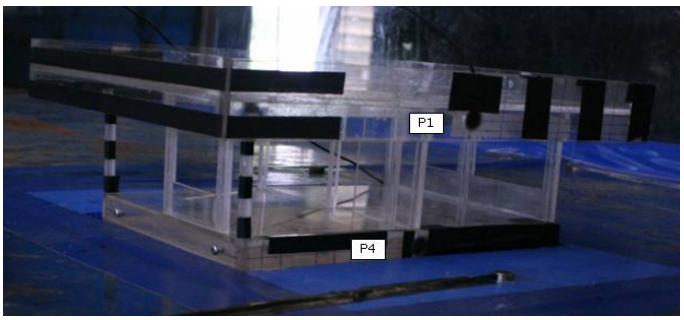

Figure 5 Model of building in wave flume.

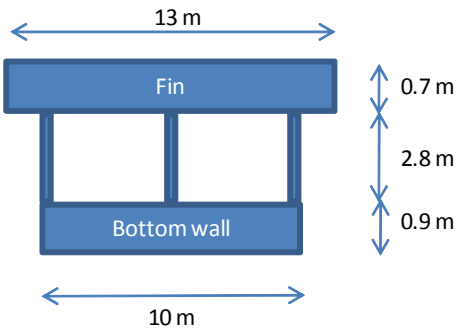

Fin	=	9.1 m^2
Column	=	5.4 m^2
Bottom wall	=	9.0 m^2
Area	=	23.5 m^2

Figure 6 Frontal areas of building submerged in flow.

3.2 Results

Figure 7 shows a typical time history of measured forces for the nominal wave height of 60 mm. The graph shows two peaks, the first peak obtained about 0.5 sec after initial impact on the bottom wall.

The second peak occurs 4.0 sec later when the flow reaches the fin. It should be noted that the maximum force at first peak does not affect the integrity of the superstructure. Therefore, the second peak, presumably in the quasi-steady state condition with most of the building submerged, is compared with the field load test result, to be described later.

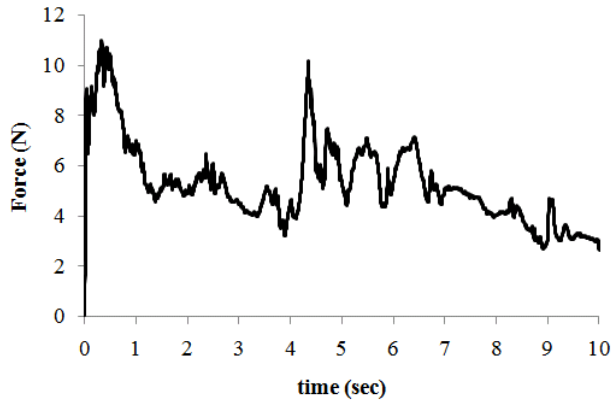

Figure 7 Typical time history of measured force for the nominal wave height of 60 mm.

Table 1 tabulates the results obtained from the tests together with the prototype scale forces determined by maintaining the Froude number similitude. In our experiment setup, we could not directly measure the maximum runup height R. Following the procedures in Lukkunaprasit et al. (2009), the theoretical formulas by Peregrine and Williams (2001), which provide time and spatial variations of the flow velocity and flow depth for bore runup, were used to estimate the equivalent maximum tsunami runup height R for the laboratory flow conditions.

Table 1 Experimental results and estimated maximum runup heights and drag force in prototype building.

Case	Model			Prototype	
	Wave height	Runup height	Drag Force	Runup height	Drag Force
	m	m	N	m	kN
1	0.065	0.40	8.0	19.94	997
2	0.065	0.40	10.2	19.94	1272
3	0.064	0.39	10.6	19.62	1324
4	0.063	0.39	11.1	19.31	1384
5	0.063	0.39	9.9	19.36	1236
6	0.064	0.39	8.2	19.67	1030
7	0.064	0.39	9.1	19.67	1133
8	0.064	0.39	6.4	19.57	802

It should be noted that the runup heights of 0.39 - 0.40 m generated in the wave flume (corresponding to 19.3 – 19.9 m in the prototype) were not a good representation of the actual condition, since the maximum runup heights at a few locations nearby the building were reported to be only about 10 - 12 m above the mean sea level. Therefore, the loads obtained from the tests would overestimate the actual value.

4. FEMA P646 TSUNAMI LOADING

FEMA-P646 (2008) proposes to use the maximum momentum flux $(hu^2)_{max}$ to estimate the maximum forces exerted by tsunami surges on buildings. In the quasi-steady state when water flows around a structure after initial surge impingement, the hydrodynamic force (or drag force) can be estimated from the well known formula:

$$F_d = \frac{1}{2}\rho C_d B h u^2 \qquad (1)$$

where h is the flow depth at the location of interest in the absence of the structure; ρ is the fluid mass density; C_d is the drag coefficient; B is the breadth of the building, and u is the flow velocity corresponding to the flow depth h. Lukkunaprasit et al. (2009) have shown that the drag force predicted by Eq. (1) using the actual values of u and h at any instant of time compares fairly well with the experimental results. However, in a practical situation, such information is not readily available except the maximum runup height, unless a refined numerical simulation of the runup is conducted with a very fine grid size (Yeh 2007). To estimate the maximum momentum flux at a location with a maximum runup height R, Yeh (2007) proposed the following expression:

$$\frac{(hu^2)_{max}}{gR^2} = 0.125 - 0.235\frac{z}{R} + 0.11\left(\frac{z}{R}\right)^2 \qquad (2)$$

where g is the acceleration due to gravity and z is the ground elevation at the building location.

5. COMPARISON OF PREDICTED SURGE FORCE WITH FIELD LOAD TEST RESULT

The surge forces exerted on the building computed based on Eqs. (1) and (2) are 178 and 340 kN corresponding to the maximum runup heights of 10 and 12 m, respectively. The FEMA P646 specified tsunami loading will now be verified with the field load test results of the damaged Meteorological building, which will be briefly described below. The detailed account of the field load test is given by Lukkunaprasit et al. (2010).

As depicted in figure 8, the loading that acted on the structure can be approximately determined by re-loading it past the state of the previous loading, which is reflected by

the degree of damage in the building before it is re-loaded.

The building was pushed over by means of static lateral loads simulating equivalent hydrodynamic forces through six hydraulic jacks bearing against a temporarily erected reaction frame. The floor and roof displacements were recorded by means of displacement transducers. The building was loaded until sufficiently more damage was observed in the structural columns as well as BW. The test was terminated at 381 kN (total load on the building) for safety reason since a major diagonal crack in BW which had a maximum crack width of 0.5 mm at the initial stage widened to a crack width of 2.5 mm which reduced to 1.5 mm residual crack upon unloading, well larger than the initial crack width. Thus, it can be concluded that the building in the damaged state was subjected to tsunami load of not more than 381 kN. In other words, this load can be regarded as an upper bound of the surge force exerted on the damaged building.

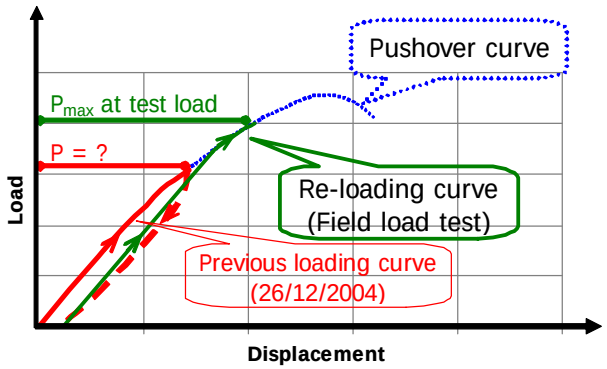

Figure 8 Schematic diagram of the re-loading curve on the remaining structure.

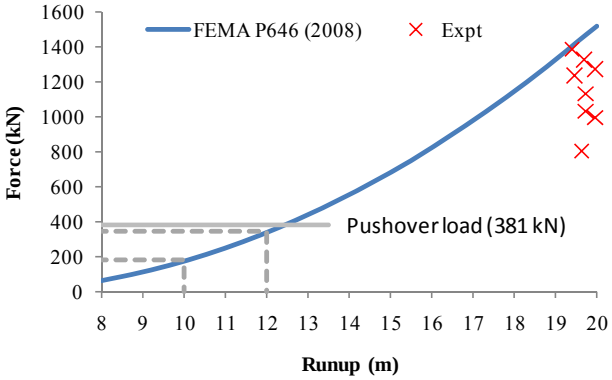

Figure 9 Comparison of the measured maximum drag forces with predictions made by Eqs. (1) and (2).

Figure 9 depicts the drag force stipulated by FEMA P646 as a function of runup height. Also shown are the experimental results which are reasonably bounded by the prediction curve. It is evident that the pushover load of 381 kN does provide an upper bound for the predicted surge force exerted on the damaged building. The predicted load of 340 kN at 12 m maximum runup height compares well with the field test result, the discrepancy being about 12%. However, should the maximum runup height be 10 m, then the difference could be as large as 50 % of the pushover load in the worst case. In view of uncertainties in the prediction of maximum runup height and for conservatism in practice, some allowance, say 15%, should be provided for the estimated value of the maximum runup height. Furthermore, an overshoot factor of 1.5 should be incorporated to account for a possibility of bore formation by subsequent waves propagating over a previously flooded runup zone (Yeh, 2007).

6. CONCLUSIONS

The tsunami surge force specification in FEMA P646 is verified with wave flume test results and pushover load of the Meteorological Department building in Phang-Nga which suffered minor structural damage from the 2004 Indian Ocean tsunami. The guidelines provide an upper bound for the experimental results. The predicted load based on an observed maximum runup height in the vicinity of the building agreed reasonably well with the pushover load of the actual building. It is recommended that an allowance of about 15% in the estimated maximum runup height should be made in view of difficulty in ascertaining the value.

Acknowledgements:

The funding from the Department of Public Works and Town and Country Planning, the Commission on Higher Education, the Royal Golden Jubilee Project of the Thailand Research Fund is gratefully acknowledged. The support of Chulalongkorn University and the Asian Institute of Technology is highly appreciated. The author greatly appreciate the valuable contributions of Prof. T. Takayama, Drs. P. Wanitchai, S. Weesakul, C. Chinnarasri, B. Stitmannaithum, and C. Chintanapakdee. The contributions of Dr. Somboon Siangchin, Mr. Surakai Banchuen and many graduate students are also acknowledged.

References:

FEMA 55 (2000), "Coastal Construction Manual, Edition 3", Federal Emergency Management Agency. Washington, D.C.

FEMA P646 (2008), "Guidelines for Design of Structures for Vertical Evacuation from Tsunamis," Federal Emergency Management Agency, Washington, D.C.

Lukkunaprasit, P. and Ruangrassamee, A. (2008), "Building damage in Thailand in 2004 Indian Ocean tsunami and clues for tsunami-resistant design," The Institution of Engineers Singapore Journal, Part A: Civil and Structural Engineering, Vol.1(1), 17–30.

Lukkunaprasit, P., Thanasisathit, N., Yeh, H. (2009), " Experimental Verification of FEMA P646 Tsunami", Journal of Disaster Research, Vol. 4, No. 6, pp. 410-418.

Lukkunaprasit, P., Ruangrassamee, A., Stitmannaithum, B., Chintanapakdee, C., and Thanasisathit, N. (2010), "Calibration of Tsunami Loading on a Damaged Building", accepted for publication in a special volume of Journal of Earthquake and Tsunami.

Peregrine, D. H. and Williams, S. M. (2001), "Swash Overtopping a Truncated Plane Beach," J. Fluid Mech., Vol.440, pp. 391-399.

Ruangrassamee, A., Yanagisawa, H., Foytong, P., Lukkunaprasit, P., Koshimura, S., and Imamura, F. (2006), "Investigation of Tsunami-Induced Damage and Fragility of Buildings in Thailand after the December 2004 Indian Ocean Tsunami," Earthquake Spectra, 22(S3), S377-S401.

USGS, http://walrus.wr.usgs.gov/tsunami/sumatraEQ/, 2008.

Yeh, H. (2007), "Design Tsunami Forces for Onshore Structures", Journal of Disaster Research, Vol. 2, No. 6, pp. 531-536.

JOINT CONFERENCE PROCEEDINGS
7th International Conference on Urban Earthquake Engineering (7CUEE) &
5th International Conference on Earthquake Engineering (5ICEE)
March 3-5, 2010, Tokyo Institute of Technology, Tokyo, Japan

NUMERICAL SIMULATION OF TSUNAMI GENERATION

Taro Kakinuma

Associate Professor, Dept. of Ocean Civil Engineering, Faculty of Science and Engineering, Kagoshima University, Japan
taro@oce.kagoshima-u.ac.jp

Abstract: Several generation processes of tsunamis due to seabed deformation have been numerically simulated without assumptions of the hydrostatic pressure and long waves. The seabed shift is described by temporal change of porosity inside each cell in the neighborhood of the seabed, while the water surface displacement is evaluated by solving an advection equation of a VOF function, which means that elevations of both sea bottom and water surface can be treated also when their movement stays inside each cell. In the cases of tsunami earthquakes or tsunamigenic earthquakes, where the location of uplift areas moves along the short axis of seabed-deformation area, the tsunamis gain remarkably high potential.

1. INTRODUCTION

In numerical computations of tsunamis due to submarine earthquakes, we usually assume that the initial displacement of water surface is equal to the permanent shift of sea bottom, after which we start calculation of tsunami propagation using a shallow-water or long-wave model. Similar calculation is performed considering multi segments also when seabed-deformation areas change their location. Tsunamis are, however, generated with time. For example, in case of "creeping," where the seabed deformation proceeds slowly, it is not difficult to imagine that the profiles are different between water surface and sea bottom because of propagation during generation of tsunamis.

Outstanding studies have been done focusing attention mainly to initial profiles of tsunamis under some assumptions. Linear analytical solutions of tsunami generation due to seabed deformation were derived by Sano and Hasegawa (1915), Syono (1936), Ichiye (1950), Takahashi (1942), Momoi (1962), Kajiura (1963), Honda and Nakamura (1951), etc., while a weakly nonlinear solution was shown by Hammack (1973). Hydraulic experiments were also performed by, for example, Hammack (1973) and Matsuyama et al. (1995), whose results were compared with those of numerical calculation by Nakayama (1983) and Matsuyama et al. (1995), respectively, using boundary element methods with velocity potential. Hwang and Divoky (1970) reproduced the field-scale phenomena of tsunami generation and propagation due to the 1964 Good Friday earthquake through a horizontally two-dimensional model with the shallow-water assumption. Ohmachi and Inoue (2008) used a three-dimensional grid system for computations of water motion, where upwelling currents as sources of tsunami generation were given on the sea bottom.

When a deformation area of seabed has a complex topography and its deformation velocity changes in space-time, the initial tsunami profile, which affects calculation results of tsunami propagation and runup, can be evaluated by considering velocity and pressure fields accurately. In this study, several generation processes of tsunamis due to seabed deformation have been numerically simulated without assumptions of hydrostatic pressure and long waves. Moreover, several cases where the uplift area of seabed changes its position are treated in the present paper. Aida (1969) performed horizontally two-dimensional linear calculation to investigate directional characteristics of tsunamis due to a dislocation progressing mainly along the long axis of seabed fault. We target uplift-dislocation movement along the short axis of seabed-deformation area, resulting in tsunami earthquakes or tsunamigenic earthquakes to increase the tsunami potential remarkably.

2. NUMERICAL MODEL

A three-dimensional VOF model, which was named STOC-VF and installed in a numerical simulator to study storm surges and tsunamis, i.e., STOC (Kakinuma and Tomita 2005), is applied to incompressible-fluid motion. Governing equations are the continuity and Reynolds-averaged Navier-Stokes equations, which are solved with a finite difference method. The Poisson equation on pressure is also solved to evaluate not only hydrostatic but also dynamic pressure. The medium porosity is considered to describe smooth shapes of the sea bottom and structure faces, around which the water velocity can be represented more accurately in numerical computations.

When a seabed uplift or subsidence occurs in very deep

water, it is efficient to use numerical cells whose size is larger than the seabed shift or water surface displacement. The seabed shift is described by temporal change of porosity inside each cell in the neighborhood of the seabed, while the water surface displacement is evaluated by solving an advection equation of a VOF function, such that elevations of both sea bottom and water surface can be treated also when their movement stays inside each cell. Accordingly, the grid system is fixed without changing the boundary shape of computational domain throughout numerical calculation of tsunami generation, propagation, and runup.

In the computations of this paper, the initial water is still with air cells on the water surface. All fixed boundaries including the sea bottom and side walls are assumed to satisfy the slip condition. The fluid density is spatially uniform and temporally constant, i.e., $\rho = 1.0\times10^{3}$ kg/m^{3}. The total viscosity ν_e is equal to 1.0×10^{-6} m^{2}/s, where any disturbance of a shorter scale than the cell size is neglected.

3. MODEL VERIFICATION IN UPLIFT CASES

Computational results are compared with the corresponding experimental data obtained by Hammack (1973). The area where $-b \le x \le b$ uplifts uniformly. The uplift shift of seabed, ζ, is given as

$$\zeta(t) = \zeta_0(1-e^{-\alpha t}) \qquad \text{when} \quad t \ge 0, \tag{1}$$

where $\alpha > 0$. The ratio b/h_0 is equal to 12.2, where h_0 is the initial water depth. The following two cases are treated in the x-z plane:

(a) Impulsive motion

$$\zeta_0 / h_0 = 0.2 \quad \text{and} \quad t_c\sqrt{gh_0}/b = 0.069, \tag{2}$$

(b) Transitional motion

$$\zeta_0 / h_0 = 0.1 \quad \text{and} \quad t_c\sqrt{gh_0}/b = 0.39, \tag{3}$$

where $\zeta(t_c) = 2\zeta_0/3$.

The grid widths Δx and Δy are equal to $0.2h_0$, while Δz is $0.05h_0$, where the number of cell along the y-axis is one. The time-step interval changes automatically depending on the Courant number.

The results of water surface displacement over the center of uplift area, where $x/h_0 = 0$, are shown in Figure 1. In the case of impulsive motion, the present calculation evaluates the water surface displacement accurately, including the short-period oscillations, whose generation should have not only linear but nonlinear mechanisms as well, for the solution of Hammack's linear theory does not show harmony with the experimental data. Also in the transitional motion, the present calculation shows good

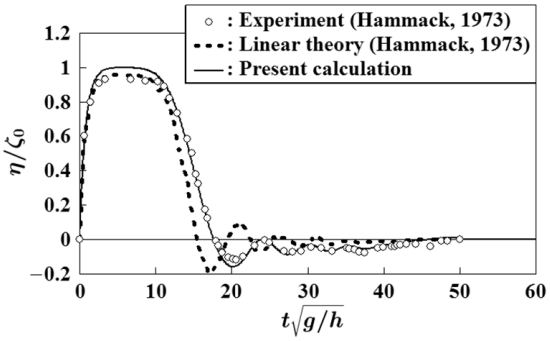

(a) Impulsive Motion

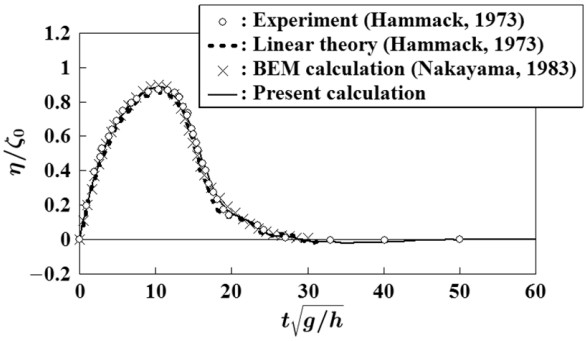

(b) Transitional Motion

Figure 1 Time Variations of Water Surface Displacement over The Center of Seabed-Uplift Area

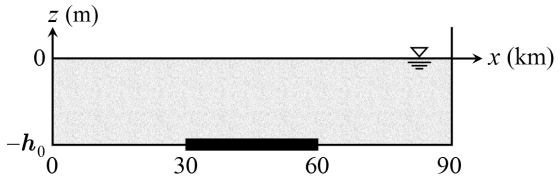

Figure 2 Definition Sketch of Calculation Domain

results, as well as the calculation performed by Nakayama (1983) using a boundary element method (BEM).

4. TSUNAMI GENERATION DUE TO SEABED DEFORMATION WHOSE RISE VELOCITY IS CONSTANT

The calculation domain is shown in Figure 2. The grid widths Δx and Δy are equal to 1 km, while Δz is 50 m, where the number of cell along the y-axis is one. The time-step interval Δt is equal to 0.5 s.

Figure 3 shows water surface profiles of tsunamis when t = 20 s due to a uniform uplift of seabed, where the initial water depth h_0 is 500, 1,000, or 4,000 m. The seabed deformation occurs inside the area where 30 km $\le x \le$ 60 km at the constant rise velocity of 0.15 m/s while 0 s $\le t <$ 20 s and stops when t = 20 s. In the numerical computations, the porosity of the lowest cells changes from 1.0 to 0.94 inside

this deformation area. According to Figure 3, we can recognize that the "initial profile" of tsunamis, whose generation depends on the initial water depth, is not always the same as the permanent shift of seabed.

Figure 4 shows velocity vectors over the seabed around one end of the deformation area when t = 20 s, where h_0 = 4,000 m. If the water depth is deep in a tsunami-generation area, the horizontal velocity over an edge or a slope of the seabed-deformation area shows a vertical distribution, which cannot be represented through a shallow-water model without dispersion terms.

Figure 5 shows water surface profiles when t = 20 s obtained using the present model (3D) and a nonlinear shallow-water model (SW). The seabed uplift is the same as that in the cases of Figure 3. The initial water depth h_0 is equal to 4,000 m. In the calculation with SW, the temporal derivative of seabed elevation, $\partial z_{\text{bottom}} / \partial t$, is considered inside the seabed-deformation area. In Figure 5, the water indicated by A, which is evaluated through 3D, is lifted up to the area B calculated by SW, such that SW overestimates the potential energy of initial tsunami. The wave length estimated by SW is shorter than that by 3D, resulting in the difference of water surface slope.

5. TSUNAMI GENERATION DUE TO SEABED DEFORMATION WHICH CHANGES ITS OCCURRENCE PLACE

Tsunami earthquakes, which were named by Kanamori (1972) and have been studied by Pelayo and Wiens (1992) etc. mainly in seismology, can generate tsunamis of a larger height than that estimated using only seismic-wave data observed before the tsunamis reach coasts. It is to clear generation mechanisms of both tsunami earthquakes, which are typified by the 1896 Meiji Sanriku earthquake, and resulting tsunamis that is important for protection against disasters. In this study the seabed deformation due to tsunami earthquakes is classified into the following groups in the view of fluid mechanics through tsunami-generation processes.

(I) Seabed deformation without interaction with water motion
- Type A: Long-duration deformation in a fixed area
- Type B: Deformation changing its occurrence place
- Type C: Deformation generating water motion affected by surroundings
- Type D: Deformation generating significant compression water waves

(II) Seabed deformation with interaction with water motion
- Type E: Deformation due to land slides
- Type F: Deformation due to inelastic ground movement
- Type G: Deformation as extravasation

(III) Seabed deformation with multiple aspects

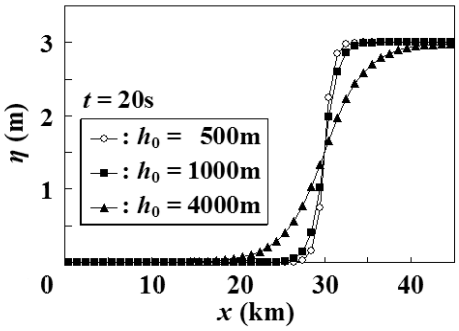

Figure 3 Initial Tsunami Profiles, Which Depend on The Initial Water Depth h_0

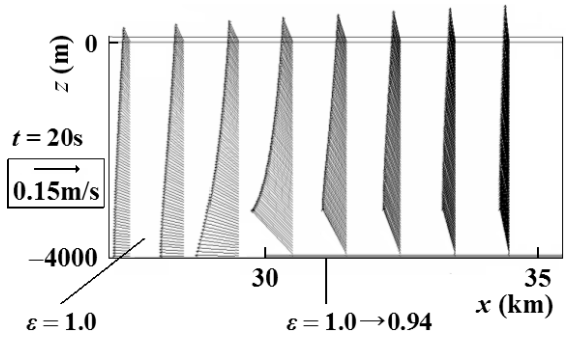

Figure 4 Water Velocity around One End (x = 30 km) of The Seabed-Uplift Area

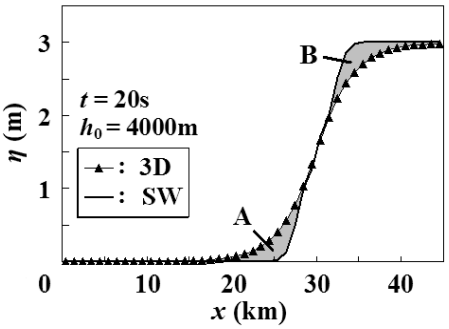

Figure 5 Initial Tsunami Profiles, Which Depend on Applied Models

In order to evaluate seabed shifts and water surface displacements of Types E, F, and G, it is necessary to solve the motion of both sea bottom and sea water simultaneously, for the seabed deformation is interacted with the water motion.

In the present paper, several cases belonging to Type B are treated. The seabed deformation of Type B is subdivided into the following three types.

Type B-1: Multistage deformation in different areas
Type B-2: Deformation changing its occurrence place

continuously

Type B-3: Multistage deformation changing its occurrence place continuously in different areas

Figure 6 shows the time variation of water surface profile for a two-stage-deformation case of Type B-1. The seabed inside the area where 50 km $\leq x \leq$ 60 km uplifts while 0 s $\leq t <$ 20 s, after which the seabed inside the area where 40 km $\leq x <$ 50 km uplifts while 50 s $\leq t <$ 70 s. The rise velocity of deformation is 0.15 m/s and the permanent shift of seabed, δ, becomes 3.0 m. The initial water depth h_0 is equal to 4,000 m. Tsunamis can grow due to succeeding stages inside different areas of seabed deformation. In the present case the almost stably propagating tsunami which has experienced two uplift stages is about twice the height of that in the corresponding one-stage-deformation case when t = 200 s. If there are two areas of dislocation, the tsunami height depends on both place and timing of the second-stage deformation of seabed.

Figure 7 shows the time variation of water surface profile for a case of Type B-2. The seabed-uplift place moves from its start point x_0, where the uplift starts when $t = 0$ s, to the end point $(x_0 - R)$ $(R > 0)$, where the uplift starts when $t = \tau$ (s), at the constant speed of R/τ. The rise velocity W is equal to 0.15 m/s throughout the seabed-deformation area, after which the uplift stops when the seabed shift becomes 3.0 m, such that the seabed deformation at the end point $(x_0 - R)$ stops when $t = \tau + 20$ s. The initial water depth h_0, the start-point position x_0, the total width of seabed-deformation area, R, and the progress duration of seabed deformation, τ, are equal to 4,000 m, 60 km, 20 km, and 70 s, respectively. In this case the tsunami which propagates towards the negative direction of x-axis when t = 200 s is more than twice the height of that in the corresponding one-stage deformation case, where the seabed-uplift area is fixed, for the seabed-uplift area chases this tsunami to be effective in growing the wave. On the other hand, the seabed-deformation area escapes from the generated waves traveling towards the positive direction of x-axis with a narrow width of uplift area which concerns the tsunami growth, resulting in low wave height and long wave length of the tsunami on this side.

Figure 8 shows the relation between the wave height of stably propagating tsunamis which have been generated and grown by seabed uplifts of Type B-2, η_{max}, and the progress speed of seabed deformation, R/τ, where the rise velocity W is equal to 0.15 m/s and h_0= 4,000 m. It should be noted that Figure 8 was obtained using the nonlinear shallow-water model without dispersion terms, i.e., SW, although 3D was applied to obtain Figs. 6 and 7. The growth rate of tsunamis on the progress sides becomes high especially when the progress speed of seabed deformation, R/τ, is close to the long-wave celerity of tsunamis in the initial water, i.e., approximately $\sqrt{gh_0}$, which is indicated with a dashed line in Figure 8.

The tsunami height η_{max} depends on both R and τ, as well as W and h_0, such that huge tsunamis, which are underestimated using only seismic ground waves, can

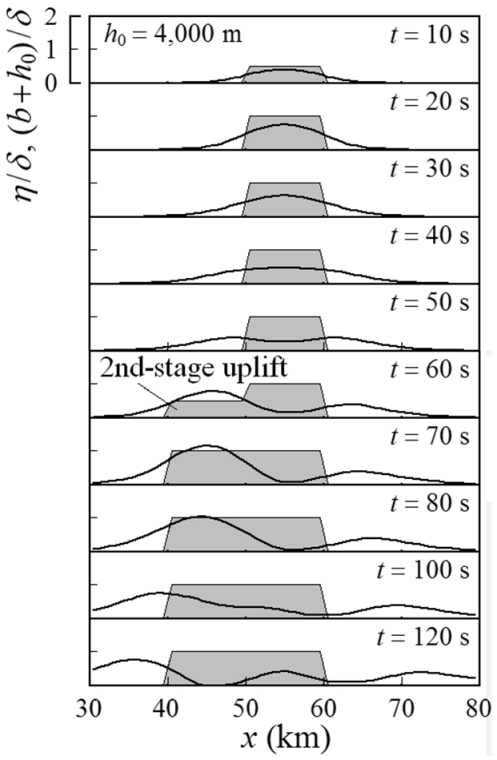

Figure 6 Time Variation of Water Surface Profile due to Two-Stage Uplifts in Different Areas of Seabed (The top faces of gray areas indicate the shapes of seabed. The second stage occurs while 50 s $\leq t <$ 70 s.)

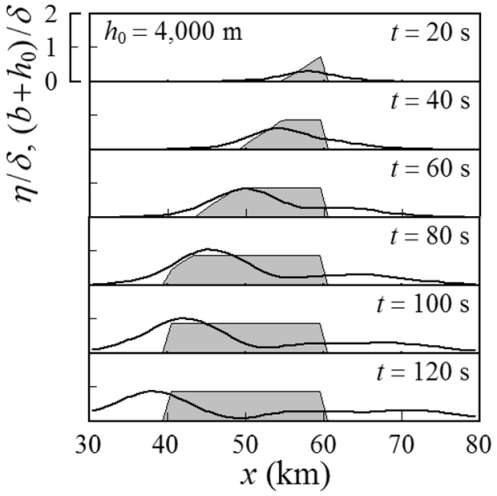

Figure 7 Time Variation of Water Surface Profile due to A Seabed Uplift Changing Its Occurrence Place Continuously (The top faces of gray areas indicate the shapes of seabed. The total width of uplift area, R, is equal to 20 km and the progress duration of seabed uplift, τ, is equal to 70 s.)

appear when the seabed deformation occurs due to dislocation of a shallow slide angle or a slow rapture velocity,

plastic movement belonging to Type E or F (e.g. Tanioka and Seno 2001), magma intrusion into sedimentary layers (Kanamori et al. 1993), etc.

6. CONCLUSIONS

Numerical computations of tsunami-generation processes due to seabed deformation in the vertical two-dimension were performed using the three-dimensional model for incompressible fluids. The seabed displacement is described by the temporal change of porosity inside numerical cells around the sea bottom, while the water surface elevation is calculated through the VOF method, which means that the present model is able to treat both sea bottom and water surface elevations also when their change stays inside each cell.

The initial profile of tsunamis, whose generation is dependent on the initial water depth, is not always identical with the permanent shift of seabed. If there are several areas or stages of dislocation, the tsunami height depends on both place and timing of the following-stage deformation of seabed. The growth rate of tsunami on the progress side of seabed deformation becomes high especially when the progress speed of seabed deformation is close to the celerity of tsunami.

Precise analyses of tsunami generation based on fluid mechanics shall contribute to discovery of unheeded types of seabed deformation including those of tsunami earthquakes.

Acknowledgements:

Sincere gratitude is extended to Mr. Minoru Akiyama, Fuji Research Institute Corporation, for beneficial help to numerical calculation.

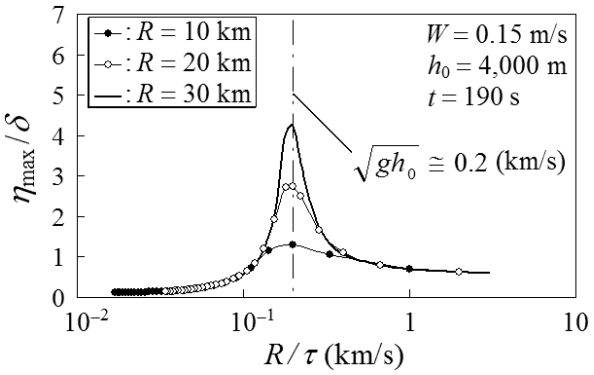

Figure 8 Relation Between Height of Stably Propagating Tsunamis, η_{max}, and Progress Speed of Seabed Uplift, R/τ (The rise velocity W is equal to 0.15 m/s. The results are shown for cases of different total width of uplift area, R.)

References:

Aida, I. (1969), "Numerical experiments for tsunamis caused by moving deformations of the sea bottom," *Bull. Earthq. Res. Inst*., **47**, 849-862.

Hammack, J. L. (1973), "A note on tsunamis: their generation and propagation in an ocean of uniform depth," *J. Fluid Mech.*, **60**, 769-799.

Honda, H. and Nakamura, K. (1951) "The waves caused by one-dimensional deformation of the bottom of shallow sea of uniform depth," *Sci. Rep. Tohoku Univ.*, Ser. 5, **3**, 133-137.

Hwang, L.-S. and Divoky, D. (1970) "Tsunami generation," *J. Geophys. Res.*, **75**, 6802-6817.

Ichiye, T. (1950) "On the theory of tsunami," *The Oceanographical Magazine*, **2**, 83-100.

Kajiura, K. (1963) "The leading wave of a tsunami," *Bull. Earthq. Res. Inst.*, **41**, 535-571.

Kakinuma, T. and Tomita, T. (2005) "Development of storm surge and tsunami simulator in oceans and coastal areas," *Proc. 29th Int. Conf. on Coastal Eng.*, ASCE, 1552-1564.

Kanamori, H. (1972) "Mechanism of tsunami earthquakes," *Phys. Earth Planet. Inter.*, **6**, 346-359.

Kanamori, H., Ekstrom, G., Dziewonski, A., Barker, J.S., and Sipkin, S. A. (1993) "Seismic radiation by magma injection: An anomalous seismic event near Tori Shima, Japan," *J. Geophys. Res.*, **98**, 6511- 6522.

Matsuyama, M., Ikeno, M., and Tanaka, H. (1995) "Laboratory experiments and numerical simulations of water surface response to sea bed rise and deformation," *Proc. Coastal Eng.*, JSCE, **42**, 226-230 (in Japanese).

Momoi, T. (1962): "General method of treatment of tsunami caused by the displacement of a portion of the bottom with an arbitrary form," *Bull. Earthq. Res. Inst.*, **40**, 309-324.

Nakayama, T. (1983) "Boundary element analysis of nonlinear water wave problems," *Int. J. num. Meth. Engng.*, **19**, 953-970.

Ohmachi, T. and Inoue, S. (2008) "Recent verification of the dynamic tsunami simulation," *5th Int. Conf. Urban Earthquake Eng.*, TIT, 425-428.

Pelayo, A. M. and Wiens, D. A. (1992) "Tsunami earthquakes: Slow-thrust faulting events in the accretionary wedge," *J. Geophys. Res.*, **97**, 15321-15337.

Sano, K. and Hasegawa, K. (1915) "On the wave produced by the sudden depression of a small portion of the bottom of a sea of uniform depth," *Bull. Cent. Met. Obs. Japan*, **2**(3), 30p.

Syono, S. (1936): "On the waves caused by a sudden deformation of a finite portion of the bottom of a sea of uniform depth," *The Geophysical Magazine*, **10**, 21-41.

Takahashi, R. (1942) "On seismic sea waves caused by deformations of the sea bottom," *Bull. Earthq. Res. Inst.*, **20**, 375-400 (in Japanese).

Tanioka, Y. and Seno, T. (2001) "The sediment effect on tsunami generation of the 1896 Sanriku tsunami earthquake," *Geophys. Res. Lett.*, **28**, 3389- 3392.

JOINT CONFERENCE PROCEEDINGS
7th International Conference on Urban Earthquake Engineering (7CUEE) &
5th International Conference on Earthquake Engineering (5ICEE)
March 3-5, 2010, Tokyo Institute of Technology, Tokyo, Japan

NUMERICAL SIMULATION OF HYDROACUOUSTIC EFFECTS IN TSUNAMI SOURCE

Sergey Kolesov[1)], Anna Bolshakova[2)], Shusaku Inoue[3)], Hiroyuki Matsumoto[4)], Mikhail Nosov[5)], and Tatsuo Ohmachi[6)]

1) Researcher Junior, Faculty of Physics, M.V.Lomonosov Moscow State University, Russia
2) Postgraduate Student, Faculty of Physics, M.V.Lomonosov Moscow State University, Russia
3) Research Associate, Department of Built Environment, Tokyo Institute of Technology, Japan
4) Research Scientist, Japan Agency for Marine-Earth Science and Technology, Japan
5) Professor, Faculty of Physics, M.V.Lomonosov Moscow State University, Russia
6) Professor, Department of Built Environment, Tokyo Institute of Technology, Japan
kolesov@phys.msu.ru, annabolshakova@list.ru, shusaku@enveng.titech.ac.jp, hmatsumoto@jamstec.go.jp, nosov@phys.msu.ru, ohmachi@enveng.titech.ac.jp

Abstract: 3D numerical model is developed to describe water layer motion in case of dynamic bottom deformation of seismic origin. The model is based on the linear potential theory of ideal homogeneous compressible fluid in the field of gravity. The model is used to simulate behavior of compressible water layer in the Tokachi-Oki 2003 tsunami source. The dynamic bottom deformation is calculated with use of the boundary element method. Comparison between JAMSTEC in-situ measurements and synthetic signals was carried out.

1. INTRODUCTION

In past decade, when JAMSTEC (Japan Agency for Marine-Earth Science and Technology) deployed a real-time observatory at the continental slope close to the islands of Japan (Hirata et al. 2002), it became possible to investigate a tsunami formation just at its source. The Tokachi-Oki earthquake of 2003 turned out to be the first strong tsunamigenic seismic event, the epicenter of which was located in the immediate vicinity of the JAMSTEC sensors (Watanabe et al. 2004, Nosov et al. 2005, Mikada et al. 2006). Analysis of the records of bottom pressure variations obtained during this event provided a unique opportunity to reveal manifestations of compressibility of water in tsunami source (Nosov et al. 2005, 2007, Nosov and Kolesov, 2007).

The necessity for taking into account the compressibility of water in describing behaviour of water column in tsunami source had been substantiated theoretically (Nosov 1999, 2000, Levin and Nosov, 2008). In case of a horizontal absolutely rigid ocean bottom the main difference in the behaviour of a compressible ocean as compared to an incompressible model medium consists in the formation of elastic oscillations of the water column, which are characterized by a discrete set of normal frequencies

$$n_n = c(1+2n)/4H\,, \qquad (1)$$

where $n = 0,1,2,3...$, H is the ocean depth and c is the sound speed in water. For typical conditions of a tsunami source the minimal normal frequency $n_0 = c/4H \sim 0.1\ Hz$ is excited most effectively. In case of a basin of variable depth, due to the cut-off frequency, elastic oscillations can not propagate upslope (Levin and Nosov, 2008). Moreover, the lowest mode of elastic oscillations can be captured by regions of local depressions of the ocean bottom (e.g. deep-water trenches).

Till the JAMSTEC records during the Tokachi-Oki 2003 earthquake the existence of the elastic oscillations of the water column at a tsunami source had not been confirmed by measurements in-situ, and, therefore, the effect remained only theoretically predicted.

To avoid confusion, the difference must be stressed between such a well-known phenomenon as the T-phase and the effects dealt with here. Not only the T-phase is related to a range of higher frequencies (>2 Hz), but it is also registered at significant distances from the source (Okal et al. 2003).

Note two features peculiar to compressibility effects that explain why they have been studied weakly. First, elastic low-frequency oscillations of a water column can be revealed only at sufficiently large depths (in the open ocean), which hinders their direct registration. Second, the compressibility effects were not quite within the line of research of tsunamis, since, owing to the significant difference in frequency ranges (tsunamis: $10^{-4} - 10^{-2}$ Hz), elastic oscillations were not considered capable of giving any contribution to a tsunami wave. Actually, such an assertion is erroneous, and the contribution of elastic oscillations to a tsunami wave can be provided by non-linear mechanisms (Novikova and Ostrovsky, 1982, Nosov and Kolesov, 2005, Nosov et al., 2008).

The present study is the first attempt to reproduce bottom pressure variations in the Tokachi-Oki 2003 tsunami source by means of 3D numerical simulations taking into

account dynamic bottom deformations and water compressibility. In this paper we continue the line that had been originated from our previous publications (Ohmachi et al. 2001, Nosov and Kolesov 2007).

2. DYNAMIC BOTTOM DEFORMATIONS

In the present technique, a total system consisting of the seawater and the underlying ground is assumed to be a weakly coupled system. On this assumption, earthquake ground motion due to seismic fault rupturing is first simulated by the boundary element method (BEM) (Kataoka, 1996). Then, seawater disturbance including tsunamis resulting from the seismic ground motion is simulated using the ground motion velocity as an input to the seawater. Formulation of these methods had been described in the paper (Ohmachi et al. 2001). Here we just outline the fault model of the Tokachi-Oki 2003 earthquake and describe simulation results.

A fault model proposed by Koketsu et el. 2004 which was based on strong dynamic motion and permanent displacement is adopted in this simulation. The fault projection and a calculation area of the ground motion simulation are shown in Figure 1. The area is extended to 350 km long in the NS direction and 350 km wide in the EW direction. The BEM element size of the seabed is 5x5 km. Employed parameters of the fault and ground are listed in Table 1. Regarding the ground, it is treated as an elastic half-space. The fault is considered as heterogeneous dislocation model with a distribution shown in Figure 2. First rupturing starts at the southeastern edge and develops in the northwestern direction with velocity of 3km/s. The total duration time of the fault rupturing is about 30 sec. The simulation is conducted within a frequency range of less than 0.5 Hz.

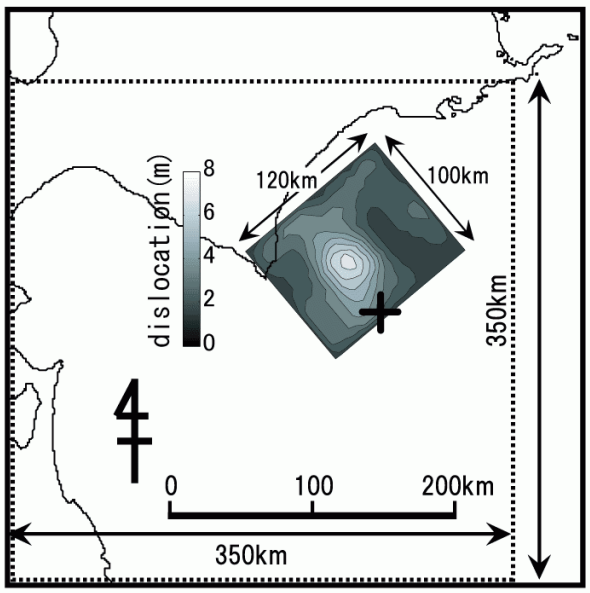

Figure 1. Fault projection (Koketsu et. el., 2004) and calculation area of the ground motion simulation. A bold cross indicates the epicenter.

1.88	2.50	2.75	3.00	3.00	2.56	2.00	2.25	2.3	2.25	2.44	1.94
2.38	3.00	3.25	3.44	3.69	3.50	3.25	3.13	3.1	3.06	2.94	2.00
2.13	2.63	2.63	3.44	4.19	3.88	3.56	3.25	2.7	2.56	2.44	1.88
1.75	2.25	2.56	3.94	4.94	4.88	3.75	2.75	2.2	2.25	2.38	2.13
1.94	2.50	2.94	4.75	6.38	6.19	4.56	2.63	1.8	2.38	2.69	2.31
2.25	2.88	3.31	5.00	6.69	7.10	5.06	2.63	1.8	2.38	2.88	2.56
2.50	3.13	3.56	4.94	5.94	5.94	4.75	2.69	1.8	2.13	2.69	2.44
2.50	3.13	3.63	4.69	5.06	4.50	3.56	2.56	1.9	1.81	2.31	2.31
2.50	3.13	3.63	4.38	4.06	3.38	2.94	2.56	1.9	1.75	2.00	1.94
2.00	2.38	2.50	2.75	2.63	2.19	2.13	1.94	1.6	1.63	1.63	1.56

1	2	3	4	5	6	7

m

Figure 2. Distribution of fault dislocation. The numbers indicate dislocation in meter

When the fault rupture finishes, permanent displacement remains above the fault projection (Figure 3). Subsidence occurs near the coastal region. On the other hand, uplifted area can be seen off shore where the JAMSTEC monitoring system is installed.

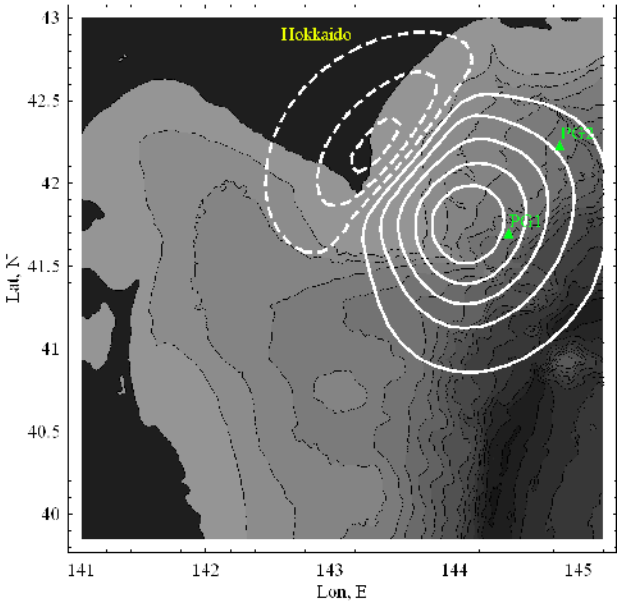

Figure 3. Calculating area. Locations of bottom pressure sensors (green triangles) and earthquake epicenter (red star) of the Tokachi-Oki 2003 earthquake. Vertical coseismic bottom deformation is shown by solid (uplift) and dashed (subsidence) white contours at 0.2-m intervals (from -0.5 to +0.9 m). Isobaths are shown at 500-m intervals.

Table 1. Parameters of the fault and ground employed in this simulation (Koketsu et. el., 2004). Rupture velocity is modified from Koketsu's model.

Depth	25 km
Dip	20°
Length	100 km
Width	120 km
Dislocation	max=6.5 m, mean=3.0 m
V_p	8.0 km/s
V_s	4.6 km/s
Rupture velocity	3.0 km/s
Density	3.3 g/cm^3

2. 3D NUMERICAL MODEL OF WATER COLUMN

Let us consider a layer, infinite in the horizontal $0xy$ plane, of an ideal incompressible homogeneous liquid of variable depth $H(x,y)$ in the field of gravity. We assume the calculation domain to be small enough to neglect the sphericity of the Earth. We shell put the origin of the Cartesian reference frame, $0xyz$, in the unperturbed free surface and direct the $0z$ axis vertically upward. The liquid is at rest until the time moment $t = 0$. To describe perturbations of water layer in the case dynamic deformation of the basin bottom, occurring in accordance with the law $\vec{h}(x,y,t) = (h_x, h_y, h_z)$, we shall resolve the problem with respect to the velocity potential $F(x,y,z,t)$ (Landau, Lifshits, 1987):

$$\frac{\partial^2 F}{\partial t^2} - c^2 \Delta F = 0, \tag{2}$$

$$\frac{\partial^2 F}{\partial t^2} = -g \frac{\partial F}{\partial z}, \quad z = 0, \tag{3}$$

$$\frac{\partial F}{\partial \vec{n}} = \left(\frac{\partial \vec{\eta}}{\partial t}, \vec{n} \right), \quad z = -H(x,y), \tag{4}$$

where $\vec{n}$ is the unit vector normal to the bottom surface. We assume the deformation of the basin bottom takes place during a time interval t, upon which the basin bottom stops. We restrict ourselves to small bottom deformations, $|\vec{h}| << H$, thus depth H as well as vector $\vec{n}$ do not depend on time. Velocity vector and dynamic pressure are related to the velocity potential by the following known formulae:

$$\vec{v}(x,y,z,t) = \nabla F, \tag{5}$$

$$p(x,y,z,t) = -\rho \frac{\partial F}{\partial t}, \tag{6}$$

where ρ is the density of liquid.

A realistic formulation of the problem under consideration should, naturally, take into account the elasticity properties of the ocean bottom. Finiteness of the bottom elasticity leads, in particular, to a gradual damping of hydroacoustic waves due to their refraction in the bottom. We can not introduce the bottom elasticity during the deformation process since the bottom movement is specified kinematically by a given law $\vec{h}(x,y,t)$. However, after the time moment $t = t$, i.e. when the bottom deformation stops, we switch from "fully reflective" boundary condition (3) to the following semi-transparent boundary condition:

$$\frac{\partial F}{\partial \vec{n}} = \frac{\partial F}{\partial t} \frac{1}{c} \frac{R-1}{R+1} \tag{7}$$

where R is amplitude reflection coefficient at the "water-bottom" boundary for a normally incident hydroacoustic wave. We estimate the reflection coefficient from the following formula:

$$R = \frac{\rho_b c_p - \rho c}{\rho_b c_p + \rho c}, \tag{8}$$

where ρ_b is density of bottom and c_p is P-wave velocity in bottom. In the region under consideration the P-wave velocity is of $8\,km/s$ and density is of $3.3\,g/cm^3$, whereas for water layer the sound velocity is of $1.5\,km/s$ and density is of $\rho = 1.03\,g/cm^3$. Thus, the reflection coefficient takes the value of $R \approx 0.89$.

The traditional explicit Finite Difference scheme (z-leveled model, rectangular grid) is used for equations (2)-(8). The condition for stability of the scheme is Courant criterion $Dt < min(Dx, Dy, Dz)/c$, where Dt is time increment, Dx, Δy and Δz are space increments. During the numerical experiments, the time increment was computed as follows: $Dt = 0.5\,Dz/c$.

Our method of approximation of the normal derivative in equation (4) and (7) had been described in details in paper (Nosov and Kolesov, 2007).

The computational domain is shown in Figure 3. It extends from 141E to 145.2E in longitude and from 39.85N to 43N in latitude (350 x 350 km). The 500 m gridded bathymetric data set of Japan Oceanographic Data Center (JODC, http://www.jodc.go.jp/) was used to build the computational grid. In calculations the following values of space increments were used: $Dx = Dy = 1000\,m$, $Dz \approx 180\,m$. The total number of the grid points was close to $5 \cdot 10^6$. The time increment was $Dt \approx 0.06\,s$. Total duration of bottom deformation was $t = 128\,s$.

The highest frequency we try to reproduce in our modeling is of 0.5 Hz. This frequency corresponds to the shortest hydroacoustic wave length of 3 km. The space increments and the time increment are small enough to perform adequate modeling.

3. RESULTS AND DISCUSSION

Figure 4 presents the change in time of the pressure near the ocean bottom registered by JAMSTEC sensors PG1 and PG2 during the Tokachi-Oki 2003 earthquake (blue curves). Particular features of the in situ measurements of the bottom pressure variations had been discussed in a number of publications (Watanabe et al. 2004, Nosov et al. 2005, 2007, Mikada et al. 2006, Nosov and Kolesov 2007). We focus here mostly on the synthetic variations of bottom pressure calculated for the positions of PG1 and PG2 sensors. The in situ records are presented here for the sake of comparison with the synthetic signals calculated by means of the 3D model described above. The synthetic signals are depicted by green curves. The red curves stand for the vertical bottom velocity represented in pressure units i.e. $p = \rho c\, \partial h_z / \partial t$. Note that such a time-history of bottom pressure one would observe in case water column was not bounded above by the free surface. It must be stressed, here, that in accordance with our numerical experiments, contribution of horizontal movements of sloping bottom in amplitude of bottom pressure variations did not exceed a few percents. Thus here

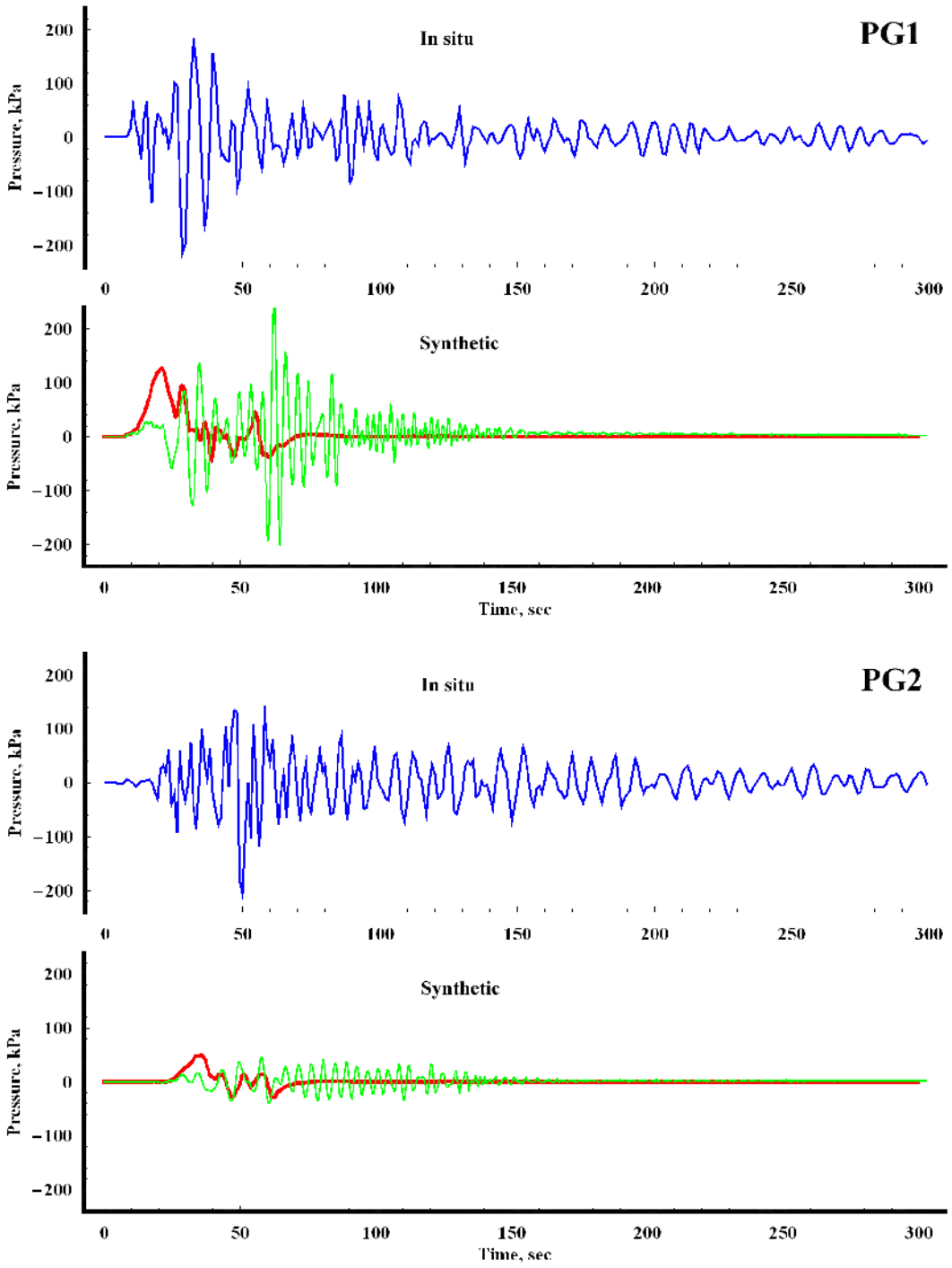

Figure 4. Variations of pressure at ocean bottom during the Tokachi-Oki 2003 earthquake: registered by JAMSTEC sensor PG1 and PG2 (blue curves), synthetic (green curves). Red curves stand for the vertical bottom velocity represented in pressure units ($p = rcv$).

and in what follows we consider only vertical component of bottom deformations.

During the first few seconds after the bottom starts moving, until the moment when the hydroacoustic waves cover the distance from the bottom to the water surface and back, the pressure just follows the bottom velocity, i.e. red and green curves are close. After that, during the following few seconds, the pressure turns out to be smaller than $r\,c\,\partial h_z/\partial t$. Indeed, reflection at the water free surface changes polarity of hydroacoustic waves; so the pressure amplitude should be decreased for a while. Later on pressure variations become quite complicated due to interference of waves that are repeatedly reflected by bottom and free surface.

There are too many factors which form the signals of bottom pressure variations: velocity field of bottom deformations, bathymetry, elastic properties of sediments and acoustic basement etc. So one can not expect an exact reproduction of in-situ measured signal in numerical simulations performed within the certain framework of simplifying assumptions and with use of huge amount of data (e.g. bathymetry). Anyway we are pleased to declare that amplitude of the in-situ and synthetic signals are of the same order of magnitude. Moreover, at the beginning, predominant periods of the in-situ signal and of the synthetic signals are also quite close. It is not surprising because the predominant period is mostly governed by the ocean depth (see eq.1). Note that thick sediment layer may noticeably diminish the predominant period (Nosov et al. 2007) and we do not consider sediments in our numerical model.

It is clearly seen from Figure 4 that later, in contrast to the in situ signal, the synthetic signal turns out to be enriched with short period components. These components are due to high-frequency hydroacoustic modes which are generated shallow water regions and propagate down the slope. In reality the high-frequency modes are not observed because of their rapid attenuation at the expense of refraction of hydroacoustic waves in the elastic bottom. It is worth mentioning here that the exponential decay time is proportional to the ocean depth (Nosov and Kolesov 2007).

4. CONCLUSIONS

JAMSTEC records during the Tokachi-Oki 2003 earthquake provided unique data on behavior of water column in tsunami source. Understanding of the physical nature of processes running in tsunami source has surely to result in capability of simulating of these natural phenomena. Present technique of numerical simulation is not capable to reproduce bottom pressure variations in tsunami source exactly. Anyway, some features of the in situ measured signal turn out to be quite close to simulated ones. It signifies consistency of employed approach. In our opinion, in order to obtain better coincidence within present technique, one should apply more detailed data on dynamic bottom deformation; also sediment layers should be taken into account. However it might be not enough, for in reality water column and bottom represent a unique whole, thus the best way to solve the problem consist in development of a fully coupling model.

Acknowledgements:

This work was supported by the Russian Foundation for Basic Research, project 07-05-00414. We are grateful to JAMSTEC for providing the data.

References:

Hirata, K., Aoyagi, M., Mikada, H., Kawaguchi, K., Kaiho, Y., Iwase, R., Morita, S., Fujisawa, I., Sugioka, H., Mitsuzawa, K., Suyehiro, K., Kinoshita, H., and Fujiwara, N. (2002), "Real-time geophysical measurements on the deep seafloor using submarine cable in the southern Kurile subduction zone," *IEEE Journal of Oceanic Engineering*, **27**(2), 170–181.

Kataoka, S. (1996), "Development of simulation methods for earthquake motion based on three-dimensional fault-ground models", Ph. D. thesis, Tokyo Institute of Technology.

Koketsu, K., K. Hikima, S. Miyazaki and S. Ide (2004), "Joint inversion of strong motion and geodetic data for the source process of the 2003 Tokachi-oki, Hokkaido, earthquake," *Earth Planets Space*, **56(**3), 329-334.

Landau, L.D., and Lifshitz, E. M. (1987), "*Fluid Mechanics, V.6 of Course of Theoretical Physics, 2nd English edition. Revised"*, Pergamon Press, Oxford-New York-Beijing-Frankfurt-San Paulo-Sydney-Tokyo-Toronto.

Levin, B.W. and Nosov, M.A. (2008), "Physics of Tsunamis," Springer.

Mikada, H., Mitsuzawa, K., Matsumoto, H., Watanabe, T., Morita, S., Otsuka, R., Sugioka, H., Baba, T., Araki, E., and Suyehiro, K. (2006), "New discoveries in dynamics of an M8 earthquake - Phenomena and their implications from the 2003 Tokachi-oki Earthquake using a long term monitoring cabled observatory," *Tectonophysics*, **426**, 95–105.

Nosov, M. A. (1999), "Tsunami Generation in Compressible Ocean," *Phys. Chem. Earth (B),* **24**(5), 437-441.

Nosov, M. A. and Kolesov, S. V. (2005), "Nonlinear tsunami generation mechanism in compressible ocean," *Vestnik Moskovskogo Universita, Ser. 3 Fizika Astronomiya*, (3), 51–54.

Nosov, M. A., Kolesov, S. V., and Denisova, A.V. (2008), "Contribution of nonlinearity in tsunami generated by submarine earthquake," *Advances in Geosciences*, **14**, 141-146.

Nosov, M. A., Kolesov, S. V., Denisova, A.V., Alekseev, A.B., and Levin, B. W. (2007), "On the near-bottom pressure variations in the region of the 2003 Tokachi-Oki tsunami source," *Oceanology*, **47**(1), 26-32.

Nosov, M. A., Kolesov, S. V., Ostroukhova, A. V., Alekseev, A.B., and Levin, B. W. (2005), "Elastic oscillations of the water layer in a tsunami source," *Doklady Earth Sciences*, **404**(7), 1097–1100.

Nosov, M.A. (2000), "On the tsunami Generation in the Compressible Ocean by Vertical Bottom Displacements," *Izvestiya, Atmospheric and Oceanic Physics,* **36**(5), 718-726.

Nosov, M.A. and Kolesov, S.V. (2007), "Elastic oscillations of water column in the 2003 Tokachi-oki tsunami source: in-situ measurements and 3-D numerical modeling," *Natural Hazards and Earth System. Sciences*, **7**, 243-249.

Novikova, L. E. and Ostrovsky, L. A. (1982), "On an acoustic mechanism of tsunami wave generation," *Oceanology*, **22**(5), 693–697.

Ohmachi, T., Tsukiyama, H., and Matsumoto, H. (2001), "Simulation of tsunami induced by dynamic displacement of seabed due to seismic faulting," *Bulletin of the Seismological Society of America*, **91**(6), 1898–1909.

Okal, E. A., Alasset, P.J., Hyvernaud, O., and Schindele`, F. (2003), "The deficient T waves of tsunami earthquakes," *Geophysical Journal International*, **152**(2), 416–432.

Watanabe, T., Matsumoto, H., Sugioka, H., Mikada, H., Suyehiro, K., and Otsuka, R. (2004), "Offshore monitoring system records recent earthquake off Japan's northernmost island," *Eos*, **85**(2), 14–15.

JOINT CONFERENCE PROCEEDINGS
7th International Conference on Urban Earthquake Engineering (7CUEE) &
5th International Conference on Earthquake Engineering (5ICEE)
March 3-5, 2010, Tokyo Institute of Technology, Tokyo, Japan

HYDRODYNAMIC ANALYSIS OF BOULDER TRANSPORTATION ON PHI-PHI ISLAND DURING THE 2004 INDIAN OCEAN TSUNAMI

K.T. Chau[1], J.Q. Bao[2]

1) Chair Professor, Dept of Civil and Structural Engineering, the Hong Kong Polytechnic University, Hong Kong
2) Post-doctoral Fellow, Dept of Civil and Structural Engineering, the Hong Kong Polytechnic University, Hong Kong
cektchau@polyu.edu.hk, cebaojq@ polyu.edu.hk

Abstract: A boulder field was found near the north tip of Laem Tong on Phi-Phi Island, Thailand after the 2004 Indian Ocean Tsunami. The largest one is a rectangular boulder of dimension 2.72m, 2.28m and 4.23m, and was found about 17.6m from the west coastline to close to Sea Gypsy Village. Shell remains were found on one side of the boulder only, suggesting that the boulder is from sea bottom. There are also impact damages at various edge of the boulder, suggesting the possible transport process and mechanism. A simple hydrodynamic model was proposed to back calculate the tsunami bore height. Parametric studies were conducted on 5 different boulder sizes (0.5m to 3m cubic boulders). It was found that the tsunami run-up height to transport boulders is most sensitive to bore periods. The dynamics of boulder transport is not included in the present analysis, and only static criteria for movement (sliding, rolling and uplifting) initiation are considered. In particular, we have ignored the bottom friction effect and only considered the energy dissipation per unit area of a bore. The energy consumed in transporting the boulder has not been taken into consideration, and hence a better theory is still needed.

1. INTRODUCTION

Boulder fields are commonly found on near shore platforms (Oak 1984, Williams and Hall 2004), which are usually transported by huge ocean waves of geological (tsunami) or meteorological (hurricane and wind-driven high-energy storm surges) origin (Noormets et al. 2004). These boulders are usually from sea bottom and transported on land by tsunami or storm surge (Noormets et al. 2004, Suanez et al. 2009, Kato and Kimura 1983).

The first author visited Southern Thailand a month after the 2004 Indian Ocean Tsunami, including Puhket, Phi-Phi Island and Khao-Lak in Thailand. Boulder fields were found on the northern part of Phi-Phi Island. The largest one is a rectangular boulder of dimension 2.72m, 2.28m and 4.23m, and was found about 17.6m from the west coastline near Laem Tong (the northern tip of Phi-Phi Island). Shell remains were found on one side of the boulder only, suggesting that the boulder is from sea bottom. This was confirmed by local fishermen. There are also impact-induced damages on various edges of the boulder, suggesting the boulder may have been lifted in the transportation process.

In this paper, a simple hydrodynamic model modified from Nott (2003) and Noormets et al. (2004) will be presented here and applied to estimate the tsunami run-up height at Phi-Phi Island.

2. FIELD INVESTIGATION

On December 26, 2004 (or the boxing day of Christmas), the worst tsunami ever recorded occurred in Indian Ocean, and it was induced by a huge earthquake of moment magnitude of 9.0 (which has been adjusted to a higher vale later) with an epicenter near Sumatra of Indonesia. This tsunami attracted much media coverage and the total death is estimated at 228,601 (up to February 19, 2005). The death tolls in Indonesia, Sri Lanka, India and Thailand are respectively 173,981, 38,195, 10,744 and 5,305. A 4-day field reconnaissance trip to Thailand was held on Feb 4-7, 2005. During the trip, we deliberately visited Phi-Phi Island because thousands of tourists died on the island. We found highly localized tsunami effect along the coastline of Phi-Phi Island. A boulder field was found along the western coastline near the north tip of Laem Tong. Figures 1-2 show the boulder field with the largest boulder of size 2.72m×2.28m×4.23m being circled, and the direction of the incoming tsunami surge is indicated by an arrow.



Figure 1 Boulder location on Phi-Phi Island



Figure 2 Boulder field on Phi-Phi Island

Figure 3 shows a close up view of the largest boulder with the first author standing in front. Note that there are remains of shells on the surface behind the first author, indicating the big boulder is transported from sea bottom. The boulder is found 17.6m from the shoreline. This information can be used to estimate the tsunami run-up height at Phi-Phi Island. Such calculation is the main purpose of the present paper.

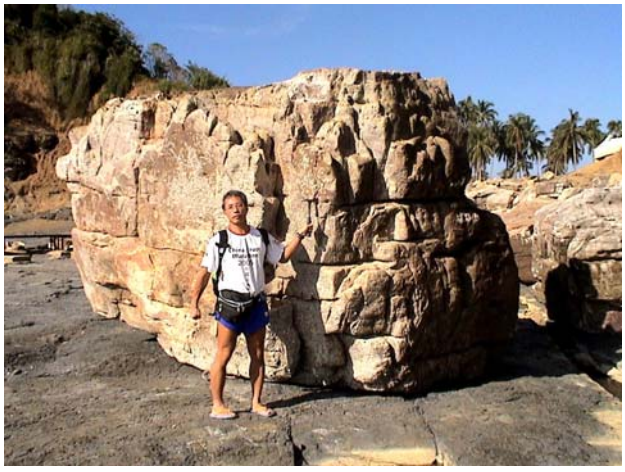

Figure 3 The largest boulder transported on land on Phi-Phi Island

3. HYDRODYNAMICAL MODELS

Clearly, the distance travel by a tsunami-transported boulder depends on the tsunami flow height, flow velocity and the size of the boulder (e.g. Nott 2003). Tsunami simulation traditionally assumes a long wavelength theory in depth water which certainly breaks down near shoreline. From videos recorded during the 2004 Sumatra Tsunami, it was clearly that the near shore surges are more like turbulent bores than long wavelength waves. The period of trains of bores is also quite different from the tsunami period of long wavelength waves in the deep sea. This information will be used in our later considerations of boulder transportation.

Motivated by the rectangular boulder shown in Fig. 3, Figure 4 shows various forces and moments induced on a submerged rectangular boulder, including the net gravity force F_G (weight subtracts the upthrust), the drag force F_d, the lift force F_l, and the friction force F_μ on the bottom. Mathematically, they can be expressed as (Nott 2003):

$$F_G = (\rho_r - \rho_w)abcg \tag{1}$$

$$F_d = C_d \rho_w u^2 ac / 2 \tag{2}$$

$$F_l = C_l \rho_w u^2 bc / 2 \tag{3}$$

$$F_\mu = \mu F_G = \mu(\rho_r - \rho_w)abcg \tag{4}$$

where ρ_w is the density of sea water equal to 1024kg/m^3, ρ_r is the density of boulder equal to 2600kg/m^3, C_d is the drag coefficient, C_l is the lift coefficient, g is the gravitational constant (or 9.81m/s), μ is the frictional coefficient equal to 0.7, and u is the flow velocity of tsunami bore, and a, b, c are the dimensions of the rectangular boulder shown in Fig. 3. The moments M_G, M_d, M_l are the moments induced by forces F_G, F_d, F_l respectively above the pivot line shown in Fig. 4. They can be expressed as:

$$M_G = [(\rho_r - \rho_w)abcg]b / 2 \tag{5}$$

$$M_d = (C_d \rho_w u^2 ac / 2)a / 2 \tag{6}$$

$$M_l = (C_l \rho_w u^2 bc / 2)b / 2 \tag{7}$$

The overturning moment M_O is the sum of M_d and M_l, whereas the resisting moment M_R is equal to M_G. For the case of totally submerged boulders, there are at least three mechanisms to start boulder transportation:

(i) sliding: when

$$F_d \geq F_\mu \tag{8}$$

the boulder will slide along the sea bottom;

(ii) rolling: when $M_O \geq M_G$, i.e.

$$M_d + M_l \geq M_G \tag{9}$$

the boulder will rotate along the sea bottom;

(iii) uplifting: when

$$F_l \geq F_G \tag{10}$$

the boulder will be lifted upward by the lift force. The first two mechanisms have been discussed in Noormets et al.

(2004) but the third one has been ignored by these authors.

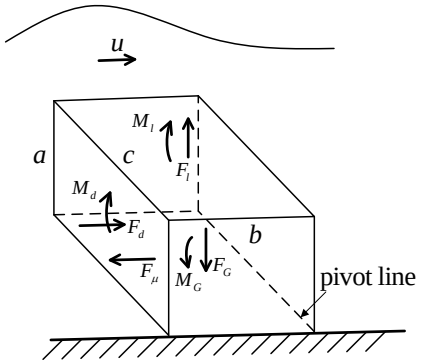

Figure 4 Hydrodynamic analysis of a fully submerged boulder

4. BOULDER TRANSPORTATION

Note that conditions (8-10) do not consider inertia and dynamic effects. They only provide the starting conditions and for subsequent dynamic movements of the boulder a very complex dynamic system needs to be solved. Such analysis is out of the scope of the present study.

Figure 5 illustrates two possible transportation routes for the case of Phi-Phi Island boulder field. The first one (Route I shown in Fig. 5) is that the boulder slides or rolls along the sea bottom, climbs up to the near shore platform, and eventually stops when F_d is less than F_μ and M_O is less than M_G. The second one (Route II shown in Fig. 5) is that the boulder is lifted up, reaches a height over the shore platform, and jumps on the shore platform. Both of these transportation routes can be separated into at least two phases, initiation phase (Phase I in Fig. 5) and stopping phase (Phase II in Fig. 5). The actual process of transportation can be very complex depending on how the tsunami bores come to shore. Of course, we can further subdivide the transportation of boulders into more stages.

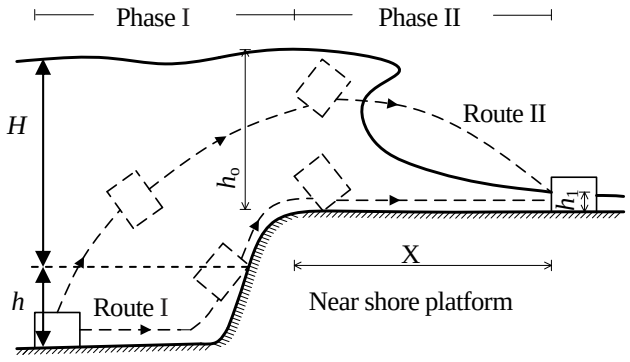

Figure 5 Scenarios of boulder transportation

4.1 INITIATION PHASE

As discussed by Noormets et al. (2004), when the tsunami height H shown in Fig. 5 is more than 0.82h (note that h is the water depth), strong turbulent bore is expected to form. For such case, flow velocity can be estimated by (Nott 2003, Noormets et al. 2004):

$$u = 2\sqrt{gH} \tag{11}$$

For the case of boulder observed on Phi-Phi Island (see Fig. 3), the estimated h is about 5m and H is about 14m from the water mark remained on higher grounds. Therefore, a strong turbulent bore should have been formed when the boulder was transported on land. If we set a = 2.28m, b = 2.72m, c = 4.23m (the boulder on Phi-Phi Island shown in Fig. 3), C_d = 2.0, C_l = 0.178, μ = 0.7 (values are adopted from Noormets et al. 2004). Substitution of (11) into (2) and (4) then the result into (8) yields the bore height to initiate movement of the big boulder originally resting on sea bottom 5m below the water surface. The boulder starts to slide when bore height is 0.68m. Similar calculation using (10) yields the bore height to lift up the boulder being 9.85m, and from (9) the least bore height to make the boulder rolling being 1.11m. When a tsunami bore comes onshore, the water level will increase from zero. Once the level is higher than 0.68m, the boulder will start to slide. When the water level further increases to 1.11m, the boulder starts to roll. Eventually, when the bore totally submerges the boulder and bore height reaches 9.85m, the boulder starts to rise by uplifting. Therefore, for the case of boulder shown in Fig. 3, the big boulder should have been transported by all sliding, rolling and uplifting. This agrees with our observation that crushing damages were found on the edges of the boulder. We should be cautious about this result as there are uncertainties in the parameters selection, which will be further discussed in later sections.

Actually, the dynamics of the boulder transport can be very complicated and equation of motions must be solved with the changing incoming bores. It is a complex process and will be very sensitive to the actual imposed bore condition as a function of time. For example, if the bore comes in as a series of surges, the boulder may slide, uplift and roll in one big surge but may stop moving after the surge passes, and may continue to move in the next surge. Since we do not have such record of surges during the tsunami, we will not attend to do that in this study.

4.2 STOPPING PHASE

No matter how a boulder is being transported from the rest position, it will eventually come into a stopping phase. When a boulder is stopped, the following criteria will be satisfied:

$$F_G \geq F_l \tag{12}$$

$$F_d \leq F_\mu \tag{13}$$

$$M_R \geq M_O \tag{14}$$

Physically, these conditions correspond to no uplifting, no frictional sliding, and no rolling. It must be pointed out that (1-8) are written for totally submerged boulder. At the final stopping position, the boulder may be partially submerged (i.e. not totally covered by water). In this case, (1-7) can be modified as

$$F_G = \rho_w abc - \rho_w abh_1 g \quad (15)$$

$$F_d = C_d \rho_w u^2 ch_1 / 2 \quad (16)$$

$$F_l \le F_G \quad (17)$$

$$F_\mu = \mu F_G = \mu(\rho_w abc - \rho_w abh_1)g \quad (18)$$

$$M_G = [(\rho_w abc - \rho_w abh_1)g]b/2 \quad (19)$$

$$M_d = (C_d \rho_w u^2 ch_1 / 2)h_1 / 2 \quad (20)$$

$$M_l \le M_o \quad (21)$$

where h_1 is the final wave height shown in Fig. 5. With these modified definitions, we can use the sliding criterion (13) to find h_1 at the instant of stopping. In addition, the no uplifting criterion (12) and the no rolling criterion (14) need to be checked as well during the stopping phase.

5. TSUNAMI RUN-UP HEIGHT

The exact process of how a bore decays with distance is a very complex phenomenon. In this paper, we follow the simplified formula proposed by Cox and Machemehl (1986). In particular, they have ignored the bottom friction effect and only considered the energy dissipation per unit area of a bore. The relation between h_1, h_0 and boulder traveled distance X (as shown in Fig. 5) is (Cox and Machemehl, 1986)

$$h_1 = (\sqrt{h_O} - \frac{5X}{T\sqrt{g}})^2 \quad (22)$$

where T is the bore period. The period of tide gauge records of the 2004 Indian Ocean Tsunami in Phuket area is in the order of 53 to 83 seconds (Synolakis and Kong 2006), but the actual period of surges pounding on the shoreline appears to be shorter than this from the recorded videos by survivors (a lot of them are available on internet). In this study, we will use 7 to 20 seconds in our parametric studies. Table 1 compiles four cubic boulders of size from 0.5m to 3.0m and the bigest boulder found on Phi-Phi Island shown in Fig. 3 (denoted as Boulder E). These boulders will be used for our parametric studies.

Note, however, that (22) gives the energy of bores propagating on land but not the energy loss due to or dynamics of boulder transportation by turbulent bores. Therefore, it can only be viewed as a very rough first approximation. A more refined theory is still required.

Table 1 Boulder dimensions, density and mass used in parametric studies

Boulder	Dimensions (m)			Density	Mass
	a	*b*	*c*	(kg/m^3)	(kg)
A	0.5	0.5	0.5	2600	325
B	1.0	1.0	1.0	2600	2600
C	2.0	2.0	2.0	2600	20800
D	3.0	3.0	3.0	2600	60200
E	2.28	2.72	4.23	2600	68205

Before we consider the traveled distance X, Figure 6 shows the effects of drag coefficient on the final bore height h_1 when the boulders stop (see Fig. 5 for the definition of h_1). It can be seen from Fig. 6 that for larger boulders the drag coefficient is of greater importance. The final bore height h_1 for smaller boulder (like boulder A) is less sensitive to the values of drag coefficient C_d, comparing to boulder E.

Once h_1 is known, we can use (22) to back calculate the tsunami run-up at coastline h_0. Such calculation gives a very simple tool to estimate the run-up by boulder transportation. Figure 7 plots the bore run-up at shoreline versus the transported distance X for various values of C_d that require to move the biggest boulder E inland. This range of C_d values is consistent with the values given by Martinuzzi et al. (2003) for a square cylinder near a wall. But the actual value of C_d for the case of a boulder resting on the sea bottom is not available in the literature. Therefore, there are uncertainties regarding its value. For the case of boulder shown in Fig. 3, at least 7m of tsunami run-up is needed to transport that boulder for a distance of 17.5m, as what we observed on Phi-Phi Island. From the water mark that we found further inland, the highest run-up is in the order of 14m. Without adjusting any parameters in our calculations and ignoring all nonlinear effect of boulder transportation, we find that this calculation can at least provide a preliminary analysis for boulder transportation.

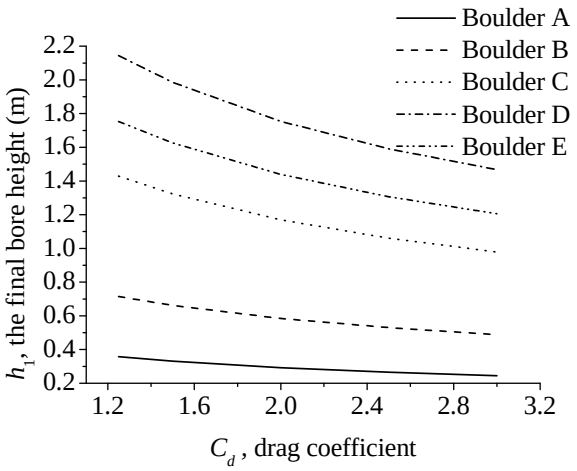

Figure 6 Final bore height h_1 versus the drag coefficient for various boulders

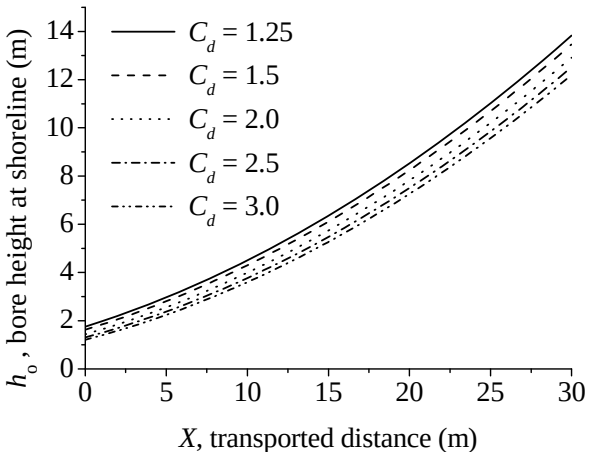

Figure 7 Tsunami run-up height h_0 versus the transported distance X for various drag coefficients for boulder E with T = 20s.

Figure 8 plots h_0 versus the transported distance X for various boulder sizes with T=20s and C_d =2.0. For example, the tsunami run-up transporting boulder E 17.5m inland would have transported the smallest boulder A 27m inland. In this calculation, we have assumed that the ground surface is flat but in reality a sloping ground is found behind boulder E on Phi-Phi Island. Therefore, we have to be cautious in our interpretation.

Figures 9-12 plots h_0 versus the period T for transported distance X of 5m, 10m, 15m and 20m respectively. It is clear that from these figures that a shorter bore period requires a higher bore run-up to transport boulders. A bore with longer period can transport boulders much easier. As mentioned earlier, the tide gauge readings on Phuket Island is about 53 to 83 seconds (Synolakis and Kong 2006), but we are skeptical about these values. They seem to correspond the period between successive surges instead of the period of bore undulations within a surge. Videos from survivors suggest that the period is much smaller than 50 seconds. We have also plotted the results for much longer period, and it turns out that the boulder size becomes unimportant. This finding is physically unreasonable. We should emphasize that the period of bores should be assigned properly to get reasonable results, and the tide gauge readings may not reflect bore undulation on shoreline.

For a fixed bore period, Figs. 9-12 show that when the transported distance increases from 5m to 20m, the tsunami run-up at shoreline may have to increase by 6 times, depending on the actual values of T. For example, for T=7 seconds, the run-up h_0 increase from 6m to 35m for the case of Boulder E.

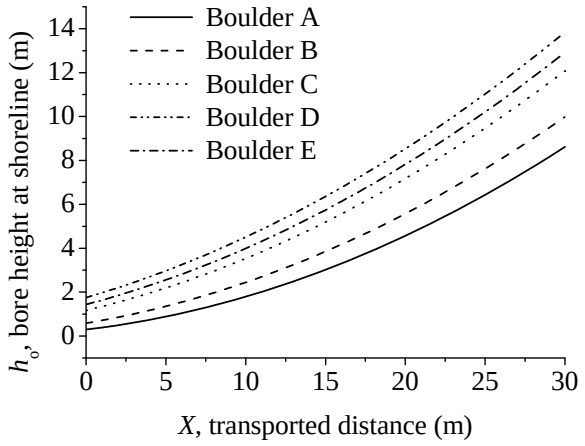

Figure 8 Tsunami run-up height h_0 versus the transported distance X for various boulders with T = 20s, C_d = 2.0

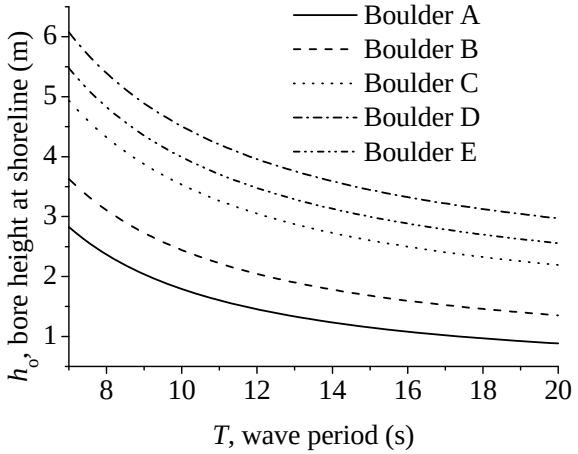

Figure 9 Tsunami run-up height h_0 versus period T for various boulders with X = 5m, C_d = 2.0

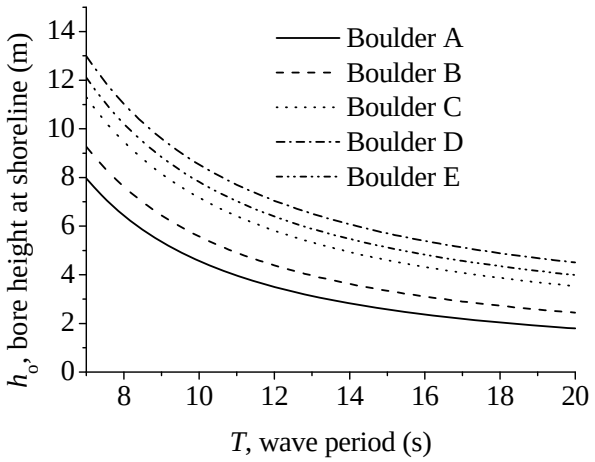

Figure 10 Tsunami run-up bore height h_0 versus period T for various boulders X = 10m, C_d = 2.0

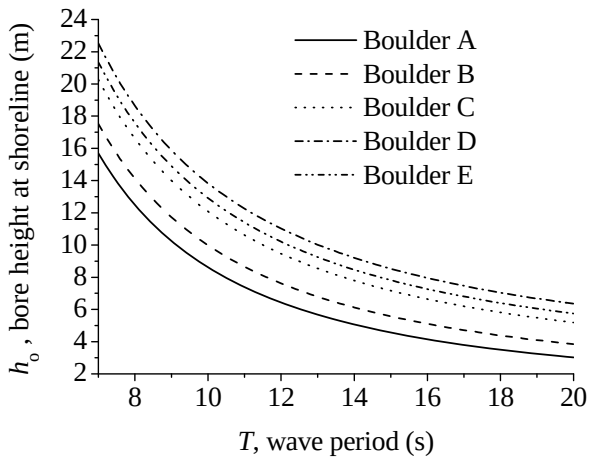

Figure 11 Tsunami run-up bore height h_0 versus period T for various boulders with X = 15m, C_d = 2.0

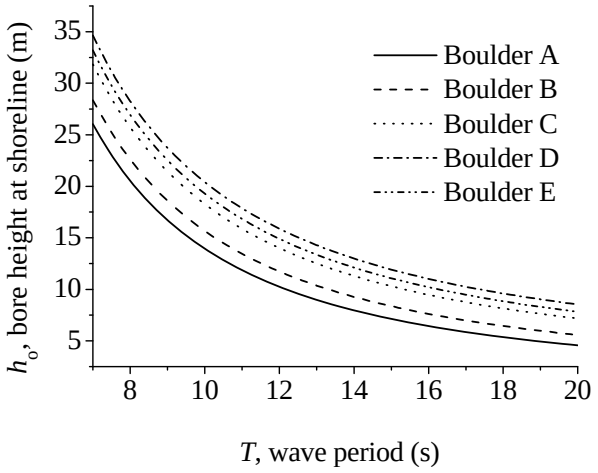

Figure 12 Final bore height h_0 versus period T for various boulders with X = 20m, C_d = 2.0

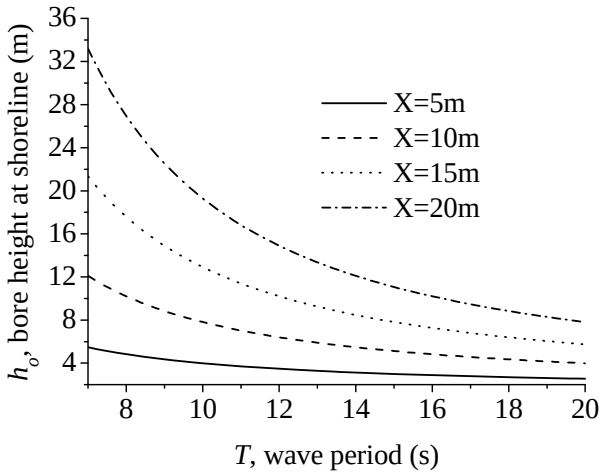

Figure13 Tsunami run-up height h_0 versus period T for boulder E with C_d = 2.0

The results of Figs. 9-12 can alternatively be plotted for various values of X for a fixed boulder size. For example, Fig. 13 plots h_0 versus T for X from 5m to 20m. For short bore period, the transported distance is very sensitive to the run-up height whereas for longer periods the transported distance X is less sensitive to the run-up height h_0.

6. DISCUSSION AND CONCLUSION

Boulders transported by tsunami bores have been reported repeatedly all over the world. In our field trip to Phi-Phi Island of Thailand, we found a big rectangular boulder of 68 tons. The hydrodynamic model considered by Nott (2003) and Noormets et al. (2004) was modified here to estimate the tsunami run-up near the northern-tip of Phi-Phi Island. By adopting the parameters used by Noormets et al. (2004) for Hawaii, we found that 0.68m of bore height at shoreline is required to initiate sliding of the big boulder located 5m below the sea level, 9.85m of bore height at shoreline is required to uplift the big boulder, and 1.11m of bore height at shoreline is required to initiate rolling. When the big boulder stopped on Phi-Phi Island, it was estimated that the bore water depth is about 1.3m to 1.7m, the exact value depending on value of drag coefficient.

Parametric studies were conducted on 5 different boulder sizes (0.5m to 3m cubic boulders), including the big boulder shown in Fig. 3. Drag coefficients have been varied from 1.25 to 3.0, the transported distance from 5m to 30m, whereas the bore periods are from 7s to 20s. It was found that the tsunami run-up height to transport boulders is most sensitive to bore periods. The period of tide gauge records of the 2004 Indian Ocean Tsunami in Phuket area is in the order of 53 to 83 seconds (Synolakis and Kong 2006), but the actual period of surges pounding on the shoreline appears to be shorter than this from the recorded videos by survivors (a lot of them are available on internet). This is the reason why we have set periods from 7 to 20 seconds in our parametric studies. Further validation for the periods of surges is still required.

Like other theoretical studies, the current hydrodynamic model adopted and modified from Nott (2003) and Noormets et al. (2004) is highly simplified. For example, the dynamics of boulder transport is not included in the present analysis, and only static criteria for movement (sliding, rolling and uplifting) initiation are considered. For example, if the bore comes in as a series of surges, the boulder may slide, uplift and roll in one big surge but may stop moving after the surge passes, and may continue to move in the next surge. Such possibility has not been considered in the current model. In addition, the bore height variation with travel distance is adopted from Cox and Machemehl (1986). In particular, they have ignored the bottom friction effect and only considered the energy dissipation per unit area of a bore. The energy consumed in transporting the boulder has not been taken into consideration. Cloutier et al. (1998) shows that suspended particles can reduce the fluid kinetic energy to a substantial amount. There are also uncertainties

concerning the life coefficient because most of the available data from literature were obtained for a fixed square cylinder in a fluid flow (Okajima et al. 1997), whereas in boulder transport problem the lift coefficient is expected to vary with the uplift process and it also change if the boulder is being rotated after uplift.

Nevertheless, our analysis suggests that the current model is accurate to the first approximation, although the error may be as large as 100%. A more sophisticated model is still required.

Acknowledgements:

The work described in this paper was fully supported by a grant from the Research Grants Council of the Hong Kong Special Administrative region, China (Project No. PolyU 5002/08P). The travel to Phi-Phi Island was supported by Dean's Reserve of FCLU. The project was partially supported by Project No. 1-BBZF of PolyU.

References:

Cloutier, D., LeCouturier., M.N., Amos., C.L., and Hill P.R. (2006), "The effects of suspended sediment concentration on turbulence in an annular flume," *Aquatic Ecology*, 40, 555-565.

Cox, J.C. and Machemehl, J. (1986), "Overload bore propagation due to an overtopping wave," *Journal of Waterway, Port, Coastal and Ocean Engineering*, 112(1), 161-163.

Kato, Y., and Kimura, M. (1983), "Age and origin of so-called "Tsunami-ishi", Ishigaki island, Okinawa prefecture," *The Journal of the Geological Society of Japan*, 89, 471-474.

Martinuzzi R.J., Bailey S.C.C., and Kopp, G.A. (2003). "Influence of wall proximity on vortex shedding from a square cylinder," *Experiments in Fluids*, 34, 585-596.

Noormets, R., Crook, K.A.W., and Felton, E.A., (2004), "Sedimentology of rocky shorelines: 3. Hydordynamics of megaclast emplacement and transport on a shore platform, Oahu, Hawai," *Sedimentary Geology*, 172, 41-65.

Nott, J., (2003), "Waves, coastal boulder deposits and the importance of the pre-transport setting,", *Earh and Planetary Sciences Letters*, 210, 269-276.

Oak, H.L., (1984), "The boulder beach: A fundamentally distinct sedimentary assemblage," *Association of American Geographers Annals*, 74, 71-82.

Okajima, A., Matsumoto, T. and Kimura, S. (1997), "Force measurements and flow visualization of bluff bodies in oscillatory flow," *Journal of Wind Engineering and Industrial Aerodynamics*, 69-71, 213-228.

Suanez, S., Fichaut, B., and Magne, R. (2009). "Cliff-top storm deposits on Banneg Island, Brittany, France: Effects of giant waves in the Eastern Atlantic Ocean." *Sedimentary Geology*, 220(1-2): 12-28.

Synolakis C.E. and Kong L. (2006). "Runup measurements of the December 2004 Indian Ocean Tsunami," *Earthquake Spectra*, 22, S67-S91.

Williams, D.M and Hall, A.M. (2004), "Cliff-top megaclast deposits of Ireland, a record of extreme waves in the North Atlantic - storms or tsunamis?," *Marine Geology*, 206(1-4), 101-117.

JOINT CONFERENCE PROCEEDINGS
7th International Conference on Urban Earthquake Engineering (7CUEE) &
5th International Conference on Earthquake Engineering (5ICEE)
March 3-5, 2010, Tokyo Institute of Technology, Tokyo, Japan

REAL-TIME TSUNAMI SIMULATION ACCELERATED BY GPU

Marlon Arce Acuna[1)], Takayuki Aoki[2)]

1) Ph.D Candidate, Department of Nuclear Engineering, Tokyo Institute of Technology, Japan
2) Professor, Global Scientific Information and Computing Center, Tokyo Institute of Technology, Japan
marlon.arce@sim.gsic.titech.ac.jp, taoki@gsic.titech.ac.jp

Abstract: In order to predict a Tsunami the Shallow Water Equations must be solved in real-time. With the introduction of GPGPU, a new revolution has been opened in high performance computing. We used CUDA to compute the simulation on the GPU which drastically accelerated the computation. A single-GPU calculation had been found to be 62-times faster than using a single CPU core. Moreover the domain was decomposed and solved on a multi-node GPU cluster. Overlapping transfers and computation further accelerated the process by hiding communication. For the GPU transfers an asynchronous copy model was used. The MPI library was used to transfer the data between nodes. A domain representing real bathymetry, with grid size 4096x8192 was used as our dataset. Our tests on TSUBAME showed excellent scalability. Results for CPU and GPU scalability are presented.

1. INTRODUCTION

A Tsunami is among the most dangerous effects caused by an earthquake. The wave created by the sudden disturbance of the ocean can travel thousands of kilometers and hit coasts with destructive power. Depending on the energy of this wave the Tsunami might create a strong and high water that washes off the coast, creating a phenomenon called run-up. This is the most dangerous part of the Tsunami since it sends the water in the shore with an enormous destructive force tearing down constructions and killing people. Countries along the Pacific Ocean are more exposed to this risk due to the high seismic activity of this region.

Therefore it is extremely important to provide these countries with a prediction and prevention tool, like a simulation to estimate the behavior of a Tsunami.

The forecasting of a Tsunami requires real-time calculation in order to give an early evacuation warning. The governing equations that model a Tsunami are called the Shallow Water Equations and their analytical solution can be found only for very simple cases, hence the need to solve them numerically which require intensive computation. The conventional approach to solve a numerical problem has been to compute on the CPU, however due to the complexity of the governing equations this approach produces results with very low performance, making it nearly impossible to obtain a real-time result unless hundreds of CPUs were used. However another important piece of hardware in the computer is the Graphics Card (GPU) which has been traditionally used to process only graphics. Due to the nature of pixels computing a GPU provides a highly parallelized environment ready to give high performance. It was not until nVIDIA introduced the Compute Unified Device Architecture, CUDA[1], in its graphics cards that they became general purpose devices instead of graphics-dedicated-only devices. Meaning that Graphics Cards could be programmed to compute almost any suitable problem, this is called General Purpose GPU, GPGPU[2] with the great performance inherent to GPUs.

This is why we embark using this new technology to increase the acceleration when solving the Shallow Water Equations. Additionally it is possible to use not only single-GPU computing but multi-GPU to improve even further the computation speed.

Pushing the envelope of acceleration, Multi-Node GPU was used on the newly introduced GPU Cluster at the Tokyo Institute of Technology's Super Computer, Tsubame and its performance was compared with that of CPUs.

2. BACKGROUND

2.1 The Shallow Water Equations

The Shallow Water Equations[3] are used to model the behavior of a Tsunami wave, these governing equations can be written in the following form:

$$U_t + F(U)_x + G(U)_y = S(U) \tag{1}$$

with:

$$U = \begin{bmatrix} h \\ hu \\ hv \end{bmatrix} \quad G(U) = \begin{bmatrix} hv \\ hvu \\ hv^2 + \frac{1}{2}gh^2 \end{bmatrix} \quad F(U) = \begin{bmatrix} hu \\ hu^2 + \frac{1}{2}gh^2 \\ huv \end{bmatrix} \tag{2}$$

where h is the water height, u and v are its velocities in the x and y direction respectively (Fig. 1), g is the gravity and S is a source term to include additional forces like Coriolis, viscosities or friction.

A directional splitting is applied to equation (1) hence computing the x-direction components and the y-direction components of the equation separately. This is done to preserve the numerical method less intensive and hence reduce the load of work in the kernel.

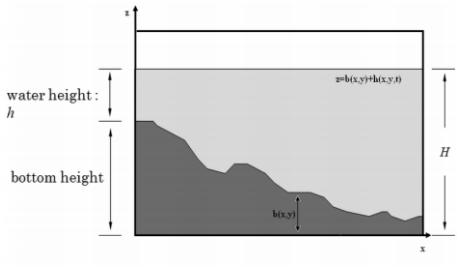

Fig. 1 Free Surface Flow under gravity

2.2 Initial Conditions

A Tsunami is generated by a strong and sudden disturbance in the water surface that propagates in the ocean [4].

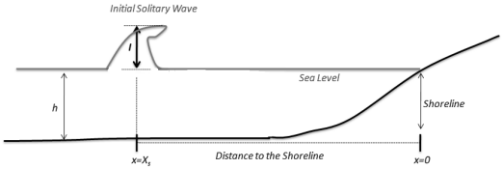

Fig. 2 Solitary Initial Wave

This disturbance usually originates from an earthquake however landslides or even meteorites could trigger a Tsunami. To simulate this initial condition a solitary wave model[5] is used as the initial wave condition (Fig. 2).
This wave is centered offshore at and has the surface profile given by:

$$\eta(x,t=0) = I \sec h^2 \gamma (x - X_s) \tag{3}$$

where $\gamma = \sqrt{3I/4}$ and I can be a dimensionless wave height ($I = I/h$).

In the simulation it is assumed an initially undisturbed flow hence the momenta *hu* and *hv* are initialized as zero in every grid point.

3. NUMERICAL METHODS

As stated before the analytical solution of the Shallow Water Equations can be found only for very simplified cases, therefore a numerical solution must be computer in order to obtain a physical simulation of realistic problems. The grid used is composed of point values and integrated values alternatively according to the numerical method.

3.1 Method of Characteristics

The Method of Characteristics[6] was used to find the point value. It can be briefly explained as follows. First the one dimensional Shallow Water equation is rewritten in the following form:

$$\frac{\partial}{\partial t}\begin{pmatrix} h \\ u \end{pmatrix} + \begin{pmatrix} u & h \\ g & u \end{pmatrix} \frac{\partial}{\partial x}\begin{pmatrix} h \\ u \end{pmatrix} \equiv \frac{\partial W}{\partial t} + A(W)\frac{\partial W}{\partial x} = 0 \tag{4}$$

Let L be a matrix that diagonalize *A*, then *L* can be found from the eigenvalues of *A*, from its eigenvectors we express equation (4) and the Riemann invariants such as:

$$\frac{D^{\pm}}{Dt}\left(\Gamma \pm \frac{u}{2}\right) = 0, \frac{D^{\pm}}{Dt} \equiv \frac{\partial}{\partial t} + \lambda^{\pm}\frac{\partial}{\partial x} \tag{5}$$

where $\Gamma \equiv \sqrt{gh}$. These are called invariants since they are values that remain constant along the curve of solution. From (5) we can estimate the point value *i* as two characteristics along C^+ and C^-. If the variables at the upstream departure points of $C^{\pm}$ are denoted by Γ_i^{n+1} and u_i^{n+1}, then the result is given by:

$$\Gamma_i^{n+1} = \frac{1}{2}\left\{\Gamma^+ + \Gamma^- + \frac{1}{2}(u^+ - u^-)\right\}$$

$$u_i^{n+1} = \frac{1}{2}\left\{u^+ + u^- + 2(\Gamma^+ - \Gamma^-)\right\} \tag{6}$$

The solution can be found at a later time by computing the intersection of the curves defined in (6).

3.2 Conservative Semi Lagrangian-IDO Method

To solve the Shallow Water Equation the CIP[7] Conservative Semi-Lagrangian IDO[8,9] Method was used. Two important reasons to work with this method are that it provides a scheme with a high accuracy and conserves mass and momentum.

The grid for this method is composed of a point value and an integrated value between the two adjacent points.

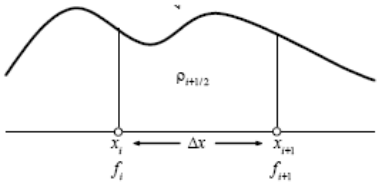

Fig. No.3 Variables for Conservative IDO

In this conservative IDO scheme the line integrated value is time-integrated at the line as a dependent variable:

$$\rho_{i+1/2} = \int_{x_i}^{x_{i+1}} f dx \tag{7}$$

The flux F between the two grid points is discretized as:

$$\frac{\partial F}{\partial x} = \frac{[F_{i+1/2} - F_{i-1/2}]}{\Delta x} \tag{8}$$

This is solved using the interpolation polynomial:

$$\Phi(x) = ax^2 + bx + f_i \tag{9}$$

which gives the dependency between the integrated value and the point value and thus proceed to time integrate using Semi-Lagrangian method for large .

4. GPU IMPLEMENTATION

4.1 Single GPU Implementation

To improve the computation performance of the simulation GPGPU was used instead of the traditional CPU computing.

First the data is loaded in the GPU, then the computing begins. Kernels are the portions of the code dedicated to program the device[10]. However the programming model is somehow different from the traditional CPU programming. Even a single GPU behaves more like a parallel environment instead of a sequential one like on CPUs, therefore from the start the GPU must be programmed in a parallel style. In the GPU the memory must be organized in Grids, Blocks and Threads which make CUDA problem-dependant. The arrangement of the memory will be reflected directly in the performance obtained, therefore is important to pay special attention and analyze the Problem. Moreover because of the different access speeds, the shared memory is preferable to be used when possible instead of the global memory because the first is about 100 times faster to be accessed.

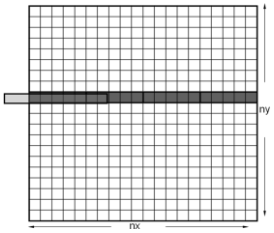

(a) X-direction

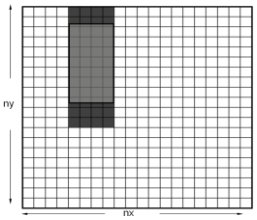

(b)*Y*-direction

Fig. 4 Shared Memory Model

Hence to improve the performance we made use of the shared memory. In the Tsunami simulation studied the GPU computes two different kernels which are launched sequentially to solve the directional splitting. For the x direction the data is loaded from global memory to shared memory in a line-like structure similar to that shown in Fig 4a. A line composed of blocks subdividing the y-length and width one is declared in the shared memory. Because of the limit of shared memory size each block compute grid points twice its size ergo each thread computed two grid points. By distributing the memory in this arrangement we assure the coalescence of the data is maintained which permits a high performance. Bank conflicts and crossed memory addresses are some important factors in low performance GPU computing.

For the y direction the shared memory model is arranged in a different shape (Fig 4b). In this case a block instead of a line is used because the fetching of data does not happen in adjacent points but rather in top and bottom ones making it a non-coalesce access thus decreasing the performance. The idea behind this arrangement is to have more threads working less which is more recommendable than having fewer ones with high loads of work.

4.2 Multi-GPU Computing

To solve the Shallow Water Equations in parallel GPU first the domain must be decomposed evenly along available CPU cores. Domain decomposition in the y direction was used in this research. Each piece of the resulting decomposed domain is then transferred to its associated GPU (Fig. 5). The GPUs cannot access data directly from others GPUs thus the CPU must be used a bridge to transfer data between neighboring GPUs.

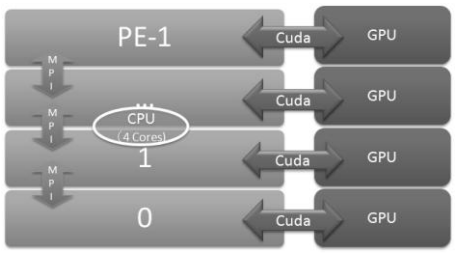

Fig. 5 Multi-GPU Decomposition

The MPI library was be used to communicate boundary data between CPUs, and the CUDA APIs were used to share data between GPU and CPU. Thus the computing procedures are: the initial data is decomposed and distributed then every GPU computes its portion of the domain, next the GPU shares its boundary values with its neighbors before the next time-step calculation.

4.3 Transfer and Communication time hiding by overlap

Analogue with traditional CPU parallel computing the data in one device cannot be accessed directly to or from another GPU.

Therefore the boundary values needed in the stencil to compute the extremes of the adjacent grid must be exchanged between neighbors manually.

This transfer is done by preparing the data in buffers and transferring them with the appropriate message passing tools. As mentioned before MPI is used for CPU to CPU transfer and CUDA is used for CPU to GPU communication.

To try to reduce the impact of the communication two

different models were tested. One model is the natural way of programming in which the communications were done synchronously with the calculation and then we tested another model in which transfers were done asynchronously, the scheme of both is shown in Fig. 6.

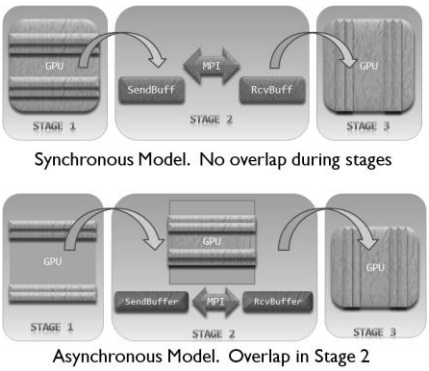

Fig. 6 CPU-GPU Communication Models

To try to reduce the impact of the communication two different models were tested. One model is the natural way of programming in which the communications were done synchronously with the calculation and then we tested another model in which transfers were done asynchronously, the scheme of both is shown in Fig. 6.

In the synchronous case the first stage consist of computing the domain in the x direction. Once every grid point has been computed the second stage is started which consist of the transfer between neighbors. The data is packed in buffer structures which are sent from the GPU to the CPU then from this to the appropriate top or bottom CPU neighbor which uploads the data to its GPU. Once this is done the final stage is executed which consists on computing in the y direction on every grid point. The disadvantage with this model is that the GPU blocks during Stage 2 waiting for the transfers to be finished.

To overcome this problem another model was tested. In the asynchronous model the stand-by disadvantage is overcome by dividing the computational domain and thus keeping the GPU running as continuous as possible. This is done by first computing only the portions of the domain that are going to be transferred. This depends entirely on the numerical method being used and its stencil however this usually requires only a few lines which is an acceptable time to divide the domain. Once this is done the GPU finishes computing the inside of the domain while at the same time the buffer transfers are being done thus overlapping the computing and the communications.

Therefore when the computing time is longer than that of the communication an even better performance can be achieved by hiding the transfer. Runtime improvements of between 5 to 10% were observed for the asynchronous over the synchronous model. Figure 7 shows results of the asynchronous transfer using 2 (7a) and 4 GPUs (7b) for four different grid sizes: 4096x4096 (labeled 4096), 2048x2048 (2048), 1024x1024 (1024) and 512x512 (512).

In Figure 7a the communication time does not represent

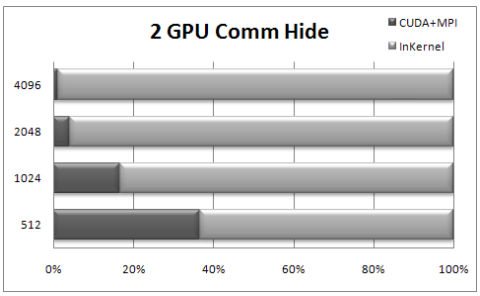

(a)2GPUs

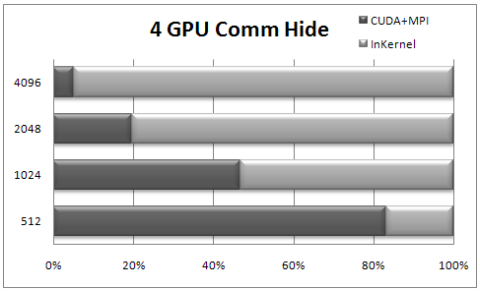

(b) 4GPUs

Fig. 7 Communication Hide using 2 (a) and 4 (b) GPUs. The dark blocks represent the percentage transfer time for CUDA and MPI and the light blocks the computing time one.

a big portion of the computing time, this is because only 2 GPUs were used and the amount of data transferred was small. In the case of the bigger domain the computing time was so large than practically it erases the communication time.

When more GPUs are used, as in Fig. 7b, the communication time became larger due to the fact that more information needs to be transferred.

Nevertheless in neither case the communications were larger than the computing which is perfect to overlap them and improve the performance.

5. RESULTS

To evaluate our scheme and the acceleration using GPGPU two adapted terrains were used with an initial wave resembling the initial Tsunami wave. Also a rendering using OpenGL was designed to provide a real-time representation of the results.

The first bathymetry, shown in Figure 8, was used to check the viability of the simulation while the second one, shown in Figure 9, was used for the actual computing and timing. Both of the datasets represent a 10kmx10km area and the same four different grid sizes were used to discretize the domain.

The initial part of the study was computed on a single machine with the following specifications: CPU: Intel Core i7 CPU920@2.67GHz; 8GB Ram memory; GPU: 4 cards nVIDIA GTX295 (installed in PCIe ports for higher speed). The code was prepared for traditional single-CPU and parallel CPU computing as well as the new single-GPU and parallel GPU computing. When a single-GPU computing

was done and compared with the single-CPU runtime an outstanding speed up performance of 62 times was found [11]. This is clearly an example of GPU computing. The speed ratio for the x-direction kernel and y-direction kernel was 10:7, the reason for this is the non-coalesced fetching of data for the y-direction kernel.

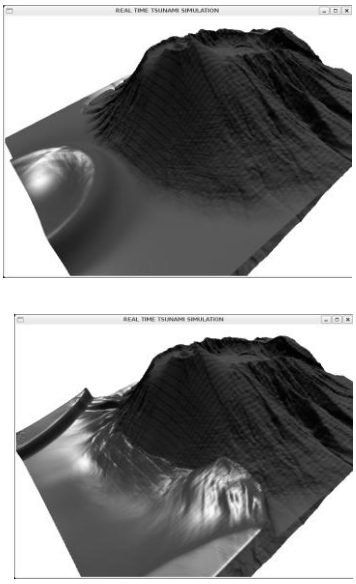

Fig. 8 Test Bathymetry I with ongoing Tsunami

A multi-GPU computing was also done in this machine; the scalability results for every grid size are shown in Fig. 10(a-d). They show the runtime rates between the multi-GPU and the single-GPU for 2 and 4 GPUs, the fine dot line represents the ideal case, the synchronous and asynchronous cases are also included. These graphs show the improved performance results for the asynchronous model which tend to approach closely to the ideal values in most of the cases. In the case of the small grid size some slow down was observed, the reason for this has to do with the characteristics of the GPU programming.

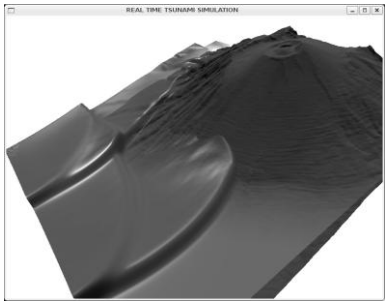

Fig. 9 Test Bathymetry II with ongoing Tsunami Simulation

It is desired that the GPU be populated and every stream processor be busy, however with a small grid size in parallel GPU produces an even smaller domain to compute on one GPU and thus this GPU becomes under populated which damages the performance. On the other hand it was found that the bigger the grid size the better the results because the computing time increases giving better chance to hide the communications.

The second bathymetry used as dataset was composed from real data for Japan`s Tohoku region, it was adapted from NASA's SRTM Mission[12] and NOAA's ETOPO[13] databases. Two datasets were used because the SRTM database does not include bathymetry while the ETOPO's resolution is not as high as that of the SRTM. Hence after downloading the desired part from their servers the dataset was processed to match the same resolution of 90m then both were merged into one single hypsometry and bathymetry dataset with a grid size of 4096x8192, covering a vast 370x735km area, the resulting dataset can be seen in Figure 11.

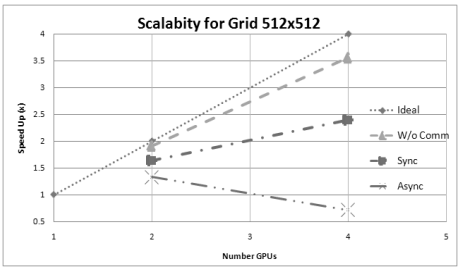

(a) 512*x*512

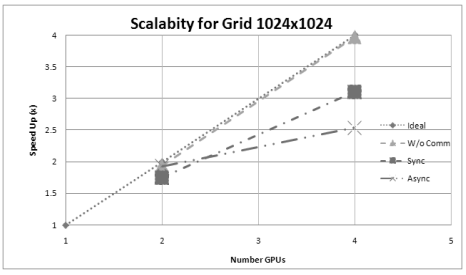

(b) 1024*x*1024

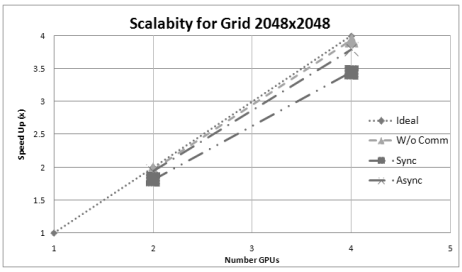

(c) 2048*x*2048

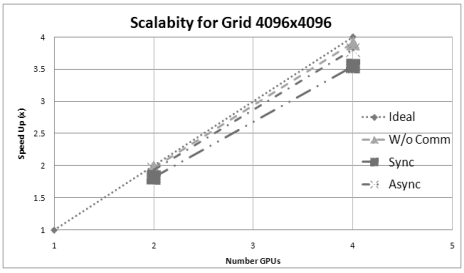

(d) 4096*x*4096

Fig. 10 Scalability results for Bathymetry II on nVIDIA's GTX295

The simulation of this bathymetry was computed using the newly introduced GPU Cluster on the Tokyo Institute of Technology's supercomputer Tsubame, which additionally has the advantage of a high speed network and thus multi-node computing was used for higher performance. This cluster consists of nVIDIA Tesla S1070 cards.

The main hardware characteristics of Tsubame are: CPU Sun Fire X4600 server (8AMD dual Core) 32 per node; 32GB Memory; GPU: Tesla S1070 (2GPU/node) and Infiniband Network Voltaire ISR 9288x8 [14].

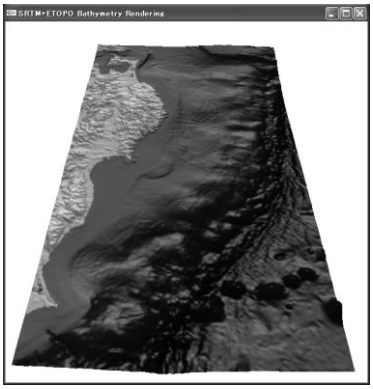

Fig. 11 Processed Real Bathymetry, Tohoku Region

The GPU cluster consist of 2 GPUs on each node and 1, 2, 4, 8, 16 and 32 total GPUs were used in our research. Also Tsubame's CPU cluster was used to compare the CPU scalability with the GPU one.

The GPU and CPU runtime results are shown in Fig. 13. In every case for the GPU runtimes the times are close or below 5 minutes: 6 min for 4GPUs, 3 min for 8GPUs, 1.5 min for 16GPUs for instance, which are optimal results for a real-time simulation since an early warning can be issued within reasonable time. Even the single-GPU case on Tsubame consumes only around 10 minutes to solve the simulation. Two screen captions of the ongoing simulation for this bathymetry at different time steps are shown in Figure 12.

In the CPU cluster computation case the results are less than under-achieved. The runtimes are orders of magnitude larger than those of the GPU runtimes. The single-CPU runtime for instance is more than 10 hours long making it clearly an unreasonable option for a real-time computing.
The scalability for CPU and GPU was estimated on Tsubame, the results are summarized in Figure 14. The dotted line represents the CPU scalability from 1 to 1024 CPU cores and the continuous line represents the GPU scalability from 1 to 16 GPU devices both in 2n increments. The scalability is calculated using the single-CPU runtime as a base.

Both scalabilities tended to be linear as the number of devices was increased. However the scalabilities clearly show the different performance between CPU and GPU. For instance around 1024 CPUs are required to match the performance of 16 GPUs, an outstanding result for GPU computing. Moreover this demonstrates the viability of multi-GPU and its excellent scaling.

If some slow down was found it could be explained due to the increase of transfer traffic, more GPUs are downloading and uploading data to and from the CPU while more CPUs are sending information with MPI through the nodes.

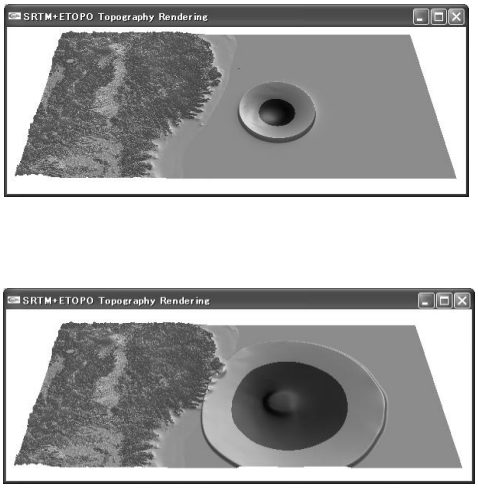

Fig. 12 Tsunami Simulation for Tohoku Region on Tsubame

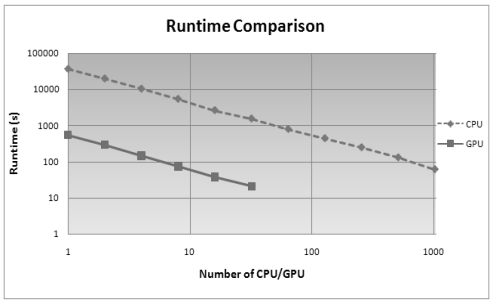

Fig. 13 CPU and GPU Runtime Results for Japan Bathymetry on Tsubame

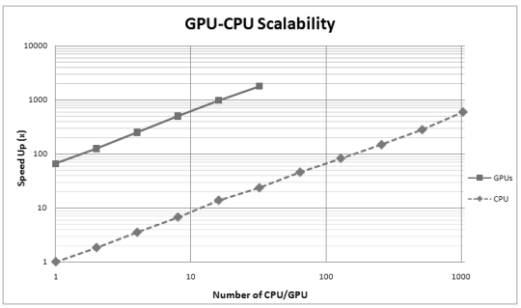

Fig. 14 CPU-GPU Scalability for Japan Bathymetry on Tsubame

The visualization of the results for the Tsunami in the Tohoku region are rendered with using OpenGL with a post-processing program specially design by ourselves for this purpose (Fig 13).

6. CONCLUSIONS

Test bathymetries were used to study the acceleration in the case of a Tsunami simulation on GPUs instead of traditional CPU computing.

The runtime results on a single machine showed and outstanding performance speed up of 62 times, demonstrating the advantage of GPGPU computing for this research.

Moreover after solving the simulation with two different data transfer models, synchronous and asynchronous, the performance was clearly improved when the asynchronous model was used. The ability of the asynchronous model to hide the communication behind the computing and thus maintaining the GPU running continuously proved to be a factor in the performance improvement, around 5% to 10% speed up was achieved.

The multi-GPU approach proved to maintain the high performance expected on a desktop machine with several GPU cards.

The CPU and GPU scalability on Tsubame showed linear tendency and close to the ideal results, nevertheless the GPU scalability showed an outstanding advantage over the CPU one. In all cases hundreds of CPU cores were needed to match the performance of a few GPUs. The multi-node computing benefited the multi-GPU computing by improving the transfer speed.

Finally based on the outstanding speed up performance results on a single machine and on Tsubame, we see the parallel GPU as a promising and revolutionizing technology to develop a warning tool for a High Performance Real-Time Tsunami Simulation.

Acknowledgements:

This research was supported in part by the Grant-in-Aid for Scientific Research (B) 19360043 of The Ministry of Education, Culture, Sports, Science and Technology (MEXT) and in part by the Japan Science and Technology Agency (JST) CREST research program: "Ultra Low-Power(ULP-HPC)".

References:

[1] *CUDA ZONE* HTTP://WWW.NVIDIA.COM

[2] HTTP://GPGPU.ORG/

[3] E.F. TORO. SHOCK-CAPTURING METHODS FOR FREE-SURFACE SHALLOW FLOWS. JOHN WISLEY&SONS LTD 2001, LONDON.

[4] SYNOLAKIS, C., P. LIU, G. CARRIER, H. YEH, TSUNAMIGENIC SEA-FLOOR DEFORMATIONS, SCIENCE, 278, 598-600, 1997.

[5] SYNOLAKIS, C.E (1991). GREEN LAW AND THE EVOLUTION OF SOLITARY WAVES. PHYS, FLUIDS A-FLUID DYN 3, 490-491

[6] MULTI-DIMENSIONAL SEMI-LAGRANGIAN CHARACTERISTIC APPROACH TO THE SHALLOW WATER EQUATIONS BY THE CIP METHODS. INTERNATIONAL JOURNAL OF COMPUTATIONAL ENGINEERING SCIENE. VOL 5, NO3. 699-730

[7] Interpolated Differential Operator (IDO) scheme for solving partial differential equations. Takayuki Aoki. Computer Physics Communications 102 (1997) 132-146

[8] T. Aoki, Comp. Phys. Comm., Vol.102, No.1-3, 132-146 (1997)

[9] Y. IMAI, T. AOKI AND K. TAKIZAWA, J. COMP. PHYS., VOL. 227, ISSUE 4, 2263-2285 (2008)

[10] CUDA PROGRAMMING GUIDE VERSION 1.1 PAG. 7

[11] GPU DRIVEN ACCELERATION FOR SOLVING THE SHALLOW WATER EQUATION. MARLON ARCE ACUÑA, TAKAYUKI AOKI. JSMES 21ST CONFERENCE, NOVEMBER 2008

[12] NASA SRTM WWW2.JPL.NASA.GOV/SRTM/INDEX.HTML

[13] NOAA WW.NGDC.NOAA.GOV/MGG/GLOBAL/GLOBAL.HTML

[14] TSUBAME PDF MANUAL : HTTP://WWW.GSIC.TITECH.AC.JP/~CCWWW/TEBIKI/TEBIKI-ENG.PDF

JOINT CONFERENCE PROCEEDINGS
7th International Conference on Urban Earthquake Engineering (7CUEE) &
5th International Conference on Earthquake Engineering (5ICEE)
March 3-5, 2010, Tokyo Institute of Technology, Tokyo, Japan

BAMBOO AS A GREEN BUILDING MATERIAL

Shyam K Paudel[1]

1) Senior Programme Officer, Coordinator of Bamboo Housing Programme, International Network for Bamboo and Rattan, Beijing 100102, PR China, Email: spaudel@inbar.int

Abstract: There has been a serious concern to look for alternative housing materials that are cheap, widely available and environmentally friendly. Bamboo is one of the best materials that have been used for centuries as a building material due to its versatile characteristics. Bamboo housing is not a new concept. It is estimated that more than a billion people live in bamboo houses mostly in developing worlds. The ecological and economical dynamics of bamboo have made it a sustainable building material.
Various testing, researches and practical experiences have revealed that bamboo has high tensile strength, high strength to weight ration and high specific load bearing capacity. Due to its long, strong and elastic nature of fibbers; bamboo is known as high resistance to the earth quake. Moreover, modern bamboo housing technology has been developed that uses engineered bamboo that can be produced through modern processing technology. This paper highlights the prospects of bamboo as an environmental friendly bamboo building for the 21st century.

1. INTRODUCTION

Bamboo is a giant grass. There are about 75 genera and 1250 species worldwide (Sharma, 1980), with total bamboo areas about 22 million hectares and with a yield of 2000 million tons (Zehui, 2007). It grows from tropical to sub-temperate regions, though the great diversity is found in sub-tropical region. It is known to be one of the fastest growing plants in the world. Its growth rate ranges from 30 cm to 100 cm per day. Bamboo grows densely sometime more than 10,000 culms per hectare and can be easily regenerated naturally. Bamboo attains its maximum size in 60-90 days of shoot sprouting and can be harvested in 3 to 6 years depending upon species. Bamboo multiplying is very easy as it expands naturally with rhizome. Its natural expansion capacity and short rotation have made it well known as an environmentally green plant.

Bamboo has a very long history for its use in various purposes such as food, shelter, furniture etc. Bamboo has been serving humanity from cradle to grave in many countries since ages in many different and ingenious ways. It has strength, flexibility and versatility and therefore is suitable material for the various types of construction.

2. BAMBOO AS A BUILDING MATERIAL

Bamboo is one of the oldest materials used for the construction of houses and other structures. Its strength, flexibility and versatility make it a suitable material for addressing every housing component when treated and used properly (Jayanetti and Follet 1998). Bamboo is relatively cheap, easy to work with and readily available in most warm climate countries. Bamboo building is highly environmental friendly than concrete and masonry buildings (Murphy and Londono, 2004). It is estimated that more than one billion people in the world live in bamboo house and in Bangladesh alone more than 70% houses are made up of bamboo (Vries, 2002).

Bamboo can be used various ways for the construction. They can be used as it is without any major processing or can be processed into panels. Based on the ways bamboo used for the construction, bamboo building technologies can be divided broadly into two types (1) bamboo building using round (unprocessed) bamboo culms and (2) bamboo building using engineered (processed) bamboo.

2.1 Bamboo building using unprocessed bamboo (culms)

Various physical and mechanical testing carried out for various species of bamboo revealed that many species of bamboos are strong enough to be used as a building material. In certain mechanical properties, bamboo even surpasses timber and concrete. However, it is difficult to generalize the properties of bamboo as it differs with the species, age, climatic factors, moisture content and different heights of the culm. Generally, the density of bamboo varies from 500 to 800 kg/m3. Bamboo possesses excellent strength properties especially tensile strength. Study shows that bamboo is as strong as wood and some species even exceed the strength of *Shorea robusta and Tectona grandis* (Sattar, 1995, table 1). An increase in strength is reported to occur at 3-4 years and

Table 1 Comparison of important strength properties of bamboos and wood of India Source: Sattar (1995)

Species	SG	MC (%)	MOR (Kg/cm2)	MOE (Kg/cm2)	MCS (Kg/cm2)
Bambusa bambos	0.65	15.5	674	65000	483
B. nutans	0.72	16	545	85000	508
B. tulda	0.71	14.9	506	82650	615
D. strictus	0.72	10.7	1184	159490	645
Tectona grandis	0.6	12	959	119600	532
Shorea robusta	0.71	12	1318	162045	641

Note: Kg/cm^2 = Kilogram per square centimeter; SG = Specific Gravity; MC = Moisture Content; MOR = Modulus of Rupture; MOE = Modulus of Elasticity; MCS = Maximum Crushing Strength.

thereafter it decreases. Therefore maturity period of bamboo is considered 3-4 years with respect to density and strength.

The comparison clearly reveals that bamboo is better in properties than that of Spruce and equal or more than steel in tensile strength. More importantly the failure in bending of bamboo is not actually totally failure. Due to its strong fibers, it first cracks unlike timber which breaks if bending fails (Janssen 2000). This quality of bamboo gives an opportunity to repair or replace failure parts of house. The elasticity of bamboo is better than wood for seismic resistant housing and as has been proved in the case of several small houses. One more advantage of bamboo over timber is that it does not have rays. Rays are mechanically weak therefore bamboo material is better in shear than timber material.

2.1.1 Existing technology of using round bamboo

There are various traditional technology and methods of building with bamboo depending upon region and bamboo species availability. Such technologies emerged from the beginning when people started to use bamboo as a building material and has been improved significantly in accordance with modern housing technology. Some of the existing technology are briefly described here.

Bahareque System: Bahreque is a traditional bamboo building (wall) system in Latin American countries mainly in Ecuador and Columbia. There are two types; hollow and solid. In solid type, horizontal bamboo laths are fixed on both sides of culms or timber frame and the space is filled with mud. In hollow type, estrilla (flattened bamboo) is fixed both sides of culm and is plastered with mud or cement mortar (Paudel and Lobovikov 2003).

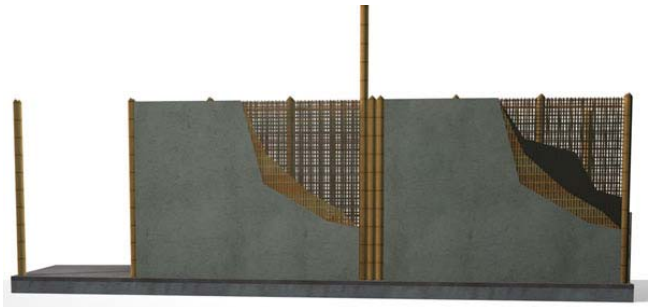

Picture 1 Hollow and Solid Bahareque walls (courtesy: Arch. Daniel Romero)

Quincha system: Quincha is also a Latin American System. There are two types of quincha. The first one is Quincha with wooden frame which is a slight modification of traditional *Bahareque*. The main structure of the wall is a wooden frame. Each side of the frame is covered with horizontally placed bamboo *esterilla* with the green side facing inwards. In some cases bamboo laths are used the fix the flattened bamboo to the wall panel. The wall is then plastered with cement mortar. The second system is Quincha with bamboo frame in which wall is fabricated with bamboo poles and flattened bamboo with the green side facing inwards. The exterior of the wall was plastered with mud and cow dung. The interior of the wall was left for the bamboo view.

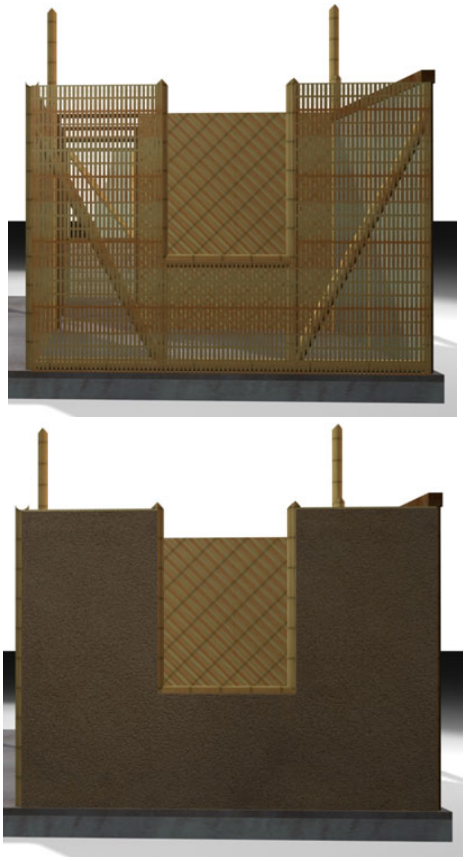

Picture 2 Quincha walls with bamboo poles (courtesy: Arch. Daniel Romero)

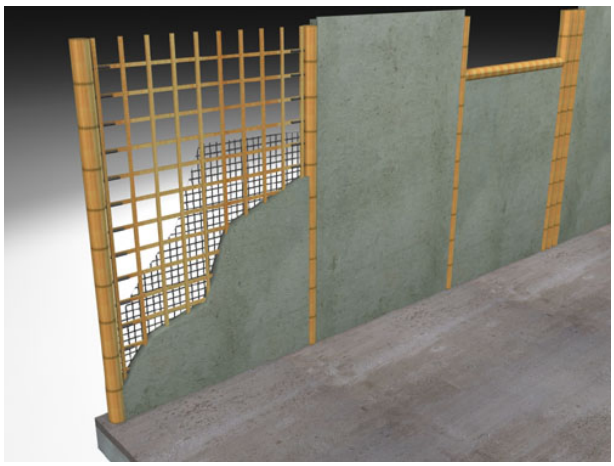

Picture 3 Grid wall system (Courtesy: Arch Daniel Romero)



Picture 4 Pre-fabricated bamboo house in Nepal (Courtesy: Himalayan Bamboo)



Picture 5 A modern bamboo house by Bamboo Technologies





Picture 6 and 7 Pre-fabricated bamboo buildings with engineered bamboo (developed and constructed by INBAR) in Beijing

Grid system: The system was developed by TRADA International in collaboration with Indian Plywood Industries Research and Training Institute (IPIRTI), Banglore India. The IPITRI bamboo-housing system is based on the principle of modular systems in which bamboo columns spaced at 1.2m center to center that act as main load bearing elements for transmission of roof dead loads. The columns are tied at the top with wooden plates and bottom is embedded in foundation concrete. The wall is made up of grid of bamboo lath and chickens mesh and plastered with cement mortar and bamboo lath and steel dowels hold spaces between columns. Roof consists of bamboo trusses, bamboo purlins and bamboo corrugated mats (Paudel, 2003).

Pre-fabricated system: Both bahareque and quincha wall can be pre-fabricated offsite and be assembled in any locations. Both traditional and modern bamboo building systems are developed with pre-fabricated he system has been modified and improved with double bamboo wall in wooden frame plastered with mortar both sides of the wall. This modified system has been used in Nepal to build low cost residential houses and community buildings. This system gives more stability and durability to the house.

2.2 Engineered bamboo building materials

It is a recent technology in bamboo housing developed in India and China. INBAR collaborated with various partners including Chinese Academy of Forestry, Fustar Bamboo, Hunan University to research and develop pre-fabricated engineered bamboo housing technology with the funding supports from Blue Moon Fund, USA. Two demonstration sites are established in Beijing to demonstrate the modern bamboo housing technology. Additionally, several other types designs and structures are developed by Hunan University, China and National Mission for Bamboo Application, India.

The engineered bamboo products developed by INBAR were designed and tested by Chinese Academy of

Forestry. According to the shape of materials used in light frame constructions, the engineered bamboo material can broadly be divided as sheathing board and bamboo lumber (Zheng et al 2009). The brief process and properties of the sh eathing board and bamboo lumber are briefly described here.

Sheathing (wall and roof board): The sheathing board is prepared through industrial process. First of all, the standard length of bamboo culms are spllited into longitudinal strips of 20 ~ 30mm wide and then into straight slivers of 1.5 ~ 3.0 mm thickness by wiping off bamboo hypodermis. Bamboo slivers are weaved into curtains or mats. Then the curtains or mats are dried to 10 ~ 12% moisture content using dryer, and immersed them in phenol-formaldehyde (PF) re sin tank for a few minutes. Finally, the bamboo curtains and mats are overlaid in odd numbers and put them in hot press. After a given period, bamboo-based panel is produced. The mechanical properties of the final product produced during the research are given below in the table.

Oriental Standard Borad (OSB) is the most commonly used structural sheathing board. According to requirements mentioned in OSB/4 level, bamboo-based plywood has met OSB standards.

Bamboo-based glued laminated lumber (glu-lam) for roof truss: The process of producing bamboo lumber is similar that of bamboo sheath. The lumber can be made by further thickening the bamboo mat board with repeated processes. In order to ensure qualities of timber, slivers should be less than 1mm. In this study, thickness of bamboo sliver is 0.5-1.0 mm.

Finger joint is the most important method to extend the length of bamboo glu-lam. Since stiffness and elasticity of such kind of bamboo-based panels is much higher, finger size should be be longer in length (31.5mm) and smaller in gradient (1/9) that that of wood .

Table 2 Mechanical properties of bamboo sheath (mat board)

properties	standard value	testing value	appendix
Bending strength /MPa	28	124.2	BS EN 300-1997, OSB/4, "load-bearing boards for use in humid conditions"
Modulus of elasticity- major axis /MPa	4800	11500	
Compression strength /MPa		71.99	
Tension strength /MPa		91.7	
Horizontal shear		8.12	JAS No.989, July 10, 2000

(Source: Zheng et al 2009)

Table 3 Mechanical properties of glu laminated bamboo lumber

Properties	standard value	testing value	appendix
Bending strength /MPa	67.5	160.9	JAS No.989, July 10, 2000, 180E
Modulus of elasticity /MPa	12000	12200	JAS No.989, July 10, 2000, 120E
Compression strength /MPa		85.47	
Tension strength /MPa		137	
Tension stiffness /MPa		17000	
Horizontal-shear strength/MPa	6.5－5.5	22.7	JAS No.989, July 10, 2000, 65V-

(Source: Zheng et al 2009)

Table 4 The advantages, disadvantages and limitations of using processed and unprocessed bamboo for housing.

	Using unprocessed bamboo	**Using processed bamboo**
Advantages	● Doesn't require big investment ● Offers flexible design ● Low technical requirements and can be done any locations where bamboo available	● Can make use of all kinds of bamboos ● Less wastage (can use much of bamboo culms) ● Can be standardized for its quality ● Large quantity production and supply is ● Can be modular and pre-fabricated ● Durable and flexible
Disadvantages and limitations	● Limited species of bamboo can be used ● Quality control problem (bamboo species, size, age etc) ● Durability depends upon the quality of bamboo and preservation ● Production and supply of houses in large quantity in a short period of time may be a problem	● Require considerable investment ● Constant supply of raw materials can be a problem. A pure bamboo forest of at least 200 hectares is required for the sustained supply bamboo raw material to a medium size industry.

Since the timber size is too large, all properties were tested in laboratory by using laminated lumber, its composition unit, with reference to Japanese agricultural standards "structural laminated veneer lumber" (No.989, July 10, 2000). The bending and shear performance have achieved higher performance level and therefore can easily be used for building construction (Zheng et al 2009).

3. ADVANTAGES AND DISADVANTAGES OF USING PROCESSED AND UNPROCESSED BAMBOOS FOR HOUSING

The both technologies have their own strengths and weakness. In certain conditions, using unprocessed bamboo could be beneficial and useful. In other situation, using processed bamboo may give better comparative advantages. The advantages and disadvantages of the technologies have been summarized in the table.

4. CONCLUSION

Bamboo is an excellent building material that offers a range of building options from very low cost to high end and therefore can meet the requirements of wider economic groups. However, there are still a few constraints and limitations that inhibit the promotion of bamboo as a building material at large. The main limitation is the misperception of people regarding bamboo as a poor men's timber. However, such perception could be altered with proper extension education such as training, workshop, demonstration of high end buildings.

The other problem of using bamboo lies within its own physical characteristics. Bamboo is a non dimensional material and is very difficult to use compared to other building material. However, technologies are being emerged to process bamboo into panels and beams that could be standardized for its dimensions as well as mechanical strengths. INBAR has recently developed a pre-fabricated modular bamboo housing system using engineered bamboo panels and beams. The engineered bamboo has a great potential to be used as a building material in the future to solve the problems associated with unsustainable building materials

References:

Jayanetti D. L. and Follet P. R. 1998 : Bamboo in Construction: An introduction. Published by TRADA and INBAR for DFID.

Murphy, R. J. Trujillo D. Londono X. (2004) "Life Cycle Assessment of a Guadua House". Paper presented to Simposio Internacional Guadua, Pereira, Colombia 27 Sept – 2 Oct, 2004.

Paudel, S. K. and Lobovikov, M. 2003. Bamboo housing: market potential for low income group. *Journal of Bamboo and Rattan,* No. 2 Vol. 4, 2003.

Paudel S.K. (2003) Bamboo School Building. INBAR: Transfer of Technology Model (TOTEM).

Paudel S.K. (2003) Proceeding of Bamboo Housing Workshop. INBAR proceeding no 10. (available at http://www.inbar.int/InfoPortal.htm)

Sattar, M. A. 1995. Traditional Housing in Asia: Present status and future prospects" Bamboo, People, The environment (1995) Vol. 3. INBAR Technical report No. 8. Editors: Ramanuja Rao I.V. and Sastry C.B. (Ed.)

Sharma, Y.M.L 1980. Bamboo in Asia Pacific Region, In Bamboo Research in Asia G. Lessard and A. Chouiard (Eds.) World Publications, Singapore, pp 99-120.

Vries, S. de. 2002. Bamboo construction Technology for housing in Bangladesh: Opportunities and constraints of applying Latin American bamboo construction technologies for housing in selected rural villages of the Chittagong Hill Tracts Bangladesh". Thesis submitted to Technical University of Eindhoven, the Netherlands.

Zehui, J. 2007 (Eds.) Bamboo and Rattan in the World. China Forestry Publishing House.

Zheng W. Xuhe C, Li G. Paudel S. (2009): Application and Demonstration of Bamboo-based Engineering Materials on Construction. Paper presented in International Conference on Modern Bamboo Structures, Bogota, Colombia, July 2009.

JOINT CONFERENCE PROCEEDINGS
7th International Conference on Urban Earthquake Engineering (7CUEE) &
5th International Conference on Earthquake Engineering (5ICEE)
March 3-5, 2010, Tokyo Institute of Technology, Tokyo, Japan

FIRE RESISTANT TESTING AND ANALYSIS OF LIGHT-GAUGE STEEL EARTHQUAKE DISASTER RELIEF SHELTERS

Q. Zhou[1], Y. Xiao[1,2] and L.Y.She[3]

1) Key Laboratory of Building Safety and Energy Efficiency, Ministry of Education, China, Institute of Modern Bamboo, Timber and Composite Structures Changsha 410082, China
2) Univ. of Southern California, Los Angeles, USA; 3) Advanced Bamboo and Timber Technologies, Ltd., Changsha, Hunan, China
quanzhou516@163.com， xiaorock@yahoo.com，sheliyong0527@163.

Abstract: This paper studies the fire resistant properties of light-gauge steel earthquake disaster relief shelters, and presents model simulations. The results showed that the light-gauge steel and Styrofoam building panels had poor fire resistance with melting at early stage of fire, while releasing toxic gases. Once the Styrofoam melted, the thin steel skins lost capability of maintaining stability. In addition, the authors conducted simulation of fire tests using fire power simulation software FDS (Fire Dynamics Simulator), and the results matched the test data well.
Key words: light-gauge steel earthquake disaster relief shelters, fire resistant properties, fire simulation, Fire Dynamics Simulator (FDS)

1 INTRODUCTION

A magnitude 8.0 earthquake occurred in SiChuan, China on May 12, 2008, and a large number of buildings, especially schools and hospitals, collapsed. An urgent need for sufficient earthquake disaster relief shelters came forth, so the safety of the light steel movable plank building was concerned. Especially the fire-resistant ability, which refers to the diffusion of heat, is a key parameter of this kind of building.

The movable plank building is a kind of building with light steel for the skeleton, sandwich panels for the wall-enclosure material, standard module for combination. With common standards, this temporary building can be easily and quickly assembled and dismantled in order to establish a green energy-saving, fast and efficient architectural system. Now the temporary housing is developing a stereotype-turnover product area with integrated production, matching of supply, and can be repeatedly made use of.

Light weight is the biggest advantage of light steel structures, its weight is 1/30 ~ 1/20 of the reinforced Concrete, 1/3 ~ 1/2 of the ordinary steel. Loads transferred to the foundation are small, thus it can significantly reduce the cost, especially for areas of poor geological conditions. In addition, it is applicable to earthquake-prone areas, since it is a kind of high-strength structure, easy for production, transportation, installation and maintenance and has small seismic response. However, it has poor fire resistance and will release much toxic gases while melting, which has seldom been researched.

2 TEST DESIGN

In Fig 1, fire test of a light steel house was conducted to research its fire-resistant properties and the damage situation. Research group assembled a light steel with size of 6.1m × 3.76m × 2.44m in laboratory, then took 100kg lumber as the fire source, equal combustion heat value of about 2000MJ (Referring to Guidelines of Transitional Construction's Technology in Earthquake Areas(2008) and Handbook of Building Materials for Fire Protection).

In order to measuring the fire situation of main structure under fire, research group installed electric thermo-couples on the each face of the wall. The couples can induce the temperatures of longitudinal and transverse direction wall, and transform the analog signal to digital signal, which can be record in the computer. The outsize point united the thermocouple wire of 0.5mm diameter, and its induce end was welded with a circular copper about 12mm diameter and 0.2mm thickness, which covering with asbestos of 30mm length and width, 2mm thickness. The inside point used the thermocouple which was compatible with the measured temperature, ensuring the change temperature did not exceed allowance.

Thermocouple should be buried under the wall more than 50mm in the isothermal section of the region, rather than measuring the wall surface air temperature. The electrical signals generated by the thermocouple transmitted directly to the recorder, and the test process, test data recording was isochronal.

According to the Guidelines of Transitional Construction's Technology in Earthquake Areas, the limiting time of fire-resisting is no less than 30minutes. In the beginning of experiment, lots of hyperthermia gas was released and the windows and doors had dissolved. When the test was carried out to 9th minutes, the bottom profiling plate had fallen down and most of the Styrofoam in roof had gasified. In the following three minutes, profiling steel plate of one longitudinal wall had broken and mostly all of Styrofoam in wall had gasified. During the trial process, the Styrofoam combustion inside the wall emitted a lot of irritating gases. Until the end of the experiment, all the walls and roof of the house were burned, profiling plate had fallen down. The main bearing components damaged in varying degrees, could not continue to load, therefore there was the danger of collapse.

3 TEST RESULTS

From the phenomena in the fire-resistant test of light steel movable plank, disadvantage of fire durability and safety property was exposed. Styrofoam occurred gasification early when fire burned the wall, and generated a large number of harmful gases. Conductivity



(a) (b) (c)

Fig 1. Fire test of light steel movable building:
(a) measured point (b) fire source (c) burning house

factor of profiling plate is great, that make it easy to let mounts of heat spread to adjacent wall. The main load-loading steel structures in fire intensity rapidly decreased, and its resistance to fire and safety became poor.

Early in this experiment, as the bottom profiling plank of the roof collapsing, heat slaked gradually and the temperature of inner wall fluctuated widely. In the meantime, At this point the Styrofoam inside wall had not happened gasification, so it could play a function of thermal insulation, and the temperature curve of exterior walls did not change with the interior wall. But approximately 20th minutes when the temperature exceeded 300 degree Centigrade, the Styrofoam was mostly dissolved, and it had lost ability of heat insulation. The trends of fluctuation about exterior and interior walls were similar, since then the heat could flow freely inside the wall.

4 SIMULATIONS

4.1 MODELING

In order to analyze the characteristics of light steel mobile house's fire-resistance and compare to test results, the modeling software FDS (Fire Dynamics Simulator) was used, which was developed by American National Standards Institute [NIST], for fire simulation. This software is commonly used to make numerical approximate solution of N-S equations in low speed heat flow, which focuses on the transfer of the fume and heat. FDS (Fire Dynamics Simulator) issued by the NIST is used to predict the flame, ventilation systems, etc. caused by smoke and air flow. Smokeview accompanied by FDS can be applied to display the results of FDS modeling graphically. In the other hand, it can be processed to gain static data once again in two-dimensional or three-dimensional contour / surface, displaying the temperature and velocity distribution of the flue gas at specified time. Under normal circumstances, calculations worked out from FDS is demonstrated graphically by Smokeview, which can be manipulated to monitor the operation status, and pre-treatment process can simulate the situation of interior furniture, vents, fire source, windows, wall, etc.. In order to accurately and quickly build FDS input file, the user is also allowed to create or edit various types of indoor Smokeview modules (such as furniture, walls, etc.), setting their size, location and surface material, for instance.

FDS adopts C language and FORTRAN90 language for edit, and the original code contains a main program and 14 sub-procedures with the length of approximately 3.5 million lines. Unless subroutines Isob.c using C language, the paragraphs procedures are written by FORTRAN90 .

Simulation was carried out basing on the actual construction settings, the thermal physical parameters were calculated in the beginning. Design information and documentation of light steel house such as thermal conductivity, specific heat capacity and thermal coefficients of steel and Styrofoam had been displayed in Table 1.

Table 1. Values of thermophysical properties of materials

material	Density (kg/m^3)	Conductivity coefficient (w/(m·k))	thickness (mm)
Steel	7850	48（588.5k）	2
Styrofoam	30	0.034 （288.5-293.5k）	40

The heat transmission coefficient of wall was calculated refer to Design standard for energy efficiency of public buildings (GB 50189-2005)

$$k = \frac{1}{\frac{1}{\alpha_i} + \sum_j \frac{\delta_j}{\lambda_j} + \frac{1}{\alpha_0}} \qquad (1)$$

k: coefficient of heat transmission
α_i: heat transfer coefficient of interior walls
α_0: heat transfer coefficient of exterior walls
δ_j: thickness of the wall
λ_j: heat conductivity coefficient of each wall

A model of 6.1m × 3.76m × 2.44m's room was set up (Fig 2), carried out in the FORTRAN programming, and the following is FDS calculation analysis and imaging which is displayed by visualization software Smokeview.

In Fig 2 there is the fire source in the yellow-center rectangle, and the yellow squares is the doors and windows. When carried out by FDS field simulation, a flat space for any fire-related parameters, including material properties, thermal conductivity and density can be recorded by SLCP.

The statement of the simulation program is as follows:

&

SURF ID = 'GYPSUM BOARD'.	Gypsum board
FYI = 'Quintiere, Fire Behavior'	Material properties, type
RGB = 0.80, 0.80, 0.70	Color
HRRPUA = 100.	Combustion heat value of
KS = 0.48.	Thermal conductivity
DENSITY = 1100.	Density
DELTA = 0.010 /	Thickness

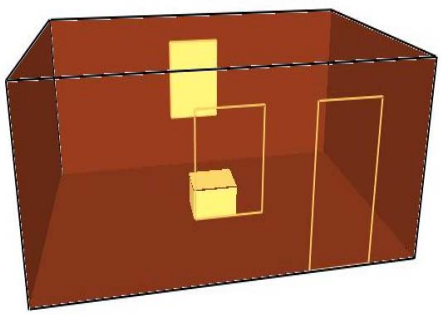

Fig 2. Simulate model

Take all above data into the model, and set the room size, simulation time, grid cell size and so on, then the Smokeview can visually display these values as well as the fire temperature inside the state.

4.2 SIMULATION RESULTS

Since the simulation data of longitudinal walls and transverse walls were similar, this paper only took the longitudinal walls into analysis. Compared and analyzed the temperature data of walls, then the interior and exterior wall surface temperature changes of light steel mobile house burn for 5 minutes and 30 minutes were show in Fig 3.

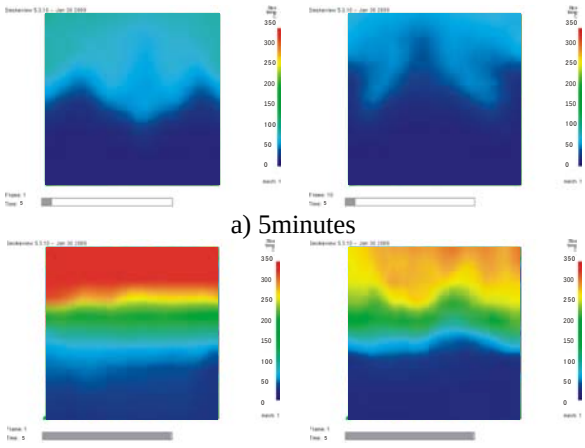

a) 5minutes

Interior surface Exterior surface

b) 30minutes

Fig 3. Longitudinal wall interior and exterior surfaces temperature simulationof light steel movable building

The temperature of the upper part was higher than the lower, and heat spread from the upper to the lower of the wall. When the simulation carried out to 5 minutes, distribution of both interior and exterior wall surface temperature was disaccord, and the limit of temperature dividing was unobvious. The temperature distribution of exterior surface of the wall was very uneven, since the gasification of Styrofoam led to the fluctuation of heat. When the simulation carried out to 30 minutes, thermal insulation performance of the wall was degrading. However, change trends of each side of the wall became similar, and the gradation of temperature distribution was distinct. There was somewhat temperature difference between each side of the wall, since the Styrofoam could still play an insulation effect.

Numerical modeling results were presented to cover time-temp relationships, temperature changes and heat distributions. The temperature of interior surface presented here is approximate 400°C, the exterior temperature was only about 120°C yet. Comparison between the experimental results and the finite element simulations in terms of time-temp relationship was also given to show validation in Fig 4.

In general, FDS simulation correlated the corresponding test results for the test reasonably well, especially for the trends of temperature rise and ultimate temperature. However, there were some different fluctuations in the curves. This may be caused by perfect gasification of Styrofoam, which was non-homogeneous in test. Another reason was the burn-damage of house body and falling down of profiling plate, leading to the redistribution of heat energy, which should be considered

in future modeling.

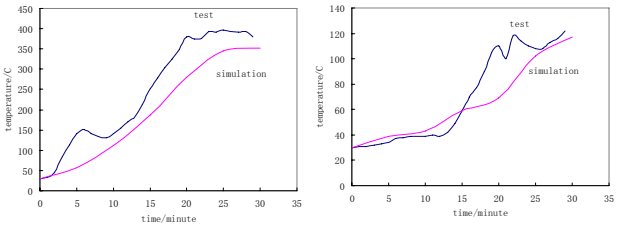

(a) (b)

Fig 4. Temperature-time curves of interior and exterior walls within test and simulation: (a) Interior walls (b) exterior walls

Fig 5 showed the relationship of temperature and time at roof's interior surface. It could be seen clearly that a large fluctuation in the test curve at 5th minute, which was due to the collapse of ceiling plate. When the profiling plate of roof fallen down, the heat space enlarged, and the heat conducted to the roof reduced.

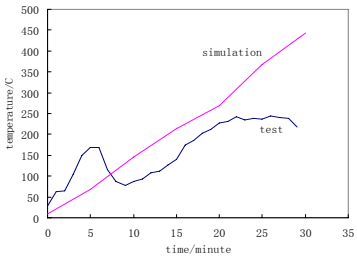

Fig 5. Temperature-time curves of interior roof surface within test and simulation

5 CONCLUTIONS

Nowadays, light steel movable plank buildings are largely used in disaster areas as tabernacle, and also widely as work shed, sentry box, etc.. Fire resistant security was test in this paper, and the whole work could be taken as a reference for manufacture，design and application of this kind of structures.

The fire resistance test results showed that: the light-gauge steel and Styrofoam building panels had poor fire resistance with melting at early stage of fire, while releasing toxic gases. This building may not collapse when fire test exceeds 30minutes which meets the fire safety requirements of transitional house, as a result trapped people have enough time to escape. However, the temperature of heat inside house rises to almost 400°C, which can not be suffered by anyone. So some ventilation devices need to be installed in the resettlement-house, then the noxious gas and high temperature air could be diffused in time. In the process of test, the fire resistance of roof could not be neglected, since the plank of roof fell down early and temperature of roof was so high.

It could be seen from the fire simulation results that there was a large temperature difference between interior and exterior walls, indicating the wall had good thermal insulation properties. But by the rising of temperature, the ability of Styrofoam's fire resistance was diminishing away, leading to consideration of adopting Rockwool instead in future which has better property.

FDS simulation correlated the corresponding test results for the tests reasonably well, despite some difference in the curves. Improvement needs to be considered in future modeling.

REFERENCES

Xue Wei, Zhang Guangjun. Fire simulation and applications. Jilin Forestry Science and Technology, 2006, 35 (6): 18-20.

David R. Lide. CRC. Handbook of Chemistry and Physics(2005)

Ministry of Housing and Urban-Rural, China. Guidelines of Transitional Construction's Technology in Earthquake Areas(2008)

Fire Dynamics Simulator (Version 4) User's Guide. Nist. 2004.

Charles A. Harper, Handbook of Building Materials for Fire Protection, McGrow–Hill Education(Asia) Co. and Chemical Industry Press(2006)

MIL-STD-2031(SH), "Fire and Toxicity Test Methods and Qualification Procedure for Composite Material Systems Used in Hull, Machinery, and Structural Applications Inside Naval Submarines," February 1991.

JOINT CONFERENCE PROCEEDINGS
7th International Conference on Urban Earthquake Engineering (7CUEE) &
5th International Conference on Earthquake Engineering (5ICEE)
March 3-5, 2010, Tokyo Institute of Technology, Tokyo, Japan

SUSTAINABLE RURAL HOUSE DESIGN IN POST-QUAKE RECONSTRUCTION

HU Rongrong [1], LIU Jiaping [2], CHENG Hui [3] and ZHOU Wei[4]

1) *Associate professor, School of Architecture, Xi'an University of Architecture and Technology, Xi'an, Shan'xi, China*
2) *Professor, School of Architecture, Xi'an University of Architecture and Technology, Xi'an, Shan'xi, China*
3) *Assistant, School of Architecture, Xi'an University of Architecture and Technology, Xi'an, Shan'xi, China*
4) *Architect, YouSe Design Institute, Kunming, Yunnan, China*
Corresponding author Email: hurongrong@live.xauat.edu.cn

Abstract: The aim of the study is to explore sustainable village reconstruction with the limitations of rural area in China after WenChuan earthquake. The earthquake that struck China on May 12th, 2008, caused extensive damage and large loss of life especially in the rural area in SiChuan province. This paper describes the field survey about the houses damages and the sustainable house design in Reconstruct Daping Village project, Pengzhou town in Sichuan province. The project focuses on improving living standards, increasing the earthquake resistance structures and preserving the local environment in addition to re-housing the population. The paper first discusses the houses behavior during the earthquake in the village based on the field survey, analyses the reasons for the poor behavior of the non-engineered houses that built recently as well as the reasons why some old traditional houses survived and almost unscathed. And the following sections briefly discuss the new houses design in the project. Basing on the safety standard of the structure and the house design is to produce a low energy and affordable eco-house with respecting of local culture and living pattern. Sustainable design strategies are applied in the design process including sustainable building materials, flexible planning with architecture and structure module idea, passive solar space heating, natural ventilation and lighting.

Keywords: post-quake reconstruction, earthquake damage, sustainable rural house, safety of structure, environment

1. INTRODUCTION

Daping village is located in Pengzhou county of Sichuan province, and only 40 kilometers from Wenchuan County, the epicenter of May twelfth earthquake 2008. Most of the buildings in Daping village were destroyed and damaged by the earthquake while the nature environment kept almost undamaged. According to the relative geological investigation the government decided to reconstruct the village on the original site.

The survey and research commenced in June 2008 just after earthquake took place. The construction began in September 2008, and before July 2009 around 80 families have moved to their new houses.

In addition to the basic purpose of reconstructing the houses as soon as possible, the project extended its main purposes to:

- Provide permanent, low cost and earthquake-resistant housing.
- To improve the indoor conditions and to meet high living requirements of the houses through better design.
- Energy efficiency designs.
- To develop rational house patterns corresponding to the local climate, culture and living styles.
- Improve the aspects of livelihoods, infrastructure, local economy and sanitation with strong consideration to the environment protection.

The following pages provide the field observations on houses damage caused by the earthquake in Daping village and a brief introduction about the new houses design in post-quake reconstruction basing on sustainable strategies.

2. RURAL HOUSES IN THE WENCHUAN EARTHQUAKE 2008

Traditional rural houses structure in Daping village is timber-frame. It consists of Chuandou wood frame, lath or wattle walls and a pitched roof covered with tiles. Burned bricks are used during last twenty years. More than two hundreds families live in Daping village. Before WenChuan earthquake, 75% of the houses in Daping village were timber-frame with different wall materials such as wood, wattle or brick. 25% of the houses were burned brick masonry and less than twenty years age. Based on the field observations month after WenChuan earthquake, the damage types of the rural houses are summarized as the following:

2.1 Timber-Frame Houses

Compared with the new built masonry houses, the timber-frame houses have resisted the earthquake better and the damage was not serious. Rarely timber-frame houses collapsed and even some traditional houses with more than one hundred years remained intact during the earthquake. Figure 1 shows that a brick masonry house collapsed, while the nearby traditional timber-frame house remained

undamaged. The traditional houses with flexible wood structure and lath or wattle walls are lightweight, which helps reduce the earthquake force. In addition, the wood elements are connected by mortise and tenon. The mortise and tenon works as a flexible semi-rigidity joints and can dissipate the energy with movement during earthquake. All the Chuandou frameworks in the traditional house are connected entirely on the main weight-bearing points using special techniques such as Chuanfang and Jiaofang to increase the integrity and stability. However, some of the traditional techniques and principles were ignored in most timber-frame houses which built last forty years and most of them were moderately damaged. The different damages occurred in timber-frame houses including:



Figure 1 a masonry house collapsed, while the nearby traditional timber-frame house remained not damaged

A) Weak joints:

The mostly damaged part in timber-frame houses was the joints that connect elements such as beam, post and purline. The joints used tenon and mortise. The load bearing capacity of the wood post was reduced if the mortise was large or multi mortises concentrated on the same section, this will weak the post and break it, causing the house collapses partly or totally under during the earthquake. Tenon (usually on the ends of beams and purlins) was pulled out from the mortise (Figure 2) or broken (Figure 3) for the lack of join length or bearing capacity. During earthquake the joints bear complicated loads with compression, tension and torsion. When the building shakes the joints with low bearing capacity will be loosened or damaged, which leads to the damage of the main load bearing elements.

B) Lack of longitudinal ties

The Chuandou wood frame used in the village is composed of three or five main posts with more than three horizontal parallel penetrating tie beams called Chuanfang. These beams offer enough stiffness on the transverse direction. However, most houses lack of the longitudinal ties. Longitudinal Chuanfang was omitted or not continued over the length of the house in some cases. Without enough supports the wood frames were not stable and the seismic load could not be transferred effectively in the longitudinal direction. Figure 4 and 5 show the inclination of the wood frame and entire house. The inclination degree reached over 15°.



Figure 2 the tenon pulled out (the beam with light color is a reinforced beam added after the earthquake)



Figure 3 the tenon was broken (the post with light color is reinforced post added after the earthquake)



Figure 4 the frame inclined



Figure 5 the entire house inclined along longitudinal direction

C) Brick masonry walls damaged

Among the timber-frame houses, the most damaged were the brick walls houses. Most of the brick walls collapsed. The un-reinforced masonry walls lack of ties with the posts. The builders attached them to the posts as envelope and filled into the wood frame part. As brittle material, the brick masonry walls tend to be stiff, weak and heavy. They attract more lateral loads than flexible light elements. Without effective connections the movements of the flexible wood frameworks and rigid wall panels couldn't be consistent. Under the large magnitude earthquake they pounded together and damaged each other (Figures 6, 7). Damage was also found that the post was broken on the top with the impact from infill wall, leading the collapse of the roof.



Figure 6 the brick masonry walls and wood frames in other parts are collapsed



Figure 7 brick masonry walls in the house collapsed

D) Other damage

Other damages including post sliding and tiles dropping were also found in timber-frame houses. Traditionally, the posts are fixed to the stone basement using tenon and mortise and tied together by Jiaofang (penetrating tie beams on the bottoms of posts). The Jiaofang was omitted and in most houses the post was placed on a stone pad or short brick pillar directly. This made the post easily to lose stability during the earthquake. Additionally, tiles were not fixed on the rafts and dropped off during earthquake.

2.2 Brick Masonry Houses

Almost all of the brick masonry houses that built without engineering support in the village have collapsed during the earthquake. The upper storey and the roof had collapsed and destroyed (Figure 8). The villagers and the builders had rare basic knowledge about the safe masonry construction. The brittle un-reinforced masonry walls with only 12 cm thickness could not bear the lateral force. Without ring beam and structural columns to tie the walls together, the long wall collapsed out of panel (Figure 9) and the corner was severely damaged.



Figure 8 the upper storey collapsed



Figure 9 longitudinal wall collapsed out of plane and the gable walls were heavily damaged

3 HOUSE DESIGN

In the new houses` design, the earthquake resistance and safety of structure was not the only main concern, additionally, designers considered availability of suitable materials and skilled labor, environmental adaptation, economy and construction speed, local culture and living patterns, energy efficiency and indoor comfort. Structure design was integrated with sustainable design strategies. Traditional skill was highly concerned and upgraded in the new design.

The traditional rural houses usually represent strongly, affordable resources and natural attitude that response well with the local environmental conditions, possessing simple ecological experiences such as disaster resistance and climate adaptation. Generally the structure of a traditional house suits the local climate. In Daping village the weather is humid all over the year. The timber frame structure gives more freedom to set the openings on walls for ventilation. In addition, the thin wattle and daub walls have well air

permeability. The tiles are put directly on the rafts without heavy and thick earth layer which is used in most rural houses in North China as insulation layer. All these approaches make the house to be lightweight and cause low seismic load, as the observation shows the old traditional houses performed much better than the recently built houses. However, the traditional houses have their own deficiencies which cannot meet the living requirement of villagers, thus, need to update.

3.1 Structure Design

The new house is lightweight structure, with the consideration of using local material also. It is therefore, planned to inherit the traditional timber-frame structure (Figure 10). Using the local natural material and traditional structure methods are important approaches for more climatic adaptation and cultural intergradations (Figure 11). The building`s materials are wood and bamboo, as both are rich in the village. These natural materials are cheap, recyclable and environmentally friendly. Some wood elements applied in various aspects in the design have been recycled and reused from previous houses.



Figure 10 traditional timber frame structure



Figure 11 a new house

Construction with these natural and local materials has an important economic advantage as could be afforded by most common villagers. Traditional housing techniques and principles are applied and upgraded to make the building seismically stable and to meet the local building codes in the new designs. To increase the seismic capacity, critical joints and the plinth are designed and reinforced by small steel accessories and nails. X braces of timber or mild steel are used over the length basing on the specification (JGJ161-2008) to increase the lateral force resistant capacity and stability in the longitudinal direction of the traditional style house. Rubble mixed with concrete individual foundations is also used for the post. Posts are tied together in both directions on the bottoms by Jiaofang. New tiles with better connection to rafts are used instead of traditional tiles. All the local builders are trained by engineers. All the houses, including public buildings have been built by the community through self-help and mutual-help progress, hence cutting the cost. The average house cost is less than 500 RMB per square meter with using self-build and some available building materials from the old houses.

3.2 Architecture Plans

The core house and module idea are used to give more flexible plan to the houses, as it is the essential idea of the rural houses design. Diverse houses plans can be obtained, altered and adjusted easily (Figure 12). According to the tradition plans and culture, the core house in its basic module consists of main living room in the center and two other rooms, one on each side. Functional and auxiliary rooms like kitchen, toilet, store room and other bedrooms can be added around the core house to meet different family numbers needs and new economy condition. The house plan form can be transfer from [−] to [L] to [U] shapes. In [L] and [U] shapes building, the wings are designed to be separate structures in order to avoid torsion in earthquake (Figure 13). For more environment integration, an eco-sanitation toilet built for each house in the courtyard. The surrounding space of the house is also designed according to the local living patterns. As a result, the new houses inherited the traditional style, the features and enhanced the occupants' satisfaction by providing more attractive and convenient places. The local people involved in the design and construction process. All the design proposals are discussed with the villagers. The residents not only interact with designers in the design but also have the right to alter a design, or even to reject other.

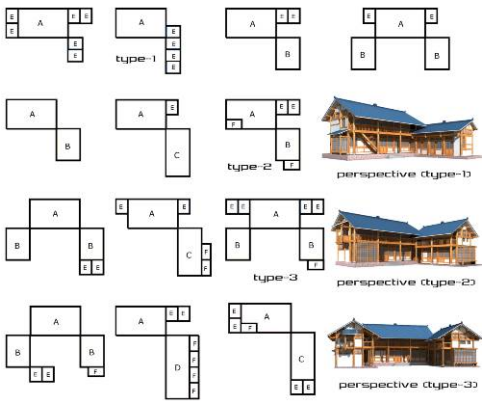

Figure 12 design idea of core house and module (A-D: basic modules with different area, E-F: functional modules)



Figure 13 separate structures on the corner

3.3 Indoor Comfort

Based on the field measurements and questionnaire investigation, the indoor environment of the old traditional houses did not meet the requirement of the villagers. In order to improve the indoor comfort using sustainable methods, the new designs are compatible with the local climate aspects, naturally energy conservation for heating, lighting and ventilation. Numerical analysis techniques are applied in the design process.

Daping village weather characterized as cold winter and cool summer. Stoves are usually used as a heating resource during winter for two months. The field`s measurements on the traditional house show that, the temperatures in indoor and outdoor are almost same in winter without using stoves. The questionnaire investigation gave a result that more than 90% of the villagers feel cold during daytime and night without stove in winter while cool in summer without air conditioning. The envelope of the traditional house is poorly insulated although its lightweight type is good for earthquake resistance. Improving the thermal environment in winter is a keystone in the new design.

New wall technique applied in the new houses design. It is easy to construct using bamboo board or wood lath and work well to improve the indoor comfort in winter. The house envelope is improved with insulation of polystyrene foam or straw earth interlining between the double wall boards, whilst respecting the necessary acoustical separation requirement. Both of the outside and inside wall boards are made of bamboo or wood panels, applying great landscape adaptation (Figures 14, 15). The combined wall can also increase the strength of the house to resist lateral forces. With adding cheap and light insulation material inside walls and roofs the indoor temperature can rise much higher comparing to the traditional house. The indoor average temperature in bedroom is 12.5℃ when the house is kept closed in January, the coldest month, without extra heating. Without using any active heating such as stove, 60% of the villagers feel acceptable and not cold in winter basing on the questionnaire investigation as about 44 families lives in new houses after the finishing of the first phase of the project.

The designs also include passive solar spaces regarding to the original house style. South-face sunrooms can be built as part of new houses or can be added to existing ones to maximize the amount of solar heat and light. Because, the sunroom will increase the cost, the building time will rely on the owners' economic condition.



Figure 14 wall made of wood lath



Figure 15 wall made of bamboo board

By using a combination of vents, operable windows and reducing the depth and width of the rooms, both natural ventilation and lighting in the new house were improved compared to the traditional house. The AIRPAK model analysis result showed in summer with windows opening the indoor wind speed of the rooms is between 0.125~0.625m/s and the mean age of air is less than 230s, when the outdoor wind speed is 1.30m/s. The basic ventilation can meet the indoor air quality requirements.

ECOTECT program is applied in the design to evaluate the daylight and visual comfort. The results under overcast sky conditions show the daylight factors of the living room and bedrooms in original traditional house are less than 1% and more than 6% in the new house, the average daylight factors and illumination of the traditional house are about 21% and 915 lux respectively, 40% and 1620 lux of the new house. The questionnaire survey of the feedback shows 90% and 73% villagers are satisfied with the natural lighting and ventilation respectively.

4 CONCLUSIONS AND DISCUSSION

The reconstruction project is based on the ecological and sustainable habitat ideas. The design is integrated with the climatic aspects and natural landscape. The building materials are wood and bamboo which are rich in the village, cheap and environmentally friendly. Traditional housing techniques and principles are applied and upgraded to make

the building seismically stable and meet local building codes in new design. The new houses inherit the traditional style and features, while the living quality is much improved, including aspects such as earthquake resistance, daylighting, natural ventilation, indoor thermal environment. The space surrounds the house is also designed according to the local living pattern.

With the influence of rapid urbanization process and higher living standard of people's pursue, in rural area in Western China, more and more traditional forms of construction for houses are being replaced with new buildings that incorporate` bricks and concrete. But both the earthquake resistance capacity and energy efficiency have not improved or even become worse. From the earthquake damage in the village we could see the old traditional construction did survive in the large earthquake, while most recently built masonry houses collapsed for lack of any technique support when they built. Compared with the local building material used in traditional rural houses, the burned brick and concrete consume much more energy when constructed, energy consumption increasing with the poor quality. Most area of Western China is seismic active area. Both the earthquake resistance and the environmental issue have become the focuses for rural houses construction. Sustainable concepts should be applied for the rural house design. The sustainable design is an integrated design process which requires close cooperation of the architects and engineers of each specialty in the whole process. With the consideration about local culture and generally low economy level, the rural houses need to be affordable. It is believed that traditional wisdom and lore in buildings may still offer wisely managed, economically effective and culturally appropriate solutions to the world's housing needs (Oliver, 1997). The ecological experiences both on disaster resistance and climate adaptation should be inherit and develop. The traditional construction where this has proven to be unsatisfactory need to make changes and improvements in order to increase the living quality of rural houses.

WenChuan earthquake should be viewed as a wake-up call: the seismic rural area where most of buildings are non-engineered is the place that needs the architectural and engineering supports most. It is necessary to make a local construction tutorial for the rural houses to guarantee the building safety considering local culture heritage. Training their own craftsmen with the tutorial for villagers is a feasible way to guide a sustainable construction of rural houses.

References:

Oliver P. (1997), "Encyclopedia of Vernacular Architecture of the World," Volume1, Cambridge University Press, Cambridge, 134

Ministry of Housing and Urban-Rural Development of the People's Republic of China(2008), JGJ161-2008 Seismic technical specification for buildings construction in town and village(in Chinese), China Architecture & Building Press, 25

JOINT CONFERENCE PROCEEDINGS
7th International Conference on Urban Earthquake Engineering (7CUEE) &
5th International Conference on Earthquake Engineering (5ICEE)
March 3-5, 2010, Tokyo Institute of Technology, Tokyo, Japan

Glubam buildings for earthquake relief in Sichuan

B. Shan[1,3] ;Y. Xiao[1,2]; L.Y. She[3]; Q. Zhou[1]; G. Chen[1]; and R.Z. Yang[1]

1) Institute of Modern Bamboo, Timber and Composite Structures (IBTCS), Hunan University, Changsha, Hunan, 410082 China
2) Department of Civil Engineering, University of Southern California, Los Angeles, CA, USA
3) Advanced Bamboo and Timber Technologies, Ltd., Changsha, China
xiaorock@yahoo.com

Abstract: Immediately after the May 12, 2008 Great Wenchuan earthquake, the authors developed a new disaster relieve temporary housing system using bamboo materials. The system built on the author's previous studies on laminated bamboo structures is an eco-friendly building system that can be made using local materials available to the Sichuan area. More than 2000 m2 classrooms and offices were constructed. The authors adopted a modular design concept to keep the fabrication cost-effective and deployment easy. The structural design was based on a procedure modified from the design guidelines for lightweight wood frame structures and was validated by testing. In room air inspection reveals that the air quality satisfies the current building standard. Full scale fire tests were conducted on both the modern bamboo shelter and the conventional light gauged steel prefab shelter. Contrasting with the poor fire performance of the conventional prefab building, the eco-friendly bamboo shelter model behaved satisfactorily.

1. INTRODUCTION

The May 12, 2008 Great Wenchuan earthquake caused significant casualties, devastated a wide area, leaving millions of people homeless. As one of the quick relief measures, the Chinese government immediately issued a guideline （Ministry of Construction of China, 2008） for construction shelters for housing people in the devastated area. According to unofficial record, a total of about seven hundred thousands shelters with a unit area of about 20m^2 were put in place within approximately three months by manufacturers throughout of China. However, most of the shelters are prefabricated light-gauge steel and styrofoam panel houses, which are not necessarily eco-friendly nor offer great comfortness.

In order to fully take the advantage of the tremendous resource of bamboo forests in the southern China, including the Sichuan Province, the Institute of Bamboo, Timber and Composite Structures (IBTCS) at the Hunan University and the Advanced Bamboo and Timber Technologies, Ltd, developed a new type of disaster relief mobile building system, based on the technology of GluBam® invented by the first author (Xiao, Y, and She, L.Y., 2007). The eco-friendly shelters were quickly deployed to some of the devastated areas in Sichuan.

This paper describes the design of the bamboo shelter and related research studies.

2. BASIC DESIGN CONSIDERATIONS

Figure 1(a) shows the basic plan of the glubam shelter unit, and Fig.1 (b) exhibits the first model unit constructed about one week after the Great Wenchuan earthquake. The shelters adopted a modular design thus the plan can be adjusted according to the needs. The modular units are connected by bolts thus is easy to manufacture and assemble. Roughly, 4~6 worker can assembler the basic unit of 22.3 square meter foot area in about 4 hours. Interior detailing is similar to the wood frame houses in the North America. The basic relief house contains two windows, fans, locations for LPG stove or bath unit, etc., satisfying basic needs for the shelter for a family of about four. The basic unit for classrooms has a foot area of 50 m^2, as shown in Fig.2.

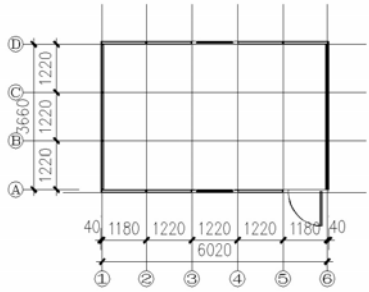

Fig. 1(a) GluBam quake shelter unit



Fig. 1(b) GluBam quake shelter unit

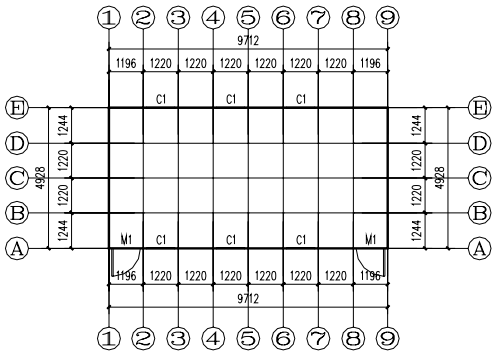

Fig. 2(a) Glubam temporary classroom design

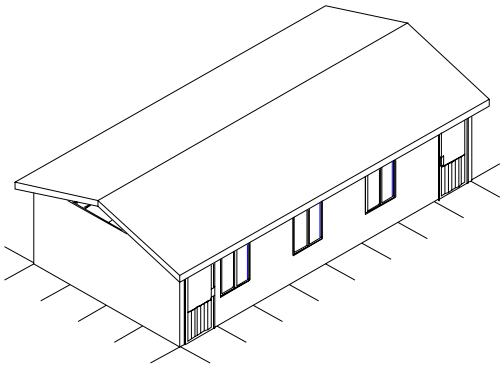

Fig. 2(b) Glubam temporary classroom design

Comparing with tents or light-gauged steel prefab shelters, the prefab glubam quake relief house has the advantages of improved heat and sound insulation, better fire proof, etc., and most importantly cost-effective. To date, more than 2000 square meters of prefab glubam shelters and temporary classrooms were deployed to five schools in Sichuan Province, and were highly appreciated by the people devastated by the disaster. Figure 3 shows the classrooms built on the campus of an elementary school in Sichuan.

3. GLUBAM MATERIALS

The main load carrying components of the bamboo shelters are made with laminated bamboo elements, trademarked as GluBam (Xiao, Y, 2007), and plybamboo sheets with a planner dimension of 2,440 mm long and 1,220 mm wide, using a processing method invented by the authors.

Table 1 Basic material properties of laminated bamboo

In-plane compressive strength	In-plane tensile strength	Bending strength	Elastic modulus
54 MPa	20 MPa	75MPa	9.4GPa

The process involves finger-jointing the sheets; surface preparations, applying two-part epoxy adhesive and pressure hardening. The properties shown in Table 1 were obtained by conducting significant amount of material tests following conventional testing methods for timber materials. The tests were conducted according to the Chinese standards.



Fig. 3 Glubam classrooms at Beijie Elementary School, Sichuan

4. LATERAL FORCE DESIGN and TESTING

The wall panels serve as the lateral force resisting system of the prefab glubam building. Each panel element has a dimension of 1.22m by 2.44m and is made by 12mm thick plybamboo strengthened by horizontal and vertical glubam grid elements of 30mm thick and 50mm to 100mm wide. Hold-down ties can be provided at the outmost edges of several panels as shown in Fig.4 (a) or at the toes of each panel element as shown in Fig.4 (b).

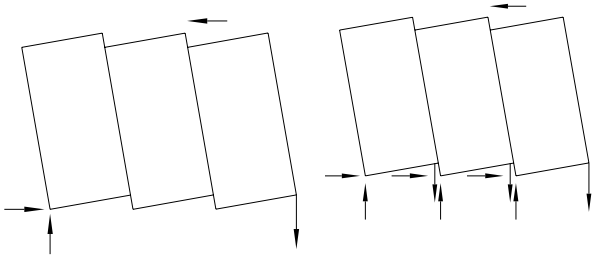

(a) (b)

Fig. 4. Lateral Force Resisting Mechanism

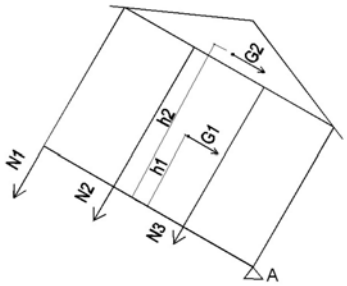

Fig. 5 Model for calculation of tie down force

The total seismic design force considered in this study was the gravity force of the building, thus the tie-down forces need to be calculated based on the model shown in Fig.5. The safety of the building was validated through a full scale model test, shown in Fig.6. As shown in Fig.6, the model was built on steel frame, which was lifted from one

side and gradually tilt the building until it became a horizontal cantilever. The tests were conducted for both the longitudinal and transverse directions of the model building.



Fig. 6 Simple full-scale lateral loading test

5. FIRE PROOF TESTING

The design specifications of the temporary shelters issued by the Ministry of Construction of China require a 30 minute fire endurance, though there is no specific regulations for testing. The authors constructed two full-scale model shelters, one made of glubam the other made of conventional prefab light gauge steel and Styrofoam panels. The models were tested them with in-room fire, burnt from 100 kg firewood, which was determined to be able to generate 2000 MJ heat, representing fire that can be generated by possible furniture.



Fig.7 .Thirty minute in-room fire damage to conventional prefab shelter model



Fig.8. Condition of Glubam shelter after 30 minute of in-room fire

The conventional light gauge steel panel building showed very poor fire resistance. After approximately 5 min. of fire burn, the ceilings fell down, revealing potential problems of prohibiting escape of occupants. After about 10 min. of fire, all the panels were severely deformed and releasing poisonous gasses from the styrofoam infill. Figure 7 shows the final condition after distinguishing the fire at 30 min. On the other hand, the glubam panel shelter model demonstrated satisfactory fire resistance. Despite of the damage of the plastic windows and door panel, the structure was intact until the termination of the fire at 30 min. After the distinguishing the fire, it was found that the gypsum board ceiling was slightly damaged directly above the firewood. Figure 8 shows the final condition of the glubam panel shelter.

6. OTHER TESTS

Tests were also conducted on various structural components, such as roof trusses in order to determine and validate the design values. In room air quality tests were conducted based on Chinese standards by certified inspecting agency, and the results validated that the glubam disaster shelter has adequate quality of in-room air quality.

7. CONCLUSIONS

A new type of prefabricated building system using laminated bamboo (GluBam®) was successfully developed based on experimental testing. More than 2000 square meters of bamboo shelters were constructed for temporary classrooms, offices and shelters in Sichuan, which was devastated by the May 12, 2008 Great Wenchuan earthquake.

Acknowledgements:

The research described in this paper was sponsored by the Institute of Bamboo, Timber and Composite Structures (IBTCS) of the Hunan University, funded by the Program for Changjiang Scholars and Innovative Research Team Project by the Ministry of Education of China (Project No. IRT0619), and Bluemoon Fund, a US non-profit organization.

References:

Ministry of Construction of China, Technical Guidelines for Construction of Earthquake Relief Temporary Shelters, May 21, 2008.

Xiao, Y.; Shan, B.; Chen, G.; Zhou, Q.; and She, L.Y. (2007), Development of A New Type of Glulam – GluBam, Proceedings of the International Conference on Modern Bamboo Structures. ICBS-2007. Changsha. China. Oct. 28-30.

She, L.Y.; Shan, B.; and Xiao, Y. (2007). Development of prefabricated bamboo mobile house. Proceedings of the International Conference on Modern Bamboo Structures. ICBS-2007. Changsha. China. Oct. 28-30.

JOINT CONFERENCE PROCEEDINGS
7th International Conference on Urban Earthquake Engineering (7CUEE) &
5th International Conference on Earthquake Engineering (5ICEE)
March 3-5, 2010, Tokyo Institute of Technology, Tokyo, Japan

BEHAVIOR OF CONCRETE HORIZONTAL-HOLE HOLLOW BLOCK MASONRY

Wu Fangbo[1], Chen Wei[1] ,Huang Hailin[1],and Zhou Xuhong [2]

1) Professor, School of Civil Engineering, Hunan University, Changsha, China
2) Professor, School of Civil Engineering and Mechanics, Lanzhou University, Lanzhou, China
wfbprof@163.com; chenwei85chen@163.com; hhlvsgenius@163.com; zhouxuhong@126.com

Abstract: There are many problems existing in the engineering application of concrete vertical-hole hollow block masonry, for instance poor thermal insulation, seepage and crack. To solve these problems, a new type concrete horizontal -hole hollow block masonry is developed. 9 groups with 54 compressive specimens of the new type masonry were tested and the deformation characteristic and failure mechanism of new type block masonry were obtained. Based on the experimental results a new compressive strength formula were proposed and the calculate results agree well with experimental results may provide some references in the construction design and engineering application. The constitutive relationship formula and elasticity modulus new block masonry have been proposed by using a logarithmic function model which lays an experimental basis for revising and improving the relevant specifications and codes for the concrete block.

1. INTRODUCTION

It cannot be denied that concrete hollow block which have many advantages such as saving energy, water and land resources can be widely used wall materials substitute for clay brick [1]. The world of common concrete hollow blocks is vertical-hole forms, such as a single row hole, double holes and multi-row holes. There are many problem existing in the engineering application of concrete Vertical-hole hollow block masonry, for instance poor thermal insulation, seepage and crack. To solve these problems, a new type concrete horizontal-hole hollow block masonry was developed (see Fig1). The new type blocks have many advantages, such as energy-saving, land conservation, environmental protection, light-weight, heat insulation, anti-cracking, seepage control and dry-laid.

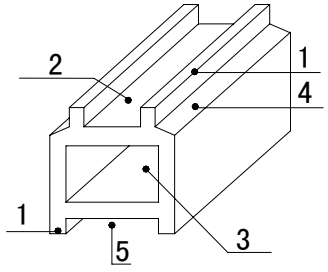

1- convex ribs; 2- groove 1;3- Horizontal-Hole;
4-gap; 5-groove 2

Figure 1 concrete horizontal -hole hollow block

In the bricklaying of the new type block, The convex ribs complete scissor bite and auto-straighten between upper and lower block, the tilted gap block the way which the water through the joint with mortar, prevent water infiltration to the wall. The horizontal hole can be inserted insulation materials to achieve the requirements of thermal insulation. The structure types of concrete horizontal -hole hollow block are different from the concrete vertical-hole hollow block. Do research on compression performance of the new type block becomes the principle problem to engineering application.

2. EXPERIMENTAL PROGRAM

2.1 Model design

The test specimens were of dimensions 290mm × 240mm × 635mm constructed with new type block of size 290mm × 240mm × 200mm and 140mm × 240mm × 200mm,see Fig1.the hole rate of the new block was 40～55%. There are nine groups testing specimens constructed with blocks of four different strengths and three of mortar and a group have nine specimens[2,3]. The compressive strength of block and mortar , see table 1. All test specimens were constructed by the same mason, thus maintaining uniform workmanship. The test specimens were cured under damp conditions for 28 days.

The block masonry were carried at the Key Laboratory of Civil Engineering of Ministry of Education, Hunan University and using an testing machine of 5,000-kN capacity. The concentrated load cell was spread over a width 300mm and 30-mm-thick steel plate fixed at the top of specimen. The test carried out step loading and the axial and lateral displacements in the specimen were measured in 2 locations over a gauge length of 250mm using two dial

gauge.

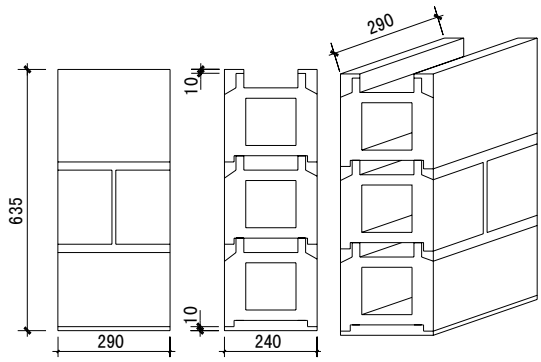

Figure 2 the size of the test specimen

Table 1 the compressive strength of block and mortar(Mpa)

	block	mortar		block	mortar
A-1	5.5	4.6	C-3	11.3	8.7
B-1	7.7	4.6	D-1	15.7	4.6
B-2	7.7	6.5	D-2	15.7	6.5
C-1	11.3	4.6	D-3	15.7	8.7
C-2	11.3	6.5			

2.2 Destruction process

The first was the stage in which the block masonry from under pressure to cracks. The specimen was in flexible working stages and the stress-strain relationship was linear, it is similar to the ordinary block masonry. The small cracks first appeared in the horizontal mortar joint of the intermediate block. For stronger mortars the cracks appeared more localized, whereas for weaker mortars the cracks in the new type block appeared dispersed. At this time the crack load is ultimate load of 60%～70%, the cracks is not developed if unload to the specimen.

The second stage, the first cracks continues to develop and when the load increased 85%～90%of the ultimate load , the cracks run through the vertical mortar joints or the height of a single block, then the vertical cracks develop gradually through the height of all new type block masonry. And the new cracks were constantly appeared and develop due to increasing load, for example appeared in the juncture of roof , floor and sidewall of a single block. The cracks would develop continued even though the specimen is unload. The concrete of the block surface exist the shedding phenomenon.

The third stage, the cracks continuous extension and widening due to the increasing load as far as the ultimate load and the specimens destroy completely. The failure form is similar to the ordinary block masonry throughout the test. The new type block specimens has its special characteristics in failure form, for example, the cracks more localized and concentrated ,it is very easy to form a main crack in the vertical mortar joints or the juncture of roof , floor and sidewall due to stress concentration, once the main cracks appeared the specimens would destroy quickly. The tests carried out clearly indicate the destructive process is more lower brittleness than the brick masonry.

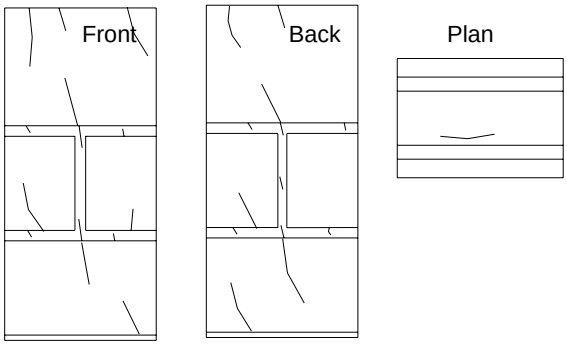

Fig 3 the crack status of the test masonry

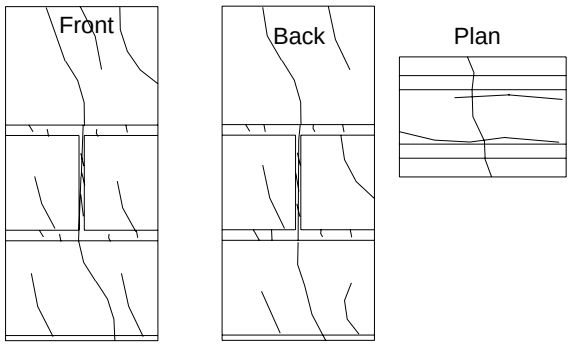

Fig 4 the failure mode of the test masonry

3. TEST RESULTS AND ANALYSIS

3.1 Compressive strength analysis

The formula to calculate the compressive strength of the masonry was generally obtained form statistical analysis lays on experimental basis, which recommended at home and abroad and have two variables, one is block strength, another is mortar strength. The formula to calculate the compressive strength at Chinese code (GB50003-2001) given by:

$$f_m = k_1 f_1^{\alpha}(1+0.07 f_2)k_2 \qquad (1)$$

Where f_m is the average of the compressive strength of the masonry, f_1 is the average of the compressive strength of the block, f_2 is the average of the compressive strength of the mortar, k_1 are the parameters of the masonry construction type, α are the parameters of the type of block, k_2 is the parameters of the mortar.

The compression method of the new type block masonry is different from the concrete vertical-hole hollow block masonry, because there are have a partially direct contact between the up and down neighbor block, the vertical pressure transfer to the down neighbor block by the mortar and the block itself before the masonry crack, once the small cracks first appeared in the mortar joint, the pressure transmission pathway become only the block itself, it would lead to accelerating the progress of the fracture of the transverse joint plate, the sidewall of block would cause the out plane moment due to the fracture of the transverse joint plate, The results are the sidewall serve as a main

bearing structure can not bring all strength into full play. Test results indicate (see table 2): the formula in Chinese Code not fit with the calculation of new type block masonry.

Table 2 the experimental results compared with the calculated test in the code

specimens	experimental results	code results	experimental / code
A-1	2.48	2.81	0.88
B-1	3.12	3.81	0.82
B-2	3.44	4.3	0.80
C-1	3.6	4.93	0.73
C-2	4.22	5.57	0.76
C-3	4.53	6.21	0.73
D-1	4.05	7.25	0.56
D-2	4.78	7.9	0.61
D-3	5.95	8.82	0.67
average variation coefficient			0.72 0.08

The result computational by the Eq.(1) about the compressive strength of new type block masonry is probably unsafe, the higher strength of the new type block the greater deviation of the result, the greater difference strength between the block and the mortar the result too. The reason is Eq.(1) is only fit with the concrete vertical-hole hollow block masonry, it is have go to suggested a formula to calculate the compressive strength of the new concrete horizontal-hole hollow block masonry. The empirical formula obtained form the regression analysis of the value of that is made by using the experiment data (see Eq.(2)) certificates that the empirical formula of fm are more right (see table.3), which lays an experimental basis for revising and improving the relevant specifications and codes for the new concrete horizontal-hole hollow block masonry.

$$f_m = 0.2 f_1 + 0.3 f_2 \qquad (2)$$

Where fm is the average of the compressive strength of the masonry, f_1 is the average of the compressive strength of the block, f_2 is the average of the compressive strength of the mortar.

Table 3 the experimental results compared with the calculated results by Eq2

specimens	experimental results	Code results	experimental / code
A-1	2.48	2.48	1.00
B-1	3.12	2.92	1.07
B-2	3.44	3.49	0.99
C-1	3.6	3.64	0.99
C-2	4.22	4.21	1.00
C-3	4.53	4.87	0.93
D-1	4.05	4.52	0.90
D-2	4.78	5.09	0.94
D-3	5.95	5.75	1.03
average variation coefficient			0.98 0.05

3.2 The constitutive relations analysis

There have be a great deal of research do about constitutive relations of masonry from different angles, many expressions under influences of different factors is suggested by the domestic and foreign scholars. The type of expressions may be summarized linear, logarithmic function, exponential function, polynomial function, rational fractional function. The logarithmic expressions(see Eq.3) is relatively simple[4], using the experimental data were treated as stress-strain curve according to logarithmic formula,then get the coefficient of concrete horizontal-hole hollow block masonry constitutive relationship formula (see table.4) and the typical stress-strain curve,see Fig 5.

$$\varepsilon = -\frac{n}{\xi} ln\left(1 - \frac{\sigma}{n f_k}\right) \qquad (3)$$

Where f_k is the compressive strength of the masonry, σ is the stress of the masonry, ξ and n are the influence-factors of the type of masonry.

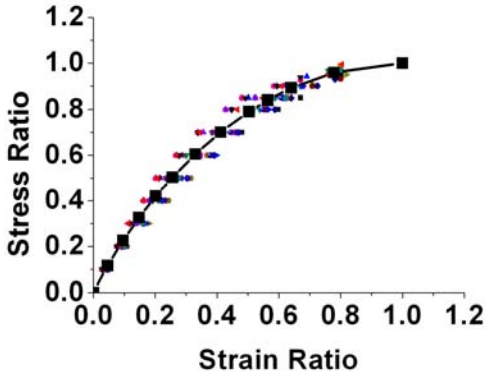

Fig 5 the typical stress-strain curve

Table4 the Values of coefficient used in constitutive relationship formula

specimens	ξ	n	specimens	ξ	n
A-1	2101	0.87	C-3	2119	0.84
B-1	2340	0.88	D-1	2310	0.81
B-2	2089	0.79	D-2	2110	0.78
C-1	1930	0.82	D-3	2040	0.85
C-2	2033	0.84			

The values of coefficient altered little when the new type block and mortar of methanol increased. In conclusion, ξ content of 2108 and n content of 0.83. In that case the constitutive relationship formula of new type concrete horizontal-hole hollow block masonry is obtained and the formula has clear physical concepts and convenience for application.

$$\varepsilon = -\frac{0.83}{2108} ln\left(1 - \frac{\sigma}{0.83 f_k}\right) \qquad (4)$$

3.3 The elasticity modulus analysis

The elasticity modulus, usually adopted as the measure

of stiffness[5,6], represent either a secant or tangent modulus. The elasticity modulus proposal in the Chinese cord been calculated as the secant from the stress-strain relationship up on 0.43 of the average of masonry compressive strength fm and suggests adopting the following formula for the tangent modulus of E. then puts the actual values of n and ξ into Eq.5 and Eq.6 were obtained which convenience for application.

$$E = tg\alpha_1 = \frac{\sigma_{0.43}}{\varepsilon_{0.43}} = \frac{0.43 f_m}{-\frac{n}{\xi} ln\left(1 - \frac{0.43}{n}\right)} \quad (5)$$

$$E = 1500 f_m \quad (6)$$

4. CONCLUSIONS

Based on the theoretical and experimental study, we have come to the main conclusions as follows:

· The deformation characteristics of concrete horizontal-hole hollow block masonry under axial compression is similar to the ordinary block masonry, there were still three stages in the entire proceeding, more lower brittleness and less crack appeared in the masonry in the test.

· The comparison between test and calculation of code shows that the calculation formula is not applicable to calculate the new type masonry and there have been a great error and probably unsafe in the result. The calculate results agree well with experimental results which used a new formula proposed in this paper and may provide some references in the construction design and engineering application.

· The constitutive relationship formula and elasticity modulus new block masonry has been proposed by using a logarithmic function model which lays an experimental basis for revising and improving the relevant specifications and codes for the concrete block.

Further studies are needed to determine the mechanical behavior of mortar in the joint and to understand the failure mechanism of masonry under compression. In particular, tests on mortar collected from actual samples in the joints and triaxial testing of mortar are needed.

References:

[1] Shi Chuxian. The thory and design of masonry structure[M]. Beijing: China Architecture and building Press, 2003.

[2] GB-50003-2001 Code for design of masonry structures[s]. Beijing: China Architecture and building Press,2002

[3] GB/T4111-1997. Test methods for the small concrete hollow block[s]. Beijing: Standards Press of China, 2003.

[4] Mohamad G, Louranco P B, Roman H R. Mechanics of hollow concrete block masonry prisms under compression: Review and prospects. Cement and Concrete Composites, 2007. 29(3): 181-192.

[5] Hamid A, Chukwunenye A O. Compression Behavior of Concrete Masonry Prisms. Journal of Structural Engineering. 1986. 112(3): p. 605-613.

[6] Koksal H O, Karakoc C, Yildirim H, Compression Behavior and Failure Mechanisms of Concrete Masonry Prisms. Journal of Materials in Civil Engineering. 2005. 17(1): 107-115.

JOINT CONFERENCE PROCEEDINGS
7th International Conference on Urban Earthquake Engineering (7CUEE) &
5th International Conference on Earthquake Engineering (5ICEE)
March 3-5, 2010, Tokyo Institute of Technology, Tokyo, Japan

Seismic design and construction of light-frame glubam houses

G. Chen[1)] , Y. Xiao[1,2)], B.Shan[1,3)], R.Z. Yang[1)], and L.Y.She[3)]

1) IBTCS, College of Civil Eng., Hunan Univ., Changsha, Hunan, 410082 China

2) Department of Civil Engineering, Univ. of S. California, Los Angeles, CA90089, USA

3) Advanced Bamboo and Timber Technologies, Ltd., Changsha, Hunan, China

xiaorock@yahoo.com,chenguo2009@126.com

Abstract: The research group led by Prof. Xiao at the Hunan University and the University of Southern California are working on developing various new types of structural elements using bamboo materials and have developed laminated bamboo elements, named as GluBam. Several mile-stone demonstration houses with 100 m^2 to 260 m^2 were completed. The design attempts are to construct these modern bamboo houses essentially following the design requirements similar to light-frame wood houses widely used in North America. Unlike conventional steel or concrete structures, bamboo buildings lack proper understanding of their structural response, particularly under the effect of severe loading conditions, such as large seismic excitations or hurricanes. This paper presents the details of the design and some special considerations for construction.

1. INTRODUCTION

Light-frame wood structures have historically performed well with regard to life-safety under natural hazard loadings such as earthquakes. Properly built wood frame structures can withstand major earthquakes and hurricanes without collapse. Many modern timber buildings have even survived showing no visible signs of damage. The advantage of wooden buildings is based on low self-weight, ductile joints and in general very regular building geometry. Being lack of forest resources in China, we must seek an alternative resource. Bamboo has several advantages as a green material that can positively influence our lives. Some of these advantages include its high strength to weight ratio which is comparable to that of steel and wood. The short maturation duration of bamboo allows for renewable architecture to turn over more rapidly（Eiichi Obataya. 2007）.

2. Construction of Modern Bamboo Buildings

The authors at the Institute of Modern Bamboo, Timber and Composite Structures (IBTCS) of the Hunan University directed by Prof. Xiao（2007）have developed several new technologies using bamboo in modern construction. This paper reports the mile-stone project of building a modern bamboo residential house in the famous Black Bamboo Park (Zizhu Yuan Park) in Beijing, which integrates all the newly invented bamboo technologies and products.

All of the structural members were prefabricated in Changsha, Hunan province, more than one-thousand kilometer away, and then transported to Beijing（Fig.1）. Figure 2-6 illustrate the construction process of bamboo building. The wall framing are consisted of laminated bamboo studs, top plates, bottom plates and headers. Studs in exterior walls of this two-story building had a cross section of about 40 mm by 84 mm, roughly equal to the size of 2×4 lumber used in the North American . The stud spacing was 406 mm in exterior walls of the first floor, whereas 610 ㎜ in the second floor. The walls are filled with heat-insulation wools. The bottom plates and top plates of wall framing usually act as a fire-stopping. The walls were sheathed with bamboo panels that were attached vertically to the wall frame. The panels were connected to the wall frame studs and top and bottom plates using nails spaced 150 mm on center along the panel edges and 300 mm along the intermediate studs. The exterior cladding included waterproof underlayment, wire mesh and stucco mortar cladding surface. The gypsum boards were attached to framing with screws spaced 305 mm on center along the panel edges and intermediate studs to form the interior sheathing of walls. The roof trusses were erected and installed on the load-bearing walls of the second story. Wood blocks were used to maintain the spacing of 610 mm between the trusses.



Fig.1 Transportation of prefabricated members



Fig.2 Floor system



Fig.3 Installation of walls



Fig.4 Heat-insulation wools in walls



Fig.5 Roof system



Fig.6 Completion of bamboo building at Zizhu-Yuan Park

3. Characteristic of Bamboo Structure

A typical structure of light-frame construction resists lateral loads through the use of horizontal floor or roof diaphragms and vertical shear walls (Faherty and Williamson 1998). The walls standing perpendicular to the lateral load collect the force and transfer it to the horizontal diaphragm. The horizontal diaphragm distributes the force to the shear walls standing in the plane of the lateral load. The shear wall then transfers the load to the foundation. A schematic diagram of the functioning of structural panels against lateral loads is shown in Figure 7.

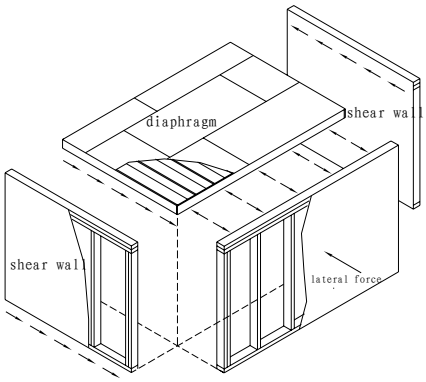

Fig.7 Transfer of lateral loads through diaphragm to shear walls

The shear wall, designed as a deep, cantilever beam, provides the support for the diaphragm. Therefore, the load the shear wall must be designed to resist is that of shear in the diaphragm at its support. In order to explain how a shear wall resists force, an explanation of its components and the forces developed with in these components will be given. The frame of a wall designed to support gravity loads can be transformed into a shear wall with the addition of two elements. These elements are sheathing panels, either oriented strand board or plywood, attached to one face of the wall and a double end stud at each end of the wall. The components of a shear wall are presented in Figure 8.

A diaphragm is a flat structural unit acting like a deep, thin beam. The term “diaphragm” is usually applied to roofs and floors. In a horizontal diaphragm, the sheathing corresponds to the web, and the chords are assumed to be the flanges. The chords are designed to carry axial forces created by the moment. These forces are obtained by resolving the

internal moment into a couple (tension and compression forces). See Fig. 9. The shear is assumed to be carried entirely by the sheathing material (Ronald E.Breyer 1998).

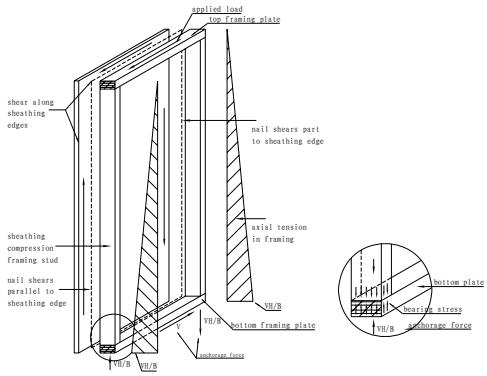

Fig.8 Forces acting on a shear wall segment

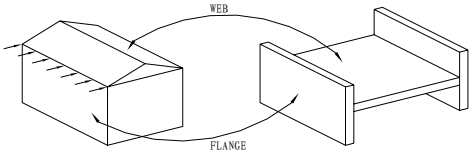

Fig.9 Deep beam analogy

The Code now has a criterion for determining when a diaphragm is flexible or rigid. This criterion involves a comparison of the diaphragm deflection Δ_D, with the shearwall story drift Δ_S. If the diaphragm deflection at mid-span Δ_D is more than twice the average shearwall drift Δ_S at the associated story (the shearwalls in the story below the diaphragm), the diaphragm is considered flexible. Otherwise, the diaphragm is considered rigid. The identification of a diaphragm as rigid or flexible is applicable whether the forces being considered are seismic or wind. In theory the deflections Δ_S and Δ_D can be determined using a fictitious unit load rather than the Code design load, since it is the relative deflections that are of interest. In practice, however, it is recommended that the deflections be calculated using Code strength level design forces for seismic and ASD forces for wind.

3.1 Seismic design of bamboo shear wall

The building is located in seismic zone 2B, and the importance factor I is 1.0. The proposed building site is 10km from a Type B seismic source. Without a geotechnical study, soil type S_D is assumed. Roof dead load D=1.91kN/m^2, floor dead load D=1.24kN/m^2, interior wall dead load D=0.39kN/m^2, exterior wall dead load D=16.29kN/m^2.

Table 1 seismic zone actor *Z*

Zone	0	1	2A	2B	3	4
Z	0	0.075	0.15	0.20	0.30	0.40

The UBC base shear formula for the main lateral force resisting system (LFRS) is

$$V = \frac{C_v I}{RT} W \le \frac{2.5 C_a I}{R} W \qquad (1)$$

where: V=seismic base shear force, W=weight of structure, C_vI/RT=velocity based seismic base shear coefficient, $2.5C_aI/R$=acceleration based seismic base shear coefficient.

The UBC provides the following formula for the fundamental period of vibration:

$$T = C_t \left(h_n\right)^{0.75} = 0.19\,\mathrm{s} \qquad (2)$$

From UBC Table 16-Q and Table 16-R, C_v=0.40, C_a=0.28,

$$T_s = \frac{C_v}{2.5 C_a} = \frac{0.40}{2.5 \times 0.28} = 0.57\,\mathrm{s} \qquad (3)$$

Base shear

$$V = \frac{2.5 C_a I}{R} W = 0.16 W \qquad (4)$$

F_x story（shearwall）Coefficients

$$F_x = \frac{\left(V - F_t\right) h_x w_x}{\sum_{i=1}^{n} w_i h_i} = 0.042 w_x h_x \qquad (5)$$

With all of the F_x story coefficients determined, the individual distributed force for designing the shearwalls can be evaluated (Table 2).

Table 2 F_x story（shear wall）force table

Story	Height h_x	Weight w_x	$w_x h_x$	Story force F_x
R	4.88	170.8	833.5	35.0
2	2.44	135.7	331.1	13.9
1	0			
Sum		306.5kN	1164.6kN.m	V=0.16W=48.9kN

3.2 Seismic design of bamboo diaphragm

The load to the roof diaphragm that is used for design of the shearwalls needs to be based on the F_x story forces from the F_x Seismic Story (Shearwall) Force table. The strength level roof diaphragm reaction can be calculated as follows:

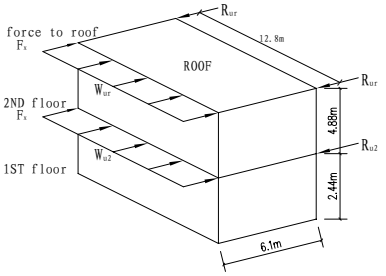

Fig.10 Seismic forces to roof and second-floor diaphragm

Load to roof diaphragm:

w_{ur}=0.042×4.88×13.5=2.77kN/m

Load to second-floor diaphragm:

w_{u2}=0.042×2.44×14.8=1.52kN/m

For both the second floor and the roof diaphragms, the seismic forces are significantly higher than the wind forces. The shearwalls, therefore, can be designed using seismic forces, because it is clear that wind will not govern either shear or overturning（Fig.10）.

4 CONCLUSIONS

A new type of glulam has been developed with bamboo as basic materials. The research showed new ways of employing the bamboo resource in sustainable construction. This innovative building in Black Bamboo Park in Beijing is the first of its kind anywhere in the world, and shows that bamboo is truly a building material for the future, for rich and poor, for the countryside and for the cities, and for all tropical and temperate climates.

Acknowledgements:

The projects described in this paper were conducted by the Institute of Bamboo, Timber and Composite Structures (IBTCS) of the Hunan University, and the Advanced Bamboo and Timber Technologies, Ltd. Supports to various phases of the projects are provided through the Program for Changjiang Scholars and Innovative Research Team Project by the Ministry of Education of China (Project No. IRT0619), Blue Moon Fund, National Natural Science Foundation (Project No. 50848008), Blue Moon Fund and the International Network for Bamboo and Rattans (INBAR). The authors warmly thank all the sponsors and collaborators.

References:

Eiichi Obataya. (2007). "Bending characteristics of bamboo (Phyllostachys pubescens) with respect to its fiber-foam composite structure."Wood Science Technology 41:385–400

Y.Xiao; B. Shan, G. Chen, Q. Zhou, R.Z Yang, L.Y. She. *（2009）* Development of laminated bamboo modern structures. Proceedings of the 11th International Conference on Non-conventional Materials and Technologies (NOCMAT 2009) 6-9 September 2009, Bath, UK.

Y. Xiao; Shan, B.; Chen, G.;Zhou, Q.; and She, L.Y. (2007), Development of A New Type of Glulam. ICBS-2007. 2007.10.

G. Chen; Y. Xiao.; B.Shan and She, L.Y. (2007), Design and construction of a two-story modern bamboo house. ICBS-2007.2007.10.

Ronald E.Breyer（1998）"Design of wood structure ASD.", McGraw-Hill, New York

ICBO（1997）,Uniform Building Code, International Conference of Building Officials, Whittier, CA

Keith Faherty, Thomas Williamson. "Wood Engineering and Construction Handbook", McGraw-Hill, 3 edition, 1998.

JOINT CONFERENCE PROCEEDINGS
7th International Conference on Urban Earthquake Engineering (7CUEE) &
5th International Conference on Earthquake Engineering (5ICEE)
March 3-5, 2010, Tokyo Institute of Technology, Tokyo, Japan

EDUCATIONAL PROGRAMS AT THE PEER CENTER THAT ENCOURAGE MULTIDISCIPLINARY UNDERSTANDING

Heidi Faison[1] and Stephen Mahin[2]

1) Outreach Director, Pacific Earthquake Engineering Research Center, University of California Berkeley, California, USA
2) Director, Pacific Earthquake Engineering Research Center, University of California Berkeley, California, USA
hfaison@berkeley.edu, mahin@berkeley.edu

Abstract: The Pacific Earthquake Engineering Research Center (PEER) is a multidisciplinary, multi-institutional research center that develops, validates and disseminates performance-based seismic design technologies for buildings and infrastructure through its many research projects. An important supplement to the research projects underway at the center is PEER's Outreach and Education Program. Recent PEER Education Projects have been targeted at students of many age levels including primary/elementary and high school level students, university undergraduates, and university graduate students in an attempt to expose them to the field research and demonstrate how many disciplines interact within earthquake engineering. Several of PEER's projects that encourage multidisciplinary understanding are explored including graduate student research workshops, laboratory field trips and lessons for elementary students, and undergraduate student internship programs.

1. INTRODUCTION TO PEER's EOT PROGRAM

The Pacific Earthquake Engineering Research Center (PEER) is a multidisciplinary, multi-institutional research center that develops, validates and disseminates performance-based seismic design technologies for buildings and infrastructure through its many research projects. Investigators from over 20 universities and several consulting companies conduct research in earthquake-related geohazard assessment, geotechnical and structural engineering, transportation, lifelines, and public policy [1]. An important supplement to the research projects underway at the center is PEER's Outreach and Education (EOT) Program.

The mission of the PEER Outreach and Education Program is "to effectively disseminate PEER research findings to PEER's constituent groups and to further promote the field of earthquake engineering (and related research) to future engineers." [2]

The first element of the EOT mission is technology transfer and dissemination of research findings. Many mechanisms are used to achieve this goal and to reach various constituent groups including faculty, practicing professionals, business industry partners, sister organizations, governments agencies, and the public. Some effective means of reaching these groups and achieving the transfer of knowledge are the PEER Report Series, the Annual Meeting, specific project-related workshops or meetings, email announcement campaigns, lectures or seminars, and regular website updates. Another successful integrated approach to technology transfer is direct involvement and collaboration by stakeholders (i.e. practicing professional engineers or funding agency representatives) on specific PEER research projects. This is regularly done during PEER projects, with the best recent example being the Tall Building Initiative project where three consulting firms were critical contributors to the research work [3].

The second element of PEER's EOT mission is encouraging the education of future earthquake engineers and growing student interest in research related to this field. In addition to these goals, the increasing focus of PEER educational programs has been on furthering multidisplinary understating of the concepts of earthquake engineering and attempting to demonstrate to students how various disciplines interact within earthquake engineering. As a multidisciplinary, multi-institutional research center, PEER research projects all have representatives from many fields participating in the research effort and the success of many projects can often be attributed to this collaboration. By showing that PEER values and actively achieves interaction between disciplines, the message of "multidisplinary understating and cooperation" resonates with students. The focus of the remainder of this paper will be on the specific education programs recently supported by the PEER Center to achieve this goal and educational mission.

Recent PEER Education Projects have been targeted at students of many age levels including primary/elementary and high school level students, university undergraduates, and university graduate students. Several of PEER's projects that encourage multidisciplinary understanding are explored including the undergraduate student internship program, graduate student research workshops, and

laboratory field trips and lessons for elementary students.

2. SUMMER INTERNSHIP PROGRAM FOR UNDERGRADUATE STUDENTS

From 1999 until 2008, PEER's successful summer internship program and Research Experience for Undergraduates Summer Internship Program provided summer internships for over 100 students at PEER affiliated research universities including UC Berkeley, UC San Diego, UC Davis, University of Washington and Stanford. These internship opportunities provided students with experience in hands-on, individualized laboratory and field research, and increased opportunities in academia and professional practice. Many of these students were from campuses without significant research focus and/or facilities that otherwise would not have been exposed to experimentation and theoretical research.

In 2009, the program was improved with some significant changes. It was decided that enhanced learning outcomes could be achieved for the participating student interns by a comprehensive internship program where the student summer projects were devised in a way that interconnected their projects with common underlying theme that would allow them to see how different disciplines can contribute to solving a specific problem. For the 2009 Internship Program this thematic focus was "seismic issues related to nonductile concrete buildings." [4]

2.1 Student Project Descriptions

Four undergraduate students were selected from a strong pool of applicants to conduct four separate but related research projects that investigated nonductile concrete buildings from the perspectives of different disciplines using varied tools.

The students were located at various sites to complete their projects on seismic hazard/risk mapping, experimental structural engineering, analytical structural engineering, and public mitigation policy. The projects were "all inclusive" so the students participated in every aspect of the research process from start to finish instead of just contributing a small trivial part of another researcher's project.

The first student project, completed by Matt Zahr, a UC Berkeley student, focused on the definition of seismic hazard as pertaining to nonductile concrete structures. His research supplemented an existing USGS web-based risk and hazard-mapping tool that is identifying seismic risks from many building types including steel, concrete and timber then generating computer based maps that identify the regional risk due to each construction material. Matt's summer work enhanced the tool's ability to differentiate between modern concrete buildings constructed with ductile concrete design and older buildings that are prone to dangerous brittle collapse due to nonductile detailing. He completed this work under the supervision of Nico Luco at United States Geological Survey, Geologic Hazards Team Office in Golden, Colorado.

The second student project, completed by Cal Poly San Luis Obispo student Victor Sanchez, focused on experimental research in structural engineering at the NEES@berkeley Laboratory. His project contributed to the research being done for the NEES Grand Challenge Project: Mitigation of Nonductile Concrete Risk. [5] Victor's research was supervised by Jack Moehle, the Grand Challenge PI involved the design, construction, and testing of a nonductile concrete column-beam joint specimen to investigate the failure mechanism from seismic loading.

The third student project, completed by Bryce Lloyd from San Jose State University, focused on analytical

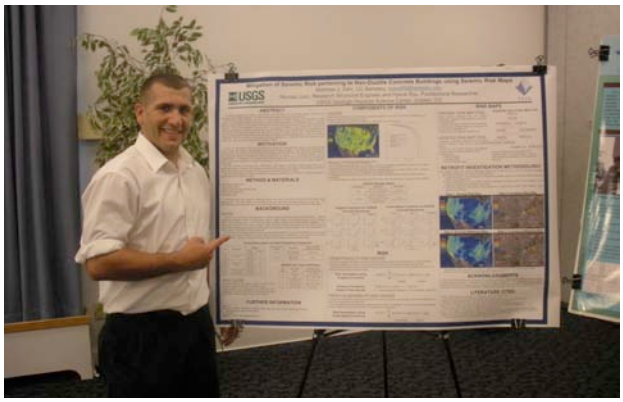

Figure 1 Matt Zahr with his 2009 Undergraduate Summer Intern Project Poster

research in structural engineering. His project involved learning some new structural analysis software to model the nonductile concrete column-beam joint specimen tested by Victor. His analysis helped with the design of the specimen and supplemented the experimental results of that specimen. Jack Moehle and his graduate student Wael Hassan supervised this project.

The fourth student project, completed by Cal Poly San Luis Obispo student Emmett Seymour, combined aspects from building inventory studies and implementation of mitigation public policy. This project was organized by the Concrete Coalition, a network of individuals, governments, institutions, and agencies with shared interest in assessing the risk associated with dangerous non-ductile concrete buildings and developing strategies for fixing them. [6] The Concrete Coalition has a project trying to determine how many nonductile concrete buildings exist in the state of California. Emmett's project helped to refine this effort by working with Professor Peter May at the University of Washington to enhance the accuracy of a regression analysis by verifying and validating data that is used to predict and quantify the number of pre-1980 concrete buildings in California. Additionally Emmett was exposed to the development of policies and ordinances that are being implemented in cities like Los Angeles to mitigate the risk of nonductile concrete structures. Emmett's project was jointly supervised by Craig Comartin, Director of the Concrete Coalition, Marjorie Greene, Special Projects Director at EERI, and Thalia Anagnos, Professor at San Jose State University, who is involved in PEER's inventory

efforts for the NEES Grand Challenge Project: Mitigation of Nonductile Concrete Risk.

2.2 Methods Used

Regular meetings were held between all four students and their advisors using computer-based interactive technologies so that the students were regularly interacting and learning from the experiences of their fellow interns. Video conferencing during these meetings allowed the students and advisors from various locations including Berkeley, San Jose, Oakland and Colorado to all easily and affordably participate in every meeting. As stated by one of the interns, "Since all of our projects were connected in some way, [these meetings] allowed us to help each other and brought us closer as a group. The webex conference calls were great ways to keep each other informed and update everybody on the progress of each project while keeping the goals of the grand challenge project in mind." [7]

During these meetings, the students were required to make PowerPoint presentations describing their projects, discussing their methods, and explaining the successes as well as challenges they were encountering during the research process. From the presentations made by each intern about their project approach and methods during these meetings, all students began to understand vast number of applications, methods and technologies that are used in research.

The student interns were also required to write a paper about their research project. This helped to develop their writing skills while also having them reflect on their project results and how their project fit into the bigger issue of nonductile concrete buildings.

In late August 2009, at the conclusion of the summer, the interns prepared posters about their research projects that they presented at the NEES Young Researcher Symposium in Buffalo, New York. They were awarded three out of seven awards given at the symposium: Victor and Bryce each won best poster presentation for their session and Matt won the overall best presentation award. The interns also presented these posters at the PEER 2009 Annual Meeting in October and attended the NEES Annual Meeting in Hawaii at the beginning at the summer. The students valued participation in these programs. "The conference in Hawaii and the symposium in Buffalo were exceptional experiences for me also. They gave me a chance to meet professionals, professors and students in the field I want to pursue. Also I was able to see the wide range of research that is currently taking place all over the world." [7]

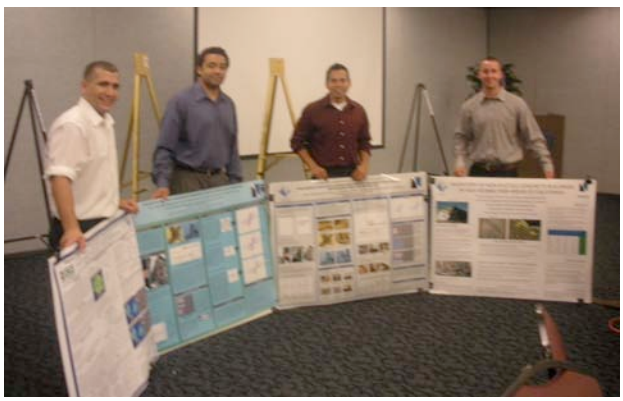

Figure 2 PEER's 2009 Undergraduate Summer Interns present their posters at the NEES Young Researcher Symposium in Buffalo, New York

Finally the interns were encouraged to create and give a presentation about their summer research experience to fellow undergraduate students their home university to ensure exposure of their experience to the largest group of undergraduate students possible.

2.3 Outcomes

The thematic approach to the internship program in 2009 exposed the interns to many seismic issues related to nonductile concrete buildings and learned how research programs using many methodologies and approaches can be designed to address a common problem.

Matt Zahr's experience showed all of the interns that advanced software can be developed to address community-wide problems, how scientific methods can be used to identify risk, and the process used to generate hazard maps, risk maps and fragility curves. According to Matt, "I really liked my project. I enjoyed coming into work everyday with an ultimate goal in mind. Previous internships that I had involved completing tiny, dead-end jobs. In this internship, Nico briefed me on some of the goals for the risk map web tool in the first couple weeks and the rest of the summer was spent working toward that goal. Once I reached those goals, I added additional options to the web tool that were outside the immediate USGS goals." [7]

Victor Sanchez's testing demonstrated the process involved in designing and constructing a test specimen, developing testing protocols, and both collecting and interpreting the resulting test data. Victor also appreciated how he was given a specific experimental test to complete from start to finish. "The fact that my project was a complete project that involved everything from ordering the material to the construction and testing of the specimen, gave me a great opportunity to experience a bit of how real research works." [7]

Bryce Lloyd's project showed the students what can be achieved and learned by computer modeling and simulation, while showing how analytical studies are integral to experimental research.

Through Emmett Seymour's project, the interns learned for the first time about social science and public policy approaches used to solve earthquake engineering issues and how this work can be used to develop mitigation policies that are acceptable to the diverse stakeholder groups including architects, engineers, government representatives, and building owners. Emmett's impression of the summer program: "This by far has been the most rewarding work experience I have had so far. I had never participated in research-based studies so everything was new to me. At Cal Poly, most of the emphasis is on undergraduate studies and

not research. This summer really opened my eyes to the research side of academia and allowed me to be involved in a way I had never been and furthered my interest in earthquake engineering." [7]

At the conclusion of the summer, the students learned as much from the other three student projects as they did from their own. They experienced first-hand how enhanced research results and understanding can be achieved from multidisciplinary involvement.

Based on the post-internship evaluation survey completed by the students, all four are planning to apply to graduate programs showing that this internship program is also achieving PEER's EOT Mission of encouraging the education of future earthquake engineers and growing student interest in research related to this field.

3. K-12 OUTREACH PROGRAM

The PEER K-12 Outreach Program is aimed at fostering enthusiasm in the science of earthquakes and earthquake engineering. Through various programs, PEER has reached out to elementary and high school students to expose them to earthquakes in a hands-on, interactive, and exciting environment. Utilizing many mediums and methods helps to activate their interest in this field of science while developing their curiosity and encouraging creativity. [8]

Having access to shaking tables and earthquake simulators at laboratories at many of our core institutions/universities, makes the PEER K-12 Program a unique asset to teachers who don't have such facilities. This gives students the unique opportunity to design their own structures from simple materials like Lego or K'NEX then have them tested on an earthquake simulator to see how they perform. Interactive programs like these make science tangible and exciting for K-12 students and show them how science and math concepts can be applied to practical problems.

3.1 Program Activity Description & Teaching Methods

The 2008-2009 K-12 outreach program at UC Berkeley successfully involved 13 bay area schools, 22 classrooms and 838 students. The program consisted of three activities for each class of students. UC Berkeley Civil Engineering graduate student, Justin Hollenback, was hired to run these activities. The 2009-2010 program is currently underway and uses the same model with a few minor improvements.

The first activity was a presentation at the classroom of an interested teacher about earthquake science and engineering. The topics included in the presentation were:

- Basic information about earthquakes (including plate tectonics and earthquake fault types)
- Explanation of why earthquakes happen
- Discussion about professions (like engineering, architecture, seismology, geology, and construction) that address the effects of earthquakes on our communities and buildings
- Teaching key building systems and components that help buildings resist earthquake shaking safely
- Learn what to do during an earthquake to be safe

The lecture was tailored to the grade level of the students and utilized many videos, physical demonstration tools and photos to maintain student interest and excitement though out the presentation. Interaction between the lecturer and the students was also encouraged in the form of questions and feedback about felt earthquake experiences of the students. For older students, the advanced high school level math and science courses required to apply to a university to study engineering were highlighted.

Second was a design activity where the students were given model kits to construct their own earthquake-resistant building structures. In groups of 4-6 students, they constructed a building with earthquake resisting features, diagonal or x-braces, that had been discussed in the presentation. In the 2009-2010 program, students also complete a worksheet during the construction of their building model, which provides a framework for the assessment of their design. The following four parts are evaluated for their building model: performance during earthquake shaking (this is determined in the third activity), its cost (determined by the calculating the number of building pieces used to construct the model), its occupiable or rentable space for use by an "owner" (determined by calculating the building's volume), and its finally its architectural creativity. This allows the students to more easily compare their models while also adding a math component to the design project.

The third activity was a field trip the PEER Laboratories at the Richmond Field Station that included tours of the nees@berkeley hybrid simulation laboratory and the Earthquake Simulator Laboratory. These tours allow the many of the students to see a research laboratory for the first time and allows them to ask questions about equipment and machinery while teaching them how it all is used to better understand earthquake behavior of structures. After the laboratory tour the students were given the opportunity to test their building models on an earthquake simulator to see how well they preformed under earthquake shaking.



Figure 3 Fifth Grade students from Allendale Elementary School in Oakland try to predict weak areas in their building designs before it is tested on the shaking table, January 2009

3.2 Outcomes

For both the 2008-2009 and the 2009-2010 forms the students have been asked to fill out evaluation forms after the final activity. From these forms, the following quotes have been extracted and the collection of pictures have been selected to demonstrate that the students are learning from the program, are actively engaged, and are enjoying the activities. [9]

"I want to learn about earthquake engineering."
- Student from Glenview Elementary School

"I learned that if you put braces on your building then it will not fall down."
- Student from Glenview Elementary School

"Always go under a table when an earthquake happens."
- Student from Webster Academy

“We would be happy to come to the lab again!"
- Student from Lincoln Elementary School

"We learned a lot of stuff. We saw things crush and the shaking table in the big one."
- Student from Webster Academy

"I learned that when earthquakes come a building could move like a boat."
- Student from Webster Academy

“It was a cool field trip."
- Student from Webster Academy

"I learned we should work together and work as a team."
- Student from Glenview Elementary School



Figure 4 First Grade students from Glenview Elementary School in Oakland watch as two of their building models are tested on the shaking table, February 2009



Figure 5 Fifth Grade students from Allendale Elementary School in Oakland cheer as their building models dramatically collapse during earthquake shaking, January 2009



Figure 6 Fifth Grade students from Webster Elementary School in Oakland watch nervously as their building models undergo their first round of shaking, May 2009

4. GRADUATE STUDENT EXPERIENCES

Graduate students get their primary support from PEER by being funded to do their doctoral research for a PEER funded project. Each of PEER’s mega projects (NEES Grand Challenge Project on Mitigation of Nonductile Concrete Risk, Tall Building Initiative, Next Generation Attenuation East and West Programs, Lifelines Program, Transportation Systems Research Program) fund many principal investigators to complete projects related to the mega project’s research objectives. Most of these principal investigators then also fund students, from one to several, depending of the quantity of work required. As a result it is common for PEER to be funding the research work of as many as 25 graduate students from over 10 university campuses who are working in a variety of disciplines and specialty focus areas.

With this network of graduate students, PEER endeavors to enhance their everyday research experiences by also creating programs that enhance their interaction with other researchers, students, practicing engineers and faculty while also exposing them to the broader earthquake engineering community.

4.1 Conference Attendance and Poster Sessions

A method frequently utilized to achieve the goal of greater interaction is providing funding for PEER students to attend conferences where they can present their research results while meeting and learning from other researchers. The best example of this effort is at PEER's Annual Meeting. [10]

Every year PEER funded graduate students are sponsored to attend the full meeting as well as present their research during a unique poster session. This poster session consists only of student posters and is always a highlight of the annual meeting. PEER faculty researchers take keen interest in the students' research work and engage them with questions. This provides a unique opportunity for students to interact with faculty from many universities as well as fellow graduate student researchers. The success of this poster presentation and meeting sponsorship is proven by the fact that over twenty-five PEER students [11] and eleven international students [12] displayed their work at the 2009 PEER Annual Meeting during a crowded two-hour poster reception with over 200 attendees.

This poster session not only brings together students from many different university campuses but it also brings together students from many disciplines. This is one of the few opportunities where students with such a diverse range of experience and background can mix on a regular basis. For example, students researching soil-structure interaction get to compare their analysis methods and software with students studying transportation and building components while students investigating network modeling tools can see what is being done by students developing models for ground motion attenuation. By allowing this flow of information between topic areas, new ideas can develop and the students are exposed to other approaches and cutting-edge developments in other fields related to earthquake engineering.



Figure 7 PEER graduate student explains his research to Peggy Hellwig, from the UC Berkeley Seismological Laboratory during the 2009 PEER Annual Meeting



Figure 8 PEER graduate students Sanaz Rezaeian from UC Berkeley and Gabriele Guerrini from the University of California, San Diego get to meet Professor Farzin Zareian from the University of California Irvine at the 2009 PEER Annual Meeting

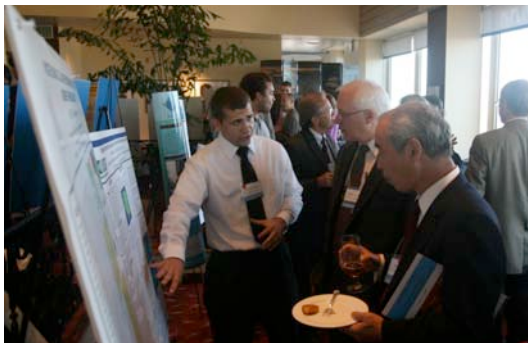

Figure 9 PEER summer intern shares is research project with international professors including Professor Akira Wada at the 2009 PEER Annual Meeting Poster Session

4.2 Young Researcher Symposiums with International Colleagues

Another recent program that is developing at the PEER Center is the sponsorship and participation in Young Researcher Symposiums. The current model is a one-day symposium for a small mixed group of international and local students a day prior to a larger international conference. The single day program consists generally of the following activities: oral presentations by some students, a small poster session by other students, a field trip to a local construction site or research lab or consulting engineering firm, and a social dinner at the end of the day.

There are several advantages of this arrangement. First, students get to meet each other prior to a big conference and start to develop familiarity, and even friendships, with their international colleagues. Second, the students get to orally present their research. Due to growing numbers of papers being submitted to conferences, there are fewer opportunities for students to orally present during the general conference proceedings so they are often put in poster sessions. While these sessions are valuable, the students miss an opportunity to enhance their personal presentation skills. By allowing students to orally present

in a Young Research Symposium, they gain experience preparing and giving oral presentations—critical skills needed as they continue their careers. Third, the advantage of having this program in advance of a larger conference is that it allows organizations to leverage their funding so that students need only to travel once but experience two separate events: the conference and the symposium.

International students attending Young Researcher Symposiums gain language practice, exposure to local construction methods during field trips, and get to interact with local students while learning about research methods in a variety of disciplines and countries. For local students, the Young Researcher Symposium provides an opportunity to learn about the work of other students and disciplines from a diverse set of experience and backgrounds. These experiences nicely supplement the research and coursework required for their degree and broaden both their skill set and their understanding of the vast realm of work done in field of earthquake engineering.

The first Young Researcher Symposium was hosted at the 2009 Center for Urban Earthquake Engineering (CUEE) Annual Meeting in Tokyo [13]. About 20 students participated: eight PEER students and twelve CUEE students and young faculty. During the 2009 PEER Annual Meeting in October, PEER hosted another Young Researcher Symposium with 25 students in attendance from PEER-affiliated universities, CUEE and Tongji University in China. According to one of the Japanese participants, who attended the symposium hosted at the PEER Annual Meeting, "I would like to express my thanks to you and PEER for inviting us to the Young Researcher Session. Six Japanese participants have enjoyed and studied a lot through the Field trip as well as the presentation. I believe that this international experience gave us large energy to create more professional and matured results in field of earthquake engineering." [14]



Figure 10 Students from PEER's Young Researcher Symposium in October 2009 at a fieldtrip to the base-isolated Cathedral of Christ the Light in Oakland, CA lead by Peter Lee and Lindsay Hu from the structural design firm Skidmore Owings and Merrill



Figure 11 Students orally present their research to an audience of their fellow international students at PEER's Young Researcher Symposium in October 2009



Figure 12 Students Ming Cheng from Tongji University in China and Nirmal Jayaram from Stanford get to know one another while looking at viscous dampers during the tour of the Caltrans Headquarter Building in Oakland, CA lead by Will Grogan from the structural design firm Degenkolb Engineers

Word about the success of these Young Researcher Symposiums has spread so several conference organizers are now considering implementing similar programs into their conferences including the 9th US National and 10th Canadian Conference on Earthquake Engineering (9USN/10CCEE) in Toronto, Canada during July 2010. [15]

5. CONCLUSIONS

Encouraging interaction amongst many earthquake engineering disciplines has long been a characteristic of

PEER's research programs. By taking this multidisciplinary approach and building it into the fabric of PEER's education programs for K-12, undergraduate and graduate students, they are experiencing a wider exposure than possible from their typical curriculum and gain enhanced understanding of earthquake engineering.

Acknowledgements:

The PEER Summer Internship Program and K-12 Education Program were made possible with funding from the George E. Brown, Jr. Network for Earthquake Engineering Simulation (NEES) operated and maintained by NEESinc under National Science Foundation cooperative agreement CMS-0402490.

Support and funding for PEER's Young Resarcher Symposium was provided by PEER, Tongji University and CUEE.

References:

[1] PEER website: http://peer.berkeley.edu/
[2] PEER Education web page: http://peer.berkeley.edu/education/research_program.html
[3] PEER's Tall Buildng Initative website: http://peer.berkeley.edu/tbi/index.html
[4] PEER's Summer Undergraduate Internship Program web page: http://peer.berkeley.edu/education/internships.html
[5] PEER's NEES Grand Challenge Project: Mitigation of Nonductile Concrete Risk website: http://peer.berkeley.edu/grandchallenge/index.html
[6] Concrete Coalition website: http://concretecoalition.org/
[7] Quote by student intern from the 2009 PEER Summer Internship Program Evaluation Survey, completed in September 2009
[8] PEER's K-12 Education Program web page: http://peer.berkeley.edu/education/k12_education.html
[9] Quote by K-12 Program student participant from the 2008-2009 Program Evaluation Forms, completed after the student's class completed the field trip in 2009
[10] PEER's 2009 Annual Meeting website: http://peer.berkeley.edu/events/annual_meeting/2009AM/index.html
[11] Listing of PEER Students from Poster Session at the 2009 PEER Annual Meeting: http://peer.berkeley.edu/events/annual_meeting/2009AM/program.html
[12] Listing of PEER Students from Poster Session at the 2009 PEER Annual Meeting: http://peer.berkeley.edu/events/2009/icaese3/program.html
[13] Article about Young Researcher Symposium at 2009 CUEE Annual Meeting: http://peer.berkeley.edu/news/2009/peer_students_japan.html
[14] Email quote from Ken Watanabe, Ph.D., Assistant Professor, Department of Civil Engineering, Graduate School of Tokyo Institute of Technology
[15] 9th US National and 10th Canadian Conference on Earthquake Engineering (9USN/10CCEE) website: http://2010eqconf.org/

JOINT CONFERENCE PROCEEDINGS
7th International Conference on Urban Earthquake Engineering (7CUEE) &
5th International Conference on Earthquake Engineering (5ICEE)
March 3-5, 2010, Tokyo Institute of Technology, Tokyo, Japan

IMPROVING SEISMIC PERFORMANCE OF BRICK MASONRY JUNCTIONS

Sekhar Chandra Dutta[1)], Parthasarathi Mukhopadhyay[2)], and Kundan Goswami[3)]

1) Professor and Head, School of Infrastructure, Indian Institute of Technology, Bhubaneswar, India
2) Asst. Professor, Dept. of Architecture, Town and Regional Planning, Bengal Engineering and Science University, Shibpur, India
3) Graduate Student, Department of Civil Engineering, Indian Institute of Technology, Kanpur, India
scdind2000@gmail.com, parthasm@gmail.com, kundanciv@gmail.com

Abstract: Unreinforced one or two storied load bearing brick masonry structures, built with combination of non-engineered bricks and mortars, are natural economic choice for the millions of inhabitants of the third world. Owing to their high compressive strength, such brick structures perform well under gravity loading. However, their resistivity to horizontal ground motion is very less due to inherent low tensile strength. The lateral load bearing capacity of such structures may be improved by ensuring proper connections at the junctions between two mutually perpendicular walls, which extends the collapse time of the out-of-plane walls. This paper in its limited scope has tried to quantify the improvement in performance of brick masonry junctions subjected to reversible lateral loading through inclusion of two types of strengthening measures viz. reinforcing with L-shaped steel bars and encasing with polypropylene bands, which leads to nominal increase in construction cost. Results show that inclusion of such reinforcements lead to increased lateral strength of masonry junctions which is even more than twice of the same exhibited by their unreinforced counterpart. Such observations may be helpful in evolving empirical design guidelines, which may be implemented at artisanal levels in the seismically active regions of the world.

1. INTRODUCTION

Millions of inhabitants of the third world countries have no other economic choice but to take shelter in single or double storied unreinforced brick masonry (URBM) structures. These masonry buildings are constructed through combination of non-engineered bricks and mortar. Bricks, being good in compression, are generally suitable for undertaking the dead and imposed loads acting vertically on the structures. However, such unreinforced structures are usually inadequate in resisting horizontal load. This is primarily because of their low tensile strength. Such structures are, therefore, susceptible to lateral thrusts generated due to the earthquake ground motions.

1.1 Connecting Corners of Masonry Walls: Qualitative Provisions

It has been observed that the isolated walls perpendicular to the direction of the earthquake shaking collapse earlier, in the form of out-of-plane failure, than those parallel to the vibrations, which suffer in-plane failure. It is this observation that prompted the different earthquake codes to recommend formation of proper connections at the junctions between two mutually perpendicular masonry walls for improving their seismic performance. This is because of the fact that when a set of mutually perpendicular walls, properly connected with each other at their junctions, suffer from earthquake ground motion, then those suffering earthquake shaking in perpendicular direction may not collapse, until those suffering earthquake vibration in parallel direction fail. Among different methods that the codes have recommended for connecting two mutually perpendicular walls, toothed joints in walls at corners and T-junctions and connection through dowels, both in alternate layers of masonry, are two important recommendations (IS: 4326-1993 and IAEE & NICEE: 2004).

1.2 Seismic Performance of URBM: Earlier Investigations

The urge for improving the seismic performance of the widely used URBM has prompted researchers in the past to conduct extensive investigation in order to enhance the lateral strength of the masonry structures through reinforcements. The concept of seismic retrofit of older masonry structures possessing substandard seismic resistance through the use of jackets or skins of composite fibres bonded with a polymer matrix to the surface has been studied by Priestley and Seible (1995) and implemented in simple design models for

enhanced shear strength and flexural ductility. The contribution of composites to the shear capacity of strengthened elements has also been studied through classical truss analogy by Triantafillou (1998). Very few investigations have also been directed to test the effectiveness of using polymeric grid reinforcement on horizontal joints (Ramos et al. 2005). It has been reported in a previous study by Kuzik et al. (2003) that the hysteresis behaviour, wall stiffness and ultimate strength are significantly affected by the amount of glass fibre reinforced polymer (FRP) sheets rather than the level of compressive axial load or the amount of steel reinforcement. The experimental results exhibited that punching shear through bricks, crushing of bricks, debonding and tensile rupture of the FRP are the modes of failure in strengthened walls that vary with the type of reinforcement and anchorage system. Experiments have also been conducted by Wang et al. (2006) to determine the interaction coefficient of the pilaster, modified coefficient, statistic coefficient and effective participation coefficient when brick masonry walls with pilasters were reinforced by glass FRP. Analyses of failure model of brick masonry walls and truss model of FRP have put forth the formulae of seismic shear capacity of reinforced brick masonry walls in concurrence with experimental results obtained from tests conducted.

Several experiments have been conducted to evaluate the out-of-plane flexural behaviour of masonry walls reinforced with glass FRP as many of the masonry structures fail in out-of-plane bending due to the lack of reinforcement (Ehsani et al. 1999, Gilstrap and Dolan 1998). In a similar study conducted by Tan and Patoary (2003), experimental values of ultimate load-carrying capacity of the strengthened walls have been found to match well with the results predicted through simple analytical models, which were developed using the principles of strain compatibility and force equilibrium. In-plane tests conducted by Elgawady et al. (2003) indicate increased lateral resistance and enhancement in ultimate drift in the upgraded specimens when they are investigated with respect to aspect ratio, fibre type, upgrading configurations, fibre structures and mortar compressive strength. Another similar study undertaken by Turek et al. (2007) revealed that the use of vertical glass FRP strips alone is able to improve the in-plane performance of URBM walls. In a previous literature (Taghdi et al. 2000), walls retrofitted with diagonal and vertical steel strip system have shown significant increase in in-plane strength and ductility behaviour. In addition, a comparative view on hysteretic behaviour of unreinforced and reinforced masonry walls has been provided in the same literature. Another recent article by Alcocer et al. (2004) also came up with the same findings. Various shaking table tests have been conducted by Meguro et al. (2005) to understand the dynamic response of masonry buildings and overall effectiveness of strengthening technique.

1.3 Need for Quantitative Guidelines

In spite of the existing provisions recommended by different national and international earthquake codes regarding strengthening of masonry walls at corner junctions, none of the investigations referred in the previous sub-section was focussed on this area. The authors, therefore, felt the necessity to conduct experiments on this area in order to identify the broad quantitative improvement due to reinforcing corners of URBM in response to reversible lateral loading. This paper, in its limited scope, has consequently attempted to investigate this issue. Further, along with the same, another popular issue of using polypropylene (PP) bands are also investigated to arrive at the understanding about quantitative levels of improvement in seismic behaviour.

2. TEST SETUP

Three L-shaped masonry corner junctions, one unreinforced and the other two strengthened as stated above, having equal legs of length 750mm, height 750mm and thickness 125mm were constructed with Class 12.5 bricks and M1 grade mortar conforming to IS: 1077-1991 and IS: 1905-1987 respectively. Thus the aspect ratio of the wall panels of the samples was unity by design. ‘Running Bond’, as illustrated in Figure 1, was used for construction of these L-shaped masonry structures in order to avoid the possibility of any portion acting as slender vertical member. In absence of proper bonds, the flexural strength and axial load carrying capacity of the masonry walls get reduced as the imposed load does not get distributed over a wide region and its intensity on a slender portion rises up.

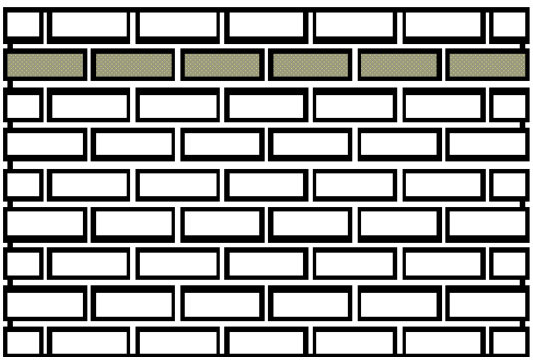

Figure 1 Masonry samples prepared in Running Bond

2.1 Unidirectional Horizontal Shaking Table

The masonry test pieces, thus set up, were mounted on an unidirectional horizontal shake table and were further cemented at the base to simulate real-life

situation. The shaking table used for simulating the earthquake thrusts have a payload capacity of 3tonnes and was subjected to sinusoidal base acceleration of frequency 10Hz, for durations of 30s with varying amplitude. The frequency level for testing the masonry junctions has been chosen as 10Hz because the natural frequencies of single storied structures lie in this range. The photograph at Figure 2 shows the URBM sample being mounted on the horizontal shaking table with a glimpse of the servo-control mechanism at the background.



Figure 2 An URBM Test Piece mounted on the Unidirectional Horizontal Shaking Table

2.2 Reinforced Brick Masonry Samples

Unlike the unreinforced one, strengthening measures for the other two masonry samples were undertaken as follows:

(a) L-shaped steel bars of diameter 8mm were provided in alternate layers at the corners of the masonry (length of each leg being 250mm), as depicted in Figure 3(a); and, (b) the walls were encased with horizontal and vertical bands of polypropylene, generally used for packaging, as shown in Figure 3(b). The average width and thickness of the PP bands were measured to be 11mm and 0.4mm respectively, and the tensile yield strength of the same was reported to be 33MPa by the manufacturer.



(a) Junction reinforced with L-shaped steel bars



(b) Encasing junction by horizontal and vertical PP bands

Figure 3 Reinforced Brick Masonry Corner Junctions during the Construction Stage

3. RESULTS AND DISCUSSION

3.1 Typical Modes of Failure

Masonry walls while behaving as in-plane may undergo four types of failure namely, (a) shear sliding or bed-joint sliding, (b) diagonal shear cracking, (c) rocking failure, and, (d) toe crushing, which are graphically represented in Figure 4. Shear sliding, as depicted in Figure 4(a), occurs when the bond between bed-joint mortar layers and bricks is weak and the frictional force developed due to vertical load along the cracks is less compared to the imposed lateral load. Diagonal shear cracking, as shown in Figure 4(b), mostly occurs when the in-plane behaving wall is square in nature. In such a case, compression is developed along one of the diagonals of the wall and tension along the other. Since masonry is weak in tension, it cannot withstand the tensile force and consequently cracks. Rocking failure, as illustrated in Figure 4(c), develops when the masonry wall is comparatively slender and is subjected to reversible lateral loading along with negligible vertical load. Toe crushing, as represented in Figure 4(d), takes place when the compressive stress developed at the toe during rocking exceeds the compressive strength of masonry elements, i.e. bricks, mortar etc.

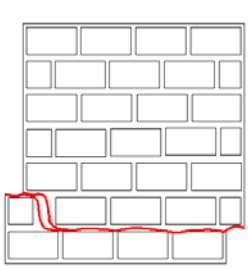

(a) Shear sliding or bed-joint sliding

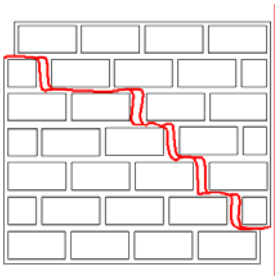

(b) Diagonal shear cracking



(c) Rocking failure

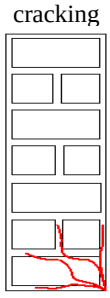

(d)Toe Crushing

Figure 4 Different Modes of In-plane Failure of URBM

3.2 Observations during shaking at different acceleration levels

The three masonry samples were subjected to shaking over a range of acceleration levels, starting from 0.20g, increased at a rate of 0.05g, until all the three samples failed. The crack patterns and failure modes at various acceleration levels were noted. However, observations corresponding to 0.25g, 0.60g and 0.80g acceleration levels are reported here, because of significant developments.

(a) Acceleration level 0.25g

The first test piece to undergo failure was the URBM sample. The two strengthened samples did not show any trace of failure at this stage. This incident confirms the assumption that reinforcing URBM wall junctions, either by L-shaped horizontal steel bars at corners, or encasing them by PP bands, improves their seismic performance. The photographs of Figure 5 represent a general view of the three samples after each were subjected to vibration on the shaking table at an acceleration level of 0.25g.



(a) URBM sample | (b) Junction reinforced with dowel bars | (c) Junction encased with PP bands

Figure 5 Performance of the three Brick Masonry Corner Junctions after Application of Sinusoidal Base Acceleration up to 0.25g

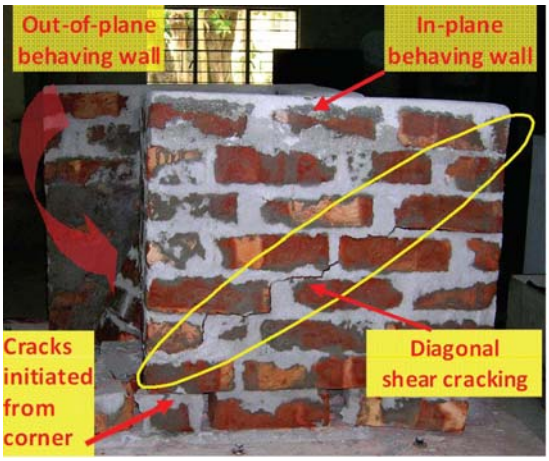

Figure 6 Collapse of both In-plane and Out-of-plane Walls of the URBM Sample at 0.25g

It can be observed from Figure 6 that both the walls forming the URBM corner junction failed. While development of diagonal shear cracks is observed in the wall parallel to the direction of the shaking (in-plane behaving wall), the other wall perpendicular to the direction of shaking simply overturned (out-of-plane behaving wall). Shear sliding in the mortar bed-joint at the second layer from the base is further observed in the in-plane behaving wall.

Overturning of the out-of-plane behaving portion of the junction at such a low acceleration level suggests relatively weaker connection with its in-plane behaving counterpart. The reason behind development of diagonal shear crack in the in-plane behaving portion of the junction may be attributed to the aspect ratio of the wall panels, whose height is equal to its length. However, development of base sliding might be due to low bond strength compared to the demand imposed by lateral load at that level.

(b) Acceleration level 0.60g

The second test piece to undergo failure was the junction reinforced with L-shaped steel bars, which failed when the acceleration level was gradually raised to 0.60g. The two photographs at Figure 7 illustrate the failures of the two walls forming the corner junction. Figure 7(b) demonstrates that the failure was due to shear sliding in the mortar bed-joint at second layer from the base in the in-plane behaving wall. It is also observed from Figure 7(a) that the out-of-plane behaving wall had shown formation of cracks at its base, but had not suffered collapse. This implies that inclusion of L-shaped steel bars of 8mm diameter helped in properly transferring the load from out-of-plane behaving wall portion to the in-plane behaving one, thereby resisting its overturning.



(a) Cracking at the base of the out-of-plane behaving wall | (b) Shear sliding failure at the mortar bed-joint in the in-plane behaving wall

Figure 7 Failure Patterns observed in the Walls Forming Corner Junction Reinforced with L-shaped Steel Bars at 0.60g

The same level of acceleration of 0.60g generated horizontal shear cracking along mortar bed-joints in the other masonry junction encased with FRP bands. This resulted in tearing of the vertical FRP bands at the bottommost portion of the out-of-plane behaving wall (refer Figure 8), probably due to the high tensile force generated by bending action of the wall.



Figure 8 Tearing of PP Bands in the Out-of-plane behaving Masonry Wall forming Corner Junction encased with PP Bands at 0.60g

(c) Acceleration level 0.80g

The third masonry junction encased with PP bands finally collapsed due to diagonal shear cracking of the in-plane behaving wall at an acceleration level of 0.80g (refer Figure 9). It is interesting to observe here that though horizontal shear cracking occurred along mortar bed-joints of both the out-of-plane and in-plane behaving walls at an acceleration level of 0.60g, yet they neither did overturn nor did suffer shear sliding failure when the acceleration reached a level of 0.80g. This incomplete failure at the junction, even though the in-plane behaving wall did actually collapse at the acceleration level of 0.80g, shows that the encasing effect of the PP bands were stronger than the tension



Figure 9 Diagonal Shear Cracking in the In-plane Failure behaving Portion of the Junction, encased with PP Bands at 0.80g

bearing capacity of the brick-mortar combination of the in-plane behaving portion of the wall.

3.3 Comparative performance of the three samples

A comparative analysis of the performance of the three types of brick masonry walls, which were put under simulated earthquake vibrations at various acceleration levels, is represented in Table 1. The table represents the failure acceleration levels and failure patterns for these masonry junctions. Comparison between the different failure acceleration levels indicates that the lateral strength of the junctions of the masonry units, reinforced by steel bars and encased by PP bands, has increased respectively to 2.4 times and 3.6 times the unreinforced one.

Table 1 Failure Acceleration Levels and Failure Patterns for the Brick Masonry Corner Junctions

Type of brick masonry junction	Failure acceleration level (g)	Failure pattern
Unreinforced	0.25	(a) In-plane behaving wall: Shear sliding failure at mortar bed-joints along with development of diagonal shear cracking initiated from corner; (b) Out-of-plane behaving wall: Failure due to overturning, initiated from corner cracking.
Reinforced with L-shaped steel bars	0.60	(a) In-plane behaving wall: Shear sliding failure at mortar bed-joints; (b) Out-of-plane behaving wall: Formation of cracks at the base of the out-of-plane behaving portion.
Encased by horizontal and vertical PP bands	0.80	(a) In-plane behaving wall: Diagonal shear failure along with horizontal shear cracks at base; (b) Out-of-plane behaving wall: Formation of horizontal shear cracking, yet did not overturn.

4. CONCLUSIONS

The failure acceleration levels and failure patterns observed from the experiments conducted on unreinforced, reinforced, and encased masonry junctions lead to the following broad conclusions.

(a) Inclusion of L-shaped steel bars and PP band encasing leads to an increase in lateral strength of masonry corner junction to the extent of upto about 2.4 times or even higher compared to the unreinforced one. However, inclusion of such reinforcements leads to nominal increase in cost of material and its subsequent construction.

(b) Among the reinforced ones, the masonry corner junction strengthened with PP band meshing has shown higher capacity. However, it failed due to diagonal shear cracking of the in-plane behaving portion after tension failure of PP bands; whereas the L-shaped steel bar reinforced junction collapsed due to shear sliding, though having lesser capacity. Pending a detailed study on use of PP band and adequate knowledge on its workmanship at mason's level, providing corner reinforcement with the frequency and length as done in here, may be an adequate codal prescription for improving seismic resistance of masonry structures. In fact, this may be a suitable choice striking balance among safety, economy, and, ease of construction.

(c) Even after strengthening, the junctions have a tendency of developing horizontal cracks at the base level of masonry structures.

Such observations may be helpful in developing empirical design guidelines for masonry structures to be built in seismically active zones of the world.

5. FURTHER SCOPE OF STUDY

In this present study, one type of steel reinforcement and another type of encasing by PP bands have been applied for observing the extent of strengthening of brick masonry corner junctions. For the sake of completeness of understanding, similar types of experiments may be conducted on masonry junctions reinforced with steel-wire mesh or glass fibre reinforced polymer (GFRP) sheets.

Further, the tests on reinforced masonry junctions include only the variation in amplitude of base excitation at a constant frequency of 10Hz. However, for generalization of guidelines, the behaviour should be studied under pulses of various frequencies and also under real earthquake time histories. A series of tests may be conducted to achieve this end.

Lastly, it needs to be mentioned that the strength properties of bricks depend upon that of the clay, and the level and extend of burning under which the bricks were manufactured. The quality of clay is not uniform throughout a vast country like India, having diverse geographic and climatic regions. Thus all the types of experiments that has been carried out and those which are proposed to be undertaken as future scope of study, need to be repeated in future, taking bricks made out of clay from different geographic regions to obtain a region specific quantitative data. All these data may be suitably collated for inclusion in the Codes.

References:

Alcocer, M. S., Arias, J. G. and Flores, L. E. (2004), "Some Developments on Performance–Based Seismic Design of Masonry Structures," *Performance-Based Seismic Design: Concepts and Implementation* edited by P. Fajfar and H. Krawinkler, PEER, Berkeley, California, 233–244.

Bureau of Indian Standards (1991), "IS: 1077-1991 (5th revision), Common Burnt Clay Building Bricks – Specification," BIS, New Delhi, India.

Bureau of Indian Standards (1987), "IS: 1905-1987 (3rd revision), Code of Practice for Structural use of Unreinforced Masonry," BIS, New Delhi, India.

Bureau of Indian Standards (2004), "IS: 4326-1993 (Reaffirmed 1998) Edition 3.2 (2002-04), Indian Standard, Earthquake Resistant Design and Construction of Buildings — Code of Practice (Second Revision) (Incorporating Amendment Nos. 1 & 2)," BIS, New Delhi, India.

Ehsani, M. R. and Saadatmanesh, H.; Velazquez-Dimas, J. I. (1999), "Behavior of Retrofitted URM Walls under Simulated Earthquake Loading," *Journal of composites for construction*, **3**(3), 134-142.

Elgawady, M. A. M., Lestuzzi, P. and Badoux, M. (2003), "Rehabilitation of Unreinforced Brick Masonry Walls Using Composites," *Proceedings of international short course on Architectural and structural design of masonry with focus on retrofitting of masonry structures and earthquake resistant design*, Dresden University of Technology, Dresden, Germany, December 7- 18.

Gilstrap, J. M. and Dolan, C. W. (1998), "Out-of-Plane Bending of FRP-Reinforced Masonry Walls," *Composites Science and Technology*, **8**(8), 1277-1284.

International Association for Earthquake Engineering & National Information Center of Earthquake Engineering (2004), "Guidelines for Earthquake Resistant non-engineered construction (English Edition)," IAEE, Tokyo & NICEE, Kanpur.

Kuzik, M. D., Elwi, A. E. and Cheng, J. J. R. (2003), "Cyclic Flexure Tests of Masonry Walls reinforced with Glass Fiber Reinforced Polymer Sheets," *Journal of Composites for Construction*, **7**(1), 20-30.

Meguro, K., Myorca, P., Guragain, R., Sathiparan, N. and Nesheli, N. (2005), "Shaking Table Experiment of Masonry Buildings and Effectiveness of PP-Band Retrofitting Technique," *Monthly Journal of Institute of Industrial Science*, University of Tokyo, **57**(6), 534-537.

Priestley, M. J. N. and Seible, F. (1995), "Design of Seismic Retrofit Measures for Concrete and Masonry Structures," *Construction and Building Materials*, **9**(6), 365-377.

Ramos, L. F., Costa, A. C. and Lourenco, P. B. (2005), "Operational Modal Analysis for Damage Detection of a Masonry Construction," *Proceedings of 1st International Operational Modal Analysis Conference*, Copenhagen, Denmark, 495-502.

Taghdi, M., Bruneau, M. and Saatcioglu, M. (2000), "Seismic Retrofitting of Low-rise Masonry and Concrete

Walls Using Steel Strips," *Journal of Structural Engineering*, American Society of Civil Engineers, **126**(9), 1017-1025.

Tan, K. H. and Patoary, M. K. H. (2003), "Strengthening of Masonry Walls against Out-of-Plane Loads Using Fiber-Reinforced Polymer Reinforcement," *Journal of Composites for Construction*, **8**(1), 79-87.

Triantafillou, T. C. (1998), "Composites: A New Possibility for the Shear Strengthening of Concrete, Masonry and Wood," *Composites Science and Technology*, **58**(8), 1285-1295.

Turek, M., Ventura, C. E. and Kuan, S. (2007), "In-Plane Shake-table Testing of GFRP-Strengthened Concrete Masonry Walls," *Earthquake Spectra*, **23**(1), 223-237.

Wang, Q., Chai, Z., Huang, Y. and Zhang, Y. (2006), "Seismic Shear Capacity of Brick Masonry Wall reinforced by GFRP," *Asian Journal of Civil Engineering (Building and Housing)*, **7**(6), 563-580.

JOINT CONFERENCE PROCEEDINGS
7th International Conference on Urban Earthquake Engineering (7CUEE) &
5th International Conference on Earthquake Engineering (5ICEE)
March 3-5, 2010, Institute of , Japan

EARTHQUAKE RESISTANCE ANALYSIS ON A DOUBLE CIRCUIT INTERMEDIATE TOWER CONSISTED OF STEEL TUBES AND ANGEL STEELS

Wang Lai[1)], Liu Ming[2)], Yang Ning[2)]

1) Professor, Shandong Provincial Key Laboratory of Civil Engineering Disaster Prevention and Mitigation (Shandong University of Science and Technology), Qingdao, China
2) Master of philosophy, College of Civil Engineering and Architecture, Shandong University of Science and Technology, Qingdao, China

wlkdtjxy@sina.com, tumuliuming@126.com

Abstract: Taking time-procedure method and using general software ANSYS, earthquake resistance of a 500 kV double circuit intermediate tower consisted of steel tubes and angel steels is analyzed when the dimensions of earthquake waves are different. In order to study the effects of dimensions of earthquake waves on the tower, changes of displacements of suspension points of conducting and ground wires are studied when dimensions of earthquake waves change from one to three. Power spectrum density of earthquake wave is also very important in time-procedure method. Fourier transform is used to transform analysis in time domain to analysis in frequency domain. Results of the analysis indicate some conclusions as follows: (1) Three dimensions of earthquake waves should be considered in time-procedure method when rare occurrence earthquake is analyzed. (2)Axial stress under 7 degree rare occurrence earthquake action is still in the elastic range.(3) Displacement of suspension points and top point of the tower mainly changes in Y direction that is perpendicular to the transmission line when wires are considered or not. (4)Reactions of the tower become weaker when the role of wires are considered in the area of I. (5)The frequency spectrum characteristics of earthquake waves have a big influence on the reactions of the tower. (6) After considering the role of conducting and ground wires, vertical displacement of the top point of the tower is smaller than the displacements of suspension points of conducting and ground wires. So members near the suspension points should be paid more attention in the process of design.

Keywords: tower consists of steel tubes and angel steels; time-procedure method; frequency spectrum characteristics; dimensions of earthquake waves; ANSYS;

1. FINITE ELEMENT MODEL OF THE TOWER-MASS

The height of the tower consisting of steel tubes and angel steels is 50m.The cross arms are made of angel steels, and the other parts are manufactured by steel tubes. The steel type of the chords is Q345B, and others are Q235B. Some physical parameters of material used are defined as follows: Elastic modulus $E_c = 2.06 \times 10^{11} Pa$; Poisson's ratio γ=0.3; Density $\rho = 7.85 \times 10^3$.

To investigate the behaviors of the tower under loading, the code ANSYS was implemented. Element Link8 in ANSYS is to simulate secondary web members in cross arms. Moreover, the other members are simulated by using the element Beam189. Normally, the stiffness of conductors plays a little role on the dynamic characteristics of the tower. Thus, the weight of mass in Z-direction is only considered, as shown in the work by Zu, Hu and Li (2006). By using the method, effects of conductors is considered. The weights of masses are calculated according to the span length of the transmission lines with the length of 500m.



Fig.1 Tower-Mass modal

2. EFFECTS OF DEMENSIONS OF EARTHQUAKE WAVES ON THE TOWER

To study the effects on the tower caused by the dimensions of earthquake waves, stress of chords, displacement of top point and suspension points are mostly studied. Earthquake fortification intensity and earthquake intensity are given as follows:

Seismic Intensity is 7(0.1g) and design earthquake group is I. To explore the effects of dimensions of earthquake waves on the tower, changes in displacements of suspension points of conducting and ground wires are studied when the dimensions of earthquake waves change from one to three. In this paper, Guangzhou Wave is used to analyze reactions of the tower.

Guangzhou Wave is designed according to the geological characteristics of Guangzhou, as shown in the work by Li, Ye, Yang and Gao (2007).There are two types of Guangzhou Waves, Guangzhou Wave I and Guangzhou Wave II. This paper adopts Guangzhou Wave I. Peak value of acceleration of Guangzhou Wave I is 100.0 cm/s^2, which lasts 12 s. Ratio of the X-component of the peak value to Y is 1:0.85, and the ratio of the X-component of the peak value to Z is 1: 0.65. In the process of analysis, the damping value applied to the time-history dynamic analysis is Rayleigh damping, $\alpha = 0.2312$, $\beta = 1.66868 \times 10^{-3}$ .Time-frequency characteristics of adjusted Guangzhou Wave are shown in Fig.2.

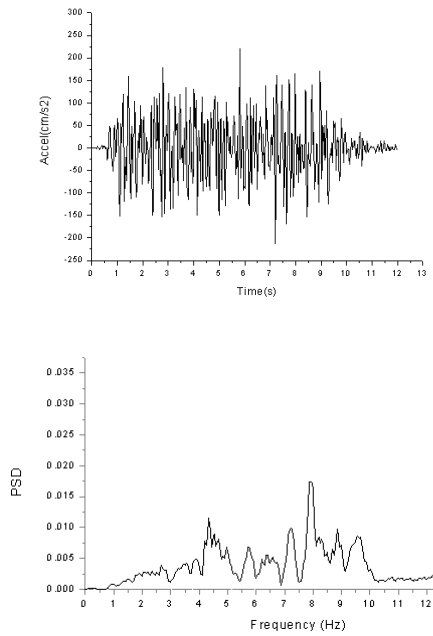

(a)

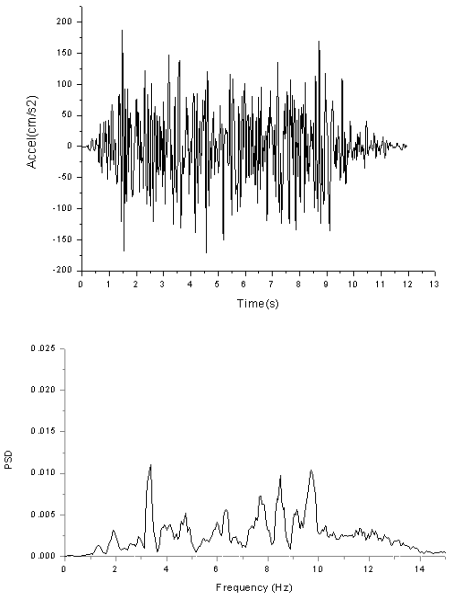

(b)

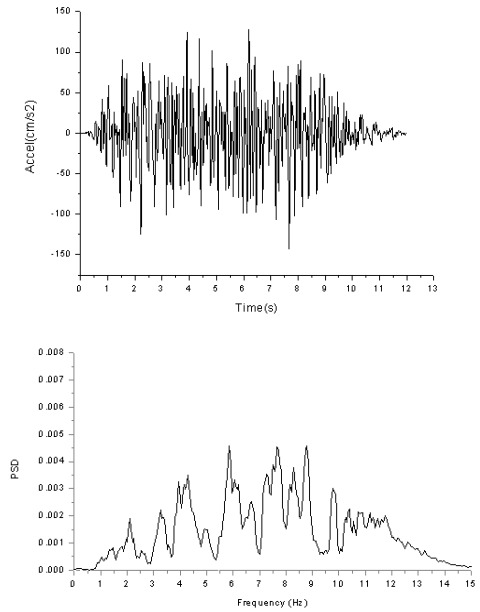

(c)

Fig.2 Characteristics of Guangzhou wave:
(a) Guangzhou wave X
(b) Guangzhou wave Y
(c) Guangzhou wave Z

2.1 Comparison of the Displacement of Suspension Points of Wires between One-dimensional and Three-dimensional Waves under 7 Degree Rare Occurrence Earthquake Action.

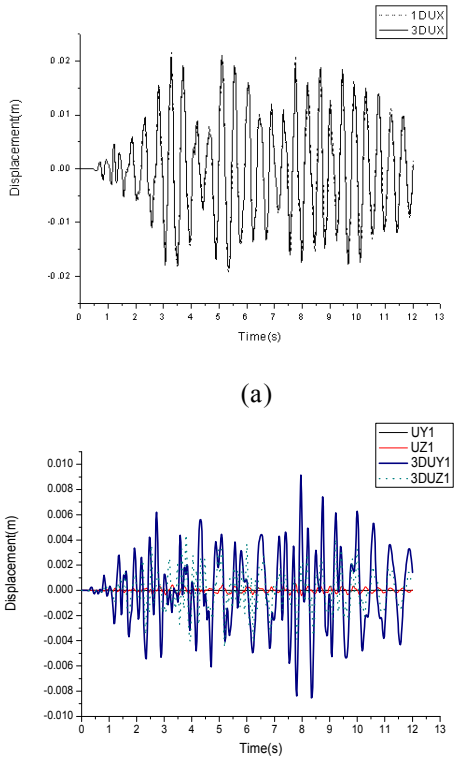

Fig3 Comparison of the displacement of suspension points of ground wires between one-dimensional and three-dimensional waves:
(a)X-component of displacement of suspension points of ground wires
(b) Y-component and Z-component of displacement of suspension points of ground wires

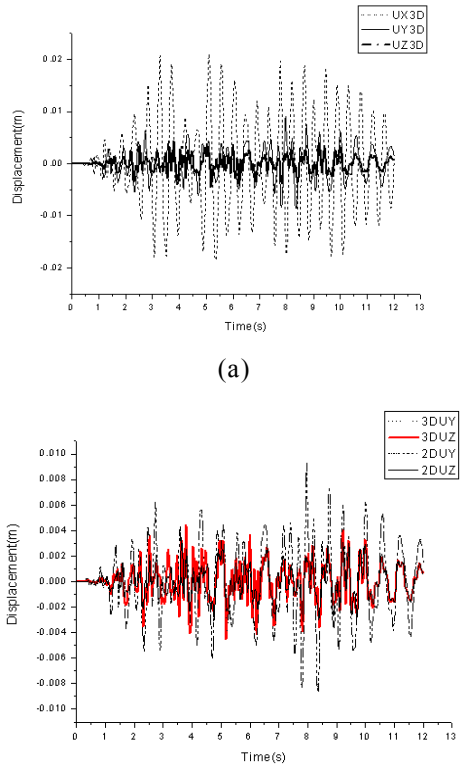

Fig.4 Comparison of displacement of node No. 477 between one-dimensional and three-dimensional waves:
(a) Displacement of the suspension point (Node 477) of ground wires excited by three-dimensional waves under 7 degree rare occurrence earthquakes
(b)Comparison of Y-component and Z-component of displacement of node 477 between one-dimensional and three-dimensional waves

As shown in figure3 (a), the X-component of displacement remains nearly the same no matter whether the tower is excited by one dimensional or three dimensional waves. X-component of displacement doesn't increase though the tower is excited by three dimensional waves. This indicates coupled excitation is not obvious.

As shown in figure3 (b), Y-component and Z-component of displacement is rarely affected. The Z-component of displacement is much larger when the tower is excited by three dimensional waves. At the same time, displacements of suspension points of conducting and ground wires in Y and Z directions are the same in quantitative rating.

Therefore, three dimensions of earthquake waves should be considered in time-procedure analysis when the rare occurrence earthquake is analyzed.

2.2 Comparison of the Displacement of Suspension Points of Wires between Two-dimensional and Three-dimensional Waves under 7 Degree Rare Occurrence Earthquake Action.

Fig.4 shows that X-component of displacement is greater than Y and Z-component of displacement. Peak value of X-component of displacement is 21mm, 5.1s.The peak value of Y-component is 10mm, 7.96s, and the maximum value of Z-component is 4mm, 3.78s.

Earthquake wave in global Y and Z directions has little influence on displacements of suspension points in X direction. This shows coupling between the horizontal and vertical earthquake waves is not obvious. Earthquake wave in global Z direction only has influence on displacements of suspension points in Z direction.

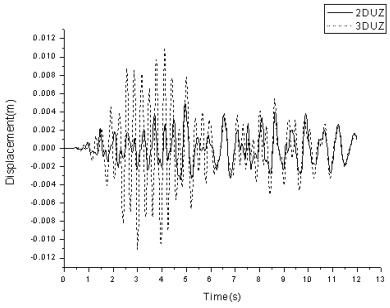

(a)

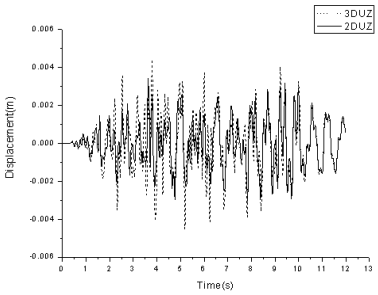

(b)

Fig.5 Comparison of displacement of suspension point of ground and conducting wires between two-dimensional and three-dimensional waves:
(a)Comparison of Z-component of suspension point (Node337) of wires between two-dimensional and three-dimensional waves
(b)Comparison of Z-component of displacement of suspension point (Node477) of between two-dimensional and three-dimensional waves

As shown in Fig.5, Z-component of displacement is very small when the tower is excited by horizontal earthquake waves.Fig.6 shows that three dimensions of earthquake waves should be considered in time-procedure method when rare occurrence earthquake is analyzed. Displacements of suspension points of wires in Y and Z direction are the same in quantitative rating. As shown in the Chinese code for seismic design of buildings, GB50011-2001, large-span structures and long-cantilevered structures for Intensity 8 or 9, and tall buildings for Intensity 9, vertical seismic action shall be taken into account. Though the Intensity of Guangzhou is 7, displacements of suspension points are obvious, thus they can not be neglected.

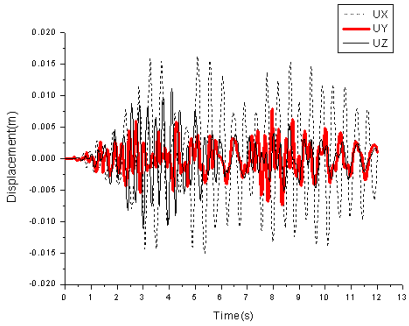

Fig.6 Displacements of suspension point of wires under 7 degree rare occurrence earthquakes (m)

3. RESEARCH ON THE CHARACTERISTICS OF FREQUENCY SPECTRUM OF RARE OCCURRENCE EARTHQUAKE WAVES WHICH CAUSE REACTION OF THE TOWER

After considering the role of wires, reaction of the tower change a lot. Power spectrum density of earthquake wave is also very important in time-procedure method.

Fourier transform is used to transform analysis in time domain to that in frequency domain. Using this method, characteristics of power spectrum density of earthquake waves under 7 degree rare occurrence earthquake actions are studied. Effects of Guangdong Wave, Qianan Wave and Kobe Wave on the tower are all studied in the area I.

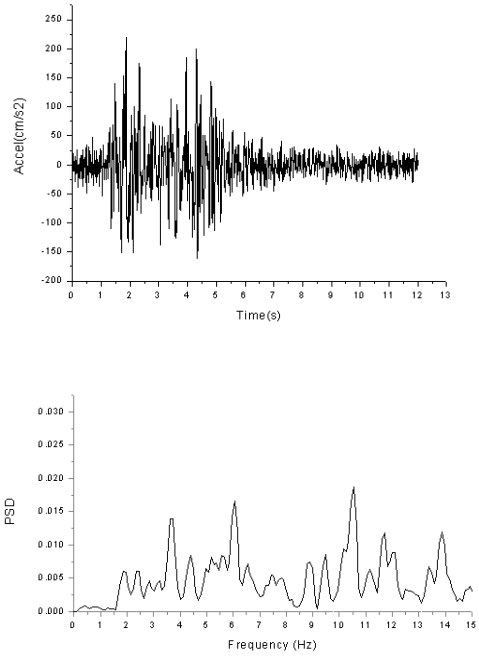

(a)

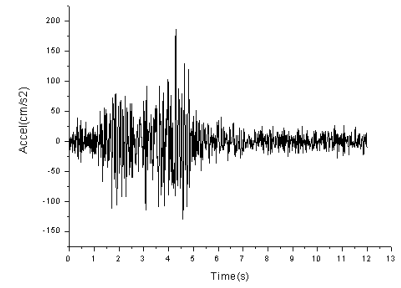

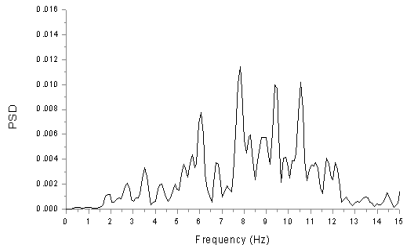

(b)

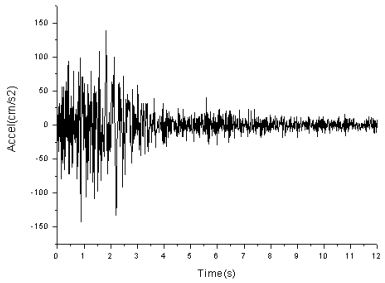

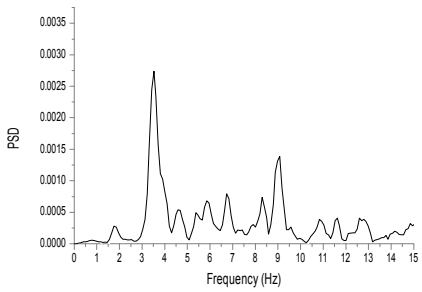

(c)

Fig7 Time-domain and frequency-domain of Qianan wave:
(a)Qianan wave 1
(b) Qianan wave 2
(c) Qianan wave 3

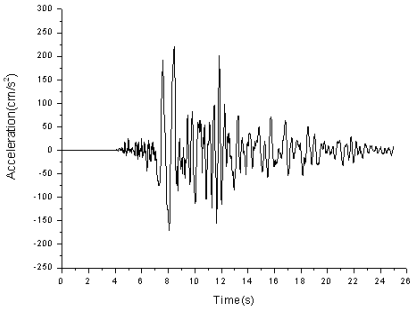

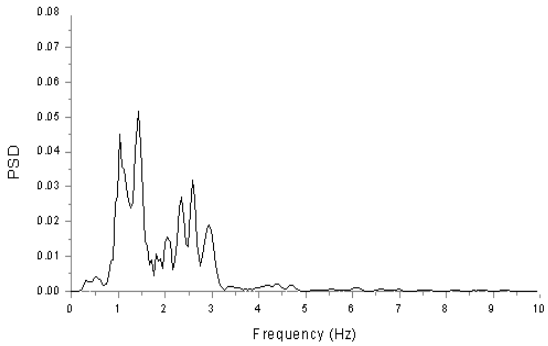

(a)

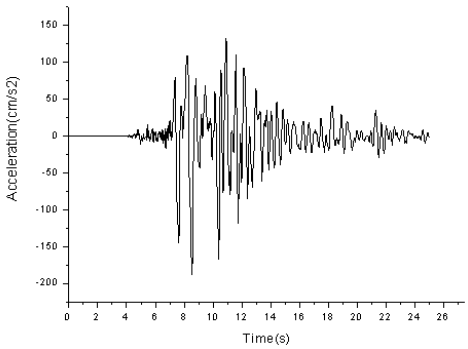

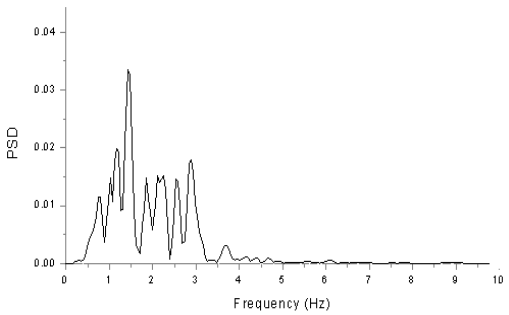

(b)

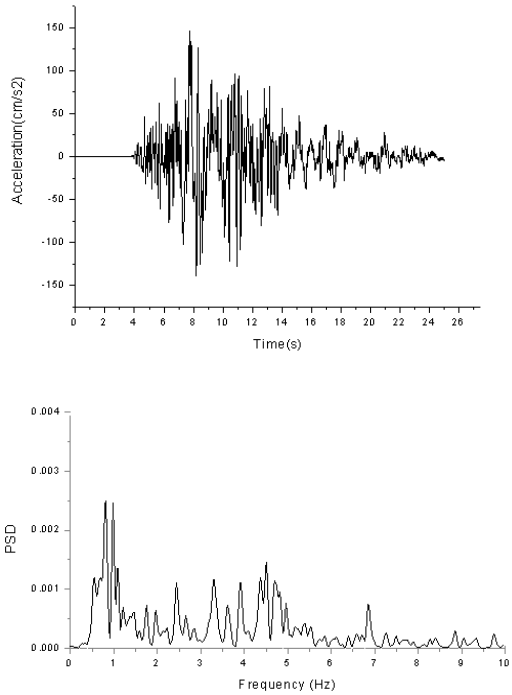

(c)

Fig.8 Kobe wave:
(a)Time-domain and frequency-domain of Kobe wave 1(E-S)
(b)Time-domain and frequency-domain of Kobe wave 2(N-S)
(c)Time-domain and frequency-domain of Kobe wave 3

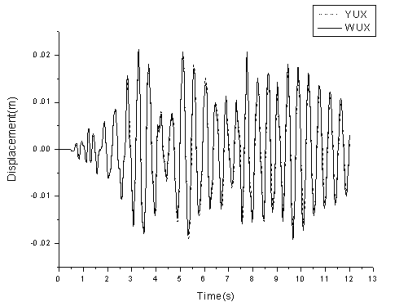

(a)

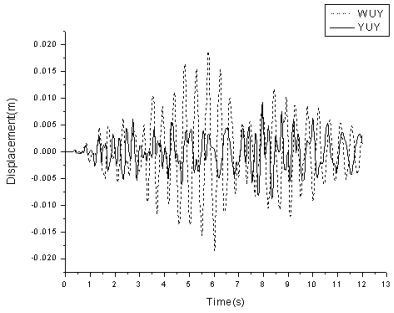

(b)

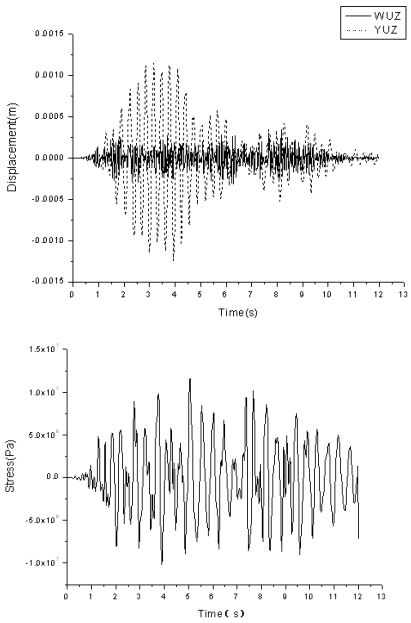

(d)

Fig.9 Time procedure analysis adopting Guangzhou wave:
(a)Comparison of X-component of displacement of top point excited by three-dimensional Guangzhou waves ("Y" stands for considering the role of conductors, "W" not)
(b) Comparison of Y-component of displacement of top point excited by three-dimensional Guangzhou waves ("Y" stands for considering the role of conductors, "W" not)
(c)Comparison of Z-component of displacement of top point excited by three-dimensional Guangzhou waves ("Y" stands for considering the role of conductors, "W" not)
(d)Axis stress of the chord near the changing slope excited by three-dimensional Guangzhou waves

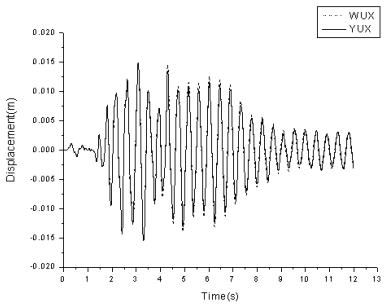

(a)

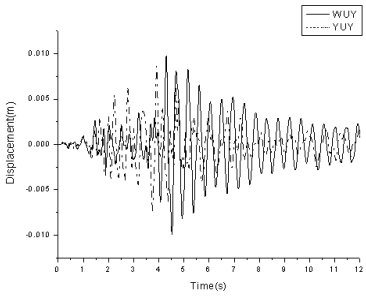

(b)

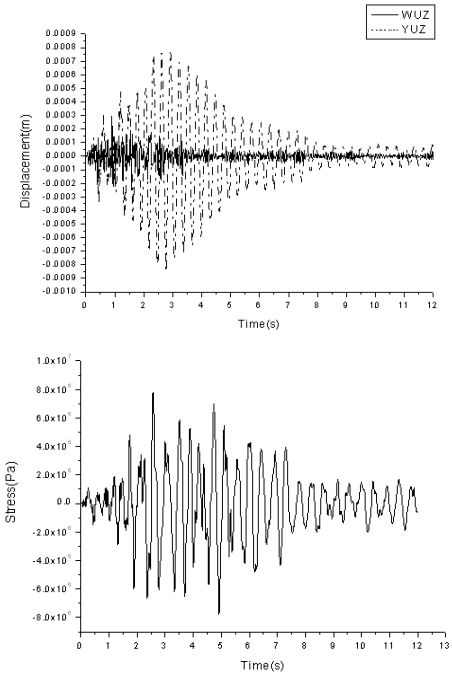

(d)

Fig.10 Time procedure analysis adopting Qianan wave:
(a)Comparison of X-component of displacement of top point excited by three-dimensional Qianan waves ("Y" stands for considering the role of conductors, "W" not)
(b)Comparison of Y-component of displacement of top point excited by three-dimensional Qianan waves ("Y" stands for considering the role of conductors, "W" not)
(c)Comparison of Z-component of displacement of top point excited by three-dimensional Guangzhou waves ("Y" stands for considering the role of conductors, "W" not)
(d)Axis stress of the chord near the changing slope excited by three-dimensional Qianan waves

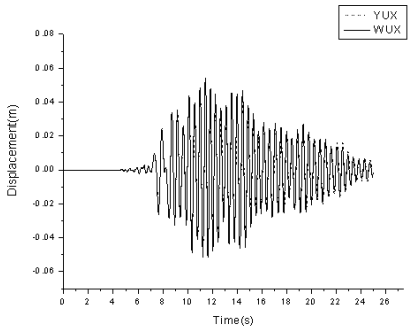

(a)

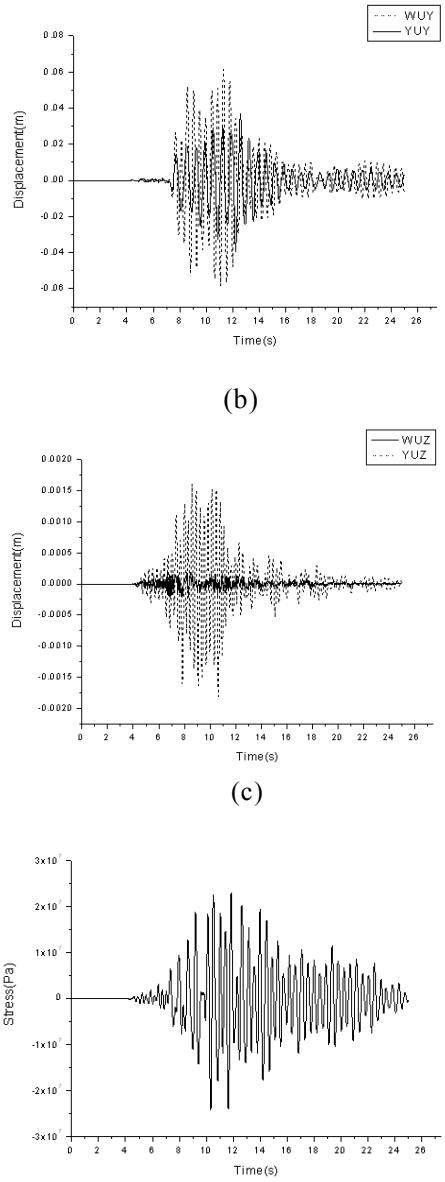

(b)

(c)

(d)

Fig.11 Time procedure analysis adopting Kobe waves:
(a)Comparison of X-component of displacement of top point excited by three-dimensional Kobe waves("Y" stands for considering the role of conductors, "W" not)
(b)Comparison of Y-component of displacement of top point excited by three-dimensional Kobe waves("Y" stands for considering the role of conductors, "W" not)
(c)Comparison of X-component of displacement of top point excited by three-dimensional Kobe waves ("Y" stands for considering the role of conductors, "W" not)
(d)Axis stress of the chord near the changing slope excited by three-dimensional Kobe waves

Some conclusions can be obtained according to Fig.7, Fig.8, Fig.9, Fig.10, and Fig.11:

(1) As shown in Fig.9 (d), Fig.10 (d) and Fig.11(d), axial stress of the chords under 7 degree rare occurrence earthquake actions is still in elastic range; it shows that seismic capacity of the double circuit intermediate tower consisted of steel tubes and angel steels is very good under 7 degree rare occurrence earthquake actions.

(2) Characteristics of frequency spectrum of earthquake waves have a significant influence on the reactions of the tower. Time traveling curves on displacements of suspension points of conducting and ground wires show that the maximum displacement is different when the tower is excited by different earthquake waves.

As shown in Fig.9 and Fig.10, the time travelling curves of Guangzhong Wave and Qianan Wave are very similar. The power spectrum density of Qianan Wave is low; therefore, the maximum displacement of Qianan Wave is smaller than that of Guangzhong Wave. As shown in Fig.10, Kobe wave is a kind of shock wave, its energy distribution lies among 1-3HZ.Reaction of the tower excited by Kobe Wave is more obvious than Qianan and Guangzhong Wave. Consequently, power spectrum density of earthquake wave plays a critical role in the analysis of earthquake resistance.

(3) Displacements of suspension points of conducting and ground wires changes no mater how the role of wires is considered or not. Changes of the Y-component of displacements that is perpendicular to the transmission line. Displacement in global Z direction of the top point of the tower becomes a little bigger after considering the mass of wires. However, total displacement of the top point is smaller.

(4) Fig.9(c), Fig.10(c) and Fig.11(c) show that the displacement in global Z direction of the top point is smaller than that of suspension point of wires.

(5) Under the respective seismic excitation of Guangzhong Wave, Qianan Wave and Kobe Wave, reaction of the tower becomes weaker if the role of wires is considered in the area of I.

4. CONCLUSIONS

(1)Three-dimensional earthquake waves should be considered in time-procedure method when rare occurrence earthquake is analyzed.

(2)Axial stress under 7 degree rare occurrence earthquake action is still in the elastic range.

(3) Displacements of suspension points and top point of the tower mainly change in Y direction that is perpendicular to the transmission line whether the role of wires is considered or not. Mass elements are used to consider the role of wires.

(4)Reactions of the tower become weaker when the role of wires is considered in the area of I.

(5)The frequency spectrum characteristics of earthquake waves have a significant influence on the reactions of the tower.

Acknowledgements:

This paper is supported by special subsidies construction of Shandong province “ Taishan Scholars” programme. This support is gratefully acknowledged.

References:

Zu B.L., Hu W.T. and Li C.X. (2006). “Estimating Seismic Responses of Transmission Towers by Finite Element Method”. Earthquake Engineering and Engineering Vibrating, 26（5）,161-166.

Li R., Ye L.Y., Yang Z.B. and Gao J.B. (2007),“Spatial Earthquake Response Analysis of Curve Bridge”. Highway Engineering，32（6）,27-29.

GB50011-2001.Code for Seismic Design of Buildings.

JOINT CONFERENCE PROCEEDINGS
7th International Conference on Urban Earthquake Engineering (7CUEE) &
5th International Conference on Earthquake Engineering (5ICEE)
March 3-5, 2010, Tokyo Institute of Technology, Tokyo, Japan

PROTECTION OF MEDITERRANEAN HISTORICAL STRUCTURES AGAINST EARTHQUAKES USING FRAGILITY CURVES

Syrmakezis A. Costas[1] and Kosta T. Margarita[2]

1) Professor, Institute of Structural Analysis & Aseismic Research, School of Civil Engineering, National Technical University of Athens, Greece
2) PhD Candidate, Research Assistant, Institute of Structural Analysis & Aseismic Research, School of Civil Engineering, National Technical University of Athens, Greece
isaarsyr@central.ntua.gr, maggiecosta@yahoo.gr

Abstract: The high importance of historical buildings and the intense seismicity of their location at the Mediterranean area, impose their present state's evaluation and if necessary, the definition of possible strengthening measures, minimization of interventions, as well as the compatibility of the materials used in their rehabilitation. Through this paper it will be presented the methodology of Fragility Curves, which takes into consideration the structural properties and the parameters characterizing the random seismic event. For the vulnerability evaluation of a structure, it is necessary to quantitatively determine its response to ground motions of different intensities. The contribution of another program called FAILURE is also very determinative, because it provides an optical indication of failing areas on wall surfaces, when the structure is subjected to a single seismic event. By processing the data from the previous software, and particularly the percentage of the total surface's damage, the fragility curves can easily be formulated. Through these curves, it is possible to distinguish the possibility of exceeding certain damage levels and also to investigate the way that each factor affects the vulnerability of the structure relatively to others.

1. INTRODUCTION

One of the most important hazards threatening heritage structures is the seismic activity, and especially its random action and intensity. In the Greek as well as in the entire Mediterranean area, the majority of cultural heritage buildings is made of masonry, which is highly vulnerable to earthquake actions. Its seismic vulnerability is mainly ought to their low tensile strength, their geometrical peculiarities, past earthquake damages and cracks, fatigue phenomena, degradation, lack of proper conservation or even incompatible human interventions.

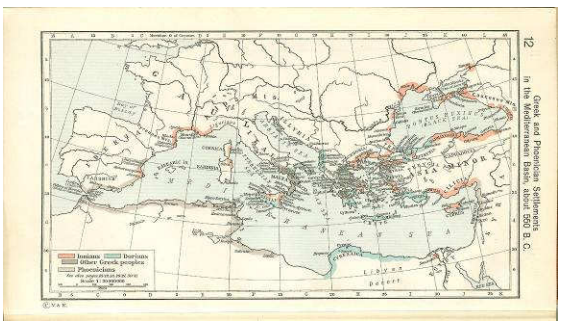

Figure 1 The Mediterranean basin

In modern societies, historical structures' architectural and social value imposes the need of their structural protection against earthquake ground motions combined with the application of special protection measures that permit reversibility and minimization of intervention.

During the last years, considerable research has been carried out in order to investigate the causes of damage and to develop technologies suitable for seismic retrofit and rehabilitation of existing masonry structures. Research has been either experimentally or analytically orientated, often focusing on the exploitation of past damage observations in order to understand the pathology of the structure before proceeding with any intervention measures. For the analytical assessment of historical structures' seismic response, two main sets of information should be taken into consideration. The first one involves structural properties (i.e. material strength, dynamic properties) and the later one concerns the parameters characterizing the seismic event (i.e. earthquake period, amplitude of vibration, direction). In both cases, many uncertainties are introduced during the structural and earthquake simulation.

In this paper, characteristic examples of historical masonry structures with various structural systems are presented and their seismic response is being investigated. These cases refer to existing outstanding historical buildings in Greece, which are:

- The Prefectorial edifice located in Rethymno, Crete
- The neoclassical residence of Prince George in Chania, Crete and
- A building made of masonry in Kazantzaki street in Sitia, Crete.

For these structures, finite element analysis is

performed using proper finite element types for each case (shell or solid types for wall design) through adequate structural program. Additionally, a qualitative and quantitative indication of structural failure, under several seismic events, is acquired, using a modified Von Mises failure criterion, adapted to masonry structures and the FAILURE software (Syrmakezis et al, 2005), that distinguishes the areas that fail using colourful elevations of the building. For the estimation of seismic vulnerability, a unique methodology is applied, incorporating both the structural and seismic uncertainties. This methodology has been developed under the scientific surveillance of Professor C.A. Syrmakezis in the Statics and Aseismic Research Laboratory at the National Technical University of Athens (Syrmakezis et al, 2005). Using the results obtained, a classification of historical masonry structures is aimed, correlating their seismic response with their dynamic properties and applied earthquake parameters.

2. DESCRIPTION OF THE STRUCTURES

2.1 The Prefectorial Edifice located in Rethymno

The Prefectorial edifice in Rethymno was constructed between 1844 and 1847 by the provincial governor of the city under the supervision of Mechmit Zeki, a very famous architect from Istanbul, in order to become the governor's residence. In 1994 and until today, the building becomes the headquarter of the prefectorial self-government in Rethymno, despite the severe damages that its structural frame has. Moreover, its interior condition imposes the need of immediate interventions. (M.T. Kosta 2008)

The building has three stories and its total length is 50.55 meters with a width that varies between 18 and 28 meters. The total area of the edifice is 3.175 m^2. The stories and the roof are made of wood and its floor plan is organized through two perpendicular axis of symmetry. In Figure 2 two general views of the edifice are being shown, one from north and the other from south.



Figure 2 Views of the Prefectorial edifice in Rethymno

2.2 The Neoclassical Residence of Prince George in Chania

This residence was built in 1882 by the architect Nikola Magouzo. During that time, it was the most suitable building to accommodate Prince George. When he resigned, it was used as military hospital, as a shelter by the Germans soldiers and finally during 1968 and 1982 as offices of Crete's historical and archeological company. (E.K. Tsatsou 2007)

This building has a ground floor, a first floor and a basement. The total area of the edifice is 293.85 m^2 and its maximum height is 10.87 meters. Its roof and stories are wooden; its masonry is made of stones from a local quarry, and also has some elements of reinforced concrete, which are partly affected by the humidity due to the sea that is near by. Although the tractors placed at the four building's corners have been corroded, they still hold the masonry satisfyingly. The floor plan is characterized by symmetry, and so are the residence's faces. In Figure 3 are being shown two general views of the edifice.



Figure 3 Views of the neoclassical residence of Prince George in Chania

2. 3 The two story Building in Kazantzaki road in Sitia

This residence was built around 1900, by some excellent technicians who came to Sitia from the island Karpathos, located at south Aegean sea. The building has two stories with a yard and an exterior staircase, which facilitates the access of the upper floor with the outdoors. (E.K. Tsatsou 2007)

The building's maximum height is 8.86 meters, the roof is wooden and the stories are made of reinforced concrete. Moreover, in the interior, the ground floor has symmetry through a main axis that divides the building. In Figure 4 are being shown two general views of the building.



Figure 4 Views of the two story building in Kazantzaki road in Sitia

3. THE STRUCTURAL MODELS

For the analysis of these case studies, a finite element model was developed using the software SAP v.10.0.1 Nonlinear (Three Dimensional Static and Dynamic Analysis of Structures).

For the structural model of the Prefectorial edifice in Rethymno city 25.964 finite elements were used. The considered parameters are masonry with modulus of

elasticity E=3,33GPa and wood with E=10GPa. The Neoclassical Residence of Prince George in Chania (3.692 finite elements) and the two story building in Kazantzaki road in Sitia (1.603 finite elements) are both modeled of stone masonry with modulus of elasticity E=1,80GPa, reinforced concrete with E=290GPa and wood with E=10GPa. These models were made so that the materials' mass could ideally be considered concentrated around the models' nodes.

Two variables were selected during the procedure; these were the tension strength and maximum ground acceleration PGA. The buildings' walls' failure was examined for 9 different mortars.

Actions applied on these models include dead and live loads, earthquake loads (PGA=0.16g, 0.24g, 0.32g, 0.40g), vertical weight loading and various combinations, according to the buildings' materials and the regulations about constructions and seismic effects.

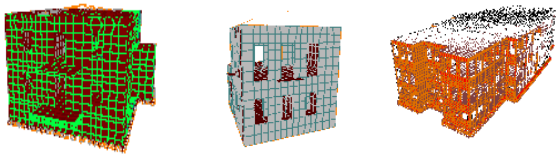

Figure 5 The finite element models of the structures

4. RESPONSE ANALYSIS

In order to evaluate the vulnerability of the structure when subjected to an earthquake event, it is necessary to determine the most vulnerable areas on the edifices. For this purpose the software "FAILURE", (C.A. Syrmakezis, P.G. Asteris 2001) was used. This software provides an optical indication of failing areas on wall surfaces, when the structure is subjected to a single seismic event and it is based on the elaboration of finite element stresses using a proper failure criterion. The criterion selected for these case studies is a modified Von Mises criterion, adapted especially for masonry structures.

The criterion is formulated by the interaction of four surfaces S1, S2, S3 and S4 as illustrated in Figure 6 (section on the horizontal plane of zero shear stress). Each surface represents a certain biaxial stress state:

- S1 represents a compression state in parallel to both principal axes
- S2 describes a stress state of tension in parallel to one principal axis and a stress state of compression in parallel to the other
- S4 exactly the reverse state and
- S3 is represents tension in parallel to both principal axes.

An element is deemed to fail when direct and shear stresses applied specify a point on the circumference or outside the shaded area, projection of the solid.

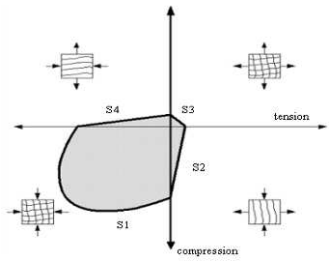

Figure 6 The modified Von Mises failure criterion

Surfaces are described by the Equations:

$$S1: \sigma_{xx}^{\ 2} + \sigma_{yy}^{\ 2} - \sigma_{xx}\sigma_{yy} + 3\tau^2 - f_{wc} = 0,$$
$$for\ \sigma xx\ and\ \sigma yy \le 0 \qquad (1)$$

$$S2: \sigma_{yy} + (1 - \sigma_{xx}/\alpha)\sqrt{f_{wc}^{\ 2} - 3\tau^2} = 0,$$
$$for\ \sigma xx \ge 0\ and\ \sigma yy \le 0 \qquad (2)$$

$$S3: \sigma xx + \sigma yy = 0,$$
$$for\ \sigma xx\ \ and\ \sigma yy \ge 0 \qquad (3)$$

S4: symmetrical to S2 in respect to the bisectional level of the first quadrant

where:

$$a = (f_{wt}/f_{wc})\sqrt{f_{wc}^{\ 2} - 3\tau^2} \qquad (4)$$

and

f_{wc} : compressive strength, f_{wt}: tensile strength

As a result, the low masonry's strength in tension in contrast with its high strength in compression has been considered.

FAILURE's input data are quantified and graphical outputs of the failed areas are produced, for each plane. Besides the illustration of the failure location, a colour output distinguishes between the four different ways of failure, which are the biaxial failure in compression and in tension, the failure in compression in parallel to one principal axis and in tension to the other, and oppositely.

The obtained results are graphically provided and presented in Figure 7. The failure is shown on the external face of the wall (a similar diagram can be produced for the internal face on wall). Red areas represent failure under biaxial tension, while green areas represent failure under biaxial tension-compression. Blue areas have not failed.

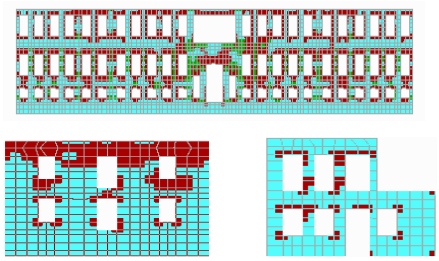

Figure 7 The finite element models of the structures

5. FRAGILITY CURVES

For a given case study, it is possible to define the ground acceleration, which is expected to have a certain damage level on the structure considered. Additionally, materials' properties and the building's response, that influence its total capacity, demand the approach of some assumptions about the ground acceleration and the area's conditions. Usually, the values of those parameters aren't very accurate – they comprise instability and uncertainty due to the nature of these factors.

By processing the data that come out from FAILURE, the fragility curves can easily be formed. After defining the areas that fail, the percentage of the total surface's damage is proposed to be calculated by the ratio A_{damage}/A_{total} (where A is the surface), and after the elaboration of the statistical results comes out the probability-density function, which indicates the possibility of the quotient's certain value by the given PGA.

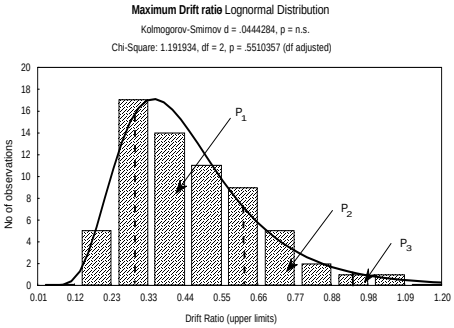

Figure 7 Diagram of density – Lognormal distribution

The possibilities P_1, P_2 and P_3 are the areas between the failure limits that define the damage levels of the construction through the probability-density function: for random values the possibility that the building's response is between the values of the damage level's rate, is being expressed.

Using fragility curves, one can distinguish the possibility of exceeding certain damage levels, as shown in Table 1.

Table 1 Damage levels

	No damage (%)	Small damage (%)	Medium damage (%)	Big damage (%)
Damage Level a	0-2.5	2.5-5	5-15	>15
Damage Level b	0-5	5-15	15-30	>30
Damage Level c	0-10	10-25	25-40	>40

According to the previous table, the possibility of exceeding damage level *a***,** for small damage is between 0-2.5%, the possibility of exceeding damage level *b* for medium damage is 15-30%, for damage level *c* for big damage is over 40%, etc.

By exporting the above percentages it can be very useful to predict the damage of a certain building caused by random earthquake's motion and to organize the interventions that may be demanded, taking under consideration the variety and the compatibility of the materials.

Then, the case studies are being compared between them using two kind of distributions (normal and lognormal) and the final assessment of the strength in tension can be analyzed, among with the buildings' seismic vulnerability.

In the following figures, the damage levels (*a*, *b* and *c*) between the two distributions and the possibility of excess for the three case studies in Chania, in Sitia and in Rethymno are depicted.

Damage level a

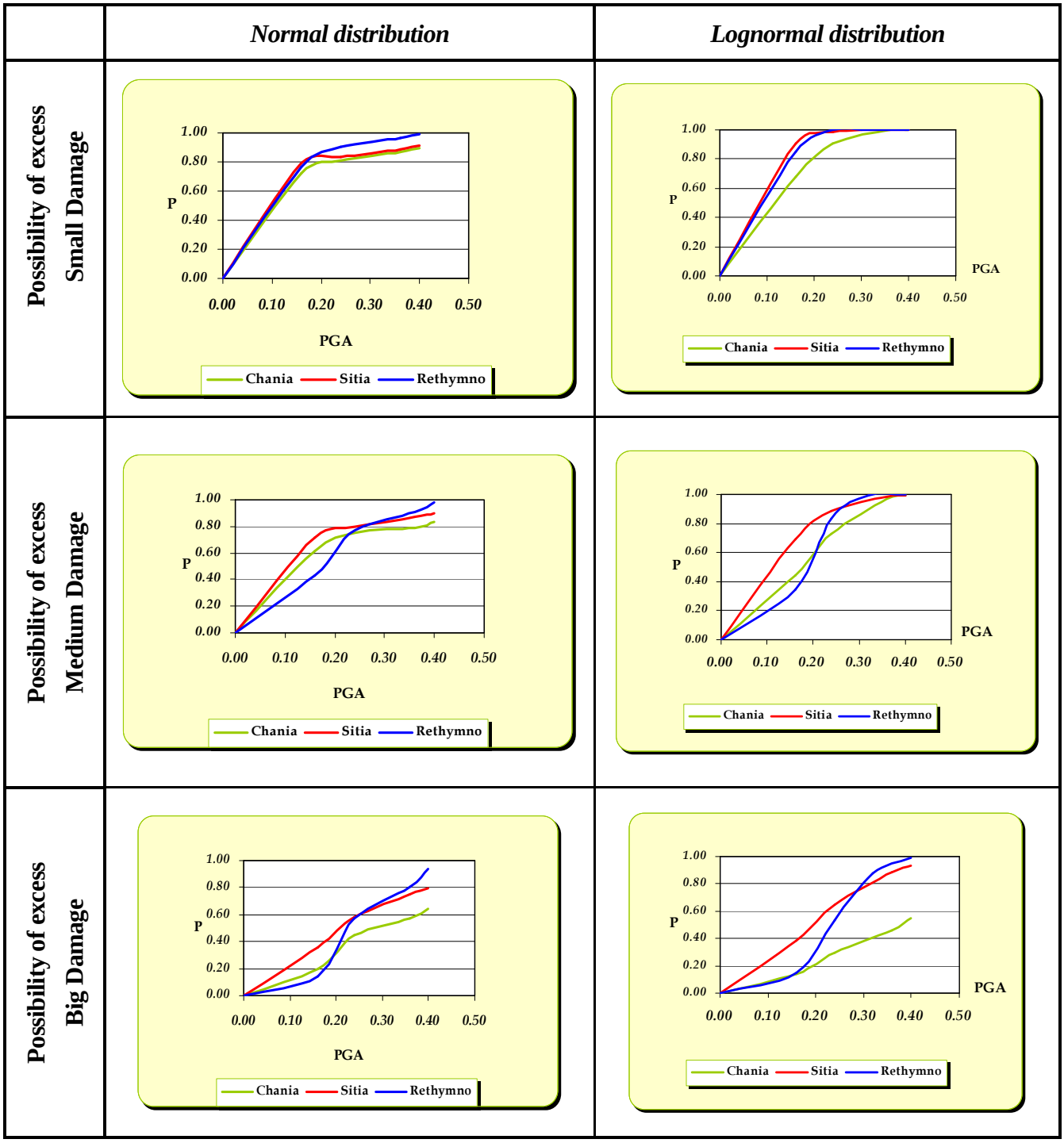

Figure 8 Damage Level a

Damage level b

	Normal distribution	*Lognormal distribution*
Possibility of excess Small Damage	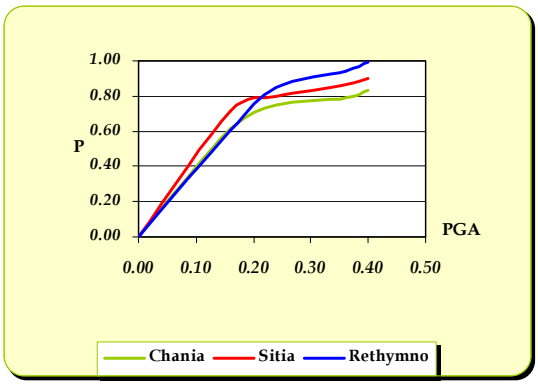	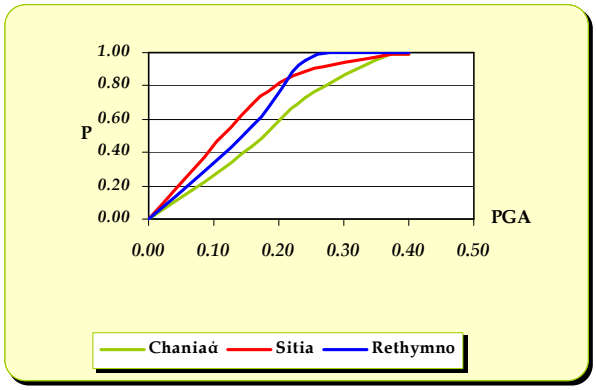
Possibility of excess Medium Damage	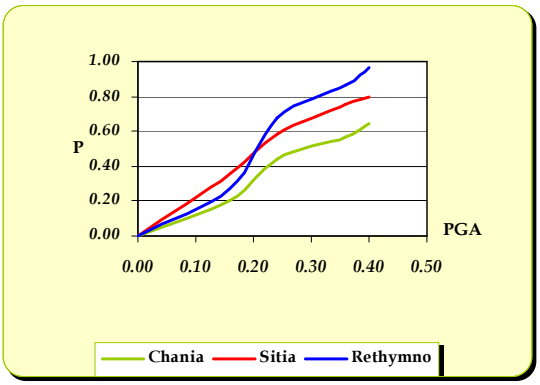	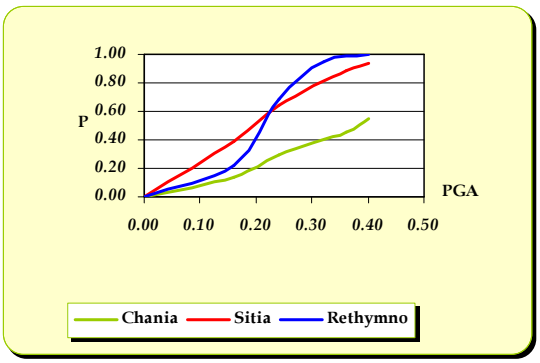
Possibility of excess Big Damage	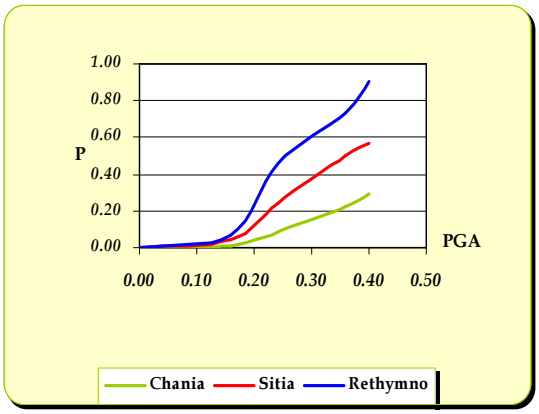	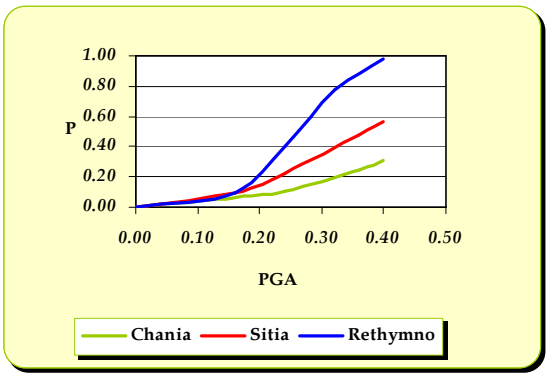

Figure 9 Damage Level b

Damage level c

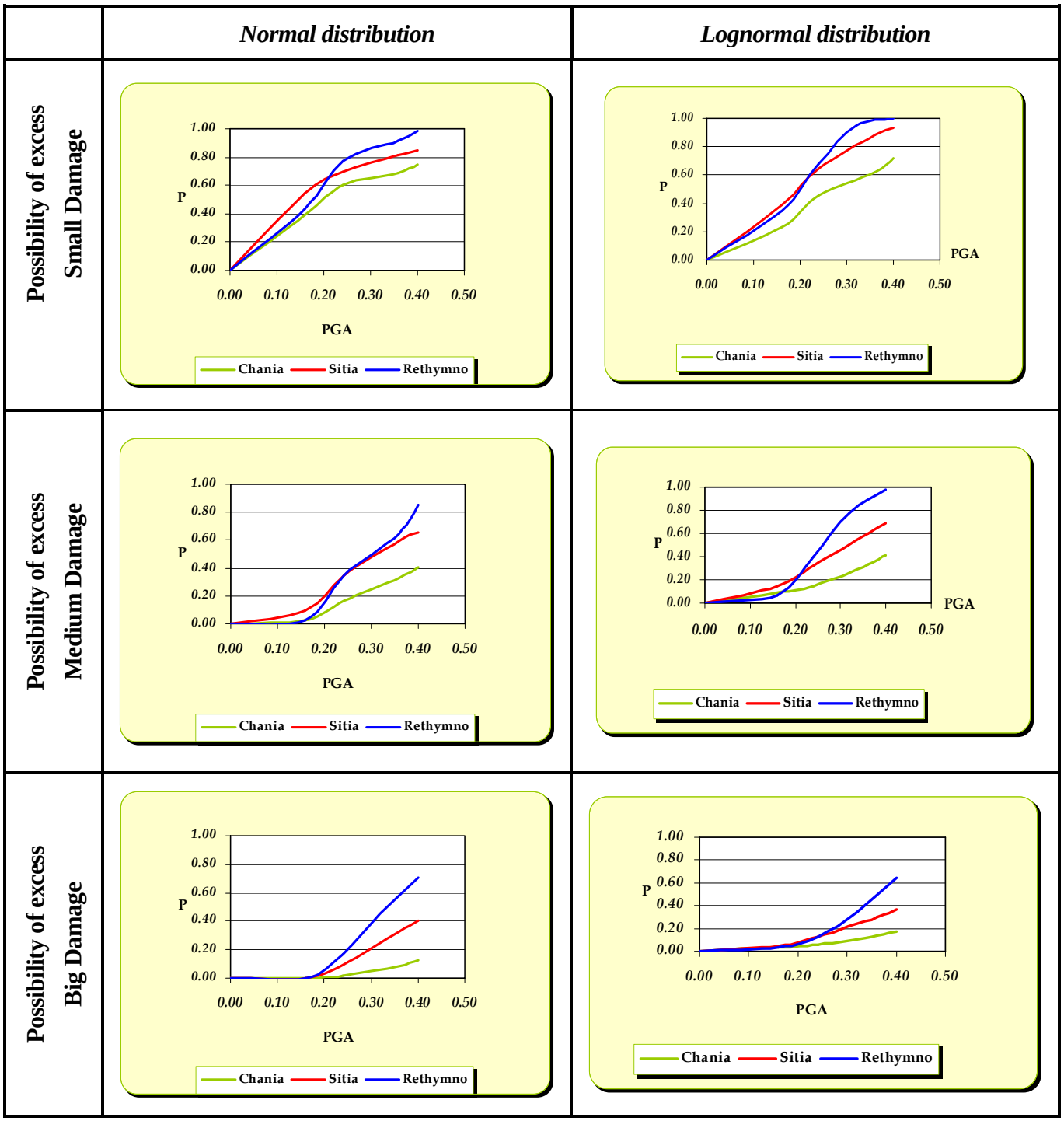

Figure 10 Damage Level c

Fragility curves are an extremely useful tool for decision-making, regarding the conservation and the restoration of the structures, especially in the case of historical monuments where reversibility is often difficult to be achieved and interventions have to be of minimum scale, so as to avoid modifications to the historical character of the structure.

Through the construction of these curves, we can easily represent the probability of certain damage ranks under the effect of various earthquakes intensities and different parameters that define the response of a different type of structures (buildings, churches and bridges). Using this family of curves, it is possible to investigate the way that each of these factors affects the vulnerability of the structures relatively to others.

Therefore, from the above diagrams, it is being concerned that when the damage's possibility increases, the diagrams' deviation becomes larger. Moreover, for the same damage value, the possibility of excess becomes larger when the PGA increases.

Also, in all diagrams, the edifice in Rethymno has higher possibilities of excess for all damage levels. And the main conclusion is that the building considered has the highest vulnerability, during a possible seismic event, among the other buildings.

6. CONCLUSIONS

The protection of the cultural heritage from the disastrous and often the irreparable consequences caused by natural enemies (such as seismic events) is very important and many times compulsory for the safeguard of the historical buildings and the maintenance of each country's cultural heritage. The post-earthquake rehabilitation and retrofitting of these structures is an important issue in the entire Mediterranean area, where many cultural heritage buildings are made of masonry. This type of structure is characterized by its low tensile strength, geometrical peculiarities, past damages due to earthquakes, degradation (cracks), lack of proper conservation and sometimes-incompatible human interventions.

A methodology for performing failure analysis has been proposed for the correlation of the earthquake intensity with the vulnerability of the structure. The modified Von Mises failure criterion for biaxial stress state has been developed in order to adapt to masonry structures.

The methodology developed leads to the construction of the fragility curves that can graphically represent the probability of certain damage ranks under the effect of various earthquakes intensities. Graphical outputs have been obtained.

The application of the methodology proposed is illustrated through three case studies, all typically masonry structures. For its reinforcement, various restoration mortars have been investigated, with diverse tensile strengths.

References:

M.T. Kosta (2008), "Comparative Research of the Static Condition of Historical Structures with the Methodology of Fragility Curves", *Postgraduate Diploma Thesis*, National Technical University of Athens, Greece.

E.K. Tsatsou (2007), "Evaluation of the seismic vulnerability of two neoclassical buildings using the Methodology of Fragility Curves", *Postgraduate Diploma Thesis*, National Technical University of Athens, Greece.

C.A. Syrmakezis, P.G. Asteris, A.K. Antonopoulos, O.A. Mavrouli (2005), "Analysis of Historical Structures using Three-Dimensional Solid Elements", *Proceedings of the Tenth International Confernce on Civil, Structural and Environmental Engineering Computing*, Rome, Italy, 29 August-2 September.

C.A. Syrmakezis, P.G. Asteris, A.K. Antonopoulos, O.A. Mavrouli (2005), "Stress-Failure Analysis of Masonry Structures under Earthquake Loadin, published in *Fracture and Failure of Natural Building Stones, Applications in the Restoration of Ancient monuments*", Chapter 3, Masonry 3.3, S.K. Kourkoulis, Springer.

C.A. Syrmakezis, P.G. Asteris, (2001) "Masonry Failure Criterion Under Biaxial Stress State", *Journal of Materials in Civil Engineering, ASCE*, Vol. 13, No. 1, January/February.

JOINT CONFERENCE PROCEEDINGS
7th International Conference on Urban Earthquake Engineering (7CUEE) &
5th International Conference on Earthquake Engineering (5ICEE)
March 3-5, 2010, Tokyo Institute of Technology, Tokyo, Japan

TOWARDS EARTHQUAKE SAFER NON-ENGINEERING HOUSES BY TECHNOLOGICAL AND SOCIAL APPROACHES

Kimiro Meguro

Director/Professor, International Center for Urban Safety Engineering,
Institute of Industrial Science, The University of Tokyo, Japan
meguro@iis.u-tokyo.ac.jp

Abstract: Damage due to past earthquakes has shown that the collapse of vulnerable houses mainly made of masonry is the main cause of casualties. As these structures, called non-engineered structures, are constructed by local people having no engineering background by using local available material without following structural code, there is no relation between their structural performance and existence and quality of the code. Therefore, establishment and/or revision of structural code cannot solve these problems. To tackle the problems considering the real situation mentioned above, I have proposed locally feasible system composed of technical and social approaches. As a technical approach, I have developed PP-band (poly-propylene band, worldwide available cheap but very strong material commonly used for packing) meshes retrofitting method. This method is very inexpensive and simple and it can be performed by the house owner him/herself. While as a social approach, I have developed several systems, such as 'two-step incentive system', 'micro earthquake insurance based or micro finance based incentive system', etc. By the integrated system proposed, house owners are encouraged to retrofit their weak structures, and structural damage and casualties due to future earthquakes would be drastically reduced. The burden which should be given to the victims by national and local governments could also be reduced very much. Moreover, other stakeholders, such as local masons, insurance companies, microfinance organizations would also have big benefit.

1. INTRODUCTION

Damage due to past and recent earthquakes, such as the 2003 Bam, 2005 Kashmir and 2006 Java, 2008 Wenchuan, and 2010 Haichi earthquakes, has shown that the collapse of vulnerable houses is the main cause of casualties. These vulnerable houses are mainly masonry structures made of unburned bricks called adobes, bricks, stones, and concrete blocks and RC frames with masonry infill wall, among others. Even if a good disaster response system, including rescue operations, and a recovery/reconstruction plan are conceived, earthquake damage, especially human casualties, cannot be reduced unless structural collapse is prevented. Therefore, it is vital to guaranty the seismic strength of new constructions as well as to upgrade the seismic capacity of existing ones. In the former case, "good construction codes", i.e. codes that are complied, are necessary. Even sophisticated, complicated codes which are difficult to interpret and put into practice are inappropriate. In addition, an efficient system to ensure the code application should also be established. For existing constructions, technical solutions which emphasize local availability, applicability, and acceptability are required. These should be accompanied by a social system which encourages retrofitting among the general population. Such system should aim at increasing people's disaster awareness and at giving incentives to house owners for retrofitting [1].

In this paper, I introduce a very efficient retrofit technique and some social systems that promote retrofitting weaker houses, and also show the great effects of the combined approaches.

2. PP-BAND MESH RETROFITTED METHOD

Masonry is the most used construction material worldwide but unfortunately very vulnerable against earthquakes. Considering these points, a technical solution for retrofitting based on polypropylene band (PP-band) meshes has been developed by the author's research group[2, 3,4]. PP-band, which is commonly used for packing, is resistant, inexpensive, durable and worldwide available and PP-band retrofit method is a simple, cheap, easy and local acceptable method. Its installation process is very simple and it can be performed by the house owner him/herself [2,3].

2.1 Performance of PP-band Mesh Retrofitted Masonry Structure

In order to verify the effects of PP-band mesh retrofit method, a number of experimental and numerical studies have been done using wallets and wall structures and 3-dimensional miniature and real scaled structures with static and dynamic loading conditions[2, 3, 4]. Due to space

limitation, this paper shows one example of shaking table experiment using unreinforced masonry and PP-band retrofitted masonry houses. The model houses used in the experiment are popular and typical single-storied houses with wooden frame roof.

Sinusoidal motions of frequencies ranging from 2Hz to 35Hz and amplitudes ranging from 0.05g to 1.4g (g: gravity acceleration) were applied to obtain the dynamic response properties of the structures. The numbers given in the Table 1 shows the loading sequence used in the tests. General trend of loading was from high frequency to low frequency and from lower amplitude to higher amplitude following the seismic intensity defined by Japan Meteorological Agency (JMA). Higher frequencies motions were skipped towards the end of the runs. The highlighted numbers in the Table 1 are the last input motion that specimen could withstand.

Table 1 Loading Sequence and The Last Run That Specimen Could Withstand

Amplitude (g)	Frequency 2Hz	5Hz	10Hz	15Hz	20Hz	25Hz	30Hz	35Hz
1.4		50						
1.2	54	49						
1.0		48						
0.8	53	47	43	40	37	34	31	28
0.6	52	45	42	39	36	33	30	27
0.4	51	44	41	38	35	32	29	26
0.2	46	25	24	23	22	21	20	19
0.1	18	17	16	15	14	13	12	11
0.05	10	09	08	07	06	05	04	03
Sweep		A-4-NR-P			01,02		A-4-NR-X	

A-4-RE-P: Brick type: A- unburned brick, B- burned brick; B-R-P-S; Surface finishing: X- Paste not applied, P- Paste applied (7.5 mm); Roof Condition: 1- no roof, 2- roof connected to two wall in direction of shaking, 3- roof connected to all four wall; Retrofitting condition: NR- Non retrofitted, RE- Retrofitted

A-4-RE-X

From the Table 1, improvement of performances of masonry house by PP-band mesh retrofit and surface finishing material on the walls can be clearly seen. Figure 1 shows the performances of non retrofitted model A-4-NR-P and retrofitted model A-4-RE-P with different JMA seismic intensities. Relation between JMA scale and Modified Mercalli Intensity (MMI) scale is also shown in the figure. Total collapse of the non-retrofitted model A-4-NR-P was observed at the 47th run with intensity JMA 5+(see Figure 2(a)) while retrofitted model A-4-RE-P performed moderate structural damage level at 47th run. Moreover, moderate structural damage level of performance was maintained until 48th run, leading to intensity JMA 6-. It should be noted again that this model survived 7 more shakings in which many runs were with higher intensities than JMA 5+ at which the non-retrofitted building collapsed before reaching to the final stage at the 54th run.

When we applied the surface finishing to above house model as shown in Figure 2(b), due to improve bond connection between PP-band and brick wall, surface plaster kept well with wall. This is not observed in non-retrofitted model. Because of this, brick unit confined effect inside the PP-band mesh is improved and it improves the overall earthquake resistant performance of the structure.

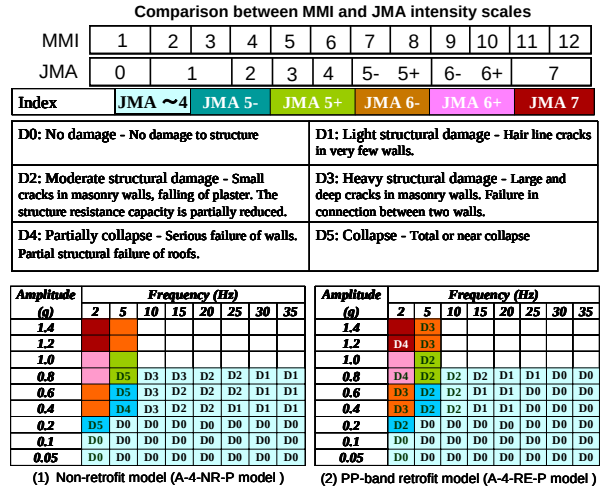

Figure 1 Performance and Damage levels of Specimen During the Experiment

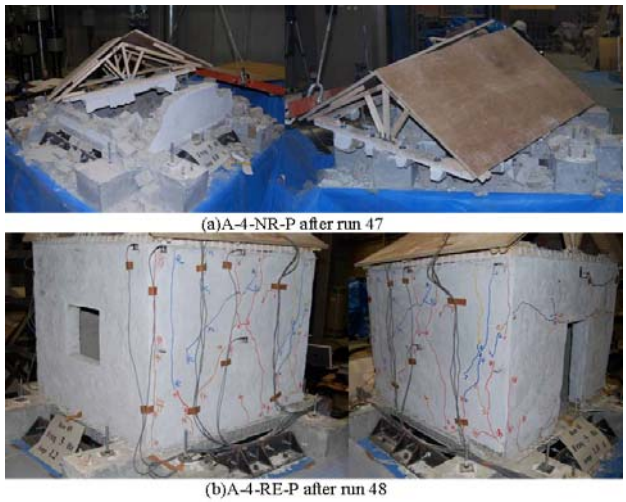

Figure 2 Photos of Damaged Specimen During Experiment

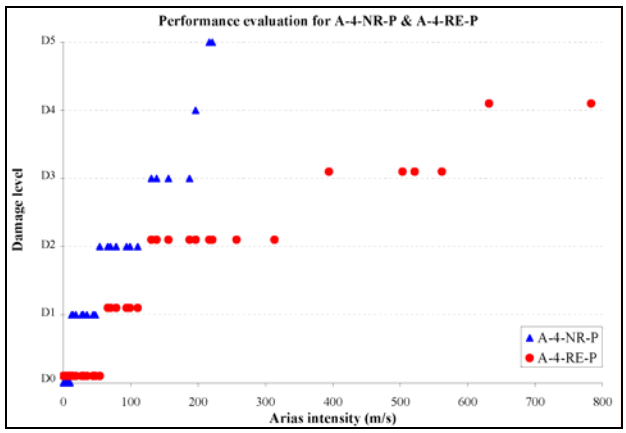

Figure 3 Performance and Damage Levels of Specimen Based on Arias Intensity

Figure 3 shows the performances of both models with Arias intensities. The Arias intensity was initially defined (Arias, 1970)[5] as equation (1).

$$I_a = \frac{\pi}{2g}\int_0^t a^2(t)dt \quad (1)$$

It is directly quantifiable through the acceleration record a(t), integrating it over the total duration of the earthquake. The arias intensity is claimed to be measure of the total energy provided by the ground. Form the results, it clearly shows that; performance of the retrofitted model was at least 4 times better than that of non-retrofitted model in terms of energy dissipation capacity.

3. THE EFFECT OF RETROFITTING

The effectiveness of retrofitting was quantitatively calculated and is exhibited using fragility functions for non-retrofitted and retrofitted structures as well as seismic intensities of MMI scale experienced in the three events such as 2003 Bam, 2005 Kashmir and 2006 Java earthquakes.

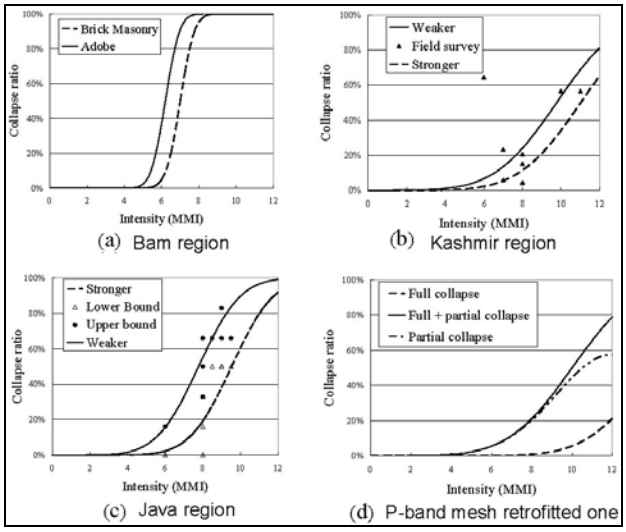

Figure 4 Fragility Functions of Houses in Different Regions

Figures 4 (a) to 4 (c) show the fragility functions of masonry houses in the regions affected by the recent earthquakes obtained from field surveys [6, 7, 8, 9]. It can be seen that the weakest houses were found in Bam area whereas the strongest ones were located in the Kashmir region. In Figure 4 (b), one of the points corresponding to the field survey data falls far from the observed trend. This point corresponds to Batagram where site effects reportedly caused strong ground amplification leading to high intensity shakes which were not reflected in the spatial intensity distributions used in this study.

As mentioned earlier, PP-band meshes were considered for retrofitting of masonry houses because they are affordable and notably improve the seismic capacity of houses. Fragility functions for PP-band mesh retrofitted houses were estimated using available experimental data. Because this data is limited, the curve was defined as the cumulative normal distribution function that best fitted the available data (Figure 4 (d)).

Table 2 Comparison of Expected Losses with and without Retrofitting Masonry Houses

Earthquake → / Item ↓	2003 Bam		2005 Kashmir		2006 Java	
	Without retrofitting	With retrofitting	Without retrofitting	With retrofitting	Without retrofitting	With retrofitting
Totally collapse house / casualty rate	1.13		3.47		33.80	
Partially collapse house / casualty rate			12.01		174.7	
Number of houses (total collapse)	49,000	8,216 (83%)	203,579	5,847 (97%)	154,098	13,080 (92%)
Number of houses (partial collapse)			196,573	67,561 (66%)	199,160	78,550 (61%)
Death toll (from total collapse)	43,200	7,271 (83%)	58,668	1,685 (97%)	4,559	387 (92%)
Death toll (from partial collapse)			16,367	5,625 (66%)	1,140	450 (61%)

* The numbers in parenthesis show the reduction in number of percentage of damaged houses and fatalities when retrofitting is implemented.

Considering the seismic intensity distribution for each event and the corresponding fragility curves for the non-retrofitted and retrofitted masonry houses, the differences in the number of collapse units were calculated as shown in Table 2. Using average house collapse / casualty ratios observed during these events, the number of casualties due to the hypothetically retrofitted houses was estimated. It can be concluded that retrofitting the houses prior to the earthquake could have led to an average reduction of over 85% and 90% in the number of fatalities and totally collapsed houses, respectively.

It is worth mentioning that the partially collapse house / casualty rate should be lower in case of the retrofitted houses because the mechanism of casualties by partially collapsed houses is different. In non-retrofitted cases, falling blocks of masonry hitting people are the major cause of death. However, in houses retrofitted by PP-band mesh, this phenomenon is prevented. Even in the case of total collapse, it takes a longer time for the retrofitted house to fail and therefore fewer casualties are expected. Because there is no data available, the same rates were used to be on the conservative side.

To promote retrofitting in developing countries, the economic issue is very important. It is expected that the house owners will undertake retrofitting spontaneously when most of them are struggling to procure more urgent basic needs. It is more realistic to recognize that they need some type of subsidy.

4. PROMOTION SYSTEM FOR SEISMIC RETROFIT

Even if technically attractive retrofit method is developed, if people's disaster imagination capability is poor, retrofit of weaker houses cannot be popular. It is impossible for human to prepare well for an unimaginable situation. We should pay much attention to increase disaster imagination of the people to understand the importance of seismic retrofit of weaker houses that is the key issue for reduction of casualty and to create some social systems by which house owners are encouraged to retrofit their own weaker houses by themselves. In this chapter, some research activities related to promotion of seismic retrofit are introduced.

4.1 Demonstration of PP-Band Mesh Retrofit Construction and Shaking Table Failure Test at the Affected Site Due to the 2005 Kashmir Earthquake

Two approaches are considered for the social system to promote retrofitting. The first is to increase people's disaster awareness. For this purpose, demonstrations at earthquake affected areas have been carried out (see Figure 5). I have introduced my research group activities in Musafarabad, one of the most affected areas by the 2005 Kashmir Earthquake. As an example, one local standard house retrofitted with PP-mesh was constructed to show the people how to built earthquake-resistant houses. Retrofitting material cost for the house was about 30US$ and the installation cost was less than 5 % of the total construction cost for the first trial by the local masons under the supervision of PP-band method experts. As a part of the demonstration, two 1/6-scale models, with and without retrofitting, were shaken with an improvised shaking table in order to increase earthquake risk awareness. This event was attended by politicians, local practitioners, mass media people, NGO/NPO representatives, and the general public. All participants could clearly understand the importance of structural strength, ease of installation, and the great effect of PP-band retrofit.

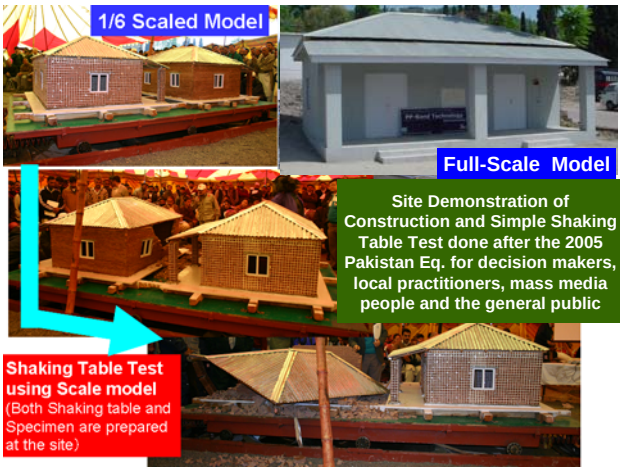

Figure 5 Demonstration of PP-band Mesh Retrofit Construction and Shaking Table Failure Test at The Affected Site Due to the 2005 Kashmir Earthquake

4.2 Proposal of the Retrofitting Incentive System

As retrofit promotion social systems, the author's research group has developed some interesting and efficient models such as the "2-step incentive system" and the "new micro-earthquake insurance based or micro finance based incentive system," etc. Due to space limitations, only the "2-step incentive system" is presented in this section.

Figure 6 shows the structure of the "2-step incentive system" proposed by the author's research group[10]. The first step is providing the house owner with the material for retrofitting plus a subsidy, α, which is given after checking that the house was properly retrofitted. This subsidy is to prevent the house owner from selling the retrofitting material and to give him/her an incentive to retrofit. When the earthquake occurs, the second step incentive is given: those who in spite of having retrofitted their houses face damage, receive larger compensation money than those who have not carried out retrofitting.

The effectiveness of the proposed system was assessed by comparing the difference in costs borne by the incentive given agency (the government for this study) and the house owner if house retrofitting were implemented at different ratios. It was assumed that ten thousand 1-story houses (total area: 72 m^2, 27 m^2 x 2 rooms, see Photo 1) were located at each MMI area. The three earthquake scenarios that have been discussed so far were considered. Unit costs for each region are shown in Table 3. To retrofit each house, around 4,500 to 5,000m of PP-band, at approximately 3,000yen in Kashimir and 7,000yen in the other regions, were needed. The total cost of retrofitting varies depending on how much of the works are done by the house owner and how much are contracted. In the calculation, other government borne costs resulting from house collapse, such as debris removal, shelter, temporary housing, among others, are not considered. Therefore, the results introduced hereinafter can be considered conservative ones.

Table 3 Unit Costs Used for the Analysis

Cost (thousand yen)	Region		
	Bam	Kashmir	Java
New construction	1620	421.2	540
Daily wage	0.96	1	0.45
Compensation (~35% of replacement cost)	600	150	200

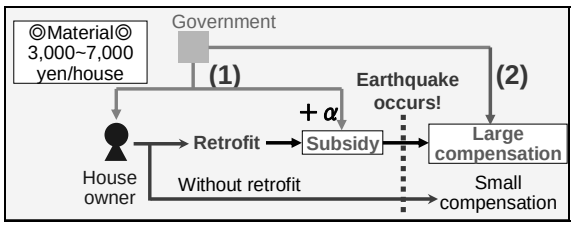

Figure 6 Scheme of 2-step Incentive System

Figures 7 and 8 show the cost borne by the house owners (as a group) if they carry out all the works and the government provides or not the 1st-step incentive (material cost + α, for example, equal to the material cost) in case of Kashmir. The different lines represent different ratios of system acceptance from 0% (no house is retrofitted) to 100% (all 10,000 houses are retrofitted.) When 10,000 houses are subjected to an intensity MMI-12, the costs borne by the owners would be approximately 3,500 million yen if retrofitting would not have been done and about 1,000 million yen when it would have been fully embraced. The difference in cost represents the money that the owners have to invest to rebuild their collapsed houses. Because the incentive money and PP-band cost are relatively low, there is no much difference between Figures 7 and 8. Consequently, the money that the government should prepare for the first step incentive is not so large.

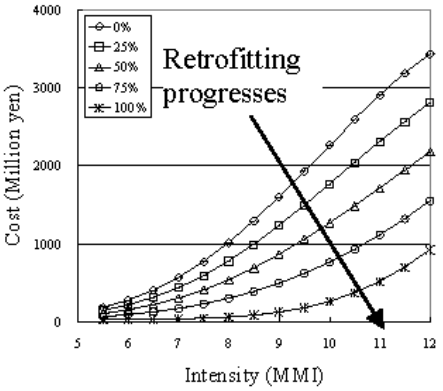

Figure 7 House Owner Borne Cost If All Works Are Done by Him/Herself and There Is No Incentive

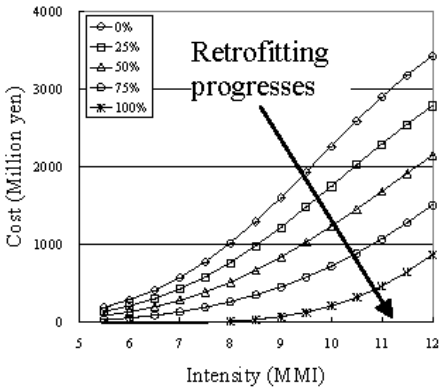

Figure 8 House Owner Borne Cost If All Works Are Done by Him/Herself and There Is Incentive

Let us now consider the cost borne by the government due to the 2nd-step incentive (i.e. compensation after the earthquake occurs). Figures 9 and 10 show the scenarios in which the owner who retrofitted his/her house receives the same or double compensation, respectively, as the owner who did nothing. Although the government expenses increase in the latter, they are still lower than carrying out no retrofitting at all. Therefore, it is concluded that even with the 2-step incentive, the government borne costs decrease if houses are retrofitted.

Figures 11 and 12 show the costs borne by the government, including the incentives with and without proposed system, for Kashmir and Java regions. Retrofitting by proposed promotion system results in less money spent on the government side.

In the previous calculations, it was considered that 10,000 houses were subjected to an each intensity of shaking. However, this is not realistic. In the real situation, there are large areas subjected to lower intensities and relatively small areas subjected to higher intensities. If this is taken into account, the costs borne by the government and the house owner can be more realistically calculated.

For each of the three earthquakes considered in this study, the actual distribution of houses and intensities experienced were used to determine the costs borne by government (Figure 13) and house owners (Figure 14) assuming that the 2-step incentive system was in place before the event. The reduction in government expenses is approximately 95.8%, 81.4% and 75.6% for Bam, Kashmir and Java earthquakes, respectively. On the side of the house owner, the reduction of expenses is even more dramatic and in some cases, the owners profit from adopting the retrofitting promotion system. This is because the government gives the subsidy (α) if retrofitting is satisfactorily carried out before the event.

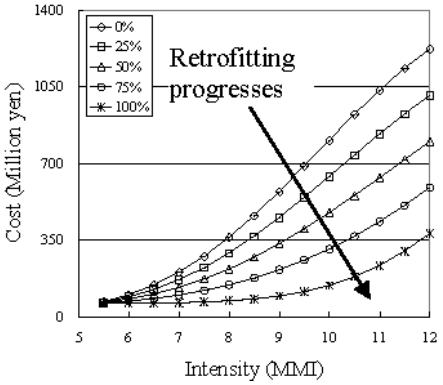

Figure 9 Government Borne Cost If Compensation Is Same for All House Owners

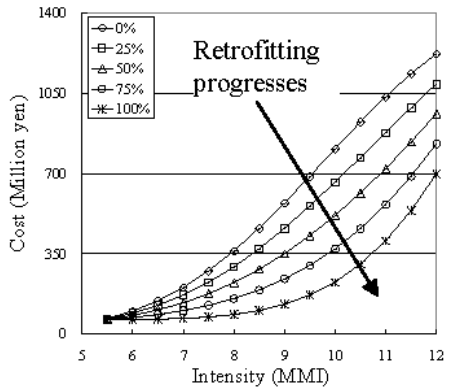

Figure 10 Government Borne Cost If Compensation Is Double for House Owners Who Retrofitted Their Houses

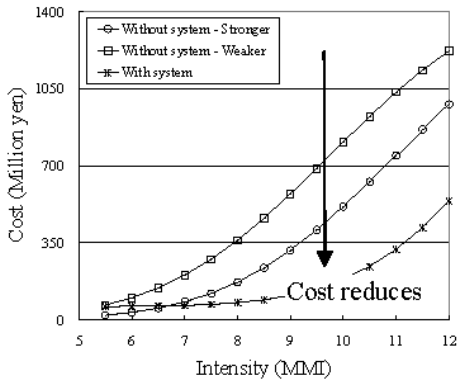

Figure 11 Total Government Borne Cost (Kashmir)

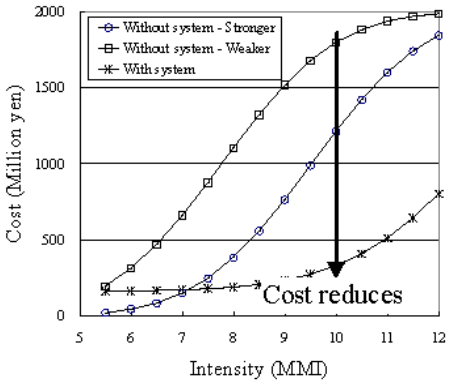

Figure 12 Total Government Borne Cost (Java)

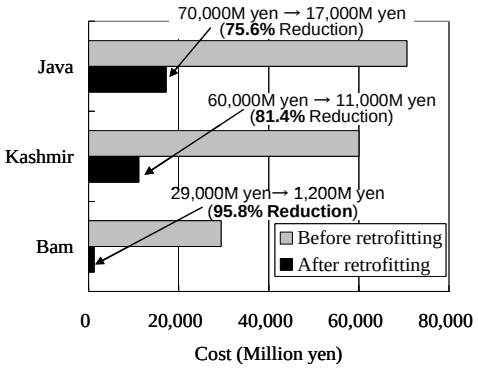

Figure 13 Total Government Borne Cost
Considering the Real Area of Seismic Intensity

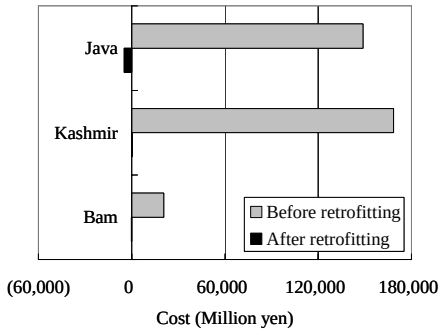

Figure 14 Total House Owner Cost
Considering the Real Area of Seismic Intensity

5. CONCLUSIONS

Retrofitting of low earthquake resistant houses is fundamental to prevent human fatalities and economic losses in future earthquakes. In spite of this, retrofitting is not progressing smoothly. For implementation of safer housing, it is important to approach by both technical and social solutions. In this paper, I have introduced the PP-band mesh retrofit method which is local available, applicable, and acceptable as one of the best technical solutions, and also, 2-step incentive system as one of my proposed social promotion systems that encourage retrofitting among the general population.

It is found that with the PP-band mesh retrofit method, both new construction and existing low earthquake resistant structures can be strengthened drastically using local available and cheap material and without requiring high skills and any change of life style of the area. And with a 2-step incentive system, house owners are encouraged to retrofit their houses before the event by receiving material for retrofitting and a subsidy upon satisfactorily carrying out the works. If after the earthquake, the retrofitted houses are affected, the owners receive double compensation than the house owners who did nothing. It was found that if this system would have been implemented before the 2003 Bam, 2005 Kashmir and 2006 Java earthquakes, the costs spend by government and house owners could have been dramatically decreased. Consequently, the number of casualties could have been reduced. Although the analysis presented did not include government expenses resulting from structural damage such as debris removal, temporary housing, shelters, compensation for casualties, etc., the benefits of the retrofitting promotion system for house owners and government were clear. It was demonstrated that by combining technological and social approaches, it is possible to verify the feasibility of implementing weak masonry house retrofitting and consequent drastic reduction of damage due to future earthquakes.

References:

1)Yoshimura, M. and Meguro, K, Basic Study on the Retrofitting Promotion System for Low Earthquake-Resistant Structures, *Proceedings of JCOSSAR2003*, (Japan, 2003).

2) Mayorca, P. and Meguro, K, Proposal of an efficient technique for retrofitting unreinforced masonry dwellings. *Proceedings of the 13WCEE*, (Vancouver, Canada, 2004), CD-ROM.

3) Meguro, K., Mayorca, P., Sathiparan, N., Guragain, R., and Nesheli, N, Shaking table tests of small scaled masonry models retrofitted with PP-band meshes. *Proceeding of the 4th International Symposium on New Technologies for Urban Safety of Megacities in Asia*, (Singapore, 2005), CD-ROM.

4) Nesheli, K., Sathiparan, N., Guragain, R., Mayorca, P., Ito, F., Kagawa, H., Tsugawa, T., and Meguro, K, Full-Scale Shaking Table Tests On Masonry Buildings Retrofitted By PP-Band Meshes, *Proc. of the 5th International Symposium on New Technologies for Urban Safety of Megacities in Asia*, (Phuket, Thailand, 2006), CD-ROM.

5) Arias, A. (1970). "A Measure of Earthquake Intensity," R.J. Hansen, ed. *Seismic Design for Nuclear Power Plants*, MIT Press, Cambridge, Massachusetts, pp. 438-483.

6) Japan Institute of Architecture, Damage Survey Report on the December 26, 2003 Bam Earthquake, Iran, (2004). (in Japanese)

7) Asian Development Bank and World Bank. Pakistan 2005 Earthquake Preliminary Damage and Needs Assessment, (2005).

8) Japan International Cooperation Agency, Survey Report for the Establishment of a Recovery and Reconstruction Project after the 2005 Kashmir, Pakistan Earthquake, (2005). (in Japanese)

9) JICA, The Study on Seismic Microzoning of the Greater Tehran Area in the Islamic Republic of Iran, (2000).

10) Iritani, S, Effects of Implementing a Low Cost PP-band Retrofitting Method for Masonry Houses. Case study for Recent Damaging Earthquakes in Developing Countries. Undergraduate Thesis, The University of Tokyo, (2007). (in Japanese)

THE INVESTIGATION AND ANALYSIS OF STRUCTURE EARTHQUAKE DAMAGE IN DUJIANGYAN

Zhong Jiangrong[1)] Lin Junqi[2)]

1) Associate professor, Institute of Engineering Mechanics, China Earthquake Administration, China

2) Professor, Institute of Engineering Mechanics, China Earthquake Administration, China

Abstract: The Great Wenchuan Earthquake (Ms8.0) occurred in the Sichuan province, China, in May 12, 2008. This incident caused enormous disaster to the region of Sichuan and Shanxi province. The historical famous city (Dujiangyan) is situated the serious disaster area of the great earthquake. The macro earthquake intensity of the urban area are Ⅷ and Ⅸ. The city has various structures in forms with a long history. It is a representative middle-small city that it includes many-ages structures. The examples of damage structure are very plentiful in the city.
After 3 months of the earthquake, the investigation group of the structures damage is founded for the city of Dujianyan. Total 8692 buildings were investigated. The gross area of buildings is about 11607.7 thousand square meters. The result manifest that the buildings of the damage degree exceeding the Moderately Damage are 3160, which accounts for 36.36% of total buildings.

The whole city macro damage of buildings is given in this paper. Then the typical building and damage status are provided. Their on-site photos are listed. The shortage of structure anti-seismic is pointed on basis of the analysis of those damage buildings in the city of Dujiangyan. This work will be contributed to the reconstruction after earthquake and the construction of city locating in the high intensity area.

1 INTRODUCTION

Dujiangyan City (Guan county) is located at the west of Chengdu Plain and the drainage of Min Jiang River. It is in the west of Sichuan province and border on the City of Chengdu on the east. It's northern latitude is from 30°44′ to 31°22′ , east longitude from 103°25′ to 103°47′ . The Dujiangyan irrigation works were set up in 256 B.C. It is the longest and subsisting unique great marine irrigation works in the world at present. The name of Dujiangyan gets from here.

Dujiangyan is 54 kilometers across from east to west and 68 kilometers from north to south. The area of the territory is 1211 square kilometers. There are 12 towns, 16townships, 2 development zones and 9 street commissions. The total population is about 550 thousands.

The Great Wenchuan Earthquake (Ms8.0) caused serious economic losses to Dujiangyan in May 12, 2008. Dujiangyan is located in the heavy disaster area of the earthquake. The whole city is lied the hybrid area that the macroscopic earthquake intensities are Ⅷ and Ⅸ. In Dujiangyan city， there were 3091 people killed, 203 people missing and 10560 people injured in the earthquake until July, 2008. Then, the event resulted in the 53,670,000,000 RMB direct economic losses. It is pleased that the 2000-years Dujiangyan irrigation works experienced the test of the earthquake of Wenchuan. It is still intact.

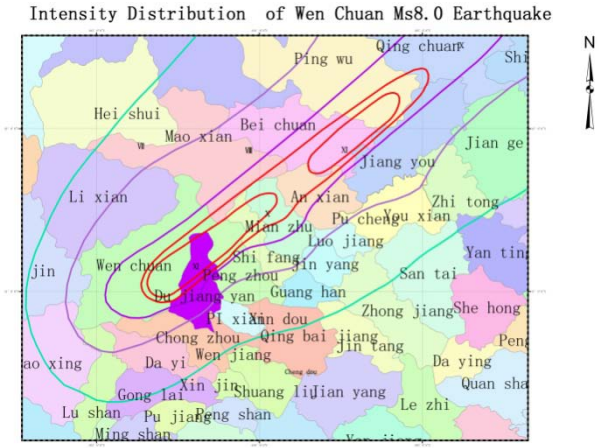

Figure 1 Distribution of Intensities around Dujiangyan

2 BRIEF INTRODUCTION OF STRUCTURE DAMAGE INVESTIGATION

Dujiangyan is a well-known historical city. It has a long history. There are plentiful forms structures inside the city. The ages of structures across a long times. There aren't only brief timber structures made in last century, but also reinforced concrete structures and tall buildings. According to the actual investigation, the structure forms are divided into masonry (MAS), reinforced concrete (RC), tall building (TB), masonry of ground floor frame (MGFF), and plant building (PB), other structure (OS).

The investigation group of structures damage is founded in the city of Dujiangyan at Aug, 2008. The IEM (Institute of Engineering Mechanics, China Earthquake Administration) is responsible for the group. It is also constituted by HIT (Harbin Institute of Technology), DUT (Dalian University of Technology), NUAA (Nanjing University of Aeronautics and Astronautics), BIT (Beijing Institute of Technology) and YTU (YanTai University).The group contains more than 30 technicians. The investigation which is aimed at the every building was in progress under cooperation of local staff. It lasted about one month by looking into the buildings one by one. The contents of investigation include the type, storey, year, pre-earthquake status, brief description of the major damage, the on-site damage causes analysis, and so on. Then photos were taken at the same time. On the basis of the damage degree of structures, 5 levels are divided into. There are Intact on the whole, Slightly Damaged, Moderately Damaged, Seriously Damaged and Ruined. The detail definitions of the levels are followed.

Intact on the whole (including Intact): The structural supporting components are intact. But a few structural un-supporting components reach a slight damage. The structure don't need be fixed and can be used as usual

Slightly Damaged means there are the visible cracks in a few structural supporting components. But there are the obvious cracks in the structural un-supporting components. The structure can be used as usual after not needing be fixed or slightly fixed.

Moderately Damaged means there are the slight cracks in the most structural supporting components and the obvious cracks in the partial ones, but there are the seriously damage in a few structural un-supporting components. The structure need be general fixed.

Seriously Damaged means there are the seriously damage in the most structural supporting components or the structure is partial collapsed. It need be capital fixed. A few structures are difficult to be fixed.

Ruined means there are the seriously damages in the most structural supporting components. The structure is on the brink of collapse or collapsed. It can't be fixed.

In the description of damage levels, 3 misty measure words mostly scopes are followed. A few is below 5%, Partial is below 30% and the most is above 50%.

3 RESULTS OF STRUCTURE DAMAGE INVESTIGATION

In this investigation, the total 8692 buildings were investigated. The gross area of structure is about 11607.7 thousand square meters. The result of investigation is listed in Table 1 by structure forms and in Table 2 by damaged levels. In the followed tables, the unit of buildings area is 10000m^2. The distribution of damage levels of the whole structure is showed in Figure 2. The distribution of every building is showed in Figure 3 by damage levels in the map. Green is Intact on the whole. Blue indicates Slightly Damaged. Yellow indicates Moderately Damaged. Purple indicates Seriously Damaged and red indicates Ruined.

Table1 Investigation Result by Structure Forms

	MAS	RC	TB	MGFF	PB	OS	Total
Num	4164	912	14	2192	141	1269	8692
Num Per	47.91	10.49	0.16	25.22	1.62	14.60	
Area	583.85	175.21	11.09	352.16	17.39	21.07	1160.77
Area Per	50.30	15.08	0.96	30.34	1.50	1.82	

Table2 Investigation Result by Damage Levels

	Intact	Slightly	Moderately	Seriously	Ruined
Num	4545	978	1363	1295	511
Num Per	52.29	11.25	15.68	14.90	5.88
Area	579.22	134.02	197.89	203.71	45.93
Area Per	49.90	11.54	17.05	17.55	3.96

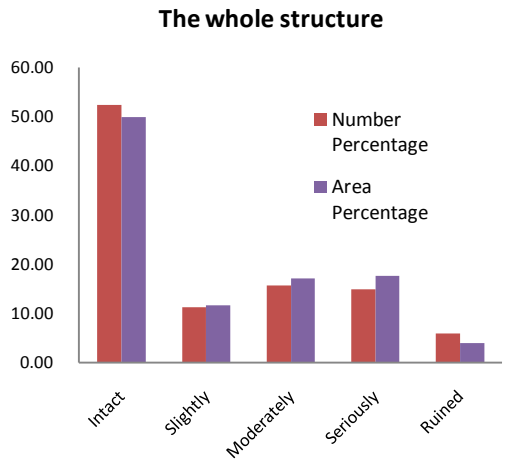

Figure 2 Damage Levels Distribution of the Whole Structure

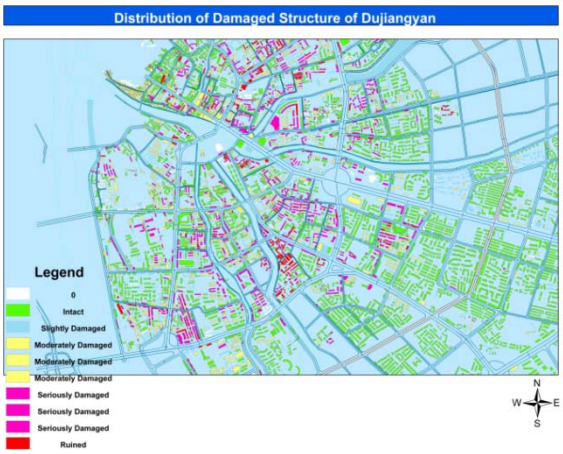

Figure 3 Distribution of the Every Damage Level Building

3.1 Masonry Structure

Masonry structure is a main form of buildings in Dujiangyan City and almost occupies the half of the whole structure. The phenomenon of seismic damage is very rich. All various damaged levels of structures can be invested in the survey. The collapses of structures, outside of walls and the big cracks of supporting-wall are the main seismic damage forms for masonry structure.

The data of investigation to the masonry structure is showed in Table 3 and Figure 4. The typical damage photos are seen in the Figure5 and 6.

Table3 Result of the MAS Structure Damage

	Intact	Slightly	Moderately	Seriously	Ruined
Num	2209	365	617	706	267
Num Per	53.05	8.77	14.82	16.95	6.41
Area	292.56	49.97	91.71	119.73	29.88
Area Per	50.11	8.56	15.71	20.51	5.12

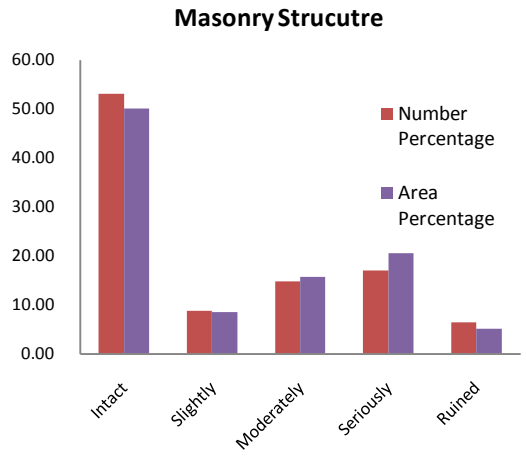

Figure 4 Distribute Diagram of the MAS Structure Damage



Figure 5 Typical Photo of the MAS Structure Damage (Seriously Damaged)



Figure 6 Typical Photo of the MAS Structure Damage (Ruined)

The followed conclusions can be given by analyzing the results of investigation. The buildings of older in age and existing obvious design blemish (such as the connect lengths of concrete pre-slabs could not satisfy the requisition of the Code, the wall bodies aren't thickness, the opening space is too much in walls) are the main reasons of masonry structure damage in Dujiangyan city.

3.2 Reinforced Concrete

The reinforced concrete structure is another main form of buildings in Dujiangyan City. The collapses of weak storey, the damage of frame column and the filling wall are the main damage forms.

The data of investigation to the reinforced concrete structure is showed in Table 4 and Figure 7. The typical damaged photos are seen in the Figure 8 and 9.

Table4 Result of the RC Structure Damage

	Intact	Slightly	Moderately	Seriously	Ruined
Num	504	145	156	98	9
Num Per	55.26	15.90	17.11	10.75	0.99
Area	82.72	36.15	33.82	19.24	3.28
Area Per	47.21	20.63	19.30	10.98	1.87

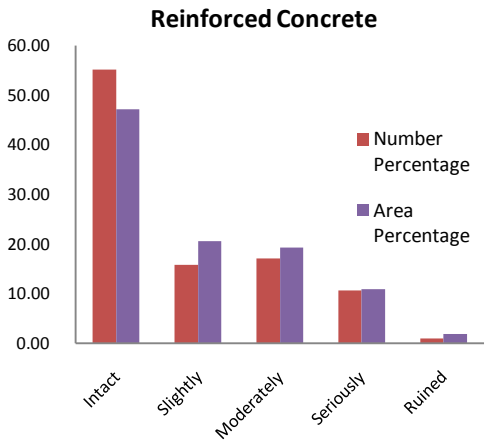

Figure 7 Distribute Diagram of the RC Structure Damage



Figure 8 Typical Photo of the RC Structure Damage (Ruined)



Figure 9 Typical Photo of the RC Structure Damage(Ruined)

3.3 Tall Building

The amount of the tall buildings is very few (only 14) in Dujiangyan City. The most damage degree is reaches the Moderately Damaged level. The main performances are the collapses and damage of filling walls. But the damage of the whole frame isn't very serious.

The data of investigation to the tall buildings is showed in Table 5. The typical damage photo is seen in the Figure 10.

Table5 Result of the TB Damage

	Intact	Slightly	Moderately	Seriously	Ruined
Num	4	2	8	0	0
Area	3.98	2.03	5.08	0	0



Figure 10 Typical Photo of the TB Damage (Moderately Damaged)

3.4 Masonry of Ground Floor Frame

The masonry of ground floor frame is a kind of structure form that has Chinese special feature. There are large number buildings in the small or middle cities at present. In the investigation of structure damage in Dujiangyan city, the main damage performance is the damage to ground frame and the upper construction, etc.

The data of investigation to the masonry of ground floor frame is showed in Table 6 and Figure11. The typical damaged photos are seen in the Figure 12.

Table6 Result of the MGFF Structure Damage

	Intact	Slightly	Moderately	Seriously	Ruined
Num	1104	232	375	398	83
Num Per	50.36	10.58	17.11	18.16	3.79
Area	178.65	39.77	61.49	62.93	9.32
Area Per	50.73	11.29	17.46	17.87	2.65

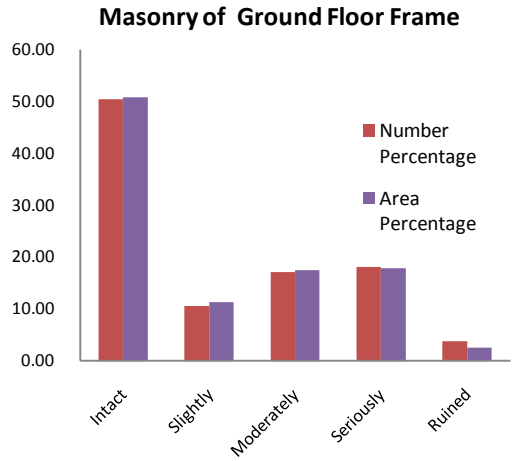

Figure 11 Distribute Diagram of the MGFF Structure Damage



Figure 12 Typical photo of the MGFF Damage (Ruined)

3.5 Plant Building

The number of the plant buildings is small in the Dujiangyan city. The more serious damage appeared the older plant buildings of masonry column.

The data of investigation to the plant buildings is showed in Table 7 and Figure13.

Table7 Result of the PB Structure Damage

	Intact	Slightly	Moderately	Seriously	Ruined
Num	72	24	23	5	17
Num Per	51.06	17.02	16.31	3.55	12.06
Area	8.58	3.21	3.91	0.53	1.16
Area Per	49.34	18.46	22.48	3.05	6.67

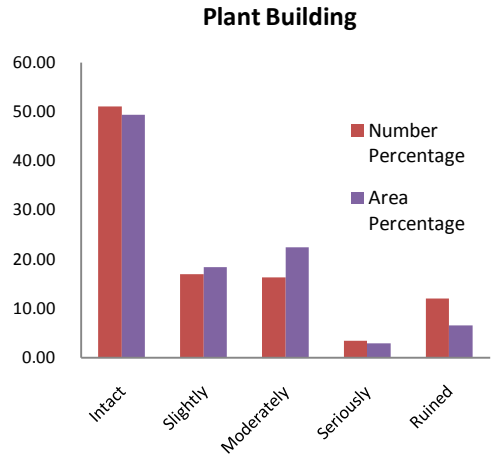

Figure 13 Distribution Diagram of the PB Structure Damage

3.6 Other Structure

The other structure includes the timber structure, stone structure and bamboo structure, etc. The buildings almost are one storey structure. The roofs are very light. So the damage also is slighter than the other forms structures.

The data of investigation to the other structure is showed in Table 8 and Figure14.

Table8 T Result of the OS Damage

	Intact	Slightly	Moderately	Seriously	Ruined
Num	652	210	184	88	135
Num Per	51.38	16.55	14.50	6.93	10.64
Area	12.72	2.87	1.91	1.28	2.29
Area Per	60.37	13.62	9.07	6.07	10.87

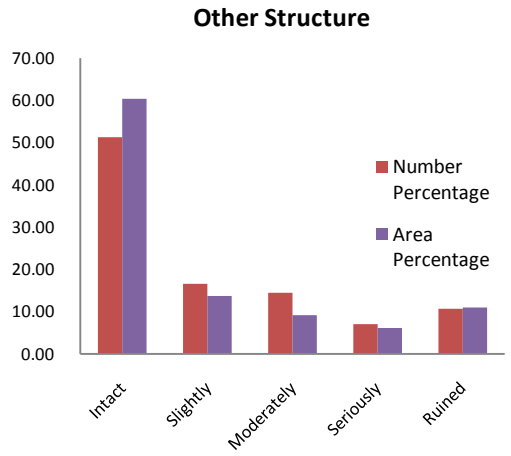

Figure 14 Distribution Diagram of the OS Damage

4 CONCLUSIONS

The original results of structures damage investigation are given in the paper. Here, the achievement belongs to the whole investigation group. Thanking for the colleagues from HIT, DUT, NUAA, BIT and YTU. The group is made up some eight teams. There are some differences in the subjective judgments for the structures damage levels in the team members. The results maybe have some errors.

Some typical photos of the important forms structure damage are given in the paper. The seasons of damage are analyzed on the basis of a large number of photographs taken on the spot. Then some conclusions are obtained.

The masonry structures of reaching seismic fortification criterion are better than others in the earthquake. Their damage degree is very slight. So, the masonry structures should be design by the seismic fortification criterion to avoid obvious disadvantage seismic factors.

Seismic concept design of the RC structure is still very important. The regular of flat and vertical surface, no obvious weak storey and a lighter roof should be considered in the design of those buildings.

Moreover, in this investigation, the damage of the older light timber structures is very slight in the earthquake. This is a problem that should be paid attention to.

Acknowledgements:

The authors acknowledge support from the "973 Project (2007CB714200)" funded by the Ministry of Science and Technology of the People's Republic of China. This support makes possible the forthcoming international conference.

Reference:

Bureau of Statistics of Dujiangyan (2008.6), "Statistical Information in Dujiangyan".

China Earthquake Administration (1998), "The Outline and Technique Guidebook on the Earthquake Spot", Earthquake Press.

The group of emergency work on the spot for Wenchuan Earthquake, China Earthquake Administration (2008.6) , "The Losses Valuation Report of the Wenchuan Ms8.0 Earthquake".

JOINT CONFERENCE PROCEEDINGS
7th International Conference on Urban Earthquake Engineering (7CUEE) &
5th International Conference on Earthquake Engineering (5ICEE)
March 3-5, 2010, Tokyo Institute of Technology, Tokyo, Japan

RETROFIT OF HISTORICAL STRUCTURES AGAINST EARTHQUAKES: A CASE STUDY ON MINARETS

A. Murat Turk[1)]

1) Assistant Professor, Civil Engineering Department, Istanbul Kultur University, Istanbul, Turkey
murat.turk@iku.edu.tr

Abstract: The paper deals with the seismic behavior and possible strengthening/retrofit strategies of block masonry historical minaret in Istanbul. Today, earthquakes are one of the most important problems that Turkey and many other countries as well. There are large number of historical mosques and large number of minarets which were built since older times. Since Turkey located in seismically active zone, the likely damage to the masonry minarets should be determined in advance and necessary precautions should be taken. The problem of seismic safety of the historical heritages have been always challenging for engineers in terms of analyzing and retrofitting of these structures due to extremely complex behavior of the material used in the construction. To achieve this objective, the minaret of historical mosque in Istanbul is chosen as a case and 3D finite element model of structure have been prepared in order to obtain possible lateral displacements, probable cracking zones and failure modes under earthquake loads. The problem becomes more complicated when the dynamic analysis is also involved. After the new developments in the dynamic testing of structures and computational methods in structural analysis, research in this field have guided some significant results about the mechanical behavior of the old buildings. These studies are essential not only in protection/retrofit viewpoint but also assessment of similar historical structures. Within this outline, the dynamic behavior of old masonry minarets, which usually exhibit vulnerable behavior under seismic loading is investigated. The results obtained from the numerical analysis have shown that the possible failure zones under seismic action can be predicted quite accurately with reasonable results, and can be used in the preservation of these minarets to guarantee their stability in case of an earthquake by strengthening/reinforcing those parts which will undergo the greatest damage (usually located at the base and the lower part of the minaret). Furthermore, the analyses are evaluated by using fiber reinforced polymer (FRP) sheets wrapped around these critical cross sections and the results are promising in terms of seismic protection of these heritages. Preservation of cultural heritage for the future generations is indispensable for every country in the modern world. Therefore, giving enough attention to protection of historical structures is one of the most important issues in highly-seismic developing countries.

1. INTRODUCTION

The earthquakes are the most important natural hazards for Turkey. Being located on the world's oldest landscape carries the problem of seismic protection of historical heritages with it. Turkey is located in one of the most seismically active regions of the world. These historical structures have experienced different levels of damage during past major earthquakes. The 1556, 1894 earthquakes that took place in Istanbul are some remarkable events. For example, after the 1894 Istanbul earthquake, 69 minarets in the city were reported as damaged, 30 of which were collapsed. Recent devastating earthquakes occurred on 17 August and 12 November 1999 that took place in northwestern part of Turkey caused damage and structural failures not only for buildings but also for minarets and mosques. The Kocaeli (M: 7.51) and Duzce (M: 7.2) earthquakes caused ruptures almost 110 km and 40 km of the North Anatolian fault, respectively. The main characteristics of ground motions observed structural damage and overall performance of existing structures during these earthquakes are given in EERI (2000) and Ramirez et al. (2000). In addition to building structures, many historical mosques and minarets either collapsed or suffered significant damage after these earthquakes. Most of the minaret structures which are slender tower type structures have performed poor structural behavior (Firat 2001, and Sezen et al. 2003).

Mosques and minarets are accepted to be the apparent symbols of religious architecture. A mosque generally includes a large gathering area roofed over by a major dome and sub-domes. In historical mosques, the main dome and the sub-domes are supported by arches and load-bearing walls. The load bearing walls generally have large openings for windows or doors. Each mosque has at least one minaret, which is a slender cylinder shaped tower with one or more balconies over its height and a conical cap at its top. The height of a minaret varies typically between 25 m and 40 m. A minaret may either have an independent foundation or the base of the minaret may be attached to the roof of the

mosque. In older mosques, solid clay bricks or stones were used in load bearing walls. Older masonry minarets were typically constructed using stone blocks, whereas lightweight stone blocks were preferred in newer construction.

Mostly, a minaret consists of three main structural parts going bottom to top. In Figure 1, two minarets of Istanbul Dolmabahce Mosque, of which west minaret of this mosque is examined as a case in this study, can be seen. The minaret footing is made by using very thick stone blocks and connected with the wall of the mosque. So the minaret can be identified as slender cantilever structure. The lower part, from bottom to the gallery, is constituted by the wall, the stairs and the core. The thickness of the wall in this part decreases along the length. Inside of the upper part, from gallery to the top of minaret is empty. The wall thickness of this part is constant along the length. Balconies are mostly used for prayers or architectural reasons create mass concentrations along the minaret's height and affect its dynamic structural response (Oguzmert 2002). The dimensions of this part are smaller than the lower part's. The conical cap part of this minaret was constructed with timber and covered with zinc. (Figure 1)



Figure 1 Side View of Dolmabahçe Mosque and Minarets

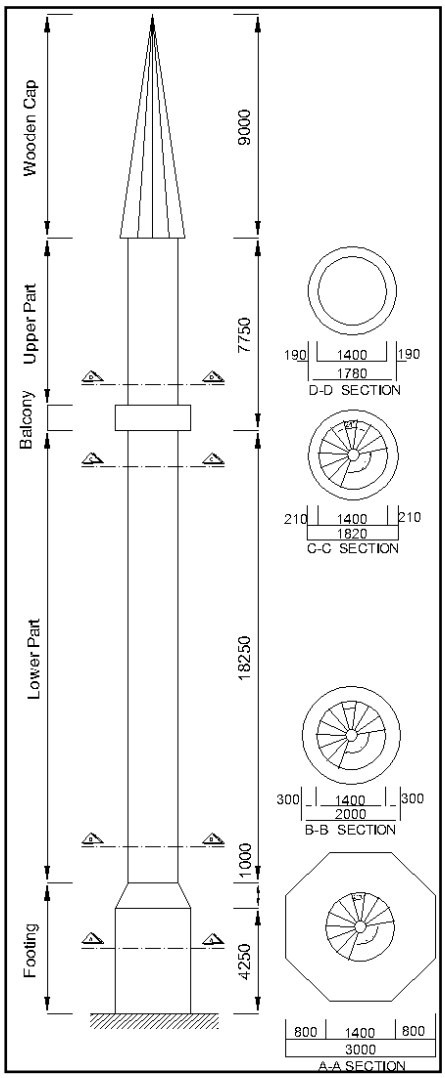

Figure 2 Geometrical and Cross-Sectional Properties of the Minarets (All dimensions are in mm.) (Oguzmert 2002)

It is essential to understand the dynamic behavior of masonry minarets to improve the life safety and to preserve and strengthen the historical monumental structures.

Due to progresses in the dynamic testing of structures and computational methods in structural analysis, studies have led some significant results about the mechanical behavior of the old structures (Cosgun 2005, Sezen et al. 2008). These types of studies are essential not only in protection point of view but also assessment of ground motion of the past events. Within this frame work, the dynamic behavior of old masonry minarets, which usually exhibit vulnerable behavior under seismic loading is investigated.

Previously a case study on the Dolmabahce Mosque minarets was conducted by a research team from Istanbul Technical University and micro tremor measurements had been recorded on the minarets and a finite element model was prepared of the minaret using shell elements with SAP2000 software. The study is concluded with the modal analysis results of the finite element model with the

proposed mechanical properties of the structural system (Oguzmert 2002).

In an other study, Sezen et al. discussed vulnerabilities and damages to 64 masonry and reinforced concrete minarets after the 1999 Kocaeli and Duzce earthquakes and investigated the seismic response of reinforced concrete minarets (Sezen et al. 2003). In addition, Dogangun et al. had analyzed and evaluated the behavior of unreinforced masonry minarets subjected to dynamic earthquake loading (2008).

2. STRUCTURAL DESCRIPTION and MATERIAL CHARACTERISTICS OF MINARET STRUCTURE

Dolmabahce Mosque was built near the Dolmabahce Palace, Istanbul with neo-classical and baroque architectural style in 1855. The mosque is located at the shores of the Bosphorus, on the south of Dolmabahce Palace. The two minarets rising from the eastern and western sides of the mosque have a strongly baroque and rococo style. Although both minarets look identically same, the west minaret keeps its original form although the other one was renovated. This study is mainly focused on the west side minaret so that the result can enlighten the real mechanical behavior of the structural system (Figure 1). As construction material, the limestone (Maktarali or kufeki limestone) has been used in the construction of all buildings in Dolmabahce Mosque. During the restoration of the Dolmabahce Palace, some experiments are performed on the stone specimens extracted from the debris of the old historical structures and old time queries. Final report of ITU on these stones is published in 2000 (Oguzmert 2002). In this report, measured mechanical properties of Maktarali limestone were given in Table 1.

Maktarali limestone (kufeki stone) had been used by Mimar Sinan, one of the most famous architects of the Ottoman Empire, in construction of almost all mosques around Istanbul. This stone belongs to Miocene formation and contains CaCO3 (93-100%). It's a natural composite material due to its matrix structure of metamorphosed sea shells.

The mechanical properties of Maktarali limestone are assumed as follows for the structural analysis: E, modulus of elasticity of uncracked section, Poisson ratio and unit weight are taken as 8856 MPa, 0.20 and 23 kN/m3 respectively. While calculating the elastic modulus E/f_c =720 ratio is taken where f_c=12.3 MPa taken from Table 1. The ratio of elastic modulus/compressive strength is given in a previous study where the mechanical properties of Maktarali limestone has been searched extensively (Erguvali et al. 1989). In other experimental studies, for the same material, typical uniaxial compressive strength/uniaxial tensile strength ratio is determined as 11-12 (Arioglu et al. 1997, Ahunbay 1988, Arioglu et al. 1999).

Table 1. Measured mechanical properties of Maktarali limestone (Oguzmert 2002)

Physical Properties	Max	Min	Average
Dry Density (kN/m^3)	24.9	23	23.9
Fully Saturated density (kN/m^3)	25.3	23.7	24.5
Compressive Strength(MPa)	19.2	12.3	16.7
Tensile Strength (MPa)	0.95	0.88	0.9
Young's Modulus(MPa)	7360	4300	5840

3. DYNAMIC ANALYSIS OF THE MINARET

In this paper, an analytical study is performed to understand the dynamic behavior of natural stone masonry minaret of historical mosque by using SAP2000 software (2009). The structure is modeled and analyzed using for different earthquake acceleration records and time history analyses and response spectrum analyses according to the Turkish Seismic Code is performed (TSC 2007).

The 3D finite element model developed by shell elements in order to study the dynamic response of the minaret is shown in Figure 1. The 3D model includes the spiral stairs made of kufeki stone and connected to the minaret walls. The dead load of the wooden cap (uppermost part of minaret) is uniformly distributed on the top of minaret wall (Figure 2). The base of the minaret is considered as fixed. Figure 1 shows that the base part of the minaret assembled to thick side wall of the mosque. No soil-structure interaction or base rotations have been taken into account.

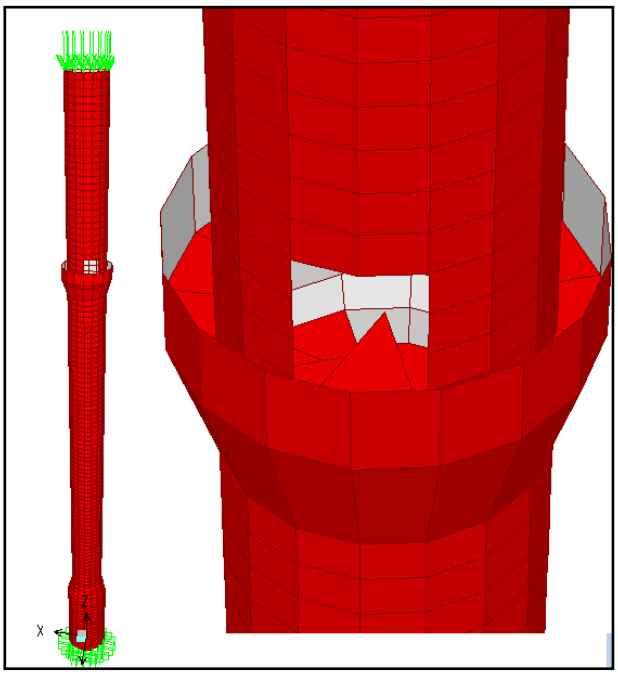

Figure 2 General view of minaret 3D FEM model and close view of balcony, door opening and stairs

In the structural model, linear elastic material behavior is assumed and the stiffness degradation is neglected. The minaret is assumed as located in a highly seismic region with weak soil layers which is assumed as in 1st seismic zone, Z4 soil class according to TSC 2007 and Type D soil class according to Eurocode 8 (2004). To simulate the elasto-plastic behavior of the minaret, R factor (seismic load reduction factor) is taken as 2 for masonry minaret according to TSC 2007 where it is recommended as 1.5 in Eurocode 8 Part 6 Annex E (q, behavior factor which is similar to R factor) for masonry towers (2004). 2 % damping ratio is assumed for dynamical analysis of such structure (Newmark et al. 1971). P-delta effect is ignored in the analysis (due to non-ductile behavior). Dynamic analysis of the minaret model is carried out using the response spectrum specified in the TSC 2007 for Z4 type soil as shown in Figure 3. In Figure 3, spectral values for previously recorded earthquakes are also given for soft soil conditions during 1999 earthquakes. Figure 3 also provides a comparison between the linear elastic acceleration response spectra calculated for soft soil conditions and those of the TSC 2007 with 2% damping for the highest seismicity in the Turkey, respectively. The elastic spectral demand obtained from TSC 2007 is comparable with the demands calculated using the recorded accelerations.

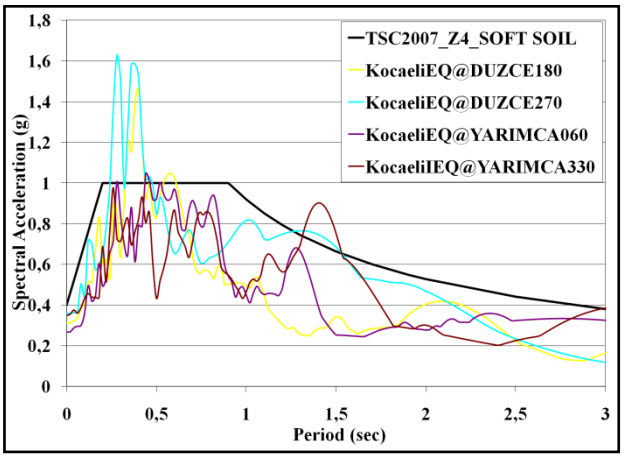

Figure 3 Absolute acceleration response spectra for Z4 soil conditions [7] and different recorded accelerations on soft soil conditions during 1999 EQ.

The first five modal periods of the minaret model (calculated from the modal analysis) and modes' contribution to the dynamic response are presented in Table 2. The fundamental period of minaret almost same calculated by modal analysis and ambient vibration measurements. The first four modes' contribution to the response is quite significant in which the first mode's participation is 34 %. The torsional mode (5th mode) has nearly no effect on the response of the minaret. In ITU study, micro tremor tests had been performed on the minaret structure and by using ambient vibrations, fundamental frequency of the minaret was measured as 0.88 Hz and first period calculated as 1.136 sec (Oguzmert 2002). The calculated first period in this study is 1.21 sec. (Table 2). 7 % difference can be assumed as negligible for practical design purposes.

Table 2 The first five modes and their participation factor

Modes	1st	2nd	3rd	4th	5th
Direction	Lateral	Lateral	Lateral	Lateral	Torsional
Period (sec)	1.21	1.21	0.20	0.20	0.08
Modal participation factor(%)	34.0	34.0	13.0	13.0	1.0

Calculated maximum lateral displacement at the top of the minaret, by utilising the response spectrum analysis and time history analyses, is shown in Figure 4. The maximum calculated displacement was 204 mm for the TSC 2007 design spectrum given for Z4 type soil conditions (soft soil). The deflected shape of the minaret shows flexure dominated lateral deformation with the largest displacement calculated at the roof. Roof height of the minaret is taken as 31.25 m without considering wooden cap. Although the minaret acts as cantilever, the deformation is smaller over the height of relatively stiff 4.25 m high base or boot. The displacement starts to increase above the transition segment at about 5.25 m.

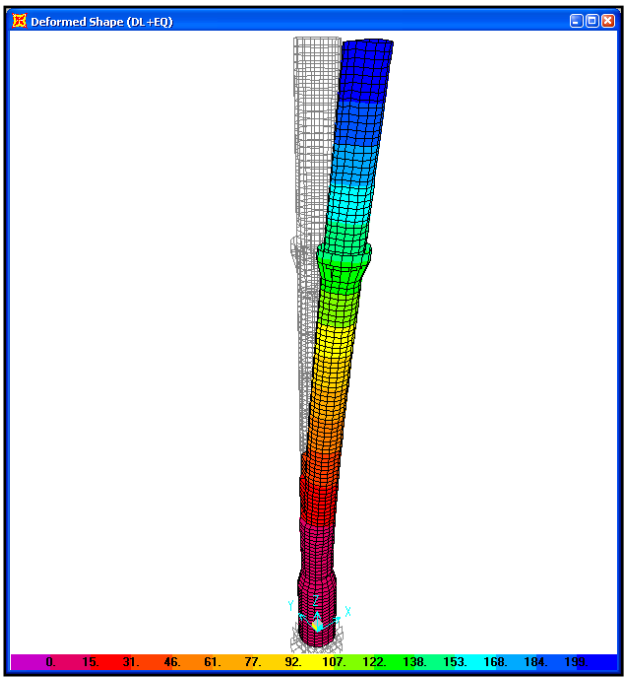

Figure 4 Deflected shape and lateral displacement over the height of minaret (in m)

Neither Turkish seismic code nor the other seismic codes contain any instructions directly related for the assessment/retrofit of slender tower structures made of block stone masonry. The Turkish earthquake code is prepared mainly for building structures, similarly its basic provisions can be used to assess the seismic capacity for the minaret. Roof drift index (δ/h) is calculated as 0.0065 which seems less than 0.01 which is given by TSC 2007 for building structures as maximum roof drift ratio for the case. In FEMA 273, 0.4 % limit drift (bed joint sliding behavior) is proposed

for collapse prevention for unreinforced masonry walls (for the walls made of hollow or solid brick clay/concrete units) (FEMA).

In literature, post-earthquake investigation of minaret failures shows that the most of masonry minarets failed at the bottom part of the cylindrical body, just above the transition zone (Firat 2001, Sezen et al. 2003). For the minaret case mentioned in this paper, the maximum values of calculated axial stresses during the FEM analysis are -11.32 MPa (compressive) and 9.20 MPa (tensile) and 0.72 MPa (shear) are shown in Figure 5 and 6. Tensile stresses are extremely higher than the tensile strength capacity of the limestone of which the maximum capacity can be taken as 1.0 MPa (Arioglu et al. 1997). High tensile stresses occurred especially lower regions causes the minaret becomes unsafe against seismic loadings. In addition, in terms of roof drift, obtained value of 0.0065 (204 mm roof displacement) seems higher for such a masonry slender structure. Under these conditions, such historical heritages appear vulnerable against strong earthquakes. On the other hand, the complex behavior of the stone material and the interface mechanics between stones may create another source of weakness. Furthermore, the conservation of historical heritages without any change on the external view should be taken into consideration while thinking about such structural intervention.

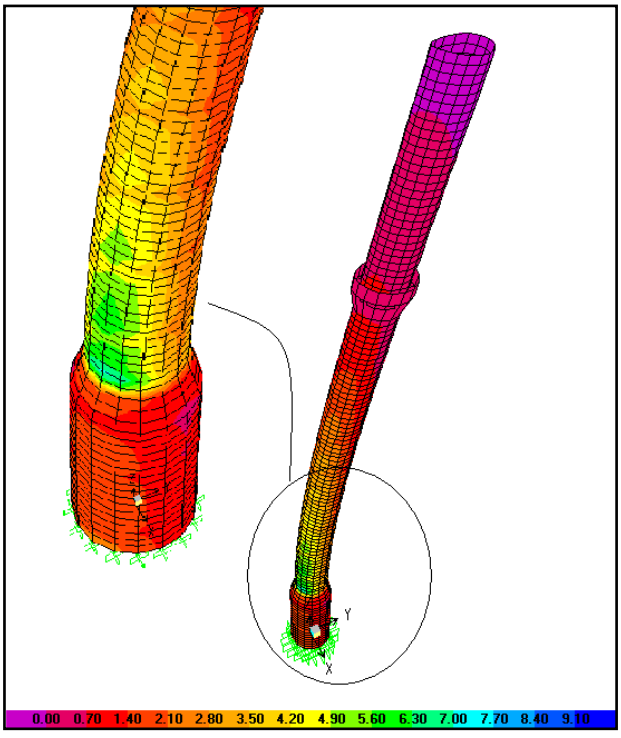

Figure 5 Axial tensile stress distribution over the height of minaret calculated by using TSC design response spectrum (in MPa)

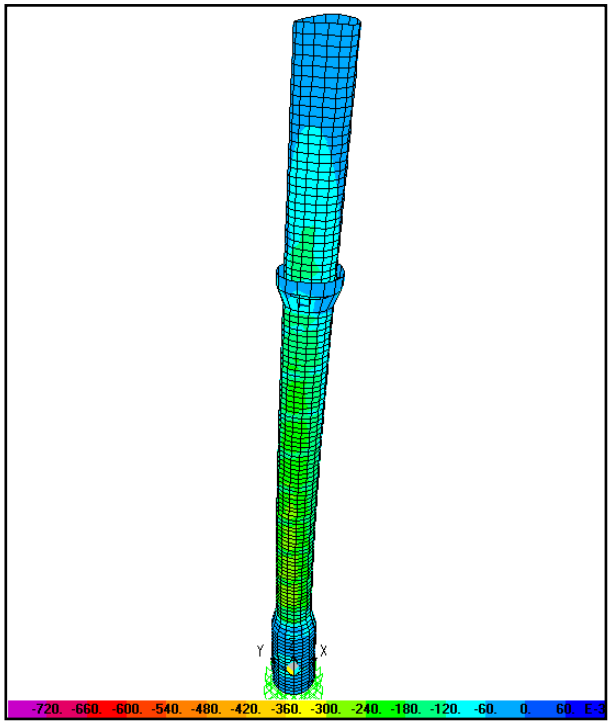

Figure 6 Shear stress distribution over the height of minaret calculated by using TSC design response spectrum (in MPa)

FRP use in such strengthening/retrofit of historical structures against earthquakes has gained importance during last few years. In order to increase the flexural capacity and shear capacity, the potential use of FRP jacketing was investigated. As it can be seen from the Figure 5 and 6, the lower part of minaret just below and over the transition zone shows such weak points in terms of axial and shear stresses. FRP wrapping around this critical zones (critical height=9.5 m from bottom of the minaret) seems easy and viable procedure in terms of strengthening/retrofit.

According to the results of available literature on structural upgrading of masonry columns by using fiber composites the following equation is proposed to calculate the compressive strength capacity of the lower part of the minaret which is continuously wrapped by FRP sheets CNR (2004) and Aiello et al. (2007).

$$f_{mcd} = f_{md} + \frac{4.g_m.t_f.b_f.\varepsilon_{fd}.}{2000.D.p_f} \quad (1)$$

where f_{mcd}= the strength of confined masonry; f_{md}=characteristic compressive strength of plain masonry; g_m=specific weight of masonry (kg/m^3) ; E_f =Elastic modulus of FRP; ε_{fd} =ultimate design strain for FRP ; t_f =thickness of FRP; b_f =width of FRP strips along the vertical direction fibers are supposed at 90° with respect to the principal axis of the column; D=diameter of the masonry column; and p_f =distance between two successive FRP strips measured by two axes.

Following parameters are used in order to calculate compressive strength increase of masonry material; f_{md}=12.3 MPa, g_m=2300 kg/m3, E_f =200000 MPa, ε_{fd} =0.004, t_f =10 mm, bf =500 mm, D=3000 mm and p_f =500 mm. The compressive strength of confined masonry is calculated as high as 25 MPa. This capacity is above the compressive stresses faced during analysis but tensile strength of the section is still less than the calculated values. Base moment due to response spectrum analysis (greater than the other time history analysis values) is calculated as 5200 kNm with the total axial load of 1920 kN for the minaret at the base.

As a result, the addition of longitudinal reinforcement like FRP strips is needed to increase the flexural capacity of the section in addition to FRP jacketing. For this purpose, a section analysis was performed by using XRACT software (2004) for the section of lower part of minaret by assuming fm=25 MPa, E_{frp} =200000 MPa, ε_{max} maximum assumed tensile strain for FRP in the given cross-section =0.01, total thickness of FRP strip (longitudinal and transversal) =10 mm, tensile strength of CFRP strips = 2800 MPa, D=3000 mm. Figure 7 shows the cross-section of lower part of minaret wrapped by FRP and Figure 8 shows the assumed stress-strain diagram of stone masonry material. Figure 9 and 10 shows the assumed stress-strain diagram of reinforced masonry material by FRP and stress-strain diagram of CFRP material respectively. In Figure 11, moment-curvature diagram of the CFRP reinforced masonry section is given and it shows that the flexural demand is met by the flexural capacity calculated for the minaret.

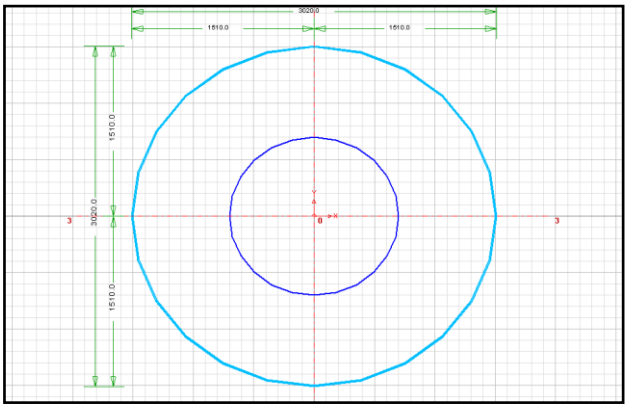

Figure 7 View of cross-section of lower part (below transition zone) of minaret wrapped by FRP

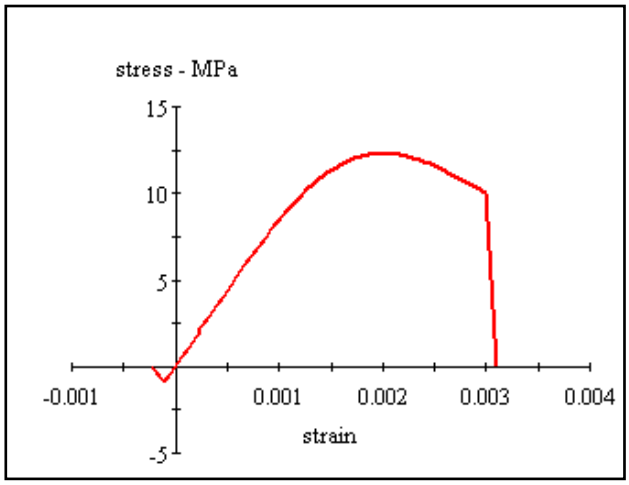

Figure 8 View of the assumed stress-strain diagram of masonry material (unconfined)

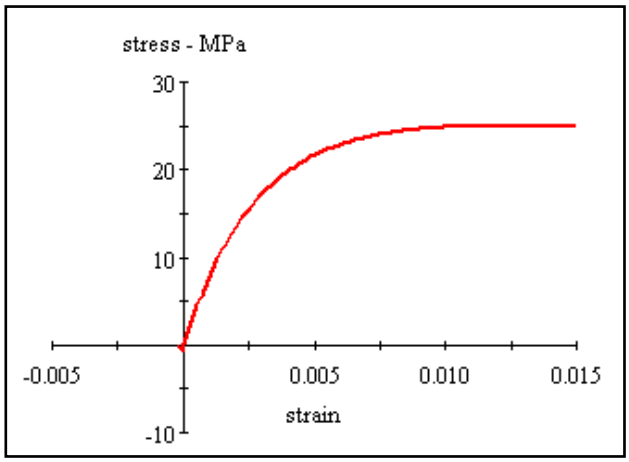

Figure 9 View of the assumed stress-strain diagram of reinforced masonry material by FRP (confined)

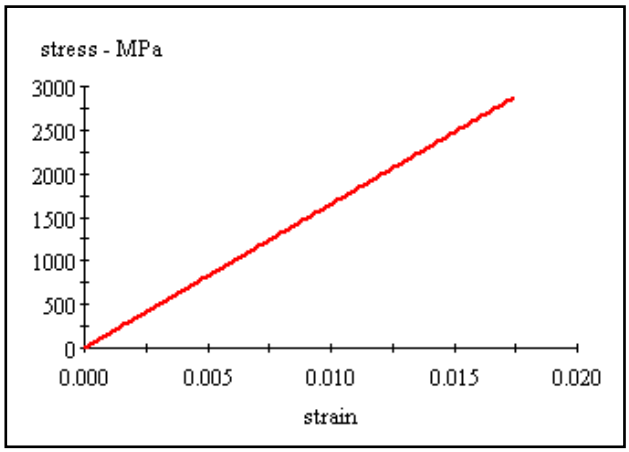

Figure 10 View of the assumed stress-strain diagram of CFRP material

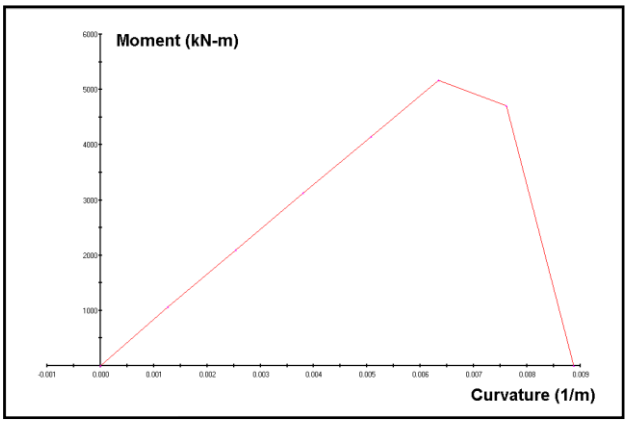

Figure 11 Moment-curvature diagram calculated for the reinforced section of lower part of minaret

4. CONCLUSIONS

This paper presents the possible failure mode for an unreinforced block masonry minaret representative of the large number of minarets currently in existence in Turkey. The results obtained from the ambient vibration and previous material tests cited have shown that the behavior under seismic action can be predicted quite accurately with reasonable results, and can be used in the assessment of these minarets to guarantee their stability in case of a code earthquake (10% probability of exceedance in 50 years, strong earthquake) by reinforcing those parts which will undergo the greatest damage (located at the base and the lower part of the minaret).

Historical structures with thick masonry walls are subjected to larger lateral earthquake forces due to their small periods of vibration. The 3D analysis performed allows distinguishing the behavior of the minaret during a seismic action, including the failure mode and the possible failure zones. Future investigations using elements or methodologies less time consuming capable of predicting crack pattern and failure modes are required. In this way, further research should be carried out in order to create special response spectra for this type of structures. Realistic seismic reduction factor (R) and damping ratio values should be investigated either by experimentally and analytically. The results obtained from the numerical analysis presented have shown that the greatest damage usually located at the base and the lower part of the minaret and jacketing of these critical cross sections by FRP sheets improves the lateral behavior and the results are promising in terms of seismic protection of these heritages.

References:

EERI (2000), "Kocaeli, Turkey Earthquake of August 17, 1999: Reconnaissance Report", *Earthquake Spectra Supplement A*, **16**. Earthquake Engineering Research Institute, Oakland, California.

Ramirez, J.A. et al. (2000), "Observations in the Cities of Duzce, Bolu and Kaynasli in Turkey after the 17 August, Kocaeli-Golcuk, and 12 November, Duzce-Bolu Earthquakes Seismological, Structural, Geotechnical and Geological Aspects", Purdue University. West Lafayette, Indiana. http://bridge.ecn.purdue.edu/~anatolia/index2.html

Firat, Y.G, (2001), "A Study of the Structural Response of Minarets in the 1999 Anatolian Earthquakes," M.Sc. Thesis. Purdue University. West Lafayette, Indiana.

Sezen, H., Firat, Y. and Sozen M.A. (2003), "Investigation of the Performance of Monumental Structures During the 1999 Kocaeli and Duzce Earthquakes," *Fifth National Conference on Earthquake Engineering*, Paper No: AE-020, Istanbul, Turkey

Oguzmert, M (2002), "Yigma Minarelerin Dinamik Davranisi", Istanbul Technical University, MSc Thesis, Istanbul.

Cosgun, C. (2005), "Silindirik Yigma Yapilarin Lif Takviyeli Polimer ile Takviye Edilmesi," MSc Thesis, Istanbul Kultur University, Istanbul.

Sezen, H., Acar, R., Dogangun, A. and Livaoglu, R. (2008) "Dynamic Analysis and Seismic Performance of Reinforced Concrete Minarets", *Engineering Structures*, **30**, 2253-2264.

SAP2000 (2009) "Integrated Software for Structural Analysis and Design," Computers and Structures Inc., California.

Dogangun, A., Acar, R., Sezen, H. and Livaoglu, R. (2008), "Investigation of Dynamic Response of Masonry Minaret Structures," *Bull Earthquake Eng*, **5**, 505-517.

Erguvanli, K., Ahunbay, Z. (1989), "Mimar Sinan İstanbul'daki Eserlerinde Kullandigi Taslarin Muhendislik Jeolojisi ve Mimari Ozellikleri," *Muhendislik Jeolojisi Bulteni*, **11**, 109-114.

Arıoglu, N. and Arıoglu, E. (1997), "Mimar Sinan'ın Sectigi Tas: Kufeki ve Cekme Dayanimi", *14. Turkiye Insaat Muhendisligi Teknik Kongresi*, Izmir.

Ahunbay, Z. (1988), "Mimar Sinan Yapilarında Kullanilan Yapim Teknikleri ve Malzeme," *Mimarbaşı Kocasinan Yaşadığı Çağ ve Eserleri*, Istanbul.

Arıoglu, E. and Arıoglu N. (1999), "Mimar Sinan'ın Tasiyici Olarak Kullandigi Kufeki Tasinin Muhendislik Gizemi," *Mimar Sinan Dönemi Yapı Etkinlikleri Sempozyumu*, Yapı Merkuzi, Istanbul.

TSC 2007 (2007), "Specification for buildings to be built in disaster areas", Ministry of Public Works and Settlement, Turkey.

Eurocode 8 (1998), "Design of Structures for Earthquake Resistance."

Eurocode 8 (1998), "Design of Structures for Earthquake Resistance", Part 6 Annex E.

Newmark, N.M. and Rosenblueth, E. (1971), "Fundamentals of Earthquake Engineering," Prentice-Hall Inc.

FEMA 273 (1997), "NEHRP guidelines for the seismic rehabilitation of buildings". Federal Emergency Management: Washington.

CNR 2004 (2004), "Guide for the Design and Construction of Externally Bonded FRP Systems for Strengthening Existing Structures," Technical Document 200/2004, Advisory Committee on Technical Recommendations for Construction of National Research Council, Italian Council of National Research, Rome.

Aiello, M.A., Micelli, F. and Valente, L. (2007), "Structural Upgrading of Masonry Columns by Using Composite Reinforcements," *Journal of Composites for Construction*, **11** (6), 650-658.

XTRACT V3.0.1. (2004), "Cross sectional x structural analysis of components," IMBSEN software systems.

JOINT CONFERENCE PROCEEDINGS
7th International Conference on Urban Earthquake Engineering (7CUEE) &
5th International Conference on Earthquake Engineering (5ICEE)
March 3-5, 2010, Tokyo Institute of Technology, Tokyo, Japan

DAMAGE ANALYSIS OF HIGH ARCH DAM INCLUDING CONTRACTION JOINT AND CRACKING NONLINEARITY

Xiaowen Yao[1)], Jianqun Jiang[2)], and Yikang Xu[3)]

1) Graduate, College of Civil Engineering and Architecture, Zhejiang University, China
2) Professor, College of Civil Engineering and Architecture, Zhejiang University, China
3) Zhejiang Design Institute of Water Conservancy and Hydroelectric Power, China
xwyao.zju@gmail.com, jianqun@zju.edu.cn, cgqas1314@163.com

Abstract: The seismic safety evaluation of high arch dam is very important for protecting the life and property safety. Due to the opening and closure of contraction joints, the arch dams exhibit nonlinear response during strong earthquakes. The revised dynamic contact force model and the continuum damage theory are employed to simulate the damage distribution on dam surface, and to investigate how the joint opening affects the stress. The dynamic analyses of a 305m-high arch dam are performed in which the reinforcements and key slots are set in the contraction joints in order to control the joint opening and thereby to control the level of the seismic damage.

1. INTRODUCTION

The recent worldwide growth of the intensity and frequency of earthquakes is of concern. In M8.0 Wenchuan earthquake (China), the 130m-high Shapai roller-compacted arch dam located near to the epicenter have actual seismic intensity of Ⅸ which is much higher than design intensity of Ⅷ with design acceleration of 0.138g. In the M6.8 Northridge earthquake (California), the acceleration recorded on the 113.5m-high Pacoima arch dam was 1.25g horizontally and 0.72g vertically, and this caused the left abutment joint to be opened by 50mm. In M7.3 Manjil earthquake (Iran), the ground acceleration, 6.8 km away from the earthquake epicenter, was 0.56g, and this caused severe cracking in the upper portion of the 106m-high Sefid Rud buttress dam (Zhou et al. 2000). It can be seen that the peak ground acceleration of a strong earthquake can far exceed the design acceleration of current earthquake resistance codes and cause some damage of the dams. Recently, several 200m and 300m high arch dams are under construction or will be constructed in the severe seismic regions of western China. The current design codes treating an arch dam as a linear monoblock can not indicate the nonlinear response of arch dams properly because the contraction joints make arch dam into a series of vertical cantilever monoliths that are commonly 20-30m wide.

A number of studies have been conducted to analyze the nonlinear behavior of arch dams including contraction joints. A series of dynamic experiments for 20 models of high arch dams were performed and show the effect of contraction joints to the seismic response and final failure (Zhou et al. 2000). The opening, closure and frictional sliding of joints in arch dams was modeled in the joint element based on penalty function by defining a nonlinear constitutive model (Zhang et al. 2000). A non-linear model was incorporated into a program to represent the partial joint opening as well as tangential displacement and to analyze the amount of energy dissipated in contraction joints during seismic events (Azmi and Paultre 2002). The dynamic contact force model was introduced into a nonlinear explicit method of time domain to consider the opening and closing effect of contraction joints on arch dams (Du and Tu, 2007).

Based on the aforementioned pioneering research, this paper focuses on the contact and material nonlinearity and their effects on nonlinear response of arch dams. Herein, the revised dynamic contact force model is first employed to analyze the nonlinear contact problems of contraction joints. Second, the continuum damage mechanics is used to establish the damage evolution equations of dam concrete. Finally, as an example of engineering application, a 305m-high arch dam under strong earthquake is studied to analyze the nonlinear response and its damage distribution.

2. REVISED DYNAMIC CONTACT FORCE MODEL

Dynamic contact force model is presented to simulate the contact nonlinear behavior of concrete under seismic loading (Liu et al.1999). As shown in Figure 1, S is a contactable interface with two side surfaces S^+ and S^-. n and t are normal vector and tangential vector respectively. At the initial time S^+ and S^- are coincident

with each other and it's assumed that the finite element nodes between S^+ and S^- are a pair of nodes. Hence, the contact process between the surfaces of the contactable joints may be simulated by the contact process between the two nodes simply.

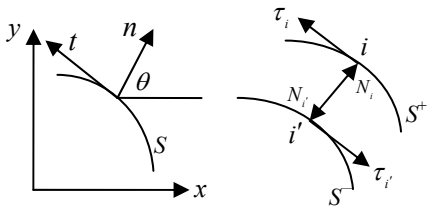

Figure 1 Model With Joints and Two Side of Contactable Interface

For any pair of nodes, i and i', the node i is located on the side of S^+ and the node i' is located on the side of S^-. N_i and τ_i are a normal contact force and a tangential contact force, respectively. Here, it is assumed that $\vec{n}$ of normal direction of S^+ is positive. The displacement of j direction at the node i can be written as

$$u_{ij}^{t+\Delta t}=\frac{\Delta t^2}{2m_i}\left[\left(Q_{ij}^t+N_{ij}^t+\tau_{ij}^t\right)-\sum_{l=1}^{n_e}\sum_{k=1}^{n}K_{ijlk}u_{lk}^t-\sum_{l=1}^{n_e}\sum_{k=1}^{n}C_{ijlk}\dot{u}_{lk}^t\right]+u_{ij}^t+\Delta t\dot{u}_{ij}^t \quad (1)$$

In which, N_{ij} and τ_{ij} are a projection of N_i and τ_i on j direction, respectively. The equation (1) also can be written as

$$u_{ij}^{t+\Delta t}=\overline{u}_{ij}^{t+\Delta t}+\Delta u_{ij}^{t+\Delta t}+\Delta v_{ij}^{t+\Delta t} \quad (2)$$

$$\overline{u}_{ij}^{t+\Delta t}=\frac{\Delta t^2}{2m_i}\left(Q_{ij}^t-\sum_{l=1}^{n_e}\sum_{k=1}^{n}K_{ijlk}u_{lk}^t-\sum_{l=1}^{n_e}\sum_{k=1}^{n}C_{ijlk}\dot{u}_{lk}^t\right)+u_{ij}^t+\Delta t\dot{u}_{ij}^t \quad (3)$$

$$\Delta u_{ij}^{t+\Delta t}=\frac{\Delta t^2}{2m_i}N_{ij}^t=\frac{N_{ij}^t}{M_i} \quad (4)$$

$$\Delta v_{ij}^{t+\Delta t}=\frac{\Delta t^2}{2m_i}\tau_{ij}^t=\frac{\tau_{ij}^t}{M_i} \quad (5)$$

$\overline{u}_{ij}^{t+\Delta t}$ is calculated from equation (3). $\Delta u_{ij}^{t+\Delta t}$ and $\Delta v_{ij}^{t+\Delta t}$, however, can not be got directly from the equations (4) and (5) in which N_{ij}^t and τ_{ij}^t are the functions of motion state at the time t and the time $t+\Delta t$. The computation methods of N_{ij}^t and τ_{ij}^t are introduced as follow respectively.

2.1 Computing N_i^t

When the contact between the nodes i and i' occurs, the relationship of the displacement and the contact force of the node i and i' can be expressed as

$$\vec{n}_i^T\left(u_i^{t+\Delta t}-u_{i'}^{t+\Delta t}\right)=0 \quad (6)$$

$$N_i^t=-N_{i'}^t \quad (7)$$

$$\tau_i^t=-\tau_{i'}^t \quad (8)$$

Substituting the equation (2) into the equation (6), there is

$$\vec{n}_i^T\left(\overline{u}_i^{t+\Delta t}+\Delta u_i^{t+\Delta t}+\Delta v_i^{t+\Delta t}-\overline{u}_{i'}^{t+\Delta t}+\Delta u_{i'}^{t+\Delta t}+\Delta v_{i'}^{t+\Delta t}\right)=0 \quad (9)$$

Because that the displacement of normal direction induced by the tangential force is zero, there exists

$$\vec{n}_i^T\cdot\Delta v_i^{t+\Delta t}=\vec{n}_i^T\cdot\Delta v_{i'}^{t+\Delta t}=0 \quad (10)$$

Equation (9) can be simplified as

$$\vec{n}_i^T\left(\overline{u}_i^{t+\Delta t}+\Delta u_i^{t+\Delta t}-\overline{u}_{i'}^{t+\Delta t}+\Delta u_{i'}^{t+\Delta t}\right)=0 \quad (11)$$

Substituting the equations (4) and (7) into the equation (11) yields

$$\begin{aligned}N_i^t&=\frac{M_iM_{i'}}{M_i+M_{i'}}\vec{n}_i\Delta_{1i}\\ \Delta_{1i}&=\vec{n}_i^T\left(\overline{u}_{i'}^{t+\Delta t}-\overline{u}_i^{t+\Delta t}\right)\end{aligned} \quad (12)$$

So $\Delta u_i^{t+\Delta t}$ and $\Delta u_{i'}^{t+\Delta t}$ can be calculated from equation (4).

2.2 Computing τ_i^t

On the other hand, the relative sliding between the nodes i and i' along tangential direction is considered after the contact between the node i and i' occurs. If there is no relative sliding, the static friction state is generated

$$\vec{t}_i^T\left(u_i^{t+\Delta t}-u_{i'}^{t+\Delta t}\right)=\vec{t}_i^T\left(u_i^t-u_{i'}^t\right) \quad (13)$$

τ_i^t must satisfy the Coulomb Friction Laws

$$\left|\tau_i^t\right|\le\mu_s\left|N_i^t\right| \quad (14)$$

Here μ_s is static friction coefficient. Substituting equation (2) into equation (13) yields

$$\begin{aligned}&\vec{t}_i^T\left(\overline{u}_i^{t+\Delta t}+\Delta u_i^{t+\Delta t}+\Delta v_i^{t+\Delta t}-\overline{u}_{i'}^{t+\Delta t}+\Delta u_{i'}^{t+\Delta t}+\Delta v_{i'}^{t+\Delta t}\right)\\ &=\vec{t}_i^T\left(u_i^t-u_{i'}^t\right)\end{aligned} \quad (15)$$

Noticing the condition $\vec{t}_i^T\Delta u_i^{t+\Delta t}=\vec{t}_i^T\Delta u_{i'}^{t+\Delta t}=0$, equation (15) can be simplified as

$$\vec{t}_i^T\left(\Delta v_i^{t+\Delta t}-\Delta v_{i'}^{t+\Delta t}\right)=\vec{t}_i^T\left[\left(\overline{u}_i^{t+\Delta t}-\overline{u}_{i'}^{t+\Delta t}\right)-\left(u_i^t-u_{i'}^t\right)\right] \quad (16)$$

Substituting equations (5) and (8) into equation (16), there is

$$\tau_i^t = \frac{M_i M_{i'}}{M_i + M_{i'}} \vec{t}_i \Delta_{2i}$$
$$\Delta_{2i} = \vec{t}_i^T \left[\left(\overline{u}_{i'}^{t+\Delta t} - \overline{u}_i^{t+\Delta t} \right) - \left(u_{i'}^t - u_i^t \right) \right] \quad (17)$$

If the result of equation (17) is not satisfied with equation (14), the dynamic friction state is generated and τ_{ij} should be given by

$$\left| \tau_i^t \right| = \mu \left| N_i^t \right| \quad (18)$$

in which μ denotes dynamic friction coefficient. If the contact state between the nodes i and i' is dynamic, the next sufficient and necessary conditions are observed

$$\text{if} \operatorname{sgn}\left(\Delta_{2i}\right) = 1, \vec{t}_i^T \left(u_{i'}^{t+\Delta t} - u_i^{t+\Delta t} \right) > \vec{t}_i^T \left(u_{i'}^t - u_i^t \right) \quad (19)$$

$$\text{if} \operatorname{sgn}\left(\Delta_{2i}\right) = -1, \vec{t}_i^T \left(u_{i'}^{t+\Delta t} - u_i^{t+\Delta t} \right) < \vec{t}_i^T \left(u_{i'}^t - u_i^t \right) \quad (20)$$

Otherwise the static friction state is generated to get the tangential contact force τ_i^t. So $\Delta v_i^{t+\Delta t}$ and $\Delta v_{i'}^{t+\Delta t}$ can be calculated from equation (5).

2.3 Model Construction

Dynamic contact force model is developed on the basis of ideal joint interface and there are several factors neglected, such as the materials in the joints, the initial contact force and initial tensile strength. Hence, the revised dynamic contact force model is discussed.

2.3.1 Initial contact force N_i^0

The initial contact force N_i^0 due to the hydrostatic pressure can be expressed as

$$\Delta_{1i}^0 = \frac{M_i + M_{i'}}{M_i M_{i'}} \vec{n}_i^T N_i^0 \quad (21)$$

When $\vec{n}_i^T \left(\overline{u}_i^{t+\Delta t} - \overline{u}_{i'}^{t+\Delta t} \right) \geq -\Delta_{1i}^0$ is satisfied, equation (12) can be revised as

$$N_i^t = \frac{M_i M_{i'}}{M_i + M_{i'}} \vec{n}_i \Delta_{1i}$$
$$\Delta_{1i} = \vec{n}_i^T \left(\overline{u}_{i'}^{t+\Delta t} - \overline{u}_i^{t+\Delta t} \right) + \Delta_{1i}^0 \quad (22)$$

2.3.2 The tension reinforcement in joints

When $\Delta_{1i} < 0$, the nodes i and i' keep separating and imply tension in reinforcements

$$\vec{n}_i^T \left(u_{i'}^{t+\Delta t} - u_i^{t+\Delta t} \right) = \frac{\vec{n}_i^T N_i^t}{K_s} \quad (23)$$

Here $K_S = E_S A_S / L_S$ represents tensile strength between the nodes i and i'. Hence N_i^t can be expressed as

$$N_i^t = \frac{1}{\frac{M_i + M_{i'}}{M_i M_{i'}} + \frac{1}{K_s}} \vec{n}_i \Delta_{1i}$$
$$\Delta_{1i} = \vec{n}_i^T \left(\overline{u}_{i'}^{t+\Delta t} - \overline{u}_i^{t+\Delta t} \right) + \frac{\vec{n}_i^T N_i^t}{K_s} \quad (24)$$

3. DAMAGE SIMULATION OF DAM CONCRETE

In conventional design methods of concrete dams, the tolerable stress of concrete is employed to evaluate the safety of dams in linear dynamic analysis. However, the cracks occur on arch dam under strong earthquake, leading to degradation of carrying capacity. There are two approaches for concrete cracking analysis. One approach uses fracture mechanics concept to model the discrete cracks observed in plain concrete. However it is limited to problems where only a few well-defined fractures are expected. For large-scale problems such as high arch dams, owing to the complexity of 3D problems, it becomes excessively complicated (Zhong et al. 2008). Another approach is the continuum damage mechanics. The fundamental notion of damage mechanics is to represent the damage state of materials by an internal variable, which directly characterizes the distribution of microcracks formed during the loading process. Each damage model established mechanical equations to describe the evolution of the internal variables and the mechanical behavior of damaged materials (Ghrib and Tinawi 1993). Some models to simulate the concrete damage have been developed (Yan, 2005; He et al. 2004; Xiong et al. 2004). In this paper, damage mechanics is employed to establish the damage evolution equation for simulating the nonlinearity of dam concrete.

The strain equivalence principle is employed to establish damage model. The damage variable D is defined as follow

$$D = 1 - E_d / E_0 \quad (25)$$

Here E_0 and E_d represent the initial elastic modulus and updated modulus of damaged element respectively. D=0 corresponds to undamaged state while D=1 implies a totally damage element. Based on the uniaxial tensile stress-strain curve recommended in the concrete specification, the concrete uniaxial tensile damage evolution equation is defined as follows:

$x \leq 1$ $$D = 1 - \left(1.2 - 0.2x^5\right)\left(1 - D_f\right) \quad (26)$$

$x>1$ $$D = 1 - \frac{1 - D_f}{\alpha_t (x-1)^{1.7} + x} \quad (27)$$

Where α_t is the parameter for descending branch of the uniaxial tensile stress-strain curve, x is defined by $x = \varepsilon / \varepsilon_f$, ε_f is peak strain, D_f is damage threshold.

Substituting the parameters of concrete into equations (26) and (27) yields a damage evolution curve as depicted in Figure 2. It can be seen that before reaching three-quarter ε_f damage is not obviously. After then the microcracks begin to propagate with the increase of the strain and the damage develops quickly. When strain exceeds 1.1 times of the peak strain the increase of damage begin to slow down. At this time the tensile strength decreases from a peak value to residual strength, together with an increase in deformation. At the end, damage is already serious but the cracks keep on growing until the ultimate tensile strain is exceeded, which means the concrete is totally damaged with D=1.

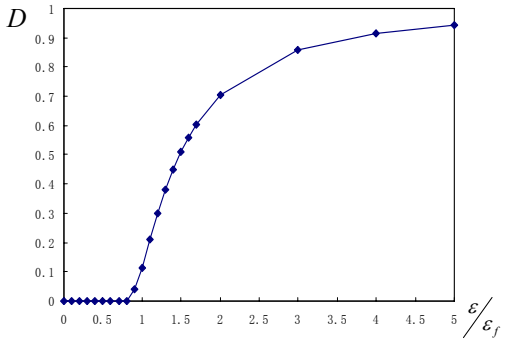

Figure 2 Damage Evolution Curve of Concrete under Uniaxial Tensile Loading

4. CASE STUDY OF THE SEISMIC RESPONSE OF AN ARCH DAM WITH JOINTS

A 305m-high arch dam with a crest length of 552.23 m, which is constructed in western China, is investigated by ABAQUS in this paper. The thickness varies from 13 m at the crest to 60 m at the base. The material properties for the concrete are: unit weight=2400 kg/m^3, modulus of elasticity=2.4×10^4 MPa, Poisson's ratio=0.167; for the foundation rock: unit weight=0, Poisson's ratio=0.25. The static loads considered here are the weight of the dam and the hydrostatic pressure of the impounded water. Lowest reservoir water with Westergaard added mass approximation is employed. The earthquake input with the maximum peak acceleration acting in the stream direction of 0.197g is shown in Figure 3.

Figure 4 shows the finite element model of the dam-foundation system discretized by 8-node hexahedron with 105361 nodes and 66015 elements. In reality 25 joints are designed for dam construction. For computational economy, fewer joints may need to be simulated in the analysis. Herein, table 1 shows five cases assumed for comparison, i.e. 0, 1 and 3 joints without considering other materials in the joint. Two additional cases are 1 joint with key slots and reinforcement respectively. Figure 5 shows the layout of 3 joints spaced approximately 60 m.

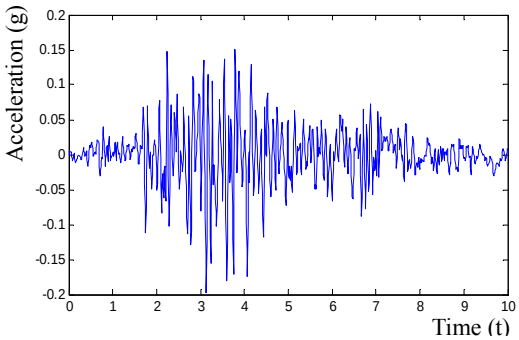

Figure 3 Input Ground Motion

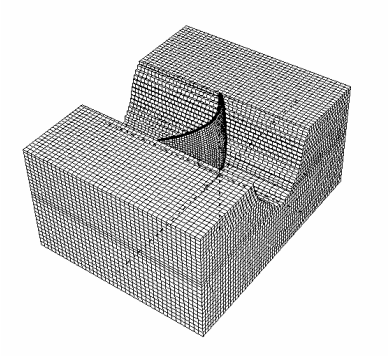

Figure 4 Finite Element Discrete Model of Arch Dam-Foundation

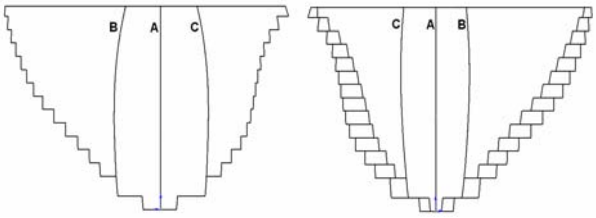

(a) Upstream Surface (b) Downstream Surface

Figure 5 Layout of The Contraction Joints

Table 1 Analytical Cases

Case	Number of Joints	Key Slots	Reinforcement
1	0	without	without
2	1	without	without
3	3	without	without
4	1	with	without
5	1	without	with

4.1 Opening of Joint A in Different Cases

The maximum opening of joint A at different height in different cases are shown in table 2. The comparisons of cases 2 and 5 show that joint reinforcements can decrease the joint opening by approximately 10% to 40% on the upstream surface and the peak value decreases

from 7.78 to 6.02 cm. It is evident that in case 3 because of joint B and joint C the opening of joint A declines by 20% to 50% with the peak value declining from 7.78 to 5.15 cm. The effect of the key slots, however, is not obvious for the opening control from the result of case 4. The analysis confirms the effectiveness of joint reinforcements for reducing the joint opening to some extent and the reduction of joint opening is a benefit to improve the dam integrity and to prevent the waterseal from damage.

Table 2 The Maximum Contraction Joint Opening Width (mm)

Scale Elevation(m)		305	295	286	277	268	258	248	238	228	218	208	198	188	178	168
Case2	US	6.36	7.06	7.56	7.78	7.78	7.5	7.10	6.47	5.66	4.68	3.59	2.50	1.53	0.67	0
	DS	4.80	3.92	3.02	2.03	1.15	0.33	0	0	0	0	0	0	0	0	0
Case3	US	5.15	4.90	4.64	4.46	4.29	4.10	3.83	3.50	3.01	2.39	1.70	1.01	0.40	0	0
	DS	3.92	3.31	2.88	2.31	1.81	1.25	0.71	0.10	0	0	0	0	0	0	0
Case4	US	6.49	7.19	7.65	7.85	7.83	7.57	7.12	6.48	5.66	4.67	3.58	2.48	1.51	0.65	0
	DS	4.63	3.76	2.88	1.91	1.05	0.24	0	0	0	0	0	0	0	0	0
Case5	US	3.98	4.74	5.14	5.50	6.02	5.96	5.86	5.58	4.99	4.19	3.24	2.28	1.40	0.576	0
	DS	3.92	3.01	2.19	1.42	0.73	0.07	0	0	0	0	0	0	0	0	0

4.2 Comparisons of Principal Stresses On The Dam Surface

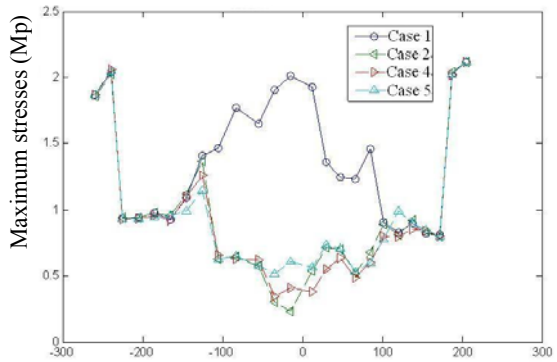

(a) Upstream Surface

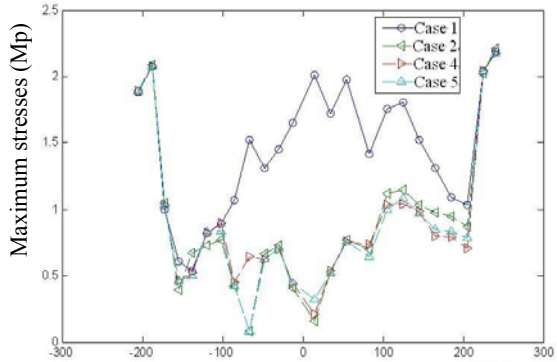

(b) Downstream Surface

Figure 6 Maximum Arch Stresses at The Top of Arch Dam

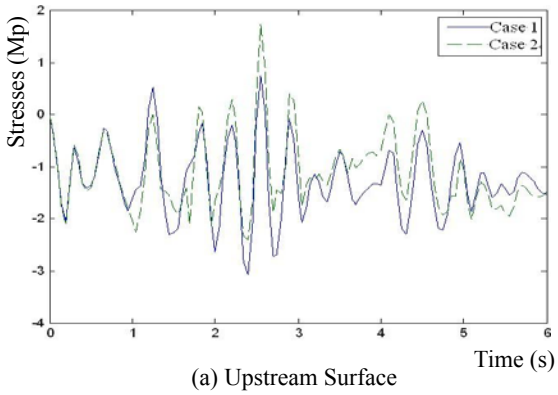

(a) Upstream Surface

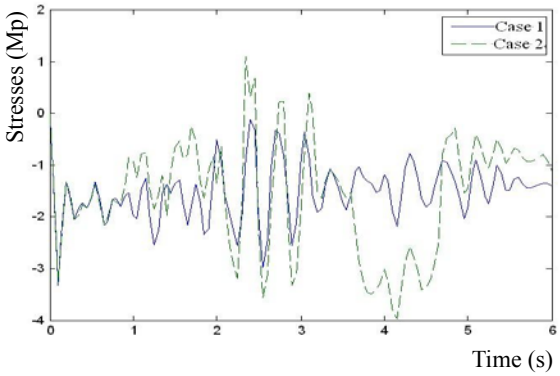

(b) Downstream Surface

Figure 7 The Histories of Stresses of Crown Cantilever

The comparisons of maximum principal tensile stresses along the axis of arch at dam crest on the surface in case 1, 2, 4 and 5 are depicted in Figure 6. It is evident that due to the joint opening, the maximum arch stresses at the crest have released dramatically in both upstream and downstream surfaces. Particularly, the stresses on the middle portion of the crest decrease from 2 to 0.2 MPa. On the other hand, compared with case 2, the effectiveness of joint reinforcements and key slots for stress redistribution is not significant. Figure 7

demonstrates the stresses histories of crest center for cantilever component. It can be seen that maximum cantilever tensile stresses increase from 0.8 to 1.7 Mpa and from 0 to 1Mpa in upstream surface and downstream surface respectively. In this case, the occurrence of horizontal cracking may be inevitable. Thus, some strengthening measures should be considered to prevent the horizontal crackings.

4.3 Damage Distribution

Figure 8 indicates the tensile damage distribution on the upstream surface of arch dam in case 1 and case 3. In case 1 cracks are mainly localized at the vicinity of central top of the dam with the damage value reaching over 0.9. Besides, some visible cracks are detected on the dam abutments. On the contrary, by considering of 3 contraction joints, there are some serious cracks on the dam abutments while only several minor cracks are detected on the other section of dam with the damage value of 0.01~0.05. It is evident that contraction joints lead the release of stresses on the arch component so that the damage of dam concrete declines significantly.

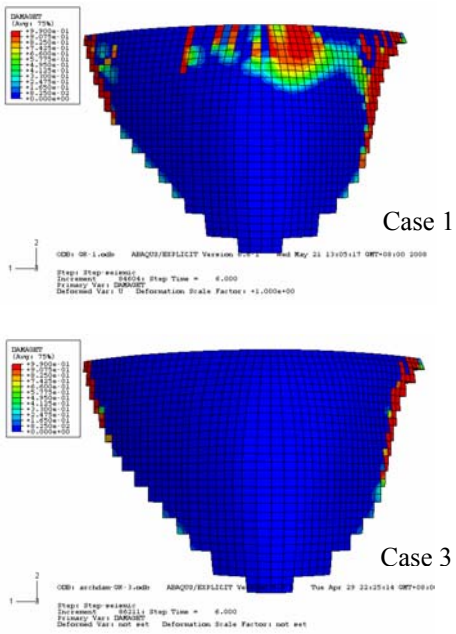

Figure 8 Damage Distribution of Dam Surface Without and With Reinforcements

5. CONCLUSIONS

In this paper, the nonlinearities of contraction joint and dam concrete are both considered to analyze the seismic response of high arch dam subjected to strong earthquake. Dynamic analyses of a 305m-high arch dam are performed and the numerical results lead to the following conclusions.

1. Adding reinforcement in the contraction joints as well as the increment of joints numbers reduced maximum joint opening significantly, particularly on the upper middle portion. However, the effect of key slots to control the joint opening is not obvious.
2. Due to the opening of contraction joints, the arch stresses decreased obviously on the top of dam and cantilever stresses in main location increase roughly.
3. For the monoblock model, the damage zones were roughly located in the top third and the abutments of the dam, whereas for jointed arch dam the damage zones were comparatively reduced and mainly existed in the abutments.

The joints cause the nonlinear responses, and the degree of this nonlinearity depends largely on the construction of the joints. Thus, it seems that using the contraction joints to control the responses and seismic damage of arch dams would be a reasonable procedure. However, some strengthening measures should be considered to control the contraction joint opening and to prevent the horizontal crackings.

References

Zhou, J., Lin, G., Zhu, T. et al (2000), "Experimental Investigation into Seismic Failure of High Arch Dams," *Journal of Structural Engineering*, 126(8), 926-935.

Zhang, C.H., Xu, Y.J., Wang, G.L. et al (2000), "Non-linear seismic response of arch dams with contraction joint opening and joint reinforcements," *Earthquake Engng Struct Dyn*, 29, 1547-1566.

Azmi, M. and Paultre, P. (2002), "Three-dimensional analysis of concrete dams including contraction joint non-linearity," *Engineering Structures*, 24, 757-771.

Du, X.L. and Tu, J. (2007), "Nonlinear seismic response analysis of arch dam-foundation systems- part Ⅱ opening and closing contact joints," *Bull Earthquake En*, 5, 121-133.

Liu, J.B., Liu S., and Du, X.L. (1999), "A Method for the Analysis of Dynamic Response of Structure Containing Non-Smooth Contactable Interfaces," *ACTA Mechanic Sinica (English Series)*, 15(1), 63–72.

Zhong, H., Lin, G. and Li, H.J. (2008), "Damage Simulation of High Arch Dams in Earthquakes," *Proceedings of the 14th World Conference on Earthquake Engineering*, Paper No. 14-0087.

Ghrib, F. and Tinawi, R. (1995), "Nonlinear Behavior of Concrete Dams Using Damage Mechanics," *Journal of Engineering Mechanics*, 121(4), 513-527.

Yan, X.R. (2005), "Application of Anisotropic Damage Model in Seismic Safety Evaluation of Concrete Dams," Dalian University of Technology, China. (in chinese)

He, M., Fu, X.L., and Xu, D.Y. (1994), "On Concrete Damage Models, *Journal of Fuzhou University (Natural Sciences Edtion)* 22(4), 109-114. (in Chinese).

Xiong, H., Fu, M.F., Luo, Q.F. (2004), "A New Subsection Curve Damage Model of Concrete," Chinese Quarterly of Mechanics, 25(3), 342-348. (in Chinese)

Xu, Y.K., Yao X.W., and Jiang, J.Q. (2009), "Damage analysis of high arch dam and joint-based seismic design," Proceedings of Earthquake Engineering and Disaster Mitigation Seminar, 645-651. (in Chinese)

JOINT CONFERENCE PROCEEDINGS
7th International Conference on Urban Earthquake Engineering (7CUEE) &
5th International Conference on Earthquake Engineering (5ICEE)
March 3-5, 2010, Tokyo Institute of Technology, Tokyo, Japan

NONLINEAR BEHAVIOR OF REINFORCED CONCRETE COLUMNS IMPACTED BY A TSUNAMI WATER-BORNE SHIPPING CONTAINER

Kavinda M. Madurapperuma [1] and Anil C. Wijeyewickrema [2]

1) Graduate Student, Department of Civil Engineering, Tokyo Institute of Technology, Japan
2) Associate Professor, Department of Civil Engineering, Tokyo Institute of Technology, Japan
ma.k.aa@m.titech.ac.jp, wijeyewickrema.a.aa@m.titech.ac.jp

Abstract: Many reinforced concrete buildings have been severely damaged or have collapsed due to impact of tsunami water-borne objects such as boats, heavy vehicles, inadequately restrained storage tanks and shipping containers. The exterior columns of a building are the most vulnerable members to such impact loads and failure of one or more columns at the lower level may result in the capacity of the remaining structural members being exceeded, which in turn could lead to collapse. In the present study, axially loaded RC columns with square and circular cross-sections are considered to investigate the force demand and nonlinear response due to impact of a tsunami water-borne shipping container. Numerical analysis is carried out using the nonlinear finite element code LS-DYNA. The shipping container is modeled using shell elements and nonlinear material behavior with strain rate effects is considered. For the column, concrete and reinforcing bars are modeled using solid and beam elements, respectively and the material strain rate effects and bond slip between concrete and reinforcing bars are taken into account. Before the container impact simulation, to validate the modeling procedure as well as the accuracy and applicability of the selected material models for the column, an axially loaded RC column subjected to lateral impact by a rigid object at mid-span is simulated and compared with experimental results available in the literature. Next, the impact simulation is carried out and the effect of container impact parameters such as speed, height above ground level, mass and orientation on peak force and impact duration are studied. In addition, the influence of container kinetic energy on the column displacement response and damage level characterized by residual axial load carrying capacity is investigated. The numerical results are compared with those obtained from current design guidelines and suitable modifications are suggested. The study highlights the importance of further consideration and refinement of current structural design guidelines for safer designs.

1. INTRODUCTION

Significant damage and the destruction of buildings, bridges and other infrastructure located in the inundation zone due to tsunamis have been reported (Synolakis et al. 2005, Ghobarah et al. 2006, Inoue et al. 2007, Kaushik and Jain 2007). The primary cause of structural failure is surge forces on structures as the area becomes inundated. To allow unrestricted flow of the water thus reducing damage due to such forces, new buildings where there are no in-fill walls on the first floor have been constructed in regions of low seismic risk (Dalrymple and Kriebel 2005, Okada et al. 2005). This type of construction is generally permitted for regions of low seismic risk where most low-rise buildings are designed only for gravity loads. However, the lower level columns of such buildings are very vulnerable to impact due to water-borne massive objects in a tsunami situation. Since columns are the primary load-carrying members, failure of one or more columns at the lower level may lead to progressive collapse of the building due to lack of alternative load paths.

Post tsunami reconnaissance surveys have reported that light-framed wood and unreinforced masonry residential buildings were severely damaged or completely destroyed due to impact of tsunami water-borne massive objects such as boats, heavy vehicles, inadequately restrained storage tanks and shipping containers (Ghobarah et al. 2006, Kaushik and Jain 2007). While it may be possible to relocate or secure most boats and heavy vehicles even with a sufficient early warning of the impending disaster it would not be possible to relocate all the shipping containers in a port within a short time. Therefore, it has been suggested that standard shipping containers could be considered as the design water-borne object in many developed coastal areas (Robertson et al. 2007).

The design standard ASCE/SEI 7-05 (ASCE 2005) and guideline FEMA P646 (FEMA 2008) specifically address the evaluation of forces acting on structural members of a building due to impact of water-borne objects. However, as discussed in Section 2 the recommended formulae are based on simplified, quasi-static, elastic analyses regardless of rate dependent nonlinear material behavior of both the water-borne object and the structural member. Both documents do not consider the dynamic interaction between the water-borne object and the structural member. However, the possible failure modes under dynamic loading

can be substantially different from the case of static loading (Miyamoto et al. 1994).

In the present study, nonlinear finite element analysis is conducted to gain a better understanding of impact between a shipping container and a RC column. In the model, material strain rate effects and bond slip between reinforcing bars and concrete are considered. To validate key aspects of the modeling procedure, as well as the accuracy and applicability of the selected material models, an axially loaded column subjected to lateral impact by a rigid object at mid-span is simulated and compared with experimental results available in the literature. Next, the container impact simulation is carried out and the effect of container impact parameters such as speed, height above ground level, mass and orientation on peak force and impact duration are studied. In addition, the influence of container kinetic energy on the column displacement response and damage level characterized by residual axial load carrying capacity is investigated.

2. EXISTING FORMULAE FOR IMPACT FORCE

The peak force F_p for head-on impact of a water-borne object given in ASCE/SEI 7-05 is

$$F_p = \frac{\pi m v}{2\Delta t}, \tag{1}$$

where m is mass of the object, v is velocity of the object and Δt is impact duration (i.e., time to reduce impact velocity to zero). This equation is based on the principle of impulse and momentum where the force time-history is assumed to be a half-sine pulse with amplitude F_p. Therefore, it is easy to show that Eq. (1) can be obtained from

$$\int_0^{\Delta t} F_p \sin\frac{\pi}{\Delta t} t \; dt = \Delta(mv) = mv, \tag{2}$$

where it is assumed in Eq. (2) that linear momentum of the water-borne object after impact is zero but this assumption may not be true for all impact scenarios. Further, there is a significant uncertainty in evaluating the duration of impact but a single value of $\Delta t = 0.03$ s has been recommended. In Section 5 it is shown that the impact duration is significantly influenced by the mass of the object and the stiffness of both the object and the structural member.

In the case of FEMA P646 the peak force is given by

$$F_p = C_m v\sqrt{k_{eff} m}, \tag{3}$$

where C_m is added mass coefficient ($C_m = 2.0$) and k_{eff} is effective contact stiffness i.e., $1/k_{eff} = 1/k_{obj} + 1/k_{st}$; in which k_{obj} is frontal stiffness of the object and k_{st} is local stiffness of the structural member in the contact region. This formula is obtained by solving the equation of motion of an undamped SDOF system and assuming linear force deformation relation for the contact. However, it is seen that Eq. (3), without the added mass coefficient is simply an application of energy conservation to the elastic collision where the sum of absorbed energies equals the kinetic energy dissipated as strain energy. Assuming a linear force deformation relation $F(x) = k_{eff} x$ where x is summation of the deformation of the structural member and the object in the contact region, the conservation of energy can be expressed as

$$\frac{1}{2} m v^2 = \int_0^{x_p} F(x)\, dx = k_{eff} \frac{x_p^2}{2}, \tag{4}$$

where x_p is the deformation that corresponds to the peak force i.e., $F_p = k_{eff} x_p$ and it is assumed that the object velocity is zero when $x = x_p$. Hence using Eq. (4) an expression for F_p van be obtained which after introducing the added mass coefficient yields Eq. (3). Although this approach is rational compared to the impulse-momentum consideration, the estimation of k_{eff} is challenging in practical applications. The mass and effective stiffness properties are provided in FEMA P646 for a few types of shipping containers but there is no information on procedures used to estimate those stiffness values. It is noted that the given k_{eff} value for $20'$ (20 foot) shipping container is quite large ($k_{eff} = 1.5 \times 10^9$ N/m) and results in a substantially high peak force. For example, the peak force acting on the structure due to impact of the 2200 kg $20'$ shipping container having a 4 m/s impact velocity (typical value in a tsunami situation) and a 0.03 s impact duration, is approximately 461 kN and 7266 kN from ASCE/SEI 7-05 and FEMA P646 (without added mass effect), respectively. This indicates that the above procedures exhibit uncertainties in the prediction of peak force and need further investigations before being used for design. This paper addresses this issue using numerical simulations and presents the results of detailed finite element analyses of impact between a $20'$ shipping container and axially loaded RC columns.

3. FINITE ELEMENT MODELLING

Crash simulation between a moving object and a RC structure is challenging because it is influenced by parameters of the impacting object (viz. geometry, mass, material properties, stiffness, impact orientation and velocity) and that of the structure (viz. geometry, inertia, material properties and stiffness) as reported by Stronge (2000). Analyses of such scenarios involve extensive use of part-to-part contact, multiple material models with strain rate effects, a combination of non-traditional elements and

large displacements, and are very often carried out using finite element codes where the main solution procedure is based on explicit time integration. The explicit solvers are more robust and computationally more efficient than implicit solvers, and well suited for complex contact problems (Zhong 1993). The general purpose finite element code LS-DYNA (2006) that includes all of these capabilities is used in the present study to analyze impact between the shipping container and the RC column.

3.1 Shipping Container Model

A general purpose steel shipping container is considered as the tsunami water-borne object in the present study. The different parts of the container which includes corrugated panels, corner posts, top side rails, bottom side rails and cross members are modeled using 4-node Belytschko-Lin-Tsay shell elements (Fig. 1).



(a) View of exterior (b) View of interior

Fig. 1. Finite element model of shipping container.

The Belytschko-Lin-Tsay element formulation results in the existence of hourglass (zero energy) modes (Khalil and Bois 2004). The errors due to hourglass modes can be reduced by using a relatively finer mesh at critical locations such as impacting surfaces of the container which in turn enhanced the accuracy of the crushing deformation of those parts. Therefore, the container model contained approximately 38,000 shell elements. Since significant yielding was expected during impact, a piecewise linear plastic material (MAT_024) was used to represent inelastic behavior of the container model (LS-DYNA 2006). Previous studies have shown that this material is computationally efficient to use with shell elements for crash simulations (Ulker et al. 2008). Steel is a rate dependent material and corresponding to a strain rate of $10\ s^{-1}$ the yield stress of mild steel is approximately double the static yield stress (Jones 1989). Therefore, rate sensitivity of the steel material used for the container model was considered in the present study using the constitutive equation originally proposed by Cowper and Symonds (Otubushin 1998),

$$\frac{\sigma_y^d}{\sigma_y^s} = 1 + (\dot{\varepsilon} / D)^{1/q} \tag{5}$$

where σ_y^d is dynamic yield stress, σ_y^s is quasi-static yield stress, $\dot{\varepsilon}$ is strain rate, D and q are material coefficients to be determined from experiments. It has been found that the material MAT_024 with the Cowper-Symonds strain rate model is capable of reproducing experimentally observed behavior of steel under dynamic loading conditions (Wu and Thomson 2007).

3.2 RC Column Model

Square and circular columns are considered in this study where peak force and residual axial capacity of the columns due to container impact is of particular interest. The constant stress solid elements and Hughes-Liu beam elements were used to represent concrete and reinforcing steel, respectively (Fig. 2(a)). The concrete in both columns is modeled using 8-node hexahedron elements. In the case of square column each element is a 25 mm cube. For the circular column elements of 25 mm thickness along the column axis direction are used. The longitudinal and transverse reinforcements are modeled using 25 mm long beam elements. The constraints provided by the foundation and the upper end at the beam-column joint are included in the model as shown in Fig. 2(b). The nodes on outer vertical surfaces of the foundation and upper end were constrained horizontally and nodes on bottom surface of the foundation were constrained vertically.

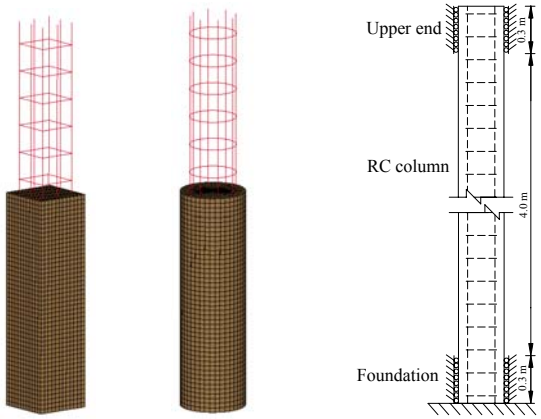

(a) (b)

Fig. 2. RC column details: (a) numerical models and (b) support conditions.

3.2.1 Material model

In the present study, the material MAT_072R3 is used to model concrete behavior (Crawford and Malvar 2006). The model includes damage and strain rate effects, and has material parameter generation capability based on the uniaxial unconfined compressive strength of concrete. Hence, it is very useful when the information of the concrete is limited or uncertain. Extensive previous studies suggested that the model provides a robust representation of concrete material behavior under uniaxial, biaxial and triaxial stress conditions (Malvar et al. 1997, Crawford and Malvar 2006). The material PLASTIC_KINEMATIC (MAT_003) is used to model longitudinal reinforcements and ties (LS-DYNA 2006). The model is bilinear representing elastic-plastic behavior and is suitable to model isotropic and kinematic hardening plasticity with the option

of including rate effects. It is a very cost effective model for reinforcing steel as suggested by previous researchers and is available for beam elements (Shi et al. 2008, Bao and Li 2009).

In the analysis of RC structures subjected to impact loads, both concrete and reinforcing steel are experienced a wide range of strain rates depending on the type loading. For instance, rates of $10^{-4} - 10^{-3}$ s^{-1} can be expected in vehicle impacts and higher strain rates, in the order of 10 s^{-1} have been achieved in drop weight impact tests (Bischoff and Perry 1991, Hentz et al. 2004). At these strain rates, for example, at 10 s^{-1} the apparent strength of concrete can increase by more than 50% in compression (Bischoff and Perry 1991) and 200% in tension (Malvar and Ross 1998). However, reinforcing steel experiences less than 20% strength increase under these strain rates thus, its effects on numerical results are insignificant (Malvar 1998). Therefore, strain rate effect only for concrete is considered in the following simulations.

3.2.2 Strain rate effect

The effect of strain rate on the compressive and tensile strength of concrete is typically represented using the *dynamic increase factor* (DIF) which is the ratio of dynamic to static strength at a given strain rate. The most comprehensive model is presented by CEB (1993) which reports DIFs for compressive and tensile strengths for a wide range of strain rates based both on test results and analytical models. Previous studies indicate that the model appears to agree well with the available experimental data particularly for compression (Malvar and Ross 1998). Hence, in the present study DIFs for compressive strength of concrete are estimated using the CEB-FIP formula,

$$\text{DIF} = \frac{f_{cd}}{f_{cs}} = \begin{cases} \left(\dfrac{\dot{\varepsilon}_d}{\dot{\varepsilon}_{cs}}\right)^{1.026\alpha}, & \dot{\varepsilon}_d \le 30 \text{ s}^{-1} \\ \gamma_s \left(\dfrac{\dot{\varepsilon}_d}{\dot{\varepsilon}_{cs}}\right)^{1/3}, & \dot{\varepsilon}_d > 30 \text{ s}^{-1} \end{cases} \tag{6}$$

where f_{cd} is dynamic compressive strength at the strain rate $\dot{\varepsilon}_d$, f_{cs} is static compressive strength at the static strain rate $\dot{\varepsilon}_{cs} = 30 \times 10^{-6}$ s^{-1}, $\log \gamma = 6.156\alpha - 2$, $\alpha = 1/(5 + 9 f_c'/f_{co}')$; in which f_c' is static uniaxial compressive strength in MPa and $f_{co}' = 10$ MPa. It is noted that Eq. (6) is valid for strain rates in the range of $30 \times 10^{-6} - 300$ s^{-1}.

Malvar and Ross (1998) proposed a formula to estimate DIFs for the tensile strength of concrete based on an excessive literature review and verified that it agrees with the experimental data more accurately than the CEB-FIP formula for tensile strength. Therefore, it is used in the present study and is given by the following formula,

$$\text{DIF} = \frac{f_{td}}{f_{ts}} = \begin{cases} \left(\dfrac{\dot{\varepsilon}_d}{\dot{\varepsilon}_{ts}}\right)^{\delta}, & \dot{\varepsilon}_d \le 1 \text{ s}^{-1} \\ \beta \left(\dfrac{\dot{\varepsilon}_d}{\dot{\varepsilon}_{ts}}\right)^{1/3}, & \dot{\varepsilon}_d > 1 \text{ s}^{-1} \end{cases} \tag{7}$$

where f_{td} is dynamic tensile strength at the strain rate $\dot{\varepsilon}_d$, f_{ts} is static tensile strength at the static strain rate $\dot{\varepsilon}_{ts} = 10^{-6}$ s^{-1}, $\log \beta = 6\delta - 2$ and $\delta = 1/(1 + 8 f_c'/f_c')$. This formula is valid for strain rates $10^{-6} - 160$ s^{-1}.

The strain rate effect is implemented in the concrete model using the above DIFs calculated at different strain rates. In their implementation Crawford and Malvar (2006) used *enhancement factor* denoted by r_f instead of DIF, and the strain rate effect was incorporated as follows. The enhanced value $\Delta\sigma_e$ of the failure surface at pressure p is desired. The "unenhanced" pressure (p/r_f) is first obtained and then the unenhanced strength $\Delta\sigma(p/r_f)$ is calculated for the specified failure surface. Finally, unenhanced strength is multiplied by the enhancement factor to give

$$\Delta\sigma_e = r_f \Delta\sigma(p/r_f). \tag{8}$$

The strength is equally enhanced along any radial stress path, including uniaxial, biaxial and triaxial tension, and uniaxial and biaxial compression.

3.2.3 Bond slip

The bond slip between the reinforcing bar and concrete is considered in the present analysis. The one-dimensional slide line, CONTACT_1D in LS-DYNA is used to model the bond slip between the reinforcing bar and concrete in a discrete manner. In this model, a string of consecutive nodes (slave nodes) related to beam elements representing reinforcing bar is forced to slide along a string of consecutive nodes (master nodes) related to concrete solid elements. This kinematic constraint is applied using a penalty method where fictitious springs are inserted between slave nodes and master nodes (Weathersby 2003). The force developed in the spring for a given slip is determined using parameters specified for the slide line model. These parameters include bond shear modulus G_s, maximum elastic slip $S_{\max}$ and exponent in damage curve h_{dmg}, and vary significantly with the concrete properties and rebar diameter. Therefore, those parameters should be obtained using corresponding pullout tests if the appropriate test data are not available. In the present study appropriate parameter sets were selected from the test data scrutinized by Shi et al. (2009).

3.3 Contact Modeling

Accurate modeling of contact between colliding objects is crucial for the prediction capability of the finite element simulations. A contact is defined by identifying specific locations that need to be checked for potential penetration of a slave node through a master surface. In crash simulations, the deformations can be very large and predetermination of contact orientation may be difficult or impossible. For this reason, the automatic contact options are recommended since it can detect penetration coming from either side of a shell element (LS-DYNA 2006). The contact type CONTACT_AUTOMATIC_SINGLE_SURFACE is used in the present analysis. With this contact type, the slave side is typically defined as a list of parts that are expected to participate actively in resisting the contact forces. The contact is considered among the parts in the slave list and no master side is defined. To obtain the resultant contact force, a force transducer is added through CONTACT_FORCE_TRANSDUCER_PENALTY option. The force transducer only measures contact forces produced by the single surface contact and does not affect the results of the simulation. With this option, both master and slave parts are defined and only those forces that develop between the master and slave parts are written to the output file.

4. VALIDATION OF FINITE ELEMENT MODEL

Since the authors have not come across any experimental work similar to the impact scenario considered in the present study, to evaluate the accuracy and reliability of the finite element models as discussed in Section 3, first the hourglass energy was checked and next the numerical model was checked with available experimental data on impact of axially loaded RC columns.

4.1 Energy considerations

The numerical model of the shipping container was tested by considering impact between the container and a 300×300 mm^2 rigid column as it can be done with minimum computational effort compared to the use of the complex RC column model. Extensive mesh refinement studies and conservation of energy checks have been carried out to ensure numerical stability of the model. The finer mesh was used in some parts of the container model. During impact the kinetic energy of the container is gradually decreased while the internal energy stored in the deformed components increase. In addition, hourglass energy increases to a maximum at rebound and then decreases. The evolution of various energy quantities are shown in Fig. 3 for the impact of a 2200 kg container with a velocity of 14 m/s on the rigid column. The results are acceptable since at rebound the maximum hourglass energy is less than 3% of the total energy. El-Tawil et al. (2005) reported a ratio of 17% for hourglass energy in the analysis of vehicle collision with bridge piers and their results were deemed to be acceptable.

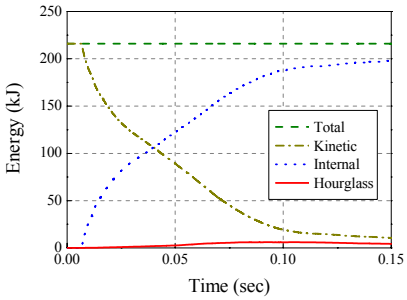

Fig. 3. Evolution of various energy quantities for the impact of a 2200 kg container with a velocity of 14 m/s on the 300×300 mm^2 rigid column.

4.2 Validation of column model with available experimental data

Experimental results of column tests reported by Louw et al. (1992) were used to evaluate the accuracy of response prediction of the RC column model. Since the behavior of RC columns subjected to transverse impact loads are significantly influenced by the level of axial load imposed on it, the selected experimental work is appropriate for the evaluation of numerical modeling techniques used in the present study. The test setup where columns were tested in a horizontal position as shown in Fig. 4(a) was used by Louw et al. (1992) to study response of axially loaded RC columns subjected to lateral impact due to a drop weight at mid-span.

Two numerical models simulating the test condition were developed in LS-DYNA. In modeling bond between reinforcing bar and concrete, one model allows for the bond slip and the other model assumes perfect bond. To model the bond slip behavior, bond shear modulus $G_s = 60$ MPa/mm, maximum elastic slip $S_{max} = 0.2$ mm and exponent in damage curve $h_{dmg} = 0.12$ are taken from Table 1 of Shi et al. (2009). However, it is noted that these values are approximate but the closest to the parameter of the experiment. The numerical analysis of these two columns subjected to the same drop weight impact as in the experiment was conducted. The comparison of the predicted and measured resultant contact force and deflection time histories at middle of the column is shown in Fig. 4(b). It is seen that considering bond slip between reinforcing bars and concrete yields better prediction of resultant peak force, duration and both peak and residual displacements compared to the perfect bond assumption. Since the parameters G_s, S_{max} and h_{dmg} used to define slide line model are approximate they may introduce some errors to the displacement response of the column. However, considering the availability of limited data particularly, information related to bond slip modeling, geometry and material properties of the drop weight, numerical results are considered to be in good agreement. Further, it is seen that the selected material models and strain rate formulae for concrete and reinforcing steel are appropriate for simulating the column response to impact loads. Therefore, modeling aspects as outlined in the above procedure were used in the following simulations.

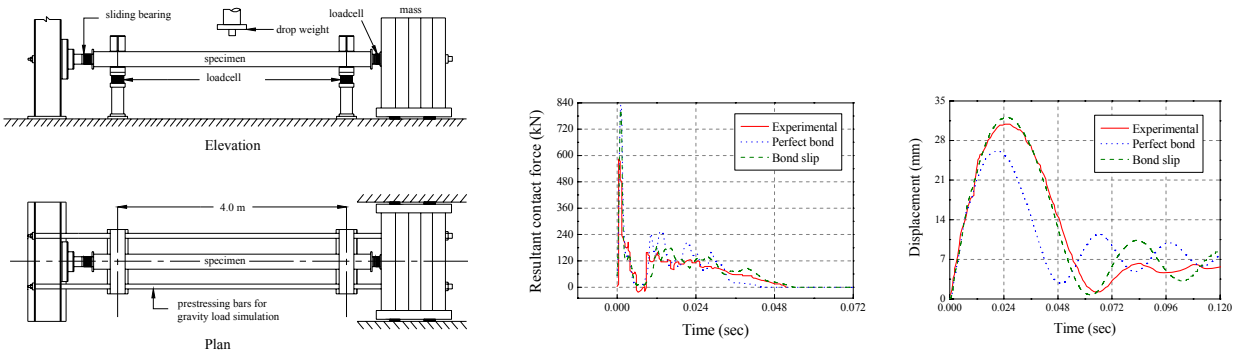

(a) (b)

Fig. 4. Drop weight impact test. (a) Test set-up (after Louw et al. 1992) and (b) resultant contact force and displacement response at middle of column.

5. CONTAINER IMPACT SIMULATION

In the present study 20′ (20 foot) ISO 1CC type steel cargo container is considered for the impact simulation (Containex 2009, Magellan 2009). The container has a length of 6.096 m, width of 2.44 m and height of 2.59 m. The tare (empty container) weight is 2200 kg and the maximum gross weight is 30,480 kg. The properties of the steel material used for modeling the container are density 7850 kg/m^3 Young's modulus 200 GPa, Poisson's ratio 0.3, yield strength 343 MPa, tensile strength 481 MPa and elongation 22% (Containex 2009). The strain rate dependent material behavior of the steel is taken into account using the coefficients $D = 40.4$ s^{-1} and $q = 5$ in the Cowper and Symonds model (Jones 1989).

In this section a building where there are no in-fill walls on the first floor to allow unrestricted flow of tsunami waves is considered. Two RC column models with square and circular sections are developed using the finite element modeling procedure described in Section 3. These columns are assumed to be located at the lower level of a three-story multi-bay RC building, supporting $6\text{ m} \times 6\text{ m}$ slabs at each floor level which carries uniformly distributed loads of 3 kN/m^2 representing live load in a typical office building, class rooms in a school or reading rooms in a library (ASCE 2005), and designed using code provisions of ACI 318-08 (ACI 2008). However, for comparison purposes the diameter of circular column is chosen to have the same cross sectional area as the square column and this also agrees with the design requirements. The section and reinforcement details are given in Table 1.

Normal weight concrete density 2400 kg/m^3 with a specified compressive strength of 37 MPa was used for all columns. The DIFs are calculated using Eqs. (6) and (7), and are given together with corresponding strain rates by a curve defined in the input file. Steel bars with yield strength of 414 MPa and 275 MPa were used for longitudinal and transverse reinforcement, respectively. The parameters for the one-dimensional slide line model in the analysis of this section are bond shear modulus $G_s = 34$ MPa/mm, maximum elastic slip $S_{\max} = 0.69$ mm and exponent in damage curve $h_{dmg} = 0.18$. In selecting these parameters, data from the pullout test conducted using the same concrete compressive strength and longitudinal bar diameter as used in the present analysis was considered (see Shi et al. (2009)). The coefficient of friction between potential contact surfaces of the container and the RC column was assumed to be 0.3.

At the beginning an axial load is applied to the column to simulate the initial stress state present in the column due to gravity loads. This force should be applied gradually from zero to the desired axial load since the analysis is explicit dynamic, and in the present analysis it takes 50 ms. The axial load applied to the column is determined based on distribution of frame loads corresponding to dead load plus 25% of the design live load. The impact is initiated when the inertial effects of the column due to the gravity loading are sufficiently small. Therefore, the initial distance between the container and the column is determined based on the specified initial velocity of the container in each analysis. The explicit dynamic analysis is continued for a sufficient period of time to capture nonlinear response of the impacted column. In the post-impact analysis stage, the residual axial load carrying capacity of the impacted column is estimated by increasing the axial load until the column is crushed (similar procedure has also been adopted by Shi et al. (2008) and Bao and Li (2009)).

Table1. Section and reinforcement details of the RC columns considered in the present study.

Column type	Cross section[a]	Longitudinal reinforcement[b]	Transverse reinforcement[b]
Square	300×300 mm^2	8-No. 5 ($\rho_l = 1.8\%$)	31-No. 3@150 mm ($\rho_v = 0.35\%$)
Circular	$D = 340$ mm	8-No. 5 ($\rho_l = 1.8\%$)	31-No. 3@150 mm ($\rho_v = 0.31\%$)

[a] D is diameter.

[b] Number of bars-diameter; No. 5: 16 mm and No. 3: 10 mm,

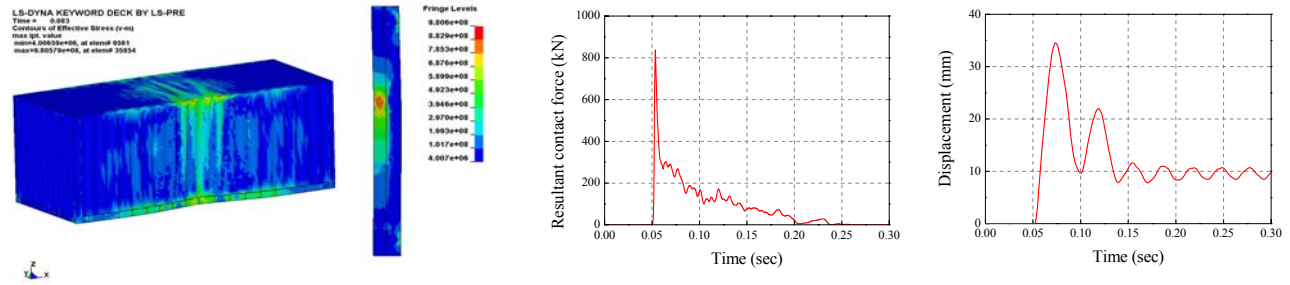

(a) (b) (c)

Fig. 5. Impact on square column by a 2200 kg container with a velocity of 8 m/s and 0.05 m above GL: (a) stress distribution, (b) resultant contact force and (c) column displacement at the location where top side rail of the container impacts.

In the present study central and eccentric impact scenarios are considered by changing the container orientation with respect to the column. The impact angles are measured anti-clockwise from the line connecting their centers of mass to the principal axis of the container (i.e., 0^0 and 90^0 represent longitudinal and transverse impact scenarios, respectively). A typical stress distribution of the impacted container and the column due to the transverse impact are shown in Fig. 5(a). The time histories of resultant contact force and lateral displacement at the location where the top side rail of the container impacts the column are shown in Figs. 5(b),(c). The impact force time-history appears to be comprised of an initial peak with high amplitude followed by comparatively low amplitude force levels that are sustained over the duration of the impact. Initially the column experiences only local deformations and stress waves are generated at the area of contact. As these deformations are very small, the impact force time-history has an early high peak. The stress wave propagates through the column depth and absorbed energy is converted into strain energy in concrete and steel reinforcement while part of it dissipates through concrete cracking. This process takes time and there is approximately a time lag of 0.02 s between the initial rises of the impact force and the peak displacement. Although it is not clear in Fig. 5(a), several oscillations occur in corrugated steel panels particularly in the impacted face of the container, result in a number of sharp spikes after the peak force as seen in Fig. 5(b). The top side rail of the container suffers extensive inelastic deformation followed by kinking of the roof panel near the contact region particularly, in a narrow area nearly equal to width of the column section. However, the deformation of the bottom side rail is not concentrated to a narrow area but distributed over large portion of the rail because the cross members in the floor structure significantly resist the lateral deformation.

The effects of container impact parameters on the resultant peak force due to the transverse impact are shown in Fig. 6 for the square column and Fig. 7 for the circular column. As shown in Figs. 6(a) and 7(a), the column geometry influences the resultant peak force due to stiffness contribution from the parallel cross members in the floor structure of the container. The square section mobilizes more of the structural system of the impacting container leading to greater contact forces than the circular section. In general the maximum peak force occurs when either top or bottom rail of the container comes into contact with the column at its mid-height, although the peak force is nearly independent of the container height above the ground level. Therefore, out of considered impact levels, maximum resultant peak force for both columns occurs when the container approaches 0.05 m above the ground level. In Figs. 6(b) and 7(b), the resultant peak force increases with increase in container mass as expected but its rate of increase tends to decrease with velocity due to stiffness degradation in the contact area of both the container and column. When the area of contact is stiff it would attract greater force but at high impact velocities, both container and column suffer damage and degradation in stiffness inevitable. The resultant peak forces and impact durations due to impact of the container with different angles are shown in Figs. 6(c) and 7(c). It is seen that the contact forces are considerably reduced in the case of longitudinal impact, since cross members are not actively participating in resisting container deformation. In general, the resultant peak force increases with container velocity but its rate of increase tends to decrease. The peak forces obtained using ASCE/SEI 7-05 and FEMA P646 are compared with the computed values from the simulation in Table 2. It is seen that the peak force determined using FEMA guideline is too conservative. In general ASCE standard provides better predictions of peak force for circular columns but underestimates for square columns particularly for low velocities.

Impact durations estimated from the simulations are presented in Figs. 8 and 9 for square and circular columns, respectively. To calculate impact duration and compare with the ASCE/SEI 7-05 (which assumes a half-sine pulse), the actual contact force time-history (as typically shown in Fig. 5(b)) is equated to a half-sine pulse with the resultant peak force as its amplitude. The actual contact duration is much higher than the computed impact duration as the container is in contact with the column for a long time due to the complexity of the impact event which involves dynamic interaction, friction effects and large plastic deformations. The idealization of half-sine pulse for the impact force time-history allows direct assessment of design provisions as outlined in Section 2.

The impact durations appear to increase almost linearly with increasing container velocity as shown in Figs. 8 and 9 for square and circular columns, respectively. Some

discrepancies particularly, at high velocities can be seen in Fig. 8(c) which is compatible with the behavior shown in Fig. 6(c). At high impact velocities both the container and column undergo plastic deformations and take longer time to rebound. It is clearly seen that the recommendation of single value for the impact duration (i.e., $\Delta t = 0.03$ s) is not correct for container impact scenarios particularly at high velocities. For the empty container, the impact duration for square column is $0.02 - 0.12$ s and for circular column is $0.04 - 0.16$ s for the velocities considered. Further, the highest impact durations for both columns can be seen for longitudinal impact cases where the container is weak in resisting deformations.

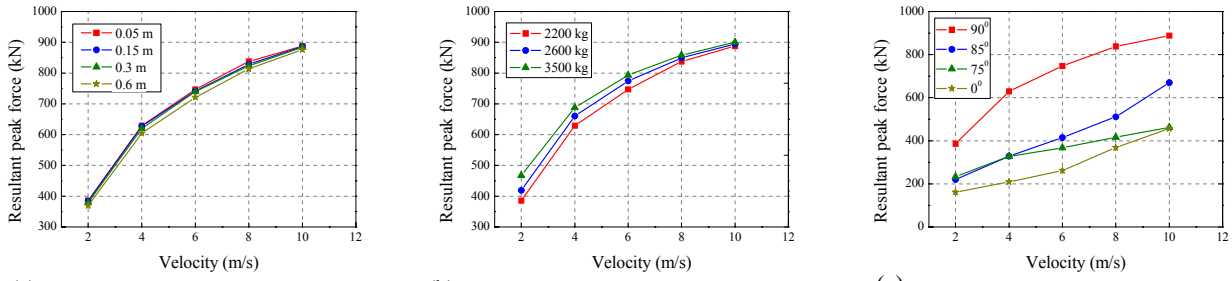

Fig. 6. Impact of container on a square column; effect of (a) container height above GL, (b) container mass and (c) impact angle on resultant peak force.

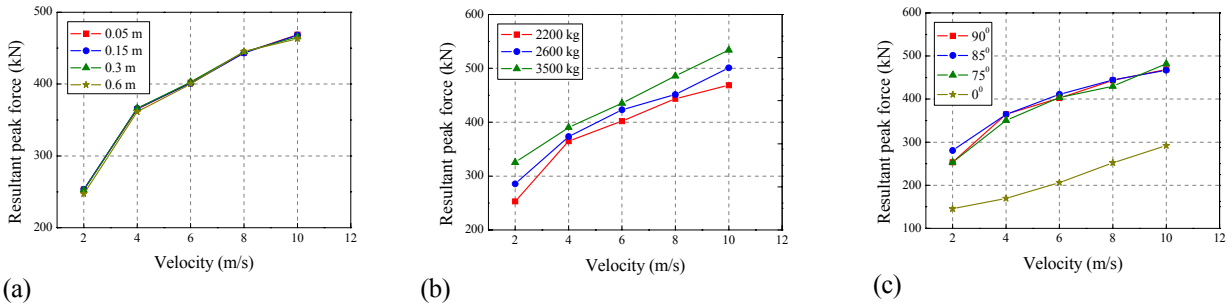

Fig. 7. Impact of container on a circular column; effect of (a) container height above GL, (b) container mass and (c) impact angle on resultant peak force.

Table 2. Comparison of peak forces due to impact of a 2200 kg container.

Velocity (m/s)	Peak force (kN)			
	ASCE/SEI 7-05 standard	FEMA P646 guideline	Present analysis	
			Square column	Circular column
2	230	3633	386	253
4	461	7266	630	365
6	691	10,899	747	402
8	922	14,533	838	443
10	1152	18,166	888	469

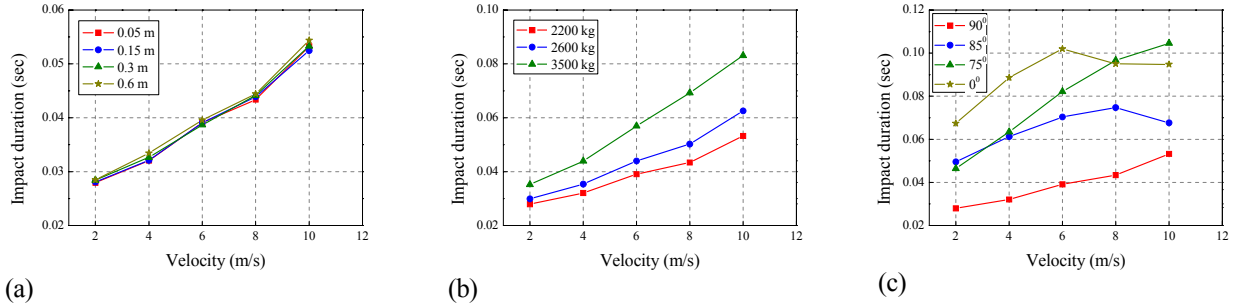

Fig. 8. Impact of container on a square column; effect of (a) container height above GL, (b) container mass and (c) impact angle on impact duration.

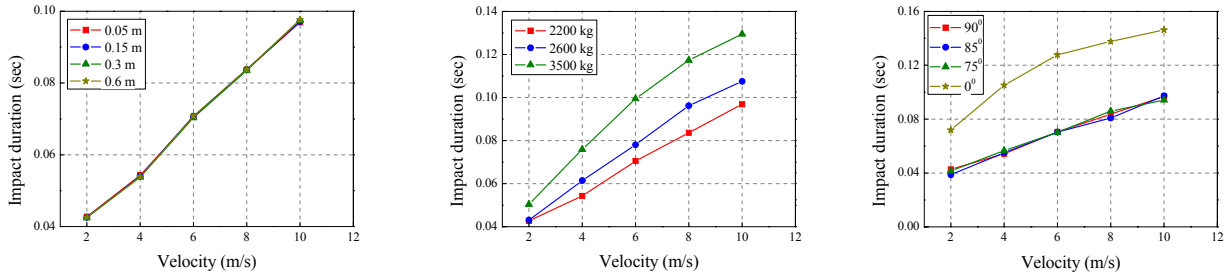

(a) (b) (c)

Fig. 9. Impact of container on a circular column; effect of (a) container height above GL, (b) container mass and (c) impact angle on impact duration.

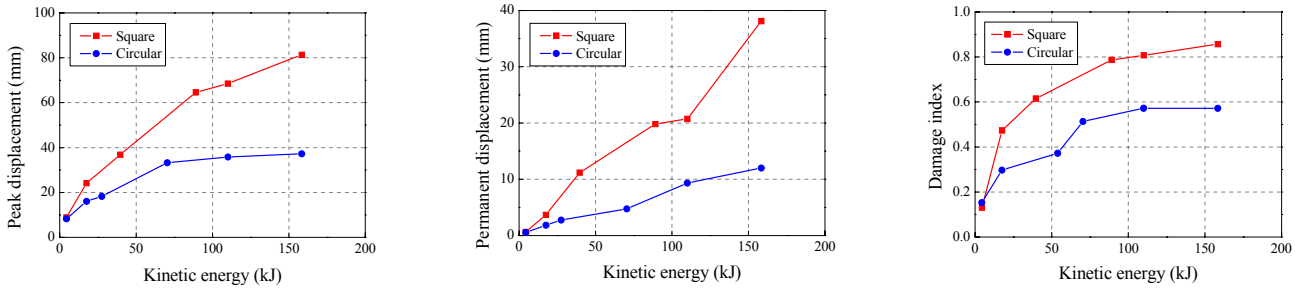

(a) (b) (c)

Fig. 10. Impact of the 2200 kg container on columns; response at the location where top side rail impacts (a) peak displacement and (b) permanent displacement, and (c) damage index.

The peak displacements and permanent displacements of the impacted columns are shown in Figs. 10(a) and (b), respectively for different container velocities indicated by its kinetic energies. These displacements are computed at the location where the top side rail of the container impacts the column. It is seen that for a given kinetic energy, the square column has much larger peak and permanent displacements than the circular column. This is because the resultant contact force on the circular column is smaller than that of square column as shown previously in Figs. 6(a) and 7(a). In addition, high confinement provided by circular ties enhances the strength of the circular column.

The damage state of the column is determined by computing a damage index which is related to the degradation of axial-load carrying capacity due to the container impact. The damage index D is defined as

$$D = 1 - P_{damaged} \Big/ P_{undamaged}, \tag{9}$$

where $P_{damaged}$ and $P_{undamaged}$ are axial load carrying capacity of damaged and undamaged column, respectively. It is seen that the column reaches to ultimate state or near collapse state when $D > 0.8$. The column damage states are shown in Fig. 10(c) for different container kinetic energies. The results show that at the same container kinetic energy, the residual axial-load carrying capacity is smaller in the case of square columns. This is because the square column suffers high damage due to the container impact, which in turn reduces axial-load carrying capacity.

6. CONCLUSIONS

The response of axially loaded RC columns due to impact of a tsunami water-borne shipping container is investigated using a comprehensive finite element model. The effect of bond slip on the column response is also studied during the validation process. It is seen that considering bond slip between reinforcing bars and concrete, results in a better prediction of column response compared to the perfect bond assumption.

The column geometry significantly affects the resultant peak force due to the container impact. The square column allows more of the structural system of the container to come into contact during the impact leading to a greater impact force. The maximum resultant peak force is seen when either top or bottom rail of the container comes into contact with the column at its mid-height. However, the height of the container above the ground level does not significantly affect the contact force on both the columns. Further, the resultant peak force is relatively small when the container is oriented along its longitudinal direction and impacts on columns. It is seen that the peak force determined using FEMA P646 is too conservative. In general ASCE/SEI 7-05 provides better predictions of peak force for circular columns when the velocity > 2 m/s but underestimates for square columns particularly for velocities ≤ 6 m/s. For the empty container, the impact duration for

square column is $0.02 - 0.12$ s and for circular column is $0.04 - 0.16$ s.

The results show that the circular column can significantly reduce the degree of damage due to container impact and subsequent collapse of the column. Both columns are damaged by flexure rather than shear. The peak force at the early stage of contact is not sufficient to cause shear failure but flexural deformation develops to a large value with the increase in container kinetic energy. The study suggests that RC buildings with circular columns at the lower level can significantly improve resistance to impact due to tsunami water-borne objects.

Acknowledgements:

The first author gratefully acknowledges a Monbukagakusho scholarship from the Japanese government. The authors are very grateful to Professor Kohji Tokimatsu, GCOE Program Leader of Center for Urban Earthquake Engineering (CUEE), Tokyo Institute of Technology, for his advice and support. Financial support from CUEE is gratefully acknowledged.

References:

ACI (2008), "Building Code Requirements for Structural Concrete (ACI 318-08) and Commentary," ACI Committee 318, American Concrete Institute, Farmington Hills (MI).

ASCE (2005), "Minimum Design Loads for Buildings and other Structures," ASCE/SEI 7-05, American Society of Civil Engineers, Reston (VA).

Bao, X. and Li, B. (2009), "Residual Strength of Blast Damaged Reinforced Concrete Columns," *International Journal of Impact Engineering*, **37**(3), 295-398.

Bischoff, P. H. and Perry, S. H. (1991), "Compressive Behavior of Concrete at High Strain Rates," *Materials and Structures*, **24**(6), 425-450.

CEB (1993), "CEB-FIP Model Code 1990," Comité Euro-International du Béton, Thomas Telford Services Ltd, London.

Containex (2009), Technical Specification," Container-Handelsgesellschaft, <http://www.containex.co.uk/dokumente/567_EN.pdf>.

Crawford, J. E. and Malvar, L. J. (2006), "User's and Theoretical Manual for K&C Concrete Model, Report TR-06-19.1, Karagozian & Case, California.

Dalrymple, R. A. and Kriebel, D. L. (2005), "Lessons in Engineering from the Tsunami in Thailand," *The Bridge*, National Academy of Engineering, **35**(2), 4-13.

El-Tawil, S., Severino, E. and Fonseca, P. (2005), "Vehicle Collision with Bridge Piers," *Journal of Bridge Engineering*, ASCE, **10**(3), 345-353.

FEMA (2008), "Guidelines for Design of Structures for Vertical Evacuation from Tsunamis," FEMA P646, Federal Emergency Management Agency, Washington (DC).

Ghobarah, A., Saatcioglu, M. and Nistor. I. (2006), "The Impact of the 26 December 2004 Earthquake and Tsunami on Structures and Infrastructure," *Engineering Structures*, **28**, 312-326.

Hentz, S., Donzé, F. V. and Daudeville, L. (2004), "Discrete Element Modelling of Concrete Submitted to Dynamic Loading at High Strain Rates," *Computers and Structures*, **82(**29-30), 2509-2524.

Inoue, S., Wijeyewickrema, A. C., Matsumoto, H., Miura, H., Gunaratna, P., Madurapperuma, K. M. and Sekiguchi, T. (2007), "Field Survey of Tsunami Effects in Sri Lanka due to the Sumatra-Andaman Earthquake of December 26, 2004," *Pure and Applied Geophysics*, **164**(2-3), 395-411.

Jones, N. (1989), "Structural Impact," Cambridge University Press, Cambridge (UK).

Kaushik, H. B. and Jain, S. K. (2007), "Impact of Great December 26, 2004 Sumatra Earthquake and Tsunami on Structures in Port Blair," *Journal of Performance of Constructed Facilities*, ASCE, **21**(2), 128-142.

Khalil, T. B. and Bois, P. D. (2004), "Finite Element Analytical Techniques and Applications to Structural Design. In Vehicle Crashworthiness and Occupant Protection, eds. Priya Prasad and Jamel E. Belwafa., American Iron and Steel Institute, Michigan, pp.388.

Louw, J. M., Maritz, G. and Loedolff, M. J. (1992), The Behaviour of RC Columns under Impact Loading," The Civil Engineer in South Africa, **34**(11), 371-378.

LS-DYNA (2006), "Theory manual," Livermore Software Technology Corporation, California.

Magellan (2009), Technical Specification for a Typical Steel Dry Cargo Container," Magellan Maritime Services GmbH, <http://www.magellan-maritime.de/cms/mdb/7/299.pdf>.

Malvar, L. J. (1998), "Review of Static and Dynamic Properties of Steel Reinforcing Bars," *ACI Materials Journal*, **95**(5), 609-616.

Malvar, L. J., Crawford, J. E., Wesevich, J. W. and Simons, D. A. (1997), "Plasticity Concrete Material Model for DYNA3D," *International Journal of Impact Engineering*, **19**(9-10), 847-873.

Malvar, L. J. and Ross, C. A. (1998), "Review of Strain Rate Effects for Concrete in Tension," *ACI Materials Journal*, **95**(6), 735-739.

Miyamoto, A., King, M. W. and Bulson, P. S. (1994), "Modeling of Impact Load Characteristics for Dynamic Response Analysis of Concrete Structures," *Proceedings of the Second International Conference on Structures under Shock and Impact*, Computational Mechanics Publications, Southampton, Boston, 71–88.

Okada, T., Sugano, T., Ishikawa, T., Ohgi, T., Takai, S. and Hambe, C. (2005), "Structural Design Method of Buildings for Tsunami Resistance (Proposed)," English Translation of the Building Letter of 2004, The Building Center of Japan, Tokyo.

Otubushin, A. (1998), "Detailed Validation of a Non-linear Finite Element Code using Dynamic Axial Crushing of a Square Tube," *International Journal of Impact Engineering*, **21**(5), 349-368.

Robertson, I. N., Riggs, H. R., Yim, S. C. S. and Young, Y. L. (2007), "Lessons from Hurricane Katrina Storm Surge on Bridges and Buildings," *Journal of Waterway, Port, Coastal, and Ocean Engineering*, ASCE, **133**(6), 463-483.

Shi, Y., Hao, H. and Li, Z-X. (2008), "Numerical Derivation of Pressure-Impulse Diagrams for Prediction of RC Column Damage to Blast Loads," *International Journal of Impact Engineering*, **35**(11), 1213-1227.

Shi, Y., Li, Z-X. and Hao, H. (2009), "Bond Slip Modelling and Its Effect on Numerical Analysis of Blast-Induced Response of RC Columns," *Structural Engineering and Mechanics*, **32**(2), 251-267.

Stronge, W. J. (2000), "Impact mechanics," Cambridge University Press, Cambridge (UK).

Synolakis, C., Okal, E. and Bernard, E. (2005), "The Megatsunami of December 26, 2004," *The Bridge*, National Academy of Engineering, **35**(2), 26-35.

Ulker, M. B. C., Rahman, M. S., Zhen, R. and Mirmiran, A. (2008), "Traffic Barriers under Vehicular Impact: from Computer Simulation to Design Guidelines," *Computer-Aided Civil and Infrastructure Engineering*, **23**, 465-480.

Weathersby, J. H. (2003), "Investigation of Bond Slip between Concrete and Steel Reinforcement under Dynamic Loading Conditions," PhD dissertation, Mississippi State University, Mississippi.

Wu, W. and Thomson, R. (2007). "A Study of the Interaction between a Guardrail Post and Soil during Quasi-Static and Dynamic Loading," *International Journal of Impact Engineering*, **34**(5), 883-898.

Zhong, Z-H. (1993), "Finite Element Procedures for Contact-Impact Problems," Oxford University Press, Oxford (UK).

JOINT CONFERENCE PROCEEDINGS
7th International Conference on Urban Earthquake Engineering (7CUEE) &
5th International Conference on Earthquake Engineering (5ICEE)
March 3-5, 2010, Tokyo Institute of Technology, Tokyo, Japan

COMPARISON OF SEISMIC RESPONSE OF SKEWED BRIDGES TO NEAR VS. FAR FIELD MOTIONS

Peyman Kaviani[1)], Farzin Zareian[2)], and Majid Sarraf[3)]

1) Graduate Student, Department of Civil and Environmental Engineering, University of California, Irvine, CA, USA
2) Assistant Professor, Department of Civil and Environmental Engineering, University of California, Irvine, CA, USA
3) Project Manager/Seismic Specialist, Parsons Corporation, Bridge and Tunnel, Irvine, CA, USA
pkaviani@uci.edu, zareian@uci.edu, majid.sarraf@parsons.com

Abstract: The seismic performance of skewed bridges during past earthquake has been complex and difficult to predict. The focus of this paper is to summarize the comparison between the seismic responses of skewed bridges to various motions for bridges with different angle of skew at their abutments. For this purpose, sensitivity analysis was performed considering a matrix of three bridges with different angle of skew in abutments varied between 0 to 60 degree, and subjecting them to near- and far field motions. The three bridge configurations are: two and three spans with single and multi-column bents. The bridges were modeled using SAP2000 program to perform nonlinear response history analysis. The results presented here show that an increase in abutment skew angle results in noticeable change in the fundamental mode of vibration and nonlinear response of bridges, particularly, significant deck rotation. In the case of a single column bent, the response is more pronounced and could lead to unseating of the bridge.

1. INTRODUCTION

Skewed bridges are commonly used as overcrossings in highway intersections and interchanges, particularly in complex intersections and in crowded urban areas where lack of space necessitates the use of skew geometries. Despite having better knowledge of their performance under service condition, their seismic response during past earthquakes has not been easily detectable. .

Much research have been conducted in regard to the seismic response of regular or straight bridges, however, there remains significant uncertainty about skewed bridge's actual behavior. Different failure scenarios, which are discussed in the studies by Ghobarah, Tso (1974), Wakefield et al. (1991), and Meng and Lui (2000), show the uncertainty to analyze the seismic response of skewed bridges during an earthquake.

Rotation and unseating of the deck is the major mode of failure in skewed bridges. For instance, the Foothill Boulevard Undercrossing experienced severe damages during the San Fernando earthquake (M_w = 6.5). This skewed bridge rotated in a horizontal plane resulting in a permanent offset of about 10 cm (Jennings 1971). Wakefield et al. (1991) concluded that the failure scenario was controlled by rigid-body motion of superstructure. In comparison to the previous studies, Meng and Lui (2000) proposed that the effects of skew angle on the overall dynamic response characteristic of the bridge are significant if the actual effect of boundary conditions can be modeled properly.

Shamsabadi et al. (2006) considered the effect of near-filed ground motion on skewed bridges. Five bridges with different geometric characteristics were modeled, Single-, two- and three span box girder bridges with single and dual column per bent supported by seat-type abutment. To consider variation in geometric characteristic, few bridge models were developed according to a modified version of the existing ones. Deck was modeled using shell element and they used nonlinear normal springs skewed to the longitudinal direction of the bridge. By changing the skewness of the abutment and implementing nonlinear response history analysis the sensitivity of bridge response to skew angle was studied. They concluded that the most sensitive seismic response of a skewed bridge is the deck rotation.

In the present article, sensitivity of skewed bridges seismic response parameters to variation of few geometric parameters is studied. Analysis has been conducted on bridges that have been recently built in California. Seismic displacement and rotation in abutments are generally captured by including longitudinal springs representing passive soil behind abutment walls. Because of the symmetry in column cross-section of all the bridge models the overall displacement is considered as the structural response parameter, but in order to study the unseating of the abutments longitudinal and transverse displacements were considered as well.

2. BRIDGE MATRIX

To investigate the sensitivity of seismic response of skewed bridges, a matrix of bridges with geometry characteristics representative of common bridges in

California have been studied. These bridges are recently designed (built after 2000) and are located in Southern California, which is a region with high seismicity. The number of spans and number of columns per bent are the parameters used to define the bridges in this study. Considering that the abutment behavior is more pronounced in seismic response of short bridges, two and three span bridges have been investigated. In addition, considering the fact that the overall torsional resistance of the bridge relies largely on the number of columns per bent, single column, and multi column bents are considered. The bridge properties are summarized as follows.

2.1 Two Span-Single Column Bent

The Jack Tone Road On-Ramp Overcrossing (Figure 1) located in city of Ripon in California, is a two-span bridge with 67.2 m total length, spans of 33.105 m and 34.095 m. The superstructure is a three-cell continuous reinforced concrete box-girder. The bent has a half-cap beam integral with the deck and a single reinforced concrete circular column in the middle. The column of the bent is 1.68 m in diameter supported on steel piles. The longitudinal reinforcing steel ratio of the column is approximately 2%. The abutments are seat-type with four elastomeric bearing pads per abutment.

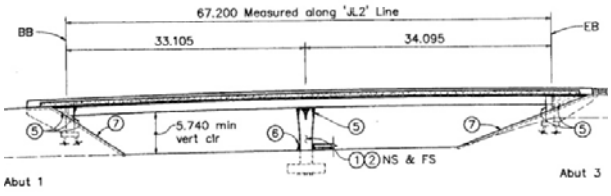

Figure 1 The Jack Tone Road On-Ramp Overcrossing Elevation

2.2 Two Span-Multi Column Bent

The La Veta Avenue Overcrossing (Figure 2) located in city of Tustin in California, is a two-span with 91.4 m total length, spans of 47.2 m and 44.2 m. The superstructure is a six-cell continuous reinforced concrete box-girder. The bent has a cap beam integral with the deck and two reinforced concrete circular columns. The column of the bent is 1.7 m in diameter supported on CIDH piles. The Longitudinal reinforcing steel ratio of the column is approximately 1.9%. The abutments are seat-type with seven elastomeric bearing pads per abutment.

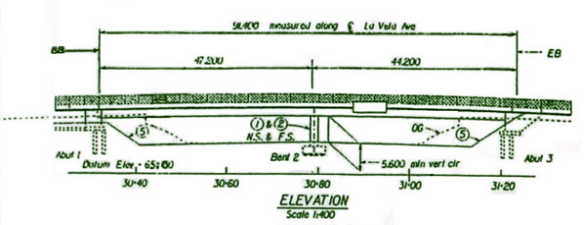

Figure 2 The La Veta Avenue Overcrossing Elevation

2.2 Three Span-Multi Column Bent

The Jack Tone Road Overhead (Figure 3) located in city of Ripon, is a three-span bridge with 127.5 m total length, spans of 47.6 m, 43.9 m and 36.0 m. The superstructure is a seven-cell continuous reinforced concrete box-girder. Intermediate bents have a cap beam integral with the deck and three reinforced concrete circular columns. The column of the bent is 1.68 m diameter supported on steel piles. The longitudinal reinforcing steel ratio of the column is approximately 2.2%. The abutments are cantilever-seat-type with nine elastomeric bearing pads per abutment. The abutment is originally is 36 degree skewed.

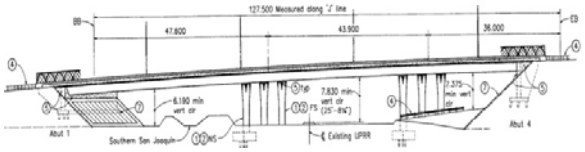

Figure 3 The Jack Tone Overhead Elevation

3. BRIDGE MODELING

The bridge structure is modeled by the structural analysis program SAP-2000 Nonlinear (2005). The present modeling assumptions mainly focuses on the modeling guidelines document prepared by Aviram et al. (2008).

The three-dimensional spine-model of the bridge structure with line elements located at the centroid of the cross sections following the alignment of the bridge is used. To capture the response of the entire bridge system and individual components under specific seismic demand characteristics, three-dimensional modeling is implemented. The developed models for the skewed bridges do incorporate nonlinear behavior of individual components. These components include column plastic hinge, abutment transverse and longitudinal springs, and abutment gap components. For simplicity of numerical simulations, the superstructure, cap beam, and foundation springs are considered as linear elastic components. Important assumptions and main aspects of modeling process of each individual component is explained in the following.

3.1 Superstructure

The superstructure elements are modeled as linear elastic beam-column elements with material properties corresponding to cracked reinforced concrete. In order to have uniform mass distribution, each span is divided to ten elastic elements. We took advantage of the Bridge Modeler component in SAP 2000 Nonlinear to define the frame properties for a box-girder cross section and the structural parameters of the section.

Cracked section properties are used in the model to obtain realistic values for the structure's period and the seismic demands generated from the analysis. I_{eff} of the box girder superstructure depends on the extent of cracking and

the effect of the cracking on the element's stiffness. I_{eff} for conventionally reinforced concrete box girder sections can be estimated between $0.5I_g$–$0.75I_g$. However, according to SDC (2004), Section 5.6.1.2. no stiffness reduction is recommended for pre-stressed concrete box girder sections ($I_{eff} = I_g$).

3.2 Cap Beam

For the multi-column bent bridge, an elastic element representing the cap beam is modeled as a frame element with a solid rectangular cross section and dimensions according to the bridge structural drawings.

The cap beam is connected through a rigid or a moment connection to the superstructure since both components are usually constructed monolithically without any joints. Because the concrete superstructure and cap beam are cast simultaneously, the superstructure's flexural stiffness enhances the torsional stiffness of the cap beam. The actual dimensions of the cap beam-superstructure system resisting torsion are greater than the cross-sectional dimensions of the cap beam element alone. The torsional constant of the cap beam J is therefore magnified by an arbitrary amplification factor of 100.

Despite the assumption adopted by Aviram et al. (2008) that assigned the calculated flexural stiffness of the cap beam from the bridge structural drawings, in the present modeling effort the flexural stiffness of the cap beam is magnified by the same amplification factor as the torsional factor (e.g., 100). As explained in the previous paragraph, simultaneous casting of cap beam and superstructure enhances the flexural stiffness of the cap beam.

3.3 Bent Column

Inelastic three-dimensional beam-column elements are used for column modeling. A beam-column element connects each of the nodes at the geometric centroid of the column cross section, using five elements to model the column. In a typical bridge structure, the bent column cross-section has a parabolic variation along the height. However, only the core section contributes in seismic response. Therefore only the core section of the bent column is modeled.

A separate segment at the column top with the length $D_{c.g.}$ (distance between box-girder centroid cross section and the column top) that represents the portion of the column embedded in the bent cap is modeled. An end (rigid) offset should be assigned in SAP2000 Nonlinear to the column top with a length of $D_{c.g}$. The offset with a rigid-zone factor of 1.0 to account for the high stiffness provided by the joint is considered.

Plastic hinges can develop at column ends near the point of fixity. The curvature of the column increases linearly with height from the point of inflection (zero moment) to the point of fixity (maximum moment). In the plastic hinge zone, the plastic moment and curvature are assumed constant. The analytical length of the plastic hinge in the column is proposed in Section 7.6.2 of SDC 2004. Eq. (1).

$$L_p = 0.08L + 0.022 f_{ye} d_{bl} \geq 0.044 f_{ye} d_{bl} \qquad (1)$$

Where: L: the column height (mm); f_{ye}: expected yield stress for A706 reinforcement (MPa); d_{bl}: Nominal bar diameter of longitudinal column diameter (mm). According to Eq. (1), the plastic hinge length depends on the column height, the longitudinal reinforcement size, and the strength of rebar.

Column hinges are modeled with fiber elements. Such modeling can incorporate the P-M-M interaction, and . represent the loss of stiffness caused by concrete cracking, yielding of reinforcing steel due to flexural yielding, and strain hardening.

3.4 Abutment

Specifically for standard bridge structures with short spans and stiff superstructure, the abutment behavior (i.e., nonlinear behavior of soil material and the soil-structure interaction) dominate the response of the bridge and the intermediate column bents. In bridge models used in this research we have employed the "Simplified" abutment model documented in Aviram et al. (2008). The general scheme of the simplified model is shown in Figure 4. In this model, the abutment is represented with a rigid element with length of d_w (superstructure width), connected through a rigid joint to the superstructure's centerline. Three nonlinear springs: Longitudinal. Transverse, and Vertical are used to connect each end of the rigid element.

In the longitudinal direction a zero length element is assigned with an elastic – perfectly – plastic (EPP) backbone curve representing the abutment backwall. The stiffness (K_{abt}) and ultimate strength (P_{bw}) of this element is obtained from section 7 of the SDC (2004). The longitudinal stiffness accounts for the gap and embankment fill response, where passive pressures are produced by the abutment back wall. The shear stiffness of the bearing pads is ignored.

In the transverse direction, a zero-length element is defined at each end of the rigid link with an assigned EPP backbone curve representing the backfill, wing wall and pile system. The abutment stiffness (K_{abt}) and back wall strength (P_{bw}) obtained for the longitudinal direction from section 7.8 of the SDC (2004) are modified using factors corresponding to wall effectiveness ($C_L = 2/3$) and participation coefficients ($C_W = 4/3$) according to Maroney and Chai, (1994). It is assumed that the wing wall length is between 1/2 to 1/3 of the back wall length. The resistance of the brittle shear keys and distributed bearing pads is ignored in this model for simplicity.

In the vertical direction, an elastic spring is defined at each end of the rigid link with a stiffness representing the stiffness of bearing pads k_v. The stiffness of the pads in compression and tension is assumed to be identical. Each bearing is assumed to have a cross-sectional area as specified on the bridge structural drawing. The distribution of the bearing pads along the stem wall and the vertical embankment stiffness are not accounted for in the model, assuming rigid soil conditions.

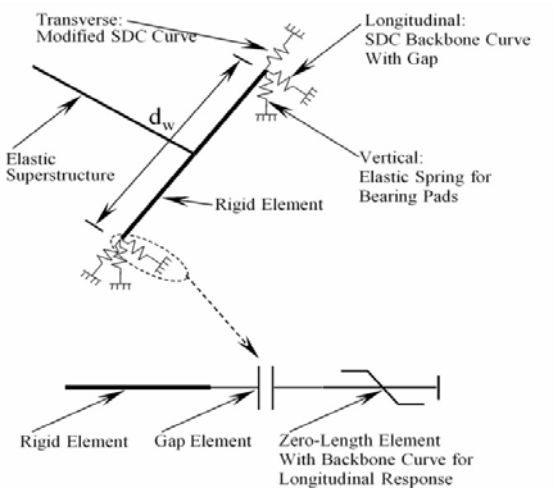

Figure 4 Simplified Abutment Model (Figure Developed According to a Similar One in Aviram et al. (2008))

4. ANALYSIS

We investigate the response of skewed bridges to variation of geometric parameters in two domains: variation in modal properties, and variation in seismic response parameters. Table 1 presents the parameters considered in this study and the range of their variation.

Table 1 Sensitivity Parameters, and Range of Variation

Sensitivity Parameters	Range of variation
Bridge Configuration	Two Span-Single Column, Two Span-Multi Column, Three Span-Multi Column
Abutment Skewness	$0^\circ, 30^\circ, 45^\circ, 60^\circ$
Ground Motion Characteristic	Near-Field Ground Motion, Far-Field Ground Motion

In applying the skew angle to the bridge models from the original non-skewed model the following assumptions are adopted:

1- the width of the superstructure in all skewed models is constant and equal to the width of the original bridge.

2- Longitudinal and transverse nonlinear springs are rotated in accordance with applied skew angles.

4.1 Modal Analysis

Modal analyses were conducted for each skew angle to determine the fundamental periods and mode shapes of the models discussed previously. Table 2 through Table 4 show first three periods and mode shapes of the bridges in regard to the variation of skewness of the abutment.

Table 2 Periods and Mode Shapes of Two Span-Single Column Bridge

Skewness		Mode		
		1	2	3
0°	Period (sec)	0.67	0.65	0.63
	Mode Shape	Long.	Trans.	Rot.
30°	Period (sec)	0.72	0.71	0.64
	Mode Shape	Rot.	Trans.	Trans./Long.
45°	Period (sec)	0.87	0.76	0.62
	Mode Shape	Rot.	Trans.	Long./Trans.
60°	Period (sec)	1.21	0.84	0.60
	Mode Shape	Rot.	Trans.	Long.

Table 3 Periods and Mode Shapes of Two Span-Multi Column Bridge

Skewness		Mode		
		1	2	3
0°	Period (sec)	1.11	0.61	0.49
	Mode Shape	Long.	Trans.	Vert.
30°	Period (sec)	1.12	0.61	0.50
	Mode Shape	Long.	Trans.	Rot.
45°	Period (sec)	1.14	0.61	0.61
	Mode Shape	Long./Trans.	Trans.	Rot.
60°	Period (sec)	1.21	0.82	0.62
	Mode Shape	Trans./Long.	Rot.	Trans.

Table 4 Periods and Mode Shapes of Three Span-Multi Column Bridge

Skewness		Mode		
		1	2	3
0°	Period (sec)	1.69	1.21	0.93
	Mode Shape	Long.	Trans.	Rot./Trans.
30°	Period (sec)	1.72	1.21	1.05
	Mode Shape	Long./Trans.	Trans.	Rot.
45°	Period (sec)	1.78	1.26	1.18
	Mode Shape	Long./Trans.	Rot./Trans.	Trans./Rot.
60°	Period (sec)	1.93	1.51	1.21
	Mode Shape	Long./Trans.	Rot.	Trans.

The natural period of bridge elongates with increase in skew angle. This phenomenon can be explained as the variation of the transverse stiffness of the abutment models and the rearrangement of each governing mode shapes. Due to implementation of gap elements in the longitudinal direction of the simplified abutment model (Figure 4), the longitudinal stiffness of the abutment model would not have any effect on the modal properties.

Seismic response of a bridge can be tracked by investigating the deformed shape of each mode of vibration. As shown in Tables 2-4, for all three bridges, the fundamental mode of vibration is the longitudinal mode, however, by increase in the skew angle the bridge tends to vibrate in the transverse direction, therefore, making the superstructure to rotate.

Variation in period elongation and mode shapes depend on the bridge geometrical characteristics. For two-span bridge the level of the variation is more pronounced in comparison to the three-span bridge. Global torsional stiffness of the bridge also affects the seismic response. For the two-span single column bridge the period elongate is more than 80% once 60 degree skewness is employed and the superstructure rotation becomes the first mode of vibration.

4.2 Response History Analysis

Nonlinear response history analysis was conducted on models with different skew angles. In order to investigate nonlinear response of models, two kinds of ground motions were considered: near-field and far-field ground motions. The effects of skew angle and ground motion characteristics on seismic performance parameters were investigated. Performance parameters considered include column drift ratio and deck rotation. The ground motion selected are two recording from the Northridge Earthquake (M_w = 6.7), one near-filed recording at the Rinaldi Receving Station (R = 6.5 km.), and one far-field recording at the Leona Valley #6 Station (R = 38.0 km.). (Need to compare and show the GM record for both, ARS curve)

The intention here is to investigate the behavior of skewed bridges to ground motions with different characteristics. The authors understand that further studies are required to extract quantitative values from such a sensitivity study. The results from nonlinear response history analysis of selected bridges are shown in Figures 5 and 6. For large skew angles, the near filed ground motion has caused the bridge to collapse, hence, no response parameter is shown on the plots. Discussion on behavior of skewed bridges to variation of structural and ground motion parameters are hereafter.

In Figure 5, the sensitivity of the column drift ratio to the skewness of the bridge abutment is illustrated. The results show that the near-field motion can cause large column deformations especially in the case of two span-single column bridges. The skewness in bridge deck and abutment enhances the rotational mode of vibration forcing large column deformation. The effect is more pronounced in single column bridge as the rotational stiffness is provided by only a single column's torsional stiffness. As can be seen in Figure 5, the effect of the abutment skewness on bridge response is less once more columns contribute the rotational stiffness of the bridge.

To investigate the unseating of the deck of skewed bridges, the sensitivity of the longitudinal displacement of the bridge abutment is studied. Our analysis shows a similarity between column drift ratio and abutment longitudinal displacement, therefore, deductions similar to those of column drift ratio can be made for the abutment longitudinal displacement.

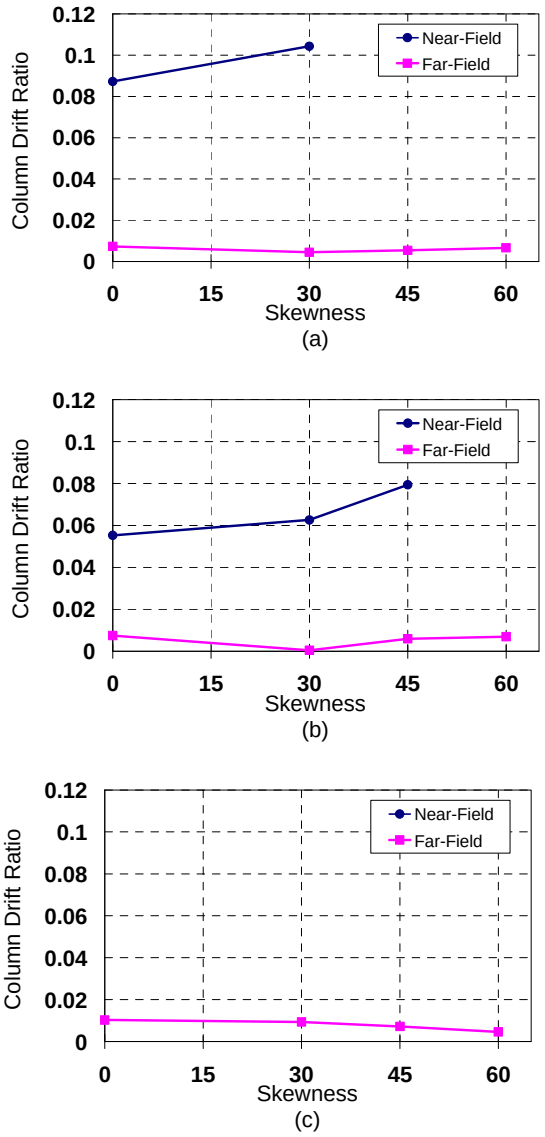

Figure 5 Column Drift Ratio Sensitivity to Skewness Angle and Ground Motion Properties: (a) Two Span-Single Column, (b) Two Span-Multi Column, and (c) Three Span-Multi Column

The unseating of the abutment as well as loss of bridge traffic capacity can be explained with deck rotation. The variation of this parameter to abutment skewness is shown in Figure 6. This parameter is the most sensitive parameter to bridge skewness. It can be seen that for angel of skew, the rotation of deck is minor. For larger skewness values, which are variable for each bridge configuration, the effect of skewness on deck rotation becomes pronounced (Figure 7). For the two span-single column bridge, this jump in deck rotation happens in skewness of 45 degrees, whereas, for the two span-multi column bridge the critical skewness is 60 degrees.

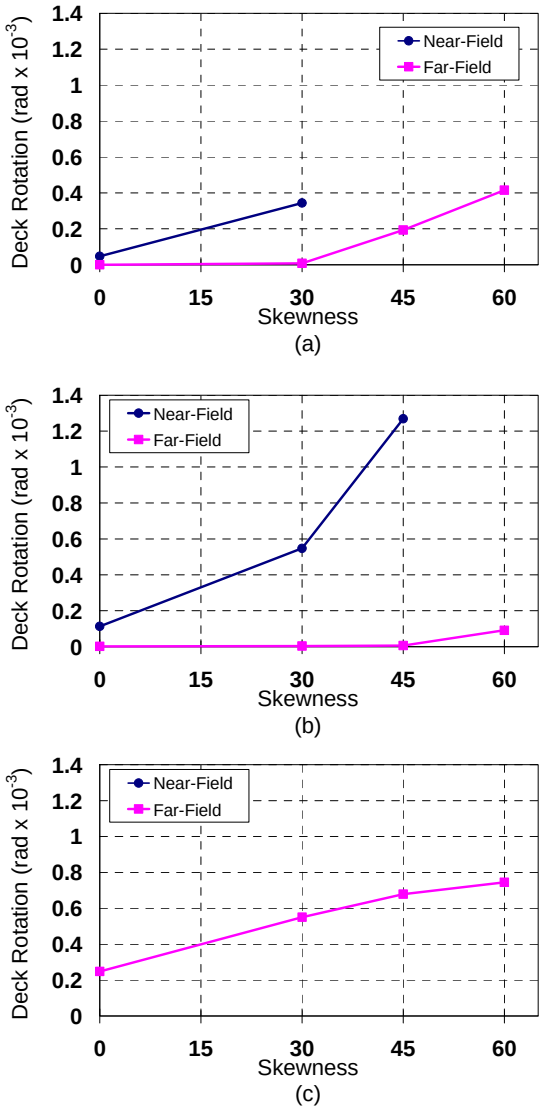

Figure 6 Deck Rotation Sensitivity to Skewness Angle and Ground Motion Properties: (a) Two Span-Single Column, (b) pan-Multi Column, and (c) Three Span-Multi Column

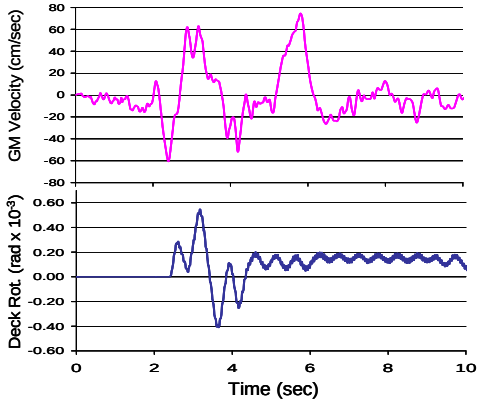

Figure 7 Response of the 30 Degree Skewed Two Span-Multi Column Bridge to the Near-Field Ground motion

5. CONCLUSION

Sensitivity of seismic response in skewed bridges to near vs. far-field motions were analyzed. Three bridge configurations were investigated: two span-single column, two span-multi column, and three span-multi column. It was shown that the angel of skew in the abutment tend to increase the amplitude of the deck ratio when a bridge is subjected to near filed ground motions.

Acknowledgements:

This study is based on work supported by the PEER Transportation Research Program under Grant No. UCLA-45782. This financial support is gratefully acknowledged. Any opinions, findings, and conclusions or recommendations expressed in this paper are those of the authors and do not necessarily reflect the views of sponsors.

References:

Jennings, P.C. (1971), "Engineering Features of the San Fernando Earthquake. Report no. EERL 71-02," California Institute of Technology.

Ghobarah, A.A. and Tso, W.K. (1974), "Seismic Analysis of Skewed Highway Bridges with Intermediate Supports," *Earthquake Engineering and Structural Dynamics*, **2**, 1315-1326.

Wakefield, R.R. Nazmy, A.S. and Billington, D.P. (1991), "Analysis of Seismic Failure in Skew RC Bridge," *Journal of Structural Engineering*, American Society of Civil Engineers, **117**(3), 972-986.

Maroney, B.H. and Chai, Y.H. (1994), "Seismic Design and Retrofitting of Reinforced Concrete Bridges," *Proceedings of 2nd International Workshop, Earthquake Commission of New Zealand*, Queenstown.

ATC (1996), "Improved Seismic Design Criteria for California Bridges: Provisional Recommendations. ATC Report No. ATC-32," Applied Technology Council.

Mckenna, F. Fenves, G.L. Scott, M.H. and Jeremic, B. (2000), "Open System for Earthquake Engineering Simulation," http://opensees.berkeley.edu.

Meng, J.Y. and Lui E.M. (2000), "Seismic Analysis and Assessment of a skew Highway Bridge," *Engineering Structure*, **22**, 1433-1452.

Caltrans SDC (2004), "Caltrans Seismic Design Criteria Version 1.3," California Department of Transportation.

CSI (2005), "SAP 2000-Linear and Nonlinear Static and Dynamic Analysis and Design of Three-Dimensional Structures: Basic Analysis Reference Manual," Computers and Structures, Inc.

Shamsabadi, A. Kapuskar, M. and Martin, G..R. (2006), "Nonlinear Seismic Soil-Abutment-Structure Interaction Analysis of Skewed Bridges," *Proceedings of Fifth National Seismic Conference on Bridges and Highways: Innovation in Earthquake Engineering for Highway Structures*, San Francisco.

Abdel-Mohti, A. and Pekcan, G. (2008), "Seismic Response of Skewed RC Box-Girder Bridges," *Earthquake Engineering and Engineering Vibration*, **7**(4), 415-426.

Aviram, A. Mackie, K.R. and Stojadinovic, B. (2008), "Effect of Abutment Modeling on the Seismic Response of Bridge Structures," *Earthquake Engineering and Engineering Vibration*, **7**(4), 395-402.

Aviram, A. Mackie, K.R. and Stojadinovic, B. (2008), "Guidelines for Nonlinear Analysis of Bridge Structures in California," Technical Report 2008/3, Pacific Earthquake Engineering Research Center, University of California, Berkeley.

JOINT CONFERENCE PROCEEDINGS
7th International Conference on Urban Earthquake Engineering (7CUEE) &
5th International Conference on Earthquake Engineering (5ICEE)
March 3-5, 2010, Tokyo Institute of Technology, Tokyo, Japan

EFFECT OF FIBER REINFORCED CEMENT COMPOSITES ON THE SEISMIC PERFORMANCE OF BRIDGE COLUMNS

Richelle Zafra[1)], Tomohiro Sasaki[2)], Kazuhiko Kawashima [3)], Koichi Kajiwara[4)] and Manabu Nakayama[5)]

1), 2) Graduate Student, Department of Civil Engineering, Tokyo Institute of Technology, Japan
3) Professor, Department of Civil Engineering, Tokyo Institute of Technology, Japan
4) Senior Researcher, Hyogo Earthquake Engineering Research Center, National Research Institute for Earth Science and Disaster Prevention, Miki, Hyogo, Japan
5) Research Fellow, Hyogo Earthquake Engineering Research Center, National Research Institute for Earth Science and Disaster Prevention, Miki, Hyogo, Japan
zafra.r.aa@m.titech.ac.jp, sasaki.t.aa@m.titech.ac.jp, kawashima.k.ae@m.titech.ac.jp, kaji@bosai.go.jp, m-nakayama@bosai.go.jp

Abstract: Fiber reinforced cement composites (FRCC) are materials that have potential for seismic applications due to their substantial strain capacity, energy absorption capacity and crack control capability. An experimental study was conducted to investigate the seismic performance of scaled bridge columns using FRCC in potential plastic hinge region. Three column models designed with the same flexural capacity were tested under combined axial load and bilateral cyclic loading. A reinforced concrete (RC), a steel fiber reinforced concrete (SFRC) and a polypropylene fiber reinforced concrete (PFRC) column were considered. The use of SFRC and PFRC was found to result in reduced cover concrete spalling and crushing on column plastic hinges and reduced transverse steel reinforcement requirements as compared to the RC column. PFRC column also showed much greater crack control capability than SFRC column. Column flexural strength and ductility, however, was not improved even with the use of SFRC and PFRC.

1. INTRODUCTION

Bridges are important structures that require a high degree of protection to ensure their functionality after a seismic event. Damage after an earthquake may render the structure unusable and may interfere with disaster recovery operation as well as affect the economy of the community. To ensure serviceability after a seismic event, attention has been drawn to the development and implementation of innovative materials to enhance the seismic performance of new and existing structures. Fiber reinforced cement composites (FRCC) have the potential for seismic applications due to their substantial strain capacity, energy absorption capacity and crack control capability (Shah and Naaman 1976, Craig et al. 1984, Parra-Montesinos 2005).

FRCC is a mixture of concrete/cement mortar and short discontinuous fibers such as steel, glass, carbon and polymer fibers such as polyethylene, polypropylene, and polyvinyl alcohol. With the addition of fibers, the brittleness of concrete is reduced due to the fibers bridging a failure crack (Shah 1992, Tjiptobroto and Hansen 1993). FRCC with fiber volume fractions of until 3% exhibit what is known as quasi-brittle behavior, that is the gradual decay of tensile stress (strain-softening) beyond the first cracking strength which corresponds to the tensile strength of the material (ACI Committee 544 1988, Li et al. 1996). Adding fibers to a concrete matrix do not significantly improve its compressive strength however the strain at peak stress is increased by the presence of any type of fiber (Hughes and Fattuhi 1977, Fanella and Naaman 1985, Ezeldin and Balaguru 1992).

Engineered cementitious composites (ECC) is a class of FRCC. Its most remarkable feature is its enhanced tensile property; strain hardening occurs in tension after the first cracking strength has been reached with multiple micro-cracks instead of a single failure crack. The rising stress is accompanied by increasing strain, thus achieving a stress-strain curve with shape similar to that of a ductile

metal. Similar to many fiber-reinforced concrete materials, the compressive strength of ECC is not significantly enhanced with the presence of fibers but the compressive strain capacity is approximately double than that of traditional FRCCs (Li 1998). ECC uses only fine aggregates in the mix to control the fracture toughness of the composite (Li et al. 1995). The lack of course aggregates in the mix results in a low composite elastic modulus. Designed based on micromechanics considerations, the fiber, cementitious matrix, and fiber/matrix interface must be of a correct combination to attain the unique properties of ECC (Li 1998).

Previous investigations have confirmed the positive effects of using FRCC for structural members subjected to cyclic loading conditions. These include the work of Filiatrault et al. (1995) wherein steel fiber reinforced concrete was used in beam-column joints. They found that the presence of steel fibers in the joint increased the shear strength and can diminish the requirements for closely spaced ties. Daniel and Loukili (2002) examined the effect of longitudinal steel ratio and steel fiber length on high-strength concrete beams under alternate cyclic bending. They found that due to the presence of fibers, cracking is delayed at the pre-peak stage and the number and length of cracks were reduced. However, at the post-peak stage, ductility was not improved with the presence of fibers due to the severe bond deterioration between longitudinal bars and the composite.

Fischer and Li (2002) studied the effect of ECC on the unilateral reverse cyclic response of small-scale cantilever beam-columns. An improvement in composite disintegration caused by a reduction in ECC spalling and crushing as well as a reduction of transverse steel reinforcement requirements were observed. Saiidi et al. (2009) investigated the effect of incorporating shape-memory alloys (SMA) and ECC on model columns subjected to simulated seismic loads. Use of SMA bars reduced permanent displacements while use of ECC substantially reduced damage in the plastic hinge. Furthermore, the combination of SMA and ECC led to larger drift capacity as compared to the conventional steel reinforced concrete column.

To achieve better understanding on the use of FRCCs for improving the seismic performance of bridge columns, bilateral cyclic loading experiments have been conducted. In particular, columns with SFRC and ECC were investigated. The columns considered have larger dimensions compared to small-scale columns previously tested by other researchers.

2. EXPERIMENTAL PROGRAM

2.1 Specimen Properties

Three 1/4.5 scaled models of a 7.5m tall, 1.7m x 1.7m square, cantilever prototype column designed based on the Japan Specifications of Highway Bridges (JRA 2002) were investigated. The scaled columns have 400mm x 400mm square cross-section with rounded corners and an effective height of 1680 mm. Shear-span ratio (cantilever height to column width) is 4.2. The columns were identical except for the material used in the potential plastic hinge region. A conventional reinforced concrete column referred herein as RC, a steel fiber reinforced concrete column referred herein as SFRC and a column using engineered cementitious composites with polypropylene referred herein as polypropylene fiber reinforced concrete (PFRC) were considered. Details of the specimens are shown in Figure 1.

The specimens were designed to have the same flexural capacity and were designed as columns with concrete without considering differing properties of the FRCC. Concrete with higher than standard nominal compressive strength $f'c$ of 60 MPa was used for the RC column. SFRC has $f'c$ of 60 MPa. PFRC with $f'c$ of 40MPa was used due to the difficulty of obtaining a mixture with $f'c$ of 60 MPa. SFRC and PFRC were used only from the footing up to a height of 600mm from the column base to minimize the cost. This height is three times the estimated plastic hinge length of one-half the column width (JRA 2002) corresponding to 200mm to avoid failure at the SFRC/PFRC-concrete interface. Above this height, regular concrete was used.

Ready-mixed concrete with a water-cement ratio of 35% and maximum aggregate size of 13 mm was used. High-range water reducing admixtures and admixtures to enhance the workability of the mix were added. The measured compressive strength at the day of the loading test, determined using the average of three standard 100mm by 200mm cylinders, is 55 MPa with a strain at peak of 0.46%.

SFRC was made by combining the ready mixed concrete, with properties earlier mentioned, with 1.0% volume of steel fibers with hooked ends. The steel fibers were made from cold drawn wires and have diameter of 0.55mm and length of 30mm. Other relevant properties of the steel fibers are summarized in Table 1. Admixtures were also used during casting to enhance the fresh properties of the mix. The measured cylinder compressive strength of SFRC is 63 MPa with a strain at peak of 0.49%.

PFRC was made by combining high-strength cement mortar, fine aggregates (maximum grain size of 0.30mm), water, and 3% volume of polypropylene fibers which is equivalent to 1.5% fiber by weight (Hirata et al 2009). The polypropylene fibers are monofilament fibers with diameter of 42.6μm and length of 12mm. Other important properties are shown in Table 1. Superplasticizers were also added to improve the workability of the mix. The measured cylinder compressive strength of PFRC is 38 MPa with a stain at peak of 0.54%.

The longitudinal steel reinforcement ratio and tie reinforcement ratio were identical in all specimens. Longitudinal reinforcement consisted of 36-10mm diameter deformed bars with nominal yield strength of 685MPa (SD685) resulting in a reinforcement ratio of 1.70%. The actual yield strength of longitudinal reinforcements is 710MPa at 0.4% strain. Tie reinforcement consisted of 6mm diameter deformed bars with nominal yield strength of 345 MPa (SD345) having 135° bent hooks. The actual yield strength of tie reinforcements is 363 MPa at 0.2% strain. Ties were spaced at 45mm (ρ_s = 0.70%) within 600mm height from the base and at 50mm spacing above (ρ_s = 0.60%). Concrete cover of 35mm was provided in all columns.

2.2 Test set-up and loading protocol

The quasi-static cyclic loading experiment was conducted under displacement control. A constant axial load of 183 KN corresponding to 1.20 MPa axial stress in the plastic hinge was applied by a vertical actuator simultaneously with a bilateral displacement applied by two lateral actuators. The applied displacement is a circular loading orbit that increases at one half of the drift ratio. Drift ratio is defined as the column top lateral displacement divided by the effective height (height from the center of the lateral actuator to the top of footing). The column was first loaded in the South (S) direction until 0.5% drift, then loaded three times by the circular orbit, then finally unloaded in S direction until the rest position (Figure 2).

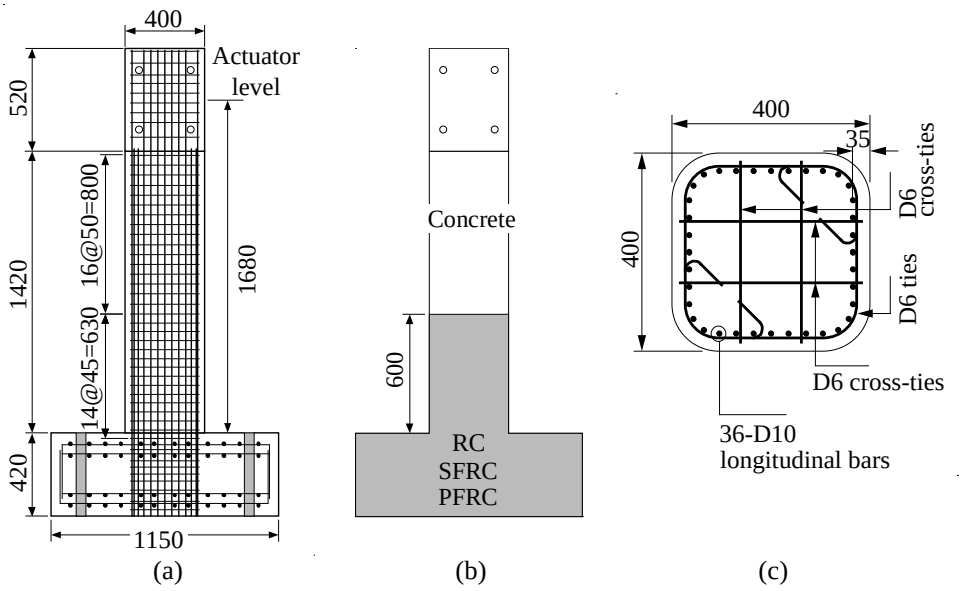

Figure 1 Specimen configuration and details: (a) reinforcement detail, (b) concrete/composite property, and (c) cross-section

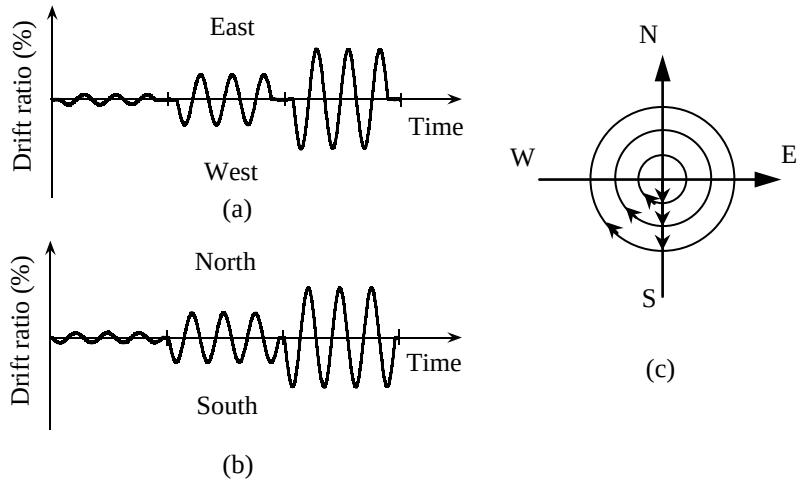

Figure 2 Loading scheme: (a) East-West component, (b) North-South component, and (c) circular displacement orbit

Table 1 Properties of fibers used

Fiber type	Steel	Polypropylene
Tensile strength (MPa)	1100	482
Young's modulus (GPa)	210	5.0
Specific gravity	7.85	0.91

Due to some problems with the lateral actuator system, a phase lag of 12.6° occurred between the North-South (NS) and East-West (EW) displacement components resulting to an elliptical loading orbit with the semimajor axis along the NE-SW direction. The P-Δ effect resulting from the vertical actuator was corrected based on Nagata et al. (2004).

The specimen footings were designed to be strong to avoid damage, minimize deformation and to avoid rocking. They were anchored to the test platform using four PC bars with 250kN prestressing force each.

A total of 70 channels per column were used to record three actuator forces, three actuator displacements, 10 linear variable differential transducers (LVDT) for translation/rotation/curvature measurements, 18 tie bar strains, and 36 longitudinal bar strains. Single electric resistance strain gages were used to monitor strains in tie and longitudinal bars at specific locations.

3. EFFECT OF FIBERS ON COLUMN CYCLIC RESPONSE

3.1 Column Damage

Figures 3 to 5 compares the observed damage at the S-face of the three columns. As observed from the experiment, damage was more severe in the SW-NE axis because of the elliptical displacement orbit hence damage at this face is shown. The observed damage at 2%, 3%, 4% and 4.5% drift loading at the SW corner are discussed.

At 2% drift ratio (Figures 3a, 4a, 5a), concrete spalling initiated at the base of RC column whereas flexural cracking initiated at the base of SFRC column. In PFRC column, only one or two flexural cracks at the base can be observed. The cracks in PFRC column were relatively short and thin compared to that of RC and SFRC because of the high tensile strength of PFRC.

At 3% drift ratio (Figures 3b, 4b, 5b), in contrast to a brittle concrete spalling and cracking in RC column, the presence of steel fibers in SFRC column transformed the cracking into a less brittle failure. Spalled cover concrete size was 50mm and larger for RC column while it is 20mm and smaller for SFRC column. The steel fibers delayed crack propagation and prevented further crack opening through the bridging action of fibers across cracks. Compared to RC and SFRC column, PFRC column sustained only numerous small, thin cracks due the presence of fibers.

At 4% drift ratio, severe cover concrete compression failure occurred within 150mm height from the base for RC column exposing longitudinal bars and two tie layers. The exposed longitudinal bars subsequently buckled. Compared to RC column, although cover compression failure occurred within 50mm height from the base for SFRC column and longitudinal bars and ties were not exposed, four (11%) longitudinal bars ruptured. In PFRC column, the number of flexural cracks at the base increased and longitudinal splitting cracks were also observed due to the tendency of the longitudinal reinforcement to buckle. Cover concrete spalling was not observed and longitudinal bars and ties were also not exposed in PFRC column. PFRC column benefitted from the higher compression strain of PFRC, providing resistance against cover spalling even at large displacements.

The extent of damage varied significantly among the three columns at 4.5% drift (Figures 3c, 4c, 5c, and 6). Whereas extensive cover and core damage was evident in RC column and limited cover spalling in SFRC column, damage in PFRC column was restricted to relatively minor cracks. In all three columns, loading was terminated at the end of 4.5% drift due to rupture of longitudinal bars. A total of 14 (39 %), 16 (44 %), 12 (33 %) longitudinal bars ruptured in RC, SFRC, and PFRC column, respectively.

3.2 Longitudinal and tie-bar strains

In the cyclic loading test, damage was severe in the SW and NE corner. Hence, because of space limitations focus will be on strains measured at the SW corner. Note that measurement of bar strains is difficult due to damage of strain gages, thus only reliable measured data will be shown. Compare

Figure 7 shows strain distribution of longitudinal bar 218mm from the column base. This height is slightly above the anticipated plastic hinge region. With a yield strain of 4,000μ, the longitudinal bars of all three columns yielded in tension at 1.5% drift ratio and that the strains were over 12,000μ at 3% drift. Variation of longitudinal bar tensile strains among the three columns was not significant. However, bar compression strains were largest in PFRC column. For example, at the first cycle of 3% drift, bar compression strain of PFRC column was 6,400μ which is 43% larger than RC column.

Strain of tie bar located 105 mm from column base is shown in Figure 8. At 3% drift, tie bar in the RC column

has already yielded while tie bars in SFRC and PFRC column have strains nearly equal to the yield strain. At 4% drift, tie strains increased to as high as 6,000μ in RC column and 4,000μ in SFRC column however tie strains in PFRC column was only about 2,000μ. As mentioned earlier, two longitudinal bars at the SW corner buckled at 4% drift in the RC column and the yielding of ties at this corner is due to the local buckling of longitudinal bars. At 4% drift, it is likely that several longitudinal bars buckled at SFRC and PFRC column based on the occurrence of longitudinal splitting cracks and rupture of bars which is related to the tie strains. The measured tie strains in SFRC and PFRC column were less compared to that of RC column. Hence, a reduction of tie strains with the use of SFRC or PFRC can result to reduced transverse reinforcement requirements. A similar observation was reported by Filiatrault et al. (1995) for SFRC columns and by Fischer and Li (2002) for PFRC columns.



(a) (b) (c)

Figure 3 Damage of RC column at S-face: (a) 2% drift, (b) 3% drift, and (c) 4.5% drift

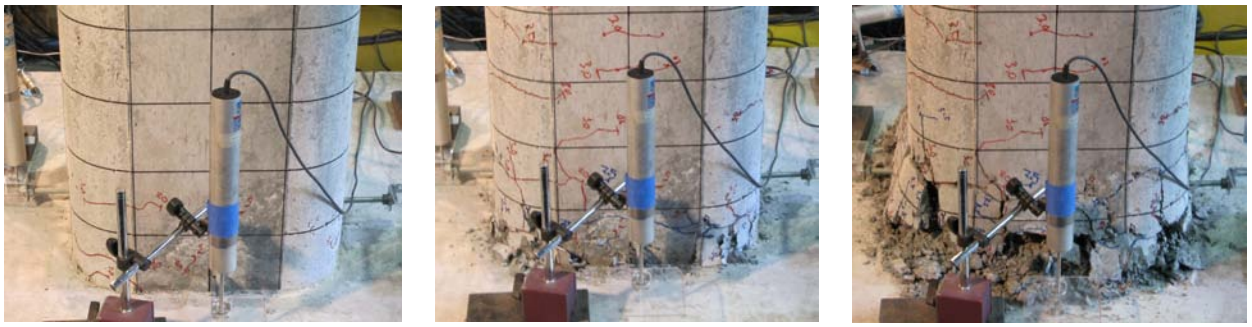

(a) (b) (c)

Figure 4 Damage of SFRC column at S-face: (a) 2% drift, (b) 3% drift, and (c) 4.5% drift

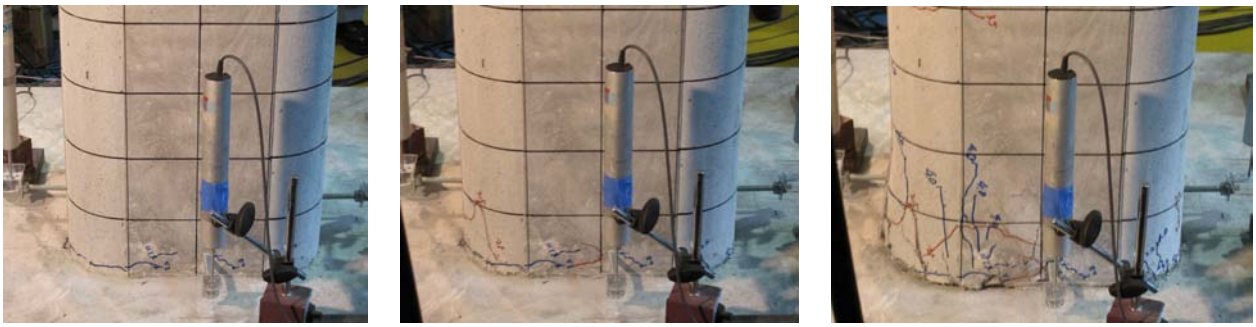

(a) (b) (c)

Figure 5 Damage of PFRC column at S-face: (a) 2% drift, (b) 3% drift, and (c) 4.5% drift

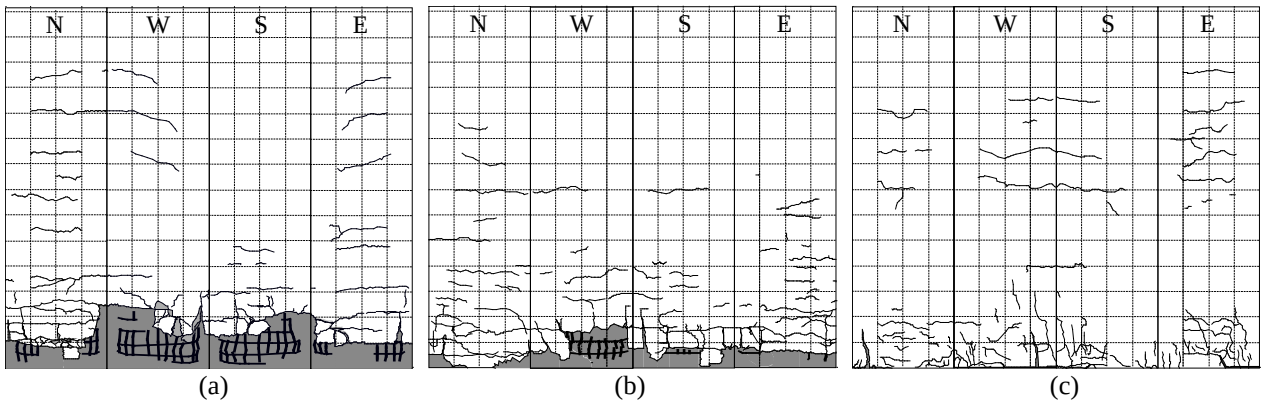

(a) (b) (c)

Figure 6 Damage of columns at the end of 4.5% drift loading: (a) RC, (b) SFRC, and (c) PFRC

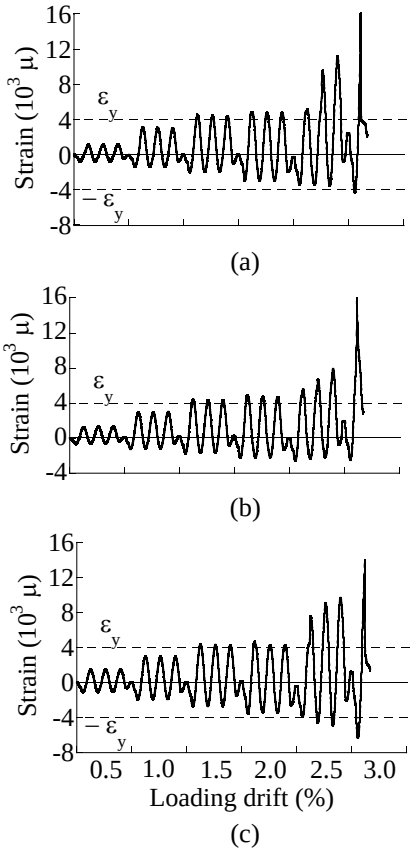

Figure 7 Strain of longitudinal bar at SW corner: (a) RC, (b) SFRC, and (c) PFRC

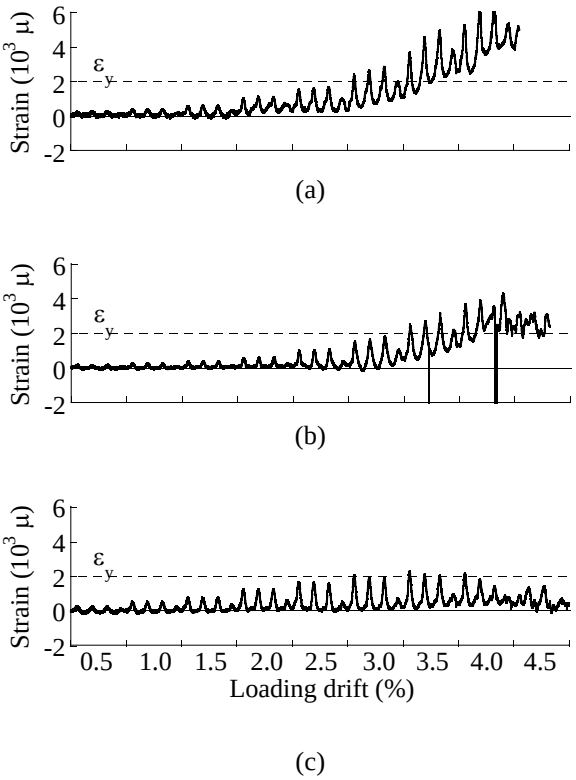

Figure 8 Strain of tie bar at SW corner: (a) RC, (b) SFRC, and (c) PFRC

3.3 Force-displacement hysteresis

Figures 9 and 10 show the lateral force vs. top lateral displacement hysteresis of the columns in the EW and NS direction, respectively. Taking the average of the maximum restoring force in the push and pull direction, then the average in the EW and NS direction, Table 2 shows that RC column reached a maximum strength of 163 KN. The measured response of RC column showed a stable and ductile response until 4% drift ratio (Figures 9a and 10a). The restoring force deteriorated to 86% of its maximum strength at 4.5% drift ratio due to extensive buckling and rupture of longitudinal bars as well as core concrete crushing.

SFRC column similarly showed a stable and ductile response until 4% drift ratio with an average maximum strength of 171 KN (Figures 9b and 10b) which is about 5%

higher than RC column due to the higher compressive strength of SFRC. The restoring force deteriorated at 4.5% drift due to rupture of 44% of longitudinal bars reducing the restoring force to 59% of its maximum strength.

PFRC column attained an average maximum strength of 158 KN which is 3% and 8% lower compared to RC and SFRC column, respectively, due to the lower compressive strength of PFRC. The difference in the flexural strength of the three columns however is not significant. PFRC column demonstrated a stable and ductile response until 4% drift ratio (Figures 9c and 10c). Although cover spalling and crushing was not observed, the restoring force decreased to 81% of its maximum strength at 4.5% drift due to rupture of 33% of the longitudinal bars.

Comparison of the lateral force vs. lateral displacement hystereses of the columns do not show the effect of SFRC and PFRC on improving flexural strength and ductility of the specimens. Although SFRC and PFRC reduced cover spalling and core crushing providing lateral stability for the longitudinal bars to endure cyclic inelastic deformations, failure of the columns was governed by rupture of longitudinal bars.

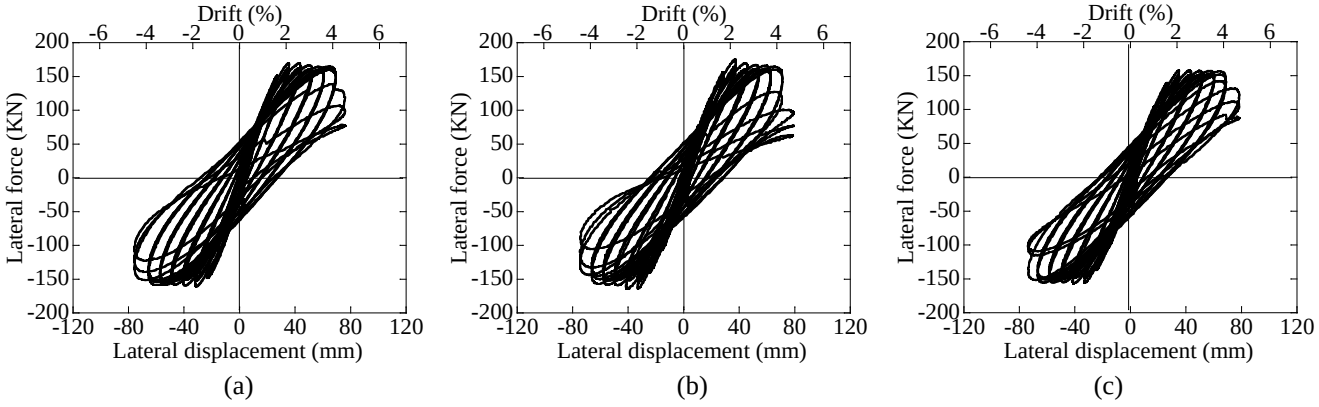

Figure 9 Lateral force vs. lateral displacement hysteresis (EW direction): (a) RC, (b) SFRC, and (c) PFRC

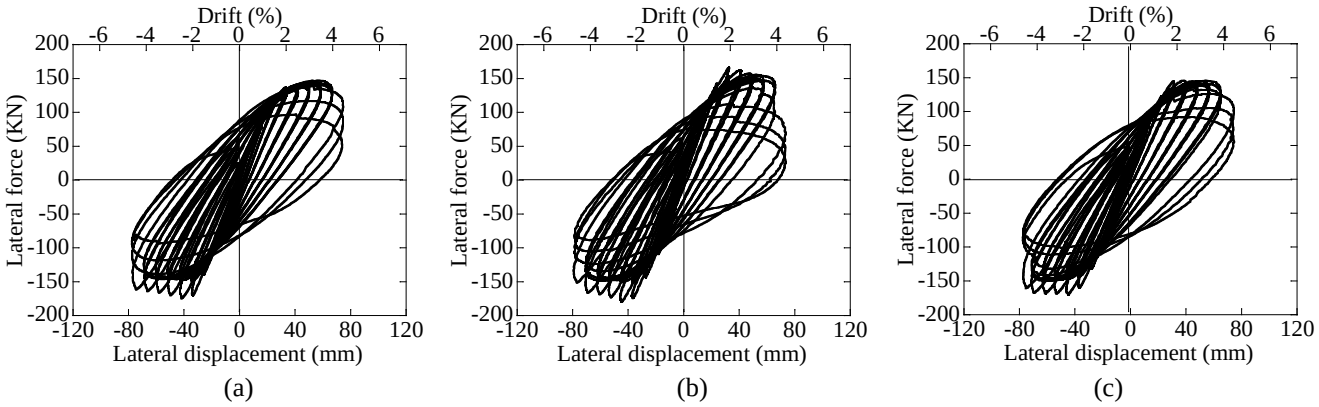

Figure 10 Lateral force vs. lateral displacement hysteresis (NS direction): (a) RC, (b) SFRC, and (c) PFRC

Table 2 Flexural strength comparison for RC, SFRC and PFRC column

Specimen	Maximum Flexural Strength (KN)						
	EW-direction			NS-direction			Average of (1) & (2)
	+	-	(1) Average	+	-	(2) Average	
RC	169.7	160.7	165.2 (100%)	145.7	175.8	160.8 (100%)	163.0 (100%)
SFRC	174.9	164.4	169.7 (103%)	164.7	180.6	172.7 (107%)	171.2 (105%)
PFRC	158.1	156.8	157.5 (95%)	145.7	170.5	158.1 (98%)	157.8 (97%)

4. CONCLUSIONS

To clarify the effect of fiber reinforced cement composites (FRCC) on the cyclic response of bridge columns, bilateral cyclic loading experiments were conducted. Based on the results presented, the following conclusions can be deduced:

1) The use of FRCC such as steel fiber reinforced concrete (SFRC) and polypropylene fiber reinforced concrete (PFRC) reduced cover concrete spalling and crushing on column plastic hinges. PFRC column showed much greater crack control capability than SFRC column.
2) Strains of ties in SFRC and PFRC columns were less compared to that of RC column. This can result in reduced tie reinforcement requirements.
3) Column flexural strength and ductility was not improved even with the presence of fibers. Although SFRC and PFRC reduced cover concrete spalling and crushing providing lateral stability for the longitudinal bars to endure cyclic inelastic deformations, column failure was governed by rupture of longitudinal bars.

Acknowledgements:

This study was conducted as part of the E-Defense Bridge Project of the National Research Institute for Earth Science and Disaster Prevention (NIED). The authors sincerely thank Hiromichi Ukon (former research fellow of NIED) and Takayoshi Hirata (Obayashi Corp.) for the material technical support. Finally, Hiroshi Matsuzaki, Assistant Professor of Tokyo Institute of Technology and students Guilian Quan, Huang Szu-chia, Yuji Kumagai, Wang Jing, Zhang Rui, Keisuke Ohta and Syota Ichikawa are gratefully acknowledged for their assistance in executing the experiments.

REFERENCES

ACI Committee 544 (1988), "Design considerations for steel fiber reinforced concrete," *ACI Structural Journal*, September-October, 563-580.

Craig, J., Mahadev, S., Patel, C., Viteri, M., and Kertesz, C. (1984), "Behavior of Joints using Reinforced Fibrous Concrete," ACI Special Publication, **81**, 125-168.

Daniel, L. and Loukili, A. (2002), "Behavior of high-strength fiber reinforced concrete beams under cyclic loading," *ACI Structural Journal*, **99**(3), 248-256.

Ezeldin, A. and Balaguru, P. (1992), "Normal and high strength fibre reinforced concrete under compression," *Journal of Materials in Civil Engineering*, **4**(4), 415-429.

Fanella, D. and Naaman, A. (1985), "Stress-strain properties of fiber reinforced mortar in compression," *ACI Journal*, July-August, 475-483.

Filiatrault, A., Pineau, S. and Houde, J. (1995), "Seismic behavior of steel-fiber reinforced concrete interior beam-column joints," *ACI Structural Journal*, **92**(5), 1-10.

Fischer, G. and Li, V. (2002), "Effect of matrix ductility on deformation behavior of steel-reinforced ECC flexural members under reversed cyclic loading conditions," *ACI Structural Journal*, **99**(6), 781-790.

Hirata, T., Kawanishi, T., Okano, M. and Watanabe, S. (2009), "Study on Material Properties and Structural Performance of High-Performance Cement Composites using Polypropylene Fiber," *Proceedings of Japan Concrete Institute*, **31**(1), 295-300.

Hughes, B. and Fattuhi, N. (1977), "Stress-strain curves for fiber reinforced concrete in compression," *Cement and Concrete Research*, **73**(1), 173-183.

Japan Road Association Specifications for Highway Bridges (2002), Maruzen, Tokyo.

Li, V. (1998), "Engineered cementitious composites (ECC) – tailored composites through micromechanical modeling," *Fiber Reinforced Concrete: Present and the Future*, N. Banthia, and A. Mufti, eds., Canadian Society of Civil Engineers, Montreal, 64-97.

Li, V., Mishra, D. and Wu, H. (1995), "Matrix design for pseudo-strain-hardening fibre reinforced cementitious composites," *Materials and Structures*, **28**, 586-595.

Li, V., Wu, H., Maalej, M. and Mishra, D. (1996), "Tensile behavior of cement-based composites with random discontinuous steel fibers," *Journal of the American Ceramic Society*, **79**(1), 74-78.

Nagata, S., Kawashima, K. and Watanabe, G. (2004) "Effect of P-Δ action of actuators in a hybrid loading test," *13th World Conference on Earthquake Engineering*, Vancouver, Canada, Paper No. 881.

Parra-Montesinos, G. (2005), "High-performance fiber reinforced cement composites: an alternative for seismic design of structures," *ACI Structural Journal*, **102**(5), 668-675.

Saiidi, M., O'Brien, M., and Sadrossadat-Zadeh, M. (2009), "Cyclic response of concrete bridge columns using superelastic nitinol and bendable concrete," *ACI Structural Journal*, **106**(1), 69-77.

Shah, S. (1992) "Do fibers increase the tensile strength of cement-based matrixes?," *ACI Materials Journal*, **88**(6), 595-602.

Shah, S. P. and Naaman, A. E (1976), "Mechanical properties of glass and steel fiber reinforced mortar," *ACI Journal Proceedings*, **73**(1), 50-53.

Tjiptobroto, P. and Hansen, W. (1993), "Tensile strain hardening and multiple cracking in high-performance cement-based composites containing discontinuous fibers," *ACI Materials Journal*, **90**(1), 16-25.

JOINT CONFERENCE PROCEEDINGS
7th International Conference on Urban Earthquake Engineering (7CUEE) &
5th International Conference on Earthquake Engineering (5ICEE)
March 3-5, 2010, Tokyo Institute of Technology, Tokyo, Japan

EFFECT OF FINGER EXPASION JOINTS ON SEISMIC RESPONSE OF BRIDGES

Guilian QUAN[1], Kazuhiko KAWASHIMA[2]

1) Graduate student, Department of Civil Engineering, Tokyo Institute of Technology, Japan
2) Professor, Department of Civil Engineering, Tokyo Institute of Technology, Japan
Zen.k.aa@m.titech.ac.jp, Kawashima.k.ae@m.titech.ac.jp

Abstract: This paper presents the effect of steel finger-type expansion joints on the overall seismic response of a bridge. For this purpose, two nonlinear hysteretic models are developed for finger expansion joints. Complex interaction of longitudinal and transverse hysteretic behavior such as slip-out, collision, and failure of fingers is included in the models. The models are implemented to seismic response analysis of a three-span simply supported bridge. It is found from the analysis that the effect of expansion joints is significant in the plastic curvature of columns at their plastic hinge and the response displacement and residual displacement of decks and columns.

1. INTRODUCTION

It becomes important to take account of the effect of expansion joints into the seismic response analysis of long multi-span continuous bridges. However research on the effect of expansion joints for the seismic response of bridges is very limited and the past efforts have been concentrated on the enhancement of durability, cold-resistance and noise-resistance of expansion joints[1)2)].

Various types of damage were developed in the past earthquakes such as the 1995 Kobe, Japan earthquake[3)]. For example, in the steel finger-type expansion joints, face-plates were detached from the slabs due to rupture of anchor bolts, fingers were bent and uplifted due to crash under extensive compression, fingers were locked together between the adjacent decks, and fingers slipped out and settled (refer to **photo 1)**. Damage of expansion joints occurred not only in Japan but also in the 1994 Northridge, USA earthquake and in the 1999 Chi Chi, Taiwan earthquake[4)5)].

Damage of expansion joints not only affects the function of bridges immediately after an earthquake but also results in a significant impact on the overall seismic response of bridges. In recent years, there have been many studies about pounding between girders. For example, Takeno and Izuno studied the usefulness of the collision velocity spectra for evaluating the pounding effect between adjacent decks[6)], and Moriyama and Yoda studied the effect of pounding based on a two-dimensional shake table experiment[7)]. Furthermore, Matsumoto and Kawashima studied possible failure modes due to the progressive failure of main structural components for a three-span simply supported bridge[8)].

In the above studies, it is assumed that bridge decks directly collide[9)], but in fact expansion joints restrain the relative movement of decks before collision. The effect of expansion joints has not yet been fully included in analysis.



Photo 1 Damage of a finger expansion joint during the 1995 Kobe earthquake

After the 1995 Kobe, Japan earthquake, elastomeric bearings as well as lead rubber bearings and high damping rubber bearings are extensive used. Although it is expected that extensive damage of bearings which occurred during past major earthquakes is mitigated by the use of elastomeric bearings, it results in an increase of deck response displacement. Consequently, it is important to take into account in analysis the effect of expansion joints on the overall bridge response. Because failure of expansion joints affects the response of bridges, it is important to clarify the failure mechanism of expansion joints.

In this paper, the effect of steel finger-type expansion joints on the overall seismic response of bridges is studied by developing two nonlinear hysteretic models of expansion joints which can take the longitudinal and transversal interaction of fingers into account[10)].

2. IDEALIZATION OF FINGER EXPANSION JOINTS

A steel finger-type expansion joint generally consists of n-set of fingers which are fixed at their base to the left deck and the other n-set of fingers which are fixed to the right deck as shown in **Fig. 1**. Relative displacement between the left and right decks is accommodated by the relative movement between the fingers fixed to the left deck and those fixed to the right deck. A finger fixed to the left deck at its base and a finger next to this finger fixed to the right deck is called as adjacent finger. Longitudinal gap between the tip of a finger and the base of the adjacent finger and the transverse gap between two adjacent fingers are called hereinafter as the longitudinal gap Δl_{EJ} and the transverse gap Δw_{EJ}, respectively. Representing the length, width and height of a finger as l_{EJ}, w_{EJ} and h, the effective finger length l_{EJe} is defined as

$$l_{EJe} = l_{EJ} - \Delta l_{EJ} \tag{1}$$

Representing the response displacement of the left and right decks in the longitudinal and transverse directions as u_k and v_k ($k = l$ and r), respectively, the longitudinal and transverse relative displacement between the two decks, Δu and Δv, are defined as

$$\begin{aligned} \Delta u &= u_r - u_l \\ \Delta v &= v_r - v_l \end{aligned} \tag{2}$$

The longitudinal and transverse lateral forces which are developed in an expansion joint corresponding to Δu and Δv are designated here as F_u and F_v. It is noted that fingers slip out from their contact position when Δu becomes larger than the effective finger length l_{EJe}.

An important mechanical property of an expansion joint is its strong hysteretic behavior depending on the relative displacements Δu and Δv. Furthermore, the hysteretic behavior in the longitudinal direction and that in the transverse direction are coupled. It should be noted here that in reality longitudinal and transverse displacements are coupled with rotation of decks about the vertical axis between the adjacent decks. However because the rotation of the decks makes the problem significantly complex, the effect of rotation is disregarded in this study for simplicity.

(1) Hysteretic behavior of an expansion joint prior to failure

Consider a set of fingers which moves in the longitudinal direction. When the tips of fingers at one side and the bases of the fingers at the other side are not in contact under compression ($\Delta u > -\Delta l_{EJ}$) or they do not slip out from their contact position under tension ($\Delta u < l_{EJe}$), the transverse relative displacement Δv is constrained within the transverse gap Δw_{EJ} ($|\Delta v| < \Delta w_{EJ}$). However, once the transverse relative displacement Δv reaches the transverse gap Δw_{EJ} ($|\Delta v| \geq \Delta w_{EJ}$), a transverse force

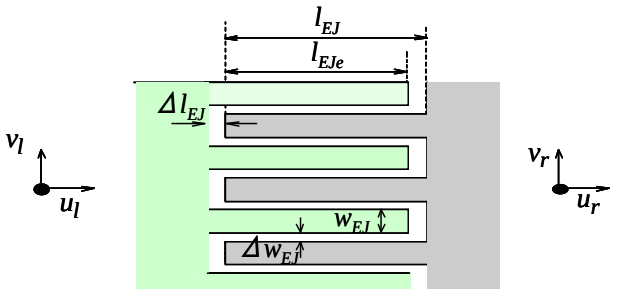

Fig. 1 Idealization structure of an expansion joint

F_v is induced, and if F_v builds up to the transverse strength of the expansion joint P_v, the expansion joint fails.

On the other hand, once fingers at one side completely slip out from the fingers at the other side in the longitudinal direction ($\Delta u \geq l_{EJe}$), the expansion joint can freely displace in the transverse direction over Δw_{EJ}. However when Δu decreases to reach l_{EJe} with the transverse displacement Δv being larger than Δw_{EJ} ($|\Delta v| \geq \Delta w_{EJ}$), the adjacent fingers collide at their tips resulting in a contact (compression) force F_u, and the fingers at both sides cannot return to their original position. If the compression force F_u reaches the longitudinal capacity P_u of the expansion joint, the expansion joint fails in compression.

It may not be theoretically impossible for an expansion joint to slip into the original position if the expansion joint transversely displaces n times $w_{EJ} + \Delta w_{EJ}$ under the condition of $\Delta u > l_{EJe}$. However, it is likely that the expansion joint suffers significant damage once the transverse relative displacement Δv becomes excessively large. Consequently it is assumed here that the expansion joint cannot slip longitudinally into the original position once the expansion joint transversely displaces over $w_{EJ} + \Delta w_{EJ}$.

Similarly, a compression force F_u is developed in an expansion joint if the tips of fingers at one side start to contact with the base of the fingers at the other side when the expansion joint is subjected to compression. If the compression force F_u reaches the compression capacity of the expansion joint P_{uc}, the expansion joint fails in compression.

It is important how to evaluate the strengths P_v, P_u and P_{uc}. Obviously, experimental verification is required for the evaluation of strengths of expansion joints, but sufficient and reliable data are hardly available at this moment. Therefore assuming that failure of an expansion joint occurs not at the connection with the slabs but in the fingers, P_v is evaluated based on the full plastic flexure strength of fingers, and P_u and P_{uc} are evaluated based on the buckling strength of fingers as

$$P_v = n \frac{w_{EJ}\, h^2 \sigma_y}{4(3/4 l_{EJ})} \tag{3}$$

$$P_u = n \frac{\pi^2 EI}{4 {l_{EJ}}^2} \tag{4}$$

$$P_{uc} = 2n\frac{\pi^2 EI}{4{l_{EJ}}^2} \tag{5}$$

in which, w_{EJ} and h : width and height of a finger, σ_y : yield stress of the fingers and EI : flexural rigidity about the weak axis (transverse direction) of a finger. P_v was evaluated by assuming that the adjacent fingers come in contact at three quarters of the finger length ($3/4\, l_{EJ}$).

Based on the above assumptions, the restoring force vs. relative displacement hysteresis of an expansion joint in the longitudinal and transverse directions may be written as

$$F_u = \begin{cases} 0 & -\Delta l_{EJ} < \Delta u < l_{EJe} \\ k_{EJu}(\Delta u + \Delta l_{EJ}) & -\Delta l_{EJB} < \Delta u < -\Delta l_{EJ} \\ & \text{and } |\Delta v| < \Delta w_{EJB} \\ k_{EJuo}(\Delta u - l_{EJe}) & \Delta l_{EJBo} \le \Delta u \le l_{EJe} \\ & \text{and } |\Delta v| > \Delta w_{EJ} \\ & \text{once after } \Delta u > l_{EJe} \end{cases} \tag{6}$$

$$F_v = \begin{cases} k_{EJv}(\Delta v - \Delta w_{EJ}) & \Delta w_{EJB} \ge |\Delta v| \ge \Delta w_{EJ} \text{ and } \Delta u < l_{EJe} \\ 0 & |\Delta v| < \Delta w_{EJ} \text{ and } \Delta u < l_{EJe} \\ 0 & \Delta u \ge l_{EJe} \\ k_{EJv}(\Delta v - \Delta v_0) & \Delta w_{EJB} \ge |\Delta v| \ge \Delta w_{EJ} \text{ and } \Delta u \le l_{EJe} \\ & \text{once after } \Delta u > l_{EJe} \\ 0 & |\Delta v| < \Delta w_{EJ} \text{ and } \Delta u \le l_{EJe} \\ & \text{once after } \Delta u > l_{EJe} \end{cases} \tag{7}$$

in which, Δu and Δv, l_{EJ}, Δl_{EJ}, l_{EJe}, w_{EJ} and Δw_{EJ} are the parameters already defined, and Δl_{EJB} : longitudinal relative displacement at the instance when a finger fails in compression, Δl_{EJBo} : longitudinal relative displacement at the instance when fingers fail in compression after fingers once slipped out and then start to contact, Δw_{EJB} : transverse relative displacement at the instance when fingers fail due to contact with adjacent fingers, Δv_0 : transverse relative displacement at the instance when fingers start to contact with the fingers at the other side after they once longitudinally slipped-out, k_{EJu} and k_{EJv} : the compressive and flexural stiffnesses of an expansion joint in the longitudinal and transverse directions, respectively, and k_{EJuo} : the longitudinal compression stiffness of an expansion joint when fingers start to contact after they once slipped out.

It should be noted in Eqs. (6) and (7) that because F_u and F_v are coupled depending on Δu and Δv, these have to be solved considering the interaction between F_u and F_v.

Fig. 2 shows the F_u vs. Δu hysteresis, and F_v vs. Δv hysteresis of an expansion joint. The hysteresis after an expansion joints fails, which will be described later, are also shown here. The stiffnesses of an expansion joint, k_{EJv}, k_{EJu} and k_{EJuo}, are defined as

$$k_{EJv} = n\frac{3EI}{(3/4 l_{EJ})^3} \tag{8}$$

$$k_{EJu} = 2n\frac{EA}{l_{EJ}} \tag{9}$$

$$k_{EJuo} = n\frac{EA}{l_{EJ}} \tag{10}$$

where, *EA* and *EI* are an axial stiffness and flexural stiffness about the weak axis, respectively. It is assumed in the evaluation of k_{EJv} by Eq. (8) that adjacent fingers contact at $3/4\, l_{EJ}$ similar to the evaluation of P_v by Eq. (3).

(2) Hysteretic behavior of an expansion joint after failure

Among several possible failure modes which could be developed in a finger expansion joint, two extreme failure modes are considered here (refer to **Fig. 2**).

a) Failure without lock of fingers

If an expansion joint fails and completely looses its restoring force either in the longitudinal or transverse direction, it is likely that the expansion joint looses the restoring force in the other direction. If an expansion joint transfers only the friction force after its failure, the resultant restoring force vs. relative displacement hysteresis of an expansion joint may be expressed as

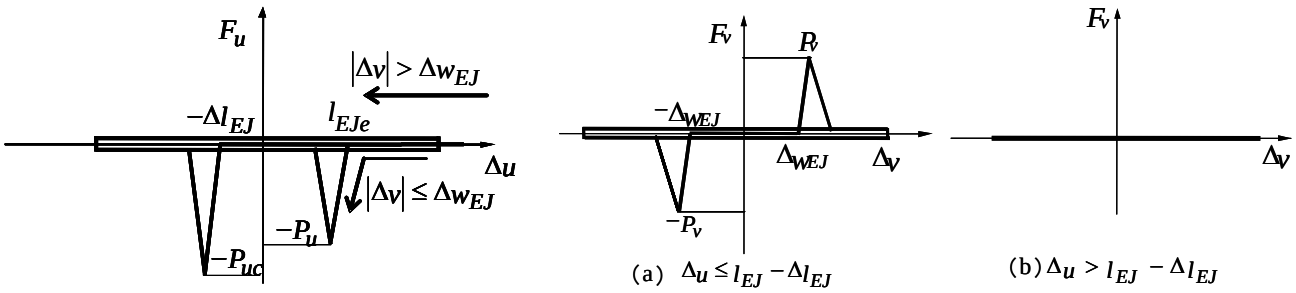

Fig. 2 Restoring force vs. relative displacement hysteresis of an expansion joint when only friction force develops after failure

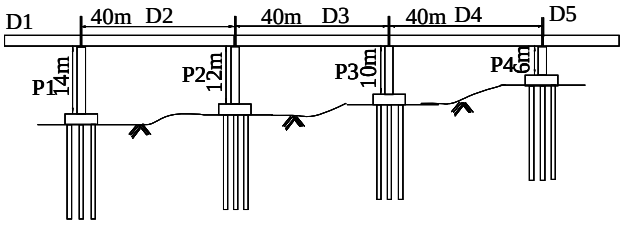

Fig. 3 Target bridge

$$F_u = \begin{cases} -P_{uc} + k_{EJuB}(\Delta u + \Delta l_{EJB}) \\ \quad \cdots\cdots -\Delta l_{EJB} + P_{uc}/k_{EJuB} \le \Delta u \le -\Delta l_{EJB} \\ \quad \text{and} \quad |\Delta v| < \Delta w_{EJB} \\ -P_u + k_{EJuB}(\Delta u - \Delta l_{EJBo}) \\ \quad \cdots\cdots \Delta l_{EJBo} + P_u/k_{EJuB} \le \Delta u < \Delta l_{EJBo} \\ \quad \text{and} \quad |\Delta v| > \Delta w_{EJ} \\ \quad \text{once after} \quad \Delta u > l_{EJe} \\ \pm F_b \qquad\qquad \cdots\cdots |\Delta v| \ge \Delta w_{EJB} \end{cases} \tag{11}$$

$$F_v = \begin{cases} -P_v + k_{EJuB}(\Delta v + \Delta w_{EJB}) \\ \quad \cdots\cdots -\Delta w_{EJB} + P_v/k_{EJuB} \le \Delta v < \Delta w_{EJB} \\ \quad \text{and} \quad \Delta u < \Delta l_{EJe} \\ P_v + k_{EJuB}(\Delta v - \Delta w_{EJB}) \\ \quad \cdots\cdots \Delta w_{EJB} < \Delta v \le \Delta w_{EJB} - P_v/k_{EJuB} \\ \quad \text{and} \quad \Delta u < \Delta l_{EJe} \\ \pm F_b \qquad \cdots\cdots \Delta u = \Delta l_{EJB} \text{ or } \Delta u = \Delta l_{EJBo} \end{cases} \tag{12}$$

in which F_b : friction force of an expansion joint after failure and k_{EJuB} : post buckling stiffness of an expansion joint. Assuming that the axial restoring force of the fingers sharply deteriorates once the fingers buckle under compression in the longitudinal direction, k_{EJuB} is evaluated as

$$k_{EJuB} = -k_{EJu} \tag{13}$$

b) Failure with lock of fingers

If only the friction force is developed at an expansion joint after its failure, it is equivalent to a kind of seismic isolation. Due to energy dissipation associated with the friction force, the deck displacement may be reduced after failure of expansion joints. However it is often the case that broken components of an expansion joint restrain the relative displacement between adjacent decks. For example, if several fingers buckle under compression and then transversely displace, the relative movement between the adjacent decks is heavily constrained. If such a lock-up of an expansion joint occurs, the failure affects the total seismic response of a bridge. Once a lock-up occurs, the lateral force

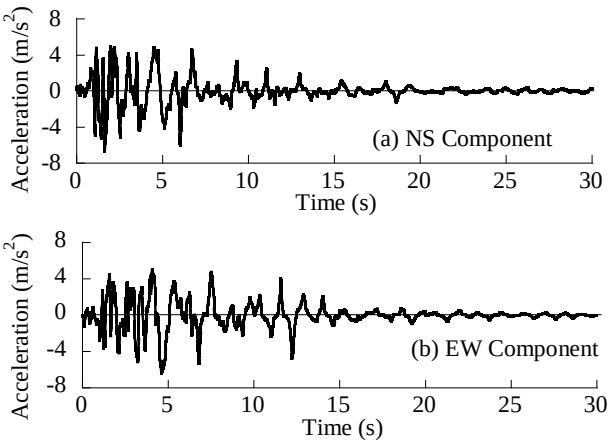

Fig. 4 Ground accelerations recorded at JR Takatori Station during the 1995 Kobe earthquake

vs. relative displacement hysteresis of an expansion joint may be expressed as

$$F_u = k_{Lu}(\Delta u - \Delta u_L) + R_{uL} \tag{14}$$

$$F_v = k_{Lv}(\Delta v - \Delta v_L) + R_{vL} \tag{15}$$

in which, k_{Lu} and k_{Lv}: stiffness of a lock-up spring in the longitudinal and transverse directions, respectively, Δu_L and Δv_L : relative displacement of an expansion joint in the longitudinal and transverse directions at the instance when an expansion joint locks-up, and R_{uL} and R_{vL} : restoring force of an expansion join in the longitudinal and transverse directions at the instance when an expansion joint locks-up.

It is assumed that the stiffness of lock-up springs, k_{Lu} and k_{Lv}, are evaluated as

$$k_{Lu} = k_{Lv} = k_{EJu} \tag{16}$$

3. IDEALIZATION OF A TARGET BRIDGE

To study the effect of expansion joints on the seismic response of a bridge, the above analytical model for an expansion joint was implemented to a three-span simply supported bridge (D2, D3 and D4) as shown in **Fig. 3**[11]. Effect of the adjacent decks (D1 and D5) was approximately taken into account in analysis by lumping half of the mass of D1 and D5 at the top of P1 and P4, respectively. The structural parameters of the target bridge are derived from reference (11). A 40-meter long and 12-meter wide deck with a mass of 628 t each is supported by 6-14 m tall cantilevered reinforced concrete piers. Type II (moderate) soil condition was assumed based on the JRA design code[12] and it was further assumed that liquefaction does not occur. The gap between each deck is 0.2m. The superstructure is supported by elastomeric bearing[13] and the columns are supported by pile foundations. A Pile foundation including the soil-structure interaction was idealized by a set of translational and rotational springs under the footing. The

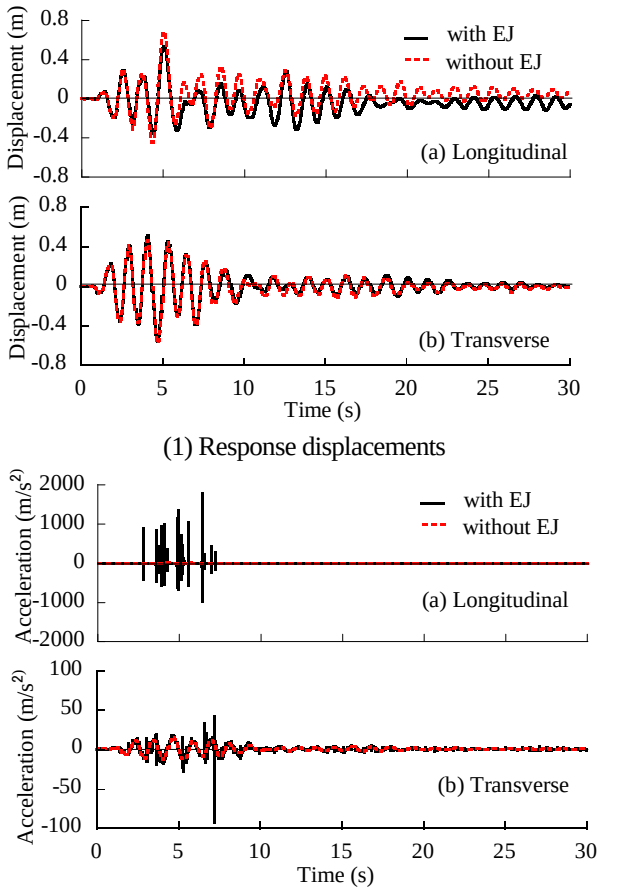

(1) Response displacements

(2) Response accelerations

Fig. 5 Response displacements and response accelerations of D3 at P3

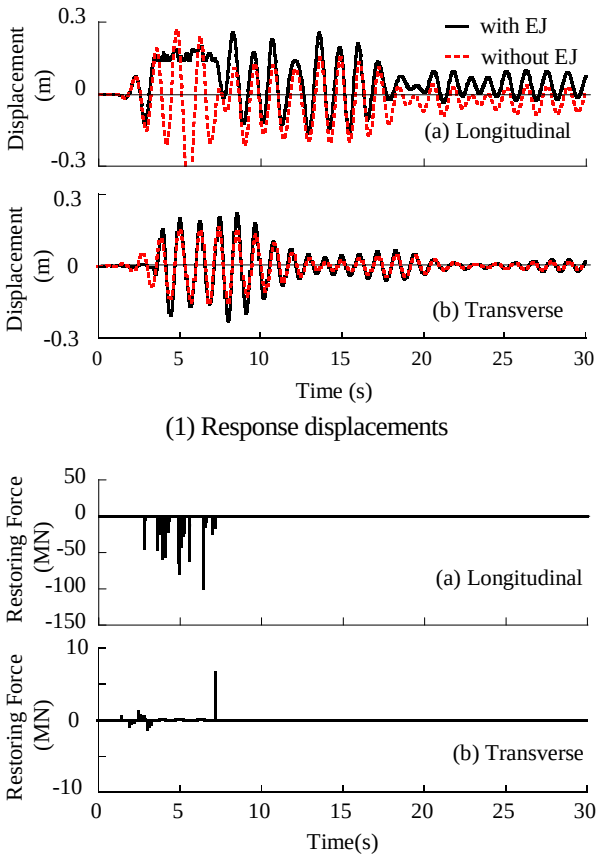

(1) Response displacements

(2) Restoring forces

Fig. 6 Response displacements and restoring forces at the expansion joint between D2 and D3

piers are idealized by fiber elements at their plastic hinge regions[14)15)]. The piers section outside of plastic hinge zone and lateral beams were idealized by elastic beam elements. The effect of damping was included in the analysis in terms of Rayleigh damping and the damping ratio is approximately 2%. The computer program "TDAP III" was used for the dynamic analysis. Time interval of the numerical integration was 1/20000 s.

Expansion joints consisting of one hundred twenty-0.275 m long, 66 mm wide and 40 mm high fingers were assumed[16)17)]. The gaps between adjacent fingers, Δl_{EJ} and Δw_{EJ}, are 0.135 m and 0.005 m, respectively. The effective length of fingers in the longitudinal direction l_{EJe} is 0.14 m. The parameters in Eqs. (3)-(5) are P_v=6.65 MN, P_u=275.5 MN, and P_{uc}=551 MN. The fault normal and parallel components of JR Takatori Station record (refer to **Fig. 4**) during the 1995 Kobe, Japan earthquake were imposed to the bridge in the longitudinal and transverse directions, respectively.

4. SEISMIC RESPONSE WITHOUT LOCK-UP OF EXPANSION JOINT

Fig. 5 shows response displacements and accelerations of D3 at P3. The responses of D3 disregarding the effect of expansion joint in the analysis are also shown in **Fig. 5** for comparison. The response displacements of D3 by disregarding the effect of expansion joints are 0.684m and 0.576m in longitudinal and transverse directions, respectively. On the other hand, response displacements of D3 became 0.543m and 0.564m in the longitudinal and transverse directions, respectively, if the effect of expansion joint is included in the analysis. Thus, the longitudinal response displacement of D3 decreases by 21% by including the effect of expansion joins in the analysis. However, there is no substantial change in the transverse response displacement. The peak longitudinal and transverse response accelerations increase from 10.93 m/s^2 and 15.41 m/s^2 to 1770 m/s^2 and 41.5 m/s^2 by including the effect of expansion joints. As will be described later, the significant increase of the peak response accelerations resulted from the pounding between fingers.

Fig. 6 (1) compares the response displacement between D2 and D3. It is important to note that the longitudinal relative displacement of expansion joint Δu keeps a value of approximately 0.14m between 3.35s to 7.19s if the effect of expansion joint is considered in analysis. It is also noted that the transverse relative displacement of expansion joint Δv does not significantly change by including the effect of expansion joint in analysis. **Fig. 6 (2)** shows the corresponding restoring forces at the expansion joint

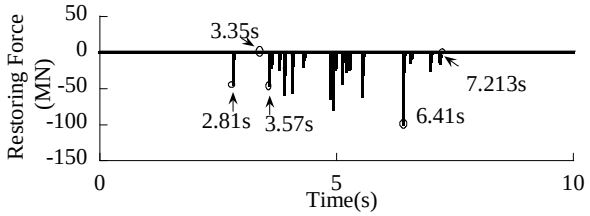

(a) Restoring force

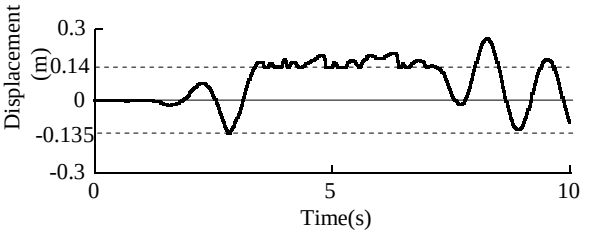

(b) Response displacement

(1) Longitudinal

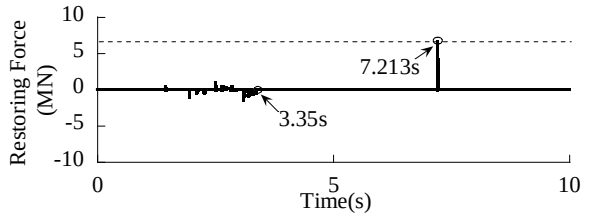

(a) Restoring force

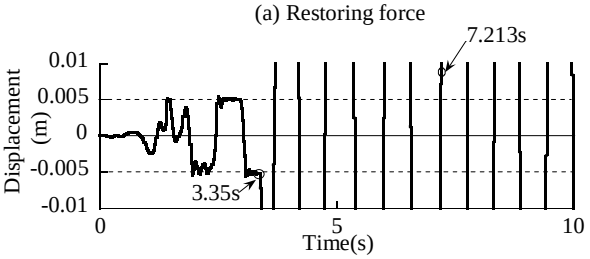

(b) Response displacement

(2) Transverse

Fig. 7 Restoring force and relative displacement of the expansion joint between D2 and D3 during a period of 0~10s

between D2 and D3 when the expansion joints are considered in analysis. While the peak restoring force at the expansion joint between D2 and D3 is 6.65 MN at 7.213 s in the transverse direction, extremely large pounding forces over 50 MN occur several times in the longitudinal direction due to collisions at the expansion joint.

Focusing on the responses between 0 to 10 s, the displacements and restoring forces presented in **Fig. 6** become as shown in **Fig. 7**. Between 0 to 3.35 s, whenever the transverse relative displacement of the expansion joint Δv reaches the gap of fingers Δw_{EJ} (= 0.005m), a restoring force F_v as large as 1.4 MN develops. On the other hand, in the longitudinal direction, tips of the fingers collide with the bases of the other side fingers at 2.81 s resulting in a longitudinal compression force F_u of 43.9 MN. Then the fingers are subjected to tension, and they completely slip out ($\Delta u \geq l_{EJe}$) at 3.35 s. Because this enables the expansion joints to freely displace in the

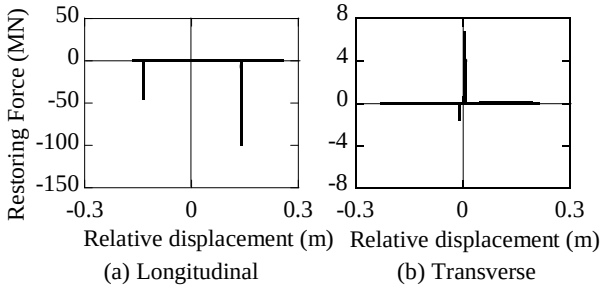

Fig. 8 Restoring force vs. relative displacement hysteresis of an expansion joint between D2 and D3

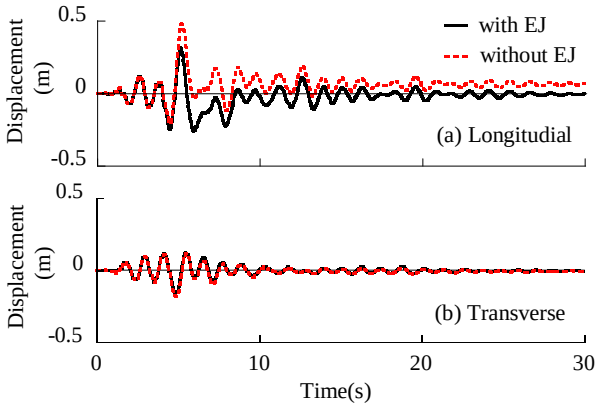

Fig. 9 Response displacements at the top of P2

transverse direction, the transverse relative displacement of the fingers Δv starts to exceed the transverse gap Δw_{EJ} (= 0.005m) at 3.35 s. Once the fingers slip out longitudinally and displace transversely larger than Δw_{EJ}, the fingers can freely move longitudinally and transversely, but they cannot slip into the original contact position no matter how they are subjected to compression. Consequently, the fingers repeatedly contact and separate due to rebound at their tips resulting in 14 times collision and separation until 7.19 s. It is the reason why longitudinal relative displacement Δu keeps nearly 0.14 m between 3.35 s and 7.19 s. The maximum pounding force during this stage is 99.5MN at 6.41 s.

The transverse relative displacement of expansion joint Δv becomes smaller than the transverse gap of the expansion joint Δw_{EJ} at 7.20 s, hence the fingers returned to their original contact position. Subsequently, because the transverse restoring force of the expansion joint F_v reaches the transverse strength P_v (= 6.65 MN), the expansion joint ruptures in the transverse direction at 7.213 s, and it also loses the function in the longitudinal direction. Following Eqs. (11) and (12), the expansion joint transfer only the friction force F_b in the longitudinal and transverse directions after its failure.

Fig. 8 shows the restoring force vs. relative displacement hysteresis of the expansion joint between D2 and D3. In the longitudinal direction, Δu and F_u reaches -0.135 m and 43.9 MN, respectively, due to collision between the tips of fingers and the bases of the other side

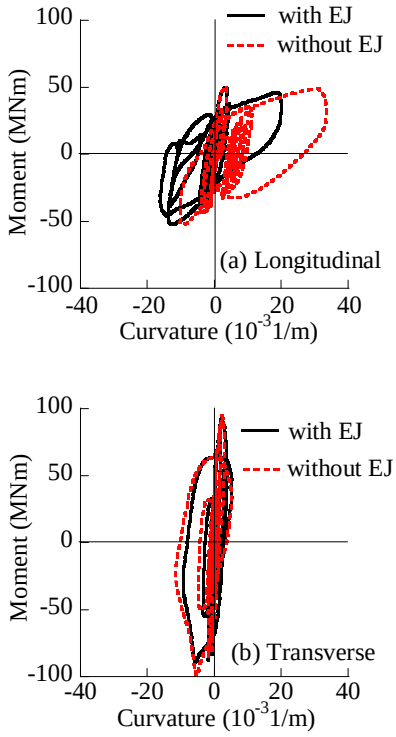

Fig. 10 Moment vs. curvature hystereses of P2 at the plastic hinge

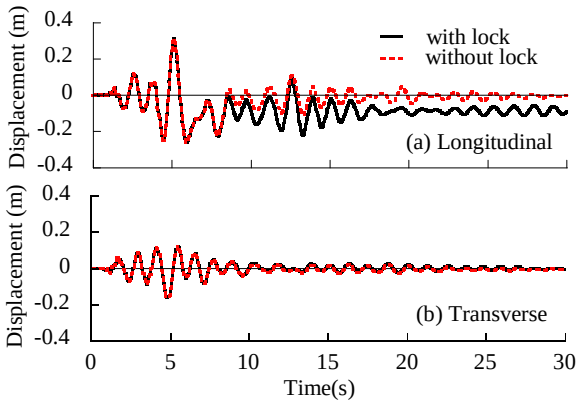

Fig. 11 Response displacements at the top of P2

fingers. The compression force induced at Δu =0.14 m results from collision between the tips of fingers after they once slip out and start to contact. On the other hand, in the transverse direction, the large relative displacement Δv of -0.23 m and 0.22 m results from free movement of the expansion joint after their rupture.

Figs. 9 and **10** show the response displacement at the top of P3 and the moment vs. curvature hysteresis of P2 at the plastic hinge, respectively. In the transverse direction, the effect of expansion joints is less significant on the column response displacement and the moment vs. curvature hysteresis, because the restraint of the expansion joints to the relative displacement Δv does not affect the column response displacement whereas it reduces the relative displacement Δv. On the other hand, the effect of expansion joints is significant in the longitudinal direction.

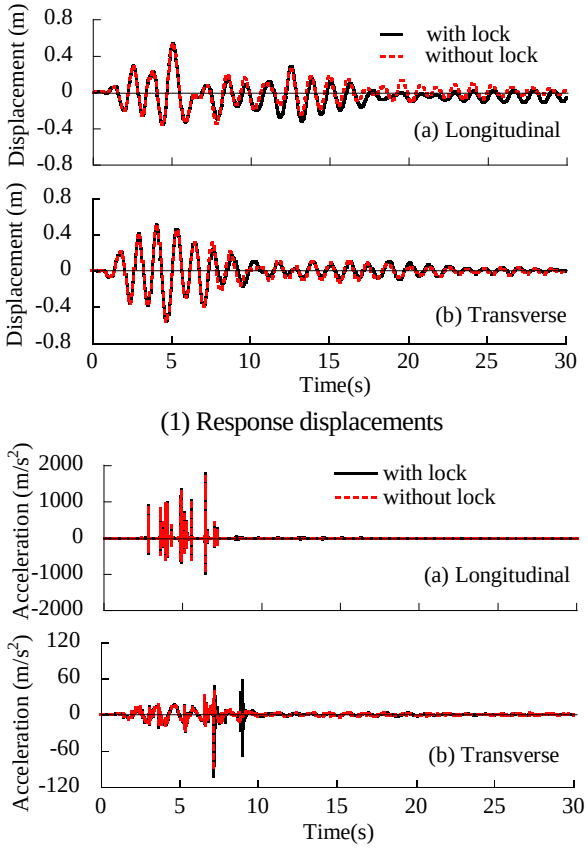

(1) Response displacements

(2) Response accelerations

Fig. 12 Response displacements and accelerations of D3 at P3

The peak response displacement at the top of P2 is 0.316 m if the effect of expansion joints is included in the analysis, and it is 65.3% of the peak column response displacement computed by disregarding the effect. Consequently, the peak curvature at the plastic hinge reduces by 40 % from 33.5×10^{-3} 1/m to 20.1×10^{-3} 1/m by considering the effect of expansion joints.

5. SEISMIC RESPONSE WITH LOCK-UP OF EXPANSION JOINT

In the above analysis, it was assumed that the expansion joints transfer only the friction force once they fail. Consequently, the expansion joints which failed have similar functions with the energy dissipators in seismic isolation. However the function of an expansion joint which suffers extensive damage under extreme ground motions is not so simple. It is often the case that fingers were badly deformed and bent resulting in locking the relative displacements Δu and Δv.

Fig. 11 shows the response displacement at the top of P2 and **Fig. 12** shows the response displacements and response accelerations of D3 at P3. The expansion joint between D2 and D3 fails and locks-up at 7.213 s. The effect of lock-up is apparent in the responses after 7.213 s. For example, virtually no residual displacement (permanent drift

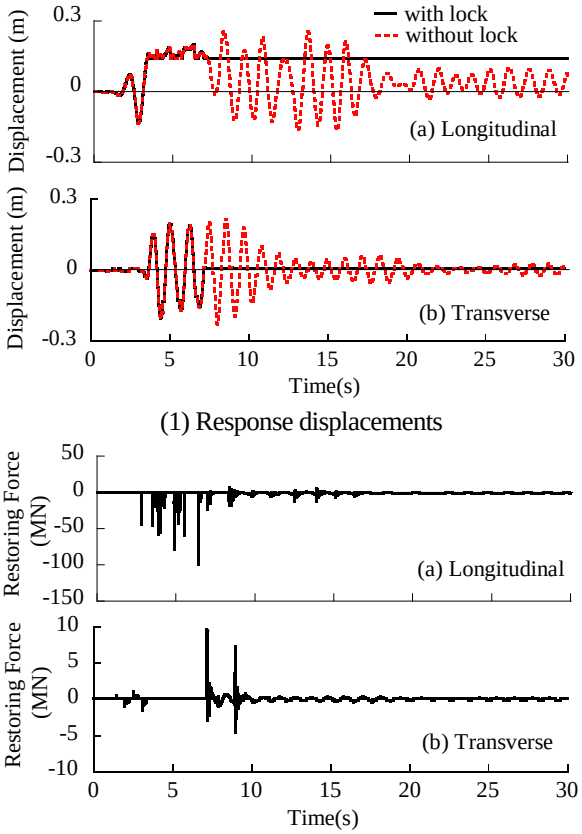

Fig. 13 Response displacement and restoring force of the expansion joint between D2 and D3

after the excitation is completed) occurs at the top of P2 if the expansion joints do not lock-up; however it increases to 0.08 m if the expansion joints lock-up. Because it is specified in the design code that the residual displacement shall be less than 1 % of the column height[14], the residual displacement of 0.08 m corresponds to 67 % of the design residual displacement. The residual displacement at the top of P3 results in the residual displacement of 0.05 m at D3. It is significantly larger than the residual displacement of 0.01 m which is computed at D3 by disregarding the effect of lock-up of the expansion joints.

Fig. 13 shows the response displacement and resultant restoring force of the expansion joint between D2 and D3. **Fig. 14** shows enlarged response of **Fig. 13** between 0 and 10 s. It is seen that the longitudinal and transverse relative displacements, Δu and Δv, are 0.138 m and 0.006 m, respectively at the instance when the expansion joint fails (7.213 s), and Δu and Δv are locked at those relative displacements if the lock-up of expansion joints is considered in analysis.

Fig. 15 shows the effect of lock-up of the expansion joints on the moment vs. curvature hysteresis of P2 at the plastic hinge. The effect of the lock-up on the peak moment and peak curvature is not significant, however, a large residual curvature is developed in the longitudinal direction associated with the residual displacement of P2 as described earlier.

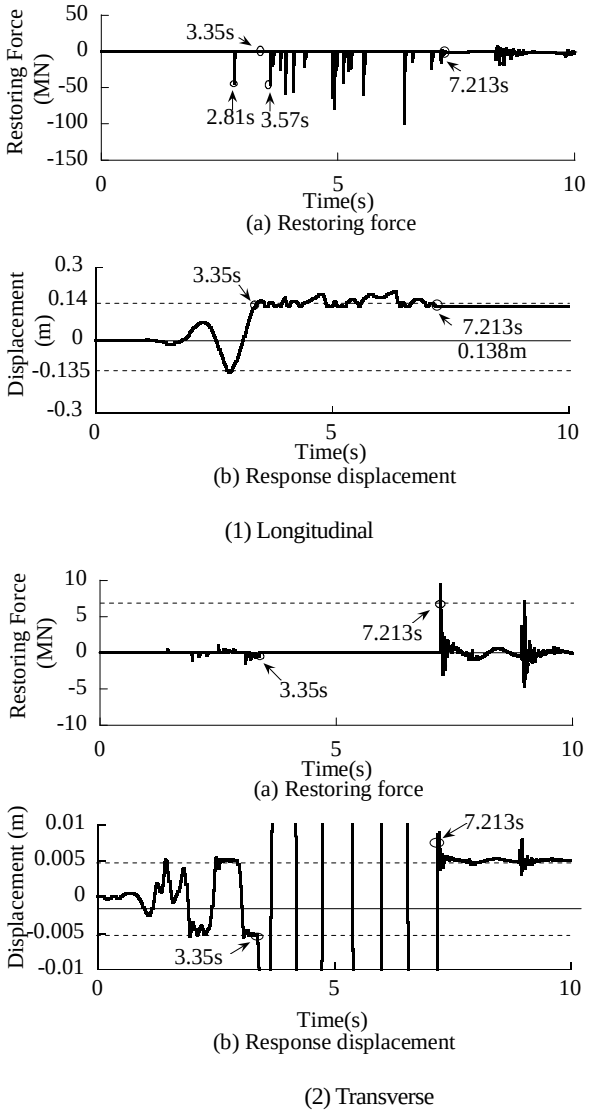

Fig. 14 Restoring force and relative displacement of the expansion joint between D2 and D3 during a period of 0~10s

6. CONCLUSIONS

A nonlinear hysteretic model of steel finger-type expansion joints was developed to investigate the effect of finger expansion joints on the seismic response of bridges and the proposed model was implemented to an analysis of a three-span simply supported plate girder bridge. Although experimental verification for the evaluation of the strength and deformation properties of expansion joints is required, the following conclusions may be deduced from the analytical results presented herein.

1) The bridge seismic response is constrained by the complex mechanism of expansion joints including constraint by fingers, pounding, slip-out, failure and lock-up. The effect of expansion joints is significant on the seismic response in the longitudinal direction.

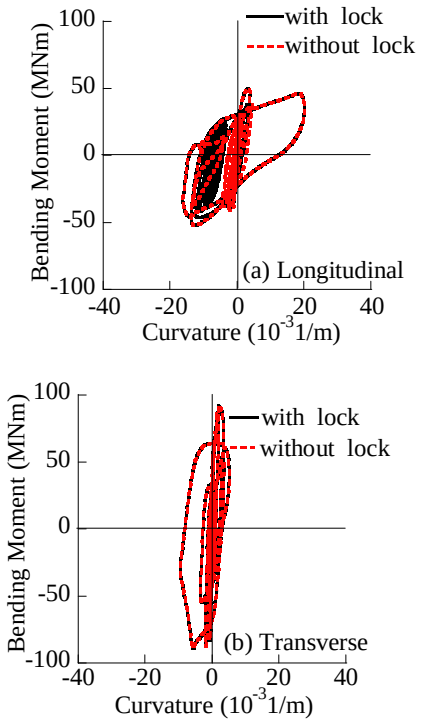

Fig. 15 Bending moment vs. curvature hystereses of P2 at the plastic hinge

2) Between the two failure models of expansion joints developed in this study, the model which assumes that expansion joints lock after failure results in more significant effect on the seismic response of the bridge than the model which assumes that the expansion joint only transfer the friction force after failure. This is because the relative displacement between the adjacent decks is more significantly restrained in the model which takes account of the lock-up.

3) The effect of expansion joints is significant on the plastic deformation of the columns, response displacement of the decks and columns and the residual displacement. Consequently, it is important to consider the realistic hysteretic behavior of the expansion joints in the seismic response analysis of bridges.

ACKNOWLEDGEMENTS:

The authors express their sincere appreciation to Dr. Masaaki Yabe, Chodai, for providing detailed information on design of expansion joints and Messrs. Tomohiro Sasaki and Takashi Matsumoto, Tokyo Institute of Technology for developing computer software for expansion joints.

REFERENCES

1) Matsumoto, Y., Yamaguchi, H., Tomida, N., Kato, T., Uno, Y., Hiromoto, Y. and Ravshanovich, K. A. (2007), "Experimental Investigation of Noise Generated by Modular Expansion Joint and Its Control," *Journal of Structural Mechanics and Earthquake Engineering*, JSCE, **63**(1), 75-92.

2) Abe, T., Kida T., Hoshino M., Kato, K. and Hsu, M. (2006), "Experimental Load-carrying Capacity and Dynamic Effect Coefficient of RC Slab and RC Beam under Running Vibration-load," *Journal of Structural Mechanics and Earthquake Engineering*, JSCE, **62**(1), 1-13.

3) Committee for Countermeasures on Seismic Damage by Kobe Earthquake (1995), "Report on the Damage of Highway Bridges due to 1995 Kobe Earthquake," Japan Ministry of Construction.

4) Yashinsky, M. (1998), "Performance of Bridge Seismic Retrofits during Northridge Earthquake," *Journal of Bridge Engineering*, ASCE, **3**(1), 1-14.

5) Yao T.H., and Chung C.F. (2004), "Seismic Effect on Highway Bridges in Chi Chi Earthquake," *Journal of Performance of Constructed Facilities*, ASCE, **18**(1), 47-53.

6) Takeno, S. and Izuno, K. (2001), "Estimation of Relative Velocity Response Considering Pounding between Adjacent Bridges during Earthquakes," *Journal of Structural Mechanics and Earthquake Engineering*, JSCE, **668**(1-54), 163-175.

7) Moriyama, T. and Yoda, T. (2000), "Experimental Study on the Effect of Pounding between the Adjacent Girders on the Falling Girders," *Journal of Structural Mechanics and Earthquake Engineering*, JSCE, **654**(I-52), 223-232.

8) Matsumoto, T. and Kawashima, K. (2008), "Effect of Pounding on the Seismic Performance of Continuous Bridges," Paper ID: S17-02-012 (CD-ROM), 14th World Conference on Earthquake Engineering, Beijing, China.

9) Kawashima, K. (1981), "An Analytical Model of Contact and Impact in Dynamic Response Analysis," JSCE, **308**, 123-126.

10) Quan, G. and Kawashima, K. (2009), "Effect of Finger Expansion Joints on Seismic Response of Bridges," *Journal of Structural Mechanics and Earthquake Engineering*, JSCE, A, **65**(1), 243-254.

11) Japan Road Association (1997), "Reference for Seismic Design of Bridges," Maruzen, Tokyo, Japan.

12) Japan Road Association (2002), "*Design Specifications of Highway Bridges*, Part-V *Seismic Design*," Maruzen, Tokyo, Japan.

13) Japan Road Association (2004), "Guide Specifications for Design of Bridge Bearings," Maruzen, Tokyo, Japan.

14) Hoshikuma, J., Kawashima, K., Nagaya, K. and Taylor, A.W. (1997), "Stress-Strain Model for Confined Reinforced Concrete in Bridge Piers," Journal of Structural Engineering, ASCE, **123**(5), 624-633.

15) Sakai, J. and Kawashima, K. (2006), "Unloading and Reloading Stress-Strain Model for Confined Concrete," Journal of Structural Engineering, ASCE, **132**(1), 112-122.

16) Japan Road Association (1970), "Guide Specifications for Expansion Joints of Bridges," Maruzen, Tokyo, Japan.

17) Japan Bridge Association (2005), "Design Guideline for Steel Expansion Joints," Tokyo, Japan.

JOINT CONFERENCE PROCEEDINGS
7th International Conference on Urban Earthquake Engineering (7CUEE) &
fifth International Conference on Earthquake Engineering (5ICEE)
March 3-5, 2010, Tokyo Institute of Technology, Tokyo, Japan

THREE DIMENSIONAL NONLINEAR ANALYSIS OF SEISMIC POUNDING BETWEEN MULTI-STORY REINFORCED CONCRETE BUILDINGS

Deepak Raj Pant [1], Anil C. Wijeyewickrema [2] and Tastsuo Ohmachi [3]

1) Graduate Student, Department of Civil Engineering, Tokyo Institute of Technology, Japan
2) Associate Professor, Department of Civil Engineering, Tokyo Institute of Technology, Japan
3) Professor, Department of Built Environment, Tokyo Institute of Technology, Japan
pant.d.aa@m.titech.ac.jp, wijeyewickrema.a.aa@m.titech.ac.jp, ohmachi@enveng.titech.ac.jp

Abstract: In this paper, a modified Kelvin-Voigt model is proposed to simulate seismic pounding between adjacent structures. The proposed model is used for three-dimensional nonlinear analysis of seismic pounding between multi-story reinforced concrete buildings. The building configuration considered consists of 8-story and 10-story buildings with equal story heights. The response of buildings is compared in terms of damage, pounding scenarios, impact forces, shear amplification factors and inter-story drift demands for two far-field and two near-field earthquakes. In order to illustrate the significance of considering energy dissipation during impact, maximum impact forces obtained using the proposed model are compared with those obtained using the linear spring model. It is concluded that, for the building configuration considered, although pounding amplifies the response of buildings, it does not initiate collapse. It is found that the pounding response is more dependent on earthquake characteristics than the gap between buildings.

1. INTRODUCTION

Adjacent buildings with insufficient separation, having different dynamic characteristics may vibrate out of phase during earthquakes causing pounding between them. Reconnaissance surveys have reported that the pounding between adjacent reinforced concrete (RC) buildings during earthquakes may lead to severe damage and even result in complete collapse (Berg and Degenkolb 1973 and Kasai and Maison 1997). However, such damage has sometimes been exaggerated as reported by Anagnostopoulos and Karamaneas (2008).

Analysis of mutual interaction of structures has gained attention of many researchers dating back from 1980's (for example Wolf and Skrikerud 1980 and Anagnostopoulos 1988) to the present time (for example Jankowski 2006, 2009a,b, Dimitrakopoulos et al. 2009 and Shakya and Wijeyewickrema 2009). Some of the crucial aspects of building pounding such as concentrated local damage, increased floor acceleration and advantageous effects of structural pounding have been researched extensively for the last two decades. Except a few (for example Filiatrault et al. 1995 and Papadrakakis and Mouzakis 1995), most of the research works are focused on numerical modeling rather than experimental study of the building pounding phenomenon. Numerical simulation of contact between adjacent structures under the action of seismic loading involves many complexities. Hence, the previous efforts have been directed towards simulating the phenomenon approximately based on some critical assumptions. The solution methods for contact-impact problems can be classified into (a) Mass point to mass point contact (i.e. stereomechanical impact), (b) Node to node one-dimensional (1D) contact, and (c) Node to surface three-dimensional (3D) arbitrary contact (Zhu et al. 2002).

The theory of stereomechanical impact also known as the classical theory of impact assumes that the impact duration is negligibly small. The initial and final states of the colliding bodies are of interest and the transient stresses and deformations in the impacting bodies are not considered. The formulation, which involves minimum mathematical difficulties, is based on the principle of conservation of momentum. The degree of plasticity of impact is incorporated through the introduction of the coefficient of restitution. This solution method has been used by several researchers to analyze seismic pounding as noted by Muthukumar and DesRoches (2006).

Node to node 1D contact is suitable when the locations of the contact points are known a priori. A contact element (composed of a spring and dashpot) or Lagrange multiplier method can be used to simulate the transient nature of structural pounding. The most widely used type of contact element model is the Kelvin-Voigt model. Many researchers have used the contact element approach to model seismic pounding (Anagnostopoulos 1988, Karayannis and Favvata 2005, Jankowski 2005, Muthukumar and DesRoches 2006, Komodromos et al. 2007 and Anagnostopoulos and Karamaneas 2008). The model has a clear physical meaning and a relatively simple algorithm, which can easily be implemented in existing finite element programs.

Node to surface 3D arbitrary contact is suitable

especially when the impact locations are not known a priori. It has a relatively complicated algorithm and a wide area of applicability including vehicle collision and metal forming. Some researchers have used this method to model seismic pounding (Papadrakakis et al. 1996, Zhu et al. 2002).

In addition to the diversity in the use of solution methods for contact-impact problems, there have been different approaches to model the colliding structures. Many previous studies on building pounding have been carried out, where the buildings are modeled as single-degree-of freedom systems (Anagnostopoulos 1988) or multi-degree-of-freedom lumped mass systems (Maison and Kasai 1992). For both cases, elastic and inelastic structural models have been employed. A more rigorous analysis based on finite element method (FEM) can be found in some publications. Papadrakakis et al. (1996) developed a 3D model for the simulation of pounding response of two or more adjacent buildings during earthquakes. The structures were modeled as multi-degree-of-freedom systems with finite elements. The analysis was based on the assumption that the contact points are not known a priori. Geometric compatibility conditions were enforced with the presence of Lagrange multipliers, thus avoiding any interface contact element. The structures were discretized with elastic elements for the simulation of columns and beams, and 4-node rectangular plane stress elements for the simulation of slabs. Mouzakis and Papadrakakis (2004) simulated 3D pounding phenomenon of two adjacent buildings during earthquakes using FEM assuming a rigid slab response. The building nonlinearities were handled with the finite element code DRAIN-TABS, which addresses inelastic flexural behavior only, ignoring inelastic shear. Similar to the case of Papadrakakis et al. (1996), the analysis was based on the assumption that the contact points are not known a priori. However, the contact points were determined geometrically without using Lagrange multiplier method. The impact was modeled assuming short duration contact. In their method, the post impact conditions are computed independently and imposed as initial conditions for the next integration step in the solution of equations. Karayannis and Favvata (2005) conducted two-dimensional (2D) pounding analysis of adjacent RC buildings with significantly varying flexibility using the program DRAIN-2DX. Beam-column elements of distributed plasticity type with fiber-based section discretization were used for the columns of the taller flexible structure. All beams and columns of shorter stiffer structure were modeled as lumped plasticity type beam-column elements. This solution strategy might have been adopted to capture the response of columns of the taller flexible structure with greater accuracy while maintaining a low computation cost. Contact elements with and without damping were used to simulate the impact. Recently, Anagnostopoulos and Karamaneas (2008) illustrated the use of collision shear walls to minimize seismic separation between the buildings. Adjacent closely spaced RC buildings with collision shear walls at the impact location were analyzed using FEM with DRAIN-2DX. Beams and columns were modeled as lumped plasticity type beam-column elements. Contact elements of Kelvin-Voigt model were used to simulate the impact. In addition, local damage of the collision shear walls due to pounding was analyzed by the means of computer program ANSYS. Jankowski (2009b) performed a nonlinear finite element analysis of seismic pounding between the main building and stairway tower of the Olive View Hospital. Three dimensional gap-friction contact elements were used to model the pounding between structures. The detailed 3D seismic pounding analysis performed using MSC.Marc is the most rigorous out of all performed so far. However, such an analysis procedure is very costly and time consuming.

Several previous studies of seismic response of structures have shown that a 3D finite element model of RC building even with 1D beam-column elements considering the spread of plasticity across the length of element can produce acceptable results. Nevertheless, the degree of accuracy depends upon the nonlinear material models used in the analysis. Such a 3D nonlinear analysis, which is also characterized by low computation cost, has not been performed so far considering the effect of pounding. However, only Karayannis and Favvata (2005) have used 2D modeling making partial use of distributed plasticity type elements. Hence, there is a strong need for further research in this area.

In the present study, nonlinear finite element analysis of seismic pounding between multi-story RC buildings using 3D frame models with 1D beam-column elements considering the spread of plasticity across the length of element is presented. A modified Kelvin-Voigt model is proposed to eliminate the limitations of conventional Kelvin-Voigt model. The proposed model is implemented in finite element program OpenSees (2009) and the analyses are performed for two far-field and two near-field earthquake records considering different gaps between the buildings. The objective of the study is to assess the effect of seismic pounding on RC members of the buildings and to evaluate the consequences of earthquake characteristics and building separation on the pounding response.

2. CONTACT ELEMENT MODELS

The *contact element approach* to solve contact-impact problems is widely used due to its clear physical meaning and simple algorithm. The schematic representation of a contact element is shown in Fig. 1. The distance between nodes i and j at at-rest condition represents the gap. The contact element is activated when two nodes come in contact and deactivates when the condition is reversed. However, there could be several models of contact elements.

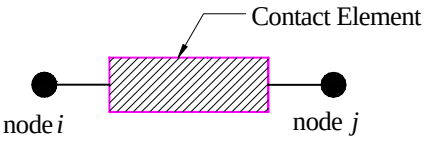

Fig. 1. Schematic representation of contact element.

2.1 Existing Contact Element Models

2.1.1 Linear spring model: This is the simplest model and represented by a linear spring. The impact force F is directly proportional to the indentation (i.e. local deformation at the contact surface), and is given by,

$$F = \begin{cases} k_s \delta & \delta > 0 \\ 0 & \delta \le 0 \end{cases}, \tag{1}$$

where k_s is stiffness of the spring element and the indentation at contact surface δ is given by,

$$\delta = u_i - u_j - gap\ , \tag{2}$$

where u_i and u_j are displacements of nodes i and j, respectively and gap is at-rest separation between the nodes. A typical impact force-indentation curve for the linear spring model for one instance of impact (i.e. approach and restitution) is shown in Fig. 2(a). Although the model is attractive due to its simplicity and ease of implementation, it does not take into account the energy dissipated during impact.

2.1.2 Kelvin-Voigt model: A Kelvin-Voigt model is represented by the combination of a linear spring and dashpot in parallel. In this model, the impact force F between the impacting bodies is,

$$F = \begin{cases} k_l \delta + c\dot{\delta} & \delta > 0 \\ 0 & \delta \le 0 \end{cases}, \tag{3}$$

where k_l is stiffness of spring element, c is the damping coefficient and relative velocity of impact $\dot{\delta}$ is,

$$\dot{\delta} = \dot{u}_i - \dot{u}_j\ , \tag{4}$$

where $\dot{u}_i$ and $\dot{u}_j$ are velocities of nodes i and j, respectively. A typical impact force-indentation curve for the Kelvin-Voigt model for one instance of impact is shown in Fig. 2(b).

The damping coefficient c in Eq. (3) can be expressed in terms of more widely used coefficient of restitution r, which is defined as the ratio of final to initial relative velocities of the colliding bodies. For low velocity impact which is generally the case during seismic pounding, the energy dissipation is assumed to be due to material damping of colliding bodies and the permanent local deformation is neglected. An expression for the damping

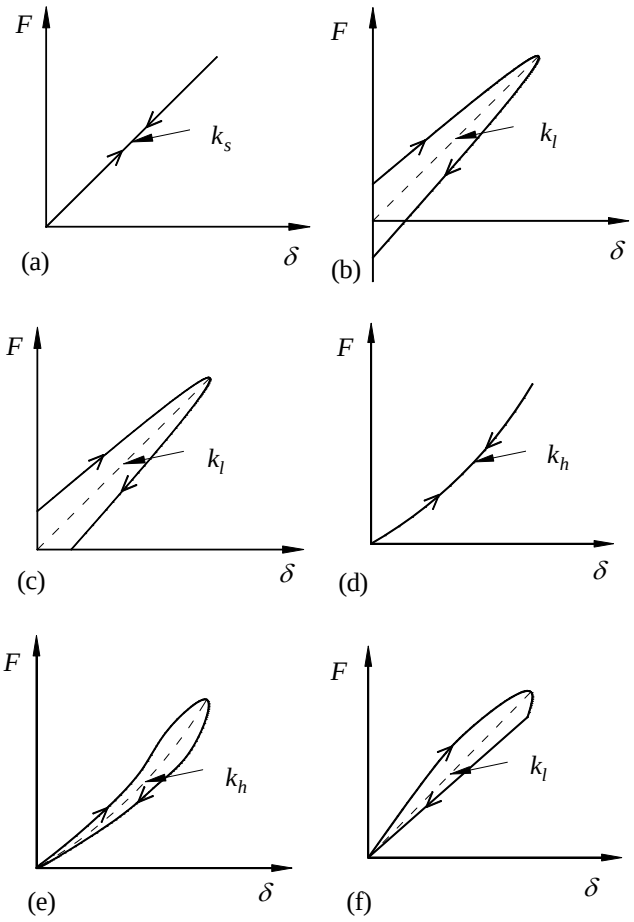

Fig. 2. Typical force-indentation curves for one instance of impact: (a) Linear spring model; (b) Kelvin-Voigt model; (c) Modified linear viscoelastic model; (d) Hertz model; (e) Hertz model with nonlinear dashpot; (f) MKV model. (F positive is a compressive force)

coefficient in the Kelvin-Voigt model proposed by Anagnostopoulos (1988, 2004) and subsequently used by other researchers (for example Zhu et al. 2002, Jankowski 2005 and Muthukumar and DesRoches 2006) is,

$$c = 2\xi\sqrt{\left(k_l m_{eff}\right)}\ , \tag{5}$$

where the stiffness k_l, in the absence of experimental studies is taken as larger of the axial stiffness of colliding bodies and the effective mass m_{eff} and damping ratio ξ are,

$$m_{eff} = \frac{m_1 m_2}{m_1 + m_2};\quad \xi = -\frac{\ln(r)}{\sqrt{\pi^2 + (\ln(r))^2}}\ , \tag{6}$$

where m_1 and m_2 are masses of colliding bodies and r is coefficient of restitution. The relationship between damping ratio ξ and coefficient of restitution r is as

shown in Fig. 3(a).

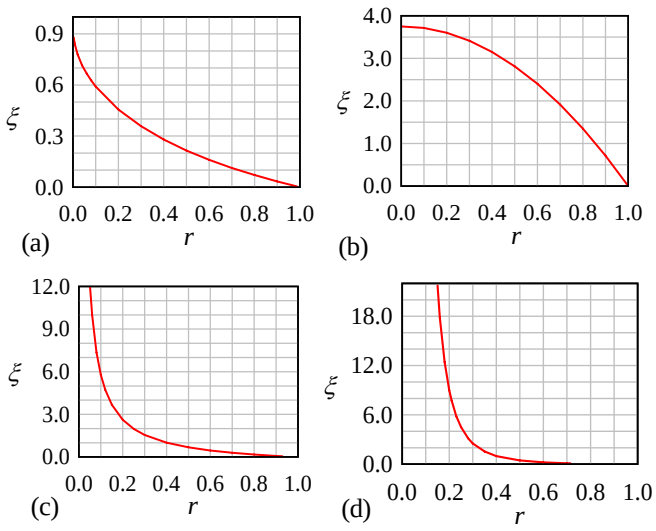

Fig. 3. Typical relationships between impact damping ratio ξ and coefficient of restitution r: (a) Anagnostopoulos (2004); (b) Lankarani and Nikravesh (1994); (c) Jankowski (2005); (d) MKV model.

Although the model is attractive due to its simplicity, there are some limitations: (a) Due to a constant damping coefficient, it shows a sudden jump of the impact force at the beginning of impact, which is not reasonable for concrete-to-concrete impact (Fig. 2b). (b) Due to the dashpot being activated even in the restitution period, the colliding bodies exert tension on each other just before the separation (Fig. 2b). (c) Effective mass m_{eff} needs to be determined to calculate c (Eq. 5). In case of buildings, this requires the determination of equivalent lumped masses at the impacting nodes, which can be done in two ways. The first way is to calculate them independent of the finite element program and second is to compute them within the finite element code. The first way is preferable because of its ease of implementation in commercial finite element programs. Extra computational effort is needed for both the ways, especially in case of multi-story buildings. (d) For a perfectly plastic impact $(r \approx 0)$, ξ should tend to infinity and for a perfectly elastic impact $(r = 1)$, ξ should be equal to zero. However, this is not the case for the relationship between ξ and r as shown in Fig. 3(a). Thus the relationship between ξ and r proposed by Anagnostopoulos (1988, 2004) assumes the system never to be over damped.

To avoid one of the major limitations discussed above i.e. the appearance of tensile impact force between the colliding bodies just before the separation, Komodromos et al. (2007) proposed a *modified linear viscoelastic model*. In this model, both the spring and dashpot are deactivated as soon as the impact force becomes zero in the restitution phase. This removes the tensile impact force part from the Kelvin-Voigt model (Fig. 2b). A typical relationship between impact force and indentation is shown in Fig. 2(c). Although the model eliminates one of the major limitations of Kelvin-Voigt model, it leaves behind a permanent deformation at the contact surface as shown in Fig. 2(c), which is not consistent with the theory of low velocity impact under consideration.

2.1.3 Hertz model: The spring of linear spring model is replaced with a nonlinear spring following the Hertz law of contact to get Hertz model. Similar to the case of linear spring model, this model also cannot include energy dissipation. The impact force F is,

$$F = \begin{cases} k_h \delta^n & \delta > 0 \\ 0 & \delta \le 0 \end{cases}, \tag{7}$$

where k_h is stiffness of spring element and n is the Hertz coefficient which is typically taken as $3/2$. Stiffness of spring element can either be determined by assuming the colliding bodies as equivalent spheres or from experiments. A typical impact force-indentation curve for Hertz model for one instance of impact is shown in Fig. 2(d).

2.1.4 Hertz model with nonlinear dashpot: This model can be represented as a combination of nonlinear spring following the Hertz law of contact and a nonlinear dashpot. The impact force F is,

$$F = \begin{cases} k_h \delta^n + c_h \dot{\delta} & \delta > 0 \\ 0 & \delta \le 0 \end{cases}, \tag{8}$$

where c_h is the damping coefficient and $n = 3/2$. A typical impact force-indentation curve for this model for one instance of impact is shown in Fig. 2(e).

Lankarani and Nikravesh (1994) obtained an expression for c_h in terms of damping ratio ξ as,

$$c_h = \xi \delta^n; \quad \xi = \frac{3k_h(1-r^2)}{4\dot{\delta}_o}, \tag{9}$$

where $\dot{\delta}_o$ is the relative velocity of impacting bodies before impact. A typical relationship between ξ and r is shown in Fig. 3(b).

The model is quite attractive from two points of views: (a) it simulates the nonlinear behavior of impact and (b) the expression of damping coefficient is independent of m_{eff}. However, since the formula for ξ in Eq. (9) has been derived based on the assumption that $r \approx 1$, the model produces inaccurate results for $r << 1$. This fact is also evident from Fig. 3(b). Furthermore, the estimation of the stiffness of spring element is not as easy as it is for Kelvin-Voigt model.

2.1.5 Nonlinear viscoelastic model: A nonlinear viscoelastic model proposed by Jankowski (2005) is similar to Hertz model with nonlinear dashpot except that now the dashpot, is only activated during the approach period of impact. The impact force F for this type of model is,

$$F = \begin{cases} k_{nl}\delta^n + c_{nl}\dot{\delta} & \delta > 0 \text{ and } \dot{\delta} > 0 \\ k_{nl}\delta^n & \delta > 0 \text{ and } \dot{\delta} \le 0 \\ 0 & \delta \le 0 \end{cases}, \quad (10)$$

where k_{nl} is stiffness of spring element, $n = 3/2$ and c_{nl} is damping coefficient given by,

$$c_{nl} = 2\xi\sqrt{\left(k_{nl}\delta^{1/2}m_{eff}\right)}. \quad (11)$$

The relationship between F and δ is similar to the one shown in Fig. 2(e) but not smooth due to the dashpot being activated only in the approach period. Jankowski (2006) relates ξ with r as,

$$\xi = \frac{9\sqrt{5}}{2}\frac{1-r^2}{r\left[r\left(9\pi-16\right)+16\right]}. \quad (12)$$

Relationship between ξ and r is as shown in Fig. 3(c), which confirms when $r \to 0$, $\xi \to \infty$ and when $r = 1$, $\xi = 0$.

The model produces more accurate results than Kelvin-Voigt model, because it simulates nonlinear nature of impact. However, the difficulty in the determination of stiffness of spring element k_{nl} and the expression of damping coefficient c_{nl} in terms of masses of colliding bodies makes it less attractive for structural pounding simulation of multi-story buildings.

2.2 Proposed Contact Element Model

A Kelvin-Voigt model seems to be the most attractive to simulate seismic pounding between multi-story buildings, if the major limitations associated with it are eliminated. Hence, a modified Kelvin-Voigt (MKV) model is proposed in this section. The MKV model is based on the assumption that most of the energy during impact is dissipated in the approach period. Previous studies have also demonstrated this fact (Goldsmith 2001). Hence, the energy dissipated in the restitution period can be neglected. Jankowski (2005) has also used this approach to propose the nonlinear viscoelastic model.

For MKV model, impact force F is expressed as,

$$F = \begin{cases} k_l\delta + c\dot{\delta} & \delta > 0 \text{ and } \dot{\delta} > 0 \\ k_l\delta & \delta > 0 \text{ and } \dot{\delta} \le 0 \\ 0 & \delta \le 0 \end{cases}. \quad (13)$$

The damping coefficient can be taken as,

$$c = \xi\delta. \quad (14)$$

The loss of kinetic energy during impact is given by,

$$\Delta E = \frac{1}{2}m_{eff}(1-r^2)(\dot{\delta}_o)^2; \quad \mathrm{r} = \left|\dot{\delta}_f\right| \Big/ \left|\dot{\delta}_o\right|, \quad (15)$$

where $\dot{\delta}_f$ is relative velocity of impacting bodies after impact.

In order to simulate this energy loss with the help of a dashpot,

$$\Delta E = \oint c\dot{\delta}\, d\delta. \quad (16)$$

Substituting the value of c from Eq. (14) in Eq. (16) and taking the limits from zero to maximum indentation, we get,

$$\Delta E = \xi\int_0^{\delta_m}\delta\dot{\delta}\, d\delta, \quad (17)$$

where δ_m is the maximum indentation during impact.

Expressing $\dot{\delta}$ in terms δ and substituting in Eq. (17), we get,

$$\Delta E = \xi\sqrt{\frac{k}{m_{eff}}}\frac{\delta_m^{\,3}}{3}. \quad (18)$$

Equating ΔE from Eq. (15) and (18), an expression for ξ can be obtained as,

$$\xi = \frac{3k_l(1-r^2)}{2r^3\dot{\delta}_o}. \quad (19)$$

Typical relationship between impact force and indentation is shown in Fig. 2(f). It is clear from the Fig. 2(f) that the sudden jump of impact force at the beginning of impact and the tensile impact force just before the separation are removed as compared to Kelvin-Voigt model (Fig. 2b). However, the curve does not possess smooth transition from approach to restitution phase due to the removal of dashpot in the latter phase, although the expression of c is independent of m_{eff}. A typical relationship between ξ and r is shown in Fig. 3(d), which shows the expected relationship between two variables. Thus, all of the major limitations of Kelvin-Voigt model are eliminated in MKV model, maintaining the simplicity and clear physical meaning of it. Furthermore, this model has been implemented in finite element program OpenSees (2009) in the form of a uniaxial material and is used to simulate seismic pounding of two multi-story RC buildings in subsequent sections.

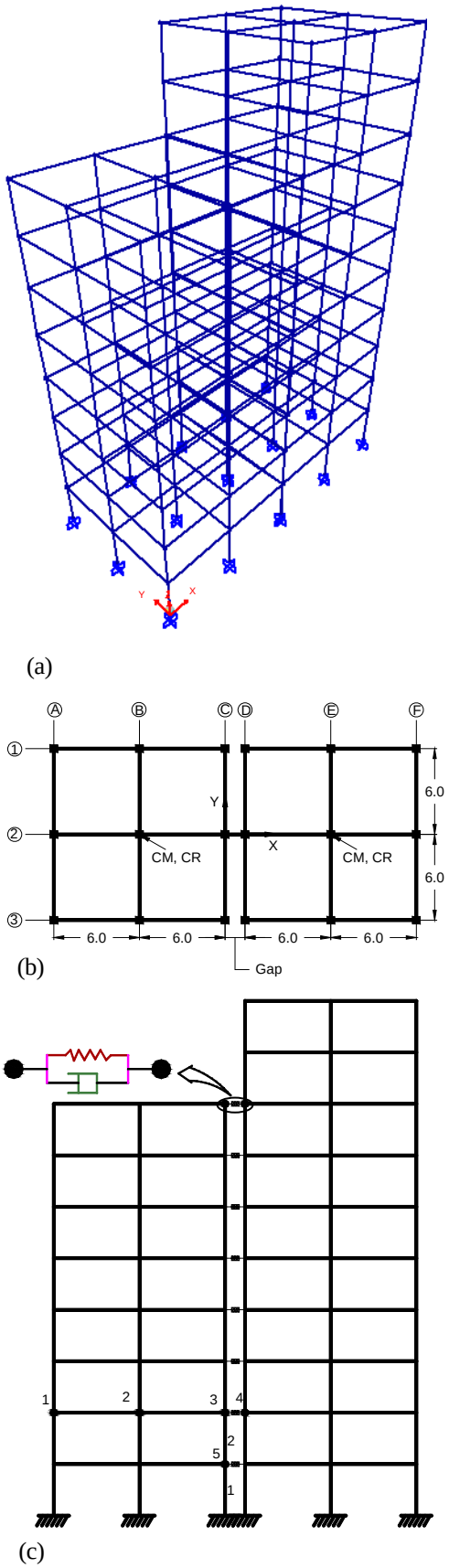

Fig. 4. Building configuration: (a) 3D view; (b) plan; (c) building frame model in XZ plane along grid 2. (All dimensions are in meters)

3. BUILDING DESCRIPTION AND MODELING

Two adjacent 8-story and 10-story RC office buildings, designed according to ACI-318-08 and IBC 2006 for site class D, are considered in the present study. Fig. 4(a) and 4(b) show the 3D view and the plan of the building configuration, respectively. Both buildings have the same story height of 3.6 m. Centre of mass (CM) and centre of rigidity (CR) of the buildings lie in same vertical plane, thus avoiding any eccentricity between them. Column section types and designed section details are given in the Appendix (Table A1 and A2).

Three dimensional frame models of buildings are used in OpenSees (2009). RC beams and columns are modeled as force-based elements with fiber-based section discretization. Material as well as geometric nonlinearities due to P-Delta effect are considered. Material models for concrete and reinforcing steel are taken to be Concrete02 and Steel02 available in OpenSees (2009), respectively. Core concrete properties are estimated using the model proposed by Mander et al. (1988). The concrete properties used in the analysis are given in Table A3. For reinforcing steel yield stress, elastic modulus and strain hardening ratio are taken to be 413.7 MPa, 1.99E5 MPa and 1%, respectively. Restraining effects of the RC slabs are incorporated by considering rigid diaphragms at each floor level.

Contact between the buildings is modeled using zero length elements as *contact elements* with uniaxial material property based on MKV model. Assuming that the contact points are known a priori, the contact elements are placed in between nodes along grids C and D at each floor level (Fig. 4b). A typical building frame section with contact elements is shown in Fig. 4(c). A value of $k_l = 93500$ kN/m used by Jankowski (2005) for concrete-to-concrete impact is also used in this study. Jankowski (2005) found that above-mentioned value of stiffness shows good correlation with experimental results provided by van Mier et al. (1991). The coefficient of restitution is taken to be 0.65 as used by other researchers for concrete-to-concrete impact (Jankowski 2005 and Anagnostopoulos and Karamaneas 2008).

4. ANALYSIS AND RESULTS

Horizontal components of two far-field (Hachinohe and El Centro) and two near-field (Kobe and Northridge) earthquake records are applied along X-direction (Fig. 4b), to evaluate the vulnerability of buildings to seismic pounding. Details of the input ground motion records are given in Table A4. The earthquakes are chosen to simulate different kinds of seismic loading on the structural system. The Hachinohe earthquake is chosen due to its high peak ground velocity (PGV), peak ground displacement (PGD) and a prolonged significant duration (D_s). The El Centro earthquake with slightly higher peak ground acceleration (PGA) than Hachinohe has a D_s nearly half of Hachinohe

and least PGV and PGD among all four earthquakes. On the other hand, the Northridge earthquake has much higher PGV and PGD than Kobe with a smaller D_s. The near-field earthquakes have high PGAs as compared to far-field earthquakes and the significant durations are very short, which implies high pulsive nature of near-field records.

Nonlinear transient analysis of buildings is carried out for different sizes of gaps between them. In the first case, the buildings are assumed to be in contact at at-rest condition (i.e. $gap = 0$), which is one of the common scenarios of RC buildings constructed mainly in developing countries. In subsequent cases, four commonly found gaps of 50 mm, 75 mm, 100 mm and 125 mm are considered. In order to demonstrate the effect of pounding on structural response, the analysis of buildings is also performed by providing a significantly large gap to avoid pounding. To illustrate the significance of considering energy dissipation during impact, buildings are also analyzed removing the dashpot from the contact element. Systems of nonlinear equations are solved using Newmark method with $\beta = 0.25$ and $\gamma = 0.5$ along with Modified Newton-Raphson technique. Rayleigh damping parameters are calculated using 5% damping ratio. The analyses for all cases are carried out up to 40 sec, with a time step of 0.005 sec.

4.1 Building Damage

In the Fig. 5(a)-(e) the vertical displacement time histories of selected nodes are plotted to assess the extent of building damage. For Hachinohe earthquake, when the pounding between buildings is not allowed, the second story columns of 8-story building fail and lose their axial load carrying capacity at nearly the same time around 32 sec as depicted by vertical displacement time history of node 3 (Fig. 5a). As it can be seen, from the Fig. 5(a) that due to failure of column 2, the irreversible deformation of node 3 is evident. Similar response was observed for nodes 2, 1 and the nodes at same location along grid 3 and grid 1. This failure progressively induces excessively large demands in other elements of building, leading to instability of system and hence non-convergence of the equilibrium equations at 32.0 sec the last time shown in the Fig. 5(a). However, the 10-story building columns do not suffer much damage and avoid collapse. The vertical displacement time history of node 4 is shown in Fig. 5(b). In contrast to node 3, excessive deformation is not observed for the node 4. On the other hand, when the buildings are placed with a small gap between them to allow pounding, the demand on critical elements decreased avoiding the failure of columns of both the buildings. This is also evident from the vertical displacement time history of node 3 for the case of 125 mm gap as shown in Fig. 5(c). Similar response was also obtained for nodes 2, 1 and the nodes at same location along grid 3 and grid 1.

For Northridge earthquake, when pounding between buildings is not allowed, columns of bottom four stories fail and lose their axial load carrying capacity at nearly the same time in very early stage of loading. For example, the vertical displacement time history of node 5 is shown in Fig. 5(d), which shows the failure of column 1 around 3 sec. Similar to the case of Hachinohe earthquake system instability occurs at 3.0 sec the last time shown in Fig. 5(d), but the 10-story building does not suffer much damage. However, in contrast to the case of Hachinohe earthquake, reducing gap between buildings to allow pounding does not avoid the collapse of 8-story building.

For Kobe and El Centro earthquakes, none of the RC members suffered collapse. As an example, the vertical displacement time history of node 5 for no pounding case of Kobe earthquake is shown in Fig. 5(e).

Hence, Hachinohe and Northridge earthquakes with very high PGD as compared to other two earthquakes are found to be destructive for the structural system especially in case of no pounding. These earthquakes first initiate the collapse of key structural elements of 8-story building and eventually cause the progression of collapse. The columns of 10-story building in the base floors with larger cross-sections as compared to 8-story building (Table A1) seem to be strong enough to avoid collapse. Thus, it can be stated that the columns of 8-story building along the periphery are not strong enough to withstand collapse due to Hachinohe and Northridge earthquakes. It is interesting to note that the Hachinohe earthquake with least PGA among all four earthquakes causes damage of 8-story building nearly towards the end of its significant duration. This could also be explained based on high PGD and prolonged D_s of this earthquake (Table A4).

4.2 Pounding Scenarios

Different scenarios of pounding are observed for different earthquakes with varying gap. Pounding does not occur for Northridge earthquake when the gap is greater than or equal to 50 mm. This is essentially because of the system instability occurring due to large damage in very early stage of loading. This further implies the large horizontal displacement of two building floors in the same direction, avoiding contact between them. As an example, horizontal displacement time histories of first floors of the two buildings for the case of 50 mm gap up to a time of 2.3 sec are shown in Fig. 5(f). Similar response was also obtained for other gap cases. Similar to the case of Northridge earthquake pounding does not occur when the gap is greater than or equal to 50 mm for El Centro earthquake. Nonetheless, in contrast to the case of Northridge earthquake, the absence of pounding is due to the lower PGA, PGD and PGV of this earthquake. In other words, the Northridge earthquake was found to be so destructive that it causes collapse of 8-story building before it can have a contact with adjacent building. However, El Centro earthquake is found to be not causing the excessive horizontal displacement of floors to induce seismic pounding. On the other hand, several instances of impact were observed in case of Hachinohe and Kobe earthquakes for different gaps between the buildings.

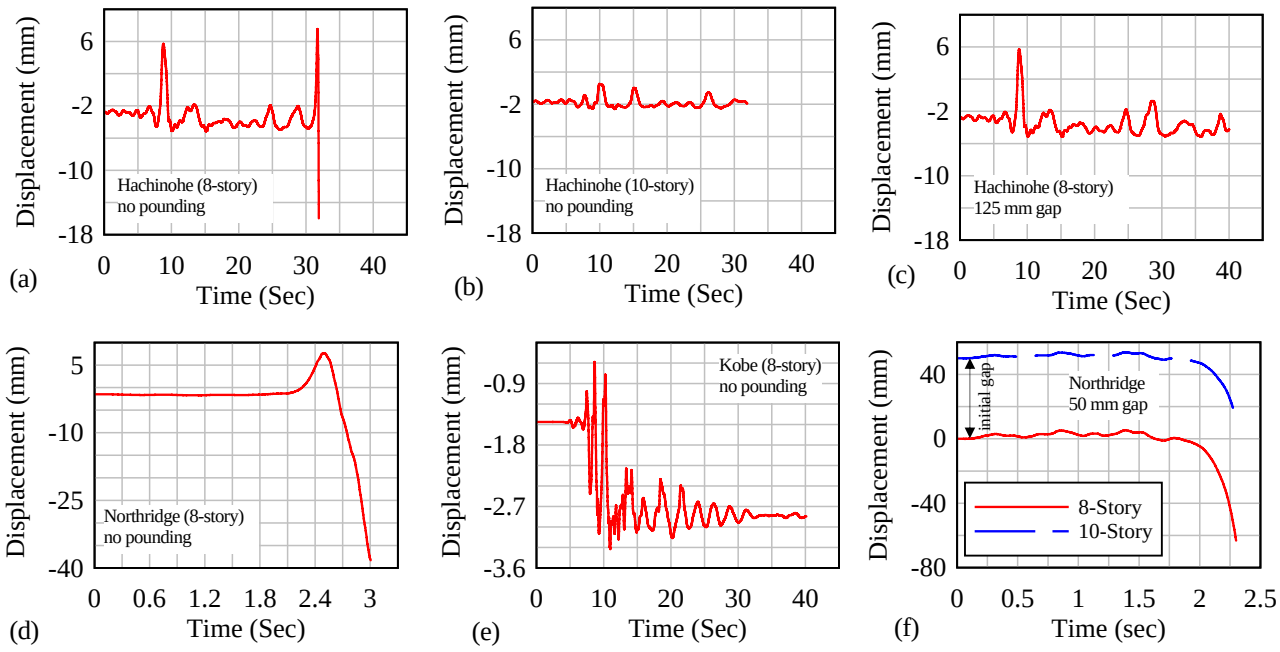

Fig. 5. Displacement time histories: (a) vertical displacement of node 3 (Hachinohe, 8-story no pounding); (b) vertical displacement of node 4 (Hachinohe, 10-story no pounding); (c) vertical displacement of node 3 (Hachinohe, 8-story 125mm gap); (d) vertical displacement of node 5 (Northridge, 8-story no pounding); (e) vertical displacement of node 5 (Kobe, 8-story no pounding); (f) horizontal displacement of first floor (Northridge, 50 mm gap).

4.3 Impact Forces, Shear Amplifications and Inter-Story Drift Demands

Maximum impact forces at each floor level for all earthquakes when the buildings are in contact at-rest (i.e. $gap = 0$) are shown in Fig. 6(a). Fig. 6(b)-6(e) show the maximum impact forces due to Hachinohe and Kobe earthquakes for increasing gap. From Fig. 6(a) it can be seen that in general impact occurs at each floor level where Kobe earthquake produces highest impact forces closely followed by El Centro, Hachinohe and Northridge. This is also consistent with the plots (Fig. 7a-e) of shear amplification factors for the case of buildings being in

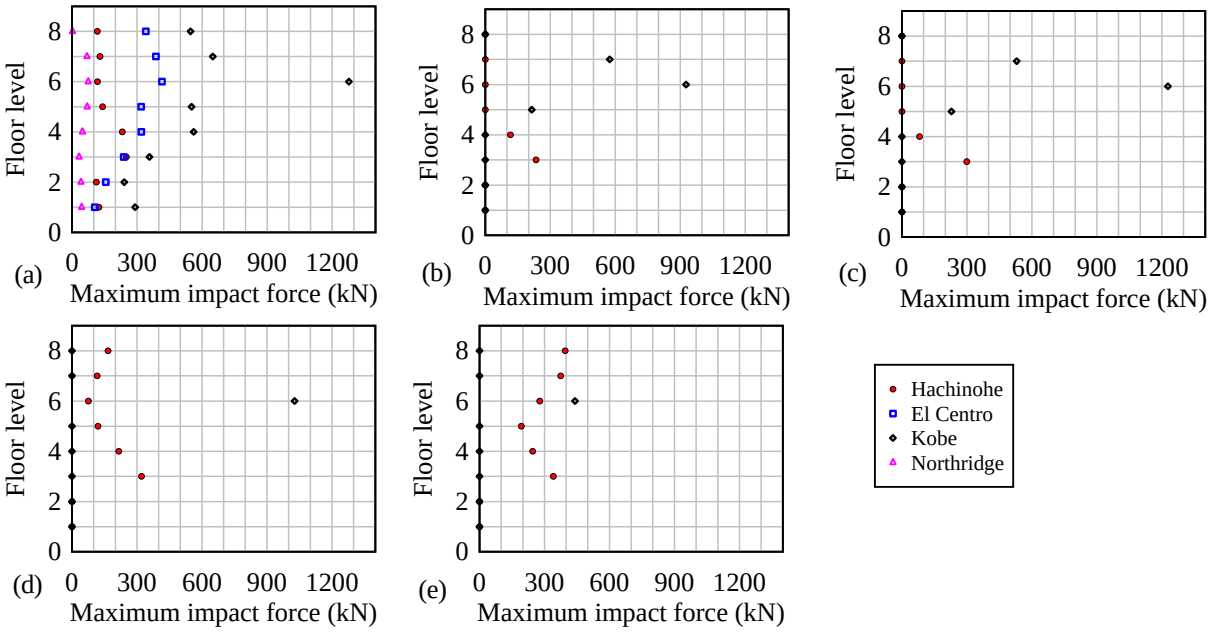

Fig. 6. Maximum impact forces at each floor level: (a) In contact; (b) 50 mm gap; (c) 75 mm gap; (d) 100 mm gap; (e) 125 mm gap. For El Centro and Northridge earthquakes, pounding only occurs when the buildings are in contact at at-rest condition.

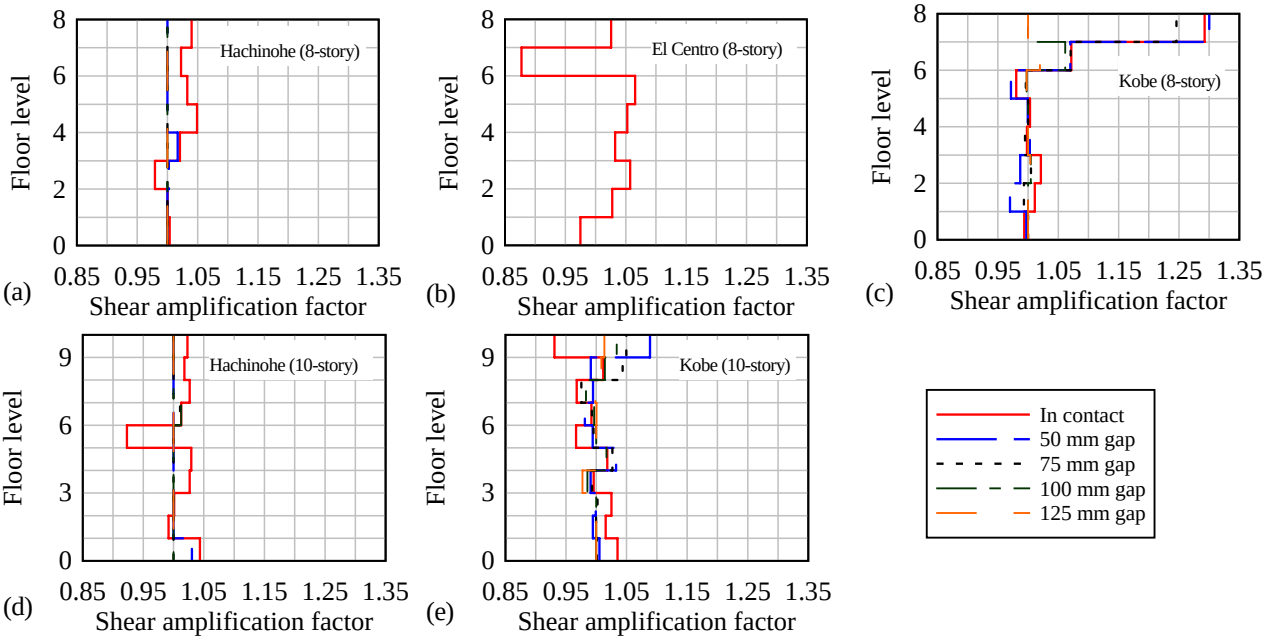

Fig. 7. Shear amplification factor: (a) Hachinohe (8-story); (b) El Centro (8-story); (c) Kobe (8-story); (d) Hachinohe (10-story); (e) Kobe (10-story).

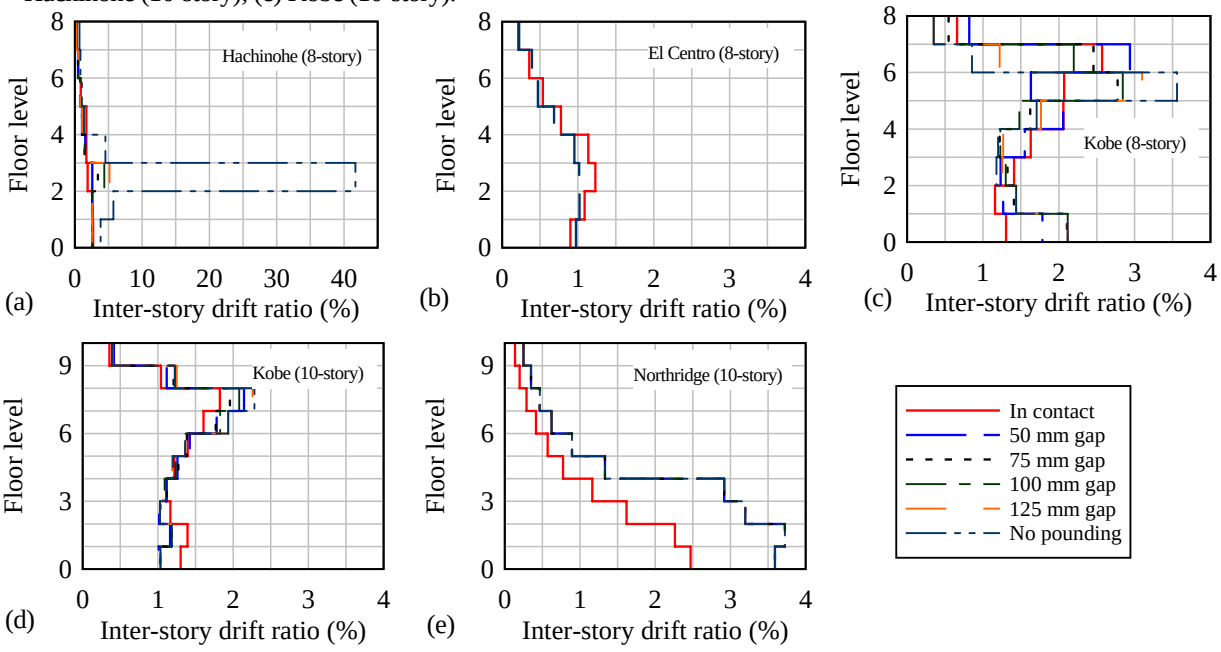

Fig. 8. Maximum inter-story drift ratio: (a) Hachinohe (8-story); (b) El Centro (8-story); (c) Kobe (8-story); (d) Kobe (10-story); (e) Northridge (10-story).

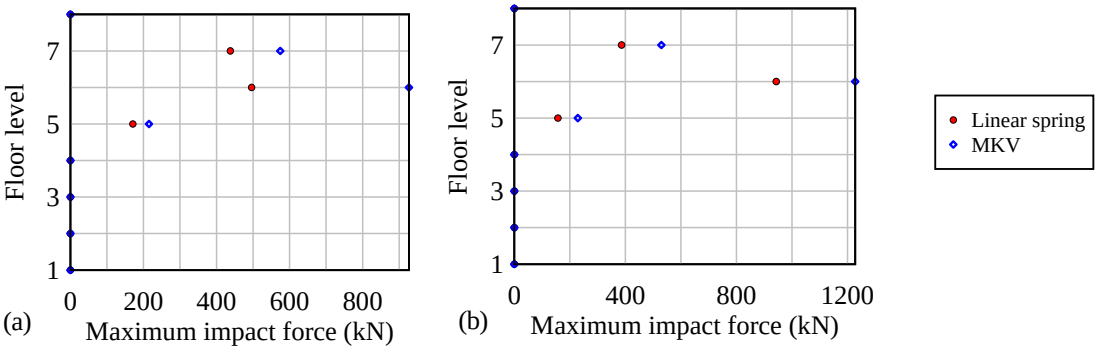

Fig. 9. Comparison of maximum impact forces at each floor level simulated by linear spring model and MKV model for Kobe earthquake: (a) 50 mm gap; (b) 75 mm gap.

contact at-rest. Shear amplification factor is defined as the ratio of maximum story shear in case of pounding to maximum story shear for no pounding case. Largest shear amplification factors are obtained in the order of Kobe, El Centro, Hachinohe and Northridge. Note that the least impact forces are obtained for the case of Northridge earthquake just before the situation when the system becomes unstable.

With increasing gap, varying response was observed for Kobe and Hachinohe earthquakes. Referring to Fig 6(a)-(e), for Kobe earthquake, the impact locations are limited to fifth, sixth and seventh floor levels for 50 mm and 75 mm gaps (Fig. 6b, c) and finally only to sixth floor level for 100 mm and 125 mm gaps (Fig. 6d, e). Maximum impact force occurs at sixth floor level in all cases (Fig 6a-e). The maximum impact forces are obtained when the buildings are in contact at-rest. The impact forces first decrease in case of 50 mm gap, next increase for 75 mm gap and again go on decreasing for 100 mm and 125 mm gaps (Fig. 6b-e). However, for Hachinohe earthquake, the impact occurring at each floor level is limited to third and fourth floor levels for the case of 50 mm and 75 mm gaps (Fig. 6b, c) and again expands to floors higher than second floor level for the case of 100 mm and 125 mm gaps (Fig. 6d, e). In general the impact force increases with increasing gap first at the lower (third and fourth) floor levels and then at lower as well as upper (sixth, seventh and eighth) floor levels (Fig. 6a-e). The varying pattern of impact forces clearly illustrates different predominant modes of vibrations of the structural system when two buildings vibrate together being in contact. Furthermore, for Kobe earthquake, maximum impact force occurs at sixth floor level for all gap sizes studied, which in general shows high shear amplification (as high as 25% more than the case of no pounding), in the floors above the impact location (Fig. 7c, e). The maximum inter-story drift for 10-story building occurs at eighth story, which shows the increased inter-story drift demand of taller building above the height of shorter building (Fig. 8 d). For 8-story building, the maximum inert-story drift occurring at sixth story is decreased due to pounding. On the other hand, the inter-story drift demand is increased above the impact location and decreased below it (Fig. 8c). However, for Hachinohe Earthquake in case of buildings being in contact at-rest, maximum shear amplification is observed nearly at mid story for 8-story building and at first story for 10-story building. The shear amplification is decreased at a gap of 50 mm but is still more than the case of no pounding. No significant shear amplification is observed for 75 mm, 100 mm and 125 mm gaps (Fig. 7a, d). Due to pounding the inter-story drift at the third story is decreased significantly which in fact is the reason for not having the failure of key load bearing elements of 8-story building and avoiding instability of the system (Fig. 8a). This is also verified by decreased shear amplification factor at the third floor level (Fig. 7a). Therefore, a clear pattern of response is not identified for varying gap.

For El Centro and Northridge earthquakes, pounding only occurs when the buildings are in contact at at-rest condition. For El Centro earthquake, the shear amplification is found to be as high as 6.5% more than the case of no pounding (Fig. 7b), which is not so significant as compared to the case of Kobe earthquake. The inter-story drift demand is found to be increased to as much as 1.25% due to pounding (Fig 8b). For Northridge earthquake, shear amplifications and inter-story drifts were found to be decreased due to pounding. For example, maximum inter-story drift ratio plot for 10-story building is shown in Fig. 8(e). However, the reduction is not found to be beneficial to avoid the collapse of stories for 8-story building and system instability.

4.4 Significance of Energy Dissipation

In order to illustrate the significance of considering energy dissipation during impact, the maximum impact forces obtained using linear spring model and proposed MKV model for 50 mm and 75 gaps in case of Kobe earthquake are compared in Fig. 9(a) and 9(b), respectively. Results for other earthquakes and gap cases are not shown here due to similarity of results. It is clear from the Fig. 9 that use of linear spring model underestimates the impact forces. The underestimation could be as large as 47% of the MKV model, as it is observed in case of 50 mm gap for Kobe earthquake at sixth floor level.

5. CONCLUSIONS

Three-dimensional nonlinear analysis of seismic pounding between 8-story and 10-story RC buildings is presented using MKV contact elements. The proposed MKV model, characterized by its high computational efficiency does not have limitations of conventional Kelvin-Voigt model. Two far-field and two near-field earthquakes are used to evaluate the effect of seismic pounding for different gaps between the buildings. In general, the response of the 8-story building is amplified due to pounding. However, the pounding response of buildings is found to be more dependent on earthquake characteristics than the gap between buildings. High impact forces resulting due to earthquakes with high PGA produce higher story shears and inter-story drift demands especially above the impact location. Important response measures are the changes in shear amplification and inter-story drift ratio, due to pounding which are decreased near the impact location and increased above it. In this scenario, pounding could be beneficial as it is proven in case of Hachinohe earthquake. By comparing linear spring model with the proposed model, it is found that, the use of energy dissipation in the model significantly affects the impact forces at floor levels.

The proposed MKV model for the solution of contact impact problems does not take into account the nonlinearity of impact and the transition between approach and restitution period of impact is not smooth. Furthermore,

1D contact element used in the analysis cannot capture sliding between the buildings during pounding. Hence, a 2D contact element would be necessary when the eccentricity in the pounding is significant. More gap cases, earthquake inputs and different building configurations need to be considered in the future to draw a general conclusion on the vulnerability of RC buildings to seismic pounding.

Acknowledgements:

The first author gratefully acknowledges a Monbukagakhusho scholarship from the Japanese government. Financial support from the project "Development of Practical Urban Earthquake Engineering Research for Mitigation of the Metropolitan Great Earthquake Disaster", is gratefully acknowledged.

References:

Anagnostopoulos, S. A. (1988). "Pounding of buildings in series during earthquakes", *Earthquake Engineering and Structural Dynamics*, **16**, 443-456.

Anagnostopoulos, S. A. (2004). "Equivalent viscous damping for modeling inelastic impacts in earthquake pounding problems", *Earthquake Engineering and Structural Dynamics*, **33**, 897-902.

Anagnostopoulos, S. A. and Karamaneas, C. E. (2008). "Use of collision shear walls to minimize seismic separation and to protect adjacent buildings from collapse due to earthquake-induced pounding", *Earthquake Engineering and Structural Dynamics*, **37**, 1371-1388.

Azevedo, J. and Bento, R. (1996). "Equivalent viscous damping for modeling inelastic impacts in earthquake pounding problems", *Eleventh World Conference on Earthquake Engineering*, Acapulco, Mexico, Paper no. 1063.

Berg, G. V. and Degenkolb, H. J. (1973). "Engineering lessons from the Managua earthquake", American Iron and Steel Institute Report.

Dimitrakopoulos, E., Nicos, M. and Kappos, A. J. (2009). "Dimensional analysis of the earthquake-induced pounding between adjacent structures", *Earthquake Engineering and Structural Dynamics*, **38**, 867-886.

Filiatrault, A., Wagner, P. and Cherry, S. (1995). "Analytical prediction of experimental building pounding", *Earthquake Engineering and Structural Dynamics*, **24**, 1131-1154.

Goldsmith, W. (2001). "Impact: The theory and physical behavior of colliding solids", Dover Publications, Inc., Mineola, New York.

Jankowski, R. (2005). "Non-linear viscoelastic modelling of earthquake-induced structural pounding", *Earthquake Engineering and Structural Dynamics*, **34**, 595-611.

Jankowski, R. (2006). "Analytical expression between the impact damping ratio and the coefficient of restitution in the non-linear viscoelastic model of structural pounding", *Earthquake Engineering and Structural Dynamics*, **35**, 517-524.

Jankowski, R. (2009a). "Experimental study on earthquake-induced pounding between structural elements made of different building materials", *Earthquake Engineering and Structural Dynamics* (in Press).

Jankowski, R. (2009b). "Non-linear FEM analysis of earthquake-induced pounding between the main building and the stairway tower of the Olive View Hospital", *Engineering Structures*, **31**, 1851-1864.

Karayannis, C. G. and Favvata, M. J. (2005). "Earthquake-induced interaction between adjacent reinforced concrete structures with non-equal heights", *Earthquake Engineering and Structural Dynamics*, **34**, 1-20.

Kasai, K., Maison, B. (1997). "Building pounding damage during the 1989 Loma Prieta earthquake", *Engineering Structures*, **19**, 195-207.

Komodromos, P., Polycarpou, P. C., Papaloizou, L. and Phocas, M. C. (2007). "Response of seismically isolated buildings considering poundings", *Earthquake Engineering and Structural Dynamics*, **36**, 1605-1622.

Lankarani, H. M. and Nikravesh, P. E. (1994). "Continuous contact force models for impact analysis in multibody systems", *Nonlinear Dynamics*, **5**, 193-207.

Maison, B. F. and Kasai, K. (1992). "Dynamics of pounding when two building collide", *Earthquake Engineering and Structural Dynamics*, **21**, 771-786.

Mander, J., B., Priestley, J. N. and Park, R. (1988). "Theoretical stress strain model for confined concrete", *Journal of Structural Engineering*, ASCE, **114**, 1804-1826.

Mouzakis, H. P. and Papadrakakis M. (2004). "Three dimensional nonlinear building pounding with friction during earthquakes", *Journal of Earthquake Engineering*, **8**, 107-132.

Muthukumar, S. and DesRoches, R. (2006). "A Hertz contact model with non-linear damping for pounding simulation", *Earthquake Engineering and Structural Dynamics*, **35**, 811-828.

OpenSees (2009). "Open system for earthquake engineering simulation". <http://OpenSees (2009).berkeley.edu>

Papadrakakis, M. and Apostolopoulou, C., Zacharopoulos, A., Bitzarakis, S. (1996). "Three dimensional simulation of structural pounding during earthquakes", *Journal of Engineering Mechanics*, ASCE, **122**(5), 423-431.

Papadrakakis, M. and Mouzakis, H. P. (1995). "Earthquake simulator testing of pounding between adjacent buildings", *Earthquake Engineering and Structural Dynamics*, **24**, 811-834.

Shakya, K. and Wijeyewickrema, A. C. (2009). "Mid-column pounding of multi-story reinforced concrete buildings considering soil effects", *Advances in Structural Engineering*, **12**(1), 71-85.

van Mier, J. G. M., Preuijssers, A. F., Reinhardt, H. W., and Monnier, T. (1991). "Load-time response of colliding concrete bodies", *Journal of Structural Engineering*, ASCE, **117**, 354-374.

Wolf, J. P. and Skrikerud, P. E. (1980). "Mutual pounding of adjacent structures during earthquakes", *Nuclear Engineering and Design*, **57**, 253-275.

Zhu, P., Abe, M. and Fujino, Y. (2002). "Modelling three-dimensional non-linear seismic performance of elevated bridges with emphasis on pounding of girders", *Earthquake Engineering and Structural Dynamics*, **31**, 1891-1913.

Appendix A

Table A1. Column section types.

Grid	Floor	8-story Building			10-story Building		
		Grid A	Grid B	Grid C	Grid D	Grid E	Grid F
1	1-3	C3	C3	C3	C2	C1	C2
	3-8	C3	C3	C3	C2	C2	C2
	8-10				C2	C2	C2
2	1-2	C3	C1	C3	C1	C1	C1
	3	C3	C2	C3	C1	C1	C1
	3-8	C3	C2	C3	C2	C2	C2
	8-10				C2	C2	C2
3	1-3	C3	C3	C3	C2	C1	C2
	3-8	C3	C3	C3	C2	C2	C2
	8-10				C2	C2	C2

Table A2. Designed beam and column sections.

Section Type		Size (mm^2)	Longitudinal Reinforcement[a]	Cover (mm)
Column	C1	600*600	8-No. 8	50
	C2	500*500	8-No. 6	
	C3	400*400	8- No. 5	
Beam		600*350	8- No. 6	60

[a] Number of bars-diameter; No. 5: 16 mm, No. 6: 20 mm and No. 8: 25 mm.

Table A3. Mechanical properties of concrete used with Concret02 material model in OpenSees (2009).

Parameters	**Unconfined Concrete**	**Confined Concrete**			
		Beam	**C1**	**C2**	**C3**
Compressive strength f_{cmx} (MPa)	-27.57	-33.09	-30.88	-31.16	-31.44
Strain at compressive strength ε_{cmax}	-2.22E-03	-2.67E-03	-2.49E-03	-2.51E-03	-2.53E-03
Crushing strength f_{cu} (MPa)	-5.51	-6.61	-6.17	-6.23	-6.28
Strain at crushing strength ε_{cu}	-4.44E-02	-5.33E-02	-4.98E-02	-5.02E-02	-5.07E-02
Unloading slope parameter λ	0.1	0.1	0.1	0.1	0.1
Tensile strength f_t (MPa)	3.86	4.63	4.32	4.36	4.40
Tension softening stiffness E_{ts} (MPa)	1.93E+03	2.32E+03	2.16E+03	2.18E+09	2.20E+03

Table A4. Input ground motion records (horizontal components).

Earthquake	**Station**	**PGA (g)**	**PGV (cm/sec)**	**PGD (cm)**	**D_s (sec)**	**Remarks**
Hachinohe (1968)	Hachinohe City	0.221g	67.42	33.92	46.86	Far-field
El Centro (1940)	USGS 117 El Centro Array #9	0.313g	29.69	13.03	24.10	Far-field
Kobe (1995)	KJMA	0.821g	81.30	17.69	8.63	Near-field
Northridge (1994)	DWP 77 Rinaldi Receiving Sta	0.825g	160.12	29.62	7.25	Near-field

JOINT CONFERENCE PROCEEDINGS
7th International Conference on Urban Earthquake Engineering (7CUEE) &
5th International Conference on Earthquake Engineering (5ICEE)
March 3-5, 2010, Tokyo Institute of Technology, Tokyo, Japan

EXPERIMENTAL TESTING OF INNOVATIVE CONFINEMENT TECHNIQUES FOR SEISMIC RETROFITTING OF RC BRIDGE COLUMNS

Moochul Shin[1] and Bassem Andrawes[2]

1) Graduate Research Assistant, Dept. of Civil and Environmental Eng, University of Illinois at Urbana-Champaign, IL, U.S.A
2) Assistant Professor, Dept. of Civil and Environmental Eng, University of Illinois at Urbana-Champaign, IL, U.S.A
mshin7@illinois.edu, andrawes@illinois.edu

Abstract: This experimental work focuses on enhancing the seismic performance of reinforced concrete (RC) bridge piers using an innovative active confinement technique. Previous attempts to apply active confinement on bridge piers using conventional materials had failed due to several problems related to the method of applying the confining pressure. The approach proposed in this paper is based on using spirals made of Shape Memory Alloys (SMAs) and relies on the SMAs recovery stress to apply the active confining pressure. Three reduced-scale columns are tested under quasi-static lateral cyclic loading. One of the columns is wrapped with prestressed SMA spirals, while another column is wrapped with glass fiber reinforced polymer (GFRP) wraps. The third column is tested in the as-built condition for comparison. The active confinement pressure provided by the SMA spirals and the passive confinement pressure provided by the GFRP wraps are chosen to be the same for comparison. The columns force versus drift results show a significant increase in the flexural ductility and energy dissipation capability of the column confined with SMA spirals compared to the as-built and GFRP wrapped columns. Further, evaluating the levels of damage sustained by the three tested columns clearly show that the SMA spiral is far more effective in mitigating the damage compared to GFRP wraps. The enhancement in the SMA retrofitted column's cyclic behavior is primarily attributed to the superior effect of active confinement in increasing the concrete strength and ultimate strain compared to passive confinement.

1. INTRODUCTION

Many of the reinforced concrete (RC) bridges catastrophic failures that occurred during past earthquakes were due to the lack of ductility and/or the insufficient shear capacity of the RC bridge piers. In order to prevent such failures, providing sufficient lateral confining pressure has proven to be one of the most effective methods to improve the strength and ductility of RC bridge piers. For several decades, many studies have focused on developing and studying numerous passive confinement techniques utilizing Fiber Reinforced Polymer (FRP) sheets or steel jackets (Samaan et al. 1998 and Li et al. 2005). Passive confinement techniques rely on the dilation of concrete to activate the confining pressure. However, the technique of applying external confining pressure, which is often known as active confinement, does not require concrete to dilate in order for the confining pressure to be activated. Previous studies have shown that actively confined concrete members exhibit better performance in terms of strength and ductility compared to passively confined members (Richart et al. 1928). Unfortunately, finding practical, effective, and reliable active confinement techniques is a challenging task that hindered the widespread application of active confinement. To address this challenge, the authors proposed earlier a new active confinement technique (Andrawes and Shin 2008; Shin and Andrawes 2009). The proposed technique is based on applying active confinement using spirals made of prestrained shape memory alloys (SMAs). In this paper the same concept is further examined experimentally on reduced-scale RC bridge columns.

2. SHAPE MEMORY ALLOYS

SMAs exhibit unique thermo-mechanical phenomena namely, superelasticity and shape memory effect (SME). SME is the ability of the SMAs to recover their original shape even after experiencing relatively large deformations (up to 8%-strain) (Vokoun et al. 2003). This unique phenomenon is primarily due to the back and forth transformation between the martensite and austenite phases on the atomic level when the temperature changes. The thermo-mechanical behavior of typical SMAs is depicted in Figure 1. At temperatures below the martensite finish temperature (M_f), SMAs exist in their martensite phase, and behave like any typical metallic materials. Hence, after the loading-unloading process, the SMA sustains large residual strain. However, if a high enough temperature is provided (higher than the austenite finish temperature, A_f), the residual strain is eliminated as the SMA transforms into its austenite

phase. This SME phenomenon is associated with large recovery stress, which depends on the alloy's composition and the level of prestrain (Otsuka and Wayman 2002). The high recovery stress of SMAs is sought in this study to apply active confining pressure on RC piers to increase their flexural ductility. In a previous study, the authors conducted experimental tests on concrete cylinders confined with NiTiNb SMA spirals (Shin and Andrawes, 2009). NiTiNb was specially utilized due to its wide thermal hysteresis, which enables SMAs to maintain their recovery stress even when the temperature drops to typical ambient temperature levels. Continually, the NiTiNb was also utilized for this study.

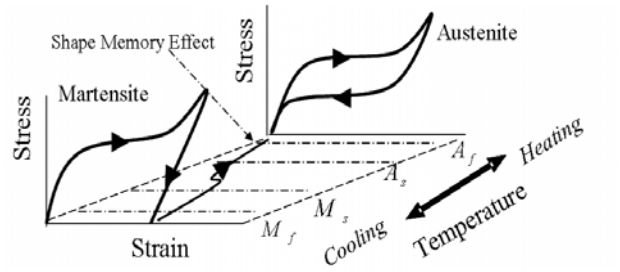

Figure 1 Thermo-mechanical behavior of typical SMAs

3. COLUMN SPECIMENS AND RETROFITTING TECHNIQUES

Three reduced-scale RC single cantilever columns were built and tested under quasi-static cyclic lateral loading. Figure 2 shows an isometric view and the cross section of the tested columns. The effective height of each column was 1270mm and its diameter was 254mm with 25.4mm concrete cover. The dimension of the footing was 1168mmx1168mmx406mm. A 445KN hydraulic actuator was mounted on the top of the column to maintain an axial load of 116KN during testing. This load represents 5% of the compression strength of the column. Eight #4 steel bars were used in the longitudinal direction and #2 (6 mm diameter) hoops were placed laterally at 102mm on center. The average compressive strength of the concrete at the time of testing was found to be 44.8MPa.

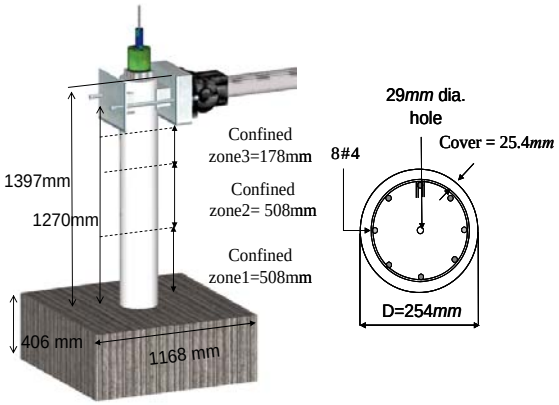

Figure 2 Schematic of the RC columns used in the tests

Figure 3 shows the test setup of the un-retrofitted column (As-built column). A 445KN hydraulic actuator was used to apply the lateral cyclic load. Four Linear Variable Differential Transformers (LVDT) were installed to capture the net displacement of the RC columns.

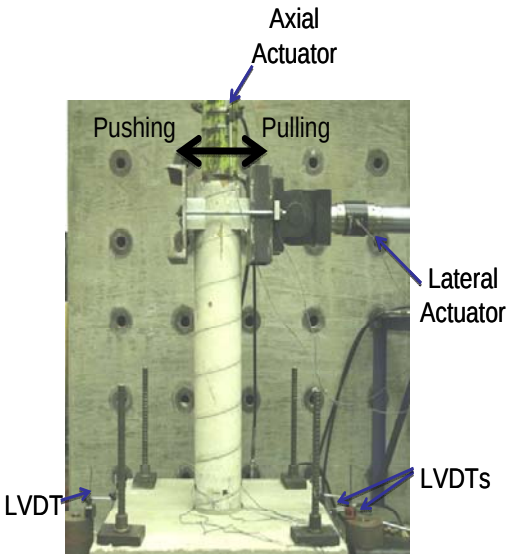

Figure 3 Test set-up of the as-built column

Each column was retrofitted using a different confining technique. One column was retrofitted entirely with GFRPs, while another column was confined with SMA spirals only at the plastic hinge zone. Table 1 shows the summary of the confinement techniques used for each column at three different zones (see Fig. 2). For the GFRP retrofitted column, GFRP sheets (0.11mm-thick) with varying number were used throughout the column height. The lower 508mm were considered to be the most critical zone (Confined zone1) and thus was wrapped with 10 layers of GFRP. In the 508mm above (Confined zone 2), the number of layers was reduced to 5, while in the top portion of the column (Confined zone 3) only 2 layers of GFRP were used. The 10, 5, and 2 layers correspond to GFRP volumetric ratio of 1.73%, 0.87% and 0.35%, respectively. For the SMA column, 2.0mm diameter SMA spirals were utilized to apply the same pressure produced by 10 layers of GFRPs at the confined zone 1. For the confined zones 2 and 3, 5 and 2 layers of GFRPs were used to wrap the column. Figure 4 shows the GFRP and SMA retrofitted columns before testing. Based on the mechanical properties of the used GFRP sheet and using an efficiency factor of 0.5 (Lorenzis and Tepfers 2003) for the GFRP jackets, the confining pressure corresponding to 10 layers of GFRP was founded to be 1.5MPa. For the SMA retrofitted column, it was found that a pitch spacing of approximately 10mm would produce the same confining pressure of 1.5MPa based on a recovery stress of 439MPa and a prestrain loss of 1.1%, which was determined in a separate study (Shin and Andrawes, 2009).

Table 1 Confinement properties of the three tested columns

	Confined Zone1	Confined Zone2	Confined Zone3
As-built Column	N/A	N/A	N/A
GFRP Column	10 layers of GFRPs	5 layers of GFRPs	2 layers of GFRPs
SMA Column	10mm pitch spacing SMA spirals	5 layers of GFRPs	2 layers of GFRPs
Confining Pressure	1.5 MPa	0.75 MPa	0.3 MPa

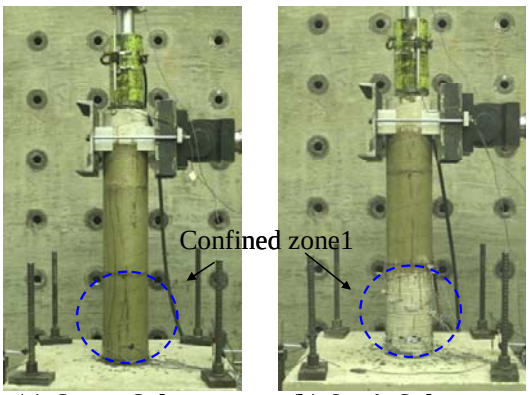

Figure 4 GFRP and SMA retrofitted columns before testing

4. LOADING PROTOCOL AND TEST RESULTS

Figure 5 shows the load protocol that was used in the test. The columns were loaded cyclically with a rate of 5.1mm/min up to 1.5% drift and 15.3mm/min thereafter. Initially a load increment of 0.5% drift was adopted until a drift of 6% was reached, after which an increment of 1% was used up until 12% drift. After reaching a drift ratio of 12%, an increment of 2% was utilized.

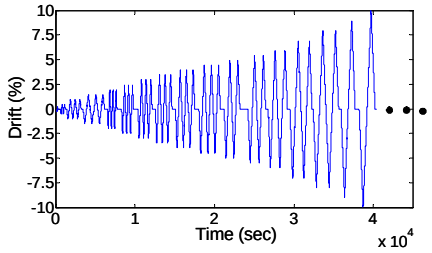

Figure 5 Loading protocol used in the study

Figure 6 shows the lateral force versus lateral drift of the three tested columns. The yielding of the longitudinal steel in the as-built column started at 1.5% drift and the column reached a maximum strength of 34.5KN at 2.8% drift. For the GFRP retrofitted column, the maximum strength recorded was 35.1KN at a drift ratio of 3.5%. After the 3.5% drift, the column started showing signs of gradual strength degradation. At 8% drift, the strength was 34.6% of the maximum strength. Finally, the maximum strength of the SMA column was found to be 36.8KN at 12% drift. After steel yielding, hardening behavior was observed, which could be attributed to the elastic behavior of the SMA spiral. The test was stopped when the load-carrying capacity lost approximately 20% of the maximum strength due to the rupture of one of the longitudinal reinforcement bars at drift of 13%. The ductility ratio (μ) was used to evaluate and compare the flexural ductility of the three columns. The ductility ratio is defined as the ratio between the drifts at the ultimate point (measured at 80% of the ultimate strength) and the yielding point. Based on this definition, the ductility ratios of the unconfined, GFRP wrapped, and SMA wrapped columns were 2.8, 3.3, and 8.0, respectively. The ductility of the SMA retrofitted column was 2.4 times that of the GFRP retrofitted column. Figure 6 clearly shows that the columns with the SMA spirals were able to sustain larger force and drift and dissipate significantly more hysteretic energy compared to that of the GFRP wrapped column. Furthermore, the GFRP retrofitted column started showing significant signs of stiffness degradation and strength deterioration at a drift ratio of 5%, while in the case of the SMA column, no signs of degradation were observed until the column reached a drift ratio of 12%.

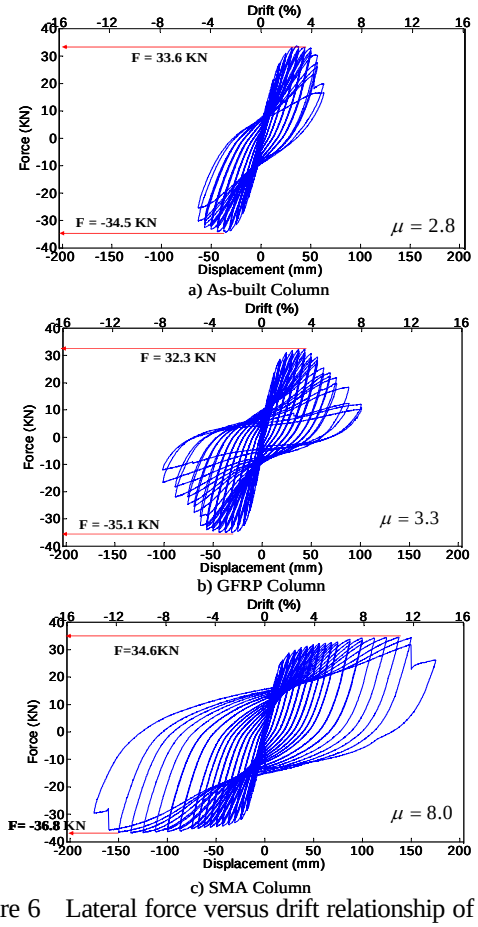

Figure 6 Lateral force versus drift relationship of the three tested columns

In order to understand the failure mechanism observed in each retrofitting technique, Figure 7 is presented. The figure shows the damage sustained by the three columns at 5% drift ratio. For the as-built column, the column was severely damaged, having completely spalled cover concrete, heavily crushed core concrete, and ruptured and buckled reinforcements (see Fig.7.a.). Also it could be seen from the figure (see Fig.7.b) that at such drift, the column wrapped with 10 layers of GFRP at the confined zone1 experienced significant damage in the form of rupture of GFRP sheets, complete spalling of the concrete cover, and significant crushing of the concrete core. However, for the case of the SMA column, only minor damage in the form of horizontal cracks in the concrete cover was observed. This limited damage could be attributed to the large active confining pressure applied by the SMA spirals, which helped in delaying the crushing of the concrete underneath.

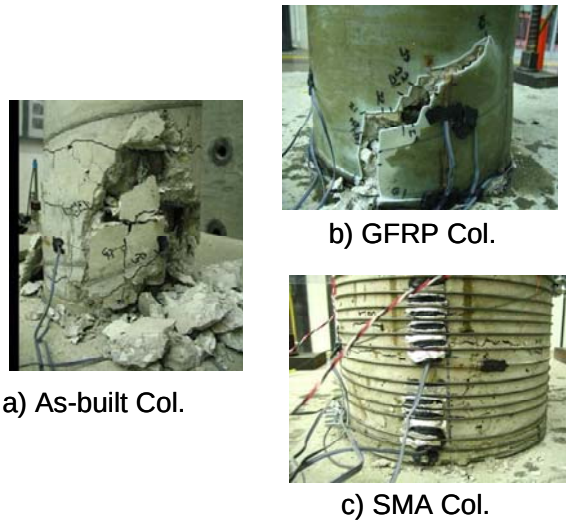

Figure 7 Damage observed in the three columns at 5% drift

5. CONCLUSIONS

This experimental study focused on investigating the application of an innovative active confinement technique for RC bridge columns using SMA spirals. Two reduced-scale RC columns were retrofitted with SMA spiral and GFRP jacket and tested under quasi-static cyclic lateral load. The behavior of the retrofitted columns was compared to that of an as-built column. The results showed that the column with the SMA spirals was able to sustain larger force and drift and dissipate more hysteretic energy compared to those of the as-built column and the GFRP retrofitted column. The maximum force reached in the cases of the as-built and GFRP columns were 34.5KN and 35.1KN, respectively, while in the case of the SMA column, the maximum lateral force was 36.8KN. The column wrapped with the SMA spiral was able to withstand a lateral drift ratio of 12% with no signs of significant damage, while the GFRP wrapped column started experiencing severe damage at a drift ratio equal to 5%. Also, using SMA spiral with 10mm pitch at the plastic hinge zone resulted in a 186% and 142% increase in the ductility ratio compared to that of the as-built and GFRP retrofitted columns, respectively, while the GFRP column showed only 18% increase in the ductility ratio compared to that of the as-built column. Moreover, the levels of damage which the tested columns sustained clearly demonstrated the superiority of the SMA spirals to the GFRP jackets in controlling the damage in the column.

References:

Andrawes, B. and Shin, M (2008), "Seismic retrofitting of bridge columns using shape memory alloys," *Proc. of SPIE 6928*, 69281K-1- 69281K-9.

Li, Y.F., Chen, S., Chang, K.C. and Liu, K.Y. (2005), "A constitutive model of concrete confined by steel reinforcements and steel jackets," *Canadian Journal of Civil Engineering,* **32**(1), 279-288.

Lorenzis LD, and Tepfers, R. (2003), "Comparative Study of Models on Confinement of Concrete Cylinders with Fiber-Reinforced Polymer Composites," *J.Composite for Construction. ASCE*, **7**(3), 219-237.

Otsuak, K. and Wayman, C.M. (2002), "Shape memory material," Cambridge University Press, New edition.

Samaan, M., Mirmiran, A., and Shahawy, M.(1998), "Model of concrete confined by fiber composites," *J. Struct. Eng.*, **124**(9), 1025-1031.

Shin, M and Andrawes, B. (2009), "Uniaxial Compression Behavior of Actively Confined Concrete Using Shape Memory Alloys," *Proceedings of the 2009 Structures Congress*, 1-8.

Richart, F.A., Brandtzaeg, A. and Brow, L.R. (1928), "A study of the failure of concrete under combined compressive stress," *Bulletin 185, University of Illinois Engineering Experiment Station*, Urbana IL.

Vokoun1, D., Kafka, V. and Hu, C.H. (2003), "Recovery stresses generated by NiTi shape memory wires under different constraint conditions," *Smart Material Structures,* **12**, 680–685.

JOINT CONFERENCE PROCEEDINGS
7th International Conference on Urban Earthquake Engineering (7CUEE) &
5th International Conference on Earthquake Engineering (5ICEE)
March 3-5, 2010, Tokyo Institute of Technology, Tokyo, Japan

EXPERIMENTAL STUDY ON STATIC AND DYNAMIC BEHAVIOR OF PP-BAND MESH RETROFITTED ADOBE MASONRY STRUCTURE

Navaratnarajah Sathiparan[1)], Paola Mayroca[2)], and Kimiro Meguro[3)]

1) Post Doctoral Fellow, Institute of Industrial Science, The University of Tokyo, Japan
2) Senior Engineer, Det Norske Veritas AS, Norway
3) Director/Professor, ICUS, Institute of Industrial Science, The University of Tokyo, Japan
sakthi@risk-mg.iis.u-tokyo.ac.jp, Paola.Mayorca@dnv.com, meguro@iis.u-tokyo.ac.jp

Abstract: This paper introduces a technically feasible and economically affordable PP-band (polypropylene bands) retrofitting for low earthquake resistant masonry structures in developing countries. Results of the material tests and shaking table tests on building models show that the PP-band retrofitting technique can enhance safety of both existing and new masonry buildings even in worst case scenario of earthquake ground motion like JMA7 seismic intensity. Therefore proposed method can be one of the optimum solutions for promoting safer building construction in developing countries and contribute earthquake disaster mitigation in future.

1. INTRODUCTION

Masonry is the most universally available and economical construction material. Individual owner used it widely around the regions and it is a highly durable form of construction because the materials used are not much affected by the elements, but the quality of the mortar and the pattern of the brick units can strongly affect the quality of the overall masonry construction. The common materials of masonry construction are burned and unburned bricks called adobe, stones and concrete blocks. Adobe masonry made of unburned bricks is the most common type of masonry. Masonry structures are generally self-made because the construction practice is simple and does not require additional energy consumption. In addition to its low cost and simple construction technology, masonry has other advantages, such as excellent thermal and acoustic properties. In spite of this, the technological development of masonry in earthquake engineering has lagged behind compared to the other structural materials like concrete and steel. Therefore, earthquake prone regions in the world have suffered a large number of casualties due to the collapse of this type of structures. This is a serious problem for the societies. Apparently, its solution is straight forward: retrofitting the existing structures. When we propose the retrofitting method in developing countries, that method should respond to the structural demand on strength and/or deformability as well as to availability of material with low cost including manufacturing and delivery, practicability of construction method and durability in each region. Considering these issues on developing appropriate seismic retrofitting techniques for masonry buildings to reduce the possible number of casualties due to future earthquakes in developing countries, a technically feasible and economically affordable PP-band (polypropylene bands; PP-band is commonly used for packing.) retrofitting technique has been developed and many different aspects have been studied by Meguro Laboratory, Institute of Industrial Science, The University of Tokyo (Mayorca P. and Meguro K., 2004).

A real scaled model test makes possible to obtain data similar to real structures. However, it requires large size testing facilities and large amount research funds, so it is difficult to execute parametric tests by using full scaled models. Therefore, in this study we performed scale model tests to understand the overall behavior of the system.

In this research, to evaluate the beneficial effects of the proposed PP-band mesh retrofitting method, diagonal shear tests and out-of-plane tests were carried out on masonry wallettes with and without retrofitting. Also, in order to understand the dynamic response of masonry houses with and without PP-band mesh retrofitting, crack patterns, failure behavior, and overall effectiveness of the retrofitting technique, shaking table tests were carried out.

2. AXIAL TENSILE TEST ON PP-BAND

Preliminary testing of the PP-band was carried out to check its deformational properties and strength. To determine the modulus of elasticity and ultimate strain, 3 bands were tested under uni-axial tensile test as shown in

Figure 1 (left). The test was carried out under displacement control method. The results are shown in Figure 1 (right). To calculate the stress in the band, its nominal cross section 15.5×0.6mm^2 was used. As the matter of fact, the band has a corrugated surface and therefore its thickness is not uniform.

All of the bands exhibited a large deformation capacity, with more than 13% axial strain. The stress-strain curve is fairly bilinear with an initial and residual modulus of elasticity of 3.2 GPa and 1.0 GPa, respectively. Given its large deformation capacity, it is expected that it will contribute to improve the structure ductility.

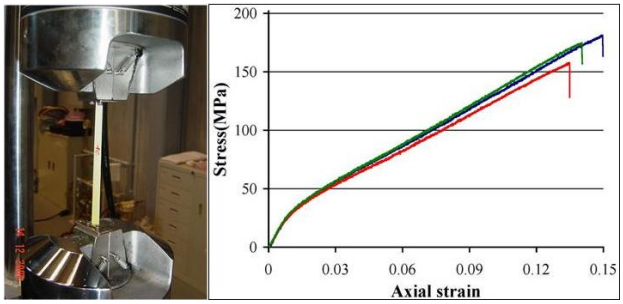

Figure 1 Tensile test setup (left) & behavior of PP-band under tension (right)

3. DIAGONAL COMPRESSION TEST

To evaluate the beneficial effects of the proposed PP-band mesh retrofit method, diagonal compression tests were carried out using masonry wallettes with and without retrofitting for unburned bricks. The wallette dimensions were 275×275×50mm^3 and consisted of 7 brick rows of 3.5 brick each. The mortar joint thickness was 5mm for both cases. A Cement/Water ratio equal to 0.33 was used.

The pitch of meshes was 40mm. Four wire connectors were used to link the meshes attached from both surfaces of the wallette. Specimens were tested 28 days after construction under displacement control. The loading rate was 0.03mm/min for the non-retrofitted case. For the retrofitted case, it was 0.03mm/min for the first 30mm vertical deflection, and then it was increased to 2mm/min for the remaining test period.

Direct compression, direct shear and bond tests were carried out to obtain masonry mechanical properties, as shown in Figure 2.

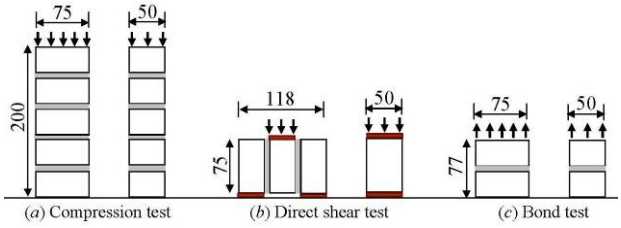

Figure 2 Direct compression, direct shear and bond test specimens (all dimensions are in mm)

Average measured mechanical properties of the masonry at the time of testing are shown below;

Compressive strength	: 4.45 MPa
Shear strength	: 0.0061 MPa
Bond strength	: 0.0056 MPa

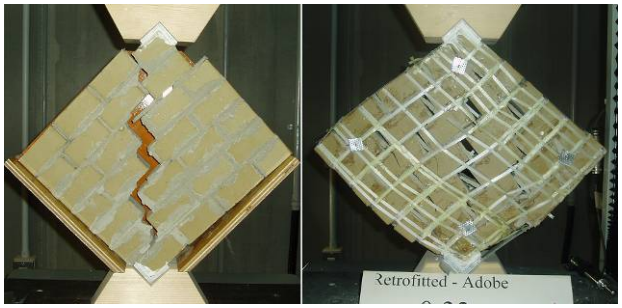

Figure 3 Failure patterns of brick masonry wallettes with and without retrofitting by PP-band mesh

Figure 3 shows the non-retrofitted and retrofitted specimens at the end of the test, which corresponded to vertical deformations equal to 1mm and 50mm, respectively. In the non-retrofitted case, the specimens split in two pieces after the first diagonal crack occurred and no residual strength was left. While in the retrofitted case, diagonal cracks appear progressively, each new crack followed by a strength drop. Although the PP-band mesh influence was not obvious before the first cracking, after it, each strength drop was quickly regained due to the PP-band mesh effect. Although at the end of the test, almost all the mortar joints were cracked, the retrofitted wallettes did not lose stability.

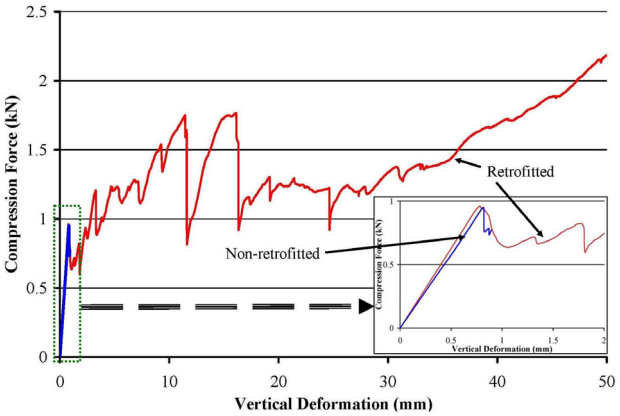

Figure 4 Force vs. vertical deformation for masonry wall specimen with and without retrofitting

Figure 4 shows the diagonal compression strength variation with vertical deformation for the non-retrofitted and retrofitted unburned brick specimens. In the non-retrofitted case, the average initial strength was 0.88kN and there was no residual strength after the first crack. While in the retrofitted case, although the initial cracking was followed by a sharp drop, at least 70% of the peak strength remained. Subsequent drops were associated with new cracks like the one observed at the deformation of 1.8mm. After this, the strength was regained by readjusting and

packing by PP-band mesh. The final strength of the specimen was equal to 2.16kN much higher than initial strength of 0.88kN.

4. OUT-OF-PLANE TEST

Out-of-plane tests were carried out in order to investigate the PP-band mesh effectiveness in walls exhibiting arching action. The nominal dimensions of these walls were 475mm×235mm; their thickness was 50mm. A total of 6 wire connectors were used to link the meshes installed on both sides of wallettes.

The Cement/Water ratio was 0.45, considering the stability of the specimens. Direct shear and bond tests were carried out to obtain masonry mechanical properties. Average measured mechanical properties of the masonry at the time of testing are shown below;

Shear strength : 0.0072 MPa

Bond strength : 0.0080 MPa

Specimens were tested 28 days after construction under displacement control. The wallettes were simply supported with a 440mm span. Steel rods were used to support the wallettes at the two ends. The masonry wallettes were tested under a line load which was applied by a 20mm diameter steel rod at the wallette mid-span. The loading rate was 0.05mm/min for the non-retrofitted case. For the retrofitted case, it was 0.05mm/min for the first 30mm vertical deflection, and then it was increased to 2mm/min for the remaining test period. The retrofitted wallettes were applied up to 70mm vertical displacement. The test setup is shown in Figure 5.

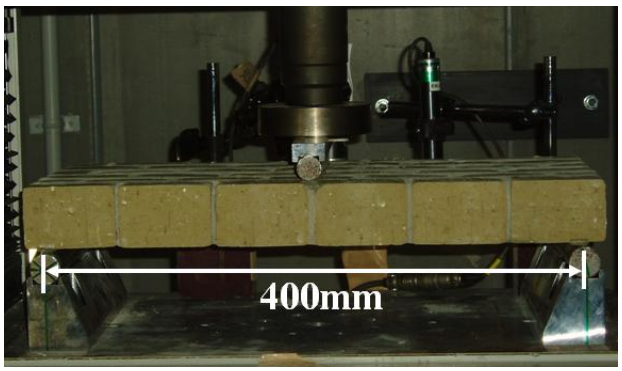

Figure 5 Out-of-plane test setup

Figure 6 shows the non-retrofitted and retrofitted masonry wallettes at the end of the test, which corresponded to a mid-span net deformation equal to 1.2mm and 70.0mm, respectively. In the non-retrofitted case, the specimens split into two pieces just after the first crack occurred at mid-span, and no residual strength was left. In the retrofitted case, on the other hand, although PP-band mesh influence was not observed before the first cracking, after it, strength was regained progressively due to the PP-band mesh effect.

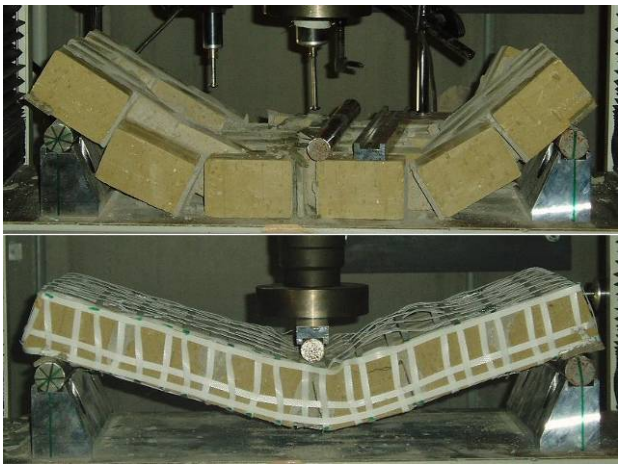

Figure 6 Failure patterns of brick masonry wallettes with and without retrofitting by PP-band mesh

Figure 7 shows the out-of-plane load variation in terms of mid-span net vertical deformation for the non-retrofitted and retrofitted wallettes. In the non-retrofitted case, the initial strength was 0.08 kN and there was some residual strength remaining for further small amount of deformation after the first crack. This behavior was observed due to interlocking between bricks and also the application of load under displacement control method.

In the retrofitted case, although the initial cracking was followed by a small drop, but strength remained closer to peak strength. After this, the strength was regained by readjusting and packing by PP-band mesh. The final strength of the specimen was equal to 0.54kN much higher than the initial strength of 0.08 kN.

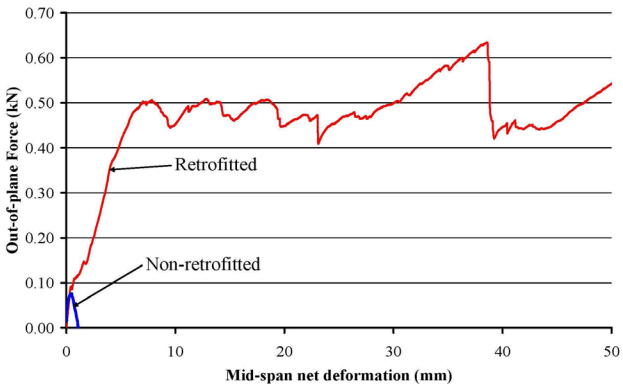

Figure 7 Out-of-plane load variation in terms of net vertical deformation

5. SHAKING TABLE TEST

By shaking table test, we tested the model's dynamic characteristics and earthquake responses under different working stages; observe and record failure modes and failure characteristic under all intensities; evaluate seismic performance of the scale model building.

5.1 Design and Constructing the Model

Considering the shaking table size and allowable loading condition, the model scaling factor adopted was 1:4 as shown in Figure 8. Two models were used for shaking table test. The dimensions of both building models were 933mmx933mmx720mm with 50mm thick walls. The sizes of door and window in opposite walls were 243mmx485mm and 325mmx245mm, respectively. Both models were represented one-storey box-like building with timber roof; one model was non-retrofitted and other model was retrofitted with PP-band mesh after construction.

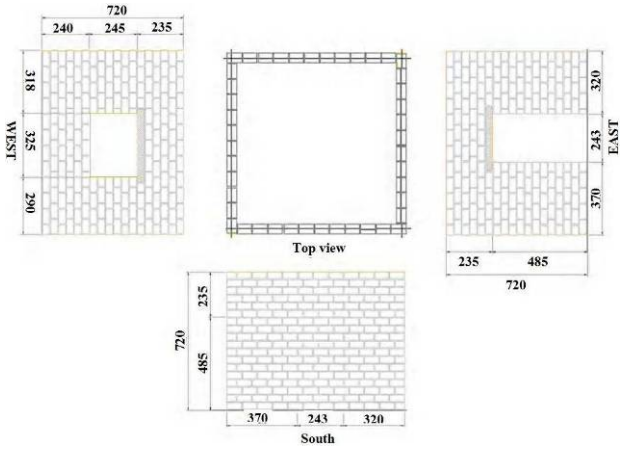

Figure 8 Model dimension (in mm)

Specimens are consisted of 18 rows of 44 bricks in each layer except openings. It took two days for construction of one specimen. The first 11 rows were constructed in first day and remaining rows were done in following day. The geometry, construction materials and mixture proportion, construction process and technique and other conditions that may affect the strength of the building models were kept identical for better comparison. The cross-section of the band used was 6mm×0.32mm and the pitch of the mesh was 40mm.

The mortar with the mixture ratio of cement, lime and sand=1:2.8:8.5 and Cement/Water ratio=0.33% was used for adobe unburned brick masonry to simulate adobe masonry buildings in developing countries. Average measured mechanical properties of the masonry at the time of testing are listed in Table 1.

Table 1 Mechanical property of masonry specimens

Strength	Non-retrofitted model (in MPa)	Retrofitted Model (in MPa)
Compression	4.28	4.36
Shear	0.0057	0.0068
Bond	0.0046	0.0046
Diagonal shear	0.041	0.045

The retrofitted procedure explained below is shown in photos (Figure 9) taken during the preparation of experimental program.

- PP-bands are arranged in meshes and connected at their intersection points using a portable plastic welder.
- Structure walls are cleaned and any loose pieces of brick should be removed.
- Straw, which placed in holes are removed. (in this experiment, during construction of model house, we put the straw in the place at approximately 200mm pitch where we required holes.) In case of existing structures, holes can be prepared by drilling through the wall.

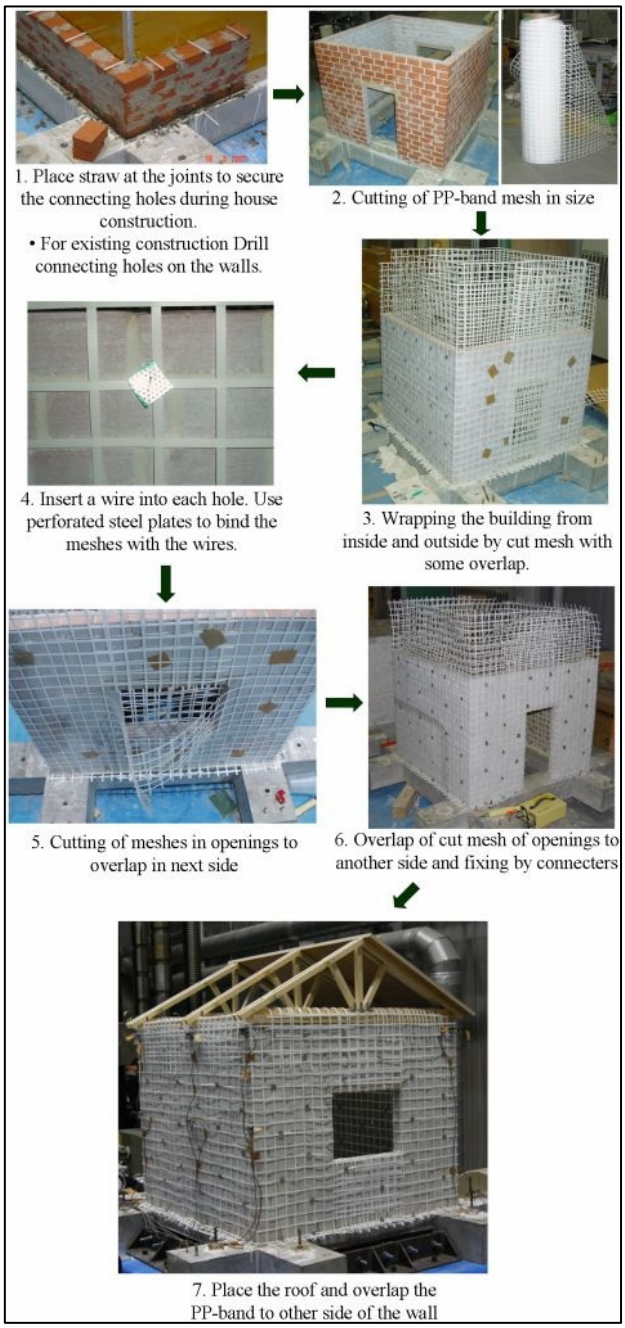

Figure 9 Retrofitting procedure

- Walls are wrapped by meshes around the corners and wall edges. The overlapping length should be long enough to accommodate sufficient wire connectors as these are the only system used to connect meshes to the structure.
- Wires are passed through wall holes and used to connect the meshes on both wall sides. In order to

prevent the wires from cutting the PP-band meshes, a plastic piece or any other stiff element is placed between the band and the wire. It is desirable to have connectors as close as possible to the wall intersections and corners.

- The top/bottom mesh edges are connected with steel wires. The bottom edge should be connected to the structure foundation as much as possible.
- Fixed connectors around the openings after the mesh was cut and overlapped on the other side.

5.2 Input Motion

Simple easy-to-use sinusoidal motions of frequencies ranging from 2Hz to 35 Hz and amplitudes ranging from 0.05g to 1.4g were applied to the specimens to obtain the dynamic response of both retrofitted and non-retrofitted structures. This simple input motion was applied because of its adequacy for later use in the numerical modeling. Figure 10 shows the typical shape of the applied sinusoidal wave input motion.

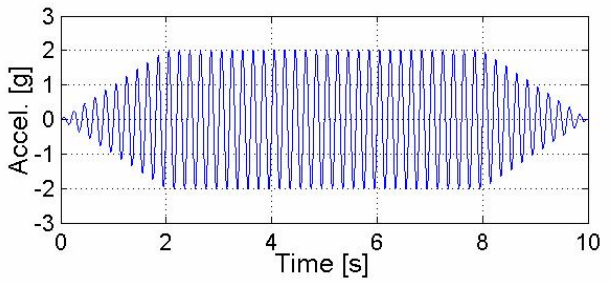

Figure 10 Typical Shape of Input Sinusoidal Motion

Loading was started with a sweep motion of amplitude 0.05g with all frequencies from 2Hz to 35Hz for identifying the dynamic properties of the models. The numbers in Table 2 indicate the run numbers. General trend of loading was from high frequency to low frequency and from lower amplitude to higher amplitude. Higher frequencies motions were skipped towards the end of the runs.

Table 2 Loading Sequence

Amplitude	Frequency							
	2	5	10	15	20	25	30	35
1.4g		50						
1.2g		49						
1.0g		48						
0.8g	53	47	43	40	37	34	31	28
0.6g	52	45	42	39	36	33	30	27
0.4g	51	44	41	38	35	32	29	26
0.2g	46	25	24	23	22	21	20	19
0.1g	18	17	16	15	14	13	12	11
0.05g	10	09	08	07	06	05	04	03
Sweep	01,02							

To assess the global and local behavior, specimens were instrumented to measure accelerations and displacements. During the tests, twenty four accelerometers, eighteen on house and six on roof were installed at the location shown in Figure 11. The number of accelerometers was 16, 4 and 4 in the exciting, transverse and vertical direction respectively.

Five lasers, in N-S direction were used to measure displacements. The locations of laser measuring instruments are shown in Figure 11. L1, L2, L3 aimed at obtaining the wall deformation at top level in the direction of shaking. Laser L4 recorded the facade wall deformation at centre. Laser L5 recorded the deformation at base. The measured data were recorded continuously throughout the tests. The sampling rate was 1/500 sec in the all runs.

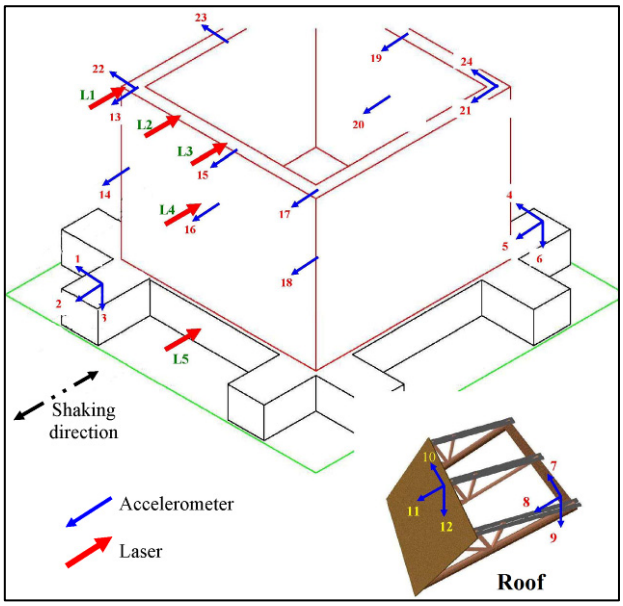

Figure 11 Location of accelerometers and lasers

5.3 Crack Propagation

In both specimens, due to shrinkage, some minor cracks were observed before the test. These cracks mainly appear closer to opening in horizontal direction. Up to the Run 21, no major crack was observed in both models.

5.3.1 Non-retrofitted model

Observed responses during test runs for non-retrofitted model were given as follows;

Run 22 - Cracks were observed from corners of the window opening and they propagated up to top and bottom layer of the wall. Still there were no major cracks observed in walls, which are in the direction of Shaking (Figure 12).

Run 28 - Cracks were observed at one of the top corners of the door opening and they propagated up to top layer of the wall.

Run 34 - Cracks propagated from openings to corners were more widen up. Cracks at bottom of the east wall and top of the north and south walls were observed.

Run 37 - Cracks appeared at the top of the north and south walls and propagated through out the whole wall. More cracks were observed in the part above the openings.

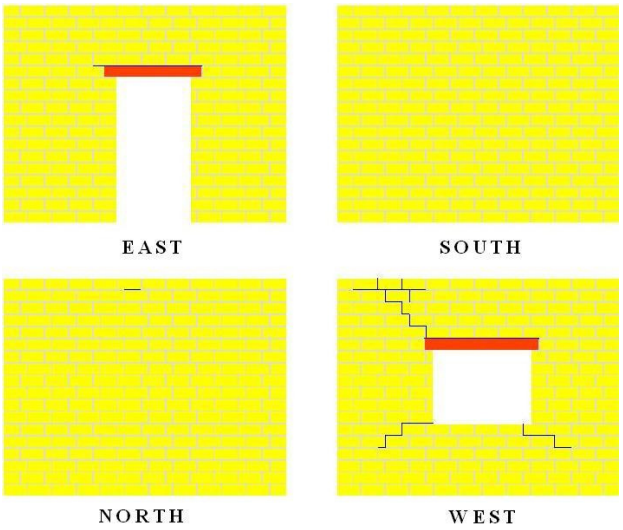

Figure 12 Crack patterns observed on non-retrofitted model after Run 22

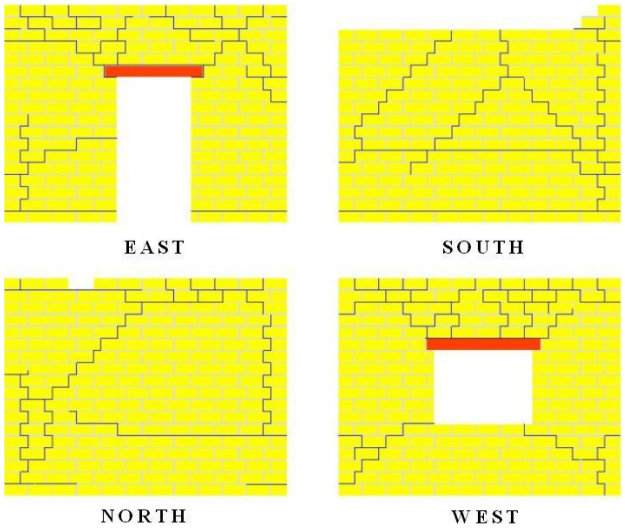

Figure 13 Crack patterns observed on for non-retrofitted model after Run 44


Figure 14 Non-retrofitted model after Run 45

Run 45 - All top part of the wall with opening was totally separated from the specimen and fallen from specimen. The roof was just supported by two walls, which were in the direction of shaking. Therefore, due to walls subjected to out-of-plane load; they were bursts outwards in shaking direction. This finally led to the structure collapse.

5.3.2 Retrofitted model

Observed responses during test runs for retrofitted model were given as follows;

Run 22 - Cracks were observed from top corner of the door opening and they propagated up to top layer of the wall. Additional cracks propagated horizontally from top and bottom of the door opening (Figure 15).

Run 31 - Cracks were observed from one side top corner of the window opening and they propagated up to top layer of the wall.

Run 34 - Cracks were observed from all corners of the window opening and they propagated to corners of the wall.

Run 40 - A long horizontal crack at the top part and couple of vertical cracks were observed in south wall. Cracks appeared in the bottom layer of the east wall propagated through to whole wall.

Run 43 - much more cracks were observed in the above part of the openings. Even though cracks propagated more wider at this level compared with non-retrofitted model, there was no brick fallen down from the wall observed.

Run 49 - Although almost all the mortar joints were cracked at the end of this run, the specimen did not lose stability.

Run 53 - Even some local failure was observed closer to door opening, the specimen did not lose stability. This input motion was 1.3 times larger acceleration and 2.7 times larger displacement than the input motion was applied in the Run 45. Another important point to mention was that the retrofitted model could sustain 8 more runs with higher input energy before this run.

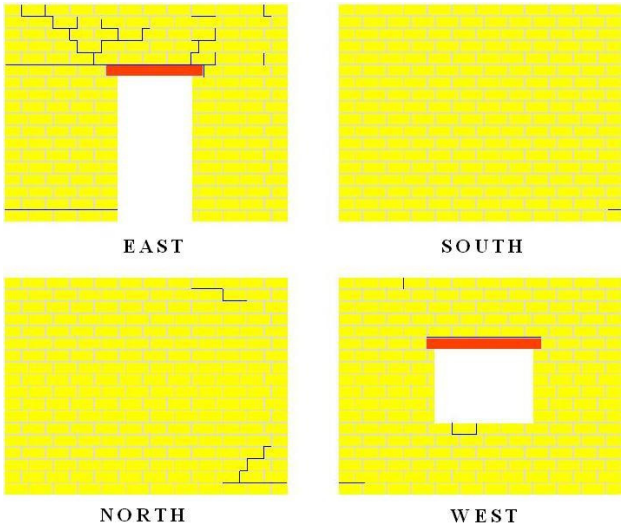

Figure 15 Crack patterns observed on retrofitted model after Run 22

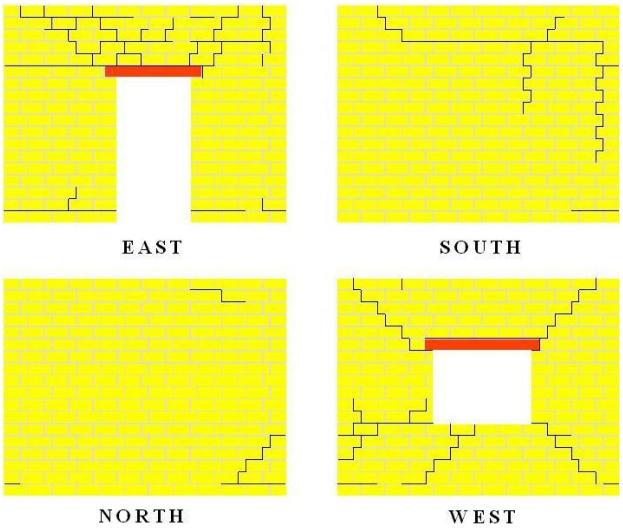

Figure 16 Crack patterns observed on for retrofitted model after Run 40

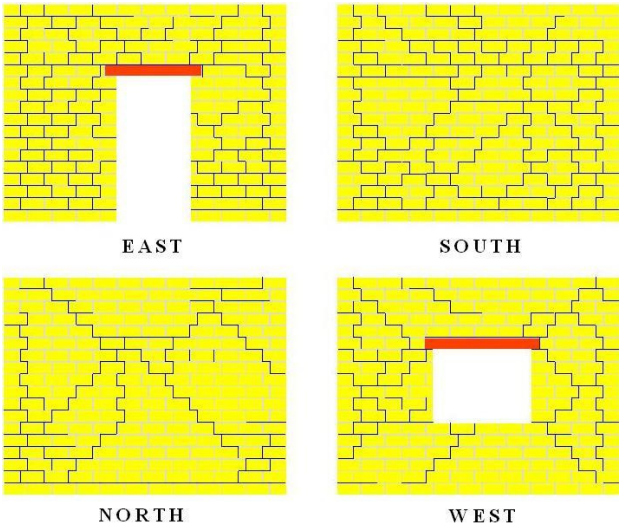

Figure 17 Crack patterns observed on for retrofitted model after Run 49

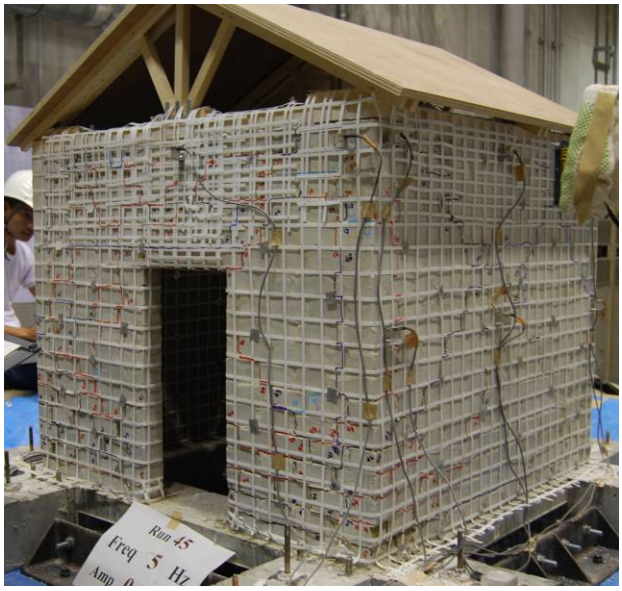

Figure 18 Retrofitted model after Run 45

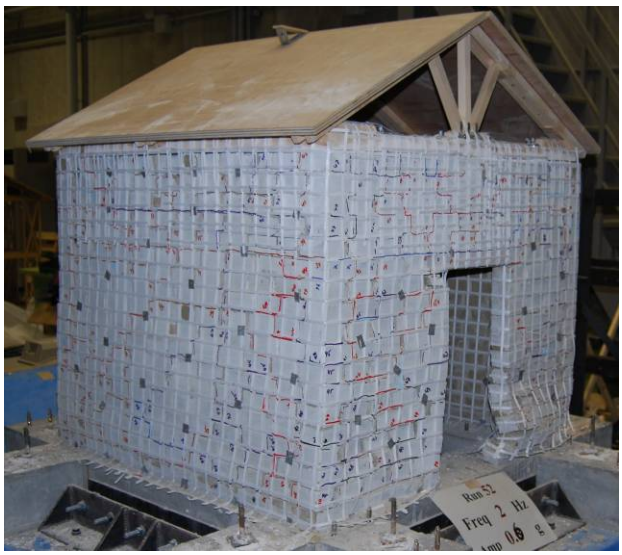

Figure 19 Retrofitted model after Run 53

At the final stage of the test, Run 53, with 50.6 mm base displacement, 8 times larger input displacement and 2.7 times larger input velocity than the Run 45 was applied. At this stage, most of the brick joints were cracked and the building had substantial permanent deformations. However, building did not loose the overall integrity as well as stability and collapse was prevented in such a high intensity of shaking. Thus, we could say that, PP-band retrofitting technique could maintain the integrity of the structural elements. Further, the retrofitted model showed the better energy dissipation mechanism as many new cracks were propagated without loosing the overall integrity and stability of the structure.

5.4 Analysis on Test Results

The performances of the models were assessed based on the damage level of the buildings at different levels of shaking.

Table 3 Damage categories

Category	Damage extension
D0: No damage	No damage to structure
D1: Light structural damage	Hair line cracks in very few walls. The structural resistance capacity did not decrease noticeably.
D2: Moderate structural damage	Small cracks were observed on masonry walls. The structure resistance capacity decreased partially.
D3: Heavy structural damage	Large and deep cracks were observed on masonry walls. Some bricks are fallen down. Failure in connection between two walls.
D4: Partially collapse	Serious failure and Partial structural failure were observed on walls and roofs, respectively. The building was in dangerous condition
D5: Collapse	Structure is totally or partially collapsed.

Performances were evaluated in reference to five levels of performances: light structural damage, moderate structural damage, heavy structural damage, partially collapse, and collapse.

5.4.1 Based on JMA Scale

The Japan Meteorological Agency seismic intensity scale (JMA) is a measure used in Japan to indicate the strength of earthquake ground motions.

Figure 20 shows the performances of model houses with different JMA intensities. Collapse of the non-retrofitted building was observed at the 45th run at intensity JMA 5-. The retrofitted building performed moderate structural damage level at the 45th run at which the non-retrofitted building was collapsed. Moreover, moderate structural damage level of performance was maintained until the 50th run. It should be noted again that this model survived 8 more shakings in which many runs were with higher intensities than JMA 5- at which the non-retrofitted building was totally collapsed before reaching to the final stage at the 53rd run.

The JMA scale was colored according to the following convention:

Index	JMA ~4	JMA 5-	JMA 5+	JMA 6-	JMA 6+	JMA 7

Amplitude	Frequency							
	2Hz	5Hz	10Hz	15Hz	20Hz	25Hz	30Hz	35Hz
1.4g								
1.2g								
1.0g								
0.8g			D3	D2	D2	D2	D2	D2
0.6g		D4	D3	D2	D2	D2	D2	D1
0.4g		D4	D3	D2	D2	D2	D2	D1
0.2g		D1	D1	D1	D1	D1	D0	D0
0.1g	D0	D0	D0	D0	D0	D0	D0	D0
0.05g	D0	D0	D0	D0	D0	D0	D0	D0

(Non-retrofitted Specimen)

Amplitude	Frequency							
	2Hz	5Hz	10Hz	15Hz	20Hz	25Hz	30Hz	35Hz
1.4g		D2						
1.2g		D2						
1.0g		D2						
0.8g	D4	D2	D2	D2	D2	D2	D1	D1
0.6g	D4	D2	D2	D2	D2	D2	D1	D1
0.4g	D3	D2	D2	D2	D2	D2	D1	D1
0.2g	D2	D1	D1	D1	D1	D1	D1	D1
0.1g	D1	D1	D1	D1	D0	D0	D0	D0
0.05g	D0	D0	D0	D0	D0	D0	D0	D0

(Retrofitted Specimen)

Figure 20 Performance evaluation based on input motion intensity by JMA scale

From these results it can be concluded that a structure retrofitted with PP-band meshes would be able to resist against strong aftershocks. Moreover, it proves that even though houses retrofitted with PP-band were cracked due to strong earthquake, it could be repaired and be expected to withstand subsequent strong shakes.

5.4.2 Based on Arias Intensity Scale

The Arias intensity was initially defined by Arias (Arias A., 1970) as

$$I_a = \frac{\pi}{2g}\int_0^t a^2(t)dt \qquad (1)$$

and was called scalar intensity. It is directly quantifiable through the acceleration record a*(t)*, integrating it over the total duration of the shaking. The arias intensity is claimed to be measure of the total seismic energy absorbed by the ground.

Figure 21 shows the performance levels of each specimen against dynamic motion based on arias intensity scale. Form the results, retrofitted model damage level performance was at least 3 times better than that of non-retrofitted model

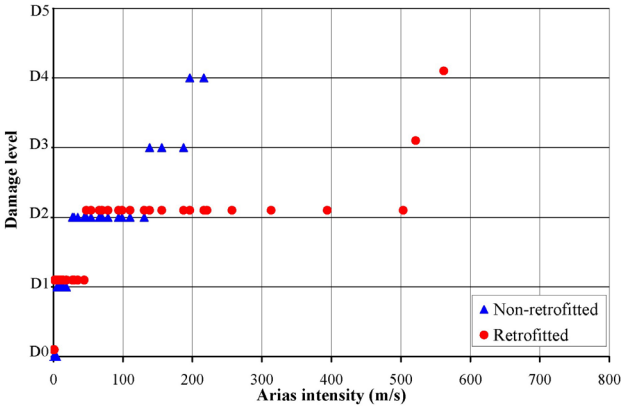

Figure 21 Performance evaluation based on arias intensity scale

6. CONCLUSION

This paper discusses the results of a series of diagonal compression tests, out-of-plane tests and shaking table tests that were carried out using non-retrofitted and retrofitted wallettes by PP-band meshes.

The diagonal compression tests showed that:

- In the retrofitted case, larger residual strength after the formation of the first diagonal shear cracks was observed. Furthermore, as deformation increased, the wallette achieved strength higher than the initial cracking strength.
- The retrofitted wallettes achieved 2.5 times larger strengths and 50 times larger deformations than the non-retrofitted wallettes did.

The out-of-plane tests showed that;

- In out-of-plane tests, the mesh effect was not observed before the wall cracked. After cracking, the mesh presence positively influenced the wallette behavior.
- The retrofitted wallettes achieved 7 times larger strengths and 60 times larger deformations than the non-retrofitted wallettes did.

The shaking table tests showed that;

- The effect of the PP-band meshes was not observed before the appearance of initial cracking. However, after cracking, they effectively helped to increase the ductility of walls parallel to the shake direction, i.e. subjected to in-plane loading, to prevent the toppling of the walls perpendicular to the shake, i.e. subjected to out-of-plane loading, and to keep the integrity of the structure by limiting corner damage. With this mechanism, PP-band mesh could avoid the typical failure modes observed in masonry structures.
- A scaled dwelling model with PP-band mesh retrofitting was able to withstand larger and more repeatable shaking than that without PP band retrofitting.
- Considering the easiness of installation and inexpensiveness of PP-band mesh, it can be considered as one of the best solutions to overcome the quality deficit of existing building stock in developing countries and therefore reduce the number of human fatalities in future seismic events.

From the all experimental results, it was found that PP-band retrofitting technique proposed can enhance safety of both existing and new masonry buildings even in the worst case scenario of earthquake ground motion like JMA 7 intensity. Therefore proposed method can be one of the optimum solutions for promoting safer building construction in developing countries and can contribute earthquake disaster in future.

References:

Mayorca P., and Meguro K., (2004). "Proposal of an efficient technique for retrofitting unreinforced masonry dwellings", *13th Conference on Earthquake Engineering,* Vancouver, Canada, Paper No.2431.

Sathiparan, N., (2008). "Experimental Study on PP-Band Mesh Seismic Retrofitting for Low Earthquake Resistant Masonry Houses", Ph.D. Dissertation, The University of Tokyo, Japan.

Sathiparan N., Mayorca P., Nesheli K., Ramesh G., and Meguro K. (2005). "In-plane and out-of-plane behavior of pp-band retrofitted masonry wallettes", *Proc. of the 4th International Symposium on New technologies for urban Safety of Mega Cities in Asia*, 18-19 Oct 2005, Nanyang Technological University, Singapore, Page 231-240.

ASTM, E72, (1997). "Standard Test Methods of Conducting Strength Tests of Panels for Building Construction", *American Society for Testing and Materials*, Philadelphia, Pa.

Roko Zarnic, Samo Gostic, Adam J. Crewe and Colin A.Taylorm, (2001). "Shaking Table Tests of 1:4 Reduced Scale Models of Masonry Infilled Reinforced Concrete Frame Buildings", *Earthquake Engineering and Structural Dynamics*, Vol.30, 819-834.

Alidad Hahemi and Khalid M.Mosalam, (2006). "Shake-table Experiment on Reinforced Concrete Structure Containing Masonry Infill Wall", *Earthquake Engineering and Structural Dynamics*. Vol 35, Page 1827-1852.

Arias, A. (1970). "A Measure of Earthquake Intensity", R.J. Hansen, ed. *Seismic Design for Nuclear Power Plants, MIT Press*, Cambridge, Massachusetts, Page 438-483.

JOINT CONFERENCE PROCEEDINGS
7th International Conference on Urban Earthquake Engineering (7CUEE) &
5th International Conference on Earthquake Engineering (5ICEE)
March 3-5, 2010, Tokyo Institute of Technology, Tokyo, Japan

EFFECT OF RUBBER BEARING'S MODELING ON SEISMIC RESPONSE OF BASE ISOLATED HIGHWAY BRIDGE

M.K. Razzaq[1], A.R. Bhuiyan[2], Y. Okui[3], H. Mitamura[4], and T. Imai[5]

1) Graduate Student, Department of Environmental Science and Civil Engineering, Saitama University, Japan
2) Assistant Professor, Department of Civil Engineering, Chittagong University of Engineering and Technology, Bangladesh
3) Professor, Department of Environmental Science and Civil Engineering, Saitama University, Japan
4) Senior Researcher, Civil Engineering Research Institute for Cold Region, PWRI, Sapporo, Japan
5) Chairman Technical Committee, Rubber Bearing Association, Tokyo, Japan
muhdkashifrazzaq@yahoo.com, arbhuiyan@yahoo.com, okui@mail.saitama-u.ac.jp, mitamura@ceri.go.jp, imaigmgb.gr.jp

Abstract: The effects of modeling of isolation bearings on the seismic response of bridges are investigated. To this end, a nonlinear dynamic analysis of a viaduct with natural rubber bearings (RBs), lead rubber bearings (LRBs) and high damping rubber bearings (HDRBs) is carried out. Three analytical models of isolation bearings are considered for comparison: the equivalent linear model, the conventional bilinear model, and the rate-dependent rheology model developed by the authors. The proposed rheology model is able to reproduce the nonlinear viscosity and the elasto-plastic behavior along with strain hardening of bearings. A numerical algorithm for solving the first order governing differential equation of the rheology model has been developed to implement the proposed model into a nonlinear dynamic analysis software. Two level-2 earthquake ground motions, applied in the longitudinal direction, are used in the analysis. The dynamic responses of the isolation bearings and the rotation responses of the plastic hinge in concrete piers are compared for different modeling. Finally, a comparative assessment of the bridge responses shows the sensitivity of modeling of isolation bearings in evaluating seismic responses of the bridge.

1. INTRODUCTION

Prior to the Hyogo-ken nanbu (H-k-n) earthquake in 1995, highway bridges were regarded as safe against even the extreme earthquake like the Great Kanto earthquake in 1923 (Kawashima et al. 1997 and Kawashima 2000). However, since the severe damage due to H-k-n earthquake, laminated rubber bearings have been used widely as an isolation system of important structures for the few decades. The base-isolation system with laminated rubber bearings is considered to be an efficient technology for providing mitigation for seismic damage for structures and equipments and has proven to be reliable and cost effective (Kelly 1997).

Three types of laminated rubber bearings are available for the base isolation devices: natural rubber bearings (RBs), lead rubber bearings (LRBs) and high damping rubber bearings (HDRBs). Of these, HDRBs exhibit nonlinear rate-dependent hysteresis (Bhuiyan et al. 2009a and Hwang et al. 2002). On the basis of the experimental observations of HDRBs, an elasto-viscoplastic rheology model has been developed by Bhuiyan et al. (2009a) considering the nonlinear rate-dependence and elasto-plastic behavior. This model is capable of reproducing the above-mentioned mechanical behavior of HDRBs. On the other hand, RBs and LRBs exhibit nonlinear elasto-plastic behavior along with comparatively weak rate-dependence (Robinson 1982 and Bhuiyan et al. 2009b). Robinson (1982) has proposed a bilinear model for representing the hysteresis behavior of LRBs, which is conceptually the same as that recommended for isolation bearings in specification of highway bridges (JRA 1996 and 2002). In the recent years, some other authors have also proposed some analytical models for RBs and LRBs; however, these models cannot reproduce the rate-dependent property (Abe et al. 2004, Kikuchi and Aiken 1997). To improve the performance of the existing models for LRBs and RBs, a rheology model based on experimental investigations has been proposed (Bhuiyan et al. 2009b) by simplifying the earlier rheology model for HDRBs (Bhuiyan et al. 2009a).

The objective of the current study is to evaluate effects of modeling of isolation bearings on the seismic responses by conducting the nonlinear dynamic analysis of a multi-span continuous highway bridge. Three types of isolation bearings, i.e. RB, LRB and HDRB, are considered in this study. The isolation bearings are modeled by the equivalent linear, the bilinear models specified by JRA (1996 and 2002) and the rheology model proposed by the authors (Bhuiyan et al. 2009a and b) for comparison.

2. MODELING OF BRIDGE

2.1 Physical Model

Figure 1 shows the physical model of a five-span continuous steel-concrete composite girder bridge isolated by laminated rubber bearings. As the laminated rubber bearings, three types of isolation bearings are considered: high damping rubber bearings (HDRBs), lead rubber bearings (LRBs) and natural rubber bearings (RBs). The isolation bearings are installed between the steel girders and the tops of the piers.

The dimensions of this model bridge including rubber bearings are determined by designing in accordance with Japanese Specifications of Highway Bridges (JRA 2002). The superstructure consists of 260 mm thick reinforced concrete slab, covered by 80 mm of asphalt pavement supported on two steel I girders. The depth of the steel girder is 2200 mm. The substructures consist of RC piers and footings supported on pile foundations. The dimensions and material properties of the bridge deck, piers with footings are given in Table 1 and those of the isolation bearings are presented in Table 2.

2.2 Analytical Model

The analytical model of the bridge system is shown in Figure 2. The entire structural system is approximated as 2-D frame. The superstructure is idealized as an elastic beam. The plastic behavior of piers is expected to concentrate at the bottom of piers, where plastic hinges are occurred. The plastic hinges of piers are modeled by the tri-linear Takeda model (Takeda et al. 1970). The superstructure, the pier cap, the pier body except the plastic zone, and the footing are modeled using the simple elastic beam elements. The foundation and soil-structure interaction are idealized by a set of linear translational and rotational springs. The superstructure and substructure of the bridge are modeled as a lumped mass system divided into a number of small discrete segments. Each adjacent segment is connected by a node and at each node two degrees of freedom are considered: horizontal translation and rotation. The vertical displacement of the piers is restrained as no significant axial shortening is expected.

In order to describe the mechanical behavior of isolation bearing, two types of analytical models of the bearings are used in the study: the rate dependent rheology model as developed by the authors (Bhuiyan et al. 2009a; 2009b) and the design models including the bilinear model and the equivalent linear model specified in JRA (2002). These two models are briefly discussed in the following sub-sections.

2.2.1 Rheology Model

The rheology model (Bhuiyan et al. 2009a; 2009b) employed in the subsequent numerical analysis is illustrated in Figure 3, where τ and γ are the average shear stress and shear strain of rubber layers, respectively. In this model, the total shear stress is decomposed into three contributions associated with a nonlinear elastic stress, an elasto-plastic stress and finally a viscosity induced overstress. The mathematical description of the model is briefly stated in Eq. (1).

Table 1 Dimensions and material properties of the piers

Properties	Specifications	
	Pier S1 & S2	Pier P1 to P4
Cross-section of the pier cap (mm^2) B1 x W1	3300x9600	2000x9600
Cross-section of the pier body (mm^2) B2 x W2	3300x6000	2000x6000
Cross-section of the footing (mm^2) B3 x W3	5000x8000	5000x8000
Number of piles/pier	4	
Young's modulus of concrete (MPa)	25000	
Young's modulus of steel (MPa)	200000	

Table 2 Properties of the isolation bearings

Dimension	Specifications		
	RB	LRB	HDRB
Length (mm)	650.0	650.0	650.0
Width (mm)	650.0	650.0	650.0
Total thickness of rubber layers (mm)	81.0	81.0	81.0
Material type	G12	G12	G12

(a) *Rheology model for HDRBs*

$$\tau = \tau_{ep}(\gamma_a) + \tau_{ee}(\gamma) + \tau_{oe}(\gamma_c) \tag{1a}$$

$$\tau_{ep} = C_1\gamma_a \quad \text{with} \quad \begin{cases} \dot{\gamma}_s \neq 0 & \text{for} \quad |\tau_{ep}| = \tau_{cr} \\ \dot{\gamma}_s = 0 & \text{for} \quad |\tau_{ep}| < \tau_{cr} \end{cases} \tag{1b}$$

$$\tau_{ee} = C_2\gamma + C_3|\gamma|^m \operatorname{sgn}(\gamma) \tag{1c}$$

$$\tau_{oe} = C_4\gamma_c \quad \text{with} \quad \tau_{oe} = A\left|\frac{\dot{\gamma}_d}{\dot{\gamma}_o}\right|^n \operatorname{sgn}(\dot{\gamma}_d) \tag{1d}$$

$$A = \frac{1}{2}\left(A_l \exp(q|\gamma|) + A_u\right) + \frac{1}{2}\left(A_l \exp(q|\gamma|) - A_u\right)\tanh(\xi\tau_{oe}\gamma_d) \tag{1e}$$

where C_i (i = 1 to 4), τ_{cr}, m, A_l, A_u, q, n, and ξ are parameters of the model to be determined from experimental data, and $\dot{\gamma}_o = 1/\sec$ (Bhuiyan 2009a).

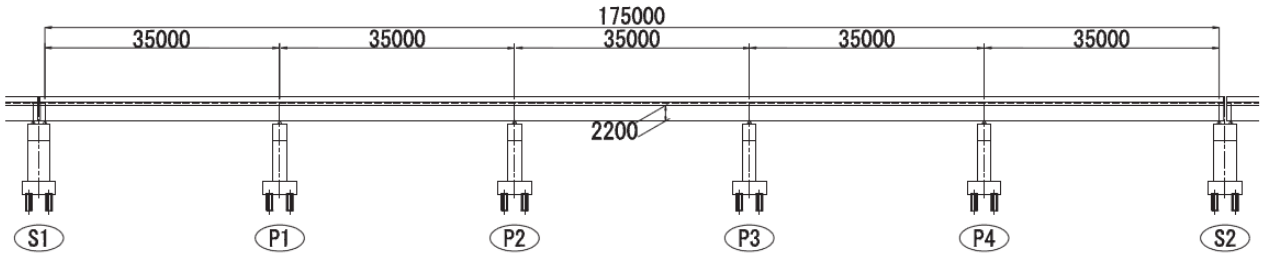

(a)

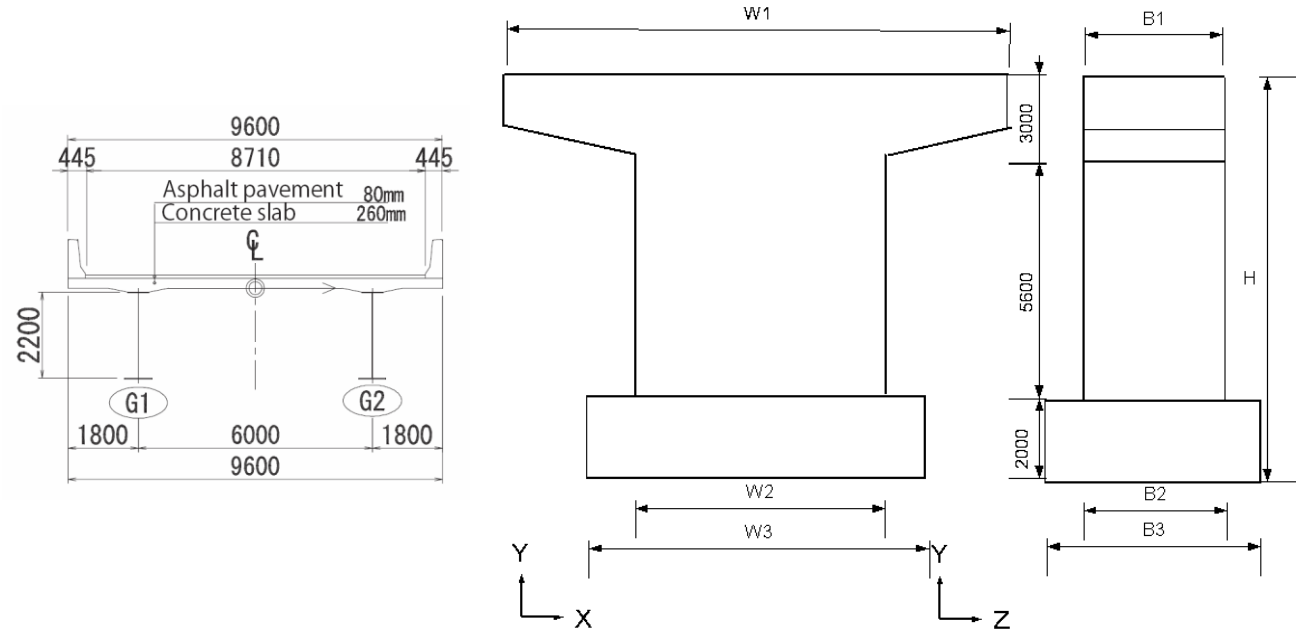

(b) (c) (d)

Figure 1 Description of the bridge (a) Longitudinal view (b) Transverse section of the superstructure (c) Transverse section of a typical pier (d) Longitudinal section of a typical pier; all dimensions are in mm.

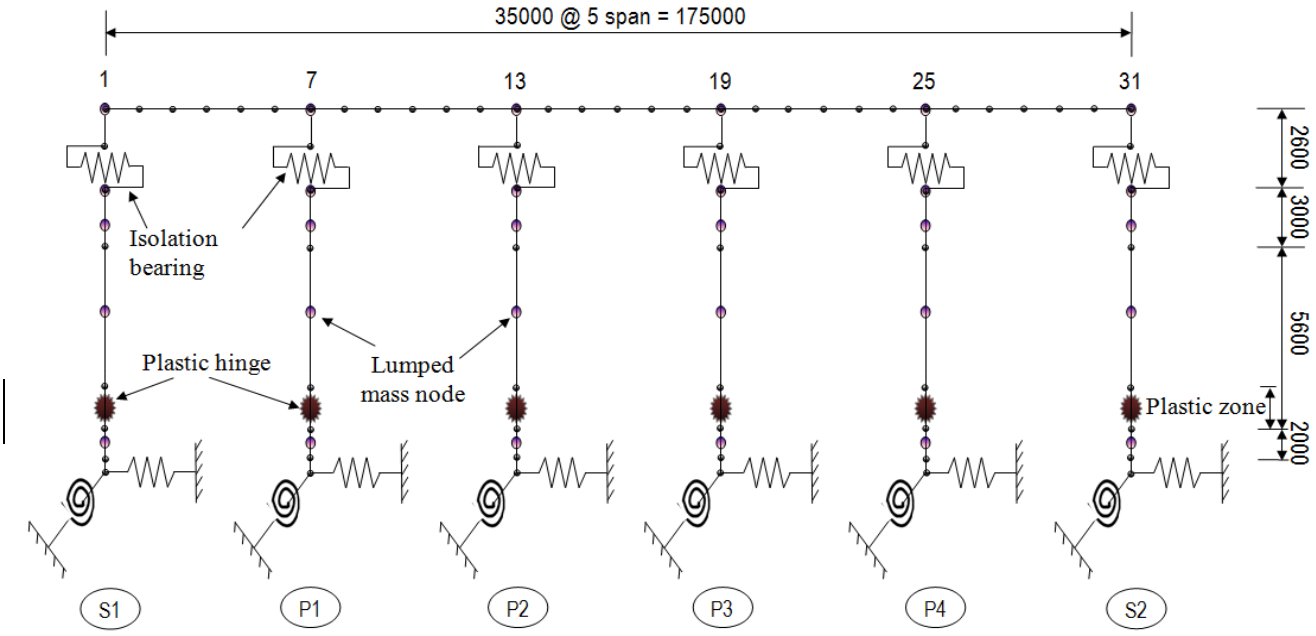

Figure 2 Analytical model of a complete bridge.

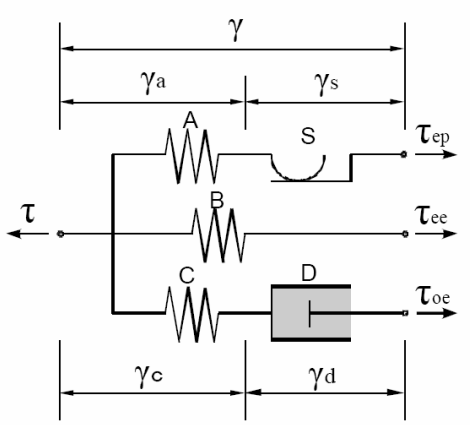

Figure 3 Rheology model structure of the isolation bearing

(b) Rheology model for LRBs and RBs

For the rheology model LRBs and RBs, the parameter *A* in Eq. (1d) is assumed to be constant on the basis of experimental results (Bhuiyan et al. 2009b). The other equations are the same as those for HDRs. The values of the parameters for HDR, LRB and RB used in the numerical analysis are listed in Table 3 and 4 respectively.

Table 3 Rate-independent parameters for the bearings

Type of Bearing	C_1 MPa	τ_{cr} MPa	C_2 MPa	C_3 MPa	C_4 MPa	*m*
HDR2	2.50	0.247	0.653	0.006	3.25	6.62
LRB1	4.25	0.190	0.710	0.003	2.35	8.42
RB2	2.05	0.112	0.883	0.006	0.40	7.23

Table 4 Viscosity parameters for the bearings

Type of Bearing	A_l MPa	A_u MPa	q	*n*	ξ
HDR2	0.351	0.272	0.344	0.224	1.252
LRB1	0.302	0.302	-----	0.272	-----
RB2	0.075	0.075	-----	0.243	-----

2.2.2 Bilinear Model

It is recognized that the isolation bearing has generally nonlinear inelastic hysteretic property. Some specifications have specified guidelines for using the bilinear model in order to represent the nonlinear inelastic hysteretic property of the HDRB and the LRB (AASHTO 2000; JRA 2002). In this case, three parameters are required to represent the hysteresis loop of HDRBs and LRBs: initial stiffness k_1, post yield stiffness k_2 and the yield strength of the bearings Q_d as shown in Figure 4. In the subsequent numerical study, these parameters are assigned for HDRB and LRB in accordance with the manual of bearings for highway bridges(JRA 2004).

2.2.3 Equivalent Linear Model

From experimental observations of RBs, it has been found that the force-displacement hysteresis loop of RBs can be approximated by the equivalent linear model (JRA 2002). Accordingly, the equivalent linear model is employed for RBs in the numerical analysis. The equivalent stiffness of the RB can be evaluated based on the nominal shear modulus G_e of the rubber material and the damping constant of the bearing is set to be 3.0%.

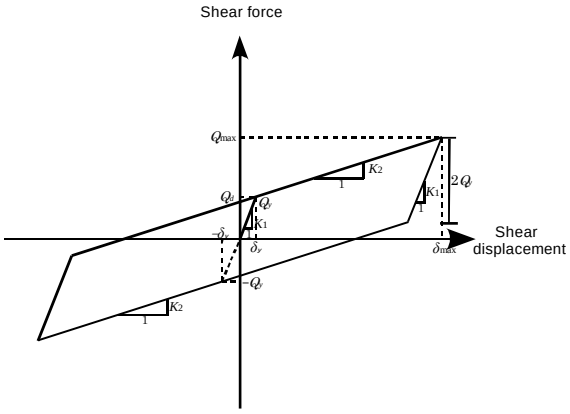

Figure 4 Bilinear relationship of the horizontal shear force-displacement of isolation bearing.

3. STRUCTURAL DAMPING

The damping constant matrix **C** for the bridge system is evaluated using the stiffness proportional damping model. The damping constant matrix is calculated by summing all the elements' damping constants. The damping constant matrix is determined by using the elemental damping constant h_j and the first natural circular frequency of the system ω_1. The damping constant matrix **C** can be written as

$$\mathbf{C} = \sum_{j=1}^{N} \frac{2h_j}{\omega_1} k_j \tag{4}$$

where h_j and k_j are, respectively, the damping constant and stiffness matrix of the jth element and *N* is the number of elements of the bridge system. The elemental damping constants for the steel girder are taken as 0.02, for the concrete part and the foundation soil taken as 0.05 and 0.2, respectively (JRA 2002).

4. EARTHQUAKE GROUND MOTIONS

The designed earthquake waves for level-2 type-I (1-2-1) and type-II (2-2-1) specified by JRA (2002) are applied to the model bridge in the longitudinal direction. Figure 6 shows the ground acceleration time history of these seismic waves.

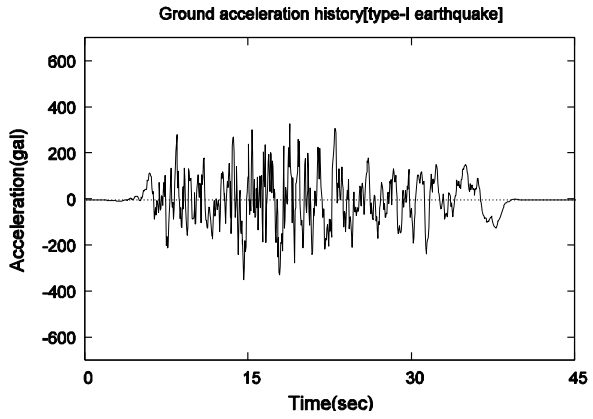

(a)

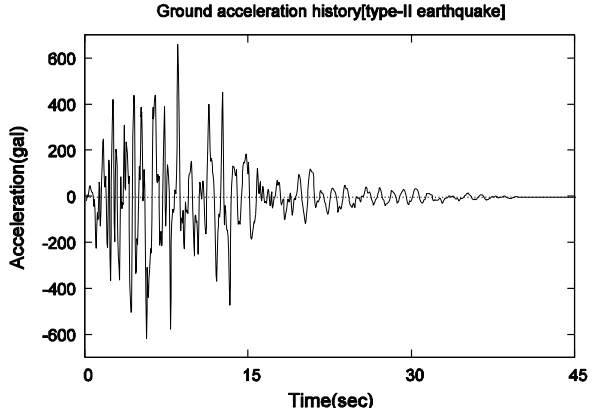

(b)

Figure 6 Ground acceleration histories used in the seismic response analysis (a) type-I (1-2-1), (b) type-II (2-2-1) earthquake ground motions.

5. SEISMIC RESPONSES OF BRIDGE

Before conducting nonlinear time history analysis of the bridge system, an eigenvalue analysis has been carried out to compute the vibration properties (natural frequencies and mode shapes of the bridge). Using the first natural frequency properties of the system, the damping matrix in Eq. (4) is obtained.

A proposed solution algorithm for the rheology model has been successfully implemented in commercially available software (Kozo Keikaku Eng. Inc., 2006). Due to symmetry of the bridge structure shown in Figure 1(a) and due to space limitation**,** only one pier's results P1 (=P4) using three isolation bearings (HDR2, LRB1 and RB2) are graphically presented and discussed herein. Figures 7, 8 and 9 represent the moment-rotation relations of the plastic hinges of the pier for level-2 type-I and type-II earthquakes, respectively. The similar trend of the responses is obtained from the shear stress-strain relations of the bearings as shown in Figures 10, 11 and 12. The effect of modeling of isolation bearings on the responses of the bridge have been clearly appeared in the comparisons of maximum shear strain (γ_{max}) occurred in the isolation bearings and the ratio of the maximum rotation to the allowable rotation (θ_{max}/θ_a) of the plastic hinge experienced for type-I and type-II earthquakes waves respectively are shown in Table 5 and 6.

Table 5 Seismic response of bridge for type-I earthquake

Type of Bearing	Type of Model	γ_{max} (Bearing)	θ_{max}/θ_a (Plastic hinge)
HDR2	Rheology	1.51	0.43
	Bilinear	1.49	0.57
LRB1	Rheology	1.71	0.46
	Bilinear	1.18	0.65
RB2	Rheology	1.87	0.62
	Eq. linear	1.89	1.17

Table 6 Seismic response of bridge for type-II earthquake

Type of Bearing	Type of Model	γ_{max} (Bearing)	θ_{max}/θ_a (Plastic hinge)
HDR2	Rheology	1.69	0.76
	Bilinear	1.72	0.86
LRB1	Rheology	1.74	0.80
	Bilinear	1.35	0.87
RB2	Rheology	1.97	0.78
	Eq. linear	2.05	0.87

6. CONCLUDING REMARKS

Effect of modeling of bearings on the seismic responses of the isolated bridge is evaluated by conducting nonlinear dynamic analyses. Two different analytical models of the isolation bearings are used in the study for conducting a comparative assessment of the seismic responses of the isolated bridge system. These two models are design model specified in manual of bearings for highway bridges (JRA 2004) and the proposed rheology model. As the design model, the bilinear model is employed for modeling LRB and HDRB; and, the equivalent linear model for RB.

It should be noted that a set of parameters corresponding to design models are estimated using the design equations as specified in JRA (2004), whereas the parameters of the proposed rheology model are estimated using experimental data conducted by the authors. In this

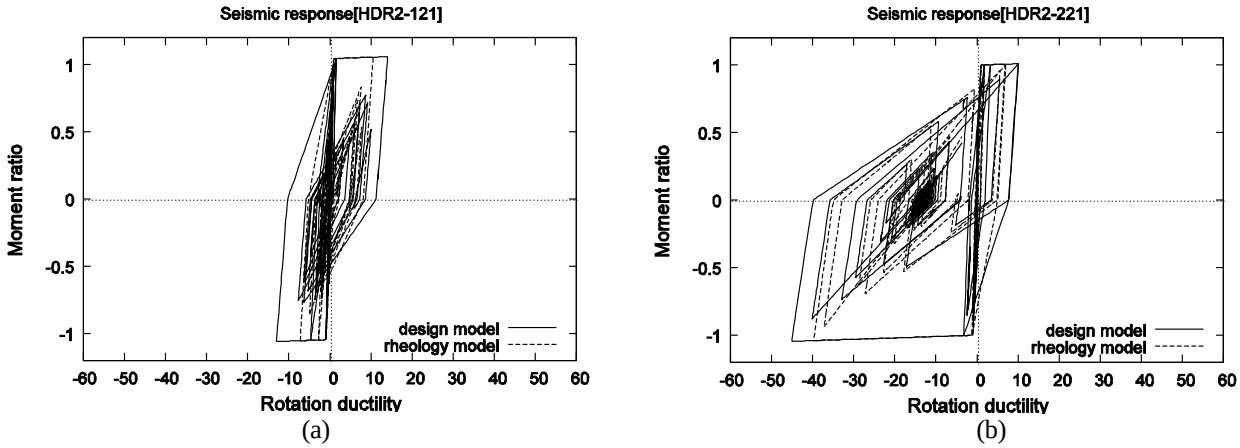

Figure 7 Moment-rotation relationships at plastic hinge of the pier P1 (=P4) as obtained for HDR2 bearings due to level-2 (a) type-I and (b) type-II earthquake ground motions; moment ratio (M/M_y) is the bending moment (M) at the level of plastic hinge divided by the yield moment (M_y) and rotation ductility is the rotation occurred at the plastic hinge level divided by the yield rotation.

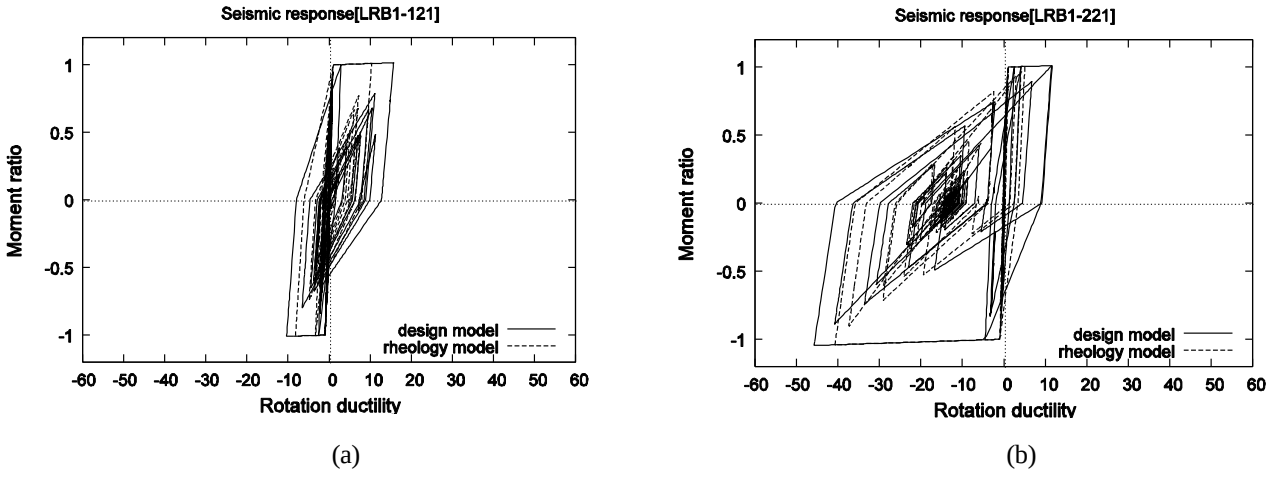

Figure 8 Moment-rotation relationships at plastic hinge of the pier P1 (=P4) as obtained for LRB1 bearings due to level-2 (a) type-I and (b) type-II earthquake ground motions; moment ratio (M/M_y) is the bending moment (M) at the level of plastic hinge divided by the yield moment (M_y) and rotation ductility is the rotation occurred at the plastic hinge level divided by the yield rotation.

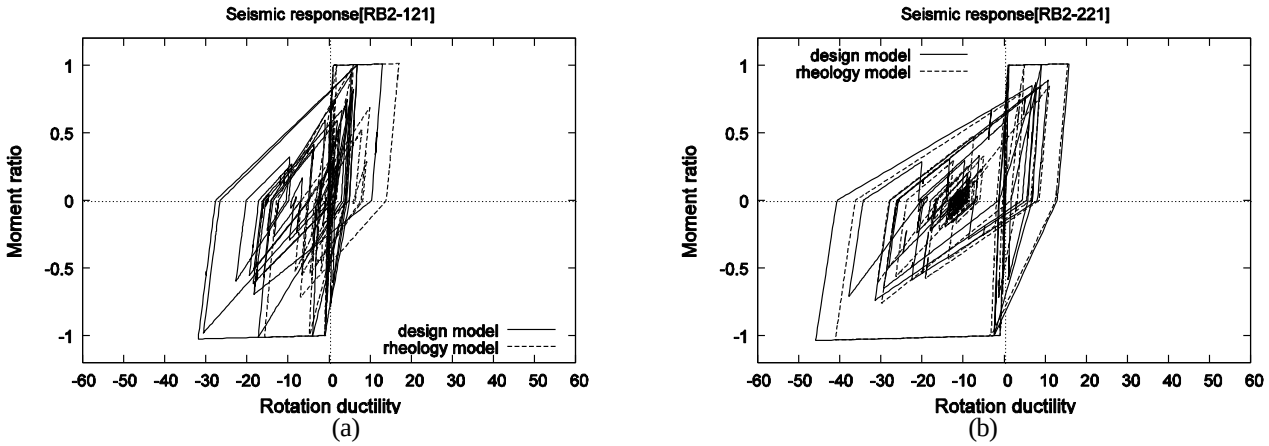

Figure 9 Moment-rotation relationships at plastic hinge of the pier P1 (=P4) as obtained for RB2 bearings due to level-2 (a) type-I and (b) type-II earthquake ground motions; moment ratio (M/M_y) is the bending moment (M) at the level of plastic hinge divided by the yield moment (M_y) and rotation ductility is the rotation occurred at the plastic hinge level divided by the yield rotation.

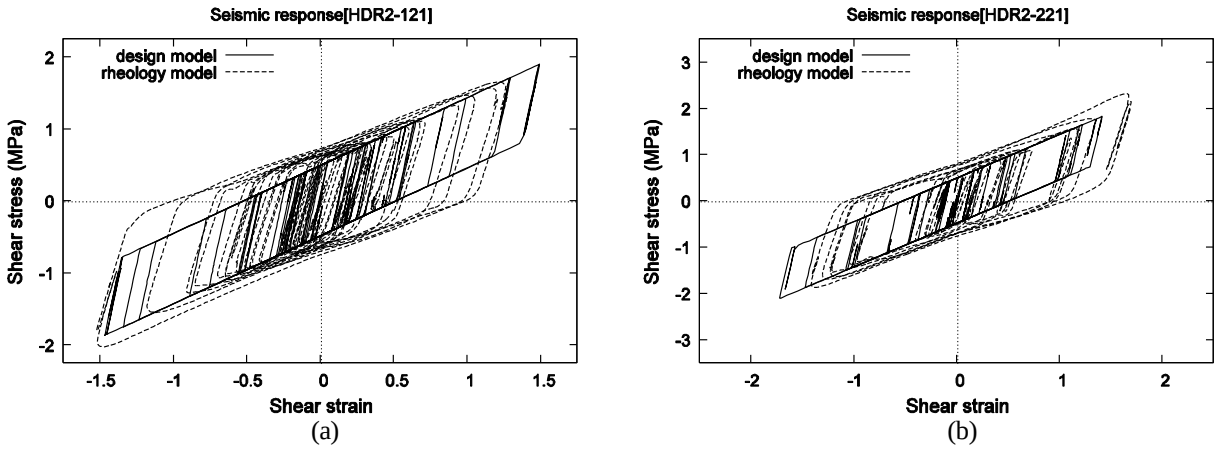

(a) (b)

Figure 10 Shear stress-strain relationships of the isolation bearing (HDR2) located at the top of the P1 (=P4) piers due to level-2 (a) type-I, (b) type-II earthquake ground motions.

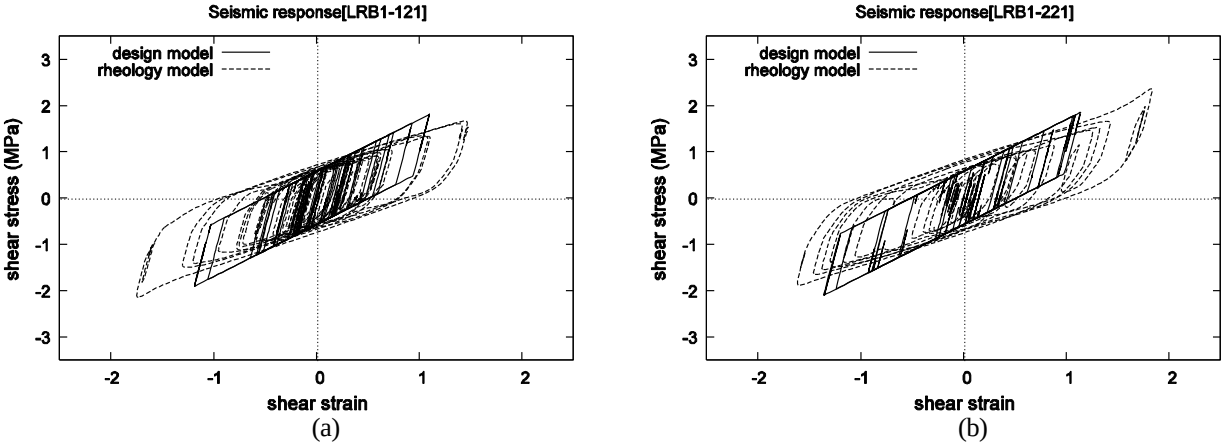

(a) (b)

Figure 11 Shear stress-strain relationships of the isolation bearing (LRB1) located at the top of the P1 (=P4) piers due to level-2 (a) type-I, (b) type-II earthquake ground motions.

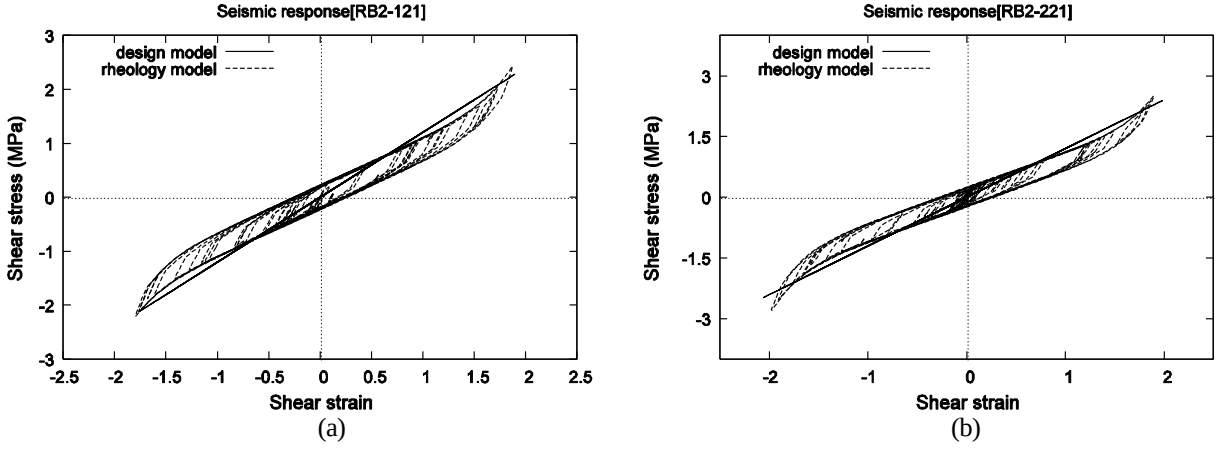

(a) (b)

Figure 12 Shear stress-strain relationships of the isolation bearing (RB2) located at the top of the P1 (=P4) piers due to level-2 (a) type-I, (b) type-II earthquake ground motions.

paper, the bridge responses are discussed in terms of the moment-rotation relations of the plastic hinges and the shear stress-strain relations of the bearings, since these responses are very crucial for seismic design of bridge systems. The effect of modeling the bearings is significantly observed in the responses indicating that a careful selection of the models of isolation bearings is very important for seismic design of an isolated bridge system.

Acknowledgements:

The experimental works were conducted by utilizing the laboratory facilities and bearings-specimens provided by Japan Rubber Bearing Association. The authors indeed gratefully acknowledge the kind cooperation extended by them. Furthermore, the authors sincerely acknowledge the funding provided by the Japan-ADB in the form of scholarships to carry out this research work.

References:

Kawashima, K. and Unjoh, S. (1997) "The Damage of Highway Bridges in the 1995 Hyogo-ken-nanbu Earthquake and Its Impact of Japanese Seismic Design", *Journal of Earthquake Engineering*, Vol.1(3), pp. 505-541.

Kawashima, K. (2000) "Seismic Performance of RC Bridge Piers in Japan: An evaluation after the 1995 Hyogo-ken nanbu earthquake." *Progress of Structural Engineering and Materials*; **2**:82-91.

Kelly, J. M, (1997). "*Earthquake resistant design with rubber"*, 2nd edition, Springer-Verlag Berlin Heidelberg, New York.

Bhuiyan, A.R., Okui, Y., Mitamura, H. and Imai, T., (2009a), "A rheology model of high damping rubber bearings for seismic analysis: identification of nonlinear viscosity", *International Journal of Solids and Structures*, 46, 1778-1792.

Hwang, J.S.,Wu, J.D., Pan, T. C., Yang, G., (2002). "A mathematical hysteretic model for elastomeric isolation bearings". *Earthquake Engineering and Structural Dynamics* 31, 771-789.

Robinson, W.H., (1982)., "Lead rubber hysteresis bearings for protecting structures during earthquakes". *Earthquake Engineering and Structural Dynamics* 10, 593-604.

Bhuiyan, A.R., Razzaq, M.K., Okui, Y., Mitamura, H. and Imai, T., (2009b), "A simplified rheology model of natural and lead rubber bearings for seismic analysis*", Proceedings of the 64th JSCE Annual Conference*, Fukuoka, Japan

Japan Road Association.(1996),"Specifications for highway bridges, Part V: Seismic design", Maruzen, Japan.

Japan Road Association.(2002),"Specifications for highway bridges, Part V: Seismic design", Maruzen, Japan.

Japan Road Association.(2004),"A Manual of bearings for highway bridges", Maruzen, Japan.

Abe, M. Yoshida, J. Fujino, Y. (2004). "Multi-axial behaviors of laminated rubber bearings and their modeling II: Modeling", *Journal of Structural Engineering* 130, 1133-1144.

Kikuchi, M. and Aiken, I.D., (1997), "An analytical hysteresis model for elastomeric seismic isolation bearings", *Earthquake Engineering and Structural Dynamics* 26, 215-231

Takeda, T., Sozen, M.A., and Nielsen, N.N.(1970), "Reinforced concrete response to simulated earthquakes."*Journal of Structural Engineering*; **96**:2557-2573.

American Association of State Highways and Transportation Officials (AASHTO) (2000), "Guide specification for seismic isolation design",2nd edition, Washington D.C., USA.

Kozo Keikaku Eng. Inc. (2006), "User's Manual of Resp-T for Windows," Version 5

JOINT CONFERENCE PROCEEDINGS
7th International Conference on Urban Earthquake Engineering (7CUEE) &
5th International Conference on Earthquake Engineering (5ICEE)
March 3-5, 2010, Tokyo Institute of Technology, Tokyo, Japan

MITIGATION OF RESIDUAL DEFORMATIONS OF RC BRIDGE PIERS USING STEEL FIBER COMPOSITE BARS AS LONGITUDINAL REINFORCEMENT

Mohamed F.M. Fahmy[1)], Zhishen Wu[2)], and Gang Wu[3)]

1) Ph.D. Candidate, Dept. of Urban& Civil Engineering, Ibaraki University, Japan
2) Professor, Dept. Urban& Civil Engineering, Ibaraki University, Japan
3) Professor, International Institute for Urban Systems Engineering, Southeast University, China
mfmf1976@yahoo.com, zswu@mx.ibaraki.ac.jp, g.wu@seu.edu.cn

Abstract: In the present study, the seismic performance of concrete columns reinforced with ordinary steel bars (OSBs) and steel fiber composite bars (SFCBs) is evaluate from the view point of required post-earthquake recoverability. Residual deformation is used as a seismic performance index to define the end of the recoverable state. Hence, the inelastic performance of 13 conventionally reinforced concrete (RC) bridge columns, available from the current literature, was scrutinized. Recoverability limit of all samples tested under the effect of low axial load ratio is corresponding to column lateral drift ratio fluctuating more or less around two. The study also showed that the axial load ratio is the only factor showing a clear effect on the residual deformations. SFCB is proposed here as an innovative longitudinal reinforcement for RC bridge columns to mitigate column residual deformations. Basalt fibers and carbon fibers, with different reinforcement ratios, were used in the production process of the new rebars. Analytical and experimental studies on concrete bridge columns reinforced with SFCBs were conducted. The residual displacement in columns with SFCBs longitudinal reinforcement was considerably less than that of conventionally reinforced column. The amount of fibers used affects the definition of the column drift at the recoverability limit, where the increase of fibers amount shifts column drift at the recoverability limit. The study indicated the beneficial effect of conventional reinforcement replacement with steel basalt-fibers composite bars (SBFCBs), rather than increasing the amount of reinforcement, where the required strength can be fulfilled with the existence of positive post-yield stiffness and the final residual displacements substantially reduce.

1. INTRODUCTION

The damages incurred by many concrete bridges under the effect of near-fault ground motions have led to the implementation of several significant improvements to bridge design codes. Recent advances in earthquake engineering favor performance-based approaches for the seismic design of new structures and for the assessment and rehabilitation of existing structures located in active seismic zones. Generally, new seismic design philosophies for bridges recommend that important bridges subject to a near-land-large-scale interplate earthquake or an inland earthquake near the structure should be able to sustain the expected maximum lateral force in the inelastic stage with limited damages, to ensure quick recoverability. Consequently, recent developments in performance-based seismic design and assessment approaches have emphasized the importance of properly assessing and limiting the residual (permanent) deformations, typically sustained by a structure after a seismic event, even when designed according to the current design code provisions Pettinga et al. (2006). To ensure post-earthquake recoverability of the various infrastructure systems, attention has been drawn to the development and implementation of innovative systems and materials in new structures to improve their performance under seismic loads. To minimize residual displacements in reinforced concrete columns, Sakai et al. (2006) reports that incorporating an unbonded prestressing strand at the center of a lightly reinforced concrete cross section can achieve restoring force characteristics similar to a conventionally designed column upon loading, but with substantially less residual displacement upon unloading. Also, Zatar and Mutsuyoshi (2002) adopted a technique that employs partially prestressed concrete for the bridge piers; and the study revealed that employing prestressing tendons in RC bridge piers could result in subsequent reductions of residual displacement. Ikeda et al. (2002) proposed a new design concept for concrete piers in which vertical prestressing was introduced only in the critical sections, e.g. the bottom portion of the pier. Saiidi et al. (2009) attempted to reduce permanent displacement and damage in concrete bridge columns subjected to strong earthquakes through incorporating supper-elastic shape memory alloy longitudinal reinforcement with conventional concrete or

engineered cementitious composites in the plastic hinge zone. The residual displacement in columns with super-elastic shape memory alloy longitudinal reinforcement was considerably less than that of conventionally reinforced columns.

The study by Kawashima et al. (1998) showed that the residual displacement response ratio spectrum depends significantly on a bilinear factor r (ratio between structure second post-yield stiffness and the initial elastic stiffness). The residual displacement ratio response spectrum is small when $r > 0.0$, and sharply increase as r approaches zero. If the residual deformations are found to be excessive, it was suggested by Chrestopoulos and Pampanin (2004) that the following design decisions are applicable; appropriately changing material properties (e.g. steel with high strain hardening), and changing the reinforcement properties and section design to increase the post-yield stiffness at a section level, since residual deformations are primarily a function of the post-yield stiffness. In the study by Iemura et al. (2004), the unbonded bar reinforced concrete structure is proposed as a high-seismic performance structure. This structure has the stable post-yield stiffness of the load-displacement relationship and it might be a suitable structure for a large-scale earthquake.

It can be concluded that residual deformation is a main seismic performance index which should be checked to investigate the required post-earthquake recoverability of structures; and incase structure has positive post-yield stiffness, residual deformation would be small. Using this index, the aim of this study is to investigate the required recoverability of bridge columns. The study is conducted on columns reinforced with ordinary steel bars and steel bars hybridized with fiber reinforced polymers (FRP). The inelastic stage of bridge column reinforced with ordinary steel bars (conventionally reinforced columns) is examined for four groups of columns available from the given literature. These groups reflect the effect of column aspect ratio, horizontal steel confinement, steel bar diameter, and axial load ratio on the required recoverability. Since the advantages of advanced composite materials (FRP) include: light weight, high strength or stiffness-to-weight ratios, corrosion resistance, and in particular, the elastic performance, steel fiber composite bars (SFCBs) are proposed as an innovative reinforcement for recoverable-structures. To investigate the controllability and recoverability of bridge columns reinforced with SFCBs, analytical studies using a computer program (Open System for Earthquake Engineering Simulation (Open SEES) (Mazzoni et al.) are applied. Furthermore, residual deformations of columns reinforced with SFCBs are examined experimentally.

2. EVALUATION OF RECOVERABILITY OF CONCRETE COLUMNS REINFORCED WITH OSBS

Four groups of rectangular RC bridge columns available from literature are studied here to investigate their recoverability after the effect of simulated seismic forces. Each group was designed by the original authors to study the effect of one parameter on the performance of RC bridge columns during the seismic action; and here the impact of these parameters on column residual deformation is the main concern. The first group is three columns (U-4, U-6, and U-7) studied by Ozcebe and Saatcioglu (1987) to examine the effect of transverse steel confinement on ductility of RC square columns subjected to simulated seismic forces. The second group is also three square columns (TP-10, TP-11, and TP-12) tested by Kawashima et al. (2000) to find out the impact of longitudinal steel bars diameter on the length of the plastic hinge zone. Nagaya and Kawashima (2001) tried to investigate the effect of column aspect ratio on the seismic performance of square RC columns through testing three columns (TP-27, TP-28, and TP-29) of the third group, with aspect ratio 2.64 to 3.75. The measurements of the columns tested by Kawashima et al. (2000) and Nagaya and Kawashima (2001), taken during the experiments, are made available online by the original authors (Kawashima et al.).The last group is four columns tested under the action of quasi-static cyclic lateral loading by Wehbe et al. (1999), where the impact of moderate horizontal confinement under different axial load ratios (10% to 24%) on the ductility and behavior of rectangular bridge columns was the main objective.

2.1 Column Residual Drift Ratio

While these tested columns achieved their ideal theoretical strengths and were able to maintain their capacities till high drift ratios, it is still necessary to define the lateral drift at which column recoverable state ends: the limit after which column can not restore its original functions after a seismic action and demolishing may be required even if damage level is light (Fahmy et al. 2009). Hence, residual deformation as an important seismic performance index is used to define the end of this state. The residual deformation, which is defined as the displacement of zero-crossing at unloading on the hysteresis loops, should not exceed 1% of the column height for a quick recovery after an earthquake (JSCE 2005). Since the preferable behavior of important bridges under the effect of major shaking is ductile-recoverable performance, the required recoverability is examined at the maximum achieved lateral strength for all columns of the current database of conventionally reinforced columns. Column residual drift ratio, defined as the ratio of residual deformation corresponding to column lateral displacement at the maximum achieved lateral strength to column height, for all columns is shown in Fig. 1. It is obvious that the residual drift of any of the examined columns is in excess of the recoverability limit. This is an indication that the control of the irrecoverable deformations of new structures is still a current challenge toward achieving the aim of ductile-recoverable structures. In order to reduce column residual deformations after an earthquake, initiatively, it is reasonable to study the effect of potentially influential design parameters. Hence, effects of column horizontal steel configuration, steel rebar diameter, aspect ratio, and axial load ratio on the residual deformations of 13 conventionally

reinforced columns are examined.

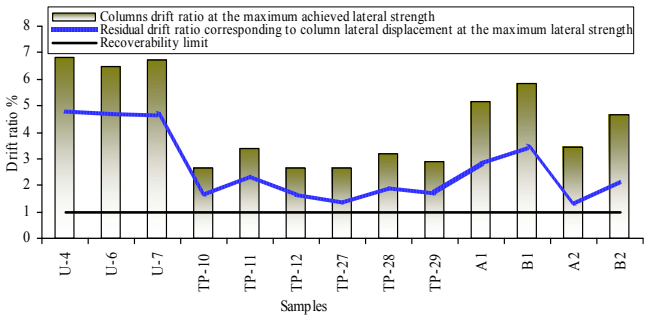

Fig.1 Investigation of recoverability of rectangular bridge columns reinforced with OSBs

Column drift ratios versus the corresponding residual drift ratios are depicted in Fig.2 for the considered samples. Fig.2 [a] shows the effect of using different transverse steel confinement on column residual deformations. There is a close similarity in the relation between column drifts and the corresponding residual deformations for the samples of this group, while the transverse steel confinement was different. Similar finding is obtained for the effect of longitudinal steel reinforcement diameter and column aspect ratio, Figs. 2 [b & c], respectively. However, the increase of the axial load ratio has to some extent an effect on column deformations. For instance, an increase of axial load ratio causes a reduction in the residual deformation, but with a significant effect on the final drift ratio. Four rectangular columns (A1, A2, B1, and B2) were tested by Wehbe et al. (1999) under different axial load ratios (10% to 24%). At the recoverability limit, columns A2 and B2, tested under the effect of 24% axial load ratios, achieved lateral drift ratio of 3.03%, however, columns A1 and B1, tested under the effect of 10% axial load ratios, could not achieve more than 2.77% and 2.64% drift ratios Fig. 2[d], respectively. And since the transverse steel confinement, longitudinal steel diameter, and column aspect did not show any significant impact on the residual deformations, the residual drift ratios versus columns drift ratios of all the examined columns are given in Fig.3 to find out, in general, the effect of axial load ratio.

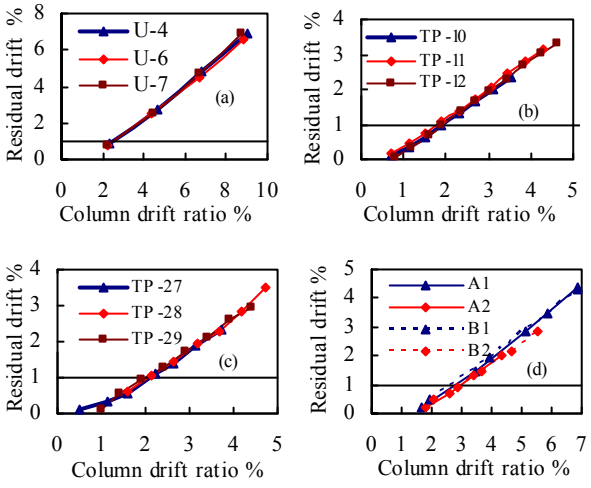

Fig. 2 Effect of (a) horizontal steel confinement, (b) steel bar diameter, (c) column aspect ratio, and (d) axial load ratio on column residual deformations

At the recoverability limit, columns studied by Kawashima et al. (2000) and Nagaya and Kawashima (2001), tested under axial load ratio less than 5%, achieved the smallest drift ratio, 1.9%; on the other hand, columns A2 and B2, tested under the effect of 24% axial load ratios, achieved the highest drift ratio (3.03%).

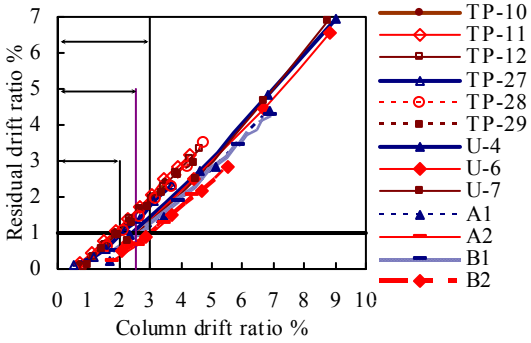

Fig.3 Effect of axial load ratio on the definition of the end point of the recoverable state of bridge columns reinforced with OSBs

3. SOURCE OF RESIDUAL DEFORMATIONS

In case RC columns tested under the action of reversed cyclic loading, it was reported by Park and Paulay (1975) that after the first yielding excursion, the moment over a large proportion of unloading and reloading loops is curried only by the steel reinforcement alone. This behavior is due to yielding of the steel in tension, causing cracks in the tension zone that do not close when the direction of moment is reversed, because of plastic elongation of the steel. During the next inelastic excursions, widening of the crack will produce additional inelastic strains in the reinforcement, which result in the penetration of yielding into the column footing, giving rise to significant extension of the reinforcement. Additional rigid-body deformation may also occur due to the slippage of the reinforcement. Consequently, column residual deformations are function of the longitudinal reinforcement deformations.

4. CONCEPT OF STEEL FIBER COMPOSITE BAR

Generally, flexural-dominated column subjected to a lateral load is damaged at the column base (plastic hinge region). Once yielding has commenced in RC column, the deformations concentrated at the plastic hinge position; hence when a column is deflected laterally in the post-elastic range, the required curvature ductility (φ/φ_y) is higher in plastic hinge region than that out of this region. The curvature (φ) is calculated from steel strains using $(\varepsilon_{st}-\varepsilon_{sc})/(d-d')$, where ε_{st} and ε_{sc} are the steel strains in the tension and compression sides of the loaded column, respectively (tensile strains taken as positive, and compression strains as negative), and d-d′ is the distance between the tension and compression steel. φ_y is the

curvature at first yield. The higher the required curvature, the higher the steel strains in the plastic hinge region. A reinforcing bar in tension develops elastic and plastic regions. The plastic region includes two subregions, consisting of yield plateau and strain hardening, Fig. 4 c. Elastic strains of a bar are recovered upon unloading, and this leaves residual strains in the inelastic regions due to plastic extension, Fig. 4. Since the unloading path follows the initial elastic slope (E_1), (Fig. 4.c), residual strains of the region of yield plateau (ε_{resp}) can be calculated from Eq. 3. Once the steel bar is stressed into the strain-hardening range, post-yielding stiffness (E_2) of the steel bar has a favored impact on the residual strains of this stage (ε_{resh}), where a reduction factor reflecting the effect of post-yield stiffness is considered, Eq. 4. However, the bilinear ratio between the post-yield and elastic stiffnesses (E_2/E_1) of the ordinary steel is very small, and its effect on the final residual strains is insignificant, namely, Eq.3 is applicable to find out the residual strain at any unloading path.

$$\varepsilon_{resp} = (\varepsilon - \varepsilon_y) \tag{3}$$

$$\varepsilon_{resh} = (\varepsilon - \varepsilon_y)\left(1 - \frac{E_2}{E_1}\right) \tag{4}$$

Residual deformations of steel bar due to plastic extension and slip can be evaluated by estimating the area under the curve representing the residual strain distribution through the embedded length of steel bar in column footing (Fig. 4.b), Alsiwat and Saatcioglu (1992). And since the aim is to reduce these deformations, increase of the slope of the post-yield stiffness is one reasonable key to lessen steel residual strains. In addition, it is crucial to prevent concentration of the plastic rotation in a short region close to the base of the column: well distributed curvature over a longer yielding zone might reduce the required curvature and in turn the corresponding steel strains.

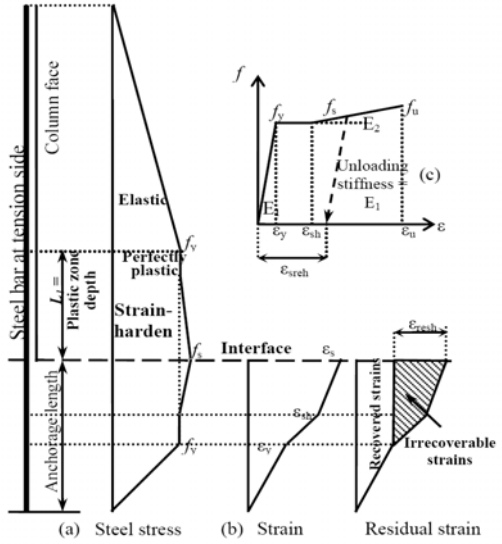

Fig.4 Schematic drawing of (a) Distribution of tension stresses of OSB, (b) Distribution of strain and residual strain of the anchored part of OSB, and (c) Stress-strain relationship of ordinary steel

To this end, hybridizing fibers with the ordinary steel reinforcement in the longitudinal direction is the adopted concept. This would enhance the inelastic response through strain hardening by the end of the elastic stage, which could be controlled depending on the type and amount of FRP used. The permanent deformations would also be reduced more due to the elastic performance of FRP, which is characterized by approximately zero residual deformations leading to unloading stiffness smaller than the elastic stiffness.

5. UNIAXIAL AND CYCLIC TENSILE BEHAVIOR OF SFCB

A wide experimental study was conducted by Wu et al. to determine the performance of SFCB under the effect of uniaxial and cyclic tensile loads. Two types of fiber were applied to produce SFCB: T700-12K carbon fiber and CBF13-2400Tex basalt fiber. Crescent-rib steel rebar with a diameter of 10 mm was used as the inner core steel bar and vinyl-ester resin was applied. Basic mechanical properties of each material can be seen in Table 1.

Table 1. Properties of components of SFCB

Type	Elastic modulus (GPa)	Yield strength (MPa)	Tensile strength (MPa)	Density (g/cm^3)	Diameter (μm)	Elongation rate (%)
Carbon fiber (T700)	230	-	3680	1.80	8	1.6
Basalt fiber (CBF13)	90	-	2250	2.63	13	2.5
Steel bar	200	420	-	7.80	10^4	15.0
Resin	3.6	-	95	1.06	-	6.1

Four types of SFCB were produced to study the effect of fibers type and amount on the performance of the new product of rebars, Table 4. Here, some of the results are presented (Figs.5 and 6), and longer treatment of this study is given by Wu et al. Fig.5 shows that the post-yield stiffness of steel bar could be controlled after hybridization with FRP, where FRP amount controls the definition of the slope value of the fulfilled post-yield stiffness and FRP type defines the end point of this stiffness. Test results revealed that the elongation rate of the fiber used is responsible about definition of end point of the achieved post-yield stiffness, where steel carbon-fiber composite bar (SCFCB) and steel basalt-fiber composite bar (SBFCB) realized different axial strains by the end of the achieved post-yield stiffness: SBFCBs have stable post-yield stiffness till a strain value almost double of that of SCFCBs. Comparison between results of OSB and SFCB specimens under the effect of repeated loading is given in Fig.6. Major and favored difference is drawn in Fig.6 (b), where residual strain of SFCB is less than that of OSB at the same level of axial strain. The possible reason of this reduction of the irrecoverable strains can be recognized from the shaded area under the unloading paths of both OSB and SFCB (Fig. 6(a)), where these areas represent the energy converting to

kinetic energy. For SFCB, kinetic energy is represented by three areas: the small triangular area *abc* represents the kinetic energy of OSB, the area *acde* represents the impact of post-yield stiffness, and the triangular *efg* represents the effect of the elastic performance of fibers used.

Table 2. SFCB test sample models

Tested samples	Diameter of inner steel bar (mm)	Type of fiber	Fiber amount (bundle)
S10-C24	10	Carbon fiber (12k)	24
S10-C40	10	Carbon fiber (12k)	40
S10-B20	10	Basalt fiber (2400tex)	20
S10-B30	10	Basalt fiber (2400tex)	30

Note: 12k expresses that each bundle of textile fiber's radical is 12000 fibers; tex is textile industry's measuring unit, indicates the weight of single bundle fiber per kilometer

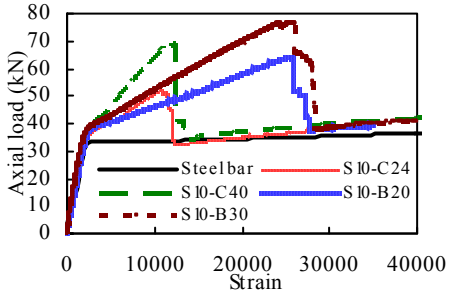

Fig.5. Load-strain relationship of steel bar, SCFCB, and SBFCB

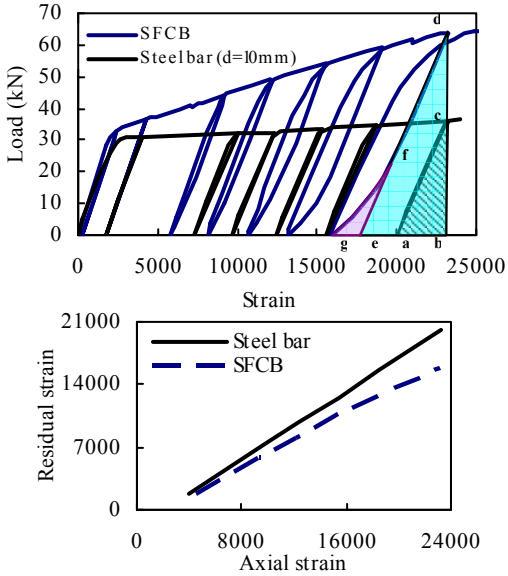

Fig.6 Comparison of cyclic response of OSB and SFCB (a) load-strain relationship, (b) Axial strain versus residual strain

6. RECOVERABILITY OF CONCRETE COLUMNS REINFORCED WITH SFCB

6.1 Analytical Studies

To investigate the performance of concrete bridges columns reinforced with SFCBs in place of ordinary rebars, analytical study using a computer program (Open SEES) were conducted. Column TP-10, tested by Kawashima et al. [14], is considered in this study as a control sample to evaluate the effectiveness of replacing its OSBs with SFCBs. Three different amounts of carbon and basalt fibers were considered (10, 20, and 30 bundles of basalt, and 12, 24, and 40 bundles of carbon). Two types of analyses were conducted for each case: pushover and cyclic loading. The computer program used has a variety of predefined material models for multiple applications that can be manipulated to fit specific criteria and properties. Since the fiber analysis remains the most economic and accurate means to capture seismic behavior of concrete structures (Spacone et al. (1992) and Mayer and Eligehausen (1998)), the fiber model was used. The constitutive relationships were based on material properties of column TP-10 (yield strength of longitudinal steel bars and horizontal reinforcement and concrete compressive strength were 377 MPa, 376MPa, and 21Mpa, respectively) and fibers (Table 1)). Column TP-10 was reinforced with 24 bars of 10mm diameter and horizontal reinforcements was 6mm diameter and 50 mm spacing. The confined concrete properties were based on Mander's model (Mander et al (1998)). The widely used Giuffré-Menegotto-Pinto model (Menegotto and Pinto 1973) is employed in this study to represent the hysteretic stress-strain behavior of OSB and also SFCB due to the absence of steel model for SFCB. The model includes the yielding, strain hardening, and Bauschinger effect of the steel bar. According to the type used for reinforcement, the failure point in the analysis was assumed. In case column is reinforced with OSBs, it was assumed to be where the calculated maximum confined core strain reaches the calculated crushing strain; but for columns reinforced with SFCBs, it was assumed to be where the maximum SFCB strain reaches the calculated ultimate strain value.

The advantages of the developed fiber-based analysis of concrete structure through the incorporation of a zero-length section element to reflect the effect of strain penetration of longitudinal bars into bridge footing was studied by Zhao and Sritharan (2007), which is adopted in this study.

6.1.1 Lateral Load-Displacement Relationship of Bridge Columns Reinforced with SFCBs

Figs.7 (a & b) show the calculated pushover curve of columns reinforced with SBFCBs and SCFCBs, respectively, in place of OSBs. The measured and calculated force-displacement of the column TP-10, tested by Kawashima et al. (2000), is superimposed on the same figures for comparison. Close correlation was evident between the measured and calculated response of column TP-10 with respect to stiffness, capacity, and the general trend in the column capacity in the nonlinear range. It should be noted in the designation of the columns reinforced with SFCBs that TP-10 denotes the details, dimensions, and material properties of column TP-10, and (+10BF, +20BF, or +30BF) and (+12CF, +24CF, and +40CF) signify the number of the hybridized bundles of basalt fibers and carbon fibers, respectively, with each steel bar of the longitudinal reinforcement.

The characteristics of the columns reinforced with SFCBs could be explained from the viewpoint of the load-displacement curves (Fig.7). It is noticeable that the initial stiffness is the same among all columns, where the replacement of OSBs with SFCBs did not cause any significant change on the yield stiffness of column TP-10; that is an advantage of the applied concept since the amount and type of fibers used will not attract additional force of the seismic input. When the deformation becomes large, all columns reinforced with SFCBs have the positive and stable post-yield stiffness. In general, the fibers hybridized with the longitudinal reinforcement of RC column work in parallel with column materials.

It is obvious from Fig. 7 that the definition of the end point of the achieved post-yield stiffness is dependent on the type of the fiber used. For instance, rupture of basalt fibers of the columns TP-10+10BF, TP-10+20BF, and TP-10+30BF is corresponding to column drift ratio of 3.0%, 3.85%, and 4.36%, respectively, however, due to the early rupture of carbon fibers these drifts are 2.3%, 2.61%, and 3.0% for the columns typified TP-10+12CF, TP-10+24CF, and TP-10+40CF, respectively. To determine the effect of fibers amount on the achieved post-yield stiffness, the bilinear factor is determined for all the columns reinforced with SFCBs. The increase of the number of basalt fibers bundles from 10 to 30 improved the bilinear factor value from 0.07 to 0.15. Also the bilinear factor of column TP-10+40CF is 0.26, which is higher than (0.1) of the column TP-10+10CF. It can be concluded that the post-yield stiffness is directly proportional to the amount of the fibers used.

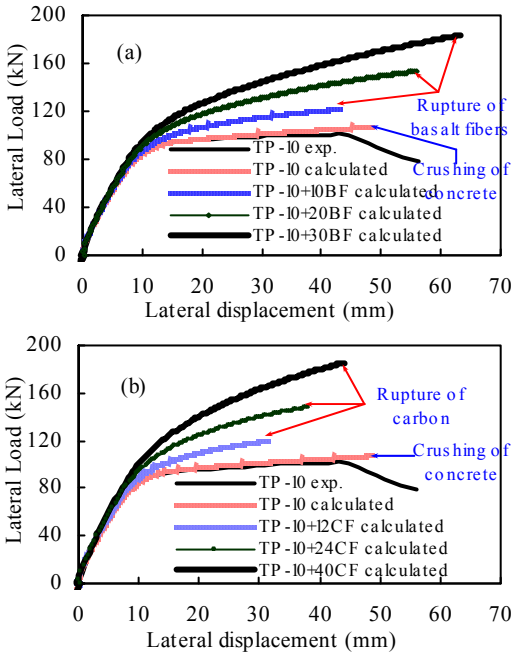

Fig.7 Lateral load-displacement envelope of column TP-10 reinforced with OSBs and those of columns reinforced with SFCBs (a) SBFCBs and (b) SCFCBs

6.1.2 Residual Deformations of Bridge Columns Reinforced with SFCBs

The pushover analytical study showed that all columns reinforced with SFCBs successfully have stable post-yield stiffnesses; hence residual deformation should be applied to investigate the recoverability of the innovative columns. The hysteresis force displacement curves of all columns (TP-10, TP10+10BF, TP-10+20BF, TP-10+30BF, TP-10+12CF, TP-10+24CF, and TP-10+40CF) were calculated using a computer program analysis based on the proposed fiber-based model. Using the cyclic loading results, the drift ratios versus columns residual drift ratios are plotted in Fig.8. Excellent correlation was observed between the experimental and analytical curves of the relationship between column drifts and the corresponding residual drift ratios of column TP-10, tested by Kawashima et al. (2000). Based on the experimental results of the column TP-10, end of the recoverable state of TP-10 locates at 1.9% lateral drift. However, Fig.8 (a) shows shifting of the end of the recoverable state of columns reinforced with SBFCBs; where lateral drifts of the columns TP-10+10BF, TP-10+20BF, and TP-10+30BF, at the recoverability limit, are 2.27%, 2.51%, and 2.8%, respectively. At the same level of lateral drift, it is evident from Fig.8 (a) that the more the amount of fibers used, the smaller the residual deformation. Similar finding is obtained for the effect of hybridization of steel bars with carbon fibers on the residual deformations, plotted in Fig.8 (b). The three columns reinforced with SCFCBs are recoverable till the failure point (column lateral displacement at which the outer carbon fibers of SCFCBs ruptured), i.e., the maximum residual drifts of the columns TP-10+12CF, TP-10+24CF, and TP-10+40CF are 0.99%, 0.97%, and 0.89%, respectively.

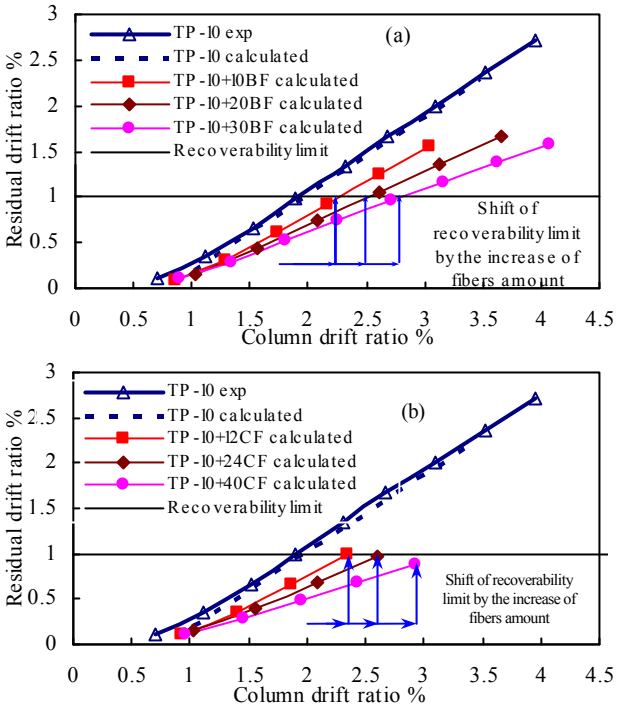

Fig.8 Relationship between drift ratio and residual drift ratio of column TP-10 reinforced with OSBs and those of columns reinforced with (a) BSFCBs and (b) CSFCBs

6.1.3 Curvature Ductility and Residual Strain of OSBs and SFCBs

Results of the analytical studies showed that the adopted concept of using steel bar hybridized with FRP in its longitudinal direction is a reasonable protecting tool, which could be applied to have the required recoverable structure after a major earthquake: structure can still carry load with the increase of the lateral deformation, and accompanied irrecoverable deformations might be reduced. It is pressing now to identify the improvement in the behavior of columns reinforced with SFCBs. Mechanical properties of longitudinal reinforcement used in the preceding analytical analyses are the cause of this change in column performance, so investigation of both curvature ductility and maximum residual strain of the longitudinal reinforcement is quite sensible to evaluate the enhancement in the performance of column reinforced with SFCBs.

It is evident from Fig. 9 (a) that the maximum curvature ductility ratio at the interface between column and footing is almost 23.2% and reduces to 6.4% at 200mm from the column base. And this mainly is due to the highest steel strain values lie in the bottom of the column, which in turn affected the column curvature distribution.

Figs.9 (b-d) detail the calculated curvature ductility of the three columns reinforced with SBFCBs at different levels of lateral drifts. And since column TP-10+30BF has the best performance from the viewpoint of ductile-recoverable structure (Figs. 7(a) and 8(a)), comparison between this column and column TP-10 is appropriate to highlight the main differences. The impact of the 30 bundles of basalt fibers hybridized with each bar of the longitudinal reinforcement of column TP-10 on its deformability can be identified from Figs.9 (a & d). At equal lateral drift of 3.36%, for instance, that amount of fibers was enough to reduce the required curvature ductility at the interface between column and footing nearly to 42% of that achieved by the conventional reinforcement. In addition, a well distribution of column curvature could be noticed from Fig. 9 (d), where the ratio of maximum curvature to yield curvature is almost 9.7% at the interface section, reduces to 7.08 % and 3.75% at 200mm and 400mm from the column base, respectively, and ends to 1.03% at 600mm.

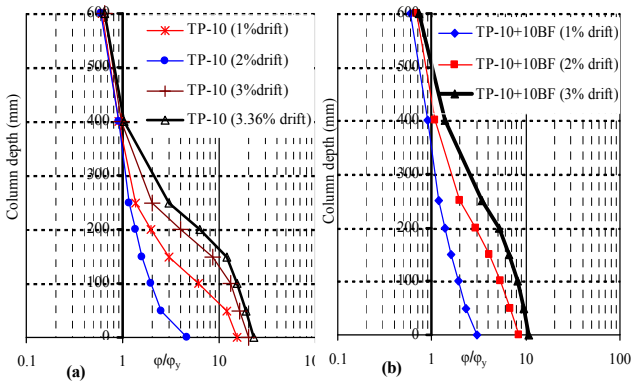

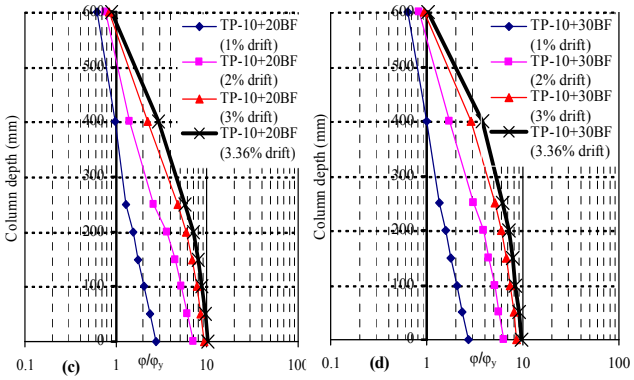

Fig. 9. Effect of hybridizing different reinforcement amount of basalt fibers with the OSBs of column TP-10 on the distribution of curvature ductility at different lateral drifts

6.2 Experimental Study of Bridge Columns Reinforced with SFCBs

To mitigate column residual deformation, it becomes clear that the contribution of longitudinal reinforcement to the lateral strength of RC column should be reduced. An experimental program was prepared and tested to verify this principle throughout the adopted concept of using SFCBs for bridge columns in place of the ordinary reinforcement. Hence, the primary objectives of this study are to test out the possibility of increasing column lateral strength capacity through the existence of post-yield stiffness using additional longitudinal fibers, rather than increasing the amount of reinforcement, and to enhance its restorability by shifting column lateral drift at the recoverability limit. The reliability of applying this concept was measured by testing three columns. Two samples typified CS10-B30 and CS10-C40 were reinforced with SFCBs, where the longitudinal reinforcement is twelve SFCBs consisted of inner steel rebar of 10-mm-diameter and outer fibers, i.e., 30 bundles of basalt fibers and 40 bundles of carbon fibers. The third column (CS14) was reinforced with twelve ordinary rebars of 14-mm-diameter. The tested specimens had square cross-section of 300x300mm and 1300-mm-tall and they were connected to a column stub of 1550x700x500mm. A photo for the product of steel bar wrapped with basalt fibers is given in Fig. 10. Lateral reinforcement of the three samples consisted of 10-mm-diameter ordinary bars with spacing of 80mm. Yield strength of the lateral reinforcement is 235 MPa. The mechanical properties of the longitudinal reinforcement are given in Table 3. The tested compressive strength of the concrete cylinder was 37.81 MPa.

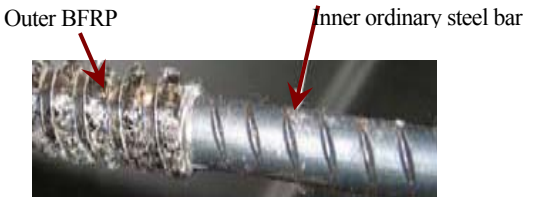

Fig.10 Product of steel basalt-fiber composite bar (SBFCB)

The columns were tested under constant axial load and reversed cyclic lateral load. An axial compressive load of

12% of column axial strength was applied by a hydraulic jack with a capacity of 3000kN. Lateral load was applied by a dynamic actuator of 1000 kN of push and pull capacity. The load cycles were divided into two phases: load control and displacement control. Load control phase was used up to yielding of the longitudinal bars, beyond that point; the test was controlled by yield displacement (Δ_y). The lateral load sequence consisted of three cycles each to Δ_y, $2\Delta_y$, $3\Delta_y$, etc. The three samples were instrumented for displacement and strain measurements. Horizontal linear variable displacement transducer (LVDT), 1100 mm from the column base, was attached to the column tip and aligned with the position of the application of lateral loading in order to measure the tip displacements. Also, strain gauges were installed on longitudinal reinforcements to measure the strains developed in the rebars.

Table 3. Properties of longitudinal reinforcement

Type	Diameter (mm)	Elastic modulus (E_1) (GPa)	Yield strength (MPa)	Post-yield stiffness (E_2) (GPa)	Ultimate strength (MPa)	E_2/E_1 (%)
Φ14	14	200	340	-	340	-
Φ10+30BF	13.19	142	312.4	16.6	691.3	11.7
Φ10+40CF	12.95	155.5	342.2	30.2	641.8	19.7

The envelopes of the measured force-drift relationships are shown in Fig.11. The curves are the average of the envelopes for the push-and-pull loadings. And this figure also for comparison shows the calculated response of column reinforced with 12 ordinary rebars of 10mm-diameter (CS10). The first stiffness was the same among the three columns reinforced with 10-mm diameter ordinary rebars or SFCBs, and it was lower than that of column S14. The lower stiffness of the columns would lead to longer vibration period for the columns and would generally reduce earthquake forces [5]. After yielding, CS10-B30 and CS10-C40 showed also a close similarity in the relation between column drifts and the corresponding lateral load till a lateral drift of 15-mm, at which light rupture sound of the carbon fibers of column CS10-C40 was noticed, and at 25-mm louder sound of the ruptured fiber was continuous till the end of the test, Fig.12(a). Column CS10-B30 was still carrying load till a lateral deformation of about 30mm, and then louder sounds at 35-mm lateral drift were due to the continuous rupture of basalt fibers, Fig.12(b). Deformation of column S14 increased without any increase in load carrying capability, and strength degradation started at lateral displacement of 35-mm due to buckling of longitudinal steel bars at the plastic hinge zone, Fig.12 (c).

Although the amount of the inner steel reinforcement of the innovative columns was almost 50% of that used to reinforce CS14, the fulfilled strength of the column CS10-B30 with the existence of post-yield stiffness was 115kN, which is nearly 92% of that achieved by the ordinary column. But, column CS10-C40 could not achieve lateral strength more than 110kN due to the early rupture of carbon fibers. The second main objective of this study was to evaluate the effect of SFCBs on residual displacements of the innovative columns in comparison with conventionally reinforced column. Fig. 13 shows the residual drift versus the lateral drift for the three columns, including the calculated residual drifts based on cyclic loading results using Open SEES. The values in Fig. 13 are based on the maximum residual drift at zero lateral loads of push-and-pull loadings. Both the measured and calculated data show that the residual drift in columns reinforced with SFCBs was considerably lower than that of CS14, indicating the beneficial effect of replacing conventional reinforcement with the SFCBs. For instance, conventionally reinforced column CS14 could not achieve lateral drift at the recoverability limit over 2.22%, but hybridizing the longitudinal steel reinforcement with FRPs shifted the end of the recoverable state of the columns CS10-B30 and CS10-C40 to 3.18% and 3.08%, respectively. Overall, the performance of the innovative columns revealed that the replacement of ordinary rebars with basalt SFCBs was effective in increasing column strength and in substantially reducing the residual drift. The practical application of the major reduction in residual drift is that the structure is more likely to remain serviceable after strong earthquake when longitudinal reinforcement is hybridized with reasonable amount of fibers used.

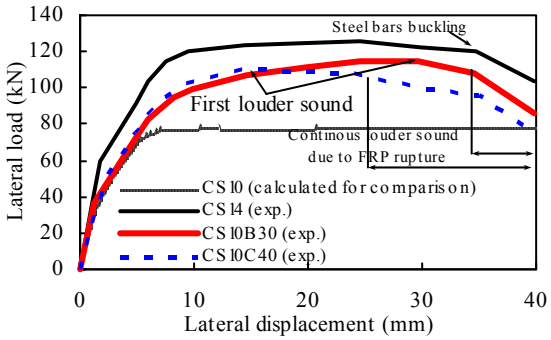

Fig.11 Comparison between lateral load-displacement relationships of the tested three columns and calculated column S10

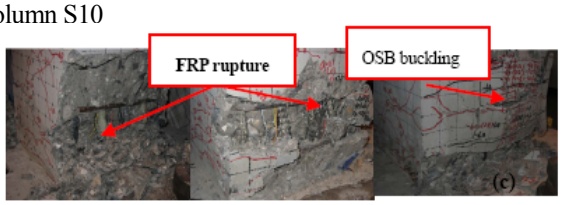

Fig.12 Ruptures of outer fibers of SFCBs (a) column CS10-C40 and (b) column CS10-B30, and (c) Buckling of OSBs of column CS14

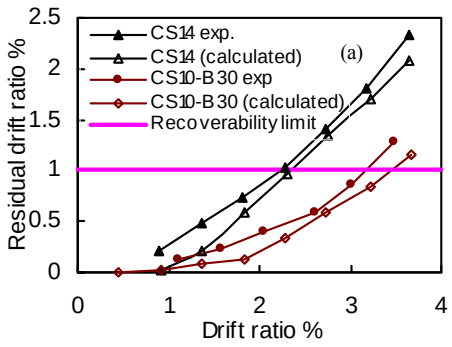

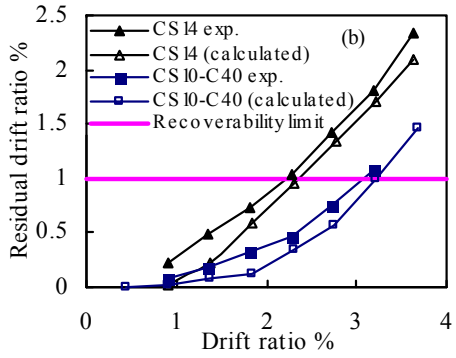

Fig. 13 Comparison between residual drift ratios of the conventionally reinforced column (CS14) and innovative columns (a) CS10-B30 and (b) CS10-C40

The hysteresis load-deformation curves calculated using a computer program analysis superimposed on the measured curves are shown in **Fig. 14**. Each column was analyzed using the measured displacement histories as loading input. The calculated curves for CS14, CS10-B30, and CS10-C40 are in an acceptable correlation with the measured curves in terms of strength, stiffness variation, and overall performance. This is an indication that modeling of the bond-slip effect with the model of Zhao and Sritharan (2007) appeared to be somewhat adequate. However, calibration of the bond-slip model based on a comprehensive experimental program on the new type of rebars is necessary to increase the accuracy of simulating the response of the innovative columns.

7. CONCLUSIONS

A study on four groups of bridge columns, focused on the inelastic performance of conventionally reinforced columns, was used to evaluate the recoverability of bridge columns and to find out the influential parameters on the required recoverability. The effect of column aspect ratio, steel bar diameter, horizontal steel configurations, and the axial load ratio on residual deformation of the tested conventionally reinforced columns was studied. The study showed that recoverability limit of all samples tested under the effect of low axial load ratio was corresponding to column lateral drift ratio fluctuating more or less around two. Also, axial load ratio is the only factor showing a clear effect on the residual deformation. Secondly, in attempt to enhance the recoverability of RC bridges, SFCB was suggested as reinforcement for a recoverable structure; residual deformation is applied also as seismic performance index. The following key conclusions were reached based on the analytical and experimental results presented in this paper:

1- Reinforcing RC bridge columns with steel fiber composite bars ensures the required post-earthquake recoverability, where column residual deformation can be mitigated.

2- Hybridizing the longitudinal steel reinforcement of ordinary RC column with FRPs did not cause any significant change on its yield stiffness, and when the deformation became large, column reinforced with SFCBs had positive and stable post-yield stiffness. The added fibers to the longitudinal reinforcement of RC column work in parallel with the column materials

3- Increasing column lateral strength using steel basalt-fibers composite bars (SBFCBs) as longitudinal reinforcement, rather than increasing the ordinary reinforcement amount, is a safe and sound design option. The first stiffness of the column reinforced with SBFCBs (10-mm inner steel diameter) was lower than that of column reinforced with 4-mm OSBs, 92% of the achieved strength by the ordinary column was fulfilled by the innovative column throughout the existence of post-yield stiffness, and column lateral drift at recoverability limit was shifted from 2.22% to 3.18%.

5- The residual displacement in columns with SFCBs longitudinal reinforcement was considerably less than that of conventionally reinforced column. The amount of fibers used affects the definition of the column drift at the recoverability limit, where the increase of fibers amount shifts column drift at the recoverability limit. The practical application of the major reduction in residual drift is that the structure is more likely to remain serviceable after strong earthquake.

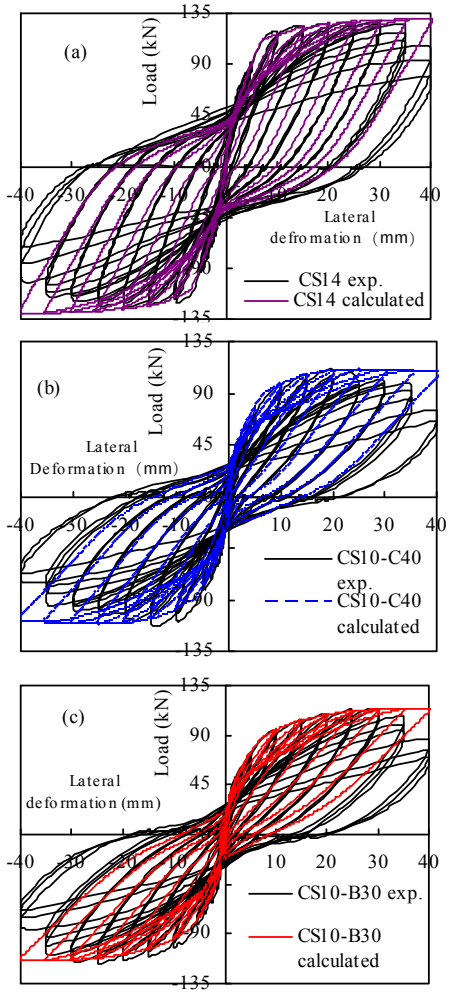

Fig. 14 Measured and calculated lateral load-deformation relationships: (a) CS14, (b) CS10-B30, and (c) CS10-C40

References:

Pettinga D, Pampanin S, Christopoulos C, Priestley N (2006), "Accounting for residual deformations and simple approaches to their mitigation," First European Conference on Earthquake Engineering and Seismology, Geneva, Switzerland.

Sakai J, Jeong H, Mahin SA (2006), "Reinforced concrete bridge columns that re-center following earthquakes," Proc. of the 8th National Conference on Earthquake Engineering, San Francisco, California, USA; Paper No. 1421.

Zatar WA, Mutsuyoshi H. (2002), "Residual displacement of concrete bridge piers subjected to near field earthquakes," ACI Struct. 99(6), 740-749.

Ikeda S, Nonaka S, Hirose S, Yamagushi T (2002), "Seismic performance of concrete piers prestressed in the critical section," Proc. of the first fib congress, Osaka congress, Japan; 47-48.

Saiidi MS, O'Brein M, Sadrossadat-Zadeh M (2009), "Cyclic response of concrete bridge columns using superelastic nitinol and bendable concrete," ACI Struct. J. 106(1), 69-77.

Kawashima K, MacRae GA, Hoshikuma J, Nagaya K. Residual displacement response spectrum. J. Struct. Enger. 1998, ASCE; 124(5): 523-530.

Chrestopoulos C, Pampanin S (2004), "Towards performance-based seismic design of MDOF structures with explicit consideration of residual deformations," ISET Journal of Earthquake Technology; 41 (1), 53-73.

Iemura H, Takahashi Y, Sogabe N. (2004), "Development of unbonded bar reinforced concrete structure," Proc. 13th World Confe. on Earthquake Enger., Vancouver, B.C., Canada: paper No. 1537.

Mazzoni S, McKenne F, Scott MH, Fenves GL, et al. Open System for Earthquake Engineering Simulation User Manual version 2.1.0. Pacific Earthquake Engineering Center, University of California, Berkeley, CA, http://opensees.berkeley.edu/OpenSees/manuals/usermanual.

Ozcebe G, Saatcioglu M (1987), "Confinement of concrete columns for seismic loading," ACI structural journal; 84(4), 308-315.

JSCE Earthquake Engineering Committee. Earthquake resistant design codes in Japan. Japan Society of Civil Engineers (JSCE) 2000, Tokyo, Japan, 150 pp.

Kawashima K, Shoji G, Sakakibara Y. A (2000), "Cyclic Loading Test for Clarifying the Plastic Hinge Length of Reinforced Concrete Piers," J. Struct. Enger., Japan; 46A: 767-776.

Nagaya K, Kawashima K. (2001), "Effect of Aspect Ratio and Longitudinal Reinforcement Diameter on Seismic Performance of Reinforced Concrete Bridge Columns,"

Report No. TIT/EERG 01-*, Tokyo Institute of Technology, Tokyo, Japan

Kawashima, K. (Cyclic loading test data of reinforced concrete bridge piers). http://seismic.cv.titech.ac.jp/en/titdata/titdata.html.

Wehbe NI, Saiidi MS, Sanders DH (1999), "Seismic performance of rectangular bridge columns with moderate confinement," ACI Struc. J.; 96(2): 248-259.

Fahmy MFM, Wu ZS, Wu G. (2009), "Seismic performance assessment of damage-controlled FRP-retrofitted RC bridge columns using residual deformations," J. Compos. Constr., ASCE, (13), 497-513.

Park R, Paulay T. (1975), "Reinforced concrete structures," John Wiley and Sons, 769pp.

Alsiwat JM, Saatcioglu M. (1992), "Reinforcement anchorage slip under monotonic loading," J. Struct. Enger. 118(9), 2421-2437.

Wu G, Wu ZS, Luo YB, Sun ZY, Hu XQ. Mechanical properties of steel fiber composite bar (SFCB) under uniaxial and cyclic tensile loads. Journal of Materials in Civil Engineering, ASCE, (submitted).

Spacone E, Filippou F, Taucer F. (1996), "Fiber beam-column model for nonlinear analysis of R/C frames-part II: applications," J. Earthquake Engineering and Structural Dynamics; 25: 727-742.

Mayer UU, Eligehausen R (1998), "Bond behavior of ribbed bars at inelastic steel strains," Proc. 2nd Inter. PhD Symposium in Civil Engineering, Budapest, hungry, 1-8.

Mander JB, Priestley MJN, Park R (1998), "Theoretical stress strain curve for confined concrete column." J. Struct. Enger., ASCE, 114(8), 1804-1826.

Menegotto M., Pinto PE (1973), "Method of analysis for cyclically loaded reinforced concrete plane frames including changes in geometry and nonelastic behavior of elements under combined normal force and bending," Proc. IABSE Symposium on Resistance and Ultimate Deformability of Structures Acted on by Well Defined Repeated Loads, Lisbon.

Zhao J, Sritharan S. (2007), "Modeling of strain penetration effects in fiber-based analysis of reinforced concrete structures," ACI Struct. J. 104(2), 133-141.

JOINT CONFERENCE PROCEEDINGS
7th International Conference on Urban Earthquake Engineering (7CUEE) &
5th International Conference on Earthquake Engineering (5ICEE)
March 3-5, 2010, Tokyo Institute of Technology, Tokyo, Japan

SEISMIC RETROFITTING OF RC COLUMNS BY CF ROPE AND ITS COMPUTATIONAL MODEL

Takumi Shimomura

Associate Professor, Department of Civil and Environmental Engineering, Nagaoka University of Technology, Japan
takumi@nagaokaut.ac.jp

Abstract: A seismic retrofitting method for RC pier and column using aramid and vinylon continuous fiber rope was developed. In this paper, series of test on load carrying behavior of RC column specimens with external continuous fiber rope under reversed cyclic load are presented. Effectiveness of continuous fiber rope to improve ductility of RC column is experimentally investigated. Load bearing mechanism of RC column with external continuous fiber rope is discussed. Based on the experimental results, a comprehensive computational model for load bearing behavior of RC column with external continuous fiber rope is proposed. Following mechanisms are considered in the model: development of plastic hinge at the bottom of the column, buckling of longitudinal reinforcement due to reversed cyclic load, spalling off of concrete cover and role of external rope to prevent spalling of concrete cover. Though it is simple, the proposed model can simulate envelope curve of load-displacement relationship of RC column and its ductility under reversed cyclic load as well as effectiveness of continuous fiber rope to improve member ductility.

1. INTRODUCTION

Since Japan is one of the earthquake prone countries, seismic retrofitting of existing concrete structure is essential matter in both building and civil engineering structures. Major seismic retrofitting method for existing reinforced concrete columns and piers are steel plate jacketing, concrete jacketing and continuous fiber sheet wrapping. The authors developed a new retrofitting method with continuous fiber (CF) rope as shown in Figure 1.

Different from conventional continuous fiber materials for concrete structures, such as continuous fiber sheets, rods and grids, CF rope can be adopted to concrete structures without epoxy resin. Therefore, some of the disadvantages of other conventional FRP reinforcements, for example difficulties in impregnating of epoxy resin, can be overcome. On the other hand, due to its lightweight and high flexibility, CF rope can be adapted to various shapes of structures and can be handled easily by hand. This makes the construction work on site easy, safe and economical. The authors have studied structural performance of concrete members reinforced with CF fiber rope (Shimomura et al. 2007, 2008). At the first stage of research, test method for tensile properties of continuous fiber rope was developed. Next, it was verified that the continuous fiber rope is effective to improve shear capacity of reinforced concrete beam when it is initially embedded in concrete as internal reinforcement. Then, it was clarified that ductility of existing concrete member under reversed cyclic load can be improved by retrofitting continuous fiber rope as external transverse reinforcement. However, CF rope that was retrofitted to concrete members as external shear reinforcement does not much increase shear capacity of the member unless bonded on the concrete tightly such with epoxy resin. Therefore, different from CF sheet, ductility of retrofitted member with CF rope can not be expressed as a function of its shear capacity nor shear-flexural capacity ratio.

In this study, a comprehensive computational model is developed, which can estimate load carrying capacity and ductility of RC column retrofitted with CF rope as external transverse reinforcement, taking into account the load carrying mechanism of CF rope in the structure based on the experimental observation.



Figure 1 Aramid Continuous Fiber rope

2. REVERSED CYCLIC LOADING TEST OF RC COLUMN SPECIMENS

2.1 Specimens and Test Method

In this paper, test results of typical three RC column specimens are presented. Specimen No.1 is a reference specimen without CF rope, while specimen No.1 and No.2 are to be retrofitted with CF rope. Details of the column

specimens before retrofitting are shown in Figure 2 and Table 1. The column specimens were designed to fail in shear after yielding of the longitudinal reinforcements. CF rope was wound by hand around the outside periphery of the columns as shown in Figure 3. Aramid CF rope was used. Spacing of CF rope is 25mm in specimen No.2 and 50mm in No.3. Steel plates were set between CF rope and the corners of the column to avoid rupture of the rope caught by concrete crack. No epoxy resin was used for bonding or anchoring CF Rope on the concrete surface.

The column specimens were tested under reversed cyclic load in horizontal direction. The loading point is 1800mm from the bottom of the column. 120kN vertical load simulating dead load was applied on the top. At first, column was loaded until yielding of longitudinal reinforcement was observed. The horizontal displacement of the column at the loading point at this stage was defined as the yield displacement (δy). Thereafter, reversed cyclic load was applied to the column specimen incrementally under deformation control, such as +1δy, -1δy, +2δy, -2δy, +3δy and -3δy. At each deformation step, three cycles of loading were repeated.

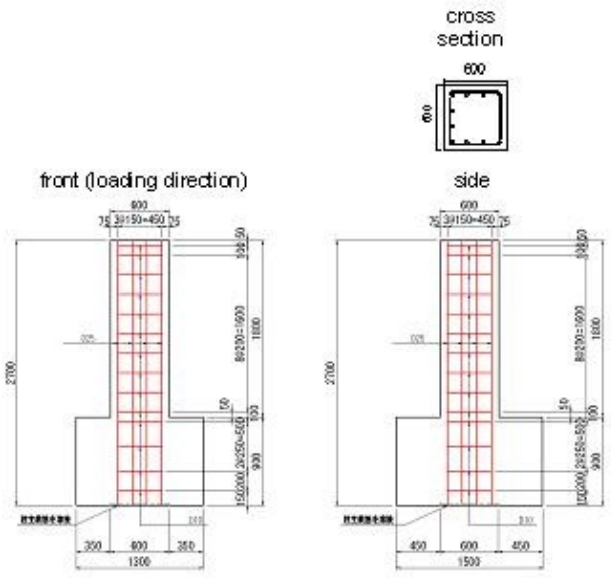

Figure 2 RC column specimen

Table 1 Test cases

Specimen	No.1	No.2	No.3
Spacing of CF rope	-	25mm	50mm
Cross sectional area of CF rope	-	11.53 mm^2	
Elastic modulus of CF rope	-	66700N/mm^2	
Longitudinal reinforcement	SD345, D25, spacing 150mm		
Transverse reinforcement	SD295, D10, spacing 200mm		
Concrete strength	28 N/mm^2		

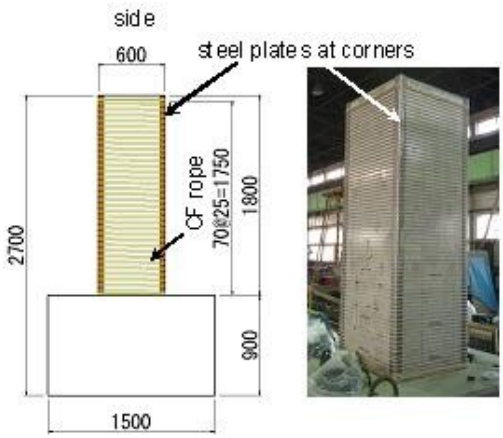

Figure 3 Retrofitting with CF rope

2.2 Test Results

With increasing of applied load, flexural cracks occurred in all specimens. Then, the cracks gradually developed in the diagonal direction. Thereafter, in case of the reference specimen No.1 without CF rope, buckling of longitudinal reinforcements and spalling-off of concrete cover were observed and the load bearing capacity suddenly decreased. On the other hand, in case of specimen No.2 and No.3 with CF rope, spalling-off of concrete nor sudden decreasing of the load was not observed. Their load gradually decreased. Figure 4 shows pictures of specimens just before the load decreased at the failure stage. Load-displacement curves of the specimens are shown in Figure 5, 6 and 7. Table 2 shows summary of the test results. Though there is no significant change in yielding load nor yielding displacement in spite of with/without CF rope, failure displacement that is defined as the displacement when the load decreases was increased by retrofitted CF rope.

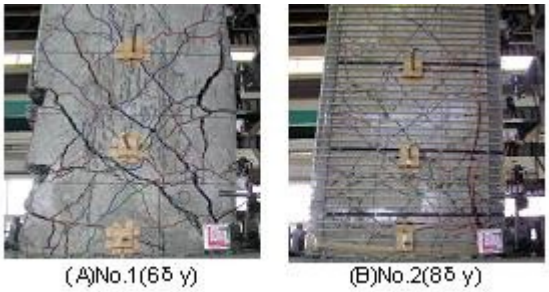

Figure 4 Crack pattern at failure

Table 2 Test results

Specimen		No.1	No.2	No.3
Spacing of CF rope		-	25 mm	50 mm
Yielding of longitudinal	Load	217.6kN	221.4kN	216.1kN
	Displacement(δ_y)	16.6mm	16.1mm	15.2mm
Failure stage (beginning of decreasing of load)	Load	267.4kN	279.4kN	271.9kN
	Displacement(δ_u)	64.6mm	85mm	73.1mm
		$5\delta_y$	$7\delta_y$	$6\delta_y$
Ductility	(δ_u /δ_y)	3.9	5.3	4.8

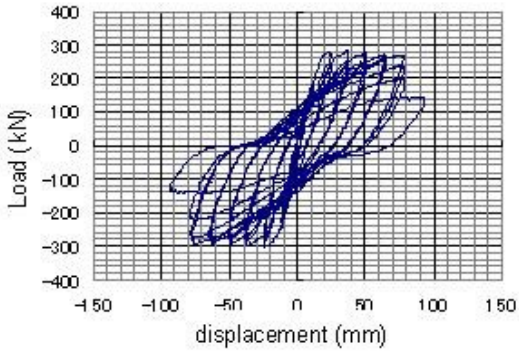

Figure 5 Load-displacement curve of Specimen No.1 (without CF rope)

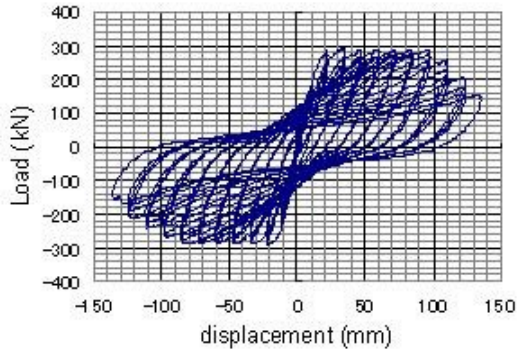

Figure 6 Load-displacement curve of Specimen No.2 (CF rope with 25mm spacing)

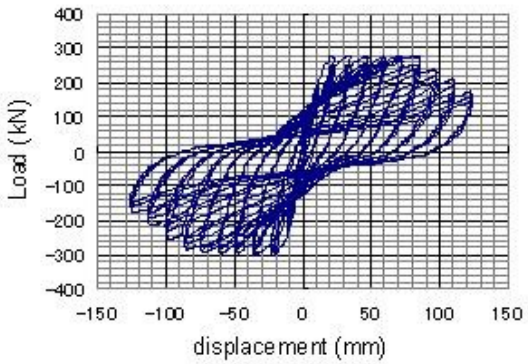

Figure 7 Load-displacement curve of Specimen No.3 (CF rope with 50mm spacing)

Figure 8 shows measured strain in CF rope at each loading step as a function of displacement. Strain of CF rope was measured by strain gauge attached on the rope at 250mm, 450mm and 650mm from the bottom of the column. According to Figure 8, strain of CF rope began to increase at the loading step of 4δy and suddenly increased around the failure stage (6 or 7δy). This implies role of CF rope in improvement of ductility of the member. With increasing in number of loading cycle, concrete cover is gradually crushed into blocks and pushed to outside by buckling of longitudinal reinforcements. When most of concrete cover is spalled off, load carrying mechanism in compression zone is no more kept. CF rope is expected to prevent spalling-off of concrete cover and maintain load carrying mechanism.

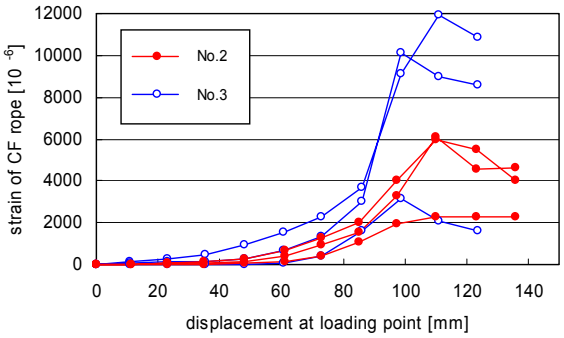

Figure 8 Strain of CF rope as a function of displacement of the member

3. MODELING OF LOAD CARRYING MECHANISM OF RC COLUMN WITH CF ROPE UNDER REVERSED CYCLIC LOADING

3.1 Outline

To estimate load-displacement curve of RC column with CF rope comprehensively, a computational model is developed. The concept of the model is to calculate ductility of the retrofitted structure based on simple assumptions concerning its load carrying mechanism that were observed in the experiment. Basic assumptions of the model are as follows.

1. Though actual column specimens are subjected to reversed cyclic load, monotonic load for one direction is considered
2. Before the yielding of the longitudinal reinforcements, load-deformation of the column is calculated ordinary flexural theory for reinforced concrete.
3. After yielding of the longitudinal reinforcements, flexural and shear cracks are represented one macro diagonal crack as shown in Figure 9 (a).
4. After yielding of the longitudinal reinforcements, deformation of the column is simulated by the rigid rotation of the separated part upper the crack as shown in Figure 9 (b). The rotation center is the tip of macro crack, which is locating at the bottom surface and xe from the compression edge.

3.2 Formulation

Deformation of the column

It is observed in the experiment that flexural cracks initially develop in horizontal direction and gradually propagate to diagonal direction with increasing in the deformation of the member. To express this tendency, direction of diagonal crack (θ) is evaluated as a function of the rotation angle of the crack (ρ).

$$\theta = m\rho \tag{1}$$

where m is a constant. From geometry, horizontal displacement of the loading point is expressed as:

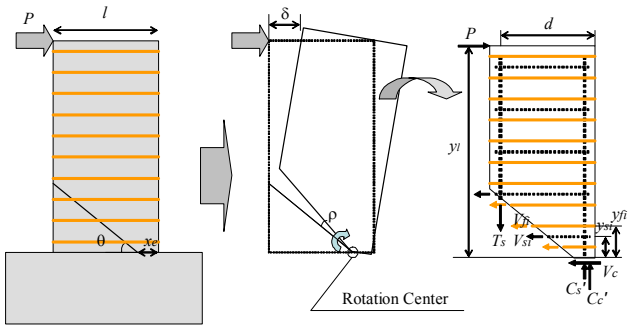

(a) RC column (b) Displacement by rigid rotation model (c) Equilibrium of external force on free body

Figure 9 Rigid rotation model for RC column under horizontal force

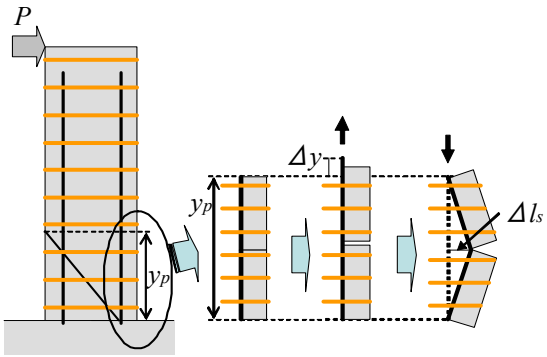

(a) RC column (b) initial (c) in tension (d) in compression

Figure 10 Expansive displacement of concrete cover under reversed cyclic load

$$\delta = \delta_y + \rho y_l \tag{2}$$

where δ_y is the displacement when longitudinal reinforcements yield.

Equilibrium in forces and bending moment

Equilibrium in horizontal forces, vertical forces and bending moment around the crack tip acting on the free body shown in Figure 9 (c) are respectively expressed as:

$$0 = V_c + \sum V_{fi} + \sum V_{si} - P \tag{3}$$

$$0 = T_s - C_c' - C_s' \tag{4}$$

$$\begin{aligned} 0 = {} & T_s(d - x_e) + \sum V_{fi} y_{fi} + \sum V_{si} y_{si} \\ & + C_c' z_c - C_s'(l - d - x_e) - P y_l \end{aligned} \tag{5}$$

where P is applied horizontal force, V_c is shear force carried by concrete, V_{fi} is tensile force of i th CF rope crossing the diagonal crack, V_{si} is tensile force of i th shear reinforcement crossing the diagonal crack, T_s is tensile force of longitudinal reinforcements in tensile side, C'_s is compressive force of longitudinal reinforcements in compression side and C'_c is integrated compressive force of concrete. Number of CF rope and shear reinforcement crossing the diagonal crack are depending on their spacing and angle and length of diagonal crack.

Strain and Stress in materials in the member

No bonding between CF rope and concrete is considered. Strain of i th CF rope is calculated from crack opening at the same position (w_i), which is a function of rotation angle (ρ).

$$\varepsilon_{fi} = \frac{w_i}{l} = \frac{\rho y_{fi}}{l} \tag{6}$$

Tensile force of i th CF rope is calculated as:

$$V_{fi} = A_f E_f \varepsilon_{fi} \tag{7}$$

where A_f is cross sectional area of one set of lateral CF rope and E_f is elastic modulus of CF rope. Strain and tensile force of i th shear reinforcement (V_{si}) is calculated by the same manner. Since longitudinal reinforcements yield already, their tensile force is:

$$T_s = A_s f_y \tag{8}$$

where A_s is cross sectional area of longitudinal reinforcements in tensile side and f_y is their yielding strength. Strain of concrete in compression edge is calculated as:

$$\varepsilon_c' = \rho \sqrt{\frac{x_e}{d}} \tag{9}$$

Strain distribution of concrete in compressive zone is evaluated based on beam theory. Stress of concrete in compression (σ'_c) is calculated by the Elasto-Plastic and Fractural model (Maekawa *et al*. 1983). Shear force carried by concrete (V_c) and compressive force of longitudinal reinforcements in compression side (C'_s) are not explicitly evaluated as functions of strain. These two variables, as well as the applied force (P), are obtained as solutions of Eq. (3), (4) and (5) under the given rotation angle (ρ).

Failure criteria

As failure criteria of the member, rupture of CF rope and failure of concrete cover are considered. When either of them is satisfied, the column is regarded as failed. Figure 10 schematically shows the latter one. Expansive displacement of concrete cover for radial direction (Δl_s) is calculated based on deformation compatibility longitudinal reinforcements and concrete cover in compression as shown in Figure 10 (d). Failure criterion of concrete cover is tentatively described in terms of its expansive displacement for radial direction (Δl_s), of which threshold value is assumed as a function of amount of

CF rope; i.e., greater limitation displacement is assumed in case of CF rope is retrofitted.

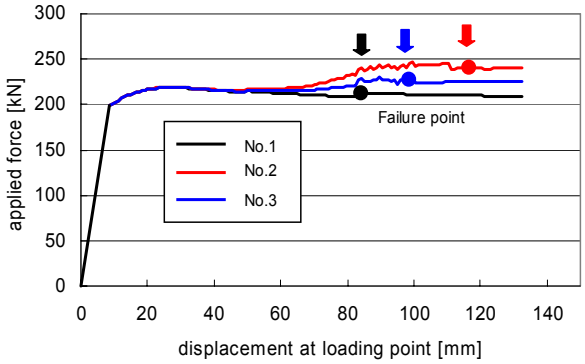

Figure 11 Calculated envelope curves of load-displacement relationship of the column specimens

4. RESULTS AND DISCUSSION

Figure 11 shows calculated envelope curves of load-displacement relationship of the column specimens No.1, 2 and 3 by the proposed model. Analytical results can well simulate experimental results in some aspects. There is no difference in load-displacement curves of three columns just after yielding of longitudinal reinforcements in spite of the existence of CF rope. With increasing of deformation, the difference among three columns is gradually emphasized. Specimen No.1 without CF rope was less ductile than Specimen with CF rope. Specimen No.3, in which CF rope is arranged in as small interval as 25mm, showed greatest ductility. However, some aspects in the experimental results can not be well simulated by the model at this moment. Though envelop of the experimental load-displacement curves descends when concrete in compression zone is failed, analytical load-displacement curve of the column with CF rope ascends slightly instead of descending around the ultimate stage. Mechanical role of CF rope at this stage should be more clarified and taken into account in the computational model in further study.

5. CONCLUSIONS

Load-carrying behavior of RC column retrofitted with external CF rope under reversed cyclic load is experimentally investigated. It is shown that CF rope can improve ductility of existing RC members by preventing spalling-off of crushed concrete in compression zone under reversed cyclic load. A comprehensive computational model predicting load-displacement curve of RC column with external CF rope was developed. It was verified that the model can simulate important tendency of load-carrying behavior of RC column with CF rope taking into consideration of role of CF rope.

Acknowledgements:

A series test of RC column with external CF rope is carried out in the joint research project among Nagaoka University of Technology, Nippon Expressway Research Institute Company Limited and Civil Engineering Research Institute for Cold Region.

References:

T. Shimomura and N. H. Phong, (2007). "Structural Performance of Concrete Members Reinforced with Continuous Fiber Rope", 8th International Symposium on Fiber Reinforced Polymer Reinforcement for Concrete Structures (FRPRCS 8), Patras.

T. Shimomura, S. Kawana and Y. Tanaka (2008). "Ductility and Shear Capacity of Reinforced Concrete Members Retrofitted with Continuous Fiber Rope", the 5th International Conference on Advanced Materials in Bridges and Structures (ACMBS-V), Winnipeg.

A. Kamiharako, K. Maruyama and T. Shimomura (1999). "Evaluation systems of capacity of reinforced concrete members retrofitted with carbon fiber reinforced polymer sheets in consideration of bond-peeling characteristics", Fourth International Symposium on Fiber Reinforced Polymer Reinforcement for Reinforced Concrete Structures (FRPRCS 4), Baltimore.

K. Maekawa and H. Okamura (1983), "Constitutive Equation of Concrete Based on the Elasto-Plastic and Fractural Model", *Concrete Journal, Japan Concrete Institute*, **21**(5), 87-99.

JOINT CONFERENCE PROCEEDINGS
7th International Conference on Urban Earthquake Engineering (7CUEE) &
5th International Conference on Earthquake Engineering (5ICEE)
March 3-5, 2010, Tokyo Institute of Technology, Tokyo, Japan

TRAIN-RUNNING SAFETY DURING SEISMICITY ON RAILWAY VIADUCT GROUP AND ITS IMPROVEMENT

Masamichi Sogabe[1], Kouji Matsuhashi[2], Keiichi Goto[3]
Yukihiro Tanimura[4] and Kiyoshi Asanuma[5]

1) Senior Researcher, Railway Dynamics Division, Railway Technical Research Institute, Japan
2) Senior Engineer, Railway Division, Pacific Consultants Co., LTD., Japan
3) Researcher, Railway Dynamics Division, Railway Technical Research Institute, Japan
4) Laboratory Head, Railway Dynamics Division, Railway Technical Research Institute, Japan
5) Laboratory Head, Structural Technology Division, Railway Technical Research Institute, Japan
sogabe@rtri.or.jp

Abstract: To evaluate train-running safety during seismicity on an entire railway line quantitatively, we should use risk analysis method. A lot of studies for seismic risk management were widely performed in various kinds of research fields. However, the study for fragility curve of train-running safety has not conducted and its basic characteristics have not obtained. Through this study, we clarified the *PGA* and *PGV* fragility curves on entire railway line based on a numerical analysis, as well as influence of train-running direction and phase difference of earthquake motions. We also investigated verification for vehicle guide device, that minimized damage when railway vehicle was derailed by a large-scale earthquake.

1. INTRODUCTION

In order to examine seismic train-running safety and effects of seismic countermeasures of an entire railway line quantitatively, establishing a risk assessment system which is intended for an entire railway line and enables us to make a precise decision for investment is essential. For an earthquake hazard curve (which indicates year exceeding probability to earthquake ground motion index) among risk assessment components, a commercial software is on sale, and much progress is made in the other research field. On the other hand, discussions on an event tree (damage pattern classification), fragility curve of each damage pattern (probability of damage occurrence to earthquake ground motion index), and cost of each damage pattern, which are unique to railway, are not accurate enough and thought to be included in critical future agenda. Especially, fragility curve associated with seismic train-running safety of railway structures has not been studied at practical level yet, and we have not grasped a true figure of it.

Against such a background, we authors have proceeded with the study on fragility curve computation. In this study, we set two goals described below.

(1) To clarify the fundamental properties of fragility curve on entire railway line in numerical experiments, specifically the effect of *PGA*, *PGV*, train-running direction and input phase difference of earthquake motion.

(2) To investigate verification for vehicle guide device on the fragility curves, that minimized damage when railway vehicle was derailed by a large-scale earthquake.

2. ANALYSIS METHOD

A program called DIASTARSIII, which analyzes dynamic interaction between railway vehicles and railway structures, was used in the numerical analysis.

2.1 Dynamic Model of Vehicle

Table 1 and Fig. 1 show a dynamic model of the vehicle. The vehicle model was created by connecting each element of a vehicle body, 2 truck frames and 4 wheelsets which were modeled at rigid masses with springs and dampers. Then, a vehicle has 31 degrees of freedom. The actual vehicle has stoppers between each element part to control significant relative displacement. In order to consider this, bi-linear non-linear springs were used for springs. In analysis, a train is composed of several vehicles. Adequacy of these dynamic models has already been verified through vibration experiment using a vibration table and a full-scale vehicle model.

Tangible vehicle specifications were assumable in reference to a recent high-speed Shinkansen train vehicle. The main input data (for an empty vehicle) were 25m of a vehicle length, 32.0t of body mass, 3.0t of truck frame mass,

Table 1 Notations of Dynamic Model of Vehicle

Items	Not.	Items	Not.	Items	Not.
Half of longitudinal distance between center pivots of fore and rear truck	L	Half of mass of car body	m	Longitudinal spring constant for air spring (half side of one truck)	K_1
Half of wheelbase	a	Half of inertial moment of car body around x axis	I_x	Longitudinal damping constant for yaw damper (half side of one truck)	C_1
Half of lateral distance between contact points of wheel and rail	b	Half of inertial moment of car body around y axis	I_y	Lateral spring constant for air spring (half side of one truck)	K_2
Half of lateral distance between yaw dampers	b_0	Half of inertial moment of car body around z axis	I_z	Damping constant for lateral damper (half side of one truck)	C_2
Half of lateral distance between axle springs	b_1	Mass of truck	M_T	Vertical spring constant for air spring (half side of one truck)	K_3
Half of lateral distance between air springs	b_2	Inertial moment of truck around x axis	I_{Tx}	Vertical damping constant for air spring (half side of one truck)	C_3
Height of center of gravity of car body from rail head	H_b	Inertial moment of truck around y axis	I_{Ty}	Longitudinal spring constant for wheelset (half side of one wheelset)	K_{wx}
Height of center of gravity of truck from rail head	H_T	Inertial moment of truck around z axis	I_{Tz}	Lateral spring constant for wheelset (half side of one wheelset)	K_{wy}
Vertical distance between center of gravities of wheelset and car body	h_1	Mass of wheelset	M_w	Vertical spring constant for axle spring (half side of one wheelset)	K_{wz}
Vertical distance between center of air spring and center of gravity of car body	h_2	Inertial moment of wheelset around x axis	I_{wx}	Vertical damping constant for axle damper	C_{wz}
Vertical distance between center of gravity of truck and center of air spring	h_s	Inertial moment of wheelset around z axis	I_{wz}	Static wheel force	P_s
Nominal radius of wheel	r				
Half of length of car body	L_c				

2.0t of wheelset mass, 200kN/m of vertical and horizontal spring constants for air-spring (half side of one truck), 25kN·s/m of damping constant for air-spring (half side of one truck), 20kN·s/m of damping constant for lateral damper (one damper of one truck), 1200kN/m of spring constant for axle spring (half side of one wheelset) and 40kN·s/m of damping constant for axle damper (half side of one wheelset). In addition, expansion gaps between each stopper were set to be 20-30mm. In this study, we used 8-car train.

Equations of motion for vehicle system in vehicle coordinate system is shown as Eq. (1) after transposing non-linear spring terms between each element to right- hand side.

$$\boldsymbol{M}^V \ddot{\boldsymbol{X}}^V + \boldsymbol{C}^V \dot{\boldsymbol{X}}^V + \boldsymbol{K}^V \boldsymbol{X}^V = \boldsymbol{F}_L^V + \boldsymbol{F}_\Gamma^V(\boldsymbol{X}^V, \boldsymbol{X}^B) + \boldsymbol{F}_N^V(\boldsymbol{X}^V) \quad (1)$$

where, affixing character V and B are the vehicle and the bridge, respectively; $\boldsymbol{X}^V$ is a displacement vector of vehicle; $\boldsymbol{M}^V, \boldsymbol{C}^V, \boldsymbol{K}^V$ are the mass, damping and stiffness matrices of vehicle, respectively; $\boldsymbol{F}_L^V$ is load vectors of wind pressure; $\boldsymbol{F}_\Gamma^V(\boldsymbol{X}^V, \boldsymbol{X}^B)$ is interaction load vectors with structure; $\boldsymbol{F}_N^V(\boldsymbol{X}^V)$ is load vectors of non-linear spring force of vehicle model assumed external forces.

2.2 Dynamic Model between Wheels and Rails

Figure 2 shows the vertical dynamic model between wheel and rail. The vertical relative displacement δz between the wheel and the rail can be shown as Eq. (2).

$$\delta_z = z_R - z_W + e_Z + e_{Z0}(y) \quad (2)$$

where, z_R and z_W were vertical displacements at the contact point of the rail and the wheel; e_Z was vertical track

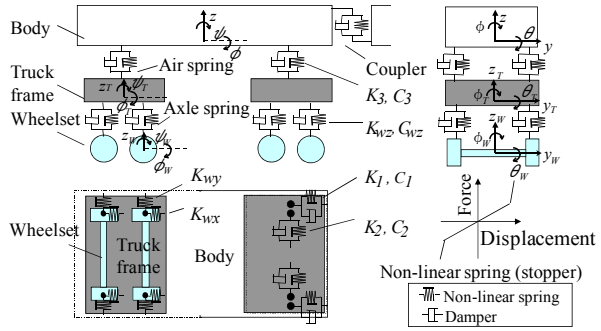

Figure 1 Vehicle Dynamic Mode

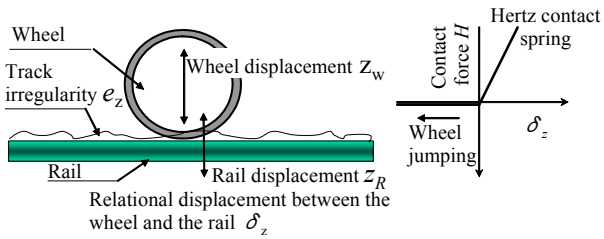

Figure 2 Vertical Dynamic Model between Wheel and Rail

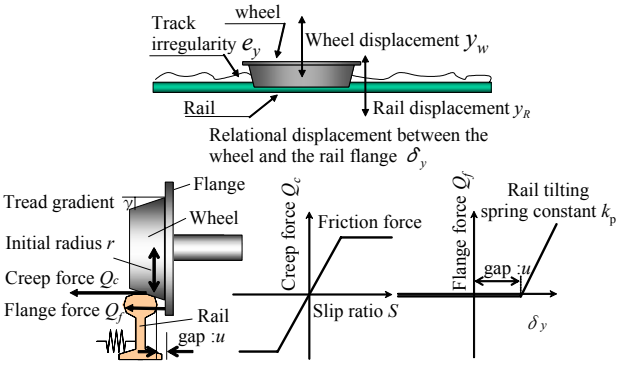

Figure 3 Horizontal Dynamic Model between Wheel and Rail

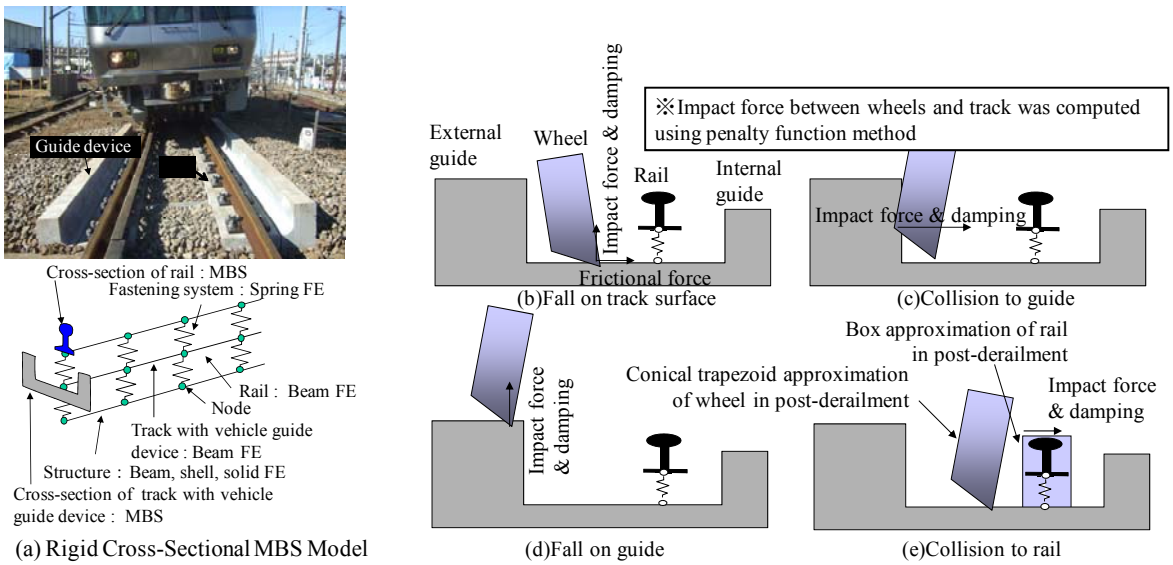

Figure 4 Dynamic Model of Wheel and Vehicle Guide Device

irregularity existing on the rail shown in Fig. 2; e_{Z0} is the amount of change of the wheel radius at the current contact point from initial wheel radius, which is shown as a function of horizontal relative displacement y between the wheel and the rail.

A contact point s and contact angle a for the relative displacement δ_z are calculated with the horizontal relative displacement y of the wheel and the rail and the contact function set in accordance with geometric shapes of the wheel and the rail. When the wheel and the rail consist of quadric surface respectively, the relation between the relative displacement δ of the wheel and the rail of the contact surface normal direction and the contact force H can be shown with the *Hertz* contact spring, as indicated in Eq. (3).

$$H = H(\delta) = H(\delta z \cdot \cos a) \tag{3}$$

The vertical component and the horizontal component of this contact force H were distributed to the wheel and the rail respectively to make the interaction force.

Figure 3 shows the horizontal dynamic model between wheel and rail. The horizontal relative displacement δy between the wheel flange and the rail can be shown as Eq. (4).

$$\delta_y = y - u(\delta_z) = y_w - y_R - e_y - u(\delta_z) \tag{4}$$

where, y is the horizontal relative displacement between the wheel and the rail; y_R and y_W are horizontal displacements at the contact point of the rail and the wheel; e_y is horizontal track irregularity existing on the rail shown in Fig. 3; $u(\delta_z)$ is the gap between the wheel flange and the rail which was shown as a function of vertical relative displacement δ_z.

A contact point s and contact angle a for the relative displacement δ_y were calculated with the vertical relative displacement δ_z of the wheel and the rail and the contact function set in accordance with geometric shapes of the wheel and the rail.

When $\delta_y<0$, it was considered that the wheel flange and the rail were not in contact. In this case, creep force Q_c acted horizontally on the contact surface of the wheel and the rail. The creep force was the tangential force caused by creep of the wheel moving forward by rolling on the rail, which can be shown as Eq. (5). This creep force was saturated with the upper limit of friction force when the creepage became high.

$$Q_c = C \cdot S_y = C \cdot (\dot{y}_w + r\dot{\phi}_w - v\varphi_w)/v \tag{5}$$

where, C is the creep coefficient; S_y is the lateral creepage; v is the train speed; r is the nominal radius.

When $\delta_y \geqq 0$, it was considered that the wheel flange and the rail were in contact. For the flange contact, only the flange pressure Q_f was considered. The flange pressure Q_f can be shown as Eq. (6) using the rail tilting spring constant k_p.

$$Q_f = k_p \cdot \delta_y \tag{6}$$

Figure 4 shows a dynamic model of each wheels and vehicle guide device, which minimized damage when railway vehicle was derailed by a large-scale earthquake. Interaction force between wheels and rails after derailment was computed by modeling the track structure including wheels and vehicle guide devices with Multi Body System (MBS). The post-derailment wheels of the used model were approximated to a divisional straight line (conical trapezoid) to speed up the analysis. A "Rigid Cross-Sectional MBS Model" with internal and external vehicle guide devices was employed for the track structure. Collision of wheels and track structure members was expressed by a non-linear collision spring. Ladder-type sleepers with a 235mm vehicle guide device (external guard type) were used as an example for analysis in this study.

Both of the two dynamic models explained above were used separately as running condition (derail or not) with

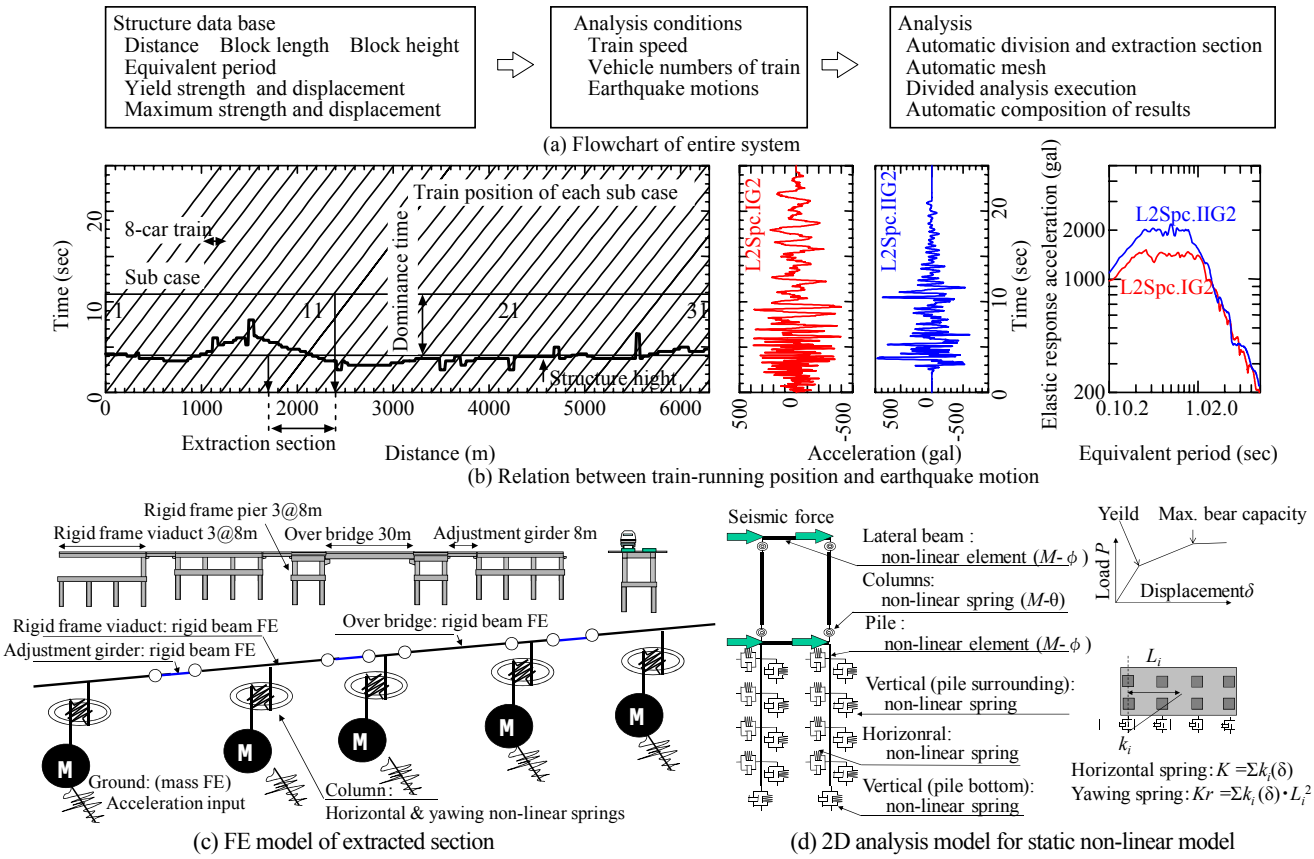

(a) Flowchart of entire system

(b) Relation between train-running position and earthquake motion

(c) FE model of extracted section

(d) 2D analysis model for static non-linear model

Figure 5 Dynamic Model of Structure

each wheelset.

2.3 Dynamic Model of Structure

Figure 5 shows the analysis system for the entire continuous structure group. This system picks up an analysis section automatically and creates an analysis model based on the structure database and analysis conditions, as shown in Fig. 5(a). After the analysis is done, the system integrates the analysis results and evaluates the entire railway line.

Structure arrangement of model line shown in Fig. 5(b) was determined based on the statistical analysis of the actual structures. In evaluating the entire railway line, loading vehicles on the entire railway and analyzing them is ideal, however; it gives structures and vehicles an extensive degree of freedom. Thus, a method to divide an 8-car train into 1 sub case, as shown in Fig. 5(b) was suggested. In this method, an extracted section of each sub case was calculated based on dominance time (time when there is the strongest power to cause derailment) predetermined for each earthquake ground motion. For example, in sub case 11, necessary extraction section has distance from 1700 to 2400m. The extracted section was modeled by Finite Elements (FE) with automatic mesh. A pre-run section and post-run section were provided as semi-infinite running section, based on average vibration characteristics of structures in the vicinity of the extracted section. Thus, accuracy of the train-running safety evaluation unit is the interval of 25m, which is the length of one car, from the viewpoint of vehicles, and from the viewpoint of the wheel axis, it is the interval of wheel axis.

In this study, the target of our analysis was a 6.3km-long double track viaduct. We set a three-span rigid-frame viaduct of adjustment girder type (block length of 24m) as a fundamental unit of the structures.

Figure 5(c) shows a specific FE model of the extracted section. Each block of the rigid frame and adjustment girder is modeled as a rigid beam element. The mass and the non-linear property of each structure are determined based on the design calculation for the actual structure (an item to input in the database). Using a 2D analysis model, a static non-linear push-over analysis is conducted on the cross-section of each column, and the relation between the load and displacement is researched. Horizontal and yawing springs on the center of gravity are computed from these obtained skeleton lines as shown in Fig. 5(d). A hysteresis model of the horizontal non-linear spring is a standard tri-linear. The damping ratio ξ of the structures were fixed to 5%.

Equations of motion for structure system is shown as Eq. (7)

$$\boldsymbol{M}^B\ddot{\boldsymbol{X}}^B+\boldsymbol{C}^B\dot{\boldsymbol{X}}^B+\boldsymbol{K}^B\boldsymbol{X}^B=\boldsymbol{F}_L^B+\boldsymbol{F}_\Gamma^B(\boldsymbol{X}^V,\boldsymbol{X}^B)+\boldsymbol{F}_N^B(\boldsymbol{X}^B) \quad (7)$$

where, $\boldsymbol{X}^B$ is a displacement vector of bridge; $\boldsymbol{M}^B,\boldsymbol{C}^B$ and $\boldsymbol{K}^B$ are the mass, damping and stiffness matrices of bridge, respectively; $\boldsymbol{F}_L^B$ is a load vector of earthquake or wind pressure of bridge; $\boldsymbol{F}_\Gamma^B(\boldsymbol{X}^V,\boldsymbol{X}^B)$ is an interaction load vector with vehicles; $\boldsymbol{F}_N^B(\boldsymbol{X}^B)$ is a load vector of

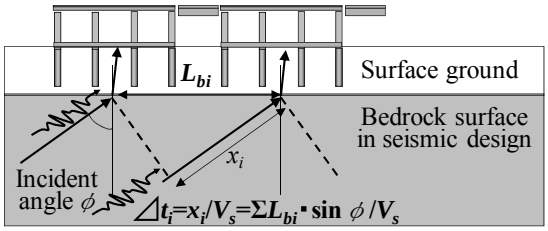

Figure 6 Time Difference of Shear Wave

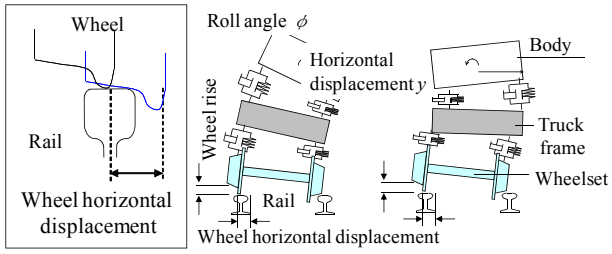

Figure 7 Derailment Mode and Criterion of Train-running Safety

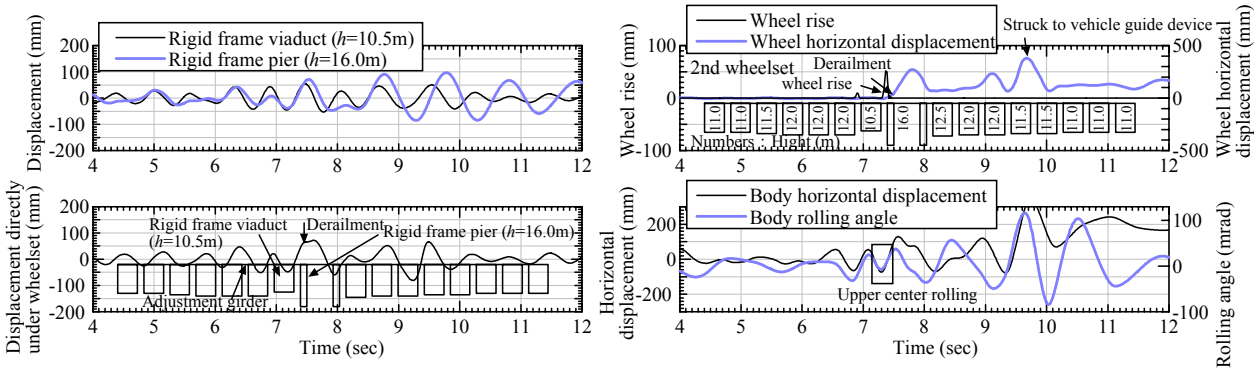

Figure 8 Example of Time Series Wave Profiles (L2 spectrum I of ocean-trench type with *PGA*=240gal)

non-linear spring force of bridge model assumed outside load.

As stipulated in Design Standards for Railway Structures and Commentary (for Seismic Design), L2 spectrum I of ocean-trench type and L2 spectrum II of inland active faults type (level 2 means large scale earthquake) were used for input earthquake ground motion. The simulated surface ground was G2 (diluvium: 0.25 and shorter ground natural period T_g). Since the vehicle response had strong non-linearity, seismic peak ground acceleration (*PGA*) was gradually and linearly increased in the study.

Figure 6 shows the setting method of seismic phase difference. The phase difference was simply computed by difference of shear wave transmission pathway as shown in Eq. (8).

$$\Delta t_i = x_i / V_s = L_{bi} \cdot \sin\phi / V_s \qquad (8)$$

where, Δt_i is arrival time difference between structure i and i -1; x_i is pathway difference of shear wave transmission between structure i and i -1; V_s is shear wave velocity in the bedrock surface in seismic design; ϕ is incident angle. In the setting, V_s=400m/s and ϕ=30° were assumed. The phase difference between each block was 0.04 (s).

2.4 Numerical Method

Equations of motion of the train and stracture shown as Eq. (1) and (7) were solved in the modal coordinates for each time increment Δt by the *Newmark* time difference scheme. Since the equations were non-linear, iterative calculations were necessary during each time increment until the unbalanced force between the train and viaduct became sufficiently small within the specified tolerance.

2.5 Evaluation Criterion

Figure 7 shows the derailment mode and the criterion of train-running safety during seismicity. The criterion used the wheel horizontal displacement in accordance with the Design Standards and Interpretation of Railway Structures (for Displacement Limits). In addition, the limit value was set to be 70mm. As the wheel horizontal displacement rapidly increase when the wheel rise exceeds the flange height (30mm), the wheel rise was also as shown in Fig. 7.

The vehicle derailment modes during an earthquake were classified broadly into upper and lower center rolling which were distinguished at less than 0.7 Hz and more than 1.3 Hz respectively. However, this was determined by phases of horizontal and rolling movements of the vehicle shown in Fig.7 (refer to Fig. 1 for the coordinate system) .

3. ANALYSIS RESULT

3.1 Time series wave profiles

Figure 8 shows an example of time series wave profiles when a derailment occurs. A response of the L2 spectrum I of ocean-trench type with *PGA*=240gal is shown. The rigid frame viaduct and pier turned out to have 50mm relative displacement at 7 seconds. It was discovered that the structural Horizontal displacement directly under the wheel axis vibrated at 2Hz and total amplitude 80mm in around 7 seconds. Wheels started rising on the adjustable girders between the rigid frame viaduct and pier, and derailment occurred when wheel horizontal displacement exceeded 70mm. The derailed wheels struck to the vehicle guide device in 9.7 seconds. The vehicle horizontal displacement and vehicle roll angle were in the same phase at the time of derailment occurrence, and it was assessed that upper center rolling resulted in derailment.

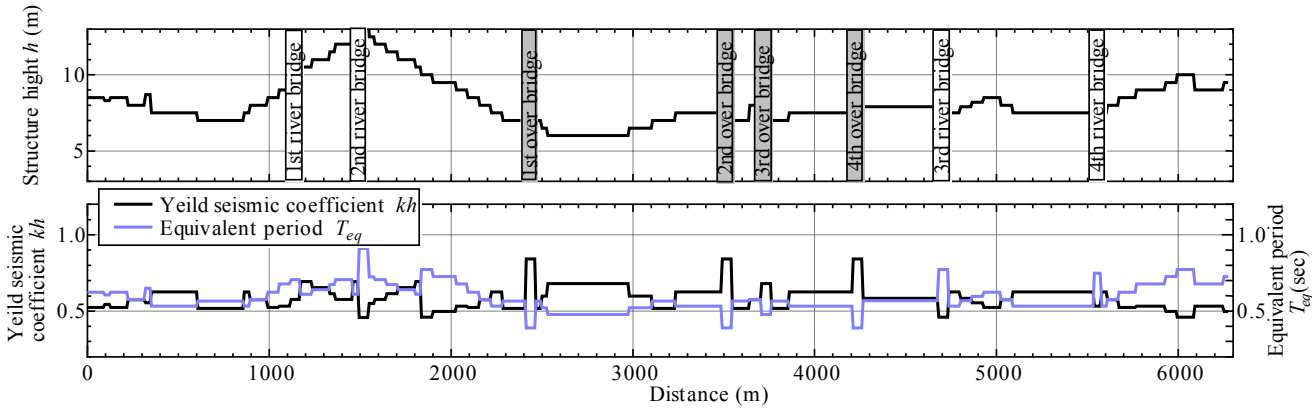

Figure 9 Specifications of Entire Model Line

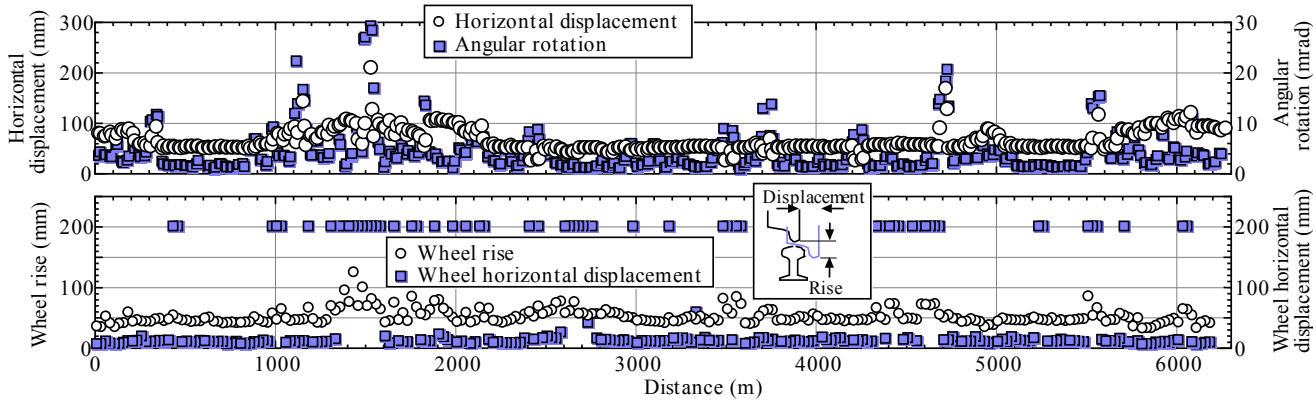

Figure 10 Maximum Response of Structure and Train (L2 spectrum I of ocean-trench type with *PGA*=240gal)

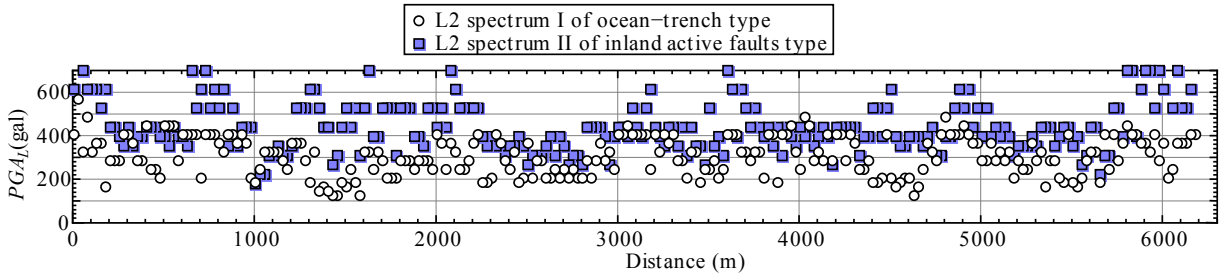

Figure 11 Limits of Peak Ground Acceleration PGA_L for Train-running Safety

3.2 Basic Characteristics of Train-Running Safety

Figure 9 and Figure 10 show specifications of the entire model line and maximum response of analysis results respectively. Structure arrangement of model line was determined based on the statistical analysis of the actual structures as described previously. A response of the L2 spectrum I of ocean-trench type with *PGA*=240gal is shown. The figure shows the maximum value of the vehicle response in each one vehicle at the running position of 8 seconds for the ocean trench type, and 6 seconds for the inland active faults type. Horizontal movement of wheels which exceeds 200mm is expressed as 200mm. Equivalent natural period of a high pier river bridge is longer than that of rigid frame viaduct, and the river bridge tends to have larger displacement. On the other hand, there is a tendency an over bridge has a shorter equivalent natural period and smaller displacement than the rigid frame viaduct do. Since angular rotations are likely to occur on the border of such structures, wheel rise and horizontal displacements were inclined to increase.

Figure 11 shows the limit of peak ground acceleration PGA_L, which contains horizontal displacement of wheel exceeding 70mm. The L2 spectrum I of ocean-trench type, which has more frequent repeats of equivalent waves, has more severe PGA_L than L2 spectrum II of inland active faults type. It indicates that PGA_L is apt to decrease at the point of vibration property change in the railway line.

3.3 Fragility Curves of Train-Running Safety

Figure 12 shows a fragility curve of seismic train-running safety of the modeled railway line. Based on the assumption in the figure, numerical analysis results shown in Fig. 11 were organized. In Fig.11, we performed running safety evaluation aimed at 248 of vehicle running position (evaluation unit was 25m length of vehicle). In Fig. 12, we firstly computed vehicle existing probability in 25m evaluation unit (about 1.5%). Probabilities of damage

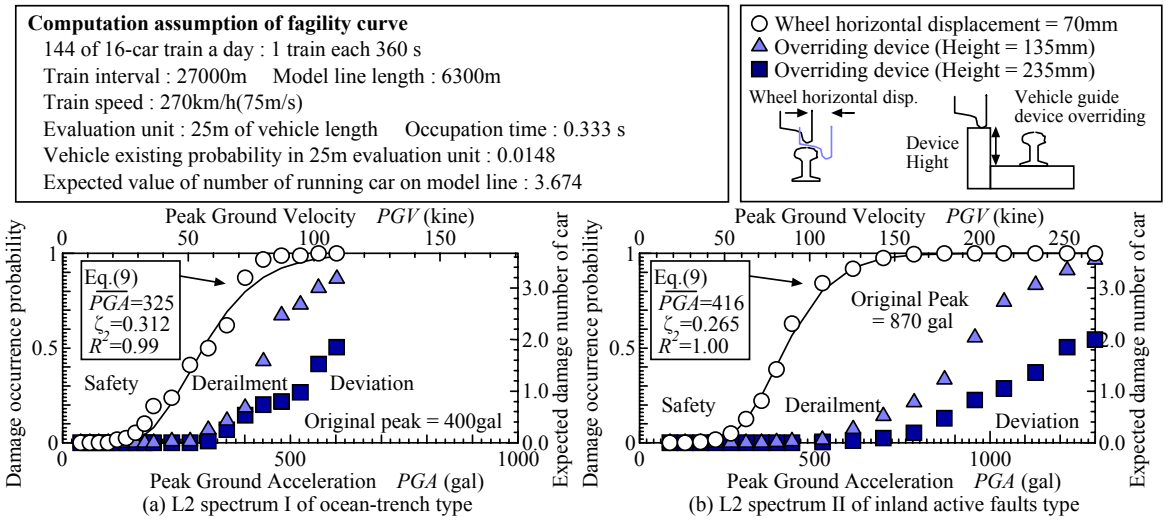

Figure 12 Fragility Curve of Seismic Train-Running Safety of Modeled Railway Line

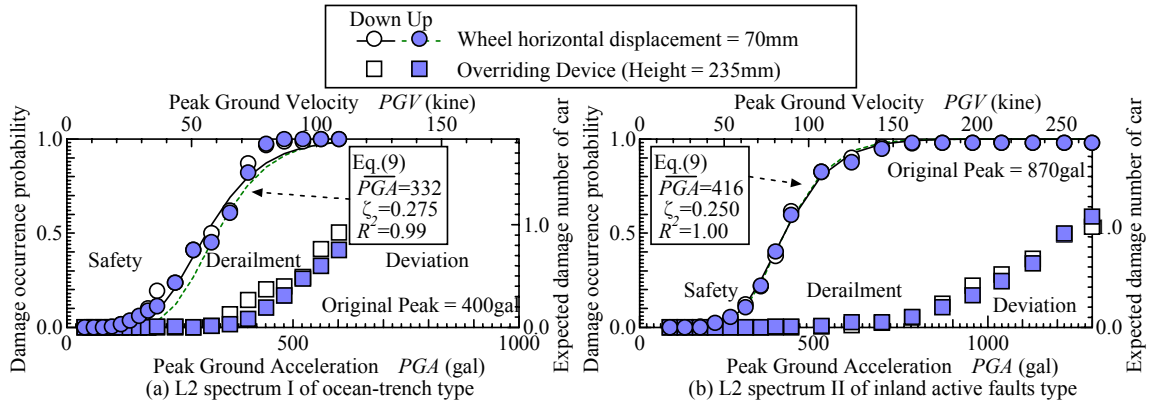

Figure 13 Effects of Vehicle Running Direction on Fragility Curve

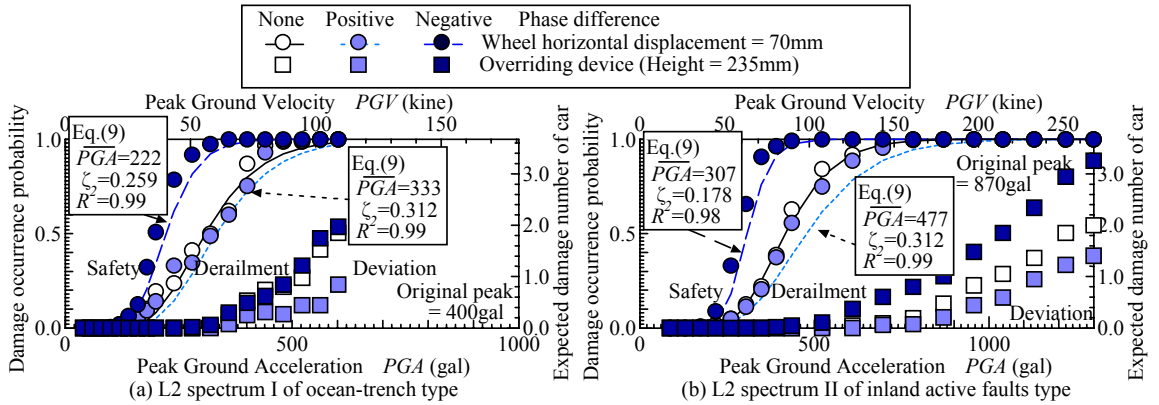

Figure 14 Effects of Earthquake Motion Phase Difference on Fragility Curve

occurrence were computed by counting derailment or deviation vehicles, increasing seismic peak ground acceleration (*PGA*) gradually and linearly. Each plot in Fig.12 becomes the fragility curves which separate safety, derailment and deviation zone respectively. In addition, we show the seismic peak ground velocity (*PGV*) as 2nd horizontal axis in Fig.12.

In the risk assessment, the fragility curves are generally expressed by the lognormal cumulative distribution function as shown in Eq. (9).

$$P_{dr}(PGA) = \Phi \frac{\ln(PGA - \overline{PGA})}{\zeta} \tag{9}$$

where, $P_{dr}(PGA)$ is probability of damage occurrence; Φ is standard normal cumulative distribution function; $\overline{PGA}$ is average *PGA* of damage occurrence; ζ is the standard deviation of lognormal distribution function.

The standard deviation of lognormal distribution function ζ became 0.32 for the L2 spectrum I of ocean-trench type, and 0.26 for L2 spectrum II of inland active faults type.

The ladder type sleepers with vehicle guide device were found out to have about 10% of deviation damage occurrence rate to original wave of each earthquake ground motion and to be very effective to large scale earthquake motions. The figure also implies that lowering the height of device (height 135mm) reduces the effect of deviation prevention performance.

Figure 13 indicates effects of a vehicle running direction on the fragility curve. The analysis target model did not show any effects of a vehicle running direction on the fragility curve.

Figure 14 indicates effects of earthquake motion phase difference on the fragility curve. The earthquake motion transmitted in the same direction as vehicles running is defined as positive, while that in the opposite direction is defined as negative. As seen in the figure, the train-running safety degrades when the earthquake motion is transmitted to the opposite direction of the vehicle running. This is because the time axis of the earthquake motion is compressed apparently due to train running. The degradation is consistent with the tendency of safety limit curve by sinusoidal wave vibration, that is, higher vibration frequency with the same amplitude increases risk of derailment.

4. CONCLUSIONS

(1) We clarified the basic characteristics of the fragility curves of train-running safety during seismicity on railway viaduct group. The standard deviation of lognormal distribution function ζ became 0.32 for the L2 spectrum I of ocean-trench type, and 0.26 for L2 spectrum II of inland active faults type.
(2) The analysis target model did not show any effects of a vehicle running direction on the fragility curve.
(3) The train-running safety degrades when the earthquake motion is transmitted to the opposite direction of the vehicle running.
(4) We clarified that vehicle guide device were very effective to large scale earthquake motions, and higher vehicle guide devices increased the effect of deviation prevention performance.

References:

Railway Technical Research Institute (1999), "Design Standard for Railway Structures (for Seismic Design)," Maruzen.

Railway Technical Research Institute (2006), "Design Standard for Railway Structures (for Displacement Limits)," Maruzen.

Sogabe, M., Harada, K. and Watanabe, T. (2009), "Vehicle Running Quality during Earthquake on Railway Viaducts," *Proceedings of the International Symposium on Speed-up, Safety and Service Technology for Railway and Maglev System 2009* (*STECH'09*), CD-ROM No.360713

Sogabe, M., Matsumoto, N., Fujino, Y., Wakui, H., Kanamori H. and Miyamoto, M. (2003), "Dynamic Response and Design of Concrete Railway Bridge in Resonance Area," *Journal of Structural Mechanics and Earthquake Engineering,* Japan Society of Civil Engineering, No. 724/I-62, 83-102.

Miyamoto, M., Matsumoto, N., Sogabe, M., Shimomura, T., Nishiyama, Y. and Matsuo, M. (2004), "Railway Vehicle Dynamic Behavior against Large-Amplitude Track Vibration – A Full-scale Experiment and Numerical Simulation," *Quarterly Report of RTRI*, Vol. 45, No. 3, 111-115

JOINT CONFERENCE PROCEEDINGS
7th International Conference on Urban Earthquake Engineering (7CUEE) &
5th International Conference on Earthquake Engineering (5ICEE)
March 3-5, 2010, Tokyo Institute of Technology, Tokyo, Japan

SHEAR RETROFITTING METHOD FOR RC BEAM USING UFC PANELS

Koji Matsumoto[1)], Kou Shibata[2)], and Junichiro Niwa[3)]

1) Post-Doctoral Fellow, Center for Urban Earthquake Engineering, Tokyo Institute of Technology, Japan
2) Master Course Student, Department of Civil Engineering, Tokyo Institute of Technology, Japan
3) Professor, Department of Civil Engineering, Tokyo Institute of Technology, Japan
matsumoto.k.ar@m.titech.ac.jp, shibata.k.ae@m.titech.ac.jp, jniwa@cv.titech.ac.jp

Abstract: Shear strengthening method for RC beams using UFC (Ultra High Strength Fiber Reinforced Concrete) panels is presented in this paper. Totally 10 specimens were prepared and UFC panels were attached by epoxy resin and anchor bolts. Experimental parameters in this study are panel thickness, panel location and existence of stirrups. Result obtained in the four point loading test shows that UFC panels considerably enhance shear carrying capacity of RC beams. In addition, shear carried by UFC panels in the experiment was quantified and then the effect of each parameter on the shear capacity was discussed. Furthermore, the experimentally observed shear carried by UFC panels was compared with computational result obtained using the fictitious diagonal crack model. As a result, failure mode of the strengthened beams was classified and the failure mechanism was investigated.

1. INTRODUCTION

In the Great Hanshin Earthquake 1995 Japan, many reinforced concrete (RC) members collapsed in shear. Hence, infrastructures were catastrophically damaged, economy slaw down and a lot of human lives were lost. To reduce social damage in the next coming great earthquake, Japan Society of Civil Engineers (JSCE) and Architectural Institute of Japan (AIJ) have revised their design code for shear of RC members. Thus, newly-constructed structures satisfy safer structural performance, however, more practical problem is repairing and strengthening of existing structures because of the financial situation in Japan and other countries.

As methods for repairing and strengthening of RC members, surface treatment, resin injection for cracks, cross-sectional restoration, steel plate attachment, FRP sheet attachment, external cable prestressing have been proposed and started to be used. However, these methods have some problems such as corrosion and heavy weight of steel plate and brittle failure of FRP material. On the other hand, UFC (Ultra High Strength Fiber Reinforced Concrete) is an advanced cementitious material which has high strength, ductility and durability (Katagiri et al. 2002). Kakei et al. conducted loading tests of UFC beams and reported that bridging effect of steel fibers contained in UFC dramatically enhance shear carrying capacity of beams (Kakei et al. 2004).

Because of the above point of view, the authors have conducted studies on strengthening method for RC members using externally bonded UFC panels (Shibata et al. 2008 and 2009). As a result, they reported that UFC panels considerably enhance shear carrying capacity and stiffness. However, it still has a problem in terms of labor cost due to its huge size.

To solve this problem, this study employs a strengthening method using strip-shaped panel, in which a number of smaller pieces of UFC panels are used. Loading test of RC beams strengthened by strip-shaped UFC panels was conducted and the shear carrying capacity, failure mechanism and failure mode was investigated.

2. OUTLINE OF THE EXPERIMENT

2.1 Experimental Parameters and Specimens

To investigate shear behavior of RC beam strengthened by strip-shaped UFC panels, loading tests of 10 specimens

Table 1 Experimental cases

Name	Panel thickness [mm]	Panel location	Shear reinforcement ratio
REF-r0	*	*	0.00
7-ABCD-r0	7.0	ABCD	
10-ABCD-r0	10.0		
14-ABCD-r0	14.0		
7-A-r0	7.0	A	
7-B-r0		B	
7-C-r0		C	
REF-r0.24	*	*	0.24
7-ABCD-r0.24	7.0	ABCD	
7-B-r0.24		B	

Meaning of the specimen name: **7-ABCD-r0.24**
Panel thickness | Panel location | Stirrup ratio

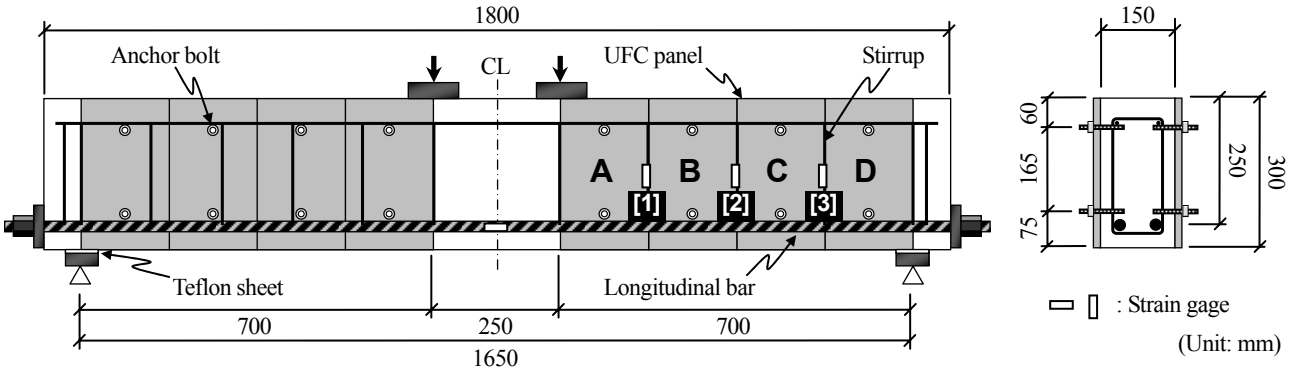

Figure 1 Dimension, reinforcing bar arrangement and panel location of the specimen.

Table 2 Mix proportion of concrete

G_{max} [mm]	W/C [%]	S/a	Unit quantity [kg/m^3]				
			W	C	S	G	AE
20	60	45	178	296	859	956	0.444

Table 3 Mix proportion of UFC

Unit quantity [kg/m^3]				Flow [mm]
W	Premix binder	Steel fiber	High performance water reducing agent	
180	2254	157	24	260±20

Table 4 Material properties except concrete

	Location	Diameter	Kind of steel	Yielding strength [MPa]
Rebar	Main bar	D22	SBPD930	1031
	Stirrup	D6	SD295	340
	Compression bar	Φ6	SR295A	342

	Compressive strength [MPa]	Tensile strength [MPa]	Elastic modulus [GPa]
UFC	211.9	10.8	50.1

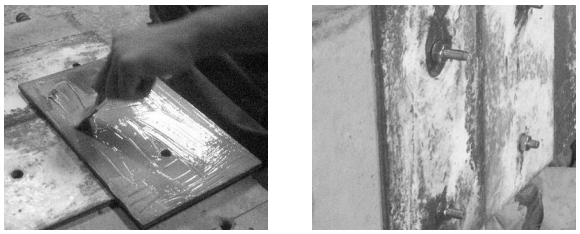

a) Epoxy resin b) Anchor bolt

Photos 1 Attaching procedure of UFC panel

listed in Table 1 were conducted. Experimental parameters are panel thickness, panel location and with or without stirrup. REF-r0 and REF-r0.24 are the reference specimens in which UFC panels are not used. 7-ABCD-r0, 10-ABCD-r0 and 14-ABCD-r0 are the specimen in which UFC panels are attached over the all span and stirrup is not used. 7-A-r0, 7-B-r0 and 7-C-r0 are the specimen in which a piece of UFC panel is attached to different location. 7-ABCD-r0.24 and 7-B-r0.24 are the specimen in which UFC panels are attached over the all span and stirrups are arranged.

Figure 1 shows dimension, reinforcing bar arrangement and panel location. As common variables for all specimens, main reinforcement ratio, shear span ratio, effective depth, specimen width and specimen height are p=2.06, a/d=2.8, d=250 mm, b=150 mm and h=300 mm, respectively. Shear reinforcement ratio of the specimens with stirrups is p_w=0.24. In this study, panel location is called A, B, C and D from the loading point as shown in Fig. 1. Name of the specimens listed in Table 1 corresponds to them. For all specimens, failure side is controlled in the right span with putting more stirrups into the left span.

2.2 Materials

Table 2 shows mix proportion of concrete. Crushed stones whose maximum diameter is 20 mm and early-strength cement were used for the coarse aggregate and cement, respectively. Table 3 shows mix proportion of UFC. UFC is consisted of water, premix binder (cement, silica fume and quartz powder premixed binder), steel fibers (15 mm length and 0.2 mm diameter, straight shape) and high performance water reducing agent. Water to binder ratio (W/B) is around 8%. Table 4 lists mechanical properties of reinforcing bar and UFC. Mechanical properties of concrete are shown in Table 5 with the experimental results.

2.3 Attaching Procedure of UFC Panels

At 7 days after casting of concrete, UFC panels were attached by epoxy resin and anchor bolts as shown in Photos 1. Two anchor bolts were used for one UFC panel. Location of the anchor bolts are also shown in Fig. 1.

2.4 Method for Loading and Measuring Items

To satisfy simple supporting condition, steel plate whose width is 65 mm was put on the pin hinge supports and antifriction pad, which is consisted of two layers Teflon sheet and grease, was inserted between the steel plate and specimen. On the top surface of specimen, gypsum was applied at the loading points, and loading plates whose width is 100 mm, steel rollers and load distribution beam were set. Load was applied by 2,000 kN Amsler type machine.

Measuring items in the experiment are load, displacement at the center of span, displacement at the supporting points, strain of the longitudinal bar, strain of the

Table 5 Mechanical properties of concrete and result of the loading test

Name	Mechanical properties of concrete			Result of loading test			
	Compressive strength [MPa]	Tensile strength [MPa]	Elastic modulus [GPa]	Shear capacity, V_u [kN]	Shear capacity of reference specimen deducting the effect of f'_c, V'_{REF} [kN]	Enhancement ratio of shear carrying capacity, n	Failure mode
REF-r0	33.2	2.1	28.4	52.8	*	*	Diagonal tension
7-ABCD-r0	32.6	2.8	28.5	62.5	52.5	0.19	Panel cracking
10-ABCD-r0	32.9	3.1	29.5	66.5	52.6	0.26	
14-ABCD-r0	32.3	2.2	29.5	64.6	52.3	0.23	Anchor pulling-out
7-A-r0	35.1	2.0	28.5	52.7	49.2	0.07	RC precedence
7-B-r0	36.6	2.2	28.2	54.3	48.7	0.12	Panel cracking
7-C-r0	33.0	2.2	28.5	52.8	52.7	0.02	RC precedence
REF-r0.24	31.9	2.7	28.7	79.7	*	*	Diagonal tension
7-ABCD-r0.24	28.4	2.7	28.0	112.1	76.7	0.46	Panel cracking
7-B-r0.24	25.1	2.2	28.2	105.9	73.6	0.44	

stirrups and crack distribution. Load was measured by the load cell in the loading machine. Displacement at the center of span and supports were measured by displacement transducers. Strain of the longitudinal bar and stirrups were measured by wire strain gages. Locations of the strain gages were also shown in Fig. 1. Crack distribution was visually observed and recorded.

3. RESULTS OF THE EXPERIMENT

3.1 Shear Capacities

Table 5 summarizes mechanical properties of concrete and result of the loading test (shear capacities, enhancement ratio of shear capacity and failure mode). Enhancement ratio of shear capacity n is a ratio of shear capacity increase to the shear capacity of non-strengthened specimen.

$$n = \frac{V_u - V_{REF}}{V_{REF}} \quad (1)$$

where, V_u is shear capacity, V_{REF} is shear capacity of non-strengthened specimen.

To eliminate the effect of concrete strength variation, shear capacity of non-strengthened specimen is multiplied by compressive strength ratio powered by 1/3 as expressed in JSCE equation for shear carried by concrete (JSCE 2002).

$$V_{REF} = \left(\frac{f'_c}{f'_{c_REF}} \right)^{1/3} \cdot V'_{REF} \quad (2)$$

where, f'_c is compressive strength of concrete, f'_{c_REF} is compressive strength of concrete of non-strengthened specimen, V'_{REF} is measured shear capacity of non-strengthened specimen.

(1) Specimens without stirrup

Enhancement ratio of shear capacity of 7-ABCD-r0, 10-ABCD-r0 and 14-ABCD-r0, in which UFC panels were attached over the all span, were 0.19, 0.26 and 0.23, respectively. That is, increase of shear capacity has a limitation from 10 mm panel thickness.

Enhancement ratio of shear capacity of 7-A-r0, 7-B-r0 and 7-C-r0, in which panel location is varied, were 0.07, 0.12 and 0.02, respectively. It indicates that location of the panel greatly affect strengthening effect on shear capacity of the beams.

(2) Specimens with stirrups

Enhancement ratio of shear capacity of 7-B-r0.24, in which a piece of UFC panel is attached at B, was 0.44. This value is about four times larger than that of the beam without stirrup (7-B-r0). On the other hand, enhancement ratio of shear capacity of 7-ABCD-r0.24, in which UFC panels were attached over the all span, was 0.46. This value is not so much different from that of 7-B-r0.24.

3.2 Load-Deflection Relationships and Crack Patterns

Figure 2 shows load-mid span deflection relationships. Broken lines represent load-deflection relationships of non-strengthened specimens. The mid span deflections were calculated as the mid span displacement subtracted by displacement at the supporting points. Figure 3 shows typical crack pattern observed in the experiment. For the specimens in which UFC panels were attached over the all span, crack patterns of both UFC panels and inside RC part are shown. Red bold lines in Fig. 3 represent critical cracks. Cracking process of each specimen is explained as follows.

(1) 7-ABCD-r0

When the load was 105.0 kN, crack occurred in the UFC panel located at B as shown in Fig. 3a-i. After that, the crack propagated with the load increasing. When the load reached to the peak (125.0 kN), crack occurred in the UFC panel located at A. After the loading test, diagonal crack of inside RC part was observed at the same location of the panel cracks as sown in Fig. 3a-ii.

(2) 14-ABCD-r0

When the load was 30.0 kN, flexural crack occurred in RC part. In this case, even the load reached to the peak

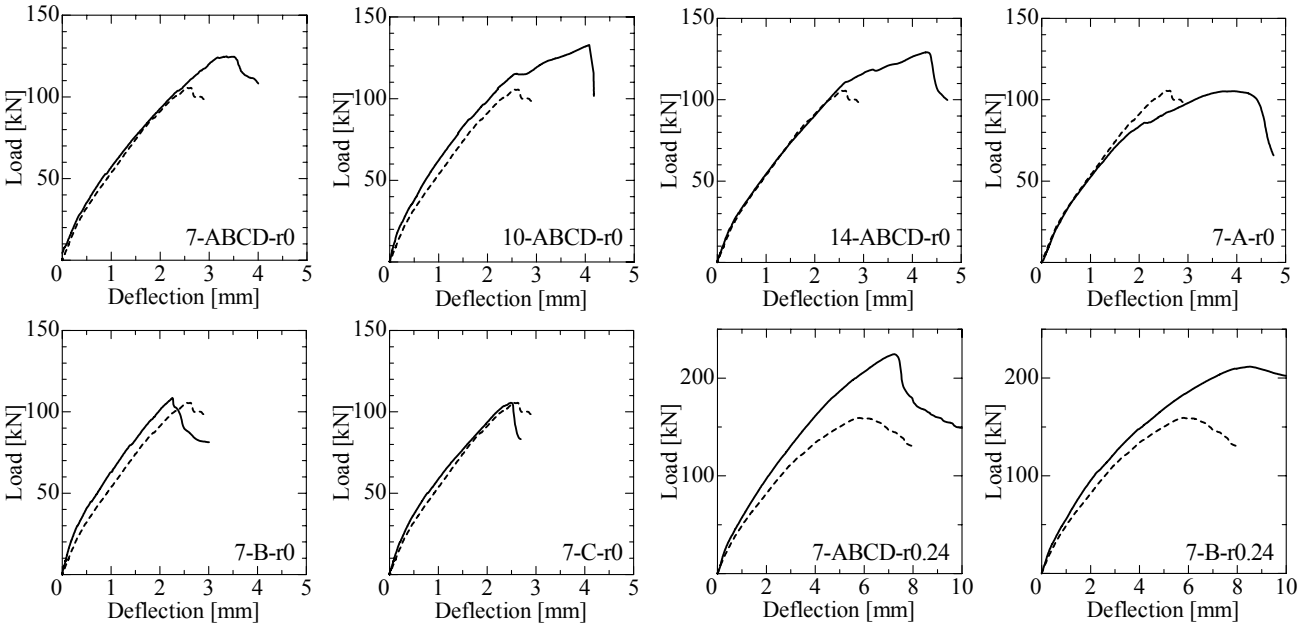

Figure 2 Load-mid span deflection relationships (Broken lines are non-strengthened specimen)

(129.2 kN), no cracks were observed in the UFC panels as shown in Fig. 3b-i. However, diagonal crack was observed in RC part similarly to that in 7-ABCD-r0 as shown in Fig. 3b-ii. After the loading test, pulling-out of the anchor bolts was observed.

(3) 7-ABCD-r0.24

When the load was 160.0 kN, crack occurred in the UFC panel located at B as shown in Fig. 3c-i. After that, the crack propagated with the load increasing. When the load reached to the peak (224.2 kN), crack occurred in the UFC panel located at A. Cracks in the UFC panels were more uniformly distributed than those in the specimen without stirrup (7-ABCD-r0).

(4) 7-A-r0

When the load was 30.0 kN, flexural crack occurred in RC part. In this case, even the load reached to the peak (105.4 kN), no cracks were observed in the UFC panels as shown in Fig. 3d. Besides, after the loading test, pulling out of the anchor bolts was not observed.

(5) 7-B-r0

When the load was 95.0 kN, diagonal crack occurred in the RC part. After that, when the load was 102.0 kN, crack occurred in the UFC panel as shown in Fig. 3e. Peak load of this specimen was 108.6 kN. Width of the crack in the UFC panel at the peak load was approximately 2 mm.

(6) 7-C-r0

When the load was 104 kN, diagonal crack occurred in RC part. After the peak load (105.6 kN), no cracks occurred in the UFC panel. Cracks in the UFC panel shown in Fig. 3f occurred in post-peak region.

(7) 7-B-r0.24

When the load was 105.0 kN, diagonal crack occurred in RC part. Load increased even after the diagonal crack appearance. When the load was 207.0 kN, crack occurred in the UFC panel as shown in Fig. 3g. Peak load of this specimen was 211.0 kN. Width of the crack in the UFC panel at the peak load was much narrower than that in

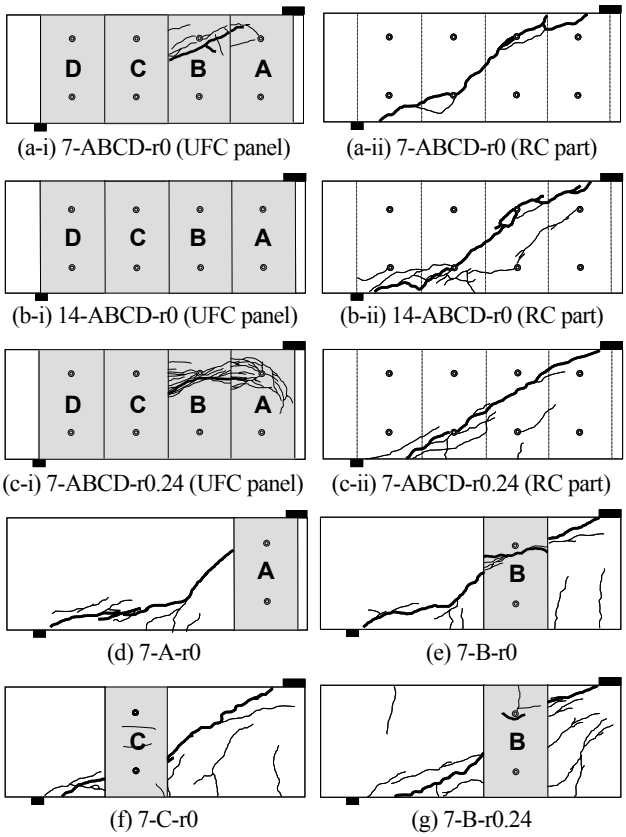

Figure 3 Crack patterns after the loading test

7-B-r0.

3.3 Load-Stirrup Strain Relationships

Figure 4 shows load-stirrup strain relationships of REF-r0.24, 7-ABCD-r0.24 and 7-B-r0.24. Stirrup [1], [2] and [3] in the legend are corresponding to those in Fig. 1. In REF-r0.24, all stirrups have not begun to be yielding at the peak load. On the other hand, in 7-ABCD-r0.24 and 7-B-r0.24, one or two stirrups have begun to be yielding, and strains of the other stirrups were larger than those in

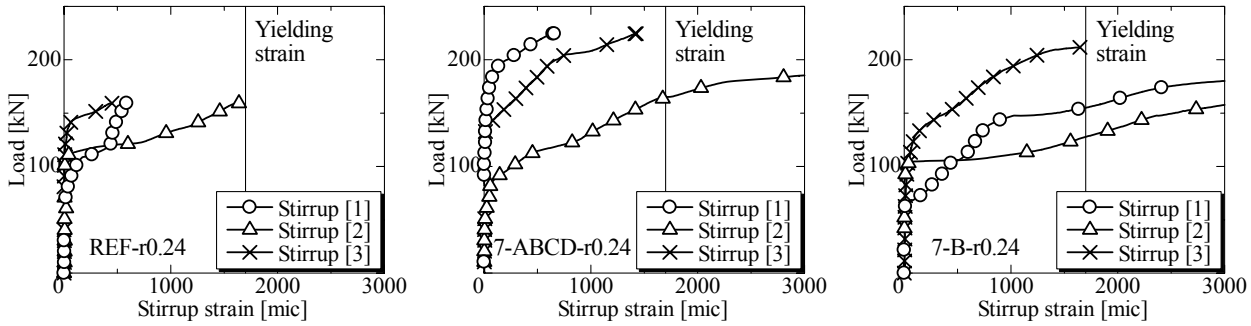

Figure 3 Load-stirrup strain relationships (Stirrup [1], [2] and [3] are corresponding to those in Fig. 1)

REF-r0.24, at the peak load. It indicates that strengthening effect of the UFC panel is not only shear carried by UFC panel itself but also enhancement of shear carried by stirrups with increasing their strain.

3.4 Failure Mode

In this study, shear failure of RC beams strengthened by UFC panels is classified to following three failure modes.

(1) Panel cracking failure

In this failure mode, cracking in UFC panel leads to shear failure as observed in 7-ABCD-r0, 10-ABCD-r0, 7-B-r0, 7-ABCD-r0.24 and 7-B-r0.24. However, width of the crack in the UFC panels at the peak load is varied in each experimental case as mentioned in Section 3.2. Crack width of the specimen with stirrups tends to be narrower than that of the specimen without stirrup. 7-C-r0 is not included to this failure mode because cracks in the UFC panel occurred in post-peak region.

(2) Anchor bolt pulling-out failure

In this failure mode, pulling-out of the anchor bolts leads to shear failure as observed in 14-ABCD-r0. As explained in Section 3.2 (2) and Fig. 3b-i, in 14-ABCD-r0, no cracks occurred in the UFC panel at the peak load and pulling-out of the anchor bolts was observed after the loading test. It means that anchor bolts had a failure because pulling force became larger than the anchorage strength before crack happens in the UFC panel.

(3) RC part precedence failure

In this failure mode, neither cracking of UFC panel nor pulling-out of anchor bolts are happen as observed in 7-A-r0 and 7-C-r0. It indicates that diagonal tension failure of RC part occurred before cracking of UFC panel or pulling-out of anchor bolt happen.

4. INVESTIGATION ON SHEAR CARRIED BY UFC PANEL

To investigate shear resisting mechanism, shear carried by UFC panel is quantified in terms of two aspects. One is experimentally observed value based on the measured data of shear capacity and strains. The other is computationally obtained value based on a simplified shear carrying model called "fictitious diagonal crack model."

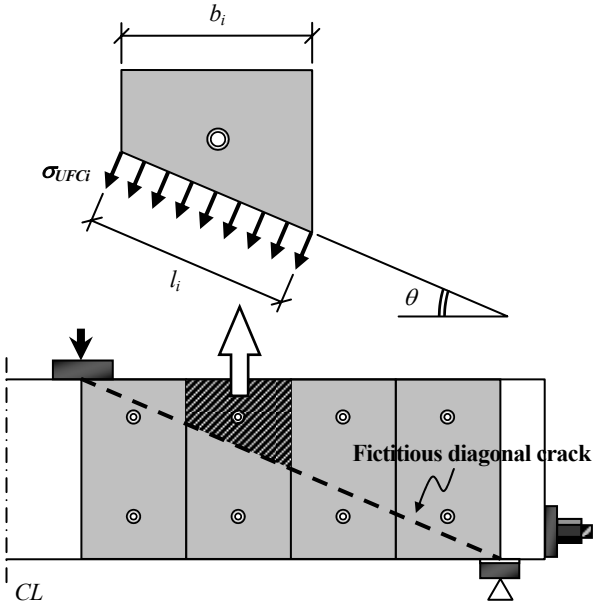

Figure 4 Fictitious diagonal crack model

4.1 Shear Carried by UFC Panels as Observed in the Experiment

Shear carried by UFC panels was calculated by subtracting shear carried by concrete and stirrups from total shear capacity obtained in the experiment. That is,

$$V_{UFC} = V_u - V_c - V_s \tag{3}$$

where, V_{UFC} is shear carried by UFC panels, V_c is shear carried by concrete, V_s is shear carried by stirrups.

In this study, shear capacity of the specimen which has no stirrups and UFC panels (REF-r0) is assumed to be shear carried by concrete. Effect of variation of concrete strength was eliminated by multiplying compressive strength ratio powered by 1/3 as well as done in Eq. (2).

$$V_c = V_{REF} \times (f_c' / f_{c-REF}')^{1/3} \tag{4}$$

Shear carried by stirrups was calculated using stirrup strains measured by strain gages. It is given by following equation.

$$V_s = \begin{cases} \sum A_s E_s \varepsilon_s & (\varepsilon_s < \varepsilon_y) \\ \sum A_s f_{wy} & (\varepsilon_s \geq \varepsilon_y) \end{cases} \tag{5}$$

Table 6 Experimentally observed and computationally obtained shear carried by UFC panels

Name	Experiment				Computation	Exp. / Comp. [1] / [2]
	Max shear force V_u [kN]	Shear carried by concrete V_c [kN]	Shear carried by stirrups V_s [kN]	[1] Shear carried by UFC panels V_{UFC} [kN]	[2] Shear carried by UFC panels V_{UFC} [kN]	
7-ABCD-r0	62.5	53.1	—	10.0	52.9	0.19
7-ABCD-r0.24	112.1	55.6	21.5	40.5	52.9	0.77
10-ABCD-r0	66.5	53.0	—	13.8	75.6	0.18
7-A-r0	52.7	56.6	—	3.5	13.3	0.26
7-B-r0	54.3	57.3	—	5.7		0.42
7-B-r0.24	105.9	58.0	43.1	14.7		1.10
7-C-r0	52.8	52.9	—	0.1		0.00

where, A_s is sectional area of stirrup, E_s is elastic modulus of stirrup, ε_s is stirrup strain, ε_y is yielding strain of stirrup, f_{wy} is yielding strength of stirrup.

4.2 Shear Carried by UFC Panels Computed by Fictitious Diagonal Crack Model

To compute shear carried by UFC, this study assumed fictitious diagonal crack model, in which linear crack from the loading point to the supporting point is assumed as shown in Fig. 4. Width of i th panel and angle of the fictitious diagonal crack are represented by b_i and θ, respectively. Crack length l_i of the i th panel is given by,

$$l_i = \frac{b_i}{\cos\theta} \tag{6}$$

Tensile stress of UFC panel is assumed to be applied in normal direction to the fictitious diagonal crack. Sectional force in normal direction to the fictitious diagonal crack is given by,

$$F_{UFCi} = \sigma_{UFCi} \cdot l_i t_i = \frac{\sigma_{UFCi} b_i t_i}{\cos\theta} \tag{7}$$

where, F_{UFCi} is sectional force of i th UFC panel in normal direction to the fictitious diagonal crack, σ_{UFCi} is tensile stress of i th UFC panel, t_i is thickness of i th UFC panel.

Tensile stress σ_{UFCi} is assumed to be tensile strength of UFC at the peak load. Eq. (7) becomes,

$$F_{UFCi} = \frac{f_{UFC} b_i t_i}{\cos\theta} \tag{8}$$

where, f_{UFC} is tensile strength of UFC.

Shear carried by UFC panel is vertical component of F_{UFCi}, therefore,

$$V_{UFCi} = F_{UFCi} \cos\theta = f_{UFC} b_i t_i \tag{9}$$

where, V_{UFCi} is shear carried by i th UFC panel.

Summation of shear carried by each UFC panel is given by,

$$V_{UFC} = \sum V_{UFCi} = f_{UFC} \sum b_i t_i \tag{10}$$

Shear carried by UFC panels based on the fictitious diagonal crack model is given by Eq. (10).

4.3 Result of the Calculation

Table 6 summarizes the result of experimentally observed and computationally obtained shear carried by UFC panel by Eq. (3) and (10), respectively. Each result is compared and shear carrying mechanism is discussed as below.

(1) Specimens without stirrup

In case of the specimens without stirrup, shear carried by UFC panels observed in the experiment became smaller than that obtained by the fictitious diagonal crack model. This is because tensile strength is used for stress of the UFC panel ($\sigma_{UFCi}=f_{UFC}$). For example, in case of 7-B-r0, crack in the UFC panel was widened approximately 2 mm at the peak load as mentioned in Section 3.2 (5). According to tension softening curve of UFC measured by Kakei et al. (Kakei et al. 2002), tensile stress of UFC is less than half of the tensile strength when crack width becomes 2 mm. Therefore, since tensile strength is directly used, computational result became overestimation. On the other hand, in case of 7-C-r0, no cracks occurred in the UFC panels at the peak load. This is because failure mode was RC part precedence failure. In this failure mode, strain of the UFC panel at the peak load is less than cracking strain. Therefore, shear carried by UFC panel became smaller.

Thus, in case of the specimens without stirrup, fictitious diagonal crack model is unreasonable because peak point of shear carried by UFC panel does not agree with the peak load.

(2) Specimens with stirrups

In case of 7-B-r0.24, ratio of experimentally observed to computationally obtained shear carried by UFC panels is 1.10. The fictitious diagonal crack model could give a reasonable result. This is because width of crack in the UFC panel was comparatively small as mentioned in Section 3.2 (2), and stress transferred in the crack was almost same as the tensile strength. On the other hand, in case of 7-ABCD-r0.24, ratio of experimentally observed to computationally obtained shear carried by UFC panels is

0.77. That is, fictitious diagonal crack model overestimated the experimental result. This is because crack did not occur in the UFC panel located at C and D in the experiment, while the computational model assumes that stress of every UFC panels reached to the tensile strength.

As discussed above, fictitious diagonal crack model is applicable to the case that crack occurs in every UFC panels and the crack width is comparatively small.

5. CONCLUSIONS

In this study, following conclusions were obtained.

1) Shear capacity of RC beams strengthened by UFC panels increases with larger reinforcement ratio when panel thickness is about 7 mm. However, it does not increase if panel thickness is over 10 mm because failure mode changes from panel cracking failure to anchor bolt pulling-out failure.
2) When UFC panels are attached near loading point and supporting point, strengthening effect becomes less because diagonal tension failure of inside RC part is preceded. That is, location of UFC panel greatly affects strengthening effect.
3) In case of RC beams with stirrups, there are two effects of UFC panel on the enhancement of shear capacity of RC beams. One is shear carried by UFC panel itself. The other is increase of shear carried by stirrups. Therefore, its strengthening effect is larger than that of RC beams without stirrup.
4) Computation of shear carried by UFC panels using fictitious diagonal crack model is applicable to the case that crack occurs in every UFC panels attached to the beams and the crack width is comparatively small.

Acknowledgements:

The authors acknowledge financial support from the Center for Urban Earthquake Engineering (CUEE) at Tokyo Institute of Technology. The authors also would like to show their gratitude to Taiheiyo Cement Corporation for providing UFC panels used in this study.

References:

Japan Society of Civil Engineers (JSCE) (2002), "Standard Specifications for Concrete Structures-Structural Performance Verification."

Kakei, T., Kawaguchi, T., Hyodo, H. and Niwa, J. (2003), "Fracture Characteristics of Ultra High Strength Fiber Reinforced Cement Composite," *Proceedings of the Conference of Japan Cement Association*, **57**, 230-231. (in Japanese)

Kakei, T., Murata, H., Niwa, J. and Hyodo, H. (2004), "Shear Behavior of Beams with the Use of Ultra High Strength Fiber Reinforced Cement Composite," *Proceedings of Japan Concrete Institute*, **26**(2), 787-792. (in Japanese)

Katagiri, M., Maehori, S., Ono, T., Shimoyama, Y. and Tanaka, Y. (2002), "Physical Properties and Durability of Reactive Powder Composite Material (DuctalR)," *Proceedings of the first fib Congress*, Session 7, 133-138.

Shibata, K., Kimura, T., Watanabe, K. and Niwa, J. (2008), "Strengthening Effect of UFC Buried Form on Load Carrying Capacity of RC Column," *Proceedings of Annual Conference of the Japan Society of Civil Engineers*, **5**(506), 1011-1012. (in Japanese)

Shibata, K., Watanabe, K., Niwa, J. and Kawaguchi, T. (2009), "Shear Strengthening Effect of UFC Panels on RC Beams," *Proceedings of Japan Concrete Institute*, **31**(2), 1633-1638. (in Japanese)

Table 1 Experimental cases

Name	Panel thickness [mm]	Panel location	Shear reinforcement ratio
REF-0	0.0	*	0.00
7-ABCD-0	7.0	ABCD	
10-ABCD-0	10.0		
14-ABCD-0	14.0		
7-A-0	7.0	A	
7-B-0		B	
7-C-0		C	
REF-0.24	0.0	*	0.24
7-ABCD-0.24	7.0	ABCD	
10-ABCD-0.24	10.0		
14-ABCD-0.24	14.0		

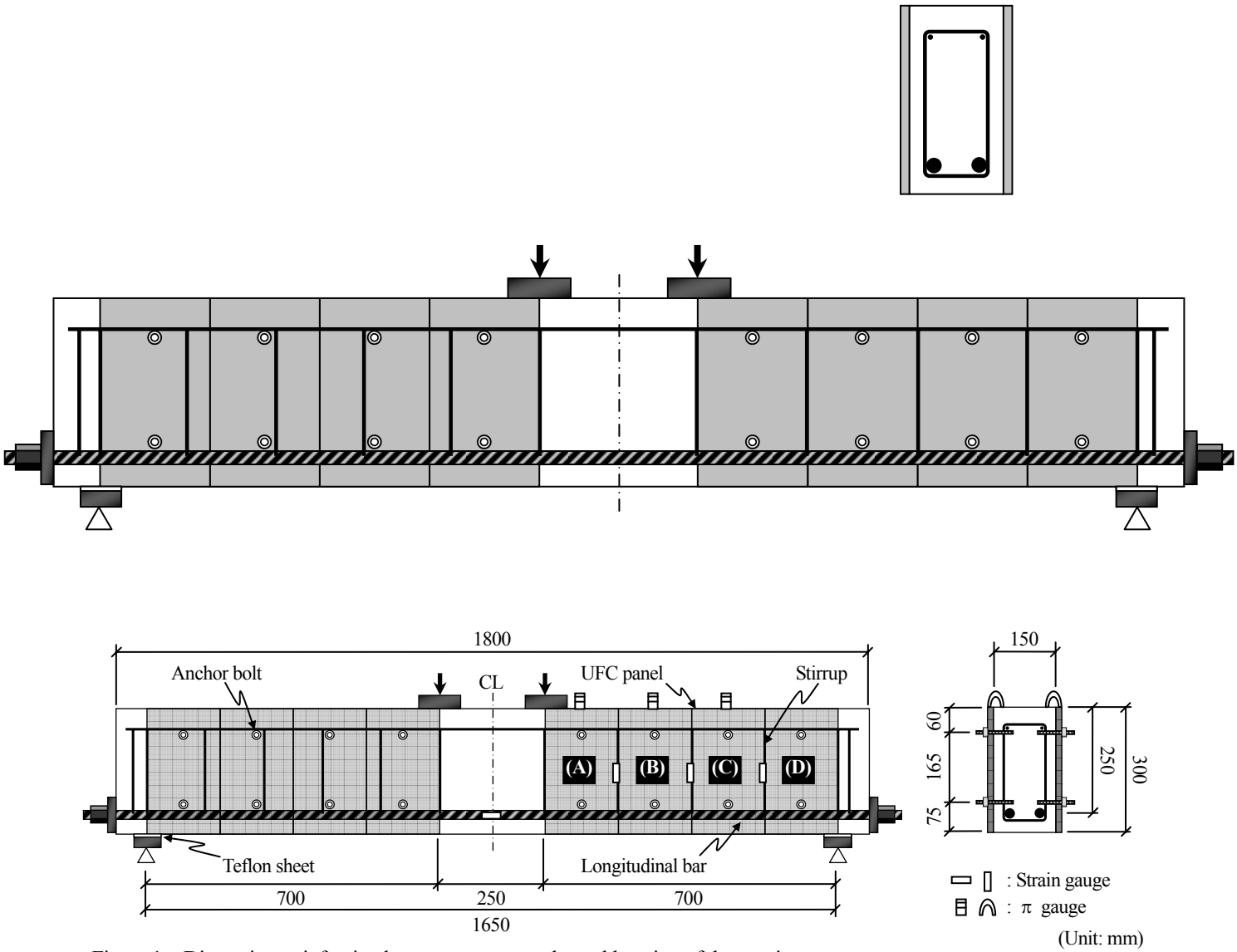

Figure 1 Dimension, reinforcing bar arrangement and panel location of the specimen.

Table 2 Mix proportion of concrete

G_{max} [mm]	W/C [%]	S/a	Unit quantity [kg/m^3]				
			W	C	S	G	AE
20	60	45	178	296	859	956	0.444

Table 3 Mix proportion of UFC

Unit quantity [kg/m^3]				Flow [mm]
W	Premix binder	Steel fiber	High-range water reducing agent	
180	2254	157	24	260±20



a) Epoxy resin



b) Anchor bolt

Photos 1 Attaching procedure of UFC panel

Table 5 Summary of the experimental result

Name	Material properties of concrete			Peak load [kN]	Shear carrying capacity [kN]	Failure mode	Angle of diagonal crack [degs]
	Compressive strength [MPa]	Splitting tensile strength [MPa]	Elastic modulus [GPa]				
REF-0	33.2			105.5	52.8	Diagonal tension	23.2
7-ABCD-0	32.6			124.9	62.5		23.2
10-ABCD-0	32.9			132.9	66.5		23.2
14-ABCD-0	32.3			129.2	64.6		23.2
7-A-0	35.1			105.2	52.6		23.2
7-B-0	36.6			108.6	54.3		23.2
7-C-0	33.0			105.6	52.8		23.2
REF-0.24	31.9	2.9	27.3	159.4	79.7		23.2
7-ABCD-0.24							23.2
7-A-0.24							23.2
7-B-0.24							23.2

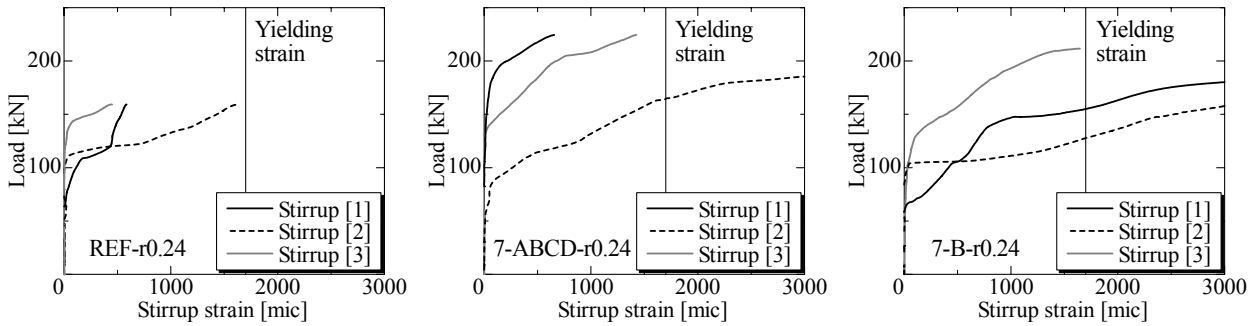

Figure 3 Load-stirrup strain relationships (Stirrup [1], [2] and [3] correspond to those in Fig. 1)

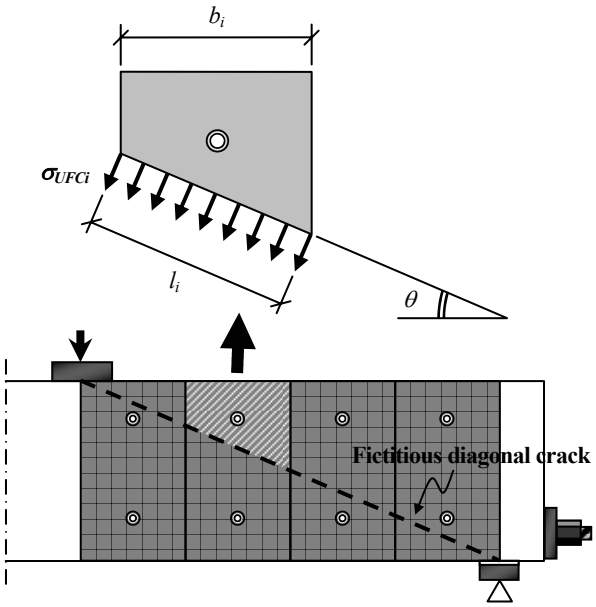

Figure 4 Fictitious diagonal crack model

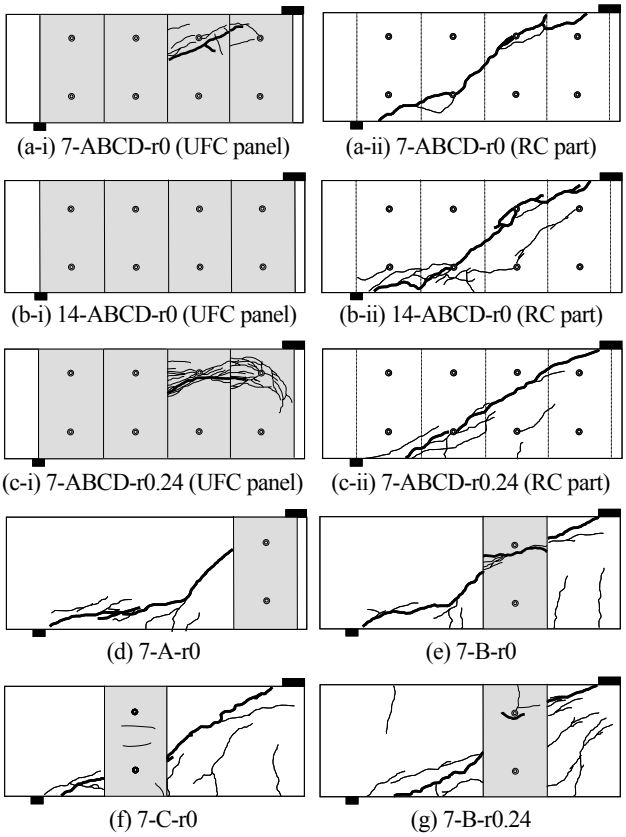

Figure 3 Crack patterns after the loading test

JOINT CONFERENCE PROCEEDINGS
7th International Conference on Urban Earthquake Engineering (7CUEE) &
5th International Conference on Earthquake Engineering (5ICEE)
March 3-5, 2010, Tokyo Institute of Technology, Tokyo, Japan

A COMPARATIVE EXPERIMENTAL STUDY ON ALTERNATIVE STRENGTHENING METHODS FOR HISTORICAL MASONRY WALL

Necdet Torunbalci[1)], Fatih Sutcu[2)]

1) Associate Professor, Department of Architecture, Istanbul Technical University, Turkey
2) Research Associate PhD, Department of Architecture, Istanbul Technical University, Turkey
necdet@itu.edu.tr, fatih.sutcu@itu.edu.tr

Abstract: Historical masonry structures may exhibit inferior performance against the lateral loads like those induced by the earthquakes. In this context, it is crucial for such structures of historical value to increase their seismic performances in order to be protected against the earthquakes. This study deals with the experimental assessment of strengthening masonry walls with alternative applications. In the experimental works conducted within the scope of the study, the brick wall specimens are strengthened on one side using carbon fibre-reinforced polymers (CFRP) and glass fibre-reinforced polymers (GFRP) in strip and sheet forms. In addition, the specimens are strengthened with self compacting concrete (SCC) as an alternate to conventional concrete. The increase of strength compared to un-reinforced masonry walls is obtained and comparisons are made between the alternate strengthening methods

1. INTRODUCTION

The majority of buildings in Turkey are masonry structures and the masonry walls are mostly made of bricks. In addition to numerous structures of monumental and historical value, the majority of the structures constructed both in the rural and urban areas are of the masonry structure type. Although masonry brick walls are known to have high vertical load bearing capacity, they are weak for lateral loading such as earthquakes. Strengthening should be provided for the structures to maintain the structural integrity that may not have been taken into consideration during the original design or construction, to increase their load-bearing capacities as a result of the change in their functional usage, eliminate the defects attributed to incorrect or insufficient application during construction and to supplement the load-bearing capacities that may be reduced as a result of the corrosion and wear in the course of time. Considering the fact that our country is in a risk region in the means of earthquakes, it is essential to strengthen the structural masonry walls.

Strengthening by shotcrete on surface of the walls coated with the steel mesh reinforcement is a popular method. However, shotcrete application is not free of any further problems in practice as the application pressure might cause major damage on a historical masonry wall. Where the conventional concrete is used, however, placing and compacting the concrete prove to be difficult due to the insufficient size of the formwork. Increasing the thickness of the concrete layer can eliminate the problem, but, this in turn gives rise to undesirable loss of footing area. Such type of strengthening is therefore not preferred, even if it greatly contributes to the structural performance. Where the self-compacting concrete is used, majority of aforementioned problems are eliminated, however, this time the original architecture of the structure is jeopardized. It can be used in cases where the authority in charge approves that the strengthening process is acceptable concerning the architectural originality. Another method still under investigation involves the strengthening of existing structural walls using Fiber Reinforced Polymer (FRP) materials. Providing practical and efficient solution where use of the concrete and steel material proves to be difficult, FRP strengthening materials obtained by the mixture of the carbon, glass and aramide with the reinforced resin provide higher tensile strength than the steel due to its fine, corrosive resistant and durable fibrous structure. Application while the structure is in use is also possible without endangering the sectional forms of the strengthened portions of the structure. Available in stripe/laminated or textile form, FRP is applied on the wall surface by the epoxy adhesive. The fibres take up the loading, while the epoxy adhesive ensures homogenous load distribution between the fibres, protecting them from the environmental effects. FRP method might effectively be used in strengthening the structures of historical value due to its virtue of preserving original architecture of the structures to a great extent.

Various experimental and analytical studies have been performed on the behaviour of the structural masonry walls under in plane, out of plane and axial loading. In a study

undertaken by Ehsani et al.(1999), the investigation is performed on the behaviour of the structural walls subject to loading acting out of the loading plane of the walls that are strengthened with CFRP materials as stripes placed in orthogonal directions to the joints on both surfaces. The study determines that CFRP stripe materials prove to be a good alternative for strengthening the structural brick walls against the lateral loads in that energy dissipation capacities are improved. Albert et.al. (2001) conducted the experimental works to determine the behaviour of the structural brick walls strengthened using carbon and glass FRPs under cyclic axial compressive loading, with various FRP forms, quantities and number of layers. Also providing the analyses on out of plane lateral loading, the study establishes that the performance of pre-damaged and non-damaged brick wall specimens strengthened using carbon fibre stripes are much better than those strengthened using glass fibres. It is also stated that strengthening using FRP is an alternative method to the existing retrofitting methods. Tan et al. (2004) in their works strengthen the brick wall specimens using FRP under three different anchoring methods. In strengthening, they use the specimens in 1000mm x 1000mm x 110mm size, with joints of 10mm. The results of experiments prove that the increase in out-of-plane strengths of the retrofitted brick wall specimens is significant. The fracture are observed in the brick wall specimens without reinforcement due to bending, whereas retrofitted ones underwent four different failure modes. Namely, the shear failure along the bricks, weakening of the bond between FRP and brick wall surfaces, formation of bending cracks and formation of tensional failure of FRP strengthening materials. In a study where 42 wall specimens subject to in-plane loading with the angle between the horizontal joints and axial force being 0°,30°,45°,60° and 90° reinforced by the laminated Glass FRP Hamid et al. (2005), it is determined that FRP has significant influence on increasing the strength and failure mode as well as extension of the rigidity of the wall. They also determine that, compared with specimens without reinforcement, the compressive strength is increased by160 – 500 %. Krevaikas at al. (2005) conduct a study where 42 brick wall specimens of 115mmx 115mm, 172.5mm x 115mm and 230mm x 115 mm sizes are reinforced with 1, 2 and 3 layers of CFRP stripes and 5 layers of GFRP and their behaviours are investigated under axial loading. It is determined, upon the experiment, that the load-bearing capacities and strains of the brick wall specimens are considerably increased. In particular, the formation of the wrap regions at the wall corners improves the stress and strength properties.

2. PURPOSE AND TEST PLAN

In this study conventional brick walls are strengthened using laminated and textile CFRP materials, textile GFRP material, self-compacting concrete (SCC) and conventional concrete (CC) on one side and the target is determining the effect of this strengthening on the behaviours and the strength of the walls with an experimental approach. The brick wall samples were mounted on the testing rig in such a way so that the bed joints formed an angle of 45°with the direction of vertical loading. Loading is exerted onto the steel shoes constructed on opposing corners of the brick masonry specimens depending on ASTM code. Within the scope of this study, it is also aimed to provide comparative analysis on, the effects of the form and quantity of CFRP, GFRP, SCC and CC and inspection of the displacements and failure modes, for which relevant specimen series were formed to correspond the resulting alternatives for respective parameters.

The experiments are consisted of 6 series with 3 brick wall specimens in the size of 185x185x45mm provided for each series. Tree brick wall specimens were used without strengthening as an additional series to represent un-reinforced masonry walls (URM). Displacements are measured by a transducer placed with 100mm nominal length as shown in Figure 1.



Figure 1. Brick wall specimens and test set up

In constructing the brick wall specimens, the mortar is used in cement: sand: water mixture ratio of 1:3.5:0.70. The mortar compressive strength is 15.63 MPa, whereas the the compressive strength of clay bricks reduced in size as to construct the brick wall specimens is 18.92 MPa. The joint size of 0.5 cm is adopted in constructing the brick wall specimens.

2.1 CFRP properties

Two types of CFRP material, namely stripe and textile CFRP were used in strengthening of the brick wall specimens. 3 specimens were used for each type.

Stripe CFRP is in laminated form of 1.2mm thickness and the uni-directional textile CFRP has 165 micron thickness. CFRP were applied on the specimen surfaces with their own adhesives. (Onar, E. 2007.) The two-part epoxy resin adhesives were prepared according to the volumetric proportion by the manufacturer. CFRP material and adhesive properties are given in Table 1.

Table 1: CFRP material and adhesive properties.

Parameter	Details
CFRP Stripe	
Tensile Ultimate Strength (MPa)	3000
Elongation at break, ε_u (%)	1.8
Tensile Modulus MPa	165000
Thickness of Layer (mm)	1.2
CFRP Textile	
Tensile Ultimate Strength (MPa)	3430
Elongation at break, ε_u (%)	1.5
Tensile Modulus MPa	230000
Thickness of Layer (mm)	165micron
Stripe adhesive	
Compressive Strength (MPa)	6
Textile adhesive	
Tensile Strength (MPa)	50
Compressive Strength (MPa)	80
Tensile Modulus MPa	3000

For stripe-type strengthening, ready-made 25mm wide laminated CFRP strips are applied first in the direction of the tensile stresses and then compressive stresses of brick wall specimens (Figure 2a).

For textile-type, however, 165 micron thick uni-directional fabric sheet, namely textile CFRP is used on all over the surface. The textile CFRP is a cheaper material as compared to the laminated CFRP and therefore, the application by textile CFRP is performed in order to keep all the cracks to be formed on the surfaces of the brick wall specimens under control (Figure 2b).

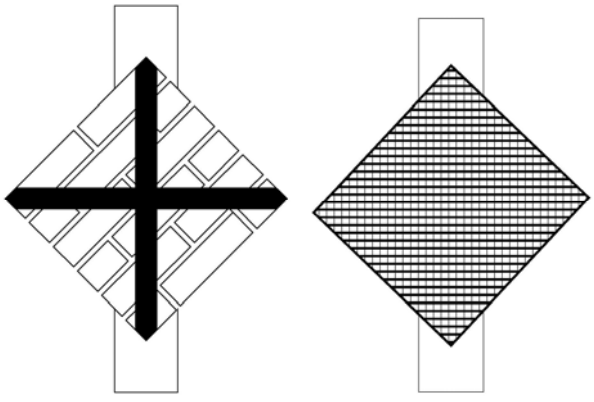

a) FRP stripe b) FRP textile

Figure 2. Strengthening types

The nomination of the CFRP strengthened specimens in a series is as follows: CFRP-S stands for brick wall specimens strengthened by CFRP stripes on one side while CFRP-T stands for brick wall specimens strengthened by CFRP textile on one side.

2.2 GFRP properties

As for strengthening with GFRP material only textile form is available. For adequate comparison with CFRP strengthening not only the surface of brick wall specimens were covered with GFRP textile but also textile-GFRP was cut in suitable stripe form and applied in stripe type as well. 3 specimens were used for each type.(Ozsarac S, 2008) GFRP was applied on the specimen surfaces with its own adhesive. The two-part epoxy resin adhesive was prepared according to the volumetric proportion by the manufacturer. GFRP material and adhesive properties are given in Table2.

Table 2: GFRP material and adhesive properties.

Parameter	Details
GFRP Textile	
Tensile Ultimate Strength (MPa)	1700
Elongation at break, ε_u (%)	2.8
Tensile Modulus MPa	65000
Thickness of Layer (mm)	165micron
Textile adhesive	
Tensile Strength (MPa)	50
Compressive Strength (MPa)	80
Tensile Modulus MPa	3000

Similar to the application with CFRP, for stripe-type strengthening, GFRP was applied in 25mm wide stripe form, first in the direction of the tensile stresses and then compressive stresses of brick wall specimens as shown in Figure 3.



Figure 3. GFRP stripe strengthening

For textile-type uni-directional fabric sheet glass FRP was used on all over the surface. The application by textile GFRP is performed in order to keep all the cracks to be formed on the surfaces of the brick wall specimens under control (Figure.4).

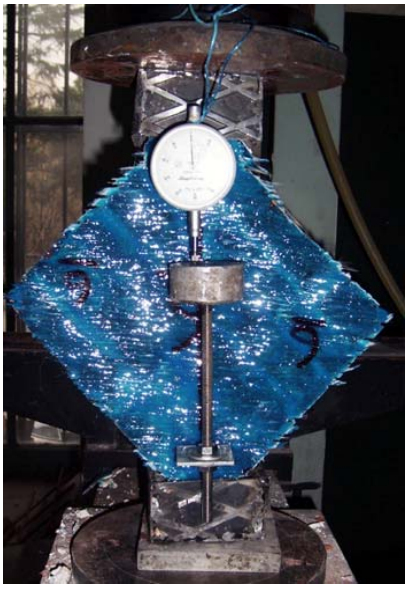

Figure 4. GFRP textile strengthening

The nomination of the GFRP strengthened specimens in a series is as follows: GFRP-S stands for brick wall specimens strengthened by GFRP stripes on one side while GFRP-T stands for brick wall specimens strengthened by GFRP textile on one side.

2.3 Concrete properties

Two types of concrete, namely, self-compacting concrete (SCC) and conventional concrete (CC) were used with steel wire mesh reinforcement for strengthening brick masonry walls. 3 specimens were used for each type. (Ediz I. 2007)

The steel wire mesh with a plain surface and a wire diameter of ø=3mm, manufactured from S500 grade steel and braided with a grid spacing of 50x50 mm, is provided to supplement the strengthening process to strengthen reinforcement. For shear connection at the interface of masonry and concrete, the mesh reinforcement was fixed 10mm in front of the surface by steel wire and epoxy. (Figure 5)

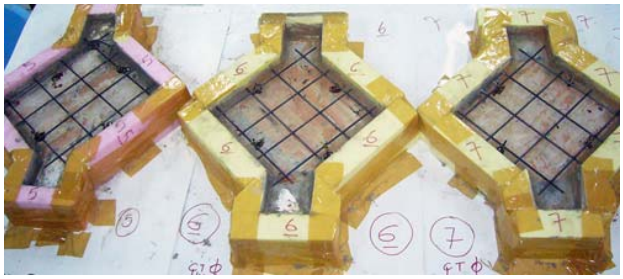

Figure 5. Fixed steel wire mesh reinforcements

For the production of self-compacting concrete with a maximum grain diameter of 10mm is used. A maximum grain diameter of 10 mm is especially preferred to have such aggregates readily entered into the brick wall samples and wire mesh reinforcement. Self-compacting concrete has a spread diameter of 75cm and specific weight of 2.350 kg/m^3.

Testing of compressing strength of the self-compacting concrete is performed on the 7th, 14th, and 28th days following concrete settling. The respective compressing strengths are determined as 40.33, 45.38 and 56.39 MPa.

While determining the compressing strength of the standard ready-mixed conventional concrete with a maximum grain diameter of 10 mm, cubic samples 150x150x150mm in size are tested. The compressive strengths on the 7th, 14th, and 28th days are determined as 24.00, 29.18 and 38.80 MPa, respectively.

3. RESULTS OF EXPERIMENTS

The maximum stress sustained by the specimens are calculated from Eq . (1) in accordance with ASTM standards [8] :

$$S_S = \frac{0.707P}{A_n} \tag{1}$$

where S_S is the shear stress based on the net area, P is the applied load and A_n is the area of the specimen calculated as in Eq. (2):

$$A_n = \left(\frac{w+h}{2}\right)tn \tag{2}$$

where *w,h* and *t* are specimen width, height and thickness, respectively and *n* is the percentage of the area of the unit that is solid, as a decimal. Average maximum strength of the URM walls subject to loading are assumed to be 100% and the test results of strengthened specimens are compared to that of URM walls.

3.1 CFRP strengthening results

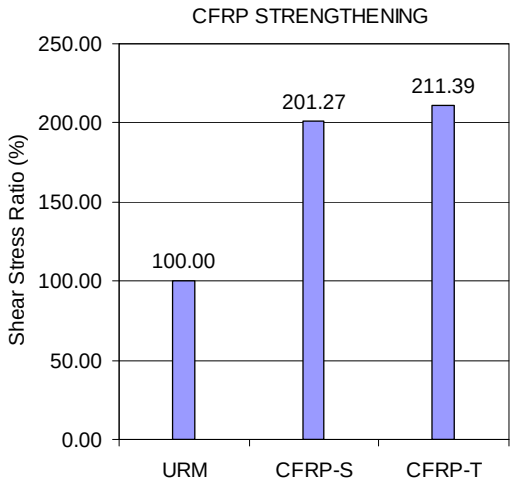

Figure 6. CFRP strengthening results

As compared with the URM brick walls, strengthening of brick wall specimens classified with CFRP on one side of the wall significantly increase the strengths of the specimens. The average strength of specimens compared to that of URM walls are shown in Figure 6 Furthermore, the increases in the degrees of the displacement are also significant compared to URM specimens.

For CFRP strengthening, the sample types exhibiting the higher failure ratings was CFRP-T which was the specimens strengthened by textile form of CFRP all over the surface. According to the comparisons, it can be concluded that strengthening of the walls on single side significantly improve their performances, irrespective of whether they are strengthened in stripe or textile type.

It is determined that the strengths of the specimens increase almost 100% as compared with that of the URM walls. Prior to failure, the cracks propagate along the portion of brick wall specimens where no strengthening is provided. In some cases, the separations are observed between FRP strips and the surface of the specimens. Complete separation is, however, not observed in any one of the specimens. Notwithstanding the occasional cases where the URM brick walls undergo instantaneous failures under ultimate loading, no fragmentation is observed for the specimens strengthened with CFRP strips. Typical failure mode of the CFRP-S specimens is illustrated in Figure 7.



Figure 7. CFRP-S failure mode

It is observed, during the failure process, that the adherences between CFRP textile and the wall surfaces are extremely crucial. It is concluded that the failure is induced on the brick internal structure. No fragmentation is observed on strengthened specimens whatsoever. As a result of the internal forces generated within brick wall specimens, they either collapse or the cracks are propagated in the bricks along the joints, which give rise to brittle fracture at the failure.

As it is the case for CFRP-S specimens, the increases in the strengths of the brick wall specimens strengthened only on one side imply that such strengthening improves the specimens behaviour. Irrespective of the type of strengthening, the application only on one side ends up with the eccentricity due to the sectional geometry turned out to be asymmetrical, resulting with the premature failure.



Figure 8. CFRP-T failure mode

3.2 GFRP strengthening results

With GFRP strengthening similar results are obtained with that of CFRP strengthening. Although the strengthening is provided on one side of the brick wall specimens, the load-bearing capacities increased significantly. (Figure 9)

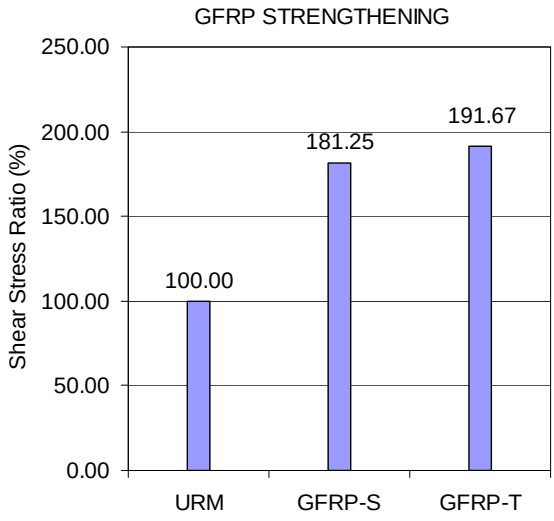

Figure 9. GFRP strengthening results

In brick wall specimens strengthened using GFRP stripe and textile, it is observed that the fragmentations of the brick wall specimens into the pieces are effectively prevented as a result of the wrapping. The plain brick walls usually collapse by formation of the cracks along the loading axis or else, in line with the joints or both the joints and the bricks. It is determined that strengthened brick wall specimens exhibit

higher strengths and besides, they are not broken into pieces. Following strengthening, plain brick wall specimens undergo significant increases in load-bearing capacity. Typical failure mode of the GFRP-S specimens is illustrated in Figure 10.



Figure 10. GFRP-S failure mode

3.3 Concrete strengthening results

Compared to those strengthened with conventional concrete, the behaviours of brick wall samples strengthened with self-compacting concrete change to great extent. The increases in failure loading capacity stand between 86 percent and 210 per cent when strengthened with conventional concrete and with self-compacting concrete, respectively. (Figure 11).

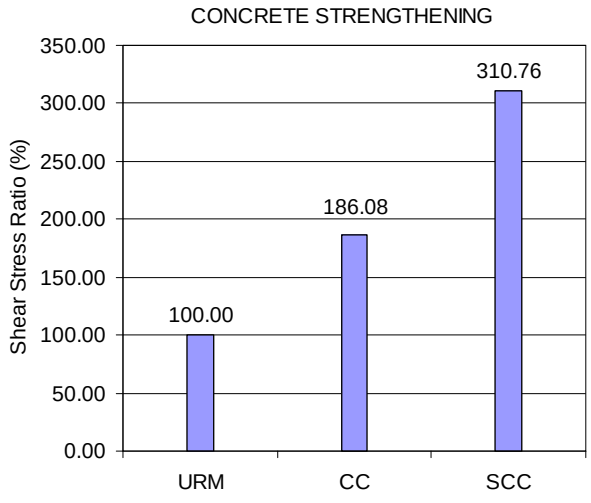

Figure 11. SCC and CC strengthening results

The improvement obtained by strengthening with the self-compacting concrete is more obvious in the behavior of wall samples. This stands on the fact that, self-compacting concrete encases the reinforcement better, the bond between self-compacting concrete and the wall is stronger, self leveling advantage and the nonporous structure of the material. Higher deformation caused by self-compacting concrete can be explained by the fact that self compacting concrete exhibits more ductile behavior compared to conventional concrete.

A typical failure mode of the SCC specimens is shown in Figure 12.



Figure 12: Failure mode of an URM wall specimen

4. CONCLUSIONS

Several observations are in general made in regard to repairing and strengthening of the masonry structural brick walls, which are remarkable enough to conduct further discussions following the experimental works on CFRP, GFRP and concrete strengthening, using specific form and types. Overall results for strength are given in Figure 13

Although the strengthening is provided on one side of the brick wall specimens, the load-bearing capacities increased in all cases and it should be recognized that the experiments are performed on single wall specimens but during a real application in an historical building the strengthening will be applied on opposite walls and will provide a symmetrical behavior in the overall structure.

As the structure in question is historical, FRP strengthening can be selected and used on one side of the walls so that the facade is kept original or covering the strengthened inner surface with a thin layer of the original stone or timber lining in order to keep the authentic look.

On the other hand, GFRP strengthening provided significant improvements in strength as well. Considering the fact that GFRP is a cheaper material, it can be a strong alternative to CFRP.

However it should be considered that environmental conditions affect resins and fibers of FRP strengthening no matter it is carbon or glass based. The mechanical properties of some FRP systems eg., tensile strength, strain, and elastic modulus, degrade under exposure to certain environments, such as salt water, chemicals, ultraviolet light, high

temperatures, high humidity, and freezing and thawing cycles. The material properties used in design should account for this degradation in accordance with the CFRP and adhesive material properties reported by manufacturers. An environmental-reduction factor for various FRP systems and exposure conditions is given by several manufacturers and scientific studies. If applied properly, FRP strengthening systems appear to offer the same or improved life cycle cost estimates compared to other strengthening systems.

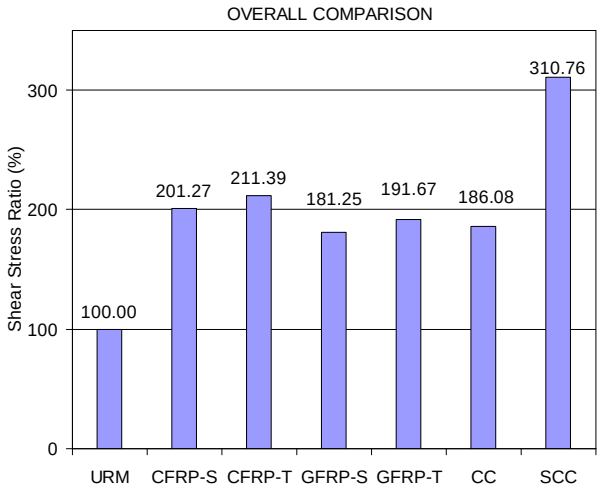

Figure 13. Over all comparison of results

As for self-compacting concrete and conventional concrete strengthening, the results show that SCC strengthening gives the highest improvement in brick wall strength. The important point here is the originality of historical structure may be jeopardized if not applied properly. Under right circumstances SCC strengthening will give highest improvements in the strength of a masonry brick wall. The impermeability of the self-compacting concrete is twice as much as compared with the conventional concrete. In strengthening the masonry structures, the service life will be improved, let alone increasing the load-bearing capacities.

Furthermore, it is possible to obtain superior surface smoothness in strengthening with SCC as compared with the conventional concrete, thanks to the self-compacting concrete's self-placing, self-levelling and nonporous strengthening properties. This also eliminates the need for the plaster, thus reducing the time and labour for strengthening. In strengthening process, the quality attributes are maintained during handling and settling of the concrete, which might be preferable. Furthermore, it is determined that the adherence obtained between the layer and the brick wall is better in case of the self-compacting concrete as compared to the standard concrete.

References:

Ediz, I. (2006) The experimental study on retrofitting of structural brick masonry walls using steel wire mesh reinforcement and self compacting concrete. M.Sc. Thesis, Institute of Science and Technology, Istanbul Technical University.

Onar, E. (2007). The Experimental study on strengthening of structural brick masonry walls using carbon fibre-reinforced polymers, M.Sc. Thesis, Institute of Science and Technology, Istanbul Technical University, 2007.

Ozsarac S. (2008) "The Experimental study on strengthening of structural brick masonry walls using glass fibre-reinforced polymers" M.Sc. Thesis, Institute of Science and Technology, Istanbul Technical University, 2008.

American Society for Testing and Materials (ASTM)(1981). "Standard test method for diagonal tension (shear) in masonry assemblages." Annual book of ASTM standards, E 519-81, Vol. 04.05

Ehsani, M.R., Saadatmanesh, H. and Velazquez-Dimas, J.I.. (1999) "Behaviour of retrofitted URM walls under simulated earthquake loading". Journal of Composites for Construction, 3-3:134-142

Albert, M.L., Elwi, A.E. and Cheng, R.J.J. (2001) "Strengthening of unreinforced masonry walls using FRPs". Journal of Composites for Construction, 5-2:170-178

Tan, K.H. and Patoary, M. K. H. (2004 ")Strengthening of Masonry Walls against Out-of-Plane Loads Using Fibre-Reinforced Polymer Reinforcement". Journal of Composites for Construction, 9-1:79–87

Hamid, A. A., El-Akhakhni, W. W., Hakam, Z. H. R. and Elgaaly, M. (2005) "Behaviour of composite unreinforced masonry-fibre-reinforced polymer wall assemblages under in-plane loading". Journal of Composites for Construction, 9-1:73–83

Krevaikas, T. D. and Triantafillou, T. C. (2005) "Masonry confinement with fibre-reinforced polymers". Journal of Composites for Construction, 9-2:128-135

JOINT CONFERENCE PROCEEDINGS
7th International Conference on Urban Earthquake Engineering (7CUEE) &
5th International Conference on Earthquake Engineering (5ICEE)
March 3-5, 2010, Tokyo Institute of Technology, Tokyo, Japan

SEISMIC RESISTANCE OF BEAM-COLUMN JOINTS IN SCALED FRAMED BRIDGES

Kabir Shakya[1], Ken Watanabe[2], and Junichiro Niwa[3]

1) Graduate Student, Department of Civil Engineering, Tokyo Institute of Technology, Japan
2) Assistant Professor, Department of Civil Engineering, Tokyo Institute of Technology, Japan
3) Professor, Department of Civil Engineering, Tokyo Institute of Technology, Japan
shakya.k.aa@m.titech.ac.jp, ken@cv.titech.ac.jp, jniwa@cv.titech.ac.jp

Abstract: In Japan, a large number of bridges have been constructed as moment resisting frames in which columns are tied together by intermediate link beam. The dense reinforcement in beams and columns of bridge causes congestion at the beam-column joints resulting in poor workability and poor performance during earthquakes. In this study, one-sixth scale beam-column T-joint composed of a column and an intermediate link beam of a framed bridge was subjected to displacement controlled quasi-static horizontal reversal load. Steel reinforcements in the test specimen were provided based on the existing design. The failure mechanism and load capacity of the specimen was investigated. The flexure plastic hinge was formed in the beam nearby the joint prior to damage of beam-column joint. Due to excessive strain in longitudinal beam rebars, internal damage occurred inside the joint. However, the cracks were not extended to the joint surface. The structure responses are expressed in terms of strain in rebars, load-displacement curve and base shear-drift ratio relationship.

1. INTRODUCTION

The moment resisting frame systems of structures are subjected to large reversal lateral loads during seismic events. The structural elements should be able to withstand these loads and also should be able to dissipate huge amount of energy in order to prevent the collapse of structures. The beam-column joint is one of the regions, where high horizontal and vertical shearing forces are induced from the adjacent beams and columns and it can initiate failure of the joints. The portion of the column within the depth of the deepest beam that frames into the column is known as beam-column joint. All the forces that are transferred by the adjacent members should be resisted by the joints. The damage and failure of joints cause severe deterioration of the overall lateral load carrying capacity of the structure and can lead to total collapse. Low amount of longitudinal and transverse reinforcement in beams and columns, insufficient amount of shear reinforcement at joints, inadequate confining effects in the potential plastic hinge regions, inappropriate anchorage detailing were most common deficiencies in old structures including bridges and buildings.

With the advancement in research, different methods and approaches were proposed to enhance the performance of beam-column joints. However, most of the researches are limited to the beam-column joints of buildings. After experiencing severe damages of bridges during Loma Prieta and Kobe earthquakes, drastic improvements have been done in the structural design of bridges. Amount of longitudinal and transverse reinforcements were increased. Special detailing of reinforcements was done to improve ductility and added cross-ties inside and in the vicinity of beam-column joints. As a result, the joints became highly congested and caused difficulty in construction. Overcongestion causes difficulty in casting which results in significant material variability and unpredictable structural performance. In Japan, a large number of railway bridges have been constructed as a moment resisting frames with intermediate link beams (Figure 1). The provision of intermediate link beams in the bridges forms T-joints.

This study deals with finding out the failure mechanism of beam-column T-joint and evaluating the load capacity. The results of displacement controlled cyclic loading experiment which was conducted on one-sixth scale beam-column T-joint are presented in this paper. The deterioration of beam-column joint was clarified by

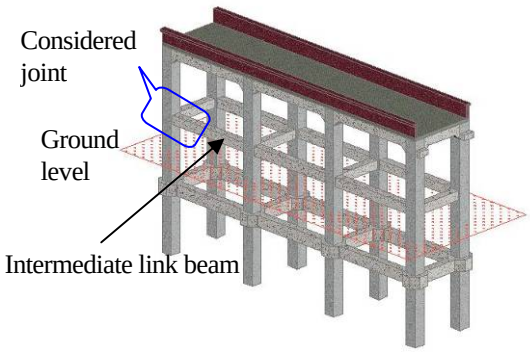

Figure 1 Framed Bridge

analysing the measured strain in longitudinal rebars and the slip amount of beam longitudinal rebars. Crack pattern observed in the specimen was used to judge the failure mechanism. Load-displacement and base shear-drift ratio relationships were also used to understand the structural behavior.

2. LITERATURE REVIEW

Abrams (1987) investigated the scale relations for reinforced concrete beam-column joints and showed that the force-deflection relations for one-quarter scale specimens were similar to those of large-scale specimens. The relation between small scale and large scale specimens was proposed for flexural strength and lateral force needed for a failure of beam-column assembly. Lowes and Moehle (1999) identified the lack of joint transverse reinforcements, short straight column bar anchorage lengths, lack of continuity between member longitudinal reinforcement and undesirable relative strengths of framing members as the main problems in the beam-column T-joints of RC bridges constructed during 1950s and 1960s. The enhancement of the joint capacity in terms of ductility and shear capacity were observed when two types of retrofit namely, addition of reinforced concrete bolsters and addition of post-tensioned reinforced bolsters to the beam, were done. Also, joint load capacity was quantified using strut-and-tie models. Based on analytical and experimental results of a beam-column connection in double-deck bridge, Mazzoni and Moehle (2001) highlighted the need of independent model of additional flexibility of joint and anchorage zones in order to consider deformations as the primary indicators of damage. The load path and the inelastic material behavior highly affected the design strengths during unidirectional and bidirectional loading. With variation in steel reinforcement arrangement at beam-column joint causes different mechanisms of shear transfer in knee and T-joints (Priestley et al. (1996)). On comparing the behavior of full-scale interior beam-column joints with and without additional vertically distributed longitudinal reinforcement at joints, considerable enhancement in strength and energy dissipation was observed. Mitra and Lowes (2007) developed mathematical model which can simulate beam-column joint response. This model can simulate the shear stress-strain response of the joint and anchorage zone response. The comparison of observed and simulated response showed very good correlation. The model showed high accuracy results in different failure modes such as joint failure prior to beam yielding, beam yielding prior to joint failure and beam yielding without joint failure.

3. EXPERIMENTAL SETUP AND MEASUREMENT SYSTEM

3.1 Material properties

Material properties, specimen dimensions, steel reinforcements etc. were chosen according to the existing design of framed bridge. The maximum size of aggregate used for casting was 10 mm. Three numbers of 100 mm × 200 mm and two numbers of 150 mm × 250 mm cylinders were cast and cured for compressive strength and tensile splitting tests, respectively. The average modulus of elasticity, average compressive strength and average tensile splitting strength were found to be 26.3 kN/mm^2, 39.8 N/mm^2 and 2.4 N/mm^2, respectively. The stress-strain curve of D6 bar obtained from tensile test (Figure 3) was used to decide the yielding of rebars during loading test. The yield strength, ultimate strength and yield strain were found to be 325 N/mm^2, 470 N/mm^2 and 1750 × 10^{-6}, respectively. The material properties of steel reinforcement and concrete are shown in Table 1.

3.2 Test specimen

The test specimen was the one-sixth scale subassembly, corresponds to half the height of columns above and below the beam and half span of the intermediate link beam (Figure 2(a)), of a framed bridge. The specimen shape and the

Table 1 Characteristics of steel reinforcement and concrete

Rebar yield stress f_y (N/mm^2)	Concrete compressive strength f_c' (N/mm^2)	Maximum aggregate (mm)	*W/C*	Mix proportion (kg/m^3)			
				Cement	Coarse aggregate	Fine aggregate	Water
(D6SD295) 295	39.8	10	0.55	291	436	811	174

Table 2 Steel reinforcement details

Longitudinal reinforcement		Shear reinforcement		Stirrup spacing (mm)	
Beam	Column	Beam	Column	Beam	Column
15 nos. D6SD295	22 nos. D6SD295	D6SD295	D6SD295	75	85

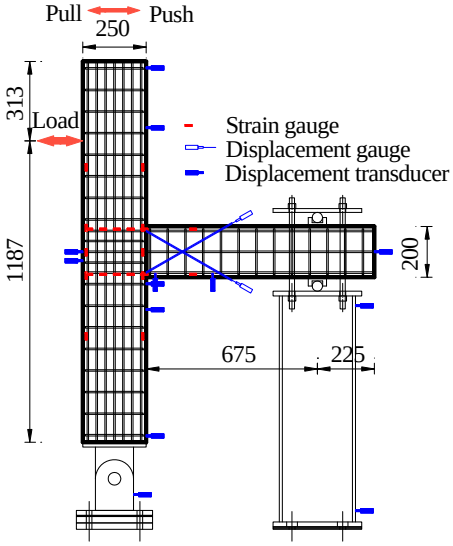

(a) Bar arrangement and measurement system

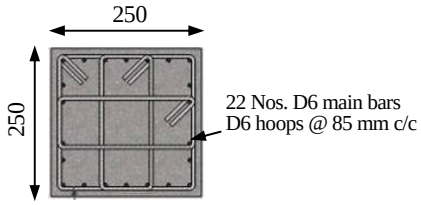

(b) Cross section of column

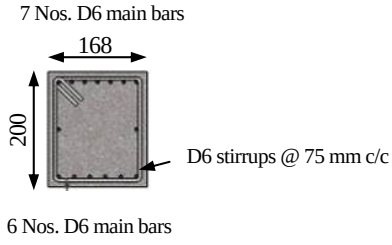

(c) Cross section of beam

Figure 2 Specimen details

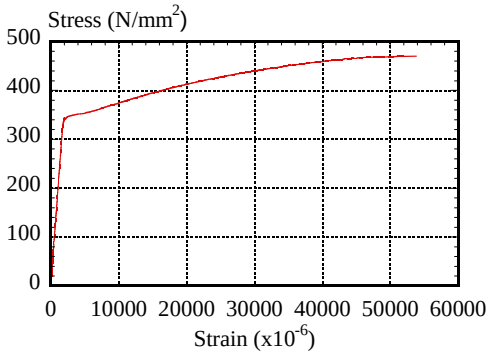

Figure 3 Stress-strain curve of D6 rebar

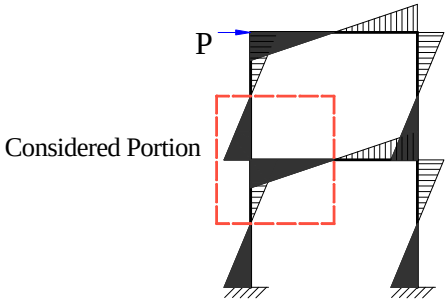

Figure 4 Moment diagram in frame due to lateral load

boundary conditions of the specimen were chosen after examining the structural response of a portal frame. The moments due to lateral load in the considered portion of portal frame (Figure 4) and the test specimen were similar. The height of column was considered as 1500 mm and length of beam from face of column to end was considered as 900 mm. The cross-sectional sizes of column and beam were 250 mm × 250 mm and 168 mm × 200 mm, respectively. The arrangement of reinforcements in column and beam were made based on the existing design of the framed bridge. Figure 2 shows the arrangement of 22 numbers of vertical rebars with hoops spaced at 85 mm center to enter in column and 15 numbers of longitudinal rebars with stirrups spaced at 75 mm center to center in beam. The clear spacing between vertical bars of column was 29 mm and that between longitudinal bars of beam was 16 mm. Hence, aggregates could pass through those spacings. All the rebars were of 6 mm diameter (D6). However, due to congestion of steel reinforcement at the joint, there was difficulty in casting. Steel reinforcements used in the test specimen are tabulated in Table 2.

3.3 Loading and instrumentation

Reversible cyclic, unidirectional lateral load was applied at the column through 200 kN displacement controlled hydraulic actuator. The lateral loading was applied in quasi-static manner with varying displacement amplitudes and varying loading rate as shown in Figure 5. The loading amplitudes were varied from 0.5 mm to 7 mm. The loading rates were varied from 0.05 mm/sec to 0.2 mm/sec. An axial load effects was neglected assuming that the effects of lateral loads were more significant than that of vertical loads.

A pin support was provided at the bottom of column while beam was rested on roller support placed above the steel column connected to loading frame. Prestressing forces were applied on the support plates in order to ensure the fixity of the supports. The supports constrained the vertical movement, however, the rotation of both column and beam were allowed. The beam was permitted for free horizontal

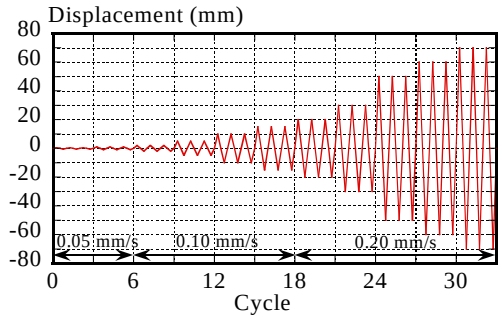

Figure 5 Applied displacement cycle and loading speed

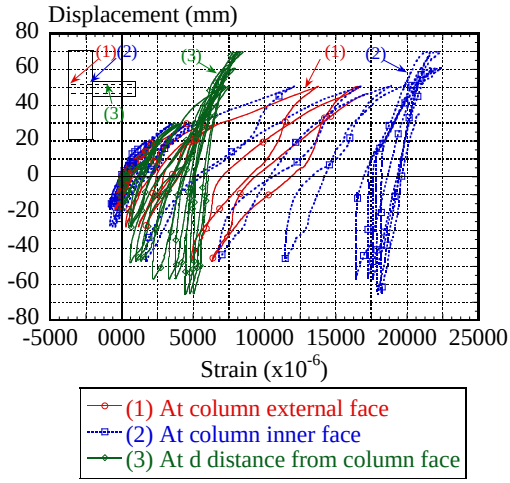

Figure 7 Strain in beam rebar

movement.

Displacement transducers, displacement gauges and strain gauges were attached at various locations to record and understand structural behavior such as deformations, slips, strains and cracking patterns under cyclic loading. The measurement system installed in the specimen is shown in Figure 2(a). Series of strain gauges were attached on the longitudinal and vertical rebars of beam and column within the beam-column joint. The strain gauges were also attached on the longitudinal and vertical rebars of beam and column at the distance of effective depths of beam and column. Displacement gauges were attached on the longitudinal bar of beam at the face of column in order to measure the bar slip. Displacement transducers were placed at various locations to measure the horizontal and vertical displacements. For the measurement of large displacement, wire type displacement transducers were used. In order to monitor displacement of supports, transducers were attached at the steel column and hinge support. Displacement at other locations can be corrected, if supports are displaced. To measure strain in concrete, gauges were pasted at different locations on the concrete surface.

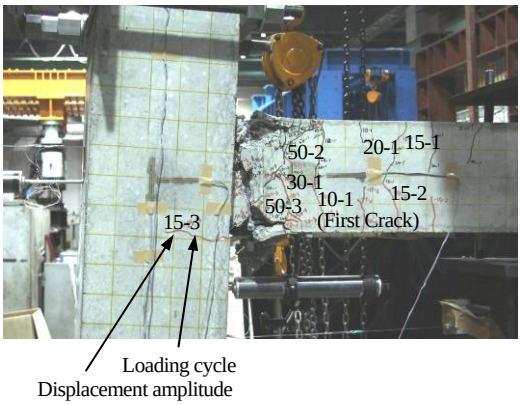

Figure 6 Crack pattern at 3rd cycle of 70 mm displacement amplitude



Figure 8 Buckling of rebars at 3rd cycle of 70 mm displacement amplitude

4. EXPERIMENTAL RESULTS AND DISCUSSIONS

4.1 Crack pattern

Crack pattern in the specimen observed by the end of the experiment is shown in Figure 6. The figure includes only the portion of the specimen where cracks were highly concentrated. The first two digits in the figure represent the displacement amplitude and last single digit indicates the number of loading cycle. For example: 50-3 represents 50 mm displacement amplitude at 3rd cycle of loading. During the first cycle of 10 mm amplitude displacement, the first crack was observed. The formation of new cracks and opening and closing of cracks continued till 50 mm displacement amplitude was applied. Only opening and closing of cracks were observed on further increasing the displacement amplitude. Spalling of concrete along with buckling of longitudinal beam rebars were noticed during the application of 60 mm horizontal displacement. The cracks were highly concentrated in the area near the column face, however, very few cracks were developed at beam-column joint. All the observed cracks were designated as flexural cracks. Due to accumulation of cracks and buckling of rebars, flexural plastic hinge was formed in the beam near the column.

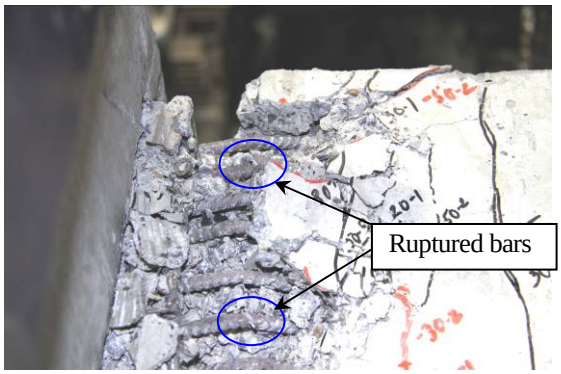

Figure 9 Rupture of rebars at 2nd ycle of 70 mm displacement amplitude

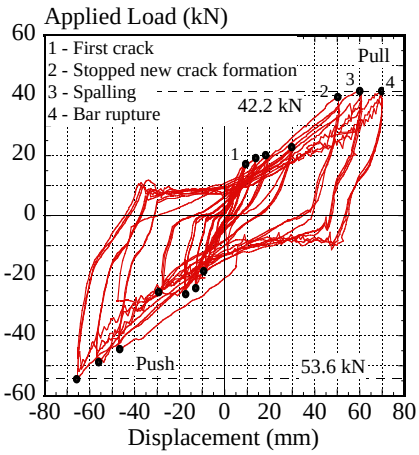

Figure 10 Load-displacement curve

4.2 Strain in rebars

In Figure 7, strains measured at three different locations on the top bar of beam are shown. The locations are the external face of column, the inner face of column and the distance of effective depth of beam from column face. The bar at all of these locations had yielded which can be clarified by comparing the strains in bars with the stress-strain relationship shown in Figure 3. The highest strain was measured at the junction between beam and column face. The reversal load induced both tensile and compressive strains in the rebars. During the application of 60 mm horizontal displacement, concrete started spalling and buckling of rebars were also observed. Buckling of rebars at the end of 3rd cycle of 70 mm horizontal displacement is shown in Figure 8. On further increasing displacement amplitude, excessive strain was induced in the rebars. Because of the excessive strain in the longitudinal beam bars, two rebars were ruptures emitting sound when the 2nd cycle of 70 mm horizontal displacement was applied. The ruptured bars are shown in Figure 9. Although strain in beam rebars exceeded the yield strain, no yielding in column rebars were recorded.

On examining the strain in rebar, it was found that the rebar at exterior column face; i.e. near the hook at the end of rebar, yielded prior to the rebar at the junction of beam and column. It indicated that the bond deterioration started from the hooks at the end of the rebars. Figure 7 also illustrates that by the end of experiment, at all the locations of bar, only tensile strains were generated. The formation of plastic hinge in beam near the column facilitated the buckling of rebars due to which high bond stresses were generated along the beam rebars in the joint. During reversal loading, although the rebars at the plastic hinge region were in compression, tensile forces were induced in the longitudinal beam rebars inside the joint because of bond deterioration. Hence, even the compression steel rebars in the beam could not contribute in bearing the compressive forces which in turns resulted in reduction of flexural strength of the beam.

The tensile force and compressive force was generated in the same longitudinal beam rebar due to application of reversal load. Due to pulling of rebars, the hooks at the end of rebars tended to straighten. It caused the stress concentration near the hook resulting in formation of localized cracks which initiated the deterioration of bond between concrete and rebars. The breakage of bond between concrete and rebars within the joint caused the slipping of rebars. Although there were cracks around the bars, it did not appear in the joint surface as the cracks were comparatively small.

4.3 Load-displacement and base shear-drift ratio relationships

The relationship between applied displacement and corresponding load recorded during the quasi-static reversal loading is expressed in terms of load-displacement curve and is shown in Figure 10. Till 30 mm horizontal displacement was applied, relatively smooth load-displacement curve was obtained. However, some spikes were appeared in the hysteresis loops upon exerting horizontal displacements of 50 mm and above. Smooth rolling of rollers was obstructed by the frictional forces. Moreover, rollers started skidding instead of rolling because of movement of roller supporting plates (Figure 11) at the higher displacement amplitudes. These two reasons caused the formation of spikes in the hysteresis loops. Furthermore, load capacity was reduced when the specimen was pulled towards the actuator than that during the specimen was pushed away from the actuator.

The load capacity of the specimen increased linearly till the horizontal displacement of 10 mm was applied. In Figure 10, the peak loads at each displacement amplitude observed after nonlinear increment of load capacity are marked. The first crack was observed during the application of first cycle of 10 mm displacement. The formations of cracks were rapid after the formation of the first crack. Hence, no significant increase in load capacity was noted upon increasing the magnitude of horizontal displacements. However, on applying 50 mm displacement, drastic increase in load capacity was recorded. Friction on rollers and difference in fixity level rollers supporting plates above and below the beam were indentified as the reasons behind the drastic increase of load capacity. Only opening and closing of cracks were observed without formation of any new

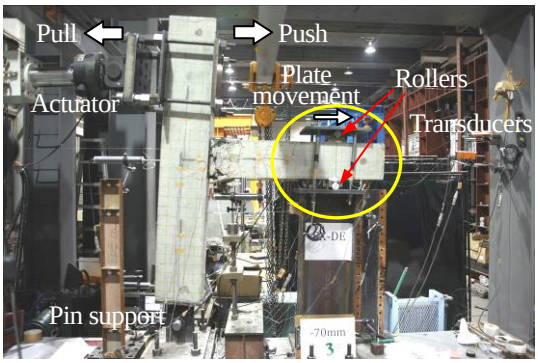

Figure 11 Displacement of roller supporting plate

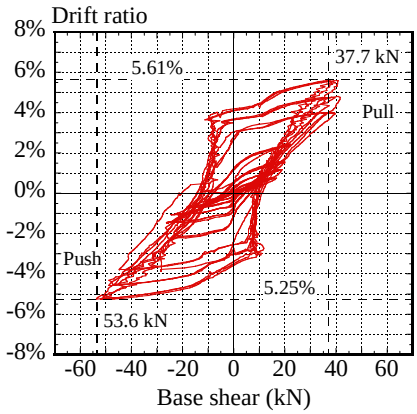

Figure 12 Base shear versus drift ratio relationship

cracks after the specimen was displaced by 50 mm. Concrete started spalling and beam longitudinal rebars started buckling when 60 mm horizontal displacement was applied. The load capacity became almost constant when the specimen was pulled towards the actuator, however, the load still increased on pushing the specimen. The load capacities of 42.2 kN and 53.6 kN were noted during pulling and pushing of the specimen during the first cycle loading of 70 mm displacement amplitude. The load capacity decreased on the further loading cycles. The shear force at the beam-column joint and shear joint capacity were calculated by following the method recommended by ACI 352R-02 and were found to be 48.5 kN and 284.8 kN, respectively. It indicates that the conservative design of beam-column joint as shear capacity of joint was very high compared to joint shear force.

In Figure 12, the relationship between base shear and drift ratio is shown. Drift ratio is defined as the ratio of displacement at the top of column relative to the bottom of the column to the height between those points. For the design of seismic resistant structures, drift ratio is one of the key parameters. The maximum drift ratio of 5.61% was found during pulling and 5.25% was found when the specimen was pushed away from the actuator. The corresponding base shears were found to be 37.7 kN and 53.6 kN. Spalling of concrete and buckling of longitudinal beam rebars including rupture of two beam rebars had occurred at these drift ratios. The damage in the structure was considered as irreparable damage.

5. CONCLUSIONS

Based on the existing design of framed bridge in Japan, a one-sixth scale beam-column joint was constructed The specimen was tested under displacement controlled quasi-static horizontal reversal load. From the experimental results following conclusions are obtained:

(1) In the considered specimen, the formation of plastic hinge in beam showed that the beam-column joint was stronger than the beam.

(2) The internal damage of beam-column joint was occurred due to excessive strain in beam rebars, however, no significant cracks were visible in surface.

(3) In compression steel of the beam, tensile force was developed during reversal loading because of bond deterioration within beam-column joint.

(4) The design of the beam-column joint was conservative because the shear capacity of beam-column joint was too high than the subjected shear at the joint.

(5) The test results indicate that in real structures of considered type, the flexural failure will occur in the beams prior to beam-column joints failure during seismic events.

Acknowledgements:

The authors are very grateful to Center for Urban Earthquake Engineering (CUEE), Tokyo Institute of Technology, for providing research fund.

References:

Abrams, D. P. (1987), "Scale Relations for Reinforced Concrete Beam-Column Joints," ACI Structural Journal, 84(6), 502-512.

Joint ACI-ASCE Committee 352, (2002), "Recommendations for Design of Beam-Column Connections in Monolithic Reinforced Concrete Structures", ACI 352R-02.

Lowes, L. N. and Moehle, J. P., (1999), "Evaluation and Retrofit of Beam-Column T-Joints in Older Reinforced Concrete Bridge Structures," ACI Structural Journal, 96(4), 519-533.

Mazzoni, S. and Moehle, J. P. (2001), "Seismic Response of Beam-Column Joints in Double-Deck Reinforced Concrete Bridge Frames," ACI Structural Journal, 98(3), 259-269.

Mitra, N. and Lowes, L. N., (2007), "Evaluation, Calibration, and Verification of Reinforced Concrete Beam-Column Joint Model," Journal of Structural Engineering, American Society of Civil Engineers, 133(1), 105-120.

Priestley, M. J. N., Seible, F. and Calvi, G. M., (1996), "Seismic Design and Retrofit of Bridges," John Wiley and Sons, Inc.

JOINT CONFERENCE PROCEEDINGS
7th International Conference on Urban Earthquake Engineering (7CUEE) &
5th International Conference on Earthquake Engineering (5ICEE)
March 3-5, 2010, Tokyo Institute of Technology, Tokyo, Japan

ROCKING BEHAVIOR OF BRIDGE PIERS WITH SPREAD FOOTING UNDER CYCLIC LOADINGS AND EARTHQUAKE EXCITATIONS

H. H. Hung[1], K. C. Chang[2], and K. Y. Liu[3]

1) Associate Research Fellow, National Center for Research on Earthquake Engineering, Taipei, Taiwan
2) Professor, Dept. of Civil Engineering, National Taiwan University, Taipei, Taiwan
3) Associate Research Fellow, National Center for Research on Earthquake Engineering, Taipei, Taiwan
hhung@ncree.org.tw

Abstract: Some spread footing foundations of real retrofitting engineering practices in Taiwan were extended to be uneconomically large due to the restriction of foundation uplift regulated in design code. Although rocking mode of spread footings induced from foundation uplift is not acceptable in current design code, some researchers have indicated that rocking itself can act as a form of isolation mechanism. Uplift of foundation can limit the earthquake forces that can be transmitted to pier base, hence to decrease the plastic deformation occurring at the plastic zone. In order to gain better understanding of the problem of rocking, and in turn have more confidence in taking the benefit of rocking mode into account in the future, a series of rocking experiments were performed in NCREE. The experimental response of six circular reinforced concrete columns with different design details were subjected to quasi static and pseudo dynamic loadings. During the tests, columns were rested on rubber pad to allow the mechanism of rocking to take place. Experimental variables include size of footing, strength and ductility capacity of columns, and level of the applied earthquake intensity. Results of each test were presented and also compared with the benchmark test with fixed base condition where foundations were constrained to the strong floor. From this comparison, the difference between the response behavior of rocking base and fixed base foundation was highlighted. These experimental results can serve as good references for future seismic evaluation and a basis for updating future design code

1. INTRODUCTION

After chi-chi earthquake, the design earthquake intensities of some area in Taiwan were shifted to a higher value; thus a great number of bridges need to be retrofitted. As the retrofitting work leads to a higher plastic moment capacity of the columns, based on capacity design, the design force for the foundation needs to be increased, too. In order to satisfy the stability check of a spread footing under the application of this plastic moment transferred from the column base, some of the retrofitting works resulted in uneconomically large spread footings. Some newly designed engineering practices also met the similar situation. This is due to the restriction of footing uplift regulated in the bridge design code. The rocking mode of a spread footing induced by foundation uplift is not favorable in the current design code. However, several studies have suggested the benefit of rocking mechanism due to foundation uplift. The uplift of the foundation can limit the earthquake forces that are transmitted to the column base, thereby decreasing the plastic deformation that occurs in the plastic zone. In addition, unless the foundation is very massive, some uplift on the tension edge of the spread footing during a major earthquake cannot be avoided. Thus, the analysis of a design for seismic retrofitting that is based on the assumption that foundation and soil are firmly bonded to each other will show unreasonable large internal forces in columns and thereby dramatically increase the cost of the retrofit. In addition, the widening and strengthening of the foundations to restrict the rocking mechanism will also force the columns to sustain most of the seismic energy and consequently the damage level to those columns will increase significantly. According to past experience, the collapse of bridges due to the failure of a spread footing is rather uncommon. For these reasons, and the fact that the retrofitting of a foundation can often be very expensive, it is reasonable to tolerate a certain amount of uplift of the foundation in the retrofit design of a bridge. In fact, foundation rocking has been conditionally accepted by some retrofitting guidelines or manuals, including FEMA (1997) for buildings, and FHWA (2006) for bridges. In Taiwan, the stability check of a spread footing was also revised recently (MOTC. 2008) to allow a certain amount of foundation uplift to occur in the ultimate state.

In the current design philosophy, the rocking mechanism of the foundation is not allowed and is not taken into account in the analysis. This is because neglecting the effect of rocking will overestimate the seismic forces applied to the structures, and lean toward conservative side for the strength design approach. However, with the ever growing interest in performance-based design approach in recent

years, the importance of a precise prediction of the behavior of the structure subjected to seismic forces is increasingly being recognized. This includes the reasonable prediction of large lateral displacements in the column top as a result of the rigid rotation due to foundation rocking. Additionally, as mentioned earlier, some uplift on the edge of a foundation is highly likely to occure under severe earthquake conditions, because in reality a spread footing is supported on the soil only through gravity loading. According to Kawashima and Nagai (2006), the rocking response in spread footing foundations was observed in the investigation of past earthquakes. Apostolou et al. (2006) also indicated several examples of structural uplift in numerous earthquakes, including Chile 1960, Alaska 1964, San Fernando 1971, Kocaeli 1999, and Athens 1999. These observations seem to indicate that even though the possible benefit gained from foundation rocking is not taken into account in the design phase, rocking did occur in the past during a severe earthquake. The insistence of not considering the effect of rocking sometimes underestimates the disadvantages that may be brought by rocking, such as large lateral displacements of the deck and permanent settlement in soils. In this regards, realistically taking the effect of rocking into consideration, including the interaction between foundation, column and soil, has gradually become an important issue in the structural design of bridges, especially for the design based on the performance-based approach.

The seismic isolation effect of the rocking mechanism has been identified in many previous studies since the pioneer work performed by Housner (1963), who noted that foundation uplift may explain the good performance of several elevated water tanks during the 1960 earthquake in Chile. Over the following few decades, several other articles were published on the study of rocking. Most of these earlier studies were performed by analytical approach, and relatively few experimental studies were carried out. Recently, with the advances in experimental technique, rocking experiments became the focus of several studies, including series of tests performed on a large centrifuge by Gajan et al. (2008) and tests performed on a shaking table by Sakellaraki et al.(2005) and Espinoza and Mahin (2006). All of these previous studies recognized the beneficial effect of rocking. However, few of them considered the coupling effect of the material nonlinearity that is involved with column plastic hinging and geometrical nonlinearity due to foundation uplift. Also, the relevant researches are not sufficiently comprehensive to provide confidence to revise the design code extensively. In order to have a better understanding about the rocking mode and its role on the overall behavior of a bridge, more experimental data and different modeling approaches are required. Therefore, in this study, a series of pseudo-dynamic tests and cyclic loading test of six reinforced concrete columns were conducted.

2. EXPERIMENTAL PROGRAM

2.1 Test Specimens

In order to investigate the coupling effect of the material nonlinearity involved with column plastic hinging and the geometrical nonlinearity due to foundation uplift, six reinforced concrete columns with two types of foundation size and three types of design details in column base were constructed. As shown in Fig. 1, these circular RC columns are all 50 cm in diameter and constructed with a clear height of 2.5 m and a height of footing 0.5 m. Their footing sizes are either B = 140 m or B = 170 m.

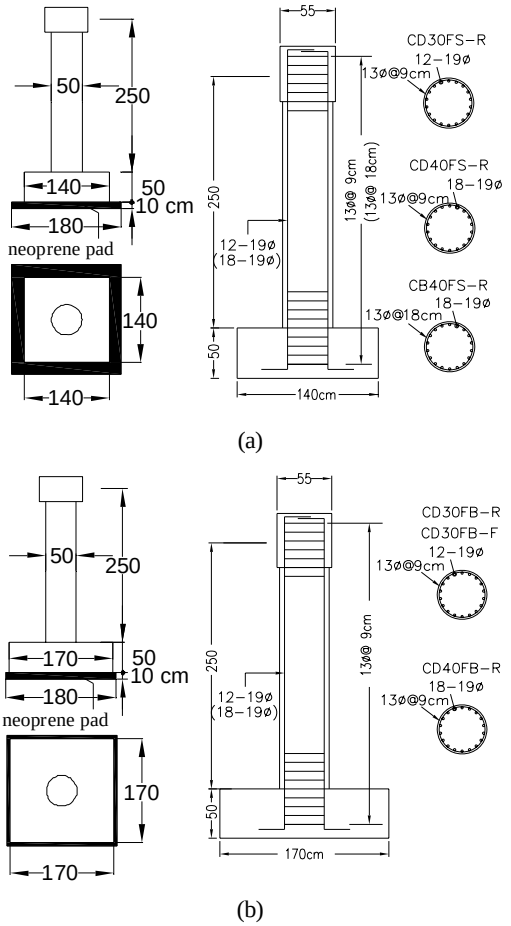

Figure 1 As-built details of model columns (a) B = 140cm, (b) B = 170cm

These columns were reinforced with three types of design details. One with 12-D19 (steel ratio = 1.75%) main reinforcements was transversely reinforced with D13 perimeter hoops spaced 9 cm (volumetric confinement ratio ρ_s = 0.012), corresponding to the case with an arrangement of transverse reinforcements that conforms to the requirement specified by the design code. The other two with 18-D19 (steel ratio = 2.63%) main reinforcements were transversely reinforced with D13 perimeter hoops spaced 9 cm and 18 cm, respectively. The one with transverse reinforcements spaced 18 cm represents a column with an insufficient volumetric confinement ratio (ρ_s = 0.006). The nominated material properties for these specimens are as follows: concrete compressive strength f_c' = 280 kg/cm^2; yield strength of main reinforcements F_y = 4200 kg/cm^2; yield strength of transverse reinforcements F_{yh} = 2800

kg/cm^2. With the combination of different sizes of footing and different design details, a total of six test columns were designed and named as CD40FS-R, CB40FS-R, CD30FS-R, CD40FB-R, CD30FB-R and CD30FB-F, respectively, as plotted in Fig. 1 and listed in Table 1. In which, characters "FS" and "FB" are denoted as cases with a footing of smaller size (B = 140 m) and of larger size (B = 170 m), respectively. Number "40" and "30" are denoted as cases with 18-D19 and 12-D19 main reinforcements, respectively; characters "CD" and "CB" are denoted as columns transversely reinforced with hoops spaced 9 cm and 18 cm, respectively; while "R" and "F" represent rocking base condition and fixed base condition, respectively. Before experimental tests, moment curvature analysis was performed for these model columns. The calculated moment-curvature curves based on the nominated material properties are shown in Fig. 2. As can be seen, the effective yield moments for specimens CD30xx.x, CD40xx,x and CB40xx.x are 329.0 kN-m, 428.3 kN-m and 426.1 kN-m, respectively.

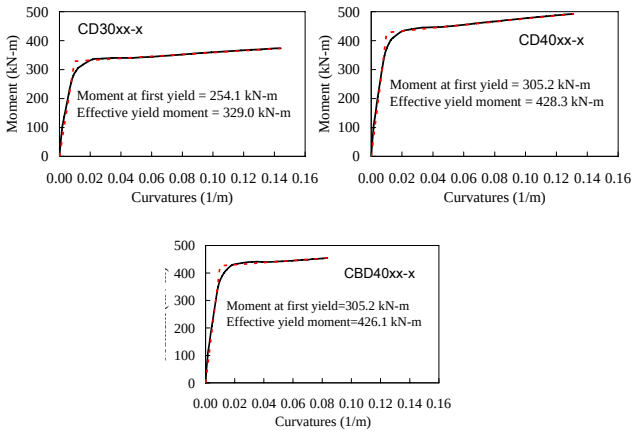

Figure 2 Moment-curvature curves of model columns

2.2 Test Setup

To clarify the difference in response behavior between columns with a rocking base condition and those with a fixed base condition, both tests with and without the footing uplift restraint were conducted. Fig. 3 illustrates the test setup. In the case where footing uplift was restrained, four tie-down rods were placed through the footing and anchored into the strong floor of the laboratory to restrain the rocking mode of the foundation (Fig. 3b). In the case where the rocking mechanism was considered (Fig. 3a), the square footings were rested on a 10 cm thick neoprene pad (Duro-60), simulating a spread footing foundation in a stiff soil. The dimension of the neoprene pad was 180 cm × 180 cm. During the test, the lateral deformation of the neoprene pad was restrained. In addition, a special apparatus with rolling balls were installed on each side of the footing to prevent torsion of the test column but allowed uplift of the footing.

During the test, a vertical axial load of 539 kN was applied to the test column through a tap beam using two vertical actuators. The vertical loading was kept constant throughout the test to simulate the tributary dead load of the deck, which is around $0.10A_g f_c^{'}$, where A_g is the gross cross-sectional area of the column. In addition, one horizontal actuator was used to apply the lateral force to the column's top to simulate the seismic loading. The location of the application force was 2.5 m from the top of the footing, and 3 m from the footing base. Under the excitation of loadings, the rotations of the foundation were monitored by six tiltmeters mounted on two sides of the foundation. Curvatures and rotations within the plastic hinge region of columns were also measured using ten tiltmeters in two lines mounted on each side of the columns along the neutral axis in the potential plastic hinge zone.

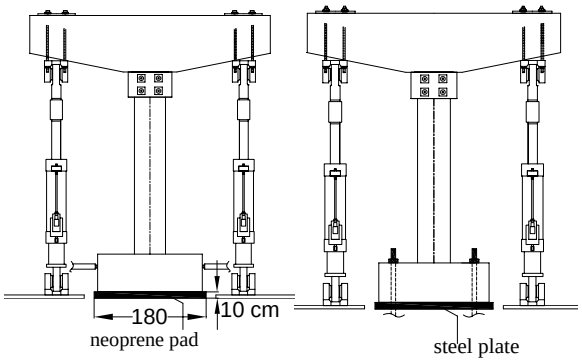

Figure 3 test setup (a) rocking bas; (b) fixed base.

2.3 Test Schedule

The test schedule is listed in Table 1, which includes pseudo-dynamic loading tests and quasi-static cyclic loading tests. The input ground motions for pseudo-dynamic tests are two artificial earthquake accelerations. As given in Fig. 4, one of these input ground motions is a code compatible medium earthquake acceleration (TH1) and the other is a code compatible design earthquake acceleration (TH2) for Nantou Pouli, a region of high seismicity in Taiwan. The peak ground accelerations for TH1 and TH2 are PGA = 100 gal and 326 gal, respectively, and the cyclic tests were performed under displacement control to a drift ratio of 7% (17.5 cm). For specimens CD40FS-R, CD30FS-R, CD40FB-R and CD30FB-R, the columns were firstly tested sequentially by two pseudo dynamic loadings, i.e., TH1 and TH2, under the rocking base condition. Then, the same specimens were subjected to a cyclic loading test. Under the rocking base condition, another specimen named CB40FS-R was also subjected to a cyclic loading test. After these tests performed in rocking base condition were competed, since no physical damage can be observed in specimens CD40FS-R and CB40FS-R, the same specimens were later constrained to the strong floor and tested by another cyclic loading test, acting as benchmark tests with fixed base condition. Another specimen named CD30FB-F that has the same design details as specimen CD30FB-R was also tested by a cyclic loading test under fixed base condition to represent a benchmark test of columns with 12-D19 main reinforcements.

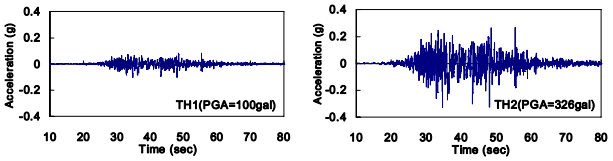

(a) (b)

Figure 4 Input ground motions for pseudo-dynamic tests: (a) TH1, (b)TH2

Table 1 Experimental test schedule

Test Specimens	Base condition	Tests
CD40FS-R	Rocking base	pseudo-dynamic test (TH1,TH2)
		cyclic loading test
	Fixed base	cyclic loading test
CD30FS-R	Rocking base	pseudo-dynamic test (TH1,TH2)
		cyclic loading test
CD40FB-R	Rocking base	pseudo-dynamic test (TH1,TH2)
		cyclic loading test
CD30FB-R	Rocking base	pseudo-dynamic test (TH1,TH2)
		cyclic loading test
CB40FS-R	Rocking base	cyclic loading test
	Fixed base	cyclic loading test
CD30FB-F	Fixed base	cyclic loading test

3. TEST RESULTS AND DISCUSSIONS

3.1 Pseudo dynamic tests of TH1 and TH2

As mentioned previously, specimens CD40FS-R, CD30FS-R, CD40FB-R and CD30FB-R were firstly supported on a neoprene pad without uplift restraint and were subjected to the pseudo dynamic test of TH1. The hysteretic responses of these tests are plotted in Figs. 5 and 6. Fig. 5 shows the lateral load versus the lateral displacement curves for the system, while Fig. 6 shows the moment versus rotation curves at the column base. In these moment-rotation curves, the rotations were obtained by taking the reading of the highest tiltmeter located at a height of 65 cm minus the reading of another tiltmeter mounted on the footing. Thus, the rotations in Fig. 6 come from the elastic and plastic flexure of the column only; whereas the lateral displacements given in Fig. 5 come from the elastic and plastic flexure of the column plus the rocking of the footing. It is evident that under the subjection of TH1 acceleration, a frequent minor earthquake, both the force-displacement curves and the moment-rotation curves almost remain linear. This result indicates that the uplift of footing was not significant and the plastic hinge was not formed as the columns experienced this minor earthquake. Other phenomenon can be observed in Figs. 5 and 6 is that the response behaviors of the specimens with the same size of footing were similar, i.e., specimens CD40FS-R and CD30FS-R had similar response behavior. Specimens CD40FB-R and CD30FB-R also behaved similarly, even though their design details of main reinforcements were different.

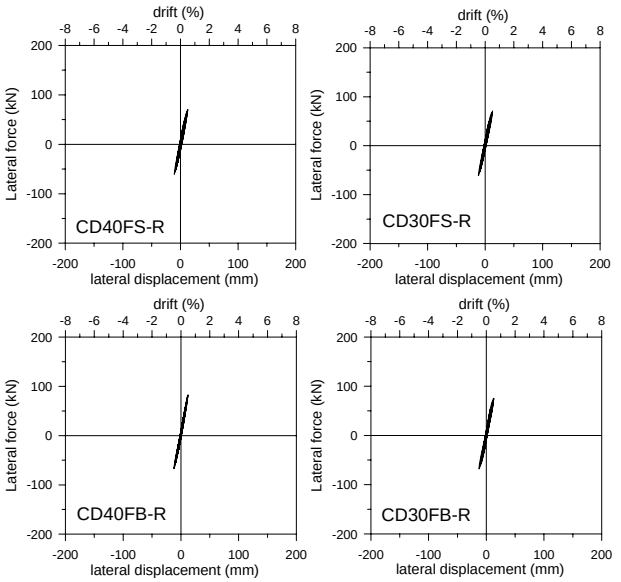

Figure 5 Lateral load-lateral displacement curves for pseudo-dynamic test of TH1.

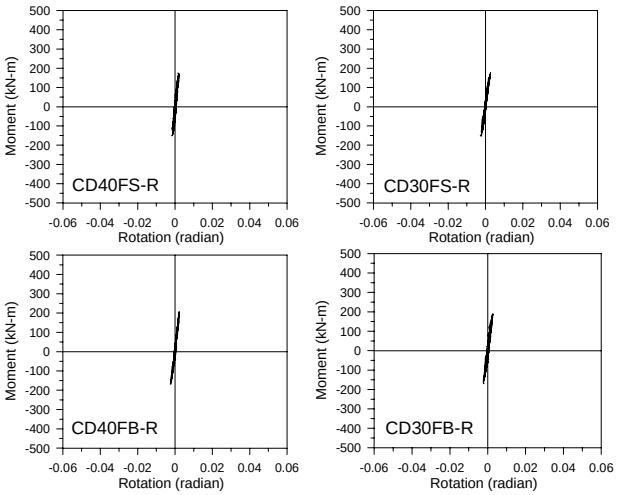

Figure 6 Moment-rotation curves at column base for pseudo-dynamic test of TH1.

After the pseudo-dynamic test of TH1, these four specimens were subjected to another pseudo-dynamic test of TH2, a code compatible design earthquake acceleration. The experimental results in the forms of lateral force versus the lateral displacement curve and moment versus the rotation curve are plotted in Figs. 7 and 8, respectively. By observing these figures, it is evident that under the subjection of a design earthquake, the plastic deformation of the columns was still not very obvious. However, at the same time, some uplift already occurred since the lateral force-displacement curves given in Fig. 7 are not linear anymore, but shows a softer stiffness as the lateral displacement increases. According to the theoretical calculation, rocking mechanism of a column with spread footing will be triggered as the base moment of footing becomes higher than M_0,

$$M_0 = \frac{BW_T}{6} \quad (1)$$

where B is the width of the footing in the direction of the bending; W_T is the total axial load applied to the footing base. For current cases with a footing size of B = 140 cm (W_T = 574 kN) and B = 170 cm (W_T = 585 kN), the footing start to uplift as the lateral force reaches 44.6 kN and 55.3 kN, respectively. These values are lower than those sustained by the columns as indicated in Fig. 7; thus uplift did occur during the subjection of design earthquake, and provided some isolation effect.

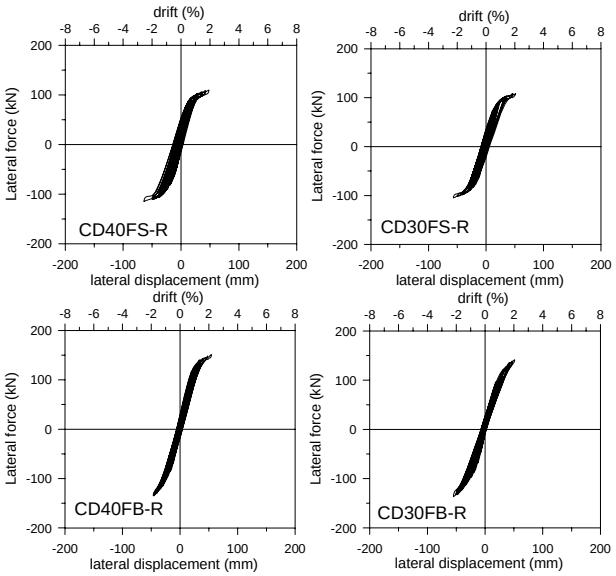

Figure 7 Lateral load-lateral displacement curves for pseudo-dynamic test of TH2.

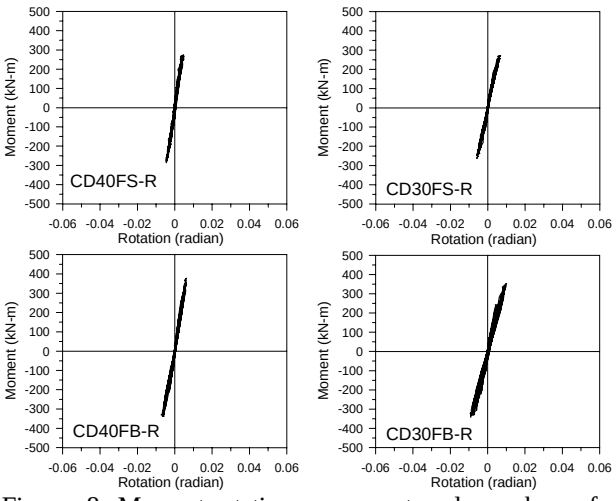

Figure 8 Moment-rotation curves at column base for pseudo-dynamic test of TH2.

Similar to last cases subjected to a frequent earthquake TH1, the response behaviors of specimens of CD40FS-R and CD30FS-R are almost the same, even though their numbers of main reinforcement are different. However, as for the specimens with footing of a larger size, .i.e., B = 170 cm, the maximum values of lateral force and moment sustained by specimens CD30FB-R are a little bit smaller than that by specimen CD40FB-R. Also, the area enclosed by the hysteresis loop of the moment-rotation curve for specimen CD30FB-R is a little bit larger than that of CD40FB-R. This is because CD30FB-R has a moment strength less than that of CD40DB-R, and it already yielded a little bit before the rocking mechanism could fully control the response behavior.

3.2 Cyclic loading tests

For test columns CD40FS-R, CD30FS-R, CD40FB-R and CD30FB-R, after pseudo-dynamic tests were completed, a cyclic loading test was applied to the same test column without uplift restraint. In order to investigate the effect of ductility, another test specimen named as CB40FS-R was also subjected to a cyclic loading test under the rocking base condition. For comparison, after these cyclic loading tests under rocking base condition were completed, another cyclic loading was applied to the same test columns CD40FS-R, CB40FS-R with uplift restraint to simulate fixed base cases and were renamed as CD40FS-F and CB40FS-F. In addition, a new specimen CD30FB-F was also tested by a cyclic loading test with uplift restraint.

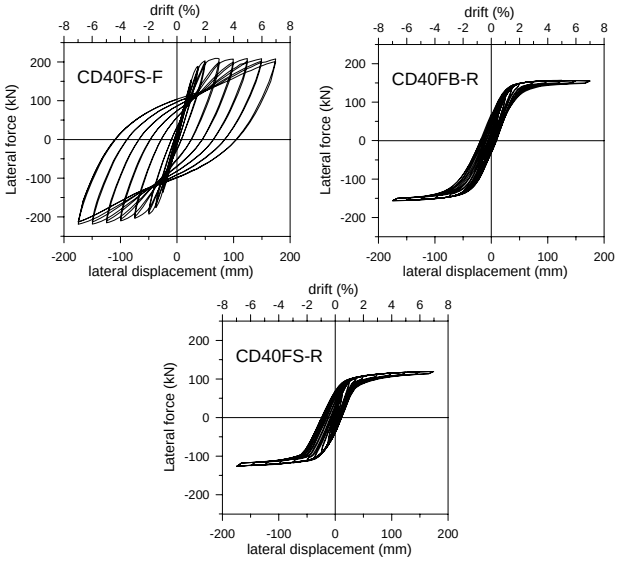

Figure 9 Lateral load-lateral displacement curves for cyclic loading test of specimens CD40xx-x.

These experimental results are plotted in Figs 9-17. Among these figures, figs. 9-11 show the experimental results of test specimens with 18-D19 main reinforcements and were transversely reinforced with D13 hoops spaced 9cm (CD40x.xx). Figs 12-14 provide the results of specimens with 18-D19 main reinforcements and were transversely reinforced with D13 perimeter hoops spaced 18 cm (CB40x.xx). Figs. 15-17 demonstrate the results of test specimens with 12-D19 main reinforcements. Again, Figs. 9, 12 and 15 are denoted as lateral force vs. lateral displacement curves and Figs. 10, 13 and 16 give moment vs. the rotation curves. Figs. 11, 14 and 17 show the vertical distribution of the curvature in the plastic hinge region for each test column. The average curvature was obtained by

taking the difference between the readings of two adjacent tiltmeters divided by the distance between them. In these figures of curvature distribution, only the results for the push direction were plotted for the sake of brevity.

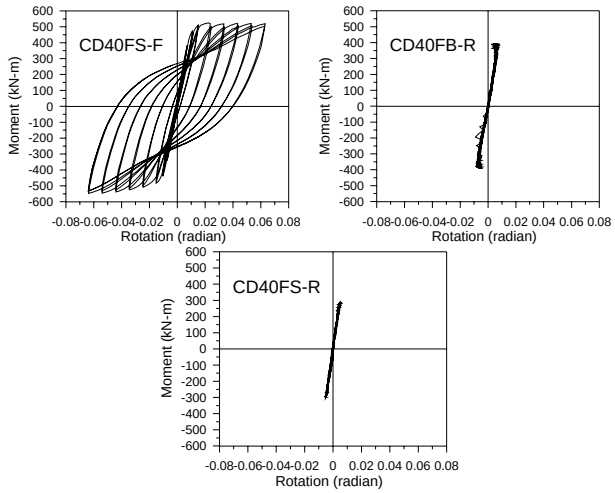

Figure 10 Moment-rotation curves at column base for cyclic loading test of specimens CD40xx-x.

In these figures, the results for fixed base cases of CD40FS-F, CB40FS-F and CD30FB-F can not only signify the capacity of the columns with the same design details, they can also represent cases with a footing of very large size. For instance, CD40FS-F in Fig. 9 can represent a case with the same design details as CD40FB-R and CD40FS-R, but with a footing of very large size. By comparing the results of CD40FS-F, CD40FB-R and CD40FS-R in Fig. 9-11, it is noted that the rocking behavior is more pronounced as the dimension of footing decreases. Also, the maximum value of lateral forces that the column sustained decreases with the decrease in footing size. According to Hung et al. (2008), if the foundation of column is allowed to rock with uplift, and the yield stress of the underlying soils is assumed to be great enough that the soil will not yield during earthquake, the shear force and bending moment that the column has to sustain will have an upper limit value given as follows,

$$V = \frac{M_2}{H} = \frac{BW_T}{2H} \tag{2}$$

$$M = V(H-h) = \frac{BW_T}{2H}(H-h) \tag{3}$$

where B is the width of the footing in the direction of the bending; W_T is the total axial load applied to the footing base; H is the distance between the location where the lateral force applies and the foundation base, and h is the height of the foundation. Thus, for current cases, the corresponding upper limit values of shear force and bending moment for specimens with a larger footing (B = 170 cm) are V = 165.8 kN and M = 414.4 kN-m. As for the specimens with a smaller footing (B = 140 cm), the corresponding upper limit values are V = 133.9 kN and M = 334.8 kN-m, respectively. In Figs. 9 and 10, these corresponding maximum values of shear forces and moments for CD40FB-R and CD40FS-R are respectively around V = 160 kN and 130 kN, M = 400 kN-m and 320 kN-m, which are close to the upper limit values calculated by Eq. (2) and (3). In addition, because the maximum values of moment, i.e., M = 400 kN-m for CD40FB-R and M = 320 kN-m for CD40FS-R, are less than the moment capacity of columns as indicated by CD40FS-F and the calculated effective yield moment from moment-curvature curves given in Fig. 2, the moment-rotation curves for both CD40FB-R and CD40FS-R are almost linear, implying that not much plastic deformation occurred in columns. Similarly, the curvatures given in Fig. 11 for both CD40FB-R and CD40FS-R are much smaller that of the fixed base case CD40FS-F, suggesting that once the rocking moment at the footing base completely govern the response, the plastic deformation occurring at the columns base can be vary minor.

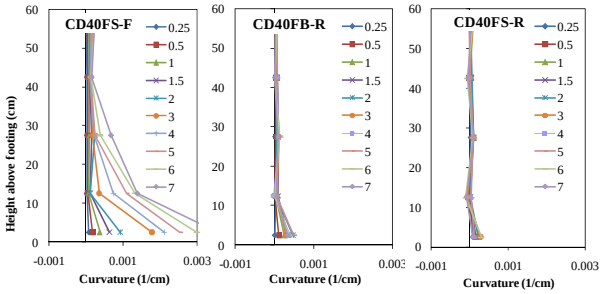

Figure 11 Curvature distributions for cyclic loading test of specimens CD40xx-x.

As for the cases with insufficient transverse reinforcements (CB40xx.x) as shown in Figs. 12-14, CB40FS-F is the benchmark test for CB40FB-R. Similarly, for the rocking case of CB40FS-R, the seismic force that the column sustained was limited to an almost constant value around V = 130 kN and M = 320 kN-m. Because the maximum value of bending moment sustained by the column was lower than its moment capacity in column base indicated by CB40FS-F and the moment-curvature curve given in Fig. 2, the plastic deformation occurring at column was minor and the corresponding moment-rotation curve shown in Fig. 13 for CB40FS-R are almost linear. The curvature distributions shown in Fig. 14 demonstrate a similar trend. The curvature in CB40FS-R is much smaller than that of the fixed base case CB40FS-F.

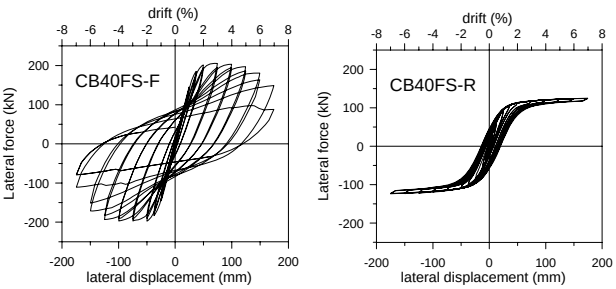

Figure 12 Lateral load-lateral displacement curves for cyclic loading test of specimens CB40xx-x.

Another trend can be observed in these figures is that the response behaviors of the rocking base cases CD40FS-R

and CB40FS-R are similar, even though the responses of the corresponding fixed bas cases CD40FS-F and CB40FS-F are different. This result confirms that the ductility demand of a column can be reduced if its upper limit value of moment due to rocking is lower than the yield moment capacity of the column base. This is because in that case, the column needs not to sustain moment with a value higher than its yield moment and will not deform into plastic state; thus the ductility capacity that allows the column to deform plastically without fracture becomes unnecessary.

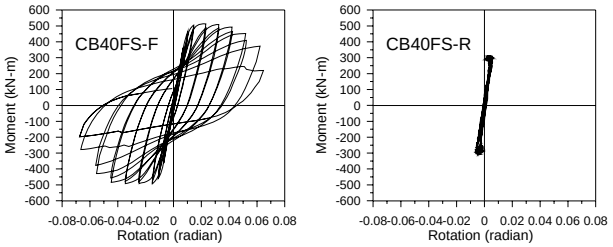

Figure 13 Moment-rotation curves at column base for cyclic loading test of specimens CB40xx-x.

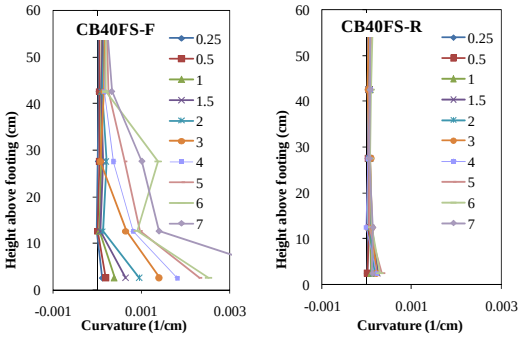

Figure 14 Curvature distributions for cyclic loading test of specimens CB40xx-x.

Figs. 15-17 plot the experimental results for specimens with 12-D19 main reinforcements (CD30xx.x). Among these specimens, CD30FB-F is the benchmark test, representing the fixed base case or case with a footing of very large size. These results demonstrate that with the decrease in footing size, the nonlinear rocking behavior becomes more significant. Consequently, the plastic deformation occurred in column base becomes minor. For instance, the moment-rotation curve for CD30FS-R shown in Fig. 16 is almost linear, while some plastic deformation was formed in CD30FB-R. Similar trend can also be observed in the curvature distribution curves in Fig. 17. For CD30FB-R, the calculated upper limit value of moment based on Eq. (2) is 414.4 kN-m, which is a value higher than the moment capacity of the column indicated by CD30FB-F in Fig. 16 and its moment-curvature curve given in Fig. 2. Therefore, before the base moment of the footing could reach its upper limit value, the column already yielded, and the moment capacity of the column governed the response behavior. On the other hand, for specimen CD30FS-R, the maximum value of bending moment sustained by column was around 320 kN-m, which is a value lower than the moment capacity of CD30FB-F indicated in Figs. 16 and 2. Thus, the column can still remain in elastic state.

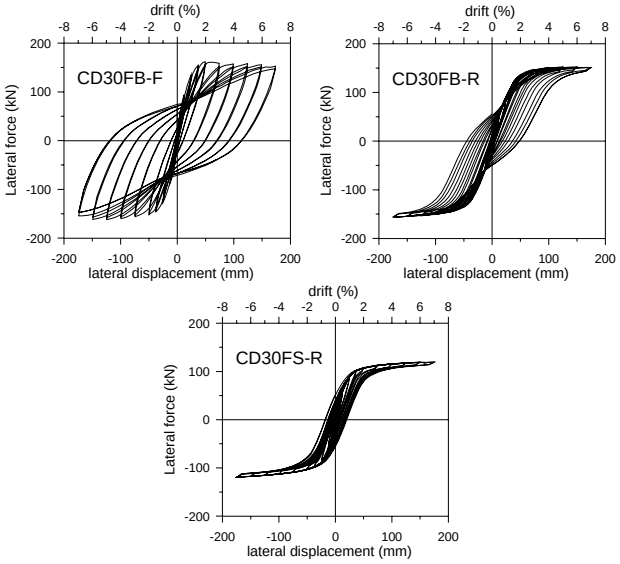

Figure 15 Lateral load-lateral displacement curves for cyclic loading test of specimens CD30xx-x.

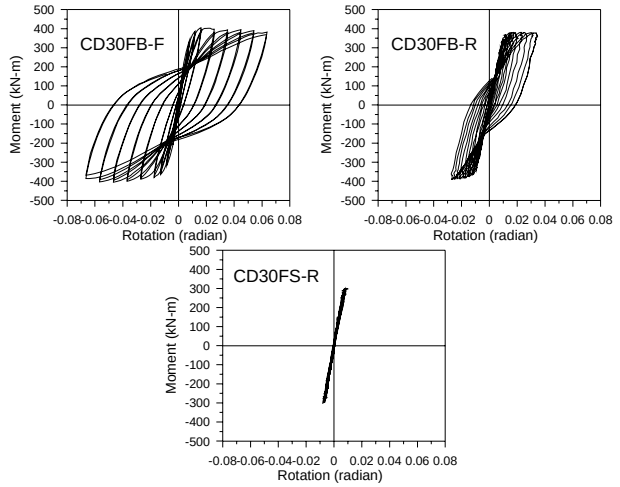

Figure 16 Moment-rotation curves at column base for cyclic loading test of specimens CD30xx-x.

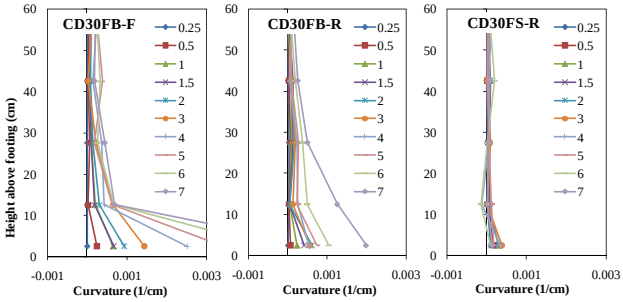

Figure 17 Curvature distributions for cyclic loading test of specimens CD30xx-x.

4. CONCLUSIONS

In this study, a series of pseudo-dynamic and cyclic loading tests of six reinforced concrete columns with different size of footing, different strength and ductility

capacity were conducted. These experiments showed that there was a significance decrease of plastic deformation at the plastic hinge of a column as a result of the energy dissipation of the inelastic rocking mechanism of the footing. In addition, if the footing of the column is allowed to rock, the base moment can be limited to a certain value. This upper limit value can be calculated based on a simple equation. If this moment limitation is lower than bending moment capacity of the column, the ductility demand of the column can be reduced. On the other hand, if this moment limitation is greater than bending moment capacity of the column, some plastic deformation will occur at the column base.

Acknowledgements:

The study reported here was funded in part by the National Science Council of Taiwan under grant number NSC 97-2625-M-492-004. The test specimens, facilities and technical support from the National Center for Research on Earthquake Engineering are also gratefully acknowledged.

References:

FEMA. (1997), NEHRP Guidelines and commentary for the seismic rehabilitation of buildings, Reports No. 273, Washington, D.C.

FHWA. (2006), Seismic Retrofitting Manual for Highway Structures: Part 1- bridges, Reports No. FHWA-HRT-05-032.

MOTC. (2008), Seismic Design Code for Highway Bridges (in Chinese)

Kawashima, K. & Nagai, T. (2006), "Effectiveness of rocking seismic isolation on bridges," 4th International Conference on Earthquake Engineering, Taipei, Taiwan, October 12-13.

Apostolou, M., Gazetas, G. & Garini, E. (2006), "Seismic response of slender rigid structures with foundation uplifting," Soil Dynamics and Earthquake Engineering, 27, 642-654.

Housner, G. W. (1963), "The behavior of inverted pendulum structures during earthquakes," Bulletin of the Seismological Society of America, 53(2), 403-417.

Gajan, S., and B. L. Kutter, (2008), "Capacity, settlement, and energy dissipation of shallow footings subjected to rocking," Journal of Geotechnical and geoenvironmental engineering (ASCE); 134(8),1129-1141.

Sakellaraki, D., G. Watanabe, and K. Kawashima, (2005), "Experimental rocking response of direct foundations of bridges," Second International Conference on Urban Earthquake Engineering, Tokyo Institute of Technology, Tokyo, Japan, March 7-8, 497-504,

Espinoza, A. and S. Mahin, (2006), "Rocking of bridge piers subjected to multi-directional earthquake excitation," Fifth National Seismic Conference on Bridge & Highways, San Francisco, CA, September 18-20.

Hung, H.H., Chang, K.C., Liu, K.Y. and Ho, T.H. (2008), A study on the rocking response of spread foundation. Report No: NCREE-08-040. (in Chinese)

JOINT CONFERENCE PROCEEDINGS
7th International Conference on Urban Earthquake Engineering (7CUEE) &
5th International Conference on Earthquake Engineering (5ICEE)
March 3-5, 2010, Tokyo Institute of Technology, Tokyo, Japan

EXPERIMENTAL STUDIES OF RATE-DEPENDENT MECHANICAL BEHAVIOR OF LAMINATED RUBBER BEARINGS

T. Imai[1], A.R. Bhuiyan[2], M. K. Razzaq[3], Y. Okui[3], and H. Mitamura[4]

[1] *Rubber Bearing Association, Japan*
[2] *Department of Civil Engineering, Chittagong University of Engineering and Technology, Bangladesh*
[3] *Department of Environmental Science and Civil Engineering, Saitama University, Japan*
[4] *Civil Engineering Research Institute for Cold Region, PWRI, Japan*

Abstract: The paper is devoted towards an experimental investigation of the rate-dependent mechanical behavior of the laminated rubber bearings under horizontal shear deformation with a constant vertical compressive load. Three types of bearings are used in this study: natural rubber bearings (RBs), lead rubber bearings (LRBs) and high damping rubber bearings (HDRBs) with ISO standard geometry. The experimental scheme is comprised of three types of test at room temperature (23±1 °C): cyclic shear (CS) test, multi-step relaxation (MSR) test, and simple relaxation (SR) test. The purpose of conducting the CS test is to identify the instantaneous behavior of the bearings; the SR test, to evaluate the viscosity induced rate-dependent behavior; and finally the MSR test, to obtain the equilibrium behavior. Moreover, a series of sinusoidal loading tests (at 0.5 Hz) are carried out at different temperatures ranging from 23°C to -30 °C. The objective of conducting the sinusoidal loading tests is to identify the basic mechanical characteristics of the bearings at different temperatures: the equivalent stiffness and damping of the bearings. The experimental results show that the viscosity induced rate-dependent behavior is more prominent in the HDR than the LRB and the RB. The viscosity induced rate-dependent behavior of the bearings is more significantly appeared in loading than in unloading. However, this typical behavior is not so significant in the RB as in the other two bearings. Furthermore, the temperature dependency of the equivalent stiffness is more remarkably emerged in the HDR and RB than the LRB, while that of the equivalent damping is more significant in the RB than the others.

1. INTRODUCTION

An isolation bearing is able to provide a structure with additional horizontal flexibility and energy dissipation. Three types of laminated rubber bearings are usually used in highway bridges for this purpose: natural rubber bearings (RBs), lead rubber bearings (LRBs) and high damping rubber bearings (HDRBs).

Several authors have conducted different loading experiments on laminated rubber bearings in order to acquire deep understanding of the mechanical properties. The work of Abe et al. (2004); Aiken et al. (1992); Kikuchi and Aiken (1997); Sano and D Pasquale (1995) can be noted. They have applied uni-directional and bi-directional horizontal shear deformations with a constant vertical compressive stress. Several types of laminated rubber bearings are used in their experimental studies. They have identified some aspects of bearings, such as hardening and dependence of the restoring forces on the maximum shear strain amplitude experienced in the past. Moreover, some of them also identified coupling effects on the restoring forces of the bearings due to deformation in the two horizontal directions. Motivated by the experimental results of bearings, different forms of analytical models for bearings are proposed by them. However, their studies are mostly related to illustrating the strain-rate independent mechanical behavior of bearings.

Very few works have been reported in literature regarding the strain-rate dependent behavior of bearings. In this regard, the work of Dall'Asta and Ragni (2006); Hwang et al. (2002) can be reported. They have studied the mechanical behavior of high damping rubber dissipating devices by conducting different experiments, such as sinusoidal loading tests at different frequencies, cyclic shear tests at different strain-rates along with relaxation tests. They have identified the strain-rate dependence of the restoring forces and subsequently developed rate-dependent analytical models. Mullin's softening behavior is also observed in the experiments (Dall'Asta and Ragni, 2006). However, separation of the rate-dependent behavior from other mechanical behavior is not elaborately addressed in their studies.

In this study, an experimental scheme was conducted at room temperature to investigate the rate-dependent mechanical behavior of the laminated rubber bearings under horizontal shear deformation with a constant vertical

compressive load. Three types of specimens with ISO standard geometry, namely HDR, LRB and RB, were used in this scheme. The experimental scheme was comprised of three types of tests: cyclic shear (CS) tests, multi-step relaxation (MSR) tests, and simple relaxation (SR) tests. The CS tests were carried out to identify the instantaneous response, and SR tests were used to identify the viscosity induced rate-dependent behavior and the MSR tests were used to obtain the equilibrium response of the bearings. In addition, a series of sinusoidal loading tests at 0.5 Hz were carried out at different temperatures ranging from 23°C to -30 ^{o}C with a view of identifying the basic mechanical characteristics of the bearing at different temperatures, such as the equivalent stiffness and damping of the bearings.

2. EXPERIMENTAL OBSERVATIONS

2.1 Specimens

Three types of bearing specimens, namely high damping rubber bearing (HDR), lead rubber bearing (LRB), and natural rubber bearing (RB) were employed in all experiments. All the specimens had square cross-sectional shape with external in-plane dimensions equal to 250 mm x 250 mm. the reinforcing steel plates had similarly a square planar geometry with external dimensions of 240 mm x 240 mm and thickness of 2.3 mm each. The dimensions and material properties of these specimens are given in Table 1. The dimensions of the test specimens were selected following the ISO standard (ISO, 2005).

2.2 Experimental Set-up and Loading Conditions

The specimens were tested in a computer-controlled servo-hydraulic testing machine at room temperature (23 ^{0}C). Displacement controlled tests, under shear deformation with an average constant vertical compressive stress of 6 MPa, were carried out. This mode of deformation is regarded as the most relevant one for application in seismic isolation. The displacement was applied along the top edge of the specimen and the force response was measured with two load cells. All data were recorded using a personal computer. Some of the experimental results are also discussed in somewhere else (Bhuiyan, 2009a; Bhuiyan et al., 2009b).

2.3 Softening Behavior

Virgin rubber exhibits a softening phenomenon, known as Mullins' effect in its first loading cycle. Due to this phenomenon, the first cycle of a stress-strain curve differs significantly from the subsequent cycles (Mullins, 1969). In order to remove the Mullins softening behavior from other inelastic phenomena, all specimens were preloaded before the actual tests. In the current work, only the specimens of SR and MSR tests were preloaded before the actual tests. The preloading was done by applying 11 cycles of sinusoidal loading at 1.75 shear strain and 0.05 Hz until stable state of the stress-strain response is achieved i.e. that no further softening occurs.

Fig. 1 (a), (b), and (c) present the typical shear stress responses obtained from the pre-loading tests on HDR, RB**,** and LRB specimens. The same loading history was applied to virgin specimens and preloaded specimens. The time interval between the preloading and the actual test loading was 30 min. The softening behavior in the first loading cycle is evident from the figures for both virgin and preloaded specimens. The Mullins softening effect is not only present in the virgin specimen but also in any preloaded specimens. This implies that Mullins effect can be recovered in quite a very short period owing to the 'healing effect' (Bueche, 1960). As can be seen from the figure, the Mullins effect is more pronounced in HDR than in LRB and RB. All the specimens show a repeatable stress response after passing through 4-5 loading cycles.

2.4 Strain-Rate Dependent Behavior

In the CS test series, a number of constant strain-rate loading tests with a range of 0.05/s to 5.5/s were conducted. Figs. 2 (a), (b), and (c) show the strain-rate dependence of shear stress responses in HDR, RB, and LRB bearings, respectively. For comparison, the equilibrium stress responses are also shown in each figure. The stress responses in the loading path contain three-characteristic features, namely high initial stiffness at low strain levels, followed by large flexibility at moderate strain levels, a large strain hardening at large strain levels. The untangling and/or the separation of weak bonds between filler particles and long chains are associated with reduction of the high initial stiffness. This typical phenomenon is regarded the 'Payne effect' (Lion, 1996).

The final increase of the stiffness is attributed to the limited extensibility of the polymer chains. When compared with the three bearings, the high initial stiffness at a low strain level and the high strain hardening at a high strain level are mostly prominent in HDR at a higher strain rate. However, weaker strain hardening in LRB than that in the other specimens at higher strain levels is also noticeable.

Table 1. Geometry and material properties of the bearings

Specifications	HDR	LRB	RB
Cross section (mm)	240X240		
Number of rubber layers	6		
Thickness of one rubber layer (mm)	5.0		
Thickness of one steel layer (mm)	2.3		
Diameter of lead plug (mm)	--	34.5	--
No. of lead plugs	--	4	--
Nominal shear modulus (MPa)	1.2		

A comparison of hysteresis loops at different strain rates shows that the size of the hysteretic loops increases with increasing the strain rates as shown in Figs.2 (a) to (c). Comparing all the bearings, the HDR demonstrates a larger hysteretic loop than the other bearings. This typical behavior can be attributed that the HDR inherits relatively high viscosity property than the other bearings. Another comparison of the shear stress responses at different strain rates shown in Figs. 2(a) to (c) indicates that the strong strain-rate dependence exists in loading, whereas much weaker strain-rate dependence is observed in unloading.

A further comparison between the loading-path responses at different strain-rates shows that with increasing strain-rate, the stresses increase due to viscosity. At higher strain rates, however, a diminishing trend in increase of stress responses is observed indicating an approach to the instantaneous state. The strain-rate dependence during loading of the bearings is illustrated in Figs.3 (a) to (c).

2.5 Viscosity Behavior

The cyclic shear tests presented in the preceding section revealed the existence of viscosity in all the specimens. Simple relaxation (SR) tests were carried out to study the viscosity behavior of the bearings. A series of SR tests at different strain levels were carried out. Figs.4 show the shear stress histories obtained from SR tests conducted at three different shear strain levels of γ = 100, 150, and 175% with a strain rate of 5.5/s in loading and unloading. The relaxation period after loading and unloading was taken to be 30 min. The stress relaxation histories illustrate the time dependent viscosity behavior of the bearings. For all specimens, a rapid stress relaxation was displayed in the first few minutes; after a while it approached asymptotically towards a converged state of responses.

From Figs.4 (a) to (c), HDR shows comparatively high stress relaxation than the other bearings. On the other hand, RB shows much lower stress relaxation than that of other bearings. These observations agree with loading/unloading dependency of rate-dependent behavior observed in the cyclic shear test as illustrated in the preceding section (Figs.2 (a) to (c)). The stress response obtained at the end of the relaxation can be regarded as the equilibrium stress response in asymptotic sense (Lion, 1996).

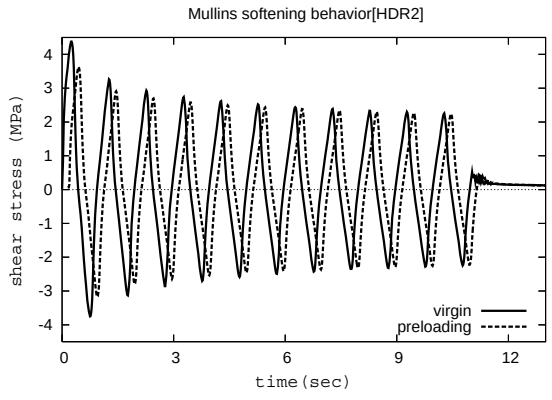

(a)

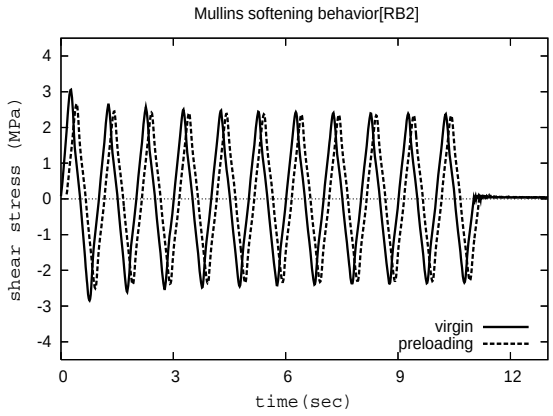

(b)

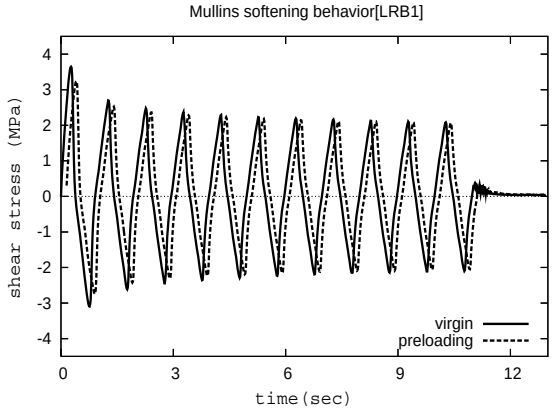

(c)

Fig. 1. 11-cycle preloading test on the bearings to remove Mullins effect; (a) HDR, (b) RB, (c) LRB; the legend indicates that the solid line in each figure shows the shear stress histories obtained from the virgin specimens and the dotted line does for the preloading specimens. For clear illustration the shear stress-strain responses are separated by 0.15 sec from each other.

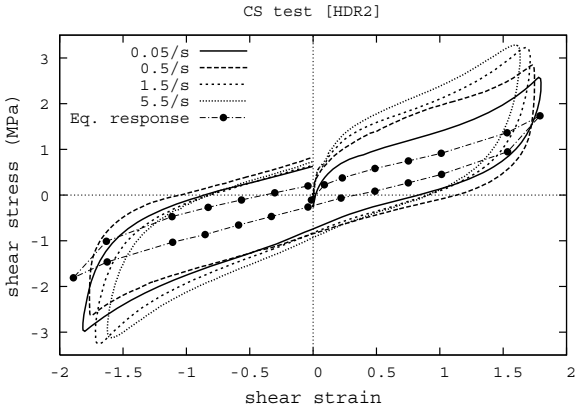

(a)

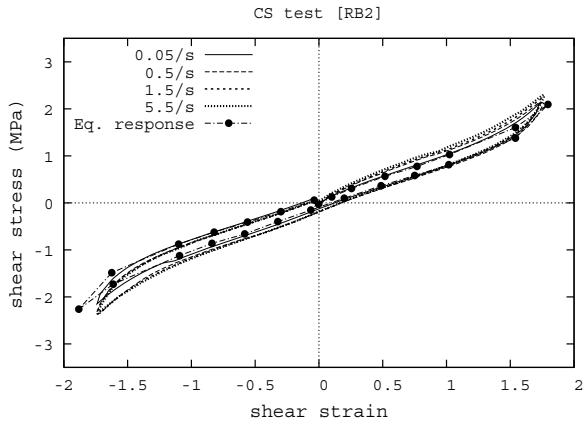

(b)

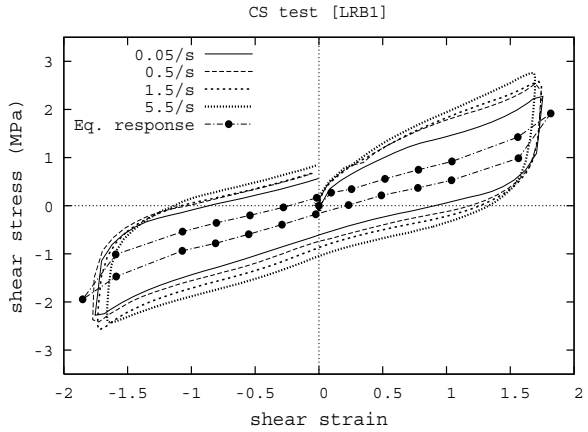

(c)

Fig.2. Shear stress-strain relationships obtained from CS tests at different strain rates of the bearings; (a) HDR, (b) RB, (c)LRB; equilibrium response as obtained from MSR tests is also presented for clear comparison.

2.6 Static Equilibrium Hysteresis

The experimental results obtained from the SR tests at different strain levels showed reduction in stress response during the hold time and approached the asymptotically converged state of responses (i.e equilibrium response). In this context, multi-step relaxation (MSR) tests were carried out to observe the relaxation behavior in loading and unloading paths and to obtain the equilibrium responses (e.g. time-independent response). The shear strain history applied in a MSR test with a maximum shear strain of 1.75 is presented in Fig. 5. In a MSR test, the applied strain is held at several constant strain levels with a relaxation period of 20 min.

Figures 6 to 8 illustrate the shear stress histories and corresponding equilibrium responses obtained in MSR tests of three bearings (HDR, RB, and LRB). At the end of each relaxation period in loading and unloading paths, the stress response converges to an almost constant stress state. The converged stress responses are identified as the equilibrium stresses in an asymptotic sense (Lion, 1996). The shear stress-strain relationships in the equilibrium state can be obtained by connecting all the asymptotically converged stress values at each strain level as shown in Figs.6(b) to 8 (b).

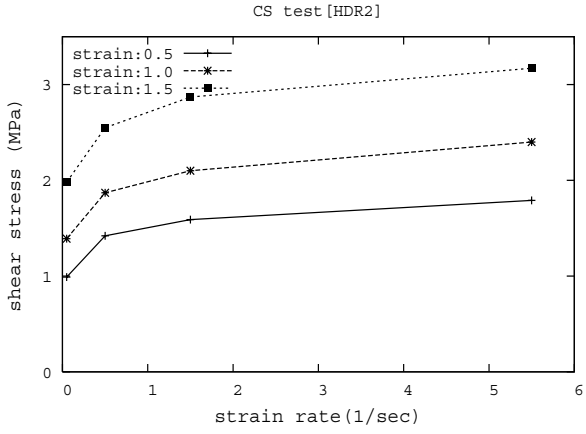

(a)

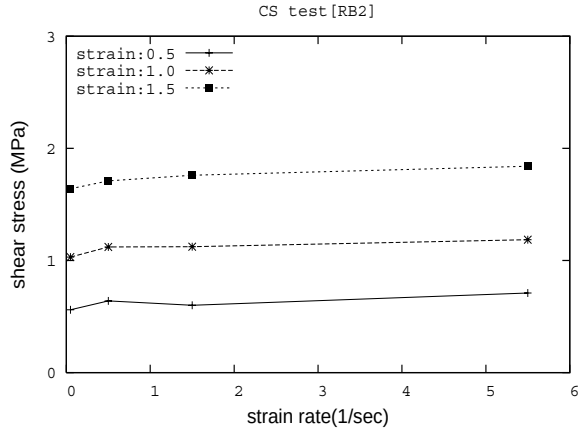

(b)

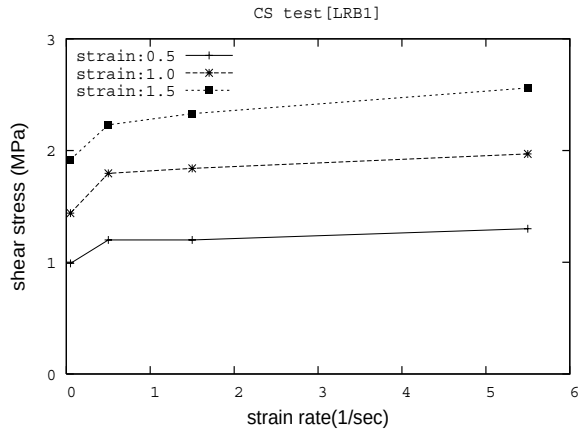

(c)

Fig.3. Shear stress response as a function of strain rates recorded from CS tests at different strain levels of the bearings; (a) HDR, (b) RB, (c)LRB.

The difference of the stresses between loading and unloading at a particular shear strain level corresponds to the equilibrium hysteresis, which can be easily visualized in the figures. This behavior may be attributed as an irreversible slip process between fillers in the rubber microstructures (Mullins, 1969), which is the resulting phenomenon of breaking of rubber-filler bonds (Bueche, 1960).

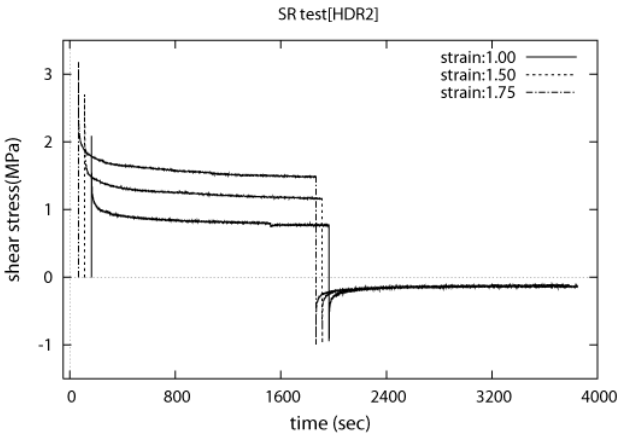

(a)

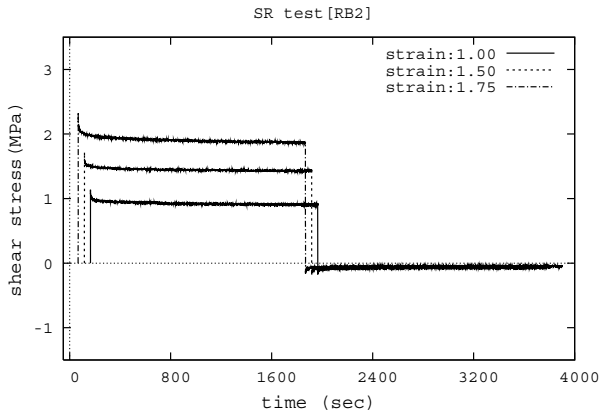

(b)

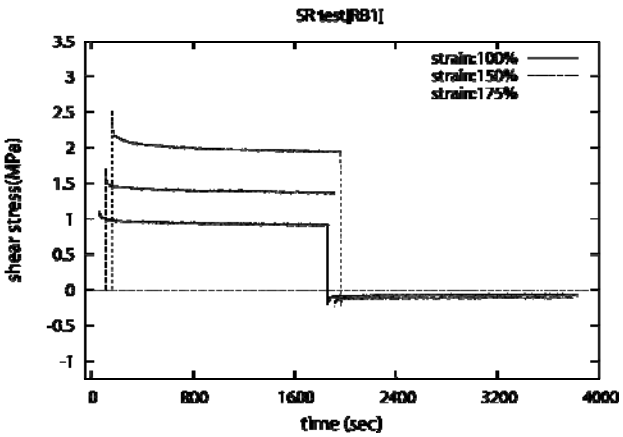

(c)

Fig. 4. Shear stress histories obtained from SR tests of the bearings at different strain levels (a) HDR, (b) RB, (c) LRB. For clear illustration, the stress histories have been separated by 50 sec from each other.

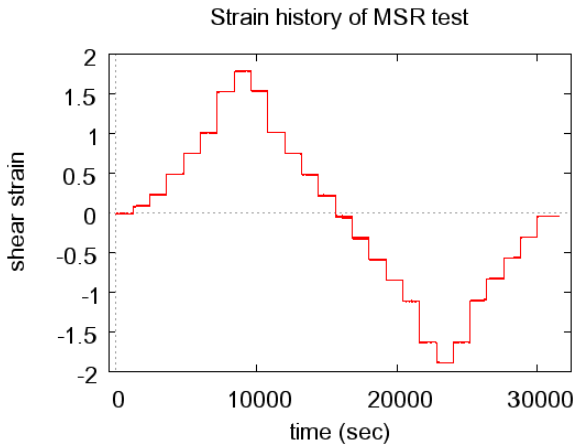

Fig.5. Applied strain histories in MSR test with 1.75 maximum strain level; a shear strain rate of 5.5/s was maintained at each loading and unloading process.

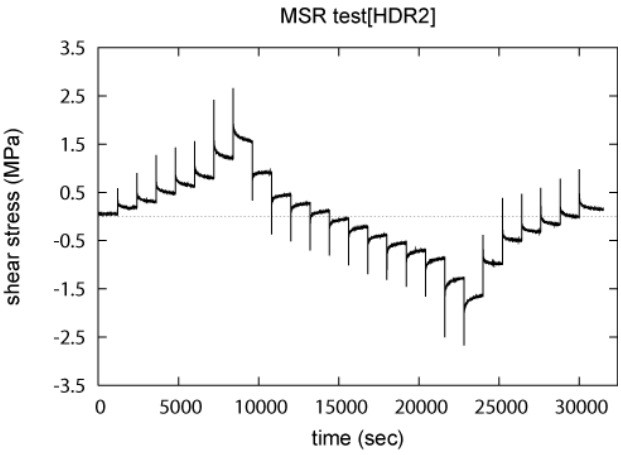

(a)

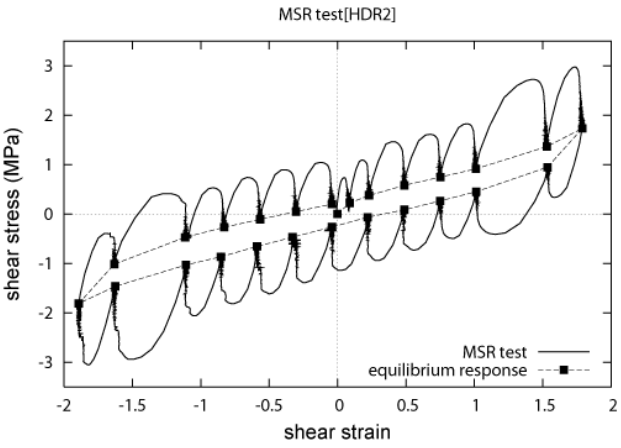

(b)

Fig. 6. MSR test results of HDR (a) stress history (b) equilibrium stress response; equilibrium response at a particular strain level shows the response, which is asymptotically obtained from the shear stress histories of MSR test.

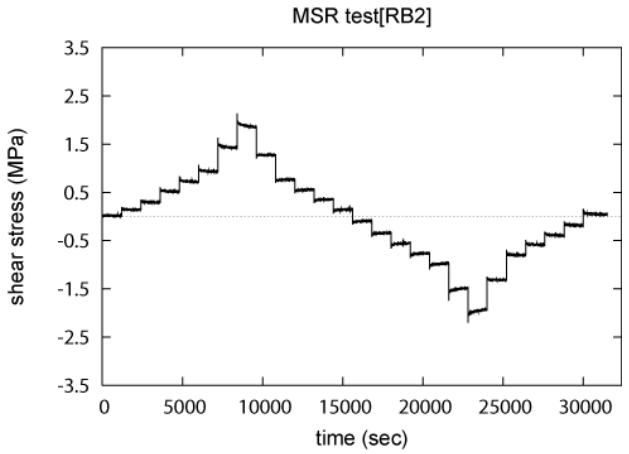

(a)

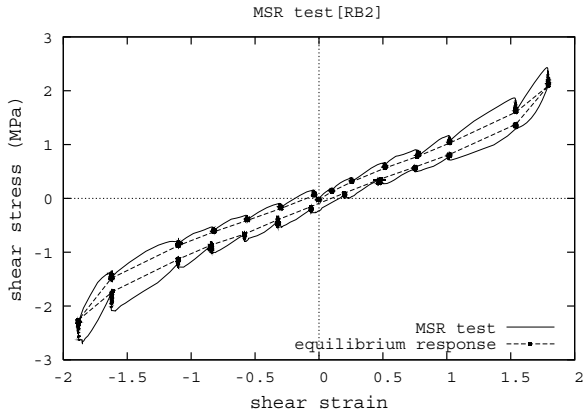

(b)

Fig. 7. MSR test results of RB (a) stress history (b) equilibrium stress response; equilibrium response at a particular strain level shows the response, which is asymptotically obtained from the shear stress histories of MSR test.

Using the stress history data of Figs. 6 (a) to 8 (a), the overstress can be estimated by subtracting the equilibrium stress response from the current stress response at a particular strain level. Comparing with the overstress for each specimen as shown in Figs.6 (a) to 8 (a), the overstress in loading period is higher than that in unloading at a given strain level. The maximum overstress was observed in HDR, while in RB it was the minimum one.

2.7 Temperature Dependent Behavior

In order to recognize temperature dependent stress-strain responses of the bearings, a series of sinusoidal loading tests of the bearings were carried out at different temperatures ranging from 23°C to -30 °C. The strain amplitude and frequency of the sinusoidal loading were assigned to 1.75 and 0.5 Hz, respectively. Figs. 9(a), (b), and (c) present the shear stress-strain responses of the HDR, RB, and LRB, respectively. These figures show that the temperature dependence of the stiffness and damping is more significantly appeared in the HDR than that in the other two bearings. Moreover, the trend of increasing the shear stress responses with decrease of temperatures is clearly evident in all the bearings. The equilibrium responses of the bearings as obtained from the MSR test results at 23 °C are also plotted along with the shear stress responses at different temperatures.

Figs. 10 (a) to (c) present the dependency of the equivalent stiffness and equivalent damping constants on temperatures. The ratios of the equivalent stiffness and damping constant at different temperatures to those at 23 °C are plotted. The temperature dependency of the equivalent stiffness is more remarkably emerged in the HDR and RB than LRB, while that of the equivalent damping is more significant in the RB than the others.

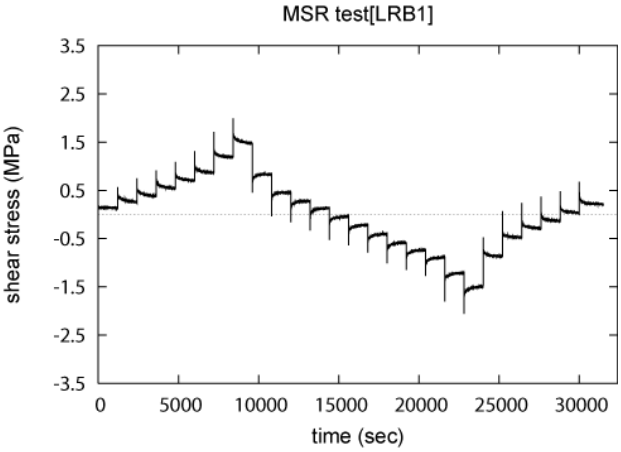

(a)

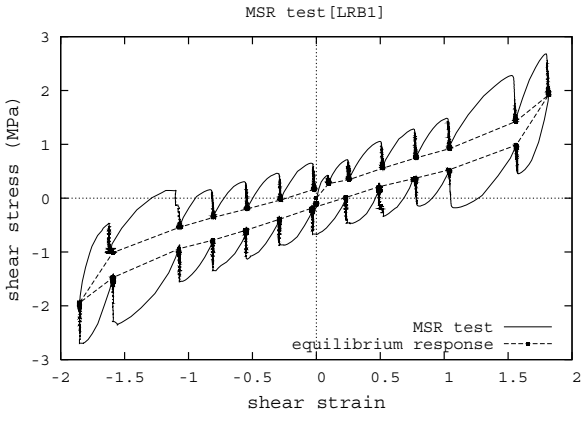

(b)

Fig. 8. MSR test results of LRB (a) stress history (b) equilibrium stress response; equilibrium response at a particular strain level shows the response, which is asymptotically obtained from the shear stress histories of MSR test.

3. CONCLUDING REMARKS

The mechanical tests under horizontal displacement along with a constant vertical compressive load demonstrated the existence of Mullins' effect in all the bearing specimens. However, with the passage of time a recovery of the softening effect was observed. A preloading sequence had been applied before simple relaxation and multi-step relaxation tests were carried out to remove the Mullins' effect.

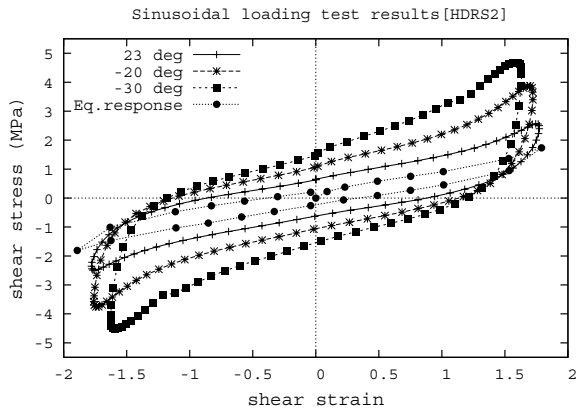

(a)

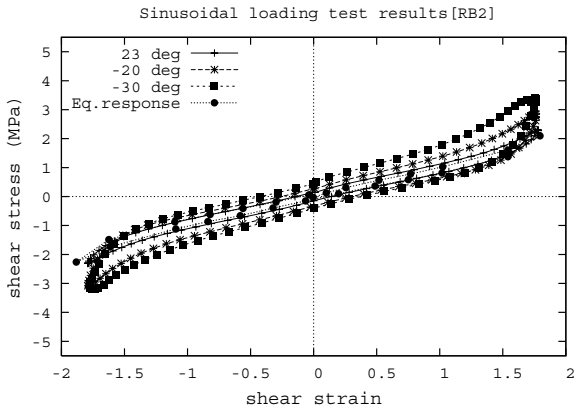

(b)

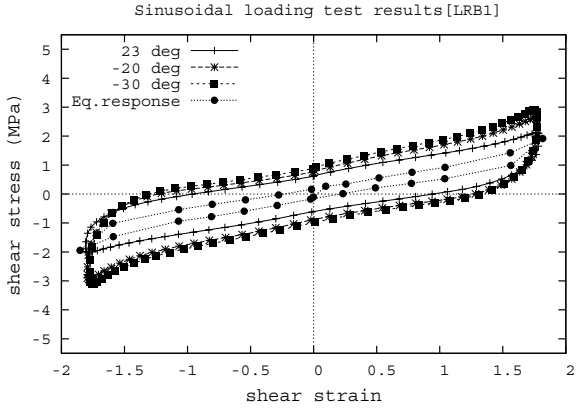

(c)

Fig. 9. Sinusoidal excitation test results of the bearings at different temperatures (a) HDR (b) RB, and (c) LRB. The legend indicates the different temperatures considered in the study.

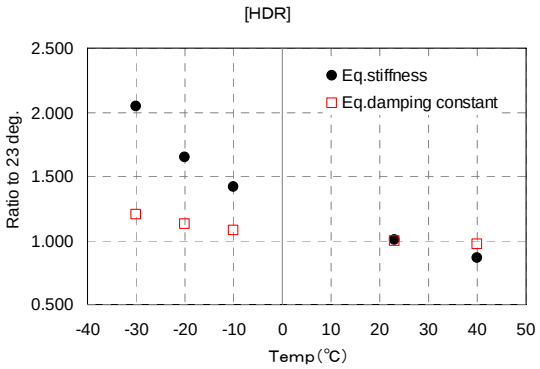

(a)

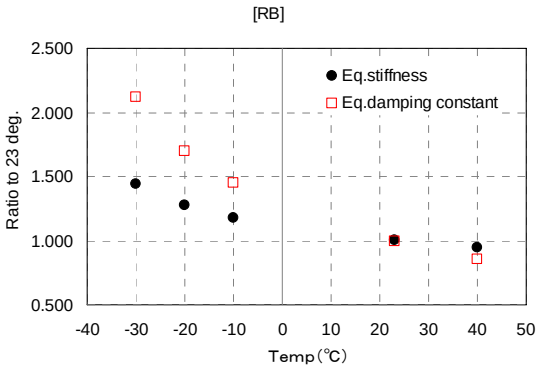

(b)

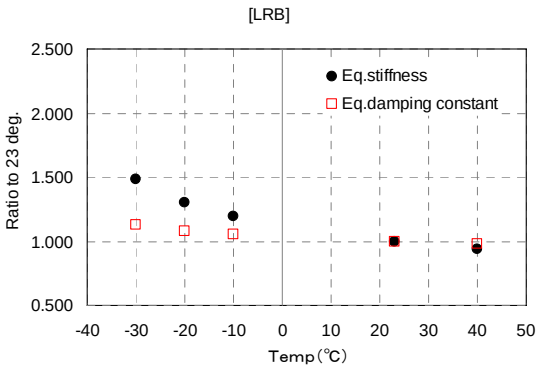

(c)

Fig. 10. Temperature dependency of equivalent stiffness and damping constant for (a) HDR (b) RB, and (c) LRB obtained from the sinusoidal loading tests.

Cyclic shear tests at different strain rates illustrated the significant strain-rate dependent hysteresis. The strain-rate dependency in the loading paths was appeared to be stronger

than in the unloading paths. The sinusoidal loading tests at different temperatures showed that the temperature dependence of the stiffness and damping is more significantly appeared in the HDR than the other two bearings. The trend of increasing the shear stress responses with decreasing temperatures is evident in all the bearings.

The simple and multi-step relaxation tests at different strain levels were carried out to investigate the viscosity property in the loading and unloading paths of the bearings. Moreover, in order to identify the equilibrium hysteresis, the multi-step relaxation tests were carried out with different maximum strain levels. When the extent of the strain-rate dependent hysteresis along with other inelastic properties were compared among the three bearings considered in the current study, these effects were found to be more significant in the HDR than the LRB and the RB. More specifically, the strain-rate dependency was more significantly appeared in the HDR than any other bearings. The viscosity property inherited in the HDR might be a possible reason behind the typical behavior of it. On the other hand, the hardening features at high strain levels were found to be more prominent in the RB and HDR than LRB.

Furthermore, temperature dependence on the shear stress-strain responses of the HDR was appeared more significantly than in the LRB and the RB. The experimental observations of the bearings as considered in the current study indicate that a rate-dependent constitutive model is indispensable for describing the mechanical behavior of the bearing.

Acknowledgements

The experimental works were conducted by utilizing the laboratory facilities and bearings-specimens provided by Japan Rubber Bearing Association. The authors indeed gratefully acknowledge the kind cooperation extended by them. The authors also sincerely acknowledge the funding provided by the Japanese Ministry of Education, Science, Sports and Culture (MEXT) in the form of scholarships to carry out this research work

Reference

Abe, M., Yoshida, J., and Fujino, Y., 2004a. Multiaxial behaviors of laminated rubber bearings and their modeling. I: Experimental study, *Journal of Structural Engineering*, **130**, 1119-1132.

Aiken, I.D., Kelly, J.M., and Clark, P.W., 1992. *Experimental studies of the mechanical characteristics of three types of seismic isolation bearings*, Proceedings of the 10th World Conference of Earthquake Engineering (WCEE), Madrid, Spain, 2280-2286.

Bhuiyan, A.R., 2009a. *Rheology modeling of laminated rubber bearings for seismic analysis*, PhD Dissertation, Saitama University, Japan.

Bhuiyan, A.R., Okui, Y., Mitamura, H. and Imai, T., 2009b. A rheology model of high damping rubber bearings for seismic analysis: identification of nonlinear viscosity, *International Journal of Solids and Structures,* **46**, 1778-1792.

Bueche, F., 1960. Moelcular basis for the Mullins effect. *Journal of Applied Polymer Science*, **4,**107-114.

Dall'Asta, A., and Ragni, L., 2006. Experimental tests and analytical model of high damping rubber dissipating devices, *Engineering Structures,* **28**, 1874-1884.

Hwang, J.S., Wu, J. D., Pan, T, C., and Yang, G., 2002. A mathematical hysteretic model for elastomeric isolation bearings, *Earthquake Engineering and Structural Dynamics,* **31**, 771-789.

International Organization of Standardization (ISO), 2005.*Elastomeric seismic-protection isolators, Part 1: Test methods*, Geneva, Switzerland.

Kikuchi, M., and Aiken, I.D., 1997. An analytical hysteresis model for elastomeric seismic isolation bearings, *Earthquake Engineering and Structural Dynamics,* **26**, 215-231.

Lion, A., 1996. A constitutive model for carbon black filled rubber: Experimental investigations and mathematical representation, *Continuum Mechanics and Thermodynamics*, **8**, 153-169.

Mullins, L., 1969. Softening of rubber by deformation, *Rubber Chemistry and Technology*, **42**, 339-362.

Sano, T., Di and Pasquale, G., 1995. A constitutive model for high damping rubber bearings, *Journal of Pressure Vessel Technology*, **117**, 53-57.

JOINT CONFERENCE PROCEEDINGS
7th International Conference on Urban Earthquake Engineering (7CUEE) &
5th International Conference on Earthquake Engineering (5ICEE)
March 3-5, 2010, Tokyo Institute of Technology, Tokyo, Japan

VISCOUS FLUID DEVICES FOR AN ITALIAN VIADUCT

Lucia Faravelli[1)], Sara Casciati[2)], and Agostino Marioni[3)]

1) Professor, Dept. of Structural Mechanics, University of Pavia, Italy
2) Assistant Professor, Dept. ASTRA, University of Catania at Syracuse, Italy
3) CEO, ALGA s.p.a., Milan, Italy
lucia@dipmec.unipv.it, saracasciati@msn.com

Abstract: Sicily is a region of medium-high seismicity. The development of a road network is still in progress and several viaducts offer non-minor design problems. For the particular case of a bridge located in the vicinity of the city of Catania, the mitigation of the seismic vibrations was pursued by viscoelastic devices of a new generation. This contribution first illustrates the bridge features, and then introduces the mechanical properties of the devices. The policy to design their locations and their comparison with other types of seismic isolation devices are eventually discussed.

1. INTRODUCTION

Throughout this paper attention is focused on the seismic isolation of bridges (Skinner et al., 1996; Soong-Dargush, 1997; Naeim-Kelly, 1999; Dicleli-Baddaram, 2006). The study is limited to passive solutions, despite active or semiactive solutions are also widely present in the literature (Faravelli-Rossi, 2002; Chu et al., 2005; Casciati et al., 2006; Soong-Dargush, 1997).

An Italian motorway viaduct is selected as case study. After a brief description of the bridge, the results of nonlinear dynamic analyses are reported. Several configurations of the bridge are studied :

1) without devices;
2) equipped with hysteretic devices,
3) equipped with cylindrical double pendulum devices;
4) and equipped with viscous fluid devices.

Comparisons are driven in terms of both stresses at the bottom of the piers and deck displacements.

2. THE CASE STUDY

The island of Sicily, in Southern Italy, is on the way to complete its motorway network. The branch connecting the Eastern towns of Catania (in the North) and Syracuse (in the South) must cross several rivers, and among them the one named Simeto. The bridge across the Simeto was designed in pre-stressed reinforced concrete with a box girder cross-section. The artwork mounts seismic devices of hysteretic type , which are distributed on the market by the company Alga s.p.a. Other typologies of isolators will be considered for the sake of a comparison, with focus on the viscous fluid devices.

An independent viaduct is dedicated to each of the two traffic lanes. Each viaduct is located far enough from the other to avoid any sort of hammering during a seismic event, so that only one viaduct will be considered in the analyses. The actual viaduct consists of nine spans, but for the purpose of evaluating the effects of different types of passive devices, it is preferable to consider a reduced model of only three spans. The resulting structure shows two lateral spans of 61 m and a central span of 92 m, for a total length of 214 m.

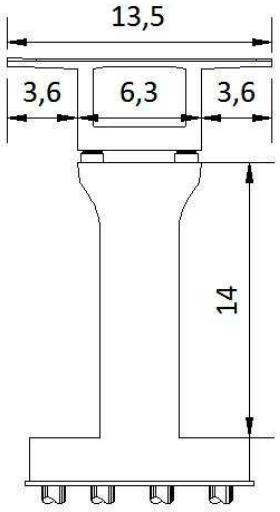

Figure 1 Pier of the bridge considered as case study. Measures in meters.

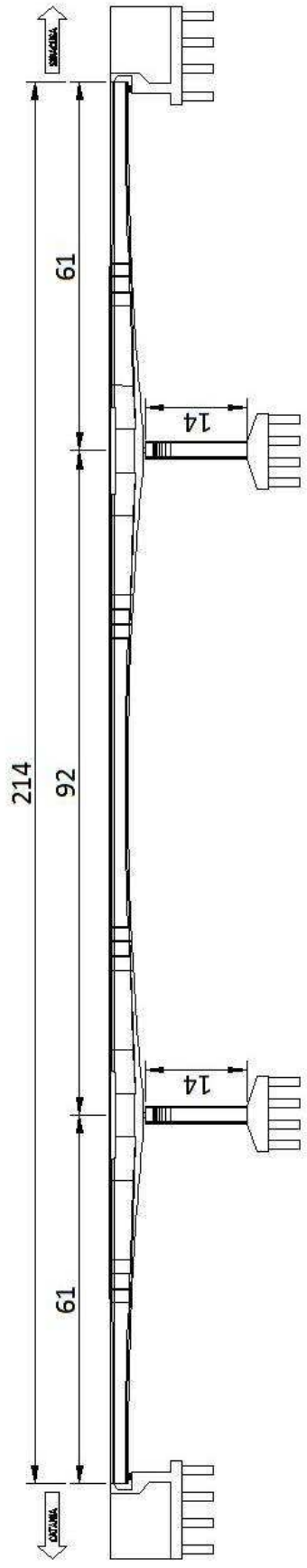

Figure 2 Longitudinal section of the three-spans bridge considered as case-study.

The height of the piers is assumed to be equal to 14 m, which represents the height of the tallest pier in the actual bridge. The box girder cross-section of the deck has a width of 13.5 m and a variable height, which is maximum at the locations of the piers and gradually decreases moving away from them. The main features of the described case study are summarized in Figures 1 and 2.

3. NUMERICAL MODEL

The general purpose finite element code SAP (CSI, 2007) was adopted for the numerical analyses. Each span was schematized by BEAM elements, in a number sufficient to provide a good approximation of the section height variability. A characteristic strength of 45 MPa was adopted for the concrete whose specific weight is γ = 25 KN/m^3. The resulting finite element model is shown in Figure 3.

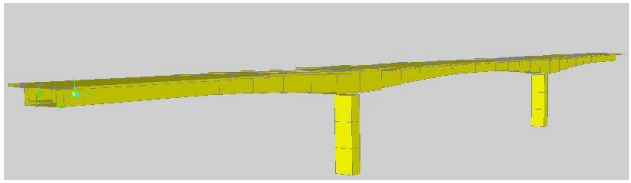

Figure 3 Finite element model of the case study.

At the supports, the distance between the box girder centroid and the actual locations of the bearings is assigned by introducing suitable BODY-CONSTRAINTS. The box girder cross-section is assumed to be fixed in the bridge transversal direction, while it can translate and rotate in the longitudinal direction. Suitable LINKS are introduced to model the interaction between the deck and the supports.

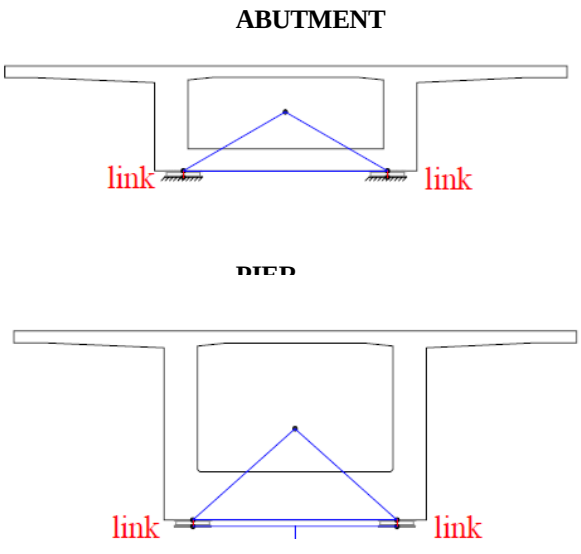

Figure 4 Links introduced to model the deck-supports interaction in order to preserve the actual locations of the devices.

In the numerical model, the piers are discretized into three finite elements in order to avoid mass concentration. Their element cross-section is constant, and the concrete material properties correspond to a strength of 35 MPa and a specific weight of 25 KN/m^3.

4. THE DEVICES

As mentioned in the Introduction, the performances of different types of seismic isolation devices are compared among them and with the one of the not isolated system. The considered devices are mainly of three types, and only two of them are currently available on the market (Marioni, 2007):

1) the hysteretic device, "Algaism";
2) and the double pendulum device, " Algapend".

The third type of devices belongs to the class of the viscous fluid dampers which are governed by the general relationship:

$$F = c\, v^{\alpha} \tag{1}$$

where F is the force on the device, v is the relative velocity of one edge with respect to the other, c is a constant for a given device, and α is a parameter in the range from 0.1 to 2 whose value depends on the adopted hydraulic circuit.

The current practice pursues the adoption of the value of 2 when the goal is to maximize the behaviour differences under low velocities associated with thermal variations and fluage, and under high velocities associated with a seismic event. In this case, the code document "prEN15129" classifies these devices as stiff links, and they are not capable to dissipate large amounts of energy.

If the main goal of the devices is the energy dissipation, the exponent in Eq. (1) should be minimized. In this case, the devices are properly named as viscous dampers, and they are classified by "prEN15129" as devices dependent on the velocity. Special care must be devoted to their re-centring capacity, which can either be relied on the structure ability, or on the device features (viscous-elastic devices).

.

5. RESULTS OF THE ANALYSES

The following figures provide a comparison of seven different configurations of the seismic isolation devices. Namely, the structure is either equipped:

1) with fluid devices and $\alpha = 0.015$;
2) with fluid devices and $\alpha = 0.15$;
3) with fluid devices and $\alpha = 0.15$, acting in multiple directions;
4) with fluid devices and $\alpha = 0.3$;
5) without devices;
6) with "Algapend" devices;
7) with "Algasism" devices.

The reported results are the mean values of different response variables and they are obtained by carrying out the simulations under three artificially generated accelerograms. The excitation is applied along both the horizontal directions: the transversal direction, which is denoted as *y*, and the longitudinal direction *x*.

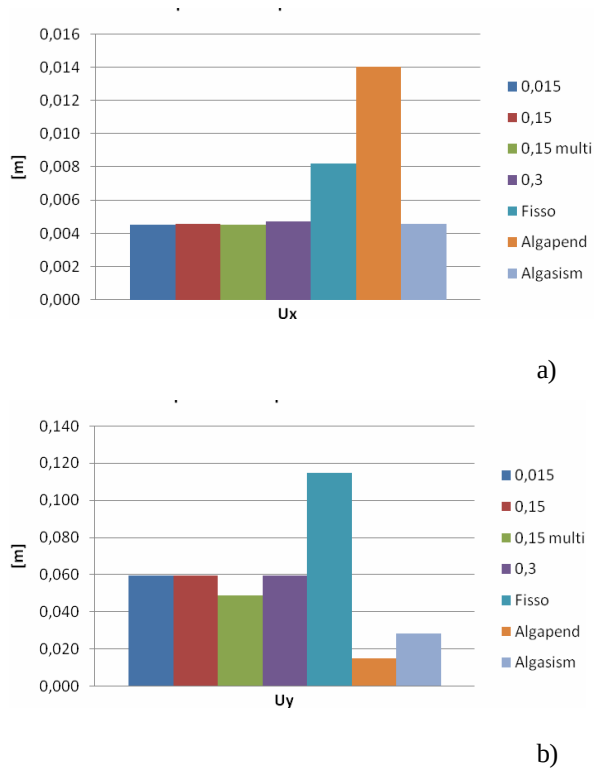

Figure 5 Comparison of the displacements at the top of the pier: a) along direction *x*; b) along direction *y*.

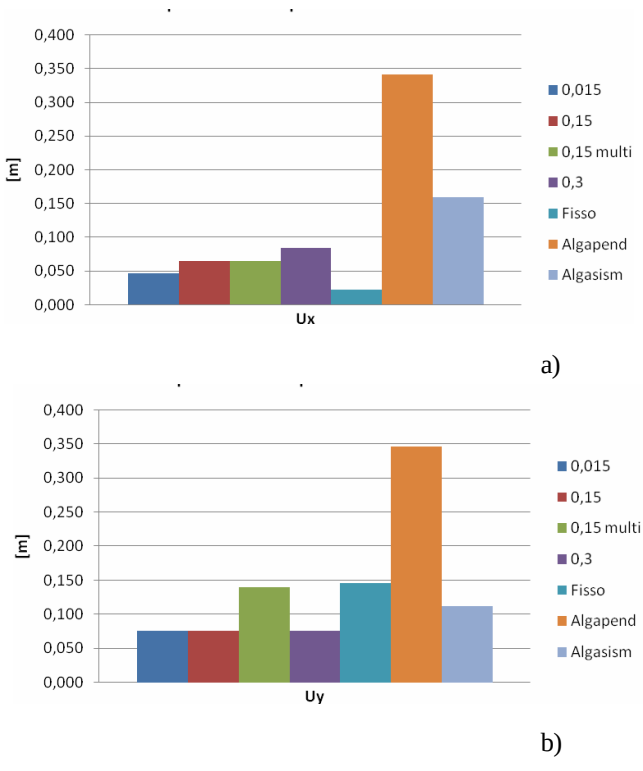

Figure 6 Comparison of the deck displacements: a) along direction *x*; b) along direction *y*.

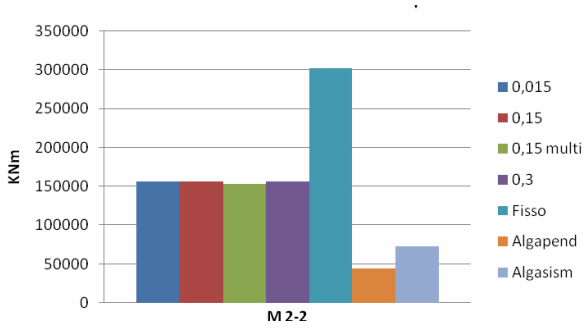

a)

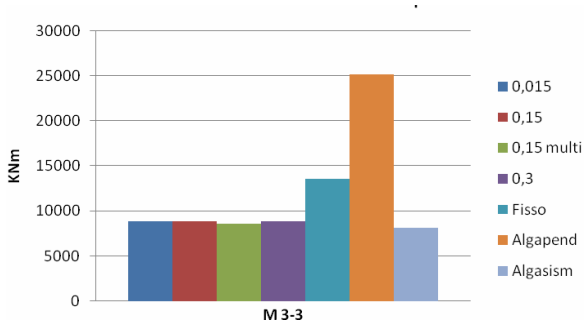

b)

Figure 7 Comparison of the bending moments at the base of the pier: a) about direction *x*; b) about direction *y*.

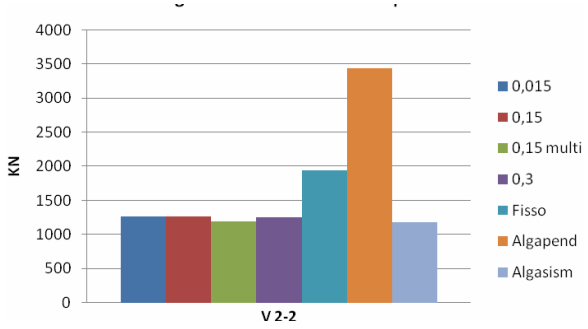

a)

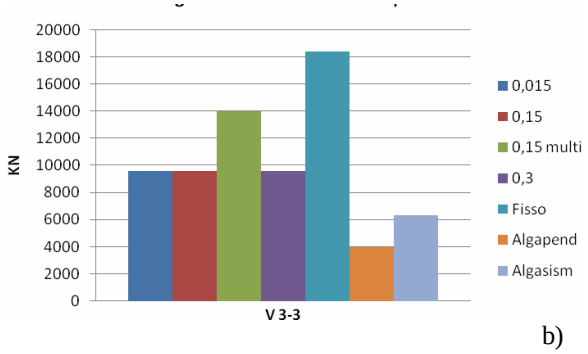

b)

Figure 8 Comparison of the shears at the base of the pier: a) along direction *x*; b) along direction *y*.

6. RESPONSE EVALUATION

In view of selecting the adequate devices in the design phase of a viaduct under consideration, several criteria were proposed in the literature, mainly as a result of benchmark studies (Agrawal et al., 2009). In the design current practice, the cost-benefit analysis is often pursued based on a qualitative framework. A possible procedure consists of identifying the main costs and benefits. A score in the range from 1 to 5 is then assigned to rank the performance of each considered item. For the three classes of considered devices, including a sliding pendulum (SP), a hysteretic device (HY) and a viscous damper (VD), three benefits and two costs were identified and evaluated. Their comparison is reported in Table 1. The ability to support the vertical loads is neglected, since it is regarded as equally satisfied by all the devices.

Table 1 Qualitative assessment of the costs and benefits for the three classes of considered devices: sliding pendulum (SP), hysteretic device (HY) and viscous damper (VD).

	SP	HY	VD
Dissipated energy	3	5	5
Period shift	5	3	3
Re-centring capacity	4	2	4
Initial cost	5	2	1
Maintenance cost	5	4	3
Total	**22**	**16**	**16**

Table 1 accounts for the increase of dissipated energy when moving from the solution relying on a sliding pendulum to those adopting other devices. Thus, hysteretic devices and viscous dampers should be preferred in areas of high seismicity, where a limitation of the displacements is required. On the other hand, the adoption of a friction pendulum scheme facilitates the ability to shift the period of the system. The friction pendulum also offers a slight advantage in the re-centring capacity, which is increased by the curvature of the sliding surface due to the vertical component of the seismic excitation.

Initial costs, as well as the maintenance costs, are definitely in favour of the friction pendulum. In this case, the maintenance costs are mainly associated to an anti-corrosion plan. Instead, for the other two systems, maintenance is required after a single seismic event. Therefore, the potential benefit of viscous dampers is, at present, not adequately supported by the associated costs.

7. CONCLUSIONS

Damage induced to bridges due to seismic excitation can be reduced in the extent that the deck and the piers are conveniently disconnected. The variety of devices which can be adopted for this purpose is rather broad.

This paper reports the results achieved on a motorway viaduct, which was recently built in Sicily and served as case study to compare the performances of three different types of passive devices. The following remarks can be driven based on the results obtained for the viscous devices of new generation. For similar stress regimes, the deck displacements decrease as the coefficient α of the viscous fluid dampers decreases. The drawback is an increase of the forces acting on the device, which therefore needs to be designed for large stresses and for wide cycles of loading/unloading.

Acknowledgements

The first two authors acknowledge support of the Athenaeum Research Funds from the University of Pavia (FAR 2009) and the University of Catania (PRA 2008), respectively. The authors are grateful to M.Sc. Enrico Bormolini who developed the numerical analyses in partial fulfillment of his duties toward the Master Degree in Civil Engineering at the University of Pavia.

References:

Agrawal, A., Tan P., Nagarajaiah S., and Zhang J. (2009). "Benchmark Structural Control Problem for Seismically Excited Highway Brige – Part I: Phase I Problem definition", *Journal of Structural Control and Health Monitoring* (16)1, 509-529.

Casciati F., Magonette G. and Marazzi F. (2006). "Technology of Semi-active Devices and Applications in Vibration Mitigation", John Wiley, Chichester and New York.

CSI (2007). "Analysis Reference Manual For SAP 2000, Etabs and Safe", Computer and Structures, Inc. Berkrley, Cal., USA

Chu, S. Y., Soong, T. T. and Reinhorn, A. M. (2005) "Active, Hybrid and Semi-active Structural Control", John Wiley, Chichester and New York

Dicleli M. and Buddaram S. (2006). "Effect of isolator and ground motion characteristics on the performance of seismic – isolated bridges". *Earthquake Engineering and Structural Dynamics*, 35(2), 233-250.

Faravelli L. and Rossi R. (2002). "Adaptive Fuzzi Control: Theory Versus Implementation", *Journal of Structural Control* (9)1, 59-73.

Naeim F. and Kelly J. M. (1999). "Design of Seismic Isolated Structures. From Theory to Practice". John Wiley, Chichester and New York.

Marioni A. (2007).Sistemi di isolamento sismico innovativi prodotti dalla Società ALGA.

Skinner R. I., Robinson W. H., McVerry G. H. (1996). "An introduction to Seismic Isolation". John Wiley, Chichester and New York.

Soong, T. T. and Dargush, G. F. (1997). "Passive Energy Dissipation System in Structural Engeneering", John Wiley, Chichester and New York.

JOINT CONFERENCE PROCEEDINGS
7th International Conference on Urban Earthquake Engineering (7CUEE) &
5th International Conference on Earthquake Engineering (5ICEE)
March 3-5, 2010, Tokyo Institute of Technology, Tokyo, Japan

NON LINEAR MODELING AND SEISMIC PERFORMANCE OF A MULTI-SPAN SIMPLY SUPPORTED VIADUCT

Sourabh Agrawal[1)] and Ashok K. Jain[2)]

1) Graduate Student, Department of Civil Engineering, Indian Institute of Technology, Roorkee, India
2) Professor, Department of Civil Engineering, Indian Institute of Technology, Roorkee, India
sourabhagrawal@aol.in, ashokjain_iitr@yahoo.co.in

Abstract: In this paper an attempt has been made to model expansion joint with due consideration of impact and separation, non-linearity of bearings, and the pounding between the adjacent spans. Discrete aero length spring elements are used to model fixed, free and guided POT-PTFE bearings. The friction force between the superstructure and the pier support is modeled by multi-linear plastic kinematic link element. A bearing is idealized as a shear element. A 3D finite element is developed and is subjected to the 1940 El Centro earthquake. Both linear and non-linear analyses were carried out. The analysis showed that the displacement of the structure relative to piers exceed the capacity of the bearings causing damage to the bearings. A linear analysis gives completely misleading results. Thus, expansion gap as well as seat width should be selected after carrying out suitable non-linear seismic analysis so as to develop a performance based seismic design of a multi-span simply supported viaduct.

1. INTRODUCTION

A three span 30 m c/c simply supported viaduct is subjected to longitudinal component of the El Centro earthquake of May 1940 on a detailed 3-dimensional model developed using a finite element package SAP2000. The pier heights were 20 m and 10 m. The expansion gap was 40 mm. Expansion gap and bearings are assessed for their influence on the variability and peak longitudinal response of critical components. The deformation in bearings, gap displacement, time of occurrence of impact, displacement of top of pier, acceleration on deck, and axial forces in the deck are monitored.

2. VIADUCT CHARACTERISTICS

2.1 The Superstructure

A three span simply supported bridge is evaluated in this paper. The bridge considered is zero-skew, concrete-slab-on girder bridge with 9.15 m wide deck, supported on single column bent. The simply supported bridge has alternating fixed and expansion bearings supporting each deck and having seat type abutments. The length of each span is 30 m. The concrete slabs of the MSSS bridge are supported by prestressed girders resting on pot bearings. The pier columns are 3000 mm in diameter and have 0.3% vertical reinforcement with 10 mm circular ties with 225 mm space. The pier labeled P1 and P2 have 20 m and 12 m heights. The design of the bridge conforms to the IRC standard specifications (IRC 6:2000 and IRC 21:2000). The longitudinal section and transverse sections are shown in Figs 1 and 2.

The expected material strength and Mander et al. (1998) stress-strain relation is used for unconfined and confined concrete as well as reinforcing steel to capture the bridge capacity and behavior.

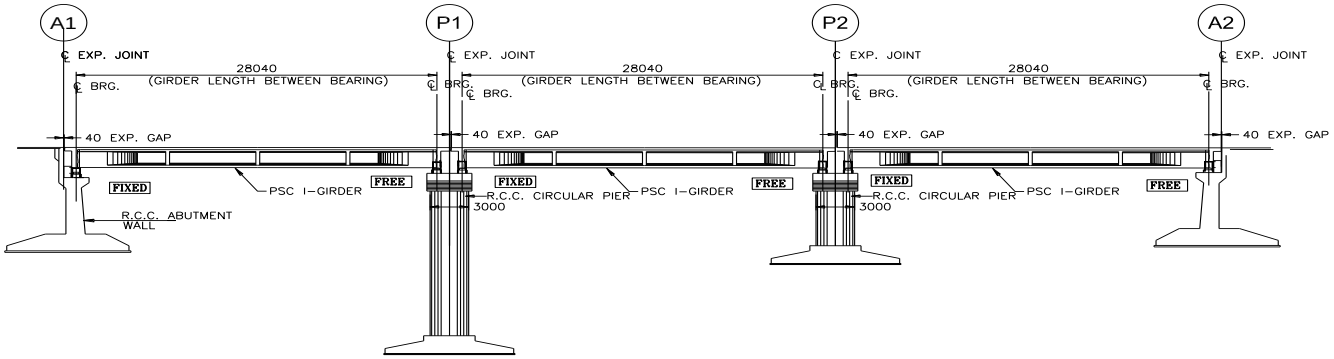

Figure 1 Longitudinal section of viaduct

The mass of the structure is calculated and is lumped at the nodes of the structure model. It is assumed that there is no live load/traffic load on the bridge, therefore, no traffic related inertia effects are considered.

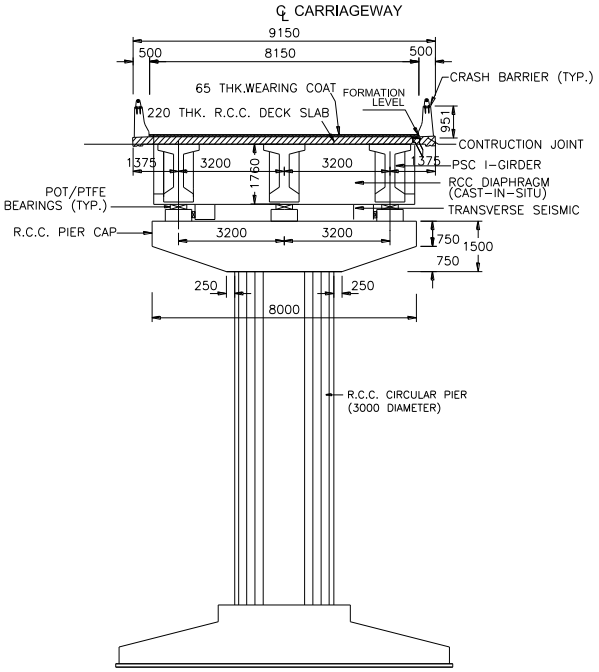

Figure 1 Transverse section of viaduct

2.2 Superstructure Modeling

Due to high axial stiffness of the superstructure, the deformation in the longitudinal and transverse directions of the bridge is negligible compared to the corresponding deformations of the bridge piers. Also, flexural and shear strength of the superstructure is much higher than that of the piers. Therefore, the superstructure is modeled using equivalent linear elastic frame elements connected through rigid links. The geometry of I girders is defined in the Section Designer of the SAP2000 software.

2.3 Pier Cap Modeling

The piercap is a concrete element connecting the superstructure and the pier. As the cross-section varies over the length from 750 mm at the edges to 1500 mm at the centre, it Is modeled as a non-prismatic section. A linear variation in the depth of a rectangular shape yields a cubic variation for EI about a vertical axis.

2.4 Pier Modeling

Each pier is modeled via a single fiber-section frame element. This element is formulated using the flexibility approach based on the exact interpolation of the internal forces (Spacone et al. 1996). The cross-section is discretized in to fibers, each fiber has a uni-axial stress-strain relationship which can be specified to represent confined concrete (core), unconfined concrete (cover) and reinforcing steel. The individual fiber behaviour is integrated to obtain a load-deformation relation for the composite reinforced concrete section. Elastic-perfectly plastic idealization for the moment-curvature relationship is assumed. The equivalent yield curvature Φ_y is found by extrapolating the line joining the origin and the point corresponding to the first yield of a reinforcing bar, up to the nominal moment capacity M_n which corresponds to a compressive strain $\varepsilon_c = 0.005$ in the extreme concrete fibre. The concrete is computed from

$$\emptyset_y = \frac{M_n}{M_y}\emptyset'_y \qquad (1)$$

Where M_y and $\emptyset'_y$ = moment and curvature at first yielding of a vertical reinforcing bar. Assuming a constant curvature over the length of the plastic hinge (L_p), the angle of rotation can be calculated as $\theta = \Phi L_p$ where L_p is calculated by (CALTRANS 2006)

$$L_p = 0.08L + 0.022f_y d_{bl} \geq 0.044f_y d_{bl} \quad [fy(MPa)] \qquad (2)$$

where L = length from the point of contraflexure to the section with maximum moment and d_{bl} = diameter of a longitudinal reinforcing bar.

2.5 Expansion joint Modeling

The expansion joints are shown in Figs. 3a, 3b and 4. at The bridge deck at column bent locations is modeled as a transverse rigid bar of length equal to the deck width right angle to longitudinal axis of the bridge to simulates the interaction between the torsional rotation of the bridge deck and the axial deformation of the columns, as well as the interaction between the in-plane rotation of the deck and lateral displacement of the columns. The transverse rigid bar is elevated to the level of the centre of gravity of the bridge deck using a set of vertical rigid elements attached to it. This is done to define accurately the vertical location of the mass of the bridge deck. The rigid vertical elements are then connected to the columns at bearing locations through rigid horizontal elements to maintain the accurate distance between the centerline of pier and centerline of the bearings arrangement.

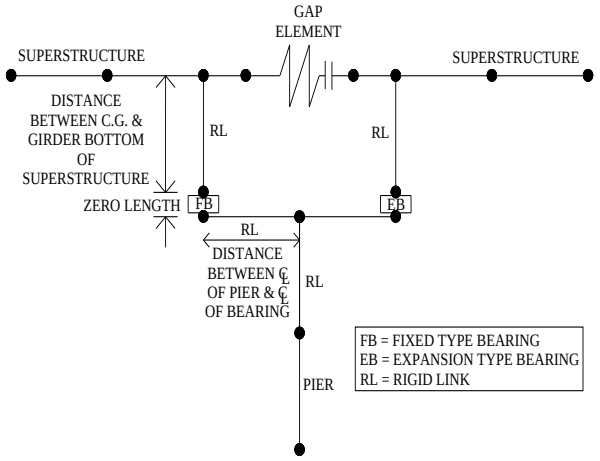

Figure 3a 2D view of Expansion joint

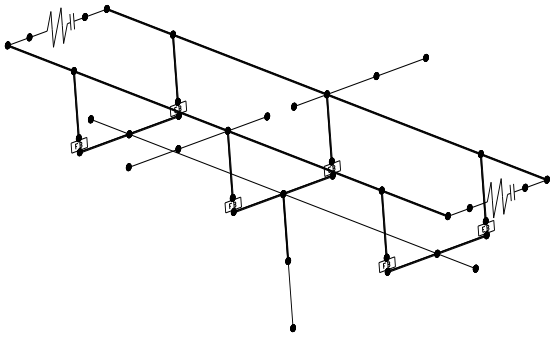

Figure 3b 3D view of Expansion joint

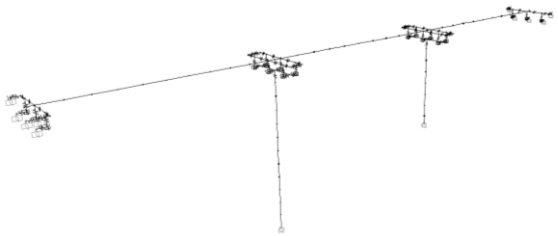

Figure 4 Three dimensional analytical model of viaduct

2.6 Bearing Modeling

Each bearing was modeled by multilinear plastic kinematic link element and is connected to the end of superstructure through a rigid link and to the top of the bent cap again through a rigid link. Fixed and movable bearings are idealized as shown in Figure 5. Based upon the degree of freedom requirements, different degrees of freedom can be given at the support point and the bearings may be classified as:

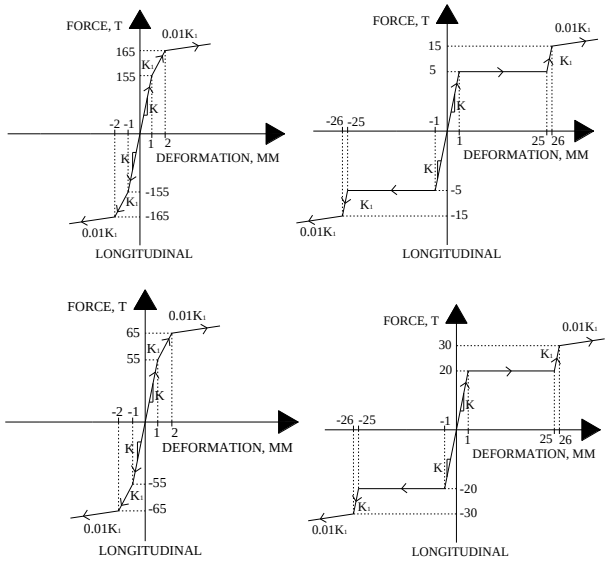

Figure 5 Force-deformation relationships: (a) Pin bearing (b) Metallic Guide bearing (c) Guided Sliding bearing and (d) Free Sliding bearing

Fixed type – Translation not permitted, rotation permitted
> combination of sliding and pin bearings
Free type – Translation permitted and rotation also permitted
> combination of free and guided bearings.

The shear capacity was determined by calculating the longitudinal forces as per IRC 6due to the following effects:
(i)Tractive effort caused through acceleration of the driving vehicles,
(ii) Braking effect due to application of brakes,
(iii) Frictional resistance offered at free bearings,
(iv) Seismic resistance offered at fixed bearings in both lateral and longitudinal directions.

The yield displacement was taken as 1mm in place of very small value (that is, elastic displacement before sliding) in order to prevent numerical instability during computations. The initial stiffness of the bolts was taken as 10 t/mm and the hardening ratio as 1% of the initial stiffness.

2.7 Gap Modeling

The gap element of Sap2000 is used to model the gap to account for the possibility of pounding longitudinal deformations close any of the gaps and to measure relative longitudinal and transverse displacements between adjacent decks. It is set as a compression only element such that the element does not offer any resistance before the closure of the gap and having stiffness proportional to the inplane axial stiffness of the colliding deck (DesRoches and Muthukumar, 2002).

The nonlinear force-deformation relationship is given by

$$F = k(d+d_o) \quad \text{if } d+d_o < 0 \qquad (3a)$$
$$= 0 \quad \text{otherwise} \qquad (3b)$$

where k = spring constant; d = deformation across the spring; and d_0 = initial gap opening.

2.8 Abutment Modeling

Abutments are earth retaining systems designed to provide unimpeded traffic access to and from the bridge. These are traditionally designed based on active and passive earth pressure theories. In this paper, a simplified spring abutment model was used. Moreover, no attempt was made to model longitudinal backfill and return walls etc.

2.9 Foundation Modeling

Fixed boundary conditions were specified at the base of the piers. No attempt was made to model the soil medium beneath the piers.

2.10 Damping Modeling

The damping mechanism is introduced in the analysis though Rayleigh damping, proportional to both mass and

stiffness.

3. COMPUTATIONAL MODEL

Two types of non-linearity are incorporated in the bridge model to properly represent anticipated response under moderate to intense levels of earthquake. The first category consists of inelastic behavior of elements and cross-sections due to non-linear stress-strain relations as well as presence of gaps and inelastic behavior of bearings. The second category consists of geometric nonlinearities that represent P-Δ effects on a structure, where equilibrium condition is determined under the deformed shape of the structure. The later non-linearity is incorporated directly in the analysis program.

4. ANALYSIS AND RESULTS

The 3D viaduct model is subjected to the first 10 second of the longitudinal component of the El Centro earthquake of May 1940. Newmark's step-by-step method of constant acceleration was adopted along with the Newton-Raphson iteration scheme for the analytical solution. The time period in the first two modes was 0.95 sec and 0.51 sec corresponding to longitudinal translation modes.

Selected results of mode shapes, response under longitudinal loading at pier P1, pier P2, fixed abutments and free abutments are shown in Figs. 6 to 8. Similarly, gap displacements at Pier P1, P2 and abutments, impact forces at Pier P1 and abutment A2 and top displacement of piers P1 and P2, accelerations at the expansion joints at P1 and P2, and axial forces in the girders at different locations are shown in Figs. 9 to 16. A summary of response parameters is also shown in Table 1.



Figure 6 (a) Fundamental longitudinal mode shape (T_1 = 0.95 s (b) First transverse mode shape (T_3 =0.45 s)

Table 1 Summary of Response Parameters

S. No.	Parameters	Pier P1	Pier P2	Abutment A1	Abutment A2
1	Bearing Deformations (mm)				
	a. Pin	0.68	0.81	4.01	--
	b. Guide	0.71	0.79	4.01	--
	c. Metallic guided	46.97	9.87	--	55.13
	d. Free sliding	46.95	9.88	--	55.13
2	Gap closing (mm)				
	a. Linear analysis	125.8	149.8	0.58	125.8
	b. Nonlinear analysis	41.19	11.03	4.2	41.19
3	Time of impact (s)	2.22	No impact	No impact	1.95
4	Pier top displacement (mm)				
	a. Linear analysis	131.6	55.69	--	--
	b. Nonlinear analysis	45.77	53.97	--	--
5	Acceleration in girder (1/g)				
	a. Left girder				
	(i). Linear analysis	0.124	0.78	--	1.06
	(ii). Nonlinear analysis	1.06	2.422	--	2.54
	b. Right girder	0.78	1.06	0.05	--
	(i). Linear analysis	1.23	1.14	2.11	--
	(ii). Nonlinear analysis				
6	Axial force in girder (1/base shear)				
	a. Left girder				
	(i). Linear analysis	0.8	0.17	--	0.08
	(ii). Nonlinear analysis	5.46	0.53	--	0.09
	b. Right girder				
	(i). Linear analysis	1.63	2.97	0.03	--

(ii). Nonlinear analysis	4.73	0.65	0.18	--

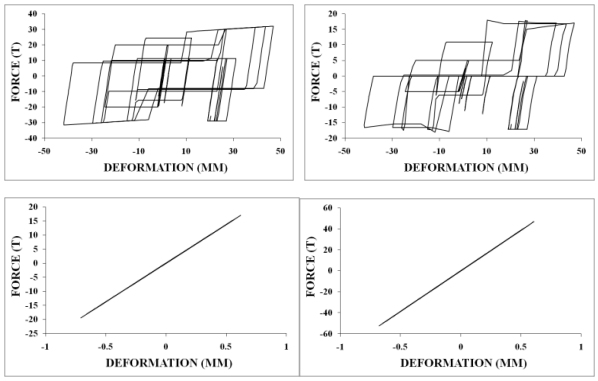

Figure 7 Response under longitudinal loading at pier P1: (a) Free Sliding bearing, (b) Metallic Guide bearing, (c) Guided Sliding bearing, (d) Pin bearing

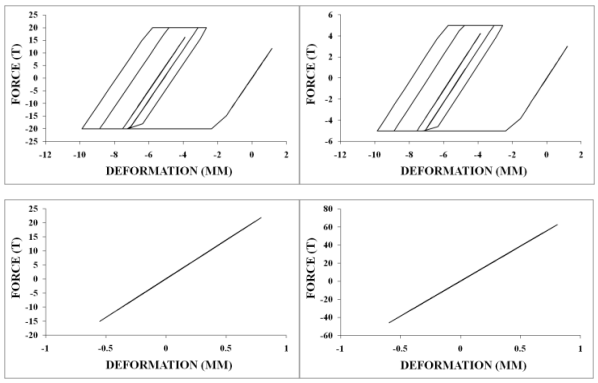

Figure 8 Response of under longitudinal loading at pier P2: (a) Free Sliding bearing, (b) Metallic Guide bearing, (c) Guided Sliding bearing, (d) Pin bearing

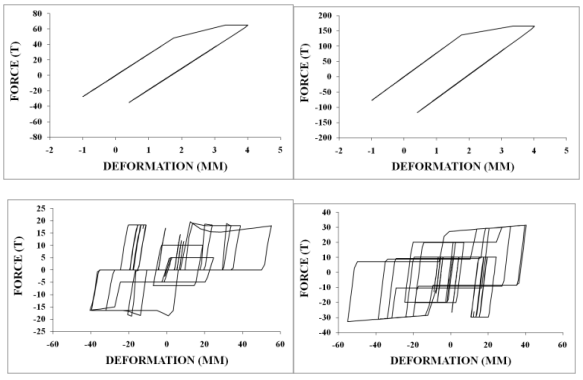

Figure 9 Response under longitudinal loading at fixed abutment A1 and free abutment: (a) Guided Sliding bearing, (b) Pin bearing, (c) Free sliding bearing, (d) Metallic Guide bearing

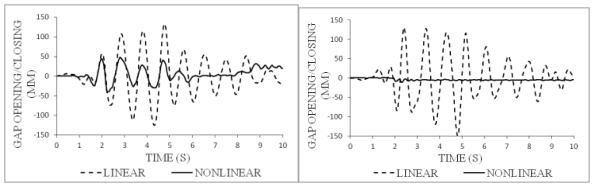

Figure 10 Gap displacement: (a) pier P1, (b) pier P2

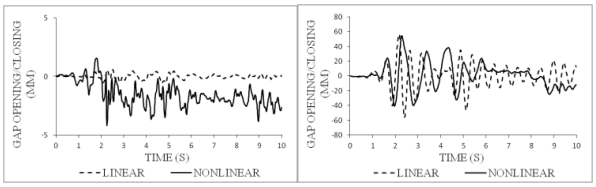

Figure 11 Gap displacement: (a) fixed abutment A1, (b) free abutment A2

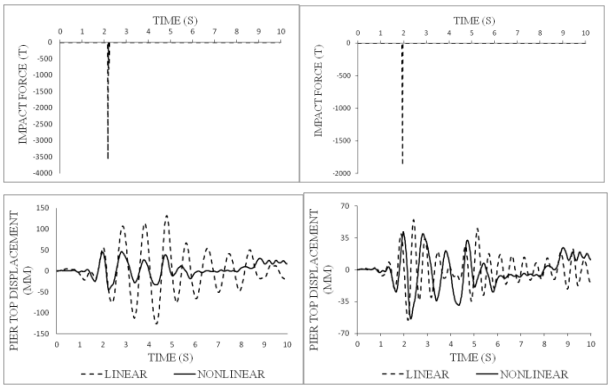

Figure 12 Impact force: (a) Pier P1 (b) abutment A2 and Top displacement (a) Pier P1, (b) Pier P2

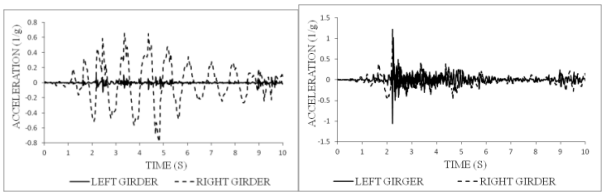

Figure 13 Acceleration at expansion joint at pier P1: (a) Linear analysis, (b) Nonlinear analysis

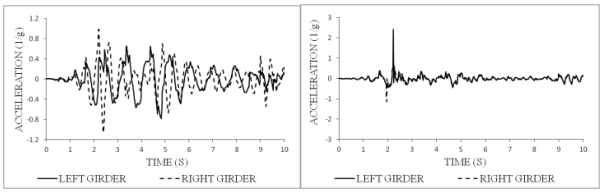

Figure 14 Acceleration at expansion joint at pier P2: (a) Linear analysis, (b) Nonlinear analysis

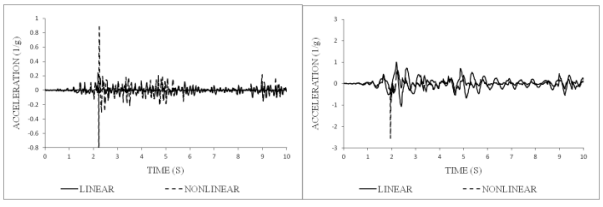

Figure 15 Acceleration in girder: (a) fixed abutment A1, (b) free abutment A2

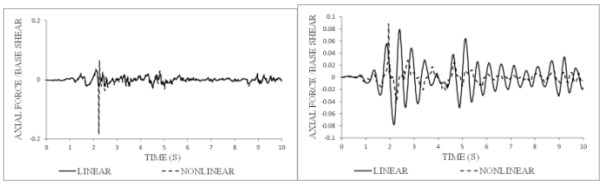

Figure 16 Axial force in girder at (a) fixed abutment A1, (b) free abutment A2

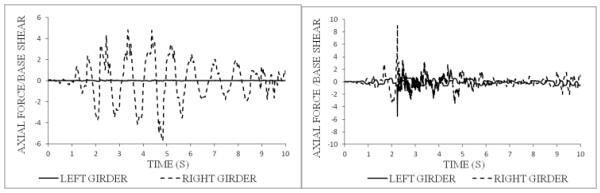

Figure 17 Axial force in girder at expansion joint at pier P1 (a) Linear analysis, (b) Nonlinear analysis

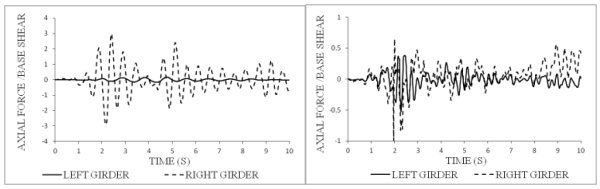

Figure 18 Axial force in girder at expansion joint at pier P2 (a) Linear analysis, (b) Nonlinear analysis

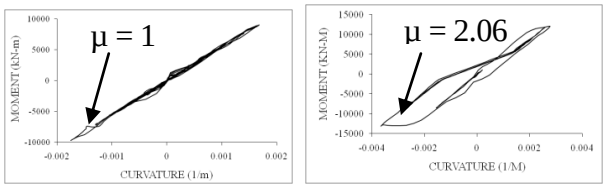

Figure 19 Moment curvature relationship at plastic hinge at (a) pier P1, (b) pier P2

5. CONCLUSIONS

Based on the results presented in this paper, it can be concluded that a non-linear analysis with appropriate modeling of the entire super-structure and sub-structure is essential to obtain meaningful results of seismic analysis of multi-span simply supported viaducts. The linear analysis results are totally misleading. The seismic performance of the viaduct can be examined with confidence besides the correct expansion gap and seat width can be determined only by carrying out non-linear analysis.

References:

Agrawal, Sourabh (2009),"Non-linear Seismic Analysis of Multi-span Simply Supported Viaduct," M. Tech. thesis, Indian Institute of Technology, Roorkee.

ATC (1981), "Seismic Design Guidelines for Highway Bridges," Report No. ATC-6, Applied Technology Council, Redwood City, CA, USA.

ATC (1996a), "Improved Seismic Design Criteria for California Bridges: Provisional Recommendations," Report No. ATC-32, Applied Technology Council, Redwood City, CA, USA.

ATC (1996b), "Improved Seismic Design Criteria for California Bridges: Resource Document," Report No. ATC-32-1, Applied Technology Council, Redwood City, CA, USA.

CALTRANS (2006),"Seismic Design Criteria" Design Manual ver. 1.4, California Department of Transportation, Sacramento, CA, USA.

DesRoches, R., and Muthukumar, S. (2002). "Effect of pounding and restrainers on seismic response of multiple–frame bridges." *Journal of Structural Engineering*, 128(7), 860-869.

IRC:21-2000. (2000,) "Standard Specification and Code of Practice for Road Bridges, Section III, Cement Concrete(Plain and Reinforced)." *The Indian Rode Congress*, New Delhi.

IRC:6-2000. (2000,) "Standard Specification and Code of Practice for Road Bridges, Section II, Load and Stresses." *The Indian Rode Congress*, New Delhi.

Mander, J. B., Kim, D. K. Chen, S.S. and Premus, G.J. (1996), "Reponse of Steel bridges Bearings to the Reversed Cyclic Loading," *Technical Report NCEER 96-0014*, Buffalo, *NY.*

Mander, J. B., Priestly, M. J. and Park, R. (1988a), "Theoretical Stress-Strain Model for Confined Concrete," *Journal of Structural Engineering*, American Society of Civil Engineers, 114(3), 1804-1826.

Mander, J. B., Priestly, M. J. and Park, R. (1988b), "Observed Stress-Strain Behaviour of Confined Concrete," *Journal of Structural Engineering*, American Society of Civil Engineers, 114(8), 1827-1849.

SAP2000 (2008), Integrated structural analysis and design software. Version 12, *Computers and Structures*, Berklley, California.

Spacone, E., Filippou, F. C., and Taucer, F. F. (1996). "Fibre beam-column model for non-linear analysis of R/C frames: Part I. formulation." *Earthquake Engng Struct. Dyn.*, 25, 711-825

JOINT CONFERENCE PROCEEDINGS
7th International Conference on Urban Earthquake Engineering (7CUEE) &
5th International Conference on Earthquake Engineering (5ICEE)
March 3-5, 2010, Tokyo Institute of Technology, Tokyo, Japan

SHAKE TABLE TEST AND NON-LINEAR DYNAMIC ANALYSIS FOR A BRIDGE MODEL USING RIGID-PLASTIC DAMPERS

Takao Okada[1], Shigeki Unjoh[2] and Jun-ichi Hoshikuma[3]

1) Researcher, Center for Advanced Engineering Structural Assessment and Research, PWRI, Japan
2) Research Coordinator for Earthquake Disaster Prevention, Research Center for Disaster Risk Management, NILIM, Japan
3) Chief Researcher, Center for Advanced Engineering Structural Assessment and Research, PWRI, Japan
okada@pwri.go.jp, unjoh-s92ta@nilim.go.jp, hosikuma@pwri.go.jp

Abstract: Various kinds of dampers for seismic response control of bridges have been developed. However, there is not unified seismic design method for bridges using structural response control devices. The objectives of this paper are to examine the dynamic response of bridges using structural response control devices and to verify the mathematical model. Shake table tests of bridge model using rigid-plastic dampers were performed to examine the dynamic responses. The nonlinear dynamic analyses using mathematical model of dampers obtained through cyclic loading tests were performed to simulate the seismic responses. The analytical results showed that the seismic responses were simulated well.

1. INTRODUCTION

Various kinds of dampers including steel damper, fluid damper, rubber damper and friction damper have been developed to control the dynamic response of bridges. The damping force characteristics are not only linear with loading velocity but also nonlinear, for example, depending on loading velocity or displacement.

The characteristics are evaluated and analytically modeled based on cyclic loading tests with each unit. However, there is not unified seismic design method for bridge system using dampers and there are few shake table tests to verify the dynamic response of bridge system using dampers.

In this research, shake table tests of bridge model using rigid-plastic dampers were performed to examine the dynamic responses and a series of dynamic analyses was conducted to evaluate the accuracy of the analytical model.

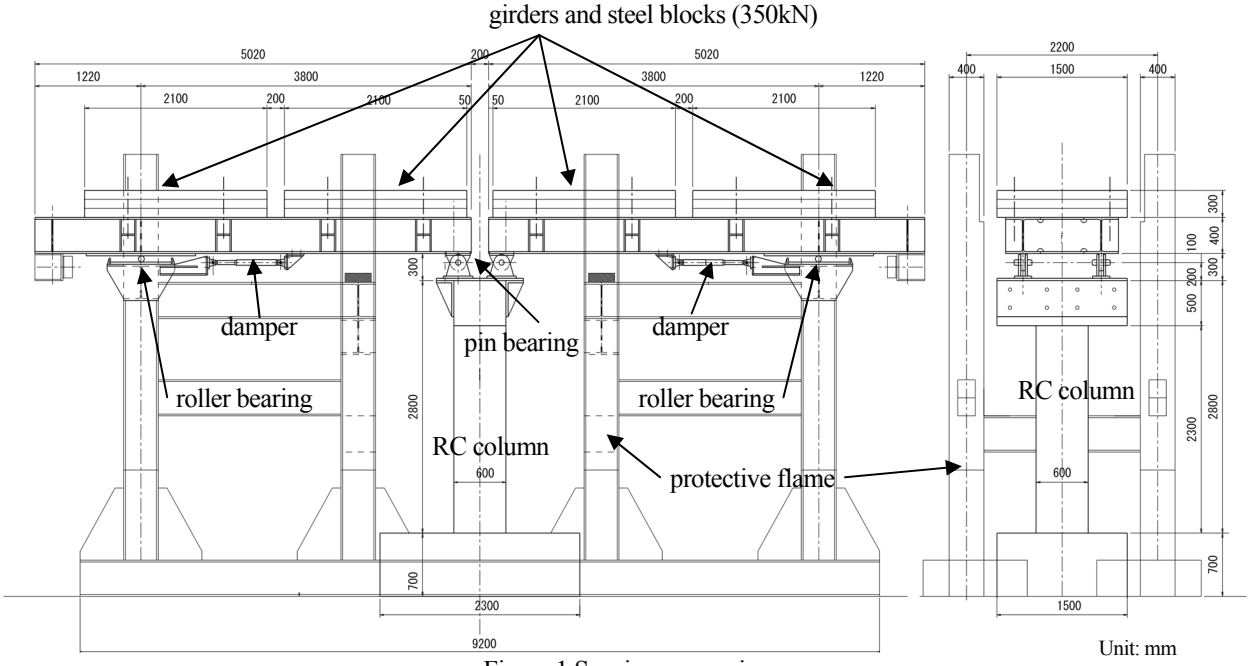

Figure 1 Specimen overview

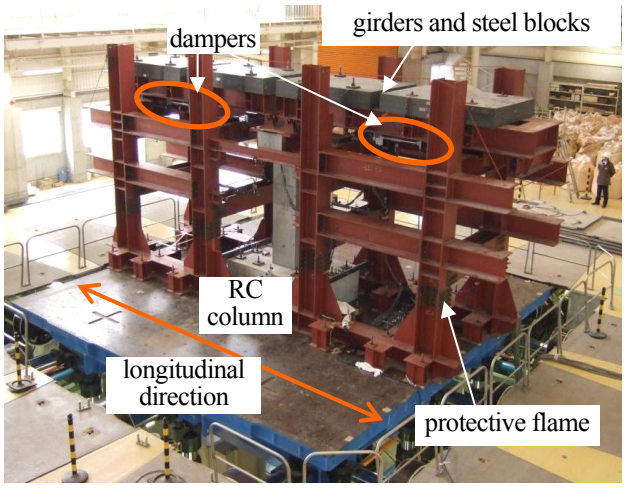

Figure 2 Test setup

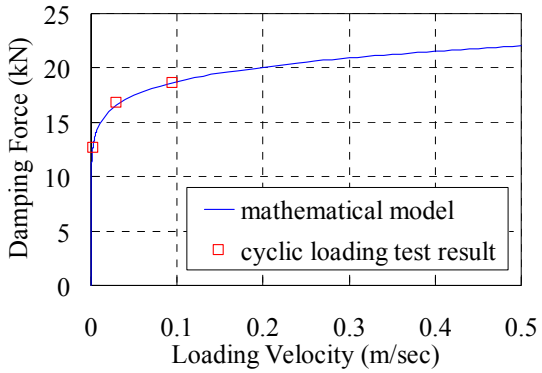

Figure 3 Damping force dependency on loading velocity

2. SHAKE TABLE TESTS

2.1 Test Setup

Figures 1 and 2 show the setup of the bridge model using dampers on the shake table. Two girders, which are assembled by H-section steel and steel blocks, are supported longitudinally by pin bearings on the top of the RC column and roller bearings were placed at each protective flame ends. Due to the setup, the inertia force of the two girders is applied to the top of the RC column in the longitudinal direction. The weight of two girders and steel blocks is 350 kN. The height of inertia force is 3m from the RC column bottom.

In this study, four rigid-plastic dampers are used to control the girder displacement and the damage of RC column. The damping force characteristic of each damper is depended on the loading velocity as shown in Figure 3. The efficiency of energy absorption is high because large damping force is generated even in low loading velocity.

Based on the cyclic loading tests, the sum of damping force of four dampers is defined in Eq. (1) below:

$$F = Cv^{\alpha} = 94.4v^{0.1} \qquad (1)$$

In which, F is the damping force (kN), C is coefficient of viscosity, α is a constant that represent the dependency of loading velocity and v is the loading velocity (m/sec).

The stroke of each damper is ± 80mm. Each two

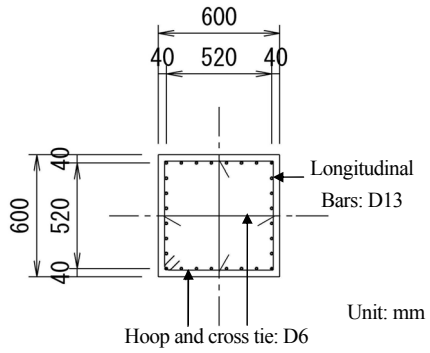

Figure 4 Cross section of bridge column specimen

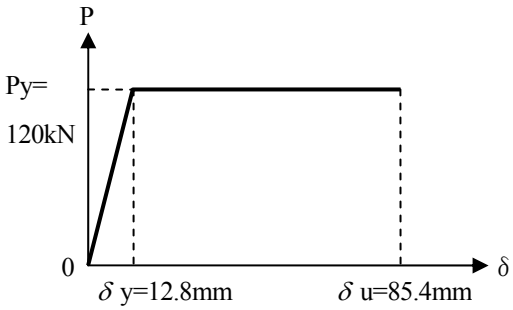

Figure 5 Relationship between horizontal force P and displacement δ

Table 1 Material properties

	f_{c0}(N/mm^2)	E_c(kN/mm^2)
Concrete	34.2	26.1
	f_{sy}(N/mm^2)	E_s(kN/mm^2)
Longitudinal bars (D13)	350.6	188.1
Hoops (D6)	345.1	193.8

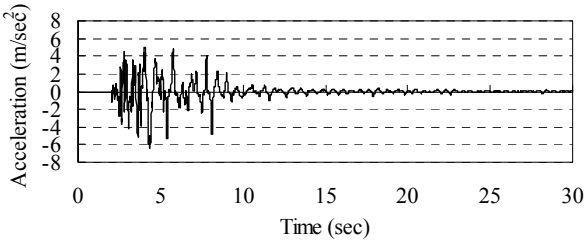

Figure 6 Input acceleration record

dampers are installed longitudinally between each end of girders and the protective flame ends, which is rigidly fixed with the shake table as shown in Figure 2.

The specimen is scaled down four times from the common RC column. The size of square cross section of the RC column is 600mm. The height of the column is 2.8m. 28 of SD295, 13-mm-diameter deformed bars are arranged as the longitudinal reinforcement. The longitudinal reinforcement ratio ρ_l is 1%, which is almost the same value of the common viaducts in Japan. SD295, 6-mm-diameter deformed bars are provided at 75mm intervals as the lateral hoops. The cross ties are arranged at the center of the cross section as shown in Figure 4.

The design strength of concrete f_{c0} is set to be 27N/mm^2. The design yield strength f_{sy} of SD295 bars are 295N/mm^2. Table 1 shows the material properties obtained from material tests. Figure 5 shows the relationship between

Table 2 maximum dynamic response

Input amplitude	acceleration		displacement	velocity	damping force		1) / 2)
	footing	girder	girder	girder	1)ovserved	2)estimated by Eq.(1)	
[%]	[m/sec^2]	[m/sec^2]	[mm]	[m/sec]	[kN]	[kN]	
30	1.7	2.7	2.1	0.07	61.4	72.7	85%
50	2.9	3.5	4.5	0.12	68.1	76.7	89%
70	3.9	4.3	9.5	0.18	74.3	79.6	93%
100	5.7	5.7	28.9	0.30	77.5	83.7	93%
120	7.2	6.1	67.8	0.47	87.8	87.6	100%

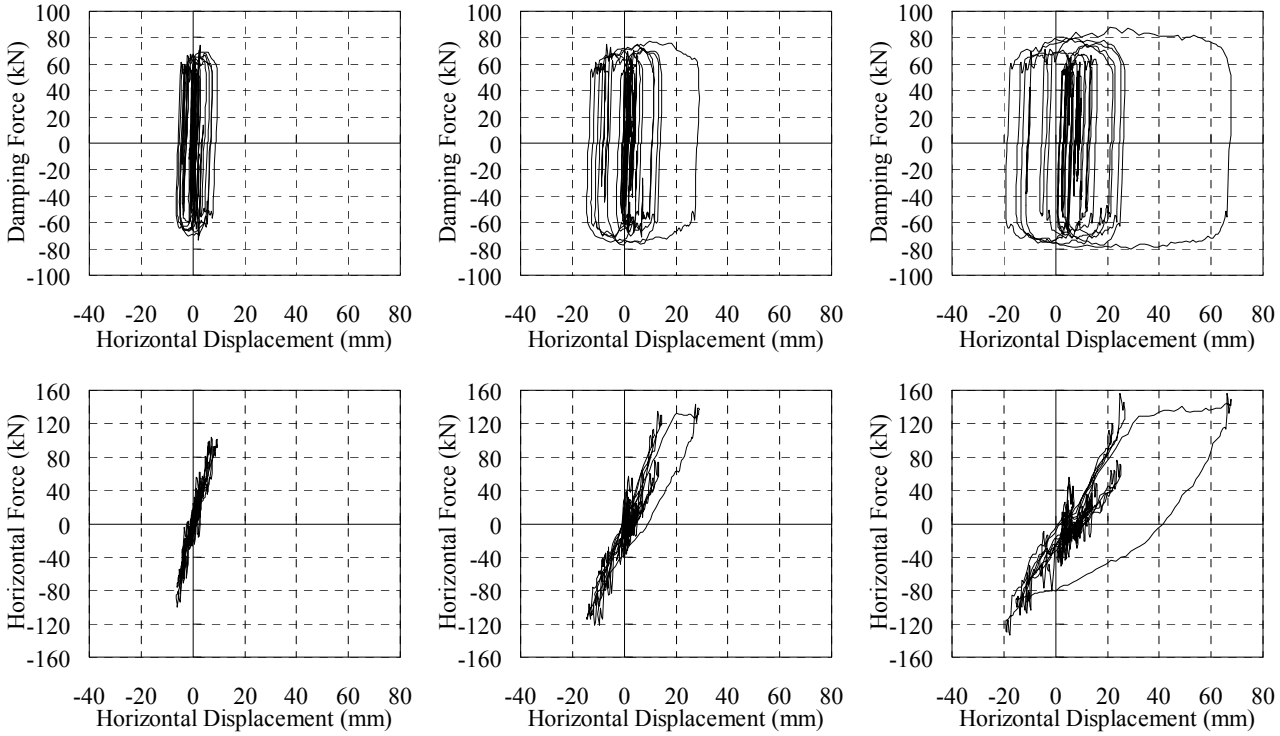

a) Input amplitude 70% b) Input amplitude 100% c) Input amplitude 120%

Figure 7 Damping force versus displacement hysteresis and column force versus displacement hysteresis

Horizontal force P and displacement δ of the RC column based on JRA specifications (2002). The yield and ultimate displacement are 12.8mm and 85.4mm.

2.2 Ground Motions and Test Sequence

Figure 6 shows the input acceleration which was observed at JR West Japan Takatori station during the 1995 Hyogo-ken Nanbu Earthquake. NS component of acceleration was input parallel with the longitudinal axis. The accelerations were not inputted transversally and vertically. The time scale was reduced to 50% because the specimen was reduced four times from the commonly envisioned RC column.

The input amplitude increased gradually because it was necessary to control the displacement within the damper stroke and to examine the dynamic response of dampers in the case where the RC column specimen was elastic and plastic. 30%, 50% and 70% of the input acceleration were used for the elastic level tests. 100% and 120% of the input acceleration were used for the nonlinear level tests.

3. TEST RESULTS

Table 2 shows the maximum responses of the girder displacement, the accelerations of the girder and the footing, the sum of generated damping force of the four dampers. Moreover, the girder velocities which were calculated based on the girder displacement time histories and the estimated damping forces based on the Eq. (1) are shown in Table 2. Figure 7 shows the response damping force of dampers versus horizontal displacement hysteresis and horizontal force and displacement hysteresis of RC column in the cases where the input amplitudes are 70%, 100% and 120%. The horizontal forces of RC column were calculated based on the inertia force of the girders minus damping force of dampers.

The stable damping forces were generated in every case regardless of the damaged level of RC column. It was verified that the maximum damper forces estimated by the Eq. (1) were generated in dynamic response, although there was a little difference between estimated and observed damping force in the case that the input amplitude is smaller.

There is a possibility that the difference was caused by the loss of velocity accuracy in these cases. The velocity was calculated from the displacement time history which includes the measurement noise. The noise has the larger influence on the velocity accuracy because the displacement is small.

4. ANALYTICAL SIMULATION

4.1 Analytical model and Procedure

Nonlinear dynamic analyses were conducted to simulate the seismic behaviors of the bridge model and to clarify the accuracy of the analytical model of dampers. The analyses were conducted continuously through a series of shake table tests to simulate the experimental condition. As input accelerations in the analyses, the acceleration data observed at RC column footing was used. The Newmark β method (β=1/4) was used as the numerical integration method. Time interval of the numerical integration was 0.002 seconds.

The bridge model is idealized as shown in Figure 8. The analytical model used is a simple beam spring-mass system which is commonly used in the usual seismic design. The girders and steel blocks are collectively idealized with one mass. The column is idealized with elastic beam elements and a nonlinear M-ϕ spring element for plastic hinge specified in the JRA specifications (2002). Two analytical models for the sum of damping force of four dampers are considered; one is a nonlinear damping element represented as Eq.(1) and the other is a simple rigid plastic spring element because the damping force characteristics is similar to sliding bearings as shown in Figure 7. Although the maximum damping force was changed in a series of shake table tests depending on the input acceleration amplitude, the maximum damping force is unchanged in order to analyze continuously in this research. The maximum damping force is 70kN which is the value calculated according to the Eq.(1) in the case that the value of v is 0.05m/sec. and is the average value in a series of shake table tests.

2% is considered as the equivalent damping ratio for RC column except the plastic hinge. The viscous damping of the bridge model system is idealized in proportion to the 1st mode damping ratio considering only stiffness matrix because the 1st mode is dominant according to the eigenvalue analysis.

4.2 Analytical Result

Table 3 shows the comparison of maximum responses value of girder displacements. The analytical simulation results using both models showed that the maximum responses displacements were evaluated well. Figure 9 shows the comparison of time histories for girder displacements, damping forces and displacement versus force of RC column hysteresis. In both analytical models, the seismic behaviors of the bridge model were simulated well. The time histories of girder displacements in using a nonlinear damping element were more accurate than in using a rigid plastic spring elements. But, the time histories of damping forces in using a rigid plastic spring element were more accurate than in using a nonlinear damping element.

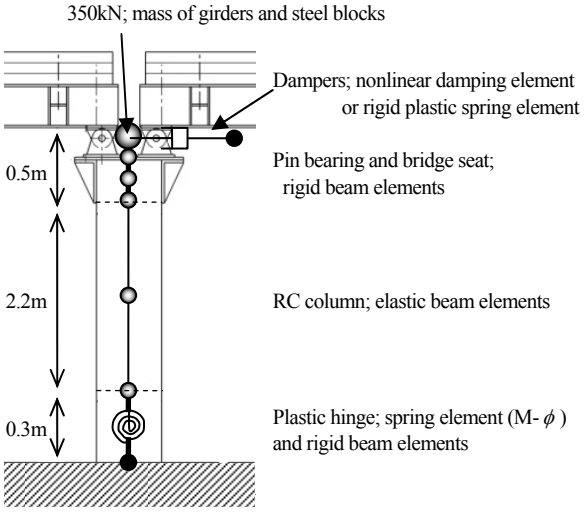

Figure 8 Analytical model

Table 3 Comparison of the horizontal displacement

Input amplitude	Test result (mm)	Analytical result (mm) and percent of test result	
		using rigid plastic spring element	using nonlinear damping element
70%	9.5	11.5 121%	11.4 120%
100%	28.9	26.2 91%	29.8 103%
120%	67.8	62.8 93%	63.5 94%

5. CONCLUSIONS

A series of shake table test of bridge model using rigid-plastic dampers were performed to examine the dynamic response and analytical simulations were conducted to evaluate the accuracy of the analytical damper model. Below are the conclusions obtained from the study:

1. The stable damping force is generated in every case regardless of the damaged level of the column. It is verified that the damper force, which are represented by Eq. (1) based on the cyclic loading tests, are generated in dynamic responses.
2. Both analytical models of dampers, using a nonlinear damping element and a rigid plastic spring element, can simulate the tested dynamic behaviors of bridge system using dampers.

References:

Japan Road Association (JRA) (2002) "Part V Seismic design, Design specifications of highway bridges," Maruzen, Tokyo, Japan.

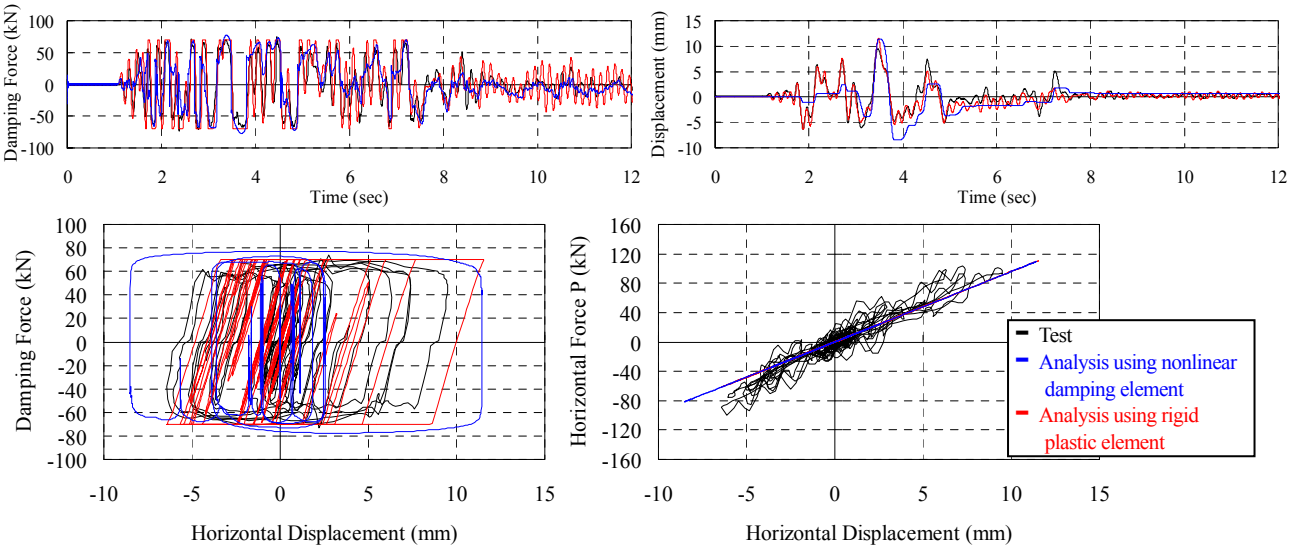

a) Input amplitude 70%

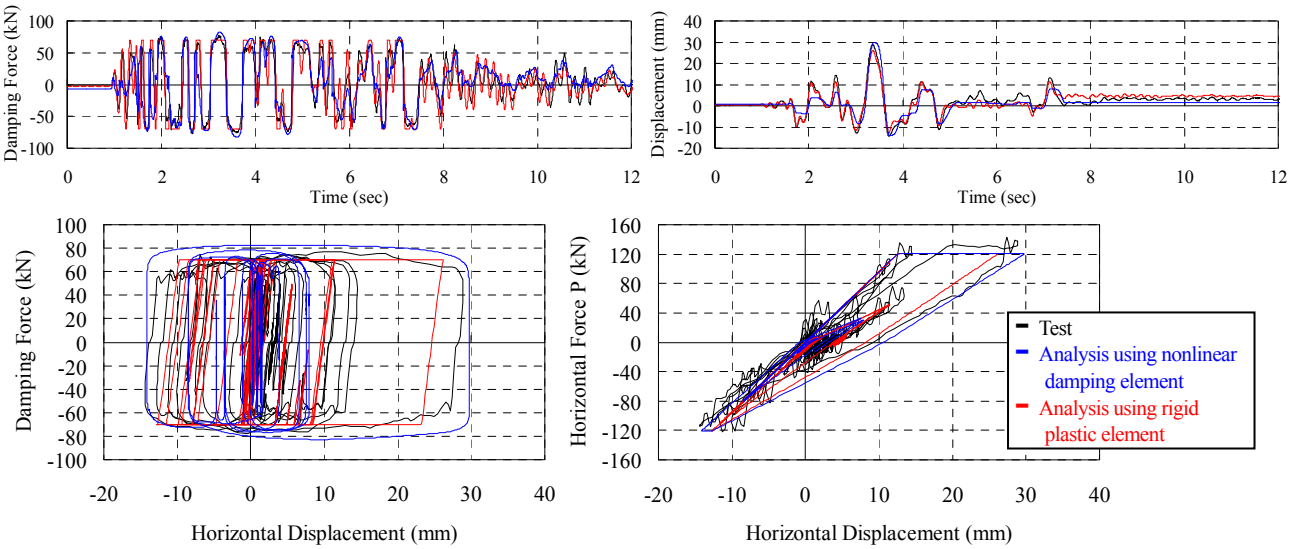

b) Input amplitude 100%

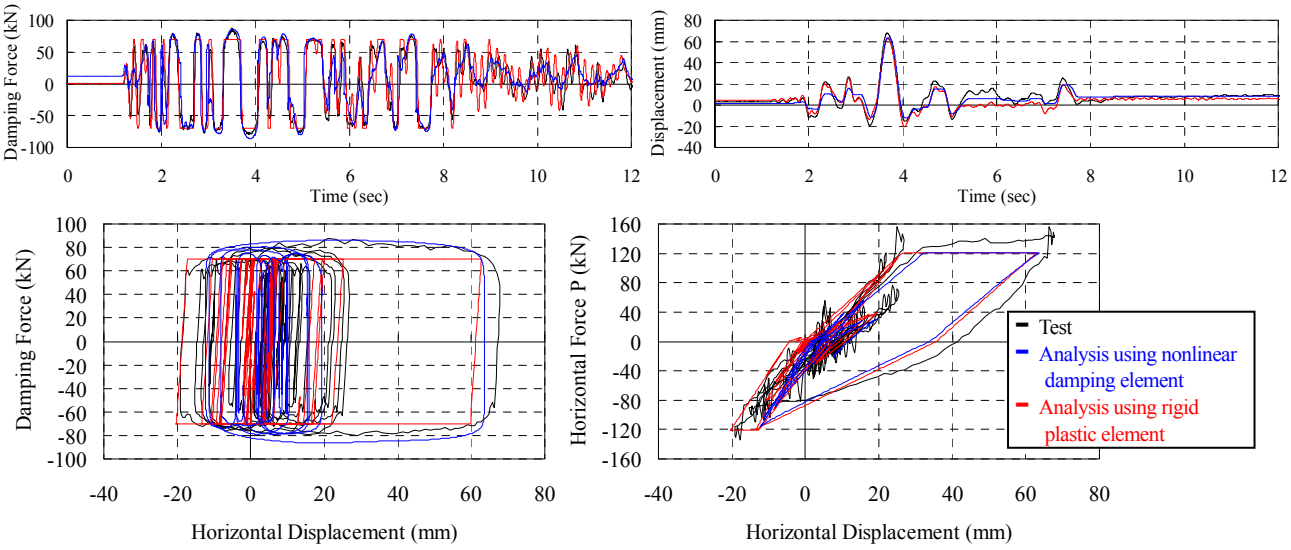

c) Input amplitude 120%

Figure 9 Compare of response displacement, damping force and hysteresis of RC column and damper

JOINT CONFERENCE PROCEEDINGS
7th International Conference on Urban Earthquake Engineering (7CUEE) &
5th International Conference on Earthquake Engineering (5ICEE)
March 3-5, 2010, Tokyo Institute of Technology, Tokyo, Japan

"COMPLETE SIMILARITIES" IN THE RESPONSE OF SEISMIC ISOLATED STRUCTURES

Nicos Makris[1] and Michalis F. Vassiliou[2]

1) Professor, Dept. of Civil Engineering, University of Patras, Greece, GR 26500
2) PhD Graduate Student, Dept. of Civil Engineering, University of Patras, Greece, GR 26500
nmakris@upatras.gr , mfvassiliou@gmail.com

Abstract: In this paper the seismic response of isolated structures supported on bearings with bilinear and trilinear behavior is revisited with dimensional analysis in an effort to better understand the relative significance of the various parameters that control the mechanical behavior of isolation systems. An isolation system that consists of lead rubber bearings or of single concave spherical sliding bearings exhibits bilinear behavior; whereas, when a double concave configuration is used the behavior is trilinear. For the case of trilinear behavior the paper shows that the presence of the intermediate slope is immaterial to the peak response of most isolated structures–a finding that shows that the response of the trilinear oscillator exhibits a complete similarity in the difference between the coefficients of friction along the two sliding surfaces as well as in the ratio of the intermediate to the final slope. This finding implies that even when the coefficient of friction of the two sliding surfaces are different, the response of isolated structures for most practical configurations can be computed with confidence by replacing the double concave spherical bearings with single concave spherical bearings with an effective radius of curvature and an effective coefficient of friction.

1. INTRODUCTION

During the last three decades seismic isolation enjoyed substantial growth, major improvements in its performance and an increasing worldwide acceptance (Skinner et al. 1993[1], Kelly 1998[2]). Several design documents are now available that offer guidelines on how to design structures equipped with this new seismic protection technology (FEMA 1997[3], 2000[4], AASHTO 1999[5], ICB 2000[6] among others.

The most widely used isolation bearings are the lead rubber bearings (Skinner et al. 1993 [1], Kelly 1998 [2]) and the spherical sliding bearings (Zayas et al. 1987[7], Constantinou et al. 1990[8], 1998[9]). Until the early years of this decade most spherical sliding bearings used involved only a single concave sliding surface, and the bilinear model was sufficient to approximate the behavior of both lead rubber and sliding spherical bearings. The only appreciable difference between the shape of the bilinear curve of the lead rubber and the sliding bearing is the size of the yield displacement, uy. In the case of the lead rubber bearing, uy, is of the order of centimeters (0.01m–0.03m) or even more; whereas, in the case of spherical sliding bearing, uy = 0.00025m = 0.25mm or even less (Mokha et al. 1990[10]).

Earlier parametric studies by Makris and Chang 2000[11] concluded that when seismic isolated structures are excited by strong ground motions, the value of the yield displacement has marginal effects on the superstructure response. This conclusion was subsequently confirmed and generalized by Makris and Black 2004a[12] via the use of dimensional analysis and it was demonstrated that the response of the bilinear oscillator exhibits a complete similarity in the normalized yield displacement.

The rapid growth of seismic isolation generated the need for more compact size, long period, bearings. Such needs are served with the double concave spherical sliding bearing–its configuration is shown schematically in Figure 1 (Hyakuda et al. 2001[13], Constantinou 2004[14], Tsai et al. 2005[15], Fenz and Constantinou 2006[16], Tsai et al. 2006[17] among others). When the double concave spherical bearing has sliding surfaces with the same coefficient of friction, μ, (no need for same radii of curvature) it becomes like a traditional single concave spherical bearing with isolation period $T_b = 2\pi\sqrt{\frac{R_1 + R_2 - h_1 - h_2}{g}}$ and coefficient of friction μ.

When the coefficients of friction along the sliding interfaces are different the behavior of the double concave friction spherical bearing is trilinear and it can be modeled using two traditional single concave spherical bearings acting on series together with a point mass representing the articulated slider. With this mathematically rigorous model one can capture the shaved portions of the hysteretic loops at the initiation and at the reversal of motion (see Figure 2) when initially, the sliding surface with the lower coefficient of friction is mobilized. Nevertheless, the implementation of two spring–slider elements in series may challenge the convergence of commercially available software which are

used routinely by practitioner engineers. This convergence challenge is accentuated when large structural systems are of interest such as multispan isolated bridges with isolation bearings and occasionally nonlinear dampers at the center piers and end abutments.

In this paper it is shown that when trilinear behavior prevails (see Figure 2) the presence of the intermediates slope, k_{tr}, and the shaving of the loops when the motion reverses, (which is the result of the difference in the coefficient of friction along the

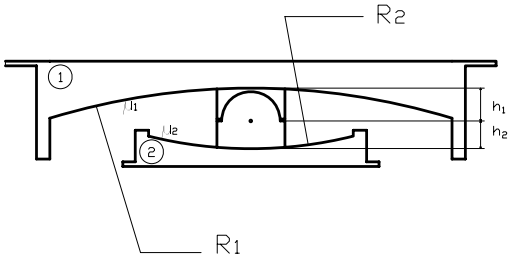

Fig. 1. Crossection of a double concave spherical sliding (DCSS) bearing with different radii of curvature

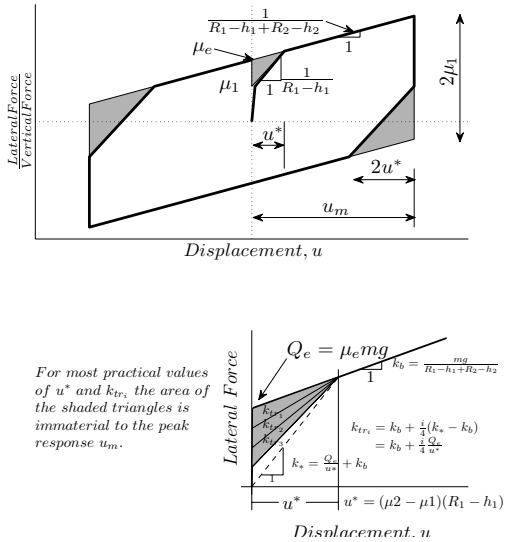

Fig. 2. Top: Generic force-displacement loop of the DCSS bearing (heavy line). Bottom: Values of the transition slope, ktr, used in this parametric study.

two interfaces) is immaterial to the response of the isolated superstructure for most practical values of the coefficients of friction used in seismic isolation of civil structures.

In more rigorous mathematical terms this finding shows that the response of the trilinear oscillator exhibits a complete similarity in the difference of the coefficient of friction along the two sliding surfaces as well as in the ratio of the intermediate to the final slope. This finding implies that under strong shaking an isolated bridge exhibits the same maximum displacement regardless whether it is supported on a double concave (R_1-h_1, R_2-h_2, μ_1, μ_2) or single concave (R_e,μ_e) spherical sliding bearing provided that

$$\frac{1}{R_e}=\frac{1}{R_1+R_2-h_1-h_2} \qquad (1)$$

and

$$\mu_e=\frac{\mu_1(R_1-h_1)+\mu_2(R_2-h_2)}{R_1+R_2-h_1-h_2} \qquad (2)$$

The existence of this complete similarity has practical significance since it eliminates the need of implementing two spring-slider elements in series and the analysis may be performed for all practical purposes with an equivalent single concave spherical sliding bearing. The permanent displacement that results from the equivalent single concave spherical bearings can be either smaller or larger than that resulting from the double concave spherical bearings, depending on the ground motion.

This study is restricted to the response analysis of an isolated deck. The effect of the transition slope of the trilinear oscillator to the response of multi-degree-of-freedom isolated structures will be the subject of a future study.

2. PARAMETERS OF THE BILINEAR SDOF OSCILLATOR

Consider a rigid deck supported on bearings that exhibit bilinear hysteretic behavior. Additional viscous dissipation can be appended if desired. The mechanical model adopted herein has been widely used for years for the modeling of either lead rubber or single concave spherical sliding bearings (Skinner et al. 1993[1], Kelly 1997[2], Constantinou et al. 1998[9], Makris and Chang 2000[11], Chang et al. 2002[18] and references reported therein) and has been systematically implemented for the response analysis of seismically isolated structures (SAP200N, OpenSEES among other commercially available software).

The bilinear model shown in Figure 3 (bottom) consists of the superposition of a linear restoring mechanism and some energy dissipation mechanism which is approximated with a parallelogram. When the yield displacement prior to flow is small as in the case of frictional dissipation (u_y = 0.2mm, Mohka et al. 1998[10]) the angles of the parallelogram tend to right angles; nevertheless, the behavior remains bilinear.

The bilinear force-displacement loop shown in Figure 3 (bottom) is uniquely defined with the isolation frequency induced by the bearings $\omega_b=\sqrt{k_b/m}=2\pi/T_b$, the characteristic strength, Q, and the yield displacement u_y. Note that the structural frequency, ω_b, is the undamped frequency of the mass, m, of the deck restrained by the stiffness of the bearings,

$\omega_b = \sqrt{k_b / m} = 2\pi / T_b$, which is the second slope of the bilinear loop. This definition is consistent with the frequency of oscillation of isolated structures supported on single-concave friction pendulum bearings with radius of curvature R. In this case

$$\omega_b = \sqrt{\frac{k_b}{m}} = \sqrt{\frac{W}{R}\frac{1}{m}} = \sqrt{\frac{g}{R}} \qquad (3)$$

The first slope K_0, of the bilinear loop

$$K_0 = \frac{Q}{u_y} + K_b \qquad (4)$$

is mostly associated with the preyielding behavior of the energy dissipation mechanism and depends primarily on the value of the yield displacement u_y. Early parametric studies by Makris and Chang 2000[11] concluded that when seismic isolated structures are excited by strong earthquakes, the value of the yield displacement has marginal effects on the superstructure response. This conclusion was subsequently confirmed and generalized by Makris and Black 2004a[12] via the use of dimensional analysis.

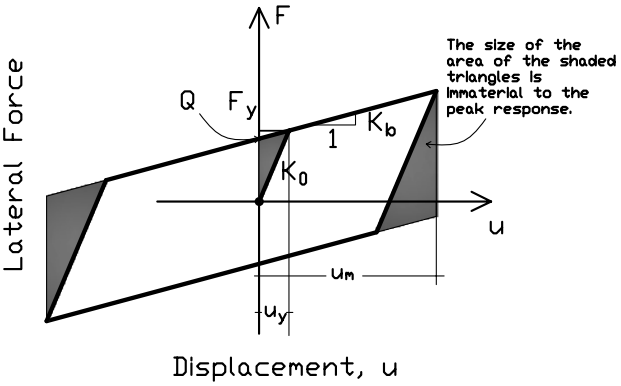

Fig. 3. Top: Rigid deck isolated on bearings that exhibit bilinear behavior. Bottom: Generic force-displacement loop.

3. TIME SCALE AND LENGTH SCALE OF PULSE-LIKE GROUND MOTIONS.

The dimensional analysis of the seismic response of inelastic structures requires a time scale and a length scale of the ground excitation. Such time scales and length scales are distinguishable in a wide class of strong ground motions most of them recorded near the source of causative faults.

The relative simple form, yet destructive potential of near source ground motions has motivated the development of various closed form expressions which approximate their leading kinematic characteristics. The early work of Veletsos et al. [19] was followed by the papers of Hall et al. [20], Heaton et al. [21], Makris [22], Makris and Chang [11], Alavi and Krawinkler [23] and more recently by the paper of Mavroeidis and Papageorgiou [24]. Physically realizable pulses can adequately describe the impulsive character of near-fault ground motions both qualitatively and quantitatively. The input parameters of the model have an unambiguous physical meaning. The minimum number of parameters is two, which are either the acceleration amplitude, a_p, and duration, T_p, or the velocity amplitude, v_p, and duration, T_p (Makris 1997[22], Makris and Chang 2000[11]). The more sophisticated model of Mavroeidis and Papageorgiou [24] involves 4 parameters, which are the pulse period, the pulse amplitude as well as the number and phase of half cycles.

The current established methodologies for estimating the pulse characteristics of a wide class of records are of unique value since the product, $a_p T_p^2 = L_p$, is a characteristic length scale of the ground excitation and is a measure of the persistence of the most energetic pulse to generate inelastic deformations (Makris and Black 2004b[25]). It is emphasized that the persistence of the pulse is a different characteristic than the strength of the pulse which is measured with the peak pulse acceleration. The reader should recall that among two pulses with different acceleration amplitude (say $a_{p1} > a_{p2}$) and different pulse duration (say $T_{p1} < T_{p2}$), the inelastic deformation does not scale with the peak pulse acceleration (most intense pulse) but with the stronger length scale (larger $a_p T_p^2$ = most persistent pulse).

The heavy line in Figure 4 (left) which approximates the long-period acceleration pulse of the NS component of the 1992 Erzinkan, Turkey, record is a scaled expression of the second derivative of the Gaussian distribution, $e^{-\frac{t^2}{2}}$, known in the seismology literature as the symmetric Ricker wavelet (Ricker 1943[26], 1944[27]) and widely referred as the "Mexican Hat" wavelet, Addison 2002[28])

$$\psi(t) = a_p \left(1 - \frac{2\pi^2 t^2}{T_p^2}\right) e^{-\frac{1}{2}\frac{2\pi^2 t^2}{T_p^2}} \qquad (5)$$

The value of $T_p = \frac{2\pi}{\omega_p}$, is the period that maximizes the Fourier spectrum of the symmetric Ricker wavelet.

Similarly, the heavy line in Figure 4 (right) which approximates the long-period acceleration pulse of the Pacoima Dam motion recorded during the February 9, 1971 San Fernando, California earthquake is a scaled expression of the third derivative of the Gaussian distribution $e^{-t^2/2}$.

Again, in equation (6) the value of $T_p = \frac{2\pi}{\omega_p}$ is the period that maximizes the Fourier spectrum of the antisymmetric Ricker wavelet.

$$\psi(t) = a_p\left(\frac{4\pi^2 t^2}{3T_p^2} - 3\right)te^{-\frac{1}{2}\frac{4\pi^2 t^2}{3T_p^2}} \quad (6)$$

The choice of the specific functional expression to approximate the main pulse of pulse–type ground motions has limited significance in this work. In the past simple trigonometric pulses have been used by the senior author (Makris 1997[22], Makris and Chang 2000[11], Makris and Black 2004[12],[25]) to extract the time scale and length scale of pulse-type ground motions. In this paper we use as alternative wavelets the symmetric and antisymmetric Ricker wavelets. A mathematically rigorous and easily reproducible methodology based on wavelet analysis to construct the best matching wavelet has been recently proposed by Vassiliou and Makris (2009)[30].

4. REVIEW OF DIMENSIONAL ANALYSIS OF THE BILINEAR SDOF OSCILLATOR

Consider a hysteretic bilinear oscillator that is described with the three parameters ω_b, Q/m and u_y *(ξ=0)*; which is subjected to a pulse type strong ground motions with a predominant acceleration pulse with duration Tp=2π/ωp and amplitude a_p. With these structural and excitation parameters the maximum inelastic displacement of the bilinear SDOF oscillator is a function of five variables

$$u_{\max} = f(\omega_b, \frac{Q}{m}, u_y, a_p, \omega_p) \quad (7)$$

The six (6) variables appearing in Equation (7), $u_{\max} \doteq$ [L] , $\omega_b \doteq [T]^{-1}$, $Q/m \doteq [L][T]^{-2}$, $u_y \doteq$ [L], $a_p \doteq [L][T]^{-2}$ and $\omega_p \doteq [T]^{-1}$, involve only two reference dimensions; that of length [L] and time [T]. According to Buckingham's Π-theorem the number of dimensionless products (Π-Terms) = [number of variables in Eq. (7) = 6] – [number of reference dimensions = 2]; therefore for the bilinear SDOF oscillators, we have 6-2 = 4 Π–terms

$$\Pi_m = \frac{u_{\max}\omega_p^2}{a_p} \quad (8)$$

$$\Pi_\omega = \frac{\omega_b}{\omega_p} \quad (9)$$

$$\Pi_Q = \frac{Q}{ma_p} \quad (10)$$

$$\Pi_y = \frac{u_y\omega_p^2}{a_p} \quad (11)$$

In deriving the Π-terms listed above we selected as repeating variables the characteristics of the pulse excitation, a_p and $\omega_p = \frac{2\pi}{T_p}$. With this selection the maximum displacement response, $u_{\max}$, is normalized with the energetic length scale $L_e = a_p/\omega_p^2$ that is a measure of the

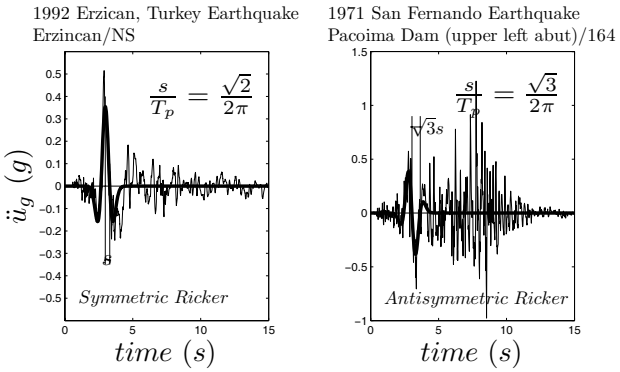

Fig. 4. Left: North-South components of the acceleration time history recorded during the 1992 Erzican, Turkey earthquake together with a symmetric Ricker wavelet. Right: Fault-normal component of the acceleration time history recorded during the 1971 San Fernando earthquake, together with an antisymmetric Ricker wavelet.

persistence of the excitation. With the four Π-terms given above the relation of the six variables appearing in equation (7) is reduced to a relation of four variables

$$\frac{u_{\max}\omega_p^2}{a_p} = \varphi\left(\frac{\omega_b}{\omega_p}, \frac{Q}{ma_p}, \frac{u_y\omega_p^2}{a_p}\right) \quad (12)$$

Pulse spectra for trigonometric pulses have been presented by Makris and Black 2004a[12] who showed that under earthquake shaking an isolated bridge exhibits the same maximum displacement regardless whether it is supported on lead rubber bearings or single concave spherical sliding bearings that exhibit the same strength and offer the same second slope (same isolation period). In mathematical terms, the dimensionless response Π_m, converges to a finite limit (neither zero nor infinity) as the dimensionless yield displacement Π_y tends to zero; and according to the theory of dimensional analysis one can simply replace Equation (12) by its limiting expression in which $\Pi_y = 0$ (Barenblatt 1996[31])

$$\lim_{\Pi_y \to 0} \frac{u_{\max}\omega_p^2}{a_p} = \varphi\left(\frac{\omega_b}{\omega_p}, \frac{Q}{ma_p}, 0\right) = finite \quad \Rightarrow \quad \frac{u_{\max}\omega_p^2}{a_p} = \varphi\left(\frac{\omega_b}{\omega_p}, \frac{Q}{ma_p}\right) \quad (13)$$

The finding that the response of the bilinear oscillator exhibits a complete similarity in the normalized yield displacement expressed by equation (13) is what is of most interest to the design structural engineer–that the exact value of the yield displacement, u_y, is immaterial to the response of the bilinear SDOF oscillator and therefore drops out of consideration. Furthermore, because of the existence of complete similarity as expressed by Equation (13), the number of arguments in the function φ( ), appearing in Equation (12) reduces by one.

5. PARAMETERS OF THE TRILINEAR SDOF OSCILLATOR

Our study proceeds with the dimensional analysis of the dynamic response of the trilinear SDOF oscillator in an effort to better understand the relative significance of the various parameters that control the mechanical behaviour of the double concave spherical sliding (DCSS) bearing.

The DCSS bearing consist of two facing concave stainless-steel surfaces as shown in Figure 1. The top and bottom concave surfaces have raddi of curvature R_1 and R_2 respectively which may be unequal. The coefficients of friction of the concave surfaces are μ_1 and μ_2, respectively which are also not necessarily equal. An articulated slider faced with an non-metallic sliding material separates the two surface. The principal benefit of the DCSS bearing is its capacity to accommodate larger displacement demands compared to the single concave spherical sliding (SCSS) bearing examined in the previous section.

When different values of coefficients of friction are used ($\mu_1 \neq \mu_2$), the force−displacement loop of the DCSS bearing is not bilinear−as is for the SCSS bearing shown in Figure 3−but rather trilinear given that at the initiation and at the reversal of motion, the bilinear loop looses the corner triangles (see Figure 2 top) when the sliding surface with the lower coefficient of friction is mobilized.

The purpose of this section is to show that the loss of the corner triangles shown with gray in Figure 2 is immaterial in the response of the isolated superstructure for most practical values of the coefficients of friction used. In mathematical terms, the paper shows that the trilinear oscillator exhibits a complete similarity in the difference between the coefficients of friction along the two sliding surfaces as well as in the ration of the intermediate to the final slope.

The trilinear force – displacement loop shown in Figure 2 is uniquely defined with the isolation frequency offered by the bearings

$$\omega_b = \sqrt{\frac{g}{R_1 - h_1 + R_2 - h_2}} \quad , \qquad (14)$$

the characteristic strength,

$$Q_e = mg\,\frac{\mu_1\left(R_1 - h_1\right) + \mu_2\left(R_2 - h_2\right)}{R_1 - h_1 + R_2 - h_2} \quad , \qquad (15)$$

the yield displacement of the equivalent bilinear system $u_{ye} \approx$ 0.25mm, which according to the previous analysis we expect to have marginal effect, the transition displacement from the second to the last slope,

$$u^* = \left(\mu_2 - \mu_1\right)\left(R_1 - h_1\right) \qquad (16)$$

and the transition frequency associated with the second slope,

$$\omega_{tr} = \sqrt{\frac{g}{R_1 - h_1}} \qquad (17)$$

In this study, while the analysis focuses on the DCSS bearings the formulation is presented for the general trilinear oscillator ($u_{ye} \neq 0$) and the result that the normalized maximum displacement exhibits a complete similarity in the normalized yield displacement is re-established.

6. PARAMETRIC ANALYSIS OF THE RESPONSE OF AN ISOLATED DECK ON DCSS BEARINGS.

Our parametric analysis to investigate the relative significance of the various parameters that control the mechanical behavior of the DCSS bearings commences with the response analysis of a rigid isolated deck as shown in the top of Figure 3 that is supported on DCSS bearings. Figure 5 top plots the relative-to-the ground deck displacement (bearing displacement) subjected to the fault-parallel OTE record from the 1995 Aigion, Greece, earthquake. Two configurations of double concave spherical bearings are used–those tested by Fenz and Constantinou (2006)[32]. The configuration of the left has a small difference between the coefficient of friction along the two sliding surfaces (μ_1=0.021, μ_2=0.038, R_1-h_1=0.726m, R_2-h_2=0.442m); whereas, the configuration on the right has a large difference in the coefficient of friction (μ_1=0.081, μ_2=0.012, R_1-h_1=0.438m, R_2-h_2=0.442m).

The displacement time histories and force-displacement loops shown in Figure 5 indicate that for the configuration on the left (small difference in the coefficient of friction), the peak displacement of the equivalent single concave spherical system (see equations (1) and (2)) is for all practical purposes the same peak displacement as the DCSS system. For the configuration on the right (large difference in the coefficient of friction) the peak displacement of the equivalent SCSS is less than 10% smaller than the peak displacement of the DCSS system. Recall that the fault parallel OTE record from the 1995 Aigion earthquake is a moderately strong motion. When a stronger motion is used which demands larger bearing displacements the behavior of the DCSS system and the SCSS are practically the same.

The response analysis presented in Figure 5 has been computed with an in-house MATLAB code (solid line) and with the SAP software (dashed lines) by connecting two spring–slider elements in series. The numerical result of the two calculations shown both on the displacement time histories and the force displacement loops are identical and this validates the solution obtained with SAP.

Returning to Figure 5 (right) the response analysis with the equivalent SCSS bearings results to zero-permanent displacement; whereas the response analysis with the DCSS bearing reaches a small permanent displacement due to the high friction μ_1=0.081 on surface one. This result is not a

general trend given that the opposite may happen depending on the fluctuations of the ground excitation that follow the main pulse.

7. DIMENSIONAL ANALYSIS OF THE TRILINEAR OSCILLATOR

Consider a trilinear oscillator that is described with the five parameters ω_b, Q_e, u_{ye}, u^* and ω_{tr} which is subjected to a pulse-type strong ground motion having a predominant acceleration pulse with duration T_p and amplitude a_p. The maximum inelastic displacement of the triliear SDOF oscillator is a function of seven variables

$$u_{\max} = f(\omega_b, \frac{Q_e}{m}, u_{ye}, u^*, \omega_{tr}, a_p, \omega_p) \qquad (18)$$

The eight (8) variables appearing in equation (18) involve only two reference dimensions; that of length [L] and time [T]. According to Buckingham's Π-theorem, the number of dimensionless products (Π-terms)=[number of variables in Eq. (15) = 8 – number of reference dimensions = 2]; therefore, for the trilinear SDOF oscillator we have 8 - 2 = 6 Π-terms. The first two Π-terms (Π_m and Π_ω) are given by equations (8) and (9) while,

$$\Pi_Q = \frac{Q_e}{ma_p} \qquad (19)$$

$$\Pi_y = \frac{u_{ye}\omega_p^2}{a_p} \neq 0 \qquad (20)$$

$$\Pi_* = \frac{u^*\omega_p^2}{a_p} \qquad (21)$$

$$\Pi_{tr} = \frac{\omega_{tr}}{\omega_p} \qquad (22)$$

As in the dimensional analysis of the bilinear oscillator in deriving the Π-terms listed above we selected as repeating variables the characteristics of the pulse excitation, a_p and $\omega_p = 2\pi/T_p$. With the six Π-terms given by equations (8), (9), (19) – (22), the elation of the eight variables appearing in equation (15) is reduced to a relation of six variables

$$\frac{u_{\max}\omega_p^2}{a_p} = \varphi(\frac{\omega_b}{\omega_p}, \frac{Q_e}{ma_p}, \frac{u_{ye}\omega_p^2}{a_p}, \frac{u^*\omega_p^2}{a_p}, \frac{\omega_{tr}}{\omega_p}) \qquad (23)$$

Range of interest of the Π-terms

- $\Pi_\omega = \omega_b/\omega_p$

Given that the majority of isolation periods used are larger than 1.5 sec ($T_p > 1.5$sec) and that energetic pulses from near source records can be as large as 3 sec, the range of interest for $\frac{\omega_b}{\omega_p}$ is $0 < \frac{\omega_b}{\omega_p} = \frac{T_p}{T_b} = \frac{3\,\text{sec}}{1.5\,\text{sec}} = 2$.

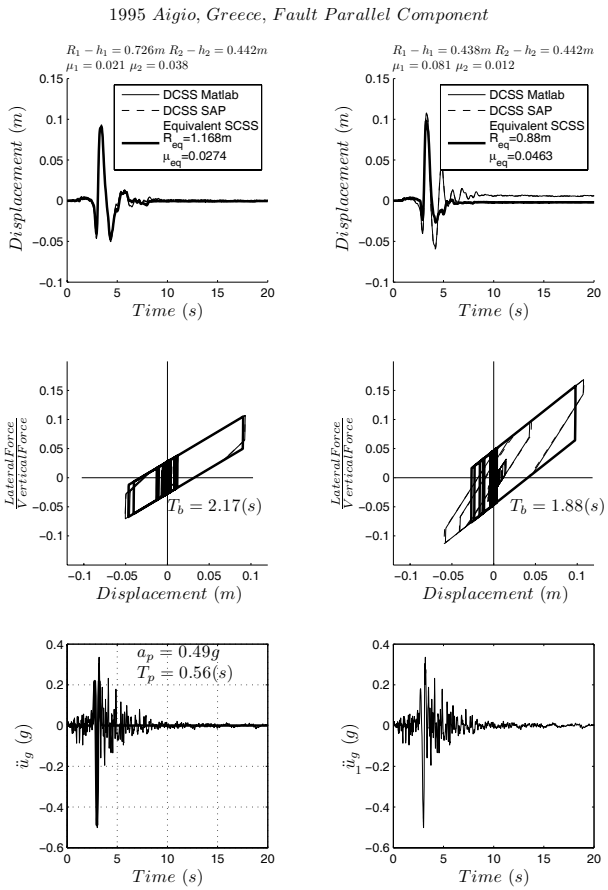

Fig. 5. Displacement time histories (top) and force-displacement loops (center) of a rigid deck isolated on double concave spherical sliding bearings (DCSS) bearings when subjected to the OTE FP acceleration record from the 1995 Aigion earthquake (bottom).

Beyond the value of $\Pi_\omega = \omega_b/\omega_p = 2$ the phenomenon of complete similarity that we intend to show becomes even stronger.

- $\Pi_Q = Q_e/ma_p$

Even for ground motions which are approximated with low amplitude acceleration pulse say a_p=0.25g and for an equivalent coefficient of friction as high as μ_e=0.05 the dimensionless product $\Pi_Q = \frac{Q_e}{ma_p} = \frac{\mu g}{a_p}$ as high as 0.2.

Accordingly $0.05 < \Pi_Q < 0.2$. For instance with thevalues of a_p=0.49g and T_p=0.56sec associated with the 1995 Aigion record shown in Figure 5 the value of $\Pi_Q = \frac{0.0274}{0.49} = 0.056$ for the configuration on the left and $\Pi_Q = \frac{0.0463}{0.50} = 0.094$ for the configuration on the right.

- $\Pi_y = u_{ye}\omega_p^2/a_p$

Given that the yield displacement of the Teflon coat before sliding along the stainless steel surface is u_y=0.2m and that u_{ye} is of the same order of magnitude , the range of interest of $\Pi_y = \frac{u_{ye}\omega_p^2}{a_p}$ is $0.0001 < \Pi_y < 0.01$

- $\Pi^* = u^* \omega_p^2 / a_p$

For the persistent near fault ground motions Π^* is well below one. However for few relative short duration pulse type ground motions such as the OTE record from the 1995 Aigion Greece earthquake and relative large values of μ_2-μ_1, Π^* may reach the value of one. For instance with the values of a_p and T_p associated with the 1995 Aigion record shown in Figure 5 the value of $\Pi^* = 0.363$ for the configuration on the left and $\Pi^* = 0.889$ for that in the right. Accordingly $0.1 < \Pi^* < 1.0$.

- $\Pi_{tr} = \omega_{tr}/\omega_p$

With reference to Figure 2 (bottom) the transition slopes k_{tr} (second slope) is bounded by

$k_b < k_{tr} < \frac{Q_e}{u^*} + k_b = k^*$. Accordingly, in terms of frequencies

$$\omega_b < \omega_{tr} < \sqrt{\frac{Q_e}{mu^*} + \omega_b^2} \qquad (24)$$

Recognizing that $\frac{Q_e}{mu^*} = \frac{\Pi_Q}{\Pi^*}\omega_p^2$, equation (24) after dividing with ω_p^2 assumes the expression

$$\Pi_\omega < \Pi_{tr} < \sqrt{\frac{\Pi_Q}{\Pi^*} + \Pi_\omega^2} \qquad (25)$$

The limiting value of $\Pi_{tr} = \sqrt{\frac{\Pi_Q}{\Pi^*} + \Pi_\omega^2}$ corresponds to the unrealistic event that the coefficient of friction along one sliding surface is zero (say μ_1=0). In our parametric study we consider that the low end value of the coefficient of friction is as low as 1/4 of the high value; therefore ,

$$\Pi_\omega^2 < \Pi_{tr}^2 < \Pi_\omega^2 + \frac{3}{4}\frac{\Pi_Q}{\Pi^*} \Rightarrow \quad \Pi_\omega < \Pi_{tr} < \sqrt{\Pi_\omega^2 + \frac{3}{4}\frac{\Pi_Q}{\Pi^*}} \quad (26)$$

Complete similarity on the dimensional yield displacement.

Figure 6 plots the dimensionless value of the solution of equation (23), $\Pi_m = u_{\max}\omega_p^2 / a_p$ as a function of $\Pi_\omega = \omega_b/\omega_p$ when Π^*=0.5 and $\Pi_{tr} = \sqrt{\Pi_\omega^2 + \frac{1}{2}\frac{\Pi_Q}{\Pi^*}}$, for three different values $\Pi_Q = Q_e/ma_p$ and different values of $\Pi_{ye} = u_{ey}\omega_p^2/a_p$ when the trilinear oscillator (rigid deck supported on DCSS bearings) is excited by an antisymmetric Ricker wavelet. Figure 6 shows that the solution for the dimensionless maximum displacement, Π_m, is nearly indifferent even when the dimensionless yield displacement of the backbone curve Π_{ye} is varied by two orders of magnitude (Π_{ye}=0.0001 – 0.01). This result indicates that the response of the trilinear oscillator exhibits a complete similarity in the dimensionless product Π_{ye}; and therefore the dimensionless product Π_{ye} drops out of consideration. Accordingly, equation (24) reduces to

$$\frac{u_{\max}\omega_p^2}{a_p} = \varphi\left(\frac{\omega_b}{\omega_b}, \frac{Q_e}{ma_p}, \frac{u^*\omega_p^2}{a_p}, \frac{\omega_{tr}}{\omega_p}\right) \qquad (27)$$

It is worth mentioning that the work of Constantinou (2004)[14] and subsequently the work of Fenz and Constantinou (2006[32], 2008[33]) silently use the result of equation (28) – that the response is insensitive to the value of the yield displacement and throughout their study they adopted that $u_{ye} = 0$

Interpretation of the Response Analysis of the DCSS

Figure 7 plots dimensionless response spectra of the trilinear oscillator for three values of the normalized strength $\Pi_Q = \frac{Q_e}{ma_p} = \frac{\mu_e g}{a_p} = 0.05,\ 0.1\ and\ 0.2$ when subjected to a symmetric Ricker wavelet (see equation (5) and Figure 4). The heavy black line plots the response of the rigid deck when supported on equivalent single concave spherical sliding bearings (backbone curve) while the other curves plot the response of the rigid deck supported on various DCSS bearings (Π^*=0.1, 0.5, 1.0) and $\Pi_{tr} = \sqrt{\Pi_\omega^2 + j\frac{\Pi_Q}{\Pi^*}}, \quad j = \frac{1}{4}, \frac{1}{2}, \frac{3}{4}$, a total of 9 combinations). The combination of $\Pi^* = 1.0$ and $\Pi_{tr} = \sqrt{\Pi_\omega^2 + \frac{3}{4}\frac{\Pi_Q}{\Pi^*}}$ corresponds to the triangles with the larger area (larger departure from the backbone loop-see Figure 2). Figure 7 indicates that the backbone heavy black line (deck on equivalent SCSS bearings) is invariably below all curves (smaller peak bearing displacements). For the case of $\Pi_Q = 0.05$ and Π_Q=0.1 (which is the majority of practical situations), the peak bearing displacements from all configurations are practically the same (complete similarity) for Π_ω<0.5 and Π_ω>1 while within the range 0.5< Π_ω<1 the response curves exhibit a mild amplification as the size of the gray triangles in Figure 2 increases.

The right plot shown in Figure 7 which is for the high-end values of the dimensionless strength $\Pi_Q = \frac{Q_e}{ma_p} = \frac{\mu_e g}{a_p} = 0.2$, indicates that the complete similarity appears in the range of interest (Π_ω<1.5) only when Π^*<0.5 and $\Pi_{tr} < \sqrt{\Pi_\omega^2 + \frac{1}{2}\frac{\Pi_Q}{\Pi^*}}$.

Figure 8 plots dimensionless response spectra of the trilinear oscillator when subjected to an antisymmetric Ricker wavelet. The response spectra in Figure 9 exhibit remarkable order and the phenomenon of complete similarity becomes most apparent in particular for the values of Π_Q<0.1 . Also note that the curves which depart the most from the heavy black backbone line are those with the stars (*) which correspond to very high values of the

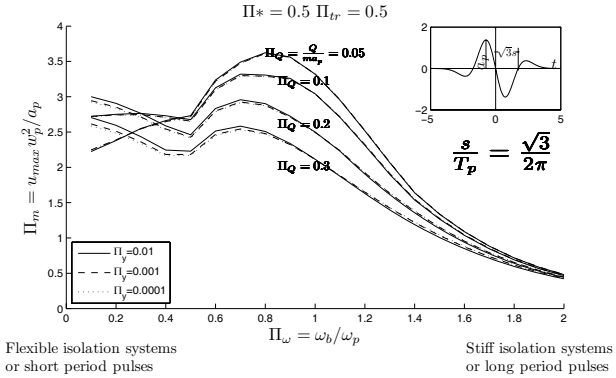

Fig. 6. Dimensionless maximum displacement spectra of a trilinear oscillator (Π*=0.5, Πtr=0.5) subjected to an antisymmetric Ricker wavelet. For a given dimensionless strength ΠQ the response is practically indifferent to two orders of magnitude variation of the dimensionless yield displacement Πye.

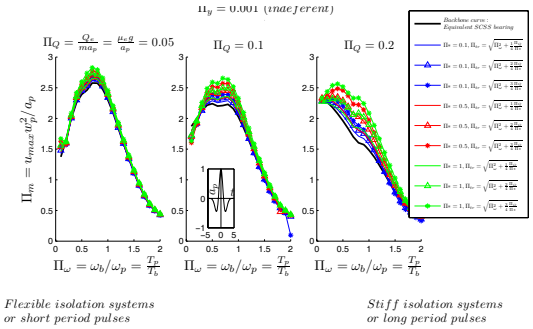

Fig.7. Dimensionless maximum inelastic displacement of a rigid deck supported on DCSS bearings with a wide range of parameters when subjected to a symmetric Ricker pulse.

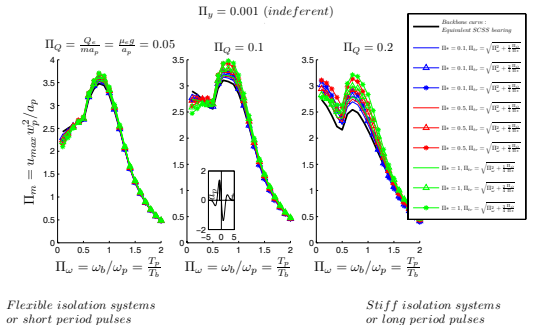

Fig. 8. Dimensionless maximum inelastic displacement of a rigid deck supported on DCSS bearings with a wide range of parameters when subjected to an antisymmetric Ricker pulse.

result of the dimensional analysis presented herein concludes that for values of $\Pi_Q \leq 0.1$ and values of $\Pi_{tr} < \sqrt{\Pi_\omega^2 + \frac{1}{2}\frac{\Pi_Q}{\Pi^*}}$ the dimensionless products Π* and Π_{tr} drop out of consideration; and therefore equation (27) further reduces to

$$\frac{u_{\max}\omega_p^2}{a_p} = \varphi\left(\frac{\omega_b}{\omega_b}, \frac{Q_e}{ma_p}, 0, any\right) \Rightarrow \quad \frac{u_{\max}\omega_p^2}{a_p} = \varphi\left(\frac{\omega_b}{\omega_b}, \frac{Q_e}{ma_p}\right) \qquad (28)$$

The finding that the response of the trilinear oscillator exhibits a complete similarity in the normalized yield displacement, Π_{ye}, in the difference between the coefficient of friction, Π*, and the ratio of the transition to the final slope, Π_{tr}, is what is of most interest to the design structural engineer. For instance, in some cases DCSS are viable alternatives due to space limitation; however, the coefficient of friction may be different due to various imperfections. The analysis presented in this paper shows that these imperfections are immaterial to the response and one can use with confidence the equivalent values of the SCSS bearings. Furthermore, because of the existence of the three complete similarities as expressed by equations (27) and (28) the number of arguments in the function φ( ) appearing in equation (23) are reduced by three (3).

8. CASE-STUDY RESPONSE OF AN ISOLATED BRIDGE

Our study to better understand the relative significance of the various parameters that control the mechanical behavior of the DCSS bearings proceeds with the response analysis of a seismically isolated bridge currently under construction in Greece in order to confirm the validity of equation (28). This case-study, is a three-span, 105m-long seismic isolated prestressed concrete bridge supported on two piers and two end abutments. The center span is 40m long; while the two end spans are 32.5m long. The two piers, M1 and M2 have respective height of 11.72m and 6.77m and they rest in pile foundations. Figure 9 shows the elevation of the bridge. At each end-abutment or pier the bridge rests on two single concave spherical sliding bearings with radius of curvature R=2.2m and coefficient of friction μ=0.045. The isolation period of the spherical bearings alone in any horizontal direction is $T_b = 2\pi\sqrt{\frac{R}{g}} = 2.98\,\text{sec}$. At the end-abutments the bridge is free to move only along the longitudinal direction, while the motion along the transverse direction is restrained in order to avoid misalignment of the rails at the deck abutment joint during earthquake shaking.
A detailed structural model of the bridge was developed with the commercially available software SAP (Computers and Structures 2007) which accounts for the flexure of the center piers and the finite stiffness of pile foundations in the horizontal, vertical, rocking and cross horizontal-rocking

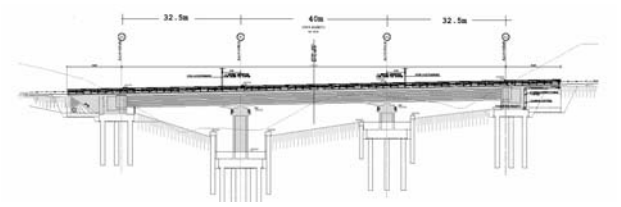

Fig. 9. Elevation of a three-span, 105m long, seismically isolated bridge.

directions (Zhang and Makris 2002[34]).

The first eigenvalue of the bridge is the longitudinal eigenvalue, $T_1=T_L= 2.992$, sec a value that is slightly larger than the SCSS bearing period, $T_b = 2\pi\sqrt{\frac{R}{g}} = 2.98$ due to the finite flexibility of the piers and piles connected in series with the spherical sliding bearings (see Figure 10).

The dynamic analysis of the bridge is also conducted by considering two configurations of double concave spherical sliding (DCSS) bearings that offer the same isolation period and same equivalent strength. The first configuration uses DCSS having the same radii (R_1-h_1=R_2-h_2=*1.1m*) and coefficient of friction μ_1=0.03 and μ_2=0.06 so that according to equation (2) $\mu_e = \frac{\mu_1+\mu_2}{2} = 0.045$.

Table 1. Earthquake records used for the dynamic response analysis of the bridge.

Earthquake	Record Station	Magnitude (Mw)	Distance (km)	PGA (g)		PGV (m/s)	
				Longitudinal Bridge Direction	Transverse Bridge Direction	Longitudinal Bridge Direction	Transverse Bridge Direction
1971 San Fernando	Pacoima Dam	6.6	11.9	1.23	1.16	1.12	0.54
1979 Imperial Valley	El Centro Array #5	6.5	27.8	0.52	0.38	0.47	0.91
1983 Coalinga	Transmitter Hill	5.8	6	1.08	0.84	0.40	0.44
1986 Kalamata	OTE Building	5.5	11	0.27	0.24	0.24	0.32
1992 Erzican,	Erzincan	6.9	13	0.50	0.52	0.64	0.84
1994 Northridge	Jensen Filter Station	6.7	13	0.42	0.59	106.2	99.30
1996 Aigio	OTE Building	6.2	20	0.50	0.54	0.43	0.48

The second configuration uses DCSS bearings with R_1-h_1=*1.7m,* μ_1=*0.04056 and* R_2-h_2=*0.5m* μ_2=*0.06*. For all three configurations, Makris and Vassiliou have shown that the computed eigenperiods are identical.

Our study proceeds with a three dimensional nonlinear time history analysis of the bridge shown in Figure 9 when subjected to the seven (7) ground motions (two dimensional excitation) listed in Table 1. Note that two of the seven earthquakes used (1986 Kalamata and 1996 Aigion) are moderately strong earthquakes with moderate displacement demands (u_{max}<0.1m).

The computed response is summarized in Figure 10 which plots maximum longitudinal deck displacement (top) and residual longitudinal displacement (bottom). Figure 10 shows that for the three configurations under investigation the maximum longitudinal displacement for each ground motion are practically the same without exhibiting any trend. Accordingly the design engineers can use with confidence the equivalent SCSS bearing for any analysis relevant to design needs. Equal interesting are the results on the permanent displacements of the bearings where the results are mixed without exhibiting any particular trend.

8. CONCLUSIONS

In this paper the seismic response of isolated structures supported on bearings with bilinear and trilinear behavior is revisited with dimensional analysis in an effort to

better understand the relative significance of the various parameters that control the mechanical behavior of isolated systems.

The paper introduces the concept of complete similarity by showing the dimensionless maximum response of both bilinear and trilinear systems exhibit a complete similarity in the dimensionless yield displacement. Given that the double concave spherical sliding bearings may be viable alternatives due to instalation limitations, the paper proceeds with a wide parametric analysis on the response of decks isolated on double concave spherical sliding bearings and concludes that for values of the dimensionless strength

$\Pi_Q = \frac{Q_e \omega_p^2}{a_p} < 0.1$ and values of the dimensionless transition slope $\Pi_{tr} = \frac{\omega_{tr}}{\omega_p} < \sqrt{\Pi_\omega^2 + \frac{1}{2}\frac{\Pi_Q}{\Pi^*}}$ the response

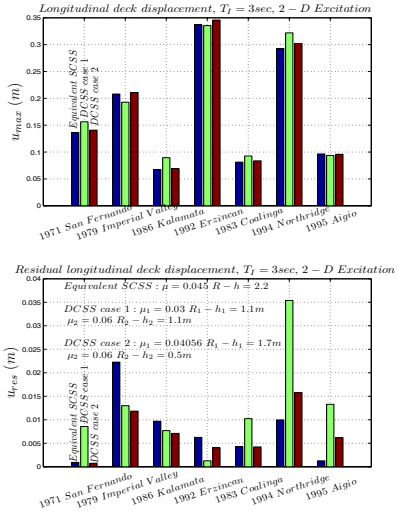

Fig.9 Comparison of peak inelastic deck displacements (top)and residual displacements (bottom) along the longitudinal direction when the bridge shown in Figure 9 is equipped with three different configurations of spherical bearings that offer the same equivalent friction and same isolation periods

of the trilinear system exhibits a complete similarity in the difference between the coefficients of friction along the sliding surface as well as in the ratio of the transition (intermediate) to the final slope.

The finding that for most practical configurations and design ground motions the response of the trilinear oscillator exhibits a complete similarity in (a) the normalized (transition) yield displacement, (b) the difference between the coefficient of friction and (c) the ratio of the intermediate to the final slope is of great interest to the design engineer since the response of a structure isolated with DCSS bearings can be computed with confidence by using the equivalent properties of the SCSS bearings.

Acknowledgements:

Partial financial support for this study has been provided to the second author by the Alexander S. Onassis Public Benefit Foundation.

References:

1.Skinner RI, Robinson WH, McVerry GH. An Introduction to Seismic Isolation. Wiley: Chichester, U.K., 1993.

2.Kelly JM. Earthquake Resistant Design with Rubber. Springer: London, 1997.

3.Federal Emergency Management Agency (FEMA). NEHRP guidelines for the seismic rehabilitation of buildings. Report No. FEMA-273 (Guidelines) and Report No. FEMA-274 (Commentary), Washington, DC, 1997.

4.Federal Emergency Management Agency (FEMA). Prestandard and commentary for the seismic rehabilitation of buildings. Report No. FEMA-356, Washington, DC, 2000.

5.AASHTO. Guide Speci:cations for Seismic Isolation Design. American Associate of State Highway and Transportation Officials, Washington, DC, 1999.

6.International Code Council (ICC), International Building Code 2000

7. Zayas VA, Low SS, Mahin SA. The FPS earthquake resisting system experimental report. EERC Technical Report, UBC/EERC-87/01, 1987.

8. Constantinou MC, Mokha AS, Reinhorn AM. Teflon bearing in base isolation. II: modeling. Journal of Structural Engineering (ASCE) 1990; 116:455–474.

9. Constantinou MC, Soong TT, Dargush GF (eds), Passive Energy Dissipation Systems for Structural Design and Retrofit, Monograph Series-1, Multidisciplinary Center for Earthquake Engineering Research, Buffalo, New York, 1998.

10. Mokha AS, Constantinou MC, Reinhorn AM. Teflon bearing in base isolation. I: testing. Journal of Structural Engineering (ASCE) 1990; 116:438–454.

11. Makris N, Chang S-P. Effect of viscous, viscoplastic and friction damping on the response of seismic isolated structures. Earthquake Engineering and Structural Dynamics 2000; 29(1):85–107.

12.Makris N, Black CJ. Dimensional analysis of bilinear oscillators under pulse-type excitations. Journal of Engineering Mechanics (ASCE) 2004; 130(9):1019 –1031.

13. Hyakuda T, Saito K, Tanaka N, Yoneki S, Miyazaki M, Sawada T. The structural design and earthquake observation of a seismic isolated building using friction pendulum system. 7th International Seminar on Seismic Isolation, Passive Energy Dissipation and Active Control of Vibrations of Structures, Assisi, Italy, 2–5 October, 2001.

14. Constantinou M. Friction Pendulum Double Concave Bearing, Technical Report, available at: http://nees.buffalo.edu/docs/dec304/FP-DC%20Report-DEMO.pdf, 2004.

15. Tsai CS, Chiang TC, Chen BJ. Experimental evaluation piecewise exact solution for predicting seismic responses of spherical sliding type isolated structures. Earthquake Engineering and Structural Dynamics 2005; 34(9): 1027–1046.

16. Fenz DM, Constantinou MC. Behavior of the double concave Friction Pendulum bearing. Earthquake Engineering and Structural Dynamics 2006; 35(11):1403–1424.

17. Tsai CS, Chen WS, Chiang TC, Chen BJ. Component and shaking table tests for full-scale multiple Friction Pendulum system. Earthquake Engineering and Structural Dynamics 2006; 35(11):1653–1675.

18. Chang, SP, Makris, N, Whittaker, AS, Thompson ACT. Experimental and analytical studies on the performance of hybrid isolation systems. Earthquake Engineering and Structural Dynamics 2002 31(2): 421–443.

19. Veletsos AS, Newmark NM, Chelepati CV. Deformation spectra for elastic and elastoplastic systems subjected to ground shock and earthquake motions. Proceedings of the 3rd World Conference on Earthquake Engineering, vol. II, Wellington, New Zealand, 1965; 663–682.

20. Hall JF, Heaton TH, Halling MW, Wald DJ. Near-source ground motion and its effects on flexible buildings. Earthquake Spectra 1995; 11(4):569 –605.

21. Heaton TH, Hall JF, Wald DJ, Halling MW. Response of high-rise and base-isolated buildings to a hypothetical Mw 7.0 blind thrust earthquake. Science 1995; 267:206–211.

22. Makris N. Rigidity–plasticity–viscosity: can electrorheological dampers protect base-isolated structures from near-source ground motions? Earthquake Engineering and Structural Dynamics 1997; 26:571–591.

23. Alavi B, Krawinkler H. Effects of near-source ground motions on frame-structures. Technical Report No. 138, The John A. Blume Earthquake Engineering Center, Stanford University, 2001.

24. Mavroeidis GP, Papageorgiou AS. A mathematical representation of near-fault ground motions. Bulletin of the Seismological Society of America 2003; 93(3):1099 –1131.

25. Makris N, Black CJ. Dimensional analysis of rigid-plastic and elastoplastic structures under pulse-type excitations. Journal of Engineering Mechanics (ASCE) 2004; 130(9):1006–1018.

26. Ricker N. Further developments in the wavelet theory of seismogram structure. Bulletin of the Seismological Society of America 1943; 33, 197-228.

27. Ricker N. Wavelet functions and their polynomials, Geophysics 1944 9, 314–323.

28. Addison P. The Illustrated Wavelet Transform Handbook: Introductory Theory and Applications in Science, Engineering, Medicine and Finance, Institute of Physics, London, UK, 2002.

29 .Vassiliou MF, Makris N, Estimating Time Scales and Length Scales in Earthquake Acceleration Records with Wavelet Analysis Bulletin of the Seismological Society of America (Submitted for Publication (2009)

30. Vassiliou MF, Makris N, Estimating time scales and length scales in earthquake acceleration records with the extended wavelet transform Report No. EEAM 2009-01, University of Patras, Greece, 2009.

31. Barenblatt GI. Scaling, Self-similarity, and Intermediate Asymptotics. Cambridge University Press: Cambridge, United Kingdom, 1996.

32. Fenz DM, Constantinou MC. Behaviour of the double concave Friction Pendulum bearing. Earthquake Engineering and Structural Dynamics. 2006; 35:1403–1424

33. Fenz DM, Constantinou MC. Spherical sliding isolation bearings with adaptive behavior: theory. Earthquake Engineering and Structural Dynamics 2008; 37(2):163–183.

34. Zhang J, Makris N. Seismic response analysis of highway overcrossings including soil–structure interaction. Earthquake Engineering and Structural Dynamics 2002; 31:1967–1991.

JOINT CONFERENCE PROCEEDINGS
7th International Conference on Urban Earthquake Engineering (7CUEE) &
5th International Conference on Earthquake Engineering (5ICEE)
March 3-5, 2010, Tokyo Institute of Technology, Tokyo, Japan

SHAKE-TABLE TESTS AND NUMERICAL STUDY OF THE SEISMIC PERFORMANCE OF NON-DUCTILE RC FRAMES WITH MASONRY INFILL WALLS

P. Benson Shing[1], Ioannis Koutromanos[2], and Andreas Stavridis[3]

1) Professor, Department of Structural Engineering, University of California, San Diego, CA, USA
2) Graduate Student Researcher, Department of Structural Engineering, University of California, San Diego, CA, USA
3) Post-doctoral Researcher, Department of Structural Engineering, University of California, San Diego, CA, USA
pshing@ucsd.edu, ikoutrom@ucsd.edu, andreas@ucsd.edu

Abstract: This paper summarizes the results of large-scale shake-table tests and numerical simulations that were carried out to investigate the seismic performance of masonry-infilled, non-ductile, RC frames. Two 2/3-scale, three-story, two-bay, masonry-infilled, nonductile RC frames were tested on a shake table. The first test specimen had no retrofit measures, while the second was strengthened with engineered cementitious composite and fiber reinforced polymeric overlays in the infill walls of the first and second stories, respectively. The tests have shown that masonry infill walls can significantly enhance the seismic resistance of a non-ductile RC frame, and have demonstrated the effectiveness of the retrofit measures. The numerical simulations presented here used both smeared and discrete crack models to capture distributed as well as localized fracture. The models have been able to simulate the load-displacement response and failure mechanisms of infilled frames in an accurate manner.

1. INTRODUCTION

In many countries, such as China and places in the Mediterranean region, reinforced concrete (RC) structures are often infilled with unreinforced brick walls, which serve as interior and exterior partitions. Such construction can also be found in many older buildings in the western United States, including pre-1930's buildings in California, and in numerous newer buildings in the midwestern and eastern parts of the country. However, even though unreinforced masonry infill walls are usually treated as non-structural components, they will interact with the bounding frames when subjected to earthquake loads.

Many engineers have recognized the benefits of infill walls in protecting a structure against earthquake loads. Nevertheless, infill walls were sometimes associated with catastrophic failures and undesired soft-story mechanisms of RC structures in a number of severe earthquake events (e.g., see EERI 2000). These failures were mostly caused by the poor quality of the structural systems, inferior infill materials, and/or the absence of infill walls in some critical locations such as open first stories. The ability to assess the performance and safety of these structures is important for retrofit decisions. However, such analysis presents a major challenge. The interaction of an RC frame with masonry infill can result in a number of possible failure mechanisms including the cracking and crushing of the infill walls and the shear failure of the columns. The lateral load resistance of an infilled frame highly depends on the failure mechanism that develops. In the US, guidelines for the evaluation of infilled frames are provided in FEMA reports (FEMA 1998, 2000), *International Existing Building Codes* (ICBO 2001), and *ASCE/SEI 41: Seismic Rehabilitation of Existing Buildings* (ACSE/SEI 2007). Nevertheless, they are far from satisfactory in terms of completeness and reliability. *ASCE/SEI 41* allows the use of nonlinear finite element models, but it does not provide any guidelines for such analysis. In addition, there are few validated simple retrofit methods that can be used for these structures.

To address the aforementioned issues, a collaborative research project has been carried out by a team of researchers from the University of California at San Diego, Stanford University, and the University of Colorado at Boulder. The research objectives are two-fold. One is to develop rational and reliable analytical methods for assessing the seismic performance of masonry-infilled RC frames, and the other is to develop effective seismic retrofit techniques. The retrofit schemes and analytical tools were validated with quasi-static tests conducted on small and large-scale frame specimens representing 1920-era construction in California. Additionally, shake-table tests were conducted on two 2/3-scale, three-story, two-bay, infilled RC frames. One was tested without retrofit measures, and the other had infill walls strengthened with engineered cementitious composite (ECC) and glass fiber reinforced polymeric (GFRP) overlays in the first and second stories, respectively. This paper summarizes the large-scale shake-table tests conducted at the NEES (Network for

Earthquake Engineering Simulation) Site at the University of California at San Diego. Furthermore, the developed computational models are described, and numerical analysis results are compared to the experimental data. Major observations and conclusions are presented.

2. PROTOTYPE BUILDING

The focal point of the experimental study was a prototype building typical of 1920-era RC construction in California. The structure is a non-ductile RC frame with unreinforced masonry infill walls on the exterior. The plan view of the structure and the elevation view of an external infilled frame, which is considered in this study, are presented in Figure 1. Although the building represents older construction, it was designed using the properties of contemporary construction materials, which were employed in the experimental investigation. A working stress design approach was used with the allowable stresses calculated

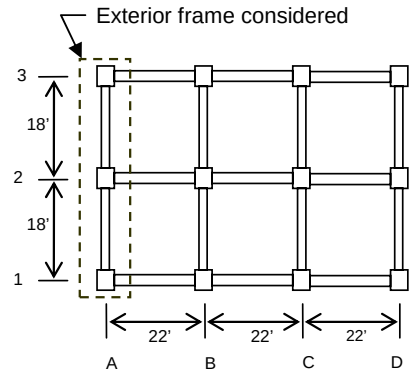

(a) Plan View

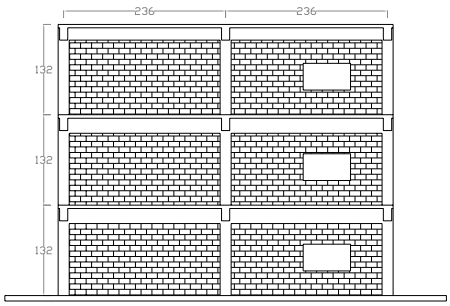

(b) Elevation View of Exterior Frame

Figure 1 Prototype Building

with the factors of safety that were used in the 1920's. In accordance with the engineering practice of that period, the RC members were designed only for gravity loads that included the self-weight, the weight of the slabs, toppings, ceilings, masonry walls, parapets, and the live load. The design live load was 75 psf for the 1st and 2nd stories, and 20 psf for the roof. The live load was reduced by 60% for the column design, and 20 and 40% for the design of the exterior and interior beams, respectively.

3. SHAKE-TABLE TESTS

Shake-table tests were conducted on two 2/3-scale models of the prototype frame shown in Figure 1b. The dimensions and reinforcement layout of the concrete frame specimens are shown in Figure 2, and the setup of the two tests is depicted in Figure 3. In the tests, the specimens were subjected to a sequence of ground motions which were scaled versions of the Gilroy record obtained in the 1989 Loma Prieta Earthquake and the NS component of the El Centro record obtained during the 1940 Imperial Valley Earthquake. The time scale of the records was compressed to satisfy the similitude requirements. The gravity load was closely simulated with added mass attached the frames at each level, but the seismic mass was smaller than the actual. This was compensated for by scaling up the acceleration and compressing the ground motion time.

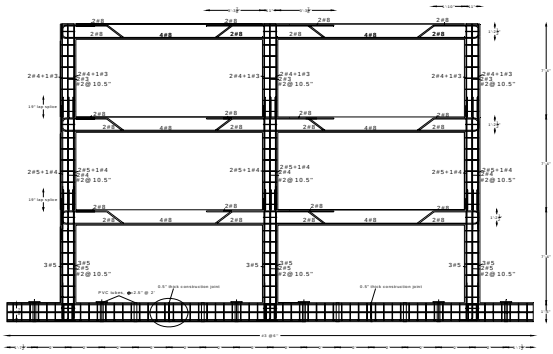

Figure 2 Design of Test Frame

To assure that the RC columns had sufficient capacity to resist the overturning moment in the second specimen, where some of the infill walls were strengthened, the columns in the two specimens had a higher quantity of flexural reinforcement than the original design. Moreover, lap splices were eliminated at the base of the bottom-story columns. All the infill walls had two wythes of brick units. The first specimen (Figure 3a) had solid infill walls in one bay and infill walls with window openings in the other. Similar to the first, the second specimen (Figure 3b) had solid infill walls in one bay and window openings in the second and third stories in the other bay. However, the solid infill in the bottom story was strengthened with an overlay of ECC, attached on each side of the wall with stitch dowels spaced at 12-in in each direction. This retrofit technique is described in Billington et al. (2009). The ECC was sprayed on the wall and had wire-mesh reinforcement and shear dowels to connect to the beam and base slab. Each overlay was about 1-in. thick near the mid-height of the wall and 2-in. thick near the top and bottom to provide appropriate cover for the shear dowels. Specimen 2 was tested under

several scenarios. At the beginning, the bottom story had an unretrofitted infill wall with a door opening in one bay. Upon the development of mild damage in the second-story infill walls, the bottom-story wall with the door opening was removed (as shown in Figure 3b), and the specimen was tested again. After the second-story walls had incurred moderate damage, they were repaired with epoxy injection and strengthened with a thin glass fiber reinforced polymeric (GFRP) overlay on one side. The GFRP overlay consisted of epoxy and one layer of bi-directional glass fabric with fibers oriented at 45° with respect to the bed joints of masonry. In addition, the masonry around the window opening was reinforced with one-foot-wide straps of uni-directional glass fabric.



(a) Specimen 1



(b) Specimen 2

Figure 3 Shake-Table Tests

In general, Specimen 1 performed well with only minor cracks after the 67% Gilroy motion. After the 100% Gilroy, the specimen had severe cracks in the bottom-story infill walls, but remained structurally stable. Shear failure developed in the middle column during the 120% Gilroy. It should be mentioned that for the original Gilroy record, the spectral intensity of the 120% motion corresponds to a representative Maximum Considered Earthquake (MCE) for Seismic Design Category D (ASCE/SEI 2005) based on the initially estimated structural period of 0.1 sec. However, the actual table motion has a spectral intensity about 50% higher,



(a) After 120% Gilroy



(b) After 120% Gilroy



(c) After 250% El Centro



(d) After 250% El Centro

Figure 4 Damage in Bottom Story of Specimen 1

while its PGA is 40% higher than the MCE. The identified fundamental period of the structure based on white-noise input varies from about 0.06 sec. initially to 0.19 sec. after the 120% Gilroy (Stavridis 2009). Damage was localized in the bottom story as shown in Figures 4a and 4b. Severe damage with shear failures in the exterior columns occurred when the specimen was subjected to the 250% El Centro as shown in Figures 4c and 4d. The wall with a window opening almost completely collapsed because of the lack of an arching mechanism to restrain the out-of-plane motion of the brick units above the opening.

Before the second-story walls in Specimen 2 were retrofitted with GFRP, they had severe cracks after the 100% Gilroy, as shown in Figures 5a and 5b, while the first story remained intact even without infill in one bay. After the repair and retrofit of the second-story walls, no further damage was observed after subsequent ground motions. However, the infill walls in the third story eventually developed cracks. No cracks were observed in the ECC, but the shear dowels connecting the ECC to the beam were damaged as evidenced by mild concrete cracking and spalling near the dowel locations as shown in Figure 5c. Noticeable sliding occurred between the ECC and the beam. While all three bottom-story columns in Specimen 1 had shear failures, Specimen 2 had only one severe shear crack developed in the beam-to-column joint right above the exterior column adjacent to the infill in the first story after the 190% El Centro, as shown in Figure 5c. The crack first developed during the 150% Gilroy.



(a) Second Story before Retrofit

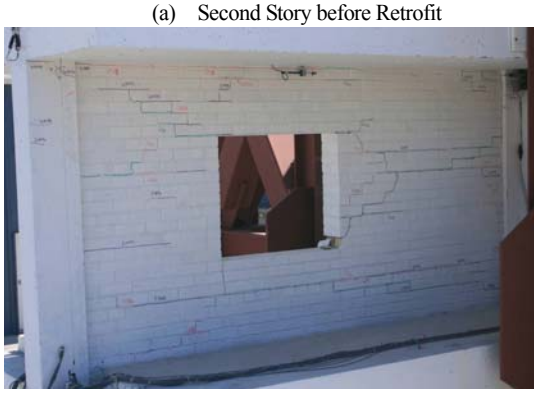

(b) Second Story before Retrofit



(c) Shear Crack at Top of First-story Column

Figure 5 Damage in Specimen 2

The bottom-story shear-vs.-story drift hysteresis curves for the two specimens are compared in Figure 6. It can be observed that even though Specimen 2 had one infill wall in the bottom story removed, the strength and stiffness of Specimen 2 were significantly higher than those of Specimen 1 due to the ECC overlays. Furthermore, the unretrofitted infill walls in Specimen 2 were found to be significantly weaker than those in Specimen 1 due to weaker mortar. This can be observed by comparing the hysteresis curves in Figures 6a and 7a. This difference is partly due to the fact that the second story gravity load was only about

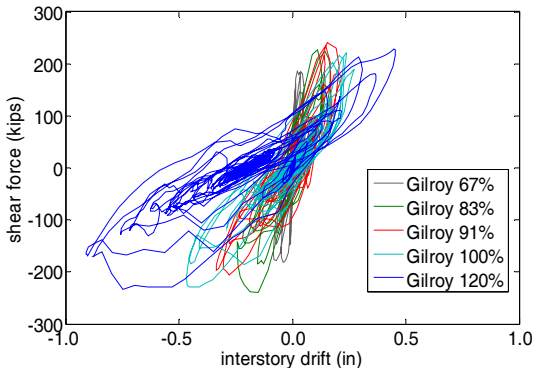

(a) Specimen 1 with No Retrofit

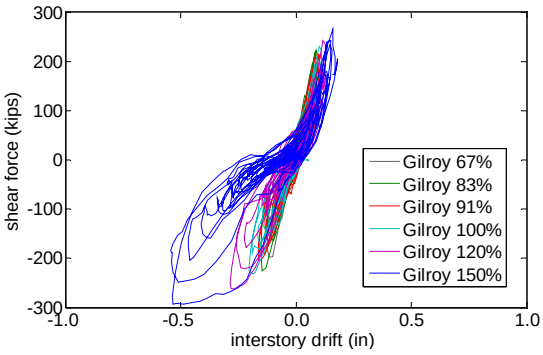

(b) Specimen 2 with ECC Retrofit and One Bttom-story Infill Removed

Figure 6 Comparison of Shear Force-vs.-Story Drift Hysteresis Curves for the Bottom Stories of the Two Shake-Table Specimens

60% of that of the bottom story. Nevertheless, a numerical study by Stavridis (2009) has shown that this difference in vertical load could not have caused such a large difference in

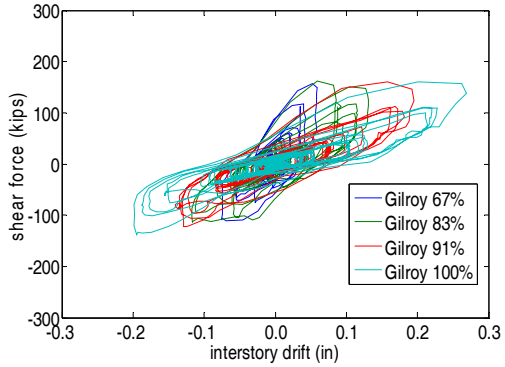

(a) Before retrofit with GFRP

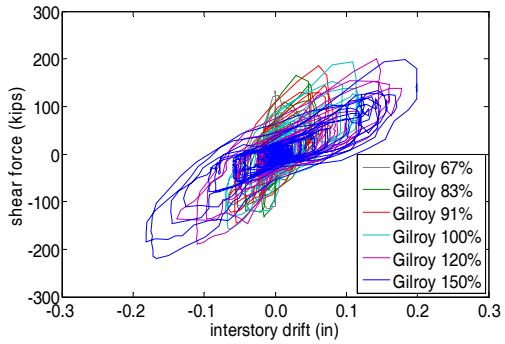

(b) After retrofit with GFRP

Figure 7 Comparison of 2nd Story Shear Force-vs.-Story Drift Hysteresis Curves Before and After Retrofit of Specimen 2

the lateral resistance. Damage developed in the second-story walls of Specimen 2 at a story shear much lower than expected. The effect of the epoxy injection and GFRP strengthening in the second story of Specimen 2 is shown in Figure 7. The repair and retrofit enhanced both the strength and stiffness. No additional damage was observed in the infill walls in the second story after the retrofit.

The drift time histories for the first two stories of the specimens under the Gilroy motion scaled to a level that is 40% higher than the Maximum Considered Earthquake (MCE) are shown in Figure 8. Specimen 2 in that test had one infill wall in the bottom story already removed. Figure 8 shows that Specimen 2 had a smaller drift in the bottom story but a much larger drift in the second story than Specimen 1. Specimen 1 exhibited a distinct weak first story which isolated the second story from any severe seismic force. As a result, no major cracks were developed in the second and third stories of the specimen.

4. FINITE ELEMENT MODELING

A finite element modeling approach has been developed to capture different possible failure mechanisms of an infilled frame under in-plane lateral loads (Stavridis and Shing 2010). It combines smeared and discrete crack models. The smeared crack approach has been commonly used to model diffused cracks in reinforced concrete structures. However, this approach suffers from some inherent limitations including the inability to capture the brittle behavior of an RC member caused by diagonal shear cracks. To overcome this deficiency, the proposed model incorporates zero-thickness interface elements to represent cracks in RC columns in a discrete fashion and to capture the fracture behavior of mortar joints in infill walls, while smeared crack elements are used to model the compressive failure in the concrete members and brick units. The reinforcing bars are modeled with elastic-plastic truss elements.

4.1 Discretization Scheme

Concrete columns, which may develop shear cracks, are modeled with the discretization scheme presented in Figure 9. The proposed scheme combines smeared crack triangular elements with line interface elements. Thus, it allows for the development of diffused cracks as well as discrete shear cracks that may dominate the behavior of a concrete member. According to the mesh geometry adopted, discrete cracks can develop at angles of 0°, 90°, and $\pm\theta$, while θ is normally close to 45° to represent shear cracks.

Reinforcing steel is modeled with truss elements, and

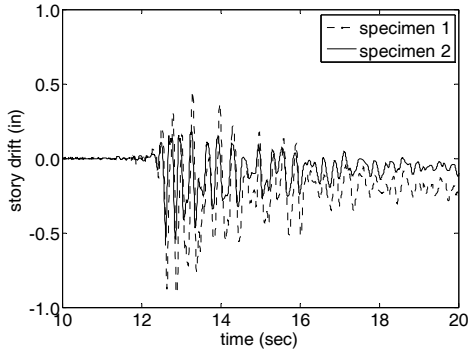

(a) 1st Story

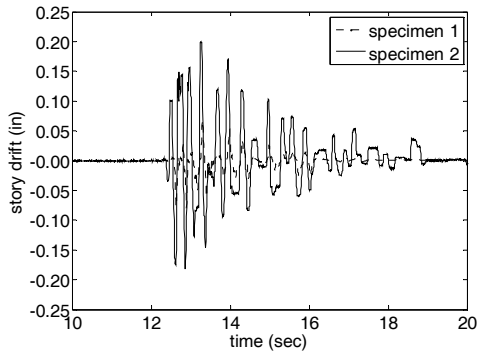

(b) 2nd Story

Figure 8 Story Drift Time Histories with Gilroy Record Scaled to 40% Higher than MCE

strategies for connecting truss elements to triangular smeared crack elements are shown in Figure 9. The area of each longitudinal bar is divided into multiple bars so that every triangular element is attached to bars at two of its nodes. For the shear reinforcement, the total steel area at each location is distributed over two bars, which are placed in a zigzag pattern. This scheme allows a crack to cross the same quantity of reinforcement as in an actual RC column.

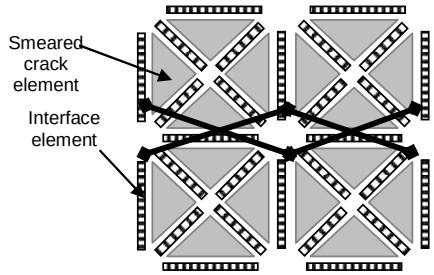

(a) With Shear Reinforcement

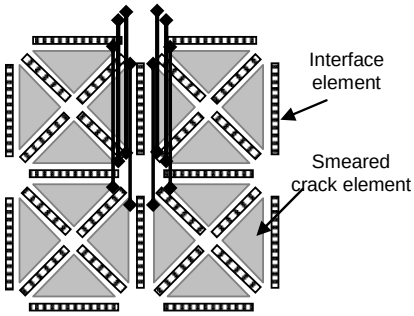

(b) With Flexural Reinforcement

Figure 9 Discretization Scheme for Reinforced Concrete Columns

Masonry walls are modeled with the scheme shown in Figure 10. Each masonry unit is modeled with two rectangular smeared crack elements that are connected with a vertical, zero-thickness interface element. The interface element is employed to model tensile splitting of a brick unit,

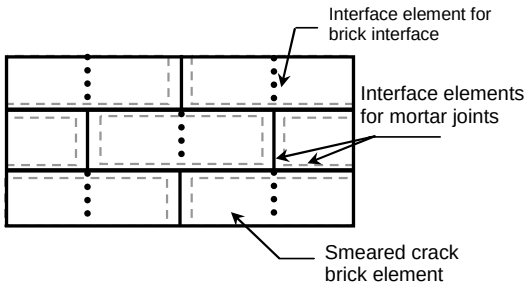

Figure 10 Discretization Scheme for Masonry Infill

and subsequent rotation and shearing of the fractured brick. Bed and head joints are modeled with interface elements that can simulate the shear sliding and opening of the joints. With this simplified approach, the failure of a brick-mortar interface is not distinguished from that of the mortar layer itself and the brick-mortar interaction is not directly accounted for as the Poisson effect of the mortar is not considered. However, the influence of the brick-mortar interaction is indirectly accounted for by having the compressive strength of the brick units to be the same as the compressive strength of masonry prisms. The stiffness of the interface elements representing mortar joints is determined so that the stiffness of the masonry assembly is properly modeled.

4.2 Constitutive Models

The smeared crack model used in this study was developed by Lotfi and Shing (1991). The uncracked material is modeled with J_2-plasticity combined with a tension cut-off surface. When the maximum principal stress reaches the tensile strength f_t' of the material, cracks initiate in a direction normal to the direction of the maximum principal stress. The cracked material is considered orthotropic with the axes of orthotropy normal and parallel to the direction of the crack. In this study, crack orientation is assumed fixed and, therefore, the axes of orthotropy remain constant. After cracking, the tensile stress is an exponentially decaying function of the strain. The compressive stress-strain relation in the orthogonal direction is modeled and calibrated in such a way that it closely matches the compressive behavior exhibited by the plasticity model to allow a smooth transition from one state to the other. Under cyclic loading, a second crack is allowed to occur at a Gauss point at 90 degrees with respect to the first when the tensile stress in the orthogonal direction exceeds the tensile strength.

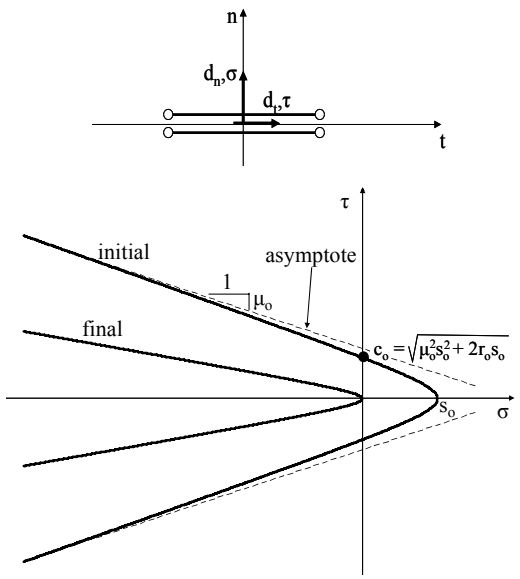

Figure 11 Failure Surface of Cohesive Interface Model

A cyclic cohesive interface model has been developed to model critical cracks in a discrete fashion (Koutromanos

et al. 2010). The yield surface is hyperbolic, as shown in Figure 11, and it evolves according to softening rules that account for the mode-I and mode-II fracture energies as well as frictional work. The interface formulation is a modified version of the model proposed by Lotfi and Shing (1994), with improvements aiming to reproduce various aspects of the cyclic behavior of a cracked interface. It is implemented as a 4-node, zero-thickness, isopararametric, line element. The model can simulate the initiation and propagation of cracks under combined normal and shear stresses. The ability of the model to capture the shear behaviour of a mortar joint is shown in Figure 12. As shown by the lower plot in the figure, the model also accounts for normal plastic compaction and dilatation under shear reversals, which can have a significant effect on the response of a confined crack. The behavior of the interface model under tensile loading, unloading, and reloading is presented in Figure 13.

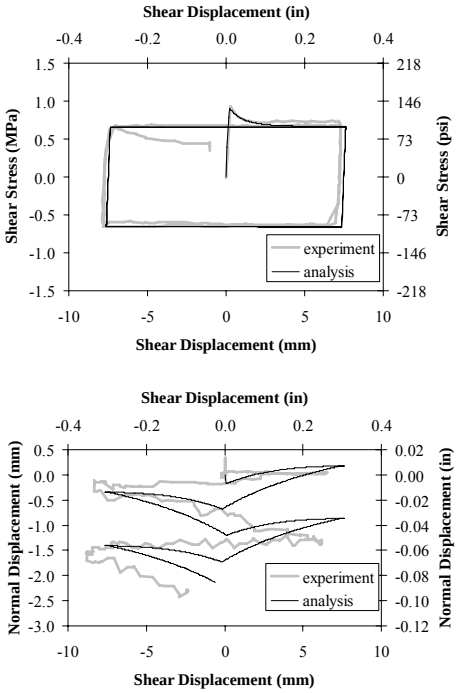

Figure 12 Shear Behavior of Mortar Joint under Constant Normal Stress

5. NUMERICAL SIMULATIONS

A quasi-static test conducted on an infilled frame at the University of Colorado at Boulder (Willam et al. 2008) was considered for the validation of the proposed finite element models. The test specimen is presented in Figure 14a. The force-displacement curves obtained in the test and analysis are compared in Figure 14b. The peak lateral load obtained in the test was 153 kips, which occurred at a drift ratio of 0.25%. A significant load drop occurred at a drift ratio of about 0.4% due to the formation of diagonal shear cracks in the concrete columns. The specimen retained a residual strength of 80 kips in the positive direction and 75 kips in the negative direction after the peak. As shown in Figure 14b, the analysis reproduced the hysteretic response, including the strength and stiffness degradation, reasonably well, but it underestimated the peak load by 15%. Figure 14c shows the crack pattern obtained in the analysis, which resembles the experimentally observed failure mechanism with the formation of diagonal and horizontal sliding shear cracks in the infill panel and shear cracks in the concrete columns.

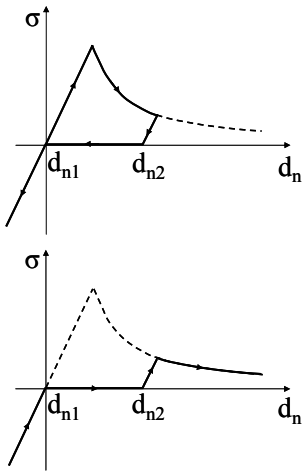

Figure 13 Tensile Behavior of Cohesive Interface

Furthermore, a pre-test nonlinear static analysis was conducted to obtain the failure mechanism and base shear-vs.-first story drift relation for the second shake-table test specimen. The ECC overlays on the first-story infill wall were modeled using the smeared-crack model with an appropriate tensile stress-strain law to simulate the ductile tensile behavior of the ECC. The second and third stories were assumed to remain linearly elastic, which is deemed acceptable since the second-story infill walls did not suffer obvious damage after they had been strengthened by the FRP overlay. The shear dowels connecting the EEC to the concrete beam and slab were simulated by elastic-perfectly plastic springs. A uniform lateral load distribution was assumed for the analysis, which was reasonable considering that the structure eventually developed a soft-story mechanism. Figure 15a shows that the non-linear base shear-vs.-drift envelope from the test results was well captured. As the deformed mesh in Figure 15b shows, a diagonal crack developed in the bottom-story masonry wall with cracks also occurring in the ECC overlay. This, however, was not observed in the test probably due to the fact that the tensile strength of the ECC assumed in the analysis was about 60% of the tensile strength subsequently obtained from material tests. These cracks, however, did not affect the resistance as the final failure mode in the analysis was governed by the yielding of the shear dowels and the

sliding between the infill and the RC beam, and the eventual shearing of the left exterior column due to the formation of a diagonal strut mechanism.

6. CONCLUSIONS

The research presented herein was part of a larger project aiming to the development of reliable analytical models and effective retrofit techniques for masonry-infilled,

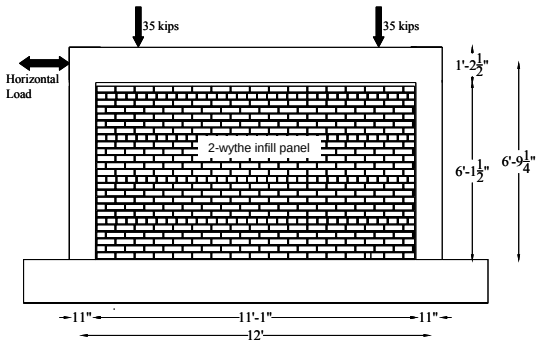

(a) Test Specimen

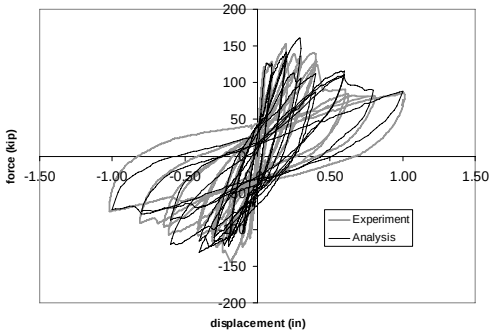

(b) Load-Displacement Response

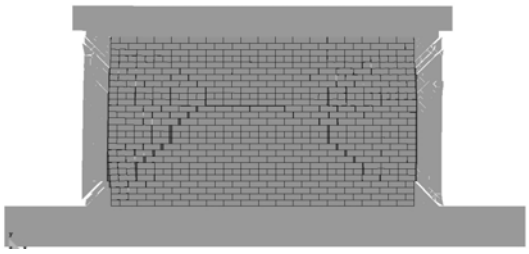

(c) Crack Pattern from Analysis

Figure 14 Comparison of Experimental and Numerical Results for a Single-Story frame

non-ductile, RC frames. Subassemblages of a prototype structure were tested to validate the proposed analytical tools and retrofit methods. These included two 2/3-scale, three-story, two-bay, infilled frame specimens, which were tested on a shake table. The experimental results have shown that unreinforced masonry infill walls can contribute significantly to the seismic resistance of a concrete frame. However, the failure behavior of such structures could be

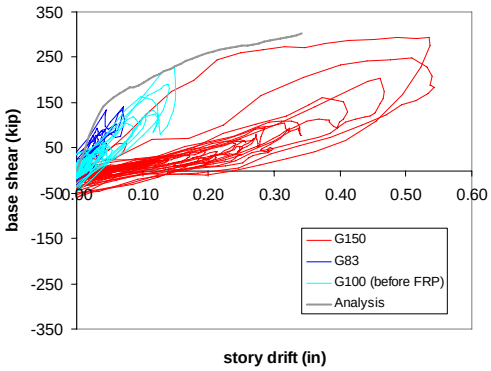

(a) Load vs. First Story Drift

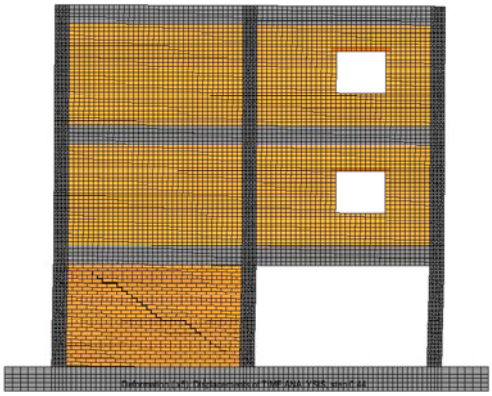

(b) Deformed Mesh

Figure 15 Analysis of Shake-Table Specimen 2

brittle, leading to a sudden collapse associated with the development of a weak-story mechanism. It has also been concluded that an infill wall with an opening could be more vulnerable to collapse because of the lack of an arching action. The effectiveness of the retrofit measures using the ECC and GFRP overlays, which can increase both the stiffness and strength of an infilled frame, has been experimentally verified. A finite element modeling strategy combining the discrete and smeared crack approaches and a cyclic cohesive interface model have been successfully developed to capture the nonlinear load-displacement response and the complicated failure mechanisms of infilled frames characterized by the shear failure of the columns and the fracture of the masonry infill.

Acknowledgments:

The study presented in this paper was supported by the US National Science Foundation Grant No. 0530709 awarded under the George E. Brown, Jr. Network for Earthquake Engineering Simulation (NEES) program. The authors would like to thank Prof.

Kaspar Willam and graduate student Ben Blackard at the University of Colorado, Boulder, and Prof. Sarah Billington and graduate student Marios Kyriakides for their contributions in this project. Input of the Professional Advisory Panel (PAP) is also gratefully acknowledged. The panel members are David Breiholz, John Kariotis, Gregory Kingsley, Joe Maffei, Ron Mayes, Paul Murray, and Michael Valley. The FRP retrofit of the masonry walls was performed by Fyfe Co. The authors are also grateful to the dedicated laboratory staff at UCSD's Englekirk Center for setting up and conducting the shake-table tests. However, the opinions expressed in this paper are those of the authors and do not necessarily represent those of the NSF, PAP, or other collaborators.

References:

ASCE/SEI (2005), "Minimum Design Loads for Buildings and Other Structures (ASCE/SEI 7-05)," ASCE/SEI, Reston, VA.

ASCE/SEI (2007), "Seismic Rehabilitation of Existing Buildings, ASCE/SEI Standard 41-06," ASCE/SEI, Reston, VA.

Billington, S.L., Kyriakides, M.A., Blackard, B., Willam, K., Stavridis, A. and Shing, P.B. (2009), "Evaluation of a Sprayable, Ductile Cement-Based Composite for the Seismic Retrofit of Unreinforced Masonry Infills," *Proceedings*, ATC & SEI Conference on Improving the Seismic Performance of Existing Buildings and Other Structures, Applied Technology Council and Structural Engineering Institute, San Francisco, CA.

Blackard, B., Willam, K., and Mettupulayam, S. (2009), "Experimental Observations of Masonry Infilled RC Frames with Openings," *ACI Special Publication SP-265*, American Concrete Institute, Farmington Hills, MI.

EERI (2000), "1999 Kocaeli, Turkey Earthquake Reconnaissance Report," *Earthquake Spectra*, Vol. 16, Issue S1.

FEMA (1998), "Evaluation of Earthquake Damaged Concrete and Masonry Wall Buildings: Basic Procedures Manual," *FEMA 306*, Federal Emergency Management Agency, Washington, D.C.

FEMA (2000), "Prestandard and Commentary for the Seismic Rehabilitation of Buildings." *FEMA 356,* Federal Emergency Management Agency, Washington, D.C.

ICBO (2001), "Guidelines for Seismic Retrofit of Existing Buildings," International Conference of Building Officials, Whittier, CA.

Lotfi, H. R. and Shing, P.B. (1994), "An Interface Model Applied to Fracture of Masonry Structures," *Journal of Structural Engineering*, ASCE, 120(1): 63-80.

Lotfi, H. R. and Shing, P. B. (1991), "An Appraisal of Smeared Crack Models for Masonry Shear Wall Analysis," *Journal of Computers and Structures*, ASCE, Vol. 120(1): 63-80.

Stavridis, A. and Shing, P.B. (2010), "Finite Element Modeling of Nonlinear Behavior of Masonry-Infilled RC Frames," *Journal of Structural Engineering* (in press).

Stavridis, A. (2009). "Analytical and Experimental Study of Seismic Performance of Reinforced Concrete Frames Infilled with Masonry Walls," Doctoral Dissertation, Department of Structural Engineering, University of California, San Diego, La Jolla, California, USA.

Willam, K., Blackard, B. and C. Citto, 2008, "Performance Evaluation of Masonry Infills subjected to Axial and In-plane Shear: Meso- and Macro Experiments and Simulations," *Proceedings*, 5th European Congress on Computational Methods in Applied Sciences and Engineering, Venice, Italy.

JOINT CONFERENCE PROCEEDINGS
7th International Conference on Urban Earthquake Engineering (7CUEE) &
5th International Conference on Earthquake Engineering (5ICEE)
March 3-5, 2010, Tokyo Institute of Technology, Tokyo, Japan

SHAKE TABLE EXPERIMENT ON REINFORCED CONCRETE BRIDGE COLUMNS USING E-DEFENSE

Kazuhiko Kawashima[1], Tomohiro Sasaki[2] and Koichi Kajiwara[3]

1) Professor, Dept. Civil Engineering, Tokyo Institute of Technology, Japan
2) Graduate student, Dept. Civil Engineering, Tokyo Institute of Technology, Japan
3) Senior researcher, Hyogo Earthquake Engineering Center,
National Research Institute for Earth Science and Disaster Prevention, Japan
kawashima.k.ae@m.titech.ac.jp, sasaki.t.aa@m.titech.ac.jp and kaji@bosai.go.jp

Abstract: This paper presents preliminary results of a large scale shake table experiment for studying the failure mechanism of three reinforced concrete bridge columns; a typical flexural dominant column in the 1970s (C1-1), a typical shear failure dominant column in the 1970s (C1-2) and a typical column designed in accordance with the current design code (C1-5). They were 7.5 m tall 1.8-2.0m diameter circular reinforced concrete columns. They were subjected to a near-filed grounds motion recorded during the 1995 Kobe, Japan earthquake. Preliminary results on the experiment and analytical correlation are presented.

Keywords: Seismic response, Bridge, RC column, Seismic design, Shake Table experiment, E-Defense

1. INTRODUCTION

Bridges are a vital component of transportation facilities; however it is known that bridges are vulnerable to the seismic effect. Bridges suffered extensive damage in past earthquakes such as 1989 Loma Prieta earthquake, 1994 Northridge earthquake, 1995 Kobe earthquake, 1999 Chi Chi earthquake, 1999 Bolu earthquake and 2008 Wenchuan earthquake. A large scale bridge experimental program was initiated in 2005 in the National Research Institute for Earth Science and Disaster Prevention (NIED), Japan as one of the three US-Japan cooperative research programs based on NEES and E-Defense collaboration. In the bridge program, it was originally proposed to conduct experiments on two model types; 1) component models and 2) system models. They are called hereinafter as C1 experiment and C2 experiment, respectively (Nakashima et al 2008).

The objective of the C1 experiment is to clarify the failure mechanism of reinforced concrete columns using models with as large section as possible. On the other hand, C2 experiment was proposed to clarify the system failure mechanism of a bridge consisting of decks, columns, abutments, bearings, expansion joints and unseating prevention devices.

C1 experiment was conducted for two typical reinforced concrete columns which failed during the 1995 Kobe earthquake (C1-1 and C1-2 experiments) and a typical reinforced concrete column designed in accordance with the current design requirements (C1-5 experiment). This paper shows preliminary results of the experiment and analysis on three C1 columns.

2. COLUMN MODELS

Photo 1 shows the experimental setup of three columns using E-Defense (Kawashima et al 2009). Two simply supported decks were set on the column and on the two steel end supports. A catch frame was set under the lateral beam of the column to prevent collapse of the column when it was excessively damaged. Tributary mass to the column by two decks including four weights was 307 t and 215 t in the longitudinal and transverse directions, respectively. The tributary mass was increased by 21 % from 307 t to 372 t in a part of C1-5 excitation.

Three full-size reinforced concrete columns as shown in Fig. 1 were constructed for the experiment. Columns used for C1-1, C1-2 and C1-5 experiments, which are called



Photo 1 C1 on E-Defense

hereinafter as C1-1, C1-2 and C1-5, respectively, are 7.5 m tall reinforced concrete columns with a diameter of 1.8 m in C1-1 and C1-2 and 2 m in C1-5. C1-1 and C1-2 are typical columns which were built in the 1970s based on a combination of the static lateral force method and the working stress design in accordance with the 1964 Design Specifications of Steel Road Bridges, Japan Road Association. Since it was a common practice prior to 1980 to terminate longitudinal bars at mid-heights, the inner and center longitudinal bars were cut off at 1.86 m and 3.86 m from the column base, respectively. The cut-off heights were determined by extending a length equivalent to a lap splicing length l_{ls} (about 30 times bar diameter) from the height where longitudinal bars became unnecessary based on the moment distribution. On the other hand, longitudinal bars were not cut-off in C1-1. C1-1 and C1-2 had the same shape, heights, bar arrangement and properties except the cut-off. As a consequence, C1-1 failed in flexure while C1-2 failed in shear, as will be described later. The shear failure due to cut-off was one of the major sources of the extensive damage of bridges in the 1995 Kobe earthquake (Kawashima and Unjoh 1997). Combination of the lateral seismic coefficient of 0.23 and the vertical seismic coefficient of +/-0.11 (upward and downward seismic force) was assumed in the design of C1-1 and C1-2.

Deformed 13 mm diameter circular ties were provided at 300 mm interval, except the outer ties at the top 1.15m zone and the base 0.95 m zone where they were provided at 150mm interval in C1-1. Ties were only lap spliced with 30 times the bar diameter. Lap splice was a common practice by the mid 1980s. The longitudinal and tie bars had a nominal strength of 345 MPa (SD345), and the design concrete strength was 27 MPa. The longitudinal reinforcement ratio P_l was 2.02 % and the volumetric tie reinforcement ratio ρ_s was 0.32 % except the top 1.15 m and base 0.95m zones where ρ_s was 0.42% in C1-1. P_l and ρ_s varied depending on the zones in C1-2; 2.02 % and 0.42 % at the base 0.95 m zone, 2.02 % and 0.32 % between 0.95 m and 1.86 m, 1.62 % and 0.21 % between 1.86 m and 3.86 m, 0.81 % and 0.11 % between 3.86 m and 4.85 m, and 0.81 % and 0.21 % at the top 1.15 m zone, respectively.

On the other hand C1-5 was designed in accordance with the 2002 JRA Design Specifications of Highway Bridges (JRA 2002). Sixty four deformed 35mm diameter longitudinal bars were provided in two layers. Deformed 22 mm diameter circular ties were set at 150 mm and 300 mm interval in the outer and inner longitudinal bars, respectively. The ties were developed in the core concrete using 135 degree bent hooks after lap spliced with 40 times the bar diameter. The nominal strength of longitudinal and tie bars and the design concrete strength were the same with those in C1-1 and C1-2 columns. The longitudinal reinforcement ratio P_l was 2.02 % and the volumetric tie reinforcement ratio ρ_s was 0.92 %

Evaluation of the seismic performance of C1-1 and C1-5 in the longitudinal direction based on the 2002 JRA code is as follows: Because the design response acceleration S_A is

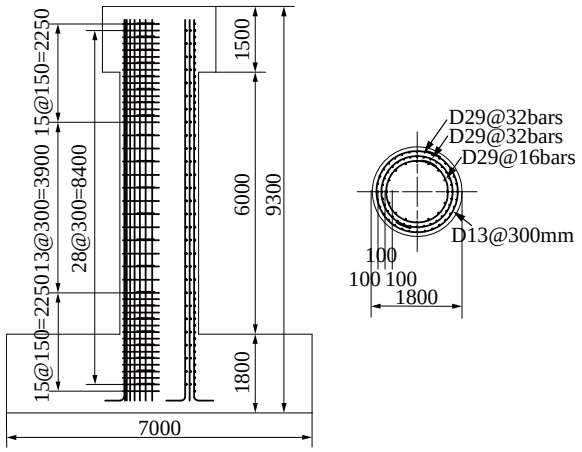

(a) C1-1

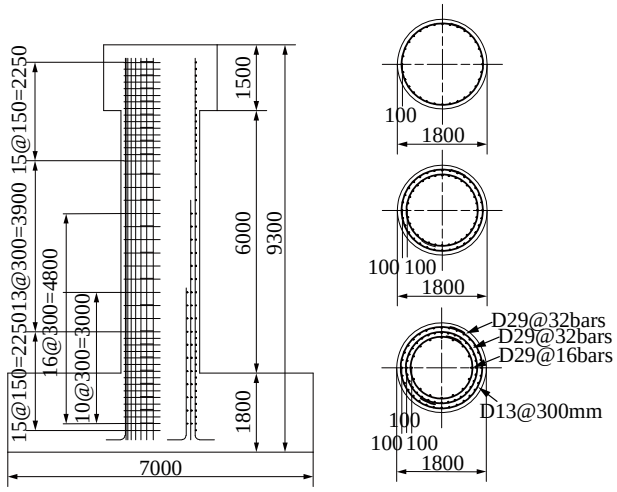

(b) C1-2

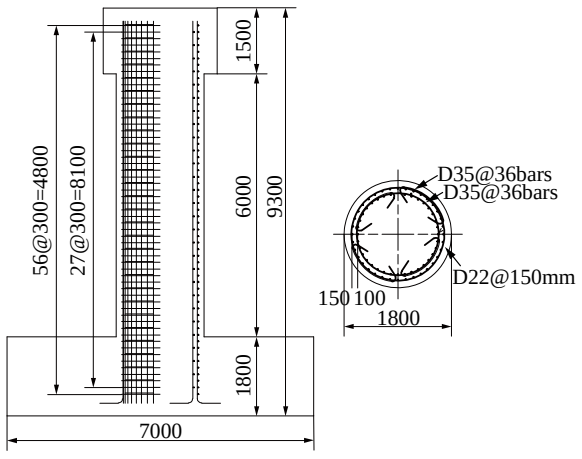

(c) C1-5

Fig. 1 C1 column models

17.15 m/s^2 for both C1-1 and C1-5, the yield displacement u_y and ultimate displacement u_u are 0.046 m and 0.099 m in C1-1 and 0.045 m and 0.231 m in C1-5. The design displacement u_d is evaluated from u_y and u_u as

$$u_d = u_y + \frac{u_u - u_y}{\alpha} \quad (1)$$

in which α depends on the type of ground motion (near-field or middle field ground motion) and the importance of the bridge. Assuming α is 1.5 for a combination of the near-field ground motion category and the important bridges category, the design displacement u_d is 0.081 m in C1-1 and 0.169 m in C1-5.

On the other hand, the displacement demand u is 0.328 m in C1-1 and 0.168 m in C1-5 because the force reduction factor is 1.58 and 2.56 respectively. Consequently, C1-1 and C1-5 were evaluated to be unsafe and safe, respectively based on the current design code.

Three columns were excited using a near-field ground motion as shown in Fig. 2 which was recorded at the JR Takatori Station during the 1995 Kobe earthquake. It was one of the most influential ground motions to structures. However duration was short. Taking account of the soil structure interaction, a ground motion with 80% the original intensity of JR Takatori record was imposed as a command to the table in the experiment. This ground motion is called hereinafter as the 100 % E-Takatori ground motion. Excitation was repeated to clarify the seismic performance of the columns when they were subjected to near-field ground motions with longer duration and/or stronger intensity. Only C1-5 was excited using 125 % E-Takatori ground motion with 21 % increased deck mass to study the seismic performance under a stronger ground motion than the JR-Takatori Station ground motion.

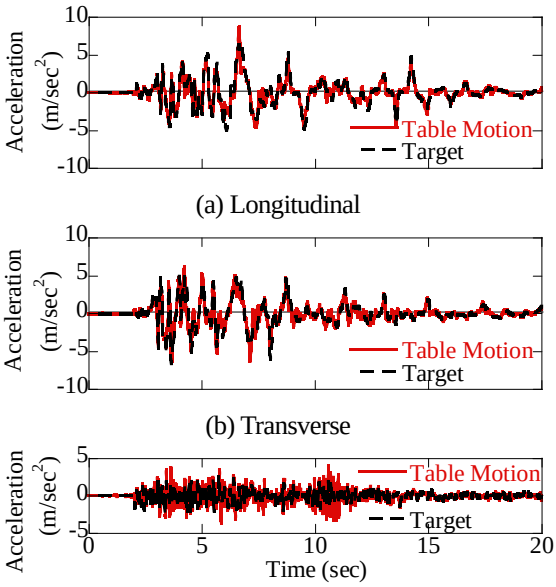

(a) Longitudinal

(b) Transverse

(c) Vertical

Fig. 2 100% E-Takatori ground motion (C1-5(1)-1 excitation)



(a) C1-1-1 excitation (8.35s)



(b) C1-1-2 excitation (7.71s)

Photo 2 Progress of damage of C1-1

3. SEISMIC PERFORMANCE OF C1-1 AND C1-5

3.1 Progress of Failure

C1-1 was subjected to the 100 % E-Takatori ground motion twice. Photo 2 shows the progress of failure at the plastic hinge on the SW surface where damage was most extensive. NS and EW direction correspond to the transverse and longitudinal directions, respectively, of the model. During the first excitation (C1-1-1 excitation), at least two outer longitudinal bars from S to W locally buckled between the ties at 200 mm and 500 mm from the base. During the second excitation (C1-1-2 excitation), both the covering and core concrete suffered extensive damage between the base and 0.7 m from the base on the SW surface. Three ties from the base completely separated at the lap splices. Eleven outer and three center longitudinal bars locally buckled between ties at 50 mm and 500 mm from the base.

On the other hand, C1-5 was subjected to the 100% E-Takatori ground motion twice (C1-5(1)-1 and C1-5(1)-2 excitations). After the mass was increased by 21 % from 307 t to 372 t, C1-5 was subjected to the 100% E-Takatori ground motion once (C1-5(2) excitation). Then C1-5 was subjected to the 125% E-Takatori ground motion twice (C1-5(3)-1 and C1-5(3)-2 excitations).

Photo 3 shows the progress of failure of C1-5 at the plastic hinge during C1-5(1)-1, C1-5(2) and C1-5(3)-2 excitations. During C1-5(1)-1 excitation, only a few flexural cracks with the maximum width of 1mm occurred around the column at the plastic hinge. Therefore it is noted that the



(a) C1-5(2) excitation (8.80s)



(b) C1-5(3)-2 excitation (7.17s)

Photo 3 Progress of damage of C1-5

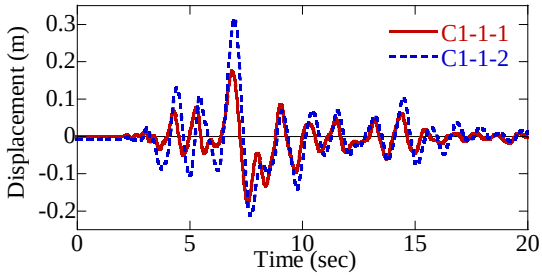

Fig. 3 Response displacement at the top of C1-1 in the principle response direction

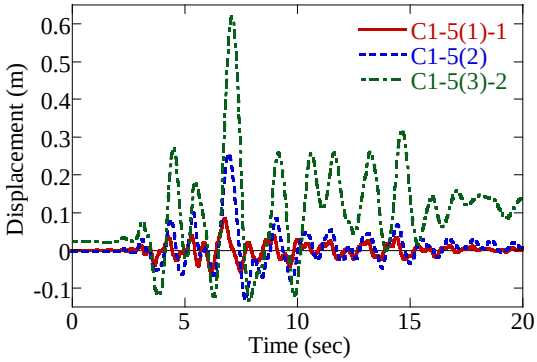

Fig. 4 Response displacement at the top of C1-5 in the principle response direction

seismic performance is enhanced in C1-5 than C1-1 under the first 100% E-Takatori excitation. The damage progressed during C1-5(2) excitation such that the covering concrete spalled off at the 500 mm base zone from WSW to SSW. During C1-5(3)-2 excitation, the failure extensively progressed. The core concrete crashed due to repeated compression, and blocks of crashed core concrete spilled out from the steel cages like explosion. Such a failure was never seen in the past quasi-static cyclic or hybrid loading experiments. Because the maximum aggregate size was 20 mm, the concrete blocks after crashed can be as small as 20-40 mm. Because the gaps of longitudinal bars and circular ties were 132mm and 128mm, respectively, it was possible for the blocks of crashed core concrete to move out from the steel cages. Furthermore twelve outer longitudinal bars and nineteen inner longitudinal bars locally buckled on SW and NE-E surfaces. The 135 degree bent hooks developed in the core concrete still existed in the original position although the core concrete around the hooks suffered extensive damage.

3.2 Response Displacement and Moment Capacity

Figs. 3 and 4 show the response displacement at the top of C1-1 and C1-5, respectively, in the principal response direction (nearly SW-NE direction). The peak displacement of C1-1 was 0.179 m (2.4 % drift) during C1-1-1 excitation while the peak displacement of C1-5 was 0.084 m (1.1 % drift) during C1-5(1)-1 excitation. Because the ultimate displacement in accordance with JRA 2002 code was 0.100 m and 0.235 m in C1-1 and C1-5, respectively, the above peak response displacements corresponded to 179 % and 36 % the ultimate displacement in C1-1 and C1-5, respectively.

Figs. 5 and 6 show the moment at the column base vs. lateral displacement at the column top hystereses of C1-1 and C1-5, respectively, in the principal response direction. The computed moment vs. lateral displacement relations based on the 2002 JRA code are also shown here for comparison. The moment capacity of C1-1 during C1-1-2 excitation was 13.41 MNm which deteriorated by 19 % from the moment capacity during C1-1-1 excitation of 16.47 MNm. On the other hand, the moment capacity of C1-5 column progressed from 19.82 MNm during C1-5(1)-1 excitation to 20.14 MNm and 24.85 MNm during the C1-5(2) and C1-5(3)-2 excitations, respectively. However since the moment capacity of C1-5 during the C1-5(3)-1 excitation was 25.54 MNm, the moment capacity of C1-5 deteriorated by 3% during C1-5(3)-2 excitation. The computed moment capacities are close to the experimental values in both C1-1 and C1-5, however the computed ultimate displacement are very conservative compared to the experiment.

4. SEISMIC PERFORMANCE OF C1-2

4.1 Progress of Failure

Photo 4 shows the progress of failure of C1-2 on NW and SE surfaces. A horizontal crack first developed at 4.10s along NW to E surface, and it progressed to a shear crack at 4.33 s. Another horizontal crack developed at 4.60s along W

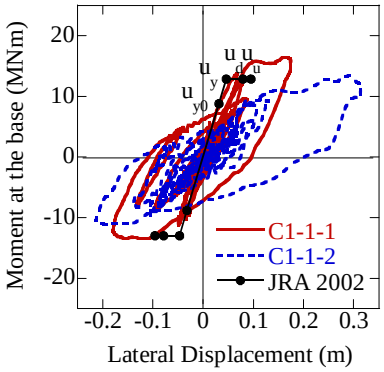

Fig. 5 Moment at the base vs. lateral displacement hysteresis of the top of C1-1 in the principle response direction

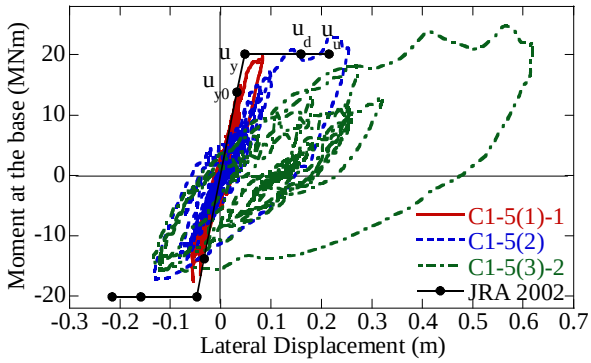

Fig. 6 Moment vs. lateral displacement hysteresis of the top of C1-5

to SE surface, and it extended to at least two diagonal cracks at 4.87s. Among two diagonal cracks developed at 4.33 s, a crack on NW surface extended to W surface, and the other crack on SE surface extended to S at 5.37s. The core concrete started to crash due to shear, and the blocks of crashed core concrete started to move out from the inside of the column near the upper cut-off on N and NW surfaces at 6.04 s. The same but more extensive failure occurred on S and SW surfaces at 6.504 s. The blocks of crashed core concrete progressively moved out from steel cages associated with the column response in the SW direction.

At 6.87 s, the bottom of lateral beam hit with the upper surface of catch frame due to excessive response displacement. Three circular tie bars completely separated at their lap splice and the longitudinal bars deformed in the outward direction. Extensive failure of core concrete and deformation of longitudinal bars progressed on W, NW, N, NE and E surfaces.

It should be noted in the above process that the failure of core concrete was extensive and a large numbers of blocks of crashed core concrete as well as deformed longitudinal bars moved out from inside of the column during very short time (less than 3 s). It was like an explosion.

4.2 Response and Shear Capacity

Fig. 7 shows response displacement of C1-2 in the principal response direction. As described above, since bottom of the lateral beam hit with the upper surface of catch



(a) NW



(b) SE

(1) 6.50s



(a) NW



(b) SE

(2) 6.87s

Photo 4 Progress of damage of C1-2

frame at 6.87s, the column response after 6.87 s was affected by this contact. Without the catch frame, the column possibly overturned. Therefore the response displacement

after this contact is plotted by dotted line in Fig. 7. At 7.125 s, right after the contact, the column response displacement reached its peak of 439.2 mm and 253.0 mm in the longitudinal and transverse directions, respectively. Residual drifts of 204.5 mm and 343.2 mm were developed after the excitation.

Fig. 8 shows the lateral force at the upper cut-off vs. lateral displacement at the column top hysteresis in the principal response direction. The hysteresis after the contact of the column with the catch frame is plotted by dotted line. The shear capacity of the column F_s was evaluated based on the truss theory as

The shear stress at the upper cut-off vs. the lateral displacement at the column top relation was evaluated as shown in Fig. 9, in which τ_c is normalized in terms of α_c and α_{pl} defined as

$$\alpha_c = \left(\frac{24}{f_c}\right)^{-1/3} \quad ; \quad \alpha_{pl} = \left(\frac{0.012}{p_l}\right)^{-1/3} \qquad (2)$$

In Fig. 9, shear stress evaluated for two 1.68m tall 400mm diameter scaled model columns with different shear vs. flexure strength ratio is included for comparison (Sasaki et al). $\tau_c / \alpha_c \alpha_{pl}$ of C1-2 is 0.68 MPa which is 15% larger than the value evaluated based on the shear equation (0.59 MPa) by Kono et al (Kono et al 1996).

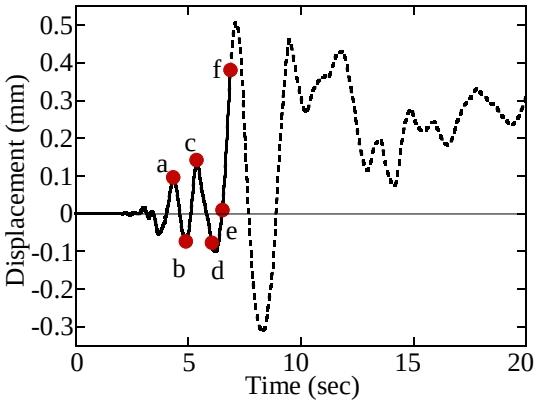

Fig. 7 Moment at the base vs. lateral displacement hysteresis of the top of C1-2 in the principle response direction

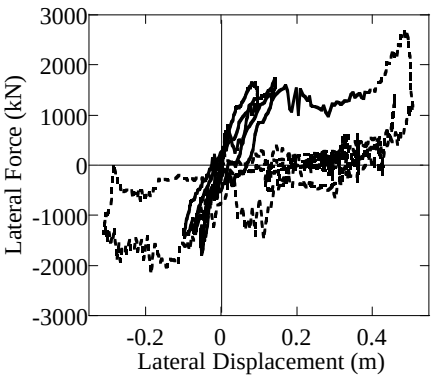

Fig. 8 Lateral force at upper cut-off vs. lateral displacement at the column top hysteresis

5. ANALYTICAL CORRELATION FOR C1-5

Analytical correlation for C1-5 during C1-5(2) and C1-5(3)-2 excitations is shown here. The column was idealized by a 3D discrete analytical model including P - Δ effect as shown in Fig. 10. The column was idealized by fiber elements. A section was divided into 400 fibers.

The stress vs. strain constitutive model of confined concrete is assumed based on Hoshikuma et al (1997) and Sakai and Kawashima (2006). The Modified Menegotto-Pinto model was used to idealize the stress vs. strain relation of longitudinal bars (Menegotto and Pinto 1973, Sakai and Kawashima 2003).

Fig. 11 shows the analytical correlation on the response displacements at the top of the column in the principal direction during C1-5(1)-1 and C1-5(2) excitations. Fig. 12 compares the measured and computed moment at the base vs. lateral displacement at the column top hystereses during the two excitations. Because nonlinear hysteretic response was still limited during C1-5(1)-1 excitation, the computed response displacement and moment vs. lateral displacement hysteresis are quite in good agreement with the experimental results, however as C1-5 suffered more damage, the accuracy of analytical prediction decreases.

Consequently, it is required to develop an analytical model that can predict the response of the columns until

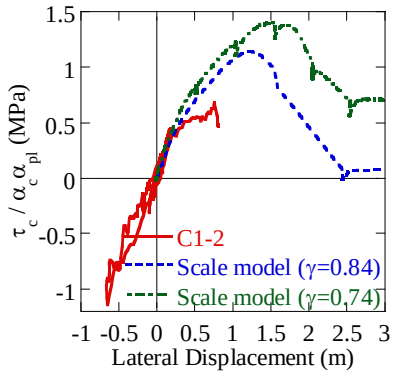

Fig. 9 Shear stress of concrete

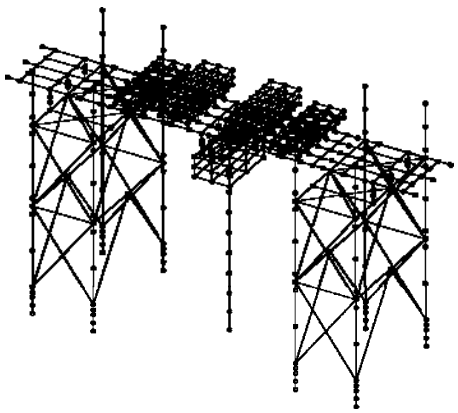

Fig. 10 Analytical model

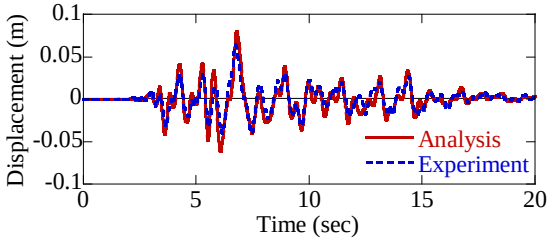

(a) Displacement

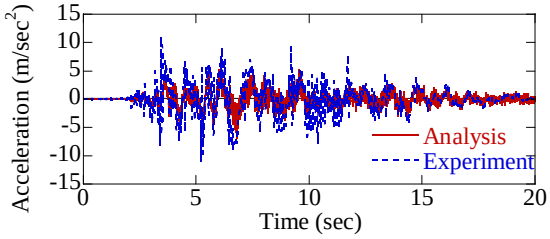

(b) Acceleration

(1) C1-5(1)-1 excitation

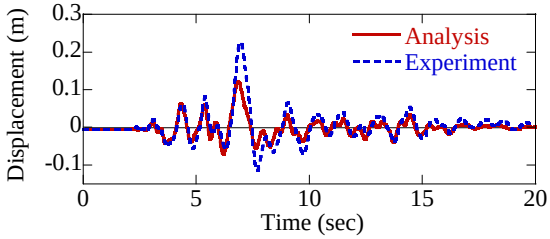

(a) Displacement

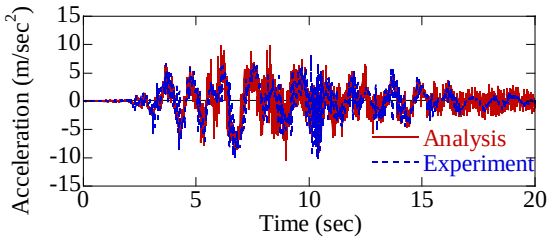

(b) Acceleration

(2) C1-5(2) excitation

Fig. 11 Analytical correlation for the response displacement and acceleration at the column top in the principle response direction

collapse for realizing reliable performance based seismic design.

6. COCLUSIONS

A preliminary result on a series of shake table experiment and analysis to three full-size reinforced concrete columns was presented. Based on the results presented herein, the following tentative conclusions may be deduced;

1) C1-1 which is a typical column in the 1970s suffered extensive damage under C1-1-1 excitation. The progress of damage during C1-1-2 excitation was extensive even

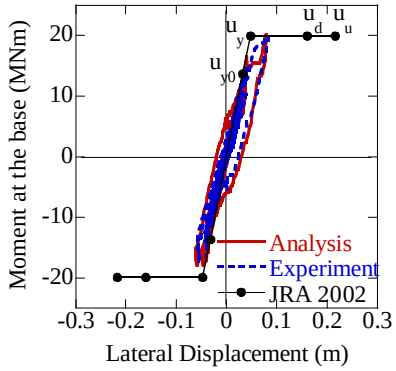

(a) C1-5(1)-1 excitation

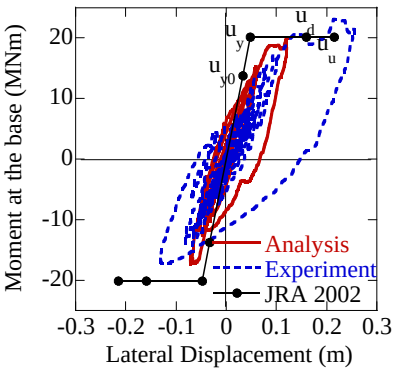

(b) C1-5(2) excitation

Fig. 12 Moment vs. lateral displacement at the column top in principle response direction

though it was anticipated before the experiment that damage would not progress unless the intensity of second excitation was much larger than that of the first excitation. This resulted from the extensive deterioration of the lateral confinement due to separation of ties at the lap splices. It is highly possible that columns without sufficient lateral confinement have a similar progress of damage during a long-duration near-field ground motion or strong aftershocks.

2) C1-5 which is a typical column in accordance with the current design criteria suffered only a few numbers of horizontal cracks with the maximum width of 1 mm under C1-5 (1)-1 excitation. The ultimate drift was 2.9 % which was 2.2 times larger than that of C1-1. Consequently, enhancement of the seismic performance of C1-5 compared to C1-1 is obvious. However the progress of failure of C1-5 was extensive when it was subjected to 25 % stronger excitation under 21% added mass (C1-5(3) excitations).Blocks of crashed core concrete spilled out like explosion from the steel cages. The seismic performance of C1-5 subjected to longer duration near-field ground motion has to be carefully evaluated.
3) C1-2 failed in shear at the upper cut-off. As soon as circular ties at the upper cut-off yielded, a small diagonal cracks developed. As they extended to several major

diagonal cracks, C1-2 completely failed in shear within less than 2.5 s since the initiation of a couple of small diagonal cracks. Concrete blocks crashed by shear and deformed longitudinal bars extensively moved out from the inside of column.

4) The lateral confinement in the flexure dominant columns is not uniform around the ties as it is currently assumed in design. More importantly, the lateral confinement of multi layered ties is very complex. Strains of ties are not similar among the multi-layered ties, and they are related to the degree of constraint exerted for preventing local buckling of longitudinal bars. Strains are generally larger in the outer ties than the inner ties. This implies that the lateral confinement by Eq. (2) can be overestimated.
5) Computed response for the flexure dominant columns is satisfactory while response undergoes the moderate nonlinear range, however accuracy of the analytical prediction deteriorates once the columns undergo the strong nonlinear range. An analytical model which can predict response of the columns until failure should be developed for enhancing the reliability of the performance based seismic design.

ACKNOWLEDGEMENTS

The C1-1, C1-2 and C1-5 experiment was conducted based on the extensive support of over 70 personnel in the Overview Committee (Chair, Professor Emeritus Hirokazu Iemura, Kyoto University), Executing Committee of Large-scale Bridge Experimental Program (Chair, Professor Kazuhiko Kawashima, Tokyo Institute of Technology), Analytical Correlation WG (Chair, Dr. Shigeki Unjoh, Public Works Research Institute), Measurements WG (Chair, Professor Yoshikazu Takahashi, Kyoto University), Dampers & Bearings WG (Chair, Dr. Masaaki Yabe, Chodai) and Blind Analysis WG (Chair, Professor Hiroshi Mutsuyoshi, Saitama University). Their strong support is greatly appreciated. The appreciation is extended to Mr. Hiromichi Ukon for his enthusiastic contribution to the project. Invaluable support and encouragement by Professor Stephen Mahin, University of California, Berkeley and Professor Ian Buckle, University of Nevada, Reno are greatly appreciated.

REFERENCES

Nakashima, M., Kawashima, K., Ukon, H. and Kajiwara, K. (2008), "Shake table experimental project on the seismic performance of bridges using E-Defense," S17-02-010 (CD-ROM), 14 WCEE, Beijing, China.

Hoshikuma, J., Kawashima, K., Nagaya, K. and Taylor, A.W. (1997), "Stress-strain model for confined reinforced concrete in bridge piers," Journal of Structural Engineering, ASCE, 123(5), 624-633.

Kawashima, K. Sasaki, T., Kajiwara, K., Ukon, H., Unjoh, S., Sakai, J., Takahashi, Y., Kosa, K., and Yabe, M. (2009), "Seismic performance of a flexural failure type reinforced concrete bridge column based on E-Defense excitation," Journal of JSCE, A, Invited paper, 1-19, JSCE.

Kawashima, K. and Unjoh, S. (1997), "The damage of highway bridges in the 1995 Hyogo-ken nanbu earthquake and its impact on Japanese seismic design," Journal of Earthquake Engineering, 1(3), 505-542.

Kono, H., Watanabe, H. and Kikumori, Y. (1996), "Shear strength of large RC beams," Technical Note, 3426, Public Works Research Institute, Tsukuba, Japan.

Menegotto, M. and Pinto, P.E. (1973), "Method of analysis for cyclically loaded R.C. plane frames including changes in geometry and non-elastic behavior of elements under combined normalized force and bending," Proc. IABSE Symposium on Resistance and Ultimate Deformability of Structures Acted on by Well Defined Repeated Loadings, 15-22.

Sakai, J. and Kawashima, K. (2006), "Unloading and reloading stress-strain model for confined concrete," Journal of Structural Engineering, ASCE, 132 (1), 112-122.

Sakai, J. and Kawashima, K. (2003), "Modification of the Giuffre, Menegotto and Pinto model for unloading and reloading paths with small strain variations," Journal of Structural Mechanics and Earthquake Engineering, JSCE, 738/I-64, 159-169.

Sasaki, T., Kurita, H., and Kawashima,K. (2008), "Seismic performance of RC bridge columns with termination of main reinforcement with inadaquate development," S17-02-009 (CD-ROM), 14WCEE, Beijing, China

JOINT CONFERENCE PROCEEDINGS
7th International Conference on Urban Earthquake Engineering (7CUEE) &
5th International Conference on Earthquake Engineering (5ICEE)
March 3-5, 2010, Tokyo Institute of Technology, Tokyo, Japan

SEISMIC PROGRESSIVE COLLAPSE OF REINFORCED CONCRETE FRAMES AND BRIDGES

David T. Lau[1] and Hartanto Wibowo[2]

1) Professor and Director, Ottawa – Carleton Bridge Research Institute, Department of Civil and Environmental Engineering, Carleton University, Ottawa, ON, K1S 5B7, Canada
2) Graduate Research Assistant, Department of Civil and Environmental Engineering, University of Nevada – Reno, Reno, NV, 89557, USA
dtl@ccs.carleton.ca, wibowoh@unr.nevada.edu

Abstract: Progressive collapse phenomenon of structures, especially bridges, is evident from structural damage and failure observed during many past major earthquakes. Many bridges failed even though they were properly designed in accordance to the provisions and requirements of the design codes at the time of their construction. Progressive structural failure is a sequence of events starting from initiation of failure of a single component, due to overstress beyond the elastic limit, to degradation of material and member properties as related to stiffness and strength that are the result of accumulation of damage effects from cyclic stress reversals until the development of collapse mechanism. To study the progressive collapse phenomenon of structures during earthquakes, analyses have been carried out of example reinforced concrete frame and bridge structures by the Applied Element Method (AEM). The AEM method takes into account fracture separation of structural components and the impact inertia load effects of falling debris. The results show the detailed failure sequence and propagation of damage in the progressive collapse of the analyzed structures. The influence of member ductility and the impact load effects from falling debris and characteristics of ground motions such as intensity, frequency content, and duration of strong shaking on the progressive collapse behaviour of reinforced concrete bridges are investigated.

1. INTRODUCTION

Progressive collapse of structures is a phenomenon in which an initial local failure spreads from structural element to other elements which eventually results in the collapse of the whole structure or to an extent disproportionate to the original failure. During earthquakes, when seismic load demand exceeds the elastic capacity of a structure, failure is initiated at a structural member or component which is the weakest link of the system. During subsequent response, the redistribution of load carried by the failed member to adjacent members may lead to overstress or exceeding load resistant capacity of the other members resulting in spread or propagation of damage until development of collapse mechanisms in seismic progressive collapse of structure. During strong shaking of severe earthquakes, repeated cyclic stress reversals and accumulation of damage effects can lead to degradation in stiffness and strength of individual structural members and the structural system. Experiences from past major earthquakes have shown that collapse of bridges can have catastrophic consequences, such as disruption to post-disaster rescue efforts and significant economic loss. In a number of post-earthquake reconnaissance studies of structural damage, the seismic performance of bridges during past earthquakes was deemed to be not satisfactory (Priestley et al. 1996, Kawashima 2000, Wallace et al. 2001, Buckle 2003, Moehle and Eberhard 2003, Han et al. 2009). In current practice of analysis and design of structures against earthquake effects, structures are designed to have the strength and deformation capacities to resist the demands of design earthquake. In ductile design of earthquake resistant structures, the ability of a structure to continue resisting severe ground shaking after initial failure that exceeds its elastic limit without significant loss of load carrying capacity depends on the amount of accumulated damage suffered by the structure. The impact of the accumulated damage and its influence on the overall seismic performance of bridge structures have not been investigated with proper detailed models and analyses.

To achieve the goal of better seismic performance of structures within the context of the Performance-Based Earthquake Engineering, it is necessary to have a thorough understanding of the complete structural response behaviour over the entire duration of seismic response from initial failure of individual structural components or members, progression of structural failure, and the influence of accumulated structural damage on the strength and stiffness of the structure to the final ultimate collapse of the structural system. To obtain insights and detailed information for improvements in understanding the seismic risk and

vulnerability of structures, accurate prediction models and analysis tools are needed for determining the complete detailed inelastic behaviour and performance of structures during earthquakes. This paper presents results obtained from a study on seismic progressive collapse analysis of reinforced concrete bridges. A better understanding and insights on the seismic performance of bridges can lead to bridge design improvement, disaster risk reduction, and better emergency preparedness. More effective and performance-based design, retrofit, and mitigation strategies can be developed to help reducing the enormous cost required for renewing the existing old bridge infrastructures.

2. APPLIED ELEMENT METHOD

The Applied Element Method (AEM), implemented in the computer software Extreme Loading for Structures (ELS), by Tagel-Din and Meguro (1999), combines the advantages of both continuum analysis models (e.g., Finite Element Method) and discrete analysis models (e.g., Discrete Element Method). The modelling approach of the AEM can easily account for element separation and contact as well as impact load from falling debris which makes it suitable as a tool for progressive collapse analysis of structures.

In the AEM, a structure is modelled by dividing it into an assembly of small rigid elements connected by springs at interfaces between adjacent elements, as shown in Figure 1. Two adjacent elements of the 2D planar frame structures as shown in Figure 1 are connected at discrete points along the element interfaces by a pair of normal and shear springs with the stiffness, K_n and K_s, given respectively as follows (Meguro and Tagel-Din 2000):

$$K_n = \frac{E\,d\,t}{a} \quad \text{and} \quad K_s = \frac{G\,d\,t}{a} \tag{1}$$

where d is the distance between springs, t is the element thickness, a is the length of the representative area, E is the material Young's modulus, and G is the material shear modulus. The spring stiffness expressions in Eq. (1) are derived based on the assumption that the deformations of the domain volume are represented by the spring deformations at the interface between the adjacent rigid elements with the dimensions d, t, and a, as depicted by the shaded area in Figure 1, subjected to given loading. In the case that reinforcement bar is present, rebar stiffness is added to the material stiffness in Eq. (1). Element rotation is resisted by a set of normal and shear springs. The contribution to rotational stiffness, K_r, from the normal springs can be calculated as follows (Meguro and Tagel-Din 2001):

$$K_r = \int_{z=-b/2}^{z=b/2} \frac{E\,t}{b}\, z^2\, dz = \frac{E\,t\,b^2}{12} \tag{2}$$

where b is the element height and z is the distance from the spring location to the centroid of the element as shown in Figure 2. In the formulation, the inelastic and nonlinear material behaviour and fracture failure of material are modelled by nonlinear stiffness properties and removal of the springs.

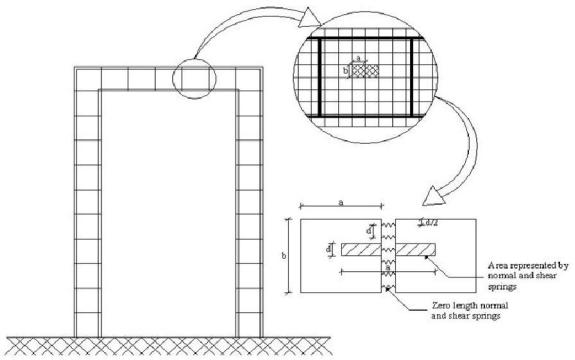

Figure 1 Elements on the Applied Element Method

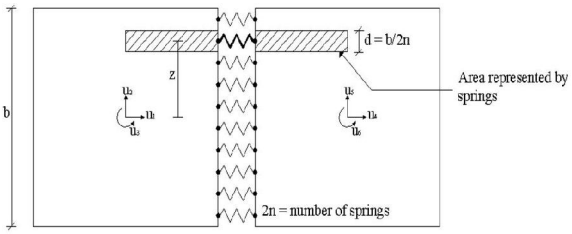

Figure 2 Normal Springs for Rotational Stiffness Calculation

In the AEM formulation, the general dynamic equation of motion in large deformation range is expressed as follows (Tagel-Din and Meguro 2000):

$$\boldsymbol{M}\,\Delta\ddot{\boldsymbol{U}} + \boldsymbol{C}\,\Delta\dot{\boldsymbol{U}} + \boldsymbol{K}\,\Delta\boldsymbol{U} = \Delta\boldsymbol{f}(t) + \boldsymbol{R}_M + \boldsymbol{R}_G \tag{3}$$

where $\boldsymbol{M}$ is the mass matrix, $\boldsymbol{C}$ is the damping matrix, $\boldsymbol{K}$ is the nonlinear stiffness matrix, and $\Delta\boldsymbol{f}(t)$ is the incremental applied load vector for a time step. $\Delta\boldsymbol{U}$, $\Delta\dot{\boldsymbol{U}}$, and $\Delta\ddot{\boldsymbol{U}}$ are the incremental displacement, velocity, and acceleration vectors respectively. $\boldsymbol{R}_M$ is the additional load vector due to the nonlinear behaviour of material and $\boldsymbol{R}_G$ is the additional load vector due to geometrical changes. Eq. (3) represents the equilibrium equation between the applied external forces and the internal forces. The solution of Eq. (3) can be obtained by numerical direct integration technique and in this case the Newmark's average acceleration method is chosen.

To follow the behaviour of concrete under compression, the Maekawa compression model (Okamura and Maekawa 1991) that describes the loading, unloading, and reloading conditions, is adopted. For modelling concrete subjected to tension, an initial stiffness is assumed for the concrete springs until they reach the cracking point. After cracking,

the spring stiffness is set to zero. The steel reinforcement material model used is the Ristic model (Ristic et al. 1986) that considers the effects of partial unloading and the Bauschinger's effect. The failure criteria are based on the principal stresses in the springs so the proper crack propagation can be followed. When the stress in a spring exceeds the critical value of the tensile resistance, the normal and shear spring forces are redistributed so that the tension stress is zero on the crack face. Some verification examples have been carried out and reported in Wibowo (2009)

3. ONE-BAY CONCRETE FRAME EXAMPLES

The period of a structure is dependent on its mass and stiffness distributions. To illustrate the damage potential of a structure as related to its mass and stiffness distributions, analyses have been carried out of a viaduct concrete frame structure. The viaduct frame has a width of 5 m and a height of 3 m and is assumed to be fixed at both column ends. The 1994 Northridge earthquake ground motion is used for this study with the stronger horizontal motion component applied in the in-plane direction of the frame.

There are two cases of beam used for this study, one is with a normal reinforcement (B1) and the other is more heavily-reinforced (B2) to represent the case of the beam remains elastic during earthquakes. There are also two types of column detailing considered in the study, one with eight #9 rebars (C1) and the other with twelve #9 rebars (C2) to provide higher ductility capacity. The transverse reinforcements are 2 legs of #4 at 200 mm. In the ELS model, each column in the numerical example is divided into a mesh of 5 x 5 equal elements in the cross-section and 30 elements along the height of the column. The beam is divided into a mesh of 5 x 5 equal elements in the cross-section and 10 elements along the length of the beam. The properties of the beam, columns, and mass of the beam of the viaduct frame are varied to obtain different values of the viaduct's fundamental period as shown in Table B1.

An interesting observation can be made when comparing the results of viaducts B2C2-B and B2C2-C. Viaduct B2C2-B does not have any separation of elements although it experiences minor cracking on the beam and columns surfaces. However, viaduct B2C2-C, as shown in Figure 3, shows significant damage at the base of the columns. These damages show that plastic hinges are formed and ductile behaviour of the structure is observed.

Although the earthquake excitation is applied in three directions (longitudinal, transversal, and vertical), the viaduct's displacement is mostly along the longitudinal direction. Figure 4 shows the displacement time history in the horizontal in-plane direction of the viaduct frame at the top of the column. The results show that the response of the viaduct frame B2C2-B resembles the time history of the excitation force as it suffers only minor damage, whereas the viaduct frame B2C2-C suffers significant damage after around 5 s and that permanent inelastic displacement is evident in the response after the earthquake excitation has ended. In comparison, the viaduct frame B2C2-C cannot sustain the moment and shear force demands as evident by the formation of the plastic hinges. However, the columns still have sufficient axial load capacity to carry the gravity load of the structure without collapse.

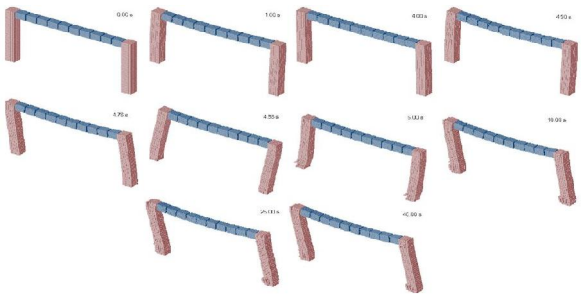

Figure 3 Deformation of Viaduct B2C2-C due to the 1994 Northridge Earthquake Excitation

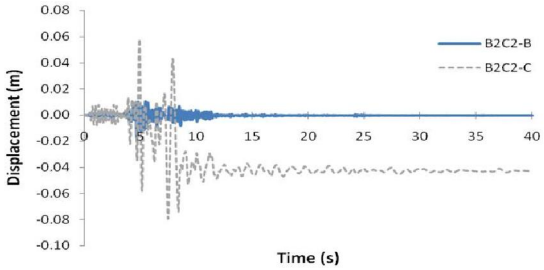

Figure 4 Displacement Time Histories of Viaducts B2C2-B and B2C2-C

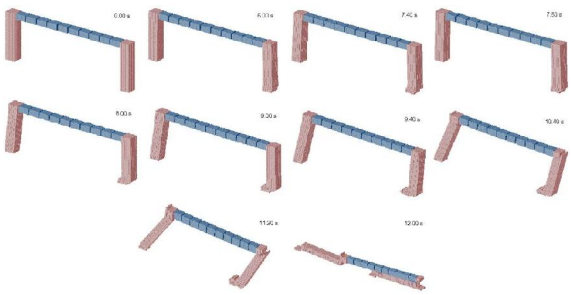

Figure 5 Deformation of Viaduct B2C1-C due to the 1994 Northridge Earthquake Excitation

When the longitudinal reinforcement in the column is reduced as in the case of viaduct B2C1-C, the damage in the plastic hinge at the base of the column is more severe and it causes the column to collapse as can be observed in Figure 5. The column does not have sufficient ductility capacity to resist the inelastic deformation demand and fails due to excessive rotation. After the column fails, the beam loses its vertical support and starts to experience excessive displacement which leads to collapse of the entire system due to instability. A brittle failure can be observed in the case of viaduct B1C2-C which has less reinforcement in the

beam as shown in Figure 6. The damage starts in the plastic hinge area of the column and spreads to the beam-column connection of the frame where separation occurs. The beam then begins to have large deflection at the point where maximum moment caused due to the combined actions of the lateral and gravity loads. After that the beam fails, it drags down the columns as the final collapse mechanism develops.

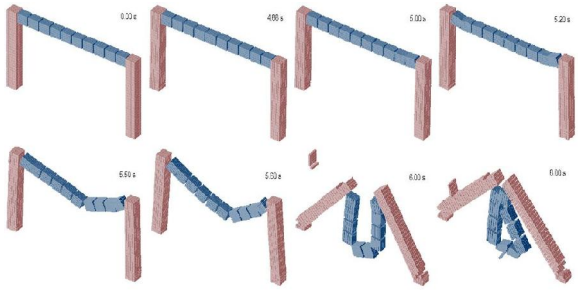

Figure 6 Deformation of Viaduct B2C2-C due to the 1994 Northridge Earthquake Excitation

4. BRIDGE MODEL AND EARTHQUAKE LOADS

The example bridge used in the present study has four 20 m bays with a total length of 80 m. The bridge superstructure dimensions and pier heights of 5.6 m, 2.8 m, and 8.4 m respectively, as shown in Figure 7. The pier base is modelled as fixed at the pier bases (Piers 2 to 4) and hinged at the abutments (Abutments 1 and 5). The longitudinal reinforcement details of the bridge are taken from the bridge model used in the study by Casarotti and Pinho (2006). In the present study, the transverse reinforcement details of the piers are determined based on the design requirements of CAN/CSA-S6-06 (CSA 2006). The bridge superstructure is a box girder 5.6 m wide and in this study, the girder is considered as reinforced concrete girder. The bridge box girder has minimum transverse reinforcements. The bridge substructures are rectangular hollow-core reinforced concrete piers. The connection between the pier and the box girder is assumed as pin, which does not transfer any moment between the box girder and the pier. The bridge's piers properties are summarized in Table B2. In the applied element model, the bridge box girder is modelled to remain elastic during earthquake response in the comparison study with previous analytical and experimental test results where elastic bridge superstructure is assumed (Casarotti and Pinho 2006). The concrete and steel properties are tabulated in Table B2. The damping ratio of the bridge in the analysis is taken as 5%.

In the applied element model of the bridge, each side of the pier cross-section is divided into a mesh of 5 x 5 equal spaced elements and in the longitudinal direction into 5 equal spaced elements per 2.8 m length. Each surface area of the box girder section (i.e., the deck, webs, and soffit) is divided into 10 x 1 elements with 50 elements per 20 m length in the longitudinal direction of the box girder. This mesh size has been found to give accurate results. Analysis using a finer mesh has been carried out without any noticeable difference in the numerical results.

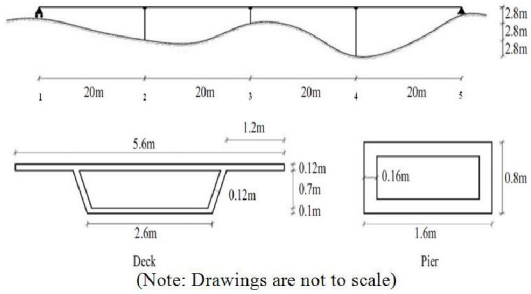

Figure 7 Bridge Elevation View and Sections (Casarotti and Pinho 2006)

The longitudinal reinforcement details of the bridge box girder are shown in Figure 8(a). The box girder is designed such that it matches the moment of inertia specified in the literature (Casarotti and Pinho 2006). The piers' longitudinal reinforcement details are divided into two types. The 2.8 m high pier follows the reinforcement detail type 1, whereas the 5.6 m high and 8.4 m high piers follow the reinforcement detail type 2. The longitudinal reinforcement details of the piers are shown in Figure 8(b).

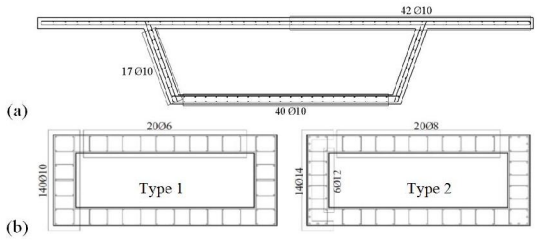

Figure 8 (a) Box Girder and (b) Piers (Casarotti and Pinho 2006) Longitudinal Reinforcement Details

Earthquake ground motion records used in the analysis are obtained from the Pacific Earthquake Engineering Research (PEER) Strong Motion Database. The earthquake records used are the 1994 Northridge, the 1995 Kobe, and the 1999 Chi-Chi earthquake records. The earthquake excitation is applied in the longitudinal (x-axis), transversal (y-axis), and vertical (z-axis) directions. A summary of the earthquake ground motions is presented in Table B3.

5. ANALYSIS RESULTS

The progression of the structural failure and collapse of the analyzed bridge due to the 1994 Northridge, the 1995 Kobe, and the 1999 Chi-Chi earthquakes are captured in Figures A1 to A3 (in Appendix A), respectively. From

observation, it can be noticed that the 1999 Chi-Chi earthquake caused the most damage to the bridge structure. Due to this earthquake, the box girder starts to fail early in the response and that actuates the short pier to bear more loads beyond its capacity and thus leads to its subsequent failure. The short pier collapses in flexure since it attracts the most seismic force. This short pier collapse also greatly reduces the load resistant capacity of the bridge resulting in the ramification effect of load shifts in the whole system which finally leads to the tall pier collapses. The collapse of the pier can also happen as a result of impact force from the failure of the box girder as can be observed in the collapse of the tall pier due to the 1995 Kobe earthquake.

The pier can also experience permanent deformation caused by the tilting and dislocation of the pier. Figure 9 shows an example of dislocation and cracks in the pier due to the 1995 Kobe earthquake excitation, where a part of the short pier is no longer completely intact at the base. The displacement time histories along the x-axis at the top of the piers caused by the 1994 Northridge, 1995 Kobe, and 1999 Chi-Chi are shown in Figures 10 to 12, respectively. The collapse of the girder results in the pier losing its lateral bracing support, then it displaces more from the dragging action of the falling girder before it is completely separated from the pier during the response.

The moment along the longitudinal direction time histories due to the three earthquakes are presented in Figure 13. The shear and axial forces of the piers can be found in Wibowo (2009). It can be seen that the internal forces also have the same patterns as the displacements. The jumps in the internal forces occur when the abutments fail and the loads from the box girder are transferred fully to the piers and when there are impact forces from the debris.

In comparing the effects of different earthquake ground motions on the progressive collapse behaviour, it is noted that the 1994 Northridge earthquake excitation with the highest peak ground acceleration causes no pier to collapse. The 1999 Chi-Chi earthquake excitation causes significant damage and collapse of the entire bridge structures including the piers. The response spectrum of the 1999 Chi-Chi earthquake ground motion show that its frequency content has higher energy in longer period range compared to the 1994 Northridge earthquake. Since the bridge softens due to strength or stiffness deteriorations after structural members start to fail and suffer damage, the period shifts in the structure to longer due to its softening and makes it more vulnerable to more severe earthquake damage.

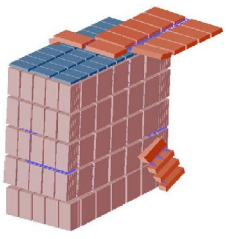

Figure 9 Dislocation and Cracks of the Short Pier due to the 1995 Kobe Earthquake Excitation

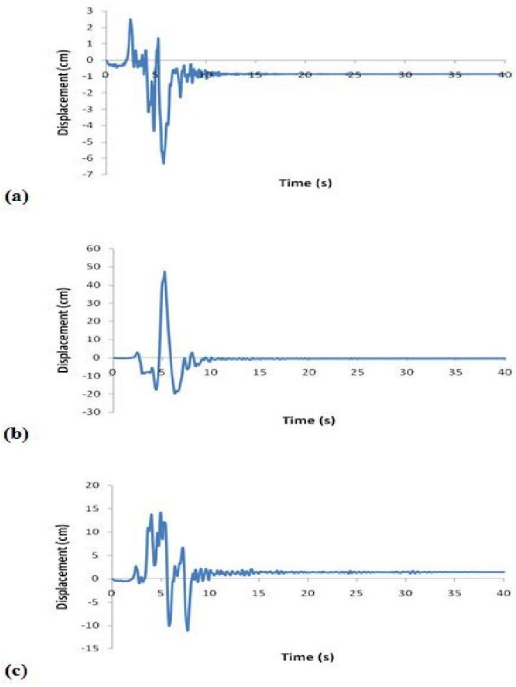

Figure 10 Displacement Time Histories of (a) Short, (b) Medium, and (c) Tall Piers due to the 1994 Northridge Earthquake Excitation

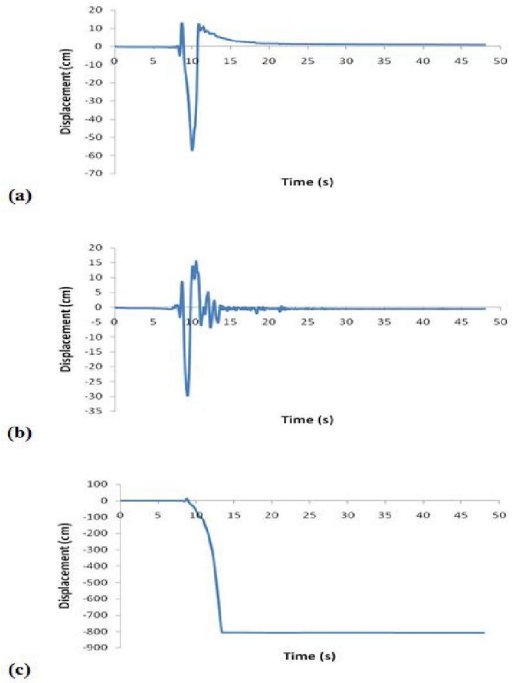

Figure 11 Displacement Time Histories of (a) Short, (b) Medium, and (c) Tall Piers due to the 1995 Kobe Earthquake Excitation

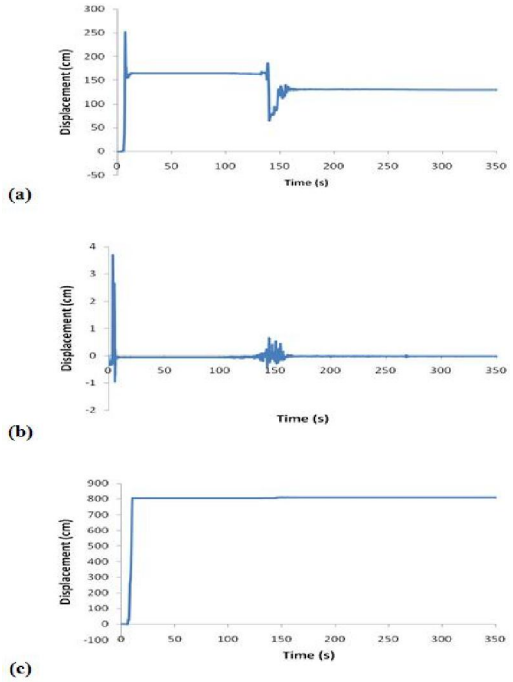

Figure 12 Displacement Time Histories of (a) Short, (b) Medium, and (c) Tall Piers due to the 1999 Chi-Chi Earthquake Excitation

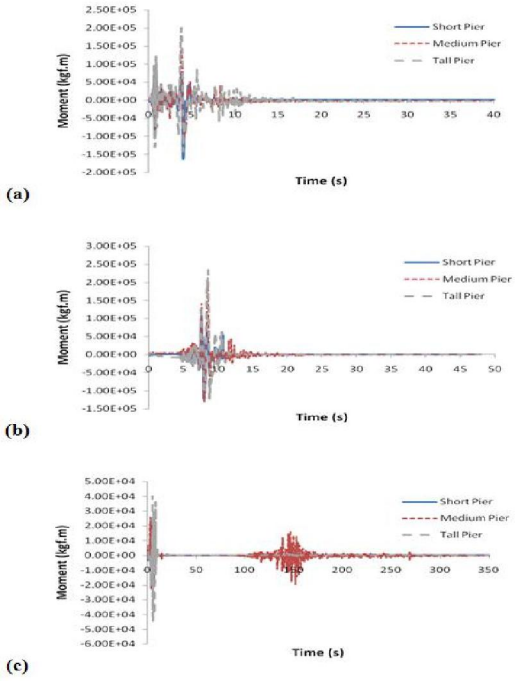

Figure 13 Moment Time Histories due to the (a) 1994 Northridge, (b) 1995 Kobe, and (c) 1999 Chi-Chi Earthquake Excitations

6. CONCLUSIONS

The Applied Element Method is a reliable tool to analyze structures to obtain insights of its collapse behaviour and possible failure modes. From the results, it can be concluded that seismic progressive collapse phenomenon is global damage behaviour of the structure. During earthquakes, part of a structure starts to fail causing redistribution of load to the remainder of the structural system and subsequent failure and development of collapse mechanisms. It is observed that the response of structures during the collapse process is highly nonlinear and influenced by the response from impact force of falling debris causing drastic changes in mass, strength, and stiffness properties of the structure during the progressive collapse process. Seismic progressive collapse simulations can help structural engineers to better design new structures, as well as to get a more comprehensive approach in devising effective retrofit strategies for old deficient bridge stock by considering the pattern and severity of the potential damage in the structure.

Acknowledgements:

The authors would like to thank Dr. Hatem Tagel-Din and Mr. Ayman El-Fouly of Applied Science International, LLC for the fruitful discussion and technical support of the software ELS. Prof. Rui Pinho of the University of Pavia is also acknowledged for providing the reinforcement details of the bridge model. This research is a part of the NSERC Strategic Network Grant Project: Canadian Seismic Research Network.

References:

Buckle, I. G. (2003), "Application of Seismic Risk Assessment Procedures to the Performance-based Design of Highway Systems," *Advancing Mitigation Technologies and Disaster Response for Lifeline Systems*, Beavers, J. E. (ed.), 886-895.

Canadian Standards Association (CSA). (2006), "CAN/CSA-S6-06: Canadian Highway Bridge Design Code," CSA International.

Casarotti, C. and Pinho, R. (2006), "Seismic Response of Continuous Span Bridges through Fiber-based Finite Element Analysis," *Earthquake Engineering and Engineering Vibration*, **5**(1), 119-131.

Han, Q., Du, X., Liu, J., Li, Z., Li, L., and Zhao, J. (2009), "Seismic Damage of Highway Bridges during the 2008 Wenchuan Earthquake," *Earthquake Engineering and Engineering Vibration*, **8**(2), 263-273.

Kawashima, K. (2000), "Seismic Performance of RC Bridge Piers in Japan: An Evaluation after the 1995 Hyogo-ken Nanbu Earthquake," *Progress in Structural Engineering and Materials*, **2**(1), 82-91.

Meguro, K. and Tagel-Din, H. (2000), "Applied Element Method for Structural Analysis: Theory and Application for Linear Materials," *Structural Engineering/Earthquake Engineering*, JSCE, **17**(1), 21s-35s.

Meguro, K. and Tagel-Din, H. (2001), "Applied Element Simulation of RC Structures under Cyclic Loading," *Journal of Structural Engineering*, ASCE, **127**(11), 1295-1305.

Moehle, J. P. and Eberhard, M. O. (2003), "Earthquake Damage to Bridges", *Bridge Engineering: Seismic Design*, Chen, W. -F. and Duan, L. (eds.), 33 pp.

Okamura, H. and Maekawa, K. (1991), "Nonlinear Analysis and Constitutive Models of Reinforced Concrete," Gihodo Co. Ltd.

Priestley, M. J. N., Seible, F., and Calvi, G. M. (1996), "Seismic

Design and Retrofit of Bridges," John Wiley & Sons Inc.
Ristic, D., Yamada, Y., and Iemura, H. (1986), "Stress-strain Based Modeling of Hysteretic Structures under Earthquake Induced Bending and Varying Axial Loads," *Research Report No. 86-ST-01*, School of Civil Engineering, Kyoto University, Kyoto, Japan.
Tagel-Din, H. and Meguro, K. (1999), "Applied Element Simulation for Collapse Analysis of Structures," *Bulletin of Earthquake Resistant Structure Research Center*, **32**, 11 pp.
Tagel-Din, H. and Meguro, K. (2000), "Applied Element Method for Dynamic Large Deformation Analysis of Structures," *Structural Engineering/Earthquake Engineering*, JSCE, **17**(2), 215s-224s.
Wallace, J. W., Eberhard, M. O., Hwang, S. -J., Moehle, J. P., Post, T., Roblee, C., Stewart, J. P., and Yashinsky, M. (2001), "Highway Bridges," *Earthquake Spectra: Chi-Chi Earthquake Reconnaissance Report*, **17**(S1), 131-152.
Wibowo, H. (2009), "Progressive Collapse Analysis of Reinforced Concrete Bridges during Earthquakes," *M.A.Sc. Thesis*, Department of Civil and Environmental Engineering, Carleton University, Ottawa, ON, Canada.

APPENDICES

A. Figures of Progression of Collapse due to Different Earthquake Excitations

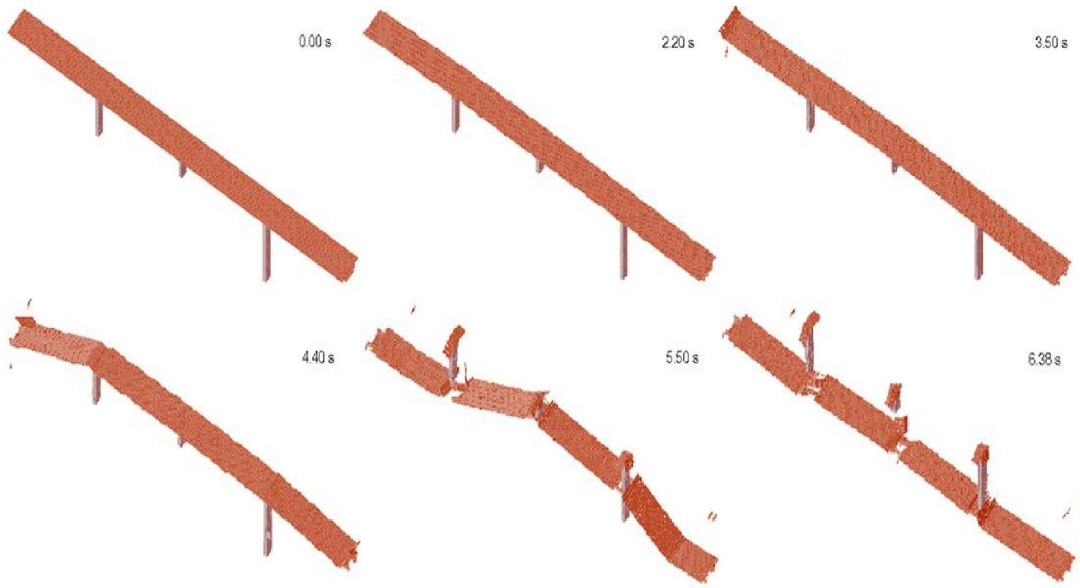

Figure A1 Progression of Collapse due to the 1994 Northridge Earthquake Excitation

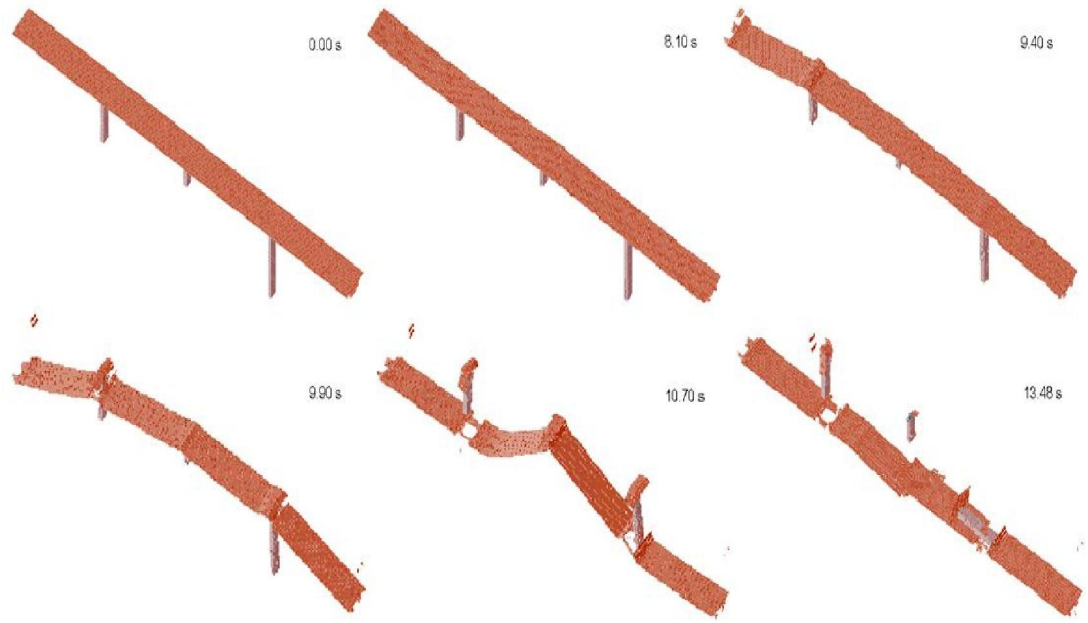

Figure A2 Progression of Collapse due to the 1995 Kobe Earthquake Excitation

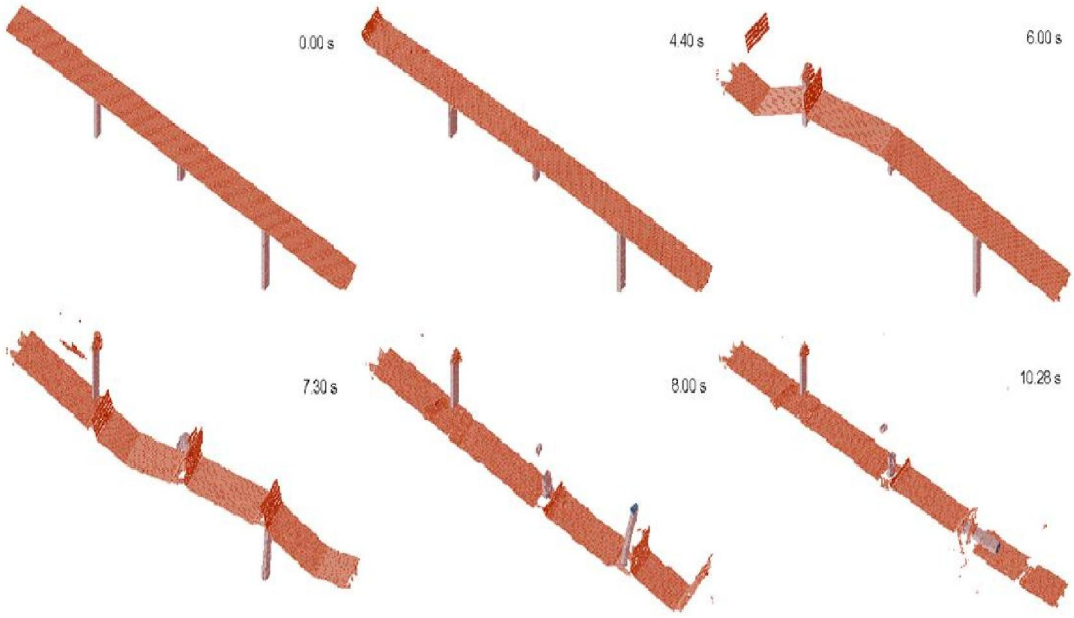

Figure A3 Progression of Collapse due to the 1999 Chi-Chi Earthquake Excitation

B. Tables

Table B1 Properties of the Verification Model

Beam	*Column*	*Mass* (kg)*	*Period (s)*	*Label*
B1	C1	0	0.047	B1C1-A
		50	0.125	B1C1-B
		150	0.243	B1C1-C
	C2	0	0.046	B1C2-A
		50	0.121	B1C2-B
		150	0.226	B1C2-C
B2	C1	0	0.046	B2C1-A
		50	0.122	B2C1-B
		150	0.226	B2C1-C
	C2	0	0.045	B2C2-A
		50	0.117	B2C2-B
		150	0.212	B2C2-C

Note: *) Mass is applied in each element of the beam

Table B2 Properties of the Bridge Model (Casarotti and Pinho 2006)

Parameter	*Concrete*			*Steel*
	Pier 2	*Pier 3*	*Pier 4*	
Compressive Strength	3.212 x 10^6 kg/m^2	3.569 x 10^6 kg/m^2	4.375 x 10^6 kg/m^2	3.6 x 10^7 kg/m^2
Tensile Strength	3.212 x 10^5 kg/m^2	3.569 x 10^5 kg/m^2	4.375 x 10^5 kg/m^2	3.6 x 10^7 kg/m^2
Strain at Unconfined Peak Stress	0.002 m/m	0.002 m/m	0.002 m/m	-
Constant Confinement Factor	1.2	1.2	1.2	-
Young's Modulus	2.549 x 10^9 kg/m^2	2.549 x 10^9 kg/m^2	2.549 x 10^9 kg/m^2	2.0389 x 10^{10} kg/m^2
Shear Modulus	1.062 x 10^9 kg/m^2	1.062 x 10^9 kg/m^2	1.062 x 10^9 kg/m^2	8.15561 x 10^9 kg/m^2
Specific Weight	2549.291 kg/m^3	2549.291 kg/m^3	2549.291 kg/m^3	7840 kg/m^3
Separation Strain	0.1	0.1	0.1	0.2
Friction Coefficient	0.8	0.8	0.8	0.8
Post-yield Stiffness Ratio	-	-	-	0.01

Table B3 Summary of the Earthquake Ground Motions

Earthquake Name	*Peak Ground Acceleration*			*Duration*
	X-Direction	*Y-Direction*	*Z-Direction*	
1994 Northridge	1.585 g	1.285 g	1.229 g	40.00 s
1995 Kobe	0.821 g	0.599 g	0.343 g	48.00 s
1999 Chi-Chi	0.821 g	0.653 g	0.337 g	360.00 s

JOINT CONFERENCE PROCEEDINGS
7th International Conference on Urban Earthquake Engineering (7CUEE) &
5th International Conference on Earthquake Engineering (5ICEE)
March 3-5, 2010, Tokyo Institute of Technology, Tokyo, Japan

PREDICTING IN-CABINET RESPONSE SPECTRUM BY USING IMPACT HAMMER TESTS

Jintao Cui[1)], Sung Gook Cho[2)], Dookie Kim[3)] , and Do-Gyeum Kim[4)]

1) Ph. D. Candidate, Department of Civil Engineering, Kunsan National University, Jeonbuk, Korea
2) Ph. D., JACE KOREA, Gyeonggi, Korea
3) Associate Professor, Department of Civil Engineering, Kunsan National University, Jeonbuk, Korea
4) Ph.D., P.E., Research Fellow, Infrastructure Research Department, Korea Institute of Construction Technology, Gyeonggi, Korea
cjt82461859@hotmail.com, sgcho76@hanmail.net, kim2kie@kunsan.ac.kr, dgkim@kict.re.kr

Abstract: An in-cabinet response spectrum prediction algorithm for electrical cabinet structures without using finite element analysis is proposed. The algorithm applies subspace system identification method to estimate the state-space models of the cabinets between the impact forces and the measured acceleration responses of the cabinets. Then the estimated model is utilized to predict the seismic responses to the equivalent earthquake forces. For the numerical verification of the proposed method, a lumped-mass beam-stick model is built and analyzed. The comparison of predicted and simulated response spectra shows a good convergence. It demonstrates that the proposed method has potential in predicting response spectra for real cabinet structures by using vibration tests.

1. INTRODUCTION

It is clearly that a great majority of the existing cabinet structures in seismically active regions are vulnerable during earthquake. Therefore, more research is needed to expand knowledge on seismic behavior and design for cabinet structures. The qualification of the device is performed by testing it to a level equal to or greater than the established response at the mounting location. The earthquake input for the device is defined in terms of an in-cabinet response spectrum (ICRS) which can be calculated from the response at the mounting location of the cabinet. Vibration tests of equipment in the nuclear industry are performed for seismic qualification, modal properties measurements, and FE model validation and verification. Djordjevic (1992) suggested the amplification factor based on in-situ modal testing to scale the floor response spectra at the base to the amplified response spectra at the location of the mounted device. U.S. Electric Power Research Institute (EPRI 1990) developed generic seismic amplification factors for electrical cabinets, bench boards, and panels that are valid for any location in the cabinets. Gupta et al. (1999) and Gupta and Yang (2002) presented the Ritz vector approaches to evaluate the ICRS based on the observations from detailed finite element (FE) analyses of 16 typical cabinets. However, the generic amplification factors are typically very conservative and tend to give unrealistic spectra. Simple methods to generate the ICRS are needed to reduce the conservatism.

The seismic capacity of electric cabinets in nuclear power plants can be normally determined by shaking table tests. However, these tests cannot be used for the cabinets that have already been installed in operating plants since the cabinets are not permitted to be removed from the plants to be mounted on the shaking table. So the impact hammer tests can be an efficient and effective way to determine the modal properties of these cabinets. The main objective of this study is to develop an ICRS prediction algorithm for electrical equipment based on subspace system identification method without using FE analysis.

2. ICRS PREDICTION

The ICRS prediction is based on the artificial earthquake generated to be compatible with the design response spectrum. Then the seismic responses under artificial earthquake are predicted and converted to ICRS.

The governing equation under a seismic motion $\ddot{u}_g$ is given as follows:

$$M\ddot{u}_r + C\dot{u}_r + Ku_r = -M\{1\}\ddot{u}_g \tag{1}$$

Where, M, C, K are the mass, damping and stiffness matrices of the cabinet structure. u_r denotes the relative displacement vector to the base motion u_g and $\{1\}$ is the column vector filled with ones. As shown in Eq. (1) u_r is the system response when the load $f_e = -M\{1\}\ddot{u}_g$ which is so-called the earthquake-equivalent force is applied to the structure.

Based on input/output measurements from impact hammer tests, the input/output relationship of the structure can be identified in the form of a discrete-time state space equation (SSE) as follows.

$$x(k+1) = Ax(k) + Bu(k) + Ke(k)$$
$$y(k) = Cx(k) + Du(k) + e(k) \quad (2)$$

where $x(k)$, $y(k)$, $u(k)$ and $e(k)$ are the input force, the response acceleration, measurement noise and state column vector at time step $k(k = 1,2,\cdots,n)$; n is the number of time steps), respectively. A, B, C, D, and K are the system matrices. There are two types of algorithms available for identification of the discrete-time SSE: 1) Prediction Error Methods (PEM) which is iterative and 2) Stochastic Subspace Identifications (SSI) which are non-iterative. This study uses the N4SID (Numerical algorithms for subspace state space system identification) which is a variant of SSI and readily available in the MATLAB system identification toolbox. N4SID has advantages over the PEM in terms of computation time and convergence.

ICRS prediction is carried out straight-forwardly by using only the earthquake-equivalent force f_e as an input to the identified SSE. Figure 1 shows the flowchart of the proposed ICRS prediction procedure.

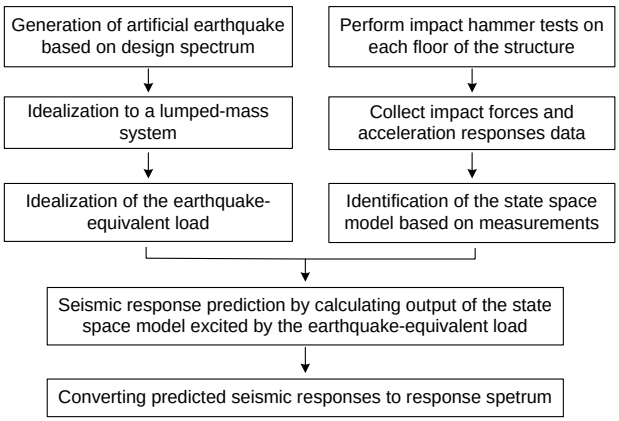

Figure 1 Flowchart of the ICRS prediction procedure

3. SUBSPACE IDENTIFICATION METHOD

The N4SID algorithm proposed by van Overschee and De Moor (1994, 1997) is a better approach than the classical system identification methods concerned with computing polynomial models as a variant of SSI. It is more closely related to linear systems theory in the engineering literatures.

The derivation of N4SID uses geometric arguments and a system theoretic approach, similar to the realization theory (Kailath 1980) and is summarized briefly in this section.

The state vector $x(k)$ is defined to be a linear combination of the past inputs and outputs

$$x(k) = Jp(k) \quad (3)$$

where $p(k)$ is referred to as the "past" for sample k. The dimension of the past is the number of lags N. The state vector $x(k)$ is calculated from data and is not specified to be a physical state of the system. After J has been calculated (as will be described below), the state vector can be estimated by Eq. (3). The state-space model matrices can then be estimated through linear regression

$$\begin{bmatrix} \hat{A} & \hat{B} \\ \hat{C} & \hat{D} \end{bmatrix} = \mathrm{cov}\left(\begin{bmatrix} x(k+1) \\ y(k) \end{bmatrix}, \begin{bmatrix} x(k) \\ u(k) \end{bmatrix}\right) \times \mathrm{cov}^{-1}\left(\begin{bmatrix} x(k) \\ y(k) \end{bmatrix}, \begin{bmatrix} x(k) \\ u(k) \end{bmatrix}\right) \quad (4)$$

The calculation of J distinguishes the various subspace algorithms from one another. In the N4SID approach, J results from a series of geometric arguments (or linear algebraic arguments) based on a set of matrix equations for the evolution of a linear system (van Overschee and De Moor 1996) based on a weighted singular value decomposition (SVD) (van Overschee and De Moor 1995) as follows:

$$svd(\mathrm{cov}(p, \bar{f})) = \begin{bmatrix} U_1 & U_2 \end{bmatrix} \begin{bmatrix} S_1 & 0 \\ 0 & S_2 \end{bmatrix} \begin{bmatrix} V_1^T \\ V_2^T \end{bmatrix} \quad (5)$$

where $\bar{f}$ is the "conditional future" estimated by the past observations $p(k)$, and S_1 is the singular value matrix with high contributions and S_2 is the singular value with negligibly small values on its diagonal.

N4SID only makes use of the lower dimensional sub-matrices with significant contributions U_1 and S_1, and ignores tiny contributions by U_2 and S_2 This is why N4SID is called a Stochastic Subspace Identification method. By inspecting the whole singular value matrix, the size of S_1 can be determined as the number of significant or non-negligible singular values in the whole singular value matrix which is equal to the order of the SSE model.

4. NUMERICAL VERIFICATION

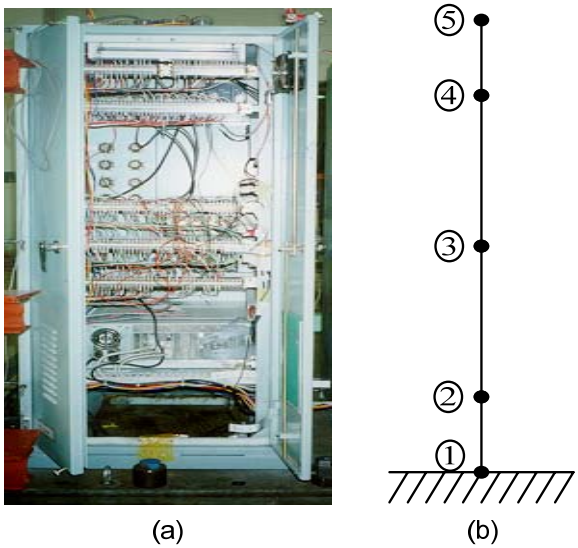

Figure 2 Cabinet and lumped-mass beam stick model:
(a) Inside view, and (b) Numerical model

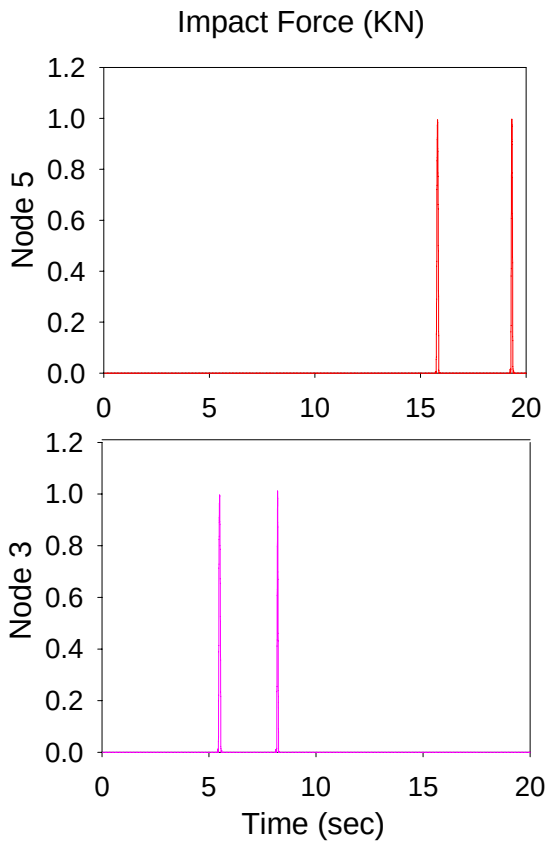

Figure 3 Instances of impact forces for input

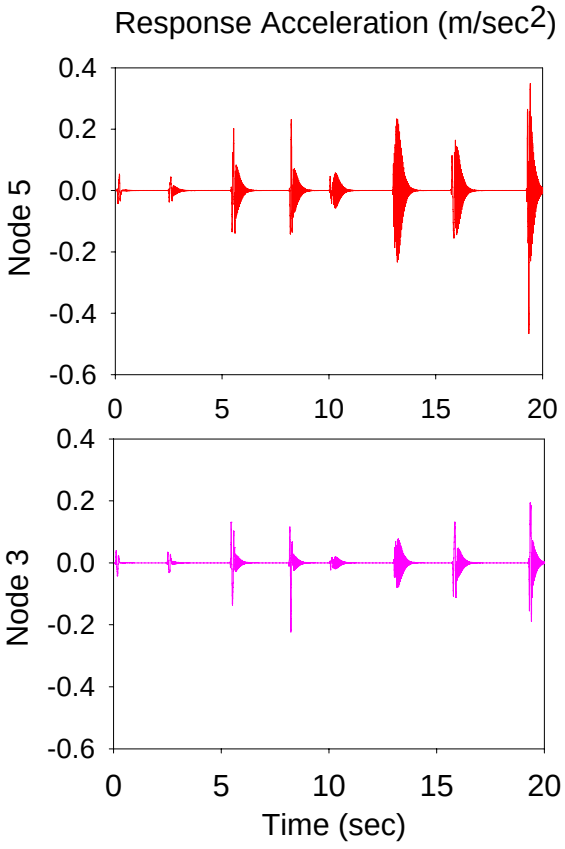

Figure 4 Instances of acceleration responses for output

Figure 2(a) shows the inside view of the cabinet structure that used for verification, and Figure 2(b) shows schematically the lumped-mass beam stick model. The impact hammer tests were performed at the four points from node 2 to node 5 continuously in time, and the acceleration responses were also collected at these nodes. So the impact forces and the acceleration responses in time domain are used as input-output data to build the state-space model. Figure 3 shows the impact forces at nodes 3 and 5 schematically while Figure 3 shows the acceleration responses.

Based on a set of the input/output measurements, a state-space equation model was identified by using N4SID. The order of the state-space equation was selected as 8 by inspecting the singular values obtained by Eq. (4) as shown in Figure 5.

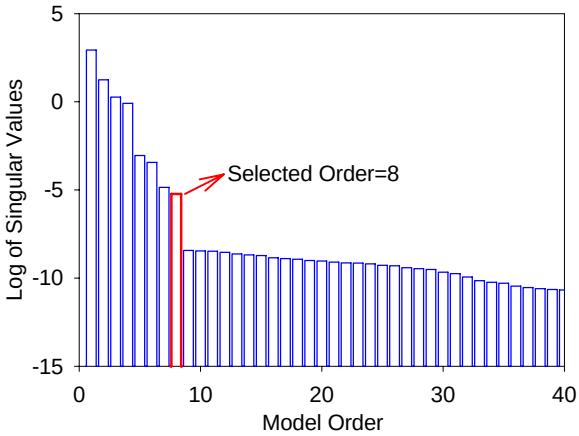

Figure 5 Model order in stochastic subspace identification

The artificial earthquakes were generated to be compatible with design response spectrum to predict ICRS as shown in Figure 6 for one set of artificial earthquake. For each of ten artificial earthquake cases, the equivalent earthquake force f_e was calculated by feeding the measured base motion $\ddot{u}_g$ into the SSE model as an input to estimate earthquake responses.

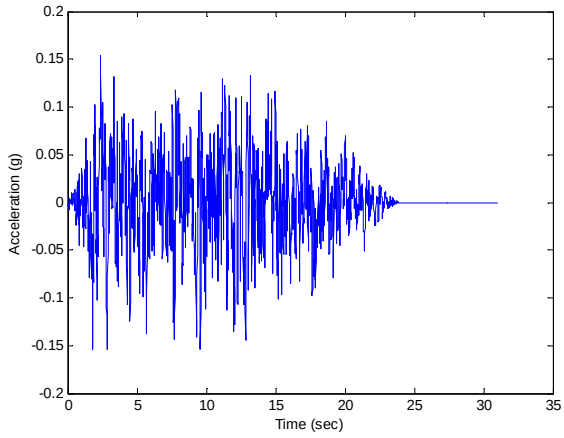

Figure 6 Artificial earthquake based on design spectrum

From the comparison of the simulated and predicted seismic responses, it can be found that the predicted responses reasonably agree with the simulated responses.

The simulated and predicted seismic responses are then converted to ICRS to verify the effectiveness of the proposed procedure. Figure 7 shows the comparison of simulated and predicted ICRS for one set of data of the top node (Node 5). The comparison of mean ICRS at node 5 from ten sets of simulated and predicted seismic responses shows a good convergence as shown in Figure 8.

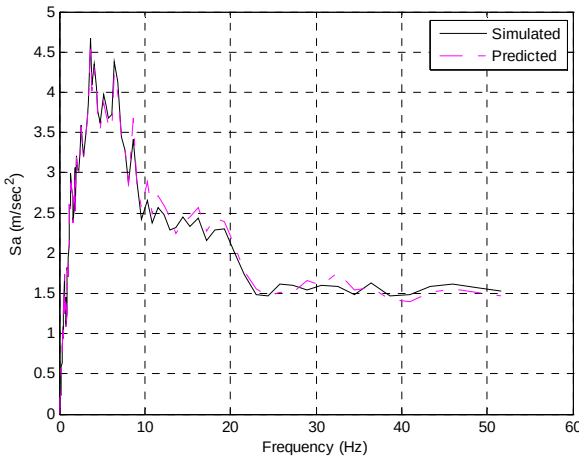

Figure 7 Comparisons of ICRS at node 5 (One set)

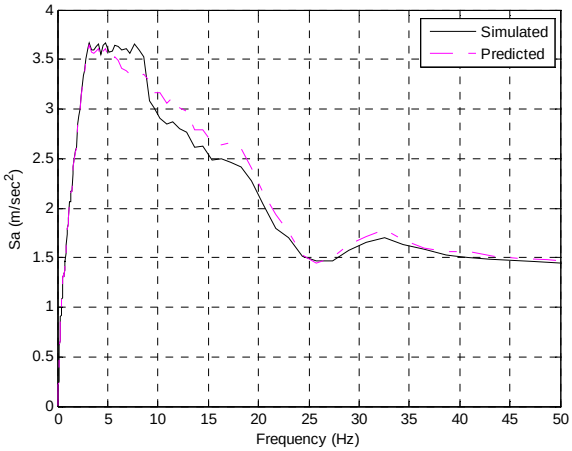

Figure 8 Comparisons of ICRS at node 5 (Mean)

5. CONCLUSIONS

This paper proposes an ICRS prediction method based on subspace identification method. The algorithm applies subspace system identification method to estimate the state-space model structures in order to build the relationship between the impact forces and the measured acceleration responses of the cabinet structures. Then the estimated state-space model is utilized to predict the seismic responses to the equivalent earthquake forces. The procedure is verified numerically on the lumped-mass beam stick model. From the comparisons of the predicted and simulated ICRS, one can note that the proposed algorithm can accurately and efficiently predict the ICRS of cabinet structures.

The proposed method is especially effective and efficient for the cabinet structures which are in operation in nuclear power plants. They are only reliable to be performed impact hammer tests but not suitable for the shaking table tests, as the cabinets which have already been installed in the operating plants are not permitted to be moved. The proposed algorithm can be developed to be a candidate algorithm for the ICRS prediction of cabinet structures.

For the further study, the experimental impact hammer tests and shaking table tests are expected to perform the verification of the proposed algorithm. Also the predicted ICRS is compared with the simulated one as well as the one based on generic seismic amplification factor proposed by EPRI. There is also a possible problem with obtaining the lumped mass matrix since exact weights of a cabinet system may not be readily available. It may be necessary to develop a way to estimate the lumped mass matrix from impact hammer tests.

Acknowledgements:

This research work presented in this paper was funded by Korea Institute of Energy Technology Evaluation and Planning (KETEP) under the Ministry of Knowledge Economy as a part of the Nuclear R&D Program. The financial support is gratefully acknowledged.

References:

Djordjevic, W., (1992), "Amplified response spectra for devices in electrical cabinets," Proc., 4th Symp. On Current Issues Related to Nuclear Power Plant Structures, Equipment and Piping, Orlando, Fla, Vol. 1992, pp.V/3-1-V/3-21.

EPRI, (1990), "Guidelines for Development of In-Cabinet Amplified Response Spectra for Electrical Benchboards and Panels," Electric Power Research Institute (EPRI), Palo alto, CA, EPRI NP-7146-M, Research Project 2925-8.

Gupta, A., Rustogi, S. K., and Gupta, A. K., (1999), "Ritz vector approach for evaluating in-cabinet response spectra," Nucl. Eng. Des., 190, 255–272.

Gupta, A., and Yang, J., (2002), "Modified Ritz vector approach for dynamic properties of electrical cabinets and control panels," Nucl. Eng. Des., 217(1-2), 49–62.

Kailath, T., (1980), "Linear Systems," Prentice Hall: Englewood Cliffs, NJ.

MIDAS Civil 2006 Online Manual, MIDAS Information Technology Co., Ltd. 2005.

van Overschee, P., and de Moor, B., (1994), "N4SID: Subspace algorithms for the identification of combined deterministic-stochastic systems," Automatica, 30, 75-93.

van Overschee, P., and de Moor, B., (1995), "A Unifying Theorem for Three Subspace System Identification Algorithms," Automatica, 31, 1853-1864.

van Overschee, P., and de Moor, B., (1996), "Subspace Identification for Linear Systems," Kluwer Academic Publishers: Boston, MA.

van Overschee, P., and de Moor, B., (1997), "Closed-loop subspace system identification," Proc. of the 36th Conference on Decision and Control, pp. 1848-1853.

JOINT CONFERENCE PROCEEDINGS
7th International Conference on Urban Earthquake Engineering (7CUEE) &
5th International Conference on Earthquake Engineering (5ICEE)
March 3-5, 2010, Tokyo Institute of Technology, Tokyo, Japan

CRACKING BEHAVIOR OF REINFORCED CONCRETE BEAMS REPAIRED WITH STRAIN HARDENING CEMENT-BASED COMPOSITE

Yuichi Uchida[1)], Seungchan Lim[2)], and Mamoru Moriyama[3)]

1) Professor, Multimedia and Information Center, Gifu University, Japan
2) Deros Japan Co., Ltd, Japan
3) Central Nippon Expressway Co., Ltd., Japan
uchida@gifu-u.ac.jp, sclim@deros-japan.co.jp, m.moriyama.aa@c-nexco.co.jp

Abstract: The cracking behavior of reinforced concrete beams patch repaired using the strain hardening cement-based composites (SHCC) was experimentally investigated. The width and number of cracks on the tension edge of the beams repaired with SHCC and the strain distribution of tensile reinforcement were measured. The crack width in SHCC was found to be 0.1 mm at the largest, with the number of cracks increasing as the load increased, without increasing the crack width. The degree of fine crack dispersion in SHCC varied depending on the thickness of SHCC and the tensile strain capacity of SHCC.

1. INTRODUCTION

A strain hardening cement-based composite (SHCC) with multiple fine cracks is characterized by its "strain hardening property," with which it increases its tensile load (or tensile stress) as its deformation (or strain) increases without causing brittle failure under tensile forces, and "multiple cracking property," with which it disperses cracks into multiple fine ones.

The patch repair is the one of repair methods for deteriorated or damaged concrete structures. Performances required of patch repair materials include strength, dimensional stability, shield ability, durability, and cohesion with the substrate. Various tests have been conducted on the mechanical properties of patch repair materials applied to tensile surface of beams (Matsubara et al. 2002), including those to investigate the applicability of SHCC as patch repair and an overlay on tensile surface (Lim et al. 2002, Fukuda et al. 2003, Kim et al. 2005). However, these studies have not clarified the degree of ductility required for patch repair materials. Also, the effect and the degree of fine crack dispersion after repair may vary depending on the degree of the ductility (ultimate tensile strain) of SHCC as a patch repair material and the thickness of SHCC patch repair.

In this study, the authors experimentally investigated the cracking behavior and load-deflection relationship of reinforced concrete beams patch repaired with two types of SHCCs having different ultimate tensile strains and different thickness of SHCC patch repair.

2. OUTLINE OF EXPERIMET

2.1 Materials

Tables 1 and 2 give the mix proportions of substrate concrete and two types of SHCCs, respectively, used in the tests.

(1) Substrate concrete

Substrate concrete was produced using normal portland cement with a density of 3.15 g/cm^3, land sand with a density of 2.58 g/cm^3 as the fine aggregate, and crushed stone with a density of 2.62 g/cm^3 and maximum size of 20 mm as the coarse aggregate with a water-cement ratio (W/C) of 49.5%.

(2) SHCC

Two types of SHCCs, a casting type and spraying type, were used. Both were made of a matrix of premixed polymer cement mortar and a blend of polyvinyl alcohol (PVA) fibers 12 mm in length and 40 μm in diameter and polyethylene (PE) fibers 9 mm in length and 12 μm in diameter with a fiber content of 2% by volume. The unit water content and slump flow of the casting-type SHCC were 286 kg/m^3 and 520 mm, respectively, whereas the unit water content and table flow of the spraying-type SHCC were 303 kg/m^3 and 147 mm, respectively. These materials were added to a geared mixer and mixed for 2 and 3 minutes for the casting and spraying types, respectively.

2.2 Outline of specimens

(1) Substrate concrete specimens

Figure 1 shows the shape and dimensions of the beam specimen. It is a double reinforced concrete beam measuring 200×300×3000 mm. The kinds of specimens are tabulated in Table 3. The thicknesses of SHCC patch repair are 10 mm,

Table 1 Mix Proportion of Substrate Concrete

W/C (%)	Unit content (kg/m^3)					Slump (cm)	Air (%)
	W	C	S	G	Ad.		
49.5	153	309	748	1082	0.96	7.5	4.0

Table 2 Mix Proportion of SHCC

Kind of SHCC	Unit content (kg/m^3)			Fiber (vol%)	Flow (mm)
	W	Premixed material	Polymer emulsion		
Casting	286	1507	34.7	2	520*[1]
Spraying	303	1640	-	2	147*[2]

*[1] Slump flow *[2] Mortal table flow

Table 3 Kinds of Specimens

Specimen	N-0	SC-10	SC-40	SC-100	SP-100
Thickness of patch (mm)	0	10	40	100	100
Type of SHCC	-	Casting			Spraying

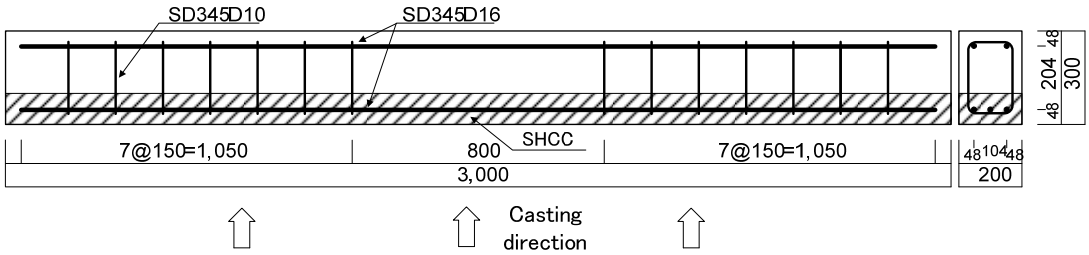

Figure 1 Dimension of Beam Specimen

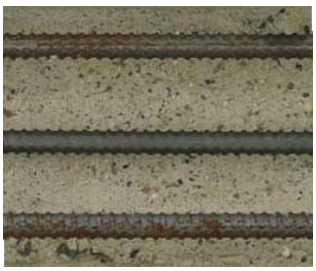

Photo 1 Surface Treatment of Construction Joint by Water Jet

40 mm and 100 mm. Two specimens were fabricated for each series, totaling ten specimens including reference unrepaired beams (N-0). Assuming bending failure, two and three threaded D16 bars (SD345) were arranged on the compression and tension sides, respectively, while D10 bars (SD345) were used as transverse bars at 150 mm intervals. Strain gauges with a gauge length of 2 mm were attached at 40 mm intervals to grooves cut in the 800 mm-long uniform bending moment zone of the central bar on the tension side of one of the two beams of each series.

Each specimen was fabricated by placing concrete with the compression side lying on the bottom of formwork. For specimens to be repaired with SHCC, concrete was placed to a predefined depth, and after air curing to an age of 14 days, the placing surface was treated with a water jet. Patching with SHCC was then carried out at an age of 4 weeks.

(2) Surface treatment of construction joint

The joint surface of specimens to be patched with SHCC was treated using a water jet with a jet pressure of 180 N/mm^2 and discharge rate of 10 *l*/min to a depth of approximately 1 to 2 mm, where coarse aggregate began to appear. The surface after treatment is shown in Photo 1.

(3) Patching

Beam specimens were patched with SHCC by casting or spraying. Patching by spraying using a spray-type SHCC was carried out by downward spraying of the as-mixed material pumped by a squeeze pump.

Patching with a casting-type SHCC was carried out by

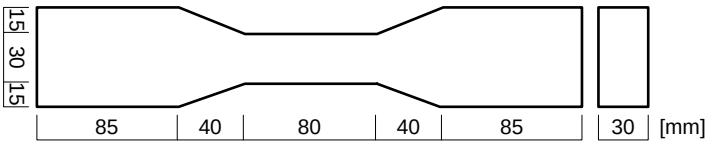

Figure 2 Tension Test Specimen of SHCC

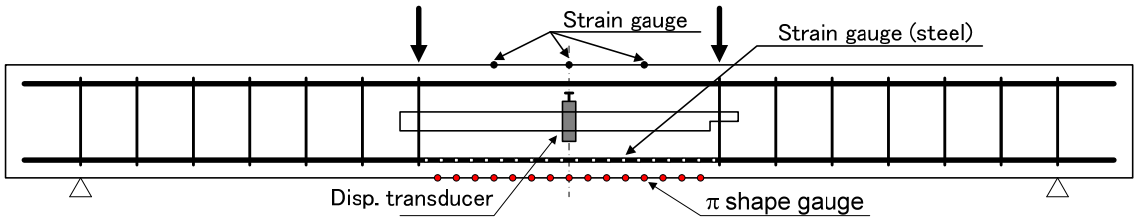

Figure 3 Flexural Loading Test

Table 4 Strength of Materials

Concrete/SHCC	Strength (N/mm^2)	
	Comp.	Flexural
Substrate	24.6	3.8
Casting	29.3	10.7
Spraying	42.8	8.0

allowing the as-mixed material to flow from the center toward both ends while applying vibration to the formwork with a mallet and vibrator, without using a tamping rod or internal vibrator.

Note that downward casting/spraying is not commonly practiced in actual repair but was adopted in this study to minimize the casting/spraying-related factors affecting the test results, as downward casting/spraying is deemed easier to do, leading to more stable results. The effect of the direction of casting/spraying will therefore have to be investigated in the future.

(4) Specimens for strength tests

Apart from beam specimens, specimens for compression, bending, and tension tests were fabricated for the substrate concrete and two SHCCs. Specimens for strength tests were also fabricated both by spraying and casting. Compression and bending specimens were cylinders 100 mm in diameter and 200 mm in height and beams measuring 100×100×400 mm, respectively.

Tension specimens of SHCC were dumbbell specimens as shown in Figure 2. Bending tests consisted of third point loading tests, whereas uniaxial tension tests were conducted by engaging the enlarged ends of specimens in the locks to transfer the tensile forces. The displacement was measured with respect to a datum length of 80 mm under loading at a rate of around 0.5 mm/min.

2.3 Flexural loading test

Figure 3 shows the flexural loading test outline for beam specimens with or without patching. The flexural loading tests consisted of four-point loading tests with a moment span of 800 mm on specimens at an age of SHCC of 1 month. In addition to the load and midspan displacement measurement, the compressive strain was measured using three strain gauges attached to the bending moment zone on the compression side (in the center of specimen length at 200 mm intervals). The crack width on the tension side was measured using 15 π shape displacement gauges with a gauge length of 50 mm continuously attached to the bending moment zone.

3. TEST RESULTS

3.1 Material strength tests

Table 4 gives the compressive and flexural strengths of each material. Figure 4 shows the uniaxial tension test results of SHCC. Whereas spraying-type specimens recorded the ultimate strain and tensile strength of 0.6% and 5.3 N/mm^2, casting-type specimens recorded the ultimate strain and tensile strength of 4.7% and 6.4 N/mm^2, respectively.

3.2 Cracking in beam specimens

(1)Overview

Figure 5 shows the cracking pattern at the uniform bending moment zone of beam specimens after the loading test. The state of cracking during the loading test in unrepaired reference specimens significantly differed from that in specimens patched with SHCC. Cracks occurred on the tension edge of unrepaired reference specimens at 150 to 200 mm intervals, with their width increasing as the load increased. On the other hand, dispersed fine cracks occurred

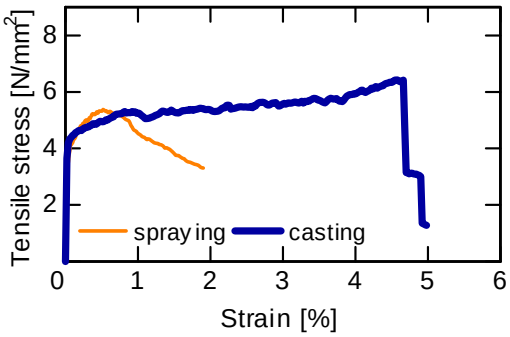

Figure 4 Tensile S-S Curve of SHCC

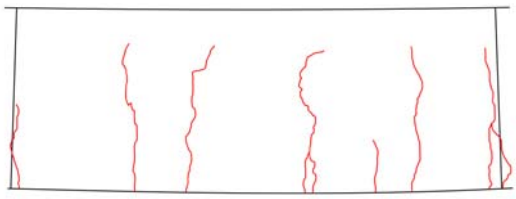

(a) N-0

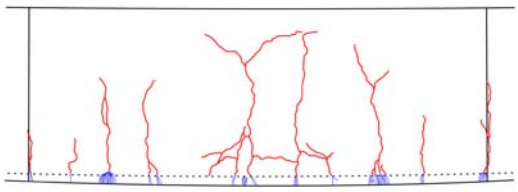

(b) SC-10

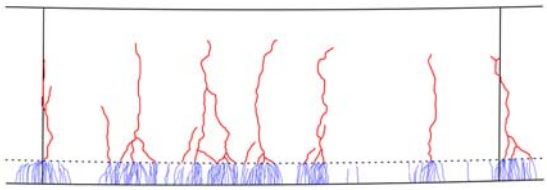

(c) SC-40

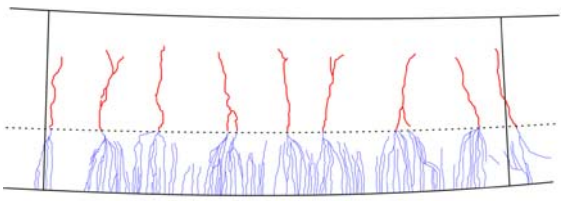

(d) SC-100

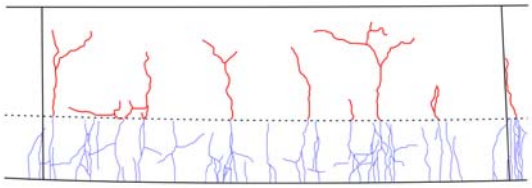

(c) SP-100

Figure 5 Cracking Pattern of Specimens

in the tension edge of specimens repaired with casting-type SHCC as the load increased. When cracking occurred in substrate concrete, the cracks in SHCC tended to concentrate on the locations of cracks in substrate concrete. However, the number of fine cracks increased meanwhile in the tension edge, without crack concentration on the tension edge (see Photo 2). Note that the crack intervals in substrate concrete were around 100 mm, being evidently narrower than in unrepaired specimens. Also, no crack was visually observed along the joint between concrete and SHCC until the yielding of reinforcement.

The fine cracks occurred in SHCC dispersed from the locations of cracks in substrate concrete toward the bottom surface of the beam. The fine crack dispersed uniformly at the bottom surface of SHCC in case of the beam having thicker patch repair.

While the behavior of spraying-type SHCC (SP-100) was similar to the casting-type, the number of cracks in SHCC was fewer than in the casting-type, which tended to partially concentrate instead of being uniformly dispersed over the moment zone. However, cracking occurred in substrate concrete at 100 to 150 mm intervals, which is a little larger than that of casting-type SHCC.

(2)Relationship between reinforcement strain and crack width

Figure 6 (a) shows the relationship between the crack width of a representative crack in the tension edge of an unrepaired specimen (N-0) measured by a π shape displacement gauge and the strain of reinforcement at the location of the crack. In this case, the crack width increased in proportion to the reinforcement strain.

Figure 6 (b) and (c) show the relationship between the

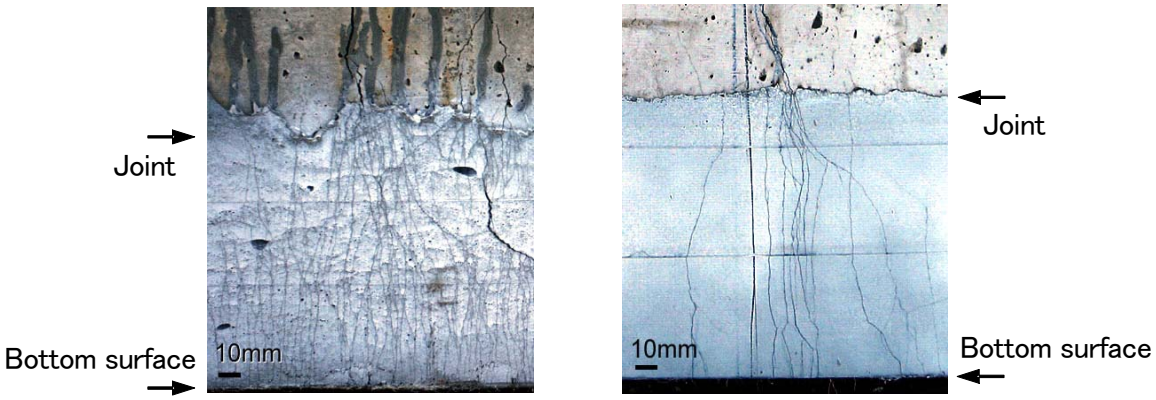

Photo 2 Cracking of SHCC

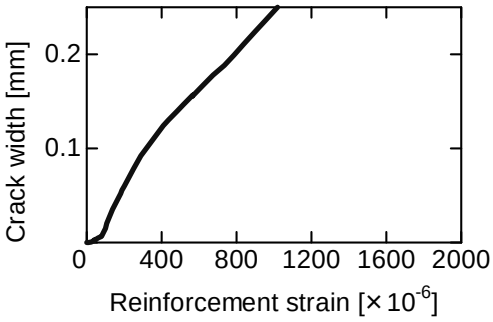

(a) N-0

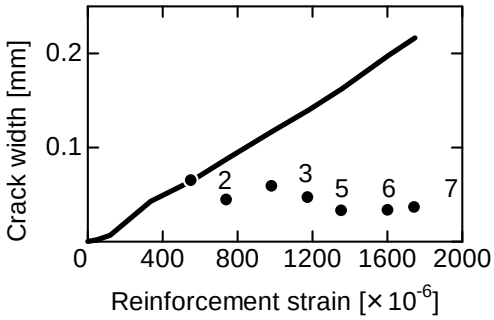

(b) SC-10

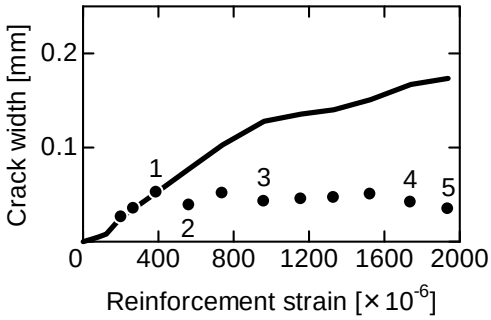

(c) SC-100

Figure 6 Crack width - reinforcement strain relationship

crack width of a representative crack measured in specimens patch repaired with casting-type SHCC (SC-10, SC-100) and the reinforcement strain. In these figures, the solid line represents the crack width measured by a π shape displacement gauge, increasing as the reinforcement strain increases. However, the slope of the curve is evidently gentler than the case of unrepaired reference specimen shown in Figure 6 (a).

For specimens repaired with SHCC, loading was stopped at every certain increment in the load to visually count the number of cracks present within the measurement length of each π shape gauge. The black circles in the figure represent the values obtained by dividing the measured displacement by the number of cracks, which correspond to the average crack width within the measurement range of each π shape gauge. Also, the numbers in the figure denote the number of cracks. Accordingly, the average crack width of specimens strengthened with SHCC is found to increase to around 0.1 mm as the reinforcement strain increases but scarcely increase thereafter by increasing the number of cracks instead.

3.3 Load-displacement relationship

Figure 7 shows the moment-curvature relationship within the uniform moment zone of specimens. The cracking load, yield load, and ultimate load of specimens strengthened with SHCC are greater than those of un-repaired specimens, showing that SHCC bears part of the tensile forces. The yield load and ultimate load of both experiment and calculation increase with the increase of the

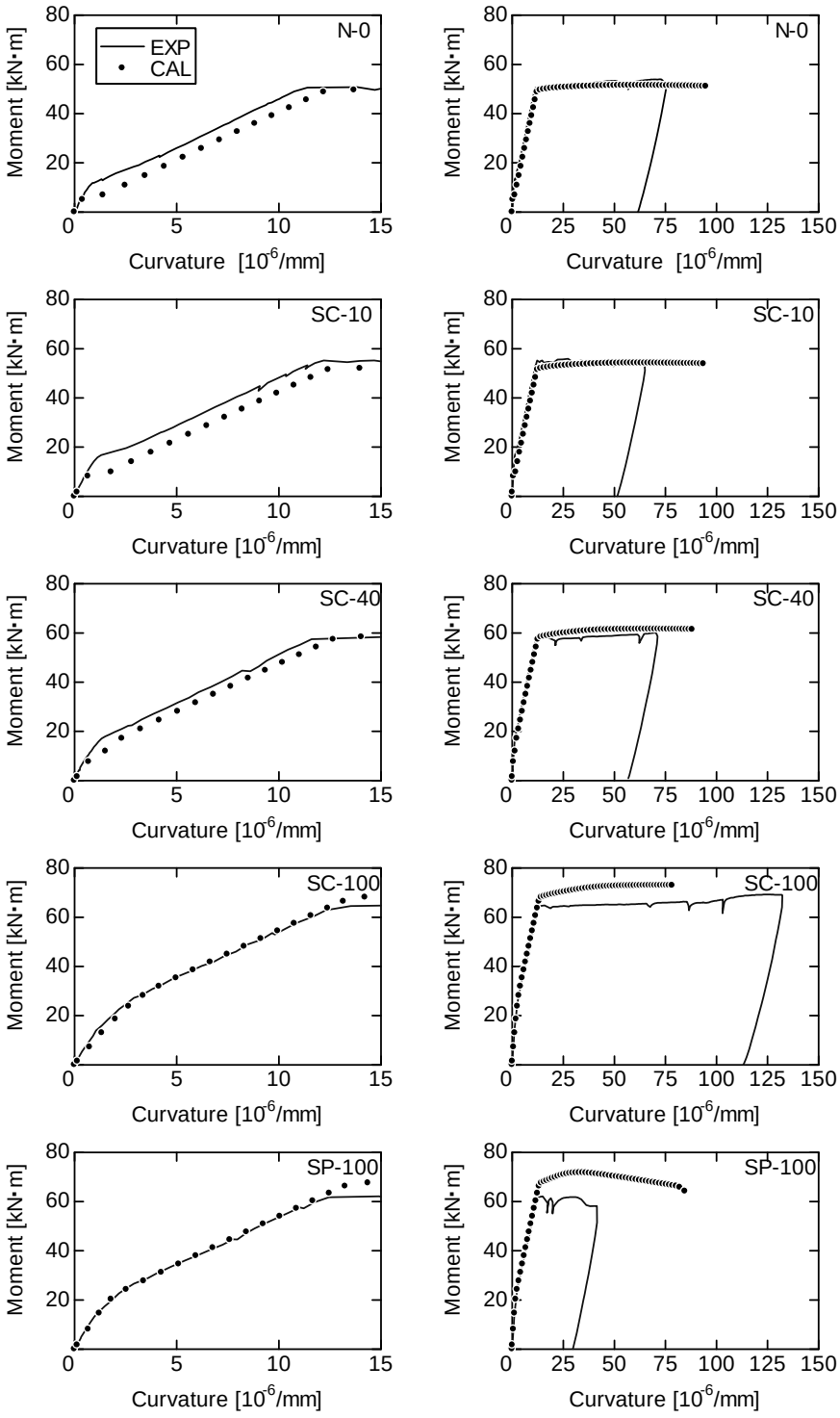

Figure 7 Moment-Curvature Relationship (Left: Initial part, Right: Whole)

thickness of SHCC patch repair.

When comparing casting and spraying applications, the yield load of specimens strengthened with the casting-type SHCC is slightly greater than the spraying type, though these were comparable until near-yield loads. It should be noted, however, that the load-bearing capacity of the spraying-type SHCC gradually decreased from immediately after yielding. This can be attributed to the loss of part of the tensile load borne by sprayed SHCC at cracked sections at an early stage, which presumably caused the concentration of deformation on the cracked sections, expediting the crush of concrete on the compression edge.

Figure 7 also shows the moment-curvature relationship calculated by a fiber model (plotted with black circles) using the stress-strain relationship of each material obtained by material testing. Note that the tension-stiffening effect was

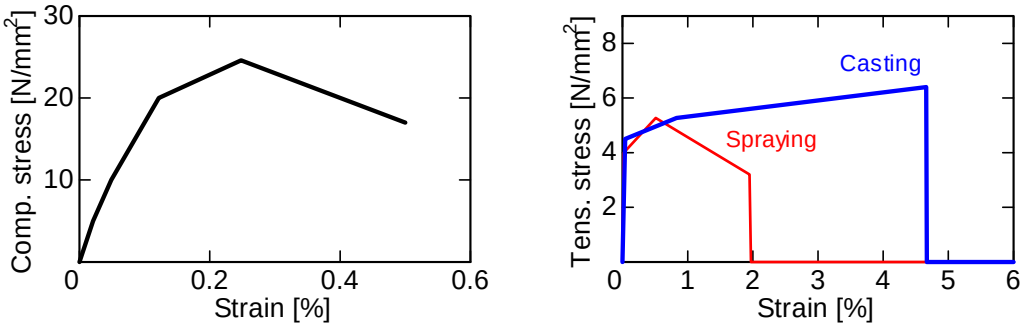

Figure 8 S-S curves used for calculation

ignored in the calculation. Also, substrate concrete was modeled to undergo brittle failure at the point of reaching the tensile strength. For SHCC, the stress-strain relationship shown in Figure 8, which is a model based on the material tests (Figure 4) was used. Reinforcement was assumed to be perfectly elastoplastic.

The calculated rigidity of unrepaired reference specimens and specimens with thin SHCC patch repair before yielding is lower than the test values. This can be attributed to disregarding of the tension-stiffening effect. On the other hand, the calculated and measured curves for specimens strengthened with a thickness of 100 mm SHCC (SC-100 and SP-100) agree well until yielding, showing that it is not necessary to consider the tension-stiffening effect, provided the tensile stress-strain relationship of SHCC is considered. Also, when comparing the calculated and measured loads at yield and thereafter, the calculated values are higher than the test values. This is presumably because the properties of SHCC placed in the specimens can differ from those of SHCC expressed by the stress-strain relationship obtained from material testing, due to the effects of size and fiber orientation. Note that the reduction in the load-bearing capacity of spraying-type SHCC that occurs after yielding while the deformation is still small is expressed by the calculation results shown in Figure 7 (b). As shown in Figure 8, this can be attributed to the difference between the ultimate values in the tensile stress-strain relationships of spray-type and casting- type SHCCs.

4. SUMMARY

The results of this study can be summarized as follows:
(1) In specimens patch repaired with SHCC, the crack width on the tension edge increased as the load increased but to no greater than around 0.1 mm. Though the tensile strain continued to increase thereafter, only the number of cracks increased, without increasing the average crack width. The crack-dispersing capability of casting-type SHCC was higher than that of spraying-type SHCC.
(2) The crack dispersability of SHCC at the bottom surface of beam specimen improved with the increase of the thickness of SHCC patch repair.
(3) As for moment-curvature relationship, the load-bearing capacity of specimens patch repaired with SHCC was larger than that of unrepaired specimens, as SHCC evidently bore part of the tensile forces. The load-bearing capacity of specimens increased with the increase of the thickness of SHCC patch repair.
(4) The calculated and measured moment-curvature relationships of specimens patch repaired with thick SHCC nearly agreed without giving consideration to the tension-stiffening effect provided the tensile stress-strain relationship of SHCC was considered.
(5) The ultimate tensile strain of spraying-type SHCC being lower than that of casting-type SHCC appeared in the behavior of beam specimens as differences in the crack dispersability and the displacement at the time when the load-bearing capacity began to decrease after yielding.

References:

Matsubara, N., Yokoyama, K., Kano, Y. and Sakata, N. (2002), "Mechanical Properties and Durability of Materials for Thickness Increment Under Bottom Surface", *Proceedings of the Japan Concrete Institute*, **24**(1), 1419-1424. (in Japanese)

Lim, Y.M., Kim, M.K., Kim, J.H.J and Shin, S.K. (2002), "Is Ductility Important for Repair Application ?", *Proceedings of the JCI International Workshop on Ductile Fiber Reinforced Cementitious Composites* (*DFRCC*), 199-208. (in Japanese)

Fukuda, I., Suda, K., Kanda, T., Sakata, N., and Hiraishi, M. (2003), "Design Method of Bending Member in Consideration of Tensile Strength of ECC", *JCI Symposium on Ductile Fiber Reinforced Cementitious Composites* (*DFRCC*)", 169-174. (in Japanese)

Kim. J.H.J., Lim Y.M. and Won, J.P.(2005), Experimental Investigation of Shear Dominant RC Beam Repaired with DFRCC at Cover Thickness, *International RILEM Workshop on High Performance Fiber Reinforced Cementitious Composites (HPFRCC) in Structural Applications*, 411-419.

JOINT CONFERENCE PROCEEDINGS
7th International Conference on Urban Earthquake Engineering (7CUEE) &
5th International Conference on Earthquake Engineering (5ICEE)
March 3-5, 2010, Tokyo Institute of Technology, Tokyo, Japan

FATIGUE BEHAVIOR OF LOAD-CARRYING CRUCIFORM JOINTS WITH WELD DEFECT UNDER CYCLIC PLASTIC STRAIN

Takeshi Hanji[1], Saiprasertkit Kawin[2], and Chitoshi Miki[3]

1) Post doctoral research fellow, Center for Urban Earthquake and Engineering, Tokyo Institute of Technology, Japan
2) Graduate student, Department of Civil Engineering, Tokyo Institute of Technology, Japan
3) Professor, Department of Civil Engineering, Tokyo Institute of Technology, Japan
hanji@cv.titech.ac.jp, saiprasertkit.k.aa@m.titech.ac.jp, miki@cv.titech.ac.jp

Abstract: In this study, fatigue behavior of load-carrying cruciform joints with incomplete penetrations under cyclic plastic strains, corresponding to the fatigue life is less than hundreds cycles, was experimentally investigated. In all specimens, fatigue cracks initiated from the weld root and propagated into the weld deposit. Crack initiation life was rather small compared with crack propagation life. This means that the propagation life is dominant in the fatigue life of the joints. Fracture surfaces under cyclic plastic strains contained dimples, which can produce an evidence of ductile crack propagation.

1. INTRODUCTION

Steel bridge piers are widely used in elevated highways in urban area, which play an important role in transportation. For example in Japan, there are more than 5000 steel piers. Their beams and columns are designed to assemble with full penetration welding, as shown in Figure 1. However at the connection, partial penetration welded joints, or fillet welded joints in the worst case, resulting from shoddy constructions are often observed. This means that the existing beam-to-column connection can be load-carrying cruciform joints with the incomplete penetration (Miki and Hirabayashi 2007), as shown in Figure 2. The incomplete penetration, called "weld defect" here, can be a fatigue crack initiation point due to high stress or strain concentration. Therefore, special care should be given to the fatigue behavior of the connections in order to prevent the failure of the piers.

Two types of limit states can be supposed at the connection. One is the serviceability limit state due to traffic load, which causes a high cycle fatigue crack, and the number of related cycles is more than 10^4. Another is the ultimate limit state due to cyclic plastic deformation like seismic load, which causes a low cycle fatigue crack, and the number of related cycles is less than 10^2. Actually, a large number of the high cycle fatigue damage has been observed at the connection, which initiated from the weld defect (Morikawa et al. 2002). Besides, the low cycle fatigue damage, which can be a trigger of brittle fracture, has been found at the connection during the Kobe Earthquake (Okashita et al. 1998). Therefore, fatigue strength of the load-carrying cruciform joints with the weld defect should be carefully investigated from low cycle to high cycle fatigue regions, corresponding to the fatigue life from tens cycles to millions cycles.

For the high cycle fatigue strength of the load-carrying cruciform joints containing the incomplete penetrations, comprehensive research has been conducted. For example, the fatigue performance of the joint has been examined, and a fatigue life estimation method based on a fracture mechanics analysis has been proposed (Frank and Fisher 1979, Miki et al. 1993). Also, fatigue tests on steel piers, which included the weld defect at their beam-to-column connection, have been performed under high cycle loading and indicated that the defect can reduce the fatigue strength of the connection (Miki et al. 2002). Meanwhile in low cycle fatigue region, there have been a small number of studies on the welded joint containing the defect, and the research focused on the fatigue behavior of butt welded joints only (Ishii and Iida 1969, Kayamori et al. 2001). Therefore, influence of the weld defect on low cycle fatigue strength of load-carrying cruciform joints has not been investigated yet.

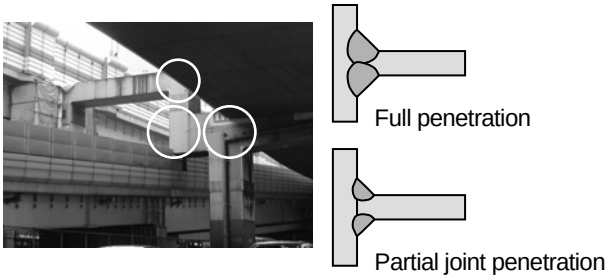

Figure 1 General view of beam-to-column connection

In this study, fatigue tests on load-carrying cruciform joints with the incomplete penetration were carried out under cyclic plastic strains, and the fatigue behavior of the joint was examined.

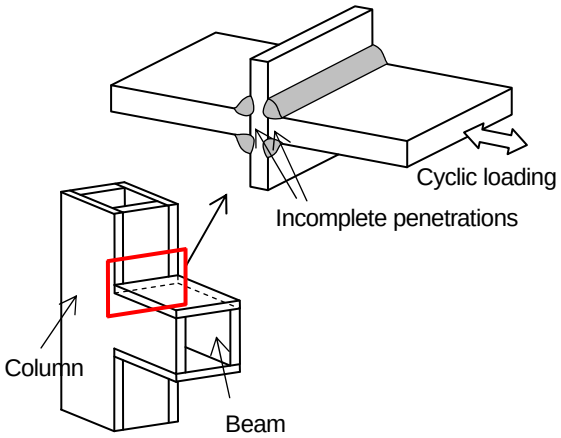

Figure 2 Load-carrying cruciform joint containing incomplete penetration

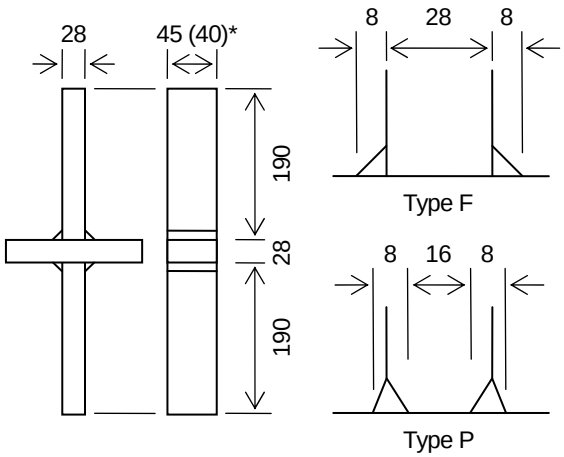

Figure 3 Specimen (* : number in a bracket show the specimen type B for fatigue tests)

2. EXPERIMENTAL METHODS

2.1 Specimen

The configurations and dimensions of the specimen are shown in Figure 3. Two types of cruciform joints were made of 490MPa class steel plate of 28mm thickness. In specimen type F, the joint was fabricated by fillet welds, while partial joint penetration groove welds were applied to specimen type P. The penetration ratio, which is defined as the ratio between the length of the unfused portion and the thickness of the loading plate, were designed to be 100% in specimen F and 60% in specimen P, respectively. The width of the specimen P for the fatigue tests was reduced to 40mm as shown in Figure 3, due to the maximum loading capacity of the testing machine.

Three different weld materials were used to vary matching conditions between the base metal and the weld deposit. The welding conditions are given in Table 1. Figure 4 shows the result of tensile tests for each material. In the test, round bar type specimens cut out from the welded joint shown in the figure were employed. The mechanical properties of the loading plate and the weld deposit obtained from the tensile tests are listed in Table 2. It can be found that all specimens used in the test are over-matched joints. The specimens were named as summarized in Table 3.

Macro etch tests were carried out to locate the heat affected zone, the deposit metal and the base metal. The etched surfaces are shown in Figure 5. Figure 6 shows the average value of the weld size (H_1, H_2), the root size (2a) and the fusion size (p) measured from the photos. Referring the research in the high cycle fatigue region (Miki et al. 1993), parameters of $2a/t_p$ and H_1/t_p in the specimen, where t_p is the thickness of loading plate, are satisfied with conditions which ensure the failures from the weld root.

2.2 Experimental Procedures

In addition to low cycle fatigue tests, tensile tests and high cycle fatigue tests, were conducted to examine the failure behavior of the specimen.

2.2.1 Tensile test

The amsler testing machine with 2000kN loading capacity applied a monotonic tensile load to the specimen. For measurements of deformation around the weld portion,

Table 1 Welding conditions

Weld material			Welding condition				
Type		Diameter (mm)	Current (A)	Voltage (V)	Speed (mm/min)	Heat input (kJ/mm)	Interpass Temperature (°C)
A	YM-24S + Ar+40%CO_2	1.2	280 ~ 300	30 ~ 32	250 ~ 300	1.7 ~ 2.1	≤ 50
B	YM-24S + Ar+10%CO_2	1.2	280 ~ 300	31 ~ 33	240 ~ 300	2.0 ~ 2.4	≤ 50
C	YM-28 + CO_2	1.2	250 ~ 270	26 ~ 28	330 ~ 380	1.1 ~ 1.3	≤ 50

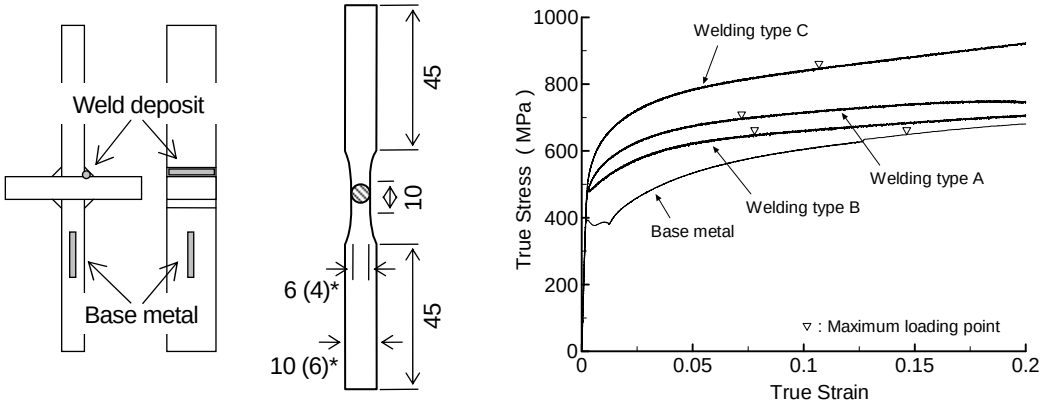

(a) Round bar specimen (b) Stress - strain relationship

Figure 4 Specimen and result of tensile test (* : number in brackets show the specimen for weld deposit)

Table 2 Mechanical properties of materials

Material		Yield stress (MPa)	Tensile stress (MPa)	Ratio of yield stresses (WD/BM)
Base metal (BM)		392	546	–
Weld deposit (WD)	A	498	637	1.27
	B	494	608	1.24
	C	565	760	1.44

Table 3 List of specimens

Welding type	Fillet weld			Partial joint penetration groove weld		
Weld material	A	B	C	A	B	C
Specimen name	FA	FB	FC	PA	PB	PC

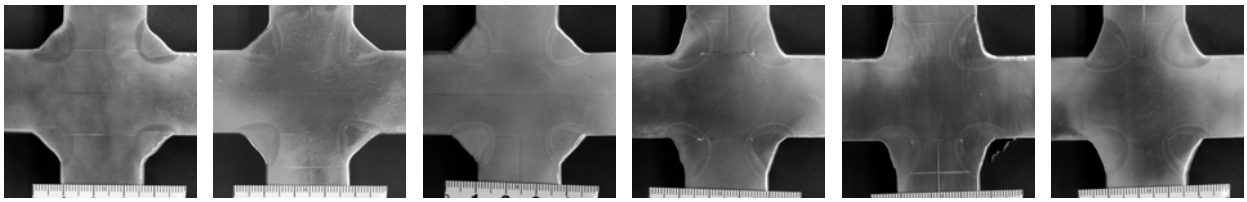

(a) Specimen FA (b) Specimen FB (c) Specimen FC (d) Specimen PA (e) Specimen PB (f) Specimen PC

Figure 5 Macro etch test result (loading direction: up-and-down)

PI displacement transducers of 50mm gauge length were mounted to both side surface of the loading plate to cross the weld roots as shown in Figure 7. The width of all specimens was 45mm.

2.2.2 Low cycle fatigue test

The fatigue testing machine was an electric hydraulic servo system with a dynamic and a static loading capacity of 300kN and 450kN. Low cycle fatigue tests were controlled by the value of the displacement transducer attached to the specimen as the tensile test, giving the displacement range of 0.18, 0.23 and 0.33mm. The ratio of the minimum and the maximum displacement was ranged from 0.06 to 0.1. Cyclic load with very low loading rate of approximately from 0.0017 to 0.0076mm/sec was applied to the specimen. For the specimen with 0.33mm displacement range, after one weld bead was penetrated by cracking, the specimen was loaded monotonically to break completely. For displacement range of 0.18 and 0.23mm, the test was stopped when the load dropped by 30% from the maximum load at initial loop. As shown in Figure 7, strain gauges were attached on the weld bead to detect the crack initiation from the root.

2.2.3 High cycle fatigue test

High cycle fatigue tests were conducted under load controlling condition. The nominal stress range, which can be obtained by dividing the load range by the measured weld throat area, was from 140 to 180MPa. The stress ratio of the test was almost 0. Sinusoidal wave with its frequency of 10Hz was used. To observe the crack propagation, beach mark tests were included during the test. The test was continued until the specimen was ruptured.

3. TEST RESULTS

3.1 Load-Displacement Relationship

The relationship between the load and the displacement in the tensile test is shown in Figure 8. The displacement is the averaged values of two PI gauges. Specimen type P shows higher load carrying capacity than specimen type F, and specimen PC is the highest. Relatively low elongation can be observed in specimen FB compared to others.

Figure 9 shows an example of the load-displacement relationship in the low cycle fatigue test. Cyclic hardening behavior cannot be found in the graph. The maximum load at each loop was picked up and related to the number of cycles in Figure 10. The ordinate shows the ratio by the maximum load of each cycle to initial cycle. The maximum load is decreasing with the load repetition.

3.2 Strain Behavior

Figure 11 indicates an example of a strain behavior in the low cycle fatigue test obtained from the strain gauge on a weld bead, where the crack first penetrated during the test. The vertical axis represents the ratio by the maximum strain of each cycle to first cycle. The strain varies just after one cycle. This means that the crack originated at the initial cycle, then the crack propagation dominate for the most part of total life of this joint. This tendency is the similar as the high cycle fatigue crack.

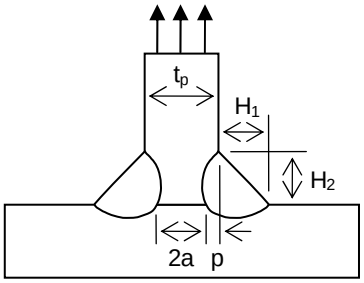

Specimen	t_p (mm)	H_1 (mm)	H_2 (mm)	2a (mm)	p (mm)	H_1/t_p	$2a/t_p$
FA	28	8.99	8.80	24.12	1.94	0.32	0.86
FB	28	9.56	9.07	24.54	1.73	0.34	0.88
FC	28	8.84	8.86	23.00	2.50	0.32	0.82
PA	28	6.11	11.31	17.34	5.33	0.22	0.62
PB	28	5.13	10.86	16.96	5.52	0.18	0.61
PC	28	6.14	11.28	17.60	5.20	0.22	0.63

Figure 6 Average values in measurements of weldment

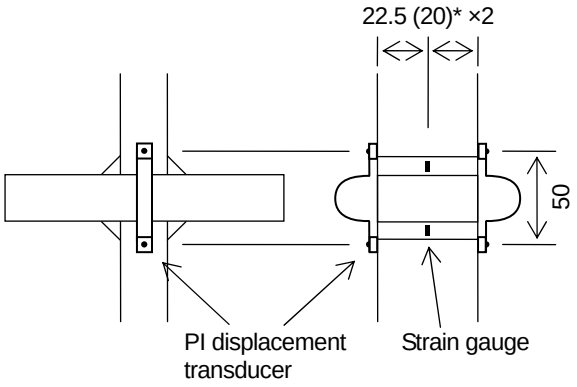

Figure 7 Gauge locations (* : number in a bracket show the specimen type B for fatigue tests)

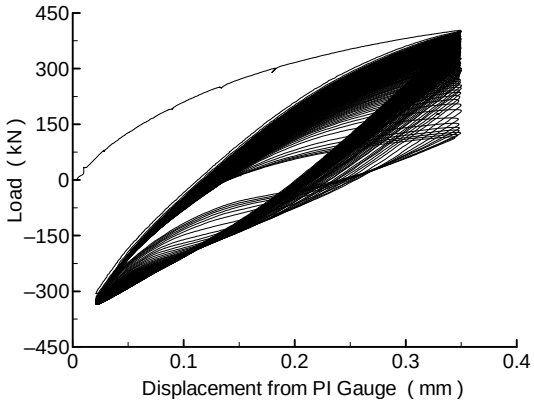

Figure 9 Load-displacement relationship in low cycle fatigue test (specimen PC)

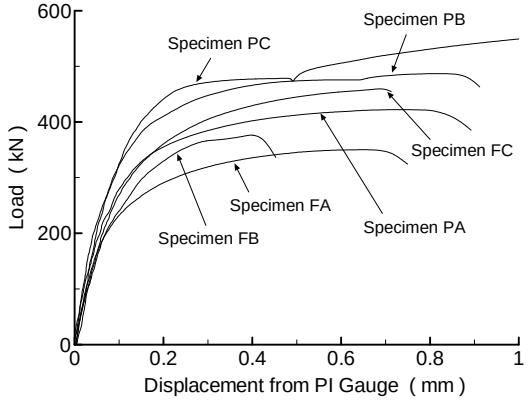

Figure 8 Results of tensile test of load-carrying cruciform joint specimens

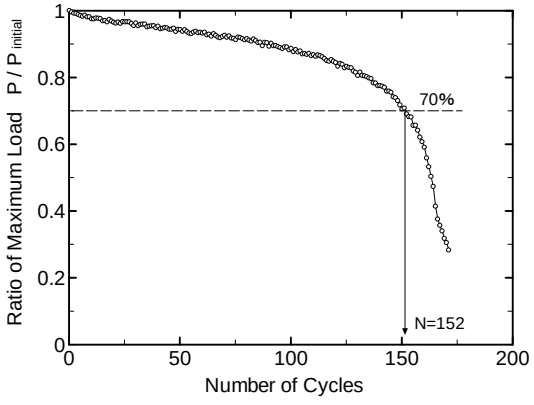

Figure 10 Relationship between the maximum load at each loop and number of cycles (specimen PC)

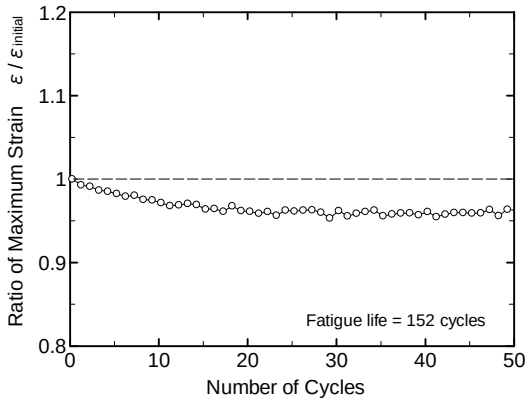

Figure 11 Relationship between the maximum strain at each loop and number of cycles (specimen PC)

3.3 Crack Propagation Path

Side surfaces of the ruptured specimen are summarized in Figures 12-14. In all specimens, the crack initiated from the weld root and propagated into the weld metal. It can be found that the angles of crack propagation are similar in the tensile and the low cycle fatigue test. Meanwhile, the crack directions in the high cycle fatigue test differ from those in the low cycle fatigue test. In the low cycle fatigue test, the crack tends to propagate into the weld deposit at a steep angle, however in the high cycle fatigue test, crack runs perpendicular to the loading direction and then begins to propagate obliquely.

The low cycle fatigue specimens applied 0.23mm displacement range was sliced at the mid-width of the specimen to measure the crack length after the load dropped by 30% from the maximum load at the first loop. The observation of the cross-section is exemplified in Figure 15. According to the measurements, the crack length ranges about from 2 to 5mm.

3.4 Fractography

Figure 16 shows examples of failure surfaces obtained in the test. A crack initiated at the weld root and propagated into the weld metal. Fractographs taken at the location close to the weld root around the mid-width are shown in Figure 17. In the figure, the fractographs of the low cycle fatigue and the high cycle fatigue test together with the tensile fracture surface are demonstrated for comparison. The weld root is located at the top side of the picture, and the crack penetrates downward. The fractograph corresponding to the low cycle fatigue test contains dimples mashed or compressed by cyclic loading (Kuwamura 1997). Similar dimple patterns can be observed in the tensile fracture surface. Moreover, the aspect failure surfaces display

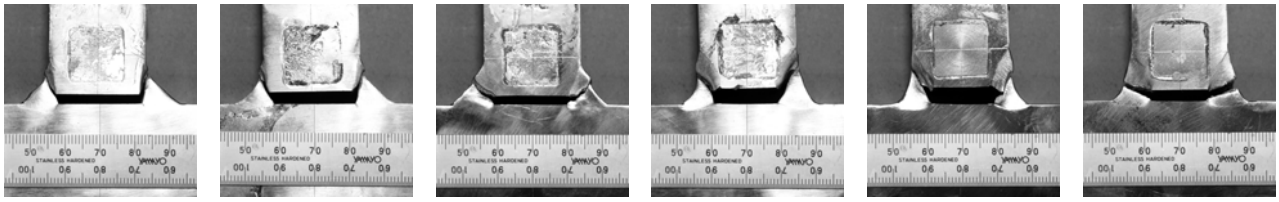

(a) Specimen FA (b) Specimen FB (c) Specimen FC (d) Specimen PA (e) Specimen PB (f) Specimen PC

Figure 12 Crack propagation path of tensile test specimen

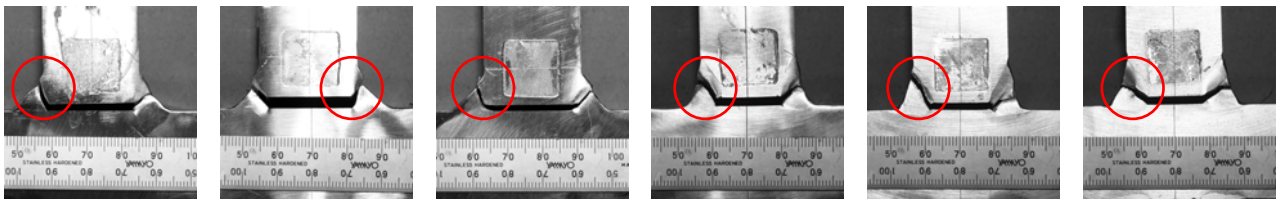

(a) Specimen FA (b) Specimen FB (c) Specimen FC (d) Specimen PA (e) Specimen PB (f) Specimen PC

Figure 13 Crack propagation path of low cycle fatigue test specimen (displacement range = 0.33mm) (circles indicate the weld bead first broken by cracking from the root)

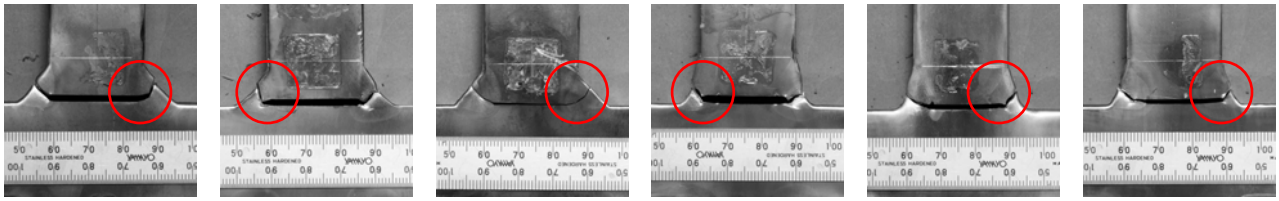

(a) Specimen FA (b) Specimen FB (c) Specimen FC (d) Specimen PA (e) Specimen PB (f) Specimen PC

Figure 14 Crack propagation path of high cycle fatigue test specimen (circles indicate the weld bead first broken by cracking from the root)

proportionally rough surface compared to that of high cycle fatigue which gives a relatively flat inclination. As a result of the fractography, it can be found that the ductile crack propagation is predominant in low cycle fatigue region.

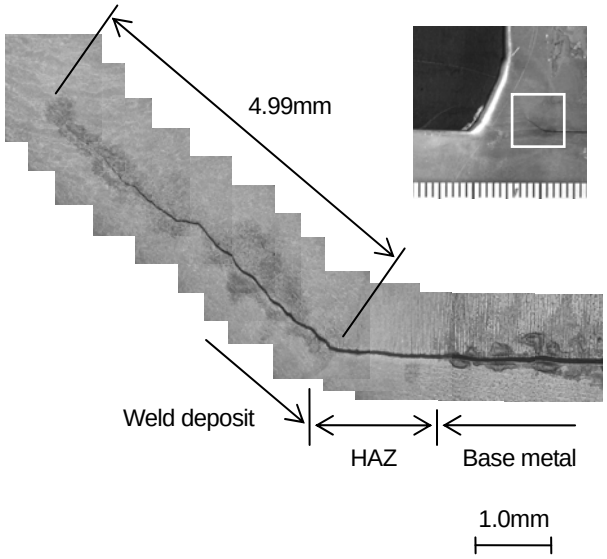

Figure 15 Crack observation (specimen PC)

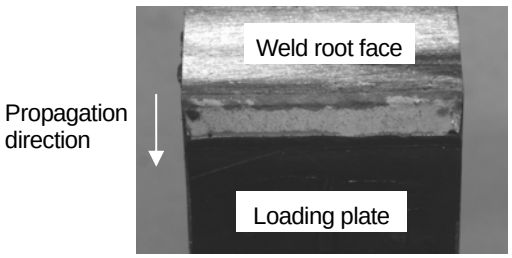

(a) Tensile test

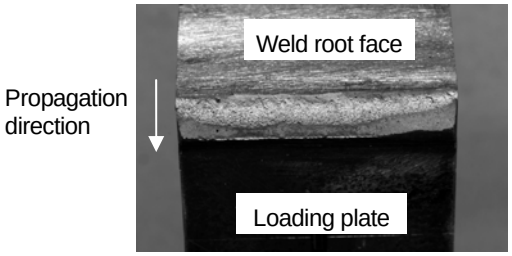

(b) Low cycle fatigue test

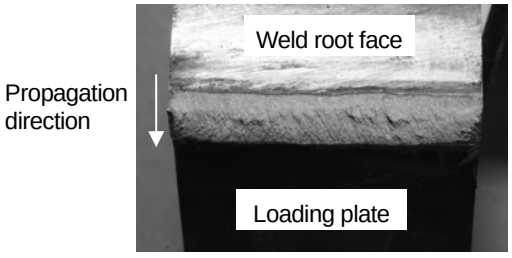

(c) High cycle fatigue test

Figure 16 Fracture surfaces (specimen FB)

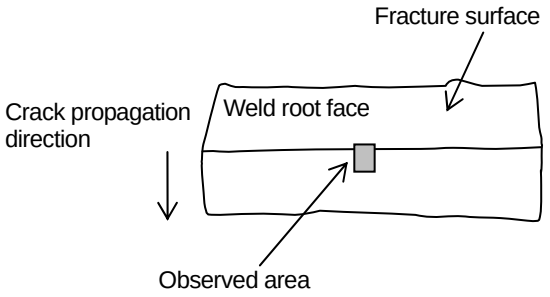

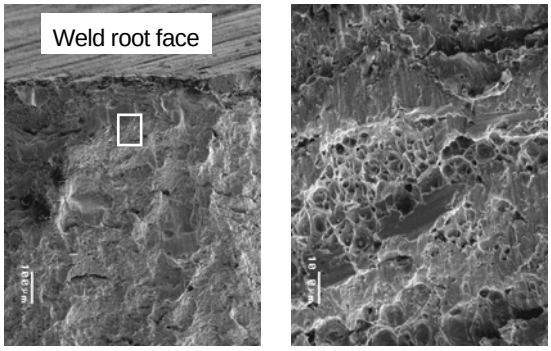

×100 ×1000

(a) Low cycle fatigue test

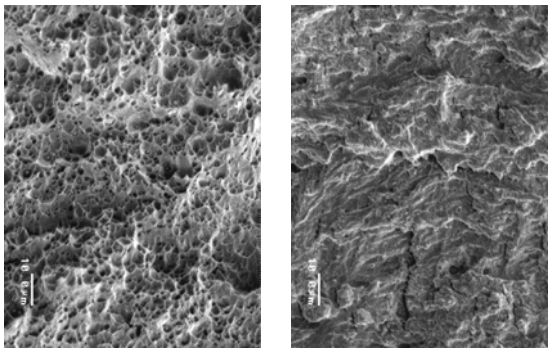

×1000 ×1000

(b) Tensile test (c) High cycle fatigue test

Figure 17 Fractographs (specimen FA)

3.5 Fatigue Lives

The results of the low cycle fatigue tests are shown in Figure 18, including those of the high cycle fatigue tests. This graph is a relationship between the nominal strain range and the fatigue life. The nominal strain for the test result is obtained by converting the nominal stress range at the measured weld throat area to the strain range with Hooke's law of elasticity. When calculating the nominal stress range, the load range at the first cycle was used. The fatigue life for the low cycle fatigue specimen was defined as the number of cycles when the maximum load decreased by 30% from the initial maximum load. For the high cycle fatigue specimen, the number of cycles to complete rupture was used as the fatigue life. In the graph, the fatigue design curves for high cycle fatigue region recommended in JSSC specification (Japanese Society of Steel Construction 1993) are also

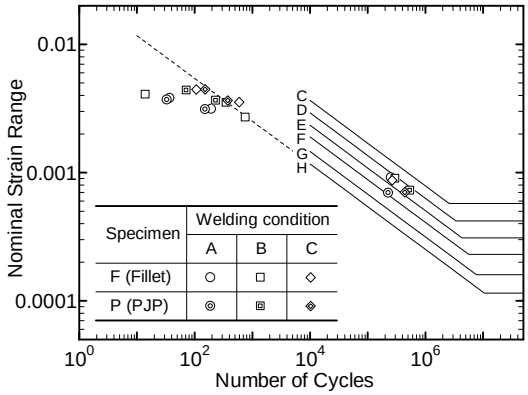

Figure 18 Fatigue lives

shown. Besides, H-class fatigue strength curve, which is the design curve for the load-carrying cruciform joints, is extended to the low cycle fatigue region with a broken line. The specimen with the welding condition A (FA, PA), which represents the relatively low load carrying capacity in the tensile test (Figure 8), tends to have shorter fatigue life than the other specimens. There is little difference in the fatigue strength between the fillet welds and the partial joint penetration groove welds. As mentioned in a past research on butt welded joints containing weld defects (Ishii and Iida 1969), the slop of the results in the low cycle fatigue region tends to be different from that in the high cycle fatigue region. It can be mentioned that the high cycle fatigue strength curve arranged by the nominal strain range at the weld throat area is not applicable to low cycle fatigue region.

4. CONCLUSIONS

Fatigue tests under cyclic plastic strains were carried out for load-carrying cruciform joints containing weld defects. The results can be summarized as followed:

1. Crack initiation point located at the weld root in the mid-width of the specimen. Then, the crack propagated through the weld deposit.
2. Fatigue life of the specimen was dominated by the crack propagation life.
3. Observations by scanning electron microscopy revealed that the fracture surfaces under cyclic plastic strains contained mashed dimples, which can produce an evidence of ductile crack propagation.
4. When arranging the fatigue life by using the nominal strain at the measured weld throat area, a slop of fatigue strength curve in low cycle fatigue region tends to be different from that in high cycle fatigue region.

Since the most of the low cycle fatigue life of the load-carrying cruciform joint with incomplete penetration can be considered as ductile crack propagation life, the non-linear fracture mechanics approach will be applied to evaluate the low cycle fatigue strength of this type of joints.

Acknowledgements:

The authors gratefully acknowledge the support of the Research Fund for Young Researchers under the Center for Urban Earthquake Engineering (CUEE) in Tokyo Institute of Technology.

References:

Frank, K.H. and Fisher J.W. (1979), "Fatigue Strength of Fillet Welded Cruciform Joints," *Journal of the Structural Division*, American Society of Civil Engineers, **105**(ST9), 1727-1740.

Ishii, Y. and Iida, K. (1969), "Low and Intermediate Cycle Fatigue Strength of Butt Welds Containing Weld Defects," *Journal of Japanese Society for Non-Destructive Inspection*, **18**(10), 443-474.

Japanese Society of Steel Construction (1993), "Fatigue design recommendations for steel structures".

Kayamori, Y., Seto, A., Masuda, T., Machida, S. and Miki, C. (2001), "Influence of Weld Defects on Very Low Cycle Fatigue Properties of Welded Joints," *ASME International*, American Society of Mechanical Engineers, PVP427, 1-8.

Kuwamura, H. (1997), "Transition between Fatigue and Ductile Fracture in Steel," *Journal of structural engineering*, American Society of Civil Engineers, **123**, 864-870.

Miki, C. and Hirabayashi, Y. (2007), "Fatigue Damage Cases due to Inappropriate Fabrication in Steel Bridge Structures," *Doboku Gakkai Ronbunshuu A*, Japan Society of Civil Engineers, **63**(3), 518-532.

Miki, C., Ichikawa, A., Sakamoto, T., Tanabe, A., Tokida, H. and Shimozato, T. (2002) "Fatigue Performance of Beam-to-Column Connections with Box Sections in Steel Bridge Frame Piers," *Journal of Structural Mechanics and Earthquake Engineering*, Japan Society of Civil Engineers, 710/I-60, 361-371.

Miki, C., Tateishi, K., Fan, H. and Tanaka, M. (1993), "Fatigue Strengths of Fillet-Welded Joints Containing Root Discontinuities," *International Journal of Fatigue*, **15**(2), 133-140.

Morikawa, H., Shimozato, T., Miki, C. and Ichikawa, A. (2002) "Study on Fatigue Cracking in Steel Bridge Piers with Box Section and Temporally Repairing," *Journal of Structural Mechanics and Earthquake Engineering*, Japan Society of Civil Engineers, 703/I-59, 177-183.

JOINT CONFERENCE PROCEEDINGS
7th International Conference on Urban Earthquake Engineering (7CUEE) &
5th International Conference on Earthquake Engineering (5ICEE)
March 3-5, 2010, Tokyo Institute of Technology, Tokyo, Japan

EFFECT OF PLATE THICKNESS ON LOW CYCLE FATIGUE STRENGTH OF CRUCIFORM WELDED JOINTS

Koji Kinoshita[1], and Kiyohiro Ueda[2]

1) Assistant Professor, Dept. of Civil Engineering, Gifu University, Japan
2) Dept. of Civil Engineering, Gifu University, Japan
kinoshita@gifu-u.ac.jp

Abstract: Welded joints of steel bridge piers may have thick plate thickness which could reduce fatigue strength of welded joints. Hence, it is necessary to grasp effect of plate thickness on fatigue strength of welded joints. In this study, the effect of the plate thickness ranging from 25mm to 40mm on low cycle fatigue strength based on nominal strain was investigated by bending fatigue tests under large plastic strain on cruciform welded joints. As a result, a decrease of low cycle fatigue strength of the welded joint with an increasing of the plate thickness is about 40%. Comparison of influence of the plate thickness on high cycle fatigue strength and low cycle fatigue strength showed higher influence of the plate thickness on low cycle fatigue strength.

1. INTRODUCTION

Welded joints of steel bridge piers may have thick plate thickness which could reduce fatigue strength of welded joints. Hence, it is necessary to consider the plate thickness for fatigue strength of welded joints.

In the Japan Society of Steel Construction (JSSC) fatigue design recommendation (JSSC (1993)), influences of plate thickness on high cycle fatigue strength of welded joints were considered. However, a general method for evaluating low cycle fatigue strength of welded joints based on nominal strain has not been established. Besides, the influences of plate thickness on the low cycle fatigue strength have not been studied enough. Thus, current evaluation method of low cycle fatigue strength based on the nominal strain does not accurately describe practical low cycle fatigue strength of welded joints of steel bridge piers.

In this study, influences of plate thickness ranging from 25mm to 40mm on low cycle fatigue strength were investigated by bending fatigue tests under large plastic strain on cruciform welded joints.

2. SPECIMENS AND TEST METHOD

2.1 Specimens

The configuration and dimensions of specimens are shown in Figure 1. The specimens reproduced the cruciform welded joint which is used to actual welded joints of beam-to-column connections of steel bridge piers. The specimens consist of two steel plates. In the JSSC fatigue design recommendation (JSSC (1993)), influences of plate thickness on high cycle fatigue strength of cruciform welded joints were considered when plate thickness is thicker than 25mm. Hence, based on the influence of plate thickness in high cycle fatigue strength, JIS SM490Y steel plates with 25mm and 40mm thickness were used. The mechanical properties of steel used in the specimens are shown in Table 1. A weld material, which has yield strength of 500N/mm2, was used. Table 2 shows conditions of each specimen.

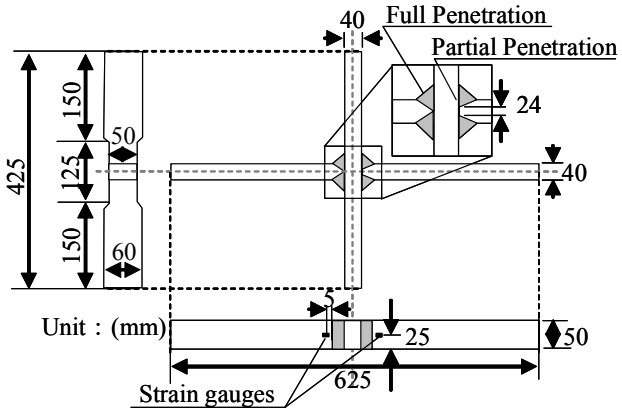

Figure 1 Configuration and dimensions of the specimen with 40mm thickness

2.2 Testing method

Test set up is shown in Figure 2. Low cycle fatigue test

were carried out with an electrohydraulic servo system fatigue test machine of maximum dynamic load 200kN. Three-point-bending tests under displacement controlled conditions were done. Loading span was 450mm. To conduct the alternating loading condition, we upset the specimens per every cycle.

Regarding an applied plastic strain range, previous studies show that during level 2 earthquake ground motion, low cycle fatigue cracks from weld toes in steel bridge piers occurred under the plastic strain range over 10% (for example, Sakano et al. (1997)). Based on previous results, applied plastic strain range at the weld toe was over 10% in this study. However, measuring the plastic strain range at weld toes is difficult because of the limit of a strain measurement. Thus, we carried out finite element method (FEM) analyses before fatigue tests in order to obtain relationship between local plastic strain range at weld toe and plastic strain range at the location of measuring strain gauge, which was located in 5mm apart from the weld toe. For the gauge location, Hanji et al. (2006) showed that the influence of strain concentration due to the weld toe on the strain 5mm apart from the weld toe is not significant. Moreover, FEM analyses describe in **3.** showed the same tendency as Hanji et al. (2006). Thus, we thought that strain 5mm apart from the weld toe is stable to measure plastic strain even though close to the weld toe, and determined the gauge location at 5mm apart from the weld toe. Consequently, we determined that applied plastic strain range for the specimens was 5% at measured strain gauge.

Figure 3 shows a history of displacement and plastic strain of the strain gauge during a low cycle fatigue test. Strain hardening was remarkable until 2 cycles, but after 2 cycles strain history was stable. The cause of a slight change of mean strain after 2 cycles was small influence of strain hardening and proper changes of mean strain of the strain gauge under cyclic loading conditions. In this study, fatigue test under displacement controlled condition after 2 cycles was done. As a result, plastic strain range was nearly same throughout the tests.

3. STRAIN CONDITION IN THE VICINITY OF THE WELD TOE FROM FEM ANALYSES ONCLUSIONS

In order to investigate local plastic strain condition in the vicinity of the weld toe prior to fatigue test, elasto-plastic FEM analyses were carried out.

3.1 FEM models

FEM models are shown in Figure 4. DIANA was used in the analyses. FEM models of the specimens with each thickness were prepared. For FEM models, considering the symmetry planes of the specimens, 1/2 models are used. The roller condition was used to both the upper surface and the bottom surface at bearing points. Solid elements were used. For the weld geometry, measured average weld size, average flank angle, and measured minimum weld radius was used.

To ensure accuracy of analytical results, the mesh size

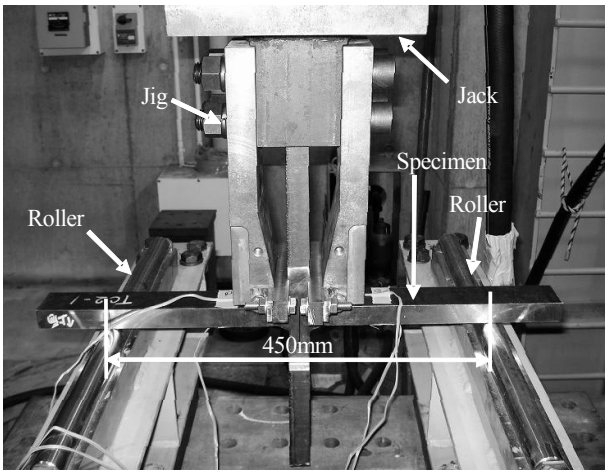

Figure 2. Test set up

Table 1. The mechanical properties of the steel

Yield Strength (N/mm^2)	Tensile Strength (N/mm^2)	Elongation (%)
411	557	31

Table 2. Condition of each specimen

Specimen	Thickness (mm)	Plastic strain range
25A-5%	25	5%(±2.5%)
40A-5%	40	5%(±2.5%)

was carefully determined based on the previous study. Hanji et al. (2006) have reported that the FEM analysis using the solid elements is reliable to predict local plastic strain of the weld toe when element mesh size in the vicinity of the weld toe is fine enough. Thus, the elements size in the weld toe is about 0.05mm in highly strain concentration area.

The yield strength of the steel and the weld material were considered in the FEM models, respectively. Young's modulus and Poisson's ratio was 200kN/mm2 and 0.3, respectively. The Bi-linear stress-strain curve was used, whose secondary slope was a reasonable one-hundredth of Young's modulus. For the behavior of the steel under the cyclic loading such as earthquakes, it is necessary to use hardening for the steel. Regarding the cyclic behavior of the steel, the bauschinger effect occurs, which is the reduction of the yield strength in the opposite loading direction. In this study, as the hardening of the steel, the kinematics hardening was used to consider the bauschinger effect of the steel. von-Mises yield criteria was used.

3.2 Analytical results

Figure 5 shows strain distributions in the longitudinal direction of the main steel plate. These results show when plastic strain at 5mm apart from the weld toe is 5%. It is thought that we can apply the local plastic strain at the weld toe over 10% when the plastic strain at strain 5mm apart from the weld toe is 5%. Figure 5 also shows a comparison between normal strain distributions and minimum principal strain distributions. Figure 5 shows that the normal strain distributions agree with the minimum principal strain

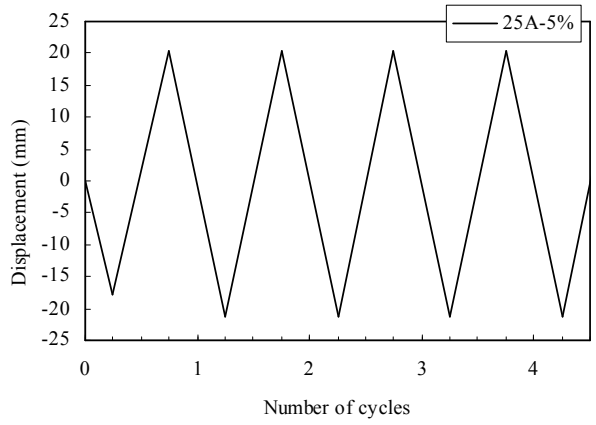

a) Displacement

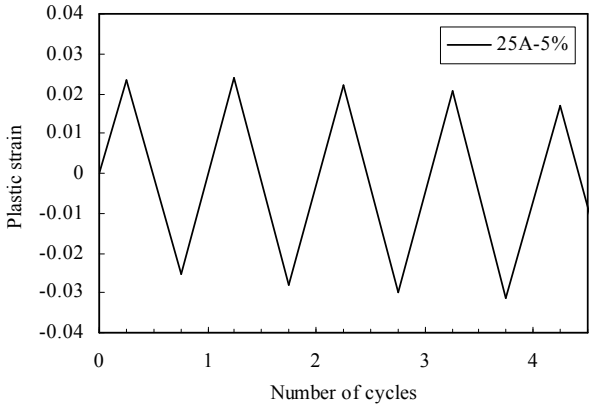

b) Plastic strain

Figure 3. History of displacement and plastic strain

distributions in both results. Thus, it can be said that low cycle fatigue strength was evaluated by using normal strain and the influence of shear stress is negligible. Moreover, from Figure 5, it can be seen that local strain of specimens with 40mm plate thickness is higher than that of specimens with 25mm. Therefore, local strain becomes higher due to increase in plate thickness. Thus, it can be expected that fatigue strength of the specimens with 40mm thickness is lower than that of the specimens with 25mm thickness.

4. FATIGUE TEST RESULTS

4.1 Crack initiations and propagations

Results of fatigue crack observations are presented in Figure 6. Crack initiations of both specimens were observed at the weld toes, and then the cracks propagated along the weld toes, and the cracks coalesced with adjacent cracks. After crack coalescences, crack propagation in the width direction was faster than that in the thickness direction. Finally, by the propagation of the cracks initiated from the weld toe, the specimens fractured in the width direction along the weld toe.

To investigate initiations of the cracks, the fracture surfaces were observed as shown in Figure 7. From Figure 7, the cracks on the specimens with both 25mm and 40mm thickness initiated from the weld toes, and these cracks

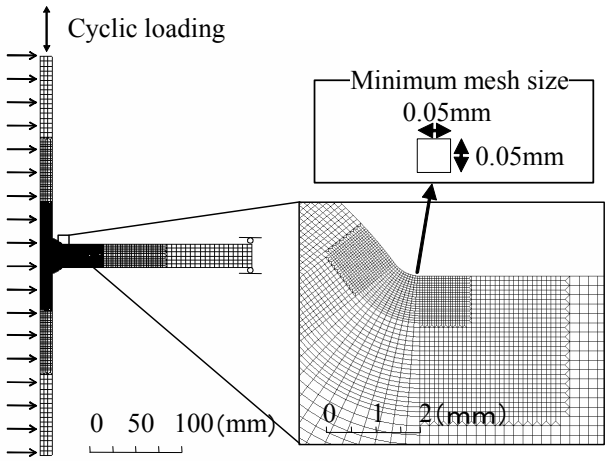

Figure 4. FEM model

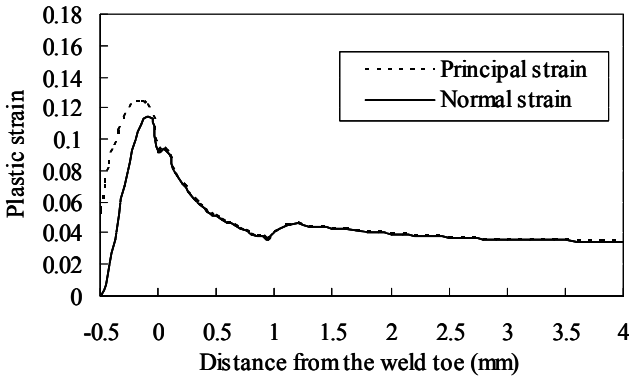

a) 25A-5%

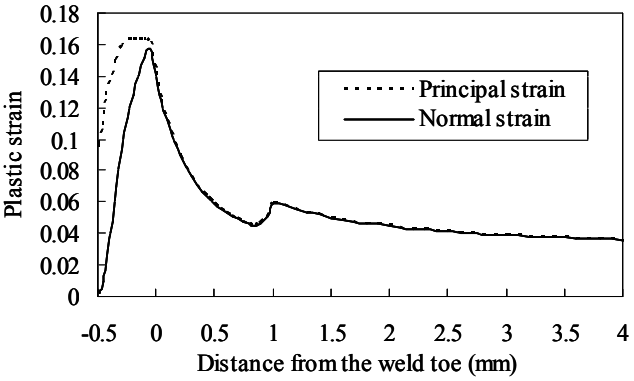

b) 40A-5%

Figure 5. Strain distribution in the longitudinal direction

propagated widely. This result indicates that the fatigue failure was governed by the cracks initiating from the weld toes.

4.2 Low cycle fatigue strength

Influences on low cycle fatigue strength of the plate thickness were examined using the relationship between plastic strain range and the number of cycles as shown in Figure 8. Figure 8 shows low cycle fatigue strength at the number of cycles when 5mm crack was detected on the specimens. Figure 8 shows that scatter of both results is small. Furthermore, by increasing the plate thickness, the fatigue strength decreased approximately by 40%.

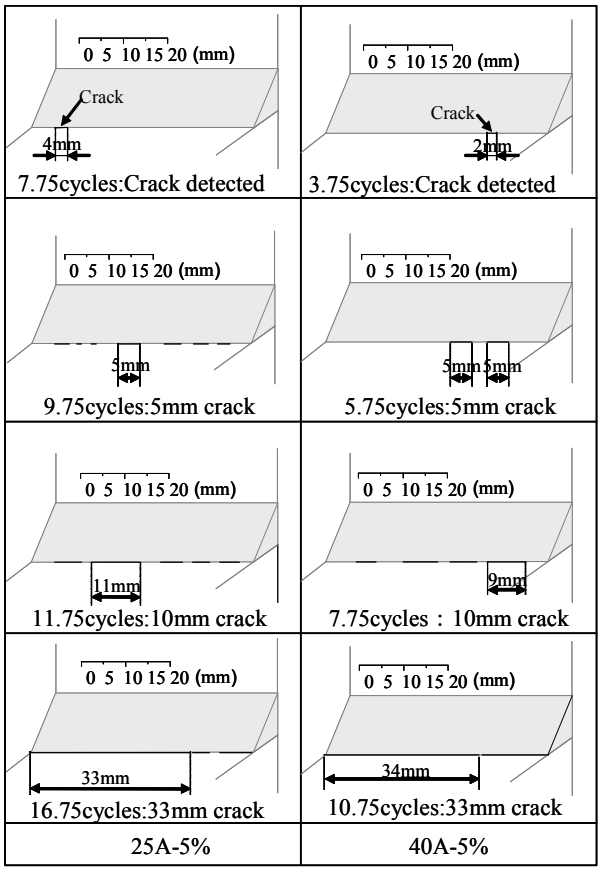

Figure 6. Crack propagation of specimens

Consequently, the increase in the plate thickness may affect low cycle fatigue strength of cruciform welded joints. This result is reasonable because local strain increases with increase in the plate thickness as mentioned in 3.2.

4.3 Comparison of influences of the plate thickness in high cycle fatigue region with that in low cycle fatigue region

According to the Fatigue Design Code of JSSC (JSSC (1993)), fatigue strength considering influences of the plate thickness in high cycle fatigue region were obtained by using following the correction coefficient C_t.

$$C_t = \sqrt[4]{\frac{25}{t}} \qquad (1)$$

where, t is the plate thickness. By using above equation, influences of the plate thickness in high cycle fatigue region were compared with that in low cycle fatigue region. The comparison of the influence of the plate thickness in high cycle fatigue region and low cycle fatigue region is shown in Figure 9. In this figure, fatigue life ratio, which indicates the following equation, was used for vertical axis.

$$fatigue\ life\ ratio = \frac{N_t}{N_{t25}} \qquad (2)$$

where, N_t is fatigue life when plate thickness is t, N_{t25} is fatigue life when plate thickness is 25mm. From Figure 9, by

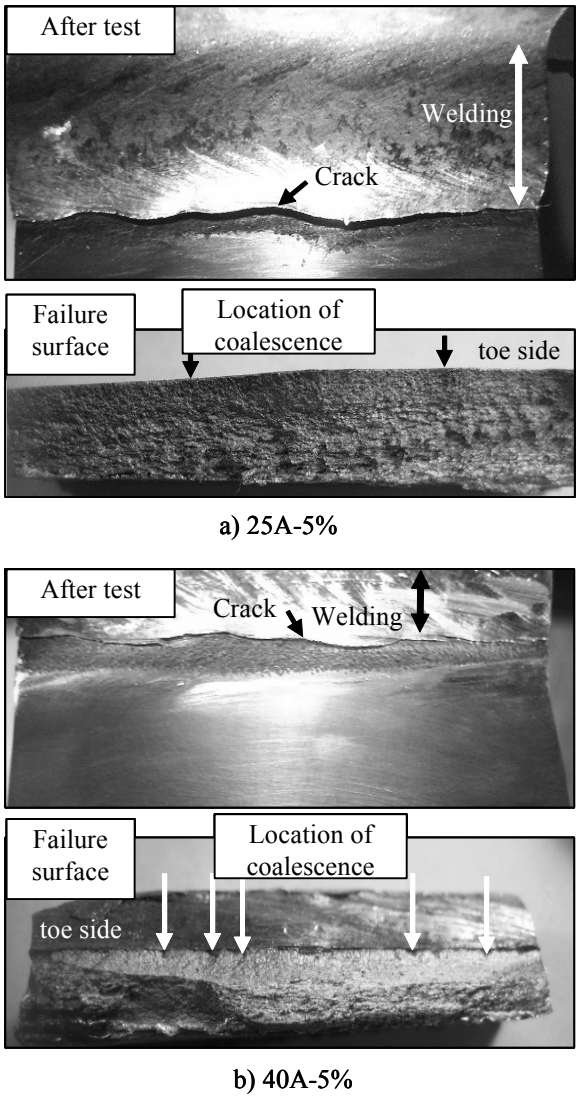

Figure 7. Fracture surface of specimens

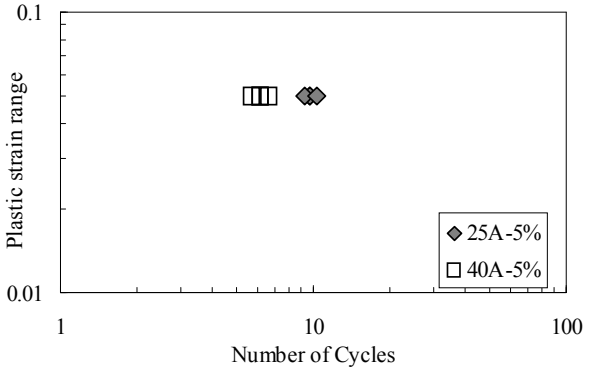

Figure 8. Low cycle fatigue test results

increasing the plate thickness from 25mm to 40mm, high cycle fatigue strength decreased by 30%. However, decrease of low cycle fatigue life by the plate thickness obtained from the low cycle fatigue tests is about 40%. Therefore, it can be found that the influence of the plate thickness in low cycle fatigue region is greater than that in high cycle fatigue region when the plate thickness is 40mm.

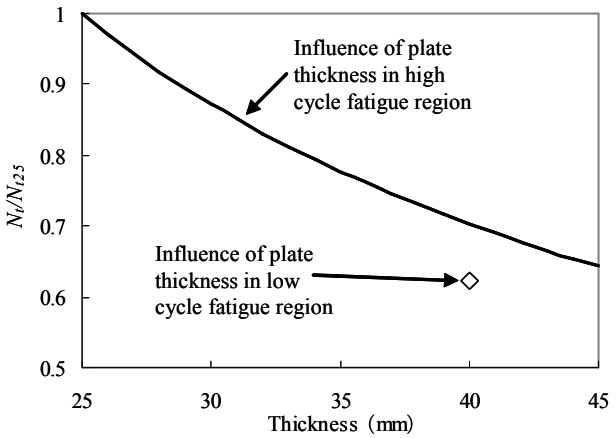

Figure 9. Comparison of influence of plate thickness in high cycle fatigue region and low cycle fatigue region

5. CONCLUSIONS

In this study, the influence of the plate thickness on low cycle fatigue strength was examined by low cycle fatigue tests using cruciform welded joints. The conclusions of this study are summarized as follows.

1) The influences of the plate thickness on fatigue crack initiation and propagation is not so significant.

2) From results of low cycle fatigue tests, it was clarified that low cycle fatigue strength decreased by 40% by increasing the plate thickness from 25mm to 40mm.

3) The influence of the plate thickness in low cycle fatigue region may be greater than that in high cycle fatigue region.

References:

Hanji et al. (2006), "Extremely low cycle fatigue assessment for welded joints based on peak strain approach," *Doboku Gakkai Ronbunshuu A*, Japan Society of Civil Engineers, 62(1):101-109.

Japan Society of Steel Construction (JSSC) (1993), "Fatigue Design Recommendation for Steel Structures in Japanese"

Sakano et al. (1997) "Low cycle fatigue behavior of steel beam-column joint", *Journal of structural mechanics and earthquake engineering*, Japan Society of Civil Engineers, 563(I-39):49-60.

JOINT CONFERENCE PROCEEDINGS
7th International Conference on Urban Earthquake Engineering (7CUEE) &
5th International Conference on Earthquake Engineering (5ICEE)
March 3-5, 2010, Tokyo Institute of Technology, Tokyo, Japan

RESIDUAL STRENGTH OF DAMAGED STEEL BRIDGE PIER WITH CIRCULAR CROSS SECTION AND ITS REPAIR METHOD

Moriaki Suzuki[1], Yoshiyuki Shimaguchi[2] and Tetsuhiko Aoki[3]

1) Associate Professor, Department of Civil Engineering, Aichi Institute of Technology, Japan
2) Graduate Student, Graduate School of Engineering, Aichi Institute of Technology, Japan
3) Professor, Department of Civil Engineering, Aichi Institute of Technology, Japan
suzuki-moriaki@aitech.ac.jp, f09703ff@aitech.ac.jp, aoki@aitech.ac.jp

Abstract: After HYOGOKEN-NANBU Earthquake in 1995 at Kobe, Japan, many researches for seismic resistance design have become actively. Especially seismic resistance design researches of steel bridge piers tend to how to strengthen them to against to severe earthquakes. For example, researches of improving the strength and the ductility by strengthen the cross section and proportion or by applying high performance materials, such as low yield steel, and so on.

But, most of the above researches are only for new bridge piers or constructed by old design codes, and these piers are not experienced severe damages caused by earthquakes. Therefore there is no guideline about repairing methods for damaged steel bridge piers. And there is no assessment techniques retrofitted piers are established until now.

In this study, firstly, we introduce repairing methods for local buckled of steel bridge piers after cyclic loading experiments. We prepared 6 damaged steel pier specimens, which had elephant foot bulge buckling at the bottom of pier, and repair them by filling concrete inside. After repairing, perform cyclic loading experiments are conducted under same load sequence, and by comparing the seismic resistance capacity between before and after repaired to discuss the reliability of repairing methods.

1. INTRODUCTION

After severe earthquake it generally needs large amount of cost and time to reconstruct infrastructures such as bridges. It is very important topics to make sure of rescue action. In Japan, many elevated bridges have been constructed in large city which have steel bridge piers. Once these kinds of infrastructures have been damaged under severe earthquake and it will make immeasurable social loss. For example, in HYOGOKEN-NANBU Earthquake in 1995 at Kobe, Japan, it takes more than one year to repair and reconstruct the highway before reopen.

Many steel bridge piers using as elevated highway bridges have circular cross section. Because which have advances on isotropic bending capacity and slenderness appearance in comparison with rectangular cross section. But after earthquake, many damages such as elephant foot bulge buckling and cracks have observed on circular cross section piers at the bottom of piers. Many researchers have been conducted to improve strength and ductility or strengthen cross section and proportion by applying high performance materials and so on. But, the subjects of these researches are only for new bridge piers or constructed bridges designed by old design codes, which have not experienced severe damages in earthquakes. Therefore, there is no guideline about repair method for damaged piers. And no assessment techniques retrofitted piers are established until now.

In this study, firstly, we introduce repairing methods for local buckled of steel bridge piers after cyclic loading experiments. We prepared 6 damaged steel pier specimens, which had elephant foot bulge buckling at the bottom of pier, and repair them by filling concrete inside. After repairing, perform cyclic loading experiments are conducted under same load sequence, and by comparing the seismic resistance capacity between before and after repaired to discuss the reliability of repairing methods.

2. SPECIMEN AND EXPERIMENT SETUP

2.1 Specimen

Table 1 shows the specifications of specimens and Figure 1 shows the general shape and cross section of specimen. And these specimens are about 1/4 scale down model from real structure. The Diameter D=600mm and the height of specimen h(=2890mm) is from bottom to loading point. These specimens have prepared for our previous experiments (Susantha et al. 2005, Hattori et al. 2006). In this table, "NC" of the specimen name means "No Core", and "CR" means "CoRe column" as previous experiment.

In this study 6 specimens have been repaired and do the same experiment, which will be described later.

Table 1 General information of specimens (Susantha et al. 2005, Hattori et al. 2006)

Specimen Name (Former exp.)	R4.5-NC/CR	R6.0-NC/CR	R12.0-NC/CR
Specimen Name (Repaired in This Study)	C1.5D-T4.5A C1.5D-T4.5B	C1.5D-T6.0A C1.5D-T6.0B	C1.5D-T12.0A C1.5D-T12.0B
Material	SS400		
Diameter : D (mm)	600		
Thickness: t (mm)	4.26	5.90	11.9
Loading Height: h (mm)	2890		
Specimen Length: h' (mm)	2600		
Moment of Inertia: I (mm^4)	3.534×10^8	4.859×10^8	9.509×10^8
Diameter Thickness Parameter: R_t	0.190	0.137	0.053
Slenderness Ratio Parameter: λ	0.351	0.354	0.316
Yield Lateral Load: Hy(kN)	118.5	158.5	250.7
Yield Lateral Displacement: δy(mm)	12.8	12.9	10.1

2.2 Experiment Setup

Figure 2 and Photo 1 shows the setup of the experiments. Vertical load is supplied by two 4400kN oil jacks connecting in a loading beam and horizontal load is supplied by one 4400kN oil jack.

In this study cyclic loading sequences have been selected. Figure 3 shows the details of loading sequences.

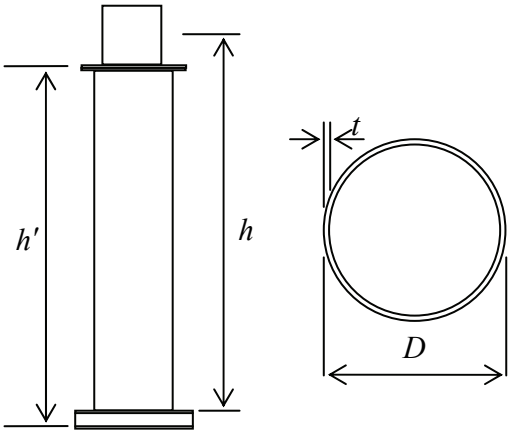

Figure 1 General shape of Specimen

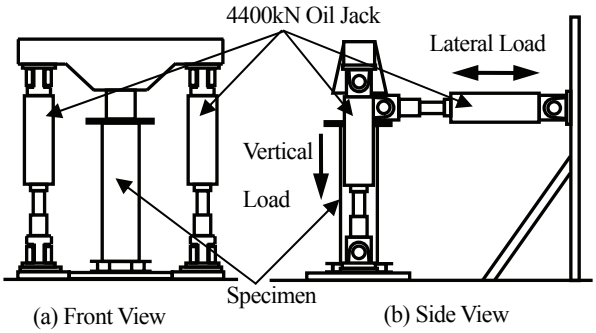

Figure2 Experiment Setup



Photo 1 Experiment Setup

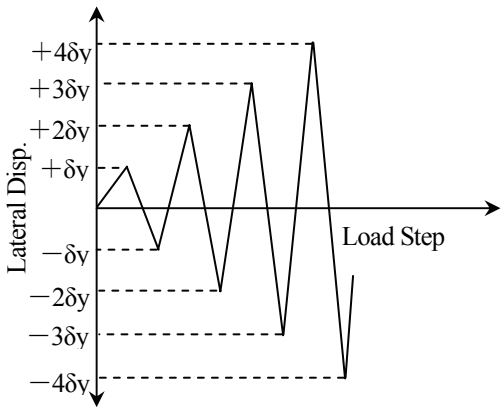

Figure 3 Loading Sequence

3. RESIDUAL STIFFNESS AND REPAIR METHOD

3.1 Damage Size and Residual Stiffness

Before the repair process, buckling damage size and residual stiffness are measured. Table 2 shows the size of damages about elephant foot bulge buckling for all specimens. Figure 4 shows the general positions of buckling damages. The residual stiffness is also measured, and both the initial and the residual stiffness are listed in Table 3. In this table, the initial stiffness indicates the strength of brand new specimen. That is, these values were obtained from former previous experiments (Susantha et al. 2005, Hattori et al. 2006). On the other hand the residual stiffness is obtained from damaged specimens. That is, the strengths obtained from the specimens before repair. And the set up of this experiment is the same system as former experiments.

From these Tables and Figure, the damages of specimens have a correlation of stiffness ratio with radius of curvature (see in Figure 5).

3.2 Repair Method

In this study the concrete-filled repair method is selected as following reasons (see Figure 6).

1) Concrete-filled column experiments for seismic retrofit have been performed in many research institutes. And the diaphragms welded inside the column have an important part in seismic performance. 2) The filled height of concrete is more effective in comparison with the concrete strength. 3) Too much amount of filled concrete will sometimes increase the strength too much. 4) Some of the material of old steel bridge piers do not suit for welding.

The purpose of this study is, recovering the stiffness to the same level as new specimen but not increasing the strength too much. And the desirable maximum strength is ±10% different from the value of a new specimen. In addition, the time cost in repairing work will not take long. Therefore, in this study Concrete-filled repair method and the height of filling in 1.5D are adopted. Table 4 shows the strength of specimens filled by concrete (Suzuki et al.1998, 1999, 2005, Morishita et al. 2000, Imanaka et al. 2004).

Table 2 Size of Damages

Specimen	Buckling Size		Radius of Curvature		
	hb (mm)	Bb (mm)	ρt (mm)	ρm (mm)	ρb (mm)
C1.5D-T4.5A	100.3	14.5	43.7	23.8	30.0
C1.5D-T4.5B	116.3	16.0	23.9	19.7	18.7
C1.5D-T6.0A	98.8	17.0	19.6	18.7	31.6
C1.5D-T6.0B	89.1	30.0	20.5	13.9	17.5
C1.5D-T12.0A	116.6	20.0	43.7	34.1	70.1
C1.5D-T12.0B	109.7	33.0	40.3	29.5	45.2

Table 3 Initial and Residual Stiffness

Specimen	Initial Stiffness	Residual Stiffness	Stiffness Ratio
	K_0 (kN/mm)	K (kN/mm)	K/K_0
C1.5D-T4.5A	8.18	5.11	0.625
C1.5D-T4.5B	8.18	3.72	0.454
C1.5D-T6.0A	10.6	5.77	0.544
C1.5D-T6.0B	10.6	4.45	0.419
C1.5D-T12.0A	18.6	14.2	0.766
C1.5D-T12.0B	18.6	10.9	0.588

Table 4 Strength of Filled Concrete

Specimen	Strength of filled concrete (N/mm^2)
C1.5D-T4.5A	30.7
C1.5D-T4.5B	34.0
C1.5D-T6.0A	35.4
C1.5D-T6.0B	26.3
C1.5D-T12.0A	34.3
C1.5D-T12.0B	27.2

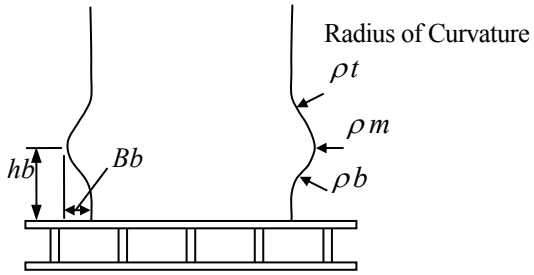

Figure 4 Schematic Drawing of Damages

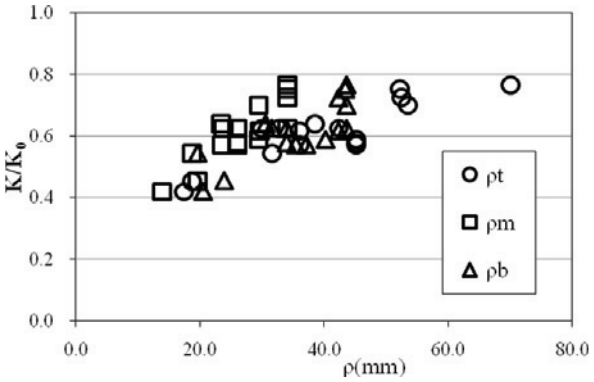

Figure 5 Stiffness Ratio - Radius of Curvature Relationship

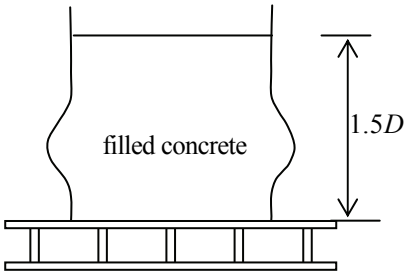

Figure 6 Concrete-Filled Repair

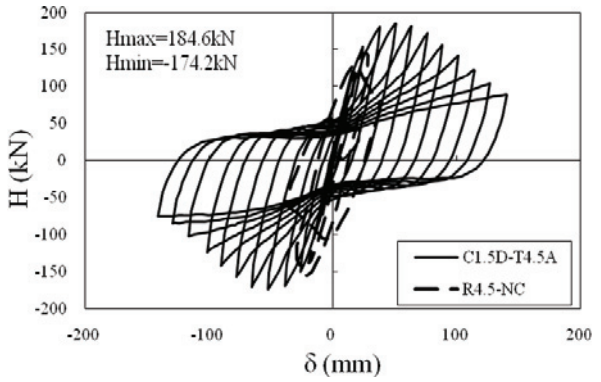

(a) C1.5D-T4.5A

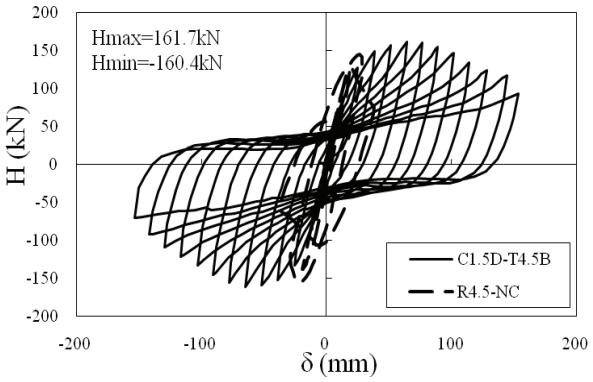

(b) C1.5D-T4.5B

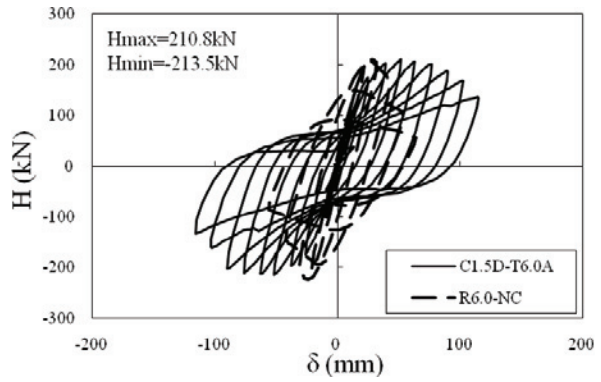

(c) C1.5D-T6.0A

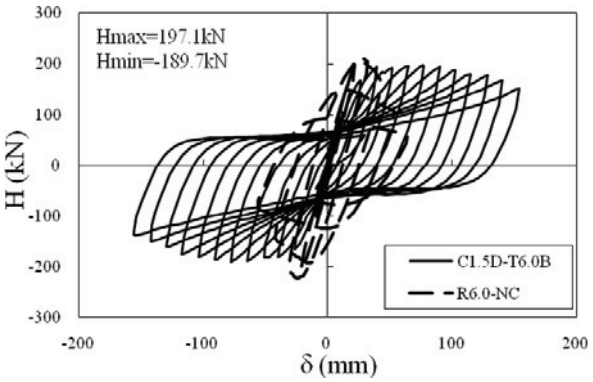

(d) C1.5D-T6.0B

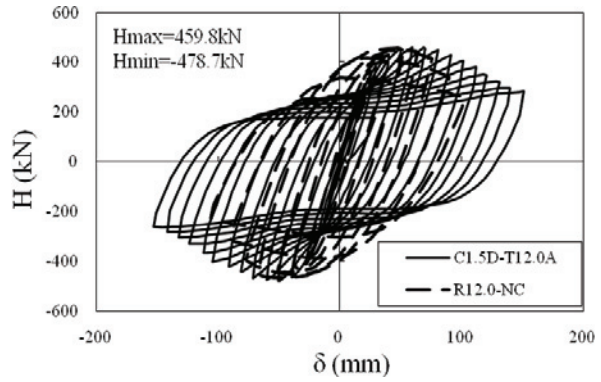

(e) C1.5D-T12.0A

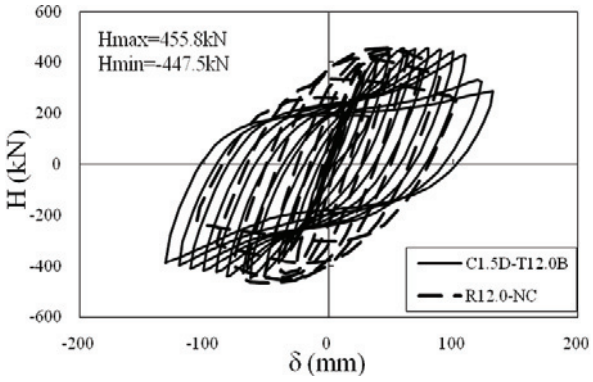

(f) C1.5D-T12.0B

Figure 7 Lateral Load-Displacement Relationships

4. RESULTS

4.1 Load-Displacement Relationship

6 repaired specimens have tested by same load sequence as previous mentioned cyclic loading (see Figure 3). The horizontal load–displacement relationships are shown in Figure 7. Vertical axis represents the lateral load and horizontal axis represents the lateral displacement. The solid hysteresis curves are the results of this study's repaired series experiments and broken lines are the results of former new series experiments.

In these figures all the hysteresis curves of repaired specimens show very stable behaviors, especially after the maximum load, in comparison with the original former experiments.

4.2 Envelope Curve

Normalized envelope curves are shown in Figure 8. Vertical axes are normalized by each yield lateral load Hy shown in Table 1 and horizontal axes are normalized by each yield lateral displacement δy corresponding to experimental yield loads listed in Table 1. Normalized maximum lateral loads (Hmax/Hy) are listed in Table 5. And the normalized lateral displacement, which correspond to maximum lateral load (δmax/δy) are listed in Table 6. From these figures and tables, maximum lateral load of C1.5D-T4.5A increases about 20% from the value of former experiment. The maximum lateral loads of other specimens are no more than 10% different with former experiments. The maximum lateral load of repaired specimen appears at around after 4δy, which is about more than twice of former experiments, except in

the cases of t=12.0mm (specimen C1.5D-T12.0A and C1.5D-T12.0B). In these cases the maximum loads appear at about 20% larger than former experiments. And it was observed that all lateral loads of repaired specimens would not decrease immediately after maximum lateral load.

4.3 Energy Absorption Capacity

Normalized energy absorption capacity E/Ee for each cycle is shown in Figure 9. Vertical axes are normalized by Ee(=Hyδy/2). As can be seen in these figures, except in the cases of t=12.0mm, energy absorption capacities of repaired specimens are larger than former experiments. But in cases of t=12.0mm, energy absorption capacity of repaired specimens are about half of former experiment.

4.4 Ductility Factor

The results of ductility factor are shown in Table 7. Ductility factor is one of the most important factors that indicate seismic resistance capacities. In this study ductility factor μ95 is defined by Figure 10 and Equation (1). Here H95 is 95% of maximum lateral load after maximum load. δ95 is lateral displacement correspond to H95. From this result all the ductility factor increased, in case of t=4.5mm and t=6.0mm the ductility factor increased from around 2 to more than 5 and in case of C1.5D-T12.0B it increased more than 10.

$$\mu 95 = \delta 95 / \delta y \qquad (1)$$

Table 5 Normalized Maximum Lateral Load

Specimen	Former (Hmax/Hy)	Repaired (Hmax/Hy)	Repaired/ Former
C1.5D-T4.5A	1.27	1.51	1.19
C1.5D-T4.5B	1.27	1.36	1.07
C1.5D-T6.0A	1.37	1.34	0.98
C1.5D-T6.0B	1.37	1.22	0.89
C1.5D-T12.0A	1.84	1.86	1.02
C1.5D-T12.0B	1.84	1.80	0.98

Table 6 Normalized Maximum Lateral Displacement

Specimen	Former (δmax/δy)	Repaired (δmax/δy)	Repaired/ Former
C1.5D-T4.5A	1.84	4.02	2.18
C1.5D-T4.5B	1.84	5.04	2.73
C1.5D-T6.0A	1.96	4.02	2.05
C1.5D-T6.0B	1.96	5.97	3.05
C1.5D-T12.0A	4.42	5.47	1.24
C1.5D-T12.0B	4.42	6.05	1.37

Table 7 Ductility Factor μ95

Specimen	Former	Repaired	Repaired/ Former
C1.5D-T4.5A	2.17	5.49	2.52
C1.5D-T4.5B	2.17	6.66	3.06
C1.5D-T6.0A	2.46	6.37	2.59
C1.5D-T6.0B	2.46	8.09	3.29
C1.5D-T12.0A	6.67	7.93	1.19
C1.5D-T12.0B	6.67	10.03	1.50

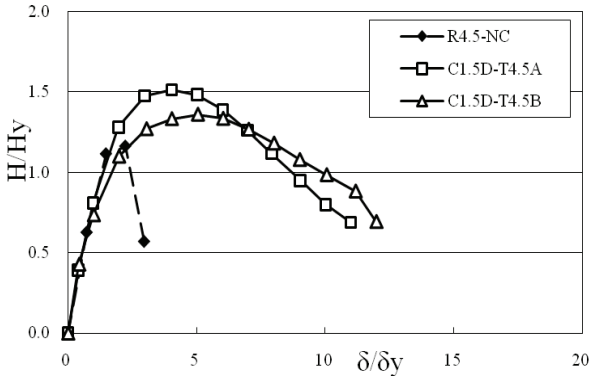

(a) t= 4.5mm

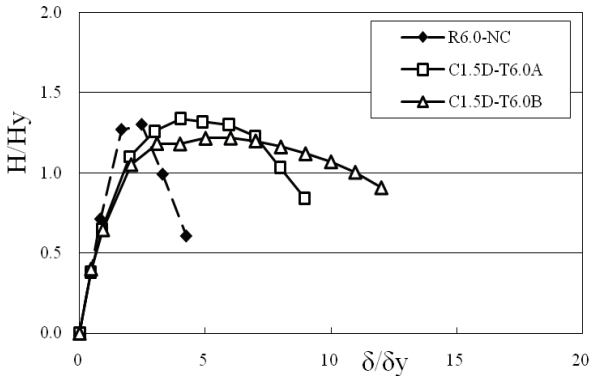

(b) t= 6.0mm

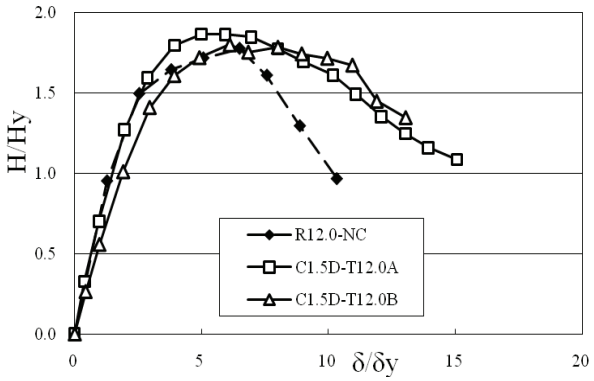

(c) t= 12.0mm

Figure 8 Envelope Curve

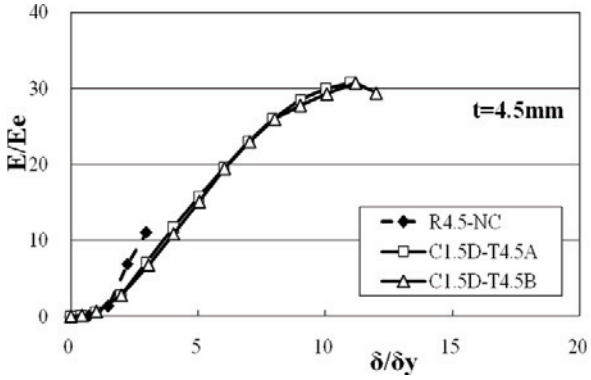

(a) t= 4.5mm

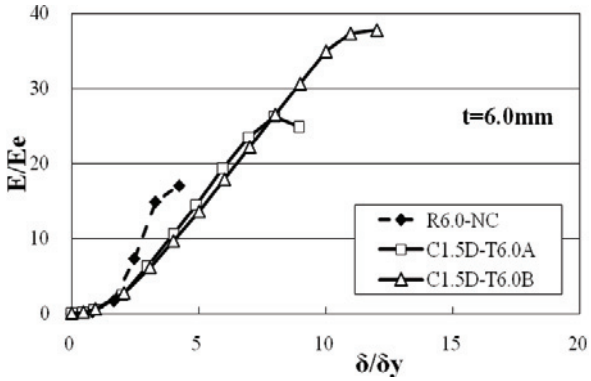

(b) t= 6.0mm

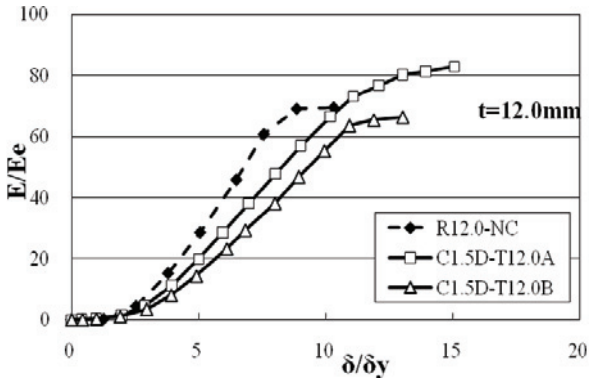

(c) t= 12.0mm

Figure 9 Energy Absorption Capacities

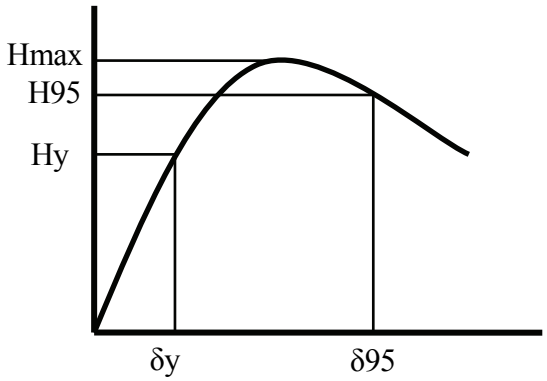

Figure 10 Definition of Ductility Factor

5. CONCLUSIONS

In this study cyclic loading tests are conducted in repaired steel bridge piers which have been damaged by loading test conducted in former researches. The conclusions are listed as below.

1) Simple Concrete-filled repair method, suggested in this study, is very effective.

2) Damage parameters such as Stiffness Ratio - Radius of Curvature have correlations with repair method.

3) All repaired specimens have good performance for maximum lateral load and energy absorption capacity in comparison with previous experiment.

4) The ductility factor increased from about 2 to more than 5, and in case of C1.5D-T12.0B it increased more than 10.

5) This repair method conducted in this study is very simple and easy method, and which have very good performances.

Acknowledgements:

The authors acknowledge support from the Seismic Resistance Experiment Center (SEIREX) in Aichi Institute of Technology. This support makes possible the experiments.

References:

Susantha, K.A.S., Aoki, T., Suzuki, M. and Hattori, M. (2005): "Innovative Method for Improving Seismic Resistance Performance of Circular Steel Tubes", *Proceedings of the First International Conference on Advances in Experimental Structural Engineering*, AESE2005 Nagoya, pp.143-150, July 2005.

Hattori, M., Aoki, T. and Suzuki, M., (2006):"Seismic Resistance Performance Test of Steel Tubes with a Compression Core Column", *Journal of Structural Engineering*, Japanese Society of Civil Engineers, Vol.52A, pp.465-475, March 2006. (in Japanese)

Suzuki, M. and Aoki, T. (1998): "Cyclic Loading Test of Steel Octagonal Section Pier Models", *Proceedings of the Second International Conference in Thin-Walled structures*, pp.779-786, December 1998.

Suzuki, M. and Aoki, T. (1999): "Repair Concept And Method of Steel Bridge Pier And It's Seismic Resistance Capacity", *6th International Conference On "Inspection, Appraisal, Repairs, Strengthening & Maintenance Of Building & Structures"*, Pp.355-360.

Morishita, M., Aoki, T. and Suzuki, M. (2000): "Experimental Study on the Seismic resistance performance of Concrete-filled Steel Tubular Columns", Journal of Structural Engineering, Japanese Society of Civil Engineers, Vol.46A, pp. 73-83, March 2000. (in Japanese)

Imanaka, A., Aoki, T. and Suzuki, M. (2004) : "Study on Repair of Damaged Circular Steel Pier", *Bulletin of Aichi Institute of Technology Vol.39 Part B*, pp.59-68, March 2004 (in Japanese).

Suzuki, M., Omatsu, H., Imanaka, A. and Aoki, T. (2005): "Seismic Resistance Capacity of Repaired Steel Bridge Piers After Severe Earthquake", *1st International Conference On Structural Condition Assessment, Monitoring And Improvement*, December 2005.

JOINT CONFERENCE PROCEEDINGS
7th International Conference on Urban Earthquake Engineering (7CUEE) &
5th International Conference on Earthquake Engineering (5ICEE)
March 3-5, 2010, Tokyo Institute of Technology, Tokyo, Japan

ELASTO-PLASTIC BEHAVIOR OF SPIRAL STEEL PIPES UNDER CYCLIC LOADING

Kiyoshi Ono[1)], Mitsuyoshi Akiyama[2)] and Hideki Naito[3)]

1) Associate Professor, Department of Civil Engineering, Tokyo Institute of Technology, Japan
2) Associate Professor, Department of Civil Engineering, Tohoku University, Japan
3) Assistant Professor, Department of Civil Engineering, Tohoku University, Japan
ono.k.ae@m.titech.ac.jp, akiyama@civil.tohoku.ac.jp, naito@civil.tohoku.ac.jp

Abstract: It has been required to decrease the construction cost of infrastructures. The application of spiral steel pipes to bridge piers is considered as one of the effective methods. Spiral steel pipes are relatively economical because they are produced in large quantities in factories. However, mechanical features of spiral steel pipes including seismic performance may be different from those of bending roll pipes. In this study, cyclic loading experiments were conducted for grasping the elasto-plastic behavior of spiral steel pipes. Furthermore, the experimental results were compared with previous experimental results and analysis results by the previous seismic evaluation methods.

1. INTRODUCTION

It has been required to decrease the construction cost of infrastructures and a lot of attempts have been conducted for reducing construction cost. As one of the effective methods, the application of spiral steel pipes to bridge piers is considered. Spiral steel pipes have been seldom used for highway bridge piers. Spiral steel pipes have been commonly used as steel pipe piles of buildings or bridges. The spiral steel pipes are manufactured in factories by continually unwinding coils and molding them spirally into pipes, with the joints being automatically welded. This enables production in large quantities, making spiral steel pipes relatively economical. However, roll forming processes of spiral steel pipes are different from those of bending roll pipes which are generally used as steel bridge piers. For this reason, mechanical features and fatigue strength of spiral steel pipes may be different from those of bending roll pipes (Kimura et al. 2001). Therefore, it is very important to grasp them in order to establish a new design method for the spiral steel pipes.

In this study, elasto-plastic behavior of spiral steel pipes is focused on as the mechanical behavior. In order to grasp the elasto-plastic behavior of spiral steel pipes, cyclic loading experiments with two specimens were conducted. On the basis of the experimental results, the seismic performance of spiral steel pipes was investigated. Furthermore, the experimental results were compared with the previous experimental results of bending roll pipes and the analysis results by the previous seismic evaluation methods for bending roll pipe piers.

2. OUTLINE OF EXPERIMENTS

2.1 Test Specimens

In this investigation, two test specimens were employed. The outline of the dimensions of test specimen is given in Figure 1 and the values of major parameters of the test specimens are listed in Table 1. In table 1, R_t is a radius thickness ratio parameter and λ is a slenderness ratio parameter of the column. The definitions of parameters mentioned above are identical to those stipulated in the 2002 design specifications (Japan Road Association 2002a; Japan Road Association 2002b) and given as follows.

$$R_t = \frac{D}{2t}\frac{\sigma_y}{E}\sqrt{3\left(1-\nu^2\right)} \tag{1}$$

$$\overline{\lambda} = \frac{1}{\pi}\sqrt{\frac{\sigma_y}{E}}\frac{2h}{r} \tag{2}$$

where D = diameter; t = plate thickness; σ_y = yield stress gained from material tests; E = Young's modulus; ν = Poisson's ratio; h= column height (distance from the bottom of the column to the point of application of horizontal load); r = radius of gyration of cross section.

The test specimens are made in SKK490. SKK490 has been commonly employed as steel pipe piles. The values of the radius thickness ratio parameter R_t applied to each specimen are different. The plate thicknesses of test specimens A9-P and A7-P are 9mm were 7mm, respectively.

2.2 Loading Condition

Each specimen was loaded with hydraulic jacks that were

installed in a fully stiff frame as shown in Figures 1and 2. In each experiment, the specified axial force as shown in Table 1 was first applied to the specimen by the vertical hydraulic jack. The axial force in Table 1 is 15% of yield axial force calculated using the nominal yield stress.

The cyclic pattern of the horizontal displacement is schematically shown in Figure 3, where δ_{yN} is calculated by the following equation. The axial load was kept constant during the cyclic experiment.

$$P_{yN} = \left(\sigma_y - \frac{N}{A}\right)\frac{Z}{h} \tag{3}$$

$$\delta_{yN} = \frac{P_{yN}h^3}{3EI} \tag{4}$$

where σ_{yN} = nominal yield stress; N = axial load during the cyclic experiment; I = moment of inertia; Z = section modulus.

3. EXPERIMENTAL RESULTS

3.1 Feature of Hysteretic Curves

Figure 4 shows horizontal load - horizontal displacement hysteretic curves and Figure 5 shows the normalized envelope curves of the hysteretic curves. The major values of experimental results are shown in Table 2. In Table 2, P_{max} is a maximum horizontal load and δ_m is a horizontal displacement at P_{max}. The triangular symbols (▲) in Figures 4 and 5 show the points where P_{max} was observed.

Figure 4 shows that the hysteretic loop size, P_{max} and

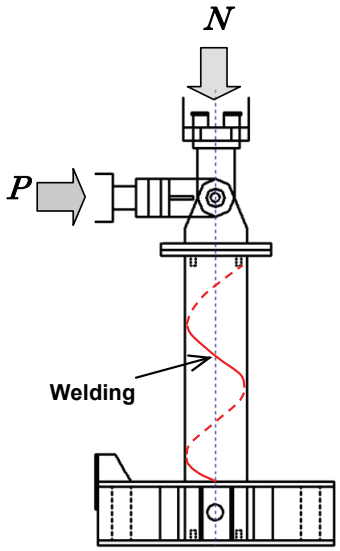

Figure 1 Test Specimen

Table 1 Major Parameters of Test Specimens

		A9-P	A7-P
Material (JIS)		SKK490	SKK490
Diameter (mm)		400	400
Thickness (mm)		9	7
Radius Thickness ratio		22.2	28.6
Area (cm^2)		111	86
Moment of inertia (cm^4)		21,138	16,691
The height of Loading point (mm)		1,805	1,805
Compressive Axial Force (kN)		522	408
Parameters calculated by nominal yield stress σ_{yN}	λ	0.33	0.32
	R_t	0.056	0.072
Parameters calculated by experimental yield stress σ_{yM}	σ_y (MPa)	470	409
	λ	0.40	0.37
	R_t	0.084	0.093

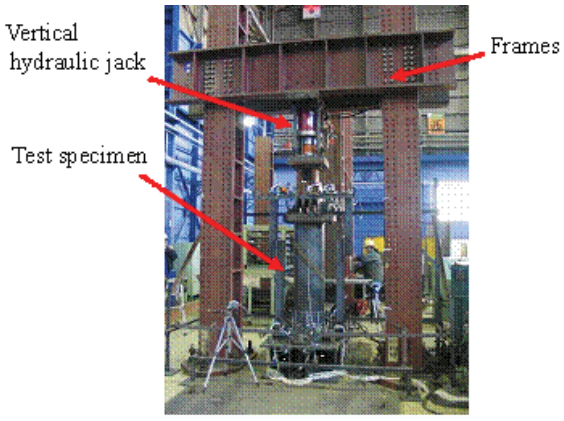

Figure 2 Test Setup

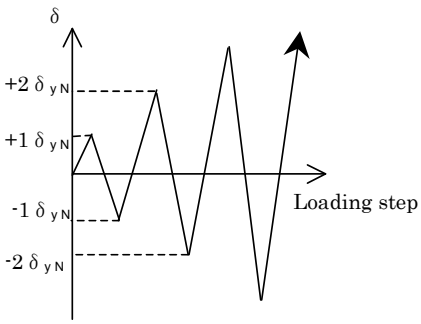

Figure 3 Cyclic Loading Pattern

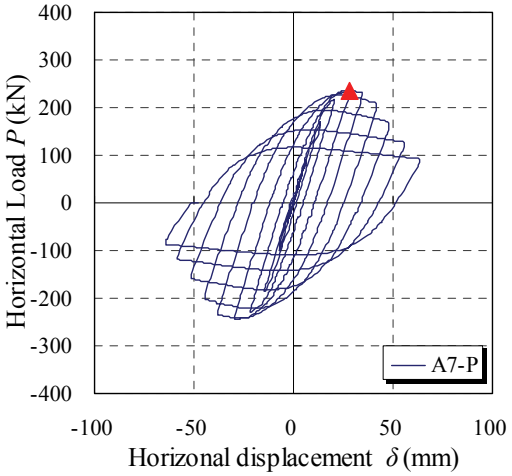

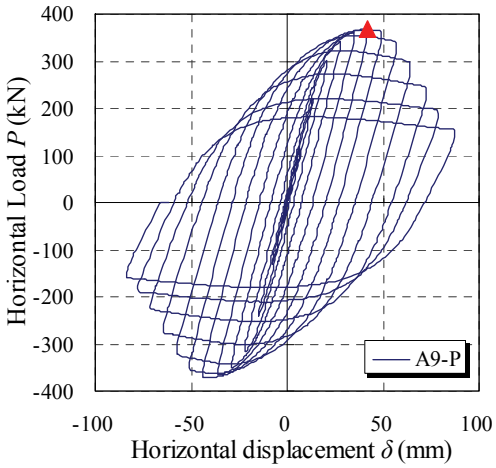

Figure 4 P-δ Relationship

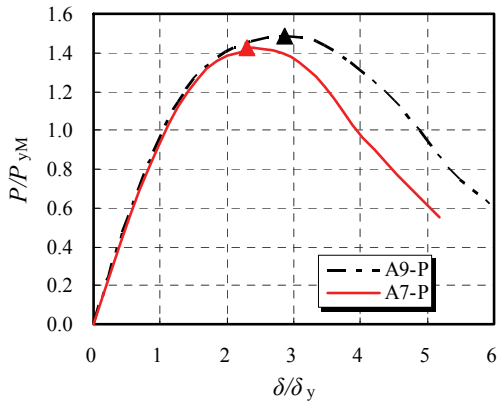

Figure 5 Envelop Curves

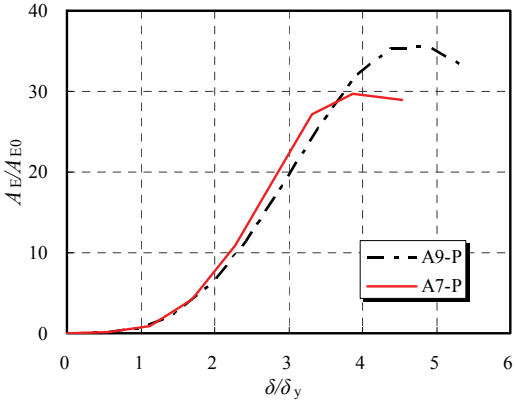

Figure 6 Absorbed Energy

Table 2 Experimental Results

Specimen	A9-P	A7-P
P_{max} (kN)	369	235
δ_m (mm)	42	28

δ_m decrease with the increase in R_t. The same tendency can be observed in envelop curves in Figure 5. And this tendency agrees with that of bending roll pipes (Public Works Research Institute 1997-1999).

3.2 Absorbed Energy

Figure 6 shows the relation of normalized absorbed energy and displacement. In horizontal load - horizontal displacement hysteretic curves, the area that horizontal load - horizontal displacement of each cycle surrounds expresses the quantity of energy absorption in the cycle. Normalized absorbed energy is calculated by dividing the absorbed energy per one cycle by the elastic energy A_{E0}, where A_{E0} is calculated by the following Eq.(5).

$$A_{E0} = \frac{1}{2} P_{yM} \delta_y \tag{5}$$

From the figure, it is observed that absorbed energy gets less with increase in R_t.

Judging From the features mentioned above, it is understood that smaller radius thickness ratio parameter R_t leads to better seismic performance of spiral steel pipes.

3.3 Buckling Modes

Figure 7 shows the buckling mode of the test specimen A7-P and Figure 8 shows that of the test specimen A9-P at the base section after the experiments. Figure 9 shows the progress of out-of-plane deformation along vertical direction at line 5 of the test specimens A7-P and A9-P. It is known by the previous study that the typical buckling mode of bending



(a) Line 1 (b) Line5

Figure 7 Buckling Mode (A7-P)



(a) Line 1 (b) Line5

Figure 8 Buckling Mode (A9-P)

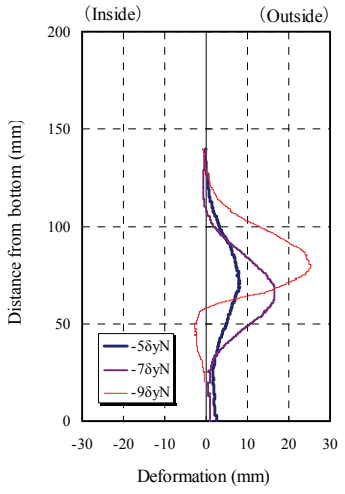

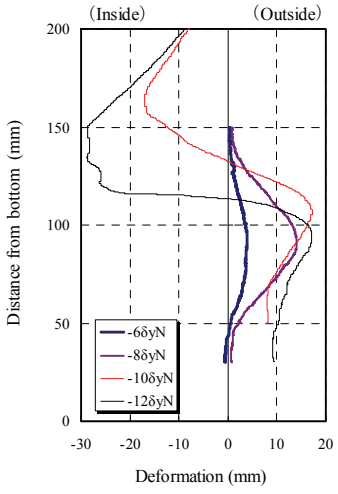

(a) A7-P (b) A9-P

Figure 9 Progress of Out-of-plane Deformation at line 5

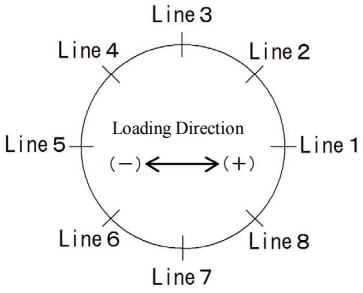

Figure 10 Location of Each Line

roll pipe piers is “elephant foot buckling”. The feature of “elephant foot buckling” is that out-of-plane deformation along the whole circumference is caused by buckling and the direction of the out-of-plane deformation is the outside of pipes (Public Works Research Institute et al.1997-1999). The buckling mode of the test specimen A7-P shown in Figure 7 was similar to that of bending roll pipes. On the other hand, it is found that the buckling mode of the test specimen A9-P shown in Figure 8 was different from the typical elephant foot buckling mode. However, the buckling mode like test specimen A9-P was observed in some test specimens of bending roll pipes in the previous study (Public Works

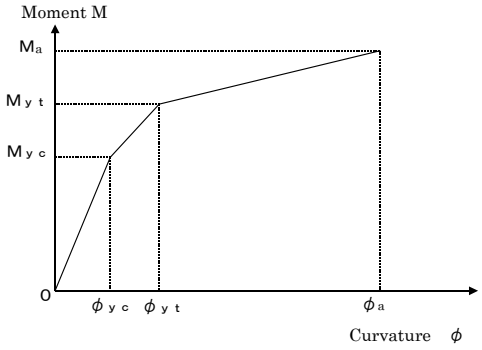

Figure 11 *M-Φ* Model

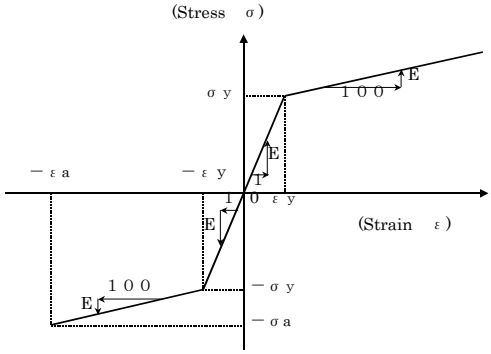

Figure 12 Stress-strain Relationship

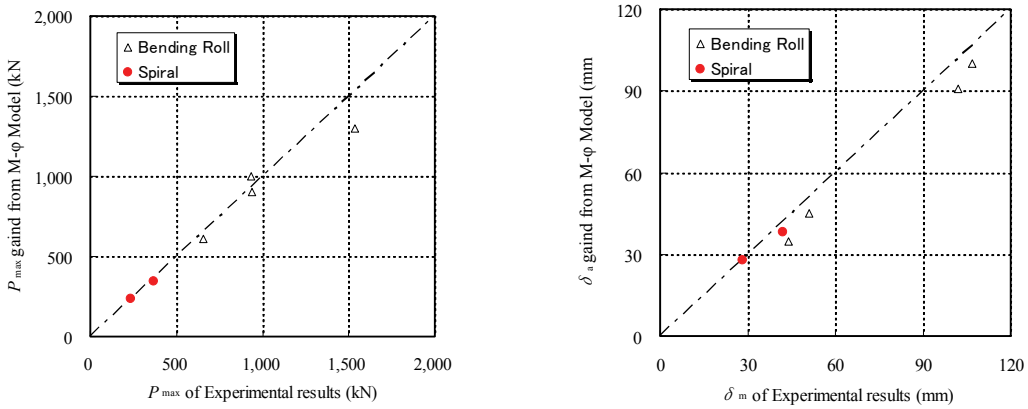

Figure 13 Comparison between Experimental Results and Analysis Results

Research Institute et al.1997-1999). It is impossible to identify the cause of the difference in buckling modes by using only experimental results in this study. Therefore, the reason why the buckling modes were different will be examined in detail in the feature works.

4. APPLICABILITY OF THE PREVIOUS SEISMIC EVALUATION METHOD

The comparison of experimental results of spiral steel pipes in this study with the previous experimental results of bending roll pipes and the analysis results by the previous seismic evaluation method for the bending roll steel pipes was conducted in order to verify whether the previous seismic design method can be applied to spiral steel pipes. P_{max} and δ_m were focused on as indexes for confirming the applicability of the previous evaluation method to the spiral steel pipes. The seismic evaluation method described in the 2002 seismic design specifications for highway bridges (Japan Road Association 2002b) was adapted as the previous seismic evaluation method.

In the 2002 seismic design specifications, *M-Φ* model as shown in Figure 11 is stipulated for evaluating seismic performance of follow steel bridge piers. The *M-Φ* model is decided based on the experimental results of bending roll pipes (Public Works Research Institute et al. 1997-1999). The point (Φ_a, M_a) of M-Φ model in Figure 11 corresponds to the point where P_{max} was observed. The following procedure is an example how to set *M-Φ* model for follow steel bridge piers with circular sections.

1) A bilinear model as shown in Figure 12 is assumed as a stress-strain curve of the steel for setting the *M-Φ* model.
2) Allowable strain ε_a corresponding to the point (Φ_a, M_a) for steel piers with circular sections is obtained by using following equation.

$$\frac{\varepsilon_a}{\varepsilon_y} = 20 - 140R_t \tag{6}$$

where ε_y = yield strain of the steel used in the target steel pier.

Here, the above Eq. (6) can be applied if the following condition is satisfied.

$$0.03 \le R_t \le 0.08, \quad 0.2 \le \lambda \le 0.4, \quad 0.0 \le N/N_y \le 0.2 \qquad (7)$$

3) The points (Φ_{yc}, M_{yc}) and (Φ_{yt}, M_{yt}) are set when the strain in the center of plate thickness at the compression side or the tension side reaches the yield strain ε_y of steel for the first time respectively.
4) The point (Φ_a, M_a) is set when the strain in the center of plate thickness at the compression side reaches the allowable strain ε_a obtained from the Eq. (6) for the first time.

$P_{\max}$ was calculated by dividing M_a by the load height h and δ_a was calculated by utilizing the curvature distribution, ignoring shear deformation and geometric non-linearity effect.

Figure 13 shows the comparison of experimental results of spiral steel pipes in this study ('●' in Figure 13) with the previous experimental results of bending roll pipes ('△' in Figure 13) and the analysis results by the previous seismic evaluation method. As shown in Figure 13, relatively good agreement between the experimental results of spiral steel pipes and analysis results by the previous seismic design method can be found. The relationship between the experimental results of spiral steel pipes and the analysis by the previous seismic evaluation method is basically similar to that between the previous experimental results of bending roll pipes and the analysis results. This fact indicates the possibility that the seismic performance of spiral steel pipes may be similar to that of bending roll pipes. In the future works, seismic performance of spiral steel pipes will be investigated in detail for developing seismic design method.

3. CONCLUSION

Cyclic loading experiments were conducted with spiral steel pipes as test specimens in order to grasp the seismic performance of spiral steel pipes. The results from experiments are concluded as follows.

- The decrease in radius thickness ratio parameter leads to the increase in the maximum horizontal load and the horizontal displacement at the maximum horizontal load as well as bending roll pipes
- Experimental results indicate a possibility that the seismic performance of spiral steel pipes may be similar to that of bending roll pipes and the previous seismic evaluation method for bending roll pipe piers may be applicable to spiral steel pipes.

References:

Kimura, Y., Ogawa, T. and Saeki, E. (2001). "The local buckling behavior of cold-formed circular tubes by different manufacturing process," Journal of Steel Construction Engineering, Vol. 8, No. 29, 27-34 (in Japanese).

Japan Road Association (2002a). Specifications for highway bridges, Part II: Steel bridges (in Japanese).

Japan Road Association (2002b). Specifications for highway bridges, Part V: Seismic Design (in Japanese).

Public Works Research Institute of the Ministry of Construction and five other organizations (1997-1999). "Ultimate Limit State Design Method of Highway Bridges Piers under Seismic Loading", Cooperative Research Report (in Japanese).

JOINT CONFERENCE PROCEEDINGS
7th International Conference on Urban Earthquake Engineering (7CUEE) &
5th International Conference on Earthquake Engineering (5ICEE)
March 3-5, 2010, Tokyo Institute of Technology, Tokyo, Japan

THE APPLICATION TO THE VIADUCT OF THE ENERGY DISSIPATION CONNECTORS OF GIRDERS IN CONSIDERATION OF AXIAL AND TRANSVERSE DIRECTIONS.

Kentaro TANAKA[1)], Masahide MATSUMURA[2)], Takeshi KITAHARA[3)], Hiroshi ZUI[4)], and Toshiyuki KITADA[5)]

1) Assistant, Department of Civil Environmental Engineering, Kanto Gakuin University, Japan
2) Department of Civil Engineering, Osaka City University, Japan
3) Professor, Department of Civil Environmental Engineering, Kanto Gakuin University, Japan
4) Professor, Department of Civil and Environmental System Engineering, Setsunan University, Japan
5) Professor, Department of Civil Engineering, Osaka City University, Japan

Abstract: In this paper, the energy absorption performance of the steel bellows as one of the energy absorbing bridge girder connectors is examined for longitudinal and transverse directions by means of a non-linear time-history analysis. The effectiveness of the steel bellows on the seismic response is verified using a three-span girder bridge model supported on lead lubber bearings.

1. INTRODUCTION

Many damage of bridges are caused due to simultaneous longitudinal and transverse seismic forces. Authors have proposed a control method in which steel bellows are connected between girders in a row or between girders and abutments as energy dissipation devices 1-4). The steel bellows can reduce longitudinal displacements of the superstructure and mitigate collision between girders or between girders and abutments which results in increased failure of super- and substructures. In this paper, the efficiency of steel bellows is investigated for both of longitudinal and transverse directions using a model of three-span continuous girders supported on lead rubber bearings. Dynamic analyses are carried out by a developed computer program against the Level 2 and Type 2 Earthquakes 5).

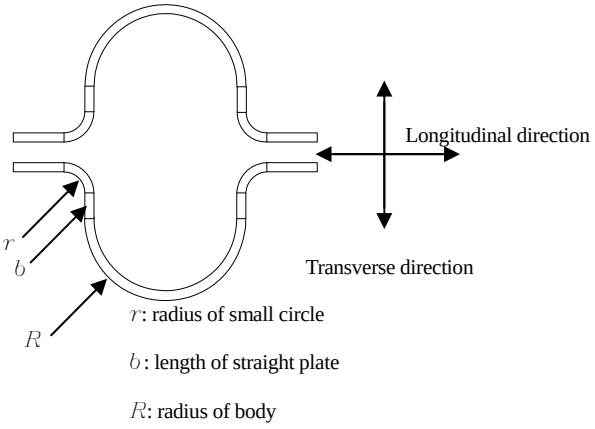

Figure 1 Cross section of steel bellows（mm）

2. STEEL BELLOWS AND ELEVATED BRIDGES MODEL USED FOR ANALYSIS

2.1 Steel bellows

Fig.1 illustrates the cross section of the steel bellows. The steel bellows connected between girders of the elevated bridges is shown in Fig.2. Two steel plates are bent in semicircular shapes and are connected to the web plates of the adjacent girders.

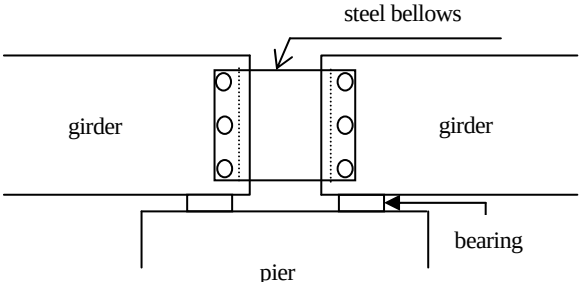

Figure 2 Setting location of steel bellows

Fig.3 illustrates the analytical model in which Ub, P and S represent the superstructure, pier and lead rubber bearings, respectively. Table 1 illustrates conditions of superstructure. The bridge superstructure consists of 4 steel girders and the characteristics of superstructure for one span length 39m are shown in Table 1. The girders are modeled as elastic beams. The piers are single columns type made of reinforced concrete. The load-displacement curve of the piers is idealized to be bi-linear characteristics as shown in Fig.4. The seismic isolation bearings are also modeled by the hysteretic bi-linear springs. The piers are designed by L1 level earthquake in JSHB. The bottom of the piers is assumed to be perfectly rigid. The acceleration time histories obtained from the actual earthquakes at the JR TAKATORI Station in the Hyogoken-Nanbu earthquake are used in the analysis. The N-S wave of the JR Takatori acceleration wave is applied to the longitudinal direction of the analytical model and E-W wave is applied to the transverse direction. Fig.5 illustrates the acceleration waves used in the analysis.

Table 2 and 3 illustrate mechanical properties of the pier and seismic isolation bearings used in the analyses. The pier is modeled as concentration mass and the force-displacement law of piers is represented by the non-linear hysteretic spring. Fig.4 illustrates the load-displacement curve of the piers and seismic isolation bearings. Table 4 illustrates the mechanical properties of the steel bellows. The steel bellows was attached for the longitudinal direction and for transverse direction. The total yield strength of bellows is determined to be about 30% ~ 40% of the superstructure.

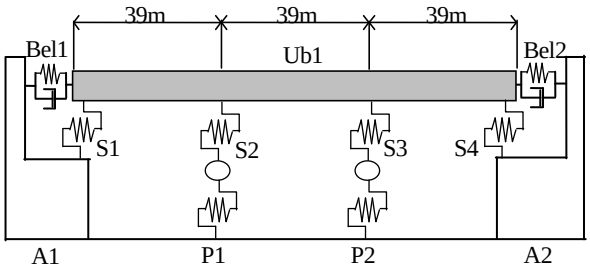

Figure 3 Analytical model

Table 1 Conditions of superstructure

Item	dimension	Value
Number of main girders	-	4
Clear width	m	9.0
Weight of girder（1 span）	kN	870
Weight of superstructure（1 span）	kN	4,250

Table 2　Mechanical properties of piers

	Reinforced concrete pier
Height	11m
Yield strength	1,230kN
Yield displacement	0.06m
Ultimate strength	1,610kN
Ultimate displacement	0.205m
Effective weight	400kN

Table 3　Mechanical properties of bearings

	On the middle piers（Q_d /W_R =0.1）	On the abutments（Q_d /W_R =0.1）
Height	0.15m	0.15m
Yield strength	425kN	212.5kN
Yield displacement	0.028m	0.028m
Initial rigidity	18,000kN/m	9,000kN/m
Secondary rigidity	2,770kN/m	1,390kN/m

Q_d /W_R　= yield load of the lead plug / weight of superstructure

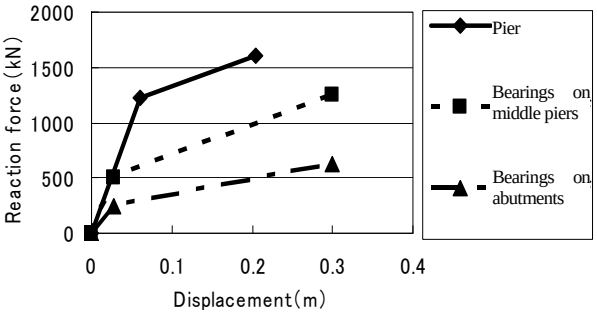

Figure 4　Reaction force and displacements curves of piers and bearings

Table 4 Mechanical properties of steel bellows

	Longitudinal direction	Transverse direction
Yield displacement	2800	3200
Yield strength	0.020	0.020
Initial rigidity	140000	160000

3. NON-LINEAR TIME-HISTORY ANALYSES

The response analyses are carried out by taking into account both of the behaviors in longitudinal and transverse direction simultaneously for the whole structure. In the analyses, it is assumed that no collision occurs for both the longitudinal and transverse directions between the girder and abutment, and the both ends of girder move freely in the both longitudinal and transverse directions against the Level 2 Type 2 earthquake.

3.1 Longitudinal direction

The cases with only LRB (without bellows), and with LRB and bellows (with bellows) are calculated. Fig.6 and 7 illustrate response results by non-linear time-history analyses. Fig.6 illustrates the time-history response of the displacement of the superstructure. Fig.7 illustrates the time-history response of the displacement of the pier. When the energy dissipation connectors is not attached (without bellows), the maximum displacements of the superstructure are about 0.57 m, and the maximum displacement of the pier is about 0.10 m as shown in Fig.6 and 7. The displacement of the pier is large and exceeds the yield displacement.

As shown in Fig.6 and 7, energy dissipation connectors is attached (with bellows), the maximum displacements of the superstructure are about 0.10 m and the maximum displacements of the pier is about 0.04 m as shown in Fig.6 and 7. We observe that the displacements of superstructure and piers can be reduced to large extent by using steel bellows.

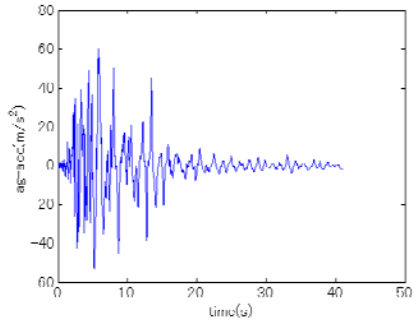

(a) N-S Direction (Longitudinal direction)

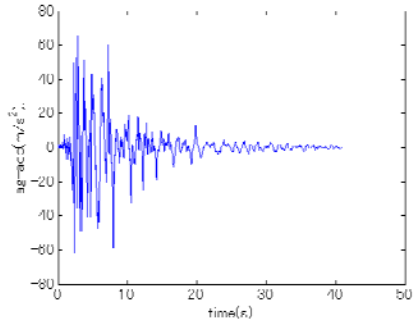

(b) E-W Direction (Transverse direction)

Figure 5 JR Takatori acceleration waves

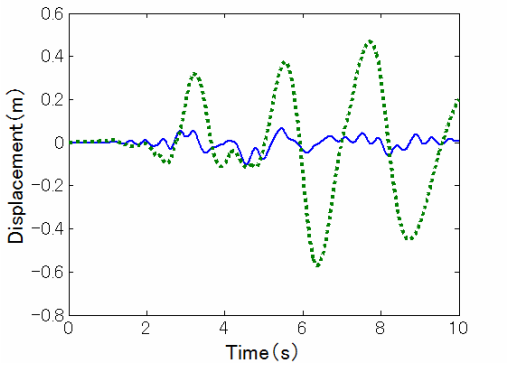

(Solid line : with bellows, Dashed line : without bellows)

Figure 6 Time histories of longitudinal direction displacement (superstructure)

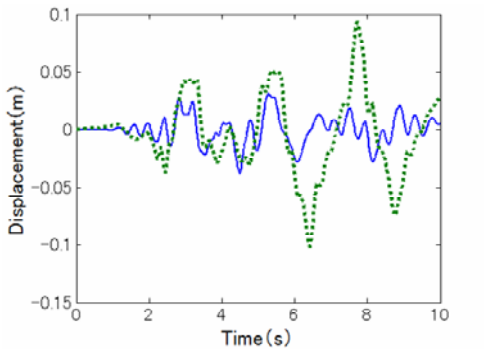

(Solid line : with bellows, Dashed line : without bellows)

Figure 7 Time histories of displacement of longitudinal direction (piers)

3.2 Transverse direction

Fig.8 and 9 illustrate the time-history response of the displacement of superstructure and piers. As shown in Fig.8 and 9, the maximum displacement of the superstructure is about 0.20 m and the maximum displacement of the pier is about 0.05 m with bellows. We must point out here that steel bellows are also effective for both displacements of superstructure and pier in the transverse direction.

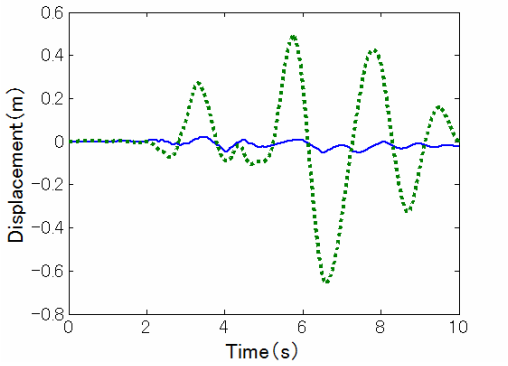

(Solid line : with bellows, Dashed line : without bellows)

Figure 8 Time histories of transverse direction displacement (superstructure)

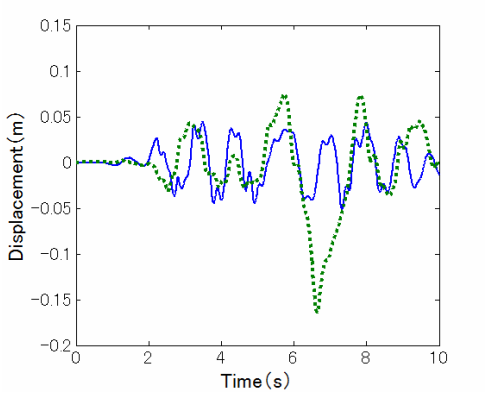

(Solid line : with bellows, Dashed line : without bellows)

Figure 9 Time histories of transverse direction displacement (piers)

3.3 Characteristics of steel bellows as energy absorbing connecters

Fig.10 illustrates the hysteretic load displacement curves of the steel bellows in the longitudinal and the transverse directions. The horizontal axis shows the displacement of the steel bellows and the vertical axis shows the force of the steel bellows. It can be confirmed that large energy absorbing is demonstrated from the load displacement history curve of the bellows.

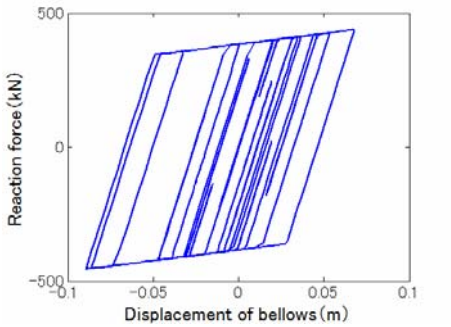

(a) Longitudinal direction

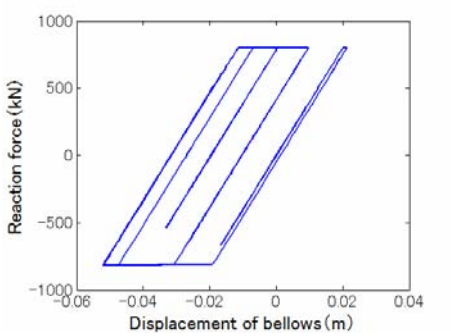

(b) Transverse direction

Figure 10 Hysteresis curve of steel bellows

3. CONCLUSIONS

The energy absorption performance and the applicability to girder bridges of the steel bellows are studied by means of the non-linear time history analyses for simultaneous biaxial seismic waves. The following conclusions are obtained:

1. The energy absorption performance of the steel bellows can be expected in the transverse direction as well as the longitudinal direction.

2. The steel bellows reduce considerably the displacement of superstructure and piers for both of longitudinal and transverse directions. Desired characteristics of steel bellows are satisfied by means of adjusting the yield strength of the bellows.

References:

K. Tanaka, H. Zui, T. Kitada, M. Matsumura, : Application of Energy Absorbing Connecters to Elevated Bridges, Steel Construction Engineering, JSSC, 10-40, pp.53-63, 2003.12 (in Japanese).

ZUI H. et al. Application of energy absorbing connecters to steel girder bridges, IABSE Symposium, towards a better built environment - innovation, sustainability, information technology, Melbourne, September 2002.

H. Zui, and Y. Namita, : Application of energy absorbing connecters to steel continuous girder bridges, 13th World Conference on Earthquake Engineering, Vancouver, B.C., Canada, August 1-6, 2004, Paper No. 3367

H. Zui, O. Ohtani and Y. Okamoto, : Mechanical Characteristics of Steel Bellows Absorbing Bridge Connecters, Steel Construction Engineering, JSSC, 9-34, pp.77-86, 2002.6 (in Japanese).

Japan Road Association, "Japanese Specifications for Highway Bridges", PartV, Seismic Design, 2002.3
(in Japanese).

JOINT CONFERENCE PROCEEDINGS
7th International Conference on Urban Earthquake Engineering (7CUEE) &
5th International Conference on Earthquake Engineering (5ICEE)
March 3-5, 2010, Tokyo Institute of Technology, Tokyo, Japan

SEISMIC FRAGILITY ANALYSIS OF LONG-SPAN CABLE-STAYED BRIDGES

Jiao Chi-yu[1)], Li Jian-Zhong[2)], and Long Pei-Heng[3)]

1) Lecture, College of Civil Engineering and traffic engineering, Beijing University of Civil Engineering and Architecture, Beijing, CHINA

2) Professor, Dept. of Bridge Engineering, Tongji University, Shanghai, CHINA

3) Associate Professor, College of Civil Engineering and traffic engineering, Beijing University of Civil Engineering and Architecture, Beijing, CHINA

jcy@bucea.edu.cn, lijianzh@mail.tongji.edu.cn, longpeiheng@bucea.edu.cn

Abstract: The 512 Wenchuan earthquake has warned us that earthquake is one of the most important risk factors in modern lifeline transportation system. As one of most important bridge types, a cable-stayed bridge belongs to the irregular bridges. Beyond the domestic and foreign criterions of seismic design, the seismic design of cable-stayed bridge was usually studied individually. In order to learn the main seismic damage characteristics of a whole kind, seismic fragility analysis of a cable-stayed bridge in longitudinal direction was done herein. The sample of cable-stayed bridge studied in this paper was based on the structural characteristics of cable-stayed bridges recently built in China. Excited by twenty ground motion waves belonging to III soil site type, the incremental dynamic analysis of cable-stayed bridge was done herein. The probabilities of difference damage state exceedance of the main tower were studied, as well as the transition pier, auxiliary pier and the piles subjected to different ground motion level. For comparing the seismic vulnerability of different components, the seismic fragility curves for different components of the sample cable-stayed bridge were developed. The research show: For upside down "Y" shape tower of the cable-stayed bridge, the vulnerable zones appear often on three positions, which are tower bottom, middle tower bottom, and top of the middle tower.

1. INTRODUCTION

Beyond the domestic and foreign criterions of seismic design, the seismic design of cable-stayed bridge was usually studied individually. Being limited to the seismic response characteristics of a single cable-stayed bridge, this research trend cannot help to learn the main seismic damage characteristics of a whole kind. On the other hand, seismic fragility analysis is becoming a popular tool to learning the seismic damage characteristics of one kind of bridge in some certain area, which is also very useful for prioritizing retrofit, pre-earthquake planning, and loss estimation.

A lot of research has been done on seismic fragility analysis of bridges in recent years. These researches can be done by two tools, one of which is empirical fragility curves; the other is analytical fragility curves. Empirical fragility curves are usually based on the reported bridge damage from past earthquakes, [Basoz 1998] and [Shinozuka 2000] have generated the empirical fragility curves of bridges in Japan and the US based on the observations of bridge damage after the 1994 Northridge earthquake and 1995 Kobe earthquake.

Analytical fragility curves are developed through seismic response data from the analysis of bridges. The fragility analysis includes three major parts: (a) the simulation of ground motions, (b) the simulation of bridges to account for uncertainty in bridge properties, and (c) the generation of fragility curves. Fragility curves can be generated by three methods. The first method is based on the statistic of frequency of the exceedance of different damage states [Shinozuka 2000]. The second method is based on the linear regressive analysis of the probabilistic seismic demand model. [Hwang, H.H.M1998.] The third method is based on the curve fitting of the capacity/demand ratio [Y.Pan, 2007].

The sample of cable-stayed bridge studied in this paper was based on the structural characteristics of cable-stayed bridges recently built in China. Because of lessen of earthquake damage of a similar type of bridge, analytical fragility curve will be a good option. The fragility curves are developed by performing nonlinear time history analyses for the bridge. A set of 200 ground motion records, with varying magnitudes, distances, and peak ground accelerations, is used in the time history analysis. The fragility curves are developed for various damage states for the bearings and columns. These individual component fragilities are obtained and compared with each other.

2. SEISMIC FRAGILITY ANALYSIS

2.1 COMPUTING MODEL

In recent years, many long span cable-stayed bridges have been built in China, as shown in Table 1.

From below, some common features of cable-stayed bridges in China can be deducted:

1) Double tower, double cable planes, and steel box girder are a popular style in recent year.

2) The main span is mainly between 600 to 800 meters.

3) Because of the similar geological conditions and mature construction crafts, pile group foundations are the optimized foundation type. Influenced by the river erosion, the pile group foundations basically are elevated pile foundations.

4) The common used tower is Diamond or "A" shape RC tower.

Based on the above observation, a sample bridge was used to resemble the significant characteristics of the cable-stayed bridges recent built in china. The span combination of the sample cable-stayed bridge is 82+262+688+262+82. An "A" shape RC tower with elevated pile group foundation was used. The tower height is 235 meters. The general scouring depth of the foundation is 19 meters. In order to consider the damage of the tower and the auxiliary piers, the fiber beam-column elements supported by the Open System for Earthquake Engineering Simulation (OpenSees) [Silvia 2007] were used. The material properties and some details about the model can be seen in a paper by Jiao Chi-Yu [2008]. In order to reduce the computation complexity, only half of the bridge was modeled and analyzed as shown in Figure 1. In the model, anti-symmetrical constraints were used in the mid span.

Table 1. Long-span cable-stayed bridges being built in china in recent years

Bridge name	**Bridge type**	**Span arrangement(m)**	**Basement**	**Height of tower (m)**	**Tower**	**Built Year**
Donghai Bridge	D* tower; D cable planes; Steel box girder;	73+132+420+132+73	pile group foundation; elevated pile foundation	147.9	Diamond shape RC tower	2005
Sutong Bridge	D* tower; D cable planes; Steel box girder;	2× 100+300+1088+300+2× 100	pile group foundation;	298	"A" shape RC tower	2008
Jintang Bridge	D* tower; D cable planes; Steel box girder;	77+218+620+218+77	pile group foundation; elevated pile foundation	210	Diamond shape RC tower	2008
Tianxingzhou Bridge	D* tower; D cable planes;	98+196+504+196+98	pile group foundation;	188.5	Diamond shape RC tower	2008
Stonecutters bridge	D* tower; D cable planes; Steel box girder	298+1018+298	pile group foundation;	295	Single column hybrid tower	2009
huanghe highway third bridge	S^{+} tower; D cable planes; Steel box girder	60+60+160+386	pile group foundation;	195.94	"A" shape RC tower	2008
Mingpu bridge	D* tower; D cable planes steel truss girder	4×60+708+4×60	pile group foundation;	200	"H" shape RC tower	2009
Xiang-shan cable-stayed bridge	D* tower; D cable planes; Steel box girder	82+262+688+262+82	pile group foundation; elevated pile foundation	219.5	Diamond shape RC tower	In built
shanghai yangtze river bridge	D* tower; D cable planes; Steel box girder	110+240+730+240+110	pile group foundation; elevated pile foundation	203.17	upside down "Y"shape RC tower	In built
Lingdingyang Bridge	D* tower; D cable planes; hybrid girder	284+950+284	pile group foundation;	259	Diamond shape RC tower	In built

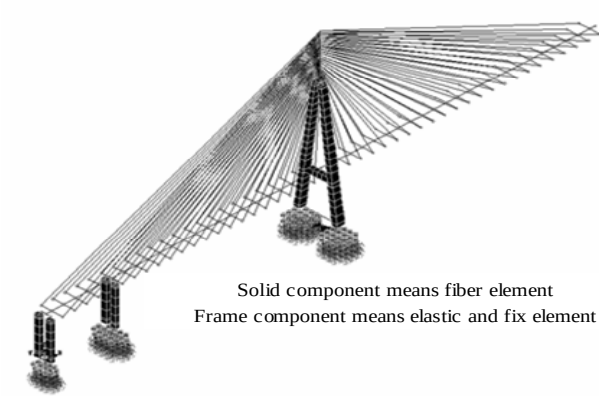

Figure 1. Cable-stayed bridge model used in this paper

2.2 DAMAGE STATE DEFINITION

A cable stayed bridge is composed of several components, such as main tower, main girder, cables, auxiliary pier, transitional pier, tower foundation, auxiliary pier foundation, and transitional pier foundation. The first aim of seismic fragility analysis in this paper is to investigate the most damageable position of each component. The second aim is to investigate the most damageable component of the whole bridge. Former studies show the cables and steel girder are the most firm components, so their vulnerability was not considered herein. For other components considering their displacement characteristics, flexural curvature at the critical section can be thought as an important symbol of each component. The axial forces under the dead load were used to calculate the most unfavorable curvature. Different damage states are decided by the material strain levels in different states. The material strain level defined [Arzoumanidis S 2005] in Tacoma new suspension bridge tower is modified herein, considering some recent research result of bridge concrete piers. The material strain levels for different states are listed in Table 2.

Table 2. Damage states and strain levels for the critical sections

Damage states	Damage description	Damage measures of strain levels
No damage	there's no crack on the concrete, the steel bars don't yield	$\varepsilon_s \le \varepsilon_y = 0.001675$
Slight damage	the spalling of the cover concrete does not occur, and the cracks were less than 1cm strain.	$0.001675 < \varepsilon_s \le \varepsilon_h = 0.015$; $\varepsilon_c \le 2\varepsilon_{co} = 0.004$
Moderate damage	the damage on the section were limited to the repairable state economically and technically	$0.015 < \varepsilon_s \le 0.55\varepsilon_{su} = 0.0495$; $0.004 < \varepsilon_{cc} \le 0.75\varepsilon_{ccu} = 0.007875$
Extensive damage	the damage on the section cannot be repaired; the tower doesn't lose bearing capacity.	$0.55\varepsilon_{su} < \varepsilon_s \le \varepsilon_{su} = 0.09$; $0.75\varepsilon_{ccu} < \varepsilon_{cc} \le \varepsilon_{ccu} = 0.0105$;
Complete damage	the component collapsed	$\varepsilon_s > \varepsilon_{su} = 0.09$; $\varepsilon_{cc} > \varepsilon_{ccu} = 0.0105$;

2.3 GROUND MOTION

To investigate the seismic fragility of the bridge, twenty ground motion records have been adopted, which are taken out from the Pacific Earthquake Engineering Research center (PEER) national ground acceleration (NGA) database. To model the most common geological condition, the earthquakes used in this paper occurred all belong to the type III, according to the Specifications of Earthquake Resistant Design for Highway Engineering in China. To reduce dispersion of the seismic response, the epicenter distance of these waves are less than 20 km, as shown in Table 3.

Table 3. Ground motion records used for seismic fragility analysis

Earthquake name	Record component	ID in paper	PGA (g)	Sa(T_1)(g)
Loma Prieta	LOMAP /NAS180	wave501	0.268	0.0203
Loma Prieta	LOMAP /NAS270	wave502	0.209	0.0408
Loma Prieta	LOMAP /EMY260	wave503	0.26	0.0251
Loma Prieta	LOMAP /EMY350	wave504	0.215	0.011
Morgan Hill	MORGAN /SFO050	wave505	0.048	0.0016
Morgan Hill	MORGAN /SFO320	wave506	0.048	0.0015

Loma Prieta	LOMAP /LKS270	wave507	0.137	0.0189
Loma Prieta	LOMAP /LKS360	wave508	0.096	0.0137
N. Palm Springs	PALMSPR /INO225	wave509	0.064	0.0086
N. Palm Springs	PALMSPR /INO315	wave510	0.117	0.0102
Loma Prieta	LOMAP /SFO000	wave511	0.236	0.0019
Loma Prieta	LOMAP /SFO090	wave512	0.329	0.0023
Northridge-01	NORTHR /WAT180	wave513	0.089	0.0005
Northridge-01	NORTHR /WAT270	wave514	0.086	0.0005
Northridge-01	NORTHR /GAR000	wave515	0.104	0.0007
Northridge-01	NORTHR /GAR270	wave516	0.103	0.0006
Northridge-01	NORTHR /WBA000	wave517	0.072	0.0003
Northridge-01	NORTHR /WBA090	wave518	0.066	0.0005
Northridge-01	NORTHR /WAI200	wave519	0.086	0.0005
Northridge-01	NORTHR /WAI290	wave520	0.069	0.0006

Then IDA analysis [Dimitrios Vamvatsikos 2003] should be done, in order to get the statistic information of seismic demand of different bridge components. Therefore, taken as an Intensity Measure (IM) for scaling, the Sa (T1=13.5s，ξ=3%) has been scaled from 0.001g to 0.028g, and the incremental step of 0.003g is adopted. The damping ratio 0.03 is used here mainly considering that the main girder and cables are made of steel.

2.4 SEISMIC FRAGILITY CURVES

The seismic fragility curves for the critical section (such as tower bottom) can be obtained by the following steps:

Step1: Calculate the section curvature demands under different intensity levels; calculate the curvature capacity under different damage state.

Step2: Take the nature logarithmic transformations of intensity measures as independent variable($\ln(Sa)$); take the nature logarithmic transformations of the demand/capacity ratio as dependent variable($\ln(S_d / S_{c4})$), by means of quadratic curve fitting these two variables[Y.Pan,2007]. By regression analysis, the mean value of $\ln(S_d / S_{c4})$ is expressed as a function of $\ln(Sa)$. The standard deviation for regression line is $\sigma = \sqrt{S_r /(n-2)}$, where *Sr*=sum of squares of the residuals with respect to the regression line, where S_d and S_{c4} are structural demand and capacity in the complete damage state.

Step3: Based on other studies, $\ln(S_d / S_{c4})$ is assumed to follow normal distribution about the regression curve for all values of analyzed *Sa*. Through regression the fragility for a specific damage-state can be computed as

$$\mu = a(\ln(Sa))^2 + b(\ln(Sa)) + c \qquad (1)$$

$$\sigma = \sqrt{S_r /(n-2)} \qquad (2)$$

By using quadratic regression, the mean is expressed as Eq. (1) with coefficients a, b, and c determined by the least-square method.

Step 4: Based on the mean and the standard deviation, by means of the below equals, we can get the fragility curve of a certain position of the section in the tower at an certain damage state.

$$P_f = P\left[\frac{S_d}{S_{c4}} \geq 1\right] = 1 - \Phi\left(\frac{\ln(1)-\mu}{\sigma}\right) = \Phi\left(\frac{\mu}{\sigma}\right) \qquad (3)$$

Taking the tower bottom section of the bridge as an example, the quadratic regression can been seen in Figure 2. The seismic fragility curve can be seen in Figure3.

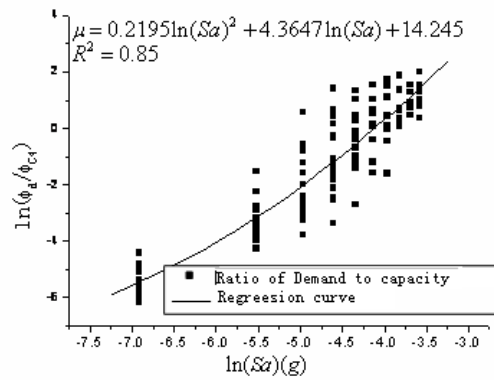

Figure 2. the regression of $\ln(Sa)$ and $\ln(S_d / S_{c4})$

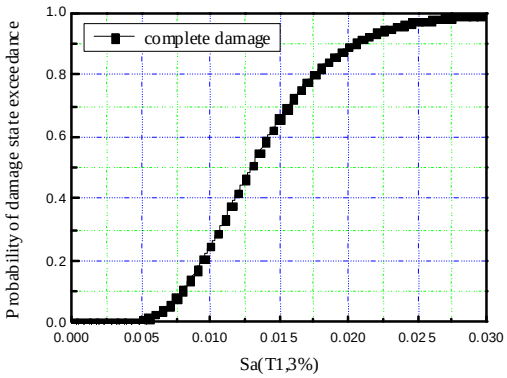

Figure 3. the seismic fragility curve of the tower bottom section

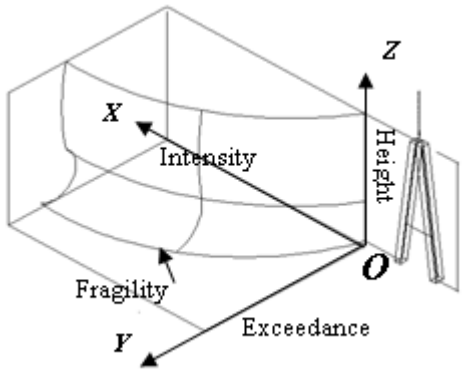

Fig.4 the exceedance probalility map introduction

Based on above methods, we can get each frailty curves of each section of the tower, plot them by the way as Figure 4, the distribution of the exceedance probability of the tower can be obtained.

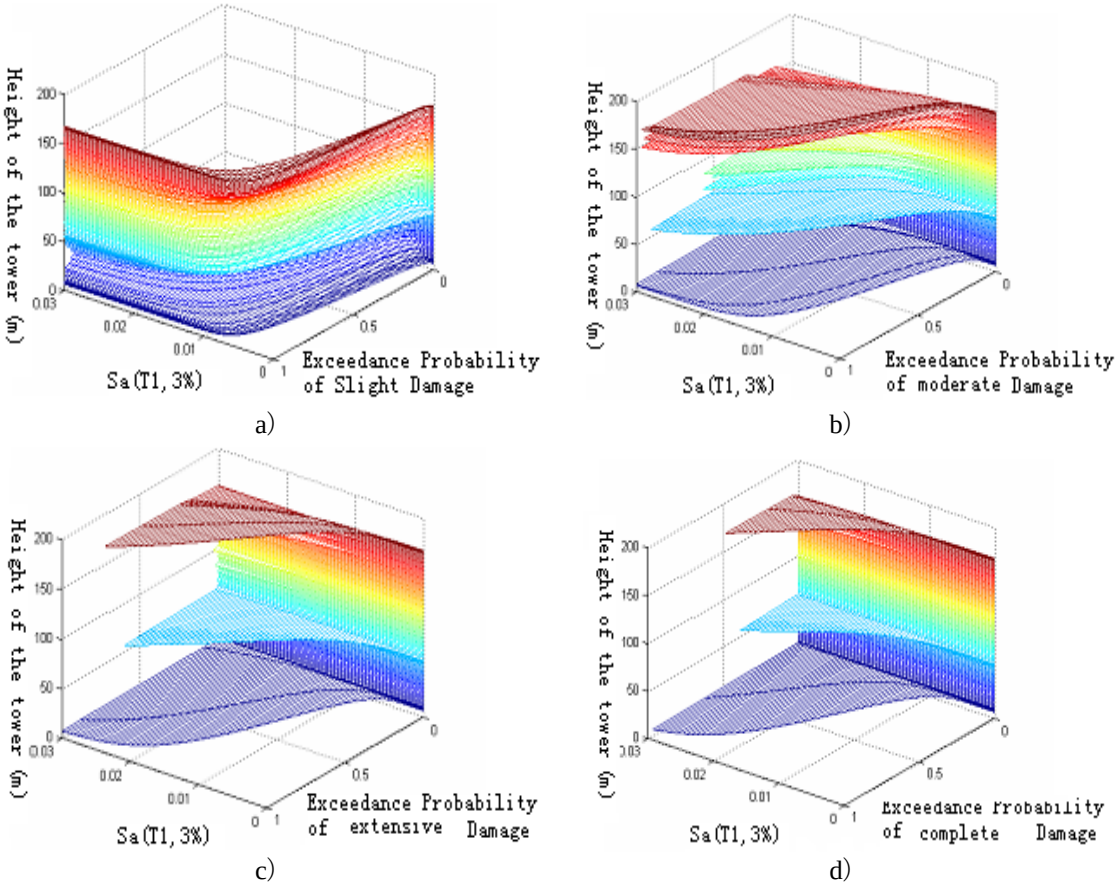

Fig.5 Exceedance probability distribution along the tower excited by longitudinal ground motions

From above, we can conclude that:

1) Under longitudinal ground motion excitation, the most damageable position of the tower mainly concentrated the damages of the tower mainly concentrate on three zones: the two pylon legs' bottoms, the two pylon legs' tops, and the middle zones of the two pylon legs' upper parts.

2) As the intensity increases, the most damageable position of the tower gradually concentrates on the pylon legs' bottoms and the two pylon legs' tops. On the other hand, with increments of the damage state severity, the two pylon legs' bottoms became the most damageable place of the tower.

By the same means, we can get the exceedance probability distribution along the auxiliary pier and the transitional of the bridge, because of the link between the girder and the pier. The most damageable position is concentrated on the bottom of the pier. Due to paper length limitations, only the exceedance probability of complete damage was shown in Figure 6 and Figure 7.

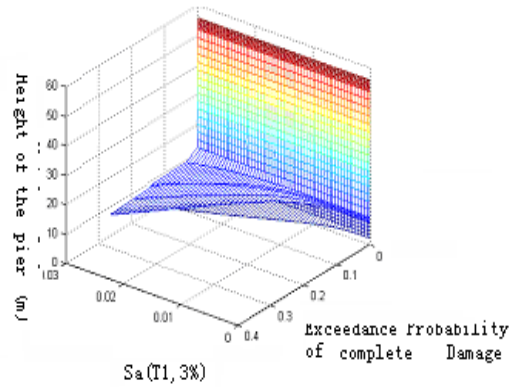

Figure 6. Exceedance probability of auxiliary pier

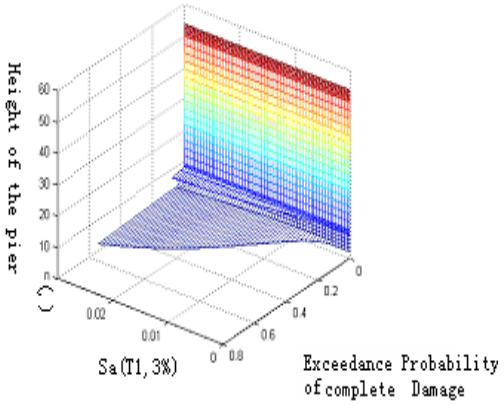

Figure 7. Exceedance probability of transitional pier

Taking the exceedance probability of the most damageable position of the whole component as the exceedance probability of the whole component and plotting different exceedance probabilities in one graph, the most damageable component of the cable-stayed bridge can be seen.

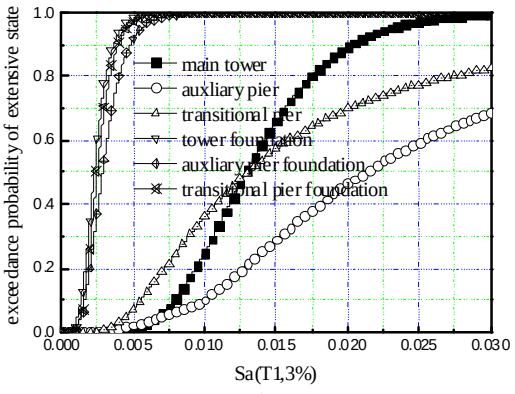

a)

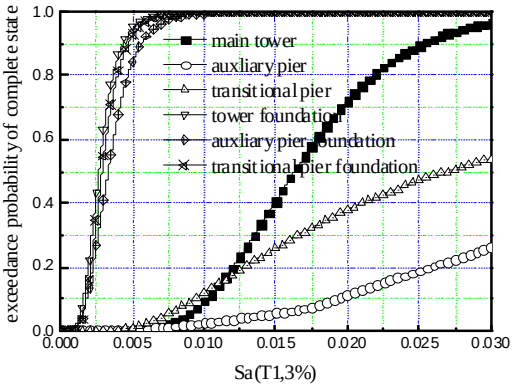

b)

Figure 8. Seismic fragility curve comparing among the component cable-stayed bridge

From above we can conclude that,

1) Under longitudinal excitation, the pile foundation especially the main tower foundation is the most damageable component.

2) The auxiliary pier is the firmest in all the component of long-span cable-stayed bridge.

3 CONCLUSION

From all the IDA analyses of the reinforced concrete tower of a cable-stayed bridge in above, seismic fragility analysis are investigated, some conclusions can be drawn as follows:

1) Seismic fragility analysis of all the components of long-span cable-stayed bridge is very helpful for engineering to investigate the most damageable component.

2) Under longitudinal excitation, the pile foundation, especially the main tower foundation, is the most damageable component.

3) By plotting the fragility curves of each important section and by comparing them, we can investigate the most damageable position.

4) Under longitudinal excitation, the damages of the tower mainly concentrate on three zones: the two pylon legs' bottoms, the two pylon legs' tops, and the middle zones of the two pylon legs' upper parts.

Acknowledgement

This research is supported by Science & Technology Program Foundation for Transportation Development in West China under Grant No. 200631882225.This research is also supported by Foundation for Cultivation of Excellent talents in Beijing under Grant No.2009B005017000003.

References:

Arzoumanidis S, Shama AA, Marlow SJ, Orsolini GO. (2005) The New Tacoma Narrows Suspension Bridge: Critical Issues in Seismic Analysis and Design. Structures 2005.New York, ASCE. p. 21-21.

Basoz, N., and Kiremidjian, A. (1998). "Evaluation of bridge

damage ata from the Loma Prieta and Northridge, CA earthquakes." Rep. No. CEER-98-0004, Multidisciplinary Center for Earthquake Engineering

Hwang, H.H.M., and Huo, J-R. Probabilistic Seismic Damage Assessment of Highway Bridges(C1998). The 6th U.S. National Conference on Earthquake Engineering, Seattle, Washington, June,.

Shinozuka M., Feng, M.Q., Lee, J., and Naganuma, T. Statistical analysis of fragility curves[J]. Journal of Engineering Mechanics, 2000, 126(12): 1224–1231

Silvia Mazzoni, Frank McKenna, Michael H. Scott, Gregory L. Fenves,et al., 2007, OpenSees Command Language Manual http: //opensees.berkeley.edu/OpenSees/user/primer.php

Y.Pan, A. K. Agrawal, M.Ghosn. Seismic Fragillity of Continuous Steel Highway Bridges in New York State[J]. Journal of Bridge Engineering 2007,12(6):689-699

Ye ai-jun et al. Study on the seismic performance of thousands meter grade cable-stayed bridges.(2007) Research Report Shanghai.

Jiao chi-yu, Li jian-zhong, Fan li-chu,(2008) Nonlinear Seismic Response Analysis and Seismic Performance Evaluation of A Reinforced-Concrete Cable-Stayed Bridge Tower Using IDA Method, 14th world conference on earthquake engineering.

JOINT CONFERENCE PROCEEDINGS
7th International Conference on Urban Earthquake Engineering (7CUEE) &
5th International Conference on Earthquake Engineering (5ICEE)
March 3-5, 2010, Tokyo Institute of Technology, Tokyo, Japan

IDENTIFYING CABLE TENSION LOSS and DECK DAMAGE IN A CABLE-STAYED BRIDGE USING A MOVING VEHICLE

Shih-Hsun Yin[1] and Chung-Yu Tang[2]

1) Assistant professor, Department of Civil Engineering, National Taipei University of Technology, Taipei,10608,Taiwan, R.O.C.
2) Graduate student, Department of Civil Engineering, National Taipei University of Technology, Taipei,10608,Taiwan, R.O.C.
shihhsun@ntut.edu.tw

Abstract: This paper presents a computational study on a new method of detecting multiple simultaneous damages in a cable-stayed bridge by use of the analysis of the vertical dynamic response of a vehicle passing the bridge. In this research, we consider that two kinds of damage including cable tension loss and deck damage may occur simultaneously at different locations. The differences between the vertical displacement responses of a vehicle passing the damaged bridge and the healthy bridge are sampled and called the relative displacement response vector of the vehicle. The proper orthogonal decomposition (P.O.D.) is utilized to decompose the relative displacement response vector of the vehicle passing the bridge with unknown multiple damages into an optimal set of basis vectors formed from the ones of the vehicle moving over the known damaged bridges. The associated system parameters variation with the unknown multiple damages can be reconstructed further.

1. INTRODUCTION

In recent years, cable stayed bridges have become more popular because they represent the best technical and economical solution to overcome long spans and provide many aesthetic options especially for communities seeking so-called signature structures and landmarks. Such long-span bridges have a long service period, require long-term durability, and suffer from heavy and fast moving loads, wind, earthquake, and environmental corrosion. Therefore, structural health monitoring systems are needed to ensure the long-term performance of these bridges. Cable tension, deck and tower deformation, and structural vibration are usually monitored by strain gauges (Ren 2007), accelerometers (Li 2006, Caicedo 2005, Macdonald 2005, and Ren 2005), laser vibrometers (Miyashita 2008, and Mehrabi 2006), polyvinylidene fluoride PVDF piezoelectric film sensors (Liao 2001 and Wang 1999), optic fiber sensors (Li 2006), and global position systems (GPS) (Li 2006 and Watson 2007). Most of these sensors are attached or embedded in structural members of a bridge. However, it takes a lot of costs and manpower to maintain sensors or replace them if needed. Instead, Yang et al. (2004 and 2005) provided the idea of using a vehicle moving over a bridge as a message carrier of the dynamic properties of the bridge, and theoretically and experimentally investigated the feasibility of extracting bridge frequencies from a passing vehicle. Compared with the aforementioned techniques of measurements, this method is cost-effective because it can reduce the number of needed sensors and the sensors installed in the vehicle are easy to maintain.

For the cable-stayed bridges, stay cables are the most critical structural elements to offer the designed load-bearing ability. Thus, monitoring of the cable tension and its variation of cable-stayed bridges is very important and necessary. Traditionally, each cable is instrumented by sensors (e.g., accelerometers), and vibratory frequencies of cables are calculated from the directly measured data or identified by some modal identification techniques from ambient vibration measurements and finite element modeling (Macdonald 2005, Ren 2005, and Weng 2008). Then, the cable tension is estimated through mathematical relationships between the frequencies and the cable force (Caicedo 2005, Miyashita 2008, Mehrabi 2006, Liao 2001, and Wang 1999). In contrast, this paper presents a preliminary and computational study on a new method of detecting tension variations of multiple cables and deck damage at different locations in a cable-stayed bridge by use of the analysis of the vertical dynamic response of a vehicle passing the bridge.

2. MATHEMATICAL MODELING

In this section, the finite element modeling of the interaction between a vehicle and a cable-stayed bridge is discussed.

The cable-stayed bridge structure is modeled as an elastic beam resting on an elastic foundation (Meisenholder 1974) or hanging on continuously distributed springs. The accuracy of the structural model has been validated in previous works through comparisons with numerical results obtained by using discrete cable system bridge models (Chatterjee 1994 and Bruno 1997). First, to take the sagging effect of a curved cable into account, the modified modulus of elasticity of the stay cable is given by Ernst (Eisenberger 1985) as

$$E_{eq} = \frac{E_s}{1+[(w_c L_h)^2 A_c E_s / 12 T_c^3]}, \tag{1}$$

where E_s is the elastic modulus of the cable, w_c is the weight of the cable per unit length, L_h is the horizontal projected length of the cable, A_c is the cross-sectional area of the cable, and T_c is the tension of the cable. Then, the equivalent vertical stiffness of the support at each cable-stay location is expressed as

$$K_{vt} = E_{eq} A_c \sin^2\theta / L_c , \tag{2}$$

where L_c is the length of the cable, and θ is the inclined angle of the cable. The vertical stiffness of equivalent continuously distributed springs as shown in Fig. 1 is obtained as

$$K_{vt}^* = K_{vt} / \Delta L . \tag{3}$$

Finally, the mass and stiffness matrices of a cable-deck element as shown in Fig. 2 are written as

$$[m_e] = \int_0^{L_e} m \langle N \rangle^T \langle N \rangle dx \tag{4}$$

$$[k_e] = \int_0^{L_e} EI \langle N'' \rangle^T \langle N'' \rangle dx + \int_0^{L_e} K_{vt}^* \langle N \rangle^T \langle N \rangle dx \tag{5}$$

where *EI* and *m* are the flexural rigidity and the mass per unit length of the deck, and $\langle N \rangle$ is a row vector containing the shape functions derived by Eisenberger (1985). Also, deck elements (common beam elements, $K_{vt}^* = 0$) are used to simulate the portion of the bridge far from the cable-stay location. The combination of cable-deck elements and deck elements is employed to model the whole cable-stayed bridge system.

The vehicle simulated as a sprung mass acts at one of the above elements as shown in Fig. 3 when it passes over the bridge. In Fig. 3, M_v is the mass of the car-body, K_v and C_v are the stiffness and damping of the suspension of the vehicle, m_w is the mass of the wheel, and x_0 is the position coordinate of the contact point of the wheel on the element. Also, z is the vertical displacement of the car-body measured from its static equilibrium position, and $\bar{y}$ is the vertical displacement of the wheel measured from the position of the undeformed bridge. Next, we assume that the wheel is perfectly rigid and in contact with the deck. Thus, $\bar{y}$ is equal to the displacement of the deck at $x = x_0$ and can be expressed as

$$\bar{y} = \langle N \rangle_{x=x_0} \{d\}, \tag{6}$$

where $\{d\}$ is the vector containing the nodal displacement and rotation of the element where the vehicle acts. The equation of motion of the sprung mass can be written as

$$M_v \ddot{z} + C_v (\dot{z} - \dot{\bar{y}}) + K_v (z - \bar{y}) = 0 . \tag{7}$$

In addition, the contact force acting on the element can be written as

$$f_c = -m_w \ddot{\bar{y}} - m_w g - M_v g - M_v \ddot{z} , \tag{8}$$

and the associated equivalent nodal load of the element can be obtained as

$$\{f_e\} = \int_0^L \langle N \rangle^T f_c \cdot \delta(x - x_0) dx , \tag{9}$$

where $\delta(x)$ is the Dirac's Delta function. The equation of motion of the element directly in contact can be expressed as

$$[m_e]\{\ddot{d}\} + [c_e]\{\dot{d}\} + [k_e]\{d\} = \{f_e\}, \tag{10}$$

where $[c_e]$ is the element damping matrix assembled from $[m_e]$ and $[k_e]$ by considering Rayleigh damping. Note that Eq. (7) and Eq. (10) are coupled since both z and $\{d\}$ are contained in these two equations.

The assembly of the sprung mass, the element directly in contact, and other elements not directly in contact can result in the equations of motion of the entire vehicle-bridge system as

$$[M]\{\ddot{D}\} + [C]\{\dot{D}\} + [K]\{D\} = \{F\}, \tag{11}$$

where $\{D\}$ denotes the system displacement vector, which contains all degrees of freedom of the vehicle and bridge, $[M]$, $[C]$, and $[K]$ are the mass, damping, and stiffness matrices of the entire system, and $\{F\}$ is the corresponding force vector. Note that $[M]$, $[C]$, $[K]$, and $\{F\}$ are functions of the acting position of the vehicle on the bridge, and must be updated at each time step during the direct integration process to account for the movement of the vehicle passing over the bridge. The system equations as given in Eq. (11) can be solved by any time integration schemes such as Runge Kutta method and Newmark-β method.

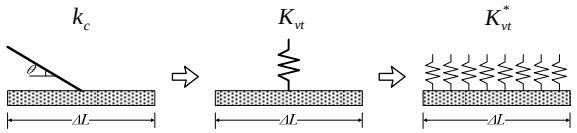

Figure 1 The schematic plots of the transition from a single cable supporting deck to equivalent continuously distributed springs supporting deck.

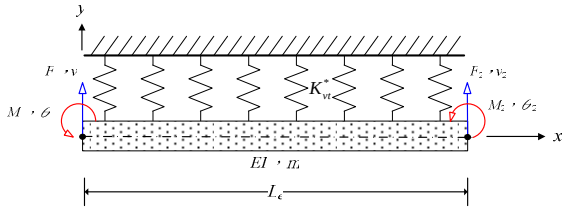

Figure 2 A cable-deck element model.

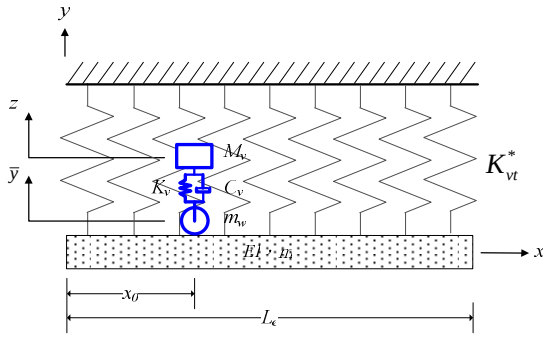

Figure 3 A sprung mass representing a vehicle acts on a cable-deck element.

3. DAMAGE DETECTION TECHNIQUE

In this study, two kinds of damage considered are stiffness reduction of the continuously distributed springs resulting from cable tension relaxation and flexural rigidity loss of the beam due to the fracture and deterioration of deck material. When the proposed damage detection technique is applied, we need to determine how many sample damage cases are considered. Each sample damage case refers to one kind of damage at one location with some damage level. These damage cases may take place simultaneously. The challenge is how to identify multiple damage cases by only use of the vertical responses of a vehicle. For this purpose, the vertical dynamic responses of the vehicle passing the healthy bridge and the bridge where all possible cases of damage are respectively imposed are simulated. Then, the differences between the vertical dynamic responses of the vehicle passing the damaged bridge and the healthy bridge are collected for all sample damage cases, and organized as column vectors in a matrix **Q** as follows

$$\mathbf{Q} = \left[\bar{\mathbf{z}}_1\ \bar{\mathbf{z}}_2 \cdots \bar{\mathbf{z}}_k\right], \tag{12}$$

where $\bar{\mathbf{z}}_k = \mathbf{z}_k - \mathbf{z}_h$, k is the number of the sample damage cases, $\mathbf{z}_k$ and $\mathbf{z}_h$ are the vectors of the vertical response of the vehicle moving over the damaged bridge for the kth sample damage case and the healthy bridge respectively, and $\bar{\mathbf{z}}_k$ is named the *relative* vertical response vector of the vehicle for the kth sample damage case. Thus, each column vector is associated with a single damage case that refers to a set of known system parameter variations. The corresponding sets of known system parameter variations to all sample damage cases are also grouped as column vectors in a matrix **P**. Then, the test damage case is considered for a general scenario where multiple damage cases occur, and the relative dynamic response vector of the vehicle for the test damage case $\bar{\mathbf{z}}_{test}$ is calculated. To evaluate the performance of the proposed technique, the parameter variations for the test case are reconstructed through P.O.D. based on the relative dynamic responses of the vehicle for all sample damage cases included in **Q.**

First, a correlation matrix **C** is calculated as $\mathbf{C} = \mathbf{Q}^T\mathbf{Q}$. The distribution of the magnitude of the eigenvalues of **C** can be used to judge if the column vectors in **Q** are linear independent. The linear independence provides the possibility of distinguishing between these sample damage cases. The number of eigenvalues m with large magnitude indicates the number of identifiable damage cases, and it dictates the minimum number of basis vectors needed for the associated parameters reconstruction. The eigenvectors v_i with i=1,…, m corresponding to the m largest eigenvalues are grouped in a matrix **V**. The proper orthogonal decomposition results in a set of optimal basis vectors arranged in a matrix **D** as

$$\mathbf{D} = \mathbf{QV}. \tag{13}$$

Next, the relative dynamic response vector of the vehicle for the test damage case $\bar{\mathbf{z}}_{test}$ can be regarded as a linear combination of these optimal basis vectors as follows

$$\bar{\mathbf{z}}_{test} = \mathbf{D}\boldsymbol{\alpha}, \tag{14}$$

where $\boldsymbol{\alpha}$ is the vector of weighting coefficients. These coefficients can be obtained by solving an underdetermined set of linear equations in a linear least squares sense as

$$\boldsymbol{\alpha} = \left(\mathbf{D}^T\mathbf{D}\right)^{-1}\mathbf{D}^T\bar{\mathbf{z}}_{test}. \tag{15}$$

Furthermore, the vector of weighting coefficients $\bar{\boldsymbol{\alpha}}$ associated with $\bar{\mathbf{z}}_1\ \bar{\mathbf{z}}_2 \cdots \bar{\mathbf{z}}_k$ to represent $\bar{\mathbf{z}}_{test}$ in a linear combination form are written as

$$\bar{\boldsymbol{\alpha}} = \mathbf{V}\boldsymbol{\alpha}. \tag{16}$$

Finally, the corresponding parameter variations to the test damage case can be identified from the known parameter variations associated with all the sample damage cases by

$$\mathbf{p}_{ident.} = \mathbf{P}\bar{\boldsymbol{\alpha}}, \tag{17}$$

which indicate the type, extent, and location of multiple

simultaneous damages for the test damage case.

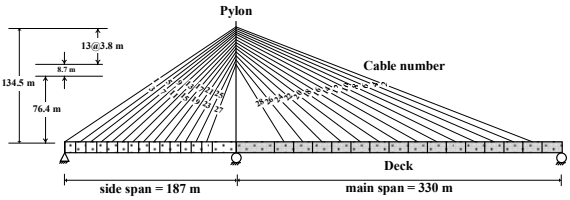

Figure 4 The structural model of the Kao Ping River Bridge in Taiwan.

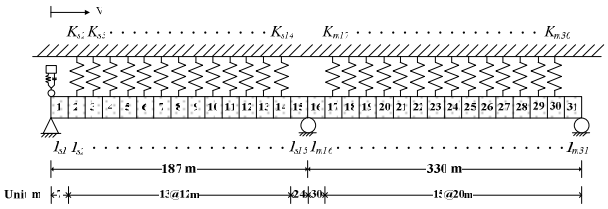

Figure 5 The bridge is divided into 31 sections based on the cable-stayed layout.

4. RESULTS

To demonstrate the proposed technique for identifying cable tension loss and deck damage in a cable-stayed bridge using a moving vehicle, a real example of a cable-stayed bridge, the Kao Ping River Bridge in Taiwan, is simulated. The bridge model is depicted as shown in Fig. 4, and the needed parameters of the bridge model are summarized in Table 1 (a) and (b). Based on the assumption in Section 2, each cable is modeled as equivalent continuously distributed springs to support the deck. Since the vertical stiffness of equivalent continuously distributed springs provided by each cable is different, the entire structural system is divided into 31 sections as shown in Fig. 5. The symbol and value of the parameters of each section for analysis are listed in Table 2. In the finite element modeling, deck elements are utilized for the first, fifteenth, sixteenth, and thirty-first sections of the bridge, and other sections of the bridge are modeled by cable-deck elements. Also, the parameters of the passing vehicle considered are summarized in Table 3.

In this study, we assume that the simulated bridge using the parameters in Table 2 can be regarded as being in a healthy state, and consider that the vehicle moves over the bridge at a constant speed of 30 m/s. Fig. 6 shows that the vertical displacement of the car-body of the vehicle varies with the location where the vehicle acts along the healthy bridge. According to the proposed damage detection technique in Section 3, we consider that 0.25% reduction of spring stiffness (K_{s2}~K_{s14} and K_{m17}~K_{m30}) and moment of inertia of deck (I_{s1}~I_{s15} and I_{m16}~I_{m31}) takes place independently. Thus, there are totally 58 damage cases called the sample damage cases. The parameters variation associated with these sample damage cases can be written in a vector form as

$$\mathbf{p}_1 = \left[\Delta K_{s2} \;\; \Delta K_{s3} \cdots \Delta K_{m30} \; \Delta I_{s1} \cdots \Delta I_{m31}\right]^T$$
$$= \left[0.025K_{s2} \;\; 0 \;\; \cdots \;\; 0\,0 \cdots 0\,0 \cdots 0\,0 \cdots 0\right]^T$$
$$\mathbf{p}_2 = \left[0 \;\; 0.025K_{s3} \;\; \cdots \;\; 0\,0 \cdots 0\,0 \cdots 0\,0 \cdots 0\right]^T$$
$$\vdots$$
$$\mathbf{p}_{58} = \left[0 \;\; 0 \cdots 0\,0 \cdots 0\,0 \cdots 0\,0 \cdots \;\; 0.025I_{m31}\right]^T$$

These column vectors are arranged in a matrix **P** as $\mathbf{P} = \left[\mathbf{p}_1 \, \mathbf{p}_2 \cdots \mathbf{p}_{58}\right]$.

Next, the vertical displacements of the car-body of the vehicle when passing all the corresponding damaged bridges at the same speed are calculated. Furthermore, the relative vertical displacements of the car-body of the vehicle for all the sample damage cases can be obtained by subtracting the vertical displacement of the car-body of the vehicle passing the healthy bridge from the ones of the vehicle moving over all the corresponding damaged bridges, and are shown in Fig. 7(a) and 7(b). Then, the relative vertical displacement vectors of the car-body for all the sample damage cases are sampled as

$$\bar{\mathbf{z}}_1 = \left[\bar{z}_1(x_1)\, \bar{z}_1(x_2) \cdots \bar{z}_1(x_n)\right]^T$$
$$\bar{\mathbf{z}}_2 = \left[\bar{z}_2(x_1)\, \bar{z}_2(x_2) \cdots \bar{z}_2(x_n)\right]^T$$
$$\vdots$$
$$\bar{\mathbf{z}}_{58} = \left[\bar{z}_{58}(x_1)\, \bar{z}_{58}(x_2) \cdots \bar{z}_{58}(x_n)\right]^T$$

where x_1, x_2, …, x_n are the locations where the vehicle acts along the bridge. To apply proper orthogonal decomposition, first, these column vectors are grouped in a matrix **Q** as $\mathbf{Q} = \left[\bar{\mathbf{z}}_1 \, \bar{\mathbf{z}}_2 \cdots \bar{\mathbf{z}}_{58}\right]$, and the correlation matrix **C** is assembled as $\mathbf{C} = \mathbf{Q}^T\mathbf{Q}$. Then, the eigenvalues of **C** are solved and plotted in Fig. 8. Fig. 8 shows that the magnitude of the eigenvalues decreases in a scale and there is no one of the eigenvalues much less than any other eigenvalues, which indicates that the relative vertical displacement vectors for all the sample damage cases ($\bar{\mathbf{z}}_1 \, \bar{\mathbf{z}}_2 \cdots \bar{\mathbf{z}}_{58}$) are linearly independent.

The above mentioned linear independence among $\bar{\mathbf{z}}_1 \, \bar{\mathbf{z}}_2 \cdots \bar{\mathbf{z}}_{58}$ is significant and provides the possibility of distinguishing between these sample damage cases. The proper orthogonal decomposition generates a set of optimal basis vectors using Eq. (13) in which the eigenvectors corresponding to the 58 largest eigenvalues are used. The measured relative displacement of the car-body of the vehicle passing the bridge with unknown damage is projected into the resulting set of optimal basis vectors. Then, the corresponding parameter variations to

the unknown damage case can be reconstructed through from Eq. (14) to Eq. (17).

To demonstrate the performance of the proposed technique to detect unknown multiple simultaneous damages, we consider 0.1% loss of K_{m28}~K_{m30} and I_{m28}~I_{m30}. The relative displacement of the car-body of the vehicle passing the damaged bridge for this case is plotted as shown in Fig. 9. The comparison between the specified parameter variations and the identified ones by the proposed method for this test case is presented in Table 4. One may find that multiple damages occurring at adjacent locations can be distinguished, and the damage type (*e.g.*, spring stiffness reduction due to cable tension loss or reduction of moment of inertia of deck) and the damage level (*i.e.* the reduction percentage) are almost accurately detected.

In addition, cable tension loss can be interrogated through the identified stiffness reduction of equivalent continuously distributed springs. By substituting Eq. (1) and (2) into Eq. (3), cable tension can be represented as

$$T_c = \left(\frac{K_{vt}^{*} w_c^{2} L_h^{2} E_s A_c L_c \Delta L}{\left(12 E_s A_c \sin^2\theta - 12 K_{vt}^{*} L_c \Delta L\right)} \right)^{1/3} .$$

When the stiffness reduction is identified, the current cable tension can be calculated by substituting the updated K_{vt}^{*} into the above equation, and the cable tension loss can be obtained further. For example, the loss percentage of the eleventh, thirteenth, and fifteenth cable causing 0.1% reduction of K_{s6}, K_{s7}, and K_{s8} are respectively 4.05%, 5.26%, and 3.14%.

5. CONCLUSIONS

In this paper, a new method of detecting multiple simultaneous damages in a cable-stayed bridge using the analysis of the vertical dynamic response of a vehicle passing the bridge is demonstrated. The vertical vibration interaction of the vehicle-cable stayed bridge system is simulated by a finite element method. Two kinds of damage including cable tension loss and deck damage are considered to occur singly or simultaneously at different locations. The unknown multiple damages can be reconstructed by decomposing the relative displacement response vector of the vehicle passing the bridge with unknown multiple damages into the ones of the vehicle moving over the bridges with known damages based on proper orthogonal decomposition. The accurate results can be obtained when two requirements are satisfied. First, a care must be taken of choosing a set of sample damage cases which covers the most likely single damage scenarios such that the system parameter variations associated with the unknown damage case lies within the range of the ones associated with the sample damage cases. Second, the relative vertical response vectors of the vehicle for all the sample damage cases are linearly independent. Note that, in addition to displacement response, velocity and acceleration responses of the vehicle can be used in the proposed method as long as the second requirement is satisfied.

Acknowledgments

The author wishes to acknowledge the National Science Council, Taiwan (R.O.C.) for the generous support of this work.

References:

Ren, W. X., Lin, Y. Q., Peng, X. L., 2007, "Field load tests and numerical analysis of Qingzhou cable-stayed bridge," J. Bridge. Eng., **12**(2), pp. 261-270.

Li, H., Ou, J. P., Zhao, X.F., Zhou, W. S., Li, H. W., Zhou, Z., and Yang, Y. S., 2006, "Structural health monitoring system for the Shandong Binzhou Yellow River Highway Bridge," Comput.-Aided Civil Infrastruct. Eng., 21(4), pp. 306-317.

Caicedo, J. M. and Dyke, S. J., 2005, "Experimental validation of structural health monitoring for flexible bridge structures," Struct. Control. Health Monit., 12(3-4), pp. 425-443.

Macdonald, J. H. G. and Daniell, W. E., 2005, "Variation of modal parameters of a cable-stayed bridge identified from ambient vibration measurements and FE modeling," Eng. Struct., 27(13), pp. 1916-1930.

Ren, W. X., Peng, X. L. and Lin, Y. Q., 2005, "Experimental and analytical studies on dynamic characteristics of a large span cable-stayed bridge," Eng. Struct., 27(4), pp. 535-548.

Ren, W. X. and Peng, X. L., 2005, "Baseline finite element modeling of a large span cable-stayed bridge through field ambient vibration tests," Comput. Struct., **83**(8-9), pp. 536-550.

Miyashita, T. and Nagai, M., 2008, "Vibiration-based Structural Health Monitoring for Bridges using Laser Doppler Vibrometers and MEMS-based Technologies," Int. J. Steel Struct., **8**(4), pp. 325-331.

Mehrabi, A. B., 2006, "In-service evaluation of cable-stayed bridges, overview of available methods, and findings," J. Bridge Eng., **11**(6), pp. 716-724.

Liao, W. H., Wang, D. H., and Huang, S. L., 2001, "Wireless monitoring of cable tension of cable-stayed bridges using PVDF piezoelectric films," J. Intell. Mater. Syst. Struct., **12**(5), pp. 331-339.

Wang, D. H., Liu, J. S., Zhou, D. G., and Huang, S. L., 1999, "Using PVDF piezoelectric film sensors for in situ measurement of stayed-cable tension of cable-stayed bridges," Smart Mater. Struct., 8(5), pp. 554-559.

Watson, C., Watson, T., Coleman, R., 2007, "Structural monitoring of cable-stayed bridge: Analysis of GPS versus modeled deflections," J. Surv. Eng.-ASCE, 133(1), pp. 23-28.

Weng, J. H., Loh, C. H., Lynch, J. P., Lu, K. C., Lin, P. Y., and Wang, Y., 2008, "Output-only modal identification of a

cable-stayed bridge using wireless monitoring systems," Eng. Struct. 30 (7), pp. 820-1830.

Yang, Y. B., Lin, C. W., and Yau, J. D., 2004, "Extracting the Bridge Frequencies from the Dynamic Response of a Passing Vehicle," J. Sound Vibr., 272(3-5), pp.471-493.

Lin, C. W. and Yang, Y. B., 2005, "Use of a passing vehicle to scan the fundamental bridge frequencies: An experimental verification," Eng. Struct., 27(13), pp. 1865-1878.

Meisenholder, S. G.., and Weidlinger P., 1974, "Dynamic interaction aspects of cable-stayed guide ways for high speed ground transportation," J Dyn. Syst. Meas. Control ASME 74-Aut-R, pp. 180–92.

Chatterjee, P. K., Datta, T. K., and Surana, C. S., 1994, "Vibration of cable-stayed bridges under moving vehicles," Struct. Eng. Int., 4(2), pp. 116–121.

Bruno, D., and Leonardi A., 1997, "Natural periods of long-span cable-stayed bridges," J. Bridge. Eng., 2(3), pp. 105–15.

Eisenberger, M. and Yankelevsky, D. Z., 1985, "Exact stiffness matrix for beams on elastic foundation," Comput. Struct., 21(6), pp. 1355-1359.

Yang, Y. B. and Yau, J. D., 1997, "Vehicle-bridge interaction element for dynamic analysis," J. Struct. Eng.- ASCE, 123 (11), pp. 1512–1518.

Table 1(a) The parameters of the cable-stayed

		Material	Young's modulus E (Nt/m^2)	Cross Section area A (m^2)	Moment Of inertia I (m^4)	Weight per unit length w (Nt/m)
Deck	Main span	steel	2.1×10^{11}	1.7421	2.9474	241817
	Side span	concrete	2.8×10^{10}	21.5967	32.608	674928
Cable		steel	1.85×10^{11}	Refer to Table 1(b)	—	Refer to Table 1(b)

Table 1(b) The parameters of the cable-stayed bridge model

	Cable number	Cross Section area A (m^2)	Weight per unit length w (Nt/m)	Cable tension T (KNt)
Main span	2	0.0444	3833.2	20250
	4	0.0183	1579.9	8910
	6	0.0255	2201.5	11230
	8	0.0183	1579.9	11440
	10	0.0201	1735.3	9820
	12	0.0249	2149.7	12660
	14	0.0255	2201.5	13670
	16	0.0246	2123.8	9770
	18	0.021	1813.0	11470
	20	0.0183	1579.9	9930
	22	0.0156	1346.8	7880
	24	0.0120	1036.0	5570
	26	0.0183	1579.9	8020
	28	0.0183	1579.9	3980
Side span	1	0.0546	4713.8	17330
	3	0.0201	1735.3	8400
	5	0.0273	2356.9	11470
	7	0.0204	1761.2	12700
	9	0.0210	1813.0	11500
	11	0.0249	2149.7	15450
	13	0.0264	2279.2	16870
	15	0.0252	2175.6	12390
	17	0.0222	1916.6	14280
	19	0.0198	1709.4	12390
	21	0.0165	1424.5	9920
	23	0.0126	1087.8	7110
	25	0.0183	1579.9	11900
	27	0.0165	1424.5	5500

Table 2 The symbol and value of the parameters of each section of the bridge model

Section number	Supporting cable number	Vertical stiffness of equivalent continuously distributed springs (Nt/m^2)		Moment of inertia of deck (m^4)	
1	—	—	—	I_{s1}	32.608
2	3	K_{s2}	490251	I_{s2}	32.608
3	5	K_{s3}	747350	I_{s3}	32.608
4	7	K_{s4}	645354	I_{s4}	32.608
5	9	K_{s5}	749093	I_{s5}	32.608
6	11	K_{s6}	1017685	I_{s6}	32.608
7	13	K_{s7}	1241953	I_{s7}	32.608
8	15	K_{s8}	1367983	I_{s8}	32.608
9	17	K_{s9}	1418302	I_{s9}	32.608
10	19	K_{s10}	1492794	I_{s10}	32.608
11	21	K_{s11}	1478974	I_{s11}	32.608
12	23	K_{s12}	1349393	I_{s12}	32.608
13	25	K_{s13}	2344085	I_{s13}	32.608
14	27	K_{s14}	2500490	I_{s14}	32.608
15	—	—	—	I_{s15}	32.608
16	—	—	—	I_{m16}	2.9474
17	28	K_{m17}	1448546	I_{m17}	2.9474
18	26	K_{m18}	1079043	I_{m18}	2.9474
19	24	K_{m19}	515769	I_{m19}	2.9474
20	22	K_{m20}	496269	I_{m20}	2.9474
21	20	K_{m21}	440588	I_{m21}	2.9474
22	18	K_{m22}	391023	I_{m22}	2.9474
23	16	K_{m23}	352074	I_{m23}	2.9474
24	14	K_{m24}	302262	I_{m24}	2.9474
25	12	K_{m25}	240987	I_{m25}	2.9474
26	10	K_{m26}	161133	I_{m26}	2.9474
27	8	K_{m27}	127268	I_{m27}	2.9474
28	6	K_{m28}	143776	I_{m28}	2.9474
29	4	K_{m29}	90912	I_{m29}	2.9474
30	2	K_{m30}	188519	I_{m30}	2.9474
31	—	—	—	I_{m31}	2.9474

Table 3 The parameters of the vehicle model

The mass of the car-body	Mass M_v=30000 kg
The stiffness and damping of the suspension system	K_v=8000 kN/m C_v=20 kN-sec/m
The mass of the wheel	m_w=2850kg

Table 4 The comparison between the specified parameter variations and the identified ones by the proposed method.

Parameters	Test variation	Identified variation
K_{s2}~K_{s14}, K_{m17}~K_{m27}	0	0.000%
K_{m28}	-0.1%	-0.098%
K_{m29}	-0.1%	-0.103%
K_{m30}	-0.1%	-0.099%
I_{s1}~I_{s15}, I_{m16}~I_{m27}	0	0.000%
I_{m28}	-0.1%	-0.100%
I_{m29}	-0.1%	-0.100%
I_{m30}	-0.1%	-0.100%

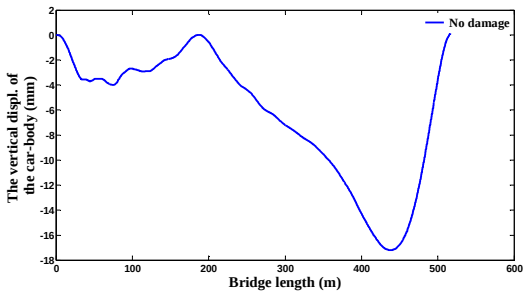

Fig. 6 The vertical displacement of the car-body of the vehicle varies with the location where the vehicle acts along the healthy bridge.

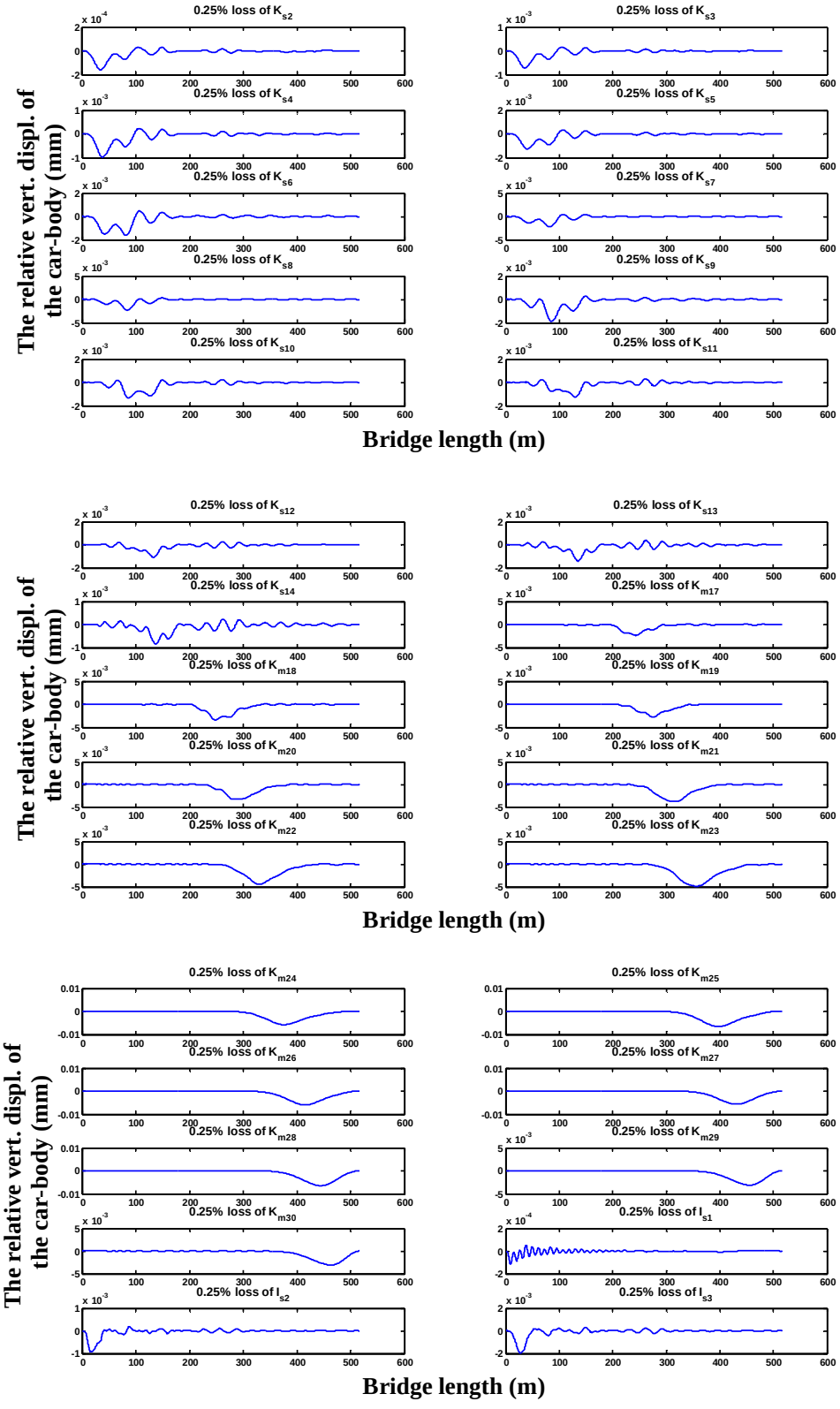

Fig. 7(a) The relative vertical displacements of the car-body of the vehicle passing the damaged bridge where 0.25% reduction of spring stiffness (K_{s2}~K_{s14} and K_{m17}~K_{m30}) and moment of inertia of deck (I_{s1}~I_{s15} and I_{m16}~I_{m31}) takes place independently.

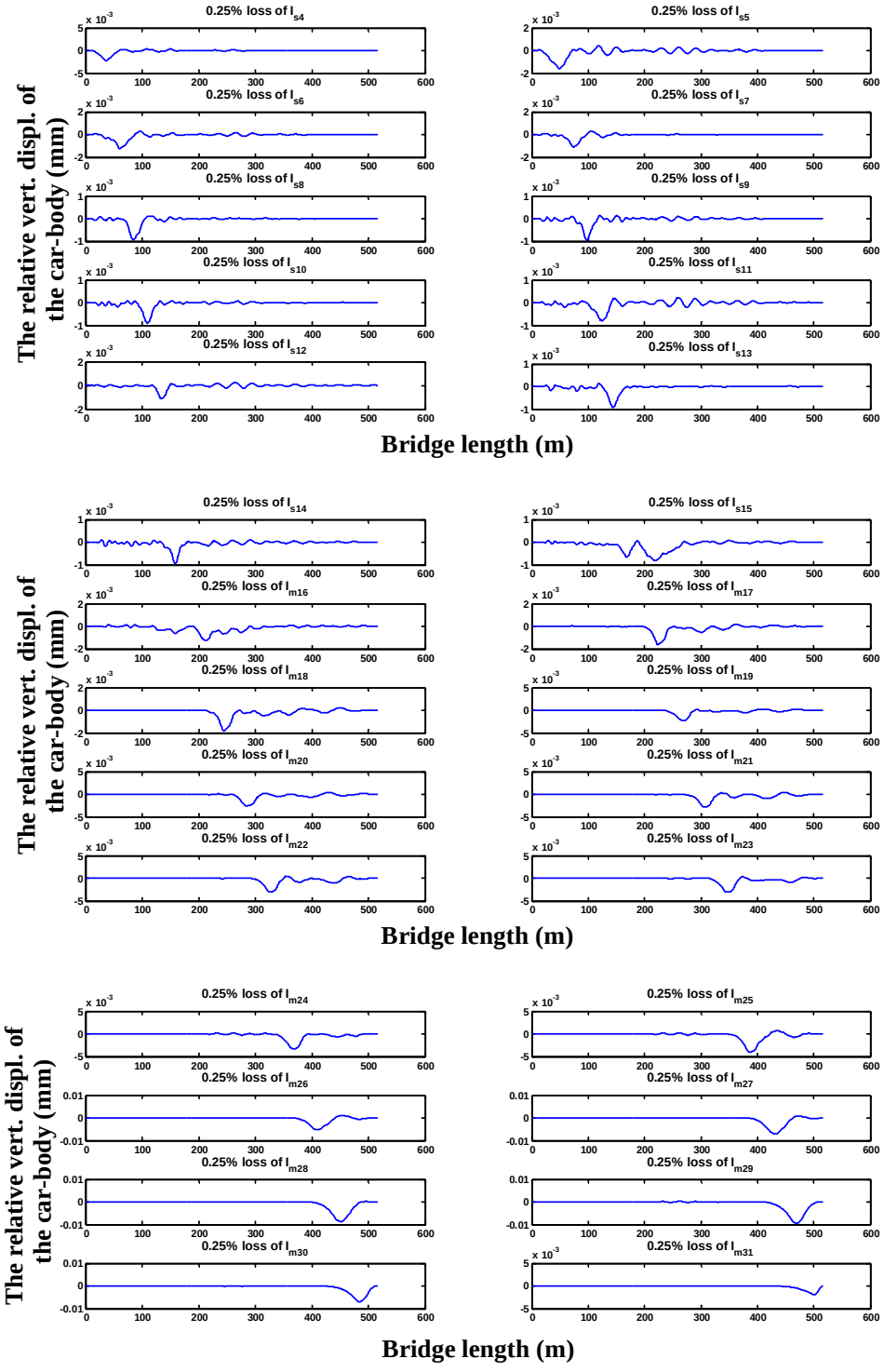

Fig. 7(b) The relative vertical displacements of the car-body of the vehicle passing the damaged bridge where 0.25% reduction of spring stiffness (K_{s2}~K_{s14} and K_{m17}~K_{m30}) and moment of inertia of deck (I_{s1}~I_{s15} and I_{m16}~I_{m31}) takes place independently.

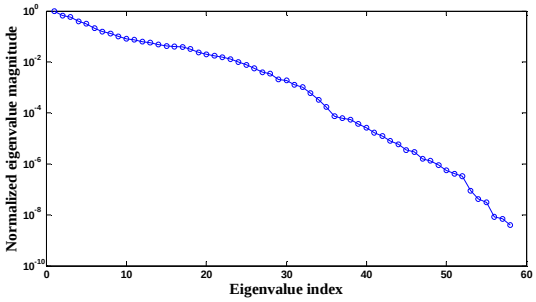

Fig. 8 The eigenvalues of the correlation matrix based on the relative vertical displacement vectors for all 58 sample damage cases ($\overline{\mathbf{Z}}_1\ \overline{\mathbf{Z}}_2\ \cdots \overline{\mathbf{Z}}_{58}$).

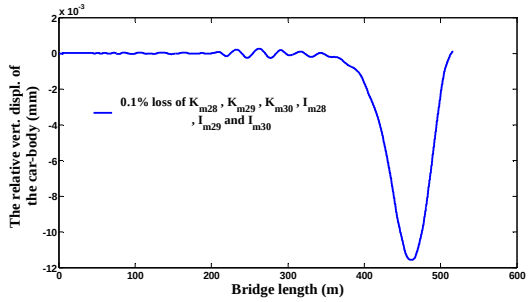

Fig. 9 The relative displacement of the car-body of the vehicle passing the damaged bridge with 0.1% loss of K_{m28}~K_{m30} and I_{m28}~I_{m30}.

JOINT CONFERENCE PROCEEDINGS
7th International Conference on Urban Earthquake Engineering (7CUEE) &
5th International Conference on Earthquake Engineering (5ICEE)
March 3-5, 2010, Tokyo Institute of Technology, Tokyo, Japan

PIEZORESISTIVE CEMENT-BASED SENSORS FOR REAL-TIME STRUCTURAL HEALTH MONITORING OF STRUCTURES DURING EARTHQUAKES

N. Banthia[1], F. Azhari[2] and B. Raheja[3]

1) Professor, Department of Civil Engineering, The University of British Columbia, Vancouver, BC, Canada
2) Sandwell Engineering Inc., 600-885 Dunsmuir Street, Vancouver, BC, Canada
3) Department of Civil Engineering, Indian Institute of Technology Delhi, Hauz Khas, New Delhi, India
banthia@civil.ubc.ca, fazhari@sandwell.com, bj_raheja@yahoo.com

Abstract: The usefulness of fiber reinforced concrete (FRC) in various civil engineering applications is indisputable. Fiber reinforced concrete has so far been successfully used in slabs on grade, shotcrete, architectural panels, precast products, offshore structures, structures in seismic regions, thin and thick repairs, crash barriers, footings and hydraulic structures. Fortunately, fiber reinforced cementitious materials based on conductive fibers, such as carbon, are also piezo-resistive. Piezo-resistivity is a unique material property which allows materials to change its electrical resistance/impedance as a result of changes in the applied stress/strain, temperature and chemical environment. FRCs are therefore smart materials that can act as low-cost sensors. This paper will discuss the piezo-resistive properties of FRC and describe the development of cement-based sensors with carbon fibers and carbon nano-tubes. Emphasis is on strain measurement, but these sensors are equally useful as chemical sensors capable of detecting pH changes, carbonation profiles, chloride ingress and corrosion detection.

1. INTRODUCTION

Bridges, buildings, turbines, aircrafts and many other engineering structures are susceptible to deficiencies due to strenuous loading and environmental conditions. These structures, when damaged or deteriorated, no longer meet the required standards and need to be repaired and rehabilitated or even rebuilt. These procedures can be very costly and time consuming if damage is not detected shortly after its occurrence.

In order to catch any deficiency in the structure's performance before any serious loss of capacity occurs, a technology has recently emerged known as Structural Health Monitoring (SHM). The purpose of SHM is to accurately monitor the behavior of an engineering structure, constantly assessing its performance and providing continuous data on its current conditions.

SHM is a multidisciplinary technology which involves structural and material design, development of sensors and actuators, signal processing, networking and communication, data mining and analysis, diagnostics and prognostics, management strategies, etc. (Inman et al, 2005).

2. SCENARIO

The sensory system is a very important component of SHM systems. Sensing devices constituting the sensory system are responsible for measuring parameters such as time, load, displacement, strain, acceleration, temperature and moisture.

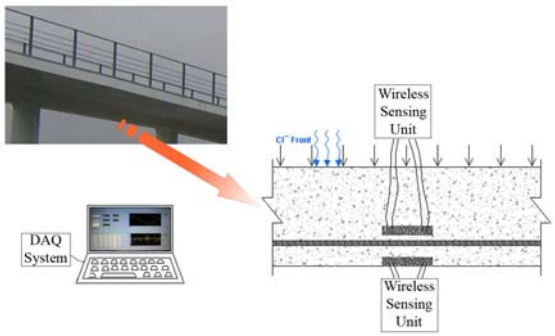

Figure 1. Proposed Application of Cement-Based Sensors in SHM of Future Structures

Because of their low cost, durability and compatibility with concrete structures, recently emerged cement-based sensors would be a very efficient replacement for current conventional sensors in SHM of concrete structures. The ultimate purpose is for these sensors to be near surface mounted or embedded in the host structure as part of a wireless SHM system that is capable of detecting strain, cracks and even corrosion (Figure 1). Made of structural material, this type of sensor can be regarded as an integral part of the structure as it does not alter the properties or appearance of the host structure. Cement-based sensors are designed to function based on the principle of piezoresistivity Piezoresistivity is defined as the dependence of electrical resistivity on strain. Materials in which the

electrical resistance changes in response to changes in the applied strain are referred to as piezoresistive materials.

In this research, smart cement-based materials are developed using either carbon fibers alone or in combination with carbon nanotubes.

2.1 Nanotechnology and Carbon Nanotubes

Nanotechnology is the science and technology of developing materials at the atomic and molecular level and generating techniques to measure and use their unique and special electrical, mechanical and chemical properties.

Discovered almost 20 years ago by Iijima (1991), carbon nanotubes (CNT) are one of the most important materials employed in nanotechnology. Carbon nanotubes are allotropes of carbon with a nanostructure that can have a length-to-diameter ratio of up to 28,000,000:1, which is significantly larger than any other material. CNT can be visualized as a modified form of graphite, where a single sheet or several sheets of graphite are seamlessly rolled into a tube structure (Makar et al., 2003). Single sheets rolled up are referred to as single-walled carbon nanotubes (SWCNT), and multiple sheets rolled up are called multi-walled carbon nanotubes (MWCNT).

Results from a study by Li et al. (2007) indicate that the addition of CNT, treated or untreated, to cement paste leads to a notable decrease in volume electrical resistivity and a distinct enhancement in the pressure-sensitive properties for cement composites.

3. EXPERIMENTAL PROGRAM

3.1 Materials

The following materials were used in the preparation of cement-based sensors:

- GU (formerly Type 10) Portland cement with specific gravity of 3.15 (W/C ratio ≈ 0.3 to 0.4).
- Densified silica fume with a specific gravity of 2.27 from Norchem, Inc. used as a densifier as well as a dispersant in the amount of 20% of the cement weight.
- K6371T Carbon Fiber DIALEAD from Mitsubishi Chemical FP America, Inc.; these coal-tar-pitch-based carbon fibers have specifications indicated in Table 1.
- Purified MWCNT, obtained from Cheap Tubes Inc., with specifications listed in Table 2.
- METHOCEL* A15 LV Methylcellulose from Dow Chemical Canada Inc. used to help disperse carbon fibers; in the amount of 0.4% of the cement weight.
- RHODOLINE 1010, which is a water base defoamer obtained from Rhodia Group; in the amount of 0.2% of the cement weight.
- Glenium 3400 NV from Master Builders, which is a polycarboxylate-based Superplasticizer with a specific gravity of 1.1.
- Copper electrodes.

Table 1. Properties of Carbon Fiber (CF)

Length (mm)	φ (μm)	S.G.	T. S.	E (GPa)	Volume Resistivity (Ω-m)
6	11	2.12	2620	634	2.3×10^{-6}

Table 2. Properties of Multi-walled Carbon Nanotubes (MWCNT)

Outer Diameter (nm)	Inside Diameter (nm)	Purity	Length (μm)	Specific Surface Area (m^2/g)	Specific Gravity	Electrical Conductivity (s/cm)
10-20	3-5	> 95 wt%	10-30	233	≈1.5	$> 10^{-2}$

3.2 Resistivity Measurements

150 mm long samples with 25 mm × 15 mm cross section and 70 mm inner-electrode spacing, as recommended by Banthia et al. (1992), were prepared using different volume fractions (V_f) of carbon fiber (CF) and MWCNT. Specimens were air cured for 24 hours before the moulds were carefully stripped.

Direct current (DC) measurement of electrical resistance has proven to be technically difficult because of the polarization effect, which causes an exponential rise in the measured resistivity (Hou et al., 2005). Therefore, resistivity measurements in this study are made using alternating current (AC). Unless otherwise noted, Agilent 4263B LCR meter at 100 kHz AC frequency was used for resistance measurements.

There are two commonly used methods for resistance measurements, two-probe and four-probe. While the two-probe technique is much simpler, error sources such as lead inductance, lead resistance and stray capacitance between the two electrodes are incorporated in the measured resistance. In the four-probe method, on the other hand, the effect of lead impedances is reduced because the current and voltage paths are separate. In the two-probe technique, the measured voltage consists of voltages from the electrodes (V_E, which is almost negligible), cement-based sensor (V_S) and contact resistance (V_C). In the four-probe method, however, V_E and V_C are eliminated and the voltage measurement consists of only the sensor voltage, V_S. Figure 2 schematically displays the equivalent circuits for two-probe and four-probe measurement techniques.

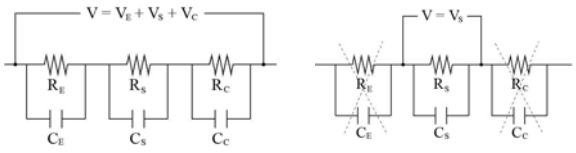

(a) (b)

Figure 2. Equivalent Circuits for (a) Two-Probe and (b) Four-Probe Measurements

role in the electrical conductivity, but as the AC frequency is increased the interface impedance decreases and thus the electrical conductivity of the composite is strongly governed by the conductive fibers (Reza at al., 2003). In addition, cement-based composites are capacitive in nature and thus, using higher frequencies reduces the reactance part of impedance.

In order to experimentally investigate the effect of current frequency on the cement-based sensors, a frequency sweep between 1 Hz and 1 MHz was completed - using a Solartron 1260 impedance/gain-phase analyzer - for

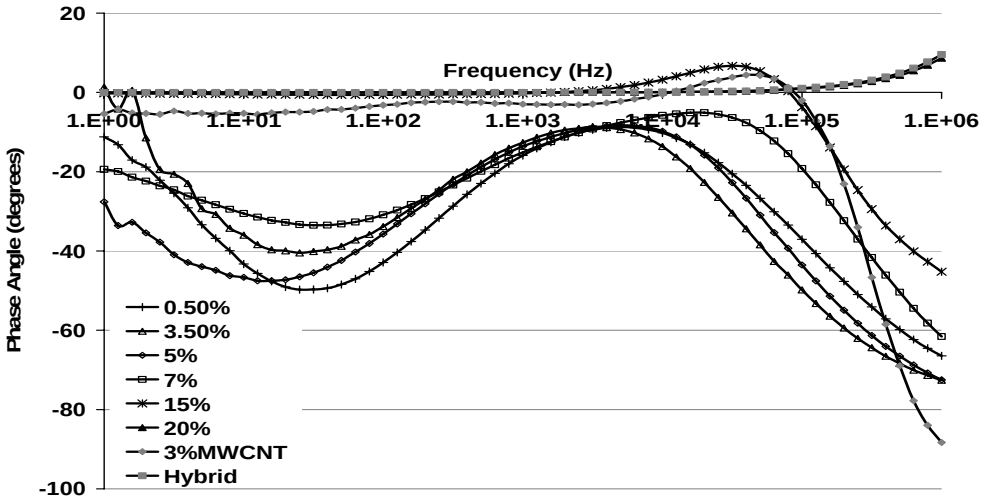

Figure 3. Phase Angle at Current Frequencies between 1Hz and 1MHz

Two-probe resistance measurements increase dramatically as the L/A (electrode spacing/electrode contact area) ratio increases, whereas the four-probe configuration is unaffected by specimen design. Therefore, the four-probe method was employed for resistivity measurements (Chiarello et al., 2005 and Azhari, 2009).

The electrical resistivity (ρ) of a material with a uniform cross section is measured as its resistance per unit length:

(1)

where
ρ = electrical resistivity in ohm meters (Ω·m)
R = electrical resistance of a uniform specimen in ohms (Ω)
A = cross-sectional area of the specimen (m^2)
ℓ = length between the measurement electrodes (m)

3.2.1 Effect of Current Frequency

The current frequency is a crucial element to be considered. Many factors may have a role in the effect of current frequency: internal factors such as fiber content and specimen geometry and external factors such as moisture and temperature. It has been found that if DC or low frequency AC is used, the cement matrix plays a dominant

specimens with different fiber contents (Figure 3).

Purely resistive impedance occurs when the phase angle (θ) is zero. Therefore, phase angles at different current frequencies were compared to find the most efficient frequency. The results, plotted in Figure 3, show that phase angle is for the most part negative, which confirms the fact that these cement-based composites are capacitive rather than inductive. For samples with fiber contents in the 0.5%-7% V_f range, phase angle values fluctuate, lowering at 1 Hz and about 10 kHz. Samples with 15% and 20% V_f of carbon fiber, 3% MWCNT specimens and the hybrid samples (15% CF + 3% MWCNT), exhibit much lower phase angle values especially at frequencies of 100 kHz and below. These samples seem to show inductive characteristics at some frequencies (where θ>0). A 100 kHz frequency was chosen.

3.2.2 Effect of Fiber Content

The addition of even a small amount of carbon fibers to cement paste significantly reduces the resistivity of the material. Conductivity increases by several orders of magnitude when the volume fraction of carbon fiber reaches a certain critical value, referred to as the percolation threshold (Xie et al., 1996).

Fiber size and shape are important factors in

determining the percolation threshold; for example, longer fibers provide higher electrical conductivity at lower fiber volume fractions, whereas the conductivity of specimens containing very short fibers increases very gradually with volume fraction (Chiarello et al., 2005).

Resistivity measurements from samples with various fiber contents, illustrated in Figure 4, indicate that the resistivity values of samples with only 0.5% V_f of carbon fiber dropped considerably (97%) compared with plain samples. The resistivity of the specimens with 0.5% Vf to ~15% V_f remained almost constant, which validates the existence of a percolation threshold. However, the resistivity values could yet be significantly decreased (up to a thousand times smaller than the values at percolation threshold) by adding more fiber to the mix; samples with 20% V_f of fiber exhibited electrical resistivity values as low as 5 Ω·cm, which was expected while these specimens were being prepared, in that there was much less cement paste than fibers and it was very difficult to mix. In order to observe the interaction between fibers and their dispersion, a series of images was obtained using a scanning electron microscope (SEM). SEM images of specimens with three different fiber contents, displayed in Figure 5, show how the increase in fiber content affects the dispersion of the fibers and in turn the electrical properties of the specimens.

The effect of different amounts of MWCNT and SWCNT is also illustrated in Figure 4. It was found that the addition of CNT at 1% or 3% V_f slightly decreases the resistivity of the cement paste. Owing to the extremely high

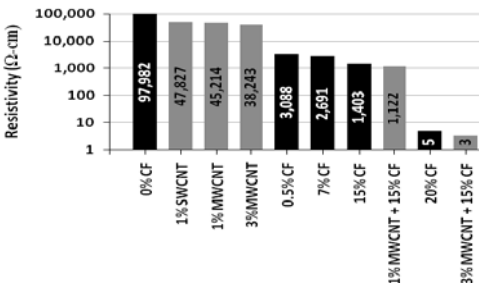

Figure 4. Resistivity Variation

conductivity values reported for CNT, this reduction was expected to be much greater, but the dispersion of CNT was very difficult to achieve even though a sonication process was used. Moreover, even if the dispersion was perfect, the extremely small size of CNT would prevent any contact or network among them in such low volume fractions. This triggered the idea of creating hybrid specimens: 1% MWCNT + 15% CF and 3% MWCNT + 15% CF; these samples yielded a lower electrical resistivity than the 15% CF and 20% CF samples, respectively.

Although the "3% MWCNT + 15% CF" hybrid and the 20% CF samples had preferable resistivity values, more suitable for the sensing application, they each had their downfalls; the former was very soft and brittle and the latter was extremely hard to prepare. Therefore samples with 15% CF or 1% MWCNT + 15% CF were selected to be used as sensor material. The entire class of such materials are hereafter called piezoresistive fiber reinforced concrete (PFRC).

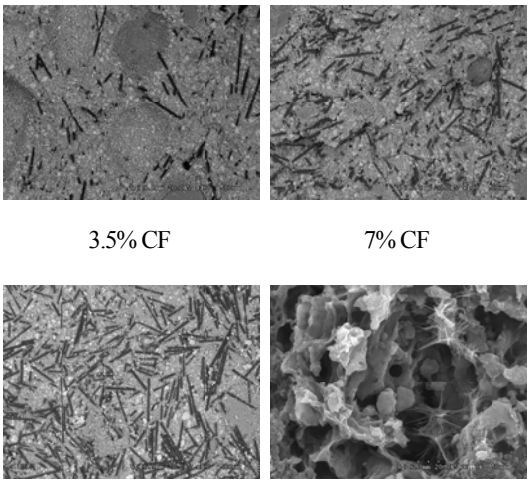

3.5% CF 7% CF

20% CF 3% MWCNT

Figure 5. SEM Images of Various Cement-Based Sensors

3.2.3 Effect of Chloride and Moisture

The electrical conductivity of cement-based sensors is through both the conductive fibers and the cementitious matrix. Conductivity of the matrix part of the conduction path is through the pore structure and is referred to as the electrolytic conductivity. The presence of moisture and chloride changes the chemical composition of the pore structure and therefore affects the electrical resistivity of cementitious composites.

To examine the effect of moisture and chloride on cement-based sensors, plain, 3.5% V_f, 7% V_f and 15% V_f samples were kept in chloride solution (100 g of NaCl dissolved in 1 L of water). Resistivity measurements were taken from the specimens at the start of the experiment, after one month of exposure and again after the specimens were completely dried using desiccators. Figure 6 shows the resistivity values of the specimens at these three stages.

While one month submersion in chloride solution caused a significant decrease in the electrical resistivities of all the specimens, the plain sample was the only one to recover most of its resistivity. The carbon fiber reinforced samples recovered only a small percentage of their original resistivity after completely drying out. The conduction path in 15% CF samples includes more fiber to fiber contact which makes them less sensitive to the presence of moisture and chloride.

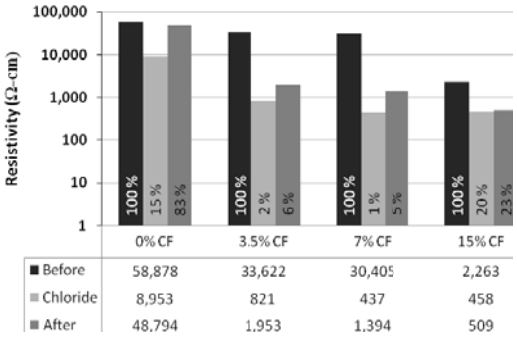

Figure 6. Effect of Chloride Solution on Electrical Resistivity of Sensors

It is important to take this effect into consideration if and where the sensors are employed in environments subjected to moisture and chloride. Coating the sensors with moisture resistant material may be a solution to this issue. It was also observed during this experiment that the plain and 3.5% CF specimens experienced some delamination and blemishes, whereas the other two samples remained unaffected, which indicates that carbon fiber reinforced cementitous composites with higher V_f of fiber are more durable when subjected to chloride ingression

4 PIEZORESISTIVITY

Changes in the electrical resistivity of piezoresistive fiber reinforced concrete (PFRC) was monitored under cyclic compression to examine their sensing abilities.

Cylindrical specimens containing either "15% CF" or "15% CF + 1% MWCNT" were prepared. 10mm strain gauges were attached to the samples to compare the results with measured strain. Specimens were loaded cyclically to 30 kN (approximately 30% of load capacity) while monitoring the response (Figure 7).

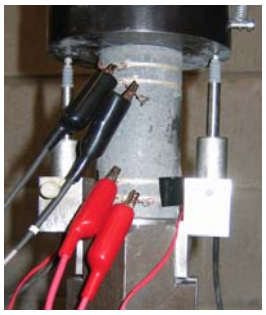

Figure 7. Sensor in Compression

In order to evaluate the sensing ability of the developed sensors, fractional change in resistivity (FCR) was compared against applied load. Fractional change in resistivity is given by:

$$FCR = \frac{\rho_t - \rho_0}{\rho_0} \qquad (2)$$

where,

ρ_t : Electrical resistivity at time t during the tests;
ρ_0 : Electrical resistivity at the beginning of the test (prior to loading)

Figure 8 and Figure 9 display the response of sensors to strain for 15% CF and 15% CF + 1% MWCNT specimens, respectively. Very good correlation between the measured FCR and strain is observed. During each loading cycle, the resistivity values decrease with the increase in compressive load, resulting in negative FCR values, and then increase to the initial value when the unloading branch of the cycle takes place. Closer examination shows that the hybrid sensors (containing both carbon fibers and carbon nanotubes) exhibit better sensitivity and repeatability to strain. Some calibration curves are given in Figure 10. Note a better gauge factor for sensor with nanotubes..

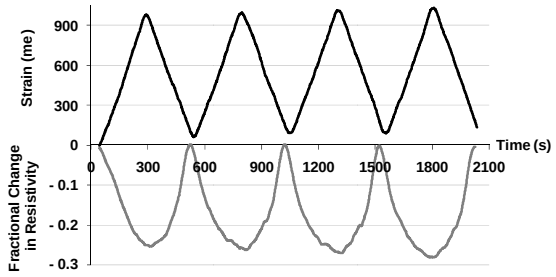

Figure 8. A 15% CF Sensor Under Cyclic Compression (30kN amplitude)

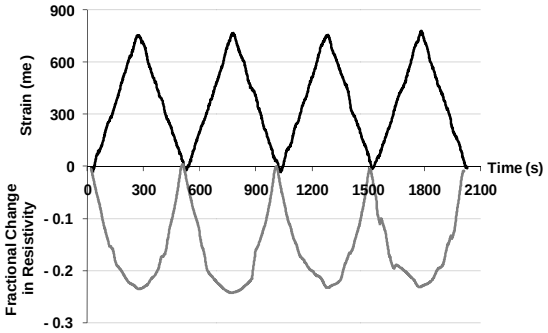

Figure 9. 15% CF +1% MWCNT sensor under cyclic compressive loading with 30kN amplitude

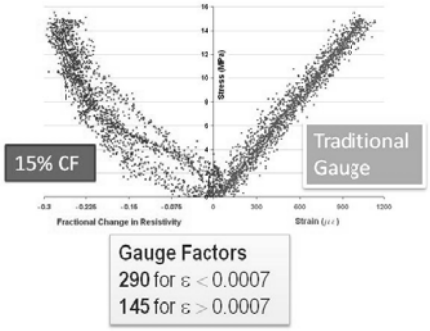

Figure 10 (a) Comparing PFRC (15% Carbon Fiber) with Traditional Sensor

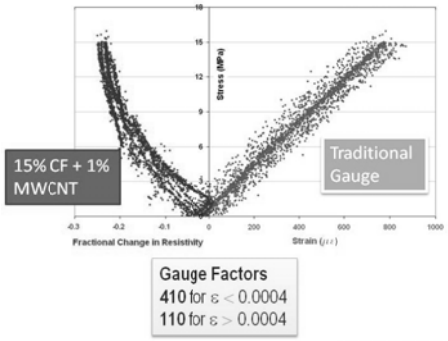

Figure 10 (b) Comparing PFRC (15% Carbon Fiber + 1% Multiwalled Carbon Nanotubes) with Traditional Sensor

5. DYNAMIC SENSING

Concrete structures in most instances are loaded at strain rates ($\dot{\varepsilon}$) approximated in our standardized tests. However, there are dynamic events in which the strain-rates may significantly exceed those obtained in standardized tests such as in fast moving traffic ($\dot{\varepsilon} = 10^{-6}$–$10^{-4} s^{-1}$), gas explosions ($\dot{\varepsilon} = 5x10^{-5} - 5x10^{-4}\ s^{-1}$), earthquakes ($\dot{\varepsilon} = 5x10^{-3} - 5x10^{-1}\ s^{-1}$), pile driving ($\dot{\varepsilon} = 10^{-2} - 10^{0}\ s^{-1}$) and aircraft landing ($\dot{\varepsilon} = 5x10^{-2}$–$2x10^{0} s^{-1}$). Sensors when used on these structures should be able to record their responses in a rapid and accurate manner. Since cement-based materials are highly strain-rate sensitive, sensors based on these materials (PFRCs) must also depict rate-effects.



Figure 11. High Strain-Rate (Impact) Tests on Sensors

Figure 11 shows high strain-rate (impact) tests on PFRC sensors obtained by using an air-gun based impact setup (Bindiganavile and Banthia; 2001a, 2001b). The specimen is held in the machine such that the top-half is stationery and the bottom half is pulled down at a high speed by an air-gun. The top half of the sensor specimen is suspended from a dynamic load cell of 5kN capacity with a resolution of 0.01 N. The displacement of the sensor specimen (ignoring the elastic deformations) during a test is measured by means of a single LVDT fixed to the moving bottom-half. The air gun operated at a peak pressure of 0.35 MPa and generated a displacement rate of 3000 mm/s. In a test the applied impact impulse (load-time curve) and resistivity signals from the sensor were recorded and some preliminary results are given in Figure 12.

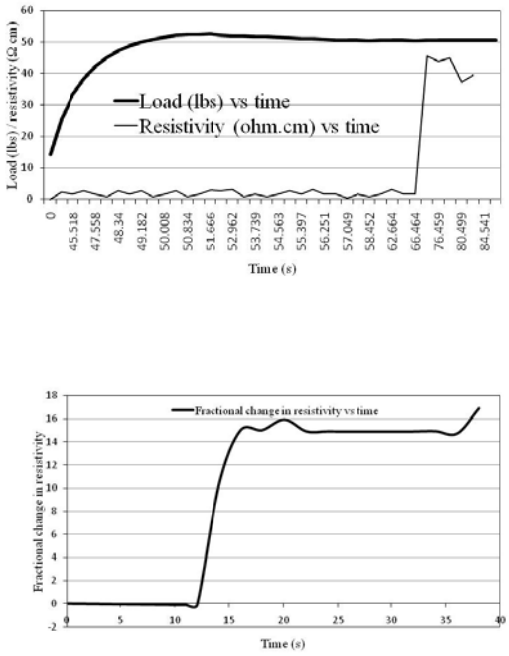

Figure 12. Dynamic Response of a PFRC Sensor

As the preliminary plots in Figure 12 indicated, while the sensor is capable of dynamic recording, there are a number of issues to be resolved. First of all, there is a lag in measurement of load and sensor response. Further, due to the lag, the FCR in the loading range remains very low. Significant amount of further work is required to derive useful information from these sensors under high strain-rate loads.

6. CONCLUSIONS

Cement-based sensors, also described as smart (self-monitoring) structural materials, have recently been developed for use in structural health monitoring (SHM) systems. These sensors are rather inexpensive, durable, very easy to manufacture and install, and best of all they possess mechanical properties similar to concrete, enabling them to perform in the same manner as the host structure. They do not alter the properties or appearance of concrete structures; hence, if integrated into the host structure, they can be regarded almost as an integral part of the structure.

The purpose of this study was to develop piezoresistive cement-based sensors for use in SHM systems by incorporating carbon fibers as well as both single-walled and multi-walled carbon nanotubes in a cement paste matrix.

The effect of fiber content, current frequency and the presence of moisture and chloride on electrical resistivity were investigated. Consequently, the piezoresistive quality of the sensors was confirmed through monitoring their response to cyclic compressive loading. The electrical resistivity of these sensors changed in response to change in strain; decreasing reversibly with the increase in compressive strain. The sensors with nano-tubes depicted a higher sensitivity than those with carbon fiber alone. Some dynamic sensing tests were carried out that showed promise, but also indicated that many issues need to be resolved before these sensors can be used for SHM during earthquakes.

Acknowledgements:

The authors acknowledge support from the Natural Sciences and Engineering Research Council and Network of Centers of Excellence: ISIS Canada.

References:

Azhari F. (2009) "Cement-Based Sensors for Structural Health Monitoring.", MASc. Thesis, http://hdl.handle.net/2429/7324

Bindiganavile, V. and Banthia, N. (2001a), Polymer and Steel Fiber Reinforced Cementitious Composites under Impact Loading, Part 1: Bond-Slip Response, ACI Materials Journal, 98(1): 10-16.

Bindiganavile, V. and Banthia, N. (2001b), Polymer and Steel Fiber Reinforced Cementitious Composites under Impact Loading, Part 2: Flexural Toughness, ACI Materials Journal, 98(1): 17-24.

Banthia N, Djeridane S, Pigeon M. (1992) "Electrical resistivity of carbon and steel micro-fiber reinforced cements." *Cem Concr Res.*;22:804-814.

Chiarello M, Zinno R. (2005) "Electrical conductivity of self-monitoring CFRC." *Cement and Concrete Composites.* 2005;27:463-469.

Iijima, S. (1991). "Helical microtubules of graphitic carbon." *Nature,* 354(6348), 56-8.

Inman, D. J., Farrar, C. R., Lopes Junior, V., and Steffen Junior, V. (2005) "Damage Prognosis for Aerospace, Civil and Mechanical System*." John Wiley & Sons Ltd, England.*

Li, G. Y., Wang, P. M., and Zhao, X. (2007). "Pressure-sensitive properties and microstructure of carbon nanotube reinforced cement composites." *Cement and Concrete Composites,* 29(5), 377-382.

Makar, J. M., and Beaudoin, J. J. (2003). "Carbon Nanotubes and their application in the construction industry." *Proceedings of 1st International Symposium on Nanotechnology in Construction.*

Reza F, Batson GB, Yamamuro JA, Lee JS. (2003). "Resistance changes during compression of carbon fiber cement composites." *J Mater Civ Eng.*;15:476-483.

Tsung-Chin Hou, and Lynch, J. P. (2005). "Conductivity-based strain monitoring and damage characterization of fiber reinforced cementitious structural components." *Smart Structures and Materials 2005: Sensors and Smart Structures Technologies for Civil, Mechanical, and Aerospace Systems,* SPIE-Int. Soc. Opt. Eng, San Diego, CA, USA, 419-29.

Xie P, Gu P, Beaudoin JJ. (1996). "Electrical percolation phenomena in cement composites containing conductive fibres." *J Mater Sci.*;31:4093-7.

JOINT CONFERENCE PROCEEDINGS
7th International Conference on Urban Earthquake Engineering (7CUEE) &
5th International Conference on Earthquake Engineering (5ICEE)
March 3-5, 2010, Tokyo Institute of Technology, Tokyo, Japan

A PRECAST CONCRETE BENT SYSTEM FOR BRIDGES IN SEISMIC REGIONS

Marc O. Eberhard[1)], John F. Stanton[2)], Jason B.K. Pang[3)], and Olafur Haraldsson[4)]

1) Professor, Department of Civil and Environmental Engineering, University of Washington, USA
2) Professor, Department of Civil and Environmental Engineering, University of Washington, USA
3) Structural Engineer, KPFF Engineers, Seattle, WA
4) Research Assistant, Department of Civil and Environmental Engineering, University of Washington, USA
eberhard@u.washington.edu, stanton@u.washington.edu, olafurh@u.washington.edu

Abstract: Precasting bridge elements offsite and erecting them quickly onsite can reduce traffic delays caused by traditional construction methods. The use of precast concrete elements in bridge substructures has been limited in seismic region, because previous systems have either been difficult to construct or are likely to perform poorly during earthquakes. A multi-disciplinary team has developed a new system that combines precast concrete columns with precast concrete cross-beams. To accelerate construction, the base of the precast column is embedded directly into its cast-in-place footing by means of a "socket" connection. At the top of the column, the precast column is connected to a precast cross-beam with a small number of large bars (e.g., #18) grouted into larger ducts (e.g., 150 mm). The ease-of-construction of this system will be evaluated during the construction of a bridge over Interstate 5. Completed and ongoing tests demonstrate that this system is expected to perform as well as a traditional cast-in-place system during earthquakes. The research also identifies the benefits and drawbacks of 1) debonding a length of the column longitudinal bars, and 2) varying the amount of steel connecting the precast column and cast-in-place footing.

1. INTRODUCTION

To reduce traffic delays and the associated societal costs, many highway agencies are seeking to develop methods to accelerate bridge construction. Such methods often also reduce environmental impacts of construction, improve worker safety, improve the quality of construction and lower life-cycle costs (Wacker et al. 2005). One approach to speeding up construction, precasting concrete members, has already been successfully used for bridge substructures in non-seismic regions (Matsumoto et al. 2001).

To facilitate fabrication and transportation, connections are typically made at the beam-column and column-foundation interfaces, which are regions of high moments and large inelastic cyclic strain reversals. It is a challenge to develop connections for these locations that are not only sufficiently robust to accommodate those cyclic loads, but are also readily constructible.

This paper describes a precast concrete bridge bent system developed to satisfy the combined needs of seismic performance and constructability. Different connection systems are used at the column-to-foundation and the cap beam-to-column interfaces, because the conditions at each location have unique constraints and offer unique opportunities. The seismic performance of the cap beam connection has already been tested and performed well. Results from those tests are presented first. The test specimens for the foundation were cast in late 2009 and are scheduled to be tested in early 2010.

2. COLUMN-TO-BEAM CONNECTION

2.1 Concept

The column-to-beam connection concept consists of bars that project from the column and are grouted into ducts in the cap beam. In the past, such designs have used a conventional arrangement of longitudinal reinforcement, consisting of, say, 18 D35 bars in a 1.5-m diameter column (18 No 11 bars in a 5-ft diameter column). In such a configuration, the numerous vertical ducts need to be small to fit between the horizontal beam bars. Fitting the 18 column bars into 18 relatively small ducts in the cap beam requires very accurate fabrication and field assembly. It is a challenge to construct such a connection.

The proposed connection is shown in Figure 1. It uses a small number of large bars to permit larger ducts and thereby facilitate the assembly on site. In a typical 1.5-m (5ft) diameter circular column, 8 D57 (No. 18) bars in 200-mm (8in.) diameter ducts are sufficient.

The major obstacle then lies in anchoring the bars in the available space, because the AASHTO LRFD Specifications require a development length in 28 MPa (4000 psi) concrete

of 2.75m (9ft), whereas the cap beam is typically only about 1m (3ft-6in.) deep.

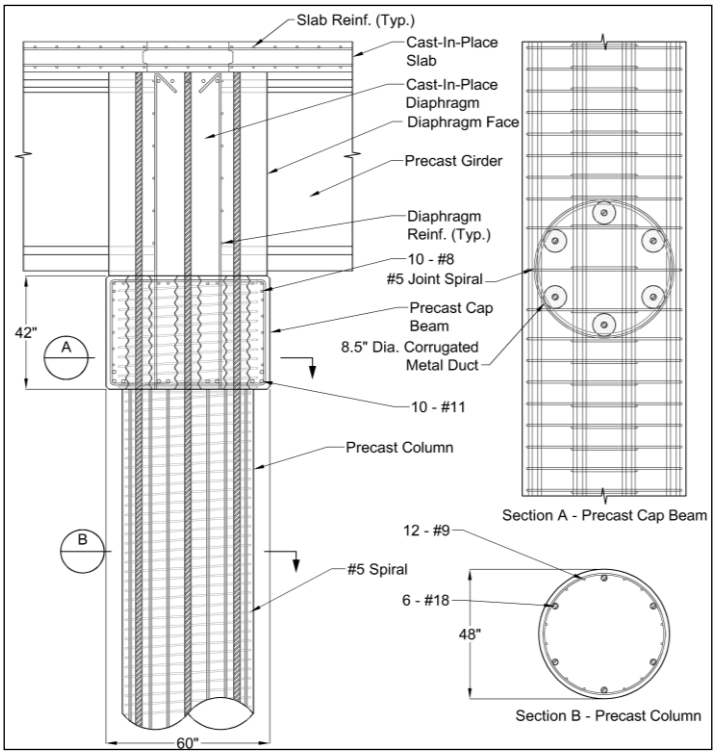

Figure 1. Full-Scale, Column-to-Beam Connection

Two approaches can be taken to solve this problem. The first is to demonstrate that the anchorage available from the grouted ducts is able to develop the bar. The second is to cast a diaphragm over the cap beam once the girders have been placed and the deck has been cast. That diaphragm, shown in Figure 1, provides additional anchorage length that can be used together with the anchorage in the ducts to resist the cyclic forces on the bar caused by seismic loading. The ducts alone then need to provide only enough development to ensure strength and stability during erection. It is likely that development to resist the yield stress under static loading, rather than the ultimate strength under cyclic loading, would be enough for that purpose.

2.2 Testing of Bar Anchorage

The anchorage characteristics of large bars were investigated by conducting full-scale monotonic, pull-out tests on D32, D45 and D57 (No. 10, 14 and 18) bars grouted into corrugated ducts. These tests confirmed that the D57 bars could be fully developed in a length significantly shorter than the depth of the cap beam (Steuck et al. 2007, 2009). Those tests combined with earlier work (Raynor et al., 2002; Precast, 2004; Moustafa et al. 1974) showed that, under static loading, the lengths needed to provide anchorage for yield and fracture were approximately 6 and 10 bar diameters, respectively. An additional allowance of 50% was suggested to account for cyclic loading.

2.3 Connection Specimens

The full-scale prototype was assumed to be a 1.2m (4ft) diameter circular column. Four sub-assemblage tests were conducted at 40% scale to evaluate the seismic performance of the proposed connection (Pang et al. 2009). The primary study variable was the anchorage conditions for the longitudinal bars. The column-to-beam test program is summarized in Table 1.

Figure 2 show the details of the scaled test specimens, which included a 445mm (17 ½-in.) deep cap beam, a 470 mm (18 ½-in.) deep portion of the diaphragm, and a 1.5m (60-in.) tall segment of the 500 mm (20-in) in diameter column. Specimen REF was a scaled model of a typical Washington State cast-in-place bridge column, with 16 D16 (16 No. 5) bars evenly distributed round the perimeter, giving a longitudinal reinforcement ratio, ρ, of 1.58 percent. The column bars were cast in place into the cap beam and diaphragm. The transverse reinforcement consists of 6 mm (1/4-in) diameter spirals spaced at 30 mm (1¼-in). This specimen provided a baseline for evaluating the performance of the proposed system.

Table 1. Column-to-Beam Connection Test Program

Specimen	Description	ρ (%)	Longitudinal Reinforcement
REF	Reference cast-in-place reinforced column	1.58	16- #5
LB-FB	Precast column with fully bonded bars	1.51	6- #8 (12- #3 for spacing)
LB-D1	Large bars debonded using Method 1	1.51	6- #8 (12- #3 for spacing)
LB-D2	Large bars debonded using Method 2	1.51	6- #8 (12- #3 for spacing)

The other three specimens, LB-FB, LB-D1, and LB-D2, represent variations of the proposed precast connection. For these connections, the columns were reinforced longitudinally with 6 D25 (#8) bars that were grouted into 100 mm (4-in.) diameter corrugated metal ducts in the cap beam and further anchored in concrete within the diaphragm, providing a longitudinal reinforcement ratio, ρ, of 1.51 percent. In Specimen LB-FB the bars were fully bonded into grouted ducts, whereas in specimens D1 and D2, two methods of local debonding were studied. The bars in LB-D1 and LB-D2 were debonded over a length of 8 bar diameters, d_b, into the cap beam using two methods. LB-D1 was debonded using a 25 mm (1-in) SCH-40 PVC pipe slit longitudinally, fitted tightly around the #8 bar, taped together,

and sealed with caulk at the ends (Method 1). LB-D2 was debonded using a 25 mm (1-in) SCH-30 PVC pipe. That pipe fitted more loosely round the bar, and provided no restraint against buckling. The detail was constructed by sliding the pipe over the bar and sealing it with caulk at the ends (Method 2).

For all precast specimens, 12 D10 (#3) bars were added to the column. Since they stopped at interface, they did no contribute to the flexural capacity; they were included purely to meet AASHTO spacing requirements. The spiral reinforcement in the columns was the same as in the reference specimen, and it continued at the same spacing into the cap beam to confine the joint region. A thin grout pad was also provided at the beam-column interface to simulate field erection of the precast pieces. Fluid, high-strength, non-shrink grout with an average compressive strength of 63 MPa (9 ksi) at 5 days was used. 420 MPa (GR 60) bars were used for the mild steel reinforcement, while 630 MPa (GR 90) wire was used for the spirals. The design concrete strength was 42 MPa (6 ksi).

2.4 Experimental Setup

Each specimen was tested under constant axial load and a cyclic lateral displacement history. The test set up is shown in Figure 2. Axial load was applied via a 10 MN (2400 kip) Baldwin Universal Test Machine, equipped with a swivel head and a low-friction sliding PTFE track. Lateral displacements were applied using a 1 MN (220-kip) MTS displacement-controlled actuator, located 1.5 m (5 ft) above the interface. The selected lateral loading protocol was a modified version of that recommended in the NEHRP Recommended Provisions (Buiding 2004), and consisted of 3 cycles at each of a series of increasing displacements.

2.5 Experimental Results

Despite the variations in construction details all four specimens had nearly identical moment-displacement response, as shown in Figure 3. The slightly variations in peak loads are mainly attributable to minor differences in the applied axial load. There was little loss in strength until the drift ratio reached at least 4 percent, despite the increasing damage accumulating in the plastic hinge region. Specimens

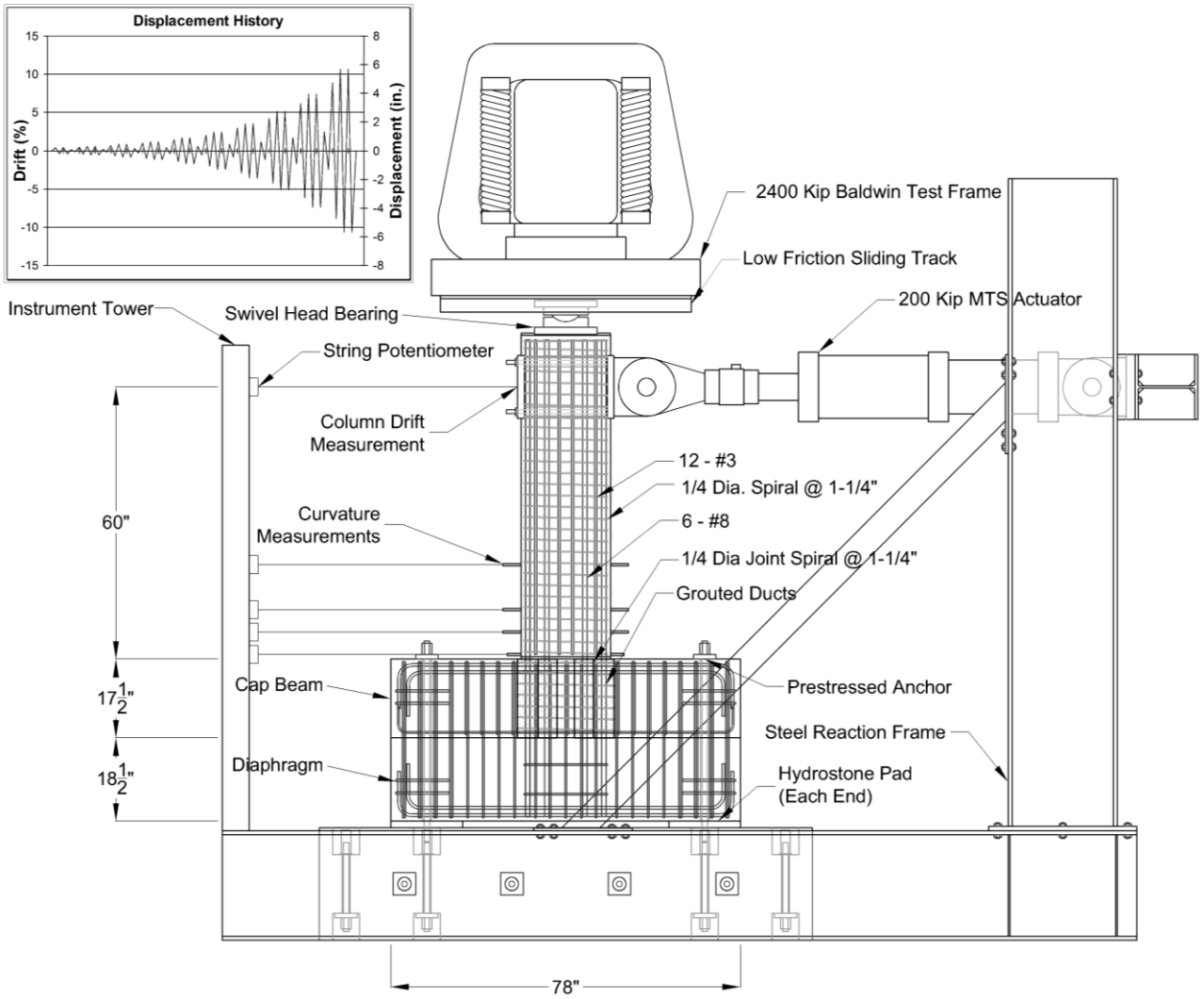

Figure 2. Experimental Setup for Column-to-Beam Connection Tests

REF, LB-FB, LB-D1, and LB-D2 maintained 80 percent of their peak lateral resistance out to drift ratios of 5.5, 5.2, 5.7, and 5.8 percent. All of these values greatly exceed the expected deformation demands for even a large earthquake.

drift levels of 2.0, 2.0, 2.4, and 2.1 percent for specimens REF, LB-FB, LB-D1 and LB-D2, respectively.

At drift levels of 5.6, 5.3, 5.7, and 5.8 percent, respectively, the most north and south bars began to buckle,

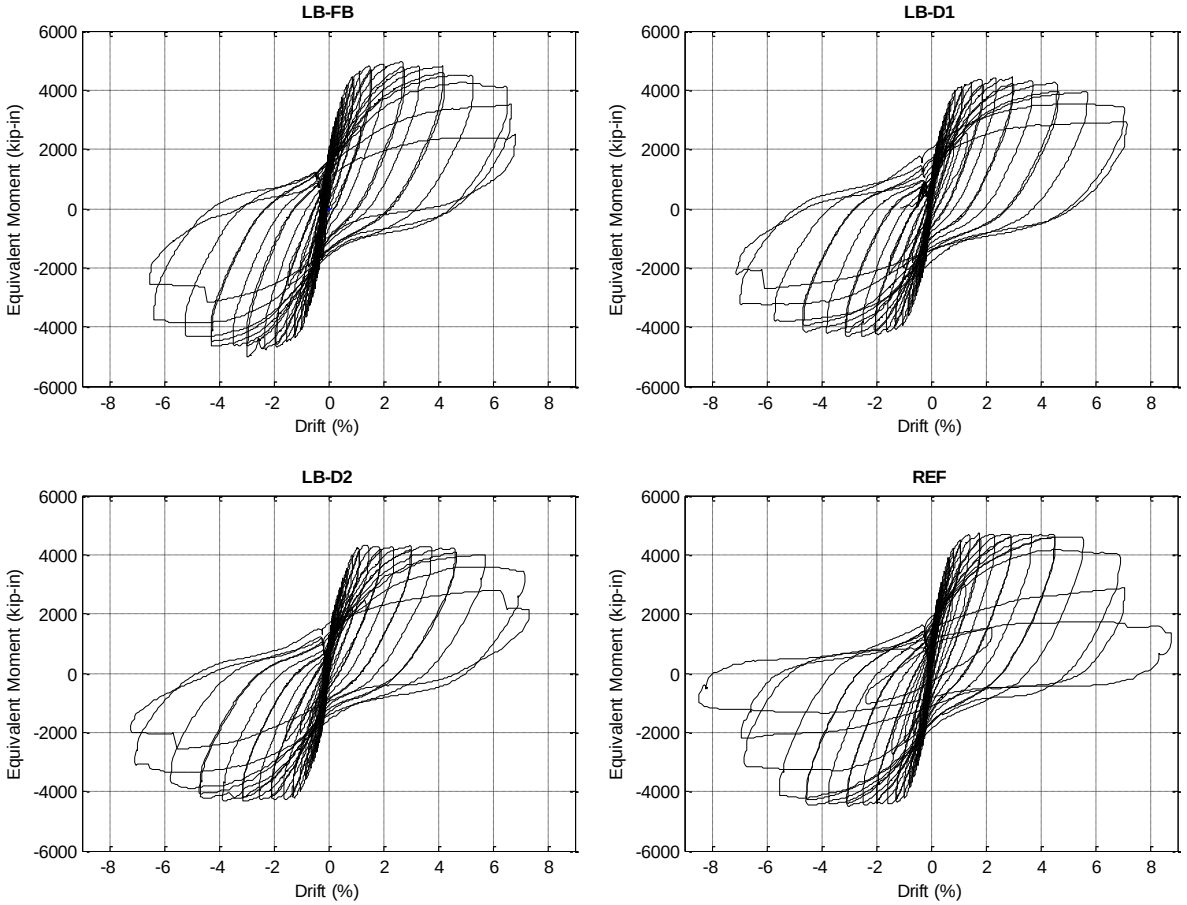

Figure 3. Moment-Drift Ratio Responses for Column-to-Beam Connection Tests

The majority of deformation for specimens LB-FB, LB-D1 and LB-D2 resulted from a large localized crack opening at the interface. Rotations measured over the bottom 38 mm (1.5 in) of the column accounted for more than 90 percent of the total column displacement. The additional 12 D10 (#3) bars in the column, which did not cross the interface, made the body of the column stronger and stiffer than the interface, so most of the deformation was forced to occur at the interface and the precast members essentially rotated as rigid bodies. This approach, in which the connection is designed to remain ductile during an earthquake, has been successfully used in precast building design and tested in the PRESSS program (Nakaki et al. 1999). In contrast, in Specimen REF, the curvature was more evenly distributed over the bottom 1 m (42 in.). of the column. The crack width at the interface was about the same as that of some of the flexural cracks above.

The observed damage was nearly identical for all specimens. Damage consisted of moderate spalling of the concrete cover and crushing of the core concrete over a plastic hinge region about 12 in. long. Spalling initiated at pushing out on the spiral. The spirals fractured when buckling was first observed or shortly thereafter.

Severe necking occurred before the spiral fractured. When the bars were next loaded in tension, they straightened and fractured. The finding that buckling occurred at almost the same drift in each specimen was surprising, given that in two specimens the bars were debonded over a length of 200 mm (8 in). The buckling always occurred in the column, whereas the debonded region was in the cap beam.

Bars in specimens LB-FB, LB-D1 and LB-D2 fractured at drift levels of 6.5, 7.1, and 7.4 percent, respectively. Bar fracture was brittle with no necking evident, and occurred approximately 6 in. above the interface, at the peak of the buckled shape. Specimen REF underwent slightly larger drifts before fracture occurred. Three bars on the north and two bars on the south fractured at a drift of 8.8 percent. It was observed that a partially fractured bar showed cracks propagating from the inner side of the buckle. This, along with the lack of necking, indicates that bar fracture occurs as a consequence of bar buckling instead of strain concentrations at the interface.

In specimens LB-D1 and LB-D2 the bars were intentionally debonded to reduce the maximum strain at the interface. Deformation in the bar was thus distributed over the debonded length rather than being concentrated at the interface crack. The debonded region was placed in the cap beam for several reasons. First, the joint region constitutes a large, relatively rigid, block of concrete that provides restraint to buckling. Second, bond stresses will distribute deeper in the beam instead of at the surface due to the superior bond in grouted ducts (Raynor et al. 2002). Last, it is a more constructible alternative, as bars could be easily sleeved for debonding after casting and prior to erection.

Despite their different capacities for inhibiting buckling, the two details performed almost identically. This is confirmed by the similarity in their force-displacement curves in Figure 3. The primary reason was that the debonding was located in the cap beam, whereas the buckling deformations occurred in the body of the column, where both specimens were identical.

The need for any debonding was also brought into question, because the anchored end of the grouted bar pulls out a conical wedge of concrete from the duct. This region then behaves as an intentionally debonded region and reduces strain concentration.

3. COLUMN-TO-FOUNDATION CONNECTION

3.1 Concept

The concept for the foundation (Figure 4) is suitable for use with spread footings and is referred to as a socket column First the column is precast, with a roughened surface in the region that will eventually be embedded in the footing. Then the foundation is excavated and, in the bottom, a small temporary slab is cast on which to set the column. The column is set, plumbed, leveled and braced, the footing steel is placed, and then the footing concrete is cast.

The constructability advantages of the system are that it is quick and simple to build, it avoids any potential problems of fit-up of bars in ducts, the column detailing can be almost identical to that of a cast in place column, and no grouting is needed.

A possible variant on the system is to cast the footing before setting the column, leaving a void in the footing into which the column can subsequently be set and grouted. While this alternative adds an extra step (grouting), it has the advantage that the top of the footing provides a solid surface to which the column braces can be attached.

The simplicity of the socket connection suggests that it could also be used at the beam-to-column interface, by creating a cap-beam with a large hole into which the precast column would fit. While this configuration is possible, the cap beam would have to be significantly wider than the column to provide sufficient beam strength at the connection. The weight of the cap beam, and the crane needed for lifting it, nust be considered in evaluating the overall economy of the system. If the bridge girders are long and approximately the same weight as the cap beam, the crane required capacity may be controlled by the girders and the large cap beam may impose no real penalty.

The longitudinal reinforcement in the column is developed at the base by mechanical anchors, rather than the traditional method of bending the bars outwards. Doing so offers the construction advantage that the precast column becomes a large concrete cylinder with no protruding reinforcement, and is therefore simpler and safer to cast and transport. It also offers a much more direct transfer of forces between the column and the footing.

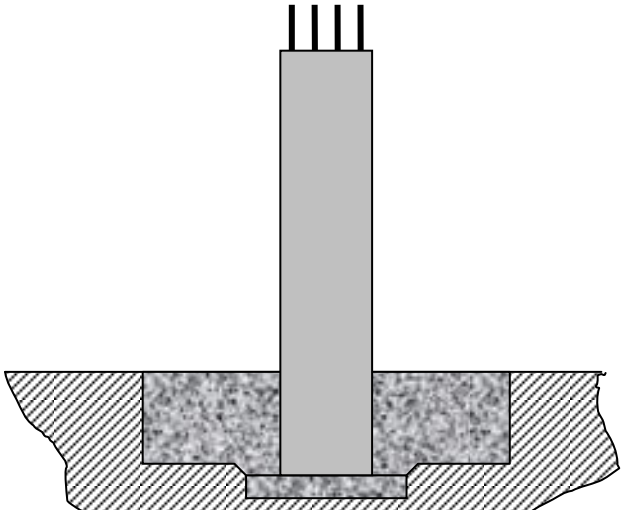

Figure 4. Column-to-Footing Connection Concept

The model proposed for use with the headed bars is very simple, and needs no top mat or tie steel, unless the "uplift" side of the footing does indeed lift off, in which case it should be reinforced to carry the cantilever moments due to the footing self-weight on the "uplift" side. The headed bars thus offer advantages for both constructability and seismic performance viewpoints. This is quite unusual: more commonly a change that benefits one imposes a disadvantage for the other.

3.2 Planned Tests

The major questions associated with the connection's seismic performance are expected to be in the transfer of forces from the column to the footing, so the planned testing focuses on them. The connection must be able to resist the cyclic column moments without significant damage to the footing, and without the column punching through the footing under gravity load.

Osanai et al. (1996) tested socket columns for buildings and concluded that, unless special conditions were satisfied, the footing depth should be at least 1.5 times the column diameter. However, the sockets they used were much smaller in plan than a typical spread footing for a bridge, so the planned tests, which are based on a footing depth/column diameter ratio of 1.0, are expected to demonstrate that the connection is strong enough to induce a plastic hinge into the column itself, just above the footing. Achieving this behavior is important, not only because it is advocated by

the AASHTO Specifications, but also because post-earthquake inspection and repair are more expensive for footings than for columns.

The first two (out of a total of 5) test specimens are shown in Figure 5. In both, the exterior of the column is roughened near the bottom to improve the transfer of shear stress. The column also extends just below the footing, to be sure that the force transfer at the node at the bottom of the column bars can take place satisfactorily.

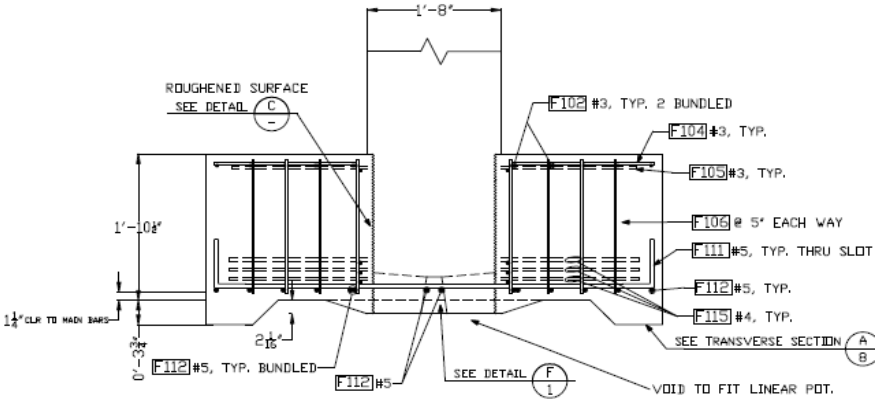

(a)

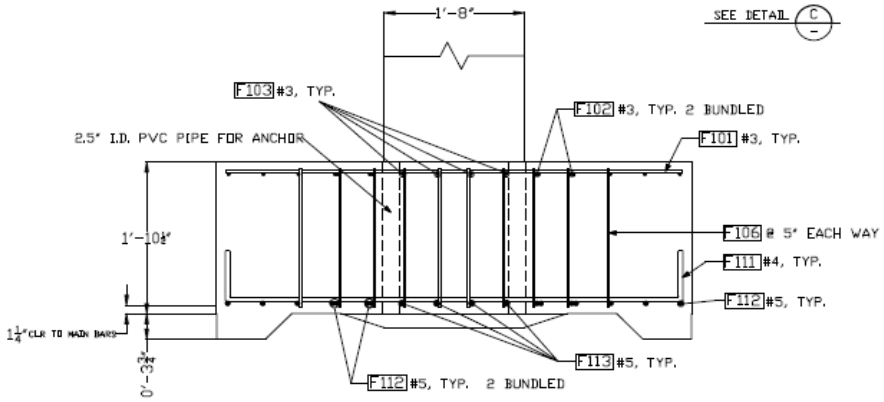

(b)

Figure 5. Drawings of Column-to-Footing Test Specimens: (a) conservative design, and (b) simpler design

Specimen A is the more conservative option. It is needed because the WSDOT has agreed to build a bridge over I-5 using the technology advocated here. The bridge is due to be bid before all the research test results are available, so a system with a very high probability of success had to be included. Two footing bars run through a slot under the column in each direction to ensure their direct engagement with the tension steel in the column. Sets of diagonal bars in the horizontal plane are placed in the top and bottom of the footing round the column. Their purpose is to act as "shear friction" steel that will provide the friction forces needed to prevent punching failure along the pc/cip interface. One set is placed in the top and three, stacked, in the bottom. Ties are included in accordance with the Caltrans recommendations (Caltrans 2006). The AASHTO Guide Specification for Seismic Design (AASHTO Guide 2009) is based on the Caltrans recommendations, but contains no tie requirements. The omission appears (Marsh, 2009) to be an oversight that is likely to be corrected, so the ties were included here in anticipation of their being required in future designs.

Specimen B was designed to determine whether the system could be simplified further. First, in each direction, the two center bars in the bottom mat of the footing steel were moved so they no longer passed under the column, but are placed just outside it. There they are bundled with the existing bar in that location. That placement frees the bottom mat to placed at any time, thereby improving constructability.

Second, the shear friction steel was reduced so that only one set of four bars was used at the top and bottom of the footing. The reasoning was that the bottom mat alone provides sufficient, provided that it can be used to provide both flexural strength and shear friction. (It should be noted that AASHTO allows some shear force to be resisted by a cohesive component of the concrete shear strength, but ACI 318 does not. In this case the cohesion component alone is theoretically sufficient to resist the axial force, which was taken as $0.1f'_cA_g$. The shear friction steel in Specimen A was designed conservatively using the ACI requirements, ignoring the cohesion component, to minimize and chance of vertical slip). One set of diagonal bars was retained at the top and bottom to act as "trimming" reinforcement at the corners of the square opening in the footing mat.

Third, the tie steel was reduced by 50%, on the basis that the Caltrans recommendations appeared to be developed for a system in which the column steel was bent out, rather than being anchored by heads. In that case the strut and tie model suggests that tie steel is largely unnecessary.

4. CONCLUSIONS

A precast concrete bridge bent system is presented that is rapid to construct and offers excellent seismic performance.

The details have been developed with extensive input from designers, the Washington State DOT, a precaster and a

general contractor. The assistance from a range of disciplines was critical to achieving the constructability goals.

The column-to-cap beam connection is made with a small number of large (D57 or No. 18) bars column grouted into ducts in the cap beam. Their small number, and the correspondingly large ducts sizes that are possible, lead to a connection that can be assembled easily on site.

The column-to-cap-beam connection has been tested under cyclic loading in three variations. All three behaved essentially identically to a cast-in-place column with similar properties. All reached a drift of approximately 6% before the longitudinal bars in the column buckled.

Two variations of the footing-to-column connection are to be tested in soon. One conservative option and one stripped-down option are to be tested. Strut and tie analyses suggest that the conservative connection detail will be stronger than the column, and that failure will occur by plastic hinging in the column, as desired. The stripped-down detail uses less steel and is simpler to construct. The constructability benefits are clear, and it is hoped that these tests will demonstrate that its seismic performance is adequate.

Acknowledgements:

The concepts were developed and tested at the University of Washington in cooperation with the Washington State Department of Transportation, Tri-State Construction, Concrete Technology Corporation and Berger/ABAM Engineers.

Support for this work was provided by the Federal Highway Administration, through their Highways for Life program, by the Washington State Department of Transportation, and by the Valle Foundation at the University of Washington. The findings and conclusions contained herein are those of the authors alone.

Thanks are extended to graduate students Kyle Steuck and Laila Cohagen, Laboratory Manager Vince Chaijaroen, Greg Ritke and the staff of Tri-state Construction, Mr. Steve Seguirant of Concrete Technology Corporation, Dr. Bijan Khaleghi and Mr. Jugesh Kapur of the WSDOT, and Dr Lee Marsh of Berger/ABAM Engineers for their valuable assistance, without which the project would not have been possible.

References:

"*AASHTO Guide Specification for LRFD Seismic Bridge Design*" (2009). AASHTO, Washington DC.

Building Seismic Safety Council for the FEMA. (2004) *"NEHRP Recommended Provisions for Seismic Regulations and for New Buildings and Other Structures (FEMA 450) 2003 Edition,"* Washington D.C.

Caltrans (2006). "*Seismic Design Criteria Version 1.4*". Caltrans, Sacramento, CA.

Marsh, L. (2009). Personal communication with J. Stanton.

Matsumoto, E., Waggoner, M., Sumen, G., Kreger, M., Wood, S., and Breen, J. (2001). *"Development of a Precast Bent Cap System,"* Center for Transportation Research, Research Project 0-1748, University of Texas at Austin.

Moustafa, S., (1989). "*Ductile Pullout Connections*". Concrete Technology Associates, CTA Bulletin 74B11. Now available from the Precast and Prestressed Concrete Institute, Chicago, IL.

Nakaki, S., Stanton, J., Sritharan, S. (1999). *"Overview of the PRESSS Five Story Precast Test Building,"* PCI Journal, V.44 N2, March-April 1999, pp 26-39.

Osanai, Y., Watanabe, F. and Okamoto, S., (1996). "*Stress Transfer Mechanism of Socket Base Connections with Precast Concrete Columns*". ACI Structural Journal, ACI, Chicago. IL. May-June, pp. 266-276.

Pang, B.K., Eberhard, M.O., and Stanton, J.F., "Large-Bar Connection for Precast Bridge Bents in Seismic Regions," to appear in Journal of Bridge Engineering, ASCE.

Precast and Prestressed Concrete Institute (2004). "*PCI Design Handbook*". 6th ed. Chicago, IL.

Raynor, D.J., Lehman, D.L. and Stanton, J.F. (2002). "*Bond-Slip Response of Reinforcing Bars Grouted in Ducts*". *ACI Str. Jo.* 99(5), Sept. pp 568-576.

Steuck, K., Pang, J., Stanton, J. and Eberhard, M. (2007) *"Anchorage of Large Bars in Grouted Ducts,"* Washington State Transportation Center Report WA-RD 684.1, Seattle, WA.

Steuck, K., Stanton, J.F. and Eberhard, M.O., "Anchorage of Large-Diameter Reinforcing Bars in Ducts," ACI Structural Journal, July-August 2009, pp 506-513.

Wacker, J., Hieber, D., Stanton, J., and Eberhard, M. (2005). "*Design of Precast Concrete Piers for Rapid Bridge Construction in Seismic Regions,"* Washington State Transportation Center Report, Seattle, WA.

Xiao, Y., Priestley, M.J.N., and Seible, F. (1996). "*Seismic Assessment and Retrofit of Bridge Column Footings*". ACI Structural Journal, ACI, Farmington Hills, MI. Jan-Feb., pp. 79-94.

JOINT CONFERENCE PROCEEDINGS
7th International Conference on Urban Earthquake Engineering (7CUEE) &
5th International Conference on Earthquake Engineering (5ICEE)
March 3-5, 2010, Tokyo Institute of Technology, Tokyo, Japan

EXPERIMENTAL STUDY ON SHEAR FAILURE MECHANISM OF CIRCULAR REINFORCED CONCRETE BEAMS

Ken Watanabe[1], Syunya Oishi[2], Moe Yonehana[2], and Junichiro Niwa[3]

1) Assistant Professor, Department of Civil Engineering, Tokyo Institute of Technology, Japan
2) Graduated Student, Department of Civil Engineering, Tokyo Institute of Technology, Japan
3) Professor, Department of Civil Engineering, Tokyo Institute of Technology, Japan
ken@cv.titech.ac.jp, oishi.s.aa@m.titech.ac.jp, yonehana.m.aa@m.titech.ac.jp, jniwa@cv.titech.ac.jp

Abstract: The objective of this research is to investigate the shear resistance mechanism of circular RC beams. According to the background of conventional equation, a series of the 4-point bending tests of circular RC beams under simple-supported condition was conducted. The contribution of cross-section shape, an arrangement of longitudinal bars and stirrups were evaluated based on the experimental results. Based on experimental results, the shear-load capacity of circular RC beams without stirrups was larger than the calculation by the conventional equation. This indicated that the effect of longitudinal bars in all circumferences should be involved in calculation. In addition, the shear carried by stirrups can be evaluated when the angle of a diagonal crack, the stress of stirrups, and the shape of stirrups were considered.

1. INTRODUCTION

Civil engineers have developed some slender reinforced concrete (RC) linear members with circular cross-section (circular RC members) for infrastructures: such as columns and piers. Standard specification of Japan society of civil engineers (JSCE 2005) has checked the shear-load capacity of circular RC linear members according to the modified truss analogy. Because the equation was developed based on experimental results of rectangular RC linear members, the specification has required replacing the equivalent square cross-section. Even longitudinal bars have been provided in all circumferences of circular RC linear members, which are conventionally used as columns and piers, only the limited number of longitudinal bars located in a quarter of a cross-section was involved for the calculation of the cross-section area of longitudinal tensile reinforcements (A_s). The effective depth (d) is assumed as the distance between the compression fiber of the equivalent square and the centroid of the longitudinal tensile reinforcements. The shape of cross-section and longitudinal bars located in all circumferences, which has been neglected in a conventional design, will affect the shear resistance mechanism.

The objective of this research is to investigate the shear resistance mechanism of circular RC beams; in particular, longitudinal bars provided in all circumferences, a shape of diagonal cracks and stirrups were discussed with the shear-load capacity of circular RC beams. In order to compare the equation in JSCE (2005), a series of 4-point bending tests of circular RC beams was conducted under the simple supported condition. Based on the experimental results, contributions of a cross-section shape, an arrangement of longitudinal bars in all circumferences, and stirrups were evaluated.

2. EXPERIMENTAL PROGRAM

2.1 Specimen Fabrication

Table 1 summarizes the mix proportion of concrete used in this study. The designed compressive strength (f'_c) of concrete at the time of the loading test was 35 N/mm^2. The maximum size of coarse aggregates (G_{max}) was 15 mm. The water-reducing admixture was added with 1.5 % of water weight.

Figure 1 illustrates the scheme of a tested circular beam. The specimen had a circular cross-section with a diameter of 300 mm, and the shear span (a) of 750 mm. The equivalent square cross-section indicated the beam width (b_w) of 266 mm, the effective depth (d) of 227 or 223 mm; the shear span to the effective depth ratio (a/d) of 3.3 or 3.4. In order to cause the shear failure in the specified shear span, more stirrups were provided in the opposite shear span than the test shear span. Specimens were longitudinally reinforced by 8 or 16 deformed steel bars of 19.1 mm in diameter; the longitudinal tensile reinforcement ratio (p_w) was 0.97 or 1.75 % when longitudinal reinforcing bars in a quarter of a cross-section were considered. CRC5-0, however, had five longitudinal bars only in a quarter of a cross-section, of which p_w was 1.75 %. The yield strength of these bars was 534 N/mm^2 as 0.2 % off-set value. These reinforcing bars were anchored by plates and bolts to ensure sufficient

Table 1 Mix proportion of concrete.

G_{max} [mm]	Water to cement ratio	Fine aggregate ratio	Unit weight (kg/m^3)						
			Water (W)	Cement (C)	Lime stone powder	Fine aggregate	Coarse aggregate	Water-reducing admixture	Viscosity improver
15	0.60	0.45	165	292	249	718	857	0.015W	0.0015C

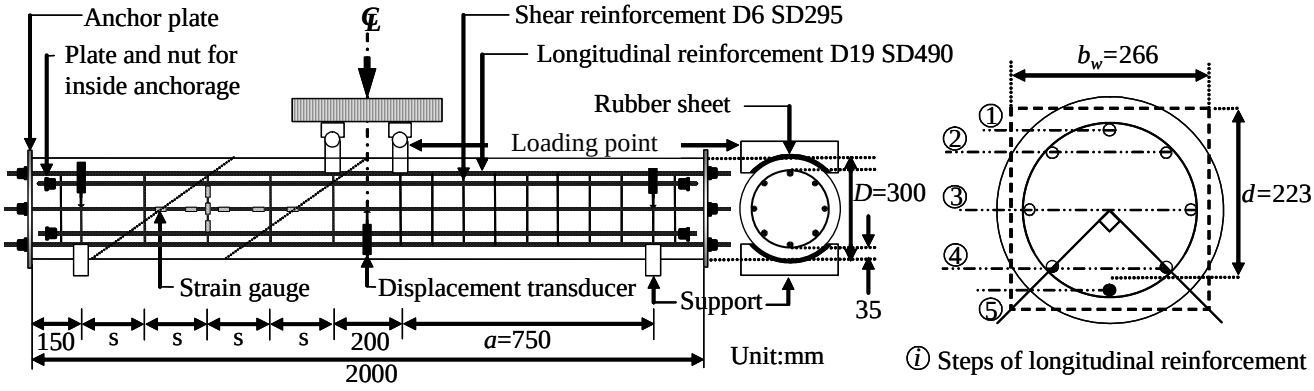

Fig. 1 Outline of tested circular RC beam.

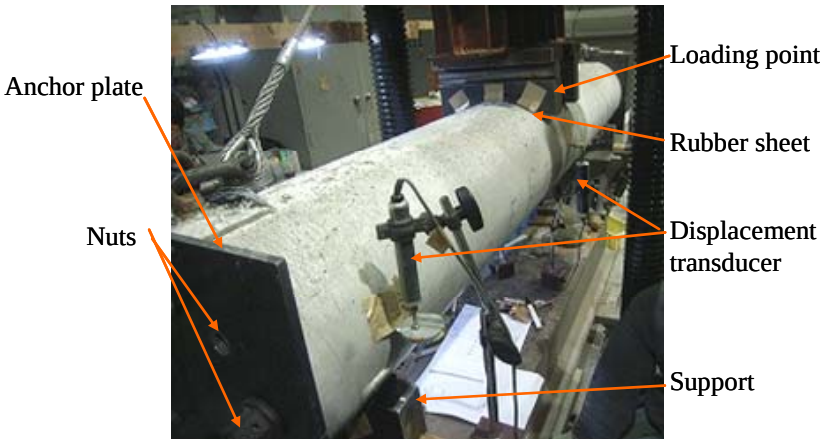

Fig. 2 Outline of loading test of circular RC beam.

anchorage. Stirrups with deformed steels of 6 mm in diameter were arranged for all specimens as stirrups with the spacing (s) to control the stirrup ratio (r_w) of 0.0 to 0.26 %. The yield strength (f_{wy}) was 342 N/mm^2.

Table 2 summarizes specifications as well as test results of specimens. A total of 6 specimens with different number of longitudinal bars and stirrups were prepared. The specimen was named according to the number of longitudinal bars and r_w; e.g. CRC8-13 was corresponding to the specimen having eight longitudinal bars and r_w=0.13 %.

The shear-load capacity of circular RC beams can be estimated according to the equations presented in the JSCE standard specifications as follows:

$$V_{cal} = V_{c_cal} + V_{s_cal} \quad (1)$$

$$V_{c_cal} = 0.20 f_c'^{\frac{1}{3}} p_w^{\frac{1}{3}} \left(\frac{1000}{d}\right)^{\frac{1}{4}} \left(0.75 + \frac{1.4}{a/d}\right) b_w d \quad (2)$$

$$V_{s_cal} = A_w f_{wy} z / s \quad (3)$$

where V_{cal}: the shear-load capacity (kN), V_c: the shear-load capacity of RC beam without stirrups (kN), V_s: the shear carried by stirrups (kN), A_s: a cross sectional area of longitudinal tensile reinforcement in a quarter of a cross section of a beam, d: the distance from extreme compression fiber of equivalent square to the centroid of the longitudinal tensile reinforcement, A_w: a cross sectional area of stirrup, and z (=(7d)/ 8) (mm).

Table 2 Comparison of the shear-load capacity between calculation and experimental results

Specimen	p_w (%)	r_w (%)	f'_c [N/mm^2]	JSCE calculation			Experiment			Comparison			Mutsuyoshi		Proposed	
				V_{c_cal} [kN]	V_{s_cal} [kN]	V_{cal} [kN]	V_{c_exp} [kN]	V_{s_exp} [kN]	V_{exp} [kN]	V_{c_exp} /V_{c_cal}	V_{s_exp} /V_{s_cal}	V_{exp} /V_{cal}	V_{cm_cal} [kN]	V_{c_exp} /V_{cm_cal}	$V_{s\delta_cal}$ [kN]	V_{s_exp} /$V_{s\delta_cal}$
CRC16-0	1.75	0	36.7	84.5	0	84.5	109.9	–	109.9	1.30	–	1.30	118.2	0.93	-	-
CRC5-0			36.4	84.5	0	84.5	86.0	–	86.0	1.02	–	1.02	90.6	0.95	-	-
CRC8-0	0.97		37.7	66.7	0	66.7	102.3	–	102.3	1.53	–	1.53	90.5	1.13	-	-
CRC8-13		0.13	37	66.3	22.5	88.8	102.3	10	112.3	–	0.44	1.26	-	-	9.5	1.05
CRC8-19		0.19	38.2	67	33.8	100.8	102.3	48	150.3	–	1.42	1.49	-	-	40.3	1.19
CRC8-26		0.26	37.7	66.7	45.1	111.8	102.3	61.7	164	–	1.37	1.47	-	-	64.2	0.96

V_{c_cal}: shear carried by concrete (calculation by eq.(2)), V_{s_cal}: shear carried by stirrups (calculation by eq.(3)), V_{cal}: shear-load capacity (calculation by eq.(1)), V_{c_exp}: shear carried by concrete (experimental result), V_{s_exp}: shear carried by stirrups (=V_{exp}- V_{c_exp}), V_{exp}: shear-load capacity (experimental result).

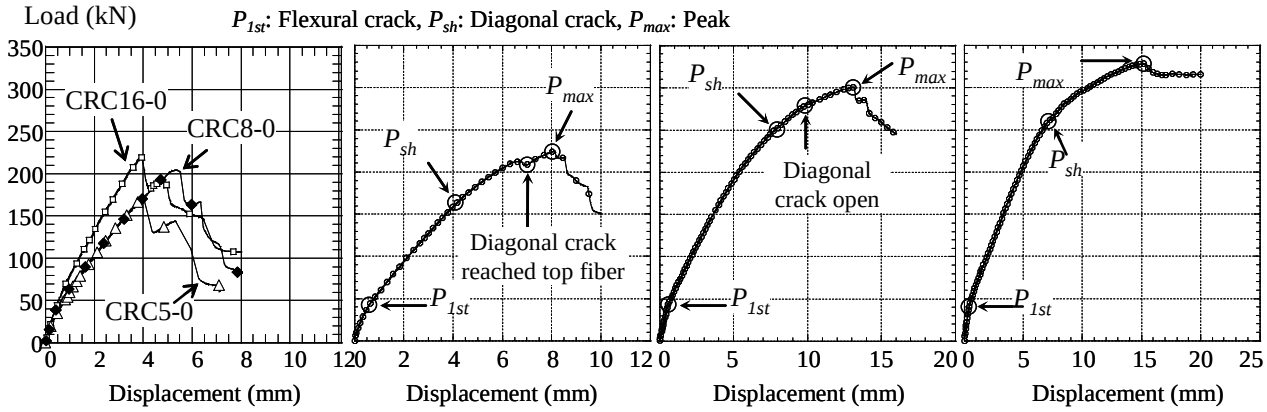

(a) No stirrup (b) CRC8-13 (c) CRC8-19 (d) CRC8-26

Fig.3 Load-displacement relationships with specific phenomenon.



(a) CRC16-0 (b) CRC8-13 (c) CRC8-19

Fig. 4 Failed specimens.

2.2 Loading and Measurements

Circular beams were subjected to a four-point bending test. The details of loading and supporting positions are illustrated in Fig. 2. Specimens were placed over roller supports, which were composed of steel plates with 50 mm width. A concentrated load was applied at the mid-span, and steel plates with width of 50 mm were provided at loading points. During the loading test, the applied load, the mid-span deflection, strain of the longitudinal reinforcement at the mid-span, and the strain of the stirrups at the middle-height were measured by using a load-cell, transducers, and strain gauges.

3. EXPERIMENTAL PROGRAM

3.1 Summary of Experimental Results

Calculations and experimental results of shear-load capacity are summarized in Table 2. Figure 3 shows the load-displacement relationship plotted by identical stirrup ratio. Figure 4 shows the test span of three failed specimen, and Fig. 5 projected the crack distribution of four specimens where the bold line represents the critical diagonal crack. β represents the angle of the critical diagonal crack with respect to the horizontal axis. There seemed to be no relation between β and r_w. The flexural crack was initiated at around 40 kN in lower fiber between two loading points, and the slope decreased gradually as shown in Fig. 3. All specimens except for CRC8-26 were designated as a diagonal tension

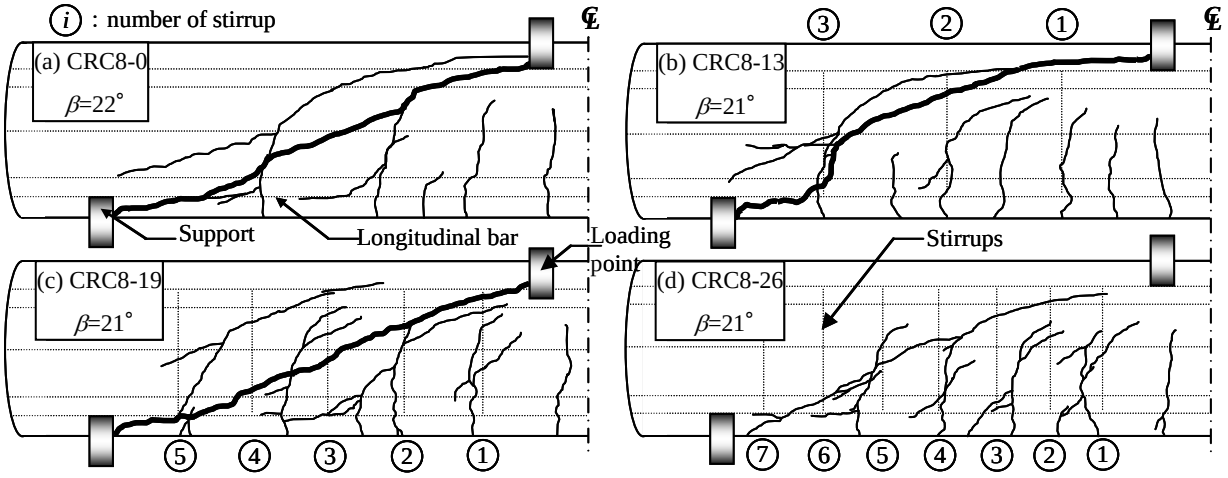

Fig. 5 Crack pattern of specimens

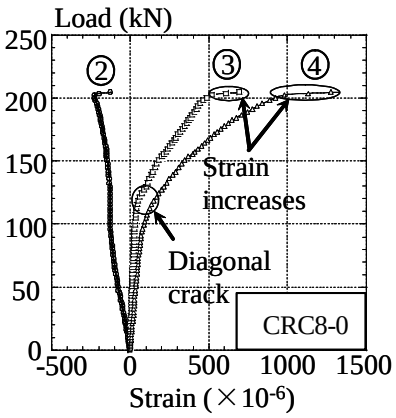

Fig. 6 Strain of longitudinal bars

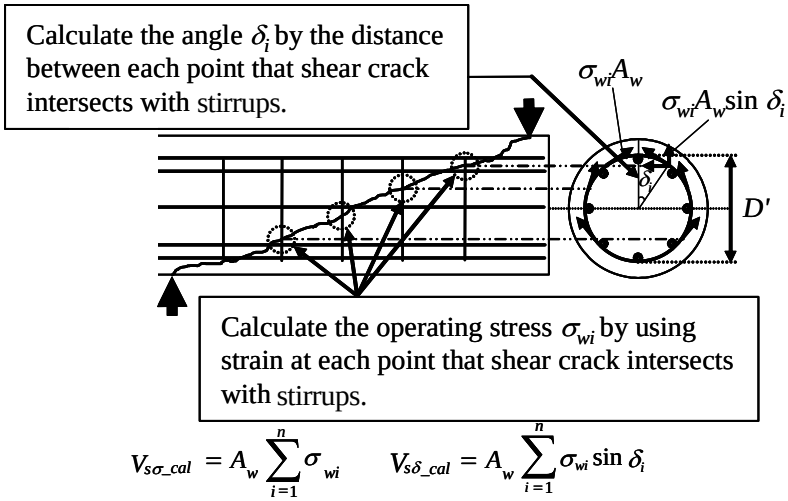

Fig. 7 Influence of shape of stirrup

failure, because the load reached peak without yielding of longitudinal bars and a remarkable diagonal crack was observed. The experimental result of CRC8-26 showed that longitudinal bars arranged in the lowest depth was yielded before a load reaching peak, the displacement increased without decreasing in the load as shown in Fig. 3. The failure mode of CRC8-26 was designated as the flexural tension failure.

3.2 Circular RC Beams without Stirrups

CRC5-0 reached the peak load just after the generation of diagonal crack. Table 2 listed the comparison of the shear-load capacity between calculation by JSCE and experimental results. The ratio of V_{c_exp}/V_{c_cal}=1.02 in CRC5-0 indicated that the conventional method by JSCE (2005) was able to predict the load at the generation of diagonal crack as well as the shear-load capasity.

On the other hands, CRC16-0 and CRC8-0 was anle to carry larger load even the diagonal crack initiated. As a result, the value of V_{c_exp}/V_{c_cal} was 1.30 or 1.53 in Table 2. It means that the current calculation method considerably underestimates the experimental result if longitudinal bars in all circumferences were neglected. Figure 6 indicated strain of longitudinal bars, of which the number is corresponding to the layer in Fig.1. When a diagonal crack intersected, the strain of longitudinal bars increased. It means that longitudinal bars contributed to carry the load. Ishibashi et al. (1985) and Mutsuyoshi and Machida (1987) reported the effect of longitudinal bars in web on the shear strength. For example, Mutsuyoshi and Machida (1987) proposed to consider the longitudinal steel bars distributed in a cross-section by Eq. (4) as:

$$A_s = \sum A_{si} \tag{4}$$

where, A_{si} is the cross sectional area of longitudinal steel bars arranged in a tensile region. Table 2 shows the shear-load capacity V_{cm_cal} calculated by Eq. (4). The value of V_{c_exp}/V_{cm_cal} was 1.13, in which the cross sectional area of

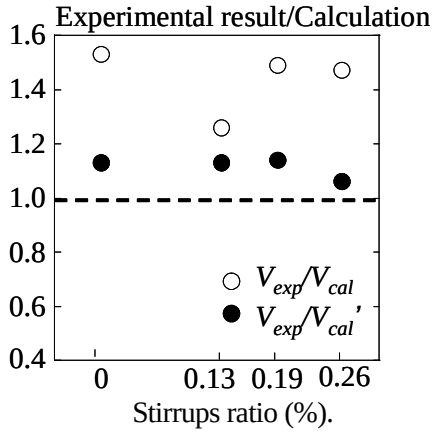

Fig. 8 Comparison of experimental and calculated results

longitudinal bars: numbered 3, 4, and 5 in Fig. 1, were considered.

3.3. Shear Carried by Stirrups

Figure 5 indicated that the angle of diagonal crack β was smaller than 45° in all specimens with stirrups. Some stirrups were not yielded or did not intersect with a diagonal crack. It means that the contribution of stirrups can not be evaluated by Eq. (3), which considered only yielded stirrups. Figure 7 explained the influence of circular shape on the shear carried by stirrups. Based on experimental results, the shear carried by stirrups was examined by following three components.

a) Angle of a diagonal crack

The angle of diagonal crack β was 21° or 22°, both were smaller than 45°. The angle of diagonal crack affected to the number of stirrups that passed the diagonal crack. This paper considered the shear-load capacity by Eq. (5) as:

$$V_{s\beta_cal} = A_w f_{wy} z \cot\beta / s \qquad (5)$$

b) Stress of stirrups

As explained in 2.1, a strain distribution in a stirrup was measured through strain gauges. According to the strain, the stress of stirrups where a diagonal crack intersected with stirrups was evaluated. Accumulation of the evaluated stress at each stirrup will corporate to understand the contribution of stirrups.

c) Shape of stirrups

Since the shape of stirrups was a circle in all specimens, the force of a stirrup occurred in a tangential direction. In order to consider the shear resistance by stirrups, the force of a stirrup in a vertical component should be considered. As reported in Kim and Mander (2005) and Jensen and Hoang (2008), the vertical component was different depending on the depth as shown in Fig. 7.

Finally, the angle of a diagonal crack, stress of stirrups evaluated by strain gauges, and the vertical component of force in stirrups were involved in the calculation and expressed as the shear carried by stirrups ($V_{s\delta_cal}$) in Table 2. The value of V_{cal}' ($=V_{cm_cal}+V_{s\delta_cal}$) was calculated and compared with V_{exp} in Fig. 8. Figure 8 also plots V_{exp}/V_{cal}. Even all V_{exp}/V_{cal}' distributed more than 1.0, it was close to 1.0 compared with V_{exp}/V_{cal}. This means that the consideration of longitudinal bars and a shape of stirrup would be effective to demonstrate the experimental result.

4. CONCLUSIONS

(1) The shear-load capacity of circular RC beams without stirrups was larger than the calculation by existing design method. This means that the longitudinal steel bars provided in all circumferences should be involved in consideration.

(2) The angle of a diagonal crack, stress of stirrups evaluated by strain gauges, and the vertical component of force in stirrups were effective to evaluate the shear carried by stirrups for circular RC members.

References:

Jensen, U. G. and Hoang, L. C. (2008), "Shear Design of Reinforced Concrete Elements with Circular Cross Section," *Eleventh East Asia-Pacific Conference on Structural Engineering & Construction (EASEC-11)*, Paper No. B05-07, pp.1-10.

JSCE (2005), "Standard specifications for Concrete Structures-2002, Structural Performance Verification."

Kim, J. H. and Mander, J. B. (2005), "Theoretical Shear Strength of Concrete Columns due to Transverse Steel," *Journal of Structural Engineering*, Vol. 131, No.1, pp1178-1179.

Mutsuyoshi, H. and Machida, A. (1987), "Shear Carrying Capacity and Deformability of RC Member with Lateral Longitudinal Reinforcement," *Proceeding of JCI*, Vol.9, No.2, pp.335-340.

Ishibashi, T., Saito, K. and Terada, T. (1985), "Effect of longitudinal bars in web on shear strength of RC beams," *Proceeding of JSCE annual conference*, Vol. 40, pp.321-322.

JOINT CONFERENCE PROCEEDINGS
7th International Conference on Urban Earthquake Engineering (7CUEE) &
5th International Conference on Earthquake Engineering (5ICEE)
March 3-5, 2010, Tokyo Institute of Technology, Tokyo, Japan

EXPERIMENTAL STUDY FOR SHEAR CAPACITY OF SEGMENTAL CONCRETE BEAMS WITH EXTERNAL TENDONS AND DRY JOINT

Dinh Hung Nguyen[1], Ken Watanabe[2], Junichiro Niwa[3], and Tsuyoshi Hasegawa[4]

1) PhD. Candidate, Graduate School of Civil Engineering, Tokyo Institute of Technology, Japan
2) Assistant Professor, Department of Civil Engineering, Tokyo Institute of Technology, Japan
3) Professor, Department of Civil Engineering, Tokyo Institute of Technology, Japan
4)Research Engineer, Research and Development Center, DPS Bridge Works Co., Ltd
nguyen@cv.titech.ac.jp, ken@cv.titech.ac.jp, jniwa@cv.titech.ac.jp, t_hasegawa@dps.co.jp

Abstract: This paper presents the results of experimental procedure of the segmental concrete beams with external tendons. The shear failure mechanism was investigated with considering the effect of the prestress level and types of segmental joint. The experimental results showed that the shear failure mechanism of segmental concrete beams with dry joint is similar to that with epoxy joint. The shear failure mechanism of segmental concrete beams with external tendons was different from that in the direct shear test. The shear capacity of segmental concrete beams with dry joint was slighter than that with epoxy joint. The experimental results from this study were compared with existing models. The results from the modified model had a good agreement with experimental results.

1. INTRODUCTION

The precast segmental construction is widely used in the bridge structures, because of substantial cost and time saving in construction. In the beginning, the internal tendon technology has been used for the segmental technology where tendons are located inside the concrete cross section. However, the problems such as leakage at epoxy joints, corrosion in tendons causes the damage of segmental bridges. So, the application of external prestressing with precast segmental structures has been used as an innovative method in the segmental concrete technology.

Segmental concrete structure with external tendons is widely used for bridges to make a longer span in construction. So, the flexure is usually considered at first. If the flexure failure occurs in the concrete structure, especially in prestressed concrete structures, there is enough time to warn people about the failure before the total collapse. However, the shear failure is usually brittle and the shear failure causes sudden collapse of a structure. The sudden collapse of Koror-Babeldaob bridge (Burgoyne and Scantlebury, 2008) was an example about the failure of a segmental concrete bridge.

The shear carrying capacity of segmental concrete beams was investigated in the direct shear test (Zhou et al., 2005). It has shown that the shear carrying capacity of dry joints was from 60% to 80% of that of epoxy joint the direct shear test. In addition, under seismic load a segmental joint may open due to the lack of longitudinal reinforcements, especially in the high seismic zone with a high shear force and moment (Megally et al. 2003) in which epoxy joint was investigate. The shear transfer across an opening segmental joint is a very complex problem for precast segmental concrete beams with external tendons. As a segmental joint opens, the area at a segmental joint to transfer shear force is reduced. It leads to the collapse of segmental beams. Therefore, it is necessary to confirm that the shear failure does not take place in the segmental concrete structure.

In segmental concrete bridges, match-cast joints are normally bonded with epoxy or strengthened with high strength mortar or grout. Match-cast joints are also dry joint for bridges wherever possible to avoid the problems in epoxy joints (Kamaitis, 1998). The objectives of this study are to investigate the shear transfer mechanism of segmental joints and the shear failure mechanism of segmental concrete beams with external tendons, such as propagation of cracks, joint opening, shear carrying capacity, by varying the joint types, i.e. epoxy and dry joints, and prestressing force. The modified model (Nguyen et al. 2010) is checked in order to confirm the applicability of the modified model for predicting the shear carrying capacity of segmental concrete beams with external tendons and a dry joint.

2. LITERATURE REVIEWS

Figure 1 shows the schematic diagrams of the modified model for predicting the shear carrying capacity of

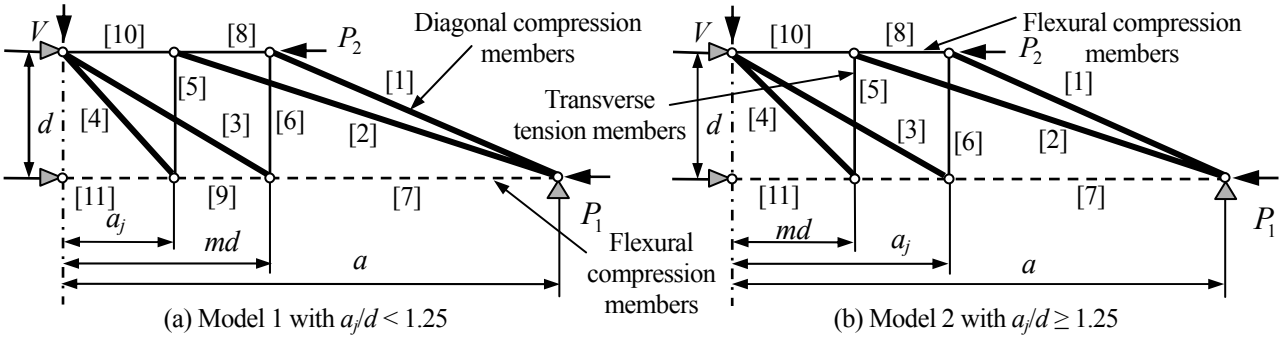

(a) Model 1 with $a_j/d < 1.25$ (b) Model 2 with $a_j/d \geq 1.25$

Figure 1 Schematic diagrams of modified model.

segmental concrete beams with external tendons and epoxy joint considering the joint position (Nguyen et al. 2010). Parameter m, $m = \cot\theta$ and θ is an angle of the concentrated stress flow from loading point inclining to beam axis, is affected by the joint position. In Model 1, the distance md is defined as the horizontal distance from the loading point to the end node of strut member [3]. The strut member [4] is provided from the bottom of the web at the edge of a segmental joint to the loading point. In Model 2, the distance md is defined as the horizontal distance from the loading point to the end node of strut member [4]. The strut member [3] is provided from the bottom of the web at the edge of a segmental joint to the loading point. From the parametric study, the equation for estimating the value of m for the Model 1 and Model 2 is shown as following Eq. (1) and (2), respectively.

$$m = 1.395\left(\frac{a_j}{d}\right)^{\frac{3}{10}}\left(\frac{a}{d}\right)^{\frac{3}{4}}(\sigma_l)^{-\frac{1}{4}} \quad (1)$$

$$m = 0.112\left(\frac{a_j}{d}\right)^{\frac{5}{7}}\left(\frac{a}{d}\right)^{\frac{1}{4}}(\sigma_l)^{\frac{5}{9}} \quad (2)$$

where a_j is the distance from the critical segmental joint to the loading point; d is the effective depth of a beam; a is the shear span; σ_l is the lower extreme fiber stress (N/mm^2).

The effects of loading plate, support plate and effective depth (Lertsamattiyakul, 2005), stirrup (Sivaleepunth et al. 2009), a/d and a_j/d ratios (Nguyen et al. 2010) were considered in formulating the horizontal thickness of a strut member. The horizontal thickness in the vicinity of loading point, t_l and support, t_s for Model 1 are shown by Eqs. (3) and (4), the values of t_l and t_s for Model 2 are shown by Eqs. (5) and (6), respectively.

$$t_l = (w_l + 0.1d)\left(\frac{b_f}{b_w}\right)^{\frac{1}{5}}\left(1+\left(\frac{A_{sv}}{b_w s}\right)^{\frac{1}{4}}\right)\left(0.167\left(\frac{a}{d}\right)^{\frac{10}{7}}\left(1+0.025\left(\frac{a_j}{d}\right)^{\frac{6}{5}}\right)\right) \quad (3)$$

$$t_s = 2(w_s + 0.1d)\left(\frac{b_f}{b_w}\right)^{\frac{1}{5}}\left(1+\left(\frac{A_{sv}}{b_w s}\right)^{\frac{1}{4}}\right)\left(0.167\left(\frac{a}{d}\right)^{\frac{10}{7}}\left(1+0.025\left(\frac{a_j}{d}\right)^{\frac{6}{5}}\right)\right) \quad (4)$$

$$t_l = (w_l + 0.1d)\left(\frac{b_f}{b_w}\right)^{\frac{1}{5}}\left(1+\left(\frac{A_{sv}}{b_w s}\right)^{\frac{1}{4}}\right)\left(0.174\left(\frac{a}{d}\right)^{\frac{7}{5}}\left(1+0.004\left(\frac{a_j}{d}\right)^{5}\right)\right) \quad (5)$$

$$t_s = 2(w_s + 0.1d)\left(\frac{b_f}{b_w}\right)^{\frac{1}{5}}\left(1+\left(\frac{A_{sv}}{b_w s}\right)^{\frac{1}{4}}\right)\left(0.174\left(\frac{a}{d}\right)^{\frac{7}{5}}\left(1+0.004\left(\frac{a_j}{d}\right)^{5}\right)\right) \quad (6)$$

where, w_l is the loading plate width; w_s is the support plate width; b_f is the width of flange; b_w is the width of web; A_{sv} is the cross sectional area of stirrup; s is the spacing of stirrups.

In order to calculate the shear carrying capacity of segmental concrete beams with external tendons and epoxy joint, the equivalent elastic analysis is utilized. The each member force, F_i is calculated based on Castigliano's second theorem, i.e. the theorem of minimum strain energy. The resistance of each member, R_i is calculated by multiplying f'_c with the softening parameter, η (Lertsamattiyakul, 2005), and the correlatively cross sectional area, A_i. The shear carrying capacity are estimated when the maximum value of ratio of F_i to R_i is equal to 1 [max $(F_i/R_i) = 1$, $i = 1$ to 4].

The modified model (Nguyen et al. 2010) is proven to provide high accuracy and simplicity in predicting the shear carrying capacity of segmental concrete beams with external tendons and epoxy joint. However, it has not yet been extended to the segmental concrete beams with external tendons and dry joint. In addition, the modified model has limited applicability for the segmental concrete beams with the stress at the lower fiber greater and equal to 10 N/mm^2.

3. TEST PROGRAM

3.1 Testing beams

Three simply supported concrete beams designed to fail in shear with a/d ratio of 3.5 were used. The beams consisted of two segments. The segmental joint was arranged in the tested shear span. The distance from the loading point to the joint position, a_j, used in these beams was 1.0d, where d was the effective depth of a beam. Test specimens were T-shaped section concrete beams with the span length of 3.2 m. Two deviators 1.367 m apart were located symmetrically with respect to the midspan, as shown in Figure 2(a). Different prestress levels and joint types were investigated in these beams. The concrete stress at the upper fiber of the all segmental beams was about 0 N/mm^2. One segmental concrete beam with epoxy joint was prestressed to obtain the concrete stress of 6 N/mm^2 at the lower fiber. The name of

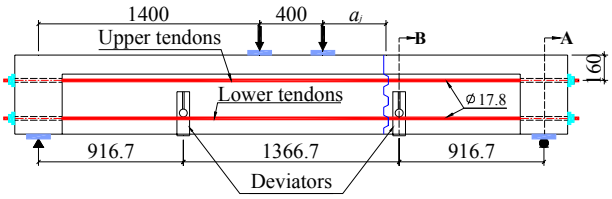

(a) General view

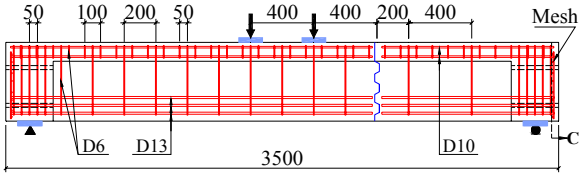

(b) Reinforcement

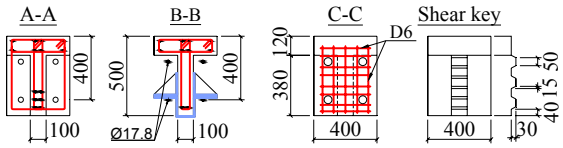

(c) Cross section (Unit: mm)

Figure 2 Detail of specimens

the beam with epoxy joint was SJ10-06. "SJ10" stands for the segmental joint with a_j of 1.0d. Two other beams were the segmental beams with dry joint. Two beams with dry joint were prestressed to obtain the concrete stress of 10 N/mm^2 and 6 N/mm^2 at the lower fiber. Therefore, name of the beams with dry joint was DSJ10-10 and DSJ10-06, respectively. "DSJ10" stands for the dry segmental joint with a_j of 1.0d. The last two numbers in the name of all segmental beams indicate the concrete stress at the lower fiber.

3.2 Materials

The arrangement of reinforcement in a beam is shown in Figure 2(b). The non-prestressed steels were deformed bars. In all the beams, six deformed bars with a nominal diameter of 12.7 mm and eight deformed bars with a nominal diameter of 9.53 mm were provided as internal longitudinal bars at the bottom and top flange, respectively. Stirrup was the type of a nominal diameter of 6.35 mm. The spacing of stirrup in the tested shear span was 400 mm. The other shear span was reinforced at an interval of 200 mm. Stirrups were also used at the top flange with an interval of 100 mm. The mechanical properties of steel bars are given in Table 1. Mesh reinforcement was utilized at the end of a beam to resist local stresses due to the prestressing force.

The match-cast method was used for casting of the segmental beams. In this method, the large segment of the beam was cast first with a wood shear key as an end formwork. Two days later formworks were removed and the large segment itself was used as an end formwork for next casting in order to provide a perfect matching between the two segments. After casting, the concrete beams were cured in the atmospheric condition. The design strength of concrete, f'_c was specified as 65.0 N/mm^2 at 28 days. The actual compressive and tensile strengths of concrete are

Table 1 Mechanical properties of reinforcements

Diameter (mm)	Yield strength (N/mm^2)	Tensile strength (N/mm^2)	Elastic modulus (kN/mm^2)	Area (mm^2)
6.35	336	522	200	31.7
9.53	479	498	200	71.3
12.7	371	512	200	126.7

Table 2 Characteristics of concrete.

Beams	Compressive strength (N/mm^2)		Tensile strength (N/mm^2)	
	Batch A	Batch B	Batch A	Batch B
SJ10-06	68.1	69.3	5.31	5.31
DSJ10-06	65.6	66.6	5.75	5.75
DSJ10-10	67.1	69.1	5.75	5.75

Note: Batch A is for large segment, Batch B is for small segment.

tabulated in Table 2.

The prestressing tendon used for the beams was of type SWPR19L ϕ17.8 mm. The yield and ultimate strengths of the tendon were 1760 N/mm^2 and 1950 N/mm^2, respectively. The external tendons were placed as shown in Figure 2(a) and were stretched 3 days before testing. Steel deviators, located in the shear spans, were attached to the beam from the bottom to ensure that there was no change in the web thickness of the test beams. Epoxy resin was used to connect concrete segments. Prestressing was introduced after assembling of concrete segments with epoxy. The compressive and tensile strengths of epoxy resin were greater than 60 N/mm^2 and 12.5 N/mm^2, respectively.

3.2 Loading Method and Measurements

The beams were subjected to a two-point loading test with a distance of 400 mm between two loading points, as shown in Figure 2. The applied load was increased monotonically by means of displacement control method until the beams were failed.

Various measuring devices were utilized in order to measure the displacement of a beam, joint opening and stress increment in the external tendons. Strain in the tendons was measured by electrical strain gauges at the middle of the external tendons. Meanwhile, displacement transducers were mounted at the midspan and the supports of a beam to monitor the vertical deflection. At the same time, transducers (T1 to T5) were placed horizontally at five levels on the segmental joints to measure the joint opening as shown in Figure 3.

4. RESULTS AND DISCUSSION

4.1 Crack Patterns and Joint Opening

Figure 4 presents the crack pattern of the beams. In DSJ10-10 and DSJ10-06, the flexural cracks formed in the maximum moment zone between the loading points. The first diagonal crack formed at the lower corner of the upper

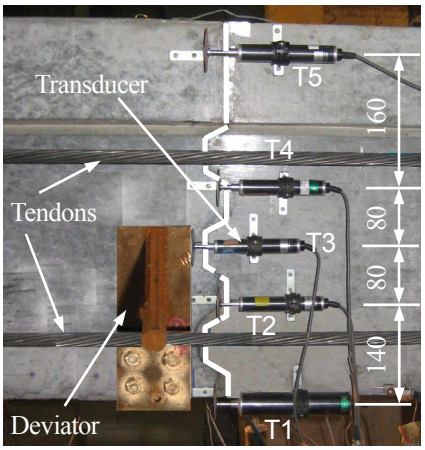

Unit: mm

Figure 3 Arrangement of transducers to measure joint opening

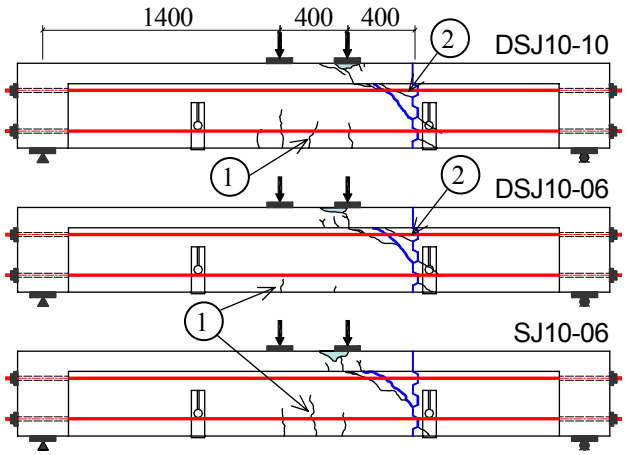

1 The fist flexural crack; 2 The first diagonal crack
Bold line is the dominant diagonal crack

Figure 4 Crack patterns

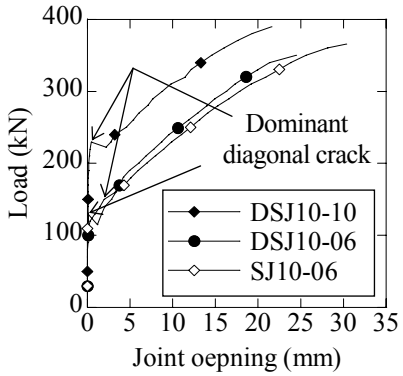

Figure 5 Load – joint opening at lower fiber

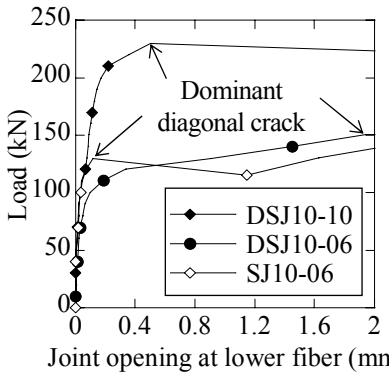

Figure 6 Load – joint opening at lower fiber before dominant diagonal crack

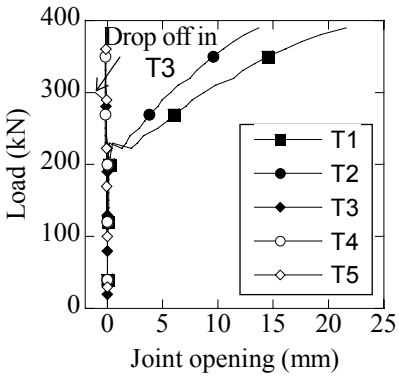

Figure 7 Load – joint opening of DSJ10-10

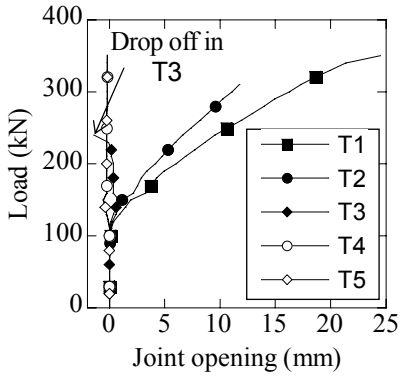

Figure 8 Load – joint opening of DSJ10-06

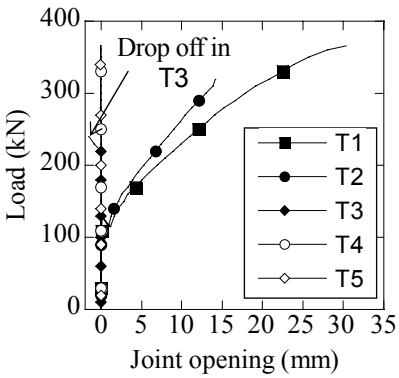

Figure 9 Load – joint opening of SJ10-06

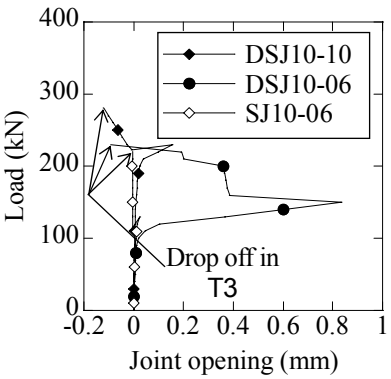

Figure 10 Load – joint opening at level of T3

key in the large segment forward the loading point. The dominant diagonal crack formed at the lower corner of the middle key in the large segment forward the loading point. At the same time of the dominant diagonal crack occurrence, the cracks at the upper corner of the middle and lower keys in the small segment also formed. In SJ10-06, after the occurrence of the flexural cracks, the dominant diagonal crack formed at the lower corner of the middle key in the large segment forward the loading point.

Figure 5 presents the joint opening at the lower fiber, measured by T1 as shown in Figure 3. In the similar prestress level, DSJ10-06 and SJ10-06, the dry joint opened larger than the epoxy joint before the occurrence of the dominant diagonal crack as shown in Figure 6. The joint opening at the lower fiber increased sharply as the dominant diagonal crack occurred. At the ultimate, the epoxy joint opened higher than the dry joint.

Figures 7, 8 and 9 show the measured joint opening. The joint opening was always detected in both T1 and T2 in all tested beams. In DSJ10-10 and DSJ10-06, the joint opening was also detected by T3 until the first diagonal crack occurred as shown in Figure 10. T3 tended to be

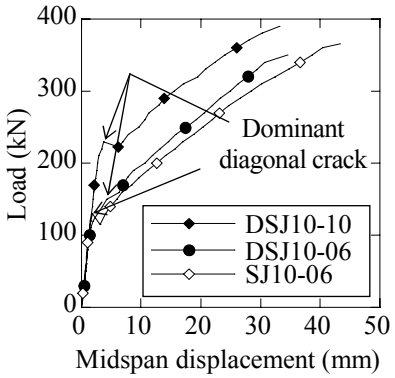

Figure 11 Load – displacement relationship

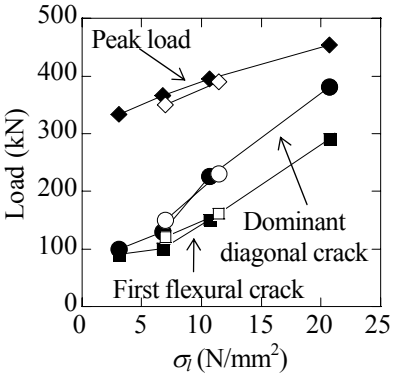

Note: Black marks for epoxy joint, White marks for dry joint

Figure 12 Load-σ_l relationship

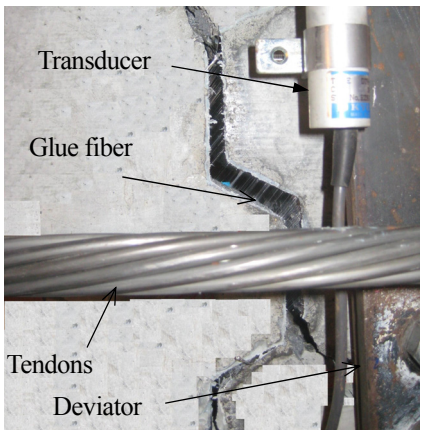

Figure 13 Glue fiber at joint opening in SJ10-06

Table 3 Test results

Beams	P_{cr} kN	P_{sh1} kN	P_{sh} kN	P_u kN	JO_1 mm	JO_2 mm
SJ10-06	100	130	130	366.1	0.12	30.3
DSJ10-06	120	130	150	350.1	1.94	24.5
DSJ10-10	160	220	230	390.2	0.50	21.6

Note: P_{cr} is load at first flexural crack; P_{sh1} is load at first diagonal crack; P_{sh} is load at dominant diagonal crack; P_u is peak load; JO_1 is joint opening at the dominant diagonal crack; JO_2 is joint opening at peak load.

compressed after the first diagonal crack occurred. T3 was attached fairly near to the deviator as shown in Figure 3. So, T3 could not obtain the opening value as the segments and the deviator were largely rotated. In SJ10-06, after the occurrence of the flexural cracks, the dominant diagonal crack formed at the lower corner of the middle key in the large segment forward the loading point.

4.2 Load-Deflection Curves

Figure 11 illustrates the load-deflection curves of tested beams. Table 3 summarizes some the measured data from experimental results. Even if there was a difference in prestress levels and types of segmental joint, at the beginning, the all segmental beams exhibited the similar linear elastic behavior. The linear behavior was prolonged until the first flexural crack occurred with the loads in Table 3. The linear behavior range was shorter when the prestress level was reduced. The loads of the first flexural crack, P_{cr} and the dominant diagonal crack, P_{sh} increased with the increase in the prestress level in the beams with dry joint. This tendency was similar to segmental beams with epoxy joint (Nguyen et al. 2010) as shown in Figure 12. The loads at the first flexural crack and the dominant diagonal crack occurred in the beams with epoxy joint was slightly smaller than those in beams with the dry joint in the similar prestress level. The ultimate capacity of DSJ10-06 was about 5% smaller than that of SJ10-06, while the ultimate capacity of DSJ10-10 is was 1% smaller than that of SJ10-10 in the previous study (Nguyen et al. 2010).

4.3 Failure Mechanism

In SJ10-06, by effect of bonding behavior of epoxy, before the occurrence of the dominant diagonal crack, joint opening was quite small, and the accumulated energy was firstly dissipated by the flexural cracks. After the occurrence of flexural cracks, the joint opened. The joint opened from the lower level up to the lower corner of the middle shear key, and then the dominant diagonal crack formed toward the loading point. The shear force transferred from the large to the small segments in the whole contact area of the segmental joint above the dominant diagonal crack. The failure at the base of lower shear key (Nguyen, et al. 2010) did not appear in SJ10-06, because the epoxy had not fully hardened yet as shown in Figure 13.

In DSJ10-10 and DSJ10-06, the load at the first flexural crack of the beams with dry joint was slightly larger than that in beams with epoxy joint at the similar prestress level. The reason is, without the bonding effect of epoxy, the joint opened largely before the occurrence of the first flexural crack as the applied load increased as shown in Figure 6. Hence, the deformation of the beams with dry joint was firstly accumulated by the joint opening. The increase in the interlock of shear keys where the joint opened with the increase in the applied load leaded to the occurrence of the flexural cracks in these beams.

Then, the joint opened up to the lower corner of the upper shear key in the large segment where the first diagonal crack formed as shown in Figure 4. The width of the first diagonal crack increased in visible. This increased the rotation of segments, the joint opening and the interlock in the lower shear keys. Then the dominant diagonal crack formed. The width of the dominant diagonal crack increased rapidly, while the width of the first diagonal crack was visibly observed to be closed again. After occurrence of the dominant diagonal crack, the height of opening joint above the dominant diagonal crack decreased again. It increased the area to transfer the shear force from the large segment to the small segment in the beams with dry joint as the dominant diagonal crack occurred.

Although there was a difference in the prestress level and joint types the shear failure mode was designated in the tested beams as the shear compression failure. Firstly, the

Table 4 Evaluation of existing equations

Beams	σ_l (N/mm^2)	P_{EXP} (kN)	Modified model		Sivaleepunth's model		Type of joint
			P_{cal} (kN)	P_{EXP}/P_{cal}	P_{cal} (kN)	P_{EXP}/P_{cal}	
SJ10-06	6.77	366.1	333.4	1.10	320.5	1.14	Epoxy
DSJ10-06	7.01	350.1	337.5	1.04	322.4	1.09	Dry
DSJ10-10	11.46	390.2	393.9	0.99	413.7	0.94	Dry
Mean				1.04		1.06	
Standard deviation				0.044		0.084	
Coefficient of variation				0.042		0.079	

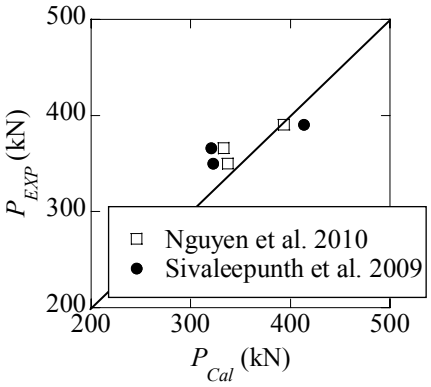

Figure 14 Validation of existing models

dominant diagonal crack was formed toward to the loading point. The final failure took place with the crushing of concrete near the loading point on the shear span.

The results from this experiment showed that the shear carrying capacity of segmental concrete beams with external tendons and dry joint was approximate to that with epoxy joint. That was different from the results in the direct shear test with dry and epoxy joints (Zhou et al., 2005). The shear transfer mechanism of the joint in segmental beams was different from that in the direct shear test. It was because of the effect of joint opening in segmental joint of segmental concrete beams.

5. EVALUATING THE EXISTING EQUATIONS

The applicability of the modified model in previous has limited for segmental beams with epoxy joint and stress at the lower fiber is greater or equal to 10 N/mm^2. The experimental results in this study are used in order to confirm the applicability of the modified model for segmental beams with dry joint and the segmental concrete beams with the concrete stress of lower than 10 N/mm^2.

The experimental results were used to compare the calculated results from the modified model (Nguyen et al. 2010) and the simplified truss model (Sivaleepunth et al. 2009). Table 4 and Figure 14 show the test results and calculated values. It shows that the modified model is capable of predicting the shear carrying capacity of segmental beams with external tendons and dry joint. The modified model can well predict the shear carrying capacity of segmental beams with external tendons and concrete stress at the lower fiber of 6 N/mm^2. Comparison of the mean value, standard deviation and coefficient of variation shows that the shear carrying capacity predicted from the modified model has higher accuracy than that from the simplified truss model.

6. CONCLUSIONS

The shear failure mechanism of segmental concrete beams with external tendons has been presented with the effect of the prestress level and type of joint in this study. The experimental results showed that the joint opening was different between segmental concrete beams with epoxy joint and dry joint before the occurrence of diagonal crack. However, the shear failure mechanism at the ultimate stage in the segmental concrete beams with external tendons and dry joint was similar to that in the segmental concrete beams with external tendons and epoxy joint. The shear failure mode in all tested segmental beams was the shear compression failure mode. The shear failure mechanism of segmental joints in segmental beams was different from that of the segmental joint in the direct shear test. The shear carrying capacity of segmental concrete beams with dry joint predicted from the modified model had higher accuracy than that from the simplified truss model. The modified model was able to predict the shear carrying capacity of segmental beams with external tendon and the concrete stress at the lower fiber of 6 N/mm^2.

References:

Burgoyne, C. and Scantlebury, R. (2008), "Lessons Learned from the Bridge Collapse in Palau," *Proceedings of the ICE*, Civil Engineering, Vol. 11, No. 6, pp. 28-34.

Zhou, X., Mickleborough, N. and Li, Z. (2005), "Shear Behavior of Joints in Precast Concrete Segmental Beams," *ACI Structure Journal*, **102**(11), 3-11.

Megally, S., Seible, F. and Dowell, R. K. (2003), "Seismic Performance of Precast Segmental Bridges: Segment–to-Segment Joints Subjected to High Flexural Moments and High Shears," *PCI Journal*, **48**(3), 72-90.

Kamaitis, Z. (2008), "Field Investigation of Joints in Precast Post-Tensioned Segmental Concrete Bridges," *Baltic Journal of Road and Bridge Engineering*, **3**(4), 198-205.

Lertsamattiyakul, M. (2005), "Simplified Truss Model for Shear Carrying Capacity of Prestressed Concrete Members," *PhD thesis*, Tokyo Institute of Technology.

Nguyen, D.H., Watanabe, K., Niwa, J. and Hasegawa, T. (2010), "Modified Model for Shear Carrying Capacity of Segmental Concrete Beams with External Tendons," *Journal of Materials, Concrete Structures and Pavements*, Japan Society of Civil Engineers, (publishing).

Sivaleepunth, C., Niwa, J., Nguyen, D.H., Hasegawa, T. and Hamada, Y. (2009), "Shear Carrying Capacity of Segmental Prestressed Concrete Beams," *Journal of Materials, Concrete Structures and Pavements*, Japan Society of Civil Engineers, **65**(1), 63-75.

JOINT CONFERENCE PROCEEDINGS
7th International Conference on Urban Earthquake Engineering (7CUEE) &
5th International Conference on Earthquake Engineering (5ICEE)
March 3-5, 2010, Tokyo Institute of Technology, Tokyo, Japan

SEISMIC RESPONSE OF R/C STRUCTURES SUBJECTED TO SIMULATED GROUND MOTIONS COMPATIBLE WITH DESIGN SPECTRUM

Dae-Han Jun[1)]

1) Associate Professor, Department of Civil & Architectural Engineering, Dongseo University, Busan, Korea
jdh@dongseo.ac.kr

Abstract: In seismic response analysis of building structures, the input ground motions have considerable effect on the nonlinear seismic response characteristics of structures. The characteristics of soil and the locality of the site where those ground motions were recorded affect the contents of ground motion time histories. Therefore, it is difficult to select appropriate input ground motions for seismic response analysis. This study describes a generation of synthetic ground motion time histories compatible with seismic design spectrum, and also evaluates the seismic response results of multi-story reinforced concrete structures by the simulated ground motions. The simulated ground motions are generated according to the previously recorded earthquake waves in the past major earthquake events. The simulated ground motion time histories have identical phase angles to the recorded ground motions, and their overall response spectra are compatible with seismic design spectrum with 5% critical viscous damping. The input ground motions applied to this study have identical elastic acceleration response spectra, but have different phase angles. The purpose of this study was to investigate their validity as input ground motion for nonlinear seismic response analysis of building structures. As expected, the response quantities by simulated ground motions presented better stability than those by real recorded ground motions. It was concluded that the simulated earthquake waves generated in this paper are applicable as input ground motions for a seismic response analysis of building structures. It was also found that the intensity of input ground motions for seismic analysis are suitable to be normalized as elastic acceleration spectra.

1. INTRODUCTION

An earthquake acceleration wave is only to represent the time histories of free field shaking of a specific site caused by an earthquake event. In other words, any one input motion adopted in the seismic response history analysis of building structures is nothing but a ground motion on a specific free field caused by an earthquake event[AIJ, 1992]. A single earthquake event can generate various ground motion time histories with different characteristics. Therefore, any one ground motion does not necessarily represent typical time histories to guarantee the seismic safety of building structures[AIJ, 2004]. It is impossible to predict ground motion characteristics that may occur in the future at a construction site because the property of the ground motion is interrelated with many factors such as fault mechanism, seismic wave propagation from source to site, and the amplification characteristics of ground. The important factors of ground motions affecting structure's response results are peak ground acceleration, frequency contents, duration of ground motion, and shapes of waveform. Though required to set input ground motions for general seismic design including these factors, it is not available at this time[Stewart et al., 2001]. Also, the input ground motions for seismic design need to correspond appropriately to various structural materials and systems. The seismic design guidelines provide an acceleration response spectrum for estimating the design seismic force of a structure. Accordingly, the input ground motion applied to the dynamic response analysis of structures would be appropriate for the ground motion history which is highly related with design seismic force.

In seismic response analysis of multi-story buildings, the selection of input ground motion and adjustment of input intensity level of the selected ground motion are most important for estimating the response results of the structure. The purpose of this study is to evaluate nonlinear response characteristics of real buildings through nonlinear time history analysis on multi-story reinforced concrete structures by inputting simulated seismic waves identical as response spectra, which was focused on design response spectrum as scaling method of the input ground motions. This study also is to evaluate its feasibility as input ground motions for the nonlinear time history analysis of actual buildings by identifying relationships between design response spectra and nonlinear seismic response results of the input ground motions.

2. GENERATION OF ARTIFICIAL GROUND MOTION

The simulation approach used in this study was to manipulate acceleration amplitudes to make acceleration response spectrum of the ground motion which is closely related to the response of structures match design response spectrum, while maintaining same phase angles characteristics of the ground motions recorded in the past earthquakes[Jun and Inoue, 1991].

3. CHARACTERISTICS OF SIMULATED GROUND MOTIONS

Figure 1 shows comparison between simulated ground motion with original recorded ground motion. Lower figures compare also target design spectra and response spectra of simulated ground motions. In the figure, it is apparent that original recorded ground motions and simulated ground motions have similar trends as phase angle characteristics are same. In addition, it is notable that response spectra of recorded ground motions are adjusted in the proximity of the design response spectrum.

Table 1 presents comparison of maximum acceleration value and its occurrence time of recorded ground motions and simulated ground motions which were developed for target response spectrum. The maximum acceleration value of the simulated ground motions adequately developed for design response spectrum is in the range of 322-426cm/sec^2. The occurrence time of the maximum acceleration values of recorded ground motions and simulated ground motions was observed to occur at the almost same time except for El Centro 1940 EW component.

4. NONLINEAR RESPONSE ANALYSIS OF MULTI-STORY FRAME STRUCTURES

4.1 Analytical Model

The analytical model of multi-story frame structures used in this study was a standard plane frame model for reinforced concrete moment resistant system, it can be generally applied in seismic design of building structure as shown in Figure 2. Modeling of the column member for nonlinear analysis utilized fiber models. The sectional dimensions and reinforcement of column and beam used in the structural model are presented in Table 2 and Figure 3, respectively. The characteristics of material are: For steel bar, elastic stiffness E_s=196GPa, yield strength f_y=392MPa; for concrete, elastic stiffness E_c=23GPa, design strength f_{ck}=24MPa. The material stress-strain relationship of concrete and reinforcement used in the analysis are presented in Figures 4 and 5.

4.1 Analysis Method

The nonlinear response analysis of ground motions was performed using CANNY-2004 software[Li, 2004]. Nonlinear time history analysis was used for nonlinear dynamic analysis and Newmark β method (β=0.25, γ=0.5) was used for numerical integration method. A Rayleigh damping was applied in the nonlinear time history analysis and horizontal input ground motion was used to perform nonlinear analysis.

4.3 Elastic Seismic Response Analysis

In elastic seismic response analysis, scaling of input ground motion is simple as the maximum response value is proportional to a prescribed ground shaking intensity level. Elastic response quantities of multi-story frame structures are determined by the dynamic property of the structural model and the elastic response spectrum characteristics of the input ground motions. The purpose of this research was to examine the variations of response results on each floor of the multi-degree-of-freedom system inputting different ground motions for the same structural model.

Here the scaling of the input ground motion was adjusted to obtain elastic response displacement of 36.5cm on the top floor (deformation angle H/100 radian, where H: total building height). Scaling factors(SF1) for elastic seismic response analysis of each input ground motion are shown in Table 1. The scale factors are modified through trial and error such that the roof displacement calculated from the scaled input ground motions accords with the target response displacement. It indicates that the recorded ground motions have the substantial change of SF1 reflecting elastic response spectrum characteristics and dynamic property of the dynamic model. However, it was previously expected that the SF1 value would be constant because the response spectrum characteristics was scaled regularly for the simulated ground motions. But a slight variation was observed as the response spectrum characteristics of each wave cannot be exactly consistent with the theoretical values of the simulated ground motions.

The seismic response results of the buildings for height-wise distribution of story displacement, inter-story drift, and story seismic force are shown in Figures 6~9 for simulated ground motions and recorded ground motions, respectively. In figure 6, the displacement distribution of lower floor was similar because the lateral displacement of the top floor was same. In the case of simulated ground motions, the response values of story displacement on all stories showed less than 3% differences, whereas the recorded ground motions in the middle stories had approximately 15% differences depending on the type of input ground motion. Figure 7 presents inter-story deformation angle distributions with input ground motions. It was verified that the response values by the simulated ground motions were less variable compared to those by the recorded ground motions.

Figures 8 and 9 represent the distribution of story seismic force and shear force on each story. Each figure shows that the response variance of the simulated ground motion is apparently smaller than that of the recorded ground motion, regardless of the input ground motions. It is also shown that the response variation of story force is greater on upper and lower stories compared to the middle stories depending on the type of the input ground motion.

4.4 Nonlinear Seismic Response Analysis

Nonlinear seismic response is different from elastic

seismic response and the response results are very complicated due to characteristics of input ground motion, dynamic property of the structures, and the influence of hysteresis model for structural component. Particularly, hysteresis model for structural member is a critical factor to determine response characteristics of multi-story frame structures. Therefore, the purpose of this analysis is to evaluate the nonlinear responses of each story of structures by changing only the input ground motion characteristics for multi-story frame structures which have same dynamic model and hysteresis characteristics. The nonlinear seismic response analysis was evaluated for story displacement, inter-story deformation, story seismic force, and story shear force just as the elastic seismic response analysis.

Here, the intensity of the input ground motion was scaled to obtain the elastic response displacement of 36.5cm on the top floor (deformation angle H/100 radian, where H: total building height) followed by evaluation of nonlinear response results of multi-story frame structures. Scaling factors (SF2) for nonlinear response analysis of each input ground motion are shown in Table 1. In Table 1, the recorded ground motions show a wide difference of scaling factors between 0.79 and 6.00 depending on the type of the ground motion. For simulated ground motions, the SF2 values were relatively less variable with coefficient range of 1.32-2.08 because the response spectrum was primarily scaled constantly for simulated ground motions.

The seismic responses of the buildings for distribution of story displacement, inter-story drift, and story seismic force are shown in figures 10~13 for simulated ground motions and recorded ground motions, respectively. In figure 10, the story displacement distribution of lower floor was similar as the roof displacement was adjusted same. In the case of the simulated ground motion waves, the response quantities of story displacement on all stories showed less than 5% differences, whereas the recorded ground motion waves in the middle stories had approximately 20% differences depending on the type of input ground motion. Both the simulated ground motion and the recorded ground motion resulted in greater difference for nonlinear response compared to elastic response. Figure 11 presents interstory drift angle distributions according to different input ground motions. It was confirmed that the response results by the simulated ground motions were less variable compared to those by recorded ground motions. Recorded ground motions in particular indicated that the response variations were greater in the middle stories. This could be due to the effect of the higher mode of the recorded ground motions.

Figures 12 and 13 represent the distribution of story seismic force and story shear force on each floor. Each figure shows that the response variances of the simulated ground motion are smaller than those of the recorded ground motion, regardless of types of input ground motions. Apparently, several waves of the recorded ground motions showed large response values compared to other ground motions. As such, these ground motions are classified as inappropriate waves to be chosen as input ground motions for seismic design, as indicated in other research[Zhai and Xie, 2007]. Likewise, the response values of the recorded ground motions in middle stories show greater variance than those of simulated ground motions. These results may be possible because the recorded ground motions had great effect on response results of the short period range corresponding to higher mode. In case of the simulated ground motion, the decrease of the short period component and amplification of the long period component resulted in relatively small effect on response results of short period structure.

When examined in the basis only results of the analytical model used in this paper, it was found from the presented figures that the response variances of simulated ground motions were smaller than those of recorded ground motions. However, the input intensity of the simulated ground motions, that is, the scaling up of the response spectrum was not always proportional to the response value of each story, and the nonlinear response value was dependent on the property of the ground motions. Furthermore, it needs to be examined how the response distribution of recorded ground motions in the middle stories had greater variance. The small variance of the response distribution of the simulated ground motions on all stories was thought to be caused by the decreased influence of the specific period component included in the ground motions. In the future, more researches need to be performed with various structural models and recorded ground motions. And also, the proposed response analysis method in this study is necessary to verify if the simulated ground motion histories generated by this study can be used as input ground motion for seismic design.

3. CONCLUSIONS

The seismic safety of building structures can be evaluated by the nonlinear behavior of structures induced by ground motions. The characteristics of input ground motions and dynamic property of the structure are important factors to affect seismic response of structures. Ground motions used in the seismic response analysis of structure include various characteristics depending on fault mechanism of earthquake, wave propagation, and amplification of soil type. As the result of the analysis, it is a difficult task to quantitatively examine all affecting factors. In seismic design, design response spectrum generally represents the response characteristics of structural model. In this study, a simulated ground motion suitable for design spectrum was developed and its feasibility for the input ground motion was evaluated through nonlinear seismic response analysis of the multi-story frame structures. The results obtained from this study can be summarized as follows.

1) The response results of simulated ground motions by each floor presented better stability than those by recorded ground motions.

2) The simulated ground motions scaled to design elastic spectrum was confirmed to show less differences in nonlinear responses by each floor.

3) The simulated ground motions generated in this paper can be applied as the input ground motions for a nonlinear response analysis of high-rise building structures.

Acknowledgements:

This work was supported by the Korea Science and Engineering Foundation(KOSEF) grant funded by the Korea government(MEST)(No. 2009-0071519)

References:

Architectural Institute of Japan.[1992] "Seismic Loading-strong motion prediction and building response(in Japanese)," Tokyo.

Architectural Institute of Japan.[2004] "Guidelines for performance evaluation of earthquake resistant reinforced concrete buildings(draft)(in Japanese)," Tokyo.

Aschheim M., Tjhin T., Cormartin C., Hamburger R. and Inel M. [2007] "The scaled nonlinear dynamic procedure," Engineering Structures, Vol. 29, 1422-1441.

Hancock J., Bommer J. and Stafford P.J. [2008] "Numbers of scaled and matched accelerograms required for inelastic dynamic analyses", Earthquake Engineering and Structural Dynamics, Vol.37,1585-1607.

Jun Dae-Han and Inoue Yutaka. [1991] "Inelastic response of single-degree-of-freedom systems subjected to artificial ground motions(in Japanese)", Journal of Structural Engineering, Vol.37B, 111-118.

Kurama Y.C.. and Farrow, K.T.[2003] "Ground motion scaling methods for different site conditions and structure characteristics", Earthquake Engineering and Structural Dynamics, Vol.32, No.15, 2423-2450.

Li Kang-Ning.[2004] "CANNY:3-dimensional nonlinear static/dynamic structural analysis computer program-User Manual," CANNY Structural Analysis, CANADA.

Moehle J.P.[2006] "Seismic analysis, design, and review for tall buildings", The Structural Design of Tall and Special Buildings, Vol.15, 495-513.

Naeim F. and Lew M.[1995] "On the Use of Design Spectrum Compatible Time Histories", Earthquake Spectra, Vo.11, No.1, 111-127.

Stewart J.P., Chiou S., Bray J.D., Graves R.W., Somerville P.G., and Abrahamson N.A.[2001] "Ground motion evaluation procedures for performance-based design," PEER-2001/09, PEER, University of California.

Zhai Chang-Hai and Xie Li-Li.[2007] "A new approach of selecting real input ground motions for seismic design: The most unfavorable real seismic design ground motions", Earthquake Engineering and Structural Dynamics, February, Vol.36, 1009-1027.

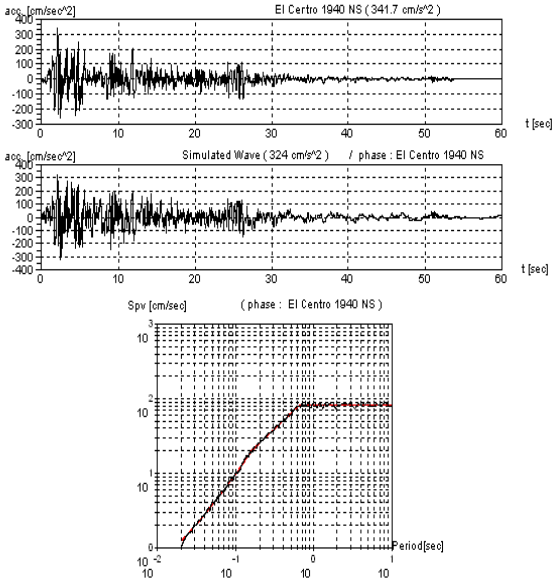

Figure 1 Comparison of El Centro 1940 NS component

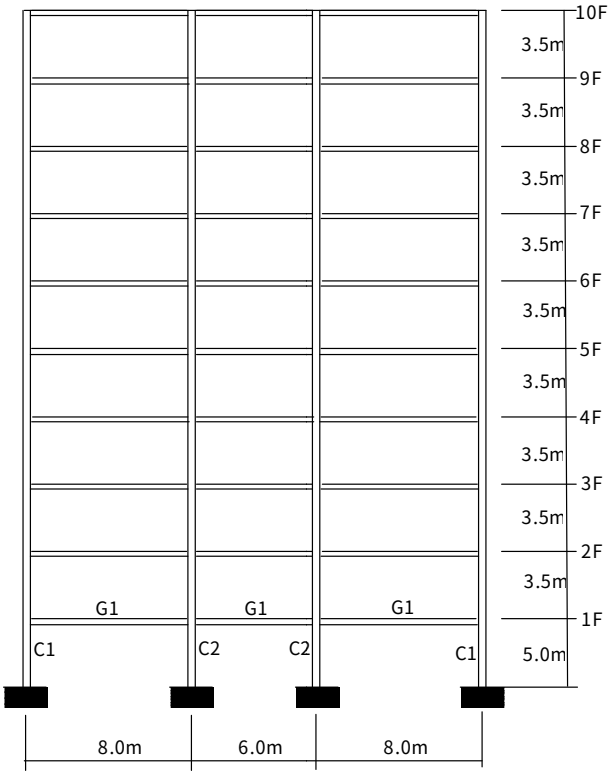

Figure 2 Structural model

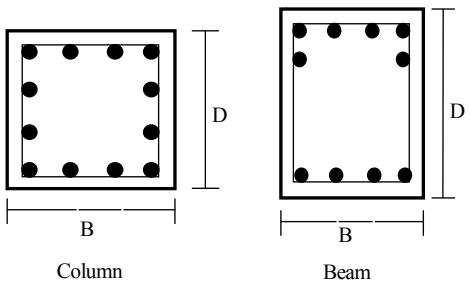

Figure 3 Member cross sections

Table 1. Comparison of maximum acceleration values for recorded and simulated ground motions(Unit: cm/sec^2, sec)

Type of ground motion wave	Recorded ground motion				Simulated ground motion			
	Max	Time	SF1*	SF2**	Max	Time	SF1*	SF2**
JMA Kobe 1995 NS	819.1	4.94	0.75	1.16	415.3	5.54	2.06	1.55
JMA Kobe 1995 EW	617.1	8.46	0.99	1.65	401.1	8.47	2.09	2.05
Taft 1952 NS	152.7	9.10	5.73	4.30	369.3	6.62	2.03	1.32
Taft 1952 EW	175.9	3.70	6.73	6.00	426.3	3.71	1.98	2.08
EL Centro 1940 NS	341.7	2.12	2.21	2.48	324.0	2.08	1.96	1.92
EL Centro 1940 EW	210.1	11.44	3.41	2.48	321.6	2.03	2.09	1.50
Mexico city 1985 NS	98.0	24.16	6.00	1.10	353.4	39.86	1.94	1.70
Mexico city 1985 EW	167.9	28.08	3.98	0.79	336.6	33.38	2.05	1.65

* SF1: Scaling Factor for elastic response analysis ** SF2: Scaling Factor for non-linear response analysis

Table 2. Member cross section and reinforcement

(a) Column (C1, C2)

Story	Size B×D(cm)	Reinforcement
1 ~ 3	60 × 60	12 – D22
4 ~ 6	50 × 60	12 – D22
7 ~ 10	50 × 50	8 – D22

(b) beam (G1)

Story	Size B×D(cm)	Upper bar*	Lower bar*
All	35 × 60	6 – D19	4 - D19

*Denotes beam`s both ends

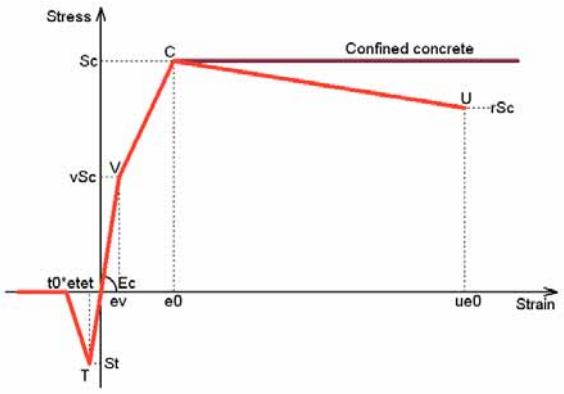

Figure 4. Stress-strain relationship of concrete

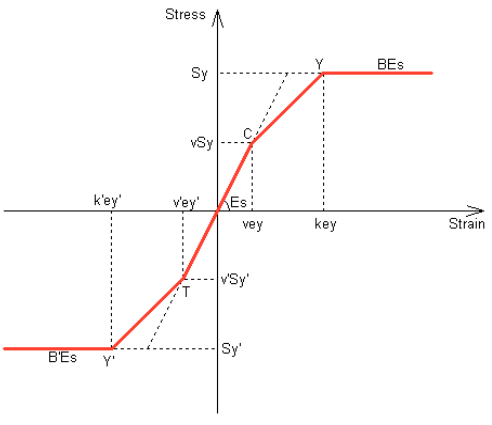

Figure 5. Stress-strain relationship of steel bar

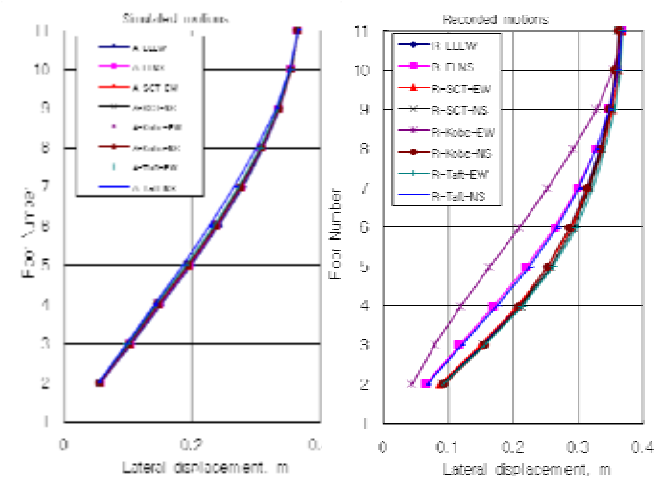

Figure 6. Distribution of story displacement

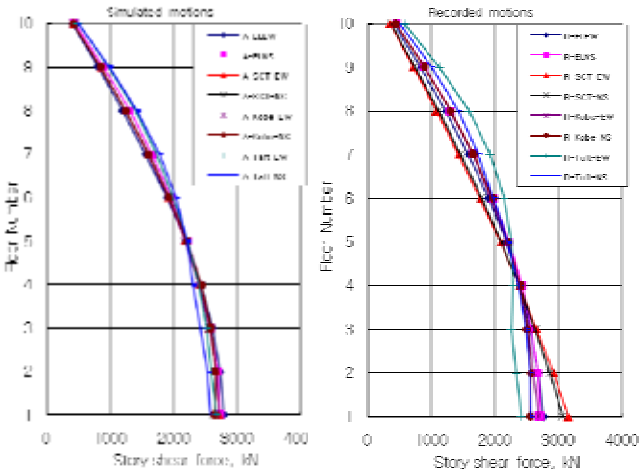

Figure 9. Distribution of story shear force

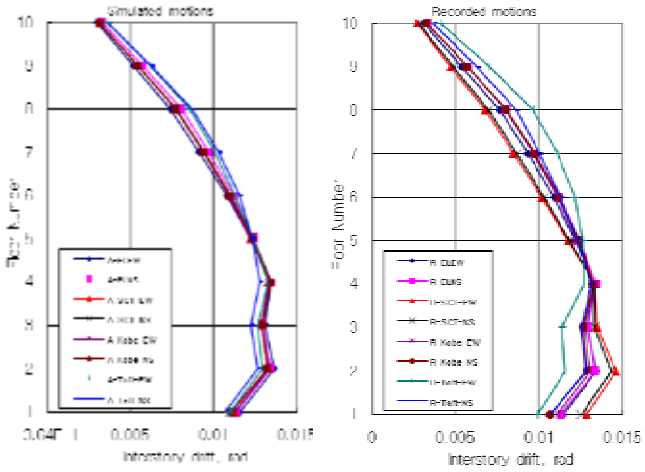

Figure 7. Distribution of inter-story deformation angle

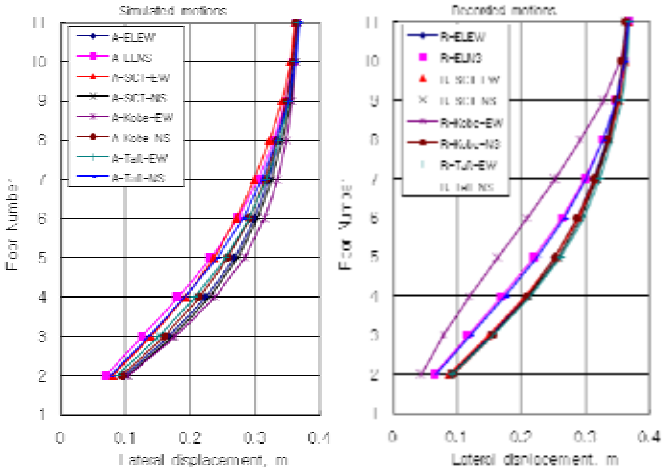

Figure 10. Story displacement distribution by non-linear analysis

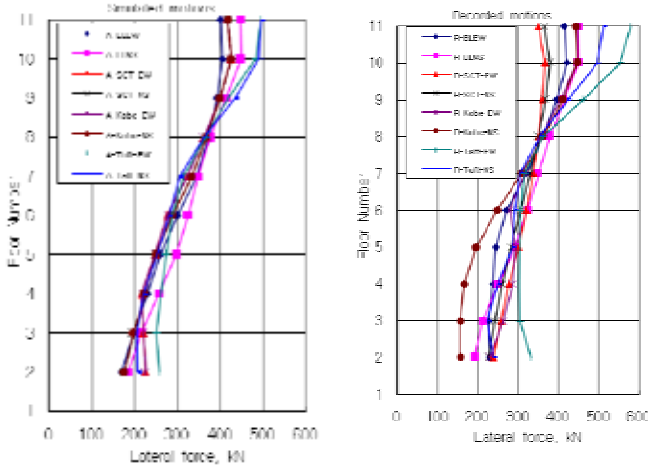

Figure 8. Distribution of story seismic force

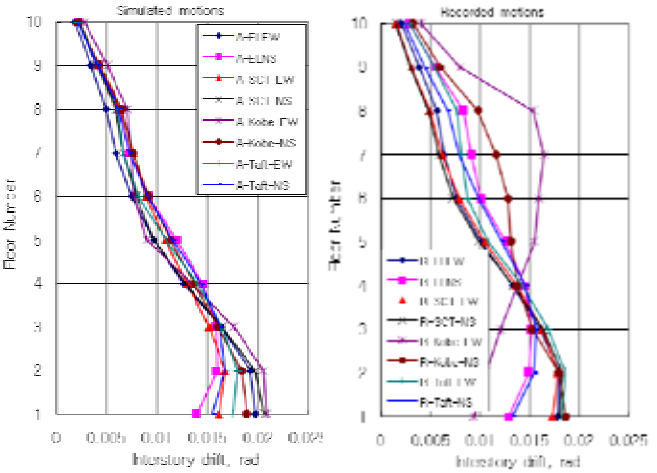

Figure 11. Story deformation angle distribution by non-linear analysis

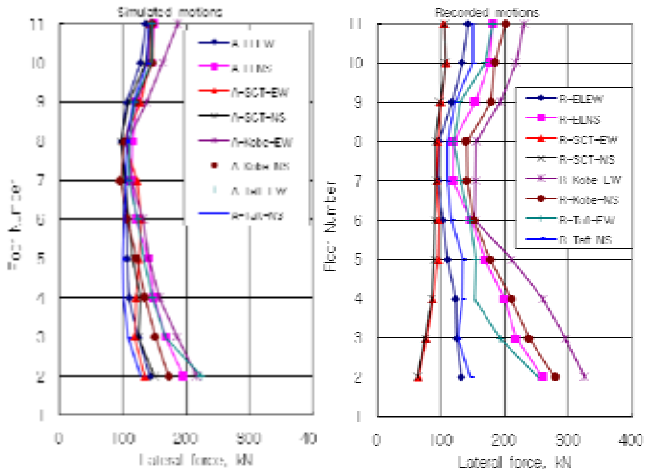

Figure 12. Story seismic force distribution
by non-linear analysis

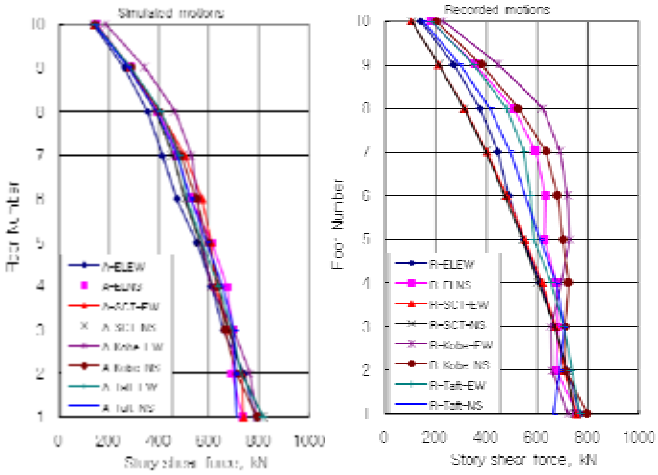

Figure 13. Story shear force by non-linear analysis

JOINT CONFERENCE PROCEEDINGS
7th International Conference on Urban Earthquake Engineering (7CUEE) &
5th International Conference on Earthquake Engineering (5ICEE)
March 3-5, 2010, Tokyo Institute of Technology, Tokyo, Japan

TESTING OF AN EARTHQUAKE-DAMAGED UNREINFORCED MASONRY BUILDING

Dmytro Dizhur[1)], Ronald Lumantarna[1)], Hossein Derakhshan[1)], and Jason Ingham[2)]

1) PhD Candidate, Department of Environmental and Civil Engineering, University of Auckland, Auckland, New Zealand
2) Associate Professor, Department of Environmental and Civil Engineering, University of Auckland, Auckland, New Zealand
ddiz001@aucklanduni.ac.nz, rlum009@aucklanduni.ac.nz, hder004@aucklanduni.ac.nz, j.ingham@auckland.ac.nz.

Abstract: In December 2007 a magnitude 6.8 earthquake had an epicentre located approximately 50 km from the city of Gisborne, New Zealand. This earthquake caused damage to a number of buildings in Gisborne, and in particular, to numerous unreinforced masonry buildings. One such building was damaged to the extent that significant post-earthquake repairs were necessary, and partial removal of two of the building's gable ended walls was required. This reconstruction allowed an opportunity for a team of researchers from the University of Auckland to conduct field tests on the building, allowing comparison with companion experiments that had previously been undertaken in a laboratory setting. This field testing involved the extraction of clay brick and mortar samples, in-situ bed joint shear tests, diagonal shear tests on samples extracted from the gabled walls, an in-situ in-plane shear test and out-of-plane testing of the gable ended wall both in the as-built condition and after the installation of a near-surface mounted (NSM) carbon fibre reinforced polymer (CFRP) retrofit solution. Testing confirmed that the boundary conditions in real buildings can significantly affect experimental response, with vertical restraint resulting in large increases in out-of-plane load capacity, and also confirmed that the near-surface mounted FRP solution is an excellent low-invasive option for seismic strengthening of unreinforced masonry. Details of the history of the building, and the methods used to undertake the field testing are reported, and experimental results are presented.

1. INTRODUCTION

Unreinforced masonry (URM) was one of the most common construction material in New Zealand prior to the 1931 Hawke's Bay earthquake (Dowrick 1998). The popularity of this form of construction has resulted in numerous URM buildings remaining throughout New Zealand, many of which are now considered to have significant national heritage value (Russell 2010). This type of construction often has insufficient strength to resist lateral earthquake forces in high and moderate seismic zones and lacks the ability to dissipate energy.

On 20 December 2007 at 8:55pm, a Richter magnitude 6.8 earthquake occurred with an epicentre located approximately 50 km from the city of Gisborne in New Zealand (GNS 2008). Even though there were no directly related fatalities, the earthquake caused damage to a number of buildings in Gisborne's central business district (CBD), which has a collection of historic buildings dating from the 1880s that are predominantly built of unreinforced masonry and timber. There were numerous instances of cracked walls and partial collapse, particularly in unreinforced masonry buildings, but most houses and commercial buildings were not significantly damaged (McClean and Wallace 2009). It has been estimated that up to 90% of the earthquake damage was attributed to over-topped parapets in unreinforced masonry buildings (Petty 2008). One such building, the B-East building of the Allen's Trade Complex, was damaged to the extent that significant post-earthquake repairs were necessary, and this required partial removal of two gable ended walls.

As most research considering seismic assessment of URM walls has been conducted using laboratory-based studies with artificial boundary conditions, in-situ testing is an important opportunity to provide data to validate the accuracy of laboratory-based studies on wall behaviour. In 2009, the reconstruction of the subject building and the removal of the aforementioned earthquake damaged end gables presented an opportunity for a team of researchers from the University of Auckland to conduct field tests on the building, allowing comparison with companion experiments that had previously been undertaken in a laboratory setting. A number of tests were performed on the building on site and in the laboratory on extracted wall samples. In particular, this field testing involved the extraction of clay brick and mortar samples, in-situ bed joint shear tests, diagonal shear tests on samples extracted from the gabled walls, an in-situ in-plane shear test and out-of-plane testing of the gable ended wall both in the as-built condition and after the installation of a near-surface mounted (NSM) carbon fibre reinforced polymer (CFRP) retrofit solution. Test results and discussions are presented here.

2. DESCRIPTION OF TESTED BUILDING

Allen's Trade Complex has had a number of varied uses throughout its life, ranging from a storage warehouse to mechanical workshop and gathering center for a community trust. The complex is comprised of five main buildings, one of which suffered significant structural damage during the 2007 Gisborne earthquake. Testing was performed on the earthquake damaged B-East building facing Pitt Street (Refer Figure 1) that was originally constructed in 1911. In 1984 the B-East building was registered as a heritage building with the New Zealand Heritage Places Trust (NZHPT), and as such the option of complete demolition of the building was not considered, and any strengthening and securing works had to be sensitive to the existing building fabric and be designed in consultation with Gisborne District Council and the NZHPT.

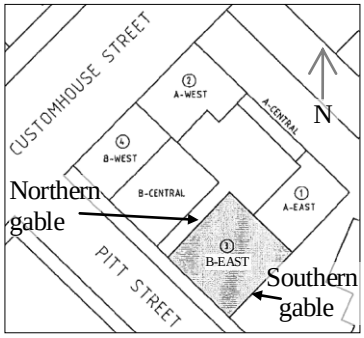

Figure 1 Allen's Trade Complex location map

The 2 storey building (shown in Figure 2) is located in the CBD of Gisborne, New Zealand, and was originally constructed of unreinforced masonry with perimeter walls comprised of 2 to 4 leaf thick solid masonry. The building has an almost square footprint of approximately 390 m^2. The first level floor diaphragm is constructed from timber joists and timber tongue and groove flooring and the roof of the building is a single gable constructed from timber framed trusses clad with corrugated iron sheets supported on wooden rafters. Both the roof and the floor diaphragms are connected to the perimeter walls using through steel anchors. The main masonry type for the original building consisted of red coloured soft bricks with soft lime/cement mortar.



(a) (b)

Figure 2 Allen's Trade Complex B-East building: (a) view facing north, (b) view facing north east

The B-East building was originally sandwiched between the existing timber framed building adjacent to the northern end gable (sharing the wall with B-East building) and the demolished building that used to be adjacent to the southern end gable. Although the exact date of demolition is uncertain, the removal of the adjacent building left the masonry of the southern end gable exposed to the environment for over a decade. There were two concrete ring beams extending along the perimeter of the building, one at approximately mid-height of the ground floor level and the second approximately at mid-height of the first floor level.

2.1 The Gisborne Earthquake Damage

During the 2007 Gisborne earthquake the B-East building suffered extensive structural damage (shown in Figure 3) to the extent that significant post-earthquake repairs were necessary and the removal of two gable ended walls was required. As a result the building was designated unstable and unsafe to occupy until reconstruction took place. Following the 2007 Gisborne earthquake it was



(a) (b)



(c)

Figure 3 B-East building damage due to 2007 Gisborne earthquake: (a) and (b) cracking of the top gable corners, (c) roof anchor pull-out

observed that there were numerous visible cracks in the vicinity of the window piers and wall corners. As shown in Figure 3 (a) and (b) the top portion of the northern gable corner separated from the cross wall, causing the entire top portion of the southern gable to permanently deform outwards from the roof diagram. The northern gable sustained less damage, with only a small number of crack locations. Due to its instability and safety considerations, the top portion of the southern end gable required demolition prior to the commencement of any testing. There were a number of locations where the anchors connecting the top of the gable to the roof diaphragm were pulled out from masonry, as shown in Figure 3 (c).

2.2 Description of Test Locations

Testing was performed only on the earthquake affected end gables which were scheduled for demolition, and occurred in two separate stages. The first stage of testing focused mainly on the in-plane behaviour and was conducted on the southern gable of B-East building. Prior to any test commencement the unstable 2 leaf portion of the gable and the upper concrete ring beam had been removed. The wall structure below the unstable portion of the gable consisted of 3 leaf thick masonry and 'masonry columns' (with increased wall thickness to 4 leafs) spaced at approximately 3000 mm. The individual test locations were selected in the 3 leaf thick masonry wall only, and the 4 leaf thick masonry columns were avoided. The second stage of testing focused on the northern gable which, apart from a few crack locations, was mostly undamaged during the earthquake. This gable consisted of a 2 leaf thick masonry wall and had a cement/lime plaster layer on the exterior surface. A mezzanine floor positioned 2500 mm above the first floor level was adjacent to both gables.

3. MATERIAL PROPERTIES

The material properties of B-East building were determined through in-situ testing and laboratory tests on samples that were extracted from walls scheduled for demolition. From visual observation, the constituent materials of the building were of average quality. The mortar joints from the northern gable were less weathered and slightly darker in colour than those from the southern gable, suggesting that the mortar from the northern gable had higher cement content.

Figure 4 illustrates the masonry type resident within the wall that was subjected to in-situ tests and sample extraction. This type of masonry was uniform throughout the building, and consisted of 75 mm × 220 mm × 105 mm red solid clay bricks, and 12 mm thick cement-lime mortar. Irregular mortar samples, single bricks and three brick high masonry prisms were extracted from the building site and tested in the laboratory.

3.1 Brick Compressive Strength

The brick compression strength was obtained using the half brick compression test method ASTM C 67-03a (ASTM 2003b). The average half brick compressive strength, f'_b, and the coefficient of variation are presented in Table 1. The bricks were classified as stiff bricks based on their physical appearance, according to the New Zealand Society for Earthquake Engineering (NZSEE 2006) guidelines for seismic assessment and strengthening of structures.

Table 1 Average half brick compressive strength (f'_b) and NZSEE (2006) suggested values

Sample Size	f'_b (MPa)	Range (MPa)	CoV	NZSEE recommendation (MPa)
9	19.4	16.5–26.1	0.158	10 – 20

The compressive strength of the bricks was found to be between 16.5 and 26.1 MPa with an average of 19.4 MPa, which is in good agreement with the NZSEE recommendation for the corresponding brick type.

3.2 Masonry prism compressive strength and Young's Modulus

Six 3-brick high masonry prisms were extracted from the northern gable of the B-East building and tested in compression in accordance with ASTM 1314 (ASTM 2003a). Displacement gauges were incorporated in the masonry prism testing setup to obtain the stress-strain response, and to calculate the Young's Modulus, which was obtained as the slope of the stress-strain curves between 0.05 and 0.33 times the maximum prism compressive strength (f'_m). The average compressive strength and Young's Modulus value (E) of the samples are presented in Table 2.

Table 2 Average masonry prism compressive strength (f'_m) and Young's Modulus (E)

Sample Size	f'_m (MPa)	f'_m CoV	E (GPa)	E CoV	E/f'_m
6	9.6	0.283	2.45	0.322	286

3.3 Mortar bed joint shear strength

The mortar bed joint shear strength was determined on-site using the in-situ shear test procedure ASTM C 1531-03 (ASTM 2003) as shown in Figure 4. A total of ten in-situ shear tests were performed, with four tests performed on the northern gable and six tests performed on the southern gable. Flatjack devices were used to apply axial precompression load during tests 2 to 5, 9 and 10. The shear test results are presented in Table 3.



Figure 4 Typical mortar bed joint shear test setup

Table 3 In-situ shear test results

Test Number	Location	Shear Strength (MPa)	Axial Precompression Load (MPa)
1	SG - exterior	0.15	0.016
2	SG - exterior	0.24	0.082
3	SG - exterior	0.25	0.180
4	SG - interior	0.16	0.007
5	SG - interior	0.13	0.230
6	SG - interior	0.19	0.310
7	NG	0.90	0.059
8	NG	0.94	0.080
9	NG	0.90	0.390
10	NG	0.69	0.470

Note: SG – southern gable, NG – northern gable

Table 3 shows that the average mortar bed joint shear strength of the southern end gable was significantly lower than that of the northern end gable. The significant difference in the mortar bed joint shear strength was attributed to a higher level of deterioration of the mortar joints in the southern gable than that in the northern gable and to the possible variation in mortar mixes during wall construction. It was observed that the bed joint shear strength was not significantly affected by the change of axial precompression load.

For this building, the cohesion values can be assumed as the average of shear strengths at different levels of axial precompression for each wall, and therefore are equal to 0.86 MPa and 0.19 MPa for the northern and southern gables respectively.

4. EXPERIMENTAL PROGRAM

On site testing was divided into two stages to reduce the interruptions for the operating construction company. The first stage of site testing involved the southern gable only, and investigated masonry in-plane behavior. In order to accuratly determine the diagonal masonry shear strength and to provide direct comparison to laboratory-built wall panels, six wall panels having approximate dimensions of 1200 mm × 1200 mm were cut, extracted and transported to the University of Auckland laboratory for testing. Due to time restrictions on site, only one wall panel was tested in diagonal shear in-situ (data not included due to equipment malfunction). To further investigate the in-plane strength capacity and the failure mechanism of the existing masonry, a push over test was performed on a 2600 mm long × 1300 mm high and 3 leaf thick wall section.

The second stage of site testing involved the northern gable and focused mainly on investigating masonry out-of-plane behavior. The particular focus was to conduct one way out-of-plane bending test on an as-built wall strip that was separated from a larger wall section. Following the completion of the as-built test the test wall was retrofitted (repaired) using the Near Surface Mounting (NSM) technique with a single CFRP strip embedded into the masonry. The purpose of the repair was to observe the effects that the NSM retrofit technique had on wall strength and stiffness.

5. WALL PANEL EXTRACTION AND DIAGONAL SHEAR TEST

5.1 Extraction Procedure

The locations of the wall panels were carefully selected to minimise the required length of masonry cutting, the cutting locations were clearly marked and the vertical cuts were made using a concrete cutting chainsaw. In order to extract the wall panels, two through penetrations per panel were made to allow lifting straps to be used. To prevent the panels from cracking or breaking during lifting and/or transportation, each wall panel was vertically strapped with two heavy duty ratchet tie downs. This secured the masonry together by applying axial force to minimise the risk of damage. Once the cutting and securing work was completed the wall panels were lifted out of the building and onto a truck using a medium sized crane, and transported to the University of Auckland in an undamaged condition. Wall panel preparation and extraction is shown in Figure 5.



(a) (b) (c) (d)

Figure 5 Wall panel preparation and extraction: (a) cutting through masonry, (b) vertical straps, (c) lifting wall panels using a medium sized crane, (d) wrapping wall panels with protective plastic

5.2 Diagonal Shear Laboratory Test

The wall panels were tested in diagonal shear (in accordance with ASTM E519 – 02) (ASTM 2002). The testing procedure involved rotation of the URM wall panel by 45° and vertical loading along one of the wall's diagonals. For testing of the wall panels extracted from B-East building the standard method was modified such that the wall remained vertical in its original orientation and the loading mechanism was rotated. The test setup is shown in Figure 6.

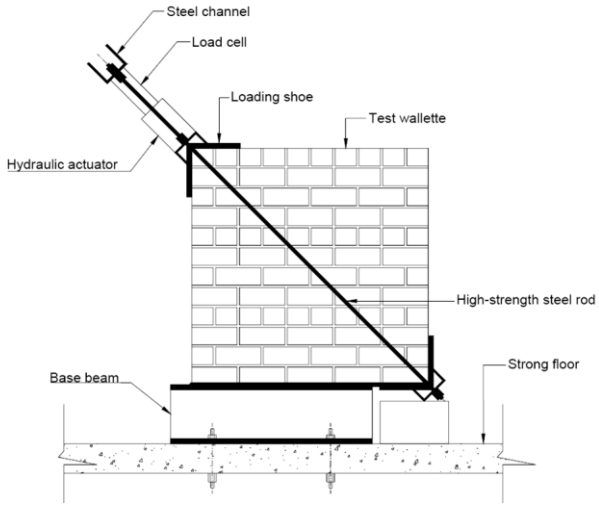

Figure 6 Diagonal shear test setup

5.3 Test Results

All wall panels failed by crack propagation through the mortar joints in a step-wise mode, with the final crack patterns illustrated in Figure 7. In order to provide direct comparison to the results obtained from laboratory-built wall panels and facilitate interpretation and use of the data by structural engineering practitioners, the wall panel displacements are reported as drift angles as shown in Figure 7. It should be noted that test panel AGW2 (as-built Gisborne wall panel 2) suffered minor damage during the setup preparation in the laboratory, resulting in the sample being pre-cracked at the 7th brick course from the bottom. This is visible in the crack pattern shown in Figure 7 (b) and is responsible for the reduction in shear stress at cracking that is illustrated in Figure 8.

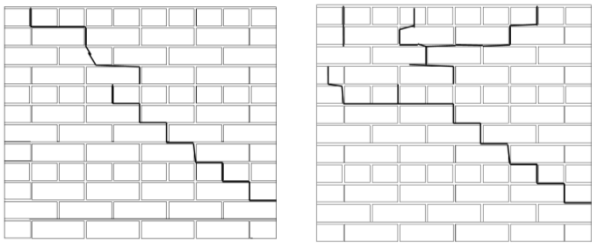

(a) (b)

Figure 7 Crack pattern: (a) AWG1 and AWG3, (b) AWG 2

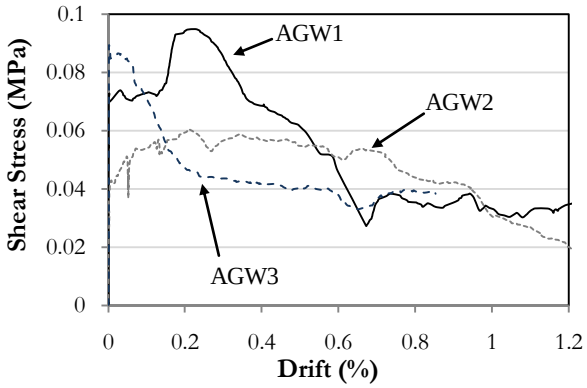

Figure 8 Shear stress - drift response for wall panels in diagonal shear

5.4 Discussion

The diagonal shear strength varied among the tests, but within reasonable limits for masonry type construction. With the exclusion of the pre-damaged wall panel AGW2 the average shear stress at cracking was 0.082 MPa, with a maximum average shear stress of 0.092 MPa. The crack pattern observed at failure closely matched the pattern obtained in laboratory-built wall panels with weaker mortar mixes (Russell 2010). For AGW1 and AGW2 the maximum shear stress was higher than the shear stress at cracking, which has not been observed in laboratory-built samples where shear stress decreased instantaneously after cracking. Table 4 compares the results from laboratory-built wall panels constructed using different mortar mixes to wall panels extracted from B-East building. The results from B-East building wall panels closely resemble values obtained from wall panels manufactured in the laboratory with 1:2:9 mortar mix (cement:lime:sand). The average maximum shear stress for the laboratory-built wall panels using a 1:2:9 mortar mix was 0.094 MPa, which compares well to the 0.082 MPa mean value obtained from B-East building wall panels. Laboratory built wall panels using a weaker mortar mix of 0:1:3 and a stronger mortar mix of 2:2:9 resulted in maximum shear stresses of 0.04 MPa and 0.50 MPa respectively, which were outside the range obtained from wall panels from the B-East building.

Table 4 Summary of wall panel diagonal shear tests

Wall panel	Shear stress at cracking (MPa)	Drift % at cracking	Maximum shear stress (MPa)	Drift % at maximum shear stress
AGW1	0.074	0.032	0.095	0.230
AGW2	0.042	0.010	0.060	0.210
AGW3	0.089	0.026	0.089	0.026
LAB1 (1:2:9)*	0.110	0.010	0.074	0.020
LAB2 (1:2:9)*	0.094	0.002	0.094	0.002
LAB3 (1:2:9)*	0.090	0.020	0.090	0.020
LAB4 (1:2:9)*	0.090	0.009	0.090	0.009
LAB5 (1:2:9)*	0.100	0.020	0.100	0.020
LAB6 (1:2:9)*	0.080	0.009	0.080	0.009
LAB7 (0:1:3)*	0.040	-	0.040	-
LAB8 (2:2:9)*	0.500	-	0.500	-

* - (1:2:9) refers to the ratio of cement:lime:sand (by volume) used in the mortar mix.

6. IN-PLANE PUSH TEST

In-plane response assessment for New Zealand URM walls currently relies on limited data obtained from laboratory-built walls in New Zealand and the NZSEE (2006) guidelines, which have primarily been developed using research data obtained from other countries. The objective of this in-situ push test was to acquire results to compare with corresponding data obtained from laboratory-based experiments.

6.1 Test Location and Setup Description

The test wall area was selected to have a maximum possible length, which was constrained by the location of the masonry columns. The selected location was on the first level of the building as illustrated in Figure 9. The test section was isolated from the rest of the wall by vertical cuts on both sides of the section and had dimensions of 2.6 m long × 1.3 m (17 bricks) high and 0.33 m wide (three leaf) with no additional axial load present apart from the wall self weight. The wall was painted white to facilitate visual detection of formed cracks during the test.

Load was applied using a hydraulic actuator positioned at the top corner of the test section using the remaining larger part of the masonry wall as a reaction point, and a manual hydraulic pump was used to gradually increase loading of the test section. In-plane wall displacement was measured using 6 portal strain gauges positioned directly on the test section (as shown in Figure 10) to detect any possible rocking and diagonal deformations. Two linear variable differential transducers (LVDTs) were positioned at the top and bottom of the test section on the opposite end from the hydraulic actuator.



Figure 9 In-plane push test location, southern gable

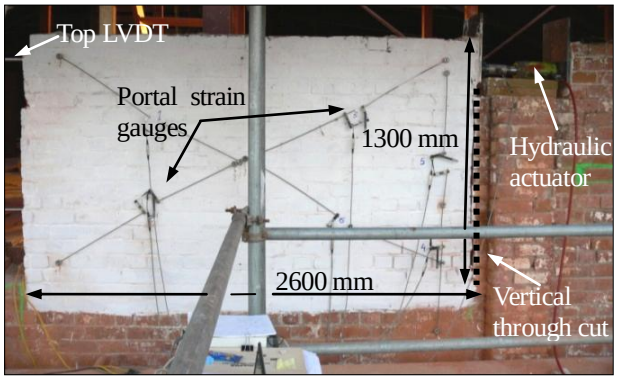

Figure 10 In-plane push test setup

6.2 Experimental Results

Initial cracking was observed at a displacement of approximately 2 mm (0.5% drift) with a corresponding base shear of 9.1 kN. With increasing loading the crack propagated from the loading side in a step-wise pattern through mortar joints and sliding of the section occurred, with the final crack pattern being as shown in Figure 11. The base shear-drift response is shown in Figure 12. Only the displacement values obtained from the top LVDT are reported here.

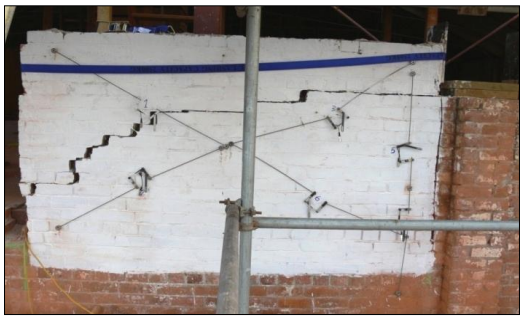

Figure 11 The crack pattern after push test

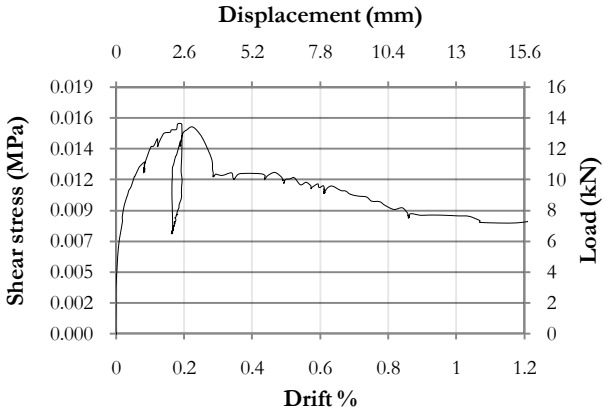

Figure 12 Base shear - drift response for in-plane push test

6.3 Discussion

During the test it was observed that the crack initiated at the loading side of the wall and gradually propagated to the opposite side, indicating that the cohesion was engaged with the increasing load levels as indicated by the changing gradient of the curve in Figure 12 between 0 and 0.2% drift. Based on simple static analysis, the applied force and the normal force due to the self weight of the test section acting on the sliding plane resulted in the coefficient of friction μ for the wall section being calculated to be 0.7.

In NZSEE (2006), the in-plane strength limit is based on sliding shear (V_s), damage in mortar joints near the point of contreflexure, diagonal tension failure and rocking. According to the observed failure mode in the wall panel, only the sliding failure mechanism is considered here. Equation 2 from NZSEE (2006) guidelines and Equation 3 from FEMA 356 (2000) are used to predict the sliding strength of the wall section. Symbols used in these expressions are given in Table 5.

$$V_s = \frac{3czt + \mu N}{1 + \frac{3\alpha_c cdt}{N}} \quad (2)$$

$$V_{bjs} = v_{me} A_n \quad (3)$$

Table 5 List of symbols

Symbol		Units
c	Cohesion	N/mm^2
z	Distance from compression fibre to line of N	mm
t	Thickness of wall	mm
N	Normal force on cross-section	N
α_c	Effective aspect ratio	
μ	Coefficient of friction	
d	Depth of member	mm
v_{me}	Cohesive strength of masonry bed joint	N/mm^2
A_n	Area of net mortared section	mm^2

Using material properties obtained from in-situ testing the sliding force was predicted to be 18.9 kN using NZSEE guidelines and 60 kN using FEMA 356. It is evident that both methods overestimated the force which initiated sliding.

7. OUT-OF-PLANE TESTS

7.1 Location and Setup Description

Two out-of-plane wall tests were conducted at the B-East building, one being in the as-build condition and one in the retrofitted (repaired) condition. A 2-leaf wall lined with 12-15 mm thick cement plaster finish on the exterior was selected for testing and was located within the southern gable as shown in Figure 13. The entire wall had dimensions of 19.8 m long × 10.8 m high with two door penetrations. In order to simplify the test and to provide possible comparison to laboratory-built specimens, a 1200 mm wide wall strip was isolated from the rest of the wall, inducing a one way bending failure. The wall strip was isolated by cutting vertically through the wall using a concrete cutting chainsaw, with vertical cuts made on an inward angle to eliminate wedging effects after wall deformations occured. Due to the presence of the mezzanine floor the maximum possible height of the wall strip was restricted to 3000 mm.

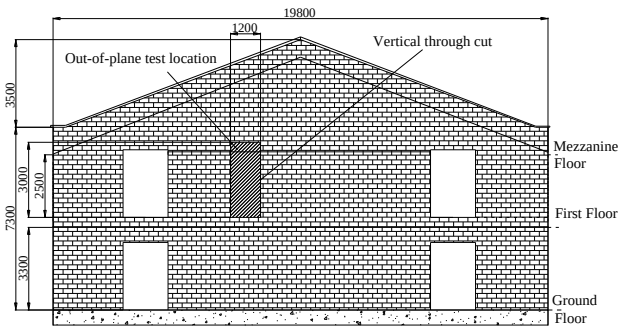

Figure 13 Southern gable elevation showing test location

Out-of-plane loading was applied by gradually inflating a 2.1 × 1.2 m Bigfoot™ vinyl airbag. To accommodate the airbag, a gap of 50 mm was left between the wall and the plywood backing. The plywood backing, measuring 2.4 m × 1.2 m, consisted of an assemblage of plywood sheets and steel angles and was supported by a reaction frame which consisted of vertical and diagonal timber members bolted to the timber floor joists to transfer horizontal load into the timber floor diaphragm. The cross-section of the setup is shown in Figure 14.

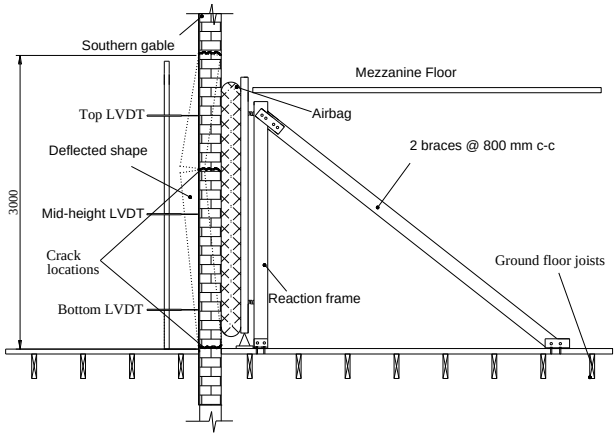

Figure 14 Out-of-plane test setup cross-section

The applied load from the airbags was transferred to the plywood backing and to the reaction frame using four S-type 10 kN load cells, which were attached between the plywood backing and reaction frame and provided horizontal stability to the plywood backing frame. To ensure that the entire load was transferred through the load cells, frictionless plates were used underneath the plywood backing. The experimental setup is shown in Figure 15 and Figure 16 (a) and closely resembled the setup successfuly used previously (Dizhur et al. 2009).

Out-of-plane displacement was measured using 3 LVDTs mounted on the opposite side of the wall. One LVDT was placed mid-height and at the wall centerline, and the second and third LVDTs were placed at 2600 mm and 600 mm above the floor level respectively, as shown in Figure 16 (b). The data from load cells and LVDTs was collected at 50 Hz using a National Instruments data acquisition system.



Figure 15 Reaction frame for out-of-plane test



(a)



(b)

Figure 16 Out-of-plane test setup: (a) Reaction frame close up, (b) LVDT locations

7.2 Retrofit Scheme

Using FRP material to retrofit URM walls is a technique for strengthening and increasing the ductility capacity of URM walls subjected to in-plane and out-of-plane earthquake loading. Externally bonded (EB) FRP sheets or plates and NSM FRP bars or strips are the two application techniques that are commonly used (Mosallam 2007, Yasser and Robert 2006). Using the NSM technique provides some protection from fire and the environment and if detailed correctly, does not adversely affect the aesthetics of the structure (Petersen and Masia 2008). In this field experiment, the simulated seismic performance of NSM FRP strip was investigated.

Following the as-built test the wall test section was retrofitted (repaired) using a single 15 mm wide and 1.2 mm thick CFRP strip (Young's modulus of 165 GPa) positioned vertically in the centre of the wall test section and extending from top to bottom, as shown in Figure 17 (b). A groove was cut into the brick through the plaster layer, using a diamond blade circular saw (5 mm thick blade) to a depth of approximately 30 mm to ensure direct bonding of the CFRP strip to the brick surface only. Two part epoxy adhesive was used to bond the CFRP strip into the groove. The groove was entirely filled with epoxy prior to CFRP strip insertion to ensure maximum bond area, and 24 hours were allocated for the epoxy to set. Figure 17 shows the installation procedure.



(a)



(b)



(c)

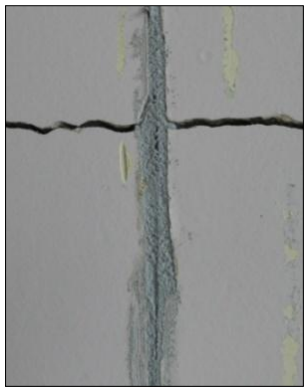

(d)

Figure 17 (a) Epoxy application (b), insertion of the CFRP strip (c), 15 mm wide CFRP strips (d), close-up of NSM repair

7.3 Experimental Results

Two semi-cyclic out-of-plane tests on the as-built wall were first performed. The pressure in the airbag was slowly and uniformly increased, and the total force exerted by the airbag onto the wall was calculated by summation of the readings from the 4 load cells. The pressure in the airbag was increased until a horizontal crack located at 1600 mm above the floor level (at 53% of the wall strip height) formed at a displacement (mid-height) of approximately 5 mm. The pressure in the airbags was further increased until a displacement of approximately 50 mm was achieved, at which point the air pressure in the airbag was released. At zero face pressure a residual displacement of approximately 15 mm was observed. The pressure in the airbag was again gradually increased until a maximum displacement of 62 mm was recorded, after which airbag pressure was again released to zero. The total lateral load – mid-height displacement response for the as-built test is shown in Figure 18. At maximum loading pressure, evidence of wall movement at the top boundary was visually detected and additional vertical, horizontal, and diagonal cracking above the tested wall strip was also observed, with cracking commencing at the wall top corners.

Following the completion of as-built wall testing, a CFRP NSM retrofit (repair) was applied, with the repaired wall tested using the same setup and boundary conditions as used for the as-built test. The pressure was increased until visible cracking within the vicinity of the strip has occurred, and the airflow was then paused (without releasing the airbag pressures) so that crack locations could be observed and marked at different stages throughout the test. Numerous new cracks formed in the vicinity of the strip and the final crack pattern is illustrated in Figure 19. The pressure in the airbag was increased until a total mid-height displacement of 130 mm was reached. At this displacement substantial wide cracking of the masonry above the tested wall strip occurred (shown in Figure 19 (c)) and due to safety considerations the pressure in the airbag was not further increased. The total lateral load - mid-height displacement response is shown in Figure 18.

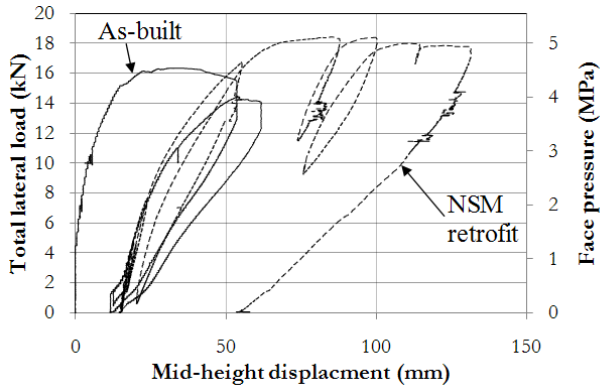

Figure 18 Total lateral force-displacement response for out-of-plane as-built and NSM repair tests

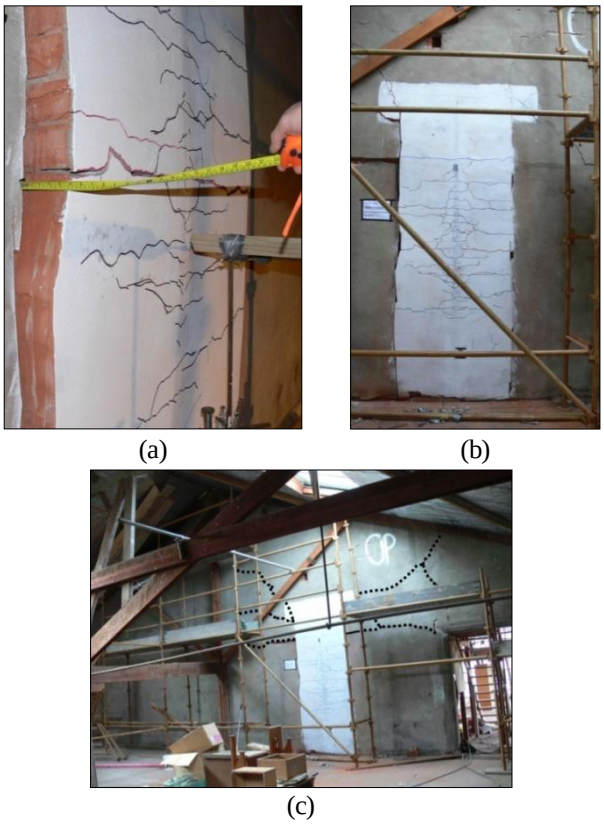

Figure 19 NSM repair - final crack pattern: (a) Wall displacement and crack pattern, (b) Overall final crack pattern, (c) Crack pattern above the test wall

7.4 Discussion

The location of crack formation at 53% of the strip height during the as-built test was comparable to the results obtained during laboratory testing of walls with similar geometry (Derakhshan et al. 2010). It is clear that the boundary conditions that are encountered in real buildings are different from those simulated in the laboratory, and that for the testing reported here the boundary condition at the top of the test wall restrained upward movement and resulted in arching action that caused cracks in the gable above the wall strip edges that propagated at approximately 45° angles away from the wall strip corner. In the second semi-cycle, shown in Figure 18, due to the pre-existing cracks the level of overburden had decreased and resulted in a 16% reduction in total lateral load.

A single CFRP NSM strip was shown to increase the post-cracking wall strength, as illustrated in Figure 18, the wall strength increased by approximately 35%. Due to a large number of newly formed cracks it is clear that there was a larger amount of energy dissipation occurring compared to the as-built condition. Even though further research is required to accurately establish the design guidelines for this type of seismic retrofit, this and previous testing have illustrated that this retrofit technique provides a simple and cost effective alternative to seismically strengthen URM buildings and their components.

8. OUT-OF-PLANE SEISMIC ASSESSMENT

Multiple sources of uncertainty are involved with the evaluation of unreinforced masonry elements. These include arbitrary variation of material properties, construction practice and structural details. NZSEE (2006) proposes a methodology for evaluation of URM walls loaded in a one-way bending condition. Although the out-of-plane tested wall in this research acted in a one-way bending condition, the behaviour was improved by the arching action arising from the top support configuration. Such arching action does not necessarily develop in an earthquake as any excitation involves the shaking of the building as a whole, and not an individual wall strip. A similar arching action also develops as a result of the contribution of the URM corners to the out-of-plane URM wall behaviour. With this analogy, the tested wall strip is assessed based upon the assumption that arching action that developed due to the existing masonry gable above the tested wall strip was comparable to that developed in walls supported by URM corners.

An overburden load equal to the weight of a masonry column above the tested wall was included in the calculations based on the NZSEE (2006) guidelines. The New Zealand Loading Standards (NZS 1170.5:2004) was used to calculate seismic demand, based on the assumption of a ductility factor of 1.0, an annual probability of exceedance of 1/500, a risk factor of 1, and a soil type of C. The seismic demand was then compared with measured performance of the tested wall, which demonstrated an out-of-plane strength of up to 129% of the seismic demand. Based on NZSEE (2006) recommendations the subject wall was estimated to have an out-of-plane strength capacity of 39% of new building standard (%NBS). Table 6 compares the results of this testing programme with that obtained using the NZSEE (2006) current recommendations, suggesting that the recommendations are overly conservative. The NZSEE (2006) procedure for out-of-plane assessment of one-way URM walls has been previously shown to be erroneous and conservative (Derakhshan et al., 2009).

Table 6: Out-of-plane assessment

Max. wall face pressure, (kPa)	Strength demand, (kPa)	Capacity/Demand × 100	%NBS (NZSEE 2006)
4.5	3.5	129%	39

9. CONCLUSIONS

The material properties of B-East building were determined by conducting in-situ testing and laboratory tests on extracted samples. The average brick compression strength was determined to be 19.4 MPa while the average three brick high prism compression strength was 9.6 MPa, with a Young's Modulus of 2.45 GPa. It was concluded that mortar bed joint shear strength did not markedly increase with increasing level of axial precompression and that the cohesion values can be assumed as the average shear strengths at different levels of axial precompression, and are equal to 0.86 MPa and 0.19 MPa for the northern and southern gables respectively.

From in-plane diagonal shear tests on extracted wall panels from B-East building it was shown that the laboratory-built wall panels composed of 1:2:9 mortar mix (cement:lime:sand) have maximum shear stress that closely matched the values obtained from the building samples. Excluding the pre-damaged wall panel AGW2, the average shear stress at cracking was 0.082 MPa and a maximum average shear stress of 0.092 MPa was obtained for B-East building wall panels.

Predictive equations for sliding failure provided by NZSEE guidelines and FEMA 356 overestimated the measured sliding strength of the wall section. The prediction by NZSEE guidelines provided a closer estimation of the actual value.

Out-of-plane in-situ testing of an as-built and a retrofitted URM wall using the NSM FRP technique was also conducted at the B-East building. The location of crack formation at 53% of the strip height was comparable to the results obtained during laboratory testing of walls with similar geometry. The out-of-plane wall behaviour subject to arching action was analogized with that of a wall subject to arching action developed by URM corners, and a comparison was made between the outcome of assessment using this experimental research and that using NZSEE (2006). The comparison suggested that the NZSEE (2006) guideline is overly conservative.

A single CFRP NSM strip was shown to increase the post-cracking wall strength by approximately 35%. Even though further research is required to accurately establish the design guidelines for this type of retrofit, this testing and further analysis have illustrated that this retrofit technique provides a simple and cost effective alternative to seismically strengthen URM buildings and their components.

The outcomes of such in-situ tests are of great assistance to understand the in-situ seismic response of heritage URM buildings, and the data acquired from such tests is essential to validate laboratory-based tests.

Acknowledgements:

The authors would like to thank Peter Smith from Spencer Holmes Ltd. and thank City Construction for providing this testing opportunity. The authors also acknowledge the support of the technical staff of the Department of Civil and Environmental Engineering at the University of Auckland, as well as Contech Limited for supplying the CFRP and epoxy. This research was conducted with financial support from the New Zealand Foundation for Research, Science and Technology.

References:

Dowrick, D. J. (1998). "Damage and intensities in the magnitude 7.8 1931 Hawke's Bay, New Zealand, earthquake." Bulletin of the New Zealand National Society of Earthquake Engineering **31**(3): 139-162.

Russell, A. P. (2010). "Seismic Assessment of In-Plane Unreinforced Masonry Walls". PhD thesis, Department of Civil and Environmental Engineering, The University of Auckland, New Zealand.

GNS. (2008). Geonet News, Issue 10: 4

McClean, R. and Wallace, P. (2009). "Towards improved national and local action on earthquake-prone heritage buildings". New Zealand Historic Places Trust.

Petty, I. (2008). "The December 20 2007 Gisborne Earthquake, the before and after story" Proceedings, 2009 New Zealand Society for Earthquake Engineering Technical Conference, Wairakei, April 11-13.

ASTM. (2000b). "Standard Test Methods for Apparent Porosity, Water Absorption, Apparent Specific Gravity, and Bulk Density of Burned Refractory Brick and shapes by Boiling Water." C 20 - 00, ASTM International, Pennsylvania, United States.

ASTM. (2008). "Standard Test Method for Compressive Strength of Hydraulic Cement Mortars (Using 2-in. or [50-mm] Cube Specimens)." C 109/C 109M - 08, ASTM International, Pennsylvania, United States.

ASTM. (2003a). "Standard Test Method for Compressive Strength of Masonry Prisms." C 1314-03b, ASTM International, Pennsylvania, United States.

ASTM. (2000a). "Standard Test Method for Measurement of Masonry Flexural Bond Strength." C 1072 - 00a, ASTM, Pennsylvania, United States.

ASTM. (2003). "Standard Test Methods for In Situ Measurement of Masonry Mortar Joint Shear Strength Index" C 1531 - 03, ASTM International, Pennsylvania, United States.

ASTM. (2003b). "Standard Test Methods for Sampling and Testing Brick and Structural Clay Tile." C 67-03a, ASTM International, Pennsylvania, United States.

New Zealand Society for Earthquake Engineering. (2006). "Assessment and improvement of the structural performance of buildings in earthquakes."

Recommendations of a NZSEE Study Group on Earthquake Risk Buildings.

Dizhur, D., Derakhshan, H., Ingham, J.M. and Griffith, M.C. (2009). "In-situ out-of-plane testing of unreinforced masonry partition walls," Proceedings, 11th Canadian Masonry Symposium, Toronto, Ontario, Canada, May 31 – June 3.

Mosallam, A. S. (2007). "Out-of-plane flexural behavior of unreinforced red brick walls strengthened with FRP composites." Composites Part B: Engineering **38**(5-6): 559-574.

Yasser, K. and D. Robert (2006). "Rehabilitation of Masonry Walls Using Unobtrusive FRP Techniques for Enhanced Out-of-Plane Seismic Resistance." Journal of Composites for Construction **10**(3): 213-222.

Tumialan, J. G., N. Galati and A. Nanni (2003). "Field Assessment of Unreinforced Masonry Walls Strengthened with Fiber Reinforced Polymer Laminates." Journal of Structural Engineering **129**(8): 1047-1056.

Petersen, R. B., Masia M.J. (2008). "Experimental Verification of Finite Element Model to Predict the Shear Behaviour of NSM FRP Strengthened Masonry Walls." Proceedings of the 14th International Brick and Block Masonry Conference, Sydney, Australia, 17-20 February, 2008.

Derakhshan, H., Ingham, J.M. and Griffith, M.C. (2009). "Out-of-plane assessment of an unreinforced masonry wall: Comparison with the NZSEE recommendations," Proceedings, New Zealand Society for Earthquake Engineering Technical Conference, Christchurch, April 3-5, paper No. 33.

Derakhshan, H., Griffith, M.C., and Ingham, J.M. (2010). " Airbag testing of unreinforced masonry walls subjected to one-way bending." ASCE Journal of Structural Engineering, under review.

SNZ (2004) "NZS 1170.5:2004 Earthquake auctions – New Zealand." Standards New Zealand.

JOINT CONFERENCE PROCEEDINGS
7th International Conference on Urban Earthquake Engineering (7CUEE) &
5th International Conference on Earthquake Engineering (5ICEE)
March 3-5, 2010, Tokyo Institute of Technology, Tokyo, Japan

COMPARISON SHAKING TABLE TEST STUDY ON SEISMIC STRENGTHENING OF SINGLE STORY MASONRY SCHOOL BUILDING

Shi Tiehua[1)], Cheng Shaoge[2)]

1) Senior Engineer, Institute of Earthquake Engineering, China Academy of Building Research, China
2) Professor, Institute of Earthquake Engineering, China Academy of Building Research, China
cabrsth@126.com, chengshaoge@163.com

Abstract: In Wenchuan Earthquake, a lot of school buildings collapsed and caused great casualty, and the china government invested much more in seismic appraisal and strengthening on school buildings. In this paper, seismic strengthening of a single story masonry school building should be undertaken because lack of seismic capacity and measures, and tie R.C. column, beam and tie tensile bar would be adopted. Additionally, the brick walls under large span roof beam were strengthened using combine masonry column method. Shaking table test of 2 models with scale 1 to 4 was carried out, one is the model without strengthening, the other is strengthening model. The models were put on the table simultaneously, the damage procedure or modal, variety of vibration characteristic, dynamic response were compared. The test shown that the structure without strengthening could only reach the seismic fortification level of 7 degree(0.10g), but after strengthening, it can satisfy the requirement of the level of 8 degree (0.30g). Finally, the seismic strengthening measures based on different seismic fortification zone was suggested.

1. INTRODUCTION

In Wenchuan Earthquake, many school buildings suffered severe damage and even collapsed with great casualty. The central government invests much more to impel the project named “Safety for school buildings”, all the school buildings need to be seismic appraised. If these buildings can not satisfy the requirements, seismic strengthening must be carried out.

Shaking table model test of a typical school building common used in countryside was carried out to evaluate the seismic behavior and the effectivity of the seismic strengthening measures. The building was a single storey masonry structure which was built in 1990s with storey height of 3.15m, depth and bay of 6m and 9m. The building was located on Site-class III, and the local seismic fortification intensity is 7 according to Chinese seismic design code. The main problems of this structure are as follows: 1) the roof is precast slab which laid on beams directly without any tie measures to the beam or each other. 2) the brick wall was improperly constructed without any tie measures at the external corner or the joints of inner and external walls. None tie-column or ring-beam was found in the masonry walls. 3) roof beams were supported directly by brick walls. 4)the strength grade of mortar is quite low and the on-site test value was about M0.4.

According to seismic appraisal result, this building can not meet the requirements of local seismic fortification. Thus, seismic strengthening measures should be adopted. The main measures are to install tie-columns at the corners and joints of inner and external walls; to establish composite columns under some of roof beams to support it; and to add ring-beams located at the same elevation with roof slab.

2. EXPERIMENTAL PROGRAMS

Two 1/4 scale models were made. Model 1 was the original building without strengthened and Model 2 was a strengthened one shown as Figure 1.1 and 1.2. Both of the models were placed simultaneously on the shaking table (Figure 2.1 and 2.2).

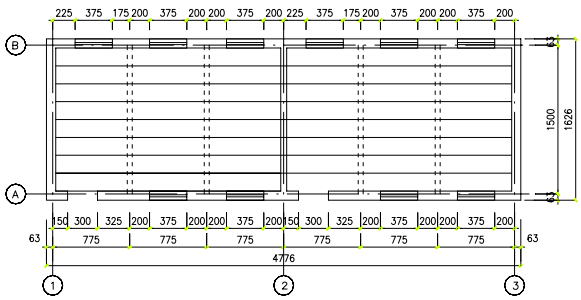

Figure 1.1 Plan of Original Structure

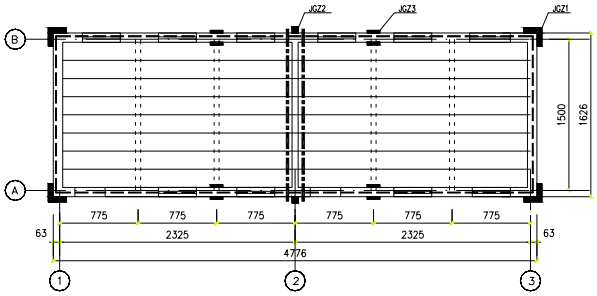

Figure 1.2 Plan of Strengthening Structure



Figure 2.1 Model 1 (without strengthening)



Figure 2.2 Model 2 (strengthened)

2.1 Similitude Law Design of Test Model

The models were made using same materials with prototype. Considering the structure is belong to distributed mass system[1], no additional weight was adopted in the test to ensure that the vertical mass distribution was the same as that of original structure. In such a case, the walls compression stress of test model and that of original structure did not match, resulting in inequivalent seismic capacity of walls. Modification of acceleration amplitude of table input was made to ensure equivalence of similarity ratio of seismic shear force and seismic shear capacity of walls. Table 1 illustrates similarity relation of main parameters.

Table 1 Dynamic Similarity of Test Model

Parameter	Scale	Parameter	Scale
Geometry size	1/4	Displacement	1/5
Elastic module	1	Stress	1/1.25
Material density	1	Mass	1/64
Period or time	1/4	Frequency	4
Acc. input	3.2	Acc. response	1/3.2
Seismic action	1/20	Seismic capacity	1/20

2.2 Fabrication of Test Model

The model was strictly fabricated with the scale and the seismic defects of original structure were reflected.

1. Bricks in the walls of test model were cut from full bricks with the scale, and scored surface was required to ensure the bonding behavior between the mortar and the bricks.
2. The strength grade of mortar in the original structure was just only M0.4. Therefore, lime and clay with the mixture ratio 1:6 were adopted in case of distortion of test due to higher strength of the mortar.
3. At the joint of longitudinal and transverse walls of test model, construction method was the same as that of original structure.
4. Precast reinforced concrete slab with the thickness 4cm was adopted. In view of the requirement of the roof system mass, none manual simulation mass was applied in the test.
5. Concrete in ring-beams and tie columns was replaced by grouting material with high fluidity.
6. The base of the model was a 20cm thick reinforced concrete slab in which bolt holes were preformed in use of mounting of the test model to the shaking table. Grooves were reserved at location of walls or tie-column to simulate the embedment of elements.

2.3 Seismic Waves

Seismic waves adopted in the test were El-Centro wave, artificial waves art1 (Site-class III, Group 1) and art2 (Site-class III, Group 2), shown as Figure 3. In the figure, normalization of peak value was handling for the acceleration time history curve. And in the test, time coordinate contraction (1/4) and acceleration magnification (3.2 times) were taken according to the dynamic similitude law.

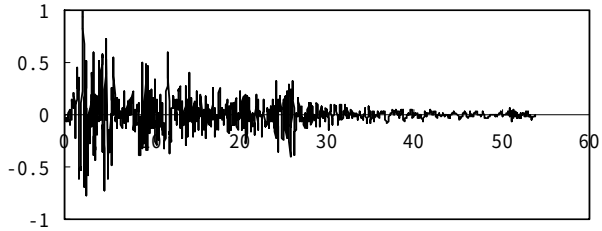

Figure 3.1 El-Centro wave time history (1940 NS)

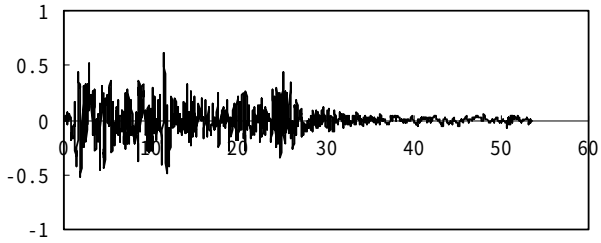

Figure 3.2 El-Centro wave time history (1940 EW)

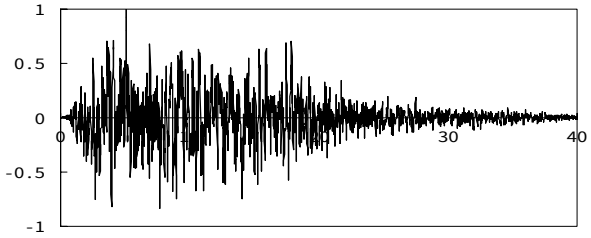

Figure 3.3 art1 wave time history

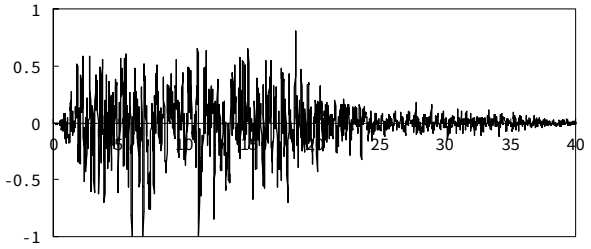

Figure 3.4 art2 wave time history

In the test, the peak value of shaking table input acceleration increased step by step. And in the process, the model suffered frequently, fortification and rarely influence of earthquakes in sequence until failure of the model. When every step was completed white noise sweep test was carried out to check the variation of natural frequency, mode curve of the structure.

It was a bi-direction earthquake simulation test, and the transverse direction was the main axis of earthquake action. In the lower peak value of acceleration input test, transverse, longitudinal and bi-directions test were implemented in sequence for every seismic wave. But in the higher peak value of acceleration input test, only bi-directions test was carried out using wave of art1.

In the test of El-Centro wave, NS and EW were the transverse and longitudinal directions input respectively. In the test of artificial wave, longitudinal acceleration time history was the same as that of transverse direction, but its amplitude was adjusted to be 0.85 times that of transverse direction.

3. TEST RESULTS AND ANALYSIS

3.1 Damages of Test Model

1. Suffering earthquake influence equal to seismic fortification intensity 7, both the test models kept in good condition and none cracks were found.

2. Suffering frequently influence of earthquake action of intensity 8 (0.30g)

Model 1(unstrengthened structure): Small cracks were found in part of windows' corners. There were slight separation from each other at the joints of inner and external transverse walls and longitudinal walls where the walls were improperly constructed as normal. Small displacement was observed between roof slab and walls.

Model 2(strengthened structure): Small cracks were also found in part of windows' corners. There were slight separation from each other at the joints of inner transverse walls and longitudinal walls where the walls were improperly constructed as normal. But none cracks were found at the joint of external transverse walls and longitudinal walls where tie columns were installed. Small cracks were observed at the corner of external transverse walls.

3. Suffering influence of earthquake action of seismic fortification intensity 7 (0.15g)

Small cracks were found in more parts of the windows' corners and the cracks that previously appeared extended. In this stage, the main damage characteristic was that evidence of slip was observed between the bottom of external transverse walls and the foundation in Model 1 (unstrengthened model).

4. Suffering influence of rarely earthquake action of intensity 7

Model 1: The previously appeared cracks developed obviously. More cracks were found and the width of cracks became larger. Integral slip occurred at the bottom of external transverse walls and obviously departure was observed between external transverse walls and longitudinal walls at their joints, shown as Figure 4.

Model 2: The previously appeared cracks developed a little. Tension cracks were found in ring-beams, shown as Figure 5.

5. Suffering influence of rarely earthquake action of intensity 7

Model 1: Slip occurred at the bottom of external transverse walls and partial damage was observed at the bottom of walls, shown as Figure 6. On top of part walls between windows cracks appeared due to push action of roof beam, shown as Figure 7.

Model 2: There was some increment of tension cracks in ring-beam, but cracks in walls were still small.


Figure 4 Slip and Departure of Walls



Figure 5 Tension Cracks in Ring-beam



Figure 6 Partial Damage at Bottom of Wall



Figure 7 Out-of-plane Cracks in Longitudinal Walls

6. Suffering earthquake action of seismic fortification intensity 8 (0.30g)

Model 1: The walls damaged severely and collapsed in local part, but the precast roof slab did not drop. For transverse walls, Complete departure occurred between bottom of transverse walls and the foundation, and obviously slip was observed in the test. Then continuous transverse cracks in walls at the elevation of roof appeared due to push and pull action of slab under longitudinal seismic action, shown as Figure 8. Cross inclined cracks were found in all transverse walls and damage of inner transverse walls was more severe that of external transverse walls, shown as Figure 9. For longitudinal walls, on top of longitudinal walls between windows out-of plane bending failure was observed due to push action of roof beam under transverse seismic action, shown as Figure 10; and these walls collapsed in local part (Figure 11). In the mean time, the walls suffered longitudinal seismic action resulting in serious cracks in corners of windows. For parapet, the corner parapet damaged and almost fell at Axis 1 (Figure 8). The whole parapet at Axis 3 collapsed. Part of parapet collapsed above the longitudinal walls.

Model 2: A principal inclined crack was observed in the middle of external transverse walls. In the longitudinal walls that did not strengthened with composite columns out-of-plane bending cracks appeared due to push action of roof beam. Failure was found in part of parapet.



Figure 8 Out-of-plane Cracks on Top of Gable



Figure 9 Inclined Cracks in Transverse Walls



Figure 10 Damage of Longitudinal Walls



Figure 11 Collapse of Longitudinal Walls

7. Suffering rarely earthquake action of intensity 8

Model 1: The test terminated.

Model 2: Slip occurred between the bottom of walls and the foundation. Cracks in transverse walls greatly developed. X-type shear cracks were observed in external transverse walls, shown as Figure 12. Out-of-plane bending cracks in longitudinal walls and notable inclined cracks in the corner of windows were also observed (Figures 13 and 14). Tension spilt occurred in the additional installed columns (Figure 15). Quite a number of parapets collapsed and fell, illustrated as Figure 16.



Figure 12 X-type Shear Cracks in Transverse Wall



Figure 13 Horizontal Cracks in Longitudinal Wall



Figure 14 Inclined Cracks at Corner of Window



Figure 15 Tension split of column



Figure 16 Fall of parapet

8. Suffering rarely earthquake action of intensity 8 (0.30g)

The test model extremely damaged. In external transverse walls, serious X-type cracks were observed and the bricks fell off (Figure 17). Destruction and loss of load-carrying capacity occurred in longitudinal walls due to push action of roof beams (Figure 18). Part of walls shifted from original position (Figure 19). Inclined cracks with large width appeared in walls below windows (Figure 20). In the additional installed columns, more cracks were found; in addition, part of longitudinal reinforced bars in them yielded and concrete crushed (Figure 21).



Figure 17 Severe Damage in Transverse Wall



Figure 18 Severe Damage in Longitudinal Wall



Figure 19 Shift of Longitudinal Wall



Figure 20 Serious Cracks in Wall Below Window

3.2 Analysis of Test Data

1. Natural frequency and mode

The test values of initial transverse basic frequency of Model 1 and Model 2 were 40.71Hz, 40.39Hz, respectively, which indicates that the transverse

frequency of structure almost keeps equal when strengthened or not. According to the dynamic similitude theory of test model, the transverse basic periods of actual structure were 0.098s and 0.099s, respectively.



Figure 21 Failure of Column

The test values of initial longitudinal basic frequency of Model 1 and Model 2 were 35.73Hz, 40.63Hz, respectively. According to the dynamic similitude theory of test model, the longitudinal basic periods of actual structure were 0.112s and 0.098s, respectively. Thus, the stiffness of structure was enhanced and its period became shorter after strengthened.

The description above shows that the transverse frequency is larger than the longitudinal frequency for the two models and so the transverse stiffness is also larger. After strengthened, little impact on transverse frequency and stiffness was observed. But the larger longitudinal frequency after strengthened indicated obvious enhancement for the longitudinal stiffness.

Figure 22 illustrates the variation of transverse basic frequency of the two models in the test with two different acceleration peak values. At the beginning of the test (before frequent earthquake action with intensity 8, 0.30g), the frequencies of the two models were close to each other without little change, which indicated that none damage occurred in both of the two models. Afterwards, frequency of the two models declined which indicated cracks appeared in the models. And in the unstrengthened model greater decline was observed indicating more serious cracks. The variation of the frequency was coincident with the crack and damage phenomena observed in the test.

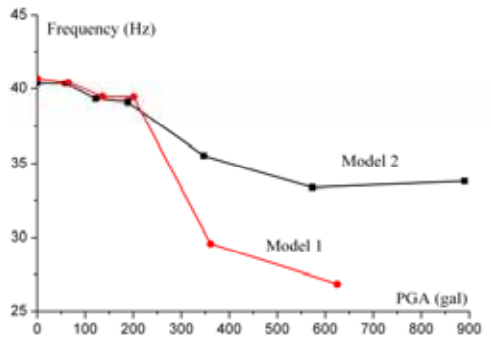

Figure 22 Variation of First Order Frequency

The test result of first order mode was shown as Figure 23, which shows the deformation was dominated by bending deformation.

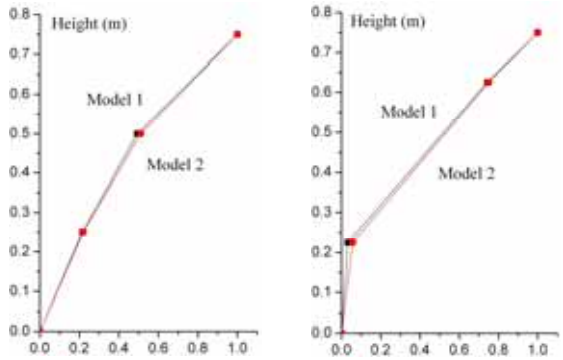

Transverse Longitudinal

Figure 23 First Order Mode

2. Acceleration response

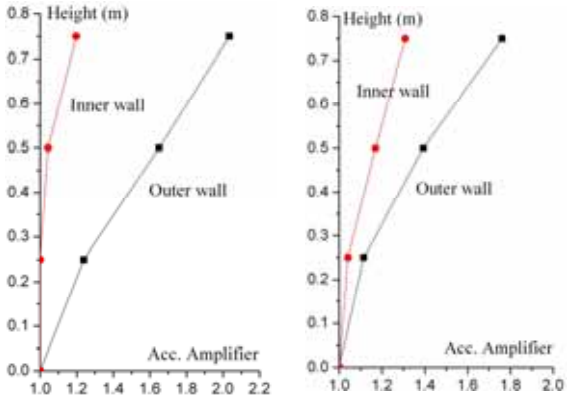

Intensity 7 (frequently) Intensity 7 (0.15g) (frequently)

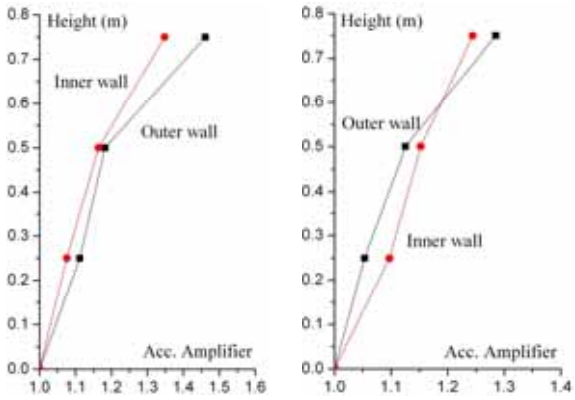

Intensity 7 (fortification) Intensity 8 (0.30g) (frequently)

Figure 24 Acc. Amplifier Curve (art1, Mode 1)

Figures 24~25 illustrate the models' test curve of transverse acceleration amplification coefficient along the height. For the unstrengthened model, there were different acceleration amplification coefficients in inner and external transverse walls, and greater seismic

response in external transverse walls was observed. This was possibly caused by insufficient stiffness of the roof resulting in inconsistent seismic response of inner and external transverse walls, and by some degree of torsion effect of the structure which would intensify the seismic response of the end of transverse walls. In addition, acceleration amplification coefficient of structure would decrease along with the increment of input seismic acceleration.

For strengthened model, there were also different acceleration amplification coefficients in inner and external transverse walls, but just the reverse, there were greater seismic response in inner transverse walls. From the analysis above, the frequency and mode of the model almost kept equal, which indicated that torsion effect could not be reduced obviously by strengthening if torsion effect existed in original structure. Therefore, inconsistent acceleration response of inner and external walls of unstrengthened model was caused mainly by insufficient stiffness of the roof. After installation of ring-beams and tie columns, integrity of the roof was enhanced and the seismic response of structure was reduced.

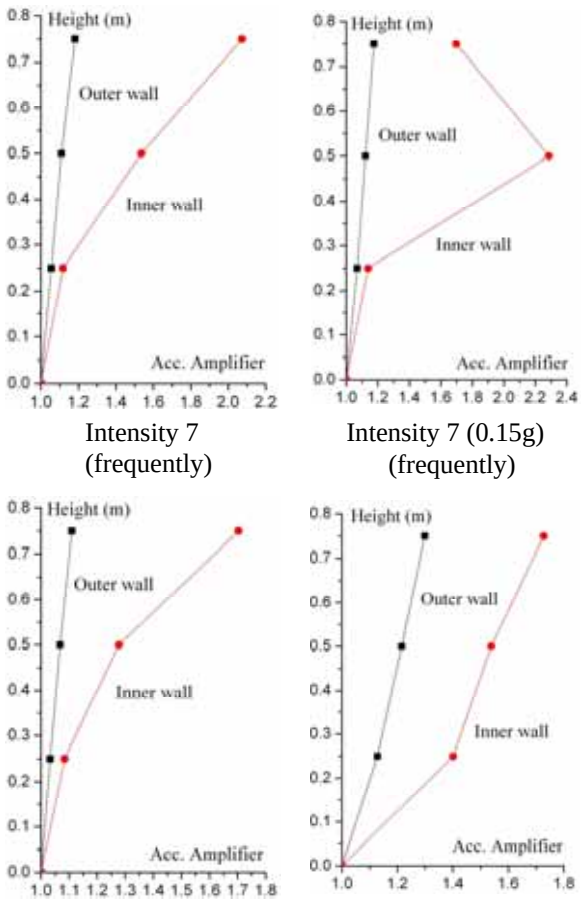

Intensity 7 (frequently) | Intensity 7 (0.15g) (frequently)

Intensity 7 (fortification) | Intensity 8 (0.30g) (frequently)

Figure 25 Acc. Amplifier Curve (art1, Mode 2)

3.3 Seismic Behavior Assessment of Model

1. Model 1 (Unstrengthened): Under frequently seismic action of intensity 8, none dominating cracks appeared in walls. Under action of seismic fortification intensity 8, severe damage occurred but the model could still be repaired. Under rarely seismic action higher than intensity 7, the model collapsed.

In general, the unstrengthened model can satisfy the goal of seismic fortification intensity 7.

2. Model 2 (Strengthened): Under frequently seismic action of intensity 8, none dominating cracks appeared in walls. Under action of seismic fortification intensity 8 (0.30g), severe damage occurred but the model could still be repaired. Under rarely seismic action of intensity 8 (0.30g), the model did not collapse.

In general, the strengthened model can satisfy the goal of seismic fortification intensity 8 (0.30g).

4. CONCLUSIONS

Through the comparison test of unstrengthened and strengthened models of this single storey school building, the following conclusions can be made from this study:

1. The original structure can satisfy the requirement of seismic fortification intensity 7, and after strengthened requirement of seismic fortification intensity 8 (0.30g) can be satisfied.
2. Severe out-of-plane damage of walls under roof beams occurred in both the models resulting in loss of seismic capacity of the structures. Therefore, the key weakness of seismic capacity exists in walls under roof beams. Improvement of seismic capacity of these walls can be achieved by installation of composite columns in them, which is also able to improve seismic capacity of the whole structure. In the test, failure occurred in some walls under beams that were not strengthened by composite columns. If these walls were strengthened, the seismic capacity of the whole structure is able to be improved more.
3. Application of strengthening methods should vary in different seismic fortification zones. In this project, the joints of transverse and longitudinal walls were constructed improperly. Therefore, it is necessary to install tie columns and ring-beams in the joints, which can satisfy the requirement of seismic fortification intensity 7. In the seismic fortification zone of intensity 8, all or part of walls that support beams should be strengthened by composite columns. And in the zone of intensity 9, concrete or mortar layer should be further applied for the strengthening of transverse walls.
4. In the test, damage occurred in parapets in both of the models under the earthquake action with identical intensity. Thus, strengthening methods could not improve the anti-collapse capacity of parapets.

Acknowledgements:

This project was funded by National Key Technology Program (2006BAJ13B01).

References:

[1]Cheng Shaoge, Yu Wen and Ge Xueli. (2007), "Study on dynamic similitude theory of adobe house scale model in shaking table test," *Journal of Disaster Prevention and Mitigation Engineering*, **27**(supplement), 360-362. (In Chinese)

[2]Industrial standard of People's Republic of China (1996), "Specification of seismic test methods for buildings(JGJ101-96)," China Architecture & Building Press. (In Chinese)

[3]Industrial standard of People's Republic of China (2009), "Technical specification for seismic strengthening of buildings (JGJ116-2009)," China Architecture & Building Press. (In Chinese)

[4]National standard collective drawings of building design (2003), "Strengthening and repair of masonry structure 03SG611," China Planning Press. (In Chinese)

JOINT CONFERENCE PROCEEDINGS
7th International Conference on Urban Earthquake Engineering (7CUEE) &
5th International Conference on Earthquake Engineering (5ICEE)
March 3-5, 2010, Tokyo Institute of Technology, Tokyo, Japan

LIFE-CYCLE COST ESTIMATION OF OPEN-TYPE WHARF BASED ON SEISMIC DAMAGE RISK

Hirohi Yokota[1)], Hiroshi Yamauchi[2)], Ema Kato[3)], and Mitsuyasu Iwanami[4)]

1) Professor, Graduate School of Engineering, Hokkaido University, Sapporo, Japan
2) Consulting Engineer, Japan Port Consultants Ltd., Fukuoka, Japan
3) Senior Researcher, Port and Airport Research Institute, Yokosuka, Japan
4) Research Team Leader, Port and Airport Research Institute, Yokosuka, Japan
yokota@eng.hokudai.ac.jp, hiroshi_yamauchi@jportc.co.jp, katoh-e@pari.go.jp, iwanami@pari.go.jp

Abstract: The number of structures in ports and harbors in which intervention is required will be increasing rapidly due to chloride-induced deterioration. Strategic maintenance and rehabilitation are necessary for the deteriorated structures to realize life extension and structural performance recovery, resulting in minimization of life-cycle costs. In this paper, several scenarios of rehabilitation are considered for a deteriorated open-type wharf taking into account the progress of deterioration and the risk of failure due to earthquakes. We examine the process how to select the most suitable scenario from the viewpoint of life-cycle cost.

1. INTRODUCTION

Civil infrastructure will be suffered from materials deterioration during the service life, which may result in degradation in structural performance such as load-carrying capacity. Accordingly, it is necessary to implement a life-cycle management strategy for existing infrastructure to keep their structural performance over required levels. To carry out the life-cycle management (Yokota et al. 2007), it is necessary to establish models to predict the progress of deterioration, to simulate the effect of materials deterioration on structural performance, and to estimate the life-cycle cost based on the aforementioned two models.

The life-cycle cost will be one of the most useful indices to make decisions for intervention. However, there have been few studies on the life-cycle cost estimation including expected restoration cost as well as maintenance and rehabilitation costs. The restoration cost should be counted because of the increase in the risk of damage due to materials deterioration against external loads.

In this paper, several rehabilitation scenarios are discussed for an existing deteriorated open-type wharf. The open-type wharf is the most vulnerable structure in ports and harbors against chloride attacks. These rehabilitation scenarios take into account the loss in structural performance due to chloride-induced deterioration and the increase in the risk of damage against seismic actions caused by the loss in structural performance. Among alternatives, the process to select the most suitable scenario is discussed from the viewpoint of the life-cycle cost including maintenance, rehabilitation, and restoration costs.

2. ESTIMATION OF LIFE-CYCLE COST

The open-type wharf discussed in this paper has two main structural components such as steel pipe piles and a reinforced concrete deck consisting beams and slabs as shown in Figure 1. The seismic performance of the wharf may be degraded by chloride-induced deterioration of its structural components during the life time. Therefore, based on the results of deterioration prediction, rehabilitation scenarios for these structural components are formulated in consideration of the risk of seismic damage.

The life-cycle cost in this paper is defined as a total sum of maintenance cost, rehabilitation cost, and restoration cost, in which the discount rate is not taken into account. The initial construction cost is not counted because this paper deals only with an existing structure.

The restoration cost is related to the risk of seismic damages of each structural component. The influence of materials deterioration on the risk of seismic damage is taken into account as follows: when thickness loss of steel pipe pile due to corrosion becomes larger than the design allowable one, it is expected to decrease in the load-carrying capacity and increase in the seismic risk. The piles above L.W.L.–1.0 m (L.W.L. refers to the monthly lowest water level) are protected by anti-corrosion coating/covering; consequently, this part does not corrode as long as the coating/covering is effective. The submerged part of the pile is delectro-chemically protected in consideration of the efficiency of cathodic protection system. The effective ratio of the cathodic protection system is set at 90 %.

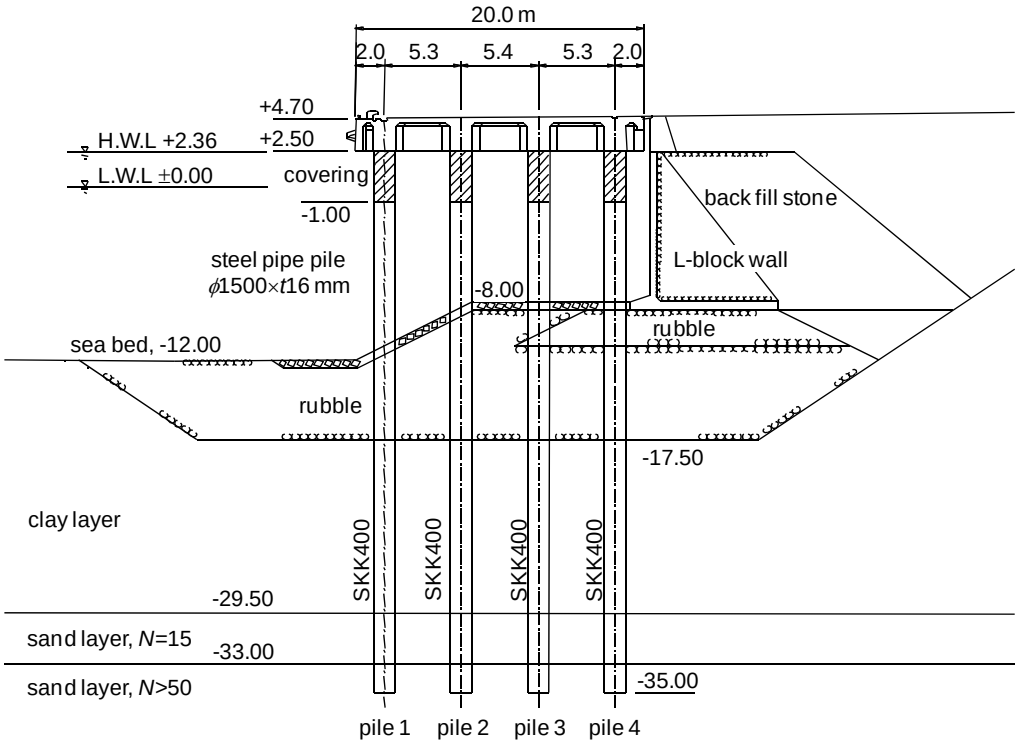

Figure 1 Cross-sectional view of the open-type wharf

The load-carrying capacity of the pile therefore starts decreasing when the corrosion protection system reaches its design life. Since seismic actions are not considered in the slab design, the effect of deterioration of the slab on the seismic risk can be ignored. Chloride-induced deterioration decreases the load-carrying capacity of the beam, which causes the increase in seismic risk.

3. FORMULATION AND EVALUATION OF SCENARIOS

3.1 Prediction of deterioration progress of deck

Chloride-induced deterioration of reinforced concrete structure is considered to progress through the initiation, propagation, acceleration, and deterioration stages (JSCE 2001). Assessment of the deck in open-type wharf is generally carried out by using the deterioration grade. The approximate relationship between the deterioration grade and the deterioration stage is indicated in Figure 2 (Yokota 2002). The current maintenance manual for port and harbor structures (PARI 2007) uses the four-grade system: Grades *d* to *a*. In this paper, however, the six-grade system: Grades 0 to V has been applied for more detailed analysis. Grades 0, I and II approximately correspond to Grade *d*, while Grades III, IV and V correspond to Grades *c*, *b* and *a*, respectively.

Before reaching Grade III, the deterioration is governed by chloride ion concentration at the position of reinforcement. During this period, no degradation in structural performance occurs because corrosion of reinforcement does not start. After that, the remaining

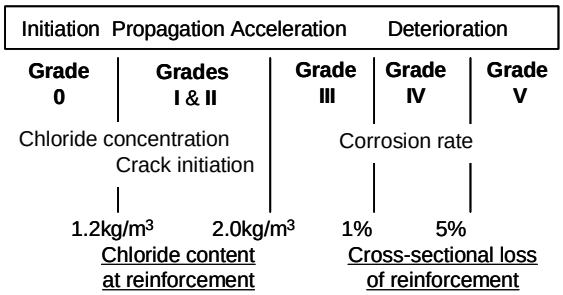

Figure 2 Progress of chloride-induced deterioration

load-carrying capacity of the deck can be approximately calculated taking into account the average cross-sectional loss of reinforcement and apparent decrease in its yield strength (Kato et al. 2008).

3.2 Formulation of rehabilitation scenario

Scenarios for rehabilitation are formulated by considering the present states of deterioration such as corrosion of pipe piles, conditions of corrosion protection, and deterioration of deck as well as the predicted result of future deterioration. Based on the result of prediction, rehabilitation methods applicable to corresponding deterioration grades and the timing of rehabilitation taken as well as renewal of materials for rehabilitation are introduced into the scenario. In this paper, since the mechanisms of re-deterioration after rehabilitation taken have not yet well

been investigated, the service lives of rehabilitation materials are set at their standard values used in the authors' past paper (Yokota et al. 2006).

3.3 Calculation of seismic damage risk

The inertial force horizontally acting on the deck due to the earthquake is taken into account for estimating the damage risk during the service life. The intensity of seismic action is represented in a seismic coefficient. Bending moment induced in the pipe pile is calculated by the ductility design method (OCDI, 2002) in which the pile head (pile-deck joint) moment is generally critical.

When the ultimate moments of beams without corrosion and with corrosion of reinforcement are denoted for $M_{u,h}$ and $M_{u,c}$ respectively, $M_{u,c}$ is smaller than $M_{u,h}$. Accordingly, decrease in load-carrying capacity of the beam with corroded reinforcement is inversely considered in terms of the equivalently enlarged seismic coefficient, $k_{h,c}$ as follows:

$$k_{h,c} = k_h / \alpha_m \tag{1}$$

$$\alpha_m = M_{u,c} / M_{u,h} \tag{2}$$

where k_h: design seismic coefficient and α_m: decreasing rate in load-carrying capacity.

The seismic performance of the wharf is verified by the ductility design method subjected to accidental seismic forces. Equation 3 shows the verification criterion based on the ductility method. $k_{h,l}$ is defined as the limit seismic coefficient when $R_a = k_{h,l}W$. In case that the seismic action larger than $k_{h,l}$ is applied, the moments at the pile head and in the ground of all the piles reach the plastic moment; therefore, all the piles remain in the fully plastic state with buckling.

$$R_a = \sqrt{2\mu_a - 1}\, P_y \geq k_h W \tag{3}$$

where R_a: load-carrying capacity (kN), μ_a: allowable ductility ratio, P_y: elastic limit force (kN), and W: vertical load such as self-weight of deck and surcharge (kN).

When corrosion at the pile head progresses, $k_{h,l}$ becomes small, which results in higher seismic damage risk. The seismic coefficient for the purpose of seismic performance verification using Equation 3 is defined as $k_{h,v}$. For design calculations of the beam, design bending moment and design shear force are determined as those subjected to $k_{h,v}$. Therefore, seismic action larger than $k_{h,v}$ is applied, the beam will be damaged.

3.4 Estimation of restoration cost

The coverage of restoration depending on the seismic intensity is summarized in Table 1. The three levels of coverage are considered based on the magnitude relation of seismic coefficients, k_h, $k_{h,v}$, $k_{h,c}$, and $k_{h,l}$.

It is possible that earthquakes occur more than once during the design service life. Therefore, number of damage occurrence should be considered according to the magnitude of seismic force. The restoration cost is defined as the summation of the products of expected number of damage and corresponding restoration cost. The expected number of damage occurrence can be calculated with Equation 4.

$$\sum_{i}^{n} E_{ni} = p_f \nu T_s$$
$$E_{nk} = \sum_{i=k}^{n} E_{ni} - \sum_{i=k+1}^{n} E_{ni} \tag{4}$$

where E_{ni}: expected number of earthquake occurrence having larger intensity than the target one during the period of T_s, p_f: probability of damage occurrence either 0 or 1, ν: annual probability of earthquake occurrence having larger seismic intensity than the target one (= $1/T_r$), T_r: return period of earthquake occurrence having larger seismic intensity than the target one (year), T_s: service life (year), and E_{nk}: expected number of earthquake occurrence having the target seismic intensity during the period of T_s.

The peak ground acceleration related to the seismic coefficient and corresponding return period can be set

Table 1 Restored areas

Seismic action	Area to be restored	Remark
$k_{h,c} \leq k_{h,v}$	No	No damage
$k_{h,v} < k_{h,c}$ $k_h \leq k_{h,l}$	Deck	Beams are damaged
$k_{h,l} < k_h$	Deck and piles	Beams are damaged. Piles are in fully plastic state with buckling.

Table 2 Summary of evaluated cases

Case	C_0 (kg/m^3) and D (cm^2/year)	Time of assessment, year	Further service life, year	$k_{h,v}$	$k_{h,l}$
1	C_0 = 9 (slab), 13 (beam) D = 1.006	15	50	0.40	0.43
2	C_0 = 5.4 (slab), 7.8 (beam) D = 0.653	15	50	0.40	0.43
3	C_0 = 9 (slab), 13 (beam) D = 1.006	25	50	0.40	0.43
4	C_0 = 9 (slab), 13 (beam) D = 1.006	15	100	0.40	0.43
5	C_0 = 9 (slab), 13 (beam) D = 1.006	15	50	0.30	0.43

according to the Technical Standards and Commentaries for Port and Harbour Facilities in Japan (OCDI, 2002). This is based on the analytical results of damaged gravity quay walls under various ground conditions. The return periods, T_r (year) are obtained by $T_r = 10^{-2.959} g\ (k_h/0.296)^{1.9}$, where g denotes for acceleration of gravity.

4. LIFE-CYCLE COST ESTIMATION

4.1 Method of estimation

Based on the evaluation process mentioned earlier, the life-cycle cost is estimated for the open-type wharf as shown in Figure 1. Five cases are considered as listed in Table 2. The other basic conditions are as follows:

- Life-cycle cost is estimated only for the main structure (decks and piles) of the wharf;
- Liquefaction of the ground is not considered for the estimation of restoration cost;
- Economic loss caused by out-of-service during rehabilitation or restoration work is not considered;
- Restoration cost is estimated as 1.5 times as much as the initial construction cost;
- Coating/covering for corrosion protection of pipe pile is renewed when it reaches its design life. The submerged part below LWL-1.0 m is strengthened at the time of design life as mentioned earlier;
- When load-carrying capacity of the beam decreases to 60% the initial one, the beam is assumed to reach the safety limit. Rehabilitation should be taken before reaching the safety limit; and
- Rehabilitation and restoration costs are expressed as the ratio to the initial construction cost of the wharf.

4.2 Prediction of the progress of deterioration

Figure 3 shows the predicted results of the progress of deterioration grade and decrease in load-carrying capacity due to deterioration of case 1. At present when 15 years have been passed since the start of service, the results of assessment show that the slab is in deterioration Grade II and the beam is in Grade III. The predicted results well fit to the assessed results.

4.3 Rehabilitation scenario

Rehabilitation of the deck will be taken at the present time or the time of deterioration grade shifting to one higher grade based on the predicted results of deterioration. Rehabilitation of the pipe pile will be taken as mentioned earlier. Figure 4 shows the expected rehabilitation cost for the steel pipe piles in its upper part. At the time of 65 years (the end of the further service life), the mortar covering case was the most economical. For the beam and slab, the similar estimation was carried out with several rehabilitation techniques. As a result, the most economical scenarios were provided by applying cathodic protection at Grade II for the slab and to applying cathodic protection at the time of reaching the safety limit of the beam.

4.4 Estimation of restoration cost against seismic damage

The decreasing rate in load-carrying capacity, α_m was calculated as shown in Figure 5. Rehabilitation was considered to be taken when the predicted deterioration grade reaches Grade III (at present), Grade IV (33 years after construction), the serviceability limit (38 years after construction), and the safety limit (43 years after construction). Deterioration actually continues more or less even after the rehabilitation, but in this calculation,

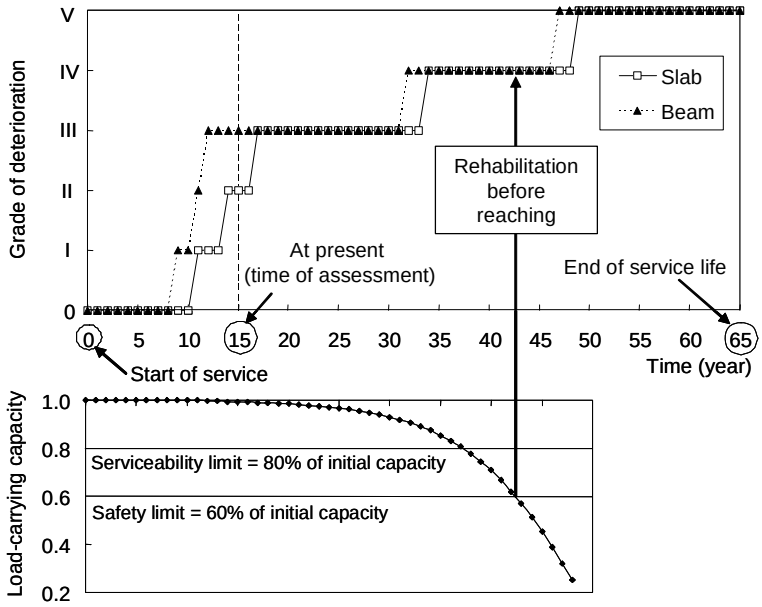

Figure 3 Predicted results of deterioration progress

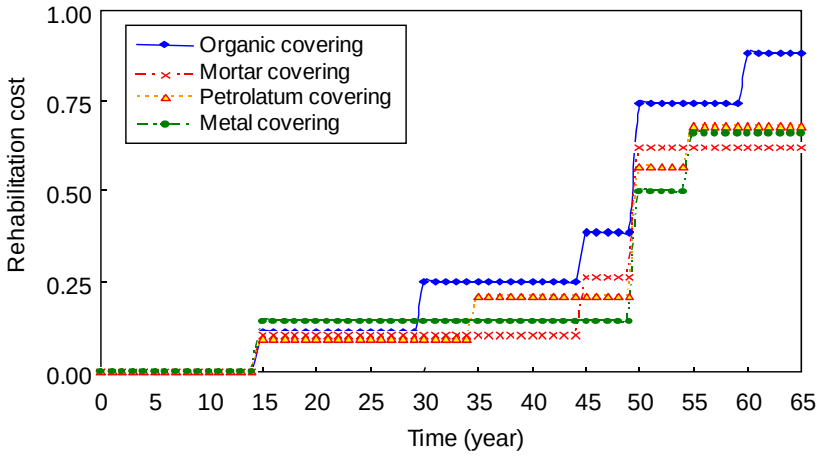

Figure 4 Estimation of rehabilitation cost for pipe pile

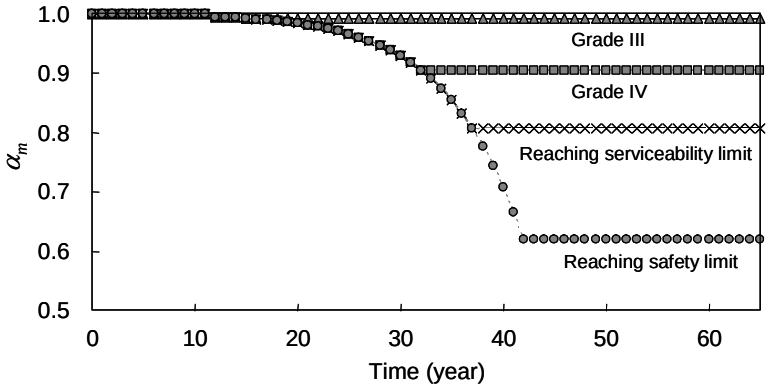

Figure 5 Decrease in α_m depending on rehabilitation timing

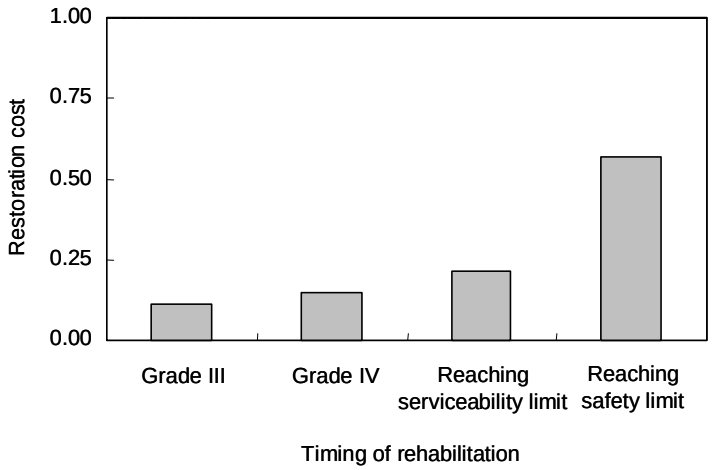

Figure 6 Estimated restoration cost

load-carrying capacity was assumed not to change during the lifetime of materials used for rehabilitation.

The estimated restoration costs are summarized in Figure 6 in case that k_h is set at 0.35. The restoration costs were counted in consideration of the expected number of earthquake occurrence, the value of $k_{h,c}$, and the timing of rehabilitation taken. The values of $k_{h,c}$ corresponding to each timing of rehabilitation shown in Figure 5 were 0.352, 0.387, 0.434, and 0.565. The cost of restoration was calculated according to each repair scenario and corresponding expected number of damage occurrence. Comparing with the case that repair was taken at the deterioration Grade III, the restoration costs were estimated about two times and four times as much as those at the serviceability limit and the safety limit, respectively.

4.5 Calculation of life-cycle cost

The estimated restoration costs showed considerable

Table 3 Estimated life-cycle cost for each scenario

Rehab. timing	Grade II			Grade III			Grade IV		
Case	SC	CP	DS	SC	CP	DS	SC	CP	DS
1	-	-	-	1.065	1.020	1.087	1.073	1.041	1.101
2	0.987	0.969	1.010	0.996	0.959	1.018	0.987	0.961	1.016
3	-	-	-	1.097	1.052	1.119	1.100	1.088	1.128
4	-	-	-	2.049	1.984	2.071	2.103	2.050	2.131
5	-	-	-	1.370	1.326	1.393	1.464	1.431	1.492

Rehab. timing	Serviceability limit			Safety limit		
Case	SC	CP	DS	SC	CP	DS
1	1.109	1.104	1.137	1.464	1.457	1.492
2	0.985	0.986	1.013	1.086	1.085	1.114
3	1.188	1.157	1.216	1.684	1.651	1.712
4	2.276	2.205	2.304	3.307	3.263	3.335
5	1.684	1.679	1.712	3.014	3.007	3.042

Note) SC: Surface coating/covering, CP: Cathodic protection, DS: Desalination

difference depending on the stage of deterioration at the time of rehabilitation. These costs were also counted to estimate the life-cycle costs. The estimated life-cycle costs for 65 years are summarized in Table 3. In each case, cathodic protection at reaching Grade III provided with the most economical results.

The representative results of life-cycle cost simulation of case 1 are shown in Figures 7 and 8. The scenario that cathodic protection is taken at Grade III showed the most economical scenario as shown in Figure 7. Comparing these scenarios, the life-cycle cost is shown in Figure 8 when cathodic protection is implemented at reaching to the safety limit state. The cost related to performance recovery against the corrosion of reinforcement accounted for about one-third of the total life-cycle cost. It also indicated that higher damage risk due to earthquake was expected because of the delays of rehabilitation.

5. CONCLUSIONS

The following conclusions are drawn from discussion on selecting the most suitable scenarios from the viewpoint of the life-cycle cost:

(1) The seismic damage risk is small when the rate of deterioration is small (case 2). In this case, the difference of rehabilitation timings does not contribute to the life-cycle cost.

(2) When the service period is long up to the time of assessment (case 3), rehabilitation is taken under more deteriorated conditions; therefore, the expected number of damages increases, which results in high restoration costs.

(3) In case of long service life (case 4), metal covering case is the most economical for rehabilitation of corrosion protection. This is because the metal covering has high durability and the number of renewal is small. When rehabilitation is taken under lower load-carrying capacity condition, the number of expected damage is large. In this case, the deck needs not only rehabilitation but also renovation.

(4) When seismic intensity is small (case 5), the difference of rehabilitation timings is most obvious compared to case 1 because seismic action has a significant effect. In this case, the number of rehabilitation taken becomes large.

This paper proposed the evaluation of rehabilitation scenarios for existing open-type wharf in consideration of chloride-induced deterioration occurring in the deck and seismic risk. The proposed method is of use to realize the life-cycle management of existing structures. However, the following further studies are required to estimate the cost and risk more accurately: how to predict the progress of deterioration and how to count economic and social losses during repair and restoration.

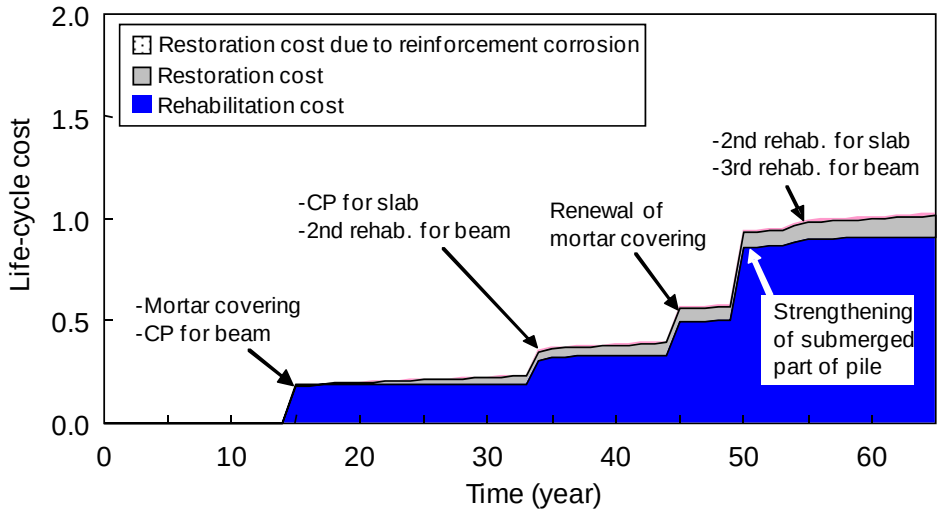

Figure 7 Estimated life-cycle cost, the beams are rehabilitated at Grade III

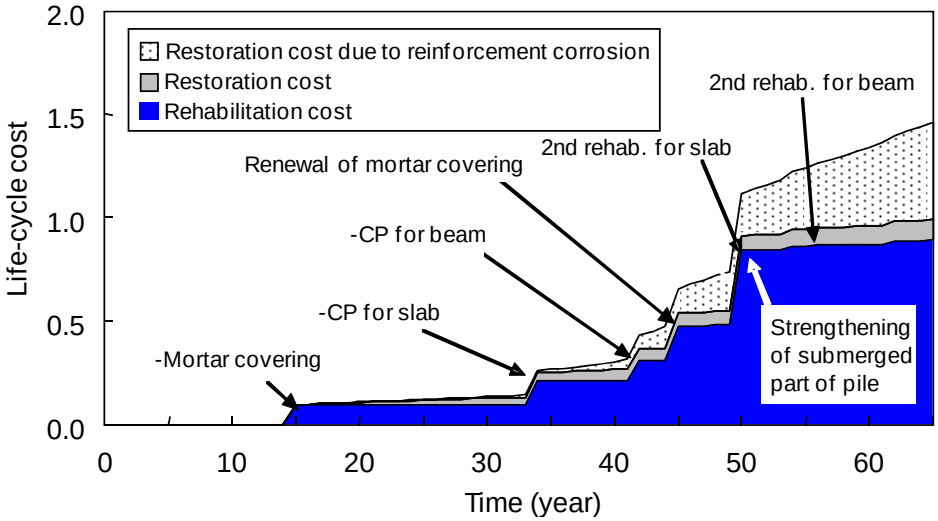

Figure 8 Estimated life-cycle cost, the beams are rehabilitated at reaching the safety limit

References:

Japan Society of Civil Engineers (2001), "Standard Specifications for Concrete Structures, Maintenance," *JSCE Guidelines for Concrete*, No.4.

Kato, E., Iwanami, M., Ito, H. and Yokota, H. (2003), "Influence of rebar corrosion on structural performance of RC beams subject to reversed cyclic loading," *Proceedings of the 9th EASEC*, Bali, RCS-205-210.

Kato, E., Iwanami, M., Yokota, H. and Hamada, H., (2008), "Corrosion characterization of reinforcing bar in existing RC structure," *Proceedings of the First International Symposium on Life-Cycle Civil Engineering*, Varenna, Lake Como, Italy, 177-182.

Overseas Coastal Area Development Institute of Japan (2002), "*Technical Standards and Commentaries for Port and Harbour Facilities in Japan*," translated from Japanese Edition in 1999.

Port and Airport Research Institute, (2007), "*Manual on Maintenance and Rehabilitation of Port and Harbor Facilities*," Coastal Development Institute of Technology.

Yokota, H., Tanabe, T. and Moriwake, A. (2002), "Maintenance management system for existing concrete marine structures. Repair, Rejuvenation and Enhancement of Concrete," *Proceedings of the International Seminar*, 37-48.

Yokota, H., Komure, K. and Takahashi, H. (2006), "Lifecycle management of concrete deck by Markov model," *Lifetime Engineering of Civil Infrastructure*, 137-149.

Yokota, H., Iwanami, M., Yamaji, T. and Kato, E. (2007), "Maintenance strategy of harbor structures in Japan based on life-cycle management," *Lifetime Engineering of Civil Infrastructure*, No.2, 229-238.

JOINT CONFERENCE PROCEEDINGS
7th International Conference on Urban Earthquake Engineering (7CUEE) &
5th International Conference on Earthquake Engineering (5ICEE)
March 3-5, 2010, Tokyo Institute of Technology, Tokyo, Japan

Shear Carrying Capacity of RC Beams Having Partially Corroded Longitudinal Reinforcement

Tomohiro Miki[1)] and Yasuhito Takeuchi[2)]

1) Associate Professor, Department of Civil Engineering, Kobe University, Japan
2) Undergraduate Student, Department of Civil Engineering, Kobe University, Japan
mikitomo@port.kobe-u.ac.jp

Abstract: This paper presents an experimental investigation to evaluate the residual structural performance of RC beams partially damaged due to steel corrosion. The acceleration corrosion test was carried out on the RC beams which were subsequently used in the loading test. From measurement instruments embedded in web concrete of the RC beams it is found that the maximum principle strain which is calculated by the measured strain increases at or before the load when a decisive diagonal crack occurs. In addition, the experiment shows the influence of corrosion cracks that are locally observed in the shear span and occurred along with the longitudinal reinforcement on the diagonal crack initiation and propagation due to the further loading.

1. INTRODUCTION

An appropriate method for the maintenance of existing structures has been required to keep the structures having their initial required performance. Deteriorations such as steel corrosion due to the permeation of chloride ions should be considered as one of the durability problems regarding reinforced concrete (RC) structures. With the deteriorated RC structures, it is required to evaluate the residual performance of the structures in a maintenance system, and hence an analytical tool to evaluate the performance of the structures is keenly needed. In the analysis for these structures, not only the material deteriorations but the interaction between concrete and steel reinforcement will be considered. This is because of that both the cross-section of the reinforcement and bond property due to expansion pressure by the corrosion products decrease when the steel corrosion occurs in the RC structures. Consequently the safety and serviceability of the structures is affected by the corrosion of steel reinforcement.

Since the shear failure can suddenly occur without any notice and result in a complete loss of structural capacity, it is certainly important to assess the shear carrying capacity of RC structural members accurately. However, it is difficult to formulate a phenomenon of RC behavior in shear witch depends on variables, including the bond property between concrete and reinforcement. Ikeda and Uji (1980) have been proposed a unified concept for the influence of bond on the shear behavior of RC beams based on their experiment and analysis. Matsuo et al. (2004) conducted the loading tests on the RC beams with or without stirrups having corrosion of reinforcements. The acceleration corrosion procedure by means of applying electric current was used to make corrosion in the steel reinforcement. The RC beams had longitudinal reinforcements with somewhat uniform condition in the shear span. It should note that the corrosion conditions of reinforcement in the actual structures may vary spatially since the surface condition of concrete structures and the environmental actions subjected to the structures depend on the site.

The final goal of this research framework is to establish a method to evaluate the performance of the RC structures using given information on the deterioration due to steel corrosion. To achieve this goal, the aim of this study is to evaluate the residual performance of RC beams having partially corroded longitudinal reinforcement by means of the experimental research. In the experiment, a developed measurement instrument embedded in the web concrete of RC beams is used to obtain the internal information in the concrete being affected by the corrosion condition of reinforcement.

2. TEST PROGRAMS

2.1 Specimens

The test program consisted in a total number of five RC beams. Details of the beam geometry and reinforcement layout are presented in Figure 1 and Table 1. As it can be seen from the figure, there are no stirrups in the shear span. The reason for such a reinforcement layout is that we want to evaluate the shear carrying capacity of the concrete itself without the help of shear reinforcement. For each concrete mix in Table 2 a beam with the dimensions of length, 1200

mm and cross-section of 200 × 150 mm was cast. In this study, a concrete with a designed compressive strength of 30 N/mm^2, obtained from uniaxial compression tests at 14 days, was considered. Maximum size of coarse aggregate was 20 mm. Early-strength Portland cement was used in the concrete mixes with an air entraining agent.

A series of test specimens are summarized in Table 3 and illustrated in Figure 2. The experimental parameters were set to be location, range and degree of the steel corrosion in the longitudinal reinforcement. The accelerated corrosion area was located at the middle of shear spans (No.2 and No.5), ranged from the middle of a shear span to the beam end (No.3 and No.4), as shown in Figure 2. As for the specimen No.4, in the anchorage zone from the support to the beams end, the current was applied additionally. The specimen No.5 had initial simulant cracks at the middle of shear spans where the accelerated corrosion was locally applied. These cracks were formed by means of thin stainless plates which are set there before concrete casting of the beam and removes after the removal of forms. The crack width was 0.2 mm.

2.2 Accelerated Corrosion Tests

Accelerated corrosion tests have been used successfully to determine the susceptibility of steel reinforcement to corrosion. The accelerated corrosion setup used in this investigation consisted of a DC power supply, plastic tanks, electrolytic solution (3% sodium chloride, NaCl by the weight of water) and stainless plates in each tank, as shown in Figure 3. The RC beam soffit was partially attached with a plastic sponge of which other side is immersed in the electrolytic solution of NaCl. The range and location of corrosion in the longitudinal reinforcement was controlled by the ones where the plastic sponge was attached with the soffit of the beams. During the accelerated corrosion test, the cumulative current per unit corrosion area (A*day/m^2) applying with a current witch is set from 0.7 to 1.7 A was controlled to induce the expected corrosion degree.

2.3 Loading Tests

To obtain the shear carrying capacity of the RC beams, a four point loading test was carried out. 2000kN universal test machine was used. For the purpose of the friction reduction at each support, a set of Teflon sheets lubricated with grease was used. During the loading test, the load, displacements at both supports and midspan, steel strain of longitudinal reinforcement, and strain in the web concrete explained detail in following section were measured.

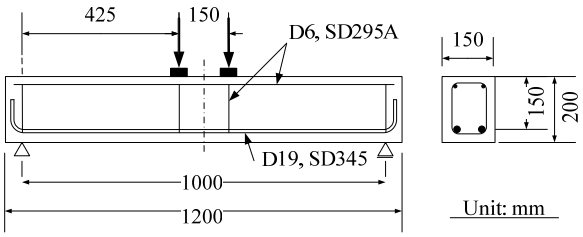

Figure 1 Details of tested beams

Table 1 Outlines of test beams

Cross-sectional width, b (mm)	150
Shear span, a (mm)	425
Effective depth, d (mm)	150
a/d	2.83
Concrete cover, side (mm)	30
Concrete cover, bottom (mm)	40.5
Cross-section of main bar A_s (mm^2)	573
$p_t = A_s/(b*d)$	1.91%

Table 2 Mixture properties

G_{max} (mm)	W/C (%)	s/a (%)	W (kg/m^3)	C (kg/m^3)	S (kg/m^3)	G (kg/m^3)	AE (ml/m^3)
20	64.9	45.0	179	276	886	945	414

2.4 Measurement of Strain in the Web Concrete

The internal strain in the web concrete within the shear span of a RC beam was measured during loading tests. Six triaxial rosette strain gages attached on an acryl plate (Tadokoro et al., 2005) which was formed and fabricated to firmly behave with surrounded concrete were embedded in the beam. This instrument with strain gages was fixed to the reinforcements for the preparation of concrete casting. For the specimens No.3 to No.5, two fabricated acryl gages, so

Table 3 Series of tested beams

Specimen	Corrosion conditions (mm)
No.1	Reference
No.2	Middle of shear span, 100
No.3	Ranged from the middle of shear span to the beam end, 312.5
No.4	Ranged from the middle of shear span to the beam end, 312.5; Additional corrosion at the anchorage zone, 100
No.5	Middle of shear span, 100 with initial cracks

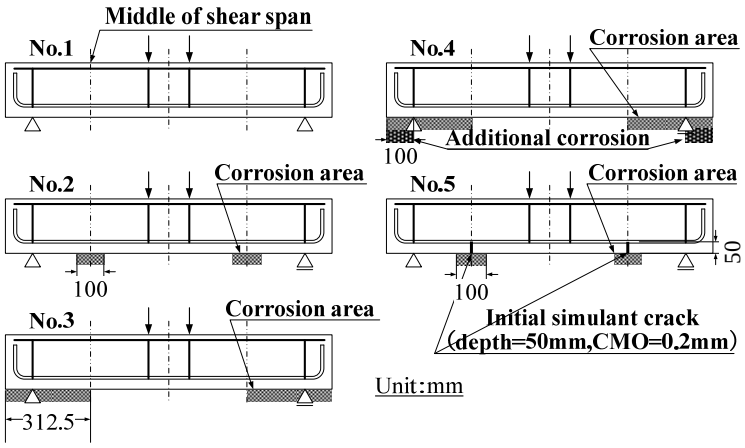

Figure 2 Outlines of the tested specimens

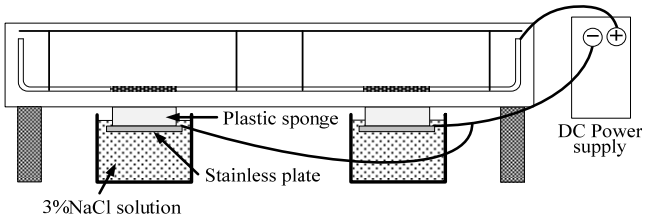

Figure 3 Test arrangement for accelerated corrosion

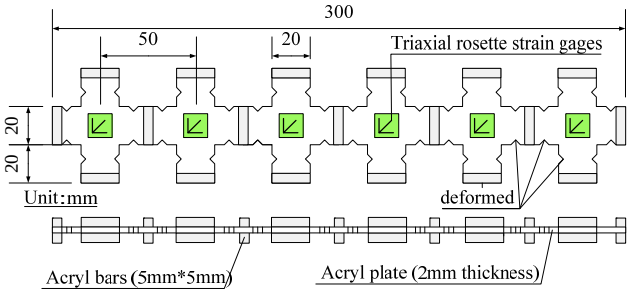

Figure 4 Details of a fabricated acryl gage

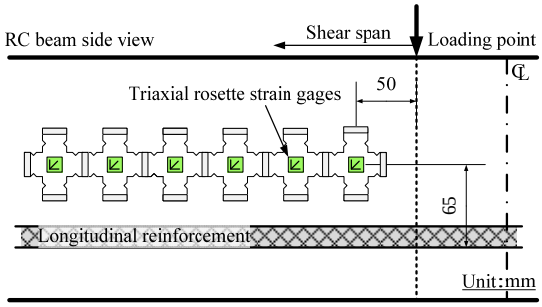

Figure 5 Location of the gages in the RC beam

that 12 measuring points was set were used in the both shear spans of the RC beams. Figures 4 and 5 illustrates details of the acryl attached the strain gages and their location set in the beam, respectively. The material properties of the acryl used in the test are summarized here; a density of 1.18 g/cm3, a tensile strength of 60 MPa, a yield strain of 4.5% and a Young's modulus in tension of 3000 MPa.

2.5 Procedure to Determine the Degree of Corrosion

The degree of corrosion was determined by the weight reduction of the steel reinforcement. In this study, the ratio of cross-sectional loss of reinforcing bar due to corrosion is defined as a ratio of the weight-loss of corroded reinforcing bar from its initial weight to that of non-corroded reinforcing bar. Tensile reinforcement was taken from the demolished RC beams after loading tests. To remove the rust on the steel reinforcement, the reinforcing bars were immersed in the 10% solution of diammonium hydrogen citrate at room temperature for 3 days. Then all reinforcing bars were divided into samples with the length of 50 mm. The ratios of cross-sectional loss were measured for each sample, and the distributions of the ratios of cross-sectional loss of reinforcing bar were measured. Therefore, the amount of corrosion can be estimated by using Eq. (1) as follows;

$$C = \frac{\Delta w}{w} \times 100 \tag{1}$$

where, Δw: weight difference between the samples of non-corroded and corroded reinforcing bars (g/mm), w: weight of non-corroded reinforcing bar (g/mm)

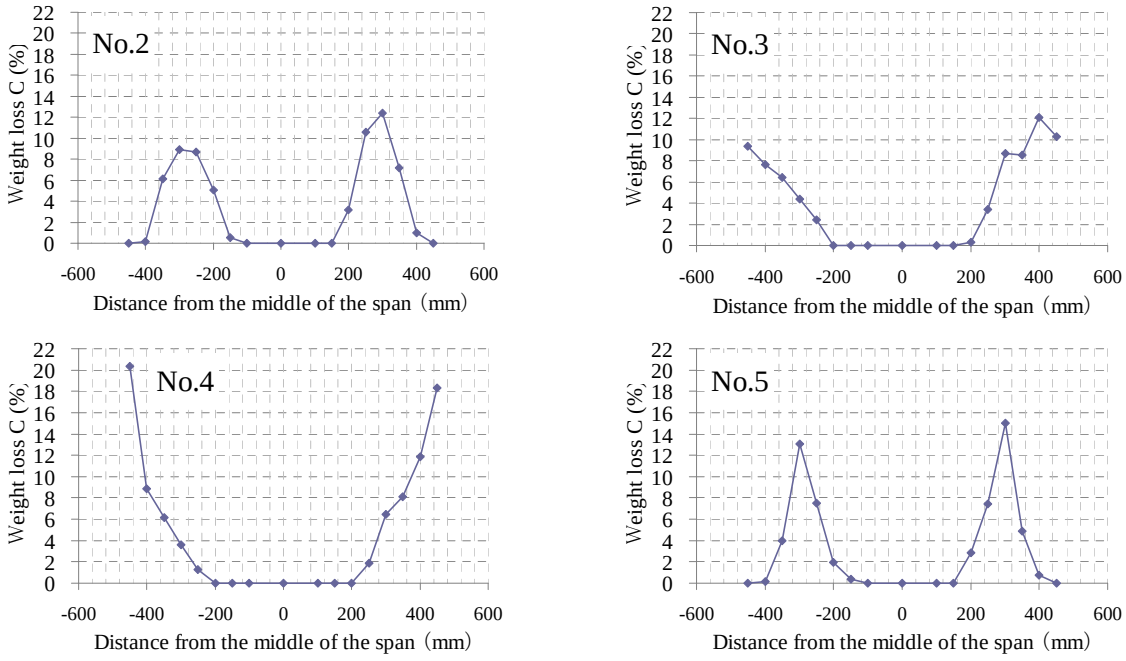

Figure 6 Distributions of cross-sectional loss of longitudinal reinforcement defined by weight reduction

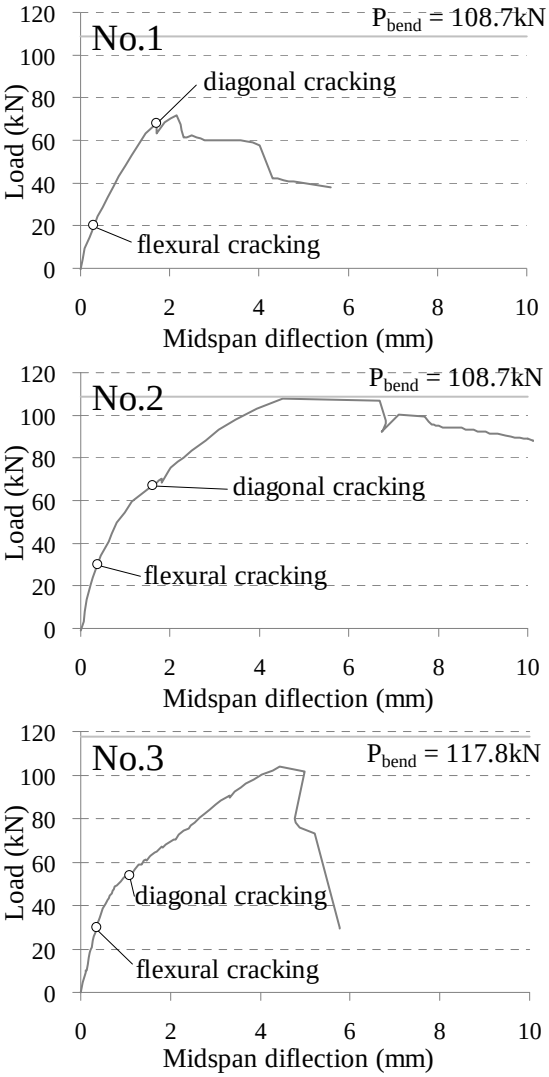

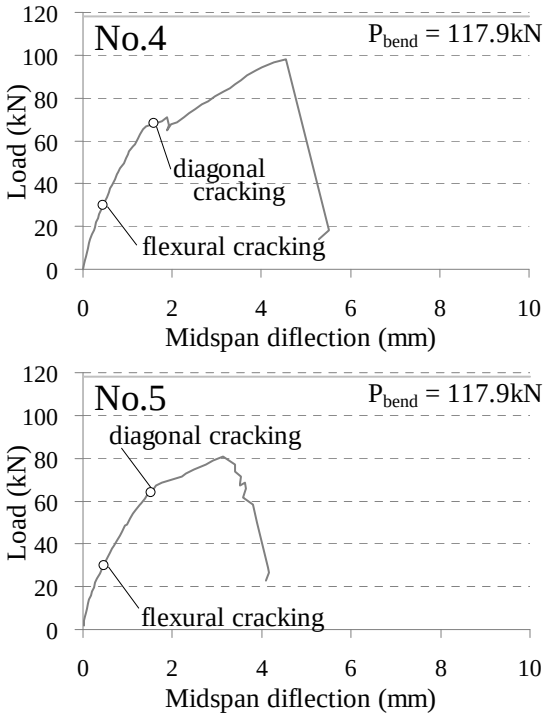

Figure 7 Load-displacement relationships

Table 4 Results of loading tests

Beam ID	f_c' (MPa)	Diagonal cracking load (kN)	Max. load (kN)	Failure mode
No.1	23.3	68	71.9	Diagonal tens.
No.2	23.3	67	107.7	Shear comp.
No.3	33.2	54	104.1	Shear comp./ Shear tens.
No.4	33.4	68	98.1	Shear comp./ Shear tens.
No.5	33.4	64	80.9	Diagonal tens.

3. TEST RESULTS AND DISCUSSION

3.1 Corrosion Tests

Figure 6 shows the distributions of cross-sectional loss of longitudinal reinforcement defined by Eq. (1) for the specimens No.2 to No.5. As can be seen in the figure, the corrosion of longitudinal reinforcement is localized within the portion and range where the accelerated corrosion was applied on purpose. The cracks along with reinforcements due to expansion of corrosion products were observed in all specimens containing the corrosion of reinforcement. In the specimen No.2 the corrosion cracks appeared along with the longitudinal reinforcement with somewhat wider range than those occurred in the specimen No.5. The specimen No.3 had cracks along with the longitudinal reinforcement in the region between the middle of shear span to the anchorage zone of the longitudinal reinforcement. As for the specimen No.4, the cracks was occurred in the similar to the specimen No.3 but more severe in the anchorage zone. Hence, the cracks occurred along with the 90° hooks at the each end of longitudinal reinforcement were observed.

3.2 Loading Tests

(1) Load-Displacement Relationships

The load-displacement relationships of all specimens are shown in Figure 7. In addition, the results of loading test are summarized in Table 4. The stiffness of all beams so that the inclination of the load-displacement curve decreases at 30kN corresponding the flexural cracking load. The stiffness of the specimens having the corroded reinforcement is similar to the control specimen No.1 until 70 kN at witch diagonal crack occurs except the specimen No.3.

As for the behavior after diagonal cracking, clear difference between corroded and uncorroded specimens can be exhibited. The specimen No.1 indicated a diagonal tension failure so that the beam failed in brittle immediately after a decisive diagonal crack widely opened. On the other hand, the load of the specimens No.2 to No.5, which are the beams having the corroded reinforcement, increased after the diagonal crack occurred, then the failure mode does not become brittle. From the results it can be expected that the failure mode changes with varying the condition of corrosion of the longitudinal reinforcement in the RC beams.

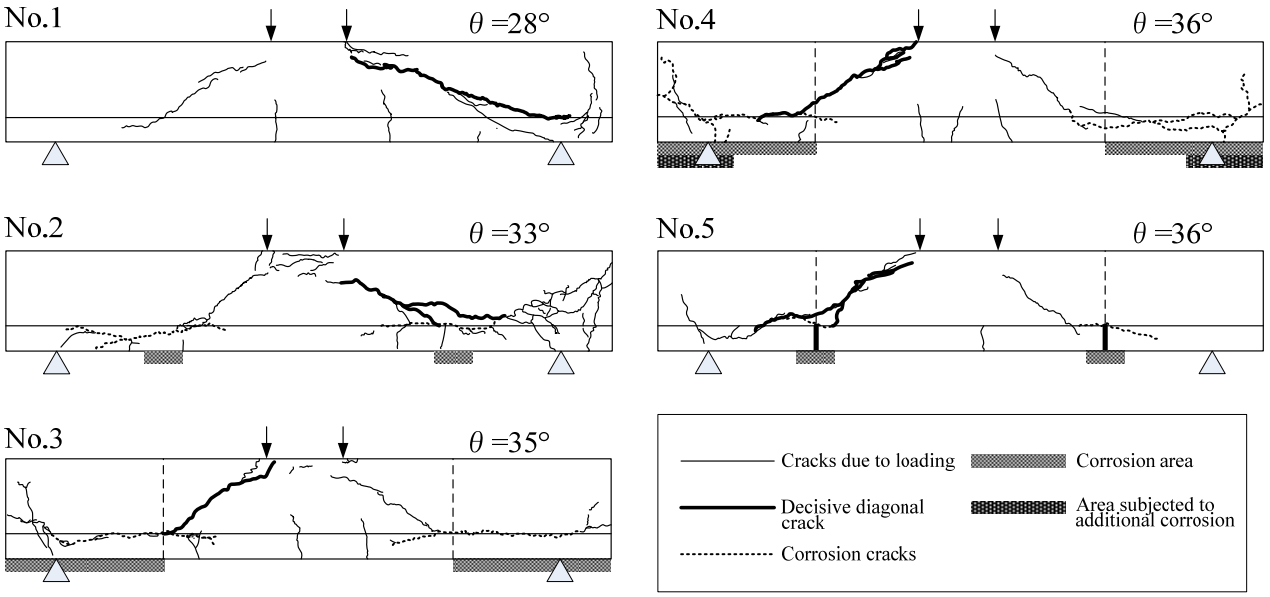

Figure 8 Crack patterns

(2) Crack Patterns of Tested Beams

The crack patterns of all beams after the loading tests are shown in Figure 8. In the figure an inclination angle of the decisive diagonal crack is also shown. Here, this inclination angle is defined as that of a linear approximation between the loading point and a crossing point of the corrosion crack to the longitudinal reinforcement, as referred the previous study (Tsunoda et al., 2008). The values of θ in Figure 8 are mean values of the inclinations estimated in the shear spans of the beams.

The decisive diagonal crack in the specimen No.1 seems to be located along with a line connecting the support and loading point. On the other hand, the specimens having the corroded reinforcement have the steeper decisive diagonal crack than in the control specimen. With the specimen No.2, diagonal cracks initially developed from the corrosion crack at an angle of around 33° with the horizontal. With further loading, it was observed that the existing corrosion crack had opened at the middle of the shear span. The final failure of the beam is caused by a crushing of the compression zone over the diagonal crack, as referred to the shear compression failure.

The specimens No.3 and No.4 had diagonal cracks from the corrosion crack. This behavior is similar to one of the specimen No.2. The experiment showed that in these beams the anchorage failure at the ends of the longitudinal reinforcement seemed to occur simultaneously with the crushing of concrete over the diagonal crack that is the vicinity of the loading point. The specimen No.5 was able to carry additional load after developing the diagonal crack at an angle of around 36°. This diagonal crack had propagated from the present corrosion crack at the middle of shear span. At ultimate stage the other crack which angle was smaller than the former subsequently occurred. This crack propagated and opened gradually and consequently resulted in the diagonal tension failure.

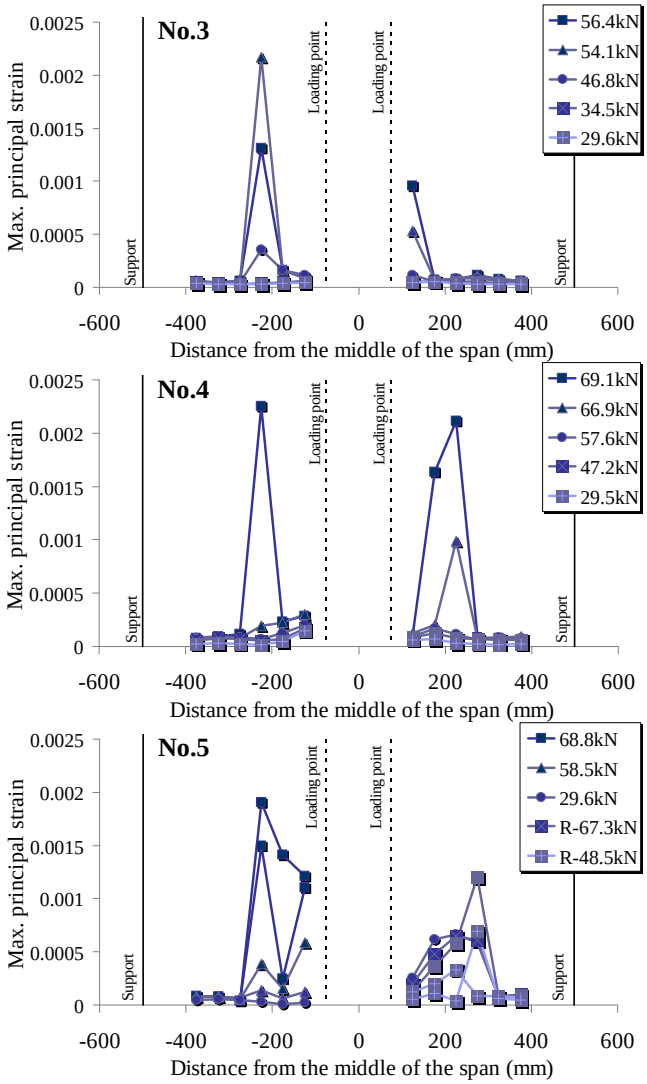

Figure 9 Concrete strain distribution in the web within the shear span

(3) Concrete Strain in the Web Concrete

As mentioned previously the internal strain in the web concrete within the shear span of a RC beam was measured during loading tests. The distribution of maximum principle strains in the specimens No.3 to No.5 is shown in Figure 9. The results indicated here were measured at the loads between of flexural cracking to of diagonal cracking of RC beams, respectively. As can be seen in the figure the strain measured near the diagonal crack significantly increased at the load when the crack occurred within the shear span.

In the specimen No.3 it is of interest to indicate the increase in the concrete strain before the diagonal cracking load of 56.4 kN. In this investigation the diagonal cracking load was determined the inclined crack initiation by the visual observation in the loading test. This result is implying that the strain condition in the web concrete was different with that at specimen surface even if the plane stress condition is assumed in the RC beam. As for the specimen No.4 this premature increase in the strain in the web concrete was not observed. The principle strain at the middle of right shear span of the specimen No.5 increased in the initial stage before the diagonal crack occurred in the shear span, implying that the initial simulant crack influenced on the response of the web concrete subjected to shear.

4. SUMMARY

In this study the accelerated corrosion tests and loading tests was carried out for five RC beams with and without the corrode reinforcement. The control RC beams with a shear span ratio a/d = 2.83 designed failed in shear. With these RC beams, the experimental investigation aims to study the influence of varying the range and location of corrosion in the longitudinal reinforcement on the shear resisting mechanism of damaged RC beams. The conclusions obtained in the present study are as follows:

1) The carrying capacity of the RC beams having locally corroded longitudinal reinforcement increases compared to the noncorroded beam.
2) The experiment shows the influence of corrosion cracks that are locally observed in the shear span and occurred along with the longitudinal reinforcement on the initiation and propagation of the decisive diagonal crack due to the further loading.
3) From the measurement instrument embedded in the web concrete of RC beams the maximum principle strain which is calculated by measured strain increases at or before the load when the decisive diagonal crack occurred.

Acknowledgements:

This research was partially supported from the Ministry of Education, Culture, Sports, Science and Technology (MEXT), Grant-in-Aid for Young Scientists (B).

References:

Ikeda, S. and Uji, K. (1980), "Studies on the Effect of Bond on The Shear Behavior of Reinforced Concrete Beams," Journal of Materials, Concrete Structures and Pavement, **293**, 101-109.

Matsuo, T., Sakai, M., Matsumura, T. and Kanazu, T. (2004), "An Experimental Study on Shear Resisting Mechanism of RC Beams with Corroded Reinforcement," Concrete Research and Technology, **15**(2), 69-77.

Tadokoro, (2005), "Effects of Shear Span Ratio on Shear Strength of RC Members with Circular Section," *Journal of Japan Concrete Institute*, **27**(2), 811-816.

Tsunoda, M., Watanabe, K., Miki, T. and Niwa, J. (2008), "Shear Behavior of RC Beams with Locally Corroded Reinforcement," *Journal of Japan Concrete Institute*, **30**(3), 1705-1710.

JOINT CONFERENCE PROCEEDINGS
7th International Conference on Urban Earthquake Engineering (7CUEE) &
5th International Conference on Earthquake Engineering (5ICEE)
March 3-5, 2010, Tokyo Institute of Technology, Tokyo, Japan

STRENGTHENING REINFORCED CONCRETE COLUMNS BY HIGH PERFORMANCE FERROCEMENT

Ivy F.Y. Ho [1] and Eddie S.S. Lam [2]

1) MPhil student, Dept. of Civil & Structural Engineering, The Hong Kong Polytechnic University, Hong Kong
2) Associate Professor, Dept. of Civil & Structural Engineering, The Hong Kong Polytechnic University, Hong Kong
ivyhofy08@gmail.com, cesslam@inet.polyu.edu.hk

Abstract: In Hong Kong, majority of our buildings are facing different degree of deterioration and requiring rehabilitation to preserve their life span. For those completed prior to the enforcement of the current Code of Practice, i.e. Code of Practice for Structural Use of Concrete 2004 ("CoP 2004"), they may not fulfill the current detailing requirement. One particular area of concern is related to the detailing of reinforced concrete columns, which is also the subject matter of this paper. Firstly, transverse reinforcement is now detailed using 135^0 hooks instead of 90^0 hooks. The latter was specified in the predecessor of CoP 2004, i.e. Code of Practice for Structural Use of Concrete 1987 ("CoP 1987"). Secondly, spacing of transverse reinforcement is greatly reduced. As a result, the existing columns may fall short of providing sufficient lateral confinement, shear capacity and ductility in accordance with the CoP 2004. It follows that strengthening of existing columns is inevitable.
Eight full-scale circular reinforced concrete columns tested to failure under axial compression. Some are strengthened with high performance ferrocement ("HPF"). The test parameters include two types of cementitious matrix and two different mesh densities. The former includes polymer mortar and fiber reinforced mortar. It is observed that specimens detailed to CoP 1987 and strengthened by HPF can achieve a load carrying capacity compatible to specimen detailed to CoP 2004. HPF strengthening is an effective way to upgrade the existing column to the current standard endowed by CoP 2004. The test results also show that confinement action provided by HPF is primarily influenced by tensile strength of rendering mortar and secondly by mesh density. The next step (which is in progress) is to develop a theory to correlate confinement action, tensile strength of rendering mortar and mesh density to load carrying capacity of columns.

1. INTRODUCTION

Hong Kong has now been well recognized as a region with moderate seismic risk. The "Seismic Ground Motion Parameter Zonation Map of China" ("GB 18306-2001") specifies that the peak ground acceleration of Hong Kong with a return period of 475 years is 0.15g on rock site. According to the Code for Seismic Design of Buildings ("GB 50011-2001"), Hong Kong is in a region with seismic intensity 7.5. However, buildings in Hong Kong are traditionally designed without seismic provisions (Lam et al. 2002). Buildings (Construction) Regulations currently in force make no provisions for seismic resistant design. According to Structural Use of Concrete 1987 ("CoP 1987"), predecessor of the current design code, it is not necessary to provide structural members with seismic detailing. The design code in force, i.e. Code of Practice for Structural Use of Concrete 2004 ("CoP 2004"), has nevertheless provided guideline on the detailing of structural members, in particular the columns, for ductility.

In respect of columns, main differences between CoP 1987 and CoP 2004 on reinforcement detail are related to the transverse reinforcement. Similarities and differences between the two codes of practice on reinforcement detail are given in Table 1.

Table 1 Detailing of CoP 1987 v. CoP 2004

	CoP 1987	CoP 2004
Main reinforcement	Usually 4-5% maximum	
Hooks	90^0 and 8d	135^0 and 6d
Overlapping of hooks	Nil	2 bars
Spacing of transverse reinforcement	≤ 12 x D; ≤ 300mm; ≤ H	≤ 6 x D; ≤ ¼ x H

(d = diameter of transverse reinforcement; D = diameter of main reinforcement; H = breadth or depth of column)

Figure 1 shows the transverse reinforcement detail as per specified in CoP 1987 and CoP 2004. In general, the columns are subjected to high axial load. The use of large spacing of transverse reinforcement (usually at 300mm) and 90^0 hooks has obvious disadvantages in seismic resistant design. As a result, the existing columns may fall short of providing sufficient confinement action, shear capacity and/or ductility as compared with those detailed to CoP 2004. It follows that strengthening of the existing columns is inevitable.

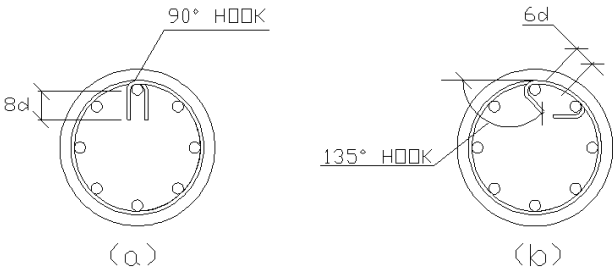

Figure 1 Detail of hooks (a) CoP 1987 and (b) CoP2004

It is the main objective of this study to develop a strengthening system for existing columns using high performance ferrocement ("HPF"). At the present stage of the study, three different types of rendering mortar are considered including cement-sand mortar and polymer or epoxy based materials. This paper reports the experimental results of 8 full-scale column specimens tested between November 2009 and January 2010, and the initial findings.

2. STRENGTHENING USING FERROCEMENT

On the subject of strengthening reinforced concrete columns, various methods have been proposed including, *inter alia*, jacketing; pre-stressing; use of fiber reinforced polymer ("FRP") and ferrocement. Among others, Ersoy et al. (1993) applied steel and concrete jacketing. Bracci et al. (1995) introduced pre-stressed concrete jacketing. Wu, Liu and Oehlers (2006) recommended the use of steel/FRP jacketing. Harries et al (2006) implemented CFRP jacketing to columns in old buildings. Unfortunately, mechanical resistance of steel/FRP jackets has to be ignored under fire due its rapid reduction in strength at moderate temperature (Han et al. 2006) and require additional fire protection. Similar difficulties were encountered using FRP or externally bonded steel plates for strengthening. For instance, Tadeu and Branco (2000) conclusion that the bonding material used in externally bond steel plate may fail in the event of a fire.

On the other hand, the use of ferrocement is more promising due to better fire resistance. Williamson and Fisher (1983) indicated that ferrocement wall has good fire resistance compatible to concrete. Kaushik et al. (1996) demonstrated that ferrocement can protect the encased column specimens when subjected to fire. Geng et al. (1998) and Cao et al. (2007) applied fiber-reinforced composites or mortar to enhance the ductility of beam-column joints. Lim et al. (2000) carried out tests on T-beams repaired by ferrocement. All in all, ferrocement has been demonstrated as a viable alternative for strengthening reinforced concrete members (ACI549.1R-93, Paramasivam et al. 2000). Other advantages of applying ferrocement are comparatively easy to construct, requiring no special technique and cost effective.

Description on ferrocement can be referred to publications by Shah et al. (1986) and Naaman (2000). It comprises multiple layers of closely spaced small-diameter wire meshes which do not allow large particles to pass through. As a result, mortar with small particle size with or without fine grain aggregates is recommended by both ACI 549.1R-93 and Naaman (2000). In the particular application considered in this study, the workability of mortar is an important factor. If the workability of mortar is too high, it may not be able to apply vertically. On the other hand, if the workability is too low, it may not be able to penetrate through the mesh layers.

3. THE SPECIMENS

Eight specimens are prepared and tested to failure under axial compression. The specimens are in full-scale of 350mm diameter and 980mm height. Concrete cover is 25mm. Specimens TPC; TA300C; TB75C and TB300C were casted in PVC moulds with internal diameter of 350mm whereas specimens TA300CS3; TA300SD1; TA300SD3 and TA300ST3 were casted in PVC moulds with internal diameter of 300mm. Specimens TA300CS3; TA300SD1; TA300SD3 and TA300ST3 were then strengthened by HPF of different compositions.

In the absence of seismic provisions, 8T25 (or 4% main reinforcement ratio) are used as the main reinforcement. Two types of transverse reinforcement detail are considered as shown in Figure 1. They are identified as A (to CoP 1987) and B (to CoP 2004) with the respective volumetric ratios of transverse reinforcement (r_s) at 0.230% and 0.918%. Basic properties of the specimens are given in Table 2. Square welded meshes were adopted and put together with different types of rendering mortar for strengthening in this research. Mechanical properties of wire meshes are given in Table 3.

Table 2 Basic properties of specimens

Specimen	Transverse reinforcement (hook)	Rendering mortar	Layers of wire meshes
TPC	Nil	Nil	Nil
TA300C	R8@300 (90^0)	Nil	Nil
TB75C	R8@75 (90^0)	Nil	Nil
TB300C	R8@300 (135^0)	Nil	Nil
TA300CS3	R8@300 (90^0)	Cement-sand	3
TA300SD1	R8@300 (90^0)	Sikadur	1
TA300SD3	R8@300 (90^0)	Sikadur	3
TA300ST3	R8@300 (90^0)	SikaTop	3

Table 3 Mechanical properties of meshes.

	Longitudinal direction	Transverse direction
Diameter (mm)	0.82	1.14
Spacing (mm)	12.7	12.6
Ultimate strength (MPa)	Nil	548
Corresponding strain	Nil	0.04874

Specimen TPC is the control specimen made of plain concrete. Specimens TA300C and TB75C are detailed in accordance with CoP 1987 and CoP 2004 respectively. It is required in CoP 2004 that the transverse reinforcement should be closely spaced at the critical region in accordance

with its axial load factor. Typical columns in Hong Kong are stocky columns with clear height around 2.5-3.0m. Thus, transverse reinforcement is generally provided at equal spacing as in critical region throughout the whole column. Configuration of transverse reinforcement of column specimen TB300C is designed in accordance with CoP 1987 but using 135^0 hooks. Reinforcement detail of specimens TA300CS3, TA300SD1, TA300SD3 and TA300ST3 are identical to specimen TA300C. They are strengthened with cement-sand mortar with three layers of meshes, SikaTop 122HB ("Sika Top") with one layer of meshes, Sikadur 41 C F Normal ("Sikadur") with 1 or 3 layers of meshes as per Table 2.

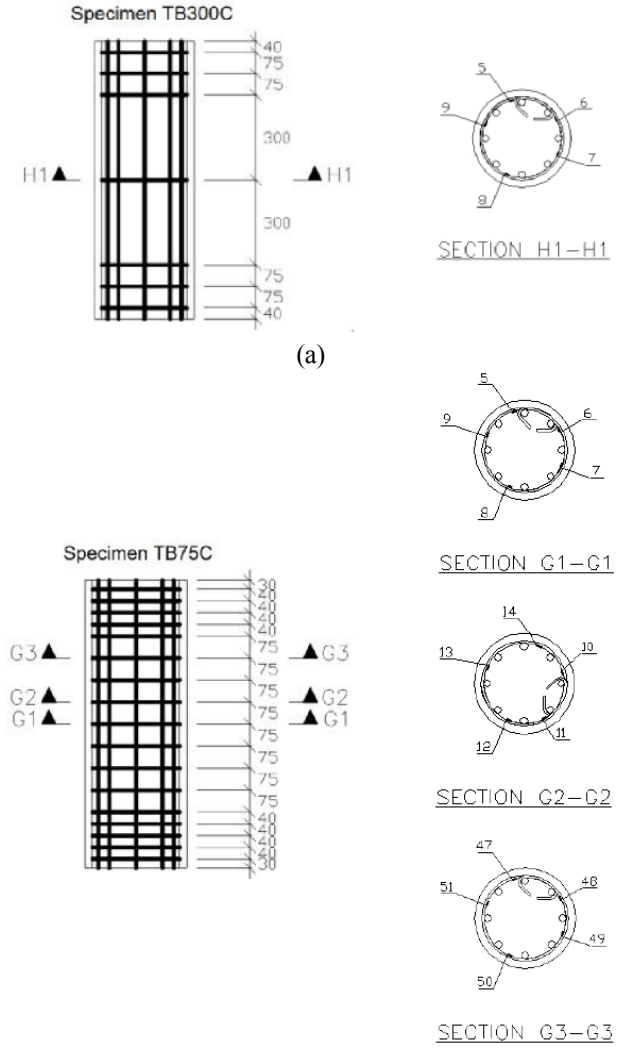

Figure 3 Reinforcement detailing to (a) CoP 1987 and (b) CoP 2004

The specimens are divided into two groups to study the influence on load carrying capacity by four parameters includes (i) angle of hooks; (ii) spacing of transverse reinforcement; (iii) tensile strength of rendering mortar and (iv) mesh densities. Specimens TPC, TA300C, TB75C and TB300C are used for studying parameters (i) and (ii). The other four specimens are strengthened with HPF as replacement of the concrete cover. These HPF strengthened specimens are used for studying parameters (iii) and (iv). An attempt in evaluating correlation between parameters (iii) and (iv) was made in this research.

Figure 3 shows typical elevation and section of the specimens. Observed zone of the specimens are at the middle portion and spacing of the transverse reinforcement is reduced by half at both ends to prevent failure at the ends. Location and identification of strain gauges installed on transverse reinforcement are also numbered in the figures. Figure 4 shows the arrangement and identification of LVDTs and rosettes. LVDTs were installed at 90^0 apart with gauge length of 400mm at the observed zone. Strain gauges are installed on the main reinforcement and transverse reinforcement (see Figures 3 and 5).

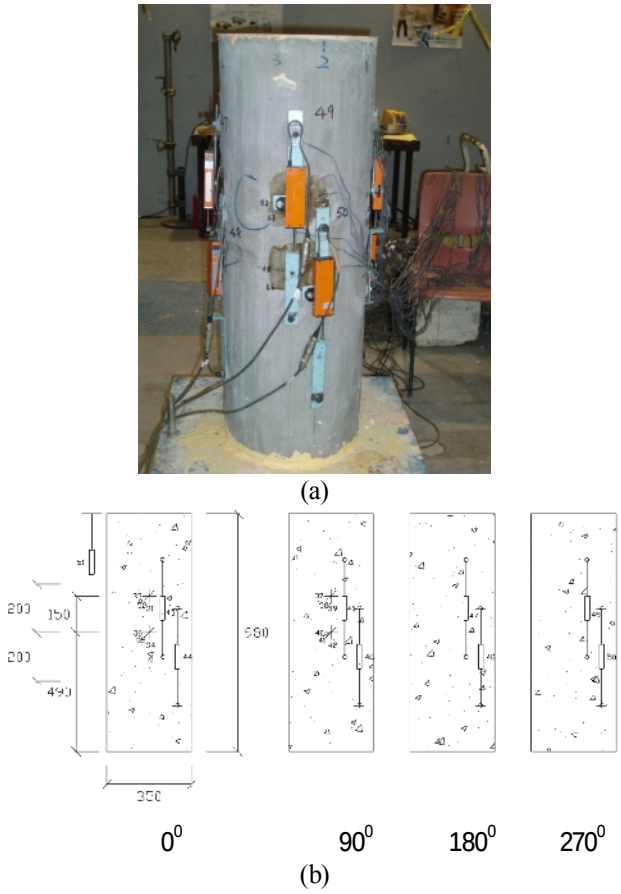

Figure 4 Arrangement and identification of LVDTs and rosettes at four directions.

Table 4 shows the material properties of rendering mortars considered in this study. They are traditional cement-sand mortar, polymer based mortar (cementitious material) and epoxy based mortar. Properties of cement-sand mortar are obtained from the compression test and tensile splitting test on a pair of 150mm cubes and 150mm x 300mm cylinders respectively whereas properties of the other materials are provided by the manufacturer.

Mix proportion of the cement-sand mortar is water-cement ratio at 0.55 and sand-cement ratio at 3.00. SikaTop is a two-component polymer modified cementitious mortar. It has high bond strength and can effectively resist passage of water and carbon dioxide. Sikadur is a solvent-free three-component mortar consists of epoxy resins and special filler. It has the highest tensile splitting strength among the three rendering materials considered in this study.

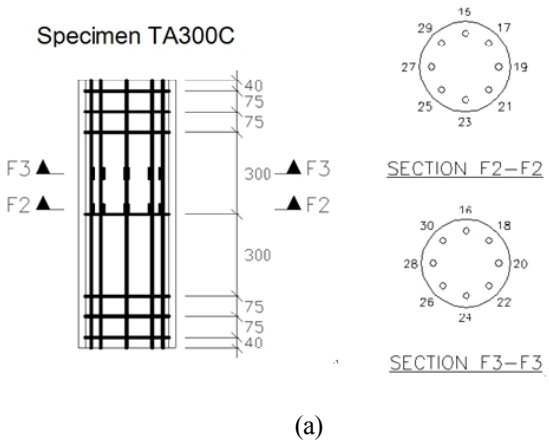

(a)

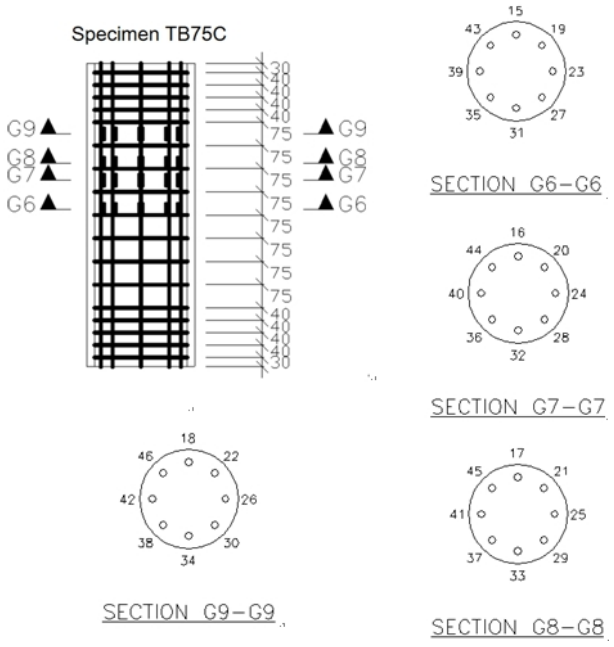

(b)

Figure 5 Arrangement and identification of strain gauges on main reinforcement detailed to (a) CoP 1987 and (b) CoP 2004.

Welded square meshes were used as reinforcement in HPF in this research. The meshes have averaged diameter and width of opening of 1.14mm and 12.60mm respectively in transverse direction and 0.82mm and 12.70mm respectively in longitudinal direction. The averaged ultimate strength of wire is 548MPa with ultimate strain of 0.04874.

The specimens were prepared from ready mix concrete. Averaged 28-day cube strength of concrete is 41.7N/mm^2 (estimated from 150mm test cubes). Measured properties of the reinforcement are given in Table 4. Table 5 lists the averaged measured properties of reinforcement.

Table 4 Properties of rendering materials (MPa)

Material	Compressive strength	Tensile splitting strength
Cement-sand mortar (10 days)	24.3	2.7
SikaTop (7days)	35.0	3.5
Sikadur (7days)	Min 59.0	Min 13.0

Table 5 Averaged measured properties of reinforcement

Diameter (mm)	Yield Strength (N/mm^2)	Ultimate Strength (N/mm^2)
25	523.0	688.0
8	369.6	456.0

A method statement was prepared to systematically outline the procedure of rehabilitation of existing reinforced concrete columns using HPF. The method statement is listed in the Appendix. Strengthening of all specimens strictly follows the method statement.

Surface of the specimens is first prepared using jack hammer to expose the embedded aggregates and transverse reinforcement as shown in Figure 6(a). Wire meshes are cut to the required dimension. Width of the wire meshes is the same as the width of the wire meshes roll (i.e. 914.40mm). Wire meshes are wrapped around the specimen layer by layer as shown in Figure 6(b). Steel wires are used to fix the position of the wire meshes. At least 100mm lap length is provided for each layer of wire meshes in accordance with the recommendation by Naaman (2000). Pressurized air is used to clean the specimen before application of the rendering mortar (see Figure 6(c)).

Rendering material is properly prepared and applied in accordance with the manufacturer's instruction. In particular, rendering material is consumed within the setting time as per specified in the manufacturer's instruction (i.e. within 1/2 hours). All specimens are air cured indoor for at least 7 days before testing. Capping material is applied to the ends of the specimens to achieve concentric and uniform loading.

Figure 7 shows the test setup. Axial load is applied through a hydraulic jack installed on a reaction frame. All specimens were tested by a Computer-Electro-Hydraulic Servo Controlled Multi-Purpose Testing System. The loading machine is displacement control with a maximum loading capacity of 10,000kN.



(a) Surface preparation



(b) Installation of mesh layers

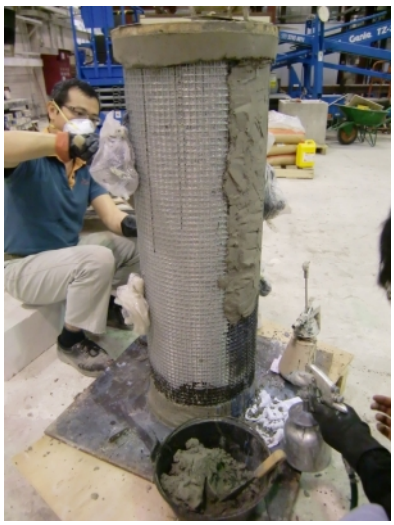

(c) Application of rendering mortar

Figure 6 HPF strengthening process.



Figure 7 Photo of test setup.

The strain rate varies in different stages. At the linear elastic portion of the load-strain curve, the strain rate is at 0.5mm/min. At the non-linear pre-peak portion, the strain rate is reduced to 0.2mm/min. When approaching the maximum load, the strain rate is further reduced to 0.1mm/min. At the post-peak region, the strain rate is 0.05mm/min. The loading test is terminated when the axial load carrying capacity of the specimen is reduced by more than 15% from the maximum.

4. TEST RESULTS

Figure 8 shows the typical modes of failure after testing. Figure 8(a) shows mode of failure of specimen TPC. It fails in a cone shape with fully developed diagonal cracks at approximately 45^0. Specimen TA300C failed in a similar manner as to specimen TB300C (see Figure 8(b)). Spalling of concrete cover and buckling of main reinforcement were observed in the observed zone. Figure 8(c) shows the mode of failure of specimen TB75C which has a relatively less serious spalling of concrete cover and buckling of main reinforcement when compared with specimen TA300C and TB300C. Figure 8(d) shows the failure condition of specimens TA300CS3. The same mode of failure is shared by specimens TA300SD1; TA300SD3 and TA300ST3. Hooks of transverse reinforcement remain intact throughout the test and sign of arching effect can also be observed in all specimens (see Figure (9)). As shown in Figure 10 vertical crack is developed in the observed zone of HPF strengthened specimens. Rendering mortar and wire meshes distorted or fractured.

Typical load-strain plots on main reinforcement and transverse reinforcement are shown in Figure 11. Strain is obtained by strain gauges installed on the reinforcement as described in Figures 3 and 5. Figure 12 shows the load-strain plot of all specimens where strain is obtained by LVDTs measuring the overall vertical displacement of specimens.

Data obtained from the tests are summarized in Table 5.

Table 5 Results of peak strength and corresponding strain of main reinforcement

Specimen	Peak strength, F_{Peak} (kN)	Corresponding strain	Concrete force, F_c (kN)
TPC	2833.4	0.00234	Nil
TA300C	3632.9	0.00300	1579.1
TB75C	4529.8	0.00728	2476.0
TB300C	3736.3	0.00305	1682.5
TA300CS3	4036.7	0.00378	1982.9
TA300SD1	4765.0	0.00421	2711.2
TA300SD3	4918.9	0.00319	2865.1
TA300ST3	4368.5	0.00702	2314.7

Note:- $F_c = F_{Peak} - A_{st}f_y$ where A_{st}=8Φ25; f_y=523MPa



(a) Specimen TPC



(b) Specimen TB300C



(c) Specimen TB75C



(d) Specimen TA300CS3

Figure 8 Typical failure modes of specimens.



Figure 9 Condition of hooks



(a)



(b)

Figure 10 Failure of HPF

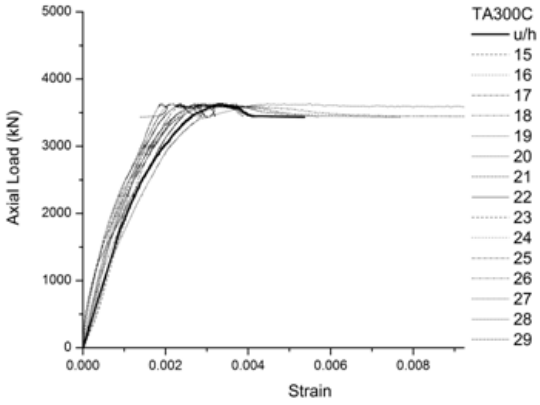

(a) Main reinforcement

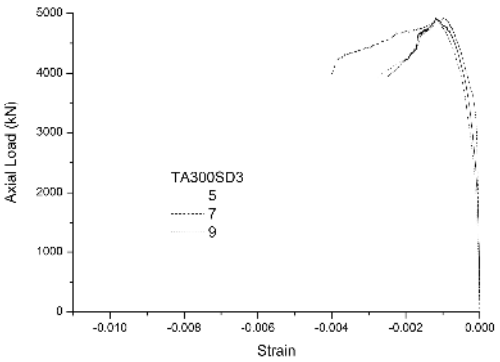

(b) Transverse reinforcement

Figure 11 Load-strain plots of (a) specimen TA300C and (b) specimen TA300SD3

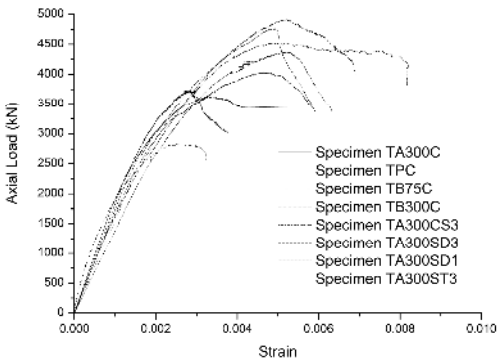

Figure 12 Load-strain plots of overall displacement (u/h)

4. CONFINEMENT ACTION

As concrete cover was not restrained by the transverse reinforcement, it is free to expand and spalls off under compression. In all the tests, concrete cover has delaminated before reaching the peak strength. When the concrete cover starts to lose its load carrying capacity due to delamination, compressive force will progressively transfer to and resist by the main reinforcement and the core concrete. As a result, the compressive strength of core concrete will have to increase to compensate for the loss in the load carrying capacity due to delamination of the concrete cover.

When a specimen is subjected to unaxial compression, lateral strain of concrete increases progressively with increasing stress. When the lateral strain of concrete reaches a critical level, there will be interaction between the core concrete and the transverse reinforcement. Transverse reinforcement will provide a confining pressure to confine the core concrete by restraining lateral expansion of concrete. It therefore enhances the overall stiffness of the specimen. The interaction works in a manner similar to the triaxial action of soil. A number of studies were carried out on this confinement effect by researchers, e.g. Richart (1929), Mander et al. (1988) and Saatcioglu and Razvi (1999). The mechanism of confinement effect is illustrated in Figure 12. Sign of arching effect can be observed in Figure 10. Compressive buckling of main reinforcement can also be seen. Besides, hooks of transverse reinforcement remain intact after testing.

Some studies have been carried out by other investigators on uniaxial compressive strength of confined concrete, for instance Mander et al. (1988), Richart et al. (1928) and Balmer (1949). It is widely accepted that uniaxial compressive strength of concrete can be enhanced significantly by proper lateral confinement. When proper confined concrete is subjected to progressive increase in uniaxial compression, lateral confinement will exercise a triaxial confining action to the core concrete. This allows the core concrete to withstand a larger applied load with change in the mode of failure.

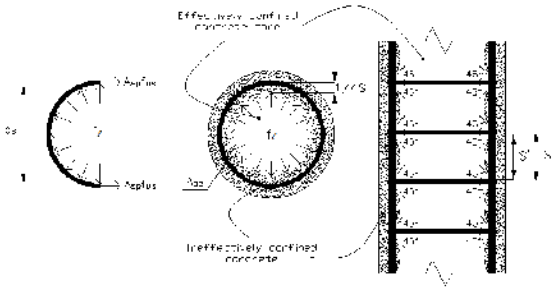

Figure 12 Mechanism of confinement action provides by circular hoops

Table 5 lists the peak strength and corresponding strain of main reinforcement. By comparing the peak strength of specimens TA300C and TB300, it seems that the variation in angle of hooks does not have significant influence to load carrying capacity of specimens.

All except specimen TA300SD1 strengthened with HPF show no sign of buckling of main reinforcement. This suggests that HPF embedded with more layers of wire meshes (i.e. higher volume fraction (V_{RL}) and specific surface (S_{RL})) performs better in restraining lateral expansion.

Specimens TA300SD1 and TA300SD3 are both rendered with Sikadur mortar. Sikadur mortar has the highest tensile strength among the other mortars (i.e. SikaTop and normal cement-sand mortar) adopted in this

research. Peak strength of specimen TA300SD3 is 3.2% higher than that of TA300SD1. This indicates that mesh density is not crucial in enhancing load carrying capacity of specimens. Specimens TA300CSD1 and TA300CSD3 achieve peak strength compatible to specimen TB75C which indicates that HPF can be an effective way to enhance load carrying capacity of column to standard endowed by CoP 2004.

After exposure of the wire meshes, it is observed that wire meshes fractured in location away from the lapping. This assures that the lap length so provided is sufficient.

Provided that the HPF layer is of identical thickness (i.e. 25mm) as of concrete cover provided in specimens without HPF strengthening, the tensile strength provides by HPF can be calculated as follow. The combined tensile strengths of different composition of HPF are listed in Table 6.

- Tensile strength of Sikadur =25 x 13=325N/mm
- Tensile strength of SikaTop=25x3.5=87.5N/mm
- Tensile strength of 1 layer of meshes= 548x (1.14^2xp/4)/12.6=44.4N/mm
- Tensile strength of 3 layer of meshes=133.1N/mm

However, these values are indicative only since we have made a presumption that tensile strength of rendering mortar is mutually exclusive with layers of meshes embedded. As HPF is reinforced with meshes with relatively small opening, it allows multiple cracks to develop in the rendering mortar under tension. Therefore, stress accumulated in the rendering mortar will be small (Naaman 2000). The overall tensile properties/ductility of HPF is then improved.

Table 6 Tensile strength provides by HPF of 25mm thick and of different mesh densities.

	1 layer of meshes (N/mm)	3 layers of meshes (N/mm)	Difference (%)
SikaTop	131.9	220.6	60
Sikadur	369.4	458.1	81

Consider the test results shown in Table 7, peak strengths (F_{Peak}) of specimens TA300SD1 and TA300SD3 are 4765.0kN and 4918.9kN. The different between these two values can be considered as the axial strength contributed by addition of 2 layers of meshes in HPF. By proportion, axial strength contributed by the 3 layers of meshes will be 230.85kN. Tensile strength of HPF is crucial to confinement action and load carrying capacity of a column. An attempt was made in this research to correlate tensile strength of HPF and load carrying capacity of specimen. Since confinement action is provided by both transverse reinforcement and HPF in specimens TA300CS3; TA300SD1; TA300SD3 and TA300ST3, an assumption is made as to consider transverse reinforcement and HPF are working as one united system. Thus, the diameter of specimen confined by this united system is 284mm (i.e. 350-2x25-2x8). Peak strength contributed by mortar, $F_{(mortar)}$ of specimen TA300CS3 is 3805.85kN which is similar to the prediction of load carrying capacity as shown below.

$$2833.4 \times \frac{284^2 \times \frac{\pi}{4} - 8 \times 491}{350^2 \times \frac{\pi}{4}} + 8 \times 491 \times \frac{523}{1000}$$

$$= 3804.2kN \approx 3850.85kN$$

Table 7 Results of peak strength and corresponding axial of main reinforcement.

Specimen Mark	Peak Strength (kN), F_{Peak}	$F_{(mortar)}$ (kN) = $F_{Peak} - F_{(mesh)}$	F_m (kN)
TPC	2833.4	2833.4	--
TA300C	3632.9	3632.9	--
TB75C	4529.8	4529.8	--
TB300C	3736.3	3736.3	--
TA300CS3	4036.7	3805.9	--
TA300SD1	4765.0	4688.0	882.2
TA300SD3	4918.9	4688.0	882.2
TA300ST3	4368.5	4137.7	331.8

By deducting $F_{(mesh)}$ of specimens TA300SD1; TA300SD3 and TA300ST3 from F_{Peak} of specimen TA300CS3, load carrying capacities contributed by rendering mortar of high tensile strength F_m were found and shown in Table 7.

Assume a quadratic relationship exists between tensile strength of rendering mortar (s_m) and F_m, the following correlation is evaluated.

$$-2.836s_m^2 + 104.724s_m^2 = F_m \qquad \text{eqn.(1)}$$

and

$$F_{Peak} = f_{co} \times (A_e - A_{st}) + A_{st} \times f_y - 2.836\sigma_m^2 + 104.724\sigma_m \qquad \text{eqn.(2)}$$

Units: s_m (MPa); F_m (kN); F_{Peak}(kN)

Further tests will be carried out to justify the above coorelation.

5. CONCLUSIONS

In this study, eight full-scale specimens with detailing in accordance with CoP 1987 and CoP 2004 were subjected to unaxial compression. Half of the specimens detailed in accordance with CoP 1987 are strengthened with HPF with different types of rendering mortar and layers of wire meshes. Preliminary conclusions are as follow:-

(i) Variation of angle of hooks does not have significant influence on load carrying capacity of specimens.
(ii) The use of closer spacing of transverse reinforcement enhances load carrying capacity of specimens.
(iii) Variation of mesh density has less significant influence on load carrying capacity of specimens in this case.
(iv) Tensile strength of mortar is crucial in achieving higher capacity of specimens.
(v) A certain correlation exists between tensile strength of mortar and peak strength of specimens.

Test results show that specimen strengthened with HPF can achieve an axial load capacity comparable to specimen detailed in accordance with CoP 2004. This indicates that

HPF can be an effective way in upgrading the existing columns to satisfy the standard endowed by CoP 2004.

Acknowledgements:

The authors are grateful to the financial support from The Hong Kong Polytechnic University and the Research Grants Council of Hong Kong (RGC No: PolyU 5206/08E).

The authors would like to thank for the technical assistance provided by the Civil Engineering Department of the South China University of Technology and the Heavy Structural Laboratory of the Hong Kong Polytechnic University.

References:

ACI 549.1R-93, "Guide for the Design, Construction, and Repair of Ferrocement", reported by ACI Committee 549, reapproved 1999.

Balmer G. G. (1949), "Shearing strength of concrete under high triaxial stress - computation of Mohr's envelope as a curve", Structural Research Laboratoty Report SP 23, US Bureau of Reclamation, 1949-10-28.

Bracci J.M., Reinhorn A.M. and Mander J.B. (1995), Seismic Retrofit of RC Buildings Designed for Gravity Loads: Performance of Structural Model," ACI Structural J, 92(6), pp. 711-723.

Cao Z., Li A., Wang Y.Y., Zhang W. and Yao Q. (2007), Experimental study on RC space beam-column joints strengthened with high strength steel wire mesh and polymer mortar, J of Southeast University (Natural Science Edition), 37(2), pp 235-239.

CoP 1987, "Code of Practice for Structural Use of Concrete 1987", Building Authority Hong Kong.

CoP 2004, "Code of Practice for Structural Use of Concrete 2004", Second Edition, The Government of the Hong Kong Special Administrative Region.

Ersoy U., Tankut A.T. and Suleiman R. (1993), Behavior of Jacketed Columns, ACI Structural Journal, 90(3), pp 249-261.

GB 50011-2001, "Code for Seismic Design of Buildings", National Standard of the People's Republic of China.

GB 18306-2001, "Seismic ground motion parameter zonation map of China".

Geng Z.J., Chajes M.J., Chou T.W. and David Yen-Cheng Pan D.Y.C. (1998), Retrofitting of RC column-to-beam connection," Composites Science and Tech, 58, pp 1297-1305.

Han L.H., Zheng Y.Q. and Teng J.G. (2006), Fire resistance of RC and FRP-confined RC columns, Magazine of Concrete Research, 58(8), pp 533-546.

Harries K.A., Ricles J.R., Pessiki S. and Sause R. (2006), Seismic retrofit of lap splices in nonductile square columns using CFR jackets, ACI Structural J, 103(6), pp 874-884.

Kaushik S.K., Singh K.K., Kumar R. and Sharma T.P. (1996), Performance of ferrocement encased concrete under fire exposure, Journal of ferrocement, 26(3), pp 191-196.

Lam, S.S.E., Xu, Y. L., Chau K. T., Wong, Y. L. and Ko, J. M. (2002). "Progress in earthquake resistant design of buildings in Hong Kong." Structural Engineering World Congress (SEWC 2002), Oct 9-12, 2002, Yokohama, Japan.

Lim C.T.E., Ong K.C.G. and Paramasivam P. (2000), Ferrocement repaired RC beams subjected to quasi-static and cyclic loading, Proceedings: 4th Int. Conf. on Repair, Rehabilitation, and Maintenance of Concrete Structures, Seoul, Korea, pp 887-907.

Mander, J.B., Priestley, M.J.N. and Park, R., (1988a), "Theoretical Stress Strain Model of Confined Concrete," Journal of Structural Engineering, ASCE, Vol. 114, No. 8, pp. 1804-1826.

Mander, J.B., Priestley, M.J.N. and Park, R., (1988b), "Observed Stress Strain Behavior of Confined Concrete," Journal of Structural Engineering, ASCE, Vol. 114, No. 8, pp. 1827-1849.

Naaman A. E. (2000), "Ferrocement and Laminated Cementitious Composites", Techno Press 3000, 2000.

Paramasivam P., Lim C.T.E. and Ong K.C.G. (2000), Ferrocement in structural upgrading and rehabilitation – an overview, Proceedings: 4th Int. Conf. on Repair, Rehabilitation, and Maintenance of Concrete Structures, Seoul, Korea, pp 253-269.

Richart F.E., Brandtzaeg A. and Brown R.L. (1928), "A study of failure of concrete under combined compressive stresses", Engineering Experiment Station Bulletin No. 185 (1928) Urbana, IL.

Saatcioglu M. and Razvi S. R. (1992), "Strength and ductility of confined concrete", Journal of Structural Engineering, Vol. 118, No. 6, June 1992, pp. 1590-1607.

Shah S.P., Lub K.B. and Ronzoni E. (1986), A summary of ferrocement construction and a survey of its durability, RILEM Committee 48-FC, Materials and Structures, 19(4), pp 297-321.

Tadeu A.J.B. and Branco F.J.F.G (2000), Shear tests of steel plates epoxy-bonded to concrete under temperature, J of Materials in Civil Engineering, 12(1), pp 74-80.

Williamson R.B. and Fisher F.L. (1983), Fire resistance of a load bearing ferrocement wall, Report no UCB-FRG-83-1, Dept of Civil Eng, U of California, Berkeley, Feb 1983.

Wu Y.F., Liu T. and Oehlers D.J. (2006), Fundamental principles that govern retrofitting of RC columns by steel and FRP jacketing, Advances in Str Eng, 9(4), pp 507-532.

Appendix:-

Method statement for column strengthening with HPF

1. General notes

1.1 This method statement provides general requirement and procedure in performing rehabilitation works on existing reinforced concrete members using HPF.

1.2 HPF comprises rendering material embedded with wire meshes applied on the surface of the substrate.
1.3 Removal of loosen and/or detached parts of the substrate is essential to achieve good bonding between the substrate and HPF.
1.4 Mock up before the commencement of the rehabilitation work.
1.5 Tests should be carried out to confirm the strength of the rendering material and compatibility of the rendering material and the substrate.
1.6 Tests should be carried out to confirm the strength of the wire meshes.
1.7 On-site demonstration should be carried out to verify and justify the method of application.

2. Surface preparation

2.1 Surface condition of the substrate should be properly prepared to receive the rendering material and in particular to prevent sagging or sliding of the rendering material during application.
2.2 Mechanical scratching, bonding agent, abrasive blasting, shot blasting and bush hammering are some of the methods in improving roughness of the substrate.
2.3 The substrate should be cleaned and free from all fine particles, dust, oil, grease, rust stains, before application of the rendering material.

3. Installation of wire meshes

3.1 Wire meshes should be in good condition. Sub-standard wire meshes, e.g. severely corroded, damaged or rusted, should not be used.
3.2 Overlapping of wire meshes should be at lease 100mm or 4 times mesh lattice width, whichever the larger.
3.3 Wire meshes should be effectively anchored to the substrate by stainless steel nails.

4. Application of the rendering material

4.1 Maximum particle size of the rendering material should not be more than ¼ of the mesh lattice width.
4.2 The rendering material should be properly prepared and applied in accordance with the manufacturer's instruction.
4.3 Properly prepared rendering material should not be consumed beyond the setting time as per specified in the manufacturer's instruction.
4.4 Properly prepared rendering material should be applied from top to bottom. In any event, spreading/belling out effect at the bottom (e.g. caused by the weight of the rendering material on the top) should be avoided.

5. Tolerances

5.1 Thickness of HPF should be the thickness of the rendering material and should fall within the range as per indicated in the table below.

Thickness of HPF (mm)	Tolerance (mm)	
25	-2.50	3.75
30	-3.0	4.50
Thickness (t) > 30	-10% t	+15% t

6. Health and safety

6.1 The contractor should observe PNRC15 on "Asbestos" and to carry out asbestos survey by a registered asbestos consultant, if appropriate.
6.2 The contractor should observe PNRC17 on "Control of Environmental Nuisance from Construction Sites" and in particular to exercise necessary control on dust emitted.
6.3 The contractor should provide all workers with suitable and adequate full/half face masks and goggles and to ensure proper use of the masks and goggles by all workers.

JOINT CONFERENCE PROCEEDINGS
7th International Conference on Urban Earthquake Engineering (7CUEE) &
5th International Conference on Earthquake Engineering (5ICEE)
March 3-5, 2010, Tokyo Institute of Technology, Tokyo, Japan

DIAGNOSIS, ANALYSIS AND RETROFITTING OF AN OLD MASONRY BUILDING IN ALGERIA

Nadir Boumechra[1)], Fabio Casciati[2)], and Karim Hamdaoui[1)]

1) Associate Professor, Department of Civil Engineering, University Abou Bekr Belkaid of Tlemcen, Tlemcen, Algeria
2) Professor, Department of Structural Mechanics, University of Pavia, Pavia, Italy
1) Assistant Professor, Department of Civil Engineering, University Abou Bekr Belkaid of Tlemcen, Tlemcen, Algeria
n_boumechra@yahoo.fr, fabio@dipmec.unipv.it, karim@unipv.it

Abstract: In this paper, the diagnosis, analysis and reinforcement of a 90 years old building in Algeria is presented. The structure under investigation, "The National Bank Agency of El Malah", although situated in a zone of low seismic activity, suffered from the damages during the Aïn Temouchent earthquake, of December 22, 1999. It was of magnitude 5.7, killed at least 28 people and made thousands of persons homeless. The building's residual damages were enough to justify questions on its availability. An analysis of the static and dynamic past and present behavior of the structure was required for its rehabilitation project. The study is the necessary preliminary step toward the optimal retrofit.

1. INTRODUCTION

Algeria is known to be part of an active tectonic structure, where the African plate collides with the Eurasian one. A zone of compression is created following these collisions and a series of thrust and normal faults have been mapped in the area. Consequently, this region is considered as the most active seismo-genetic area in the Western part of the Mediterranean Sea. The area has a rich history of seismicity and experienced many destructive earthquakes such as the worst one of 1365, which completely destroyed the city of Algiers. Reports on other earthquakes that struck Northern Algeria in 1716, 1887, 1910, 1922, and 1934 are also available in the archives of the "Centre de recherche en astronomie astrophysique et géophysique" (CRAAG, 1994). Several more moderate earthquakes occurred in that region in recent years (Benouar and Laradi 1996). On October 10, 1980, the city of El Asnam (today Chlef) was severely damaged by a magnitude 7.1 earthquake killing roughly 3000 people. The same city, during the French colonization period, had been heavily damaged on September 9, 1954, by a magnitude 6.7 earthquake which killed more than 1000 people. Five other damaging earthquakes, of magnitude 5.4 or higher, were reported in the country in the short period from 1989 to 2000 (such as Aïn Temouchent 1999 (5.7) and Beni Ourtilane 2000 (5.6)). Recently, a magnitude 6.8 earthquake surprised the city of Boumerdes and killed at least 2278 people in May 21, 2003 (Boughacha et al. 2004).

The town of Aïn Temouchent is located in the North West of Algeria, at mid-distance between the economic town of Oran and the historical citadel of Tlemcen. During the 20th century, the region, which was previously of weak seismic activity, recorded seven earthquakes of magnitude larger than 5. In December 22, 1999, at 19h37mn30s, the province of Aïn Temouchent was shot by an earthquake that was felt in all the Algerian West till the East of Morocco. The earthquake caused a lot of damages, 28 dead, 3000 homeless families in addition to a great panic in the population. More that 2000 buildings were reached including 39% hardly damaged with 15% to be demolished. The village of Ain Lâalem was completely destroyed; the villages of Ain Tolba and Sidi Ben Adda were half destroyed.

The earthquake's epicenter was located by the Algerian seismic network at the coordinates 35.25°N - 01.30°W, on the locality of Aïn-Allem (20km in the Western South of Aïn Temouchent). Results of the study by Yelles-Chaouche et al. (2004) showed that the maximum intensity of this earthquake I_0 was VII (MSK), its depth was 4.0km, with 5sec of dislocation duration and 5.7 of magnitude (Figure 1). By using the InSAR technique (Interferometric Satellite Aperture Radar images), Belabbes et al. (2009) gave evidence, on the fold named Berdani in the Western North of Aïn Kihal and close to the basin of Tafna, of cumuli of geological slips due to cycles of earthquakes indicated by a defect of geological fold and quaternary deposits on the fold to the North-West of Aïn Kihal village. Moreover, a seismic moment of 4.7×10^{17} N.m and a maximum engendered slip of 1m to 5km of depth over 20km length resulted from the same study. Following this earthquake, the area of Aïn Temouchent initially classified as zone of weak seismicity (reference acceleration coefficient = 0.08*g) in the Algerian

seismic code RPA99 (RPA 99, 1999) is reclassified into a zone of moderate seismicity (reference acceleration coefficient = 0.15*g) in the updated version of 2003 (RPA99, 2003).

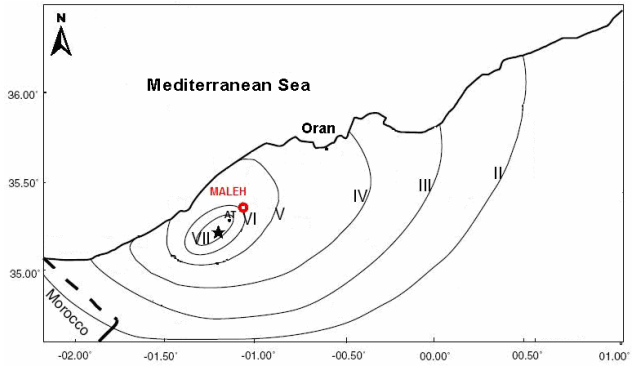

Figure 1 Iso-seismal map of the Aïn-Temouchent earthquake (Yelles-Chaouche et al. 2004)

El Malah is a small town located at 12km in the North-West of Aïn Temouchent and 60km from Oran. It was called by the Romans Flumen Salsum, then Rio Salado during the Spanish colonial occupation. El Malah was a village devoted to agricultural activity, specialized in the vineyard, but it had a significant expansion at the beginning of the 19th century, since it is located on the road axis between Tlemcen and Oran. Administrative buildings, the covered market and many social constructions have been built since 1887. The National Bank building was built in the 19th century French traditional architecture that characterizes the aesthetic facades on the principal boulevard of the village. During the December 22, 1999 earthquake, several buildings were damaged; some of them were demolished later. Among the damaged buildings, the National Bank which suffered moderate damages (degree 2, according to the criteria of the EMS.98 (European Macroseismic Scale)).

A retrofit study required an historical survey on the building and a study of its composition and its structure. This allowed the authors to understand the origin of some particular cracks. Following this analysis a proposal for the structural reinforcement was formulated. The performance evaluation of this solution was compared with those of the old and previous configurations by carrying out numerical simulations.

2. THE CASE STUDY

The bank branch building was realized in 1920 by the colonial administration. The building, which is of 19th century French classic conception, consists of a banking service in the ground floor, an apartment in the first floor and a deposit room in the second floor (Figure 2). Many doors and windows are observed in the ground floor. Along the external walls of the first floor, windows and door-windows are regularly distributed on. These openings are rhythmic with a symmetrical disposition, proportional and apparently in addition to other architectural characteristics, peculiar of classical French buildings (Petruccioli 1992). With its trapezoidal plan (21.80m of length, 16.00m of width and 11.00m of height), the building shows an angular orientation towards the North compared to the surrounding streets. The facades are richly decorated by bulky corbels which carry the balconies as well as some floral motifs. The slabs levels are clearly marked by architectural elements.

The structure is made of masonry with external stone bearing walls (60cm thickness), internal solid brick bearing walls (20cm thickness) and separation solid bricks walls (10cm thickness). The slabs are composed of steel I-beams (IPN140 and IPN160) with a clay-tile arched floor. A central solid brick staircase is carried by steel beams anchored to the walls.

A scouring operation of the external and internal walls' plaster showed that changes were made from the original plan. Following a historical research on the building and a reading of some old photographs, it became evident that since the fifties, transformations have been carried out. The three doors on the angular part of the facades were transformed into windows. Moreover a broad opening on the internal longitudinal bearing was introduced to realize a large counter, some doors and supplementary intermediate partitions were also added (Figure 2). The past decision of introducing these transformations, though innocent and unconscious, had negative consequences on the stability of the structure especially when facing seismic events.



Figure 2 General view on the bank branch (recent photo)

3. DEFINITION OF BUILDING MATERIALS

As classic buildings of 19th century, the bank branch is built on thick bearing walls. The external walls are made of masonry stones and protected by a covering plaster. The wall device is an assembly of not squared stones called hardcore, where the coarse aspect requires a rough coat: a mix of sand and lime that imitates the color of the calcareous stone.

Inside the building, an intermediate bearing wall reinforces the structure on the longitudinal axis. This wall, of 20cm, is built of solid clay bricks with a variable thickness mortar (from 2cm to 5cm) made of sand and lime (Figure 3).

During the diagnosis, operations of plaster wall scouring and exploration of the walls were made, where some parts of solid clay bricks and specimens were taken around windows and doors. Compression tests on solid bricks were carried out at the structural laboratory of the Civil Engineering Department at Tlemcen University, Algeria. The measured average compression strength is of 16.18MPa (Figure 4) (Table 1).



(a) (b)

Figure 3 (a) Stone and (b) brick bearing walls



(a) (b)

Figure 4 (a) Brick specimens , (b) Compression test

Table 1 Laboratory tests results on solid clay brick specimens (compression test)

Specimen	Compressive strength (MPa)
C1	12.571
C2	15.491
C3	16.811
C4	22.974
C5	13.291
C6	15.952

The slabs, of traditional type, are made of steel I-beams (IPN140 or IPN160) with clay-tile arched floors, a higher beaten ground filling and finally a tiling plaster (Figures 5 and 6). Considering the proximity of the site to the sea (around 14km) and the oldness of the building, a more or less important corrosion in the steel beams is observed. The lack of internal and external maintenance increases this deterioration status.



Figure 5 Lower side view of the mixed slab

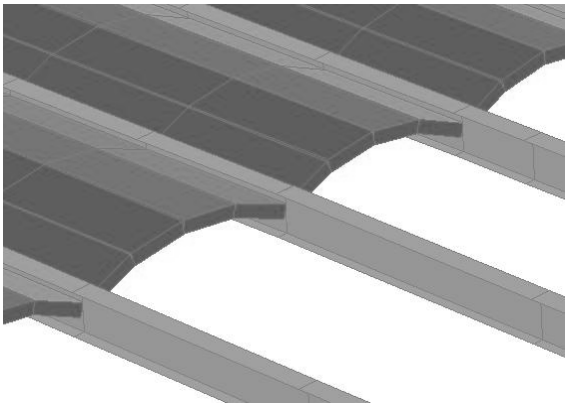

Figure 6 Composition of the traditional mixed slab

The stone and the clay bricks bearing walls are composite materials (mortar + stone/brick + mortar). Their composition is heterogeneous and irregular with nonsymmetrical elasticity and elastic limits. Several researches showed that the determination of the materials' physical and mechanical characteristics is approximate and based on empirical formulas (Brencich et al. 2005 and Domede et al. 2009). The Switzerland masonry standards give a procedure to estimate the mechanical masonries characteristics on the basis of the compressive strengths of the basic material (stone or brick), in addition to the type of mortar (SIA – V.117 1995). Based on these data, the choice of the mechanical characteristics is summarized in Table 2.

Concerning the steel of the slab's beams, the normalized characteristics are as follows: density 7.80, modulus of elasticity 21.10^4 MPa and Poisson's ratio 0.30.

Table 2 Physical and mechanical characteristics of the structure's masonries

	Stone	Brick
Density of masonry (d)	2.20	1.90
Compressive strength of the stone (σ_{MAX}) (MPa)	23.00	16.18 (measured)
Modulus of elasticity of masonry (E) (MPa)	$1.90\ 10^3$	$1.50\ 10^3$
Poisson's ratio (ν)	0.10	0.10

4. ANALYSIS OF STRUCTURAL PATHOLOGIES

The diagnosis carried out on the building highlighted two types of damages: those caused by the oldness of the building and those caused by the Aïn Temouchent earthquake of 1999.

For the first type, degradations are basically the damages in the terrace's sealing (with consequent accelerated degradation of the terrace's slab), the corrosion of the steel beams (Figures 5), and the degradation of some parts of the plaster, of the facade's architectural elements and of the balcony plaster corbels. Of course, this is clearly due to the absence of any building maintenance program.

Other different damages appeared just after the earthquake of December 22, 1999. But they were highlighted only after the scouring of the internal and external walls plaster. Deep diagonals cracks appeared on the internal solid brick bearing wall both at the ground level and on the first floor (Figures 7a). Vertical dislocations were also observed, in the corners inside the solid brick walls. For the external stone bearing walls, some cracks are noted around the openings (windows, doors and door-windows), but because of the presence of steel beams lintels on the top of the openings, they were of minor length and depth, (Figure 7b). Dissociations are also observed between the slabs and the walls; they were apparently due to the strong movements of the slabs, which were more flexible than the walls. Some parts of the internal walls underwent irreversible lateral shift (displacement from 2 to 5cm). On the other hand, no damages were noted on the chimneys, balcony plaster corbels and facade cornices, which usually are rather fragile elements.

Detailed static and dynamic structural analyses are thus necessary to understand the degree of warning caused the by earthquake effects.



(a)



(b)

Figure 7 (a) Deep cracks rose after the earthquake of December 22, 1999. (b) Cracks near the openings

5. ANALYSES OF THE STRUCTURAL BEHAVIOR

5.1 Building's numerical modeling

A realistic numerical analysis of the structural behavior must be consistent with the geometry of the building, with its materials characteristics and with the static and dynamic applied actions. The built model, within the Sap2000 software environment (SAP, 2007), took into account the exact walls' position, the steel beams of floors, the stairs, the openings as well as the steel lintels. The numerical analysis comprised the two configurations "before" and "after" the man-made "transformations" on the structure.

The numerical model of the initial configuration is composed of 4064 shell elements and 730 frame elements, so that 24174 degrees of freedom are considered (Figure 8).

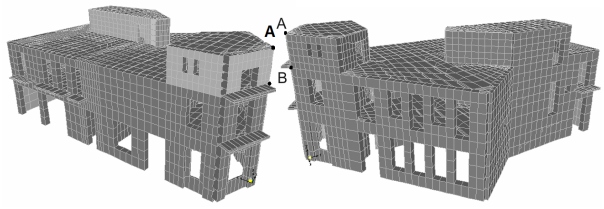

Figure 8 Finite elements model: East and West sides View

5.2 Response analysis in the past and present configurations

The static analysis for the serviceability limit state load condition gave the maximum compression stresses as following: in the external stone walls σ_{max}=-0.593MPa and in the internal solid brick walls σ_{max}=-0.402MPa. These values are rather low if compared with the average strength of masonry in Table 2.

A modal analysis was carried out on the structure before and after transformation (Figure 9). It is useful to observe, that for the first three modes, the difference of the natural periods is negligible.

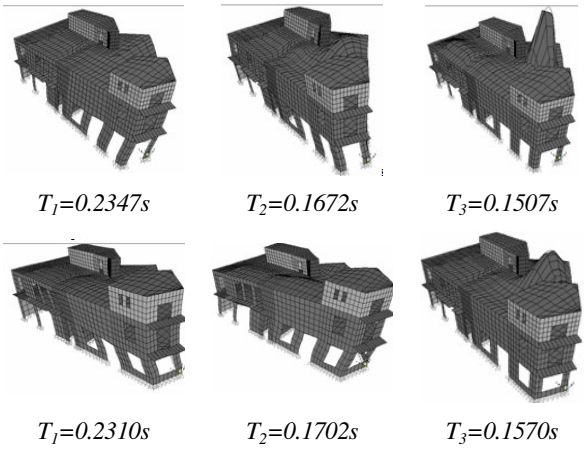

Figure 9 The first three mode shapes before (top) and after (bottom) transformations

5.3 Rehabilitation proposal

Considering the stiffness deficit of the intermediate bearing wall after the past modifications, the observed bad state of the slabs as well as the advanced corrosion of the steel beams, a plan for the building rehabilitation was conceived to save the structure. The following operations were included:

i- Renovation of slabs in mixed steel-concrete slabs with the replacing of the old and corroded I-beams by new IPE180 elements;

ii- Reinforcement of the intermediate bearing wall by a discrete reinforced concrete 3D portal frame, connected to the old structure and being able to take again the totality of the intermediate wall corresponding loads (Figure 10);

iii- Repair of the active deep cracks by reinforcing the corresponding masonry; sewing by steel reinforcements and injection of special grout;

iv- Renewal of the internal and external wall plaster and coats. The original construction material (2 hydraulic lime volumes + 1 cement volume + 1 sand volume) is respected, but reinforced by a fine steel grid;

v- Reinforcement of the of the large doors perimeter by discrete reinforced concrete stiffeners.

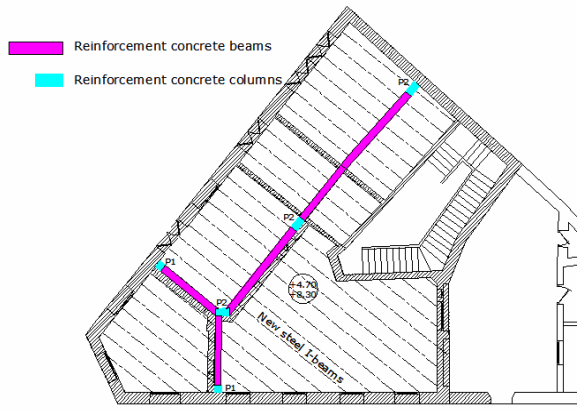

(a)

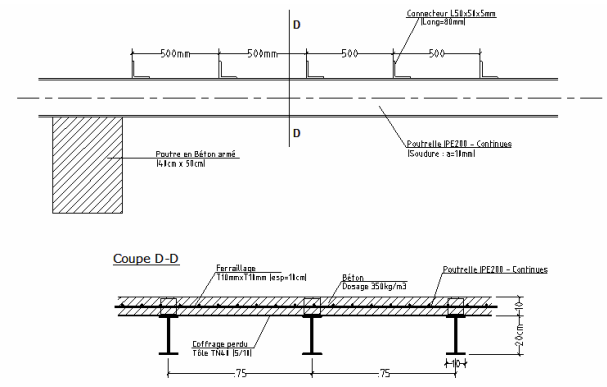

(b)

Figure 10 (a) A plan view of the reinforcement. (b) Details of the new steel-concrete floor

5.4 Comparative study and seismic response

Following these rehabilitation actions, a rather faithful numerical model was developed to correctly evaluate the behavior of the rehabilitated structure.

The modal vibration analysis of this structure shows significant reduction of periods (from -15% to -20%) for the three first modes (Figure 11) with similar deformed modal shapes.

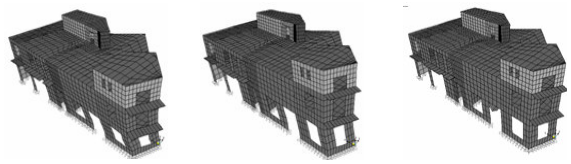

T_1=0.1852s T_2=0.1420s T_3=0.1335s

Figure 11 The new first three vibration's modes (after structural rehabilitation)

For the evaluation of the seismic dynamic behavior, the seismic response was studied for some numerically generated accelerograms (Faravelli, 1988).

It was interesting to generate and use artificial accelerograms corresponding to the Aïn Temouchent December, 22, 1999 earthquake, by non-stationary simulation. The selected process is the Sabetta and Pugliese method (Sabetta and Pugliese 1996), which is defined on the basis of three parameters: the magnitude, the epicenter distance, and underground soil conditions. The basement of the site is defined according to one of the three cases: stiff, not very deep or deep. In the case of this study, the relevant parameters are as follows:

- Magnitude: M_W = 5.7 (Aïn Temouchent earthquake: December, 22, 1999);
- Epicenter distance: 25km (Distance Aïn Allem - El Malah);
- The soil is supposed not very deep (according to the geological study of the site).

From these data, a program was developed to generate single horizontal artificial accelerometers. Five artificial accelerometers were generated and used for this study (Figure 12). For the five generated simulations, the peak ground acceleration is estimated Pga=0.0831*g, the peak velocity Pgv=4.8902cm/s and the duration of the generated ground motion strong phase: T_{tot}=14.1538s. Both x and y artificial earthquake horizontal directions are analyzed. The maximum response in the two directions is considered.

The study includes also the use of the spectral response according to the new seismic zoning as given by the updated para-seismic code (RPA99, 2003), by taking in account a referential acceleration A=0.15*g (seismic return period: 500 years) and of a shallow soil (Figure 13). The mean response spectrum induced by the five generated artificial earthquakes is done and compared to the standard design spectrum. It is clear, that the simulated earthquakes have a low acceleration for periods larger than T=0.26*g .

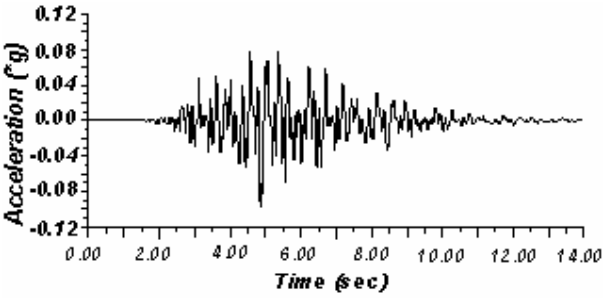

Figure 12 One of the five generated artificial time histories

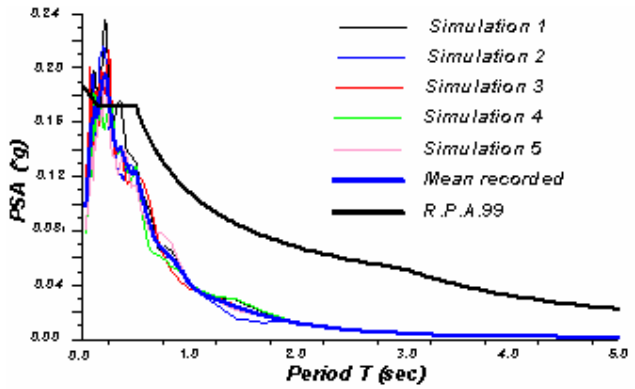

Figure 13 Comparison between the RPA99 spectrum and acceleration of the site and the mean recorded simulations

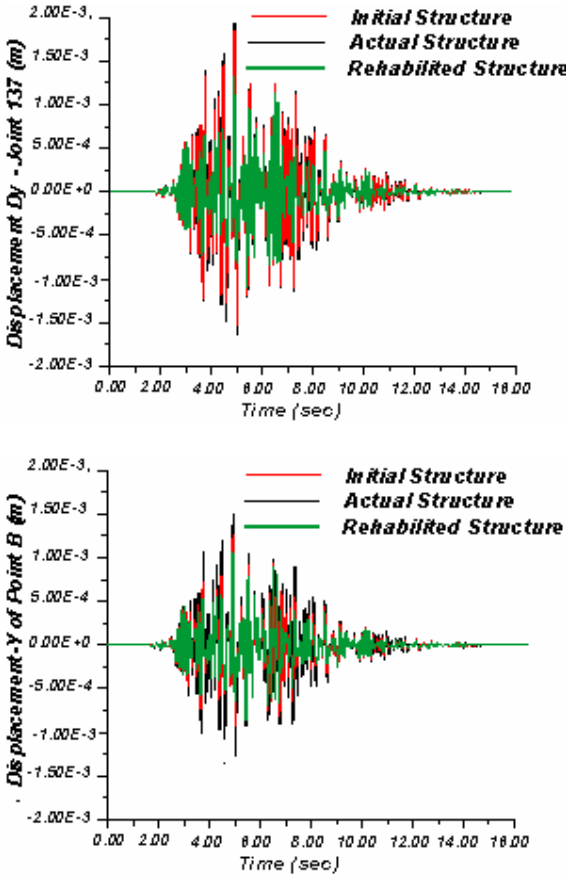

Figure 14 The y-displacement of the points A and B in the time for the first simulation

The temporal dynamic analysis, carried out for the different generated accelerograms, used the linear modal history method. The modal spectral analysis took into account the first twenty vibration modes. Displacements, in y direction, of nodes A and B (as marked in Figure 8) are considered as reference elements to be considered for the analysis and the comparison.

The displacements of nodes A and B are plotted to give a preliminary idea about the structural behavior of the three examined configurations. It is observed, in Figure 14, that the displacement in points A and B increased by approximately 6% after the man-made and seismic damages. When analyzing the rehabilitated structure behavior, it is outlined that the global stiffness of the structure increases. The displacements of the referred points A and B decrease of 20-30%. The rehabilitated structure is appreciated to work, much better than the initial structure.

6. CONCLUSIONS

Traditional masonry structures made by stones and solid clay-bricks perform satisfactorily under gravitational loads, but badly during earthquakes. This is essentially due to the development of tensile stresses in the walls. These bearing walls are designed to equilibrate loadings and external actions. In this paper, the consequences of modifications to them were studied in a specific case study.

The external bearing walls made by stone masonry contribute significantly to the resistance of the building. This is mainly due to their thickness and composition which is not easily susceptible to cracks as the solid clay brick walls. The irregular arrangements of stones in the wall offer a good strength than any regular brick walls. During an earthquake excitation, parts of solid brick walls underwent irreversible deformations, without reaching partial ruptures. The ductility of masonry materials is emphasized. The effectiveness of the steel ties on the top of each opening is remarkable.

An opening, was created, after the building complete,, in the intermediate wall of the first floor. It caused a weakening of the seismic structural strength, made evident by diagonal cracks in the brick walls at higher floors.

The selected system of reinforcement was developed on the basis of following criterion:

1- to provide again the longitudinal wind-bracing of the intermediate bearing wall;

2- to integrate a new system, whose typology is different from the old one, but compatible in the physical and mechanical senses;

3- and, finally, to ensure the effectiveness of this reinforcement without disturbing the initial behavior of the structure.

Acknowledgements

The cooperation effort whose results are summarized in this paper was made possible under the shield of the International Cooperation grant assigned by the Italian Ministry of University and Research (MIUR). The support of the University of Tlemcen is also acknowledged.

References

Belabbès, S., Meghraoui, M., Çakir, Z. and Bouhadad, Y. (2009), "InSAR analysis of a blind thrust rupture and related active folding: the 1999 Ain Temouchent earthquake (Mw 5.7, Algeria) case study", *Journal of Seismology*, **13**(4), 421-432.

Benouar, D. and Laradi, N. (1996), "A Reappraisal of the Seismicity of the Maghreb Countries – Algeria, Morocco, and Tunisia", *Journal of Natural Hazards*, **13**(3), 275-296.

Boughacha, M.S., Ouyed, M., Ayadi A. and Benhallou, H. (2004), "Seismicity and seismic hazard mapping of northern Algeria: Map of Maximum Calculated Intensities (MCI)", *Journal of Seismology*, **8**(1), 1–10.

Brencich, A. and Gambarotta, L. (2005), "Mechanical response of solid clay brickwork under eccentric loading. Part I: Unreinforced masonry", *Journal of Materials and Structures*, **38**(2), 257-266.

CRAAG -Centre de Recherche en Astronomie, Astrophysique et de Géophysique-. (1994), "Les séismes en Algérie de 1365 a` 1992". *CRAAG Report*, Algiers, Algeria. (In Frensh)

Domède, N., Pons, G., Sellier, A. and Fritih, Y. (2009), "Mechanical behaviour of ancient masonry", *Journal of Materials and Structures*, **42**(1), 123-133.

Faravelli, L. (1988), "Stochastic modeling of the seismic excitation for dynamic purposes", *Journal of System for Probabilistic Engineering Mechanics*, **3**(4) 189-195.

Olivito, R.S. and Strump, P. (2001), "Fracture mechanics in the characterisation of brick masonry structures", *Journal of Materials and Structures*, **34**(4), 217-223.

Petruccioli, A. (1992), "Alger 1830-1930 : Pour une lecture typologique des immeubles d'habitation", *Environmental Design, Journal of the Islamic Environmental Design Research Center*, **1**(2), 104-117.

RPA – Règlement Parasismique Algérien RPA99-, (1999).

RPA – Rrèglement Parasismique Algérien RPA99v2003-, (2003).

Sabetta, F. and Pugliese, A. (1996), "Estimation of response spectra and simulation of nonstationary earthquake ground motions", *Bulletin of the Seismological Society of America*, **86**(2), 337-352.

SAP, (2007), [Computer Program], Non Linear Version 11.0.0, Computers and Structures,Inc., Berkeley, California.

SIA-V.117 (1995), "Normes Suisses – Maçonnerie", *Société Suisse des Ingénieurs et Architectes*.

Yelles-Chaouche, A.K., Djellit, H., Beldjoudi, H., Bezzeghoud, M. and Buforn, E. (2004), "The Ain Temouchent (Algeria) Earthquake of December 22nd, 1999", *Journal of Pure and Applied Geophysics*, **161**(3), 607–621.

JOINT CONFERENCE PROCEEDINGS
7th International Conference on Urban Earthquake Engineering (7CUEE) &
5th International Conference on Earthquake Engineering (5ICEE)
March 3-5, 2010, Tokyo Institute of Technology, Tokyo, Japan

3-D BLIND ANALYSES OF FULL-SCALE 5-STORY BUILDING WITH STEEL DAMPERS

Naohiro Nakamura[1)], Takuya Suzuki[2)], Soshi Nakamura[2)], Masashi Yamamoto[1)], Takayuki Sone[2)], and Harumi Yoneda[2)]

1) Chief Researcher, R&D Institute, Takenaka Corporation, Japan
2) Researcher, R&D Institute, Takenaka Corporation, Japan
nakamura.naohiro@takenaka.co.jp, suzuki.takuya@takenaka.co.jp, nakamura.soushi@takenaka.co.jp, yamamoto.masashia@takenaka.co.jp, sone.takayuki@takenaka.co.jp, nishimura.harumi@takenaka.co.jp

Abstract: The E-Defense Steel Research Team held the 2009 blind analysis contest for a full-scale 5-story steel building, which used steel dampers and viscous dampers. Our team was fortunate enough to win Category 1 (3D Analysis, Steel damper) in the contest. This paper explains the analysis model and the results. When 15% of the amplitude of Takatori waves was input, all the structural members and dampers remained in the linear condition. For the 100% input, the structural members remained in the linear condition but the dampers showed nonlinear behavior. The employed Menegotto-Pinto model closely described the nonlinear behavior of the dampers, so the analysis results closely matched the test results.

1. INTRODUCTION

The E-Defense Steel Research Team (Leader: Kazuhiko Kasai, Tokyo Institute of Technology) has been testing various full-scale steel frames using the world's largest three-dimensional shaking table located at Miki City, Hyogo Prefecture, Japan. (K. Kasai et al (2010))

The team held the 2009 blind analysis contest for a full-scale 5-story steel building, which used Japanese steel dampers in the first test, and American viscous dampers in the second one. (T. Hikino et al (2010))

Each participant predicted the responses before and after the test, and the closest predictions to the test results received awards. Because the actual loadings would be determined during the testing based on observed response, the contest consisted of two parts: a pre-test analysis based on anticipated earthquake loadings, and a post-test analysis using the actual loadings. The building analytical model for the post-test analysis must be identical with that for the pre-test analysis.

The contest was categorized by the combination of damper type and analysis type. Two types of dampers and two types of analysis methods, 3D and 2D analyses, were considered. Thus, there were awards for four winners in total, one from each category.Our team was fortunate enough to win Category 1 (3D Analysis, Steel damper) in the contest. This paper explains the analysis model and the results.

2. ANALYSIS MODEL

2.1 Basic Concept

Figure 1 shows the analysis model and Table 1 shows the parts and element types modeled. The parts modeled are columns, beams, floor slabs, partition walls and steel dampers; the external walls are not modeled. Because it was predicted that the input earthquake motion used for this study would remain within the elastic range in the main frame, parts other than the dampers are treated as linear. The overall model has 488 nodal points, 451 elements, and 1,534 degrees of freedom.

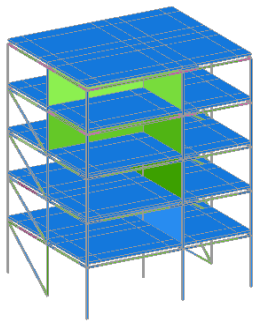

Figure 1 Analysis model

Table 1 Parts and element types modeled

Parts	Element Type	Remarks
Columns and beams	Beam element	Linear
Floor slabs	Shell element	Linear
Non-structural materials (Partition walls)	Shell element	Linear
Dampers (Plastic parts)	Truss element	Non-linear
Dampers (Elastic parts)	Beam element	Linear

2.2 Modeling The Entire Frame

The columns and beams are modeled by linear beam elements, while the panel zones of joints are not modeled. Thus, the stiffness of the panel zones is considered by increasing the stiffness of beam end elements. It is seemed that the horizontal haunches of beam flanges, gusset plates of damper attachments, rib plates, etc. will also increase the stiffness of the frame. This increase of stiffness is, along with the stiffness of the panel zone, also considered as a stiffness increase of the end beams. The stiffness increase was set to conform with the stiffness of the frame in the total sense, with reference to actual-size testing and analysis of joints performed in research related to this shaking test (K. Kaneko et al (2007,2008), M. Yonetani et al (2008)).

The floor slab is modeled using linear shell elements. The stiffness of the slab is the value when the entire slab section is assumed to be of concrete. , The slab is modeled to the height of the slab center and is joined by corresponding beam element node points and rigid body elements.

The partition walls are modeled as linear shell elements with their stiffness set with reference to past test results (Y. Matsuoka et al (2008)). The stiffness of the walls is set as the average stiffness when the predicted story drift of 1/100 occurs, causing vibration. As a result, the stiffness equal to 1.5/1,000 of the stiffness of concrete of the same thickness is used. A previous study confirmed that the presence or absence of non-structural materials does not greatly affect the results.

2.3 Modeling Dampers

The restoring force properties of the steel dampers are represented by a second-order function which was set by treating the increase in stress caused by the increase in strain amplitude as the yield judgment function, and the curved part caused by the Bauschinger effect is represented by the Menegotto-Pinto model (H. Yamazaki et al (2005)). Figure 2 shows how the restoring force properties are modeled.

This restoring force model represents the increase of stress caused by the increase of strain amplitude as the yield judgment function in order to consider the strain amplitude dependency, permitting behavior to be represented by hardening when the strain gradually rises and softening when the strain gradually falls. There are a total of seven parameters: initial stiffness (linear constant), three kinds of coefficients of yield judgment second-order functions, one kind used to set the secondary gradient of the polygonal line designated based on the dotted line in Figure 2, and two kinds used to set the Menegotto-Pinto model which is a curve model based on this polygonal line model.

The parameters necessary to determine these restoring force properties are set based on the results of dynamic testing in the paper "Sample Steel Damper Tests for Blind Analysis Contest", which is shown by the contest organizer. Table 2 shows the set parameter values and Figure 3 shows their correspondence with the test results. The restoring force model is defined based on the stress–strain relationship, and is set for the plastic parts of all dampers.

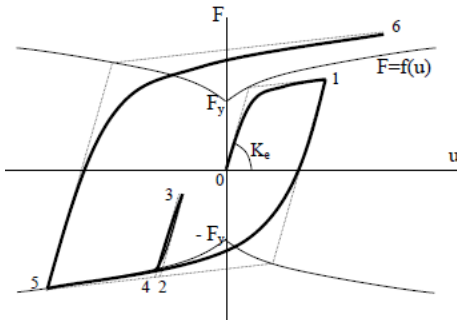

Figure 2 Restoring force model of steel dampers

Table 2 Parameters used (set as the stress–strain relationship)

Parameter	Value
Yield curve zero-order coefficient (kN/m^2)	320000
Yield curve first-order coefficient (kN/m^2)	50000
Yield curve second-order coefficient (kN/m^2)	-400
Secondary stiffness ratio	0.005
Curve parameter R0	7
Curve parameter a1	6
Curve parameter a2	0.009

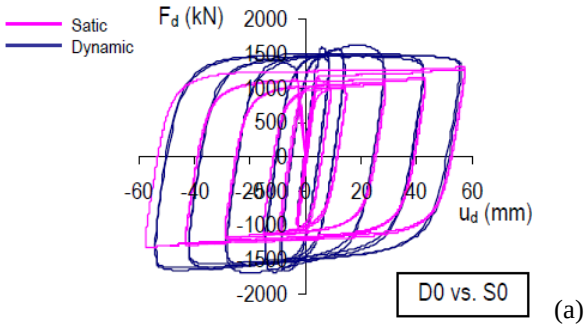

(a)

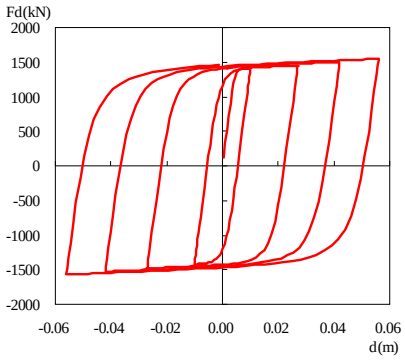

(b)

Figure 3 Correspondence of test results with the restoring force model
(a) Test results ("Sample Steel Damper Tests for Blind Analysis Contest"), and (b) Restoring force model

3. ANALYSIS RESULTS

The analyses were performed with input waves set at 15% and 100% of the recorded amplitude of Takatori waves. Each analysis result was compared with the test results.

3.1 15% Input test

The maximum absolute floor displacements for both the X and Y directions are shown in Figure 4, and the maximum absolute floor accelerations for both directions are shown in Figure 5. In both figures, the analysis results were compared with the measured experimental results. The analysis and measured results agree in both figures. In this test, the structural members remained in the linear condition.

Figure 6 compares the maximum absolute story drift

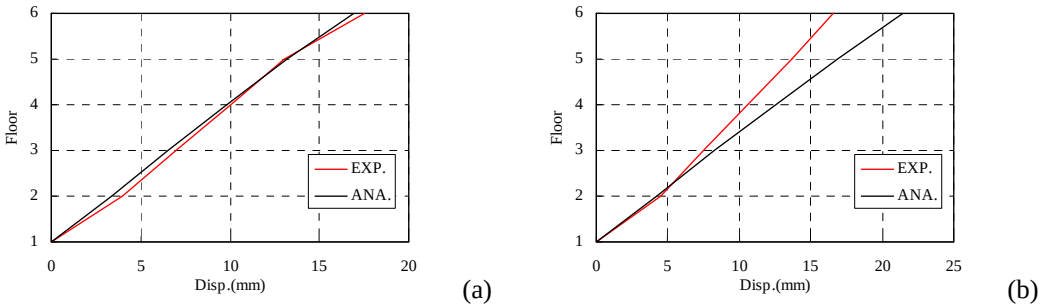

Figure 4 Comparison of maximum absolute floor displacement (15% Input)
(a) X direction, and (b) Y direction

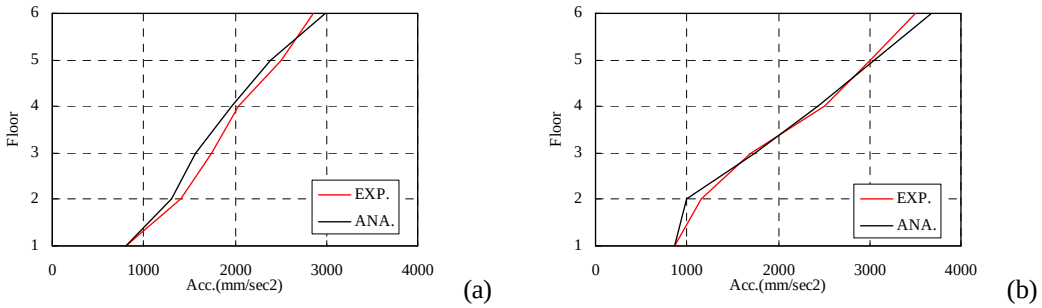

Figure 5 Comparison of maximum absolute floor acceleration (15% Input)
(a) X direction, and (b) Y direction

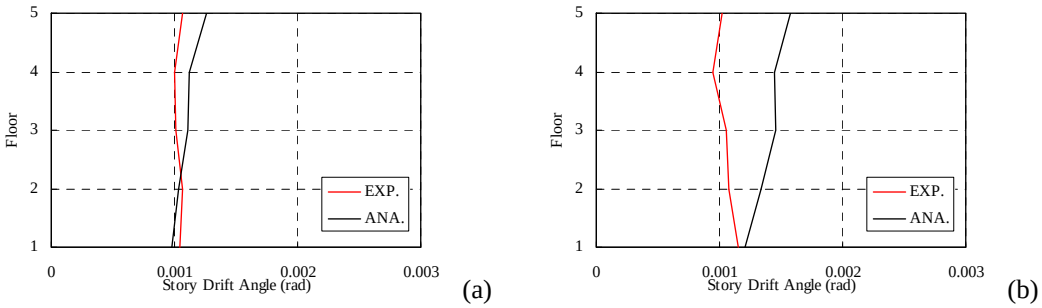

Figure 6 Comparison of maximum absolute story drift angle (15% Input)
(a) X direction, and (b) Y direction

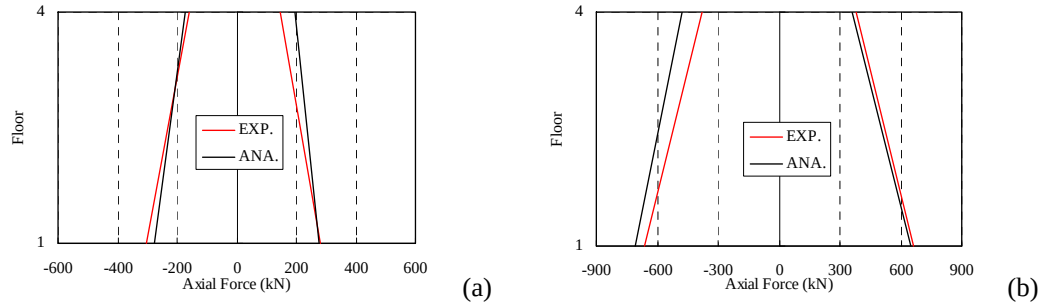

Figure 7 Comparison of axial forces of 1st and 4th story dampers (15% Input)
(a) X direction, and (b) Y direction

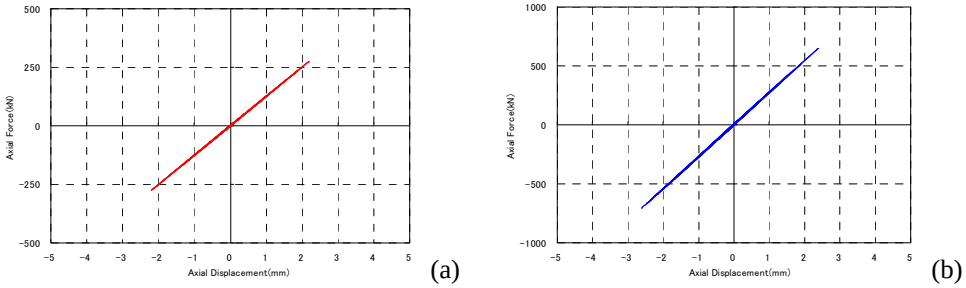

Figure 8 Relation between axial force and axial displacement of 1st story (15% Input)
(a) X direction, and (b) Y direction

angle for both directions. Some differences can be seen between the analysis and test results.

Figure 7 compares the axial forces of dampers for both directions, for the dampers in the 1st and 4th stories. All the figures showed good agreement between the analysis and test results. Figure 8 shows the relation between axial force and axial displacement of the 1st story damper for both directions; it can be seen that these dampers stayed in the linear condition.

3.2 100% input test

The maximum absolute floor displacements for both

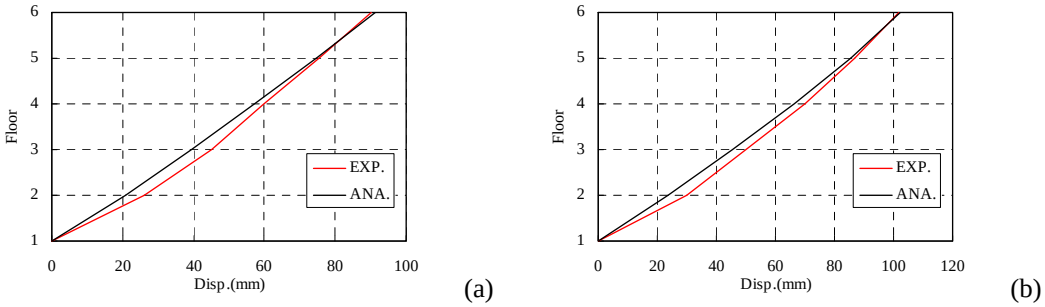

Figure 9 Comparison of maximum absolute floor displacement (100% Input)
(a) X direction, and (b) Y direction

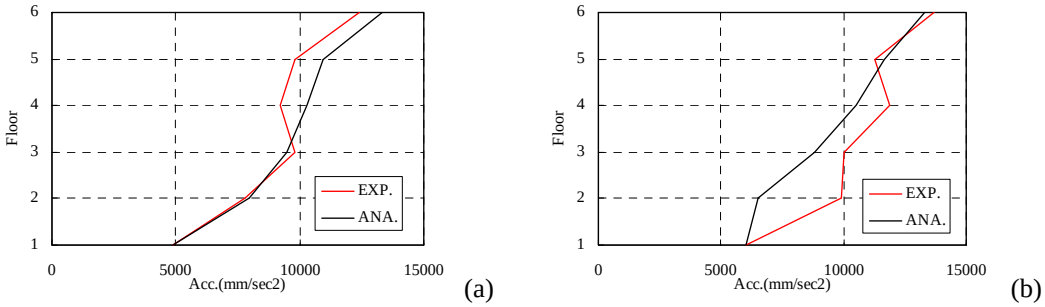

Figure 10 Comparison of maximum absolute floor acceleration (100% Input)
(a) X direction, and (b) Y direction

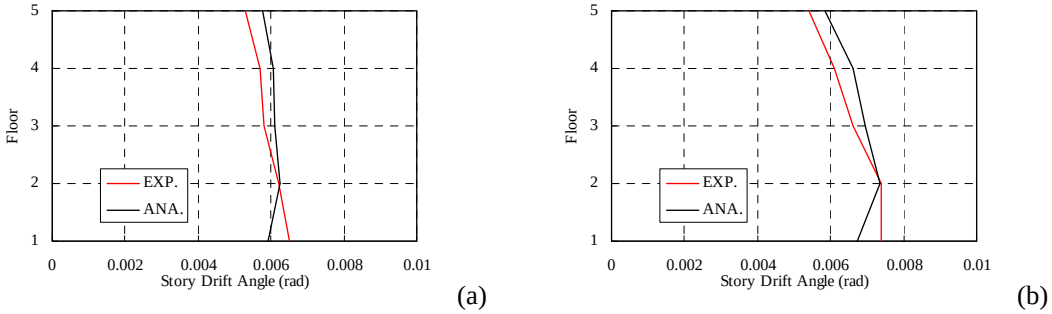

Figure 11 Comparison of maximum absolute story drift angle (100% Input)
(a) X direction, and (b) Y direction

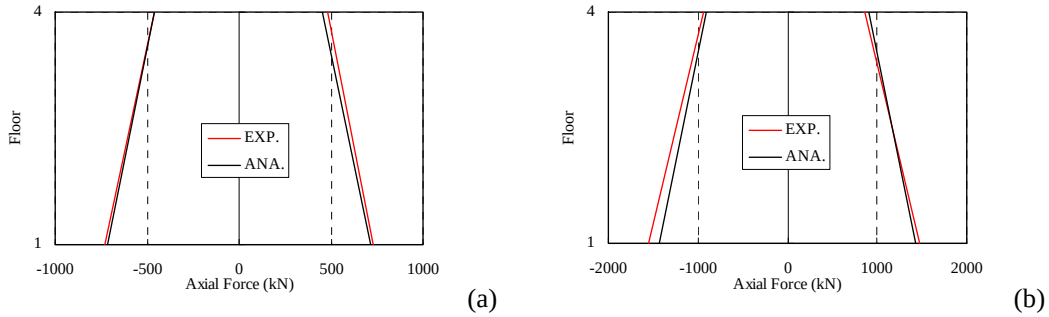

Figure 12 Comparison of axial forces of 1st and 4th story dampers (100% Input)
(a) X direction, and (b) Y direction

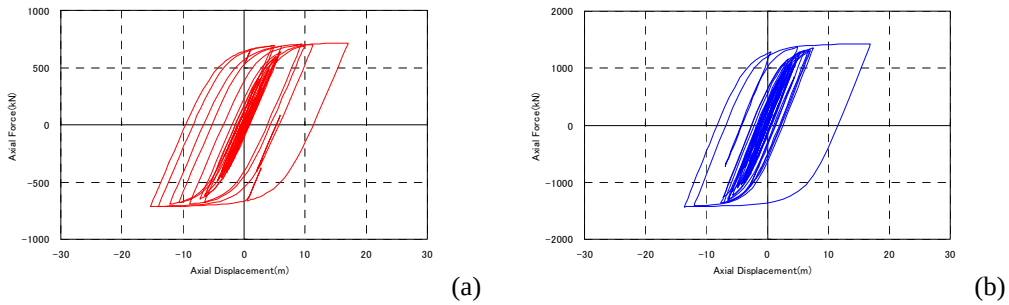

Figure 13 Relation between axial force and axial displacement of 1st story (100% Input)
(a) X direction, and (b) Y direction

the X and Y directions are shown in Figure 9, and the maximum absolute floor accelerations for both directions are shown in Figure 10. In both figures, the analysis results almost agree with the measured experimental results.

Figure 11 compares the maximum absolute story drift angle for both directions. The analysis results agree with the measured experimental results.

Figure 12 compares the axial forces of dampers for both directions, for the dampers in the 1st and 4th stories. All the figures showed good agreement between the analysis and test results. Figure 13 shows the hysteresis curves of the 1st story damper for both directions; these dampers showed nonlinear behavior.

It is considered that the employed Menegotto-Pinto model closely describes the nonlinear behavior of the dampers, so the analysis results closely matched the test results.

4. CONCLUSIONS

The E-Defense Steel Research Team held the 2009 blind analysis contest for a full-scale 5-story steel building, which used steel dampers and viscous dampers. Our team was fortunate enough to win Category 1 (3D Analysis, Steel damper) in the contest, and this paper explained the analysis model and the results.

When 15% of the amplitude of Takatori waves was input, all the structural members and dampers remained in the linear condition. For the 100% input, the structural members remained in the linear condition but the dampers showed nonlinear behavior. It is considered that the employed Menegotto-Pinto model closely described the nonlinear behavior of the dampers, so the analysis results showed good agreement with the test results.

References:

K. Kasai et al (2010): FULL-SCALE SHAKE TABLE TESTS OF 5-STORY STEEL BUILDING WITH VARIOUS DAMPERS, JOINT CONFERENCE PROCEEDINGS, 7th International Conference on Urban Earthquake Engineering (7CUEE) & 5th International Conference on Earthquake Engineering (5ICEE), 2010, Tokyo

T. Hikino et al (2010): OVERVIEW OF 2009 E-DEFENSE BLIND ANALYSIS CONTEST RESULTS, JOINT CONFERENCE PROCEEDINGS, 7th International Conference on Urban Earthquake Engineering (7CUEE) & 5th International Conference on Earthquake Engineering (5ICEE), 2010, Tokyo

K. Kaneko, K. Kasai, S. Motoyui et al (2007): “FE Analysis and Performance Assessment for Subassemblies in a Full-Size Damped Steel Building Specimen: E-Defense Experimental Projects for Steel Buildings - Part17, 18”, Summaries of technical papers of Annual Meeting Architectural Institute of Japan. C-1, Structures III, 2007, pp.1087-1090

M. Yonetani, Y. Azuma, K. Kasai et al (2008): “Hybrid-control Experiments on Full-Scale Subassemblies with Beam-Column-Gusset Connections for Passive-Controlled Steel Buildings: E-Defense Experimental Projects for Steel Buildings - Part 35”, Summaries of technical papers of Annual Meeting Architectural Institute of Japan. C-1, Structures III, 2008, pp.861-862

K. Kaneko, K. Kasai, Y. Azuma et al (2008): “Post-Buckling Analysis for Subassembly Specimen with Beam-Column-Gusset Connection in Passively-Controlled Steel Structures: E-Defense Experimental Projects for Steel Buildings - Part 38”, Summaries of technical papers of

Annual Meeting Architectural Institute of Japan. C-1, Structures III, 2008 pp.867-868

Y. Matsuoka et al (2008): “SEISMIC RESPONSE OF NON-STRUCTURAL PARTITION WALLS AND HANGING CEILING SYSTEMS”, Journal of structural and construction engineering. Transactions of AIJ 73(632) pp.1857-1864

H. Yamazaki et al (2005): “Curved Hysteresis Model of Structural Steel under Cyclic Loading: Part 1 Analytical Model”, Summaries of technical papers of Annual Meeting Architectural Institute of Japan. C-1, Structures III, 2005 pp.745-746

“Sample Steel Damper Tests for Blind Analysis Contest” (Downloadable Information)

JOINT CONFERENCE PROCEEDINGS
7th International Conference on Urban Earthquake Engineering (7CUEE) &
5th International Conference on Earthquake Engineering (5ICEE)
March 3-5, 2010, Tokyo Institute of Technology, Tokyo, Japan

2-D BLIND ANALYSES OF FULL-SCALE 5-STORY BUILDING WITH STEEL DAMPERS

Harumi Yoneda[1)], Masashi Yamamoto[2)] , Takayuki Sone[1)] , Naohiro Nakamura[2)], Takuya Suzuki[1)] and Soshi Nakamura[1)]

1) Researcher, Takenaka Research and Development Institute, Japan
2) Chief Researcher, Takenaka Research and Development Institute, Japan
nishimura.harumi@takenaka.co.jp, yamamoto.masashia@ takenaka.co.jp, sone.takayuki@takenaka.co.jp, nakamura.naohiro@takenaka.co.jp, suzuki.takuya@takenaka.co.jp, nakamura.soushi@takenaka.co.jp

Abstract: A blind analysis contest has been conducted in conjunction with the full-scale experiment of a five-story steel building with dampers in March 2009 at the E-Defense shaking table facility. The purpose of the contest is to stimulate development of computational methods and efficient modeling techniques for analysis. In this report, the methods of modeling and simulation, and the results of nonlinear time history analysis of the winner of the category of 2-D analysis with steel dampers are presented.

1. INTRODUCTION

Shaking table tests of a full-scale five-story steel frame building specimen with dampers were carried out in March 2009 at the E-Defense shaking table facility. For the result of these tests, a blind analysis contest was hosted by National Research Institute for Earth Science and Disaster Prevention. (Kasai et al. (2010) and Hikino et al. (2010)). This contest continues to the previous contest in 2007.

The contest has four categories by the combination of analysis type (2-D and 3-D analyses) and the damper type. The authors are the winner of category 3 (2-D analysis with steel damper). In this study, the analytical method and results by the authors are reported.

2. ANALYTICAL MODEL

2.1 Outline

The subject of previous contest in 2007 was collapse test of full-scale four-story steel frame building by the shaking table. The authors were winner of category of 2-D/ researcher in that contest. In the contest in 2009, the frame model composed in 2007 was modified and used, and the analytical method same as the previous contest was applied (Ohsaki et al. (2008)).

The frame model for this analysis is shown in Figure 1. This model consists of line elements, hinge elements and panel-zone elements. In addition, damper elements were newly applied. The mass elements are centralized and located at panel zones.

In modeling and analysis, the following properties are taken into consideration based on pre-estimation.

a) P-Δ effect is neglected, because it is estimated to be small enough in this range of excitation.
b) M-N interaction is not considered because the response is estimated to be within elastic range.
c) There are three structural frames in direction of analysis. But steel dampers are placed in only one structural frame. When modeling 2-D frame, sections of each element are simply combined.
d) Influence of orthogonal frame is neglected.
e) Influence of biaxial bending is neglected.
f) Influence of non-structural components is neglected, because it is estimated to be small.

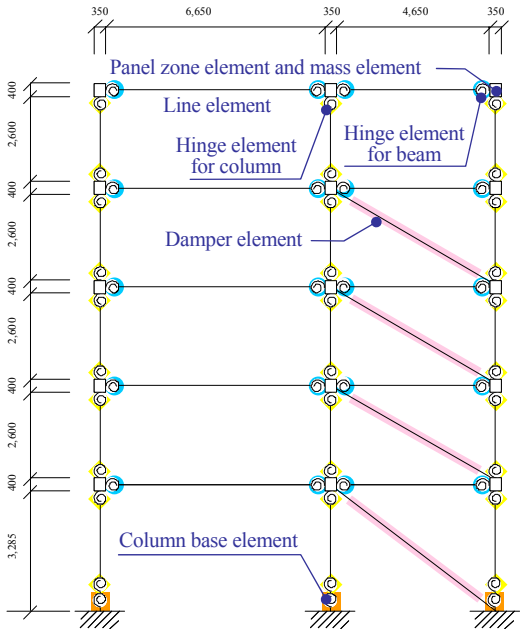

Figure 1 The frame model (unit: mm)

g) Considering composite beam effect, the stiffness and strength of the beams are magnified. The magnification ratio is 1.69 to 2.07, which was calculated by another analysis.
h) Column bases are modeled, but whose stiffness value is set sufficiently large because of its little influence.

Especially, a), b) and h) are different from the previous analysis. Although the hinges and panel-zones were modeled as elasto-plastic, all the elements remained in elastic range as a result of time-history analysis.

The number of elements is 97, and the number of degrees of freedom is 113. The damping matrix is proportional to the stiffness matrix of the line elements only, and the damping factor for the first mode is 0.02.

2.3 Damper model

As a hysteresis model of steel, Menegotto-Pinto model is well known (Figure 2 (a)). This model uses curved hysteresis model whose yield point rises according to increase of amplitude. Yamazaki et al. modified the model considering asymmetry positive and negative input amplitude (Yamazaki et al. (2006), Sadasue et al. (2006) and Sorazyo et al. (2006), Figure 2 (b) and (c)). The authors used this modified model as a plastic portion of damper (see Table 2) except for hysteretic rule of elastic region. About hysteretic rule of elastic region, the authors applied the original Menegotto-Pinto model.

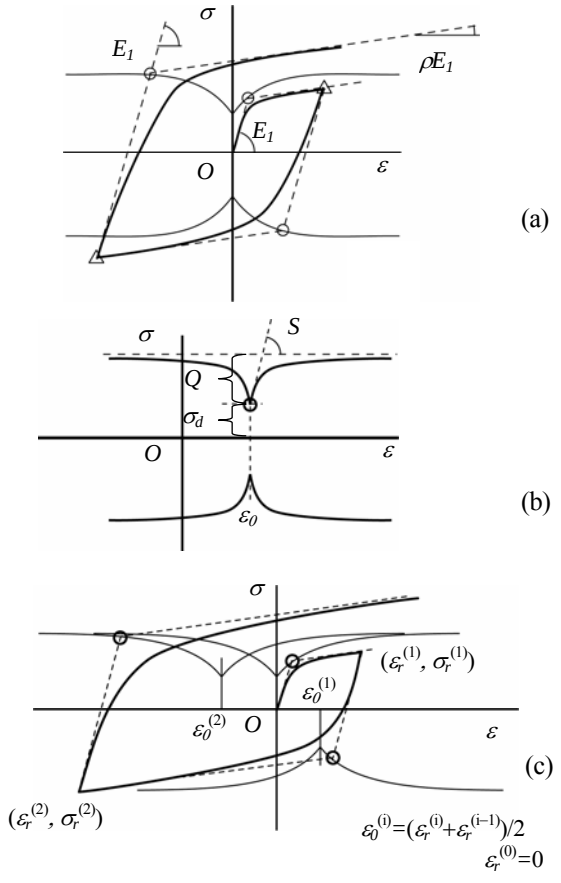

Figure 2 Steel damper Model: (a) Menegotto-Pinto model, (b) Modified yield judgment function and (c) Moving of the modified yield judgment function

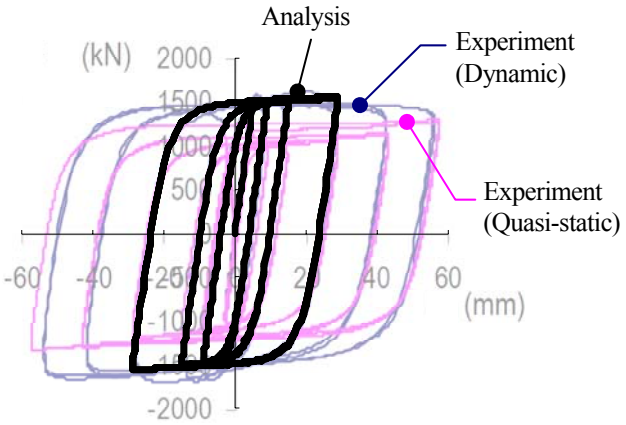

Figure 3 Comparison between experiments and analysis of damper unit

Table 1 Parameters of damper

Story	S (N/mm^2)	Q (N/mm^2)	E (N/mm^2)	σ_d (N/mm^2)	R_0	a_1	a_2	ρ
1, 2	50	190	240000	335	40	37	0.02	0.006
3, 4	50	190	205000	335	40	37	0.02	0.006

Table 2 Axial stiffness of the damper except for plastic portion

Story	Axial stiffness (kN/mm)			
	Gasset Plates	Connection Portion	Elastic Portion	Total
1	2966	5471	3391	1227
2	2896	5471	3138	1181
3	2962	3608	1972	882.1
4	2449	3608	1972	838.5

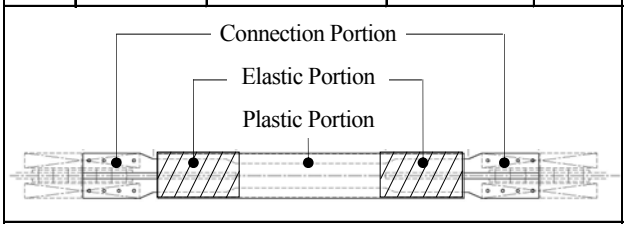

Although the parameters of the model based on the specimen test are shown in the reference (Sadasue et al. (2006)), the authors identified these parameters by themselves based on the test results of a damper unit provided by the contest organizer. The parameters are shown in Table 1. Young's modulus E was evaluated based on material test results of steel damper provided by the organizer.

Comparison between the test results and result of this analysis model are shown in Figure 3. Although the tests were conducted to large displacement, analytical results are shown only in the range of expected displacement in the shaking table test.

Axial stiffness of the damper except for plastic portion was evaluated and shown in Table 2. The stiffness of gasset plates was separately evaluated by FEM analysis, because of their complex shape.

Damper element in Figure 1 consists of the plastic portion described above and the other portions modeled as springs with stiffness shown in Table 2 in series.

2.4 Eigenvalue analysis

To investigate basic property of analytical model, eigenvalue analysis was conducted with initial stiffness.

The periods of the four lowest modes of this model are 0.483s, 0.170s, 0.091s and 0.069s. The periods of the four lowest modes of the model without damper are 0.679s, 0.213s, 0.109s and 0.0707s. By steel damper, first order natural period becomes 71 percent of the frame without damper.

3. ANALITICAL METHOD

3.1 Calculating Method

In this analysis, linear model was composed by putting temporary elastic spring in place of nonlinear element, and then differential force from original nonlinear element is fed back. Block diagram is shown in Figure 4. Although a time-lag will occur in the analysis, accuracy is ensured by making time step small (less than 0.002s). The stiffness of these temporary elastic springs was defined as second stiffness for panel-zone and 1/1000 of initial stiffness for the others.

3.2 Time history analysis

Equation of motion is expressed by

$$[M]\{\ddot{x}\}+[C]\{\dot{x}\}+[K]\{x\}=-[M]\{1\}\ddot{a}+\{f\} \qquad (1)$$

where $[M]$: mass matrix, $[C]$: damping matrix, $[K]$: stiffness matrix, $\{x\}$: displacement vector, $\ddot{a}$: earthquake acceleration, $\{f\}$: feedback external force, dot means differential.

Ordinary differential equations by state space representation are shown in Eq. (2). In which, components of observed vector Y are absolute acceleration and displacement.

$$\begin{cases} \dot{X} = AX + Bu \\ Y = CX + Du \end{cases} \qquad (2)$$

where

$$A=\begin{bmatrix} -[M]^{-1}[C] & -[M]^{-1}[K] \\ [I] & [O] \end{bmatrix},\quad B=\begin{bmatrix} -\{1\} & [M]^{-1} \\ \{0\} & \{0\} \end{bmatrix},$$

$$C=\begin{bmatrix} -[M]^{-1}[C] & -[M]^{-1}[K] \\ [O] & [I] \end{bmatrix},\quad D=\begin{bmatrix} \{0\} & [M]^{-1} \\ \{0\} & \{0\} \end{bmatrix},$$

$$X=\begin{Bmatrix} \{\dot{x}\} \\ \{x\} \end{Bmatrix},\quad u=\begin{Bmatrix} \ddot{a} \\ \{f\} \end{Bmatrix},\quad Y=\begin{Bmatrix} \{\ddot{x}\}+\{1\}\ddot{a} \\ \{x\} \end{Bmatrix},$$

$$[I]=\begin{bmatrix} 1 & & O \\ & 1 & \\ & \ddots & \\ O & & 1 \end{bmatrix},\quad [O]=\begin{bmatrix} 0 & \cdots & 0 \\ \vdots & \ddots & \vdots \\ 0 & \cdots & 0 \end{bmatrix} \qquad (3)$$

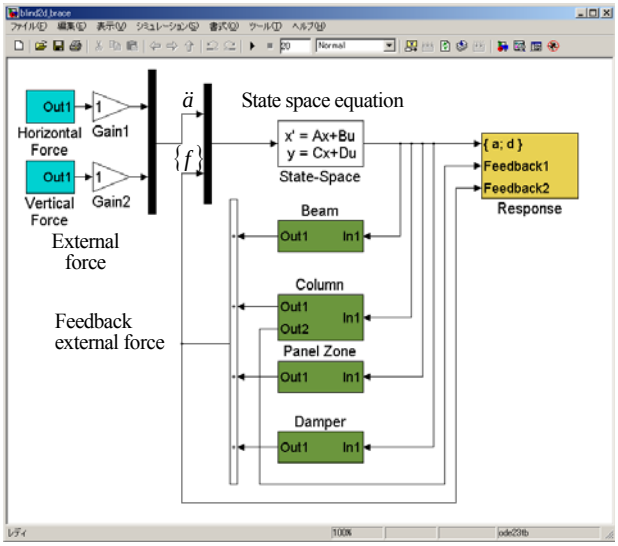

Figure 4 Block diagram

Although Eq. (1) is expressed for input in one direction, matrix A, B, C and D is expanded to two directions (horizontal and vertical) .

MATLAB/Simulink version 7.0 (R2007b) was used for the analysis. Analytical solver in this analysis used variable time step, however, the maximum step time was set as 0.002s in order to ensure sufficient degree of accuracy. The linear solver was 'ode23tb' of MATLAB (Shampine et al. (1996)).

3.3 Calculation of strains

In this model, three structural frames had been combined into one. Therefore axial forces and bending moments have to be distributed to each structural frame for calculation of strains.

Steel dampers were installed in only one structural frame. Assuming that damper's axial force only flows to column connected with the damper, the axial force of the column from which vertical component of the damper's force was subtracted is distributed to three columns according to section area. To obtain axial force of the column connected with the damper, vertical component of the damper's force was added. The bending moments were distributed according to proportion of second moment of area.

The strain of the column was calculated neglecting the bending moment, because the target strain gage was at the point where the influence of the bending moment is small. The section force of the girder was obtained from that of column. Using this section force, the strain of the girder was calculated.

4. ANALYTICAL RESULT

The seismic motion used in the tests was the 1995 Hyogo-ken Nanbu Earthquake Takatori wave. The input motion was scaled to 15%, 40%, 50%, 70% and 100%. The scales of the wave, for which the responses are to be predicted, are 15% for elastic behavior and 100% for

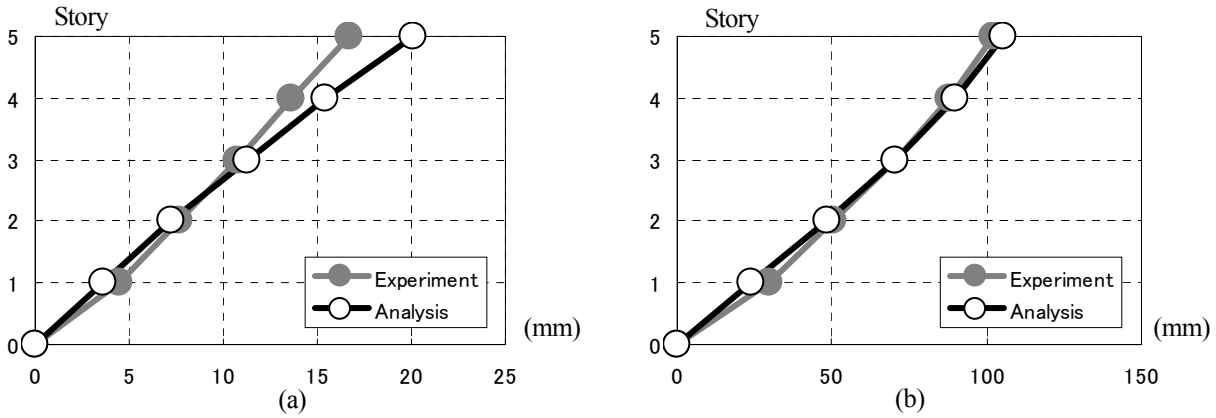

Figure 5 Maximum relative displacement in each story: (a) 15% input and (b) 100% input

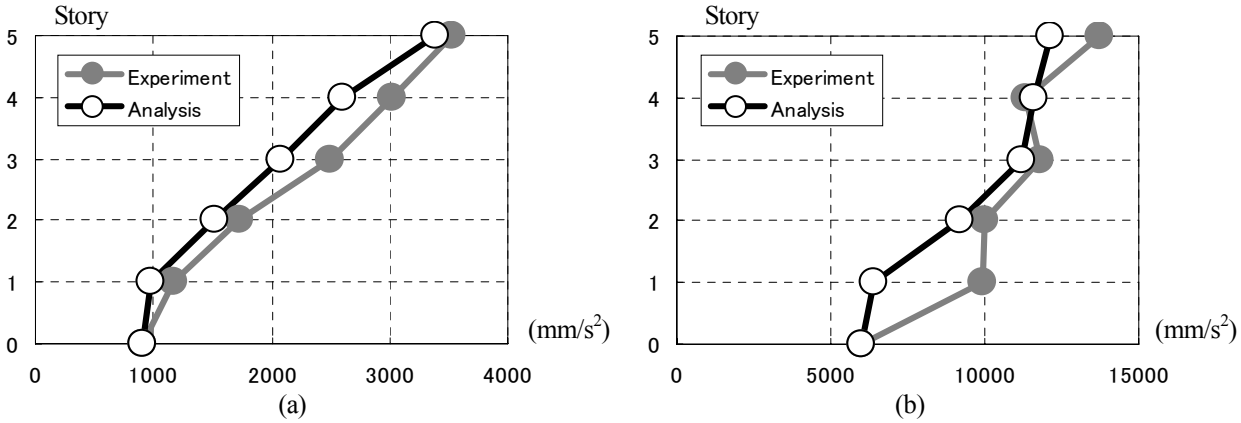

Figure 6 Maximum absolute acceleration in each story: (a) 15% input and (b) 100% input

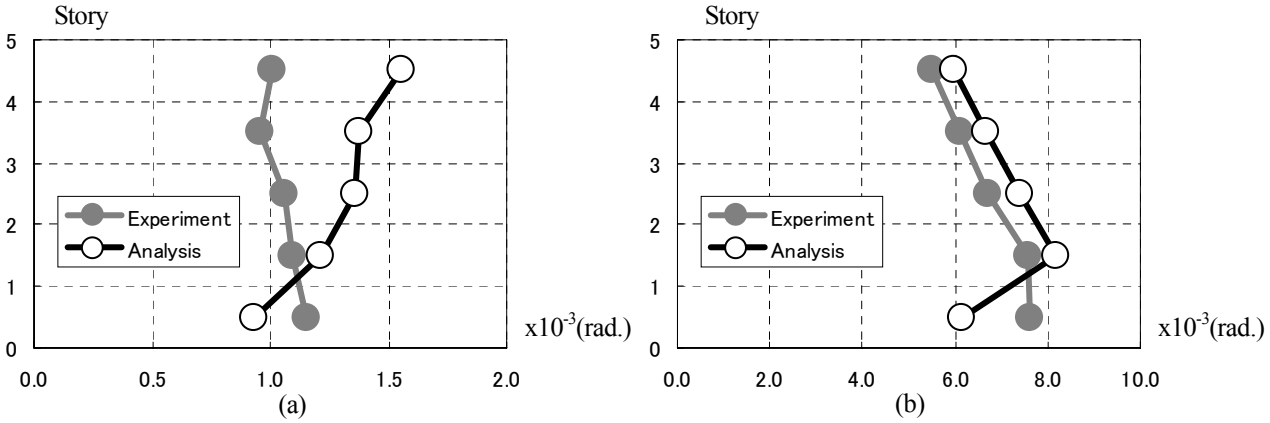

Figure 7 Maximum drift angle in each story: (a) 15% input and (b) 100% input

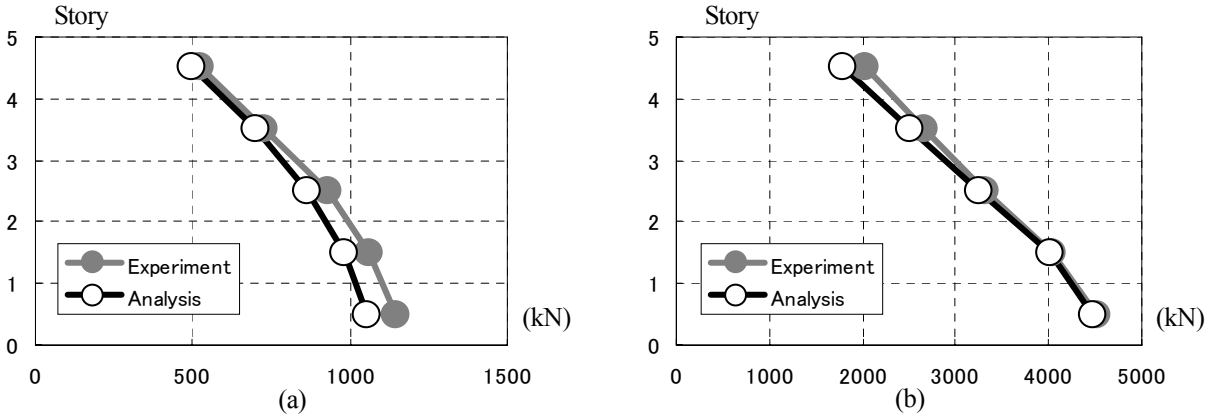

Figure 8 Maximum story shear in each story: (a) 15% input and (b) 100% input

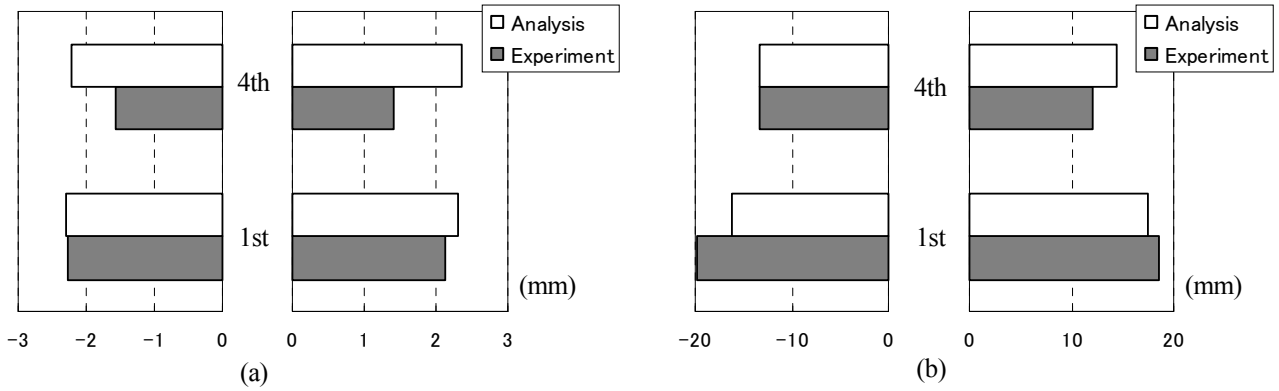

Figure 9 Maximum axial deformation of damper: (a) 15% input and (b) 100% input

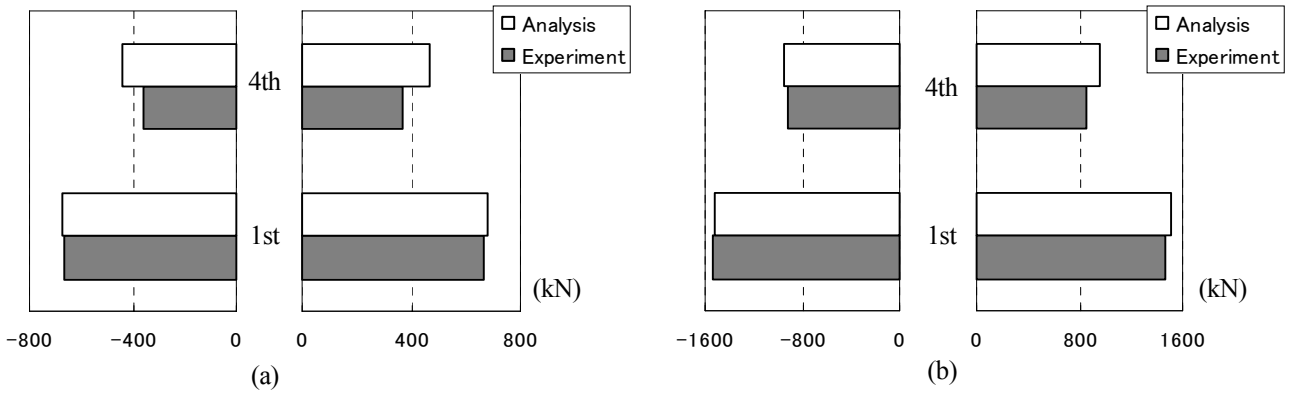

Figure 10 Maximum axial force of damper: (a) 15% input and (b) 100% input

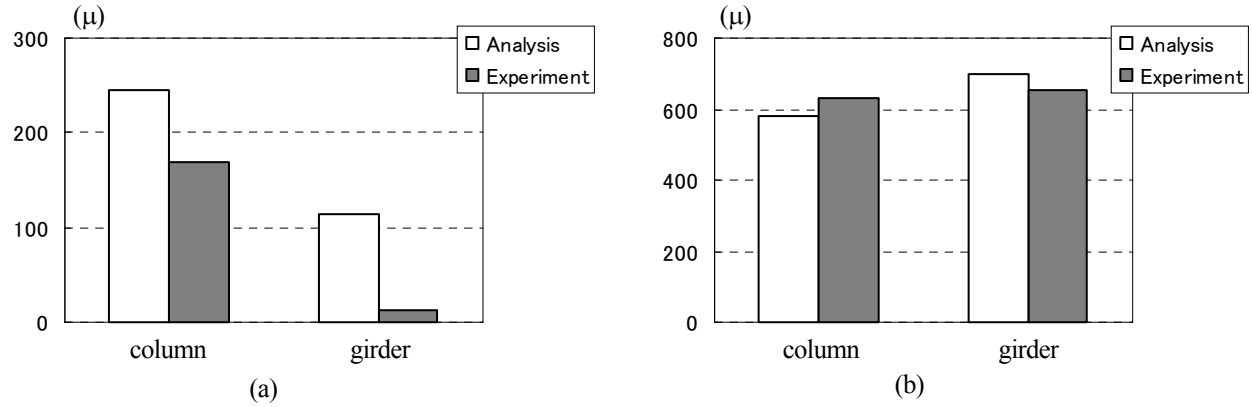

Figure 11 The strain of column and girder: (a) 15% input and (b) 100% input

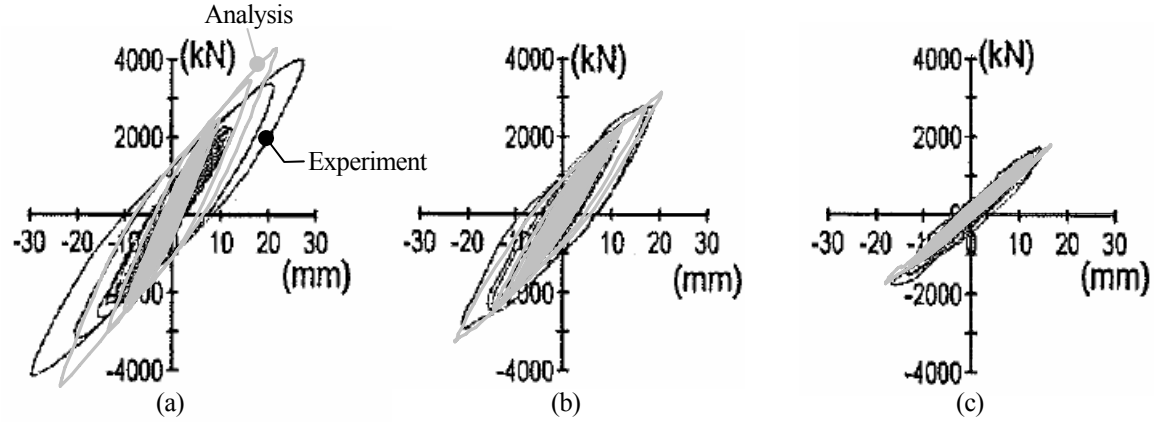

Figure 12 Relation between shear force and relative story displacement: (a) 1st story, (b) 3rd story and (c) 5th story

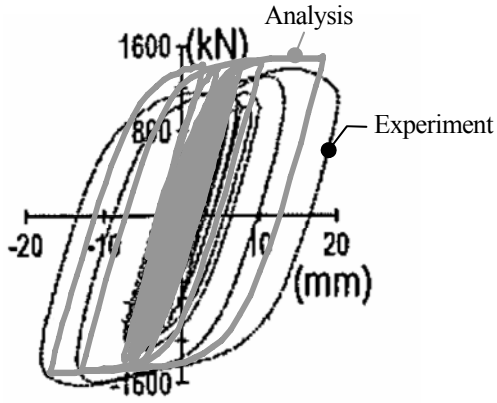

Figure 13 Relation between axial force of damper and axial deformation of damper at first story

elastoplastic behavior of steel damper. In the analysis for 100% input, the effect of residual strain and stress by the previous tests were considered.

Analytical results are described below compared to experimental results. Experimental value is not official, because experimental results are not provided by the organizer and the authors read the value from the figures on published report.

Maximum displacement, absolute acceleration, drift angle and story shear in each story are shown in Figure 5 to Figure 8.

Analytical maximum displacement and story shear in both 15% and 100% input are corresponding with experiment very well. Maximum absolute accelerations also almost agree with experiment except for first story under the 100% input. Analytical results are smaller than experimental results.

About maximum drift angle under the 15% input, the experimental result becomes smaller as the story becomes higher. On the other hand, analytical result is bigger as the story becomes higher. Analyses under the 100% input almost agree with experiments except for first story.

The result of damper deformation, axial force and the strain of column and girder are shown in Figure 9 to Figure 11.

About damper deformation and axial force under the 15% input, analytical results of first story correspond with experimental results and that of fourth story are bigger than experimental results. Damper deformation and axial force are almost same as experiment under the 100% input.

About the strain, the difference is big under the 15% input, especially analytical strain of the girder was greatly overestimated. Both strains of column and girder match well under the 100% input.

The relation between story shear and relative story displacement under the 100% input is shown in Figure 12 (Kasai et al. (2009)). The analytical results at third story and fifth story correspond with the each experimental result very well. About first story, gradient of the hysteresis loops of analytical result is bigger than that of test results. The stiffness of analysis was overestimated. That is why the difference of acceleration and drift angle at first story arose.

The relation between deformation and axial force of damper at first story under the 100% input is shown in Figure 13 (Kasai et al. (2009)). Although second stiffness is a little smaller than that by experiment, analytical damper force matches to experiments well. Initial stiffness also agrees between analysis and experiment. Then, it is conclude that the overestimate of stiffness of first story is due to the model of frame without damper, not of damper.

5. CONCLUSIONS

The analytical method applied in blind analysis contest 2009 in category 3 (2-D analysis with steel damper) was described. By modeling steel damper accurately, the responses were able to predict well. Since the stiffness of the frame at first story was overestimated, the response at first story was different from experiment. So far, the cause of difference of the stiffness at first story remains unknown.

Acknowledgements:

The authors express their appreciation to the contest organizers and National Research Institute for Earth Science and Disaster Prevention of having given such opportunity.

References:

Kasai, K., Ito, H., Ooki, Y., Motoyui, S., Ishii, M., Ozaki, H., and Hikino, T. (2010), "Full-scale shake table tests of 5-story steel building with various dampers," *Proceedings of the 7th CUEE and 5th ICEE Joint Conference*.

Hikino, T., Ohsaki, M., Kasai, K., and Nakashima, M., (2010), "Overview of 2009 E-Defense blind analysis contest results," *Proceedings of the 7th CUEE and 5th ICEE Joint Conference*.

Ohsaki, M., Kasai, K., Yamamoto, M. and Kiriyama, S. (2008), "2-D Analysis Methods for 2007 Blind Analysis Contest" *Proc. 14th World Congress of Earthquake Engineering (14WCEE)*, S17-03-005.

Yamazaki, H, Kasai, K., Kaneko, H. and Ono, Y. (2006), "Curved Hysteresis Model of Structural Steel under Cyclic Loading: Part 3 Modify of Analysis Model," *Summaries of tech. papers of Annual Meeting AIJ*, **C-1**, 935-936. (in Japanese)

Sadasue, K., Kasai, K., Yamazaki, H, Ono, Y. and Kaneko, H. (2006), "Curved Hysteresis Model of Structural Steel under Cyclic Loading: Part 4 Experimental Work and Decision Method of Material Characteristic Value," *Summaries of tech. papers of Annual Meeting AIJ*, **C-1**, 937-938. (in Japanese)

Sorazyo, S., Kasai, K., Sadasue, K., Yamazaki, H, Ono, Y. and Kaneko, H. (2006), "Curved Hysteresis Model of Structural Steel under Cyclic Loading: Part 5 Verification of Analytical Model," *Summaries of tech. papers of Annual Meeting AIJ*, **C-1**, 939-940. (in Japanese)

Shampine, L. F. and Hosea M. E. (1996), "Analysis and Implementation of TR-BDF2," *Applied Numerical Mathematics*, **20**, 21 - 37.

Kasai, K., Ito, H., Motoyui, S., Ozaki, H., Ishii, M., Kajiwara, K. and Hikino, T. (2009), "Full-Scale Tests on Value-Added Performance of 5-Story Building with Various Dampers Commercially Available," *International Symposium on Seismic Response Controlled Buildings for Sustainable Society*, OS-6.

JOINT CONFERENCE PROCEEDINGS
7th International Conference on Urban Earthquake Engineering (7CUEE) &
5th International Conference on Earthquake Engineering (5ICEE)
March 3-5, 2010, Tokyo Institute of Technology, Tokyo, Japan

2- AND 3-D BLIND ANALYSES OF FULL-SCALE 5-STORY BUILDING WITH VISCOUS DAMPERS

Tadamichi Yamashita[1)], Jun Kawabata[1)], Masayuki Ninomiya[2)], Norikazu Sakaba[2)] and Yukimori Yanagawa[3)]

1) Structural Design Department, Osaka Office, Kozo Keikaku Engineering Inc., Japan
2) Structural Design Department, Tokyo Office, Kozo Keikaku Engineering Inc., Japan
3) Disaster Prevention Consulting Department, Kozo Keikaku Engineering Inc., Japan

E-mail: tad-yamashita@kke.co.jp, jun@kke.co.jp, mninomiy@kke.co.jp, sakaba@kke.co.jp, yanagawa@kke.co.jp

Abstract: A blind analysis contest has been conducted in conjunction with full-scale 5-story building specimens with two damper types in March 2009 at the E-Defense shake-table facility. The purpose of the contest is to stimulate development of computational methods and efficient modeling techniques for steel frame buildings with various dampers. The building shaking-table tested repeatedly, inserting and replacing each of four damper types, i.e., steel damper, oil damper, viscous damper, and viscoelastic damper. This blind analysis contest is categorized by the combination of two damper types (steel and viscous damper) and two analysis types (3-D and 2-D analysis) into four categories. Authors' group participated in all categories, and won first place in the 3-D (viscous damper) and 2-D (viscous damper) categories. In this report, we present the methods of modeling and the result of seismic analysis in these two winning categories.

1. INTRODUCTION

Founded as a structural design firm in 1956, Kozo Keikaku Engineering Inc., where the authors work at, has expanded its line of business to a variety of fields in structural design as well as software development that helps design flow. We have entered this contest in all categories, aiming to serve test cases for RESP-F3T (our newly-developed 3-D analysis software of general purpose) at the same time. Our team has won first place in 2 categories that are assigned with viscous dampers in steel building in 3-D and 2-D model. In this paper are described the analysis models and results of seismic response simulations in these 2 award-winning categories as well as the technical tips for further accuracy improvement.

2. MODEL OF FIVE-STORY STEEL FRAME

We created the detailed structural model for the blind analysis contest using three approaches of modeling principally, such as modeling the steel frame building, modeling the viscous damper including brace and other members, and modeling the viscous damping of steel frame itself (without viscous dampers). (Figure 2.1) First, the steel frame building and the viscous damper system were modeled based upon the design specification and experimental result of the viscous damper distributed by National Research Institute for Earth Science and Disaster Prevention (NIED). The viscous damping of steel frame was modeled by our original approach. Instead of using the typical damping model, we created a model by ourselves, evaluated it and then employed it as analysis model.

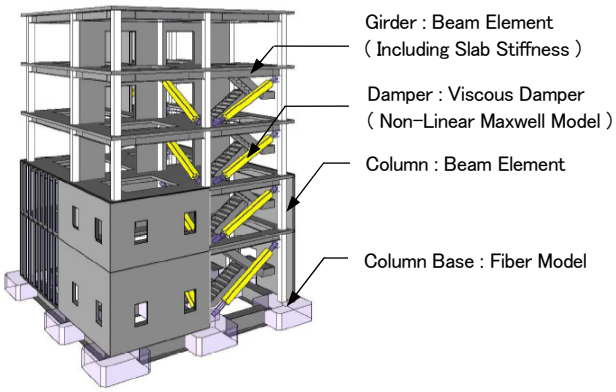

Figure 2.1 Structural Model (3 - D analysis)

Weight appraisal of the steel building (except the viscous damper systems) was determined by the calculation based on the design specification, referring to the figures disclosed by NIED, which are shown in the parenthesis in the table below. (Table 2.1)

Table 2.1 Comparison of the Weight Distribution

[kN]

Story	Floor (Include stairs)	Steel frame	Exterior wall	Interior wall Steel sash	Equipment items Weight , etc	Total weight
5th	506 (498)	88 (88)	0 (0)	9 (10)	834 (834)	1445 (1451)
		28 (21)				
4th	362 (366)	81 (72)	0 (0)	17 (20)	273 (273)	770 (779)
		47 (47)				
3rd	366 (373)	89 (89)	0 (0)	13 (14)	284 (284)	800 (820)
		62 (60)				
2nd	401 (406)	90 (87)	47 (43)	10 (7)	215 (215)	811 (824)
		70 (67)				
1st	368 (373)	91 (91)	127 (98)	5 (4)	199 (199)	825 (844)
		83 (80)				

※( ) Figures indicate the disclosed calculational data by NIED.

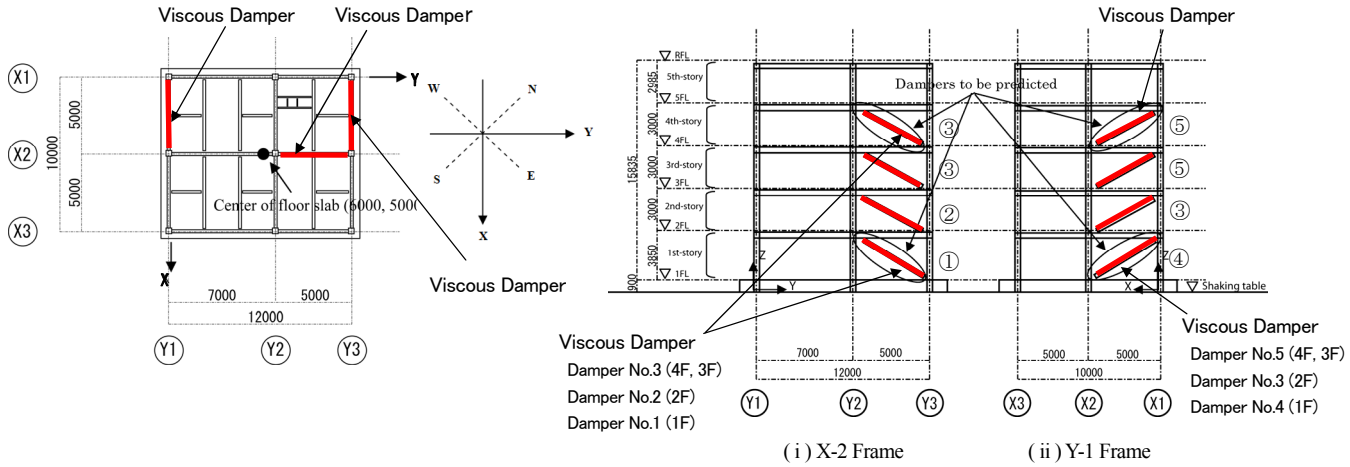

(a) Horizontal Plan

(b) Elevational Plan

(i) X-2 Frame (ii) Y-1 Frame

Figure 2.2 5-Story Steel Building with Viscous Dampers

Table 2.2 Modulus of Eccentricity for 5-Story Steel Building

Story	Eccentric Distance ex (mm)	Eccentric Distance ey (mm)	Spring Radius j x (mm)	Spring Radius j y (mm)	Modulus of Eccentricity Rex	Modulus of Eccentricity Rey
5th	150	220	6210	6420	0.036	0.023
4th	200	150	6190	6390	0.025	0.033
3rd	210	190	6090	6310	0.032	0.035
2nd	150	110	6140	6390	0.018	0.024
1st.	40	270	6270	6430	0.043	0.006

(※Japanese Seismic Design Index : Rex、Rey)

Table 2.3 Modeling and Analysis Method in Each Category

Categorie (Viscous Damper)	2-D Analysis	3-D Analysis
Structural Model	3-D Model ※YZ-Plane only	3-D Model
Number of DOFs	3 (Y, Z, YZ)	6 (X, Y, Z, XY, YZ, ZX)
Method of Time Integration	Newmark - β (β = 0.25)	Newmark - β (β = 0.25)
Time Step Increment	0.0001	0.00005

Table 2.1 shows the weight distribution by member type. Compared to the figures we calculated based upon the design specification, the figures disclosed by NIED have small discrepancies but are all higher than the calculated ones with the numerical error of approximate 2 % in every story.

The steel building is installed with viscous dampers as shown in Figure 2.2. The modeling technique of the steel building alone shall be described in this chapter. (Modeling the viscous damper system is illustrated in the following chapter.)

・Model of Steel Elements

As for the tension strength of columns and girders, yield strength of each member was defined based on the distributed result of material experiment.

・Model of Concrete

The compressive strength of concrete was specified with the experimental result obtained 90 days after casting. (Young modulus: 3.004×10^4 N / mm ^{2})

・Composite Beam Model

Assuming the girder as a composite beam with slab, its section modulus and neutral axis were calculated in accordance with "***Design Recommendations for Composite Constructions***" by Architectural Institute of Japan. The effective width of slabs was determined with reference to ***Standard for Structural Calculation of Reinforced Concrete Structures***.

・Description of Member Model

Both columns and girders were modeled as beam elements and the girder haunch was modeled as rigid zone.

・Details of the Model of Column Hinge

M-N correlation was applied to the hinge axis area of each member.

・Column-Base Model

The column bases were built as fiber models with rotational springs fully fixed.

・Model of Slabs

Assumption of rigid floor was applied for slab modeling.

After creating the model with the aforesaid specifications for each material, the modulus of eccentricity were obtained for steel frame building without damper systems. (Table 2.2) The eccentricity of strength was not calculated, assuming that the steel frame would stay mostly within the elastic region. As shown in Table 2.2, the eccentricity ratio of each story of the steel frame has the maximum value of 0.043 on the 1st story (X-direction) and 0.02 ~ 0.04 on the other stories in each direction. Having these figures, we determined that the steel building for this analysis contest scarcely has eccentricity impact. Therefore, the structural models for 2-D and 3-D categories of this blind analysis contest were built in 3-D, creating 2-D models from 3-D in YZ-plane: Y-translation, Z-translation, and X-rotation (rotation with respect to X-axis). The analysis model and method are represented in Table 2.3.

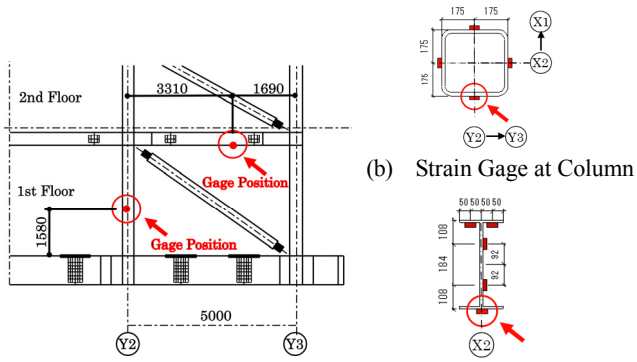

(a) X2-Elevation (b) Strain Gage at Column (c) Strain Gage at Girder

Figure 2.3 Specified Point of Strain Frame

The column strain was calculated from the axial strain and bending strain. Obtaining the axial strain from the axial force of column, and the bending strain by calculating the bending moment at the strain gage point shown in Figure 2.3 based on the bending moment of the base and top of column, the column strain was gained by summing those figures dynamically.

As shown in Figure 2.3, specifying the strain locations at girder as nodal points in the analysis model, the girder strain was calculated from the axial force and bending moment at those specified nodal points. The axial strain was calculated from axial cross-sectional area of girder with consideration of the effective width of slab when it has compressive axial force, while it was calculated from the axial cross-section of the girder only when it has tensile axial force. The bending strain was calculated respectively for each neutral axis of positive and negative moment, and thus the section modulus was obtained.

3. MODEL OF VISCOUS DAMPERS

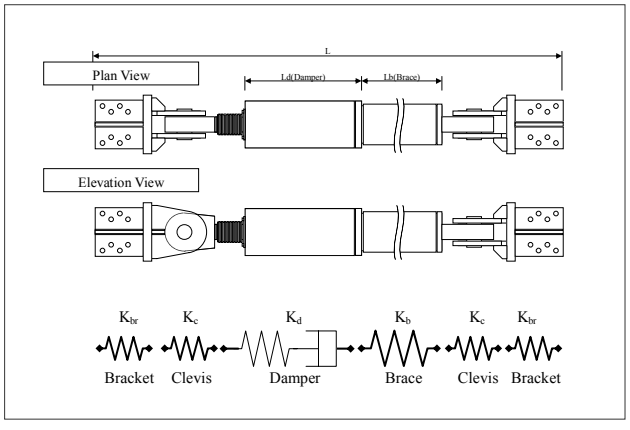

Figure 3.1 Model of Viscous Damper (Maxwell Model)

The viscous damper that is employed for this blind analysis contest is called "Non-Linear Maxwell Model", whose dashpot exerts damping force proportional to the power of the velocity, α. (Figure 3.1)

Table 3.1 Characteristics of Maxwell Model (Non-Linear)

Frame	Story	Damper No.	C_d (kN/(mm/s))$^{0.38}$	K_d (kN/mm)
X2 (Y2-3)	4th	3	98	193
	3rd	3	98	193
	2nd	2	196	438
	1st	1	196	438
Y1,Y3 (X1-2)	4th	5	49	Conjecture
	3rd	5	49	Conjecture
	2nd	3	98	193
	1st	4	98	193

While the coefficient of damping (Cd) of the viscous damper installed in the steel building and α, the power of the velocity are provided by its manufacturer, and the stiffness of the viscous damper (K_d) was determined in reference to the experimental data of the damper alone, we had to conjecture the coefficient of viscous damping for the dampers with $C_d = 49$ kN/(mm/s)$^{0.38}$. (Table 3.1)
Likewise, another model of viscous damper with coefficient damping value of $C_d = 131$ kN/(mm/s)$^{0.38}$ was also distributed (but not installed in the building) as a referential data for theorizing the damper stiffness K_d. Based on all of those damper characteristics, the damper stiffness K_d was determined.

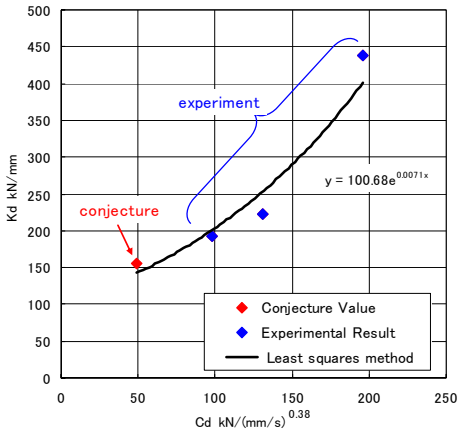

Figure 3.2 C_d - K_d Relation of Viscous Dampers

Figure 3.2 represents the correlation between the coefficient of damping C_d and the damper stiffness K_d, referring to the distributed specimen data of the viscous damper. Having no experiments done, the coefficient of damping of the model with the coefficient of damping of $C_d = 49$ kN/(mm/s)$^{0.38}$ needed to be speculated by the least squares method as shown in Figure 3.2. In this calculation, the stiffness K_d corresponding to the model with the coefficient of damper of $C_d = 49$ kN/(mm/s)$^{0.38}$ (one without any experimental data) becomes too small when assuming the coefficient of damper C_d and the damper stiffness K_d to have linear relation. Instead, we adopted relation with index function to have variants in curvature, which was $K_d = 155$ kN/(mm/s).

Table 3.2 Stiffness of Damper, Brace, Clevis and Bracket

(kN/mm)

Frame	Story	K_d	K_b	K_c	K_{br}	$K_{maxwell}$
X2 (Y2-3)	4th	193	816	13783	6070	145
	3rd	193	816	13783	6994	146
	2nd	438	2037	21921	8716	323
	1st	438	1353	21921	8716	299
Y1,Y3 (X1-2)	4th	155	770	13832	7335	122
	3rd	155	770	13832	7335	122
	2nd	193	816	13783	6070	145
	1st	193	600	13783	6994	137

The viscous damper is modeled with components coupled in series as shown in Figure3.1. The total stiffness of the viscous damper including brace and other members is calculated using Maxwell equations (Eq 3.1) with the stiffness of the viscous damper alone K_d, the stiffness of the brace K_b, the stiffness of the clevis K_c, and the stiffness of the bracket K_{br}. (Table 3.2)

$$\frac{1}{K_{maxwell}} = \frac{1}{K_d} + \frac{1}{K_b} + 2\frac{1}{K_c} + 2\frac{1}{K_{br}} \qquad (3.1)$$

Since the viscous damper is connected eccentrically from the center line of the girder, the mounting angle was tuned by setting additional nodal points in vertical direction for columns with consideration for eccentric moment. The gusset plate mounted on the damper on steel frame side is connected in series, assessing the stiffness of the plate.

4. SELECTED MODAL DAMPING RATIOS

Table4.1 Periods and Participation Factors for 3-D Model

Mode	Period (sec)	Participation factor				Notes
		X-direction	Y-direction	Z-direction	XY-direction	
1	0.747	-0.058	1.230	0.003	-82.700	1st mode(Y-dir.)
2	0.724	1.230	0.073	0.000	50.800	1st mode(X-dir.)
3	0.649	-1.170	0.664	0.003	1.240	1st mode(XY-dir.)
4	0.234	-0.011	0.463	-0.008	-140.000	
5	0.228	0.465	0.013	0.001	14.500	
6	0.206	0.444	-0.069	0.004	-0.496	
7	0.120	0.029	0.240	0.006	14.700	
8	0.119	0.234	-0.035	-0.001	5.150	
9	0.106	0.242	0.033	0.001	-0.389	
10	0.079	-0.081	-0.105	0.507	-2.160	
11	0.079	0.136	0.016	0.835	3.700	1st mode(Z-dir.)
12	0.078	-0.061	0.096	0.246	-9.180	

※XY-direction : Rotational direction

The viscous damping model of typical low-rise buildings is stiffness proportional damping. If this model was applied to the steel frame building of this blind analysis contest, the viscous damping would have resulted inevitably in high value for higher modes due to the lack of dynamic interaction with ground. Furthermore, the viscous damping in Z- direction (vertical) for 1st mode needs to be specified at minimum value in order to simulate three directions in X, Y, and Z simultaneously.

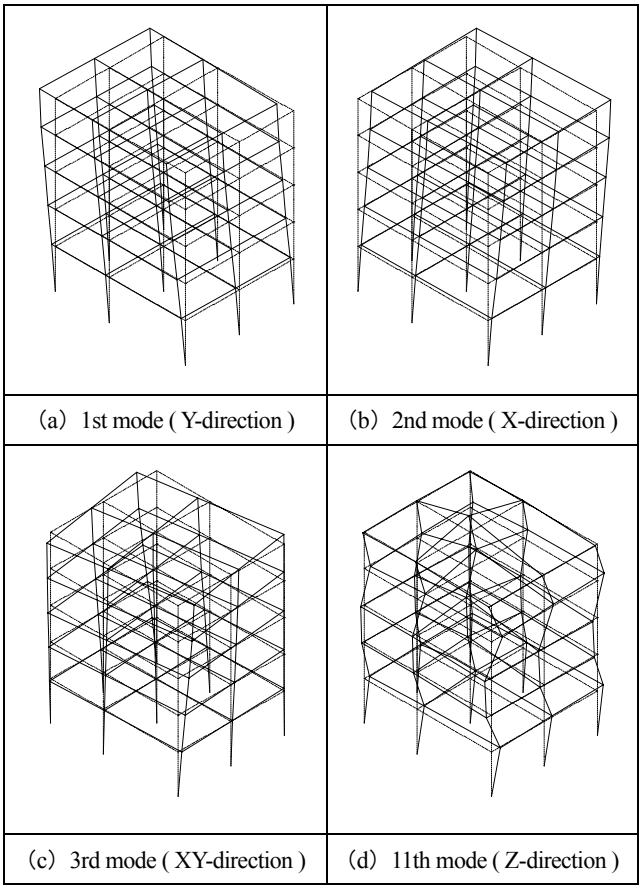

(a) 1st mode (Y-direction) (b) 2nd mode (X-direction)

(c) 3rd mode (XY-direction) (d) 11th mode (Z-direction)

Figure 4.1 Modes of 5-Story Building without Dampers

Therefore, Rayleigh damping model was applied, which is used relatively in common for high-rise buildings to determine the viscous damping for the analysis model.

Assuming the damping matrix to be proportional to a combination of the mass and the stiffness matrices, Eq 4.1 shall be obtained.

$$C = a0 \cdot [M] + a1 \cdot [K] \qquad (4.1)$$

Given Eq 4.1, modal damping ratio (h_n) leads to the following relation between two constants ($a0$, $a1$) and one frequency (ω_n) for Rayleigh damping. (Eq 4.2)

$$h_n = \frac{a0}{2 \cdot \omega_n} + \frac{a1 \cdot \omega_n}{2} \qquad (4.2)$$

Once, the damping constants h_i, h_j regarding the two vibration frequency ω_i, ω_j are specified in Eq 4.2, a set of simultaneous equations is established for invariables $a0$, $a1$. In the other words, damping constants h_i , h_j can be back-calculated by specifying the two constants $a0$, $a1$.

Thus we sought and extracted the constants $a0$, $a1$ that have 3%, 3%, 1% as damping ratio of steel frame itself (without viscous damper) in X, Y, Z in the first mode, using linear programming. (Figure 4.2) The first modal damping ratio for X and Y direction were specified as 3 %, anticipating the high damping effect by the relatively high ratio of the mounted materials (exterior-wall etc) on the steel frame compared to the typical buildings.

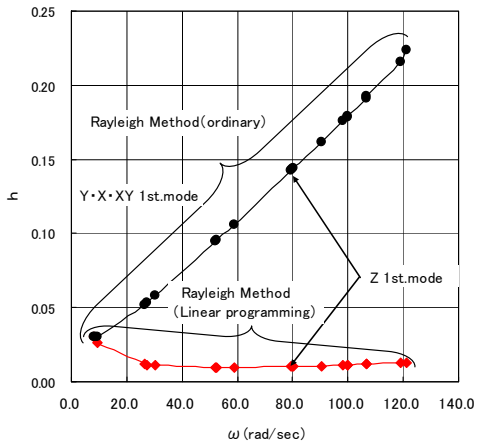

Figure 4.2 Selected by Modal Damping Ratios
(Linear Programming Method)

The value of constants $a0$ and $a1$ are detected and extracted for targeted damping ratio in 2-D and 3-D models by linear programming as shown in Table 4.2.

Table4.2 Target Modal Damping Ratios in Each Category

Categorie (Viscous Damper)	2-D Analysis	3-D Analysis
Target Modal Damping Ratio (1st Mode for each direction)	Y : 3 % , Z : 1 %	X : 3 % , Y : 3 % , Z : 1 %
a0	0.4864	0.4935
a1	0.0001745	0.0001736

5. 3 – D PREDICTION OF SEISMIC RESPONSE

Figures 5.2(a) ~ 5.3(b) indicate the maximum response acceleration and the maximum story shear force in X and Y-direction. (Seismic motion inputs were set as 0.4-scale and full-scale wave.

As can be seen in Figure 5.2(a), the experimental result (dotted line) and the analysis result (solid line) of the maximum response acceleration in X-direction are quite similar when shaken by 0.4-scale and full-scale of Takatori wave. The distribution in Figure 5.2(b) shows that the response acceleration in Y-direction has the same tendency as Figure 5.2(a) regardless to the input levels, however, their experimental results (dotted line) are much higher than the analysis results (solid line) on the top story. Studying the curves of acceleration spectra shown in Figure 5.1(a), the 1st natural period of experimental building is conceivably slightly shorter than the one of analysis model (Y-direction:T = 0.747(s)).

As for the maximum story shear force represented in Figures 5.3(a)(b), the prediction error of the experimental result of maximum response acceleration (dotted line) and the calculated result (solid line) was directly reflected on the conjectured value of maximum story shear force, since the figures of weight appraisal had very little differences between the figures NIED distributed and the one that we calculated based on the design specification.

Figures 5.4(a)～5.5(b) indicate the maximum response displacement and the maximum drift angle in X and Y-direction. (Seismic motion inputs were set as 0.4-scale and full-scale.

Comparing the maximum response displacement in X and Y-direction with 0.4-scale as in Figures 5.4(a)(b), the analysis result (solid line) is slightly less than the experimental result (dotted line). Nevertheless, the results are quite consistent. On the other hand, the maximum response displacement in X-direction with full-scale input is much higher in analysis (solid line) than experimental result (dotted line). The displacement spectra trend in Figure 5.1(b) and the speculation in Reference 2) indicate that the 1st natural period of experimental building is shorter than the one of analysis model (X-direction:T=0.724(s)) in not only Y-direction, but also in X-direction.

Studying the tendency of the displacement spectra, we have noticed that the maximum response displacement in Y-direction is also increased in the region of shorter period than the 1st natural period (Y-direction:T=0.747(s)) of analysis model when shaken in full-scale of Takatori wave. Assuming the 1st natural period of experimental building is around this period range, the discrepancies of experimental result (dotted line) and analysis result (solid line) are quite explainable.

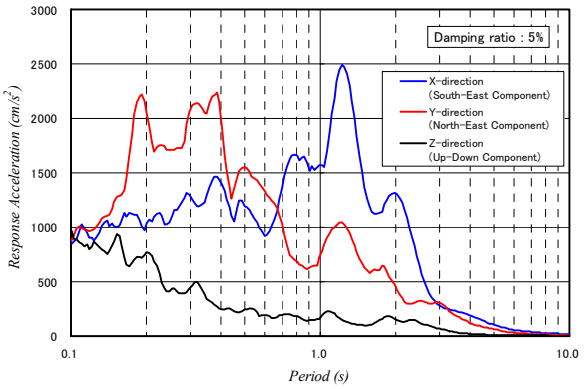

Figure 5.1(a) Acceleration Spectra for the JR Takatori Station Records
(Measured Acceleration of the Shaking-Table)

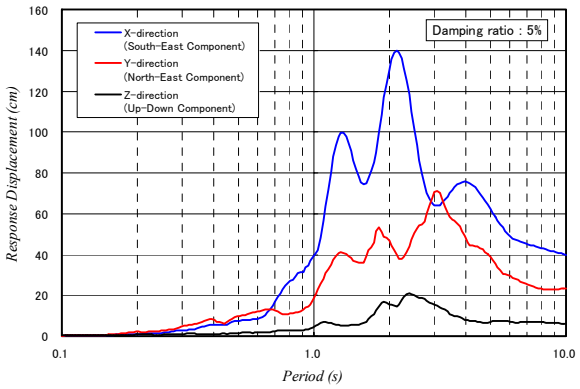

Figure 5.1(b) Displacement Spectra for the JR Takatori Station Records
(Measured Acceleration of the Shaking-Table)

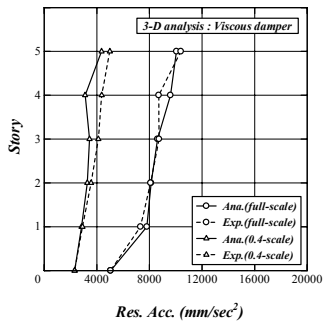

Figure 5.2(a) Maximum Response Acceleration in X-Direction

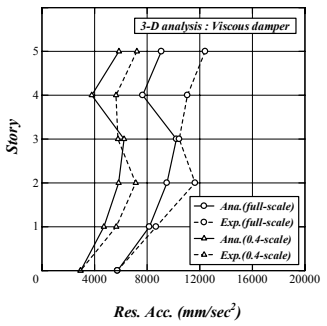

Figure 5.2(b) Maximum Response Acceleration in Y-Direction

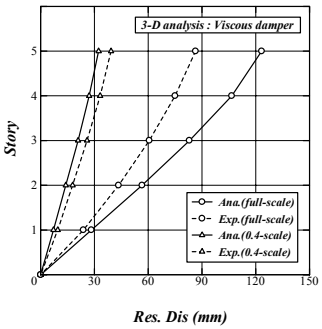

Figure 5.4(a) Maximum Response Displacement in X-Direction

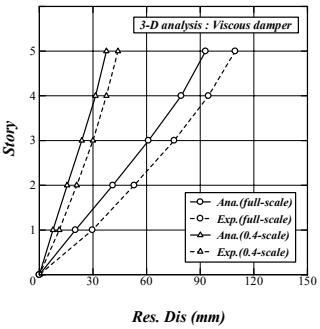

Figure 5.4(b) Maximum Response Displacement in Y-Direction

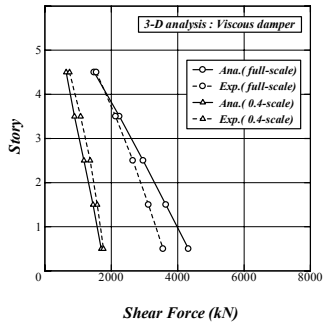

Figure 5.3(a) Maximum Story Shear Force in X-Direction

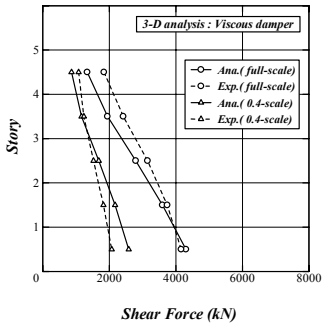

Figure 5.3(b) Maximum Story Shear Force in Y-Direction

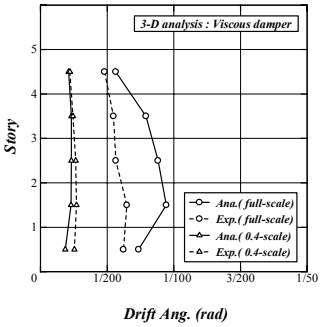

Figure 5.5(a) Maximum Drift Angle in X-Direction

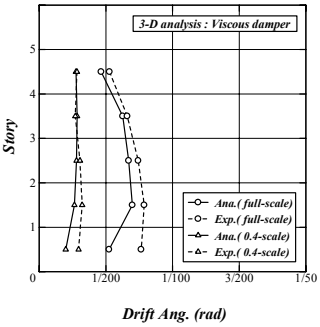

Figure 5.5(b) Maximum Drift Angle in Y-Direction

Furthermore, presuming that the 1st natural period of experimental building is shorter than the one of analysis model, the similarities of experimental result (dotted line) and analysis result (solid line) in maximum response acceleration as well as maximum response displacement for 0.4-scale of Takatori wave shown in Figures 5.2(a)(b) and Figures 5.4(a)(b) indicate the damping ratio of the steel frame itself (without dampers) has been specified slightly too high and it needs to be specified for each input level respectively.

The maximum drift angle shown in Figures 5.5(a)(b) have mostly the same prediction error as the maximum response displacement in the experimental result (dotted line) and the analysis result (solid line). The maximum drift angle for full-scale of Takatori wave, especially, has very little discrepancy between the experimental result on 1st story and the one immediately upper 1st story (2nd story) compared with the analysis results. Considering above and the fact that the story height of 1st story is taller than the other stories, the shear deformation ratio can be relatively high as a consequence of the loose connection of the pin joint at both edges of dampers, which, in fact, is reported in References 2) and 3).

Figures 5.6(a) ~ 5.9(b) show relations between the axial force and deformation of the viscous dampers that installed on the 1st and 4th stories in X-2 frame and Y-1 frame as shown in Figure 2.2. (Seismic motion inputs were set as 0.4-scale and full-scale of Takatori wave.

As can be seen in Figures 5.6(a) ~ 5.7(b), the relation of axial force and deformation of dampers installed on X and Y-directions for 0.4-scale of Takatori wave is quite consistent in the experimental result (dotted line; envelop region) and the analysis result (solid line; Hysteresis Loop), that is to say, the simulation illustrates the experimental outcome with high accuracy.

Looking at Figures 5.8(a) ~ 5.9(b), the relation of axial force and deformation of dampers installed on X and Y-directions for full-scale of Takatori wave has some larger analysis deformations (solid line) in X-direction than experimental deformations (dotted line), yet, the axial force of dampers are simulated fairly accurately. Moreover, despite the prediction error of analysis and experiment on 1st story, the relation between axial force and deformation of dampers in Y-direction is accurately calculated for the dampers installed on 4th story.

Table 5.1 Maximum Axial Strain at Column and Girder [μ]

Position	Dimension	0.4 scale wave	1.0 scale wave
Column	3-D	**349.9 Modified** (311.9)	**730.6 Modified** (534.7)
	2-D	279.7 (311.9)	472.5 (534.7)
Girder	3-D	317.9 (227.2)	557.8 (638.6)
	2-D	320.2 (227.2)	561.3 (638.6)

※( ) Figures indicate the disclosed experimental data.

Figures shown in Table 5.1 are the respective strain values of columns and girders at the gage point specified in Figure 2.3. (Seismic inputs were set as 0.4-scale and full-scale of Takatori wave. The values of column strain in 3-D analysis shown in Table 5.1 include modifications in this paper (modified the miscalculation by external processing of result of time historical response analysis).

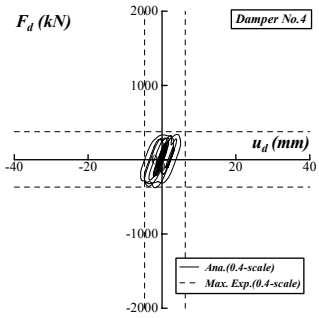

Figure 5.6(a) Force - Deformation Relation of Viscous Damper for 0.4-Scale Wave (1F:X-Direction)

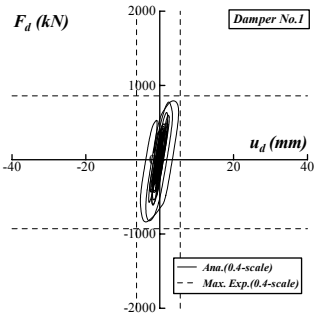

Figure 5.6(b) Force - Deformation Relation of Viscous Damper for 0.4-Scale Wave (1F:Y-Direction)

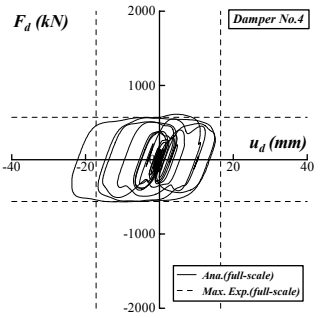

Figure 5.8(a) Force - Deformation Relation of Viscous Damper for Full-Scale Wave (1F:X-Direction)

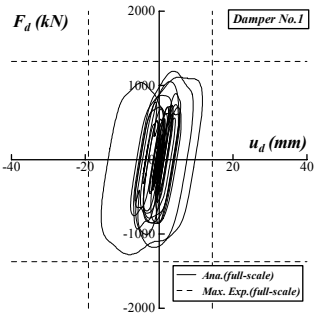

Figure 5.8(b) Force - Deformation Relation of Viscous Damper for Full-Scale Wave (1F:Y-Direction)

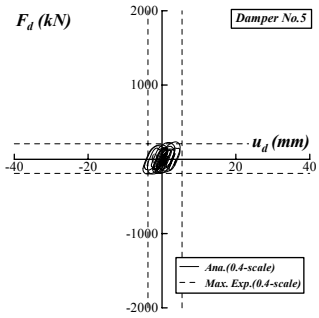

Figure 5.7(a) Force - Deformation Relation of Viscous Damper for 0.4-Scale Wave (4F:X-Direction)

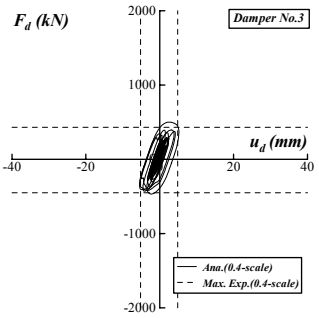

Figure 5.7(b) Force - Deformation Relation of Viscous Damper for 0.4-Scale Wave (4F:Y-Direction)

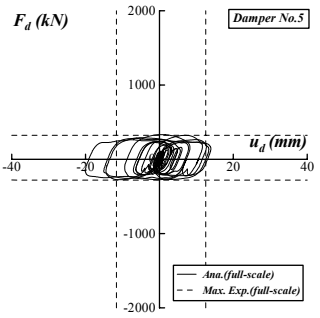

Figure 5.9(a) Force - Deformation Relation of Viscous Damper for Full-Scale Wave (4F:X-Direction)

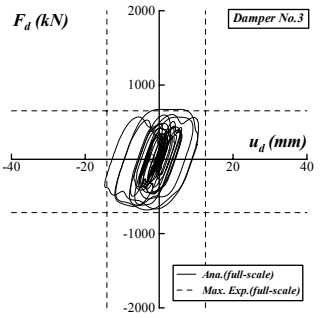

Figure 5.9(b) Force - Deformation Relation of Viscous Damper for Full-Scale Wave (4F:Y-Direction)

The results in Table 5.1 indicate approximate 10-40% errors in axial strain of both columns and girders, and the highest error can be found in columns in 3-D analysis for full-scale of Takatori wave. On the other hand, the analysis result of columns in 3-D with 0.4-scale wave is similar to that of experiment. Besides this, looking back the result of maximum story shear force shown in Figure 5.3(a) as well as the maximum drift angle in Figure 5.5(a), it is implied that the analysis result were higher than the experimental result due to the much higher maximum shear force in analysis (solid line) than experiment (dotted line) on 1st story for full- scale of Takatori wave.

The girder strain for 0.4-scale wave has greater value in analysis than experiment result, while it is less for full-scale wave. This is accountable by studying in conjunction with the result of maximum story shear represented in Figure 5.3(b), having the relation between analysis and experimental result corresponding to the maximum response shear force.

Finally, we reported that the analysis results in 2-D have few discrepancies with the results in 3-D that are shown in this paper. The experimental results are not equivalent to the official data disclosed, but are estimated figures based upon the examination outcome in NIED site. (http://www.blind-analysis.jp/)

6. CONCLUSIONS

Reviewing the analysis model and seismic response analysis results in 2 award-winning categories (categories assigned with viscous dampers in 3-D and 2-D) in this paper, we have found useful technical tips in terms of accuracy enhancement.

1) Comparing the 1st natural period of experimental building and the one of analysis model, the former tends to be shorter than the latter. This tendency causes significant impact on the seismic response analysis result of buildings whose 1st natural period are within short period region.
2) The viscous damper systems including brace and other components can be modeled accurately by Maxwell model. However, loose connections of the pin joint of damper need to be reduced as much as possible in order to maximize the damping force of the device as well as to improve the accuracy of the simulation.
3) The viscous damping model of the building that has comparatively short first natural period can be optimized by applying the individual modal damping and specifying mostly the same damping ratio from 1st to higher modes, provided that there isn't any dynamic interaction (radiation damping) with ground at all. Thus the model can duplicate the phenomena accurately.
4) The viscous damping of the building must be specified in accordance with the seismic input level. The damping ratio of the analysis model should be slightly less for 0.4-scale than for full-scale of Takatori wave.
5) The accuracy of 2-D simulation can be as high as 3-D by creating 2-D model from 3-D (limited to the two directional model), provided the eccentricity (of stiffness or of strength) of the building is small.

Acknowledgements:

The authors acknowledge support of Mr. Mitsuhiro Saito (Disaster Prevention Consulting Department, Kozo Keikaku Engineering Inc.), Mr. Tetsushi Inubushi (Structural Design Department, Osaka Office, Kozo Keikaku Engineering Inc.) and Ms. Eiko Kawamura (Overseas Marketing and Corporate Development Dept.) for these analyses and completing this paper, with sincere gratitude to their assistance.

References:

1)K.Kasai, Y.Ooki, M.Ishii, H.Ozaki, H.Ito, S.Motoyui T.Hikino, and E.Sato. (2008), "VALUE-ADDED 5-STORY STEEL FRAME AND ITS COMPONENTS: PART1 FULL-SCALE DAMPER TESTS AND ANALYSES," ***The 14th World Conference on Earthquake Engineering***, S17-01-013.

2)Y.Ooki, K.Kasai, S.Murata and Y.Yamazaki. (2009), "Shaking Machine Test of the Full Scale Value-Added 5-Story Steel Building: E-Defense Experimental Projects for Steel Building Part48," ***Summaries of Technical Papers of Annual Meeting Architectural Institute of Japan***, C-1, 749-750.

3)M.Yonetani, K.Kasai, Y.Ooki, H.Ito and T.Hikino. (2009), "Result of Shaking Table Test of 5-Story Steel Frame with Viscous Damper: E-Defense Experimental Projects for Steel Building Part45," ***Summaries of Technical Papers of Annual Meeting Architectural Institute of Japan***, C-1, 743-744.

JOINT CONFERENCE PROCEEDINGS
7th International Conference on Urban Earthquake Engineering (7CUEE) &
5th International Conference on Earthquake Engineering (5ICEE)
March 3-5, 2010, Tokyo Institute of Technology, Tokyo, Japan

OVERVIEW OF 2009 E-DEFENSE BLIND ANALYSIS CONTEST RESULTS

Tsuyoshi Hikino[1], Makoto Ohsaki[2], Kazuhiko Kasai[3] , and Masayoshi Nakashima[4]

1) Researcher, National Research Institute for Earth Science and Disaster Prevention, Japan
2) Associate Professor, Dept. of Architecture and Architectural Engineering, Kyoto University, Japan
3) Professor, Structural Engineering Research Center, Tokyo Institute of Technology, Japan
4) Professor, Disaster Prevention Research Institute, Kyoto University, Japan
hikino@bosai.go.jp, ohsaki@archi.kyoto-u.ac.jp, kasai@serc.titech.ac.jp, nakashima@archi.kyoto-u.ac.jp

Abstract: A blind analysis contest has been conducted in conjunction with the full-scale tests of passively-controlled five-story steel building frames in March 2009 at E-Defense shake table facility. The purpose of the contest is to stimulate development of computational methods and efficient modeling techniques for steel structures. In this report, in addition to the rules and the procedures of the contest, statistical data are presented for the types and parameter values for analysis employed by the participants of the contest, and the key factors to accurate estimation of passively-controlled steel structures are investigated.

1. INTRODUCTION

A blind analysis contest has been conducted in conjunction with the full-scale tests of passively-controlled five-story steel building frames in March 2009 at E-Defense shake table facility. The frame has five stories and 2×2 spans as shown in Figure 1. Passive dampers are located in 1st, 2nd, 3rd, and 4th stories. The details of the building frames with steel dampers and viscous dampers, respectively, can be referred to Kasai et al. (2010). This blind analysis contest is the third contest of E-Defense following the contests of the four-story steel building frame in 2007 (Ohsaki et al. 2008) and the steel bridge in 2008. Outline of the E-Defense tests on full-scale steel buildings is presented in Kasai et al. (2007).

The contest has been carried out by the Blind Analysis Contest Committee (Contest organizer: Makoto Ohsaki, Kyoto University), which did tasks including announcement, distribution of data, answering questions, and judgment. The Damper and Isolation System Working Group (Leader: Kazuhiko Kasai, Tokyo Institute of Technology) supplied the experimental data for the passively-controlled five-story building. The purpose of this blind analysis contest is to stimulate development of computational methods and efficient modeling techniques for prediction of seismic responses of passively-controlled steel frames. The final goal of the series of contests is to improve seismic performance of steel frames through numerical simulation.

In this paper, the details of the contest rule and the results including key factors adopted by participants for accurate estimation of responses are reported.

The methods and results of the winners may be consulted to the papers by Nakamura et al. (2010), Yoneda et al. (2010), and Yamashita et al. (2010).

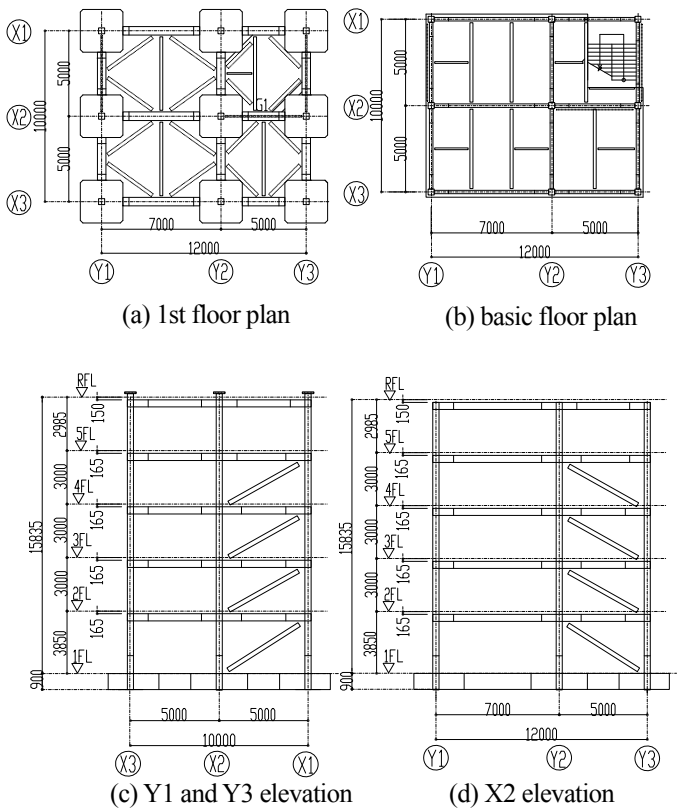

(a) 1st floor plan (b) basic floor plan

(c) Y1 and Y3 elevation (d) X2 elevation

Figure 1 Plan and elevation of the 5-story steel building specimen

2. CONTEST RULE

2.1 Difficulties of the Blind Analysis Contest

The main difficulties of the contest are summarized as follows:

i. The actual motion of the table is not known before the test due to the inevitable small control error of the shake table.
ii. The shake table tests are conducted consecutively with increasing levels of seismic motion, and the seismic level of the subsequent test is decided according to the actual response of the current test.
iii. The property of the concrete material is measured only a few days before the test.

Therefore, the following two-step process has been adopted for the contest:

i. The contest consists of two parts; i.e., *pre-test analysis* based on anticipated seismic motions, and *post-test analysis* using the actual table acceleration.
ii. The building frame model and the analysis procedure for the *post-test analysis* must be identical to those for the *pre-test analysis* except for the property of concrete material and the input accelerations.

In order to incorporate the effects of residual deformations appropriately in the simulation results, the table accelerations of the sequence of all the major tests are distributed to the participants.

2.2 Category of the Contest and Input Accelerations

The contest is categorized by the types of analysis models and dampers. Analysis models are classified to 3D-analysis and 2D-analysis, and the damper types are steel and viscous. The categories are:

Category1: 3D-analysis, Steel damper
Category2: 3D-analysis, Viscous damper
Category3: 2D-analysis, Steel damper
Category4: 2D-analysis, Viscous damper

The participants compete in each category, and consequently, the four winners are selected.

The input motion is the JR-Takatori wave of the 1995 Hyogo-ken Nanbu Earthquake that is scaled to various levels. The sequence of major tests and the target levels for which the responses are to be predicted for each category are as follows:

i. Steel damper: Tests were conducted for 15%, 40%, 50%, 70% and 100%, and the contest targets are 15% and 100%.
ii. Viscous damper: Tests were conducted for 40%, 50%, 60%, 70%, 83% and 100%, and the contest targets are 40% and 100%.

The measured table accelerations for all the tests are distributed to the participants.

2.3 Data to be provided and submitted

In order to focus on the essential analysis parameters, not only structural geometry data, but also supplemental information was distributed by the committee through website:

i. Structural geometry:
plan, elevation, cross-sectional properties of structural members, and detailed description of the specimen including connections to non-structural components.
ii. Details of loading conditions:
weights of parts and non-structural components.
iii. Preliminary analysis results:
pushover analysis and preliminary time-history analysis carried out by the committee (Kasai et al. 2008).
iv. Material test results:
properties of steel and concrete, which are obtained by the tests based on Japanese specification (results of concrete material are available after the test).
v. Time-history and response spectrum of seismic motion:
ideal acceleration for pre-test analysis, and measured acceleration for post-test analysis.

The data to be submitted for the pre-test analysis and post-test analysis are specified as follows:

i. Predicted responses:
maximum absolute values of relative displacement from base and absolute acceleration at each floor; maximum absolute values of story shear and story drift angle; maximum and minimum values of axial deformations and axial forces of the dampers in the 1st and 4th stories in Y1 and X2 sections for 3D-analysis and in X2 section only for 2D-analysis.
ii. Maximum absolute value of strain at a specified point in an elastic state.
iii. Description of computational environment, model and method for analysis:
name of program; type of availability of program (commercial, research purpose); name of computer; CPU time; number of degrees of freedom; constitutive models; definition of damping; method of time integration, etc.
iv. Input files to the analysis program:
data in ASCII format; all the non-default values such as damping factor, hardening parameters, etc.;(Input echo of the analysis program is preferred, while the geometry data such as nodal coordinates and node-element relations are not needed).
v. Supplemental data:
figures illustrating the deformation and plastification; relation between force and deformation of a damper; time histories of shear force; drift angle of a story, and so on.

2.4 General Remarks

The supplementary remarks of the contests were informed as follows:

i. The responses in X- and Y-directions should be presented for 3D-analysis, while only Y-directional responses are to be presented for 2D-analysis.

ii. The target levels of pre-test analysis are only Takatori 100% for both categories, while the levels of post-test analysis are Takatori 15% for steel damper, and 40% for viscous damper in addition to Takatori 100% for both categories.
iii. Any modeling method including frame model, lumped mass model, FEM, etc., can be used for prediction of the responses.
iv. Shake table tests are carried out from small levels to large levels by gradually increasing levels in both steel and viscous damper tests. Therefore, the measured acceleration records of shaking table are distributed for all levels of motions. The participants are free to use any method and engineering judgment for evaluating the effect of residual deformation.
v. The maximum absolute values of relative displacement and absolute acceleration are evaluated on the upper surface at the center of each floor slab.
vi. Formulas for computing story drift and story shear, as well as the weight of each story from the measured displacements and accelerations, respectively, are given by the committee.
vii. Predictions shall be in SI units (mm, kN, sec, rad) and each number should have four significant figures. For example, a story drift angle can be reported as 0.01234rad.

Table 1 Numbers of teams in each category

	S3	V3	S2	V2	TOTAL
Japan	8	2	3	2	15
Taiwan	3	4	4	4	15
U.S.	2	4	3	3	12
China	2	4	0	0	6
N.Z.	1	0	0	0	1
Italy	1	0	0	0	1
Canada	0	0	1	0	1
UAE	0	0	0	1	1
TOTAL	17	14	11	10	52

Note) S3: Category1 3D-analysis, Steel damper
V3: Category2 3D-analysis, Viscous damper
S2: Category3 2D-analysis, Steel damper
V2: Category4 2D-analysis, Viscous damper

Table 2 Numbers of types of softwares and modeling elements adopted in each category

		3D-analysis		2D-analysis	
Items	Damper type Subtotal	Steel 17	Viscous 14	Steel 11	Viscous 10
Types of softwares	Commercial Research Personal	8 4 (1) 5 (2)	9 (1) 2 (1) 3 (1)	5 5 (3) 1 (1)	5 (2) 3 2 (1)
Types of modeling elements	Line Fiber Line+Fiber Shell Line+Shell Others N/A	8 1 (1) 3 1 1 (1) 3 (1) 0	5 (1) 0 5 (1) 0 3 (1) 0 1	6 (3) 2 (1) 2 0 0 1 0	8 (2) 0 1 (1) 0 1 0 0

Note) The number within parenthesis means the number of within third place.

2.5 Method of Judgment

The judgment process is summarized as follows:

i. Compare the RMS errors for each response quantity, which is computed from

$$E_k = \sqrt{\sum_j (F_{k,j} - F^*_{k,j})^2} \quad (1)$$

Here, $F_{k,j}$ is the analysis result and $F^*_{k,j}$ is the test result of the kth response quantity at the jth floor/story, respectively, and E_k is the RMS error of the kth response quantity. Note that only the responses in the 1st and 4th stories are considered for the deformation and axial force of dampers. It is possible to normalize $F_{k,j} - F^*_{k,j}$ by $F^*_{k,j}$ before summation. However, in this case the errors of the small responses are magnified. Therefore, we did not make normalization in this contest.

ii. The point b_i for the ith response quantity is 8 for the minimum error, 5 for the second, 3 for the third, and 1 for the fourth. The total point P is computed as follows, and the team/individual with maximum total point will be the winner for each category:

$$P = \sum_{i=1}^{n} b_i \quad (2)$$

Here, n is the number of response quantities.

iii. The judgment is carried out completely anonymously recognizing each participant only by the ID number.
iv. In each category, up to and including the third place winners are announced and all the participants are asked to disclose their names and affiliations.

3. RESULTS OF THE CONTEST

The numbers of teams who submitted the post-test results are shown in Table 1. As is seen, we had more than ten teams in each category, although some of 2D-analysis and 3D-analysis are duplicate. The numbers of types of softwares adopted in each category are shown in Table 2, where "commercial" means any commercially available software package, "research" means free software that may possibly be used for commercial purpose, and "personal" means in-house program developed for own use. The numbers of types of modeling elements are also listed in Table 2. "Line" indicates the conventional beam-column line elements including hinge elements. "Line+Fiber" means that fiber elements are used for beams and columns, while line elements are adopted for dampers.

"Line+Shell" means that line elements are used for beams, columns and dampers, and shell elements are used for slabs and partition walls. "Others" include the combination of line, fiber and shell elements which do

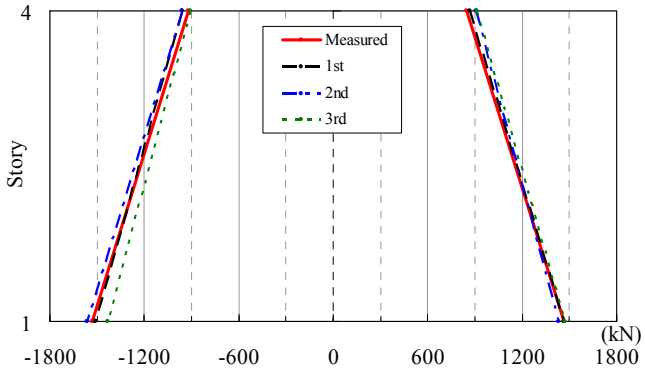

(a) Axial force of 1st and 4th story dampers

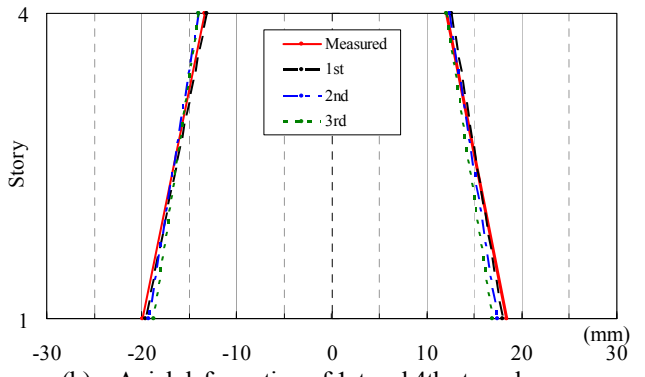

(b) Axial deformation of 1st and 4th story dampers

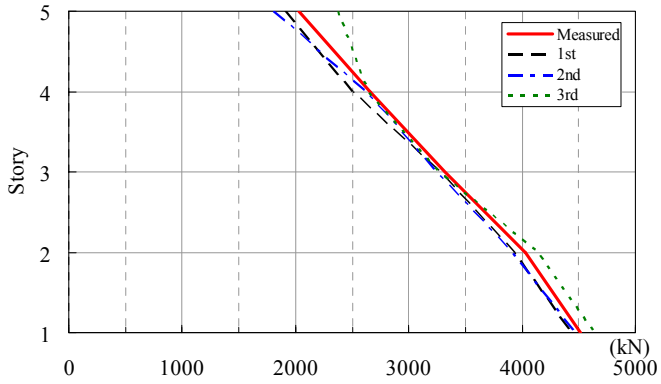

(c) Maximum absolute story shear

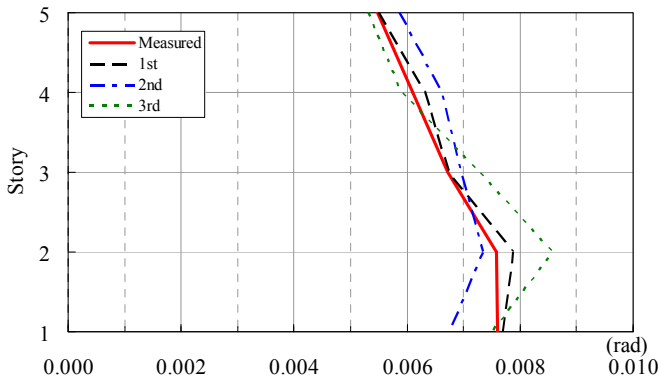

(d) Maximum absolute story drift angle

Figure 2 Measured and best three teams of each response quantities in Y-direction at Takatori 100% shaking, category1 (3D-analysis, Steel damper)

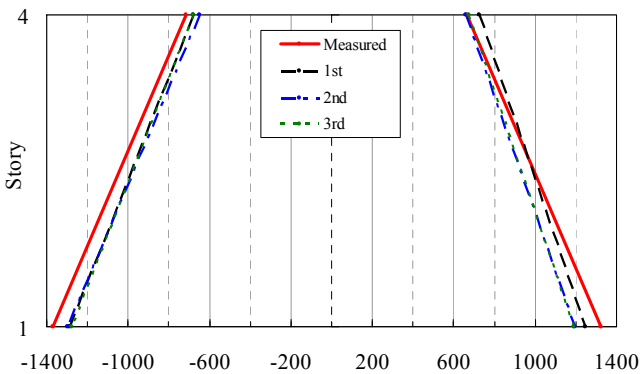

(a) Axial force of 1st and 4th story dampers

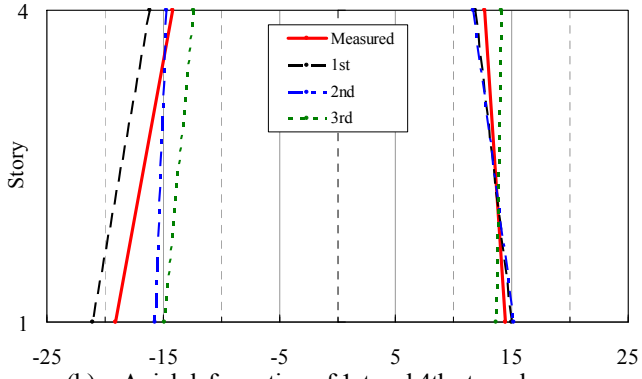

(b) Axial deformation of 1st and 4th story dampers

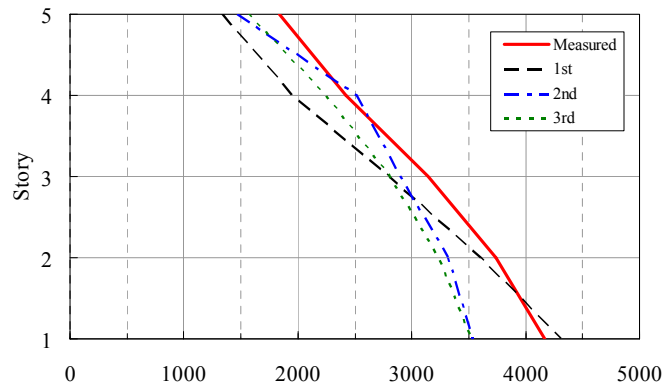

(c) Maximum absolute story shear

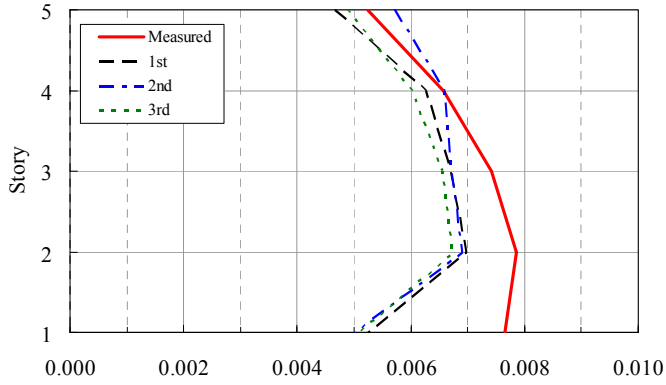

(d) Maximum absolute story drift angle

Figure 3 Measured and best three teams of each response quantities in Y-direction at Takatori 100% shaking, category1 (3D-analysis, Viscous damper)

not apply to above types.

In Table 2, the numbers in parentheses are those in best three teams in each category, where we had two third-place winners with the same point for 2D-analysis of steel damper. As is seen, line elements are most commonly used and lead to very accurate results, while only one team used a shell element.

Figure 2 and Figure 3 shows the results of the best three teams of category1 (3D-analysis, Steel damper) and category2 (3D-analysis, Viscous damper), respectively. The estimated responses as well as the measured data are plotted for each response quantity in Y-direction at Takatori 100% input. Highly accurate prediction is observed from figures.

4. STATISTICAL INVESTIGATION OF RESULTS

The parameters for analysis and selection of key factors that have significant effect on the analysis results of the teams in each category are shown in Table 3, which gives the following observations:

- 3D-analysis generally has larger DOFs, which result in larger CPU time, than 2D-analysis.
- All the best three teams in all categories, which are called best three teams for simplicity, utilize the results of material tests. The Menegotto Pinto model leads to better results than the bilinear model.
- Some of the best three teams did not consider composite beam effect or assumption of rigid floor.
- The 1st natural frequencies of the pure frame estimated by the best three teams range between 0.60 sec and 0.80 sec, which agree within good accuracy with the experimental results.
- Geometrical nonlinearity need not be considered for a good estimation, because the maximum interstory drift angle is less than 1/100.
- Most of the teams, including the best three teams, employed the Rayleigh damping with the damping ratio 0.02 for the 1st mode.
- The Newmark-β method is used by most of the teams, and no improvement in accuracy is observed from a time increment smaller than 0.01 sec.

5. CONCLUSIONS

The details of 2009 E-Defense Blind Analysis Contest have been reported. The rules and procedures of the contest have been presented followed by the general difficulties in blind analysis contest. The contest results and the key factors for accurate estimation of the responses are discussed in view of various parameters and methodologies of analysis.

Compared with the results of the previous contest on total collapse analysis, better prediction has been observed mainly by the best three teams in each category. More detailed investigation will be made in our future study to clarify the key factors for accurate estimation of seismic responses of passively-controlled frames.

Table 3 The distribution of adopted key factors by the participants

		3D-analysis		2D-analysis	
Items	Damper type Subtotal	Steel 17	Viscous 14	Steel 11	Viscous 10
CPU time	Less than 5 min. 5 to 60 min. 60 to 600 min. Over 600 min. N/A	4 4 4 (2) 3 (1) 2	1 6 (2) 3 3 (1) 1	2 (1) 4 (2) 4 (1) 0 1	2 4 (2) 3 (1) 1 0
DOFs	Less than 200 200 to 1000 1000 to 2000 Over 2000 N/A	2 4 (1) 5 (2) 5 1	1 (1) 3 6 (2) 4 0	5 (2) 2 (1) 3 (1) 1 0	4 (3) 0 5 1 0
Material test results	Use Do not use	13(3) 4	14 (3) 0	10 (4) 1	10 (3) 0
Constitutive model of Steel damper	Bilinear RO *2 MP *3 Other N/A	6 2 2 (2) 3 (1) 3	- - - - -	0 1 4 (3) 5 (1) 1	- - - - -
Composite beam	Consider Do not consider	11(2) 6 (1)	5 (1) 9 (2)	9 (4)	5 (3) 5
Rigid floor assumption	Use Do not use	11(1) 6 (2)	11 (2) 3 (1)	11 (4) 0	8 (3) 2
Period of pure frame in Y-dir.	Less than 0.60 0.60 to 0.70 0.70 to 0.80 Over 0.80	1 6 (3) 4 6	0 5 (2) 5 (1) 4	2 4 (3) 3 (1) 2	0 4 (2) 3 (1) 3
Period of frame with Steel damper in Y-dir.	Less than 0.50 0.50 to 0.55 0.55 to 0.60 Over 0.60	4 (2) 6 (1) 4 3	- - - -	3 (1) 5 (3) 3 0	- - - -
Geometrical nonlinearity	Consider Do not consider	9 (1) 8 (2)	8 4 (3)	5 (2) 6 (2)	5 (1) 5 (2)
Damping type	Rayleigh Stiffness-proportional Other N/A	8 3 0 6	5 (2) 1 (1) 0 8	6 (3) 1 (1) 1 3	6 (2) 1 (1) 1 2
Damping ratio	Less than 0.02 0.02 0.03 Over 0.03 N/A	2 8 (2) 3 (1) 1 3	1 6 (2) 2 2 3 (1)	1 5 (2) 2 (1) 0 3 (1)	1 (1) 6 (1) 0 0 3 (1)
Method of integration	Newmark-β HHT *4 Modal Other	12(3) 3 1 1	8 (3) 1 2 3	8 (3) 0 1 2 (1)	6 (1) 0 2 2 (2)
Time step Δt (sec.) for integration	Δt≤0.001 0.001<Δt<0.01 Δt =0.01 0.01<Δt N/A	4 (1) 6 (1) 6 (1) 0 1	2 (1) 4 (1) 6 (1) 1 1	6 (2) 3 (1) 2 (1) 0 0	2 (1) 3 (2) 5 0 0

Note) *1 N/A: Not available from the documents
*2 RO: Ramberg Osgood model
*3 MP: Menegotto Pinto model
*4 HHT: Hilber-Hughes-Taylor

Acknowledgements:

This study is a part of "NEES/E-Defense collaborative research program on steel structures," and was pursued by the Damper and Isolation System Working Group. The Japan team leader for the overall program and WG is Kazuhiko Kasai, Tokyo Institute of Technology, and the Contest organizer is Makoto Ohsaki, Kyoto University. The authors acknowledge the support by the members of WG and the Blind Analysis Committee, also the financial support provided by the National Research Institute for Earth Science and Disaster Prevention. Valuable cooperation from participants is greatly acknowledged.

References:

Kasai, K., Ito, H., Ooki, Y., Motoyui, S., Ishii, M., Ozaki, H., and Hikino, T. (2010), "Full-scale shake table tests of 5-story steel building with various dampers," *Proceedings of the 7th CUEE and 5th ICEE Joint Conference*.

Ohsaki, M., Kasai, K., Hikino, T., and Matsuoka, Y. (2008), "Overview of 2007 blind analysis contest results," *Proceedings of the 14th World Conference on Earthquake Engineering*, Paper No. S17-03-004.

Ohsaki, M., Kasai, K., Yamamoto, M., and Kiriyama, S. (2008), "2-D analysis methods for 2007 blind analysis contest," *Proceedings of the 14th World Conference on Earthquake Engineering*, Paper No. S17-03-005.

Ohsaki, M., Kasai, K., Thiagarajan, G., Yang, Y., and Komiya, Y. (2008), "3-D analysis methods for 2007 blind analysis contest," *Proceedings of the 14th World Conference on Earthquake Engineering*, Paper No. S17-03-007.

Kasai, K., Ooki, Y., Motoyui, S., Takeuchi, T., and Sato, E., (2007), "E-Defense tests on full-scale steel buildings: Part1 - Experiments using dampers and isolators," *Proceedings of the Structures Congress 2007,* 247-17.

Nakamura, N., Suzuki, T., Nakamura, S., Yamamoto, M., Sone, T., and Yoneda, H. (2010), "3-D blind analyses of full-scale 5-story building with steel dampers," *Proceedings of the 7th CUEE and 5th ICEE Joint Conference*.

Yoneda, H., Yamamoto, M., Sone, T., Nakamura, N., Suzuki, T., and Nakamura, S. (2010), "2-D blind analyses of full-scale 5-story building with steel dampers," *Proceedings of the 7th CUEE and 5th ICEE Joint Conference*.

Yamashita, T., Kawabata, J., Ninomiya, M., Sakaba, N., Yanagawa, Y. (2010), "2- and 3-D blind analyses of full-scale 5-story building with viscous dampers," *Proceedings of the 7th CUEE and 5th ICEE Joint Conference*.

Kasai, K., Ooki, Y., Ishii, M., Ozaki, H., Motoyui, S., Hikino, T., and Sato, E., (2008), "Value-added 5-story steel frame and its components: Prat1-Full-scale damper tests and analyses," *Proceedings of the 14th World Conference on Earthquake Engineering*, Paper No. S17-01-013.

JOINT CONFERENCE PROCEEDINGS
7th International Conference on Urban Earthquake Engineering (7CUEE) &
5th International Conference on Earthquake Engineering (5ICEE)
March 3-5, 2010, Tokyo Institute of Technology, Tokyo, Japan

NUMERICAL SIMULATION OF UNDERGROUND PIPELINE UNDER LATERAL NON-UNIFORM EARTHQUAKE WAVE EXCITATION AND COMPARISON WITH SHAKING TABLE TESTS

Xiaoyu Qi[1)], Jun Chen[2)]

1) Master of Engineering, Dept. of Building Engineering, College of Civil Engineering, Tongji University, China,
2) Associate Professor, State Key Laboratory for Disaster Reduction in Civil Engineering, Tongji University, China
windfly-2004@163.com,cejchen@tongji.edu.cn

Abstract：This paper investigates the numerical simulation of underground pipeline under lateral non-uniform earthquake wave excitation by a three-dimensional finite element model based on ABAQUS. In particular, the Drucker-Prager model is adopted for modeling soil and the soil-structure interface and initial stress field are also considered in the numerical model. The acceleration time histories are taken as the input at the bottom of each box. The calculated soil and pipeline acceleration, displacement and strains are compared with that obtained in shaking table tests in terms of time history, amplification factor, spectrum and patterns. The comparison demonstrates that the proposed modeling methodology can capture the main features of the pipeline under non-uniform earthquake excitation and therefore can be adopted for further parametrical analysis.

Keys Words: underground pipeline; shaking table test; non-uniform excitation; finite element model

1 Introduction

Safety of underground pipelines in lifeline system, including communication network, water supply, gas supply and sewage system, under earthquake attack is of great importance for the function of modern cities, and certain industries as well. Many recent major earthquakes, such as the ChiChi Earthquake in Taiwan, the Wenchuan Earthquake in Sichuan China, has demonstrated again that lifeline system pipelines could be severely damaged in the earthquake causing serious problems for the rescue and recovery after the earthquake. Figure 1 is a photo of pipeline damage during the Wenchuan Earthquake.

Being a long line-type underground structure, the underground pipeline is very vulnerable to spatial distribution of earthquake wave termed as the non-uniform earthquake wave excitation. Compared with researches on seismic responses analysis of underground pipeline under uniform earthquake excitation, the performance of pipeline under non-uniform excitation has not yet be well understood.



Figure 1 pipeline damage during the Wenchuan Earthquake.

In this connection, this paper investigates the numerical simulation of underground pipeline under lateral non-uniform earthquake wave excitation. The effectiveness and

feasibility of the proposed finite element model is validated by comparison of numerical results with that obtained in a shaking table test.

2 Shaking Table Tests

A series tests were conducted on pipelines using two shaking tables to simulate non-uniform earthquake excitation. Therefore, two identical laminar shear boxes are used to simulate the non-uniform soil excitation to underground pipelines. The overall dimension of each box is 3.2m×2m×1.92m (L×W×H) with inner soil dimension as 3m×1.8m×1.87m (L×W×H). The laminar shear box consists of 16 steel frames, which are numbered as 1 to 16 from bottom to top. The width and height of every steel frame are 100mm with the clearance of each frame as 21.3mm. Figure 2 shows the full view of the shaking table test of underground pipeline. Detailed of the shear box can be found in Shi et al. (2009). During the test, the two boxes vibrate in a direction perpendicular to the axis of the pipe, which is defined as lateral direction in this paper.

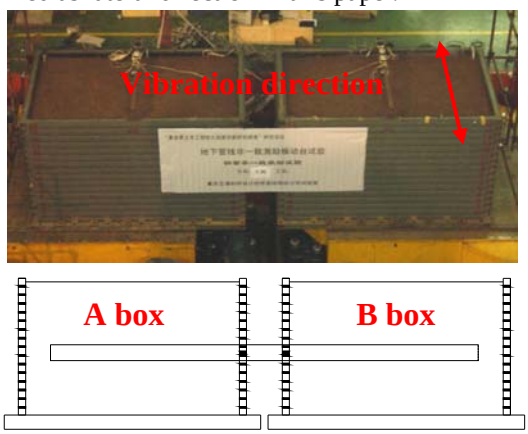

Figure 2 the full view of the shaking table test

As showed in the figure 2 and figure 3, the steel pipe of this test is 6m long, which is buried in the soil.

The soil in this experiment is the clay taken from upper reaches of the Yangtze River with the Poisson's ratio as 20.0%, the inner friction angle as 27.9 and cohesion as 24.4kPa. The soil is compressed by laminar and the underground pipeline is made of jointed seal steel tube.

A series of shaking table tests has been carried out with different peak acceleration levels varying from 0.1g to 1.0g. Figure 3a shows the 1# input acceleration time history (PGA=1.0g) for A-box in the test, while Figure 3b shows 2# input acceleration time history (PGA=1.0g) for B-box.

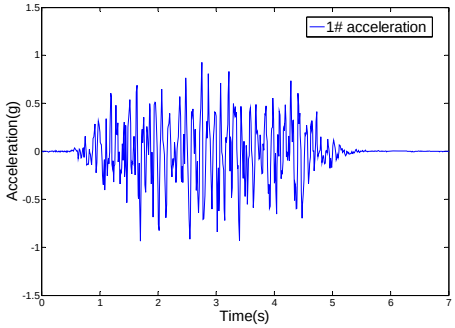

(a) 1# input acceleration

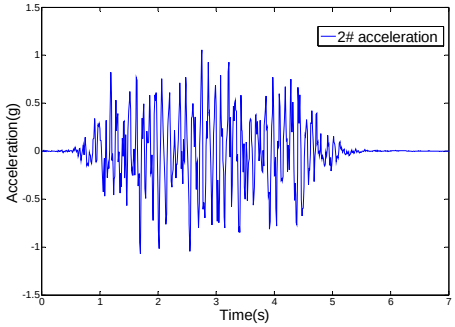

(b) 2# input acceleration

Figure 3 the input acceleration time history (PGA=1.0g)

In the shaking table test, accelerometers (A), displacement transducers (AD, BD), and strain gauges (W) are used to record the responses of the soil, the laminar shear box and pipeline respectively. Figure 4 shows the layout of all the sensors.

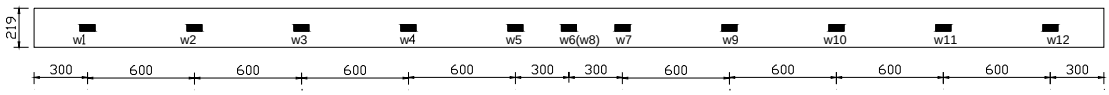

(a) strain gauges

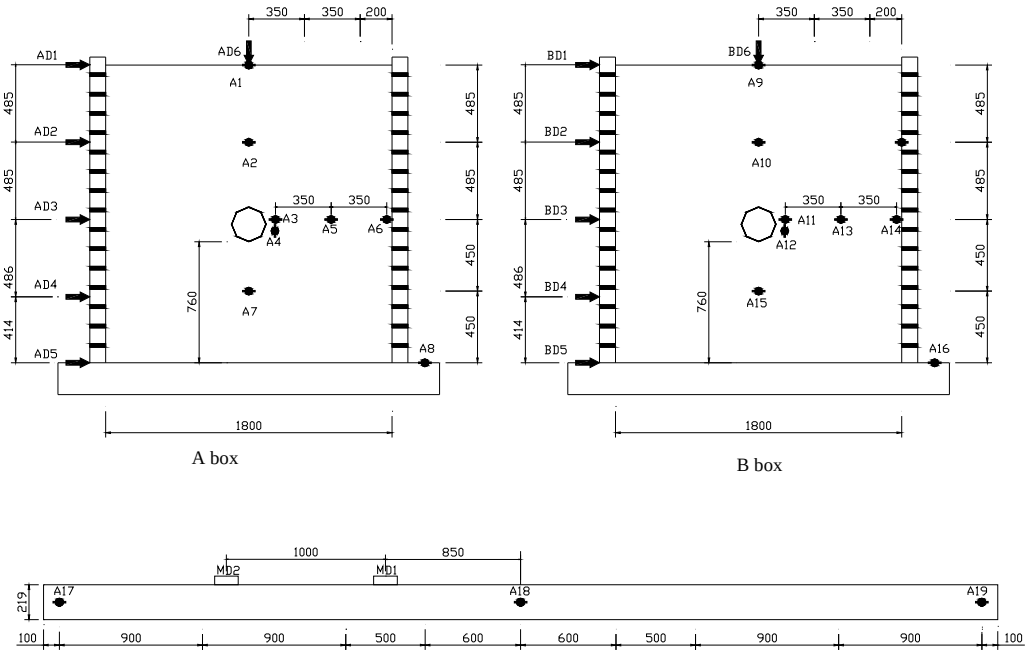

(b) accelerometers and displacement transducers

Figure 4 the layout of sensor

3 Numerical modeling

The laminar shear model box used in the test leads to shear type deformation of soil in the vibration direction. The main factors considered for modeling the laminar shear box are the inertia force and the boundary constraint effect. In our model, shell elements are used to model the box but with small rigidity, which means the elastic modulus are set same with soil. The slippage and the separation between the box and the soil are ignored. The mass of box equally distributes over the shell unites so as to consider the inertia force caused by mass of model box.

Comparing with soil, the rigidity of steel can be considered as infinity. The soil is constrained inside the steel frames. All nodes of the boxes in same height are deemed to have same displacements along the input direction of earthquake wave. Also the vertical displacement of the nodes on lateral side of boxes is constrained.

The Drucker-Prager model is adopted to simulate the soil. To simulate initial stress fields accurately is essential to the subsequent analysis. Coefficient of the lateral pressure 'at rest' is taken as 0.429 in this paper.

Shell elements are used to model the pipeline. Elastic modulus is taken the same as steel, which is 200GPa, a constant Poisson' ratio of 0.2 is adopted.

In this paper, contact elements of ABAQUS are used to realize the soil-pipe contact analysis, maser-slaver surface is also defined. For stiffness of pipe is larger than soil, pipe surface is defined as master surface, and the soil surface in interface as slave surface. Contact properties are given to maser-slaver surface, with the coulomb friction factor be 0.282.

For the numerical calculation, the acceleration time histories (under PGA of 0.1g, 0.3g,0.6g,1.0g) are input at the bottom of each box.

Figure 5 shows the finite element model of the test.

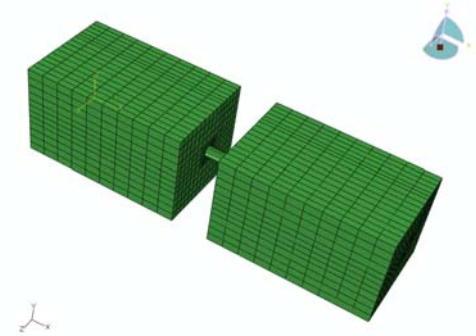

Figure 5 the finite element model

4 Comparison of numerical and experimental results

The applicability and reliability of the proposed numerical model are verified by comparing the computed results and experimental measurements in terms of time history, amplification factor, spectrum and patterns.

Figure 6 shows the Mises stress diagram of soil in initial stress fields and pipe at 4.8s under PGA of 1.0g. (Amplification factor of deformation is 1000)

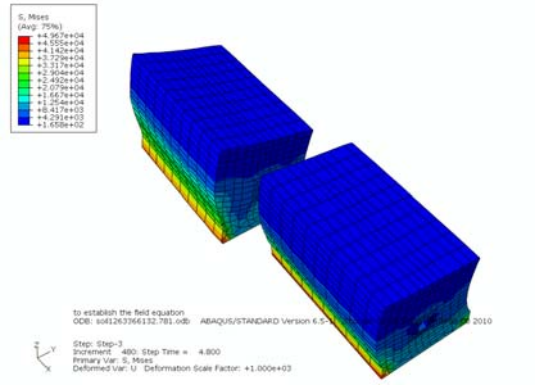

(a) The responses of soil

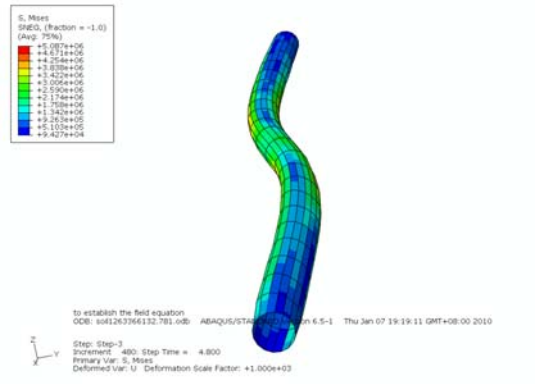

(b) The responses of pipe

Figure 6 Mises stress and deformation at 4.8s under PGA of 1.0g

The calculated accelerations amplitude time histories of node A15 in Box B is compared with the experimental measurements for test case with peak ground acceleration (PGA) of 0.1g, 0.3g, 0.6g and 1.0g. Figure 7 shows that the acceleration scale factors have the similar trend, but there is some difference under PGA of 0.1g. This is mainly because of the higher noise of telecom signals under shaking condition.

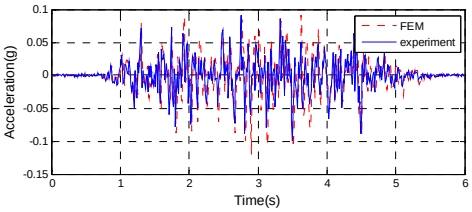

(a)0.1g

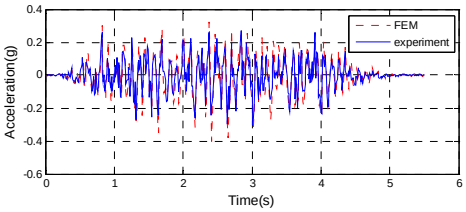

(b)0.3g

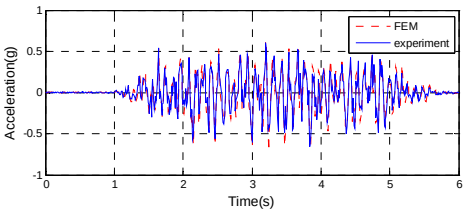

(c)0.6g

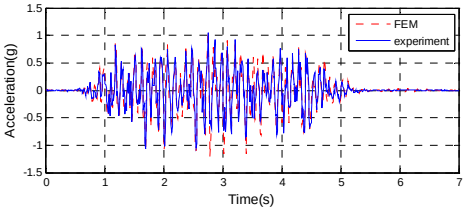

(d)1.0g

Figure 7 the acceleration of node A15

Figure 8 shows the comparison of the acceleration amplification factors along depth of soil of Box B under PGA of 0.6g and 1.0g. The calculation results and experimental results agree well with each other.

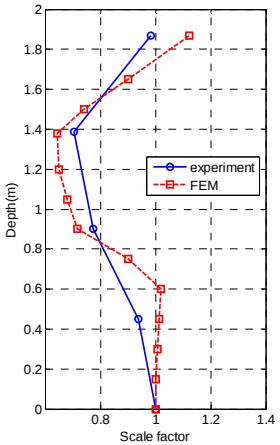

(a)0.6g

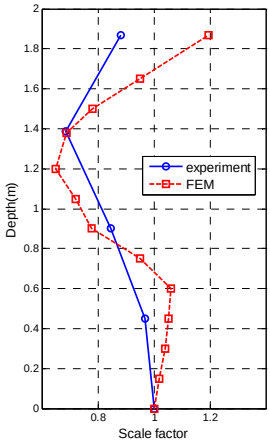

(b)1.0g

Figure 8 the acceleration amplification factors of box B

Figure 9 shows the comparison of power spectrum calculation results and actual testing result of Node A15 in Box B under PGA of 0.6g and 1.0g. The peak ground of acceleration and the relevant frequency agree well with each other.

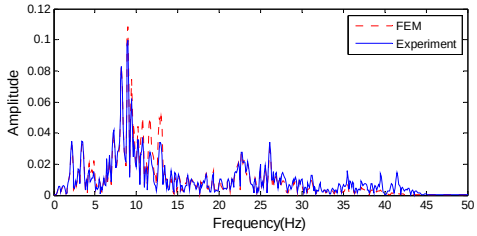

(a)0.6g

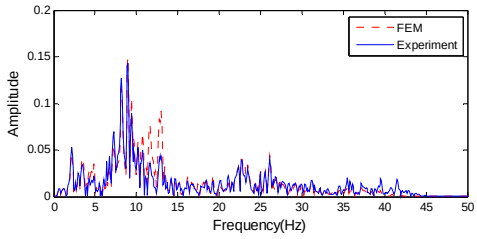

(b)1.0g

Figure 9 power spectrum of Node A15 in Box B

Figure 10 shows the comparison of displacement time history of BD3 around pipelines in Box B under PGA of 0.1g, 0.3g, 0.6g and 1.0g. It can be seen that the displacement amplitude scale is consistent except of the difference under test case of 0.1g. This result also makes great foundation for correct simulation of pipe-soil interaction and pipeline reaction.

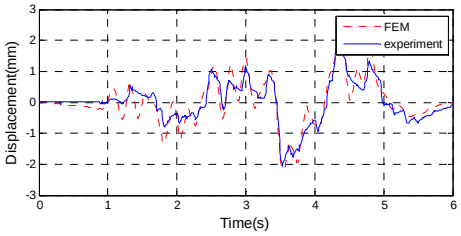

(a)0.1g

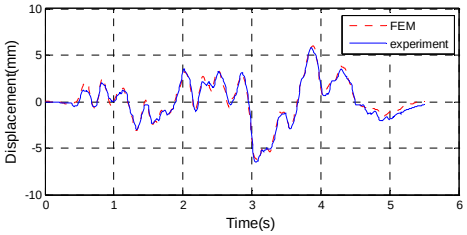

(b)0.3g

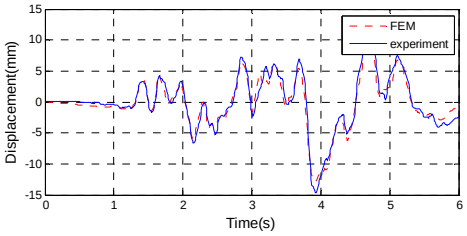

(c)0.6g

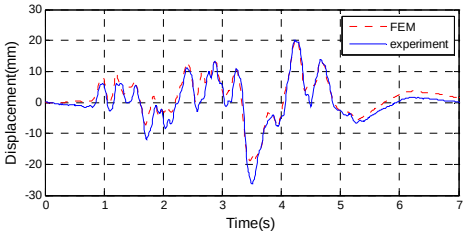

(d)1.0g

Figure 10 displacement time history of BD3

Figure 11 compares the lateral direction strain of node W10 between analysis results and the test under 0.3g and 0.6g input acceleration. The computed results show well consistency with the experimental results, which prove that the contact elements used in this paper can well simulate the dynamic nonlinear property of interface.

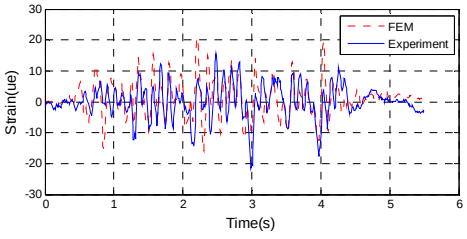

(a)0.3g

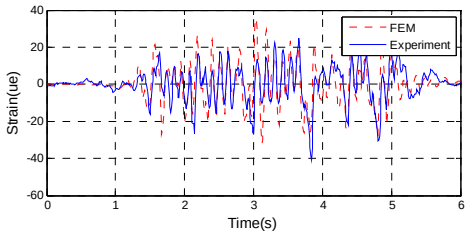

(b)0.6g

Figure 11 lateral direction strain of node W10

Figure 12 compares the max strain along the pipeline. Since the earthquake wave excitation is in lateral direction, the max strain in the middle of the pipe should be smaller. The computed results match this trend well, but the experimental result may be affected by the accuracy of the strain gauges under lateral direction excitation.

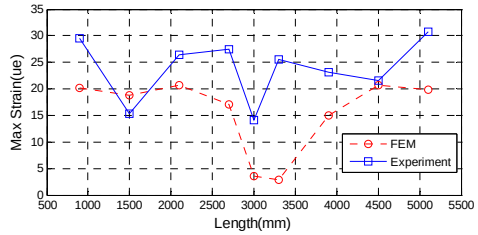

(a)0.3g

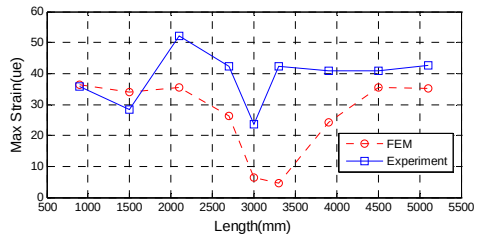

(b)0.6g

Figure 12 max lateral direction strain along the pipe

5 Concluding Remarks

Three-dimensional finite element model of underground pipeline system under non-uniform earthquake wave excitation is studied in this paper. Also the modeling method is discussed and the calculation results and experimental results are compared.

The results and comparison show that the numerical simulated results can capture the main features of the pipeline under non-uniform earthquake excitation with experimental results. The modeling method of the test model is proved to be acceptable, also the applicability and reliability of the proposed model is validated.

Acknowledgement:

The authors gratefully acknowledge the financial support to this study from Key Project in the National Science & Technology Pillar Program (Grant NO. 2006BAJ03B03), Research Fund for Young Teacher supported by State Key Laboratory for Disaster Reduction in Civil Engineering (SLDRCE08-C-03).

References:

"ABAQUS version 6.5 Documentation." (2005)

Chen Bo, Lu Xilin and Li Peizhen.(2002), "Modeling of dynamic soil-structure interaction by ANSYS program." Earthquake engineering and engineering vibration, **22**(1), 126-131. (in Chinese)

MENG Hail, CHEN Jun LI Jie. (2008), "Shaking Table Test of Soil-pipe Dynamic Interaction under Non-uniform Earthquake Wave Excitation." Chinese Journal of Underground Space and Engineering, **4**(5), 853-859. (in Chinese)

Prasad S.K. Towhata I. and Chandradhara G. P. etc. (2004), "Shaking table tests in earthquake geotechnical engineering." Current Science, **87**(10), 1398-1404.

Shinozuka M. and Deodatis G. (1996), "Simulation of multi-dimensional Gaussian stochastic fields by spectral representation." Applied Mechanics Review, **49**(1), 29-53.

SHI Xiao-jun, CEHN Jun, LI Jie. (2009), "Design and Verification of Dual-direction Shear Laminar Box for Shaking Table Test." Chinese Journal of Underground Space and Engineering, **5**(2), 254-261. (in Chinese)

Qin Wang, Jun Chen and Jie Li. (2008), "Three Dimensional Numerical Simulation of Underground Pipeline Under Non-uniform Earthquake Wave Excitation and Comparison with Shaking Table Test." The Fifth China-Japan-US Trilateral Symposium on Lifeline Earthquake Engineering

Yang Lin-de, Yang Chao and Ji Qian-qian etc. (2003), "Shaking table test and numerical calculation on subway station structures in soft soil," Journal of Tongji University, **31**(10), 1135-1140. (in Chinese)

JOINT CONFERENCE PROCEEDINGS
7th International Conference on Urban Earthquake Engineering (7CUEE) &
5th International Conference on Earthquake Engineering (5ICEE)
March 3-5, 2010, Tokyo Institute of Technology, Tokyo, Japan

CONSIDERATION ON PROCESS OF SEISMIC RETROFIT USING ENVIRONMENTALLY FRIENDLY MATERIALS IN EXISTING BRIDGE.

Jang, Won-Rak[1], Jeon, Gyoo-Shick[2], Kim, Eun-Kyum[3], and Park, Chul-Sung[4]

1) Team leader, Civil Department of Seoul Metro, Korea
2) Chief Director, CMR Technology Institute, Korea
3) Professor, Seoul National University of Technology, Korea
4) Team leader, No.4 Technical Department of Seoul Metro, Korea
jj5080@empal.com, gsjeon@korea.com, ke6507@snut.ac.kr, sungtwa@hanmail.net

Abstract: Earthquake resistant design of subway system has very important role in prevention of urban disasters. Specially, bridge structure which is consisted of cantilever column is very weak structure about earthquake as proved from experience of Kobe earthquake. The Seoul Metropolitan Subway Corporation has achieved the retrofit construction about highway bridge area which is built by cantilever column for several years. And we have the retrofit plan about the total area of bridge including underground structure such as station building by effect of Wenchuan earthquake. Recently Korea Highway Corporation and the Ministry of Construction are doing fairly other aspect with retrofit method that is achieved in Japan. That is, the retrofit methods that are achieved in the Korea change the bridge bearing like as isolation bearing and install the damper or shear-key, not trying to increase the ductility of pier itself like as wrapping method with thin steel plate. It is originated in burdensome of retrofit method such as traffic control in downtown, do not considering the satisfaction of rebar detail on past specification like as no joint in main rebar and the interval of lateral rebar. Therefore, in this paper, we would like to review the retrofit procedure that is achieved in the Korea, and introduce the simple mechanization method to extend the ductility developed in the Korea.

1. INTRODUCTION

Since the Kobe Earthquake that broke out in 1995, Korea has also focused on the seismic designs, resulting in the continued seismic improvement efforts for the existing bridges as well as the new ones. Recovering from its harsh experiences from the Earthquake, Japan revised its Bridge Design Code in 1997, and undertook bridge retrofitting efforts with the steel plate reinforcing methods employed on most of the concrete piers of the existing bridges built based on the old design version. It may safely be said that most of the concrete piers of the bridges in Japan had been given the steel plate reinforcement works. As for such reinforcement works for the existing bridges in Korea, however, the methods designed to improve ductility of the piers themselves have been hardly employed, and most of the methods chosen were only limited to such simple ones as the replacement of the bridge bearings with the isolating pads, and the installation of the shear keys or the dampers. But, isn't it strange? While Japan considers the methods for improving ductility of the piers of the bridges constitute an essential part of the reinforcement works for the existing bridges built based on the old version seismic design methods, they are still a matter of choice for such bridges in Korea. These different approaches between the two countries may not be successfully explained by any possible difference in their design seismic force, and it could still less be accounted for by the argument that such reinforcement works are not necessary as the Korea's past design details on tie bars and the connection of re-bars were enough to secure sufficient ductility even from the current standards. If we can say that, with the seismic design force employed in Korea, such passive load distributing methods are sufficient for allowing us to go without any reinforcement works for the piers of the existing bridges, then the arguments from work sites to the effect that the excessive amount of the tie bars the current specifications have required for new bridges since the adoption of the seismic design have rendered on-site concrete pouring works by far tougher and are lowering structural safety may be considered well-grounded, and the current design details related to the use of re-bars may be misguiding provisions that help waste the taxpayers' money.

2. ROAD AND BRIDGE FACILITY IN KOREA

The Korea belongs to the country that construction is fairly lively worldwide. But, road because belong to that is still feeble if penetration of road compares with the main OECD countries as Table-1, Investment of country for traffic network such as road, bridge and railroad is forecasted that is continued continuing. Traffic policy of the Korea have developed laying stress on expressway over the

latest 20 ~ 30 years, and the construction of expressway has accomplished with bridge and tunnel by the topographical effect of Korea peninsula. Also, The bridges which is constructed to expressway have continues span and long span than that under administration of general province, and seismic grade is also higher than general province. It can be said that seismic design standard of bridge was enforced regularly from 1996 years by effect of Kobe earthquake, and before designed bridge is wholly lacking anti-seismic countermeasure in Korea. We have executed retrofit procedure for non seismic bridge from the 2000s. Therefore, saying too much is not even if there is almost for completion phase in the present. Earthquake resistant design is achieved rightfully by relation that bridge of expressway is importance bridge, but bridges belonging to province belong to bridge that mostly earthquake resistant design is not achieved. In step that anti seismic procedure is almost completed, we can talk that was wholly lacking the method to improve the ductility.

Table 1 Road Penetration of the Main OECD Country

Nation	*Length (km)*	*Population (1000P)*	*Area (1000km²)*	*Vehicle (1000V)*	*Road Ratio*
Korea	104,236	48,747	99.7	16,794	1.46
USA	6,378,254	294,043	9,629	230,428	3.79
France	894,300	60,144	552	35,144	4.91
Germany	230,735	82,476	357	48,560	1.34
Spain	664,649	41,060	506	22,156	4.61
Britain	371,913	59,251	243	30,970	3.10
Japan	1,171,647	127,654	387	73,993	6.34

Table 2 Bridge Classification by Administration in Korea

		Total	Express	Control by Govern.	Control by S.Province	Etc.
Total	Number (ea)	22,871 (100%)	5,923 (26%)	5,302 (23%)	1,115 (5%)	10,531 (46%)
	Length (km)	1,987 (100%)	697 (35%)	490 (25%)	231 (12%)	570 (28%)

Table 3 Seismic Design Bridge of Expressway in Korea

Total Number	Seismic Design	Non Seismic Design		
		Sub Total	Urgency	Exception
5,825 (100%)	4,165 (71.5%)	1,660 (28.5%)	660 (11.3%)	1,000 (17.2%)

3. CONCEPT OF SEISMIC DESIGN

The design specifications from any part of the world as well as from Korea do not prescribe that the seismic designs code should be anything that absolutely guarantees the structural safety from the given design earthquakes. This is because the economical aspect of the matter makes the securing of the absolute structural stability almost impossible as long as we do not find any construction materials that are better and more economical than the gravels and sand, the most inexpensive materials we know. Accordingly, the basic concepts of the seismic designs as provided in the Bridge Design Code are; 1) to minimize the casualties, (2) to prevent the overall structural collapse, while allowing partial damages, and (3) to help maintain the basic functions of the bridges. Therefore, the provisions simply provide that, in an earthquake weaker in magnitude than the design seismic force, the substructure elements should be able to resist it within the elastic region to suffer only limited damages, while, in the an earthquake greater than that, all or part of the structures should not collapse. In an effort to enable the structural engineers to easily put into practice the concept of the plastic design without elaborating in a complicate manner, the bridge design codes in a number of the nations including the U.S.A. are employing such values as the response modification factors, which are being explained to comprise the three concepts of "the marginal strength of the materials", "the ductility factor" based on the principle of energy conservation proposed by N. M. Newmark (1973), and "the structural redundancy."

4. A REVIEW ON THE SEISMIC PERFORMANCE ASSESSMENT METHODS

4.1 Seismic performance assessment methods of Korea

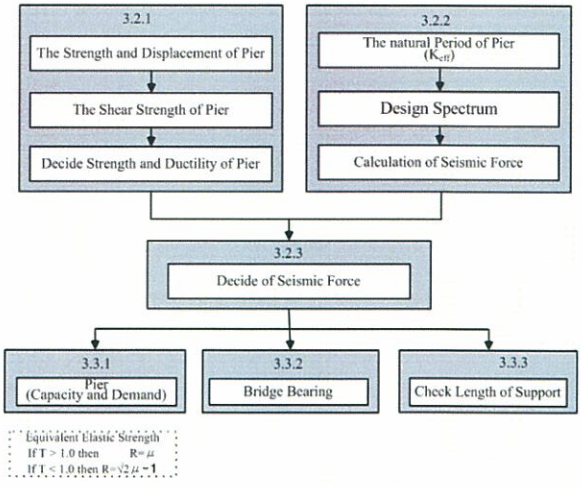

Figure 1 The Procedure of Seismic Retrofit in Korea

The "Guidelines on the Seismic Reinforcement of the Non-seismic Bridges" published by the Korea Expressway Corporation in October, 2005 recommends that, for the assessment of the magnitude of the elastic seismic forces the piers of the bridges are assumed to have in consideration of the displacement ductility ratio, the equivalent elastic strength as per the natural period be estimated by applying the equal displacement principle and the energy conservation principle proposed by N. M. Newmark (1973). Therefore, the engineers estimate the elastic seismic forces by applying the rules based on their respective natural periods and accept them as those of the existing bridges without any trace of doubt, and determine the reinforcement of the piers of such bridges by comparing them with the

design seismic forces through seismic interpretation. In the seismic design methods, however, only the energy conservation principles were applied for the response modification factors irrespective of the periods in consideration of the safety side, an essential perspective in design, but in the seismic performance assessment methods, it needs to be reviewed in the aspect of safety that the equal displacement principle was separately made to be applied for the structures having at least 1.0 second of the natural period.

4.2 Principle Proposed by N.M Newmark (1973)

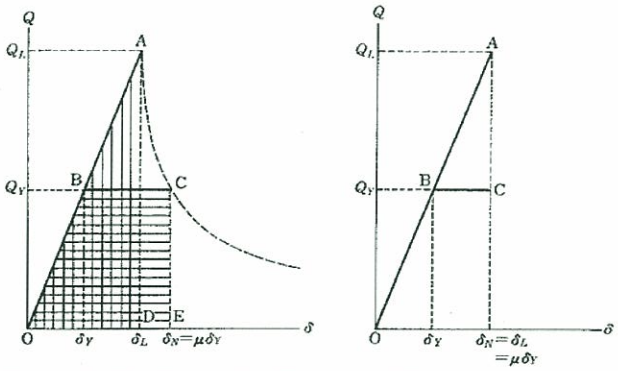

Figure 2 The Principle of Energy and Displacement

The principle proposed by N.M Newmark amounts to a simple explanation of the non-linear analyses that, with the Elasto Perfectly Plastic model applied, the results of the analyses of the structures based on elasticity and those of which that are conducted to the plastic region reducing the yield strength are similar to the energy input into the structures in the relatively short-period region, while, in the relatively long-period region, the displacements generated are generally uniform despite a different yield strength applied. In other words, the energy conservation principle in the short-period region means that, in the case of the short natural period of the structures, the absolute amount progressing to plasticity is huge because of the high frequency of vibrations while the seismic waves are progressing, and the equal displacement principle in the long-period region amounts to a simple indication that such amount is not huge in the long period of frequency due to the low frequency of vibrations in the long-period of the natural period. N.M Newmark did not mention that the boundary line determining the above two principles should be about one second of the natural period, and the calculations conducted by a good seismological experts since N.M. Newmark suggest that the trends can be different based on the hysteretic model adopted and the periodic characteristics of the seismic waves. Therefore, he is being revered as a pioneer who well organized the results of the non-linear analyses, which were hard to estimate in the 1970s, when the computer technologies had yet to emerge, not as a person who discovered a new principle. The Chapter V: Seismic Designs (pp.316~pp.318) from Japan's Bridge Design Code that was revised in 1997 states that "as the vibration frequencies of the structural system become longer, the estimations of the non-linear responses based on the energy conservation principle generally decrease, and the equal displacement principle adequately applies instead. However, as the separate applications of the energy conservation principle and the equal displacement principle require a lot further studies, we are going to uniformly apply the energy conservation principle on the general frequency range of the bridges in the aspect of the safety side.

4.3 Assessment of the effective stiffness

During the last decade, the Earthquake Engineering Society of Korea has been holding technological seminars aimed at helping the civil engineers having limited experiences in the seismic design improve their practical capabilities. An introduction on the effective stiffness of the bents of the bridges was made at its 6th seminar, and the contents are still being consulted as a reliable reference by those civil engineers who intend to reduce seismic loads by lengthening the estimations of the natural periods. As has been stated at the end of the seminar, however, the shear stiffness may be employed in the assessment of the internal force, and the engineers are advised to keep in mind the fact that the employment of the shear stiffness in the structural analysis of the displacements results in the displacement less than the actual ones. The estimations of the natural period of the structures play a decisive role in determining the magnitude of the seismic force inflicted upon the structures, and the use of the effective stiffness that is 0.5 times the elastic stiffness in the estimations of the natural period of the piers of the bridges results in $\sqrt{2}$ times in the estimations of the natural period, leading to being assessed as the structures that exceed 1.0 second in the general bridge category. Along with the decrease of the seismic load due to the trends of these structures towards the long periods, the application of the equal displacement principle in the assessment of the equivalent holding internal force can lead to the high assessment of the equivalent elastic stiffness, and this is being suggested as a well-grounded foundation for such an argument that the reinforcement works for the piers of the existing bridges are not necessary.

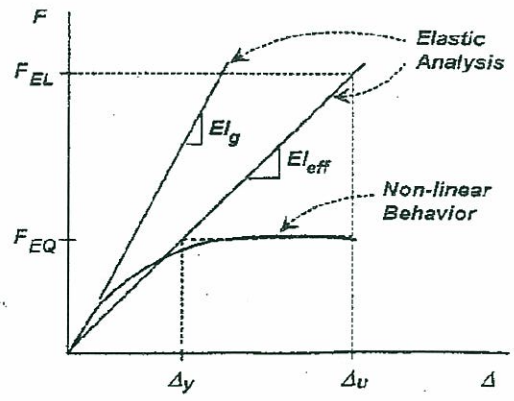

Figure 3 Effective Stiffness and Normal Stiffness

4.4 The seismic reinforcement methods for the existing bridges being employed in Japan

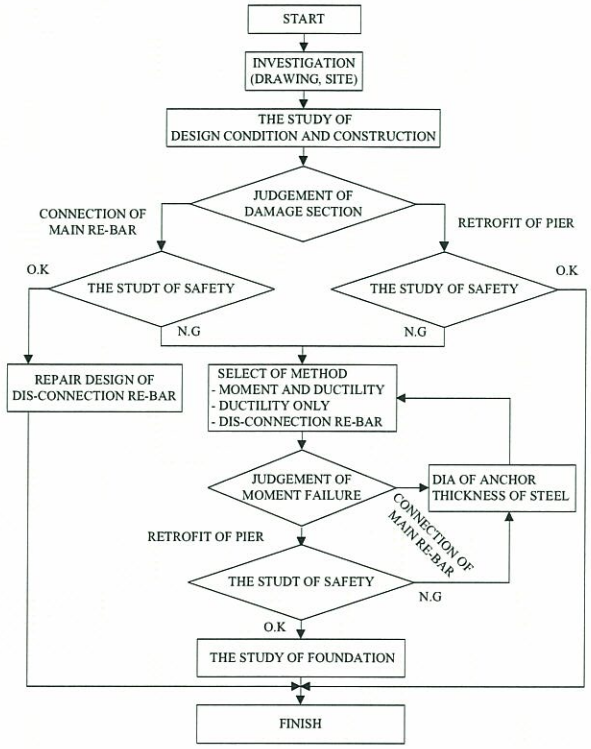

Figure 4 The Procedure of Seismic Retrofit in Japan

The past specifications of Japan established during the times when there were not many records on earthquakes also allowed the adjustment of the joints of the main re-bars and the reduction of the cross section of re-bars based on the magnitude of the bending moments that are estimated by location. For the economic reasons during the past years when re-bars were relatively expensive to be used in the civil/building structures, a sufficient amount of re-bars were used on the lower part of the structures that have the high bending moments, while on the upper part of the structures were used a minimum amount of re-bars that barely satisfied the minimum amount required. Therefore, Japan's seismic reinforcement methods stipulate that, on the assumption that damages occur in the reduced cross section of re-bars when the calculation results in less than 1.2 as per the formula provided in (1), the reinforcement works should be undertaken for those part, and, when higher than 1.2, the next steps should proceed on the assumption that damages occur on the lower part of the piers of the bridges. This regulation is wishing to secure the ductility regardless of size of section in case there is disconnection of main reinforcement. On the other hand, preferential reinforcement proceedings for disconnection of this main reinforcement were not prepared in seismic retrofit guideline of the Korea.

$$\frac{M_{Tyo}}{h_t} \geq 1.2 \quad : \text{Damages to lower part of pier}$$
$$M_{Byo} / h_B < 1.2 \quad : \text{Damages to rebar disconnect part} \qquad (1)$$

About method of construction here no detailed introduce, but various reinforcement method that construct by manpower without using equipment is developed. One of interesting method is method that close pillar consecutively as fiber of laminate like as compress for emergency measure.

5. CHAIN WRAPPING DEVICE SYSTEM FOR RETROFIT

Usual fiber reinforcement methods have strengthened with carbon fiber and glass fiber that is consisted of two dimensions. But, these methods of construction have restriction in size of fiber and could not but have connection area. Therefore, this fiber reinforcement method causes handicap in connection area and have shortcoming that could not display enough performance of reinforcement method. Display effect such as circle tie bar by serving bandage of laminate linked infinitely in form of compress that is used in emergency measure. But, this belt fiber could not secure homogeneity of quality in case of make manpower construction and there was shortcoming that external appearance is not smart. But, efficiency can expect improvement of construction quality as well as is high if supply at the speed that is fixed depending on speed of manpower gluing by self-feeding device of light weight consisted of self-propelled type.

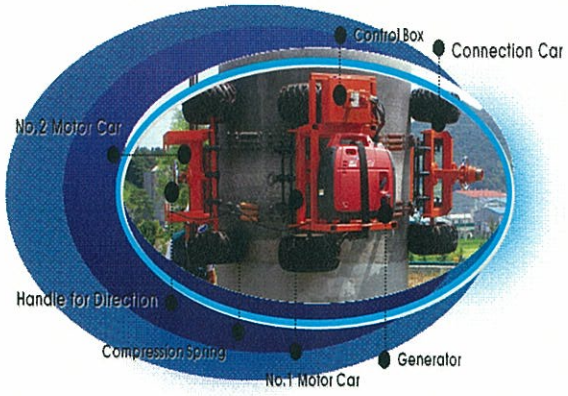

Photo 1 The Wrapping Device System

Photo 1 displays machine of automatic fiber retrofit method that is developed in CMR Technology Institute of Korea. Machine is consisted of form that assembly is available, and each part has weight that conveyance is available by manpower. And can connect sequentially because unit vehicles consisted of tire according to size of pier use compression spring. Can control angle of progress direction and speed controlling handle established on a forefront car by wireless. Also, width and kind of belt that material feeder is supplied by attachment is available random are possible by various method. There is point that automation method is expedient about circle pier but uncomfortable accompanies in covering of automation device about quadrilateral pier. But, enabled that attach device that is accessory about quadrilateral pier. Photo 2 and Photo 3 display the photograph about circle pier and quadrilateral pier.



Photo 2 Circle Pier on Han-River Bridge



Photo 3 Quadrilateral Pier on Han-River Bridge

The following explains reinforcement effects for before and after that strengthen by this retrofit method about railway bridge with brick structure of non reinforcement. Railroad bridge in Korea that is constructed by Japan before 1945 is still using with small scale repair and is expected with weakness about anti-seismic because of consisted by non reinforcement structure. About brick structure of railroad bridge pier, retrofit method that enlarges the sectional area from outside is considered, but there are a lot of problems that should consider decreasing the sectional area that water passes. Therefore, suggested retrofit method not to reduce the sectional area that changes the brick structure to reinforce structure by attaching the equivalent tie bar and re-bars. Closed outside to fiber glass equivalent to tie bar after attach correspond to vertical re-bars as photo 4. Establishment divides into occasion handled from lower part to upside contiguously and occasion that put and constructs interval. There was enlargement effect about 89% after reinforcement compares before reinforcement and there was effect that displacement measure at top of pier decreases about 58%~80%.



Photo 4 Pier of Railroad Bridge with Non-Reinforcement

6. CONCLUSIONS

We conducted this study to further look into the current situation in which the measures to secure the ductility of the piers of the bridges are seldom taken in the seismic reinforcement works for the existing bridges that are conducted based on the reinforcement guidelines for the conventional bridges and tried to provide the alternative seismic design methods for such bridges. We introduced about glass fiber retrofit method being consisted of serial belt developed in Korea.

1. The retrofit method should be selected confirming the actual situation of re-bar and tie bar in existing bridge. In according to past design standard, there must be disconnection in main re-bar on lower part of bridge pier. But, it is real condition that the detail re-bar situation is not confirmed in constructed drawings. Plan that can confirm the re-bar situation of existing bridge should be considered.
2. In the seismic performance assessment methods for the existing bridges, the assessment of the equivalent holding internal force by employing the equal displacement principle on such structures whose natural period is longer than 1.0 second can result in the overestimations of the internal force, and, at the same time, the application of the effective stiffness in the assessment of the natural period can possibly be employed as a useful excuse for such argument that the securing of ductility may not be required.
3. For such bents of the bridges having significant problems with the structural details of the re-bars compared to the current specifications, including the joints of the main re-bars of the existing bridges, the measures to secure the minimum ductility should be undertaken with first priority.

"This work is financially supported by Korea Ministry Environment(MOE) ET-Human resource development Project"

References : Korea Expressway Corp. "Guidelines on the Seismic Reinforcement of the Non-seismic Bridges" in 2005

Center for Urban Earthquake Engineering (CUEE)
Tokyo Institute of Technology

O-okayama Office
Department of Architecture and Building Engineering
Tokyo Institute of Technology
M1-39 2-12-1 O-okayama, Meguro-ku, Tokyo, Japan 152-8550
Tel: +81-(0)3-5734-3200 Fax: +81-(0)3-5734-3200

Suzukakedai Office
Department of Built Environment
Tokyo Institute of Technology
G3-11 4259 Nagatsuta-cho, Midori-ku, Yokohama, Japan 226-8502
Tel: +81-(0)45-924-5576 Fax: +81-(0)45-924-5199

Email:office@cuee.titech.ac.jp/
URL:http://www.cuee.titech.ac.jp/